ENCYCLOPEDIA
OF
VIBRATION

Editor-in-Chief

S BRAUN

Editors

D EWINS

S S RAO



ACADEMIC PRESS

A Division of Harcourt, Inc.

San Diego San Francisco New York Boston
London Sydney Tokyo

This book is printed on acid-free paper.

Copyright © 2002 by ACADEMIC PRESS

All Rights Reserved.
No part of this publication may be reproduced or transmitted in any form or by any means, electronic or mechanical, including photocopying, recording, or any information storage and retrieval system, without permission in writing from the publisher.

Academic Press
A division of Harcourt, Inc.
Harcourt Place, 32 Jamestown Road, London NW1 7BY, UK
http://www.academicpress.com

Academic Press
A division of Harcourt, Inc.
525 B Street, Suite 1900, San Diego, California 92101-4495, USA
http://www.academicpress.com

ISBN 0-12-227085-1

Library of Congress Catalog Number: 2001092782

A catalogue record for this book is available from the British Library

Access for a limited period to an online version of the Encyclopedia of Vibration is included in the purchase price of the print edition.

This online version has been uniquely and persistently identified by the Digital Object Identifier (DOI)

10.1006/rwvb.2001

By following the link

http://dx.doi.org/10.1006/rwvb.2001

from any Web Browser, buyers of the Encyclopedia of Vibration will find instructions on how to register for access.

If you have any problems with accessing the online version, e-mail:
idealreferenceworks@harcourt.com

Typeset by Bibliocraft, Dundee, Scotland
Printed and bound in Great Britain by MPG Books Ltd, Bodmin, Cornwall, UK

02 03 04 05 06 07 MP 9 8 7 6 5 4 3 2 1

Editors

EDITOR-IN-CHIEF

S Braun
Technion – Israel Institute of Technology
Faculty of Mechanical Engineering
Haifa 32000
Israel

EDITORS

D Ewins
Imperial College of Science, Technology and Medicine
Department of Mechanical Engineering
Exhibition Road
London SW7 2BX, UK

S S Rao
University of Miami
Department of Mechanical Engineering
PO Box 248294, Coral Gables,
FL 33124-0624, USA

Editorial Advisory Board

R Bigret
22 Rue J Varnet
93700 Drancy
France

P Cawley
Imperial College of Science, Technology & Medicine
Department of Mechanical Engineering
Exhibition Road
London SW7 2BX, UK

R Craig
University of Texas
Aeronautical Engineering and Engineering Mechanics Department
Austin TX 78712, USA

B Dubuisson
33 Rue Saint Hubert
60610 La Croix Saint Ouen
France

R Eshleman
Vibration Institute
6262 S. Kingery Highway
Willowbrook
IL 60514, USA

M Geradin
Universite de Liège
LTAS Dynamique des Structures
Institut de Mecanique et Genie Civil
Chemin des Chevreuils 1
4000 Liège, Belgium

J Hammond
University of Southampton
Institute of Sound and Vibration Research
Southampton SO9 5NH, UK

S Hayek
Pennsylvania State University
112 EES Building
University Park
PA 16802-6812, USA

D Inman
Virginia Polytechnic Institute & State University
Department of Engineering Science and Mechanics
310 NEB, Mail Code 0261
Blacksburg
VA 24061-0219, USA

M Lalanne
Laboratorie de Mecaniques des Structures
Institut National des Sciences Appliquees de Lyon
LMSt - Batiment 113 20
avenue Albert Einstein
69621 Villeurbanne Cedex, France

M Link
Universitat Gesamthoschule Kassel
Fachgebiet Leichtbau
Moenchebergstrasse 7,
D34109 Kassel, Germany

K McConnell
Iowa State University
AEEM
Black Engineering Building
Ames, IA 50011, USA

D E Newland
University of Cambridge
Department of Engineering
Trumpington Street
Cambridge CB2 1PZ, UK

N Okubo
Chuo University Faculty of Science & Engineering
Department of Precision Mechanical Engineering
1-37-27 Kasuga
Bunkyo-ku, Tokyo, Japan

M Radeş
Universitatea Politehnica Bucuresti
Department of Engineering Sciences
313 Splaiul Independentei
79590 Bucuresti
Romania

S Rakheja
Concordia University
Department of Mechanical Engineering
1455 de Masonneuve Blvd W
Montreal, Quebec H3G 1M8
Canada

G Rosenhouse
Technion – Israel Institute of Technology
Faculty of Civil Engineering
Technion City
Haifa 32000, Israel

S Shaw
Michigan State University
Department of Mechanical Engineering
A321 Engineering Building
East Lansing, MI 48824-1226, USA

M Sidahmed
Université de Technologie de Compiègne
Heuristique et Diagnostic des Systèmes Complexes
Centre de Recherches de Royallieu
BP 20529
60205 Compiègne, France

H S Tzou
University of Kentucky
Department of Mechanical Engineering
Dynamics and Systems Laboratory
Lexington, KY 40506, USA

Foreword

Vibration is usually defined in dictionaries as rhythmic motion back and forth. It has attracted the curiosity of humans since people have had time to contemplate the natural world. In the sixth century BC, Pythagoras had related harmonic intervals to ratios of lengths of a vibrating string. In 1581, Galileo had observed that the period of a simple pendulum is (nearly) independent of the amplitude of vibration. A century later the basic principles of dynamics were put on a firm basis by I. Newton. Further development of the science of mechanics was led by L. Euler (1707–83). Most of the analytical tools now used in vibration studies were available by the year 1788, when *Mécanique Analytique* was published by J.L. Lagrange. The first book devoted entirely to the theory of vibration was volume I of Lord Rayleigh's *Theory of Sound* (1887). It became the model for the classical vibration textbooks of Timoshenko (1928), and DenHartog (1934). Subsequent texts have followed much the same pattern, with the addition of matrix notation and linear algebra after the engineering-science revolution of the sixties.

Vibration is a fascinating physical phenomenon, well worth studying on its own merits. In many applications, vibration is harnessed for useful purposes, e.g., to make music, to drive vibrational transport systems, or provide frequency standards in clocks and precision instruments. In many other applications, vibration is an undesired intruder that interferes with the normal operation of the system, creating noise, and developing stresses that may cause fatigue failure.

Engineers have been dealing with vibration problems since the beginning of the industrial revolution and the introduction of the steam engine. With each new mode of transportation and each new technology, there often appears an unexpected vibrational challenge. The interaction of steam-driven trains with relatively flexible metal bridges produced unexpected problems of vibration and fatigue in the 19th century. At the beginning of the 20th century, cities began to install central electric power stations and engineers were faced with a variety of vibration problems associated with the rotor dynamics of turbine generator sets. By the end of World War I, the diesel engine had become a popular medium-power prime mover. A rash of fatigue failures in diesel engine shafting spurred work on the torsional vibration of crank-shafts. A major technological effort of the period between World War I and II was the development of airplanes and helicopters. The unexpected vibrational challenge for aircraft was the phenomenon of wing flutter, while the new problem for helicopters was the phenomenon of ground resonance. In 1940 the Tacoma Narrows suspension bridge developed large self-excited torsional vibrations in a moderate wind and failed dramatically. The challenge to explain this completely unexpected result kept vibration experts busy for decades.

The latter half of the 20th century saw a great expansion of high technology. As new technologies proliferated, job opportunities for vibration engineers multiplied. The new technologies also provided vastly improved tools for the vibration engineer. Particularly important has been the development of improved sensors and actuators. It is interesting to compare the vast array of optical, electrical, magnetic, piezoelectric, eddy-current, and laser transducers available to the engineer today, with the situation faced by the pioneers in torsional vibration, who had no way of detecting the presence of large vibrations, superposed on the steady rotation of the shaft, until the shaft failed.

Perhaps the most important technical advance of the last half-century has been the development of the digital computer. The computer is now an essential part of most vibration measurement systems, and the computational power it has unleashed has provided important support for many theoretical advancements.

After World War II, the development of rocket propulsion and space flight introduced vibration engineers to the topic of random vibration and the requirements for large wide-band shakers and sophisticated data-processing instrumentation. Instrumentation based on analog principles was soon replaced by digital processors. The fast Fourier transform (FFT) was conceived in 1965, and a decade later, commercial instruments based on the FFT were on the market. Soon digital analyzers capable of performing experimental modal analysis became available. At the same time, computer software for performing finite element analysis and boundary element analysis was being applied to the dynamic analysis of complicated real structures. The difficulty in reconciling the experimental measurements with the analytical predictions, beyond the first few modes of a structure, remains a challenge for vibration engineers.

During the past half-century, important advances in the theory of nonlinear vibrations have been made, including the clarification of the concept of chaotic response from a deterministic system. Much of the supporting work would not have been possible without high-speed digital computers.

A present trend in vibration technology is the inclusion of vibration considerations in the preliminary design of products. The old tradition of waiting until a prototype was available, and hoping that any vibration problem that arose could be cured with a quick fix (which did not impact the primary design goals) is gradually giving way to early consideration of the vibrational problems of the product. In some industries, machinery is being delivered with vibration sensors already installed, so that the customer can monitor the performance, or diagnose the cause of a malfunction. Another present trend is the miniaturization of sensors and actuators using microelectromechanical elements (MEMS).

The field of vibration is now so broad that no single person can keep up-to-date in all its branches. Furthermore, it is impossible to squeeze all the essential information into a single book. The editors of the present *Encyclopedia of Vibration* have performed a valuable service to the field by dividing the subject matter into 168 chapters and selecting experts to create authoritative chapters on the individual topics. The result is a three-volume encyclopedia, which will be of great value to practicing vibration engineers and theorists. The encyclopedia will also be useful as a general reference, and as a guide to students, and professionals in neighboring fields.



Stephen H. Crandall
Ford Professor of Engineering, Emeritus
Massachusetts Institute of Technology

Preface

We are surrounded by vibrations, some of them generated by nature, others by human-built devices. While some are harmless, many have adverse effects. These can affect human well-being or health, cause malfunctioning of devices, or result in life-threatening situations. Vibrating patterns may also carry information, which when deciphered correctly can convey important knowledge.

This three-volume reference work focuses on aspects of vibration which are of interest mainly to practicing and research engineers. Even within this specific audience, vibration problems span multidisciplinary aspects, and we thus believe there is a need for a reference work, geared to the specific area of vibration, covering as many relevant examples as possible.

The more classical topics of vibration engineering are naturally covered: basic principles, sound radiation by vibrating structures, vibration isolation, damping principles, rotating systems, wave propagation, nonlinear behavior, and stability. Modern aspects developed in the last two decades also have a prominent place. To mention just a few, these include software and computational aspects, testing and specifically modal testing/modeling, active vibration control, instrumentation, signal processing, smart materials, and vibration standards. Specific entries address analysis/design aspects as encountered in aeronautical, civil, and mechanical engineering: vibration abatement, seismic vibrations, civil engineering structures, rotating machines and surveillance, aircraft flutter, and the effect of vibrations on humans.

In view of the large scope of topics addressed, the type and depth of presentation had to be adapted to the style of concise alphabetical entries, and some compromises were necessary in the choice of topics. More 'classical' aspects suffer somewhat at the expense of more modern topics, due to our opinion that more information sources are already available for them. Carefully chosen references appearing under the 'further reading' sections are however given for them. In addition, at the end of each entry there is a cross-referencing 'see also' section where the reader is directed to other entries within the *Encyclopedia* which contain additional and/or related information. In view of the large scope of topics chosen, the type and depth of presentation had to be adapted to specific entries. Unified symbols and notation have been used to some extent, but when deemed preferable, superceded by those commonly accepted in specific areas. The table of contents lists entries in an intuitive alphabetical form, and any topic not found through the contents list can be located by referring to the index which appears in each volume. Useful reference data can be found in the appendices, which also appear in each volume.

An online version of the *Encyclopedia* will be available to all purchasers of the print version and will have extensive hypertext links and advanced search tools. Leading authorities have contributed to this work. Together with our advisory board they should receive the main credit for this important source of knowledge. My personal thanks are naturally extended to them, but even more so to my colleagues and co-editors, Dave Ewins and Singiresu Rao, without whose constant help this task would have been impossible. Special thanks are due to Dr Carey Chapman and Lorraine Parry from the Academic Press Major Reference Work team for their encouragement and help extended to us at every stage.

Simon Braun
Editor-in-Chief

Guide to Use of the Encyclopedia

Structure of the *Encyclopedia*

The material in the *Encyclopedia* is arranged as a series of entries in alphabetical order. Some entries comprise a single article, whilst entries on more diverse subjects consist of several articles that deal with various aspects of the topic. In the latter case the articles are arranged in a logical sequence within an entry.

To help you realize the full potential of the material in the *Encyclopedia* we have provided three features to help you find the topic of your choice: contents list, cross-references, and index.

Contents lists

Your first point of reference will probably be the contents list. The complete contents list appearing in each volume will provide you with both the volume number and the page number of the entry. On the opening page of an entry containing more than one article, a contents list is provided so that the full details of the articles within the entry are immediately available.

Alternatively, you may choose to browse through a volume using the alphabetical order of the entries as your guide. To assist you in identifying your location within the *Encyclopedia*, a running headline indicates the current entry and the current article within that entry.

You will find dummy entries in the following instances:

1. Where obvious synonyms exist for entries.
   For example, a dummy entry appears for Structural Damping which directs you to Hysteretic Damping where the material is located.
2. Where we have grouped together related topics.
   For example, a dummy entry appears for Magnetorheological Fluids which leads you to Electrorheological and Magnetorheological Fluids where the material is located.
3. Where there is debate over the given entry title and whether readers would intuitively find the topic they are trying to locate under that title.
   For example, a dummy entry appears for Vibration Absorbers which directs you to Absorbers, Vibration where the material is located.
4. Where there is debate over whether diverse subjects should comprise several single articles, or one entry consisting of several articles.
   For example, a dummy entry appears for Smart Materials which directs you to the entries Electrorheological and Magnetorheological Fluids, Electrostrictive Materials, Magnetostrictive Materials, Piezoelectric Materials, and Shape Memory Alloys.

Dummy entries appear in both the contents list and the body of the text.

Example
If you were attempting to locate material on diagnostics via the contents list the following information would be provided:

DIAGNOSTICS *See* BEARING DIAGNOSTICS; DIAGNOSTICS AND CONDITION MONITORING, BASIC CONCEPTS; GEAR DIAGNOSTICS; NEURAL NETWORKS, DIAGNOSTIC APPLICATIONS

The page numbers of these entries are given at the appropriate location in the contents list.

If you were trying to locate the material by browsing through the text and you looked up Diagnostics then the following would be provided:

DIAGNOSTICS *See* **BEARING DIAGNOSTICS; DIAGNOSTICS AND CONDITION MONITORING, BASIC CONCEPTS; GEAR DIAGNOSTICS; NEURAL NETWORKS, DIAGNOSTIC APPLICATIONS**

Cross-references

To direct the reader to other entries on related topics, a 'see also' section is provided at the end of each entry.

Example
The entry Wave propogation, Waves in an Unbounded Medium includes the following cross-references:

See also: **Nondestructive testing**, Sonic; **Nondestructive testing**, Ultrasonic; **Ultrasonics**; **Wave propagation**, Guided waves in structures; **Wave propagation**, Interaction of waves with boundaries.

Index

The index will provide you with the volume number and page number of where the material is located, and the index entries differentiate between material that is a whole article, is part of an article, or is data presented in a table. On the opening page of the index detailed notes are provided. Any topic not found through the contents list can be located by referring to the index.

Color Plates

The color figures for each volume have been grouped together in a plate section. The location of this section is cited both in the contents list and before the 'See also' list of the pertinent articles.

Appendices

The appendices appear in each volume.

Contributors

A full list of contributors appears at the beginning of each volume.

Contributors

Agnes, G
1489 Fudge Drive
Beavercreek
OH 45434
USA

Ahmadian, M
Virginia Tech
Advanced Vehicle Dynamics Laboratory
Department of Mechanical Engineering
Blacksburg, VA 24061-0238
USA

Ahmed, A K W
Concordia University
Department of Mechanical Engineering
Montreal
Quebec
Canada

Bajaj, A
Purdue University
Department of Mechanical Engineering
West Lafayette
IN 47907-1288
USA

Banks, H T
North Carolina State University
Center for Research - Science Comput.
324 Harrelson Hall, Box 8205, CRSC
Raleigh, NC 27695-8105
USA

Bauchau, O
Georgia Institute of Technology
Atlanta
GA 30332-0710
USA

Baz, A
University of Maryland
Department of Mechanical Engineering
2137 Engineering Building
College Park, MD 20742
USA

Benson, D J
University of California, San Diego
Division of Mechanical Engineering
Department of Applied Mechanics and
Engineering Sciences
9500 Gilman, La Jolla, CA 92093
USA

Bert, C W
University of Oklahoma
Department of Mechanical Engineering
865 Asp Avenue, Room 202
Norman, OK 73019
USA

Bigret, R
22 Rue J Varnet
93700 Drancy
France

Book, W
Georgia Institute of Technology
School of Mechanical Engineering
Room 472 Manufacturing Research Center
813 Ferst Drive, Atlanta, GA 30332-0405
USA

Braun, S
Technion - Israel Institute of Technology
Faculty of Mechanical Engineering
Haifa 32000
Israel

Cai, G Q
Florida Atlantic University
Center for Applied Stochastics
Boca Raton
FL 33431
USA

Cardona, A
INTEC
Grupo de Technologia Mecanica
Guemes 3450
RA-3000, Santa Fe
Argentina

Castellini, P
Universitá di Ancona
Dipartimento Di Meccanica
Via Brecce Bianche
1-60131 Ancona
Italy

Chou, C S
National Taiwan University
Taipei
Taiwan
Republic of China

Constantinides, T
Imperial College of Science, Technology and Medicine
Engineering Department, Room 812
Exhibition Road
London SW7 2BT
UK

Cooper, J E
School of Engineering
University of Manchester
Oxford Road
Manchester M13 9PL
UK

Craig, Jr R R
University of Texas
Aeronautical Engineering and Engineering Mechanics Department
Austin TX 78712
USA

D'Aubrogio, W
University of L'Aquila
Dipartimento di Energetica
Roio Poggio
67040 L'Aquila
Italy

Dalpiaz, G
University of Bologna
Faculty of Mechanical Engineering
2, 40136 Bologna
Italy

David, A
Auburn University
Nonlinear Systems Research Laboratory
Department of Mechanical Engineering
Auburn, AL 36849
USA

Devloo, P
Universidade Estadual de Campinas
Faculdade de Engenharia Civil
Caixa Postal 6021
13083-970 Campinas São Paulo
Brazil

Dimentberg, M F
Worcester Polytechnic Institute
Mechanical Engineering Department
Worcester
MA 01609
USA

Doebling, S
Los Alamos National Laboratory
ESA - EA, M/S P946, PO Box 1663
NM 87545
USA

Drew, S J
The University of Western Australia
Department of Mechanical and Materials Engineering
Nedlands 6709, Perth
Western Australia
Australia

Dubuisson, B
33 rue Saint Hubert
60610 La Croix Saint Ouen
France

Dyne, S
University of Southampton
Institute of Sound and Vibration Research
Southampton
SO17 1BJ
UK

Elishakoff, I
Florida Atlantic University
Department of Mechanical Engineering
Boca Raton
FL 33431-0991
USA

Elliott, S J
The University of Southampton
Institute of Sound and Vibration Research
Southampton SO17 1BJ
UK

Ewins, D J
Imperial College of Science, Technology and Medicine
Department of Mechanical Engineering
Exhibition Road
London SW7 2BX
UK

Farhat, C
University of Colorado
Department of Aerospace Engineering Sciences
Campus Box 429
Boulder, CO 80309
USA

Farrar, C
Los Alamos National Laboratory
ESA - EA, M/S P946, PO Box 1663
NM 87545
USA

Fassois, S D
University of Patras
Stochastic Mechanical Systems (SMS) Group
Faculty of Mechanical and Aeronautical Engineering
GR 265 00 Patras
Greece

Feeny, B F
Michigan State University
Department of Mechanical Engineering
2555 Engineering Building
East Lansing, MI 48824
USA

Feldman, M
Technion - Israel Institute of Technology
Faculty of Mechanical Engineering
Haifa 32000
Israel

Flatau, A
National Science Foundation
Dynamic Systems and Control Program
4201 Wilson Blvd. Suite 545
Arlington VA 22230
USA

Fuller, C R
Virginia Tech
Department of Mechanical Engineering
Blacksburg
VA 24061-0238
USA

Gandhi, F
The Pennsylvania State University
Department of Aerospace Engineering
233 Hammond Building
University Park, PA 16802
USA

Gern, F H
Center for Intelligent Material Systems and Structures (CIMSS)
Virginia Polytechnic Institute and State University
New Engineering Building, Room 303
Blacksburg, VA 24061-0261
USA

Giurgiutiu, V
University of South Carolina
Department of Mechanical Engineering
300 S. Main Street, Room A222
Columbia, SC 29208
USA

Griffin, M J
The University of Southampton
Human Factors Research Unit
Institute of Sound and Vibration Research
Southampton SO17 1BJ
UK

Griffin, S
AFRL/VSSV
3550 Aberdeen Ave SE
Kirtland AFB
NM 87117-5748
USA

Haddow, A
Michigan State University
Department of Mechanical Engineering
East Lansing
MI 48824
USA

Hallquist, J
Livermore Software Technology Corporation (LSTC)
97 Rickenbacker Circle
Livermore
CA 94550
USA

Hann, F
University of Notre Dame
Department of Civil Engineering
Notre Dame
IN 46556-0767
USA

Hartmann, F
University of Kassel
Dept. Baustatik, Fb 14
Kurt-Wolters-Str 3
D-34109 Kassel
Germany

Hayek, S I
Pennsylvania State University
112 EES Building
University Park
PA 16802-6812
USA

Holmes, P J
Princeton University
Department of Mechanical and Aerospace Engineering
Princeton
New Jersey 08544
USA

Ibrahim, R
Wayne State University
Mechanical Engineering
Detroit, MI 48202
USA

Inman, D
Virginia Polytechnic Institute and State University
Department of Engineering Science and Mechanics
310 NEB, Mail Code 0261
Blacksburg, VA 24061-0219
USA

Kapania, R
Virginia Polytechnic Institute and State University
Department of Aerospace and Ocean Engineering
Blacksburg
VA 24061-0203
USA

Kareem, A
University of Notre Dame
Department of Civil Engineering
Notre Dame
IN 46556-0767
USA

Kijewski, T
University of Notre Dame
Department of Civil Engineering
Notre Dame
IN 46556-0767
USA

Klapka, I
Université de Liège
Laboratoire des Techniques Aéronautiques et Spatiales
Dynamique des Structures
rue E Solvay 21, B-4000, Liège
Belgium

Kobayashi, A S
University of Washington
Department of Mechanical Engineering
Seattle, WA 98195
USA

Krishnan, R
University of Maryland at College Park
Department of Aerospace Engineering
3180 Engineering Classroom Building
College Park
MD 20742-3015
USA

Krousgrill, C M
Purdue University
School of Mechanical Engineering
West Lafayette
IN 47907-1288
USA

Leissa, A W
Ohio State University
Department of Mechanical Engineering
206 W. 18th Ave
Columbus, OH 43210-1154
USA

Lesieutre, G A
Pennsylvania State University
Department of Aerospace Engineering
153G Hammond Building
University Park, PA 16802
USA

Li, C J
Rensselaer Polytechnic Institute
Department of Mechanical Engineering,
Aeronautical Engineering, and Mechanics
110 8th Street
Troy, NY 12180
USA

Lieven, N A J
Bristol University
Department of Aerospace Engineering
Queens Building, University Walk
Bristol, BS8 1TR
UK

Lin, Y K
Florida Atlantic University
Center for Applied Stochastics
Boca Raton
FL 33431
USA

Link, M
Universität Gesamthoschule Kassel
Fachgebiet Leichtbau
Mönchebergstrasse 7
D34109 Kassel
Germany

Lowe, M J S
Imperial College of Science, Technology and Medicine
Department of Mechanical Engineering
Exhibition Road
London, SW7 2BX
UK

Ma, F
University of California
Department of Mechanical Engineering
Berkeley
California, CA 94720
USA

Maddux, G E
PO Box 203
Tipp City
OH 45371 - 9435
USA

Maia, N M M
Instituto Superior Technico
Department de Engenharia Mecanica
Av Rovisco Pais
1049-001 Lisboa
Portugal

Marcondes, J
San Jose University
Packaging Department
One Washington Square
San Jose, CA 95192-0005
USA

McConnell, K
Iowa State University Ames
AEEM
Black Engineering Building
Iowa 50011
USA

McKee, K
Rensselaer Polytechnic Institute
Department of Mechanical Engineering, Aeronautical Engineering, and Mechanics
110 8th Street
Troy, NY12180
USA

Mucino, V H
West Virginia University
Mechanical and Aerospace Engineering
Room 351
PO Box 6106, Morgantown WV 26506-6106
USA

Naeim, F
John A Martin & Associates, Inc.
1212 S. Flower Street
Los Angeles, CA 90015
USA

Natori, M C
Institute of Space and Astronautical Science
Kanagawa
Japan

Niemkiewicz, J
Techonology Transfer Manager
Maintenance and Diagnostic (M&D) LLC
440 Baldwin Tower
Eddystone, PA 19022
USA

Norton, M P
The University of Western Australia
Department of Mechanical and Materials Engineering
Nedlands 6709, Perth
Western Australia
Australia

Pan, J
University of Western Australia
Department of Mechanical and Materials Engineering
Nedlands 6709, Perth
Western Australia
Australia

Perkins, N C
University of Michigan
Mechanical Engineering and
Applied Mechanics Department
Ann Arbor
MI 48109
USA

Peterka, F
Academy of Sciences of the Czech Republic
Institute of Thermomechanics
182 00 Prague 8, Doplejskova 5
The Czech Republic

Pierre, C
University of Michigan
Mechanical Engineering and Applied Mechanics
College of Engineering, 2202 GG Brown Building
2350 Hayward Street, Ann Arbor, MI 48109-2125
USA

Pinter, G A
North Carolina State University
Center for Research - Science Comput.
324 Harrelson Hall, Box 8205, CRSC
Raleigh, NC 27695-8105
USA

Prasad, M G
Stevens Institute of Technology
Department of Mechanical Engineering
Hoboken
NJ 07030
USA

Rade, D
Federal University of Uberlandia
Mechanical Engineering Department
Campus Santa Monica
PO Box 593, 38400-902 Uberlandia, MG
Brazil

Radeş, M
Universitatea Politehnica Bucharesti
Department of Engineering Sciences
313 Splaiul Independentei
79590 Bucuresti
Romania

Ram, Y M
Louisiana State University
Mechanical Engineering Department
Baton Rouge
LA 70803
USA

Ramulu, M
University of Washington
Department of Mechanical Engineering
Seattle, WA 98195
USA

Randall, R B
University of New South Wales
School of Mechanical and Manufacturing Engineering
Sydney 2052, New South Wales
Australia

Rao, S S
University of Miami
Department of Mechanical Engineering
PO Box 248294, Coral Gables
FL 33124-0624
USA

Revel, G M
Università di Ancona
Dipartimento di Meccanica
Via Brecce Bianche
1-60131 Ancona
Italy

Rivin, E
Wayne State University
Mechanical Engineering
2100W Engineering Building
Detroit, Michigan 48202
USA

Rixen, D
Delft University of Technology
PO Box 5
2600 AA Delft
The Netherlands

Robert, G
Samtech SA
Rue des Chasseurs-Ardennais, 8
B-4031 Liège
Belgium

Rosenhouse, G
Technion - Israel Institute of Technology
Faculty of Civil Engineering
Technion City
Haifa 32000
Israel

Schmerr, Jr, L W
Iowa State University
Center for NDE, Aerospace Engineering and Engineering Mechanics
211A Applied Science Complex II, 1915 Scholl Road
1915 Scholl Road, Ames, IA 50011
USA

Sciulli, D
5725 Cedar Way #301
Centerville
VA 20121
USA

Scott, R A
University of Michigan
Department of Mechanical Engineering and Applied Mechanics
2206 G. G. Brown Building
Ann Arbor, MI 48109
USA

Sestieri, A
Università Degli Studi di Roma
Dipartimento Meccanica e Aeronautica
Via Eudossinia 18
I - 00184 Roma
Italy

Shaw, S
Michigan State University
Department of Mechanical Engineering
A321 Engineering Building
East Lansing, MI 48824-1226
USA

Shteinhauz, G D
The Goodyear Tire Rubber Company
Tire-Vehicle Engineering Technology
Technical Center D/460G
PO Box 353, Akron, Ohio 44309-3531
USA

Sidahmed, M
Université de Technologie de Compiègne
Heuristique et Diagnostic des Systèmes Complexes
Centre de Recherches de Royallieu
BP 20529
60205 Compiègne
France

Sieg, T
Paulstra Industries Inc.
Carlsbad, CA
USA

Silva, J M M
Instituto Superior Tecnico
Departmento de Engenharia Mecanica
Av Rovisco Pais
1049-001 Lisboa
Portugal

Sinha, S
Auburn University
Nonlinear Systems Research Laboratory
Department of Mechanical Engineering
Auburn, AL 36849
USA

Smallwood, D
Sandia National Laboratories
PO Box 5800
Albuquerque
NM 87185-0865
USA

Snyder, R
University of Maryland at College Park
Department of Aerospace Engineering
3180 Engineering Classroom Building
College Park, MD 20742-3015
USA

Soedel, W
Purdue University
School of Mechanical Engineering
West Lafayette
IN 47907
USA

Soong, T T
State University of New York at Buffalo
MCEER
107 Red Jacket Quadrangle
Buffalo, NY 14261-0025
USA

Spencer, Jr, B F
University of Notre Dame
Department of Civil Engineering
Notre Dame
IN 46556-0767
USA

Stanway, R
The University of Sheffield
Department of Mechanical Engineering
Mappin Street
Sheffield S1 3JD
UK

Steffen, Jr, V
Federal University of Uberlandia
Mechanical Engineering Department
Campus Santa Monica
PO Box 593, 38400-902 Uberlandia, MG
Brazil

Steindl, A
Vienna University of Technology
Wiedner Hauptstrasse 8-10
A-1040 Vienna
Austria

Stiharu, I
Concordia University
Department of Mechanical Engineering
1455 de Masonneuve Blv W
Montreal, Quebec H3G 1M8
Canada

Sun, J-Q
University of Delaware
Department of Mechanical Engineering
Newark, DE 19716
USA

Sunar, M
King Fahd University of Petroleum and Minerals
Department of Mechanical Engineering
PO Box 1205
Dhahran 31261
Saudi Arabia

Tang, J
The Pennsylvania State University
Department of Mechanical Engineering
157 E Hammond Building, University Park
PA 16802
USA

Tomasini, E P
Università di Ancona
Dipartimento Di Meccanica
Via Brecce Bianche
1-60131 Ancona
Italy

Tordon, M J
University of New South Wales
School of Mechanical and
Manufacturing Engineering
Sydney 2052, New South Wales
Australia

Troger, H
Vienna University of Technology
Wiedner Hauptstrasse 8-10
A-1040 Vienna
Austria

Tzou, H S
University of Kentucky
Department of Mechanical Engineering
Dynamics and Systems Laboratory
Lexington, KY 40506
USA

Uchino, K
The Pennsylvania State University
134 Materials Research Laboratory
University Park
PA, 16802-4800
USA

Ungar, E E
Acentech Incorporated
33 Moulton Street
Cambridge
MA 02138-1118
USA

Vakakis, A
University of Illinois
Department of Mechanical and Industrial Engineering
140 Mechanical Engineering Building,
1206 West Green Street
Urbana, IL 61801
USA

Varoto, P S
Escola de Engenharia de São Carlos, USP
Dept. Engenharia Mecanica
Av.Dr. Carlos Botelho, 1465, CP 359
São Carlos - SP - 13560-250
Brasil

Vorus, W S
University of New Orleans
School of Naval Architecture and Marine Engineering
College of Engineering
New Orleans, LA 70148
USA

Wang, K W
The Pennsylvania State University
Department of Mechanical Engineering
157 E Hammond Building, University Park
PA 16802
USA

Wereley, N M
University of Maryland at College Park
Department of Aerospace Engineering
3180 Engineering Classroom Building
College Park, MD 20742-3015
USA

White, P
The University of Southampton
Institute of Sound and Vibration Research (ISVR)
Southampton, SO9 5NH
UK

Wickert, J
Carnegie Mellon University
Department of Mechanical Engineering
Pittsburg
PA 15213-3890
USA

Wright, J
University of Manchester
School of Engineering
Oxford Road
Manchester M13 9PL
UK

Yang, B
University of Southern California
Department of Mechanical Engineering
Los Angeles
CA 90089-1453
USA

Zacksenhouse, M
Technion - Israel Institute of Technology
Faculty of Mechanical Engineering
Haifa 32000
Israel

Zu, J W
University of Toronto
Department of Mechnical and Industrial Engineering
5 King's College Road
Toronto, Ontario
Canada M5S 3G8

CONTENTS

VOLUME 1

A

ABSORBERS, ACTIVE *G Agnes* 1

ABSORBERS, VIBRATION *V Steffen, Jr* *D Rade* 9

ACTIVE ABSORBERS *See* ABSORBERS, ACTIVE 26

ACTIVE CONTROL OF CIVIL STRUCTURES *T T Soong* *B F Spencer, Jr.* 26

ACTIVE CONTROL OF VEHICLE VIBRATION *M Ahmadian* 37

ACTIVE ISOLATION *S Griffin* *D Sciulli* 46

ACTIVE VIBRATION CONTROL *See* ACTIVE CONTROL OF VEHICLE VIBRATION; ACTIVE ISOLATION; ACTIVE VIBRATION SUPPRESSION; ACTUATORS AND SMART STRUCTURES; DAMPING, ACTIVE; FEED FORWARD CONTROL OF VIBRATION; FLUTTER, ACTIVE CONTROL; HYBRID CONTROL. 48

ACTIVE VIBRATION SUPPRESSION *D Inman* 48

ACTUATORS AND SMART STRUCTURES *V Giurgiutiu* 58

ADAPTIVE FILTERS *S J Elliott* 81

AEROELASTIC RESPONSE *J E Cooper* 87

ANTIRESONANCE *See* RESONANCE AND ANTIRESONANCE 98

AVERAGING *S Braun* 98

B

BALANCING *R Bigret* 111

BASIC PRINCIPLES *G Rosenhouse* 124

BEAMS *R A Scott* 137

BEARING DIAGNOSTICS *C J Li* *K McKee* 143

BEARING VIBRATIONS *R Bigret* 152

BELTS *J W Zu* 165

BIFURCATION *See* DYNAMIC STABILITY 174

BLADES AND BLADED DISKS *R Bigret* 174

BOUNDARY CONDITIONS *G Rosenhouse* 180

BOUNDARY ELEMENT METHODS *F Hartmann* 192

BRIDGES *S S Rao* 202

C

CABLES *N C Perkins* 209

CEPSTRUM ANALYSIS *R B Randall* 216

CHAOS *P J Holmes* 227

CHATTER *See* MACHINE TOOLS, DIAGNOSTICS 236

COLUMNS *I Elishakoff* *C W Bert* 236

COMMERCIAL SOFTWARE *G Robert* 243
COMPARISON OF VIBRATION PROPERTIES 256
Comparison of Spatial Properties *M Radeş* 256
Comparison of Modal Properties *M Radeş* 265
Comparison of Response Properties *M Radeş* 272
COMPONENT MODE SYNTHESIS (CMS) *See* THEORY OF VIBRATION, SUBSTRUCTURING 278
COMPUTATION FOR TRANSIENT AND IMPACT DYNAMICS *D J Benson J Hallquist* 278
COMPUTATIONAL METHODS *See* BOUNDARY ELEMENT METHODS; COMMERCIAL SOFTWARE; COMPUTATION FOR TRANSIENT AND IMPACT DYNAMICS; CONTINUOUS METHODS; EIGENVALUE ANALYSIS; FINITE DIFFERENCE METHODS; FINITE ELEMENT METHODS; KRYLOV-LANCZOS METHODS; LINEAR ALGEBRA; OBJECT ORIENTED PROGRAMMING IN FE ANALYSIS; PARALLEL PROCESSING; TIME INTEGRATION METHODS. 286
CONDITION MONITORING *See* DIAGNOSTICS AND CONDITION MONITORING, BASIC CONCEPTS; ROTATING MACHINERY, MONITORING. 286
CONTINUOUS METHODS *C W Bert* 286
CORRELATION FUNCTIONS *S Braun* 294
CRASH *V H Mucino* 302
CRITICAL DAMPING *D Inman* 314

D

DAMPING IN FE MODELS *G A Lesieutre* 321
DAMPING MATERIALS *E E Ungar* 327
DAMPING MEASUREMENT *D J Ewins* 332
DAMPING MODELS *D Inman* 335
DAMPING MOUNTS *J-Q Sun* 342
DAMPING, ACTIVE *A Baz* 351
DATA ACQUISITION *R B Randall M J Tordon* 364
DIAGNOSTICS AND CONDITION MONITORING, BASIC CONCEPTS *M Sidahmed* 376
DIAGNOSTICS *See* BEARING DIAGNOSTICS; DIAGNOSTICS AND CONDITION MONITORING, BASIC CONCEPTS; GEAR DIAGNOSTICS; NEURAL NETWORKS, DIAGNOSTIC APPLICATIONS 380
DIGITAL FILTERS *A G Constantinides* 380
DISCRETE ELEMENTS *S S Rao* 395
DISKS *D J Ewins* 404
DISPLAYS OF VIBRATION PROPERTIES *M Radeş* 413
DISTRIBUTED SENSORS AND ACTUATORS *See* SENSORS AND ACTUATORS 431
DUHAMEL METHOD *See* THEORY OF VIBRATION: DUHAMEL'S PRINCIPLE AND CONVOLUTION 431
DYNAMIC STABILITY *A Steindl H Troger* 431

E

EARTHQUAKE EXCITATION AND RESPONSE OF BUILDINGS *F Naeim* 439
EIGENVALUE ANALYSIS *O Bauchau* 461

ELECTRORHEOLOGICAL AND MAGNETORHEOLOGICAL FLUIDS *R Stanway* 467
ELECTROSTRICTIVE MATERIALS *K Uchino* 475
ENVIRONMENTAL TESTING, OVERVIEW *D Smallwood* 490
ENVIRONMENTAL TESTING, IMPLEMENTATION *P S Varoto* 496
EQUATIONS OF MOTION *See* THEORY OF VIBRATION: EQUATIONS OF MOTION 504

VOLUME 2

F

FATIGUE *A S Kobayashi M Ramulu* 505
FE MODELS *See* DAMPING IN FE MODELS; FINITE ELEMENT METHODS 513
FEEDFORWARD CONTROL OF VIBRATION *C R Fuller* 513
FFT METHODS *See* TRANSFORM METHODS 520
FILTERS *See* ADAPTIVE FILTERS; DIGITAL FILTERS; OPTIMAL FILTERS 520
FINITE DIFFERENCE METHODS *S S Rao* 520
FINITE ELEMENT METHODS *S S Rao* 530
FLUID/STRUCTURE INTERACTION *S I Hayek* 544
FLUTTER *J Wright* 553
FLUTTER, ACTIVE CONTROL *F H Gern* 565
FORCED RESPONSE *N A J Lieven* 578
FOURIER METHODS *See* TRANSFORM METHODS 582
FREE VIBRATION *See* THEORY OF VIBRATION: FUNDAMENTALS 582
FRICTION DAMPING *R Ibrahim* 582
FRICTION INDUCED VIBRATIONS *R Ibrahim* 589

G

GEAR DIAGNOSTICS *C J Li* 597
GROUND TRANSPORTATION SYSTEMS *A K Waizuddin Ahmed* 603

H

HAND-TRANSMITTED VIBRATION *M J Griffin* 621
HELICOPTER DAMPING *N M Wereley R Snyder R Krishnan T Sieg* 629
HILBERT TRANSFORMS *M Feldman* 642
HUMAN RESPONSE TO VIBRATION *See* GROUND TRANSPORTATION SYSTEMS; HAND-TRANSMITTED VIBRATION; MOTION SICKNESS; WHOLE-BODY VIBRATION 649
HYBRID CONTROL *J Tang K W Wang* 649
HYSTERETIC DAMPING *H T Banks G A Pinter* 658

I

IDENTIFICATION, FOURIER-BASED METHODS *S Braun* 665
IDENTIFICATION, MODEL-BASED METHODS *S D Fassois* 673
IDENTIFICATION, NON-LINEAR SYSTEMS *See* NON-LINEAR SYSTEM IDENTIFICATION 685
IMPACTS, NON-LINEAR SYSTEMS *See* VIBRO-IMPACT SYSTEMS 686

IMPULSE RESPONSE FUNCTION *See* THEORY OF VIBRATION: IMPULSE RESPONSE FUNCTION 686
INTENSITY *See* VIBRATION INTENSITY 686
INVERSE PROBLEMS *Y M Ram* 686
ISOLATION, ACTIVE *See* ABSORBERS, ACTIVE; ACTIVE CONTROL OF VEHICLE VIBRATION; ACTIVE ISOLATION 690
ISOLATION VIBRATION – APPLICATIONS AND CRITERIA *See* VIBRATION ISOLATION, APPLICATIONS AND CRITERIA 690
ISOLATION VIBRATION – THEORY *See* VIBRATION ISOLATION THEORY 690

K

KRYLOV-LANCZOS METHODS *R R Craig Jr* 691

L

LAGRANGE METHOD *See* BASIC PRINCIPLES; THEORY OF VIBRATION, ENERGY METHODS 699
LAPLACE TRANSFORMS *See* TRANSFORM METHODS 699
LASER BASED MEASUREMENTS *E P Tomasini G M Revel P Castellini* 699
LINEAR ALGEBRA *C Farhat D Rixen* 710
LINEAR DAMPING MATRIX METHODS *F Ma* 721
LIQUID SLOSHING *R A Ibrahim* 726
LOCALIZATION *C Pierre* 741

M

MACHINERY, ISOLATION *See* VIBRATION ISOLATION, APPLICATIONS AND CRITERIA. 753
MAGNETORHEOLOGICAL FLUIDS *See* ELECTRORHEOLOGICAL AND MAGNETORHEOLOGICAL FLUIDS 753
MAGNETOSTRICTIVE MATERIALS *A Flatau* 753
MATERIALS, DAMPING *See* DAMPING MATERIALS 762
MEASUREMENT *See* LASER BASED MEASUREMENT; SEISMIC INSTRUMENTS, ENVIRONMENTAL FACTORS; STANDARDS FOR VIBRATIONS OF MACHINES AND MEASUREMENT PROCEDURES; TRANSDUCERS FOR ABSOLUTE MOTION; TRANSDUCERS FOR RELATIVE MOTION 762
MEMBRANES *A W Leissa* 762
MEMS, APPLICATIONS *I Stiharu* 771
MEMS, DYNAMIC RESPONSE *I Stiharu* 779
MEMS, GENERAL PROPERTIES *I Stiharu* 794
MODAL ANALYSIS, EXPERIMENTAL 805
Basic Principles *D J Ewins* 805
Measurement Techniques *J M M Silva* 813
Parameter Extraction Methods *N M M Maia* 820
Construction of Models from Tests *N M M Maia* 824
Applications *D J Ewins* 829
MODE OF VIBRATION *D J Ewins* 838
MODEL UPDATING AND VALIDATING *M Link* 844
MODELS, DAMPING *See* DAMPING MODELS 856

MODES, NON-LINEAR SYSTEMS *See* NON-LINEAR SYSTEMS MODES 856
MODES, ROTATING MACHINERY *See* ROTATING MACHINERY, MODAL CHARACTERISTICS 856
MONITORING *See* DIAGNOSTICS AND CONDITION MONITORING, BASIC CONCEPTS, ROTATING MACHINERY, MONITORING 856
MOTION SICKNESS *M J Griffin* 856

N

NEURAL NETWORKS, DIAGNOSTIC APPLICATIONS *M Zacksenhouse* 863
NEURAL NETWORKS, GENERAL PRINCIPLES *B Dubuisson* 869
NOISE 877
Noise Radiated from Elementary Sources *M P Norton J Pan* 877
Noise Radiated by Baffled Plates *M P Norton J Pan* 887
NONDESTRUCTIVE TESTING 898
Sonic *S Doebling C Farrar* 898
Ultrasonic *L W Schmerr Jr* 906
NONLINEAR NORMAL MODES *A F Vakakis* 918
NONLINEAR SYSTEM IDENTIFICATION *B F Feeny* 924
NONLINEAR SYSTEM RESONANCE PHENOMENA *A Bajaj C M Krousgrill* 928
NONLINEAR SYSTEMS, OVERVIEW *N C Perkins* 944
NONLINEAR SYSTEMS ANALYSIS *A Bajaj* 952

O

OBJECT ORIENTED PROGRAMMING IN FE ANALYSIS *I Klapka A Cardona P Devloo* 967
OPTIMAL FILTERS *S J Elliott* 977

P

PACKAGING *J Marcondes* 983
PACKAGING, ELECTRONIC *See* ELECTRONIC PACKAGING 990
PARALLEL PROCESSING *D Rixen* 990
PARAMETRIC EXCITATION *S C Sinha A David* 1001
PERTURBATION TECHNIQUES FOR NONLINEAR SYSTEMS *S Shaw* 1009
PIEZOELECTRIC MATERIALS AND CONTINUA *H S Tzou M C Natori* 1011
PIPES *S S Rao* 1019
PLATES *A W Leissa* 1024

VOLUME 3

R

RANDOM PROCESSES *M F Dimentberg* 1033
RANDOM VIBRATION *See* RANDOM VIBRATION, BASIC THEORY; RANDOM PROCESSES, STOCHASTIC SYSTEMS 1040
RANDOM VIBRATION, BASIC THEORY *M F Dimentberg* 1040
RESONANCE AND ANTIRESONANCE *M Radeş* 1046

RESONANCE, NON LINEAR SYSTEMS *See* NON LINEAR SYSTEM RESONANCE PHENOMENA; STOCHASTIC SYSTEMS 1055
ROBOT VIBRATIONS *W Book* 1055
ROTATING MACHINERY *See* ROTATING MACHINERY, ESSENTIAL FEATURES; ROTATING MACHINERY, MODAL CHARACTERISTICS; ROTATING MACHINERY, MONITORING; ROTOR DYNAMICS; ROTOR STATOR INTERACTIONS; BALANCING; BLADES AND BLADED DISKS 1064
ROTATING MACHINERY, ESSENTIAL FEATURES *R Bigret* 1064
ROTATING MACHINERY, MODAL CHARACTERISTICS *R Bigret* 1069
ROTATING MACHINERY, MONITORING *R Bigret* 1078
ROTOR DYNAMICS *R Bigret* 1085
ROTOR–STATOR INTERACTIONS *R Bigret* 1107

S

SEISMIC INSTRUMENTS, ENVIRONMENTAL FACTORS *K McConnell* 1121
SENSORS AND ACTUATORS *H S Tzou C S Chou* 1134
SHAPE MEMORY ALLOYS *H S Tzou A Baz* 1144
SHELLS *W Soedel* 1155
SHIP VIBRATIONS *W S Vorus* 1167
SHOCK *J Marcondes P. Singh* 1173
SHOCK ABSORBERS *See* SHOCK ISOLATION SYSTEMS 1180
SHOCK ISOLATION SYSTEMS *M Radeş* 1180
SIGNAL GENERATION MODELS FOR DIAGNOSTICS *M Sidahmed G Dalpiaz* 1184
SIGNAL INTEGRATION AND DIFFERENTIATION *S Dyne* 1193
SIGNAL PROCESSING, CEPSTRUM *See* CEPSTRUM ANALYSIS 1199
SIGNAL PROCESSING, MODEL BASED METHODS *S Braun* 1199
SMART MATERIALS *See* ELECTRORHEOLOGICAL AND MAGNETORHELEOLOGICAL FLUIDS; ELECTROSTRICTIVE MATERIALS; MAGNETOSTRICTIVE MATERIALS; PIEZOELECTRIC MATERIALS; SHAPE MEMORY ALLOYS 1208
SOUND *See* VIBRATION GENERATED SOUND, FUNDAMENTALS; VIBRATION GENERATED SOUND, RADIATION BY FLEXURAL ELEMENTS 1208
SPECTRAL ANALYSIS, CLASSICAL METHODS *S Braun* 1208
SPECTRAL ANALYSIS, MODEL BASED METHODS *See* SIGNAL PROCESSING, MODEL BASED METHODS 1223
SPECTRAL ANALYSIS, WINDOWS *See* WINDOWS 1223
STABILITY *See* DYNAMIC STABILITY 1224
STANDARDS FOR VIBRATIONS OF MACHINES AND MEASUREMENT PROCEDURES *J Niemkiewicz* 1224
STOCHASTIC ANALYSIS OF NON LINEAR SYSTEMS *Y K Lin G Q Cai* 1238
STOCHASTIC SYSTEMS *M F Dimentberg* 1246
STRUCTURAL DAMPING *See* HYSTERETIC DAMPING 1252
STRUCTURAL DYNAMIC MODIFICATIONS *A Sestieri W D'Ambrogio* 1253
STRUCTURE-ACOUSTIC INTERACTION, HIGH FREQUENCIES *A Sestieri* 1265

STRUCTURE-ACOUSTIC INTERACTION, LOW FREQUENCIES *A Sestieri* 1274
SUBSTRUCTURING *See* THEORY OF VIBRATION, SUBSTRUCTURING 1283
SUPERPOSITION *See* THEORY OF VIBRATION, SUBSTRUCTURING 1283
SVD *See* LINEAR ALGEBRA 1283

T

TESTING, MODAL *See* MODAL ANALYSIS, EXPERIMENTAL: APPLICATIONS; MODAL ANALYSIS, EXPERIMENTAL: BASIC PRINCIPLES; MODAL ANALYSIS, EXPERIMENTAL: CONSTRUCTION OF MODELS FROM TESTS; MODAL ANALYSIS, EXPERIMENTAL: MEASUREMENT TECHNIQUES; MODAL ANALYSIS, EXPERIMENTAL: PARAMETER EXTRACTION METHODS 1285
TESTING, NONLINEAR SYSTEMS *A Haddow* 1285
THEORY OF VIBRATION 1290
Fundamentals *B Yang* 1290
Superposition *M G Prasad* 1299
Duhamel's Principle and Convolution *G Rosenhouse* 1304
Energy Methods *S S Rao* 1308
Equations of Motion *J Wickert* 1324
Substructuring *M Sunar* 1332
Impulse Response Function *R K Kapania* 1335
Variational Methods *S S Rao* 1344
TIME–FREQUENCY METHODS *P White* 1360
TIRE VIBRATIONS *G D Shteinhauz* 1369
TOOL WEAR MONITORING *M Sidahmed* 1379
TRANSDUCERS FOR ABSOLUTE MOTION *K G McConnell* 1381
TRANSDUCERS FOR RELATIVE MOTION *G E Maddux* *K G McConnell* 1398
TRANSFORM METHODS *S Braun* 1406
TRANSFORMS, HILBERT *See* HILBERT TRANSFORMS 1419
TRANSFORMS, WAVELETS *P White* 1419
TRANSMISSION *See* VIBRATION TRANSMISSION 1435
TRANSPORTATION SYSTEMS *See* GROUND TRANSPORTATION SYSTEMS 1435

U

ULTRASONICS *M J S Lowe* 1437
ULTRASONICS, NONDESTRUCTIVE TESTING *See* NONDESTRUCTIVE TESTING: ULTRASONIC 1441

V

VARIATIONAL METHODS *See* THEORY OF VIBRATION: VARIATIONAL METHODS 1443
VEHICLES, ACTIVE VIBRATION CONTROL *See* ACTIVE CONTROL OF VEHICLE VIBRATION 1443
VIBRATION ABSORBERS *See* ABSORBERS, VIBRATION 1443
VIBRATION GENERATED SOUND 1443
Fundamentals *M P Norton* *S J Drew* 1443
Radiation by Flexural Elements *M P Norton* *S J Drew* 1456
VIBRATION INTENSITY *S I Hayek* 1480

VIBRATION ISOLATION THEORY *E Rivin* 1487
VIBRATION ISOLATION, APPLICATIONS AND CRITERIA *E Rivin* 1507
VIBRATION PROPERTIES, COMPARISON *See* COMPARISON OF VIBRATION PROPERTIES: COMPARISON OF MODAL PROPERTIES; COMPARISON OF VIBRATION PROPERTIES: COMPARISON OF RESPONSE PROPERTIES; COMPARISON OF VIBRATION PROPERTIES: COMPARISON OF SPATIAL PROPERTIES 1521
VIBRATION TRANSMISSION *S I Hayek* 1522
VIBRO-IMPACT SYSTEMS *I F Peterka* 1531
VISCOUS DAMPING *F Gandhi* 1548

W

WAVE PROPAGATION 1551
Guided Waves in Structures *M J S Lowe* 1551
Interaction of Waves with Boundaries *M J S Lowe* 1559
Waves in an Unbounded Medium *M J S Lowe* 1565
WAVELETS *See* TRANSFORMS, WAVELETS 1570
WHOLE-BODY VIBRATION *M J Griffin* 1570
WIND-INDUCED VIBRATIONS *T Kijewski F Hann A Kareem* 1578
WINDOWS *S Braun* 1587

Z

Z TRANSFORMS *See* TRANSFORM METHODS 1597

GLOSSARY Gi–Gvi
APPENDICES Ai–Axviii
INDEX Ii–Ixxxii
COLOUR PLATE SECTIONS
Volume 1 292–293
Volume 2 812–813
Volume 3 1308–1309

A

ABSORBERS, ACTIVE

G Agnes, Beavercreek, OH, USA

Copyright © 2001 Academic Press

doi:10.1006/rwvb.2001.0190

Active vibration absorbers combine the benefits of mechanical vibration absorbers with the flexibility of active control systems. Mechanical vibration absorbers use a small mass coupled to the structure via a flexure (in some form) to add a resonant mode to the structure. By tuning this resonance, the vibration of the structure is reduced. Two limitations on the performance of mechanical vibration absorbers are the mechanism's strokelength and the added mass.

The active vibration absorber replaces the flexure and mass with electronic analogs. Active vibration absorbers can achieve larger effective strokelengths with less mass added to the system. In addition, they can be implemented via strain actuators located in regions of high strain energy instead of large displacement as required by mechanical vibration absorbers – a benefit for some applications.

The drawback to active vibration absorbers is the need for power and electronics. Higher cost and complexity results from the custom analog circuits which must be built or the digital controllers which must be implemented. Finally, unlike mechanical vibration absorbers, active vibration absorbers can lead to spillover, destabilizing the system.

In the following sections, the equations of motion for three common implementations are discussed: the piezo-electric vibration absorber, positive position feedback control and the active vibration absorber. Other combinations of position, velocity, and acceleration feedback are possible (depending on sensor availability) but will not be discussed herein.

Piezo-electric Vibration Absorber

Piezo-electric materials act as a transformer between mechanical and electrical energy. Common forms include a ceramic (PZT) and a polymer (PVDF). When a piezo-electric material undergoes strain, electrical charge is produced on its electrode. By creating a resonant electrical shunt via a resistor and inductor, an electrical resonator is formed. (The piezo-electric material acts as a capacitor in an L–R–C circuit.) By tuning the resonant frequency, the vibration of the structural system is reduced. In practice, inductances on the order of kilohenries are required for low-frequency modes. The inductor is therefore often implemented as an active circuit, requiring power to operate. Hence the piezo-electric vibration absorber is considered an active vibration absorber.

Equations of Motion

A modal model of a structure containing piezo-electric materials can be idealized as shown in **Figure 1**. The base system consists of a mass constrained by a structural spring, K_S, and a piezo-electric spring, K_P, arranged in parallel. The displacement of the structure, X, is to be minimized by a tuned resonant circuit, with charge Q, on the piezo-electric electrodes. The system thus has two-degrees-of-freedom or four states.

The linear constitutive equations for piezo-electric materials, simplified for one-dimensional transverse actuation are:

$$\begin{Bmatrix} E_3 \\ T_{11} \end{Bmatrix} = \begin{bmatrix} 1/\varepsilon^S & -h_{31} \\ -h_{31} & c^D \end{bmatrix} \begin{Bmatrix} D_3 \\ S_{11} \end{Bmatrix} \qquad [1]$$

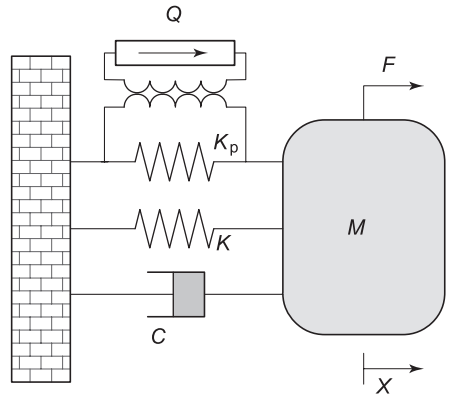


Figure 1 The piezo-electric vibration absorber.

The views expressed in this article are those of the author and do not reflect the official policy or position of the United States Air Force, Department of Defense, or the US Government.

Here, the standard IEEE notation is used (i.e., E is electric field, T is stress, D is electrical displacement, S is strain, ε^S is electrical permittivity, h is the piezo-electric coupling constant, and c^D is the elastic modulus). Assuming a standard patch-like application, these equations may be rewritten in terms of variables more convenient for this study. The equations for piezo-electric spring are thus:

$$\begin{Bmatrix} V \\ F \end{Bmatrix} = \begin{bmatrix} 1/C_{\mathrm{P}}^S & -H \\ -H & K_{\mathrm{P}}^D \end{bmatrix} \begin{Bmatrix} Q \\ X \end{Bmatrix} \qquad [2]$$

where V is the voltage or the piezo-electric electrode, F is the force of the spring, Q is the charge flowing into the patch electrodes, X is the displacement of the spring, C_{P}^S is the capacitance of the patch under constant strain, K_{P}^D is the stiffness of the piezo-electric spring under constant charge, and H is the electromechanical coupling parameter. Note that coefficients in these equations can be modified for more complicated geometries, but would assume a similar form.

Placing an inductive–resistive (LR) shunt across the electrodes of the piezo-electric spring, the equations of motion for the mass in **Figure 1** are:

$$M\ddot{X} + C\dot{X} + K_{\mathrm{P}}^D X + K_{\mathrm{S}} X - HQ + = F(t) \qquad [3a]$$

$$L\ddot{Q} + R\dot{Q} + \frac{1}{C_{\mathrm{P}}^S} Q - HX = 0 \qquad [3b]$$

Here, L is the shunt inductance; R, the shunt resistance; M, the structural mass; and $F(t)$ is an external disturbance.

These equations are next nondimensionalized:

$$\ddot{x} + 2\zeta\dot{x} + x - \frac{\omega_{\mathrm{e}}}{\omega^D}\alpha q = f(t) \qquad [4a]$$

$$\ddot{q} + r\left(\frac{\omega_{\mathrm{e}}}{\omega^D}\right)^2 \dot{q} + \left(\frac{\omega_{\mathrm{e}}}{\omega^D}\right)^2 q - \frac{\omega_{\mathrm{e}}}{\omega^D}\alpha x = 0 \qquad [4b]$$

with the nondimensional quantities used in eqns [4a] and [4b] defined as:

$$\begin{aligned} \omega^D &= \sqrt{\left(\frac{\mathrm{K_S} + K_{\mathrm{P}}^D}{M}\right)} & \omega_{\mathrm{e}} &= \frac{1}{\sqrt{(LC_{\mathrm{P}}^S)}} \\ \alpha^2 &= \tilde{K}_{31}^2 = \frac{K^E}{K + K^E}\frac{k_{31}^2}{1 - k_{31}^2} & r &= RC_{\mathrm{P}}^S\omega^D \\ q &= \sqrt{(L)}Q & x &= \sqrt{(M)}X \end{aligned} \qquad [5]$$

Time has been nondimensionalized such that $t = \omega^D T$. Note that eqns [4a], [4b] and [5] differ from those in the literature since the constant charge (or shorted) stiffness, K^D, of the piezo-electric spring is used in place of the usual constant voltage stiffness, K^E. This simplifies the tuning. Also note, that the coupling term is the generalized electromechanical coupling coefficient, $\tilde{K}_{31}$, which can be determined experimentally – as a modal quantity.

These equations are of the same form as those for the mechanical vibration absorber. The coordinates x and q are proportional to the system displacement and shunt charge, respectively, thus maintaining physical significance. In the next section, the equations of motion for a single-degree-of-freedom structure under positive position feedback control will be derived of this same form. First, however, the tuning and response of the PVA will be considered.

Controller Design

The design of a piezo-electric vibration absorber involves three factors: $\tilde{K}_{ij}$, L and R. The value of $\tilde{K}_{ij}$ is maximized by locating the piezo-electric material in areas of high strain energy. This constant may be determined as a modal constant by considering either the open- and short-circuit resonant mode:

$$\tilde{K}_{ij} = \sqrt{\left[\frac{(\omega^D)^2 - (\omega^E)^2}{(\omega^E)^2}\right]} \qquad [6]$$

or analytically by:

$$\tilde{K}_{ij} = \sqrt{\left[\frac{(\omega^E)^2 - (\omega^*)^2}{(\omega^E)^2}\frac{k_{ij}^2}{1 - k_{ij}^2}\right]} \qquad [7]$$

where ω^* is the natural frequency with the mass of the piezo-electric device included, but its stiffness neglected.

Given the piezo-electric coupling coefficient, a broadband vibration absorber analagous to Den-Hartog's equal peak implementation can be formed by setting:

$$\omega_{\mathrm{e}} = \omega^E\sqrt{\left(1 + K_{ij}^2\right)} = \omega^D \qquad [8]$$

$$r = \sqrt{(2)}\frac{K_{ij}}{\left(1 + K_{ij}\right)^{3/2}} \qquad [9]$$

For multimodal applications, numerical optimization must be used to determine the proper electrical network to suppress the vibration of the structure.

System Response

The response of a single-degree-of-freedom system to harmonic excitation is shown in **Figure 2**. The tuning

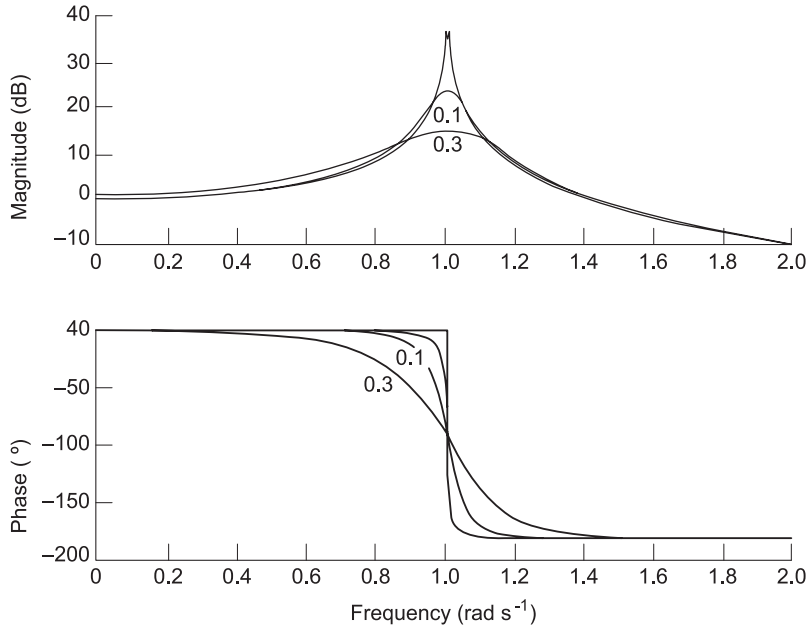


Figure 2 PVA frequency response as the piezo-electric coupling varies.

in eqns [8] and [9] was used. As the piezo-electric coupling is increased, the response of the system decreases. In practice, the piezo-electric coupling is generally limited to at most 0.3.

The impulse response of the system with the $\alpha = 0.2$ and the shunt tuned as presented above is shown in **Figure 3**. Note the system response is damped. The low coupling factors and the fragile nature of piezo-ceramics limit the application of piezo-electric vibration absorbers when higher damping is desired. In the next section, another implementation of an active vibration absorber is discussed: positive position feedback control.

Positive Position Feedback

Modern control design is traditionally performed using first-order dynamical equations. The positive position feedback (PPF) algorithm developed by Goh and Caughey and implemented by Fanson and Caughey uses second-order compensation, allowing physical insight to vibration control by active modal addition. In this algorithm, a position signal is compensated by a second order filter for feedback control. For linear systems, the PPF controller is stable even in the presence of unmodeled actuator dynamics. In addition it is possible to transform the dynamical equations to modal space and design independent second-order feedback compensators for individual modes. Many numerical and experimental implementations of the PPF control scheme may be found in the vibrations literature.

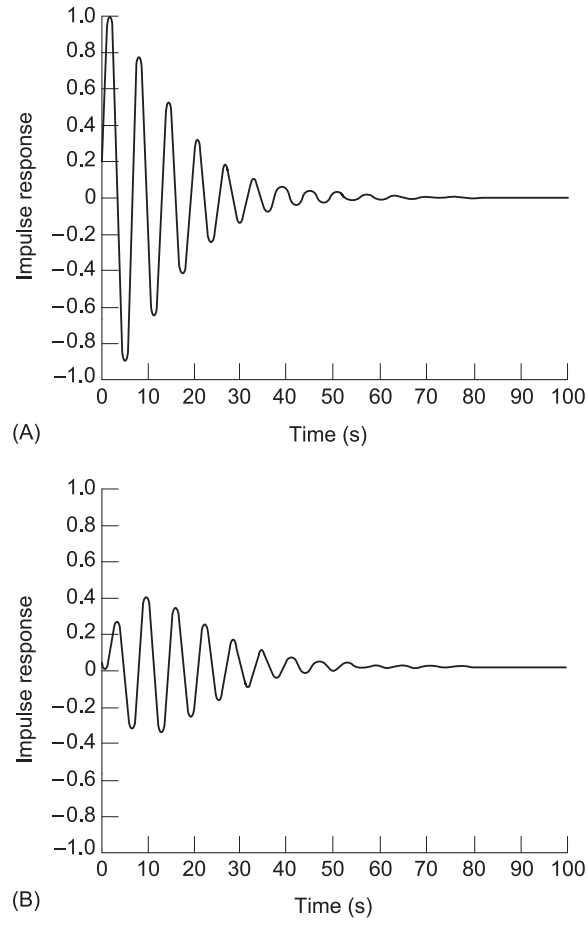


Figure 3 PVA results for a single-degree-of-freedom system with $\alpha = 0.2$. (A) System; (B) controller.

Equations of Motion

A modal model of a structure containing an actuator can be idealized as shown in **Figure 4**.

A single-degree-of-freedom with mass, M, viscous damping, C, and stiffness, K, is driven by an external force, F. The displacement, X, of M is controlled by an actuation force, U. The equations of motion are:

$$M\ddot{X} + C\dot{X} + KX = F + U \qquad [10]$$

Introducing the usual nondimensional parameters:

$$\frac{C}{M} = 2\zeta\omega, \quad \frac{K}{M} = \omega^2, \quad \frac{f}{M} = f, \quad \frac{U}{M} = u \qquad [11]$$

Equation [10] can be nondimensionalized. For positive position feedback, U is defined:

$$u = g\omega_c^2 x_c \qquad [12a]$$

$$\ddot{x}_c + 2\zeta_c\omega_c\dot{x}_c + \omega_c^2 x_c = g\omega_c^2 x \qquad [12b]$$

The sensor and controller gains, H and G, have been set equal (as is conventional) and defined as $G = H = g\omega_c^2$. The equations of motion for the combined system are therefore:

$$\ddot{x} + 2\omega\zeta\dot{x} + \omega^2 x = g\omega_c^2 x_c + f \qquad [13a]$$

$$\ddot{x}_c + 2\zeta_c\omega_c\dot{x}_c + \omega_c^2 x_c = g\omega_c^2 x \qquad [13b]$$

Controller Design

Using eqns [13a] and [13b], a controller with prescribed closed loop damping ratio ξ_p can be found. The design requires three factors: g, ω_c and ζ_c. The value of g is determined such that actuator saturation is avoided. In practice, this may require experimentally setting g for the worst case disturbance.

Again a broadband vibration absorber analogous to the equal peak tuning can be determined. Given the feedback gain, the controller is tuned by setting:

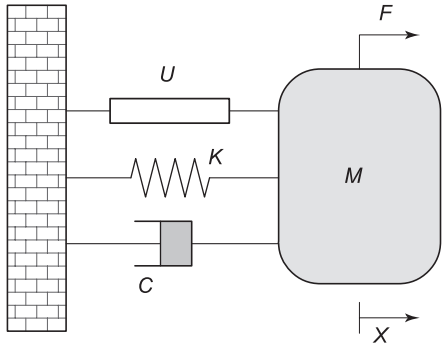


Figure 4 An actuated structure.

$$\omega_c = \omega\sqrt{(1+g^2)} \qquad [14]$$

$$\zeta_c = \sqrt{\left[\frac{(\omega_c g)^2}{*\left(1+(\omega_c g)^2\right)^3}\right]} \qquad [15]$$

For low values of g this leads to 'equal peak' results similar to the piezo-electric vibration absorber. Using this tuning law, the variance in system natural frequency, damping ratio, and pole locations are plotted in **Figure 5** as the gain is varied. Note that this law is not an equal peak law at higher values of g.

For multimodal application, numerical optimization must be used to determine the proper parameter

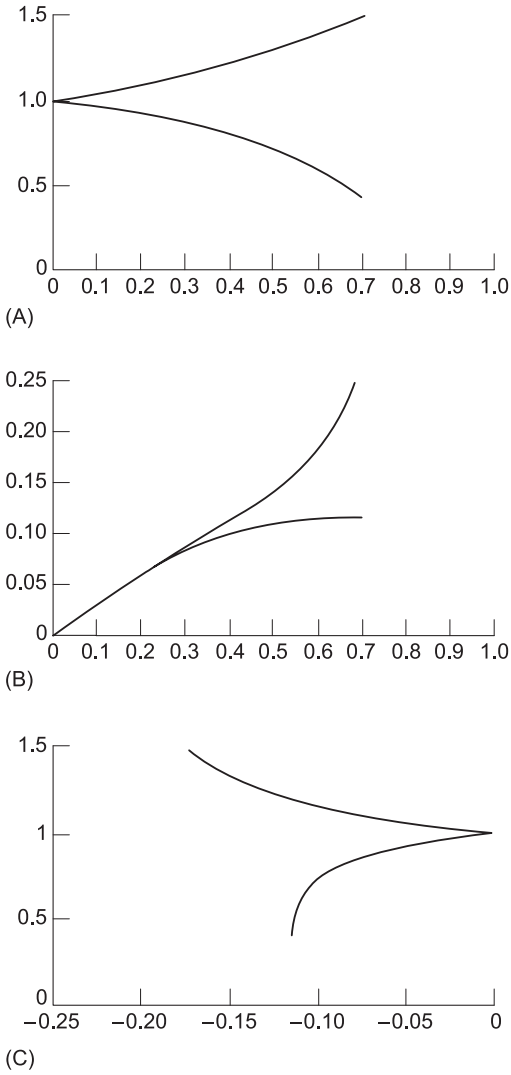


Figure 5 Positive position feedback results for a single-degree-of-freedom system as feedback gain is increased from 0 to 0.7. (A) Natural frequencies; (B) damping ratio; (C) pole locations.

set which suppresses the vibration of the structure. Often traditional output control optimization algorithms are used to design the controller.

System Response

The response of a single-degree-of-freedom system to harmonic excitation is shown in **Figure 6**. The tuning discussed in the previous section was used. As the gain of the PPF system increased, the response of the system decreases. However, with higher gains, the damping of the two modes does not remain equal.

The impulse response of the system with $g = 0.2$ and the controller tuned as presented above is shown in **Figure 7**. Note the system response is damped; however, also note that the actual control force required is $g\omega_c^2$ times the controller state which is plotted. For the system this amounts to dividing the plot in **Figure 7B** by 5.

Active Vibration Absorber

The active vibration absorber (AVA) is another implementation of a second-order compensator. It can be generalized to use a combination of position, velocity and acceleration feedback, but, in this section, only acceleration feedback is considered. Positive position feedback is a version of the more general implementation with the direct feedthrough term neglected. The advantage of AVA is that unlike PPF, the gain can be increased without fear of instability of the controlled mode. However, in contrast to the PPF controller, the AVA control law does not roll off at higher frequencies. This can lead to spillover (instability) when implemented in multimodal systems, limiting the achievable gain.

Equations of Motion

Again, a modal model of a structure containing an actuator can be idealized as shown in **Figure 4**. The displacement, X, of M is controlled by an actuation force, U. The equations of motion are:

$$M\ddot{X} + C\dot{X} + KX = F + U \qquad [16]$$

Introducing the usual nondimensional parameters:

$$\frac{C}{M} = 2\zeta\omega \quad \frac{K}{M} = \omega^2 \quad \frac{f}{M} = f \quad \frac{U}{M} = u \qquad [17]$$

Equation [16] can be nondimensionalized. For the active vibration absorber, u is defined:

$$u = \ddot{x}_c - g^2\ddot{x} \qquad [18a]$$

$$\ddot{x}_c + 2\zeta_c\omega_c\dot{x}_c + \omega_c^2 x_c = gx \qquad [18b]$$

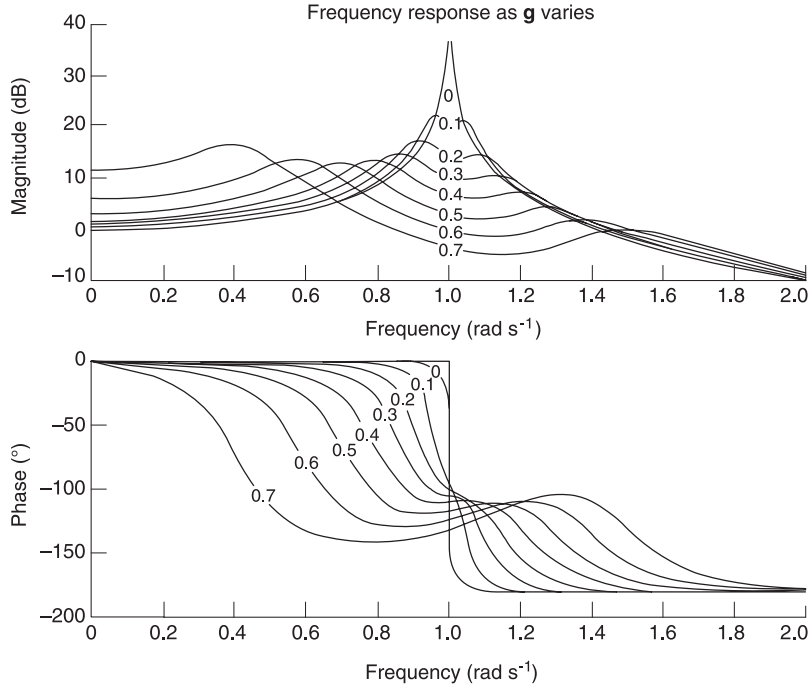


Figure 6 PPF frequency response as the gain varies.

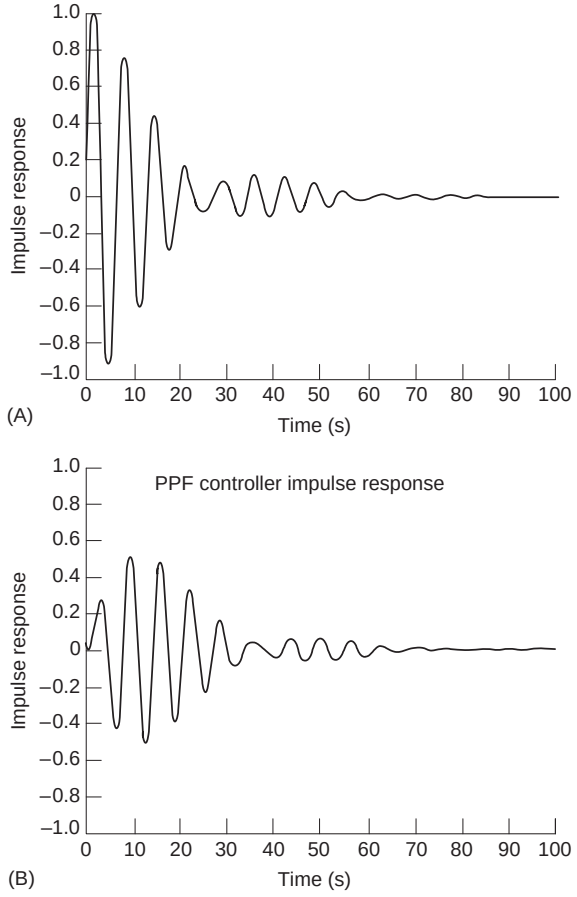


Figure 7 PPF results for a single-degree-of-freedom system with $g = 0.2$. (A) System; (B) controller.

The equations of motion for the combined system are therefore:

$$(1+g^2)\ddot{x} - g\ddot{x}_c + \omega^2 x = f \qquad [19a]$$

$$-g\ddot{x} + \ddot{x}_c + 2\zeta_c\omega_c\dot{x}_c + \omega_c^2 x_c = 0 \qquad [19b]$$

This equation can be transformed into a mechanical analogy by performing a similarity transformation:

$$\begin{Bmatrix} x \\ x_c \end{Bmatrix} = \begin{bmatrix} 0 & 1 \\ 1 & g \end{bmatrix} \begin{Bmatrix} q_c \\ q \end{Bmatrix} \qquad [20]$$

The nondimensional equations written for comparison are:

$$\ddot{q}_c + 2\zeta_c\omega_c q_c + g2\zeta_c\omega_c q + \omega_c^2 q_c + g\omega_c^2 q = 0 \qquad [21a]$$

$$\ddot{q} + g2\zeta_c\omega_c q_c + g^2 2\zeta_c\omega_c q + g\omega_c^2 q_c + (\omega^2 + g^2\omega_c^2)q = 0 \qquad [21b]$$

Note that while q still represents the motion of the mass, x, $q_c = x_c - gx$. Thus the motion of the mass is combined with the electrical degree-of-freedom. The control force required is $g\ddot{q}_c$.

Controller Design

Using eqns [19a] and [19b], a controller which minimizes the resonant amplitude of the system (acting as an optimal damped mechanical vibration absorber) can be obtained.

$$\omega_c = \frac{\omega}{1+g^2} \qquad [22a]$$

$$\zeta_c = \frac{1}{g^2}\sqrt{\left[\frac{g^2}{4(1+g^2)^3}\right]} \qquad [22b]$$

The larger g^2 is, the lower the amplitude of the response in a manner analogous to the mass ratio of a mechanical vibration absorber. These values lead to 'equal peak' results similar to the piezo-electric vibration absorber. Using these values, the variance in system natural frequency, damping ratio, and pole locations are plotted in **Figure 8**.

System Response

The response of a single-degree-of-freedom system to harmonic excitation is shown in **Figure 9**. The tuning discussed in the previous section was utilized. As the gain of the AVA system increased, the response of the system decreases. The damping of the two peaks is uniform unlike the damping of the PPF controller.

The impulse response of the system is shown in **Figure 10**. This response is similar to that PPF response. Recall however, that the control force required is a function of acceleration for the AVA controller.

Summary

The piezoelectric vibration absorber, positive position feedback, and active vibration absorbers all allow electrical analogies of mechanical vibration absorbers. The choice amongst these implementations will depend on the knowledge of the system dynamics, availability of suitable actuators or sensors, and other application specific criteria. Each provides an effective method of vibration suppression without the strokelength and mass limitation of the mechanical vibration absorber albeit with greater cost and complexity.

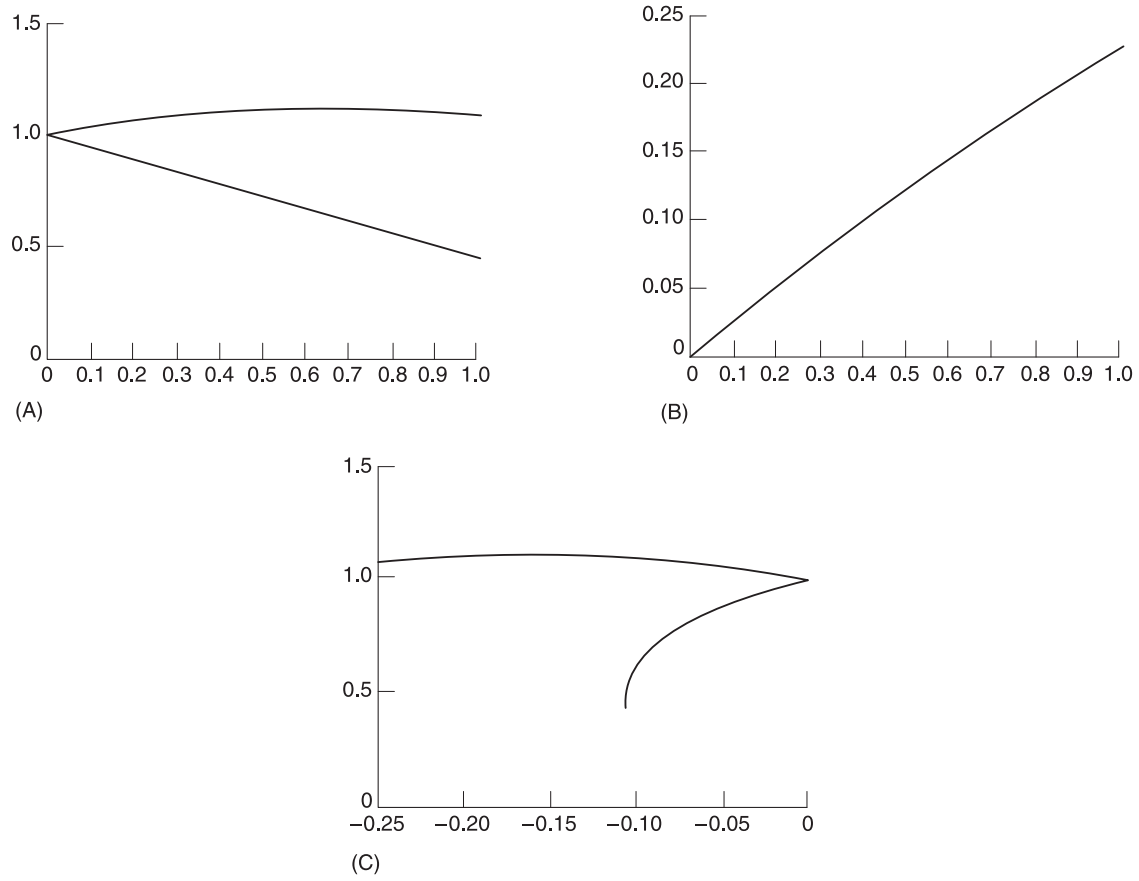


Figure 8 Active vibration absorber results for a single-degree-of-freedom system as feedback gain is increased from 0 to 1.0. (A) Natural frequencies; (B) damping ratio; (C) pole locations.

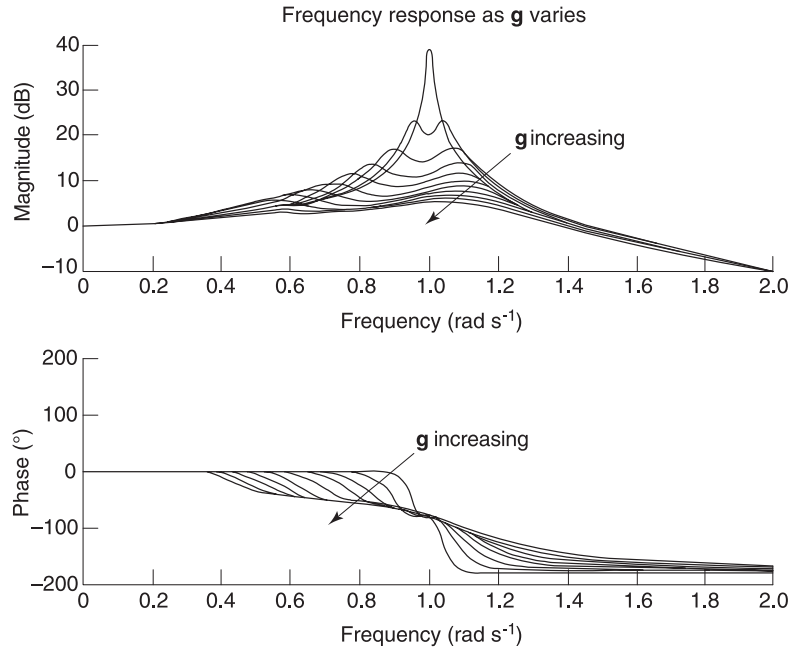


Figure 9 AVA frequency response as the gain varies.

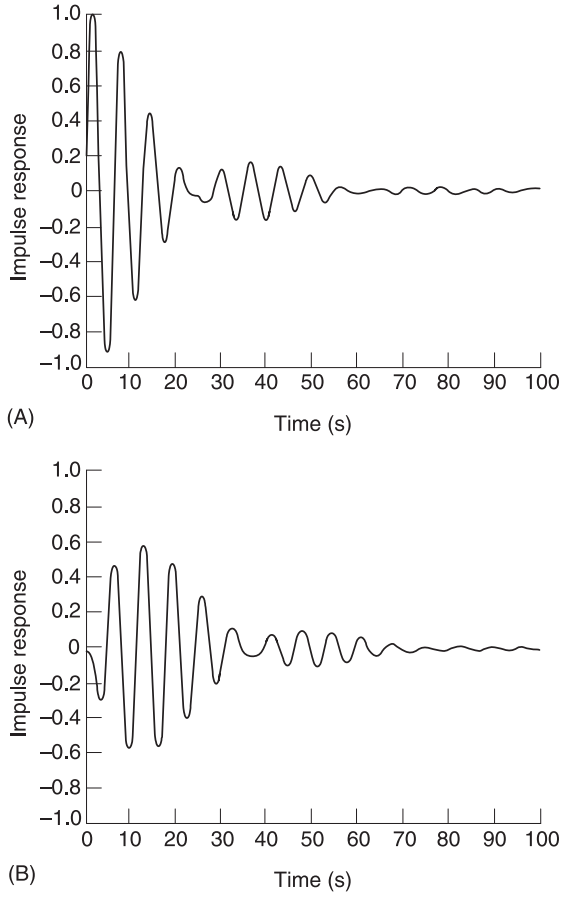


Figure 10 AVA results for a single-degree-of-freedom system with $g = 0.2$. (A) System; (B) controller.

Nomenclature

c^D	elastic modulus
C	capacitance
D	electrical displacement
E	electric field
F	force
$F(t)$	external disturbance
G	controller gain
h	piezo-electric coupling constant
H	sensor gain
K	stiffness
L	shunt inductance
M	structural mass
Q	charge
R	shunt resistance
S	strain
T	stress
U	actuation force
V	voltage
X	displacement
ε	permittivity
ξ	damping ratio

See also: **Absorbers, vibration**; **Active control of civil structures**; **Active control of vehicle vibration**; **Vibration isolation, applications and criteria**; **Vibration isolation theory**

Further Reading

Agnes GS (1995) Active/passive piezoelectric vibration suppression. *Journal of Intelligent Materials, Systems, and Structures* 6:482–7.

American Institute of Aeronautics and Astronautics (1987) *Proceedings of the 28th AIAA/ASME/ASCE/AHS/ACS Structures, Structural Dynamics and Materials Conference*, April, Monterey, CA.

American Institute of Aeronautics and Astronautics (1994) *Proceedings of the 35th AIAA/ASME/ASCE/AHS/ACS Structures, Structural Dynamics and Materials Conference*, April, Hilton Head, SC.

Baz A, Poh S, Fedor J (1992) Independent modal space control with positive position feedback. *Transactions of the ASME* 114:96–103.

Caughey TK (1995) Dynamic response of structures constructed from smart materials. *Smart Materials and Structures* 4:A101–A106.

DenHartog JP (1985) *Mechanical Vibrations*. New York: Dover Books.

Dusch JJ (1995) *Active Vibration Suppression: Stability and Design in Second Order Form*. PhD thesis, SUNY at Buffalo.

Fanson JL, Caughey TK (1987) Positive position feedback control for large space structures. In *Proceedings of the 28th AIAA/ASME/ASCE/AHS/ACS Structures, Structural Dynamics and Materials Conference* 87–0902. April, Monterey, CA.

Fanson JL, Caughey TK (1990) Positive position feedback control for large space structures. *AIAA Journal* 28(4).

Flotow AH Von, Beard A, Bailey D (1994) Adaptive tuned vibration absorbers: tuning laws, tracking agility, sizing, and physical implementations. *Proceedings Noise-Conference 94*.

Forward RL (1979) Electronic damping of vibrations in optical structures. *Journal of Applied Optics*, 18:690–7.

Goh CJ, Caughey TK (1985) On the stability problem caused by finite actuator dynamics in the collocated control of large space structures. *International Journal of Control* 41(3):787–802.

Hagood NW, Flotow A Von (1991) Damping of structural vibrations with piezoelectric materials and passive electrical networks. *Journal of Sound and Vibration* 146:243–68.

Hollkamp JJ (1994) Multimodal passive vibration suppression with piezoelectric materials and resonant shunts. *Journal of Intelligent Materials Systems and Structures* 5:49–57.

Hollkamp JJ, Starchville TF (1994) A self-tuning piezoelectric vibration absorber. In *Proceedings of the 35th AIAA/ASME/ASCE/AHS/ACS Structures, Structural Dynamics and Materials Conference* 94–1790. April, Hilton Head, SC.

Jaffe B, Cook R, Jaffe H (1971) *Piezoelectric Ceramics*. New York: Academic.

Lee-Glauser G, Juang J-N, Sulla JL (1995) Optimal active vibration absorber: Design and experimental results. *Journal of Vibration and Acoustics* 117:165–171.

Sun JQ, Jolly MR, Norris MA (1995) Passive, adaptive, and active tuned vibration absorbers. *Trans. ASME Combined Anniversary Issue Journal of Mechanical Design and Journal of Vibration and Acoustics*, 117(B):234–42.

ABSORBERS, VIBRATION

V Steffen, Jr and D Rade, Federal University of Uberlandia, Uberlandia, Brazil

Copyright © 2001 Academic Press

doi:10.1006/rwvb.2001.0176

Introduction

Dynamic vibration absorbers (DVAs), also called Vibration Neutralizers or Tuned Mass Dampers, are mechanical appendages comprising inertia, stiffness, and damping elements which, once connected to a given structure or machine, named herein the primary system, are capable of absorbing the vibratory energy at the connection point. As a result, the primary system can be protected from excessively high vibration levels. In practice, DVAs can be included in the original system design or can be added to an existing system, often as part of a remedial course of action.

Since their invention by Frahm at the beginning of the twentieth century, dynamic vibration absorbers have been extensively used to mitigate vibrations in various types of mechanical systems. A very well-known application is the so-called Stockbridge damper, widely used to reduce wind-induced vibrations in overhead power transmission lines. In a remarkable engineering application, a 400-ton absorber has been designed for Citicorp Center, a 274-m high office building in New York City, for suppressing primarily the contribution of the first vibration mode in wind-induced oscillations. In a similar application, two 300-ton DVAs have been installed in the John Hancock Tower, in Boston, Massachussets. The dynamics of television towers are particularly favorable for the use of pendulum-like DVAs, which have been applied, for example, to the towers of Alma-Ata and Riga, in the former Soviet Union.

Due to their technological relevance both in the academic and industrial domains, DVAs are still a subject of permanent interest. New applications include devices used to stabilize ship roll motion, to improve the comfort of users when walking on pedestrian bridges, to attenuate vibrations transmitted from the main rotor to the cockpit of helicopters, and to improve machine tool operation conditions, to mention just a few examples. Military applications have also been developed. The use of DVAs to reduce the dynamic forces transmitted to an aircraft due to high rates of fire imposed on the canon motion can be mentioned as another example.

In practical applications, DVAs can be found in various configurations, intended for the attenuation of either rectilinear or angular motion. The simplest setup is that formed by a single mass attached to the primary system through a linear spring. This configuration is named the 'undamped dynamic vibration absorber'. As will be shown later, in designing an undamped DVA to attenuate harmonic vibrations, the values of its physical parameters (stiffness and inertia) must be chosen according to the value of the excitation frequency and it is then said that the DVA is tuned. The undamped DVA may become ineffective when the excitation frequency deviates, even slightly, from the nominal tuning frequency. In order to provide a mechanism for energy dissipation and to enlarge the effective bandwidth of the absorber, damping can be introduced into the DVA. In most applications, a viscous damping model is used, although viscoelastic and Coulomb-type dampers can be found in certain cases. In general, a DVA is designed to attenuate vibrations generated by a purely harmonic excitation. However, in several situations, vibrations are produced by periodic forces containing various harmonic components. In this case, multiple DVAs can be used, each one tuned to a specific frequency component. It is also possible to use distributed-parameter structural elements, such as beams or plates, as dynamic absorbers. Besides the ease of physical realization, the main interest in using these configurations is related to the fact that the DVA can be tuned to various frequency values simultaneously.

All the configurations mentioned above form the class of 'passive' DVAs, defined as those containing exclusively passive, time-independent, components. For this type of absorber, tuning can be achieved only by physically constructing inertia, stiffness and damping elements with adequate values. When the excitation frequency changes, which is likely to occur in many cases, the absorber becomes mistuned and less effective. To overcome this limitation, active DVAs have been developed. Besides the passive elements, they contain an actuator which applies a control force calculated according to an adequate control law. This strategy provides self-tuning capability to the DVA, over a finite frequency band.

In the following sections the basic theory of passive and active dynamic vibration absorbers are presented, as well as some special configurations.

Undamped Dynamic Vibration Absorbers

Figure 1 illustrates an undamped two-degree-of-freedom system, where the subsystem (m_p, k_p) represents the primary system, whose vibrations are to be attenuated, and the subsystem (m_a, k_a) represents the dynamic vibration absorber. The primary system is assumed to be excited by an external harmonic force with constant amplitude and constant circular frequency, given by:

$$f(t) = F_0 e^{i\omega t} \qquad [1]$$

Using Newton's laws, the following equations of motion are obtained for the two-degree-of-freedom system, in terms of the coordinates defined in **Figure 1**:

$$m_p \ddot{x}_p + (k_p + k_a)x_p - k_a x_a = f \qquad [2a]$$

$$m_a \ddot{x}_a + k_a(x_a - x_p) = 0 \qquad [2b]$$

The steady-state harmonic responses are written:

$$x_p(t) = X_p e^{i\omega t} \qquad [3a]$$

$$x_a(t) = X_a e^{i\omega t} \qquad [3b]$$

Upon substitution of eqns [3] in eqns [2], the following set of frequency-dependent algebraic equations involving the amplitudes of the harmonic responses is obtained:

$$X_p(-m_p\omega^2 + k_p + k_a) - k_a X_a = F_0 \qquad [4a]$$

$$-k_a X_p + X_a(-m_a\omega^2 + k_a) = 0 \qquad [4b]$$

Solving eqns [4], the following expression is obtained for the amplitudes:

$$\frac{X_p}{(X_p)_{st}} = \frac{\left[1 - (\omega/\omega_a)^2\right]}{\left[1 + (k_a/k_p) - (\omega/\omega_p)^2\right]\left[1 - (\omega/\omega_a)^2\right] - (k_a/k_p)} \qquad [5a]$$

$$\frac{X_a}{(X_p)_{st}} = \frac{1}{\left[1 + (k_a/k_p) - (\omega/\omega_p)^2\right]\left[1 - (\omega/\omega_a)^2\right] - (k_a/k_p)} \qquad [5b]$$

where:

$$\omega_p = \sqrt{\left(\frac{k_p}{m_p}\right)} \quad \omega_a = \sqrt{\left(\frac{k_a}{m_a}\right)} \quad (X_p)_{st} = \frac{F_0}{k_p} \qquad [6]$$

are, respectively, the natural frequency of the primary system, the natural frequency of the absorber, when both are considered as separate single-degree-of-freedom systems, and the static displacement of the primary mass.

In eqn [5a], it can be seen that the amplitude X_p vanishes when the excitation frequency ω coincides with the natural frequency of the DVA, ω_a. In this situation, the amplitude of the response of the DVA mass is obtained by introducing $X_p = 0$ in eqn [4a]:

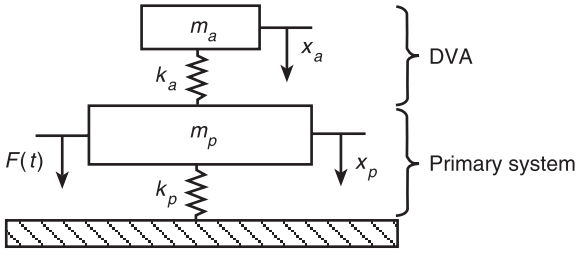


Figure 1 Schematic representation of an undamped DVA connected to a primary system.

$$X_a|_{\omega=\omega_a} = -\frac{F_0}{k_a} \qquad [7]$$

In eqn [7] the minus sign indicates that there is a phase shift of 180° between the excitation force and the response of the DVA mass. **Figure 2** illustrates the variation of X_p with ω, according to eqn [5a]. It can be seen that an antiresonance is generated at $\omega = \omega_a$. Thus, to achieve complete attenuation of harmonic vibrations with a given frequency ω, the values of the inertia and stiffness parameters of the undamped DVA must be selected so as to satisfy $\omega = \sqrt{(k_a/m_a)}$. **Figure 2** also shows the amplitudes of the response of the primary system without the DVA. It can be seen that with the addition of the DVA, two resonance peaks are generated in the frequency response and vibration reduction is achieved only within the frequency band limited by points A and B. Since this bandwidth is generally small, even slight modifications in the forcing frequency and/or in the DVA parameters can lead to a significant decrease in the attenuation capability of the absorber. This is the major drawback of the undamped DVAs.

At this point, the following comments are made regarding the practical design of undamped DVAs. In any physical realization, the interest is to have a DVA with a small mass. This means that the mass ratio, defined as $\mu = m_a/m_p$ should be kept as small as possible (values of μ up to 5 percent are generally acceptable). However, eqns [6b] and [7] state that small values of the secondary mass correspond to small values of the DVA stiffness and high amplitude of vibration of the secondary mass. This last fact has direct implication in the fatigue life of the resilient element of the DVA.

In many circumstances the interest is to reduce the amplitude of vibration of the primary system in the vicinity of its resonance frequency. In these cases, the DVA must be tuned so that its natural frequency coincides with the natural frequency of the primary system, that is:

$$\frac{k_a}{m_a} = \frac{k_p}{m_p} \qquad [8]$$

In this case, eqns [5] can be rewritten in terms of dimensionless parameters, as follows:

$$\frac{X_p}{(X_p)_{st}} = \frac{1 - g^2}{(1 - g^2)(1 - g^2 + \mu) - \mu} \qquad [9a]$$

$$\frac{X_a}{(X_p)_{st}} = \frac{1}{(1 - g^2)(1 - g^2 + \mu) - \mu} \qquad [9b]$$

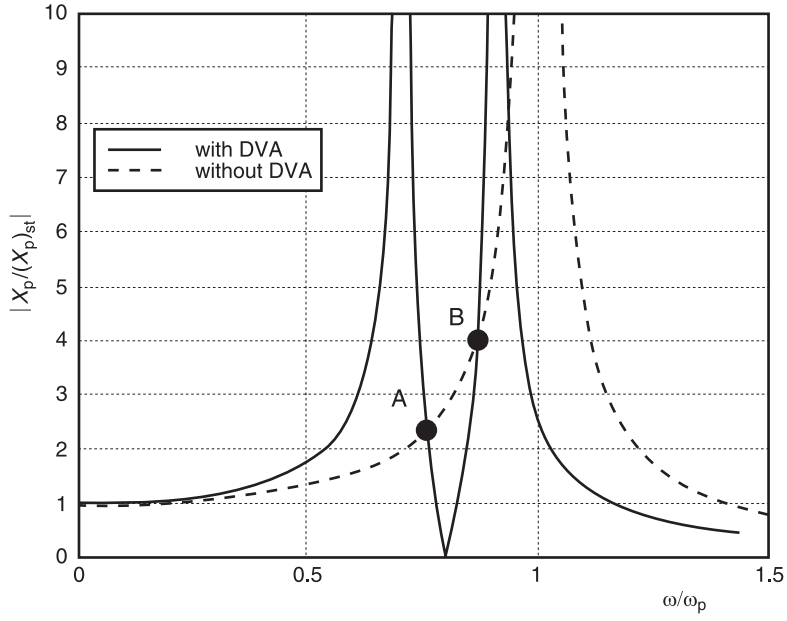


Figure 2 Typical variation of the amplitude of the response of the primary X_p with the excitation frequency ω for $\omega_a/\omega_p = 0.8, m_a/m_p = 0.1$.

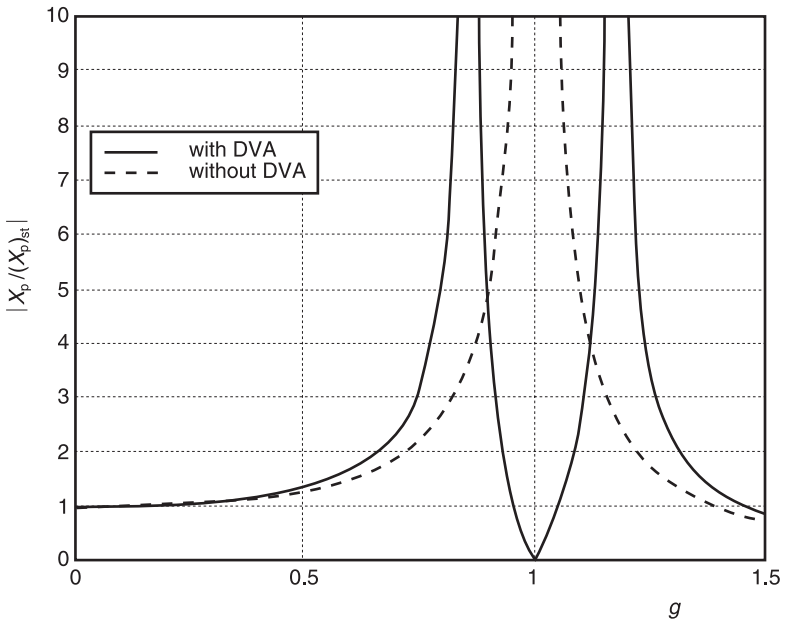


Figure 3 Typical variation of the amplitude of the response of the primary X_p with the excitation frequency ω for $\omega_a/\omega_p = 1.0$, $\mu = 0.1$.

where the dimensionless parameters are defined as $g = \omega/\omega_p$ (forcing frequency ratio) and $\mu = m_a/m_p$ (mass ratio).

The roots of the denominator of eqns [9] define the natural frequencies of the two-degree-of-freedom system (primary system + DVA), given by:

$$g^2 = 1 + \frac{\mu}{2} \pm \sqrt{\left[\mu + \left(\frac{\mu^2}{4}\right)\right]} \qquad [10]$$

Eqns [9] show that for $g = 1$ the primary mass will not vibrate while the absorbing mass will vibrate with amplitude $X_a = -(X_p)_{st}/\mu$. A typical plot of eqn [9a] is shown in **Figure 3**.

Viscously Damped Dynamic Vibration Absorbers

The effective bandwidth of a DVA can be enlarged by introducing a damping element responsible for energy dissipation. Moreover, damping facilitates a reduction of the amplitude of relative motion between the primary and the secondary masses, thus rendering less critical the fatigue of the resilient element of the DVA. **Figure 4** illustrates a viscously damped DVA (m_a, c_a, k_a) attached to an undamped primary system (m_p, k_p). Assuming that a harmonic excitation force given by $f(t) = F_0 e^{i\omega t}$ acts on the primary mass, the equations of motion for this two-degree-of-freedom system are written:

$$m_p\ddot{x}_p + k_p x_p + k_a(x_p - x_a) + c_a(\dot{x}_p - \dot{x}_a) = F_0 e^{i\omega t} \qquad [11a]$$

$$m_a\ddot{x}_a + k_a(x_a - x_p) + c_a(\dot{x}_a - \dot{x}_p) = 0 \qquad [11b]$$

The resulting steady-state amplitude for the primary and DVA masses are found to be given by:

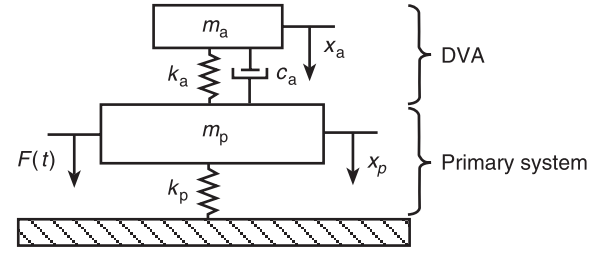


Figure 4 Scheme of a viscously damped DVA connected to a primary system.

$$X_p = F_0 \frac{k_a - m_a\omega^2 + i\omega c_a}{(k_p - m_p\omega^2)(k_a - m_a\omega^2) - m_a k_a \omega^2 + i\omega c_a (k_p - m_p\omega^2 - m_a\omega^2)} \quad [12a]$$

$$X_a = -F_0 \frac{k_a + i\omega c_a}{(k_p - m_p\omega^2)(k_a - m_a\omega^2) - m_a k_a \omega^2 + i\omega c_a (k_p - m_p\omega^2 - m_a\omega^2)} \quad [12b]$$

Similarly to what has been done when developing the formulation for the undamped DVA, the following parameters are introduced: $\mu = m_a/m_p$, mass ratio; $\omega_a = \sqrt{(k_a/m_a)}$, undamped natural frequency of the DVA considered separately; $\omega_p = \sqrt{(k_p/m_p)}$, undamped natural frequency of the primary system considered separately; $f = \omega_a/\omega_p$, turning factor; $g = \omega/\omega_p$, forcing frequency ratio; $c_c = 2m_a\omega_p$, critical damping; $\zeta = c_a/c_c$, damping ratio; $(X_p)_{st} = F_0/k_p$, static displacement of the primary mass. Thus, eqns [12] can be rewritten in terms of the dimensionless parameters as follows:

$$\frac{|X_p|}{(X_p)_{st}} = \sqrt{\left\{\frac{(2\zeta g)^2 + (g^2 - f^2)^2}{(2\zeta g)^2(g^2 - 1 + \mu g^2)^2 + [\mu f^2 g^2 - (g^2 - 1)(g^2 - f^2)]^2}\right\}} \quad [13a]$$

$$\frac{|X_a|}{(X_p)_{st}} = \sqrt{\left\{\frac{(2\zeta g)^2 + f^4}{(2\zeta g)^2(g^2 - 1 + \mu g^2)^2 + [\mu f^2 g^2 - (g^2 - 1)(g^2 - f^2)]^2}\right\}} \quad [13b]$$

Figure 5 illustrates a typical variation of the amplitude X_p with the forcing frequency ratio, for different values of the damping factor ζ. As can be seen, for $\zeta = 0$ the system behaves like an undamped two-degree-of-freedom system, with response amplitudes tending to increase indefinitely at each of the two resonance frequencies. As the amount of damping is progressively increased, the system behaves like a typical damped two-degree-of-freedom system and eventually exhibits the apparent behavior of a single-degree-of-freedom system with mass $(m_1 + m_2)$ when the two masses become virtually connected through the dashpot. It can also be seen that all curves intercept at points P and Q, named 'invariant points'. Eqn [13b] can be expressed as:

$$\frac{|X_a|}{(X_p)_{st}} = \sqrt{\frac{A\zeta^2 + B}{C\zeta^2 + D}} \quad [13c]$$

where A, B, C, and D are functions of f and g, only. The characterization of the invariant points is based on the fact that the identity $A/C = B/D$ holds, regardless of the value of the damping factor. **Figures 6** and **7** show the influence of the damping ratio ζ and the tuning factor f on the frequency response of the primary mass. It can be seen that the response amplitudes at the invariant points vary when the tuning factor is changed. For the purpose of optimal design of a damped DVA, it is desired to find a set of values (ζ_{opt}, f_{opt}) to ensure a response curve which is as flat as possible. Based on the behavior illustrated in **Figures 5–7**, this optimal configuration is achieved when both the invariant points are adjusted to equal heights and the response curve presents null slope at one of them. It makes marginal difference which invariant point is taken. According to the development originally presented by Den Hartog, imposing these conditions to the frequency response given by eqn [13a], the following expression for the optimal tuning ratio is obtained:

$$f_{opt} = \frac{1}{1 + \mu} \quad [14]$$

The expressions for the optimal damping ratios that ensure zero slope at each invariant point are:

$$\zeta_P^2 = \frac{\mu[3 - \sqrt{(\mu/\mu + 2)}]}{8(1 + \mu)^3} \qquad \zeta_Q^2 = \frac{\mu[3 + \sqrt{(\mu/\mu + 2)}]}{8(1 + \mu)^3}$$

Den Hartog suggests to take the average between the two values provided by the equations immediately above as the optimal value of the damping ratio, as given by:

$$\zeta_{opt} = \sqrt{\left[\frac{3\mu}{8(1 + \mu)^3}\right]} \quad [15]$$

An optimally shaped frequency response curve is indicated in **Figure 7**.

DVAs for Viscously Damped Primary Systems

Dynamic vibration absorbers are likely to be added only to lightly damped systems, since highly damped

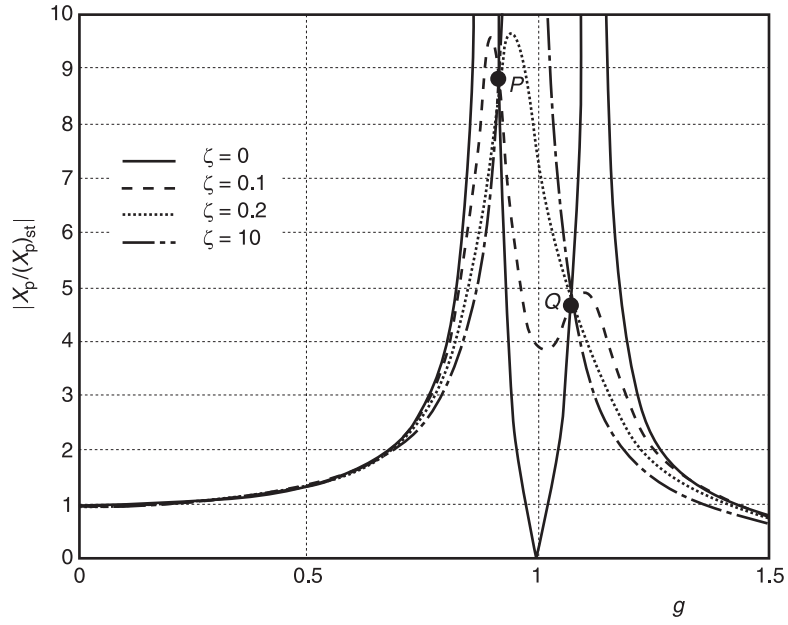


Figure 5 Influence of damping on the frequency response of the primary mass $f = 1$, $\mu = 1/20$.

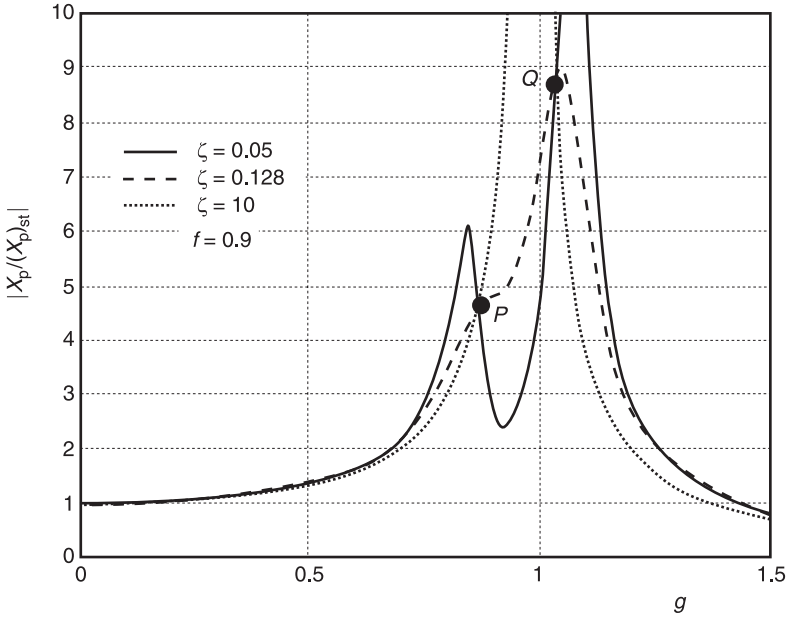


Figure 6 Frequency response of the primary mass for different values of the damping ratio and $f = 0.90$.

systems usually present moderate vibration levels which do not require any additional attenuation. However, special situations may be found where it is intended to design DVAs taking into account the damping of the primary system. Such a situation is illustrated in **Figure 8**. For this two-degree-of-freedom system, the following equations of motion are written:

$$m_p\ddot{x}_p + (c_p + c_a)\dot{x}_p - c_a\dot{x}_a + (k_p + k_a)x_p - k_a x_a = F \quad [16a]$$

$$m_a\ddot{x}_a + c_a\dot{x}_a - c_a\dot{x}_p + k_a x_a - k_a x_p = 0 \quad [16b]$$

From eqns [16], and using the same procedure as the one adopted for the undamped primary system, the

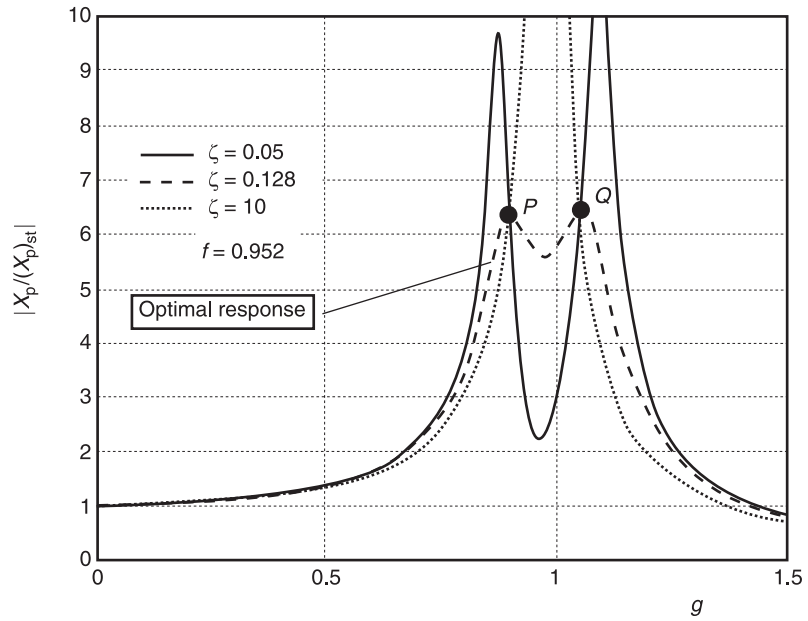


Figure 7 Frequency response of the primary mass for different values of the damping ratio and $f = 0.952$.

following expression is obtained for the frequency response of the primary system in terms of dimensionless parameters.

$$\frac{|X_p|}{(X_p)_{st}} = \sqrt{\left\{\frac{(2\zeta_a g)^2+(g^2-f^2)^2}{\left[2\zeta_a g(1-g^2-\mu g^2)+2\zeta_p \mu g(f^2-g^2)\right]^2+\left[\mu f^2 g^2-(g^2-1)(g^2-f^2)\right]^2}\right\}} \qquad [17]$$

where:

$$\zeta_a = \frac{c_a}{2m_a\omega_p} \quad \text{and} \quad \zeta_p = \frac{c_p}{2m_a\omega_p}$$

and the other dimensionless parameters remain the same as those already defined for the case of the undamped primary system.

As opposed to eqn [13a], eqn [17] does not admit the existence of invariant points in the frequency response curves, since Eqn [17] cannot be put in the form of Eqn [13c] with $A/C = B/D$. As a result, Den Hartog's optimization procedure does not apply. In this case, to obtain the optimal values of the tuning ratio and absorber damping ratio, numerical optimization has to be carried out. For this purpose an objective function related to the maximum response amplitude must be defined and minimized with respect to the DVA parameters. Such an optimization procedure was implemented by Warburton and Yorinde, resulting in the values presented in **Table 1**. It can be seen that, for small values of the primary system damping, little influence of this damping on the values of the optimal parameters f_{opt} and ζ_a^{opt} is noticed.

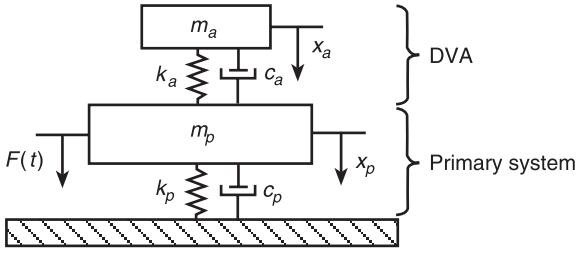


Figure 8 Scheme of a damped DVA connected to a damped primary system.

Optimal Design of Damped DVAs Applied to Multi-degree-of-freedom Primary Systems

Single-degree-of-freedom primary systems are rarely encountered in practical applications. Instead, real-world mechanical systems for which vibration protection is pursued are more conveniently modeled either as multi-degree-of-freedom discrete systems or continuous distributed parameter systems. The procedure for the optimum design of damped DVAs applied to

Table 1 Optimal values of DVA parameters for viscously damped primary systems

Mass ratio	*Primary system damping*	*Optimal values*		*Values of g for equal peaks*	
	$\zeta_p = c_p/2m_p\omega_p$	f_{opt}	$\zeta_{opt} = c_a/2m_a\omega_a$	g_1	g_2
0.01	0	0.9901	0.061	0.960	1.030
	0.01	0.9886	0.062	0.956	1.032
	0.02	0.9869	0.064	0.953	1.033
	0.05	0.9807	0.068	0.942	1.034
	0.1	0.9663	0.073	0.923	1.030
0.1	0	0.9091	0.185	0.848	1.059
	0.01	0.9051	0.187	0.843	1.058
	0.02	0.9009	0.188	0.838	1.058
	0.05	0.8875	0.193	0.823	1.054
	0.1	0.8619	0.199	0.795	1.043
1.0	0	0.499	0.448	0.487	0.928
	0.01	0.494	0.448	0.481	0.924
	0.02	0.489	0.449	0.476	0.921
	0.05	0.473	0.454	0.462	0.904
	0.1	0.446	0.455	0.434	0.882

Adapted with permission from Warburton GB and Yorinde EO (1980) Optimum absorber parameters for simple systems. *Earthquake Engineering and Structural Dynamics*, 8: 197–217. John Wiley.

single-degree-of-freedom undamped primary systems can be extended to these types of systems, using a modal approach, developed in the following.

The main idea is to apply an optimization criterion in the vicinity of a particular natural frequency of the primary system. Several DVAs can be designed independently for each individual vibration mode. For this purpose it is assumed that the natural frequencies of the primary system are sufficiently well separated and that the masses of the DVAs are small enough not to modify significantly the natural frequencies of the primary system. **Figure 9** shows schematically a damped DVA attached to an undamped multi-degree-of-freedom primary system, modeled by inertia matrix **M** and stiffness matrix **K**. The indicated coordinates x_c and x_f correspond to the coordinates to which the DVA is attached and the excitation force is applied, respectively. In the general case of multi-dimensional systems, these coordinates may correspond to either displacements or rotations. To attenuate the vibrations in the vicinity of the nth natural frequency of the primary system, it is assumed that the responses are dominated by this particular mode. Thus, the vector of time responses of the primary system can be written:

$$\mathbf{x}(t) = \psi_n q_n(t) \qquad [18a]$$

and, in particular, for the forcing and coupling coordinates:

$$x_f(t) = \psi_{fn} q_n(t) \qquad [18b]$$

$$x_c(t) = \psi_{cn} q_n(t) \qquad [18c]$$

In the equations above, ψ_{fn} and ψ_{cn} designate the components of the nth eigenvector corresponding to the excitation and coupling coordinates, respectively,

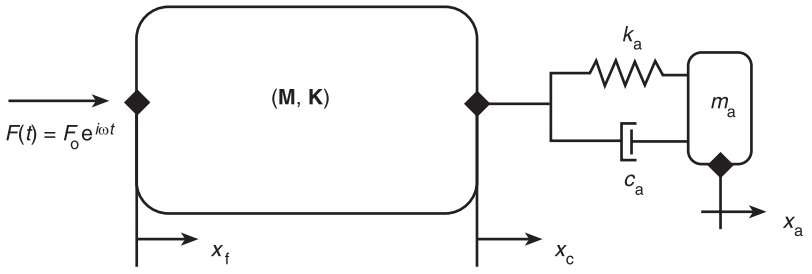


Figure 9 Schematic representation of a damped DVA attached to a multi-degree-of-freedom primary system.

and $q_n(t)$ is the generalized coordinate associated with the nth vibration mode. It is also assumed that the nth eigenvector is normalized so as to satisfy:

$$\psi_n^{\mathrm{T}}\mathbf{M}\psi_n = M_n \qquad [19a]$$

$$\psi_n^{\mathrm{T}}\mathbf{K}\psi_n = M_n\omega_n^2 \qquad [19b]$$

where M_n and ω_n are, respectively, the generalized mass and the natural frequency associated with the nth vibration mode of the primary system. In order to formulate a generalized substructuring theory, the following quantities are defined for the coupled system (primary system + DVA):

- Kinetic energy: $T = \frac{1}{2}\dot{\mathbf{x}}^{\mathrm{T}}\mathbf{M}\dot{\mathbf{x}} + \frac{1}{2}m_{\mathrm{a}}\dot{x}_{\mathrm{a}}^2$ [20a]
- Strain energy: $V = \frac{1}{2}\mathbf{x}^{\mathrm{T}}\mathbf{K}\mathbf{x} + \frac{1}{2}k_{\mathrm{a}}(x_{\mathrm{a}} - x_{\mathrm{c}})^2$ [20b]
- Rayleigh dissipation function: $F = \frac{1}{2}c_{\mathrm{a}}(\dot{x}_{\mathrm{a}} - \dot{x}_{\mathrm{c}})^2$ [20c]
- Virtual work of the excitation force: $\delta W^{nc} = F\mathrm{e}^{\mathrm{i}\omega t}\delta x_{\mathrm{f}}$ [20d]

Introducing eqns [18] into eqns [20], taking into account relations [19], and employing Lagrange's equations, the following equations of motion are obtained:

$$M_n\ddot{q}_n + c_{\mathrm{a}}\psi_{cn}^2\dot{q}_n - c_{\mathrm{a}}\psi_{cn}\dot{x}_{\mathrm{a}} + \left(M_{\mathrm{p}}\omega_n^2 + k_{\mathrm{a}}\psi_{cn}^2\right)q_n - k_{\mathrm{a}}\psi_{cn}x_{\mathrm{a}} = \psi_{\mathrm{f}n}F\mathrm{e}^{\mathrm{i}\omega t} \qquad [21a]$$

$$M_{\mathrm{a}}\ddot{x}_{\mathrm{a}} - c_{\mathrm{a}}\psi_{cn}\dot{q}_n + c_{\mathrm{a}}\dot{x}_{\mathrm{a}} - k_{\mathrm{a}}\psi_{cn}q_n + k_{\mathrm{a}}x_{\mathrm{a}} = 0 \qquad [21b]$$

At this point the concepts of effective mass $(M_{\mathrm{eff}})_n$ and effective stiffness $(K_{\mathrm{eff}})_n$ are introduced, according to:

$$\tfrac{1}{2}(M_{\mathrm{eff}})_n\dot{x}_{\mathrm{c}}^2 = \tfrac{1}{2}\dot{\mathbf{x}}^{\mathrm{T}}\mathbf{M}\dot{\mathbf{x}} \qquad [22a]$$

$$\tfrac{1}{2}(k_{\mathrm{eff}})_n x_{\mathrm{c}}^2 = \tfrac{1}{2}\mathbf{x}^{\mathrm{T}}\mathbf{K}\mathbf{x} \qquad [22b]$$

As can be seen from the eqns [22], the effective mass can be interpreted as the mass that, once placed at the connection point, yields the same value of kinetic energy as that of the primary system. Similar interpretation is reserved to the effective stiffness, in terms of strain energy. Introducing eqns [18] into eqns [22] and taking into account relations [19], the effective parameters are expressed as:

$$(M_{\mathrm{eff}})_n = \frac{M_n}{\psi_{cn}^2} \qquad [23a]$$

$$(K_{\mathrm{eff}})_n = M_n\omega_n^2 \qquad [23b]$$

Assuming steady-state harmonic motion with frequency ω, by manipulating eqn [21] and using eqns [18], the following expression for the harmonic amplitude at the coupling coordinate is obtained:

$$\frac{|X_{\mathrm{c}}|}{(X_{\mathrm{est}})_n} = \psi_{cn}\psi_{\mathrm{f}n}\left\{\frac{(2\zeta_n g_n)^2 + \left(g_n^2 - f_n^2\right)^2}{(2\zeta_n g_n)^2\left[g_n^2 - 1 + (\mu_{\mathrm{eff}})_n g_n^2\right]^2 + \left[(\mu_{\mathrm{eff}})_n f_n^2 g_n^2 - \left(g_n^2 - 1\right)\left(g_n^2 - f_n^2\right)\right]^2}\right\} \qquad [24]$$

where the parameters are defined as follows:

$$(\mu_{\mathrm{eff}})_n = \frac{m_{\mathrm{a}}}{(M_{\mathrm{eff}})_n} \qquad g_n = \frac{\omega}{\omega_n} \qquad f_n = \frac{\omega_{\mathrm{a}}}{\omega_n}$$
$$(X_{\mathrm{est}})_n = \frac{F_0}{(K_{\mathrm{eff}})_n} \qquad \omega_{\mathrm{a}} = \sqrt{\frac{k_{\mathrm{a}}}{m_{\mathrm{a}}}} \qquad \zeta_n = \frac{c_{\mathrm{a}}}{2m_{\mathrm{a}}\omega_n} \qquad [25]$$

Comparing eqns [24] and [13a], it can be seen that the same dependence on the excitation frequency and dimensionless parameters is present in both. Thus, using the correspondences $\zeta \Longleftrightarrow \zeta_n$ and $\mu \Longleftrightarrow (\mu_{\mathrm{eff}})_n$ it is possible to extend the optimization procedure developed for single-degree-of-freedom primary systems to discrete multi-degree-of-freedom or continuous distributed parameter systems, by treating each vibration mode separately.

In the example illustrated in **Figure 10**, the primary system is a simply-supported beam, simulated by finite elements, the properties of which are given in **Table 2**. The values of the first three natural frequencies and the components of the mode shapes corresponding to the vertical displacement of point B are given in **Table 3**. The mode shapes are normalized so that the generalized masses M_n are numerically equal to the mass of the beam. A damped DVA is optimally designed to attenuate the vibrations in the vertical direction at point B in the frequency band neighboring the second natural frequency. Choosing the effective mass ratio $\mu_{\mathrm{eff}} = 0.02$, according to the procedure previously described, the following computations lead to the optimal values of the DVA parameters:

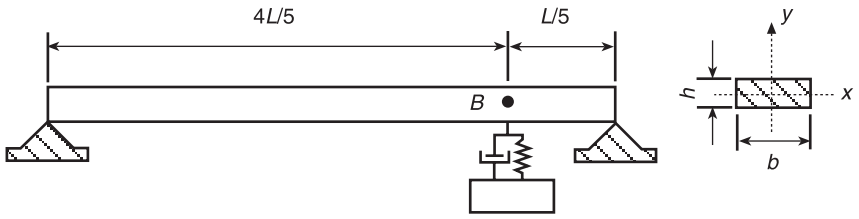


Figure 10 Beam-like primary system.

$$M_{\text{eff}} = \frac{M_{\text{p}}}{\psi_{\sigma c}^2} = \frac{2.54}{1.36^2} = 1.37$$

$$\zeta_{\text{opt}} = \sqrt{\frac{3\mu_{\text{eff}}}{8(1+\mu_{\text{eff}})}} = \sqrt{\frac{3 \times 0.02}{8(1+0.02)}} = 0.09$$

$$f_{\text{opt}} = \frac{\omega_{\text{a}}}{\omega_2} \Rightarrow k_{\text{a}} = m_{\text{a}}\left(f_{\text{opt}}\omega_2\right)^2 = 3.85 \times 10^4\,\text{N m}^{-1}$$

$$f_{\text{opt}} = \frac{1}{1+\mu_{\text{eff}}} = \frac{1}{1+0.02} = 0.98$$

$$m_{\text{a}} = \mu_{\text{eff}} M_{\text{eff}} = 0.02 \times 1.37 = 0.03\,\text{kg}$$

$$\zeta_{\text{opt}} = \frac{c_{\text{a}}}{2m_{\text{a}}\omega_2} \Rightarrow c_{\text{a}} = 6.25\,\text{N m}^{-1}\,\text{s}$$

Figure 11 shows the frequency response for the coordinate to which the optimal DVA is attached, superimposed on the same frequency response of the primary system without the DVA. It can be seen that the resonance peak corresponding to the second natural frequency has been significantly damped. **Figure 12** shows the plots of the frequency response in the vicinity of the second natural frequency for different values of the damping ratio and a unique value of the tuning ratio, demonstrating the existence of the invariant points.

Table 2 Physical and geometrical characteristics of the beam-like primary system

Property	*Value*
Young modulus	$E = 2.1 \times 10^{11}\,\text{N m}^{-2}$
Mass density	$\rho = 7800\,\text{kg m}^{-3}$
Beam length	$L = 763.0\,\text{mm}$
Cross-section width	$b = 36.6\,\text{mm}$
Cross-section height	$h = 11.4\,\text{mm}$
Second moment of area about x axis	$I = 4518.7\,\text{mm}^4$
Total mass	2.54 kg

Special Configurations of Dynamic Vibration Absorbers

Although the theory presented above has been developed for the attenuation of translational motion of vibrating systems, it can be readily extended to DVAs intended for reducing rotational vibrations. Moreover, besides their classical representation as shown by **Figure 1**, DVAs can assume various constructive forms according to the specific application desired. In the following, some of these special configurations are reviewed.

Torsional Dynamic Vibration Absorbers

Torsional vibrations of internal combustion engines and other rotating systems can be controlled by using torsional vibration absorbers. Such an arrangement is shown in **Figure 13A**. The primary system is represented by inertia J_{p} and torsional stiffness $k_{T_{\text{p}}}$, and the absorber is represented by inertia J_{a} and torsional stiffness $k_{T_{\text{a}}}$. Viscous damping is provided by oil inside a housing rigidly connected to the primary system, in such a way that a dissipative torque given by $c_{\text{T}}(\dot{\theta}_{\text{p}} - \dot{\theta}_{\text{a}})$ is generated. An equivalent translational two-degree-of-freedom system is shown in **Figure 13B**. Since the dynamic equations of motion are similar for both systems, the formulae obtained for the translational DVA and the procedure to obtain its optimal design remain applicable for the torsional system. The equivalence between the parameters of the translational and torsional systems is indicated in **Table 4**.

Table 3 Modal characteristics of the beam-like primary system

Mode	*Natural frequency (Hz)*	*Mode-shape component*
1	46.10	−0.84
2	184.2	1.36
3	414.3	−1.33

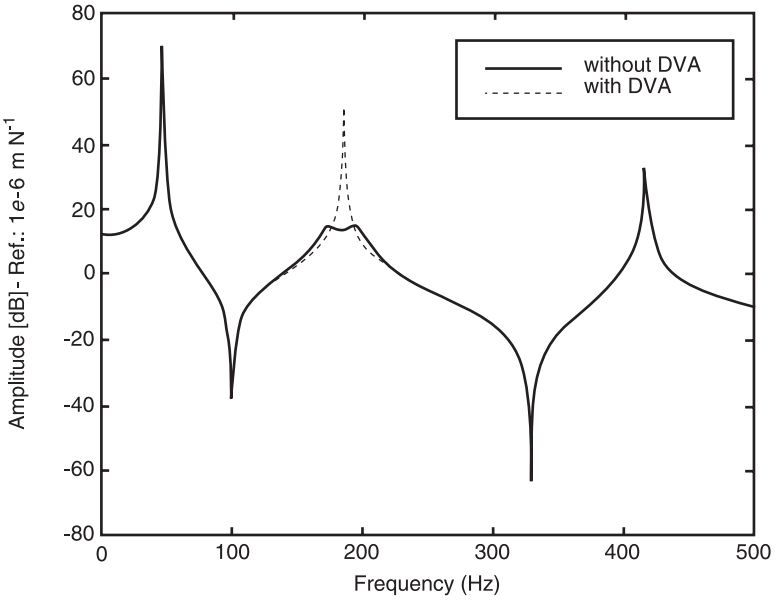


Figure 11 Frequency response corresponding to the coupling coordinate.

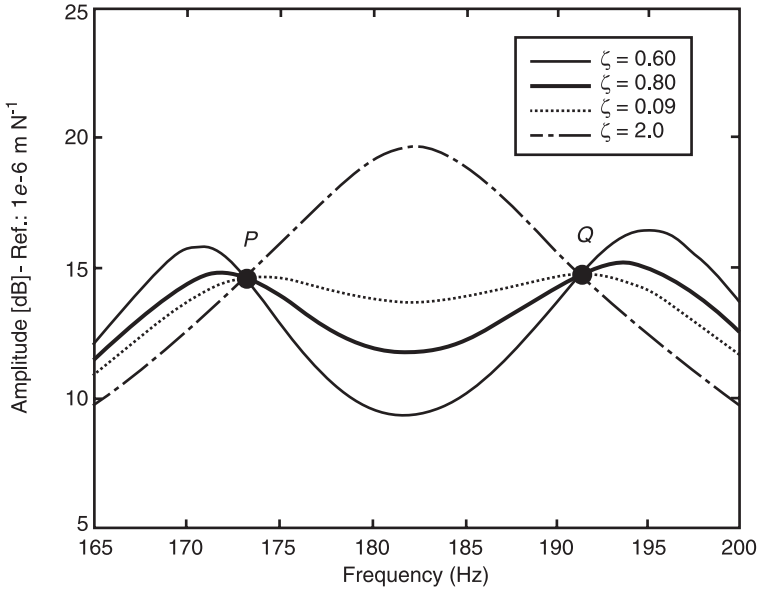


Figure 12 Illustration of the invariant points in the vicinity of the second natural frequency.

The Gyroscopic Dynamic Vibration Absorber

The roll motion of ships can be reduced by installing a large gyroscopic fixed to the hull, as shown in **Figure 14**. This arrangement is called gyroscope of Schlick and consists of a heavy gyroscope rotating at a high speed about a vertical axis. The roll motion of the ship induces the gyroscope to precess in the plane of symmetry along the length of the ship. Optionally, the precession motion can be damped by introducing an energy dissipation device. Neglecting damping, the equations of motion for the coupled system (ship + gyro) are written:

$$J_s\ddot{\phi} + J\Omega\dot{\theta} + k_r\phi = \tau_s \qquad [26a]$$

$$J_g\ddot{\theta} - J\Omega\dot{\phi} + Wa\theta = 0 \qquad [26b]$$

where $a =$ distance between precession axis and gyro's center of gravity; $J =$ polar moment of inertia

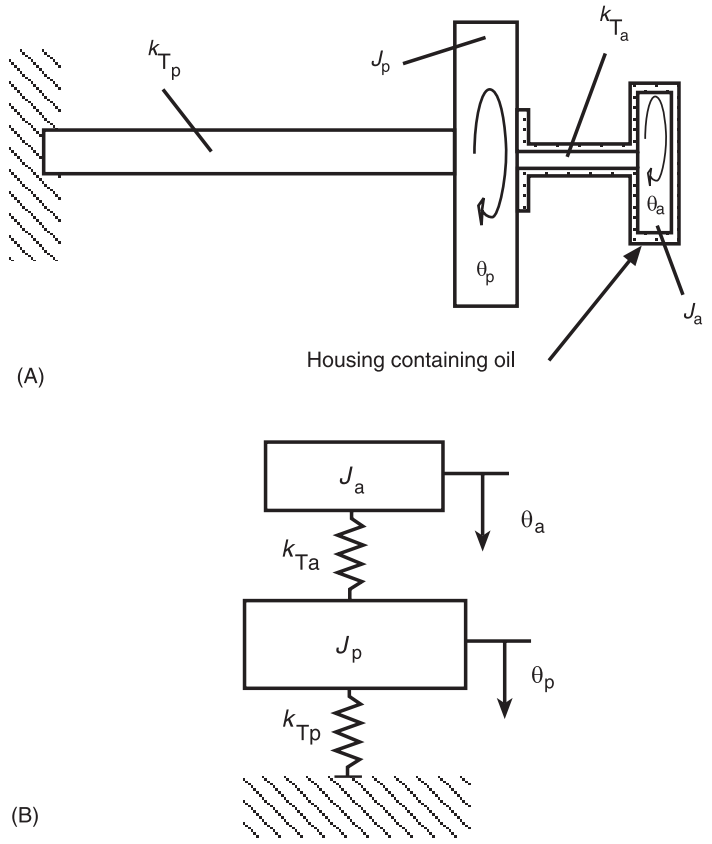


Figure 13 (A) Scheme of a torsional system with DVA and (B) equivalent rectilinear system.

Table 4 Equivalence between translational and torsional parameters

	Translational system	*Torsional system*
Inertia of the primary system	m_p (kg)	J_p (kg m^2)
Stiffness of the primary system	k_p (N m^{-1})	k_{Tp} (N.m rad^{-1})
Inertia of the DVA	m_a (kg)	J_a (kg m^2)
Stiffness of the DVA	k_a (N m^{-1})	k_{Ta} (N.m rad^{-1})
Damping of the DVA	c_a (N.s m^{-1})	c_{Ta} (N.m.s rad^{-1})

of the gyro; J_s = mass moment of inertia of the ship about its longitudinal axis; J_g = mass moment of inertia of the gyro about the precession axis; k_r = stiffness associated with roll motion; W = gyro's weight; ϕ = roll angle of the ship; θ = precession angle of the gyro; Ω = rotational speed of the gyro; τ_s = external excitation torque applied to the ship. As indicated in **Figure 14**, the gyro's center of gravity is situated below the precession axis. This ensures that the gyro is submitted to a restoring gravitational torque about the precession axis.

Assuming harmonic excitation:

$$\tau_s = T_s e^{i\omega t} \qquad [27]$$

the steady-state solution to eqns [26] is written:

$$\phi = \Phi e^{i\omega t} \qquad [28a]$$

$$\theta = \Theta e^{i\omega t} \qquad [28b]$$

After some algebraic manipulation, the following expression is obtained for the frequency response corresponding to the roll motion of the ship:

$$\Phi = \frac{Wa - \omega^2 J_g}{(k_r - \omega^2 J_s)(Wa - \omega^2 J_g) - (J\Omega\omega)^2} T_s \qquad [29]$$

It can be readily seen from eqn [29] that the roll motion is completely eliminated when the numerator vanishes, i.e.:

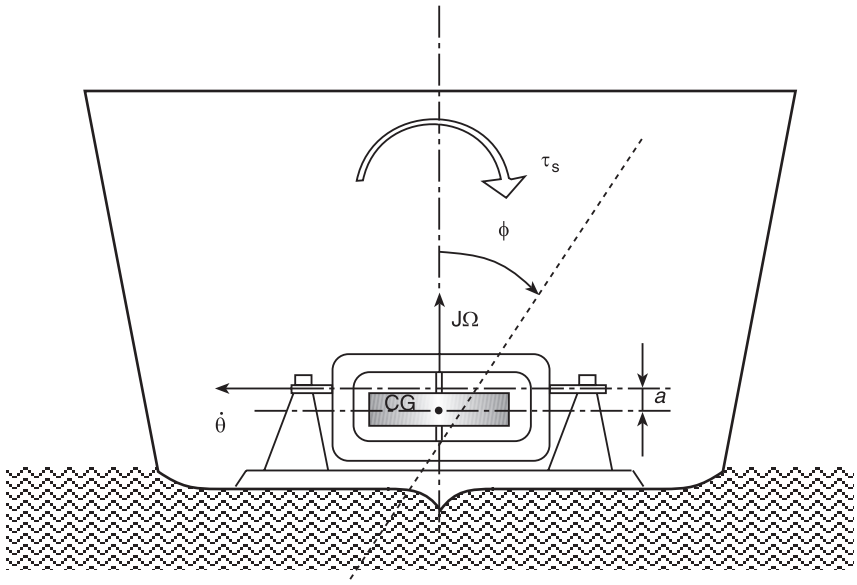


Figure 14 Sketch of a gyroscopic DVA used to attenuate ship roll motion.

$$\omega = \sqrt{\left(\frac{Wa}{J_g}\right)} \qquad [30]$$

Thus, the gyroscope parameters can be chosen so as to achieve tuning to the excitation frequency according to eqn [30].

It can be demonstrated that, when the precession motion is viscously damped, the expression for the frequency-response function associated to the roll motion is similar to eqn [13a], and allows for invariant points. Thus, the gyroscopic system can be optimally designed by using Den Hartog's procedure in the same way as it is applied to rectilinear damped DVAs.

The Centrifugal Pendulum Vibration Absorber

In the torsional vibration of rotating systems, it is generally the case that the excitation occurs at the same frequency as the rotational speed or at a multiple n of this frequency. For example, a shaft that drives a propeller can be subjected to torsional vibrations whose frequency is given by the number of blades of the propeller times the rotation speed. In such systems, a configuration of vibration absorber which has been frequently used is the centrifugal pendulum, depicted in **Figure 15**. The equations of motion for the two-degree-of-freedom system (flywheel + pendulum) can be written as:

$$\left(\frac{J}{mRl}+\frac{R}{l}+\frac{l}{R}+2\right)\ddot{\theta}+\left(\frac{l}{R}+1\right)\ddot{\psi}+\frac{k_T}{mRl}\theta=\frac{\tau}{mRl} \qquad [31a]$$

$$\left(1+\frac{R}{l}\right)\ddot{\theta}+\ddot{\psi}+\frac{\Omega^2 R}{l}\psi=0 \qquad [31b]$$

where J = mass moment of inertia of the flywheel; k_T = torsional stiffness of the shaft; l = length of the pendulum; m = mass of the pendulum; n = ratio between the excitation frequency and the angular velocity of the flywheel (order of vibration); R = distance between the center of the flywheel and the pivoting point of the pendulum; θ = angular coordinate describing the torsional vibration of the flywheel; ψ = angular coordinate describing the oscillation of the pendulum; Ω = angular velocity of the flywheel. Assuming steady-state harmonic vibration, one writes:

$$\tau = T\,e^{in\Omega t} \qquad \theta = \Theta\,e^{in\Omega t} \qquad \psi = \Psi\,e^{in\Omega t} \qquad [32]$$

and manipulation of eqns [31] leads to the following relation between the amplitudes of torsional vibration of the shaft and oscillation of the pendulum:

$$\frac{\Theta}{\Psi}=\frac{R-ln^2}{n^2(l+R)} \qquad [33]$$

It can be readily seen that if the geometry of the system is designed such that $R/l = n^2$, the torsional vibration of the flywheel is completely cancelled. In this case, the pendulum behaves as a DVA tuned to a given multiple of the excitation frequency.

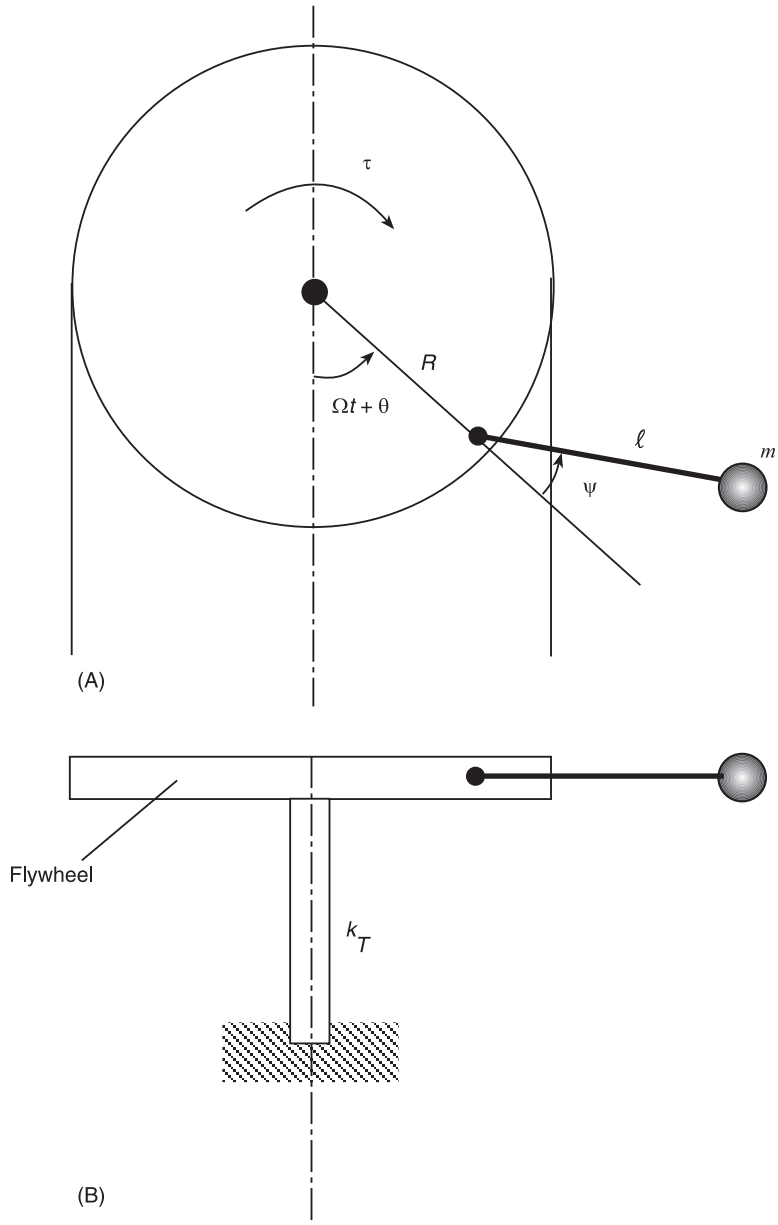


Figure 15 Scheme of a centrifugal pendulum DVA applied to a rotating system. (A) Top view; (B) side view.

Active Dynamic Vibration Absorbers

In applications requiring attenuation capability over a broad frequency band, active DVAs can be a very interesting solution. Moreover, active DVAs offer the possibility of automatic real-time tuning to the excitation frequency varying within a frequency band. Active DVAs are understood as those having an active element (actuator) installed in parallel with the passive elements supporting the reactive mass, as shown in **Figure 16**. The force impressed by the actuator is calculated through a previously defined control law. It is important to point out, however, that active DVAs have some drawbacks, such as energy consumption and instability.

Various control laws can be used, involving either absolute or relative dynamic responses. In the following, for illustration, the theory of an active DVA based on a control law expressed as a linear combination of relative displacement, velocity and acceleration responses is developed.In the system represented by **Figure 16** the control force applied by the actuator is assumed to be expressed as:

$$u(t) = -[\alpha(\ddot{x}_a - \ddot{x}_p) + \beta(\dot{x}_a - \dot{x}_p) + \gamma(x_a - x_p)] \quad [34]$$

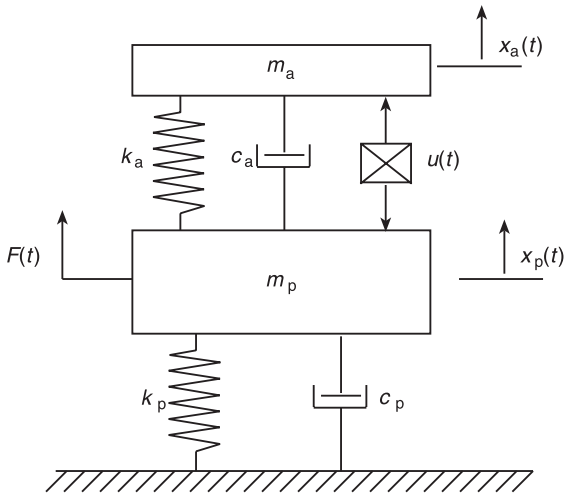


Figure 16 Schematic representation of a primary system with an active DVA.

where α, β, and γ are, respectively, the feedback gains for acceleration, velocity, and displacement signals.

The matrix equation of motion for the two-degree-of-freedom system is written as:

$$\mathbf{M}\ddot{\mathbf{x}} + \mathbf{C}\dot{\mathbf{x}} + \mathbf{K}\mathbf{x} = \mathbf{F} \qquad [35]$$

where:

$$\mathbf{M} = \begin{bmatrix} m_a + \alpha & -\alpha \\ -\alpha & m_p + \alpha \end{bmatrix}$$
$$\mathbf{C} = \begin{bmatrix} c_p + c_a + \beta & -(c_a + \beta) \\ -(c_a + \beta) & c_a + \beta \end{bmatrix}$$
$$\mathbf{K} = \begin{bmatrix} k_p + k_a + \gamma & -(k_a + \gamma) \\ -(k_a + \gamma) & k_a + \gamma \end{bmatrix}$$
$$\mathbf{x} = \begin{Bmatrix} x_p \\ x_a \end{Bmatrix} \quad \mathbf{F} = \begin{Bmatrix} f \\ 0 \end{Bmatrix}$$

As can be seen in the previous equations, the parameters β and γ can be interpreted as damping and stiffness parameters, which are added to the corresponding passive elements of the absorber. The same interpretation cannot be given the parameter α, since it also appears in the off-diagonal positions of the mass matrix.

The characteristic equation of the system is written in the Laplace domain as:

$$a_0 s^4 + a_1 s^3 + a_2 s^2 + a_3 s + a_4 = 0 \qquad [36]$$

where:

$$\begin{cases} a_0 = m_a\alpha + m_p(m_a + \alpha) \\ a_1 = (m_p + m_a)(c_a + \beta) + c_p(m_a + \alpha) \\ a_2 = k_p(m_a + \alpha) + c_p(c_a + \beta) + (k_a + \gamma)(m_p + m_a) \\ a_3 = c_p(k_a + \gamma) + k_p(c_a + \beta) \\ a_4 = k_p(k_a + \gamma) \end{cases} \qquad [37]$$

As in every application of active control, it is important to carry out a study of the stability of the system. Using the Routh–Hurwitz stability criterion, based on the expressions of the coefficients of the characteristic equation, as given by eqn [37], it can be shown that stability is ensured, provided that the following inequalities are satisfied by the feedback gains:

$$\alpha > \frac{-m_p m_a}{(m_p + m_a)} \qquad [38a]$$

$$\beta > -c_a \qquad [38b]$$

$$\gamma > -k_a \qquad [38c]$$

The feedback gains can be adjusted so as to tune the absorber to an arbitrarily chosen value of the excitation frequency. Using the equations of motion [35] and assuming harmonic excitation $F = F_0 e^{i\omega t}$, the frequency response of the primary mass is found to be expressed as:

$$\frac{X_a}{F_0} = \frac{-(m_a + \alpha)\omega^2 + i\omega(c_a + \beta) + k_a + \gamma}{a_0\omega^4 - ia_1\omega^3 - a_2\omega^2 + ia_3\omega + a_4} \qquad [39]$$

For the case of an undamped DVA without velocity feedback ($c_2 = \beta = 0$), from [39] it can be seen that the response vanishes when:

$$\omega^2 = \frac{k_a + \gamma}{m_a + \alpha} \qquad [40]$$

Thus, it is possible to cancel the harmonic vibrations at a given frequency ω by adjusting the values of the feedback gains γ and/or α so as to satisfy eqn [40] and the stability conditions given by [38a] and [38c].

Considering the particular case of an undamped primary system and a control law without acceleration feedback ($c_p = 0, \alpha = 0$), eqn [39] can be expressed as follows:

$$\left(\frac{X_p k_p}{F_0}\right)^2 = \frac{(2\zeta g)^2 + (g^2 - f^2)^2}{(2\zeta g)^2 (g^2 - 1 + \mu g^2)^2 + [\mu g^2 f^2 - (g^2 - 1)(g^2 - f^2)]^2} \quad [41]$$

where:

$$\mu = \frac{m_a}{m_p}; \qquad \omega_a = \sqrt{\left(\frac{k_a + \gamma}{m_a + \alpha}\right)}; \qquad \omega_p = \sqrt{\left(\frac{k_p}{m_p}\right)}$$

$$g = \omega/\omega_p; \qquad f = \omega_a/\omega_p; \qquad \zeta = \frac{c_a + \beta}{2 m_a \omega_p} \quad [42]$$

Eqn [41] has the same form as eqn [13a] developed for purely passive DVAs. As a result, the optimization procedure based on the invariant points also holds for the active DVA. Thus, assuming that the values of the passive elements are not varied, the optimization of the DVA can be achieved by finding an optimal set of feedback gains. Introducing eqns [42] into eqns [14] and [15], the following expressions for the optimal gains are obtained:

$$\gamma_{opt} = \left(\frac{\omega_p}{1 + \mu}\right)^2 m_a - k_a \quad [43a]$$

$$\beta_{opt} = 2\sqrt{\left[\frac{3\mu}{8(1 + \mu)^3}\right]} \omega_p m_a - c_a \quad [43b]$$

To illustrate the procedure for optimal design of an active DVA, consider an undamped primary system, for which the parameters take the following values:

$$m_p = 1.0 \text{ kg}, \quad k_p = 10\,000 \text{ N m}^{-1}, \quad c_p = 0$$

The passive parameters of the DVA are chosen as:

$$m_a = 0.1 \text{ kg}, \quad k_a = 1000 \text{ N m}^{-1}, \quad c_a = 0$$

Eqns [43] are used to determine the following optimal values of the feedback gains γ and β:

$$\gamma_{opt} = -173.55 \text{ N m}^{-1} \quad \beta_{opt} = 3.36 \text{ Ns m}^{-1}$$

Figure 17 shows the influence of the active DVA on the frequency system response of the primary system as compared to the response of this system without DVA and with the purely passive undamped DVA.

Final Remarks and Future Perspectives

In the previous sections, only DVAs comprising stiffness and damping elements exhibiting linear behavior have been considered. However, studies have demonstrated that nonlinear DVAs generally provide a suppression bandwidth much larger than linear absorbers. As a result, in spite of a more involved theory and design procedure, nonlinear vibration absorbers have received much attention lately.

Although only harmonic excitations were considered here, the reader should be aware of the fact that dynamic vibration absorbers have been extensively used to attenuate other types of vibrations, such as transient and random. In such cases, the optimal design is generally carried on by using time domain-based procedures.

The study and development of techniques related to smart materials represent new possibilities of vibration reduction in mechanics and mechatronics. The physical properties of such materials can be modified by controlled modifications of some environmental parameters. To mention a few examples, the viscosity (damping capacity) of electrorheological and magnetorheological fluids can be varied by applying external electric and magnetic fields, respectively. The geometry of components made of shape memory alloys can be changed by applying temperature variations. Some researchers have considered the possibility of using such smart materials to conceive self-tunable adaptive vibration absorbers. Furthermore, the possibility of dissipating mechanical energy with piezoelectric material, such as piezoelectric ceramics, shunted with passive electrical components has been investigated by various authors in this decade. The four basic kinds of shunt circuits are: inductive, resistive, capacitive, and switched. If a piezoelectric element is attached to a structure, it is strained as the structure deforms and part of the vibration energy is converted into electrical energy. The piezoelectric element behaves electrically as a capacitor and can be combined with a so-called shunt network in order to perform vibration control. Shunting with a resistor and inductor forms a RLC circuit introducing an electrical resonance which, in the optimal case, is tuned to structural resonances. The scheme of such an arrangement is depicted in **Figure 18**. The inductor is used to tune the shunt circuit to a given resonance of the structure and the resistor is responsible for peak amplitude reduction of a particular mode. The inductive shunt or resonant circuit shunt presents a vibration suppression effect that is very similar to the classical dynamic vibration absorber. The classical DVA stores part of the kinetic energy of the primary

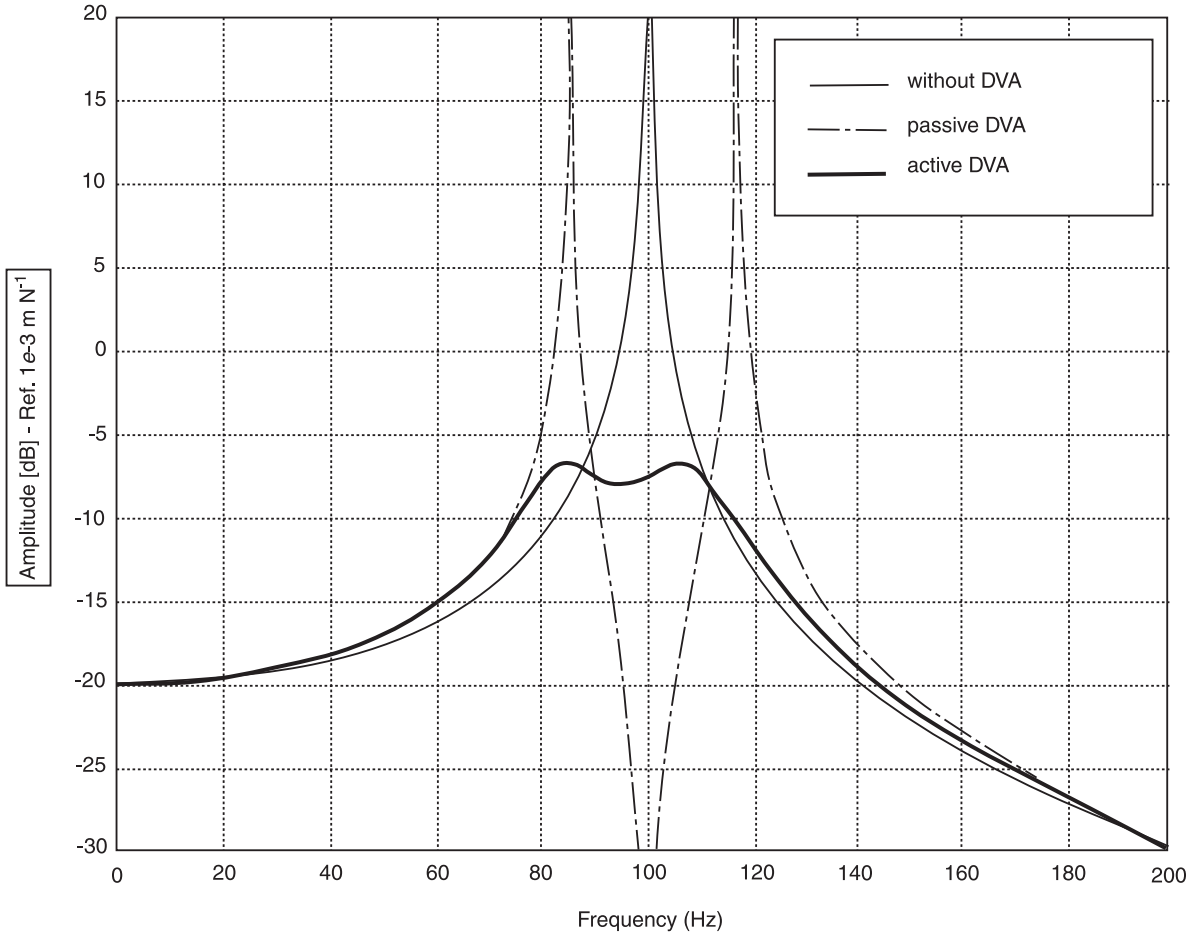


Figure 17 Frequency response of the primary system.

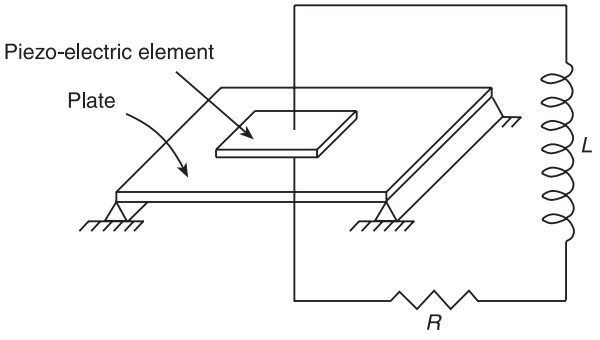


Figure 18 Scheme of a resonant circuit shunt used for vibration attenuation.

system, while the resonant circuit shunt is designed to dissipate the electrical energy that has been converted from mechanical energy by the piezoelectric. A multimode damper can be obtained by adding a different shunt for each suppressed mode in such a way that attenuation can be obtained for a given number of frequencies.

Nomenclature

f	tuning factor
g	forcing frequency ratio
J	inertia
l	length
W	weight
X	amplitude
μ	mass ratio
ψ	angular coordinate
θ	precession angle
τ	external excitation torque
Φ	roll angle
Ω	rotational speed/angular velocity

See also: **Absorbers, active**; **Active control of civil structures**; **Active control of vehicle vibration**; **Active isolation**; **Damping, active**; **Flutter, active control**; **Ship vibrations**; **Shock isolation systems**; **Theory of vibration**, Fundamentals; **Vibration isolation theory**; **Viscous damping**.

Further Reading

Den Hartog JP (1956) *Mechanical Vibrations*, 4th edn. McGraw-Hill Book Company.

Hagood NW and von Flotow A (1991) Damping of structural vibrations with piezoelectric materials and passive electrical networks. *Journal of Sound and Vibration* 146: 243–268.

Harris CM (1988) *Shock and Vibration Handbook*, 3rd edn, McGraw-Hill Book Company.

Inman DJ (1989) *Vibration with Control, Measurement and Stability*. Prentice-Hall.

Korenev BG and Reznikov LM (1993) *Dynamic Vibration Absorbers. Theory and Practical Applications*. John Wiley.

Nashif AD, Jones DIG and Henderson JP (1985) *Vibration Damping*. John Wiley.

Newland DE (1989) *Mechanical Vibration Analysis and Computation*. Longman Scientific and Technical.

Snowdon JC (1968) *Vibration and Shock in Damped Mechanical Systems*. John Wiley.

Sun JQ, Jolly MR and Norris MA (1995) Passive, adaptive and active tuned vibration absorbers – a survey. *Trans. ASME Combined Anniversary Issue Journal of Mechanical Design and Journal of Vibration and Acoustics* 117: 234–242.

ACTIVE ABSORBERS

See **ABSORBERS, ACTIVE**

ACTIVE CONTROL OF CIVIL STRUCTURES

T T Soong, State University of New York at Buffalo, Buffalo, NY, USA

B F Spencer, Jr., University of Notre Dame, Notre Dame, IN, USA

Copyright © 2001 Academic Press

doi:10.1006/rwvb.2001.0189

Introduction

In civil engineering structural applications, active, semiactive, and hybrid structural control systems are a natural evolution of passive control technologies such as base isolation and passive energy dissipation. The possible use of active control systems and some combinations of passive and active systems, so-called hybrid systems, as a means of structural protection against wind and seismic loads has received considerable attention in recent years. Active/hybrid control systems are force delivery devices integrated with real-time processing evaluators/controllers and sensors within the structure. They act simultaneously with the hazardous excitation to provide enhanced structural behavior for improved service and safety. Remarkable progress has been made over the last 20 years. As will be discussed in the following sections, research to date has reached the stage where active systems have been installed in full-scale structures. Active systems have also been used temporarily in construction of bridges or large-span structures (e.g., lifelines, roofs) where no other means can provide adequate protection.

The purpose of this article is to provide an assessment of the state-of-the-art and state-of-the-practice of this exciting, and still evolving, technology. Also included in the discussion are some basic concepts, the types of active control systems being used and deployed, and their advantages and limitations in the context of seismic design and retrofit of civil engineering structures.

Active, Hybrid, and Semiactive Control Systems

An active structural control system has the basic configuration shown schematically in **Figure 1A**. It consists of: (1) sensors located about the structure to measure either external excitations, or structural response variables, or both; (2) devices to process the measured information and to compute necessary control force needed based on a given control algorithm; and (3) actuators, usually powered by external sources, to produce the required forces.

When only the structural response variables are measured, the control configuration is referred to as feedback control since the structural response is continually monitored and this information is used to make continual corrections to the applied control forces. A feedforward control results when the control forces are regulated only by the measured excitation, which can be achieved, for earthquake inputs, by measuring accelerations at the structural base. In the case where the information on both the response quantities and excitation is utilized for control design, the term feedback–feedforward control is used.

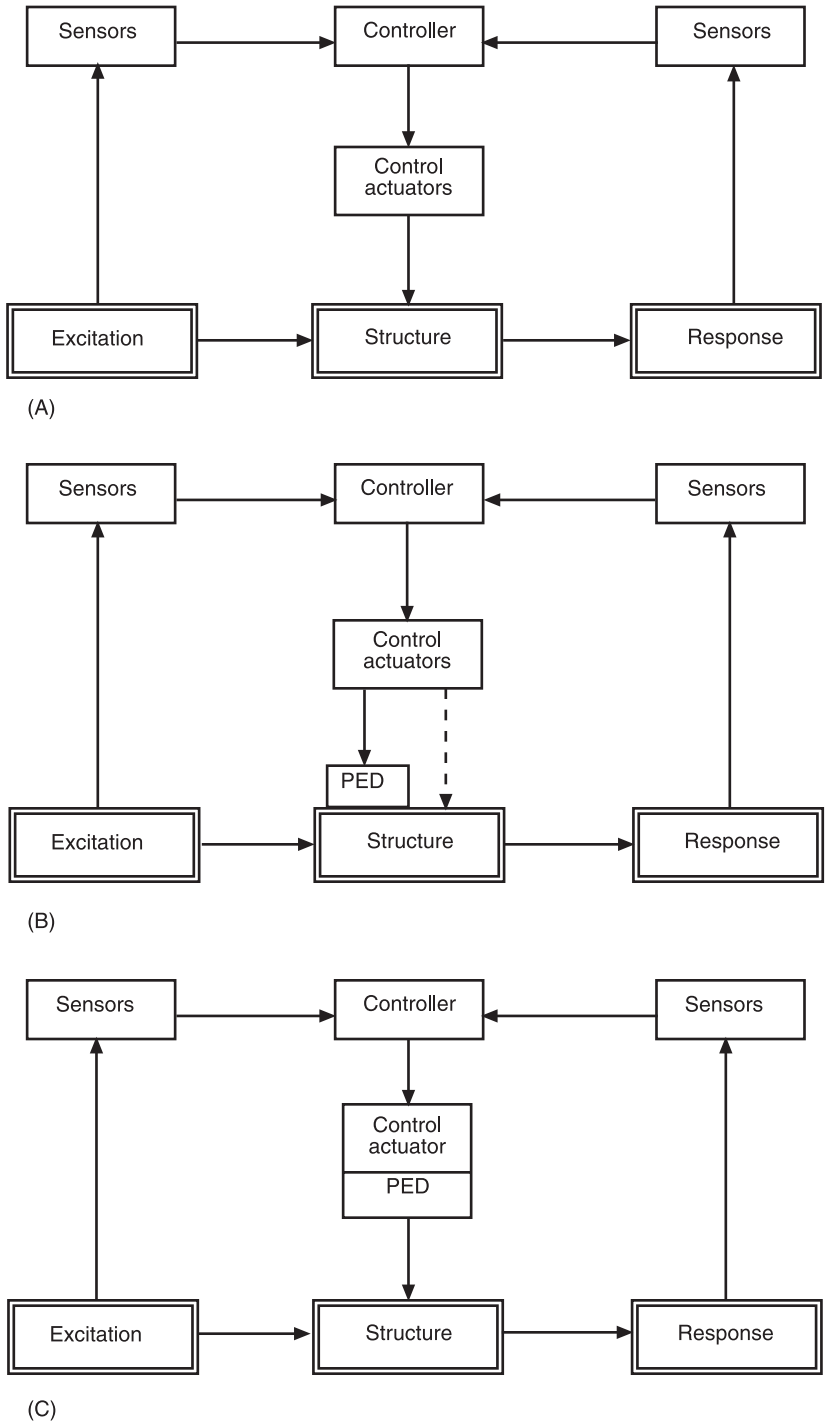


Figure 1 Structure with various schemes. (A) Structure with active control; (B) structure with hybrid control; (C) structure with semiactive control. PED, passive energy dissipation.

To see the effect of applying such control forces to a linear structure under ideal conditions, consider a building structure modeled by an n-degree-of-freedom lumped mass-spring-dashpot system. The matrix equation of motion of the structural system can be written as:

$$\mathbf{M}\ddot{x}(t) + \mathbf{C}\dot{x}(t) + \mathbf{K}x(t) = \mathbf{D}u(t) + \mathbf{E}f(t) \qquad [1]$$

where $\mathbf{M}$, $\mathbf{C}$, and $\mathbf{K}$ are the $n \times n$ mass, damping and stiffness matrices, respectively, $x(t)$ is the n-dimensional displacement vector, the m-vector $f(t)$ represents the applied load or external excitation, and

r-vector $u(t)$ is the applied control force vector. The $n \times r$ matrix $\mathbf{D}$ and the $n \times m$ matrix $\mathbf{E}$ define the locations of the action of the control force vector and the excitation, respectively, on the structure.

Suppose that the feedback–feedforward configuration is used in which the control force $u(t)$ is designed to be a linear function of measured displacement vector $x(t)$, velocity vector $\dot{x}(t)$ and excitation $f(t)$. The control force vector takes the form:

$$u(t) = \mathbf{G}_x x(t) + \mathbf{G}_{\dot{x}} \dot{x}(t) + \mathbf{G}_f f(t) \qquad [2]$$

in which $\mathbf{G}_x$, $\mathbf{G}_{\dot{x}}$, and $\mathbf{G}_f$ are respective control gains which can be time-dependent.

The substitution of eqn [2] into eqn [1] yields:

$$\begin{aligned} \mathbf{M}\ddot{x}(t) + (\mathbf{C} - \mathbf{D}\mathbf{G}_{\dot{x}})\dot{x}(t) + (\mathbf{K} - \mathbf{D}\mathbf{G}_x)x(t) \\ = (\mathbf{E} + \mathbf{D}\mathbf{G}_f)f(t) \end{aligned} \qquad [3]$$

Comparing eqn [3] with eqn [1] in the absence of control, it is seen that the effect of feedback control is to modify the structural parameters (stiffness and damping) so that it can respond more favorably to the external excitation. The effect of the feedforward component is a modification of the excitation. The choice of the control gain matrices $\mathbf{G}_x$, $\mathbf{G}_{\dot{x}}$, and $\mathbf{G}_f$ depends on the control algorithm selected.

In comparison with passive control systems, a number of advantages associated with active control systems can be cited; among them are: (1) enhanced effectiveness in response control; the degree of effectiveness is, by and large, only limited by the capacity of the control systems; (2) relative insensitivity to site conditions and ground motion; (3) applicability to multihazard mitigation situations; an active system can be used, for example, for motion control against both strong wind and earthquakes; and (4) selectivity of control objectives; one may emphasize, for example, human comfort over other aspects of structural motion during noncritical times, whereas increased structural safety may be the objective during severe dynamic loading.

While this description is conceptually in the domain of familiar optimal control theory used in electrical engineering, mechanical engineering, and aerospace engineering, structural control for civil engineering applications has a number of distinctive features, largely due to implementation issues, that set it apart from the general field of feedback control. In particular, when addressing civil engineering structures, there is considerable uncertainty, including nonlinearity, associated with both physical properties and disturbances such as earthquakes and wind, the scale of the forces involved can be quite large, there are only a limited number of sensors and actuators, the dynamics of the actuators can be quite complex, the actuators are typically very large, and the systems must be failsafe.

It is useful to distinguish between several types of active control systems currently being used in practice. The term hybrid control generally refers to a combined passive and active control system, as depicted in **Figure 1B**. Since a portion of the control objective is accomplished by the passive system, less active control effort, implying less power resource, is required.

Similar control resource savings can be achieved using the semiactive control scheme sketched in **Figure 1C**, where the control actuators do not add mechanical energy directly to the structure, hence bounded-input bounded-output stability is guaranteed. Semiactive control devices are often viewed as controllable passive devices.

A side benefit of hybrid and semiactive control systems is that, in the case of a power failure, the passive components of the control still offer some degree of protection, unlike a fully active control system.

Full-scale Applications

As alluded to earlier, the development of active, hybrid, and semiactive control systems has reached the stage of full-scale applications to actual structures. **Figure 2** shows that, up to 1999, there have been 43 installations in building structures and towers, most of which are in Japan (**Table 1**). In addition, 15 bridge towers have employed active systems during erection. Most of these full-scale systems have been subjected to actual wind forces and ground motions and their observed performances provide invaluable information in terms of: (1) validating analytical and simulation procedures used to predict actual system performance; (2) verifying complex electronic–digital–servohydraulic systems under actual loading conditions; and (3) verifying the capability of these systems to operate or shut down under prescribed conditions.

Described below are several of these systems together, in some cases, with their observed performances. Also addressed are several practical issues in connection with actual structural applications of these systems.

Hybrid Mass Damper Systems

As seen from **Table 2**, the hybrid mass damper (HMD) is the most common control device employed in full-scale civil engineering applications. An HMD is a combination of a passive tuned mass damper (TMD) and an active control actuator. The ability of

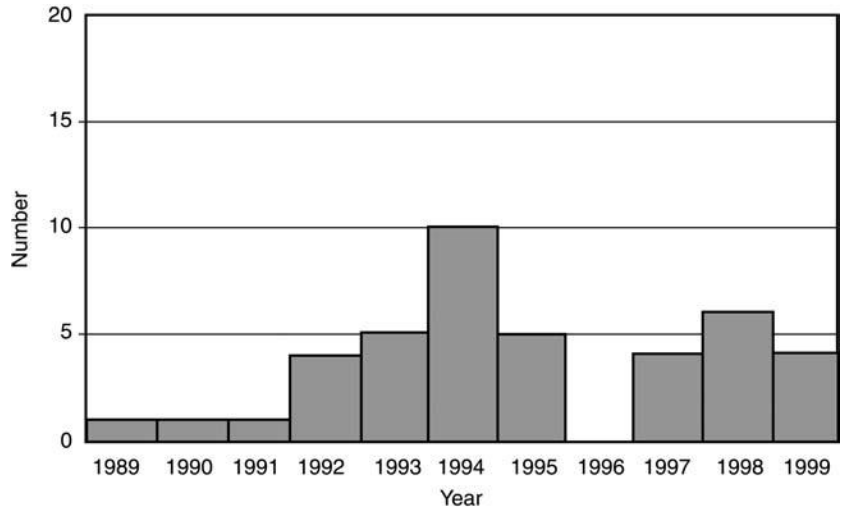


Figure 2 Active control – number of installations.

Table 1 System applications

Country	*Number*[a]
Japan	39
Others	4

[a] Up to 1999.

Table 2 System configurations

Type	*Number*[a]
Hybrid mass damper	33
Others	10

[a] Up to 1999.

this device to reduce structural responses relies mainly on the natural motion of the TMD. The forces from the control actuator are employed to increase the efficiency of the HMD and to increase its robustness to changes in the dynamic characteristics of the structure. The energy and forces required to operate a typical HMD are far less than those associated with a fully active mass damper system of comparable performance.

An example of such an application is the HMD system installed in the Sendagaya INTES building in Tokyo in 1991. As shown in **Figure 3**, the HMD was installed atop the 11th floor and consists of two masses to control transverse and torsional motions of the structure, while hydraulic actuators provide the active control capabilities. The top view of the control system is shown in **Figure 4**, where ice thermal storage tanks are used as mass blocks so that no extra mass needs to be introduced. The masses are supported by multistage rubber bearings intended for reducing the control energy consumed in the HMD and for insuring smooth mass movements.

Sufficient data were obtained for evaluation of the HMD performance when the building was subjected to strong wind on 29 March 1993, with peak instantaneous wind speed of $30.6\,\mathrm{m\,s^{-1}}$.

An example of the recorded time histories is shown in **Figure 5**, giving both the uncontrolled and controlled states. Their Fourier spectra using samples of 30-s durations are shown in **Figure 6**, again showing good performance in the low-frequency range. The response at the fundamental mode was reduced by 18% and 28% for translation and torsion, respectively.

Variations of such an HMD configuration include multistep pendulum HMDs (as seen in **Figure 7**), which have been installed in, for example, the Yokohama Landmark Tower in Yokohama, the tallest building in Japan, and in the TC Tower in Kaohsiung, Taiwan. Additionally, the DUOX HMD system which, as shown schematically in **Figure 8**, consists of a TMD actively controlled by an auxiliary mass, has been installed in, for example, the Ando Nishikicho Building in Tokyo.

Active Mass Damper Systems

Design constraints, such as severe space limitations, can preclude the use of an HMD system. Such is the case in the active mass damper or active mass driver (AMD) system designed and installed in the Kyobashi Seiwa Building in Tokyo and the Nanjing Communication Tower in Nanjing, China.

The Kyobashi Seiwa Building, the first full-scale implementation of active control technology, is an

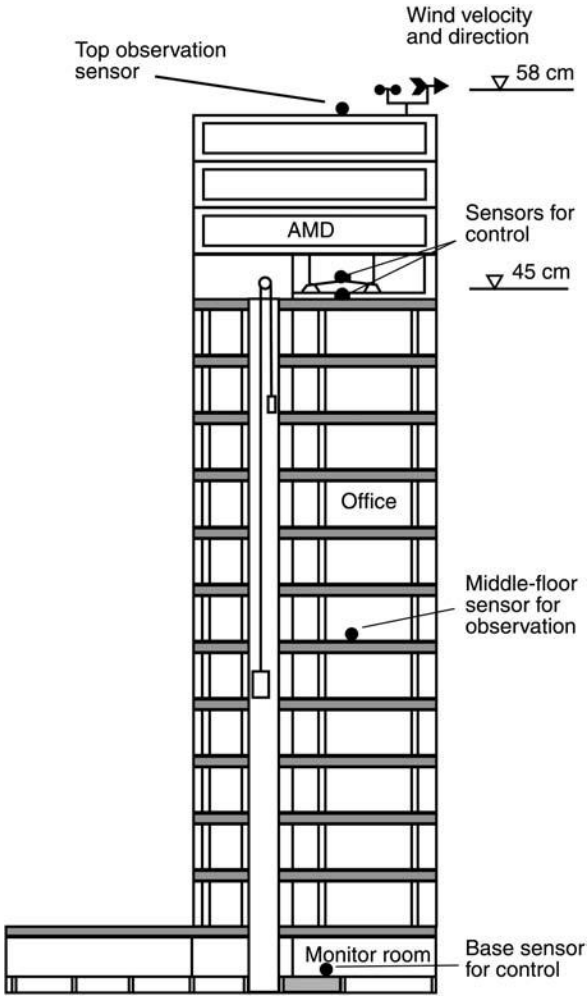


Figure 3 Sendagaya INTES building with hybrid mass damper. AMD, active mass damper.

11-story building with a total floor area of 423 m^2. As seen in **Figure 9**, the control system consists of two AMDs where the primary AMD is used for transverse motion and has a weight of 4 tons, while the secondary AMD has a weight of 1 ton and is employed to reduce torsional motion. The role of the active system is to reduce building vibration under strong winds and moderate earthquake excitations and consequently to increase comfort of occupants in the building.

Semiactive Damper Systems

Control strategies based on semiactive devices appear to combine the best features of both passive and active control systems. The close attention received in this area in recent years can be attributed to the fact that semiactive control devices offer the adaptability of active control devices without requiring the associated large power sources. In fact, many can operate on battery power, which is critical during seismic events when the main power source to the structure may fail. In addition, as stated earlier, semiactive control devices do not have the potential to destabilize (in the bounded input/bounded output sense) the structural system. Extensive studies have indicated that appropriately implemented semiactive systems perform significantly better than passive devices and have the potential to achieve the majority of the performance of fully active systems, thus allowing for the possibility of effective response reduction during a wide array of dynamic loading conditions.

One means of achieving a semiactive damping device is to use a controllable, electromechanical, variable-orifice valve to alter the resistance to flow of a conventional hydraulic fluid damper. A schematic of such a device is given in **Figure 10**. Such a system was implemented, for example, in a bridge to dissipate the energy induced by vehicle traffic.

More recently, a semiactive damper system was installed in the Kajima Shizuoka Building in Shizuoka, Japan. As seen in **Figure 11**, semiactive hydraulic dampers were installed inside the walls on both sides of the building to enable it to be used as a disaster relief base in postearthquake situations. Each

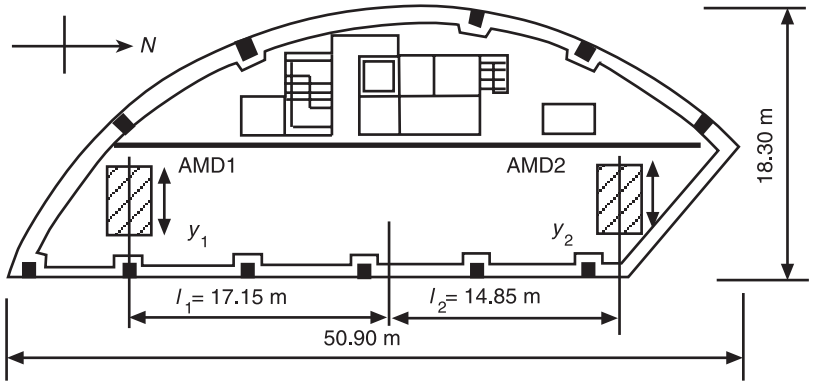


Figure 4 Top view of hybrid mass damper. AMD, active mass damper.

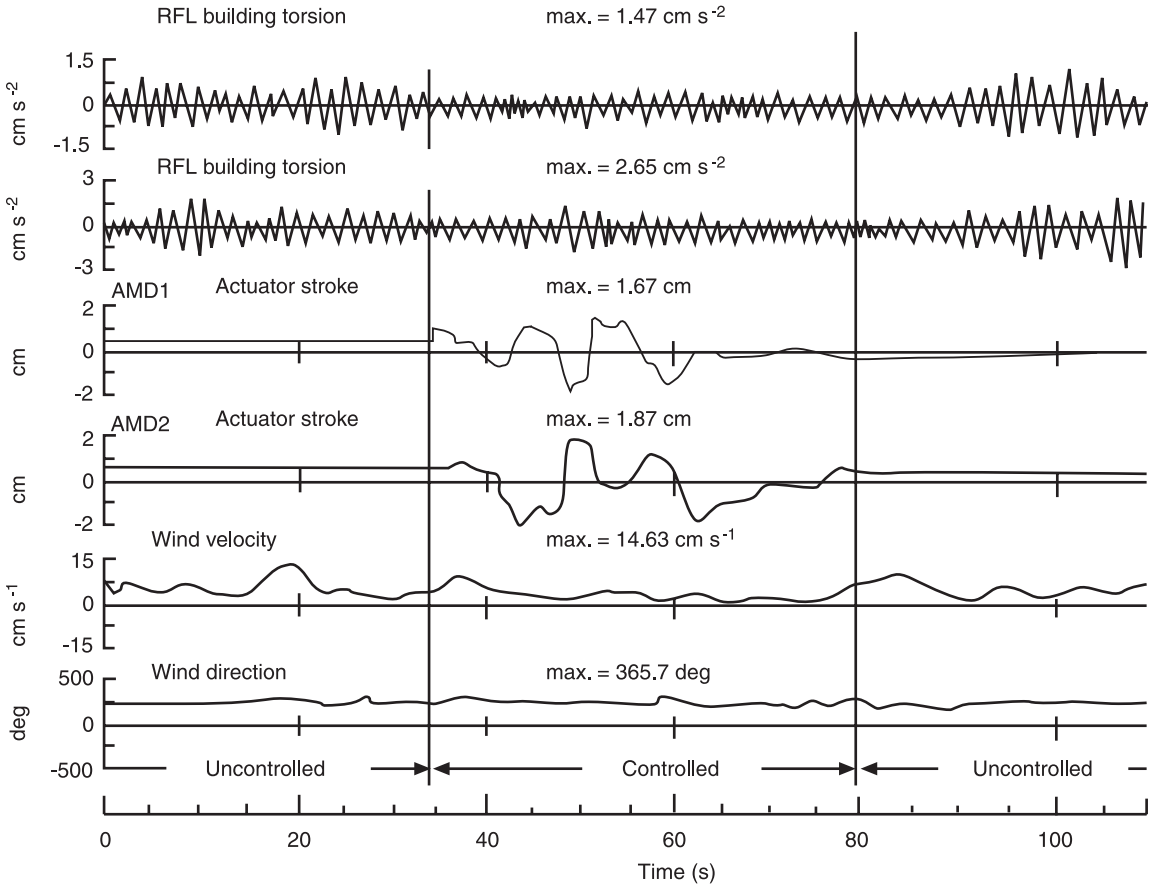


Figure 5 Response time histories (23 March 1993). AMD, active mass damper.

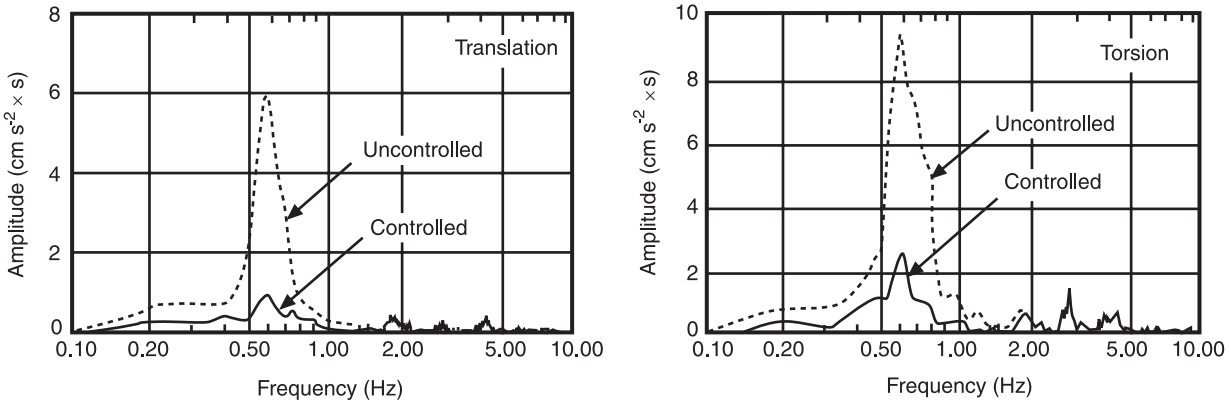


Figure 6 Response Fourier spectra (23 March 1993).

damper contains a flow control valve, a check valve, and an accumulator, and can develop a maximum damping force of 1000 kN. **Figure 12** shows a sample of the response analysis results based on one of the selected control schemes and several earthquake input motions with the scaled maximum velocity of $50\,\mathrm{cm\,s^{-1}}$, together with a simulated Tokai wave. It is seen that both story shear forces and story drifts are greatly reduced with the control system activated. In the case of the shear forces, they are confined within their elastic-limit values (indicated by E-limit) while, without control, they would enter the plastic range.

Semiactive Controllable Fluid Dampers

Another class of semiactive devices uses controllable fluids, schematically shown in **Figure 13**. In comparison with semiactive damper systems described

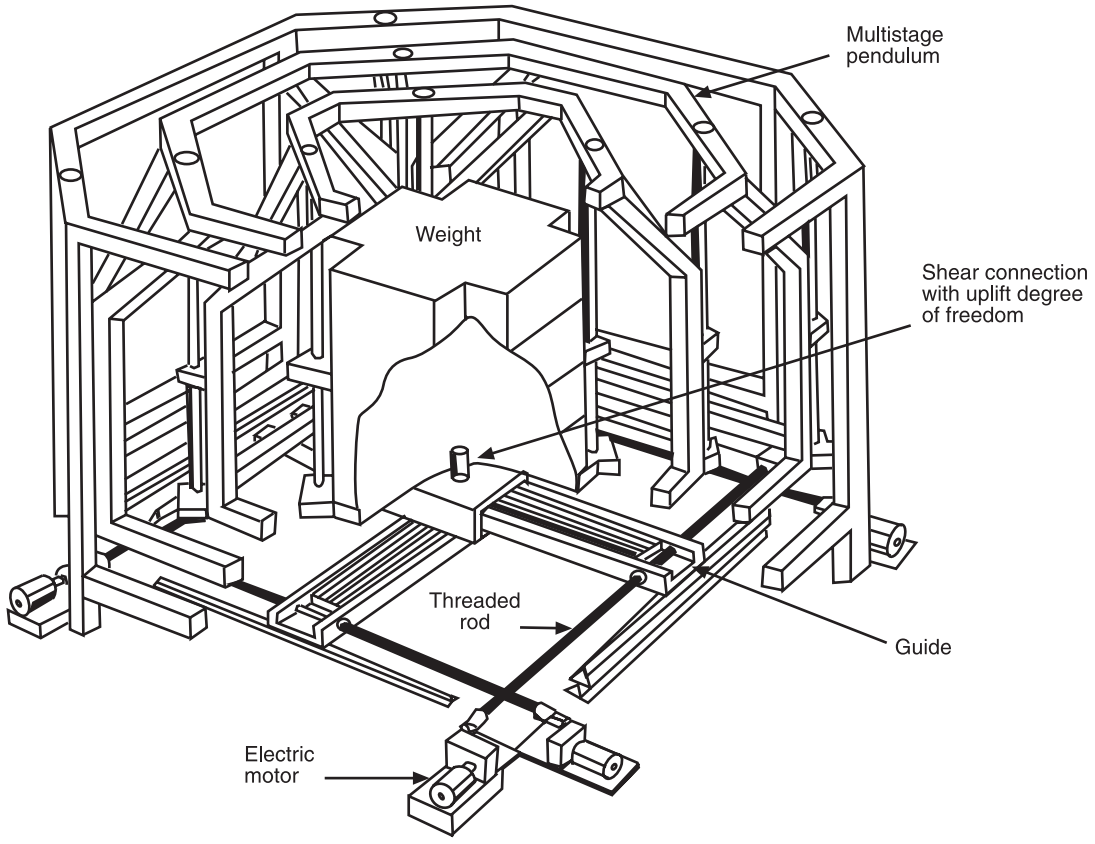


Figure 7 Hybrid mass damper in Yokohama Landmark Tower.

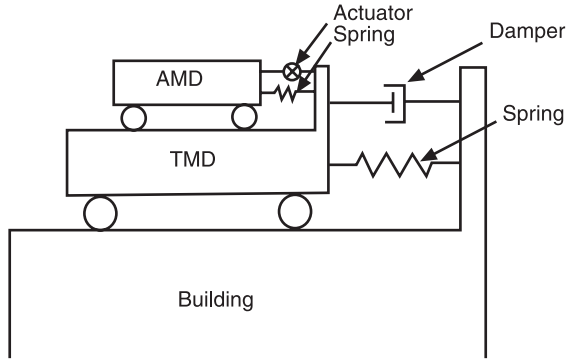


Figure 8 Principle of DUOX system. AMD, active mass damper; TMD, tuned mass damper.

above, an advantage of controllable fluid devices is that they contain no moving parts other than the piston, which makes them simple and potentially very reliable.

The essential characteristics of controllable fluids is their ability to change reversibly from a free-flowing, linear, viscous fluid to a semisolid with a controllable yield strength in milliseconds when exposed to an electric (for electrorheological (ER) fluids) or magnetic (for magnetorheological (MR) fluids) field.

In the case of MR fluids, they typically consist of micron-sized, magnetically polarizable particles dispersed in a carrier medium such as mineral or silicone oil. When a magnetic field is applied to the fluid, particle chains form, and the fluid becomes a semisolid and exhibits viscoplastic behavior. Transition to rheological equilibrium can be achieved in a few milliseconds, allowing construction of devices with high bandwidth. Additionally, it has been indicated that high yield stress of an MR fluid can be achieved and that MR fluids can operate at temperatures from -40°C to 150°C with only slight variations in the yield stress. Moreover, MR fluids are not sensitive to impurities such as are commonly encountered during manufacturing and usage, and little particle/carrier fluid separation takes place in MR fluids under common flow conditions. Further, a wider choice of additives (surfactants, dispersants, friction modifiers, antiwear agents, etc.) can generally be used with MR fluids to enhance stability, seal life, bearing life, and so on, since electrochemistry does not affect the magnetopolarization mechanism. The MR fluid can be readily controlled with a low-voltage (e.g., 12–24 V), current-driven power supply outputting only 1–2 A.

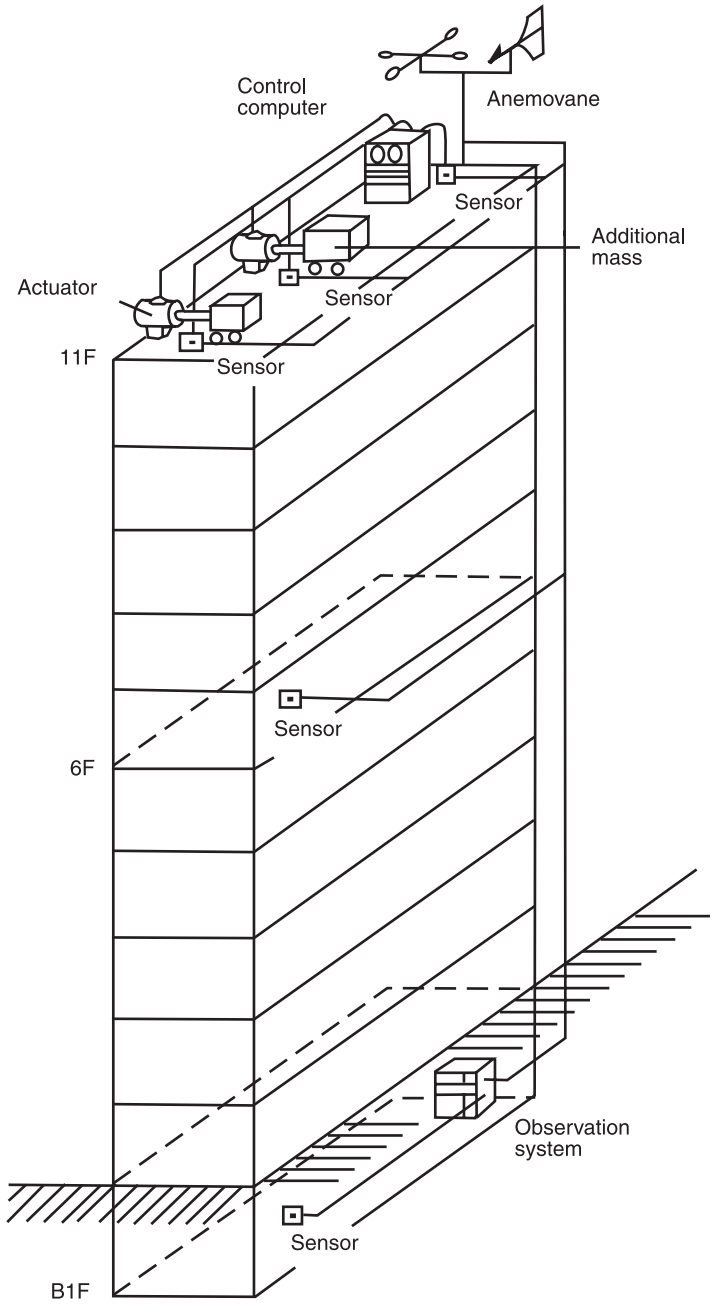


Figure 9 Kyobashi Seiwa building and active mass damper.

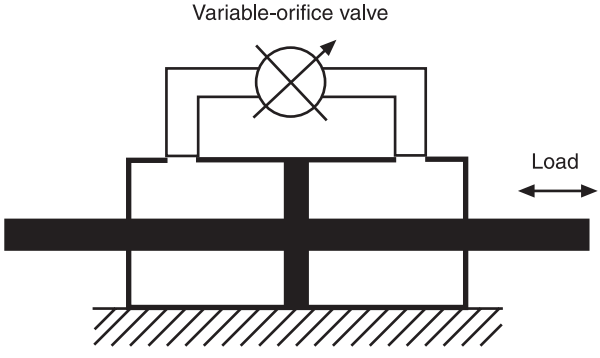


Figure 10 Schematic of variable-orifice damper.

While no full-scale structural applications of MR devices have taken place to date, their future for civil engineering applications appears to be bright. There have been published reports on the design of a full-scale, 20-ton MR damper, showing that this technology is scalable to devices appropriate for civil engineering applications. At design velocities, the dynamic range of forces produced by this device is over 10 (**Figure 14**), and the total power required by the device is only 20–50 W.

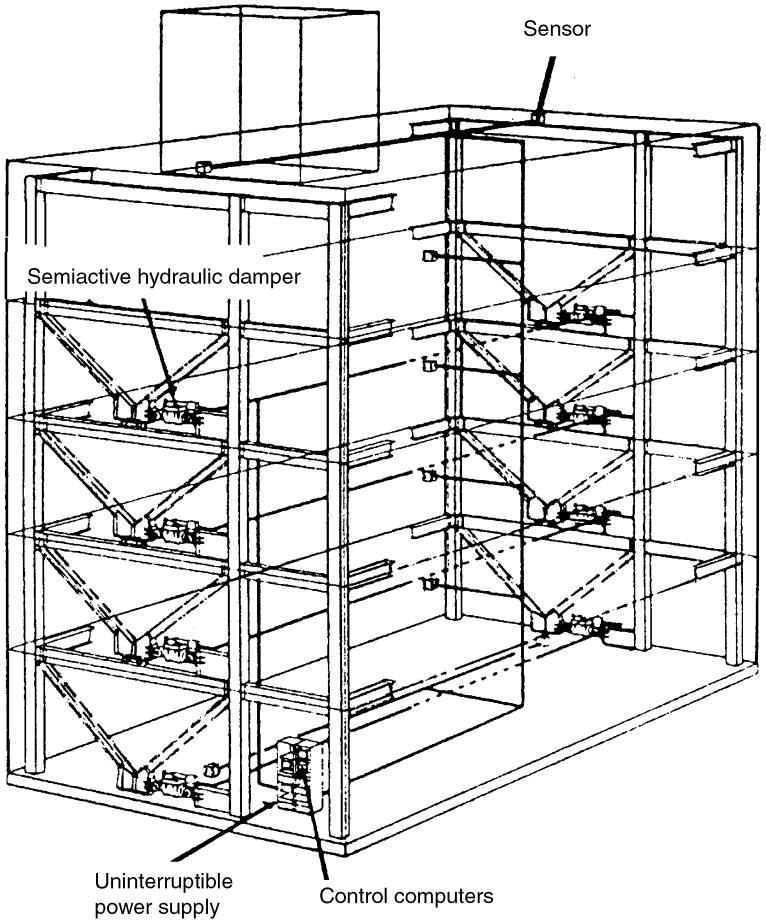


Figure 11 Semiactive hydraulic damper in the Kajima Shizuoka building.

Concluding Remarks

An important observation to be made in the performance observation of control systems such as those described above is that efficient active control systems can be implemented with existing technology under practical constraints such as power requirements and stringent demand of reliability. Thus, significant strides have been made, considering that serious implementational efforts began less than 15 years ago. On the other hand, there remains a significant distance between the state-of-the-art of active control technology and some originally intended purposes for developing such a technology. Two of these areas are particularly noteworthy and they are highlighted below.

1. Mitigating higher-level hazards. In the context of earthquake engineering, one of the original goals for active control research was the desire that, through active control, conventional structures can be protected against infrequent, but highly damaging earthquakes. The active control devices currently deployed in structures and towers were designed primarily for performance enhancement against wind and moderate earthquakes and, in many cases, only for occupant comfort. However, active control systems remain to be one of only a few alternatives for structural protection against near-field and high-consequence earthquakes.

   An upgrade of current active systems to this higher level of structural protection is necessary, since only then can the unique capability of active control systems be realized.
2. Economy and flexibility in construction. Another area in which great benefit can be potentially realized by the deployment of active control systems is added economy and flexibility to structural design and construction. The concept of active structures has been advanced. An active structure is defined here as one consisting of two types of load-resisting members: the traditional static (or passive) members that are designed to support basic design loads, and dynamic (or active) members whose function is to augment the structure's capability in resisting extraordinary dynamic

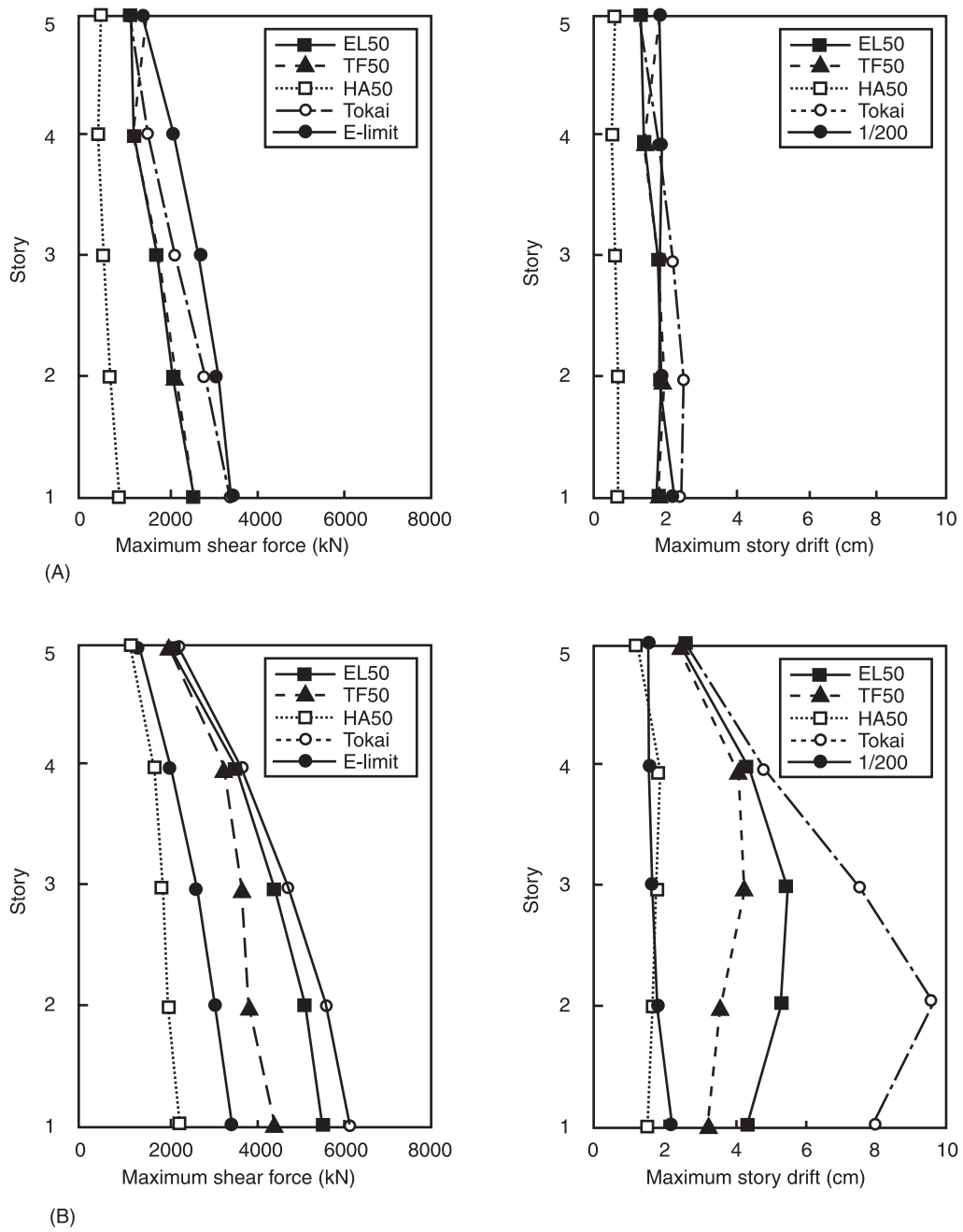


Figure 12 Maximum responses (El Centro, Taft, and Hachinohe waves with 50 cm s^{-1} and assumed Tokai waves). (A) With semi-active hydraulic damper control; (B) without control.

loads. Their integration is done in an optimal fashion and produces a structure that is adaptive to changing environmental loads and usage.

Note that an active structure is conceptually and physically different from a structure that is actively controlled, as in the cases described above. In the case of a structure with active control, a conventionally designed structure is supplemented by an active

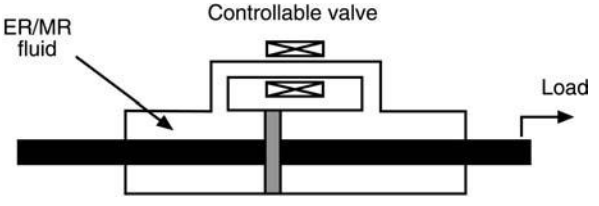


Figure 13 Schematic of controllable fluid damper. ER, electrorheological; MR, magnetorheological.

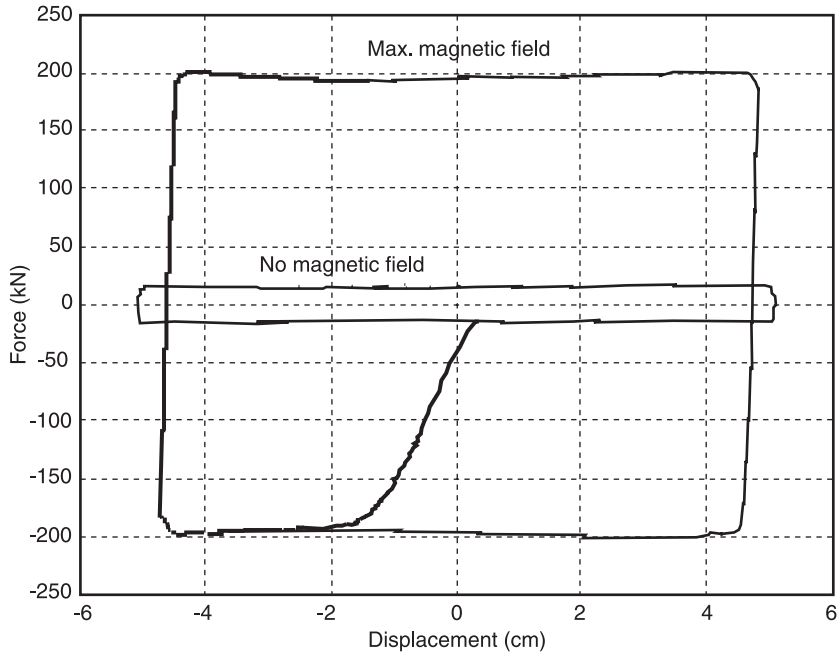


Figure 14 Force–displacement loops at maximum and zero magnetic fields.

control device that is activated whenever necessary in order to enhance structural performance under extraordinary loads. Thus, the structure and the active control system are individually designed and optimized. An active structure, on the other hand, is one whose active and passive components are integrated and simultaneously optimized to produce a new breed of structural systems. This important difference makes the concept of active structures exciting and potentially revolutionary. Among many possible consequences, one can envision greater flexibilities which may lead to longer, taller, slender, or more open structures and structural forms.

See Plates 1,2,3.

See also: **Damping, active**; **Hybrid control**.

Further Reading

Carlson JD and Spencer BF Jr. (1996) Magneto-rheological fluid dampers for semi-active seismic control. In: *Proceedings of the 3rd International Conference on Motion and Vibration Control*, Chiba, Japan. Japan Society of Mechanical Engineers, Tokyo, Japan, Vol. III, pp. 35–40.

Carlson JD and Weiss KD (1994) A growing attraction to magnetic fluids. *Machine Design*, pp. 61–64.

Housner GW, Bergman LA, Caughey TK *et al.* (1997) Structural control: past, present, and future. *Journal of Engineering Mechanics* 123: 897–971.

Kobori T (1994) Future direction on research and development of seismic-response-controlled structure. *Proceedings 1st World Conference on Structural Control* (GW Houser, SF Masri and AG Chassiakos, eds), International Association for Structural Control, Los Angeles, CA, pp. 19–31.

Kobori T (1999) Mission and perspective towards future structural control research. *Proceedings of the 2nd World Conference on Structural Control*, Kyoto, Japan. (T Kobori, Y Inoue, K Seto, H Iemura and A Nishitani, eds), John Wiley, Chichester, UK, pp. 25–34.

Patten WN (1999) The I-35 Walnut Creek bridge: an intelligent highway bridge via semi-active structural control. In: *Proceedings of 2nd World Conference on Structure Control*, Kyoto, Japan (T Kobori, Y Inoue, K Seto, H Iemura, A Nishitani, (eds), John Wiley, Chichester, UK, pp. 427–436.

Soong TT (1990) *Active Structural Control: Theory and Practice*. New York, NY: Wiley.

Soong TT and Manolis GD (1987) Active structures. *Journal of Structural Engineering* 113: 2290–2301.

Soong TT, Reinhorn AM, Aizawa S and Higashino M (1994) Recent structural applications of active control technology. *Journal of Structural Control* 1: 5–21.

Spencer BF Jr, Carlson JD, Sain MK and Yang G (1997) On the current status of magnetorheological dampers: seismic protection of full-scale structures. In: *Proceedings of American Control Conference*, American Automatic Control Council, pp. 458–462, Albuquerque, NM.

Spencer BF Jr, Yang G, Carlson JD and Sain MK (1999) Smart dampers for seismic protection of structures: a full-scale study. In: *Proceedings of 2nd World Conference on Structure Control*, Kyoto, Japan (T Kobori, Y Inoue, K Seto, H Iemura, A Nishitani, eds), John Wiley, Chichester, UK, pp. 417–426.

ACTIVE CONTROL OF VEHICLE VIBRATION

M Ahmadian, Virginia Tech, Blacksburg, VA, USA

Copyright © 2001 Academic Press

doi:10.1006/rwvb.2001.0193

Introduction

Perceived comfort level and ride stability are two of the most important factors in a vehicle's subjective evaluation. There are many aspects of a vehicle that influence these two properties, most importantly the primary suspension components, which isolate the frame of the vehicle from the axle and wheel assemblies. In the design of a conventional primary suspension system, there is a tradeoff between the two quantities of ride comfort and vehicle stability, as shown in **Figure 1**. If a primary suspension is designed to optimize the handling and stability of the vehicle, the operator is often subjected to a large amount of vibration and perceives the ride to be rough and uncomfortable. On the other hand, if the primary suspension is designed to be soft and 'cushy', the vibrations in the vehicle are reduced, but the vehicle may not be too stable during maneuvers such as cornering and lane change. As such, the performance of primary suspensions is always limited by the compromise between ride and handling. Good design of a passive suspension cannot eliminate this compromise but can, to some extent, optimize the opposing goals of comfort and handling.

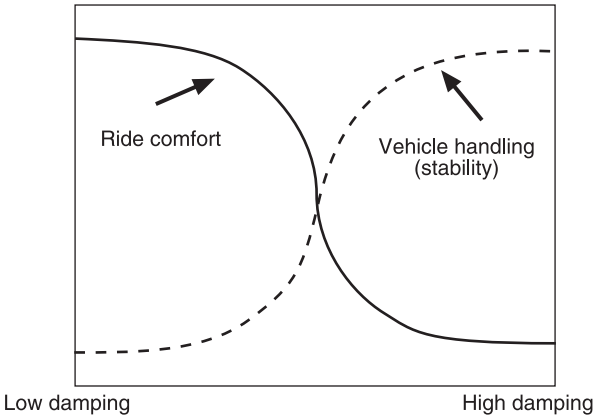


Figure 1 Vehicle vibration and handling compromise due to suspension damping.

Passive Suspensions

A passive suspension system is one in which the characteristics of the components (springs and dampers) are fixed. These characteristics are determined by the suspension designer, according to the design goals and the intended application. A passive suspension, such as shown in **Figure 2**, has the ability to store energy via a spring and to dissipate it via a damper. **Figure 2** represents one-quarter of a vehicle, and therefore is commonly referred to as 'quarter-car model'. The mass of the vehicle body (sprung mass) and tire–axle assembly (unsprung mass) are defined respectively by m_b and m_a, with their corresponding displacements defined by x_b and x_a. The suspension spring, k_s, and damper, c_s, are attached between the vehicle body and axle, and the stiffness of the tire is represented by k_t.

The parameters of a passive suspension are generally fixed to achieve a certain level of compromise between reducing vibrations and increasing road holding. Once the spring has been selected, based on the load-carrying capability of the suspension, the damper is the only variable remaining to specify. Low damping yields poor resonance control at the

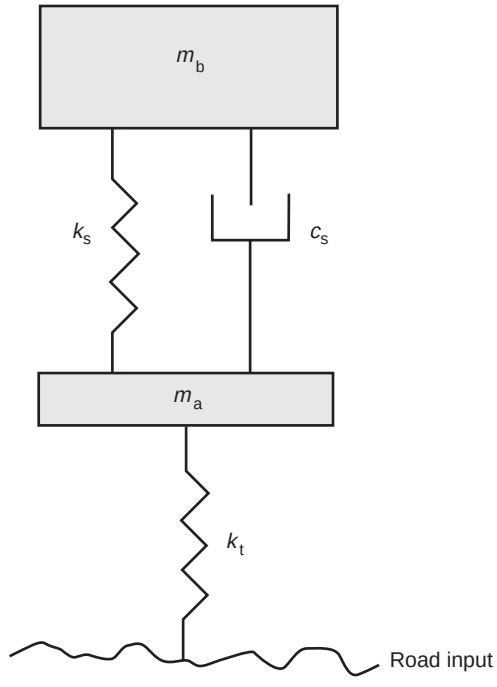


Figure 2 Passive suspension.

natural frequencies of the body (sprung mass) and axle (unsprung mass), but provides the necessary high-frequency isolation required for lower vibrations and a more comfortable ride. Conversely, large damping results in good resonance control at the expense of lower isolation from the road input and more vibrations in the vehicle.

Adjustable Suspensions

An adjustable suspension system combines the passive spring element found in a passive suspension with a damper element whose characteristics can be adjusted by the operator. As shown in **Figure 3**, the vehicle operator can use a selector device to set the desired level of damping based on a preference for the subjective feel of the vehicle. This system has the advantage of allowing the operator occasionally to adjust the dampers according to the road characteristics. It is, however, unrealistic to expect the operator to adjust the suspension system to respond to time inputs such as potholes, turns, or other common road inputs.

Active Suspensions

In an active suspension, the passive damper, or both the passive damper and spring, are replaced with a force actuator, as illustrated in **Figure 4**.

The force actuator is able both to add and dissipate energy to and from the system, unlike a passive damper, which can only dissipate energy. With an active suspension, the force actuator can apply force independent of the relative displacement or velocity across the suspension. Given the correct control strategy, this results in a better compromise between ride comfort and vehicle stability as compared to a passive system, as shown in **Figure 5** for a quarter-car model.

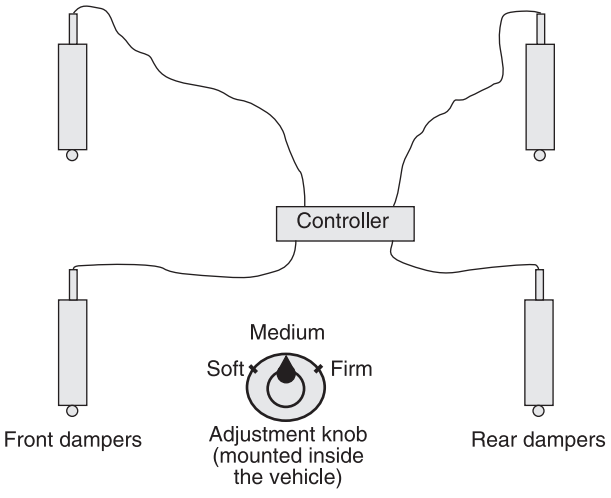


Figure 3 Schematics of a driver-adjustable suspension.

Semiactive Suspensions

Semiactive suspensions were first proposed in the early 1970s. In this type of system, the conventional spring element is retained, but the damper is replaced with a controllable damper, as shown in **Figure 6**.

Whereas an active suspension system requires an external energy source to power an actuator that controls the vehicle, a semiactive system uses external power only to adjust the damping levels and operate an embedded controller and a set of sensors. The controller determines the required damping force based on a control strategy, and automatically commands the damper to achieve that damping force. The force achieved by the damper can simply be in two levels: a minimum and a maximum damping force, as shown in **Figure 7A**. This type of system is typically referred to as an on–off (bang–bang) semiactive suspension. Alternatively, the damping force can be adjusted in a range of damping bound by the minimum and maximum damping, as shown in **Figure 7B**. This is commonly called damping. Several studies have shown that one can get nearly all of the benefits of an active suspension with a continuously variable semiactive system, without the complications and costs inherent to active suspensions.

Semiactive Control Methods

In semiactive suspensions, the damping force is adjusted by a controller that may be programmed with any number of control schemes. The control schemes that are commonly used for vehicle suspensions include:

- on–off skyhook control
- continuous skyhook control
- on–off groundhook control
- hybrid control
- fuzzy logic damping control

The succeeding paragraphs describe these control methods in more detail.

On–Off Skyhook Control

In on–off skyhook control, the damper is controlled by two damping values. Illustrated earlier in **Figure 7A**, these are referred to as maximum and minimum damping. The determination of whether the damper is to be adjusted in real time to either its maximum or minimum damping state depends on the product of the relative velocity across the damper and

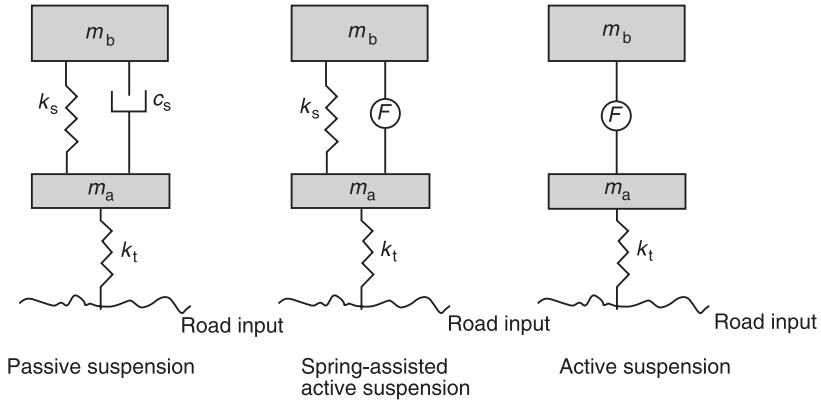


Figure 4 A schematic comparison of passive and active suspensions.

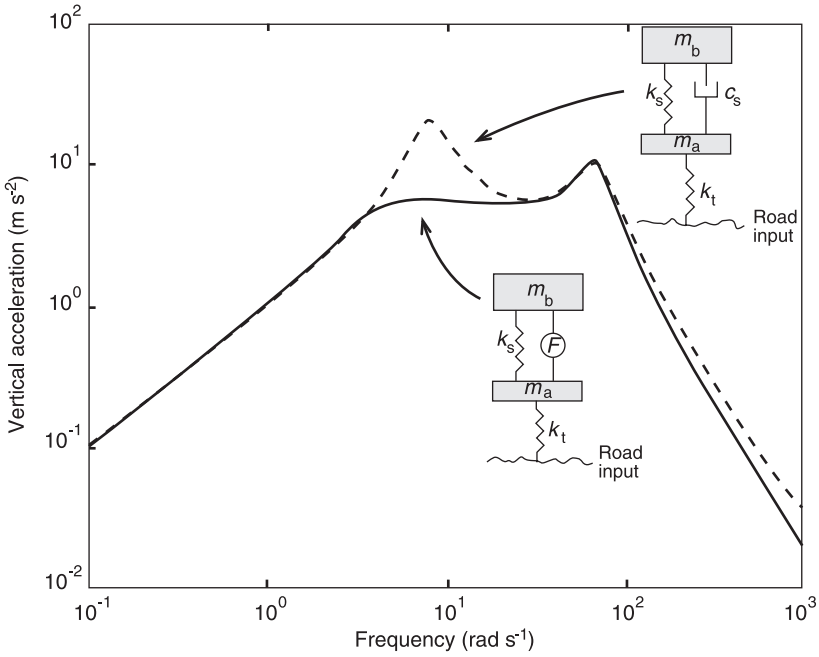


Figure 5 Passive and active suspension comparison.

the absolute velocity of the vehicle body, as illustrated in **Figure 8.** If the product is positive or zero, the damper is adjusted to its maximum state, otherwise the damper is set to the minimum damping. For the quarter-car model of **Figure 6,** this concept is summarized by:

$$v_b v_{rel} > 0, \quad c_s = \text{maximum damping} \qquad [1a]$$

$$v_b v_{rel} < 0, \quad c_s = \text{minimum damping} \qquad [1b]$$

The variables v_b and v_{rel} represent the body velocity and the relative velocity across the suspension (i.e., between the body and the axle), respectively. The logic of the on–off skyhook control policy is as follows. When the relative velocity of the damper is positive, the force of the damper acts to pull down on the vehicle body; when the relative velocity is negative the force of the damper pushes up on the body. Thus, when the absolute velocity of the vehicle body is negative, it is traveling downwards and the maximum value of damping is desired to push up on the body, while the minimum value of damping is desired to continue pulling down on the body. If, however, the absolute velocity of the body is positive and it is traveling upward, the maximum value of damping is desired to pull down the body, while the minimum

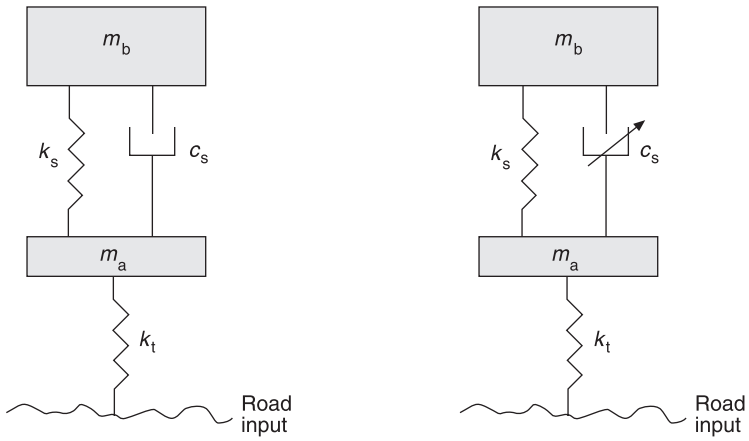


Figure 6 A schematic comparison of passive and semiactive suspensions.

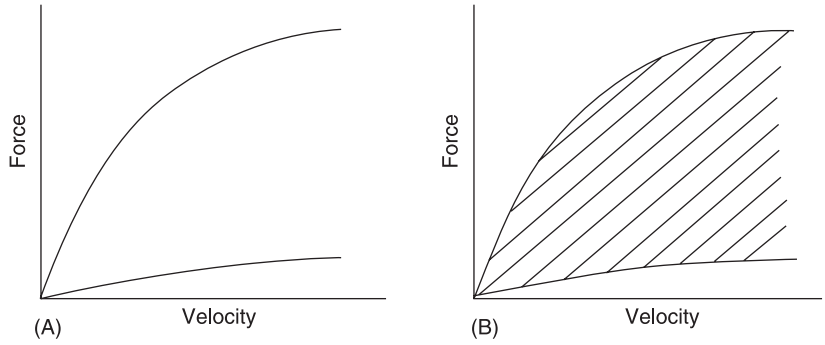


Figure 7 Range of damping values. (A) On–off semiactive; (B) continuously variable semiactive.

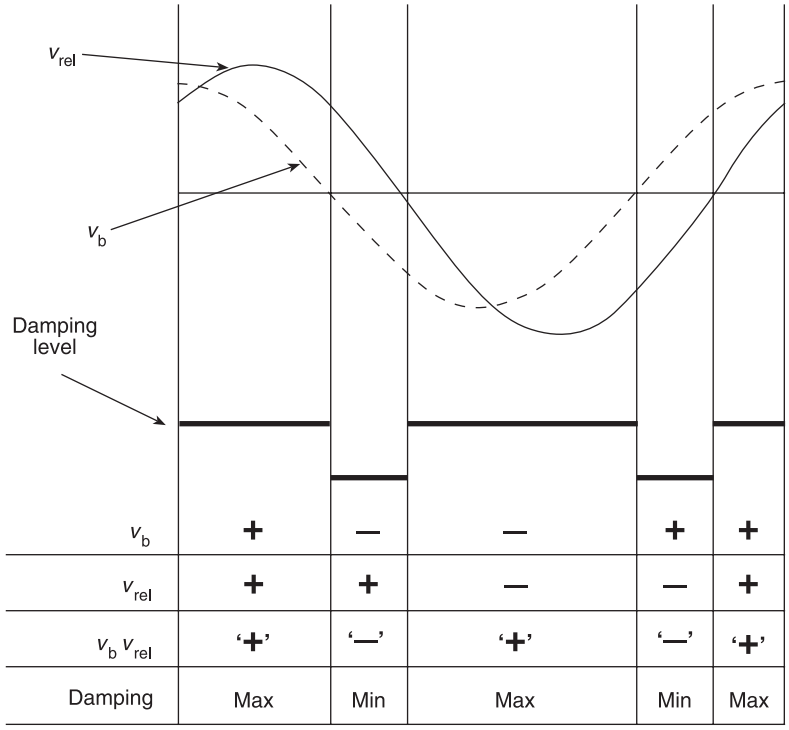


Figure 8 On–off skyhook control.

value of damping is desired to further push the body upward. The on–off skyhook semiactive policy emulates the ideal body displacement control configuration of a passive damper 'hooked' between the body mass and the 'sky' as shown in **Figure 9**; hence, the name 'skyhook damper'.

Continuous Skyhook Control

In continuous control, the damping force is not limited to the minimum and maximum states alone, as was the case for the on–off skyhook control. As illustrated in **Figure 7B** the damper can provide any damping force in the range between the minimum and maximum limits. This will enable the semiactive suspension to achieve a performance that is closer to the ideal skyhook configuration shown in **Figure 9.**

In continuous skyhook control, the low state remains defined by the minimum damping value, while the high state is set equal to a constant gain value multiplied by the absolute velocity of the vehicle body, bounded by the minimum and maximum damping force of the damper:

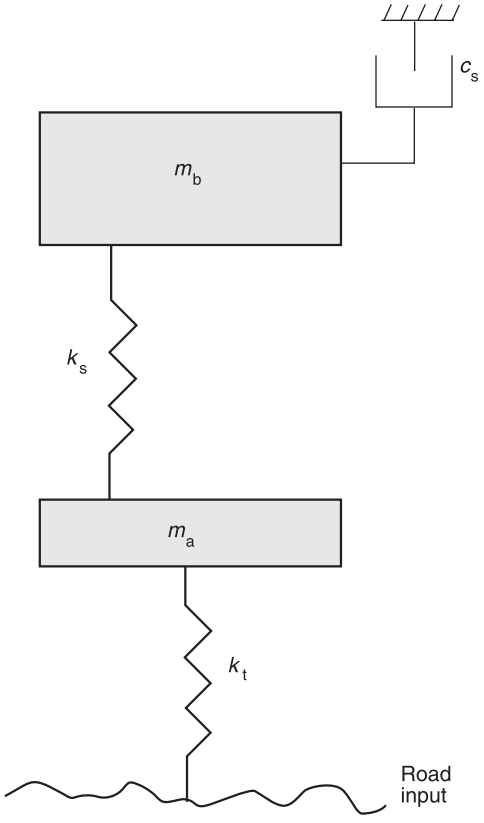


Figure 9 Idealized illustration of semiactive skyhook control.

$$v_b v_{rel} \geq 0, \quad c_s = \max \{\text{Minimum damping}, \min[G \times v_b, \text{maximum damping}]\} \qquad [2a]$$

$$v_b v_{rel} < 0, \quad c_s = \text{minimum damping} \qquad [2b]$$

The constant gain G in eqn [2a] is selected, empirically, such that the allowable damping range shown in **Figure 7B** is fully utilized.

On–Off Groundhook Control

In on–off groundhook control, the damper is also controlled by two damping values referred to as minimum and maximum damping. The determination of which damping value the damper needs to adjust to is made based on the product of the relative velocity across the suspension and the absolute velocity of the axle. As shown in **Figure 10,** if the product of the relative velocity across the suspension and absolute velocity of the axle is negative or zero, the damper is adjusted to its maximum damping. Otherwise, the damper is adjusted to its minimum value. For the quarter-car model of **Figure 2**, this concept is summarized by:

$$v_a v_{rel} < 0, \quad c_s = \text{maximum damping} \qquad [3a]$$

$$v_a v_{rel} > 0, \quad c_s = \text{minimum damping} \qquad [3b]$$

The variable v_a represents the axle velocity. The logic for the on–off groundhook control policy is similar to the on–off skyhook control policy, except that control is based on the unsprung mass. When the relative velocity of the damper is positive, the force of the damper acts to pull up on the axle; when the relative velocity is negative, the force of the damper pushes down on the tire mass. When the absolute velocity of the axle is negative, however, it is traveling downward and the maximum value of damping is desired to pull up on the axle, while the minimum value of damping is desired to continue pushing down on the axle. But, if the absolute velocity of the axle is positive and it is traveling upward, the maximum value of damping is desired to push down on the axle, while the minimum value of damping is desired to pull the axle upward. The on–off groundhook semiactive policy emulates the ideal axle displacement control configuration of a passive damper 'hooked' between the axle and the 'ground' as shown in **Figure 11**, hence, the name 'groundhook damper'.

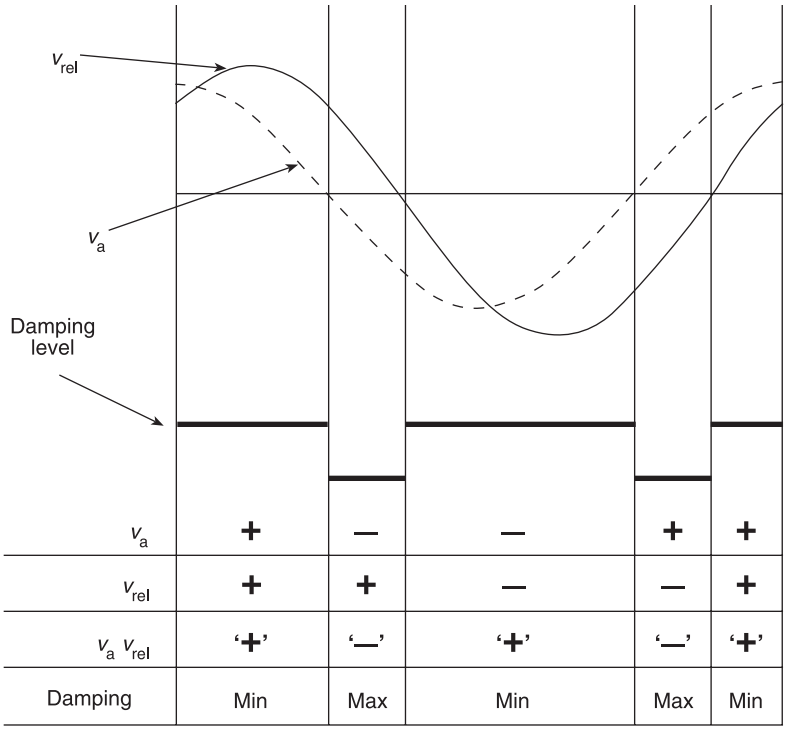


Figure 10 On–off groundhook control.

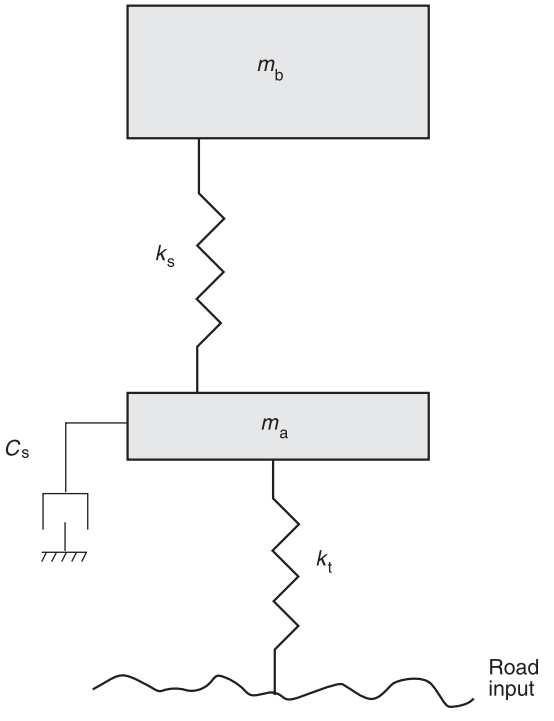


Figure 11 Idealized illustration of semiactive groundhook control.

Hybrid Control

An alternative semiactive control policy, known as hybrid control, combines the concept of skyhook and groundhook control to take advantage of the benefits of both. With hybrid control, the system can be set up to function as a skyhook or groundhook controlled system, or a combination of both, as shown in **Figure 12.** Mathematically, hybrid control policy is a linear combination of the formulation of the skyhook and groundhook control, and can be expressed as:

$$\left.\begin{array}{ll} v_b v_{rel} > 0 & \sigma_{SKY} = v_b \\ v_b v_{rel} < 0 & \sigma_{SKY} = 0 \end{array}\right\}$$

$$F_{SA} = G[\alpha\sigma_{SKY} + (1-\alpha)\sigma_{GND}]$$

$$\left.\begin{array}{ll} -v_a v_{rel} > 0 & \sigma_{GND} = v_a \\ -v_a v_{rel} < 0 & \sigma_{GND} = 0 \end{array}\right\} \qquad [4]$$

The variables σ_{SKY} and σ_{GND} are the skyhook and groundhook components of the damping force, α is the relative ratio between the skyhook and groundhook control, and G is a constant gain that is chosen in the same manner as described earlier for eqn [2a]. When $\alpha = 1$, hybrid control reduces to pure skyhook control, and when $\alpha = 0$, it becomes groundhook control.

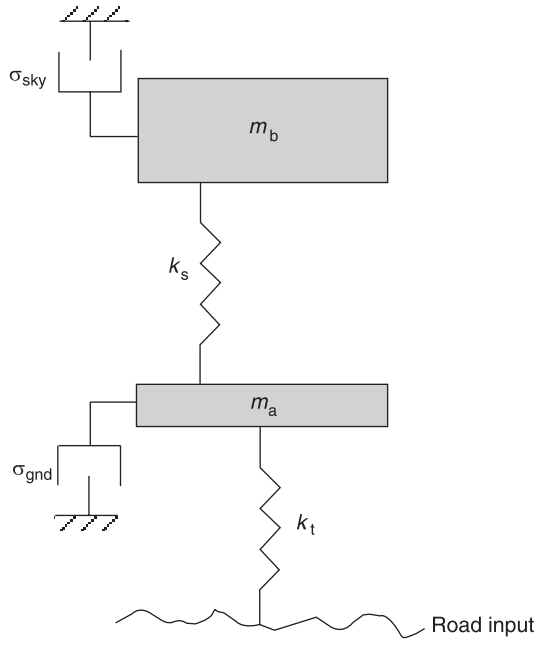


Figure 12 Idealized illustration of semiactive hybrid control concept.

Fuzzy Logic Control

Fuzzy logic control of semiactive dampers is another example of continuous control illustrated in **Figure 7B**. The output of the controller as determined by the fuzzy logic that may exist anywhere between the minimum and maximum damping states. Fuzzy logic is used in a number of controllers because it does not require an accurate model of the system to be controlled. Fuzzy logic works by executing rules that correlate the controller inputs with the desired outputs. These rules are typically created through the intuition or knowledge of the designer regarding the operation of the controlled system. No matter what the system, there are three basic steps that are characteristic to all fuzzy logic controllers. These steps include the fuzzification of the controller inputs, the execution of the rules of the controller, and the defuzzification of the output to a crisp value to be implemented by the controller. These steps will be explained in succeeding paragraphs.

Step One: Fuzzification

The first step of the fuzzy logic controller is the fuzzification of the controller inputs. This is accomplished through the construction of a membership function for each of the inputs. The possible shapes of these functions are infinite, though very often a triangular or trapezoidal shape is used. For simplicity, an example of a triangular-shaped membership function used to describe the controller input, x, is shown in **Figure 13.** The number of memberships assigned may be any number of linguistic variables.

The three linguistic variables assigned to the example of **Figure 10** are negative (N), zero (Z), and positive (P), and are correspondingly assigned values of -1, 0, and $+1$. Once the membership function is assigned for each input, the actual fuzzification of the inputs is performed. First, the input is read as a crisp value. Say, for example, that the input, x, is entered as -0.6. A line is drawn from the x-axis at -0.6 to indicate its point of intersection with each component of the membership function, as detailed in **Figure 14**.

In **Figure 14**, the intersection of the x value of -0.6 crosses Z at a weighting function of 0.4 and crosses N at a weighting function of 0.6. In linguistic terms, an input of -0.6 is considered to be 40% zero and 60% negative. These are the fuzzified values of the crisp input, x. Once this process has been performed for all the inputs into the controller, the fuzzification step of the fuzzy logic controller is complete and the rules of the controller are executed.

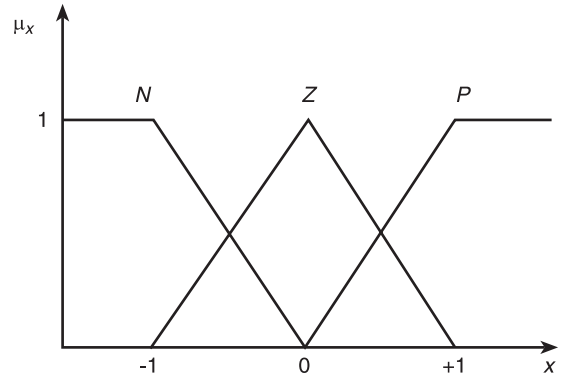


Figure 13 Triangular-shaped input membership function example.

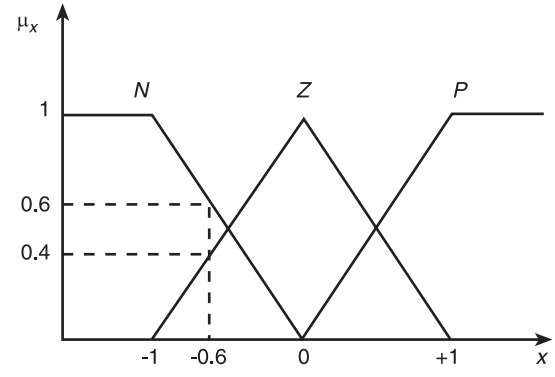


Figure 14 Input intersection with memberships.

Step Two: Execution of Rules

In order to create the rule-base of the controller, the membership function of the output must first be defined. Take, for example, the triangular-shaped membership function for the output, y, shown in **Figure 15**. The linguistic variables assigned to the output are defined as: small (S), medium small (MS), medium (M), medium large (ML), and large (L), and are given the values of 2, 4, 6, 8, and 10, respectively.

Now that the derivation of the controller output membership function is complete, the rule-base of the controller may be created. Suppose two inputs exist, x_1 and x_2, that are each defined by the membership function of **Figure 13**; and one output exisits, y, defined by **Figure 15**. For each possible input combination of x_1 and x_2, a value for the output, y, is linguistically defined. An example of a possible rule-base is shown in **Figure 16**.

The rules of **Figure 16** may also be described as a series of IF–THEN statements. For instance:
IF

$$x_1 = N$$

and

$$x_2 = N$$

THEN

$$y = S$$

and:

IF

$$x_1 = N$$

and

$$x_2 = Z$$

THEN

$$y = MS$$

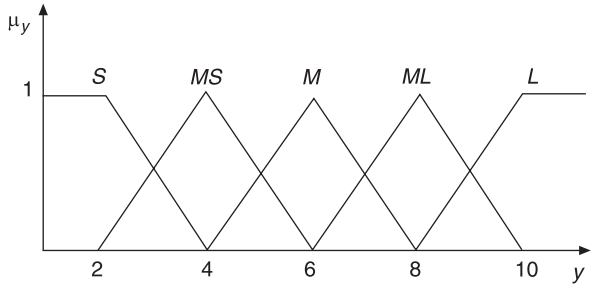


Figure 15 Triangular-shaped output membership function example.

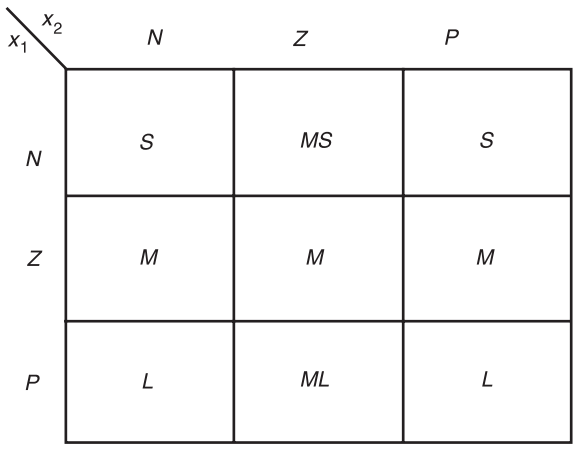


Figure 16 Rule table example.

and so forth, until all the rules of the table are described. The table in **Figure 16** has a total of nine rules.

Now suppose that, after fuzzification, x_1 is found to be 40% zero and 60% positive, and x_2 is found to be 50% zero and 50% positive. In other words: $\mu_{x_1,\,N} = 0$, $\mu_{x_1,\,Z} = 0.4$, $\mu_{x_1,\,P} = 0.6$, $\mu_{x_2,\,N} = 0.5$, $\mu_{x_2,\,Z} = 0.5$, and $\mu_{x_2,\,P} = 0.5$. The rules are applied by assigning the output variable with the minimum (or maximum, depending on the defuzzification method to be applied) weighting function described by the rules. Applying the rule:
IF

$$x_1 = P$$

and

$$x_2 = P$$

THEN

$$y = L$$

with the fuzzified values of x_1 and x_2, the rule becomes:
IF

$$x_1 = 0.6P$$

and

$$x_2 = 0.5P$$

THEN

$$y = \min(0.6,\ 0.5)L = 0.5L$$

In other words, $y(0.6P,\ 0.5P)$ is $0.5L$, where the output weighting function $\mu_y(x_1 = P, x_2 = P)$ is 0.5. Applying this procedure to the inputs defined by this example, the fuzzy outputs become:

$$\begin{array}{lll} y(0.0N, 0.0N) = 0.0S & y\,(0.0N, 0.5Z) = 0.0MS & y(0.0N, 0.5P) = 0.0S \\ y\,(0.4Z,\ 0.0N) = 0.0M & y(0.4Z, 0.5Z) = 0.4M & y(0.4Z, 0.5P) = 0.4M \\ y(0.6P, 0.0N) = 0.0L & y\,(0.6P,\ 0.5Z) = 0.5ML & y(0.6P, 0.5P) = 0.5L \end{array}$$

These fuzzy outputs now go through the defuzzification process to determine a single, or crisp, controller output value.

Step Three: Defuzzification

Defuzzification is the process of taking the fuzzy outputs and converting them to a single or crisp output value. This process may be performed by any one of several defuzzification methods. Some common methods of defuzzification include the max or mean–max membership principles, the centroid method, and the weighted average method. The weighted average method was used for this research. It should be noted that the weighted average method is only valid for symmetrically shaped output membership functions.

The weighted average method for finding the crisp output value, y^*, is accomplished by taking the sum of the multiplication of each weighting function, μ_y, with the maximum value of its respective membership value, $\bar{y}$, and dividing it by the sum of the weighting functions. This concept is presented in eqn [5]:

$$y^* = \frac{\sum \left[\mu_y(\bar{y}) \times \bar{y}\right]}{\sum \mu_y(\bar{y})} \qquad [5]$$

Applying the weighted average defuzzification method to the example discussed above, the crisp output, $y*$, of the controller is calculated by:

$$y^* = \frac{(0.4M + 0.4M + 0.5ML + 0.5L)}{(0.4 + 0.4 + 0.5 + 0.5)} = 7.67 \qquad [6]$$

Recall from **Figure 16** that the maximum values of the linguistic variables M, ML, and L were respectively defined as 6, 8, and 10. A crisp output of 7.67 is thus calculated and applied to the system being controlled. At this point, the current controller inputs are read, and the steps of the fuzzy logic controller are repeated.

Nomenclature

G	constant gain
L	large
M	medium
ML	medium large
MS	medium small
N	negative
P	positive
S	small
y^*	crisp output value
Z	zero

See also: **Damping, active**; **Damping measurement**.

Further Reading

Ahmadian M (1999) On the isolation properties of semiactive dampers. *Journal of Vibration and Control*, 5: 217–232.

Inman DJ (1994) *Engineering Vibration*. Prentice Hall.

Ioannou PA, Sun J (1996) *Robust Adaptive Control*. Prentice Hall.

Jamshidi M, Nader V, Ross TJ (1993) *Fuzzy Logic and Control, Software and Hardware Applications*. New Jersey: Prentice-Hall.

Karnopp D, Crosby MJ, Hardwood RA (1974) Vibration control using semi-active force generators. *Journal of Engineering for Industry*, 96: 619–626.

Milliken WF, Milliken DL (1995) *Race Car Vehicle Dynamics*. Warrendale, PA: Society of Automotive Engineers.

Ross TJ (1995) *Fuzzy Logic with Engineering Applications*. New York: McGraw-Hill.

Widrow B, Stearns SD (1985) *Adaptive Signal Processing*. Prentice Hall.

Widrow B, Walach E (1996) *Adaptive Inverse Control*. Prentice Hall.

Zadeh LA (1965) Fuzzy sets. *Information and Control* 8: 338–353.

ACTIVE ISOLATION

S Griffin, Kirtland AFB, NM, USA

D Sciulli, Centerville, VA, USA

Copyright © 2001 Academic Press

doi:10.1006/rwvb.2001.0191

Control Approaches – Feedforward versus Feedback

Active isolation control approaches can be broadly grouped into one of two categories: feedback and feedforward control. There are also control approaches which include some combination of both. For instance, it is often necessary to consider secondary or feedback paths in feedforward control and, under special circumstances, adaptive feedforward control has an equivalent feedback interpretation.

Feedforward Control

In the case where active isolation of periodic or otherwise predictable excitations is desired, feedforward control is usually the simplest approach to attaining performance goals. In order for feedforward control to be effective, a disturbance sensor signal must be available that is well correlated with the motion of the system to be controlled. In addition, application of feedforward control requires an error sensor and an actuator. The necessary components of feedforward control when the goal is single-degree-of-freedom active isolation of sensitive equipment on a moving base are shown in **Figure 1**.

In the case of **Figure 1**, the actuator provides the secondary force, f_s, and the feedforward controller commands the secondary force in a way that minimizes the error signal, e. The measure of how well correlated the disturbance sensor signal is with the motion of the system to be controlled is the coherence, γ_{dx}, between the error signal, e, and the disturbance signal, x. The explicit relationship between controlled-output power spectral density, O_c, and uncontrolled-output power spectral density, O_u, and coherence is given by:

$$\frac{O_c}{O_u} = 1 - \gamma_{dx}^2 \qquad [1]$$

For a linear time-invariant system with no external noise on either the error or disturbance signal, the coherence is 1 at all frequencies and it is theoretically possible to obtain a zero-controlled power spectral density at all frequencies. In realistic implementations, sensor noise and system nonlinearities constrain the actual value of coherence to a value of less than 1. Eqn [1] provides a convenient measure of achievable feedforward control performance before control implementation.

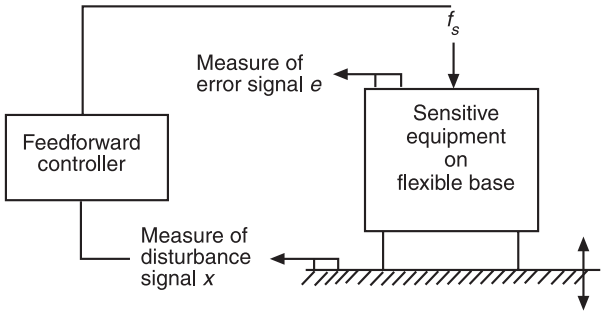


Figure 1 Feedforward control schematic.

Feedback Control

If the excitation is random or unpredictable and a disturbance sensor cannot make a coherent measurement, feedback control is the favored approach. In order to implement a feedback control approach, it is necessary to have a mathematical model that characterizes the structural dynamics of the system. Unlike feedforward control, there is no predictive measurement of the maximum achievable performance attainable with feedback control. Control performance is adversely affected by model errors and limited by stability margins. A control design and simulation must be accomplished to estimate maximum achievable control performance within stability margins. In general, feedback control requires a control sensor, an error sensor, and an actuator. The necessary components of feedback control when the goal is active isolation of sensitive equipment on a moving base are shown in **Figure 2**. In cases when only local isolation is required or when the components to be isolated can be considered as rigid, the feedback sensor can also serve as the error sensor. In the case of **Figure 2**, the actuator provides the secondary force, f_s and the feedback controller commands the secondary force in a way that minimizes the control signal, y. The error signal, e, provides a secondary measure of control performance.

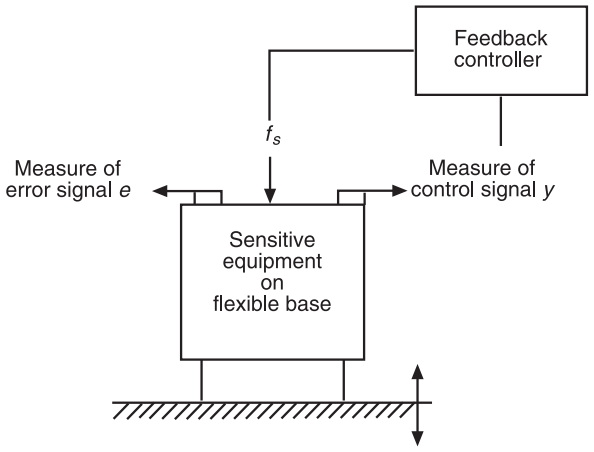


Figure 2 Feedback control schematic.

Equivalence of Feedback and Feedforward Control

Since the form of the feedforward control filter is dependent on both the path between the disturbance and the system to be controlled and the nature of the disturbance, it is often necessary to make the feedforward control filter-adaptive. Adaptation of the feedforward controller is accomplished by feeding back the error sensor signal to an adaptive feedforward filter, as shown in **Figure 3**, applied to the same system considered in **Figure 1**.

Since the adaptation of the feedforward controller is dependent on the error signal, a feedback path is introduced into the system. For the case of sinusoidal disturbance, there is an equivalent feedback controller which exhibits exactly the same performance characteristics as the feedforward controller.

Actuation Approaches

Many different actuators are available and have found application in both practical and experimental active isolation systems. Traditional active isolation actuators include hydraulic and electromagnetic drives. Force and displacement limits of actuators based on hydraulic drives depend on the energy-producing mechanism and the fluidic circuit which makes up the actuator. As such, hydraulic actuators have been

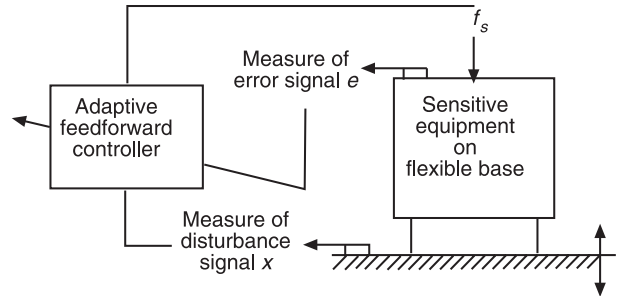


Figure 3 Feedforward control with adaptive path.

employed in systems as large as earthquake simulators and as small as miniature valves. Linear force and displacement limits of actuators based on electromagnetic voice coils of 100 lb (45 kg) and 0.5 in (12.5 mm) are readily available commercially. Greater performance is possible but may require a custom design. An example of a hydraulic active isolation system is the fully active suspension on high-performance Lotus race cars. In these systems, hydraulic actuators are located at each wheel and force is provided by a reservoir and pump system. The active suspension car is programmed to keep the car parallel to the road at all times, thus minimizing roll and pitch. An example of an electromagnetic active isolation system is the vibration isolation and suppression system VISS experiment. In this system, voice coil actuators form a hexapod mount which actively isolates an infrared telescope from the spacecraft bus.

Active isolation actuators which incorporate active materials include piezoceramic magnetostrictive and magnetorheological materials. **Table 1** compares the actuation properties of these commercially available active materials. Piezoceramic properties are for PZT 5H and magnetostrictive properties are for Terfenol-D. Blocked stress is the product of maximum strain and modulus.

Since piezoceramic materials tend to exhibit relatively high force and low stroke, they are often combined with a hydraulic or mechanical load-coupling mechanism to multiply motion at the expense of applied force.

An example of an active isolation system that uses piezoceramic actuators is the satellite ultraquiet isolation technology experiment (SUITE). In this

Table 1 Comparison of actuation properties of piezoceramic, magnetostrictive, and magnetorheological materials

	Material	*Activation*	*Maximum strain*	*Blocked stress*
Piezoceramic	Ceramic	Electric field	0.13%	79 MPa
Magnetostrictive	Metal alloy	Magnetic field	0.2%	59 MPa
Magnetorheological	Fluid	Magnetic field	Not applicable	Not applicable

experiment, viscoelastic damped piezoceramic actuators form a hexapod mount to isolate a sensitive instrument from a spacecraft bus. An example of an actuator that uses a magnetostrictive material is the Terfenol-D-based reaction mass actuator (RMA) made by SatCon Technologies. This actuator is being investigated for use in helicopter noise and vibration control. Finally, an example of a linear actuator that uses a magnetorheological fluid is the linear pneumatic motion control system made by LORD Corporation. This technology is also available in dampers and brakes.

In applications where maximum power draw is constrained, stored electrical energy is limited, or weight is constrained, it is also necessary to compare the relative efficiency of each of the actuation approaches. To make a fair comparison of efficiency between actuation materials, it is necessary to include control and power electronics and energy storage. This becomes a complicated question, since the choice of power electronics will drastically affect the power or energy efficiency metric that is selected. If the actuator that is incorporated into the active isolation system is considered in terms of its closed-loop electrical impedance, the real part of the impedance is directly related to the mechanical work and mechanical losses that are associated with the actuator. This represents the minimum amount of energy necessary to accomplish active isolation, and the ideal amplifier would supply this energy with 100% efficiency. Taking the example of a piezoceramic actuator, the closed-loop electrical impedance is highly capacitive and contains a large complex component. A linear amplifier is very inefficient at driving a capacitive load, so the total system weight using this approach would have to include sufficient batteries and passive or active cooling to allow for inefficiency. Conversely, a properly designed switching amplifier is much more efficient at driving a capacitive load and would result in a lower system weight.

See also: **Actuators and smart structures**; **Feedforward control of vibration**.

Further Reading

Anderson E, Evert M, Glaese R *et al.* (1999) Satellite Ultraquiet Isolation Technology Experiment (SUITE): electromechanical subsystems. *Proceedings of the 1999 SPIE Smart Structures and Materials Conference*, 3674: 308–328.

BEI Kimco Magnetics Division. *Voice Coil Actuators: An Applications Guide*. BEI Sensors and Systems Company.

Cobb R, Sullivan J, Das A *et al.* (1999), Vibration isolation and suppression system for precision payloads in space. *Smart Materials and Structures* 8: 798–812.

Fenn R, Downer J, Bushko D *et al.* (1996) Terfenol-D driven flaps for helicopter vibration reduction. *Smart Materials and Structures* 5: 49–57.

Fuller C, Elliot S and Nelson P (1996) *Active Control of Vibration*. San Diego, CA: Academic Press.

Maciejowski J (1989) *Multivariable Feedback Design*. Addison-Wesley.

Ross CF (1980) Active control of sound. PhD thesis, University of Cambridge, England.

Sievers L and von Flotow A. Comparison and extensions of control methods for narrowband disturbance rejection. *IEEE Transactions Signal Processing* 40: 2377–2391.

Warkentin, D (1995) Power amplification for piezoelectric actuators in controlled structures. PhD thesis, Massachusetts Institute of Technology.

Widrow B and Stearns SD (1985) *Adaptive Signal Processing*. Englewood Cliffs, NJ: Prentice-Hall.

Williams D and Haddad W (1997) Active suspension control to improve vehicle ride and handling. *Vehicle System Dynamics* 28: 1–24.

ACTIVE VIBRATION CONTROL

See **ACTIVE CONTROL OF VEHICLE VIBRATION; ACTIVE ISOLATION; ACTIVE VIBRATION SUPPRESSION; ACTUATORS AND SMART STRUCTURES; DAMPING, ACTIVE; FEED FORWARD CONTROL OF VIBRATION; FLUTTER, ACTIVE CONTROL; HYBRID CONTROL.**

ACTIVE VIBRATION SUPPRESSION

D Inman, Virginia Polytechnic Institute and State University, Blacksburg, VA, USA

Copyright © 2001 Academic Press

doi:10.1006/rwvb.2001.0192

Vibration suppression is a constant problem in the design of most machines and structures. Typically vibration reduction is performed by redesign. Redesign consists of adjusting mass and stiffness values or adding passive damping in an attempt to reduce

vibration levels to acceptable values. Vibration isolation, vibration absorbers and constrained layer damping treatments are all traditional methods of controlling vibration levels by passive means. Indeed, if passive redesign or add-on techniques allow desired vibration levels to be met, then a passive approach to vibration suppression should be used. However, if passive techniques cannot achieve desired vibration levels within design and operational constraints then an active control method should be attempted as addressed in this article.

Active control consists of adding an applied force to the machine, part or structure under consideration in a known way to improve the response of a system: in this case to suppress vibrations. Control concepts for mechanical systems originated with radar work during World War II and the subject has developed its own special jargon. The object to be controlled (machine, part or structure) is often called the 'plant'. Control methods for linear plants (the only type considered here) can be divided into two main categories: frequency domain methods (also called classical control) and state space methods (also called modern control). Control methods are further classified as open-loop or closed-loop. In an open-loop control, the control force is independent of the response of the system, while in a closed-loop system the control force applied to the system (called the input) depends directly on the response of the system. Closed-loop control can be further divided into feedforward control or feedback control. Feedforward control is most often used in acoustic and wave applications while feedback is most often used in vibration suppression. Here we focus on closed-loop feedback control.

Closed-loop feedback control consists of measuring the output or response of the system and using this measurement to add to the input (control force) to the system. In this way the control input is a function of the output called closed-loop control. There are a variety of methods for choosing the control force and several common methods are presented here at an introductory level.

Single-Degree-of-Freedom Systems

Single-degree-of-freedom systems are used here to introduce the basic concepts for control. Consider first a single-degree-of-freedom system with an applied force (mass normalized), denoted by $u(t)$ rather than the usual notation of $f(t)$ to remind us that the force is a control force derived from an actuator rather then a disturbance. The equation of motion is written as:

$$\ddot{x}(t) + 2\zeta\omega_n\dot{x}(t) + \omega_n^2 x(t) = Ku(t) \qquad [1]$$

where ζ and ω_n are the usual damping ratio and undamped natural frequency, respectively. The scalar constant K is called the gain and is a parameter that can be adjusted to change the magnitude of the applied force. Taking the Laplace transform of eqn [1] with zero initial conditions yields:

$$\frac{X(s)}{U(s)} = \frac{K}{s^2 + 2\zeta\omega_n s + \omega_n^2} = KG(s) \qquad [2]$$

Here the capital letters indicate the Laplace transform of the variable and s is the complex valued Laplace variable.

Eqn [2] also defines the transfer function $G(s)$ that characterizes the dynamics of the plant. Eqn [2] is represented symbolically by the block diagram of **Figure 1**. Block diagrams have formal rules of manipulation that reflect the equations they represent. Open-loop control design consists of choosing the form of $u(t)$ (or $U(s)$ in the Laplace domain) and adjusting the gain K until a desired response characteristic is obtained. If the control force, $u(t)$, is chosen by looking at the response in $x(t)$ in the time domain, called time domain design, the value of K can be seen to directly adjust the maximum value of the steady-state response as well as the amplitude of the transient terms. Picking the form of $U(s)$ and K in the Laplace domain is referred to as frequency domain design. In frequency domain design, the magnitude and phase plots are examined as $U(s)$ and K are adjusted. Choosing the form of $U(s)$ (or $u(t)$) and the value of K are referred to as designing the control law. Note that compared to passive control there are more parameters to choose from in shaping the response.

As an example of open-loop control design suppose that $x(t)$ corresponds to the angular motion of a shaft and the $G(s)$ is the dynamics of a motor-load system. Suppose also that it is desired to move the shaft from its current position to 20°. Then the control law design consists of choosing K and $u(t)$ to force $x(t) = 20°$. The solution would be to choose $u(t)$ to be a step function and K to have a value determined

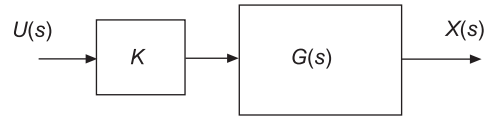


Figure 1 The block diagram of the open-loop system represented by eqn [2].

by setting the magnitude of the steady-state response equal to 20°.

The concept of a closed-loop system is illustrated in **Figure 2**. In the closed-loop case the form of the control law $u(t)$ depends on the response $x(t)$. A common choice for this is called position and derivative (PD) control. This assumes that the velocity and position can be measured and then used to form the control force. This is illustrated in **Figure 2** where the control law $H(s)$ has the following form:

$$H(s) = g_1 s + g_2 \qquad [4]$$

The constant g_1 is called the velocity gain and g_2 is called the position gain. These gains reflect measurement factors and other constants involved in the electronics yet are adjustable to produce a desired response. The equation of motion corresponding to the closed-loop system of **Figure 2** is:

$$\ddot{x}(t)+(Kg_2 + 2\zeta\omega_n)\dot{x}(t) + (Kg_1 + \omega_n^2)x(t) = Ku(t) \qquad [5]$$

In the frequency domain the input–output transfer function becomes:

$$\frac{X(s)}{U(s)} = \frac{K}{s^2 + (Kg_2 + 2\zeta\omega_n)s + (Kg_1 + \omega_n^2)} \qquad [6]$$

Note from eqns [4] and [5] that the effective damping ratio and natural frequency are adjusted by tuning the gains g_1 and g_2. Thus the response of the system to the input $u(t)$ can be adjusted.

To see the impact that PD control has on the design process, define an equivalent damping ratio, ζ^e and natural frequency ω^e. Then from eqn [5]:

$$\omega_n^e = \sqrt{Kg_1 + \omega_n^2} \text{ and } \zeta^e = \frac{Kg_2 + 2\zeta\omega_n}{2\omega_n^e} \qquad [7]$$

Thus the effective frequency and damping ratio can be tuned by adjusting the gains g_1 and g_2, providing two additional design parameters.

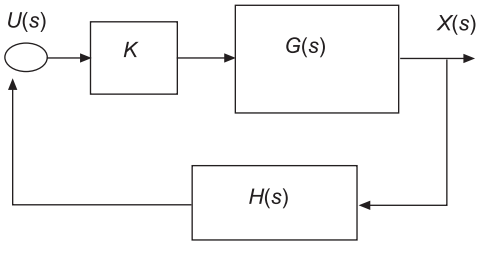


Figure 2 Block diagram for closed-loop feedback control representing eqn [5].

The passive design process will chose the best possible values of m, c, and k so that the response has the desired properties. However, these values and hence ω_n and ζ, will be subject to physical constraints such as static deflection, mass limitations, and material properties. Thus the desired frequency and damping ratio may not be obtained because of these limitations. In this case active control is implemented to provide two additional parameters, g_1 and g_2, to adjust in order to produce the desired response. Active control, or PD control as introduced here, allows additional freedom in shaping the response to meet desired specifications. The control gains are not subject to the same sorts of physical constraints that the mass, damping and stiffness are, so that the desired response can often be achieved when passive design fails. The control gains are usually adjusted electronically or hydraulically. However, g_1 and g_2 are expensive, as they require sensor and actuator hardware as well as electronics. The gains are also subject to other physical constraints such as available current and voltage, actuator stroke length and force limitations. Active control provides additional help in cases where passive design fails, but at a cost.

An additional problem with implementing active control can be seen by realizing that an active control device is 'adding' energy to the system to cancel vibration. However, if an error is made in sign or calculation, then the closed-loop system could become unstable. For example if the design requirements call for a reduced frequency, then the coefficient of g_1 would be negative. If in addition, the exact value of m or k were not known, the coefficient of $x(t)$ could be driven negative causing the response to grow without bound and become unstable.

Velocity and position feedback control, also called PD control, is an example of full-state feedback. For a single-degree-of-freedom system there are two state variables: the position and the velocity. The idea of state variables comes from the thought in mathematics that a single nth order differential equation may be represented as n-first-order differential equations. The state variables come from the transformation from nth order to first order. For example eqn [1] can be written as the two, coupled first-order equations:

$$\begin{aligned} \dot{x}_1(t) &= x_2(t) \\ \dot{x}_2(t) &= -2\zeta\omega_n x_2(t) - \omega_n^2 x_1(t) + Ku(t) \end{aligned} \qquad [8]$$

Here the new variables $x_1(t)$ and $x_2(t)$ are called the state variables and are the position and velocity, respectively:

$$x_1(t) = x(t) \text{ and } x_2(t) = \dot{x}(t)$$

In this case the use of both state variables in the feedback loop is called full-state feedback because all of the states are used to form the control law. Thus for a single-degree-of-freedom system, full-state feedback and PD control are the same. In this way, the example of PD control may be easily extended to multiple-degree-of-freedom systems. The equations of motion represented in the form of eqn [8] is called the state space formulation and allows a productive connection between dynamics, vibration and control with the mathematics of linear algebra.

Multiple-Degree-of-Freedom Systems

Multiple-degree-of-freedom systems arise in both machines and structures. Many of these have dynamics governed by linear, time invariant, ordinary differential equations that may be written in the following form:

$$\mathbf{M}\ddot{\mathbf{q}} + \mathbf{D}\dot{\mathbf{q}} + \mathbf{K}\mathbf{q} = \mathbf{f} \qquad [9]$$

Here $\mathbf{M}$, $\mathbf{D}$ and $\mathbf{K}$ are the usual mass, damping and stiffness matrices defined in such a way as to be positive definite and symmetric and $\mathbf{f}$ is the vector of applied forces. Note that $\mathbf{D}$ is used instead of the traditional $\mathbf{C}$, because of the need to interface with the notation of control theory. The vector $\mathbf{q}$ is used to denote the generalized displacement vector (with velocity and acceleration denoted by overdots) commonly used in the Lagrangian formulation of the equations of motion. These coefficient matrices can be derived from Newton's laws in the case of lumped parameter systems, or from some approximation of a set of partial differential equations in the case of a distributed mass system. Eqn [9] is a system of coupled second-order, ordinary differential equations with constant coefficients. Because of the symmetry and definiteness the coefficient matrices for structures, the solution to eqn [9] is stable, perhaps asymptotically stable.

The majority of control theory has developed around systems of first-order differential equations cast in what is called state space form introduced in eqn [8]. For more than one degree-of-freedom, the state equations are also given in matrix form by:

$$\dot{\mathbf{x}} = \mathbf{A}\mathbf{x} + \mathbf{B}\mathbf{u} \qquad [10]$$

$$\mathbf{y} = \mathbf{C}\mathbf{x} \qquad [11]$$

$$\mathbf{u} = \mathbf{G}\mathbf{y} \qquad [12]$$

Here $\mathbf{y}$ is the vector representing the measured combinations of states $\mathbf{x}$, called a state vector. The matrix $\mathbf{B}$ denotes positions of the applied control forces contained in the vector $\mathbf{u}$, and is often called the control input matrix. The matrix $\mathbf{C}$ contains the locations where sensors are placed that measure the various states. Control law refers to how the vector $\mathbf{u}$ is chosen. A common choice, called output feedback, is to choose $\mathbf{u}$ according to the law eqn [12] and measurement eqn [11], where $\mathbf{G}$ is a gain matrix chosen to satisfy some performance or stability condition. If the matrix $\mathbf{C}$ reflects measurements of every state (i.e., if $\mathbf{C}$ is an identity matrix), then the control law becomes $\mathbf{u} = \mathbf{G}\mathbf{C}\mathbf{x} = \mathbf{G}\mathbf{x}$ and is called full-state feedback.

The various theories and numerical algorithms that are centered on the state space formulation expressed by eqns [10]–[12] overshadow results developed in the physical coordinates of eqn [9]. In fact, numerous high level programs exist for solving control problems associated with the state space formulation. None the less, in order to put equations derived from Newton's law or Euler–Lagrange formulations of eqn [9] into a first-order or state space form, the natural properties of the coefficient matrices (bandedness, definiteness and symmetry) are lost. Furthermore, the order of the vector $\mathbf{x}$, is twice that of the vector $\mathbf{q}$ and the physical importance of the entries may be lost. The relationship between the physical coordinate description given by eqn [9] and the state space formulation given by eqn [10] is simply:

$$\mathbf{x} = \begin{bmatrix} \mathbf{q} \\ \dot{\mathbf{q}} \end{bmatrix} \mathbf{A} = \begin{bmatrix} \mathbf{I} & \mathbf{0} \\ -\mathbf{M}^{-1}\mathbf{K} & -\mathbf{M}^{-1}\mathbf{D} \end{bmatrix} \qquad [13]$$

Note that if there are n degrees-of-freedom, then the vector $\mathbf{x}$ is $2n \times 1$ and the state matrix $\mathbf{A}$ is $2n \times 2n$. Also note that the identity matrix $\mathbf{I}$ is $n \times n$ and the $\mathbf{0}$ here denotes and $n \times n$ matrix of zeros. Thus given the physical model in eqn [9], the state space model can be easily constructed.

Modal Control

Modal control is a popular method of providing control laws for structures because it appeals to the simplistic and intuitive notions of single-degree-of-freedom systems. In addition, much of structural dynamics analysis and testing centers around modal methods making modal approaches a natural place to start understanding control. Mathematically, modal control derives its power from consideration of matrix decoupling transformations. Modal control methods developed in two distinct disciplines: control theory and structural dynamics. Basically the use of

modes in control theory is different from that in structural dynamics and hence from that in structural control. In control, the theory of modal control refers to collapsing the problem into a series of first-order, ordinary differential equations that are decoupled and hence easily solved. Modal methods in control theory center around the Jordan canonical form of the state space matrix given by eqn [13]. In structural dynamics, modal control refers to a series of decoupled second-order ordinary differential equations, motivated by an understanding of single-degree-of-freedom/oscillators which provides both a set of decoupled equations to analyze and the physical intuition and experience of (structural) modal analysis.

The goal of both the state space (first-order) and the physical space (second-order) modal control approaches is to essentially find a nonsingular, coordinate transformation that takes the equations of motion into a canonical, or decoupled form. In the state space this amounts to looking for the Jordan form of a matrix and the resulting system will be completely decoupled as long as there are no repeated (nonsimple) eigenvectors. That is the system of eqn [10] can be written as a set of first-order decoupled equations by simply applying the Jordan transformation. In the physical space, the attempt to look for a transformation that decouples the equations of motion amounts to looking at whether or not the mass weighted eigenvectors of the stiffness matrix can be used as system eigenvectors. The existence of modally decoupled control laws depends on the conditions under which two matrices share common eigenvectors. This condition is that two symmetric matrices share the same eigenvectors if and only if they commute.

First, let $\mathbf{f}(t)$ become the control-input vector $\mathbf{Bu}(t)$. Then assume that the mass matrix $\mathbf{M}$ is nonsingular. Then use the transformation:

$$\mathbf{q} = \mathbf{M}^{-1/2}\mathbf{r} \qquad [14]$$

where the exponent refers to the positive definite matrix square root. (Numerically it is better to use the Cholesky factors of the mass matrix rather than the matrix square root.) Substitution of eqn [14] into eqn [9] and multiplying by $\mathbf{M}^{-1/2}$ from the left yields:

$$\ddot{\mathbf{r}} + \tilde{\mathbf{D}}\dot{\mathbf{r}} + \tilde{\mathbf{K}}\mathbf{r} = \mathbf{M}^{-1/2}\mathbf{Bu}(t) \qquad [15]$$

Here, the coefficients are:

$$\tilde{\mathbf{D}} = \mathbf{M}^{-1/2}\mathbf{D}\mathbf{M}^{-1/2} \text{ and } \tilde{\mathbf{K}} = \mathbf{M}^{-1/2}\mathbf{K}\mathbf{M}^{-1/2} \qquad [16]$$

which we call the mass normalized damping and stiffness matrices, respectively. Two symmetric matrices commute if and only if they have the same eigenvectors. These eigenvectors form a complete set because the matrices in eqn [16] are carefully constructed to be symmetric. Thus the matrix $\mathbf{P}$ formed by combining the normalized mode shapes as its columns becomes a modal matrix which will decouple both of the coefficient matrices in eqn [15]. To see this, substitute $r = \mathbf{Pz}$ into eqn [15] and premultiply by $\mathbf{P}^T$ to obtain the n modal equations

$$\ddot{z}_i + 2\zeta_i\omega_i\dot{z}_i + \omega_i^2 z_i = (\mathbf{P}^T\mathbf{M}^{-1/2}\mathbf{Bu})_i \qquad [17]$$

Here, ζ_i and ω_i are the modal damping ratios and natural frequencies, respectively, and the subscript refers to the ith element of the vector $\mathbf{z}$. This decoupled form results if and only if the matrices in eqn [9] commute, or if and only if

$$\mathbf{D}\mathbf{M}^{-1}\mathbf{K} = \mathbf{K}\mathbf{M}^{-1}\mathbf{D} \qquad [18]$$

This last condition is a necessary and sufficient condition for the system of eqn [9] to possess normal modes (which are real valued) and to decouple as indicated in eqn [15]. Thus with condition [18] satisfied, the system may be analyzed using modal analysis. Furthermore, the undamped mode shapes are, in fact, also the physical mode shapes of the damped system.

The idea behind modal control is to assume that the damping in the system is such that eqn [18] is satisfied, use the transformation $\mathbf{P}$ to decouple the equations and then choose the individual control inputs $(\mathbf{P}^T\mathbf{M}^{-1/2}\mathbf{u}(t))_i$ to shape each individual mode to have a desired behavior. In particular, suppose that state feedback is chosen as the form of the control law. Then the closed loop system will have the form:

$$\mathbf{M}\ddot{\mathbf{q}} + \mathbf{D}\dot{\mathbf{q}} + \mathbf{K}\mathbf{q} = -\mathbf{G}_v\dot{\mathbf{q}} - \mathbf{G}_p\mathbf{q} \qquad [19]$$

where G_v and G_p are gain matrices to be chosen in the control design. The gain matrices are now chosen to force the closed-loop system to have the desired modal behavior. Under the modal transformation, and using the idea of full-state feedback, the modal equations all reduce to the form given in eqn [7] for the singe-degree-of-freedom case. This procedure can also be carried out in the state space coordinate system of eqns [10]–[12].

For simplicity, consider the single-input single-output case (siso) which collapses the input matrix $\mathbf{B}$ to the vector $\mathbf{b}$, and the measurement matrix $\mathbf{C}$ to the vector $\mathbf{c}$. Furthermore, assume that gain matrix is the identity matrix ($\mathbf{G} = \mathbf{I}$). Let $\mathbf{P}$ denote the matrix of eigenvectors that transforms the state matrix $\mathbf{A}$ into a

diagonal matrix of eigenvalues (denoted Λ) and perform the transformation $\mathbf{x} = \mathbf{P}\mathbf{z}$ on eqns [10] and [11]. Substitution of eqn [12] into eqn [11] and substituting the result into eqn [10], yields:

$$\dot{\mathbf{z}}(t) = \mathbf{\Lambda}\mathbf{z}(t) + \mathbf{b}\mathbf{c}^T\mathbf{z}(t) \qquad [20]$$

Here the vector $\mathbf{z}$ is the modal state vector and the matrix $\mathbf{\Lambda}$ is a diagonal (or Jordan form) matrix of the (complex) eigenvalues of the system. If the structure is underdamped, the eigenvalues appear in complex conjugate pairs of the form:

$$\begin{aligned}\lambda_i &= -\zeta_i\omega_i - \omega_i\sqrt{(1-\zeta_i^2)}\mathrm{j} \\ \lambda_{i+1} &= -\zeta_i\omega_i + \omega_i\sqrt{(1-\zeta_i^2)}\mathrm{j}\end{aligned} \qquad [21]$$

where j is the imaginary unit. The elements of the matrix $\mathbf{b}\mathbf{c}^T$ are now chosen to modify the eigenvalues of the closed loop system to provide the desired response. To see this possibility note that eqn [20] can be written as:

$$\dot{\mathbf{z}}(t) = \underbrace{(\mathbf{\Lambda} + \mathbf{b}\mathbf{c}^T)}_{\hat{\mathbf{A}}}\mathbf{z}(t) \qquad [22]$$

The dynamics of the closed-loop system are characterized by the closed-loop state matrix:

$$\hat{\mathbf{A}} = \mathbf{\Lambda} + \mathbf{b}\mathbf{c}^T \qquad [23]$$

Various methods of choosing the values of $\mathbf{b}\mathbf{c}^T$ exist in the control literature.

Controllability and Observability

An important aspect of controlling structures is the placement of sensors and actuators. This can be seen by examining eqn [17] and focusing on the control-input term:

$$(\mathbf{P}^T\mathbf{M}^{-1/2}\mathbf{B}\mathbf{u})_i \qquad [24]$$

If this term is small, not much energy is being put into the ith mode. This means that the control effort $\mathbf{u}(t)$ will have a very difficult time changing the ith mode. On the other hand, if the value of the term given in eqn [24] is large, the choice of $\mathbf{u}(t)$ will have a great effect on the ith mode. This leads to the concept of controllability. Basically, if the value of eqn [24] is zero for some value of i, then the ith mode is said to be uncontrollable because the applied control has no effect on this mode. On the other hand, if it is non-zero, then the ith mode is said to be controllable. If every mode is controllable then the system is said to be controllable. Most structures are controllable by the nature of their connectivity. However, the real issue is how controllable is a given mode. The larger the value of eqn [24] the more likely the control effort will be able to change the desired mode to its desired state. The concept of controllability is defined without reference to modes, but modes are used here to connect the idea to vibrations. Note that if $\mathbf{B}$ happens to be orthogonal to a column of the modal transformation, then that particular mode will not be controllable. This corresponds to the concept known to most structural test engineers that exciting a mode by placing a shaker at a node of a mode will not excite the mode at all. Thus one significant control design task is the placement of actuators so that the modes of interest have high values of modal controllability.

A similar concept called observability applies to sensor placement. The locations of the sensors, as captured by the matrix $\mathbf{C}$, determine if a given mode can be measured by the sensors. If the mode cannot be measured it is also difficult to control.

Spillover

Another significant consideration in controlling the vibration of structures is that of spillover. Spillover addresses the issue of designing a control law to suppress the response of a group of modes and neglecting other modes. Such is the case if the model used in the control design is a reduced-order model as is common practice in structural dynamics. Control and observation spillover can be explained by a simple partitioning of eqn [20] into two groups of modes at index k. This yields:

$$\begin{aligned}\begin{bmatrix}\dot{\mathbf{z}}_k \\ \dot{\mathbf{z}}_{2n-k}\end{bmatrix} &= \begin{bmatrix}\mathbf{\Lambda}_k & 0 \\ 0 & \mathbf{\Lambda}_{2n-k}\end{bmatrix}\begin{bmatrix}\mathbf{z}_k \\ \mathbf{z}_{2n-k}\end{bmatrix} \\ &+ \begin{bmatrix}\mathbf{b}_k\mathbf{c}_k^T & \mathbf{b}_k\mathbf{c}_{2n-k}^T \\ \mathbf{b}_{2n-k}\mathbf{c}_k^T & \mathbf{b}_{2n-k}\mathbf{c}_{2n-k}^T\end{bmatrix}\begin{bmatrix}\mathbf{z}_k \\ \mathbf{z}_{2n-k}\end{bmatrix}\end{aligned} \qquad [25]$$

Here, the vectors $\mathbf{P}^{-1}\mathbf{b}$ and $\mathbf{c}^T\mathbf{P}$ are partitioned according to:

$$\mathbf{P}^{-1}\mathbf{b} = \begin{bmatrix}\mathbf{b}_k \\ \mathbf{b}_{2n-k}\end{bmatrix} \quad \text{and} \quad \mathbf{c}^T\mathbf{P} = \begin{bmatrix}\mathbf{c}_k^T & \mathbf{c}_{2n-k}^T\end{bmatrix} \qquad [26]$$

Note that while the state matrix transforms into a diagonal form, the second matrix containing the control hardware parameters has clear off-diagonal terms. If $\mathbf{b}_{2n-k}$ and $\mathbf{c}_{2n-k}$ both happen to be zero, then the closed-loop system also decouples into modal

form. Unfortunately, if these are not zero, the off-diagonal terms couple the first k modes with the last $2n-k$ modes, spoiling the modal form. The term $\mathbf{b}_{2n-k}$ gives rise to modal coupling due to control action (called control spillover) and the term $\mathbf{c}_{2n-k}$ gives rise to modal coupling due to observation or measurement (called observation spillover). The coupled term $\mathbf{b}_{2n-k}\mathbf{c}_{2n-k}^T$ represents the control action that 'spills over' into the uncontrolled modes $(2n-k)$ in the situation where the control law is designed considering only the first k modes. If this term is large, then the performance, or even stability, of the closed-loop system will be lost. While this explanation is made in state variable form, the argument also holds true in the physical coordinates.

Eqn [26] also provides an opportunity to comment on model reduction. One simple model reduction method is to transform the system into modal form and then drop the higher modes $(2n-k)$. The question of model reduction then becomes one of asking how many modes should we keep in the model (i.e., how large should k be)? For open-loop analysis this question may be answered satisfactorily by looking at the modal participation factors and picking k accordingly. The difficulty in closed-loop control is that a satisfactory choice of k in the open-loop case may not be satisfactory in the closed-loop case because of the influence of the control and observation spillover terms. Thus, it is desired to find means of control that drive these coupling and spillover terms to zero. Using a large number of sensors and actuators can eliminate or minimize the spillover terms.

Pole Placement

State feedback refers to requiring the feedback control law to be a linear combination of only the state variables (velocity and position). Once state feedback is chosen as the form for the control force, there are several other possible control laws. One possibility is to use pole placement. Pole placement in structural control consists of determining desired modal damping ratios and natural frequencies. Once these are specified, eqns [21] are used to change these into eigenvalues, called the desired eigenvalues and denoted by λ_{di}. These are then formed into a diagonal matrix denoted by $\mathbf{\Lambda}_D$. Let $\mathbf{P}$ denote the matrix of eigenvectors that transforms the state matrix $\mathbf{A}$ into a diagonal matrix of eigenvalues (denoted $\mathbf{\Lambda}$) and perform the transformation $\mathbf{x} = \mathbf{Pz}$ on eqns [10] and [11]. Substitution of eqns [12] into [11] and substituting the result into eqn [10], yields:

$$\dot{\mathbf{z}}(t) = \left(\mathbf{\Lambda} + \mathbf{BGC}^T\right)\mathbf{z}(t) \qquad [27]$$

which is in modal coordinates. The goal of the pole placement technique is to force the eigenvalues, or poles, of eqn [27] to have the desired eigenvalues by choosing, $\mathbf{B}$, $\mathbf{G}$, and $\mathbf{C}$ so that:

$$\begin{aligned} \left(\mathbf{\Lambda} + \mathbf{P}^T\mathbf{BGC}^T\mathbf{P}\right) &= \mathbf{\Lambda}_D \quad \text{or} \\ \mathbf{BGC}^T &= \mathbf{P}(\mathbf{\Lambda}_D - \mathbf{\Lambda})\mathbf{P}^T \end{aligned} \qquad [28]$$

The last expression guides the designer for the choice of the gain matrix ($\mathbf{G}$) and the placement of the sensors ($\mathbf{C}$) and the actuators ($\mathbf{B}$). Here $\mathbf{P}$ and $\mathbf{\Lambda}$ are known from the open-loop state matrix, and $\mathbf{\Lambda}_D$ is given by the desired modal information. For full-state feedback, the matrices $\mathbf{C}$ and $\mathbf{B}$ may be taken as the identity matrix and eqn [28] yields a simple solution for the gain matrix that will provide a closed-loop system with exactly the desired damping ratios and natural frequencies.

The calculation for the gain matrix looks straightforward, but solving eqn [28] for $\mathbf{G}$ can be difficult unless $\mathbf{B}$ and $\mathbf{G}$ are nonsingular and well conditioned (requiring full-state feedback). There are a variety of pole placement algorithms each solving specialized problems and dealing with the difficulty of using a small number of sensors and actuators ($\mathbf{B}$ and $\mathbf{C}$ singular, or output feedback). Another difficulty is partial pole placement. This refers to the case where it is desired to assign only a few of the poles and to leave the other poles alone, as is often the case in design. It should also be pointed out that the larger the difference between the open-loop poles, $\mathbf{\Lambda}$, and the desired poles, $\mathbf{\Lambda}_D$, the more gain and hence the more power and force required by the controller.

A more radical version of pole placement is called eigenstructure assignment. Eigenstructure assignment refers to a control law that aims to produce a closed-loop system with both desired eigenvalues (poles or natural frequencies and damping ratios) and desired eigenvectors (mode shapes). The calculation for the gain matrix $\mathbf{G}$ to perform eigenstructure assignment is not presented here. Rather it is important to note that one cannot exactly specify any desired mode shape for the closed-loop system, but rather the assigned mode shapes are somewhat determined by the nature of the original state matrix, $\mathbf{A}$. Thus, while one can completely specify desired natural frequencies and damping ratios and compute a closed-loop control providing these specified poles, one cannot do the same for desired mode shapes. Rather, the desired mode shapes must be modified according to the original system dynamics. This is not surprising to structural engineers who have worked in model updating as it is well known there that the analytical model and the test data must be fairly close before updating is successful.

Optimal Control

The question of whether or not there is a best control system is somewhat answered by methods of optimal control. Optimal control is a closed-loop method devised using variational methods to find a control law $\mathbf{u}(t)$ that minimizes a quadratic 'cost function' containing the response of the system. One simple approach to optimal control is to compute the control, $\mathbf{u}(t)$ that minimizes the square of the response, $\mathbf{x}(t)$, subject to the constraint that the response satisfies the equation of motion. This constrained optimization problem produces controls that are independent of the modal model of the structure. The optimization procedure also allows one to include the control force as part of the cost function. In this case the cost function becomes:

$$J = \int_0^t \left(\mathbf{x}^T(t)\mathbf{Q}\mathbf{x}(t) + \mathbf{u}^T(t)\mathbf{R}\mathbf{u}(t)\right) \mathrm{d}t \qquad [29]$$

Here the matrices $\mathbf{Q}$ and $\mathbf{R}$ are weighting matrices that are chosen by the designer to balance the effect of minimizing the response with that of minimizing the control effort. Optimal control with this sort of cost function is referred to as the linear quadratic regulator (LQR) problem. Specifically the LQR problem is to minimize eqn [29] subject to eqn [10] and initial conditions. If full-state feedback is used (that is if $\mathbf{u} = -\mathbf{G}\mathbf{x}$), then the solution to the LQR problem leads to:

$$\mathbf{u}(t) = -\mathbf{R}\mathbf{B}^T S(t)\mathbf{x}(t) \qquad [30]$$

Here $S(t)$ is the solution to the Riccati equation:

$$\mathbf{Q} - S(t)\mathbf{B}\mathbf{R}^{-1}S(t) + \mathbf{A}^T S(t) + S(t)\mathbf{A} + \frac{\mathrm{d}S(t)}{\mathrm{d}t} = 0 \qquad [31]$$

which must be solved numerically. Steady-state solutions are found by assuming the derivative of $S(t)$ to be zero and that the system is controllable (more precisely: that pair A, B are controllable). The restrictions are that the matrix $\mathbf{R}$ must be symmetric and positive definite and that the matrix $\mathbf{Q}$ must be symmetric and positive semidefinite. Fortunately there are several numerical algorithms for solving the steady-state-matrix Riccati equation.

Optimal control is the only control methodology discussed here that allows the designer some clear method of restricting the amount of control energy expended while designing the controller. The other methods, such as pole placement, can potentially lead to solutions that call for more control effort than is practically available. The $\mathbf{R}$ term in the LQR cost function allows the excessive use of control energy to be penalized during the optimization. The designer adjusts $\mathbf{Q}$ to reduce the vibration to acceptable levels and adjusts $\mathbf{R}$ to reduce the control effort to meet available control forces. Commercial codes are available for computing the optimal control given the equations of motion, sensor locations and actuator locations.

Compensators

Compensation is a technique of essentially adding dynamics to a system to compensate for its open-loop performance. The idea is very similar to that of a passive vibration absorber. In the case of a vibration absorber an additional spring-mass system is added to the plant. This additional degree-of-freedom is used to absorb a harmonic input, causing the base system or plant to remain free of vibration. In control theory, the compensator, as it is called, adds dynamics to a system to change its performance to obtain a more desirable response.

A good example of the difference between state feedback and compensation is to consider the vibration isolation design. It is well known that isolators are designed by choosing the stiffness to be low enough to avoid the resonance peak yet high enough to provide low static deflection. Increased damping, which lowers the peak, unfortunately raises the magnitude in the region of isolation. Thus the designer is often left with the dilemma of adding damping to improve shock isolation and at the same time reducing the performance of the vibration (steady-state) isolation. If state feedback is used in an attempt to provide an active isolator that provides good performance across the entire spectrum, the same difficulty arises because state feedback for a single-degree-of-freedom system can only change damping and stiffness. To solve this problem, new dynamics must be added to the system. These new dynamics are effectively a compensator.

One popular example of compensation in structural control is called positive position feedback (PPF). To illustrate the formulation consider the single-degree-of-freedom system (or alternately, a single mode of the system):

$$\ddot{x} + 2\,\zeta\,\omega_n\,\dot{x} + \omega_n^2\,x = b\,u \qquad [32]$$

where ζ and ω_n are the damping ratio and natural frequency of the structure, and b determines the level

of force into the mode of interest. The PPF control is implemented using an auxiliary dynamic system (compensator) defined by:

$$\begin{aligned} &\ddot{\eta} + 2\,\zeta_f\,\omega_{nf}\,\dot{\eta} + \omega_{nf}^2\,\eta = \omega_{nf}^2\,x \\ &u = \frac{g}{b}\,\omega_{nf}^2\,\eta \end{aligned} \qquad [33]$$

Here ζ_f and ω_{nf} are the damping ratio and natural frequency of the controller and g is a constant. The particular form of eqn [33] is that of a second-order compensator. The idea is to choose the PPF frequency and damping ratio so that the response of this mode has the desired behavior. Combining eqns [32] and [33] gives the equations of motion in their usual form, which are, assuming no external force:

$$\begin{bmatrix} \ddot{x} \\ \ddot{\eta} \end{bmatrix} + \begin{bmatrix} 2\zeta\omega_n & 0 \\ 0 & 2\zeta_f\omega_{nf} \end{bmatrix} \begin{bmatrix} \dot{x} \\ \dot{\eta} \end{bmatrix} + \begin{bmatrix} \omega_n^2 & -g\omega_{nf}^2 \\ -\omega_{nf}^2 & \omega_{nf}^2 \end{bmatrix} \begin{bmatrix} x \\ \eta \end{bmatrix} = \begin{bmatrix} 0 \\ 0 \end{bmatrix} \qquad [34]$$

This is a stable closed-loop system if the 'stiffness' matrix is positive definite. That is if the eigenvalues of the displacement coefficient matrix are all positive. This condition is satisfied if:

$$g\omega_{nf}^2 < \omega_n^2 \qquad [35]$$

Notice that the stability condition only depends on the natural frequency of the structure, and not on the damping or mode shapes. This is significant in practice because when building an experiment, the frequencies of the structure are usually available with a reasonable accuracy while mode shapes and damping ratios are much less reliable.

This stability property is also important because it can be applied to an entire structure eliminating spillover by rolling off at higher frequencies. That is, the frequency response of the PPF controller has the characteristics of a low-pass filter. The transfer function of the controller is:

$$\frac{U(s)}{X(s)} = \frac{g\omega_{nf}^4}{b\left(s^2 + 2\zeta_f\omega_{nf}\,s + \omega_{nf}^2\right)} \qquad [36]$$

illustrating that it rolls off quickly at high frequencies. Thus the approach is well suited to controlling a mode of a structure with frequencies that are well separated, as the controller is insensitive to the unmodeled high frequency dynamics. Thus if cast in state space, the term $\mathbf{b}_{2n-k}$ in eqn [25] is zero and no spillover results. In many ways, the PPF active feedback control scheme is much like adding a vibration absorber that targets each mode of interest.

Stability and Robustness

Two important considerations in designing a control system are those of stability and robustness. Most of the structures and machines that mechanical engineers deal with are open-loop stable. However, adding control to such systems has the potential to make the closed-loop system unstable. This usually occurs because the physical parameters in the system and/or the disturbance forces are not known exactly. This uncertainty leads in a natural way to the concept of stability and performance robustness. As an example of robustness, consider the simple suspension design that produces a damping ratio resulting in a smooth ride and not too much static deflection. Now if the vehicle is overloaded, then the damping ratio decreases and the static deflection increases, both serving to ruin the performance (ride). The amount the vehicle can be loaded (mass change) before acceptable performance is lost is a measure of the performance robustness of the design.

Stability robustness refers to how much the parameters of the system may be changed before stability is lost. For instance, suppose a control system is designed to reduce damping in the system in order to provide a really fast responding machine. The effective control reduces damping based on the amount of natural damping in the system. However, if that amount of natural damping is greatly overestimated, it is possible to design a controller that will subtract too much damping and render the closed-loop system unstable. The amount of damping in the original system then becomes a measure of stability robustness. Stability robustness indicates the amount of error that can be tolerated in the system's parameters before the system is in danger of losing stability.

As an example of one robustness condition, consider a control law that regulates the difference between the closed-loop response and the desired response of a system. A good measure of performance of this control system is then whether or not the steady-state error is zero. The system is said to be robust if there exists a control that regulates the system with zero steady-state error when subjected to variations in the state matrix $\mathbf{A}$, the control input matrix $\mathbf{B}$, or the sensor matrix $\mathbf{C}$.

An example of a stability robustness condition consider the closed-loop system with full-state feedback defined by:

$$\dot{\mathbf{x}} = (\underbrace{\mathbf{A} + \mathbf{BG}}_{\mathbf{A}'})\mathbf{x} \qquad [37]$$

Next suppose that the closed-loop matrix $\mathbf{A}'$ is subject to some error (either in $\mathbf{A}$, $\mathbf{B}$ or $\mathbf{G}$), defined by the matrix of errors $\mathbf{E}$. The exact value of $\mathbf{E}$ is not known, but it is reasonable to assume that bounds on the elements of $\mathbf{E}$ are known. Let each element of the uncertainty matrix be bounded in absolute value by the same number ε, so that:

$$|\mathbf{E}_{ij}| < \varepsilon \qquad [38]$$

Then it can be shown that the closed-loop system of eqn [37] will be asymptotically stable if:

$$\varepsilon < \frac{1}{2n}\left(\frac{1}{\sigma_{\max}(\mathbf{F})}\right) \qquad [39]$$

Here n denotes the number of degrees of freedom in the system and $\sigma_{\max}(\mathbf{F})$ is the largest singular value of the matrix $\mathbf{F}$. The matrix $\mathbf{F}$ is a solution of the Liapunov matrix equation

$$\mathbf{A}'\mathbf{F} + \mathbf{F}\mathbf{A}' = -2\mathbf{I} \qquad [40]$$

Here the matrix $\mathbf{I}$ is the $2n \times 2n$ identity matrix. Numerical algorithms must be used to solve the Liapunov equation. In this way the maximum allowable variation in either $\mathbf{A}$ or $\mathbf{B}$ can be determined. Variations falling within less then ε will not spoil the stability of the closed-loop response. However, this particular result does not give any information about performance.

The concept of robust control designs has been the focus of a great deal of research. Unfortunately a majority of the literature focuses on stability robustness, while structural control is usually more concerned with performance robustness. None the less, useful methods exist, which are beyond the scope of the introduction presented here.

Limitations

Numerous other control methods exist that may be adapted to the structural control problem. However, one item often ignored in the literature and in design is the need to match the actuation and sensing requirements of the control law to physically available hardware. In particular, the force and stroke and time constant of each actuator must be matched with the force, stroke and time constant required of the structure to be controlled. For instance if the actuator takes of the order of a second to respond, then it is doubtful that the actuator will be capable of controlling transient vibrations that are over in less then a second. The key elements in control, beyond the theoretical methods discussed here, are force, stroke, time constant, and location of actuators and sensors. These represent the hardware issues that cannot be ignored in any successful application of feedback control for vibration suppression of structures and machines.

Another limitation of control design is that of model order. Most control designs are straightforward to compute for plants that are of low order (say less than five or six degrees-of-freedom). However, in order to obtain good models of the plant, larger-order finite element models are often used. Hence many control designs focus on ways to control a reduced-order model without losing performance or stability through spillover. Several methods for dealing with control in the presence of model reduction exist and others are still being researched.

The question of control when the plant or actuators have significant nonlinear effects has also been addressed in the literature but is not summarized here. Nonlinear behavior forms a constant concern and several methods exist for controlling structures with nonlinear deformations, rigid body motions and nonlinear damping elements. Just as nonlinear structural analysis is very case dependent, so is nonlinear control.

Nomenclature

$\mathbf{A}$	state matrix
$\mathbf{B}$	control input matrix
$\mathbf{C}$	sensor matrix
$\mathbf{D}$	damping matrix
$\mathbf{E}$	matrix of errors
g_1	velocity gain
g_2	position gain
$\mathbf{G}$	gain matrix
$\mathbf{I}$	identity matrix
$\mathbf{Q}$, $\mathbf{R}$	weighting matrices
$\mathbf{\Lambda}$	diagonal matrix

See also: **Active control of civil structures**; **Active control of vehicle vibration**; **Absorbers, active**; **Damping models**; **Vibration isolation, applications and criteria**; **Vibration isolation theory**.

Further Reading

Clark RL, Saunders WR, Gibbs GP (1998) *Adaptive Structures: Dynamics and Control*. New York: Wiley.

Fuller CR, Elliot SJ, Nelson PA (1996) *Active Control of Vibration*. London: Academic Press.

Inman DJ (1989) *Vibration with Control Measurement and Stability*. Englewood Cliffs: Prentice Hall.
Meirovitch L (1990) *Dynamics and Control of Structures*. New York: Wiley.
Skelton RE (1988) *Dynamic Systems and Control*. New York: Wiley.
Soong TT (1990) *Active Structural Control: Theory and Practice*. Harlow: Longman and New York: Wiley.

ACTUATORS AND SMART STRUCTURES

V Giurgiutiu, University of South Carolina, Columbia, SC, USA

Copyright © 2001 Academic Press

doi:10.1006/rwvb.2001.0197

Introduction

The subject of smart structures and induced-strain actuators has attracted considerable attention in recent years. Smart structures offer the opportunity to create engineered material systems that are empowered with sensing, actuation, and artificial intelligence features. The induced-strain active materials actuators are the enabling technology that makes adaptive vibration control of smart structures realizable in an optimal way. Some generic concepts about smart structures and induced-strain active materials actuators will be given first. Then, details will be presented about piezo-electric, electrostrictive, magnetostrictive, and shape memory alloy materials that are used in the construction of induced-strain actuators. Guidelines for the effective design and construction of induced-strain actuation solutions will be provided. Details about sensory, actuatory, and adaptive smart structures will be provided, together with some examples. Conclusions and directions for further work are given last.

Smart Structures: Concepts

The discipline of adaptive materials and smart structures, recently coined as adaptronics, is an emerging engineering field with multiple defining paradigms. However, two definitions are prevalent. The first definition is based upon a technology paradigm: 'the integration of actuators, sensors, and controls with a material or structural component'. Multifunctional elements form a complete regulator circuit resulting in a novel structure displaying reduced complexity, low weight, high functional density, as well as economic efficiency. This definition describes the components of an adaptive material system, but does not state a goal or objective of the system. The other definition is based upon a science paradigm, and attempts to capture the essence of biologically inspired materials by addressing the goal as creating material systems with intelligence and life features integrated in the microstructure of the material system to reduce mass and energy and produce adaptive functionality.

It is important to note that the science paradigm does not define the type of materials to be utilized. It does not even state definitively that there are sensors, actuators, and controls, but instead describes a philosophy of design. Biological systems are the result of a continuous process of optimization taking place over millennia. Their basic characteristics of efficiency, functionality, precision, self-repair, and durability continue to fascinate scientists and engineers alike. Smart structures have evolved by biomimesis; they aim at creating man-made structures with embedded sensing, actuation, and control capabilities. **Figure 1** shows how the modern engineer might try to duplicate nature's functionalities with man-made material systems: composite materials to replicate the biological skeleton; piezo and optical sensors to duplicate the five senses; piezo and shape memory alloy actuators to replicate the fast twitch and slow twitch muscles; artificial intelligence networks to mimic the motor control system, etc. Such innovative developments have been spurred by the revolutionary emergence of commercially available smart active materials and their sensing and actuation derivatives.

Active Materials Actuators

The term 'smart materials' incorporates a large variety of revolutionary material systems that exhibit sensing and actuation properties similar to that of the living world. Of these, some smart materials may have only sensing properties, others may exhibit both sensing and actuation. An example of the former are the optical fiber sensors, and composite materials incorporating such fibers in their fibrous structure. Of the latter, a most obvious example is that of piezoelectric ceramics that can both sense and create mechanical strain. We will not cover the smart sensing materials here. Concentrating our attention on actuating smart materials, we notice that their list is

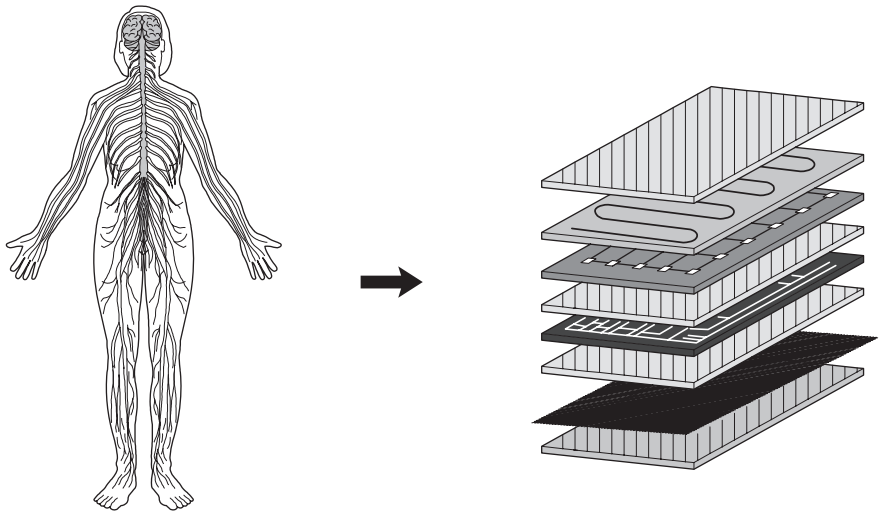


Figure 1 (see Plate 4). Biomimesis parallelism between the human body and a smart material system.

long and varied. A raw categorization may distinguish several large classes:

1. Piezo-electric (PZT), electrostrictive (PMN), and magnetostrictive (Terfenol-D) materials that directly convert an externally applied electric or magnetic field into induced strain through a direct physical effect at microstructural level (similar to the thermal expansion effect). Such materials come as piezo and electrostrictive ceramics, piezoelectric polymers, and magnetostrictive alloys.
2. Shape memory alloys (SMA) that produce induced-strain actuation through a metallurgical phase transformation triggered by the crossing of certain temperature thresholds (Martensitic to Austenitic transformation). The induced-strain effect of SMA materials is the result of the strain states not being carried over from one metallurgical phase into the other phase. Thus, a material deformed (say, stretched) in the Martensitic phase will return to the undeformed state when transformed into the Austenitic phase, with the overall result being a net change in shape (i.e., length).
3. Electrochemical actuators, which are base on the change of volume that takes place during electrically controlled chemical reactions.
4. Chemomechanical actuators, which start with biological muscle and continue with several 'artificial muscle' materials based on net-linked collages, polyelectrolyte gels, conducting polymers, etc. One example is provided by the electroactive polymers Nafion® and Flemion® that display remarkable large strains when used as wet membranes.

Also mentioned by some authors are certain smart materials that change their effective damping properties in response to electric and magnetic stimuli:

1. Electrorheological fluids (ERF), which are suspensions of micron-sized high-dielectric-strength particles in an insulating base oil, able to modify their effective viscosity and shear strength in response to electric fields.
2. Magnetorheological fluids (MRF), which are suspension of micron-sized ferromagnetic particles able to modify their effective viscosity and shear strength in response to magnetic fields.

In the present discussion, we will focus our attention on the piezo-electric, electrostrictive, magnetostrictive, and shape memory alloy materials, and explain how they can be used in the construction of active-materials actuators.

Actuators are devices that produce mechanical action. They convert input energy (electric, hydraulic, pneumatic, thermic, etc.) to mechanical output (force and displacement). Actuators rely on a 'prime mover' (e.g., the displacement of high-pressure fluid in a hydraulic cylinder, or the electromagnetic force in an electric motor) and on mechanisms to convert the prime mover effect into the desired action. If the

prime mover can impart a large stroke, direct actuation can be effected (e.g., a hydraulic ram). When the prime mover has small stroke, but high frequency bandwidth, a switching principle is employed to produce continuous motion through the addition of switched incremental steps (e.g., some electric motors). Like everywhere in engineering, the quest for simpler, more reliable, more powerful, easier to maintain, and cheaper actuators is continuously on. In this respect, the use of active-materials solid-state induced-strain actuators has recently seen a significant increase. Initially developed for high-frequency, low-displacement acoustic applications, these revolutionary actuators are currently expanding their field of application into many other areas of mechanical and aerospace design. Compact and reliable, induced-strain actuators directly transform input electrical energy into output mechanical energy. One application area in which solid-state induced-strain devices have a very promising future is that of translational actuation for vibration and aeroelastic control. At present, the translational actuation market is dominated by hydraulic and pneumatic pressure cylinders, and by electromagnetic solenoids and shakers.

Hydraulic and pneumatic cylinders offer reliable performance, with high force and large displacement capabilities. When equipped with servovalves, hydraulic cylinders can deliver variable stroke output. Servovalve-controlled hydraulic devices are the actuator of choice for most aerospace (**Figure 2**), automotive, and robotic applications. However, a major drawback in the use of conventional hydraulic actuators is the need for a separate hydraulic power unit equipped with large electric motors and hydraulic pumps that send the high-pressure hydraulic fluid to the actuators through hydraulic lines. These features can be a major drawback in certain applications. For example, a 300-passenger airplane has over a kilometer of hydraulic lines spanning its body, from the engines to the most remote wing tip. Such a network of vulnerable hydraulic piping can present a major safety liability, under both civilian and military operation. In ground transportation, similar considerations have spurred automobile designers to promote the 'brake-by-wire' concept that is scheduled to enter the commercial market in the next few years. In some other applications, the use of conventional actuation is simply not an option. For example, the actuation of an aerodynamic servo-tab at the tip of a rotating blade, such as in helicopter applications, cannot be achieved through conventional hydraulic or electric methods due to the prohibitive high-g centrifugal force field environment generated during the blade rotation.

At present, electro-mechanical actuation that directly converts electrical energy into mechanical energy is increasingly preferred in several industrial applications. The most widely used high-power electro-mechanical actuators are the electric motors. However, they can deliver only rotary motion and need to utilize gearboxes and rotary-to-translational conversion mechanisms to achieve translational motion. This route is cumbersome, leads to additional weight, and has low-frequency bandwidth. Direct conversion of electrical energy into translational force and motion is possible, but its practical implementation in the form of solenoids and electrodynamic shakers is marred by typically low-force performance. The use of solenoids or electrodynamic shakers to perform the actuator duty-cycle of hydraulic cylinders does not seem conceivable.

Solid-state induced-strain actuators offer a viable alternative (**Figure 3**). Though their output displacement is relatively small, they can produce remarkably high force. With well-architectured displacement amplification, induced-strain actuators can achieve

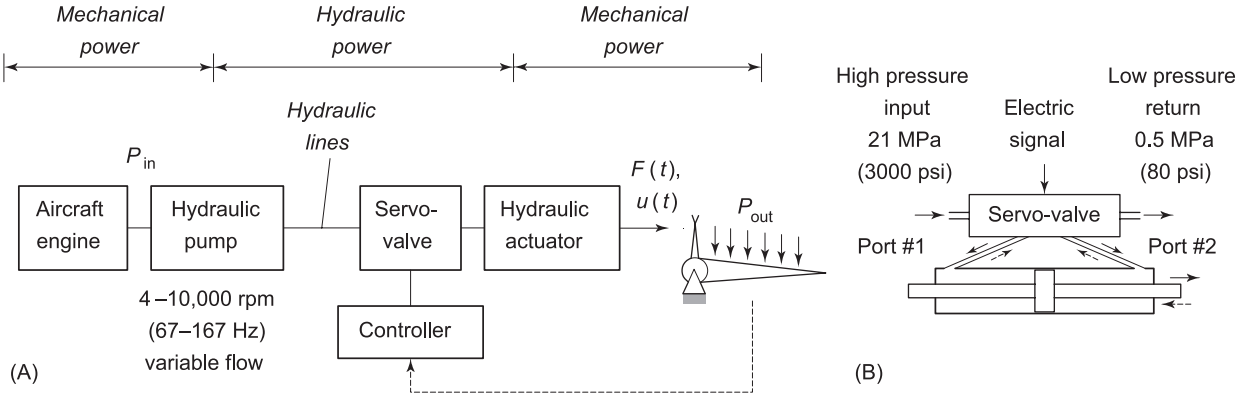


Figure 2 Conventional hydraulic actuation system: (A) flight controls of modern aircraft: (B) details of the servo-valve controlled hydraulic cylinder.

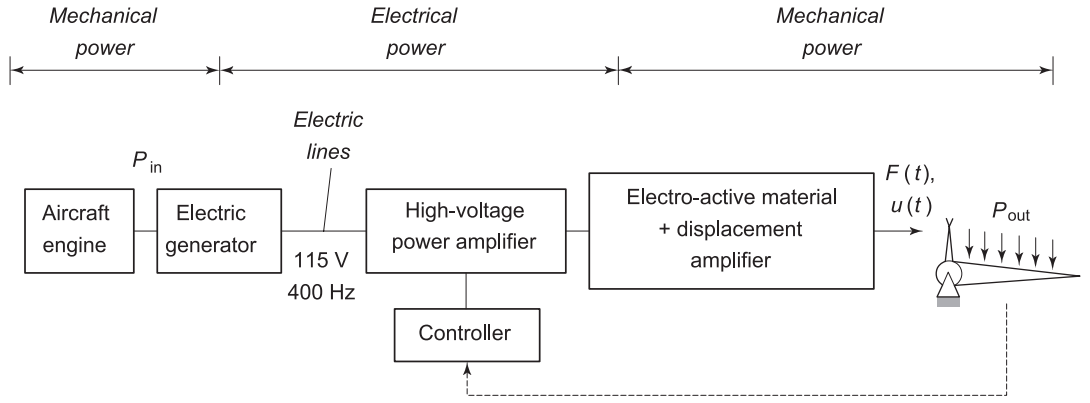


Figure 3 Schematic representation of a solid-state induced-strain actuated flight control system using electro-active materials.

output strokes similar to those of conventional hydraulic actuators, but over much wider bandwidth. Additionally, unlike conventional hydraulic actuators, solid-state induced-strain actuators do not require separate hydraulic power units and long hydraulic lines, and use the much more efficient route of direct electric supply to the actuator site.

The development of solid-state induced-strain actuators has entered the production stage, and actuation devices based on these concepts are likely to reach the applications market in the next few years. An increasing number of vendors are producing and marketing solid-state actuation devices based on induced-strain principles.

Piezo-electric and Electrostrictive Materials

Piezo-electricity

Piezo-electricity (discovered in 1880 by Jacques and Pierre Curie) describes the phenomenon of generating an electric field when the material is subjected to a mechanical stress (direct effect), or, conversely, generating a mechanical strain in response to an applied electric field. Piezo-electric properties occur naturally in some crystalline materials, e.g., quartz crystals (SiO_2), and Rochelle salt. The latter is a natural ferroelectric material, possessing an orientable domain structure that aligns under an external electric field and thus enhances its piezo-electric response. Piezo-electric response can also be induced by electrical poling of certain polycrystalline materials, such as piezo-ceramics (**Figure 4**).

The application of a high poling field at elevated temperatures results in the alignment of the crystalline domains; this alignment is locked in place when the high temperatures are removed. Subsequently, the poled ceramics response to the application of an applied electric field or mechanical stress with typical piezo-electric behavior. The distortion of the crystal domains produces the piezo-electric effect. Lead zirconate titanate, $PbZrO_3$, is commercially known as PZT. To date, many PZT formulations exist, the main differentiation being between 'soft' (e.g., PZT 5–H) and 'hard' (e.g., PZT 8). Within the linear range, piezo-electric materials produce strains that are proportional to the applied electric field or voltage. Induced strains in excess of 1000 μstrain (0.1%) have become common. These features make piezo-electric materials very attractive for a variety of sensor and actuator applications.

Modeling of Piezo-electric Behavior

For linear piezo-electric materials, the interaction between the electrical and mechanical variables can be described by linear relations (ANSI/IEEE Standard

Table 1 Mechanic and dielectric properties for piezo-electric (PZT-5, PZT-8) and electrostrictive (PMN EC-98) materials

Property	*Soft PZT-5 Navy Type VI*	*Hard PZT-8 Navy Type III*	*PMN EC-98*
$\rho\,(kg\,m^{-3})$	7600	7600	7850
k_{31}	0.36	0.31	0.35
k_{33}	0.71	0.61	0.72
k_{15}	0.67	0.54	0.67
$d_{31}\,(\times 10^{-12}\,m\,V^{-1})$	−270	−100	−312
$d_{33}\,(\times 10^{-12}\,m\,V^{-1})$	550	220	730
$d_{15}\,(\times 10^{-12}\,m\,V^{-1})$	720	320	825
$g_{31}\,(\times 10^{-3}\,Vm\,N^{-1})$	−9.0	−11.3	−6.4
$g_{33}\,(\times 10^{-3}\,Vm\,N^{-1})$	18.3	24.9	15.6
$g_{15}\,(\times 10^{-3}\,Vm\,N^{-1})$	23.9	36.2	17
$s_{11}^{E}\,(\times 10^{-12}\,m^2\,N^{-1})$	15.9	10.6	16.3
Poisson ratio	0.31	0.31	0.34
$s_{33}^{E}\,(\times 10^{-12}\,m^2\,N^{-1})$	20.2	13.2	21.1
Curie temp. (°C)	200	350	170
Mechanical Q_m	75	900	70

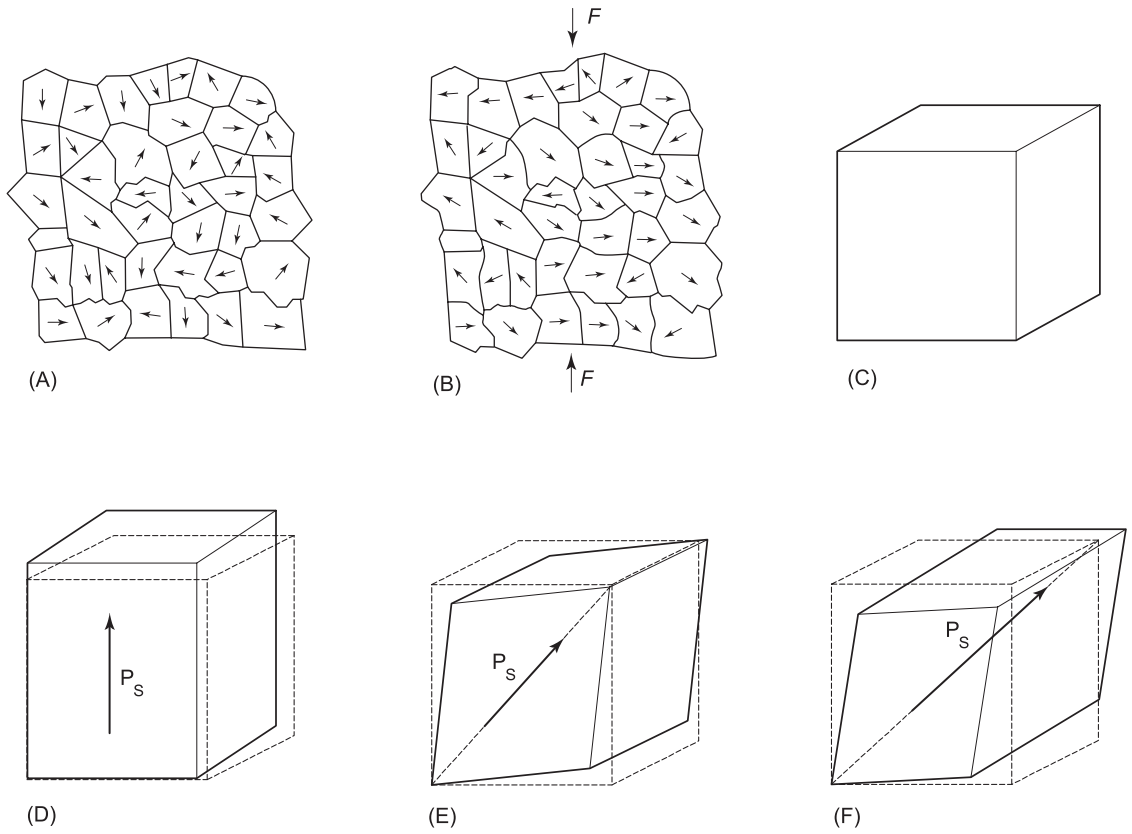


Figure 4 Illustration of piezo-electric principles: (A) un-stressed piezo-electric material has the electric domains randomly oriented; (B) stressing produces orientation of the electric domains perpendicular to the loading direction; (C) cubic phase, stable above the Curie temperature, no piezo-electricity; (D) tetragonal phase; (E) orthorhombic phase; (F) rhombohedral phase.

176–1987). A tensorial relation between mechanical and electrical variables is established in the form:

$$\begin{aligned} S_{ij} &= s^E_{ijkl} T_{kl} + d_{kij} E_k + \alpha^E_i \theta \\ D_j &= d_{jkl} T_{kl} + \varepsilon^T_{jk} E_k + \tilde{D}_m \theta \end{aligned} \qquad [1]$$

where S_{ij} is the mechanical strain, T_{ij} is the mechanical stress, E_i is the electrical field, D_i is the electrical displacement (charge per unit area), s^E_{ijkl} is the mechanical compliance of the material measured at zero electric field $(E = 0)$, ε^T_{jk} is the dielectric constant measured at zero mechanical stress $(T = 0)$; d_{kij} is the piezo-electric displacement coefficient that couples the electrical and mechanical variables, θ is the absolute temperature, α^E_i is the coefficient of thermal expansion under constant electric field; $\tilde{D}_j$ is the electric displacement temperature coefficient. The stress and strain are second-order tensors, while the electric field and the electric displacement are

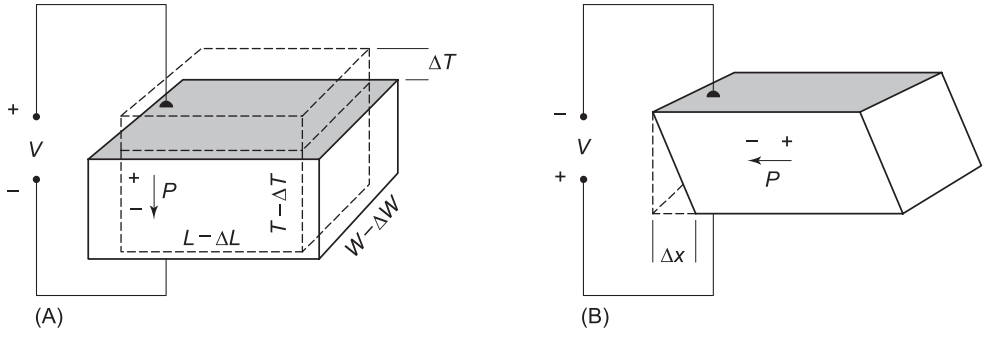


Figure 5 Basic induced-strain responses of piezo-electric materials: (A) axial and transverse strain; (B) shear strain.

first-order tensors. The superscripts, T, D, E, signify that the quantities are measured at zero stress, or zero current, or constant electric field, respectively. The second equation reflects the direct piezo-electric effect, while the first equation refers to the converse piezo-electric effect.

In engineering practice, the tensorial eqn [1] is rearranged in matrix form using the six-component stress and strain vectors, $(\mathbf{T}_1, \ldots, \mathbf{T}_6)$ and $(\mathbf{S}_1, \ldots, \mathbf{S}_6)$, where the first three components represent direct stress and strain, while the last three represent shear. **Figure 5** illustrates the physical meaning of these equations in the case of simple polarization. **Figure 5A** shows that an electric field $E_3 = V/t$ applied parallel to the direction of polarization $(E_3||P)$ induces thickness expansion $(\varepsilon_3 = d_{33}E_3)$ and transverse retraction $(\varepsilon_1 = d_{31}E_3)$. **Figure 5B** shows that, if the field is perpendicular to the direction of polarization $(E_3 \perp P)$, shear deformation is induced $(\varepsilon_5 = d_{15}E_3)$.

Electromechanical coupling coefficient is defined as the square root of the ratio between the mechanical energy stored and the electrical energy applied to a piezo-electric material. For direct actuation, we have $\kappa_{33} = d_{33}/\sqrt{(s_{11}\varepsilon_{33})}$, while for transverse actuation $\kappa_{31} = d_{31}/\sqrt{(s_{11}\varepsilon_{33})}$.

Electrostrictive Materials

Electrostrictive ceramics are ferroelectric ceramics that contain both linear and quadratic terms:

$$\begin{aligned} S_{ij} &= s^E_{ijkl}T_{kl} + d_{kij}E_k + M_{klij}E_kE_l \\ D_j &= d_{jkl}T_{kl} + \varepsilon^T_{jk}E_k \end{aligned} \qquad [2]$$

Note that the first two terms in the first equation are the same as for piezo-electric materials. The third term is due to electrostriction, with M_{klij} being the electrostrictive coefficient. In general, the piezo-electric effect is possible only in noncentrosymmetric materials, whereas the electrostrictive effect is not limited by symmetry and is present in all materials. A common electrostrictive compound is lead–magnesium–niobate, or PMN. Commercially available PMN formulations are internally biased and optimized to give quasilinear behavior, but do not accept field reversal. **Figure 6A** compares induced-strain response of some commercially available piezo-electric, electrostrictive, and magnetostrictive actuation materials. It can be seen that the electrostrictive materials have much less hysteresis, but more nonlinearity.

Piezo-polymers

Polyvinylidene fluoride (PVDF or PVF_2), is a polymer with strong piezo-electric and pyroelectric properties. In the α phase, PVDF is not polarized and is used as a common electrical insulator among many other applications. To impart the piezo-electric properties, the α phase is converted to the β phase and polarized. Stretching α-phase material produces the β phase. After surface metallization, a strong electric field is applied to provide permanent polarization. The flexibility of the PVDF overcomes some of the drawbacks associated with the piezo-electric ceramics brittleness. As a sensor, PVDF provides higher voltage/electric field in response to mechanical stress. Their piezo-electric g-constants (i.e., the voltage generated per unit mechanical stress) are typically 10–20 times

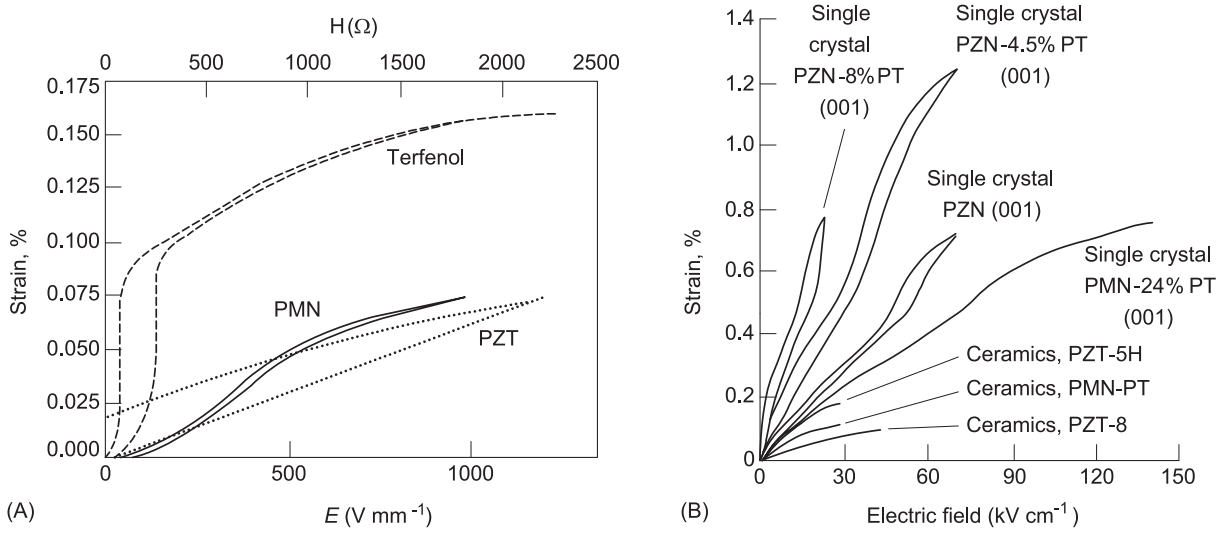


Figure 6 Strain vs electric field behavior of induced-strain materials: (A) currently available materials; (B) new $<001>$ oriented rhombohedral crystals of PZN–PT and PMN–PT compared to current piezo-electric ceramics.

larger than for piezo-ceramics. PVDF film also produces an electric voltage in response to infrared light due to its strong pyroelectric coefficient. However, the use of PVDF materials as actuators is inappropriate for most structural applications due to their low elastic modulus which cannot generate large actuation forces.

New Piezo-electric Materials

New piezo-electric materials with much larger induced-strain capabilities are currently being developed in research laboratories. Very promising are the single crystal materials: single crystals of PZN–PT, a relaxor pervoskite $Pb(Zn_{1/3}Nb_{2/3})O_3$–$PbTiO_3$, have been studied. Strain levels of up to 1.5 percent, and reduced hysteresis have been reported. The response of these new materials can be an order of magnitude larger than that of conventional PZT materials (see curves in **Figure 6B**. When building actuators from PZN–PT material, one must take into account the strong dependence of the piezo-electric properties on the crystal orientation. This imposes certain design restrictions in comparison with conventional piezo-ceramics. Commercial production of induced strain actuators based on these new materials has been undertaken by TRS Ceramics, Inc., and a prototype PZN–PT actuator with a maximum strain of around 0.3% has been reported.

Advantages and Limitations of Piezo-electric and Electrostrictive Actuation Materials

Piezo-electric ceramics, e.g., PZT, are essentially small-stroke large-force solid-state actuators with very good high-frequency performance. However, they also display certain limitations. The most obvious limitation is that, in many engineering applications, some form of mechanical amplification is required. Other limitations are associated with electrical breakdown, depoling, Curie temperature, nonlinearity, and hysteresis.

1. Electrical breakdown may happen when an electric field applied in the poling direction exceeds the dielectric strength of the material, resulting in electrical arcing through the material and short-circuit. Electrical breakdown also destroys the piezo-electric properties of the material.
2. Depoling may happen when an electric field is applied opposite to the poling direction, resulting in degradation of the piezo-electric properties or even polarization in the opposite direction. The depoling field (or coercive field) may be as low as half of the electrical breakdown field.
3. Curie temperature. At temperatures close to the Curie temperature, depoling is facilitated, aging and creep are accelerated, and the maximum safe mechanical stress is decreased. For typical PZT materials, the Curie temperature is about 350°C. The operating temperature should generally be at least 50°C lower than the Curie temperature.
4. Nonlinearity and hysteresis. Actual piezo-ceramics are nonlinear and hysteretic (**Figure 6**). Hysteresis is due to internal sliding events in the polycrystalline piezo-electric material. Upon removal of the electric field, remnant mechanical strain is observed. Hysteresis of common piezo-electric may range from 1 to 10%. Under high frequency operation, hysteresis may generate excessive heat, and loss of performance may occur if the Curie temperature is exceeded.

The main advantage of electrostrictive materials over piezo-electric materials is their very low hysteresis. This could be especially beneficial in high-frequency dynamic applications, which could involve considerable hysteresis-associated heat dissipation. The main disadvantage of electrostrictive materials is the temperature dependence of their properties.

Magnetostrictive Materials

Magnetostrictive materials expand in the presence of a magnetic field, as their magnetic domains align with the field lines. Magnetostriction was initially observed in nickel cobalt, iron, and their alloys but the values were small (<50 μstrain). Large strains ($\sim$ 10 000 μstrain) were observed in the rare-earth elements terbium (Tb) and dysprosium (Dy) at cryogenic temperatures (below 180 K). The compound Terfenol-D ($Tb_{.3}Dy_{.7}Fe_{1.9}$), developed at Ames Laboratory and the Naval Ordnance Laboratory (now Naval Surface Weapons Center), displays magnetostriction of up to 2000 μstrain at room temperature and up to 80°C and higher.

Modeling of the Magnetostrictive Materials

The magnetostrictive constitutive equations contain both linear and quadratic terms:

$$\begin{aligned} S_{ij} &= s^E_{ijkl} T_{kl} + d_{kij} H_k + M_{klij} H_k H_l \\ B_j &= d_{jkl} T_{kl} + \mu^T_{jk} H_k \end{aligned} \qquad [3]$$

where, in addition to the already defined variables, H_k is the magnetic field intensity, B_j is the magnetic flux density, and μ^T_{jk} is the magnetic permeability under constant stress. The coefficients d_{kij} and M_{klij} are defined in terms of magnetic units. The magnetic

field intensity, H, in a rod surrounded by a coil with n turns per unit length is related to the current, I, through the relation:

$$H = nI \qquad [4]$$

Advantages and Limitations of Magnetostrictive Actuators

Magnetostrictive materials, like Terfenol-D, are essentially small-stroke large-force solid-state actuators that have wide frequency bandwidth. However, they also display certain limitations. The most obvious one is that, in actuation applications, some form of mechanical amplification is required. The main advantage of magnetoactive actuation materials over electroactive materials may be found in the fact that it is sometimes easier to create a high intensity magnetic field than a high intensity electric field. High electric fields require high voltages, which raise important insulation and electric safety issues. According to eqn [4], high magnetic fields could be realized with lower voltages using coils with a large number of turns per unit length, through which a high-amperage current flows.

An important limitation of the magnetoactive materials is that they cannot be easily energized in the two-dimensional topology, as when applied to a structural surface. This limitation stems from the difficulty of creating high-density magnetic fields without a closed magnetic circuit armature. For the same reason, the magnetoactive induced-strain actuators will always require additional construction elements besides the magnetoactive materials. While a bare-bones electroactive actuator need not contain anything more than just the active material, the bare-bones magnetoactive actuator always needs the energizing coil and the magnetic circuit armature. For this fundamental reason, the power density (either per unit volume or per unit mass) of magnetoactive induced-strain actuators will always remain below that of their electroactive counterparts.

Shape Memory Alloys

Another class of induced-strain actuating materials, with much larger strain response but low frequency bandwidth, is represented by shape memory alloys. Shape memory alloys (SMA) materials are thermally activated ISA materials that undergo phase transformation when the temperature passes certain values. The metallurgical phases involved in this process are the low-temperature martensite and the high-temperature austenite. When phase transformation takes place, the SMA material modifies its shape, i.e., it has 'memory'. The SMA process starts with the material being annealed at high-temperature in the austenitic phase (**Figure 7**). In this way, a certain shape is 'locked' into the material. Upon cooling the material transforms into the martensitic phase, and adopts a twinned crystallographic structure. When mechanical deformation is applied, the twinned crystallographic structure switches to a skew crystallographic structure. Strains as high as 8% can be achieved through this de-twinning process. This process gives the appearance of permanent plastic deformation, though no actual plastic flow took place. In typical actuator applications, this process is used to store mechanical energy by stretching SMA wires.

Upon heating, the martensitic phase changes into austenite and the shape initially imposed by annealing is recovered. In this way, the permanent deformation created through de-twinning of the martensitic phase is removed, and the material returns to its initial state

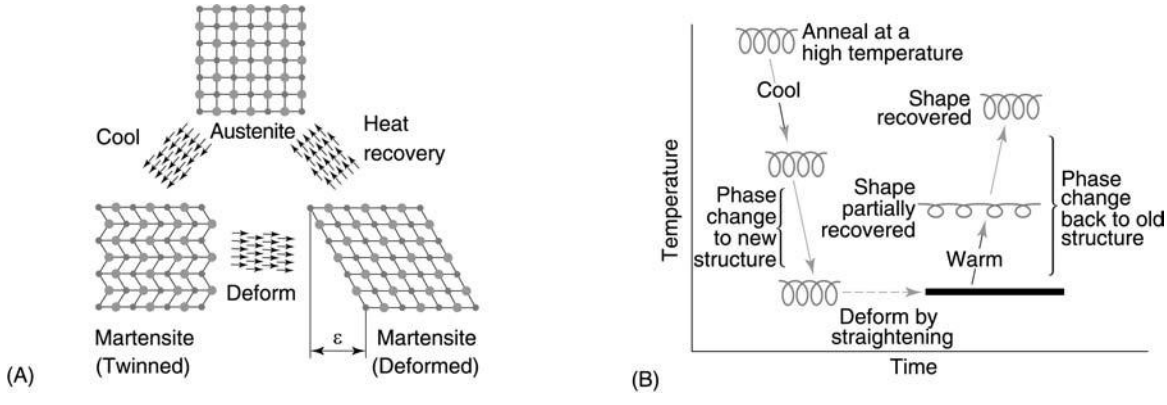


Figure 7 (see Plate 5). Principles of SMA materials: (A) change in crystallographic structure during cooling and heating; (B) associated component-shape changes, using a coil spring as an example.

memorized during annealing at austenite temperatures. If recovery is mechanically prevented, restraining stresses of up to 700 MPa can be developed. This is the one-way shape memory effect, which is a one-time only deployment at the end of which full recovery of the initial state is obtained. For dynamic operations, a two-way shape memory effect is preferred, in order that cyclic loading and unloading is attained. Two-way shape memory effect can be achieved through special thermomechanical 'training' of the material. In such cases, repeated activation of SMA strains is possible in synch with heating–cooling cycles (**Figure 8**). Many materials are known to exhibit the shape–memory effect. They include the copper alloy systems of Cu–Zn, Cu–Zn–Al, Cu–Zn–Ga, Cu–Zn–Sn, Cu–Zn–Si, Cu–Al–Ni, Cu–Au–Zn; Cu–Sn, the alloys of Au–Cd, Ni–Al; Fe–Pt; and others. The most common shape–memory alloy is the nickel–titanium compound, Nitinol^{TM}, discovered in 1962 by Buehler *et al*. at the Naval Ordnance Laboratory (NOL).

During heating, the change from martensite to austenite starts at temperature A_s and finishes at temperature A_f. During cooling, the reverse change from austenite to martensite starts at temperature M_s and finishes at temperature M_f. Note that $A_s < A_f$, while $M_s > M_f$. In the interval (A_s, A_f) on heating, and (M_s, M_f) on cooling, two phases coexist in temperature-dependent volume fractions. The values of the phase-transition temperatures can be varied with alloy composition and stress level. In fact, in SMA materials, stress and temperature act in opposition such that an SMA material brought to austenite by heating can be isothermally forced back to martensite by stressing. Shape–memory alloys composition can be tuned to start the austenite transformation at almost any predetermined temperature in the range $-50°C$ to $62°C$.

In addition to 'memory', SMA materials have other remarkable properties: phase-dependent elastic modulus, superelasticity, and high internal damping. In most metals, the elastic modulus decreases with temperature: in SMA materials it actually increases, since the modulus of the high-temperature austenitic phase can be up to three times larger than that of the low-temperature martensitic phase.Superelasticity is associated with the fact that strains of up to 12% can be accommodated before actual plastic deformation starts to take place. Superelasticity is displayed by low-A_f SMA materials, which are austenitic at room temperature. As stress is applied, the superelastic SMA material undergoes phase transformation and goes into martensite. Upon unloading, the austenite phase is recovered, and the material returns to the zero-stress zero-strain state, i.e., displays superelastic properties (**Figure 9**). Though full strain recovery has been achieved, the recovery is nonlinear and follows a hysteretic path. The internal damping of the SMA materials is associated with the hysteresis curve enclosed by the loading–unloading cycle. The area within this cycle is orders of magnitude larger than for conventional elastic materials.

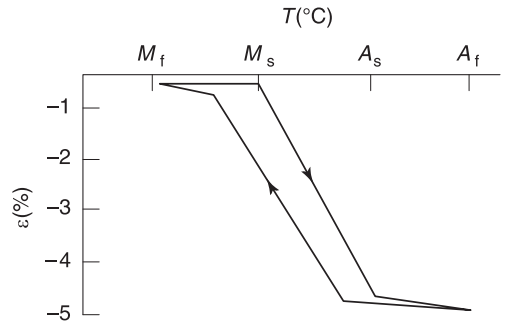


Figure 8 Schematic representation of strain recovery through the SMA effect in a two-way shape memory alloy.

Modeling of SMA Materials

Since the mechanical behavior of SMA materials is closely related to the microscopic martensitic phase transformation, the constitutive relations developed for conventional materials such as Hooke's law and plastic flow theory are not directly applicable. Hence, specific constitutive relations, which take into consideration the phase transformation behavior of SMA, have been developed. Two approaches are generally used: (i) the phenomenological (macroscopic) approach, based on extensive experimental work; and (ii) the physical (microscopic) approach using fundamental physical concepts. Hybrid approaches that combine both approaches to obtain a more accurate description and prediction of the SMA material behavior have also been used. Tanaka's model, based on the concept of the free-energy driving force, considers a one-dimensional metallic material undergoing phase transformation. The state variables for the material are strain, ε, temperature, T, and martensitic fraction, ξ. Then, a general state variable, Λ, is defined as:

$$\Lambda = (\bar{\varepsilon}, T, \xi) \qquad [5]$$

The Helmholtz free energy is a function of the state variable Λ. The general constitutive relations are then derived from the first and second laws of thermodynamics as:

$$\bar{\sigma} = \rho_0 \frac{\partial \Phi}{\partial \varepsilon} = \sigma(\bar{\varepsilon}, T, \xi) \qquad [6]$$

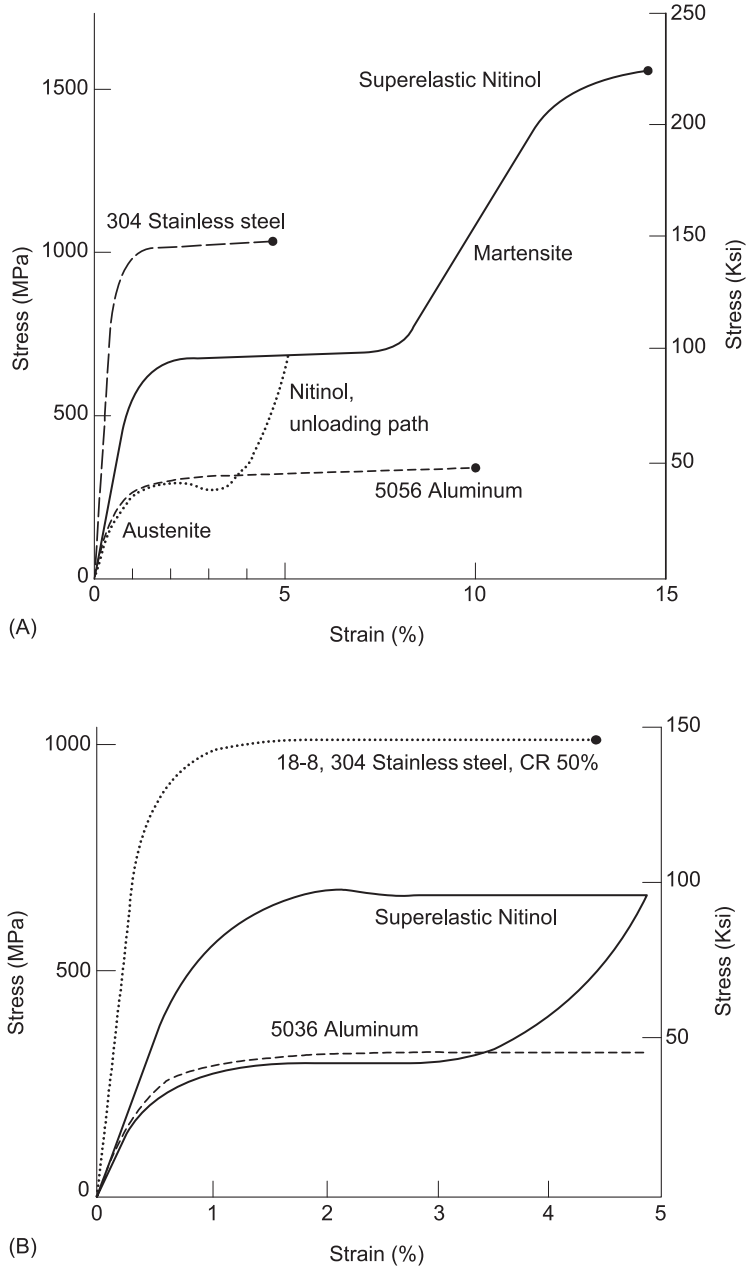


Figure 9 Stress–strain curves of superelastic Nitinol and other metallic wires: (A) overall behavior; (B) zoom-in on the low-strain range.

The stress is a function of the martensite fraction, an internal variable. Differentiation of eqn [6] yields the stress rate equation:

$$\dot{\bar{\sigma}} = \frac{\partial \sigma}{\partial \bar{\varepsilon}}\dot{\bar{\varepsilon}} + \frac{\partial \sigma}{\partial T}\dot{T} + \frac{\partial \sigma}{\partial \xi}\dot{\xi} = D\dot{\bar{\varepsilon}} + \Theta\dot{T} + \Omega\dot{\xi} \quad [7]$$

where D is Young's modulus, Θ is the thermoelastic tensor, and Ω is the transformation tensor, a metallurgical quantity that represents the change of strain during phase transformation. The Martensite fraction, ξ, can be assumed as an exponential function of stress and temperature:

$$\begin{aligned} \xi_{M\to A} &= \exp\left[A_a(T - A_s) + B_a\sigma\right], \\ \xi_{A\to M} &= 1 - \exp\left[A_m(T - M_s) + B_m\sigma\right] \end{aligned} \quad [8]$$

where A_a, A_m, B_a, B_m are material constants in terms of the transition temperatures, A_s, A_f, M_s, M_f. Time integration of eqn [7] yields:

$$\sigma - \sigma_0 = D(\varepsilon - \varepsilon_0) + \theta(T - T_0) + \Omega(\xi - \xi_0) \quad [9]$$

It is convenient to adopt a cosine model for the phase transformation, i.e.:

$$\xi_{A\to M} = \frac{\xi_M}{2}\{\cos[a_A(T - A_s) + b_A\sigma] + 1\},$$
$$\xi_{M\leftarrow A} = \frac{1 - \xi_A}{2}\{\cos[a_M(T - M_s) + b_{M\sigma}] + 1\} + \frac{1 + \xi_A}{2} \quad [10]$$

where

$$a_A = \frac{\pi}{A_f - A_s}, \quad a_M = \frac{\pi}{M_s - M_f},$$
$$b_A = -\frac{a_A}{C_A}, \quad b_M = -\frac{a_M}{C_M}$$

while C_M and C_A are slopes

Advantages and Limitations of SMA Actuation

The main advantage of SMA materials is their capability to produce sizable (up to 8%) actuation strains. In addition, they have inherent simplicity since only heating (readily available through the electric Joule effect) is needed for actuation. Main limitations of the SMA actuators are the poor energy conversion efficiency, and the low bandwidth of the heating/cooling process which can only achieve a few Hz, at the very best.

Effective Implementation of Induced-strain Actuation

Design and Construction of Piezo-electric and Electrostrictive Actuators

An electroactive solid-state actuator consists of a stack of many layers of electroactive material (PZT or PMN) alternatively connected to the positive and negative terminals of a high-voltage source (**Figure 10A**). Such a PZT or PMN stack behaves like an electrical capacitor. When activated, the electroactive material expands and produces output displacement. The PZT or PMN stacks are constructed by two methods. In the first method, the layers of active material and the electrodes are mechanically assembled and glued together using a structural adhesive. The adhesive modulus (typically, 4–5 GPa) is at least an order of magnitude lower than the modulus of the ceramic (typically, 70–90 GPa). This aspect may lead to the stack stiffness being significantly lower than the stiffness of the basic ceramic material. In the second method, the ceramic layers and the electrodes are assembled in the 'green' state. Then, they are fired together (co-fired) under a high isostatic

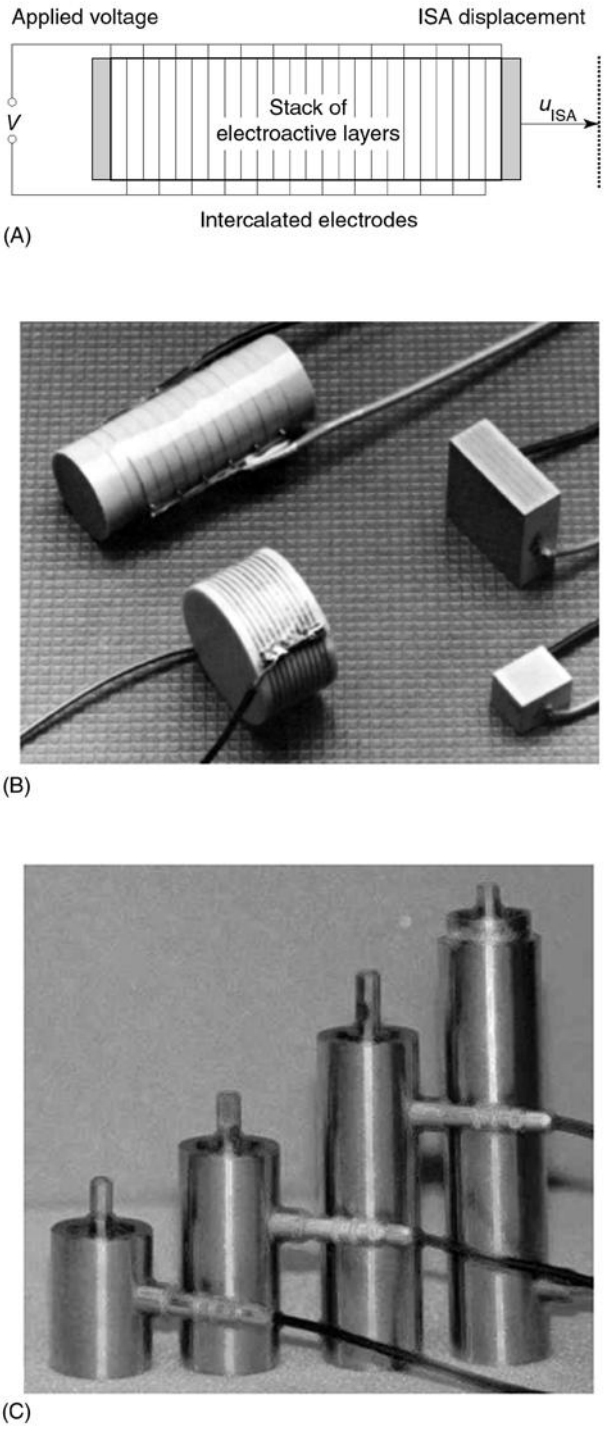


Figure 10 Induced strain actuator using a PZT or PMN electroactive stack: (A) schematic; (B) typical commercially available cofired stack from EDO Corporation; (C) a range of Polytec PI actuators heavy-duty actuators.

pressure (HIP process) in the processing oven. This process ensures a much stiffer final product and, hence, a better actuator performance. However, the processing limitations, such as oven and press size, etc., do not allow the application of this process to anything else but small-size stacks.

The PZT and PMN stacks may be surrounded by a protective polymeric or elastomeric wrapping. Lead wires protrude from the wrapping for electrical connection. Steel washers, one at each end, are also provided for distributing the load into the brittle ceramic material. When mounted in the application structure, these stacks must be handled with specialized knowledge. Protection from accidental impact damage must be provided. Adequate structural support and alignment are needed. Mechanical connection to the application structure must be such that neither tension stresses nor bending are induced in the stack since the active ceramic material has low tension strength. Hence, the load applied to the stack must always be compressive and perfectly centered. If tension loading is also expected, adequate prestressing must be provided through springs or other means. For applications, the stack can be purchased as such (**Figure 10B**), or encapsulated into a steel casing which provides a prestress mechanism and the electrical and mechanical connections (**Figure 10C**).

Figure 11 compares the response of two commercially available actuators, one piezo-electric, the other electrostrictive. It can be seen that both have about the same maximum induced-strain value, as it can be readily verified by dividing the maximum displacement by the actuator length. Both material types display quasilinear behavior. The piezo-electric actuator allows some field reversal (up to 25%, according to manufacturer), which make the total stroke larger. On the other hand, the electrostrictive actuator has much less hysteresis, i.e., less losses and less heating in high-frequency regime.

Design and Construction of Magnetostrictive Actuators

Magnetostrictive materials can be also used to produce an effective actuator. **Figure 12A** shows the typical layout of a magnetostrictive actuator. It consists of a Terfenol-D bar surrounded by an electric coil and enclosed into an annular magnetic armature. The magnetic circuit is closed through end caps. In this arrangement, the magnetic field is strongest in the cylindrical inner region filled by the Terfenol-D bar. When the coil is activated, the Terfenol-D expands and produces output displacement. The Terfenol-D bar, the coil, and the magnetic armature are assembled with prestress between two steel-washers and put inside a protective wrapping to form the basic magnetoactive induced-strain actuator. Though the Terfenol-D material has been shown to be capable of up to 2000 μstrain, its behavior is highly nonlinear in both magnetic field response and the effect of compressive prestress. Manufacturers of magnetostrictive actuators optimize the internal prestress and magnetic bias to get a quasilinear behavior in the range of 750–1000 μm m^{-1}. **Figure 12B** shows the displacement–magnetic field response for a typical large-power magnetostrictive actuator (ETREMA AA–140J025, 200 mm long, $\approx$1 kg weight, 0.140 mm peak-to-peak output displacement).

Principles of Induced-Strain Structural Actuation

In structural applications, the induced ISAs must work in direct relation with the actuated structure,

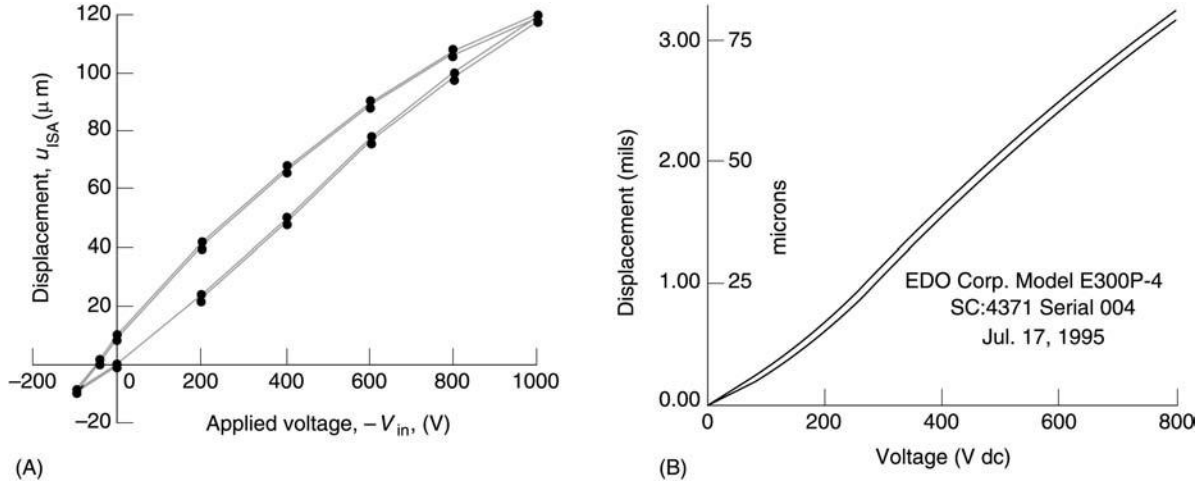


Figure 11 The induced-strain displacement vs applied voltage for typical electroactive actuators: (A) Polytec PI P-245.70 PZT stack, 99 mm long (Giurgiutiu *et al.*, 1997); (B) EDO Corporation model E300P PMN stack, 57 mm long.

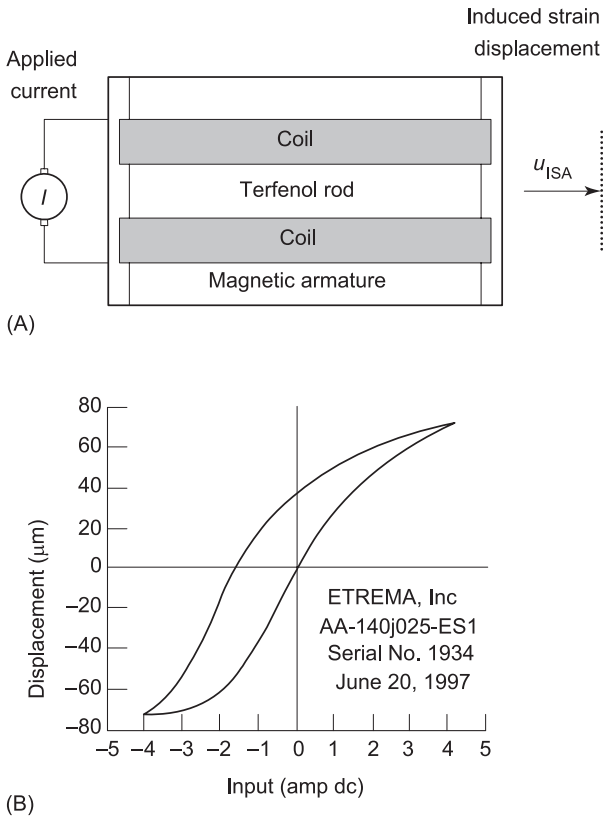


Figure 12 (A) Schematic construction of a magnetostrictive (Terfenol-D) solid-state actuator; (B) typical response curve (actuator model AA140J025-ES1, ETREMA, Inc.).

and special attention must be given to their interaction. The main differentiating feature between active materials actuators and conventional actuators lies in the amount of available displacement. The induced-strain effect present in active materials results in output displacements that seldom exceed 100 μm (0.1 mm). In a conventional actuator, e.g., a hydraulic cylinder, displacement of the order of several millimeters can be easily achieved, and if more displacement is needed, additional hydraulic fluid could be pumped in. In contrast, an ISA has at its disposal only the very limited amount of displacement generated by the induced-strain effect. This limited displacement needs to be carefully managed, if the desired effect is to be achieved. Under reactive service loads, the internal compressibility of the active materials actuator 'eats-up' part of the induced-strain displacement, and leads to reduced output displacement (**Figure 13A**). If the external stiffness, k_e, is reduced, the force in the actuator is also reduced, and more displacement is seen at the actuator output end. For a free actuator, i.e., under no external reaction, the output displacement is maximum. However, no active work is being done in this case since the force is zero. At the other extreme, when the actuator is fully constrained, the force is maximum, but no work is again performed since the displacement is zero. An optimum is attained between these two extremes, and this optimum can be best described in terms of stiffness match principle. Under static conditions, the stiffness match principle implies that the external stiffness (i.e., the stiffness of the application) and the internal stiffness of the actuator are equal, which gives a stiffness ratio with value $r = 1$. As shown in **Figure 13B**, $r = 1$ corresponds to maximum energy situation.

Under dynamic conditions, this principle can be expressed as dynamic stiffness match or impedance match. **Figure 13C** shows a solid-state ISA operating against a dynamic load with parameters $k_e(\omega)$, $m_e(\omega)$, and $c_e(\omega)$. The actuator is energized by a variable voltage, $v(t)$, which sends a time-varying current, $i(t)$. The actuator output displacement and force are, $u(t)$ and $F(t)$, respectively. The complex stiffness ratio is given by

$$\bar{r}(\omega) = \bar{k}_e(\omega)/\bar{k}_i \qquad [11]$$

where $\bar{k}_e(\omega) = (k_e - \omega^2 m_e) + i\omega c$ is the complex external stiffness of the dynamic load, and $\bar{k}_i$ is the complex internal stiffness of the ISA.

Power and Energy Extraction from ISAs

Using the definition, mechanical power = force $\times$ velocity, and assuming harmonic motion, the complex power is expressed as $\bar{P} = \frac{1}{2}\bar{F}\bar{v}^*$, where, $\bar{v}^*$ is the complex conjugate of $\bar{v}$, and $\bar{v} = i\omega\bar{u}$. Output mechanical power and energy is written as:

$$\begin{aligned}\bar{P}_{mech} &= \tfrac{1}{2}\bar{k}_e\bar{u}(i\omega\bar{u})^* \\ &= -i\omega\frac{\bar{r}(\omega)}{[1+\bar{r}(\omega)][1+\bar{r}(\omega)]^*}\left(\tfrac{1}{2}\bar{k}_i\hat{u}_{ISA}^2\right)\end{aligned} \qquad [12]$$

$$\bar{E}_{mech} = \tfrac{1}{2}\bar{k}_e\bar{u}(\bar{u})^* = \frac{\bar{r}(\omega)}{[1+\bar{r}(\omega)][1+\bar{r}(\omega)]^*}\left(\tfrac{1}{2}\bar{k}_i\hat{u}_{ISA}^2\right) \qquad [13]$$

The maximum output power and energy are attained at the dynamic stiffness match condition:

$$P_{out}^{max} = \omega\tfrac{1}{4}E_{mech}^*, \quad E_{out}^{max} = \tfrac{1}{4}E_{mech}^* \qquad [14]$$

where:

$$E_{mech}^* = \tfrac{1}{2}k_i\hat{u}_{ISA}^2$$

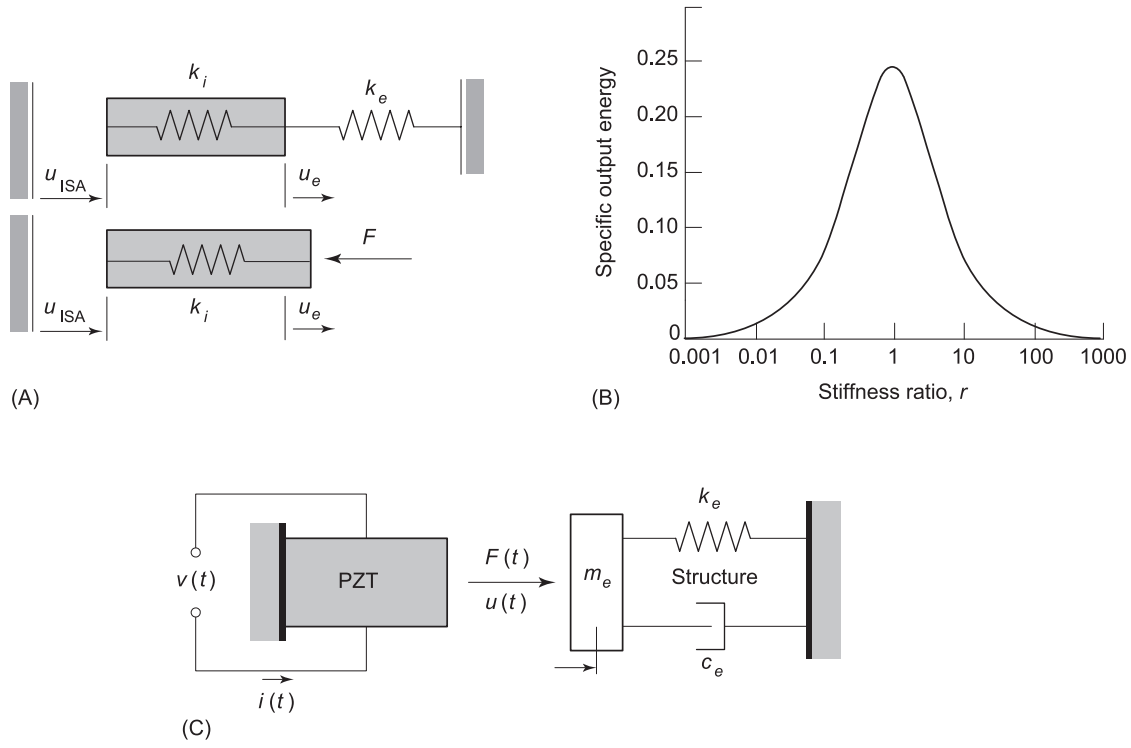


Figure 13 Schematic of the interaction between an active material actuator and an elastic structure: (A) the active displacement, u_{ISA}, is partially lost due to the actuator internal compressibility, such that the resulting external displacement, u_e, is always less; (B) maximum energy extraction is attained when the internal and external stiffness match; (C) under dynamic conditions, the frequency dependent dynamic stiffness must be used.

Electrical Input Power and Energy

From the electrical side, note that, for frequencies well below the actuator free resonance (typically, 1–10 kHz, depending on length), the wave propagation effects can be ignored, and the equivalent input admittance as seen at the actuator terminals is:

$$Y_C(\omega) = i\omega C\left[1 - \kappa_C^2 \frac{\bar{r}(\omega)}{1 + \bar{r}(\omega)}\right] \qquad [15]$$

where:
$\kappa^2 = d^2/(\bar{s}\bar{\varepsilon})$ and $\bar{s} = (1 - i\delta_s)s$, $\varepsilon = (1 - i\delta_\varepsilon)\varepsilon$, δ_s is the hysteresis internal damping coefficient of the actuator, δ_ε is the dielectric loss coefficient of the actuator, $d = (u_{ISA}/V)(t/l)$, $\varepsilon = (C/A)(t^2/l)$, $s = A/lk_i$, l is the stack length, t is the layer thickness, A is the stack cross-sectional area, and u_{ISA} is the dynamic free stroke at voltage V, while $\kappa_C^2 = d^2/s\varepsilon = k_i u_{ISA}^2/CV^2$ is the effective full-stroke electromechanical coupling coefficient of the actuator. For magnetoactive actuators, $\kappa_L^2 = k_i u_{ISA}^2/LI^2$ and

$$Z_L(\omega) = i\omega L\left[1 - \kappa_L^2 \frac{\bar{r}(\omega)}{1 + \bar{r}(\omega)}\right] \qquad [16]$$

The input electrical power can be evaluate as $(1/2)Y_C V^2$ for capacitive loads, and $(1/2)Z_L I^2$ for inductive loads, where the frequency dependent Y_C and Z_L are given by eqns [15] and [16], respectively. When the DC bias effects are included, expressions that are slightly more complicated need to be used.

Design of Effective Induced-strain Actuators

The design of effective piezo actuators is particularly difficult due to the small displacement generated by these materials. However, the forces that can be generated by a piezo actuator can be very large; are only limited by the inherent stiffness and compressive strength of the piezo material; by its effective area. For most practical applications, displacement amplification of the induced strain displacement is employed. The effective design of the displacement amplifier can 'make or break' the practical effectiveness of a piezo actuator. The most important parameter that needs to be optimized during such a design is the energy extraction coefficient defined as the ratio between the effective mechanical energy delivered by the actuator and the maximum possible energy that can be delivered by the actuator in the stiffness–match condition.

Of extreme significance in the design of an effective ISA is the amount of energy available for performing external mechanical work. **Figure 14** presents comparison of the energy density per unit volume for some commercially available ISAs under static and dynamic regimes. Typical energy density values are in the range 2.71–15.05 J dm^{-3} (0.292–1.929 J kg^{-1}) under static conditions, and 0.68–3.76 J dm^{-3} (0.073–0.482 J kg^{-1}) under dynamic conditions. Power densities of up to 23.6 kW dm^{-3} (3.0 kW kg^{-1}) at 1 kHz are predicted. The overall efficiency of active-material actuation depends, to a great extent, on the efficiency of the entire system that includes the active-material transducer, the displacement amplification mechanisms, and the power supply.

Power Supply Issues in Induced Strain Actuation

Since ISAs can operate in the kHz range, eqn [14], in conjunction with **Figure 14**, indicates the opportunity for the generation of large output power densities. However, a number of practical barriers need to be overcome before this can be achieved: (i) the capability of power supply to deliver kVA reactive power; (ii) the dissipation of the heat generated in the active material due to internal losses (hysteresis) that can be in the range 5–10% of the nominal reactive input power; and (iii) the electromechanical system resonance that sets upper frequency limits.

The power supply aspects of induced-strain actuation are currently being addressed by using specialized power supplies (switching amplifiers) that are able to handle reactive loads much better than conventional linear amplifiers. The switching amplifiers (**Figure 15**) utilize high frequency pulse width modulation (PWM) principles and solid-state switching technology to drive current in and out of the capacitive load presented by the induced-strain piezo-electric actuator. In this process, a high-value inductance ballast is utilized (**Figure 15A**). To simultaneously achieve optimal actuator performance and minimum weight, the switching amplifier design has to be performed using a complete model that includes adequate representation of the actuator and external load dynamics (**Figure 15B**).

The difficulty connected with the electric-supply may seem less severe when using magnetoactive devices, such as Terfenol-D actuators, because they are current driven and require lower voltages at low frequencies. At present, the low-voltage power supply technology is predominant and cheaper than the high-voltage technology, which somehow facilitates the use of magnetostrictive actuators.

The effect of adaptive excitation on the current and power requirements, and on the displacement output from a heavy-duty piezo-electric actuator driving a smart structure near the electromechanical resonance is shown in **Figure 16**. The actuator was assumed to have $k_i = 370\,\text{kN mm}^{-1}$ internal stiffness, $C = 5.6\,\mu\text{F}$ internal capacitance, 3.5 kHz resonance, and output displacement $u_m \pm u_a = 22.5 \pm 37.5\,\mu\text{m}$ when driven by a voltage $V_m \pm V_a = -375 \mp 625\,\text{V}$. The external mechanical load was assumed to have a matched static stiffness, a mechanical resonance of 30 Hz,

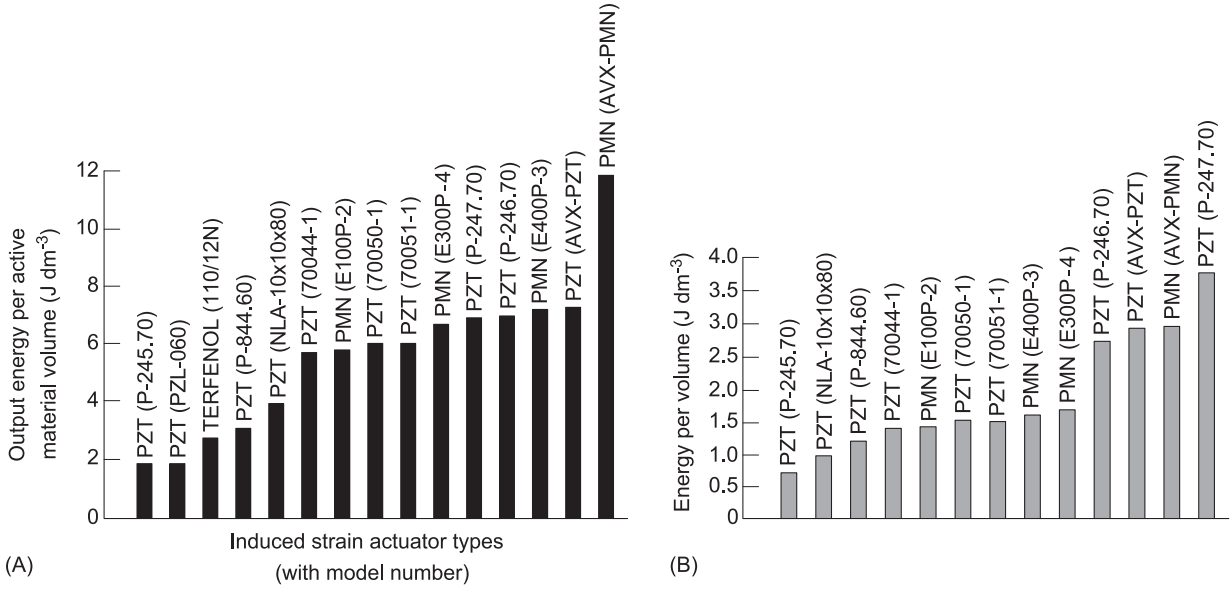


Figure 14 Specific energy output capabilities of a selection of commercially available induced-strain actuators: (A) static operation; (B) dynamic operation.

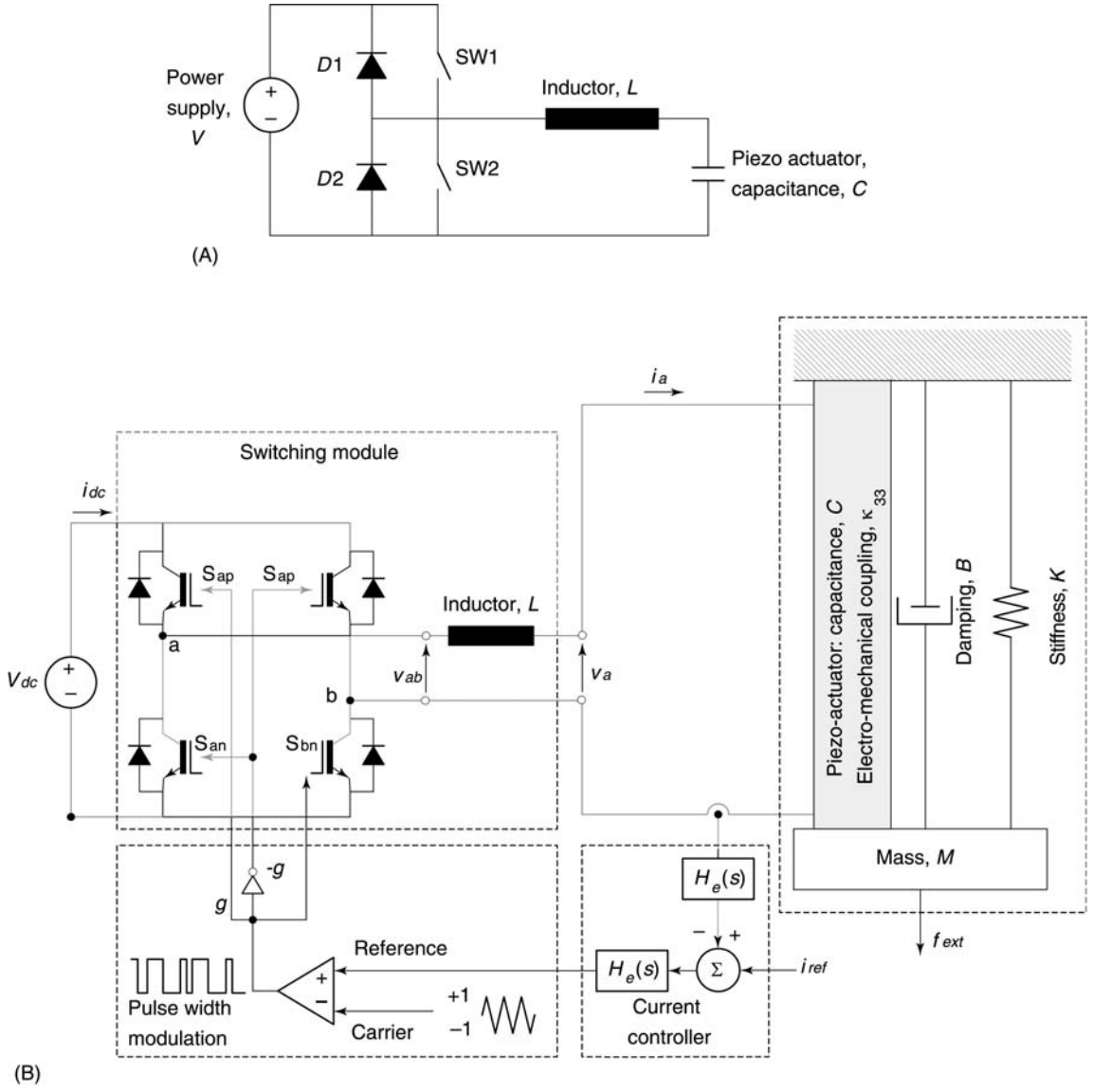


Figure 15 (see Plate 6). Power supplies for active material actuators: (A) principle of switching power supplies for high reactive load; (B) schematic of the supply system incorporating the switching module, current controller, pulse width modulator, and the piezo-actuator-external load assembly.

and a 1% internal damping. The system was assumed driven by a 1 kVA amplifier, with up to 1000 V voltage and 1 A current. As show in **Figure 16**, the electromechanical system incorporating the structure and the embedded actuator displays an electromechanical resonance at 42.42 Hz. Without adaptive excitation, i.e., under constant voltage supply, the current demands are very large, the actuator experiences a displacement peak that may lead to its destruction, and the required power is excessive. When adaptive excitation was simulated, both the displacement and the current could be kept within bounds, while the power requirements became more manageable and kept within the 1 kVA capability of the power amplifier.

Smart Structures

The concept of smart structures has largely evolved by biomimesis and under the influence of Asimov's three laws of robotics. In the biological world, plants and animals alike react to the environment in order to protect their existence, or to acquire the much needed nourishment. For example, the sharp heat from an open flame would instantly make someone retract his hand. It would also, most probably, make the person shout 'ouch!'. In the engineering world, smart structures are viewed as adaptive systems fitted with sensors, actuators, and command-control processors that could take automatic actions without specific human interventions.

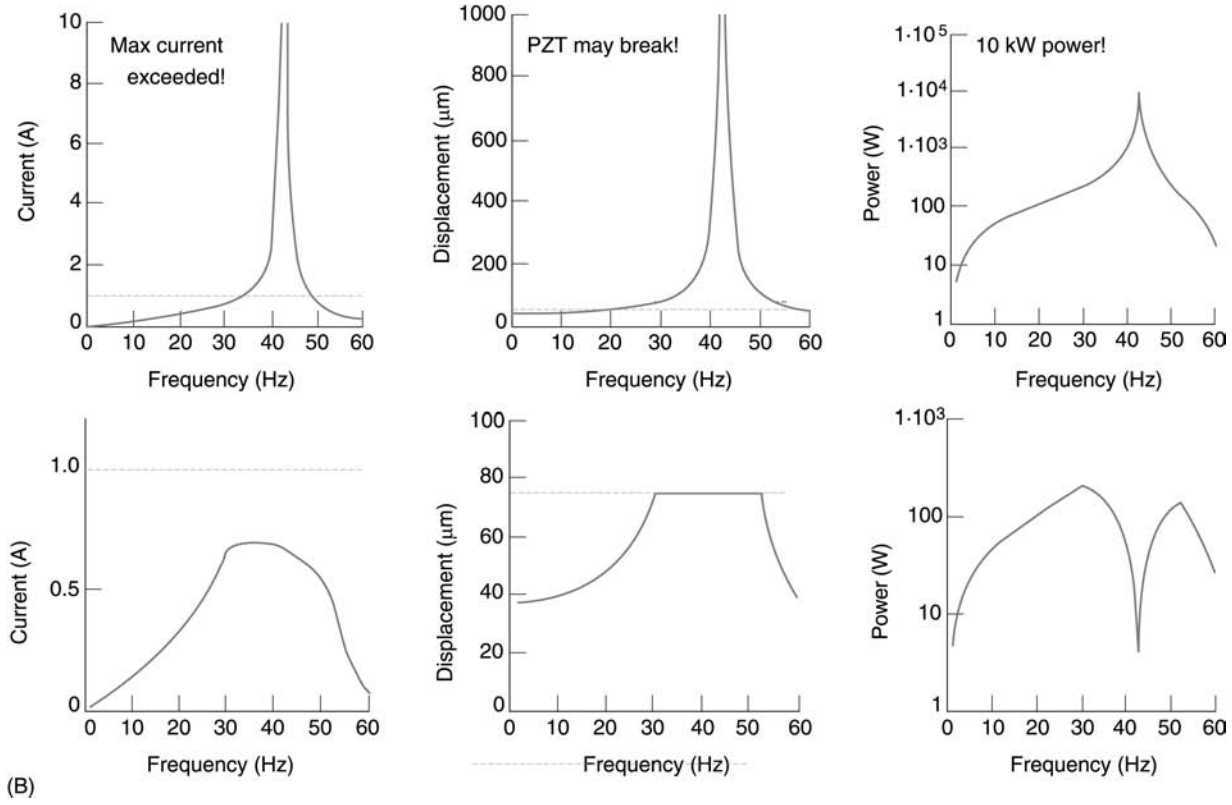


Figure 16 Adaptive excitation of piezo-electric actuators near embedded electromechanical resonance: (A) under constant voltage excitation, the current demands are very large, the actuator may break, and the required power is excessive; (B) with adaptive excitation, both the displacement and the current are kept within bounds, and the power becomes manageable.

Sensory Smart Structures

Sensory smart structure attributes are found in even the simplest single-cell micro-organism (**Figure 17A**). A bridge fitted with smart structure characteristics has been conceptualized. Such a 'smart' bridge (**Figure 17B**) would be expected to 'sense' the environment, react accordingly, and 'tell' what is happening by sending alarm signals that announce that strength and safety are diminishing, and appropriate action is needed. In this example, a smart structure is seen that is capable of automatic health monitoring, damage detection, and failure prevention.

Adaptive Actuation Smart Structures

Another class of smart structure is that fitted with adaptive actuation. Nature offers the ideal example of adaptive actuation. A pair of antagonistic muscles (*musculus biceps brachii* and *musculus triceps brahii*) ensures exact and precise position control during the most difficult maneuvers of our arms. The skeletal muscles of the human arm are attached at a small-displacement high-force position, well-suited for the induced-strain muscle actuation (**Figure 18A**). As a catapulting twitch is performed, the nonlinear skeletal kinematics effects a favorable response during which the distance between the thrown weight and the elbow joint decreases while the perpendicular distance between the muscle tendon and the joint increases, such that the overall force required in the muscular actuator decreases as the catapulting motion develops.

In fact, once the weight has been put in motion, the biceps muscle can reduce the contracting signal and even stop before the end of the catapulting motion. In the same time, the antagonistic triceps muscle can start its braking action before the end position has been achieved, such that a smooth transition is achieved. This remarkable feat is accomplished through complex adaptive control architecture, as depicted in **Figure 18B**. An engineering building incorporating adaptive structural response is presented in **Figure 18C**. This smart structure not only senses and processes the external stimuli, but also takes mechanical action. When the vibration excitation from a gust of wind or earthquake is endangering the structural integrity through excessive resonance response, action is taken in the variable stiffness

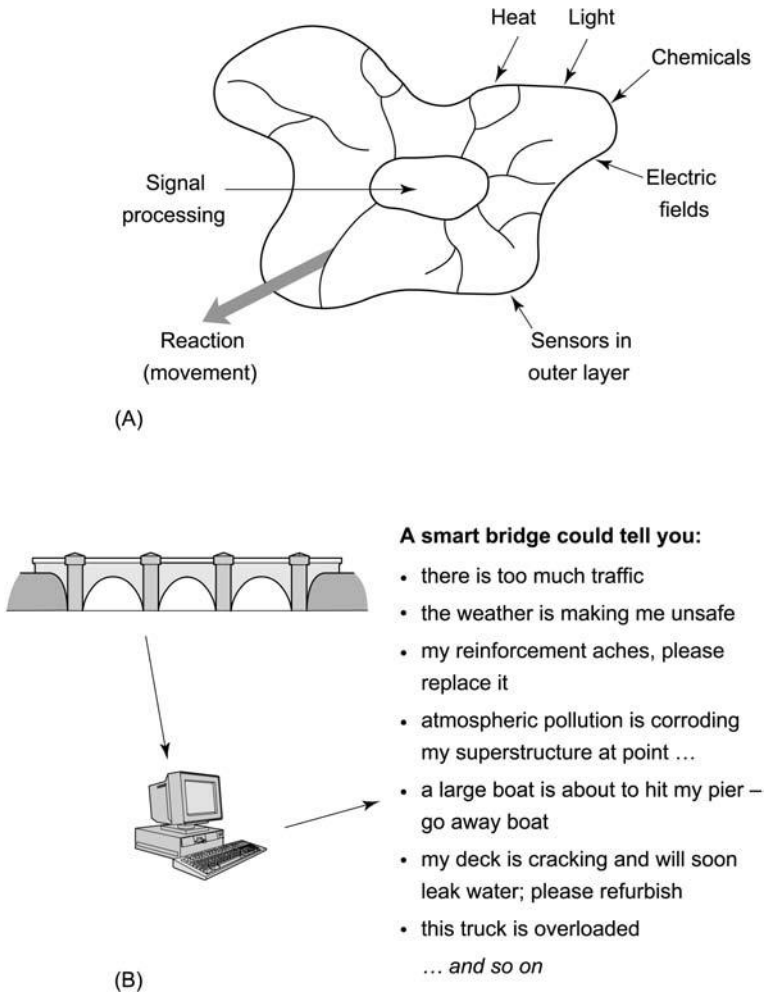


Figure 17 Sensory smart structures: (A) single cell micro-organism viewed as a sensory smart structure; (B) smart structure concept applied to a bridge.

members such that the structure's natural frequency is shifted and the resonance is avoided. This natural frequency shift achieved through stiffening or relaxing of active structural members resembles the bracing of one's muscles when trying to attain steadiness in a challenging situation. Besides resonance avoidance, smart structures can also attempt to dissipate energy through active and passive mechanisms, or to prevent a nonlinear vibrations or aeroelastic effect from building up through vibration cancellation.

Applications of Shape Memory Alloys to Vibration Control

Because of its biocompatibility and superior resistance to corrosion, shape memory alloys such as Nitinol have gained wide usage in the medical field as bone plates, artificial joints, orthodontic devices, coronary angioplasty probes, arthroscopic instrumentation, etc. In engineering, these materials have been used as force actuators and robot controls. They also offer vibration control potentials based on three important principles: (i) the three to four times increase in elastic modulus in the transition from martensitic to austenitic phase; (ii) the creation of internal stresses; and (iii) the dissipation of energy through inelastic hysteretic damping. These effects can be practically realized either as additional components to be retrofitted on existing structures, or as hybrid composite materials containing embedded SMA fibers.

The increase in elastic modulus is used in the active properties tuning (APT) vibration control method. As SMA wires are activated by heating with electric current or other methods, their modulus increases threefold from 27 GPa to 82 GPa. Depending on the structural architecture and on how much SMA material is used, this may result in a sizable change in the effective structural stiffness, and a considerable frequency shift away from an unwanted resonance.

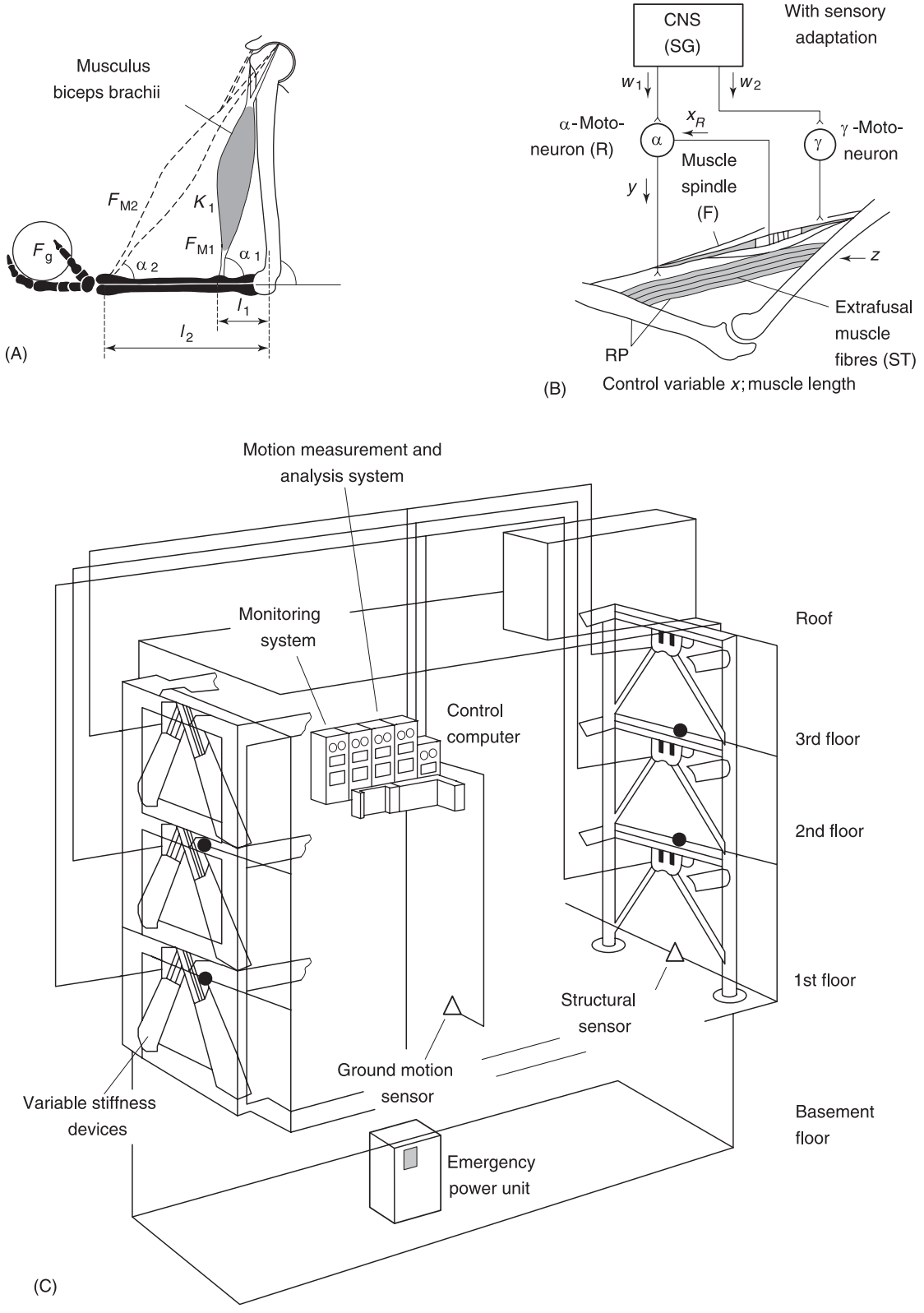


Figure 18 Concepts in adaptive smart structures actuation: (A) kinematic of an arm muscle; (B) muscle control system with sensory adaptation; (C) schematic of an earthquake-resistant variable-stiffness building (KaTRI No.21 in service in Tokyo, Japan).

The activation speed, which depends on the heating rate, is usually sufficient to achieve acceptable structural control. The recovery, however, depends on the rate of cooling, and hence takes place much more slowly.

The creation of internal stresses is used in the active strain energy tuning (ASET) method. The activation of stretched SMA fibers can make them shrink by 4–8% and thus create considerable contractile stress in the support structure. If the SMA fibers are placed inside beams or plates, active frequency control can be readily achieved, since the presence of inplane compressive stresses can considerably change the beams' and plates' natural frequencies. One ready application of this effect is the avoidance of critical speeds during the run-up and run-down of high-speed shafts.

Applications of Electro- and Magnetoactive Materials to Vibration Control

Active materials are well suited for vibration and aeroelastic control. Electroactive (PZT and PMN) and magnetoactive (Terfenol-D) actuators can be used as translational actuators to replace conventional devices, or as surface-bonded actuators to induce axial and bending strains in the host structure. In the former case, the strain induced parallel to the field direction is utilized, as, for example, in piezoelectric stacks. In the latter case, the strain induced transverse to the direction of the applied field is used. Translational ISAs are ideal in retrofit situations when the replacement of a conventional actuator with a 'smart' actuator is sought. Surface-bonded actuation is a completely new engineering concept, which is specific to the smart structures world. Bonded electroactive actuator wafers have been used successfully to control the shape of deformable mirrors. In the stack configuration, they have been used for impact dot-matrix printing. Advantages over conventional electromagnetic actuators included order-of-magnitude higher printing speeds, order-of-magnitude lower energy consumption; and reduced noise emissions. A tunable ultrasonic medical probe composed of electroactive elements embedded in a polymer matrix has also been developed. Electro- and magneto-active materials can be used to enhance structural damping and reduce vibrations. Two mechanisms are available: (i) direct approach, in which the vibration energy is dissipated directly through the electromechanical interaction between the active material and the host structure; (ii) indirect approach, in which the active material is used to enhance the damping properties of a conventional damping treatment. The dissipation of vibration energy through the electromechanical interaction of the active materials with the host structure can be achieved either passively or actively. Since the active material is connected to the structure undergoing vibration, the deformation of the active material follows the deformation of the structure. As the structure deforms during vibrations, the active material takes up the strain and transforms it into an oscillatory electrical field.

For passive active-material vibration suppression, the induced electric field is used to drive currents into an external resistance thus dissipating the energy through Ohmic heating (**Figure 19**). In order to dissipate selected frequencies, RCL tuning principles are applied. In active vibration suppression, the active material is used to produce vibration input in antiphase with the external disturbance, thus resulting in noise and vibrations cancellation. In this case, the energy is dissipated in the heat sink of the driver–amplifier circuit. The active material can be also used to enhance the damping properties of a conventional damping material through the 'constraint layer damping effect'. Conventional vibration damping treatments utilize the dissipation properties of viscoelastic materials that mainly operate in shear. The shear can be enhanced if, on top of the damping layer, an extra layer of active material is added that deforms in antiphase with the base structure. Thus, the damping layer between the active material layer and the base structure is subjected to a much larger differential shear strain than in the absence of the active layer.

For illustration, two current aerospace smart structure projects are discussed. One project is aimed at the reduction of noise and vibrations in helicopter rotors (**Figure 20**). The other project is addressing the buffet vibrations alleviation in a fixed wing aircraft (**Figure 21**). The smart materials actuation rotor technology (SMART) rotor blade program, under way at Boeing (Mesa), is tasked to test the feasibility of using active materials actuators for rotor blade control to reduce noise and vibrations, improve ride qualities, and extend the service life. The conceptual design of the SMART rotor blade program calls for the simultaneous satisfaction of two important operational requirements: (i) reduction of blade vibration through in-flight rotor track and balance adjustments; and (ii) reduction and counteraction of aerodynamically induced noise and vibration through an actively controlled aerodynamic surface. The first objective is achieved with a slow-moving trim tab controlled through a bidirectional SMA actuator (**Figure 20**). The second objective is met with a fast-moving control flap actuated by piezo-ceramic stacks through a stroke-amplifier.

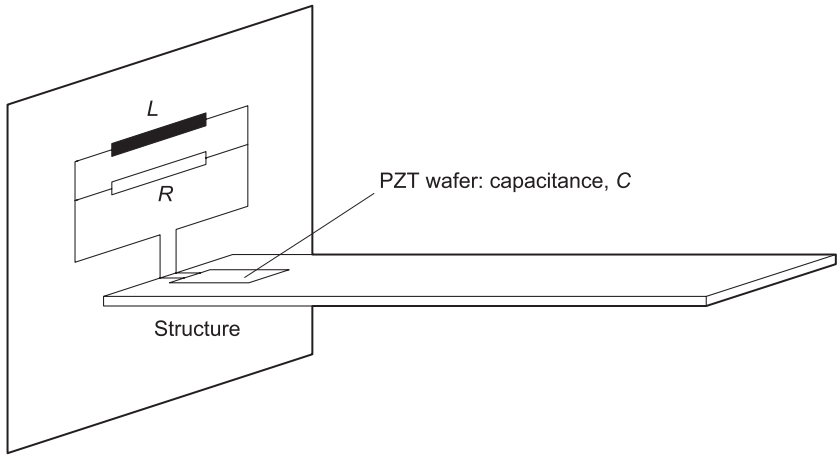


Figure 19 Tuned shunt circuit for vibration control. *L*, inductor; *R*, resistor.

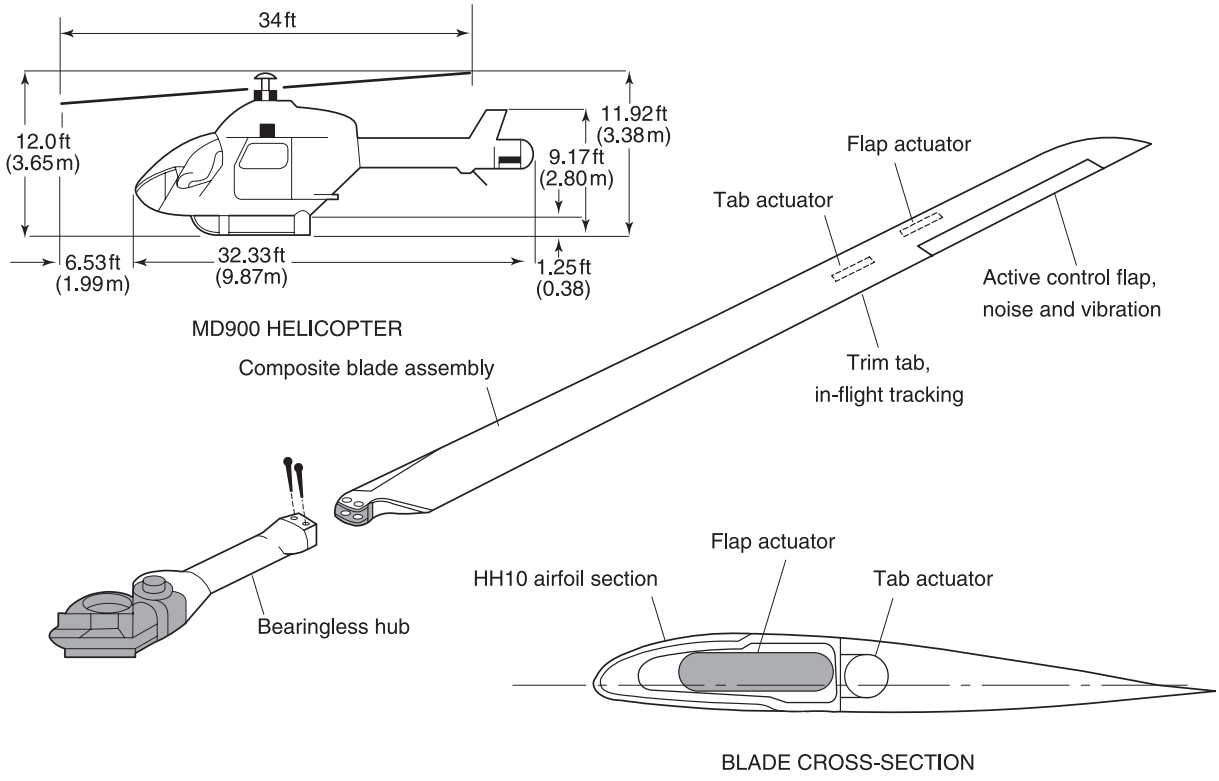


Figure 20 MD 900 helicopter and hingeless blade displaying the planned trim tab for in-flight tracking and active control flap for noise and vibration reduction.

The second smart structures project to be discussed here relates to aircraft tail buffeting. Tail buffeting is a significant concern for aircraft fatigue and maintenance. The actively controlled response of buffet affected tails (ACROBAT) program studied active materials solutions to resolve the buffet problems of the F/A–18 twin-tail aircraft. A 1/6-scale full-span model was tested in the NASA Langley transonic dynamics tunnel. The portside vertical tail was equipped with surface-bonded piezo-electric wafer actuators, while the starboard vertical tail had an active rudder and other aerodynamic devices. During

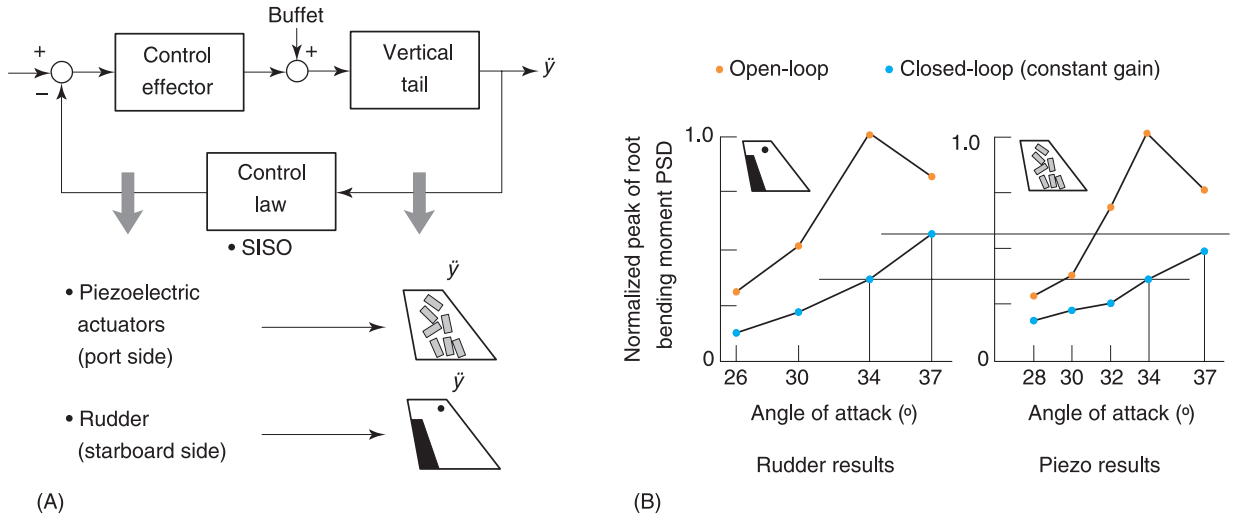


Figure 21 ACROBAT tail buffet alleviation experiments: (A) single-input single-output (SISO) control law design for active rudder and piezo-electric wafers excitation; (B) power spectrum density (PSD) peak values for the root bending moment at the first bending resonance.

the wind tunnel tests, constant-gain active control (**Figure 21A**) was able to reduce power spectral density of the first bending resonance by as much as 60% (**Figure 21B**).

Adaptive Algorithms for Smart Structures Control

Implementation of control algorithms in smart structures architecture is subject to attentive scrutiny. Conventional application of classical control algorithms is only the first step in this process. Much better results are obtained if modern adaptive control is used, such that the resulting smart structure can react to changes in the problem-definition parameters. Actual structural designs are very complex, nonlinear in behavior, and subject to load spectra that may be substantially modified during the structures service life. Under such adverse situations, the resulting uncertainty in the controlled plant dynamics is sufficient to make 'high-performance goals unreachable and closed-loop instability a likely result'. To address this problem, at least three adaptive control approaches are advocated: (i) adaptive signal processing methods; (ii) model reference adaptive control (MRAC); and (iii) self tuning regulators (STR). Though different in detail, all three aim at the same goal, i.e., to eliminate the effect of variations in disturbance signature and plant dynamics on the smart structure's performance. Many adaptive signal processing algorithms operate in the feedforward path. For example, an acoustic cost function was used in conjunction with structural inputs in controlling far-field acoustic pressures to achieve aircraft cabin noise cancellation. MRAC and STR are mainly associated with adaptive feedback structural control. **Figure 22** illustrates the adaptive feedback and feedforward concepts in an adaptively controlled smart structure. The disturbance input, $u_d(z)$, is fed through the feedforward compensator, $K_{ff}(z)$, and summated with the error signal, $e(z)$, modulated through the feedback compensator, $K_{fb}(z)$, to generate the control signal, $u_c(z)$. The error signal, $e(z)$, is obtained in the classical control fashion by subtracting the resulting output, $y_e(z)$, from the required reference signal, $r(z)$. The blocks $P_{de}(z)$ and $P_{ce}(z)$ represent the plant's response to disturbance and control, respectively. The feedforward compensator, $K_{ff}(z)$, is adaptively modified in response to trends noticed in the output signal, $y_e(z)$, by the adaptive algorithm block that could typically be a least-mean-squares (LMS) method applied to the coefficients of a finite impulse response (FIR) filter. A cost functional incorporating a measure of the output, $y_e(z)$, or a time-averaged gradient (TAG) descent algorithm may be used. Use of hybrid control architecture combines the feedback and feedforward principles to achieve best performance when complex disturbances incorporating both persistent and impulsive components are present.

Conclusion

The concepts of induced-strain actuation and smart structures have been reviewed and briefly discussed. ISAs are based on active materials that display dimensional changes when energized by electrical, magnetical, or thermal fields. Piezo-electric, electrostrictive, magnetostrictive, and shape memory alloy

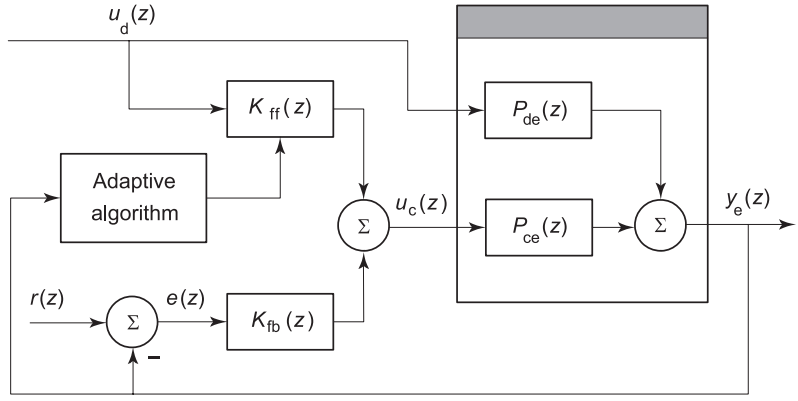


Figure 22 Schematic representation of smart structure with adaptive hybrid control capabilities.

materials have been presented and analyzed. Of these, piezo-electric (PZT), electrostrictive (PMN), and magnetostrictive (Terfenol-D) materials have been shown to have excellent frequency response (1–10 kHz, depending on actuator length), high force (up to 50 kN on current models), but small induced-strain stroke capabilities (typically, 0.1 mm for 0.1% strain on a 100 mm actuator). With this class of ISAs, displacement amplification devices need always to be incorporated into the application design. In contrast, the shape memory alloy (Nitinol) materials have large induced-strain stroke capabilities (typically, 4 mm for 4% strain on a 100 mm actuator), but low-frequency response (< 1 Hz).

The effective implementation of induced strain actuation was discussed and guidelines for achieving optimal energy extraction were presented. As different from conventional actuation techniques, induced-strain actuation can only rely on a limited amount of active stroke, and this has to be carefully managed. It has been shown here that the stiffness and impedance matching principles can produce the maximum energy extraction from the ISA and ensure its transmission into the external application. Details of these principles, together with typical energy density values for various ISAs have been given. It was found that, for dynamic applications, as much as $3.76\,\mathrm{J\,dm^{-3}}(0.482\,\mathrm{J\,kg^{-1}})$ could be extracted under dynamic conditions. Power densities of up to $23.6\,\mathrm{kW\,dm^{-3}}(3.0\,\mathrm{kW\,kg^{-1}})$ were predicted at 1 kHz.

In summary, one can conclude that the potential of smart materials in structural applications has been clearly demonstrated through laboratory research in many institutions around the world. However, the field is still in its infancy and further research and development is required to establish smart materials as reliable, durable, and cost-effective materials for large-scale engineering applications.

Nomenclature

A	cross-sectional area
B	magnetic flux density
D	electrical displacement; Young's modulus
E	electrical field
F	force
H	magnetic field intensity
I	current
l	length
M	electrostrictive coefficient
P	power
S	strain
t	thickness
T	stress; temperature
V	voltage
ε	strain
μ	magnetic permeability
ξ	martensitic fraction
Λ	state variable
Θ	thermoelastic tensor
Ω	transformation tensor

See Plates 4,5,6.

See also: **Electrostrictive materials**; **Magnetostrictive materials**; **Piezoelectric materials and continua**; **Shape memory alloys**.

Further Reading

Anon (1988) IEEE standard on piezoelectricity, ANSI/IEEE Std 176–1987, Institute of Electrical and Electronics Engineers, Inc., New York.

Bank R (1975) *Shape Memory Effects in Alloys*, p. 537. New York: Plenum.

Clark AE (1992) High power rare earth magnetostrictive materials. In: Rogers CA and Rogers RC (eds). *Proc. Recent Advances in Adaptive and Sensory Materials*, pp. 387–397. Lancaster, PA: Technomic Publishing.

Clark RL, Saunders, WR, Gibbs G (1998) *Adaptive Structures – Dynamics and Control*. Wiley.
Culshaw B (1996) *Smart Structures and Materials*. Artech House Publishers.
Duerig TW, Melton KN, Stockel D, Wayman CM (1990) *Engineering Aspects of Shape Memory Alloys*. Butterworth-Heinemann.
Fuller CR, Elliot SJ, Nelson PA (1996) *Active Control of Vibration*. London: Academic Press.
Funakubo H (1987) *Shape Memory Alloys*. New York: Gordon and Breach.
Giurgiutiu V (2000) Active-materials induced-strain actuation for aeroelastic vibration control. *Shock and Vibration Digest* 32(5): 335–368.
Giurgiutiu V, Craig A, Rogers CA (1997) Power and energy characteristics of solid-state induced-strain actuators for static and dynamic applications. *Journal of Intelligent Material Systems and Structures* 8: 738–750.
Janocha H (1999) *Adaptronics and Smart Structures*. Springer-Verlag.
Lachisserie, E du Tremolet de (1993) *Magnetostriction – Theory and Applications*. CRC Press.
Moses RW (1997) Active vertical tail buffeting alleviation on a twin-tail fighter configuration in a wind tunnel. *CEAS International Forum on Aeroelasticity and Structural Dynamics 1997*, Rome, Italy, June 17–20.
Nachtigall W (1999) Adaptronic systems in biology and medicine. In: Janocha H (ed.), *Adaptronics and Smart Structures*. Springer.
Park S-E, Shrout TR (1997) Ultrahigh strain and piezoelectric behavior in relaxor ferroelectric single crystals. *Journal of Applied Physics* 4(82): 1804–1811.
Rao SS, Sunar M (1999) Recent advances in sensing and control of flexible structures via piezoelectric materials technology. *Applied Mechanics Reviews* 52(1): 1–16.
Straub FK, King RJ (1996) Application of smart materials to control of a helicopter rotor. *SPIE Symposium on Smart Structures and Materials*, February 26–29, San Diego, CA.
Tanaka K, Iwasaki R (1985) A phenomenological theory of transformation superplasticity. *Engineering Fracture Mechanics* 21(4): 709–720.
Udd E (1995) *Fiber Optic Smart Structures*. Wiley.

ADAPTIVE FILTERS

S J Elliott, The University of Southampton, Institute of Sound and Vibration (ISVR), Southampton, UK

Copyright © 2001 Academic Press

doi:10.1006/rwvb.2001.0059

In the article on optimal filters (see **Optimal filters**) we saw that the optimum finite impulse response (FIR) filter, which minimizes the mean-square error for the model problem shown in **Figure 1** of that article, can be directly calculated from a knowledge of the autocorrelation properties of the reference signal and the cross-correlation between the reference and desired signal. In a practical problem, these auto- and cross-correlation functions would have to be estimated from the time histories of these signals, which would require a considerable amount of data in order to calculate accurately. It was also assumed that the reference and desired signals are stationary, since otherwise their correlation properties will change with time. The calculation of the optimal filter with I coefficients involves the inversion of the $I \times I$ autocorrelation matrix. Although this matrix has a special form (it is symmetric and Toeplitz), and efficient algorithms can be used for its inversion, the computational burden is still proportional to I^2 and so can be significant, particularly for long filters. The matrix inversion may also be numerically unstable if the matrix is ill-conditioned.

Another approach to determining the coefficients of such a filter would be to make them adaptive. Instead of using a set of data to estimate correlation functions, and then using these to calculate a single set of optimal filter coefficients, the data are used sequentially to adjust the filter coefficients gradually so that they evolve in a direction which minimizes the mean-square error. Generally, all the filter coefficients are adjusted in response to each new set of data, and the algorithms used for this adaptation use a considerably smaller number of calculations per sample than the total number of calculations required to compute the true optimal coefficients. As well as converging towards the optimal filter for stationary signals, an adaptive filter will also automatically readjust its coefficients if the correlation properties of these signals change. The adaptive filter is thus capable of tracking the statistics of nonstationary signals, provided the changes in the statistics occur slowly compared with the convergence time of the adaptive filter.

Steepest Descent Algorithm

The most widely used algorithm for adapting FIR digital filters is based on the fact that the error surface for such filters has a quadratic shape, as shown in **Figure 2** of the article on optimal filters (see **Optimal filters**). This suggests that, if a filter coefficient is

adjusted by a small amount, which is proportional to the negative of the local gradient of the cost function with respect to that filter coefficient, then the coefficient is bound to move towards the global minimum of the error surface. If all the filter coefficients are simultaneously adjusted using this gradient descent method, the adaptation algorithm for the vector of filter coefficients may be written as:

$$\mathbf{w}(\text{new}) = \mathbf{w}(\text{old}) - \mu \frac{\partial J}{\partial \mathbf{w}}(\text{old}) \qquad [1]$$

where μ is a convergence factor and $\partial J/\partial \mathbf{w}$ was defined in eqn [14] of the article on optimal filters (see **Optimal filters**).

For the model problem shown in **Figure 1** of that article, the vector of derivatives is given by eqn [15], and using the definitions given in eqns [7] and [8] of that article, this can be written as:

$$\frac{\partial J}{\partial \mathbf{w}} = -2E[\mathbf{x}(n)\mathbf{x}^{\mathrm{T}}(n)\mathbf{w} - \mathbf{x}(n)d(n)] \qquad [2]$$

The measured error signal is given by:

$$e(n) = d(n) - \mathbf{x}^{\mathrm{T}}(n)\mathbf{w} \qquad [3]$$

and so the vector of derivations may also be written as:

$$\frac{\partial J}{\partial \mathbf{w}} = -2E[\mathbf{x}(n)e(n)] \qquad [4]$$

To implement the true gradient descent algorithm, the expectation value of the product of the error signal with the delayed reference signals would need to be estimated to obtain eqn [4], probably by time-averaging over a large segment of data, and so the filter coefficients could only be updated rather infrequently.

The suggestion made in the seminal paper by Widrow and Hoff was that, instead of infrequently updating the filter coefficients with an averaged estimate of the gradient, the coefficients be updated at every sample time using an instantaneous estimate of the gradient, which is sometimes called the stochastic gradient. This update quantity is equal to the derivative of the instantaneous error with respect to the filter coefficients:

$$\frac{\partial e^2(n)}{\partial \mathbf{w}} = -2\mathbf{x}(n)e(n) \qquad [5]$$

The adaptation algorithm thus becomes:

$$\mathbf{w}(n+1) = \mathbf{w}(n) + \alpha \mathbf{x}(n)e(n) \qquad [6]$$

where $\alpha = 2\mu$ is the convergence coefficient, which is known as the LMS (least mean-square) algorithm, and this has been very widely used in a variety of practical applications, for example in adaptive electrical noise cancellation, adaptive modeling and inversion and adaptive beam forming. A block diagram indicating the operation of the LMS algorithm is shown in **Figure 1**.

Properties of the LMS Algorithm

In order to guarantee convergence it is not only necessary to ensure that the mean value of the filter coefficients converge but also that their mean square value converges. In theory, this can be ensured provided the convergence coefficient α is positive, but below a certain value which is proportional to the mean-square value of the reference signal, i.e.:

$$0 < \alpha < \frac{2}{I\overline{x^2}} \qquad [7]$$

where I is the number of coefficients and $\bar{x}^2 = E[x^2(n)]$ is the mean-square value of $x(n)$. This has been found to give a reasonable estimate of the maximum stable value of the convergence coefficient in many practical simulations.

The convergence rate of the LMS algorithm is not uniform, however, but depends on the shape of the multidimensional error surface formed by plotting the mean-square error against each of the FIR filter coefficients. If a section is taken through this surface, the resulting graph is guaranteed to be quadratic, but its shape depends on exactly which combination of filter coefficients is included in the section, and the autocorrelation properties of the reference signal. If we consider the combination of filter coefficients corresponding to the eigenvectors of the autocorrelation matrix (eqn [10] of the article on optimal filters; see **Optimal filters**) then the steepness of the quadratic sections along these directions, which are called the principal axis of the error surface, are defined by the

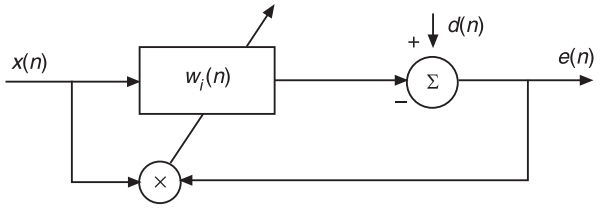


Figure 1 Diagrammatic representation of an FIR filter, with coefficients w_i at the nth sample time, being adapted using the LMS algorithm.

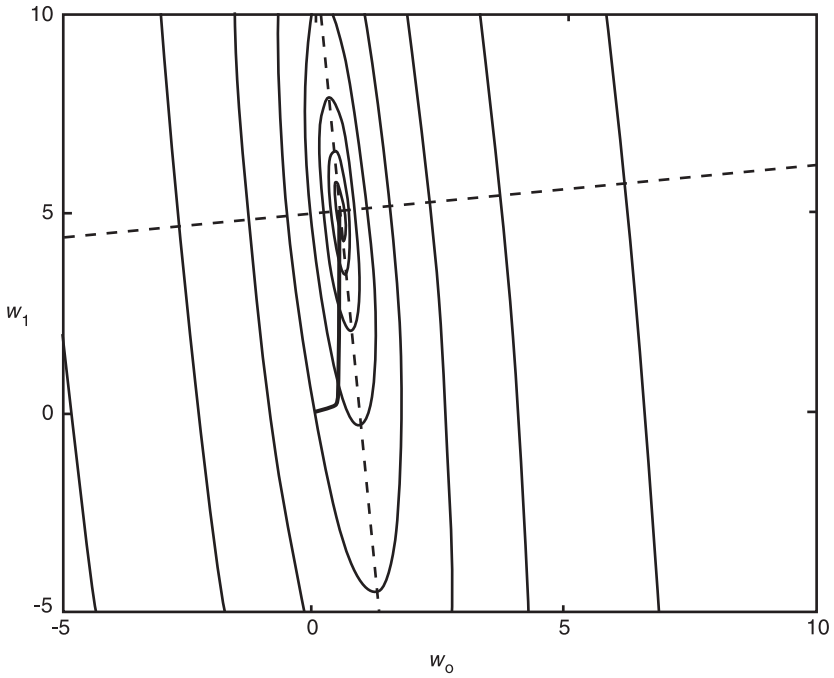


Figure 2 Contour map of an example error surface showing the trajectory of the average behavior of the LMS algorithm. Also shown are the principal axes of the error surface.

eigenvalues of the autocorrelation matrix, as illustrated in **Figure 2**. The LMS algorithm will, on average, follow the steepest descent path down this error surface, as also illustrated in **Figure 2**. The average convergence of the LMS algorithm along one of the principle axes would be exponential, with a time constant (in samples) given by:

$$\tau_i \approx \frac{1}{2\alpha\lambda_i} \qquad [8]$$

where λ_i is the eigenvalue of the autocorrelation matrix corresponding to this principal axis. In practice, the convergence of the algorithm is associated with all principal axes at once, although clearly that associated with the largest eigenvalue, $\lambda_{\max}$, decays fastest and that associated with the smallest eigenvalue, $\lambda_{\min}$, decays most slowly. **Figure 3** shows the average reduction in the level of the average mean-square error as the LMS descends the error surface, shown in **Figure 2**. This has two exponential decays, corresponding to the two eigenvalues of the autocorrelation matrix in this case, which are different by a factor of 100. The ratio of the smallest time constant to the largest for such a decay can be expressed using eqn [8] as:

$$\frac{\tau_{\min}}{\tau_{\max}} = \frac{\lambda_{\min}}{\lambda_{\max}} \qquad [9]$$

The convergence properties of the LMS algorithm are thus determined by the eigenvalue spread of the autocorrelation matrix of the reference signal. A physical interpretation of the eigenvalue spread can be obtained from an interesting relationship between the eigenvalues of the autocorrelation matrix and the power spectral density, which can be used to show that:

$$\frac{\lambda_{\max}}{\lambda_{\min}} < \frac{S_{xx,\max}}{S_{xx,\min}} \qquad [10]$$

where $S_{xx,\,\max}$ and $S_{xx,\,\min}$ are the maximum and

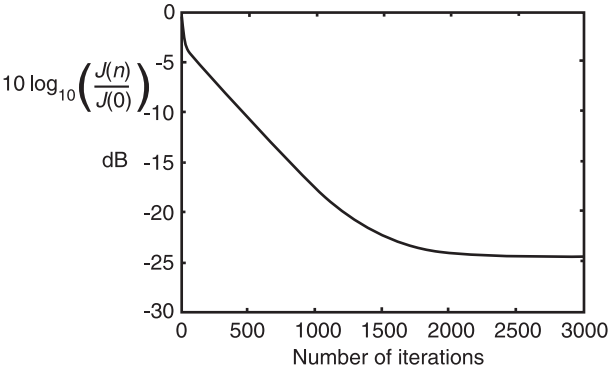


Figure 3 The average convergence behavior of the LMS algorithm in the case in which two modes converge at different rates.

minimum values of the power spectral density of the reference signal, $x(n)$.

The Recursive Least-squares (RLS) Algorithm

In order to overcome the slow convergence of the steepest descent-based LMS algorithm when faced with a large eigenvalue spread, algorithms based on faster optimization techniques, such as Newton's method, have been developed. Writing the mean-square error (J) in the quadratic form used in the article on optimal filters (see **Optimal filters**), $J = \mathbf{w}^{\mathrm{T}}\mathbf{A}\mathbf{w} + 2\mathbf{w}^{\mathrm{T}}\mathbf{b} + c$ where $\mathbf{A}$ is the autocorrelation matrix of the reference signal, Newton's algorithm may be written as an extension of eqn [1] as:

$$\mathbf{w}(\text{new}) = \mathbf{w}(\text{old}) - \mu\mathbf{A}^{-1}\frac{\partial J}{\partial \mathbf{w}}(\text{old}) \qquad [11]$$

The RLS algorithm is a practical form of Newton's algorithm which at each new sample time, n, minimizes the exponentially weighted mean-square error given by:

$$J(n) = \sum_{l=0}^{n} \lambda^{n-l}\varepsilon^2(l) \qquad [12]$$

where λ is the forgetting factor and $\varepsilon(l)$ is the error which would be produced if the current values of the filter coefficients had been used for all previous samples, i.e.:

$$\varepsilon(l) = d(l) + \mathbf{w}^{\mathrm{T}}(n)\mathbf{x}(l) \qquad [13]$$

By calculating the values of the $\mathbf{A}$ matrix and $\partial J/\partial \mathbf{w}$ associated with the cost function given by eqn [12] and using these in eqn [11], the RLS algorithm may be derived which can be written as:

$$\mathbf{w}(n+1) = \mathbf{w}(n) - \alpha(n)\mathbf{A}^{-1}(n-1)\mathbf{x}(n)e(n) \qquad [14]$$

where the time-varying convergence coefficient is equal to:

$$\alpha(n) = \frac{1}{\lambda + \mathbf{x}^{\mathrm{T}}(n)\mathbf{A}^{-1}(n-1)\mathbf{x}(n)} \qquad [15]$$

and in order to avoid the inverse of a matrix having to be calculated at every sample, the inverse of the $\mathbf{A}$ matrix is calculated intervals using the matrix inversion lemma, to give:

$$\mathbf{A}^{-1}(n) = \lambda^{-1}\mathbf{A}^{-1}(n-1) - \alpha(n)\lambda^{-1}\mathbf{A}^{-1}(n-1)\mathbf{x}(n)\mathbf{x}^{\mathrm{T}}(n)\mathbf{A}^{-1}(n-1) \qquad [16]$$

There are also various approaches to fast RLS algorithms, in which the number of operations required to implement the adaptive filter is of the order of I where I is the number of filter coefficients, instead of the order of I^2, as required to implement eqns [14], [15], and [16] above.

Another potential method of improving the convergence characteristics of the time domain LMS algorithm is to use the normalized frequency domain LMS algorithm. This algorithm can also significantly reduce the computation requirements for the adaptive filter if the filter has a large number of coefficients. There are also several other benefits to frequency–domain adaptation when considering feedforward and feedback controllers.

Block LMS Algorithm

Let us return to eqn [1], which describes the general philosophy of adaptation using the method of steepest descent:

$$\mathbf{w}(\text{new}) = \mathbf{w}(\text{old}) - \mu\frac{\partial J}{\partial \mathbf{w}}(\text{old}) \qquad [17]$$

and the expression for the vector of derivatives, eqn [4]:

$$\frac{\partial J}{\partial \mathbf{w}} = -2E[\mathbf{x}(n)e(n)] \qquad [18]$$

In deriving the normal LMS algorithm, we used the instantaneous version of these derivatives to update the filter coefficients. Another approach would be to calculate the average value of $\mathbf{x}(n)e(n)$ over N samples and use this to update the filter coefficients only every N samples, so that:

$$\mathbf{w}(n+N) = \mathbf{w}(n) + \frac{\mu}{N}\sum_{l=n}^{n+N-1}\mathbf{x}(l)e(l) \qquad [19]$$

This algorithm is called the block LMS algorithm. This can have similar convergence properties to the LMS algorithm, since the filter coefficients change less frequently but by larger amounts, provided the filter does not converge too quickly compared with the block size, N. The main difference between the LMS algorithm and the block LMS algorithm is that the former uses a recursive averaging of the gradient

estimate whereas the latter uses a finite moving average. The quantity used to update the filter coefficients in eqn [19] can be regarded as an estimate of the cross-correlation function between the reference signal, $x(n)$, and the error signal, $e(n)$, which can be written as:

$$\hat{R}_{xe}(m) = \frac{1}{N}\sum_{l=n}^{n+N-1} x(l-m)e(l) \qquad [20]$$

This estimate of the cross-correlation function needs to be calculated for $m = 0$ to $I - 1$, where I is the number of filter coefficients being adapted. The most efficient implementation of the block LMS algorithm occurs when $N = I$, and under these conditions the block LMS algorithm requires N^2 multiplications every N samples and thus has about the same computational requirements as the normal LMS algorithm. If N is large, then it would be more computationally efficient to calculate the estimated cross-correlation function from an estimate of the power spectral density, using the fast Fourier transform (FFT) to calculate the discrete Fourier transform (DFT) of blocks of reference and error signals. In order for this estimate of the cross-correlation function to be unbiased, however, some care needs to be taken to prevent circular correlation effects, such as the use of the overlap–save method. This involves taking $2N$-point FFTs and adding N zeros to the error data block before taking the FFT. Only the causal part of the cross-correlation function is used to update the filter, and so half the length of the point cross-correlation function is discarded. This requires an operation similar to that denoted $\{\}_+$ in eqn [29] of the article on optimal filters (see **Optimal filters**) and involves an inverse FFT of the spectral density, the setting to zero or windowing of the noncausal part of the resulting cross-correlation function, and taking an FFT of the result. The adaptation algorithm for the filter coefficient in the kth frequency bin can thus be written as:

$$W_{\text{new}}(k) = W_{\text{old}}(k) + \alpha\{X^*(k)E(k)\}_+ \qquad [21]$$

where $X(k)$ is the DFT of $2N$ points of $x(n)$, * denotes complex conjugation, and $E(k)$ is the DFT of N points of $e(n)$ padded with N zeros, assuming the overlap save method is used to prevent circular correlation. This algorithm is called the fast LMS (FLMS) algorithm, and is exactly equivalent to the block LMS algorithm.

Once the reference signal and filter response are available in the frequency domain, further computational savings can be made by also performing the convolution required to obtain the filter output in the frequency domain, so that:

$$Y(k) = W(k)X(k) \qquad [22]$$

from which the time history must be obtained by taking the inverse FFT (IFFT) and only using the last N points to avoid circular convolution effects. The block diagram of the complete frequency domain LMS algorithm is shown in **Figure 4**.

The implementation of the frequency domain adaptation of the filter, and the convolution of the reference signal with the reference signal thus

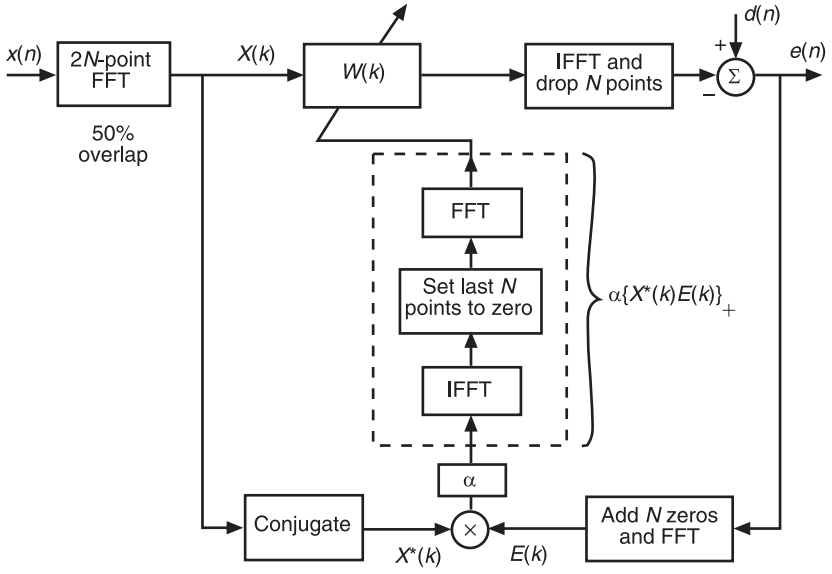


Figure 4 Block diagram of a frequency domain implementation of the LMS algorithm.

uses five $2N$-point FFTs, where $N = I$ and I is the number of adaptive filter coefficients. If each $2N$ point FFT requires $2N\log_2 2N$ operations, then frequency domain adaptive filtering requires about $10N\log_2 2N$ operations every N samples, or $10\log_2 2N$ operations per sample. This can be compared with N operations per sample to adapt the coefficients using the normal LMS, and N operations per sample, for the normal time domain convolution of the reference signal and filter coefficients. The frequency domain implementation of the LMS algorithm thus requires a factor of about $N/5\log_2 2N$ fewer computational operations compared with its direct implementation. For a 512-point filter this corresponds to a computational saving of about a factor of 10.

Frequency-dependent Convergence Coefficients

Apart from the computational advantages, it may also be possible to use the frequency domain implementation to improve the convergence properties of the LMS algorithm. This was originally suggested by Ferrara, who argued that in the frequency domain the error signal in a given frequency bin, $E(k)$, is only a function of the filter coefficient in the same bin, $W(k)$, and so each of the frequency domain filter coefficients converge independently. If this were the case the convergence coefficient could be selected independently for each bin, so that the adaptation algorithm becomes:

$$W_{\text{new}}(k) = W_{\text{old}}(k) + \{\alpha(k)X^*(k)E(k)\}_+ \qquad [23]$$

The convergence coefficients used in the adaptation of the individual frequency bins could be normalized by the average power in each frequency bin, for example, so that:

$$\alpha(k) = \frac{\alpha'}{\mathrm{E}\left[|X(k)|^2\right]} \qquad [24]$$

where α' is a single normalized convergence coefficient. For some applications, this normalization of the frequency-dependent convergence coefficient has been found to improve considerably the convergence rate of the adaptive filter.

Unfortunately, if a frequency-dependent convergence coefficient is used in eqn [23], the adaptive filter is not guaranteed to converge towards the optimum causal Wiener filter. This problem is particularly severe when the adaptive filter is used as a linear predictor, and is caused by spurious components in the causal part of the Fourier transform of $\alpha(k)X^*(k)E(k)$, in eqn [23], which arises because of the interaction between the causal parts of the Fourier transform of $\alpha(k)$ with the noncausal parts of the Fourier transform of $X^*(k)E(k)$.

A solution to this problem can be obtained by deriving a frequency domain adaptive algorithm directly based on Newton's method, which can be written as:

$$W_{\text{new}}(k) = (1-\alpha)W_{\text{old}}(k) + \alpha\hat{W}_{\text{opt}}(k) \qquad [25]$$

where α is the convergence coefficient and $\hat{W}_{\text{opt}}(k)$ is an estimate of the optimum causal filter. We have seen in the article on optimal filters (see **Optimal filters**) that the optimum causal filter can be written in the frequency domain as:

$$W_{\text{opt}}(\mathrm{e}^{\mathrm{j}\omega T}) = \frac{1}{F(\mathrm{e}^{\mathrm{j}\omega T})}\left\{\frac{S_{xd}(\mathrm{e}^{\mathrm{j}\omega T})}{F^*(\mathrm{e}^{\mathrm{j}\omega T})}\right\}_+ \qquad [26]$$

where $F(\mathrm{e}^{\mathrm{j}\omega T})$ and $F^*(\mathrm{e}^{\mathrm{j}\omega T})$ are the spectral factors of $S_{xx}(\mathrm{e}^{\mathrm{j}\omega T})$. In the discrete frequency domain we can obtain an estimate of the optimum causal filter from the current block of data as:

$$\hat{W}_{\text{opt}}(k) = \frac{1}{\hat{F}(k)}\left\{\frac{X^*(k)D(k)}{\hat{F}^*(k)}\right\}_+ \qquad [27]$$

where $\hat{F}(k)$ is the estimated spectral factor of $S_{xx}(k)$, which could in practice be obtained by taking the Hilbert transform of $\sqrt{S_{xx}(k)}$.

We can now write $D(k)$ as $E(k) + W(k)X(k)$, so that eqn [27] can be expressed as:

$$\hat{W}_{\text{opt}}(k) = \frac{1}{\hat{F}(k)}\left\{\frac{X^*(k)E(k)}{\hat{F}^*(k)}\right\}_+ + \frac{1}{\hat{F}(k)}\left\{\frac{W(k)X^*(k)X(k)}{\hat{F}^*(k)}\right\}_+ \qquad [28]$$

The average value of the term $X^*(k)X(k)/\hat{F}^*(k)$ in this equation is equal to $\hat{F}(k)$, and since $W(k)\hat{F}(k)$ is entirely causal, the final term in eqn [28] will, on average, be equal to $W(k)$. Using eqn [28] in eqn [25], a form of the frequency domain Newton's algorithm is obtained, which may be written as:

$$W_{\text{new}}(k) = W_{\text{old}}(k) + \alpha^+(k)\{\alpha^-(k)X^*(k)E(k)\}_+ \qquad [29]$$

where $\alpha^+(k) = \sqrt{2}/\hat{F}(k)$, which corresponds to an entirely causal time sequence, and $\alpha^-(k) = (\alpha^+(k))^*$

which corresponds to an entirely noncausal time sequence. In this algorithm the bin-normalized convergence coefficient given by eqn [24] has essentially been split into two parts and since only the noncausal part is used inside the causality constraint in eqn [29], this does not cause noncausal components of the Fourier transform of $X^*(k)E(k)$ to affect the adaptation of the filter, which thus converges to the optimal causal filter.

Adaptive filters are used to cancel electrical interference in measurement systems and also as the basis for practical feedforward and feedback controllers in active vibration control.

Nomenclature

$\mathbf{A}$	autocorrelation matrix
$e(n)$	error signal
I	number of filter coefficients
J	mean-square error
S_{xx}	power spectral density
$x(n)$	reference signal
α	convergence coefficient
λ	eigenvalue
μ	convergence factor
τ	time constant

See also: **Adaptive filters**; **Digital filters**; **Signal processing, model based methods**.

Further Reading

Clarkson PM (1993) *Optimal and Adaptive Signal Processing*. Boca Raton, FL, CRC Press.

Elliott SJ (2001) *Signal Processing for Active Control*. Academic Press.

Elliott SJ, Rafaely B (2000) Frequency-domain adaptation of causal digital filters. *IEEE Transactions on Signal Processing*, **48**(5).

Ferrara ER (1985) *Frequency-domain Adaptive Filtering in Adaptive Filters*. Cowan CFN and Grant PM (eds) 145–179. Englewood Cliffs, NJ: Prentice Hall.

Haykin S (1996) *Adaptive Filter Theory*, 3rd edn. Englewood Cliffs, NJ: Prentice Hall.

Rabiner LR, Gold B (1975) *Theory and Application of Digital Signal Processing*. Englewood Cliffs, NJ: Prentice Hall.

Shynk JJ (1992) Frequency-domain and multirate adaptive filtering. *IEEE Signal Processing Magazine*, January, 14–37.

Widrow B, Hoff ME Jr (1960) Adaptive switching circuits. *IRE WESCON Conv. Rec.* Pt.4. 96–104.

Widrow B, Stearns SD (1985) *Adaptive Signal Processing*. Englewood Cliffs, NJ: Prentice Hall.

AEROELASTIC RESPONSE

J E Cooper, University of Manchester, Manchester, UK

Copyright © 2001 Academic Press

doi:10.1006/rwvb.2001.0125

Introduction

Aircraft are subjected to a wide range of static (i.e., steady) and dynamic loads in flight and also on the ground. Combined with the inherent flexibility of the structure, these dynamic loads result in vibration. Gusts and dynamic maneuvers can cause the limit loads to be exceeded; however, in most cases structural failure would occur due to fatigue. Consideration should also be made regarding the discomfort caused by the responses to the pilot or passengers, and also the consequent malfunctioning of equipment and systems.

Care must be taken at the design stage to ensure that the static and dynamic responses stay within acceptable limits of deformation and load on production aircraft, otherwise costly redesigns will have to be made. Both the civil and military airworthiness regulations, that dictate how aircraft must be certified to fly, have several sections devoted to loads. If new technologies or ideas are being applied that are not accounted for in the regulations, then the engineers have to discuss the way forward for certification with the authorities.

This item provides a brief overview of an immense subject area, with a wealth of literature and work in the aerospace community being devoted to each of the topics covered. The problems associated with a number of critical phenomena are described. The classical flutter phenomenon is covered in a different item (see **Flutter**).

Flight Loads

Flight loads include all loads that can occur in any part of the flight envelope. Typically, the most critical design cases occur in flight.

Steady Maneuvers

The loads on an aircraft increase during maneuvers and these are often the critical design cases, particularly for military aircraft. The loads must be calculated, first by determining the lift and inertia forces (obtained from application of D'Alembert's principle), and then determining the internal loads (e.g., bending moments, torques) from which the resulting stresses can be found.

Balance Calculations

If an aircraft is considered in accelerated flight (**Figure 1**), the overall lift due to the wings and tail $L = L_W + L_T$ is balanced by the inertia force nW, where W is the weight and n is known as the load factor, defined as

$$\text{Load factor } n = (\text{total lift developed})/(\text{weight of aircraft})$$

The load factor n is produced by the aircraft accelerating upwards at $(n-1)g$, where g is the acceleration due to gravity. In straight and level flight, $n = 1$ and thrust $T = \text{drag } D$. In a particular maneuver, it is possible to calculate the value of the load factor from which the total lift can be found. The distribution of lift between the wing and tailplane and the thrust required in the maneuver may be determined from moment equilibrium.

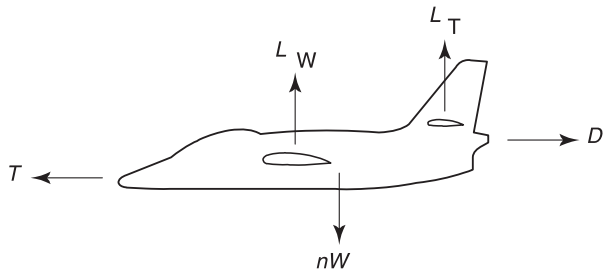


Figure 1 Balance forces on aircraft in accelerated flight.

Internal Loads

Although the external loads discussed above are in overall equilibrium, they do not have the same distribution over the structure. Consider the aircraft in **Figure 2** with a fuselage mass of typically two times that of the wings (dependent on the position of the power plant and the fuel storage) whereas nearly all of the lift is distributed over the wings. The difference in load distribution gives rise to internal loads, namely shear force, torque and bending moment distributions along the wings, fuselage, etc. It is traditional to consider the aircraft in sections (**Figure 3**). The inertia and lift forces can be estimated from the results of the balanced calculations. The shear force, torque and bending moment can then be determined at the junction of each section by equilibrium considerations. Nowadays, once the lift distribution is known, the loads and resultant stresses can be found using finite element (FE) models.The designer needs to consider the critical parts (most highly stressed) of the structure and to ensure that they do not exceed ultimate stresses during any desired maneuvers. These highly stressed areas are also going to be the areas where failure due to fatigue may occur. During the design process, trade-off studies may be conducted to change the design if these stresses are considered too high.

Maneuver Envelope

Rather than specifying a whole range of maneuvers of varying severity and speed, the airworthiness requirements define a maneuver envelope that show the combinations of load factor n and speed v that an aircraft has to be able to withstand. **Figure 4** shows a typical envelope for a commercial aircraft.

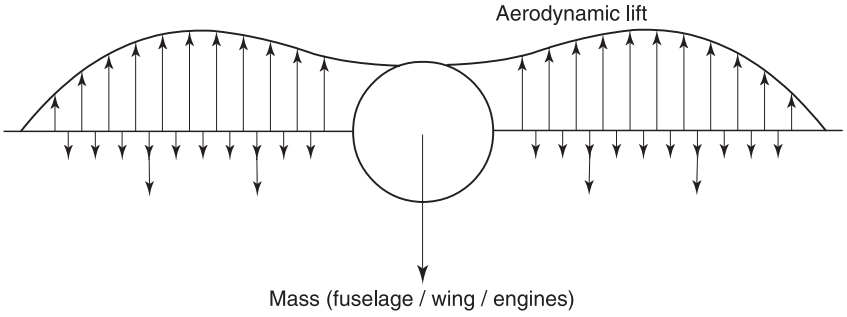


Figure 2 Aerodynamic and mass load distributions.

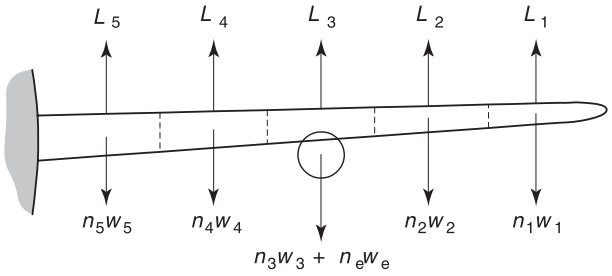


Figure 3 Sectional distribution of loads.

The envelope is constructed knowing the design cruise and dive speeds v_C, v_D, as well as the maximum maneuvering load factor (usually 2.5 for commercial aircraft).

Dynamic Maneuvers

Pilot Induced Maneuvers

The airworthiness regulations define a number of maneuvers that must be considered, e.g., (i) step input; (ii) sinusoidal motion of the controls at various frequencies.

An aeroelastic model that includes both rigid-body and flexible modes must be used in the form of

$$\begin{bmatrix} A_{rr} & A_{rf} \\ A_{rf} & A_{ff} \end{bmatrix} \begin{bmatrix} \ddot{q}_r \\ \ddot{q}_f \end{bmatrix} + \begin{bmatrix} B_{rr} & B_{rf} \\ B_{rf} & B_{ff} \end{bmatrix} \begin{bmatrix} \dot{q}_r \\ \dot{q}_f \end{bmatrix} + \begin{bmatrix} C_{rr} & C_{rf} \\ C_{rf} & C_{ff} \end{bmatrix} \begin{bmatrix} q_r \\ q_f \end{bmatrix} = \begin{bmatrix} U_r \\ U_f \end{bmatrix}$$

where subscripts r and f refer to rigid and flexible terms, respectively. These equations can be solved in time for given inputs U, and consequently nonlinear terms can be catered for.

On some aircraft, maneuver load alleviation systems are implemented to reduce the loads on critical parts of the aircraft structure. By sensing the maneuvers that the aircraft is being asked to perform, the control surfaces may be moved in such a way as to reduce the loads while still undertaking the maneuver.

Gusts

Aircraft are often subjected in flight to motion of the air in the form of gusts. These gusts can impose considerable loads on aircraft and may come from all directions:

1. vertical gusts load the wing, fuselage and horizontal tail (**Figure 5**);
2. lateral or 'side' gusts, loading the fuselage, vertical tail and pylons;
3. longitudinal or 'head-on' gusts which may cause important loads on flap structures.

Since the recognition during the First World War that these effects produced significant loads, gust design criteria have been formulated, which have evolved over the years and are still under development.

For civil aircraft, gust load cases are often the most critical for load design, and are also one of the main fatigue loading sources for the structure. A further important consideration is the aircraft dynamic response due to gusts in terms of passenger comfort. Although military type aircraft structures are generally maneuver load critical, for specific parts of the structure, such as flexible outer wing sections and store pylons, gusts may determine the critical design load cases, particularly at high speed/low level conditions.

The analysis of the response to, and resulting loads from, gusts takes one of two possible approaches; (i) each gust is considered as a separate discrete event; (ii) the gusts are considered as a random turbulent

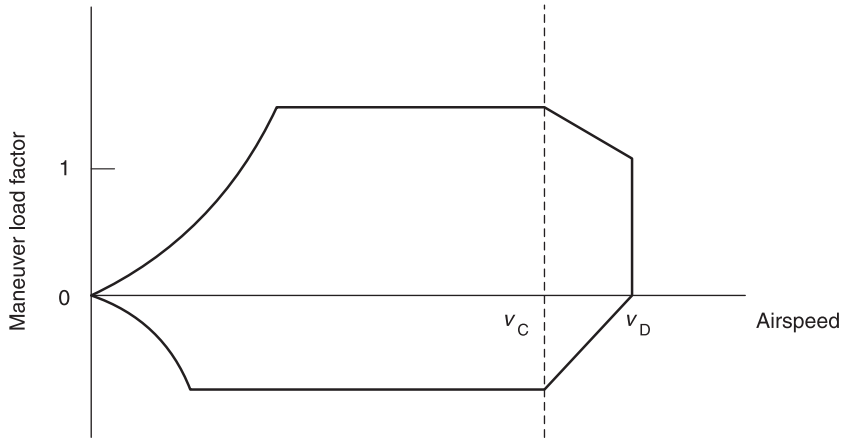


Figure 4 Maneuver envelope.

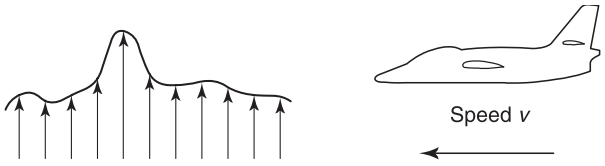


Figure 5 Aircraft encountering vertical gusts.

sequence. All major current airworthiness codes include two sets of gust criteria based on concepts. The discrete gust criterion is typically 'worst case': the highest load resulting from a particular time sequence must be taken. This discrete case is included to safeguard against sudden 'stand-alone' gusts that can occur in practice. The continuous turbulence criterion is based upon a consistent model of the atmospheric turbulence defining design loads based on an averaged response and considering all possible gust lengths that prevail in random turbulence.

Discrete gusts The basic loading mechanism of gusts is schematically illustrated in **Figure 6** for motion in the vertical plane. A rigid aircraft flying with speed v, entering an upward gust with velocity w, experiences a sudden change in angle of incidence $\Delta\alpha = w/v$. The gust gives rise to an additional lift proportional to v^2 and $\Delta\alpha$.

Such an analysis was first considered in the 1920s. In reality, the above model is a gross oversimplification of a number of effects that must be considered in order to give accurate response and loads predictions:

1. The abrupt or 'sharp-edged' gust indicated in **Figure 6** is physically impossible. A real gust must have some distance over which its velocity builds up. A number of different shapes have been considered over the years, with the '1 – cos' gust shape (shown in **Figure 7**) being included in almost all current airworthiness regulations.
2. Due to unsteady aerodynamic effects, a sudden change in angle of incidence does not immediately result in a proportional change in lift. These effects are modeled by the Kussner function shown in **Figure 8**. Consequently, the aircraft has time to respond to the gust, thus reducing the gust-imposed load in comparison to the 'sharp-edged' gust case.
3. The gust is not only going to impart a lift force on the wings, but also onto the tail surfaces at some fixed time delay (depending on the speed and the geometry). This so-called 'penetration effect' will result in a pitch motion being imparted to the aircraft.
4. The aircraft is flexible, thus the resulting motion and load will depend on the size and frequency characteristics of the gust as well as the vibration characteristics of the aircraft.
5. Modern aircraft are becoming increasingly nonlinear in their behavior. The nonlinearities can be structural (e.g., free-play), aerodynamic (e.g., transonic shock effects), or control system based (e.g., nonlinear control laws) and these effects must be considered in the gust design calculations. The prediction of maximum gust loads is much more complicated for nonlinear aircraft as the law of superposition does not hold in any analysis.

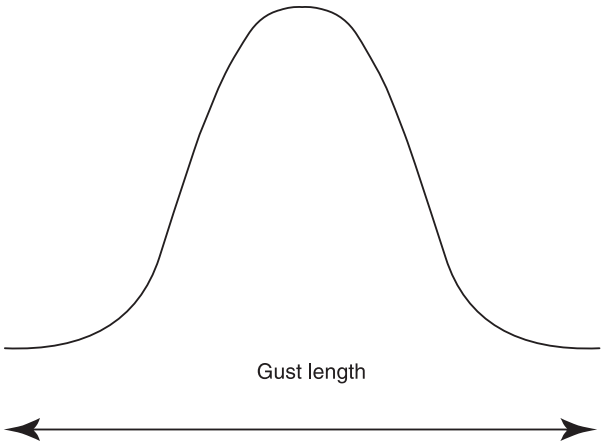


Figure 7 'I – Cosine' gust.

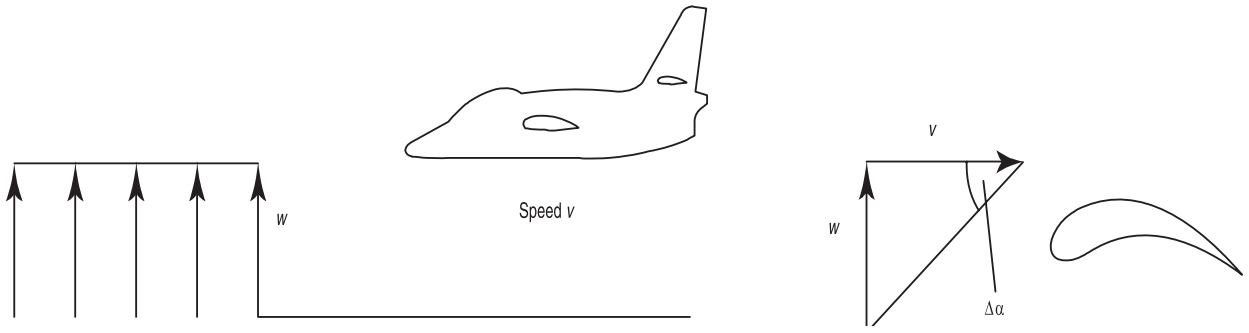


Figure 6 Aircraft encountering a sharp-edged gust.

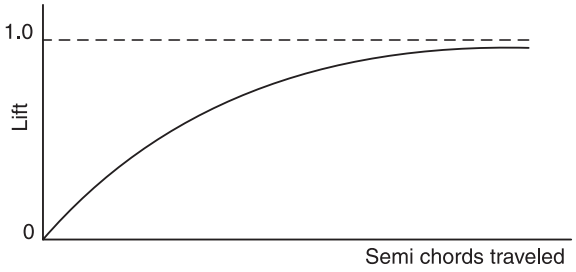


Figure 8 Kussner function: lift due to flight in a sharp-edged gust.

For many years, the main airworthiness codes included simplifying assumptions with regard to the length of the gust (e.g., a '1 − cos' gust of 25 wing chords). The response of a rigid aircraft in heave due to a sharp-edged gust resulted in very simple gust-response expressions. The well-known 'Pratt formula' introduced a gust load alleviation factor (multiply the predicted loads by 0.7 typically) to allow crudely for gust velocity build-up and unsteady aerodynamic effects. The gust envelope shown in **Figure 9** shows the flight points that needed to be considered.

Discrete tuned gusts With the growing size and increasing flexibility of aircraft, the above assumptions became more and more unacceptable. Hence, the major airworthiness codes currently demand a full dynamic response calculation. The mathematical model used to calculate the gust response is similar to that used for flutter calculations (see **Flutter**) but includes additional unsteady aerodynamic terms to account for the gust loading. The response is determined by integration of the equations in the time domain.

As the physical length of the gust affects the frequency content of the load time history, and hence the structural response, a range of gust lengths has to be considered. The gusts giving the highest loads (the discrete tuned gust) is taken for design calculations. The magnitude of the peaks reduces at shorter gust wavelengths and higher altitudes because the energy in the turbulence decreases in these cases.

Recent work has investigated methods of finding the gust sequence (e.g., a combination of several '1 − cos' gusts) that gives rise to the greatest response and loads. The techniques have been extended to consider nonlinear aircraft.

Continuous turbulence methods Measurements in flight reveal a pattern of gusts resembling a random process of continuous turbulence. This notion led in the early sixties to the development of additional design guidelines. Over short periods of time, such a random process may be considered as stationary with gaussian properties. Over longer periods of time, the standard deviation or gust intensity is not a constant, but varies randomly with a given probability function.

The turbulence is often considered to have a 'von Karman' power spectral density function derived from matching experimental data, shown in **Figure 10**, describing how the energy in the process is distributed over frequency.

The response power spectral density can be found by multiplying the known aircraft transfer function (derived from the full aeroelastic model; see **Flutter**) by the 'von Karman' power spectral density. This operation gives the RMS of the response parameter. It is then possible to determine load RMS values that can be used for design purposes. Recent advances have extended the continuous turbulence approach to deal with nonlinear aircraft.

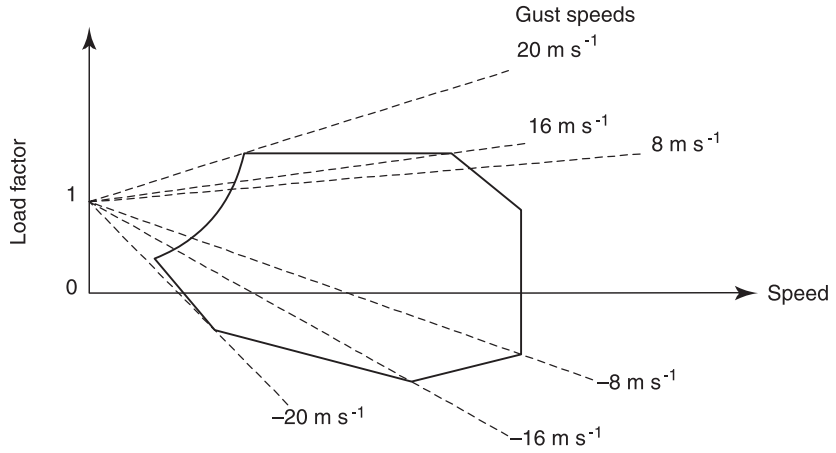


Figure 9 Gust envelope.

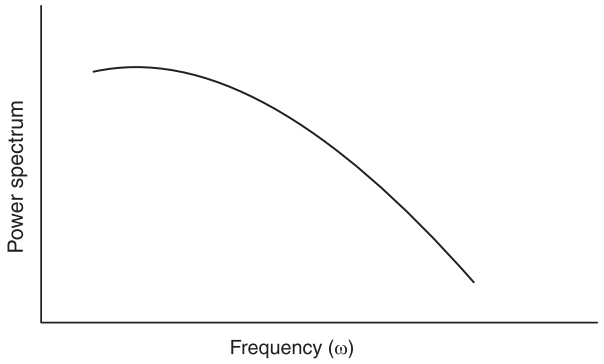


Figure 10 Von Karman gust spectrum.

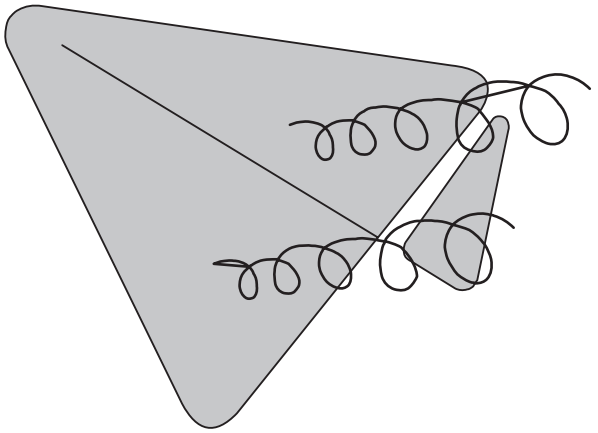


Figure 11 Tail buffet on delta wing fighter aircraft.

Active Gust Alleviation Systems

A common approach to reduce gust loads, particularly in terms of increasing passenger comfort, is to make use of an active gust alleviation system. By sensing the response of the aircraft as it encounters a gust, the control surfaces may be moved to counteract the effect and reduce the loads. Any flight control system (FCS) may well perform this function anyway. It should be noted that by alleviating the wing root bending moment, the fatigue life of the control surfaces and attachments are often drastically reduced.

Buffet and Buffeting

Buffet is defined as the aerodynamic excitation due to a separated flow. It is usually random and covers a wide frequency range, but is dependent upon the geometry and the flight condition. In some cases the buffet can be periodic and exist at individual frequencies.

Buffeting is the response resulting from the excitation of the buffet. The term originated in 1930 following a fatal accident that was attributed to the aircraft being subjected to gust loading. These gusts led to a sharp increase in the effective angle of incidence (see section on gusts) with the consequent formation of flow separation over the wing. The tail was subjected to intense vibrations (given the name buffeting) due to the turbulent wake and this resulted in structural failure. Buffeting will occur on aircraft if the vibration modes of the tail or wing structure are excited by the buffet. It rarely produces an instant catastrophic failure; however, the loads can be severe and consequently fatigue problems can result.

Fin buffet/buffeting of delta wing fighter aircraft When high angles of attack maneuvers are undertaken, turbulent flow detaches itself from the wings and meets the fin (**Figure 11**). Although this effect is desirable to enable lateral control of the aircraft, the fin can experience severe loads (up to 400*g* has been measured) due to the buffeting. The fatigue life of the fin can be used up in a few hours. Buffet can also be caused due to airbrakes and cavities in the structure. Twin-fin fighter aircraft are particularly susceptible to buffet and there is a significant effort underway worldwide to reduce/eliminate the difficulty. Approaches under investigation include:

1. The use of MEMS on the wing surfaces to eliminate the turbulent flow (see **MEMS, general properties**)
2. SMART devices on the fin to reduce the resulting vibration
3. Aerodynamic devices on the fin to counteract the buffeting
4. Aerodynamic devices upstream to influence the vortex characteristics

Buffet/buffeting of commercial aircraft Although commercial aircraft do not reach such high angles of attack as fighter aircraft, the buffeting problem can still occur. In this case, passenger comfort also needs to be taken into consideration. Separated flow can occur on the main wing surfaces, particularly on application of wing control surfaces, and if this impinges on the tail, then not only the tail modes may be excited but also those of the fuselage.

One major difficulty with design against buffeting is that it is still extremely difficult and impractical to produce a predictive model of buffet. Consequently, wind tunnel model testing must be undertaken in order to predict the buffet behavior. Once an appreciation of the frequency characteristics of the buffet and the geometry of the flow has been gained, it is possible to make response predictions using the aircraft mathematical model (assumed mode or finite element) and to construct any design changes that may be required.

Acoustic Excitation

High levels of acoustic excitation due to jet efflux and turbulent fluid flow have been experienced on the skin panels of modern jet aircraft, particularly on short take-off and vertical landing (STOVL) aircraft such as the Harrier. This high intensity noise environment is often combined with very high temperatures, e.g., at some points on the structure the sound pressure could be in the region of 180 dB with panel temperatures over 1500 °C. There is a high likelihood of fatigue damage occurring in such an environment.

Similar problems are likely to occur with the new generation of stealth aircraft as power-plant and stores will be internal. When the cavities have to be opened, for instance when a store is to be dropped, extremely high noise levels will occur. Civil aircraft are also susceptible to such difficulties on the flaps and rear fuselage, etc. Much work is being undertaken to investigate approaches (e.g., passive damping technology, smart materials and devices, and MEMS) in order to reduce the severe problems that will have to be overcome.

Gunfire Loads

Repetitive gunfire blasts impart pulses that can cause vibration levels typically twice that occurring in normal flight. These vibrations occur at distinct frequencies as shown in **Figure 12**. The aircraft structure, and the equipment within, must be cleared to withstand the vibration levels due to gunfire.

Store Release

When stores are released from military aircraft (or even dropping aid parcels from transport aircraft) an impulse is imparted onto the structure and the aircraft will respond dynamically. The designer needs to ensure that this response is not significant, bearing in mind that the mass distribution and aerodynamic characteristics have changed. Care has also to be taken in the design to guarantee that the store jettisons safely rather than rebounding back onto the aircraft.

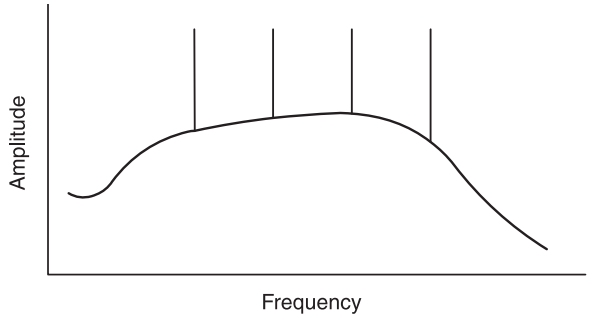


Figure 12 Typical flight vibration spectra including gunfire.

Birdstrike

All aircraft fly with the likelihood of hitting one or more birds in flight. The airworthiness regulations lay down strength criteria that every aircraft must meet. Certification is usually met through ground testing. The leading edges of the wings and tailplane, as well as the canopy and radome, must be constructed so that they can survive such an incident. Ingestion of birds into jet engines is also a problem that must be considered particularly for large diameter civil aircraft engines.

Hammershock

Jet engines cannot operate in supersonic flow conditions, therefore the intakes and ducts of supersonic aircraft need to be designed so that subsonic conditions occur at the engine (**Figure 13**). At the limits of engine performance, it is possible for the airflow into the engine to distort, resulting in an engine surge. This surge in turn causes a pressure wave called hammershock to occur in the duct. This wave advances at high speed (typically 400 m s^{-1}) down the duct in the opposite direction to the airflow. The wave causes a pressure in the duct of up to three times the usual steady-state pressure that in turn leads to a dynamic response.

The engine intake and duct structure are designed to withstand the stresses due to maneuver loads, the steady-state operating pressure, and critically the hammershock loads. It is not possible at present to predict the hammershock pressures, so experimental measurements on the ground and in flight are taken. These measurements can then be used with a structural FE model to predict the resultant stresses and to make any design modifications that may be necessary.

Ground Loads

The landing gear of an aircraft undertakes two functions: to absorb the energy due to the vertical descent on landing, and to enable the aircraft to maneuver on the ground. A complete analysis of the behavior of the aircraft during both phases of operation is essential so that the undercarriage is designed to be strong enough and also to ensure that no other component fails. The airworthiness regulations dictate how the undercarriage should be cleared for each aircraft.

Landing Loads

Aircraft are subjected to significant forces during landing, especially in the special case of landing on an aircraft carrier. The characteristics of these loads are dependent upon the landing gear. There are a number of variables that must be considered:

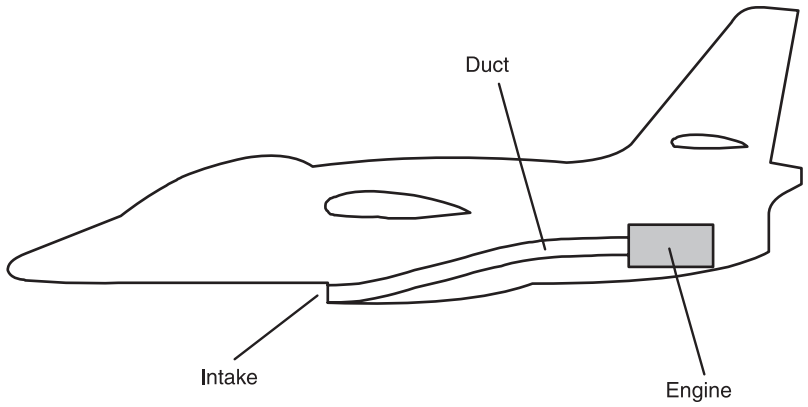


Figure 13 Typical intake of a jet fighter.

- limit descent velocity at the design landing weight (typically $3\,\mathrm{m\,s^{-1}}$ for transports and land based fighters (not trainers), $6\,\mathrm{m\,s^{-1}}$ for carrier based aircraft),
- undercarriage and tyre energy absorption characteristics (nonlinear),
- aircraft attitude relative to the ground,
- distribution of the aircraft mass,
- lift acting on the aircraft at the impact point,
- friction coefficient between the tyre and the ground,
- rotation of the aircraft on take-off.

The analysis of the aircraft response should consider the following behavior:

- landing gear dynamic characteristics,
- spin up loading due to forces that accelerate the wheel up to the ground speed,
- spring back once the wheel has reached the ground speed and the sliding friction has gone to zero, the strain energy stored by the undercarriage's rearward bending motion is released and the undercarriage returns to its original orientation with a sizeable inertia load,
- rigid-body response of the aircraft,
- dynamic response of the aircraft.

A typical commercial aircraft would make a conventional two-point landing (nose gear does not contact the ground until the main undercarriage has absorbed all the energy from the descent) as shown in **Figure 14**. However, the cases of three-wheel (nose gear critical case) and one-wheel landings must also be considered. In each case the loads and resulting motions must be analyzed to ensure that structural integrity is maintained.

Runway Loads

These are usually defined as the loads resulting from taxiing including turning, braking applied during take-off (e.g., an aborted take-off) or landing, as well as towing, jacking and tethering (tying down an aircraft in a very high wind). Of particular interest are the loads on the nose undercarriage when the brakes have been applied suddenly, causing an increase in the vertical load on the nose gear due to the pitching moment of the aircraft. Similarly, the forces due to the application of the spoilers, brakes, thrust reversers, brake parachute deployment and arrestor wire engagement need to be considered.

Shimmy

In the 1930s, the air pressure in car tyres was reduced with the object of producing a smoother ride. This change produced an effect known as 'shimmy' that consisted of a self-excited unstable rotational oscillation of the front wheels about the vertical axis. The problem was eventually cured through independent spring suspension of the front wheels. Shimmy is not restricted solely to pairs of wheels on a common axis, but has been observed on single castored wheels such as on supermarket trolleys and, more importantly, on aircraft nose and main undercarriages where its

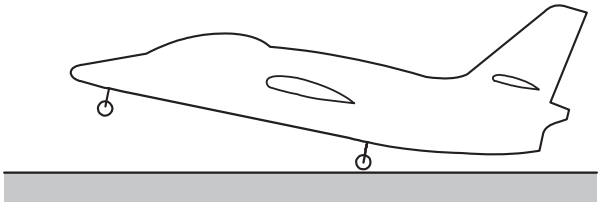


Figure 14 Conventional two-point (main undercarriage) landing.

occurrence can be disastrous. The coupling of the torsion and bending modes, analogous to flutter, leads to an unstable motion.

The analysis of the shimmy problem is made very complex due to the dynamics of the tyre (viscoelastic material, nonlinear friction and deformation characteristics). Experimental tests are performed to verify the design calculations.

Other Aircraft Aeroelastic Phenomena

Classical linear flutter is considered in **Flutter**. In this section, a number of related phenomena that have nonlinear response characteristics are described.

Limit Cycle Oscillations

If an aircraft that behaves linearly is flown fast enough, flutter will occur. In practice though, aircraft are nonlinear in their vibration behavior and these nonlinearities can produce phenomena known as limit cycle oscillations (LCOs). LCOs are characterized as bounded instabilities, as shown in **Figure 15**, where it can be seen that the amplitude initially increases but then stops growing. This effect can arise due to nonlinearities occurring in the:

- structure – freeplay, backlash, cubic stiffening,
- aerodynamics – moving shocks, other transonic aerodynamic effects,
- control system – time delays, nonlinear control laws.

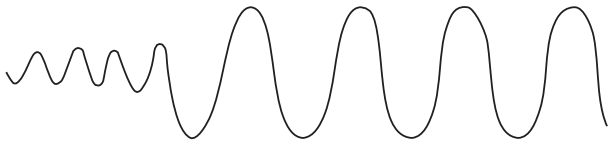


Figure 15 Typical limit cycle oscillations.

As LCOs are not immediately destructive, they can be considered as a fatigue problem. However, they are extremely difficult to predict as an accurate nonlinear model is required. At present, a large amount of computer simulation is needed to do this. However, as modern aircraft are becoming more flexible and nonlinear, consequently, LCOs are becoming more of a problem. Research is currently being directed towards methods that can predict LCOs without the need for vast amounts of testing or computer simulation. Such methods will speed up the flight test procedure whilst improving safety by giving an improved predictive capability.

Aeroservoelasticity

Modern aircraft contain a range of active control technology including flight control systems (FCSs), gust alleviation systems, flutter suppression systems, etc., that can combine with the usual aeroelastic phenomena. The FCS detects a motion (which it assumes is the uncommanded aircraft rigid-body response) and tries to correct it. In the worst case, the frequency of activation commanded coincides with the structural mode frequency being corrected, leading to a potentially unstable condition. This interaction is illustrated by the 'aeroservoelastic pyramid' in **Figure 16**. The entire system including feedback must be included in all stability calculations and the siting of motion sensor units is critical. It is

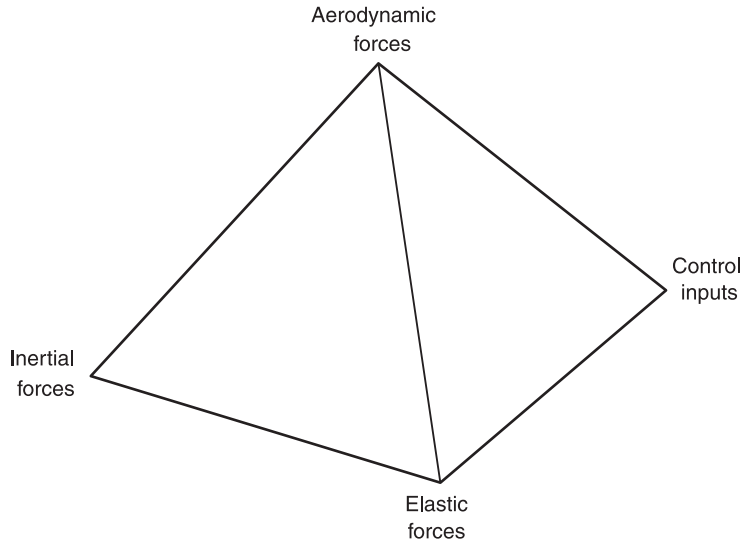


Figure 16 Aeroservoelastic pyramid.

possible for the control system to interact with the structure in such a way that unstable oscillations can occur. The control system is likely to contain nonlinearities and these can give rise to phenomenon such as LCOs.

Panel Flutter

When there is supersonic flow past a thin panel, there is the possibility of self-excited oscillations of the panel normal to its plane. Consider the panel in **Figure 17**. The pressure acting on the plate is proportional to the dynamic pressure and the local slope of the surface. Therefore, a symmetric slope distribution leads to an unsymmetrical pressure loading which tends to deform the surface of the plate into a more complicated shape. As the dynamic pressure increases, the plate loses its ability to maintain equilibrium and a response limited LCO occurs due to nonlinear stiffening effects at higher amplitudes. The solution to this problem is to increase the stiffness of the panel through the use of larger or more stringers/ribs. Other solutions include increasing the tension in the panel. Recent work has investigated the use of shape memory alloys to do this, using the temperature increase associated with supersonic flight to take the alloys beyond the activation temperature.

Control Surface Buzz

This is a LCO-type phenomenon that occurs in the transonic flight regime. At transonic speeds there will be a shock wave acting on the airfoil. Any movement of the shock will result in a difference in aerodynamic forces with a consequent change in deflection of the aerofoil, but in particular of the control surface itself.

Consider the aerofoil with flap in **Figure 18**. In this case, the flap is entirely in subsonic flow as the shock is on the aerofoil surface. A similar type of response occurs at slightly higher speeds when the shock is on the control surface. Oscillation of the flap causes a fore-and-aft motion of the shock waves that changes the aerodynamic moments acting on the control surface. The resulting change in deflection of the control surface results in further movement of the shock waves. The resulting motion is amplitude limited, but can result in deflections of up to ± 10 degrees causing severe problems for the pilot. The phenomenon also causes undesirable vibration and fatigue damage.

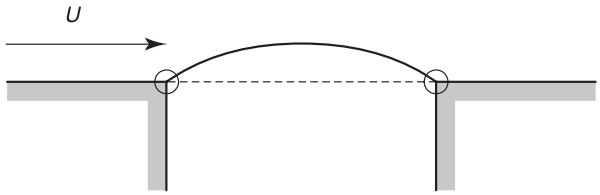


Figure 17 Panel flutter.

Stall Flutter

If the angle of incidence of an airfoil exceeds its stall angle, then stall will occur. Stall flutter is a LCO-type phenomenon that can occur in propellers, helicopter rotors, compressor/turbine blades as well as aircraft wings. It is characteristically a torsion type motion shown in **Figure 19** and consists of the following stages:

1. the aerofoil angle of incidence θ increases dynamically, increasing the lift;
2. the angle of attack exceeds the stalling angle, separation occurs, and the lift reduces;
3. with the lift reduced, the angle of attack reduces, until is passes the stalling angle;
4. the flow reattaches and the cycle is repeated.

Stall flutter is not immediately catastrophic, but may lead to fatigue problems. For structures such as aircraft wings, or turbine blades, the phenomenon will occur at the tip, where the twist will be largest.

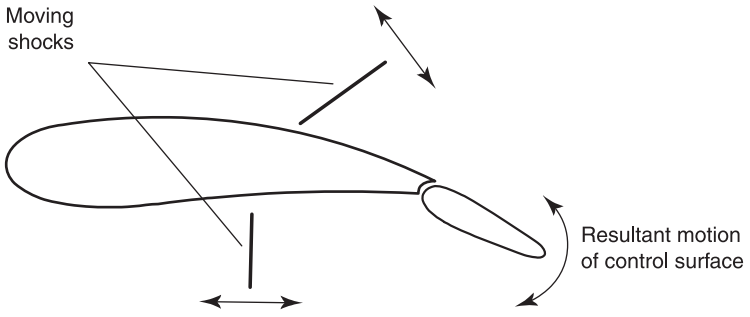


Figure 18 Control surface buzz.

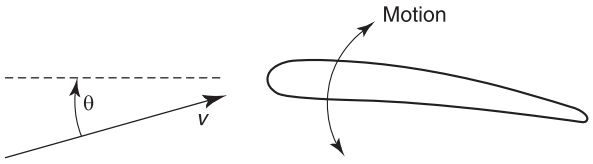


Figure 19 Typical stall flutter.

Another Aeroelastic Phenomenon

For completeness, a number of important aeroelastic phenomenon are included, however, these are not directly relevant to aircraft.

Aerodynamically Induced Negative Damping

It can be shown that most simple cross-section shapes, except a smooth circle, produce an aerodynamic force in the direction of motion. This is equivalent to having a negative angle of lift curve slope and will produce an unstable response. Such shapes can occur through the build-up of ice on the structure. The phenomenon can occur on electric transmission lines giving rise to the phenomenon known as 'galloping'.

Vortex Shedding

Under the correct flow conditions, the flow around a bluff body produces a regular pattern of alternating vortices known as a von Karman vortex street (**Figure 20**). These vortices produce a sinusoidal force acting on the body perpendicular to the flow. For a cylinder, the frequency ω (in Hz) of the shedding is related to the diameter D(m) and wind speed v (m s^{-1}) via the Strouhal number S such that

$$S = \frac{\omega D}{v} = 0.21$$

If the frequency of the shed vortices is the same as one of the natural frequencies of the structure, then large vibrations can result. Although it is possible for this loading to cause the structure to fail through the ultimate load being exceeded, failure is more likely to occur through fatigue.

The effect is exacerbated by an effect known as 'lock-in' where the vortex shedding frequency is forced to remain at the critical structural frequency at a range of speeds below and above the critical speed. The design of bridges, chimneys, submarine periscopes, etc. must take this phenomenon into account. Aerodynamic devices are used commonly nowadays to either ensure that the flow remains attached, or to break up the regular formation of the vortexes.

See also: **Flutter**; **Structural dynamic modifications**.

Further Reading

AGARD–SMP Report 815 (1997) Loads and requirements for Military Aircraft.

Bisplinghoff RL, Ashley H, Halfman RL (1996) *Aeroelasticity*. Dover.

Dowell EH, Curtis HC, Scanlan RH, Sisto F (1989) *A Modern Course in Aeroelasticity*. Kluwer.

ESDU Item 84020 *An Introduction to time-dependent aerodynamics of aircraft response, gusts and active controls*.

Fung YC (1993) *An Introduction to the Theory of Aeroelasticity*. Dover.

Lomax TL (1995) *Structural Loads Analysis for Commercial Transport Aircraft: Theory and Practice*. AIAA Education Series.

Niu MCY (1988) *Airframe Structural Design*. Conmilit Press Ltd.

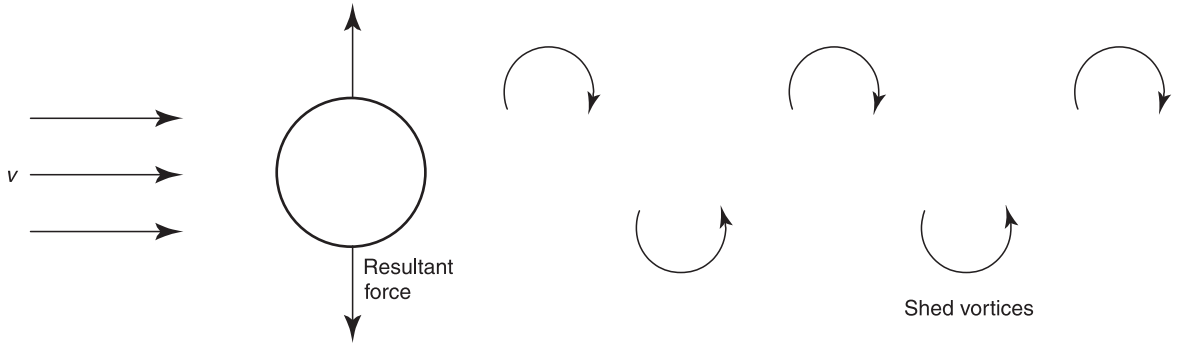


Figure 20 Vortex shedding.

ANTIRESONANCE

See **RESONANCE AND ANTIRESONANCE**

AVERAGING

S Braun, Technion – Israel Institute of Technology, Haifa, Israel

Copyright © 2001 Academic Press

doi:10.1006/rwvb.2001.0049

General

Computations of averages are necessary in many signal-processing tasks, whenever uncertainties result from random components in the analyzed signal. Averaging operations are thus performed in simple computations like those of root mean square (RMS) values, up to operations on vectors like time domain (synchronous) averaging (TDA) and power spectral density (PSD) averaging. Batch and recursive realizations are possible. The recursive procedures also enable the obtaining of properties of decaying memory, more suitable for situations involving some nonstationarity.

All these averaging procedures are extensively used in the processing of vibration signals, and available on most dedicated analyzing systems.

Basic operations

Given a sequence x_n, the most basic operation of averaging is given by:

$$y = \frac{1}{N}\sum_{n=1}^{N} x_n \qquad [1a]$$

where N is the number of elements in the sequence. Often a different weight is given to the samples, as per:

$$y = \sum_{n=1}^{N} w_n x_n \qquad [1b]$$

Eqn [1a] corresponds to the more general case of eqn [1b] with $w_n = 1/N$. The weights w_n are often chosen according to the importance or confidence of the data.

For dynamic signals, we often use moving averages (MAs). This is given by:

$$y_n = \sum_{k=0}^{N-1} w_n x_{n-k} \qquad [2]$$

and shown in **Figure 1**. The sequence w is called a window (see **Windows**) and often is intended to concentrate the (moving) averaging operation around the windows duration.

Specific cases are shown in **Figure 2**. The first case (**Figure 2A**) shows a rectangular window with $w_n = 1/N$; an average is computed each time for the data within the sliding window. A typical example is the continuous monitoring of the RMS value of a signal. For random signals, the random error of the computed RMS is approximately inversely proportional to $1/\sqrt{N}$, and can be controlled by averaging N elements of:

$$X_{\mathrm{RMS}} = \left(\frac{1}{N}\sum_{k=0}^{N-1} x_k^2\right)^{0.5}$$

or by the equivalent MA expression for time-varying RMS values:

$$X_{\mathrm{RMS}_n} = \left(\frac{1}{N}\sum_{k=0}^{N-1} x_{n-k}^2\right)^{0.5}$$

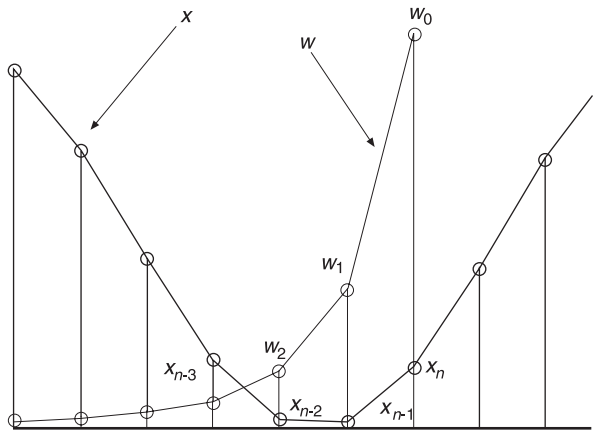


Figure 1 Moving average with window.

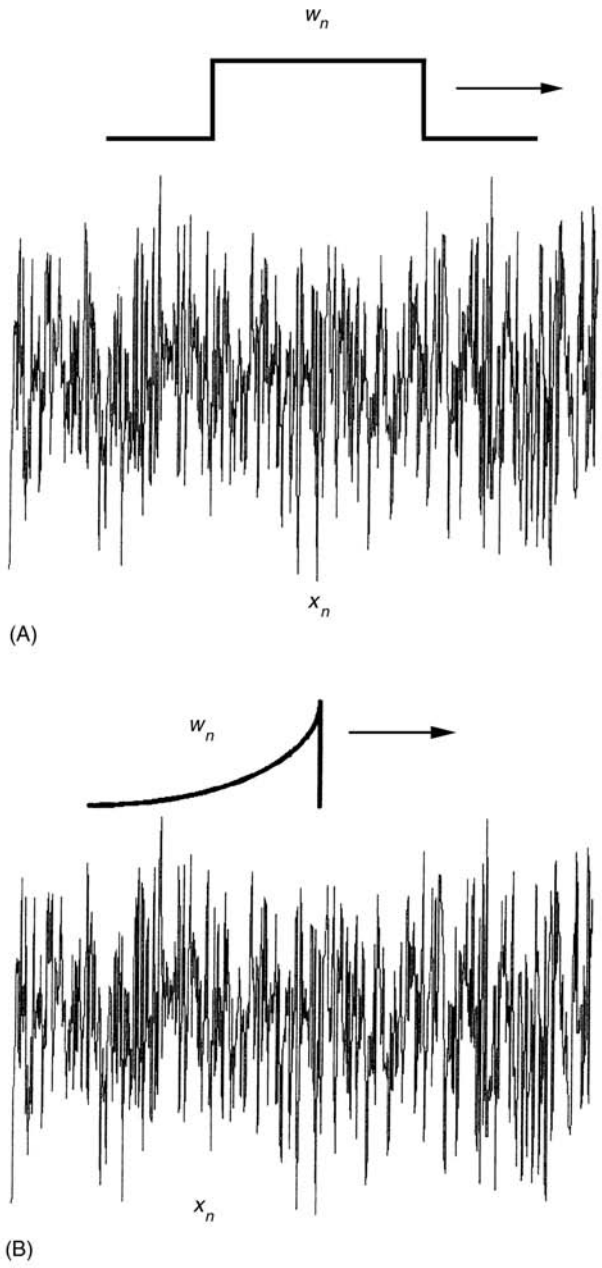


Figure 2 Moving average: (A) rectangular window; (B) exponential window.

An exponential window is shown in **Figure 2B**, where a forgetting effect is achieved for past data, less and less weight being given to data more distant in the past.

The Frequency Response of the Moving Average

It is convenient to consider the MA as a linear filter, where a new y_n is produced for each new input x_n. For the windows shown in **Figure 2** we obviously get a smoothing effect, hence the operation is equivalent to some low pass filter. The filter's bandwidth must be inversely proportional to the windows effective duration (which must be defined according to a specific criterion).

The MA filter can be analyzed in the frequency domain, describable by $H(\omega)$, its frequency response function (FRF). This can be conveniently undertaken via the Z transform (see **Transform methods**).

For the rectangular window, N increases as each new x_n occurs:

$$Y(z) = \frac{1}{N}\sum_{k=0}^{N-1} X(z)z^{-k} \qquad [3]$$

and the FRF is computed by substituting $z = \exp(j\omega\Delta t)$, Δt the time interval between samples and computing:

$$Y(\omega) = \frac{1}{N}\sum_{k}^{N-1} X(\omega)\exp(-j\omega k\Delta t) \qquad [4a]$$

$$H(\omega) = \frac{1}{N}\sum_{k}^{N-1} \exp(-j\omega k\Delta t) \qquad [4b]$$

The filter's response is shown in **Figure 3**. The magnitude of H consists of a main lobe and secondary lobes attenuated with frequency. Zeros occur at locations $f = 1/N$.

In addition to the finite-length MA filter, an infinitely operating MA can be used, as shown in **Figure 4**. The average is still computed via:

$$y_n = \frac{1}{n}\sum_{k=1}^{n} x_k \qquad [5a]$$

but with n increasing with each incoming data sample. This is equivalent to a filter with time-dependent parameters. Comparing this to **Figure 3**, the width of the main lobe will decrease as N increases (see **Figure 5**).

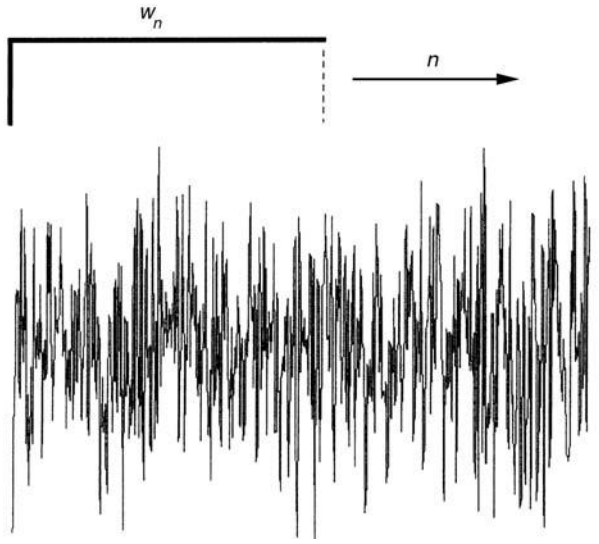


Figure 4 Running moving average with increasing number of samples.

Recursive Averaging Filters

Recursive computations are often preferred to batch ones, as close to real-time processing is possible. For n increasing as each new x_n occurs, eqn [5b] can be cast is the recursive form:

$$y_n = y_{n-1} + \frac{x_n - y_{n-1}}{n} \qquad [5b]$$

the average y_n is updated at each step, and a diminishing weight (with n) is applied to the difference between the incoming data and the prior average. The frequency response of **Figure 5** obviously applies.

A modified averaging process can be used by replacing the variable n in eqn [5b] by a constant parameter N_1. The corresponding recursive equation can be rewritten as:

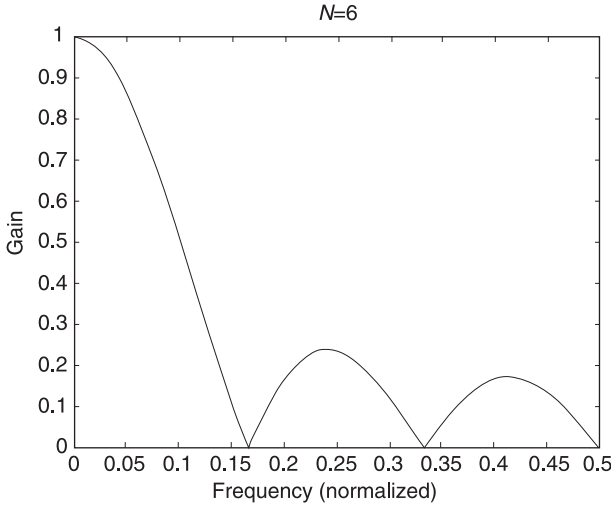


Figure 3 Frequency response function of moving average with rectangular window.

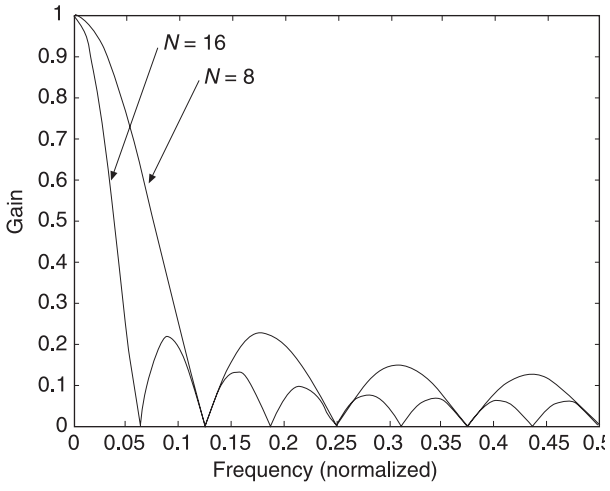


Figure 5 Frequency response function of running moving average for $N = 8$ and $N = 16$.

$$y_n = (1-\alpha)y_{n-1} + \alpha x_n \qquad [6]$$

where $\alpha = 1/N_1$. This is sometimes called exponential recursive averaging. The FRF of the equivalent filter:

$$H(z) = \frac{\alpha}{1-(1-\alpha)z^{-1}} \qquad [7a]$$

is:

$$H(\omega) = \frac{\alpha}{1-(1-\alpha)\exp(-j\omega\Delta t)} \qquad [7b]$$

is shown in **Figure 6**, the impulse response in **Figure 7**. The equivalent time constant for $\alpha \gg 1$ is approximately equal to N_1. In this averaging process, gradually decreasing weight is given to past samples. The bandwidth of the FRF is inversely proportional to α, and no zeros or secondary lobes result.

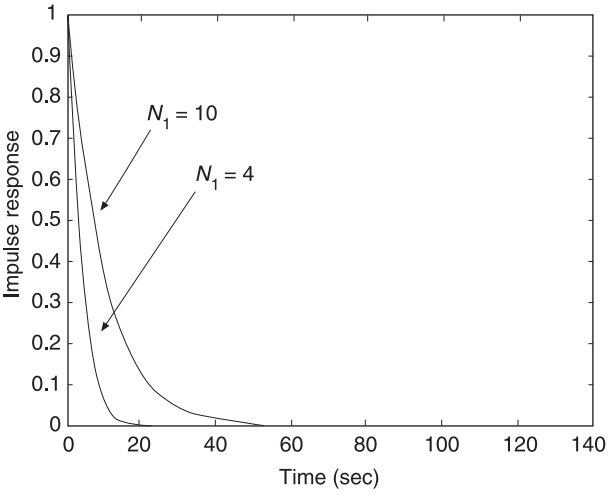


Figure 7 Impulse response of exponential moving average for $N_1 = 4$ and $N_1 = 10$.

Time Domain Averaging (TDA)

One of the most powerful and practical methods of extracting periodic signals from a composite signal is based on averaging signal sections of the period (frequency) sought. An *a priori* knowledge of the frequency sought is obviously necessary. This method is also known as synchronous averaging.

Regular TDA

The principle is shown in **Figure 8**, whereby signal elements separated by one (known) period are averaged. Signal elements which are of the frequency sought will be unaffected by the averaging process. All other components will be attenuated, and will converge to zero as the process is repeated indefinitely.

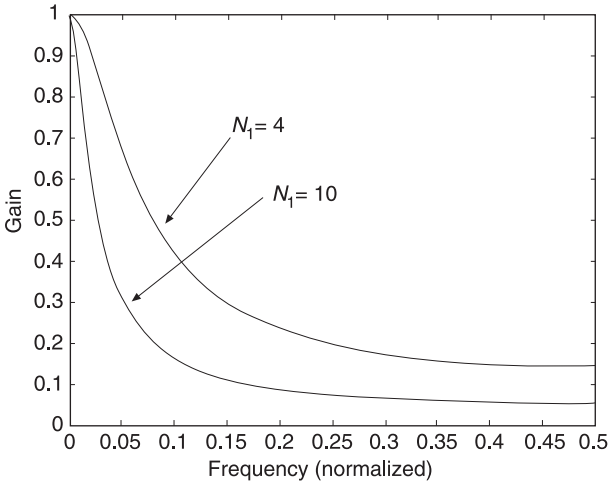


Figure 6 Frequency response function of exponential moving average for $N_1 = 4$ and $N_1 = 10$.

Knowledge of the period can also be based on appropriate acquisition of a synchronizing signal. The method is thus extensively used in analyzing vibration (and other) signals acquired from rotating machinery, where synchronizing trigger signals are easily available via suitable hardware solutions (see **Data acquisition**).

The mathematical description of the averaging process is given by:

$$y(n\Delta t) = \frac{1}{N}\sum_{r=0}^{N-1} x(n\Delta t - rM\Delta t) \qquad [8]$$

where M is the number of elements per period, and N the number of sections averaged.

This has similarities to eqn [3], and the process can be analyzed as a filtering process. The frequency response can be computed via the Z transform as:

$$H(z) = \frac{1}{N}\frac{1-z^{-MN}}{1-z^{-N}} \qquad [9]$$

$$H(f/f_p) = \frac{1}{N}\frac{\sin(\pi N f/f_p)}{\sin(\pi f/f_p)} \qquad [10a]$$

$$\phi_H(f/f_p) = -\pi(N-1)f/f_p \qquad [10b]$$

where:

$$f_p = \frac{1}{MN\Delta t} \qquad [10c]$$

is the frequency of the periodic component to be extracted.

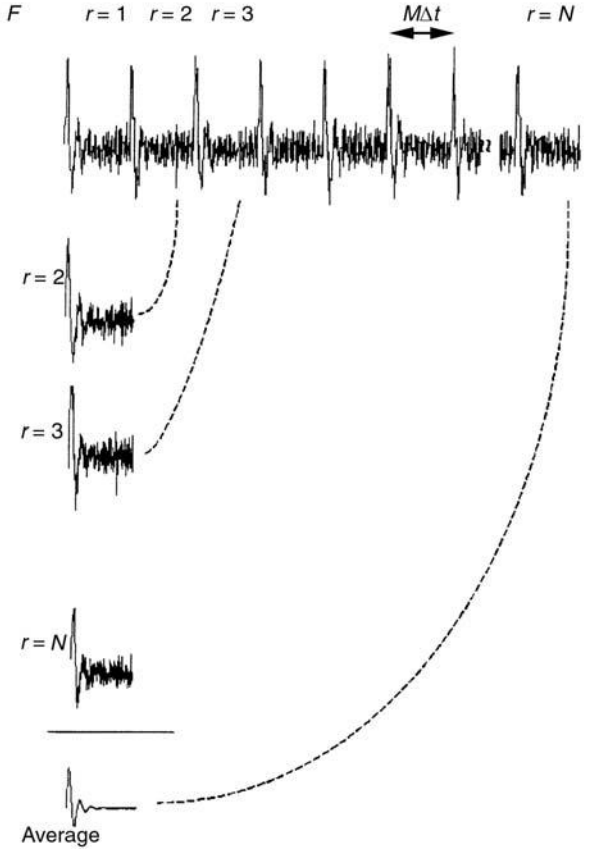


Figure 8 Principle of time domain averaging.

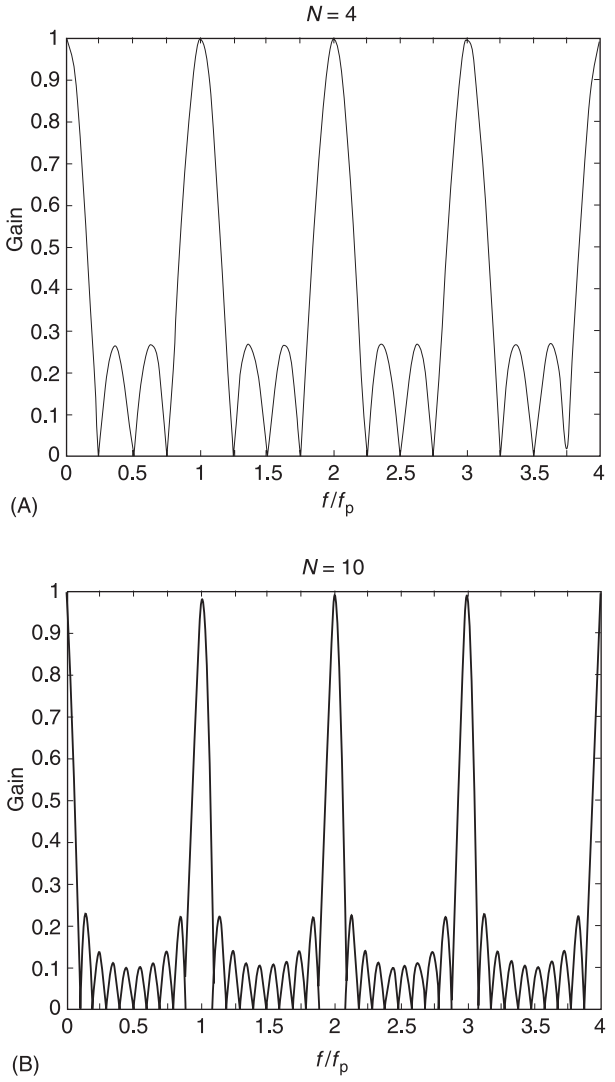


Figure 9 Frequency response function of exponential TDA, $H(f/f_p)$: (A) $N_1 = 4$; (B) $N_1 = 10$.

The FRF is shown in **Figure 9**. It has the form of a 'comb' filter, with main lobes centered around integer multiples of the synchronizing frequency f_p.The gain at these frequencies is 1, and the phase shift zero, hence the fundamental and harmonic components of the periodic signal are extracted exactly. All other components however, are attenuated. The zeros of the FRF are separated by:

$$f/f_p = k/N \quad k = 1, 2, \ldots$$

The bandwidth of the main lobe is thus inversely proportional to the number of sections averaged.

Recursive Schemes for TDA

The recursive algorithms described above can be applied as well. The algorithm:

$$y_r(n\Delta t) = y_{r-1}(n\Delta t) + \frac{x_r(n\Delta t) - y_{r-1}(n\Delta t)}{r} \quad [11a]$$

where y_r is the running average at the rth period. The algorithm is very efficient, only two vector additions and one division are necessary per averaging, and real-time operating systems (for frequency ranges typical of mechanical vibration tasks) exist. The results are obviously equivalent to those described above. Additional versatility can be achieved by using the exponential averaging of eqn [6], resulting in:

$$y_r(n\Delta t) = y_{r-1}(n\Delta t) + \frac{x_r(n\Delta t) - y_{r-1}(n\Delta t)}{N_1} \quad [11b]$$

The resulting FRF is shown in **Figure 10**. It has again the form of a comb filter, but only one lobe exists around each center frequency. Their lobes function is given by eqn [4b], the bandwidth dictated by the parameter N_1.

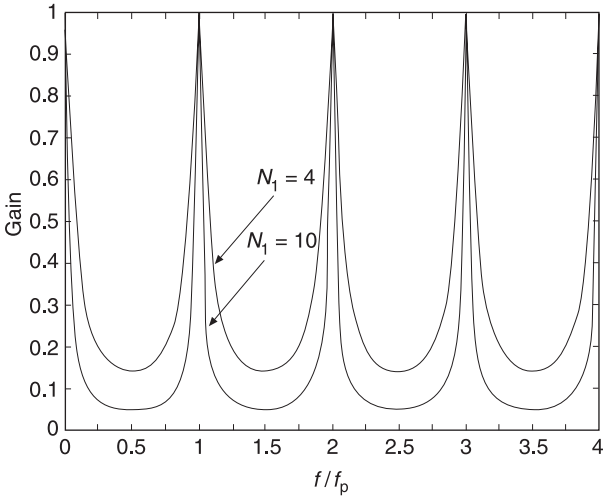


Figure 10 Frequency response function of exponential TDA, $H(f/f_p)$ for $N_1 = 4$ and $N_1 = 10$.

Performance of TDA

Rejection of unwanted components The rejection of unwanted components is a function of their properties. Denoting the signal $x(n\Delta t)$ as a sum of a periodic component $s(n\Delta t)$ and noise $e(n\Delta t)$, where the noise includes all the signal elements not periodic within $1/f_p$:

$$x(t) = s(t) + e(t) \qquad [12]$$

we may estimate the attenuation of $e(t)$ for the cases when it is broadband random or harmonic.

For additive broadband random noise, the averaging process will attenuate the RMS of the noise according to eqn [14a]. An example is given in **Figure 11**, where a periodic signal in the form of decaying oscillations is corrupted by random noise. This shows the result of the averaging, considered as a filtering process, where a new output is generated for each new input. In practice, only M points of the last averaging operation, i.e., one period only, would be shown, as in **Figure 8**. The improvement in the signal-to-noise ratio as the number of averages increases is evident.

For additive harmonic noise, the attenuation of $e(t)$ is a function of its frequency, according to the frequency response of the averaging filter (**Figure 9**). An upper bound of this attenuation can be based on the maxima of the secondary lobes, resulting in:

$$H_{\max}(k) = \left[N \sin\left(\pi f/f_p\right)\right]^{-1} \qquad [13a]$$

$$\frac{f}{f_p} = (k - 0.5)/N \qquad [13b]$$

An example is shown in **Figure 12**. It can be noted that the increase in the attenuation of the noise with N has an oscillatory character. The number of averages N, necessary to achieve a given attenuation, is given by:

$$\left.\begin{array}{ll} \text{Broadband noise} & N > (1/NR)^2 \\ \text{Harmonic noise} & N > \left[NR \sin\left(\pi f/f_p\right)\right]^{-1} \end{array}\right\} \qquad [14]$$

where NR is the desired noise reduction of the interfering signal components.

Comparisons between regular and exponential averaging The exponential averaging achieves a fading memory property. For regular averaging see eqn [11a], as the number of incoming data samples (and hence N, the number of available periods) increases, the bandwidth of the comb filter main lobes becomes narrower and narrower, with increased rejection of unwanted components. With exponential averaging (see eqn [11b]) the bandwidth is fixed, and after a transient stabilizing time, the rejection of the interfering signals stays constant. This is shown in **Figure 13**.

One advantage of exponential averaging is due to the decaying memory of the process. The effect of a single artifact or time-localized interference will slowly disappear as future data become available. An example is shown in **Figure 14**, extracting a periodic signature from broadband noise, while a single disturbing transient occurred once. Comparing exponential averaging to the regular one, the fading effect of the transient can easily be controlled by N_1 (see eqn [11b]), the approximate decaying memory length.

Variable periods and the effect of jitter In many practical cases, the period of the signal of interest may not be constant. An example could be the vibratory response of an impacted structure, where many transient responses could be averaged. A triggered mode of data acquisition (see **Data acquisition**) could then be used, where a limited and fixed number of data points would be acquired after each trigger. In such a case, the interval between the transient responses would not inhibit the use of the averaging method. An example is shown in **Figure 15**. Comparison with **Figure 8** shows that the averaged result would extract the exactly repeating component following the trigger. Obviously both regular and exponential averaging could be used.

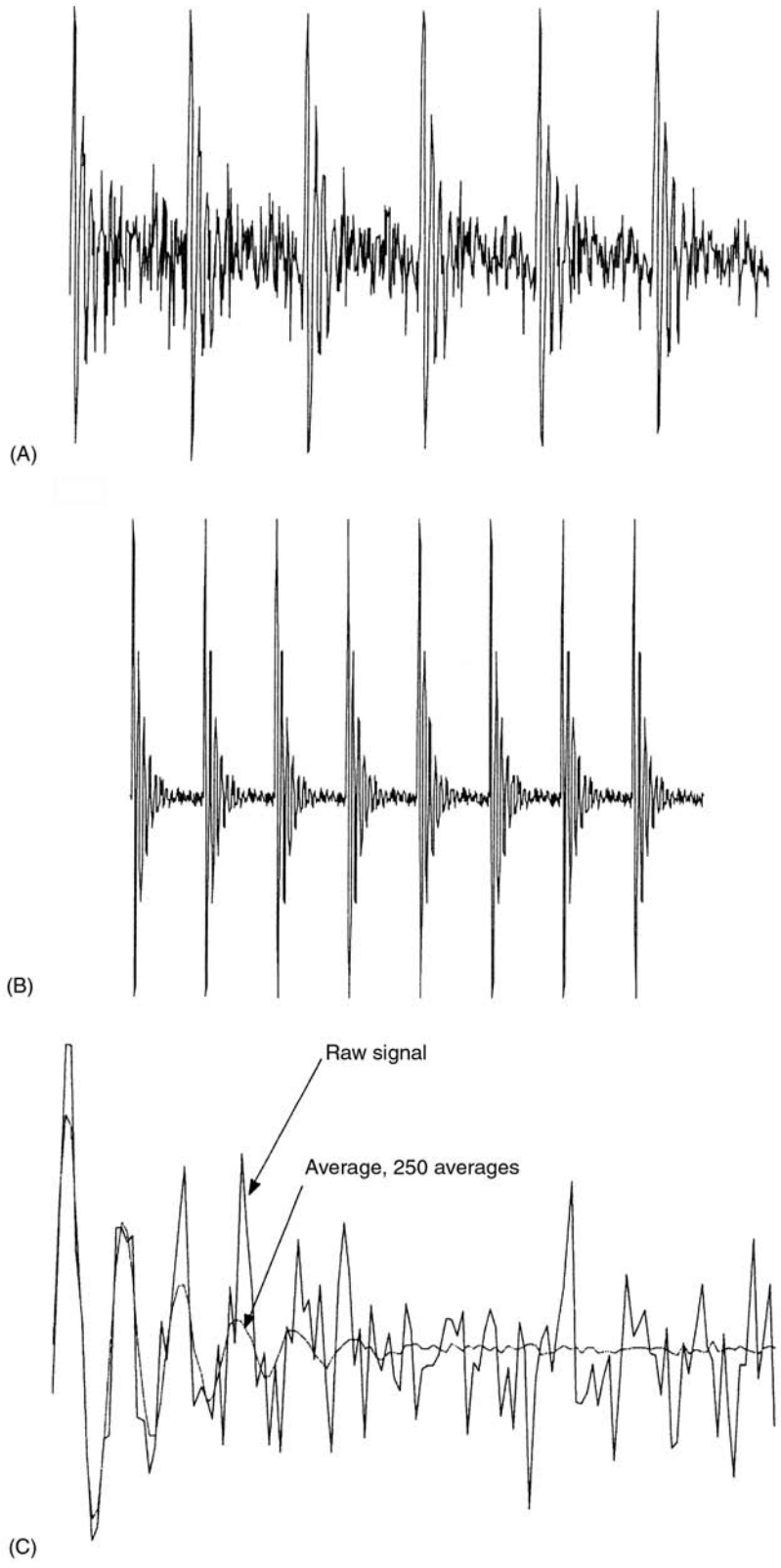


Figure 11 Rejection of broadband random interfering signal by TDA: (A) signal for periods 2 to 8; (B) signal for periods 200 to 208; (C) single raw signal period and result of 250 averages.

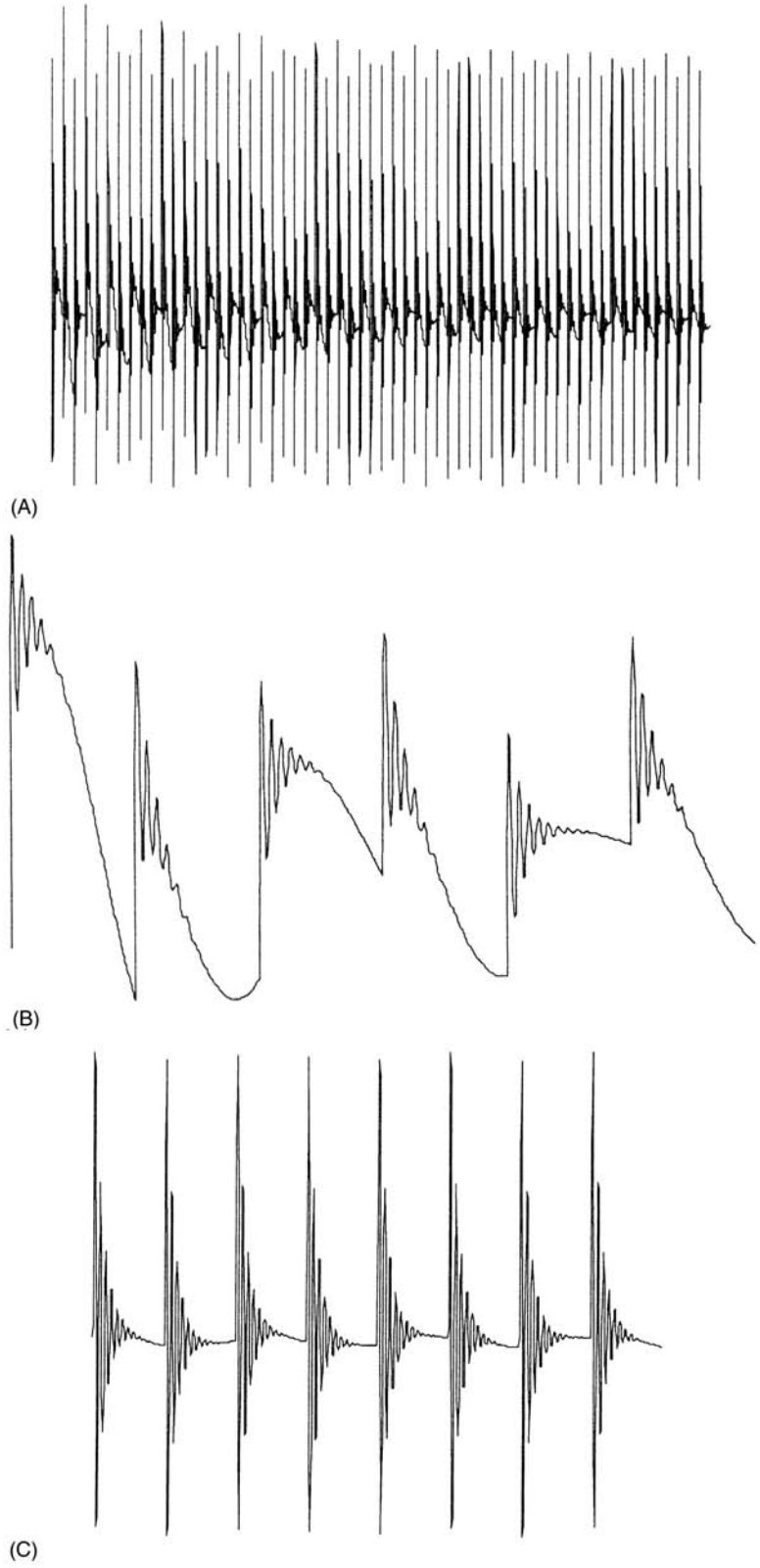
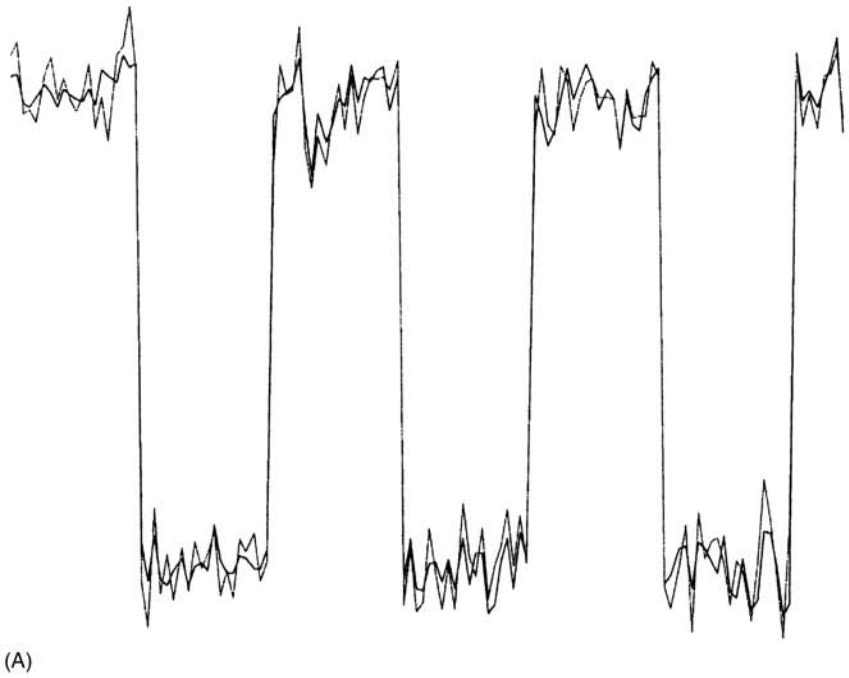
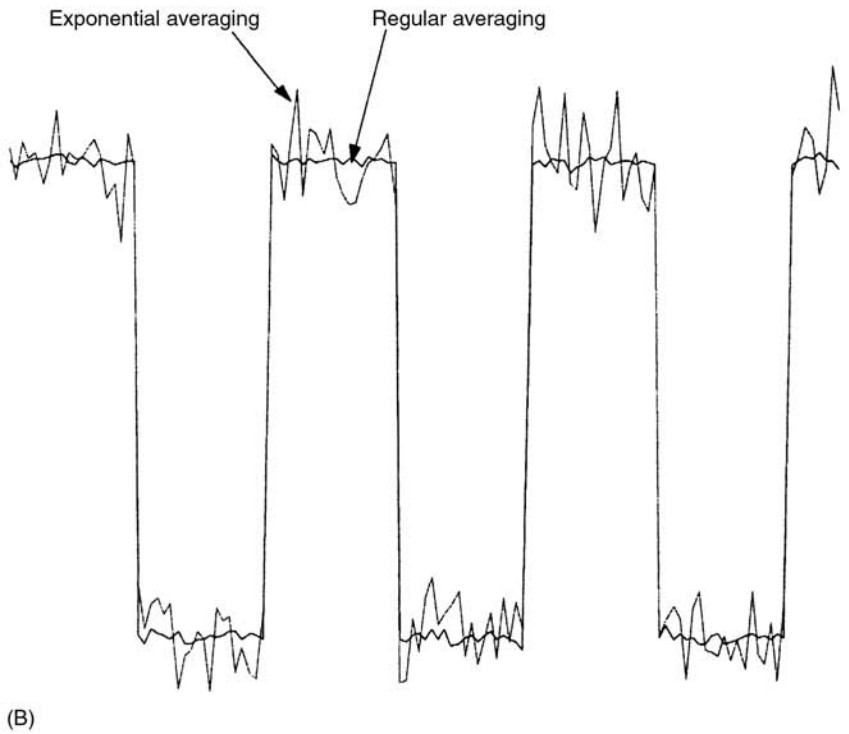


Figure 12 Rejection of harmonic interference by TDA: (A) signal for periods 20–80; (B) signal for periods 2–8; (C) signal for periods 200–208.



(A)



(B)

Figure 13 Regular and exponential TDA for square signal and broadband random interference: (A) N_1 and N same order of magnitude; (B) $N \gg N_1$.

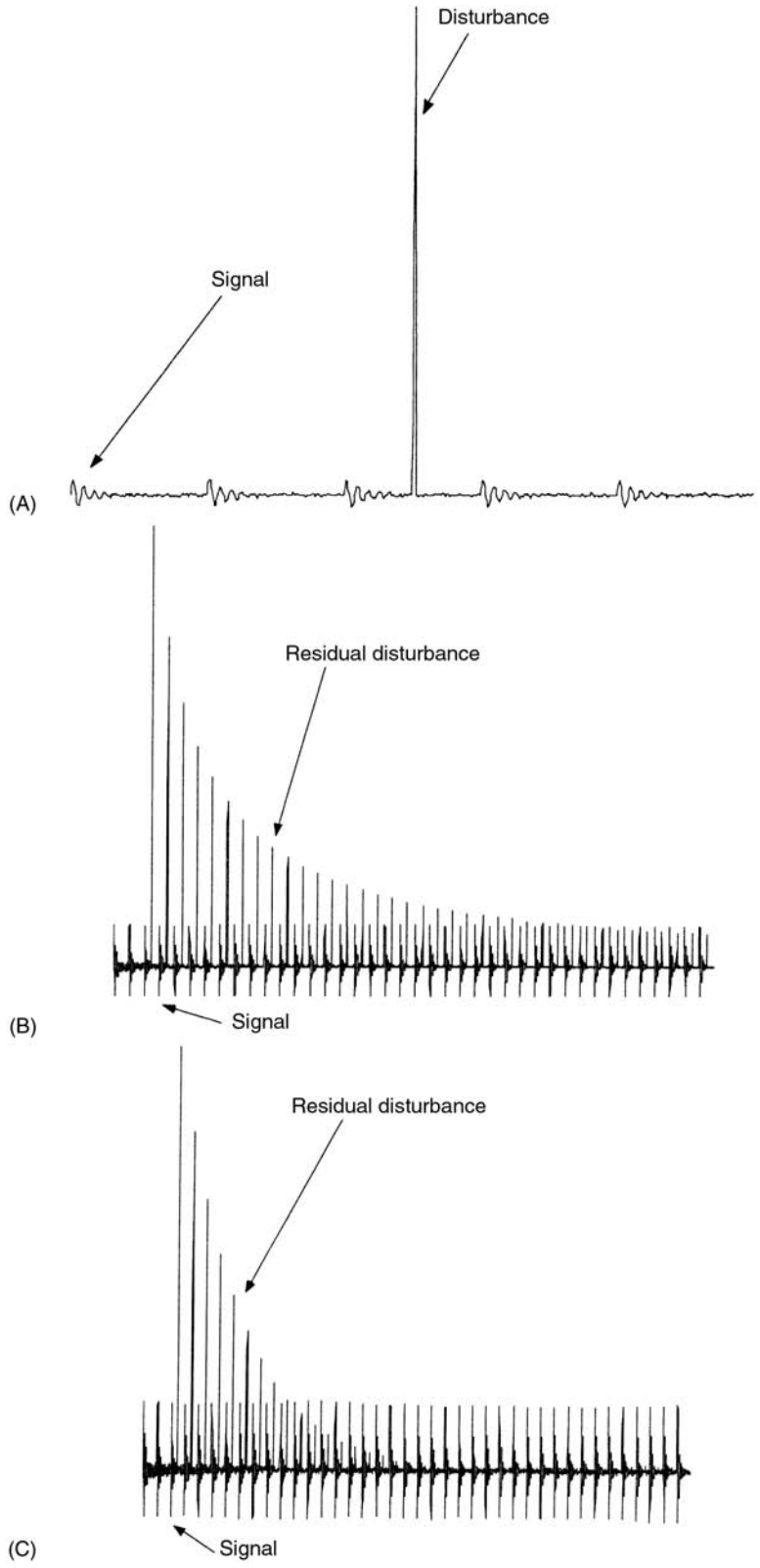


Figure 14 Rejection of single artifact disturbance by TDA: (A) occurrence of artifact disturbance; (B) rejection with regular TDA; (C) rejection with exponential TDA.

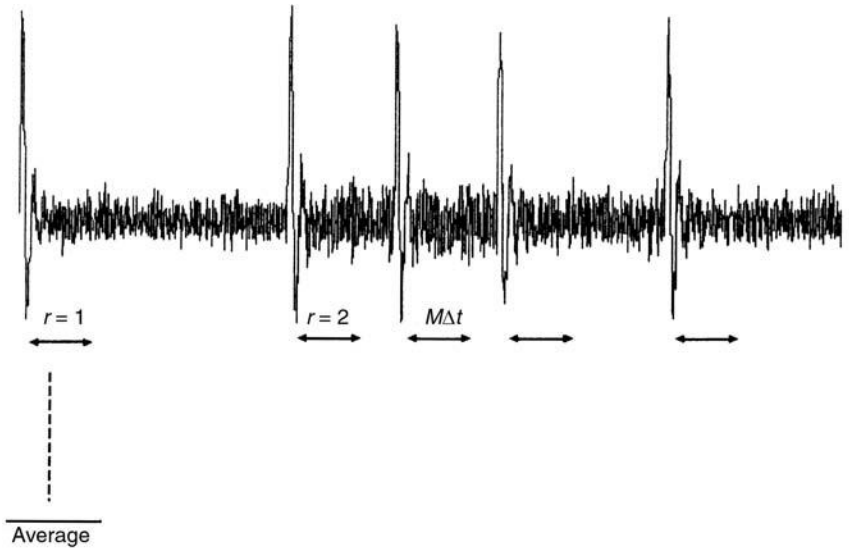


Figure 15 TDA with triggered data acquisition.

Another example occurring in practice is that of small variations between consecutive periods. As an example, when dealing with vibrations of rotating machinery, speed fluctuations may be induced by changes of loads and other affecting variables. Large fluctuations can decrease and even nullify the magnitude of extracted periodic components.

An example is shown in **Figure 16A**. A random fluctuation of 2% (RMS) in the period is assumed. Also shown is the average of 100 periods, compared to the case of zero fluctuation, and the resulting attenuation is evident.

The effect of jitter can be recognized by averaging signal sections which correspond to a multitude of the desired period. At least two periods should be extracted to notice the effect. **Figure 16B** shows the result of averaging 100 sections. It can be noticed that the magnitude of the first half of the averaged signal is larger than that of the second one. This effect is traced to the fact that the effect of the jitter is larger for data points more distanced from the start of the averaged section. The larger the number of periods in the averaged section, the more pronounced the effect towards the end of the section. Obviously the price paid for increasing this section length is that more data points are needed for the same number of averaged sections.

Averaging in the Frequency Domain

Computation of PSD

Often there is a need to average descriptors of data in the frequency domain. In the computations of the PSD, segmentation of the data (with possible overlapping processing) is used in order to decrease random errors whenever random components exist in the signal. The PSDs of the segmented sections are averaged (see **Windows; Spectral analysis, classical methods**).

Recursive schemes are usually implemented, and the averaging effect can often be followed in real time. Both regular and exponential averaging can be used, obviously in the frequency domain. The exponential averaging is better suited to situations involving nonstationarities. **Figure 17** shows the PSD of a stationary random process with an additive component – a harmonic signal with time-dependent increasing frequency. Instantaneous PSD, based on one segment at a time, can follow the frequency changes, but the random error of the PSD would not be controlled. In regular averagings, the 'smearing' due to changing frequency is evident. This is much less pronounced in the exponential averaging scheme, the decaying memory 'forgets' some of the initial frequencies, the corresponding peak would be much stronger. Commercial analyzers sometimes have a 'peak' averaging mode. This is not an averaging operation; the global maximum values of segment's PSD is retained.

Extraction of Periodic Signals via Averaging in Time and Frequency

The time domain averaging is aimed at extracting periodic signals from a composite signal. Averaging the PSD is aimed at reducing the random error of the PSD estimate. However, when the frequency domain description of the periodic component only is sought,

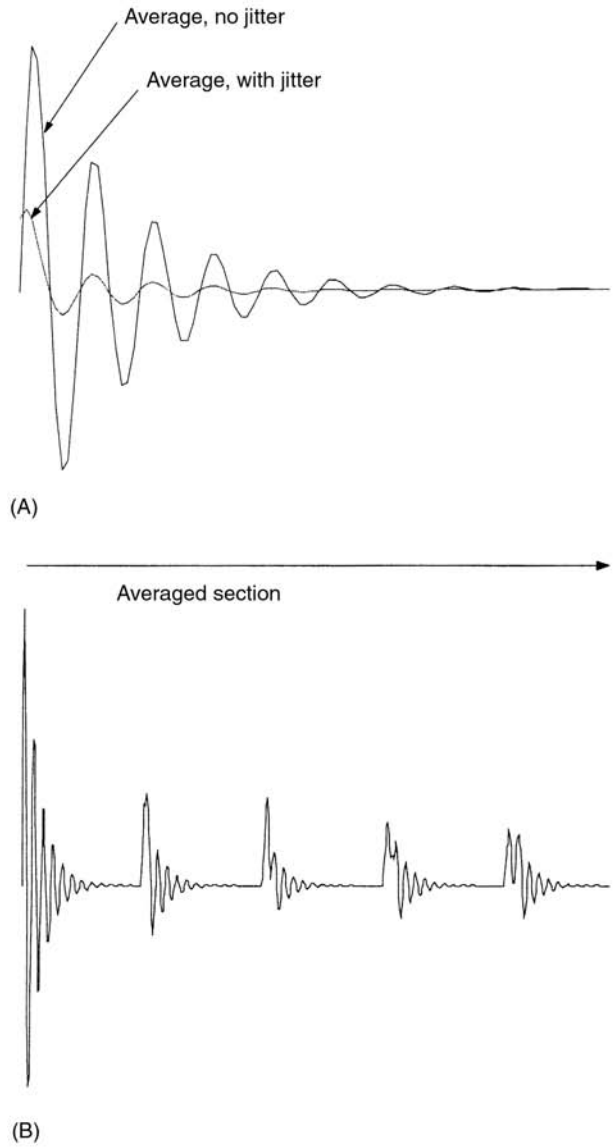


Figure 16 TDA in the presence of jitter: (A) TDA with and without jitter – sections of single period averaged; (B) TDA with jitter – sections of multiple periods averaged.

then two equivalent procedures are possible. Both assume knowledge of the frequency of the signal sought, whether via hardware triggering or external knowledge. Both procedures are shown in **Figure 18**. In the first, an FFT computation follows extraction via TDA. In the second, FFT operations (without squaring for PSD) are performed on each segment, and then averaged. Both procedures reject components not synchronous with the frequency sought (whether deterministic or random). The first procedure is slightly more efficient (one averaging vs one FFT operation).

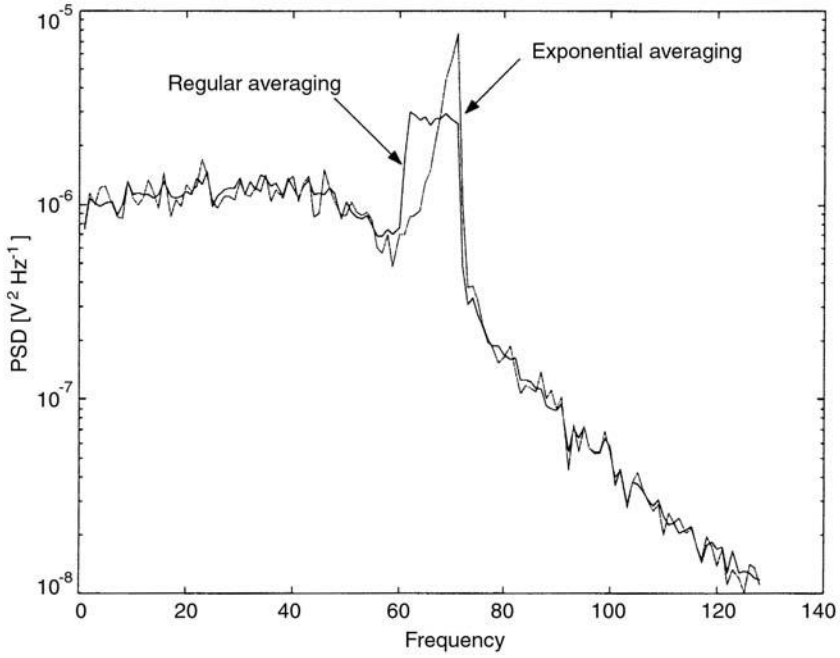


Figure 17 Averaging for computation of PSD – composite signal including harmonic component of varying frequency: regular and exponential averaging.

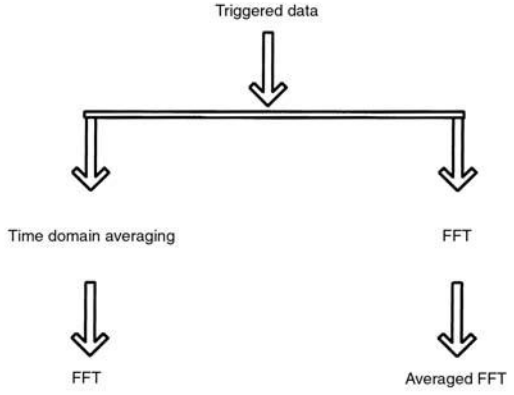


Figure 18 Equivalent procedure for the DFT of the periodic component.

Nomenclature

f	frequency (Hz)
f_p	frequency of periodic component
ω	radial frequency (rad s^{-1})

See also: **Data acquisition**; **Spectral analysis, classical methods**; **Transform methods**; **Windows**.

Further Reading

Braun S (1986) *Mechanical Signature Analysis*, London: Academic Press.

B

BALANCING

R Bigret, Drancy, France

Copyright © 2001 Academic Press

doi:10.1006/rwvb.2001.0093

Introduction

The center of gravity of a rotor does not generally coincide with the geometrical axis of rotation. Neither are the axial moments on inertia of these elements parallel to the rotation axis. These deviations from the ideal situation result from inaccuracies during the machining and assembly process, and result in vibrations whose frequency equal the frequency of rotation.

The vibrations can be attenuated by a balancing procedure by i masses attached to the rotor. These m_i masses of small dimension, at distances d_i from the axis of rotation and angular position θ_i, generate couples $m_i d_i$. The centrifugal forces generated oppose the forces and couples, and will reduce the magnitude of vibrations (unless the malfunction causing the vibrations are too severe).

When the maximum rotation frequency $\Omega_{\max}$ is less than that of the first natural flexural mode, ω_1, say $\Omega_{\max} \leq 0.8\omega_1$, the rotor is considered as being rigid. The balancing can be achieved by $i = 2$ balancing masses, which can be determined (by an appropriate procedure) at any speed inferior to $\Omega_{\max}$. When $\Omega_{\max} \geq 0.8\omega_i$, the rotor is considered as flexible. Balancing may necessitate $i > 2$ masses, determined at more than one rotational speed.

Balancing is undertaken by dedicated balancing machines by the manufacturer. It can also be performed on site, sometimes with an improved attenuation of vibrations. The balancing is aimed at attenuated vibration levels, as determined by contract (or standard), but need to consider technological constraints.

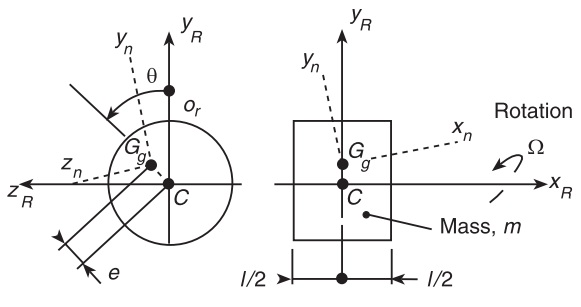


Figure 1 Rotor element. C is the geometric center of the median section profile (barycenter); $Cx_Ry_Rz_R$ is the referential linked to element; G_g is the mass element barycenter; $G_gx_ny_nz_n$ is the principal axes of central inertia ellipsoid.

Set of Forces and Rotating Couples: Balancing

In the article on definitions and characteristics of rotating machines (see **Rotating machinery, essential features**) elementary unbalance and unbalance torsion around the line of rotation are defined. In the chapter on dynamics of rotating machinery (see **Rotor dynamics**) the performance of the De Laval rotor which is subject to centrifugal force caused by elementary unbalance is studied. Moment due to run out on the disk is defined.

Definitions: Eccentricity and Elementary Run Out

Figure 1 shows elements which induce rotating forces. The axis Cx_R is part of the rotor axis, the geometric centers of section profiles. In rotation under the effect of centrifugal forces, as well as other forces, this axis becomes a left line around which the sections rotate. The terms associated with the element are: C, geometric center of the profile of the median section or center of gravity; $Cx_Ry_Rz_R$, frame of reference for the element; G_g, element mass center of gravity; $G_gx_ny_nz_n$, principal axes of central inertia ellipsoid; $\overrightarrow{CG_g}$, eccentricity (e, θ); $\overrightarrow{CG_g}m$, unbalance (em, θ); $\overrightarrow{CG_g}m\Omega^2$, rotating force unbalance $(em\,\Omega^2, \theta)$. The moments of mass intertia produced in $Cx_Ry_Rz_R$ (close to $G_gx_Ry_Rz_R$) Ix_Ry_R, Ix_Rz_R, induce rotating couples which are in proportion to

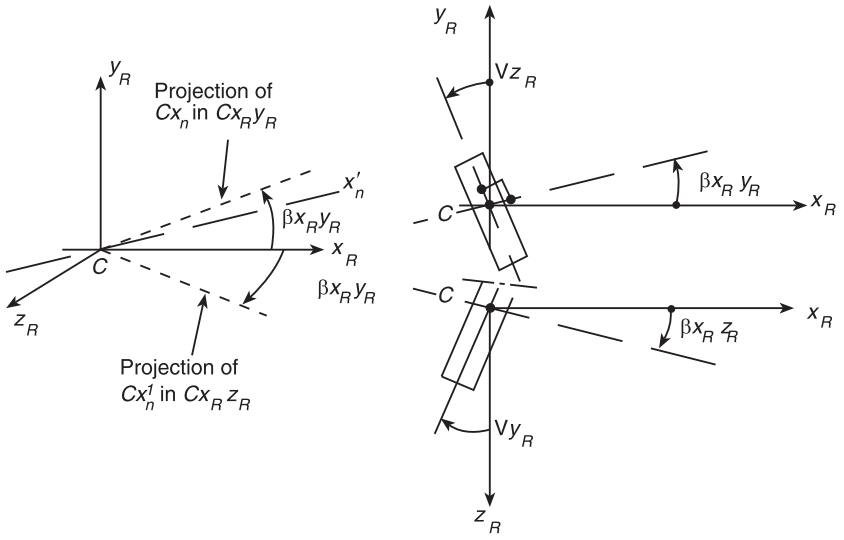


Figure 2 Rotor element. Angles linked to inertia products.

Ω^2. Inertia products arise from the angles $\beta x_R y_R$ and $\beta x_R z_R$ (**Figure 2**). For an element which is thin compared to its radial dimensions

$$\beta_{x_R y_R} = \frac{Ix_R y_R}{Ix_R x_R - Iy_R y_R} \quad \beta_{x_R z_R} = \frac{Ix_R z_R}{Ix_R x_R - Iz_R z_R} \quad [1]$$

where $Ix_R x_R$, $Iy_R y_R$, $Iz_R z_R$ are moments of mass inertia in relation to Cx_R, Cy_R, Cz_R. The small angles β characterize run out which are generally designated Vz_R and Vy_R. $\overrightarrow{CG_g}$, $Ix_R y_R$, $Ix_R z_R$ are caused by manufacturing or assembly faults, transformations of materials, or deteriorations. For a thin disk of mass m and radius R:

$$Ix_R y_R = -\frac{mR^2}{4} Vz_R, Ix_R z_R = -\frac{mR^2}{4} Vy_R$$

Definitions: Set of Unbalance and Run Out

Let there be a rotor of axis $0x_R$ in a rigid state, without any deformations. The geometric centers of sections perpendicular to right-angle $0x_R$ are at $0x_R$ (**Figure 3**). Eccentricity $e(x)$ of an element of size $\Delta x(\rightarrow \mathrm{d}x)$ defines the position of the mass center of gravity $0xg$. The arrangement $e(x)$ defines the set which can be characterized by a resultant, and a resultant moment which on rotation induces excitations at frequency Ω. In the frame of reference $G_r x_R y_R z_R$, unbalance which results from set of eccentricity $e(x)$ has the following components:

$$\text{For } G_r y_R: \quad my_G = \int_{x_0}^{x_l} e_y(x)\mu(x)\,\mathrm{d}x$$
$$\text{For } G_r z_R: \quad mz_G = \int_{x_0}^{x_l} e_z(x)\mu(x)\,\mathrm{d}x \quad [2]$$

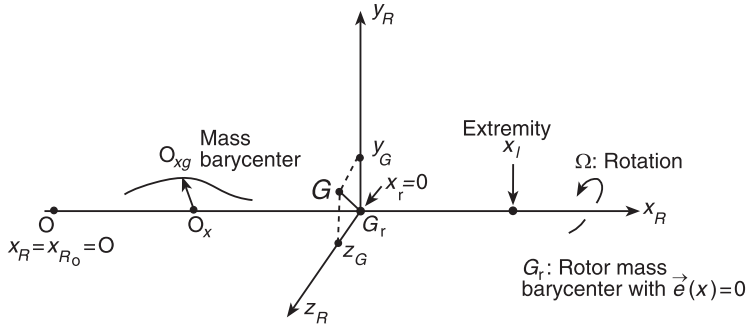


Figure 3 Rotor eccentricities. $G_r x_R y_R z_R$ is linked to the rotor.

where y_G, z_G are coordinates of the center of gravity of mass G; m is the rotor mass; $\mu(x)$ is the mass by unit of length; my_G and mz_G are components of initial unbalance resultants. They are independent of the position of G_r, but dependent on the direction of $G_r y_R$ and $G_r z_R$. The resultant is expressed by:

$$m\,\overrightarrow{G_rG} \rightarrow \begin{cases} \text{module } m\sqrt{y_G^2 + z_G^2} \\ \text{angular position } \theta \rightarrow \text{tg } \theta = z_G/y_G \end{cases}$$

In the frame of reference $G_r x_R y_R z_R$ the moment resultant from the set of eccentricities has the components:

$$\begin{aligned} &\text{For } G_r y_R\text{: } M_r y_R = \int_{x_0}^{x_l} e_z(x)\mu(x)(x - x_r)\,\mathrm{d}x \\ &\text{For } G_r z_R\text{: } M_r z_R = \int_{x_0}^{x_l} e_y(x)\mu(x)(x - x_r)\,\mathrm{d}x \end{aligned} \qquad [3]$$

$M_r y_R$ and $M_r z_R$ are components of the initial moment of unbalance. They depend on the position of G_r and the direction of $G_r y_R$ and $G_r z_R$. The moment can be represented by a vector $\overrightarrow{M}_r$ in the same way as the resultant. In general, let $\overrightarrow{V}_1 \ldots \overrightarrow{V}_i$ (where $i = 1 \pm n$) a set of vectors applied to $0_1 \ldots 0_i \ldots$. At 0 this set can be reduced to a resultant:

$$\overrightarrow{R}_0 = \sum_{i=1}^{n} \overrightarrow{V}_i$$

and at a moment:

$$\overrightarrow{M}_0 = \sum_{i=1}^{n} \overrightarrow{00_i} \wedge \overrightarrow{V_i}$$

At:

$$0';\ \overrightarrow{R}'_0 = \overrightarrow{R}_0;\quad \overrightarrow{M}'_0 = \overrightarrow{M}_0 + \overrightarrow{00'} \wedge \overrightarrow{R}_0$$

The result is independent of the point of reduction. The resultant moment depends on it.

Forces arise from the vectors of eccentricity. Couples are a result of run out vectors. They are connected to the line of rotation (**Figure 4**).

In G_r, the central inertia ellipsoid is defined by: the moments of inertia $I_{x_R x_R}, I_{y_R y_R}, I_{z_R z_R}$, moments of inertia produced $I_{x_R y_R}, I_{x_R z_R}$. During rotation the excitations at frequency Ω are caused by $I_{x_R y_R}$ and $I_{x_R z_R}$.

$$\begin{aligned} I_{x_R y_R} &= \int_{\text{volume}} xy\rho(x,y)\,\mathrm{d}V \\ I_{x_R z_R} &= \int_{\text{volume}} xz\rho(x,z)\,\mathrm{d}V \end{aligned} \qquad [4]$$

where x, y, z are coordinates of the center of an element of volume $\mathrm{d}V$ and specific mass $\rho(x, y)$; $\rho(x, z)$.

The moments of inertia depend on the direction of axes $G_r y$ and $G_r z$. They can be defined at any point.

Balancing

Balancing is a procedure which arranges on the rotor elements of slight dimensions (of small mass) which, creating unbalance and so rotating forces, reduce forces and initial rotating couples. Balancing can be carried out at a rotating speed which is much less than the first critical flexion speed, in a flexible condition. The quality of balancing is appreciated by rotor vibration amplitude, nonrotating situations, forces perpendicular to the links, levels of sound, or other features. Their modules must be less than the limits which may be agreed under contract. The vocabulary of balancing is the subject of standards ISO 1925 and AFNOR E 90–002.

Rigid States

Introduction to Balancing

Figure 5 shows an isotrope arrangement of rotor and links which is affected by a line of eccentricity, which is obscured in the fixed plane $0xy$. The line of eccentricity is also projected in the plane $0xz$ which is perpendicular to $0xy$. Taking into account only the

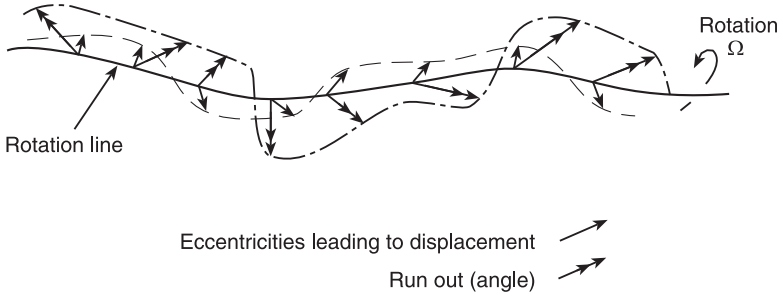


Figure 4 Eccentricities leading to displacement.

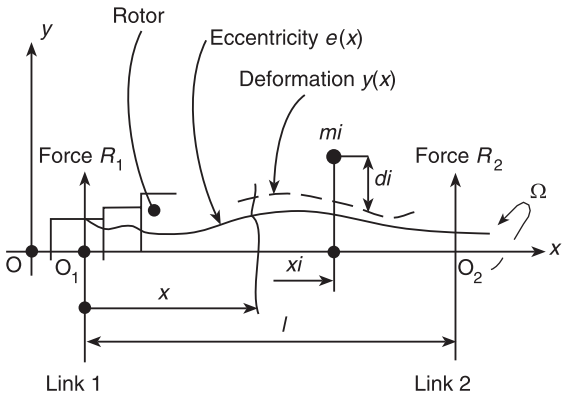


Figure 5 Rotor links: eccentricity.

plane $0xy$ does not restrict the conclusions that can be drawn.

Balance results in the solution to the two equations:

$$\int_{0_1}^{0_2} [e(x) + y(x)]\Omega^2 \mu(x)\, dx + \sum_i m_i(d_i + y(x))\Omega^2 + R_1 + R_2 = 0 \quad [5]$$

$$\int_{0_1}^{0_2} [e(x) + y(x)]x\Omega^2 \mu(x)\, dx + \sum_i m_i(d_i + y(x))x_i\Omega^2 + R_2 l = 0 \quad [6]$$

where $\mu(x)$ is the linear mass; m_i is the mass of corrective element i; and x_i is the position of the chosen balancing plane. Balancing is satisfactory when:

$$R_1 \leq R_{1L}; \quad R_2 \leq R_{2L} \quad [7]$$

The condition, which is theoretically strictly rigid, is expressed by:

$$y(x) = y_1 + ax \qquad a = \frac{y_2 - y_1}{l} \quad [8]$$

where y_1 and y_2 are amplitudes at right-angles to the links; $y_1 = R_1/Z_1$; $y_2 = R_2/Z_2$ where Z_1 and Z_2 are impedances perpendicular to the links; $R_1 = R_{1L}$; $R_2 = R_{2L}$; $y_1 = y_{2L} = R_{2L}/Z_2$; $\Omega = \Omega_{\max}$.

Eqns [5] and [6] make it possible to calculate corrective balancing masses:

$$m_1 d_1, m_2 d_2$$

where d_1 and d_2 are chosen to be large values in order to have m_1 and m_2 small.

Where $R_{1L} = R_{2L} = 0$, the two corrective balancing masses are independent of Ω. Practically, taking into account rotor deformation, it is necessary to verify that quality criteria are satisfied whatever the value of Ω in the rigid state.

Balancing of Eccentricities and Shadows: Vectoral Expressions

With run out and eccentricities, two corrective balancing masses make it possible to balance in a strictly rigid condition following the relations (**Figure 6**):

$$\overrightarrow{B_{c1}} + \overrightarrow{B_{c2}} + \overrightarrow{B_0} = 0$$
$$\overrightarrow{B_{c1}} \wedge \overrightarrow{C_0 0_1} + \overrightarrow{B_{c2}} \wedge \overrightarrow{C_0 0_2} + \overrightarrow{M_0} = 0$$

The positions of the balancing planes are fixed: they must allow the corrective elements, or masses, to be attached.

The set can be carried to a point $G_0'(C_0')$:

$$\overrightarrow{B}_0' = \overrightarrow{B_0}$$
$$\overrightarrow{M}_0' = \overrightarrow{C_0 C_0'} \wedge \overrightarrow{B_0} + \overrightarrow{M_0}$$

At 0_1, for balancing with $\overrightarrow{B}_{c1}$ and $\overrightarrow{B}_{c2}$.

$$\overrightarrow{B_{01}} = \overrightarrow{B_0} = -\left(\overrightarrow{B_{c1}} + \overrightarrow{B_{c2}}\right)$$
$$\overrightarrow{M_0} + \overrightarrow{C_0 0_1} \wedge \overrightarrow{B_0} = -\overrightarrow{M_{01}} = -\left(\overrightarrow{0_1 0_2} \wedge \overrightarrow{B_{c2}}\right)$$

The module of $\overrightarrow{B}_{c2}$ is large if $|\overrightarrow{0_1 0_2}|$ is small. Taking into account technological limitations, it may not be possible to achieve balancing, in particular when the run out of a thin disk must be compensated by two mass elements arranged on each of its faces.

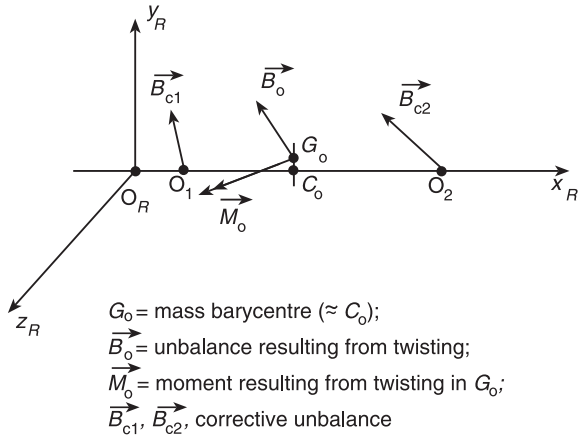


Figure 6 Unbalance and moments.

At the first balancing time, the direction of resulting unbalance was determined by setting out the two journal bearings on narrow horizontal tempered steel tracks to reduce friction moment caused by roller bearings. The mass center of gravity was placed under the tracks in a vertical direction. After several attempts, suitable corrective unbalance placed the rotor in the position fixed by the operator. Static unbalance was also corrected. When the size of the elements or disks on the shaft was significant, a moment could exist. Its correction required rotation in order to remedy dynamic unbalance. Today, for thin disks and for mediocre qualities, static balance is determined in this manner.

Balancing

In the planes P_1 and P_2, which are perpendicular to $0x_R$, let us arrange the elements E_1 and E_2 of mass M_1 and M_2 at $\overrightarrow{d}_1$ and $\overrightarrow{d}_2$ of $0x_R$ (**Figure 7**); this *a priori* arrangement of two elements is justified *a posteriori* by the solution which can be obtained thus.

The components of unbalance are:

For P_1: $m_1 d_{1y} = b_{1y}$; $m_1 d_{1z} = b_{1z}$
For P_2: $m_2 d_{2y} = b_{2y}$; $m_2 d_{2z} = b_{2z}$

The set of unbalance, which is corrective for perfect balancing, must:

- Cancel the resultant of the initial set of eccentricities, defined by eqn [2]
- Cancel the moment of initial set of eccentricities, defined by eqn [3] and the moment caused by products of inertia defined by eqn [4]

With eqn [2] canceling will necessitate:

$$\begin{aligned} m y_G + m_1 d_{1y} + m_2 d_{2y} &= 0 \\ m z_G + m_1 d_{1z} + m_2 d_{2z} &= 0 \end{aligned} \qquad [9]$$

Using eqns [3] and [4] canceling the moment is achieved when:

$$\begin{aligned} -I_{x_R z_R} + M_{rz} + m_1 d_{1y} x_1 + m_2 d_{2y} x_2 &= 0 \\ I_{x_R y_R} + M_{ry} + m_2 d_{1z} x_1 + m_2 d_{2z} x_2 &= 0 \end{aligned} \qquad [10]$$

x_1 and x_2 are fixed in the position of the balancing planes. In the referential $G_r yz$, connected to the rotor, it is demonstrated that excitation along $G_r y_R$ and $G_r z_R$ is defined by $I_{x_R y_R}\Omega^2$ and $I_{x_R z_R}\Omega^2$. Balancing masses $\overrightarrow{b}_1$ and $\overrightarrow{b}_2$ modify $l_{x_R y_R}$ and $I_{x_R z_R}$, and cancel them to achieve perfect balance. In eqn [10], unbalance appears in explicit form.

Eqns [9] and [10] make it possible to calculate corrective unbalances:

$$\begin{aligned} m_1 d_{1y} &= b_{1y} & m_1 d_{1z} &= b_{1z} \\ m_2 d_{2y} &= b_{2y} & m_2 d_{2z} &= b_{2z} \\ d_1 y, d_{1z} &\rightarrow & \sqrt{d_{1y}^2 + d_{1z}^2} &= \left|\overrightarrow{d_1}\right| \\ d_2 y, d_{2z} &\rightarrow & \sqrt{d_{2y}^2 + d_{2z}^2} &= \left|\overrightarrow{d_2}\right| \end{aligned}$$

must be chosen: large values in order that m_1 and m_2 are small, according to technological possibilities. y_G, z_G, $I_{x_R y_R}$, $I_{x_R z_R}$, M_{rz}, M_{ry} are not known, but are derived from the balancing procedure.

Specific examples

- $y_G = z_G = 0$

Using eqn [9]:

$$\begin{aligned} m_1 d_{1y} &= -m_2 d_{2y} \rightarrow b_{1y} = -b_{2y} \\ m_1 d_{1z} &= -m_2 d_{2z} \rightarrow b_{2z} = -b_{2z} \end{aligned}$$

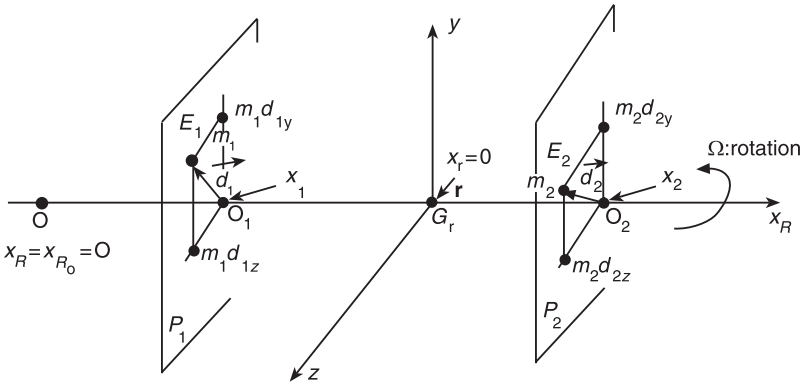


Figure 7 Unbalance $m_1\overrightarrow{d}_1 = \overrightarrow{b}_1$, $m_2\overrightarrow{d}_2 = \overrightarrow{b}_2$.

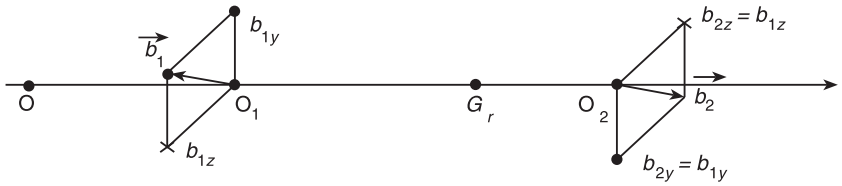


Figure 8 Corrective balancing masses: $\vec{b}_1$ and $\vec{b}_2$ for $y_G = z_G = 0$.

Using eqn [10]:

$$\begin{aligned} I_{x_R z_R} + M_{rz} + b_{1y}(x_1 - x_2) &= 0 \\ I_{x_R y_R} + M_{ry} + b_{1z}(x_1 - x_2) &= 0 \end{aligned} \qquad [11]$$

Figure 8 shows corrective balancing masses $\vec{b}_1$ and $\vec{b}_2$ which form a couple. Their direction is identical; their sense is opposite. They depend on x_1 and x_2.

- $y_G = z_G = 0, \quad M_{rz} = M_{ry} = 0$

Using eqn [11]:

$$\frac{I_{x_R z_R}}{x_2 - x_1} = b_1 y \quad \frac{I_{x_R y_R}}{x_2 - x_1} = b_1 z$$

Let us consider a thin disk ($2l$) placed on a rotor, with a run out defined by the angle V_z (**Figure 9**), corresponding to a rotation vector $\vec{V}_z$, following $0z_R$.

It is easy to show:

$$I_{x_R y_R} \approx -\frac{mR^2}{4} V_z \qquad [13]$$

Similarly:

$$I_{x_R z_R} \approx \frac{mR^2}{4} V_y$$

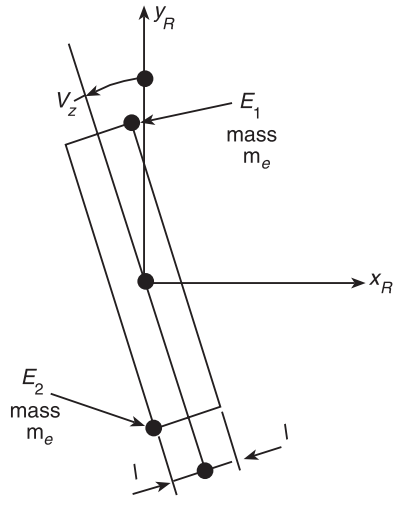


Figure 9 Disk: radius R, mass m, run out V_z.

The balancing which corrects $I_{x_R y_R}$ can be done using elements E_1 and E_2 to produce a product of inertia:

$$2m_e R\left(-V_z + \frac{l}{R}\right)R \qquad [14]$$

Considering the products of inertia according to x_R and y_R, balancing is achieved taking into account eqns [13] and [14] using elements E_1 and E_2 of mass m_e, so that:

$$m_e = \frac{m}{8}\frac{1}{\frac{1}{V_z}\frac{l}{R} - 1}$$

If $l/R \approx V_z$, m_e is large, and so balancing cannot be achieved. A similar situation may arise with regard to $I_{x_R z_R}$.

- $I_{x_R z_R} = I_{x_R y_R} = 0$

The components of corrective balancing mass:

$$\begin{aligned} m_1 d_{1y} &= b_{1y}; \quad m_1 d_{1z} = b_{1z} \\ m_2 d_{2y} &= b_{2y}; \quad m_2 d_{2z} = b_{2z} \end{aligned}$$

can be determined using eqns [9] and [10]. The two corrective balancing masses $\vec{b}_1$ and $\vec{b}_2$ depend on x_1 and x_2.

In vector form, balancing is expressed in G_r, 0_1, 0_2 by:

$$\begin{aligned} &m\overrightarrow{G_r G} + \overrightarrow{b_1} + \overrightarrow{b_2} = 0 \\ &\overrightarrow{M_r} + \overrightarrow{G_r 0_1} \wedge \overrightarrow{b_1} + \overrightarrow{G_r 0_2} \wedge \overrightarrow{b_2} = 0 \end{aligned}$$

In another form:

$$m\overrightarrow{G_r G} + \overrightarrow{b_c} = 0 \quad \overrightarrow{M_r} + \overrightarrow{M_c} = 0$$

At a point G_r':

$$\begin{aligned} &m\overrightarrow{G_r G} + \overrightarrow{b_c} = 0 \\ &\overrightarrow{M_r} + \overrightarrow{G_r G_r'} \wedge m\overrightarrow{G_r G} + \overrightarrow{M_c} + \overrightarrow{G_r G_r'} \wedge \overrightarrow{b_c} = 0 \end{aligned}$$

Notes In industrial applications, perfect balancing is not obtained. Eqns [9] and [10] are not satisfied.

The quality of balancing is characterized by residual unbalance, after balancing. They are defined by standards which propose modules of residual unbalance for a crusher which are greater than those of a gyroscope.

Standards

Standards ISO 1940/1, 1940/2 and AFNOR NF E 90600 propose criteria and methods to estimate the quality by residual amplitudes of force and vibration. A factor of quality G is also used. Modules of residual unbalance at right-angles to links 1 and 2 must be less than:

$$|b_{Li}|\left(\mathrm{kg\,mm^{-1}}\right) = G\frac{M_i}{\Omega} \quad i = 1, 2 \qquad [15]$$

where $M_i \times 9.81\,\mathrm{m\,s^{-2}}$ is the weight on link $i(N)$; Ω is the maximum rotation speed (rad $\mathrm{s^{-1}}$); G is defined as a function of the machine type (mm $\mathrm{s^{-1}}$); $G = 630$ for crankshaft arrangements; and $G = 0.4$ for precision mills and gyroscopes.

When set results from eccentricity e of mass center of gravity G_g (**Figure 10**), unbalance is equal to Me. Initial unbalance at right-angles to the links is:

At 1: $M_1 e$; at 2: $M_2 e$ where $M_1 = M(l_2/l)$; $M_2 = M(l_1/l)$.
If $e \leq G/\Omega$ balancing is not necessary.

Using eqn [15], at the limit residual eccentricities at G_g at 1 and 2 are equal to G/Ω. Its relation to initial eccentricity is equal to $G/\Omega e$. For a compressor, pump, or electric motor, $G = 6.3$. Where $M_1 = M_2 = 500\,\mathrm{kg}$, $\Omega = 314\,\mathrm{rad\,s^{-1}}$ (3000 rpm), $|b_{L_1}| = |b_{L_2}| \approx 10\,\mathrm{kg\,mm^{-1}}$. Let there be 20 g at 500 mm neighboring eccentricity of 20 μm. Quality can be defined perpendicular to the links by the relationship R_f of amplitude of residual rotating force, to static force caused by gravity. Where $l_1 = l_2$ and Me at G_g (**Figure 10**):

$$R_f = \frac{e\,\Omega^2}{9.81\,\mathrm{m\,s^{-2}}} \qquad [16]$$

R_f is independent of rotor mass. For $R_f = 0.1$, $\Omega = 314\,\mathrm{rad\,s^{-1}}$ ($\rightarrow$3000 rpm); $G = 3.13$:

$$e \approx 10\ \mu\mathrm{m}$$

When torsion is reduced to Me and $M_1 = M_2$:

$$G = \frac{9810\ R_f}{\Omega}$$

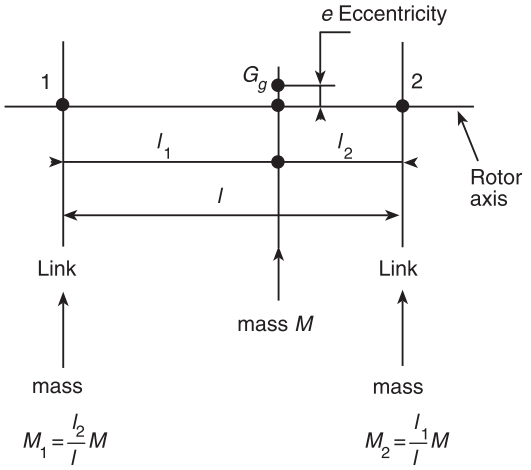


Figure 10 Unbalance M_l at the mass barycenter G_g.

So that the quality fixed by R_f is identical to that fixed by G, G has to vary as $1/\Omega$. Where R_f is 0.1; $\Omega = 314$ rad $\mathrm{s^{-1}}$; $G \approx 3.13$.

When the set is a result of a central axis of inertia at angle γ of the axis (**Figure 11**), where γ is small and a thin disk, l_d, in relation to radius R:

$$R_f = \frac{2\left(I_{x_R x_R} - I_{y_R y_R}\right)\gamma\ \Omega^2}{9.81\ \mathrm{m\ s^{-2}} Ml} \qquad [17]$$

For couple unbalance which, at right-angles to the links, balance couple due to γ are:

$$|b_{L1}| = |b_{L2}| = \frac{\left(I_{x_R x_R} - I_{y_R y_R}\right)\gamma}{l} = \frac{9.81}{2}\frac{M}{\Omega^2} R_f$$

where:

$$I_{y_R y_R} = \frac{I_{x_R x_R}}{2} = \frac{MR^2}{4}; \quad M = \pi R^2 l_d l$$

$$R_f = \frac{\Omega^2 \gamma}{2 \times 9.81}\frac{R^2}{l}$$

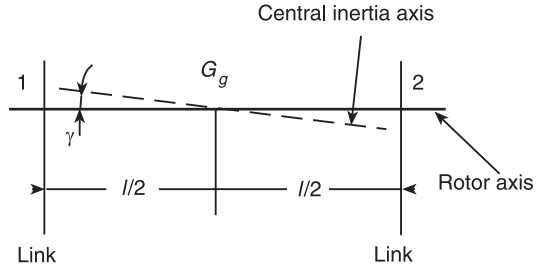


Figure 11 Couple due to γ.

where $R_f = 1$, $\Omega = 314\,\text{rad}\,\text{s}^{-1}$; $l = 2\,\text{m}$; $R = 0.5\,\text{m}$; $\gamma = 1.59 \times 10^{-4}\text{rad} \rightarrow \approx 0.092°$. Where $l_d = 0.1\,\text{m}$; $\rho = 7800\,\text{kg}\,\text{m}^{-3}$; $M = 612\,\text{kg}$. $|b_{L_1}| = |b_{L_2}| = 305 \times 10^{-5}\,\text{kg m} \rightarrow 61\,\text{g}$ at 0.5 m in two planes 2 m apart.

To obtain $R_f = 0$, after balancing, two opposing unbalances equal to $122\,\text{g} \times 0.5\,\text{m}$ must be set out in two planes at $l/4 = 0.5\,\text{m}$ on both sides of G_g, the mass of corrective elements must be equal to 1.22 kg. It is probable that technological limitations do not permit their implantation, despite the low value of γ (**Figure 12**).

Balancing Machines

Rotor balancing in a rigid state is carried out by dedicated machines which generate by themselves a minimum amount of vibration. They permit to determine the residual of unbalance and uncertainties associated with them. Vibration sensors are mounted on nonrotating parts of the machine. The corrective unbalance is determined by a computer. Standard ISO 2953 deals with balancing machines.

Rotors can be arranged in simple machines or in the stator of the affected machine.

Flexible State

Modal Description: General Case

The article on modal characteristics (see **Rotating machinery, modal characteristics**) defines the components of vibrations due to excitation:

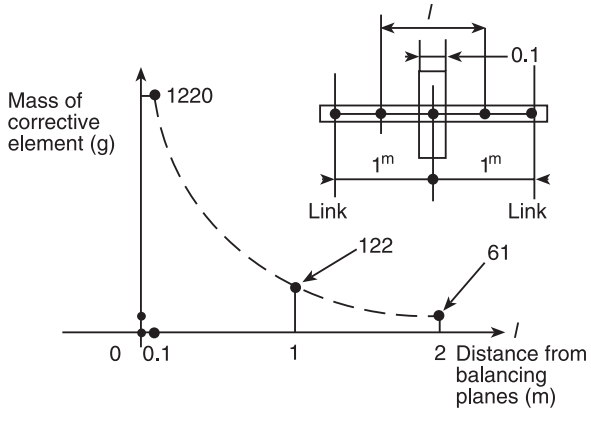


Figure 12 Mass of corrective element at 0.5 m from rotation axis.

$$U_k = \sum_l \frac{U_{kl}^d}{\alpha_{ll}(i\Omega - p_l)} \Big[\ldots + U_{ql}^g (me)_q \exp i\psi_q + U_{(q+1)l}^g \Big(-i(me)_q \exp i\psi_q \Big) + \ldots \Big] \Omega^2 \quad [18]$$

where Ω is the rotation speed; U_k is the component related to displacement $u_k = |U_k| \cos(\Omega t + \varphi_k)$; where φ_k is the argument for U_k. k marks out the direction point (in the plane $0xy$ or $0xz$) of observation of relative vibration between rotor and bearing, absolute of the nonrotating structure. Other components may be considered, for example $\dot{u}_k = -\Omega |U_k| \sin(\Omega t + \varphi_k)$ expressed by $-i\Omega U_k$, and forces perpendicular to the links; p_l is the complex natural frequency: $p_l = \delta_l + i\omega_l$ and $p_l = \delta_l - i\omega_l$, $i^2 = -1$; $\delta_l < 0$: attenuation factor (stability); ω_l is the natural damped frequency; U_{kl}^d is the component of natural mode at right-angles associated with p_l in the point-direction k, associated with U_k; α_{ll} is the component determined by biorthogonality relations: $U_{kl}^d U_{\cdot l}^g / \alpha_{ll}$ is independent of arbitrary standards defining natural modes. $U_{\cdot l}^g$ is the component of natural left-hand mode associated with p_l in the point-direction $\cdot$, $U_{\cdot l}^g$ can be composed of different components from that of U_k^{dl}, an angle, for example, when it expresses excitation by a couple due to run outs of a thin disk characterized by angles V_y, V_z.

Components of unbalance in rotor radial sections $q, s, t, \ldots$ are in general counterbalanced by displacement components of left-hand modes of geometric centers of these sections $(q, s, t, \ldots)$:

$$U_{ql}^g (me)_q \exp i\psi_q$$
$$U_{(q+1)l}^g \Big[-i(me)_q \exp i\psi_q \Big]$$

where U_{ql}^g and $U_{(q+1)l}^g$ are displacement components of the geometric center of section q; $(me)_q \exp i\psi_q$; $(me)_q \exp i\psi_q$: components of unbalance $(me)_q . \psi_q$ in section q; terms of eqn [18] between parentheses, modal excitation, is designed by modal unbalance. For each natural frequency p_l, it intervenes in displacement U_k in the same way: it is independent of k. $B_l = [\ldots U_{ql}^g (me)_q \exp i\psi_q + \ldots]$.

Eqn [18] assumes linear components: proportionality between displacement and exciters.

Slow Rotation Speed: Rigid State

For the first natural frequency ($\omega_1 < \omega_2 < \omega_3 \ldots \delta_1$ small), modules of $i\Omega - p_1$ and $i\Omega - p_1^*$ are: $[(\Omega - \omega_1)^2 + \delta_1^2]^{1/2}$. Where $\Omega \ll \omega_1$, if these terms are small, in relation to terms corresponding to $\omega_2 \ldots$ eqn [18] leads to expression of U_k in a rigid state:

$$U_k \approx \frac{U_{k1}^d B_1 \Omega^2}{\alpha_{ll}[i(\Omega-\omega_1)-\delta_1]} + \frac{U_{k1}^{d*} B_1^{\oplus} \Omega^2}{\alpha_{ll}^*[i(\Omega+\omega_1)-\delta_1]} \quad [19]$$

$\tilde{B}_l^{\oplus}$ is a result of B_l by substituting $U_{\ddot{.}}^{g*}$ for $U_{\ddot{.}}^{g}$. In a rigid state the first natural left-hand mode is written:

$$U_{.l}^g = a_1^g x. + b_1^g$$
$$U_{.l}^{g*} = \bar{a}_1^g x. + b_1^{g*}$$

where a_1^g, b_1^g are complex constants and x is the abscissa of sections $q, q+2, q+4\ldots$.

Two unbalances at abscissa x_{c1} and x_{c2} (balancing planes) make it possible to reduce, and even cancel at speed $\Omega|B_1|$ and $|B_1|$: this is the balancing in a rigid state.

Reduction to Two Terms

When $\omega_{l-1} \ll \Omega \ll \omega_{l+1}$; $\delta_l \ll \omega_l$, $\delta_{l-1} \ll \omega_{l-1}$; $\delta_{l+1} \ll \omega_{l+1}$, the modal decomposition eqn [18] is reduced to two terms only defined in the article on modal characteristics (see **Rotating machinery, modal characteristics**). The model is of a De Laval rotor.

Speed Close to Critical Speed

When rotation speed is close to natural frequency ($\Omega \approx \omega_l$) and thus close to critical speed and:

$$\delta_l \ll \omega_l; \quad \omega_{l-1} \ll \omega_l \ll \omega_{l+1}$$

modal decomposition is reduced to two terms (see **Rotating machinery, modal characteristics**) distinguishing between unbalance $(me)_r \exp i\psi_r$ and $(me)_s \exp i\psi_s$. In the radial planes r and s:

$$U_k \approx \frac{U_{kl}^d}{\alpha_{ll}(i\Omega - p_l)}\left[E_l + \left(U_{rl}^g - iU_{(r+1)l}^g\right)(me)_r \times \exp i\psi_r + \left(U_{sl}^g - iU_{(s+1)l}^g\right)(me)_s \exp i\psi_s\right]\Omega^2 + \frac{U_{kl}^{d*}}{\alpha_{ll}\left(i\Omega - p_l^*\right)}\left[E_l^{\oplus} + \left(U_{rl}^{g*} - iU_{(r+1)l}^{g*}\right)(me)_r \times \exp i\psi_r\left(U_{sl}^{g*} - iU_{(s+1)l}^{g*}\right)(me)_s \exp i\psi_s\right]\Omega^2$$

where E_l = modal excitation which performs on unbalance and run out factored with Ω^2: it is modal unbalance; E_l can perform from initial peaks which are not factored with Ω^2. $E_l^{\oplus}$ is a result of E_l substituting $U_{\ddot{.}}^{g*}$ and $U_{\ddot{.}}^{g}$.

When $\Omega = \Omega_0 \approx \omega_l$ $|U_k|$ can be canceled by $(me)_r \exp i\psi_r$ and $(me)_s \exp i\psi_s$; that is to say, by two unbalances in an identical way balancing in a rigid state. When initial peaks are zero, the domain of variation Ω, around Ω_0 in which amplitude is acceptable is in general more drawn out than when there exist initial peaks.

Balancing Procedure by Influence Coefficients

Direct Definition of Influence Coefficients

Vibration V_n – relative, displacement absolute of displacement speed (see **Rotating machinery, monitoring**) – of a force in point-direction n is due to unbalance test B_{mt} in a section plan m of rotor at speed Ω by an influence coefficient:

$$C_{nm}(\Omega) = \frac{|V_{nt}| \exp i\varphi_{nt}}{|B_{mt}| \exp i\varphi_{mt}} \quad [20]$$

According to **Figure 13**:

$$|V_n| = A_{nt}; \; |B_{mt}| = m_t R$$

Taking into account the influence of initial vibration:

$$C_{nm}(\Omega) = \frac{|V_{nt}| \exp i\varphi_{nt} - |V_{no}| \exp i\varphi_{no}}{|B_{mt}| \exp i\psi_{mt}} \quad [21]$$

Two tests are necessary to measure V_{no} and V_{nt} with B_{mt}. $C_{nm}(\Omega)$ is independent of B_{mt} if the performance of the arrangement of machine and measuring system and analysis is linear and repeatable.

Definition of Influential Coefficients by Modal Decomposition

Modal decomposition (eqn [18]) permits expression of $C_{nm}(\Omega)$ to be defined by eqn [20]:

$$C_{nm}(\Omega) = \sum_l \frac{U_{nl}^d}{\alpha_{ll}(i\Omega - p_l)}\left(U_{ml}^g - U_{(m+1)l}^g\right)\Omega^2 \quad [22]$$

In general, $|C_{nm}(\Omega)|$ is maximal in the neighborhood of critical speeds: $\Omega \approx \omega_l$.

Corrective Unbalance and Residual Vibration Forces

Vibration is connected to unbalance by matrix $\mathbf{C}$ of influence coefficients:

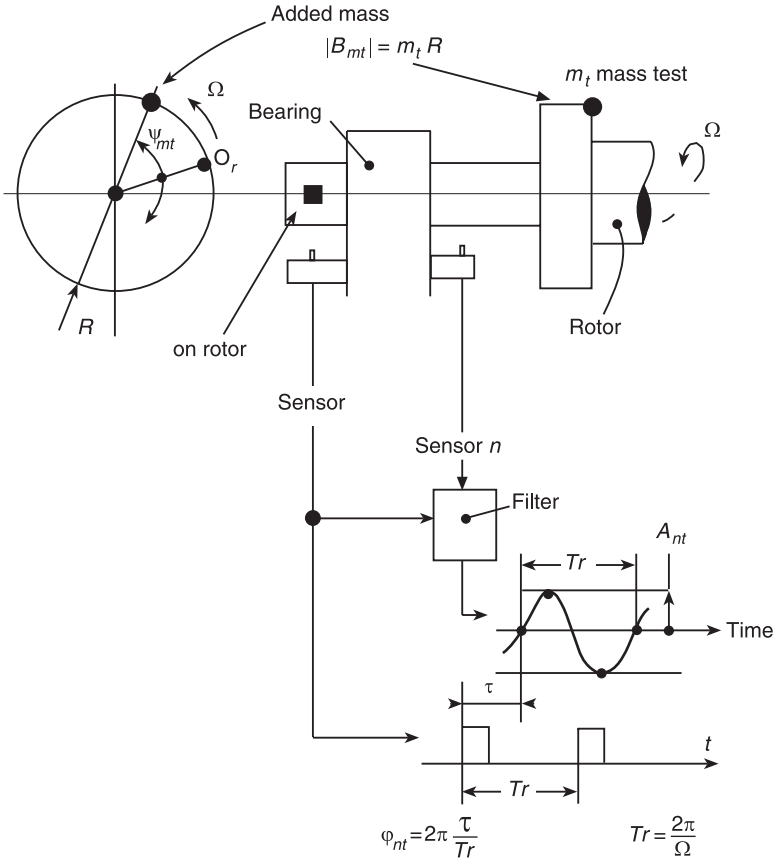


Figure 13 Elements defining influential coefficients. A_{nt}, amplitude; φ_{nt}, phase difference; m_tR, unbalance module; φ_{mt}, angular position of unbalance.

$$\begin{array}{cc} \text{Speed} & \text{Sensor} \\ \boldsymbol{\Omega}_1 & C_1 \\ & C_2 \\ \cdots & \vdots \\ \boldsymbol{\Omega}_q & C_k \\ \cdots & \vdots \\ & C_l \\ \boldsymbol{\Omega}_p & \vdots \end{array} \begin{bmatrix} V_1 \\ V_2 \\ \vdots \\ V_3 \\ \vdots \\ \vdots \\ V_N \end{bmatrix} = \underbrace{\begin{bmatrix} C_{11} & \cdots & C_{1m} \\ & \vdots & \\ & C_{nm} & \\ & \vdots & \\ C_{1M} & \cdots & C_{NM} \end{bmatrix}}_{\text{Coefficients of influence}} \underbrace{\begin{bmatrix} B_1 \\ \vdots \\ B_m \\ \vdots \\ B_M \end{bmatrix}}_{\text{Unbalance}} \rightarrow \mathbf{V} = \mathbf{CB}$$

Certain speeds can be critical speeds. Nominal speed is generally taken into account. The number of vibrations is equal to the number of speeds when these speeds are all different.

Forces perpendicular to the links can be introduced. In the matrix $\mathbf{V}$ given in eqn [23], relative vibrations $V_{Li}^1 V_{Li}^2$ measured in the same radial plane at right-angles to link *Li* in two perpendicular directions, noted 1 and 2, are marked out to form:

$$\mathbf{V}_L = \left[V_{L1}^1 V_{L1}^2 \ \cdots \ V_{Li}^1 V_{Li}^2 \ \cdots \right]^{\mathrm{T}}$$

Forces are expressed by impedance matrices $\mathbf{Z}_i$ (see **Bearing vibrations**).

$$\begin{bmatrix} \mathbf{I} & | & & & \mathbf{O} \\ - & - & - & - & - \\ & | & \mathbf{Z}_1 & & \\ & | & & \ddots & \\ \mathbf{O} & | & & & \mathbf{Z}_l \end{bmatrix} \begin{bmatrix} \mathbf{V} \\ \mathbf{V}_L \end{bmatrix}$$

$$= \begin{bmatrix} \mathbf{I} & | & & & \mathbf{O} \\ - & - & - & - & - \\ & | & \mathbf{Z}_1 & & \\ & | & & \ddots & \\ \mathbf{O} & | & & & \mathbf{Z}_l \end{bmatrix} \begin{bmatrix} \mathbf{C} \\ \mathbf{C}_L \end{bmatrix} \begin{bmatrix} \mathbf{B_1} \\ \vdots \\ \mathbf{B_M} \end{bmatrix} = \begin{bmatrix} \mathbf{V} \\ \mathbf{F}_L \end{bmatrix}$$

where $\mathbf{I}$ is the unit matrix. Lines of the matrix $\mathbf{C}_L$ are the lines of the matrix $\mathbf{C}$ associated to the vibrations: $V_{Li}^1 V_{Li}^2 \ldots V_{Li}^1 V_{Li}^2$.

$$\mathbf{F}_L = \begin{bmatrix} \mathbf{Z}_1 & & \\ & \ddots & \\ & & \mathbf{Z}_i \end{bmatrix} \mathbf{V}_L$$

forces perpendicular to the links.

The matrices $\mathbf{Z}_i$ can be calculated. They allow the determination of the forces which are necessary to the constructor to define the machine.

Corrective unbalances $\mathbf{B}_c$ in the corrective planes $1 \ldots m \ldots M$ which cancel, or reduce, initial vibratory amplitude $\mathbf{V}_0$ resulting from eqn [23]:

$$\mathbf{B}_C = \mathbf{C}^{-1}\mathbf{V}_0 \exp i\pi \qquad [24]$$

Residual vibration is zero:

$$\mathbf{V}_r = \mathbf{V}_0 + \mathbf{C}\mathbf{B}_C = \mathbf{0} \qquad [25]$$

$\mathbf{C}^{-1}$ exists if $N = M$ and if the determinant of $\mathbf{C} \neq 0$. If $M > N$ it is necessary to augment N where $M \leq N$. If $N > M$, the number of equations is greater than the unknown number B.

Optimization permits control of vibrations. With matrix $\mathbf{A}$ at M lines and N columns, eqn [23] leads to:

$$\mathbf{B}_C = [\mathbf{A}\mathbf{C}]^{-1}\mathbf{A}\mathbf{V}_0 \exp i\pi$$
$$\mathbf{V}_r = \left[\mathbf{I} + [\mathbf{A}\mathbf{C}]^{-1}\mathbf{A} \exp i\pi\right]\mathbf{V}_0$$

where $\mathbf{I}$ is unit matrix. Matrix $\mathbf{A}$ is acceptable if the modules of residual vibration and corrective unbalance are less than limits characterizing the quality:

$$\frac{|V_{nr}|}{|V_{nr}|_L} < 1 \qquad n = 1, 2 \ldots N$$
$$\frac{|B_{mc}|}{|B_{mc}|_L} < 1 \qquad m = 1, 2 \ldots M \qquad [26]$$

A first solution, which is often satisfactory, is obtained with $\mathbf{A} = \mathbf{C}^{\mathrm{T}}$ which expresses optimization by least-squares, where T denotes transposition.

When the inequalities [26] are not satisfied, improvements can be achieved by diagonal weighting matrices $\mathbf{P}_V$ on vibration, $\mathbf{P}_b$ on unbalance:

$$\mathbf{B}_C = \left[\mathbf{C}^{\mathrm{T}}\mathbf{C}\right]^{-1}\mathbf{C}^{\mathrm{T}}\mathbf{P}_V\mathbf{V}_0 \exp i\pi$$
$$\mathbf{V}_r = \left[\mathbf{I} + \mathbf{P}_b\mathbf{C}\left[\mathbf{C}^{\mathrm{T}}\mathbf{C}\right]^{-1}\mathbf{C}^{\mathrm{T}}\mathbf{P}_V \exp i\pi\right]\mathbf{V}_0$$

When $\mathbf{C}$ is square ($N = M$):

$$\mathbf{V}_r = [\mathbf{I} + \mathbf{P}_b\mathbf{P}_V \exp i\pi]\mathbf{V}_0$$

residual amplitudes are generally not zero, unless $\mathbf{P}_b\mathbf{P}_V = \mathbf{I}$. The use of weightings does not always appear to be justified.

As a complement to the weightings, vibration and unbalance can be suppressed. This degeneration brings about suppression of lines or columns in matrix $\mathbf{C}$.

The diagonal terms of $\mathbf{P}_V$ and $\mathbf{P}_b$ can be adjusted by servo-control subjected to eqn [26]. An automatic iterative process can lead to a solution or instability characterized by variations of eqn [26] around 1. In this case a modification of the law of servo-control can be carried out, or the limits $|V_{nr}|_L$, $|B_{mc}|_L$ can be increased or modified.

Instability can lead to the assumption that the problem posed does not have a solution: $N - M$ can seem too large, the limits too weak, the positions of the balancing planes may be bad, initial amplitudes are too raised.

Maintenance

When the performance is linear and repeatable, matrix $\mathbf{C}$ of influencing coefficients, which are intrinsic to a machine, on memory on a computer disk, thanks to quality maintenance can be used so that the rotor is in a rigid or flexible state. The minimum number of tests is equal to 2 (it is equal to $M + 2$ when the influencing coefficient matrix is to be determined).

An abnormal situation can be seen when the matrix $\mathbf{C}$ used does not permit reduction of vibration. It is

then possible that the procedure modifies vibration amplitude which arise from other excitations than unbalance. A balancing procedure must be engaged after a diagnosis which makes it possible to find out the causes of variations in vibratory amplitude.

Measuring and Analysis

Vibration is measured and analyzed to find out components whose frequency is equal to rotation frequency. Discrete Fourier transforms are edited by Bode graphs or polar (Nyquist) graphs: amplitudes and phases as a function of rotation speed. Measurement is carried out in steady state, at constant speed, or transient state where there is increase or reduction in rotation speed Ω. The transitory mode proves useful for extracting amplitude and phases at critical speed with reasonable accuracy, so long as the gradient $|d\Omega/dt|$ is less than a limit which enables the machine to be in a state which is close, or tangent, to a permanent state. The measuring system must acquire signals at speeds $\Omega_0 + n\Delta\Omega (n = 0, 1, 2 \dots)$ with an increment $\Delta\Omega$ which is even smaller for small damping ($\xi = 1/2Q_{3dB}$). The damping controls the amplitude around critical speed (**Figure 14**). $\Delta\Omega < \Delta\Omega_{cr}/6$ is generally suitable.

Discretization of signals can be done in synchronous or free mode. Using discrete Fourier transform, the synchronous mode makes it possible to determine components whose frequencies are multiples ($n = 1 \dots K$) of rotation speed (harmonic spectrum). K is independent of speed Ω. Using discrete Fourier transform, free mode permits determination of components whose frequencies are between f_{mini} and f_{maxi} (spectra). f_{mini} and f_{maxi} are independent of speed Ω.

Measuring the signal by a magnetic sensor of displacement, fixed on the nonrotating structure, a look at a rotor measuring track (**Figure 15**) results from movement (vibration) of the geometric center C profiled and:

- Gaps ($\varepsilon_e, \varepsilon_i \dots$) between this profile and the circumference of the average profile
- Variations in the magnetic permeability and resistivity between 0 and 360° of the measuring track
- Permanent magnetic spot on the measuring track

These three components constitute a noise (run-out) which it is necessary to deduct from the signal measured to obtain vibration, used for preliminary diagnosis before balancing and in its realization.

The noise is measured at slow rotation speed when the displacement from the geometric center C is negligible. Balancing carried out with noisy signals can lead to increases or decreases in vibration. For example, the maximum acceptable peak-to-peak level, resulting from all spectral components, is, according to standard ISO 7919–3, for industrial machines, equal to $L(\mu m)$ peak-to-peak $= 4800/\sqrt{N(rpm)}$ where N is the nominal speed on a turbine, a compressor, a pump at 10 000 rpm; $L = 48\,\mu m$ peak-to-peak. Balancing carried out without subtraction of a noise equal to $10\,\mu m$ peak-to-peak can lead – when the spectrum is made up by the only component of rotation frequency – to an amplitude of vibration between 19 and $29\,\mu m$ ($24 \pm 5\,\mu m$) peak-to-peak 38 and $58\,\mu m$. The combination of response to rotating forces and speed of rotation Ω with the fundamental component of noise can produce antiresonances. Measuring and acquisition of signals must be made simultaneously on the arrangement of Q sensors and the sensor which indicates

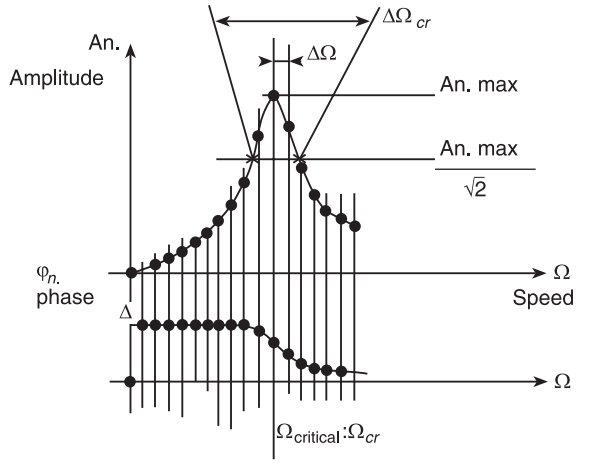


Figure 14 Increment $\Delta\Omega$ of signal acquisition. $Q_{3dB} = \Omega_{cr}/\Delta\Omega_{cr}$ = amplifiction factor at 3 dB.

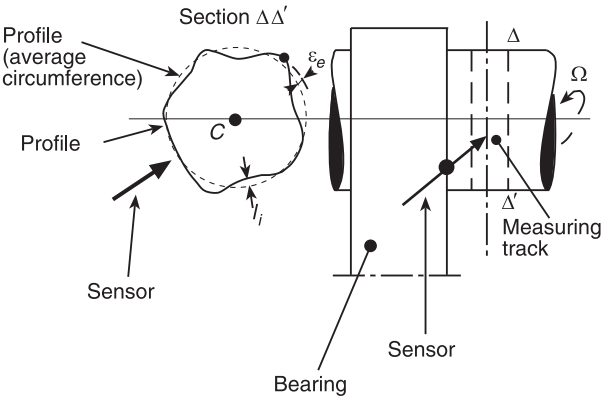


Figure 15 Fault of form: ($\varepsilon_e, \varepsilon_i$).

rotation (measurement of speed and determination of phases) in order to reduce uncertainty caused by faults in repeatability: a system capable of measuring simultaneously $(Q+1)/R$ signals lead to k tests on conditions which, in general, may not be identical, and so affected by repeatability faults. In addition, the difference in price of a system of $Q+1$ tracks and to $(Q+1)/k$ tracks must be compared to the difference in price between k tests and a test.

Software

The balancing procedure necessitates dedicated software. This makes it possible to take into account a large number of vibrations (50 ...) and balancing planes (10 ...); the signal components, chosen as a function of rotation speed on Bode graphs, automatically pass from the measuring, acquisition, and analysis system to the computer which carries out the subtraction of noise and simultaneously treats absolute vibration (nonrotating parts) and relative vibration (rotor and nonrotating parts) following the bases defined above, proposed corrective unbalance and associated residual vibration.

As for the rotors in a rigid state, the corrective unbalances for normal situations are small in general, at critical speeds, particularly since damping is weak. Complementary software enables these procedures: composition and decomposition of unbalance, average signal, unbalance imposed to calculate vibration; composition of signals to determine elliptical pathways, evaluation of the quality of balancing by the length of the ellipse axis; coefficients of nonrepeatability and nonlinearity.

It is still useful to manage and monitor a large number N of vibrations, even when the number M of corrective unbalance is low (1, 2). $N \gg M$ is useful when the rotor is in a flexible state in a special casing under vacuum, or in the structure of the machine on site.

Diagnostics: Limit Values

The procedure of amplitude reduction (balancing) results from diagnostics capable of pinpointing its need and/or that of other operations.

Reduction in amplitude may make it possible to obtain linear performance (following reduction in amplitude of harmonic components of rotation speed), passing critical speed without risk of contact between the rotor and the stator, rotating forces which are weaker than static forces at right-angles to the bearings, and an increase in the lifespan of ball bearings or roller bearings (see **Bearing vibrations**).

The limit values $|V_{nr}|_L$ of vibration amplitude permits quality apprecation in respect of limit values $|B_{mc}|_L$ of unbalance modules, imposed by technology. The textbook on charges and standards (see **Rotating machinery, monitoring**) must be consulted for the definition of limit values. The fuzziness of certain standards makes it possible to negotiate and make agreements between users and constructors.

Example

The machine comprises an electric motor, including two rotors. Two elastic couplings are arranged between the rotors. Links are established by ball bearings. Vertical vibration is measured by accelerometers on the motor stator (numbers 1 and 2) and on each of four rotor bearings (numbers 3–6). Corrective unbalances are placed in four planes: one close to the motor coupling (P_1) and one and two on the rotors (P_2, P_3, and P_4). Measurements are carried out when there is an increase in speed (temporary rate of flow) after maintaining speed at a constant level to obtain a permanent thermal rate of flow. The matrix of influential coefficients comprises 72 terms. Corrective unbalance and residual unbalance are calculated by the least-squares matrix (matrix $\mathbf{C}^{\mathrm{T}}$). There is little uncertainty caused by repeatablity faults – several percent on amplitude. **Table 1** shows conditions and results. Ten critical speeds are used. Reduction is important at critical speed; theoretical and measured amplitudes are similar.

See also: **Bearing vibrations**; **Rotating machinery, essential features**; **Rotating machinery, modal characteristics**; **Rotating machinery, monitoring**; **Rotor dynamics**; **Spectral analysis, classical methods**; **Standards for vibrations of machines and measurement procedures**.

Further Reading

Adams ML Jr (1999) *Rotating Machinery Vibration. From Analysis to Troubleshooting*. New York: Marcel Dekker.

Bigret R (1980) *Vibrations des Machines Tournantes et des Structures*. [*Vibrations of Rotating Machines and Structures.*] *Paris: Technique et Documentation Lavoisier.*

Bigret R (1997) *Stabilité des Machines Tournantes et des Systèmes. [Stability of Rotating Machines and Systems.]* Simlis, France: CETIM.

Bigret R, Feron J-L (1995) *Diagnostic, Maintenance, Disponibilité des Machines Tournantes.* [*Diagnostics, Maintenance, Availability of Rotating Machines.*] Paris: Masson.

Boulenger A, Pachaud S (1998) *Diagnostic Vibratoire en Maintenance Préventive*. [*Vibratory Diagnostics and Preventive Maintenance.*] Paris: Dunod.

Childs D (1993) *Turbomachinery Rotordynamics*. Chichester: John Wiley.

Table 1 Balancing

Sensor accelerometer no.	*Speed (rpm)*	*Critical speed*	*Amplitude ($mm\,s^{-1}$ peak)*		
			Initial (to be reduced)	*Residual*	
				Theoretical	*Measured*
1	1496	Yes	3.32	0.77	1
1	1696	Yes	5.40	1.78	1
1	1960	Yes	10.36	1.10	1.1
2	1408	No	0.80	1.08	0.6
2	1680	Yes	2.16	1.78	0.4
2	1960	Yes	4.90	2.30	0.8
3	1660	Yes	3.20	1.10	0.1
3	1856	Yes	2.90	0.33	0.2
3	2048	No	1.60	1.39	1.1
4	1612	Yes	7.36	0.13	1.7
4	1856	No	6.92	0.65	0.8
4	2048	No	9.80	1.11	1.2
5	1328	No	2.76	1.02	0.5
5	1564	Yes	11.20	0.37	1.2
5	1984	No	11.62	1.64	1.2
6	1328	No	5.40	1.84	0.2
6	1548	Yes	18.60	1.55	1.5
6	1984	No	13.60	2.32	1.8

Corrective unbalance (g mm): P_1=161; P_2=195; P_3=450; P_4 = 203.

Dimentberg FM (1961) *Flexural Vibrations of Rotating Shafts*. London: Butterworths.

Frêne J, Nicolas D, Dequeurce, Berthe D, Godet M (1990) *Lubrification Hydrodynamique – Paliers et Butées. [Hydrodynamic Lubrication – Bearings and Thrust.]* Paris: Eyrolles.

Gasch R, Pfützner (1975) *Rotordynamik, Eine Einführung*. Berlin: Springer Verlag.

Genta G (1999) *Vibration of Structures and Machines*. Berlin: Springer Verlag.

Lalanne M, Ferraris G (1990) *Rotordynamics Prediction in Engineering*. Chichester: John Wiley.

Morel J (1992) *Vibrations des Machines et Diagnostic de leur Etat Mécanique*. [*Machine Vibrations and Diagnostics of their Mechanical Condition*] Paris: Eyrolles.

Tondt A (1965) *Some Problems of Rotor Dynamics*. London: Chapman & Hall.

Vance JM (1988) *Rotordynamics of Turbomachinery*. Chichester: John Wiley.

BASIC PRINCIPLES

G Rosenhouse, Technion - Israel Institute of Technology, Haifa, Israel

Copyright © 2001 Academic Press

doi:10.1006/rwvb.2001.0088

Vibrations of bodies including motions and deformation waves under the action of forces can be approximated by the application of physical models and mathematical tools. Here the two main branches of the theory, which are the vectorial approach and the calculus of variations, are presented. Next, the basic rules of the vectorial approach are reviewed. Then the development and variants of the calculus of variations is linked to the theory of vibrations. Some examples help to understand the use of the formulae.

Background

Mechanical vibrations involve phenomena that are periodic in time, and can also be generalized to nonperiodic phenomena. In order to predict them it is necessary to be familiar with their basic parameters, including:

1. The independent variables, the time, t, and the location, $\mathbf{r}$, in a spatial reference frame. In a Cartesian orthogonal system of coordinates $Oxyz$ (**Figure 1A**) the radius vector is given by its components as:

$$\mathbf{r} = x\mathbf{i} + y\mathbf{j} + z\mathbf{k} \qquad [1]$$

2. The kinematics parameters that depend on t and $\mathbf{r}$: displacements, $\mathbf{u}$ velocities, $\mathbf{v}$, and accelerations, $\mathbf{a}$. In a Cartesian orthogonal system of coordinates $Oxyz$ (**Figure 1B**) the velocity is given by its components as:

$$\mathbf{v} = \lim_{\Delta t \to 0} \frac{\Delta \mathbf{r}}{\Delta t} = \lim_{\Delta t \to 0} \frac{\mathbf{r}(t + \Delta t) - \mathbf{r}(t)}{\Delta t} = \frac{\mathrm{d}\mathbf{r}}{\mathrm{d}t} = D\mathbf{r}$$
$$\Rightarrow \mathbf{v} = \dot{\mathbf{r}} = \dot{x}\mathbf{i} + \dot{y}\mathbf{j} + \dot{z}\mathbf{k} \qquad [2]$$

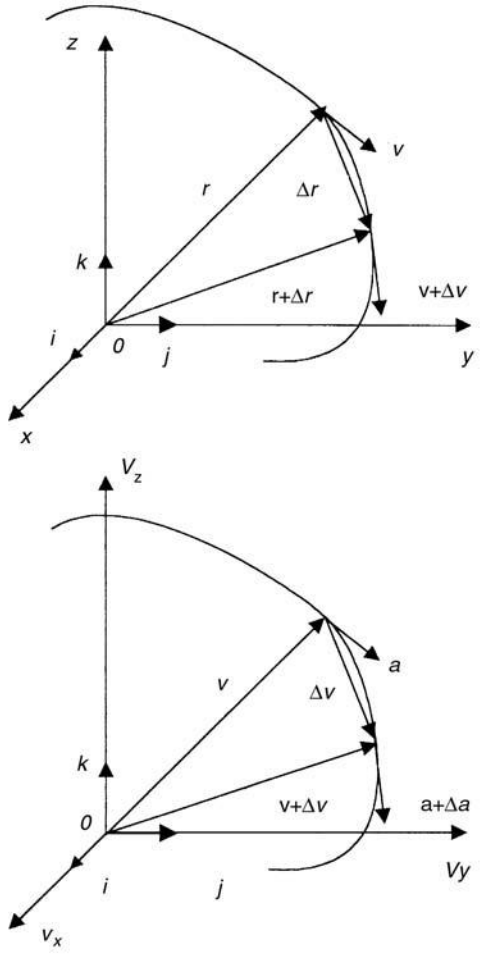


Figure 1 Independent variables of mechanics in a spatial Cartesian orthogonal reference frame.

3. Similarly, the acceleration is:

$$\mathbf{a} = \dot{\mathbf{v}} = \lim_{\Delta t \to 0} \frac{\Delta \mathbf{r}}{\Delta t} = \lim_{\Delta t \to 0} \frac{\dot{\mathbf{r}}(t + \Delta t) - \mathbf{r}(t)}{\Delta t} = \frac{\mathrm{d}\dot{\mathbf{r}}}{\mathrm{d}t}$$
$$= D^2\mathbf{r} \Rightarrow \mathbf{a} = \ddot{\mathbf{r}} = \ddot{x}\mathbf{i} + \ddot{y}\mathbf{j} + \ddot{z}\mathbf{k} \qquad [3]$$

4. The physical measures: mass, m, force, $\mathbf{F}$, inertia, spring constant, k, damping factor.
5. Parameters that are specific to vibrations: period, T, frequency, $f = 1/T$, amplitude, A, generalized coordinates, q, and number of degrees-of-freedom.
6. Specific terms: particle, rigid body, matter, harmonic motion, small displacements, finite displacements.

The basic principles on which the theory of vibration relies are from two main branches: the vectorial approach, based on the laws of Newton (1643–1727), and the principle of virtual work, mentioned by Leonardo da Vinci (1452–1519). The fundamentals of dynamics were proposed in the 17th century by Galileo Galilei (1564–1642). Descartes (1596–1650) recognized the basic idea of infinitely small motions, and John Bernoulli (1667–1748) made the final formulation of the principle of virtual displacements. D'Alembert (1718–1783) developed a basic principle in dynamics, Lagrange (1736–1813) developed a differential approach, and Hamilton (1805–1865) used an integral form, describing the energy principles of mechanics concerning vibrations, and extended the principle of virtual work to kinetics. Simplified solutions of dynamics problems where derived by energy considerations and approximating functions have been developed by Rayleigh (1842–1919) and Ritz (1878–1909). The above-mentioned outstanding research workers are only some of the many who have contributed to the area of mechanical vibrations.

The Vectorial Approach

Vibration modeling is based on the laws of dynamics. These laws are mostly axiomatic, being generalized results of observations over many centuries. The laws of dynamics were summarized in the monumental book *Principia Mathematica*, written by Isaac Newton in 1687. These laws, together with the principle of conservation of mass and the relevant constitutive law, combine the equations of motion and the boundary conditions in the examined material space. The three basic laws of dynamics are:

> Law 1: Every body preserves at its state of rest, or of uniform motion in a right line, unless it is compelled to change that state by forces impressed thereon.

Galileo first discovered this law in 1638.

> Law 2: The alteration of motion is ever proportional to the motive force impressed, and is made in the direction of the right line in which that force is impressed.

In this fundamental law of dynamics, Newton refers to the quantitative value of motion, or momentum $m\mathbf{v}$ change under the action of the force $\mathbf{F}$ on a body. m is the instantaneous proportionality coefficient of the material body that is defined as mass. $\mathbf{v}$ is the instantaneous velocity of the body. If the direction of motion is $\mathbf{r}$ then the second law implies that:

$$\mathbf{F} = m\frac{\mathrm{d}(m\mathbf{v})}{\mathrm{d}t} = \frac{\mathrm{d}\left(m\dfrac{\mathrm{d}\mathbf{r}}{\mathrm{d}t}\right)}{\mathrm{d}t} \qquad [4]$$

An example of varying mass occurs, for example, to a rocket, at the stage where it loses fuel, during flight. Where the mass remains constant, the second law becomes:

$$\mathbf{F} = m\frac{\mathrm{d}^2\mathbf{r}}{\mathrm{d}t^2} = m\mathbf{a}; \quad \mathbf{a} = \frac{\mathrm{d}^2\mathbf{r}}{\mathrm{d}t^2} \qquad [5]$$

where $\mathbf{a}$ is the acceleration of the body.

Newton's second law can be extended to rotation, where the force $\mathbf{F}$ along $\mathbf{x}$ is replaced by a moment M_T about $\mathbf{r}$, $\mathbf{r}$ is replaced by the rotation θ about $\mathbf{r}$, and mass m is replaced by the polar moment of inertia I_p about the x axis.

The second law can also be extended to the action of resultant forces on the body.

> Law 3: To every action there is always an equal opposed reaction, or the mutual actions of two bodies upon each other are always equal, and directed to contrary parts.

An important principle linked to Newton's second law is the dynamic equilibrium concept suggested by D'Alembert (1743). D'Alembert's principle says that when a body in a fixed system is forced by a resultant $\mathbf{R} = \sum_{i=1}^{n} \mathbf{F}_i$ of n forces, then Newton's second law defines its absolute acceleration, $\mathbf{a}$. However, if the reference system moves at the same velocity as the body, the observer will note that the body is in rest, or equilibrium. This can occur since $\mathbf{R}$ is balanced by the inertia force $-m\mathbf{a}$ (**Figure 2**):

$$\mathbf{P} = \mathbf{R} - m\mathbf{a} = 0 \qquad [6]$$

For a system of n bodies (**Figure 2**):

$$\sum_{i=1}^{n} \mathbf{P}_1 = \sum_{i=1}^{n} (\mathbf{R}_i - m\mathbf{a}) = 0 \qquad [7]$$

The resultant force is obtained by the vectorial rule of the parallelogram, as presented by Newton (1687). The rule follows Aristotle's assumption that a force is proportional to speed: 'A body by two forces conjoined will describe the diagonal of a parallelogram, in the same time that it would describe the sides, by these forces apart'. At that time the parallelogram of velocities was known. In fact, Leonardo da Vinci had already defined in his way the terms 'force' and 'moment', and suggested combinations of forces into a resultant force (**Figure 3**).

Varignon's (1654–1722) contribution was the superposition of moments. He introduced the rule that the moment of the result of two forces, at a chosen point, equals the algebraic sum of moment of the two forces.

An important rule in vibrations of deformable bodies is that when a deformable free body is subjected to action of forces in equilibrium, this equilibrium is kept when the body becomes rigid.

Calculus of Variations

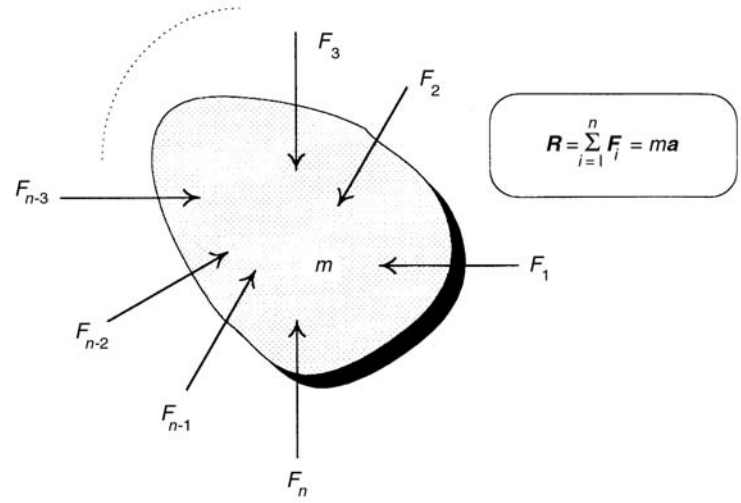
The theory of variations has many applications, and it allows for the derivation of basic principles. It deals with maximal and minimal problems determining the values of independent variables $(x_1, x_2, x_3 \ldots x_n)$ for which the function $y(x_1, x_2, x_3 \ldots x_n)$ has either a maximum or minimum value. In its fundamental description, a definite integral that has an integrand composed of unknown functions (one or more), and their derivatives, is given. These unknown functions are solved in such a way that the integral, usually of the form, if F contains derivatives of y to the first order:

$$I = \int_{x_1}^{x_2} [F(x, y, y')]\,\mathrm{d}x; \quad y' = \frac{\mathrm{d}y}{\mathrm{d}x} \qquad [8]$$

will be of either minimum or maximum value.

Euler's Equations

Given two points, A_1 and A_2 in the $(x,\ y)$ plane, it is necessary to find for eqn [8] the admissible arc A_1A_2 that minimizes I (**Figure 4A**). Such admissible arcs are usually continuous and consist of a finite number of arcs. The tangent of each arc varies continuously, but the whole curve may have corners. The admissible curves joining A_1 and A_2 can be given as:



Dynamic equilibrium following d'Alembert's principle

1. for a single body: $\boldsymbol{P} = \boldsymbol{R} - m\boldsymbol{a} = 0$

2. for a system of bodies: $\sum_{i=1}^{n} \boldsymbol{P}_i = \sum_{i=1}^{n} (\boldsymbol{R}_i - m_i \boldsymbol{a}_i) = 0$

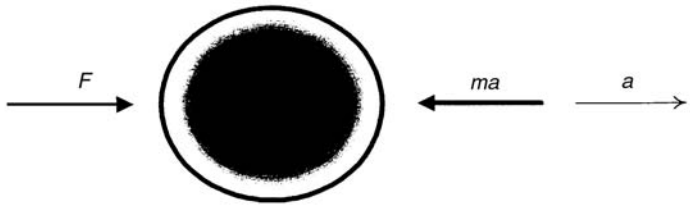


Figure 2 D'Alembert's principle.

$$y = y(x) + \alpha\eta(x) \qquad [9]$$

where $\eta(x)$ is an arbitrary function that vanishes at A_1 and A_2. $y = y(x)$ is the minimizing function. Substituting eqn [8] in eqn [9] yields:

$$I(\alpha) = \int_{x_1}^{x_2} F[x; y + \alpha\eta(x); y' + \alpha\eta'(x)]\,\mathrm{d}x \qquad [10]$$

To minimize $I(\alpha)$ for $\alpha = 0$, it is necessary that:

$$I'(0) = \int_{x_1}^{x_2} \left[F_y\eta(x) + F_{y'}\eta'(x)\right]\mathrm{d}x = 0; \qquad F_y = \frac{\partial F(x,y,y')}{\partial y}; \quad F_{y'} = \frac{\partial F(x,y,y')}{\partial y'} \qquad [11]$$

By integrating the parts and satisfying the end conditions, the following version of Euler's equation results in:

$$F_y - \frac{\mathrm{d}F_{y'}}{\mathrm{d}x} = 0 \qquad [12]$$

The last equation must be satisfied conditionally by every function $y = y(x)$ that minimizes or maximizes eqn [8]. There are additional conditions, which are more complicated, that are needed to secure the maximization or minimization of eqn [8], which in most cases are suspended. A more explicit version of Euler's equation is:

$$F_{y'y'}y'' + F_{y'y}y' + F_{y'x} - F_y = 0; \quad F_{y'y'} = \frac{\partial^2 F}{\partial y'^2}; \quad F_{y'x} = \frac{\partial^2 F}{\partial y'\partial x} \qquad [13]$$

The solutions of eqn [12] are called extremals and the resulting curves are called extremal arcs. In either case, y must able to be differentiated twice and F three times in order to discover whether the result is extremal.

(A) A superposition of forces
Leonardo da Vinci
Codex Arundel.
The Trustees of the British Museum,
London

(B) A study equilibrium
Leonardo da Vinci
Codex Madrid I.
Biblioteca National, Madrid
and McGraw-Hill

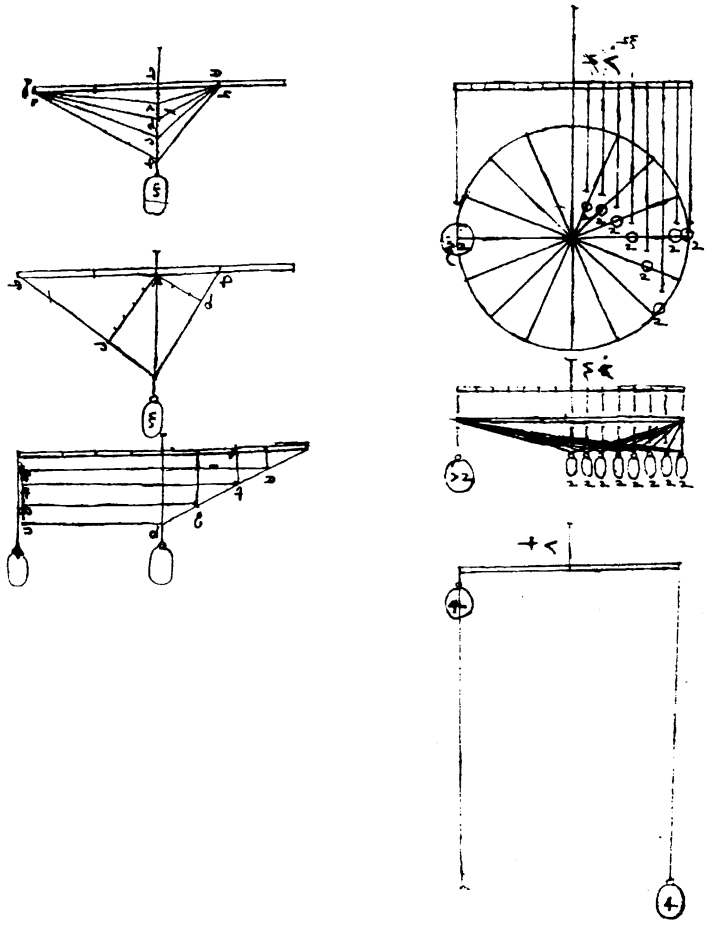


Figure 3 (A) Superposition and (B) equilibrium by Leonardo da Vinci.

The functional may depend on more then one function:

$$I = \int_{A_1}^{A_2} F\left(x, y_1, y_2 \ldots y_n, y_1', y_2' \ldots y_n'\right) \, \mathrm{d}x \qquad [14]$$

and the end conditions at A_1 and A_2. As a result, and since it is possible to vary only one function at a time, a set of n Euler equations results in:

$$F_{y_i} - \frac{\mathrm{d}}{\mathrm{d}x} F_{y_i'} = 0; \qquad i = 1, 2, 3 \ldots n \qquad [15]$$

Euler's equation can be further generalized to include derivatives of higher order:

$$I = \int_{A_1}^{A_2} F\left(x, y(x), y'(x) \ldots y^{(n)}(x)\right) \mathrm{d}x \qquad [16]$$

and the end conditions at A_1 and A_2. For the extremum of the functional I, the following Euler–Poisson equation must be satisfied:

$$\frac{\partial F}{\partial y} - \frac{\mathrm{d}}{\mathrm{d}x}\frac{\partial F}{\partial y'} + \frac{\mathrm{d}^2}{\mathrm{d}x^2}\frac{\partial F}{\partial y''} - \frac{\mathrm{d}^3}{\mathrm{d}x^3}\frac{\partial F}{\partial y'''} + \cdots + (-1)^n \frac{\mathrm{d}^n}{\mathrm{d}x^n}\frac{\partial F}{\partial y^{(n)}} = 0 \qquad [17]$$

This is an equation of the order $2n$, and y must be able to be differentiated $2n$ times, while F must be able to be differentiated $n + 2$ times: once in order to examine if the result yields an externum.

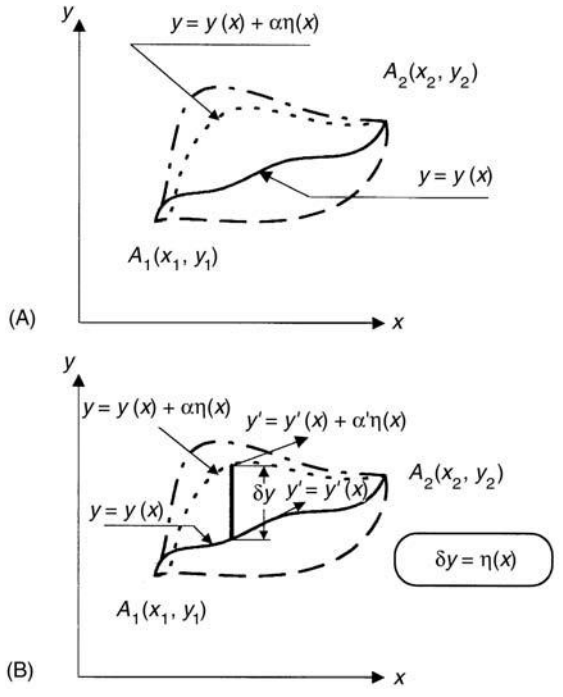


Figure 4 Variations in a curve between two stationary points.

If the functional depends on several functions and their higher derivatives:

$$I = \int_{A_1}^{A_2} F\Big(x_1, y_1, y_1' \ldots y_1^{(n1)}, x_2, y_2, y_2' \ldots y_2^{(n2)} \ldots x_m, y_m, y_m' \ldots y_m^{(nm)}\Big)\,\mathrm{d}x \qquad [18]$$

and the end conditions at A_1 and A_2 then, for extremum, the following set of equations has to be satisfied:

$$\frac{\partial F}{\partial y_i} - \frac{\mathrm{d}}{\mathrm{d}x}\frac{\partial F}{\partial y_i'} + \frac{\mathrm{d}^2}{\mathrm{d}x^2}\frac{\partial F}{\partial y_i''} - \frac{d^3}{\mathrm{d}x^3}\frac{\partial F}{\partial y_i'''} + \cdots + (-1)^{ni}\frac{\mathrm{d}^{ni}}{\mathrm{d}x^{ni}}\frac{\partial F}{\partial y_i^{(ni)}} = 0; \qquad i = 1, 2 \ldots m \qquad [19]$$

The functional can also be dependent on several independent variables:

$$I[z(x_1, x_2 \ldots x_n)] = \iint \ldots \int_D F(x_1, x_2 \ldots x_n, z, p_1, p_2 \ldots p_n)\,\mathrm{d}x_1\mathrm{d}x_2 \ldots \mathrm{d}x_n;$$
$$p_i = \frac{\partial z}{\partial x_i} \qquad [20]$$

and the end conditions at A_1 and A_2. Then for extremum, variation of I is used:

$$\delta I = \delta \iint \ldots \int_D F(x_1, x_2 \ldots x_n, z, p_1, p_2 \ldots p_n)\,\mathrm{d}x_1\,\mathrm{d}x_2 \ldots \mathrm{d}x_n = \iint \ldots \int_D (F_z\delta z + F_{p1}\delta p_1 + F_{p2}\delta p_2 + \cdots + F_{pn}\delta p_n)\mathrm{d}x_1\,\mathrm{d}x_2 \ldots \mathrm{d}x_n = 0 \qquad [21]$$

and the following set of equations must be satisfied:

$$F_z - \sum_{i=1}^{n}\frac{\partial}{\partial x_i}F_{p_i} = 0 \qquad [22]$$

In the specific case of two independent variables, $z = z(x_1, x_2)$, Euler–Lagrange or Ostrogradsky (1801–1861) equation results. Likewise, other cases may be developed.

Notes

1. As mentioned by Bolza (1931), Weierstrass has proven that a continuous function $y(x)$ that has isolated discontinuities in its first or second derivatives has a minimum value for I if it satisfies Euler's equation in any interval between successive discontinuities. This is in addition to conditions that must be satisfied at the points of discontinuity of the derivatives.
2. If F has several unknown functions $(y, z \ldots)$, it is necessary to satisfy the separate Euler's equation for $y, z \ldots$ for a stationary value of I.

Another way of proving Euler's equation is by the method of variations. Now $\eta(x)$ is defined as an incremental change, δy, in the neighborhood of the function $y(x)$ that minimizes or maximizes the integral [8] (**Figure 4B**). δy is defined as variation, and the analysis involved with δy is called the calculus of variations. Important relations in the calculus of variations are at each x between A_1A_2:

$$\eta'(x) = \frac{\mathrm{d}(\delta y)}{\mathrm{d}x} = \delta\frac{\mathrm{d}y}{\mathrm{d}x};$$
$$\delta F(y) = F(y + \delta y) - F(y) = \frac{\partial F}{\partial y}\delta y = F_y\delta y;$$
$$\delta F(x, y, y') = \delta F(y, y') = \frac{\partial F}{\partial y}\delta y + \frac{\partial F}{\partial y'}\delta y' = F_y\delta y + F_{y'}\delta y' \qquad [23]$$

Since $y(x)$ obeys the minimax condition it is stationary, and:

$$\delta \int_{A_1}^{A_2} F(x, y, y')\,\mathrm{d}x = \int_{A_1}^{A_2} \delta F(x, y, y')\,\mathrm{d}x = \int_{A_1}^{A_2} \left[F_y \delta y + F_{y'} \delta y'\right] \mathrm{d}x = 0 \quad [24]$$

then, using integration by parts and the fact that the variation is an arbitrary function of x, this leads to Euler's equation [12].

The calculus of variations can be used in dynamics in general and in the theory of vibrations specifically if the time t is introduced as an independent variable. In a three-dimensional space (x_1, x_2, x_3) we have:

$$I = \int_{t_0}^{t_1} \mathrm{F}(t, x_1, x_2, x_3, \dot{x}_1, \dot{x}_2, \dot{x}_3)\,\mathrm{d}t \quad [25]$$

An extremum is sought for this functional by finding functions that satisfy the end conditions: $x_i(t_0) = x_{i0}$; $x_i(t_1) = x_{i1}$; $i = 1, 2, 3$ at each specific problem.

In many cases the spatial coordinates are constrained (e.g., the length in a spherical pendulum is: $L = \sqrt{x_1^2 + x_2^2 + x_3^2}$). This constraint can be written as: $C(t, x_1, x_2, x_3) = 0$, and for $\partial C/\partial x_3 \neq 0$, x_3 can be extracted: $x_3 = f(t, x_1, x_2)$. This relation leads to the unconstrained extremum problem:

$$\hat{I} = \int_{t_0}^{t_1} \hat{F}(t, x_1, x_2, \dot{x}_1, \dot{x}_2)\,\mathrm{d}t \quad [26]$$

with the relation:

$$\hat{F}(t, x_1, x_2, \dot{x}_1, \dot{x}_2) = \Psi\left(t, x_1, x_2, f(t, x_1, x_2), \dot{x}_1, \dot{x}_2, \frac{\mathrm{d}}{\mathrm{d}t} f(t, x_1, x_2)\right) \quad [27]$$

For an extremum the functions x_i must satisfy the Euler's equations:

$$\hat{F}_{x_i} - \frac{\mathrm{d}}{\mathrm{d}t}\hat{F}_{\dot{x}_i} = 0; \quad i = 1, 2 \quad [28]$$

Also, the extremalizing functions and the involved Lagrange multiplier function must satisfy the Euler's equations:

$$\hat{F}_{x_i} - \frac{\mathrm{d}}{\mathrm{d}t}\hat{F}_{\dot{x}_i} = \lambda C_{x_i}; \quad i = 1, 2, 3 \quad [29]$$

The Equation of Flexural Motion Obtained by the Calculus of Variations

To illustrate the use of the calculus of variations in the theory of vibrations, we find the equation of motion for a beam (**Figure 5**). The total virtual work obtained by the variation δ along the beam is:

$$\delta I = \int_0^L (-M\delta v'' - q\delta v + m\ddot{v}\delta v)\,\mathrm{d}x = 0, \quad \xi' = \frac{\partial \xi}{\partial x}; \quad \dot{\xi} = \frac{\partial \xi}{\partial t} \quad [30]$$

We modify the first term in eqn [30]:

$$\int_0^L (-M\delta v'')\,\mathrm{d}x = -M\delta v'\big|_0^L + M_{,x}\delta v\big|_0^L - \int_0^L M_{,xx}\delta v\,\mathrm{d}x = -\int_0^L M_{,xx}\delta v\,\mathrm{d}x$$

and get:

$$\delta I = \int_0^L \left(-M_{,xx} - q + m\ddot{v}\right)\delta v\,\mathrm{d}x = 0$$

Since $M = -EIv' \Rightarrow M_{,xx} = -(EIv'')''$, and the virtual work equals zero whatever δy is, the resulting equation becomes:

$$-M_{,xx} - q + m\ddot{v} = 0 \quad \text{or} \quad \left(EI_{,xx}\right)_{,xx} - q + m\ddot{v} = 0 \quad [31]$$

Generalized Coordinates of a System

If the displacements $\mathbf{u}$ of a body are defined in terms of m coordinates, and if there are r equations of constraints among these displacements, then the rest of the coordinates, $n = m - r$, are independent. These n independent coordinates, that specify completely the configuration (displacements and forces) of the system, are defined as generalized coordinates, $\mathbf{q}$. The number of generalized coordinates of a system is also its number of degrees-of-freedom. If it is possible to extract a set of independent coordinates in a mechanical system, then the system is holonomic. However, if the resulting set of equations of a system does not permit extraction of the constraints, then the system is nonholonomic. Usually, the systems are holonomic. In a holonomic system it is possible to transform $\mathbf{u}$ into $\mathbf{q}$ by a transform matrix $\mathbf{C}$: $\mathbf{u} = \mathbf{Cq}$. For

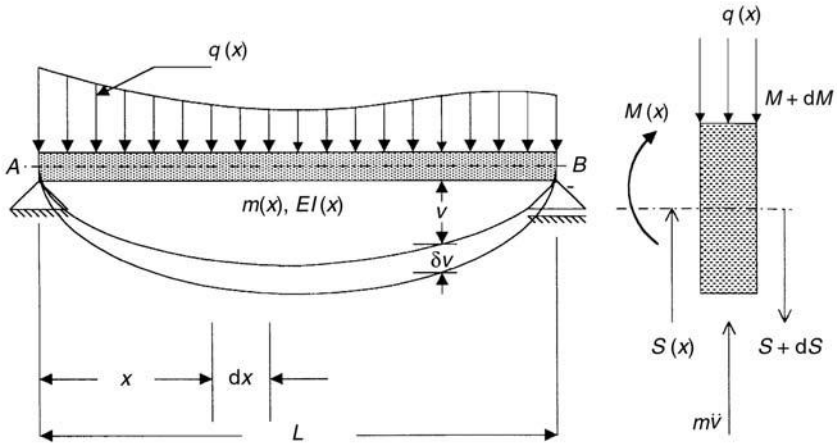


Figure 5 Variation in a deflection line of a beam.

example, if the kinetic energy of a holonomic set of linked rigid bodies m_j is $T = \frac{1}{2}\sum_j m_j \dot{u}_j^2$, then the displacements u_j can be given in term of generalized coordinates $u_j = u_j(q_1, q_2, q_3 \ldots)$:

$$\mathrm{d}\mathbf{u} = \sum_k \frac{\partial u_j}{\partial q_k}\mathrm{d}q_k; \quad \mathrm{d}\mathbf{u} = \mathbf{C}\,\mathrm{d}\mathbf{q}; \quad C_{jk} = \frac{\partial u_j}{\partial q_k} \qquad [32]$$

A virtual displacement is an arbitrary small displacement. A system of n degrees-of-freedom has n possible independent virtual displacements. A virtual work is the work done by forces that act during the virtual displacement: $\delta W = \mathbf{Q}^{\mathrm{T}}\delta\mathbf{q} = \mathbf{F}\delta\mathbf{u}$. $\mathbf{Q}$ are generalized forces in accordance with the generalized coordinates, and $\mathbf{F}$ are the forces that correspond to $\mathbf{u}$.

As an example, D'Alembert's principle can be given in terms of virtual displacements:

$$\delta W = \sum_j m_j \ddot{u}_j \delta u_j = \sum_j F_j \delta u_j \qquad [33]$$

Hamilton's Principle

Hamilton's principle is one of the most fundamental principles in vibration analysis. It leads to the basic equations of dynamics and elasticity. It is based on the assumption that when a system moves from a state at a time t_1 to a new state at the time t_2, in a Newtonian route, then the actual route out of all the possible ones obeys stationarity. This condition leads to Hamilton's principle:

$$\delta \int_{t_1}^{t_2} (T - V)\,\mathrm{d}t = \delta \int_{t_1}^{t_2} L\,\mathrm{d}t = 0; \qquad [34]$$
$$L = T - V = \text{Lagrangian}$$

where T is the kinetic energy of the system and V is the potential energy of the system. The Lagrangian L can be written in that case of elasticity in the form $L = U - K + A$, where A is the potential energy of the system, U is the strain energy of the system, and K is the overall kinetic energy of the system.

In terms of generalized coordinates, Hamilton's principle obtains the form:

$$\int_{t_1}^{t_2} \sum_j \left\{ -\frac{\mathrm{d}}{\mathrm{d}t}\left(\frac{\partial T}{\partial \dot{q}_j}\right) + \frac{\partial T}{\partial q_j} + Q_j \right\} \partial q_j\,\mathrm{d}t = 0 \qquad [35]$$

It is noted here that, for calculation of the kinetic energy of a system, Koenig's theorem can be used. This theorem states that the total kinetic energy of a rigid body of mass M is the kinetic energy of a particle of mass M that moves with the center of gravity of the body, plus the kinetic energy of the motion relative to the center of gravity of the body (as if it were fixed).

Lagrange Equations

While Hamilton's principle has an integral form, Lagrange equations are differential and describe an instantaneous situation. Lagrange equations carry the form:

$$\frac{\mathrm{d}}{\mathrm{d}t}\left(\frac{\partial T}{\partial \dot{q}_j}\right) - \frac{\partial T}{\partial q_j} + Q_j = 0;\ j = 1, 2 \ldots n \qquad [36]$$

The generalized forces can include external forces, Q_{Aj}, internal elastic forces, $Q_{Ej} = -\partial U/\partial q_j$, and damping forces, Q_{Dj}. Hence:

$$\frac{\mathrm{d}}{\mathrm{d}t}\left(\frac{\partial T}{\partial \dot{q}_j}\right) - \frac{\partial T}{\partial q_j} + \frac{\partial U}{\partial q_j} - Q_{Dj} = Q_{Aj};\ j = 1, 2 \ldots n \qquad [37]$$

In a conservative system, the potential energy due to potential sources is: $V(q_1, q_2, q_3 \ldots)$, and Lagrange's equation becomes:

$$\frac{\mathrm{d}}{\mathrm{d}t}\left(\frac{\partial T}{\partial \dot{q}_j}\right) - \frac{\partial T}{\partial q_j} + \frac{\partial V}{\partial q_j} = 0 \quad \text{or} \quad \frac{\mathrm{d}}{\mathrm{d}t}\left(\frac{\partial L}{\partial \dot{q}j}\right) - \frac{\partial L}{\partial q_j} = 0;$$
$$L = T - V;\ j = 1, 2 \ldots n \qquad [38]$$

Lagrange's equation is also useful in the case of dependent coordinates. Assume a set of m coordinates x_i; r of which are dependent and have the relations:

$$C_j(x_1, x_2, x_3 \ldots x_m) = 0; \quad j = 1, 2 \ldots r \qquad [39]$$

then, by using Lagrange multipliers, the Lagrangian can be formulated by coordinates, not all of which are independent:

$$L = L_0 + \sum_j \lambda_j C_j(x_1, x_2 \ldots x_m) \qquad [40]$$

The equations of motion become:

$$\frac{\partial L}{\partial x_i} - \frac{\mathrm{d}}{\mathrm{d}t}\frac{\partial L_0}{\partial x_i} + \sum_j \lambda_j \frac{\partial C_j}{\partial x_i} = 0; \quad i = 1, 2 \ldots n \qquad [41]$$

Hence, an equation of motion that represents the D'Alembertian sum of forces exists for each coordinate. Each multiplication of force by virtual displacement generates a contribution to the total virtual work that should be zero. Also, in the case of dependent coordinates, it is necessary that the virtual work will be zero. However, two separate conditions are necessary to insure:

$$\left(\frac{\partial L}{\partial x_i} - \frac{\mathrm{d}}{\mathrm{d}t}\frac{\partial L_0}{\partial x_i} + \sum_j \lambda_j \frac{\partial C_j}{\partial x_i}\right)\delta x_i = 0; \quad i = 1, 2 \ldots n \qquad [42]$$

One is the set of $n = m - r$ equations of motion and the second is involved with the r constraint equations.

Rayleigh's Principle

Rayleigh's principle and the fundamental equations of dynamics enable derivation of the theory of vibrations. When a conservative system vibrates freely, the total mechanical energy is constant. If the initial state is 0 and another state is defined by 1, then the sum of the kinetic and potential energies in the two states is the sum:

$$T_0 + V_0 = T_1 + V_1 \Rightarrow T_0 = V_1 \qquad [43]$$

In simple harmonic motion the average energies are $\overline{T} = 0.5T_0$; $\overline{V} = 0.5V_0 \Rightarrow \overline{T} = \overline{V}$. Since, in linear vibrations:

$$T = 0.5\sum_{i=1}^{n}\left(\dot{u}_i^2\right);$$
$$V = 0.5\sum_{i=1}^{n}\left(\omega_i^2 u_i^2\right) \Rightarrow \qquad [44]$$
$$\overline{T} = \overline{V} = 0.25\sum_{i=1}^{n}\left(A_i^2\omega_i^2\right)$$

then, using $\bar{T} = \bar{V}$ or $T_0 = V_1$ enables one to determine the natural frequency for a conservative 1-degree-of-freedom system. When the system has several degrees of freedom, the equation $\bar{T} = \bar{V}$ or $T_0 = V_1$ can be used for each mode, provided its modal shape can be approximated. This usually leads to frequencies that are higher by some percent than the natural frequencies.

A scheme of a one-dimensional straight element of length l, loaded by a distributed mass $m(x)$ and discrete masses M_i, is given in **Figure 6** to illustrate Rayleigh's principle.

Assuming a deflection shape $\phi(x)$ that approximates one modal shape, such that the deflection is given by $y = y_0\phi(x)$, then the system is approximated into a single-degree-of-freedom one, with an equivalent mass, $M_{\mathrm{eq}}(a)$ at $x = a$. The equivalent mass is calculated as:

$$\frac{1}{2}M_{\mathrm{eq}}(a)\dot{y}_0^2\phi^2(a) = \frac{1}{2}\left\{\sum_{i=1}^{n}\left(M_i\dot{y}_0^2\phi^2(i)\right) + \int_{(1)}\left(m(x)\dot{y}_0^2\phi^2(x)\right)\mathrm{d}x\right\}$$

or

$$M_{\mathrm{eq}}(a) = \frac{1}{\phi^2(a)}\left\{\sum_{i=1}^{n}\left(M_i\phi^2(i)\right) + \int_{(1)}\left(m(x)\phi^2(x)\right)\mathrm{d}x\right\} \qquad [45]$$

Obviously:

$$\frac{M_{eq}(a)}{M_{eq}(b)} = \frac{\phi^2(b)}{\phi^2(a)}; \quad \frac{K_{eq}(b)}{K_{eq}(a)} = \frac{\phi^2(b)}{\phi^2(a)}$$

and, the approximate frequency is calculated as:

$$\omega^2(a) = \omega^2(b) = \frac{K_{eq}(a)}{M_{eq}(a)} = \frac{K_{eq}(b)}{M_{eq}(b)} \qquad [46]$$

Example: given a fixed steel beam of a profile INP 30 (a standard I profile made of steel, common in Europe, with moment of inertia $I = 9800\,\text{cm}^4$, and Young's modulus $E = 2.1 \times 10^4\,\text{kN m}^{-1}$). See **Figure 7**. It is assumed that the deflection line carries the form:

$$y(x) = \frac{1}{2} y_0 \left[1 - \cos\left(\frac{2\pi x}{L}\right)\right] = y_0 \phi(x)$$

The maximum deflection of the beam under concentrated load P at its center is $f_{max} = PL^3/192EI$, and the equivalent spring constant becomes:

$$K_{eq} = \frac{192EI}{L^3} = 3.165 \times 10^5\,\text{N m}^{-1}$$

The equivalent mass is derived from the equation: $\frac{1}{2} M_{eq} \dot{y}_0^2 = \frac{1}{2} m \dot{y}_0^2 \int_0^L \phi^2\, dx$. The result is $M_{eq} = \frac{3}{8} mL = 3750\,\text{Ns}^2\,\text{m}$. Hence, following eqn [43], the radian frequency becomes:

$$\omega^2 = 84\,\text{rad}^2\,\text{s}^{-2} \rightarrow \omega = 9.165\,\text{rad s}^{-1}$$

The equivalent spring constant relates the force to displacement and to the static deflection of the vibrating element at the generalized coordinate. Hence it is important in this case to calculate the static deflection at that coordinate. In many cases the examined structure is indeterminate and its static analysis can be supported by the theorem of Castigliano (1847–1884) and of Menabrea (1809–1896). This theorem

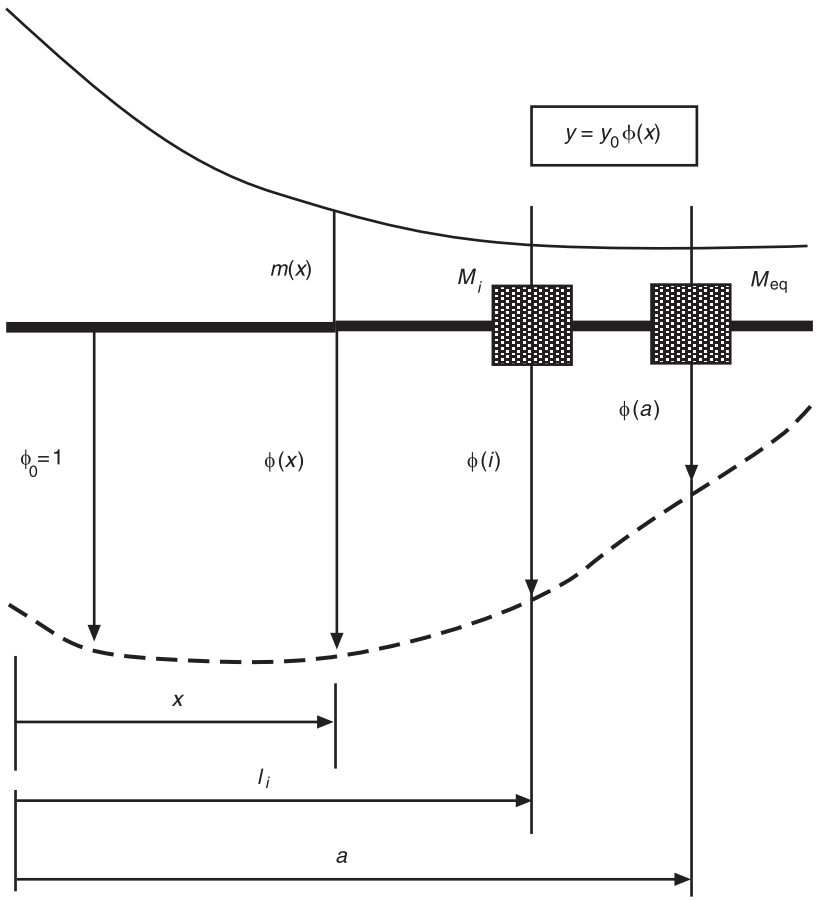


Figure 6 A scheme to illustrate Rayleigh's method.

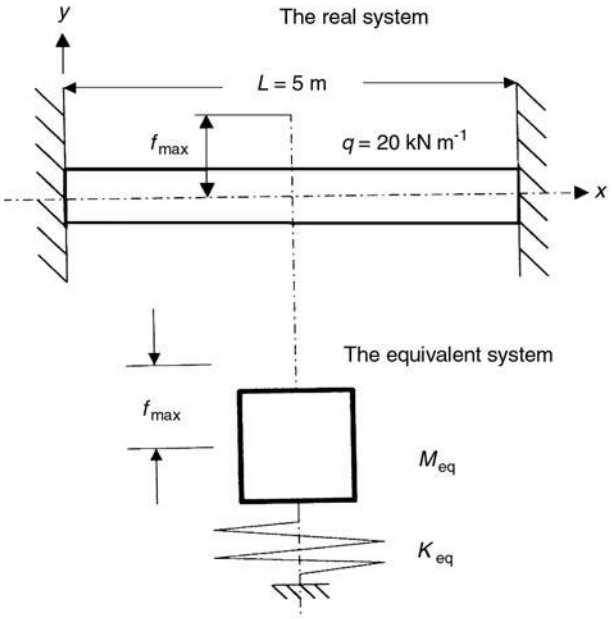


Figure 7 Equivalent mass and spring constant.

of the minimum strain energy says that each system brings its internal (potential) energy to the minimum.

Rayleigh's principle can also be used for the first and the higher modes $\phi_j(x)$ of a beam. The maximum kinetic energy of the beam in the jth mode (**Figures 5–7**) is:

$$T_{\max j} = \frac{1}{2}\int_0^L m\dot{v}_j^2 \mathrm{d}x = \frac{1}{2}f_{\max j}^2 \int_0^L m\omega_j^2\phi_j^2(x)\,\mathrm{d}x$$
$$= \frac{1}{2}f_{\max j}^2\omega_j^2 M_{\mathrm{eq}\,j} \qquad [47]$$
$$M_{\mathrm{eq}\,j} = \int_0^L m\phi_j^2(x)\,\mathrm{d}x$$

The maximum potential energy of the beam is:

$$U_{\max} = \frac{1}{2}\int_0^L \frac{M_j^2}{EI}\mathrm{d}x = \frac{1}{2}\int_0^L EI\left(\frac{\mathrm{d}^2 v_j}{\mathrm{d}x^2}\right)^2 \mathrm{d}x$$
$$= \frac{1}{2}f_{\max j}^2 \int_0^L EI\left(\frac{\mathrm{d}^2\phi_j}{\mathrm{d}x^2}\right)^2 \mathrm{d}x = \frac{1}{2}K_{\mathrm{eq}\,j}f_{\max j}^2 \qquad [48]$$
$$K_{\mathrm{eq}} = \int_0^L EI\left(\frac{\mathrm{d}^2\phi_j}{\mathrm{d}x^2}\right)^2 \mathrm{d}x$$

Hence, the natural frequency of the jth mode is:

$$\omega_j^2 = \frac{K_{\mathrm{eq}\,j}}{M_{\mathrm{eq}\,j}} = \frac{\int_0^L EI(x)\left[\phi_j''(x)\right]^2 \mathrm{d}x}{\int_0^L m_j(x)\left[\phi_j(x)\right]^2 \mathrm{d}x} \qquad [49]$$

Rayleigh–Ritz or Ritz Method

The Rayleigh–Ritz method enables one to reduce an infinite number of degrees-of-freedom of a system into a finite number, which makes analysis possible and easier. The method relies on the approximation of the possible deformation shapes of the system, following the basic idea beyond Rayleigh's principle. A proper combination of these deformation shapes is supposed to reproduce roughly the expected overall vibration pattern and natural frequencies. Following the Ritz method the family of curves over which the values of the functional are calculated is obtained by a linear combination of functions:

$$\phi(x) = \sum_{i=1}^{n} \alpha_i\varsigma_i(x); \quad i = 1, 2, 3 \ldots n \qquad [50]$$

Here, α_i are constants and ς_i are functions that satisfy certain end conditions. Hence, the shape of the function ϕ is determined by ς_i while its values are determined by the coefficients α_i. The functional I turns to be a function of the coefficients α_i:

$$I = \Psi(\alpha_1, \alpha_2 \ldots \alpha_n) \qquad [51]$$

where the condition of obtaining an extremum dictates the following set of n equations:

$$\frac{\partial\Psi}{\partial\alpha_i} = 0; \quad i = 1, 2 \ldots n \qquad [52]$$

The solution of the coefficients α_i yields the values of the function $y(x)$ for which the functional obtains the approximate extremal value. The more suitable the choice of the family of function, the more exact the solution will be.

The method also applies to the solution of problems with functionals that depend on several functions of one or more independent variables. For example, the Rayleigh–Ritz method can be used for the analysis of flexural vibrations of a beam. The jth natural frequency of the beam satisfies the ratio given in eqn [49]. Using this equation and eqns [51] and [52] results in:

$$\frac{\partial}{\partial \alpha_1}\frac{\int_0^L EI(x)\left[\phi_j''(x)\right]^2 \mathrm{d}x}{\int_0^L m_j(x)\left[\phi_j(x)\right]^2 \mathrm{d}x} = 0 \qquad [53]$$

Substituting the expression [50] in eqn [53] leads to a set of linear equations that solve the $\alpha_i s$. However, in order to avoid a trivial solution, the determinant of coefficients of this set of equations should be zero, which yields the frequency equation for the various modes of vibrations. Now eqn [50] is again used to find the mode shape, having solved the jth natural frequency and the ratios of the $\alpha_i s$.

Galerkin's Method

In a similar way to that of Ritz's method, Galerkin's method combines a family of curves for which the values of the functional I are obtained follow eqn [50]. The difference is in that each function has to satisfy all the end conditions of the problem. This means that, for all the combinations $\delta v = 0$, the solution is that of a problem with fixed ends. The condition for extremum obtains in this case the form:

$$\delta I = \int \Psi(\alpha_1, \alpha_2 \ldots \alpha_n)\delta y \, \mathrm{d}x = 0 \qquad [54]$$

This equation has to be satisfied for any arbitrary δy. A set of n equations for the n unknowns α_i is obtained by a sequential choice of z_i for δy. In many cases Galerkin's method coincides with that of Ritz. However, whenever the solution is not the same, Galerkin's method is more exact for the same number of terms. The reason is that the end conditions are satisfied *a priori* by this method.

The method also applies to the solution of problems with functionals that depend on several functions of one or more independent variables.

We demonstrate now this method for the natural vibrations of a beam to illustrate the point. The virtual work of the beam of constant EI is:

$$\int_0^L \left[\left(EI_{,xx}\right)_{,xx} + m\ddot{v}\right]\delta v \, \mathrm{d}x = 0 \qquad [55]$$

A deflection curve of the beam is assumed to have the form and variation:

$$\begin{aligned} v(x,t) &= \zeta(x)\exp(i\omega t) \\ \delta v(x,t) &= \delta\zeta(x)\exp(i\omega t) \end{aligned} \qquad [56]$$

Substitution in eqn [55] yields:

$$\exp(i\omega t)\int_0^L \left[\left(EIv_{,xx}\right)_{,xx} - m\omega^2 v\right]\delta v \, \mathrm{d}x = 0 \qquad [57]$$

Assume a solution of the form:

$$\bar{v}(x) = \sum_{j=1}^{n} \alpha_j \zeta_j(x);$$

and:

$$\delta\bar{v}(x) = \sum_{i=1}^{n} \delta\alpha_j \zeta_j(x) \qquad [58]$$

Since $\delta\alpha_j$ is arbitrary, it is possible to make all the virtual displacements zero. Then for each k the following equation is obtained:

$$\int_0^L \left[\left(EI\bar{v}_{,xx}\right)_{,xx} - m\omega_k^2\bar{v}\right]\bar{v}_k \, \mathrm{d}x = 0 \qquad [59]$$

After calculating the integral and using the orthoganality rules, the result for the natural frequency becomes:

$$\omega_k^2 = \frac{4k^4\pi EI}{mL^4} \qquad [60]$$

Dunkerley's Method

While Rayleigh's method yields the upper bound of the natural frequencies, Dunkerley's method (1894) suits the lower bound. The method originally estimates the fundamental frequency in a multidegree-of-freedom system, with the eigenvalue problem:

$$L(u) = \omega^2 M(u) = 0 \qquad [61]$$

For:

$$M(u) = \sum_{i=1}^{m} M_i(u) \qquad [62]$$

the partial problem is self-adjoint and fully defined if its fundamental frequency is known. Hence:

$$L(u) = \omega_i^2 M_i(u) = 0 \qquad [63]$$

and, using Galerkin's method, Dunkerley's frequency, ω_{D}, becomes:

$$\frac{1}{\omega_{1\mathrm{D}}^2} = \sum_{i=1}^{m} \frac{1}{\omega_{1i}^2}; \quad \omega_{1\mathrm{D}}^2 \le \omega_1^2 \qquad [64]$$

Here, ω_1 is the exact fundamental mode, and ω_{li} are the fundamental frequencies of the partial problems.

The natural frequencies of the second and higher modes are often much higher than the fundamental one. A scheme of an example is given in **Figure 8**. A cantilever of length L has evenly distributed mass m, with $mL = M$, and a concentrated mass at its end. The first natural frequency for the distributed mass is $\omega_{11}^2 = 3.515^2(EI/ML^3)$, and the first natural frequency for the concentrated mass is $\omega_{12}^2 = 3.00(EI/ML^3)$. The first frequency of the whole system is calculated following eqn [64]:

$$\frac{1}{\omega_{1D}^2} = \frac{1}{\omega_{11}^2} + \frac{1}{\omega_{12}^2} \rightarrow \omega_{1D}^2 = \frac{\omega_{11}^2\omega_{22}^2}{\omega_{11}^2 + \omega_{12}^2} = \frac{3.515^2 \times 3.00}{3.515^2 + 3}\frac{EI}{ML^3} = 2.41\frac{EI}{ML^3}$$

This value is the lower bound. The upper bound, ω_{1R}, is found by Rayleigh's method:

$$\omega_{1R}^2 = \frac{3EI}{(1 + \frac{33}{140})ML^3} = 2.43\frac{EI}{ML^3}$$

The exact first frequency is somewhere between ω_{1D} and ω_{1R}.

Maxwell's Theorem of Reciprocity

Maxwell's theorem of reciprocity (1831–1879) states that deflection at a point A in the direction **a**, due to a unit force acting along **b**, is equal to deflection at the point B, in the direction **b**, caused by a unit force acting along **a**. This theorem is useful in solving vibration problems since it does not deny D'Alembertian forces.

As an example, we seek the two natural frequencies of a weightless simply supported beam that supports two masses at A and B (**Figure 9**).

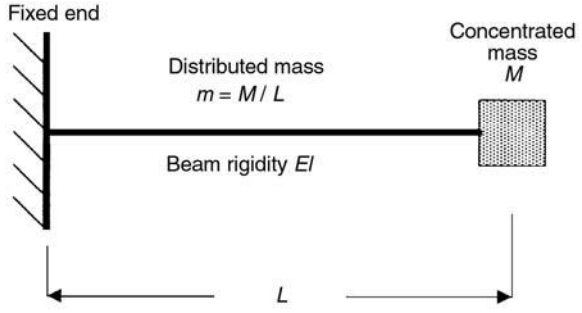


Figure 8 A cantilever beam supporting a mass at its end.

If f_{ij} is the deflection at j due to the force at i, then the deflection at A is:

$$\begin{aligned} v\mathrm{A} &= -m_\mathrm{A}\ddot{v}_\mathrm{A}f_{\mathrm{AA}} - m_\mathrm{B}\ddot{v}_\mathrm{B}f_{\mathrm{BA}}; \\ v_\mathrm{B} &= -m_\mathrm{A}\ddot{v}_\mathrm{A}f_{\mathrm{AB}} - m_\mathrm{B}\ddot{v}_\mathrm{B}f_{\mathrm{BB}} \end{aligned} \quad [65]$$

and following Maxwell's theorem, $f_{\mathrm{AB}} = f_{\mathrm{BA}}$. The assumed solutions are:

$$v_i = \bar{v}_i \ \sin\ (\omega t), \quad i = A, B \quad [66]$$

and by substitution into eqn [65] we obtain:

$$\begin{aligned} (1 - m_\mathrm{A}\omega^2 f_{\mathrm{AA}})\bar{v}_\mathrm{A} - m_\mathrm{B}\omega^2 f_{\mathrm{AB}}\bar{v}_\mathrm{B} = 0; \\ -m_\mathrm{A}\omega^2 f_{\mathrm{AB}}\bar{v}_\mathrm{A} + (1 - m_\mathrm{B}\omega^2 f_{\mathrm{BB}})\bar{v}_\mathrm{B} = 0 \end{aligned} \quad [67]$$

In order to avoid a trivial solution, the determinant of coefficients has to be zero, and this yields two natural frequencies:

$$\begin{aligned} \omega_{1,2} &= \sqrt{\frac{1}{m_\mathrm{A}\chi_{\mathrm{AB}}}} \\ \chi_{\mathrm{AB}} &= \frac{f_{\mathrm{AA}} + \vartheta f_{\mathrm{BB}}}{2} \pm \sqrt{\frac{(f_{\mathrm{AA}} - \vartheta f_{\mathrm{BB}})^2}{4} + \vartheta f_{\mathrm{AB}}^2} \\ \vartheta &= \frac{m_\mathrm{B}}{m_\mathrm{A}} \end{aligned} \quad [68]$$

Nomenclature

a	accelerations
C	transform matrix
F	force
l	length
L	Lagrangian; length
M	mass
Q	generalized forces
r	radius vector
u	displacements
v	velocities
ω_D	Dunkerleys frequency

See Plate 7.

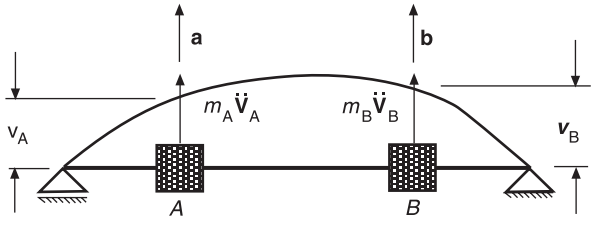


Figure 9 A simply supported beam with two concentrated masses.

See also: **Theory of vibration**, Equations of motion; **Theory of vibration**, Variational methods; **Wave propagation**, Waves in an unbounded medium.

Further Reading

Argyris JH and Kelsey S (1960) *Energy Theorems and Structural Analysis*. London: Butterworth.

Bolza O (1931) *Lectures on the Calculus of Variations*. New York: Stechert-Hafner.

Collatz L (1948) *Eigenvertprobleme und ihre numerische Behandlung*. New York: Chelsea.

D'Alembert J (1743) *Traite de Dynamique* (see also Dugas, 1955)

Dugas RA (1955) *History of Mechanics*. New York: Central Book.

Duhem PMM (1905–1906) Les Origines de la Statique (two volumes). Paris. See also: *The Evolution of Mechanics*, translated by M Cole. The Netherlands: Sijhoff of Noordhoff, Alphen an den Rijn. (Translation of *L'Evolution de la Mechanique*).

Dunkerley S (1894) On the whirling and vibration of shafts. *Philosophical Transactions of the Royal Society of London (Series A)* 185: 279–360.

Galerkin BG (1915) Bars and plates. Series in certain problems of elastic equilibrium of bars and plates. *Vestnik inzhenerov i tekhnikov* 19: 17–26.

Hart IB (1925) *The Mechanical Investigations of Leonardo da Vinci*. Chicago: Open Court

Keller EG (1947) *Mathematics of Modern Engineering*, vol. II. New York: Dover.

Lagrange L (1788) *Mechanique Analytique*. Paris. (The complete works of Lagrange were edited by Serret and Darboux, *Oeuvres de Lagrange*, 14 vol. (1867–1892)).

Lanczos C (1970) *The Variational Principles of Mechanics*, 4th edn. Toronto: University of Toronto Press.

Langhaar HL (1962) *Energy Methods in Applied Mechanics*. New York: John Wiley.

Newton I (1995: originally 1687) *The Principia*. New York: Prometheus Books.

Ritz W (1908) Ueber eine neue Methode zur Luesung gewisser Variationsprobleme der Mathematichen. *Physik J. für reine und angewandte Mathematik* 135: 1–61.

Temple G and Bickley WG (1956) *Rayleigh's Principle*. New York: Dover (by special arrangement with Oxford University Press).

Weinstock R (1952) *Calculus of Variations*. New York: McGraw-Hill.

Wittaker ET (1944) *A Treatise on the Analytical Dynamics of Particles and Rigid Bodies*, 4th edn. Dover (by special arrangement with the Cambridge University Press and the Macmillan Co. first edition 1904).

BEAMS

R A Scott, University of Michigan, Ann Arbor, MI, USA

Copyright © 2001 Academic Press

doi:10.1006/rwvb.2001.0128

Introduction

The topic treated is the transverse vibrations of single-span uniform beams with constant cross-sections. Detailed results are given for Euler–Bernoulli beams subjected to various boundary conditions. Results for a Timoshenko beam are presented for the pin–pin case.

Transverse Beam Vibrations

Euler–Bernoulli Beam Theory

Treated are external loads, cross-sections, and materials such that the motions are planar. The beam transmits a shear force, V, and a bending moment M (the x-axis is along the undeformed neutral axis of the beam and $f(x, t)$ is the external lateral force per unit length). Neglecting shear deformations and rotary inertia, the equation of motion for the homogeneous beam of cross-sectional area A is:

$$\frac{\partial^4 v}{\partial x^4} + \frac{\rho A}{EI}\frac{\partial^2 v}{\partial t^2} = \frac{f(x,t)}{EI} \qquad [1]$$

Here, v is the transverse deflection of the neutral axis, E and ρ are Young's modulus and density, respectively, and I is the area moment of inertia about the z-axis. V and M are related to v by:

$$M = EI\frac{\partial^2 v}{\partial x^2} \qquad [2]$$

$$V = -EI\frac{\partial^3 v}{\partial x^3} \qquad [3]$$

Free motions The solution to eqn [1] for free vibrations ($f = 0$) is:

$$v(x,t) = h(x)\ \sin\ (\omega t) \qquad [4]$$

where:

$$h(x) = c_1\ \sin\ \beta x + c_2 \cos \beta x + c_3 \sinh \beta x + c_4 \cosh \beta x$$
$$\beta = \left(\rho A \omega^2 / EI\right)^{1/4}$$

and c_1, c_2, c_3, c_4 are arbitrary constants. Application of boundary conditions gives an equation – the frequency equation – for the determination of β (and hence ω) and expressions for the ratios of the cs, which then yield the associated mode shapes. Some commonly occurring boundary conditions are found using eqns [2], [3], and [4]: (i) pinned edge: $h = \mathrm{d}^2h/\mathrm{d}x^2 = 0$; (ii) fixed edge: $h = \mathrm{d}h/\mathrm{d}x = 0$; (iii) free edge: $\mathrm{d}^2h/\mathrm{d}x^2 = \mathrm{d}^3h/\mathrm{d}x^3 = 0$. Results for some standard configurations follow. Tabulation of the first five natural frequencies are given, together with a sample of selected mode shapes.

1. *Pin–pin*:
   Frequency equation: $\sin \beta_n L = 0 \Rightarrow \beta_n L = n\pi$, $n = 1, 2 \ldots$.
   Mode shapes: $h_n(x) = c_n\ \sin\ (n\pi x/L)$
   The c_n are arbitrary scale factors and here and in the sequel are set equal to 1. L is the length of the beam.

2. *Fixed* $(x = 0)$ – *free*$(x = L)$:
   Frequency equation: $\cos \beta_n L \cosh \beta_n L = -1$
   Mode shapes:

$$h_n(x) = \sin\ \beta_n x - \sinh \beta_n x - \left(\frac{\sin\ \beta_n L + \sinh \beta_n L}{\cos \beta_n L + \cosh \beta_n L}\right)(\cos \beta_n x - \cosh \beta_n x).$$

See **Table 1**.

3. *Fixed–fixed*:
   Frequency equation: $\cos \beta_n L \cosh \beta_n L = 1$
   Mode shapes:

$$h_n(x) = \sin\ \beta_n x - \sinh \beta_n x + \left(\frac{\sin\ \beta_n L - \sinh \beta_n L}{\cos \beta_n L - \cosh \beta_n L}\right)(\cos \beta_n x - \cosh \beta_n x).$$

See **Table 2**.

4. *Free–Free:*
   Frequency equation: $\cos \beta_n L \cosh \beta_n L = 1$
   This is the same as in the fixed–fixed case. However the mode shapes are different.
   Mode shapes:

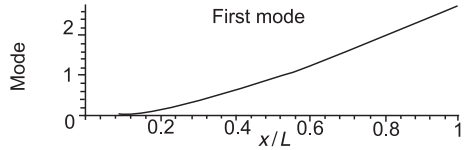
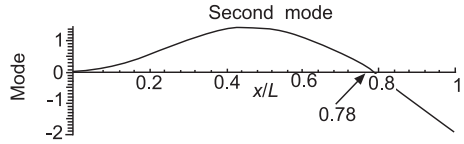
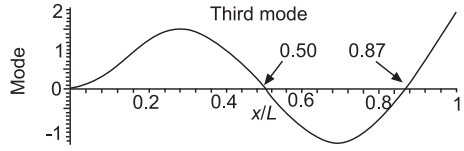
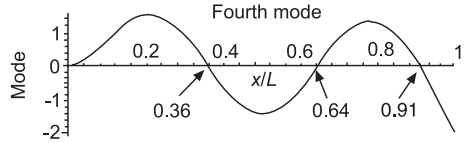
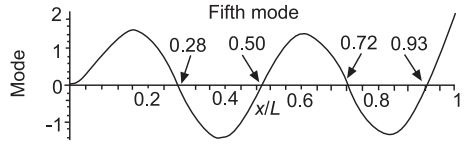
$$h_n(x) = \sin\ \beta_n x + \sinh \beta_n x + \left(\frac{\sin\ \beta_n L - \sinh \beta_n L}{\cos \beta_n L - \cosh \beta_n L}\right)(\cos \beta_n x + \cosh \beta_n x)$$

5. *Fixed* $(x = 0)$ – *pin*$(x = L)$:
   Frequency equation: $\sin\ \beta_n L \cosh \beta_n L = \sinh \beta_n L \cos \beta_n L$
   Mode shapes:

$$h_n(x) = \sin\ \beta_n x + \left(\frac{\sinh \beta_n L - \sin\ \beta_n L - \sinh \beta_n x}{\cos \beta_n L - \cosh \beta_n L}\right)(\cos \beta_n x - \cosh \beta_n x).$$

See **Table 3**.

Table 1 Roots for fixed–free case

n	$\beta_n L$	*Mode shape*
1	1.8751	
2	4.6941	
3	7.8548	
4	10.9955	
5	14.1372	

6. *Pin* (*at* $x = 0$)*–linear spring* (*at* $x = L$; *rate* k):
The boundary conditions at $x = L$ are $d^2h/dx^2 = 0, \quad d^3h/dx^3 = (k/EI)h$
Frequency equation: $(\beta_n L)^3 (\sin \beta_n L \cosh \beta_n L - \cos \beta_n L \sinh \beta_n L) = 2q_k \sin \beta_n L \sinh \beta_n L$
where q_k, which is essentially the ratio of the spring stiffness and beam stiffness, is given by $q_k = k/(EI/L^3)$. See **Table 4**.
Mode shapes:

$$h_n(x) = \sin \beta_n x + \frac{\sin \beta_n L}{\sinh \beta_n L} \sinh \beta_n x$$

Shown in **Figure 1** is a plot of the lowest root $\beta_1 L$ vs q_k. It is seen that, after $q_k > 50$, $\beta_1 L$ rapidly approaches the pin–pin value: $\beta_1 L = \pi$. For example, for $q_k = 350$, the difference is of the order of 1.4 percent.

7. *Fixed* (*at* $x = 0$)*–linear spring* (*at* $x = L$):
Frequency equation: $(1 + \cos \beta_n L \cosh \beta_n L)(\beta_n L)^3 = (\cos \beta_n L \sinh \beta_n L - \cosh \beta_n L \sin \beta_n L)\, q_k$
Mode shapes:

$$h_n(x) = \sin \beta_n x - \sinh \beta_n x - \left(\frac{\sin \beta_n L + \sinh \beta_n L}{\cos \beta_n L + \cosh \beta_n L}\right)(\cos \beta_n x - \cosh \beta_n x).$$

See **Table 5**.
Note that for $q_k = 0.1$ the difference between $\beta_1 L$ and the fixed–free root is only about 0.8 percent.

8. Pin (*at* $x = 0$) – *rotational spring (at* $x = L$; *rate* G):
The boundary conditions at $x = L$ are $d^3h/dx^3 = 0$, $d^2h/dx^2 = -(G/EI)\, dh/dx$
Frequency equation: $(-\cos \beta_n L \sinh \beta_n L + \cosh \beta_n L \sin \beta_n L)(\beta_n L) = 2q_r \cos \beta_n L \cosh \beta_n L$
where $q_r = G/(EI/L)$
Mode shapes:

$$h_n(x) = \sin \beta_n x + \frac{\cos \beta_n L}{\cosh \beta_n L} \sinh \beta_n x.$$

See **Table 6**.

Table 2 Roots for fixed–fixed case

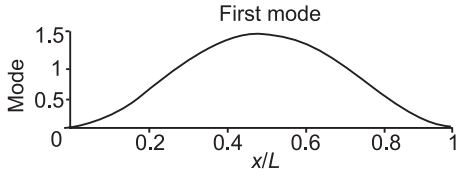
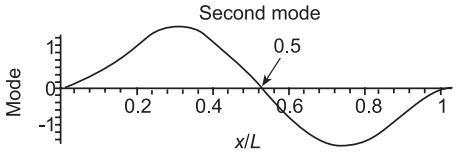
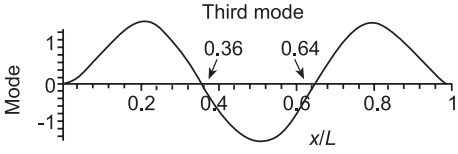
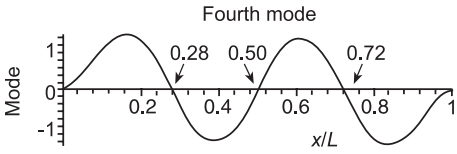
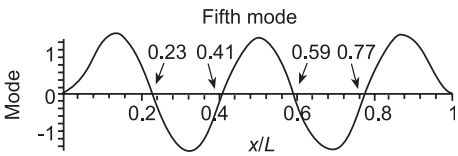
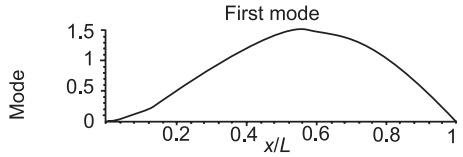
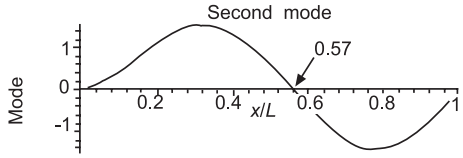
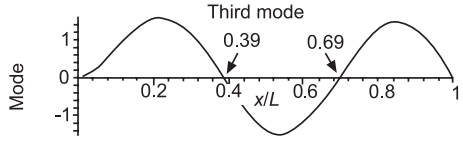
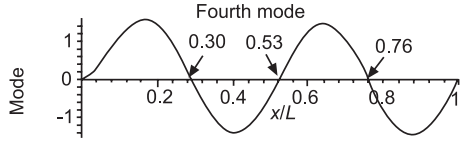
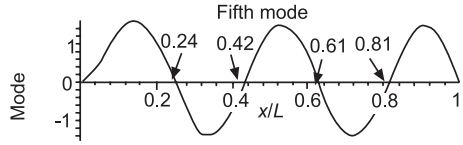
n	$\beta_n L$	*Mode shape*
1	4.7300	
2	7.8532	
3	10.9956	
4	14.1372	
5	17.2788	

Table 3 Roots for fixed–pin case

n	$\beta_n L$	*Mode shape*
1	3.9266	
2	7.0686	
3	10.2102	
4	13.3518	
5	16.4934	

9. *Fixed (at $x = 0$)–rotational spring (at $x = L$)*:
Frequency equation: $(1 + \cos\beta_n L \cosh\beta_n L)(\beta_n L) = -q_r(\cos\beta_n L \sinh\beta_n L + \cosh\beta_n L)$
Mode shapes:

$$h_n(x) = \sin\beta_n x - \sinh\beta_n x + \left(\frac{\cos\beta_n L + \cosh\beta_n L}{\sin\beta_n L - \sinh\beta_n L}\right)(\cos\beta_n x - \cosh\beta_n x)$$

See **Table 7**.
Note that for $q_r = 0.1$, the difference between $\beta_1 L$ and the lowest fixed–free root is only about 1.4 percent.

10. *Fixed (at $x = 0$)–mass loaded (at $x = L$; rigid mass m)*:
The boundary conditions at $x = L$ are $d^2h/dx^2 = 0$, $d^3h/dx^3 = -(m\omega^2/EI)h$
Frequency equation: $1 + \cos\beta_n L \cosh\beta_n L = q_m\beta_n L(\cos\beta_n L \sinh\beta_n L - \sin\beta_n L \cosh\beta_n L$
where q_m, which is the ratio of the external mass to the mass of the beam, is given by $q_m = m/\rho AL$.
Mode shapes:

$$h_n(x) = \sin\beta_n x - \sinh\beta_n x - \left(\frac{\sin\beta_n L + \sinh\beta_n L}{\cos\beta_n L + \cosh\beta_n L}\right)(\cos\beta_n x - \cosh\beta_n x).$$

See **Table 8**.
If the inertia of the beam is ignored and it is simply treated as a spring with a spring rate $k_e = 3EI/L^3$, then $\omega_1 = (k_e/m)^{1/2}$. This gives $\beta_1 L = (3/q_m)^{1/4}$. A correction to this expression is $\beta_1 L = [3/(q_m + 0.23)]^{1/4}$. The exact values of $\beta_1 L$ and the two approximate values are shown in **Figure 2** as a function of q_m. Note that for $q_m > 2$, the approximate value is very accurate.

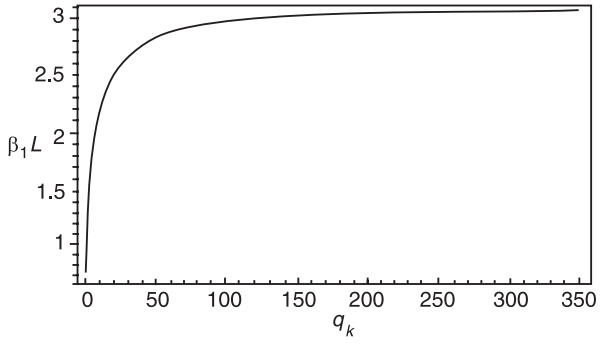


Figure 1 Lowest root vs stiffness ratio.

Table 4 Roots for pin–linear spring case

$q_k = 0.1$		$q_k = 1.0$		$q_k = 10.0$	
n	$\beta_n L$	n	$\beta_n L$	n	$\beta_n L$
1	0.7397	1	1.3098	1	2.2313
2	3.9283	2	3.9432	2	4.0954
3	7.0689	3	7.0714	3	7.0974
4	10.2103	4	10.2111	4	10.2120
5	13.3518	5	13.3522	5	13.3560

Table 5 Roots for fixed–linear spring case

$q_k = 0.1$		$q_k = 1.0$		$q_k = 10.0$	
n	$\beta_n L$	n	$\beta_n L$	n	$\beta_n L$
1	1.8901	1	2.0100	1	2.6389
2	4.6951	2	4.7038	2	4.8757
3	7.8550	3	7.8568	3	7.0974
4	10.9956	4	10.9963	4	11.0031
5	14.1372	5	14.1375	5	14.1407

Table 6 Roots for pin–rotational spring case

$q_r = 0.1$		$q_r = 1.0$		$q_r = 10.0$	
n	$\beta_n L$	n	$\beta_n L$	n	$\beta_n L$
1	0.7314	1	1.1916	1	1.5007
2	3.95132	2	4.1197	2	4.5298
3	7.08250	3	7.1901	3	7.5856
4	10.2199	4	10.2985	4	10.6609
5	13.3592	5	13.4210	5	13.7503

Table 7 Roots for fixed–rotational spring case

$q_r = 0.1$		$q_r = 1.0$		$q_r = 10.0$	
n	$\beta_n L$	n	$\beta_n L$	n	$\beta_n L$
1	1.9022	1	2.0540	1	2.2912
2	4.7156	2	4.8686	2	5.2887
3	7.8673	3	7.9657	3	8.3531
4	11.0045	4	11.0782	4	11.4321
5	14.1442	5	14.2029	5	14.5243

11. *Fixed (at $x = 0$)–rigid rotor (at $x = L$; mass moment of inertia J)*:
The boundary conditions at $x = L$ are $d^2h/dx^2 = 0$, $d^2h/dx^2 = (J\omega^2/EI)\, dh/dx$
Frequency equation: $1 + \cos\beta_n L \cosh\beta_n L = q_J(\beta_n L)^3(\sinh\beta_n L \cos\beta_n L + \sin\beta_n L \cosh\beta_n L)$
where $q_J + J/\rho AL^3$

Mode shapes:

$$h_n(x) = \sin\ \beta_n x - \sinh \beta_n x + \left(\frac{\cos \beta_n L + \cosh \beta_n L}{\sin\ \beta_n L + \sinh \beta_n L}\right)(\cos \beta_n x - \cosh \beta_n x).$$

See **Table 9**.

Forced motions For $f \neq 0$ in eqn [1], the steady-state response can be obtained using modal analysis. With the exception of boundary conditions involving mass and inertia loads, the mode shapes are orthogonal in the sense:

$$\int_0^L h_n(x)h_m(x)\,\mathrm{d}x = \begin{cases} 0, & n \neq m \\ I_n \equiv \int_0^L h_n^2(x)\,\mathrm{d}x, & n = m \end{cases}$$

Using this property, the steady-state response is given by:

$$v(x,t) = \sum_{j=1}^{\infty} \eta_j(t) h_j(x)$$

where the $\eta_j(t)$ are determined from:

$$\ddot{\eta}_j + \omega_j^2 \eta_j = \frac{1}{\rho A I_j} \int_0^L f(x,t) h_j(x)\,\mathrm{d}x$$

the ω_j being the natural frequencies of the system. For example if $f(x, t) = f_0 \sin \omega t$, f_0 constant:

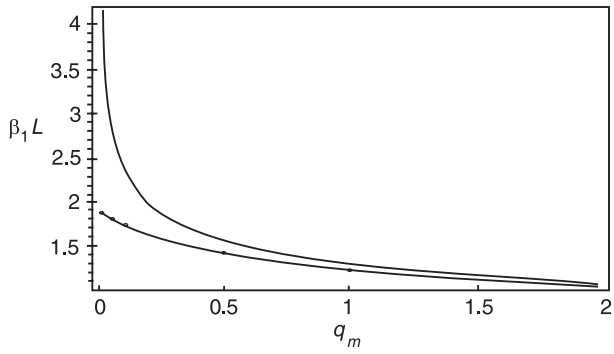


Figure 2 Lowest root vs mass ratio.

$$\ddot{\eta}_j + \omega_j^2 \eta_j = \frac{f_0}{\rho A I_j} \sin\ \omega t \int_0^L h_j(x)\,\mathrm{d}x \equiv \Theta_j f_0 \sin\ \omega t$$

Thus:

$$\eta_j = \frac{f_0 \Theta_j}{\omega_j^2 - \omega^2} \sin\ \omega t$$

and:

$$v(x,t) = f_0 \left\{ \sum_{j=1}^{\infty} \frac{\Theta_j}{\omega_j^2 - \omega^2} h_j(x) \right\} \sin\ \omega t$$

clearly showing the occurrence of resonances at $\omega = \omega_j$.

Timoshenko Beam Theory

In Timoshenko beam theory, rotary inertia and deflections due to shear are taken into account. The coupled equations of motion for v and the bending slope ψ are (lateral force = 0):

Table 8 Roots for fixed–mass loaded case

$q_m = 0.01$		$q_m = 0.05$		$q_m = 0.1$		$q_m = 0.5$		$q_m = 1$		$q_m = 2$	
n	$\beta_n L$	n	$\beta_n L$	n	$\beta_n L$	n	$\beta_n L$	n	$\beta_n L$	n	$\beta_n L$
1	1.8568	1	1.7912	1	1.7227	1	1.4200	1	1.2479	1	1.0762
2	4.6497	2	4.5127	2	4.3995	2	4.1111	2	4.0311	2	3.9826
3	7.7827	3	7.5863	3	7.4511	3	7.1903	3	7.1341	3	7.1027
4	10.8976	4	10.6609	4	10.5218	4	10.2984	4	10.2566	4	10.2340
5	14.0149	5	13.7503	5	13.6142	5	13.4210	5	13.3878	5	13.3701

$$A\rho\frac{\partial^2 v}{\partial t^2} - A\kappa G\left(\frac{\partial^2 v}{\partial x^2} - \frac{\partial \psi}{\partial x}\right) = 0 \qquad [5]$$

$$EI\frac{\partial^2 \psi}{\partial x^2} + A\kappa G\left(\frac{\partial v}{\partial x} - \psi\right) - I\rho\frac{\partial^2 \psi}{\partial t^2} = 0 \qquad [6]$$

where G is the shear modulus and κ is the Timoshenko shear coefficient. Vibration solutions to eqns [5] and [6] are of the form: $v = h(x)\sin\omega t$, $\psi = g(x)\sin\omega t$, where:

$$h(x) = c_1\cos\delta s^2 x/L + c_2\ \sin\ \delta s^2 x/L + c_3\cosh\gamma s^2 x/L + c_4\sinh\gamma s^2 x/L \qquad [7]$$

$$Lg(x) = c_1\Gamma_t\sin\ \delta s^2 x/L - c_2\Gamma_t\cos\delta s^2 x/L + c_3\Gamma_h\sinh\gamma s^2 x/L + c_4\Gamma_h\cosh\gamma s^2 x/L \qquad [8]$$

$$\delta,\gamma = \left\{\pm\frac{1}{2}\left(s_h^2 + R^2\right) + \frac{1}{2}\left[\left(S_h^2 - R^2\right)^2 + \frac{4}{s^4}\right]^{1/2}\right\}^{1/2},$$
$$s = \beta L,\ R^2 = \frac{I}{AL^2},\quad s_h^2 = \frac{EI}{\kappa GAL^2} = \frac{ER^2}{\kappa G}$$
$$\Gamma_t = s^2\left(s_h^2 - \delta^2\right)/\delta,\quad \Gamma_h = s^2\left(s_h^2 + \gamma^2\right)/\gamma$$

In arriving at the above solutions it has been assumed that:

$$\left[\left(s_h^2 - R^2\right)^2 + \frac{4}{s^4}\right]^{1/2} > \left(s_h^2 + R^2\right)$$

If this condition (which should be monitored in numerical work) is not true, then the terms involving c_3 and c_4 in eqns [7] and [8] have to be replaced by:

$$c_3\cos\varepsilon s^2 x/L + c_4\ \sin\ \varepsilon s^2 x/L,$$
$$c_3\Gamma_n\ \sin\ \varepsilon s^2 x/L - c_4\Gamma_n\cos\varepsilon s^2 x/L$$

where:

$$\varepsilon = \left\{\frac{1}{2}\left(s_h^2 + R^2\right) - \frac{1}{2}\left[\left(s_h^2 - R^2\right)^2 + \frac{4}{s^4}\right]^{1/2}\right\}^{1/2}$$
$$\Gamma_n = s^2\left(s_h^2 - \varepsilon^2\right)/\varepsilon$$

Some common boundary conditions are: (i) pinned edge: $h = \mathrm{d}g/\mathrm{d}x = 0$; (ii) fixed edge: $h = 0, g = 0$; (iii) free edge: $\mathrm{d}g/\mathrm{d}x = 0, \mathrm{d}h/\mathrm{d}x - Lg = 0$.

Pin–Pin

- Frequency equation: $\sin\delta s^2 = 0$.
- Mode shapes:

$$h_n(x) = c_n\sin\delta s^2 x/L - \left(\frac{\sin\delta s^2}{\sinh\gamma s^2}\right)\sinh s^2\gamma x/L$$

Results for the Timoshenko beam are not universal; definite properties and geometries have to be specified. For a solid circular beam of radius a, $R = a/L$ and κ is taken to be 0.75. For steel $E/G = 2(1+\nu)$, ν being Poisson's ratio, taken to be 0.33. **Figure 3** shows a plot of the ratio of the lowest root for the Timoshenko beam divided by that for the Euler beam as a function of the aspect ratio R. For large L, there is excellent agreement between the two roots. Note that for $R = 0.2$, there is about a 20% drop-off, the Euler root being the smaller.

Table 9 Roots for fixed–inertia loaded case

$q_J = 0.01$		$q_J = 0.05$		$q_J = 0.1$		$q_J = 0.5$		$q_J = 1$		$q_J = 2$	
n	$\beta_n L$	n	$\beta_n L$	n	$\beta_n L$	n	$\beta_n L$	n	$\beta_n L$	n	$\beta_n L$
1	1.8396	1	1.7075	1	1.5771	1	1.1597	1	0.9873	1	0.8357
2	3.7818	2	2.8882	2	2.6482	2	2.4219	2	2.3932	2	2.3791
3	5.8267	3	5.5602	3	5.5286	3	5.5039	3	5.5009	3	5.4993
4	8.7207	4	8.6550	4	8.6472	4	8.6409	4	8.6402	4	8.6398
5	11.8122	5	11.7871	5	11.7840	5	11.7816	5	11.7813	5	11.7811

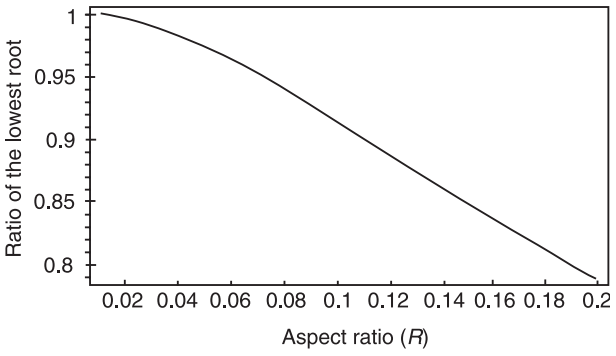


Figure 3 Timoshenko/Euler lowest roots vs aspect ratio.

Nomenclature

a	radius
A	cross-sectional area
E	Young's modulus
G	shear modulus
I	inertia
M	bending moment
R	aspect ratio
v	transfer deflection
V	shear force
ψ	bending slope
ρ	density
κ	Timoshenko shear coefficient

See Plate 8.

See also: **Finite element methods**; **Shock**.

Further Reading

Blevins RD (1984) *Formulas for Natural Frequency and Mode Shape*. Malabar, FL: Krieger.

Cook RD, Malkus DS, Plesha ME (1989) *Concepts and Applications of Finite Element Analysis*, 3rd edn. New York: John Wiley.

Harris CM (ed.) (1996) *Shock and Vibration Handbook*, 4th edn. New York: McGraw-Hill.

Huang, TC (1961) The effect of rotatory inertia and of shear deformation on the frequency and normal mode equations of uniform beams with simple end conditions. *Journal of Applied Mechanics, Transactions of the ASME* 579–584.

Zu JW, Han RPS (1992) Natural frequencies and normal modes of a spinning Timoshenko beam with general boundary conditions. *Journal of Applied Mechanics, Transactions of the ASME* 59: 197–204.

BEARING DIAGNOSTICS

C J Li and K McKee, Rensselaer Polytechnic Institute, Troy, NY, USA

Copyright © 2001 Academic Press

doi:10.1006/rwvb.2001.0200

Roller Bearing

Figure 1A illustrates the cross-section of an angular contact ball bearing. It shows the angle of contact, and the diameters of outer race, rollers, inner race and pitch circle. **Figure 1B** illustrates the cross-section of a taper roller bearing. It shows the angle o'f contact, and the diameters of outer race (cup), inner race (cone), and rollers. The primary excitations of vibration are the contact forces between the rollers and the raceways, and the rollers and the cage. The frequencies of these contacts are directly related to the roller passing frequency on the raceways, the roller spinning frequency, and the cage spinning frequency which can be theoretically estimated with the equations in **Table 1**.

Failure Modes

Bearing failure modes include corrosion, wear, plastic deformation, fatigue, lubrication failures, electrical damage, fracture, and incorrect design. Out of these, classical localized defects result from fatigue, and certain distributed defects have fairly distinct vibration patterns which will be detailed below. However, the vibration patterns of other failure modes are, in general, not easy to predict, let alone detect and diagnose at onset. While some of them do eventually lead to localized defects, others give almost no vibration warning and therefore call for means other than vibration analysis.

Localized Defects

The most common failure mode of a properly installed and operated rolling element bearing is localized defects such as fatigue spall, which occur when a sizable piece of material on the contact surface is dislodged during operation, mostly by fatigue

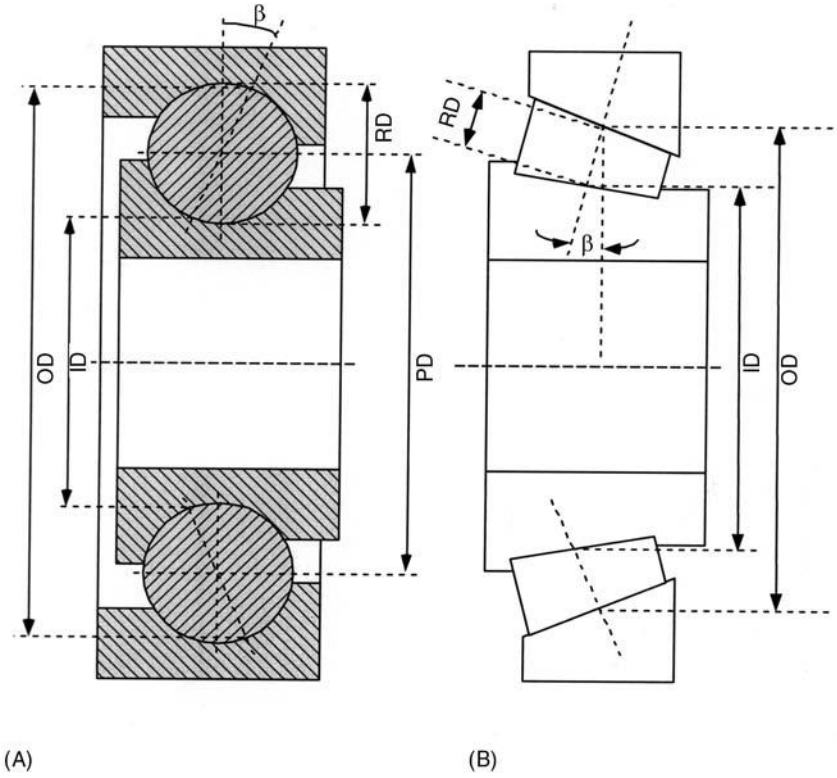


Figure 1 Cross-section. (A) Ball bearing; (B) taper roller bearing.

cracking under cyclic contact stressing. In addition, the bearing cage can fail due to overload or poor lubrication. Thus, a failure alarm for a rolling element bearing is often based on the detection of the onset of localized defects.

Signature-generating Mechanism

During bearing operation, wide-band impulses are generated when rollers pass over a defect at a frequency determined by shaft speed, bearing geometry, and defect location. The frequency, which is often termed characteristic defect frequency, can be estimated as f_{rpi}, f_{rpo} and $2xf_{rs}$ (**Table 1**) for an inner race, outer race and roller defect, respectively. Some of the vibration modes of the bearing and its surrounding structure, or even the sensor, will be excited by the periodic impulses, and a distinct signature will be generated by such ringings. The leading edge of each ringing usually comprises a sharp rise that corresponds to the impact between a roller and the defect. The ringing then decays due to damping. (It is like driving over a pothole.) Therefore, the signature of a damaged bearing consists of exponentially decaying vibration ringings that occur quasiperiodically at the

Table 1 Important bearing frequencies

	Ball bearing	*Taper roller bearing*
Inner race roller passing frequency (f_{rpi})	$\frac{n(f_o - f_i)(1 + (RD/PD)\cos\alpha)}{2}$	$n(f_o - f_i)\frac{OD}{OD + ID}$
Outer race roller passing frequency (f_{rpo})	$\frac{n(f_o - f_i)(1 - (RD/PD)\cos\alpha)}{2}$	$n(f_o - f_i)\frac{ID}{OD + ID}$
Cage rotating frequency (f_c)	$\frac{f_i(1 - (RD/PD)\cos\alpha)}{2} + \frac{f_o(1 + (RD/PD)\cos\alpha)}{2}$	$\frac{f_i \times ID + f_o \times OD}{OD + ID}$
Roller spinning frequency (f_{rs})	$\frac{(f_o - f_i)}{2}\frac{PD}{RD}(1 - ((RD/PD)\cos\alpha)^2)$	$(f_o - f_i)\frac{ID}{RD}\frac{OD}{OD + ID}$

n = number of rollers, f_o = outer race rotating speed (rps), f_i = inner race rotating speed (rps), OD = outer race diameter, ID = inner race diameter, RD = roller diameter, PD = pitch circle diameter, α = contact angle.
These equations were derived under the assumption that it is pure rolling contact (no slipping, skidding, etc.) and perfect geometry even under load. One would expect some deviations under actual conditions.

characteristic defect frequency. **Figure 2** shows an example of bearing vibration which has the distinct pattern of periodic ringings. It is sometimes considered as the resonance being amplitude-modulated at the characteristic defect frequency. However, this pattern will begin to fade and become more random as localized defects develop around the races and the rollers. (Then, it is like driving a car on a gravel road.)

The above model does not include many factors such as: radial loading, variation due to transmission path between the signal source and the transducer, misalignment, unbalance, pre-load, and manufacturing defects.

The dominant effect of radial loading is modulation. Assuming a stationary outer race, an inner-race defect rotates around at shaft frequency. Under a radial load, the bearing vibration will be modulated periodically at shaft frequency as the defect goes in and out of the loading zone. For a defect on a roller revolving at the cage frequency, a radial load will result in a modulation at cage frequency. For a defect on the stationary outer race, no modulation will be produced.

Cage fault is different from other localized defects in its signal generating mechanism. It does not usually produce sharp impacts that excite narrow-band bearing resonance. When a cage develops a weak point such as deformation or breakage, a modulation of the wide-band bearing vibration at the cage's rotating speed is common.

Diagnostic Algorithms

Statistical parameters When periodic ringings due to a localized defect become dominant, bearing vibration becomes impulsive. The following statistical parameters have been used as diagnostic parameters for detecting bearing localized defects. For a discrete vibration signal, $x(n)$, let N and $\bar{x}$ denote the length and the mean, respectively. Then:

$$\text{Peak-to-valley} = \max\left(x(n)\right) - \min\left(x(n)\right) \quad [1]$$

$$\text{RMS} = \sqrt{\left(\frac{1}{N}\sum_{i=1}^{N}\left(x(i)-\bar{x}\right)^2\right)} \quad [2]$$

$$\text{Crest Factor} = \frac{\text{Peak to valley}}{\text{RMS}} \quad [3]$$

$$\text{Kurtosis} = \frac{\frac{1}{N}\sum_{i=1}^{N}\left(x(i)-\bar{x}\right)^4}{\text{RMS}^4} \quad [4]$$

$$\begin{aligned}&\text{probability density function}\\ &p(x \le x(n) \le x+\Delta x)\\ &= \frac{\text{No. of } x(n) \text{ between } x \text{ and } (x+\Delta x)}{N}\end{aligned} \quad [5]$$

A common drawback of these time domain techniques is that they cannot provide information about the location of a defect because they do not take advantage of the characteristic defect frequencies. While the peak-to-valley value is expected to increase due to the periodic ringings, a single noise spike can throw it off and it is also sensitive to changes in operating conditions such as loading and speed. The root mean square (RMS) is not sensitive at the initial stage of damage because a few short-lived, not very large ringings would not change the overall RMS much and operating conditions also affect it. The crest factor provides a normalized peak-to-valley which should be somewhat less sensitive to changes in operation conditions. Kurtosis' quadruple power emphasizes larger amplitudes in defect-induced ringings and therefore is more sensitive to bearing defects than the RMS. The probability density function is expected to have larger tails for a damaged bearing. However, kurtosis, crest factor, and probability density function will fall back to undamaged levels as localized defects spread around races and rollers.

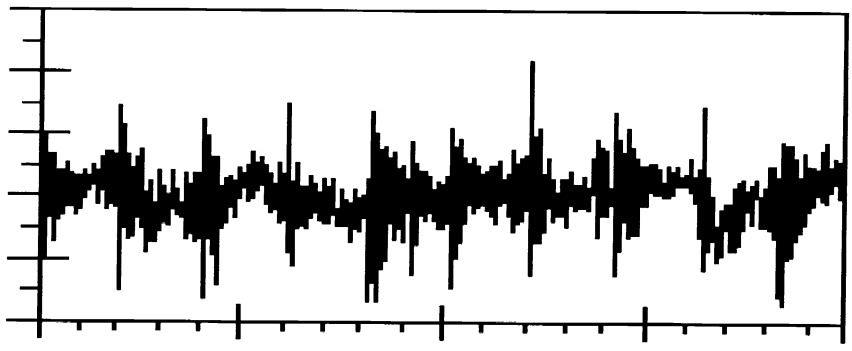


Figure 2 Vibration signal of a bearing with an outer-race defect.

In general, the success of these parameters depends on finding a frequency band that is dominated by bearing ringings. Otherwise, they indicate a change in something other than the condition of the bearing. It was reported that good results can be obtained from higher frequency bands such as 10–20 kHz and 20–40 kHz, where the structure resonance is usual. While it is easy to find some band that works to some extent, the optimal result is difficult to obtain because there is no simple way to predict a bearing structure's natural frequencies, and which one will be excited.

Although trending can be used with these statistical parameters, some of them have been toted as single-shot diagnostic variables that have an absolute threshold and therefore do not need historical data. For example, kurtosis is said to have a value of about 3.0 for a relatively random vibration from an undamaged bearing. Any value significantly higher than 3, say 4.5, is therefore considered as a sign of a bearing fault. Crest factor and probability density function are sometimes considered as single-shot variables. Realistically, these variables are just too simple to offer single-shot diagnosis under all circumstances.

Shock pulse counting This method takes advantage of transducer resonance. When a roller runs over a localized defect, the impact produces a pressure wave. When this pressure wave reaches the transducer, it frequently rings the resonance of the transducer. The number of vibration peaks above a certain threshold during a fixed length of time is then used as a damage indicator. Typically, the transducer is selected to have a resonance frequency between 25 and 40 kHz to avoid the usual machine noise. Due to its simplicity, it is implemented in a couple of off-the-shelf bearing monitoring systems. However, there are few theoretical guidelines about setting the threshold and it has limited use when there are sources of shock pulses other than a roller bearing. Furthermore, as a time domain method, it cannot determine the location of the defect.

High-frequency resonance technique (HFRT) This is probably one of the best known bearing diagnostic algorithms: it is also known as amplitude demodulation, demodulated resonance analysis, and envelope analysis. The technique band-pass filters a bearing signal to remove low-frequency mechanical noise and then estimates the envelope of the filtered signal. (Enveloping can be accomplished with a rectifier followed by a smoothing operation, or a squaring operation followed by an analog or digital low-pass filter. In addition, the Hilbert transform can also be used if a computer is available.)

The periodicity of the envelope signal, like the one shown in **Figure 3**, is then estimated by spectral analysis or autocorrelation, and compared with the characteristic defect frequencies. If a match is found, the bearing is declared to be damaged.

Obviously, this technique will give the best result if the passing band is chosen to include one or more excited resonances. For simple machines, good results can often be obtained with a fixed passing band with low cut-off placed between 5 and 10 kHz and high cut-off between 25 and 40 kHz. For complex machines such as helicopter transmission, selecting a passing band to include resonances and avoid gear meshing harmonics may not be easy. Varying speed, and therefore meshing harmonics, further compounds the problem.

Synchronized averaging This algorithm can be used as a preprocessing technique to enhance the signal-to-noise ratio. The technique consists of first

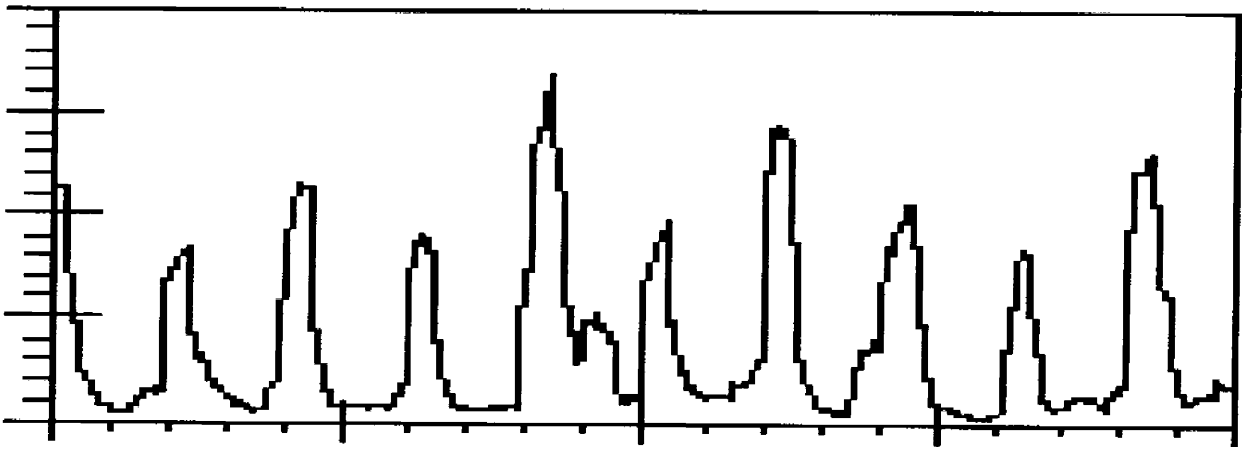


Figure 3 Envelope of the band-pass-filtered signal in **Figure 2**.

calculating the period of repeated ringings by inverting the characteristic defect frequency and then ensemble averaging consecutive segments of a bearing vibration, each one period long. Signals that cannot fit full waves in the period will be attenuated while signals that do will remain. In the original work, only the RMS of the average was calculated. Other diagnostic algorithms can certainly be applied as appropriate.

Cepstral analysis As shown in **Figure 2**, localized defects produce periodic ringings. The spectrum of such a vibration contains a characteristic defect frequency and its harmonics with the larger magnitude around the excited resonance(s). Since the energy of the bearing vibration is spread across a wide frequency band, it can easily be buried by noise. Therefore, spectral analysis will not be effective. The cepstrum, which was initially defined as the 'power spectrum of the logarithmic power spectrum', is useful in detecting spectrum periodicities, such as families of harmonics of bearing defect frequencies, by reducing a whole family of harmonics into a single cepstral line:

$$\begin{aligned} x_c(\tau) &= F\left[\ln|X(\omega)|^2\right] \quad \text{(original definition)} \\ \text{or:} \quad &= F^{-1}[\ln[X(\omega)]] \text{ where } X(\omega) = F(x(t)) \end{aligned} \qquad [6]$$

Cepstral analysis has been shown to be very effective in bearing diagnosis. However, it has not received much acceptance, perhaps because it is more difficult to compute and interpret than the output of, say, the HFRT.

Wavelet transform For a continuous signal $x(t)$, the wavelet transform (WT) is defined as:

$$W_x(a,b) = \int g^{*(a,b)}(t)x(t)\,\mathrm{d}t \qquad [7]$$

where * denotes the complex conjugate, and $g(t)$ represents the mother wavelet, e.g.:

$$\begin{aligned} g(t) &= \exp(-\sigma t)\ \sin(\omega_0 t) \quad \text{for } t = 0 \\ \text{and:} \quad g(t) &= -g(-t) \quad \text{for } t < 0 \\ g^{(a,b)}(t) &= \frac{1}{\sqrt{a}} g\left(\frac{t-b}{a}\right) \end{aligned} \qquad [8]$$

where a is the dilation parameter which defines a baby wavelet for a given value, and b is the shifting parameter.

For a given a, carrying out WT over a range of b is like passing the signal through a filter whose impulse response is defined by the baby wavelet. Therefore, one may consider WT as a bank of band-pass filters defined by a number of a's. The salient characteristic of the WT is that the width of the passing band of the filters is frequency-dependent. Therefore, the WT can provide a high-frequency resolution at the low-frequency end while maintaining good time localization at the high-frequency end. This is advantageous for processing transient bearing ringings.

When applied to a bearing signal as a preprocessing tool, the passing band of one or more of the filters could overlap with some of the resonances that are being excited by the roller defect impacts. This results in an enhanced signal-to-noise ratio. For example, **Figure 4** shows a bearing vibration measured from a roller-damaged bearing. (Note that it is already high-pass-filtered.) The periodic ringings are not obvious. **Figure 5** is the result of WT with one of the baby wavelets. The periodic ringings can be seen more readily and therefore easily identified by, say, an envelope analysis.

By breaking up a broad-band bearing signal into a number of narrow-band subsignals and then scanning them for evidence of bearing defect, WT avoids the risk of selecting a wrong band that does not include any resonance and then missing the defect. The price is that one has to repeat the same bearing diagnostic algorithm on more than one subsignal.

Time–frequency distribution for bearing monitoring The periodic ringings can be revealed or accentuated with time–frequency distributions which give an account of how energy distribution over frequencies changes from one instant to the next. Examples of such distributions include the spectrogram (short-time Fourier transform), Wigner–Ville distribution, and Choi–Williams distribution (CWD).

Figure 6 is a CWD of a bearing signal. Horizontal stripes correspond to the periodic ringing due to a ball passing on an outer-race defect. It is clear that the resonance occurs at 10, 18, and 22 kHz. When compared to WT, which has a better time localization of the ringing, CWD gives a better frequency resolution at high frequencies at a higher computational cost.

The drawback of time–frequency distributions is the medium-to-high computational cost and two-dimensional image-like output, which is usually troublesome for a computer to interpret.

Bicoherence As shown in **Figure 2**, localized defects produce repetitive ringings. The spectrum of such a vibration contains a characteristic defect frequency and its harmonics, with the largest magnitude around



Figure 4 Bearing vibration with inner-race defect.



Figure 5 Wavelet transform of the vibration in **Figure 4**.

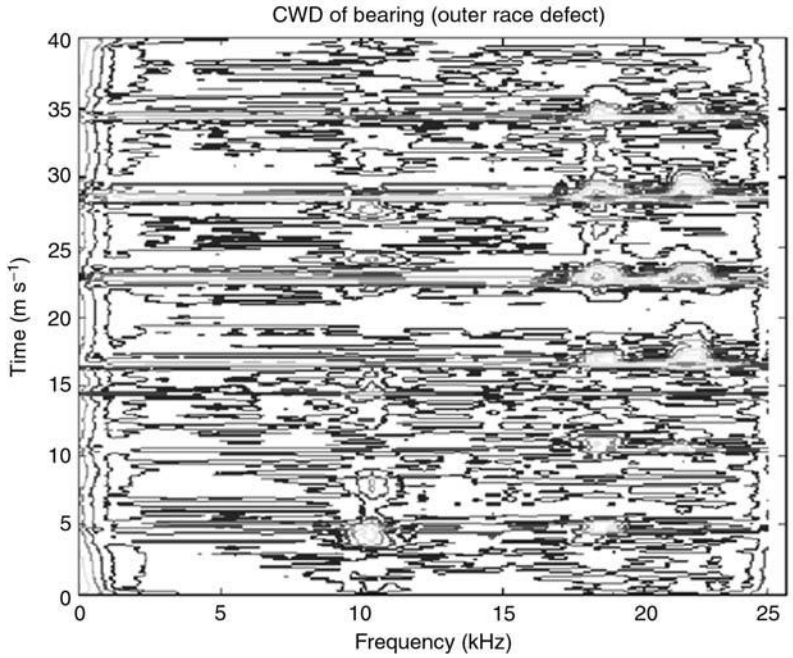


Figure 6 Choi–Williams distribution of bearing vibration with outer-race defect.

the excited natural frequencies. These harmonics are the Fourier components of a periodic signal, and therefore have a fixed phase relationship with one another.

Bicoherence, defined below, quantifies the phase dependency among the harmonics of the characteristic defect frequency, which increases when a bearing is damaged:

$$b^2(f_1, f_2) = \frac{|E[X(f_1)X(f_2)X^*(f_1+f_2)]|^2}{E\left[|X(f_1)X(f_2)|^2\right]E\left[|X(f_1+f_2)|^2\right]} \quad [9]$$

where $E[\,]$ denotes the expected value, and $X(f_i)$ denotes the complex frequency component from the Fourier transform. In this case, f_i would be one of the harmonics of the characteristic defect frequency. For example, f_1 and f_2 can be chosen as f_{rpi} and $2f_{rpi}$.

Because bicoherence is based on phase, it works even when the ringings are less than dominant. For example, **Figure 7** shows bearing vibration signals from a good bearing and another with a damaged roller. Although one cannot see the repeated ringing patterns in the bad bearing signal, bicoherence plots can tell them apart (**Figure 8**). While bicoherence outperfoms traditional algorithms such as HFRT, it

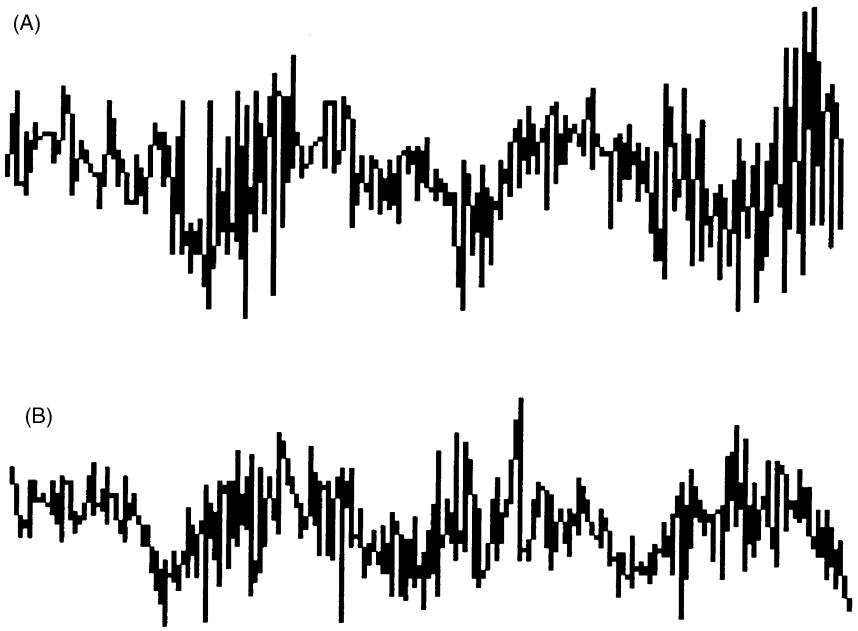


Figure 7 Bearing vibrations. (A) Good bearing signal; (B) bad bearing signal.

is one of the most expensive algorithms in terms of computation cost and data length.

Cage fault When a cage develops a weak point such as deformation or breakage, a modulation of the wide-band bearing vibration at the cage's rotating frequency is common. Traditional bearing diagnostic algorithms such as narrow-band envelope analysis are not effective in detecting this kind of wide-band modulation. One way to determine if a modulation is happening at the cage rotating frequency is to perform a synchronized average, at the cage rotating period, on the envelope of the bearing vibration. The average is then examined for once-per-cage-rotation phenomena. Alternatively, bandwidth-weighted demodulation can be used.

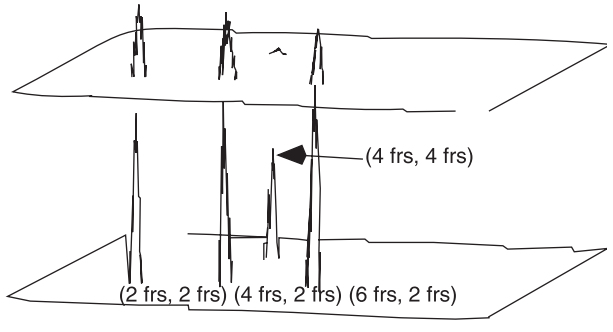


Figure 8 Bicoherence values of good bearing and roller-damaged bearings at four frequency pairs.

Summary of localized defect diagnostic algorithms A significant number of the afore-mentioned algorithms look for the distinct pattern of repeated ringings (**Figure 2**) associated with the onset and the early stage of damage. Consequently, they suffer from the limitation that they will fall back to the undamaged levels as localized defects spread and the distinct pattern fades away as rollers strike different local defects almost simultaneously all the time. In other words, they do not trend well while damage evolves and this is a problem for the prognosis of bearing life. In addition, since a resonance excited at the onset of a defect may no longer be excited at a later stage, using a band-pass filter to zoom on to a resonance can have its downside of missing another defect-excited resonance later.

Distributed Defects

In addition to localized defects, distributed defects such as off-size rollers and waviness of components are another class of bearing problems. While distributed defects are not generally failures *per se*, they often lead to excessive contact forces and vibrations which in turn lead to premature failures. Fortunately, analysis of vibration spectra is often adequate to diagnose this kind of faults.

A bearing without any distributed defect is considered first. Under a thrust load, roller forces act on the races to produce a deflection. **Figure 9** shows how roller forces act on the inner race. As the rollers and races rotate, the forces and the deflection become periodic. Thus, a vibration sensor located at the inner race would sense vibrations at f_{rpi} and its harmonics. Similarly, a sensor at the outer race would sense vibration at f_{rpo} and its harmonics. **Table 2** gives the frequency associated with a number of conditions while the inner race is stationary.

Table 2 Frequencies associated with various distributed defects

Conditions	*Frequencies (sensor at inner race)*
One roller off size (k: 1, 2, ... etc.)	$k(f_{rpi}/n)$
Misaligned outer race	Side band $k(f_{rpi}/n)\pm f_o$
Waviness in outer race (m = number of full waves around the circumference)	Side band $k(f_{rpi}/n)\pm mf_o$

From Meyer *et al.* (1980).

Journal Bearing

Figure 10 shows the three basic parts to a journal bearing: the outer housing, the journal, and the lubricant. The outer housing is a cylindrical shaft, which contains a hollow core large enough to create a close fit between itself and the journal. In addition to confining the path of the journal's orbit, it provides radial support to the journal through direct contact or by aiding in the creation of the oil wedge. A small clearance space between the outer housing and the journal is necessary: in order to assist in the assembly of the journal and the bearing, to provide space for the addition of the lubricant, to accommodate thermal expansion of the journal, and to anticipate any journal misalignment. Within this small clearance space resides the lubricant which provides the basic function of lubricating the journal and outer housing contact, as well as producing the load-carrying capability of the journal bearing and possibly attenuating the vibrations of the rotors. This load-carrying capability is a result of the pressure that is developed by the viscous effects within the thin film lubricant. A more complex journal bearing that is commonly used is the tilt-pad journal bearing. This type of journal bearing contains the same components as the simple bearing, with the added feature of tilt pads. Tilt pad journal bearings are used for their innate ability better to handle rotor-dynamic instability problems; however, they provide less damping than the simple bearing. Consequently, if vibrations occur due to other sources aside from the bearing, then the amount of damping provided by the bearing may arise as an issue.

Diagnostic Algorithms

Unlike roller bearings, whose vibration has simple and distinct patterns that can mostly be predicted from the geometry, journal bearings, while simple-looking, are rather complicated in their dynamics. Since journal bearings are only one part of a rotating machine, the analysis of the bearings must take into consideration vibrations caused by the flexible journal, fluid and rotor dynamics, and any outside sources of vibration acting on the system. Consequently, this type of analysis usually becomes complicated, and results in no clear vibration patterns associated with most of the failure modes. This is why the tools for the diagnosis of a journal bearing stagger are lacking.

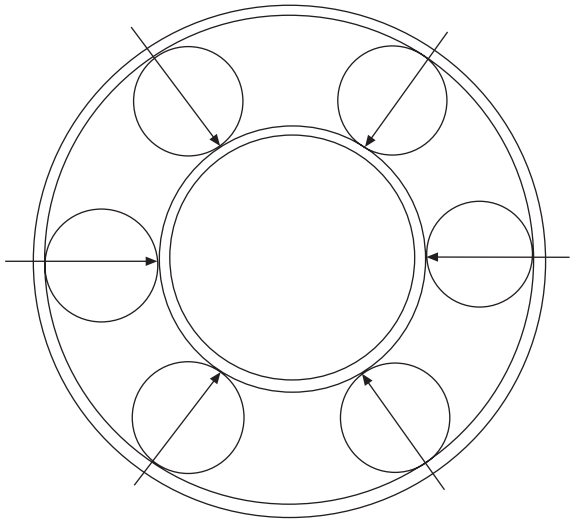


Figure 9 Roller forces acting on inner race.

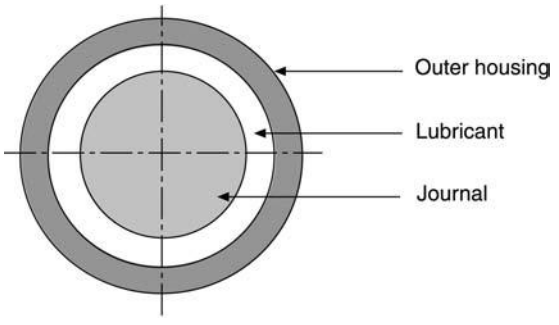


Figure 10 Simple journal bearing.

'Whirl' refers to a circulating path the journal takes within the bearing resulting from large vibrations of the journal. Proximity sensors can be placed at perpendicular positions to the orbit of the shaft. These sensors would allow the monitoring of the position of the orbit, and notify the user of the misalignment, the amount of clearance existing, and the range of motion of the journal. The user would be warned if the motion of the journal exceeds a certain allowable envelope of motion.

An accelerometer can be placed on the outer housing to measure the frequency and amplitude of the housing vibrations which do not have a straightforward relationship with journal whirl. Based on the vibrations taken from the bearing's normal conditions, abnormal conditions can be detected. For example, in cases where the bearing's housing is supported on springs rather than secured directly to an immobile object, chaotic motion is found at intermediate speed ranges, and disappears at low and high speeds. At low and high speeds, different distinct subharmonic frequency components in the *X*- and *Y*-direction of the bearing are excited. However, during intermediate speeds, there is a rich spectrum of excited frequencies in both directions, which results in vibrations with comparatively large amplitudes that may induce fatigue failure.

Misalignment occurs when the journal's centerline does not coincide with the bearing's centerline. This is caused by combinations of rotational movements about a pivot point in the longitudinal cross-section and translational movements of the journal in the vertical and horizontal axis in the radial cross-section. Misalignment results from assembling or manufacturing errors, off-centric loads, shaft deflection such as elastic and thermal distortions, and externally imposed misaligned moments. A side-effect of the misalignment is the creation of a converging wedge geometry, known as the oil wedge, between the journal and the outer housing. In addition, misalignment contributes to the whirl by changing the threshold speed at which instability occurs. It is able to change the journal bearing's load-carrying capability, increase its frictional power loss, alter the fluid film thickness, change the dynamic characteristics such as system damping and critical speeds, and modify the vibrations as well as the overall stability of the system. One of the most significant effects of misalignment is its ability to produce a substantial amount of vibration when the frequency of the rotor's vibrations is a harmonic of the rotational speed of the journal.

Hot spots found on a journal, which ultimately develop into thermal bends, are results of the Newkirk effect. These hot spots are quite common, resulting from the contact of the rotor with the bearing or due to a temperature difference across the diameter of the journal. In the latter case, the temperature difference is a result of the differential shearing in the oil film. This phenomenon, in conjunction with the system running near a critical speed of the journal, can generate unstable vibrations in the bearing.

Under normal, low journal velocity conditions, the journal resides at an equilibrium position that is determined by its velocity. However, as the speed increases and approaches a threshold speed of instability, the journal's stability becomes compromised. Speeds above the threshold speed cause a self-excited oscillation to occur, during which the whirling motion of the journal is increased by its own rotational energy. This is dangerous if the oscillations are of large magnitude. If the journal suddenly becomes unstable, this is called subcritical bifurcation. On the other hand, if the journal gradually becomes unstable, it is called supercritical bifurcation. Subcritical bifurcation is also possible under the threshold speed when the rotor is given small perturbations by an outside force. Consequently, factors such as constant and imbalance loads on the journal are considered important when preventing bifurcation.

Vibrations can also occur from the lack of an oil wedge. Oil wedges, which are responsible for the load-carrying capability of the journal bearing, can be prevented from forming if the load is too heavy, the journal speed is too slow, or there is a lack of lubrication. In all three cases, metal-to-metal contact occurs, thus causing vibrations in the bearing.

Seizure, which results in a complete halt of the journal's movement, is a serious common problem. This mode of failure can result from the lack of an oil wedge (dry rubbing) which leads to highly localized heating, inadequate heat release from the system, and thermal expansion of the journal. In the third case, the journal may thermally expand faster than the bearing housing, causing the clearance between the journal and the bearing to disappear and metal-to-metal contact to occur. In the case of tilt pad bearings, thermal expansion of the tilt pads can produce the same phenomenon.

See also: **Balancing**; **Diagnostics and condition monitoring, basic concepts**.

Further Reading

Arumugam P, Swarnamani S and Prabhu BS (1997) Effects of journal misalignment on the performance characteristics of three-lobe bearings. *Wear* 206: 122–129.

Braun S and Datner B (1979) Analysis of roller/ball bearing vibration. *Journal of Mechanical Design* 101: 118–125.

Chen CL and Yau HT (1998) Chaos in the imbalance response of a flexible rotor supported by oil film bearings with non-linear suspension. *Nonlinear Dynamics* 16: 71–90.

de Jongh FM and Morton PG (1996) The synchronous instability of a compressor rotor due to bearing journal differential heating. *Journal of Engineering for Gas Turbines and Power–Transactions of the ASME* 118: 816–823.

Deepak JC and Noah ST (1998) Experimental verification of subcritical whirl bifurcation of a rotor supported on a fluid film bearing. *Journal of Tribology – Transactions of the ASME* 120: 605–609.

Elkholy AH and Elshakweer A (1995) Experimental analysis of journal bearings. *Journal of Engineering for Gas Turbines and Power–Transactions of the ASME* 117: 589–592.

Howard I (1994) *A Review of Rolling Element Bearing Vibration 'Detection, Diagnosis, and Prognosis'*. DSTO-RR-0013. Melbourne, Australia: DSTO Aeronautical and Maritime Research Laboratory.

Jang JY, Khonsari MM and Pascovici, MD (1998) Thermohydrodynamic seizure: Experimental and theoretical analysis. *Journal of Tribology–Transactions of the ASME* 120: 8–15.

Li CJ and Ma J (1992) Bearing localized defect detection through wavelet decomposition of vibrations. In: Pusey H and Pusey S (eds), *Proceedings of 46th General Meeting of Mechanical Failures Prevention Group*, 7–9 April, Virginia Beach, Virginia, pp. 53–62. Willowbrook, IL: Vibration Institute.

Li CJ, Ma J, Hwang B and Nickerson GW (1991) Pattern recognition based bicoherence analysis of vibrations for bearing condition monitoring. In: Liu TI, Meng CH and Chao NH (eds), *Proceedings of Symposium on Sensors, Controls and Quality Issues in Manufacturing*, ASME Winter Annual Meeting, 1–6 December, Atlanta, GA, PED – vol. 55, pp. 1–11. New York: ASME.

Limmer JD and Li CJ (1997) A case study in cage fault detection using bandwidth-weighted demodulation. In Burroughs CB (ed.) *Proceedings of NOISE-CON 97*, 15–17 June, State-College, PA, pp. 189–194. Poughkeepsie, New York: Noise Control Foundation.

Meyer LD, Ahlgren FF and Weichgrodt B (1980) An analytic model for ball bearing vibrations to predict vibrations response to distributed defects. *Journal of Mechanical Design* 102; 205–210.

Monmousseau P, Fillon M and Frene J (1998) Transient thermoelastohydrodynamic study of tilting-pad journal bearings – application to bearing seizure. *Journal of Tribology – Transactions of the ASME* 120: 319–324.

Su YT and Lin SJ (1992) On initial fault detection of a tapered roller bearing: frequency domain analysis. *Journal of Sound and Vibration* 155(1): 75–84.

White MF and Chan SH (1992) The subsynchronous dynamic behavior of tilting-pad journal bearings. *ASME Journal of Tribology* 114: 167–173.

BEARING VIBRATIONS

R Bigret, Drancy, France

Copyright © 2001 Academic Press

doi:10.1006/rwvb.2001.0092

Sealing systems and elements connected to the rotor play a part in guiding the rotor. Coupling between rotors falls into the link category. This article describes the characteristics of links.

Introduction

Rotors in rotating machinery are guided by links. They are classified into three categories:

1. Fluid
2. Roller bearings
3. Magnetic field

Forces are transmitted to nonrotating parts. They are a result of associated impedance:

- To links
- To sealing systems
- To elements connected to the rotor, such as wheels.

Functions

Links must allow:

- Fixed-precision guidance to avoid rotor–stator contact
- Minimum wear and tear to reduce machine unavailability
- Removal of heat, in particular from the rotor
- Minimization of leaks
- Neutralization or removal of impurities
- Minimum loss through friction, for economy and low-level heating

In 1987, in the USA, the American Society of Mechanical Engineering (ASME) estimated that 11% of consumption was lost through friction; in 1996 France it was valued at 1.6% of gross national product.

Through their impedance, links contribute to the dynamic behavior of rotating machines, their stability and vibratory levels, in particular at critical speed. Their optimization complements that of rotors and stators, their function and performance.

Fluid Links

Fluid links offer contacts which are dry or hydrodynamically lubricated. In 1902 Richard Stribech (1861–1950) proposed a function which makes it possible to distinguish four zones within a bearing (**Figure 1**). Zone 1 falls within the province of tribology. The term 'tribology' was invented in 1968 and encompasses the study of friction, wear, lubrication, and the design of bearings.

Contacts may be:

- Surface: friction is oily; pressure is 1–1000 bar. This is the sphere of bearings, thrust, and sealing systems.
- Hertzian: surfaces are separated by films formed in a chemical reaction between materials and additives contained in the fluid (the oil). This process is elastohydrodynamic. The pressure is 1000–25 000 bar. This is the sphere of gears and roller bearings.
- Dry, nonlubricated: there may be microsoldering and particles may become loose, which reduces friction.

In zone 2, a hydrodynamic effect separates the surfaces which remain in contact at their rough patches. In zone 3, a hydrodynamic laminary film, in which the fluid trickles are parallel, separates the surfaces when:

$$\Re = \frac{\rho V}{\mu} J < 1000$$

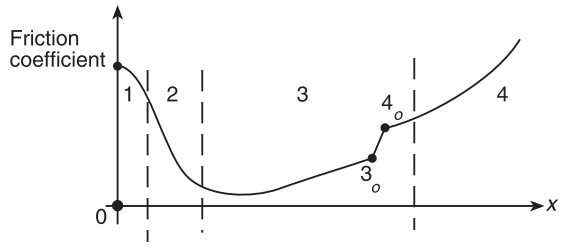


Figure 1 Stribech curve. x, film thickness; $\mu\Omega/F$ where μ = viscosity; Ω = rotation speed; F = force.

where $\Re$ = average Reynolds number, ρ = fluid volume mass; V = speed, ΩR, where Ω = rotation speed and R = radius; μ = fluid viscosity; and J = radius clearance. (Reynolds (1842–1912) was an English engineer who defined the principles of lubrification in 1884–86 and coefficients of similarity in 1883.)

In zone 4, the flow is turbulent hydrodynamic with $\Re > 2000$, even 1000. Between 3_0 and 4_0, so-called Taylor rotors may be seen in the direction of the bearing axis. This instability is due to radial centrifugal forces of inertia which are related to tangential forces of viscosity.

Hydrodynamic laminary lubrication is currently used in rotating machines. Lubrication limits in zones 1 and 2 occur when the machine is started up and stopped.

At the time of construction of the pyramid of Kheops in Egypt (around 2700 years BC), the Egyptians did not know about the wheel. They used to pull blocks of stone on ramps tilted at most at 9°; these ramps were made of bricks lubricated by silt from the Nile. Some 2400 years BC, this was how the statue of Ti was moved. In Mesopotamia, 2500 years BC, the palace doors of the sultans of the Ottoman empire would turn on *crapaudines*, using steam pressure. In China around the year 900, iron bearings were used, and in the Middle Ages iron and bronze axles and bearings were developed. Leonardo da Vinci (1452–1519) used an alloy comprising 30% copper and 70% tin. Today antifriction bearings contains 80% tin. Research continued with the Frenchman Amontons, who in 1699 published *On Resistance Caused in Machines*; Euler (1707–83), who was Swiss, distinguished between static and dynamic friction, while Coulomb (in 1782) discussed simple machines and proposed the friction coefficients which are used today.

Bearings

Fluid bearings – which are often oil bearings – are useful and necessary in the basic rotating machinery used in industry. They allow:

- Optimization of impedance to the rotor for stability; passage of critical speed and normal function with vibrations and force transmitted to low-amplitude bearings
- Adaptation to moderate misalignment
- The possibility to remove calories by fluid, of which a small part is used for lubrication

Precautions must be taken to:

- Avoid impurity and debris by filtering
- Insure constant temperature of the fluid

- Avoid wear and tear at low speed when the machine starts up and stops when the film is not formed
- Insure emergency supply

The cylindrical bearing shown in **Figure 2** enables to define the elements which permit characterization of normal performance. The rotor section turns around *C*. The surface of the rotor section is cylindrical and parallel to the surface of the bearing. A thin fluid film is formed between the rotor section and the bearing. In general, the surface is affected by geometrical faults, which require precautions for machine monitoring and diagnostics. Colinearity $\overrightarrow{C_oC_m}$ results from the static form: $\overrightarrow{W}$ possibly results from rotating force $\overrightarrow{W_t}$. If $|\overrightarrow{W_t}|$ varies over one revolution, the path of C is influenced by the variation in C_m.

If $\overrightarrow{C_oC_m}$ is constant and if $h(\theta, t)$ is included in the limits which permit linear performance, the path of the center *C* of the whirl is an ellipse. C_m is fixed. The

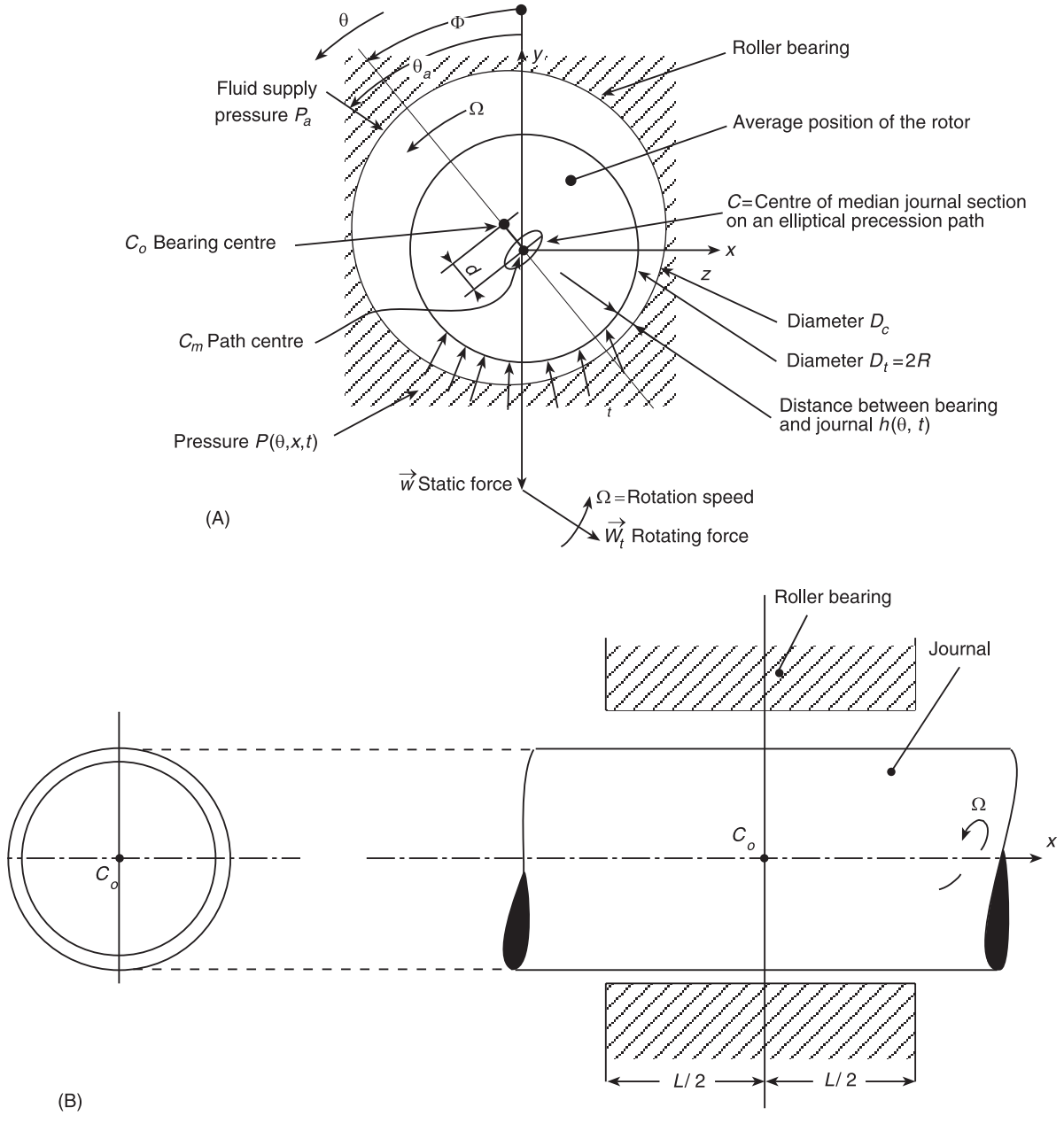


Figure 2 Rotor bearing–journal, where $t =$ time, $L =$ bearing length; unbalance of the axis: $\left|\overrightarrow{C_oC_m}\right| = d$; Radius clearance: $D_c/2 - R = J$; $\overrightarrow{W}$ and $\overrightarrow{W_t}$ are applied to *C*.

minimum value of $h(\theta, t)$ depends on the nature of the materials of the rotor and the bearing. It may be close to 30 μm, or may even be less. The field of pressure (p, θ, x, t) balances the forces applied on C.

Supply is generally between 1.5, and 6 bars absolute, in a weak pressure zone opposed to its maximum [average $p(\theta, x)$]. In this zone, when d is significant $(d/J > 0.5)$, theoretical pressure is negative; practically, there exists cavitation and pressure is equal to the pressure of saturating steam, which may be ≈ 0.4 bar at 30°C; when $d = 0$, there is no cavitation but the arrangement of rotor and bearing may become unstable. An increase in supply pressure reduces the cavitation zone.

When $\Re < 1000$, the angle ϕ and $|\overrightarrow{C_oC_m}|$ which characterize the average position, the stiffness k_{ij} and damping coefficient f_{ij} (either positive or negative) expressed by $K_{ij} = k_{ij}(J/W), F_{ij} = f_{ij}(J/W)\,\Omega$ $(i = x, z; j = y, z)$ and characterize dynamics, depending on $L/2R$ and Summerfeld number:

$$S = \frac{\mu\Omega RL}{\pi W}\left(\frac{R}{J}\right)^2 \qquad [1]$$

where μ is the viscosity and the Reynolds number $\Re = \rho\Omega RJ/\mu$ must be less than 1000. When $\Re > 1000$ laminary, the flow becomes turbulent. When $\Re > 2000$, it is extremely turbulent.

Stiffness and damping coefficients which form the impedance in a radial plane are obtained by the Reynolds equation:

$$\frac{\partial}{\partial\theta}\left[(1+\varepsilon\cos\theta)^3\frac{\partial p}{\partial\theta}\right] + R^2\,\frac{\delta}{\delta x}\left[(1+\varepsilon\cos\theta)^3\frac{\partial p}{\partial x}\right] = -6\mu\left(\frac{R}{J}\right)^2\left[\left(\Omega - 2\frac{\mathrm{d}\phi}{\mathrm{d}t}\right)\varepsilon\ \sin\ \theta - 2\frac{\mathrm{d}\varepsilon}{\mathrm{d}t}\cos\theta\right] \qquad [2]$$

where $h = J(1 + \varepsilon\cos\theta)$; $\varepsilon = d/J$.

This equation is developed via the Navier equations with the following hypotheses:

- Constant viscosity
- Negligible mass of the fluid
- Incompressible fluid
- Constant pressure over the thickness of the film
- Speed of the fluid in contact with the journal equal to ΩR, zero in contact with the bearing

Many types of boundary conditions may be assumed:

- That of Gümbel
  $p(\theta, x) = 0$
  where $\pi < \theta - \theta_a < 2\pi$
  $p(\theta = \theta_a, x) = p_a = 1$ bar absolute
- That of Reynolds, which is more often used:
  $\delta p/\delta x = \delta p/\delta z = 0$ and $p = p_a$ when $z = z_s \rightarrow$ function of x
  $p(\theta = \theta a, x) = p_a$; $p = p_a$ for supply, $p = 0$ at $x = \pm L/2$

The solution to eqn [2] may be obtained analytically for large L (= length of bearing) is $(\partial p/\partial x = 0)$ and small L is $(\partial p/\partial\theta = 0)$. This solution was obtained in 1952 by Ocvirk for the so-called Ocvirk bearing where $L/2R \leq 0.5$.

This is more easily expressed by the method of finite elements which, balancing energy, allows viscosity corresponding to temperature to be used for each element. A more complete formulation makes it possible to take into account the moment and rotation around the axes C_{my} and C_{mz} (**Figure 2**); the link is represented by eight stiffnesses and eight damping coefficients.

Bearing and Corner

A bearing made up of a thin fluid film tolerates significant charges. The same applies to a fluid corner. **Figure 3** shows a fluid corner and a bearing composed of a partial arc. For the corner, the Reynolds equation leads to:

$$W = \frac{6\mu VlL_1^2}{J_2^2(r-1)^2}\quad\left(\ln r - 2\frac{r-1}{r+1}\right)$$

For the partial bearing, d, θ, stiffness k_{ij}, and the damping coefficients f_{ij} are defined by the Sommerfeld number S. Where $\mu = 0.1$ Pa s (for water at 20°C, $\mu = 0.001$); $V = 31.4\ \mathrm{m\,s^{-1}}$ $(R = 0.1$ m; $\Omega = 314\ \mathrm{rad\,s^{-1}} \rightarrow 3000$ rpm); $J_2 = 0.1833$ mm; $r = 2.2$ (for W_{maxi}; $J_1 = 0.40326$ mm); $L_1 = 209$ mm; $l = 153$ mm $(l/L_1 = 0.732$; $S = 320\ \mathrm{cm^2})$; $\beta = 10^{-3}$ rad (0.06 deg); $\alpha = 100$ deg; $J = 0.2$ mm; $L = 2R = 0.2$ m $(L/2R = 1)$ Length $2\pi R100/360 = 174$ mm. Force W is close to 10^5 N. For the corner, $\Re \approx 92$. Average pressure $\approx 3.13 \times 10^6$ Pa. Power lost through viscosity is defined by: force × speed $= \mu\Omega R\omega$ surface $\times\ \Omega R \approx 17\,200\,W$. Average pressure $\approx 3.13 \times 10^6$ Pa.

For the partial arc, $\Re \approx 63$; $S = 0.5$. Average pressure on the projected section (between 1 and 2) $\approx 3.5 \times 10^6$ Pa; $d \approx 0.02$ mm $(d/J = 0.1)$, $\theta \approx 55$ deg; $d_f = 0.18$ mm $(d_f/J = 0.9)$ where $W = 10^5$N. The force W is significant, if the film is thin.

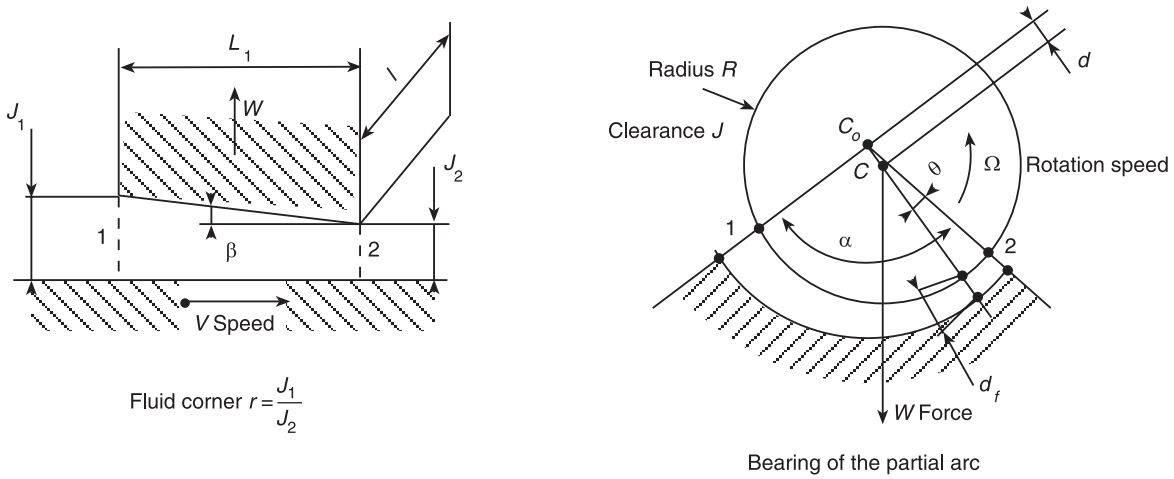


Figure 3 Bearing corner. Pressure in 1 = pressure in 2 (atmospheric pressure). Fluid viscosity, μ. Disregarded marginal leak.

Diversity of Bearings

Figure 4 shows forms used in industry: at fixed geometry (with two, three, or four lobes) with oscillating runners (one, two, three, four, five runners). When the mass of the runners is negligible, there is no static force:

$$k_{xy} = k_{yx} = f_{xy} = f_{yx} = 0$$

This property facilitates the achievement of stability which is discussed in **Rotor dynamics**. The oscillating runner was introduced in the USA by Kinsbury in 1905.

The minimum recommended radial clearance J_m is a function of speed and diameter D: for 60 rpm, $D = 710$ mm, $J_m = 0.16$; $2J_m/D \rightarrow 0.04\%$. For 40 000 rpm, $D = 25$; $J_m = 0.04$; $2J_m/D \rightarrow 0.16\%$. Temperature can be measured by thermocouples placed in the neighborhood of contact surfaces of the bearings and runners.

In linear performance, forces and displacements are linked by a transfer matrix, displacement impedance, and isochrome for frequency ω:

$$\begin{bmatrix} F_y \\ F_z \end{bmatrix} = \begin{bmatrix} Z_{yy} & Z_{yz} \\ Z_{zy} & Z_{zz} \end{bmatrix} \begin{bmatrix} y \\ z \end{bmatrix} \rightarrow \mathbf{F} = \mathbf{ZD} \qquad [3]$$

The terms used in eqn [3] are complex members: Z depends on ω and on rotation speed $\boldsymbol{\Omega}$. When the velocities are substituted for the displacements, the square matrix is one of impedance: its inverse is an admittance, or mobility. The isotropy is expressed by:

$$Z_{yy} = Z_{zy} \quad Z_{yz} = -Z_{zy}$$

The term Z_{00} depends on the viscosity ($\rightarrow$ temperature) and on the vector of colinearity $\overrightarrow{C_oC_m}$ (**Figure 2**) affected by misalignment (see **Rotator stator interactions**). When variations in $\overrightarrow{C_oC_m}$ are significant, the

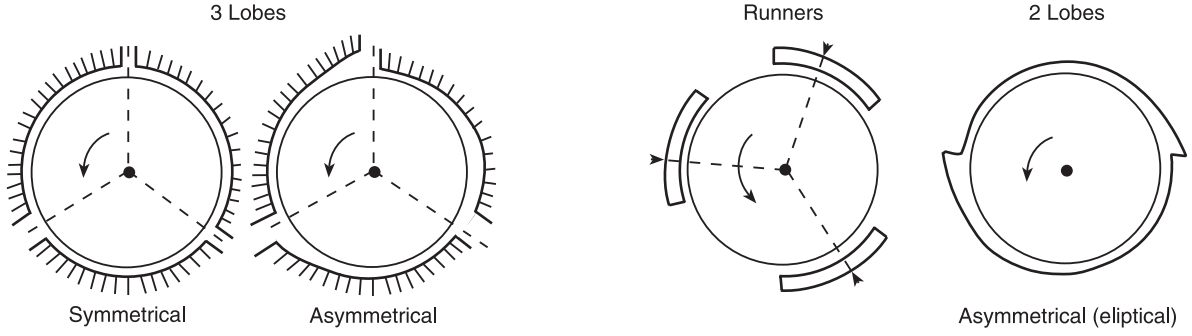


Figure 4 Bearings at fixed geometry, with oscillating runners.

term Z_{00} causes a nonlinear behavior which increases the number of spectral components.

Specificities

Links play a large part in achieving a significant margin of stability ($\Omega_{max} \ll \Omega_{limit}$) at low-level vibration amplitudes and critical speed.

If the bearing material is correctly chosen, even with a lack of oil, then the amount of damage may be limited.

Guidance of the rotors and their vertical support may be obtained hydrostatically by bearings and thrust, in which fluid and oil are introduced under pressure; these devices enable the machine to operate at very slow rotational speed. In particular, they are used to insure, without wear and tear, slow rotor rotation before and after their use in turbomachines submitted to high temperatures.

The experimental determination of stiffness and damping coefficients of bearings and thrust requires special installations which permit to control excitation forces for constant rotation speed.

Thrust with fluid enables axial guidance of the rotors, classically for hydraulic turbines on a vertical axis and for turbomachines. Thrust utilizing fluid or oil corners formed by 'tilt pads' rotation on a pellet fixed between them are handled by the blocks at fixed geometry or by oscillating runners, which were first introduced into Australia by Michell in 1905 (**Figure 5**). Thrust may bring two fixed pellets, partly rotating pellets. Axial force may reach 5×10^6 N where $D \approx 1800$ mm and axial clearance ≈ 0.7 mm.

Roller Bearings

In Malta, which was inhabited from the end of the fifth millennium BC, stone rollers enabled stone blocks to be moved 5 km when megaliths were being constructed. The Egyptians were not aware of the wheel, but were able to use wooden spheres ($\phi \approx 75$ mm) to move stones for the pyramids, as well as statues. In Central America from the fourth to the 15th century the Mayans used logs to move heavy objects. A roller bearing comprising eight marbles was drawn by Leonardo da Vinci in 1501–2. Suriray gave it its current configuration in 1870: this is an example of art preceeding manufacturing. This then became technical in 1940 and then in 1960 was associated with lubrication and heat removal.

Roller bearings using ball bearings, rollers, and needles are shown in **Figure 6**. Manufacturing tolerance may be close to 1 μm. The impedance to the rotor is large. Special arrangements permit an angular distances between the rotor axis and the axis of the outer cage. Displacements and mislalignments between bearings induce radial forces which may lead to damage.

Roller Bearings

Between rotors guided by roller bearings, the use of flexible couplings avoids damage. Damping arises because of elastomer or rubber rings between the outer cage and the bearing, or through a fluid film of oil supplied by a pump. This arrangement requires specific and precise mechanical adaptations which must not affect machine reliability. The coefficients damping and stiffness are combined to form an impedance matrix.

Certain roller bearings require lubrication by oil or the flow of a fluid, which may also remove heat generated by the rotor.

The lifespan of a rolling bearing depends on:

- Rotation speed
- Static force
- Dynamic or rotating force
- The environment: temperature and displacement

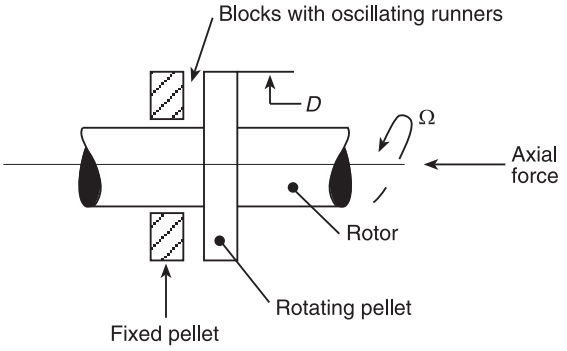


Figure 5 Thrust.

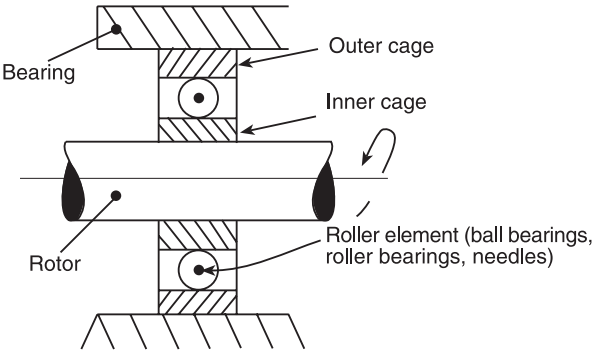


Figure 6 Roller bearings.

Uncertainties concerning dynamic force may be important. The reduction of dynamic force by balancing increases the lifespan. For example, the lifespan as determined by a statistic, drawn from experimental studies, may be defined for ball bearings by:

$$D = \frac{a}{60}\frac{10^6}{N}\left(\frac{C}{P}\right)^3$$

where a is the constant related to reliability; to material, and to the environment; N = speed (rpm); C = dynamic charge; P = equivalent dynamic charge determined according to operating conditions. Balancing which, for a bearing at 3600 rpm ($\phi_{ext} = 190$ mm; $\phi_{int} = 75$) reduces C to $1/5C$, leads to an increase in lifespan from 230 to 430 days. The stiffness of a ball bearing is defined by:

$$K_r\left(\frac{\text{da N}}{\text{mm}}\right) = \frac{W}{\delta_r} = \frac{\cos\alpha}{2.5\times10^{-3}}(WD_b)^{1/3}$$

where W = radial force (da N); D_b = diameter of the ball bearings; α = contact angle. Stiffness results from Hertzian theory where there are fewer deformations at the elastic limits; K_r is not independent of W, where $W = 5\times10^4$ N; $D_b = 10$ mm (outer diameter $\approx$ 110 mm; inner diameter $\approx$ 60 mm); $\alpha = 0$; $K_r \approx 1.5\times10^8$ (N m^{-1}). Speed must be less than 10 000 rpm, depending on the desired lifespan. The stiffness of a rolling bearing is greater than that of a ball bearing.

The performance of a roller bearing is defined by its N dm (rpm $\times$ average diameter in mm), which is close to 1.5×10^6; at a maximum, it is 3×10^6, which may be 46 mm at 65 000 rpm. The outer ring diameter may be several meters: it was 4 m for the drill head for the Channel Tunnel. Roller bearings make it possible to handle thrust.

Sensors may be installed in roller bearings to monitor their state of vibration, to measure useful rotation speed for the Antilocking System (ABS), which avoids wheel locking. A car uses 50 roller bearings; a high-speed train uses 500, a plane 800, and a paper machine 2000.

Aeronautical motors use numerous roller bearings which permit low-speed rotation without causing damage, and which leave a considerable time between their wear, tear (when they are being monitored) and their destruction and which time they are quickly and easily replaced.

Magnetic Links

Figure 7 shows the relations between mechanical, magnetic, and electric phenomena. Magnetic flow and battery voltage are coupled to the mechanical. Magnetoelectric phenomena falls within this category.

Figure 8 shows the principle of the radial lift of a rotor submitted to force F (gravity or others). When I is constant and e is small:

$$F_m = \frac{B^2S}{2\mu_0} \qquad [4]$$

where B is the magnetic induction in the air gap of length e (in Tesla); S = active surface (penetration of flow in the rotor); μ_0 = permeability of space $= 1.25\times10^{-6}$ (system: meter, kg, second, Tesla).

When the permeability of rotor and stator, within a magnetic field, is very great in relation to μ_0:

$$B \approx \frac{NI\mu_0}{2e} \qquad [5]$$

where N = number of electromagnetic spikes and I = current in amps.

From eqns [4] and [5], it follows that:

$$F_m = \frac{(NI)^2S}{8e^2}\mu_0; \quad \frac{\mathrm{d}F_m}{\mathrm{d}e} = \frac{-(NI)^2S\mu_0}{4e^3} = \frac{-2F_m}{e}\mathrm{d}e$$

When e decreases ($\mathrm{d}e \to \Delta e < 0$), F_m increases ($\mathrm{d}F_m \to \Delta F_m > 0$): the system is intrinsically unstable. This instability is a result of a negative stiffness of the order of -5×10^7 N m^{-1}. Stability is obtained by a loop which takes its information from a sensitve sensor at $\Delta e_m = \Delta e$; a seconday loop uses magnetic flow. With sheet metal (iron silicium 3%), $B_{max} = 1.5$ T; $S = 1$ cm^2; $F_m = 9$ da N; where $e = 0.5$ mm, $(\mathrm{d}F_m/\mathrm{d}e) = 360$ N^{-1}.

The pressure is equal to 90 da N cm^{-2} $\to 9\times10^5$ Pa. The pressure is small relative to the pressure which can be achieved with fluids. $NI = 600$ A rev^{-1} where $I = 20$ A ($2 < I < 40$ at 300 V); $N = 30$ rev. When $F_m = 100\,000$ N, using eqn [4] $S_i = 1100$ cm^2. With the arrangement shown in **Figure 9**, $S = \frac{4}{6}(\pi D/4)\, l_m\, k$ where $k = 0.9$; ($\to$ curvature) and l_m: breadth, where $D = 0.2$ m (partial arc bearing, $l_m = 1.17$ m).

The classical arrangement of a magnetic circuit (containing rotor and stator) is shown in **Figure 10.** Magnetic forces generated as per the principle in **Figure 8** oppose static and rotating forces such that

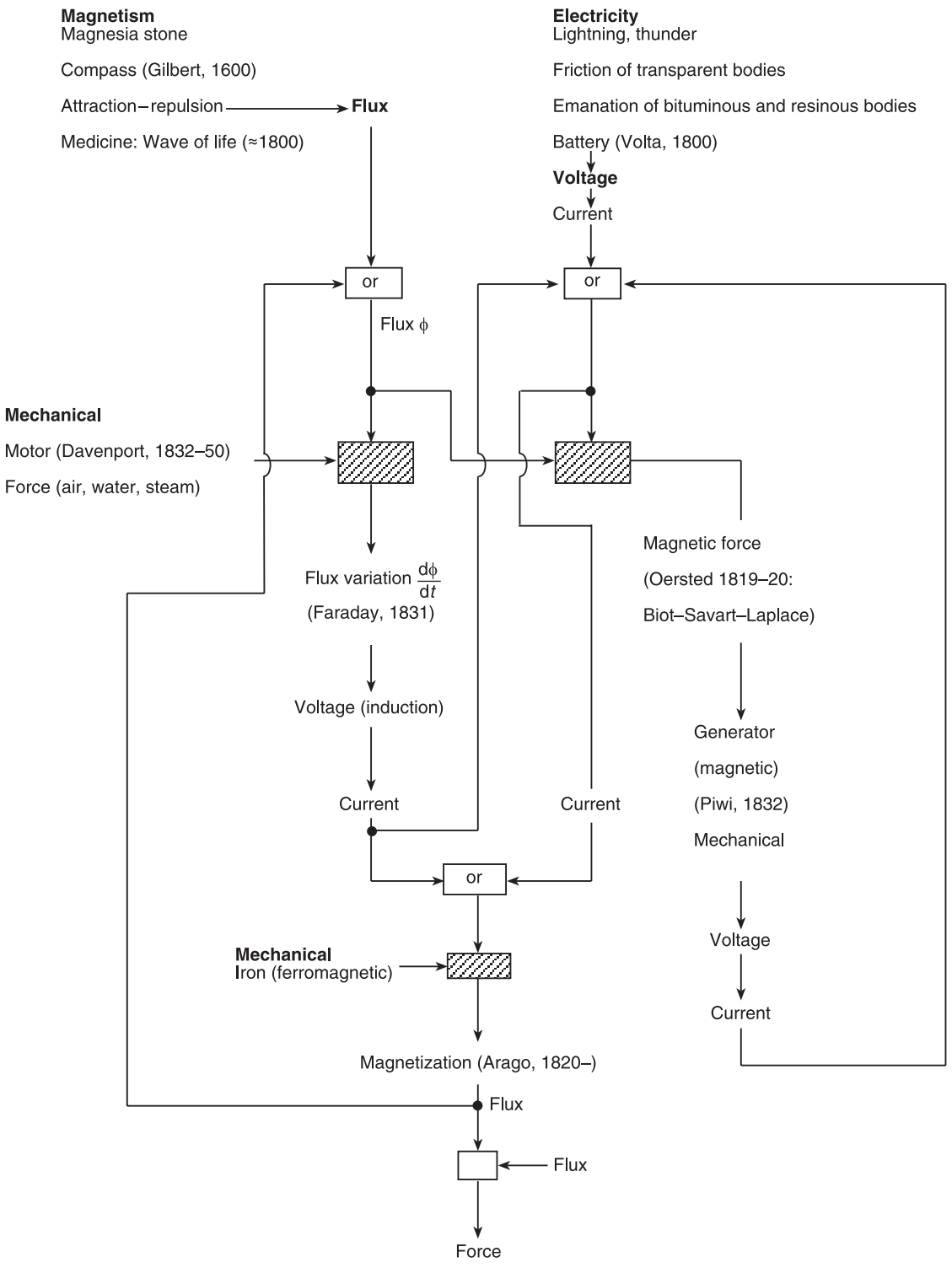


Figure 7 Magnetic–electric–mechanical synergy.

the displacement relative to center C (**Figure 8**) is slight; the maximum force (static and dynamic) is close to $F_m(\mathrm{N}) \approx \alpha D\,(\mathrm{cm})\, l_m\,(\mathrm{cm})$; $\alpha = 40$ for silicium sheet metal, 80 for cobalt sheet metal; $0.3 \leq e \leq 0.6$ mm where $D \leq 100$ mm; $0.6 < e \leq 2$ when $100 < D \leq 1000$; $N_{\mathrm{maxi}} = 180\,000$ rpm.

Speed is limited to $200\,\mathrm{m\,s^{-1}}$ (if diameter is 127 mm at 30 000 rpm then it is 1270 mm at 3000 rpm) by constraints in the rotor ferromagnetic sheet metal, which are less at the elastic limits. $F_{m\mathrm{maxi}} \approx 100\,000$ N. The peripheral speed V of a disk of constant thickness is related to the constraint σ at the center (tangential = radial) by the following relation: $V^2 = [\gamma/(3+\nu)](\sigma/\rho)$ where $\nu = 0.3$: Poisson coefficient and ρ: volume mass. When $V = 200\,\mathrm{m\,s^{-1}}$, $\rho = 7800\,\mathrm{kg\,m^{-3}}$, constraint σ is equal to $1.29 \times 10^8\,\mathrm{N\,m^{-2}}$. This value is less than the elastic limit.

Stability and performance which permit operation beyond critical speed at low-level vibrations are obtained by the corrective circuit and secondary loop (**Figure 8**). Interactions between the circuits associated with each of the electromagnets are possible, even between the circuits associated with n machine bearings, where $n = 2, 3, \ldots$. For horizontal rotors, when the rotating forces are less than the force of gravity, the number of magnetic forces may be less than four.

When rotors are supported and guided by links, fluid, or roller bearings, static magnetic forces may be zero. Losses result from joule losses in coils. Losses by Foucault currents depend on the circumferential speed of permeability and thickness e_t of sheet metal of the foliated circuits ($\mathrm{loss} = \beta(l_t)^2$ where $e_t = 0.1-1$ mm). Losses by hysteresis are slight in comparison to loss by Foucault current.

The power, P, which is lost by Foucault current is in proportion to the force F_m:

$$\frac{P}{F_m}\left(\frac{W}{N}\right) \approx 5 \times \frac{e_t^2(\mathrm{m})}{h(\mathrm{m})}[\pi D(\mathrm{m}) f_r(\mathrm{Hz})]^2 \lambda$$

where f_r = rotation frequency; $3 \leq \lambda \leq 4$ obtained through tests; where $e_t = 5 \times 10^{-4}(\mathrm{m})$; $h = 5 \times 10^{-2}(\mathrm{m})$; $fr = 50\,(\mathrm{Hz})$; $\lambda = 3.5$; $D = 0.2$ m; $P/F_m = 8.63 \times 10^{-2}\,(W/N)$ when $F_m = 10^5$ N; $P \approx 8630$ (W).

Magnetic sensors are arranged in radial planes, close to the electromagnetic planes. They are supplied by high-frequency tension, modulated by variations in l_m (**Figure 8**). Their sensitivity is in the range of 20 and 50 mV $\mu\mathrm{m}^{-1}$. Signals developed by captors at 180° (a couple) are treated by a Wheatstone bridge assembly. Couples at 60° and others, may be used. These arrangements enable to eliminate certain imperfections of the measuring track.

The canceling out of vibration at frequency f_a of the magnetic stator circuit – and thus of the bearing on which it is fixed – can be obtained by canceling, at f_a, the corrective circuit module and function of transfer (**Figure 8**). Consequently, rotor vibration at f_a is a result of excitatory forces at f_a.

Landing devices avoid destruction caused by failure of the magnetic link; in general, they are comprised of ball bearings mounted on the rotor or the stator. The radial clearance is close to half of magnetic clearance; this is useful when assembling, disassembling.

Magnetic links permit axial guidance by thrust and magnetic axial bearing. It uses an identical principle to that of radial guidance. The landing arrangement comprises ball bearings or roller bearings. The max-

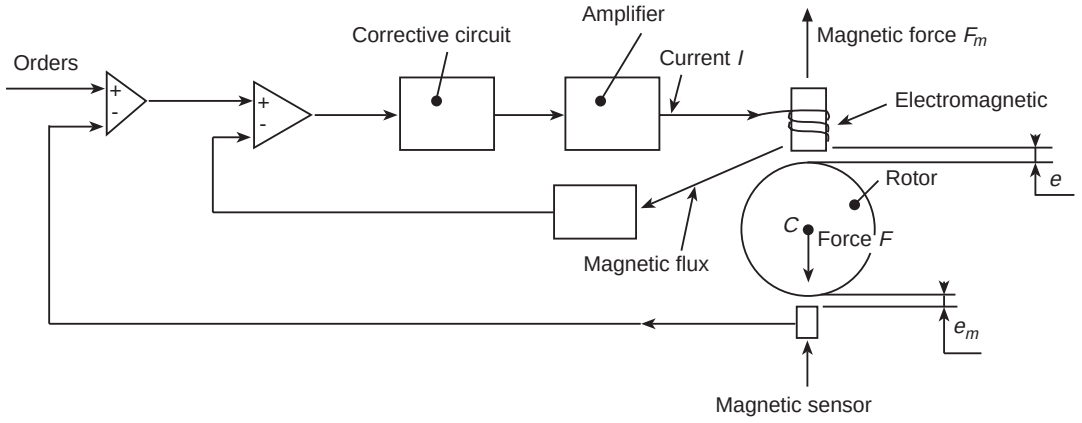


Figure 8 Principles of rotor magnetic lift.

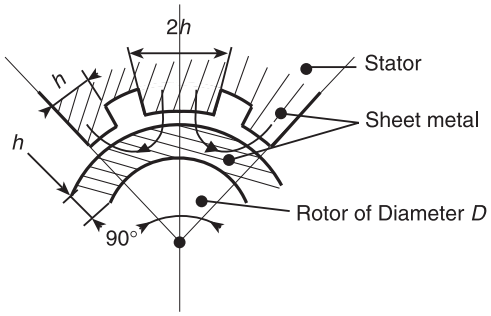


Figure 9 Magnetic circuits.

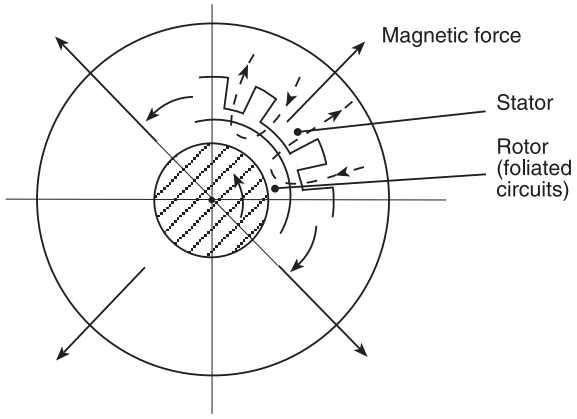


Figure 10 Magnetic circuits.

imum speed is close to 350 m s^{-1}; the maximum force is close to 350 000 N.

To monitor vibratory components, signals delivered by the sensors are processed and compared to the limits; the temperature may also be measured (see **Rotating machinery monitoring**).

Magnetic links are used in gyroscopes, machine tools, cryogenic turbopumps, compressors, vacuum pumps, and centrifuges. They may be associated with fluid links or bearings to optimize dynamic characteristics. This results in an increase in the margin of stability, and a reduction of amplitude at resonance.

As an example, for aluminum manufacturing an electric pin at 40 000 rpm permits 1200 cm^3 of turnings per minute and very slight faults on the manufactured surface. This result is obtained by optimizing the transfer function of the servo-control in order to eliminate spectral components caused by tool impact.

Comparison

Table 1 enables to compare different properties of two fluid links and a magnetic link. Variations are possible to obtain optima which would take into account other constraints.

For the corner shown in **Figure 3**, the force W expressed as a function of $r = J_1/J_2$ has a maximum for $r = 2.2$. This calculation is adopted here. As a result, $\Delta W/\Delta J_1 \approx 0$ where $r > 2.2$: $\Delta W/\Delta J_1 < 0$ and $r < 2.2$: $\Delta W/\Delta J_1 > 0$.

Sealing Systems

Leaks reduce the output and the machine performance. They may pollute the environment. Harmful leaks are essentially seen between rotor and stator at the rotor edges and perpendicular to the disk, the bladed motor or receptive wheels. **Figure 11** shows four arrangements.

The clearance J must be minimum, but sufficient to avoid contact between rotor and stator undergoing displacements and relative vibration. In the arrangement 1, contact is tolerable, to the detriment of an increase in clearance. The contact may lead to local rotor overheating, as a result of flexural deformation which may increase vibration.

Table 1 Comparison of radial links at charge force: 10^5 N, speed: $V = 31.4$ m s^{-1}

	Fluid		*Magnetic* (**Figures 8** and **9**)
	Corner (**Figure 3**)	*Partial arc* (**Figure 3**)	
Rotation speed (rpm)	0	3000	Whatever ($V < 200$ m s^{-1})
Viscosity (Pa s)	0.1	0.1	
Clearance (mm)	0.29 (average)	0.2 (to radius)	0.5 (to radius)
Supporting surface (cm^2)	320	288 (projected 307)	1100
Length (mm)	209	174 ($\phi = 200$)	105 ($\phi = 200$)
Width (mm)	153	200	1170
Stiffness (N m^{-2})	≈ 0	1.5×10^9	3.6×10^5
Loss (W)	$\approx$ 10 760 viscosity	$\approx$ 17 200 viscosity	$\approx$ 8630 − 3000 rpm Foucault currents

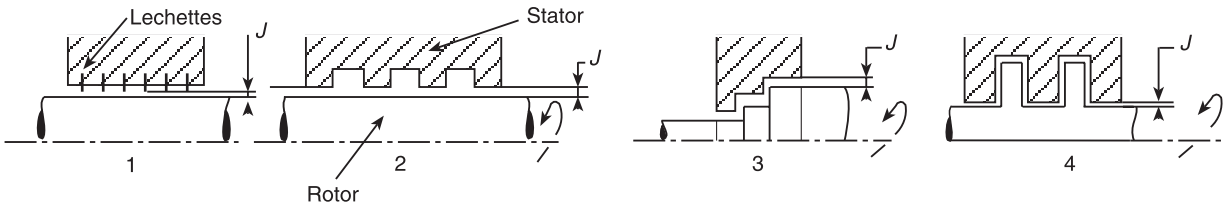


Figure 11 Sealing systems.

Figure 12 shows a mobile element device, with seals. When the slight clearance J is cancelled, the seal is displaced radially without harm. Oil films between seals and rotor insure sealing. **Figure 13** shows *lechettes* (so-called in France) used on disks.

Sealing systems are characterized by impedance matrices which may strongly influence the static and dynamic performance, and may cancel the stabilizing effect of the bearings. Such situations can be seen on boiler supply pumps which force back the flow of water at several hundred bars, and on the turbopumps of satellite launchers.

Since the study of Lomakin in 1957, research was undertaken in how to realize impedance matrices. For a blindfold steam turbine disk, the following matrix relation is assumed:

$$\begin{bmatrix} f_y \\ f_z \end{bmatrix} = \begin{bmatrix} 0 & \dfrac{0.6T}{DH} \\ \dfrac{-0.6T}{DH} & 0 \end{bmatrix} \begin{bmatrix} y \\ z \end{bmatrix}$$

where f_y, f_z are components of force in two perpendicular directions; y, z are displacement components; T = disk couple; D = average blade diameter; and H = blade height.

For a pump with radial diffusion:

$$\begin{bmatrix} f_y \\ f_z \end{bmatrix} = \frac{R}{\rho A V^2} \begin{bmatrix} -2 & 0.7 \\ -0.7 & 2 \end{bmatrix} \begin{bmatrix} y \\ z \end{bmatrix}$$

where R is the outer wheel radius; l is the fluid volume mass; A is the section of fluid exit; $V = \Omega R$, where Ω is the rotation speed. The terms of the second diagonal which are of equal and opposing sign express a tangential force which reduces the margin of stability.

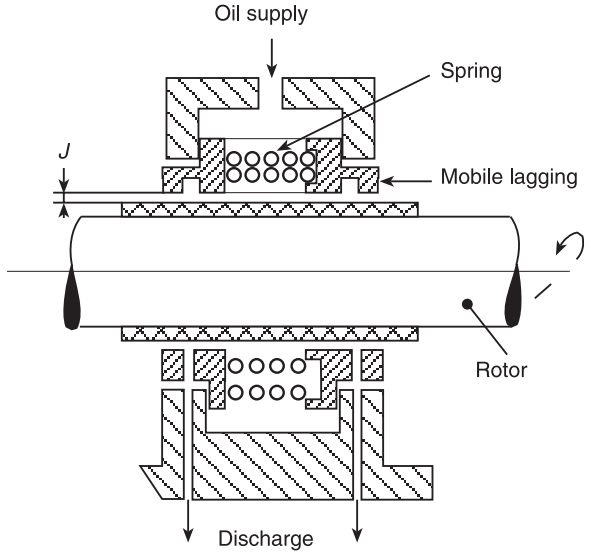


Figure 12 Sealing system with lagging.

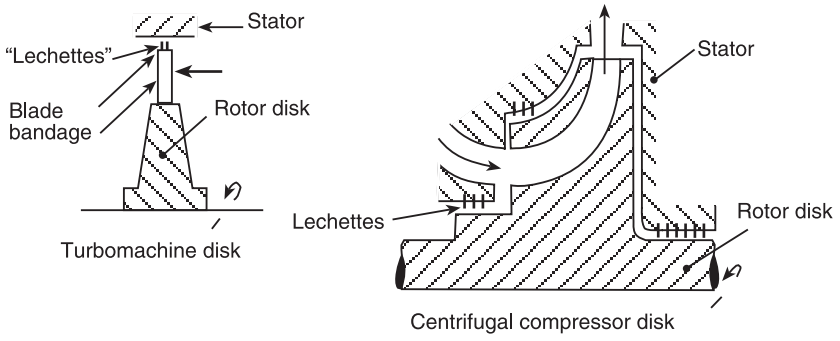


Figure 13 Sealing systems on disks.

Coupling

Couplings create a link between two rotors. The coupling comprises two elements (disks and coupling element) fixed on rotors and by one of the link elements: membrane, disk, blades, cable, cogs, elastomers, universal joints, magnetic field, fluid. Couplings:

- facilitate rotor construction as well as rotor assembly and transport
- enable to fix limits of furniture from different constructors: electric motor, pump
- can enable relative displacement between bearings, without significant variation of forces perpendicular to bearings; in this regard roller bearings are generally not very tolerant (see **Rotator stator interactions**)
- enable decoupling of rotors without displacing them
- enable organization of devices for damping torsion vibrations
- can reduce the transmission of axial forces

Couplings use various technological arrangements which makes them flexible (supple) or rigid. Flexible couplings are used for low-level power: for example, 3 MW at 40 000 rpm with cogs. An acceptable transmitted couple depends on the rotation speed, for example, 5 MW at 600 rpm (80 000 da N m^{-1}), 2.5 MW at 950 rpm. Rigid couplings are used for high power: 10 MW at 3000 rpm, 1500 MW at 1500 rpm.

Coupling may be permanent – the more classic type – or temporary (such as a clutch).

Coupling may be affected by faults which modify the vibratory performance, the transient and spectral signal forms, which may then detect them.

Coaxiality faults between rigid coupling plateaux are a result of wear and tear or slippage between disks caused by significant transient torque. They induce rotating forces at the rotation speed.

Deterioration and significant linear misalignments (coaxiality fault) and angular misalignments result in spectral components of frequency $(p/q)\Omega$, where p and q are integers, and Ω is rotation speed.

Example: Disc Contact of a Flexible Coupling

A flexible coupling is shown schematically in **Figure 14**. The amplitude of the fundamental component of horizontal vibration of a bearing containing a ball bearing is shown in **Figure 15**.

Around critical speed (≈26.2 Hz) of the initial state, the slope, $dA/d\Omega$, is great when $d\Omega/dt > 0$; $dA/d\Omega$ is normal when $d\Omega/dt < 0$. After balancing, the slopes are normal, hysteresis subsists.

The amplitude of the fundamental component of relative vertical vibration close to a bearing next to the coupling is shown in **Figure 16**. Significant slopes $dA/d\Omega$ and hysteresis appear. This amplitude is shown in **Figure 17** where $d = 3$ mm: the maximum amplitude is reduced (from ≈700 μm to ≈300 μm), critical speed is reduced (from ≈26 Hz to ≈2520 Hz), and the slope is normal. The anomaly, which balancing blurs, disappears on structuring d from 1 to 3 mm to suppress nonlinearity.

The solutions to the Duffing equation with damping, presented in the article on **Rotor–stator interactions** compared to the measures shown in **Figures 15** and **16** support the hypothesis of nonlinearity in elastic forces.

See also: **Rotating machinery, essential features**; **Rotating machinery, monitoring**; **Rotor dynamics**; **Rotor stator interactions**.

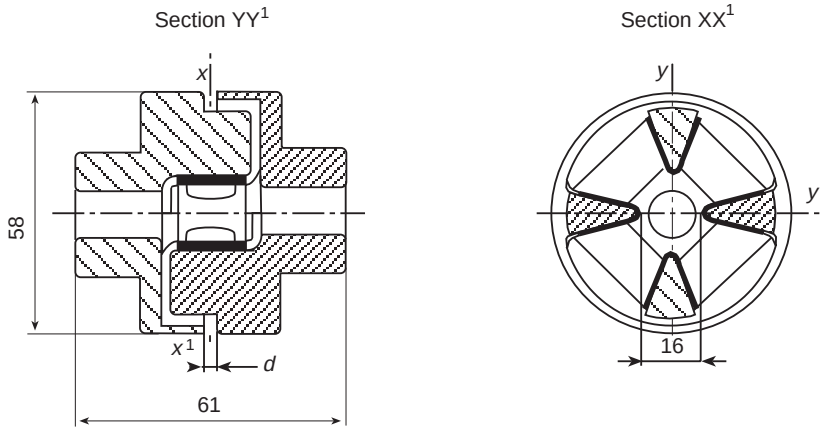


Figure 14 Coupling.

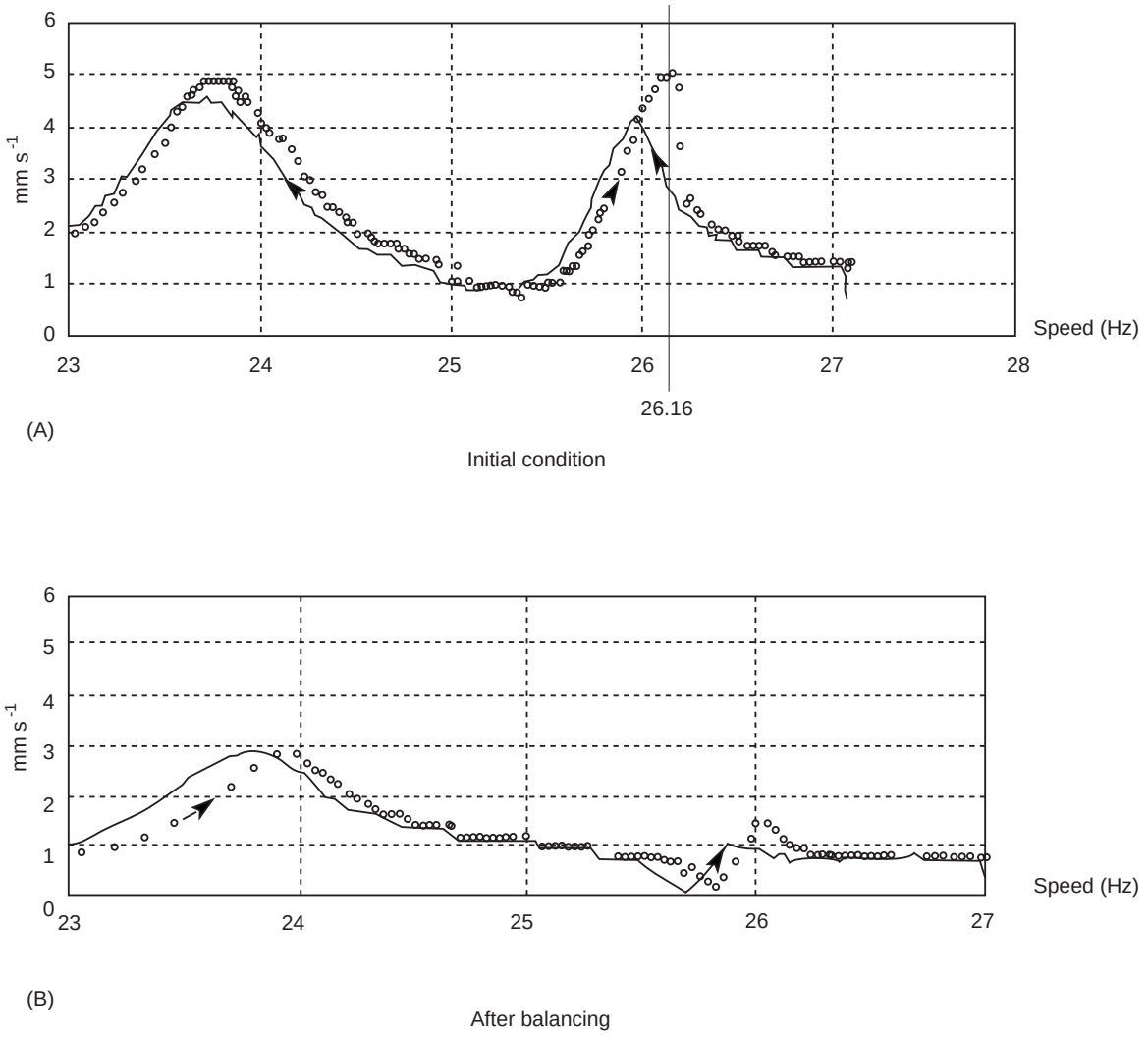


Figure 15 (A, B) Bearing vibration (fundamental component).

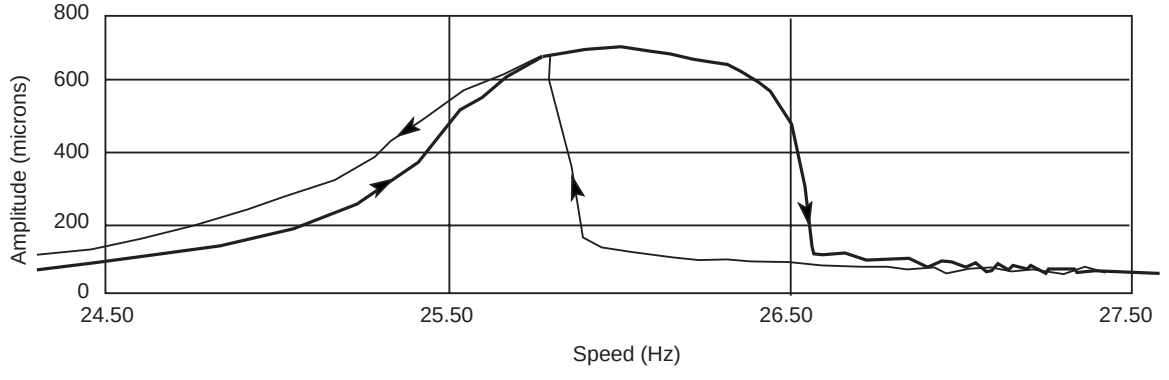


Figure 16 Relative speed (fundamental component). $d = 1$ mm (see **Figure 14**).

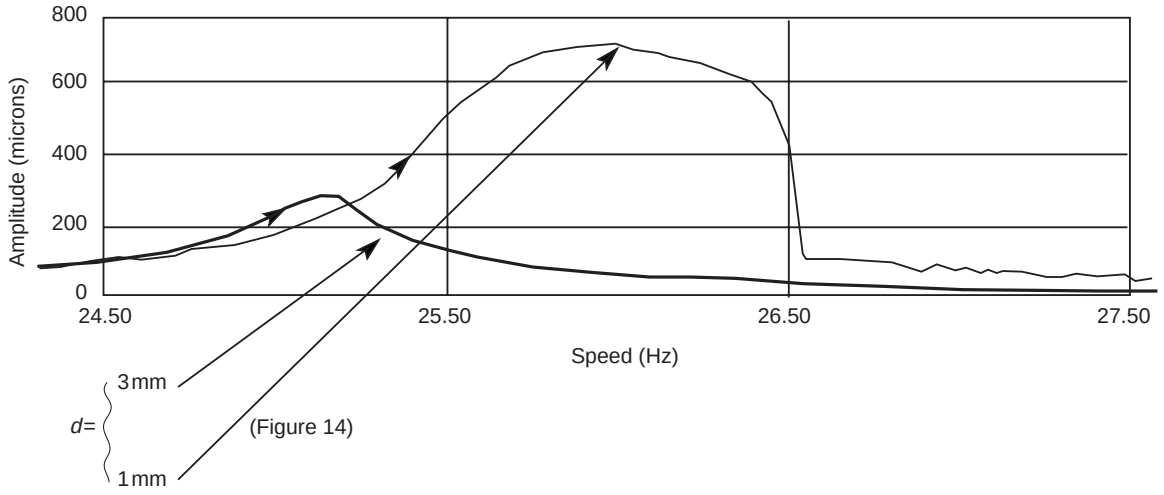


Figure 17 Relative vibration (fundamental component).

Further Reading

Adams ML Jr (1999) *Rotating Machinery Vibration. From Analysis to Troubleshooting*. New York: Marcel Dekker.

Bigret R (1980) *Vibrations des Machines Tournantes et des Structures. [Vibrations of Rotating Machines and Structures.]* Paris: Technique et Documentation Lavoisier.

Bigret R (1997) *Stabilité des Machines Tournantes et des Systèmes. [Stability of Rotating Machines and Systems.]* Simlis, France: CETIM.

Bigret R, Feron J-L (1995) *Diagnostic, Maintenance, Disponibilité des Machines Tournantes. [Diagnostics, Maintenance, Availability of Rotating Machines.]* Paris: Masson.

Boulenger A, Pachaud S (1998) *Diagnostic Vibratoire en Maintenance Préventive. [Vibratory Diagnostics and Preventive Maintenance.]* Paris: Dunod.

Childs D (1993) *Turbomachinery Rotordynamics*. Chichester: John Wiley.

Dimentberg FM (1961) *Flexural Vibrations of Rotating Shafts*. London: Butterworths.

Frêne J, Nicolas D, Dequeurce, Berthe D, Godet M (1990) *Lubrification Hydrodynamique – Paliers et Butées. [Hydrodynamic Lubrication – Bearings and Thrust.]* Paris: Eyrolles.

Gash R, Pfützner (1975) *Rotordynamik. Eine Einführung*. Berlin: Springer Verlag.

Genta G (1999) *Vibration of Structures and Machines*. Berlin: Springer Verlag.

Lalanne M, Ferraris G (1990) *Rotordynamics Prediction in Engineering*. Chichester: John Wiley.

Morel J (1992) *Vibrations des Machines et Diagnostic de leur Etat Mécanique. [Machine Vibrations and Diagnostics of their Mechanical Condition.]* Paris: Eyrolles.

Tondt A (1965) *Some Problems of Rotor Dynamics*. London: Chapman & Hall.

Vance JM (1988) *Rotordynamics of Turbomachinery*. Chichester: John Wiley.

BELTS

J W Zu, University of Toronto, Toronto, Ontario, Canada

Copyright © 2001 Academic Press

doi:10.1006/rwvb.2001.0130

Belts are commonly used in power transmission through belt drives. A power transmission belt is a flexible element subject to initial tension moving in the axial direction. Belts and belt drive systems may exhibit complex dynamic behavior, severe vibrations, and excessive slippage of belts under certain operating conditions.

The vibration analysis of a single belt span assumes that the belt span is uncoupled from the rest of the system. The vibration analysis of belt drives considers the whole drive system, including each belt span and all the pulleys in the system.

Stationary Belts

The simplest model to describe the transverse vibration of a belt is to assume that the belt is stationary by

ignoring the transport speed of the belt. The string theory and the Euler–Bernoullie beam theory are combined to obtain the equation of motion for free vibration of a stationary belt with length L as:

$$\rho\frac{\partial^2 w}{\partial t^2} - T\frac{\partial^2 w}{\partial x^2} + EI\frac{\partial^4 w}{\partial x^4} = 0 \qquad [1]$$

where w is the transverse displacement of the belt, ρ is the mass per unit length, T is the initial tension of the belt and EI is the bending rigidity. If the belt span is assumed to be constrained under simply supported boundary conditions, the nth natural frequency ω_n is obtained as:

$$\omega_n^2 = \omega_{sn}^2 + \omega_{bn}^2 \qquad [2]$$

where:

$$\omega_{sn} = \left(\frac{n\pi}{L}\right)\sqrt{\frac{T}{\rho}} \qquad [3]$$

is the nth natural frequency of a string and:

$$\omega_{bn} = \left(\frac{n\pi}{L}\right)^2\sqrt{\frac{EI}{\rho}} \qquad [4]$$

is the nth natural frequency of a simply supported beam. It is shown from experiments that the fundamental natural frequency of a stationary belt calculated by the string theory alone can accurately predict the relationship between natural frequencies and tension, except for short belt spans. **Figure 1** shows the influence of the bending rigidity on the natural frequencies where the correction factor ψ_n is defined as:

$$\omega_n = \omega_{sn}\psi_n \qquad [5]$$

where:

$$\psi_n^2 = 1 + n^2\pi^2\varepsilon^2 \quad \text{and} \quad \varepsilon^2 = EI/(TL^2)$$

Moving Belts

A moving belt belongs to a class of axially moving continua. There are three types of vibrations for a moving belt, transverse vibration, torsional vibration, and axial vibration, as shown in **Figure 2**. Among the three vibration modes, transverse vibration is the dominant one and is of main interest to industry. Torsional and axial vibrations in a moving belt also exist, but are much less important in most cases.

A Moving String Model for Transverse Vibration

The bending rigidity of a belt may often be neglected with small errors. In the absence of bending stiffness,

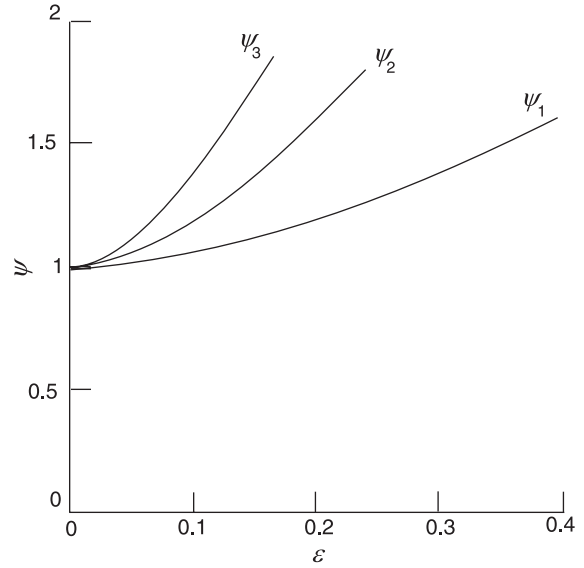


Figure 1 The influence of bending rigidities.

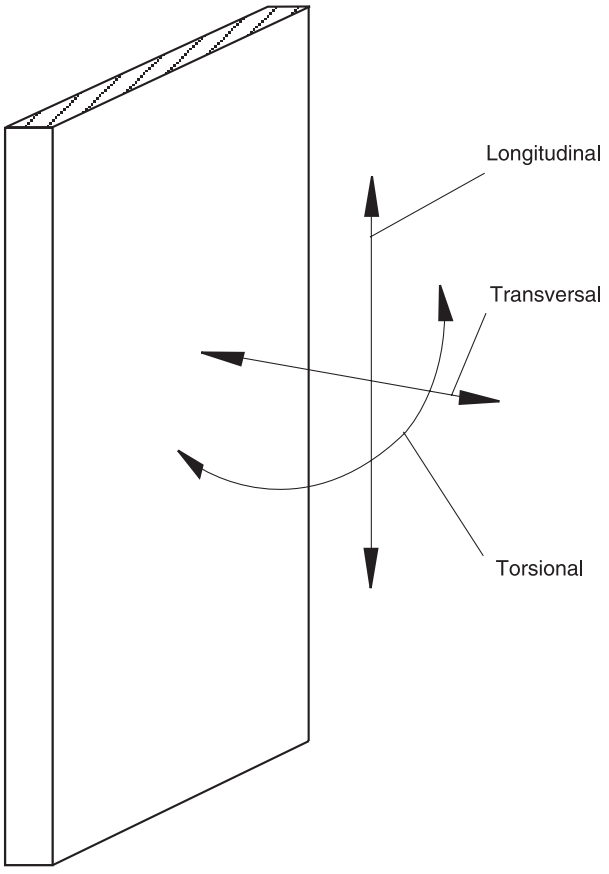


Figure 2 Three vibration modes of a belt segment.

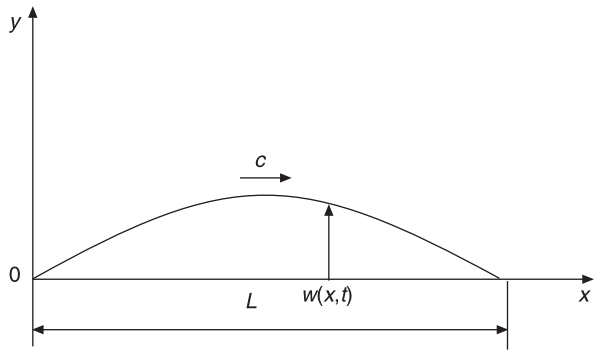


Figure 3 A prototypical model a moving belt.

the belt can be modeled as an axially moving string. A moving string model is commonly used to describe the transverse vibration of a moving belt as long as the thickness of the belt is relatively small and the belt material is flexible enough such as automotive serpentine belts.

One important characteristic of a moving belt is that the axial velocity of the moving belt introduces two convective Coriolis acceleration terms which are not present in the equivalent stationary belt. As a result, a moving belt is a gyroscopic system described by one symmetric and one skew-symmetric operator. The linear equation of motion for free vibration of a moving belt shown in **Figure 3** is given by:

$$\rho\frac{\partial^2 w}{\partial t^2} + 2\rho c\frac{\partial^2 w}{\partial x \partial t} + \left(\rho c^2 - T\right)\frac{\partial^2 w}{\partial x^2} = 0 \qquad [6]$$

where c is the transport speed of the belt and A is the area of cross-section of the belt. The boundary conditions are:

$$w = 0 \quad \text{at } x = 0 \text{ and } x = L \qquad [7]$$

The nth natural frequency is obtained as:

$$\omega_n = n\pi\left(1 - v^2\right) \qquad [8]$$

where $v = c\sqrt{\rho A/T}$ is the nondimensional transport speed. As the critical transport speed parameter $v_c = 1$ at which the transport speed c equals the transverse wave speed in the corresponding stationary string, the natural frequency of each mode vanishes. In **Figure 4**, the first three natural frequencies of a moving belt as a function of the transport speed parameter in the range of a stationary string and a critical string are presented.The eigenfunctions governing free vibration of a moving belt are complex and speed-dependent resulting from the Coriolis acceleration term. The real and imaginary components of the orthonormal eigenfunctions are given by:

$$\psi_n^{\mathrm{R}}(x) = \frac{1}{n\pi}\sqrt{\frac{2}{1-v^2}}\ \sin\ (n\pi x)\cos\ (n\pi v x) \qquad [9]$$

$$\psi_n^{\mathrm{I}}(x) = \frac{1}{n\pi}\sqrt{\frac{2}{1-v^2}}\ \sin\ (n\pi x)\ \sin\ (n\pi v x) \qquad [10]$$

Figure 5 shows the first three complex, orthonormal eigenfunctions of a moving belt at $v = \frac{1}{2}$. The real component is represented by solid lines and the imaginary component is represented by dotted lines.

Nonlinear Effect on Transverse Vibration

There exist primarily two nonlinear sources in a moving belt: geometric nonlinearity and material nonlinearity.

For geometric nonlinearity, it is observed from experiments that at very small amplitudes the belt behaves linearly, but nonlinearities occur at amplitudes well within the range of those observed in practical operations. The equation of motion to consider large transverse vibration of a moving string may be given by:

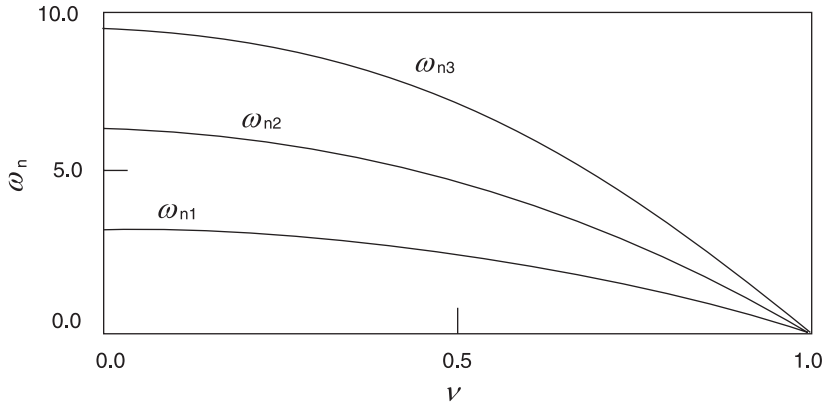


Figure 4 The first three natural frequencies of a moving belt with the change of the transport speed.

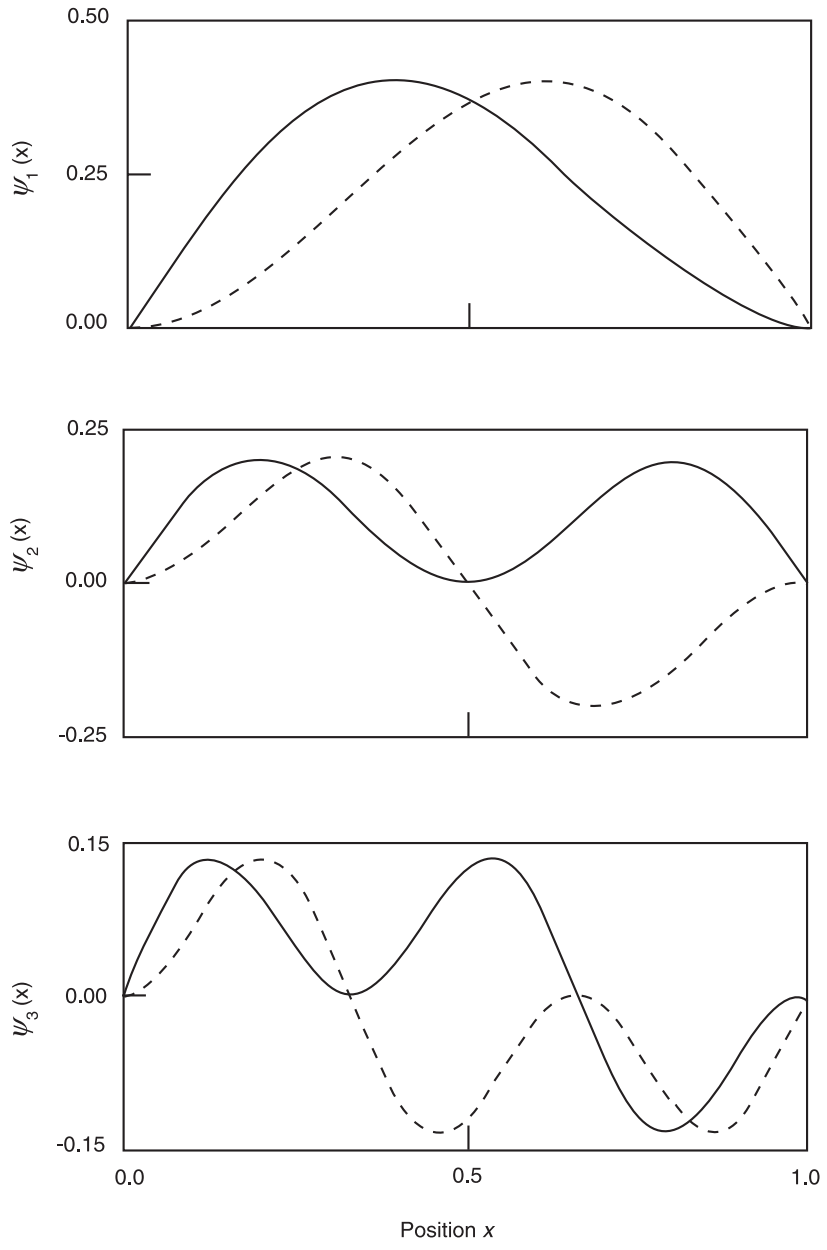


Figure 5 The first three complex, orthonormal eigenfunctions of a moving belt at $v = \frac{1}{2}$: real component (solid), imaginary component (dashed).

$$\rho\frac{\partial^2 w}{\partial t^2} + 2\rho c\frac{\partial^2 w}{\partial x \partial t} + \left(\rho c^2 - T\right)\frac{\partial^2 w}{\partial x^2} + \frac{3}{2}\frac{\partial^2 w}{\partial x^2}\left(\frac{\partial w}{\partial x}\right)^2 (T - AE) = 0 \qquad [11]$$

The natural frequencies of a nonlinear moving string depend on the initial tension, the transport speed and the amplitude of the vibration. An approximate expression to predict the nth nonlinear frequency is as follows:

$$\omega_n^2 = n^2\pi^2\left(1 - v^2\right) + \frac{9}{32}n^4\pi^4\frac{EA}{T}(w^*)^2 \qquad [12]$$

where $w*$ is the nondimensional amplitude defined as the amplitude of transverse vibration divided by the span length. The second term in eqn [12] represents the effect of nonlinearities on the natural frequencies. The influence of this term becomes larger as the transport speed increases. The second term is also directly proportional to the belt tensile modulus EA. Furthermore, eqn [12] indicates that nonlinear effects

are much more pronounced for higher modes and that nonlinear effects can only be neglected for small amplitudes and high tensions.

Another source of nonlinearity comes from the belt material. The belt material is usually assumed to be linear elastic. However, experiments show that the stiffness of the belt is a function of the belt peak-to-peak strain. An empirical formula for belt stiffness as a function of peak-to-peak strain is in the form of a linear term plus an exponential decaying term. The nonlinear stiffness makes the resonant frequency shifted to smaller value and the amplitude of the resonant vibration smaller.

Parametrically Excited Transverse Vibration

Tension fluctuations cause parametrically excited vibrations and they are the main source of excitation in automotive belts. For parametrically excited moving belts, the constant tension T in eqn [6] becomes a function of time and its fluctuation is characterized as a small periodic perturbation $T_1 \cos \Omega t$ on the steady state tension T_0, i.e.,

$$T = T_0 + T_1 \cos \Omega t \qquad [13]$$

where Ω is the frequency of excitation. For automotive belt drives, these belt tension variations arise from the loading of the pulley by the belt-drive accessories (e.g., air conditioning compressor). They may also arise from pulley eccentricities. These tension fluctuations may parametrically excite large amplitude transverse belt vibrations and adversely impact belt life.

For nonlinear moving belts, there are one trivial solution and two nontrivial solutions (limit cycles) for steady-state dynamic response of parametrically excited vibrations. There exists a lower boundary for the nontrivial limit cycles.

There are two possible parametric resonances: the summation resonance, where the excitation frequency is the sum of any two natural frequencies; and the difference resonance, where the excitation is the difference between any two natural frequencies. Primary resonance, where the excitation frequency is twice the natural frequency, is a special case of summation resonance. For summation resonance, it is found that the first nontrivial limit cycle is always stable while the second nontrivial limit cycle is always unstable.

Transverse Vibration of Viscoelastic Moving Belts

Belts are usually composed of some metallic or ceramic reinforced materials like steel-cord or glass-cord and polymeric materials such as rubber. Most of these materials exhibit inherently viscoelastic behavior. The viscoelastic characteristic can effectively reduce the vibration of moving belts without suffering from greatly reduced natural frequencies. It is found that for nonlinear moving belts, viscoelasticity leads to the upper boundary of nontrivial limit cycles in addition to the lower boundary observed for elastic moving belts. In other words, viscoelasticity narrows the stable region of the first limit cycle and the unstable region of the second limit cycle.

A Moving Beam Model for Transverse Vibration

A moving beam model can be adopted to predict the transverse vibration of a moving belt if the belt is stiff and thick, such as V belts. The linear equation of motion of a moving Euler–Bernoullie beam model is given by:

$$\rho \frac{\partial^2 w}{\partial t^2} + 2\rho c \frac{\partial^2 w}{\partial x \partial t} + \left(\rho c^2 - T\right) \frac{\partial^2 w}{\partial x^2} + EI \frac{\partial^4 w}{\partial x^4} = 0 \qquad [14]$$

The natural frequency for a simply supported moving beam can be calculated by:

$$\omega = p^2 \left(\frac{EI}{\rho L^4}\right)^{1/2} \qquad [15]$$

where p^2 is a parameter determined by solving the equation:

$$c^2 \sigma \delta (\cos 2c - \cosh \delta \cos \sigma) + \left(c^2 - \delta^2\right) \sinh \delta \sin \sigma = 0 \qquad [16]$$

in which:

$$C = \frac{c}{2} \left(\frac{\rho L^2}{EI}\right)^{1/2}, \quad \sigma^2 = p^2 + c^2 \quad \text{and} \quad \delta^2 = p^2 - C^2$$

The variation of the first natural-frequency parameter p^2 with nondimensional velocity C is shown in **Figure 6**.

Torsional Vibration

Torsional vibration is usually not important compared with the transverse vibration of a moving belt, particularly for a single belt. However, if the width of a belt is much bigger compared with a string (this might be the case for toothed belt used in sychronous drives), or if a whole belt drive system is considered, the belt may exhibit twisting or torsional vibrational modes. In this case, the belt is observed to twist along its longitudinal center-line. By ignoring

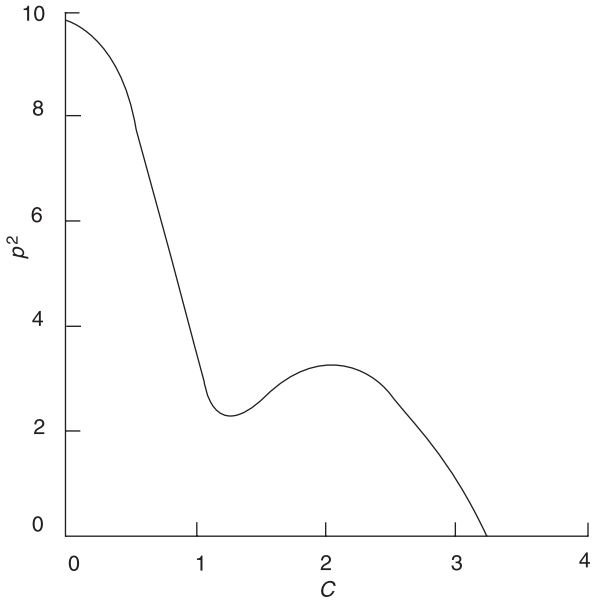


Figure 6 The variation of the first natural-frequency parameter p^2 of a moving beam with the transport speed parameter C.

the coupling between the transverse vibration and the torsional vibration, the equation of motion for torsional vibration θ of a moving belt is given by:

$$\frac{\partial^2\theta}{\partial t^2} + 2c\frac{\partial^2\theta}{\partial x \partial t} + \left(c^2 - c_0^2\right)\frac{\partial^2\theta}{\partial x^2} = 0 \qquad [17]$$

in which the torsional wave velocity c_0 is:

$$c_0^2 = 4\left(\frac{b}{h}\right)^2\frac{G}{\rho} + \frac{T}{\rho b h} \qquad [18]$$

where b and h are the width and height of the cross-section of a belt. Note that eqn [18] is identical in form to eqn [6] for transverse vibration of a moving string. Therefore, analysis and results from the transverse vibration apply to the torsional vibration.

Axial Vibration

Axial vibration of a moving belt is very small compared with transverse vibration. In most cases, axial motion is not important, since axial vibration has much higher natural frequencies. Therefore, a quasi-static assumption can be employed to describe axial motion.

Belt Drives

Belt drives are used in many mechanical systems for power transmission. **Figure 7** shows a typical automotive belt drive system where a single polyvee belt drive powers all the accessories, including alternator, power steering, water pump, tensioner, and so on.

Two distinct types of vibration modes occur for a belt drive: (i) rotational modes and (ii) transverse modes. In rotational modes, the pulleys rotate about their spin axes and the belt spans act as axial springs. In transverse modes, the belt spans vibrate transversely, as discussed in the previous section on moving belts. Both types of vibration are harmful to the system performance. Rotational motions induce dynamic belt tension and the attendant problem of belt fatigue, dynamic bearing reaction, structure-borne noise, and bearing fatigue. Transverse vibrations also induce dynamic tensions, and may directly radiate noise.

For belt drive systems with fixed-center pulleys, the rotational and transverse modes are uncoupled and thus can be modeled by a multi-degree-of-freedom rotational system and by a moving belt model for each belt span, respectively. However, for belt drives with a nonfixed-center pulley, such as the tensioner pulley in the automotive serpentine belt drive system, the rotational and transverse modes are linearly coupled through the rotation of the tensioner arm.

Two commonly adopted models for vibration analysis of automotive serpentine belt drive systems are presented here.

Discrete Spring–Mass Model

The discrete spring–mass model ignores the transverse vibration of the belt and treats each belt spring as an axial spring. Thus, the belt drive is approximated as a multi-degree-of-freedom system where each pulley's moment of inertia is associated with one rotational degree-of-freedom, as shown in **Figure 8**. Such a discrete spring–mass model is used to describe the rotational vibration mode of the belt drive system. The prescribed harmonic crankshaft speed fluctuation due to the cylinder engine operation serves as the excitation of the system. Based on this model, the equation of motion for each fixed center pulley is given by:

$$I_j\ddot{\theta}_j = R_j\left(T_{j-1} - T_j\right) - c_j\dot{\theta}_j + Q_j, \quad j = 2, 3, \ldots, n \qquad [19]$$

where R_j is the jth pulley's radius ($j = 1, 2, \ldots, n$), I_j is the jth pulley's moment of inertia including the accessory driven by this pulley and any shaft extension and couplings, c_j is the jth pulley's rotational

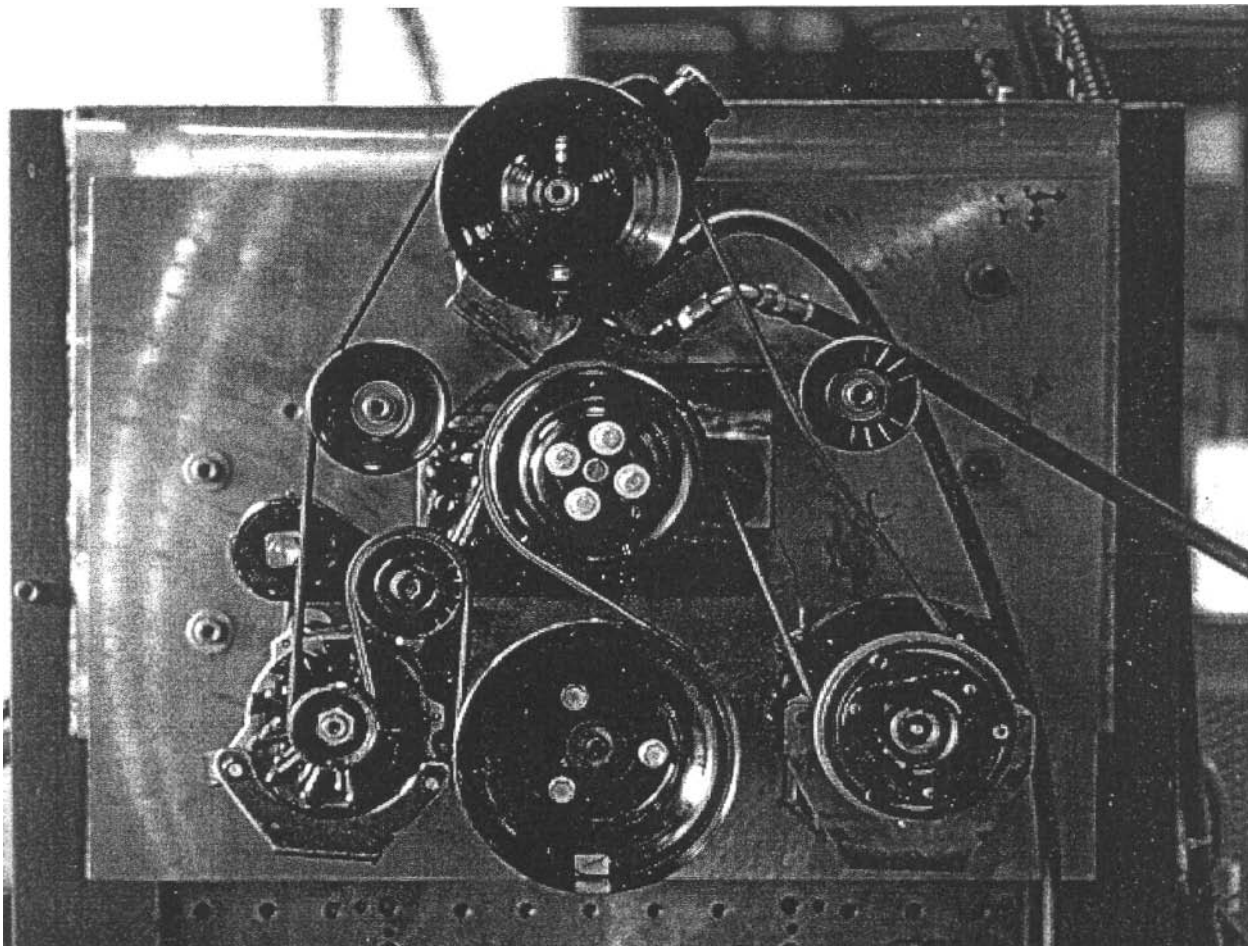


Figure 7 A typical automotive belt drive system.

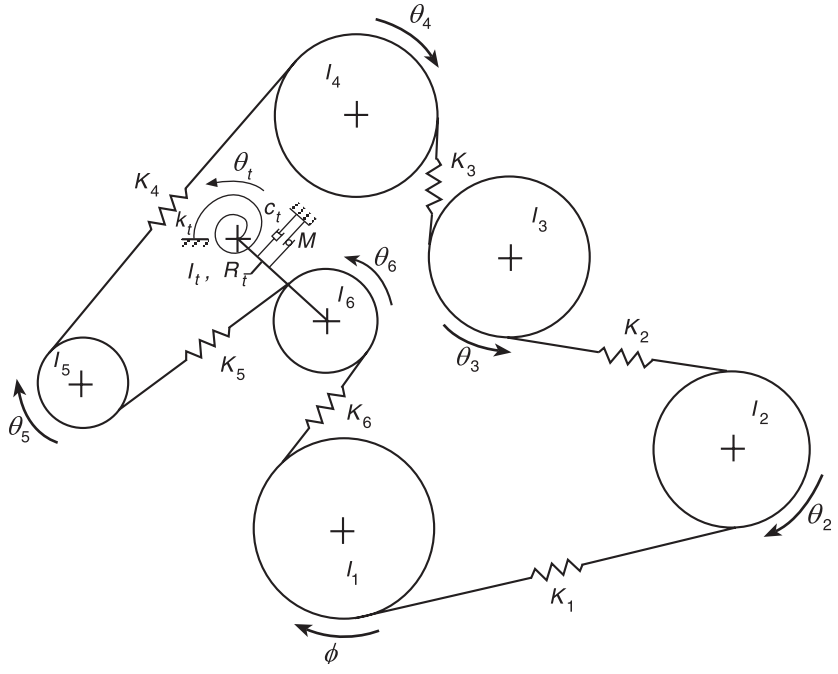


Figure 8 A discrete automotive belt drive system.

damping, Q_j is the dynamic torque requirement of the jth pulley and T_j is the jth belt span tension. The tensioner pulley can be any number from 2 to n and the first pulley is always defined as the crankshaft pulley.

The equation of motion for the tensioner arm is given by:

$$I_t\ddot{\theta}_t = -T_{j-1}L_t \sin\left(\theta_t - \beta_j\right) - T_jL_t \sin\left(\theta_t - \beta_j\right) - c_t\dot{\theta}_t - k_t(\theta_t - \theta_{t0}) + Q_{t0} \quad [20]$$

where I_t is the moment of inertia of the tensioner arm and T_{j-1} and T_j are the two belt tensions acting on the tensioner pulley. In addition, β_j is the angle between the tensioner arm and the vertical line at equilibrium state, R_t is the length of the tensioner arm, θ_t is the dynamic angle of the tensioner arm, c_t is the external viscous damping acting on the tensioner arm, k_t is the rotational stiffness of the tensioner arm, and M denotes the dry friction torque (Coulomb damping torque) acting on the tensioner arm.

For a practical accessory belt drive system, the magnification ratio of the dynamic response of each component with the change of the excitation frequency is shown in **Figure 9**. It is shown that the alternator has the largest magnification ratio.

Hybrid Discrete–Continuous Model

The hybrid model for an automotive belt drive system captures the coupling between discrete rotational vibration of pulleys and the continuous transverse vibration of belt spans. **Figure 10** shows a prototypical belt drive system where $\theta_i\,(i = 1,\ 4)$ is the rotation from equilibrium of the ith discrete element (pulleys or tensioner arm), $w_i\,(i = 1,\ 3)$ is the transverse deflection of span i from equilibrium, J_i and r_i are the mass moment of inertia and radius of the ith discrete element, and l_i is the length of belt span i. The linear equations of motion of the coupled system are composed of three equations of motion for the three continuous belt spans, three equations of motion for the discrete pulleys 1, 2, 4 and the equation of motion for the tensioner arm rotation θ_4. The linear coupling between the transverse vibration of the continuous belt and the rotational vibration of the pulleys are reflected from the equation of motion of the tensioner arm.

Figure 11 shows a prototypical three-pulley serpentine belt drive system called baseline system. The physical properties of the system are given in **Table 1**. The first transverse and rotational vibration mode shapes of the system are shown in **Figures 12** and **13**. It is seen from the mode shapes that there is a significant coupling between the span's transverse vibration and the tensioner arm's rotational vibration.

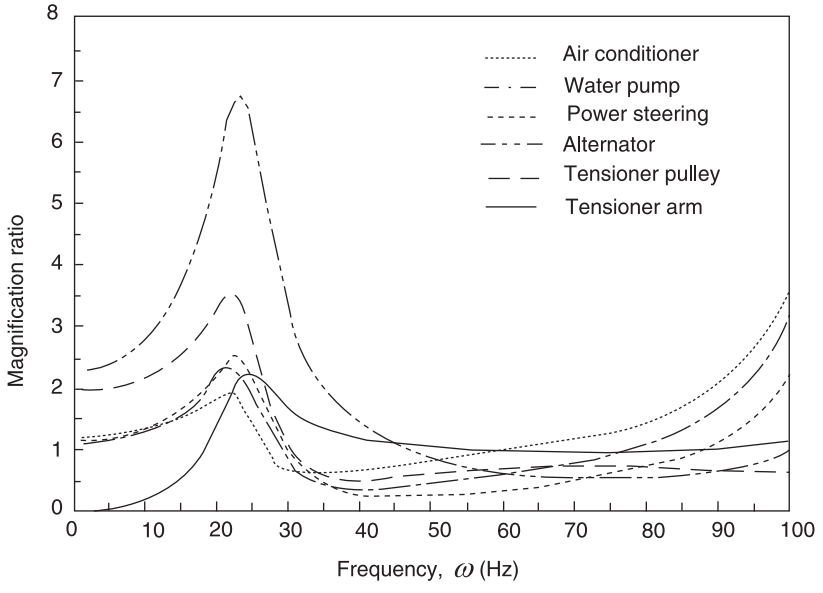


Figure 9 Dynamic response of an automotive belt drive system.

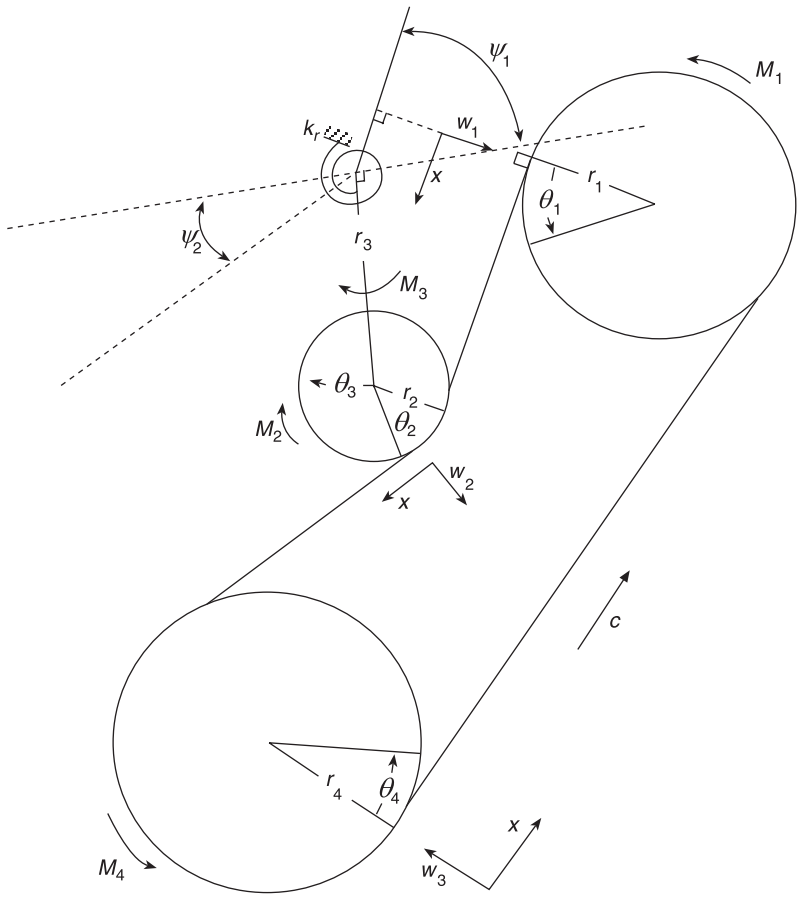


Figure 10 A prototypical belt drive system.

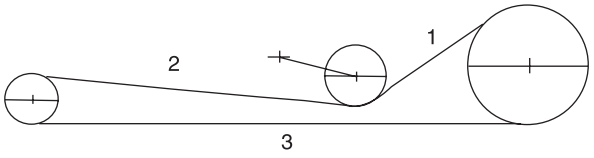


Figure 11 A three-pulley baseline system.

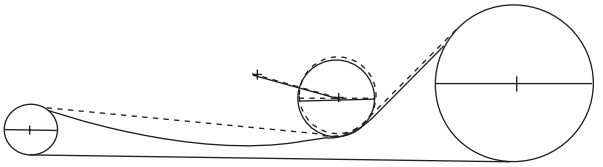


Figure 12 Transverse vibration mode of span 2 of the baseline system (50.53 Hz). Continuous line, mode shape; dashed line, baseline system.

Nomenclature

A	area of cross section
c	torsional wave velocity
C	nondimensional velocity
EA	belt tensile modulus
EI	bending rigidity
I	inertia
L	length
M	dry friction torque
T	tension
ψ	correlation factor
ρ	correction factor
Ω	fequency of excitation

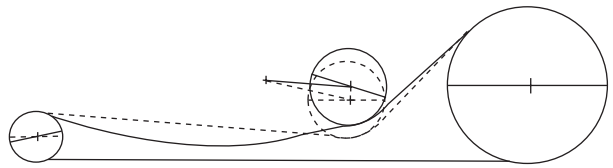


Figure 13 Rotational vibration mode of the baseline system (62.18 Hz). Continuous line, mode shape; dashed line, baseline system.

Table 1 The physical properties of a three-pulley baseline system.

	Pulley 1	*Pulley 2*	*Tensioner arm*	*Pulley 4*
Spin axis coordinates	(0.5525, 0.0556)	(0.3477, 0.05715)	(0.2508, 0.0635)	(0.0, 0.0)
Radii (m)	0.0889	0.0452	0.097	0.02697
Rotational inertia	0.07248	0.00293	0.001165	0.000293
Other physical properties	Belt modulus: $EA = 170\,000\,\text{N}$, $m = 0.1029\,\text{kg m}^{-1}$, Tensioner spring constant: $k_r = 54.37\,\text{N m rad}^{-1}$, Tensioner pulley mass: 0.302 kg (baseline) 0.378 kg (modified)			

See also: **Nonlinear normal modes**; **Nonlinear system identification**; **Nonlinear systems analysis**; **Nonlinear systems, overview**.

Further Reading

Abrate S (1992) Vibrations of belts and belt drives. *Mechanism and Machine Theory* 27: 645–659.

Mockensturm EM, Perkins NC, Ulsoy AG (1996) Stability and limit cycles of parametrically excited, axially moving strings. *ASME Journal of Vibration and Acoustics* 118: 346–351.

Wickert JA, Mote CD Jr (1990) Classical vibration analysis of axially moving continua. *ASME Journal of Applied Mechanics* 57: 738–744.

Zu JW *Static and Dynamic Analysis and Software Development of Automotive Belt Drive Systems*. Internal Final Report to Tesma International Inc.

BIFURCATION

See **DYNAMIC STABILITY**

BLADES AND BLADED DISKS

R Bigret, Drancy, France

Copyright © 2001 Academic Press

doi:10.1006/rwvb.2001.0094

Introduction and Definition

In a turbomachine, a fluid flows across blades mounted on a rotor which is made up of one or more disks with moving blades. When fluid is released, it provides energy to the blades and the rotor works as an engine. On compression, the fluid receives energy from the blades and the rotor acts as a receptor.

In hydraulic machines the function of the blade is as a paddle, whereas when it is larger it works as a blade. Blades are either acted upon by the fluid (motor) or act on the fluid (receptor). Based on the laws of aerodynamics and thermodynamics, blades serve a particular function with great efficiency. Centrifugal, aerodynamic, and hydrodynamic forces all set blades in motion.

A study carried out by VGB (Essen, Germany) from 1973 to 1977 on 76 steam turbines operating at 64–365 MW noted that there were 50 breakdowns in 28 of the 76 turbines. Of these, 80% were caused by moving blades. Were the blades the cause of the breakdown? Blade reliability is an important factor in machine reliability.

In general, stationary blades which are linked to the stator are connected to moving blades which direct the fluid. These fixed, stationary blades are also acted on by aerodynamic and hydrodynamic forces.

Instability

Bladed disks are acted on by three types of aerodynamic force:

1. Anisotropy
2. Particular phenomena
3. Erratic fluctuations in pressure

Anisotropy arises as a result of flow from the radial field of pressure and wakes, which are as wide as the thickness of the blades and stator obstacles. At speed Ω the bladed disks are excited by frequencies:

$$F_{cx} = h\Omega/2\pi$$
$$h = 1, 2, 3 \ldots$$

The amplitude of the components can be high ($\nu n_d \to h$):

$$\nu n_d \Omega/2\pi \quad (\nu = 1, 2, 3 \ldots)$$

where n_d is the number of blades, distributors and stator elements above the disk.

Particular phenomena may be seen at low flow rates, when the fluid does not follow the path designated by the blades. This stalling produces rotating fields at speed $\pm\Omega_t$ in relation to the stator, and at speed $\Omega_{tr} = \Omega \pm \Omega_t$ in relation to the disks which are excited at the following frequencies:

$$f_{ex,t} = m\frac{\Omega \pm \Omega_t}{2\pi}$$

where $m = 1, 2, 3 \ldots$. Observation of high-power turbines shows that $0.3 \leq |\Omega_t|/\Omega \leq 0.7$.

These three forms of excitation may create resonances when:

1. The frequency of excitation is close to a natural disk frequency $\omega_q/2\pi$ (where natural frequency $p_q = \delta_q + i\omega_q$ where $i^2 = -1$; $q = 1, 2, 3 \ldots$) at speed Ω: $h\Omega \approx \omega_q$ or $m(\Omega \pm \Omega_t) \approx \omega_q$
2. The number of nodal diameters n of the natural mode q of the rotational disk, connected to ω_q is equal to h or m.

During resonance, vibration waves, which are fixed in relation to the rotating stator, are rotating in relation to the bladed disk at speed ω_q. The component at ω_1, without a nodal diameter, cannot cause resonance. There may be instability of the limit cycle resulting from a coupling between disk vibration and fluid, in particular in axial compressors. It may be difficult to distinguish between this instability and a forced rate of flow from aerodynamic excitation caused by a rotating field.

Strains

Dynamic strains on the body of the blade, and on its base which is in contact with the disk, are due to a forced rate of flow, resonances, or eventual instability. For a fixed lifespan, which is often important, the maximum acceptable level of dynamic strain is even less when the static strain increases as a result of centrifugal and aerodynamic force (driving or resisting torque).

Table 1 shows the static strains on two turboalternator blades.

The lifespan of high-power steam turbines used by Electricité de France is close to 40 years. A machine working at 600 MW at 3000 rpm, using fossil fuel, contains 4468 moving blades. Machines operating at 1000 MW and 1500 rpm and using nuclear fuel contain 9749 blades, while machines working at 1500 MW, which were first brought into use in 1996, contain 4350 blades. This is a notable reduction.

For low-pressure steam expansion towards the condenser (whose temperature is dependent on that of the cold source, for example 35°C gives rise to 55 mbar), the necessary section for the steam flow imposes a compromise between the number of low-pressure rotors, the diameter of the last disk, and the length of its blades. This section is longer where there are two low-pressure flows in parallel, than when there are three flows. The natural frequencies of the blades and their strains play an essential role in this compromise.

Table 1 Static strains on two turboalternator blades

Steam turbine		*Bladed disk: last stage, low pressure*						
Power (MW)	*Speed* (rpm)	*Power* (MW)	*No. of blades*	*Blade length* (mm)	*Blade mass* (kg)	*Base centrifugal force* (N)	*Maximum static base strain* ($N\,m^{-2}$)	
							Centrifugal force	*Torque*
860 (fossil)	3600	17	78	885	23	2×10^6	1.5×10^8	0.12×10^8
1000 (nuclear)	1500	19.6	138	1220	39	1.22×10^6	0.278×10^8	0.123×10^8

Causes and Consequences of Breakdowns

The driving forces and thus the strains are weak when the distances between the trailing and leading edges of the stator and rotor blades are sufficient for a trickle of fluid to reorganize, beyond the journal zone, as also happens when there are obstacles in the flow. Large gaps make it possible to avoid siren noises, which are particularly annoying in ventilation circuits. However, large gaps may reduce efficiency. In general, stator blades are subject to less dangerous vibration than rotor blades.

The blades of compressors and fans which function at low flow and under unstable conditions (pumping) at frequencies of several hertz are subject to significant strain which may lead to breakdown.

A blade breaking may lead to the machine being destroyed and this may even spark off a greater catastrophe. Breakdown is caused by fatigue as a result of large dynamic strains which are manifested as cracks, and transiently raised thermal gradients. Where there is instability (flutter), the strain may be greater than that seen with the forced rate of flow caused by the harmonics of the rotation speed, and thus the lifespan may be noticeably shorter. If part of a broken blade falls free in the stator, it may destroy other blades, and may well end in catastrophe.

The unbalance created by a broken blade generates a rotating force. For example, for a blade of the last disk of a low-pressure rotor, with 8.5 bar absolute downstream of a 15 MW turbine operating at 7600 rpm: in this case, the rotating force is equal to $mr\Omega^2 = 0.3 \times 0.28(\pi.7600/30)^2 = 53150\,\text{N}$.

The ratio of the rotating force to the static charge at right-angles to the bearings can be high: for a turbine operating at 15 MW, it is $53150/3826 \approx 14$. Deterioration in the bearings, in the sealants, and of the contacts between the rotor and the stator may lead to chaos.

Misalignments and rotating forces from other causes – such as the receiving structure being deformed, coaxiality problems, rotor shaft, cracked rotor, instability, short axial distance between the rotor and stator as a result of differential expansion – can lead to contact between the blades and the stator, as a consequence of deterioration and chaos.

The presence of water within steam, or cavitation within the pump and turbine, may cause erosion of the blades. These erosions affect the natural frequencies; they may cause harmful resonance and greater unbalance, leading to a breakdown in the links. Flowing fluids can leave deposits on the blades, such as soot on fan blades; when these deposits come loose they create unbalance. The blades need to be cleaned: introducing grains of rice to the machine helps loosen any deposits.

Technology

Blades are fixed by an integrated base radiating out from the edge of the disk, in various ways. Axial rivets may be used. Where gas turbines work with gas at high temperature (800–1000°C), the play between the base and the disk permits transient differences in expansion, and low levels of strain.

Blades may be connected together at the top with shrouds which are in contact with each other. Wires or shrouds attached to the body of the disk may also be used. Such connectivities between blades may prevent dangerous vibration resonance. This connectivity may not be acceptable for particularly long blades, because of the strain involved.

In some sets of blades, in particular in turboreactors, masses – so-called 'candies' – are placed on the platform at the base of the disks. These masses, which come into contact through centrifugal force, create friction which reduces vibration.

Natural frequencies and their associated natural modes characterize the disk and blade set-up and even the rotor. When the natural frequencies of the disks and rotor are much greater than those frequencies which are liable to provoke unacceptable resonance, only those blades, whether connected or standing alone, fixed on the disks are taken into account when evaluating the vibratory rate of flow. This situation is common in fans where only a few blades (≤ 10) are soldered on to a massive rotor element.

On certain axial compressors the influence of the disks and rotors may have a minimal effect on the vibration of thin blades.

Hydraulic turbine wheels, pumps, and radial compressors may be extracted from the same metallic blocks from which the blades are cut. The frequencies and natural modes are related to the total wheel assembly.

Technological considerations are taken into account when defining procedures to determine frequencies and natural modes by theoretical models and experiments. As a manufacturer's control or to define the limits of a study, approaches are generally made on isolated elements, such as a free fitted blade or a nonbladed disk.

Pulsations and Natural Modes of a Disk

Figure 1 shows a naturally axially vibrating disk. This is characterized by two nodal diameters and one nodal circle, on which the level of vibration is very low.

The number of diameters and nodal circles increases with natural frequency. The natural frequencies, ω_{nc}, of a thin cylindrical disk without damping, are defined by:

$$\omega_{nc} = \frac{\alpha_{nc}}{r^2}\sqrt{\frac{D}{\rho h}}$$

where $r =$ radius, $D = Eh^3/12(1-\nu^2)$; $h =$ thickness; $E =$ elasticity modulus, $\nu =$ Poisson coefficient; $\rho =$ volume mass; $n =$ number of nodal diameters; and $c =$ number of nodal circumferences.

Where $n = 1$, whether the center of the disk is fixed or free, $\alpha_{11} = 20.52$ when $c = 1$; $\alpha_{12} = 59.86$ when $c = 2$.

Neglecting the increase in natural frequencies with rotation speed Ω, resonance can be shown by:

$$\Omega = \begin{cases} \omega_{11} \\ \omega_{12} \end{cases}$$

when the disk rotates in a field of fixed force which has a component of frequency Ω ($h = 1$; first harmonic for $n = 1$).

Technological requirements lead to bladed disks whose form is more complex than that of the disk shown in **Figure 1**. Their modal shape is defined by components in axial and tangential directions. On the whole, the radial components are weak. Nodal lines may be moving: they constitute nodal zones.

When the natural frequencies of rotating disks are high in comparison to frequencies from driving forces, isolated blades are resonant when the frequency of the exciting force is the same as the natural eigenvalues of the blades.

Example

The following example is an evaluation of the resonant frequencies of a low-pressure bladed disk from an 860-MW turbine. The characteristics of this disk are shown in **Table 1**.

In a test rotor ($l = 2990$ mm; two bearings) 78 blades are mounted. They are linked together by arches of wire (stanchion: 200 mm^2 section). The outside diameter is 3140 mm; the rotor is contained in a casing under vacuum (pressure ≈ 3 mbar absolute). The blades pass through two fixed magnetic fields at 180° which excite them. The deformations (strains) are measured by extensometers.

Figure 2 is a schematic of the measuring system. **Figure 3** shows a Campbell diagram, dating from 1924. The resonances at the intersection $f = hN$, and the frequency of the bladed disk. These are close to the natural frequencies, ω_q, which are associated to the mode waves at order h (nodal diameters). Nodal circles may exist in the four groups depicted.

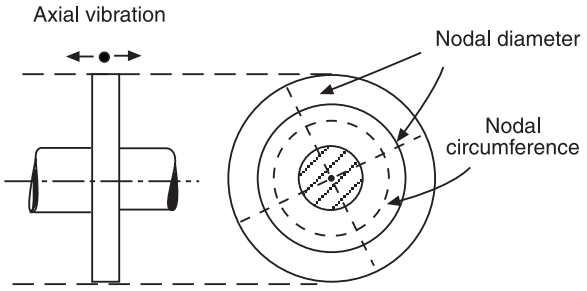


Figure 1 Vibrating disk.

Figure 4 shows a resonance at the nominal speed of 3600 rpm.

Analyses during Rotation and at Rest ($f_r = 0$)

Measuring systems incorporating rotating contacts to transmit signals are used for on-site analysis and in workshops. **Figure 2** shows the structure of one such system. Natural frequencies may be adjusted to shorten the blades mounted on the disks, preventing resonance during machine use. On-site, dynamic strains are measured with reference to power, flow, and pressure at the condenser. As an example, a reduction in power of the nominal value W_0 at $0.13W_0 = W_r$ can lead to an increase in strain: $\sigma_r/\sigma_0 \approx 6.3$. For flow from Q_0 to $Q_r = 0.2Q_0$, $\sigma_r/\sigma_0 \approx 2$. For pressure from P_0 to $P_r = 0.2P_0$, $\sigma_r/\sigma_0 \approx 5$.

The increase in strain arises from rotor and flow. These phenomena may cause instability occurring on natural frequencies related to the order of a wave.

The frequencies and natural waves of the bladed disks are established at zero speed; they are excited by harmonic forces and the responses measured with a seismic or magnetic sensor. Modal analysis procedures using specific software can also be used; the frequencies and natural modes are obtained faster than with simple methods.

Great uncertainty occurs for the value of natural frequency computed from natural frequencies which are determined at zero speed. This is the influence of the centrifugal forces which directly act as stiffening and modify the contacts between the blades, between the blades and the disk, and even between the disk and the rotor shaft.

The influence may be approximated for the first natural frequencies by:

$$f_{dr} = \sqrt{f_{d0}^2 + \alpha f_r^2}$$

where f_{dr} = natural frequency of the rotating disk; f_{d0} = natural frequency of the disk at zero speed; and f_r = rotation speed. The value of α can be estimated by comparing the natural frequency f_{d0} calculated at zero rotation speed, to the frequency of resonance f_{dr}, which is related to the rotation speed f_{rr}:

$$\alpha = \frac{f_{dr}^2 - f_{d0}^2}{f_{rr}^2}$$

Measured natural frequencies can be used to tune the mathematical model. An algorithm can then calculate the natural frequencies from rotation speed.

For the bladed disk shown in the Campbell diagram (**Figure 3**), at resonance on the sixth harmonic, $\alpha \approx 10$.

The modification of the contacts, often more important if there are significant imperfections (tightenings or loosenings, which give rise to anisotropy), can cause important variations in natural frequencies as a function of rotation speed. In this regard, the connectivity between the blades (beyond their stiffening role) causes homogenization, which minimizes the influence of local imperfections.

The results of on-site rotation measurement, or measurements made in the casing, at zero speed can be used to tune theoretical models.

Studies are currently underway to monitor the vibratory conditions of blades *in situ*. These studies incorporate measurement and analysis of the movement of the blade edges by the radial captors, as well as vibrations of the fixed parts (bearings) and the rotors to detect the vibrating components of both fixed and moving blades.

When breaking blades cause violent variations in vibration intensity, whether increasing or decreasing, the machine must be shut down to avert catastrophe.

Models

Mathematical models are obtained by three-dimensional finite-element methods. The disks are generally taken into account in this, as is the rotor. Uncertainty about conditions at the limits, at right-angles to the contacts, and variations in rotation speed, temperature, and time (creep) may be important. Models make it possible to estimate their influence, for example, variation in link stiffness of some of the disk blades.

Experimental studies on elementary physical models make it possible to extract useful sizes for resetting models.

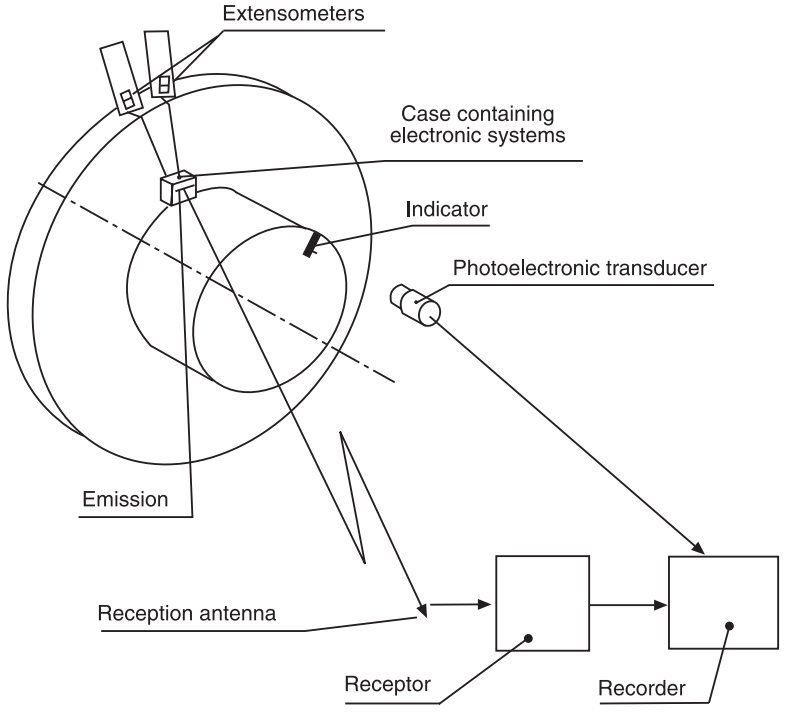


Figure 2 System for measuring strain on rotating blades.

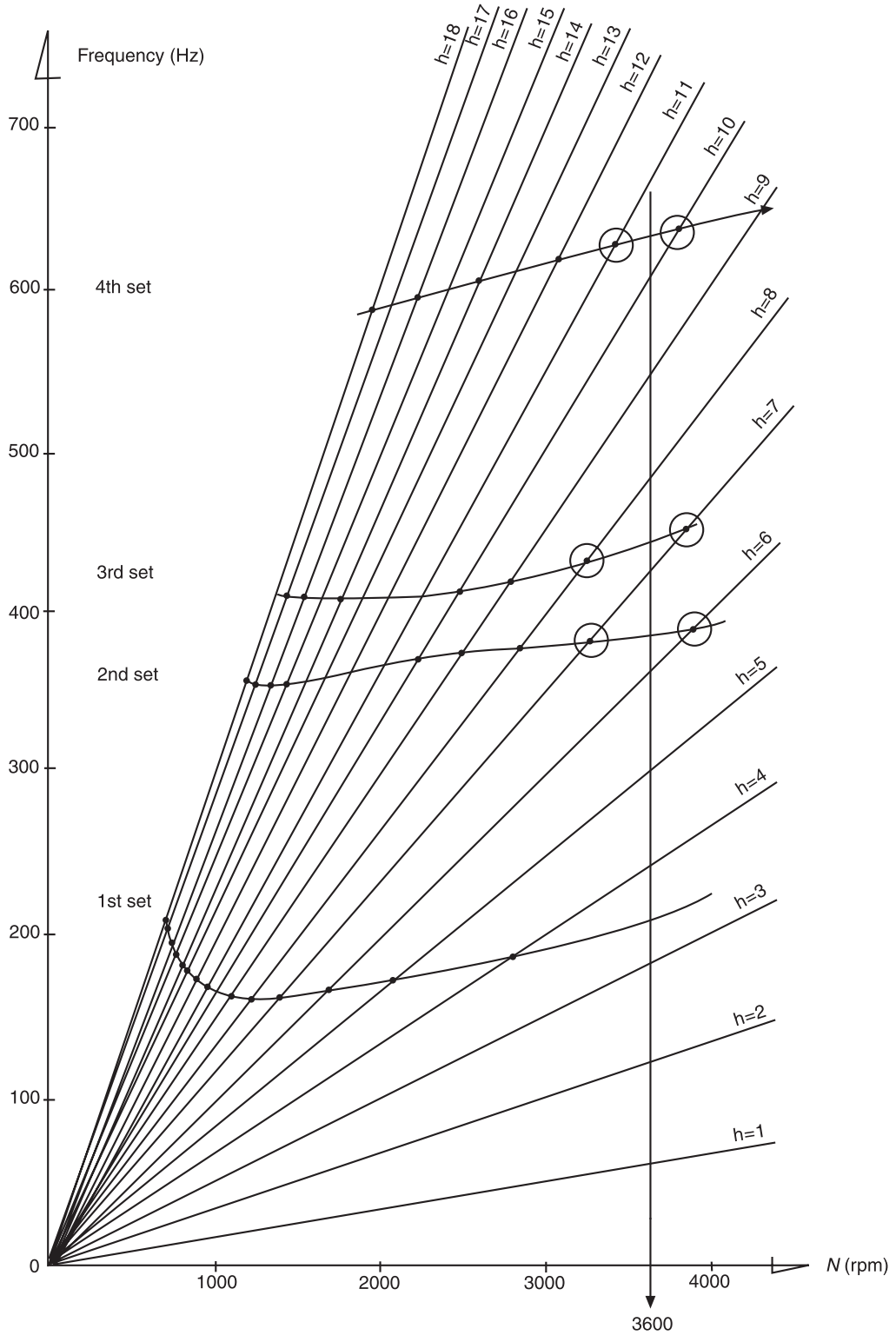


Figure 3 Resonances (•) of a bladed disk. *h*: Harmonic order of speed. Modified from Campbell.

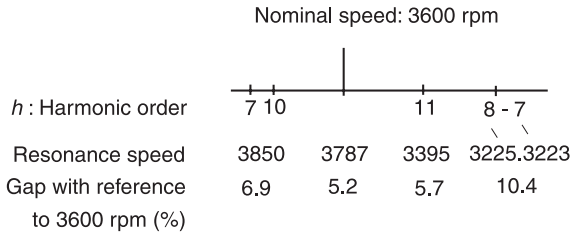


Figure 4 Resonances.

Aeroelasticity can be introduced to study behavior, which is particularly relevant for conditions of turbomachine stability, as well as aviation compressors and pumps, which are widespread because of their hydroelasticity.

See also: **Discs**; **Rotating machinery, essential features**; **Rotating machinery, monitoring**; **Rotor dynamics**.

Further Reading

Adams ML Jr (1999) *Rotating Machinery Vibration. From Analysis to Troubleshooting*. New York: Marcel Dekker.

Bigret R (1980) *Vibrations des Machines Tournantes et des Structures. [Vibrations of Rotating Machines and Structures.]* Paris: Technique et Documentation Lavoisier.

Bigret R (1997) *Stabilité des Machines Tournantes et des Systèmes. [Stability of Rotating Machines and Systems.]* Simlis, France: CETIM.

Bigret R, Feron J-L (1995) *Diagnostic, Maintenance, Disponibilité des Machines Tournantes. [Diagnostics, Maintenance, Availability of Rotating Machines.]* Paris: Masson.

Boulenger A, Pachaud S (1998) *Diagnostic Vibratoire en Maintenance Préventive. [Vibratory Diagnostics and Preventive Maintenance.]* Paris: Dunod.

Childs D (1993) *Turbomachinery Rotordynamics*. Chichester: John Wiley.

Dimentberg FM (1961) *Flexural Vibrations of Rotating Shafts*. London: Butterworths.

Frêne J, Nicolas D, Dequeurce, Berthe D, Godet M (1990) *Lubrification Hydrodynamique – Paliers et Butées. [Hydrodynamic Lubrication – Bearings and Thrust.]* Paris: Eyrolles.

Gasch R, Pfützner (1975) *Rotordynamik. Eine Einführung*. Berlin: Springer Verlag.

Genta G (1999) *Vibration of Structures and Machines*. Berlin: Springer Verlag.

Lalanne M, Ferraris G (1990) *Rotordynamics Prediction in Engineering*. Chichester: John Wiley.

Morel J (1992) *Vibrations des Machines et Diagnostic de leur Etat Mécanique. [Machine Vibrations and Diagnostics of their Mechanical Condition.]* Paris: Eyrolles.

Tondt A (1965) *Some Problems of Rotor Dynamics*. London: Chapman & Hall.

Vance JM (1988) *Rotordynamics of Turbomachinery*. Chichester: John Wiley.

BOUNDARY CONDITIONS

G Rosenhouse, Technion - Israel Institute of Technology, Haifa, Israel

Copyright © 2001 Academic Press

doi:10.1006/rwvb.2001.0089

The present article reviews the effect of boundaries and obstacles on generation of vibrations in solid bodies. We distinguish between a point motion and vibrations in one-, two-, and three-dimensional spaces. The article also deals with special effects, such as change from wave propagation into the state of vibrations via boundary conditions, flanking through joints, coupling between longitudinal and flexural waves, elastic mountings, nonreflecting boundary conditions, moving boundaries and semi-definite systems.

Background

A homogeneous isotropic elastic infinite medium does not reflect waves. Hence, when a source radiates mechanical (acoustic) energy into an infinite medium it does not turn into vibration in the sense of standing waves. On the other hand, existence of ends or inhomogeneities of the medium influence the displacement field within the medium by causing reflections that can lead to vibration patterns. Another effect

that occurs generally at the boundaries is the transmission of mechanical energy into or out of the medium. Even along a rigid boundary, the mechanical energy is not totally reflected and some of it disappears through a thermodynamic process of absorption. Vibrations can occur at a point and in any spatial dimension.

A typical point vibration is the motion of a mass of a single-degree-of-freedom 'mass-spring' unit. A one-dimensional vibration occurs longitudinally in a rod by an axial excitation force, axially by torque and laterally in a beam by a dynamic transverse load. Two-dimensional vibrations occur in-plane and out-of-plane in plates. Vibrations of shells can be like that of vibration of surfaces that are described in three dimensions. Vibrations also occur in three-dimensional bodies, as in a piezoelectric transducer built of a layered block. Determination of vibrations in any of these dimensions involves satisfying both the governing field equations and the boundary conditions.

Boundary Conditions for a Longitudinal Wave

If a longitudinal mechanical wave propagates in x-direction, and a boundary exists at x_0, it causes reflection. The simplest boundary conditions are:

1. A rigid end that does not allow for displacements, u:

$$u(x_0, t) = 0 \qquad [1]$$

2. A free end where no stress, σ_x, exists on the surface:

$$\left.\frac{\partial u(x,t)}{\partial x}\right|_{x_0} = 0 \qquad [2]$$

See **Figure 1**. If E is Young's modulus, and x_0 is an interface between two media, 1 and 2, then continuity of displacements and equality of stresses on both sides of the interface yield interface conditions:

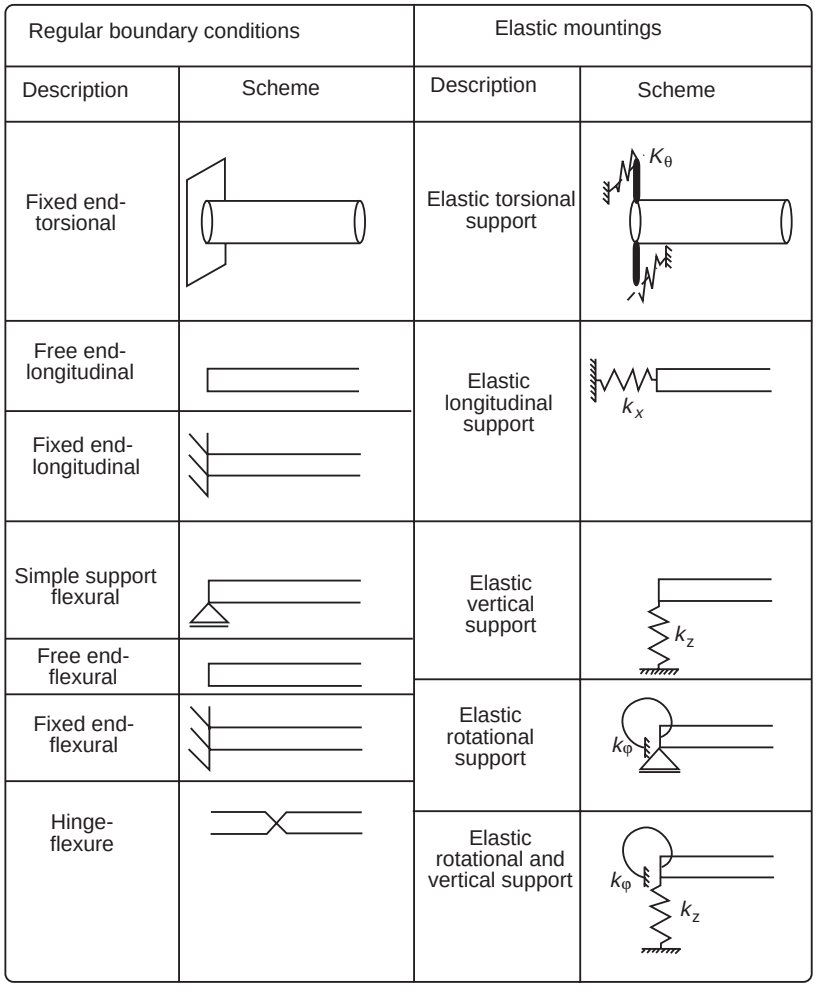


Figure 1 Ends and elastic mountings of rods and beams.

$$(u_1 - u_2)_0 = 0, \quad E_1 \frac{\partial u_1}{\partial x} - E_2 \frac{\partial u_2}{\partial x}\bigg|_{x_0=0} = 0 \qquad [3]$$

Eqn [3] also expresses the interface conditions for longitudinal waves.

A specific important case is the boundary interaction of a harmonic wave of radian frequency ω. Such a wave in a complex form is:

$$\begin{aligned} u(\omega, x, t) &= \hat{C}_1(\omega) \exp\left[i(kx - \omega t + \psi_1)\right] + \hat{C}_2(\omega) \\ &\quad \times \exp\left[-i(kx + \omega t + \psi_2)\right] \\ &= C_1(\omega) \exp\left[i(kx - \omega t)\right] + C_2(\omega) \\ &\quad \times \exp\left[-i(kx + \omega t)\right] \end{aligned} \qquad [4]$$

where $k = \omega/c$ is the wave number, and c is the velocity of propagation of the wave. Only the real part is to be taken into account in the last equation for physical interpretation. The first term in the right-hand side of eqn [4] is a wave propagating in x-direction, while the second one is propagating in the opposite direction. ψ_1 and ψ_2 are the phases of the two terms respectively. A whole signal can be built of harmonic components, and when this dependence is continuous, the Fourier integral is used:

$$u(x,t) = \int_{-\infty}^{\infty} \left\{ \begin{array}{c} C_1(\omega) \exp\left[i(kx - \omega t)\right] \\ +C_2(\omega) \exp\left[-i(kx + \omega t)\right] \end{array} \right\} \mathrm{d}\omega \qquad [5]$$

One harmonic term can suffice to illustrate the effect on the boundary conditions. We consider one term that propagates towards $x = 0$ within the domain $-\infty < x \leq 0$:

$$u(\omega, x, t) = C_1(\omega) \exp\left[i(kx - \omega t)\right] \qquad [6]$$

Assume a rigid boundary at $x = 0$, then by satisfying eqn [1] at $x_0 = 0$, a reflected wave that propagates opposite x in the domain $-\infty < x \leq 0$ occurs. This wave component has the same frequency and magnitude of amplitude as the incident wave, but the reflected amplitude has a negative sign. Hence, due to the specific boundary condition, the displacement function of the rod becomes:

$$u(\omega, x, t) = 2iC_1 \ \sin\ (kx) \exp\left(-i\omega t\right); \ -\infty < x \leq 0 \qquad [7]$$

For a free end at $x = 0$, and the same incident wave, eqn [2] has to be satisfied. Again, a reflection occurs with the same frequency and magnitude of amplitude, but with a positive sign of the amplitude, and the result becomes:

$$u(\omega, x, t) = 2C_1 \cos\,(kx) \exp\left(-i\omega t\right); \ -\infty < x \leq 0 \qquad [8]$$

Given two semiinfinite rods that are firmly connected at $x = 0$, the properties of the whole rod are Young's modulus E_1 and density ρ_1 at $x < 0$ and E_2 and ρ_2 at $x > 0$. $u(\omega, x, t) = C_1(\omega) \exp\left[i(kx - \omega t)\right]$ of eqn [6] propagates within the domain $-\infty < x \leq 0$ towards $x = 0$. In this case a reflection wave with a reflection coefficient R and a transmitted wave with a transmission coefficient Tr are needed in order to satisfy the boundary conditions (eqn [3]), while the frequency of these added waves is the same as that of the incident wave. R and Tr are defined by Fresnel formulae:

$$\begin{aligned} R &= \frac{\sqrt{\rho_1 E_1} - \sqrt{\rho_2 E_2}}{\sqrt{\rho_1 E_1} + \sqrt{\rho_2 E_2}} = \frac{n - m}{n + m}; \\ Tr &= \frac{2n}{n + m}; \quad n = \frac{c_1}{c_2}; \quad m = \frac{\rho_2}{\rho_1} \end{aligned} \qquad [9]$$

From Wave Propagation to Vibrations via Boundary Conditions

Disturbing a rod from its rest conditions by $u(x, 0) = 0; 0 < x < L$, without external excitation when $t > 0$, then the rod should obey the longitudinal homogeneous wave equation:

$$\frac{\partial^2 u}{\partial t^2} - c^2 \frac{\partial^2 u}{\partial x^2} = 0; \quad t > 0 \qquad [10]$$

This homogeneous second-order differential equation with constant coefficients has a solution of the form:

$$u(x,t) = \hat{u}(x) \exp\left(-i\omega t\right) \qquad [11]$$

Substituting eqn [11] into eqn [10] yields:

$$\frac{\partial^2 \hat{u}}{\partial x^2} + k^2 \hat{u} = 0; \quad k = \frac{\omega}{c} \qquad [12]$$

The solution to the last equation is:

$$\hat{u} = C \ \sin\ (kx) \qquad [13]$$

Eqn [13] has to satisfy the boundary conditions of the rod. Say that the rod is fixed at $x = 0$ and $x = L$, which means $\hat{u}(0) = u(L) = 0$, then the boundary condition at $x = 0$ is satisfied identically. However, the boundary condition at $x = L$ dictates $\sin\,(kx) = 0$, which leads to a series of discrete possible motions satisfying:

$$k_n = \frac{n\pi}{L};\ n = 1, 2, 3 \ldots$$

or:

$$\omega_n = \frac{n\pi c}{L};\ n = 1, 2, 3 \ldots \qquad [14]$$

Hence, due to the boundary conditions also under excitation, the vibrations of the rod can carry in general only a combination of specific mode shapes $\phi_n(x)$:

$$\hat{u}_n(x) = \hat{C}_n \phi_n(x) = \hat{C}_n \ \sin\left(\frac{n\pi x}{L}\right) \qquad [15]$$

For other boundary conditions other mode shapes are suitable.

The total solution for free vibrations carries the form:

$$u(x,t) = \sum_{n=1}^{M} [C_n \phi_n(x) \exp(i\omega_n t)]; \quad C_n = \hat{C}_n \exp(i\psi_n) \qquad [16]$$

$\hat{C}_n$ and ψ_n are arbitrary and depend on the initial conditions.

Longitudinal Elastic Mounting

Between the states of free and fixed-end conditions, a state of elastic support with a reactive force that limits the motion can be constructed. The larger the displacement at the end, then the larger is the reactive force. Such a situation can occur if, for example, a spring is attached to the end of the rod and constrained at its other end (**Figure 1**). If k_x is the spring constant in x-direction, then the boundary condition is:

$$\left.\frac{\partial u(x,t)}{\partial x}\right|_{x_0} = \frac{k_x u(x_0,t)}{ES} \qquad [17]$$

where S is the cross-section area of the rod.

Boundary Conditions for a Torsion Wave

Torsion vibration of a rod is one-dimensional, like longitudinal vibration. In fact, the angle of rotation $\theta(x, t)$ replaces the longitudinal displacement $u(x, t)$, the torque $M_T(x, t)$ replaces the axial force $F(x, t)$, the polar cross-sectional moment of inertia I_p replaces the cross-section area S, the shear modulus of elasticity G replaces Young's modulus E, and the velocity of torsion wave propagation c_T replaces the velocity of propagation of the longitudinal wave c. The rest is analogous. Hence, the regular torsion boundary conditions are:

1. A rigid end that does not allow for rotation:

$$\theta(x_0, t) = 0 \qquad [18]$$

2. A free end where no torque, $M_T = GI_p(\partial\theta/\partial x)$, exists:

$$\left.\frac{\partial\theta(x,t)}{\partial x}\right|_{x_0} = 0 \qquad [19]$$

The homogeneous equation of torsion motion is also analogous to the longitudinal one:

$$\frac{\partial^2\theta}{\partial x^2} + \frac{1}{c_T^2}\frac{\partial^2\theta}{\partial t^2} = 0 \qquad [20]$$

Boundary Conditions for a Beam

Lateral (Flexural) Vibrations

The effect of boundary conditions on both natural frequencies and normal modes is shown in this section for a straight beam with different end conditions. Generally, in a three-dimensional problem there are six resultant generalized force components that can act on the cross-section of the beam (three forces and three moments); **Figure 2** (bottom). However, most two-dimensional models of beams are satisfactory, as shown in **Figure 2** (top). The beam in this case has a length L, cross-section area S, rigidity EI, density ρ, and mass per unit length m. I is the moment of inertia of the cross-section, around the z-axis, through the center of gravity.

The free (without external excitation) deflection $v(x, t)$ of the beam is given by the following fourth-order differential equation:

$$EI\frac{\partial^4 v}{\partial x^4} + \rho S\frac{\partial^2 v}{\partial t^2} - \rho I\frac{\partial^4 v}{\partial t^2 \partial x^2} = 0 \qquad [21]$$

In the case of negligible rotary inertia, which is a common situation, the equation of motion becomes:

$$EI\frac{\partial^4 v}{\partial x^4} + \rho S\frac{\partial^2 v}{\partial t^2} = 0; \quad \text{or} \quad r_0^2\frac{E}{\rho}\frac{\partial^4 v}{\partial x^4} + \frac{\partial^2 v}{\partial t^2} = 0; \quad r_0 = \sqrt{\frac{I}{S}} \qquad [22]$$

The most common boundary conditions, ignoring axial forces, are defined **Table 1** and **Figure 1**.

The general solution to eqn [22] for a wave propagating in x-direction is $v(x, t) = C_1\phi(x) \exp(-i\omega t)$

Table 1 Various flexural boundary conditions

Type of boundary or joint	*Conditions*
Free boundary	$d^2\phi/dx^2 = 0;\ d^3\phi/dx^3 = 0$
Clamped boundary	$\phi = 0;\ d\phi/dx = 0$
Pinned or simply supported boundary	$\phi = 0;\ d^2\phi/dx^2 = 0$
Sliding boundary	$d\phi/dx = 0;\ d^3\phi/dx^3 = 0$
An internal hinge	$d^2\phi/dx^2 = 0$

and, when substituted in the equation of motion, leads to the ordinary differential equation for $\phi(x)$:

$$\frac{d^4\phi(x)}{dx^4} - k^4\phi = 0; \quad k = \sqrt[4]{\frac{\rho}{Er_0^2}}\sqrt{\omega} \qquad [23]$$

The general solution for the ω is:

$$v(x,t) = C_1 \exp[i(kx - \omega t)] + C_2 \exp[-i(kx - \omega t)] + C_3 \exp[kx - i\omega t]C + {}_4 \exp[-kx - i\omega t];$$
$$k = \sqrt[4]{\frac{\rho}{Er_0^2}}\sqrt{\omega} \qquad [24]$$

The two last terms on the right-hand side of eqn [24] are nonpropagating harmonic oscillations, that appear mostly near the beam ends or obstructions along the beam. The first two are propagating in x-direction and in the opposite, at the phase velocity:

$$c_{ph} = \pm\frac{\omega}{k} = \sqrt[4]{\frac{Er_0^2}{\rho}}\sqrt{\omega} \qquad [25]$$

As in the case of longitudinal waves, boundary conditions cause reflection of bending waves. $v(\omega, x, t) = C_1(\omega) \exp[i(kx - \omega t)]$ eqn [24] propagates within the domain $-\infty < x \leq 0$ towards $x = 0$,

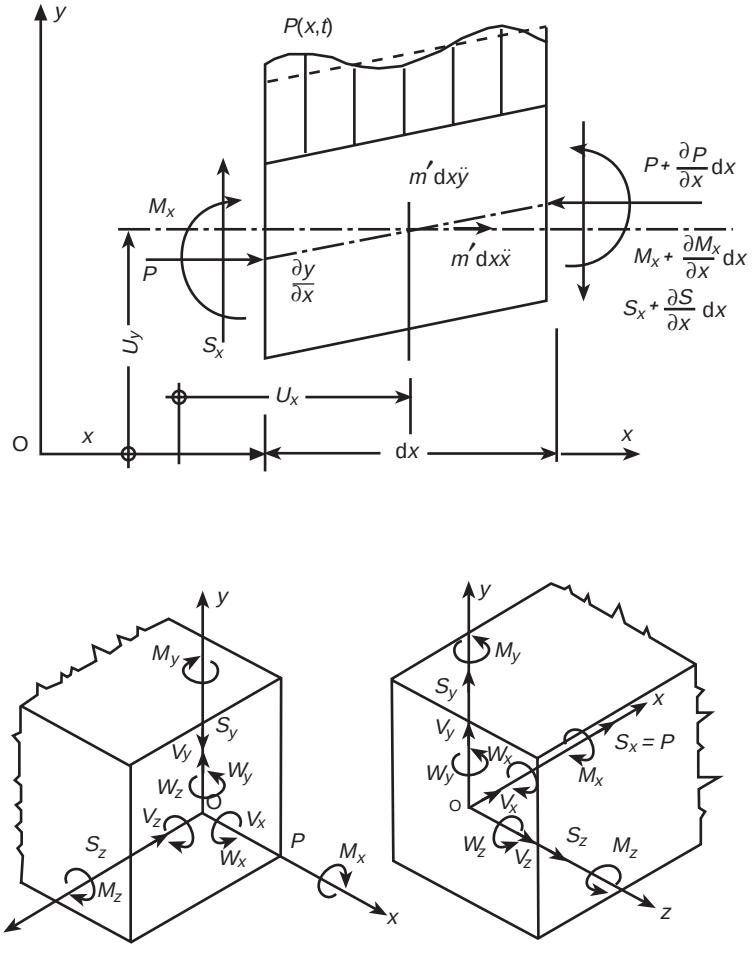


Figure 2 Notation of displacements and forces.

where the beam is clamped ($\phi = 0$; $d\phi/dx = 0$). In this case a reflected wave with a reflection coefficient R and the evanescent wave of a coefficient V are needed in order to satisfy the specified boundary conditions, while the frequency of these added waves is the same as that of the incident wave. Introducing into eqn [24]:

$$C_1 = C; \quad C_2 = RC; \quad C_3 = VC; \quad C_4 = 0 \qquad [26]$$

and using the boundary conditions of a fixed end, the reflection and evanescence coefficients are:

$$R = \frac{1-i}{1+i}; \quad V = \frac{-2i}{1+i} \qquad [27]$$

and finally, the solution of the sound field for the fixed end becomes:

$$v(x,t) = C\left\{\exp\left[i(kx-\omega t)\right] + \frac{1-i}{1+i} \times \exp\left[-i(kx-\omega t)\right] - \frac{2i}{1+i}\exp\left[kx - i\omega t\right]\right\} \qquad [28]$$

Excluding the cases where the boundary or support is elastically held against deflection and rotation and ignoring longitudinal effects, the lateral mode shapes can be defined as $\phi_n(x/L)$; $n = 1, 2, 3\ldots$ In the cases presented in the example the mode shapes carry the form:

$$\phi_n\left(\frac{x}{L}\right) = \cosh\left(\vartheta_n\frac{x}{L}\right) + \cos\left(\vartheta_n\frac{x}{L}\right) - \xi_n\left[\sinh\left(\vartheta_n\frac{x}{L}\right) + \sin\left(\vartheta_n\frac{x}{L}\right)\right]; \quad n = 1,2,3\ldots \qquad [29]$$

and the nth natural frequency:

$$f_n = \frac{\vartheta_n^2}{2\pi L^2}\sqrt{\frac{EI}{m}}; \quad n = 1,2,3\ldots \qquad [30]$$

The values of ϑ_n and ξ_n depend on the boundary conditions and on the nth mode shape.

A relatively simple example is of a simply supported beam of length L, where $\phi = 0$; $d^2\phi/dx^2 = 0$ at $x = 0$ and $x = L$. These boundary conditions lead to the following two characteristic equations:

$$\begin{bmatrix} \sin(kL) & \sinh(kL) \\ -\sin(kL) & \sinh(kL) \end{bmatrix}\begin{bmatrix} C_1 \\ C_2 \end{bmatrix} = \begin{bmatrix} 0 \\ 0 \end{bmatrix} \qquad [31]$$

For a nonzero solution we have:

$$\sin(kL) = 0 \rightarrow k_n = \frac{n\pi}{L}; \; n = 1,2,3\ldots \rightarrow \omega_n = \sqrt{\frac{Er_0^2}{\rho}}\left(\frac{n\pi}{L}\right)^2 \qquad [32]$$

and:

$$v_n = C\sin(k_n x)\exp(-i\omega t) \qquad [33]$$

Illustration of the Effect of Boundary Condition of a Beam

The coefficients ϑ_n and ξ_n for various boundary conditions and modes are given in **Table 2**. A comparison of the effect of the various boundary conditions considered in **Table 2** shows how different boundary conditions lead to significantly different modes and natural frequencies.

Elastically Mounted Beams

Between the states of free and fixed supports there are states of elastic mountings. The elastic mounting allows for deflection and rotation under the action of forces and moments respectively (**Figure 1**). The boundary condition in this case equalizes the action and reaction at the mounting. The elastic reaction can be against the linear motion, rotation or both, as can be seen from **Figure 1**. The use of such boundary conditions is demonstrated by the following example.

Given a beam as shown in **Figure 3**; m is the mass per unit length of the beam, and L is the span of the beam. The beam is simply supported at A and elastically mounted at B. k_z is the spring constant of the beam. The natural frequency of the beam is sought. If the reaction of the beam at B is $R_B = mgL/2$, then $v_B = R_B k_z$ is the deflection at B. The natural radian frequency can be estimated by Rayleigh's method. If the midspan of the beam is considered as the location of the equivalent mass, then the equivalent mass and spring constant are respectively:

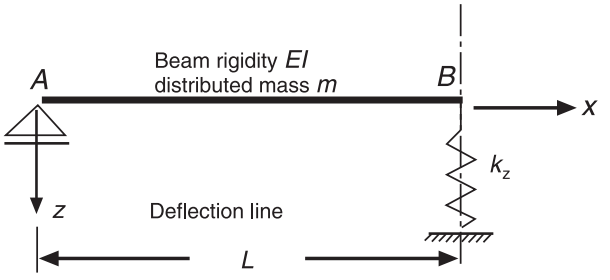


Figure 3 Elastically mounted beam.

Table 2 The coefficients ϑ_n and ξ_n for various boundary conditions and modes

Boundary conditions →	*Free–free*	*Clamped–free*	*Clamped–pinned*	*Clamped–clamped*	*Clamped–sliding*
ϑ_1	4.73004074	1.87510407	3.92660231	4.73004074	2.36502037
ϑ_2	7.85320462	4.69409113	7.06858275	7.85320462	5.49780392
ϑ_3	10.9956078	7.85475744	10.21017612	10.9956079	8.63937983
ϑ_4	14.1371655	10.99554073	13.35176878	14.1371655	11.78097245
ϑ_5	17.2787597	14.13716839	16.49336143	17.2787597	14.92256510
$\vartheta_n, n > 5$	$0.5\pi(2n+1)$	$0.5\pi(2n-1)$	$0.25\pi(4n+1)$	$0.5\pi(2n+1)$	$0.25\pi(4n-1)$
ξ_1	0.982502215	0.734095514	1.000777304	0.982502215	0.982502207
ξ_2	1.000777312	1.018467319	1.000001445	1.000777312	0.999966450
ξ_3	0.999966450	0.999224497	1.000000000	0.999966450	0.999999933
ξ_4	1.000001450	1.000033553	1.000000000	1.000001450	0.999999993
ξ_5	1.999999937	0.999998550	1.000000000	0.999999937	0.999999993
$\xi_n, n > 5$	~ 1.0	~ 1.0	1.0	1.0	1.0

$$M_{\text{eq}} = \frac{m^2 gL\left\{\dfrac{25L^6}{2\times 384^2 EI} + \dfrac{1}{12k_z^2} + \dfrac{5}{384}\dfrac{L^2}{\pi EIk_z}\right\}}{\left(\dfrac{5}{384}\dfrac{L^2}{EI} + \dfrac{1}{4k_z}\right)^2};$$
$$K_{\text{eq}} = \frac{48EIk_z}{L^3k_z + 12EI} \qquad [34]$$

and:

$$\omega^2 = \frac{K_{\text{eq}}}{M_{\text{ek}}} \qquad [35]$$

It should be noted that, if the spring's constant at the support is complex, then it absorbs vibration energy. In this case we talk about damped supports.

Joints that Couple Longitudinal and Flexural Waves

Structures encounter a variety of joints, and examples are presented in **Figure 4**. a-1 and a-2 describe obstructions, a-3 to a-5 illustrate additional elements that differ from the original elements, a-6 is a corner, a-7 depicts columns within a wall, a-8 and a-9 are schemes of T joints. All the other examples stand for a variety of branching elements, including hinged ones. There have been results where coupling during flanking is ignored (**Figure 5**; see Further reading).

An extended solution has been developed, taking into account simultaneously axial forces shear and moments at a joint in a two-dimensional problem (**Figure 6**). This extension was verified experimentally, and used to analyze a variety joints and structures (**Figure 7**).

Three-dimensional Boundary Value Problems in Mechanics

The fundamental boundary value problems of elasticity involve prescribed distribution of data over the surface of the body. These can be of two types:

1. Displacement: u_i, $i = 1, 2, 3$
2. External forces: $t_{(n)i}$, $i = 1, 2, 3$

Hence, it is reasonable to present the problem to be solved in terms of either displacements or stresses. The state of stress and deformation in an anisotropic material involves a stress (τ_{kl}, $k, l = 1, 2, 3$)–strain (e_{ij}, $i, j = 1, 2, 3$) relation using repeated indices for the summation convention, as follows:

$$e_{ij} = d_{ijkl}\tau_{kl} \qquad [36]$$

where d_{ijkl} is the tensor of elastic compliance. In the case of an isotropic material we have:

$$e_{ij} = \frac{1}{2\mu}\left(\tau_{ij} - \frac{\lambda}{2\mu + 3\lambda}\tau_{kl}\delta_{ij}\right) \qquad [37]$$

where λ and μ are the Lamé coefficients and δ_{ij} is the delta of Kronecker.

As mentioned before, the prescribed boundary conditions are to be expressed either by displacements or stresses. In the first case the strains are given in terms of displacements:

$$e_{ij} = 0.5\left(u_{i,j-}u_{j,i}\right) \qquad [38]$$

In the second case, the following constitutive relations give the strains:

$$e_{ij} = d_{ijkl}\tau_{kl} \text{ or } e_{ij} = \frac{1}{2\mu}\left(\tau_{ij} - \frac{\lambda}{2\mu + 3\lambda}\tau_{kl}\delta_{ij}\right) \qquad [39]$$

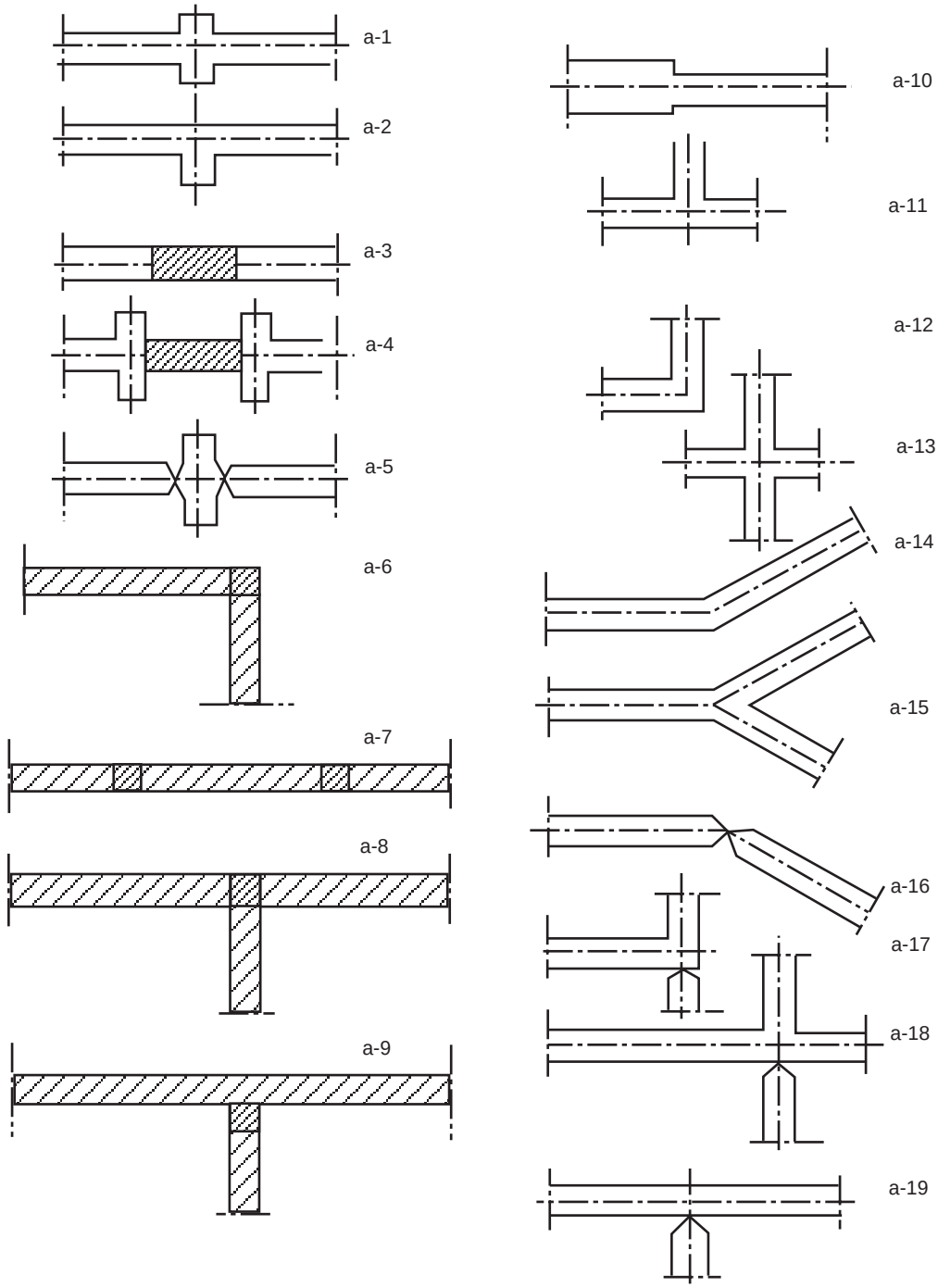


Figure 4 Various kinds of single joints.

The compatibility equations are:

$$e_{ij,kl} + e_{kl,ij} - e_{ik,jl} - e_{jl,ik} = 0 \qquad [40]$$

They are satisfied if the displacements are sufficiently regular functions of position. The dynamic equilibrium equations are:

$$\tau_{ij,i} + F_i = \rho u_{i,tt} \qquad [41]$$

F_i designates body force, ρ is density and t denotes time. For unknown displacements only, the dynamic equilibrium equations become:

$$\mu u_{i,kk} + (\lambda + \mu) u_{kk,i} + F_i = \rho u_{i,tt} \qquad [42]$$

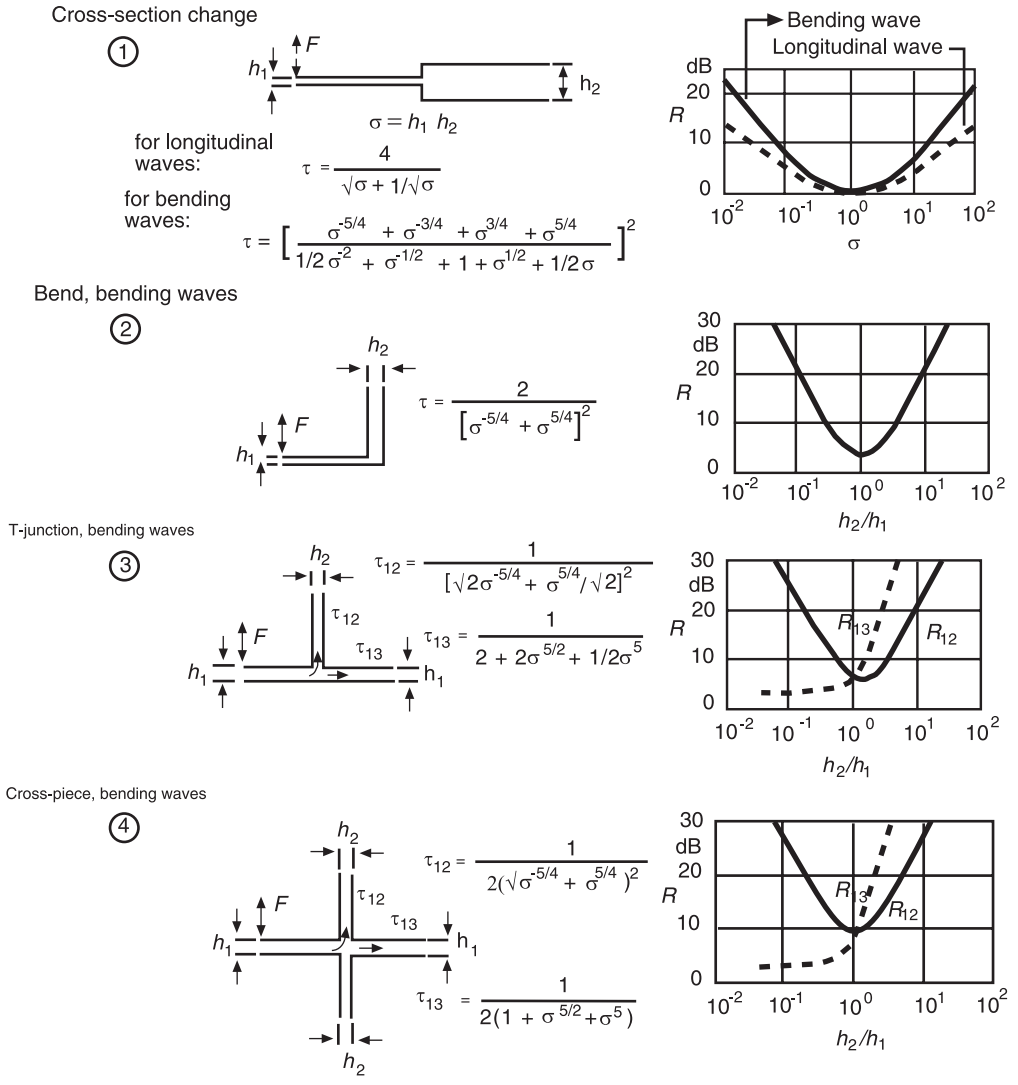


Figure 5 Flanking through joints. From Heckl M (1981) The tenth Richard Fairey memorial lecture: sound transmission in buildings. *Journal of Sound Vibration* 77: 165–180 with permission

Consequently, the boundary value problem includes the last field equation and the boundary conditions of displacements:

$$u_i = u_{i0} \text{ over } \Gamma_u = \Gamma \qquad [43]$$

Γ is the boundary of the investigated domain Ω.Γ coincides in this case with the boundary Γ_u of the prescribed displacements.

If prescribed tractions are imposed on the boundary, the equilibrium equation [41] and the compatibility condition [40] are to be obeyed, using Hooke's law for compatibility. Yet, satisfaction of the dynamic equilibrium equations does not automatically satisfy the deformation equations. This problem of mismatch between the equilibrium equation and compatibility has already been addressed (Further reading). At the boundary surface, the following equation has to be satisfied:

$$t_{(n)i} = \tau_{ij} \text{ over } \Gamma_\tau = \Gamma \qquad [44]$$

where n_i is the external normal. Γ is the boundary of the investigated domain Ω, which coincides in this case with boundary, Γ_τ, of prescribed tractions.

There are also cases where over a part, Γ_u, of the boundary Γ, the displacements are prescribed, and on the other part, Γ_τ, the tractions are prescribed. In the last case, we have $\Gamma_u + \Gamma_\tau = \Gamma$.

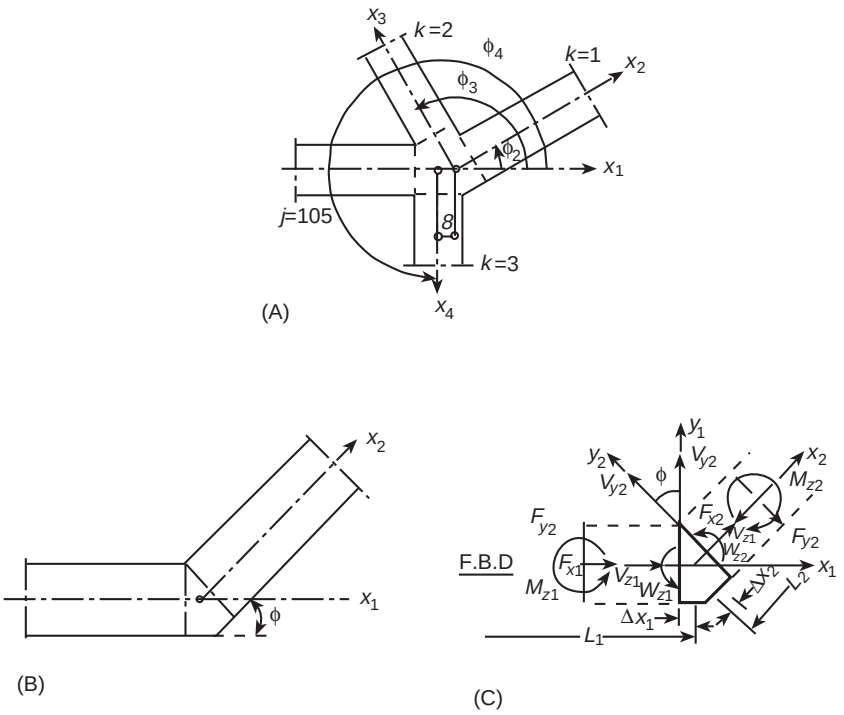


Figure 6 Flanking through a joint: (A) Branched joint; (B) bent one-dimensional wave guide; (C) free body diagram of a bend. From Rosenhouse G (1979) Acoustic wave propagation in bent thin-walled wave guides. *Journal of Sound Vibration* 67: 469–486 with permission.

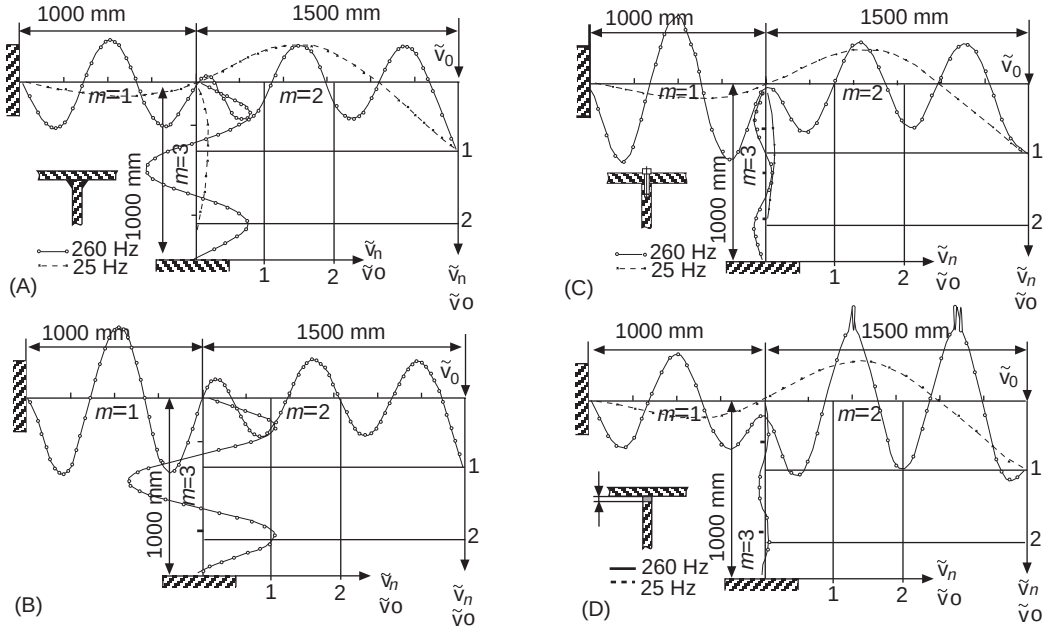


Figure 7 Sound transmission through a joint – theory and experiment. From Rosenhouse G, Ertel H and Mechel FP (1981) Theoretical and experimental investigations of structure-borne sound transmission through a 'T' joint in a finite system. *Journal of the Acoustic Society of America* 70: 492–499.

Moving Boundaries

As has been shown up to now, the boundary conditions are a major influence on the resulting vibrating field. If they are forced to move in certain ways, such as in the case of longitudinally moving support, they can form sources of vibration and sound. Such special boundary conditions have specific effects. Typical moving boundaries of technological interest are rotating blades. This is a rather complicated motion that sometimes involves a longitudinal motion as well, as in airplanes and helicopters. The forces that act on the blades enforce vibrations. This subject relates to the study of aerodynamics (see Further reading).

Moving boundaries also appear in contact problems of elastic bodies. When two elastic bodies collide, their contact area varies as a function of the contact force. Compatibility, equilibrium, and constitutive relations are to be satisfied at the contact area, and the definition of these begins with the simple models of Hertz and are supported today by numerical techniques.

Moving boundaries may be a consequence of nonmechanical processes. An example is the definition of domains in a melting/solidification of a certain material. The definition of the moving melting front is Stefan's problem. This varying boundary (interface) problem can combine with a vibration problem.

Nonreflecting boundaries

Earthquakes are geophysical mechanical sources of vibrations. Such sources radiate energy from distant locations in a domain that can be considered for the purpose of structural analysis to be theoretically infinite. However, estimates of vibrations generated in such large domains are difficult, especially if they are done numerically. Ways of confining the domain of analysis were sought as a result. A finite domain, where the vibration field is calculated, is cut out from the infinite one, yet defining boundary conditions that replace the removed infinite space at the cut or artificial boundary, without changing the vibration field within the investigated domain (**Figure 8**).

Nonreflecting boundaries mean local impedance matching. However, this necessity can lead to a more complicated formulation in order to secure nonreflecting transmission of all the components of stress and displacement along the whole artificial boundary. This leads to an integral (nonlocal) formulation of the boundary conditions.

Semidefinite systems

In many problems the whole system is moving under certain excitation forces. It might be a moving elastic elongated body. Ignoring air resistance, the boundary

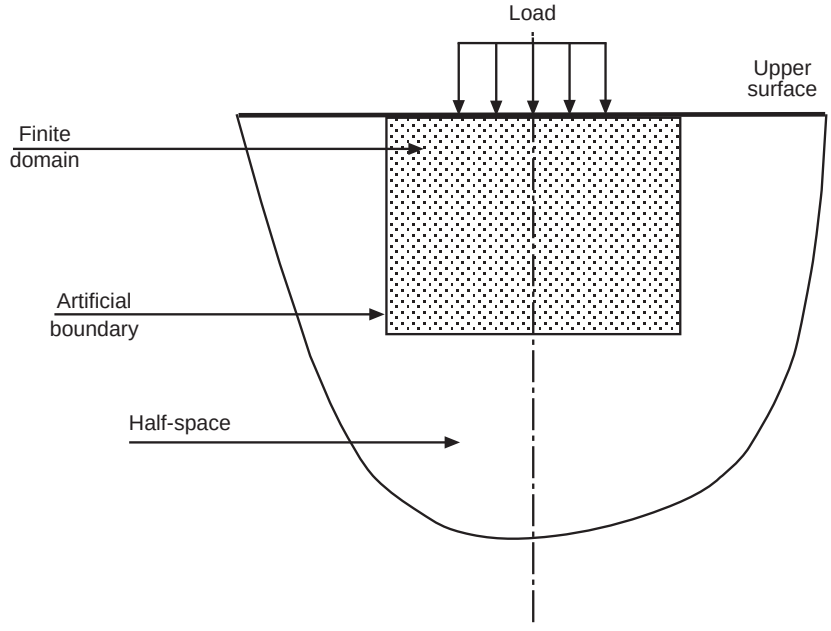


Figure 8 Nonreflecting boundaries in a half-space.

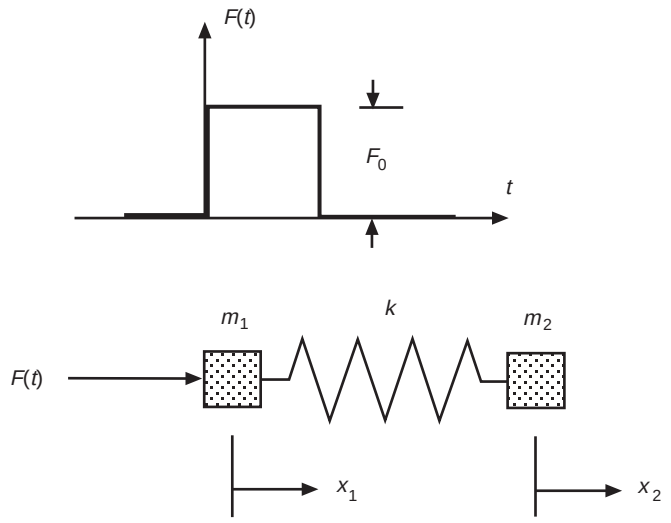


Figure 9 A semidefinite system of two masses linked by a spring.

conditions at the ends of the body can be defined as free–free. A simple example is shown in **Figure 9**. Two masses, m_1 and m_2, are linked together by a spring with a constant k. The behavior of this system depends on the excitation function. If the excitation is a rectangular pulse of constant amplitude in the range $0 < t < t_0$, then, within the range of excitation, the average velocity of the whole system will rise linearly, and at the same time the masses will oscillate about the center of gravity of the system. Later, when no additional energy is supplied to the system, the average velocity will not change, but the masses will continue to oscillate.

Nomenclature

E	Young's modulus
EI	rigidity
$F(x, t)$	axial force
G	shear modulus of elasticity
I	moment of inertia
L	length
R	reflection coefficient
S	cross-section area of rod
Tr	transmission coefficient
ρ	density
$\theta(x, t)$	angle of rotation

See also: **Basic principles**; **Beams**; **Structural dynamic modifications**; **Theory of vibration**, Variational methods; **Vibration isolation theory**; **Wave propagation**, Interaction of waves with boundaries.

Further Reading

Blevins RD (1977) *Flow-Induced Vibration*. New York: Van Nostrand Reinhold.

Chang TC and Craig RR (1969) Normal modes of uniform beams. *Journal of Engineering Mechanics Division, American Civil Engineers* 95: 1027–1031.

Crank J (1984) *Free and Moving Boundary Problems*. Oxford: Clarendon Press.

Goldsmith W (1960) *Impact*. London: Edward Arnold.

Heckl M (1981) The tenth Richard Fairey memorial lecture: sound transmission in buildings. *Journal of Sound Vibration* 77: 165–189.

Johnson KL (1987) *Contact Mechanics*. New York: Cambridge University Press.

Keller JB and Givoli D (1989) Exact non-reflecting boundary conditions. *Journal of Computational Physics* 82: 172–192.

Prager W and Synge JL (1947) Approximations in elasticity based on the concept of function space. *Quarterly Journal of Applied Mathematics* 5: 241–269.

Rosenhouse G (1979) Acoustic wave propagation in bent thin-walled wave guides. *Journal of Sound Vibration* 67: 469–486.

Rosenhouse G, Ertel H and Mechel FP (1981) Theoretical and experimental investigations of structureborne sound transmission through a 'T' joint in a finite system. *Journal of the Acoustic Society of America* 70: 492–499.

BOUNDARY ELEMENT METHODS

F Hartmann, University of Kassel, Kassel, Germany

Copyright © 2001 Academic Press

doi:10.1006/rwvb.2001.0111

The boundary element method is an integral equation method. Approximations are made only on the boundary or surface of the problem domain. No interior mesh of elements need be specified and at each interior point the governing differential equation is satisfied exactly.

This reduction of the dimension of the problem is the main advantage of the method. In cases where the domain extends to infinity, as in potential flow problems or in seismic wave problems, this advantage is even more striking because the equation governing the infinite domain is reduced to an integral equation over the boundary of the domain.

The boundary element method is applicable to most of the classical problems of mechanics. The method requires that the problem is linear – although the method nowadays is also applied successfully to nonlinear problems – and that a fundamental solution of the governing equation is known.

In the following sections we shall concentrate on the fundamental principles behind the boundary element method and show how it is applied to time harmonic and transient problems in vibration analysis.

Fundamental Solutions

From a physical point of view, the boundary element method is a method of sources or potentials. The smallest source is a point load whose magnitude oscillates in time (harmonic problems) or a short impulse which hits the structure at a time, T, for an infinitesimal small time step $\mathrm{d}t$ as in transient problems.

Mathematically speaking the point sources are Dirac δ functions and the solution of the corresponding field equations, for example, the Poisson equation:

$$-\Delta u(y) = \delta(y - x)$$

are called fundamental solutions:

$$g_0(y, x) = \frac{1}{2\pi} \ln r \quad r = |y - x|$$

They are homogeneous solutions of the differential equation at all points y which do not coincide with the source point, x. Typically these functions are symmetric with respect to the source point x and field point y, so that $g_0(y, x) = g_0(x, y)$. At the source point, x, they exhibit the $1/r$ (or higher) behavior in the stresses – here it is actually the slope:

$$\frac{\partial}{\partial v} g_0(y, x) = \frac{1}{2\pi} \frac{1}{r} \left(r_{,y1}\, v_1 + r_{,y2}\, v_2 \right)$$

which guarantees that in the limit the integral of the stresses over any circle centered at the source point x tends to the unit point load (**Figure 1**).

$$\lim_{r \to 0} \int_{\Gamma_r} \frac{1}{2\pi r} \mathrm{d}s = \int_0^{2\pi} \frac{1}{2\pi r} r \, \mathrm{d}\varphi = 1$$

Fundamental solutions are also called free space Green's functions because they formulate the response of the infinite medium to the action of a point load. If the same load is applied to, say, a circular plate, then boundary conditions must be met and we speak of a Green's function, $G_0(y, x)$. If we know what happens to a structure under the action of a point load, we can instantly formulate the answer to a load p spread over any patch Ω_p:

$$u(x) = \int_{\Omega_p} G_0(y, x) p(y) \, \mathrm{d}\Omega y$$

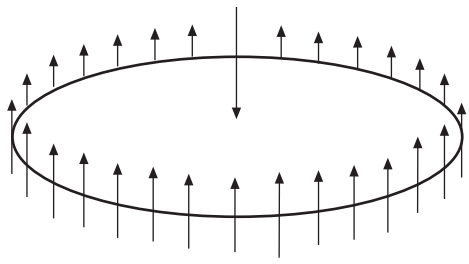


Figure 1 Point source.

This explains why the boundary element method is also called a method of influence functions.

Influence functions are linear by nature: they are L_2-scalar products between kernel functions and domain or boundary layers. For the boundary element method to be applicable the physical nature of the problem must therefore be linear and we must know the fundamental solution of the governing equation – the response of the infinite medium to a point load or point excitation.

The Direct Method

Most of the linear differential operators in physics, for example, the Laplacian, are of even order, say $2m$, they are self-adjoint and we have an identity such as:

$$G(u,\hat{u}) = \int_\Omega -\Delta u\hat{u}\,\mathrm{d}\Omega + \int_\Gamma \frac{\partial u}{\partial n}\hat{u}\,\mathrm{d}s - \int_\Omega \nabla u\cdot\nabla\hat{u}\,\mathrm{d}\Omega = 0$$

which allows us to formulate Green's second identity as well:

$$\begin{aligned} B(u,\hat{u}) &= G(u,\hat{u}) - G(\hat{u},u) \\ &= \int_\Omega -\Delta u\hat{u}\,\mathrm{d}\Omega + \int_\Gamma \frac{\partial u}{\partial n}\hat{u}\,\mathrm{d}s \\ &\quad - \int_\Gamma u\frac{\partial\hat{u}}{\partial n}\,\mathrm{d}s - \int_\Omega u(-\Delta\hat{u})\,\mathrm{d}\Omega = 0 \end{aligned}$$

on any domain Ω with boundary Γ where u and $\hat{u}$ are smooth enough, $u, \hat{u}\in C^2(\Omega)$. The B stands for Betti. In elastodynamics the equivalent identity goes under the name of Graffi's theorem.

If we substitute for $\hat{u}$ the fundamental solution, consider the identity on the punctured domain $\Omega_\varepsilon = \Omega - N_\varepsilon(x)$ (**Figure 2**) and let the radius ε of the cut-out N_ε tend to zero:

$$\lim_{\varepsilon\to 0} B(u, g_0[x])_{\Omega_\varepsilon} = 0 \qquad [1]$$

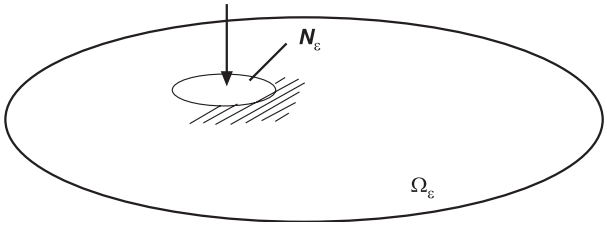


Figure 2 Punctured domain.

then we obtain an integral representation for the field u:

$$c(x)u(x) = \int_\Gamma \left[g_0(y,x)\frac{\partial u(y)}{\partial v} - \frac{\partial g_0(y,x)}{\partial v}u(y)\right]\mathrm{d}s_y + \int_\Omega g_0(y,x)p(y)\,\mathrm{d}\Omega_y \qquad [2]$$

where $c(x)$ is the characteristic function:

$$= c(x) \begin{cases} 1 & x\in\Omega \\ \Delta\varphi/2\pi & x\in\Gamma, \quad \Delta\varphi = \text{angle at the boundary point} \\ 0 & x\in\Omega^c \quad \text{(outside)} \end{cases} \qquad [3]$$

Hence we can compute the solution u of the field equation at any interior point x by a series of L_2-scalar products of known kernel functions and boundary layers and (one or more) domain functions p.

In the case of the Laplacian where $2m = 2$, the two kernel functions

$$\left(g_0(y,x), \quad \frac{\partial}{\partial v}g_0(y,x)\right)$$

are problem-independent, while the $2m$ boundary layers $(u(y), \quad \partial u(y)/\partial v)$ are not. They are the boundary values of the solution u. For a boundary value problem to be consistent with the physical nature of the problem, only m of these $2m$ boundary values can be prescribed. If a boundary value, say the slope $\partial u/\partial n$ is given, then the conjugated boundary value – the function u in this case – is unknown.

To find these unknown boundary layers we have to take the point x in the integral representation (2) to the boundary. By this maneuver the integral representation becomes an integral equation. It formulates a coupling condition between the trace of u on the boundary and the slope $t = \partial u/\partial n$ of u, which means that on each portion of the boundary either one of these boundary functions determines the other.

To solve this integral equation numerically we subdivide, as in a finite element method, the boundary curve (2-D) or the surface (3-D) into a mesh of small boundary elements (**Figure 3**) and approximate the boundary functions by piecewise linear or quadratic nodal functions $\phi_i(x), \psi_i(x)$:

$$u(x) = u_i\varphi_i(x) \quad t(x) = t_i\psi_i(x)$$

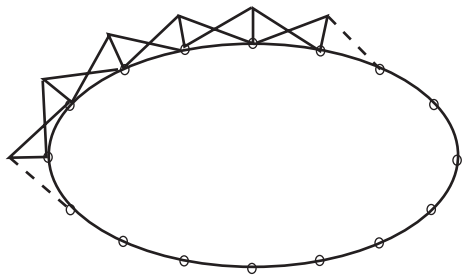


Figure 3 Boundary elements.

and we determine the unknown nodal values of u or t respectively either by a collocation method or by Galerkin's method and so obtain a linear system of equations:

$$\mathbf{Hu} = \mathbf{Gt} + \mathbf{p} \qquad [4]$$

where (in a collocation method) the coefficient matrices:

$$H_{kj} = c\left(x^k\right)\delta_{kj} + \int_\Gamma \frac{\partial}{\partial v} g_0\left(y, x^k\right)\varphi_j(y)\,\mathrm{d}s_y$$

$$G_{kj} = \int_\Gamma g_0\left(y, x^k\right)\psi_j(y)\,\mathrm{d}s_y$$

contain the influence of the boundary layers $\phi_j(x)$ and $\psi_j(x)$ on the collocation point x^k on the boundary. The vector $\mathbf{p}$ lists the influence of the distributed load p on the same points:

$$p_k = \int_\Omega g_0\left(y, x^k\right)p(y)\,\mathrm{d}\Omega_y$$

Fortunately, in most applications we can transform this domain or volume integral into an equivalent boundary integral or we have vanishing body forces or zero initial conditions so that the computation of this volume integral is not needed.

After we have solved this system (4) for the unknown nodal values we can calculate with [2] the field $u(x)$. The technique outlined here is basically the direct boundary element method.

If we multiply eqn [4] from the left with the inverse of the matrix $\mathbf{G}$ and the matrix $\mathbf{F}$, where:

$$F_{ij} = \int_\Gamma \varphi_i \varphi_j\,\mathrm{d}s$$

then we obtain a nonsymmetric finite element stiffness matrix $\mathbf{K} = \mathbf{F}\mathbf{G}^{-1}\mathbf{H}$.

Symmetric Formulations

Because the kernel $\partial g_0/\partial v$ depends on the normal vector $\boldsymbol{\nu}$ at the integration point, the matrix $\mathbf{H}$ is not symmetric and in addition both matrices $\mathbf{G}$ and $\mathbf{H}$ are fully populated.

If the lack of symmetry is a problem, then we can mix the influence function for u with the influence function for the slope:

$$c_1(x)u_{,1}(x) + c2(x)u_{,2}(x) = \int_\Gamma \left[g_1(y,x)\frac{\partial u}{\partial v}(y) - \frac{\partial}{\partial v}g_1(y,x)(u(y) - u(x))\right]\mathrm{d}s_y + \int_\Omega g_1(y,x)p(y)\,\mathrm{d}\Omega_y \qquad [5]$$

where the c_i are the two characteristic functions:

$$c_i(x) = \begin{cases} n_i, & x \in \Omega \\ \dot{c}_i(x), & x \in \Gamma \\ 0, & x \in \Omega^c \end{cases}$$

with the following boundary values:

$$\dot{c}_1(x) = \frac{1}{2\pi}[(\varphi + \tfrac{1}{2}\ \sin\ 2\varphi)n_1 + \sin^2\varphi n_2]_{\varphi_2}^{\varphi_1} \qquad [6]$$

$$\dot{c}_2(x) = \frac{1}{2\pi}[\sin^2\varphi n_1 + (\varphi - \tfrac{1}{2}\ \sin\ 2\varphi)n_2]_{\varphi_2}^{\varphi_1} \qquad [7]$$

The kernel g_1 is the normal derivative of the kernel g_0:

$$g_1(y,x) = \frac{\partial}{\partial n_x}g_0(y,x) = -\frac{1}{2\pi r}(r_{,x1}\,n_1 + r_{,x2}\,n_2)$$

If we put the point x in eqn [5] on the boundary we obtain an additional integral equation or coupling condition between the two boundary values u and $\partial u/\partial n$. In more abstract terms the two coupling conditions in eqns [2] and [4] can be stated as:

$$\frac{1}{2}\begin{bmatrix}\partial^0 u \\ \partial^1 u\end{bmatrix} = \int_\Gamma \begin{bmatrix}\partial_y^0\partial_x^0 g_0 & \partial_y^1\partial_x^0 g_0 \\ \partial_y^0\partial_x^1 g_0 & \partial_y^1\partial_x^1 g_0\end{bmatrix}\begin{bmatrix}+\partial^1 u \\ -\partial^0 u\end{bmatrix}\mathrm{d}s_y + \begin{bmatrix}\partial_x^0 g_0 \\ \partial_x^1 g_0\end{bmatrix}p\,\mathrm{d}\Omega_y$$

The kernels of the single integral operators are products of the boundary operators ∂_y^i and ∂_x^j and the zero-order fundamental solution g_0. By a proper combination of these two integral equations – on Γ_t where the slope t is unknown we formulate the first

integral equation and on Γ_u where u is unknown the second integral equation – and by using Galerkin's method instead of simple collocation, we obtain a symmetric system matrix for the unknown nodal values.

This system of integral equations is typical for the boundary element method. Given an equation of order $2m$ there are $2m$ boundary values $\partial^j u$ which satisfy a system of $2m$ integral equations on the boundary. The higher we go in this hierarchy of integral equations, the more singular the kernels become. Note that the calculation of the coefficients G_{kj} and H_{kj} near the diagonal, if the collocation point x^k lies near or even on the patch of elements where the shape function ϕ_j lives, is not a real problem. On straight elements we can usually integrate analytically and on curved elements we can still use some semianalytical procedures which render well-behaved expressions for even hypersingular integrals. In this regard the limit [1] holds all the answers.

The Indirect Method

In mathematical terms the influence function [2] is the sum of a single-layer potential, a double-layer potential, and a volume potential. The first two potentials are homogeneous solutions of the governing equation while the volume potential has a so-called reproducing kernel. It solves the equation $-\Delta u = p$.

To have a homogeneous solution, either the single-layer or double-layer potential would therefore suffice:

$$u(x) = \int_\Gamma g_0(y,x)a(y)\,\mathrm{d}s_y \quad v(x) = \int_\Gamma \frac{\partial g_0(y,x)}{\partial v} b(y)\,\mathrm{d}s_y$$

Techniques based on this approach are called indirect methods because the boundary layers $a(y)$ and $b(y)$ are not the boundary values of the solution:

$$\lim_{x\to\Gamma} u(x) = \int_\Gamma g_0(y,x)a(y)\,\mathrm{d}s_y$$

$$\lim_{x\to\Gamma} v(x) = \frac{\Delta\varphi}{2\pi} b(x) + \int_\Gamma \frac{\partial g_0(y,x)}{\partial v} b(y)\,\mathrm{d}s_y$$

We would like to have $u(x)\to a(x)$ and $v(x)\to b(x)$. This makes it difficult to control and predict the behavior of the boundary layers. But the indirect method has a long tradition: it is identical with the approach of classical potential theory. The sudden popularity of boundary element methods must certainly be attributed to the switch from the indirect method to the direct method. The direct method is much more transparent than the indirect method because it allows engineers to state problems in mechanical terms rather than using artificial boundary layers. Many of the features we have outlined here are common to all boundary element formulations. In the following we shall look at specific differential equations and see how the boundary element approach evolves.

Harmonic Oscillations

If the excitation is harmonic, $p(x,t) = p(x)\cos(\omega t + \varphi)$, then the response of the structure, the medium, is also harmonic. This is an important case, not only because transient problems are easier to solve but also because transient problems can be reduced to harmonic-type problems by applying a Fourier or a Laplace transform.

Helmholtz Equation

An important part in dynamics is played by the wave equation which governs, for example, the vibration of a stretched membrane. The response of a membrane to harmonic excitations:

$$-\Delta v + \rho v = b(x,t) = p_1(x)\cos\omega t + p_2(x)\ \sin\ \omega t$$

can be stated in the form:

$$v(x,t) = v_1(x)\cos\omega t + v_2(x)\ \sin\ \omega t$$

If we write:

$$b(x,t) = \Re\left\{p(x)\mathrm{e}^{-i\omega t}\right\} \quad p(x) = p_1(x) + ip_2(x)$$

and:

$$v(x,t) = \Re\left\{u(x)\mathrm{e}^{-i\omega t}\right\} \quad u(x) = u_1(x) + iu_2(x)$$

then this leads to the Helmholtz equation:

$$-\Delta u(x) - \lambda u(x) = p(x) \quad \lambda = \rho\omega^2$$

for the complex valued amplitude $u(x)$. Associated with these differential equations is the identity:

$$G(\hat{u},u) = \int_\Omega (-\Delta\hat{u} - \lambda\hat{u})u\,\mathrm{d}\Omega + \int_\Gamma \frac{\partial\hat{u}}{\partial n}u\,\mathrm{d}s - \int_\Omega \nabla\hat{u}\cdot\nabla u\,\mathrm{d}\Omega + \int_\Omega \lambda\hat{u}u\,\mathrm{d}\Omega = 0$$

If we formulate the second identity $B(\hat{u},u) = G(\hat{u},u) - G(u,\hat{u}) = 0$ with the fundamental solutions:

$$g_0(y,x) = \frac{-i}{2} H_0^{(1)}(\lambda r) \text{ (2-D) (Hankel function)}$$

$$g_0(y,x) = -\frac{1}{4\pi r} e^{i\lambda r} \text{ (3-D)}$$

$$g_1(y,x) = \frac{\partial}{\partial n_x} g_0(y,x)$$

then we obtain the influence function for $u(x)$:

$$c(x)u(x) = \int_\Gamma \left[g_0(y,x) \frac{\partial u}{\partial v}(y) - \frac{\partial}{\partial v} g_0(y,x) u(y) \right] ds_y + \int_\Omega g_0(y,x)(-\Delta u(y) - \lambda u(y))\, d\Omega_y$$

and the normal derivative:

$$c_j(x) u_{,j}(x) = \int_\Gamma \left[g_1(y,x) \frac{\partial u}{\partial v}(y) - \frac{\partial}{\partial v} g_1(y,x)(u(y) - u(x)) \right] ds_y + \int_\Omega g_1(y,x)(-\Delta u(y) - \lambda u(y))\, d\Omega_y$$

The characteristic functions are the same functions as in eqns [3] and [6]. Note that in exterior problems Sommerfeld's radiation condition:

$$\lim_{r\to\infty} \left(\frac{\partial u}{\partial n} - i\lambda u \right) = 0 \quad r = |y - x|$$

is satisfied automatically. The Helmholtz equation appears in many wave propagation problems in acoustics as well as in fluid dynamics.

Elastic Solids (2-D and 3-D)

The vibrations v of an isotropic, homogeneous linear elastic solid satisfy the differential equations:

$$-c_2^2 \Delta v - (c_1^2 - c_2^2) \nabla \text{div}\, v + \ddot{v} = \frac{1}{\rho} b(x,t) \qquad [8]$$

where the constants:

$$c_2 = \left(\frac{\mu}{\rho} \right)^{1/2} \quad c_1 = \left(\frac{2\mu}{\rho} \left(\frac{1-\nu}{1-2\nu} \right) \right)^{1/2}$$

are the isochoric velocity $c_2\ (= c_s)$, or s-wave velocity, and the irrotational velocity $c_1\ (= c_p)$, or p-wave velocity (**Figure 4**). Harmonic excitations:

$$\frac{1}{\rho} b(x,t) = p_1(x) \cos \omega t + p_2(x) \sin \omega t$$

and harmonic displacement fields:

$$v(x,t) = v_1(x) \cos \omega t + v_2(x) \sin \omega t$$

can be considered as the real parts of complex-valued functions:

$$\frac{1}{\rho} b(x,t) = \Re \left\{ p(x) e^{-i\omega t} \right\} \quad v(x,t) = \Re \left\{ u(x) e^{-i\omega t} \right\}$$

where:

$$p(x) = p_1(x) + i p_2(x) \quad u(x) = v_1(x) + i v_2(x)$$

If we substitute these expressions into eqn [8], then we obtain the following system of equations for the complex-valued amplitude:

$$-c_2^2 \Delta u - (c_1^2 - c_2^2) \nabla \,\text{div}\, u - \omega^2 u = p(x)$$

To this system belong the identities:

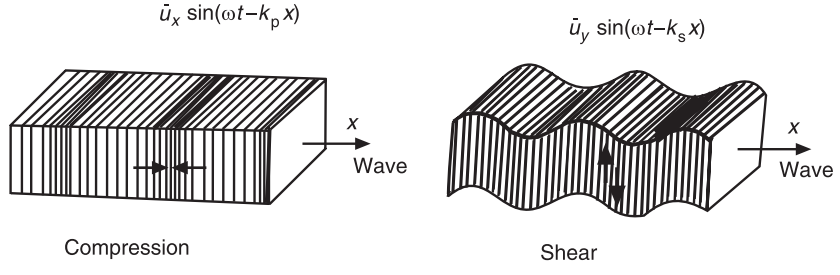


Figure 4 Compression and shear waves in a solid.

$$G(\hat{u},u)=\int_{\Omega}\left(-L\hat{u}-\omega^2\hat{u}\right)\cdot u\,\mathrm{d}\Omega+\int_{\Gamma}\tau(\hat{u})\cdot u\,\mathrm{d}s$$
$$-E(\hat{u},u)+\int_{\Omega}\omega^2\hat{u}\cdot u\,\mathrm{d}\Omega=0$$
$$B(\hat{u},u)=G(\hat{u},u)-G(u,\hat{u})=0$$

The operator $-L$ denotes the operator in eqn [8] without the inertial forces and $E(\hat{u}, u)$ is the associated energy product. The fundamental solutions of eqn [8] are:

$$U_{ij}=\frac{1}{4\pi\rho c_2^2}\left[\psi\delta_{ij}-\chi r_{,i}r_{,j}\right]$$

where:

$$\psi=\frac{1}{r}\left[\mathrm{e}^{-i\omega r/c_2}\left(1-\frac{c_2^2}{\omega^2r^2}+\frac{c_2}{i\omega r}\right)-\frac{c_2^2}{c_1^2}\left(-\frac{c_1^2}{\omega^2r^2}+\frac{c_1}{i\omega r}\right)\mathrm{e}^{-i\omega r/c_1}\right]$$
$$\chi=\left(-\frac{3c_2^2}{\omega^2r^2}+\frac{3c_2}{i\omega r}+1\right)\frac{\mathrm{e}^{-i\omega r/c_2}}{r}-\frac{c_2^2}{c_1^2}\left(-\frac{3c_1^2}{\omega^2r^2}+\frac{3c_1}{i\omega r}+1\right)\frac{\mathrm{e}^{-i\omega r/c_1}}{r}$$

and the components of the associated traction vectors are:

$$T_{ij}=\frac{1}{4\pi}\left[\left(\frac{\mathrm{d}\psi}{\mathrm{d}r}-\frac{1}{r}\chi\right)\left(\delta_{ij}r_{,v}+r_{,j}v_i\right)-\frac{2}{r}\chi\left(v_jr_{,i}-2r_{,i}r_{,j}r_{,v}\right)-2\frac{\mathrm{d}\chi}{\mathrm{d}r}r_{,i}r_{,j}r_{,v}+\left(\frac{c_1^2}{c_2^2}-2\right)\left(\frac{\mathrm{d}\psi}{\mathrm{d}r}-\frac{\mathrm{d}\chi}{\mathrm{d}r}-\frac{2}{r}\chi\right)r_{,i}v_j\right]$$

If we formulate with the three fundamental solutions $g_0^i=\{U_{ij}\}$ the limit:

$$\lim_{\varepsilon\to0}B\left(g_0^i,u\right)_{\Omega_\varepsilon}=0$$

then we obtain three influence functions for the complex-valued amplitude:

$$C_{ij}(x)u_j(x)=\int_{\Gamma}\left[U_{ij}(y,x)t_j(y)-T_{ij}(y,x)u_j(y)\right]\mathrm{d}s_y+\int_{\Omega}U_{ij}(y,x)p_j(y)\,\mathrm{d}\Omega_y$$

The terms $C_{ij}(x)$ are the same characteristic functions as in steady-state problems. The method can easily be extended to include material damping, viscous elastic effects, anisotropy, and thermoelasticity. It has found widespread use in the analysis of soil–structure interaction, beginning with the calculation of dynamic stiffness matrices of rigid foundations with as little as 6 degrees-of-freedom up to the complete analysis in the frequency domain of the interaction between the soil and a complete building.

Kirchhoff Plates

We mention Kirchhoff plates because they are governed by a fourth-order equation. The application of boundary element methods differs little from the standard approach based on Betti's principle (or Rayleigh–Green identity in plate bending). The response of a plate to a harmonic excitation:

$$K\Delta\Delta v+p\ddot{v}=b(x,t)=p_1(x)\cos\omega t+p_2(x)\ \sin\ \omega t$$

where ρ = specific mass $\times$ plate thickness is a harmonic oscillation:

$$v(x,t)=v_1(x)\cos\omega t+v_2(x)\ \sin\ \omega t$$

If we formulate as before:

$$v(x,t)=\Re\left\{w(x)\mathrm{e}^{-i\omega t}\right\}\quad b(x,t)=\Re\left\{p(x)\mathrm{e}^{-i\omega t}\right\}$$

where:

$$w(x)=w_1(x)+iw_2(x)\quad p(x)=p_1(x)+ip_2(x)$$

then the differential equation for the complex-valued amplitude $w(x)$ becomes:

$$K\Delta\Delta w(x)-\rho\omega^2w(x)=p(x)\qquad[9]$$

Associated with this equation are the identities:

$$G(\hat{w},w)=\int_{\Omega}\left(K\Delta\Delta\hat{w}-\rho\omega^2\hat{w}\right)w\,\mathrm{d}\Omega+\int_{\Gamma}\left(\hat{V}_nw-\hat{M}_n\frac{\partial w}{\partial n}\right)\mathrm{d}s+\sum_e\left[\hat{F}(x^e)w(x^e)-\hat{w}(x^e)F(x^e)\right]-E(\hat{w},w)+\int_{\Omega}\rho\omega^2\hat{w}w\,\mathrm{d}\Omega=0$$
$$B(\hat{w},w)=G(\hat{w},w)-G(w,\hat{w})=0$$

The integral $E(\hat{w}, w)$ is the energy product of the static problem.The fundamental solution of the differential eqn [9] is:

$$g_0(\lambda r) = icJ_0(\lambda r) + cY_0(\lambda r) + dK_0(\lambda r)$$

where:

$$\lambda = \frac{\omega^2}{\rho K} \quad c = \frac{1}{8\lambda^2} \quad d = \frac{1}{4\pi\lambda^2}$$

With these tools one can easily solve time-harmonic problems in plate bending for arbitrarily shaped plate geometries and arbitrary boundary conditions. Note that the boundary element method is also applicable to Mindlin–Reissner plates.

Eigenvalues

Formulations of harmonic problems (formulations in the frequency domain) with homogeneous boundary conditions and zero body forces result after a proper rearrangement of the system $\mathbf{Hu} = \mathbf{Gt} + \mathbf{p}$ in a homogeneous system of equations:

$$\mathbf{A}(\omega)x = 0$$

Because the coefficients of $\mathbf{A}$ are complex-valued functions of ω, free vibration analysis by the boundary element method must be done by a determinant search method. This is an indication of the fact that in the boundary element method continuous mass distribution is preserved, resulting in an infinite number of natural frequencies.

As a result, the boundary element method is not particularly efficient at calculating, say, the eigenmodes of a plate or more generally of a bounded domain Ω (infinite domains do not have eigenmodes). The method still retains its edge over domain-type methods but the search for the eigenvalues is certainly cumbersome and standard numerical routines for such tasks are not applicable.

To reformulate the problem as a finite element-like eigenvalue problem, one could either do a Taylor expansion of the matrix $\mathbf{A}$:

$$[\mathbf{A}(0) + \omega\mathbf{A}'(0)]u = 0$$

or one could use the mass matrix method which leads to the system:

$$\mathbf{Fu} + \mathbf{M\ddot{u}} = \mathbf{Gt}$$

The mass matrix approach is a general method for both steady-state and transient problems in which use is made of the static fundamental solutions and the resulting volume integrals are converted into surface integrals which eventually lead to the mass matrix.

Transient Problems

In transient problems the boundary element method can fully utilize its potential. In infinite domains the radiation condition is automatically satisfied and there are no artificial boundaries with reflecting waves.

In steady-state problems and time harmonic problems, the derivation of Betti's principle starts with the integral:

$$\int_0^l -EAu''\hat{u}\,\mathrm{d}x$$

In transient dynamics, the L_2-scalar product is replaced by a convolution:

$$\int_0^l (-EAu'' + \mu\ddot{u}) * \hat{u}\,\mathrm{d}x$$

If we apply integration by parts to this integral then we obtain the first identity for the axial displacement of a beam under dynamic loads:

$$\begin{aligned} G(u,\hat{u}) = &\int_0^l (-EAu'' + \mu\ddot{u}) * \hat{u}\,\mathrm{d}x + [N * \hat{u}]_0^l \\ &- \int_0^l \mu[\dot{u}(x,t)\hat{u}(x,0) - \dot{u}(x,0)\hat{u}(x,t)]\,\mathrm{d}x \\ &- \int_0^l \left(\frac{N * \hat{N}}{EA} - \mu\dot{u} * \hat{\dot{u}}\right)\mathrm{d}x = 0 \end{aligned}$$

and therefore also the second identity, Betti's principle, $B(\hat{u}, u) = G(\hat{u}, u) - G(u, \hat{u}) = 0$. The fundamental solution, which now has a singularity in space and time:

$$-EAg_0''(y,x;t,\tau) + \mu\ddot{g}_0(y,x;t,\tau) = \delta(y-x)\delta(t-\tau)$$

is the response of an infinite bar to a concentrated force $\hat{P} = 1$ which acts at the time mark t and at the point x. If we formulate the second identity with this function and a regular function u, then we obtain an influence function for u and thus automatically the coupling condition between the boundary data of u. Formally this condition differs from the coupling condition of the static case only by the two stars:

$$\mathbf{H} * \mathbf{u} = \mathbf{G} * \mathbf{f} + \mathbf{d}(t)$$

which indicate the convolution. Explicitly, these conditions read:

$$\int_0^t H_{ij}(t-\tau)u_j(\tau)\,\mathrm{d}\tau = \int_0^t G_{ij}(t-\tau)f_j(\tau)\,\mathrm{d}\tau + d_i(t)$$
$$i = 1, 2 \qquad [10]$$

The vector $\mathbf{d}(t) = \{d_i(t)\}$ represents the influence of the distributed forces and the initial conditions.

The system (10) is a system of two Volterra integral equations for the end displacements $u_i(t)$ and end forces $f_i(t)$. This is the typical situation in transient boundary element analysis. (In 2-D and 3-D problems, the number of Volterra integral equations is equal to the number of nodal values.) In time-dependent problems, influence means convolution. We have to verify that at each time step t_i the wave is compatible with its own history and this means that the boundary displacements and boundary stresses have to satisfy Volterra integral equations at each point of the time axis.

The analysis therefore consists of two steps: first, a discretization of the time axis into a sequence of equally spaced time intervals with a constant or linear variation of displacements and tractions over each time interval, and second, a discretization of the boundary Γ into boundary elements over each of which a constant or linear distribution of displacements and tractions is assumed.

The Wave Equation

To the wave equation:

$$-c^2\Delta u(x,t) + \ddot{u}(x,t) = p(x,t)$$

belong the identities:

$$G(u,\hat{u}) = \int_\Omega \left(-c^2\Delta u + \ddot{u}\right) \times \hat{u}\,\mathrm{d}\Omega + \int_\Gamma c^2 \frac{\partial u}{\partial n} \times \hat{u}\,\mathrm{d}s - c^2 \int_\Omega \nabla u \times \nabla \hat{u}\,\mathrm{d}\Omega - \int_\Omega (u \times \hat{u})\,\mathrm{d}\Omega + \int_\Omega \left[\dot{u}_0\hat{u} + u_0\dot{\hat{u}}\right]\mathrm{d}\Omega = 0$$

and $B(\hat{u}, u) = G(\hat{u}, u) - G(u, \hat{u}) = 0$. Next, we consider a load case where a concentrated force $\hat{P}$ acts at point x. We assume that the magnitude of the force changes with time according to a given function $f(\tau)$, of which we only require that it has a 'quiet past':

$$f(\tau) = 0 \quad \tau \le 0 \quad \dot{f}(0) = 0$$

The corresponding solution of the wave equation is:

$$\hat{u}(y,x,\tau) = \frac{1}{c^2 4\pi r} f\left(\tau - \frac{r}{c}\right)$$

Let us assume that $u = u(y, \tau)$ is a smooth solution of the differential equation:

$$-c^2\Delta u + \ddot{u} = p(y,\tau)$$

If we formulate Betti's principle with these two solutions and let the function $f(t)$ converge uniformly to a Dirac function $\delta(t-\tau)$, then we obtain the result:

$$\begin{aligned} c(x)u(x,t) = &\int_\Gamma \frac{r_\nu}{4\pi r^2}\left[u\left(y, t-\frac{r}{c}\right) + \frac{r}{c}\dot{u}\left(y, t-\frac{r}{c}\right)\right]\mathrm{d}s_y \\ &+ \int_\Gamma \frac{1}{4\pi r}\frac{\partial u}{\partial \nu}\left(y, t-\frac{r}{c}\right)\mathrm{d}s_y \\ &+ \int_\Omega \frac{1}{4\pi c^2 r}\delta\left(t-\frac{r}{c}\right)\dot{u}(y,0)\,\mathrm{d}\Omega_y \\ &+ \int_\Omega \frac{1}{4\pi c^2 r}\dot{\delta}\left(t-\frac{r}{c}\right)u(y,0)\,\mathrm{d}\Omega_y \\ &+ \int_\Omega \hat{u}(y,x,\tau) \times p(y,\tau)\,\mathrm{d}\Omega_y \end{aligned} \qquad [11]$$

The integrals of the initial data are equivalent to:

$$\int_\Omega \frac{1}{4\pi c^2 r}\delta\left(t-\frac{r}{c}\right)\dot{u}(y,0)\,\mathrm{d}\Omega_y = tM_{x;ct}[\dot{u}(y,0)]$$

and:

$$\int_\Omega \frac{1}{4\pi c^2 r}\dot{\delta}\left(t-\frac{r}{c}\right)u(y,0)\,\mathrm{d}\Omega_y = \frac{\partial}{\partial t}\left(tM_{x;ct}[u(y,0)]\right)$$

where:

$$M_{x;ct}[u] = \frac{1}{4\pi}\int_0^{2\pi}\int_0^{\pi} u\left(x + ct\nabla_y r, 0\right)\ \sin\ \vartheta\,\mathrm{d}\vartheta\,\mathrm{d}\varphi$$
$$r = |y - x|$$

is the average value of $u(y, 0)$ on a sphere with radius

ct and center at x. Eqn [11] is the influence function for the solution $u(x, t)$ of the three-dimensional wave equation.

Dynamic Displacement Fields

Associated with the system of differential equations:

$$-c_2^2\Delta u - (c_1^2 - c_2^2)\nabla \operatorname{div} u + \ddot{u} = p(y,\tau) \qquad [12]$$

are the identities:

$$\begin{aligned} G(u,\hat{u}) = \int_\Omega & \left(-c_2^2\Delta u - (c_1^2 - c_2^2)\nabla \operatorname{div} u + \ddot{u}\right) \times \hat{u}\, d\Omega \\ & + \int_\Gamma \tau(u) \times \hat{u}\, ds - \int_\Omega (u \times \hat{u})\, d\Omega \\ & + \int_\Omega \left[\dot{u}_0 \cdot \hat{u}(y,t) + u_0 \cdot \dot{\hat{u}}(y,t)\right] d\Omega \\ & - E^*(u,\hat{u}) = 0 \end{aligned}$$

and $B(\hat{u}, u) = G(\hat{u}, u) - G(u, \hat{u}) = 0$, where:

$$\begin{aligned} E^*(u,\hat{u}) &= \int_\Omega \sigma_{ij} \times \hat{\varepsilon}_{ij}\, d\Omega = \int_\Omega S(u) \times E(\hat{u})\, d\Omega \\ &= \int_\Omega E(u) \times S(\hat{u})\, d\Omega \end{aligned}$$

denotes the convolution of the energy product between the stress and strain tensors $S(u)$ and $E(\hat{u})$. By proceeding as in the case of the wave equation, we obtain the influence function for the transient displacement field of a solid:

$$\begin{aligned} C(x)u(x,t) + \int_\Gamma & \left[T(y,x,\tau) \times u(y,\tau) \right. \\ & \left. - U(y,x,\tau) \times t(y,\tau)\right] ds_y \\ & - \int_\Omega U(y,x,\tau) \times p(y,\tau)\, d\Omega_y \\ & + \int_\Omega [U(y,x,t)\, \dot{u}_0(y,t) \\ & - \dot{U}(y,x,t) u_0(y,t)]\, d\Omega_y = 0 \end{aligned}$$

where the convolutions can be expressed as:

$$\begin{aligned} U_{ij} \times t_j &= u_{ij}(y,x,t;t_j(y,t)) \\ T_{ij} \times u_j &= t_{ij}(y,x,t;u_j(y,t)) \\ U_{ij} \times p_j &= u_{ij}(y,x,t;p_j(y,t)) \end{aligned}$$

This results in

$$\begin{aligned} U_{ij} \times t_j &= u_{ij}(y,x,t;t_j) \\ &= \frac{1}{4\pi\rho r}\left\{(3r_{,i}r_{,j} - \delta_{ij}) \int_{1/c_1}^{1/c_2} \lambda t_j(x, t - \lambda r)\, d\lambda \right. \\ &\quad + r_{,i}r_{,j}\left[\frac{1}{c_1^2} t_j\left(y, t - \frac{r}{c_1}\right) - \frac{1}{c_2^2} t_j\left(y - \frac{r}{c_2}\right)\right] \\ &\quad \left. + \frac{\delta_{ij}}{c_2^2} t_j\left(x, t - \frac{r}{c_2}\right)\right\} \\ &= \frac{1}{4\pi\rho r}\left\{(3r_{,i}r_{,j} - \delta_{ij})\left[H\left(t - \frac{r}{c_1}\right)\right.\right. \\ &\quad \times \int_{r/c_1}^{t} \tau t_j(y, t - \tau)\, d\tau \\ &\quad \left.\left. - H\left(t - \frac{r}{c_2}\right) \int_{r/c_2}^{t} \tau t_j(y, t - \tau)\, d\tau\right] \frac{1}{r^2} \right. \\ &\quad + r_{,i}r_{,j}\left[\frac{1}{c_1^2} H\left(t - \frac{r}{c_1}\right) t_j\left(y, t - \frac{r}{c_1}\right)\right. \\ &\quad \left. - \frac{1}{c_2^2} H\left(t - \frac{r}{c_2}\right) t_j\left(y, t - \frac{r}{c_2}\right)\right] \\ &\quad \left. + \frac{\delta_{ij}}{c_2^2} H\left(t - \frac{r}{c_2}\right) t_j\left(y, t - \frac{r}{c_2}\right)\right\} \end{aligned}$$

where:

$$H(x) = \begin{cases} 1, & 0 < x \\ 0, & x < 0 \end{cases}$$

is the Heaviside function which acts like a cut-off function and expresses the causality condition. To reach points at a distance r the wave needs the time $t_r = r/c_i$ and as long as t is smaller, $t - t_r = t - r/c_i < 0$, all is quiet at that point, so that only those points y influence the point x, whose distance r satisfies the inequality $t - r/c_i > 0$. Note that, to insure the causality condition numerically for nonconvex domains, the discretization must not be too coarse.

Fourier and Laplace transforms

We can eliminate from eqn [12] the time variable either by a Fourier transformation or by a Laplace transformation:

$$\tilde{u}(x,\omega) = \frac{1}{2\pi}\int_{\infty}^{+\infty} u(x,t)\,\mathrm{e}^{i\omega t}\,\mathrm{d}t$$

$$\tilde{u}(x,s) = \int_{0}^{\infty} u(x,t)\,\mathrm{e}^{st}\,\mathrm{d}t$$

In this respect we speak of the transition from the time domain into the frequency domain. The Fourier transformation leads to the following system of differential equations:

$$-c_2^2\Delta\tilde{u} - \left(c_1^2 - c_2^2\right)\nabla\,\mathrm{div}\,\tilde{u} - \omega^2\tilde{u} = \tilde{p}(x,\omega)$$

and the Laplace transformation to the system:

$$-c_2^2\Delta\tilde{u} - \left(c_1^2 - c_2^2\right)\nabla\,\mathrm{div}\,\tilde{u} + s^2\tilde{u} = \tilde{p} + s\,u_0 + \dot{u}_0$$

which is identical to the first system if we substitute for $s = i\omega$. The fundamental solutions are the fundamental solutions of the harmonic problem and therefore we can solve the boundary value problem of the Laplace transform by the boundary element method as well.

The only problem is that we must solve the boundary value problem for a whole range of complex-valued parameters s and then apply a (numerical) inverse transformation from the frequency domain back into the time domain:

$$u(x,t) = \frac{1}{2\pi i}\int_{\beta-i\infty}^{\beta+i\infty} \tilde{u}(x,s)\,\mathrm{e}^{st}\,\mathrm{d}s$$

to obtain the original solution.

One of the computational problems in the Fourier-transformed domain is that of fictitious eigenfrequencies, which naturally holds also true for time harmonic problems. These are frequencies corresponding to the eigenvalues of the associated interior problem that render the system matrix singular.

Summary

The boundary element method is a numerical method for the approximate solution of partial differential equations but it is deeply rooted in the mechanical and mathematical properties of the governing equations.

The method can be applied successfully to a wide range of dynamic problems (**Figure 5**), of which we have only mentioned a few: soil–structure interaction problems, fluid–structure interaction problems, the dynamic analysis of underground structures, of pile groups, of vibration isolation devices, of the scattering of waves, of wave diffraction. It can also be applied to study the dynamics of structural elements such as beams and plates. The main advantages of the boundary element method are the reduction of the dimensionality of the problem and the high accuracy of results.

See also: **Continuous methods**; **Eigenvalue analysis**; **Fluid/structure interaction**; **Transform methods**.

Further Reading

Antes H and Panagiotopoulos PD (1992) *Boundary Integral Approach to Static and Dynamic Contact Problems*. Basel: Birkhäuser Verlag.

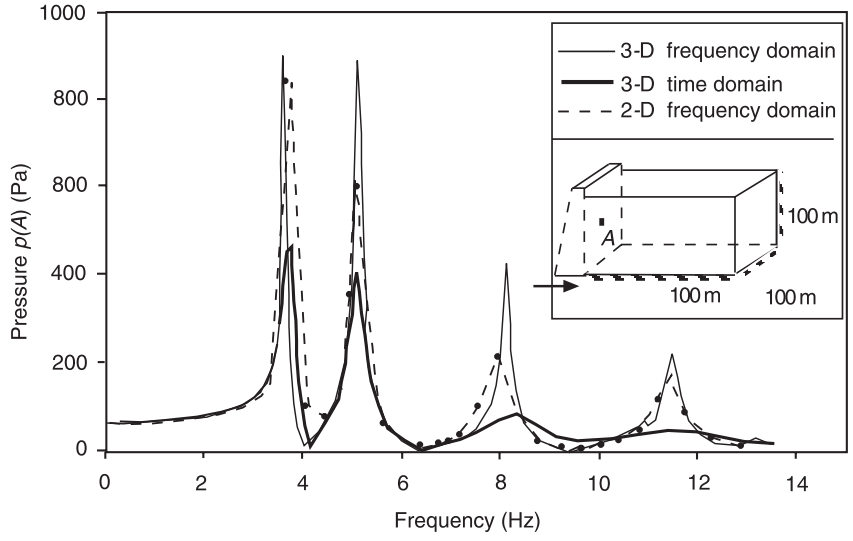


Figure 5 Fluid–structure interaction.

Balaš J, Sládek J and Sládek V (1989) *Stress Analysis by Boundary Element Methods*. Amsterdam: Elsevier

Banerjee PK (1994) *Boundary Element Method in Engineering*. London: McGraw Hill.

Banerjee PK and Kobayashi S (1992) (eds) *Advanced Dynamic Analysis by Boundary Element Methods. Developments in Boundary Element Methods*, vol. 7: London: Elsevier Applied Science.

Beer G and Watson JO (1992) *Introduction to Finite and Boundary Element Methods for Engineers*. Chichester: John Wiley.

Beskos DE (1987) Boundary element methods in dynamic analysis. *Applied Mechanical Review* 40: 1–23.

Beskos DE (1997) Boundary element methods in dynamic analysis. part II (1986–1996). *Applied Mechanical Review* 50: 149–197.

Bonnet M (1999) *Boundary Integral Equation Methods for Solids and Fluids*. Chichester: John Wiley.

Brebbia CA, Telles JCF and Wrobel LG (1984) *Boundary Element Techniques*. Berlin: Springer Verlag.

Do Rego Silva (1994) *Acoustic and Elastic Wave Scattering Using Boundary Elements*. Southampton: Computer and Mechanical Publishing.

Dominguez J (1993) *Boundary Elements in Dynamics*. Southampton: Computer and Mechanical Publishing/ London: Elsevier Applied Science.

Hartmann F (1989) *Introduction to Boundary Elements*. Berlin: Springer-Verlag.

Kitahara M (1985) *Boundary Integral Equation Methods in Eigenvalue Problems of Elastodynamics and Thin Plates*. New York: Elsevier.

Manolis GD and Beskos DE (1988) *Boundary Element Methods in Elastodynamics*. London: Unwin Hyman.

Manolis GD and Davies TG (eds) (1993) *Boundary Element Techniques in Geomechanics*. London: Elsevier Applied Science.

BRIDGES

S S Rao, University of Miami, Coral Gables, FL, USA

Copyright © 2001 Academic Press

doi:10.1006/rwvb.2001.0127

Introduction

The natural frequencies of vibration play a major role in determining the impact factors of highway bridges. The dynamic response of bridges under traveling loads is important in the design of highway and railway bridges. The study of vibration of bridges under traveling loads was started in the middle of the nineteenth century when railroad bridge construction began. The problem was studied by several investigators including Krylov, Timoshenko, and Inglis. The problem of vibration of a uniform beam subject to a constant transverse force moving with constant velocity was studied by Krylov in 1905. The solution of a beam subject to a traveling pulsating load was given by Timoshenko in 1908. Inglis (1938) presented a systematic analysis of the vibration of bridges by considering the influence of factors such as moving loads, damping and spring stiffness of the suspension of the locomotive. When a steam locomotive crosses a bridge, the balance weights attached to the driving wheels, for the purpose of minimizing the inertia effects of the reciprocating parts, will cause hammer-blows on the rails that result in the vibration of the bridge. Although hammer-blows will not be present when an electric locomotive crosses a bridge, there will be some vibration, with a smaller amplitude, due to the moving load. Vibration is also caused by the rail joints and track irregularities.

Natural Frequencies of Bridges

The first flexural frequency of vibration of a bridge is required for the computation of the dynamic load allowance, also called the impact factor, for its major components. A bridge can be modeled as a uniform beam when the width is uniform, the span is much larger than the width and the angle of skew is less than 20°. Typical bridges that can be approximated as uniform beams are shown in **Figure 1**. The first flexural natural frequency of a simply supported single-span uniform beam, in Hertz, is given by:

$$f_s = \frac{\pi}{2L^2}\sqrt{\left(\frac{EI}{m}\right)} \qquad [1]$$

where L is the span, E is Young's modulus, I is the moment of inertia and m is the mass per unit length. The first flexural natural frequency of a multispan bridge, with symmetric span about its center line and uniform flexural rigidity, can be determined as:

$$f_m = cf_s \qquad [2]$$

where f_s is the first flexural natural frequency of the largest span single bridge in isolation, given by eqn

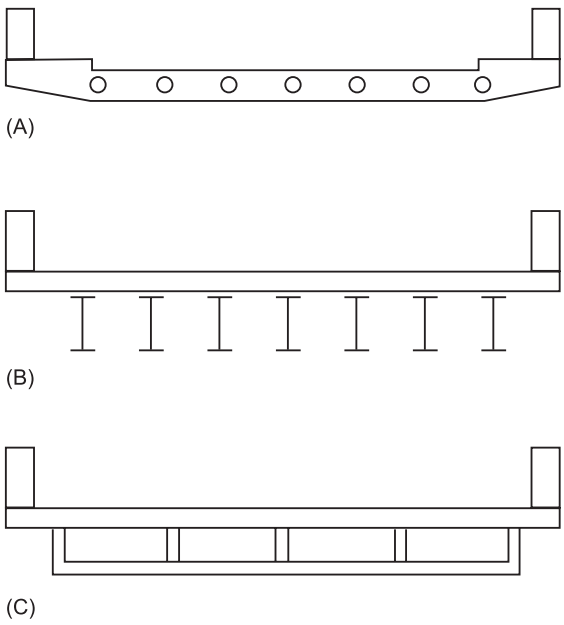


Figure 1 Cross-sections of typical bridges that can be approximated as uniform bridges. (A) Voided slab bridges; (B) slab-on-girder bridges; (C) cellular bridge.

[1], and c is a constant that depends on the number of spans and the ratio of spans. The constant c is shown in **Figure 2** for two-, three-, and four-span bridges.

Many highway bridge codes permit the use of static analysis for moving loads provided that the loads are converted into equivalent static loads. The equivalent static load is determined by multiplying the actual load by (1 + IF) where IF is the impact factor or the dynamic load allowance. A typical variation of the impact factor with the first natural frequency of the bridge is shown in **Figure 3**.

Dynamic Response using Harmonic Analysis

The bridge is modeled as a uniform simply supported beam for simplicity. When the beam is subject to the time-varying distributed load:

$$f(x,t) = f(x)\ \sin\ \omega t \qquad [3]$$

where the function, $f(x)$, can be expanded into a sum of harmonic components using Fourier series as:

$$f(x) = \sum_{n=1}^{\infty} f_n\ \sin\ \frac{n\pi x}{L} \qquad [4]$$

where:

$$f_n = \frac{2}{L}\int_0^L f(x)\ \sin\ \frac{n\pi x}{L}\,\mathrm{d}x \qquad [5]$$

When the load on the beam is uniform with $f(x) = f_0$, the Fourier coefficients are given by:

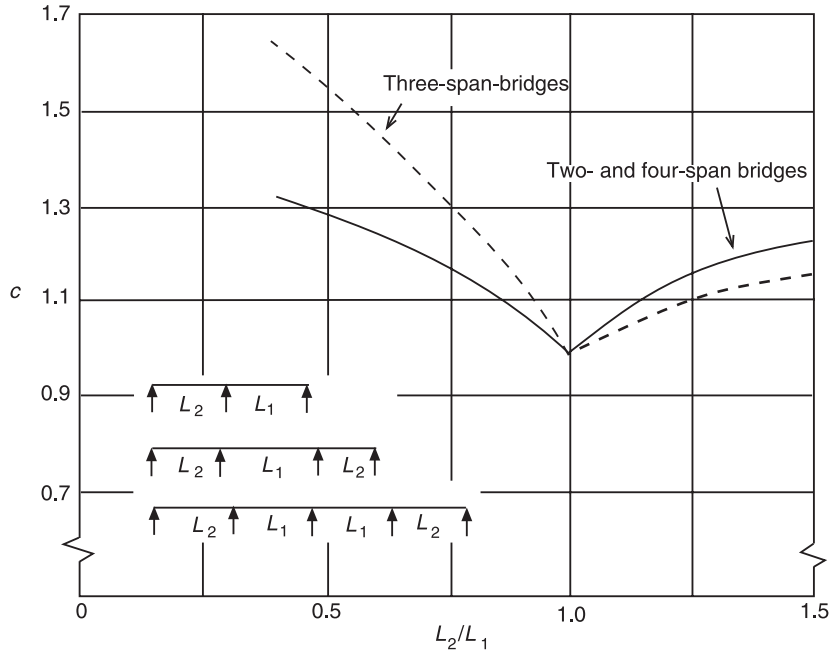


Figure 2 Variation of c with L_2/L_1.

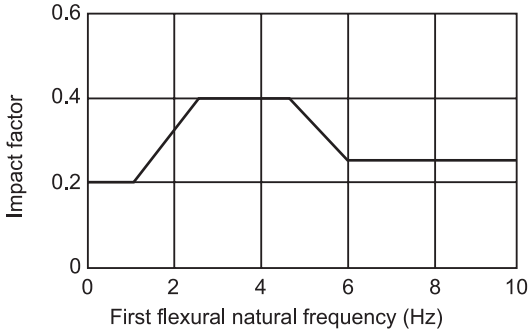


Figure 3 Variation of impact factor for nonwood components.

$$f_n = \begin{Bmatrix} 4f_0/n\pi, & n = 1,3,5,\ldots \\ 0, & n = 2,4,6,\ldots \end{Bmatrix} \quad [6]$$

If the load acts at one point of the beam (at $x = a$) with a sinusoidal variation as:

$$f(x) = \begin{Bmatrix} F_0, & x = a \\ 0, & x \neq a \end{Bmatrix} \quad [7]$$

then the Fourier coefficients are given by:

$$f_n = \frac{2F_0}{L} \sin \frac{n\pi a}{L} \quad [8]$$

By finding the response of the beam to individual harmonic components of the load, the total response of the beam can be determined using superposition. This method is known as harmonic analysis. The equation of motion of the beam subject to a harmonically varying load is given by:

$$EI\frac{\partial^4 y}{\partial x^4} + \rho A\frac{\partial^2 y}{\partial t^2} = f_n \sin \frac{n\pi x}{L} \sin \omega t \quad [9]$$

where y is the transverse deflection, E is Young's modulus, I is the moment of inertia, ρ is the density, A is the cross-sectional area and L is the length of the beam. Using the initial conditions:

$$y(x,0) = \frac{\partial y}{\partial t}(x,0) = 0 \quad [10]$$

the solution of eqn [9] can be expressed as:

$$y(x,t) = \frac{L^4 f_n}{EI\pi^4\left[n^4 - \left\{(\omega/\omega_1)^2\right\}\right]} \sin \frac{n\pi x}{L} \times \left(\sin \omega t - \frac{\omega}{n^2\omega_1} \sin n^2\omega_1 t\right) \quad [11]$$

where ω_n is the nth natural frequency of the beam:

$$\omega_n = \frac{n^2\pi^2}{L^2}\sqrt{\left(\frac{EI}{\rho A}\right)} \equiv n^2\omega_1; \quad n = 1,2,3,\ldots \quad [12]$$

The total response of the beam, considering all harmonic components of the load, is given by:

$$y(x,t) = \frac{L^4}{EI\pi^4}\sum_{n=1}^{\infty} \frac{f_n \sin (n\pi x/L)}{\left[n^4 - (\omega/\omega_1)^2\right]} \times \left(\sin \omega t - \frac{\omega}{n^2\omega_1} \sin n^2\omega_1 t\right) \quad [13]$$

Vibration due to Concentrated Traveling Load

When a concentrated load, F_0, moves along a uniform beam with constant velocity, v_0, as shown in **Figure 4**, the time-varying load can be expressed as, using $a = v_0 t$ and $\omega_0 = (\pi v_0/sL)$:

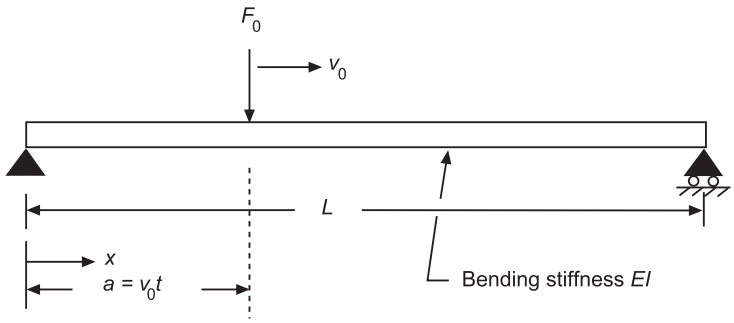


Figure 4 Constant load moving along a beam.

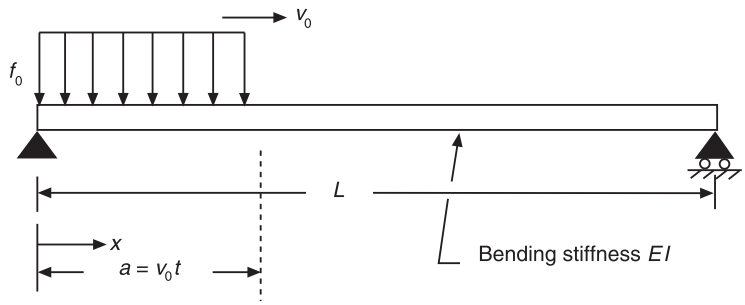


Figure 5 Distributed moving load.

$$f(x,t) = \frac{2F_0}{L}\sum_{n=1}^{\infty} \sin\ \frac{n\pi x}{L}\ \sin\ n\omega_0 t \qquad [14]$$

and the response of the beam is given by:

$$y(x,t) = \frac{2F_0L^3}{EI\pi^4}\sum_{n=1}^{\infty} \frac{\sin\ (n\pi x/L)}{\left\{n^4 - (n\omega_0/\omega_1)^2\right\}} \times \left(\sin\ n\omega_0 t - \frac{\omega_0}{n\omega_1}\ \sin\ n^2\omega_1 t\right) \qquad [15]$$

Vibration due to Distributed Traveling Load

When a uniformly distributed load of intensity f_0 per unit length moves along a uniform beam with constant velocity, v_0, as shown in **Figure 5**, the time-varying load can be represented as, assuming that the leading edge of the load reaches a distance $a = v_0 t$ from $x = 0$ in time t:

$$f(x,t) = \frac{4f_0}{\pi}\sum_{n=1}^{\infty}\frac{1}{n}\ \sin\ \frac{n\pi x}{L}\ \sin^2 n\omega_0 t = \frac{2f_0}{\pi}\sum_{n=1}^{\infty}\frac{1}{n}\ \sin\ \frac{n\pi x}{L}(1 - \cos 2n\omega_0 t) \qquad [16]$$

with:

$$\omega_0 = \frac{\pi v_0}{L} \qquad [17]$$

The response of the beam can be expressed as:

$$y(x,t) = \frac{2f_0L^4}{EI\pi^5}\sum_{n=1}^{\infty}\left\{\frac{1}{n^5}\ \sin\ \frac{n\pi x}{L} + (-1)^n\frac{1}{n}\frac{1}{\left[n^4 - (n\omega_0/\omega_1)^2\right]}\ \sin\ \frac{n\pi x}{L}\cos 2n\omega_0 t\right\} \qquad [18]$$

If ω_0/ω_1 is very small, eqn [18] can be approximated as:

$$y(x,t) \approx \frac{4f_0L^4}{EI\pi^5}\sum_{n=1}^{\infty}\frac{1}{n^5}\ \sin\ \frac{n\pi x}{L}\ \sin^2 n\omega_0 t \approx \frac{2f_0L^4}{EI\pi^5}\sum_{n=1}^{\infty}\frac{1}{n^5}\ \sin\ \frac{n\pi x}{L}(1 - \cos 2n\omega_0 t) \qquad [19]$$

Vibration due to Pulsating Traveling Load

When a harmonically varying concentrated load moves along a uniform beam with constant velocity as shown in **Figure 6**, the time-varying load can be expressed as, using $\omega_0 = (\pi v_0/L)$:

$$f(x,t) = \frac{2F_0}{L}\left(\sum_{n=1}^{\infty}\ \sin\ \frac{n\pi x}{L}\ \sin\ n\omega_0 t\right)\sin\ \omega t \qquad [20]$$

The response of the beam can be approximated by the first harmonic term of the infinite series as:

$$y(x,t) \approx \frac{\delta}{2}\ \sin\ \frac{\pi x}{L}\left\{\frac{\cos\ (\omega - \omega_0)t - \cos\ \omega_1 t}{1 - [(\omega - \omega_0)/\omega_1]^2} - \frac{\cos\ (\omega + \omega_0)t\cos\ \omega_1 t}{1 - [(\omega + \omega_0)/\omega_1]^2}\right\} \qquad [21]$$

where δ represents the deflection of the beam at the middle due to the load F_0 given by:

$$\delta = \frac{2F_0L^3}{EI\pi^4} \qquad [22]$$

Vibration of Railroad Track

The railroad track can be modeled as an infinitely long uniform beam on a Winkler foundation

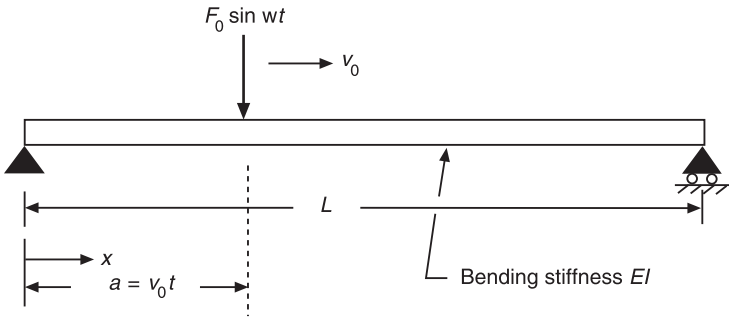


Figure 6 Harmonically varying moving load.

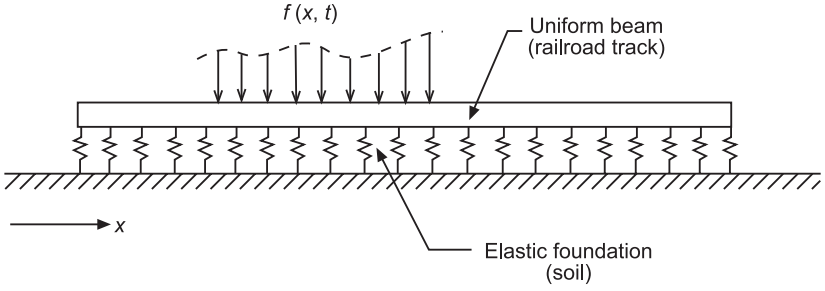


Figure 7 Modeling of a railroad track.

(**Figure 7**). When a distributed load $f(x, t)$ acts on the railroad track, the transverse deflection of the track is governed by the equation:

$$EI\frac{\partial^4 y}{\partial x^4} + m\frac{\partial^2 y}{\partial t^2} + ky = f(x,t) \qquad [23]$$

where EI is the bending stiffness and m is the mass per unit length of the track, k is the foundation modulus and $f(x, t)$ is the external load:

$$f(x,t) = f(x - v_0 t) \qquad [24]$$

Using $z = x - v_0 t$, eqn [23] can be rewritten as:

$$EI\frac{\mathrm{d}^4 y(z)}{\mathrm{d}z^4} + mv_0^2\frac{\mathrm{d}^2 y(z)}{\mathrm{d}z^2} + ky(z) = f(z) \qquad [25]$$

If $f(x, t)$ is a concentrated load F_0 moving along the track with a constant velocity v_0, the equation of motion is taken as:

$$EI\frac{\mathrm{d}^4 y}{\mathrm{d}z^4} + mv_0^2\frac{\mathrm{d}^2 y}{\mathrm{d}z^2} + ky = 0 \qquad [26]$$

and the load F_0 is incorporated into the solution as a known shear force at $z = 0$. The solution of eqn [26] can be expressed as:

$$y(z) = a_1 \mathrm{e}^{(\alpha+\mathrm{i}\beta)z} + a_2 \mathrm{e}^{(\alpha-\mathrm{i}\beta)z} + a_3 \mathrm{e}^{-(\alpha+\mathrm{i}\beta)z} + a_4 \mathrm{e}^{-(\alpha-\mathrm{i}\beta)z} \qquad [27]$$

where $\mathrm{i} = \sqrt{(-1)}$:

$$\alpha = d\sqrt{(1-c)}, \quad \beta = d\sqrt{(1+c)},$$
$$c = \left(\frac{v_0}{v_{\mathrm{cri}}}\right)^2, \qquad v_{\mathrm{cri}} = \left(\frac{4EIk}{m^2}\right)^{1/4},$$
$$d = \left(\frac{k}{4EI}\right)^{1/4}$$

and the constants $a_i, i = 1, 2, 3, 4$, are determined using the conditions:

$$y = \frac{\mathrm{d}^2 y}{\mathrm{d}z^2} = 0 \quad \text{at } z = \infty \qquad [28]$$

$$\frac{\mathrm{d}y}{\mathrm{d}z} = 0, \quad EI\frac{\mathrm{d}^3 y}{\mathrm{d}z^3} = \frac{F_0}{2} \quad \text{at } z = 0 \qquad [29]$$

Thus the response of the railroad track can be expressed as:

$$y(z) = \frac{F_0 e^{-\alpha(x-v_0t)}}{4EI(\alpha^2+\beta^2)} \times \left[\frac{1}{\alpha}\cos\beta(x-v_0t) + \frac{1}{\beta}\sin\beta(x-v_0t)\right] \quad [30]$$

From this solution, the maximum dynamic deflection of the track can be found to occur at $x = v_0t$ with a magnitude y_{max}:

$$y_{max} = \frac{dF_0}{2k\left[\left(1 - v_0^2/v_{cri}^2\right)\right]^{1/2}} \quad [31]$$

Nomenclature

A	cross-sectional area
c	constant
E	Young' modulus
EI	bending stiffness
f	frequency
F_0	concentrated load
I	moment of inertia
k	foundation modulus
L	span length of beam
m	mass
v	velocity
y	transverse deflection
δ	deflection of beam
ρ	density

See also: **Damping, active**; **Damping materials**; **Damping measurement**.

Further Reading

American Association of State Highway and Transportation Officials (AASHTO) (1977). *Standard Specifications for Highway Bridges*. Washington DC.

Bakht B, Jaeger LG (1985). *Bridge Analysis Simplified*. New York: McGraw-Hill.

Cain BS (1940). *Vibration of Rail and Road Vehicles*. New York: Pitman.

Cusens AR, Loo YC (1974). Application of the finite strip method in the analysis of concrete box bridges. *Proceedings of the Institute of Civil Engineers* 57(II): 251–273.

Inglis CE (1934). *A Mathematical Treatise on Vibrations in Railway Bridges*. Cambridge: Cambridge University Press.

Inglis CE (1938–1939). The vertical path of a wheel moving along a railway track. *Journal of the London Institution of Civil Engineers* 11: 262–288.

Ministry of Transportation and Communications (1983). *Ontario Highway Bridge Design Code (OHBDC)*, 2nd edn. Ontario, Canada: Downsview.

Rao SS (1995). *Mechanical Vibrations*, 3rd edn. Reading, Mass: Addison-Wesley.

Timoshenko S (1927–1928). Vibration of bridges. *Transactions of the American Society of Mechanical Engineers* 49–50 (II): 53–61.

Volterra E, Zachmanoglou EC (1965) *Dynamics of Vibrations*, Columbus, OH: C. E. Merrill Books.

C

CABLES

N C Perkins, University of Michigan, Ann Arbor, MI, USA

Copyright © 2001 Academic Press

doi:10.1006/rwvb.2001.0135

is subsequently used to describe linear vibration characteristics. Extensions to this linear theory of cable vibration are then mentioned that generalize results to include a broader range of applications and also nonlinear effects.

Introduction

Cables can be viewed as the one-dimensional structural analogs to membranes. As with membranes, the structural stiffness of cables derives from the equilibrium tension created by applied preloads (see **Membranes**). In contrast to other one-dimensional structural elements such as beams and rods, cables are generally considered to lack torsional, flexural, and shear rigidities (see **Columns**). Under static loading, cables are also curved and the equilibrium curvature induces behaviors in cables that are also found in other curved structural elements including arches (one-dimensional) and shells (two-dimensional) (see **Shells**).

The overall flexibility of cables renders them useful in a wide range of applications, particularly those requiring long, flexible, or readily deployable structural elements. In addition to carrying loads as structural elements, cables are also commonly used to transmit power, electrical signals, and optical signals across long distances. Consider, for instance, the diverse uses of cables in ocean engineering applications, some of which are depicted in **Figure 1**. These include mooring lines for vessels, platforms and buoys, towing lines, umbilicals, tethers, instrumentation arrays, etc. Cables play a dominant role in power distribution systems where they serve as conducting elements. They also serve as major load-transmitting elements when used in guyed towers, as cable trusses in suspended roofs, and in cable-stayed bridges (see **Bridges**).

The objective of this article is to review the fundamental characteristics of cable vibration and to summarize the associated analytical models that may be used to predict dynamic cable response. To this end, a general model for a suspended cable is reviewed that

Nonlinear Model of a Suspended Cable

Consider an elastic cable of length L that is suspended between two supports, as shown in **Figure 2**. Under the action of gravity (g) the cable will sag in the vertical plane and achieve an equilibrium shape in the form of a catenary (see dashed curve in **Figure 2**). Following a disturbance, the cable may then vibrate about this equilibrium and achieve the three-dimensional shape shown by the solid curve in **Figure 2**.

To describe this dynamic response from equilibrium, we will introduce three unit vectors that are defined by the equilibrium shape. These include the unit tangent vector $\mathbf{l}_1$, the unit normal vector $\mathbf{l}_2$, and the unit binormal vector $\mathbf{l}_3$. The dynamic response about equilibrium is then decomposed as:

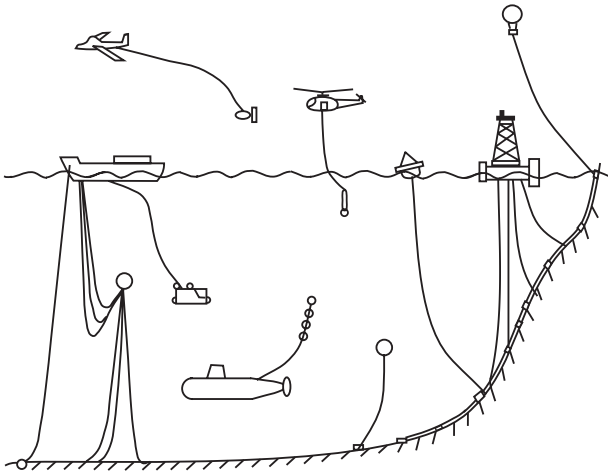


Figure 1 Applications of cables in ocean engineering. Adapted with permission from Choo Y, and Casarella MJ (1973) A survey of analytical methods for dynamic simulation of cable-body systems. *Journal of Hydronautics* 7: 137–144.

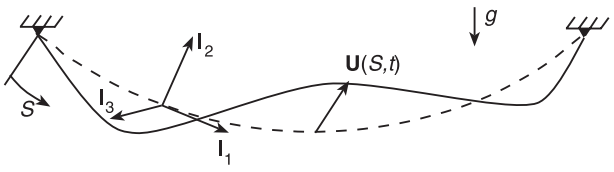


Figure 2 Definition diagram for suspended cable. Dashed curve represents the (planar) equilibrium shape of the cable and the solid curve represents a three-dimensional motion about equilibrium. The orthonormal triad $(\mathbf{l}_1, \mathbf{l}_2, \mathbf{l}_3)$ consists of the tangential, normal, and binormal unit vectors defined by the equilibrium shape.

$$\mathbf{U}(S,T) = U_1(S,T)\mathbf{l}_1 + U_2(S,T)\mathbf{l}_2 + U_3(S,T)\mathbf{l}_3 \tag{1}$$

in which S denotes the arc length coordinate measured along the equilibrium shape of the cable starting from the left support, T denotes time, and U_1, U_2, and U_3 denote the dynamic displacement of the cable in the tangential, normal, and binormal directions, respectively. The components (U_1, U_2) define the in-plane motion of the cable, while the component (U_3) defines the out-of-plane motion.

The cable is assumed to be a one-dimensional continuum obeying a linear elastic law for cable extension and possessing no flexural, shear or torsional rigidity. With these assumptions, the strain – displacement relation for cable extension is given by:

$$\varepsilon = P(S)/EA + \varepsilon_d(S,T) \tag{2a}$$

where $P(S)$ denotes the equilibrium cable tension, EA is the cross-sectional stiffness, and:

$$\varepsilon_d(S,T) = U_{1,S} - KU_2 + \frac{1}{2}\left[(U_{1,S} - KU_2)^2 + (U_{2,S} + KU_1)^2 + (U_{3,S})^2\right] \tag{2b}$$

is the (nonlinear) dynamic strain. In addition, K denotes the equilibrium curvature and the notation $(\,)_{,S}$ denotes partial differentiation with respect to S. The nonlinear equations of motion describing three-dimensional response about equilibrium are:

(tangential direction)

$$\begin{aligned}&\left[P(U_{1,S} - KU_2)\right]_{,S} \\ &+ \left[EA\varepsilon_d(1 + U_{1,S} - KU_2)\right] \\ &- \left[(P + EA\varepsilon_d)K(U_{2,S} + KU_1)\right] = \rho U_{1,TT}\end{aligned} \tag{3a}$$

(normal direction)

$$\begin{aligned}&\left[(P + EA\varepsilon_d)(U_{2,S} + KU_1)\right]_{,S} \\ &+ PK(U_{1,S} - KU_2) \\ &+ EA\varepsilon_d K(1 + U_{1,S} - KU_2) = \rho U_{2,TT}\end{aligned} \tag{3b}$$

(binormal direction)

$$\left[(P + EA\varepsilon_d)U_{3,S}\right]_{,S} = \rho U_{3,TT} \tag{3c}$$

in which ρ denotes the cable mass/length. For the suspension illustrated in **Figure 2,** the boundary conditions:

$$U_i(0,T) = U_i(L,T) = 0, \quad i = 1,2,3 \tag{3d}$$

describe the illustrated fixed supports.

The nonlinear equations of cable motion above contain the nonconstant coefficients $P(S)$ and $K(S)$ that describe the equilibrium state of the cable. For the catenary of **Figure 2** with level supports, these are given by:

$$P(S) = \sqrt{P_o^2 + [\rho g(S - L/2)]^2} \tag{4a}$$

$$K(S) = \frac{\rho g P_o}{P_o^2 + [\rho g(S - L/2)]^2} \tag{4b}$$

in which P_0 is the (characteristic) tension at the midspan of the equilibrium cable.

Linear Model of Shallow Sag Cable

We shall now focus on the technically important case of a suspended cable under relatively high tension such that the amount of sag at the midspan does not exceed (approximately) one-eighth of the distance between the supports. Such a cable is frequently referred to as a shallow sag cable for which there is a well established linear theory of vibration.

To obtain this theory, we begin by approximating the equilibrium tension eqn [4a] and curvature eqn [4b] as constants (retain first term in Taylor series expansion about the cable midspan):

$$P(S) \approx P_O \tag{5a}$$

$$K(S) \approx K_O = \rho g / P_O \tag{5b}$$

Next, we introduce two wave speeds:

$$c_t = \sqrt{(p_O/\rho)} \qquad [6a]$$

$$c_l = \sqrt{(EA/\rho)} \qquad [6b]$$

which have the interpretation of the speed of propagation of transverse waves along a taut string and longitudinal waves along an elastic rod, respectively (see **Wave propagation**, Guided waves in structures). Clearly the longitudinal wave speed is orders of magnitude greater than the transverse wave speed as $EA \gg P_O$. Recognizing this, it then follows that the equation of motion in the longitudinal direction (eqn [3a]) can be approximated by an equation of statics (eliminate the inertia term $\rho U_{1,TT}$) since longitudinal waves will propagate orders of magnitude faster than transverse waves. This assumption is referred to as the quasistatic stretching assumption and is valid for low-order modes of cable vibration. Finally, we eliminate all the nonlinear terms in the equations of motion to obtain the linear theory. The linear equations are then simplified further by ordering each term and retaining the largest of these. The resulting equations of linear free vibration are:

(Normal direction)

$$P_O U_{2,SS} - \frac{K_O^2 EA}{L} \int_0^L U_2 \, \mathrm{d}S = \rho U_{2,TT} \qquad [7a]$$

(Binormal direction)

$$P_O U_{3,SS} = \rho U_{3,TT} \qquad [7b]$$

with the boundary conditions:

$$U_i(0,T) = U_i(L,T) = 0, \quad i = 2,3 \qquad [7c]$$

describing fixed supports. Note that the equation of motion in the binormal (out-of-plane) direction (eqn [7b]) reduces to the classical wave equation for a taut string. Similarly, the equation of motion in the normal direction (eqn [7a]) is also that for a taut string with the added integral term that accounts for the first-order stretching of the cable centerline. The equation of motion in the tangential direction can be integrated to yield:

$$U_1(S,T) = K_O \left[\int_0^S U_2(\eta,T) \, \mathrm{d}\eta - \frac{S}{L} \int_0^L U_2(\eta,T) \, \mathrm{d}\eta \right] \qquad [7d]$$

Thus, the tangential displacement U_1 can now be computed from knowledge of the normal displacement U_2. This reduction from three variables to two follows from the use of the quasistatic stretching approximation.

Natural Frequencies and Vibration Modes

Eqns [7a] and [7b] are uncoupled in the normal and binormal displacement components U_2 and U_3. Thus, there exists two families of vibration modes, one for in-plane modes associated with eqn [7a] and one for out-of-plane modes associated with eqn [7b] (see **Figure 3**). Three-dimensional linear motions about equilibrium can therefore be decomposed into these two families of vibration modes as suggested in **Figure 3**.

Out-of-plane modes As noted above, the equation describing the out-of-plane vibration of a shallow sag cable is identical to that of a taut string with static tension P_O (the static tension at the midspan of the cable). The natural frequencies and mode shapes can be found by solving the eigenvalue problem associated with the equation of motion (eqn [7b]) and the boundary conditions (eqn [7c]). Doing so yields the natural frequencies:

$$\omega_n = (n\pi c_t/L)\,\mathrm{rad\,s^{-1}}, \; n = 1,2,\ldots \qquad [8a]$$

and mode shapes:

$$\nu_n(S) = C_n \sin(n\pi S/L), \; n = 1,2,\ldots \qquad [8b]$$

in which C_n is an arbitrary constant (frequently selected to satisfy a normalization condition).

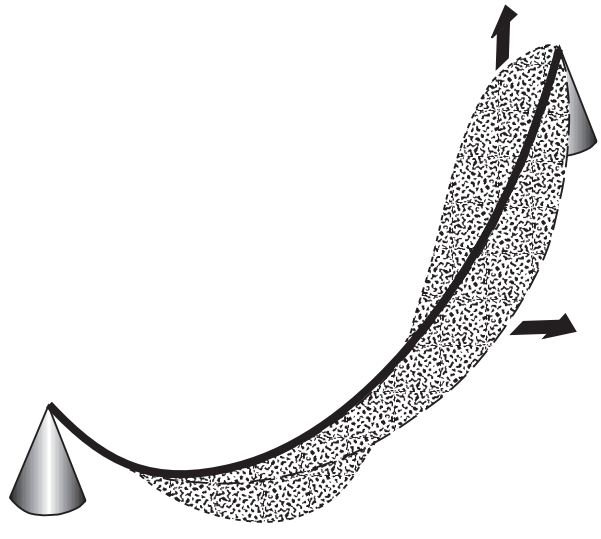


Figure 3 Three-dimensional, linear motions of a sagged cable about equilibrium can be described using two families of vibration modes, namely in-plane modes and out-of-plane modes.

In-plane modes The in-plane modes of a shallow sag cable can be found by formulating the eigenvalue problem associated with eqn [7a] and the boundary conditions in eqn [7b]. Doing so reveals that there are two distinct classes of in-plane modes. One class constitutes all mode shapes that are antisymmetric with respect to the midspan of the cable; that is, all mode shapes that are odd functions about the point $S = L/2$. For these modes, the second term in eqn [7a] vanishes (since an odd function integrated over symmetric limits is zero). Physically, these mode shapes do not induce first-order stretching of the cable centerline. As a result, the equation of in-plane motion is now identical to that of the out-of-plane modes and therefore the antisymmetric in-plane modes and natural frequencies are equivalent to those of the antisymmetric out-of-plane vibration modes.

Antisymmetric in-plane vibration modes

$$\omega_n = (n\pi c_t/L) \text{ rad s}^{-1},\ n = 2, 4, 6, \ldots \qquad [9a]$$

with mode shapes:

$$v_n(S) = C_n \sin(n\pi S/L),\ n = 2, 4, 6, \ldots \qquad [9b]$$

in which C_n is again an arbitrary constant.

The second class of in-plane modes constitutes all mode shapes that are symmetric with respect to the midspan of the cable; that is, all mode shapes that are even functions about the point $S = L/2$. For these modes, the second term in eqn [7a] does not vanish in general and therefore these modes induce first-order stretching of the cable centerline.

Symmetric in-plane vibration modes The mode shapes for the symmetric in-plane modes are:

$$v_n = C_n\left[\sin\left(\frac{\omega_n}{2c_t}S\right)\sin\left(\frac{\omega_n}{2c_t}(S-L)\right)\right],\quad n = 1, 3, 5, \ldots \qquad [10a]$$

in which C_n is an arbitrary constant and ω_n is the corresponding natural frequency that satisfies the characteristic equation:

$$\tan\left(\frac{\omega_n L}{2c_t}\right) = \frac{1}{2}\left[\frac{\omega_n L}{c_t} - \left(\frac{\omega_n L}{c_t}\right)^3/\lambda^2\right] \qquad [10b]$$

Here, the quantity:

$$\lambda^2 = \frac{c_l^2}{c_t^6}(gl)^2 \qquad [10c]$$

is a nondimensional quantity commonly referred to as the cable parameter. The cable parameter represents a ratio of two sources of stiffness, namely, stiffness due to elasticity (through the longitudinal wave speed c_l) and stiffness due to tension (through the transverse wave speed c_t). This single parameter can be used to classify the vibration properties of cable suspensions as described below.

Figure 4 illustrates how the natural frequencies of the in-plane cable modes depend upon the cable parameter. For convenience, the natural frequencies plotted in this figure are nondimensionalized by dividing by the natural frequency of the fundamental out-of-plane cable mode ($n = 1$ in eqn [8a]). The frequencies are plotted as functions of the parameter λ/π. Note that small values of this parameter correspond to a highly tensioned cable and/or small axial stiffness. For example, large P_0 implies large c_t, which implies small λ/π. Conversely, large values of this parameter correspond to less tension (greater sag) and larger axial stiffness. For example, large EA implies large c_l, which implies large λ/π. Note that the natural frequencies of the out-of-plane modes are independent of the parameter λ/π, as are the natural frequencies of the antisymmetric in-plane modes. In both of these cases, the natural frequencies are simply those of a taut string. By contrast, the natural frequencies of the symmetric in-plane modes depend on λ/π. To understand this dependence, we discuss first the vibration characteristics for the two limiting cases $\lambda/\pi \to 0$ and $\lambda/\pi \to \infty$.

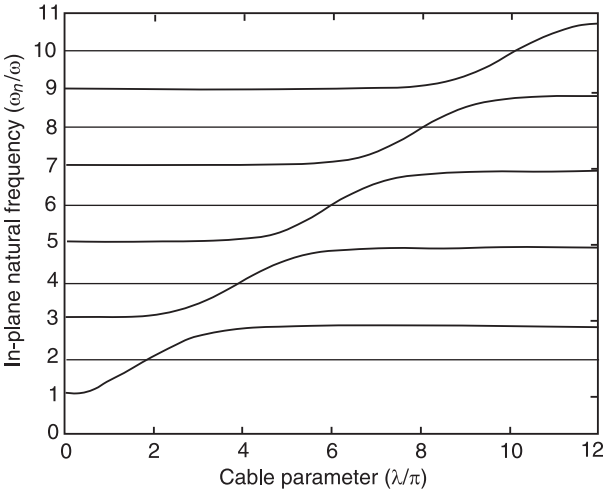


Figure 4 Cable in-plane natural frequency spectrum as a function of the parameter λ/π. The natural frequencies are normalized with respect to the fundamental out-of-plane natural frequency, $\omega = \pi c_t/L$.

Limiting case $\lambda/\pi \to 0$: the taut string For this limiting case, the characteristic equation for the symmetric in-plane modes, eqn [10b], reduces to:

$$\tan\left(\frac{\omega_n L}{2c_t}\right) \to \infty \qquad [11a]$$

and admits the roots:

$$\omega_n = (n\pi c_t/L) \text{ rad s}^{-1}, \quad n = 1, 3, 5, \ldots \qquad [11b]$$

Thus, the symmetric in-plane modes of an elastic and sagged cable reduce to those of a taut string in the limit of large tension (vanishing sag). Consequently the classical taut string model is fully recovered in this limit. In **Figure 4**, the natural frequencies for all of the in-plane modes correspond to the simple integer values (1, 2, 3 ...) in the limit $\lambda/\pi \to 0$. The natural frequencies for all of the out-of-plane modes are, of course, independent of λ/π and correspond to those of a taut string as mentioned above.

Limiting case $\lambda/\pi r \to \infty$: the inextensible cable (chain) For this limiting case, the characteristic equation for the symmetric in-plane modes (eqn [10b]) reduces to:

$$\tan\left(\frac{\omega_n L}{2c_t}\right) = \frac{1}{2}\left[\frac{\omega_n L}{c_t}\right] \qquad [12]$$

This is precisely the characteristic equation of an inextensible cable or chain with small sag. The roots of this equation are the limiting values of the natural frequencies for the symmetric in-plane modes as $\lambda/\pi \to \infty$. In this limit, the cable no longer stretches and all mode shapes induce deformations that satisfy an inextensibility constraint (derivable from the condition $\varepsilon_d = 0$ in eqn [2b]).

General case: the elastic sagged cable The model above provides a continuous transition between the two limiting cases. For small values of λ/π, the model describes a simple taut string. For large values of λ/π, the model describes a sagged but inextensible cable. It is important to note that the (simpler) theory of a sagged but inextensible cable cannot reduce to that of a taut string in the limit of vanishing sag. In this limit, the cable must stretch in response to first-order (linear) deformations. Thus, cable elasticity must be included in any cable theory that might be used near this limit.

The transition of the elastic cable model from a taut string to an inextensible cable is clearly seen in **Figure 4**. For example, follow the curve that defines the first (symmetric) mode of a taut string for $\lambda/\pi \to 0$ starting at the left of **Figure 4** and then proceeding to the right. There is a rapid increase in this quantity near $\lambda/\pi = 2$ where the first natural frequency is also equivalent to the second natural frequency. This point is often referred to as the first crossover point. Second- and higher-order crossover points at $\lambda/\pi = n$, $n = 4, 6, 8 \ldots$ define the transition of the second- and higher-order symmetric in-plane modes. These crossover points represent the values of the cable parameter where a particular symmetric in-plane mode for an elastic cable is evolving from that of a taut string to that of an inextensible cable (chain). During this transition, the mode shape induces cable stretching and undergoes qualitative changes, as discussed below.

Figure 5 illustrates the transition of the fundamental symmetric in-plane mode as one varies the parameter λ/π through the first crossover point. Starting at the bottom of this figure where $\lambda/\pi = 1$, this mode resembles the fundamental mode of a taut string and appears as one-half of a sine wave. As λ/π increases, the tangent at the boundaries rotate to the degree that they become horizontal when the suspension is tuned to the crossover point $\lambda/\pi = 2$. With any further increase in λ/π, the tangents at the boundaries rotate more and create two interior nodes near the boundaries; see mode shape corresponding to $\lambda/\pi = 2.5$. These nodes migrate inwards with further increases in λ/π, until they reach their limiting positions as observed for the case $\lambda/\pi = 4$. At this point, this mode shape now resembles the third mode of a taut string, yet it corresponds to the second mode of a

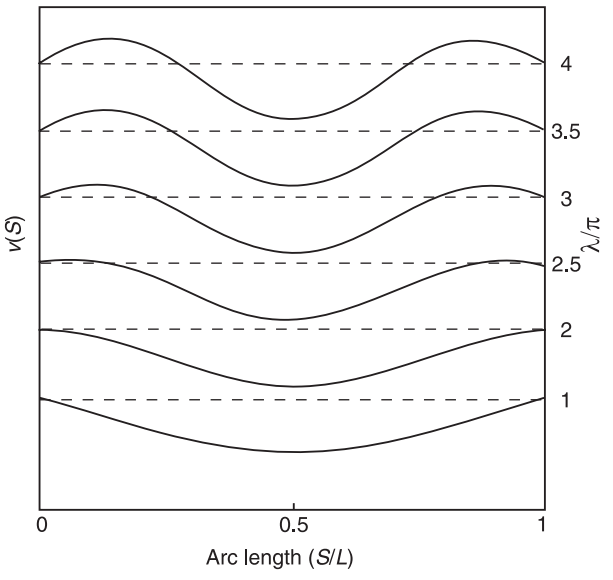


Figure 5 Evolution of fundamental symmetric in-plane mode as the parameter λ/π is varied through the crossover point $\lambda/\pi = 2$.

sagged cable. This is the limiting shape of the first symmetric mode and it induces no stretching of the cable centerline in keeping with the fact the cable model for this mode is equivalent to that of a inextensible cable (chain). Similar transitions occur for all higher-order symmetric modes; namely, each of these gain two interior nodes as the parameter λ/π is increased through the corresponding crossover point.

Extensions of Linear Theory

The linear theory for a shallow sag cable reviewed above provides the basis for many extensions. For instance, specialized theories exist for shallow sag cables that have inclined supports, multispan cables (e.g., transmission lines), translating cables, and cables supporting attached masses, to name a few. In addition, numerous studies have considered possible nonlinear responses of cables, and in doing so have revealed response characteristics that are qualitatively different from predictions based on the linear theory above. A brief review of some nonlinear characteristics is provided here as they significantly differ from what is described above.

To begin, consider a simple experiment as depicted in the schematic of **Figure 6**. In this experiment, a small length of cable is suspended between a fixed support at the right and a movable support at the left. The motion of the left support is controlled by an electromechanical shaker that provides harmonic motion along the cable tangent. This excitation causes the cable to oscillate about its equilibrium configuration. An optical probe positioned somewhere along the cable records these oscillations in the normal and binormal directions (see **Figure 2**).

In this experiment, the tension (sag) of the cable is adjusted so that $\lambda/\pi \approx 2$, i.e., the suspension is tuned to the first crossover. As a consequence, the natural frequency for the fundamental symmetric in-plane mode is approximately twice that of the fundamental out-of-plane mode. The experiment proceeds by adjusting the excitation frequency to be equal to the frequency of the fundamental symmetric in-plane mode. Thus, this mode is resonantly excited and one would anticipate that the cable oscillates in this mode within the equilibrium plane. This expectation, however, is only partially met as can be seen in the experimental results of **Figure 7**.

Figure 7 illustrates the orbit traced by a representative cross-section of the cable as viewed in the normal–binormal plane. Thus, planar motion (motion restricted to the equilibrium plane) will appear as a vertical line in this figure. As the excitation amplitude is slowly increased, the motion begins as planar and then becomes decidedly nonplanar. **Figure 7A** corresponds to the lowest level of excitation and the response is planar as predicted by the linear theory. A modest increase in this excitation leads to a proportional increase in the planar response as seen in **Figure 7B**. A further increase in the excitation,

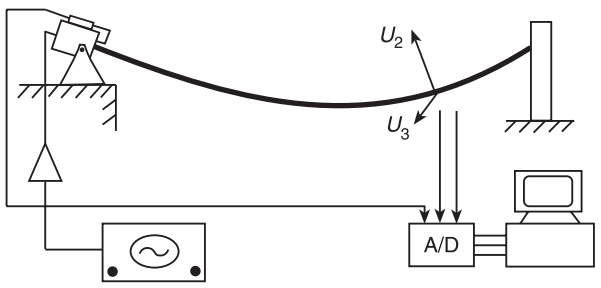


Figure 6 Schematic of a laboratory experiment illustrating nonlinear cable response. The cable is suspended between a fixed support at the right and an electromechanical shaker at the left. Reproduced with permission from Perkins NC (1992) Modal interactions in the non-linear response of elastic cables under parametric/external excitation. *International Journal of Non-linear Mechanics* 27(2): 233–250.

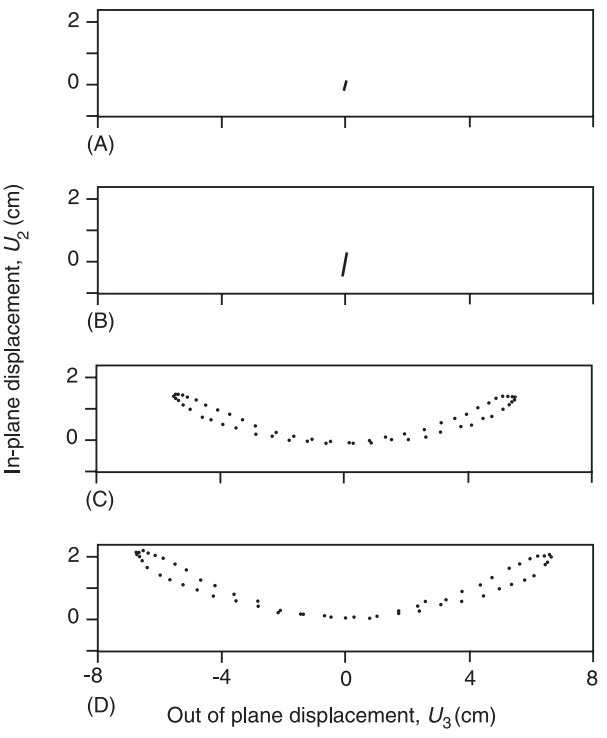


Figure 7 Experimental measurements showing motion of cable cross-section in the normal–binormal plane. Excitation amplitude increases from (A) to (B) to (C) to (D). Reproduced with permission from Perkins NC (1992) Modal interactions in the non-linear response of elastic cables under parametric/external excitation. *International Journal of Non-linear Mechanics* 27(2): 233–250.

however, generates a sizable out-of-plane motion component and the closed orbit shown in **Figure 7C**. Increasing the excitation further yet magnifies this nonplanar motion which cannot be predicted by the linear theory.

Note from **Figures 7C** and **7D** that the nonplanar response forms a closed loop (periodic motion) in the normal–binormal plane. For this particular loop, the cable completes two cycles of motion in the normal direction for every one cycle of motion in the binormal direction. This two-to-one relation in the response frequencies suggests the source of this interesting motion. Further experimental evidence reveals that this motion is produced by two cable modes; namely the fundamental symmetric in-plane mode and the fundamental out-of-plane mode. As mentioned above, these two modes have natural frequencies in a two-to-one ratio when the cable is at the first crossover point as in the experiment. The nonplanar motion observed here results from a nonlinear coupling of these two cable modes. The support excitation resonantly drives the in-plane mode and the in-plane mode is strongly coupled to the out-of-plane mode through the nonlinearities associated with nonlinear (finite) stretching of the cable centerline, (see **Nonlinear system identification**). In particular, there exists a two-to-one internal resonance of these two cable modes that leads to the resulting nonplanar motion (see **Nonlinear system resonance phenomena**). This internal resonance destabilizes the (linear) planar motion through a pitchfork bifurcation. This fact is illustrated in the experimental results of **Figure 8** which shows how the amplitudes of the in-plane displacement (a_2) and the out-of-plane displacement (a_3) vary with the excitation amplitude. Notice that the planar (linear) motion corresponds to the straight line in this figure that begins at the origin. This planar motion ultimately loses stability and is replaced by a periodic nonplanar response that is actually dominated by the out-of-plane motion component.

Numerous studies similar to this have revealed a rich variety of nonlinear responses. These include other classes of internal resonances including one-to-one internal resonances and internal resonances involving multiple (more than two) cable modes. It is important to recognize that these motions develop precisely because of the influence of nonlinear stretching. Thus, they cannot be predicted using a linear theory for cable dynamics.

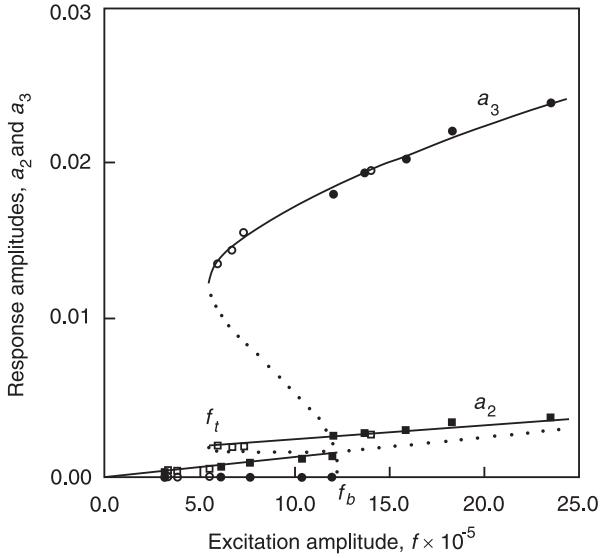


Figure 8 Summary of experimental results showing the amplitudes of the in-plane (a_2) and out-of-plane motion (a_3) components as the excitation amplitude is varied. Solid (open) symbols denote data collected while increasing (decreasing) the excitation amplitude. Reproduced with permission from Perkins NC (1992) Modal interactions in the non-linear response of elastic cables under parametric/external excitation. *International Journal of Non-linear Mechanics* 27(2): 233–250.

Nomenclature

EA	cross-sectional stiffness
g	gravity
K	equilibrium curvature
$P(S)$	equilibrium cable tension
T	time
ρ	cable mass/length

See Plates 11, 12.

See also: **Bridges**; **Columns**; **Membranes**; **Nonlinear system identification**; **Nonlinear system resonance phenomena**; **Shells**; **Wave propagation**, Guided waves in structures.

Further Reading

Cheng SP, Perkins NC (1992) Closed-form vibration analysis of sagged cable/mass suspensions. *ASME Journal of Applied Mechanics* 59: 923–928.

Choo Y, Casarella MJ (1973) A survey of analytical methods for dynamic simulation of cable-body systems. *Journal of Hydronautics* 7: 137–144.

Irvine HM (1981) *Cable Structures*. Cambridge, MA: MIT Press.

Irvine HM, Caughey TK (1974) The linear theory of free vibrations of a suspended cable. *Proceedings of the Royal Society of London* A341: 299–315.

Perkins NC (1992) Modal interactions in the non-linear response of elastic cables under parametric/external excitation. *International Journal of Non-linear Mechanics* 27(2): 233–250.

Perkins NC, Mote CD Jr. (1987) Three-dimensional

vibration of travelling elastic cables. *Journal of Sound and Vibration* 114(2): 325–340.
Simpson A (1966) Determination of the in-plane natural frequencies of multispan transmission lines by a transfer matrix method. *IEE Proceedings* 113(5): 870–878.
Triantafyllou MS (1984) Linear dynamics of cables and chains. *Shock and Vibration Digest* 16: 9–17.
Triantafyllou MS (1984) The dynamics of taut inclined cables. *Quarterly Journal of Mechanics and Applied Mathematics* 37: 421–440.
Triantafyllou MS (1987) Dynamics of cables and chains. *Shock and Vibration Digest* 19: 3–5.
Triantafyllou MS (1987) Dynamics of cables, towing cables and mooring lines. *Shock and Vibration Digest* 23: 3–8.

CEPSTRUM ANALYSIS

R B Randall, University of New South Wales, Sydney, Australia

Copyright © 2001 Academic Press

doi:10.1006/rwvb.2001.0055

Introduction

The cepstrum has a number of variants, definitions, and realizations, but all involve a (Fourier) transform of a logarithmic spectrum, and are thus a 'spectrum of a spectrum'. This is in fact the reason for the name 'cepstrum' and a number of related terms coined, by reversing the first syllable, in the original paper by Bogert, Healy, and Tukey, and discussed here in the section on terminology. However, the autocorrelation function is the inverse Fourier transform of the corresponding autospectrum and so is equally a spectrum of a spectrum. What really distinguishes the cepstrum is the logarithmic conversion of the spectrum before the second transform. In response spectra, this converts the multiplicative relationship between the forcing function and transfer function (from force to response) into an additive one which remains in the cepstrum. This gives rise to one of the major applications of the cepstrum. Another property of the logarithmic conversion is that it often makes families of uniformly spaced components in the spectrum, such as families of harmonics and sidebands, much more evident, so that the final transform is able to reveal and quantify them and their spacing. This gives rise to a further range of applications of the cepstrum in vibration analysis. Note, however, that the cepstrum, being based on logarithmic conversions of dimensionless ratios, in general gives no information on the absolute scaling of signals. All such information is contained in the first (or zero 'quefrency') component in the cepstrum, which is often modified, or a combination of several factors.

Terminology

In the same way as 'cepstrum' is formed from 'spectrum' by reversing the phoneme of the first syllable, the original authors proposed a number of terms which are still found in the cepstrum literature, and which are useful to distinguish properties or operations associated with or carried out in the cepstrum domain. The most useful, which are used in this section, are 'quefrency' the x-axis of the cepstrum, which has the units and dimensions of time, 'rahmonics' a series of uniformly spaced components in the cepstrum, and often coming from a family of harmonics in the log spectrum, and a 'lifter', the equivalent of a filter, but realized by windowing in the cepstrum domain. Thus, a 'shortpass lifter' is analogous to a lowpass filter. Other terms such as 'gamnitude' and 'saphe' are of dubious usefulness.

Definitions and Formulae

The original definition of the cepstrum by Bogert, Healy, and Tukey was the 'power spectrum of the logarithm of the power spectrum', but this has been largely superseded by the definition as the 'inverse Fourier transform of the logarithm of a spectrum'. If the spectrum is a power spectrum, there are two differences with respect to the original definition:

1. The second transform is inverse rather than forward, but since the power spectrum is a real, even function, this only gives a difference in scaling. It is more logical to carry out an inverse transform on a function of frequency.
2. Forming the power (amplitude squared) spectrum of the result makes it irreversible and puts more weight on the largest peaks. It precludes applications involving liftering in the cepstrum, followed by transformation back to the log spectrum.

Moreover, the new definition can be extended to the case where the spectrum (and thus the logarithmic

spectrum) is complex, and the whole process is reversible back to the time domain.

Thus, the cepstrum is defined as:

$$C(\tau) = F^{-1}\{\log[X(f)]\} \quad [1]$$

where:

$$X(f) = F[x(t)] = A(f)\exp[j\phi(f)] \quad [2]$$

in terms of its amplitude and phase, so that:

$$\log[X(f)] = \ln[A(f)] + j\phi(f) \quad [3]$$

When $X(f)$ is complex, as in this case, the cepstrum of eqn [1] is known as the 'complex cepstrum' although since $\ln[A(f)]$ is even and $\phi(f)$ is odd, the complex cepstrum is real-valued.Note that, by comparison, the autocorrelation function can be derived as the inverse transform of the power spectrum, or:

$$R_{xx}(\tau) = F^{-1}\left[|X(f)|^2\right] = F^{-1}\left[A^2(f)\right] \quad [4]$$

When the power spectrum is used to replace the spectrum $X(f)$ in eqn [1], the resulting cepstrum, known as the 'power cepstrum' or 'real cepstrum', is given by:

$$C_{xx}(\tau) = F^{-1}\{2\ln[A(f)]\} \quad [5]$$

and is thus a scaled version of the complex cepstrum where the phase of the spectrum has been set to zero.

Another type of cepstrum which is useful in some cases is the 'differential cepstrum', which is defined as the inverse transform of the derivative of the logarithm of the spectrum. It is most easily defined in terms of the Z-transform (which can replace the Fourier transform for sampled functions) as:

$$C_d(n) = Z^{-1}\left\{z\frac{(\mathrm{d}/\mathrm{d}z)[H(z)]}{H(z)}\right\} \quad [6]$$

where n is the quefrency index, and can be directly calculated from a time signal as:

$$C_d(n) = F^{-1}\left\{\frac{F[nx(n)]}{F[x(n)]}\right\} \quad [7]$$

Among other things this has the advantage that the phase of the (log) spectrum does not have to be 'unwrapped' to a continuous function of frequency, as is the case with the complex cepstrum of eqn [1].

Where the frequency spectrum $X(f)$ in eqn [1] is a frequency response function (FRF) which can be represented in the Z-plane by a gain factor K and the zeros and poles inside the unit circle, a_i and c_i, respectively, and the zeros and poles outside the unit circle, $1/b_i$ and $1/d_i$, respectively (where $|a_i|, |b_i|, |c_i|, |d_i| < 1$), then it has been shown by Oppenheim and Schafer that the complex cepstrum is given by the analytical formulae:

$$\begin{aligned} C(n) &= \ln(K), && n = 0 \\ C(n) &= -\sum_i \frac{a_i^n}{n} + \sum_i \frac{c_i^n}{n}, && n > 0 \\ C(n) &= \sum_i \frac{b_i^{-n}}{n} - \sum_i \frac{d_i^{-n}}{n}, && n < 0 \end{aligned} \quad [8]$$

in terms of quefrency index n.

Since the cepstrum is real, the complex exponential terms in eqn [8] can be grouped in complex conjugate pairs so that a typical pair of c_i terms, for example, can be replaced by $(2/n)\,C_i^n\cos(n\alpha_i)$ where $C_i = |c_i|$ and $\alpha_i = \angle c_i$. This represents an exponentially damped sinusoid, further damped by the hyperbolic function $1/n$. **Figure 1** compares the cepstrum with the impulse response function (IRF) for a single-degree-of-freedom (SDOF) system which has one pair of poles and no zeros. On a logarithmic amplitude scale, zeros of the FRF (antiresonances) are like inverted poles (resonances) so it is no surprise that the corresponding terms in the cepstrum have inverted sign.

Taking the derivative of the log spectrum in the Z-domain to obtain the differential cepstrum results in multiplication by n in the cepstrum, so that a typical term becomes $2C_i^n\cos(n\alpha_i)$, an exponentially damped

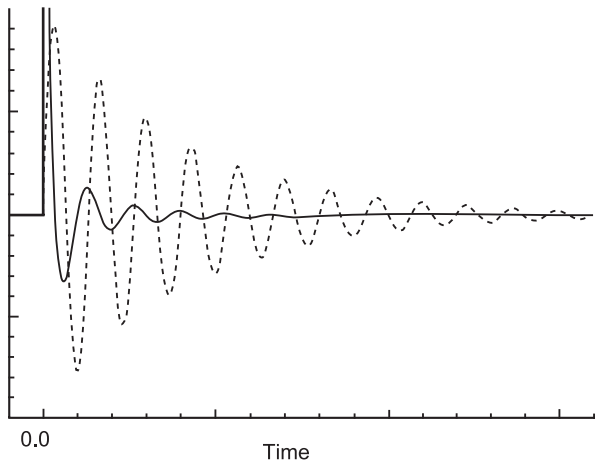


Figure 1 The impulse response (dashed line) of a single-degree-of-freedom system and the corresponding cepstrum (continuous line).

sinusoid without the hyperbolic weighting, so that its form is similar to that of the IRF. This is useful in that techniques which have been developed to curve fit parameters to the IRF can be directly applied to the differential cepstrum. This is the second advantage of the differential cepstrum.

Note that for functions with minimum phase properties, which applies to FRFs for many physical structures, there are no poles or zeros outside the unit circle (the b_i and d_i vanish) and thus there are no negative quefrency terms in eqn [8], so that the cepstrum (and differential cepstrum) are causal. By normal Hilbert transform relationships (see **Hilbert transforms**) this means that the real and imaginary parts of the corresponding Fourier transform, the log amplitude and phase of the spectrum, are related by a Hilbert transform, and only one has to be measured. It also means that the complex cepstrum can be obtained from the corresponding power cepstrum (which is real and even) by doubling positive quefrency terms and setting negative quefrency terms to zero. In this case also, the phase of the spectrum does not have to be measured or unwrapped.

Phase Unwrapping

As mentioned above, the spectrum phase in eqn [1] must be unwrapped to a continuous function of frequency before the inverse transform is carried out, whereas often the phase is obtained as a principal value between $\pm\pi$. **Figure 2** shows a typical example. Simple phase-unwrapping algorithms make a decision based on whether the phase jump between adjacent samples is $> \pi$ or $< \pi$. This can be in error in regions of rapid phase change. Tribolet has devised a more reliable phase-unwrapping algorithm, but perhaps a simpler way of avoiding problems is to use a finer interpolation in the spectrum, by padding time records with zeros up to a sufficient multiple of their original length that the phase jumps between adjacent frequency samples are no longer ambiguous. After unwrapping, the phase function can be decimated back to the original sample rate.

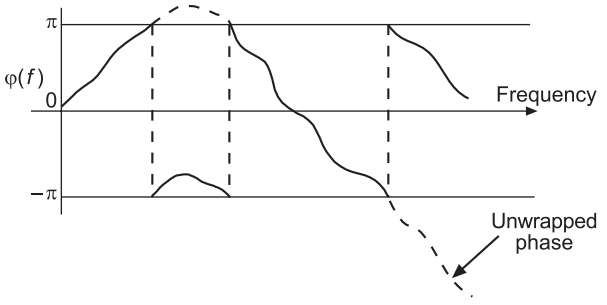


Figure 2 An example of unwrapped phase as determined from the principal values between $\pm\pi$.

Applications of the Power Cepstrum

The major application of the power cepstrum in machine vibrations is to detect and quantify families of uniformly spaced harmonics, such as arise from periodic added impulses (bearing faults, missing turbine blades, faulty valve plate in a reciprocating compressor) and sidebands, such as arise from amplitude and phase modulation of discrete carrier frequencies (faults in gears which modulate the common gearmesh frequency at lower frequencies corresponding to the individual gear rotational speeds).

Faults in Bearings

Figure 3 gives an example of the development of an outer race fault in a ball bearing in a high-speed gearbox driven by a gas turbine, and shows the (log) spectra on the left and the cepstra on the right. Even at the early stages of the fault (24 August 1981) there is a dramatic change in the cepstrum, with a new series of rahmonics appearing in addition to the component corresponding to the shaft speed (RPM). In addition to this detection sensitivity, the other advantages given by the cepstrum are:

1. Since the position of the first rahmonic represents (the reciprocal of) the average harmonic spacing throughout the whole spectrum, the value is much more accurate than can be obtained by measuring the spacing between individual harmonics. Of course, the same accuracy can be obtained by adjusting a finely tunable harmonic cursor on to the spectrum pattern, but even then the cepstrum may be useful in suggesting spacings to try.
2. The fact that the shaft speed quefrency is 4.1 times the quefrency of the unknown component means that its corresponding frequency is 4.1 times the shaft speed. In this case it immediately identified the source as corresponding to the outer race frequency for a particular bearing in the gearbox (which had 10 balls and an effective ball-diameter-to-pitch-diameter ratio of 0.18).
3. Once again, because of the averaging effect across the whole spectrum, the first rahmonic exhibits much less variation with time than the individual harmonics in the spectrum, and thus makes a more valid trend parameter when tracing the course of the fault development. **Figure 4** illustrates this. The higher rahmonics are affected by a number of artifacts and do not add much more information except to confirm the periodicity.

By way of contrast, **Figure 5** compares the (log) power spectrum and its corresponding cepstrum for one of the cases in **Figure 3**, with the (linear) power spectrum for the same case, and its corresponding

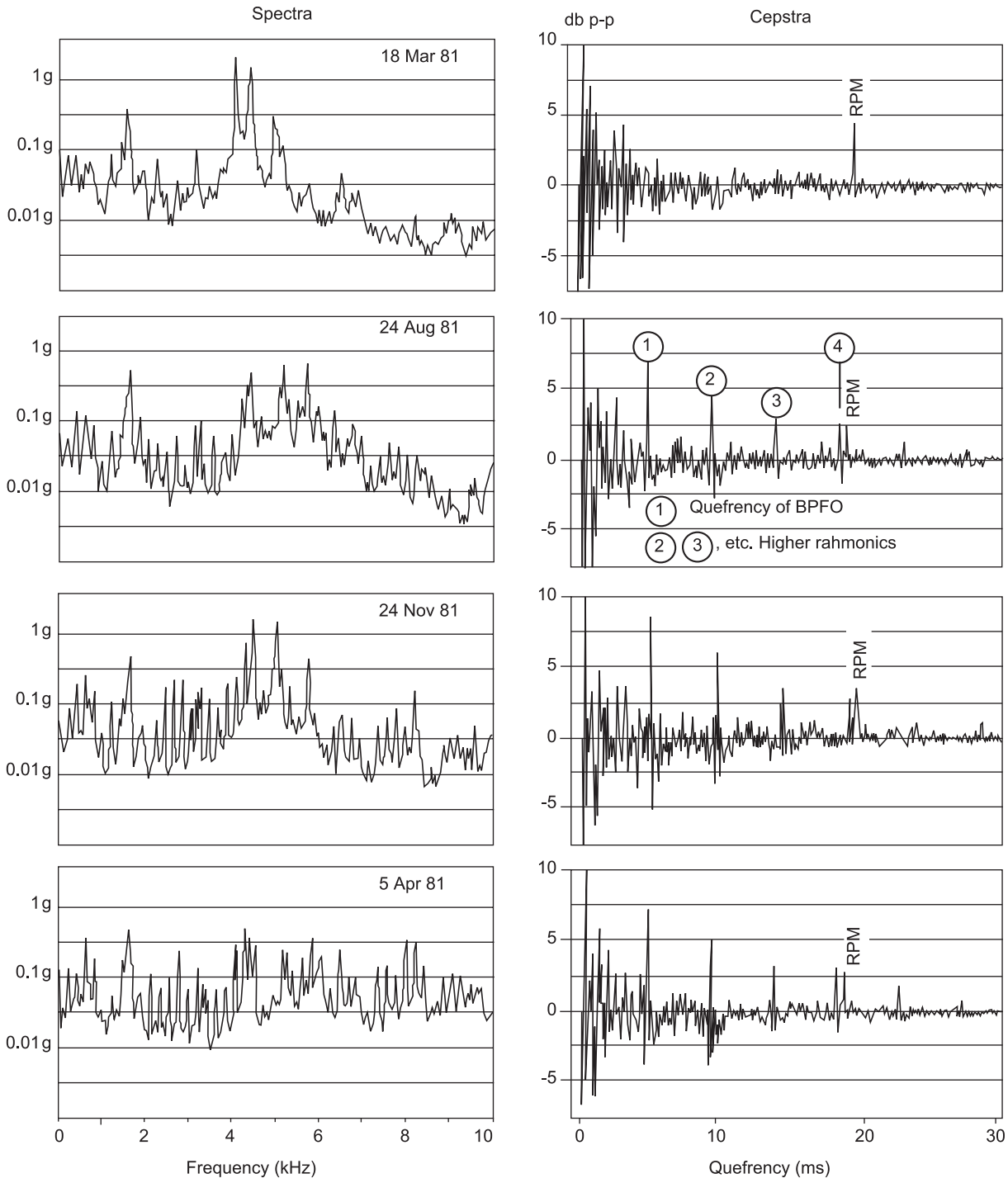


Figure 3 Development of a bearing outer race fault with time as manifested in the (logarithmic) spectrum and cepstrum. Note that variation in load affects some unrelated discrete frequency components, particularly in the range, 4 – 5 kHz.

autocorrelation function. The latter contains no information about the bearing fault; only a beat corresponding to the frequency difference between the two highest spectral peaks.

Thus the cepstrum can be useful in all three phases of condition monitoring: fault detection, diagnosis, and prognosis.

Note that the cepstrum can only be used for bearing fault diagnosis when the fault generates discrete harmonics in the spectrum. This is usually the case for high-speed machines, where resonances excited by the fault represent a relatively low harmonic order of the ballpass frequencies involved, but is often not the case for slow-speed machines, where this order

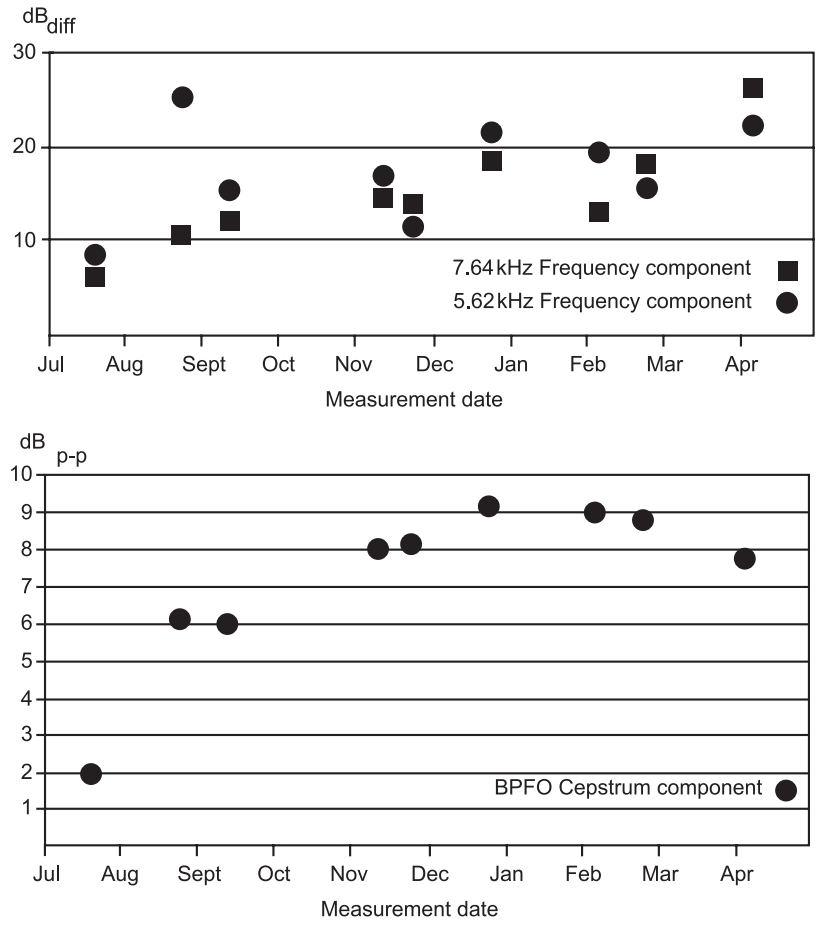


Figure 4 Comparison of trend information given by two typical ballpass frequency harmonics and the corresponding first rahmonic in the cepstrum. BPFO, ballpass frequency, outer race.

may be in the hundreds or even thousands, and these high harmonics are often smeared together. It should be noted that 'envelope analysis', where the envelope obtained by amplitude demodulation of the band-pass-filtered signal is frequency-analyzed, can be used in either case.

Note also that the cepstra in this case have been scaled in terms of 'dB peak-to-peak'. Such practical points are discussed below.

Faults in Turbomachines

The French electrical authority (Electricité de France, EDF) has demonstrated the application of the power cepstrum to the detection of missing blades in a steam turbine. Each missing blade gives rise to an impulse once per revolution as the misdirected steam flow interacts with the stator at the measurement point. This results in the growth of a large number of harmonics of the shaft speed (50 Hz) in the mid-frequency range, and a corresponding growth in the rahmonics of 20 ms in the cepstrum. Only the first rahmonic of the cepstrum needs to be monitored to detect this pattern in the spectrum.

Faults in Gears

Figure 6 illustrates a number of ways in which the power cepstrum can be useful for gear analysis. The degree of modulation of the gearmesh signal by each of the meshing gears is indicated by the corresponding families of rahmonics in the cepstrum, although to separate the sidebands from low harmonics of the shaft speeds (which may have another cause), it is advisable to edit the log spectrum before calculating the cepstrum, for example by only retaining that part of the spectrum above half the toothmesh frequency (but perhaps extending to several harmonics of it). The comparison of **Figure 6B** with **6A** shows that such editing considerably reduces the influence of one gear (121 Hz speed) so that the other (50 Hz speed) is dominant. However, some time later, when the

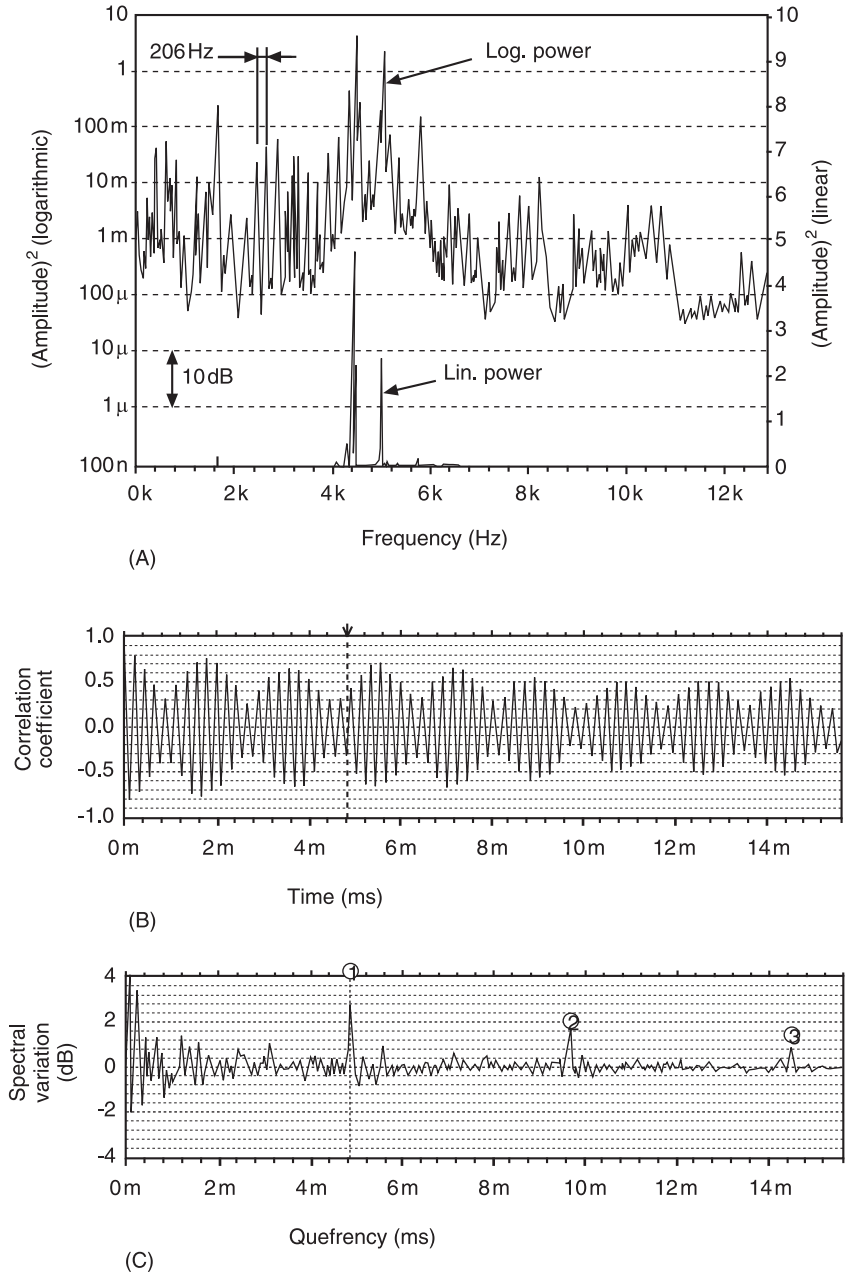


Figure 5 Effect of linear vs logarithmic amplitude scales in the power spectrum. (A) Power spectrum on linear scale (lower curve) and on logarithmic scale (upper curve). (B) Autocorrelation function (obtained from linear representation). (C) Cepstrum (obtained from logarithmic representation). The circled numbers are rahmonics of 4.85 ms, which corresponds to the 206 Hz spacing of the BPFO ballpass frequency harmonics that can be seen in the logarithmic spectrum (but not the linear spectrum). This frequency is 4.1 times the shaft speed.

121 Hz shaft developed some misalignment, it is seen to give increased components in the cepstrum, even with the same editing (**Figure 6C**). **Figure 6D** shows how liftering in the cepstrum can be used to remove one family of sidebands, allowing the other to be more easily visualized. The same can be achieved by synchronous averaging, but requires a tacho signal to synchronize the averaging.

Practical Points in Calculating the Power Cepstrum

Log amplitude spectra are normally represented on a dB scale, and the dB units can be retained for the cepstrum (as there is no interaction with the units of phase). As in **Figure 3**, the amplitude of the cepstrum can be scaled in 'dB peak-to-peak' on the tacit assumption that the harmonic pattern is continuous

and stationary, but in any case that the values obtained are the average values for the section of spectrum analyzed. The value represents in some sense the average protrusion of the harmonic/sideband pattern above the base noise level, and is thus very signal-dependent as well as depending on such artifacts as the analysis bandwidth (relative to the harmonic/sideband spacing) and the type of window function used for the original analysis (e.g. Hanning, flattop). Even so, it is often meaningful to make comparisons between cepstra measured under the same operating conditions on the same machine (where the base noise level could be taken to be constant) and analyzed in the same way. Note that the reference level for the dBs in principle only affects the zero quefrency value of the cepstrum, so in practice it is often convenient to place it in the middle of the range of dB values so that the zero quefrency component in the cepstrum does not dominate the dynamic range and reduce the accuracy of higher quefrency values. This can be achieved in practice by taking the dBs with respect to any reference, and then subtracting the mean dB value.

Increase in a family of harmonics/sidebands will only be detected if the lower amplitude limit is a constant noise level rather than a 'bridging' between adjacent components a fixed number of dB below the peaks. This can occur if the spacing between the latter is not sufficiently greater than the analysis bandwidth. As a rule of thumb, the spacing between adjacent components should be at least 6–8 spectral lines if Hanning weighting is used.

This latter requirement will often mean that it is necessary to use a zoom rather than baseband spectrum in order to obtain sufficient resolution, and then there is another practical point to be aware of. **Figure 7** shows the cepstra obtained from two zoom spectra, slightly displaced from each other in center frequency. Because the harmonic pattern no longer passes through the effective 'zero' frequency, it is seen that there is no longer necessarily a positive peak in the cepstrum corresponding to the harmonic spacing, but there can even be positive and negative peaks on either side of a zero crossing. The same effect can occur with baseband spectra, in cases where a sideband spacing is not an exact subharmonic of the carrier frequency, such as in signals from rolling element bearings and planetary gearboxes. This problem can be very easily solved by making use of Hilbert transform theory (see **Hilbert transforms**). If the cepstrum calculation is carried out on the one-sided spectrum (positive frequencies only), then the resulting cepstrum will be analytic and complex (not to be confused with the 'complex cepstrum', which is real) and a peak will always be found at the correct quefrency in the amplitude of this complex function. **Figure 7** illustrates this for the two zoom spectra. Note that any editing or 'liftering' would have to be done on the complex function. The dB values of the one-sided spectrum should be doubled to maintain unchanged scaling, and it should be zero-padded to the same size as the two-sided spectrum.

Applications of the Complex Cepstrum

For a linear single-input multiple-output (SIMO) system, the relationship between the input (force) and the transfer function (or FRF) in measured signals for each response point is given by:

$$x(t) = f(t) \otimes h(t) \qquad [9]$$

in the time domain, where $\otimes$ represents convolution;

$$X(f) = F(f) \cdot H(f) \qquad [10]$$

in the frequency domain, where $\cdot$ represents multiplication;

$$\log [X(f)] = \log [F(f)] + \log [H(f)] \qquad [11]$$

after taking logs, and:

$$C_X(\tau) = C_F(\tau) + C_H(\tau) \qquad [12]$$

in the cepstrum (or differential cepstrum).

Thus, subtraction of one component in the cepstrum corresponds to deconvolution or inverse filtering in the time domain.

One of the applications of this is the removal of echoes and reflections in signals, as these can be modeled as a convolution with a delayed delta function. Thus, if the primary signal is $x(t)$, and it has an echo scaled by factor $a(< 1)$ and with delay time t_o, it can be represented as $x(t) \otimes [\delta(t) + a\delta(t - t_o)]$ and its spectrum as the product of the two Fourier transforms, or $X(f) \cdot [1 + a \exp(-2\pi f t_o)]$, whose log amplitude and phase are those of $\log(X(f))$ with an additive periodic component in both, which varies with period $1/t_o$ Hz. The cepstrum is thus the sum of the cepstrum of the original function and a series of rahmonics corresponding to the added periodic function, with a spacing of t_o. Provided the original cepstrum is shorter than t_o, these rahmonics can easily be removed by liftering, and the echo thus removed. **Figure 8** gives an example where two equispaced echoes have been removed even though they overlap the original function.

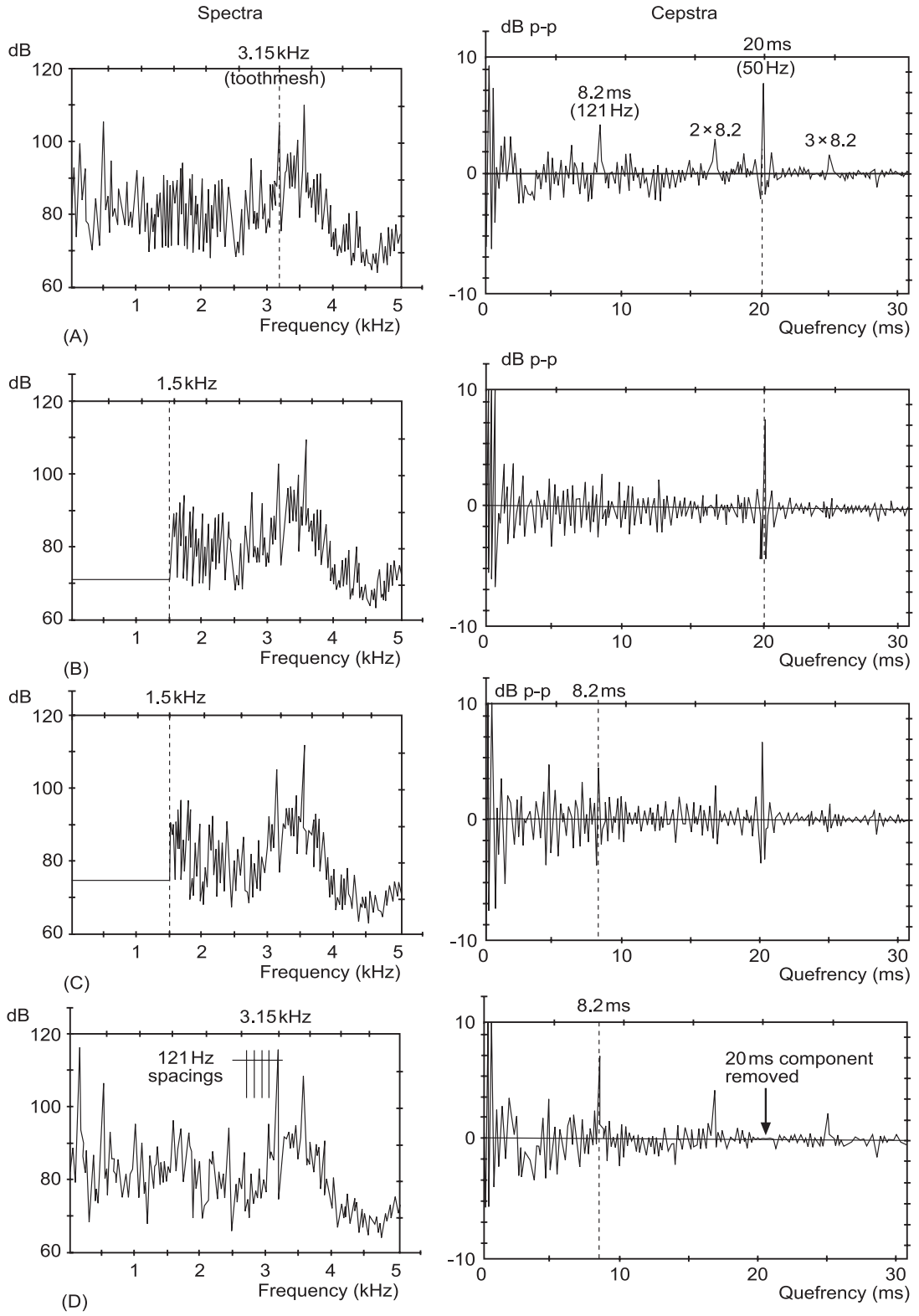


Figure 6 The effects of editing in the spectrum and cepstrum. (A) Original baseband spectrum including both low harmonics and sidebands around a gearbox toothmesh frequency. Cepstrum shows effects from both gear speeds (50 Hz and 121 Hz). (B) Effect of removing low harmonics up to approximately half the toothmesh frequency. The 50 Hz gear now dominates in the cepstrum. (C) Effect of deterioration in alignment of 121 Hz shaft. The effects of this shaft are now evident in the cepstrum, even after editing the spectrum. (D) Effect of removing the cepstral components of one gear (50 Hz) in the cepstrum (from the unedited baseband spectrum) and transforming back to the log spectrum, where the harmonics and sidebands from the other gear (121 Hz) are made more evident.

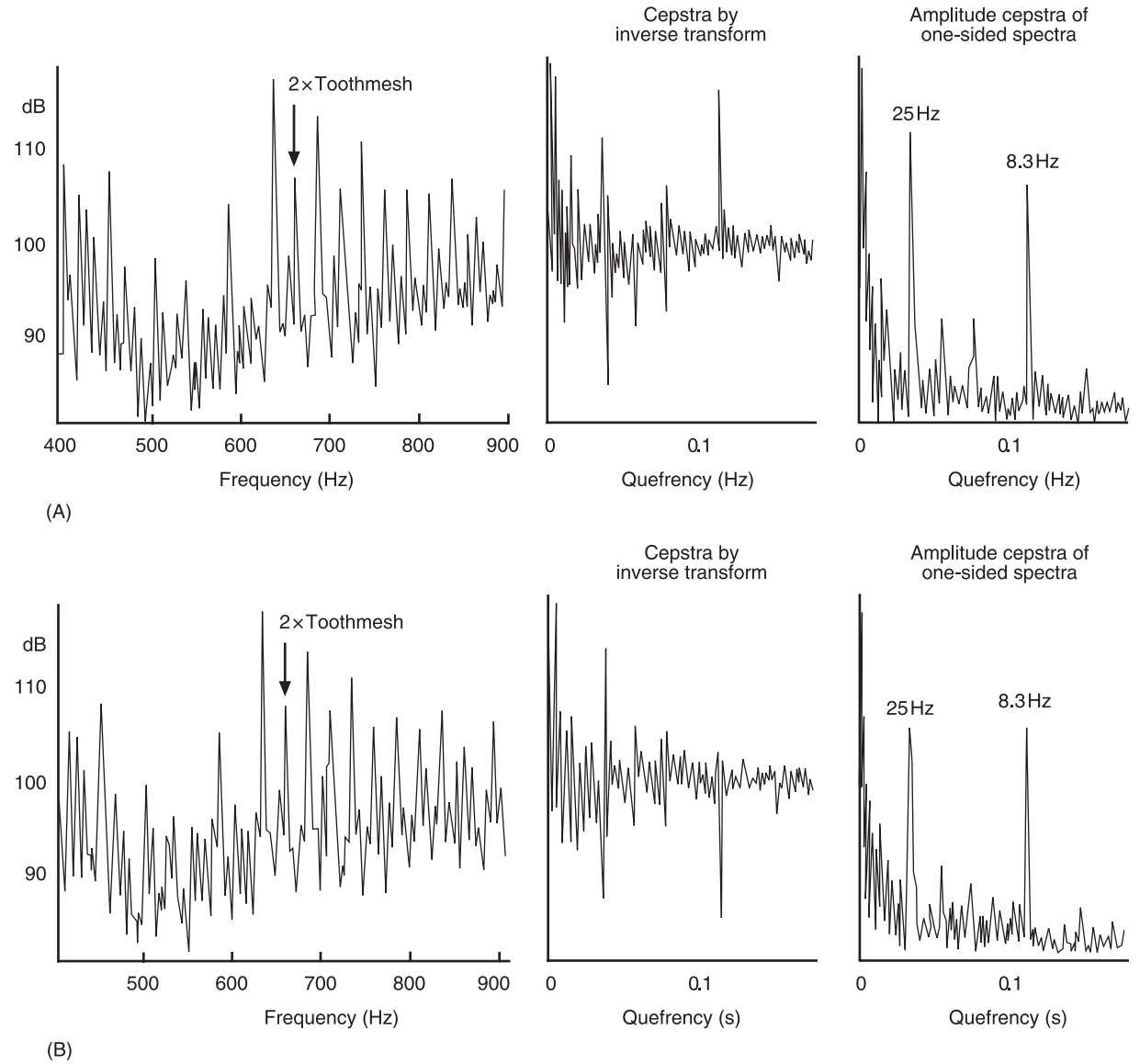


Figure 7 Obtaining cepstra from zoom spectra, by the formal definition (inverse transform of log spectrum) and as the amplitude of the analytic signal obtained from the one-sided spectrum. (A) and (B) represent two slightly displaced zoom spectra from the same signal. Note that the amplitude cepstra indicate the sideband spacings more clearly.

In vibration signals from gears it can be shown that the force at the mesh and the transfer function from the mesh to the measurement point, largely separate in the cepstrum, in that the forcing function is periodic and most of it concentrates at rahmonics corresponding to the toothmesh frequency and individual shaft speeds. Removing these with a suitable 'comb lifter' allows the remaining part of the log spectrum, dominated by the transfer function, to be reproduced by a forward transform. This can reveal whether resonance peaks have changed, and thus whether measured changes are due to changes at the source or in the signal transmission path. **Figure 9** shows the results of such a manipulation in a case where a small number of teeth on the drive pinion of a ball mill were cracked. The resonances in the transfer function are virtually unchanged, demonstrating that the entire change is due to the cracked teeth affecting the mesh force.

Another case where the forcing function and transfer function are well separated in the cepstrum is when a structure is excited by a forcing function with a relatively flat and smooth log spectrum such as the impulse from a hammer blow. In this case the force cepstrum is very short, and the higher-quefrency part of the response cepstrum dominated by the transfer function. The poles and zeros of the FRF can be extracted from this region of the cepstrum (or

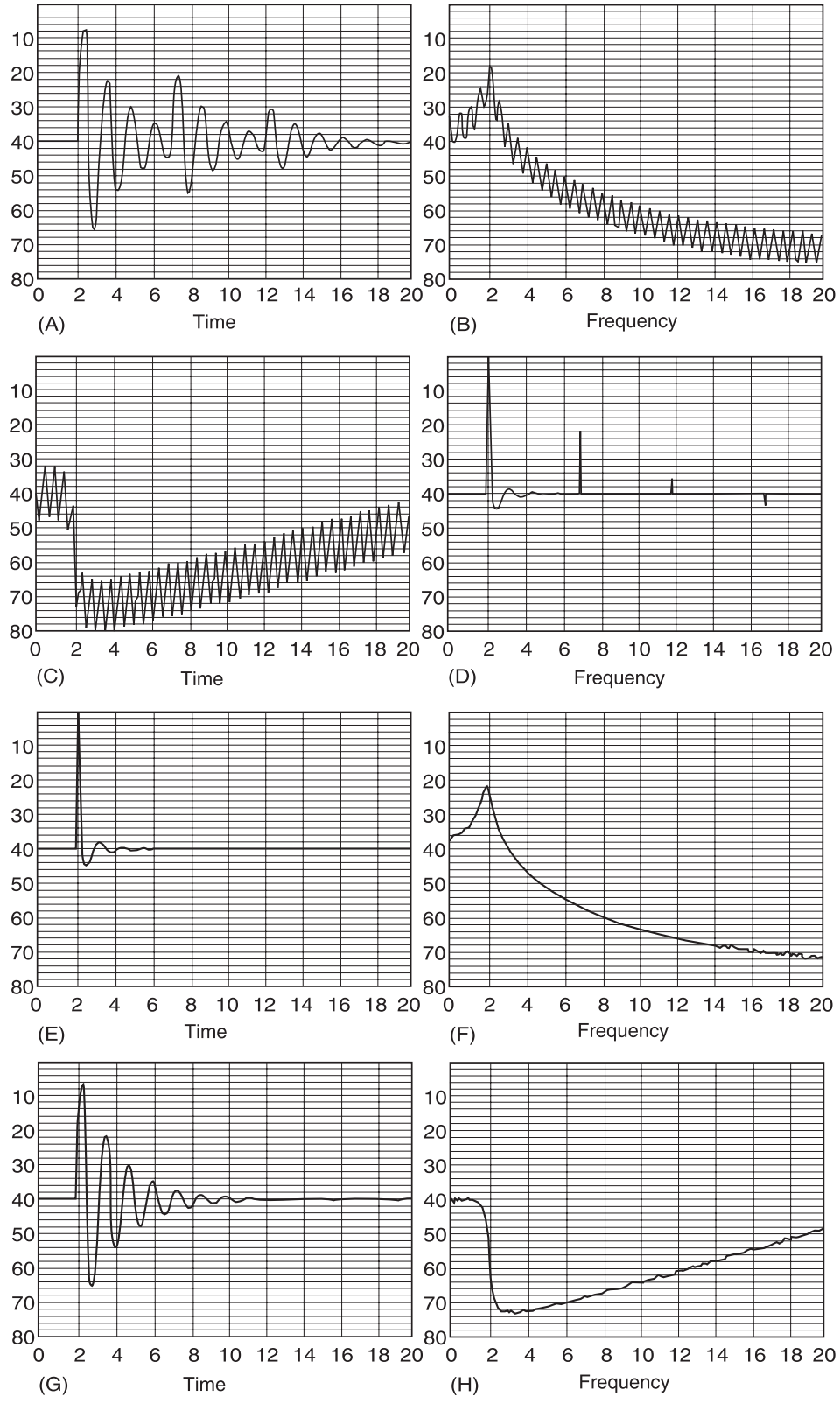


Figure 8 Echo removal using the complex cepstrum. (A) Original signal with two equispaced echos. (B) Log amplitude and (C) phase spectra from (A). (D) Complex cepstrum from (B) and (C). (E) Edited cepstrum after removing rahmonics due to delay. (F) Log amplitude and (G) phase spectra after forward transformation of (E). (H) Time signal by inverse transformation of the complex spectrum obtained by exponentiation of (F) and (G).

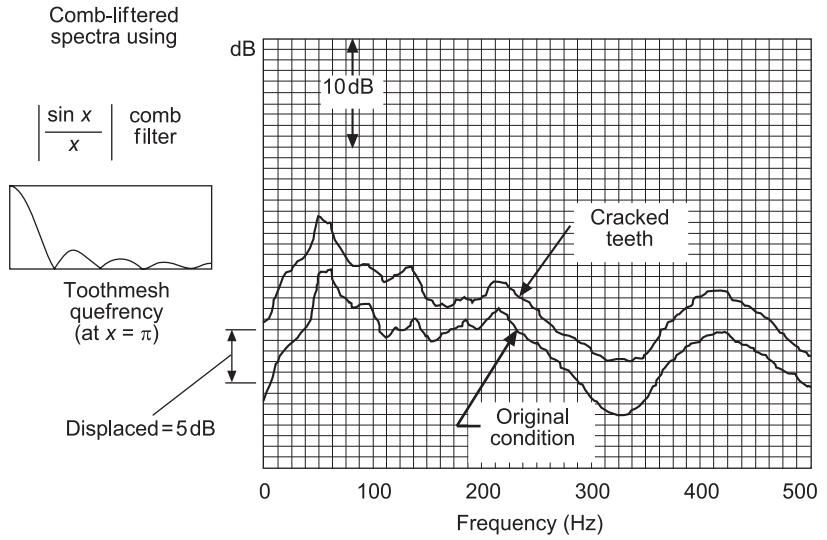


Figure 9 Use of liftering in the cepstrum to separate the effects of the forcing function (gearmesh signal with and without cracked teeth) and the transfer function in the response spectra. Toothmesh rahmonics have been removed by a tailored $|\sin x/x|$ comb lifter (of which the $1/x$ part is a shortpass lifter). The resulting comb-liftered spectra (displaced 5 dB for ease of comparison) indicate that resonance frequencies are unchanged.

differential cepstrum) by curve-fitting expressions of the form of eqn [8], using a nonlinear least-squares optimization algorithm, or from the differential cepstrum by treating it in the same way as a free decay impulse response using the Ibrahim time domain (ITD) method. Note that the latter cannot distinguish between poles and zeros, as there is no absolute time zero, but if measurements are made at several points, use can be made of the fact that the poles are global parameters while the zeros are unique to the different FRFs. It has been found that the poles and zeros within the measurement range are not sufficient in themselves to regenerate the FRF, as the shape is also affected by unmeasured out-of-band modes. However, these effects can be compensated for by in-band 'phantom zeros' (as they usually are in normal modal analysis) and are relatively insensitive to small changes in the pole and zero positions. This means that, once an initial measurement has been made (or perhaps an estimate by finite element modeling), changes in the modal properties of the object can be tracked using response measurements only. **Figure 10** gives an example where phantom zeros determined from FRF measurements on a free–free beam were used in conjunction with updated poles and zeros, extracted by curve-fitting response cepstra, to make estimates of the new FRFs in a case where a milled slot in the middle of the beam had changed some natural frequencies by as much as 10%. An initially determined scaling constant was also used in this

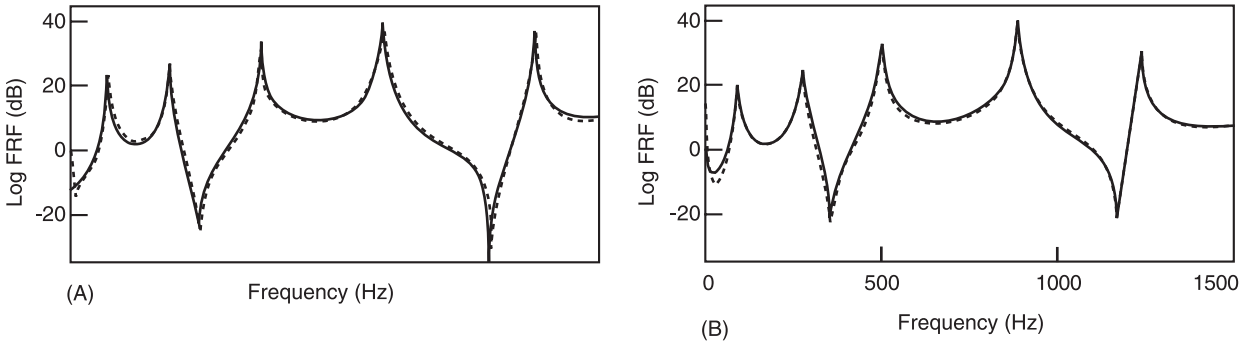


Figure 10 Updating frequency response functions (FRFs) from response measurements obtained by impulsive excitation of a free–free beam. (A) Original measurement. (B) Measurement with a half-depth slot at midspan. Dotted lines – measured FRFs. Solid lines – FRFs reconstructed from poles and zeros extracted by curve-fitting response cepstra. The reconstructed FRF in (B) uses phantom zeros and a scaling factor obtained from the original measured FRF in (A). Note the reduction in frequency of the symmetric (i.e., odd-numbered) modes in (B).

case, as the scaling factor of the FRF cannot be separated in the zero quefrency value of the response cepstrum.

The complex cepstrum has been used by Lyon and others to aid in the inverse filtering process of reconstituting diesel engine cylinder pressure signals from external measurements, typically acceleration of the engine block or head. Small changes in the pole/zero positions mean that they often do not cancel each other in the inverse filtering process, and the resulting pole/zero pair disrupts the estimated pressure signal. Short-pass liftering in the cepstrum smooths the result, giving improved estimates.

Scaling the Complex Cepstrum

Note from eqn [3] that the complex cepstrum has components from both the log amplitude and phase of the spectrum, so the log amplitude should be scaled in nepers (natural log of the amplitude ratio) to agree with the radians of the phase function. The complex cepstrum can then also be scaled in nepers. There are 8.7 dB per neper.

Nomenclature

K	gain factor
n	quefrency index
$\otimes$	convolution

See also: **Gear diagnostics**; **Hilbert transforms**; **Signal processing, model based methods**.

Further Reading

Berther T, Davies P (1991) Condition monitoring of check valves in reciprocating pumps. *Tribology Trans*. 34: 321–326.

Bogert BP, Healy MJR, Tukey JW (1963) The quefrency alanysis of time series for echoes: cepstrum, pseudo-autocovariance, cross-cepstrum, and saphe cracking. In *Proceedings of the Symposium on Time Series Analysis*, by Rosenblatt M (ed), pp. 209–243, New York: John Wiley.

Childers DG, Skinner DP, Kemerait RC (1977) The cepstrum: a guide to processing. *Proceedings of the IEEE* 65: 1428–1443.

Gao Y, Randall RB (1996) Determination of frequency response functions from response measurements. Part I: Extraction of poles and zeros from response cepstra. Part II: Regeneration of frequency response functions from poles and zeros. *Mechanical Systems and Signal Processing* 10: 293–317, 319–340.

Lyon RH, Ordubadi A (1982) Use of cepstra in acoustical signal analysis. *ASME J. Mech. Des.* 104: 303–306.

Oppenheim AV, Schafer RW (1989) *Discrete Time Signal Processing*. New Jersey: Prentice-Hall.

Randall RB (1987) *Frequency Analysis*, 3rd edn, Chapt. 8, Cepstrum Analysis. Copenhagen: Bruel and Kjaer.

Sapy G (1975) Une application du traitement numérique des signaux au diagnostic vibratoire de panne: la détection des ruptures d'aubes mobiles de turbines. *Automatisme* XX: 392–399.

Tribolet JM (1977) A new phase-unwrapping algorithm. *IEEE Trans. Acoust. Speech Signal Proc*. ASSP-25: 170–177.

CHAOS

P J Holmes, Princeton University, Princeton, NJ, USA

Copyright © 2001 Academic Press

doi:10.1006/rwvb.2001.0039

Introduction

Basic ideas and techniques from the theory of dynamical systems are reviewed and applied to analyze and understand chaotic vibrations. Single-degree-of-freedom, periodically forced, nonlinear oscillators are treated; the canonical examples being the pendulum, the Duffing and the van der Pol equations. After sketching some history, the key ideas of Poincaré maps and invariant manifolds are introduced, followed by a simple mathematical example (the doubling map), which illustrates deterministic chaos and a major tool for its analysis: symbolic dynamics. Then, using regular perturbation methods, it is shown that chaotic solutions occur in a broad class of nonlinear oscillators, including Duffing's equation, and the difficulty of proving the existence of 'strange attractors' – motions displaying sensitive dependence on initial conditions that attract almost all initial conditions – is discussed. The article ends with a brief note on sources and types of nonlinearity likely to lead to chaos, and some pointers to the (enormous) literature.

A Brief History

Henri Poincaré's studies of celestial mechanics, in particular of the three-body problem, led him to discover complex motions in deterministic Hamiltonian classical mechanics; he also provided the groundwork

for much of the modern qualitative theory of dynamical systems (chaos theory). Poincaré's work was followed by that of George Birkhoff in the US, Andronov and Pontryagin in the USSR, and a remarkable paper on the van der Pol equation by Cartwright and Littlewood, arising from British radar development work in World War II. This latter was the first explicit example of a periodically forced nonlinear oscillator having chaotic solutions; subsequently studied by Levinson, it led Smale in 1960 to create the horseshoe map, and thus complete part of the story begun by Poincaré. Shortly after Smale's work (but before its publication), Ueda, working with an analog computer, independently discovered chaotic motions in a variant of the forced van der Pol system, and Lorenz published his now celebrated example of an autonomous three-dimensional system. See Further Reading.

Poincaré Maps and Invariant Manifolds

Dynamical systems theory addresses nonlinear differential equations and iterated mappings, bringing a geometrical and topological approach to complement perturbative and other analytical methods (see **Perturbation techniques for nonlinear systems**). The study of qualitative behavior is emphasized; solutions of the differential equation:

$$\dot{x} = f(x);\ x \in R^{n} \qquad [1]$$

are viewed as flowlines evolving in the state or phase space, R^{n}. A key idea is that the behavior of a nonlinear system near a nondegenerate equilibrium or periodic orbit can be deduced by linearization and successive Taylor series approximations; geometrically, local stable and unstable manifolds exist. These manifolds are smooth (hyper-) surfaces, tangent at the equilibrium or periodic orbit to the eigenspaces belonging to exponentially decaying and growing linearized solutions, and invariant under the flow defined by eqn [1]. This is the main consequence of the stable manifold theorem. The local manifolds, which are related to nonlinear normal modes, are defined in a neighborhood of the orbit in question, but they can be extended globally by following solutions backwards and forwards in time, and their structure determines the asymptotic behavior of solutions starting nearby. See **Figure 1A**, which shows the stable and unstable manifolds (= separatrices, here) of the saddle point $(\theta, v) = (\pm\pi, 0)$ corresponding to the inverted (unstable) equilibrium of the damped pendulum, whose governing equation can be written in nondimensional form as:

$$\dot{\theta} = v,\ \dot{v} = -\sin\theta - \delta v \qquad [2]$$

Note that the local stable manifold of the 'downward' equilibrium $(\theta, v) = (0, 0)$ includes a full neighborhood of that point: it has no unstable manifold; indeed, almost all solutions eventually approach (0, 0); those that do, belong to its domain of attraction. In the above, 'nondegenerate' means that all eigenvalues of the system linearized at the fixed point have nonzero real parts; such points are also called hyperbolic. Both equilibria are hyperbolic in **Figure 1A**.

Periodically forced oscillators, such as the Mathieu, Duffing and van der Pol equations, or the pendulum itself, require a three-dimensional phase space for their definition as dynamical systems. We think of time, t, as a third 'dependent' variable, ϕ, as here, for the negative stiffness Duffing equation:

$$\begin{aligned} &\dot{x} = y, \quad \dot{y} = x - \delta y - x^{3} + \gamma\cos(\phi), \\ &\dot{\phi} = \omega; \quad (x, y, \phi) \in R^{2} \times S^{1} \end{aligned} \qquad [3]$$

Since the excitation $\gamma\cos(\omega t)$ is periodic, we can identify time or ϕ-slices equally spaced by 2π and roll up the ϕ-axis into a circle S^{1}. The phase space therefore resembles a solid torus: see **Figure 1B**.

In this phase space we fix a cross-section $\Sigma_0 = \{\phi = 0\}$, and consider the Poincaré map, P, obtained by integrating eqn [3] with initial conditions $(x(0), y(0)) = (x_0, y_0) \in \Sigma$ until the solution first returns to Σ_0. This implicitly defines a difference equation or discrete dynamical system:

$$P(x_0, y_0) = (x_1, y_1)$$

or, in general

$$(x_{n+1}, y_{n+1}) = P(x_n, y_n) \qquad [4]$$

Orbits $\{P^{k}(x)\}_{k=0}^{\infty}$ of eqn [4] are discrete sequences of points, not smooth curves, as in the usual phase portraits like that of **Figure 1A**; see **Figure 1B**. Harmonic responses of period $(2\pi/\omega)$ of eqn [3] correspond to fixed points of P, and $(2m\pi/\omega)$-periodic subharmonics to m-periodic cycles of P. Periodic orbits can be attractors (asymptotically stable), neutrally stable (Liapunov stable but not asymptotically stable), of saddle type, or repellors (both unstable). A saddle-type orbit, being itself one-dimensional (topologically a circle), has a two-dimensional sheet of solutions approaching it and a two-dimensional sheet of solutions leaving its stable and unstable manifolds, which intersect Σ_0 in curves (**Figure 1B**). Hence the invariant manifolds of a saddle point p in a two-dimensional

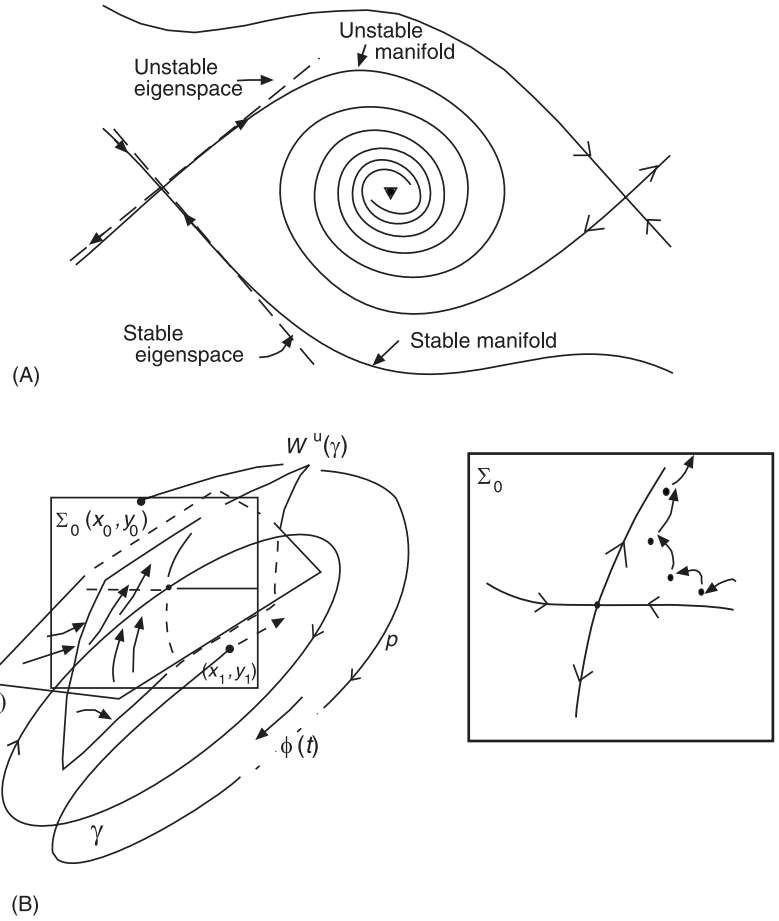


Figure 1 Stable and unstable manifolds (A) for a fixed point: an equilibrium of a 'free' nonlinear oscillator, the damped pendulum; (B) for a periodic orbit, illustrating a cross-section Σ_0 and the Poincaré map P.

map P resemble saddle separatrices for a two-dimensional flow (**Figure 1A**), but there is a crucial difference: the stable and unstable manifolds of a saddle point p for a map can cross at homoclinic points. These are points q which approach (= incline towards) p under both forward and backward iteration: $P^n(q) \to p \text{as} |n| \to \infty$. A heteroclinic point is one which approaches distinct fixed points p_1 and p_2 under forward and backward iteration. If the tangents to the manifolds at the intersection point are distinct, the homoclinic (heteroclinic) point is called transverse. As Poincaré realized, such points are associated with extremely sensitive dependence on initial conditions, and what is now commonly called chaos. Before illustrating homoclinic points and their consequences, a simple motivating example is described.

Symbolic Dynamics and Chaos

Consider a mathematical toy: the one-dimensional piecewise linear map defined on the interval $[0, 1] \subset R$ by:

$$h(x) = \left\{ \begin{array}{ll} 2x & \text{if } 0 \leq x < \frac{1}{2} \\ 2x - 1 & \text{if } \frac{1}{2} < x \leq 1 \end{array} \right\} \qquad [5]$$

and illustrated in **Figure 2**. An orbit of h is the sequence $\{x_n\}_{n=0}^{\infty}$ obtained by successively doubling the initial value x_0 and subtracting the integer part at each step; for example: $0.2753 \mapsto 0.5506 \mapsto 1.1012 = 0.1012 \mapsto 0.2024 \mapsto 0.4048 \mapsto \ldots$

To understand the sensitive dependence on initial conditions and its consequences, we represent the numbers in $[0, 1]$ (the phase space of this dynamical system) in binary form. This is the idea of symbolic dynamics. Let:

$$x_0 = \frac{a_1}{2} + \frac{a_2}{2^2} + \frac{a_3}{2^3} + \cdots + \frac{a_k}{2^k} + \cdots \qquad [6]$$

where each coefficient a_j takes the value 0 or 1. It follows that:

$$x_1 = h(x_0) = 2\left(\sum_{j=1}^{\infty} \frac{a_j}{2^j}\right) = a_1 + \frac{a_2}{2} + \frac{a_3}{2^2} + \frac{a_4}{2^3} + \cdots$$

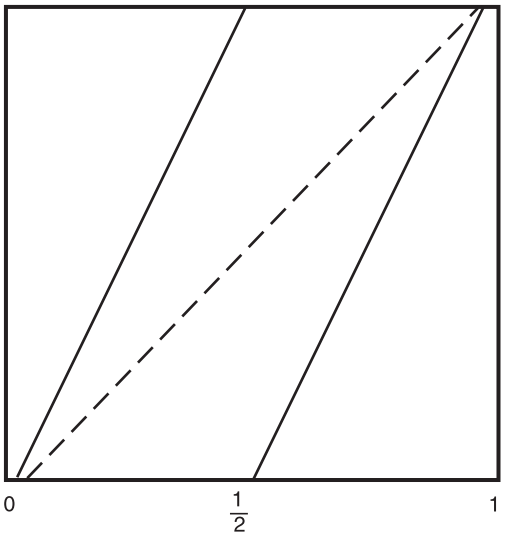


Figure 2 The doubling map, h.

Since each time the integer part is removed (a_1, here), the kth iterate gives:

$$x_k = h^k(x_0) = \sum_{j=k+1}^{\infty} \frac{a_j}{2^{j-k}} \qquad [7]$$

Thus, applying h is equivalent to shifting the binary point and dropping the leading coefficient in the binary representation: $(a_1a_2a_3a_4\ldots)\mapsto(a_2a_3a_4\ldots)$, just as multiplication by 10 shifts the decimal point. In this operation the leading symbol is removed and information is lost. If x_0 were known to infinite accuracy, with all a_ks specified for $1 \leq k < \infty$, at each step the current state x_k would still be known exactly. But, given knowledge of only the first N binary places $(a_1, a_2, \ldots a_N)$, after N iterations, it cannot even be determined whether the state x_{N+1} lies above or below $\frac{1}{2}$. Moreover, even if two initial conditions differ only at the Nth binary place, so that the points lie within $(\frac{1}{2})^{N-1}$, after N iterations they lie on opposite sides of $\frac{1}{2}$ and thereafter behave essentially independently. Here is the sensitive dependence: the dynamics amplifies small errors.

The binary representation shows that to every infinite sequence of 0s and 1s there corresponds a number between zero and one, and vice versa. Thus, for any random sequence (e.g., obtained by tossing a coin: heads = 0, tails = 1), there is an initial state $x_0 \in [0, 1]$ such that the orbit $h^k(x_0)$ realizes the chosen sequence. Hence the map has infinitely many random orbits. There are also infinitely many periodic orbits, corresponding to repeating sequences such as 001001001.... However, since a number picked at random is almost always irrational (the irrational numbers form a set of full measure), typical behavior is chaotic rather than periodic.

The binary representation also shows that a dense orbit exists. Consider the sequence a^* formed by concatenating all possible sequences of lengths 1, 2, 3, ... end to end: $a^* = 0\ 1\ 00\ 01\ 10\ 11\ 000\ 001\ldots$. As one iterates and drops leading symbols, every possible subsequence of any given length appears at the head. This implies that the orbit of the point x^* corresponding to a^* contains points which approximate, to any desired accuracy, every point in the interval [0, 1] and so $\{h^k(x^*)\}_{k=0}^{\infty}$ is a dense orbit. The symbol sequences also allow one to enumerate the periodic orbits simply by listing all distinct (i.e., non-shift-equivalent) sequences of lengths 1, 2, 3, ... which do not contain lower period subsequences (**Table 1**). Asymptotically, there are $\approx 2^N/N$ orbits of period N.

This example embodies the three key characteristics of a chaotic invariant set $V \subset R^n$ for a map P: $R^n \to R^n$:

1. Sensitive dependence on initial conditions: There is a $\beta > 0$ such that, for any $x \in V$ and any neighborhood $U \ni x$, no matter how small, there exists a point $y \in U$ and an integer $k > 0$ such that $|P^k(y) - P^k(x)| > \beta$; i.e., almost all orbits eventually separate.
2. The periodic points are dense in V.
3. There is a dense orbit in V.

The final condition implies that V cannot be decomposed into simpler elements. The dense orbit contains segments passing arbitrarily close to any given point in V and so almost all orbits must 'fill out' V without getting 'stuck' in simple periodic motions.

Below it is shown that the presence of transverse homoclinic orbits in a Poincaré map implies that chaotic dynamics occurs of precisely the same type as that just described.

Table 1 Enumerating periodic orbits for h

Length	*Sequences*	*Number of orbits*
1	0, 1	2
2	01 (=10)	1
3	001, 011	2
4	0001, 0011, 0111	3
5	00001, 00011, 00101, 00111, etc.	6
6	.....	9
.	.....	.
.	.....	.
25	.....	1 342 176
.	.....	.

Perturbing Separatrices: Melnikov's Method

Melnikov developed a perturbative method for detecting homoclinic orbits in periodically perturbed nonlinear systems that have smooth separatrices connecting saddle points prior to perturbation, such as eqns [2] and [3] with $\delta = 0$ and $\gamma = 0$. Letting x denote the two-dimensional vector (x, y) or (θ, ν), one may write the perturbed equation as:

$$\dot{x} = f(x) + \varepsilon g(x,t)\ ;\ 0 \le \varepsilon \ll 1 \qquad [8]$$

noting that $g(x, t)$ is T-periodic in t. Assume that for $\varepsilon = 0$ the unperturbed system is Hamiltonian, with $f(x) = (\partial H/\partial y,\ -\partial H/\partial x)^{\mathrm{T}}$ and (energy) function $H(x, y)$ constant on solutions. (This assumption is not essential, but leads to a simpler expression in eqn [11] below.) Assume further that $x = p_0$ is a hyperbolic saddle point with eigenvalues $\pm\lambda \neq 0$, and that there is a homoclinic (separatrix) loop $q_0(t)$ to p_0: see **Figure 3A**. The fact that p_0 is nondegenerate (hyperbolic), along with perturbation and invariant manifold theory, implies that it perturbs to a small T-periodic orbit $\gamma_\varepsilon = p_0 + O(\varepsilon)$, and that solutions $x^{\mathrm{s}}_\varepsilon, x^{\mathrm{u}}_\varepsilon$ in the stable and unstable manifolds respectively of γ_ε can be written as power series in ε: $x_0 + \varepsilon x_1^{\mathrm{s,\,u}} + O(\varepsilon^2)$, uniformly convergent on semi-infinite time intervals. Substituting these expansions into eqn [5] and equating zeroth and first-order terms yields:

$$\dot{x}_0 = f(x_0), \quad \dot{x}_1^{\mathrm{s,u}} = Df(x_0)x_1^{\mathrm{s,u}} + g(x_0, t) \qquad [9]$$

where Df denotes the matrix of first partial derivatives.

Now consider the quantity:

$$d(t_0) = f(x_0(0))^{\perp} \cdot \left(x^{\mathrm{s}}_\varepsilon - x^{\mathrm{u}}_\varepsilon\right) \qquad [10]$$

which measures the distance between the perturbed stable and unstable manifolds at a selected point $x_0(0)$, projected on to the normal $f(x_0(0))^{\perp}$ to the unperturbed solution (= level sets of H), on the cross-section Σ_{t_0} (**Figure 3B**). $d(t_0)$ may be approximated to first-order via the power series for x^{s} and x^{u}, and a short computation using eqn [9] leads to the expression:

$$\begin{aligned} d(t_0) &= \varepsilon M(t_0) + \mathrm{O}\left(\varepsilon^2\right) \\ M(t_0) &= \int_{-\infty}^{\infty} f(q_0(t))^{\perp} \cdot g(q_0(t),\, t + t_0)\, \mathrm{d}t \end{aligned} \qquad [11]$$

It follows that, if the Melnikov function $M(t_0)$, has simple zeroes, then the stable and unstable manifolds of the fixed point, p_ε, of the Poincaré map corresponding to γ_ε, intersect transversely. As shown below, $M(t_0)$ may be explicitly calculated in specific examples, even though the perturbed Poincaré map, P_ε, is effectively uncomputable (except numerically).

If one (transverse) homoclinic point, q, exists, then every image, $P^k(q)$, is also homoclinic: there is a homoclinic orbit. In fact, considering images of small arcs contained in $W^{\mathrm{s}}(p_\varepsilon)$ and $W^{\mathrm{u}}(p_\varepsilon)$ near q under the map P, we see that the global manifolds must intersect repeatedly in a homoclinic tangle (**Figure 3C**). Poincaré described this 'tissue ... with infinitely fine mesh' and noted that nothing could better represent the complexity of three-body problem. But he went no further in analyzing the structure of orbits associated with the tangle: that awaited the work of Birkhoff and Smale.

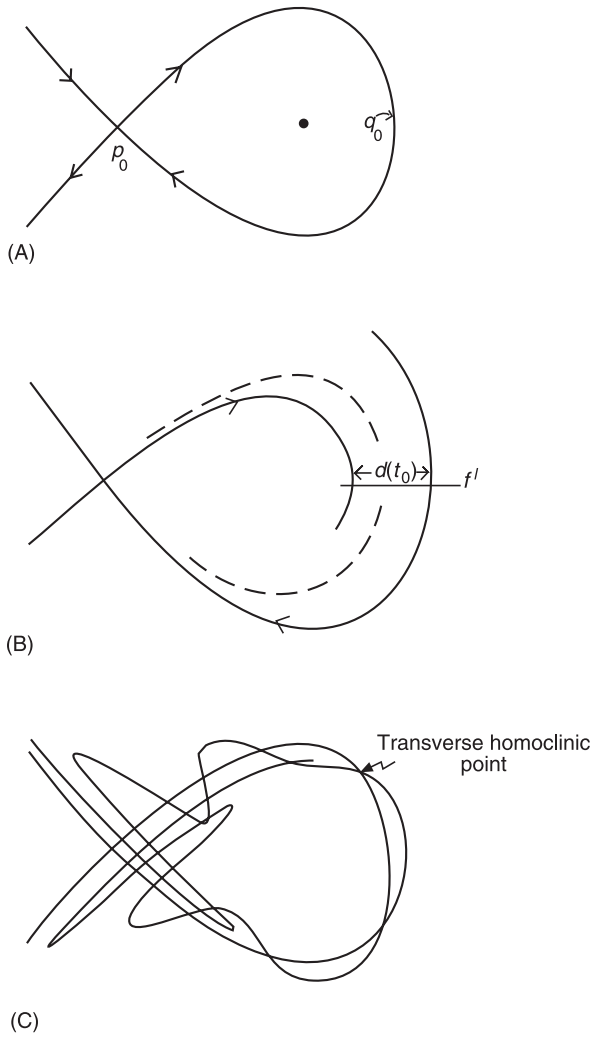


Figure 3 (A) The unperturbed homoclinic loop; (B) the distance estimate for splitting of stable and unstable manifolds in the perturbed Poincaré map; (C) the homoclinic tangle.

Smale's Horseshoe and Chaos

Before presenting an example from nonlinear oscillations, the connection between homoclinic points and chaos, promised above, is made. **Figure 4A** shows a rectified version of **Figure 3B**. Consider the effect of the map P_ε on a rectangular strip, S, containing p_ε, a homoclinic point q_ε, and partially bounded by pieces of $W^s(p_\varepsilon)$ and $W^u(p_\varepsilon)$. Successive applications of P_ε compress S along $W^s(p_\varepsilon)$ and stretch it along $W^u(p_\varepsilon)$, so that for sufficiently large n, the nth image $P_\varepsilon^n(S)$ assumes the horseshoe shape, also shown in **Figure 4A**.

This suggests the following piecewise-linear map F, which approximates P_ε^n. F is defined on the unit square, and takes the lower rectangle H_0 of height γ^{-1} into the left-hand strip V_0 of width λ, and the upper rectangle H_1 of height γ^{-1} into the right-hand strip V_1 of width λ, rotating the latter by π. Here $\lambda < 1/2$, $\gamma > 2$. The image of the central strip is the arch connecting V_0 and V_1 (**Figure 4B**). The key to understanding F (and hence P_ε) is in the description of the set, Λ, of points which never leave S under forward or backward iteration of F. These points must lie in either H_0 or H_1 and V_0 or V_1 (e.g., if they lie in the middle strip, they leave S on the next application of F). Moreover, for their second forward and backward iterates to lie in S, they must inhabit the intersections of four horizontal and four vertical strips H_{ij}, V_{ij} of widths γ^{-2} and λ^2 respectively, also shown in **Figure 4B**, or else they will land in a middle strip after one iterate. Continuing inductively, we find that Λ is a Cantor set: an uncountably infinite 'cloud' of points, containing no open sets, and every point of which is a limit point of other points in the set.

As shown above, symbol sequences may be uniquely assigned to the points of Λ, but now they are doubly infinite, since F is an invertible map.

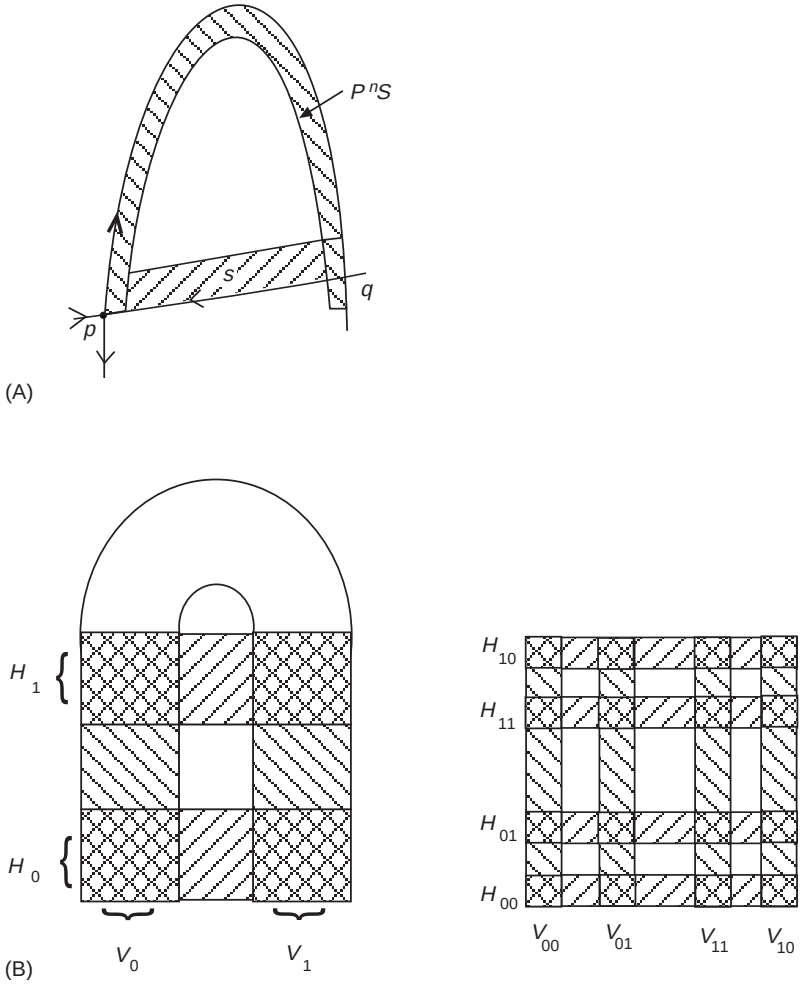


Figure 4 Smale's horseshoe: (A) S and $P^n(S)$; (B) the strips H_j and V_j.

Specifically, associate a sequence $a(x) = \{a_k(x)\}_{-\infty}^{+\infty}$ with each $x \in \Lambda$, via the rule:

$$a_k(x) = \left\{ \begin{array}{ll} 0 & \text{if } F^k(x) \in H_0 \\ 1 & \text{if } F^k(x) \in H_1 \end{array} \right\} \qquad [12]$$

The shift map σ defined on the space S of doubly infinite sequences of 0s and 1s captures the behavior of F restricted to Λ much as in the semiinfinite binary arithmetic shown above. In particular, to every sequence there corresponds a unique point $x \in \Lambda$ and vice versa, and the action of F on Λ is equivalent or topologically conjugate to that of shifting sequences under σ on S. We therefore have the same accounting of periodic points presented in **Table 1**, along with an uncountable infinity of nonperiodic orbits, and infinitely many homoclinic and heteroclinic orbits corresponding to sequences having periodic heads (tails) in the infinite past (future). All these orbits are of unstable saddle type, due to the linear horizontal contraction and vertical expansion of F on H_0 and H_1, and Λ displays sensitive dependence on initial conditions.

The fact that F is linear on H_0 and H_1 is not crucial to this analysis; all one needs is uniform bounds on contraction and expansion, and so it can be shown that all these conclusions follow for the nonlinear map, P_ε^n, resticted to a neighborhood of the homoclinic point q_ε. This leads to the:

> Smale–Birkhoff homoclinic theorem: Let $P{:}\Sigma \mapsto \Sigma$ be a smooth invertible map with a transverse homoclinic point q to a hyperbolic saddle point p. Then, for some $n < \infty$, P has a hyperbolic invariant set Λ on which P^n is topologically conjugate to a shift on two symbols.
>
> Corollary: Λ contains a countable infinity of periodic, homoclinic and heteroclinic orbits, an uncountable infinity of 'chaotic' orbits, and a dense orbit.

Birkhoff's name properly belongs here, since he proved that near every homoclinic point there is an infinite set of periodic orbits: essentially those that circulate near the homoclinic orbit $\{P^k(q)\}_{k=-\infty}^{\infty}$, marking time for arbitrarily long near the saddle point. In symbolic terms, these have sequences with periodically repeating blocks of the form 000 ... 0001 and 000 ... 0011.

We cannot however conclude that almost all, or even a set of positive measure, of orbits of the map behave chaotically, for in constructing Λ we eliminated all orbits which leave S. These orbits may approach stable sinks or attracting periodic cycles.

Chaos in Duffing's Equation: Strange Attractors?

Holmes and Moon provided early analyses of Duffing-type equations modeling the forced vibrations of a buckled beam. Experiments were carried out with a cantilever buckled by magnetic forces and subject to transverse sinusoidal oscillation at the base (**Figure 5**). This led to a considerable amount of research on chaotic vibrations. Including only the fundamental beam mode, and modeling the magnetic forces on the tip by a simple cubic term with negative linear stiffness, one arrives at the nondimensionalized equation:

$$\dot{x} = y, \quad \dot{y} = x - x^3 + \varepsilon(\gamma \cos(\omega t) - \delta y); \quad 0 \le \varepsilon \ll 1 \qquad [13]$$

This is eqn [3], with an explicit small parameter included to denote weak damping and forcing. Note that the nonlinearity is 'large' and present in the unperturbed ($\varepsilon = 0$) limit: this is crucial so that there is a homoclinic loop to perturb from. The unperturbed phase portrait is shown in **Figure 6A**; note the two potential wells surrounding the 'buckled' equilibria and the saddle separatrices bounding these wells. Solutions in these separatrices or homoclinic loops are given by:

$$(x_0(t),\ y_0(t)) = \left(\pm\sqrt{2}\ \mathrm{sech}\, t,\ \mp\sqrt{2}\ \mathrm{sech}\, t\ \tanh t\right) \qquad [14]$$

Inserting these expressions in the Melnikov function (eqn [11]) and evaluating in this case we obtain:

$$\begin{aligned} M(t_0) &= \int_{-\infty}^{\infty} y_0(t)[\gamma \cos(\omega(t+t_0)) - \delta y_0(t)]\, \mathrm{d}t \\ &= -\frac{4\delta}{3} + \sqrt{2}\gamma\pi\omega\ \mathrm{sech}\left(\frac{\pi\omega}{2}\right) \sin \omega t \end{aligned} \qquad [15]$$

This calculation yields a critical force/damping ratio:

$$\left.\frac{\gamma}{\delta}\right|_{\mathrm{crit}} = \frac{4\cosh(\pi\omega/2)}{3\sqrt{2}\pi\omega} \qquad [16]$$

which must be exceeded for the stable and unstable manifolds to intersect and transverse homoclinic orbits to exist. It represents a necessary condition for homoclinic chaos involving orbits which pass back and forth from one (unperturbed) potential well to the other, and, via the Smale–Birkhoff theorem, a sufficient condition for the existence of a horseshoe. Note that it is obtained by an explicit calculation.

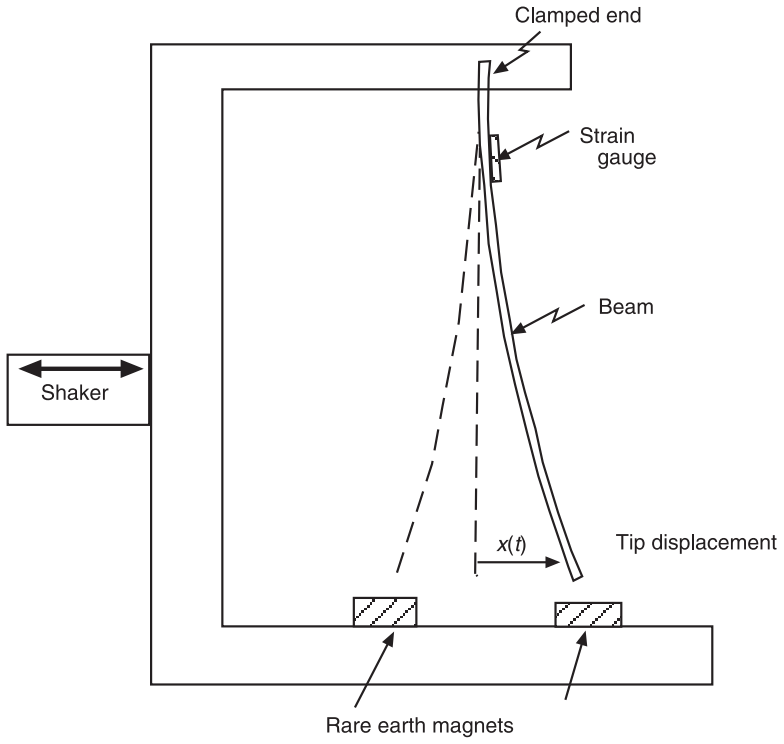


Figure 5 The magnetically buckled cantilever beam.

Figure 6B shows numerical computations of segments of the stable and unstable manifolds; the transverse intersections are clearly visible. For $\omega = 1$ the critical ratio is 0.7530 ... and for $\varepsilon\delta = 0.25$, the manifolds are observed to touch at $\varepsilon\gamma \approx 0.19$, within 1% of the predicted value 0.18825 ... .

Along with the chaotic orbits associated with the horseshoe, the damping term $-\varepsilon\delta y$ of eqn [13] makes possible the construction of a large trapping region: a bounded region D (a topological disk) into which the Poincaré map eventually draws all orbits (Liapunov functions are helpful in this construction). We may then define the attracting set $A \subset D$ as:

$$A = \bigcap_{k=0}^{\infty} P^{k}(D)$$

More generally, an attracting set is a compact invariant set which attracts a full neighborhood of solutions (its stable manifold has dimension equal to that of the phase space).

Here A clearly contains the horseshoe Λ, but it may also contain (many) 'simple' attractors, such as stable periodic orbits. Indeed, numerical studies of the Duffing equation for parameter values above but near the critical ratio (eqn [16]) reveal that almost all orbits eventually approach one or other of the two stable periodic orbits which develop from the fixed points $(x, y) = (\pm 1, 0)$ for $\varepsilon\gamma \neq 0$; this is sometimes called transient chaos. As $\varepsilon\gamma$ increases for fixed $\varepsilon\delta$ and ω, numerical simulations indicate that these orbits lose stability and eventually almost all solutions behave chaotically forever. **Figure 7A** shows an example, for the same parameter values as **Figure 6B**; the corresponding time series is shown in **Figure 7B**; such signals display broad band power spectra. Comparing **Figures 7A** and **6B**, note how the orbit appears to lie 'along' the unstable manifold $W^{u}(p_{\varepsilon})$: it appears that A is the closure of $W^{u}(p_{\varepsilon})$ (the manifold and its limit points).

To qualify as a genuine strange attractor, one has to show that almost all orbits explore the whole of A: this is accomplished if the existence of an orbit dense in A can be proven, not merely one dense in Λ. This has not been proved for the Duffing equation; it is currently impossible to rule out the possibility of stable periodic cycles, and the persistently chaotic behavior of **Figure 7** may be a numerical artefact. It has been proved for closely related Poincaré maps, including a specific example – the quadratic Hénon map – but there is currently no generally applicable method available to achieve it, nor a computable condition that provides both necessary and sufficient conditions for chaos in specific differential equations such as eqn [13].

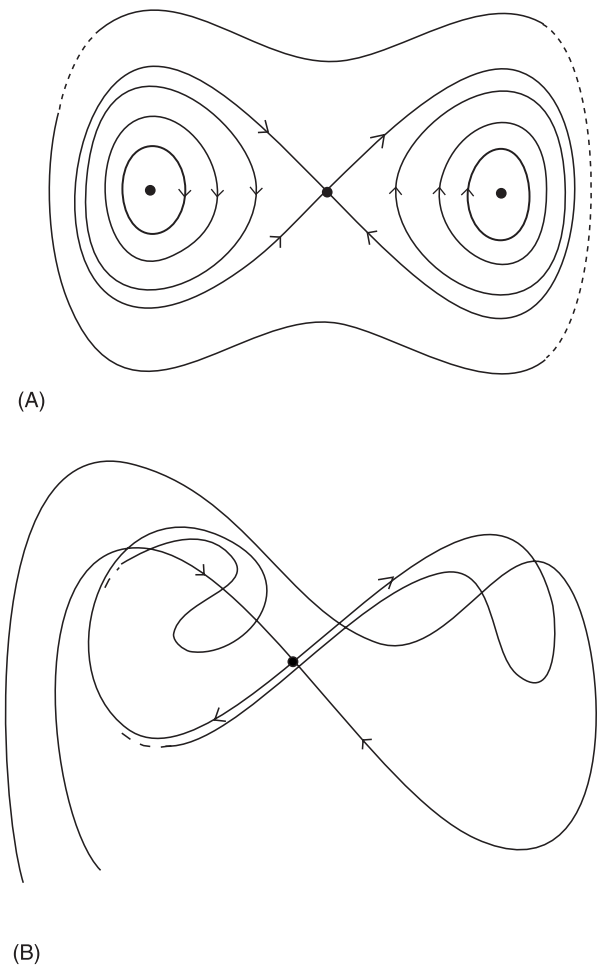


Figure 6 The unperturbed phase portrait ($\varepsilon = 0$) (A) and the perturbed Poincaré map (B) of the Duffing equation (eqn [13]): $\varepsilon\gamma = 0.30, \varepsilon\delta = 0.25, \omega = 1$, showing intersections of stable and unstable manifolds.

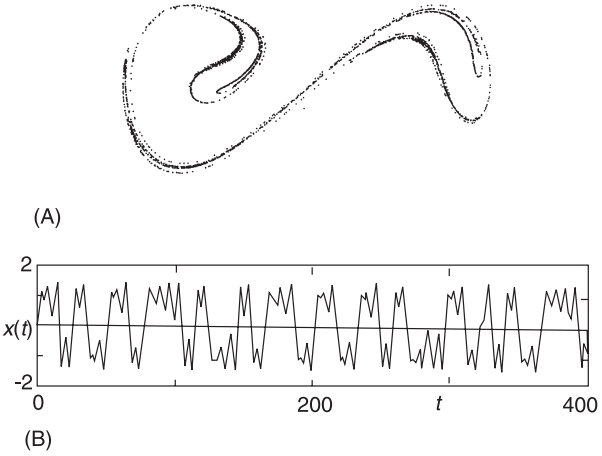


Figure 7 (A) An orbit of the Poincaré map of the Duffing equation (eqn [13]): $\varepsilon\gamma = 0.30, \varepsilon\delta = 0.25, \omega = 1$; (B) the corresponding time series.

Sources of Nonlinearity and Chaos

We have already met one source of nonlinearity in the example above: restoring forces in postbuckling behavior. Large amplitudes in general lead to nonlinear effects, through geometry alone (as in the pendulum), via nonlinear constitutive effects due to large strains, or both. Contact problems often lead to restoring forces of piecewise linear type, for example the wheel flange/rail contact in rail vehicle dynamics, or gears and mechanisms with play. Dissipation can also be strongly nonlinear, a common example being stick–slip friction. Inherent (convective) nonlinearities in fluid dynamics lead to nonlinear effects in fluid–structure interactions. Bang-bang control, or smoothed versions thereof, also leads to strongly nonlinear effects (see article **Nonlinear systems, overview**).

From a phase space perspective, the key properties necessary for chaos are present in the simple doubling map example. One must have (exponential) expansion in at least one dimension, coupled with a cutting or folding mechanism which prevents orbits from simply escaping to infinity. Strong nonlinearity or large amplitudes are generally required for this. Chaos can occur in undamped (conservative, Hamiltonian) systems, where it is associated with behavior in the 'gaps' between quasiperiodic motions associated with the Kolmogorov–Arnold–Moser theorem, but the presence of damping is generally necessary for trapping regions and strange attractors.

Nomenclature

Df	matrix of first partial derivatives
$M(t_0)$	Melnikov function
P	Poincaré map
R^n	state or phase space
Λ	Cantor set

See Plates 13, 14, 15.

See also: **Nonlinear normal modes**; **Nonlinear system identification**; **Nonlinear systems, overview**; **Perturbation techniques for nonlinear systems**; **Testing, nonlinear systems**.

Further Reading

Cartwright ML and Littlewood JE (1945) On nonlinear differential equations of the second order, i: The equation: $\ddot{y} + k(1 - y^2)\dot{y} + y = b\lambda k \cos(\lambda t + a)$, k large. *Journal of the London Mathematical Society* 20: 180–189.

Glendinning P (1995) *Stability, Instability and Chaos*. Cambridge, UK: Cambridge University Press.
Guckenheimer J and Holmes PJ (1983) *Nonlinear Oscillations, Dynamical Systems and Bifurcations of Vector Fields*. New York: Springer-Verlag.
Holmes PJ (1979) A nonlinear oscillator with a strange attractor. *Philosophical Transactions of the Royal Society of London A* 292: 419–448.
Holmes PJ and Moon FC (1980) A magneto-elastic strange attractor. *Journal of Sound and Vibration* 65: 275–296.
Moon FC (1987) *Chaotic Vibrations*. New York: John Wiley.
Palis J and Takens F (1993) *Hyperbolicity and Sensitive Chaotic Dynamics at Homoclinic Bifurcations*. Cambridge, UK: Cambridge University Press.
Poincaré HJ (1892–1899) *Les méthodes nouvelles de la mécanique celeste*, vols 1–3. Paris: Gauthiers-Villars. Translation (1993) edited by Goroff D: New York: American Institute of Physics.
Smale S (1967) Differentiable dynamical systems. *Bulletin of the American Mathematical Society* 73: 747–817.
Strogatz S (1994) *Nonlinear Dynamics and Chaos*. Reading, MA: Addison Wesley.
Ueda Y (1993) *The Road to Chaos*. Santa Cruz, CA: Ariel Press.

CHATTER

See **MACHINE TOOLS, DIAGNOSTICS**

COLUMNS

I Elishakoff, Florida Atlantic University, Boca Raton, FL, USA

C W Bert, University of Oklahoma, Norman, OK, USA

Copyright © 2001 Academic Press

doi:10.1006/rwvb.2001.0131

A column is a slender structural member subjected to axial compressive force. If the compressive load is excessive, a column may fail by structural instability, called buckling. Buckling may be by general column instability or, in the case of a thin-walled member (angle, box, channel, or I cross-sections), by local buckling.

The purpose of this section is not to discuss column buckling, but rather to discuss vibration of columns. Free vibration analysis of prismatic columns, tapered columns, and thin-walled sections is covered in separate subsections.

It should be mentioned at the outset that compressive loading decreases the natural frequencies of lateral vibration relative to their unloaded values. In fact, vibration is one of the ways to determine experimentally the buckling load by a nondestructive means. In contrast, application of loading in tension increases the natural frequencies of lateral vibration. Such a member is usually called a tie bar but is not covered here.

Free Lateral Vibration of Uniform Columns

Problem Formulation

A slender column of uniform cross-section (area A) and length L is made of a linearly elastic material (elastic modulus E) and subjected to a constant axial compressive force P. The governing partial differential equation of motion for lateral vibration is:

$$EI\frac{\partial^4 w}{\partial x^4} + P\frac{\partial^2 w}{\partial x^2} + \rho A\frac{\partial^2 w}{\partial t^2} = 0 \qquad [1]$$

where I is the centroidal area moment of inertia, t is time, w is the lateral deflection, x is the axial position coordinate, and ρ is the density of the material. Since the problem is linear, the vibration can be taken as harmonic in time, i.e.:

$$w(x,t) = W(x)\cos\omega t \qquad [2]$$

where $W(x)$ is known as the mode shape and ω is the circular natural frequency. Now eqn [1] becomes an ordinary differential equation:

$$EI\frac{\mathrm{d}^4 W}{\mathrm{d}X^4} + PL^2\frac{\mathrm{d}^2 W}{\mathrm{d}X^2} - \rho AL^4\omega^2 W = 0 \qquad [3]$$

where $X \equiv x/L$.

A combination of two boundary conditions must be specified for each end, making a total of four for the fourth-order differential eqn [3]. The sets of classical boundary conditions for each end, taken here as $X = 0$ just as an example, are:

1. clamped: $W(0) = 0, \quad W'(0) = 0$
2. pinned (simply supported): $W(0) = 0, \; W''(0) = 0$
3. free: $W''(0) = 0, \; W'''(0) + (P/EI)W'(0) = 0$
4. guided (sliding): $W'(0) = 0, \; W'''(0) = 0$

[4]

where a prime denotes a derivative with respect to X.

Direct Analytical Solution

The general solution of eqn [3] can be expressed as:

$$W(X) = C_1 \sinh \alpha X + C_2 \cosh \alpha X + C_3 \sin \beta X + C_4 \cos \beta X \quad [5]$$

where $C_1 \ldots C_4$ are constants of integration to be determined from the boundary conditions and:

$$\left\{ \begin{matrix} \alpha \\ \beta \end{matrix} \right\} z = \left[\mp \bar{P} + \sqrt{\bar{P}^2 + \bar{\omega}^2} \right]^{1/2} \quad [6]$$

Here $\bar{P} = PL^2/2EI$ is the dimensionless axial force and $\bar{\omega} = \omega L^2 \sqrt{\rho A/EI}$ is the dimensionless natural frequency. Satisfaction of the four boundary conditions, two at each end, lead to four homogeneous algebraic equations in the coefficients $C_1 \ldots C_4$. To guarantee a nontrivial solution, the determinant of the coefficients must be zero. This leads to a standard eigenvalue problem with a characteristic frequency equation, in which the dimensionless frequencies are the eigenvalues, of which there are an infinite number.

As an example, consider the case of a column that is clamped at $X = 0$ and pinned at $X = 1$. Then the characteristic frequency equation which comes from vanishing of the frequency determinant is:

$$\begin{aligned} &\left(-\bar{P} + \sqrt{\bar{P}^2 + \bar{\omega}^2}\right)^{1/2} \\ &\times \cosh\left(-\bar{P} + \sqrt{\bar{P}^2 + \bar{\omega}^2}\right)^{1/2} \sin\left(\bar{P} + \sqrt{\bar{P}^2 + \bar{\omega}^2}\right)^{1/2} \\ &- \left(\bar{P} + \sqrt{\bar{P}^2 + \bar{\omega}^2}\right)^{1/2} \sinh\left(-\bar{P} + \sqrt{\bar{P}^2 + \bar{\omega}^2}\right)^{1/2} \\ &\times \cos\left(\bar{P} + \sqrt{\bar{P}^2 + \bar{\omega}^2}\right)^{1/2} = 0 \end{aligned} \quad [6]$$

The fundamental dimensionless frequency $\bar{\omega}$ as a function of $\bar{P}$ is listed in column 2 of **Table 1**. These are exact values.

Table 1 Dimensionless frequency $\bar{\omega}$; as a function of dimensionless compressive load $\bar{P}$ for a clamped-free homogeneous column

$\bar{P}$	*Exact*	*Lower bound*	*Upper bound*
0.1	14.644	14.627	14.645
0.2	13.823	13.791	13.829
0.3	12.946	12.900	12.961
0.4	12.001	11.943	12.031
0.5	10.971	10.903	11.022
0.6	9.8263	9.7513	9.9124
0.7	8.5229	8.4448	8.6607
0.8	6.9707	6.8954	7.1947
0.9	4.9377	4.8757	5.3403

Bokaian suggested the following expression for $\bar{\omega}$:

$$\bar{\omega} = \bar{\omega}_0 \left(1 - \gamma \bar{P}/\bar{P}_{cr}\right)^{1/2} \quad [7]$$

where $\bar{\omega}_0$ is the dimensionless natural frequency for the same mode but in the absence of axial load, $\bar{P}_{cr}$ is the dimensionless critical axial load for buckling at the same mode, and γ is a dimensionless factor depending only on the set of boundary conditions, as tabulated in **Table 2**.

Hohenemser and Prager's Approximate Lower Bound

Hohenemser and Prager derived the following expression for ω for pinned–pinned boundary conditions:

$$\bar{\omega} = \bar{\omega}_0 \left(1 - \bar{P}/\bar{P}_{cr}\right)^{1/2} \quad [8]$$

It has been shown that the Hohenemser–Prager equation always gives a lower bound, although it is exact in three cases (**Table 2**): pinned–pinned, pinned–guided, and guided–guided. The dimensionless numerical results from the Hohenemser–Prager formula for the clamped-free case are listed in column 3 of **Table 1**.

Table 2 Factor γ for various end conditions

End conditions	γ	*End conditions*	γ
Free–guided	0.925	Clamped–pinned	0.978
Clamped–free	0.926	Pinned–pinned	1.000
Clamped–clamped	0.970	Pinned–guided	1.000
Clamped–guided	0.970	Guided–guided	1.000
Free–free	0.975	Free–pinned	1.130

Approximate Upper Bound Based on the Energy Method

The Rayleigh quotient (see Continuous methods) for lateral vibration of a homogeneous column is:

$$\omega^2 = \left[\int_0^L EI\left(\frac{\mathrm{d}^2 w}{\mathrm{d}x^2}\right)^2 \mathrm{d}x - P\int_0^L \left(\frac{\mathrm{d}w}{\mathrm{d}x}\right)^2 \mathrm{d}x\right] \Big/ \left[\int_0^L \rho A w^2\,\mathrm{d}x\right] \quad [9]$$

or, in dimensionless form:

$$\bar{\omega}^2 = \left[\int_0^1 (W'')^2 \mathrm{d}X - 2\bar{P}\int_0^1 (W')^2 \mathrm{d}X\right] \Big/ \left[\int_0^L W^2 \mathrm{d}X\right] \quad [10]$$

In principle, one can use any function $W(X)$ for the mode shape provided that it at least satisfies the geometric boundary conditions. However, if it satisfies the generalized force type as well, greater accuracy can be obtained. A very convenient mode shape function is the eigenfunction for the free vibration of a homogeneous beam without axial force. Such functions and the integrals of their squares and of the squares of their first and second derivatives were first tabulated by Young and Felgar, and Felgar; see also many vibration textbooks.

For the example of a clamped-pinned beam, the Rayleigh results are given in column 4 of **Table 1**. It is seen that the bounds are quite close for low values of $\bar{P}$, but the relative differences increase as $\bar{P}$ is increased.

Extensions and Application

The effect of an elastic foundation may be included by adding a term, $-kw$, to the left side of eqn [1] or by adding a term, $+\int_0^L kw^2 \mathrm{d}x$, to the numerator of the right side of eqn [9]. Here k is known as the foundation modulus and has units of force per length squared. The effect, of course, is to increase the natural frequencies.

A distributed axial loading occurs, for instance, when a vertical column is subjected to its own dead weight. This effect can be included by adding a term

$$+\frac{\partial}{\partial x}\left(qx\frac{\partial w}{\partial x}\right)$$

to the left side of eqn [1] or by adding a term

$$-\int_0^L qx\left(\frac{\partial w}{\partial x}\right)^2 \mathrm{d}x$$

to the numerator of the right side of eqn [9]. Here q is the distributed axial loading and has units of force per unit length. The result is that the reduction in the natural frequencies is not as severe as it is for a uniform loading equal to the integral $\int_0^L q\mathrm{d}x$.

Sometimes columns are loaded by a concentrated axial load applied at an intermediate point within the column. Kunukkasseril and Arumugam studied this effect for both pinned–pinned and clamped–clamped end conditions. In certain applications, it is desirable to use prestressing to resist applied loadings. Kerr showed both analytically and experimentally that, provided the prestressing force passes through the centroids of the beam cross-sections, prestressing has no effect whatsoever on the natural frequencies.

Since the work of Massonet in 1940, the idea of using the lateral vibration of a column to determine the buckling load experimentally in a nondestructive manner has been known. Most of this work has been based on the Hohenemser–Prager formula, eqn [8], rather than the more general Bokaian relation, eqn [7], so caution is advised.

Free Vibration of Stepped and Tapered Columns

To model the vibration of a column with discrete steps, one can use any of the following approaches:

1. Direct analytical solution using mode shapes of the form of eqn [5] for each uniform-cross-section segment
2. The energy method using eqn [9], with A and I being step function of x
3. Galerkin method, using as the governing equation eqn [3], with A and I being step functions of x
4. Finite element method

To model the vibration of a column with a smoothly varying cross-section, direct analytical solution is usually not feasible and may be impossible. For the energy and Galerkin methods, the area A and moment of inertia I must be appropriate smoothly varying functions of x.

Effect of Transverse Shear Flexibility

Slender columns are those having large values of the effective slenderness ratio, L_e/R, where L_e is the effective length (length equivalent to that of a pinned–pinned column) and R is the radius of gyra-

tion. For such columns, the ordinary Bernoulli–Euler bending theory is adequate. However, for short columns or slender columns constructed of highly shear-flexible material (such as most composite materials), this theory is inadequate. Instead, Bresse–Timoshenko theory, which includes both transverse shear deformation and rotatory inertia, must be used. For this theory, eqn [9] must be modified as follows:

$$\omega^2 = \left\{\int_0^L \left[EI\left(\frac{d^2w}{dx^2}+\frac{d\beta}{dx}\right)^2 + KGA\gamma^2 - P\left(\frac{dw}{dx}\right)^2\right]dx\right\} \Big/ \left\{\int_0^L \left[\rho A w^2 - \rho I\left(\frac{dw}{dx}+\beta\right)^2\right]dx\right\} \quad [11]$$

Here G is the transverse shear modulus, I is the centroidal area moment of inertia, K is known as the shear correction coefficient (usually taken to be $\pi^2/12$ (≈ 0.822) or $5/6$ (≈ 0.833) for homogeneous material), and β is the shear rotation angle. It was shown that the effect of transverse shear deformation is much larger, for practical cross-sections, than the effect of rotatory inertia, but both effects reduce the natural frequency. Thus, it is inconsistent to use Rayleigh bending theory (which considers rotatory inertia but not transverse shear deformation) rather than Bresse–Timoshenko theory.

Free Vibration of Thin-walled Columns

In the preceding subsections, it was tacitly assumed that all cross-sections of a column were doubly symmetric, i.e., symmetric about both the x and y centroidal axes. However, in the cross-sections of many practical column structures, there is often a finite distance between the geometric center (centroid) and the elastic center (shear center). This eccentricity produces a coupling between bending action and twisting action. Also, thin-walled structures are susceptible to warping action.

The following additional symbols are introduced:

- C, C_W, torsional and warping constants
- I_x, I_y, moments of inertia about the x and y axes
- r_0, polar radius of gyration of cross-section with respect to the shear center
- u, v, w, displacements in the x, y, z directions
- x_0, y_0, coordinates of the centroid of the cross-section with respect to the shear center
- ϕ, angle of rotation of cross-section
- $(\,)_{,z}$, $\partial(\,)/\partial z$, etc.

The strain energy can be written as:

$$U = \frac{1}{2} \times \int_0^L \left[EI_y(u_{,zz})^2 + EI_x(v_{,zz})^2 + GC(\phi_{,z})^2 + EC_W(\phi_{,zz})^2\right]dz \quad [12]$$

The potential energy due to the external compressive load P is:

$$V = -\frac{P}{2} \times \int_0^L \left[(u_{,z})^2 + (v_{,z})^2 + r_0^2(\phi_{,z})^2 - 2y_0u_{,z}\phi_{,z} + 2x_0v_{,z}\phi_{,z}\right]dz \quad [13]$$

The kinetic energy is:

$$T = (\rho A/2) \times \int_0^L \left[(u_{,t})^2 + (v_{,t})^2 - 2y_0u_{,t}\phi_{,t} + 2x_0v_{,t}\phi_{,t} + r_0^2(\phi_{,t})^2\right]dz \quad [14]$$

The variational principle is:

$$\delta(U + V - T) = 0 \quad [15]$$

As an illustrative example, the case of pinned (universal-joint) ends is considered. Then:

$$u(z,t)/A_x = v(z,t)/A_y = \phi(z,t)/A_\phi = \sin(\pi z/L)\cos\omega t \quad [16]$$

and the modified Lagrangian functional $\bar{L}$ is:

$$\bar{L} \equiv (4L/\pi^2)(U + V - T) = (P_y - P - \tilde{\omega}^2)A_x^2 + (P_x - P - \tilde{\omega}^2)A_y^2 + (P_\phi - P - \tilde{\omega}^2)r_0^2A_\phi^2 + 2(P + \tilde{\omega}^2)y_0A_xA_\phi - 2(P + \tilde{\omega}^2)A_yA_\phi \quad [17]$$

where:

$$P_i \equiv EI_i\pi^2/L^2 \quad \text{for } i = x, y$$
$$P_\phi \equiv GC + EC_W(\pi^2/L^2)$$
$$\tilde{\omega}^2 \equiv \rho AL^2\omega^2/\pi^2$$

Application of eqn [15] yields three simultaneous homogeneous equations in the amplitudes A_i. To guarantee a nontrivial solution, the following determinant of the coefficients must vanish:

$$\begin{vmatrix} P_y - P - \tilde{\omega}^2 & 0 & (P+\tilde{\omega}^2)y_0 \\ 0 & P_x - P - \tilde{\omega}^2 & -(P+\tilde{\omega}^2)x_0 \\ (P+\tilde{\omega}^2)y_0 & -(P+\tilde{\omega}^2)x_0 & (P_\phi - P - \tilde{\omega}^2)r_0^2 \end{vmatrix} = 0 \quad [18]$$

In the general case ($x_0 \neq 0, y_0 \neq 0, r_0 \neq 0$), eqn [18] becomes a cubic in $\tilde{\omega}^2$, i.e., there is triple coupling. For the case of a singly symmetric cross-section (say, $y_0 = 0$), eqn [18] is quadratic in $\tilde{\omega}^2$.

Nonlinear Vibration of Columns

In the usual vibration theory of columns, the assumption is made that one end of the column is unrestrained in the axial direction. Hence, deflections are inextensional. In technical practice, one often encounters immovable hinges; then the effect of the axial force on the vibration mode shape must be investigated. Nonlinear free vibration of elastic columns under axial compression was first analyzed by Woinowsky-Krieger. The effect of initial imperfections – deviations from the ideal straight state – was studied by Elishakoff, Birman, and Singer.

The governing differential equation is obtained by replacing the first term in eqn [1] by $EI\partial^4(w - w_0)/\partial x^4$, where $w_0 = w_0(x)$ is the initial imperfection. In new circumstances, in which $w(x, t)$ is the total deflection, the compressive force P in eqn [1] is now given by:

$$P = P_0 - (AE/2L)\int_0^L \left[\left(\frac{\partial w}{\partial x}\right)^2 - \left(\frac{\partial w_0}{\partial x}\right)^2\right] \mathrm{d}x \quad [19]$$

where P_0 is the external compressive force applied to the column. The initial conditions are:

$$w(x,0) = w_0(x) = a_0 \sin \pi X; \quad \dot{w}(X,0) = 0 \quad [20]$$

where the dot denotes partial differentiation with respect to time. Assuming that both the initial imperfection and total deflection have the shape of a half-sine wave, one has:

$$w(x,t) = aF(t) \sin \pi X \quad [21]$$

where a is the amplitude of the total deflection. Substitution into eqn [1] suitably modified as described above and using the Bubnov–Galerkin method (nonlinear version of the Galerkin method discussed in the article on **Continuous methods**), one obtains the following ordinary differential equation:

$$\ddot{F} + \left[\omega^2 - 2k^4(a_0/a)^2\right]F + 2k^4F = \frac{P_{cr}}{P_{cr} - P_0}\frac{a_0}{a}\omega^2 \quad [22]$$

For an imperfection-free column, *aequiv*0 and eqn [22] reduces to the equation for that case. Note that the presence of the initial imperfection makes the equation nonhomogeneous. Eqn [22] was solved exactly in terms of the normal elliptic integral of the first kind by Elishakoff *et al*.

Following various previous investigators, the term 'throw' is used here for nonlinear vibrations instead of 'amplitude' in linear vibrations. Elishakoff *et al*. showed that, in some intervals of variation of P_0/P_{cr}, the imperfect column can have frequencies in excess of its perfect-column counterparts. Also, the initial imperfection appears to decrease the frequency of nonlinear free vibration of elastic columns under moderate compression. Nevertheless, there are columns in which the vibration frequency increases due to initial imperfections, when P_0 approaches P_{cr}. Such an increase is characteristic for columns with small values of vibration throw to cross-sectional radius of gyration. Nonlinear vibration of a buckled column under harmonic excitation was studied by Tseng and Dugundji, who found that the buckled column is characterized by soft-spring behavior at small vibration throws before snap-through, and hard-spring-type behavior after snap-through.

A model structure, namely a three-hinge, rigid-element column system constrained laterally by a nonlinear spring, was studied in detail by Elishakoff, Birman, and Singer. They studied the static behavior and then superimposed small vibrations $w(t)$ on it. The spring force was taken as:

$$F = k_1\hat{w} + k_2\hat{w}^2 + k_3\hat{w}^3 \quad [23]$$

where $k_1/2$ constitutes a nondimensional buckling load and $\hat{w}$ is a nondimensional static deflection. The coefficients $a \equiv k_2/k_1$ and $b \equiv (k_2/k_1) - 0.5$ were introduced. If $b = 0$ and $a \neq 0$, the structure is said to be asymmetric; if $a = 0$ and $b \neq 0$, the structure is called symmetric; whereas if $a \neq 0$ and $b \neq 0$, the structure is nonsymmetric.

The following formulas were derived. For the asymmetric case, the nondimensional frequency squared is given by:

$$\bar{\omega}^2 = (1 - P/P_{cr})\left[1 + 4aw_0(P/P_{cr})(1 - P/P_{cr})^{-2}\right]^{1/2} \quad [24]$$

A structure that is imperfection-sensitive for buckling turns out to be imperfection-sensitive for vibration as well, for $aw_0 < 0$, $\bar{\omega}^2 < 1 - P/P_{cr}$. In other words, initial imperfections reduce the natural frequency found by the Hohenemser–Prager formula. For an imperfection-sensitive structure, the natural frequency increases with the magnitude of w_0 compared with that of a perfect structure.

For the symmetric structure, eqn [24] is replaced by:

$$\left(1 - \frac{P}{P_{cr}} + \frac{\bar{\omega}^2}{2}\right)\left[\frac{\bar{\omega}^2 - (1 - P/P_{cr})}{3b}\right]^{1/2} = \frac{3}{2}\frac{P}{P_{cr}}w_0 \quad [25]$$

Eqn [25] implies that for the structure to be vibrationally imperfection-sensitive (i.e., with decreased frequency as a result of imperfection), the coefficient b must be negative, as in the case of static buckling. For $b > 0$, the natural frequency increases with w_0.

Random Vibration of Columns

There are numerous works devoted to random vibration of elastic structures. Apparently the first study devoted to the case of beams was by Eringen in 1957, while random vibration of columns was first studied by Elishakoff in 1987. The governing eqn [1] is modified by adding a damping term, $c\partial w/\partial t$, on the left side and by adding the transverse loading, $q(x, t)$, on the right side.

The autocorrelation function of the loading is taken as the 'rain-on-the-roof' excitation, represented by a space- and time-wise ideal white noise:

$$R_q(x_1, x_2, t_1, t_2) = (R/L)\delta(x_1 - x_2)\delta(\tau) \quad [26]$$

where R is a positive constant, x_1 and x_2 are spatial coordinates, $\delta(x)$ is the Dirac delta function, and $\tau = t_2 - t_1$ is the time lag.

The following result was obtained for the deflection autocorrelation function at zero time lag:

$$\begin{aligned} R_w(X_1, X_2, 0) = \frac{RL^2}{8\pi^2 EIc\beta}\Bigg(&2|X_1 - X_2| \\ &- (X_1 - X_2)^2 - 2(X_1 + X_2) + (X_1 + X_2)^2 \\ &+ \frac{2}{\pi\sqrt{\beta}}\frac{1}{\sin\pi\sqrt{\beta}}\left\{\left(\cos\pi\sqrt{\beta}\right)[1 - (X_1 + X_2)]\right. \\ &\left. - \left(\cos\pi\sqrt{\beta}\right)[1 - |X_1 - X_2|]\right\}\Bigg) \end{aligned} \quad [27]$$

where $X_1 \equiv x_1/L$, $X_2 \equiv x_2/L$, and $\beta \equiv P/P_{cr}$. As the axial compression reaches its critical value, i.e., as β tends to unity, $\sin\pi\sqrt{\beta}$ tends to zero and the autocorrelation function of deflection increases without bound. When β goes to zero, eqn [27] reduces to Eringen's result for a beam (no axial loading):

$$R_W(X, X, 0) = RL^2X^2(1 - X)^2 \Big/ 6EI \quad [28]$$

Elishakoff showed that the presence of axial compression increases the mean-square response of the column.

The effect of randomness in elastic modulus and/or other material properties on stressed structures was studied by Hart. He developed a method for calculating statistics of natural frequencies and vibrational mode shapes of a structure acted upon by external static loading. In order to formulate a geometric stiffness matrix for the structure, it is necessary, in general, to solve a static response problem to obtain the axial forces in each structural member. Then this geometric stiffness is added to the elastic stiffness matrix and the eigenvalue problem is solved to obtain natural frequencies and mode shapes. The eigenvalue problem of the discretized structure can be written as:

$$\mathbf{M}\ddot{\mathbf{W}} + (\mathbf{K}_e - \mathbf{P}\mathbf{K}_G)\mathbf{W} = \mathbf{0} \quad [29]$$

where $\mathbf{K}_e \equiv$ elastic stiffness matrix, $\mathbf{K}_G \equiv$ geometric stiffness matrix, $\mathbf{M}$ is the mass matrix, and $\mathbf{W}$ and $\ddot{\mathbf{W}}$ are the vectors of the system's deflections and accelerations, respectively. When $P = P_{cr}$, the system's fundamental natural frequency is zero. Let $r_1, r_2 \ldots r_m$ be random structural parameters. A linear probabilistic structural model uses multiple Taylor series expansions for an arbitrary natural frequency:

$$\begin{aligned} \omega_j(r_1, r_2, \ldots r_m) = {} & \omega_j[E(r_1) \ldots E(r_m)] \\ & + \sum_{\alpha=1}^{m} \left.\frac{\partial\omega_j}{\partial r_\alpha}\right|_{r_\alpha = E(r_\alpha)} [r_\alpha - E(r_\alpha)] \end{aligned} \quad [30]$$

where $E(r_\alpha) \equiv$ mean value of the αth random structural parameter, and $\partial\omega_j/\partial r_\alpha \equiv$ sensitivity derivative.

The mean value of the natural frequency can be expressed as:

$$E(\omega_j) = E[\omega_j(r_1, r_2, \ldots r_m)] \quad [31]$$

and the mean-square value is obtained as:

$$\mathrm{Var}(\omega_j) = \sum_{\alpha=1}^{m}\sum_{\beta=1}^{m} \left.\frac{\partial \omega_j}{\partial r_\alpha}\right|_{r_\alpha = E(r_\alpha)} \left.\frac{\partial \omega_j}{\partial r_\beta}\right|_{r_\beta = E(r_\beta)} \mathrm{Cov}(r_\alpha, r_\beta) \qquad [32]$$

where $\mathrm{Cov}(r_\alpha, r_\beta)$ is the covariance given by:

$$\mathrm{Cov}(r_\alpha, r_\beta) = E\{[r_\alpha - E(r_\alpha)][r_\beta - E(r_\beta)]\} \qquad [33]$$

and $E(\ )$ denotes mathematical expectation. In a particular example of a two-column structure, Hart showed that the mean value of the natural frequency is a nonlinear function of the ratio $\beta = P/P_{cr}$ and vanishes when $\beta = 1$. The mean-square value of the natural frequency increases with an increase of β.

More recently, use of finite element analysis in the stochastic setting was put forward for eigenvalue problems with uncertainties by Nakagiri.

Nomenclature

A	cross-sectional area
a	amplitude of total deflection
a	k_2/k_1
a_0	amplitude of initial imperfection
A_x, A_y, A_ϕ	coefficients of u, v, and ϕ expressions
b	$(k_2/k_1)-0.5$
C	torsional constant
b_i	constants of integration
Cov	covariance
C_W	warping constant
c	damping coefficient
E	elastic modulus
$E(r_\alpha)$	expected mean value of ( )
F	dimensionless deflection in eqn [21]
F	spring force
G	shear modulus
I	centroidal area moment of inertia
I_x, I_y	moments of inertia about x and y axes
K	shear correction coefficient
$\mathbf{K}_e$	elastic stiffness matrix
$\mathbf{K}_G$	geometric stiffness matrix
k	foundation modulus
k	$(\pi/L)(Ea^2/\rho)^{1/4}$
k_i	stiffness coefficients in eqn [23]
L	column length
$\overline{L}$	modified Lagrangian functional
$\mathbf{M}$	mass matrix
P	axial compressive force
P_0	external compressive force
P_x, P_y, P_ϕ	coefficient in eqn [17]
$\overline{P}$	dimensionless axial compressive force
$\overline{P}_{cr}$	dimensionless critical axial load
q	distributed axial loading
R	positive constant in equation
R_q	cross-sectional
R_W	deflection autocorrelation function
r_i	random structural parameters
r_0	cross-sectional polar radius of gyration relative to the shear center
T	kinetic energy
t	time
t_1, t_2	time values at start and end
U	strain energy
u, v, w	displacements in the x, y, z directions
V	potential energy due to P
Var	mean-square value of natural frequency
W	mode shape
$\mathbf{W}$	vector of deflections
w	column deflection
$\hat{w}$	nondimensional static deflection
W_0	initial imperfection
X	x/L
X_1, X_2	X_1/L, X_2/L
x	axial position coordinate
x, y	centroidal axes in the cross-section
x_1, x_2	spatial coordinates
x_0, y_0	coordinates of cross-sectional centroid relative to the shear center
z	axial position coordinate
α, β	parameters defined in eqn [6]
β	shear rotation angle
β	P/L_{cr}
γ	factor appearing in eqn [7]
δ	Dirac delta-function
ρ	material density
ϕ	angle of rotation of cross-section
τ	$t_2 - t_1$
ω	natural frequency
ω_j	arbitrary natural frequency
$\bar{\omega}$	dimensionless natural frequency
$\bar{\omega}_0$	dimensionless natural frequency in absence of axial force
$(\ )'$	derivative with respect to X
$(\ )_{,z}$	derivative with respect to z

See also: **Continuous methods**; **Eigenvalue analysis**.

Further Reading

Banerjee JR and Williams FW (1985) Further flexural vibration curves for axially loaded beams with linear or parabolic taper. *Journal of Sound and Vibration* 102: 315–327.

Bokaian A (1988, 1989) Natural frequencies of beams under compressive axial loads. *Journal of Sound and Vibration* 126: 49–65; author's reply 131: 351.

Elishakoff I (1987) Generalized Eringen problem: influence of axial force in random vibration response of simply supported beam. *Structural Safety* 4: 255–265.
Elishakoff I (1999) *Probabilistic Theory of Structures*. New York: Dover.
Elishakoff I, Birman V and Singer J (1984) Effect of imperfections on the vibrations of loaded structures. *Journal of Applied Mechanics* 51: 191–193.
Elishakoff I, Birman V and Singer J (1985) Influence of initial imperfections on nonlinear free vibrations of elastic bars. *Acta Mechanica* 55: 191–202.
Eringen AC (1957) Response of beams and plates to random loads. *Journal of Applied Mechanics* 24: 46–52.
Hart GC (1973) Eigenvalue uncertainty in stressed structures. *Journal of Engineering Mechanics* 99: 481–494.
Hohenemser K and Prager W (1933) *Dynamik der Stabwerke*. Berlin: Springer.
Kerr AD (1976) On the dynamic response of a prestressed beam. *Journal of Sound and Vibration* 49: 569–573.
Kunukkasseril VX and Arumugam M (1975) Transverse vibration of constrained rods with axial force fields. *Journal of the Acoustical Society of America* 57: 89–94.
Mujumdar PM and Suryanarayan S (1989) Nondestructive techniques for prediction of buckling loads – a review. *Journal of the Aeronautical Society of India* 41: 205–223.
Nakagiri S (1984) Structural system with uncertainties and stochastic FEM. *JSME Transactions Series A* 30: 1319–1329.
Tseng W-Y and Dugundji J (1971) Nonlinear vibrations of a buckled beam under harmonic excitation. *Journal of Applied Mechanics* 37: 467–476.
Woinowsky-Krieger S (1950) The effect of an axial force on the vibration of hinged bars. *Journal of Applied Mechanics* 17: 35–36.

COMMERCIAL SOFTWARE

G Robert, Samtech SA, Liege, Belgium

Copyright © 2001 Academic Press

doi:10.1006/rwvb.2001.0010

Introduction

A lot of engineer work is done nowadays using commercial computer software. To deal with large projects, engineers construct numerical models to simulate the real world, thanks to the performances of fast digital processors. Such models allow the engineer to test choices during the design process. In the field of mechanical engineering, finite element analysis (FEA) is the most popular way to investigate structural behavior without experiment. In principle, finite element method (FEM) allows one to build a mathematical model of a given structure and to predict its behavior by numerical computation, given boundary, and initial conditions.

The scope of this article is to present some FEA commercial software. We have limited the choice of software because the goal is not to compare software, but rather to give an overview of FEA software capabilities. The question is not Which software exists? but What does the existing software offer the user? It must be noted that the software is presented at a given moment in its history. It is clear that software is constantly being improved: most have a new version released about once a year.

History

Software dedicated to structural analysis first appeared in the mid 1960s. It was initially used in advanced technology such as aeronautical and space industries. At that time, software focused on efficient computation rather than user-friendliness: it did not matter that the process was tortuous provided that the result achieved were correct. Nevertheless, at this first stage, FEM proved its ability to predict structural behavior. In some situations it appeared as a cost-effective alternative to testing procedure and an efficient way of reducing design cost and time. As a result, these computational techniques spread to more and more engineering sectors.

Factors contributing to software evolution include the following:

Analysis of More and More Complex Structures

The aim is not only to analyze structures with complex geometries, but also to analyze complex assemblies, made up of a large number of parts. The number of degrees of freedom may range from a few to several millions. To solve large systems, new algorithms have been implemented, which use parallel and vector processing. Also Graphical User Interface and database systems have evolved in order to process a large amount of data. This evolution has followed the improvement of graphical and digital processors.

Analysis of More and More Complex Situations

To make an accurate model of a structure, it is necessary to take into account many factors influencing its behavior. For example, to analyze the effects of an explosion on a given structure, a model is made of the structure itself and the surrounding fluid as well as interaction between both. Analysis of such situations led software designers to develop multiphysical simulation. In addition to coupled equations between different physical variables, FEM addresses the problem of interactions between several parts of the same structure, including contact detection and simulation.

Reduction of the Time Devoted to Design

The target of high profitability has reduced the length of the design stage. Adaptation of FEA software to this economic reality requires improvement in usability and of interoperability. That is, software must be easy to use and its integration to the design environment must be as complete as possible.

Change of Software User Itself

During the first years of FEA, the interaction between programmers and users was so strong that often the same people both wrote and ran the software. This time is now passed and it must be borne in mind that the user's background does not include a good command of computer science and a theoretical knowledge of numerical methods. Programmers, and programs, must provide sufficient information both to check input and validate output.

Application Fields in Dynamics

FEM applies to continuous media. It allows one to compute static or dynamic equilibrium of the media subject to initial and boundary conditions. FEM is broadly used to resolve equations related to solid and fluid mechanics, heat transfer, and electromagnetism. In the specific domain of vibration analysis, FEM is used to compute natural frequencies and corresponding vibration modes as well as dynamic response in time, possibly including nonlinearities. Different types of analyses are listed below.

Modal Analysis

The prediction of natural frequencies of a structure is useful so that one can understand fundamental dynamic behavior and avoid the risk of resonance during service. Direct applications of modal analysis are, for example, computation of critical speed of rotating machines and noise reduction by vibration isolation of structures.

Transient Response

This is the most general dynamic response. At a given time, arbitrarily set to zero, initial displacements and velocities are known at any point of the structure and motion or forces are prescribed at some points. Transient response results from the time integration of equations of motion. Solution techniques vary according to the range of natural modes that are excited. At low frequency, modal methods and implicit time integration are generally used, whereas explicit time integration is better suited to high frequency. A typical example of transient loading is increasing pressure in an enclosure. At low speed, implicit integration will give good results. At high speed, if a shock wave ensues, it will become necessary to use explicit software.

Periodic Response

For structures subject to periodic loading, such as an unbalanced mass in rotating machines, it is of interest to predict the response during one of the repetitive load cycles. Excitation may include one or more harmonics. In the case of single harmonics, the response is called harmonic forced response. Modal solution methods are used with linear systems. Techniques such as equivalent linearization or finite elements in time are used in the presence of nonlinearities.

Random Response

In some cases, loading is so erratic that it is better described in a probabilistic way. A typical example is the force profile transmitted by the suspension of a car running on an uneven road. We characterize the excitation – force or motion – by a power spectral density (PSD), which gives the distribution of power in a frequency range. Solution techniques are close to those of the single harmonic case. Response is also expressed in terms of PSD. From the PSD, it is possible to compute statistical moments of the random process and to derive quantities of physical meaning such as root mean square (RMS) value, standard deviation or peak value.

Response Spectrum

This solution technique is widely used in earthquake engineering. It is based on the maximum response of a Single Degree of Freedom (SDOF) oscillator. A response spectrum is obtained by plotting frequency versus the maximum response of several oscillators with different natural frequencies but the same damping to a given input transient signal to a given input transient signal of short duration. Responses may be expressed in terms of displacement, velocity,

or acceleration. For a real structure, the response spectrum provides the maximum response for each mode, according to its frequency and damping. Modal responses are then accumulated using combination rules such as Square Root of Sum of Squares (SRSS). The result is the probable maximum response of the structure. Response spectra are also known as shock spectra.

Software Quality Assurance

After initially being research tools, FEA software has now become an industrial product. Its use is conditioned not only by technical aspects, but also by economical aspects. To play its part efficiently, software must fulfill quality requirements. There are several organizations that have established rules and criteria for software quality assurance (QA), including:

- American National Standards Institute (ANSI).
- Federal Aviation Administration (FAA).
- Institute of Electrical and Electronic Engineers (IEEE).
- International Standards Organization (ISO).
- National Agency for Finite Elements and Standards (NAFEMS).
- Nuclear Regulatory Commission (NRC).

Most of these organizations have acquired international status. NAFEMS, based in the UK, is specially dedicated to FEA. It aims 'to promote the safe and reliable use of finite element technology'. Since 1983, this organization has promoted the development of many benchmarks which are used worldwide to qualify and compare FEA software.

The Developer's Side

This section summarizes important aspects contributing to quality that are directly under the developer's responsibility.

Validation Software must provide a correct response to a correct input. It must be reliable. The software vendor should maintain a library of tests related to all its options. Most tests must have accepted references, such as analytical references.

Integration The developer must ensure good integration of the software with the hardware. Products must run efficiently on various available platforms. Efficiency implies that algorithms should take the best advantage of computers, considering the number of operations to perform.

Maintenance FEA software has a long life cycle. Most such software has been on the market for more than 10 years. To continue to be competitive over a long time, software must prove its maintainability and flexibility. Maintainability refers to the ease of bug fixing, while flexibility is the ability to incorporate new functionalities.

Training and support FEA vendors should provide information to support the customer. This includes an installation guide, user's manuals, theoretical references, tutorial and examples, as well as release notes. Documentation must be such that information is easy to find. In addition, it is important to organize training sessions and to propose a hot-line service ready to help users.

The User's Side

There are quality factors that must be checked by the customer, even if the customer has no direct influence on them. Using the same criteria:

Validation The user's responsibility starts with the choice of software. The first rule is that software must meet the user's needs. For instance, if a given problem requires nonlinear analysis, the user must ensure that the software includes adequate formulations. The user's validation is not reduced to a technical choice. It also includes more subjective aspects such as the ease of use.

Integration The customer must make sure that software will be correctly integrated in its working environment. For example, the user should check that it interfaces completely with other software, including office tools and CAD or CAM, including possible testing programs.

Maintenance FEA software may be used throughout a long-term project. The user is then concerned with the availability of new releases and compatibility. For that purpose, it is important that each software output can be clearly identified, with release number, date, and type of result. Possible incompatibilities must be traced and documented. Error reports must be regularly provided. They must include possible bypass when available.

Training and support The fact that a software computes correct results when given the correct input is not a guarantee of success when using it. FEA software is a tool and, as such, one has to learn to use it. Moreover, it is not sufficient to learn about all the possible options: the analyst has to know why and

when to use them. Appropriate training must comprehensively establish the correspondence between physics and models. For advanced analysis, FEA vendors generally complete their offer by direct support and by engineering services.

Presentation of FEA Software

As stated in the introduction, this part presents a limited number of commercial FEA software packages. This information has been kindly supplied by software companies which have agreed to contribute to this review. The NAFEMS maintains a more complete list of FEA software and its internet home page contains various links to vendors' sites and other sites related to FEA and numerical computation, including Computational Fluid Dynamics (CFD).

ABAQUS

Developer Hibbitt, Karlsson & Sorensen, Inc., 1080 Main Street, Pawtucket, RI 02860, USA.

General description Advanced, general-purpose, finite element system for the solution of large complex problems.

Main features ABAQUS programs are used throughout the world to simulate the physical response of structures and solid bodies to load, temperature, contact, impact, and other environmental conditions. They are state-of-the-art software for linear and nonlinear analysis of large models. Major market segments include automotive, aerospace, defense, offshore, civil, power generation, consumer products, and medical devices.

First and latest releases

First version Version 1.0, 1978.

Current version Version 5.8, October 1998.

Quality assurance Complies with requirements of ISO 9001 and ASME/ANSI NQA-1.

Documentation Documentation includes user's manual, example problems manual, theory manual, verification manual, and tutorial manual.

Service and support Unlimited technical support is provided to customers, as well as a wide range of training courses, engineering services, and code customization.

Availability Network and nodelock licenses are available. There are offices and representatives in most industrialized countries worldwide.

Computer environment Cray C90/T90 (Unicos 10); Cray J90/YMP (Unicos 10); Cray T90 IEEE (Unicos 10); Digital Alpha (Unix 4.0); Fujitsu VX/VPP (UXP/V); HP-PA7000 (HP-UX 10.20); HP-PA8000 (HP-UX 10.20); HP-PA8000 (HP-UX 11.0); IBM RS6000 (AIX 4.1.5); Intel (Windows-NT 4.0); NEC SX-4 (Super UX R7.2); SGIR4000/R5000 (Irix 6.2); SGI R8000/R10000 (Irix 6.2); Sun UltraSparc (Solaris 2.6).

Interfaces with other software

Geometry IGES, SAT (ACIS), DXF.

CAD and preprocessors Catia, CADFix, Femap, FemGV, HyperMesh, I-DEAS, MSC/Aries, MSC/Patran, Pro/Mesh, TrueGrid.

Postprocessor Catia, CADFix, Ensight, Femap, FemGV, HyperMesh, I-DEAS, MSC/Aries, MSC/Patran, TrueGrid.

Analysis Adams, C-Mold, DADS, Zencrack.

ANSYS

Developer ANSYS, Inc., Southpointe, 275 Technology Drive, Canonsburg, PA 15317, USA.

General description The ANSYS program is a flexible, robust package for design analysis and optimization.

Main features ANSYS is capable of making various types of analyses, including linear and nonlinear structural, steady-state and transient thermal, and coupled-field analysis. In its Multiphysics version, ANSYS allows design engineers and analysts to look at the interaction of structural, thermal, fluid flow, and electromagnetic effects on the same model.

First and latest releases

First release ANSYS, 1970.

Latest release ANSYS 5.4, 1998.

Quality assurance Complies with requirements of ISO 9001 and ASME/ANSI NQA-1.

Documentation Documentation set includes analysis guides (one for each discipline), command and element references, theory manual, workbook, and

verification manual. User's guides on advanced topics are also available.

Service and support The customer services department provides service and support through multiple programs that ensure the customer's success. Services range from hot-line support to training courses and include consulting and customization services to tailor the ANSYS program to meet individual engineering requirements.

Availability A network of distributors provides licensing and customer support in the USA, Canada, Brazil, Western Europe, Israel, India, East Asia, and Australia.

Computer environment Digital Alpha UNIX, Digital Alpha NT, HP 7000/8000 Series, HP Exemplar, IBM RS/6000, Silicon Graphics, Sun Solaris, CRAY, Intel PC (Windows NT and 95).

Other products ANSYS/LS-DYNA, explicit dynamic solver.

Interfaces with other software

CAD and preprocessors AutoCAD, CADDS, CATIA, I-DEAS, MicroStation Modeler, Pro/Engineer, Solid Designer, Solid Edge, Unigraphics.

Postprocessor I-DEAS, PATRAN, Pro/Engineer.

Analysis ABAQUS, ALGOR, COSMOS/M, NASTRAN, STARDYNE, WECAN.

COSMOS/M

Developer Structural Research & Analysis Corp., 12121 Wilshire Boulevard, 7th Floor, Los Angeles, CA 90025, USA.

General description A general-purpose finite element analysis package for structural, thermal, fluid flow, and electromagnetics analysis.

Main features

Structural Linear stress, strain, displacement; frequency; buckling; nonlinear static and dynamic; dynamic response; fatigue; design optimization analyses.

Thermal Linear and nonlinear steady-state and transient thermal analysis.

Fluids Laminar/turbulent, incompressible, subsonic/transonic/supersonic compressible, transient and much more.

First and latest releases

First release COSMOS/M 1.0–1985

Latest release COSMOS/M 2.0–1998

Quality assurance A strict quality assurance procedure has been in place since 1990 (over 1800 problems of all types, sizes, and options have been tested and new ones are added continuously).

Documentation A complete set of documents is available, including user's guide, command reference, basic analysis modules, advanced modules manuals, verification and examples, and manuals of theory.

Service and support The training and consulting department offers regular training classes for the basic and advanced modules of the product. The technical support department provides support by phone, e-mail, and fax on all aspects of the program to all customers with maintenance contracts.

Availability Available through distributors, retailers, and directly from SRAC.

Computer environment PCs running Windows NT/95.

UNIX workstations: IBM, SGI, HP, Sun, DEC.

Other products COSMOS/Works, COSMOS/Edge, COSMOS/M for Helix, COSMOS/M DESIGNER II, COSMOS/M for Eureka, COSMOS/M ENGINEER, COSMOS/Wave.

Interfaces with other software

CAD and preprocessors SolidWorks, Solid Edge, Helix Design System, MicroStation Modeler, IronCAD, CADKEY, AutoCAD, Eureka Gold 97, Pro/ENGINEER, DesignWave, Hypermesh, FEMAP.

Postprocessor Pro/FEM-POST (Pro/ENGINEER), FEMAP.

Analysis ANSYS, NASTRAN (MSC and UAI), Patran, I-Deas.

MSC/NASTRAN

Developer MacNeal-Schwendler Corp., 815 Colorado Boulevard, Los Angeles, CA 90041–1777, USA.

General description MSC's principal product, MSC/NASTRAN, is the industry's leading FEA program and has proven its accuracy and effectiveness over many years. It is constantly evolving to take

advantage of the newest analytical capabilities and algorithms for structural analysis.

Main features MSC/NASTRAN is a general-purpose analysis program offering a wide variety of analysis types. These include linear statics, normal modes, buckling, heat transfer, dynamics, frequency response, transient response, random response, response spectrum analysis, and aeroelasticity. Most material types can be modeled, including composites and hyperelastic materials. Advanced features include superelements (substructuring), component mode synthesis, and DMAP (a tool kit for creating custom solutions in support of proprietary applications).

In addition to analyzing structures, you can use MSC/NASTRAN to optimize designs automatically. You can optimize statics, normal modes, buckling, transient response, frequency response, acoustics, and aeroelasticity. This can be done simultaneously, with both shape and sizing design variables. Weight, stress, displacement, natural frequency, and many other responses can be used as either the design objective (which can be minimized or maximized) or as design constraints. In addition, you can synthesize the design objective and constraints via user-written equations, making possible capabilities such as updating a model to match test data. MSC/NASTRAN is the only FEA program that does this automatically.

First and latest releases

First release In 1971.

Latest release MSC/NASTRAN V70.5 was released in June 1998.

Quality assurance MSC/NASTRAN's internal QA program is fully documented in a number of publications.

Documentation A full range of documentation is available in both electronic and paper versions. This includes user manuals, theory manual, numerical methods manual, demonstration and verification problem manuals, and many more, including compact user guides for most analysis topics.

Service and support Primary customer support and training is provided by local MSC offices spread worldwide and is backed up by a comprehensive internal system. MSC is also keen to work with customers as part of a 'quickstart' program to make them as effective as possible, as quickly as possible. As well as analysis applications, MSC's engineering service projects range from software integration and customization to a complete company-wide engineering process review.

Availability MSC/NASTRAN is available from over 50 MSC offices in 17 countries plus many more full service distributors and agents spread worldwide.

Computer environment MSC/NASTRAN is available for a wide range of hardware and software platforms, including PC (Windows 95, 98 and NT), SGI, HP, DEC, SUN, IBM unix workstations, and many Supercomputer platforms.

Related products MSC/Acumen, MSC/AFEA, MSC/AKUSMOD, MSC/AMS, MSC/CONSTRUCT, MSC/DropTest, MSC/DYTRAN, MSC/FATIGUE, MSC/FlightLoads, MSC/InCheck, MSC/MVISION, MSC/NVH Manager, MSC/PATRAN, MSC/SuperModel, MSC/SuperForge, MSC/Ultima.

Interfaces with other software

CAD and preprocessors MSC/NASTRAN data formats have become a standard in many industries. This has led to the availability of interfaces to most CAD and preprocessors. MSC also supplies its own interfaces to most major systems via MSC/PATRAN. Direct interfaces are available to Catia, ProEngineer, Euclid, CADDS 5, and Unigraphics packages as well as all Parasolid-based and ACIS-based systems.

Postprocessor MSC/NASTRAN is supported by most commercial postprocessing systems.

Analysis MSC/NASTRAN may be combined with many other analysis packages, either via data transfer using a standard data format, or via a number of programming options that enable direct process-to-process communication.

SAMCEF

Developer SAMTECH S.A., 25 Boulevard Frère Orban, 4000 Liège, Belgium.

General description General-purpose finite element package for linear and nonlinear, structural, and thermal analyses.

Main features SAMCEF is composed of several analysis modules that are interconnected. For the nonlinear part, module MECANO performs static, kinematic, or dynamic analyses on flexible mechanisms modeled with nonlinear structural finite elements and kinematic rigid or flexible joints. The module ROTOR offers a powerful design tool

dedicated to rotating machines. All modules are piloted either by menus or by a fully parameterized command language.

First and latest releases

First release SAMCEF in 1965.

Latest release SAMCEF 8.0 was released in 1998.

Quality assurance Since 1990, a quality control and validation procedure has been integrated to the life cycle of the software.

Documentation The complete documentation is available on HTML format. This includes primer manual, reference manual for the commands, user's manuals (one for each analysis module), and example problems manual.

Service and support Training sessions are regularly organized at company headquarters and at subsidiaries. Advanced courses are organized either on-site or at SAMTECH. A hot-line is accessible in each subsidiary. In addition, experienced engineers provide consultancy and customization services.

Availability SAMCEF is available directly from SAMTECH and its subsidiaries. Networks of regional and international distributors are reselling SAMTECH products in many countries.

Computer environment All products run on UNIX platforms (CRAY, DEC, HP, IBM, SGI, SUN) and on Windows NT (PCs).

Other products

BOSS Quattro An application manager for optimization, parametric, statistic, and correlation studies.

SAMCEF Design An innovative technology pre- and postprocessor for several FEA softwares.

Interfaces with other software

Geometry IGES.

CAD and preprocessors CATIA, I-DEAS/Master Series, MSC/Patran.

Postprocessor I-DEAS/Master Series, MSC/Patran.

Analysis MSC/NASTRAN.

Technical Description of FEA Software

Finite Element Models

Meshing The mesher divides the geometry into several cells, each cell being a finite element (**Table 1**). The adaptive mesher permits automatic modification of the mesh according to error computation from a previous analysis. The aim is to improve the precision of results (mainly stresses). Rezoning techniques give details of the stress distribution in some regions of an existing mesh.

Standard elements It is considered that standard elements are those which are required to modelize most mechanical parts. They are trusses, beams, membranes, shells, and solids. Many variants exist (**Table 2**). According to geometry considerations, the formalism used to describe structures can be particularized. We generally distinguish between two- and three-dimensional problems. Axisymmetric structures expanded in Fourier series and semiinfinite media are other forms of idealization. Depending on the software, all standard elements do not necessarily exist for all formalisms.

Nonstandard elements Nonstandard elements include specialized elements that are useful to express rigid or flexible links between degrees of freedom. The list given in **Table 3** is not exhaustive.

Table 1 Meshing tools

	ABAQUS	*ANSYS*	*COSMOS*	*NASTRAN*	*SAMCEF*
ID mesh generator	√	√	√	√	√
Plane mesh generator	√	√	√	√	√
Surface mesh generator	√	√	√	√	√
Volume mesh generator	√	√	√	√	√
Mesh editor	√	√	√	√	√
Junction of different meshes	√	√	√	√	√
Error computation	√	√	√	√	√
Adaptive meshing	√	√			
Rezoning, submodeling	√	√	√	√	

Table 2 Standard finite elements

	ABAQUS	*ANSYS*	*COSMOS*	*NASTRAN*	*SAMCEF*
Axisymmetry	MSV	SV	SV	MSV	MSV
Fourier expansion	SV	SV	S	MSV	BSV
Plane stress	TBM	TBM	M	TM	TBM
Plane strain	V	V	V	MV	MV
Generalized plane strain	V		V	MV	V
3D	TBMSV	TBMSV	TBV	TBMSV	TBMSV
3D p-element		SV		BMSV	
Semiinfinite	V	V			

Table 3 Specialized elements

Element	*ABAQUS*	*ANSYS*	*COSMOS*	*NASTRAN*	*SAMCEF*
Pipe	√	√	√	√	√
Cable	√	√	√		√
Gasket	√				
Bushing	√	√		√	√
Bearing					√
Spring	√	√	√	√	√
Dashpot	√	√	√	√	√
Point inertia	√	√	√	√	√
Rigid body element	√	√	√	√	√
Kinematic joints	√	√	√	√	√
Superelement	√	√	√	√	√
Contact	√	√	√	√	√
Airbag	√				
Accelerometer	√				
Monitored volume	√				√
Hydrostatic fluid element	√				
User-defined element	√	√		√	√

Geometric nonlinearity Geometric nonlinearity conditions the amplitude of motion or deformation that a structure can reach during simulation. Formulations such as Eulerian and arbitrary Eulerian Lagrangian (ALE) are adapted to flow analysis (**Table 4**).

Materials The finite element discretization process considers the material at a macroscopic level and supposes that it is continuous. But microscopic structure of material may reveal macroscopic anisotropy (**Table 5**). The FEM allows one to introduce anisotropic properties in constitutive laws. A typical anisotropy is the one present in composite materials.

A material is said to be nonlinear when stresses are not proportional to strains. Material behaviors are divided into three categories: material elasticity supposes that the stresses derive from a strain potential; plasticity expresses the material yielding; and viscoplasticity concerns deformations that depend on strain rate (**Tables 6–10**).

Boundary conditions Once the structure geometry and materials have been described, it is necessary to specify how the structure interacts with the external world. Prescribed conditions refer to known values that are imposed to a set of degrees of freedom (**Table 11**). Loads refer to any forces, whether distributed or not, that are applied to the structure (**Table 12**). Such conditions are given as functions of time or frequency, according to the type of analysis.

Analyses

Linear Analyses

The linearity assumption imposes that the coefficients appearing on both sides of the equation of motion do not depend on the motion itself. This assumption is reasonable if the stresses are proportional to strains and if the displacements remain small during the analysis.

Table 4 Geometric nonlinearities

Formulation	*ABAQUS*	*ANSYS*	*COSMOS*	*NASTRAN*	*SAMCEF*
Large displacement	S	S	SM	S	S
Large rotation	S	S	SM	S	S
Large strain	S	S	SM	S	S
Updated Lagrange	S		SM	S	
Eulerian	SM				
Arbitrary Eulerian Lagrangian	SM				

S, Solid structure; M, material flow.

Table 5 Material anisotropy

Orientation	*ABAQUS*	*ANSYS*	*COSMOS*	*NASTRAN*	*SAMCEF*
Isotropy	BMSV	BMSV	BMSV	BMSV	BMSV
Orthotropy	BMSV	MSV	MSV	MSV	MSV
Anisotropy	BMSV	MSV	MSV	MSV	MSV
Multilayer	MSV	SV	SV	BMS	MSV

B, Beam; M, membrane; S, shell; V, solid volume.

Table 6 Elastic materials

Elasticity	*ABAQUS*	*ANSYS*	*COSMOS*	*NASTRAN*	*SAMCEF*
Linear elasticity	√	√	√	√	√
Time-dependent viscoelasticity	√	√	√	√	√
Frequency-dependent viscoelasticity	√				√
Hypoelasticity	√	√			
Hyperelasticity (Mooney)	√	√	√	√	√
Hyperelasticity (Ogden)	√	√	√		√
Hyperelasticity (Arruda–Boyce)	√				
Hyperelasticity (Bergstrom–Boyce)	√				
Hyperelasticity (polynomial)	√				
Porous elasticity	√				

Table 7 Plastic materials

Plasticity	*ABAQUS*	*ANSYS*	*COSMOS*	*NASTRAN*	*SAMCEF*
Von Mises yield criterion	√	√	√	√	√
Drucker–Prager criterion	√	√	√	√	√
Mohr–Coulomb criterion	√			√	
Rankine criterion	√				
Gurson criterion	√				√
Associated flow rule	√	√	√		√
Nonassociated flow rule	√	√			
Isotropic hardening	√	√	√	√	√
Kinematic hardening	√	√	√	√	√
Combined hardening	√	√	√	√	√
Soil CAP model	√				
Foam model	√	√	√		√
Concrete cracking/crushing	√				
Jointed rock	√				
Cam-clay plasticity	√				
Ramberg–Osgood plasticity	√	√	√	√	√
Johnson and Cook plasticity	√				
Krieg anisotropic plasticity					

Table 8 Viscoplastic materials

Viscoplasticity	*ABAQUS*	*ANSYS*	*COSMOS*	*NASTRAN*	*SAMCEF*
Steady-state hardening	√	√			√
Time hardening	√	√			
Strain hardening	√	√			√
Isotropic hardening	√	√		√	√
Kinematic hardening	√	√		√	√
Damage law					√
Lemaître law	√				√
Chaboche law	√				√

Table 9 Failure models

Failure models	*ABAQUS*	*ANSYS*	*COSMOS*	*NASTRAN*	*SAMCEF*
Maximum stress	√	√	√	√	√
Maximum plastic strain	√			√	
Tsai–Hill (composite)	√	√	√	√	√
Tsai–Wu (composite)	√	√	√	√	√
Azzi–Tsai–Hill (composite)	√				
Hashin (composite)	√				√
Breakable connections	√				
User-defined criterion	√			√	√

Table 10 Definition of materials

Facilities	*ABAQUS*	*ANSYS*	*COSMOS*	*NASTRAN*	*SAMCEF*
Thermal expansion	√	√	√	√	√
Temperature-dependent coefficients	√	√	√	√	√
Material damping	√	√	√	√	√
Material removal and addition	√				
User-defined material	√	√	√		√
Material database			√		

Table 11 Prescribed conditions

Prescribed conditions	*ABAQUS*	*ANSYS*	*COSMOS*	*NASTRAN*	*SAMCEF*
Functions (of time or frequency)	√	√	√	√	√
Local frames	√	√	√	√	√
Fixation	√	√	√	√	√
Prescribed displacement	√	√	√	√	√
Prescribed velocity	√	√	√	√	√
Prescribed acceleration	√	√	√	√	√
Initial displacement	√	√	√	√	√
Initial velocity	√	√	√	√	√
Pretension (bolt loading)	√	√	√	√	√

In linear dynamics, an economical way of solving the equations of motion is to expand the solution (displacements) as a series of lower-frequency modes. The technique applies for relatively low-frequency excitations. The mode acceleration method improves the solution by adding to the response the static contribution of unknown highest-frequency modes. Reactions and stresses benefit dramatically from that correction (**Tables 13** and **14**)

Nonlinear Analyses

The solution of a nonlinear problem usually requires an iterative procedure on all the degrees of freedom of

Table 12 Loads

Loading	*ABAQUS*	*ANSYS*	*COSMOS*	*NASTRAN*	*SAMCEF*
Point forces	√	√	√	√	√
Follower point forces	√	√	√	√	√
Pressure	√	√	√	√	√
Hydrostatic pressure	√	√	√	√	√
Global surface tractions			√	√	√
Centrifugal forces	√	√	√	√	√
Coriolis forces	√	√	√		√
Global acceleration (translation)	√	√	√	√	√
Global acceleration (rotation)	√	√	√	√	√

Table 13 Linear structural analyses

Type of analysis	*ABAQUS*	*ANSYS*	*COSMOS*	*NASTRAN*	*SAMCEF*
Static	√	√	√	√	√
Vibration mode extraction	√	√	√	√	√
Mode extraction in a prescribed range	√	√	√	√	√
Transient response (modal)	√	√	√	√	√
Transient response (direct solver)	√	√	√	√	√
Harmonic response (modal)	√	√	√	√	√
Harmonic response (direct solver)	√	√		√	√
Response spectrum	√	√	√	√	√
Random response	√	√	√	√	√
Campbel diagrams (rotor dynamics)					√
Buckling	√	√	√	√	√

Table 14 Advanced linear analyses

Options	*ABAQUS*	*ANSYS*	*COSMOS*	*NASTRAN*	*SAMCEF*
Mode acceleration method (modal response)			√	√	√
Initial stress stiffening	√	√	√	√	√
Centrifugal stiffening	√	√	√	√	√
Modal damping	√	√	√	√	√
Proportional damping (K, M)	√	√	√	√	√
Viscous damping	√	√	√	√	√
Hysteretic damping (harmonic response)		√		√	√
Gyroscopic matrix		√		√	√
Node-to-node contact	√	√	√	√	√

the structure. In transient static analysis, excitation depends on time- but rate-dependent phenomena (friction, damping, etc.) and inertial effects are neglected. Kinematics studies the motion of bodies, and does not take into account inertial effects and other forces (**Table 15**).

Linear Perturbation Analyses

Linear perturbation analysis means a linear analysis at the vicinity of a nonlinear equilibrium configuration (**Table 16**). An example is the computation of vibration modes of a cable submitted to large deflection in a gravity field.

Interactions

These concern interactions between parts of the model (**Table 17**).

Coupled Analyses

Direct coupling analysis introduces simultaneous coupling between two or more different physical unknowns. It is separate from indirect coupling involving two sequential separate analyses. The commonest indirect coupling case is computational thermomechanics with precomputed temperatures. Here, we consider only coupling with mechanics (**Table 18**).

Table 15 Nonlinear structural analyses

Type of analysis	*ABAQUS*	*ANSYS*	*COSMOS*	*NASTRAN*	*SAMCEF*
Static	√	√	√	√	√
Kinematic	√	√	√		√
Transient static	√	√	√	√	√
Transient dynamic	√	√	√	√	√

Table 16 Linear perturbation analysis

Type of analysis	*ABAQUS*	*ANSYS*	*COSMOS*	*NASTRAN*	*SAMCEF*
Static response	√	√	√	√	√
Dynamic response	√	√	√	√	√
Vibration mode extraction	√	√	√	√	√
Eigenvalue buckling prediction	√	√	√	√	√

Table 17 Interactions within structures

Interaction type	*ABAQUS*	*ANSYS*	*COSMOS*	*NASTRAN*	*SAMCEF*
Node-based contact	√	√	√	√	√
Element-based contact			√	√	√
Surface-based contact	√	√	√		√
Rigid–flexible contact	√	√	√	√	√
Flexible–flexible contact	√		√	√	√
Eroding contact					
Friction	√	√	√	√	√
Multipoint constraint	√	√	√	√	√
Cyclic symmetry	√		√	√	√
Periodic symmetry	√		√	√	
Feedback and control systems	√	√		√	√

Table 18 Coupled analyses

Physics	*ABAQUS*	*ANSYS*	*COSMOS*	*NASTRAN*	*SAMCEF*
Compressible fluid flow		I	I		
Incompressible fluid flow		I	I		
Pore fluid flow	D		I		
Acoustic radiation	DI	D	D	D	D
Heat transfer	DI	I	I	I	I
Piezoelectricity	D	D	I		
Magnetic		I	I		
Electromagnetic		I	I		

D, direct coupling; I, indirect coupling.

Solution Methods

Solver

Basically, the solver is that part of the program dedicated to solving a linear system of equations. It allows one to obtain directly the linear static response. To solve nonlinear problems or dynamic ones, it is usually coupled to iterative procedures. Solver efficiency often determines the overall performance of the program. It is why solvers are generally adapted to specific computer architectures (**Table 19**).

Eigenvalue Extraction

The Lanczos method is widely used to compute natural modes and frequencies of large systems. The block Lanczos method is a variant which iterates with a set of vectors instead of a single one. When extracting many modes, the efficiency of the technique is

Table 19 Equation solvers

Solver	*ABAQUS*	*ANSYS*	*COSMOS*	*NASTRAN*	*SAMCEF*
Bandwidth reduction	√	√	√	√	√
Iterative (PCG)		√	√	√	√
Frontal (wavefront solver)	√	√		√	√
Multifrontal	√	√	√	√	
Augmented Lagrangian					√
Sparse storage	√	√	√	√	
Nonsymmetric	√	√		√	√
Complex		√	√	√	√
Parallel (shared memory)	√	√	√	√	√
Parallel (distributed memory)	√			√	
Vector processing	√			√	

improved by operating several spectral shifts in order to localize the frequencies in successive subintervals (**Table 20**).

Nonlinear Equilibrium

To converge to an equilibrium at each load increment (statics) or at each time step (dynamics), iterative procedures are used that are based on the well-known Newton or tangent method (**Table 21**). In statics, the loads are usually applied step by step; when there is a risk of buckling or snap-through, increments must be applied according to a continuation method (arc length, Riks, etc.). In dynamics, the size of the time step conditions the size of load increments. In the general case, the loads depend on the configuration reached by the structure and must be computed at each iteration.

Time Integration

In transient dynamics, the displacements are obtained by integrating the equations of motions (**Table 22**). Schemes of the Newmark family are the most widely used. Since the range of excited frequencies may change during the response according to changes in the loading or in the structure itself, automatic time stepping may dramatically reduce the CPU time for a given accuracy.

Substructuring

Substructuring is a technique used to condense the degrees of freedom of a linear structure (**Table 23**). Stiffness, mass, and other matrices and loads are reduced from their initial size to a smaller number of degrees of freedom. Analyses are performed using condensed matrices and results are recovered *a pos-*

Table 20 Eigenvalue algorithms

Algorithm	*ABAQUS*	*ANSYS*	*COSMOS*	*NASTRAN*	*SAMCEF*
Lanczos	√	√	√	√	√
Block Lanczos	√	√	√	√	√
Subspace iteration	√	√	√		
Inverse power			√	√	
Nonsymmetric				√	√
Complex		√	√	√	

Table 21 Nonlinear solution techniques

Nonlinear iterations	*ABAQUS*	*ANSYS*	*COSMOS*	*NASTRAN*	*SAMCEF*
Newton–Raphson	√	√	√	√	√
Modified Newton–Raphson	√	√	√	√	√
Quasi-Newton	√		√	√	
Line search	√	√	√	√	√
Continuation method	√	√		√	√
Automatic convergence control	√	√	√	√	√
Automatic static stepping	√	√	√	√	√

Table 22 Time integration

Time integration	*ABAQUS*	*ANSYS*	*COSMOS*	*NASTRAN*	*SAMCEF*
Central difference	√	√	√		
Hilber–Hughes–Taylor	√				√
Newmark	√	√	√	√	√
Automatic time stepping	√	√	√	√	√
Restarts	√	√	√	√	√

Table 23 Substructuring

Substructuring	*ABAQUS*	*ANSYS*	*COSMOS*	*NASTRAN*	*SAMCEF*
Guyan reduction	√	√	√	√	√
Craig–Bampton reduction		√		√	√
MacNeal reduction			√	√	
Superelement scaling	√		√		√
Superelement rotation	√	√	√	√	√
Superelement reflection	√	√	√	√	
Prestressed superelement created after a linear or nonlinear analysis	√				√
Use of superelement in nonlinear analysis (small rotations)	√	√		√	√
Use of superelement in nonlinear analysis (large rotations)		√			√

teriori for the whole set of degrees of freedom. The method is statically exact but gives approximate results in dynamics. The condensed matrices form a superelement which is useful to export a model from one software to another. It is possible to impose large rotations to a superelement in a nonlinear analysis.

See also: **Computation for transient and impact dynamics**; **Eigenvalue analysis**; **Finite element methods**; **Krylov-Lanczos methods**; **Nonlinear systems analysis**; **Structural dynamic modifications**.

Further Reading

Adams ML Jr (1999) *Rotating Machinery Vibration. From Analysis to Troubleshooting*. New York: Marcel Dekker.

Craveur J-C (1996) *Modélisation des Structures*. Paris: Masson.

Hinton E (ed.) (1992) *Introduction to Nonlinear Finite Element Analysis*. Glasgow: Nafems.

Martin J-P (1987) *La qualité des Logiciels. Du Bricolage à l'Industrialisation*. Paris: Afnor Gestion.

Robert G (1993) Finite element quality control. In: *Proceedings of the Fourth International Conference on Quality Assurance*, pp. 279–290. Glasgow: NAFEMS.

SFM (1990) *Guide de Validation des Progiciels de Calcul des Structures*. Paris: Afnor Technique.

COMPARISON OF VIBRATION PROPERTIES

Comparison of Spatial Properties

M Radeş, Universitatea Politehnica Bucuresti, Bucuresti, Romania

Copyright © 2001 Academic Press

doi:10.1006/rwvb.2001.0162

Spatial properties of structural dynamic models are presented in the form of mass, stiffness, and damping matrices. For gyroscopic systems, such as rotor-bearing systems, one can add gyroscopic and circulatory matrices. The static flexibility matrix, i.e., the inverse of the stiffness matrix, is also of interest because it is measurable.

The mass and stiffness matrices can have the full dimension of the finite element model (FEM) or

can be reduced to the size of the test analysis model (TAM), for comparisons based on experimental data. The TAM is a reduced representation of the structure, whose degrees-of-freedom (DOFs) correspond to the instrumented DOFs in modal testing.

A comparison of spatial properties is, in principle, desirable, because it reveals not only the extent of discrepancy between analytical and test-derived models, but also the areas on the structure where these errors might originate.

However, experimentally-derived models are not only truncated or incomplete, but are also nonunique, being computed either from an intermediate truncated modal model, or directly from the small-size response model. The result is that any direct comparison of analytical and test-derived spatial properties at the full size of the FEM is meaningless.

One can consider the comparison of reduced spatial properties, i.e., of the mass and stiffness matrices reduced to the size of the TAM, or of their inverses. Again, a direct comparison is inconclusive. Instead, the experimental mode shapes can be used either to correct the reduced analytical mass and stiffness matrices, or to assess their goodness based on orthogonality constraints.

Comparison of Reduced Mass Matrices

It is useful to compare TAM mass matrices, $\mathbf{M}_{\mathrm{TAM}}$, obtained by different model reduction methods, either on the same test modal vectors, or on reduced analytical modal vectors. The comparison is based on the orthogonality of the reduced mass matrices with respect to either the test or the analytical modal vectors.

The test orthogonality matrix (**TOR**), defined as:

$$\mathbf{TOR} = (\mathbf{\Phi}_{\mathrm{TEST}})^{\mathrm{T}}\mathbf{M}_{\mathrm{TAM}}\mathbf{\Phi}_{\mathrm{TEST}}$$

is used as a measure of the robustness of the TAM reduction method, i.e., the ability of the TAM to provide TOR matrices that resemble the identity matrix, when the FEM has inaccuracies. The matrix Φ_{TEST} contains the measured modal vectors as columns.

The generalized mass matrix is:

$$\mathbf{GM} = \left(\mathbf{\Phi}^{\mathrm{R}}_{\mathrm{FEM}}\right)^{\mathrm{T}}\mathbf{M}_{\mathrm{TAM}}\mathbf{\Phi}^{\mathrm{R}}_{\mathrm{FEM}}$$

where $\mathbf{\Phi}^{\mathrm{R}}_{\mathrm{FEM}}$ is the matrix of target analysis modes reduced to the measured DOFs. It is used as an indicator of the goodness of the TAM mass matrix, revealing errors in the TAM due to the reduction process. It should approximate to the identity matrix. The cross-orthogonality matrix (**XOR**):

$$\mathbf{XOR} = \left(\mathbf{\Phi}^{\mathrm{R}}_{\mathrm{FEM}}\right)^{\mathrm{T}}\mathbf{M}_{\mathrm{TAM}}\mathbf{\Phi}_{\mathrm{TEST}}$$

is a less stringent check of robustness, since the test modal vectors are only used once in the calculation. Note that the TAM accuracy, i.e., its ability to predict the dynamic response of the structure to operating environments, is assessed by comparison of modal frequencies and mode shapes, i.e., of test and TAM modal properties.

Reduced Mass Matrices

In the reduction process, the TAM degrees-of-freedom (DOFs) are referred to as the active (a) DOFs. The other DOFs used in the FEM are called omitted (o) DOFs.

If the FEM coordinate vector, $\mathbf{u}$, is partitioned as:

$$\mathbf{u} = \begin{Bmatrix} \mathbf{u}_a \\ \mathbf{u}_o \end{Bmatrix}$$

where $\mathbf{u}_a$ contains the active DOFs and $\mathbf{u}_o$ contains the omitted DOFs, the transformation from the full set of FEM DOFs to the TAM DOFs can be defined as:

$$\mathbf{u} = \mathbf{T}\mathbf{u}_a$$

The transformation matrix, $\mathbf{T}$, is used to calculate the reduced mass and stiffness matrices:

$$\mathbf{M}^{\mathrm{R}}_{\mathrm{A}} = \mathbf{T}^{\mathrm{T}}\mathbf{M}_{\mathrm{A}}\mathbf{T} \qquad \mathbf{K}^{\mathrm{R}}_{\mathrm{A}} = \mathbf{T}^{\mathrm{T}}\mathbf{K}_{\mathrm{A}}\mathbf{T}$$

where $\mathbf{M}_{\mathrm{A}}$ and $\mathbf{K}_{\mathrm{A}}$ are the full-size analytical FEM matrices, usually partitioned according to the a and o sets as:

$$\mathbf{M}_{\mathrm{A}} = \begin{bmatrix} M_{aa} & M_{ao} \\ M_{oa} & M_{oo} \end{bmatrix} \qquad \mathbf{K}_{\mathrm{A}} = \begin{bmatrix} K_{aa} & K_{ao} \\ K_{oa} & K_{oo} \end{bmatrix}$$

The form of the transformation matrix, $\mathbf{T}$, depends on the reduction method. Four of the most popular reduction methods are presented below.

Guyan–Irons Reduction (Static Condensation)

In the Guyan–Irons reduction, the displacements in the o set are described by a set of static shapes called constraint modes. They are calculated so as to minimize the total strain energy. The transformation matrix has the form:

$$\mathbf{T}_{\mathrm{S}} = \begin{bmatrix} \mathbf{I} \\ -\mathbf{K}^{-1}_{oo}\mathbf{K}_{oa} \end{bmatrix} = \begin{bmatrix} \mathbf{I}_a \\ \mathbf{G}_{oa} \end{bmatrix}$$

where $\mathbf{G}_{oa}$ enters the constraint equation between the a and o DOFs $\mathbf{u}_o = \mathbf{G}_{oa}\mathbf{u}_a$ and $\mathbf{I}_a$ is the identity matrix of size equal to the number of a DOFs.

Improved Reduced System

The improved reduced system (IRS) method is an improved static condensation, involving minimization of both strain energy and the potential energy of applied forces. It includes a static approximation for the inertia terms discarded in the static condensation.

The IRS transformation matrix is:

$$\mathbf{T}_{\mathrm{IRS}} = \begin{bmatrix} \mathbf{I}_a \\ \mathbf{G}_{oa} + \mathbf{K}_{oo}^{-1}(\mathbf{M}_{oa} + \mathbf{M}_{oo}\mathbf{G}_{oa})\mathbf{M}_a^{-1}\mathbf{K}_a \end{bmatrix}$$

where:

$$\mathbf{M}_a = \mathbf{T}_{\mathrm{S}}^{\mathrm{T}}\mathbf{M}_{\mathrm{A}}\mathbf{T}_{\mathrm{S}} \quad \mathbf{K}_a = \mathbf{T}_{\mathrm{S}}^{\mathrm{T}}\mathbf{K}_{\mathrm{A}}\mathbf{T}_{\mathrm{S}}$$

are the condensed mass and stiffness matrices obtained using the Guyan–Irons reduction.

Modal TAM

Consider the full-square FEM mode shape matrix partitioned in the form:

$$\mathbf{\Phi} = \begin{bmatrix} \mathbf{\Phi}_a \\ \mathbf{\Phi}_o \end{bmatrix} = [\mathbf{\Phi}_t \quad \mathbf{\Phi}_r] = \begin{bmatrix} \Phi_{at} & \Phi_{ar} \\ \Phi_{ot} & \Phi_{or} \end{bmatrix}$$

where the subscript t denotes the target modes, i.e., the FEM mode shapes used in the reduction procedure, and the subscript r denotes the residual modes, i.e., all the other analytical modes. Note that $\mathbf{\Phi}_t = \mathbf{\Phi}_{\mathrm{A}}$ and $\mathbf{\Phi}_{at} = \mathbf{\Phi}_{\mathrm{A}}^{\mathrm{R}}$ (see **Comparison of vibration properties: Comparison of modal properties**).

The modal TAM transformation matrix, $\mathbf{T}_{\mathrm{M}}$, is given by:

$$\mathbf{T}_{\mathrm{M}} = \begin{bmatrix} \mathbf{I}_a \\ \mathbf{\Phi}_{ot}\mathbf{\Phi}_{at}^{+} \end{bmatrix}$$

where the superscript + indicates the pseudoinverse. The matrix $\mathbf{\Phi}_{at}$ has more rows than columns and is full-column rank. The modal TAM provides an exact reduction provided that there are no modeling errors in the FEM. The modal TAM is a variant of the more general system-equivalent reduction/expansion process (SEREP).

Hybrid TAM

An improved TAM can be derived from the modal TAM by incorporating static modes with the target modes. The hybrid TAM transformation matrix, $\mathbf{T}_{\mathrm{H}}$, is given by:

$$\mathbf{T}_{\mathrm{H}} = \mathbf{T}_{\mathrm{S}} + (\mathbf{T}_{\mathrm{M}} - \mathbf{T}_{\mathrm{S}})\mathbf{\Phi}_{at}\mathbf{\Phi}_{at}^{\mathrm{T}}\mathbf{M}_{at}$$

where $\mathbf{M}_{at}$ is the modal TAM mass matrix for the target modes satisfying the orthogonality relationship:

$$\mathbf{\Phi}_{at}^{\mathrm{T}}\mathbf{M}_{at}\mathbf{\Phi}_{at} = \mathbf{I}_t$$

where $\mathbf{I}_t$ is the identity matrix of order equal to the number of target modes. The hybrid TAM combines the accuracy of the modal TAM with the robustness of the static TAM.

Test Orthogonality Check

An indirect comparison of the TAM mass matrices, obtained by the four reduction methods presented above, can be made based on the test mode shapes and the mixed orthogonality check TOR. A typical result is illustrated in **Figures 1–4**, presenting the TOR matrices calculated from four different reduced mass matrices. The reference FEM of the structure, having about 45 000 DOFs, has been reduced to a 120-DOFs TAM, having 15 flexible natural modes between 5.2 and 34.3 Hz.

The largest off-diagonal terms occur in the TOR matrix of the modal TAM (**Figure 3**), especially for the higher residual modes. This can be an indication that the spatial resolution given by the selected response measurement points (the a set) is insufficient to make the target modes linearly independent and observable – an important outcome of such a comparison process.

The hybrid TAM shows a slight improvement on the modal TAM, due to the inclusion of static modes with the target modes (**Figure 4**). Surprisingly, the static TAM performs better than the modal TAM, showing smaller off-diagonal terms (**Figure 1**). The IRS TAM yields the best reduced-mass matrix, producing the lowest off-diagonal elements in the TOR matrix (**Figure 2**).

While the modal TAM gives the best match in frequencies and target modes, its prediction capability is low outside the frequency range spanned by the selected target modes. The static TAM, implemented as the Guyan reduction in many computer programs, performs better in orthogonality checks, but is dependent on the selection of a DOFs and generally requires more a DOFs to give comparable accuracy. However, these types of comparisons are usually problem-dependent.

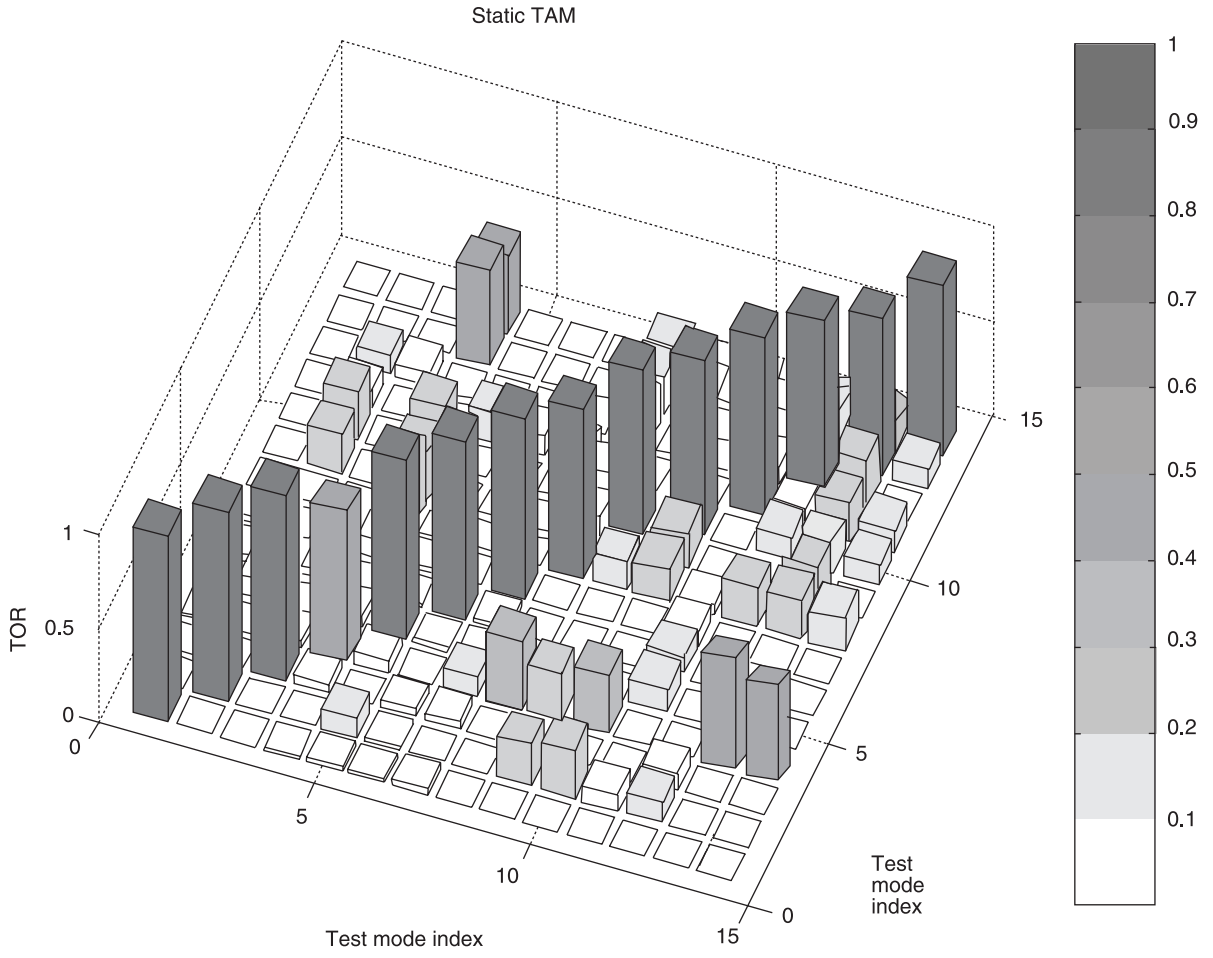


Figure 1

Mass and Stiffness Error Matrices

Different techniques can be used to update the mass and stiffness matrices, based on an incomplete set of modal frequencies and mode shapes derived from measurements. Assuming that the measured modal vectors are correct, the mass matrix can be updated by minimization of the cost function:

$$J_{\mathrm{M}} = \left\| \mathbf{M}_{\mathrm{A}}^{-1/2} (\mathbf{M}_{\mathrm{U}} - \mathbf{M}_{\mathrm{A}}) \mathbf{M}_{\mathrm{A}}^{-1/2} \right\|$$

subject to the orthogonality constraint:

$$\left(\mathbf{\Phi}_{\mathrm{X}}^{\mathrm{E}}\right)^{\mathrm{T}} \mathbf{M}_{\mathrm{U}} \mathbf{\Phi}_{\mathrm{X}}^{\mathrm{E}} = \mathbf{I}$$

where $\mathbf{M}_{\mathrm{A}}$ is the original estimate of the full-size FEM mass matrix, $\mathbf{M}_{\mathrm{U}}$ is the updated mass matrix, and $\mathbf{\Phi}_{\mathrm{X}}^{\mathrm{E}}$ is the matrix of expanded modal vectors. The weighting by $\mathbf{M}_{\mathrm{A}}^{-1/2}$ allows for differences in the magnitudes of the elements of the two mass matrices.

A 3D plot of the error matrix:

$$\mathbf{\Delta M} = \mathbf{M}_{\mathrm{U}} - \mathbf{M}_{\mathrm{A}}$$

helps to track the updating process and to localize parts of the structure where the inertia properties are poorly defined.

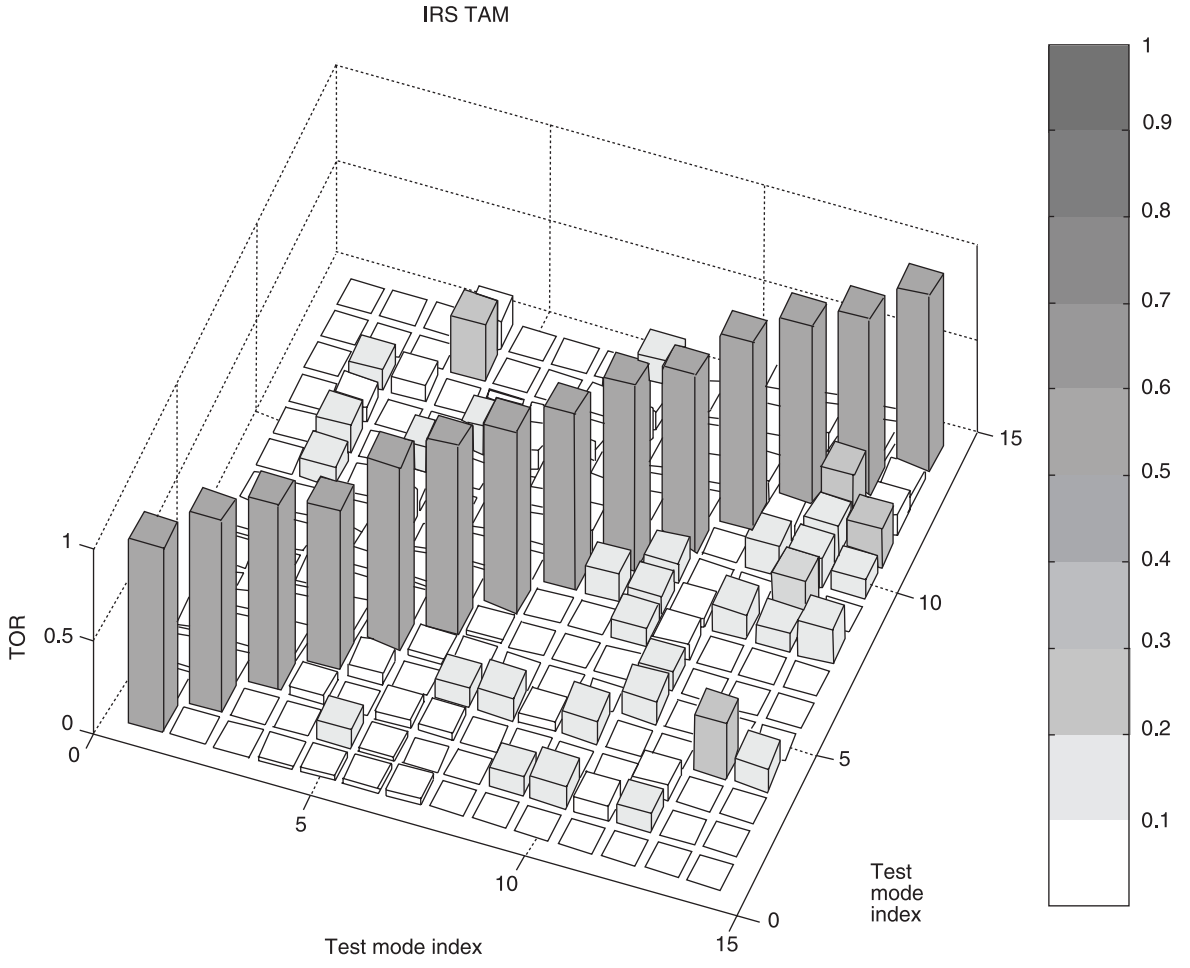


Figure 2

After the calculation of $\mathbf{M}_{\mathrm{U}}$, the stiffness matrix can be obtained by minimization of:

$$J_K = \left\| \mathbf{M}_{\mathrm{A}}^{-1/2} (\mathbf{K}_{\mathrm{U}} - \mathbf{K}_{\mathrm{A}}) \mathbf{M}_{\mathrm{A}}^{-1/2} \right\|$$

subject to constraints that enforce the stiffness symmetry, the stiffness orthogonality condition, and the equation of motion.

The stiffness error matrix:

$$\boldsymbol{\Delta}\mathbf{K} = \mathbf{K}_{\mathrm{U}} - \mathbf{K}_{\mathrm{A}}$$

can be presented in a graphical form like the mass error matrix (**Figure 5**).

It must be borne in mind that mode shape expansion can render the direct comparison of spatial properties meaningless. Direct updating methods are usually unable to preserve the connectivity of the structure. The updated matrices are usually fully populated, while analytical matrices are banded or sparse, so that local discrepancies have no physical meaning.

Early updating methods, referred to as error matrix methods, were conceived to estimate directly the

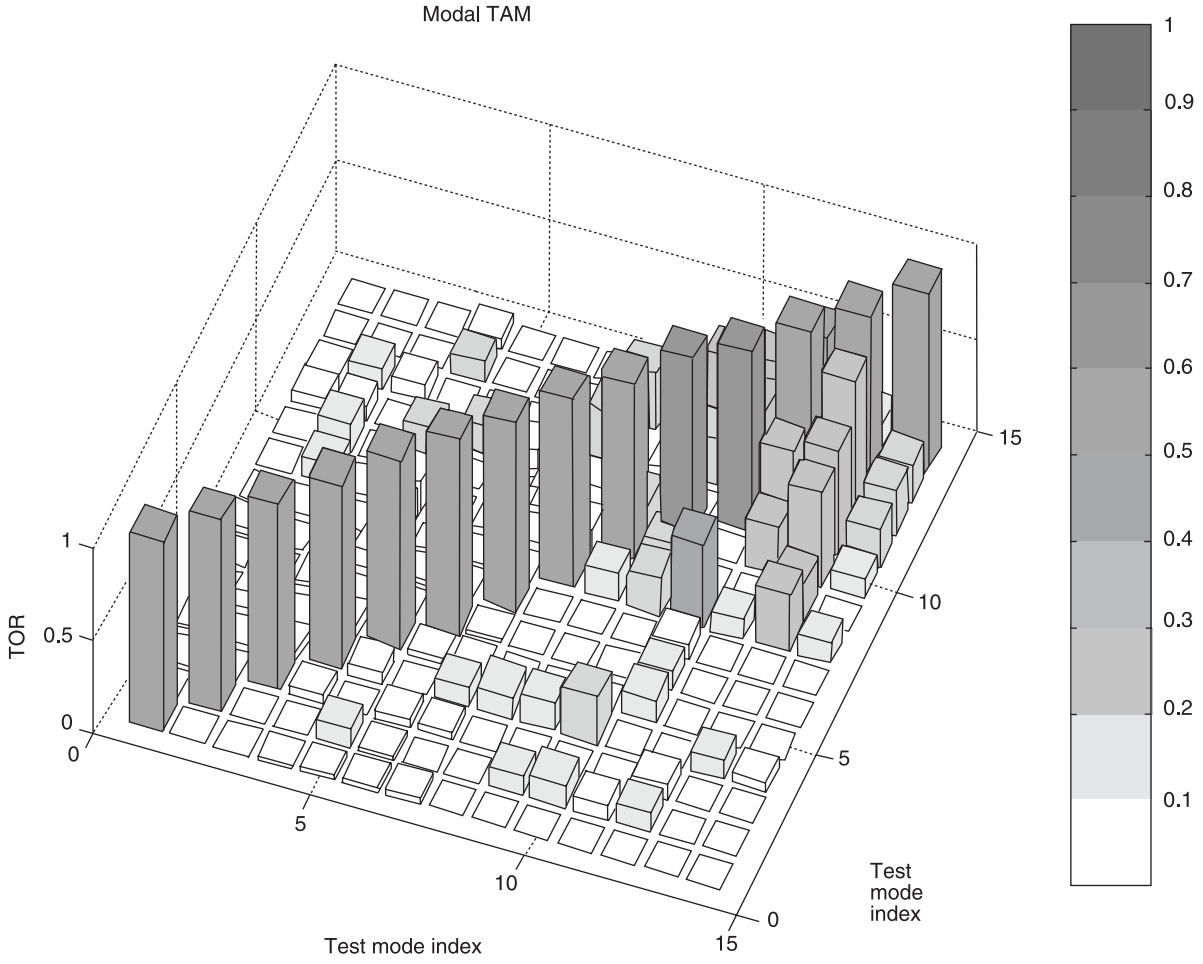


Figure 3

error in the system matrices, expressed as the difference between the measured and the predicted matrix.

Due to the incompleteness of experimental data, the stiffness error matrix:

$$\mathbf{\Delta K} = \mathbf{K}_{\mathrm{X}} - \mathbf{K}_{\mathrm{A}}$$

is calculated either as:

$$\mathbf{\Delta K} \cong \mathbf{K}_{\mathrm{A}}\left(\mathbf{K}_{\mathrm{A}}^{-1} - \mathbf{K}_{\mathrm{X}}^{-1}\right)\mathbf{K}_{\mathrm{A}}$$

or, using modal data to express the pseudoflexibility matrices, as:

$$\mathbf{\Delta K} = \mathbf{K}_{\mathrm{A}}\left(\mathbf{\Phi}_{\mathrm{A}}\left[\frac{1}{\omega_{A}^{2}}\right]\mathbf{\Phi}_{\mathrm{A}}^{\mathrm{T}} - \mathbf{\Phi}_{\mathrm{X}}\left[\frac{1}{\omega_{\mathrm{X}}^{2}}\right]\mathbf{\Phi}_{\mathrm{X}}^{\mathrm{T}}\right)\mathbf{K}_{\mathrm{A}}$$

where $\mathbf{\Phi}_{\mathrm{X}}$ is the reduced mass-normalized mode shape matrix from tests and $\mathbf{\Phi}_{\mathrm{A}}$ is calculated with the corresponding modes from the FEM. A similar approach, applied to the mass matrix, yields the mass error matrix:

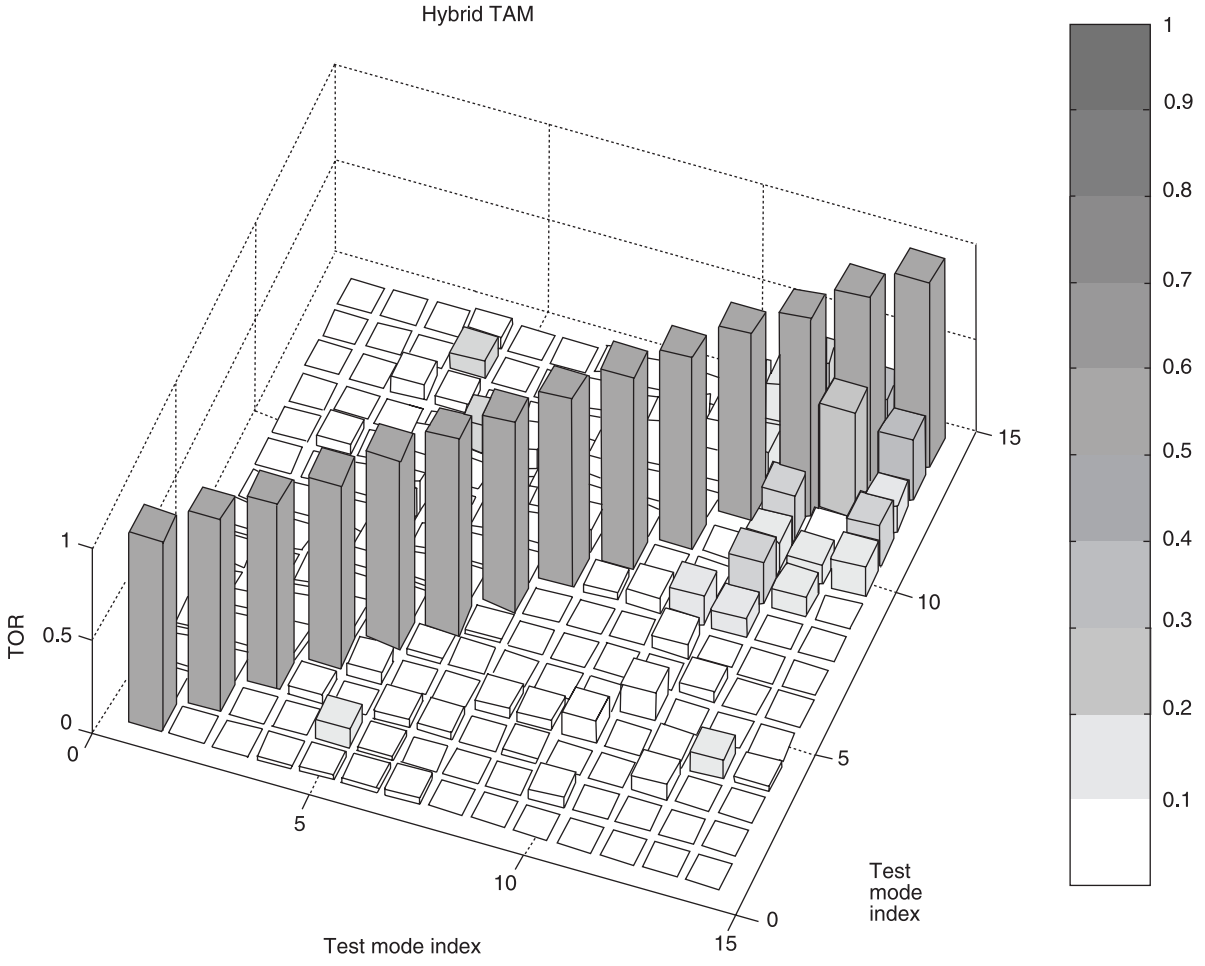


Figure 4

$$\mathbf{\Delta M} = \mathbf{M}_{\mathrm{A}}\left(\mathbf{\Phi}_{\mathrm{A}}\mathbf{\Phi}_{\mathrm{A}}^{\mathrm{T}} - \mathbf{\Phi}_{\mathrm{X}}\mathbf{\Phi}_{\mathrm{X}}^{\mathrm{T}}\right)\mathbf{M}_{\mathrm{A}}$$

The stiffness error matrix has been presented in graphical form using the alternative mesh format from **Figure 6**.

For large FEM, plots like those shown in **Figures 5** and **6** become impractical. Comparisons of spatial properties can be carried out at the reduced size of the TAM. They are only instruments to assess the accuracy of a given procedure and should not be used to locate inconsistencies in the compared models because the reduction process destroys the connectivity of the structure.

Finally, it should be emphasized that in any test/analysis correlation there are three main sources of errors: (1) FEM inaccuracies, (2) test mode shape measurement and identification errors, and (3) reduction/expansion errors. Additionally, errors due to the real normalization of measured complex modes must be taken into account.

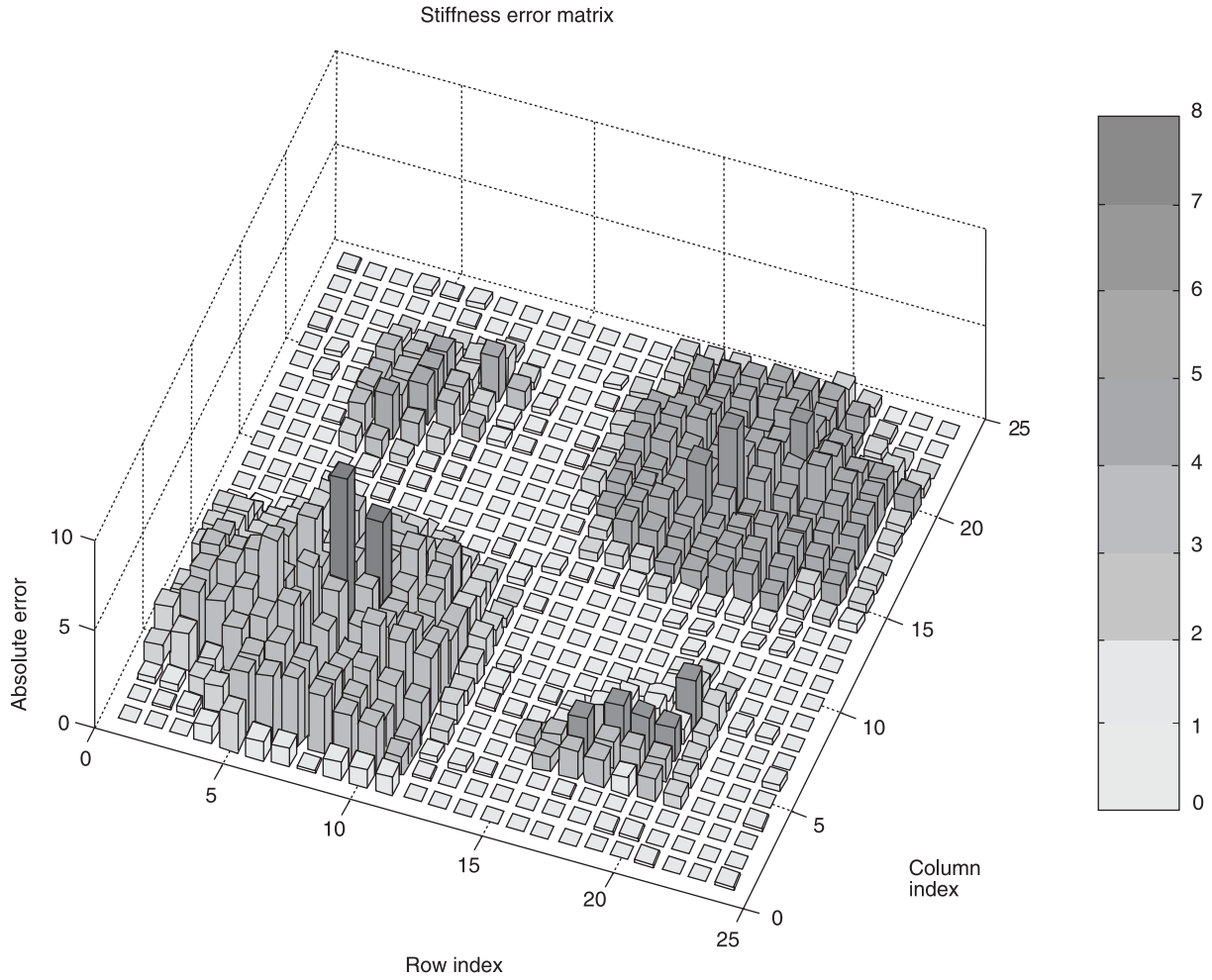


Figure 5

Nomenclature

a	active
GM	generalized mass matrix
I	identity matrix
M	mass matrix
o	omitted
r	residual
t	target
T	transformation matrix
TOR	test orthogonality matrix
XOR	cross orthogonality matrix
ΔK	stiffness error matrix
ΔM	mass error matrix

See also: **Comparison of vibration properties**: Comparison of modal properties; **Comparison of vibration properties**: Comparison of response properties; **Model updating and validating**.

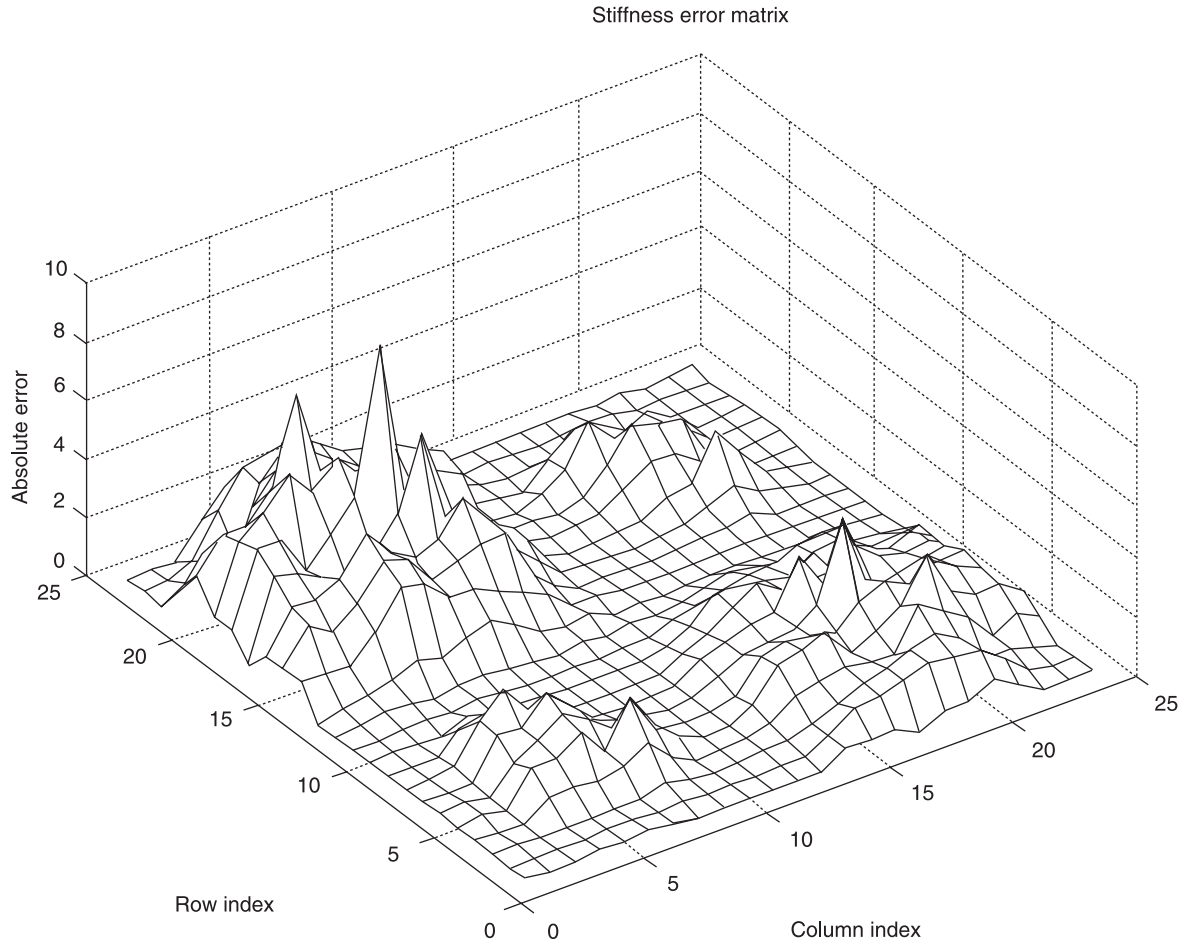


Figure 6

Further Reading

Ewins DJ (2000) *Modal Testing: Theory, Practice and Application*, 2nd edn. Baldock, UK: Research Studies Press.

Freed AM and Flanigan ChC (1991) A comparison of test-analysis model reduction methods. *Sound and Vibration* 25: 30–35.

Friswell MI and Mottershead JE (1995) *Finite Element Model Updating in Structural Dynamics*. Dordrecht: Kluwer.

Guyan RJ (1965) Reduction of stiffness and mass matrices. *AIAA Journal* 3: 380.

Irons BM (1963) Eigenvalue economisers in vibration problems. *Journal of the Royal Aeronautical Society* 67: 526–528.

Kammer DC (1987) Test-analysis model development using an exact model reduction. *International Journal of Analytical and Experimental Modal Analysis* xx: 174–179.

Kammer DC (1991) A hybrid approach to test-analysis modal development for large space structures. *Journal of Vibrations and Acoustics* 113: 325–332.

O'Callahan JC (1989) A procedure for an improved reduced system (IRS) model. *Proceedings of the 7th International Modal Analysis Conference*, Las Vegas, pp. 17–21.

O'Callahan JC (1990) Comparison of reduced model concepts. *Proceedings of the 8th International Modal Analysis Conference*, Kissimmee, Florida, pp. 422–430.

O'Callahan JC, Avitable P, Madden R and Lieu IW (1986) An efficient method of determining rotational degrees of freedom from analytical and experimental modal data. *Proceedings of the 4th International Modal Analysis Conference*, Los Angeles, California, USA, pp. 50–58.

O'Callahan JC, Avitable P and Riemer R (1989) System equivalent reduction expansion process (SEREP). *Proceedings of the 7th International Modal Analysis Conference*, Las Vegas, Nevada, USA, pp. 29–37.

Comparison of Modal Properties

M Radeş, Universitatea Politehnica Bucuresti, Bucuresti, Romania

Copyright © 2001 Academic Press

doi:10.1006/rwvb.2001.0174

Modal properties that are compared usually include: natural frequencies, real mode shape vectors, modal masses, modal kinetic and strain energies. For systems with complex modes of vibration one can add modal damping ratios and complex mode shapes. Left-hand modal vectors, modal participation factors, and reciprocal modal vectors are also considered in some applications. A test-analysis comparison is meaningful only for matched modes, i.e., for correlated mode pairs (CMPs). These are estimates of the same physical mode shape and their entries correspond one-to-one with their counterparts. Mode matching (pairing) is an essential step before any comparison can be undertaken.

In order to make it possible to compare experimental and finite element method (FEM) results, a reduced test-analysis model (TAM) is often used. This is represented by the mass and stiffness matrices computed for the test degrees-of-freedom (DOFs) only. Comparison of modal vectors can be done at the reduced order of the TAM or at the full order of the FEM. Reduction of the physical mass matrix or expansion of test modal vectors bring inherent approximations in the comparison criteria.

There are three main kinds of comparison: (1) analytical-to-analytical (FEM-to-FEM, TAM-to-TAM, and TAM-to-FEM); (2) experimental-to-experimental; and (3) analytical-to-experimental. The third type will be considered in more detail below.

It is useful to compare: (1) measured mode shapes against modal vectors determined by an analytical model; (2) estimates of the same test modal vector obtained from different excitation locations; (3) estimates of the same modal vector obtained from different modal parameter identification processes using the same test data; (4) one test mode shape before and after a change in the physical structure caused by a wanted modification, by damage or by operation over time.

Direct Numerical Comparison

Scalar quantities, such as natural frequencies, modal damping ratios, norms of modal vectors, modal masses, and modal energies are usually compared by simple tabulation of the relative error. Simple comparison of two columns of natural frequencies is meaningless without prior mode matching based on mode shape data. Mode pairing is done using the modal assurance criterion (MAC) described in a later paragraph. If there is one-for-one correspondence between the rth and the qth modes, then the following discrepancy indicators are used:

the relative modal frequency discrepancy:

$$\varepsilon_\omega = \frac{|\omega_r - \omega_q|}{\omega_r} \cdot 100$$

the relative modal damping discrepancy:

$$\varepsilon_\zeta = \frac{|\zeta_r - \zeta_q|}{\zeta_r} \cdot 100$$

the relative mode shape norm difference:

$$\varepsilon_\psi = \text{abs}\frac{|\boldsymbol{\psi}_r^{\mathrm{H}}\boldsymbol{\psi}_r| \; - \; |\boldsymbol{\psi}_q^{\mathrm{H}}\boldsymbol{\psi}_q|}{|\boldsymbol{\psi}_r^{\mathrm{H}}\boldsymbol{\psi}_r|} \cdot 100$$

For some aerospace structures, having about 20 flexible modes up to 50 Hz, modeling accuracy criteria typically specify values $\varepsilon_\omega \leq 5\%$. Comparative values for mode shape and damping ratio discrepancies are $\varepsilon_\psi \leq 10\%$ and $\varepsilon_\zeta \leq 25\%$, respectively.

Direct Graphical Comparison

A straightforward way to compare two compatible sets of data is by making an X–Y plot of one data set against the other. The method can be used to compare the natural frequencies from two different models. For well correlated data, the points of the resulting diagram should lie close to a straight line of slope equal to 1. If the approximating straight line has a slope different from 1, this indicates a bias error due to either calibration or erroneous material property data. Large random scatter about a 45° line indicates poor correlation or bad modeling.

The procedure can be applied to the mode shapes of correlated mode pairs. Each element of a test mode shape is plotted against the corresponding element of the analytical modal vector. For consistent

correspondence, the points should lie close to a straight line passing through the origin. If both modal vectors are mass-normalized, then the approximating line has a slope of ± 1.

Modal Scale Factor

If the two mode shape vectors have different scaling factors, it is useful to determine the slope of the best line through the data points. This is calculated as the least squares error estimate of the proportionality constant between the corresponding elements of each modal vector.

For real vectors, it is a real scalar referred to as the modal scale factor (MSF), defined as:

$$\mathrm{MSF}(r,q) = \frac{\boldsymbol{\psi}_r^{\mathrm{T}}\boldsymbol{\psi}_q}{\boldsymbol{\psi}_r^{\mathrm{T}}\boldsymbol{\psi}_r}$$

where $\boldsymbol{\psi}_r$ be the test vector and $\boldsymbol{\psi}_q$ the compatible analytical vector. For complex vectors, the superscript T is replaced by H (hermitian) and the MSF is a complex scalar.

The MSF gives no indication on the quality of the fit of data points to the straight line. Its function is to provide a consistent scaling factor for all entries of a modal vector. It is a normalized estimate of the modal participation factor between two excitation locations for a given modal vector.

Orthogonality Criteria

The most relevant way to assess the validity of a set of modal vectors is the orthogonality check. In order to use orthogonality checks, it is necessary to compute: (1) an FEM of the tested structure; (2) an analytical mass matrix reduced to the test DOFs; and/or (3) a set of test mode shapes expanded to the FEM DOFs.

The mass-orthogonality properties of FEM real mode shapes can be written as:

$$\boldsymbol{\Phi}_{\mathrm{A}}^{\mathrm{T}}\mathbf{M}_{\mathrm{A}}\boldsymbol{\Phi}_{\mathrm{A}} = \mathbf{I}$$

where $\boldsymbol{\Phi}_{\mathrm{A}}$ is the modal matrix at the full FEM order, $\mathbf{M}_{\mathrm{A}}$ is the FEM full-order mass matrix and $\mathbf{I}$ is the identity matrix.

For the TAM, the mass-orthogonality condition becomes

$$\boldsymbol{\Phi}_{\mathrm{A}}^{\mathrm{RT}}\mathbf{M}_{\mathrm{A}}^{\mathrm{R}}\boldsymbol{\Phi}_{\mathrm{A}}^{\mathrm{R}} = \mathbf{I}$$

where $\mathbf{M}_{\mathrm{A}}^{\mathrm{R}}$ is the reduced TAM mass matrix (see **Comparison of vibration properties: Comparison of spatial properties**) and $\boldsymbol{\Phi}_{\mathrm{A}}^{\mathrm{R}}$ contains the modal vectors reduced to the measured DOFs and mass-normalized with respect to $\mathbf{M}_{\mathrm{A}}^{\mathrm{R}}$.

Modal Auto-orthogonality

A mixed orthogonality test of the set of measured modal vectors $\boldsymbol{\Phi}_{\mathrm{X}}$ is often done to check the quality of the measurement data. The test orthogonality (TOR) matrix is defined as:

$$\mathbf{TOR} = \boldsymbol{\Phi}_{\mathrm{X}}^{\mathrm{T}}\mathbf{M}_{\mathrm{A}}^{\mathrm{R}}\boldsymbol{\Phi}_{\mathrm{X}}$$

If the measured modal vectors are orthogonal and mass-normalized with respect to the reduced mass matrix $\mathbf{M}_{\mathrm{A}}^{\mathrm{R}}$, then **TOR** will be the identity matrix. Test guidelines specify $\mathrm{TOR}_{rr} = 1.0$ and $|\mathrm{TOR}_{rq}| < 0.1$.

Modal Cross-Orthogonality

A cross-orthogonality test is performed to compare the paired modal vectors, the measured ones with the analytical vectors.

A cross-generalized mass (CGM) matrix, defining a cross orthogonality (XOR) criterion, can be constructed with mass-normalized modal vectors either at the TAM size:

$$\mathbf{XOR}_{\mathrm{TAM}} = \boldsymbol{\Phi}_{\mathrm{X}}^{\mathrm{T}}\mathbf{M}_{\mathrm{A}}^{\mathrm{R}}\boldsymbol{\Phi}_{\mathrm{A}}^{\mathrm{R}}$$

or at the full FEM size:

$$\mathbf{XOR}_{\mathrm{FEM}} = \boldsymbol{\Phi}_{\mathrm{X}}^{\mathrm{ET}}\mathbf{M}_{\mathrm{A}}\boldsymbol{\Phi}_{\mathrm{A}}$$

where $\boldsymbol{\Phi}_{\mathrm{X}}^{\mathrm{E}}$ contains the test modal vectors expanded to the full FEM DOFs.

For perfect correlation, the leading diagonal elements XOR_{rr} should be larger than 0.9, while the off-diagonal entries $|\mathrm{XOR}_{rq}|$ should be less than 0.1. Use of the reduced mass matrix $\mathbf{M}_{\mathrm{A}}^{\mathrm{R}}$ raises problems. One must differentiate reduction errors from discrepancies between the FEM and the test model.

When the reduced TAM mass matrix is obtained by the system equivalent reduction expansion process (SEREP) method, XOR is referred to as a pseudo-orthogonality criterion (POC). It is demonstrated that $\mathrm{POC}_{\mathrm{TAM}} = \mathrm{POC}_{\mathrm{FEM}}$. In this case, the full FEM mass matrix is not needed to compute either $\mathbf{M}_{\mathrm{A}}^{\mathrm{R}}$ or $\mathrm{POC}_{\mathrm{TAM}}$ because:

$$\mathbf{M}_{\mathrm{A}}^{\mathrm{R}} = \left(\boldsymbol{\Phi}_{\mathrm{A}}^{\mathrm{R}+}\right)^{\mathrm{T}}\boldsymbol{\Phi}_{A}^{R+}$$

where the superscript + denotes the pseudoinverse and $\boldsymbol{\Phi}_{\mathrm{A}}^{\mathrm{R}}$ is the rectangular matrix of analytical target modes reduced at the test DOFs.

An average measure of the correspondence between the compared modal vectors is given by the RMS value of either the off-diagonal elements in the **XOR** matrix or of the entries in the matrix calculated as the difference between the **XOR** matrix and the identity matrix. If only the diagonal elements are considered, then the mean deviation from one of these elements:

$$\text{mean}|XOR - 1| = \frac{1}{L}\sum_{l=1}^{L}\left|\left(\boldsymbol{\phi}_{\text{X}}^{\text{E}}\right)_l^{\text{T}}\mathbf{M}_{\text{A}}(\boldsymbol{\phi}_{\text{A}})_l - 1\}\right|$$

where L is the number of CMPs, gives an indication that the modal expansion fails to provide physically sound modal vectors.

Cross-orthogonality criteria cannot locate the source of discrepancy in the two sets of compared mode shapes. Large off-diagonal elements in the cross-orthogonality matrices may occur simply because they are basically small differences of large numbers. Also, modes having nearly equal frequencies may result in (linear combinations of) analysis modes rotated with respect to the test modes, case in which the off-diagonal elements of **XOR** are skew-symmetric.

Modal Vector Correlation Coefficients

The Modal Assurance Criterion

One of the most popular tools for the quantitative comparison of modal vectors is the modal assurance criterion (MAC). It was originally introduced in modal testing in connection with the MSF, as an additional confidence factor in the evaluation of a modal vector from different excitation locations.

When an FRF matrix is expressed in the partial fraction expansion form, the numerator of each term represents the matrix of residues or modal constants. Each residue matrix is proportional to the outer product of one modal vector and the corresponding vector of the modal participation factors. Each column of the residue matrix is proportional to the respective modal vector. One can obtain estimates of the same modal vector from different columns of the residue matrix. MAC has been introduced as a measure of consistency and similarity between these estimates.

If the elements of the two vectors are used as coordinates of points in an $X - Y$ plot, the MAC represents the normalized least squares deviation of corresponding vector entries from the best straight line fitted to the data, using the MSF. The concept can be applied to the comparison of any pair of compatible vectors. The MAC is calculated as the scalar quantity:

$$\text{MAC}(r,q) = \frac{\left|\boldsymbol{\psi}_r^{\text{H}}\boldsymbol{\psi}_q\right|^2}{\left(\boldsymbol{\psi}_r^{\text{H}}\boldsymbol{\psi}_r\right)\left(\boldsymbol{\psi}_q^{\text{H}}\boldsymbol{\psi}_q\right)}$$

where the form of a coherence function can be recognized. An equivalent formulation is:

$$\text{MAC}(r,q) = \frac{\left|\boldsymbol{\psi}_r^{\text{T}}\boldsymbol{\psi}_q^{*}\right|^2}{\left(\boldsymbol{\psi}_r^{\text{T}}\boldsymbol{\psi}_r^{*}\right)\left(\boldsymbol{\psi}_q^{\text{T}}\boldsymbol{\psi}_q^{*}\right)}$$

where T denotes the transpose and * the complex conjugate. It has been introduced as a mode shape correlation constant, to quantify the accuracy of identified mode shapes. Note that the modulus in the numerator is taken after the vector multiplication, so that the absolute value of the sum of product elements is squared.

The MAC takes values between 0 and 1. Values larger than 0.9 indicate consistent correspondence whereas small values indicate poor resemblance of the two shapes. The MAC does not require a mass matrix and the two sets of vectors can be normalized differently. The division cancels out any scaling of the vectors.

If $\boldsymbol{\psi}_r$ and $\boldsymbol{\psi}_q$ are the rth and qth columns of the real modal matrix $\boldsymbol{\Psi}$, then, using the cross-product (Gram) matrix $\mathbf{G} = \boldsymbol{\Psi}^{\text{T}}\boldsymbol{\Psi}$, the MAC can be written as:

$$\text{MAC}(r,q) = \frac{G_{rq}^2}{G_{rr}G_{qq}} = \cos^2\theta_{rq}$$

where $G_{rq} = \boldsymbol{\psi}_r^{\text{T}}\boldsymbol{\psi}_q$ is the inner product and θ_{rq} is the angle between the two vectors. This equation has the form of a coherence function, indicating the causal relationship between $\boldsymbol{\psi}_r$ and $\boldsymbol{\psi}_q$. The MAC is also a measure of the squared cosine of the angle between the two vectors. It shows the extent to which the two vectors point in the same direction.

Nonconsistency, i.e. near zero MAC values, can be the result of system nonlinearity, nonstationarity, an invalid parameter identification algorithm, and orthogonal vectors. Consistency, i.e., near unity MAC values, can result from different scaling of the same vector, incompleteness of the measured vectors, testing with other sources of excitation than the desired one, and coherent noise.

MAC Matrix

Given two sets of compatible modal vectors, a MAC matrix can be constructed, each entry defining a certain combination of the indices of the vectors belonging to the two sets. The ideal MAC matrix cannot be a unit matrix because the modal vectors are not directly orthogonal, but mass-orthogonal (**Figure 1A**). However, the MAC matrix indicates which individual modes from the two sets relate to each other. If two vectors are switched in one set, then the largest entries of the MAC matrix are no more on the leading diagonal and it resembles a permutation matrix. The two large off-diagonal elements show the indices of the switched vectors, as illustrated in **Figure 1B**. **Figure 2** is the more often used form of **Figure 1B**.

The MAC can only indicate consistency, not validity, so it is mainly used in pretest mode pairing. The MAC is incapable of distinguishing between systematic errors and local discrepancies. It cannot identify whether the vectors are orthogonal or incomplete.

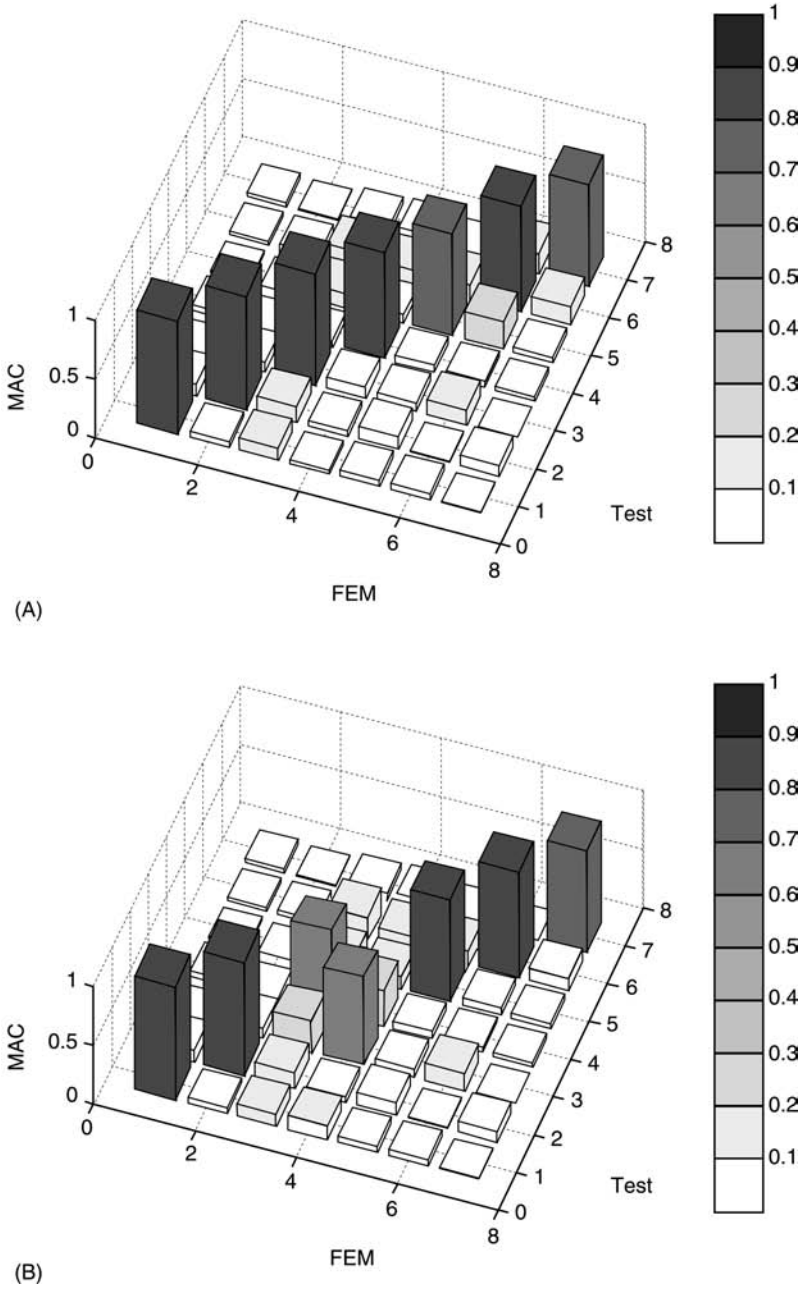


Figure 1 3D plots of MAC matrices: (A) seven correlated mode pairs, (B) switched modes 3 and 4.

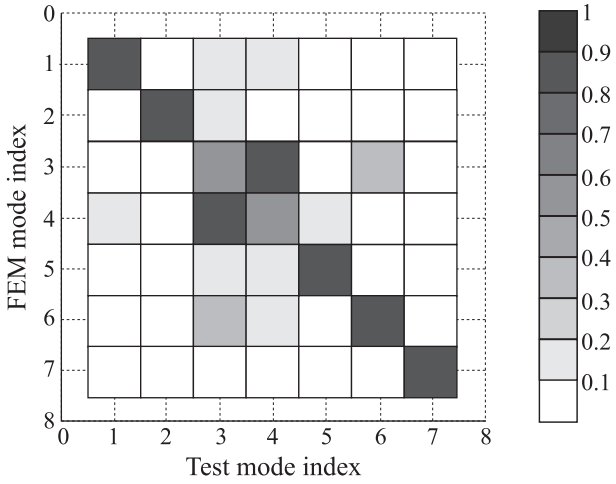


Figure 2 2D plot of MAC matrix.

An overall mode shape error indicator may be calculated from

$$\varepsilon_\phi = \left[1 - \frac{1}{L}\sqrt{\left(\sum_{l=1}^{L}(\mathrm{MAC})_l^2\right)}\right] \cdot 100$$

where L is the number of CMPs.

For axisymmetric structures that exhibit spatial phase shifts between test and analysis mode shapes, improved MAC values can be obtained by the rotation of mode shapes prior to correlation. For test mode shapes that contain multiple diametral orders, a special Fourier MAC criterion has been developed, using the first two primary Fourier indices.

The MAC is often used to assess the experimental vectors obtained by modal testing, especially when an analytical mass matrix is not available, and to compare test modal vectors with those calculated from FEM or TAM. The success of this apparent misuse is explained by two factors. First, test modal vectors usually contain only translational DOFs because rotational DOFs are not easily measured. If rotational DOFs were included in the modal vectors, the MAC would yield incorrect results. In this case it will be based on summations over vector elements of incoherent units, having different orders of magnitude. Second, for uniform structures, the modal mass matrix is predominantly diagonal and with not too different diagonal entries. In these cases, the MAC matrix is a good approximation for a genuine orthogonality matrix.

It should be underlined that a modal vector containing both translational and rotational DOFs cannot be simply scaled, and it has to be normalized with respect to the mass matrix. For example, if all linear displacements are multiplied by a factor of two, then the rotations are not doubled. It is the mass matrix that does the correct job, containing both masses and mass moments of inertia, which multiply linear and angular accelerations, respectively.

Normalized Cross-Orthogonality

A modified MAC, weighted by the mass or the stiffness matrix, referred to as the normalized cross-orthogonality (NCO) is defined as:

$$\mathrm{NCO}(r,q) = \frac{\left|\boldsymbol{\psi}_r^{\mathrm{H}}\mathbf{W}\boldsymbol{\psi}_q\right|^2}{\left(\boldsymbol{\psi}_r^{\mathrm{H}}\mathbf{W}\boldsymbol{\psi}_r\right)\left(\boldsymbol{\psi}_q^{\mathrm{H}}\mathbf{W}\boldsymbol{\psi}_q\right)}$$

where the weighting matrix $\mathbf{W}$ can be either the mass or the stiffness matrix. In the first case, it is sensitive to local modes with high kinetic energy, in the second case it is sensitive to regions of high strain energy. Applying the NCO separately, using the analytical mass and stiffness matrices, it is possible to locate sources of inadequate modeling. However, one must be careful to differentiate inherent reduction errors from discrepancies between the FEM and test data.

The NCO is able to use two arbitrarily scaled modal vectors. It defines the CMPs more clearly than the MAC. The square root version of NCO is being also used as a cross-orthogonality check based on mass-normalized modal vectors.

AutoMAC

The AutoMAC addresses the spatial (or DOF) incompleteness problem. The MAC can show correlation of actually independent vectors. If the number of DOFs is insufficient to discriminate between different mode shapes, it is possible that one analytical modal vector can appear to be well correlated with several experimental vectors.

It is necessary to check if the number of DOFs included in the model is sufficient to define all linearly independent mode shapes of interest. This check can be done using the AutoMAC, which correlates a vector with itself based on different reduced DOF sets. Spatial aliasing is shown by larger-than-usual off-diagonal elements of the AutoMAC matrix.

Degree-of-Freedom Correlation

In the comparison of two sets of modal vectors, one of the issues of interest is the influence of individual DOFs on the vector resemblance. The spatial dependence of the previously presented correlation criteria can be misleading. On one side, unacceptable large off-diagonal terms in cross-orthogonality matrices can correspond to large errors in points of very

small shape amplitude. On the other hand, very small off-diagonal elements of the XOR matrix do not necessarily indicate unrelated vectors.

A series of criteria have been developed to reveal the DOF dependence of the discrepancy between modal vectors. Their interpretation is not obvious and caution must be taken in their use as indicators of modeling accuracy.

Coordinate Modal Assurance Criterion

The coordinate MAC (COMAC) is used to detect differences at the DOF level between two modal vectors. The COMAC is basically a row-wise correlation of two sets of compatible vectors, which in MAC is done column-wise. The COMAC for the jth DOF is formulated as:

$$\mathrm{COMAC}(j) = \frac{\left(\sum_{l=1}^{L} \left|(\phi_{\mathrm{A}})_{jl}(\phi_{\mathrm{X}})_{jl}^{*}\right|\right)^{2}}{\sum_{l=1}^{L}(\phi_{\mathrm{A}})_{jl}^{2} \cdot \sum_{l=1}^{L}(\phi_{\mathrm{X}})_{jl}^{*}2}$$

where l is the index of the CMP, $(\phi_{\mathrm{A}})_{jl}$ is the jth element of the lth paired analytical modal vector, and $(\phi_{\mathrm{X}})_{jl}$ is the jth element of the lth paired experimental modal vector. Both (sets of) modal vectors must have the same normalization.

The COMAC is applied only to CMPs after a mode pairing using the MAC. It is a calculation of correlation values at each DOF, j, over all CMPs, L, suitably normalized to present a value between 0 and 1. The summation is performed on rows of the matrix of modal vectors, in a manner similar to the column-wise summation in the MAC. However, at the numerator, the modulus sign is inside the summation, because it is the relative magnitude at each DOF over all CMPs that matters.

The only thing the COMAC does is to detect local differences between two sets of modal vectors. It does not identify modeling errors, because their location can be different from the areas where their consequences are felt. Another limitation is the fact that COMAC weights all DOFs equally, irrespective of their magnitude in the modal vector.

The simplest output of the computation is a list of COMAC values between 0 and 1, which help to locate the DOFs for which the correlation is low. These DOFs are also responsible for a low value of MAC. The COMAC can be displayed as a bar graph of its magnitude against the DOF index (**Figure 3**).

Enhanced Coordinate Modal Assurance Criterion

A different formulation, also loosely called COMAC, is:

$$\mathrm{COMAC}(j) = 1 - \mathrm{ECOMAC}(j)$$

where the enhanced coordinate modal assurance criterion (ECOMAC) is defined as:

$$\mathrm{ECOMAC}(j) = \frac{\sum_{l=1}^{L} \left|(\phi_{\mathrm{A}})_{jl} - (\phi_{\mathrm{X}})_{jl}\right|}{2L}$$

The ECOMAC is the average difference between the elements of the modal vectors. It has low values for correlated vectors. It is sensitive to calibration and phase shifting errors in test data. The ECOMAC is dominated by differences at DOFs with relatively large amplitudes.

Normalized Cross-orthogonality Location

A different criterion that avoids the phase sensitivity is the normalized cross-orthogonality location (NCOL), defined as:

$$\mathrm{NCOL}(j) = \frac{\sum_{l=1}^{L}\left((\phi_{\mathrm{X}})_{jl}(\phi_{\mathrm{A}})_{jl} - (\phi_{\mathrm{A}})_{jl}^{2}\right)}{\sum_{l=1}^{L}(\phi_{\mathrm{A}})_{jl}^{2}}$$

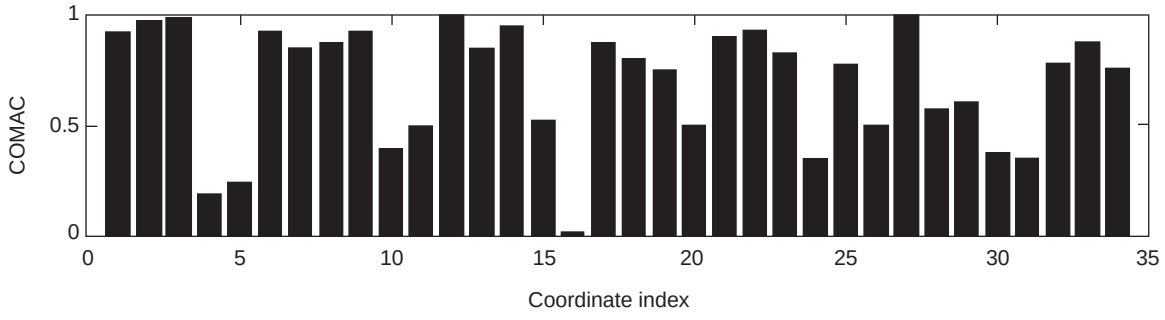


Figure 3 Bar graph plot of the COMAC.

NCOL is a DOF-based normalized cross-orthogonality check which contains neither mass nor stiffness terms. It allows the inclusion of phase inversions that are important near nodal lines.

Modulus Difference

The modulus difference (MD) is defined as the column vector formed by the differences between the absolute values of the corresponding elements of two paired modal vectors:

$$\mathrm{MD}(l) = \left|(\phi_{\mathrm{A}})_l\right| - \left|(\phi_{\mathrm{X}})_l\right|$$

The modulus difference matrix:

$$\mathbf{MDM} = [\mathrm{MD}(1) \quad \mathrm{MD}(2) \quad \ldots \quad \mathrm{MD}(\mathrm{L})]$$

can be displayed as a 3D graph showing the locations of low correlation between two sets of modal vectors.

Coordinate Orthogonality Check

The coordinate orthogonality check (CORTHOG) determines the individual contribution of each DOF to the magnitude of the elements of the cross-orthogonality matrix. If the $\mathrm{XOR}_{\mathrm{TAM}}$ for the $r - q$ mode pair and the $k - l$ DOF pair is written in the double sum form:

$$\mathrm{XOR}_{rq}^{jk} = \sum_{j=1}^{L}\sum_{k=1}^{L}\left((\phi_{\mathrm{X}})_{jr} m_{jk} (\phi_{\mathrm{A}})_{kq}\right)$$

where m_{jk} are elements of the analytical mass matrix, it can be seen that each off-diagonal element results from a summation of contributions from all DOFs. If (ϕ_{X}) is replaced by (ϕ_{A}), then the double sum represents elements of the analytical orthogonality matrix. The CORTHOG is the simple difference of the corresponding triple product terms in the two matrices, summed for the column index of DOFs:

$$\mathrm{CORTHOG}(j)_{rq} = \sum_{l=1}^{L}\left(\left(\phi_{\mathrm{X}}\right)_{jl} m_{jl}\left(\phi_{\mathrm{A}}\right)_{lq} - \left(\phi_{\mathrm{A}}\right)_{jr} m_{jl}\left(\phi_{\mathrm{A}}\right)_{lq}\right)$$

The CORTHOG can also be displayed as a bar graph of its magnitude against the DOF index.

Other Comparisons

Other comparisons have also been used for FEM/TAM correlation. Modal kinetic energy and modal strain energy comparisons are being used to assess the TAM validity or to locate dynamically important DOFs. Modal effective mass distributions are also used to compare important modes. Orthogonality relations between left and right modal vectors of gyroscopic systems, as well as between inverse modal vectors and their related mode shape vectors are also used in updating procedures.

Nomenclature

$\mathbf{I}$	identity matrix
L	number of CMPs
$\mathbf{M}$	mass matrix
$\mathbf{MDM}$	modulus difference matrix
$\mathbf{TOR}$	test orthogonality matrix
$\mathbf{XOR}$	cross orthogonality matrix
$\boldsymbol{\psi}_q$	compatible analytical vector
$\boldsymbol{\psi}_r$	test vector
$\boldsymbol{\Phi}$	modal matrix
$\boldsymbol{\Psi}$	real modal matrix

See also: **Comparison of Vibration Properties**, Comparison of Spatial Properties; **Modal analysis, experimental**, Applications; **Modal analysis, experimental**, Construction of models from tests; **Modal analysis, experimental**, Parameter extraction methods; **Model updating and validating**.

Further Reading

Allemang RJ (1980) *Investigation of Some Multiple Input/Output Frequency Response Function Experimental Modal Analysis Techniques*. PhD thesis, University of Cincinnati.

Blaschke PG, Ewins DJ (1997) The MAC revisited and updated. *Proceedings of the 15th International Modal Analysis Conference*, Orlando, Florida, USA, pp 147–154.

Chen G, Fotsch D, Imamovic N, Ewins DJ (2000) Correlation methods for axisymmetric structures. *Proceedings of the 18th International Modal Analysis Conference*, San Antonio, Texas, USA, pp 1006–1012.

Ewins DJ (2000) *Modal Testing: Theory, Practice and Application*, 2nd edn. Taunton, UK: Research Studies Press.

Fotsch D, Ewins DJ (2000) Application of MAC in the frequency domain. *Proceedings of the 18th International Modal Analysis Conference*, San Antonio, Texas, USA, pp 1225–1231.

Heylen W, Lammens S, Sas P (1997) *Modal Analysis Theory and Testing*. Leuven, Belgium: K. U. Leuven.

Imamovic N, Ewins DJ (1995) An automatic correlation procedure for structural dynamics. *International Forum on Aeroelasticity and Structural Dynamics*, Manchester, pp 56.1–56.12.

O'Callahan JC, Avitable P, Riemer R (1989) System equivalent reduction expansion process (SEREP). *Proceedings of the 7th International Modal Analysis Conference*, Las Vegas, Nevada, USA, pp 29–37.

Pappa RS, Ibrahim SR (1981) A parametric study of the Ibrahim time domain modal identification algorithm. *Shock and Vibration Bulletin* 51(3): 43–71.

Comparison of Response Properties

M Radeş, Universitatea Politehnica Bucuresti, Bucuresti, Romania

Copyright © 2001 Academic Press

doi:10.1006/rwvb.2001.0175

Compared response functions usually include Frequency Response Functions (FRFs), Operating Deflection Shapes (ODSs), and Principal Response Functions (PRFs). In the following, the presentation will be focused on the comparison of FRFs. ODSs can be compared in the same way as mode shape vectors (see **Comparison of vibration properties: Comparison of modal properties**). There are three main kinds of comparison: (1) analytical-to-analytical; (2) experimental-to-experimental; and (3) analytical-to-experimental. The last is of interest in structural modification (see **Structural dynamic modifications**) and model updating (see **Model updating and validating**) procedures and will be considered as the default case.

Comparison of Individual Response Functions

A typical FRF contains hundreds of values so that a graphical format is the most appropriate for comparisons. Diagrams of the FRF magnitude as a function of frequency are satisfactory for most applications. Bode diagrams, showing both the magnitude and the phase variation with frequency, are often used. Nyquist plots for selected parts of the frequency response are preferred when detailed information around a resonance is required. A visual inspection is usually sufficient to determine the similarities or lack of agreement between two FRFs.

The simplest comparisons may include: (1) FRFs measured using different excitation levels, as a linearity check; (2) FRFs measured or calculated switching the input and output points, as a reciprocity check; (3) FRFs measured or calculated before and after a structural modification, to show its effect on the system response; (4) FRFs calculated for different models and levels of damping; and (5) FRFs calculated before and after a data reduction that is intended to eliminate the noise and the linearly-related redundant information.

It is customary to use an overlay of all the FRFs, measured from all combinations of input and output coordinates, and to count the resonance peaks as a preliminary estimation of the model order.

Comparisons of measured and predicted FRFs may include: (1) FRFs calculated with different numbers of terms included in the summmation, to check the effect of residual terms and whether a sufficient number of modes have been included; (2) a measured FRF and the corresponding regenerated analytical curve, calculated from an identified modal model; (3) an initially-unmeasured FRF curve, synthesized from a set of test data, and the corresponding FRF curve obtained from a later measured set of data, to check the prediction capability of the analytical model.

Three factors must be borne in mind when analytically generated FRF curves are used in the comparison. First, the way the damping has been accounted for in the theoretical model; second, the fact that the analytical FRFs are usually synthesized from the modal vectors of the structure and depend on the degree of modal truncation; and third, when the compared FRFs originate from two models, one model being obtained by a structural modification of the other, the comparison must take into account the frequency shift and the change of the scale factor in the FRF magnitude. For instance, if the reference stiffness matrix is modified by a factor of α, the frequencies in the modified model increase by a factor of $\sqrt{\alpha}$, while the FRF magnitudes of an undamped model decrease by a factor of α.

Generally, in the correlation of measured and synthesized FRFs in an updating process, the pairing of FRFs at the same frequency has no physical meaning. As several physical parameters at the element level are modified, an average frequency shifting exists at each frequency line, so that an experimental frequency, ω_X, will correspond to a different analytical frequency, ω_A.

A global error indicator, calculated as the ratio of the Euclidean norm of the difference of two FRF vectors measured at discrete frequencies and the norm of a reference FRF vector, is of limited practical use. Visual inspection of two overlaid FRF curves can be more effective in localizing discrepancies (**Figure 1**).

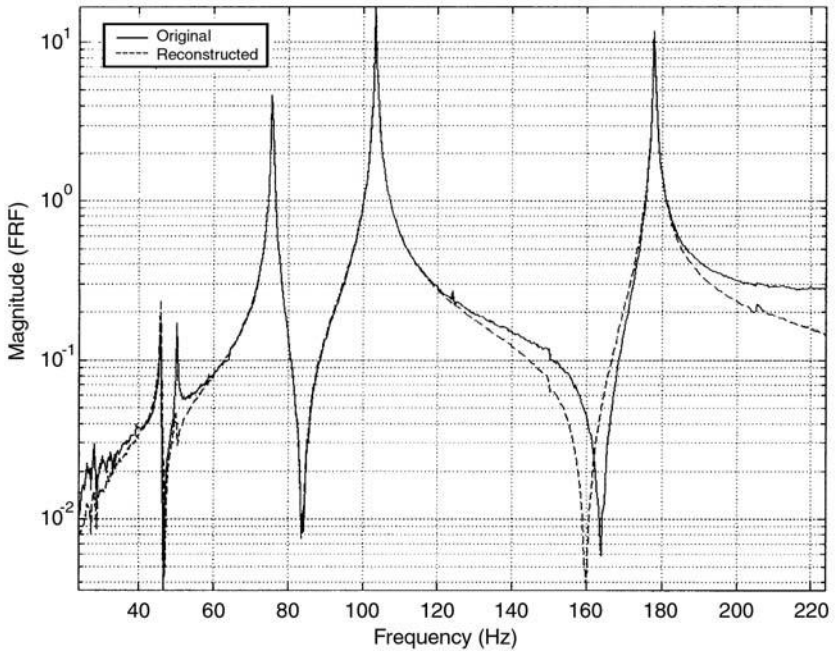


Figure 1 Measured and reconstructed FRFs.

Comparison of Sets of Response Functions

An FRF data set is usually measured at a larger number of response measurement points, N_o, than the number of input (reference) points, N_i. The measured FRF matrix $\mathbf{H}_{N_o \times N_i}(\omega)$ contains values measured at a single frequency, ω. If measurements are taken at N_f frequencies, then a complete set of FRF data is made up of N_f matrices, of row dimension N_o, and column dimension N_i. In a typical modal test, at least one column of the FRF matrix is measured. For structures with close or coincident natural frequencies, FRF elements from several such columns are measured. In order to compare several FRFs simultaneously it is necessary to use some frequency response correlation coefficients.

Frequency Response Assurance Criterion

Consider a complete set of $N_o N_i$ FRFs, measured at N_o response locations and N_i excitation locations, each containing values measured at N_f frequencies. A Compound FRF (CFRF) matrix, of size $N_f \times N_o N_i$ can be constructed such that each row corresponds to different individual FRF values at a specific frequency, and each column corresponds to a different input/output location combination for all frequencies:

$$\mathbf{A}_{N_f \times N_o N_i} = \begin{bmatrix} \mathbf{H}_{11} & \mathbf{H}_{21} & \dots & \mathbf{H}_{jl} & \dots \end{bmatrix}$$

where $\mathbf{H}_{jl}$ is an N_f-dimensional FRF column vector, with response at location j due to excitation at l.

Each column of the CFRF matrix is an FRF. If the magnitudes of its elements are plotted as a function of frequency, then an FRF curve is obtained. The columns of the CFRF matrix are (temporal) vectors that can be compared using the Modal Assurance Criterion (MAC) approach (see **Comparison of vibration properties: Comparison of modal properties**), i.e., calculating a correlation coefficient equal to the squared cosine of the angle between the two vectors.

The Frequency Response Assurance Criterion (FRAC), defined as:

$$\mathrm{FRAC}(j,l) = \frac{\left|\mathbf{H}_{Xjl}^{\mathrm{H}} \mathbf{H}_{Ajl}\right|^2}{\left(\mathbf{H}_{Xjl}^{\mathrm{H}} \mathbf{H}_{Xjl}\right)\left(\mathbf{H}_{Ajl}^{\mathrm{H}} \mathbf{H}_{Ajl}\right)}$$

is used to assess the degree of similarity between measured $\mathbf{H}_X$ and synthesized $\mathbf{H}_A$ FRFs, or any compatible pair of FRFs, summed across the frequency range of interest.

The FRAC is a spatial correlation coefficient, similar to the Coordinate Modal Assurance Criterion (COMAC) (see **Comparison of vibration properties:**

Comparison of modal properties), but calculated like the MAC. It is a measure of the shape correlation of two FRFs at each j, l input/output location combination. The FRAC can take values between 0 (no correlation) and 1 (perfect correlation). The FRAC coefficients can be displayed in a FRAC matrix, of size $N_o \times N_i$, which looks different from the usual MAC matrix, the diagram of each column resembling a COMAC plot.

Response Vector Assurance Criterion

The transposed CFRF matrix can be written as:

$$\left(\mathbf{A}^{\mathrm{T}}\right)_{N_o N_i \times N_f} = \left[\mathbf{H}(\omega_1) \quad \mathbf{H}(\omega_2) \quad \ldots \quad \mathbf{H}(\omega_f) \quad \ldots\right]$$

where each column contains all $N_o N_i$ FRFs, measured at a certain frequency, $\omega_f (f = 1, 2, \ldots, N_f)$, for N_o output locations and N_i input locations.

A temporal vector correlation coefficient can be defined using the columns of the $\mathbf{A}^{\mathrm{T}}$ matrix. If the column vector $\mathbf{H}(\omega_f)$ contains only the N_o entries from the lth input point, then the Response Vector Assurance Criterion (RVAC) is defined as:

$$\mathrm{RVAC}(\omega_f, l) = \frac{\left|\mathbf{H}_l^{\mathrm{H}}(\omega_f)\mathbf{H}_l(\omega_f)\right|^2}{\left(\mathbf{H}_l^{\mathrm{H}}(\omega_f)\mathbf{H}_l(\omega_f)\right)\left(\mathbf{H}_l^{\mathrm{H}}(\omega_f)\mathbf{H}_l(\omega_f)\right)}$$

This contains information from all response degrees-of-freedom simultaneously and for one reference point, at a specific frequency. The RVAC is analogous to the MAC and takes values between 0 (no correlation) and 1 (perfect correlation). Each N_o dimensional column is a response vector, i.e., the vector of displacements at all N_o response measurement points, calculated or measured at a given frequency, so that the RVAC can also be applied to the correlation of ODSs.

When the analytical model is undamped, the complex values of the measured FRFs should be converted into real ones, using an approximation of the type:

$$\mathbf{H}_{\mathrm{real}} = \mathrm{abs}\left(\mathbf{H}_{\mathrm{complex}}\right) \otimes \mathrm{sign}\left(\mathrm{Re}\,\mathbf{H}_{\mathrm{complex}}\right)$$

The RVAC coefficients can be displayed in a plot (**Figure 2**) of the type used for the MAC. However, the RVAC matrix, of size $N_f \times N_f$, yields a much denser diagram, plotted at several hundred frequency values, and hence it is more difficult to interpret. It helps in the selection of frequencies for correlation, within the intervals with high values of RVAC, where the Finite Element Model (FEM) data are close to the test data.

If the analytical FRF is calculated at N_f analytical frequencies, ω_A, and the test FRF is measured at N_f experimental frequencies, ω_X, then a Frequency Domain Assurance Criterion (FDAC) can be defined, whose real version is:

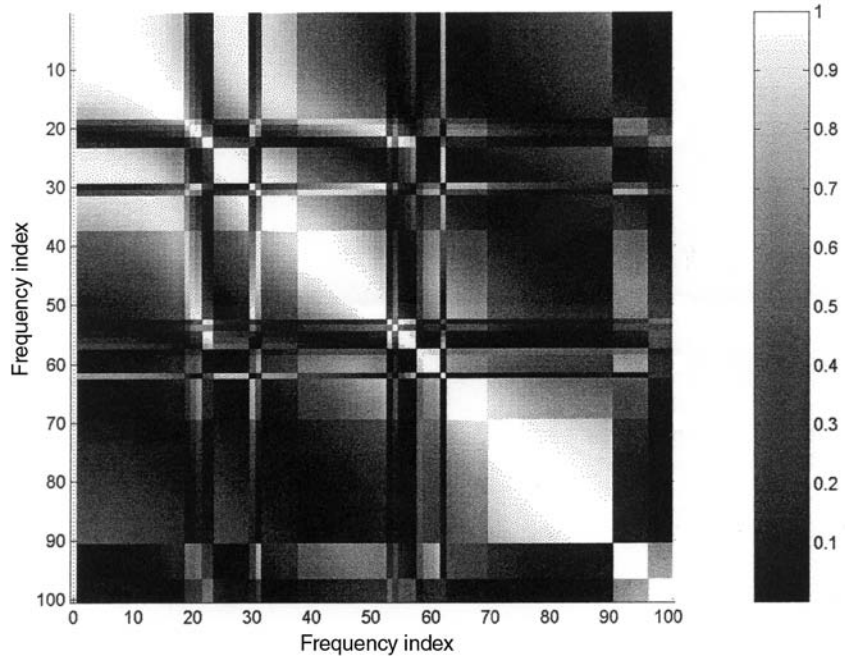


Figure 2 RVAC matrix.

$$\mathrm{FDAC}(\omega_A, \omega_X, l) = \frac{\mathbf{H}_X(\omega_X)_l^{\mathrm{T}} \mathbf{H}_A(\omega_A)_l}{\left|\mathbf{H}_X(\omega_X)_l^{\mathrm{T}} \mathbf{H}_X(\omega_X)_l\right| \quad \left|\mathbf{H}_A(\omega_A)_l^{\mathrm{T}} \mathbf{H}_A(\omega_A)_l\right|}$$

where $\mathbf{H}_A(\omega_A)$ is the analytical FRF at any analytical frequency, ω_A, and $\mathbf{H}_X(\omega_X)$ is the experimental FRF at any experimental frequency, ω_X.

Using experimental FRFs converted to real values, the FDAC is calculated as the cosine of the angle between the FRF column vectors, with values between -1 and 1, to take into account the phase relation between the FRF vectors. Note that the original version of FDAC, still used in many publications, had the numerator squared, like the MAC, and was thus insensitive to the phase lag between the FRFs. A typical FDAC matrix, calculated for the same data as **Figure 2**, free of frequency shifts, is illustrated in **Figure 3**. Lightly shaded zones indicate good frequency correlation.

While the FRAC is a coordinate correlation measure across all frequencies, the RVAC and FDAC coefficients represent the correlation between two sets of FRFs at specific frequencies across the full spatial domain. The RVAC cross-correlates each frequency line with every other measured frequency line, across the spatial domain. In a way, the MAC can be considered as the RVAC evaluated only at the natural frequencies.

The reader must be warned that in some publications the RVAC is loosely referred to as the FRAC and the first variant of FDAC is similar to the RVAC. The FRAC is sometimes compared to the COMAC, but the calculation is different. The modulus in the numerator is taken after the vector multiplication, like in the MAC, and not inside the summation, for each term of the scalar product, as is taken in the COMAC.

Correlation of response properties is a relatively new technique. Frequency response correlation coefficients must be applied with great care, using stiffness factors to adjust for frequency shifts and being aware of the approximations introduced by the inclusion of an arbitrary damping model in the analysis. A global frequency shift between the experimental and predicted FRFs leads to a biased correlation coefficient even if the FRFs are otherwise identical. Selection of frequency points is a key factor in any FRF-based correlation.

Using magnitudes or logarithm values instead of complex values can give better results, especially for lightly-damped structures whose FRFs exhibit large differences in the order of magnitude and the phase angles. When the damping updating is not of interest, it is useful to choose the frequency points away from resonances and antiresonances, though the largest discrepancies noticed visually occur in these regions. The FRAC coefficients are more sensitive to resonances and less sensitive to antiresonances heavily affected by modal truncation.

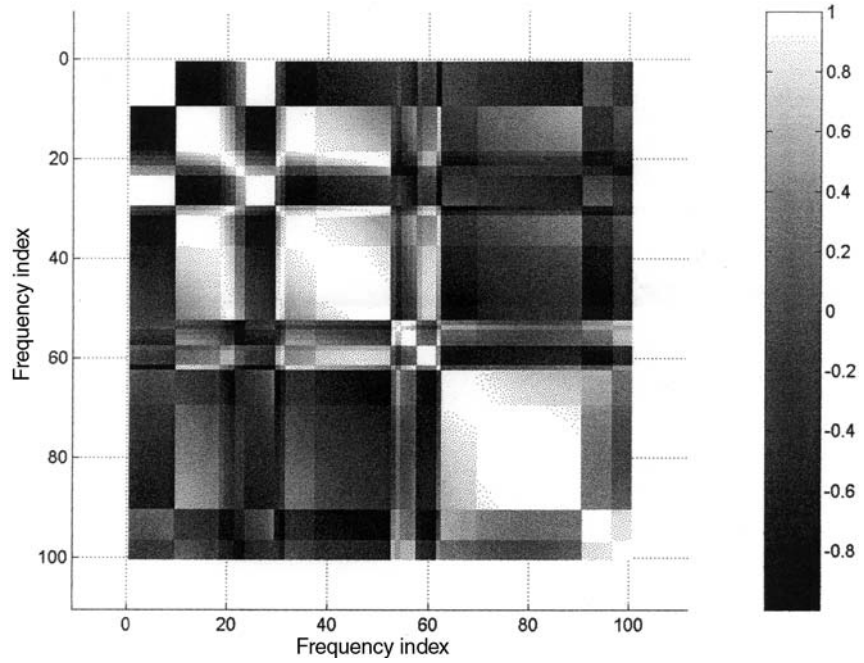


Figure 3 FDAC matrix.

The FRAC and RVAC are useful tools for examining the level of correlation of FRF data used in frequency-based model-updating procedures.

Comparison of Principal Response Functions

The singular value decomposition of the CFRF matrix is of the form:

$$\mathbf{A}_{N_f \times N_o N_i} = \mathbf{U}_{N_f \times N_o N_i} \mathbf{\Sigma}_{N_o N_i \times N_o N_i} \mathbf{V}^{\mathrm{H}}_{N_o N_i \times N_o N_i}$$

The columns of the matrix $\mathbf{U}$ are the left singular vectors. They contain the frequency information, being linear combinations of the original FRFs that form the columns of $\mathbf{A}$. The diagonal matrix of singular values, $\mathbf{\Sigma}$, incorporates the amplitude information. The columns of the matrix $\mathbf{V}$ are the right singular vectors. They represent the spatial distribution of the amplitudes from $\mathbf{\Sigma}$.

If $N_r = \mathrm{rank}(A)$, then the PRFs are defined as the first N_r left singular vectors of $\mathbf{A}$ scaled by their associated singular values. The matrix of the PRFs is thus:

$$(\mathbf{P}_r)_{N_f \times N_r} = (\mathbf{U}_r)_{N_f \times N_r} (\mathbf{\Sigma}_r)_{N_r \times N_r}$$

The plot of the left singular vectors of the CFRF matrix is used as the left singular vectors mode indicator function, or the U-Mode Indicator Function (UMIF), to locate frequencies of the dominant modes and to reveal multiple modes.

PRFs are left singular vectors, scale shifted in magnitude by multiplication with the corresponding singular value. They can be used to eliminate redundant, linearly dependent information and noise, and to estimate the rank and condition of the FRF test data.

The first six, twelve and twenty PRFs of a typical CFRF matrix are plotted in **Figures 4–6**. Inspection of such overlays with an increased number of PRFs reveals an upper group of six noise-free curves, more or less clearly separated from a lower group of 'noisy' curves. The number of distinct curves in the upper group is a good estimate of the rank of the CFRF matrix. Retaining only these PRFs, a rank-limited FRF matrix can be reconstructed by multiplying the truncated PRF matrix with the Hermitian of the matrix of corresponding right singular vectors.

Correlation coefficients similar to the FRAC and RVAC can be computed for the PRFs to characterize the average behavior of a structure in a given frequency band, especially in the medium frequency range.

See also: **Comparison of Vibration Properties**, Comparison of Spatial Properties; **Comparison of Vibration Properties**, Comparison of Modal Properties

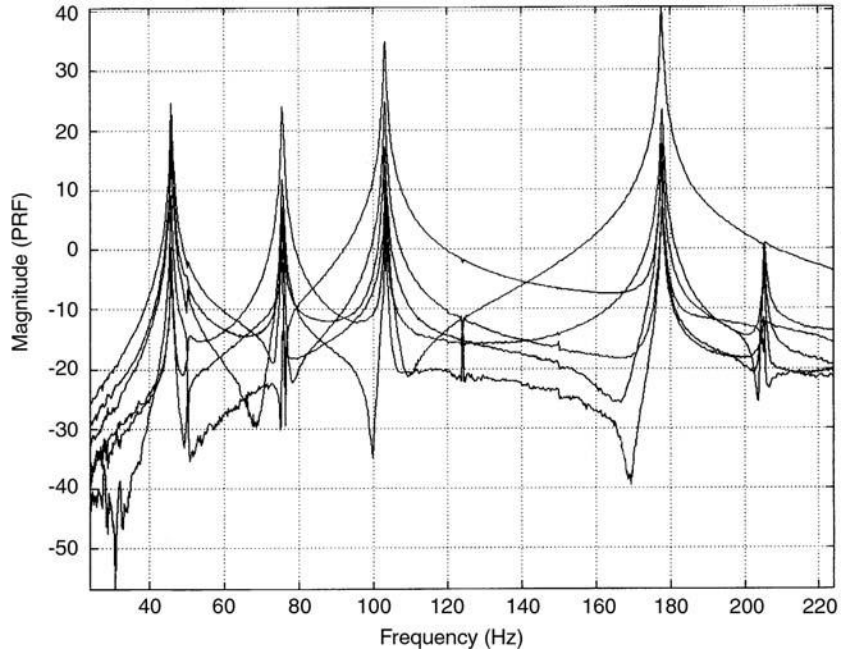


Figure 4 First six PRFs of a typical test CFRF matrix.

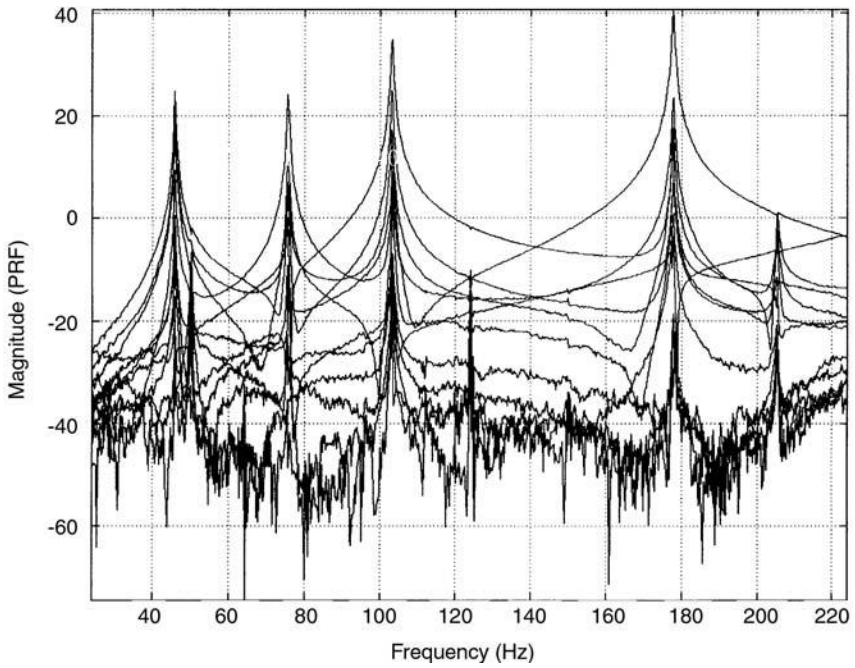


Figure 5 First twelve PRFs of the same matrix as in **Figure 4**.

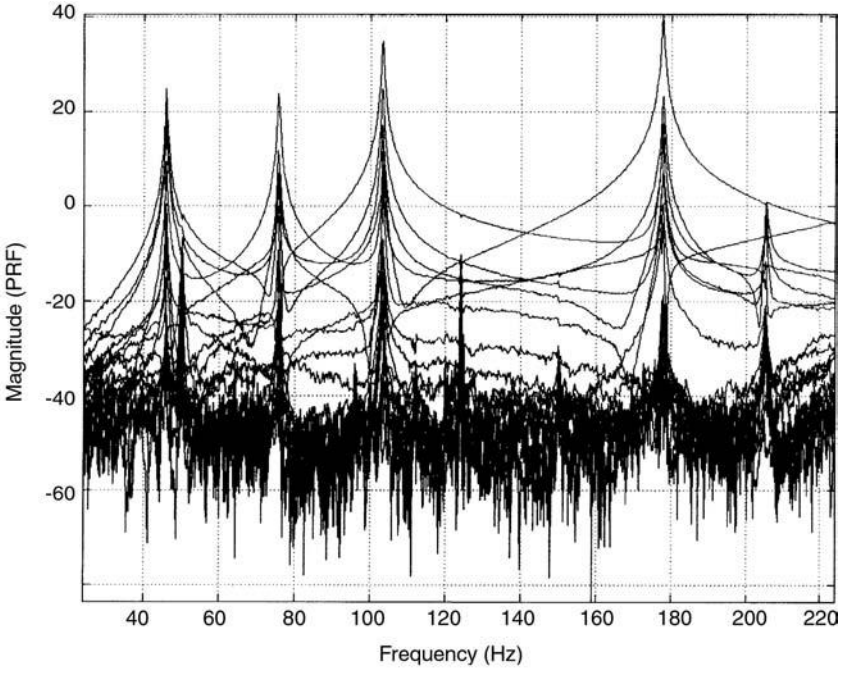


Figure 6 First twenty PRFs of the same matrix as in **Figures 4** and **5**.

Further Reading

Allemang RJ, Brown DL (1996) Experimental modal analysis. In: *Shock and Vibration Handbook*, 4th edn., pp. 21.1–21.74. McGraw Hill.

Avitable P (1999) *Modal Handbook*. Merrimack, NH: Dynamic Decisions Inc.

Ewins DJ (2000) *Modal Testing: Theory, Practice and Application*, 2nd edn. Taunton, UK: Research Studies Press.

Heylen W, Lammens S, Sas P (1997) *Modal Analysis Theory and Testing*. Leuven: K. U. Leuven.

Pascual R, Golinval JC, Razeto M (1997) A frequency domain correlation technique for model correlation and updating. In: *Proceedings of the 15th International Modal Analysis Conference*, Orlando, Florida, pp 587–592.

COMPONENT MODE SYNTHESIS (CMS)

See **THEORY OF VIBRATION, SUBSTRUCTURING**

COMPUTATION FOR TRANSIENT AND IMPACT DYNAMICS

D J Benson, University of California, San Diego, La Jolla, CA, USA

J Hallquist, Livermore Software Technology Corporation (LSTC), Livermore, CA, USA

Copyright © 2001 Academic Press

doi:10.1006/rwvb.2001.0006

Introduction

Transient and impact dynamics problems typically occur over short periods of time, ranging from nanoseconds to milliseconds, and have large deformations and rotations, high strain rates, and nonlinear boundary conditions. Specialized computational methods are used as an efficient solution to problems with this particular combination of characteristics. These methods have evolved from the finite element and finite difference methods used for solving quasistatic and dynamic structural problems. This article focuses on the differences between the computational methods used for transient and impact dynamics and those used to solve more traditional types of problems in structures and solid mechanics.

Typical applications of explicit codes include automotive crashworthiness and occupant protection, bird strike on jet engine fan blades and aircraft structures, industrial processes such as sheetmetal stamping, and defense applications involving ordnance design. To handle such a wide range of problems modern-day explicit codes have many capabilities, including a variety of contact algorithms, a large library of constitutive models for an extensive range of material behavior, equations of state for modeling the response of materials under high pressure, and various forms of adaptive remeshing.

Computational Methods for Transient and Impact Dynamics

Formulations that are intended for transient and impact dynamics share several characteristics that set them apart from methods intended to solve quasistatic and traditional dynamic problems for structures and solid mechanics. Most of the formulations for transient and impact dynamics can be derived from either the finite element or finite difference perspective. In fact, many of the algorithms used in finite element impact calculations by engineers were originally developed by physicists at the national laboratories for the finite difference formulations used to analyze nuclear weapons.

The global solution strategy typically uses:

1. Explicit time integration.
2. Lumped mass matrices.
3. Contact algorithms.
4. Algorithms for mapping solutions from distorted to undistorted meshes.

The elements have:

1. Linear interpolation functions.
2. Uniformly reduced (one-point) spatial integration.
3. Hourglass control to eliminate zero-energy modes.
4. A shock viscosity to resolve stress waves.

Global Solution Strategies

Time Integration

For typical structural dynamics problems, the step size is governed by the accuracy required by the engineer and the truncation error of the time integration method. In contrast, the mechanics of transient and impact calculations governs the time step size. For example, the time step size required to resolve the propagation of a stress wave is the amount of time the wave takes to cross an element. Therefore, computational formulations for impact problems minimize the cost of each time step by using explicit time integration methods.

The second-order accurate central difference method is the time integration method that is most commonly used in codes for impact calculations. Given the accelerations and displacements at time

step n and the velocity at $n + 1/2$, the solution is advanced in time to step $n + 1$ with second-order accuracy using the explicit formulas:

$$\mathbf{v}^{n+1/2} = \mathbf{v}^{n-1/2} + \Delta t^n \mathbf{a}^n \quad [1]$$

$$\mathbf{x}^{n+1} = \mathbf{x}^{n-1} + \Delta t^{n+1/2} \mathbf{v}^{n+1/2} \quad [2]$$

subject to the time step size limitation:

$$\Delta t \leq S \cdot \frac{2}{\omega_{\max}} \left(\sqrt{\zeta_{\max}^2 + 1} - \zeta_{\max} \right) \quad [3]$$

where S is a time step safety scale factor, $\omega_{\max}$ is the maximum natural frequency, and $\zeta_{\max}$ is the corresponding damping ratio.

The time step size is recalculated every time step because the maximum eigenvalue and the damping change with time. A simple bound:

$$\omega_{\max} \leq 2s \max_{e=1}^{\text{Elements}} \left(\frac{c_e}{l_e} \right) \quad [4]$$

on the maximum natural frequency is usually calculated instead of solving the eigenvalue problem, where s is a factor determined by the element formulation, l is a characteristic length for the element and c is the sound speed. This quantity is evaluated for every element, and the largest calculated value is mathematically guaranteed to be an upper bound on the actual value of $\omega_{\max}$ for the system.

Lumped Mass Matrix

A lumped mass matrix is used instead of the consistent mass matrix because:

1. Inverting a lumped mass matrix is trivial.
2. It requires less storage.
3. It eliminates spurious oscillations in the acceleration.

The accelerations at the nodes are calculated by solving Newton's equation:

$$\mathbf{a} = \mathbf{M}^{-1} \{ \mathbf{F}_{\text{external}} - \mathbf{F}_{\text{internal}} \} \quad [5]$$

where $\mathbf{F}_{\text{external}}$ is the vector of external applied loads due to boundary conditions and gravity, and $\mathbf{F}_{\text{internal}}$ is the vector of internal forces due to the stress in the structure.

The lumped mass matrix M is trivial to invert because it is diagonal. Each acceleration component is simply calculated as $a_i = F_i / M_{ii}$, which avoids the expense of solving a system of simultaneous linear equations, the single largest computational cost in traditional structural calculations.

Since minimizing the cost of each time step is a major concern in developing a formulation for transient and impact problems, the minimization of the storage requirements is also important because the cost of reading and writing information from a hard disk for a traditional finite element formulation is larger than the computational cost of an explicit time step. A lumped mass matrix therefore permits the solution of much larger problems than a consistent mass matrix for a fixed amount of memory.

When an impact applies a sudden load on the boundary of a finite element mesh, an acceleration field that is in the direction of the applied force is expected. A consistent mass matrix, which inertially couples the nodes, often results in an oscillatory acceleration field, with nodes accelerating in the direction opposite of the applied force. This error, which has been analyzed theoretically, can only be eliminated from impact calculations by using a lumped mass matrix.

Contact Algorithms

Impact calculations require contact algorithms to impose the contact forces required to keep exterior surfaces from passing through each other. Ideally, the penetration of surfaces through each other is held to zero by an exact enforcement of the contact constraints, but in practice this is difficult to achieve. Most of the current methods permit the surfaces to penetrate slightly, and the small violation of the contact constraint has no adverse effect for most problems. During the early years of computational mechanics, 'gap elements' required nodes on opposite surfaces to come in direct contact to prevent penetration. Large deformation problems have surfaces that undergo large relative slip, and therefore the nodes that were opposite each other at the beginning of the calculation are remote from each other by the end of it. Furthermore, during large slip, node-on-node contact is impossible to maintain unless the mesh moves relative to the material, which introduces its own complications.

Contact algorithms for impact calculations have two aspects that may be considered independently: calculating the contact locations, and calculating the forces to prevent penetration.

Calculating contact locations Contact is described in terms of a node and its location relative to the exposed edge or face of an element. In the remaining discussion, the exposed element boundary will be referred to as a 'surface segment'. When there are two distinct surfaces, they are called 'master' and 'slave' surfaces in the literature. Buckling calculations have a single surface which contacts itself as the

buckles form, and special contact search algorithms have been developed for handling this situation. Some contact algorithms are sensitive to which surface is designated the master surface, while symmetric methods, where the distinction is immaterial, are more robust.

The contact locations are calculated by a combination of global and incremental searches. Global searches are more expensive than the incremental searches, and are performed as infrequently as possible. A brute force search strategy for a global search checks for contact between each node on the slave surface and the surface segments on the master surface. The cost of this strategy is proportional to the number of slave nodes, N_n^s, times the number of master surface segments, N_s^m. Incremental searches check for contact between a slave node and the last surface segment it contacted. If they are no longer in contact, the search continues over the surface segments that are contained in the neighborhood of the last contacting segment. The cost of the incremental search is therefore proportional to N_n^s times the average number of surface segments in the incremental search (which is typically on the order of 4–10 for three-dimensional calculations). A typical computational strategy is to perform a brute force search at the start of a calculation to determine the initial contacts, and to update the contact points with the incremental searches for the duration of the calculation.

Global searches are performed many times during buckling calculations because the incremental searches frequently fail when a surface contacts itself. The brute force approach for the global search is not acceptable because of its cost, and a more sophisticated method, called a bucket sort, is used instead. The central idea is relatively simple, but the actual programming is complicated for an efficient, robust implementation. A bucket sort starts by dividing the space surrounding the mesh into the 'buckets' which are Δx by Δy by Δz. The size of the bucket is problem-dependent, and it is determined automatically by the sorting algorithm. Bucket *ijk* contains the region $[x_i,\ x_{i+1}]\times[y_j,\ y_{j+1}]\times[z_k,\ z_{k+1}]$ and

$$x_{i+1} = x_i + \Delta x \quad y_{j+1} = y_j + \Delta y$$
$$z_{k+1} = z_k + \Delta z \qquad [6]$$

The bucket *ijk* associated with a point (x, y, z) is calculated by:

$$i = \text{int}(x/\Delta x) + 1 \quad j = \text{int}(y/\Delta y) + 1$$
$$k = \text{int}(z/\Delta z) + 1 \qquad [7]$$

and a list of the nodes inside the bucket and contact segments that intersect it is stored. To determine which contact segments are close to a node in bucket *ijk*, only the contact segments listed in bucket *ijk* and in the 26 buckets surrounding *ijk* are considered. The cost of the global search is therefore proportional to the number of nodes and the average number of contact segments stored in a block of 27 buckets. Most of the contact segments within a bucket can be eliminated with simple checks and only a few require a detailed check. The cost of the global search is therefore reduced to a small multiple of the cost of the incremental search.

During the incremental search, the point of contact between a node and the surface segment is calculated in terms of the surface segments' isoparametric coordinates (ξ_1, ξ_2) by solving the closest point minimization problem:

$$J = \frac{1}{2}\left(\left(x^s - \sum x_k^m N_k(\xi_1,\xi_2)\right)^2 + \left(y^s - \sum y_k^m N_k(\xi_1,\xi_2)\right)^2 + \left(z^s - \sum z_k^m N_k(\xi_1,\xi_2)\right)^2\right) \qquad [8]$$

which generates two nonlinear equations. The node is potentially in contact if the isoparametric coordinates lie between -1 and $+1$, otherwise the search proceeds to the next segment. The depth of the penetration, δ, is:

$$\delta = -(\mathbf{x}^s - \mathbf{x}^m(\xi_1,\xi_2)) \cdot \mathbf{n}(\xi_1,\xi_2) \qquad [9]$$

where $\mathbf{n}$ is the exterior normal to the contact segment:

$$\mathbf{n}(\xi_1,\xi_2) = \frac{\frac{\partial \mathbf{x}^m}{\partial \xi_1} \times \frac{\partial \mathbf{x}^m}{\partial \xi_2}}{\left\|\frac{\partial \mathbf{x}^m}{\partial \xi_1} \times \frac{\partial \mathbf{x}^m}{\partial \xi_2}\right\|} \qquad [10]$$

Calculating the contact force The contact force acts along the surface normal to resist the interpenetration of the two surfaces and its magnitude may be calculated using a penalty method, Lagrange multipliers, or an augmented Lagrangian formulation.

The penalty method applies a force that is a function of the depth of penetration. In most codes, the force is linear, $F = k\delta\mathbf{n}$, which has the desirable property of conserving energy. The value of the penalty stiffness is a function of the material properties of the two contacting surfaces and the sizes of the elements at the contact point. While the idea of using a simple linear spring to resist penetration may seem overly simplistic, it works well in calculations ranging

from automobile crashworthiness simulations to the design of munitions.

Until recently, Lagrange multiplier methods were never used in impact calculations because they generate systems of coupled equations over the contacting surfaces in their standard form. Their primary advantage is the contact constraints are enforced exactly. Explicit Lagrange multiplier methods have recently been proposed which avoid this difficulty by introducing assumptions that decouple the equations. In their explicit form, Lagrange multiplier methods resemble a penalty method with a stiffness that is a function of the time step size, and the contact constraint is no longer enforced exactly. The time dependence of the surface stiffness with this method results in small errors in the conservation of energy.

Augmented Lagrangian methods try to combine the Lagrange multiplier method with the penalty method to gain the advantages of both. Although they have enjoyed some success in implicit formulations, they have yet to be used in codes for impact calculations.

Mapping Solutions from Distorted to Undistorted Meshes

The finite element or finite difference mesh distorts as the calculation progresses, which reduces the accuracy of the solution and the time step size. Eventually, the mesh may become too distorted to continue the calculation. A strategy for mapping the solution from the distorted mesh to an undistorted mesh is therefore required. At this time, the most popular strategies are periodic rezoning, arbitrary Lagrangian Eulerian (ALE) formulations, and Eulerian formulations.

While the three approaches differ considerably in their implementation, they possess many similarities. First, the qualities that are desired in the remapping schemes are the same: conservation of solution variables (e.g., momentum); second-order accuracy; and to avoid introducing oscillations into the solution. Second, the simulation time is fixed during the mapping process, i.e., it does not proceed simultaneously with the evolution of the solution variables, an approach that is referred to as 'operator splitting' in the literature on ALE and Eulerian formulations. Third, the functional representation of the solution variables on the old mesh is usually different (and of higher order) than the one used during the evolution of the solution. Fourth, the sequence of the mapping process is first, determine if a new mesh and a mapping are required; second, generate the new mesh; third, project the solution from the old mesh on to the new mesh, and fourth, restart the calculation with the new mesh.

Periodic rezoning The calculation is stopped periodically either by manual intervention or by the program itself (e.g., based on some measure of mesh distortion), and the solution is projected from the old mesh to a completely new mesh. The new mesh has nothing in common with the old mesh other than the shape of the material boundaries. Originally, the new mesh was generated by the analyst, but automatic mesh generation algorithms are advanced enough today that most of the new meshes are generated automatically. If the new mesh is generated by the analyst, the number of rezones in a calculation is typically on the order of 10, while automatic mesh generation schemes may redefine the mesh up to 100 times.

The rezoning scheme has to identify which elements of the old mesh overlap an element in the new mesh. Search algorithms that are similar to the global contact search algorithms are used, and they frequently account for a major part of the mapping cost.

Once the overlapping elements are found, the mapping of the solution usually proceeds in one of two ways. The generality of the periodic rezoning projection makes achieving both conservation and second-order accuracy very difficult. Either the solution is interpolated from the old mesh, which results in a loss of conservation, or a 'completely conservative' mapping scheme calculates the exact integral average for the new solution values. The completely conservative scheme is significantly more expensive and difficult to program than interpolating the new values, but for problems where strong solution gradients are present, it gives a superior answer.

ALE and Eulerian formulations ALE formulations permit the mesh to move relative to the material continuously as the solution evolves. The most common form of the ALE formulation is the simplified ALE or SALE formulation, which permits only one material in an element. This simplification means that the nodes on a material boundary can only move tangentially to the boundary, which limits its usefulness since elements near the boundaries are frequently the most distorted. Eulerian formulations use a spatially fixed mesh, and materials flow through it. An element may therefore contain several materials, as may a general ALE formulation.

Since the material moves relative to the mesh each time step (or sometimes every few time steps), the mapping procedure is performed thousands of times during a calculation. Speed and accuracy are therefore at a premium. While a first-order accurate mapping method may be adequate for 10 periodic rezones, it is too diffusive to be used thousands of

times during a calculation, and a minimum of second-order accuracy is a practical necessity. The mapping algorithms, also called transport or advection algorithms, are based on computational fluid dynamics algorithms for the Euler equations. Speed is obtained by keeping the same topology for the new and old meshes and limiting their relative displacement to some fraction of the element width.

Element Technology

Linear Interpolation Functions

The displacements, velocities, and accelerations are interpolated linearly and the stresses are piecewise constants in the elements used in transient and impact calculations. Their advantages over higher-order approximations are:

1. They possess symmetries and antisymmetries that reduce their computational cost relative to higher-order elements far more than a casual inspection would suggest.
2. Linear elements are very robust and are not prone to the singularities that occur in higher-order elements when the nodes are not uniformly spaced.
3. Linear interpolation simplifies the geometric calculations in the contact and mapping algorithms.
4. The zero-energy modes due to reduced integration are more readily suppressed in comparison to higher-order elements.
5. For a given nodal spacing, linear elements permit larger time steps than higher-order elements.

The primary disadvantage of linear elements relative to higher-order elements is that they are too stiff with full integration and too soft with reduced integration. Triangular and tetrahedral elements, in particular, are especially prone to locking with incompressible (plastic) flow for some meshes.

Uniformly reduced integration Only a single integration point is used for linear elements, which reduces the required central processing unit time and memory for the stress by factors of four and eight in two and three dimensions respectively. For quadratic elements, the speed gain would only be a factor of two to three.

Zero-energy mode control One byproduct of uniformly reduced integration is the occurrence of zero-energy or hourglass modes. The shape of the zero-energy modes is a function of the element geometry. Since a zero-energy mode does not produce a strain, no stress is generated to resist it, and the modes may grow without bound unless additional stiffness or damping terms are introduced to resist it. Conversely, since a mode produces no strain, it does not affect the accuracy of the stresses in the calculation. Problems only occur when the modes become large enough to turn the elements inside out or distort the contact geometry.

Zero-energy modes are suppressed by calculating their magnitude, and then adding a force that opposes them. Assuming that the magnitude of the mode, h, is calculated by:

$$h = \mathbf{H} \cdot \mathbf{v} \qquad [11]$$

the viscous force, $\mathbf{F}_h$, opposing the zero energy mode is:

$$\mathbf{F}_h = -ch\mathbf{H} = -c\mathbf{H} \otimes \mathbf{H}^{\mathrm{T}}\mathbf{v} \qquad [12]$$

or, if a stiffness form is used, the force is:

$$\mathbf{F}_h = -k \int_0^t h\mathbf{H}\, \mathrm{d}t \qquad [13]$$

and it is stored as a solution variable with incremental update performed each time step.

Shock viscosity Shocks propagate via a thermodynamically irreversible process and appear as jump discontinuities in the solution variables. Their accurate resolution and propagation are critical for solving high-speed impact problems. Oscillations will occur behind the jump in the stress unless some form of damping, which is called the shock viscosity, is included in the calculation. The physical thickness of a shock is typically on the order of microns, but in computational practice, they are smeared over three to six elements regardless of the element size. Although this introduces a large error in the shock width itself, the critical aspects of the shock, namely its speed and the stress states on either side of it, are accurately calculated.

The standard form of shock viscosity, q, a function of the volume strain rate, $\dot{\varepsilon}_v$, is:

$$q = -\rho \ell \dot{\varepsilon}_v (c_1 C + c_2 |\ell \dot{\varepsilon}_v|) \qquad [14]$$

and it differs little from the one originally introduced by von Neumann and Richtmeyer to solve shock problems in the design of the atom bomb (they did not include the linear term). The shock viscosity is treated like a contribution to the pressure for the calculation of the nodal forces.

Example Transient and Impact Calculations

The calculations shown in this section were performed with LS-DYNA3D, developed and marketed by Livermore Software Technology Corporation. It incorporates many advanced capabilities that are not available in the public domain version of DYNA3D, which was originally developed by John Hallquist. While the code runs on everything from PCs to massively parallel computers, the calculations shown here were performed on workstations.

Airbag Deployment

Transportation engineering is currently one of the largest applications areas for explicit finite element methods. Since the safety of the occupants is a major concern, accurate detailed modeling of the impacts between the occupants and the vehicle is a necessity. One of the more challenging modeling aspects is the deployment of the airbags in automobiles. In this example, shown in **Figure 1**, the airbag is initially folded into the center of the steering wheel. A control volume model of the combustion of the propellant located in the steering wheel hub determines the gas pressure in the bag during its inflation. Special element technology and material models were developed to model the dynamic response of the airbag material accurately.

Crashworthiness Simulations

The first crash simulation of a full vehicle model, including the suspension, tires, and other running gear, was performed with DYNA3D in 1986. It had a little over 4000 elements and required over 20 h of computing on the Cray-XMP supercomputer at Lawrence Livermore National Laboratory. Today, calculations with 10–100 times as many elements are routinely performed by automobile manufacturers to enhance the safety of modern vehicles and reduce the number of prototypes required for crashworthiness testing.

Many of the stronger components, such as the engine, are modeled as rigid bodies. In regions removed from the impact, analysts use a coarse computational mesh or rigid bodies to minimize the cost of the calculation. The impact area requires detailed modeling. For example, automobiles typically have thousands of spot welds which may fail during an impact, and each spot weld in the impact area is individually modeled.

As in the previous example, the largest challenge is modeling the contact during the crash. Most of the contact involves interior structural components which are not visible in **Figure 2**. For example, some of the interior sheetmetal structure is designed to buckle in an accordion mode to absorb the impact energy. The contact interactions are so extensive that all the surfaces on all the front-end components are treated as potential contact surfaces in the calculation.

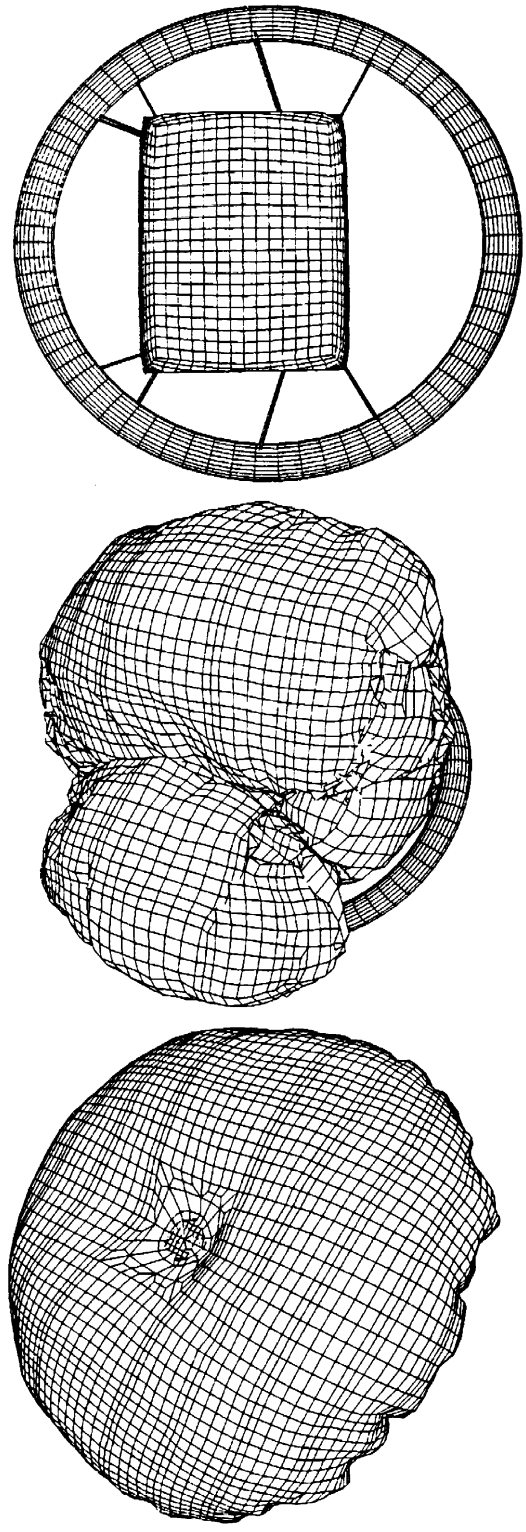


Figure 1 The simulation of the deployment of an airbag.

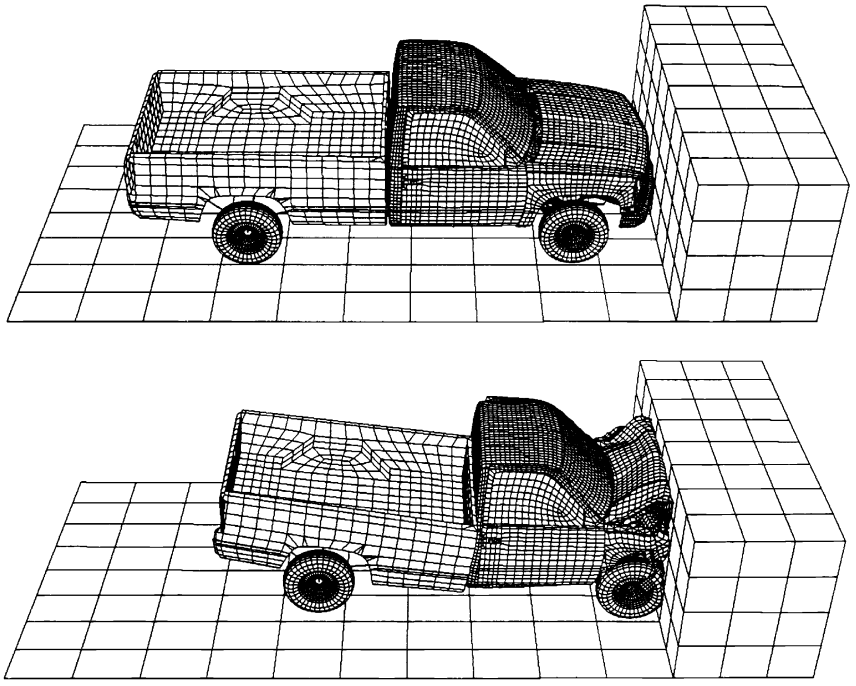


Figure 2 Crashworthiness analysis of a truck. Truck graphics courtesy of National Highway Traffic Safety Administration and National Crash Analysis Center.

Sheetmetal Forming

The buckling patterns, and therefore the energy absorbed by the structure, are very sensitive to the manufacturing process. Current crashworthiness simulations do not account for the plastic work and thinning caused by the sheetmetal forming process; however, they will do so in the near future.

Sheetmetal-forming simulations are used to aid in the design of the dies, which greatly reduces the time and cost to bring a product to market. Before simulations were possible, engineers designed the dies based on their experience and the dies were altered by tool and die makers on the production floor until they produced acceptable parts.

Explicit finite element methods are capable of simulating sheetmetal-forming processes with greater speed and accuracy than current implicit methods. Very fine meshes are required to resolve the sharp bends and the wrinkles caused by inadequate die designs. Adaptive mesh refinement automatically adds elements to the mesh (**Figures 3**

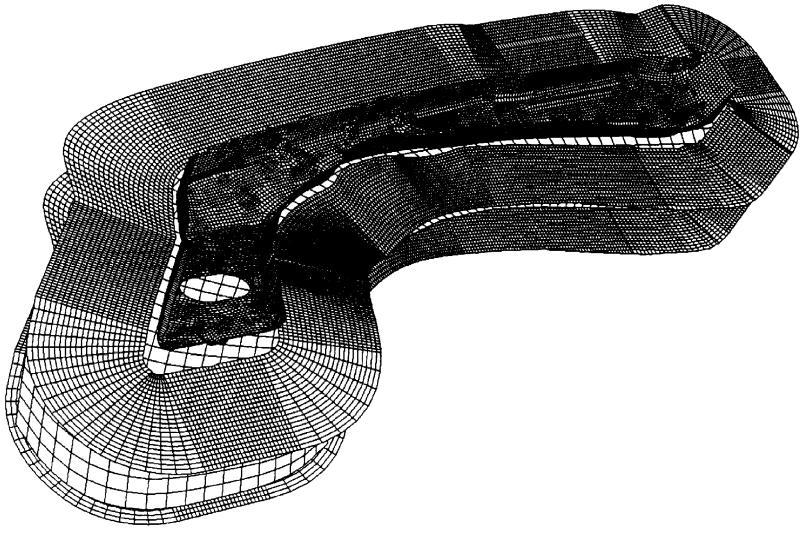


Figure 3 The initial configuration of the dies and the blank.

and 4) during the calculation. Various criteria, e.g., element distortion, determine when a single quadrilateral element should be split into four elements, adding one level of local mesh refinement. The maximum number of levels (typically two to four) is specified in the input file to prevent the adaptive algorithm from generating a mesh that is too large for the available computer resources.

In comparison to the 60 ms duration of a vehicle crash, the timescale of a metal-forming operation is extremely long. Since inertial forces are not important in metal forming, the density of the metal blank can be scaled up to permit the explicit finite element code to take larger time steps. Care must be taken with this strategy, since scaling the density to too large a value will create spurious inertial effects.

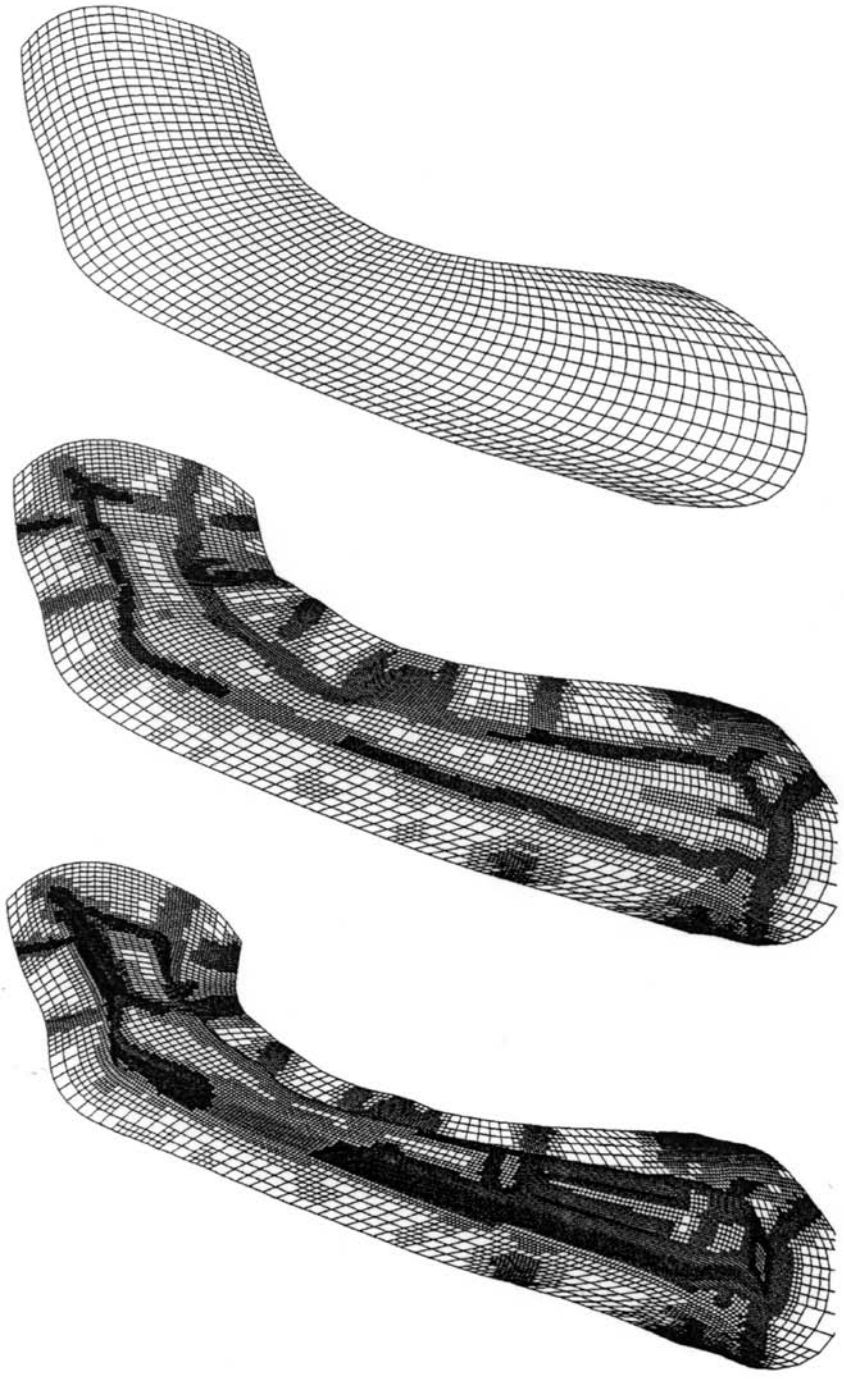


Figure 4 A sequence showing the deformation of the blank and its adaptive mesh refinement.

Nomenclature

c	speed of sound
h	magnitude of the mode
l	length
M	lumped mass matrix
q	shock viscosity
S	time step safety scale factor
δ	depth of penetration
ζ	damping ratio
ω	frequency

See also: **Computation for transient and impact dynamics**; **Commercial software**; **Crash**; **Discrete elements**; **Dynamic stability**; **Eigenvalue analysis**; **Finite difference methods**; **Finite element methods**; **Helicopter damping**; **Krylov-Lanczos methods**; **Shock**; **Ship vibrations**; **Structural dynamic modifications**; **Tire vibrations**; **Wave propagation**, Waves in an unbounded medium.

Further Reading

Bathe KJ (1995) *Finite Element Procedures*. Prentice Hall.

Belytschko TB and Hughes TJR (eds) (1983) *Computational Methods for Transient Analysis*, vol. 1. North-Holland.

Hughes TJR (1987) *The Finite Element Method, Linear Static and Dynamic Finite Element Analysis*. Prentice Hall.

Irons B and Ahmad S (1980) *Techniques of Finite Elements*. John Wiley.

Kikuchi N and Oden JT (1988) *Contact Problems in Elasticity: A Study of Variational Inequalities and Finite Element Methods*. SIAM.

Oden JT (1972) *Finite Elements of Nonlinear Continua*. McGraw-Hill.

Simo JC and Hughes TJR (1998) *Computational Inelasticity. Interdisciplinary Applied Mathematics*, vol. 7. Springer Verlag.

Zienkiewicz OC and Taylor RL (1991) *Finite Element Method*, vols 1 and 2, 4th edn. McGraw-Hill.

COMPUTATIONAL METHODS

See **BOUNDARY ELEMENT METHODS; COMMERCIAL SOFTWARE; COMPUTATION FOR TRANSIENT AND IMPACT DYNAMICS; CONTINUOUS METHODS; EIGENVALUE ANALYSIS; FINITE DIFFERENCE METHODS; FINITE ELEMENT METHODS; KRYLOV-LANCZOS METHODS; LINEAR ALGEBRA; OBJECT ORIENTED PROGRAMMING IN FE ANALYSIS; PARALLEL PROCESSING; TIME INTEGRATION METHODS**.

CONDITION MONITORING

See **DIAGNOSTICS AND CONDITION MONITORING, BASIC CONCEPTS; ROTATING MACHINERY, MONITORING.**

CONTINUOUS METHODS

C W Bert, The University of Oklahoma, Norman, OK, USA

Copyright © 2001 Academic Press

doi:10.1006/rwvb.2001.0009

Continuous methods of vibration analysis are applicable to continuous structural elements such as one-dimensional (1-D) members (strings, bars, beams, and columns), 2-D members (membranes, thin plates, and thin shells), and 3-D members (blocks, thick plates, and thick shells). These methods are called continuous to distinguish them from discrete methods, such as finite difference, collocation, finite element, transfer matrix, boundary element, differential quadrature, quadrature element, etc.

The present discussion is limited to linear vibration analysis; see **Nonlinear systems analysis**. Furthermore, since forced vibration of linear systems can always be expanded in terms of the free vibration modes (see **Modal analysis, experimental**, Parameter extraction methods), the present section is limited to free vibration. Finally, although continuous methods can be applied to damped as well as undamped systems, damping introduces considerable complexity and thus is omitted here. In summary, the present section treats free vibration of undamped, linear, continuous systems.

All problems of the present class lead to self-adjoint eigenvalue problems (see **Eigenvalue analysis**). It is rather dry and not very informative to discuss the general free vibration problem, so here a model problem has been selected. It is the axial vibration of a slender bar of rectangular cross-section gently tapered in planform but uniform in thickness so that 1-D theory is adequate.

In order to provide a yardstick with which to evaluate the various approximate methods, first the model problem is solved exactly in closed form. Then it is solved using the ordinary Rayleigh method, the noninteger-power Rayleigh method, the Ritz (or Rayleigh–Ritz) method, several versions of the complementary energy method, and the Galerkin method. All of the approximate methods mentioned yield upper bounds for the fundamental frequency. Thus, several methods of estimating the lower bound are also presented. Finally, the problem is solved by an alternative exact method, the differential transformation method.

Formulation and Classical Solution

Free vibration problems may be formulated in the form of integral equations or differential equations. The latter formulation is more convenient and is used here. The governing differential equation of motion may be obtained using a differential element or by Hamilton's principle. For the present model problem, the result is:

$$\frac{\partial}{\partial x}\left(A(x)E(x)\frac{\partial u}{\partial x}\right) - m(x)\frac{\partial^2 u}{\partial t^2} = 0 \qquad [1]$$

where $A(x)=$ cross-sectional area, $E(x)=$ elastic modulus, $m(x)$ = mass per unit length, $t=$time, $u=$axial displacement, and $x=$axial position coordinate.

The classical boundary conditions associated with the problem are:
Fixed end:

$$u(x_B, t) = 0 \qquad [2a]$$

Free end:

$$A(x_B)E(x_B)\frac{\partial u}{\partial x}(x_B, t) = 0 \qquad [2b]$$

where x_B may be either 0 or L.

In the present case:

$$A(x) = 2A_0 x/L \qquad [3]$$

$$m(x) = 2m_0 x/L \qquad [4]$$

and E is constant. Here A_0 and m_0 are constants (reference area and reference mass, respectively), and L is the length of the bar.

To be specific, the free end, boundary condition [2b], is taken to be at $x = 0$ and the fixed end, boundary condition [2a], is taken to be at $x = L$.

Since eqn [1] is linear, the axial displacement can be expressed as:

$$u(x, t) = W(X)e^{i\omega t} \qquad [5]$$

where W is called the mode shape, $X \equiv x/L$, and ω is the natural frequency. Then the governing equation of motion can be expressed as:

$$\frac{d}{dX}\left(X\frac{dW}{dX}\right) + k^2 XW = 0 \qquad [6]$$

where $k^2 \equiv (m_0 L^2/A_0 E)\omega^2$. The associated boundary conditions are:

$$\lim_{X\to 0}[(AE/L)(dW/dX)] = 0$$

or:

$$\lim_{X\to 0}[X\,dW/dX] = 0 \qquad [7]$$

and:

$$W(1) = 0 \qquad [8]$$

Eqn [6] can be rewritten as:

$$\frac{d^2 W}{dX^2} + \frac{1}{X}\frac{dW}{dX} + k^2 W = 0 \qquad [9]$$

which is easily identified as the Bessel equation of rank 0.

The general solution for the mode shape is:

$$W(X) = D_1 J_0(kX) + D_2 Y_0(kX) \qquad [10]$$

where D_1, D_2 are constants and J_0 and Y_0 are zero-

order Bessel functions of the first and second kind. The dimensionless frequency is given by:

$$\bar{\omega} = k = \left(m_0 L^2 / EA_0\right)^{1/2} \omega \qquad [11]$$

For the present boundary conditions, $D_2 = 0$ and the various zeros of the Bessel function of the first kind and of rank zero, $J_0(\bar{\omega}) = 0$ are the values of $\bar{\omega}$ for the corresponding mode shapes. The five lowest values are:

$$\bar{\omega} = 2.4048,\ 5.5201,\ 8.6537,\ 11.7915,\ 14.9309$$

Ordinary Rayleigh Method

This method, sometimes known as the Rayleigh quotient, is based on equating the maximum potential and maximum kinetic energies. The maximum potential energy stored in each cycle of vibration is:

$$\begin{aligned} U_{\max} &= \frac{1}{2L}\int_0^1 EA(X)\left(\frac{\mathrm{d}W}{\mathrm{d}X}\right)^2 \mathrm{d}X \\ &= (EA_0/L)\int_0^1 X\left(\frac{\mathrm{d}W}{\mathrm{d}X}\right)^2 \mathrm{d}X \end{aligned} \qquad [12]$$

The maximum kinetic energy due to the vibration is:

$$\begin{aligned} T_{\max} &= \frac{\omega^2 L}{2}\int_0^1 m(X)[W(X)]^2 \mathrm{d}X \\ &= m_0 \omega^2 L \int_0^1 X W^2 \mathrm{d}X \end{aligned} \qquad [13]$$

Equating $U_{\max}$ and $T_{\max}$ yields the Rayleigh quotient:

$$\bar{\omega}^2 = \frac{m_0 L^2}{EA_0}\omega^2 = \frac{\int_0^1 X(\mathrm{d}W/\mathrm{d}X)^2 \mathrm{d}X}{\int_0^1 X W^2 \,\mathrm{d}X} \qquad [14]$$

which is an upper-bound approximation for $\bar{\omega}^2$.

A simple polynomial approximation for the fundamental mode shape which satisfies eqns [7] and [8] is:

$$W(X) = C\left(1 - X^2\right) \qquad [15]$$

where C is a constant.

Using this expression in eqn [14] yields $\bar{\omega}^2 = 6$ or $\bar{\omega} = 2.4495$, which is approximately 1.9% higher than the exact solution.

The mode shape function for a prismatic (uniform cross-section) beam is simply:

$$W(X) = C\cos(\pi X/2) \qquad [16]$$

which also satisfies the boundary conditions [7] and [8] of the present problem. Substitution of eqn [16] into eqn [14] yields $\bar{\omega} = 2.4146$, which is only approximately 0.41% higher than the exact value.

Noninteger Power Rayleigh Method

It was first suggested by Rayleigh and much later further developed by Robert Schmidt (1981) that the power of X in the mode shape function need not be an integer, i.e.:

$$W(X) = C(1 - X^n);\ n > 0 \qquad [17]$$

Substituting mode shape [17] into the Rayleigh quotient [14] yields an expression for $\bar{\omega}^2$ that is a function of n only:

$$[\bar{\omega}(n)]^2 = \frac{n}{1 - \dfrac{4}{n+2} + \dfrac{1}{n+1}} \qquad [18]$$

Since the Rayleigh quotient is an upper bound to the natural frequency (here the fundamental frequency), then the value of n which minimizes $\bar{\omega}(n)$ is the best or optimal value. In the present problem, the optimal value of n is 1.414, which yields $\bar{\omega}_{\min} = 2.4142$, only 0.39% higher than the exact solution. The optimization involved in this approach led Laura and Cortinez to call it the 'optimized Rayleigh or Galerkin method'.

Complementary Energy Method

Bhat used the concept of a d'Alembert reversed effective force and the principle of complementary energy. The reversed effective force at a dimensionless position X can be expressed as:

$$P(X) = -\omega^2 L \int_0^X m(X) W(X)\,\mathrm{d}X + C_1 \qquad [19]$$

where C_1 is a constant of integration, which is zero in the present problem since the bar is free at $X = 0$.

The maximum complementary energy can be expressed as:

$$U^{C}_{\max} = \frac{L}{2}\int_0^1 \frac{[P(X)]^2}{EA(X)}\,dX \qquad [20]$$

Now equating $T_{\max}$ and $U^{C}_{\max}$ from eqns [13] and [20] and using $P(X)$ from eqn [19], one obtains the following result for the square of the natural frequency for general $A(X)$ and $m(X)$ distributions:

$$\omega^2 = \frac{E}{L^2}\frac{\int_0^1 m(X)[W(X)]^2\,dX}{\int_0^1 \frac{\left[\int_0^X m(X)W(X)\,dX\right]^2}{A(X)}\,dX} \qquad [21]$$

For the model problem in which $A(X)$ and $m(X)$ are expressed as in eqns [3] and [4], respectively, eqn [21] becomes:

$$\bar{\omega}^2 = \frac{\int_0^1 X[W(X)]^2\,dX}{\int_0^1 \frac{\left[\int_0^X XW\,d\right]^2}{X}\,dX} \qquad [22]$$

Using eqn [15] for the mode shape in eqn [22], one obtains $\bar{\omega} = 2.4121$, which is only 0.30% higher than the exact value. The considerable reduction in error from 1.9% for the ordinary Rayleigh method to 0.30% for the complementary energy method, using the same mode shape function for each, is due to the avoidance of derivatives of W in eqn [22].

Noninteger Power Complementary Energy Method

Bert *et al.* combined Bhat's version of the complementary energy method (see preceding subsection) with the use of a noninteger power mode shape function. Thus, using mode shape function [17] in eqn [22], one obtains:

$$\bar{\omega}^2 = \frac{n^2/(n+1)}{\dfrac{1}{(n+2)^2} - \dfrac{2}{n+4} + \dfrac{n+2}{8}} \qquad [23]$$

The optimal value of n is 1.40, which yields $\bar{\omega} = 2.4055$, only 0.029% higher than the exact value.

Rayleigh–Ritz or Ritz Method

Rayleigh suggested the use of multiple shape functions in conjunction with application of Hamilton's principle to obtain a set of N homogeneous linear algebraic equations in the coefficients. According to Crandall, this idea was implemented by Ritz in 1909 and thus we have two alternative names for the same method: Rayleigh–Ritz or Ritz method.

The advantages of this method are twofold:

- more accurate determination of the fundamental natural frequency and its associated mode shape
- determination of higher natural frequencies and their associated mode shapes

In practice, if one wants to determine N natural frequencies, one must use N shape functions. Let:

$$W(X) = \sum_{i=1}^{N} C_i W_i(X) \qquad [24]$$

Also, define the Lagrangian energy functional as:

$$I \equiv \lambda T'_{\max} - U_{\max} \qquad [25]$$

where $T'_{\max} \equiv T_{\max}/\bar{\omega}^2$ and $\lambda \equiv \bar{\omega}^2$.

Then application of Hamilton's principle leads to the following $N \times N$ set of homogeneous linear algebraic equations in the coefficients C_i:

$$\partial I/\partial C_i = 0; \quad i = 1, 2 \ldots N \qquad [26]$$

As an example, we consider the same tapered bar problem analyzed previously. Now we take the case of $N = 2$ as an example, using $W_1 = \cos(\pi X/2)$ and $W_2 = \cos(3\pi X/2)$. This leads to:

$$\begin{bmatrix} k_{11} - \lambda m_{11} & k_{12} - \lambda m_{12} \\ k_{21} - \lambda m_{21} & k_{22} - \lambda m_{22} \end{bmatrix} \begin{Bmatrix} C_1 \\ C_2 \end{Bmatrix} = \begin{Bmatrix} 0 \\ 0 \end{Bmatrix} \qquad [27]$$

where:

$$k_{ij} \equiv \int_0^1 X\left(\frac{dW_i}{dX}\right)\left(\frac{dW_j}{dX}\right)dX$$
$$m_{ij} \equiv \int_0^1 XW_iW_j\,dX \qquad [28]$$

To guarantee a nontrivial solution of eqn [27], the determinant of the coefficients must be set equal to zero. This leads to an $N \times N$ determinant which is an

N-degree polynomial equation in λ. In the present case, this is the following quadratic equation:

$$(m_{11}m_{22} - m_{12}^2)\lambda^2 - (k_{11}m_{22} + k_{22}m_{11} - 2k_{12}m_{12})\lambda + k_{11}k_{22} - k_{12}^2 = 0 \quad [29]$$

The results are:

$$\bar{\omega}_1 = 2.4062, \quad \bar{\omega}_2 = 5.5298$$

The value of $\bar{\omega}_1$ is only 0.058% higher than the exact value. This is a considerable improvement over the one-term solution (Rayleigh method) which was 0.41% higher than the exact value. The second harmonic value $\bar{\omega}_2$ could not be obtained at all from the one-term solution. Here it is not only obtained, but its value is only 0.175% higher than the exact value.

Galerkin Method

According to Crandall, the Galerkin method was originated in 1915 by B.G. Galerkin and it is based on minimizing the error in an assumed-mode method by making the error orthogonal to a weighting function. In this method, the weighting function is taken to be the function W_i itself. The method can have a one-term solution and the result is identical to eqn [14] for the ordinary Rayleigh method. It can also be implemented as a multiterm solution form and then it coincides with the Rayleigh–Ritz method. In fact, some texts do not distinguish between the Rayleigh, Rayleigh–Ritz, and Galerkin methods.

So long as the Galerkin method is equivalent to the Rayleigh or Rayleigh–Ritz method, only the geometric boundary conditions need be satisfied by the trial function(s). However, it is cautioned that the resulting Galerkin-method equations are not always equivalent to the Rayleigh or Rayleigh–Ritz equations and in this general case, all of the boundary conditions, force type (such as eqn [2a]) as well as geometric type (such as eqn [2b]) must be satisfied. Furthermore, the upper-bound property of the Rayleigh and Rayleigh–Ritz methods no longer holds.

Lower-bound Approximations

In many practical problems of free vibration, it may be more important to obtain a lower-bound approximation to a given natural frequency than an upper bound. A popular lower-bound approximation is known as the enclosure theorem. If the governing ordinary differential equation is expressed as:

$$L(W) - \lambda MW = 0 \quad [30]$$

where L is a differential operator, M is a function of position X, and $\lambda(\equiv \bar{\omega}^2)$ is the eigenvalue. Now λ^* is defined as:

$$\lambda^* \equiv \frac{L(W)}{MW}; \quad 0 \le X \le 1 \quad [31]$$

Then, the theorem says that λ is contained in the interval:

$$\lambda^*_{\min} \le \lambda \le \lambda^*_{\max}$$

In the present problem:

$$L(W) = \frac{\mathrm{d}}{\mathrm{d}X}\left(X\frac{\mathrm{d}W}{\mathrm{d}X}\right); \quad MW = -XW$$

First, let's consider the trigonometric solution, eqn [16]. Then eqn [31] gives:

$$\lambda^* = \frac{\pi}{2}\left[\frac{\pi}{2} + \frac{1}{X}\tan\frac{\pi X}{2}\right]$$

and:

$$\lambda^*_{\min} = \lambda^*\big|_{X=0} = \frac{\pi}{2}\left(\frac{\pi}{2} + 1\right) \text{ or } \bar{\omega}_{\min} = 2.0095$$

This gives a very wide spread from $\bar{\omega}_{\min}$ to $\bar{\omega}_{\max}$ (2.0095–2.4146).

Now let's take a look at the power function solution in eqn [17]. Eqn [31] gives:

$$\lambda^* = \frac{n^2X^{n-2}}{1 - X^n}$$

and:

$$\lambda^*_{\min} = \left.\frac{n^2X^{n-2}}{1 - X^n}\right|_{X=0}$$

It is noted that if $n > 2$, $\lambda^*_{\min} = 0$ and if $n < 2$, $\lambda^*_{\min}$ increases without limit. Thus, it is clear that the only usable value of n in so far as the enclosure theorem is concerned is $n = 2$. Then $\lambda^*_{\min} = 4$ or $\bar{\omega}_{\min} = 2.0000$, not as good as the previous lower bound.

Bert found that the following equation, proposed by Ku, was an excellent predictor of the lower bound for the buckling load of a column:

$$\bar{P}_{LB} = \bar{P}_R - \left[\bar{P}_R\left(\bar{P}_R - \bar{P}_T\right)\right]^{1/2} \qquad [32]$$

where $\bar{P}$ denotes the dimensionless critical load and subscripts R and T denote Rayleigh and Timoshenko, respectively. The vibrational analog of eqn [32] is:

$$\bar{\lambda}_{LB} = \bar{\lambda}_R - \left[\bar{\lambda}_R\left(\bar{\lambda}_R - \bar{\lambda}_C\right)\right]^{1/2} \qquad [33]$$

where $\bar{\lambda}(\equiv\omega^2)$ is the dimensionless eigenvalue, and subscripts R and C denote the Rayleigh quotient (eqn [14]) and the complementary energy quotient (eqn [22]). For the present case, disregarding the difference between $n = 1.41$ and $n = 1.40$, $\bar{\omega}_R = 2.4142$ and $\bar{\omega}_c = 2.4055$. Then eqn [33] gives $\bar{\lambda}_{\mathrm{LB}} = 5.7435$ or $\bar{\omega}_{\mathrm{LB}} = 2.3966$, which is only 0.34% below the exact value.

Differential Transformation Method

This relatively new technique is an exact series solution of a linear or nonlinear differential equation. The method is based on the Taylor series expansion of an arbitrary function $w(x)$ at a point $x = 0$:

$$w(x) = \sum_{k=0}^{\infty}\left(x^k/k!\right)\left[\frac{\mathrm{d}^k w}{\mathrm{d}x^k}\right]_{x=0} \qquad [34]$$

The differential transformation (DT) of $w(x)$ is defined as:

$$W(k) = \frac{1}{k!}\left[\frac{\mathrm{d}^k w}{\mathrm{d}x^k}\right]_{x=0} \qquad [35]$$

where the capital letter denotes the DT of the same letter in lower case. The inverse DT is:

$$w(x) = \sum_{k=0}^{\infty} x^k W(k) \qquad [36]$$

The governing differential equation for the mode shape of an axially vibrating, linearly tapered bar is rewritten from eqn [9] as:

$$xw_{,xx} + w_{,x} + \bar{\omega}^2 xw = 0; \quad 0 \le x \le 1 \qquad [37]$$

where $(\,)_{,x}$ denotes $\mathrm{d}(\,)/\mathrm{d}x$, etc.

To take the differential transform of eqn [37], the table of transforms in **Table 1**, based on eqns [35] and [36], is necessary.

Then the DT of eqn [37] is:

$$\sum_{j=0}^{k}\delta(j-1)(k-j+1)(k-j+2)W(k-j+2) + (k+1)W(k+1) + \bar{\omega}^2\sum_{j=0}^{k}\delta(j-1)W(k-j) = 0 \qquad k = 0, 1\ldots\infty \qquad [38]$$

The boundary conditions are eqns [8] and [7], which in the present notation are:

$$w(1) = 0; \quad w_{,x}(0) = 0 \qquad [39]$$

and transform to:

$$\sum_{k=0}^{\infty} W(k) = 0; \quad \sum_{k=0}^{\infty} kx^{k-1}W(k) = W(1) = 0 \qquad [40a, b]$$

To illustrate the procedure for finding the eigenvalues, with the use of eqn [40b], eqn [38] yields:

$$W(2) = \frac{-1}{4}\bar{\omega}^2 W(0), \quad W(3) = W(5) = 0, \quad W(4) = \frac{1}{64}\bar{\omega}^4 W(0) \qquad [41]$$

Substitution of eqns [41] into eqn [40a] yields:

$$\left(1 - \frac{1}{4}\bar{\omega}^2 + \frac{1}{64}\bar{\omega}^4\right)U(0) = 0 \qquad [42]$$

Table 1 Table of differential transforms (DT)

Original function	DT
$f(x)g(x)$	$\sum_{j=0}^{k} F(j)\,G(k-j)$
$w_{,x}(x)$	$(k+1)W(k+1)$
$w_{,xx}(x)$	$(k+1)(k+2)W(k+2)$
x	$\delta(k-1) = \begin{cases} 1 & \text{if } k = 1 \\ 0 & \text{if } k \neq 1 \end{cases}$

which has roots ±2.8284. The positive real root (2.824) is the eigenvalue for $N = 5$. To obtain more accurate results more terms are needed and the results are tabulated in **Table 2**.

It is clear that more terms are needed to calculate the second mode than the first and that convergence is from above.

A Two-dimensional Problem and a Galerkin Solution

As the model two-dimensional problem, a uniform thickness, thin, rectangular plate made of isotropic material and clamped on all four edges is considered. For these particular boundary conditions there is no known closed-form solution. In fact, the only set of boundary conditions for which there are closed-form solutions is simply supported on all four sides.

The plate has a rectangular planform and the origin of the Cartesian coordinate system is in the midplane of the plate and at its center. The plate is of length 2a and 2b in the x and y directions and its thickness (in the z direction) is h. For small-amplitude, out-of-plane, free vibration, the governing partial differential equation is:

$$-D\left(w_{,xxxx} + 2w_{,xxyy} + w_{,yyyy}\right) = \rho h w_{,tt} \qquad [43]$$

where $w(x, y, t)$ is the plate deflection, ρ is the density of the plate material, and $(\,)_{,tt} \equiv \partial^2(\,)/\partial t^2$, etc. The flexural rigidity, denoted by D, is given by:

$$D = \frac{Eh^3}{12(1-\nu^2)} \qquad [44]$$

Since the problem is linear, the deflection can be assumed to be the product of the mode shape $W(x, y)$ and a harmonic time function:

$$w(x, y, t) = W(X, Y)\mathrm{e}^{i\omega t} \qquad [45]$$

where $X \equiv x/a$ and $Y \equiv y/b$.

Then the governing equation becomes:

$$W_{,XXXX} + 2\lambda^2 W_{,XXYY} + \lambda^4 W_{,YYYY} - \rho h a^4 \omega^2 W = 0 \qquad [46]$$

where $\lambda \equiv b/a$ is the plate aspect ratio.

There are three popular mode shapes used in connection with Galerkin or Rayleigh–Ritz analyses of plate vibration:

1. Polynomial. This is the simplest and it turns out to be the most accurate for the all-clamped-edge conditions considered here.
2. Trigonometric. This gives accurate results for all simply supported edge conditions but a very poor result for the present case.
3. Beam functions. These are the exact solutions for free vibration of a uniform beam, but the expressions are unwieldy. They have the advantage of being able to approximate higher modes, not just the fundamental one.

Here, for simplicity and accuracy, the polynomial form is chosen:

$$W(X, Y) = W_0\left(1 - X^2\right)^2\left(1 - Y^2\right)^2 \qquad [47]$$

The Galerkin integral then becomes:

$$\int_{-1}^{1}\int_{-1}^{1}\left(W_{,XXXX} + 2\lambda^2 W_{,XXYY} + \lambda^4 W_{,YYYY} - \frac{\rho h a^4 \omega^2}{D} W\right) \times \left(1 - X^2\right)^2\left(1 - Y^2\right)^2 \mathrm{d}X\,\mathrm{d}Y = 0 \qquad [48]$$

Performing the integration yields:

$$\bar{\omega} \equiv a^2(\rho h/D)^{1/2}\omega = \left[31.5\left(1 + \lambda^4\right) + 18\lambda^2\right]^{1/2} \qquad [49]$$

Dimensionless fundamental frequencies obtained by various methods for the case of a square plate ($\lambda = 1$) are listed in **Table 3**.

Table 2 Dimensionless frequencies obtained by the *DT* technique versus number of terms, *N*

Mode	N	*5*	*7*	*9*	*10*	
1st		2.8284	2.3916	2.4056	2.4048	(exact value)
	N	*10*	*12*	*20*	*21*	
2nd		5.9893	5.4059	5.5183	5.5201	(exact value)

Plate 1 Active Control of Civil Structures. Actuator used in the Hybrid Mass Damper System in INTES.



Plate 2 Active Control of Civil Structures. Variable Stiffness System used in Kajima Research Laboratory.

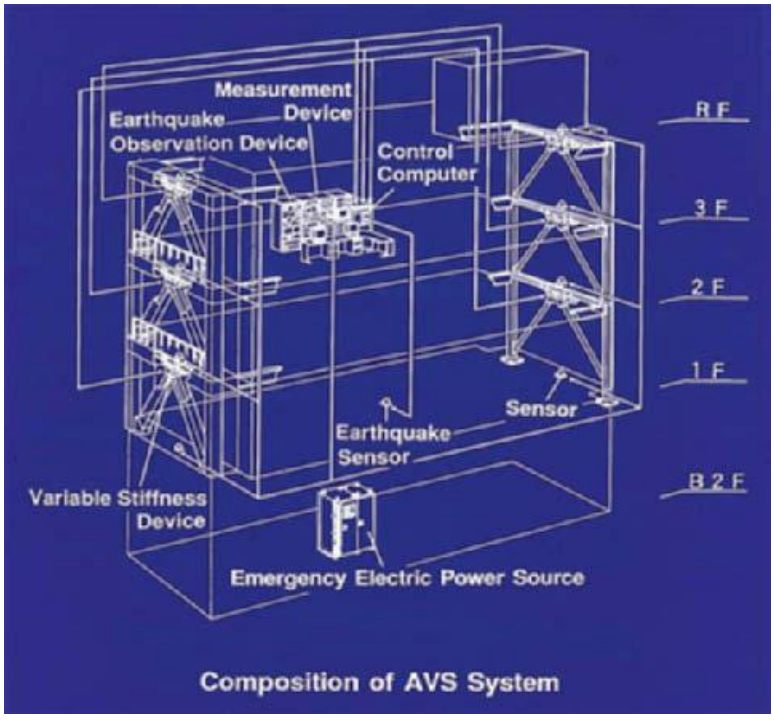
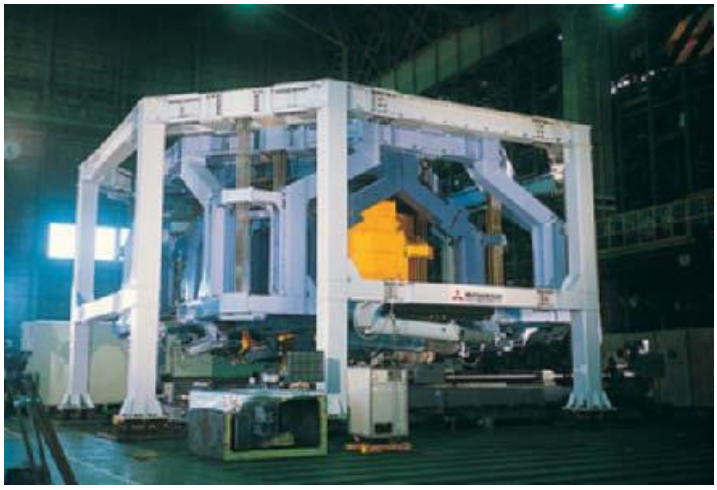


Plate 3 Active Control of Civil Structures. The Hybrid Mass Damper used in the Landmark Tower.



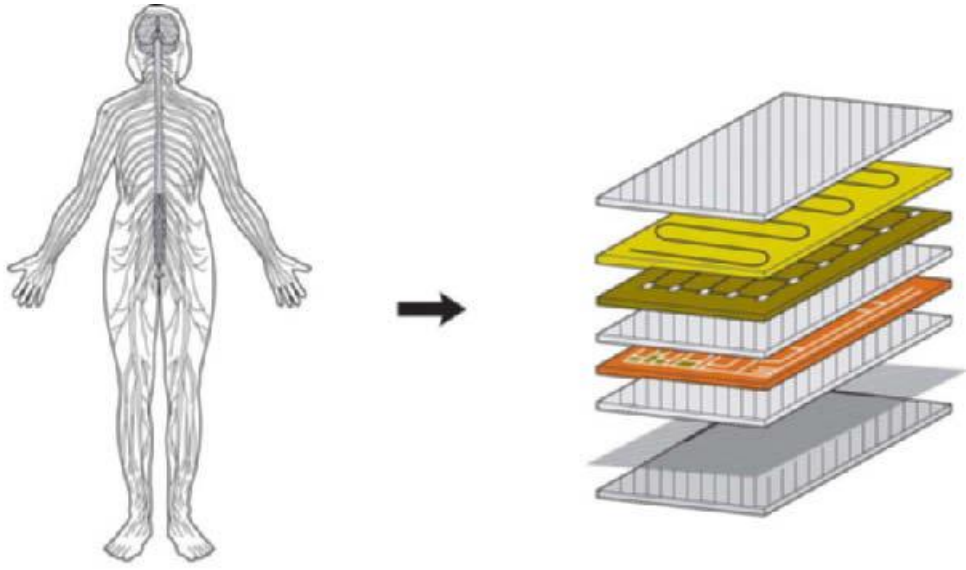


Plate 4 Actuators and Smart Structures. Biomimesis parallelism between the human body and a smart material system.

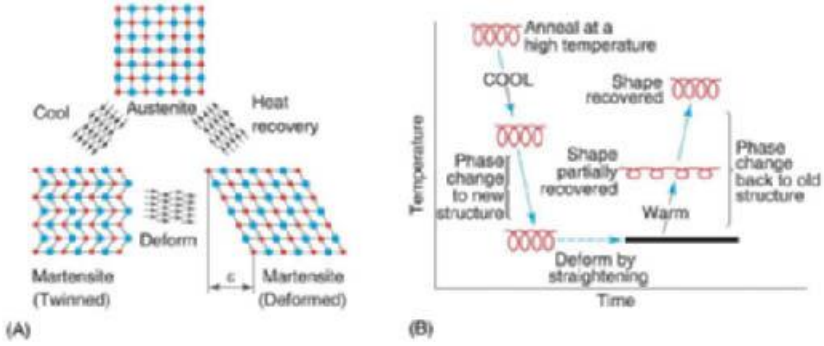


Plate 5 Actuators and Smart Structures. Principles of SMA materials: (A) change in crystallographic structure during cooling and heating; (B) associated component-shape changes, using a coil spring as an example.

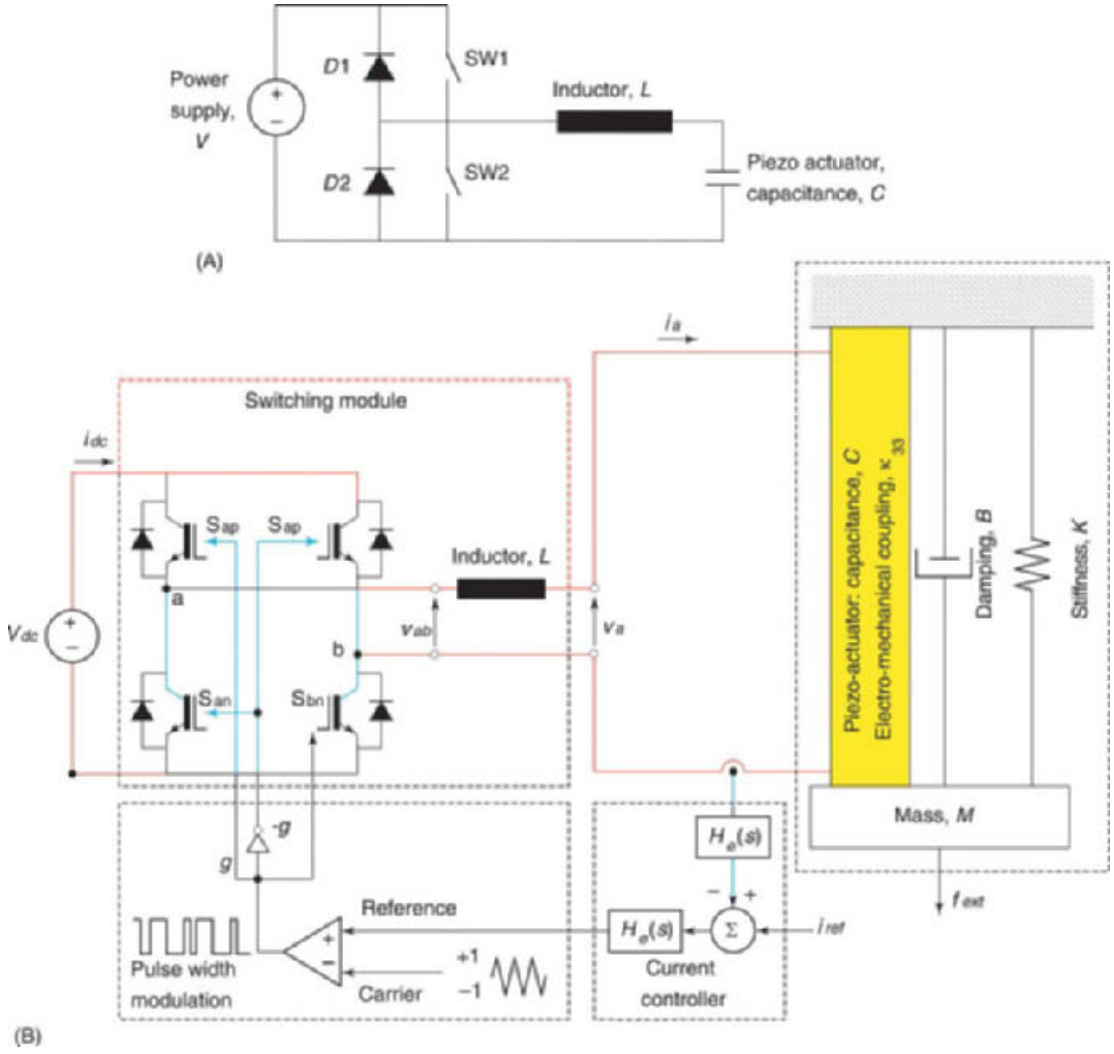


Plate 6 Actuators and Smart Structures. Power supplies for active material actuators: (A) principle of switching power supplies for high reactive load; (B) schematic of the supply system incorporating the switching module, current controller, pulse width modulator, and the piezo-actuator-external load assembly.



Plate 7 Basic Principles. Joseph Louis Lagrange (1736-1813). Italian-French mathematician. (With permission from Mary Evans Picture Library).



Plate 8 Beams. Leonard Euler, Swiss mathematician. From a picture by A. Lorgnal in the collection of the Institute of France. (BBC Hulton Picture Library).



Plate 9 Bridges. The Millennium Bridge, London, UK. (With permission from Tony Kyriacou).



Plate 10 Bridges. View of the transporter bridge which spans the River Tees at Middlesborough in the UK. The bridge was constructed in 1911 to replace the old ferryboat crossing there. It is a total of 260m wide and around 68m high. A cradle suspended from the main girder ferries cars and passengers across the 174m stretch of water in about 2 minutes. (With permission from Science Photo Library).

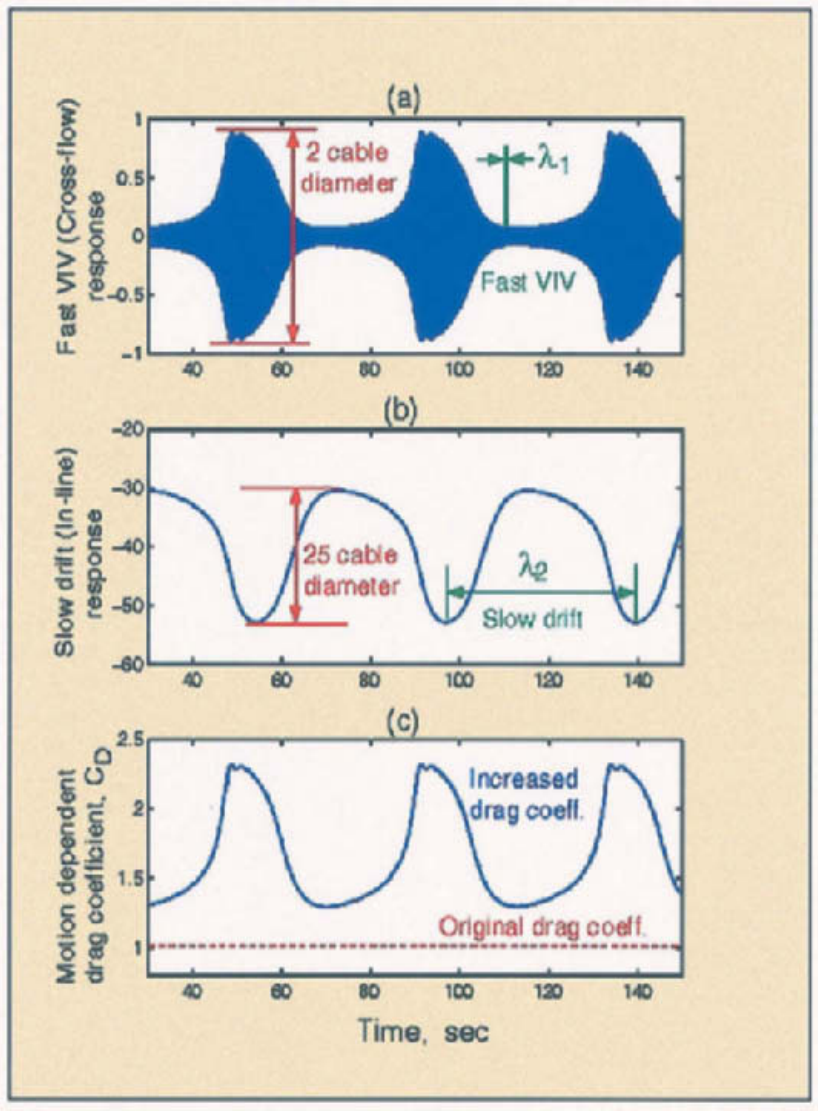


Plate 11 Cables. Coupled fast and slow response of cable-buoy system (a) fast (small amplitude) cross-flow vortex-induced vibration of the cable and an antidote; (b) slow (large amplitude) in-line drift of the cable at the upper end; (c) variation of the drag coefficient due to modulations of the cross-flow amplitude.

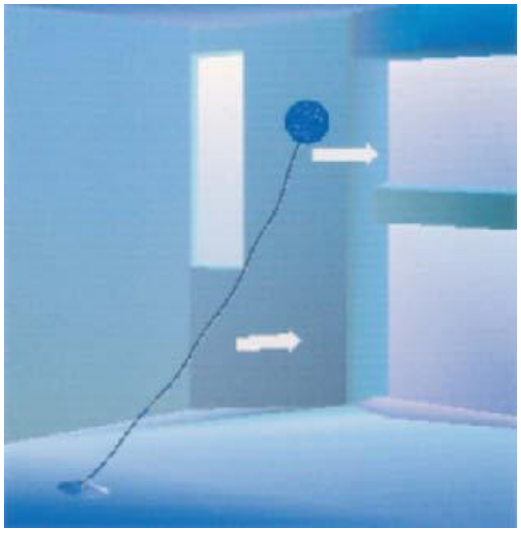


Plate 12 Cables. Underwater cable-buoy system with uniform current parallel to the cable equilibrium plane.

Plate 13 Chaos. Chaotic systems: head-on collision of two dipolar vortices in a stratified fluid environment. The original vortices, dyed orange and green, have exchanged a partner to form two new (mixed) dipoles which are moving at roughly right angles to the original direction of travel, that is, towards the top and bottom of the image. The green fluid was injected from the right, the orange from the left. Dipolar vortices are relevant to turbulence in large-scale geophysical systems such as the atmosphere or oceans. Turbulence in fluid systems is one example of a chaotic system. (With permission from Science Photo Library).



Plate 14 Chaos. Fractal basin boundary for a magnetopendulum system. This colorful picture is a fractal basin boundary for a magnetopendulum system. $\theta + \delta\theta + \sin(\theta) = f\cos(\theta)\cos(\omega t)$, when $\delta = 0.25$, $\omega = 1.0$, and $f = 1.40$ (the homoclinic bifurcation value is 0.798) in the state space $(\theta, d\theta/dt)$. The blue represents initial points which have counterclockwise rotating solutions. The black represents the points whose solutions never settle down in a time interval of 90π computer seconds.

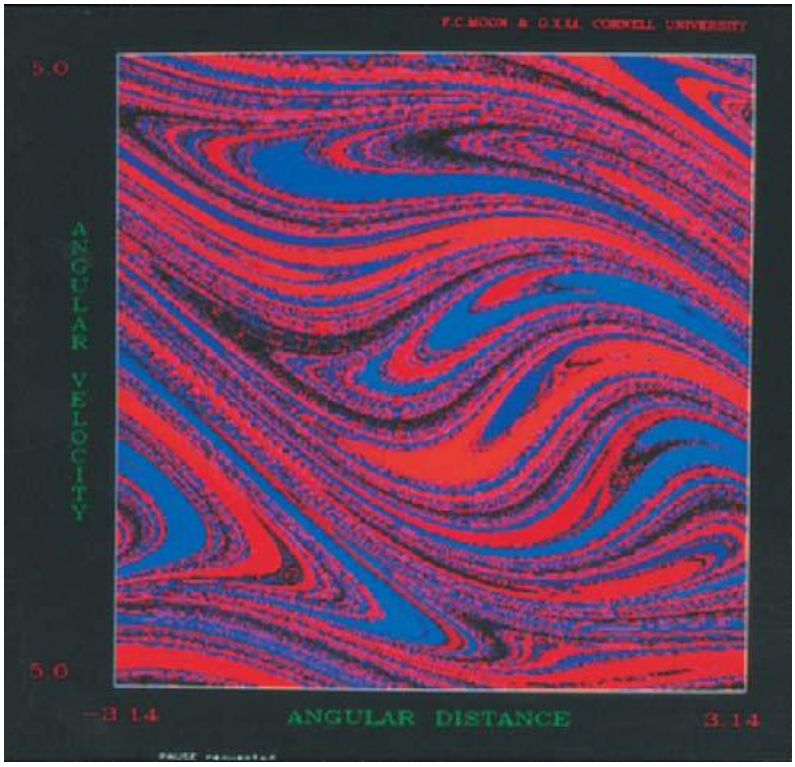
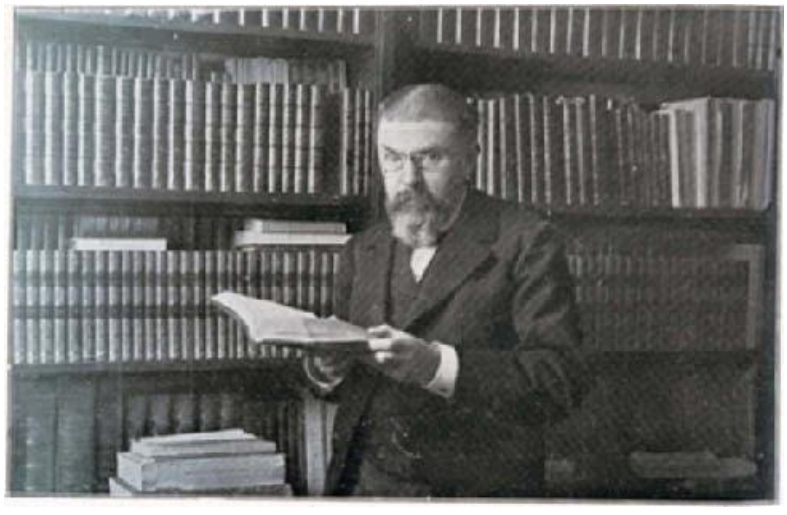


Plate 15 Chaos. Jules Henri Poincare (1854-1912). French mathematician. (With permission from Mary Evans Picture Library).



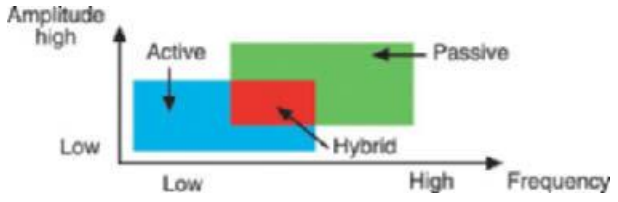


Plate 16 Damping, Active. Operating range of various damping methods.

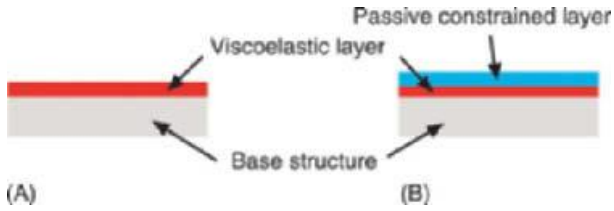


Plate 17 Damping, Active. Viscoelastic damping treatments. (A) Free; (B) constrained



Plate 18 Damping, Active. Shunted piezoelectric treatments.

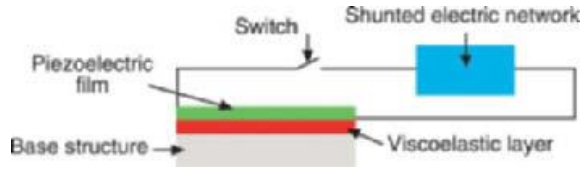


Plate 19 Damping, Active. Damping layers with shunted piezoelectric treatments.

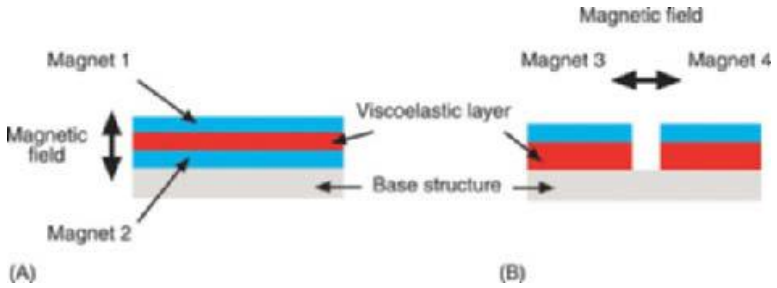


Plate 20 Damping, Active. Configurations of the MCLD treatment (A)2 Compression MCLD; (B) shear MCLD.

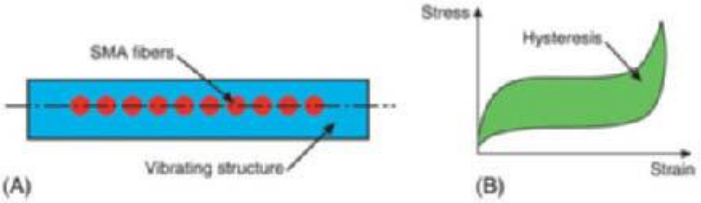


Plate 21 Damping, Active. Damping with shape memory fibers. (A) SMA-reinforced structure; (B) superelastic characteristics.

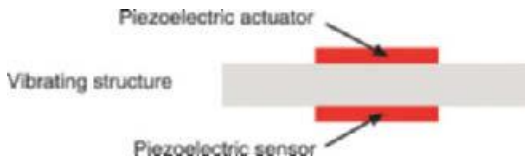


Plate 22 Damping, Active. Active damping

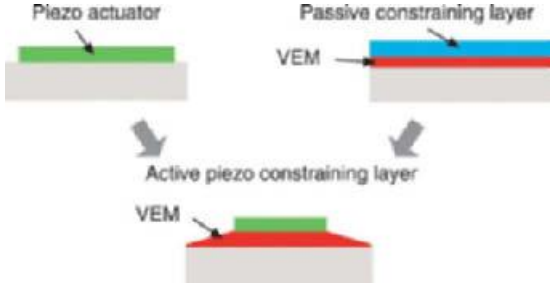


Plate 23 Damping, Active. Active constrained layer damping treatment.

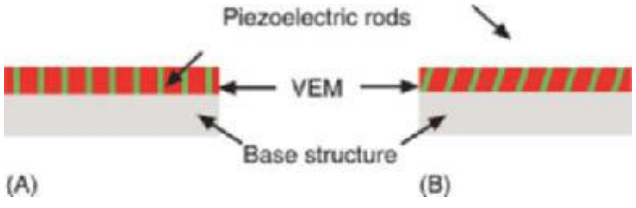


Plate 24 Damping, Active. Active piezoelectric damping composites.

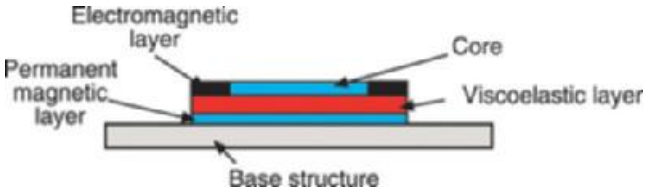


Plate 25 Damping, Active. Electromagnetic damping composite (EMDC).

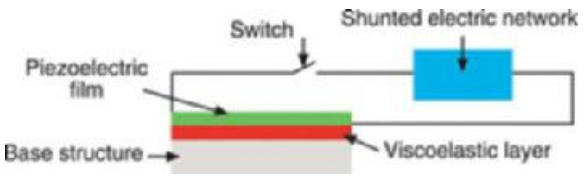


Plate 26 Damping, Active. Damping layers with shunted piezoelectric treatments.

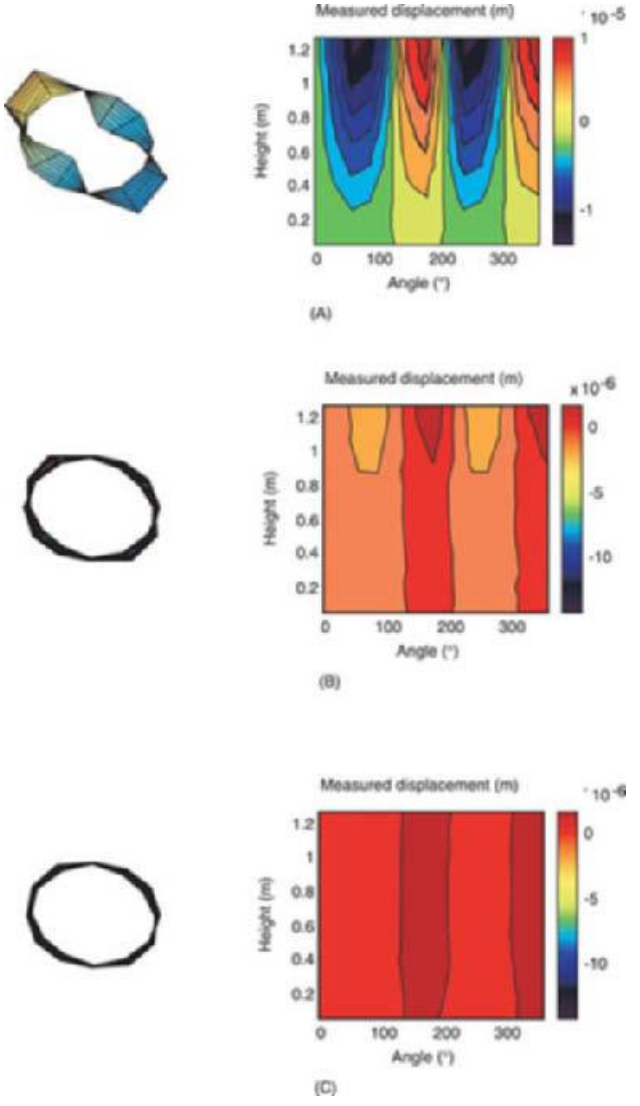


Plate 27 Damping, Active. Experimental results using laser vibrometer before and after control for mode (1,2). (A) PLCD; (B) ACLD (open actuator); (C) ACLD (two actuators).

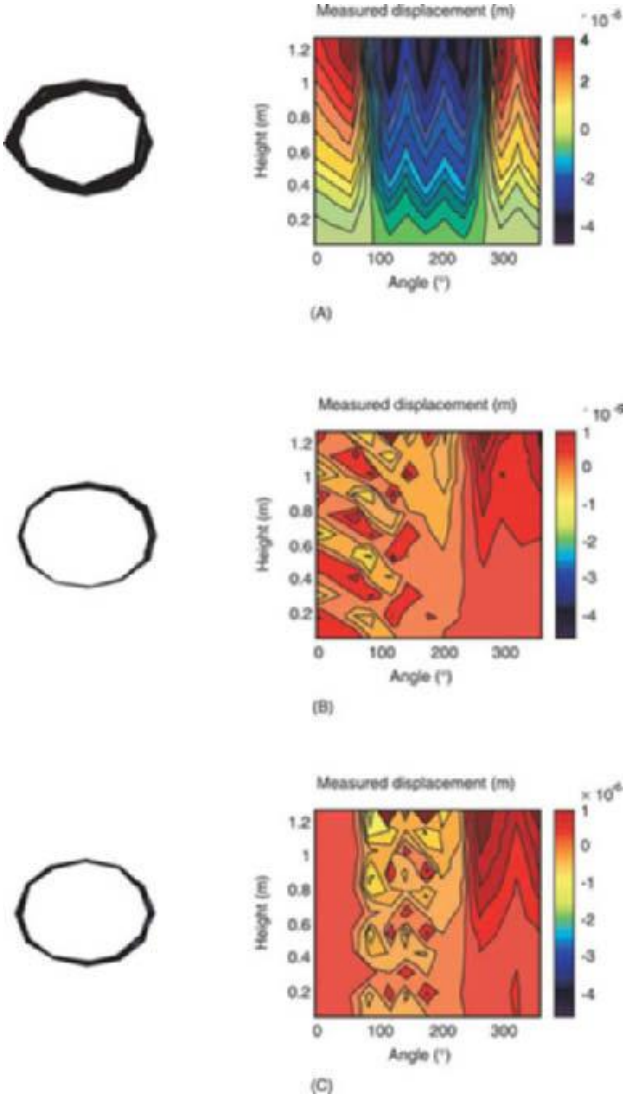


Plate 28 Damping, Active. Experimental results using laser vibrometer before and after control for mode (1,1). (A) PCLD; (B) ACLD (one actuator); (C) ACLD (two actuators).



Plate 29 Earthquake Excitation and Response of Buildings. Earthquake damage. Collapsed road bridges after an earthquake. Earthquakes are caused when sections of the earth (tectonic plates) move against each other to relieve stress. Photograph of highway near Watsonville in California, USA, in 1990. California lies on the boundary between the North American and Pacific plates. (With permission from Science Photo Library).

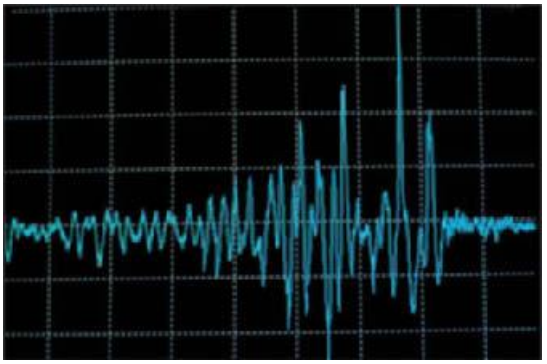


Plate 30 Earthquake Excitation and Response of Buildings.
Kobe earthquake seismograph. Screen display of a seismograph of the Kobe earthquake of 16 January 1996. The horizontal divisions represent acceleration along a north-south line with the third line from top representing zero acceleration. The vertical divisions represent time intervals of five seconds. Kobe, Japan, was struck by an earthquake which measured 7.1 on the Richter scale. Image recorded at the University of Tokyo. (With permission from Science Photo Library).



Plate 31 Earthquake Excitation and Response of Buildings.
1999 Taiwan earthquake. Apartment block with extensive damage.

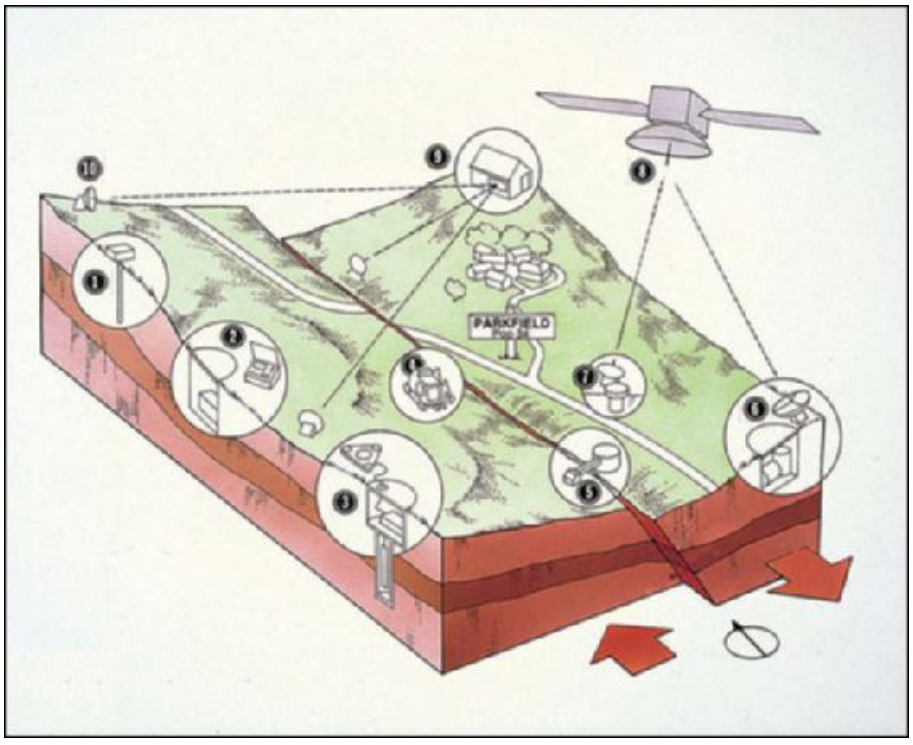


Plate 32 Earthquake Excitation and Response of Buildings. Diagram of Parkfield earthquake prediction experiment, showing instrumentation: (1) seismometer in hole to record microquakes; (2) magnetometer to record magnetic field; (3) near-surface seismometer to record larger shocks; (4) VIBREOSIS truck that creates shear waves to probe the earthquake zone; (5) creepmeter to record surface movement; (6) strainmeter to monitor surface deformation; (7) sensors in water well to monitor groundwater level; (8) satellite relaying data to US Geological Survey; (9) laser to measure surface movement by bouncing beams on reflectors (10). Arrows show crustal plates movements along San Andreas fault. (With permission from Science Photo Library).

Table 3 Dimensionless fundamental frequencies for square plates by different methods

Method used	*No. of terms used*	$\bar{\omega}$	*% error*
Exact (Tomotika)		8.9966	
Rayleigh–Ritz (trigonometric)	36	8.9975	0.010
Rayleigh–Ritz (polynomial)	4	8.9998	0.036
Galerkin (polynomial)	1	9.0000	0.038
Galerkin (trigonometric)	1	9.3060	3.440

It can readily be seen that the present one-term polynomial Galerkin solution is quite close to higher-term Rayleigh–Ritz solutions and the exact solution, while the one-term trigonometric Galerkin solution gives a poor result.

Acknowledgment

The assistance of Ms Huan Zeng with the differential transformation method is gratefully acknowledged.

Nomenclature

$A(\ )$	Cross-sectional area (variable)
A_o	reference area coefficient
a	plate half-length
b	plate half-width
C	coefficient
C_i	constants of integration
D	plate flexural rigidity
E	elastic modulus
f, g	functions of x
F, G	transforms of f and g
h	plate thickness
I	Lagrangian energy
J_o	zero-order Bessel function of first kind
k	constant in eqn [6]
k_{ij}	coefficient defined in eqn [28]
L	length of bar
$L(W)$	differential operator operating on W
M	function of X
$m(x)$	mass per unit length as function of x
m_{ij}	coefficients defined in eqn (28)
m_o	reference mass coefficient
N	number of terms
n	exponent
$P(X)$	reversed effective force
$T_{\max}$	maximum kinetic energy
$T'_{\max}$	$T_{\max}/\bar{\omega}^2$
t	time
$U_{\max}$	maximum potential energy per cycle
$U^C_{\max}$	maximum complementary energy per cycle
u	axial displacement
W	mode shape function
$W(k)$	differential transform of $w(x)$
$w(x)$	function of x
X	x/L
X	x/a
x	axial position
Y	y/b
Y_o	zero-order Bessel function of second kind
y	transverse position
λ	$\bar{\omega}^2$
λ	a/b
λ^*	$L(W)/MW$
$\bar{\lambda}_i$	various values of $\bar{\omega}^2$
ν	Poissons ratio
ω	natural frequency
$\bar{\omega}$	dimensionless natural frequency
$(\ )_{,tt}$	$\partial^2(\ )/\partial t^2$

See also: **Eigenvalue analysis**; **Modal analysis, experimental**, Parameter extraction methods; **Nonlinear systems analysis**.

Further Reading

Batdorf SB (1969) On the application of inverse differential operators to the solution of cylinder buckling and other problems. In: *Proceedings, AIAA/ASME 10th Structures, Structural Dynamics, and Materials Conference*, New Orleans, LA. ASME, New York, pp. 386–391.

Bert CW (1987a) Application of a version of the Rayleigh technique to problems of bars, beams, columns, membranes, and plates. *Journal of Sound and Vibration* 119: 317–326.

Bert CW (1987b) Techniques for estimating buckling loads. In: Cheremisinoff PN, Cheremisinoff NP and Cheng SL (eds). *Civil Engineering Practice*, vol. 1: *Structures*. Lancaster, PA: Technomic, pp. 489–499.

Bert CW, Jang SK and Striz AG (1988) Two new approximate methods for analyzing free vibration of structural components. *AIAA Journal* 26: 612–618.

Bhat RB (1984) Obtaining natural frequencies of elastic systems by using an improved strain energy formulation in the Rayleigh–Ritz method. *Journal of Sound and Vibration* 93: 314–320.

Collatz L (1948) *Eigenwertprobleme*. New York: Chelsea, p. 135.

Crandall SH (1956) *Engineering Analysis*. New York: McGraw-Hill.

Ku AB (1977) Upper and lower bound eigenvalues of a conservative discrete system. *Journal of Sound and Vibration* 53: 183–187.

Laura PAA and Cortinez VH (1986) Optimization of eigenvalues when using the Galerkin method. *AIChE Journal* 32: 1025–1026.

Malik M and Dang HH (1998) Vibration analysis of continuous systems by differential transformation. *Applied Mathematics and Computation* 96: 17–26.

Meirovitch L (1967) *Analytical Methods in Vibrations*. New York: Macmillan.

Rao SS (1995) *Mechanical Vibrations*, 3rd edn. Reading, MA: Addison Wesley.

Rayleigh Lord (Strutt JW) (1870) On the theory of resonance. *Philosophical Transactions, Royal Society (London)* A161: 77–118. See also: Rayleigh Lord (1945) *Theory of Sound*, vol. 2, 2nd edn. New York: Dover Publications.

Schmidt R (1981) A variant of the Rayleigh–Ritz method. *Industrial Mathematics* 31: 37–46.

Singer J (1962) On the equivalence of the Galerkin and Rayleigh–Ritz methods. *Journal of the Royal Aeronautical Society* 66: 592.

CORRELATION FUNCTIONS

S Braun, Technion – Israel Institute of Technology, Haifa, Israel,

Copyright © 2001 Academic Press

doi: 10.1006/rwvb.2001.0170

Introduction

The notion of correlation is one of the most basic ones in the description of data, and especially joint descriptions. Joint descriptions between data points, whether from single or joint data sets, can describe patterns existing in the data. Correlation functions and matrices are often used to define or describe the patterns and dynamic behavior of vibration signals and vibrating systems.

The following first recalls basic correlation concepts, and their application to time functions. Stochastic random processes can be described by their autocorrelation as well as the spectral density function, and the relation between these presentations is described next. The possibility of using correlation concepts to define nonstationary random data is almost immediate.

Processing discrete data often involves the notion of the correlation matrix, which is briefly defined.

Classic as well as modern FFT based, computational schemes are described, including some notions of the variability of the estimated parameters.

The last part of the entry briefly describes some engineering applications, all relevant to aspects of vibration processing: the detection of delays in dispersionless propagation, spiking filters, and AR modeling. Adaptive line enhancer and adaptive noise cancellation applications conclude the entry.

Correlation Functions

Basic concepts for assessing the degree of linear dependence between two data sets x_k and y_k are based on covariance and correlation coefficients. The correlation coefficient R is then:

$$R = \frac{\sum_k x_k y_k}{\left(\sum_k x_k^2\right)^{1/2}\left(\sum_k y_k^2\right)^{1/2}} \qquad [1]$$

A specific example for which $R = 0.7$ is shown in **Figure 1**.

The notion of these descriptors of dependence can be extended to time-history data. Thus we have the covariance function between the time data $x(t)$ and $y(t)$ as:

$$C_{xy}(\tau) = E\left[\{x(t) - \mu_x\}\left\{y(t+\tau) - \mu_y\right\}\right] \qquad [2]$$

where $E[.]$ denotes expectations, $\mu_x = E[\{x(t)\}]$, and $\mu_y = E[\{y(t)\}]$. For zero-mean functions, we may use the cross-correlation function:

$$R_{xy}(\tau) = E[x(t)y(t+\tau)] \qquad [3]$$

which for continuous functions would be computed as:

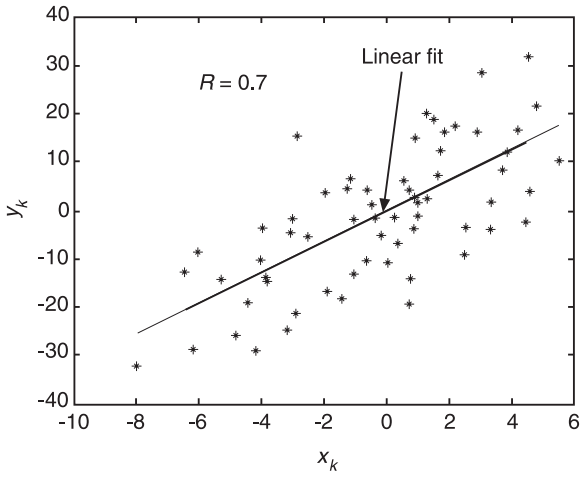


Figure 1 Linear dependence between two data sets.

$$R_{xy}(\tau) = \lim \frac{1}{T} \int_0^T x(t)y(t+\tau)\,\mathrm{d}t \qquad T \to \infty \qquad [4]$$

For the special case where $x(t) = y(t)$ we have the autocovariance and autocorrelation functions $C_{xx}(\tau)$ and $R_{xx}(\tau)$. Some general properties of the autocorrelation function are: first, the autocorrelation function is an even function of τ:

$$R_{xx}(\tau) = R_{xx}(-\tau) \qquad [5a]$$

and secondly, for $\tau = 0$:

$$R_{xx}(0) = \sigma_x^2 + \mu_x^2 \qquad [5b]$$

where $\sigma_x^2 = E[(x - \mu_x)^2]$ is the variance of $x(t)$. For zero-mean data (the prevalent case for vibration signals) $R_{xx}(0)$ is the mean square and thus also the power (the square of the RMS) of the signal. The cross-correlation function has the inequality:

$$\left|R_{xy}(\tau)\right| \leq \left[R_{xx}(0)R_{yy}(0)\right]^{1/2} \qquad [6]$$

It is instructive to note that tests for linear dependence are not necessarily applied to time data. Expressions analogous to the time domain correlation concept can be found in well known vibration engineering applications. One example is the coherence function (see **Spectral analysis, classical methods**) used to test the linear dependence between spectral estimates. It is given by:

$$\gamma^2(\omega) = \frac{S_{xy}(\omega)S_{xy}^*(\omega)}{S_{xx}(\omega)S_{yy}(\omega)} \qquad [7]$$

where * denotes the complex conjugate. This is actually the correlation coefficient (squared) in the frequency domain, i.e., computed for each frequency ω.

Another example concerns the comparison of the spatial deflection of vibrating structures. The analytical mode shapes ϕ_a computed via FE analysis are compared with experimentally derived ones ϕ_{ex}. The mode shapes are associated with a modal frequency and in the general case are complex vectors. They are often compared by the modal assurance criterion (MAC), defined as:

$$\mathrm{MAC}\left[(\phi_a)_i(\phi_{ex})_j\right] = \frac{\left|(\phi_a)_i^{\mathrm{T}}(\phi_{ex}^*)_j\right|^2}{\left[(\phi_a)_i^{\mathrm{T}}(\phi_a^*)_j\right]\left[(\phi_{ex})_i^{\mathrm{T}}(\phi_{ex}^*)_j\right]} \qquad [8]$$

where i and j are the indices or the modal frequencies. Again this can be recognized as a correlation coefficient for deflection data (see **Comparison of vibration properties: Comparison of modal properties**).

Stochastic Processes: Correlation and Power Spectral Density Functions

Random phenomena are represented by the notion of a stochastic process. A random variable with a probability distribution function (as well as joint probability distribution functions between any sets of times) is associated to each point in time. This is the probability description of a random phenomenon, extended to $\pm\infty$ at any time, and also itself in the $\pm\infty$ region. This set is called an ensemble, and any measured signal is then considered as one realization of such an ensemble. As in any statistical approach, the measured data are considered as one of the many sets which might have occurred.

Moments of the stochastic process should, in principle, be computed across the ensemble, i.e., via ensemble averaging. A stationary process would be one where the probability distribution functions, and hence the moments, would be invariant with time.

Random processes that have nontime varying mean and autocorrelation functions (depending only on τ) are sometimes called wide-sense stationary. For stationary processes, we assume in practice that the process has the so-called ergodic property, enabling us to compute the moments via time averages. These averages are computed via the single time function (the acquired signal), i.e., the realization of the stochastic process which is observed. While the notion of the ensemble is the basic one for stochastic processes, it has very little practical effect. In what follows all descriptions of the random phenomena are time based averages, i.e., computable via a single time record.

The power spectral density (PSD), denoted by S, for a continuous wide-sense stationary process is defined as the Fourier transform of the autocorrelation function.

$$S_{xx}(\omega) = \int_{-\infty}^{0} R_{xx}(\tau) \exp\ (-j\omega\tau)\, d\tau \qquad [9a]$$

$$R_{xx}(\tau) = \frac{1}{2\pi} \int_{-\infty}^{\infty} S_{xx}(\omega) \exp\ (j\omega\tau)\, d\omega \qquad [9b]$$

These Fourier transform-based definitions are often denoted by a double arrow notation:

$$R_{xx}(\tau) \longleftrightarrow S_{xx}(\omega) \qquad [10]$$

The definitions in eqn [9] are known as the Wiener-Khintchine theorem.

Correlation Functions for Nonstationary Signals

In the previous section it was implicitly assumed that correlation functions computed for finite signal sections would be independent of the specific time intervals chosen. In the more general case, it must be assumed that:

$$R_{xy}(t, \tau) = E[x(t)y(t + \tau)] \qquad [11]$$

may be a function of the variable t, the time. This is the case for non-stationary signals, where the statistical signal properties are not invariant with time. The case: $R_{xx}(t, \tau) = R_{xx}(\tau)$ is a special case of time invariance, which applies to stationary signals. Eqn [11] in conjunction with eqn [9] can be used to define time varying spectra as:

$$S(t, \omega) = \int R(t, \tau) \exp\ (-j\omega\tau)\, dt \qquad [12]$$

The time-dependent autocorrelation function can be chosen in more than one way. Using eqn [12], we can define the Wigner–Ville distribution (WVD) as a basic tool for the analysis of nonstationary signals (see **Time–frequency methods**).

Examples of Correlations and Spectra for Random Signals

We first note that for the case:

$$R(\tau) = S_0\delta(\tau)$$
$$R_{xx}(0) = \frac{1}{2\pi} \int_{-\infty}^{\infty} S_{xx}(\omega)\, d\omega = \int_{-\infty}^{\infty} S_{xx}(f)\, df \qquad [13]$$

where $R_{xx}(0)$ is the total power (we assume zero mean), and the PSD is interpreted to be the distribution of the total power in the frequency domain. It should be noted that the power tends to infinity, and this case, which is possible mathematically, will never exist exactly in practice.

Next, using eqn [9] we consider some examples involving some idealized situations. These can often help in defining general properties.

Example 1 This concerns a possible definition (and intuitive understanding) of white noise. Assuming a constant PSD of value S_0 covering the infinite frequency range $\pm\infty$, we compute the autocorrelation as an impulse function. The autocorrelation being an impulse, there is zero correlation between two signal points separated by any incremental time, a completely memory-less phenomenon. White noise is obviously a mathematical notion.

Example 2 This concerns a constant PSD limited to f_{max}, of magnitude equal to S_0. The autocorrelation is then:

$$R_{xx}(\tau) = 2S_0 f_{max} \frac{\sin\ (2\pi f_{max}\tau)}{(2\pi f_{max}\tau)} \qquad [14]$$

and is shown in **Figure 2C**. The first zero crossing of

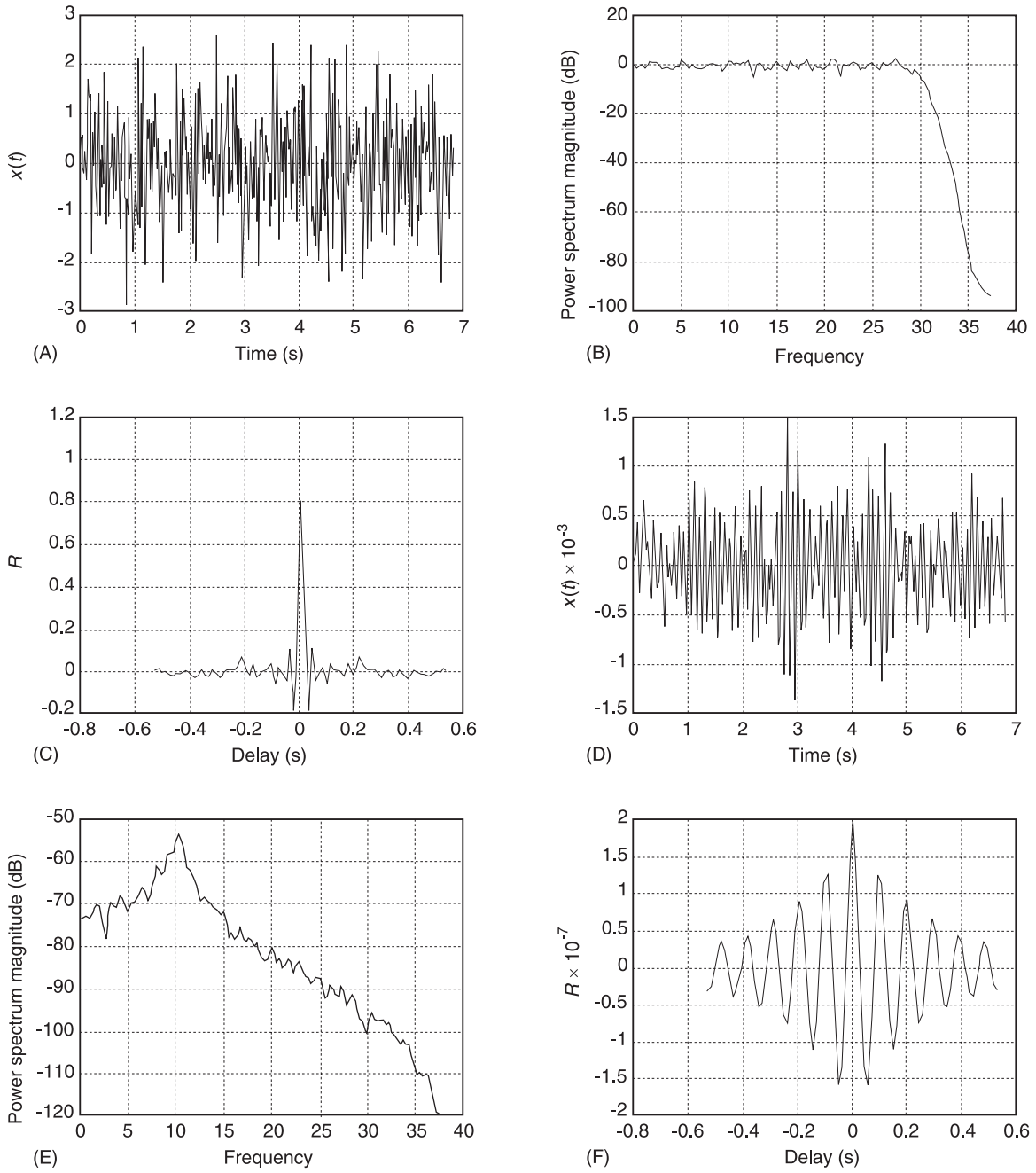


Figure 2 PSD vs aotocorrelation of random signals. (A) Wideband noise, time domain; (B) wideband noise, PSD; (C) wideband noise, autocorrelation; (D) narrowband noise, time domain; (E) narrowband noise, PSD; (F) narrowband noise, autocorrelation.

R_{xx} occurs for $\tau = 1/2f_{\max}$, and this is roughly the memory of the process, the time interval for which there is still a correlation between the signal samples. The smaller the bandwidth, $f_{\max}$, the longer this memory will be.

Example 3 Here we show a narrowband PSD, typical of a mass-spring-damper (SDOF) system excited by a white noise with a PSD equal to S_0:

$$R_{xx}(\tau) = S_0 \frac{\pi S f_0}{2} \exp\ (-2\pi\zeta f_0 \tau) \cos\ (2\pi f_0 \tau) \quad [15]$$

where f_0 is the natural frequency and ζ is the damping ratio. This is shown in **Figure 2F**. While the autocorrelation is oscillatory (dictated by f_0), the duration in the correlation domain is inversely proportional to the bandwidth in the frequency domain.

The Correlation Matrix

The products of correlation values (for the range of delay indices) can be arranged in a matrix form known as the correlation matrix. Many digital modeling and filtering operations involve the use of such matrices.

For discrete data, the autocovariance and autocorrelation sequences are important second-order characterizations. For the discrete sequence $\mathbf{x} = [x(0)\, x(1) \ldots\, x(p)]^{\mathrm{T}}$.

These are defined via the $(p+1) \times (p+1)$ outer product:

$$\mathbf{x}\mathbf{x}^{\mathrm{T}} = \begin{bmatrix} x(0)x(0) & x(0)x(1) & \ldots & x(0)x(p) \\ x(1)x(0) & x(1)x(1) & \ldots & x(1)x(p) \\ \vdots & & & \\ x(p)x(0) & x(p)x(1) & \ldots & x(p)x(p) \end{bmatrix} \quad [16]$$

For a wide-sense stationary process, the autocorrelation $\mathbf{R}_x$ matrix is based on the expectation of eqn [16]:

$$\mathbf{R}_x = E(\mathbf{x}\mathbf{x}^{\mathrm{T}}) = \begin{bmatrix} r_x(0) & r_x(1) & r_x(1) & r_x(p) \\ r_x(1) & r_x(0) & r_x(1) & r_x(p-1) \\ \vdots & & & \\ r_x(p) & r_x(p-1) & & r_x(0) \end{bmatrix} \quad [17]$$

Computational Aspects

Direct computations: These are based on eqns [2]–[4]. Two estimates can be computed. The unbiased version is:

$$R_{xy}(\tau) = \frac{1}{T-\tau} \int_0^{T-\tau} x(t)y(t+\tau)\, \mathrm{d}t \quad [18a]$$

and the biased one is:

$$R_{xy}(\tau) = \frac{1}{T} \int_0^{T} x(t)y(t+\tau)\, \mathrm{d}t \quad [18b]$$

For the discrete, unbiased case we have:

$$R_{xy}(k) = \frac{1}{N-|k|} \sum_{n=0}^{N-1-|k|} x(n)y(n+|k|) \quad [19a]$$

and for the discrete biased case we have:

$$R_{xy}(k) = \frac{1}{N} \sum_{n=0}^{N-1} x(n)y(n+|k|) \quad [19b]$$

For both types of estimate, the variance tends to zero with the signal length going to infinity:

$$\mathrm{var}\left[\hat{R}_{xy}\right] \to 0 \text{ for } N \to \infty \quad [20]$$

and the estimates are thus consistent.

The variance of the computed estimate is slightly less for the unbiased case, but there are some computational advantages which can be realized (using specific matrix formulations) when using the biased version.

Modern computational methods: These use eqn [9]. Spectral densities are computed first, utilizing the highly efficient Fast Fourier Transform (FFT) algorithm, and correlation functions are then computed as inverse Fourier transforms of these, again using the FFT algorithm:

$$\begin{aligned} r_{xy}(\tau) &= F^{-1}\left[S_{xy}(\omega)\right] \\ S_{xy} &= \frac{\Delta t}{N} X^*(k)Y(k) \end{aligned} \quad [21]$$

where $x(k) = \mathrm{FFT}[x(n)]$ and $y(k) = \mathrm{FFT}[y(n)]$. Some specific computational techniques are involved in such an approach, in order to avoid the so-called 'circular' properties of correlation functions which have been computed in such a manner.

Statistical Properties of the Correlation Estimators

Asymptotic expressions for the variance of the estimators are available for the specific case of band-limited white noise signals. The normalized standard deviation is then:

$$e_{Rxy(\tau)} = \left[\frac{1+\rho_{xy}^{-2}}{N}\right]^{1/2} \quad [22]$$

and the correlation coefficient is:

$$\rho_{xy}(\tau) = \frac{R_{xy}(\tau)}{\left[R_{xx}(o)R_{yy}(o)\right]^{1/2}}$$

Two tendencies can be noted from eqn [22]. First, the variance tends to zero as the data length (or number of samples for the discrete case) goes to infinity. As has already been mentioned, the estimator

is consistent. Second, the statistical error grows as the correlation coefficient decreases. The error becomes unpredictable when there is zero correlation between values. Such a property is very common for estimators which describe cross-properties between two parameters or functions.

Correlation Functions and Matrices in some Engineering Applications

Linear Systems

Some basic input/output relations may be based on correlation functions. When $x(t)$ is the excitation of a system with an impulse response $h(t)$, the response $y(t)$ is (**Figure 3**):

$$y(t) = h(t) \otimes x(t) \qquad [23]$$

where $\otimes$ denotes the convolution operator. It is simple to show that:

$$R_{xy} = h \otimes R_{xx} \qquad [24]$$

and for the specific case of x white noise:

$$R_{xx}(\tau) = \delta(\tau) \qquad [25a]$$

$$R_{xy}(\tau) = h(\tau) \qquad [25b]$$

Dispersionless Multipath Propagation

Figure 4 shows a scheme with propagation delays, τ_k, in each path.The resulting impulse response is:

$$h(t) = \sum_k h_k(t) = \sum_k h(t - \tau_k) \qquad [26]$$

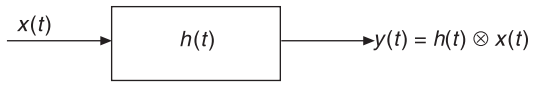


Figure 3 Impulse response and linear systems.

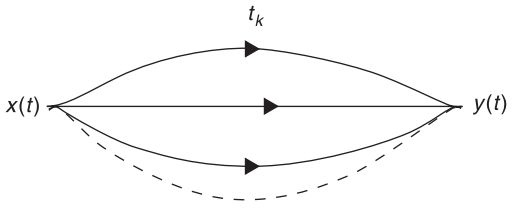


Figure 4 Multipath propagation.

The convolution operation being commutative, this yields:

$$R_{xy}(\tau) = R_{xx}(\tau) \otimes \sum_k h(t - \tau_k) \qquad [27]$$

and R_{xy} peaks at locations where $t = \tau_k$. One method of identifying propagation delays is thus based on peak localization. This is a viable option when the propagating signals are random power signals, when a simple time pattern is not evident. As with any parameter identified from random signals, the variance of the peak's location is an uncertainty in the extracted delay. The normalized error for this location is:

$$e_{\tau_k} \approx 0.6 \left[\frac{1 + \delta_{xy}^{-2}}{N} \right]^{1/4} \qquad [28]$$

From eqn [27] it can be seen that h is 'smeared' by R_{xx}, unless x is white noise.

Figure 5 deals with the sums of a signal and its delayed versions. Three delayed components are added, with delays of 2 ms, 3.9 ms, and 5 ms, respectively. Three cases with varying degrees of signal bandwidth are shown. For the wideband case, all three delays are recognizable as approximate impulses in the cross-correlation function. The smearing of R_{xy} with the narrowing of the signal's bandwidth is evident. The delays of 3.9 ms and 5 ms (**Figure 5F**) are not resolved in the case with the narrowest bandwidth.

From

$$S_{xy}(\omega) = H(\omega) S_{xx}(\omega) \qquad [29]$$

we can attempt to compute $H(\omega) = S_{xy}(\omega)/S_{xx}(\omega)$ and via an inverse Fourier transform compute $h(t)$ directly and obtain a clearer distribution of peaks. But ill conditioning could occur as H would have negligible magnitude in some frequency ranges, and more advanced techniques are then indicated.

Examples of applications can be found in situations where the propagation velocity is known (as in airborne and body-borne acoustic waves). Estimation of delays can then help in determining signal sources, for those cases where the involved geometrical propagation paths can be identified (**Figure 6**).

Investigation of flow regimes in pipes is another example. For flows involving stocastic velocity fluctuations, the average delay between two spatial locations can be estimated using correlation techniques (**Figure 7**).

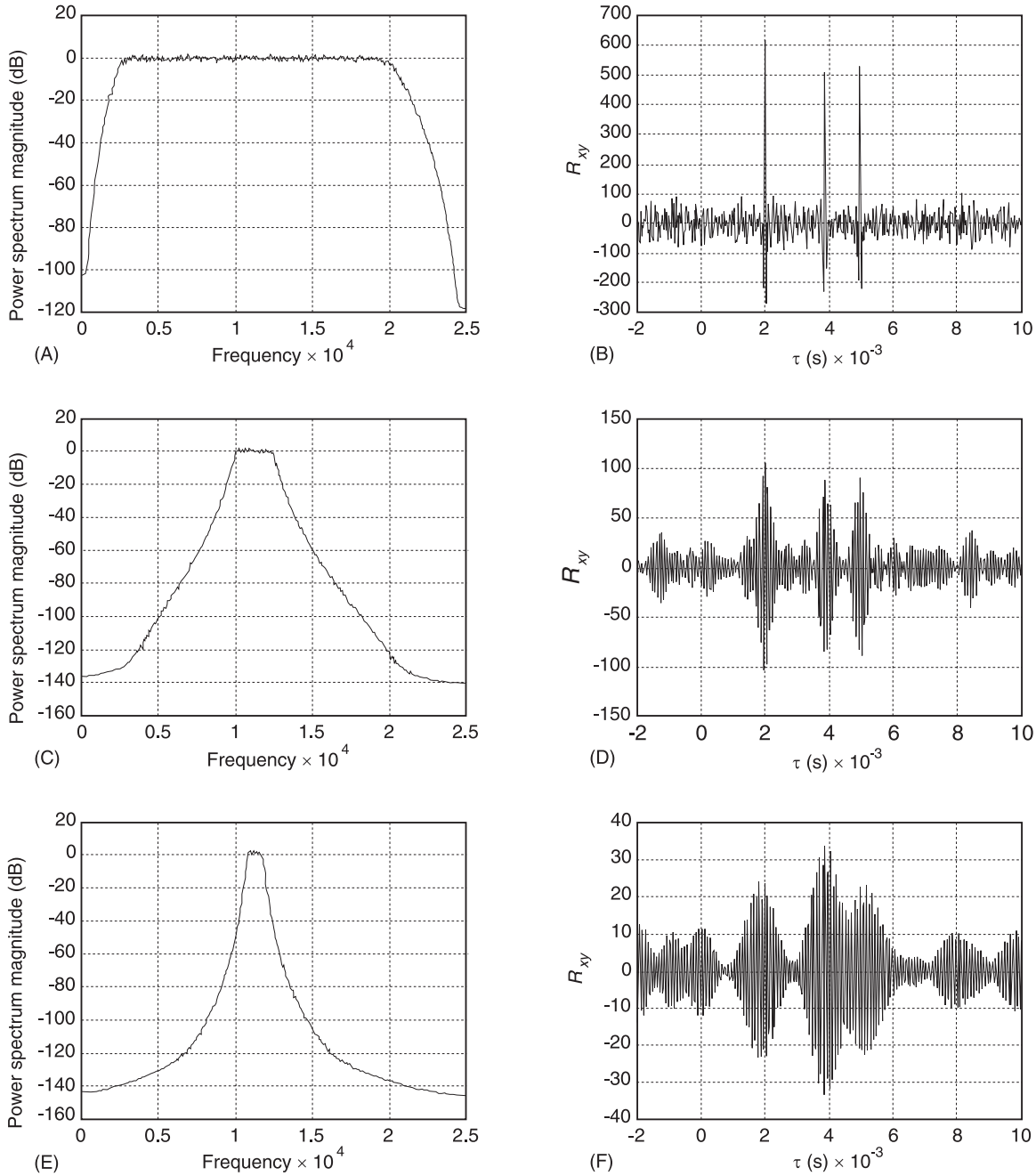


Figure 5 Dispersionless multipath propagation example. (A) Wideband signal, PSD; (B) wideband signal, autocorrelation; (C) intermediate bandwidth signal, PSD; (D) intermediate bandwidth signal, autocorrelation; (E) narrowband signal, PSD; (F) narrowband signal, autocorrelation.

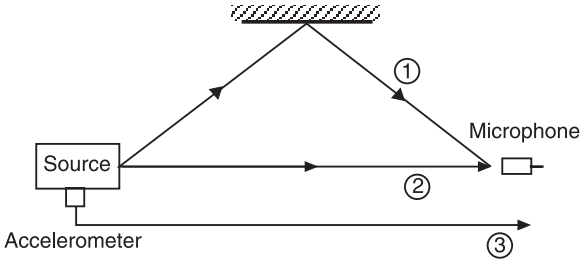


Figure 6 Source and propagation path problem.

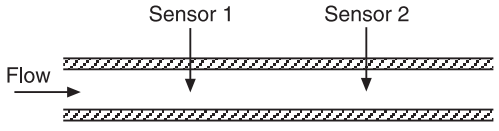


Figure 7 Flow propagation.

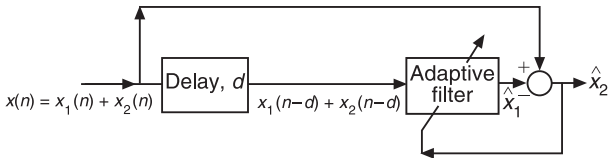


Figure 8 Adaptive line enhancement.

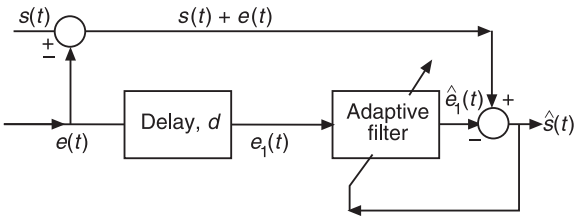


Figure 9 Adaptive noise cancellation.

Filtering and modeling

Correlation matrices find wide application in the area of signal processing, for signal modeling, filtering, etc. As an example, we mention a spiking filter used when an impulsive signal is smeared by the propagation medium, as in seismic signal processing. Shaping the measured signal $x(n)$ is achieved by the filter $h(n)$ such that $x(n) \otimes h(n) = \delta(n)$. The filter coefficients $\mathbf{h}$ are then computed using:

$$\mathbf{R}_x\mathbf{h} = x^*(0)\begin{bmatrix}1\\0\\0\\\cdot\\\cdot\\\cdot\\0\end{bmatrix} \qquad [30]$$

Models of signals are widely used in areas of spectral analysis, diagnostics, etc. An example of a model for measuring signal x is the autoregressive (AR) model:

$$x_i = -\sum_{k=1}^{p} a_k x_{i-k} + w_i \qquad [31]$$

The vector of the model's parameters is then computed using:

$$\mathbf{Ra} = \sigma^2\mathbf{I} \qquad [32]$$

with

$$\mathbf{I} = [1\ 0\ 0\ \ldots\ 0]^{\mathrm{T}}$$

See **Adaptive filters** for application.

An example of the adaptive line enhancement (ALE) procedure is shown in **Figure 8**. This can be applied in situations where a composite signal which includes both broadband and narrowband signals is to be decomposed. The objective can be to extract either the narrowband or the broadband component. The narrowband signal can be an approximate harmonic signal, like those found in rotating machinery vibrations. The method is based on the fact that the narrowband signals tend to have longer autocorrelation durations than the broadband ones.

For the composite signal:

$$x = x_1 + x_2$$

where τ_1 and τ_2 denote the respective autocorrelation lags beyond which the autocorrelations of x_1 and x_2 become negligible. Then $\tau_2 < \tau_1$.

The delay d shown in **Figure 8** is chosen such that $\tau_2 < d < \tau_1$.The delayed signal component $x_2(n-d)$ is not correlated with $x_2(n)$, while the delayed component $x_1(n-d)$ is still correlated with $x_1(n)$. The adaptive filter adjusts its weights so as to cancel x_1, the component which is correlated with $x_1(n-d)$. The output of the filter will be an estimate x_1 of x_1. The subtraction results in x_2, or if desired, x_1 can be used for further processing. The method has been applied to composite vibration signals in order to enhance periodic components mixed with broadband random ones.

An adaptive noise cancellation (ANC) scheme is shown in **Figure 9**. This is a more general case of the earlier application. It can be used to cancel an interfering signal $e(t)$ from a composite signal $s(t) + e(t)$, in those cases where another reference signal $e_1(t)$ is available.

The requirement is that $e_1(t)$ must be highly correlated with $e(t)$. (Full correlation is obviously described in the hypothetical case shown in **Figure 9**.) The adaptive filter adjusts its weight so as to generate an estimate $e(t)$ of the interfering signal. The scheme is widely used for acoustic noise cancellation, where the interfering signal is often either periodic or mostly harmonic. The correlated reference signal can often be obtained from vibration measurements, as in cases where harmonic vibrations generate that part of the acoustic signal which needs to be attenuated/cancelled. ANC has also found applications in vibration base diagnostics of rotating machinery (see **Diagnostics and condition monitoring, basic concepts**).

Nomenclature

d	delay
$e(t)$	interfering signal
$E[.]$	expectations
f_0	natural frequency
$h(t)$	impulse response
R	correlation coefficient
S	power spectral density
$y(t)$	response

See also: **Time–frequency methods**; **Hilbert transforms**; **Adaptive filters**; **Spectral analysis, classical methods**

Further Reading

Bendat JS, Piersol AG (1993) *Engineering Applications of Correlation and Spectral Analysis*. New York: Wiley.

Hayes MH (1996) *Statistical Digital Signal Processing and Modeling*. New York: Wiley.

CRASH

V H Mucino, West Virginia University, Morgantown, WV, USA

Copyright © 2001 Academic Press

doi: 10.1006/rwvb.2001.0164

Automotive collisions are responsible for many fatalities every year and a public safety concern in every country for automakers, transportists and governments alike. According to the International Road Traffic Accident Database (IRTAD), in 1998 alone, averages of 13 fatalities and 480 injury accidents per 100 000 population were registered among the 29 participating countries in Europe, North America, Asia and Australia. Yet, this statistic is the result of a decreasing trend in the past two decades reflecting, among other things, the significant technological advances in the automotive field aimed at enhancing 'crashworthiness' of vehicles.

Crashworthiness by itself is not a characteristic or feature that can be measured or quantified, but it relates to the capacity of a vehicle structure and occupant restraint system to protect the occupants in the event of a collision. The main objectives being to reduce the likelihood and severity of injuries to vehicle occupants and ultimately, to reduce the fatality rates in vehicle collisions. Crashworthiness concepts are also being applied to aircraft structures and heavy-duty vehicles to enhance survivability of occupants in the event of a crash.

Vehicle accidents have always been a concern to auto makers. But it was not until the early 1970s, together with the advent of supercomputers, that the key issues relating to the mechanics of automotive collisions acquired such significant relevance to trigger the development of what is known today as the area of crashworthiness.

Central to the development of the crashworthiness area is the use of explicit finite element (FE) techniques to conduct computer simulations of collisions. These techniques have been developed to address the nonlinear transient solid mechanics of high-speed colliding structures, which involve the elastic and plastic stress wave propagation through solid continua and the characteristic nonlinear crushing behavior of structures. Crashworthiness applications have been extended to include human body structures and the interactions between vehicle, occupants and restraining devices.

Yet, many challenges lie ahead. New advanced materials are being used in vehicles to reduce weight (for fuel economy purposes) and to enhance crashworthiness. Many of these materials are yet to be adequately characterized in order to take full advantage of their applicability in vehicle structures. Representation of human body structures for simulation purposes is another area where the challenges are plentiful, from the mechanical characterization of human tissue to the classification and determination of injury thresholds for various types impact. Ultimately, the integration of crashworthiness advances in vehicle systems design is a challenge, which seems to be within reach, given the strides in computer technology.

Introduction

Crashworthiness has emerged as a multidisciplinary area that is now at the very heart of vehicle design and transportation systems in general. It addresses the mechanics of colliding structures and the interactions

between vehicles and occupants, in such detail that realistic simulations are now not only possible, but within reach of a record number of engineers involved with vehicle design, the overall objectives being to reduce the likelihood and severity of injury to humans and of fatality rates in vehicle collisions.

The issues in crashworthiness are plentiful; high speed colliding and crushing structures, biomechanics of the human body dynamic response in collisions, passenger restraint systems such as seat-belts, airbags, interior padding and energy absorbing materials, just to mention a few. From the experimental side, the use of rather sophisticated dummies has also called for advanced design and modeling of dummies that can be used effectively as human surrogates to verify various vehicle crashing scenarios.

Essential in the study of crashworthiness of vehicles, is the study of energy dissipation characteristics of colliding vehicle structures and the interactions between occupants and vehicle. From the simulation standpoint, the development of explicit FE approaches together with advanced contact algorithms has enabled the study of crashworthiness phenomena. However, the development of crashworthiness technologies has had several parallel tracks, the most important ones being the supercomputer development track, the vehicle collision track and the numerical solid mechanics track.

The Supercomputer Track

This was triggered by the development of the CRAY-1 supercomputer in the early 1970s by Seymour Cray. With a top speed of 100 megaflops, the first supercomputer provided the capability for vectorized processing, which in turn enabled applications where large numbers of computations were required, such as in nonlinear solid mechanics and computational fluid dynamics. Since then, several generations of CRAY supercomputers have provided an exponential growth in speed and parallel processing capability. Today's CRAY-SV1ex, released in 1999, is several orders of magnitude faster and more computationally efficient than the first supercomputers (with faster multistreaming vector processors at 7.2 billion calculations per second, memory size of 128 gigabytes), providing the capacity for the analysis of very large models in record turn-around times. FE models of vehicles for crashworthiness purposes can easily have several millions degrees of freedom with a large number of nonlinear relationships, making the solution processes iterative in nature and convergence-sensitive, thus requiring vast computational capabilities.

Parallel to the development of supercomputer technology, microprocessor and high-resolution graphics technologies have combined to enable and foster the development of sophisticated and computationally intense applications such as explicit FE codes for realistic simulations and visualization of crashworthiness phenomena.

On the Vehicle Collision Track

Vehicle manufacturers worldwide were confronted with government regulations to address occupant protection in vehicle collisions in the mid-1960s. In the USA, the first federal motor vehicle safety standard (MVSS 209: Motor Vehicle Safety Standard, by the US-National Highway Traffic Safety Administration (NHTSA)) related to crashworthiness became effective on 1 March 1967. By 1976, in the USA there were 15 specific MVSSs related to crashworthiness as shown in **Table 1**. Several of these standards relate directly to the issues currently addressed by crashworthiness analysis codes. For example, standard MVSS-203, first issued in 1968, requires a vehicle to be crash-tested (frontal collision) at $48\,\mathrm{km\,h^{-1}}$ (30 mph) against a rigid wall. These standards called for engineering assessment of vehicle

Table 1 USA-NHTSA Federal motor vehicle safety standards (MVSS) related to car crashworthiness

Motor Vehicle Safety Standard (MVSS) no.	*Description*	*Effective date*	*Last revision*
201	Occupant protection in interior impact	1–1–68	9–1–2000
202	Head restraints	1–1–69	
203	Impact protection for the driver from the steering control system.	1–1–68	9–1–81
204	Steering control rearward displacement	1–1–68	9–1–91
205	Glazing materials	1–1–68	
206	Door locks and door retention components	1–1–68	1–1–72
207	Seating systems	1–1–68	1–1–72
208	Occupant crash protection	1–1–68	9–1–91
209	Seat belt assemblies	3–1–67	
210	Seat belt assembly anchorages	1–1–68	7–1–71
212	Windshield mounting	1–1–70	9–1–78
213	Child restraint systems	4–1–71	1–1–81
214	Side impact protection	1–1–73	9–1–98
216	Roof crush resistance	9–1–75	9–1–94
219	Windshield zone intrusion	9–1–76	4–3–80

designs, which in turn, triggered the development of a variety of engineering tools and approaches to assess crashworthiness of vehicles and occupant response. New standards and revisions to existing standards are published in the Federal Register. These standards represent the minimum safety performance requirements for motor vehicles. The basic premise is that the 'public is to be protected against unreasonable risk of crashes occurring as a result of the design, construction, or performance of motor vehicles and is also protected against unreasonable risk of death or injury in the event crashes do occur'.

Early studies of crashworthiness relied almost completely on experimental barrier impact tests that produced data, which were used later on, to help explain the dynamic response of colliding vehicles. In some of these tests, mannequins were used to provide some idea of human response in vehicle frontal crashes. Kamal and Lin produced one of the first models for vehicle collisions based on nonlinear mass-spring elements, whose characteristics were derived experimentally.

Frontal collisions were first addressed by the standard MVSS-203 ($48\,\mathrm{km\,h^{-1}}$ rigid barrier frontal crash), given the frequency of their occurrence (roughly 50% of collisions). In such a collision, the passenger cabin is supposed to maintain its integrity by not allowing large structural deformations. The kinetic energy of the vehicle is to be dissipated by large plastic deformations of the front-end of the vehicle, which in turn, acts as a cushion to the passenger compartment. Deformations in the order of 800 mm (32 in) can take place in a time interval of approximately 120 ms, which produces strain rates between 1 and 100 per second. Under these conditions, the passenger cabin experiences decelerations of the order of 20*g*. Unrestrained occupants colliding with the vehicle interior may experience even higher deceleration rates, illustrating the importance of restraining devices. The rather costly nature of experimental tests and the limited predictability of collision events based on experimental data triggered the interest in simulation. The experimental programs however, highlighted some of the most important issues in solid mechanics that needed to be addressed, namely the large plastic deformations, strain rate dependency of materials, plastic and elastic stress wave propagation, local buckling and fracture/rupture of materials in the 120 ms of collision duration.

On the Solid Mechanics Track

Melosh and Kelly envisioned the requirements for the development of FE methods for crashworthiness analysis and outlined the issues to be addressed in order to make it possible. In the early 1970s, a number of studies pointed out the importance of local deformations and local geometry instabilities to conduct the structural response of colliding structures, issues that are central to crashworthiness analysis of structures. McIvor *et al*., Armen *et al*. and Welch *et al*. put forward important studies for crashworthiness simulations of structural components using FEs, in which the phenomena of local deformations and nonlinear elasto-plastic material behavior was considered.

The development of one of the most widely used FE codes for crashworthiness, DYNA3D, started in the mid 70s by Hallquist at Lawrence Livermore Laboratory. This code captured the essence of high-speed impact solid mechanics phenomena, for military and civilian applications, from projectile penetration to vehicle collisions. In 1979, DYNA3D was reprogrammed for the CRAY-1 supercomputer with more sophisticated sliding interfaces than the previous version. In 1981, new material formulations and the problem of penetration of projectiles was successfully simulated by the use of sliding interfaces. In 1990 LS-DYNA3D is released with added capabilities to represent fabric materials for seat belts and airbags and composite glass models. Parallel to that, pre and postprocessing codes (INGRID and TAURUS) were developed to interface with LS–DYNA3D and currently, there are versions of DYNA3D for PC and desktop workstations. Meanwhile, several other codes have emerged with various capabilities that allow for similar functions. For the most part, these codes seem to provide consistency in the applications. Other codes commercially available that are capable of simulating collisions of large structures effectively are PAM-CRASH, ADINA, MADYMO, WHAMS, and ABAQUS. The latter has useful data base descriptions of crash dummy models that are widely used for vehicle–occupant interaction assessment.

Three special features that distinguished this code were (i) explicit time integration schemes for the equations of motion; (ii) the application of advanced contact algorithms to allow for sliding surfaces with friction and nonpenetrating contact surfaces; and (iii) the use of 'economic' one-point-integration elements with 'hourglassing energy control' options to monitor convergence (hourglassing energy is associated to the zero energy deformation modes and is briefly described below). Additionally, this program was developed to include a wide array of nonlinear materials, including strain rate dependent materials and viscoelastic materials, rubber, honeycomb, and composite materials among others.

Many other standard commercial FE codes such as ANSYS, IDEAS–MS, PATRAN and CATIA among others, now provide import/export functions to interface with some of the crashworthiness codes, making the modeling and data preparation more readily available to many engineering analysts.

Brief Description of Crashworthiness Codes Based on DYNA3D

All the FE crashworthiness codes share the same basic principles of computational mechanics. The use of explicit time integration algorithms, the use of 'economic' elements, the formulation of various constitutive models for engineering materials, the re-zoning of the meshes using advection algorithms and the use of similar contact–impact algorithms. Some variations exist on special interface representations between structural components, but in general they all share similar or equivalent features. A brief description of the key features of a crashworthiness code is provided next.

Spacial Discretization

DYNA3D uses an updated Lagrangian formulation based on the weak form integral of the virtual work principle. Economic isoparametric elements with one integration Gauss point and diagonal mass matrices are used, for which viscous or stiffness hourglass energy can be used to control the zero energy modes associated to the one point of integration scheme. The structural elements include springs, lumped masses, discrete dampers, beams, trusses, solids (tetrahedron, wedges and brick) and shells (quadrilateral and triangular), the Hughes and Liu shells, also the Belytscho–Schwer beam and Belytschko–Tsy shell. Solid elements use the Flanagan–Belytschko constant stress, exact volume integral. **Table 2** shows the type of elements available in DYNA3D for structural representations.

Table 2 Element types available in DYNA3D

Element no.	*Type of element*
1	Solid elements (brick and tetrahedron)
2	Belytschko beam
3	Hughes–Liu beam
4	Belytchko–Lin–Tsay shell
5	C^0 triangular shell
6	Marchertas–Belytchko triangular shell
7	Hughes–Liu shell
8	Eight-node solid shell element
9	Truss element
10	Membrane element
11	Discrete elements and masses

Arbitrary Lagrangian Eularian (ALE) Advection

This is a re-zoning approach, which is needed to maintain consistency between solution requirements and the FE mesh. The rezoning consists of a Lagrangian time step followed by an advection or remap step. In this process the solution is stopped and the mesh is adjusted to the deformed geometry in such a way that elements are not highly distorted (smoothing). The solution is then mapped from the old mesh to the new one until the next step. While advection is different from adaptive FE meshing, both techniques can be used to enhance accuracy and convergence of a solution where nonlinear large displacements occur and where high gradients of the response variables occur.

Time Integration

A central difference explicit time integration algorithm is used to integrate the resulting equations of motion. This scheme is conditionally stable but does not require the use of implicit iterative techniques. The central difference approach requires that for each time step Δt, the current solution be expressed as:

$$\dot{x}^{n+1/2} = \dot{x}^{n-1/2} + \Delta t^n \ddot{x}^n \qquad [1]$$

$$x^{n+1} = x^n + \Delta t^{n+1/2} \dot{x}^{n+1/2} \qquad [2]$$

The difference with implicit methods of integration is that in explicit schemes, the solution to the current time step depends only on the solution of previous steps, thus avoiding the costly iterations on each time step to determine the unknown solution at the current time step (required in implicit schemes). The result is that no iterations are necessary at each time step. The drawback with explicit methods is the stability, which can only be controled by taking rather small time steps, as the error is proportional to the square of the time step. The Courant stability criterion must be used, which requires the solution not to propagate through an element faster than the dilatational wave speed of the material. This requirement gives rise to the need for rather refined meshes to provide numerical stability. Monitoring the energies of the system becomes the key to controling the stability of the solution.

Boundary Conditions

Several loading conditions can be simulated. Direct nodal loads, line and surface pressures and body loads are available. Kinematic boundary conditions are also allowed through prescribed displacements, velocities and accelerations; fixed nodes and displacement

constraints in the form of nodal-degree-of-freedom relationships. Another type of boundary conditions that can be considered are the 'contacting surfaces' where collision is to occur. These boundary conditions can be treated by means of the contacting and sliding surfaces described next.

Sliding Interfaces

The use of advanced impact contact algorithms is another unique feature of this program, allowing for various types of contacting surfaces. DYNA3D supports 22 types of interfaces. Master–slave surface concept is used to define contacting interfaces. Single surface can be defined as a 'slave only' surface, in such a way that each node is monitored to prevent penetration through the surface. This type of surface can effectively capture the 'accordion folding' behavior of crushing thin shell elements commonly found in vehicle crashes. The 22 types of interface can support sliding with friction; tied and sliding only interfaces can also be defined. Rigid 'master surfaces' can also be used. Interface definitions can be used to define lines and surfaces where contact is prescribed or where master lines in tiebreaking definitions can be used.

Constitutive Equations Library

The availability of a wide range of constitutive models is another essential feature of this code. From the elastic isotropic to the nonlinear elastic, orthotropic, visco-elastic, elasto-plastic and strain dependent material formulations. Near incompressible materials (rubber) and fluid material formulations, composite materials and fabric type materials are also possible. DYNA3D has about 120 material models and allows for 'user defined' material characterizations. This provides a very powerful capability to formulate sophisticated materials.

The constitutive equations used in the calculations can be expressed as:

$$\sigma_{ij}^{*} = \sigma_{ij}^{*}\left(\dot{\varepsilon}_{ij}\right) \qquad [3]$$

$$\dot{\sigma}_{ij} = \sigma_{ij}^{*} + \sigma_{ik}\omega_{kj} + \sigma_{jk}\omega_{ki} \qquad [4]$$

$$\dot{\varepsilon}_{ij} = \frac{1}{2}\left(\frac{\partial \dot{x}_i}{\partial x_j} + \frac{\partial \dot{x}_j}{\partial x_i}\right) \qquad [5]$$

$$\omega_{ij} = \frac{1}{2}\left(\frac{\partial \dot{x}_i}{\partial x_j} - \frac{\partial \dot{x}_j}{\partial x_i}\right) \qquad [6]$$

where σ_{ij}^{*} is the Jaumann rate of the Cauchy stress, $\dot{\sigma}_{ij}$ is the material derivative of the stress, $\dot{\varepsilon}_{ij}$ is the strain rate tensor, and ω_{ij} is the spin rate tensor. This constitutive model can be effectively used in the case of large deformation, where rigid body rotations may occur.

A variety of special materials formulations are also available through equations of state, to deal with cases where extremely large pressures take place, such as in the case of explosive materials

Basic Formulation in DYNA3D

Momentum Conservation Principle

The formulation is based on equations of motion derived from the momentum conservation principle, which can be expressed as follows:

$$\sigma_{ij,j} + \rho f_i = \rho \ddot{x}_i \qquad [7]$$

the traction boundary conditions $\sigma_{ij}\mathbf{n}_i = t_i(t)$ on boundary ∂b_1, displacement boundary conditions $x_i(X_a, t) = D_1(t)$ on boundary ∂b_2, and contact discontinuity $(\sigma_{ij}^{+} - \sigma_{ij}^{-})n_i = 0$ along the interior boundary ∂b_3, for $x_i^{+} = x_i^{-}$, where σ represents the Cauchy stress, ρ is the density and f_i is the body force, $\ddot{x}$ is the acceleration, the comma designates a covariant differentiation, and $\mathbf{n}_i$ is a unit vector normal to the boundary ∂b.

The energy equation can be integrated in time for energy balance and state evaluations. The equation is given by:

$$\dot{E} = Vs_{ij}\dot{\varepsilon}_{ij} - (p+q)\dot{V} \qquad [8]$$

which yields the weak form of the equation of equilibrium, where variation δx_i satisfies all boundary conditions on ∂b_2 as follows:

$$\int_{v} \left(\rho \ddot{x}_i - \sigma_{ij,j} - \rho f\right) \delta x_i \, \mathrm{d}v + \int_{\partial b_1} \left(\sigma_{ij} n_j - t_i\right) \delta x_i \, \mathrm{d}s + \int_{\partial b_2} (\sigma_{ij}^{+} - \sigma_{ij}^{-}) n_i \, \delta x_i \, \mathrm{d}s = 0 \qquad [9]$$

Application of the stationarity conditions leads to the virtual work principle and the following expression:

$$\delta\pi = \int_{v} \rho \ddot{x}_i \, \delta x_i \, \mathrm{d}v + \int_{v} \sigma_{ij} \, \delta x_{i,j} \, \mathrm{d}v - \int_{v} \rho f_i \, \delta x_i \, \mathrm{d}v - \int_{\partial b_1} t_i \, \delta x_i \, \mathrm{d}s = 0 \qquad [10]$$

This variation can be integrated by assembling the individual integrals of each FE yielding the global

(over m elements) FE equilibrium equations as follows:

$$\sum_{m=1}^{n}\left\{\int_{v_m}\rho\mathbf{N}^{\mathrm{T}}\mathbf{N}a\,\mathrm{d}v+\int_{v_m}\mathbf{B}^{\mathrm{T}}\sigma\,\mathrm{d}v-\int_{v_m}\rho\mathbf{N}^{\mathrm{T}}b\,\mathrm{d}v-\int_{\partial b_1}\mathbf{N}^{\mathrm{T}}t\,\mathrm{d}s\right\}^{m}=0 \quad [11]$$

Subsequently, the explicit central difference method is used to integrate the equations of motion.

Vibrations and Shock Wave Propagation

Colliding structures are in reality vibration systems subjected to impact loads that excite various natural modes and produce elastic and plastic waves traveling at various speeds through the structure. The crushing behavior is characterized by local buckling as a result of the impulse, the bulk viscosity and associated shock waves, the natural modes of the structure and the energy release from the crushing behavior. Given the relevance of wave propagation phenomena in the analysis of colliding structures, several issues are extremely important in the application of crashworthiness procedures. Specifically, the relationships between the speed of sound through the material, the frequencies of the natural modes of vibration, the critical damping, the time step required to maintain numerical stability and the mesh size used in the model. All these features are reflected in the models used, which are in general nonlinear.

On the Contact Algorithms

DYNA3D uses three approaches for dealing with the impact contact and sliding interfaces of models. The methods are known as the 'kinematic constraint method', the 'penalty method' and the 'distributed parameter method'. In the first method, constraints are imposed to the global equations by a transformation of the nodal displacement component of the 'slave' nodes along the contact interfaces. This way only the global degrees of freedom of each master node are coupled. This method requires consistent zoning of the interfaces. In the 'penalty method', artificial interference springs are placed normal to the contacting surfaces on all the penetrating nodes. The spring elements are assembled in the global stiffness matrix and their modulus is determined based on the elements in which the nodes reside. This is a stable method and produces little noise for hourglassing modes. However, for relatively large interface pressures, the stiffness has to be scaled up and the time step reduced. In such cases, the third method 'distributed parameters' is recommended. This last method is used primarily for 'sliding' interfaces, in which the internal stress in each element in contact determines the pressure distribution for the corresponding master surface. Accelerations are updated after mass and pressure distributions on the master surface are completed. With these three algorithms, most contact conditions can be simulated. See **Table 3**.

Table 3 Contact interfaces in DYNA3D

Type of interface	*Description*
1	Sliding only for fluid/structure or gas/structure interfaces
2	Tied
3	Sliding, impact, friction
4	Single surface contact
5	Discrete nodes impacting surface
6	Discrete nodes tied to surface
7	Shell edge tied to shell surface
8	Nodes spot weld to surface
9	Tiebreak interface
10	One-way treatment of sliding impact friction
11	Box-material limited automatic contact for shells
12	Automatic contact for shells
13	Automatic single surface with beams and arbitrary orientations
14	Surface-to-surface eroding contact
15	Node-to-surface eroding contact
16	Single surface eroding contact
17	Surface-to-surface symmetric constraint method
18	Node-to-surface constraint method
19	Rigid-body to rigid-body contact with arbitrary force/deflection curve
20	Rigid nodes to rigid-body contact with arbitrary force/deflection curve
21	Single-edge contact
22	Drawbead

Economic Elements and Hourglassing

Explicit time integration schemes call for the so-called 'economic' finite elements. These are isoparametric element formulations with one integration or Gauss point, to minimize the computational time. These type of integration give rise to the possibility of 'zero energy' modes, which produce the 'hourglass mode shapes' with zero energy. This is an undesirable effect and must be prevented. To illustrate, let us consider the strain rate for an eight-node solid element:

$$\dot{\varepsilon}_{ij}=\frac{1}{2}\left[\sum_{k=1}^{8}\frac{\partial\phi_k}{\partial x_i}\dot{x}_j^k+\frac{\partial\phi_k}{\partial x_i}\dot{x}_i^k\right] \quad [12]$$

If diagonally opposite nodes have identical velocities, then the strain energy rates are identically zero ($\dot{\varepsilon}_{ij} = 0$), that is when the following 'hourglassing' conditions occur:

$$\dot{x}_i^1 = \dot{x}_i^7, \quad \dot{x}_i^2 = \dot{x}_i^8, \quad \dot{x}_i^3 = \dot{x}_i^5, \quad \dot{x}_i^4 = \dot{x}_i^6 \qquad [13]$$

Hourglass modes can be avoided by the use of artificial forces consistent with the orthogonal nature of the modes, ($\Gamma_{\alpha k}$) and related to the element volume and material sound speed. The nodal velocities for these modes are given by:

$$h_{i\alpha} = \sum_{k=1}^{8} \dot{x}_i^k \Gamma_{\alpha k} = 0 \qquad [14]$$

And the resisting hourglass forces are defined as:

$$f_{i\alpha}^k = a_h h_{i\alpha} \Gamma_{\alpha k} \quad \text{and} \quad a_h = Q_{hg} \rho v_e^{2/3} \frac{c}{4} \qquad [15]$$

where Q_{hg} is an empirical constant defined between 0.05 and 0.15. Refined finite element meshing of components tends to reduce the hourglassing modes, which otherwise produce artificial energies in excess of the initial energy of the system.

Component Crashworthiness Roles

Upon a collision, the components of a vehicle–occupant system play a certain role or function. In general, the key functions are:

1. *Energy absorption of colliding elements*. Generally, the elements that are to make contact first with another vehicle, object or barrier in a collision are intended to absorb energy upon impact by collapsing in controlled modes, acting as dampers to the passenger cabin. Bumpers and front rails of vehicles are typical structural elements intended to dissipate energy in case of collisions. The frontal rails connecting to the bumper supports for example are now designed with 'crush initiators', as intended imperfections in the form of notches on strategic locations, to ensure the collapse occurs in a prescribed manner.

   Polyurethane-foam filled tubing and honeycomb sandwich panels are components typically used to provide higher stiffness at reduced weights while providing additional energy absorbing capabilities. Crashworthiness codes such as DYNA3D are capable of using these types of structural components and strain rate dependent materials for crashworthiness analyses.

2. *Energy absorption of interior surfaces*. Occupants of colliding vehicles can be subject to severe impacts with interior elements and surfaces of the vehicle. A primary concern was the likelihood of contact between the occupant's head and the interior hard surfaces of the vehicle, such as the A–pillar (front), the B–pillar (mid-post), the dashboard (passenger side) and the steering wheel.

   The use of polyurethane foam materials for interior cushioning is mainly intended to reduce the severity of impact on the head, as designated by the term known as 'head injury criteria' (HIC), which is expressed as follows:

$$\text{HIC} = (t_2 - t_1) \left[\frac{1}{(t_2 - t_1)} \int_{t_1}^{t_2} \ddot{x}(t)\, \mathrm{d}t \right]_{\max}^{2.5} \qquad [16]$$

   The time interval for which this equation applies is approximately 15 ms and the interval must be taken in such a way that the maximum value of HIC is obtained. If the value reaches a value of 1000, severe injury to the head is likely to occur. Using this criteria, the most important state variable is the head's *cg* overall acceleration.

   While HIC is a standard accepted index for assessment of vehicle passenger performance under collision loads, HIC alone is not sufficient to describe the mechanism of head injury. For that matter not only the head is important; head–neck complex as well as thorax response and lower limb interaction with vehicle interior are all important indicators of crashworthiness of a particular vehicle.

3. *Structural integrity of passenger cabin*. While some structural elements are meant to dissipate energy in the event of a collision, the structural members that comprise the passenger cabin are meant to maintain the structural integrity. This means allowing only minimum deformations and keeping the occupant space envelope from being invaded. For this purpose, the structural components of the passenger cabin are designed to provide high stiffness and strength. Some of the members in a cabin are intended to provide rollover protection, others are intended to provide lateral impact protection. In all cases the stiffness-to-weight ratio is very important due to the trend towards lighter and more efficient vehicles. Polyurethane foam-filled tubing profiles and honeycomb-sandwiched panels can provide increased stiffness properties at reduced weights. Another important function of the passenger cabin structural elements is to prevent intrusion of objects into

the passenger space envelope. Reinforced vehicle doors are examples of elements that provide that kind of protection in the case of lateral impacts.

4. *Occupant restraint systems*. It was stated above that in the case of a frontal collision, the decelerations of an unrestrained occupant could be an order of magnitude larger than that of the passenger cabin. Thus, the occupant restraint systems have as main function to reduce the magnitude of the decelerations of the occupant. Two types of restraint systems are used in vehicles. The passive ones are the seat belts, and the active ones are air bags. Modeling seat belts requires the use of elements that can interface with the occupant and vehicle and provide membrane stiffness only. Crashworthiness FE codes permit the use of 'fabric' material that provides the membrane properties needed to model the seat belt; the number of points of anchorage, their location and the amount of 'slack' in the belt being the key design factors to consider.

   Air bags provide active protection in the case of a collision. At issue is the presence of a cushion between the passenger and the hard surfaces of the vehicle interior immediately after a collision. The issues involve the inflation pressure level required for deployment of the airbag in the first few milliseconds following the collision and the interaction with the occupant afterward. But in cases of proximity of occupant and passenger prior to the collision, the airbag deployment itself may produce injuries to the occupant depending on the inflation pressure and the resulting head accelerations after deployment. Airbags are primarily aimed at reducing head injuries. Thus the HIC can also be applied for the assessment of airbag adequacy. Some airbags have also been considered to protect the occupants from lateral impacts.

Bioengineering Considerations

Human Body Structures

A major effort in crashworthiness technology development has been directed at the representation of human body structures for crashworthiness study. From the kinematics point of view, a human body can be represented as an articulated system with kinematic degrees of freedom, certain mass distribution and some degree of flexibility and relative motion stiffness.

Three approaches have been followed in crashworthiness studies. The first approach uses models that capture human body segment mobility and general mass distribution. These models can produce useful information about general displacements, velocities and accelerations of body segments during a collision, but do not capture the nature of the human body internal anatomy and thus, they cannot be used to assess detailed interactions between vehicle and occupants.

The second approach is to model the structure of dummies, which in turn are designed with the sole purpose of mimicking the human body response in experimental vehicle collisions for crashworthiness assessments. The development of the 'Hybrid III Family' is the result of many years of crashworthiness technology development pursuing biofidelity between the dummies and the human body for the 50-percentile male, female, and children of several ages. MADYMO^{TM} code provides a database for modeling validated standard dummies.

The third approach is to model human body structures in such a way that human body compliance in terms of flexibility and inertia are taken into consideration in the analyses. The FE models that have been developed in this area are intended to describe the dynamics of human body structures involved in vehicle collisions and to produce a better understanding of the likely injuries that occupants may possibly sustain. A number of models can be found in literature for head–neck complex, for thorax and spine complex and for lower extremities that reflect anatomically correct features.

There are two key issues in modeling human body structures; one is the complex geometry of body parts, including bones and internal organs. This task is extremely tedious but has been advanced greatly by the availability of the 'visible human project'. Yet, the development of accurate FE models calls for appropriate material characterization of body tissue, from various bone structures to soft tissue and membrane materials. One example that illustrates the importance of material characterization can be found in modeling of the human head for impact assessment. Several FE models have been proposed with material properties for the brain tissue

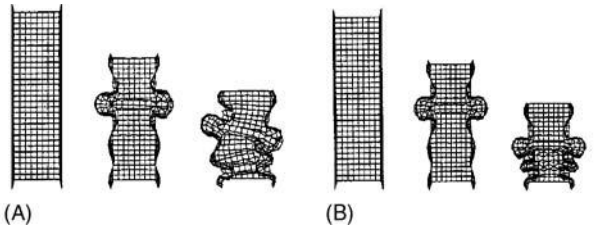


Figure 1 Impact crushing behavior of a square tubing with (A) and without (B) a mild load offset (0.2 mm/300 mm length).

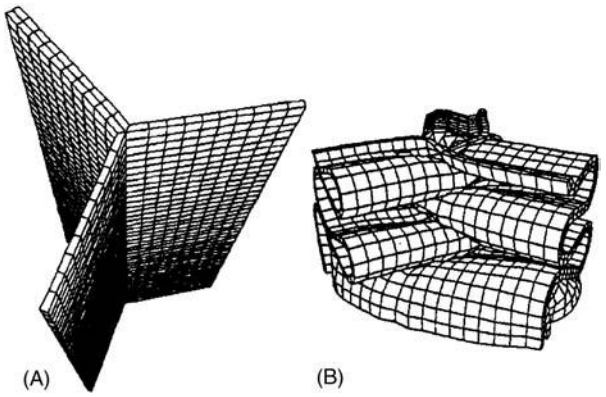


Figure 2 Honeycomb cell segment crushing under axial loading. (A) Honeycomb cell segment; (B) honeycomb cell segment crushing under axial load.

that produces a different response. At issue is how the material properties affect the standards used to assess head injury, specifically, the HIC.

Application Examples

Application examples can be found in many fields, from the solid mechanics general examples (cylindrical shells under axial impact) to automotive structures under various collision scenarios. **Figure 1** shows the crushing of a square tubing under axial impact loading. Notice the accordion folding of the walls of the tube in such a way that the surface produces contact with itself as it folds. The use of a 'single surface' contact is illustrated in this example. The same figure illustrates the effect of a mild load

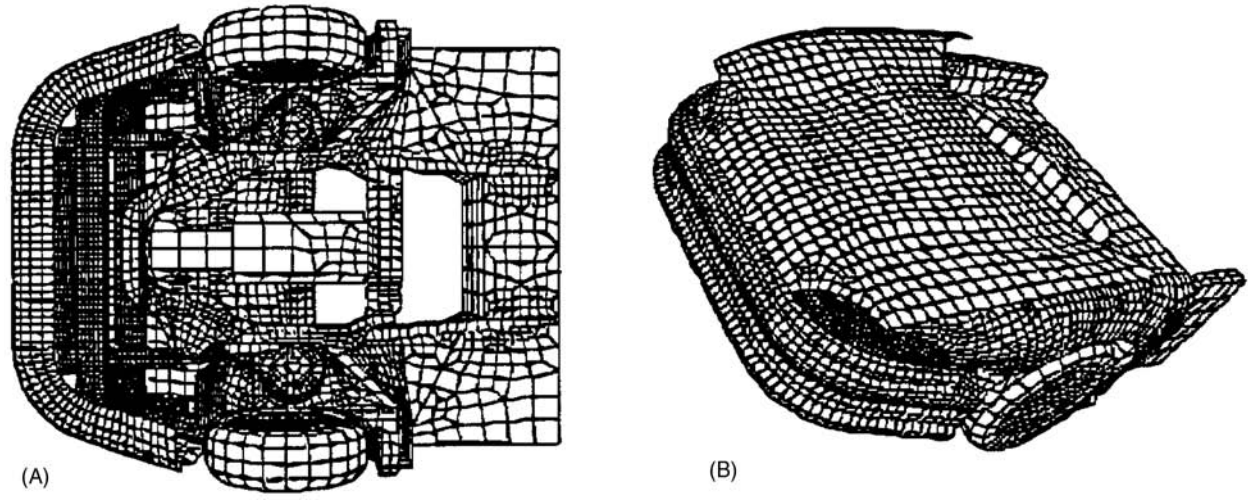


Figure 3 Example of a vehicle front-end used in a frontal collision simulation. (A) Under view; (B) isometric view.

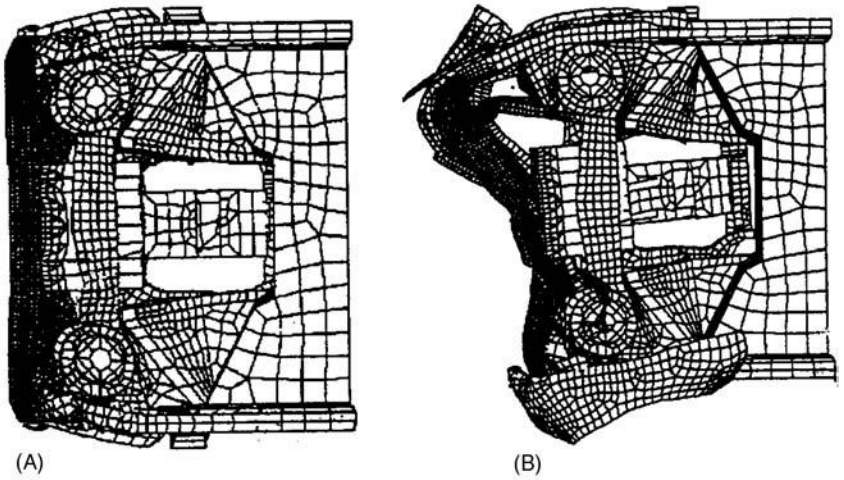


Figure 4 Examples of frontal collision simulation of a midsize vehicle. (A) Frontal collision of front end of vehicle against rigid wall (under view); (B) offset frontal collision of front end of vehicle against rigid wall (under view).

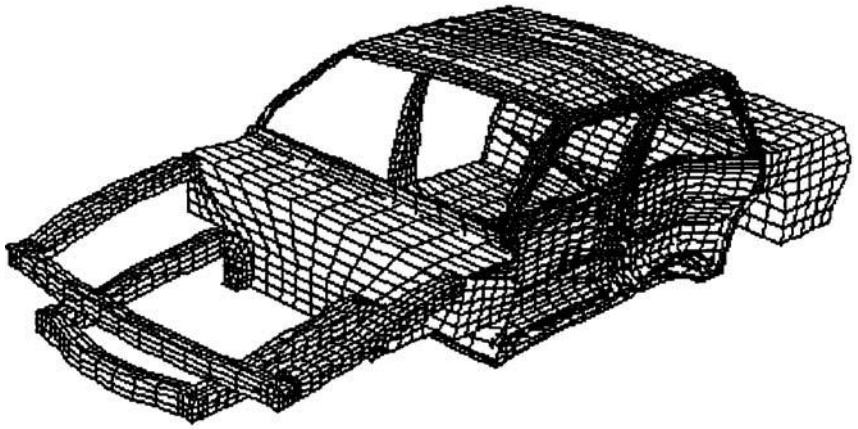


Figure 5 Example of a passenger cabin used in a lateral collision simulation.

offset of 0.02 mm over the length of the tube (300 mm), producing asymmetric crushing. A similar example shows the analysis of a cell segment of a honeycomb arrangement under crushing axial loads. **Figure 2** illustrates the crushing modes that can be used to characterize a honeycomb material using the 'user-defined' material 26 in DYNA3D. A more classical application of crashworthiness is illustrated in the front-end model of a midsize sedan for the purpose of frontal collision assessment (see **Figure 3**). Such a model can be used for several frontal collision scenarios, as illustrated in **Figure 4**, illustrating a frontal collision against a rigid wall and against an offset collision.The case of a lateral collision is illustrated in **Figure 5**. The structural integrity of the passenger cabin becomes the central issue, as well as the performance of the doors with reinforcing bars. The US–NHTSA maintains a public website with a variety of generic FE models, developed for the purpose of crashworthiness assessments of vehicles under various loading conditions. A variety of vehicle models are included, compact, midsize sedans, sports utility vehicles, pickup trucks, school bus, etc. In addition, some models have been developed to address human body response in a colliding vehicle. One such model is shown in **Figure 6**, demonstrating a compact vehicle running against a rigid wall. The occupant has received significant attention in the crashworthiness studies. One example is the study of restraint systems in the event of a collision. At issue is the deceleration of the occupant following the collision. **Figure 7** illustrates the model of an occupant, represented by the model of a dummy, and the response under frontal impact. Seat belts (and airbags as well) are modeled using membrane elements, capable of carrying tension but not compression. Another important application of crashworthiness is the study of human body structures to impact loads. Crashworthiness studies have been successfully applied for the study of the dynamic response of different human parts to impact. An example is the response of the human head. **Figure 8** shows a model

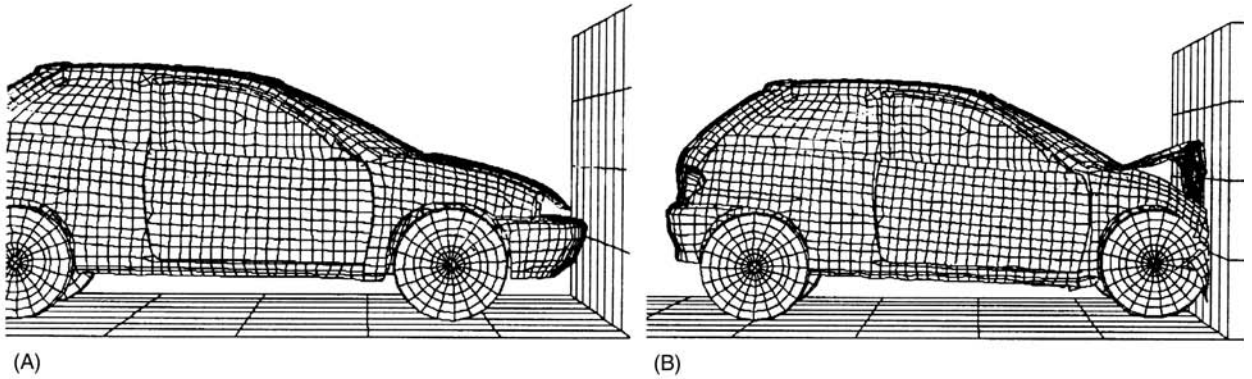


Figure 6 Compact vehicle simulation of a frontal collision against a rigid wall.

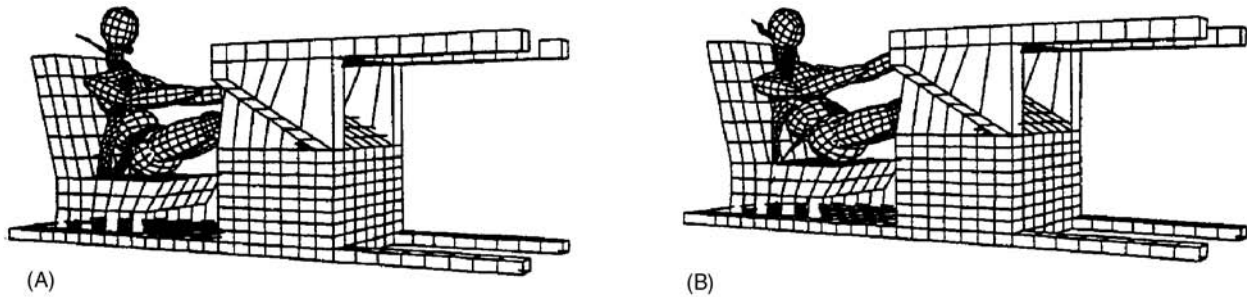


Figure 7 Example of a passenger restraint system (seat belt) under frontal collision.

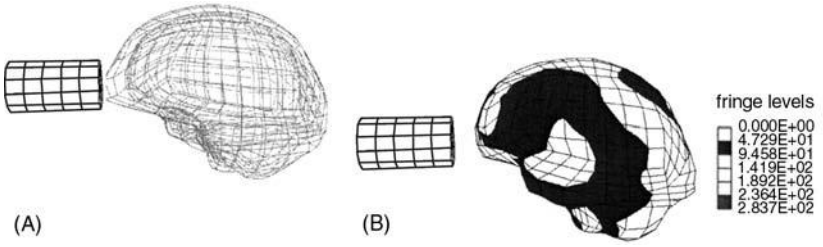


Figure 8 Human head under frontal impact. (A) Skull brain cavity and brain mass; (B) brain mass stress response immediately after impact (at 5 ms).

developed in which the brain cavity is modeled (skull and brain mass) and then subjected to a frontal impact. The stress waves on the brain mass can be analyzed using visco-elastic materials for the brain mass and elastic properties for the skull. At issue are the maximum pressures developed in the brain mass and the effect of the visco-elastic vs elastic brain material assumptions.

Conclusions

Crashworthiness has matured into a multidisciplinary area with a wide range of applications: in vehicle design, aircraft design, military ballistics, bioengineering, sports gear design, metal forming processes, particle impact erosion, cold working processes. The disciplines involved in the development of crashworthiness include computational mechanics, fluid–structure interactions, materials science, composite materials, honeycomb stiffened structures, polyurethane foam filled tubing, glass breaking, etc.

Yet certain areas remain a challenge to the crashworthiness technologies. Specifically, the mechanisms of fracture mechanics and the failure of intricate materials like composite laminates, and braided composite materials. Fluid–structure interaction as well as gas–structure interactions are clearly applications where challenges lie ahead.

An important challenge lies ahead in terms of applying crashworthiness principles for the study and prevention of fatal accidents involving heavy-duty vehicles. In the case of heavy-duty tanker trucks for example, the sloshing dynamics may produce instabilities that can cause rollover accidents. Substance containment to prevent spills and collision with transportation structures are topics yet to be fully addressed using crashworthiness techniques.

Perhaps one of the most important challenges lying ahead is in the comprehensive integration of crashworthiness principles in the design practice that relates not only to vehicles but to other systems, such as aircraft structures, transportation structures, and the ever challenging area of human structures.

Nomenclature

$\mathbf{B}$	strain-displacement matrix
E	total energy
f_i	body force
f^k_{ia}	hourglass resisting force
h_{ia}	nodal velocities
HIC	head injury criterion
$\mathbf{N}$	interpolation function matrix
p	pressure
q	bulk viscosity
Q_{hg}	empirical constant

s_{ij}	deviatoric stress
t	time parameter
v_m	element volume
V	relative volume
x^n	displacement at the nth time increment
x^n	velocity at the nth time increment
x^n	acceleration at the nth time increment
δx	virtual displacement
δ_{ij}	Kronecker delta
$\delta\pi$	variation of energy functional
ε_{ij}	strain tensor
$\dot{\varepsilon}_{ij}$	strain rate tensor
ϕ_k	shape function
Γ_{ak}	hourglass mode
ρ	density
σ_{ij}	stress tensor
σ^*_{ij}	Jaumann rate of the Cauchy stress
$\dot{\sigma}_{ij}$	material derivative of the stress
ω_{ij}	spin rate tensor
∂b_i	domain boundary i
$\partial/\partial x$	partial differentiation operator with respect to x

See also: **Active control of vehicle vibration**; **Basic principles**; **Computation for transient and impact dynamics**; **Finite element methods**.

Further Reading

Aida T (2000) *Study of Human Head Impact: Brain Tissue Constitutive Models*. PhD Dissertation, University West Virginia, May.

Allison D (1995) *Seymour Cray Interview*. http://american-history.si.edu/csr/comphist/cray.htm.

Armen H, Pifko A, Levine H (1975) *Nonlinear Finite Element Techniques for Aircraft Crash Analysis*. Aircraft Crashworthiness Symposium, Cincinnati, pp. 517–548.

Belytscho T, Schwer L, Klein MJ (1977) Large displacement transient analysis of space frames. *International Journal for Numerical and Analytical Methods in Engineering* 11: 65–84.

Belytscho T, Tsay CS (1981) Explicit algorithms for nonlinear dynamics of shells. *AMD* 48: 209–231.

Belytscho T, Tsay CS (1983) A stabilization procedure for the quadrilateral plate element with one-point quadrature. *International Journal of Numerical Methods in Engineering* 19: 405–419.

Flanagan DP, Belytscho T (1981) A uniform strain hexahedron and quadrilateral and orthogonal hourglass control. *International Journal of Numerical Methods in Engineering* 17: 679–706.

Hallquist JO (1976) *A Procedure for the Solution of Finite Deformation Contact-Impact Problems by the Finite Element Method*. University of California: Lawrence Livermore National Laboratory, rept. UCRL-52066.

Hallquist JO (1996) *Preliminary User's Manuals for DYNA3D and DYNAP (Nonlinear Dynamic Analysis of Solids in Three Dimensions)*. University of California: Lawrence Livermore National Laboratory, rept. UCID-17268 (Rev. 1, 1979).

Hallquist JO, Gourdeau GL, Benson DJ (1985) Sliding interfaces with contact-impact in large-scale Lagrangian computations. *Computer Methods in Applied Mechanics and Engineering* 51; 107–137.

Hughes TJR, Liu WK (1981) Nonlinear finite element analysis of shells: part I, two dimensional shells. *Computer Methods in Applied Mechanics* 27: 167–181.

Hughes TJR, Liu WK (1981) Nonlinear finite element analysis of shells: part II, three dimensional shells. *Computer Methods in Applied Mechanics* 27: 331–362.

Kamal MM (1970) Analysis and simulation of vehicle to barrier impact. *SAE Transactions* 79: 1498–1503.

Kamal MM, Wolf JA (1977) Finite element models for automotive vehicle vibrations. In: *ASME Finite Element Applications in Vibration Problems*, presented at the Design Engineering Technical Conference, Chicago, IL, Sept. 26–28.

Kan S, FHWA/NHTSA *National Crash Analysis Center*, Public Finite Element Model Archive. http://www.ncac.gwu.edu/archives/model/index.html.

Lin KH (1973) A rear-end barrier impact simulation model for uni-body passenger cars. *SAE Transactions* 82: pp. 628–634.

Macmillan RH (1970) *Vehicle Impact Testing*. SAE paper no. 700404. Warrendale, PA: International Automobile Safety Conference Compendium.

Martin DE, Kroel CK (1967) Vehicle crash and occupant behavior. Paper no. 670034. *Transactions of the SAE* 76: 236–258.

McHenry RR, Naab KN (1966) Computer simulation of the crash victim: a validation study. *Proceedings of the Tenth Stapp Car Crash Conference*. November pp. 126–163.

McIvor IK Wineman AS, Wang HC (1975) *Large Dynamic Plastic Deformation of General Frames*. Twelfth Meeting of the Society of Engineering Science, University of Texas, October, pp. 1181–1190.

Melosh RJ (1972) *Car-Barrier Impact Response of a Computer Simulated Mustang*. DOT-NHTSA Report DOT-HS-091-1-125A.

Melosh RJ, Kelly DM (1967) The potential for predicting flexible car crash response. *SEA Transactions* 76: 2835–2842.

OECD *International Road Traffic and Accident Database, Brief Overview*. IRTAD. http://www.bast.de/irtad/english/irtadlan.htm.

Ruan JS, Khalil T, King AI (1991) Human head dynamic response to side impact by finite element modeling. *ASME Journal of Biomechanical Engineering* 113: 276–283.

US National Library of Medicine, *The Visible Human Project*. http://www.nlm.nih.gov/research/visible/visible–human.html.

US–DOT, National Highway Traffic Safety Administration *The Federal Motor Vehicle Safety Standards and Regulations Brochure*. http://www.nhtsa.dot.gov/cars/rules/import/FMVSS/SN219.

USA Office of the Federal Register. *The Code of Federal Regulations*, title, 49, subtitle B, chapter V, part 571, subpart B, section 571.216.

Van Leer B (1977) Towards the ultimate conservative difference scheme. IV. A new approach to numerical convention. *Journal of Computational Physics* 23: 276–299.

Welch RE, Bruce RW, Belytscho T. (1976) *Finite Element Analysis of Automotive Structures Under Crash Loadings*. Report no. DOT-HS-810 847. U.S. Department of Transportation.

Wilson RA (1970) A review of vehicle impact testing: how it began and what is being done. Paper no. 700414. *SAE Transactions* 79:1498–1503.

Yang KY, Wang KH (1998) *Finite Element Modeling of the Human Thorax*. http://www.nlm.nih.gov/research/visible/vhpconf98/AUTHORS/YANG/YANG.HTM.

CRITICAL DAMPING

D Inman, Virginia Polytechnic Institute and State University, Blacksburg, VA, USA

Copyright © 2001 Academic Press

doi: 10.1006/rwvb.2001.0061

Critical damping is defined for linear, single-degree-of-freedom systems with viscous damping. It is based on the three stable solutions to a second-order, ordinary differential equation with constant coefficients and corresponds to the case of repeated, real roots in the characteristic equation. Physically, critical damping corresponds to that value of damping that separates oscillation from nonoscillation of the free response. Thus, critical damping is also the minimum amount of damping that a spring-mass-damper system can have and not vibrate. If such a system has a smaller than critical amount of damping it will oscillate.

Critical damping is also the numerical value used to nondimensionalize damping parameters to produce a damping ratio. Experimentalists and analysts alike use the percent critical damping as a dimensionless parameter for describing the amount of damping in a system. Percent critical damping is also used in performance specifications and in design.

Although critical damping is defined for a single-degree-of-freedom, spring-mass-damper system, it is also routinely applied to modal equations where it appears as a modal damping ratio. The modal damping ratio extends the concept of critical damping to multiple-degree-of-freedom systems. The same is true for systems described by distributed mass models. The extension of the concept of critical damping to both lumped and distributed mass models is straightforward, yet somewhat buried in mathematical details.

Definition of Critical Damping

Critical damping is defined for a single-degree-of-freedom, spring-mass-damper arrangement, as illustrated in **Figure 1**. The equation of motion for this system is found from Newton's law and the free-body diagram to be:

$$m\ddot{x}(t) + c\dot{x}(t) + kx(t) = 0 \qquad [1]$$

Here $x(t)$ is the displacement in meters, $\dot{x}(t)$ is the velocity in meters per second, $\ddot{x}(t)$ is the acceleration in meters per second per second, m is the mass in kilograms, k is thestiffness in Newtons per meter and c is the damping coefficient in Newton second per meter or kilograms per second. Eqn [1] is written in dimensionless form by dividing the expression by the mass. This yields:

$$\ddot{x}(t) + 2\zeta\omega_n\dot{x}(t) + \omega_n^2 x(t) = 0 \qquad [2]$$

Here the undamped natural frequency is defined to be:

$$\omega_n = \sqrt{k/m} \qquad [3]$$

(in radians per second) and the damping ratio is defined to be:

$$\zeta = \frac{c}{2m\omega_n} = \frac{c}{2\sqrt{km}} \qquad [4]$$

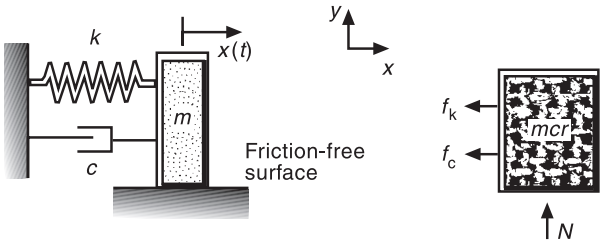


Figure 1 A single-degree-of-freedom system and free-body diagram.

which is dimensionless.

To solve the differential equation given in eqn [2], a solution of the form $x(t) = Ae^{\lambda t}$ is assumed and substituted into eqn [2] to yield:

$$\lambda^2 + 2\zeta\omega_n\lambda + \omega_n^2 = 0 \qquad [5]$$

which is called the characteristic equation in the unknown parameter λ. This process effectively changes the differential eqn [2] into a quadratic algebraic equation with a well-known solution. The value of λ satisfying eqn [5] is then:

$$\lambda = -\zeta\omega_n \pm \omega_n\sqrt{\zeta^2 - 1} \qquad [6]$$

which are the two roots of the characteristic equation. It is the radical expression that gives rise to the concept of critical damping. If the radical expression is zero, that is, if:

$$\zeta^2 = 1 \qquad [7]$$

the system of **Figure 1** is said to be critically damped. If $\zeta = 1$, then the corresponding damping coefficient c is called the critical damping coefficient, c_{cr}, by:

$$c_{cr} = 2m\,\omega_n = 2\sqrt{km} \qquad [8]$$

obtained by setting $\zeta = 1$ in eqn [4].

The mathematical significance of $\zeta = 1$ is that the two roots given in eqn [6] collapse to a repeated real root of value $\lambda = -\omega_n$. The solution to the vibration problem given in eqn [1] then becomes:

$$x(t) = (a_1 + a_2 t)e^{-\omega_n t} \qquad [9]$$

where the constants of integration a_1 and a_2 are determined by the initial conditions. Substituting the initial displacement, x_0, into eqn [10] and the initial velocity, v_0, into the derivative of eqn [10] yields:

$$a_1 = x_0, \quad \text{and} \quad a_2 = v_0 + \omega_n x_0 \qquad [10]$$

Critically damped motion is plotted in **Figure 2** for two different values of initial conditions. Notice that no oscillation occurs in this response.

The motion of critically damped systems may be thought of in several ways. First, a critically damped system represents a system with the smallest value of damping coefficient that yields aperiodic motion. If $\zeta > 1$, the roots given in eqn [6] are distinct, real roots giving rise to solutions of the form:

$$x(t) = e^{-\zeta\omega_n t}\left(a_1 e^{-\omega_n\sqrt{\zeta^2-1}\,t} + a_2 e^{+\omega_n\sqrt{\zeta^2-1}\,t}\right) \qquad [11]$$

which also represents a nonoscillatory response. Again, the constants of integration a_1 and a_2 are determined by the initial conditions. In this aperiodic case, the constants of integration are real valued and are given by:

$$a_1 = \frac{-v_0 + \left(-\zeta + \sqrt{\zeta^2 - 1}\right)\omega_n x_0}{2\omega_n\sqrt{\zeta^2 - 1}} \qquad [12]$$

and

$$a_2 = \frac{-v_0 + \left(\zeta + \sqrt{\zeta^2 - 1}\right)\omega_n x_0}{2\omega_n\sqrt{\zeta^2 - 1}} \qquad [13]$$

Such a response is called an overdamped system and does not oscillate, but rather returns to its rest position exponentially.

If the damping value is reduced below the critical value, so that $\zeta < 1$, the discriminant of eqn [6] is negative, resulting in a complex conjugate pair of roots. These are:

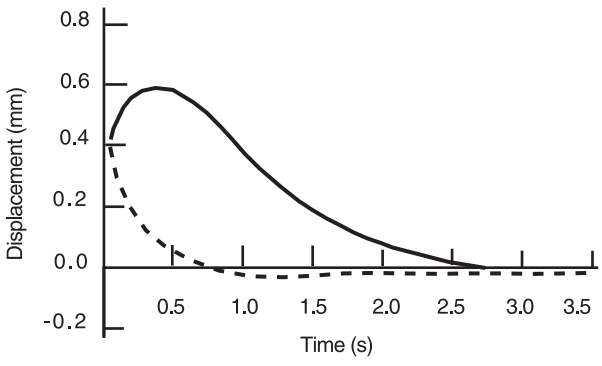


Figure 2 The critically damped response for two different initial conditions.

$$\lambda_1 = -\zeta\omega_n - \omega_n\sqrt{1-\zeta^2}\,j \qquad [14]$$

and:

$$\lambda_2 = -\zeta\omega_n + \omega_n\sqrt{1-\zeta^2}\,j \qquad [15]$$

where $j = \sqrt{-1}$ and:

$$\sqrt{1-\zeta^2}\,j = \sqrt{(1-\zeta^2)(-1)} = \sqrt{\zeta^2-1} \qquad [16]$$

The solution of eqn [1] is then of the form:

$$x(t) = \mathrm{e}^{-\zeta\omega_n t}\left(a_1\mathrm{e}^{j\sqrt{1-\zeta^2}\omega_n t} + a_2\mathrm{e}^{-j\sqrt{1-\zeta^2}\omega_n t}\right) \qquad [17]$$

where a_1 and a_2 are arbitrary complex valued constants of integration to be determined by the initial conditions. Using the Euler relations for the sine function, this can be written as:

$$x(t) = A\mathrm{e}^{-\zeta\omega_n t}\sin(\omega_\mathrm{d} t + \phi) \qquad [18]$$

where A and ϕ are constants of integration and ω_d, called the damped natural frequency, is given by:

$$\omega_\mathrm{d} = \omega_\mathrm{n}\sqrt{1-\zeta^2} \qquad [19]$$

The constants A and ϕ are evaluated using the initial conditions. This yields:

$$A = \sqrt{\frac{(v_0 + \zeta\omega_n x_0)^2 + (x_0\omega_\mathrm{d})^2}{\omega_\mathrm{d}^2}}, \qquad \phi = \tan^{-1}\left[\frac{x_0\omega_\mathrm{d}}{v_0 + \zeta\omega_n x_0}\right] \qquad [20]$$

where x_0 and v_0 are the initial displacement and velocity. Note that for this case $(0 < \zeta < 1)$ the motion oscillates. This is called an underdamped system. Hence, if the damping is less then critical, the motion vibrates, and critical damping corresponds to the smallest value of damping that results in no vibration. Critical damping can also be thought of as the value of damping that separates nonoscillation from oscillation.

The concept of critical damping provides a useful value to discuss level of damping in a system, separating the physical phenomenon of oscillation and no oscillation. Often when reporting levels of damping, the percent of critical damping is provided. The percent critical damping is defined as $100\zeta\%$ or:

$$\frac{c}{c_\mathrm{cr}} \times 100 \qquad [21]$$

Normal values for ζ are very small, such as 0.001, so that percent critical damping is of the order of 0.1–1%. However, viscoelastic materials, hydraulic dampers, and active control systems are able to provide large values of percent critical damping.

Critical damping viewed as the minimum value of damping that prevents oscillation is a desirable solution to many vibration problems. Increased damping implies more energy dissipation, and more phase lag in the response of a system. Reduced damping means more oscillation, which is often undesirable. Adding phase to the system slows the response down and in some cases this may be undesirable. Hence, critical damping is a desirable tradeoff between having enough damping to prevent oscillation and not so much damping that the system uses too much energy or causes too large a phase lag.

An example of the use of critical damping is in the closing of a door. If the mechanism has too much damping, the door will move slowly and too much heat will exchange between the inside and outside. If too little damping is used the door will oscillate at closing and again too much air and heat is exchanged. At critical damping the door closes without oscillation and a minimum amount of air and heat are exchanged. The needle gauges used in tachometers and speedometers in automobiles provide additional examples of critically damped systems. The needle operates as a torsional spring with critical damping. Too much damping would make the gauge slow to reach the actual value and too little damping would cause the needle to vibrate.

Critical Damping in Lumped Parameter Models

The concept of critical damping may be defined for multiple-degree-of-freedom systems. First consider the model used for such systems. A linear multiple-degree-of-freedom system may be modeled by the vector differential equation:

$$\mathbf{M}\ddot{\mathbf{x}}(t) + \mathbf{C}\dot{\mathbf{x}}(t) + \mathbf{K}\mathbf{x}(t) = 0 \qquad [22]$$

where **M**, **C**, and **K** are the usual mass, damping, and stiffness matrices, respectively. These coefficient matrices are real-valued and of size $n \times n$ where n is the number of degrees of freedom. Each matrix is assumed to be positive-definite and symmetric. The vector $\mathbf{x}(t)$ is an $n \times 1$ vector of displacements with the over dots denoting the time derivatives yielding velocity and acceleration.

The system described by eqn [22] may be divided into two important subclasses depending on the nature of the damping matrix **C**. Either the equations of motion [22] can be decoupled into n independent equations with real constant coefficients or they cannot. A necessary and sufficient condition for the equations to decouple is:

$$\mathbf{C}\mathbf{M}^{-1}\mathbf{K} = \mathbf{K}\mathbf{M}^{-1}\mathbf{C} \qquad [23]$$

If eqn [22] holds, then such systems are sometimes said to have classical, proportional, or modal damping. In this case the modal matrix of the undamped system can be used to decouple the equations of motion into n single-degree-of-freedom systems. Let **P** be the modal matrix (the matrix with columns made up of the mode shapes of the undamped system, normalized with respect to the mass matrix **M**, such that $\mathbf{P}^{-1}\mathbf{M}\mathbf{P} = \mathbf{I}$, the $n \times n$ identity matrix). Then substitution of $\mathbf{x} = \mathbf{P}\mathbf{r}$ in eqn [1] and multiplying by $\mathbf{P}^{-1}$ yields:

$$\ddot{\mathbf{r}} + \mathbf{P}^{-1}\mathbf{C}\mathbf{P}\dot{\mathbf{r}} + \mathbf{P}^{-1}\mathbf{K}\mathbf{P}\mathbf{r} = 0 \qquad [24]$$

If eqn [23] holds, then each of the coefficient matrices is diagonal and of the form:

$$\mathbf{P}^{-1}\mathbf{C}\mathbf{P} = \begin{bmatrix} 2\zeta_1\omega_1 & 0 & \dots & 0 \\ 0 & 2\zeta_2\omega_2 & \dots & 0 \\ \vdots & \dots & \ddots & \vdots \\ 0 & \dots & \dots & 2\zeta_n\omega_n \end{bmatrix}$$

and:

$$\mathbf{P}^{-1}\mathbf{K}\mathbf{P} = \begin{bmatrix} \omega_1^2 & 0 & \dots & 0 \\ 0 & \omega_2^2 & \dots & 0 \\ \vdots & \dots & \ddots & \vdots \\ 0 & \dots & \dots & \omega_n^2 \end{bmatrix} \qquad [25]$$

Thus eqn [24] can be written as the n decoupled modal equations:

$$\ddot{r}_i(t) + 2\zeta_i\omega_i\dot{r}_i(t) + \omega_i^2 r_i(t) = 0 \qquad [26]$$

Here ζ_i are defined to be the modal damping ratios and if each one has the value 1, then each mode of the system is critically damped. Consequently the critical damping matrix, $\mathbf{C}_{cr}$, is defined to be:

$$\mathbf{C}_{cr} = \mathbf{P}\begin{bmatrix} 2\omega_1 & 0 & \dots & 0 \\ 0 & 2\omega_2 & \dots & 0 \\ \vdots & \dots & \ddots & \vdots \\ 0 & \dots & \dots & 2\omega_n \end{bmatrix}\mathbf{P}^{-1} \qquad [27]$$

This is the value of damping matrix that causes each mode to be critically damped.

The critical damping matrix may be used to define the condition of underdamping, overdamping, and critical damping for a lumped-mass system that satisfies eqn [23]. The following conditions hold for the system of eqn [1]:

1. If the matrix $\mathbf{C} = \mathbf{C}_{cr}$, each mode is critically damped.
2. If the matrix $\mathbf{C} - \mathbf{C}_{cr}$ is positive-definite, each mode is overdamped.
3. If the matrix $\mathbf{C}_{cr} - \mathbf{C}$ is positive-definite, each mode is underdamped.
4. If the matrix is $\mathbf{C} - \mathbf{C}_{cr}$ indefinite, some modes may oscillate and some will not.

If the commutivity condition of eqn [23] is not satisfied, these conditions are still valid. However, if eqn [23] holds, these conditions are both necessary and sufficient. In the case that eqn [23] is not satisfied, the idea of a 'mode' changes to include phase information and the decoupled equations given in eqn [26] are no longer valid. In this case the damping conditions stated here refer to the system eigenvalues which are of the form:

$$\lambda_i = -\zeta_i\omega_i \pm \omega_i\sqrt{\zeta_i^2 - 1} \qquad [28]$$

where ζ_i is one, greater than one or less than one for every value of i depending on the definiteness of the matrix $\mathbf{C} - \mathbf{C}_{cr}$.

The critical damping matrix can be defined in terms of the mass and stiffness matrix much like the critical damping coefficient of the single-degree-of-freedom system is defined in terms of the scalar values of mass and stiffness in eqn [8]. It can be shown through a series of simple matrix manipulations that eqn [27] may be written as:

$$\mathbf{C}_{\text{cr}} = 2\mathbf{M}^{1/2}\left(\mathbf{M}^{-1/2}\mathbf{K}\mathbf{M}^{-1/2}\right)^{1/2}\mathbf{M}^{1/2} \qquad [29]$$

Here the exponent refers to the positive-definite matrix square root of a matrix (not the square root of each element). Note that eqn [29] reduces to the scalar definition of eqn [8] if the matrices are collapsed to scalar values.

Critical Damping in Distributed Parameter Models

The concept of critical damping can also be extended to elastic systems governed by systems of partial differential equations used to model rods, beams, plates, and shells. The equations of motion of such systems may be symbolically represented by the operator equation:

$$\begin{aligned}&\rho(\mathbf{x})\mathbf{u}_{tt}(\mathbf{x},t) + L_1\mathbf{u}_t(\mathbf{x},t) + L_2\mathbf{u}(\mathbf{x},t) = 0, \quad \mathbf{x}\in\Omega\\ &\text{and} \quad B\mathbf{u}(\mathbf{x},t) = 0, \quad \mathbf{x}\in\partial\Omega\end{aligned} \qquad [30]$$

Here $\mathbf{u}(\mathbf{x}, t)$ represents the deflection in three space (u_x, u_y, u_z), $\mathbf{x}$ represents a position along the surface in three space (for example: x, y, z, in rectangular coordinates), the subscripts denote partial time derivatives, $\rho(\mathbf{x})$ is the density, Ω is the domain in which $\mathbf{x}$ is defined, and the differential operators L_1 and L_2 represent damping and stiffness respectively. The operator B denotes the boundary conditions and $\partial\Omega$ represents the boundary. As an example, for a uniform, clamped-free beam, subject to air damping, the following holds: $\rho =$ constant, $\mathbf{x}$ becomes the scalar length along the neutral axis of the beam, $\mathbf{u}$ becomes the scalar deflection perpendicular to the neutral axis of the beam, Ω becomes the interval $(0, l)$ where l is the length of the beam and the clamp is at the origin, $\partial\Omega$ consists of the two points 0 and l, the operator $L_1 = c$, a constant damping coefficient, and L_2 is given by the familiar beam stiffness:

$$L_2 = \frac{\partial^2}{\partial x^2}\left(EI(x)\frac{\partial^2(\cdot)}{\partial x^2}\right) \qquad [31]$$

The boundary operator B expresses the usual boundary conditions:

$$\begin{aligned}&Bu = 0 \Rightarrow u(0,\ t) = 0, \quad u_x(0,\ t) = 0,\\ &\frac{\partial}{\partial x}\left(EI\frac{\partial^2 u(l,\ t)}{\partial x^2}\right) = 0, \quad EI\frac{\partial^2 u(l,\ t)}{\partial x^2} = 0\end{aligned} \qquad [32]$$

These equations are subject to some more technical conditions to define the operators properly in rigorous mathematical terms. These mathematical conditions may be found in the Further Reading section.

The concept of critical damping for systems described by eqn [30] parallels that of the matrix case given by that of eqn [29]. However, in the operator case, careful attention must be paid to the boundary conditions and the existence of derivatives. The modal decoupling condition is similar and requires that $L_1L_2 = L_2L_1$ for certain boundary conditions. In this case, the modal damping ratios can be defined exactly as in eqn [26] where the total solution takes on the form:

$$\mathbf{u}(\mathbf{x},t) = \sum_{i=1}^{\infty} r_i(t)\phi_i(\mathbf{x}) \qquad [33]$$

where the $\phi_i(\mathbf{x})$ are the mode shapes (or eigenfunctions) of the undamped system. As before, the critical damping condition corresponds to $\zeta_i = 1$ for every value of the index i.

To represent a critical damping operator as in eqn [29] it is first necessary to make eqn [30] monic by either dividing through by $\rho(\mathbf{x})$ or making a change of variables. Assuming that eqn [30] is thus normalized, the critical damping operator becomes:

$$L_{\text{CD}} = 2L_2^{1/2} \qquad [34]$$

defined on an appropriate domain (boundary conditions). Here the square root again refers to the operator square root that has a precise mathematical definition and rules for computing. It practice it is often easier to compute the square of the critical damping operator, defined by $L_{\text{CD}}^2 = 4L_2$. In most systems it is likely that only one mode will be critically damped.

The concept of critical damping has been defined for linear vibrating systems with viscous damping. Achieving the exact state of critical damping is often difficult and requires a large amount of damping not usually available in natural materials. However critical damping serves as an important analytical expression to separate the two distinct phenomena of vibration versus exponential decay without oscillation in a system's time response.

Nomenclature

a_1, a_2	constants of integration
B	boundary operator
$\mathbf{I}$	$n \times n$ identity matrix
l	length

L_1, L_2	differential operators
$\mathbf{P}$	modal matrix
$\mathbf{u}$	scalar deflection
ρ	density

See also: **Damping materials**; **Damping measurement**; **Viscous damping**.

Further Reading

Den Hartog JP (1956) *Mechanical Vibration*, 4th edn. New York: McGraw Hill.

Inman DJ (1989) *Vibrations: Control, Measurement and Stability*. Upper Saddle River, NJ, USA: Prentice Hall.

Inman DJ (1996) *Engineering Vibration*, revised edn. Upper Saddle River, NJ, USA: Prentice Hall.

D

DAMPING IN FE MODELS

G A Lesieutre, Penn State University, University Park, PA, USA

Copyright © 2001 Academic Press

doi:10.1006/rwvb.2001.0021

Damping in structural systems is the result of a multitude of complex physical mechanisms (**Figure 1**). For this reason, structural designers do not often use physics-based damping models for analysis. (In fact, such models are not generally available.) In practice, most analysts use linear, finite element structural models and relatively simple mathematical models of damping.

Because such damping models do not accurately describe the underlying physics, the resulting damped structural model may only capture the general effects of damping (e.g., decaying free vibration) without capturing the details (e.g., phase differences between the motion at various points when the structure executes harmonic response). As a result, approximate values for damping parameters are often used for initial design analysis, and improved using experiments.

Finally, many common damping models have specific deficiencies that limit their utility under some circumstances. These deficiencies may sometimes justify the use of higher-fidelity models having stronger physical foundations.

Viscous Damping

Consider an elastic (undamped) nongyroscopic linear structure. Application of the finite element modeling method yields a discretized matrix equation of motion having the following general form:

$$\mathbf{M}\ddot{\mathbf{x}} + \mathbf{K}\mathbf{x} = \mathbf{f}(t) \qquad [1]$$

where $\mathbf{M}$ and $\mathbf{K}$ are the system mass and stiffness matrices, and $\mathbf{x}$ and $\mathbf{f}$ are $N \times 1$ vectors of global nodal displacements and forces, respectively. Analysis of the eigenvalue problem associated with the unforced matrix equation yields normal modes of vibration, each comprising a real eigenvector (discrete mode shape) $\boldsymbol{\psi}_r$; and a natural frequency (corresponding to undamped harmonic vibration) ω_r. The associated structural response has the form:

$$\mathbf{x}(t) = \boldsymbol{\psi}_r \, \mathrm{e}^{i\omega_r t} \qquad [2]$$

The 'natural' extension of the linear equation of motion [1] to include damping involves the addition of a matrix term multiplying the vector of nodal velocities:

$$\mathbf{M}\ddot{\mathbf{x}} + \mathbf{C}\dot{\mathbf{x}} + \mathbf{K}\mathbf{x} = \mathbf{f}(t) \qquad [3]$$

$\mathbf{C}$ is called the viscous damping matrix.

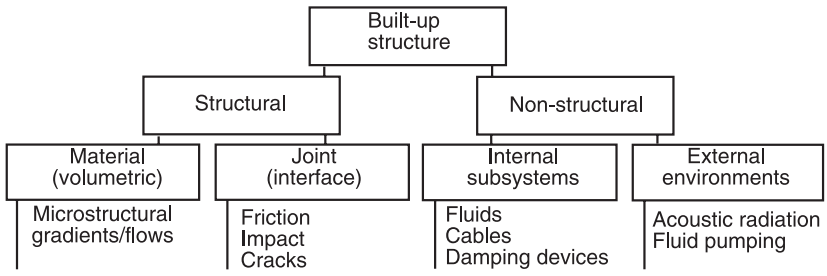


Figure 1 Damping in built-up structures is the result of many physical mechanisms acting in concert.

Elemental Viscous Damping

In a finite element context, $\mathbf{C}$ may be understood to be assembled from elemental viscous damping matrices and discrete viscous devices. As such, it can be expected to have symmetry and definiteness properties like those of $\mathbf{K}$. Furthermore, that part of $\mathbf{C}$ associated with elemental viscous damping has a matrix structure (connectivity) similar or identical to that of $\mathbf{K}$.

The basis for an elemental viscous damping matrix must necessarily be the constitutive equations of the material from which the modeled structural member is made. In this case, the common linear elastic constitutive equations are augmented such that part of the instantaneous stress σ is proportional to the strain rate $\dot{\varepsilon}$:

$$\boldsymbol{\sigma} = \mathbf{E}\boldsymbol{\varepsilon} + \mathbf{F}\boldsymbol{\varepsilon} \qquad [4]$$

One of the deficiencies of the viscous damping model is that the constitutive behavior described by [4] does not represent the observed behavior of structural or damping materials very well, except perhaps over a very limited frequency range. As a result, structural analysts have difficulty obtaining material strain rate coefficients $\mathbf{F}$ for most materials – materials scientists do not try to determine such properties because the basic structure of the underlying model is inadequate.

Viscous Damping of Structures

Analysis of the eigenvalue problem associated with the general unforced, damped matrix equation of motion [3] yields complex normal modes of vibration, each comprising a complex eigenvector (discrete mode shape) $\boldsymbol{\psi}_r$; and a complex natural frequency (corresponding to damped oscillatory vibration) s_r. The associated structural response has the form:

$$\mathbf{x}(t) = \boldsymbol{\psi}_r \, \mathrm{e}^{s_r t} \qquad [5]$$

where, assuming oscillatory motion, s_r is often expressed as:

$$s_r = -\zeta_r \omega_r + i\omega_r \sqrt{1 - \zeta_r^2} \qquad [6]$$

In eqn [6], ζ_r is the modal damping ratio, and ω_r is the magnitude of the complex natural frequency. If s_r can be represented in this oscillatory form, then its complex conjugate is also a complex natural frequency of the system.

Proportional Viscous Damping

Proportional viscous damping is a subset of viscous damping in which the viscous damping matrix $\mathbf{C}$ is a linear combination of the mass and stiffness matrices $\mathbf{M}$ and $\mathbf{K}$:

$$\mathbf{C} = \beta\mathbf{M} + \gamma\mathbf{K} \qquad [7]$$

As a consequence of not representing material behavior well, some deficiencies of the (proportional) viscous damping model are observed at the structural level.

Consider first the case of proportionality to the stiffness matrix. For simple structures, in which single material elastic and strain rate coefficients, $\mathbf{E}$ and $\mathbf{F}$, are assumed to represent material behavior adequately, the following relationship may be defined:

$$\boldsymbol{\sigma} = \mathbf{E}\boldsymbol{\varepsilon} + \gamma\mathbf{E}\dot{\boldsymbol{\varepsilon}} \qquad [8]$$

Analysis then shows that modal damping increases monotonically with frequency, with a slope of +1 on a log–log scale:

$$\zeta_r = \frac{\gamma}{2}\omega_r \quad (\omega_r;\ \zeta_r \leq 1) \qquad [9]$$

One result of this is that all modes having a natural frequency greater than $2/\gamma$ are overdamped; that is, in unforced motion, they do not respond in an oscillatory manner. Such behavior is not representative of that of most structures and is a serious deficiency of this viscous damping model. Many structures exhibit modal damping that depends only weakly on frequency and, when the source is material-based, generally increases, then decreases with frequency over a broad frequency range.

In the more general situation that includes proportionality to the mass matrix, modal damping is given by:

$$\zeta_r = \frac{\beta}{2\omega_r} + \frac{\gamma}{2}\omega_r \qquad [10]$$

Furthermore, the same real eigenvectors (discrete mode shapes) that diagonalize the mass and stiffness matrices of the undamped problem also diagonalize the viscous damping matrix $\mathbf{C}$. This feature is probably the greatest attraction of the proportional damping model.

One deficiency of this model, however, is associated with proportionality to the mass matrix. In the event that a structure of interest possesses a rigid body (zero-frequency) mode, that mode will have

nonzero damping. In addition, the general trend of modal damping indicated by this model first decreases with increasing frequency (with a slope of -1 on a log–log scale), then increases.

Finally, note that only the simplest structures will be made of a single material or be governed by single elastic and strain rate coefficients. And even assuming that the viscous damping model is reasonable over some frequency range, different materials will exhibit different ratios of strain rate to elastic coefficients. Thus, the proportional damping model must be regarded in practice as a mathematical curiosity. An analyst who uses a viscous damping model should be prepared to use complex modes.

Despite its drawbacks, viscous damping is a simple way of introducing damping in a structural model and may be adequate under some circumstances (for example, when accuracy is only needed over a small frequency range). Perhaps the greatest utility of the viscous damping model is the possibility of determining (identifying) a viscous damping matrix from experiments. Although such a damping matrix would not be element-based, a desirable feature, it might represent damping adequately for the purposes of continuing analysis.

Structural or Hysteretic Damping

The structural, or hysteretic, or complex stiffness damping model is motivated by a desire to obtain modal damping with frequency dependence weaker than that which results from the use of the viscous damping model. This model may developed by defining a frequency-dependent viscous damping matrix, or by using the complex modulus model of material behavior. Common to both approaches is a fundamental assumption of forced harmonic response. In practice, damping is also assumed to be closely related to stiffness (because both are associated with deformation), and independent of mass.

Frequency-dependent Viscous Damping

Observing from eqn [9] that, for stiffness-proportional damping, modal damping increases monotonically with modal frequency, one might be inclined to modify a single-modulus elemental viscous damping matrix by dividing by a frequency:

$$\mathbf{C}_{\text{hysteretic}} = \frac{1}{\Omega}\mathbf{C}_{\text{viscous}} = \frac{\gamma}{\Omega}\mathbf{K} \qquad [11]$$

where Ω is interpreted as a forcing frequency. In this case, and for a simple structure with single material elastic and strain rate coefficients, eqn [3] is initially modified as:

$$\mathbf{M}\ddot{\mathbf{x}} + \frac{\gamma}{\Omega}\mathbf{K}\dot{\mathbf{x}} + \mathbf{K}\mathbf{x} = \mathbf{f}\,e^{i\Omega t} \qquad [12]$$

then, considering the relationship of velocity to position in forced harmonic response:

$$\begin{aligned}\mathbf{x}(t) &= \mathbf{x}\,e^{i\Omega t}\\ \dot{\mathbf{x}}(t) &= i\Omega\mathbf{x}(t)\end{aligned} \qquad [13]$$

leads to:

$$\mathbf{M}\ddot{\mathbf{x}} + (1 + i\gamma)\mathbf{K}\mathbf{x}(t) = \mathbf{f}\,e^{i\Omega t} \qquad [14]$$

Finally, using the result that $\mathbf{x}(t)$ is harmonic at the forcing frequency, this may be expressed as:

$$\left[-\Omega^2\mathbf{M} + (1 + i\gamma)\mathbf{K}\right]\mathbf{x}(\Omega) = \mathbf{f} \qquad [15]$$

Note that this approach leads essentially to a complex stiffness matrix, as shown in eqn [14]. In addition, the response vector, $\mathbf{x}(\Omega)$, as in eqn [15], is generally complex, indicating possible phase differences between the response and the forcing, as well as between responses at multiple points.

Material Complex Modulus

The basis for an elemental hysteretic damping matrix must be the constitutive equations of the material from which the modeled structural member is made. In this case, response to harmonic forcing is considered, and the single-modulus linear elastic constitutive equations are modified to include a material loss factor, η:

$$\boldsymbol{\sigma}(\Omega) = (1 + i\eta)\mathbf{E}\boldsymbol{\varepsilon}(\Omega) \qquad [16]$$

The material loss factor is essentially the phase difference in forced harmonic response between an applied stress and the resulting strain. It may also be regarded as the fractional energy dissipation per radian of motion. Materials scientists commonly measure loss factors, sometimes as a function of frequency, temperature, and amplitude. Note that real materials with nonzero loss factors exhibit stiffnesses that vary with frequency and temperature.

Eqn [16] can also be expressed in a form that includes multiple material moduli and loss factors:

$$\boldsymbol{\sigma}(\Omega) = [\mathbf{E}' + i\mathbf{E}'']\boldsymbol{\varepsilon}(\Omega) \qquad [17]$$

where $\mathbf{E}'$ is associated with storage moduli and $\mathbf{E}''$ with loss moduli. An elemental stiffness matrix may then be modified as:

$$\mathbf{K}^* = \mathbf{K}' + i\mathbf{K}'' \qquad [18]$$

And when the use of a single material modulus suffices, eqn [18] may be expressed as:

$$\mathbf{K}^* = (1 + i\eta)\mathbf{K}' \qquad [19]$$

In this case, and recalling that forced harmonic response is assumed, the structural equations of motion (3) may be initially modified as:

$$\mathbf{M}\ddot{\mathbf{x}} + (1 + i\eta)\mathbf{K}\mathbf{x}(t) = \mathbf{f}(t) = \mathbf{f}\, e^{i\Omega t} \qquad [20]$$

This is identical to eqn [14]. Using the result that $\mathbf{x}(t)$ is harmonic at the forcing frequency, this may be expressed in the same form as eqn [15]:

$$\left[-\Omega^2\mathbf{M} + (1 + i\eta)\mathbf{K}\right]\mathbf{x}(\Omega) = \mathbf{f} \qquad [21]$$

The damped structural model described by eqns [15] and [21] has some deficiencies, but also has considerable utility in practice.

First of all, this model is not generally useful for obtaining direct time response, as it essentially describes frequency response. However, when the time domain forcing function in eqn [20] is not harmonic, but nevertheless has a Laplace transform, it may be possible to find the response via inverse transformation using the elastic–viscoelastic correspondence principle.

In practice, an eigenvalue problem based on eqn [20] may be posed. Assuming the time response indicated in eqn [5], a complex natural vibration frequency results. If a single global loss factor can be isolated, as in eqn [20], such proportional hysteretic damping results in real eigenvectors or mode shapes. And for light damping, the modal damping ratio is approximately half of the loss factor. In the general case, complex eigenvectors result. Frequency-dependent stiffness and damping can be accommodated via iteration.

One difficulty with this eigenvalue problem is that the decaying time response postulated in eqn [5] differs from the forced harmonic response assumption underlying this damping model [13]. In practice, the accuracy of natural frequencies and mode shapes determined using this method may decrease with increasing loss factor(s).

This hysteretic damping model is ideal, however, for frequency response analysis [21]. Furthermore, loss factors and stiffnesses can, in principle, be functions of frequency:

$$\begin{aligned}\left[-\Omega^2\mathbf{M} + (1 + i\eta(\Omega))\mathbf{K}(\Omega)\right]\mathbf{x}(\Omega) &= \mathbf{f} \\ \left[-\Omega^2\mathbf{M} + [\mathbf{K}'(\Omega) + i\mathbf{K}''(\Omega)]\right]\mathbf{x}(\Omega) &= \mathbf{f}\end{aligned} \qquad [22]$$

Because high-damping viscoelastic materials that are sometimes used to enhance structural damping exhibit significant frequency-dependent stiffness and damping, this feature is especially useful in practice.

Viscous Modal Damping

Modal analysis, or modal superposition, is an efficient means of obtaining the dynamic response of linear structures. In this approach, the time response is determined using a number of modes that is small relative to the number of physical degrees of freedom in a finite element model. Either real or complex mode shapes may be used, along with either real or complex natural frequencies.

The most common use of modal superposition involves the solution to the undamped eigenvalue problem (real modes and real natural frequencies). The modal equations of motion and initial conditions have the form:

$$\ddot{\boldsymbol{\alpha}} + \boldsymbol{\omega}_r^2\boldsymbol{\alpha} = \boldsymbol{\Psi}^{\mathrm{T}}\mathbf{f}(t) \qquad [23]$$

$$\begin{aligned}\boldsymbol{\alpha}(0) &= \boldsymbol{\Psi}^{\mathrm{T}}\mathbf{M}\mathbf{x}(0) \\ \dot{\boldsymbol{\alpha}}(0) &= \boldsymbol{\Psi}^{\mathrm{T}}\mathbf{M}\dot{\mathbf{x}}(0)\end{aligned} \qquad [24]$$

where $\boldsymbol{\alpha}$ is an $M\times 1 (M \ll N)$ vector of modal coordinates, $\boldsymbol{\Psi}$ is a (real) $N\times M$ matrix of mass-normalized columnal eigenvectors, and $\boldsymbol{\omega}_r^2$ is a diagonal $M \times M$ matrix of squared undamped natural frequencies. Damping may be included in eqn [23] by adding a viscous modal damping term:

$$\ddot{\boldsymbol{\alpha}} + 2\boldsymbol{\zeta}_r\boldsymbol{\omega}_r\dot{\boldsymbol{\alpha}} + \boldsymbol{\omega}_r^2\boldsymbol{\alpha} = \boldsymbol{\Psi}^{\mathrm{T}}\mathbf{f}(t) \qquad [25]$$

where ζ_r is the modal damping ratio of mode r, and $2\boldsymbol{\zeta}_r\boldsymbol{\omega}_r$ is a diagonal modal damping matrix.

Once the modal response is found, the physical response is determined using:

$$\mathbf{x}(t) = \boldsymbol{\Psi}\boldsymbol{\alpha}(t) \qquad [26]$$

This approach can be modified to use complex mode shapes and/or natural frequencies.

Modal Damping Ratios

For many structures, eqn [25] gives results of satisfactory accuracy. Once this approach is selected for

use, a main problem becomes determining appropriate modal damping ratios.

Experience One approach is based on personal or organizational experience with similar structures. Although there is no assurance that this approach will yield correct values for any modes, it can provide a valuable starting point for analysis. For example, values of modal damping in the range from 0.003 to 0.03 might be appropriate for lightly damped, built-up aerospace structures.

Complex stiffness Alternate approaches to estimating modal damping may proceed by establishing a lower bound based on material loss factor contributions. Such approaches are especially effective when high-damping materials are used to augment nominal lightly damped structures. An example of this kind of approach is the use of modal analysis of a complex stiffness-based model to yield a complex natural frequency and associated modal damping.

Modal strain energy Another materials-based approach is the modal strain energy method. In this approach, a modal loss factor is a weighted sum of material loss factors:

$$\zeta_r \cong \frac{1}{2}\eta_r = \frac{1}{2} \sum_{\substack{i \\ \text{materials}}} \eta_i \frac{U_{ri}}{U_r} \qquad [27]$$

The weighting terms are the fraction of modal strain energy stored in each material (or component), usually estimated from analysis of an undamped model. The modal damping ratio is approximately half of the modal loss factor.

Other Damping Models

For some applications that require high model fidelity, the damping models described in the preceding may be inadequate. An example of such an application might be a structural dynamic model that is to be used as the basis for the design of a high-performance feedback controller. Some of the main deficiencies of models considered to this point include the following.

Viscous damping yields modal damping that tends to increase with frequency, in a manner inconsistent with observations. Proportional damping, either related to the mass matrix, or for multicomponent structures, should be regarded as a mathematical curiosity.

Hysteretic (complex stiffness) damping, while capable of accommodating frequency-dependent damping and stiffness, and of yielding better estimates of modal damping, cannot be used directly to determine structural response to arbitrary dynamic loading. However, the combination of either the complex stiffness or modal strain energy method, along with a viscous modal damping model, often yields acceptable results. Limitations of this approach usually stem from neglecting phase differences in response (using real modes), from neglecting frequency-dependent properties, from sacrificing mode orthogonality by including frequency-dependent properties, or from unusually high, perhaps localized, damping.

Several damping models suitable for use with finite element analysis have been developed to address such shortcomings. The emphasis here is on models that are compatible with linear analysis, thus neglecting friction and other models.

Fractional Derivative

Fractional derivative models provide a compact means of representing relatively weak frequency-dependent properties in the frequency domain. For example, a single material complex modulus might be represented as:

$$E^*(i\omega) = \frac{E_0 + E_1(i\omega)^m}{1 + b(i\omega)^m} \qquad [28]$$

where E_0, E_1, b, and m are material properties, with $+m$ being the slope of the loss factor on a log–log plot versus frequency, at frequencies below that at which peak damping is observed. Values for m range from nearly 0 to 1, with $\frac{1}{2}$ being typical.

Although developed as a time domain model, the fractional derivative approach, as a means of determining dynamic response, suffers at present from the need for special mathematical and computational tools.

Internal Variable Viscoelastic Models

Another approach to capturing viscoelastic (frequency- and temperature-dependent) material behavior in a time domain model involves the introduction of internal dynamic coordinates. Several such models are available and, although they differ in some respects, they share many common features. A one-dimensional mechanical analogy of material behavior (**Figure 2**) aids understanding of the general structure of such models.

The deformation of this system is described primarily by the stress, σ, and the total strain, ε, but its apparent stiffness is affected by the dynamics of an internal strain, ε_A. If this system is subjected to harmonic forcing, its apparent stiffness and damping

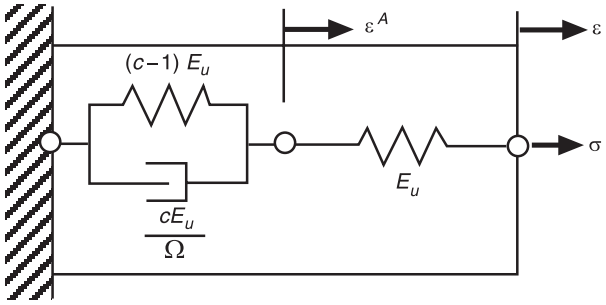


Figure 2 The standard three-parameter anelastic solid.

vary with frequency. At very high frequencies, the internal dashpot is essentially locked, the material modulus is E_u, and the damping is low. At very low frequencies, the internal dashpot slides freely, the modulus is lower, and the damping remains low. At some intermediate frequency, the damping reaches a peak value.

The peak loss factor and change in modulus both depend on the strength of the coupling between the total strain and the internal strain, $1/(c-1)$. The frequency at which peak damping is observed, very nearly Ω, is related to the inverse of the relaxation time for the internal strain.

With a single internal variable, the loss factor is proportional to frequency at low frequencies, and inversely proportional at high frequencies. Weaker frequency dependence can be introduced by using multiple internal fields, each having its own relaxation dynamics. Temperature effects can be included by using a shift function that essentially increases the relaxation rate of the internal fields with increasing temperature.

Such internal variable models are quite compatible with finite element structural analysis methods. In one approach, additional nodal displacement coordinates, identical to those of an elastic element, are introduced to model the internal system. The internal field is then interpolated in the same way as the total displacement field. Additional first-order equations of motion are then developed to describe the relaxation (creep) behavior of the internal system and its coupling to the total displacements. The boundary conditions for the internal coordinates are implemented just as those for the corresponding total displacements are, with the additional elimination of strain-free motion.

Eqn [29] shows the general structure of the finite element equations with a single set of internal coordinates. In this form, **K** is calculated using the high-frequency material stiffness. Evidently, higher accuracy comes at a cost of additional coordinates and material properties.

$$\begin{bmatrix} M & \\ & \end{bmatrix}\begin{Bmatrix} \ddot{x} \\ \end{Bmatrix} + \begin{bmatrix} 0 & 0 \\ 0 & \frac{c}{\Omega}K \end{bmatrix}\begin{Bmatrix} \dot{x} \\ \dot{x}_A \end{Bmatrix} + \begin{bmatrix} K & -K \\ -K & cK \end{bmatrix}\begin{Bmatrix} x \\ x_A \end{Bmatrix} = \begin{Bmatrix} f(t) \\ 0 \end{Bmatrix} \quad [29]$$

Such internal variable approaches have advantages over more conventional approaches in that they yield linear time domain finite element models, the frequency-dependent elastic and dissipative aspects of structural behavior are represented in fixed (not frequency-dependent) system matrices, modal damping is calculated concurrently with modal frequency without iteration, the resulting complex modes more accurately reflect the relative phase of vibration at various points, and modal orthogonality is preserved.

Nomenclature

E	material elastic coefficient
F	material strain rate coefficient
ε	strain
η	material loss factor
σ	stress
Ω	forcing frequency

See also: **Comparison of Vibration Properties**, Comparison of Spatial Properties; **Discrete elements**; **Finite element methods**; **Hysteretic damping**; **Modal analysis, experimental**, Basic principles; **Model updating and validating**; **Viscous damping**.

Further Reading

Bagley RL and Torvik PJ (1986) On the fractional calculus model of viscoelastic behavior. *Journal of Rheology* 30: 133–155.

Enelund M and Josefson, BL (1997) Time-domain finite element analysis of viscoelastic structures with fractional derivative constitutive relations. *AIAA Journal* 35: 1630–1637.

Johnson AR (1999) Modeling viscoelastic materials using internal variables. *Shock and Vibration Digest* 31: 91–100.

Johnson CD (1995) Design of passive damping systems. *Journal of Mechanical Design* 117B: 171–176.

Johnson CD and Kienholz DA (1982) Finite element prediction of damping in structures with constrained viscoelastic layers. *AIAA Journal* 20: 1284–1290.

Lesieutre GA and Bianchini E (1995) Time domain modeling of linear viscoelasticity using anelastic displacement fields. *Journal of Vibration and Acoustics* 117: 424–430.

Lesieutre GA and Govindswamy K (1996) Finite element modeling of frequency-dependent and temperature-dependent dynamic behavior of viscoelastic materials in

simple shear. *International Journal of Solids and Structures* 33: 419–432.
McTavish DJ and Hughes, PC (1993) Modeling of linear viscoelastic space structure. *Journal of Vibration, Acoustics, Stress, and Reliability in Design*, 115: 103–110.
Mead DJ (1999) *Passive Vibration Control*. Chichester: John Wiley.
Meirovitch L (1980) *Computational Methods in Structural Dynamics*. Alphen aan den Rijn, The Netherlands: Sijthoff & Noordhoff.
Nashif AD, Jones DIG and Henderson JP (1985) *Vibration Damping*. New York, NY: John Wiley.
Pilkey W and Pilkey B (eds) (1995) *Shock and Vibration Computer Programs: Reviews and Summaries*. Arlington, VA: Shock and Vibration Information Analysis Center, Booz Allen & Hamilton.
Soovere J and Drake ML (1984) *Aerospace Structures Technology Damping Design Guide*. AFWAL-TR-84-3089. Dayton, OH: U.S. Air Force.

DAMPING MATERIALS

E E Ungar, Acentech Incorporated, Cambridge, MA, USA

Copyright © 2001 Academic Press

doi:10.1006/rwvb.2001.0014

What is a Damping Material?

A damping material is a solid material that dissipates (that is, converts into heat) a significant amount of mechanical energy as it is subjected to cyclic strain. Most damping materials are not useful structural materials themselves, but typically are combined with structural elements so that the resulting combination is structurally viable and relatively highly damped. A damping material configuration that is applied to a structural component usually is called a 'damping treatment'.

Although granular materials and viscous liquids can provide considerable energy dissipation in some applications, these usually are not regarded as damping materials. Even though so-called high-damping metal alloys are more highly damped than common metals, their damping generally is not high enough for these to be considered damping materials in the present sense. Almost all practical damping materials are polymeric plastics or elastomers – but some other materials can also dissipate considerable energy in some temperature and frequency ranges.

Characterization of Material Properties

Damping materials are often called 'viscoelastic', because they combine energy dissipation (viscous) with energy storage (elastic) behavior. Characterization of the properties of such a material requires two parameters; one associated with energy storage, and one, with energy dissipation.

If a sinusoidal compressive stress represented by the phasor[†] $\sigma(\omega)$ acts on an element of a damping material, so as to produce a strain represented by the phasor $\varepsilon(\omega)$, one may write the complex dynamic modulus $E(\omega)$ as:

$$E(\omega) = \sigma(\omega)/\varepsilon(\omega) \equiv E' + jE'' \equiv E'[1 + j\eta] \quad [1]$$

The real part E' of the complex modulus is known as the 'storage modulus' because it is associated with energy storage, and the imaginary part $E'' = \eta E'$ is known as the 'loss modulus' because it is associated with energy dissipation. The 'loss factor' obeys:

$$\eta = E''/E' \quad [2]$$

The values of E', E, and η generally vary with frequency and with other parameters, as discussed later.

In steady sinusoidal vibration at a given frequency:

$$\eta = D/2\pi W \quad [3]$$

where D denotes the energy dissipated in unit volume of the element per cycle and where $W = E'[\varepsilon(\omega)]^2/2$ represents the energy stored in unit volume of the element at instants when the strain is at its maximum.

The complex shear modulus $G(\omega)$, its real and imaginary parts, and the corresponding loss factor may be defined entirely analogously to the complex compression modulus $E(\omega)$ and its components. According to elasticity theory, the modulus of elasticity in compression E is related to the shear modulus G via Poisson's ratio ν by:

[†] The phasor $Y(\omega)$ of a sinusoidally time-dependent variable $y(t) = Y_0\cos(\omega t - \phi)$ is a complex quantity $Y(\omega) = Y' + jY''$ defined so that $y(t) = \mathrm{Re}\{Y(\omega)\,e^{-j\omega t}\}$. The phasor accounts both for the amplitude $Y_0 = |Y(\omega)|$ and for the phase angle $\phi = \arctan(Y''/Y')$.

$$G = \frac{E}{2(1+\nu)} \quad [4]$$

and therefore:

$$\nu = \frac{E}{2G} - 1 \quad [5]$$

Application of this relation to the complex compression and shear moduli implies that Poisson's ratio is complex, unless the loss factors associated with the two moduli are equal. For most materials the two loss factors indeed are equal for all practical purposes; thus, their Poisson's ratio can be taken as real.

Measurement of Material Properties

The most direct approaches to determination of the complex compression or shear modulus of a material involve measurements on samples whose shapes or sizes are such that application of a force in an appropriate direction results in an essentially uniform or in another reliably predictable strain distribution in the sample. For example, one may evaluate the complex shear modulus of a material at a given frequency by applying a known sinusoidal shear force at the given frequency to one face of a thin flat sample, whose other face is restrained from moving, and observing the magnitude of the resulting shear displacement, together with its phase angle relative to the applied force. Such measurement approaches are simple in concept, but generally involve considerable practical difficulties and relatively complex apparatus. Nevertheless, such apparatus is necessary for the measurement of the amplitude-dependences of the complex moduli.

The moduli of most viscoelastic materials, however, are practically independent of the strain amplitude up to stains of perhaps 5% or more. Thus, one can determine the damping of such materials by approaches in which the strain amplitude is permitted to vary during a measurement. These approaches include measurement of the rate of decay of free vibrations or of the resonance bandwidth of a test system that includes a sample of the damping material.

The simplest and most widely-used measurement approaches employ metal reeds (plate strips, or beams with thin rectangular cross-sections) which have thin layers of damping material bonded to one or both of their faces. A test reed is clamped to a rigid support at one end, and the other end is excited magnetically at one of its resonances at a time. The loss factor of the coated reed is evaluated either from the observed rate of decay of the reed's vibration after the excitation has been turned off, or from measurement of the bandwidth of the resonance. The flexural stiffness of the coated reed is determined from its mass-per-unit length and the resonance frequency, using the classical relations applicable to an elastic cantilever beam. The stiffness and loss factor of the bare metal reed are determined similarly. The properties of the damping material then are calculated by means of well-established equations that indicate how the flexural stiffness and loss factor or the reed with attached damping material layer(s) depend on the dimensions of the reed and of the attached layer(s) and on the moduli and loss factors of the bare reed and the damping material. These measurement approaches are the subject of recent standards.

Typical Behavior of Damping Materials

The dynamic properties (moduli and loss factors) of a damping material generally vary markedly with frequency and temperature. They usually vary only a little with strain amplitude up to quite large strains and generally depend only to a minor extent on static preload and on exposure to long-duration cyclic loading.

Figures 1A and **1B** shows how the real (storage) shear modulus and the loss factor in shear of a representative damping material vary with frequency and temperature. **Figure 1A** shows graphs of these two quantities as functions of frequency at several constant temperatures. **Figure 1B** shows the same data plotted upon a temperature–frequency plane, in order to permit one to visualize the trends more easily.

At a given frequency, the modulus varies drastically with temperature, starting from large values at low temperatures and progressing to small values at high temperatures via a range of intermediate temperatures in which the rate of change is greatest. At low temperatures the material is said to be in its 'glassy' state and at high temperatures, in its 'rubber-like' state. At high temperatures – beyond those covered by the plots – the material becomes very soft and tends toward the behavior of a viscous liquid. The region in which rapid changes occur is called the 'glass transition region'; the temperature at which the modulus changes most rapidly is termed the 'glass transition temperature'. The highest loss factor values occur at or near this temperature.[†]

[†] Although **Figure 1** pertains to shear properties, the figure also indicates the behavior of the material's properties in extension–compression. A material's loss factor in compression–extension is the same as that in shear for all practical purposes, and the modulus values for compression–extension are higher than those for shear by a nearly constant factor of about 3. Poisson's ratio for plastics and elastomers is about 0.33 in the glassy region and nearly 0.5 in the transition and rubber-like regions, so that E/G is between 2.7 and 3, according to eqn [4]. The latter value applies essentially throughout the regions of primary interest in damping applications.

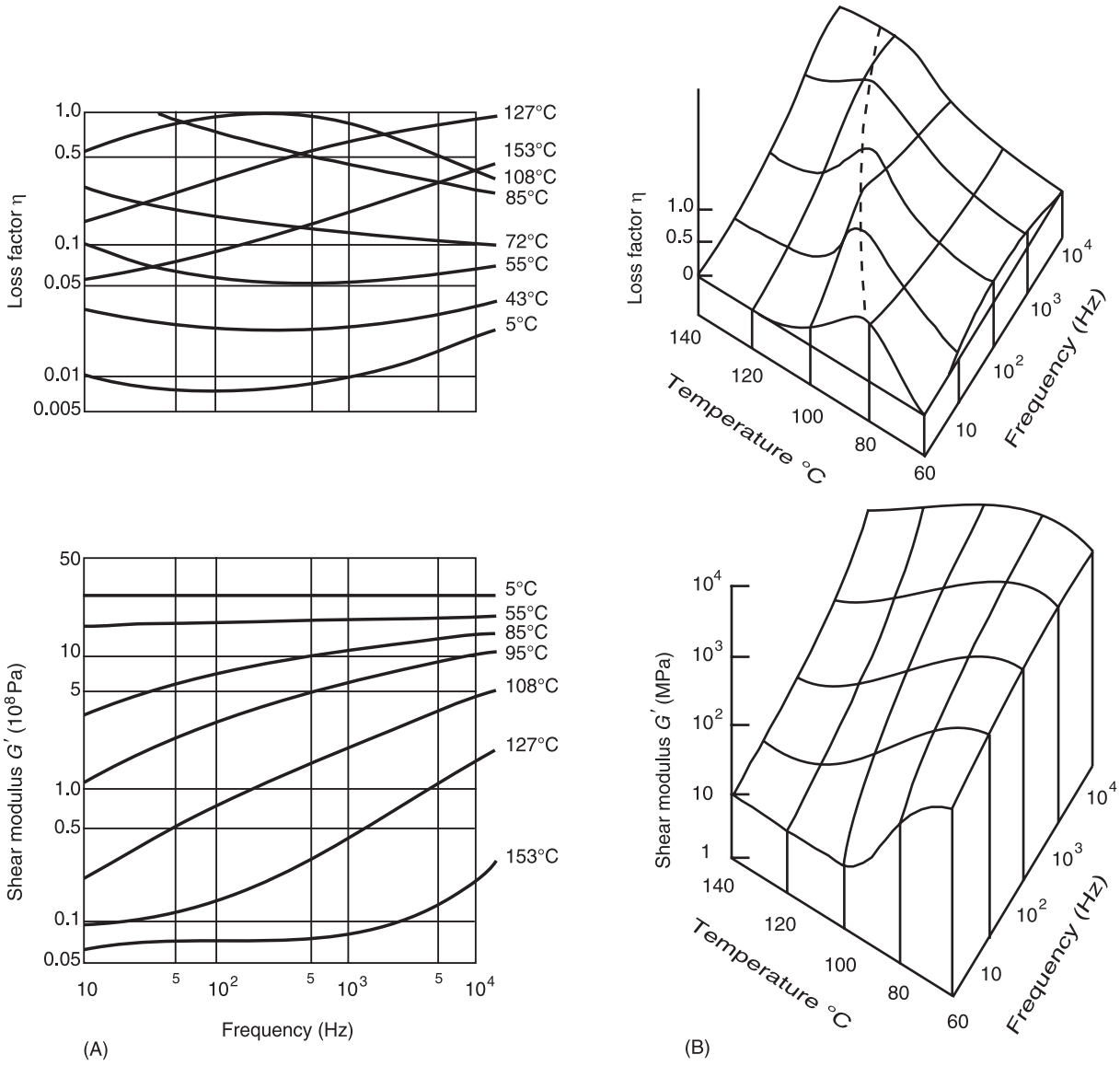


Figure 1 Dependences of shear modulus and loss factor of a damping material on frequency and temperature: (A) shown as functions of frequency at constant temperatures; (B) shown as plots upon temperature–frequency plane. Adapted from Ungar EE (1992) Structural damping. In: Beranek LL, Ver IL (eds) *Noise and Vibration Control Engineering*, ch. 12. New York: John Wiley.

The variation with frequency of the material properties at constant temperature is similar to their variation with temperature at constant frequency. At a constant temperature, the modulus progresses from small values at low frequencies to high values at high frequencies via an intermediate region in which the change is relatively rapid. Again, the highest loss factor values occur in the area of the most rapid modulus changes. This similarity has led to the concept of 'temperature–frequency equivalence'. According to this concept, if one starts with the material at a given temperature and frequency, one observes the same change in the material properties due to a temperature increase (or increase) by a given amount as from a suitably selected decrease (or increase) in the frequency.

The general behavior of many materials is similar to that illustrated by **Figures 1A** and **1B**, but the actual values of the properties depend on the specific materials. Storage moduli as great as 10^8 kPa (or 10^7 psi) may occur in the glassy region, and moduli as small as 10 kPa (1 psi) may occur in the rubbery region. For a given material, the modulus values in the glassy region may be three or four orders of magnitude greater than those in the rubbery region.

The loss factor values in the glassy region usually are small, typically between 10^{-3} and 10^{-2}, whereas in the rubbery region they tend to be of the order of 0.1

for many materials. In the transition region, the loss factors of good damping materials generally approach 1 and for some materials may reach 2. The transition region may extend over only 20 °C for some materials or over more than 200 °C for others. Commercial materials that are intended for use in given temperature ranges typically have their glass transition temperatures in the middle of these ranges. At constant temperature, the transition region may extend over one to four decades of frequency. The loss factor curves for materials with wider transition ranges typically exhibit flatter peaks and lower maximum values than similar curves for materials with narrower transition ranges.

Figures 1A and **1B** correspond to a material consisting of a single viscoelastic component – that is, of a single polymeric material (with or without nonpolymeric admixtures). Such a material has a single transition region and, correspondingly, its loss factor curve exhibits a single peak, as illustrated by the figure. The behavior of materials consisting of two or more viscoelastic components with different transition regions is more complex. The loss factor curve for such a material may have two or more peaks, and the slope of the modulus curve for such a material may not change monotonically with temperature and frequency.

Presentation of Material Data

Material property data may be presented in the form of a series of curves giving values of the modulus and loss factor at various temperatures as functions of frequency, as in **Figure 1A**. Data may also be presented in terms of curves representing the values of these parameters at various frequencies as functions of temperature. Instead of curves of the real modulus, or in addition to these curves, one may also show curves of the imaginary (loss) modulus or of the magnitude of the complex modulus. Because the various moduli are simply related, so that one can readily be calculated from the other, the following discussion focuses on the same parameter set as that used in **Figures 1A** and **1B**.

By shifting the various curves that show the modulus variations with frequency at different constant temperatures along the frequency axis, these curves can be arranged to form a single continuous smooth curve. The same is true also for the loss factor curves, if they are shifted by the same amounts as the modulus curves. (Analogous statements also apply to shifting curves obtained at different constant frequencies along the temperature axis.) This shifting, the possibility of which is a consequence of the aforementioned temperature–frequency equivalence, permits one to show the modulus and loss factor data for a single-transition material for all frequencies and temperatures as functions of a single 'reduced frequency' parameter, as illustrated in **Figure 2**.

The reduced frequency is defined as the product of the actual frequency and of a 'shift factor' α_T that depends on the temperature as determined from the shifting required to make all the curves coalesce into continuous ones. The dependence of the shift factor on temperature may be given by an equation, by a separate plot, or – more conveniently – by a nomogram superposed on the data plots as in **Figure 2**. Presentation of data as in **Figure 2** is the subject of an international standard.

Analytical models have been developed that use empirical data obtained in limited frequency and temperature ranges to characterize a material's behavior outside of these ranges. These models generally have been confined to single-transition materials and have been of limited practical utility. Such models, as well as plots like **Figure 2**, can lead to significant errors if they are used for extrapolations outside of the regions for which measured data are available.

Practical Considerations

The dynamic properties of a sample of a polymeric material depend not only on its basic chemical composition (that is, on the monomers that make up the material), but also on several other factors. These include the material's molecular weight spectrum (the distribution of molecular chain lengths), the degree of cross-linking, and the amounts and types of included plasticizers and fillers. Experience has shown that even samples taken from the same production batch of a given material may exhibit considerably different modulus and loss factor values.

The differences may be even greater for samples taken from different, nominally identical, batches of a material. It thus is important that damping materials for critical applications be obtained from experienced suppliers who can guarantee the performance of their materials, and that these materials be specified and accepted not on the basis of their chemical compositions, but on the basis of their dynamic properties in the frequency and temperature ranges of concern.

Nomenclature

D	energy dissipated per cycle in unit volume
E'	real part of $E(\omega)$; storage modulus
E''	imaginary part of $E(\omega)$; loss modulus

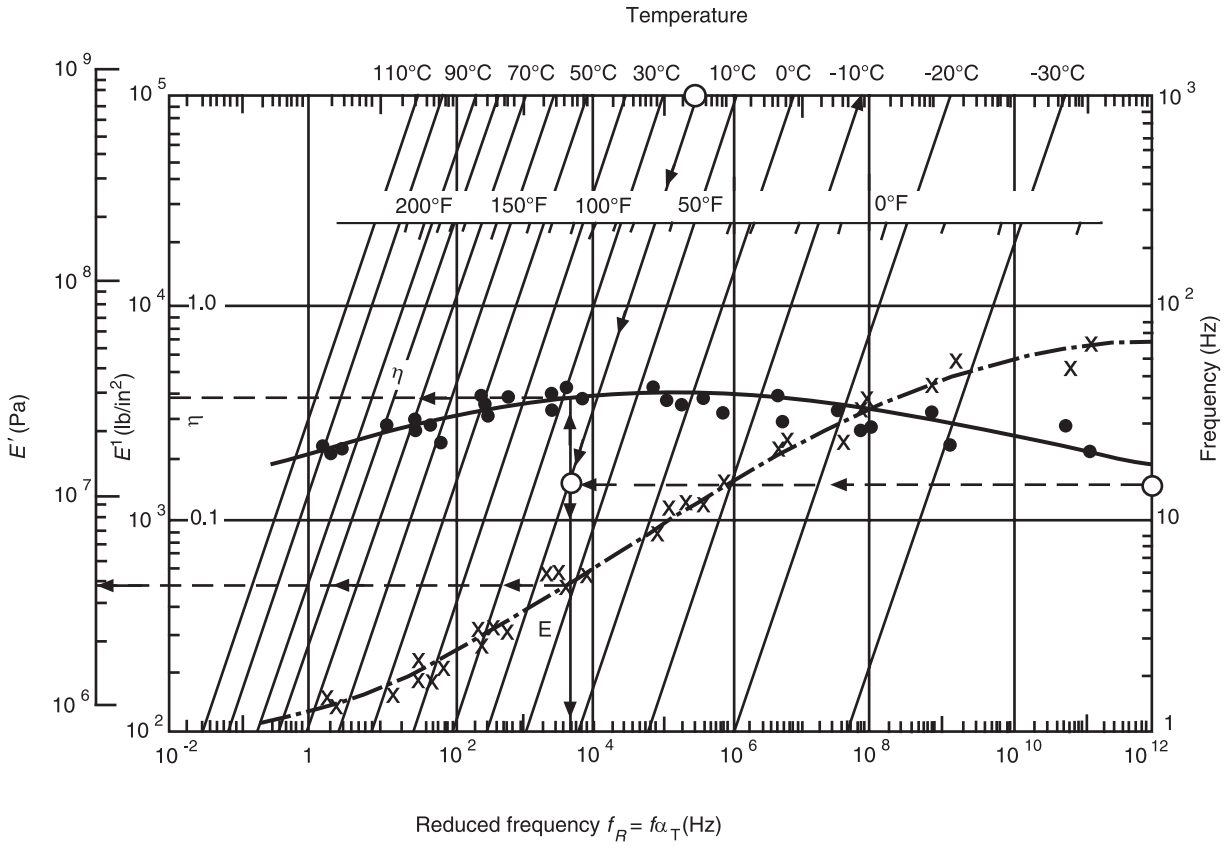


Figure 2 Reduced frequency plot of elastic modulus E' and loss factor η of a viscoelastic material. Points indicate measured data to which curves like those of **Figure 1** were fitted. Nomograph superposed on data plot facilitates determination of reduced frequency f_R corresponding to frequency f and temperature T. Use of nomograph is illustrated by dashed lines: for $f = 15$ Hz and $T = 20$ deg C one finds $f_R = 5\times10^3$ Hz and $E' = 3.8\times10^6$ Pa, $\eta = 0.36$. Adapted from Ungar EE. (1992) Structural damping. In: Beranek LL, Ver IL (eds) *Noise and Vibration Control Engineering*, ch. 12. New York: John Wiley.

$E(\omega)$	complex modulus in extension–compression (complex Young's modulus)
G	shear modulus
W	time-wise maximum energy stored per unit volume
$\varepsilon(\omega)$	strain phasor
ν	Poisson's ratio
$\sigma(\omega)$	stress phasor
ϕ	phase angle

See also: **Damping in FE models**; **Damping measurement**; **Hysteretic damping**.

Further Reading

Anon (1971) DIN 53 440, *Biegeschwingungsversuch. Bestimmung von Kenngrössen Schwingungsgedämpfter Mehrschichtsysteme (Flexural Vibration Test. Determination of Parameters of Vibration-damped Multi-layer Systems)*. Berlin: Deutsches Institut für Normung.

Anon (1991) ISO Standard 10112–1991 *Damping Materials: Graphic Presentation of Complex Modulus*. Geneva: ISO.

Anon (1998) ANSI Standard S2.23-1998, *Single Cantilever Beam Method for Measuring the Dynamic Mechanical Properties of Viscoelastic Materials*. New York: ANSI.

Anon (1998) ASTM Standard E756-98, *Test Method for Measuring Vibration-damping Properties of Materials*. West Conshohocken, Pennsylvania: Am. Soc. for Testing Materials.

Ferry JD (1970) *Viscoelastic Properties of Polymers*, 2nd edn. New York: John Wiley.

Nashif AD, Jones DIG, Henderson JP (1985) *Vibration Damping*. New York: John Wiley.

Ungar EE (1992) Structural damping. In Beranek LL, Ver LL (eds) *Noise and Vibration Control Engineering*, ch. 12. New York: John Wiley.

Ungar EE, Kerwin EM Jr. (1962) Loss factors of viscoelastic systems in terms of energy concepts. *Journal of the Acoustical Society of America* **34**(7): 954–7.

DAMPING MEASUREMENT

D J Ewins, Imperial College of Science, Technology and Medicine, London, UK

Copyright © 2001 Academic Press

doi:10.1006/rwvb.2001.0020

Introduction

Damping is one of the properties of vibrating structures that is the most difficult to model and to predict. As a result, it is more frequently required to conduct tests to measure damping than the other parameters in vibrating systems. This short article summarizes the different approaches to measuring damping levels in practical structures, and some of the difficulties that may be encountered in doing so.

As explained elsewhere (see **Damping models**), damping is the name given to a variety of different physical mechanisms which all share the common feature that they convert mechanical energy into heat, thereby reducing levels of vibration at the expense of the temperature of the vibrating structure. There are basically three approaches to the experimental determination of damping levels:

- measuring the energy absorption characteristic directly
- measuring the rate at which damping reduces the vibration of a structure
- measuring the extent to which damping limits resonance peak amplitudes.

Before explaining the methods involved in measuring damping, it is appropriate to restate the different damping parameters that are in common use, and these are: ζ = critical (viscous) damping ratio; η = (structural) damping loss factor $\sim 2\zeta$ (at resonance); δ = logarithmic decrement $\sim 2\pi\zeta$ (at resonance), and Q = dynamic magnification factor $\sim(1/2\zeta)$; $(1/\eta)$ (see **Damping models**).

Basis of Vibration Measurement Procedures

The principles upon which the three main damping measurement procedures are based can be simply illustrated using a simple theoretical model which uses the classical viscous dashpot as the mathematical model of a damping element. **Figure 1A** shows such a damper element in parallel with a simple undamped spring. If this spring–dashpot element is subjected to a harmonically varying force, $f(t) = F_0 e^{i\omega t}$, then the trace of an $f-x$ plot is as shown in **Figure 1B**, the curve tracing out an ellipse centered on a straight line of slope k. The area contained by the loop represents the energy dissipated in one cycle of vibration ($E = \pi c X_0^2 \omega$) and thus the level of damping present in the system. This area can be expressed in nondimensional form as the ratio of Area1 (energy dissipated) to Area2 (energy stored) revealing a dimensionless damping ratio. For a simple SDOF system at resonance ($\omega = \omega_0$), this energy ratio can be shown to be equal to $4\pi\zeta$, thus providing a direct means of measuring the damping in such a simple system.

Figure 2A shows a complete SDOF mass–spring–dashpot system and **Figure 2B** shows a typical plot of the response of that system to a transient input. This plot displays the characteristic free decay of all damped systems and the form of the resulting time-history is heavily influenced by the damping in the

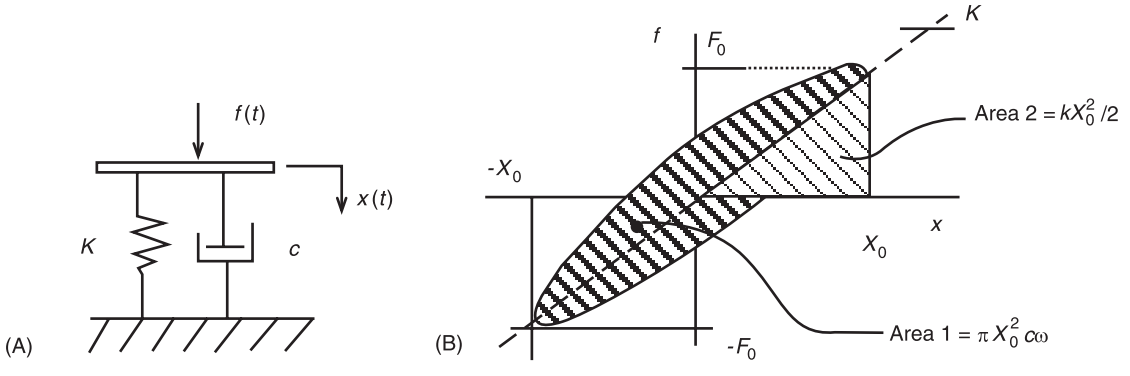


Figure 1 (A) Basic spring–dashpot model for damper, (B) force–displacement characteristic for spring–dashpoint system.

system, c. The frequency of successive oscillations is always the same, at ω'_0, and the rate of decay (envelope) of successive peaks is governed by the exponential expression: $e^{-\omega'_0 t}$. The ratio of successive peak amplitudes is given by: $\Delta = e^{2\pi\zeta}$, or in its more usual form, $\delta = \log_e \Delta \sim 2\pi\zeta$, thereby providing another simple method (the logarithmic decrement or 'log dec' method) of extracting damping estimates from the free vibration of the structure. The exact formula for estimating damping from these free decay curves is:

$$\zeta = \frac{\delta}{\sqrt{(4\pi^2 + \delta^2)}}$$

The third approach to damping measurement can be made using the forced harmonic vibration response characteristics and is based on the form of the classical resonance curve, shown in **Figures 2C** and **2D**. In the first of these, **Figure 2C**, there is a simple construction that is used to estimate damping whose features are shown in the diagram:

- the maximum response level, $\hat{H}$
- two points (frequencies, ω_1 and ω_2) at which the response is 0.707 $\hat{H}$ (the so-called 'half-power points') and these parameters can be used to estimate the damping form:

$$\zeta = (\omega_2 - \omega_1)/2\omega_0$$

The alternative Nyquist plot presentation of the response characteristic, shown in **Figure 2D** provides a different perspective of this same region of the resonance response, but permits a more general formula to be used to estimate the damping:

$$\zeta = \frac{(\omega_a - \omega_b)}{2\omega_0(\omega_a \tan(\theta_a/2) + \omega_b \tan(\theta_b/2))}$$

It should be noted that the formulas presented here are, strictly, approximate but that they are well within any measurement uncertainty for systems with light damping ('light' generally means a critical damping ratio, or loss factor, of less than about 5–10%). In fact, there is an exact version of each of these simple formulas, and it is that which is used in the software that is generally employed to perform the calculations that reveal the damping estimates. Nevertheless, it serves the purpose here of explanation by showing the simple versions.

Practical Considerations

The above formulas provide the basis for estimating damping from any of three different types of test.

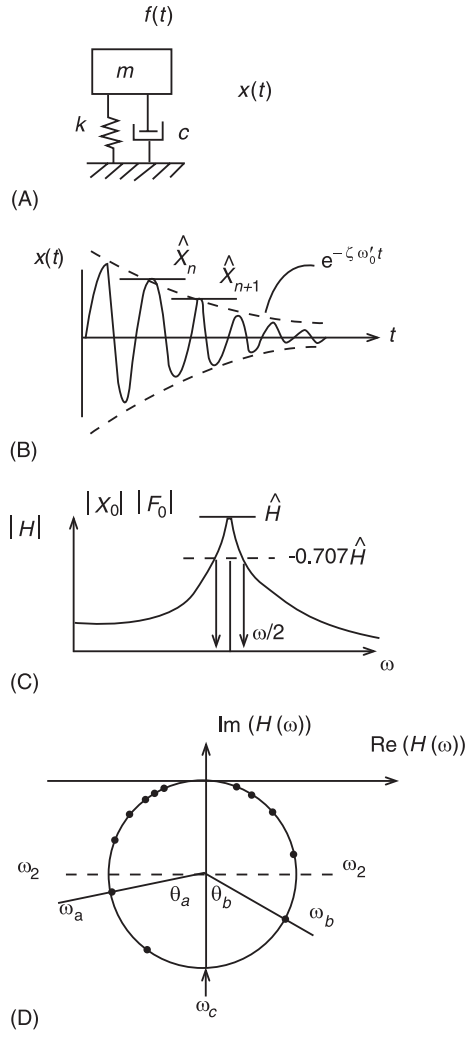


Figure 2 (A) SDOF mass–spring-dashpot system; (B) free vibration response of damped SDOF system; (C) forced response characteristic for SDOF system (modulus plot); (D) forced response characteristic for SDOF system (Nyquist plot).

Indeed, all three are widely used in practice (see **Modal analysis, experimental: Basic principals**).

However, there are a number of complications that often arise when applied to practical structures, and it is worthwhile to list some of these here. The first difficulty that is often encountered is due to the fact that most practical structures are more complicated than the single DOF system used here to illustrate the principles of measurement and so the actual time records, or response curves, are generally more complex than those shown in **Figures 2B–D**. Examples of a typical multi-DOF system responses are sketched in **Figure 3**. In each of these examples, it can be shown that the actual response is the linear summation of several SDOF component responses, each of which has the form of those shown previously in **Figure 2**. Thus, we might expect that if we can extract the

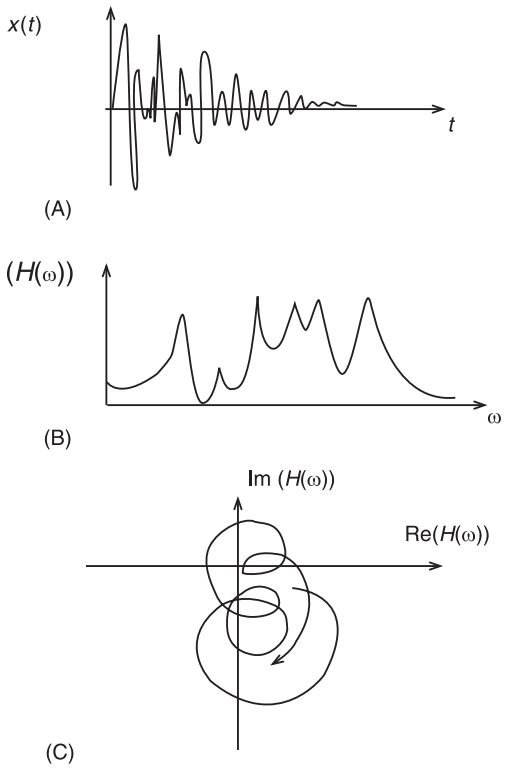


Figure 3 MDOF system. (A) Free vibration response of system (B) modulus response plot for system; (C) Nyquist response plot for system.

individual components of response, such as those shown in **Figure 3**, into their individual modal components, then each of these might take the form of the plots shown in **Figure 2B–D**, and thus be amenable to analysis by one of the three methods above to determine the damping. Sometimes, this complication is such that only a single resonance peak is apparent in a region where, in fact, there are many modes and this almost always leads to a significant overestimation of the damping levels.

The second difficulty that occurs in practice results from the fact that many sources of damping in real

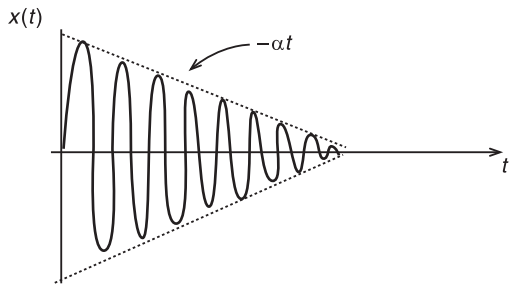


Figure 4 Free vibration response of nonlinear SDOF system.

structures have much more complicated behavior than indicated by the theoretical expressions above. At best, they do not conform exactly to the viscous-type model of the basic damping mechanism used in the formulas, and at worst they are often not linear in their underlying behavior. As a result, it is not possible to extract a single value for the damping: in nonlinear systems, this quantity is often amplitude-dependent. Thus we sometimes obtain free-decay curves such as that shown in **Figure 4**, which displays a linear, rather than exponential, decay characteristic. This is a common feature in systems with dry friction as the source of damping and it is clear that a different damping ratio will be found if we base our estimate on the first few cycles of response than if we use the later cycles. In this case, the damping ratio, or more strictly, the 'equivalent damping factor' increases as the vibration amplitude drops. This is a well known phenomenon of friction-damped systems and it can be seen clearly in these methods of measuring damping.

We often use this concept of equivalent damping when measuring damping in practical structures. Essentially, the equivalent damping factor, or ratio, is that level of viscous (or, sometimes, structural) damping that dissipates the same energy as the actual mechanism which is being measured. This can be seen graphically in **Figure 5**, which shows an actual-system force–deflection characteristic (**Figure 5A**) alongside

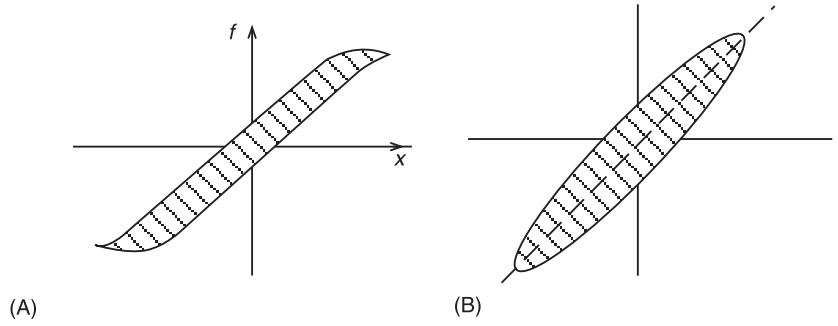


Figure 5 Force–deflection characteristic: (A) hysteresis behavior; (B) viscous dashpot model.

the expected behavior based on the SDOF mass–spring–dashpot model (**Figure 5B**). By choosing a dashpot rate, c, such that the area in the loop of **Figure 5B** is equal to that of the hysteresis characteristic displayed in **Figure 5A**, we can define an equivalent damping model for the measured system.

Accuracy and Reliability of Damping Estimates

In the same way that damping is the most difficult of the standard vibration properties to model, so it tends to be the most difficult to measure accurately. This difficulty is in large part because of the complexity of the real behavior and the relative simplicity of the models used to represent it. However, there are also several practical (measurement) factors which serve to make damping measurements inaccurate and it is appropriate to record here that these errors tend to be all in the same sense. Measurement difficulties associated with noisy signals, and with signal conditioning and processing, as well as the complications discussed above, generally tend to result in damping estimates which are too high, and rarely in ones which are too low by comparison with the correct values. This result is not a conservative one, from a practical point of view, because it is usually required to determine how little damping there is in a practical structure and estimates which are too high indicate a better state of affairs (i.e., that there is more damping present) than is really the case. It is advisable to bear this comment in mind, especially when repeat measurements give significant differences in estimates from one test to the next, where a uniform result might be expected.

Nomenclature

c	dashpot rate
E	energy
$\hat{H}$	maximum response level
Q	dynamic magnification factor
δ	logarithmic decrement

See also: **Damping models**; **Damping, active**; **Modal analysis, experimental**, Basic principles; **Modal analysis, experimental**, Measurement techniques; **Modal analysis, experimental**, Construction of models from tests.

Further Reading

Ewins DJ (2000) *Modal Testing: Theory, Practice and Application*. Taunton, UK: Research Studies Press.

Inman DJ (1994) *Engineering Vibration*. Englewood Cliffs, NJ: Prentice Hall.

DAMPING MODELS

D Inman, Virginia Polytechnic Institute and State University, Blacksburg, VA, USA

Copyright © 2001 Academic Press

doi:10.1006/rwvb.2001.0060

Energy dissipation in vibrating systems is an extremely significant physical phenomenon. Yet damping models remain an illusive research topic. Part of the reason for the lack of definitive damping models is that measurements of damping properties must be dynamic. On the other hand, measurements of stiffness and inertia can be made from static experiments. The need for dynamic experiments in order to verify analytical damping models has resulted in a great deal of difficulty in determining the nature of energy dissipation in a variety of structures and machines. The other fact that makes damping a difficult phenomenon to model is that it is inherently nonlinear, frequency dependent and temperature dependent. There are numerous sources of damping in structures and machines. Sliding friction and the energy dissipation of material moving in air provide the dominant sources of external damping. Sliding friction also exists as an internal cause of damping in jointed structures. Other common sources of internal damping are grouped together and called material damping. The physical sources of various material-damping mechanisms are not presented here; rather some general models are presented based on phenomenological data. Here some basic models that characterize the most common methods of modeling are reviewed.

Viscous Damping

The response of a simple, single-degree-of-freedom, spring-mass model predicts that the system will oscillate indefinitely. However, everyday observation indicates that most freely oscillating systems eventually die out and reduce to zero motion. This experience suggests that the typical undamped single-degree-of-freedom model needs to be modified to account for this decaying motion. The choice of a representative model for the observed decay in an oscillating system is based partially on physical observation and partially on mathematical convenience. The theory of differential equations suggests that adding a term to the undamped equation:

$$m\ddot{x}(t) + kx(t) = 0 \qquad [1]$$

of the form $c\dot{x}$, where c is a constant, will result in an equation that can be solved and a response $x(t)$ that dies out. Physical observation agrees fairly well with this model and it is used successfully to model the damping, or decay, in a variety of mechanical systems. This type of damping, called viscous damping, is the most basic attempt to model energy dissipation in vibrating systems. Viscous damping forms the most common model used in lumped mass, single- as well as multiple-degree-of-freedom systems.

While the spring forms a physical model for storing potential energy and hence causing vibration, the dashpot, or damper, forms the physical model for dissipating energy and hence damping the response of a mechanical system. A dashpot can be thought of as a piston fitted into a cylinder filled with oil. This piston is perforated with holes so that motion of the piston in the oil is possible. The laminar flow of the oil through the perforations as the piston moves causes a damping force on this piston. The force is proportional to the velocity of the piston, in a direction opposite that of the piston motion. This damping force, denoted by f_c, has the form:

$$f_c = c\dot{x}(t) \qquad [2]$$

where c is a constant of proportionality related to the oil viscosity. The constant c, called the damping coefficient, has units of force per velocity: Ns/m, or kg/s. The force f_c is referred to as linear viscous damping.

In the case of the oil-filled dashpot, the constant c can be determined by fluid principles. However, in most cases, equivalent effects occurring in the material forming the device provide this damping force. A good example is a block of rubber (which also provides stiffness) such as an automobile motor mount, or the effects of air flowing around an oscillating mass. An automobile shock absorber provides another example of a viscous damper (in its linear range of operation). In all cases in which the damping force f_c is proportional to velocity, the schematic of a dashpot is used to indicate the presence of this force in free-body diagrams. Unfortunately, the damping coefficient of a system cannot be measured statically as can the mass or stiffness of a system.

Combining eqns [1] and [2], the standard equation of motion of a spring-mass-damper system becomes:

$$m\ddot{x}(t) + c\dot{x}(t) + kx(t) = 0 \qquad [3]$$

The solutions of this linear differential equation decay with time exponentially agreeing with the dissipation of energy expected from physical observation. Depending on the relative value of the damping coefficient, the solution will oscillate and decay (underdamped) or just exponentially decay (overdamped and critically damped).

It is useful to divide eqn [3] by the mass and write the result as:

$$\ddot{x}(t) + 2\zeta\omega_n\dot{x}(t) + \omega_n^2 x(t) = 0 \qquad [4]$$

Here the natural frequency and damping ratio are defined as:

$$\omega_n = \sqrt{\left(\frac{k}{m}\right)} \quad \text{and} \quad \zeta = \frac{c}{2\sqrt{(km)}} \qquad [5]$$

respectively. The solution to eqn [3] given initial conditions on the position, x_0, and velocity, v_0, for the underdamped case ($0<\zeta<1$) is then simply:

$$x(t) = \sqrt{\left(\frac{(v_0 + \zeta\omega_n x_0)^2 + (x_0\omega_d)^2}{\omega_d^2}\right)} e^{-\zeta\omega_n t} \times \sin\left(\omega_d t + \left[\frac{x_0\omega_d}{v_0 + \zeta\omega_n x_0}\right]\right) \qquad [6]$$

Here the damped natural frequency is defined as:

$$\omega_d = \omega_n\sqrt{(1-\zeta^2)} \qquad [7]$$

It is important to realize that viscous damping as defined by the constant c and the nondimensional version ζ, does not come from a physical modeling exercise or a fundamental mechanics principle, such as Hooke's law, but is used because it results in the solution, given in eqn [6], that matches the physical observation in many situations. Hence, the viscous

damping model is useful because first, it adds energy dissipation to the vibration problem of eqn [1], and secondly, it provides an analytical solution to the vibration problem with energy dissipation. This form assumes that the damping is a linear, time invariant phenomenon chosen to be viscous, or proportional to velocity, motivated by the ability to solve the resulting equation of motion.

An attempt to rationalize the use of the viscous damping term can be found in elasticity. Here the stress–strain relationship (Hooke's law) is modified to become:

$$\sigma(x,t) = E\varepsilon(x,t) + c\dot{\varepsilon}(x,t) \qquad [8]$$

Here σ is the stress as a function of position (x) and time (t), ε is the strain as a function of position and time, the over dot indicates differentiation with respect to time (hence, strain rate), c is a damping coefficient, and E is the elastic modulus. This relationship can be used to generate equations of motion in the form of eqn [4] (on a modal basis) from first principles. Eqn [8] is called the Kelvin–Voigt model of damping and is represented schematically by a spring and damper in parallel, forming the most basic procedure for including linear viscous damping in lumped-mass systems.

Coulomb Damping

Sliding friction, also termed Coulomb damping, is the damping force commonly used to model friction arising from relative motion of two surfaces. Such damping arises in certain kinds of joints in structures and is most commonly used to model the damping in sliding mechanisms. Coulomb damping is characterized by the force:

$$f_c = F(\dot{x}) = \begin{cases} -\mu N & \dot{x} > 0 \\ 0 & \dot{x} = 0 \\ \mu N & \dot{x} < 0 \end{cases} \qquad [9]$$

where f_c is the dissipation force, N is the normal force (see any introductory physics text), and μ is the coefficient of sliding friction (or kinetic friction). Because of the switching nature of the Coulomb force it is nonlinear and hence the resulting equation of motion is nonlinear. The Coulomb damping force can be written as the signum function, denoted sgn (τ), and defined to have the value 1 for $\tau>0$, -1 for $\tau<0$, and 0 for $\tau = 0$. A spring-mass system with Coulomb damping has the equation of motion:

$$m\ddot{x} + \mu mg \text{ sgn } (\dot{x}) + kx = 0 \qquad [10]$$

Since this differential equation is nonlinear, it cannot be solved directly using analytical methods such as the variation of parameters or the method of undetermined coefficients. Rather, eqn [10] can be solved by breaking the time intervals up into segments corresponding to the changes in direction of motion (i.e., at those time intervals separated by ($\dot{x} = 0$). Alternatively, eqn [10] can be solved numerically.

Nonlinear vibration problems are much more complex than linear systems. Their numerical solutions, however, are often fairly straightforward. Several new phenomena result when nonlinear terms are considered. Most notably, the idea of a single equilibrium point of a linear system is lost. In the case of Coulomb damping, a continuous region of equilibrium positions exists, corresponding to the maximum static friction force. This single fact greatly complicates the analysis, measurement, and design of vibrating systems with nonlinear terms.

Several things can be noted about the free response with Coulomb friction vs the free response with viscous damping. First, with Coulomb damping the amplitude decays linearly with slope given by (g is the acceleration due to gravity):

$$-\frac{2\mu mg\omega_n}{\pi k} \qquad [11]$$

rather than exponentially as does a viscously damped system. Second, the motion under Coulomb damping comes to a complete stop, at a potentially different equilibrium position than when initially at rest. However, the motion under viscous damping oscillates around the single equilibrium of $x = 0$ and approaches zero exponentially. Third, the frequency of oscillation of a system with Coulomb friction is ω_n, the undamped natural frequency, while the frequency of oscillation of the viscously damped system is the damped natural frequency as given in eqn [7].

Coulomb friction, as defined above by eqn [9], is a fairly accurate description of the behavior of many machine and structural components. However, as with all theories there are a number of more advanced descriptions of sliding friction as discussed elsewhere in this encyclopedia (see **Friction damping**).

Material Damping

One approach to modeling damping from linear viscoelasticity is to expand on eqn [8] and hypothesize that the one-dimensional stress–strain relationship is:

$$\begin{aligned} a_0\sigma + a_1\dot{\sigma} + a_2\ddot{\sigma} + a_3\dddot{\sigma} + \cdots \\ = b_0\varepsilon + b_1\dot{\varepsilon} + b_2\ddot{\varepsilon} + b_3\dddot{\varepsilon} + \cdots \end{aligned} \qquad [12]$$

Here each of the coefficients a_i and b_i are constants and the stress σ, and the strain ε, both depend on position and time. The over dots represent time derivatives. Various damping models follow from eqn [12] by setting various combinations of the coefficients to zero. For instance, if all of the coefficients except a_0 and b_0 are zero, then Hooke's law results. Keeping the first two terms in this expansion leads to:

$$\sigma(x,t) + a_1\dot{\sigma}(x,t) = E_r[\varepsilon(x,t) + \tau_\sigma\dot{\varepsilon}(x,t)] \qquad [13]$$

which is called the Kelvin model or standard linear model. Here E_r is called the relaxed modulus of elasticity and the over dots are again time derivatives. If a_1 in eqn [13] is zero then eqn [13] reduces to eqn [8] and equations of the form of eqn [3] result. Another popular model resulting from eqn [12] is the Maxwell model:

$$a_0\sigma(x,t) + a_1\dot{\sigma}(x,t) = b_1\dot{\varepsilon}(x,t) \qquad [14]$$

The Maxwell model can be visualized as a spring and damper in series. All of the different models derived from eqn [12] can be thought of as various series and parallel combinations of springs and dampers connected as lumped elements.

Some of the constitutive relationships derived from eqn [12], when used in energy methods or in Newton's law, yield equations of motion with linear viscous behavior. For example, one model of an Euler–Bernouli beam with strain rate damping (C_D) moving in air (γ) is:

$$\rho\frac{\partial^2 u(x,t)}{\partial t^2} + \gamma\frac{\partial u(x,t)}{\partial t} + \frac{\partial^2}{\partial^2 x} \times\left(C_D I\frac{\partial^3 u(x,t)}{\partial^2 x\partial t} + EI\frac{\partial^2 u(x,t)}{\partial^2 x}\right) = 0 \qquad [15]$$

Here $u(x, t)$ is the displacement of the beam, E is the elastic modulus, and I is the cross-sectional area moment of inertia about the z-axis. It is important to note that in such models the damping terms also appear in the boundary conditions. For instance at a free end, with strain-rate damping as given in eqn [15], the boundary conditions are:

$$EI\frac{\partial^2 u}{\partial x^2} + C_D I\frac{\partial^3 u}{\partial t\partial x^2} = 0 \text{ at the free boundary}$$
$$-\frac{\partial}{\partial x}\left(EI\frac{\partial^2 u}{\partial x^2} + C_D I\frac{\partial^3 u}{\partial t\partial x^2}\right) = 0 \text{ at the free boundary} \qquad [16]$$

This model corresponds to Kelvin–Voigt damping offering resistance to the bending moment. Such models give reasonable predictions of the time response and decay rates for vibrating beams made of metals when compared with vibration experiments. However, the damping coefficients (γ and C_D) must be determined by parameter identification methods and experimental data.

Complex Stiffness and Modulus

The complex modulus approach to representing various damping mechanisms follows from eqn [12] by simply taking the Laplace transform of the expression and evaluating the transform variable along the imaginary axis. However, an easier way to visualize the complex modulus approach is to examine the Kelvin–Voigt damping model under harmonic excitation. Using the exponential form of harmonic excitation the equation of motion becomes:

$$m\ddot{x}(t) + c\dot{x}(t) + kx(t) = F\,e^{j\omega t} \qquad [17]$$

Here ω is the driving frequency and F is the amplitude of the applied force. The symbol j denotes the imaginary unit. Assuming a steady state solution of the form $x(t) = X\,e^{j\omega t}$ and substituting this into eqn [17] results in:

$$-m\omega^2 X\,e^{j\omega t} + (k + j\omega c)X\,e^{j\omega t} = F\,e^{j\omega t} \qquad [18]$$

Again using the substitution $X\,e^{j\omega t} = x(t)$ yields:

$$m\ddot{x}(t) + \underbrace{(k + j\omega c)}_{k'}x(t) = F\,e^{j\omega t} \qquad [19]$$

In this form, the complex stiffness is evident from the coefficient of $x(t)$ and has the form:

$$k' = k + j\omega c \qquad [20]$$

This also leads to the concept of the complex modulus. The complex stiffness is often referred to as the Kelvin–Voigt complex stiffness.

If experiments are performed and used to compute the energy dissipated per cycle under sinusoidal excitation, many engineering materials exhibit damping of the form $C_d X^2$ where:

$$C_d = \pi c\omega \qquad [21]$$

The constant c is the normal viscous damping coefficient. This is referred to as the Kimball–Love observation. Solving this for a damping force, the following frequency dependent damping force is obtained:

$$f_c = \left(\frac{b}{\omega}\right)\dot{x}(t) \qquad [22]$$

Here the constant b is the measured value of $b = (C_d)/\pi$. The corresponding equation of motion is:

$$m\ddot{x}(t) + \frac{b}{\omega}\dot{x}(t) + kx(t) = 0 \qquad [23]$$

This illustrates a system with frequency dependent damping. Here however, the interpretation of the value of ω is somewhat fuzzy. Some interpret it to be the driving frequency in steady state, but this denies the use of eqn [23] for transient analysis. Furthermore, the form of eqn [23] does not satisfy the condition of causality for physically realizable systems. Under harmonic excitation, the complex stiffness and the frequency dependent form of eqn [20] are equivalent.

The frequency-dependent form given by eqn [23] has been adapted to free vibration by hypothesizing the damping force:

$$f_c = b\left|\frac{x(t)}{\dot{x}(t)}\right|\dot{x}(t) \qquad [24]$$

This is causal, allows numerical simulation, but results in a nonlinear differential equation of motion.

Viscoelastic Damping

Viscoelastic damping arises from materials that are rubber like in nature, called viscoelastic materials (VEM). Viscoelastic damping is exhibited in polymeric and glassy materials as well as in some enamel materials. Viscoelastic materials are often added to metal structures (which typically have very low damping) and devices to increase the amount of system damping. Examples are rubber mounts and constrained layer damping treatments. The classical theory of elasticity states that for sufficiently small strains, the stress in an elastic solid is proportional to the instantaneous strain and is independent of the strain rate. In a viscous fluid, according to the theory of hydrodynamics, the stress is proportional to the instantaneous strain rate and is independent of the strain. Viscoelastic materials exhibit both solid and fluid characteristics. Such materials include plastics, rubbers, glasses, ceramics, and biomaterials. Viscoelastic materials are characterized by constant-stress creep and constant-strain relaxation. Their deformation response is determined by both current and past stress states or, conversely, the current stress-state is determined by both current and past deformation states. It may be said that viscoelastic materials have 'memory'; this characteristic constitutes one foundation on which their mathematical modeling may be based. In polymers, material damping is a direct result of the relaxation and recovery of the long molecular chains after stress.

Linear viscoelastic materials may be defined by either differential or integral relationships. The differential model is presented in eqn [12]. Boltzmann in 1876 initiated a linear hereditary theory of material damping by formulating an integral representation of the stress–strain relation resulting in a damping force of the form:

$$f_c = \int_{-\infty}^{t} G(t,\tau)x(\tau)\,\mathrm{d}\tau \qquad [25]$$

Here t is the current time, x is the displacement and G is the hereditary kernel. The term hereditary is used because the instantaneous deformation depends on all of the stresses previously applied to the system as well as depending on the stress at the current time. It is common to take the time dependence of the hereditary kernel to be a difference so that eqn [25] becomes:

$$f_c = \int_{-\infty}^{t} G(t-\tau)x(\tau)\,\mathrm{d}\tau \qquad [26]$$

Motivated by Boltzmann's hypothesis, a general hereditary integral for the stress–strain relation was later proposed (1947) of the form:

$$\sigma(t) = E_0\varepsilon(\tau) + \int_0^t k(t-\tau)\,\frac{\mathrm{d}\varepsilon(\tau)}{\mathrm{d}\tau}\,\mathrm{d}\tau \qquad [27]$$

Here, $k(t-\tau)$ is the relaxation modulus and E_0 represents an instantaneous modulus of elasticity. Eqn [27] can be thought of as a generalization of the Kelvin model. This expression can also be written in terms of the creep compliance $J(t)$ as:

$$\varepsilon(\tau) = \int_0^t J(t-\tau)\,\frac{\mathrm{d}\sigma(\tau)}{\mathrm{d}\tau}\,\mathrm{d}\tau \qquad [28]$$

Various methods of modeling the relaxation modulus have led to a number of useful methods of modeling hysteretic type damping (see **Damping models**).

In practice, the damping related to VEM, as described by eqn [27], is characterized by a single number, the loss modulus or loss factor. The loss factor is derived analytically from the complex stiffness description given in eqn [20]. Rewriting eqn [20] as:

$$k' = k(1 + \bar{\eta}j) \qquad [29]$$

defines the loss factor to be:

$$\bar{\eta} = \frac{c}{k}\omega \qquad [30]$$

Here ω is the driving frequency and the concept is defined only in the steady state under harmonic excitation. This shows clear frequency dependence. In terms of a material property, the complex modulus may also be written in a factored form:

$$E' = E(1 + \eta j) \qquad [31]$$

where η is now the material loss factor which is also frequency dependent. Tests show that these values depend heavily on both frequency and temperature.

Eqn [31] is written for the extensional modulus. However, most of the damping produced in VEM comes from shear effects. The relationship between the shear modulus, G', and extensional modulus is given from the elasticity theory through Poisson's ratio, v, to be:

$$E' = 2(1 + v)G' \qquad [32]$$

Typical values of Poisson's ratio are about 0.5 for elastomeric materials at room temperatures, so that $E = 3G$. However, Poisson's ratio is both frequency and temperature dependent. For example, at lower temperatures Poisson's ratio is closer to 0.33. Unfortunately, Poisson's ratio is very difficult to measure.

A typical VEM is chosen in design applications based on plots of loss factor vs temperature and loss factor vs frequency. Basically the loss factor η is considered to be a function of both driving frequency and temperature; $\eta = \eta(\omega T)$. While no mechanics model of the temperature dependence is presented, the values of η are measured at various temperatures and plotted for a fixed frequency. In addition, for a fixed temperature, values of η are measured at a variety of frequencies for a fixed temperature. These plots are then provided as design guides for working with damping treatments for the purpose of vibration reduction (see **Damping materials**).

The complex modulus is also both frequency and temperature dependent. Eqn [31] can be written for the complex shear modulus as a temperature and frequency dependent quantity:

$$G'(\omega, T) = G(\omega, T)(1 + \eta(\omega, T)j) \qquad [33]$$

The complex notation provides a way to measure the phase angle between the applied stress and the resulting strain in cyclic loading. The real and imaginary parts of the complex shear modulus are widely used in the VEM industry to characterize damping materials. The real part, $G(\omega T)$, is called the storage modulus or shear modulus, and the imaginary part, $G(\omega T)\eta(\omega T)$, is called the loss modulus. The loss factor provides a measure of the energy dissipation capacity of the material, while the storage modulus provides a measure of the stiffness of the material. Basically the shear modulus determines how much energy goes into the VEM and the loss factor determines how much of that energy is dissipated.

A great deal of effort has been invested by industry in characterizing viscoelastic materials in terms of their temperature and frequency dependence. Testing of viscoelastic materials can be divided into two main categories: resonant testing and nonresonant testing. Nonresonant tests are often called complex stiffness tests and use a sample VEM fixed to a rigid mount and loaded in shear. The force and deformation are measured. The phase angle between the force and the deformation then provides a measure of the damping. The ratio of in-phase force to displacement provides a measure of the storage modulus.

The resonant testing method provides an indirect measure of damping and stiffness by using modal parameters. Basically, a beam-like specimen is excited (randomly) and a modal analysis yields the damping and frequency, from which the loss factor (equal to twice the damping ratio at resonance) and stiffness (hence storage modulus) are determined (ASTM E756-98).

These temperature and frequency dependencies are difficult to model in any analytical sense. Experiments show that temperature variations in damping are much more drastic then frequency variations. While good models of these dependencies do not exist at the system level, experimental data can be used to approximate the inclusion of these effects in finite element modeling, as discussed in **Damping in FE models**.

Equivalent Viscous Damping

Most of the damping models listed here are nonlinear and/or frequency and temperature dependent. In fact,

accurate modeling of damping quickly leads to nonlinear terms. The effects of nonlinearity and frequency dependence render the models difficult to use in vibration analysis. In particular, the most common method of modeling structures for vibration analysis is the finite element method, which has difficulty with even the basic linear viscous behavior. As a result, some effort has been spent to produce 'equivalent' linear viscous models. It is important to note that while these models express the energy dissipated accurately, the linearized models do not render the same physical behavior. For instance, the linear version will not have multiple equilibrium points.

The equivalent viscous damping of any single-degree-of-freedom damping model is obtained by examining the response of the system in steady state under sinusoidal excitation. The energy dissipated per cycle of the forced response is then computed for a linear viscous damper. Next the same calculation is made for the identical system (i.e., same mass and stiffness) with the nonlinear damping mechanism. These two expressions for the energy dissipated per cycle are then compared and the equivalent linear, viscous damping coefficient, c_{eq} is derived. The results of such calculations can be found in most introductory texts on vibration and are summarized for some common damping mechanisms in **Table 1**.

The value of equivalent viscous damping from **Table 1** can then be used in place of the actual mechanism. This results in a linear equation of motion that can be solved in close form to simulate the nonlinearly damped system. Most often such calculations are used to approximate the magnitude of the steady-state response of the nonlinear system for design purposes. The method must be treated only as a crude approximation because the nonlinear system exhibits additional phenomena that are not present in the equivalent linear system. For example, the response of a system with Coulomb friction under steady-state excitation will chatter under harmonic loads with amplitudes near the maximum static friction force. This behavior would be completely missed by the equivalent, linear viscous form.

As an example of the use of equivalent viscous damping factors, consider a system with nonlinear air damping. A single-degree-of-freedom system with velocity squared damping, a linear spring and harmonic input is described by:

$$m\ddot{x} + \alpha \text{ sgn } (\dot{x})\dot{x}^2 + kx = F_0 \cos \omega t \qquad [34]$$

The equivalent viscous damping coefficient from **Table 1** is:

Table 1 Damping models and equivalent linear models.

Name	*Damping force*	c_{eq}	*Source*
Linear viscous damping	$c\dot{x}$	c	Slow fluid
Air damping	a sgn $(\dot{x})\dot{x}^2$	$8a\omega X/3\pi$	Fast fluid
Coulomb damping	β sgn $\dot{x}$	$4\beta/\pi\omega X$	Sliding friction
Displacement-squared damping	d sgn $(\dot{x})\dot{x}^2$	$4dX/3\pi\omega$	Material damping
Solid, or structural, damping	b sgn $(\dot{x})\lvert x\rvert$	$2b/\pi\omega$	Internal damping

$$c_{eq} = \frac{8}{3\pi}\alpha\omega X \qquad [35]$$

The value of the magnitude, X, can be approximated for near resonance conditions to be ($f_0 = F_0/m$):

$$X = \sqrt{\left(\frac{3\pi m f_0}{8\alpha\omega^2}\right)} \qquad [36]$$

Combining these last two expressions yields an equivalent viscous damping value of:

$$c_{eq} = \sqrt{\left(\frac{8m\alpha f_0}{3\pi}\right)} \qquad [37]$$

Using this value as the damping coefficient results in a linear system of the form:

$$m\ddot{x} + c_{eq}\dot{x} + kx = F_0 \cos \omega t \qquad [38]$$

This provides a linear approximation to eqn [34]. **Figure 1** is a plot of the linear system with equivalent

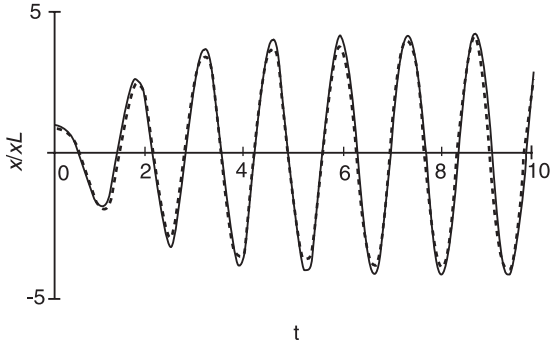


Figure 1 The displacement of the equivalent viscous damping (—) and the displacement of the nonlinear system (- - -) vs time for the case of $\alpha = 0.5$.

viscous damping and a numerical simulation of the full nonlinear eqn [38] for the value of the parameter $\alpha = 0.5$ that depends on the drag coefficient. Further simulations show that the larger the drag coefficient the greater the error is in using the concept of equivalent viscous damping. Note from the plot that the frequency of the response looks similar, but the amplitude of oscillation is slightly over estimated by the equivalent viscous damping technique, rendering it conservative in design.

Numerical simulation has become cheap, and well understood. In the case of single-degree-of-freedom systems it is best to simulate the full nonlinear system rather then to use the approximation. Repeated simulations can offer design information that is more accurate then using the equivalent viscous damping approach. However, if a closed form design formula is needed, then the 'equivalence' listed in **Table 1** will be useful.

Nomenclature

c	constant
C_D	strain rate damping
E	modulus of elasticity
f_c	damping force
F	amplitude of the applied force
g	acceleration due to gravity
G	hereditary kernel
I	inertia
j	imaginary unit
t	time
v	velocity
X	magnitude
σ	stress
ε	strain
η	material loss factor

See also: **Damping in FE models**; **Damping materials**; **Viscous damping**.

Further Reading

Bandstra JP (1983) Comparison of equivalent viscous damping and nonlinear damping in discrete and continuous vibrating systems. *ASME Journal of Vibration, Acoustics, Stress and Reliability in Design* 105: 382–392.

Banks HT, Wang Y, Inman DJ (1994) Bending and shear damping in beams: frequency domain estimation techniques. *ASME Journal of Vibration and Acoustics* 116(2): 188–197.

Bert CW (1973) Material damping: an introductory review of mathematical models, measures and experimental techniques. *Journal of Sound and Vibration* 29(2): 129–153.

Inman DJ (2001) *Engineering Vibration*, 2nd edn. Upper Saddle River, NJ: Prentice Hall.

Lazan BJ (1968) *Damping of Materials and Members in Structural Mechanics*. London: Pergamon Press.

Nashif AD, Jones DIG, Henderson JP (1985) *Vibration Damping*. New York: Wiley.

Osiñski Z (ed.) (1998) *Damping of Vibrations*. Rotterdam: A.A. Balkema.

Snowden JC (1968) *Vibration and Shock in Damped Mechanical Systems*. New York: Wiley.

Sun CT, Lu YP (1995) *Vibration Damping of Structural Elements*. Englewood Cliffs, NJ: Prentice Hall.

DAMPING MOUNTS

J-Q Sun, University of Delaware, Newark, DE, USA

Copyright © 2001 Academic Press

doi:10.1006/rwvb.2001.0019

Introduction

Mounts are commonly used to reduce the energy transmission from one mechanical system to another. They are also referred to as vibration isolators. Mounts are often designed to provide damping in the transmission path for vibration isolation. Damping is therefore incorporated in the mounting system for energy dissipation. There is a compromise between the inclusion of proper damping and the isolation performance of the mounting system. This article presents the common designs of mounts with various built-in damping mechanisms.

Special mounting systems are also discussed in this *Encyclopedia* (see Active Mounts in article **Active control of vehicle vibration**; and Isolation of Machinery in Buildings in article **Active control of civil structures**.

Basic Concepts of Mounting System

There are two types of applications with a mounting system, as illustrated in **Figure 1**. The first is to isolate

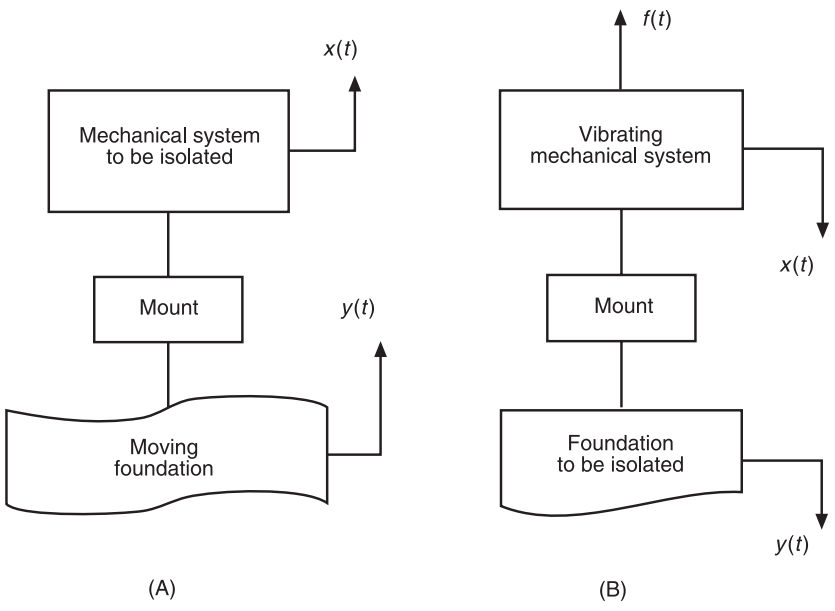


Figure 1 Two typical applications of mounting systems.

mechanical systems from based excitations. Applications of this type include earthquake isolation of buildings, isolation of high-precision instruments from ground motions, and isolation of passengers from rough road-induced vibrations of automobiles. The second is to isolate vibrating systems from the foundation. Applications of this type include reducing the dynamic forces transmitted to the foundation that are generated by vibrating heavy machines and home appliances.

Mounting systems are characterized by the quantity called transmissibility. For the moving foundation problem, an absolute transmissibility can be defined as:

$$(T_A)_d = \frac{X}{Y}, \quad (T_A)_v = \frac{\dot{X}}{\dot{Y}}, \quad (T_A)_a = \frac{\ddot{X}}{\ddot{Y}} \qquad [1]$$

where $(T_A)_d$, $(T_A)_v$, and $(T_A)_a$ are the absolute displacement, velocity, and acceleration transmissibilities. X, $\dot{X}$, and $\ddot{X}$ are the amplitudes of the absolute displacement, velocity and acceleration of the isolated system. Y, $\dot{Y}$, and $\ddot{Y}$ are the amplitudes of the absolute displacement, velocity, and acceleration of the foundation. When the foundation motion is harmonic, and the entire system is linear, these three transmissibilities are equal. In practice, it is often more convenient to use the relative displacement across the mount as a parameter to characterize the system. Let Z, $\dot{Z}$, and $\ddot{Z}$ be the amplitudes of the relative displacement, velocity, and acceleration across the mount. We can define a relative transmissibility as:

$$(T_R)_d = \frac{Z}{Y}, \quad (T_R)_v = \frac{\dot{Z}}{\dot{Y}}, \quad (T_R)_a = \frac{\ddot{Z}}{\ddot{Y}} \qquad [2]$$

For the force isolation problem, the transmissibility is defined as the ratio of the force F_t transmitted to the foundation to the dynamic force F_d acting on or generated by the vibrating mechanical system:

$$T_f = \frac{F_t}{F_d} \qquad [3]$$

Passive Damping in Mounts

Various damping mechanisms can be built in a mount. **Table 1** presents a list of commonly used damping. For the mount with eletrorheological (ER) fluid or magnetorheological (MR) fluid in **Table 1**, the damping force of the mount is controllable, and the system is called semiactive. Active damping is normally provided by a force actuator that is part of a closed-loop control system. The active and semiactive damping will be discussed later.

Consider a single-degree-of-freedom (SDOF) system, as shown in **Figure 2**. The equation of motion for the system is given by:

$$m\ddot{x} + D(\dot{z}) + kz = f(t) \qquad [4]$$

For linear viscous damping $D(\dot{z}) = c\dot{z}$, the transmissibility can be obtained in closed form. Assume that the base excitation $y(t)$ is harmonic with frequency ω and $f(t) = 0$; we have:

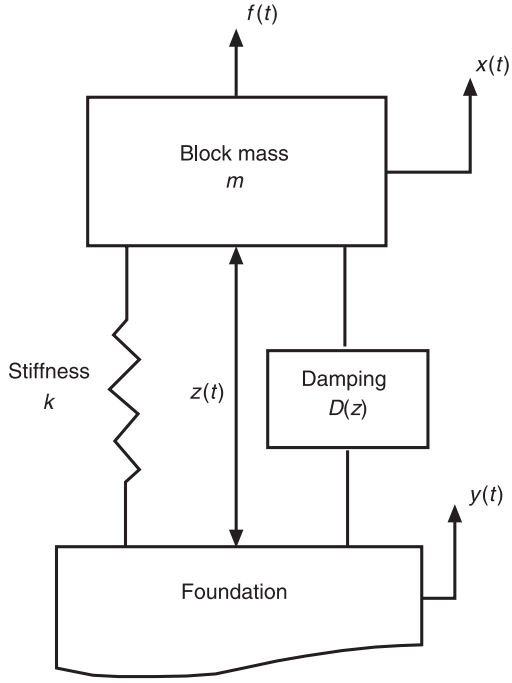


Figure 2 A single-degree-of-freedom example of directly coupled damping in mounting systems.

$$(T_A)_d = \sqrt{\frac{1+4\zeta^2 r^2}{(1-r^2)^2+4\zeta^2 r^2}}\, e^{-i\phi}$$
$$\phi = \tan^{-1}\left(\frac{2\zeta r^3}{(1-r^2)+4\zeta^2 r^2}\right) \qquad [5]$$

where $\zeta = c/2\sqrt{mk}$ is the damping ratio, $r = \omega/\omega_n$ is the frequency ratio. $\omega_n = \sqrt{k/m}$ is the natural frequency of the mount. The amplitude and phase of the transmissibility are shown in **Figure 3**. The effect of damping on vibration isolation is clearly shown in the amplitude plot. For $r \le \sqrt{2}$, damping suppresses the resonant response of the mounting system, and is thus beneficial. For $r > \sqrt{2}$, damping actually increases the transmitted vibration level. However, the mount is typically designed to operate in the frequency range $\omega \gg \omega_n$, i.e., $r > \sqrt{2}$; damping is less beneficial in this higher-frequency range. This observation of the effect of damping on the transmissibility is common to other types of damping.

Table 1 Damping mechanisms for mounting systems

Type of damping	*Damping force*
Linear viscous	$-c\dot{z}$
Dry friction	$-\mu\,\mathrm{sgn}(\dot{z})$
Power-law	$-c_n\lvert\dot{z}\rvert^n\,\mathrm{sgn}(\dot{z})$
Hysteretic	$-c(\omega)\dot{z}$
Electrorheological fluids	$-f_y(E)\,\mathrm{sgn}(z) - c(E)\dot{z}$
Magnetorheological fluids	$-f_y(H)\,\mathrm{sgn}(z) - c(H)\dot{z}$
Active damping	$-K_D\dot{z}$
Skyhook active damping	$-K_s\dot{x}$

E, electric field strength in the electrorheological fluid; *H*, magnetic field strength in the magnetorheological fluid; K_D, feedback gain in active damping.

When the damping is nonlinear, it is often very difficult to obtain analytical solutions for the transmissibility. A common approach to obtain approximate solutions in order to design a mount is the method of equivalent linearization. The method proposes to find an equivalent linear viscous damping to replace the nonlinear damping. The closed-form solution for the linear system then becomes available. For example, an equivalent linear system to eqn [4] is given by:

$$m\ddot{x} + c_{eq}\dot{z} + kz = f(t) \qquad [6]$$

The equivalent linear viscous damping coefficient c_{eq} can be determined such that the error $e(t) = c_{eq}\dot{z} - D(\dot{z})$ is minimized. When the system is harmonic, the following mean square error over a period is minimized with respect to c_{eq}:

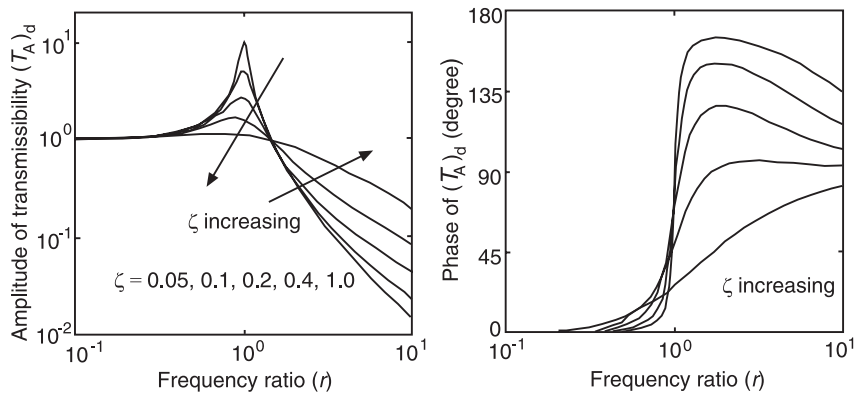


Figure 3 Effect of viscous damping on the amplitude and phase of the absolute displacement transmissibility of the simple mount.

$$J = \frac{1}{\tau}\int_0^{\tau} e^2(t)\,\mathrm{d}t \qquad [7]$$

where τ is the period of the harmonic motion. The equivalent linear viscous damping coefficient is given by:

$$e_{\mathrm{eq}} = \frac{\int_0^{\tau} \dot{z}D(\dot{z})\,\mathrm{d}t}{\int_0^{\tau} \dot{z}^2\,\mathrm{d}t} \qquad [8]$$

When the motion is random, the mean square error and the equivalent linear viscous damping coefficient are given by:

$$J = E\left[e^2(t)\right], \quad e_{\mathrm{eq}} = \frac{E[\dot{z}D(\dot{z})]}{E[\dot{z}^2]} \qquad [9]$$

where $E[\cdot]$ is the mathematical expectation operator. As an example, consider a quadratic nonlinear damping element given by $D(\dot{z}) = c_2\dot{z}^2\mathrm{sgn}(\dot{z})$. The magnitude of the displacement transmissibility is given by:

$$\left|(T_{\mathrm{A}})_{\mathrm{d}}\right| = \sqrt{\frac{1+4\zeta_{\mathrm{eq}}^2 r^2}{(1-r^2)^2+4\zeta_{\mathrm{eq}}^2 r^2}} \qquad [10]$$

where:

$$4\zeta_{\mathrm{eq}}^2 r^2 = \frac{1}{2}\left[\sqrt{(1-r^2)^4+\left(\frac{16c_2\omega_{\mathrm{n}}^2 Y_0 r^4}{3\pi k}\right)^2} - \left(1-r^2\right)^2\right]$$

Y_0 is the magnitude of the harmonic motion of the base excitation. The phase of the transmissibility based on the equivalent linear system has the same form as the one given in eqn [5]. **Figure 4** shows the magnitude and phase of the transmissibility. The parameter α shown in the figure is defined as $\alpha = c_2\omega_{\mathrm{n}}^2 Y_0 k^{-1}$. The effect of damping is very similar to that for the system with linear viscous damping.

The method of equivalent linearization can be applied to the mounting system with nonlinear damping and nonlinear stiffness. It provides a quick solution for design engineers. However, when the nonlinearity is strong, caution should be exercised when interpreting the results.

Elastically Coupled Damping

The damping element in the mount shown in **Figure 2** is directly coupled. Another common arrangement is to couple the damping element elastically in the mount, as shown in **Figure 5**. The elastic coupling introduces a half-degree-of-freedom, leading to an equation of motion for the system that is third-order. The equation of motion for the system with linear viscous damping $D(\dot{z}) = c\dot{z}$ is given by:

$$\frac{mc}{k_1}\dddot{x} + m\ddot{x} + c\frac{k_1+k}{k_1}\dot{z} + kz = f(t) + \frac{c}{k_1}\dot{f}(t) \qquad [11]$$

Assume that the base excitation $y(t)$ is harmonic with frequency ω and $f(t) = 0$; we have:

$$(T_{\mathrm{A}})_{\mathrm{d}} = \sqrt{\frac{1+4\zeta^2 r^2\left(\frac{\gamma+1}{\gamma}\right)^2}{(1-r^2)^2+4\zeta^2 r^2\left(\frac{\gamma+1-r^2}{\gamma}\right)}}\,\mathrm{e}^{-i\phi}$$

$$\phi = \tan^{-1}\left(\frac{2\zeta r^3}{(1-r^2)+4\zeta^2 r^2\left(\frac{(\gamma+1)(\gamma+1-r^2)}{\gamma^2}\right)}\right) \qquad [12]$$

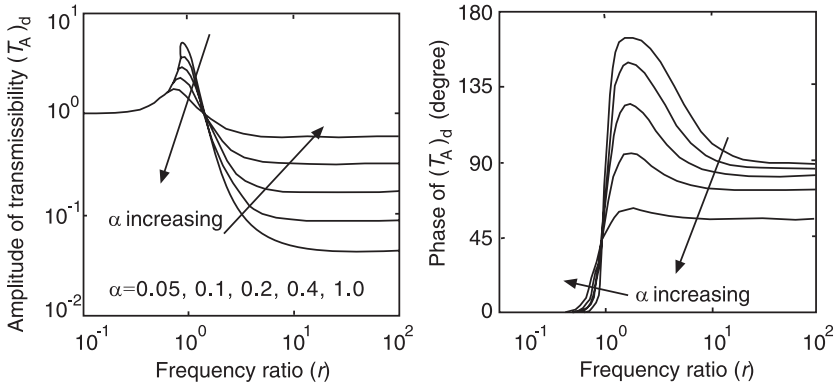


Figure 4 The amplitude and phase of the absolute displacement transmissibility of a SDOF mount with quadratic nonlinear damping.

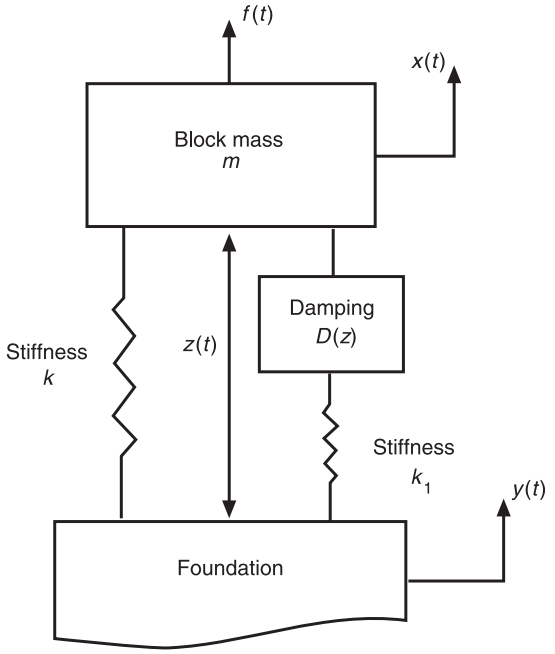


Figure 5 Elastically coupled damping in mounting systems.

where $\gamma = k_1/k$ is the stiffness ratio. The magnitude and phase of the transmissibility are shown in **Figure 6**.

The elastic coupling has also been generalized to include dynamic coupling in the mount. **Figure 7** shows three mounts with a tuned vibration absorber. In fluid-elastic mounts, this dynamic coupling is even magnified by means of a leverage mechanism. A schematic of such a mount is shown in **Figure 8**. There are many design variations of commercial mounts with different leveraging mechanisms.

The additional resonance of the vibration absorber provides another degree of freedom that can help improve the mount performance. A notch in the frequency response can be created to eliminate effectively a tonal disturbance by properly tuning the vibration absorber. The transmissibility of a typical commercial fluid-elastic mount with tuned fluid inertia track is shown in **Figure 9**. For more discussions on vibration absorber, see **Absorbers, vibration**.

Multidirectional Mounting Systems

The mounts discussed so far are unidirectional for one-degree-of-freedom systems. Practical applications often involve multiple degrees of freedom and multidirectional motion. Schematics of two multidirectional and multiple-degree-of-freedom mounting systems are shown in **Figure 10**.

The design and analysis of such mounts are generally more difficult and involved. A useful concept for evaluating multidirectional mounting systems is the mount effectiveness. This concept is particularly well suited to mount design for flexible structural systems.

Consider a mounting system for isolating a vibrating source, such as aircraft engines, from the base, such as the aircraft fuselage. Let $\mathbf{v}_h$ be the vector consisting of all the generalized velocity components of the base at the mounting points when the vibrating source is rigidly connected to the structure. $\mathbf{v}_i$ is the vector consisting of the same velocity components of the base at the mounting points when the vibrating source is connected to the structure via the mount. Then, a matrix $\mathbf{E}_v$ can be found as a function of the system impedance matrices, such that:

$$\mathbf{v_h} = \mathbf{E}_v \mathbf{v_i} \qquad [13]$$

A similar effectiveness matrix can also be defined for the transmitted generalized forces at the mounting points. The spectral norm of the complex matrix $\mathbf{E}_v$

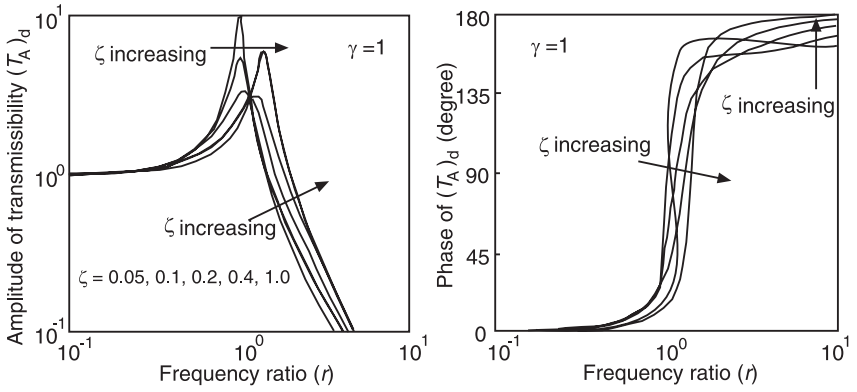


Figure 6 The amplitude and phase of the absolute displacement transmissibility of a SDOF mount with elastically coupled linear viscous damping. The stiffness ratio $\gamma = 1.0$.

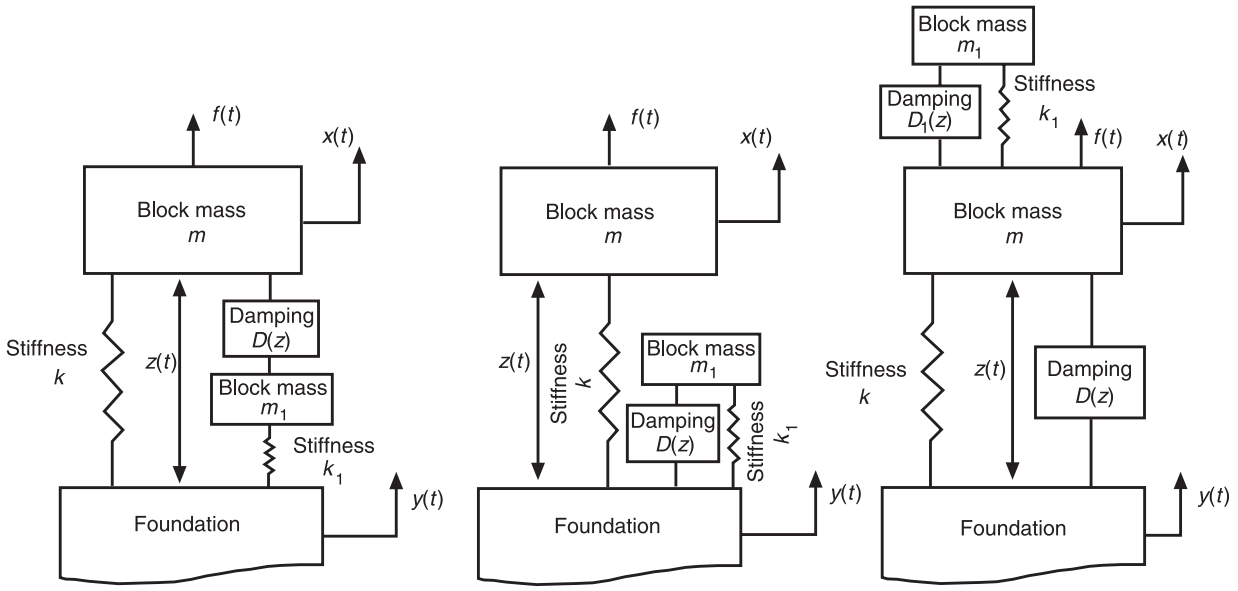


Figure 7 Examples of dynamically coupled mounts with vibration absorber.

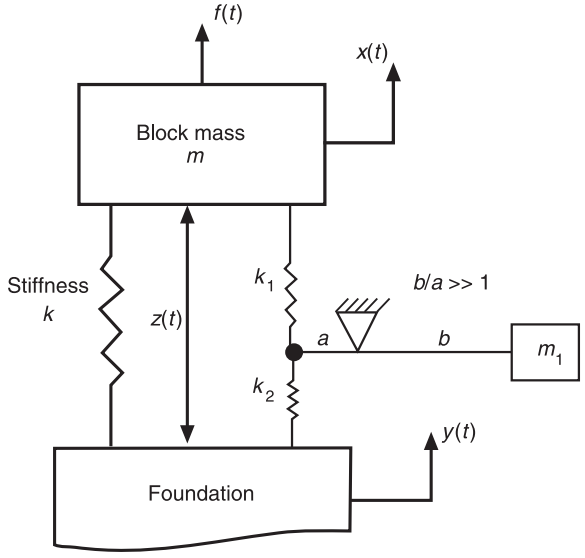


Figure 8 A dynamically coupled mount with a leveraged vibration absorber. Such a leverage mechanism is widely used in commercial fluid-elastic mounts.

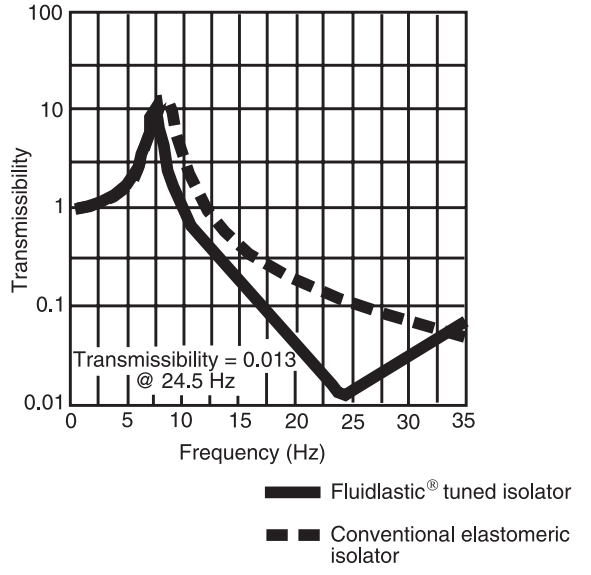


Figure 9 The transmissibility of a typical commercial fluid-elastic mount with a tuned and leveraged vibration absorber in the form of fluid inertia track. Courtesy of Lord Corporation. Continuous line, Fluidlastic® tuned isolator; dashed line, conventional elastomeric isolator.

can be used to characterize the performance of the mounting system:

$$\|\mathbf{E}_{\mathbf{v}}\| = \sigma_{\max}(\mathbf{E}_{\mathbf{v}}) \qquad [14]$$

where $\sigma_{\max}(\mathbf{E}_{\mathrm{v}})$ is the largest singular value of $\mathbf{E}_{\mathrm{v}}$. The spectral norm is the matrix equivalent of the scalar magnitude. It helps to extend the mount design procedure for unidirectional systems to multi-directional and multiple-degree-of-freedom mounting systems.

Active and Semi-Active Damping in Mounts

Linear system analysis, presented above, has shown that the effect of damping on vibration isolation is beneficial in suppressing the resonant response of the mounting system in the frequency ratio range $r \leq \sqrt{2}$, and becomes less desirable for $r > \sqrt{2}$. In the application when the base has to go through a start-up

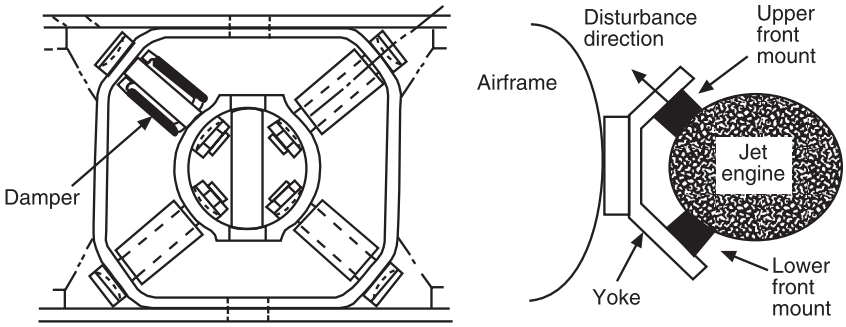


Figure 10 Examples of mounts having multiple degrees of freedom. Courtesy of Lord Corporation.

transient, the mount has to be designed to isolate the vibration for a wide range of frequencies before the system settles down to steady state with $r>\sqrt{2}$. It is hence desirable to have an adjustable damping.

An active control system can provide such a damping with proper sensing and feedback strategies. Furthermore, the feedback gain can be shaped in the frequency domain. In other words, the feedback gain can be selected as a function of frequency.

Consider the mount with active damping $-K_D\dot{z}$, listed in **Table 1**. Note that the feedback signal is the relative velocity within the mount. Assume that the feedback gain K_D is shaped so that the closed-loop damping ratio ζ_D in the range $0 < r < \sqrt{2}$ is unit, and drops to 0.001 for $r > \sqrt{2}$. This is an idealization of the relative velocity feedback. The resulting amplitude and phase of the displacement transmissibility are shown in **Figure 11**. Clearly, active controls have a great potential to create superior isolation performance. The performance shown in the figure is very difficult to duplicate with pure passive damping.

Generally, a control force actuator is used to physically provide active damping in the mount. With active systems, other feedback strategies can be implemented that will lead to better performance than the one shown in **Figure 11**. A very successful control concept is the so-called skyhook damping. A schematic of the skyhook damper is shown in **Figure 12**.

Consider a simple example of velocity feedback $-K_s\dot{x}$. The displacement transmissibility of the mount is then given by:

$$(T_A)_d = \sqrt{\frac{1+4\zeta^2 r^2}{(1-r^2)^2+4(\zeta+\zeta_s)^2 r^2}}\, e^{-i\phi}$$
$$\phi = \tan^{-1}\left(\frac{2\zeta r^3}{(1-r^2)+4(\zeta+\zeta_s)^2 r^2}\right) \qquad [15]$$

where ζ is the passive damping ratio of the mount, and ζ_s is the damping ratio due to the feedback. **Figure 13** shows the magnitude and phase of the displacement transmissibility. It is clear that skyhook damping can provide much better vibration isolation over a broad range of frequencies.

For more discusssions on real-time issues of the feedback control design, see section on Feedback

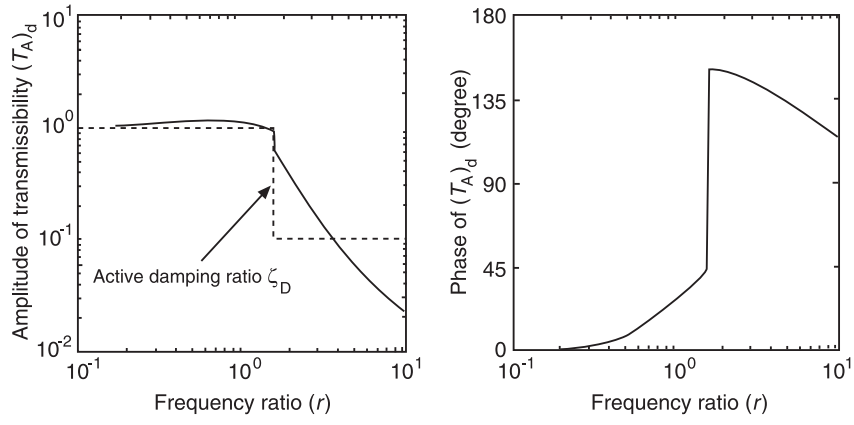


Figure 11 The magnitude and phase of the transmissibility with active damping using relative velocity feedback. The active damping ratio ζ_D (dashed line) is shaped in the frequency domain, and is a mathematical idealization.

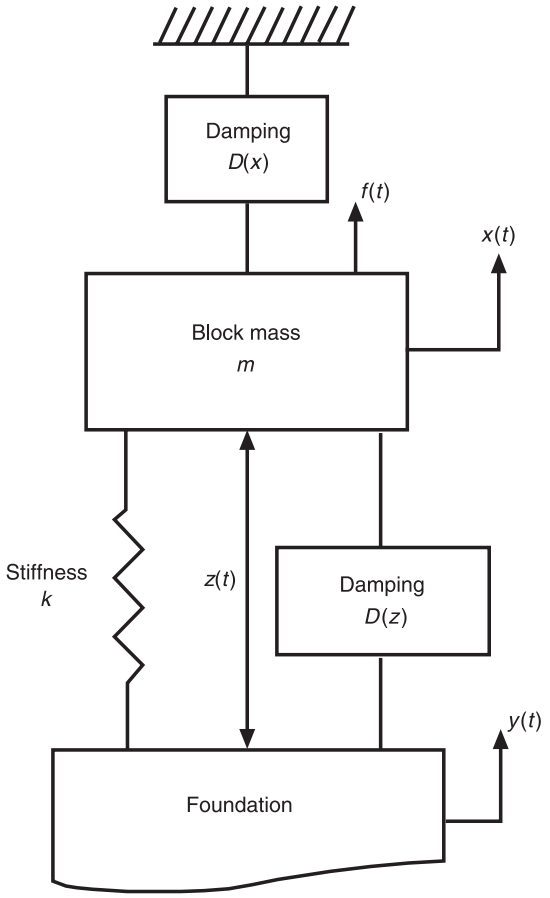


Figure 12 Schematic of a mount with skyhook damping.

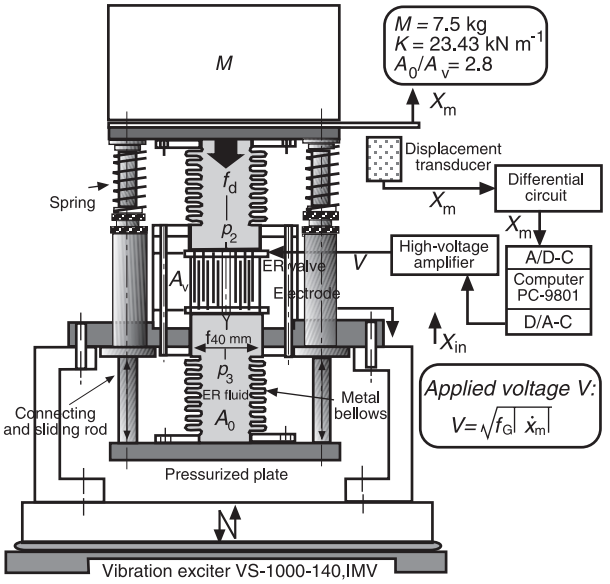


Figure 14 Vibration isolator system using an antagonized bellows ER damper and its control system. From Jolly MR and Nakano M (1998) *Properties and Applications of Commercial Controllable Fluids. Actuator 98*. Bremen, Germany, with permission.

Control in the article **Active control of civil structures**. Active systems can provide better vibration isolation, and are more expensive and less reliable than passive systems. Semi-active damping represents a compromise between passive and active systems. Mounts with ER and MR fluids can provide a range of damping. **Figures 14** and **15** show an ER fluid vibration isolation system and MR fluid vibration dampers. These devices are commercially available.

Figure 16 shows typical damping forces of a MR damper as a function of the current input to the coil. When this damper is used in a vibration isolation system, the transmissibility of the system can be improved substantially.

Figure 17 shows the magnitude of transmissibility of a system with a MR damper. The vibration isolation performance is comparable with the active system in the lower-frequency range. At higher frequencies, however, the high-level passive damping of MR fluids becomes less advantageous, and cannot be reduced by the control system. Nevertheless, the

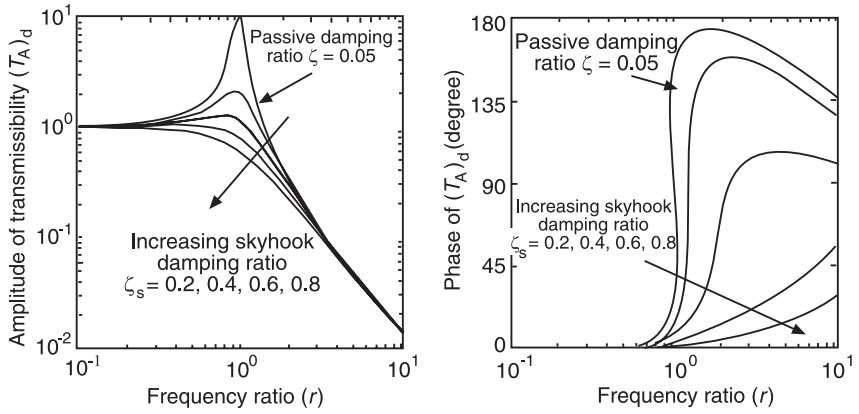


Figure 13 The magnitude and phase of the transmissibility with active skyhook damping.

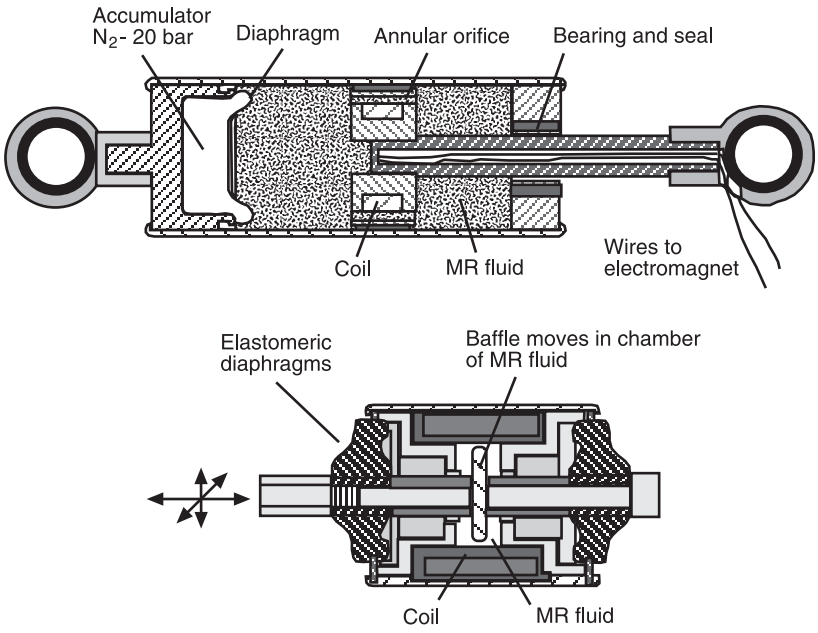


Figure 15 Examples of commercially available MR fluid vibration damper. From Jolly MR and Nakano M (1998) *Properties and Applications of Commercial Controllable Fluids. Actuator 98*. Bremen, Germany, with permission.

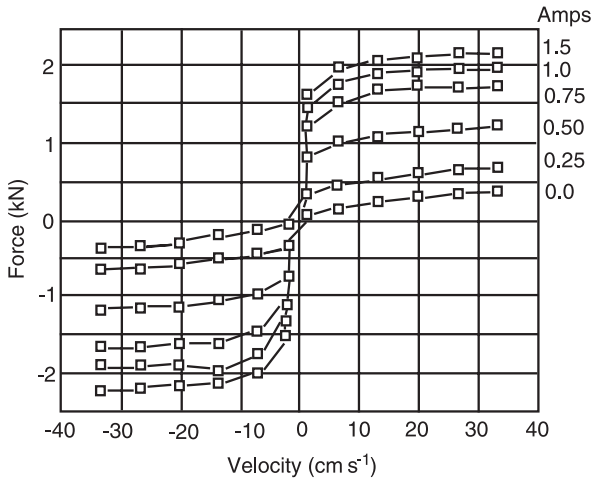


Figure 16 Damping force of the MR damper as a function of current input to the coil. From Jolly MR and Nakano M (1998) *Properties and Applications of Commercial Controllable Fluids. Actuator 98*. Bremen, Germany, with permission.

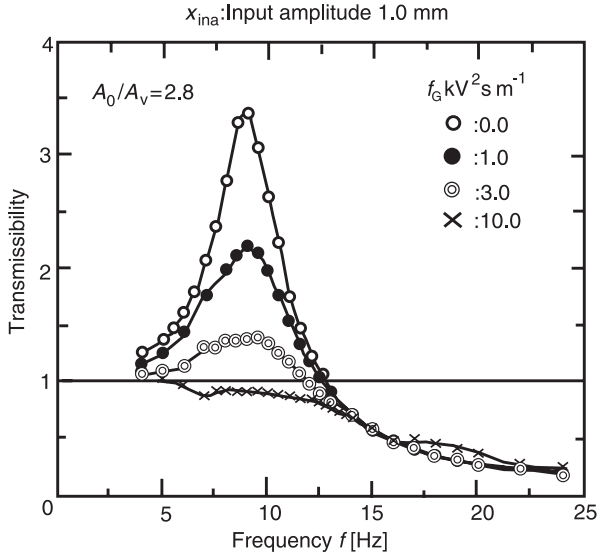


Figure 17 Magnitude of transmissibility of SDOF vibration isolator system using ER damper controlled by nonlinear feedback of absolute mass velocity. From Jolly MR and Nakano M (1998) *Properties and Applications of Commercial Controllable Fluids. Actuator 98*. Bremen, Germany, with permission.

semi-active isolation system using controllable fluids such as ER and MR fluids is fail-safe, and requires much simpler electronics to implement.

Nomenclature

$E[\cdot]$	expectation operator
F_d	dynamic force
F_t	transmitted force
γ	stiffness ratio
τ	period of harmonic motion
ζ_D	active damping ratio

See also: **Absorbers, vibration**; **Active control of civil structures**; **Active control of vehicle vibration**.

Further Reading

Avallone EA and Baumeister T III (eds) (1978) *Marks' Standard Handbook for Mechanical Engineers*. New York: McGraw-Hill.

Beards CF (1996) *Engineering Vibration Analysis with Application to Control Systems*. New York: Halsted Press.

Dimarogona A (1996) *Vibration for Engineers*. Upper Saddle River, New Jersey: Prentice Hall.

Harris CM and Crede CE (eds) (1996) *Shock and Vibration Handbook*. New York: McGraw-Hill.

Jolly MR and Nakano M (1998) *Properties and Applications of Commercial Controllable Fluids. Actuator 98*. Bremen, Germany.

Karnopp D (1995) Active and semi-active vibration isolation. *50th Anniversary Issue of ASME Journal of Mechanical Design and Journal of Vibration and Acoustics* 117: 177–185.

Lord Corporation (1997) *Rheonetic Linear Damper RD-1001/RD-1004 Product Information Sheet*. Cary, North Carolina.

Rao SS (1995) *Mechanical Vibrations*. New York: Addison-Wesley.

Ruzicka JE and Derby TF (1971) Influence of damping in vibration isolation. In: *The Shock and Vibration Monograph Series, SVM-7*. Washington, DC: Shock and Vibration Information Center, United States Department of Defense.

Snowdon JC (1968) *Vibration and Shock in Damped Mechanical Systems*. New York: John Wiley.

Sun JQ, Norris MA and Jolly MR (1995) Passive, adaptive and active tuned vibration absorbers – a survey. *50th Anniversary Issue of ASME Journal of Mechanical Design and Journal of Vibration and Acoustics* 117: 234–242.

Swanson DA and Miller LR (1993) Design and mount effectiveness evaluation of an active vibration isolation system for a commercial jet aircraft. *Proceedings of AIAA/AHS/ASEE Aerospace Design Conference* paper no. AIAA-93-1145.

Swanson DA, Miller LR and Norris MA (1994) Multidimensional mount effectiveness for vibration isolation. *Journal of Aircraft* 31: 188–196.

Thomson WT and Dahleh MD (1998) *Theory of Vibration with Applications*. Upper Saddle River, New Jersey: Prentice Hall.

DAMPING, ACTIVE

A Baz, University of Maryland, College Park, MD, USA

Copyright © 2001 Academic Press

doi:10.1006/rwvb.2001.0195

Passive, active, and/or hybrid damping treatments are recognized as essential means for attenuating excessive amplitudes of oscillations, suppressing undesirable resonances, and avoiding premature fatigue failure of critical structures and structural components. The use of one form of damping treatments or another in most of the newly designed structures is becoming very common in order to meet the pressing needs for large and lightweight structures. With such damping treatments, the strict constraints imposed on present structures can be met to insure their effective operation as quiet and stable platforms for manufacturing, communication, observation, and transportation.

This article presents the different types of passive, active, and hybrid damping treatments. Emphasis is placed on presenting the fundamentals of active constrained layer damping (ACLD), one of the most commonly used class of hybrid treatments, which combines the attractive attributes of both the passive and active treatments.

Types of Passive, Active, and Hybrid Damping Treatments

Various passive, active, and hybrid damping control approaches have been considered over the years employing a variety of structural designs, damping materials, active control laws, actuators, and sensors. Distinct among these approaches are the passive, active, and hybrid damping methods.

It is important here to note that passive damping can be very effective in damping out high-frequency excitations whereas active damping can be utilized to control low-frequency vibrations, as shown in **Figure 1**. For effective control over a broad frequency band, hybrid damping methods are essential.

Passive Damping

Passive damping treatments have been successfully used, for many years, to damp out the vibration of a wide variety of structures ranging from simple beams to complex space structures. Examples of such passive damping treatments are given below.

Free and constrained damping layers Both types of damping treatments rely in their operation on the use of a viscoelastic material (VEM) to extract energy

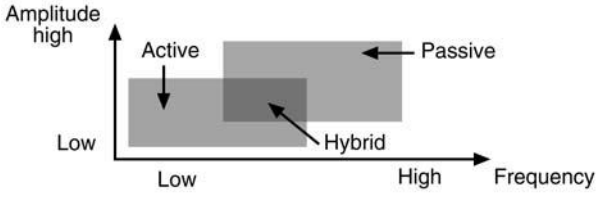


Figure 1 (See Plate 16). Operating range of various damping methods.

from the vibrating structure, as shown in **Figure 2**. In the free (or unconstrained) damping treatment, the vibrational energy is dissipated by virtue of the extensional deformation of the VEM, whereas in the constrained damping treatment more energy is dissipated through shearing the VEM.

Shunted piezoelectric treatments These treatments utilize piezoelectric films, bonded to the vibrating structure, to convert the vibrational energy into electrical energy. The generated energy is then dissipated in a shunted electric network, as shown in **Figure 3**, which is tuned in order to maximize the energy dissipation characteristics of the treatment. The electric networks are usually resistive, inductive, and/or capacitive.

Damping layers with shunted piezoelectric treatments In these treatments, as shown in **Figure 4**, a piezoelectric film is used to constrain passively the deformation of a viscoelastic layer which is bonded to a vibrating structure. The film is also used as a part of a shunting circuit tuned to improve the damping characteristics of the treatment over a wide operating range.

Magnetic constrained layer damping (MCLD) These treatments rely on arrays of specially arranged permanent magnetic strips that are bonded to viscoelastic damping layers. The interaction between the magnetic strips can improve the damping characteristics of the treatments by enhancing either the compression or the shear of the viscoelastic damping layers, as shown in **Figure 5**.

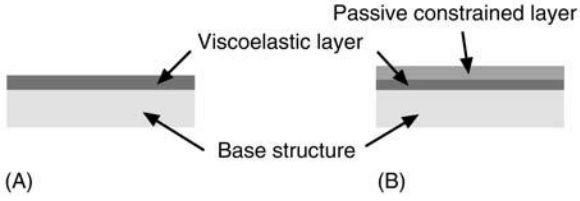


Figure 2 (See Plate 17). Viscoelastic damping treatments. (A) Free; (B) constrained.



Figure 3 (See Plate 18). Shunted piezoelectric treatments.

In the compression MCLD configuration of **Figure 5A**, the magnetic strips (1 and 2) are magnetized across their thickness. Hence, the interaction between the strips generates magnetic forces that are perpendicular to the longitudinal axis of the beam. These forces subject the viscoelastic layer to cross the thickness loading, which makes the treatment act as a Den Hartog dynamic damper. In the shear MCLD configuration of **Figure 5B**, the magnetic strips (3 and 4) are magnetized along their length. Accordingly, the developed magnetic forces, which are parallel to the beam longitudinal axis, tend to shear the viscoelastic layer. In this configuration, the MCLD acts as a conventional constrained layer damping treatment whose shear deformation is enhanced by virtue of the interaction between the neighboring magnetic strips.

Damping with shape memory fibers This damping mechanism relies on embedding superelastic shape memory fibers in the composite fabric of the vibrating structures, as shown in **Figure 6A**. The inherent hysteretic characteristics of the shape memory alloy (SMA), in its superelastic form, are utilized to dissipate the vibration energy. The amount of energy dissipated is equal to the area enclosed inside the stress–strain characteristics (**Figure 6B**). This passive mechanism has been successfully used for damping out the vibration of a wide variety of structures, including large structures subject to seismic excitation.

Active Damping

Although the passive damping methods described above are simple and reliable, their effectiveness is limited to a narrow operating range because of the significant variation of the damping material

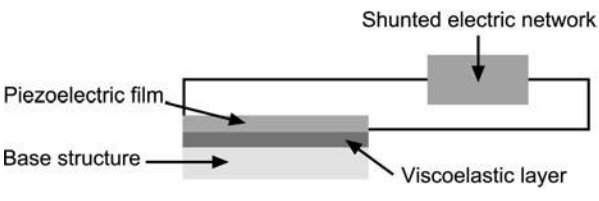


Figure 4 (See Plate 19). Damping layers with shunted piezoelectric treatments.

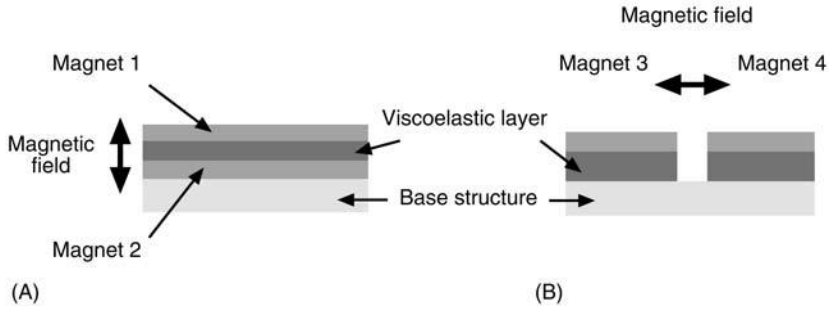


Figure 5 (See Plate 20). Configurations of the MCLD treatment. (A) Compression MCLD; (B) shear MCLD.

properties with temperature and frequency. It is therefore difficult to achieve optimum performance with passive methods alone, particularly over wide operating conditions. Hence various active damping methods have been considered. All of these methods utilize control actuators and sensors of one form or another. The most common types are made of piezoelectric films bonded to the vibrating structure, as shown in **Figure 7**.

This active control approach has been successfully used for damping out the vibration of a wide variety of structures ranging from simple beams to more complex space structures.

Hybrid Damping

Because of the limited control authority of the currently available active control actuators, and because of the limited effective operating range of passive control methods, treatments which are a hybrid combination of active damping and passive damping treatments have been considered. Such hybrid treatments aim at using various active control mechanisms to augment the passive damping in a way that compensates for its performance degradation with temperature and/or frequency. These treatments also combine the simplicity of passive damping with the effectiveness of active damping in order to insure an optimal blend of the favorable attributes of both damping mechanisms.

Active constrained layer damping This class of treatments is a blend between a passive constrained layer damping and active piezoelectric damping, as shown in **Figure 8**. The piezofilm is actively strained so as to enhance the shear deformation of the viscoelastic damping layer in response to the vibration of the base structure.

Active Piezoelectric damping composites (APDC) In this class of treatments, an array of piezoceramic rods embedded across the thickness of a viscoelastic

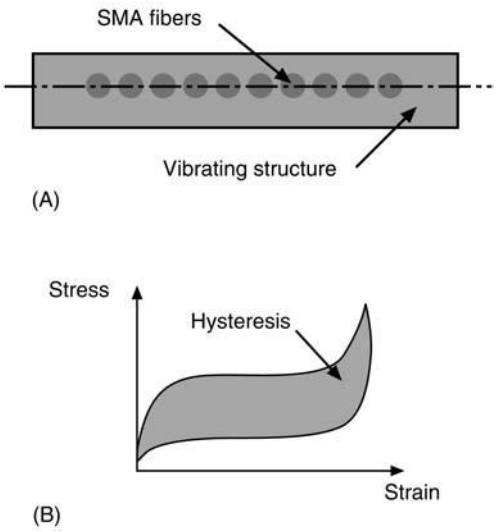


Figure 6 (See Plate 21). Damping with shape memory fibers. (A) SMA-reinforced structure; (B) superelastic characteristics.

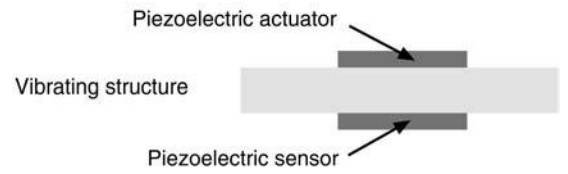


Figure 7 (See Plate 22). Active damping.

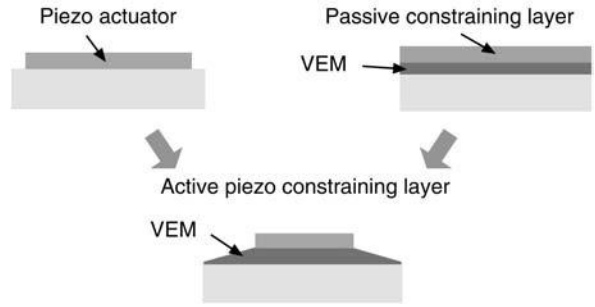


Figure 8 (See Plate 23). Active constrained layer damping treatment.

polymeric matrix is electrically activated to control the damping characteristics of the matrix that is directly bonded to the vibrating structure, as shown in **Figure 9**. The figure displays two arrangements of the APDC. In the first arrangement, the piezorods are embedded perpendicular to the electrodes to control the compressional damping and in the second arrangement, the rods are obliquely embedded to control both the compressional and shear damping of the matrix.

Electromagnetic damping composites (EMDC) In this class of composites, a layer of viscoelastic damping treatment is sandwiched between a permanent magnetic layer and an electromagnetic layer, as shown in **Figure 10**. The entire assembly is bonded to the vibrating surface to act as a smart damping treatment. The interaction between the magnetic layers, in response to the structural vibration, subjects the viscoelastic layer to compressional forces of proper magnitude and phase shift. These forces counterbalance the transverse vibration of the base structure and enhance the damping characteristics of the viscoelastic material. Accordingly, the EMDC acts in effect as a tunable Den Hartog damper with the base structure serving as the primary system, the electromagnetic layer acting as the secondary mass, the magnetic forces generating the adjustable stiffness characteristics, and the viscoelastic layer providing the necessary damping effect.

Active shunted piezoelectric networks In this class of treatments, shown in **Figure 11**, the passive shunted electric network is actively switched on and off in response to the response of the structure/network system in order to maximize the instantaneous energy dissipation characteristics and minimize the frequency-dependent performance degradation.

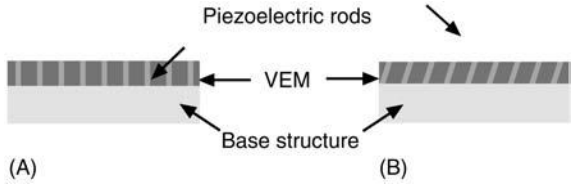


Figure 9 (See Plate 24). Active piezoelectric damping composites. (A) Perpendicular rods; (B) Inclined rods.

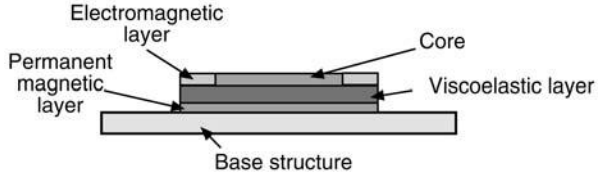


Figure 10 (See Plate 25). Electromagnetic damping composite (EMDC).

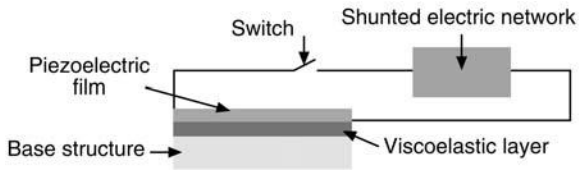


Figure 11 (See Plate 26). Damping layers with shunted piezoelectric treatments.

Basics and Characteristics of a Typical Hybrid Treatments

Emphasis is placed here on presenting the theory and the performance characteristics of one of the most widely used class of active/passive hybrid damping treatments, the ACLD treatment.

The ACLD treatment is a new class of hybrid damping treatments which has a high energy dissipation-to-weight ratio compared to conventional constrained or unconstrained damping layer configurations.

The ACLD consists of a conventional passive constrained layer damping which is augmented with efficient active control means to control the strain of the constrained layer, in response to the structural vibrations, as shown in **Figure 12**. The viscoelastic damping layer is sandwiched between two piezoelectric layers. The three-layer composite ACLD when bonded to a vibrating surface acts as a smart constraining layer damping treatment with built-in sensing and actuation capabilities. The sensing is provided by the piezoelectric layer which is directly bonded to the vibrating surface. The actuation is generated by the other piezoelectric layer which acts as an active constraining layer. With appropriate strain control, through proper manipulation of the sensor output, the shear deformation of the viscoelastic damping layer can be increased, the energy dissipation mechanism can be enhanced, and structural vibration can be damped out.

In this manner, the ACLD provides a viable means for damping out the vibration as it combines the attractive attributes of passive and active controls. This makes the ACLD particularly suitable for critical applications where the damping-to-weight ratio is important, e.g., aircraft and automobiles.

Concept of active constrained layer damping The effect of interaction between the sensor and the actuator on the operation of the ACLD can best be understood by considering the motion experienced by

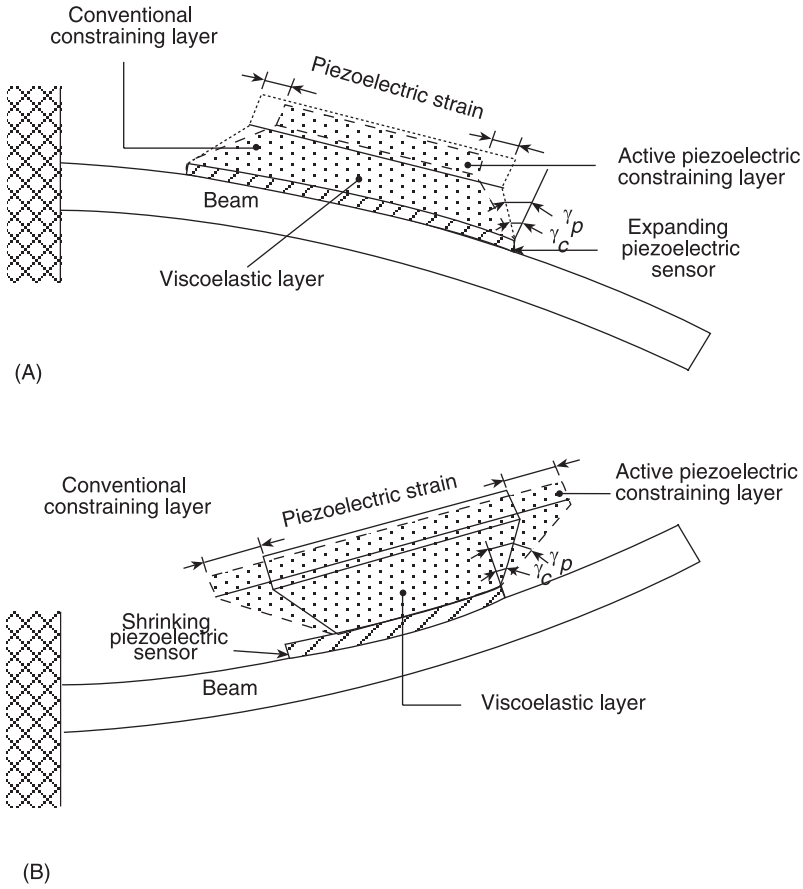


Figure 12 (A, B) Operating principle of the active constrained layer damping.

a beam during a typical vibration cycle. In **Figure 12A**, as the beam moves downward away from its horizontal equilibrium position, the sensor which is bonded to the outer fibers of the beam will be subjected to tensile stresses, generating accordingly a positive voltage, V_s, by the direct piezoelectric effect. If the sensor voltage is amplified, its polarity is reversed and the resulting voltage, V_c, is fed back to activate the piezoelectric constraining layer; the constraining layer will shrink by virtue of the reverse piezoelectric effect. The shrinkage of the active constraining layer results in a shear deformation angle, γ_p, in the viscoelastic layer, which is larger than the angle, γ_c, developed by a conventional passive constraining layer, as indicated in **Figure 12A**.

Similarly, **Figure 12B** describes the operation of the ACLD during the upward motion of the beam. During this part of the vibration cycle, the top fibers of the beam as well as the piezoelectric sensor experience compressive stresses and a negative voltage is generated by the sensor. Direct feedback of the sensor signal to the active constraining layer makes it extend and accordingly increases the shear deformation angle to γ_p as compared to γ_c for the conventional constraining layer.

The increase of the shear deformation of the viscoelastic layer, throughout the vibration cycle, is accompanied by an increase in the energy dissipated. Furthermore, the shrinkage (or expansion) of the piezoelectric layer during the upward motion (or during the downward motion) produces a bending moment on the beam which tends to bring the beam back to its equilibrium position. Therefore, the dual effect of the enhanced energy dissipation and the additional restoring bending moment will quickly damp out the vibration of the flexible beam. This dual effect, which does not exist in conventional constrained damping layers, significantly contributes to the damping effectiveness of the smart ACLD. In this manner, the smart ACLD consists of a conventional passive constrained layer damping which is augmented with the described dual effect actively to control the strain of the constrained layer, in response to the structural vibrations. With appropriate strain control strategy, the shear deformation of the viscoelastic damping layer can be increased, the energy dissipation mechanism can be enhanced, and vibration can be damped out. One possible strategy is direct feedback of the sensor voltage to power the active constraining layer. Other strategies will rely on

feeding back both the sensor voltage and its derivative to obtain proportional and derivative control action. With such a strategy, additional damping can be imparted to the vibrating beam system and the versatility of active controls can be utilized to improve considerably the damping characteristics of the ACLD.

Therefore, the ACLD relies in its operation on a blend between the attractive attributes of both active and passive controls. In other words, the simplicity and reliability of passive damping are combined with the low weight and high efficiency of active controls to achieve high damping characteristics over broad frequency bands. Such characteristics are essential to the optimal damping of vibration.

Also, it is essential to note that the ACLD provides an excellent and practical means for controlling the vibration of massive structures with the currently available piezoelectric actuators without the need for excessively large actuation voltages. This is due to the fact that the ACLD properly utilizes the piezoelectric actuator to control the shear in the soft viscoelastic core – a task which is compatible with the low control authority capabilities of the piezoelectric materials currently available.

Furthermore, it is important to note that the ACLD configuration described in **Figure 12** is only one of many possible configurations. For example, the ACLD can be arranged in a multilayer configuration or in discrete patches distributed at optimal locations over the vibrating structure. Other possible configurations are only limited by our imagination.

Finite element modeling of shells treated with ACLD **Figure 13** shows the transverse cross-section of a thin cylindrical shell treated partially with ACLD treatments. The shell has longitudinal length a, average circumferential length b, average radius R, and thickness h. The thickness of the viscoelastic core and the piezoelectric actuator are h_c and h_p, respectively.

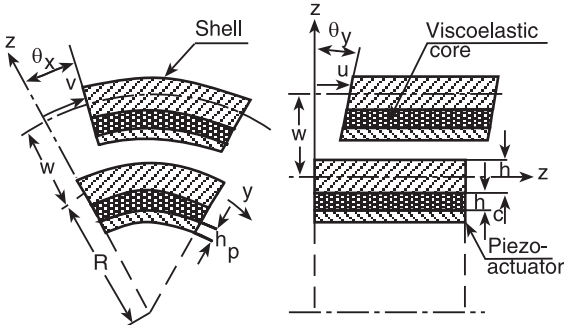


Figure 13 Geometrical and kinematical parameters of the shell/ACLD system.

Displacement fields In case of constrained layer damping analysis, the layer-wise theories have been used continuously. For sandwiched or laminated structures, the use of the layer-wise theories involves more generalized displacement variables than a single first-order shear deformation theory needs. This results in a large number of global degrees-of-freedom in the case of finite element analysis, which eventually proves to be cost-ineffective.

Hence, the longitudinal and circumferential deformations u and v, respectively, at any point of the shell/ACLD system, are represented by the first-order shear deformation theory (FSDT):

$$\begin{aligned} u(x,y,z,t) &= u_0(x,y,t) + z\theta_x(x,y,t) \\ v(x,y,z,t) &= v_0(x,y,t) + z\theta_y(x,y,t) \end{aligned} \quad [1]$$

in which x and y are the longitudinal and circumferential coordinates, respectively; z is the radial coordinate; u_0 and v_0 are the generalized displacements at any point of the reference plane ($z = 0$); θ_x, θ_y are the rotations of the normal to the reference plane about the y- and x- axes, respectively. According to the FSDT the radial displacement, w is assumed to be constant through the thicknesses of the cylinder, the viscoelastic core and the piezoelectric actuator.

The generalized displacement variables are separated into translational $\mathbf{d}_t^{\mathrm{T}}$ and rotational variables $\mathbf{d}_r^{\mathrm{T}}$ as follows:

$$\mathbf{d}_t = [u_0 \quad v_0 \quad w]^{\mathrm{T}}; \quad \mathbf{d}_r = [\theta_x \quad \theta_y]^{\mathrm{T}} \quad [2]$$

Strain displacement relations Applying Donnell's theory for strain displacement relations and using eqn [1], the strain vector at any point of the shell/ACLD system can be expressed as:

$$\boldsymbol{\varepsilon} = \mathbf{Z}_1\boldsymbol{\varepsilon}_t + \mathbf{Z}_2\boldsymbol{\varepsilon}_r \quad [3a]$$

where the generalized strain vectors $\boldsymbol{\varepsilon}_t$, $\boldsymbol{\varepsilon}_r$ are given by:

$$\begin{aligned} \boldsymbol{\varepsilon}_t &= \left[\frac{\partial u_0}{\partial x} \quad \frac{\partial v_0}{\partial y} + \frac{w}{R} \quad \frac{\partial u_0}{\partial y} + \frac{\partial v_0}{\partial x} \quad \frac{\partial w}{\partial x} \quad \frac{\partial w}{\partial y} - \frac{v_0}{R}\right]^{\mathrm{T}} \\ \boldsymbol{\varepsilon}_r &= \left[\frac{\partial \theta_x}{\partial x} \quad \frac{\partial \theta_y}{\partial y} \quad \frac{\partial \theta_x}{\partial y} + \frac{\partial \theta_y}{\partial x} \quad \theta_x \quad \theta_y\right]^{\mathrm{T}} \end{aligned} \quad [3b]$$

and the transformation matrices $\mathbf{Z}_1$ and $\mathbf{Z}_2$ are given in Appendix A.

Constitutive equations The constitutive equation for the material of the piezoelectric constraining layer is:

$$\boldsymbol{\sigma}^3 = \mathbf{C}^3\left[\boldsymbol{\varepsilon}^3 - \boldsymbol{\varepsilon}_p\right] \quad [4]$$

where $\boldsymbol{\sigma}$ represents the stress vector; $\mathbf{C}$ is the elastic constant matrix, the superscript 3 denotes the piezoelectric layer number 3 and the piezoelectrically induced-strain vector $\boldsymbol{\varepsilon}_p$ for a biaxially polarized actuator layer is given by:

$$\boldsymbol{\varepsilon}_p = \bar{\boldsymbol{\varepsilon}}_p V \quad [5]$$

with:

$$\bar{\boldsymbol{\varepsilon}}_p = \left(1/h_p\right)[d_{31} \quad d_{32} \quad 0 \quad 0 \quad 0]^{\mathrm{T}}$$

where d_{31}, d_{32} denote the piezoelectric strain constants and V, the applied voltage, respectively.

The constitutive equations for the materials of the shell and the viscoelastic core are given by:

$$\boldsymbol{\sigma}^L = \mathbf{C}^L\boldsymbol{\varepsilon}^L, \quad (L = 1, 2) \quad [6]$$

where the superscripts 1 and 2 identify the shell and the viscoelastic core, respectively.

System energies The potential energy T_p of the overall system is given by:

$$T_p = \frac{1}{2}\sum_{L=1}^{3}\int_{h_{L+1}}^{h_L}\int_0^b\int_0^a \boldsymbol{\varepsilon}^{L\mathrm{T}}\boldsymbol{\sigma}^L \,\mathrm{d}x\,\mathrm{d}y\,\mathrm{d}z - \int_0^b\int_0^a \boldsymbol{\Delta}_{z=h_1}^{\mathrm{T}} f^s \,\mathrm{d}x\,\mathrm{d}y \quad [7]$$

and the kinetic energy T_k is given by:

$$T_k = \frac{1}{2}\sum_{L=1}^{3}\int_{h_{L+1}}^{h_L}\int_0^b\int_0^a \rho^L\dot{\boldsymbol{\Delta}}^{L\mathrm{T}}\dot{\boldsymbol{\Delta}}^L \,\mathrm{d}x\,\mathrm{d}y\,\mathrm{d}z \quad [8]$$

in which ρ with superscript L is the mass density of the Lth layer, $\boldsymbol{\Delta}$, is the vector of absolute displacements (u, v, w) and $\mathbf{f}^s$ is the vector of surface traction.

The whole continuum is discretized by an eight-noded two-dimensional isoparametric element. The generalized displacement vectors for the ith$(i = 1, 2, ..., 8)$ node of the element are then given by:

$$\mathbf{d}_{ti} = [u_{0i} \quad v_{0i} \quad w]^{\mathrm{T}}; \quad \mathbf{d}_{ri} = \left[\theta_{xi} \quad \theta_{yi}\right]^{\mathrm{T}} \quad [9]$$

and the generalized displacement vector at any point within the element is given by:

$$\mathbf{d}_t = \mathbf{N}_t\mathbf{d}_t^e; \quad \mathbf{d}_r = \mathbf{N}_r\mathbf{d}_r^e \quad [10]$$

where:

$$\begin{aligned}
\mathbf{d}_t^e &= \left[\mathbf{d}_{t1}^{\mathrm{T}} \quad \mathbf{d}_{t2}^{\mathrm{T}} \quad \ldots \quad \mathbf{d}_{t8}^{\mathrm{T}}\right]^{\mathrm{T}}\\
\mathbf{d}_r^e &= \left[\mathbf{d}_{r1}^{\mathrm{T}} \quad \mathbf{d}_{r2}^{\mathrm{T}} \quad \ldots \quad \mathbf{d}_{r8}^{\mathrm{T}}\right]^{\mathrm{T}}\\
\mathbf{N}_t &= [N_{t1} \quad N_{t2} \quad \ldots \quad N_{t8}]\\
\mathbf{N}_r &= [N_{r1} \quad N_{r2} \quad \ldots \quad N_{r8}]\\
N_{ti} &= n_i\mathbf{I}_t \quad \text{and} \quad \mathbf{N}_{ri} = n_i\mathbf{I}_r
\end{aligned}$$

with $\mathbf{I}_t$ and $\mathbf{I}_r$ being the identity matrices of appropriate dimension and n_i the shape functions of natural coordinates.

Using eqns [2], [3b], [9], and [10], the generalized strain vectors at any point within the element can be expressed as:

$$\boldsymbol{\varepsilon}_t = \mathbf{B}_t\mathbf{d}_t^e, \quad \boldsymbol{\varepsilon}_r = \mathbf{B}_r\mathbf{d}_r^e \quad [11]$$

in which the nodal strain displacement matrices are given by:

$$\mathbf{B}_t = [\mathbf{B}_{t1} \quad \mathbf{B}_{t2} \ \ldots \ \mathbf{B}_{t8}]$$

and:

$$[\mathbf{B}_r] = [\mathbf{B}_{r1} \quad \mathbf{B}_{r2} \ \ldots \ \mathbf{B}_{r8}]$$

The various submatrices $\mathbf{B}_{ti}$ and $\mathbf{B}_{ri}$ are given in Appendix A.

Finally, using eqns [3a], [4]–[6], and [11] in eqns [7] and [8], the strain energy of the eth typical shell element augmented with ACLD treatment can be expressed as:

$$\begin{aligned}
T_p^e = \frac{1}{2}\int_0^{a^e}\int_0^{b^e}\Big[&\mathbf{d}_t^{e\mathrm{T}}\mathbf{B}^{\mathrm{T}}\mathbf{D}_{tt}\mathbf{B}\mathbf{d}_t^e + \mathbf{d}_t^{e\mathrm{T}}\mathbf{B}_t^{\mathrm{T}}\mathbf{D}_{tr}\mathbf{B}_r\mathbf{d}_r^e.\\
&+ \mathbf{d}_r^{e\mathrm{T}}\mathbf{B}_r^{\mathrm{T}}\mathbf{D}_{rt}\mathbf{B}_t\mathbf{d}_t^e + \mathbf{d}_r^{e\mathrm{T}}\mathbf{B}_r^{\mathrm{T}}\mathbf{D}_{rr}\mathbf{B}_r\mathbf{d}_r^e\\
&- \int_{h_4}^{h_3}\left(\mathbf{d}_t^{e\mathrm{T}}\mathbf{B}_t^{\mathrm{T}}\mathbf{Z}_1^{\mathrm{T}}\mathbf{C}^3\boldsymbol{\varepsilon}_p + \mathbf{d}_r^{e\mathrm{T}}\mathbf{B}_2^{p\mathrm{T}}\mathbf{Z}_2^{p\mathrm{T}}\mathbf{C}^3\boldsymbol{\varepsilon}_p\right)\mathrm{d}z\Big]\,\mathrm{d}x\,\mathrm{d}y\\
&- \int_0^{a^e}\int_0^{b^e}\left(\mathbf{d}_t^{e\mathrm{T}}\mathbf{N}_t^{\mathrm{T}} + \mathbf{d}_t^{e\mathrm{T}}\mathbf{N}_r^{\mathrm{T}}\right)\mathbf{f}^s\,\mathrm{d}x\,\mathrm{d}y
\end{aligned} \quad [12]$$

and the kinetic energy of the element can be obtained as:

$$T_k^e = \frac{1}{2}\int_0^{a^e}\int_0^{b^e} (\rho^1 h + \rho^2 h_c + \rho^3 h_p)\mathbf{d}_t^{e^{\mathrm{T}}}\mathbf{N}_t^{\mathrm{T}}\mathbf{N}_t\dot{\mathbf{d}}_t^e \, \mathrm{d}x \, \mathrm{d}y \qquad [13]$$

in which a^e and b^e are the longitudinal and circumferential lengths of the element, respectively. The various rigidity matrices $\mathbf{D}_{tt}, \mathbf{D}_{tr}, \mathbf{D}_{rt}$ and $\mathbf{D}_{rr}$ appearing in eqn [12] are given in Appendix B. Since the present study deals with thin shell analysis, the rotational inertia of the element has been neglected when estimating the kinetic energy of the element.

Equations of motion Applying Hamilton's variational principle, the following equations of motion for the element are obtained:

$$\mathbf{M}^e\ddot{\mathbf{d}}_t^e + \mathbf{K}_{tt}^e\mathbf{d}_t^e + \mathbf{K}_{tr}^e\mathbf{d}_r^e = \mathbf{F}_{at}^e V + \mathbf{F}_t^e \qquad [14]$$

$$\mathbf{K}_{rt}^e\mathbf{d}_t^e + \mathbf{K}_{rr}^e\mathbf{d}_r^e = \mathbf{F}_{ar}^e V + \mathbf{F}_r^e \qquad [15]$$

in which the various elemental matrices $\mathbf{M}^e$, $\mathbf{K}_{tt}^e$, $\mathbf{K}_{tr}^e$, $\mathbf{K}_{rt}^e$ and $\mathbf{K}_{rr}^e$; the electroelastic coupling vectors $\mathbf{F}_{at}^e$, $\mathbf{F}_{ar}^e$, and the excitation force vectors $\mathbf{F}_t^e$, $\mathbf{F}_r^e$ are defined in Appendix B. It may be mentioned here that in case of an element without ACLD treatment, the electroelastic coupling vectors $\mathbf{F}_{at}^e$ and $\mathbf{F}_{ar}^e$ do not appear in eqns [14] and [15].

The elemental equations are assembled in such a manner to obtain the global equations of motion so that each actuator can be activated separately as follows:

$$\begin{aligned}\mathbf{M}\ddot{\mathbf{X}}_t + \mathbf{K}_{tt}\mathbf{X}_t + \mathbf{K}_{rr}\mathbf{X}_r &= \sum_{j=1}^{n}\mathbf{F}_{at}^j V^j + \mathbf{F}_t \\ \mathbf{K}_{rt}\mathbf{X}_t + \mathbf{K}_{rr}\mathbf{X}_r &= \sum_{j=1}^{n}\mathbf{F}_{ar}^j V^j + \mathbf{F}_r\end{aligned} \qquad [16]$$

where $\mathbf{M}$ and $\mathbf{K}_{tt}, \mathbf{K}_{tr}, \mathbf{K}_{rr}$ are the global mass and stiffness matrices; $\mathbf{X}_t, \mathbf{X}_r$ are the global nodal generalized displacement coordinates; $\mathbf{F}_t, \mathbf{F}_r$ are the global nodal force vectors corresponding to translational and rotational coordinates, n is the number of ACLD patches and for the jth ACLD patch the global nodal electroelastic coupling vectors are given by:

$$\mathbf{F}_{at}^j = \sum_m \mathbf{F}_{at}^e \quad \text{and} \quad \mathbf{F}_{ar}^j = \sum_m \mathbf{F}_{ar}^e \qquad [17]$$

with m being the number of elements per ACLD treatment. Invoking the boundary conditions, the global rotational degrees-of-freedom can be condensed to obtain the global equations of motion in terms of the global translational degrees-of-freedom only as follows:

$$\mathbf{M}\ddot{\mathbf{X}}_t + \mathbf{K}^*\mathbf{X}_t = \sum_{j=1}^{n}[\mathbf{F}_{at}^j - \mathbf{K}_{tr}\mathbf{K}_{rr}^{-1}\mathbf{F}_{ar}^j]V^j + \mathbf{F} \qquad [18]$$

in which $\mathbf{K}^* = \mathbf{K}_{tt} - \mathbf{K}_{tr}\mathbf{K}_{rr}^{-1}\mathbf{K}_{rt}$ and $\mathbf{F} = \mathbf{F}_t - \mathbf{K}_{tr}\mathbf{K}_{rr}^{-1}\mathbf{F}_r$.

Control law In the active control strategy, each actuator is supplied with the control voltage proportional to the radial velocity at the points on the outer surface of the cylinder which correspond to midpoint of the free width of the ACLD patches. Thus the control voltage for the jth actuator can be expressed in terms of the derivatives of the nodal global degrees-of-freedom as:

$$V^j = -K_d^j\mathbf{e}^j\dot{\mathbf{X}}_t \qquad [19]$$

where K_d^j is the controller gain and $\mathbf{e}^j$ is a unit vector with unity as the only nonzero element corresponding to that global degree-of-freedom, the derivative of which is fed back to the actuator.

Substitution of eqn [19] into eqn [18] yields the final damped equations of motion as:

$$\mathbf{M}\ddot{\mathbf{X}}_t + \mathbf{K}^*\mathbf{X}_t + \mathbf{C}_d\dot{\mathbf{X}}_t = \mathbf{F} \qquad [20]$$

where:

$$\mathbf{C}_d = \sum_{j=1}^{n} K_d^j\left[\mathbf{F}_{at}^j - \mathbf{K}_{tr}\mathbf{K}_{rr}^{-1}\mathbf{F}_{ar}^j\right]\boldsymbol{\varepsilon}^j$$

Eqn [20] can be formulated to compute the frequency response function (FRF) when the shell/ ACLD system is subjected to harmonic excitations using the mechanical impedance approach.

Performance of shells with ACLD treatment In this section, the performance of shells treated with two ACLD patches is evaluated by comparing their FRFs using the finite element model developed earlier in this article. The numerical results are compared with experimental results.

Materials The shell considered is made of a stainless steel shell: Young's modulus $E_1 = 210\,\mathrm{GN\,m^{-2}}$, Poisson's ratio $v_1 = 0.3$ and the density $\rho^1 = 7800\,\mathrm{kg\,m^{-3}}$. The material of the acrylic-based viscoelastic core has a complex shear modulus $G_2 = 20(1 + 1.0i)\,\mathrm{MN\,m^{-2}}$ and density $\rho^2 = 1140\,\mathrm{kg\,m^{-3}}$. The piezoelectric actuator is an active polymeric film (PVDF). Its Young's modulus E_3, Poisson ratio v_3 and

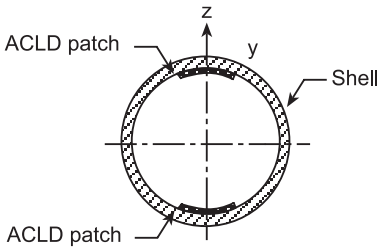


Figure 14 Cross-section of the shell/ACLD system.

density ρ^3 are 2.25 GN m^{-2}, 0.28 and 1800 kg m^{-3}, respectively. The values of the piezoelectric strain constants d_{31} and d_{32} are 23×10^{-12} and 3×10^{-12} m V^{-1}, respectively.

Numerical and experimental results A clamped-free cylinder with $R = 0.1016$ m, $a = 1.27$ m and $h = 0.635$ mm is chosen to demonstrate the performance of the ACLD as compared to passive constrained layer damping (PCLD) treatments. Experiments are conducted using this cylinder. The arrangement of the experimental setup is schematically described in **Figure 14**. Two patches of ACLD treatment are used which are bonded 180° apart on the inner surface of the cylinder, as shown in **Figure 15**. The length and width of each patch are 0.508 m and 0.1016 m, respectively. The shell is excited with swept sinusoidal excitations at its free end by the speaker. The outputs of two collocated accelerometers are sent to phase shifters and then to power amplifiers. The output of the amplifiers is used to activate the piezo-constraining layers. The velocity feedback is insured by properly adjusting the phases of the phase shifters.

The natural frequencies of the cylinder are computed using the finite element model and are also

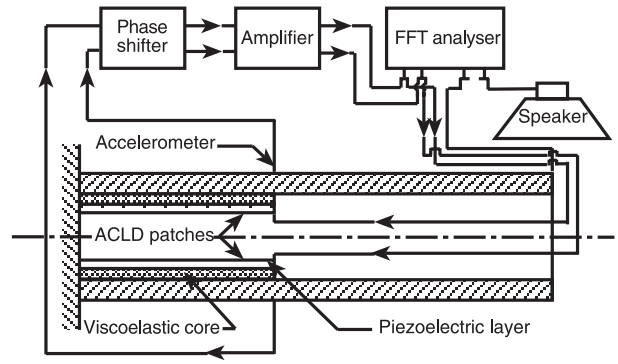


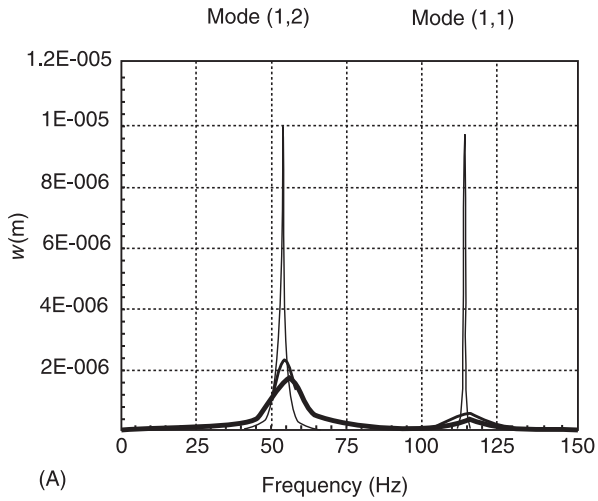
Figure 15 Schematic diagram of the shell/ACLD system.

experimentally determined. **Table 1** shows a comparison between the theoretical predictions and the experimental results. The numerical estimations are slightly higher than the experimental values. This can be attributed to the fact that the clamped end is not ideal and geometrical imperfections are inherent due to the manufacturing process of the cylinder.

Figures 16A and **16B** display the numerically and experimentally determined FRFs of the shell/ ACLD system at the free end of the cylinder $(a, 0, h/2)$, respectively. The figure shows the amplitudes of radial displacements when the piezoelectric-constraining layers in both the patches are passive and active, with different control gains. These figures clearly

Table 1 Comparison of natural frequencies (Hz) of the shell/ ACLD system

Mode	*Finite element model*	*Experiment*
(1, 2)	54.06	51.2
(1, 1)	113.62	113



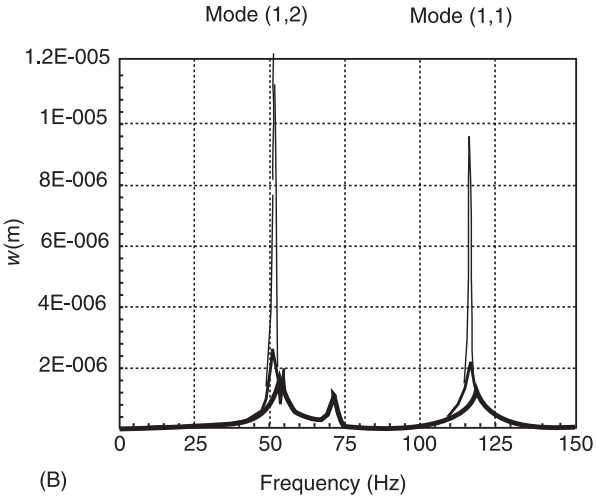


Figure 16 FRF of the shell/ACLD system when both piezoelectric patches are active. (A) Numerical; (B) experimental. (—) PCLD, (—) $k_d = 5E5$, (—) $k_d = 9E5$.

reveal that the ACLD treatments significantly improve the damping characteristics of the shell over the PCLD. A comparison between parts (A) and (B) shows that maximum values of the uncontrolled radial displacement of the shell obtained numerically at the point $(a, 0, h/2)$, considered here match with that obtained experimentally with close accuracy. The controlled responses indicate that the attenuated amplitudes for the first mode $(1, 2)$ of vibration differ negligibly. In the case of the second mode $(1, 1)$, the numerical predictions are slightly lower than the experimental results. The numerical predictions of the maximum voltages required to control the mode $(1, 2)$ match closely with the experimental results, as presented in **Table 2**. However, the numerical predictions for the control voltages for the mode $(1, 1)$ are higher than those obtained experimentally. In order to identify the modes and the modal contents after the control, the surface of the cylinder is scanned using a laser vibrometer, as shown in **Figures 17** and **18** for modes $(1, 2)$ and $(1, 1)$, respectively. It is clear from these figures that significant attenuation is obtained with the activation of the controller.

Figure 19 illustrates the numerical and experimental results for the case when only one of the piezoelectric-constraining layers is active. In this case also, the numerical predictions matched well with the experimental results. However, numerical predictions for the control voltages differ from the experimental results but are within the acceptable limit, as shown in **Table 2**.

Concluding Remarks

A brief description is presented here of the different types of passive, active, and hybrid damping treatments that have been successfully applied to damping out the vibration of a wide variety of structures. Emphasis is placed on presenting the theory and performance characteristics of one of the most commonly used hybrid treatments, the ACLD. It is important to note that the hybrid ACLD treatment has been shown to be very effective in damping out broadband vibrations as compared to conventional PCLD treatment, without the need for excessively high control voltages.

It is equally important to emphasize that, although the concepts presented are utilized to control the vibration of shells, these concepts have been successfully applied to the control of vibrations and sound radiation of beams, plates, and shells. In all these studies, it is shown that hybrid treatments provide effective and globally stable means for controlling structural vibration and acoustics without any adverse effects, such as those generated by control spillover or even by failure of the controller. Accordingly, these treatments provide a failsafe means of attenuating vibration and noise radiation, which is essential for reliable operation of critical structures. More importantly, the hybrid treatments can also be designed to insure robust operation in the presence of uncertainties in the structural parameters or in the operating conditions.

Appendix A

Forms of Matrices $\mathbf{Z}_1$, $\mathbf{Z}_2$, $\mathbf{B}_{ti}$ and $\mathbf{B}_{ri}$

Transformation Matrices $\mathbf{Z}_1$ and $\mathbf{Z}_2$

The explicit forms of the transformation matrices, $\mathbf{Z}_1$ and $\mathbf{Z}_2$ appearing in eqn [3] are:

$$\mathbf{Z}_1 = \begin{bmatrix} 1 & 0 & 0 & 0 & 0 \\ 0 & 1 & 0 & 0 & 0 \\ 0 & 0 & 1 & 0 & 0 \\ 0 & 0 & 0 & 1 & 0 \\ 0 & 0 & 0 & 0 & 1 \end{bmatrix}$$

and:

$$\mathbf{Z}_2 = \begin{bmatrix} z & 0 & 0 & 0 & 0 \\ 0 & z & 0 & 0 & 0 \\ 0 & 0 & z & 0 & 0 \\ 0 & 0 & 0 & 1 & 0 \\ 0 & 0 & 0 & 0 & 1 - \dfrac{z}{R} \end{bmatrix}$$

Submatrices $\mathbf{B}_{ti}$ and $\mathbf{B}_{ri}$

The submatrices $\mathbf{B}_{ti}$ and $\mathbf{B}_{ri}$ $(i = 1, 2, \ldots 8)$ of the nodal strain displacement matrices, $\mathbf{B}_t$ and $\mathbf{B}_r$, in eqn [11] are obtained as:

Table 2 Maximum control voltage

Mode	*Approach*	*One actuator gain* $= 3.5 \times 10^5$	*One actuator gain* $= 8 \times 10^5$	*Two actuators gain* 5×10^5	*Two actuators gain* $= 9 \times 10^5$
(1, 2)	Finite element model	82	100	49.01	61.23
	Experiment	70	80	47.82	64.00
(1, 1)	Finite element model	50	70	34.60	40.00
	Experiment	64	84	20.20	26.00

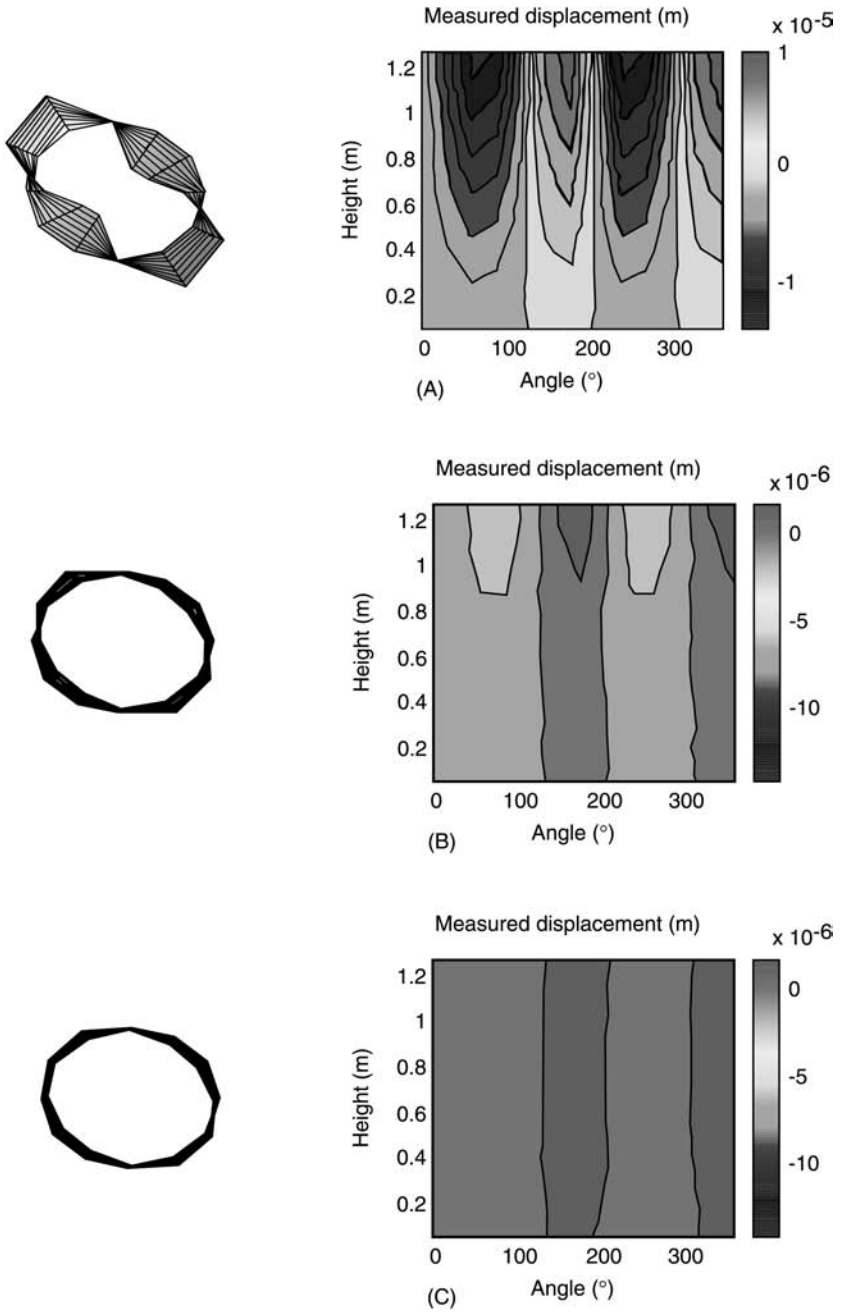


Figure 17 (See Plate 27). Experimental results using laser vibrometer before and after control for mode (1, 2). (A) PLCD; (B) ACLD (one actuator); (C) ACLD (two actuators).

$$\mathbf{B}_{ti} = \begin{bmatrix} n_{i,x} & 0 & 0 \\ 0 & n_{i,y} & 1/R \\ n_{i,y} & n_{i,x} & 0 \\ 0 & 0 & n_{i,x} \\ 0 & -1/R & n_{i,y} \end{bmatrix} \quad \text{and} \quad \mathbf{B}_{ri} = \begin{bmatrix} n_{i,x} & 0 \\ 0 & n_{i,y} \\ n_{i,y} & n_{i,x} \\ 1 & 0 \\ 0 & 1 \end{bmatrix} \quad \text{where:}$$

$$n_{i,x} = \frac{\partial n_i}{\partial x} \quad \text{and} \quad n_{i,y} = \frac{\partial n_i}{\partial y}$$

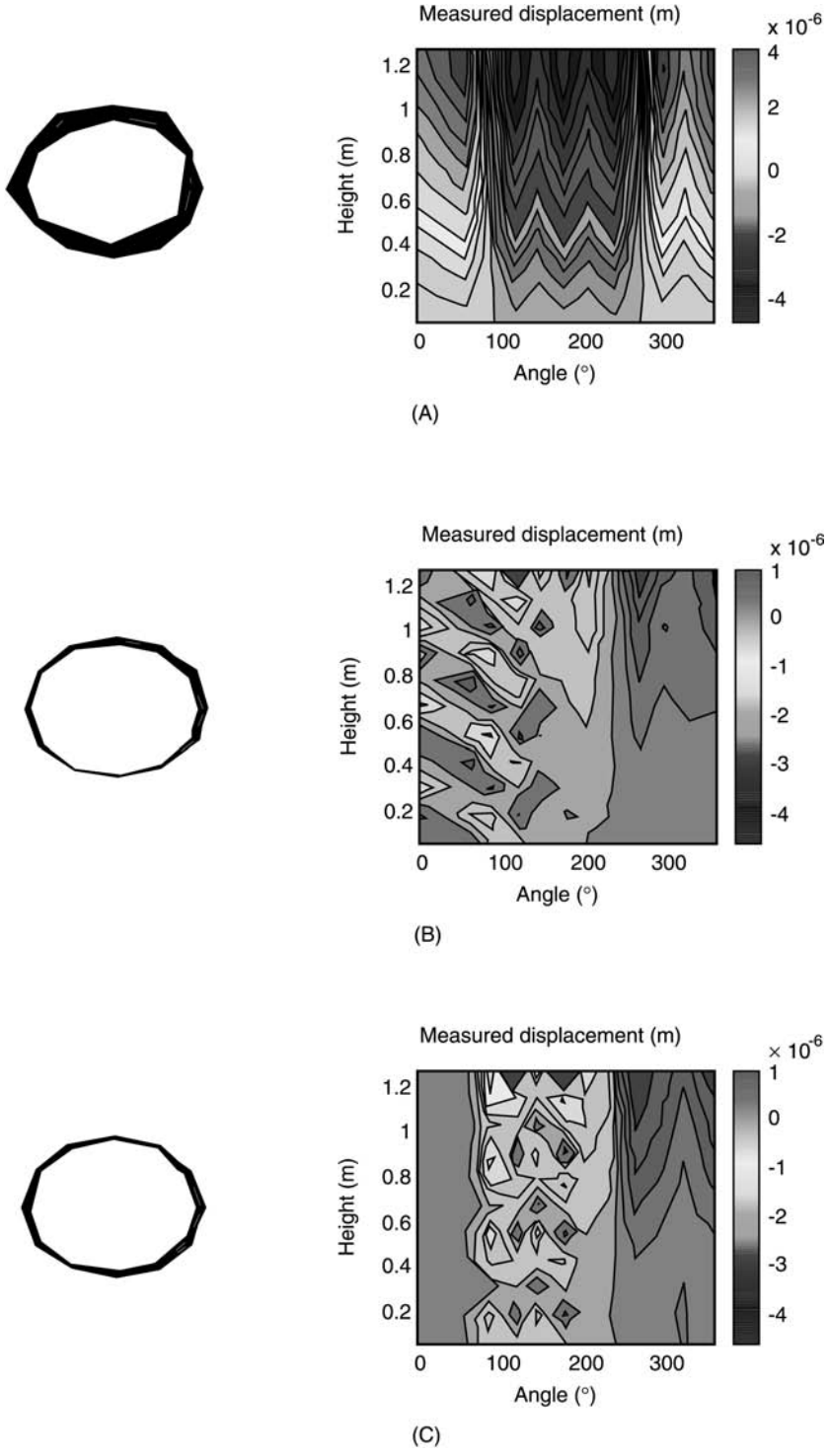


Figure 18 (See Plate 28). Experimental results using laser vibrometer before and after control for mode (1, 1). (A) PCLD; (B) ACLD (one actuator); (C) ACLD (two actuators).

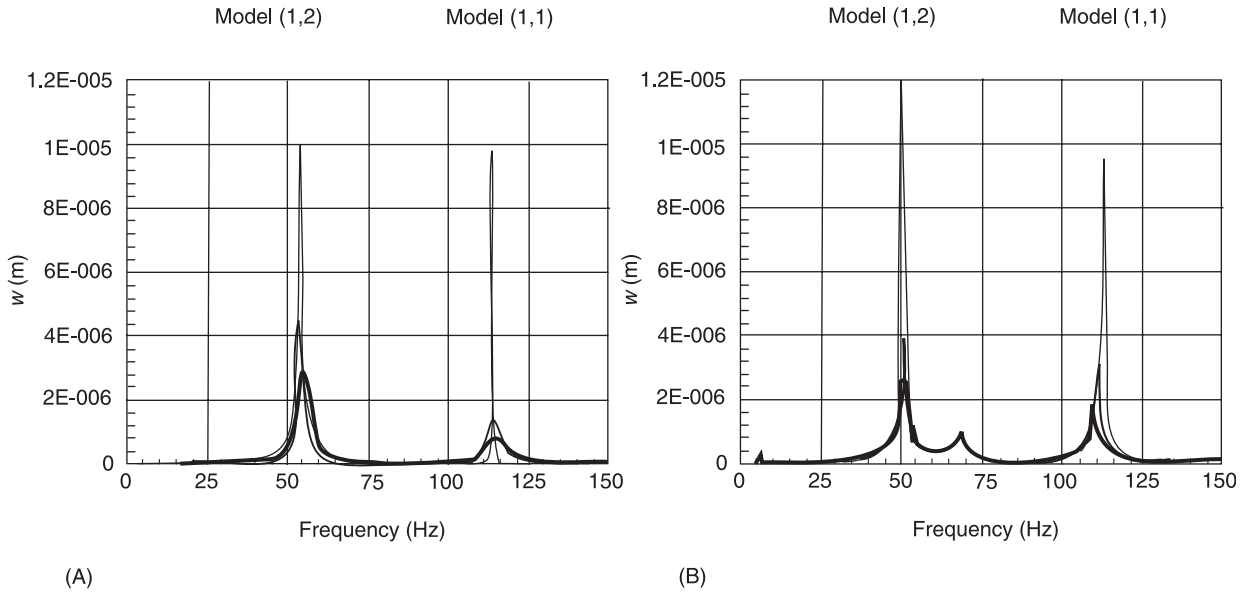


Figure 19 FRF of the shell/ACLD system when one of the piezoelectric layers is active. (A) Numerical; (B) experimental. (—) PCLD, (—) $k_d = 3.5E5$, (—) $k_d = 8E5$.

Appendix B

Rigidity and Elemental Matrices

Rigidity Matrices

The various rigidity matrices $\mathbf{D}_{tt}$, $\mathbf{D}_{tr}$, $\mathbf{D}_{rt}$ and $\mathbf{D}_{rr}$ appearing in eqn [12] are defined as:

$$\mathbf{D}_{tt} = \sum_{L=1}^{3} \int_{h_{L+1}}^{h_L} \mathbf{Z}_1^{\mathrm{T}} \mathbf{C}^{\mathrm{L}} \mathbf{Z}_1 \, \mathrm{d}z,$$

$$\mathbf{D}_{tr} = \sum_{L=1}^{3} \int_{h_{L+1}}^{h_L} \mathbf{Z}_1^{\mathrm{T}} \mathbf{C}^{\mathrm{L}} \mathbf{Z}_2 \, \mathrm{d}z,$$

$$\mathbf{D}_{rt} = \mathbf{D}_{tr}^{\mathrm{T}}$$

and:

$$\mathbf{D}_{rr} = \sum_{L=1}^{3} \int_{h_{L+1}}^{h_L} \mathbf{Z}_2^{\mathrm{T}} \mathbf{C}^{\mathrm{L}} \mathbf{Z}_2 \, \mathrm{d}z$$

Elemental Matrices

In eqns [14] and [15], the elemental mass matrix $\mathbf{M}^e$ and the elemental stiffness matrices $\mathbf{K}_{tt}^e$, $\mathbf{K}_{tr}^e$, $\mathbf{K}_{rt}^e$ and $\mathbf{K}_{rr}^e$ are defined as:

$$\mathbf{M}^e = \frac{1}{2} \int_0^{a^e} \int_0^{b^e} \left(\rho^1 h + \rho^2 h_c + \rho^3 h_p\right) \mathbf{N}_t^{\mathrm{T}} \mathbf{N}_t \, \mathrm{d}x \, \mathrm{d}y$$

$$\mathbf{K}_{tt}^e = \frac{1}{2} \int_0^{a^e} \int_0^{b^e} \mathbf{B}_t^{\mathrm{T}} \mathbf{D}_{tt} \mathbf{B}_t \, \mathrm{d}x \, \mathrm{d}y$$

$$\mathbf{K}_{tr}^e = \frac{1}{2} \int_0^{a^e} \int_0^{b^e} \mathbf{B}_t^{\mathrm{T}} \mathbf{D}_{tr} \mathbf{B}_r \, \mathrm{d}x \, \mathrm{d}y$$

$$\mathbf{K}_{rt}^e = \mathbf{K}_{tr}^{e^{\mathrm{T}}}$$

and:

$$\mathbf{K}_{rr}^e = \frac{1}{2} \int_0^{a^e} \int_0^{b^e} \mathbf{B}_r^{\mathrm{T}} \mathbf{D}_{rr} \mathbf{B}_r \, \mathrm{d}x \, \mathrm{d}y$$

The elemental electroelastic coupling vectors $\mathbf{F}_{at}^e$ and $\mathbf{F}_{ar}^e$ as well as the elemental exciting force vectors $\mathbf{F}_t^e$ and $\mathbf{F}_r^e$ appearing in eqns [14] and [15] are defined as:

$$\mathbf{F}_{at}^e = \frac{1}{2} \int_{h_4}^{h_3} \int_0^{a^e} \int_0^{b^e} \mathbf{B}_t^{\mathrm{T}} \mathbf{Z}_1^{\mathrm{T}} \mathbf{C}^3 \bar{\boldsymbol{\varepsilon}}_p \, \mathrm{d}x \, \mathrm{d}y$$

$$\mathbf{F}_{ar}^e = \frac{1}{2} \int_{h_4}^{h_3} \int_0^{a^e} \int_0^{b^e} \mathbf{B}_r^{\mathrm{T}} \mathbf{Z}_2^{\mathrm{T}} \mathbf{C}^3 \bar{\boldsymbol{\varepsilon}}_p \, \mathrm{d}x \, \mathrm{d}y$$

$$\mathbf{F}_t^e = \int_0^{a^e} \int_0^{b^e} \mathbf{N}_t^{\mathrm{T}} \mathbf{f}^s \, \mathrm{d}x \, \mathrm{d}y$$

and:

$$\mathbf{F}_r^e = \int_0^{a^e} \int_0^{b^e} \mathbf{N}_r^{\mathrm{T}} \mathbf{f}^s \, \mathrm{d}x \, \mathrm{d}y$$

Nomenclature

a	longitudinal length
b	circumferential length
$\mathbf{B}$	submatrix
$\mathbf{C}$	elastic constant matrix
$\mathbf{D}$	rigidity matrix
E	Young's modulus
h	thickness
$\mathbf{I}$	identity matrix
R	radius
T	energy
u	longitudinal deformation
v	circumferential deformation
V	voltage
$\mathbf{Z}$	transform matrix
$\boldsymbol{\varepsilon}$	strain vector
$\boldsymbol{\sigma}$	stress vector
ρ	density
ν	Poisson's ratio

See plates 16, 17, 18, 19, 20, 21, 22, 23, 24, 25, 26, 27, 28.

See also: **Absorbers, vibration**; **Active control of civil structures**; **Active control of vehicle vibration**; **Noise**, Noise radiated by baffled plates; **Noise**, Noise radiated from elementary sources; **Vibration generated sound**, Fundamentals; **Vibration generated sound**, Radiation by flexural elements; **Vibration isolation, applications and criteria**; **Viscous damping**.

Further Reading

Arafa M and Baz A (2000) Dynamics of active piezoelectric damping composites. *Journal of Composites Engineering: Part B* 31: 255–264.

Baz A (1996) Active constrained layer damping. US Patent 5,485,053.

Baz A (1997) Magnetic constrained layer damping. *Proceedings of 11th Conference on Dynamics and Control of Large Structures*, May, Blacksburg, VA, pp. 333–344.

Baz A (1999) Passive magnetic damping composites. In Szulc JH and Rodellar J (eds) *Smart Structures*, pp. 19–25. Dordrecht: Kluwer.

Baz A and Poh S (2000) Performance characteristics of the magnetic constrained layer damping. *Journal of Shock and Vibration* 7: 81–90.

Ghoneim H (1995) Bending and twisting vibration control of a cantilever plate via electromechanical surface damping. In Johnson C (ed.) *Proceedings of Smart Structures and Materials Conference*, vol. SPIE-2445, pp. 28–39.

Greaser E and Cozzarelli F (1993) Full cyclic hysteresis of a Ni-Ti shape memory alloy. *Proceedings of DAMPING '93*, 24–26 February, San Francisco, CA, vol. 2, pp. ECB 1–28.

Lesieutre GA (1998) Vibration damping and control using shunted piezoelectric materials. *The Shock and Vibration Digest* 30 (3): 187–195.

Nashif A, Jones D and Henderson J (1985) *Vibration Damping*. New York: Wiley.

Omer A and Baz A (2000) Vibration control of plates using electromagnetic compressional damping treatment. *Journal of Intelligent Materials and Structures Systems* (to be published).

Preumont A (1997) *Vibration Control of Active Structures*. Dordrecht: Kluwer.

Ray M, Oh J and Baz A (2000) Active constrained layer damping of thin cylindrical shells. *Journal of Sound and Vibration*, 240: 921–935.

Reader W and Sauter D (1993) Piezoelectric composites for use in adaptive damping concepts. *Proceedings of DAMPING '93*, 24–26 February, San Francisco, CA, pp. GBB 1–18.

DATA ACQUISITION

R B Randall and M J Tordon, University of New South Wales, Sydney, Australia

Copyright © 2001 Academic Press

doi:10.1006/rwvb.2001.0142

Background

In order to process analog signals digitally it is necessary to convert them into digital form. The object of a data acquisition system is to collect and record data from physical phenomena in the real world, which by nature are continuous in both amplitude and time. This can be a labour-intensive process, which in its simplest form involves reading values from instruments and recording the observations on a data sheet. Even in this simple form we are representing a continuous signal by values recorded at discrete times with a limited number of discrete digits. Advances in digital computers have provided efficient and fast means of collecting and processing signals represented and stored in digital form. **Figure 1** shows a schematic diagram of a general data acquisition (DAQ) system.

A transducer changes a physical phenomenon into an electrical signal. The aim is to produce electrical signals which represent the physical phenomena investigated, while at the same time minimizing the

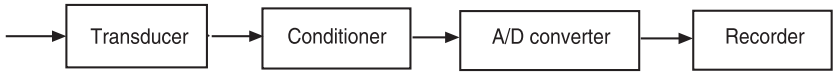


Figure 1 Schematic diagram of a general data acquisition system. A/D, analog-to-digital.

influence of other physical phenomena present in the real world.

The conditioner modifies the signal from the transducer to provide signals suitable for the analog-to-digital (A/D) converter. The conditioning often includes amplification, isolation, and filtering.

The output from the conditioner is applied to the input of the A/D converter, which may contain additional circuits such as a multiplexer and sample-and-hold amplifier, followed by the converter itself.

The A/D converter is followed by a recorder (digital memory). The recorded data should be in a form suitable for processing and/or presentation, and are thus sometimes preprocessed in real time before storage.

The way in which the data acquisition should be done depends to a large extent on what the data files are to be used for, and some confusion has arisen because of the differences between the two main areas of application:

1. Applications analogous to those of a digital oscilloscope. Here, the signals themselves are to be recorded and viewed, with the most important requirement being the visual similarity to the original signal. It is perhaps desired to extract parameters such as peak and root mean square (RMS) values. This case also applies to data-logging of very slowly changing signals such as temperature and (mean) pressure, perhaps in order to use the current value in calculations triggered by an external event.
2. Applications involving further processing (such as filtering) of the data, with actual or implicit transformation to the frequency domain.

Aliasing

In the latter case it is imperative that the signals be low-pass filtered before digitization so as to avoid problems with aliasing. This is a phenomenon whereby high frequencies before sampling appear as lower frequencies after sampling, and there is no way of knowing what the original frequency was. It can be avoided by low-pass filtering the signals before sampling, but on the other hand this can distort their shape. **Figure 2** shows two high-frequency signals that have been sampled at too low a sampling frequency, so that the sampled signal appears to be at low frequency.

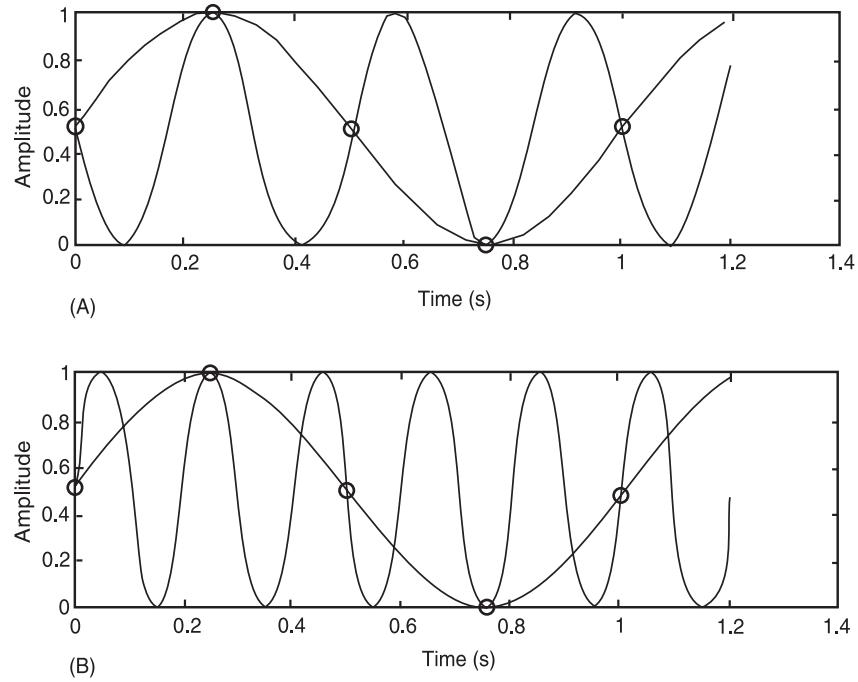


Figure 2 Higher frequencies interpreted as lower frequencies by sampling at too low a frequency (4 Hz). (A) 3 Hz as 1 Hz; (B) 5 Hz as 1 Hz.

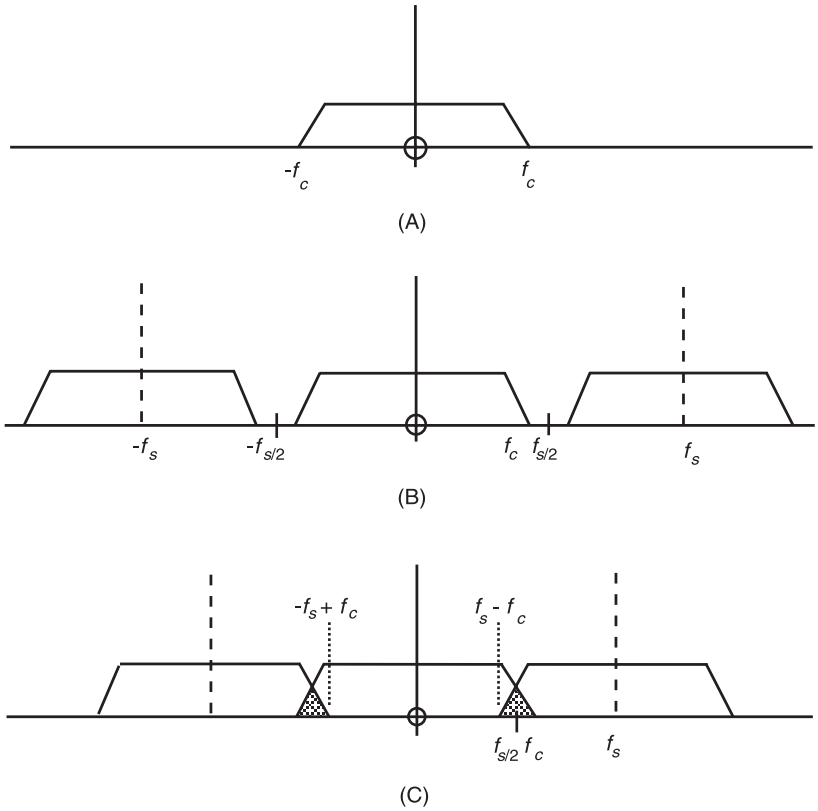


Figure 3 (A) Spectrum of a continuous band-limited signal with maximum frequency f_c. (B) Spectrum of a digitized signal with sampling frequency $f_s > 2f_c$. (C) Spectrum of a digitized signal with sampling frequency $f_s < 2f_c$. Note that frequency $\pm f_c$ is aliased to $\pm(f_s - f_c)$.

To understand the relationship between the frequencies before and after sampling it is best to look at the sampling process in the frequency domain. Sampling a signal can be treated as multiplying it by a train of delta functions (sampling functions) with spacing Δt, where sampling frequency $f_s = 1/\Delta t$. By the convolution theorem, the spectrum of the sampled signal is thus the convolution of the spectra of the original signal and that of the delta function train (itself a train of delta functions with spacing f_s). As illustrated in **Figure 3**, this means that the spectrum of the sampled signal is a periodic repetition of the original spectrum with period f_s in the frequency domain. Thus, if the original signal is low-pass filtered so as to contain no components outside the range $\pm f_s/2$, there will be no overlap in the periodic spectrum, and in principle it would be possible to regain the original signal by using a low-pass filter to remove all components outside the range $\pm f_s/2$. On the other hand, if the original signal bandwidth is greater than $\pm f_s/2$, there will be an overlap in the spectrum of the sampled signal, with no possibility of separating the mixed components with a low-pass filter. It can be seen that frequencies which can be confused with frequency f_0 are given by the formula $nf_s \pm f_0$ (in **Figure 2**, with $f_s = 4$ Hz, both 5 Hz and 3 Hz give samples corresponding to 1 Hz).

Figure 4 illustrates the differences between the two types of applications as mentioned above. It shows an asymmetric rectangular wave, sampled with and without low-pass filtering.

Without low-pass filtering, the appearance is much closer to that of the original signal, and for example a more accurate estimate of the peak value could be obtained. On the other hand, it is evident that its spectrum has a lot of invalid frequency components (since it is periodic it would only contain harmonics of the fundamental frequency) and these would remain in any further processing of the signal. The low-pass filtered signal no longer has the original rectangular shape (it can be considered to have the step response of the low-pass filter after each step) but on the other hand the spectrum is now correct up to the cut-off frequency of the low-pass filter, and further processing would be valid up to that frequency.

Antialiasing Filter Specifications

Where the signal is to be further processed, and thus aliasing errors must be limited, it has become fairly

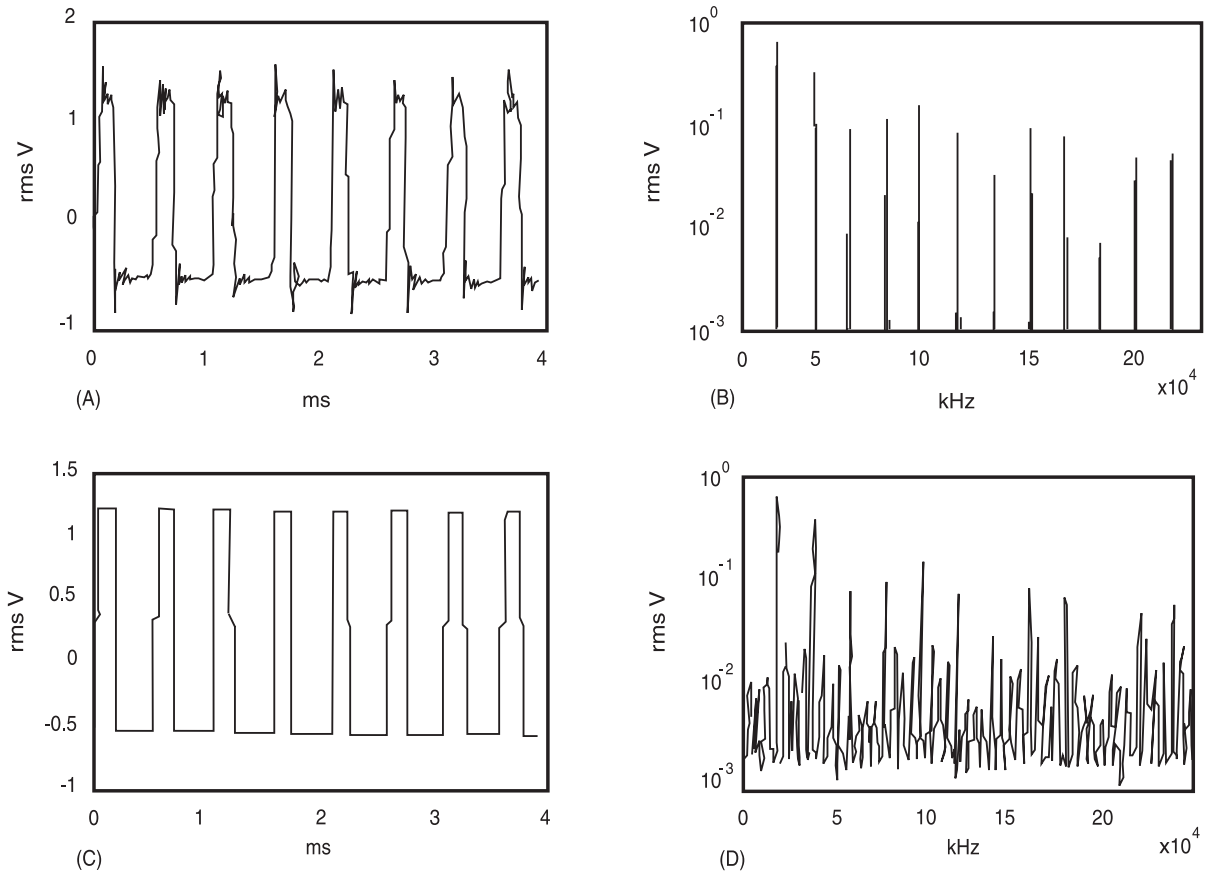


Figure 4 Digitization with and without antialiasing filters. (A) Time signal with filter. (B) Spectrum with filter. (C) Time signal without filter. (D) Spectrum without filter.

standard to utilize approximately 80% of the calculated spectrum, i.e., 400 lines out of 512 calculated, or 800 lines out of 1024. In **Figure 5**, it is seen that this requires a low-pass filter roll-off of 120 dB per octave, to ensure that components folded back into the measurement band are attenuated by at least 77 dB, to put them below the dynamic range. Elliptic filters are commonly used to achieve such roll-off, with a fixed stopband rejection. The first antialiasing filter used on the signal before digitization must of course be analog, but after fault-free digitization, digital filters can be used to filter to a lower frequency, before decimating the signal to a lower sample rate. As digital signal processing (DSP) boards become cheaper and faster, it is becoming more attractive to use simpler initial analog filters, or even the natural fall-off of the signal itself at, for example, 6 dB per octave, and digitize the signals at a very high sample rate. To avoid having to store massive amounts of data, the signals can then be

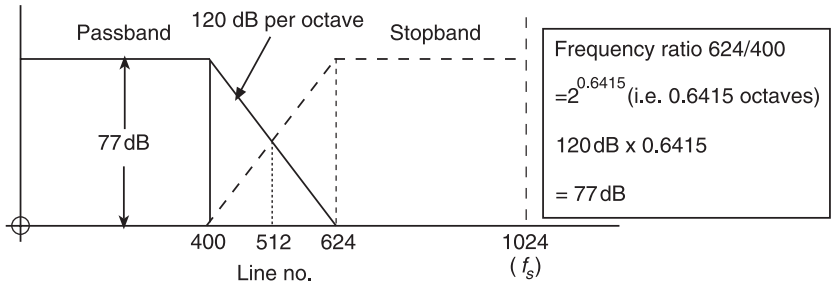


Figure 5 Antialiasing filter specification (120 dB per octave) to give $>$ 77 dB attenuation in the passband (400 lines) with sampling frequency f_s at line no. 1024.

decimated to a much lower sample rate, using digital filters operating in real time. The delta-sigma converter (see below) represents one example of this.

The major advantage of digital filters, apart from any cost comparisons, is that they can be made to have identical properties, and thus give perfect matching between channels that are converted simultaneously. Moreover, multiplexing of the same hardware units can be used to increase the number of effective filters, and the order of the filters, as the speed of the units increases. In the latter connection, it is worth pointing out that by being able to calculate at twice the rate of the incoming data, it is possible for a single digital low-pass filter to decimate by any power of two, by repeatedly decimating by a factor of two (one octave). Each time the filter reduces the frequency content of the signal (relative to the sampling frequency) to one-half of the current value, this permits the sampling frequency to be halved by discarding every second sample. This also means that, in each lower octave, only half the number of samples have to be processed in a given time, and if the number per unit time in the highest octave is S, the total number to be processed is $S(1 + \frac{1}{2} + \frac{1}{4} + ...) = 2S$.

A/D Converter Specifications

The specifications of the A/D converter determine the major performance parameters of the data acquisition system. The basic parameters of the A/D converter (ADC) include the resolution, maximum sampling rate, accuracy, dynamic range, nonlinearity (and many others).

The basic specifications of the DAQ system provide information on both capabilities and accuracy of the system. They include number of channels, sampling rate, resolution, and input range.

Analog inputs In practice we collect more than one variable so the system should include provisions for collecting data from multiple channels. The input channels can be single-ended or differential. Single-ended inputs are referenced to a common ground and due to a higher level of noise they are typically used for high-level (>1 V) input signals. Differential inputs on the other hand respond to a potential difference between two terminals. Noise or other signals present in both terminals, referred to as common-mode voltage, are cancelled out. The term common-mode voltage range describes the ability of the system to reject common-mode voltage signals.

Sampling rate Sampling rate specifies how often the conversion takes place. A faster sampling rate will provide a better representation of the original signal. To avoid aliasing, the signal must be sampled at least at twice the frequency of the maximum frequency component of the input signal, as discussed above. However, for the applications where no antialiasing filters are used, the sampling rate is typically much higher, say 10–20 times the highest frequency to be viewed, so as not to distort the appearance of the signal.

Sampling methods Due to the cost of the ADC, the DAQ system often contains only one ADC and uses a multiplexer to switch between channels. The data channels may then be sampled in sequence so that only one conversion is taking place at any one time. This method of sampling is suitable for applications where the exact time relationship between sampled signals is not important. If the time (and phase) relationships between input signals are important the inputs must be sampled simultaneously. To achieve simultaneous sampling we need sample-and-hold circuitry for each input channel, which will allow simultaneous sampling and subsequent sequential conversion of instantaneous values of input signals.

Multiplexing Multiplexing is a technique for measuring several signals with a single ADC. The multiplexer selects one input channel at a time and routes the signal to the ADC for digitizing. The effective sampling rate per channel is reduced by a factor equal to the number of channels sampled.

Resolution Resolution is the smallest signal increment that can be detected by a measurement system. Resolution can be expressed in bits, as a proportion, or in percent of full scale. For example, if a system has 8-bit resolution, this corresponds to one part in 256, and 0.39% of full scale. The higher the resolution, the smaller the detectable voltage change. **Figure 6** shows a sine wave obtained by an ideal 3-bit ADC, which divides the analog range into eight divisions. Each division is represented by a binary code between 000 and 111. It can be seen that quantization of the input signal introduces irreversible loss of information.

Range Range refers to the minimum and maximum voltage levels that the ADC can span. The range of the ADC can be changed by selecting a different amplifier gain. The range, resolution, and gain of the DAQ system determine the smallest detectable change in voltage. This change in voltage corresponds to the least significant bit (LSB) of the digital number and is often called the code width. The ideal code width is found by dividing the voltage range by the expression (gain times number of codes). For example, DAQ

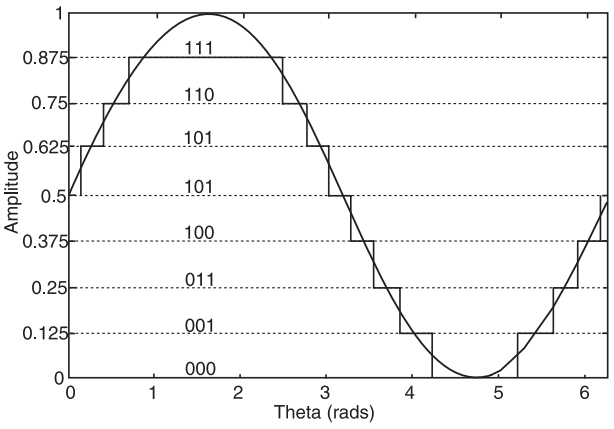


Figure 6 Example of quantized sine wave (version b, 3 bits).

system with input range 0–10‘V, gain 100 and 16-bit ADC will have code width 10 V / (100 × 65536), i.e., 1.5 μV.

Critical Parameters of Analog Inputs

The parameters mentioned above, such as sampling rate, resolution, and range, describe the overall limitation of the DAQ system. Additional parameters, such as nonlinearity, relative accuracy, settling time, and noise specifications, are needed to describe the actual performance of the DAQ system.

Nonlinearity The plot of the voltage versus the output code for an ideal ADC should be a straight line. Deviation from the straight line is specified as nonlinearity. Several terms are used to express this property. Differential nonlinearity (DNL) is a measure in LSB of the worst-case deviation of the analog code widths from their ideal value of 1 LSB. A perfect DAQ system has a DNL of 0 LSB. A good DAQ system will have a DNL within ± 0.5 LSB. Nonlinearity (or integral nonlinearity) is a measure of the worst-case deviation from the ideal transfer function (a straight line) of the system expressed in percent of full-scale range (FSR).

Relative accuracy The relative accuracy of an ADC is a measure in LSBs of the worst-case deviation from the ideal transfer function of a straight line. It can be obtained by sweeping an applied voltage through the range and digitizing it. Plotting the digitized points results in an apparent straight line. If we subtract an actual straight line from the apparent straight line, as shown in **Figure 7**, we can see the deviations from zero across the range. The maximum deviation from zero as a proportion of the FSR is the relative accuracy of the DAQ system. The relative accuracy includes all nonlinearity and quantization errors. It does not include offset and gain errors of the circuitry feeding the ADC.

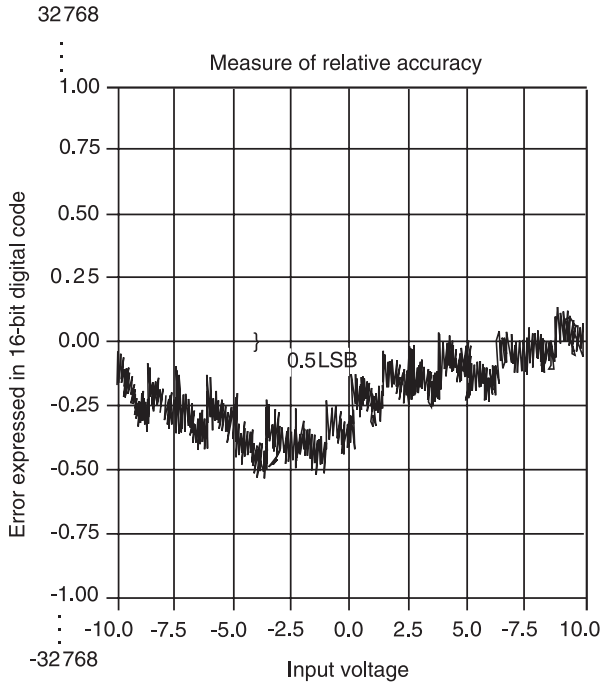


Figure 7 Deviation of encoded values from the ideal straight line. Courtesy of National Instruments 1996.

Settling time In systems with a multiplexer we have to take into account the time required for the signals at the input of the ADC to settle after changing channels. The duration required by the system to settle to a specified accuracy is called the settling time.

Discretization Errors, Dynamic Range

The process of converting a discrete-time signal into a digital signal by expressing each sample value as a finite number of digits is called quantization. The process of quantization is a many-to-one mapping and is both nonlinear and noninvertible and as such results in loss of information. Loss of information is directly linked to the number of discrete levels available for the process. The resulting digital information is stored in words of finite length expressed in bits. A wordlength of B bits can represent $N = 2^B$ different discrete levels. The signal-to-noise ratio (SNR) is used to quantify the effect of quantization noise (errors) resulting from the finite word length of the conversion.

Figure 8 shows an example of a quantized sine wave using a wordlength of 3 bits. The normalized (from 0 to 1) continuous signal is represented by eight codes representing equally spaced steps. The step size

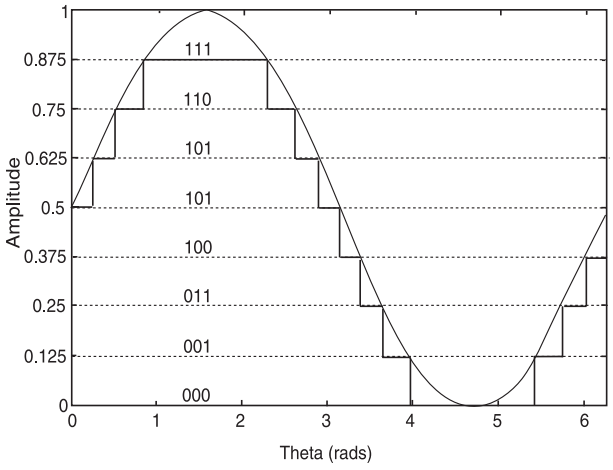


Figure 8 Example of quantized sine wave (version a, 3 bits).

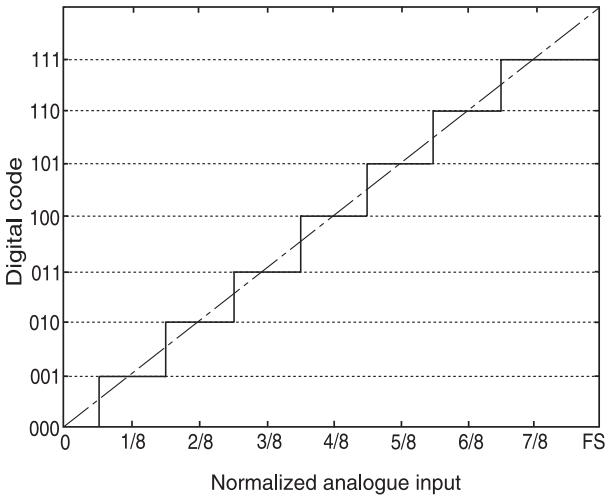


Figure 9 Analog-to-digital conversion (3 bits).

is called the quantum Δ and is equal to the width of the LSB of the ADC. The quantum represents the distance between any two successive code levels. The step size Δ of a quantizer with word length B bits and assuming unity-normalized range is $\Delta = 2^{-B}$.

Note that, for the allocation of codes as shown in **Figure 8**, the quantization error q for any particular conversion is in the range $0 \leq q \leq \Delta$ with the mean value $+0.5\Delta$. It is however possible to shift the range covered by each individual code by 0.5Δ, thus rounding the input conversion in the range $-0.5\Delta \leq q \leq +0.5\Delta$ with zero mean value. An example of this arrangement is shown in **Figure 6**. The disadvantage of this arrangement is that the first code 000 now covers a range of 0.5Δ while the last code 111 covers the range 1.5Δ. This loss of symmetry however does not cause major problems for an ADC with a large number of quantization levels. **Figure 9** shows the corresponding input–output characteristic of a 3-bit quantizer.

If we assume that the quantization noise is uncorrelated with the input signal sequence and that it has probability density function uniformly distributed over the range $(-0.5\Delta, +0.5\Delta)$, i.e., it can be represented by white noise, we can obtain a mathematical model of the quantizer, as shown in **Figure 10**. This model is used to express the effect of quantization noise and to calculate the SNR of the ADC as a function of word length B. The effect of the additive noise can be quantified by evaluating the signal-to-noise (power) ratio as SNR = 10 $\log_{10}$ (P_x/P_e) where P_x is the input signal power and P_e is the power of the quantization noise. P_e for white noise is:

$$P_e = \frac{\Delta^2}{12} = \frac{2^{-2B}}{12} \qquad [1]$$

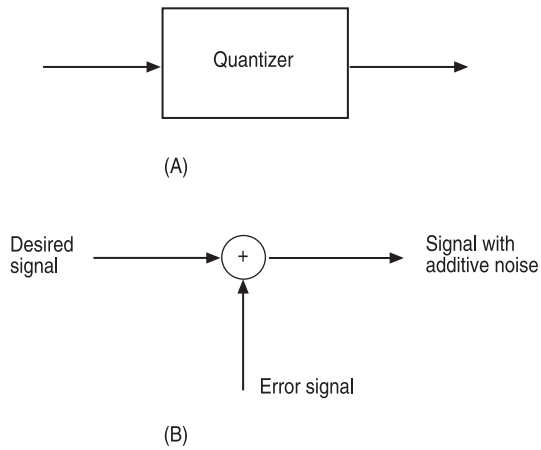


Figure 10 Mathematical model of additive noise for the quantization errors in analog-to-digital conversion. (A) Actual system; (B) mathematical model.

The input signal is often assumed to be a sinusoidal signal with magnitude spanning the whole range of the ADC. In the case of normalized input signal range the magnitude of the input signal is $\frac{1}{2}$ and the corresponding power is:

$$P_x = \frac{1/2^2}{2} = \frac{1}{8} \qquad [2]$$

The SNR of the ADC can then be expressed as:

$$\text{SNR} = 10 \ \log_{10}\left(\frac{12}{8}2^{2B}\right) = 6.02\,B + 1.76 \qquad [3]$$

in dB and represents the theoretically achievable value. If the input signal does not span the whole input range of the ADC, the SNR can be greatly

reduced. This also shows the importance of matching the magnitude of the input signal with the input range of the ADC, using a conditioning amplifier.

The maximum value of the SNR corresponding to a sine wave spanning the whole input range of the ADC is also known as the dynamic range of the ADC.

Sigma-Delta Converters

A sigma-delta modulating ADC is a circuit that samples at a very high rate with lower resolution than is needed and, by means of feedback loops, pushes the quantization noise above the frequency range of interest. It is based on the noise-shaping technique performed by a delta modulator. The most popular form of noise-shaping quantization was given the name delta sigma modulation but due to a misunderstanding the words delta and sigma were interchanged and thus today both names delta sigma and sigma delta are in use. The out-of-band noise is typically removed by digital filters. The basic principle of operation of the converter relies on oversampling and averaging.

Conventional converters require use of antialiasing quality analog filters, high-precision analog circuits, and are susceptible to noise and interference. The advantage of the conventional ADC is the use of a relatively low sampling rate, usually the Nyquist rate of the signal (i.e., twice the signal bandwidth).

Oversampling converters can use simple and relatively high-tolerance analog components, but require fast and complex digital signal-processing stages. They modulate the analog input into a simple digital code, usually single-bit words, at a frequency much higher than the Nyquist rate. Because the sampling rate usually needs to be several orders of magnitude higher than the Nyquist rate, oversampling methods are best suited for relatively low-frequency signals. The major advantage of these converters is that they provide a low-cost conversion method with high dynamic range for low-bandwidth input signals such as high-accuracy transducer applications.

An important difference between conventional and oversampling converters concerns testing and specifying their performance. With conventional converters there is a one-to-one correspondence between the input and output sample values and hence one can describe their accuracy by comparing the corresponding input and output samples. In oversampling converters each input sample contributes to a number of output samples which are then digitally filtered.

Oversampling

Figure 5 shows the antialiasing requirements for a conventional ADC. To satisfy the Nyquist sampling theorem, and utilize a maximum of the available passband, we need a very steep transition from the passband to the stopband, which in turn requires a complex analog low-pass filter. If we oversample the input signal by using a sampling frequency f_{s2}, which is much higher than the required Nyquist frequency, as shown in **Figure 11**, then we are able to relax the requirements for the width of the transition band and the solution can be as simple as the use of the first-order low-pass filter.

Noise Considerations

The limiting factor in the resolution of an ADC is quantization noise (quantization error). Assuming that the quantization error is random it can be treated as white noise. The quantization noise power and RMS quantization voltage for an ADC is given by the equation:

$$e_{rms}^2 = \frac{q^2}{12} \quad \text{or} \quad e_{rms} = \frac{q}{\sqrt{12}} \qquad [4]$$

A quantized signal sampled at frequency f_s has all of its noise power folded into the frequency band $0 <= f <= f_s/2$. Assuming that we can model the noise as white noise, the power spectral density of the noise is given by:

$$E(f) = e_{rms}^2 \left(\frac{2}{f_s}\right) \qquad [5]$$

If we are dealing with a bandwidth of interest f_0 (i.e., the maximum frequency of interest of the input signal is f_0) we can get the expression for the RMS value n_0 of the noise in the bandwidth of interest as:

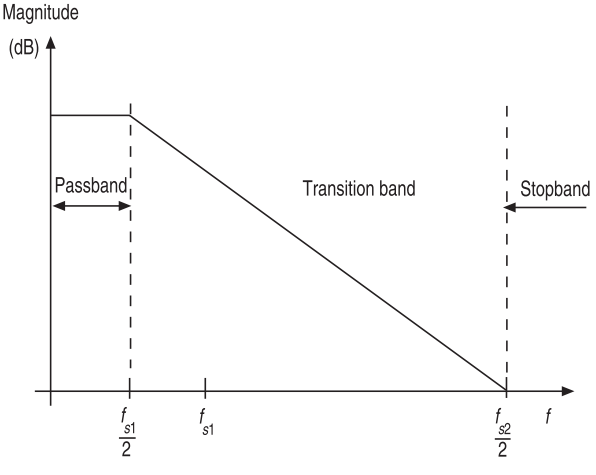


Figure 11 Antialiasing frequency response requirement for an oversampling analog-to-digital conversion.

$$n_0 = e_{rms}\left(\frac{2f_0}{f_s}\right)^{1/2} \quad [6]$$

where n_0 is in-band quantization noise. The quantity $f_s/2f_0$ is generally referred to as the oversampling ratio (OSR). The above equation shows that the oversampling theoretically reduces the inband quantization noise by the square root of the OSR. It is important to remember that this requires additonal filtering which can be done digitally so that the overall low-pass filter characteristic, which will be a combination of the antialiasing filter as shown in **Figure 11** and the digital filter required to reduce the inband noise, should have a characteristic which is close to the low-pass filter shown in **Figure 5**.

Sigma-Delta Modulator

A simple example of a first-order sigma-delta ADC is shown in **Figure 12**. A differential amplifier at the input amplifies the difference between the analog input voltage and the output of a 1-bit digital-to-analog converter (DAC). The input amplifier performs the function of a summing point. The signal then passes through an integrator which in its simplest form can be implemented as a capacitor. The output of the integrator is compared with zero level in a comparator. The comparator in turn controls the 1-bit DAC. The sigma-delta ADC, often called a charge-balancing ADC, tries to balance the charge on the integrating capacitor at zero level. This is achieved by rapid switching between a full-scale positive (+FS) and full-scale negative ($-$FS) voltage so that the resulting duty cycle is uniquely linked to the magnitude of the input voltage (bipolar in this case). As an example, a duty cycle of 50% would be required to balance zero input voltage, and 75% for half full-scale voltage.

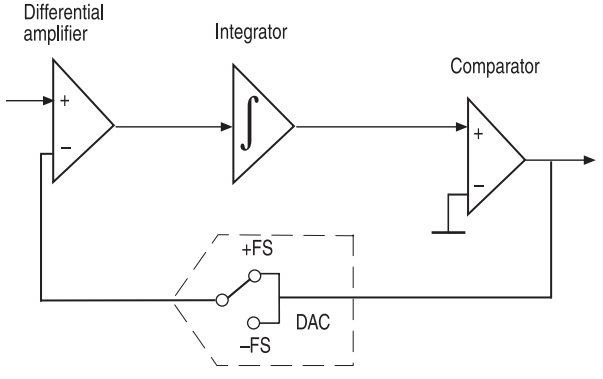


Figure 12 Simple charge-balancing analog-to-digital conversion. +FS, full-scale positive; $-$FS, full-scale negative; DAC, digital-to-analog converter.

A general sigma-delta ADC can be seen in **Figure 13**. A sample and hold (S/H) amplifier is used at the input of the converter to maintain a stationary input during conversion. A digital filter connected to the output of the comparator is used to convert the information about the input voltage level to the corresponding digital format (effectively a count of the duty cycle, with a count over more samples giving more output bits). It is usually the case that this smoothing filter also performs the process of decimation to reduce the output sampling frequency without loss of information of the input signal.

The integrator in the sigma-delta modulator (SDM) provides for further reduction in noise. As the quantizing noise as expressed in eqn [4] has to pass through an integrator present in the SDM the noise will be further reduced and will be proportional to $(2f_0/f_s)^{3/2}$ in the case of a first-order integrator, and $(2f_0/f_s)^{5/2}$ in the case of a second-order integrator. The noise of an Mth-order modulator will be proportional to:

$$\left(\frac{2f_0}{f_s}\right)^{M+0.5} \quad [7]$$

i.e., doubling the sampling frequency will decrease the in-band quantization noise by $3(2M + 1)$ dB. Considering the fact that one extra bit of resolution reduces the noise by 6 dB, doubling the OSR will in theory increase the resolution by $(M + 0.5)$ bits. This can lead to over 20 bits of resolution.

Data Acquisition Modes

Triggering

To avoid excessive storage of data, in particular for high-frequency signals, it is often desirable to be able to base the storage on detection of some event such as

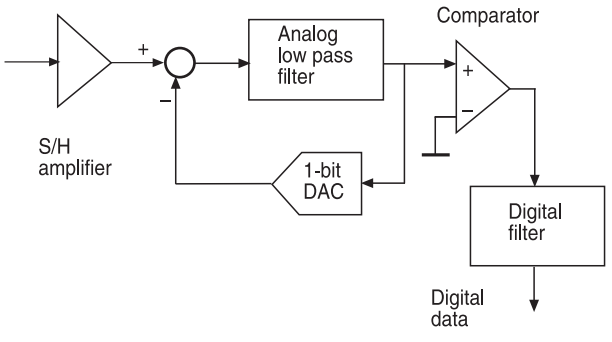


Figure 13 General sigma-delta analog-to-digital conversion. S/H, sample and hold; DAC, digital-to-analog converter.

exceedance of a specified level. Normally, however, it will be desired to capture also the signal immediately prior to the trigger event. The normal way to achieve this is to record continuously in a circular buffer, and use the trigger to define when the recording is to stop. In this case the data record can consist of anything from one complete memory length before the trigger point to any later section of data. It would be typical to continue recording for 90% of the record length after the trigger point so as to include 10% before it (**Figure 14**). The trigger level can be defined in terms of the original analog signal, before or after low-pass filtering, which requires analog hardware, or on the digital value after A/D conversion, which can be achieved by soft- or firmware. The latter is not always satisfactory, as the required low-pass filtering might remove a short trigger event requiring high frequencies to describe it. The trigger can be based on the value of one of the channels being recorded or an external signal (analog or digital). Where the external signal is unrelated to the sampling clock of the ADC, an uncertainty of up to one sample spacing may result. This may appear trivial, but represents 360° of phase of the sampling frequency, and approximately 140° of phase of a typical highest-frequency component. As described below, in cases where this is important, it is desirable to generate the sampling clock signal from the same events as are used for triggering (e.g., a once-per-rev tacho signal).

External Sampling

There are a number of reasons why it is sometimes desirable to generate the sampling signal externally, in addition to the one just mentioned. The main one, which serves as a typical example, is to achieve order analysis of signals originating from rotating machines. Due to changes in speed, large or small, the number of samples corresponding to a shaft rotation will vary and thus the various harmonics of that shaft speed will appear at different frequencies or smear over a range of frequency. If the sampling is linked to the shaft speed, to give a fixed number of samples every revolution, every shaft harmonic (or order) will appear in a fixed line of a frequency spectrum, thus aiding interpretation (**Figure 15**). Since the number of periods of rotation in a record length can be made integer, it is not necessary to use a window such as Hanning in fast Fourier transform (FFT) spectrum analysis, and each harmonic of the fundamental frequency will be completely concentrated in a single spectral line. Note that, in a machine with several shafts, it can usually only be arranged for this to apply to one shaft at a time, and typically this would be done in order to carry out synchronous averaging with respect to that shaft. Where the different shafts are geared together, it would only be necessary digitally to resample the signal (see below) to obtain an integer number of revolutions of another shaft in the record length, but where the different shafts are independent (e.g., in an aero gas turbine engine) the whole sampling would have to be done with respect to another tacho signal.

External sampling signals In order to achieve order tracking, there are several different options for obtaining the sampling signal:

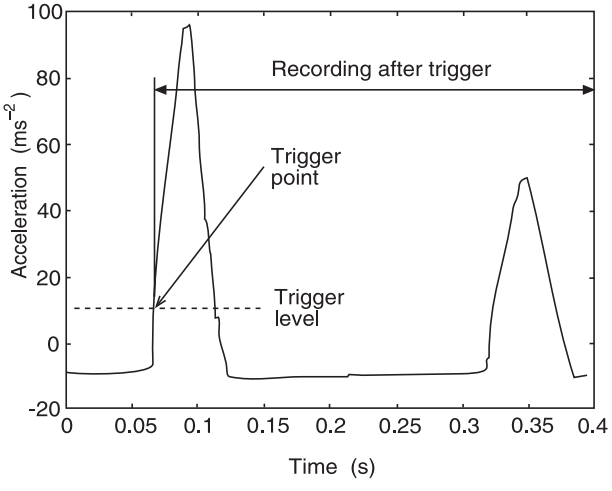


Figure 14 Example of use of a trigger to get pretrigger information.

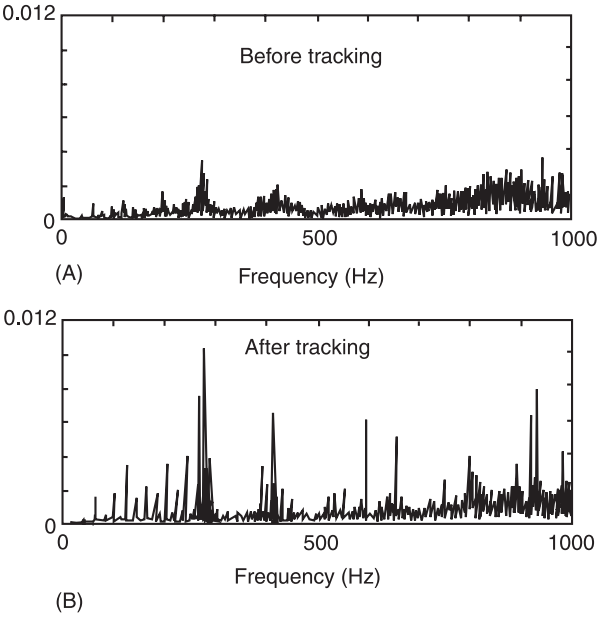


Figure 15 Use of tracking to avoid smearing of shaft speed-related components.

1. *Shaft encoder*: A shaft encoder gives a series of pulses at equal angular intervals (e.g., 1024 per rev) and thus the sampling is on a shaft angle basis. Note that this removes phase modulation effects that might be of interest, for example in gear vibrations.
2. *Frequency multiplier*: A frequency multiplier is based on a phase-locked-loop (PLL) which locks on to a signal such as a once-per-rev tacho signal and produces a fixed number of pulses per basic period of the locked frequency. Both the phase-locked frequency and the multiplied frequency are actually produced by dividing a much higher frequency. Because the PLL is an analog device, it has a finite response time, and does not respond instantaneously to sudden changes in the input frequency, even when able to maintain phase-lock. Because the multiplied signal is based on the much lower frequency input signal, the sampled signal still retains phase modulation information at frequencies higher than the fundamental frequency (for example, in the vicinity of a gearmesh frequency in a gearbox where the gear rotational speed is the input to the frequency multiplier).
3. *Software resampling*: Signals sampled at a fixed sampling rate can be resampled using digital interpolation techniques to a fixed number of samples per fundamental period of one or more tacho signals which are sampled simultaneously with the other signals. This does not suffer from the finite response time of PLLs, by resampling the data in real time or postprocessing already recorded data, and thus has many advantages. Because of its importance this topic is treated separately.

Software Resampling Schemes for Tracking

The simplest technique is to detect the first sample after each trigger point and then convert each block of data starting with these samples (and containing an integer number of samples N_i) to a fixed number of samples N_o greater than the largest value of N_i in any of the blocks. Such interpolation can be achieved by transforming each block into the frequency domain, padding the (two-sided) spectrum to the required size N_o with zeros around the Nyquist frequency, and then inverse transforming back to a time record of size N_o as required. This suffers from the disadvantage that the first sample of each block and the number of samples in each block has a possible error of one sample spacing. The error can be reduced by first increasing the sampling rate of all signals (including the tacho signals) by a large factor of, say, eight or 16, and then simply choosing the nearest sample to that calculated by the interpolation formula, based on the more accurate trigger definition. The maximum error will then correspond to one sample spacing of the higher sample rate. If performed block by block using FFT transforms, even though the transform size will be quite large, use can be made of the most efficient FFT by making both forward and inverse transforms a power of two (whereas for the above method, the forward transform may be any size, including prime numbers). The oversampling by a fixed integer factor can alternatively be done in real time using a digital low-pass filter, as illustrated in **Figure 16** for a factor of four. Three zeros are inserted between each original sample, which increases the sampling frequency by a factor of four without changing the spectrum.

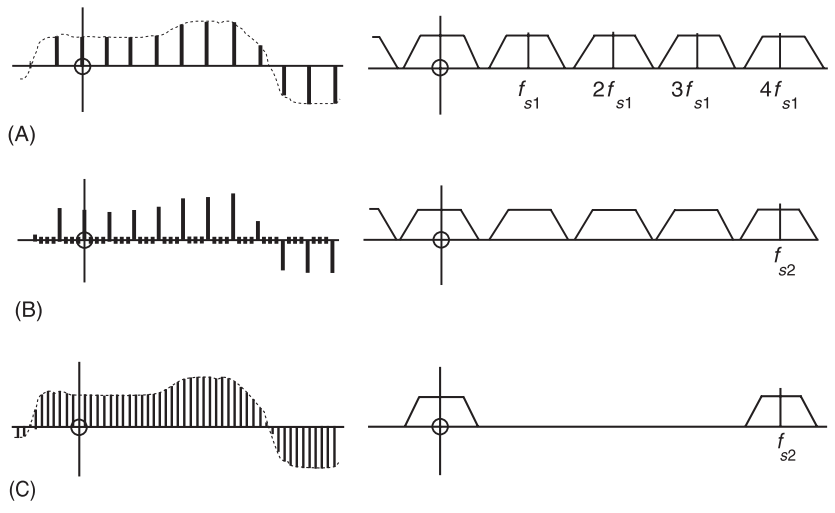


Figure 16 Digital resampling with four times higher sampling frequency. (A) Signal sampled at f_{s1} and its spectrum. (B) Addition of zeros which changes sampling frequency to f_{s2}. (C) Low-pass filtration and rescaling.

Low-pass filtration (and scaling up by a factor of four) produces an interpolated signal at the higher sampling rate but with a frequency content corresponding to the original low-pass filter (before sampling).

Interpolation in the time domain gives more flexibility, allowing the curve joining the data points to be progressively smoother depending on the order. Selecting the nearest sample (i.e., treating the basic function as a series of steps) is the same as convolving the data points with a rectangular function of width equal to the sample spacing. Linear interpolation (joining the samples with a series of straight lines) is the same as convolving the data points with a triangular function of base width twice the sample spacing (the convolution of the previous rectangular function with itself). This convolution in the time domain corresponds to a multiplication in the frequency domain with the Fourier transform of the convolving function, in the first case a $\sin x/x$ function, and the second a $(\sin x/x)^2$ function. The effect of these multiplying functions is not only through their low-pass filtration effect, but also by virtue of the aliasing of higher-order sidelobes because of the resampling. A good choice is a cubic spline interpolation, which has less low-pass filter distortion than linear interpolation, and also less aliasing from sidelobes (**Figure 17**). An efficient procedure assumes that the machine shaft speed changes with constant acceleration steps (linear speed variation and quadratic phase angle variation) and matrix methods are used to calculate the times corresponding to equal angle intervals at which the data are resampled.

Nomenclature

B	word length of a quantizer
dB	decibel
f	frequency
e	voltage
f_s	sampling frequency
q	quantization error
S	number of samples per unit time
M	order of a modulator
N	number of samples
n_0	in-band quantization noise
P	signal power
t	time
Δ	quantization step
E	noise power spectral density

See also: **Signal integration and differentiation**; **Signal generation models for diagnostics**;

Further Reading

Analog Devices Application Note AN-389. *Using Sigma Delta Converters – Part 2*. Norwood, Massachusetts.

Candy JC and Temes GC (eds) (1991) *Oversampling Delta-Sigma Data Converters – Theory, Design, and Simulation*. Piscataway, NJ: IEEE Press.

House R (1997) National Instruments Application Note 092. *Data Acquisition Specifications – a Glossary*. Austin, Texas: National Instruments.

McFadden PD (1989) Interpolation techniques for time domain averaging of gear vibration. *MSSP* 3:87–97.

Miner GF and Comer DJ (1992) *Practical Data Acquisition for Digital Processing*. New Jersey: Prentice-Hall.

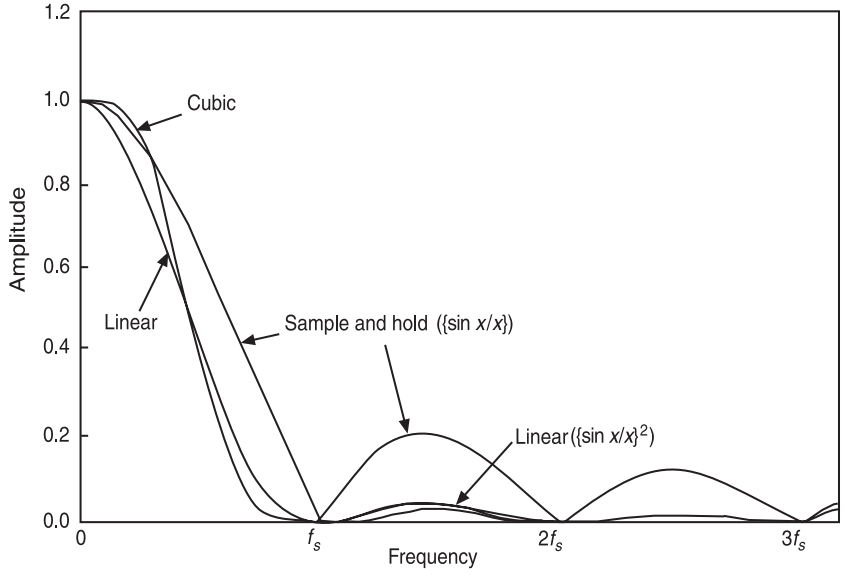


Figure 17 Frequency characteristics for three interpolation functions. Note that the upper side lobes fold back into the measurement range. Cubic interpolation gives best low-pass characteristic and lowest side bands. From McFadden (1989) with permission.

National Instruments (1996) National Instruments Application Note 007. *Data Acquisition Fundamentals*. Austin, Texas: National Instruments.
Oppenheim AV and Schafer RW (1989) *Discrete-time Signal Processing*. New Jersey: Prentice-Hall.
Potter R and Gribler M (1989) *Computed Order Tracking Obsoletes Older Methods*. SAE paper 891131. Warrendale, PA: SAE International.
Proakis JG and Manolakis DG (1989) *Introduction to Digital Signal Processing*. New York: Macmillan.

DIAGNOSTICS AND CONDITION MONITORING, BASIC CONCEPTS

M Sidahmed, Université de Technologie de Compiègne, Compiègne, France

Copyright © 2001 Academic Press

doi:10.1006/rwvb.2001.0147

Introduction

Diagnostics and condition monitoring is a multidisciplinary subject combining various techniques and areas of knowledge: mechanical engineering, reliability techniques, measurement procedures, signal processing, data analysis, and expert or knowledge-based systems. The objectives of diagnostics and condition monitoring of machinery include:

- Control of the machinery, safety is vital when dealing with high power or dangerous machines.
- Optimizing the availability of machines by avoiding unexpected shutdowns. This is particularly true for critical machines in a continuous production process.
- Implementation of condition-based maintenance, or more specifically predictive maintenance, for which the operations are planned according to various constraints (cost, production, failure condition, etc.).

This explains the importance of such techniques which are extensively used in industry.

Diagnostic and condition monitoring is based on the measurements of physical parameters on the machines in order, after specific processing, to assess the state of the machines and to identify any existing failures that may give rise to catastrophic damage. For any physical parameters, it obeys some general principles and methodology which we will describe. Vibration diagnostics and condition monitoring is then considered.

General Principles

Machine Deterioration

Figure 1 shows a typical machinery deterioration time curve (a classical 'bathtub' diagram). Three periods can be distinguished: period 1 corresponds to the running-in, in which early (or young) failures may occur. The failure probability, which is high at the beginning, will decrease by the end of the period. Period 2 is normally the longer period of normal operation of the machine in which the failure probability is lower and is constant. In period 3, failures will occur as a consequence of wear and the probability of failure increases rapidly.

Within the context of condition monitoring and diagnostics, we are concerned with failures which may influence any physical parameters and have a more or less evolutionary process. For sudden unforeseen failures, monitoring is of little value.

Principle and Vocabulary

The general principle of a diagnostic process used in condition monitoring is presented in **Figure 2**. Five steps are clearly identified:

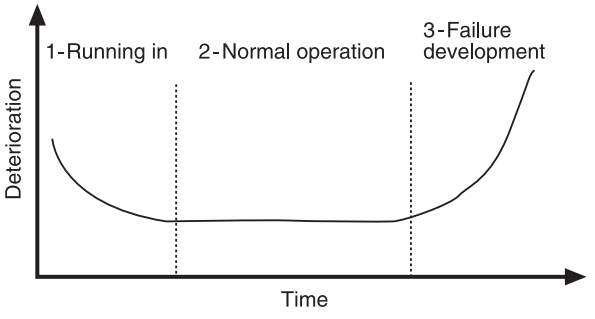


Figure 1 Deterioration time curve for machinery.

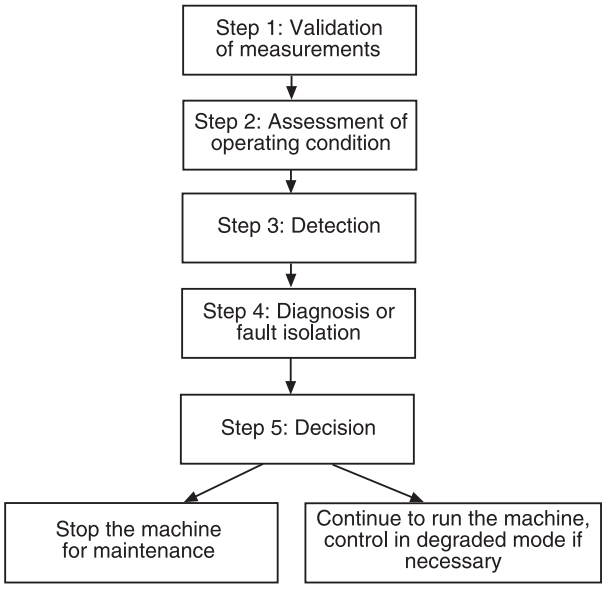


Figure 2 Steps in the diagnosis process.

Step 1: data measurement and validation The information is taken from sensors and measurement systems that have to be reliable. This step is of importance because 'bad' measurements generate a wrong diagnosis. When dealing with complex systems with numerous sensors, this step is critical. Various techniques have been developed to detect invalid measurements, these include: sensor redundancy, comparison to static or dynamic limits, and analytical redundancy.

Step 2: Operating condition assessment This step allows us to define a 'reference signature' which is able to characterize the state of the machine (healthy or faulty), but can also be related to various kinds of faults. The signature may be more or less complex. This step is very important and is a preliminary to the diagnostic process. It makes use of the machine characteristics, the type of physical measurements and the effects of the faults, i.e., the symptoms. It obviously requires the 'knowledge' of faults that may occur on the machine, and their criticality, to be able to define the most suitable signature. For complex machinery, failure mode effects and criticality analysis (FMECA) may be conducted first. It should be noted that in the case of vibration measurements, the signature is obtained by vibration signal processing.

Step 3: Detection Detection is the procedure which decides, from real observations, whether or not the system or machine is operating normally. We 'compare' the signature characterizing the healthy state to the one extracted from the real measurement. The fault is not defined. Comparing the signature belongs to decision theory and is often done using statistical decision theory.

Step 4: Diagnosis This is the art of identifying a machine condition from symptoms. Diagnosis also implies an assessment of the 'gravity' of the fault which is difficult to evaluate in practice. Several authors use the term 'fault isolation' for the process consisting of the identification of a fault from a specified fault set. However, we will use the term diagnosis instead of fault isolation. When a signature is related to a specific fault, steps 3 and 4 may be imbedded in one-step detection/diagnosis. This case often happens in vibration condition monitoring.

Step 5: Decision The operator has to decide whether to stop the machine for maintenance and repair, or to continue operating. In this last case, operating in a degraded mode may be important. This step, known as 'prognosis', is perhaps the more complex one: it is necessary to predict the future machine condition from the past and present symptoms. It is a key point in a diagnostic system. Good prognosis enables the selection of the best time for maintenance and is essential to industry. Many mathematical or statistical trending algorithms are generally used in association with diagnostic software or systems but the results are quite limited. The reason is that the remaining life of a machine depends on the environment, the stress history of the machine and indeed the wear. Work has to be done to adapt the mathematical or stochastic models for fatigue-life estimation and cumulative damage, which have been developed in the 'reliability' community.

Simple example A simple example is given in **Figure 3**. One may consider the extraction of a parameter from the measurement which completely characterizes one fault. During the normal life of the machine, we take periodical measurements. The extracted parameter will be distributed within the limits corresponding to the good condition. This parameter will be over the limit when the fault

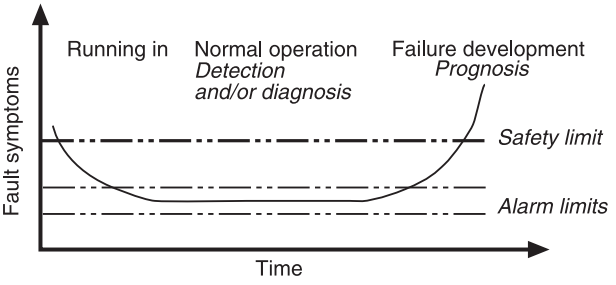


Figure 3 Limits of symptoms: from detection/diagnosis to prognosis.

appears. If the parameter has a known (estimated) probability distribution, then a statistical test may be derived. Note that in this case, the detection and diagnostic processes are the same. Prognosis is necessary to predict the 'safety limit'.

Methods Used for Machinery Condition Monitoring

Various methods are used for condition monitoring, they depend on the physical parameters to be measured and processed to deliver the diagnostic. Each method has advantages and drawbacks, thus it is advantageous to combine the different methods to obtain more reliable results.

Oil analysis Most of the machinery requires lubricants to minimize wear, for example diesel engines, turbines, or components such as gear boxes or rolling bearings. Oil analysis may give information on the lubricant quality and on the wear metal contamination. This last point is used for diagnosis. In complex machinery, this technique may complement vibration analysis in order to provide a more reliable diagnosis. This method suffers, however, from difficulties in collecting 'good' oil samples.

Nondestructive techniques 'Active' techniques (ultrasonics, radiography, etc.) are used to determine the state of various materials: homogeneity, stress, cracks, and quality of welding. The control of specific parts of the rotating machine (blades, shafts, etc.) may be carried out. Passive techniques such as acoustic emission (AE) take advantage of the sound waves emitted by materials when growing cracks or localized constraints are present. Sound waves have very high frequency components and are amplified by resonant sensors (from about 100 kHz to a few Mhz). The complexity of sound propagation in structures makes the interpretation difficult. AE is used for incipient detection but not for diagnosis. This technique is used extensively for tool wear monitoring. Some applications have been developed for incipient detection of faults in rolling bearings.

Infrared or thermographic analysis Infrared cameras are used to detect differences in surface temperatures which may be due to specific faults. This technique appears to be more suitable for the diagnosis of faults in electrical or electromechanical equipment (e.g., transformers).

Current analysis This is used for the detection and diagnosis of electrical problems in motor driven rotating equipment. This technique is of interest because it is not intrusive, the information being available on the motor power cables. Various models exist which allow us to establish the symptoms related to various faults. The capability of current analysis to diagnose mechanical faults has been established (the motor sensing the mechanical load variations) but is still under investigation.

Vibration analysis This is the most widely used technique for diagnosing faults in rotating machines, this is due to three reasons:

- Signal generation models associated with the major faults generating dynamic efforts and then vibrations, have been developed. This gives a good knowledge of the symptoms of the faults, and reliable reference signatures.
- The technique is not intrusive and does not require the machine and then the production to be stopped (thus we may consider vibration monitoring as a kind of nondestructive testing)
- The sensors are low cost and, in general, reliable, the associated data analysis systems are increasingly powerful.

In recent years emphasis has been placed on the development of advanced signal processing techniques for incipient fault detection and diagnosis. These are detailed in the next section. We may also note, that standards have been developed to classify machine vibrations into acceptable or nonacceptable vibration levels. These levels are derived from very simple processing such as power in the band (10–1000 Hz). These deterministic levels are used as detection limits (**Figure 3**). The diagnostic ability of these limits is very limited. It should be noted that vibration frequency analysis standards are currently under development.

The various techniques for condition monitoring and diagnostics may be used for quality control of components that are to be tested during production. They are usually used for low-cost components such as small DC motors, automotive gearboxes, etc.

The detection and diagnostic procedures may be developed in real time when we deal with controlled machinery (for machine tools it is necessary to detect a tool breakage in real time). In general, when real time is required, detection is addressed rather than diagnosis. In most cases, for rotating machines, signature analysis techniques are carried out periodically.

Vibration Condition Monitoring and Diagnostic

Vibration Signatures

Vibration monitoring is suitable to detect faults generating dynamics giving rise to vibrations that may be

measured with sensors fixed to a fixed part of the machine, mainly the bearing cases. These faults generate vibrations with specific characteristics which are linked to the machine kinematics which have to be defined with details (rotation speed, number of rotating elements, characteristics of rolling bearing, etc). **Table 1** summarizes the symptoms of various faults in rotating machines with a fundamental rotating speed, f_r. These results are obtained from signal generation models developed for rotating machines and show that vibrations due to faults in various components give rise to signals with:

- high frequency components at shaft rotation speed and harmonics
- amplitude and phase modulation
- possible repetitive impulses
- broadband noise.

According to the signal generation models, 'signatures' that emphasize the frequency characteristics of the signals may be used such as:

- frequency domain analysis (Fourier power spectral density)
- cepstral analysis, especially when numerous harmonics are expected
- envelope analysis
- time frequency analysis for nonstationary phenomena occurring during run-up and run down
- more advanced methods such as the bispectrum or spectral correlation function.

Statistical 'signatures' based on the time domain characteristics are used mainly for impact detection:

- RMS value and crest factor
- kurtosis value which is sensible to impacts
- repetitive variance analysis
- wavelet decomposition.

It should be noted that vibration condition monitoring using signature analysis has an important drawback. It is necessary to compare the signatures in the same operating conditions (same rotation frequency and load). Statistically based signatures are less subject to small variations in operating conditions (e.g., kurtosis).

Detection

Detection is essentially based on fixed limits. These limits are fixed from a reference operating condition. Various measurements are generally used to estimate a probability distribution to derive statistical levels.

Table 1 Vibration symptoms for various faults in rotating machines (f_r fundamental rotating frequency)

Excitation sources	*Main frequency components*	*Direction*	*Other characteristics*	*Comments*
Unbalance	$1 \cdot f_r$	Radial	Elliptic orbit	
Misalignment	$1 \cdot f_r$, $2 \cdot f_r$ and higher harmonics	Axial, radial	Double orbit	
Gear system (f_m meshing frequency, f_{r1} and f_{r2} shaft rotation frequencies, m and n integers)	Modulated meshing frequency and harmonics $m \cdot f_m \pm n \cdot f_{r1}$ $m \cdot f_m \pm n \cdot f_{r2}$	Radial and axial, depends on the gear type	Amplitude and phase modulation	Several components are present, even under good conditions
Blades passing (k number of blades)	$k \cdot f_r$, f_r	Radial, axial	High level	Modulation may exit
Oil whirl or whip in journal bearings	0.42 to $0.48 \cdot f_r$	Radial		
Rolling bearings	Impact rates and harmonics, related to defects (inner and outer races, rolling elements, cage)	Radial, axial		Excitation of structural resonances in the high frequency range may exit
Induction machines (f_s synchronous frequency)	$1 \cdot f_r$, $1 \cdot f_s$, $2 \cdot f_s$	Radial, axial		
Turbulence	Wideband	Radial, axial	$1/f$ characteristic of the spectrum	
Cavitation in pumps	High frequency	Radial, axial		Random vibration
Clearance	Random impacts	Radial, axial		
Alternative machines (combustion engines, compressors)	Repetitive impacts			Each impact has specific spectral content
Structural resonances	Resonance frequency	Radial, axial		May be excited

We may note that, model-based signal processing methods (ARMA models) are good candidates for deriving statistical detection limits by inverse filtering.

Diagnostic

When parameters derived from signal processing are uniquely related to faults, then the preceding detection step also provides the diagnosis. As shown in **Table 1**, various faults in rotating machines may have similar symptoms. It is then difficult to attribute a simple symptom to each specific fault, and additional processing is needed. Heuristic rules may be used to remove some ambiguities. This field is covered by expert or knowledge-based systems.

In complex machines, signal processing may not be sufficient to differentiate various faults. Pattern recognition techniques such as neural networks may be used. Such techniques make use of training data sets which are not easy to acquire on real machinery.

Conclusion

Diagnostics and condition monitoring is an efficient technique for predictive maintenance and safety control. It is based on physical measurements on the machinery, that are sensible to faults that happen and evolve. There are various techniques. Vibration analysis is used extensively for rotating machine diagnostics because of the existence of signal generation models, which make possible the extraction of parameters related to various faults. Advanced signal processing techniques which allow us to carry out the incipient and reliable diagnosis of complex and critical machines need to be developed.

See also: **Bearing diagnostics**; **Gear diagnostics**; **Nondestructive testing**, Sonic; **Nondestructive testing**, Ultrasonic; **Tool wear monitoring**; **Vibration isolation, applications and criteria**; **Vibration isolation theory**.

Further Reading

Braun SJ (1986) *Mechanical Signature Analysis*. London: Academic Press.

Collacot RA (1979) *Vibration Monitoring and Diagnostic*. New York: Wiley.

Mitchell JS (1981) *Machinery Analysis and Monitoring*. Tulsa, Penn Well Books.

Natke HG, Cempel C (1997) *Model-aided Diagnosis of Mechanical Systems: Fundamental Detection, Localisation, Assessment*. Berlin: Springer Verlag.

DIAGNOSTICS

See **BEARING DIAGNOSTICS; DIAGNOSTICS AND CONDITION MONITORING, BASIC CONCEPTS; GEAR DIAGNOSTICS; NEURAL NETWORKS, DIAGNOSTIC APPLICATIONS**

DIGITAL FILTERS

A G Constantinides, Imperial College of Science, Technology and Medicine, London, UK

Copyright © 2001 Academic Press

doi:10.1006/rwvb.2001.0050

System Function of Discrete-time Systems

Digital filters are a fundamental signal processing operation of universal applicability. They have a series of properties on which design procedures are based. These are outlined below. The ideal frequency amplitude characteristics are given in **Figure 1**. These characteristics correspond to lowpass, highpass, bandpass, and bandstop digital filters. They are not realizable with finite order transfer functions, as it will be indicated at a later stage but they serve a useful purpose in providing target responses to design procedures.

In a block diagram form the action of a digital filter (or of any system for that matter) may be symbolically represented as shown in **Figure 2**.

Let the input signal be $\{x(n)\}$ of the z-transform $X(z)$, and the output signal $\{y(n)\}$ of the z-transform be $Y(z)$. We define the transfer function of the system as $G(z) = Y(z)/X(z)$, and with $Y(z) = G(z)X(z)$ it is evident that when $X(z) = 1$ then $G(z) = Y(z)$, i.e.,

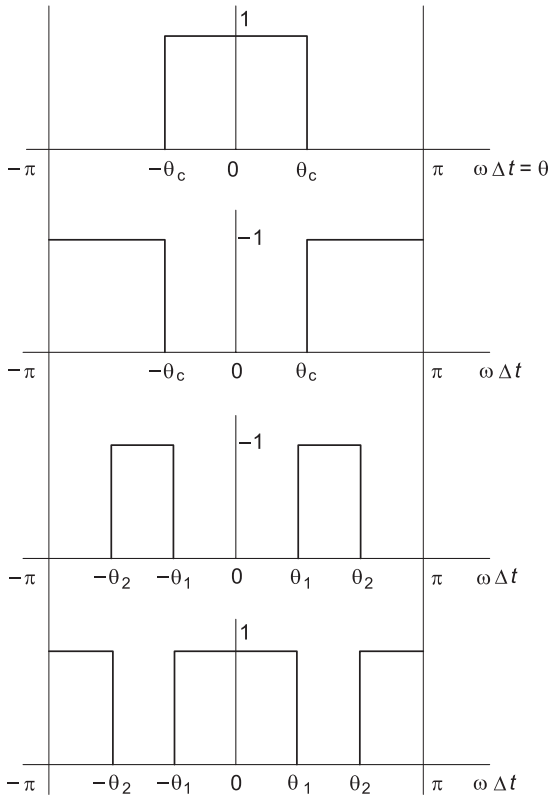


Figure 1 Ideal frequency amplitude characteristics.

$G(z)$ is the z-transform of the impulse response $h(n)$, where:

$$G(z) = \sum_{n=0}^{\infty} h(n) z^{-n}$$

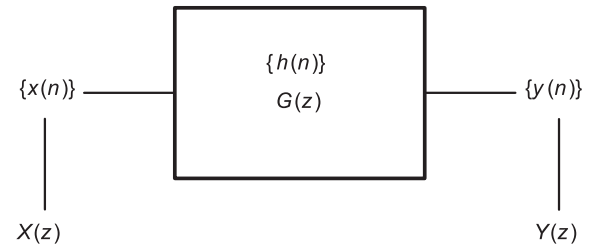


Figure 2 Block diagram of digital filter.

Hence a convolution relationship exists, which can be written as:

$$y(n) = \sum_{r=0}^{\infty} h(r) x(n-r)$$

It is clear that the transfer function of a digital filter is defined once the impulse response of the filter is specified. It would appear therefore that all one has to do in a design procedure is to determine the impulse response of one of the cases shown in the figure appropriate to the application in mind, and the task is completed.

The impulse response of the ideal lowpass filter of cutoff frequency θ_c and constant group delay τ is given by:

$$h(n) = \left(\frac{\theta_c}{\pi}\right) \frac{\sin\theta_c(n\Delta t - \tau)}{\theta_c(n\Delta t - \tau)}$$

as is shown in **Figure 3**.

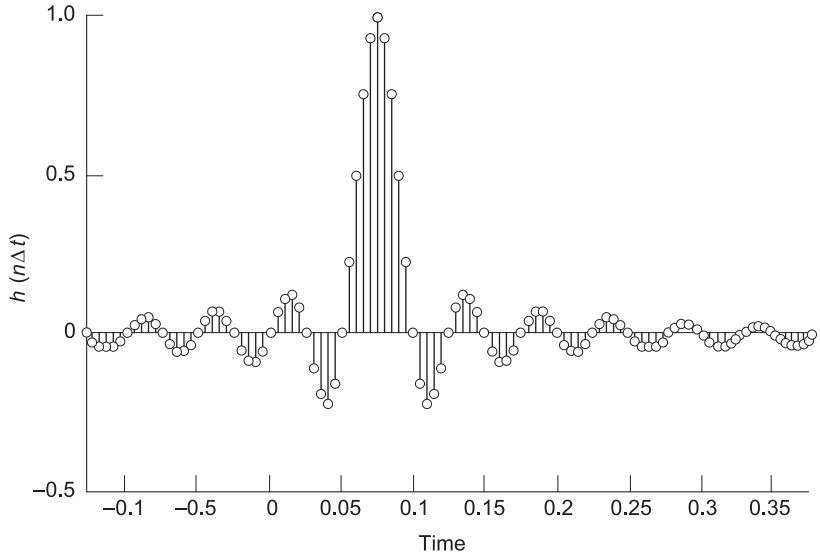


Figure 3 Ideal lowpass impulse response.

It is clear that this impulse response not only exists for negative values of time but also extends to infinity in the positive and negative directions. It is, in effect, anticipating the input to the filter. Evidently, much more needs to be done, in order to determine a realizable digital filter transfer function. To appreciate the range of tasks and constraints, and to have a proper perspective on the design processes involved, we need to examine some fundamental properties of transfer functions for discrete time systems.

If the input is the sampled sinusoidal signal $x(n) = e^{j\omega n\Delta t}$ with Δt as the sampling period we have:

$$y(n) = \sum_{r=0}^{\infty} h(r)e^{j\omega(n-r)\Delta t} = e^{j\omega n\Delta t}G(e^{j\theta})$$

where:

$$G(e^{j\theta}) = \sum_{r=0}^{\infty} h(r)e^{-jr\theta} = G(z)|_{z=e^{j\theta}} \quad \text{and} \quad \theta = \omega\Delta t$$

For discrete time real systems the amplitude response is then:

$$A(\theta) = |G(z)|_{z\,\text{on}\,C}$$

where C: $|z| = 1$ while the phase response is given as $\phi(\theta) = \arg\ \lfloor G(z)|_{z\,\text{on}\,C}\rfloor$. On the unit circle C:

$$G(e^{j\theta}) = \sum_{n=0}^{\infty} h(n)e^{-jn\theta} = A(\theta)e^{j\phi(\theta)}, \quad \theta = \omega\Delta t$$

It follows that $A(\theta) = A(-\theta)$ (even function) and $\phi(-\theta) = -\phi(\theta)$ (odd function). Moreover $dA(\theta)/d\theta = 0$ at $\theta = 0$. Further, from $G(e^{j\theta}) = A(\theta)e^{j\phi(\theta)}$ we have:

$$\frac{dG(e^{j\theta})}{d\theta} = e^{j\phi(\theta)}\frac{dA(\theta)}{d\theta} + A(\theta)j\frac{d\phi(\theta)}{d\theta}e^{j\phi(\theta)}$$

and in this equation we can use the group delay given as:

$$-\frac{d\phi(\theta)}{d\omega}\bigg|_{\theta=\omega T} = \tau(\omega)$$

to yield:

$$\frac{dG(e^{j\theta})}{d\theta} = e^{j\phi(\theta)}\frac{dA(\theta)}{d\theta} + jA(\theta)e^{j\phi(\omega)}\left(-\frac{\tau(\omega)}{\Delta t}\right)$$

This form at $\theta = 0$ with the left-hand side can be expressed in terms of $h(n)$ produces:

$$A(0)\frac{\tau(0)}{\Delta t} = \sum_{n=0}^{\infty} nh(n)$$

A simplification can be put into effect here, by using the notion of the center of gravity of $h(n)$ defined as:

$$\mu_h = \frac{\sum_{n=0}^{\infty} nh(n)}{\sum_{n=0}^{\infty} h(n)} = \frac{\sum_{n=0}^{\infty} nh(n)}{G(0)}$$

and hence we have:

$$A(0)\frac{\tau(0)}{\Delta t} = G(0)\mu_h \quad \text{or} \quad \tau(0) = \mu_h\Delta t$$

i.e., the center of gravity of a signal at the output of a linear system will be delayed by $\tau(0)$.

Group Delay for Discrete Time Systems

An expression for the group delay can be obtained from the following considerations. Let:

$$G(z)|_{z=e^{j\theta}} = |G(e^{j\theta})|e^{j\phi(\theta)}\,\theta = \omega\Delta t$$

so that

$$\frac{1}{2}\ln\left(G(e^{j\theta})\right) = \frac{1}{2}\ln\left(G(e^{-j\theta})\right) + j\phi(\theta)$$

and hence the phase response is given as:

$$\phi(\theta) = -\frac{j}{2}\ln\left(\frac{G(e^{j\theta})}{G(e^{-j\theta})}\right)$$

The group delay is given by:

$$\tau_g(\theta) = -\frac{d\phi(\theta)}{d\theta}\frac{d\theta}{d\omega} = -T\frac{d\phi(\theta)}{d\theta}$$

and hence one obtains:

$$\tau_g(\theta) = \frac{\Delta t}{2}\left[z\frac{G'(z)}{G(z)} + z^{-1}\frac{G'(z^{-1})}{G(z^{-1})}\right]_{z=e^{j\theta}}$$

where $G'(u) = dG(u)/du$, i.e., the prime indicates differentiation with respect to the argument of the function.

Signal Flow Graphs

An important concept in the study and implementation of algorithms for general digital signal processing and for digital filters is that of signal flow graphs (SFGs). Essentially they embody the essence of the interacting relationships that yield the specific input/output results. Linear time invariant discrete time systems can be made up from three basic elements namely storage, scaling, and summation.

Storage In the digital signal processing literature this is sometimes known as 'Delay', or 'Register'. Its SFG representation and mathematical description are given in **Figure 4**. The output from this element is essentially the same as the input delayed by one sampling instant.

Scaling In the digital signal processing literature this is sometimes known as weight, product, and multiplier. Two frequently encountered SFG representations and their mathematical description are given in **Figure 5**. The output from this element is essentially the same as the input delayed by one sampling instant

Summation In the digital signal processing literature this is sometimes known as adder, or accumulator. Its SFC representation and mathematical description are given in **Figure 6**. The output from this element is essentially the sum of its inputs and this operation is assumed to be carried out instantly. A simple digital filtering equation such as $y_n = a_1 y_{n-1} + a_2 y_{n-2} + b x_n$ can be represented in terms of the SFC, employing these elements and is shown in **Figure 7**.

Conversely, the system equation, which is essentially the algorithmic form of the input/output relationship may be obtained from the interconnected components. Such interconnections are termed the realization structure. A realization structure can be computable when all the loops in it contain delays, normally of integer multiples of the sampling period, or it can be noncomputable if there exist some loops that contain no delays.

An important operation in the study concerning the behavior of realization structures is that of transposition. Transposition of a SFG is the process of reversing the direction of signal flow on all transmission paths while keeping their transfer functions the same. The adders are replaced by nodes, and nodes by adders. For a single-input/output SFG the transpose SFG has the same transfer function overall, as the original.

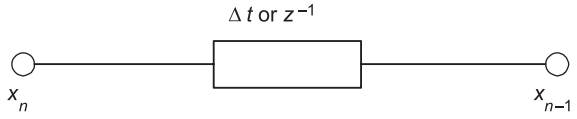


Figure 4 Storage.

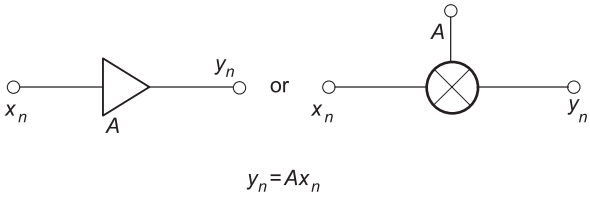


Figure 5 Scaling.

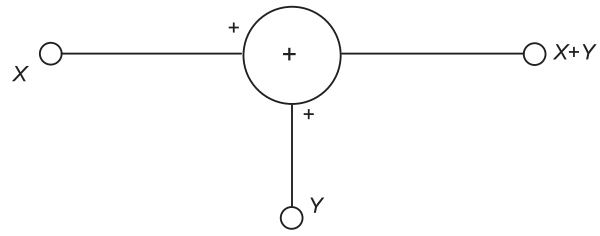


Figure 6 Summation.

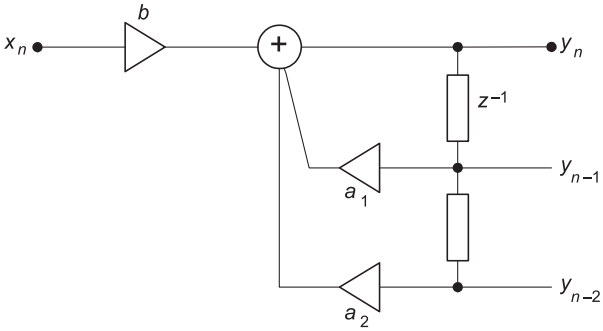


Figure 7 Simple digital filtering.

Structures

As already mentioned these are the computational schemes embodying the individual interactions between the realization elements that yield the overall input/output relationships. For a given transfer function, there are many realization structures. Each structure has different properties with respect to coefficient sensitivity and finite register computations. When the number of delays used in a structure is equal to the order of the transfer function the structure is termed canonic. Some standard forms are:

Direct form I Let us assume that the transfer function is given by:

$$G(z) = \frac{Y(z)}{X(z)} = \frac{\sum_{i=0}^{n} a_i z^{-i}}{1 + \sum_{i=1}^{m} b_i z^{-i}}$$

The numerator of the above transfer function has a realization structure as shown in **Figure 8**. This is known as a direct form realization. It is a standard form for finite impulse response (FIR) transfer functions (i.e., when the denominator above is constant). The numerator realization alone is canonic. The denominator of the above transfer function has a direct form realization structure shown in **Figure 9**. This is also a canonic realization. The cascaded interconnection of these two realization structures produces the so-called direct form I. The structure produced by this cascaded interconnection is noncanonic. There are many other alternative ways of producing individual realization structures of the direct form. For example, one can immediately proceed by using the principle of SFG transposition as mentioned earlier. Alternatively one can develop specific decomposition algorithms for this purpose.

The direct form is a simple structure but not used extensively in demanding applications because its performance degrades rapidly due to finite register computation effects.

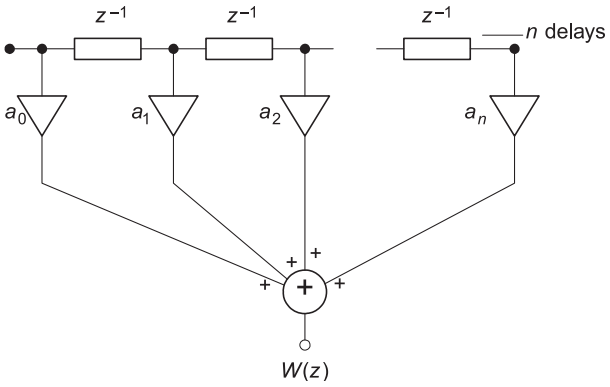


Figure 8 Direct form realization.

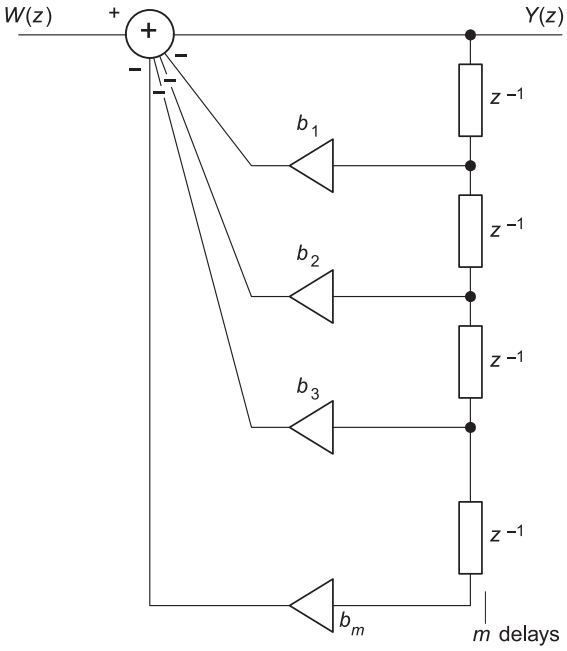


Figure 9 Canonic realization.

Direct form II A canonic form can be obtained by a more careful interconnection of the above components. A simple analysis of the structure (**Figure 10**) shows that it has the required transfer function and the lowest number of delays consistent with its order.

Cascade form By expressing the numerator and denominator polynomials as factors of polynomials of lower degree we can produce different structures. The cascaded interconnection of the individual realizations produce a large number of alternative realizations for the given transfer function. Reduction of the effects due to finite register length can be achieved by a suitable selection of factors. In general:

$$G(z) = \prod_i G_i(z)$$

and for second-order blocks:

$$G_i(z) = \frac{a_{0i} + a_{1i} z^{-1} + a_{2i} z^{-2}}{1 + b_{1i} z^{-1} + b_{2i} z^{-2}}$$

or for first-order blocks:

$$G_i(z) = \frac{a_{0i} + a_{1i} z^{-1}}{1 + b_{1i} z^{-1}}$$

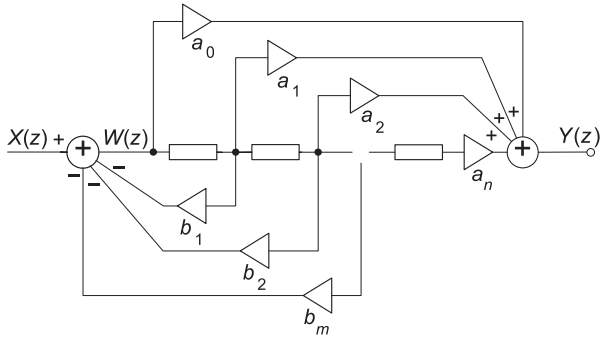


Figure 10 Simple analysis of canonic structure.

Figure 11 is a canonic realization for the second-order transfer function, or indeed for the first-order case, when the quadratic terms are taken to be zero.

Parallel form Let the transfer function be expressed as:

$$G(z) = g + \sum_{i=1}^{k} G_i(z)$$

The individual transfer functions $G_i(z)$ are as in the cascade realization with $a_2 = 0$. The parallel interconnection in which each subtransfer function takes the same input and their outputs are summed to produce the overall output, yields the parallel form.

Filtering

The digital signal processing operations aimed at removing a frequency or a band of frequencies from a given signal is called digital filtering. The complete removal of a single frequency is a relatively straightforward matter. Indeed, if the given is $\{x_n\}$ and the generated signal (output) is $\{y_n\}$ the algorithm below will remove a single frequency of value $\omega_0 = \theta_0/\Delta t$, where Δt is the sampling period:

$$y_n = x_n - 2\cos\theta_0 x_{n-1} + x_{n-2}$$

An example is shown in **Figure 11** where we also show the frequency response of the transfer function of this operation, which is given by:

$$G(z) = 1 - 2\cos\theta_0 z^{-1} + z^{-2}$$

However, the entire suppression of a band of frequencies as is required by the ideal frequency responses discussed above, is not possible as can be seen from the following argument.

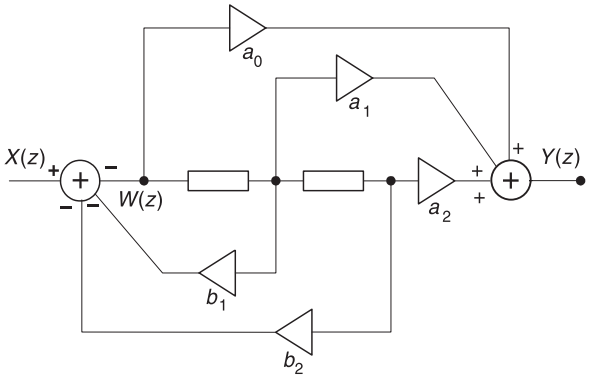


Figure 11 Canonic realization.

Suppression of a frequency band

The transfer function of a real digital filter is required to be a rational function of z^{-1} (i.e., a ratio of two polynomials in z^{-1}). A real and rational transfer function $H(z)$ cannot suppress a band of frequencies completely, i.e., $H(z)$ cannot be zero for $z = e^{j\theta}$ and θ over a band of frequencies in (θ_1, θ_2), $\theta_2 \neq \theta_1$. This may be demonstrated as follows. To produce a zero at say $\theta = \theta_0$ we must have in the numerator of $H(z)$ a factor of the form (as seen from the previous example) $(z^2 - 2\cos\theta_0 z + 1) = (z - e^{j\theta 0})(z - e^{-j\theta 0})$. Therefore for one zero within the band of (normalized) frequencies (θ_1, θ_2) the factor is of the form $(z^2 - 2\cos\theta_{0i} z + 1)\theta_1 \leq \theta_{0i} \leq \theta_2$.

Since there are an infinite number of points in the band we need factors in the numerator as:

$$\prod_{i=1}^{\infty} (z^2 - 2\cos\theta_{0i} z + 1) \quad \theta_{01} = \theta_1, \quad \theta_{0\infty} = \theta_2$$

Clearly the result is of infinite degree and is not a rational function. Hence it cannot be the transfer function of a real digital filter. However, in practice one may be satisfied not with the complete suppression of a frequency band but with its attenuation to an acceptable level that depends on the application. This is the pivotal consideration for all design techniques, taken either implicitly or explicitly.

Finite Impulse Response Filters

The transfer function of a FIR digital filter is essentially a polynomial of the form:

$$H(z) = \sum_{n=0}^{N-1} h(n)\, z^{-n}$$

The length of the filter impulse response is the number of coefficients N. While this kind of transfer function is sometimes called 'all-zero', strictly speaking it has as many poles as the order $(N-1)$ all of which are located at $z = 0$. The zeros can be placed anywhere on the z-plane and their location dictates the form of the frequency response. A great advantage of FIR filters is their ability to produce a linear phase response and yet allow freedom to shape the amplitude response as required.

Linear phase For linear phase response the impulse response is required to be such that $h(n) = \pm h(N-1-n)$. It can be seen then that for N even we have:

$$
\begin{aligned}
H(z) &= \sum_{n=0}^{(N/2-1)} h(n)\, z^{-n} \pm \sum_{n=N/2}^{N-1} h(n)\, z^{-n} \\
&= \sum_{n=0}^{(N/2)-1} h(n)\, z^{-n} \\
&\quad \pm \sum_{n=0}^{(N/2)-1} h(N-1-n)\, z^{-(N-1-n)} \\
&= \sum_{n=0}^{(N/2)-1} h(n)[z^{-n} \pm z^{-m}], \quad m = N-1-n
\end{aligned}
$$

which on taking the positive sign becomes on C: $|z| = 1$, i.e., with $z = \mathrm{e}^{\mathrm{j}\theta}$ and $\theta = \omega\Delta t$:

$$
\begin{aligned}
H(\mathrm{e}^{\mathrm{j}\theta}) &= \mathrm{e}^{-\mathrm{j}\theta((N-1)/2)} \\
&\quad \times \sum_{n=0}^{(N/2)-1} 2h(n) \cos\left(\theta\left(n - \frac{N-1}{2}\right)\right)
\end{aligned} \tag{1}
$$

while with the negative sign it becomes:

$$
\begin{aligned}
H(\mathrm{e}^{\mathrm{j}\theta}) &= \mathrm{e}^{-\mathrm{j}\theta((N-1)/2)} \\
&\quad \times \sum_{n=0}^{(N/2)-1} \mathrm{j}2h(n) \sin\left(\theta\left(n - \frac{N-1}{2}\right)\right)
\end{aligned} \tag{2}
$$

It should be noted that the antisymmetric case adds $\pi/2$ rads to the phase, with a discontinuity at $\theta = 0$.

For N odd we write the transfer function as:

$$
\begin{aligned}
H(z) &= \sum_{n=0}^{((N-1)/2)-1} h(n)\, [z^{-n} \pm z^{-m}] \\
&\quad + h\left(\frac{N-1}{2}\right) z^{-((N-1)/2)}
\end{aligned} \tag{3}
$$

On taking the positive sign we have on C: $|z| = 1$:

$$
\begin{aligned}
H(\mathrm{e}^{\mathrm{j}\theta}) &= \mathrm{e}^{-\mathrm{j}\theta[(N-1)/2]} \\
&\quad \times \left\{ h\left(\frac{N-1}{2}\right) + \sum_{n=0}^{(N-3)/2} 2h(n) \cos\left[\theta\left(n - \frac{N-1}{2}\right)\right] \right\}
\end{aligned} \tag{4}
$$

while with the negative sign we obtain:

$$
\begin{aligned}
H(\mathrm{e}^{\mathrm{j}\theta}) &= \mathrm{e}^{-\mathrm{j}\theta[(N-1)/2]} \\
&\quad \times \left\{ 0 + \sum_{n=0}^{(N-3)/2} 2\mathrm{j}\, h(n) \sin\left[\theta\left(n - \frac{N-1}{2}\right)\right] \right\}
\end{aligned} \tag{5}
$$

It should be noted that for the antisymmetric case to have a linear phase we require $h((N-1)/2) = 0$. The phase discontinuity is as for N even.

The cases most commonly used are (1) and (3), for which the amplitude characteristic can be written as a polynomial in $\cos\theta/2$.

FIR filters are implicitly stable, can be designed to have linear phase when their impulse response is symmetric or antisymmetric about its midpoint, and they can have low computational noise. But in order to satisfy a set of attenuation specification their order needs to be much higher than the corresponding infinite impulse response digital filters.

The real transfer function

$$
H(z) = \sum_{n=0}^{N-1} h(n)\, z^{-n}
$$

with symmetries on the impulse response $\{h(n)\}$ for linear phase will have zeros disposed on the z-plane in a special form. Because it is real, the zeros that are complex must appear in complex conjugate form. Moreover, because of the symmetries in the impulse response, in general, a zero and its inverse will also be present, i.e., it has zeros at $\left[\rho_i \mathrm{e}^{\pm\mathrm{j}\theta_i}\right]^{\pm 1}$ where ρ_i has value other than 1. With zeros on the unit circle (which, of course, produce zero gain at their respective frequencies) the zeros do not have to have this quadrantal symmetry, but they need to be in complex conjugate form.

There are four cases that one needs to examine for linear phase responses.

1. Symmetric ($h(n)$, odd N). The amplitude response may be zero at 0 or $\pi/\Delta t$.
2. Symmetric ($h(n)$, even N). The amplitude response is always zero at $\pi/\Delta t$.
3. Antisymmetric ($h(n)$, odd N). The amplitude response is always zero at 0 and $\pi/\Delta t$.
4. Antisymmetric ($h(n)$, even N). The amplitude response is always zero at 0.

These general properties indicate the possible options prior to a design. For example one cannot use case (2) for highpass filters because of its transmission zero at zero frequency.

Design of FIR Filters

The obvious approach is to determine the ideal impulse response and then to take a finite number

of terms symmetrically disposed about its midpoint. This would produce ripples of increasing height near an abrupt change in the amplitude, and to reduce these the 'Window method' has been produced. Essentially it involves the following steps:

1. Start with ideal infinite duration $\{h(n)\}$.
2. Truncate $\{h(n)\}$ to finite length (this produces unwanted ripples that increase in height near discontinuity).
3. Modify $\{h(n)\}$ as $\tilde{h}(n) = h(n)w(n)$ where the weight $w(n)$ is called the window and may be chosen from a wide range of available functions.

Notice that in practice steps (2) and (3) are taken together by having the window zero outside the chosen interval. There are many windows with different properties that may be selected. Commonly used windows are:

Name of window $w(n)$	*Range of time index* $\lvert n\rvert<(N-1)/2$:
Rectangular	1
Bartlett	$1-(2\lvert n\rvert/N)$
Hann	$1+\cos((2\pi n)/N)$
Hamming	$0.54+0.46\cos((2\pi n)/N)$
Blackman	$0.42+0.5\cos((2\pi n)/N)$ $-0.08\cos(4\pi n/N)$
Kaiser	$J_0\left[\beta\sqrt{\left(1-\left(\frac{2n}{N-1}\right)^2\right)}\right]\Big/J_0(\beta)$

where $J_0(x)$ is the zero-order Bessel function of the second kind, and β is a parameter that may be chosen according to the filter performance needs as indicated in **Table 1**. **Figure 12** shows the ideal lowpass impulse response symmetrically centered around the zero frequency point, in which form it is used for the application of the window method. This will result in essentially a linear phase response. Some examples are shown in **Figure 13**. Attention should be paid not only to the attenuation discrimination between passband and stopband but also to the passband behavior. The consequences of product involved in the modification of the impulse response can be examined from the frequency domain by making use of the following relationships.

Table 1

β	*Normalized transition width*	*Minimum stopband to passband discrimination in dB*
2.12	1.5/*N*	30
4.54	2.9/*N*	50
6.76	4.3/*N*	70
8.96	5.7/*N*	90

Windows: Products of Signals: Parseval's Theorem

In a general case let $\{u(n)\}$ and $\{w(n)\}$ be the given signal of z-transforms $U(z)$ and $W(z)$, respectively.

Let us form a new signal given by $y(n) = w(n)u(n)$. We need to determine the z-transform of this new signal. We can now use the definition of the z-transform and the inverse z-transform relationship as follows:

$$Y(z) = \sum_{n=0}^{\infty} w(n)\, u(n)\, z^{-n}$$

$$= \sum_{n=0}^{\infty} w(n) \left[\frac{1}{2\pi \mathrm{j}} \oint_c U(\xi)\, \xi^n\, \frac{\mathrm{d}\xi}{\xi}\right] z^{-n}$$

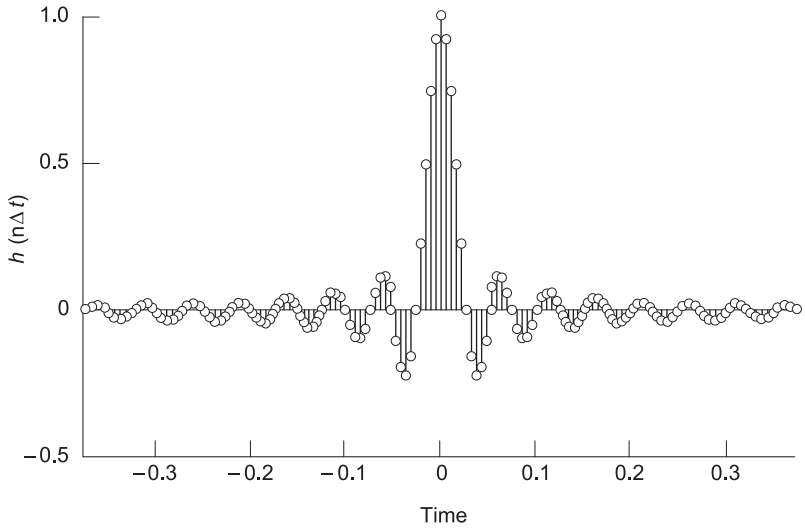


Figure 12 Ideal lowpass impulse response.

Next Page

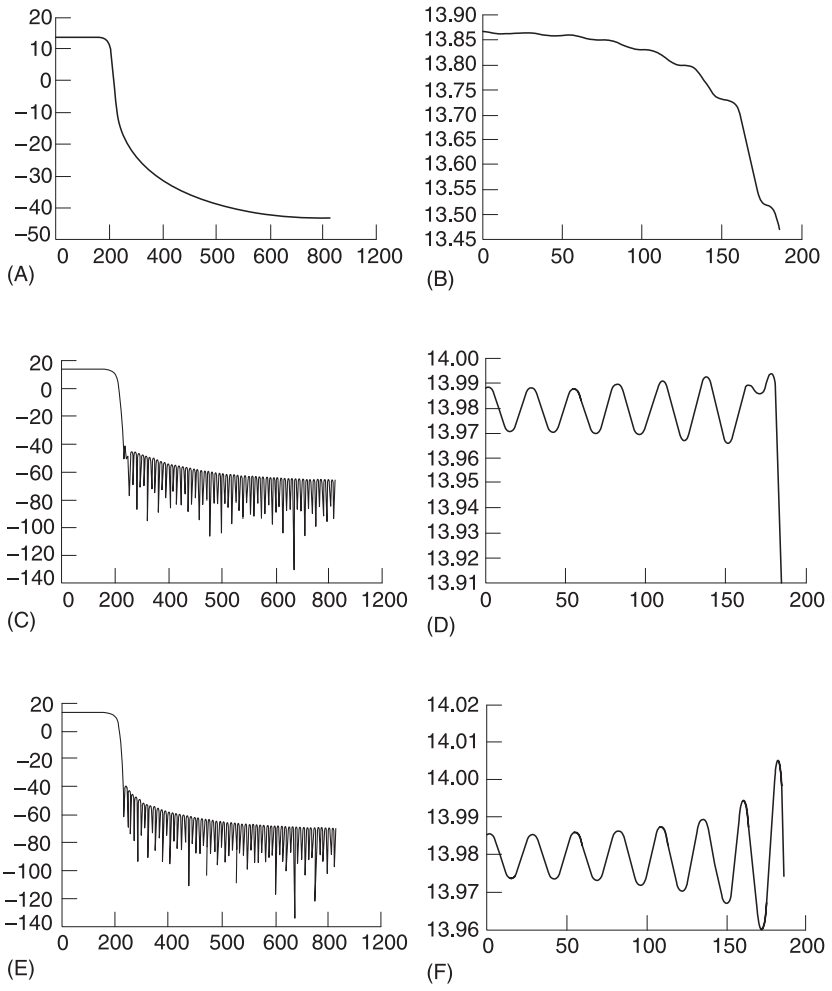


Figure 13 Examples of window technique. (A) Entire response of triangular window, (B) passband response of triangular window, (C) entire response of Hamming window, (D) passband response of Hamming window, (E) entire response of Kaiser window, (F) passband response of Kaiser window.

or

$$Y(z) = \frac{1}{2\pi \mathrm{j}} \oint_c U(\xi) \left[\sum_{n=0}^{\infty} w(n)\ (\xi^{-1}\ z)^{-n} \right] \frac{\mathrm{d}\xi}{\xi}$$

and hence

$$Y(z) = \frac{1}{2\pi \mathrm{j}} \oint_c U(\xi)\ W(z\xi^{-1})\ \frac{\mathrm{d}\xi}{\xi}$$

However, on the unit circle $\xi = \mathrm{e}^{\mathrm{j}\phi}$, $z = \mathrm{e}^{\mathrm{j}\theta}$ and $\theta = \omega \Delta t$, therefore in the frequency domain we can write:

$$Y(\mathrm{e}^{\mathrm{j}\theta}) = \frac{1}{2\pi} \int_{-\pi}^{\pi} U(\mathrm{e}^{\mathrm{j}\phi})\ W(\mathrm{e}^{\mathrm{j}(\theta-\phi)})\ \mathrm{d}\phi$$

This is a convolution relationship in the frequency domain, which can symbolically be written as:

$$Y = U * W$$

A bonus arising from the above is that if $u(n) = w(n) = x(n)$ and are all real signals and for $z = 1$ then:

$$\sum_{n=0}^{\infty} [x(n)]^2 = \frac{1}{2\pi \mathrm{j}} \oint_c |X(z)|^2 \frac{\mathrm{d}z}{z} = \frac{1}{2\pi} \int_{-\pi}^{\pi} \left|X(\mathrm{e}^{\mathrm{j}\theta})\right|^2 \mathrm{d}\theta$$

This is Parseval's relationship. (Actually it is much older than Parseval in that it dates from the nineteenth century from the works of Lord Rayleigh.)

It can now be seen that the use of a window would produce a reduction of the ripples or 'sidelobe levels'.

Previous Page

Let us consider the simple Hann window to appreciate this point, i.e.:

$$w(n) = 0.5 + 0.5\ \cos\ \left(\frac{2\pi n}{N-1}\right)$$

for:

$$-\frac{(N-1)}{2} \leq n \leq \frac{(N-1)}{2}$$

and 0 otherwise. Take this window to be formed as a product $w(n) = c(n)w_R(n)$ where $c(n)$ is an infinite duration version of $w(n)$ the spectrum of which is given by:

$$C(e^{j\theta}) = \pi\delta(\theta) + 0.5\pi\delta\left(\theta - \frac{2\pi}{N-1}\right) + 0.5\pi\delta\left(\theta + \frac{2\pi}{N-1}\right)$$

while $w_R(n)$ is the rectangular window of spectrum:

$$W_R(e^{j\theta}) = \sum_{n=-(N-1)/2}^{(N-1)/2} e^{-jn\theta} = \frac{\sin\ (N\theta/2)}{\sin\ (\theta/2)}$$

Since products in the time domain involve convolutions in the frequency domain we see that the delta functions will essentially replicate the spectrum of the rectangular window at the first zero-crossings. Hence the positive excursions in its response will approximately cancel the negative ones while extending somewhat the transition band. However, the window method is somewhat indirect in that it does not examine the specifications in the frequency domain. At any rate there is no direct control over the frequency domain performance. The 'frequency sampling method' is meant to provide such control at least at preselected frequency points.

Frequency Sampling Technique

Let $H(r)$ be the values of the transfer function $H(z)$ at the points $z_r = \exp(j\theta_r)$, $r = 0, 1, ..., N-1$. Assume that $H(z)$ is a general transfer function and hence of the form:

$$H(z) = \sum_{n=0}^{\infty} h(n)\ z^{-n}$$

If N values of z are available we can set up only N linear equations of the form:

$$H(r) = \sum_{n=0}^{\infty} h(n)\ z_r^{-n}, \quad r = 0,\ 1, ..., N-1$$

and hence only N terms of $\{h(n)\}$ can be determined. Hence the upper summation limit is $N-1$, i.e.:

$$H(r) = \sum_{n=0}^{N-1} h(n)\ z_r^{-n}, \quad r = 0,\ 1, ..., N-1$$

We can think of the problem as an interpolation and in terms of the Lagrange interpolation formula we have:

$$H(z) = \sum_{r=0}^{N-1} H(r) \prod_{\substack{i=0 \\ i\neq r}}^{N-1} \frac{(z^{-1} - z_i^{-1})}{(z_r^{-1} - z_i^{-1})}$$

Let:

$$C(z) = \prod_{i=0}^{N-1} (z^{-1} - z_i^{-1})$$

so that:

$$H(z) = C(z) \sum_{r=0}^{N-1} \frac{H(r)}{(z^{-1} - z_r^{-1})} \frac{1}{\prod_{\substack{i=0 \\ i\neq r}}^{N-1} (z_r^{-1} - z_i^{-1})}$$

This expression has a signal flow graph of the form given in **Figure 14** where:

$$C(z) = \prod_{i=0}^{N-1} (z^{-1} - z_i^{-1})$$

$$A(r) = H(r) \frac{1}{\prod_{\substack{i=0 \\ i\neq r}}^{N-1} (z_r^{-1} - z_i^{-1})}$$

If the points at which the required response values are chosen to be equidistant in frequency, i.e., if $z_i = \exp(i\theta_0)$, $\theta_0 = 2\pi/N$ and $i = 0, 1, 2, ..., N-1$, then z_i are the N roots of 1, and hence:

$$C(z) = \prod_{i=0}^{N-1} (z^{-1} - e^{-ji\theta_0}) = z^{-N} - 1$$

Moreover:

$$\prod_{\substack{i=0 \\ i\neq r}}^{N-1} (z_r^{-1} - z_i^{-1}) = \prod_{\substack{i=0 \\ i\neq r}}^{N-1} (z^{-1} - z_i)\big|_{z=z_r} = \frac{C(z)}{z^{-1} - z_r^{-1}}\bigg|_{z=z_r}$$

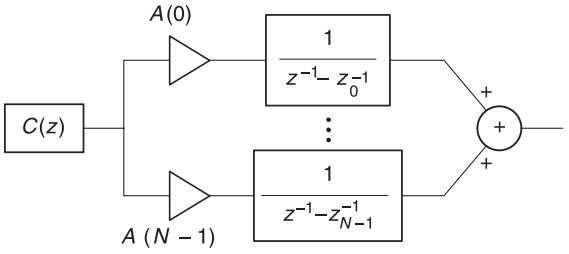


Figure 14 Signal flow graph.

which from the L'Hopital rule gives:

$$\left.\frac{Nz^{-(N-1)}}{1}\right|_{z=z_r} = Nz_r^{-(N-1)}$$

i.e.:

$$A(r) = H(r)\frac{z_r^{(N-1)}}{N}$$

Thus:

$$H(z) = \frac{z^{-N}-1}{N}\sum_{r=0}^{N-1} H(r)\, z_r^{(N-1)}\, \frac{1}{z^{-1}-z_r^{-1}}$$

and making use of $z_r^{(N-1)} = z_N^N z_r^{-1} = z_r^{-1}$ we obtain:

$$H(z) = \frac{1-z^{-N}}{N}\sum_{r=0}^{N-1} H(r)\, \frac{1}{1-z^{-1}z_r}$$

where $z_r = e^{j\pi r}$ and $\theta_r = (2\pi/N)r$.This is precisely the form one would obtain by means of discrete Fourier transforms. An example is shown in **Figure 15**. Frequency sampling technique with 128 samples, 32 of which are of unity value (lowpass) and 96 are set to zero value (the high frequency part). The phase is linear.

An important question is concerned with the estimation of the length N (i.e., the number of coefficients) of the impulse response. A simple empirical formula can be used for an approximate estimate as follows:

$$N = \frac{A}{20}\,\frac{f_s}{\Delta f}$$

where A is the discrimination in dB between the passband and stopband attenuation levels, Δf is the transition band between passband and stopband, and f_s is the sampling frequency. The last two quantities are in real frequencies.

However, the approach that can guarantee a performance within a set of prescribed specifications is based on the optimization of the amplitude response, in which the parameters of the optimization process are the filter coefficients. This becomes particularly straightforward in the linear phase case as all pertinent relationships are linear and hence guaranteed and unique optima are then available in the coefficient search space. A solution through the Remez exchange algorithm has been implemented with almost universal current use, with a Chebyshev or minimax objective function. The aim under this form of objective function is to design FIR filters in such a way that the maximum deviations of the frequency response from a set of prescribed specifications are minimized.

Minimax design From earlier considerations we can write the frequency (magnitude or amplitude) response as:

$$|H(\theta)| = P(\theta)\, Q(\theta)$$

where the various factors for the four cases, are indicated in **Table 2**. The phase response is given by $\phi(\theta) = ((N-1)/2)\theta$ in all four cases. With $D(\theta)$ as the desired response and $W(\theta)$ as a suitably chosen weighting function we can write the error expression as:

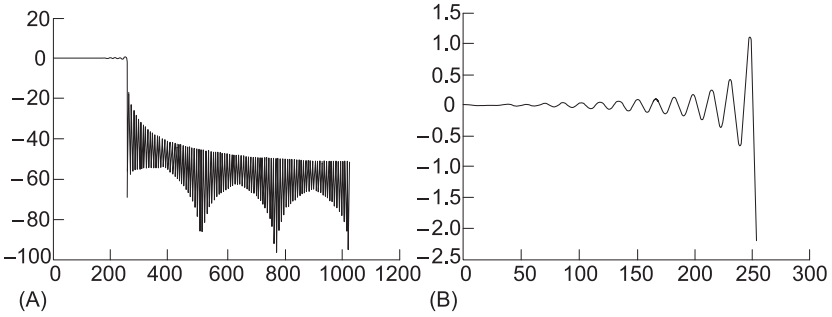


Figure 15 Frequency sampling technique. (A) Entire response, (B) passband response.

Table 2

Case	$Q(\theta)$	$P(\theta)$
1	1	$\sum \tilde{a}(n) \cos(n\theta)$
2	$\cos(\theta/2)$	$\sum \tilde{b}(n) \cos(n\theta)$
3	$\sin \omega\Delta t$	$\sum \tilde{c}(n) \cos(n\theta)$
4	$\sin(\theta/2)$	$\sum \tilde{d}(n) \cos(n\theta)$

$$E(\theta) = W(\theta)[D(\theta) - P(\theta)\, Q(\theta)]$$

or:

$$E(\theta) = W(\theta)Q(\theta)\left[\frac{D(\theta)}{Q(\theta)} - P(\theta)\right]$$

i.e.:

$$E(\theta) = W'(\theta)[D'(\theta) - P(\theta)]$$

The problem is then cast as in the optimization context, where we optimize:

$$\underset{\{h(n)\}}{\text{minimize}} \left\{ \underset{\theta \in \Theta}{\max} E(\theta) \right\}$$

The above is satisfied if and only if the error $E(\theta)$ has $(M+1)$ extremal values on $\Theta(M = (N-1)/2)$. Specifically, when the weighting function $W(\theta)$ is constant then the error is equiripple, i.e., at consecutive extremal frequencies we have $E(\theta_i) = -E(\theta_i + 1)$. The problem is linear and can be solved easily using several techniques by computer (e.g., linear programming, Remez exchange algorithm, etc.). **Figure 16** shows an example for an order 128 and normalized cutoff and transition frequencies of 0.25 and 0.3, respectively.

IIR Digital Filter Design Principles

The design of infinite impulse response (IIR) digital filter transfer functions can be approached from two different perspectives. The first assumes the existence of an analog filter transfer function and then seeks to transform this into a digital form via suitable transformations. The other approach involves no such assumptions and attempts to effect the design directly from the prescribed specifications.

IIR digital filter design from analog filters The fundamental assumption made here is that there is an analog filter, $H(s)$, that can meet the frequency domain filtering requirements, and we seek to transform this transfer function, $G(z)$, into a form appropriate for use in the discrete-time domain.

The problem has been approached from a range of points of view.

1. Matched z-transform assumes that the analogue transfer function is of the form:

$$H(s) = \frac{\sum_{i=0}^{n} (s + a_i)}{\sum_{i=0}^{m} (s + b_i)}$$

Then use is made of the fact that a typical factor $(s + \lambda)$ in the numerator or denominator would correspond, in the z-domain to a typical factor $(1 - z^{-1}e^{-\lambda\Delta t})$. This is so in order to keep the frequency domain correspondence equivalent (i.e., with $z = e^{sT}$ it can be seen that the z-domain factor would correspond to the same s-value as the s-domain factor).

Therefore a factor-by-factor replacement produces:

$$G(z) = \frac{\sum_{i=0}^{n} \left(1 - z^{-1}e^{-a_i\Delta t}\right)}{\sum_{i=0}^{m} \left(1 - z^{-1}e^{-b_i\Delta t}\right)}$$

Note, however, that the frequency response of $G(z)$ is assumed on the circumference of the unit circle and not along a straight line (i.e., the imaginary axis) as is the case for $H(s)$. Thus the retention of the finite poles and zeros achieved by this approach does not guarantee that the two filter transfer functions would have corresponding frequency responses. Observe, in addition, that the zeros at $\pm\infty$ of $H(s)$ are not mapped to $G(z)$ in the above equation and an additional factor for these is required of the form $(1 + z^{-1})^{m-n}$ known as the guard filter. Even with the incorporation of the guard filter, the correspondence between the analog and digital filter responses of $H(s)$ and $G(z)$ is tenuous. However, the correspondence improves for higher than normal sampling rates (i.e., with significant oversampling). An example is shown in **Figure 17**.

2. Invariant Impulse Response Method
In this approach the analog transfer function is expressed in the form:

$$H(s) = \sum_i \frac{A_i}{s + \beta_i}$$

where the parameters A_i, β_i are either real or are complex if they occur in complex conjugate pairs.

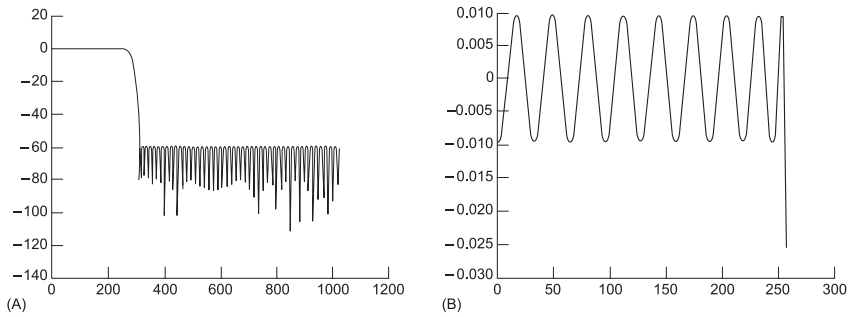


Figure 16 Minimax technique. (A) Entire response, (B) passband response.

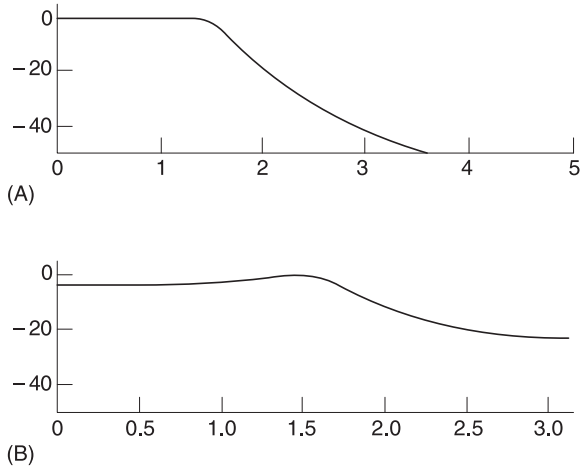


Figure 17 (A) Analog filter response. (B) Matched pole-zero filter response.

The impulse response of $H(s)$ is therefore given by $h(t) = \sum_i A_i e^{-\beta_i t}$. The next step is to sample $h(t)$ to obtain the impulse response $\{h(n\Delta t)\}$ of the corresponding digital filter, i.e., $h(n\Delta t) = \sum_i A_i e^{-\beta_i n\Delta t}$.

On taking the z-transform of this sampled impulse response we obtain the transfer function:

$$G(z) = \sum_i \frac{A_i}{1 - z^{-1}e^{-\beta_i \Delta t}}$$

This transfer function is taken to be the digital filter transfer function.

This approach is very simple to use, moreover $G(z)$ is stable when $H(s)$ is stable. However, there are problems with respect to aliasing or folding of the analog filter spectrum. In order to obtain reasonable responses we need to sample at rates, which are much higher that need be, as **Figure 18** shows.

An alternative concept in this range of techniques involves s-plane to z-plane transformations. The principle is as follows: obtain $G(z)$ from $H(s)$ by replacing the complex variable s by an appropriate function $f(z)$. A very simple solution, which is not entirely satisfactory, is to employ the so-called backward difference formula. Essentially from the complex variable domain, this formula can be seen as a first-order approximation of the correspondence between z and s. Let us write $z^{-1} = e^{-s\Delta t}$ and let us further expand the exponential in a Taylor series and retain the first two terms to obtain $z^{-1} = 1 - s\Delta t$. This can be rearranged to yield $s = (1 - z^{-1})/\Delta t$. However, in a transfer function $H(s)$ there are powers of s higher than the first, for which we use $s^n = \left[(1 - z^{-1})/\Delta t\right]^n$. A simple example is as follows. Let $H(s) = 1/(s + a)$. Then we obtain:

$$G(z) = \frac{1}{[(1 - z^{-1})/\Delta t] + a}$$

Figure 19 shows the two frequency responses. In order to appreciate the limitations of this approach let us re-express the relationship between the complex variables as follows:

$$z = \frac{1}{1 - s\Delta t}$$

In order to see whether or not we will always obtain stable digital filter transfer functions let us set $s\Delta t = \alpha + j\Omega$ so that:

$$|z| = \frac{1}{\sqrt{\left((1 - \alpha)^2 + \Omega^2\right)}}$$

It can be seen that whenever $\alpha<0$ then $|z|<1$, and hence the left-hand side of the s-plane maps to the inside of the unit circle. This means that we shall always obtain stable digital filter transfer functions from stable analog filter transfer functions.

The correspondence between the frequency responses is seen by writing:

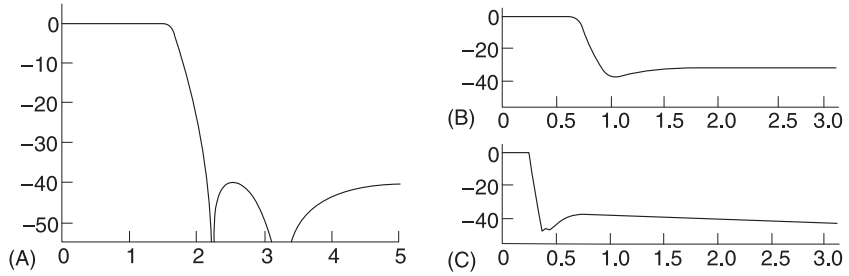


Figure 18 Different sampling frequencies. (A) Prototype analog filter response, (B) impulse invariance filter response oversampled $\times 1.5$, (C) impulsive invariance filter response oversampled $\times 4$.

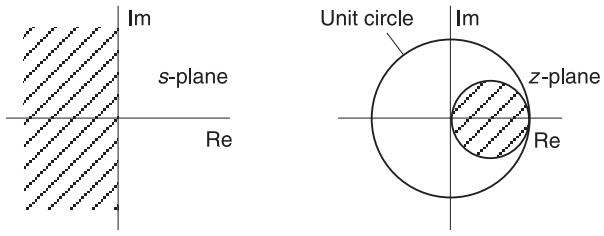


Figure 19 Frequency responses.

Table 3

$G(z)$	*Available* $H(s)$
Stable	Stable
Real and rational in z^{-1}	Real and rational in s
Order n	Order n
Lowpass cutoff Ω_c	Lowpass cutoff θ_c

$$z = \frac{1}{2}\left[1 + \frac{1 + s\Delta t}{1 - s\Delta t}\right]$$

so that when $s = \mathrm{j}\Omega$ it can be written as:

$$z = \frac{1}{2}\left[1 + \mathrm{e}^{\mathrm{j}2\tan^{-1}\Omega\Delta t}\right]$$

i.e., the complex variable z will be located on a circle of radius $1/2$ shifted by $1/2$ when the complex variable s is on the imaginary axis.

Forward difference: In a manner similar to that above we obtain $z = 1 + s\Delta t$. However, for $s = \alpha + \mathrm{j}\Omega$ it can be seen that $|z|>1$ and hence it leads to unstable transfer functions $G(z)$.

The method that is used extensively is the bilinear transform outlined below.

Bilinear transformation A simple way to derive the bilinear transformation is to view it as mapping between the two planes. In this sense let us begin with a table of properties and requirements of the transfer functions $G(z)$ and $H(s)$, respectively. The required transformation will operate as follows. To obtain $G(z)$ we shall replace s in $H(s)$ by a function $f(z)$. Hence in view of the relationships in **Table 3**, $f(z)$ must be a real and rational function in z and of order one. Hence we can write $f(z)$ as:

$$f(z) = \frac{az + b}{cz + d}$$

Now let us make it specific to a desired form of filtering. Let us assume that the given analog filter transfer function $H(s)$ is lowpass, and we need a lowpass digital filter transfer function $G(z)$. Under these requirements we have the following correspondence between points on the s-plane and on the z-plane. The point $s = 0$ is mapped onto the point $z = 1$ and hence $f(1) = 0$, i.e., $a + b = 0$. Further, the point $s = \pm\mathrm{j}\infty$ is mapped onto the point $z = -1$ yielding $f(-1) = \pm\mathrm{j}\infty$, i.e., $c - d = 0$. Thus we obtain:

$$f(z) = \left(\frac{a}{c}\right)\frac{z - 1}{z + 1}$$

The ratio (a/c) is fixed from the correspondence at one more point that can be taken to be the cutoff frequency $\theta_c = \omega_c\Delta t \leftrightarrow \Omega_c$ for $z = \mathrm{e}^{\mathrm{j}\theta}$ on C: $|z| = 1$. The transformation on the unit circle becomes:

$$f(z)|_c = \left(\frac{a}{c}\right)\mathrm{j}\tan\frac{\theta}{2}$$

and hence the cutoff frequency correspondence becomes:

$$\mathrm{j}\Omega_c = \left(\frac{a}{c}\right)\mathrm{j}\tan\frac{\theta_c}{2}$$

Therefore the bilinear transformation takes the form:

$$s = \left(\frac{\Omega_c}{\tan(\omega_c \Delta t/2)}\right)\frac{1-z^{-1}}{1+z^{-1}}$$

For stability considerations we write:

$$z = \frac{(1+s)A}{(1-s)A}A = \frac{\tan(\omega_c \Delta t/2)}{\Omega_c} > 0$$

and set $sA = \tilde{a} + j\tilde{\Omega}$. Then we have:

$$|z|^2 = \frac{(1+\tilde{\alpha})^2 + \tilde{\Omega}^2}{(1-\tilde{\alpha})^2 + \tilde{\Omega}^2}$$

i.e., the region outside the unit circle $|z|>1$ corresponds to $\tilde{\alpha}>0$ which is the right-hand half s-plane, the region inside the unit circle corresponds to $\tilde{\alpha}<0$ which is the left-hand half s-plane (where the poles of a stable $H(s)$ are located), and the circumference of the unit circle corresponds to $\tilde{\alpha} = 0$. Hence the stable region is mapped into a stable region (**Figure 20**). **Figure 21** shows aspects of the bilinear transformation.

It is possible to transform a given digital filter transfer function into others by using allpass transformations. Indeed, if the given digital filter transfer function is lowpass then **Table 4** gives the required transformations for the target filter transfer function. All frequencies are taken to be normalized, i.e., a typical value is given by $\theta = \omega\Delta t$ where ω is the angular frequency (in rad s^{-1}) and Δt is the sampling period (in s). Thus to transform a lowpass digital filter with cutoff frequency, β, to the target filter with the target requirements we must replace z^{-1} by the corresponding transformation. The response shown in **Figure 22A** is obtained by applying the bilinear transform to the analog filter response used earlier in the impulse invariance method. The response in **Figure 22B** is that of bandpass filter obtained by applying the lowpass to bandpass digital filter transformation. For a wider perspective the reader should consult the references given below.

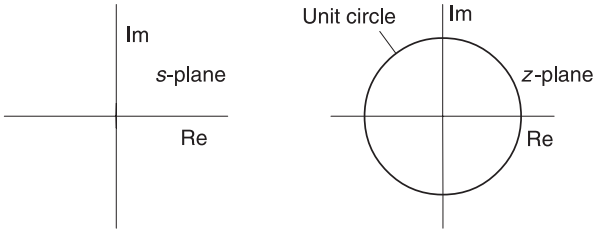


Figure 20 Stable regions.

Table 4

Target filter	*Transformation*	*Associated design formulas*
Lowpass cutoff θ_c	$\dfrac{z^{-1}-\alpha}{1-\alpha z^{-1}}$	$\alpha = \dfrac{\sin\left(\dfrac{\beta-\theta_c}{2}\right)}{\sin\left(\dfrac{\beta+\theta_c}{2}\right)}$
Highpass cutoff θ_c	$-\dfrac{z^{-1}-\alpha}{1+\alpha z^{-1}}$	$\alpha = -\dfrac{\cos\left(\dfrac{\beta-\theta_c}{2}\right)}{\cos\left(\dfrac{\beta+\theta_c}{2}\right)}$
Bandpass cutoff θ_1, θ_2 center θ_0	$-\dfrac{z^{-2}-\dfrac{2\alpha k}{k+1}z^{-1}+\dfrac{k-1}{k+1}}{\dfrac{k-1}{k+1}z^{-2}-\dfrac{2\alpha k}{k+1}z^{-1}+1}$	$\alpha = \cos\theta_0 = \dfrac{\cos\left(\dfrac{\theta_2+\theta_1}{2}\right)}{\cos\left(\dfrac{\theta_2-\theta_1}{2}\right)}$ $k = \cot\left(\dfrac{\theta_2-\theta_1}{2}\right)\tan\dfrac{\beta}{2}$
Bandstop cutoff θ_1, θ_2 center θ_0	$\dfrac{z^{-2}-\dfrac{2\alpha}{1-k}z^{-1}+\dfrac{1-k}{1+k}}{\dfrac{1-k}{1+k}z^{-2}-\dfrac{2\alpha}{1+k}z^{-1}+1}$	$\alpha = \cos\theta_0 = \dfrac{\cos\left(\dfrac{\theta_2+\theta_1}{2}\right)}{\cos\left(\dfrac{\theta_2-\theta_1}{2}\right)}$ $k = \tan\left(\dfrac{\theta_2-\theta_1}{2}\right)\tan\dfrac{\beta}{2}$

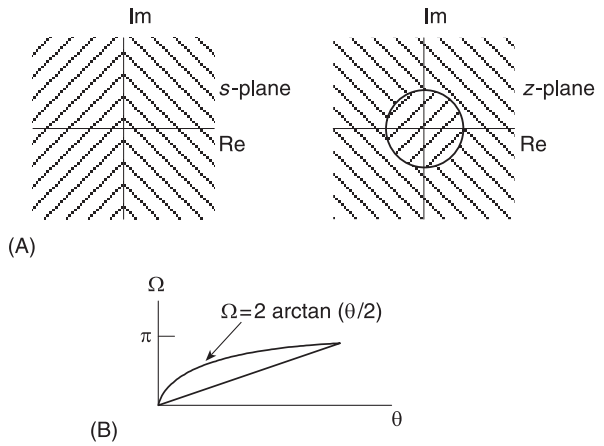


Figure 21 Bilinear transformation. (A) Correspondence in the regions on the two planes related to the bilinear transformation, i.e., the left-half of the *s*-plane maps to the inside of the unit circle in the *z*-plane and the right-half of the s-plane maps to the outside of the unit circle. (B) Nonlinear mapping between the continuous-time frequency variable Ω and the discrete-time normalized frequency variable $\theta = \omega\Delta t$.

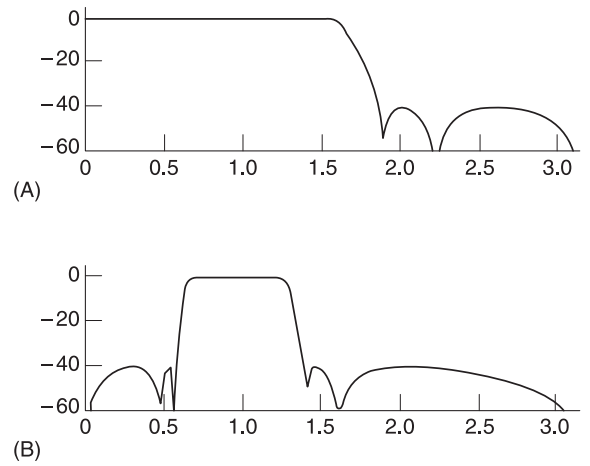


Figure 22 Digital filter response. (A) Lowpass; (B) bandpass.

See also: **Signal processing, model based methods**; **Spectral analysis, classical methods**; **Transform methods**; **Windows**.

Further Reading

Antoniou A (1982) Accelerated procedure for the design of equiripple non recursive digital filters. *IEE Proceedings, Pt C* 129: 1–10 (see *IEE Proceedings, Pt C* 129: 107 for errata).

Antoniou A (1993) *Digital Filters: Analysis, Design, and Applications*, 2nd edn. New York: McGraw Hill.

Constantinides AG (1970) Spectral transformations for digital filters. *IEE Proceedings* 117: 1585–1590.

Lim YC (1983) Efficient special purpose linear programming for FIR filter design. *IEEE Transactions on Acoustics, Speech and Signal Processing* ASSP-31: 96–98.

Lim YC, Constantinides AG (1979) New integer programming scheme for nonrecursive digital filter design. *Electronic Letters* 15: 812–813.

Lim YC, Parker SR, Constantinides AG (1982) Finite wordlength FIR filter design using integer programming over a discrete coefficient space. *IEEE Transactions Acoustics, Speech and Signal Processing* ASSP-30: 661–664.

McClellan JH, Parks TW, Rabiner LR (1973) A computer program for designing optimum FIR linear phase digital filters. *IEEE Transactions on Audio and Electroacoustics*, AU-21: 5–526.

Oppenheim AV, Schafer RW (1975) *Digital Signal Processing*. Englewood Cliffs, NJ: Prentice Hall.

Proakis JC, Manolakis DG (1992) *Digital Signal Processing Principles, Algorithms and Applications*, 2nd edn. New York: Macmillan.

Rabiner LR (1971) Techniques for designing finite duration impulse response digital filters. *IEEE Transactions on Communication Technology* COM-19: 188–195.

Rabiner LR, Gold B (1975) *Theory and Application of Digital Signal Processing*. Englewood Cliffs, NJ: Prentice Hall.

Regalia PA, Mitra SK, Vaidyanathan PP (1988) The digital all-pass filter: A versatile signal processing building block. *Proceedings of the IEEE* 76: 19–37.

DISCRETE ELEMENTS

S S Rao, University of Miami, Coral Gables, FL, USA

Copyright © 2001 Academic Press

doi:10.1006/rwvb.2001.0108

A vibrating system basically consists of three components or elements: a spring or elastic element that stores the potential energy; a mass or inertia element that stores the kinetic energy; and a damping element that dissipates the energy. The vibration of a system involves the transfer of its kinetic energy to potential energy and potential energy to kinetic energy, alternately. Thus, if the damper is absent, the system will undergo oscillations with constant amplitude in which the sum of potential and kinetic energies will remain constant. On the other hand, if the damper is present, energy must be supplied externally to sustain oscillations with constant amplitude.

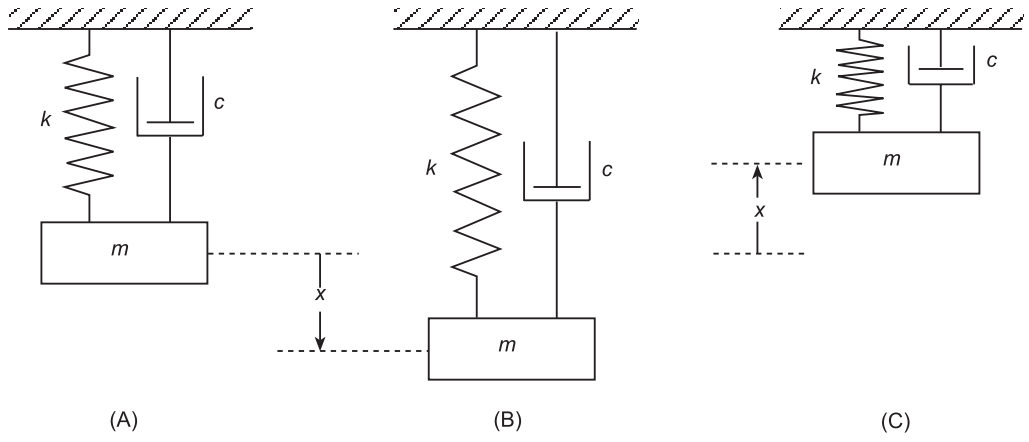


Figure 1 (A)–(C) A spring–mass–damper system.

As an example, consider the spring-mass-damper system shown in **Figure 1**, in which the mass oscillates in the vertical direction. **Figure 1A** denotes the mass in static equilibrium position. Let the mass be released after giving it an initial displacement x (downwards), as shown in **Figure 1B**. At this position, the mass will have a zero velocity and hence its kinetic energy will be zero. Also, at this position, the spring is stretched by an amount x; hence it will have a strain or potential energy. Since the spring force acts upwards, the mass starts moving upwards from the bottom-most position. When the mass reaches the static equilibrium position with $x = 0$, all the potential energy of the spring will have been converted into kinetic energy. As the mass has attained its maximum velocity (in the upward direction), the mass will not stop at this position; it will continue to move upwards until its velocity reduces to zero (**Figure 1C**). At the uppermost position, the kinetic energy will be zero but the strain or potential energy of the system will be maximum. Thus the kinetic energy has been converted into potential energy. Again, owing to the downward spring force, the mass starts to move downwards with progressively increasing velocity and passes the static equilibrium position again. At the static equilibrium position, the system will have maximum kinetic energy and zero potential energy. This process repeats and the the mass will have an oscillatory motion. In the absence of a damper, the oscillations continue forever. However, in the presence of a damper, the amplitude of oscillations gradually diminishes owing to dissipation of energy.

Torsional Systems

The vibration of a rigid body about an axis is known as rotational or torsional vibration. The basic elements of a rotational system are known as the torsional spring, mass moment of inertia, and torsional damper, analogous to the spring, mass, and damper of a translational or linear system.

Modeling of Discrete Elements

The basic elements of a vibratory system can be modeled as continuous (distributed) or discrete (lumped) elements. If the elements are continuous the governing equations will be partial differential equations, which are more difficult to solve. On the other hand, if the elements are discrete the governing equations will be ordinary differential equations, which are relatively easier to solve. Hence it is desirable to approximate the elements as discrete elements. Although there are no unified rules or guidelines available for modeling continuous elements as equivalent discrete ones, engineering intuition, energy balance, and equilibrium considerations can be used in most cases. In the modeling process, care must be taken to insure that the approximation process yields results that are reasonably accurate.

Mass or Inertia Elements

Although mass is distributed throughout a body, it can be considered as a lumped or point mass located at the center of mass of the body. Whenever a mass (m) undergoes acceleration ($\ddot{x}$), the force developed (F) is given by $F = m\ddot{x}$, according to Newton's second law of motion. The kinetic energy associated with a mass moving at a velocity v is given by $E = \frac{1}{2}mv^2$. Basically, three methods can be used to find the equivalent lumped mass of a body. These methods are based on using: (i) engineering intuition; (ii) equivalence of masses; and (iii) equivalence of kinetic energies. The engineering intuition method can be seen with reference to the multistorey building

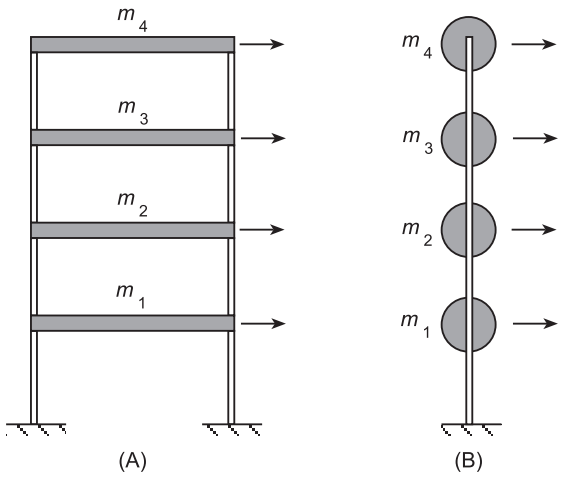


Figure 2 A multistorey building frame.

frame shown in **Figure 2A**. Usually the masses of columns can be neglected compared to the masses of the floors. Hence the masses of the floors can be assumed to be lumped masses, as shown in **Figure 2B**. The method of using equivalence of mass can be explained with reference to the connecting rod shown in **Figure 3A**. In an internal combustion engine, one end of the connecting rod (O_1) rotates while the other end (O_2) reciprocates. Thus, part of the mass of the connecting rod undergoes rotary motion while the remaining part undergoes reciprocating motion. The connecting rod can be replaced by two lumped or point masses m_1 and m_2, as shown in **Figure 3B**. The values of m_1 and m_2 can be determined using the conditions that: (i) the total mass must be the same for both systems; (ii) the center of mass must be the same for both systems; and (iii) the moment of inertia must be the same for both systems, which yield the relations:

$$m = m_1 + m_2 \qquad [1]$$

$$ml_2 = m_1(l_1 + l_2) \qquad [2]$$

$$I_0 = m_1 l_1^2 + m_2 l_2^2 \qquad [3]$$

where I_0 is the mass moment of inertia about the center of mass of the original connecting rod. Since m, I_0, and l_1 are usually known, eqns [1]–[3] can be solved to find the values of m_1, m_2, and l_2.

The use of equivalence of kinetic energy can be illustrated with reference to the bar under axial motion (**Figure 4A**). To determine the equivalent lumped mass M at the free end, we equate the kinetic energies of the two systems:

$$\frac{1}{2}Mv^2 = \frac{1}{2}\int_{x=0}^{1} \rho A\, \mathrm{d}x(\dot{x})^2 \qquad [4]$$

where A is the cross-sectional area and ρ is the density. Assuming that the velocity, $\dot{x}$, varies linearly from zero at the fixed end to v at the free end, eqn [4] can be evaluated to find:

$$\frac{1}{2}Mv^2 = \frac{1}{2}\int_{x=0}^{1} \left(\frac{xv}{l}\right)^2 \rho A\, \mathrm{d}x = \frac{1}{2}\frac{\rho A}{l^2}v^2\left(\frac{l^3}{3}\right) \qquad [5]$$

which gives the equivalent mass as:

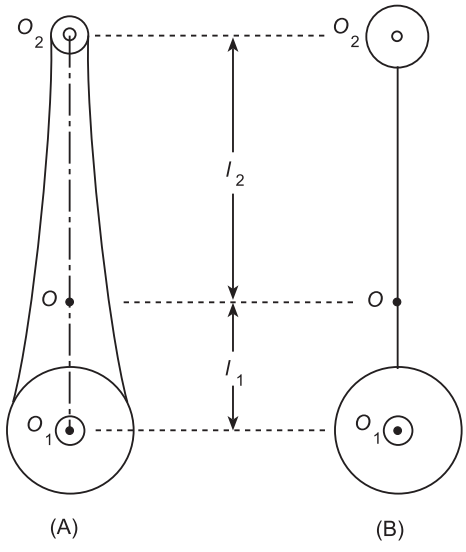


Figure 3 A connecting rod.

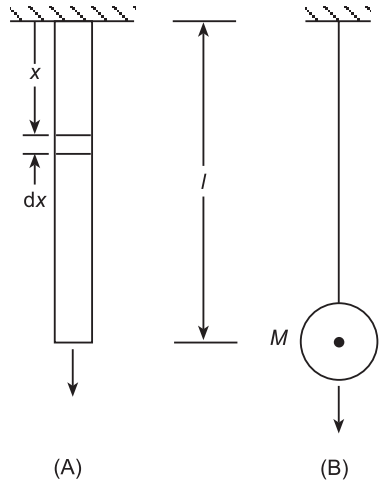


Figure 4 A bar under axial motion.

$$M = \frac{\rho A l}{3} = \frac{m}{3} \qquad [6]$$

where m denotes the mass of the bar. **Table 1** gives the equivalent masses of some typical mass or inertia elements.

Spring or Elastic Elements

A linear spring is a mechanical element that develops a force (F) proportional to the amount of deformation (x) it undergoes, as $F = kx$ where the constant of proportionality, k, is called the spring stiffness, spring constant, or spring rate. The force acts in a direction opposite to that of deformation. Helical springs and elastic members such as beams, plates, and rings can be considered as spring elements. For simplicity, a spring element is assumed to have no mass or damping. The energy stored in a linear spring due to a deformation x is given by the area under the force–deformation curve of **Figure 5A** as $E = \frac{1}{2}kx^2$. Although the force–deformation behavior of a linear spring is as shown in **Figure 5A**, most practical springs behave nonlinearly, as shown in **Figure 5B**. The nonlinear behavior is related to the nonlinear stress–strain curve exhibited by most elastic materials. A nonlinear spring can be approximated as a linear spring in the neighborhood of any specific deformation ($\tilde{x}^*$). For this, consider the Taylor series approximation of the spring force, $f(\tilde{x})$, about $\tilde{x}^*$:

$$f(\tilde{x}) = f(\tilde{x}^*) + \frac{\mathrm{d}f}{\mathrm{d}\tilde{x}}(\tilde{x}^*)(\tilde{x} - \tilde{x}^*) + \frac{1}{2}\frac{\mathrm{d}^2 f}{\mathrm{d}\tilde{x}^2}(\tilde{x}^*)(x - \tilde{x}^*)^2 + \ldots \qquad [7]$$

By neglecting terms involving higher derivatives of $f(\tilde{x})$, eqn [7] can be used to express the incremental force developed, $F = f(\tilde{x}) - f(\tilde{x}^*)$, for the net deformation, $x = \tilde{x} - \tilde{x}^*$, as $F = kx$ where $(k = \mathrm{d}f(\tilde{x}^*)/\mathrm{d}\tilde{x})$ can be considered as the spring stiffness (**Figure 5C**). The spring constants of some typical elastic elements are given in **Table 2**.

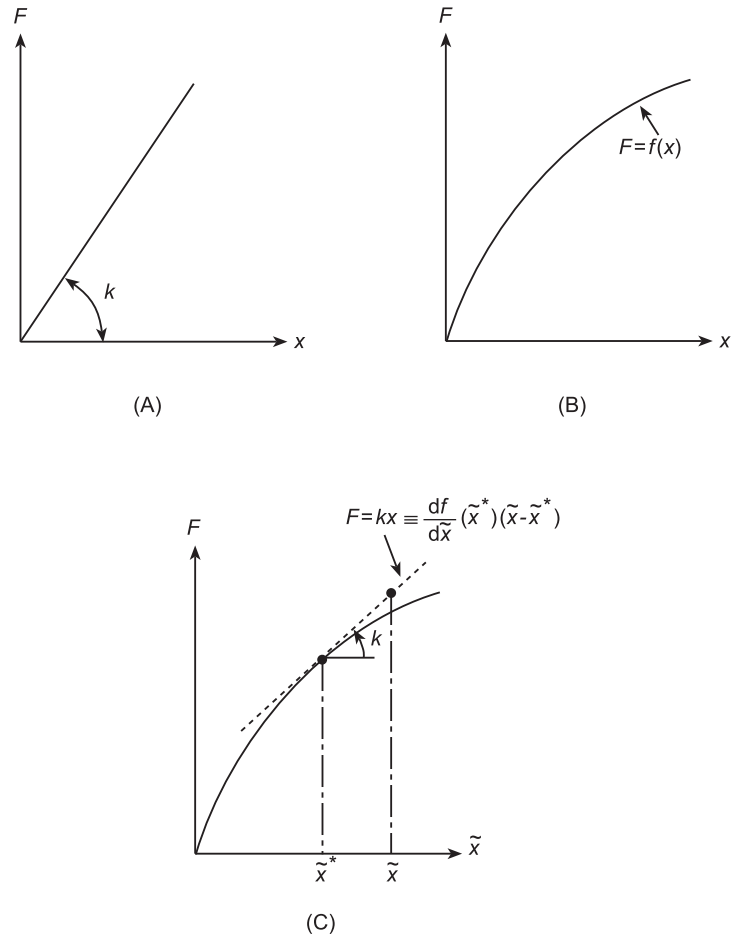


Figure 5 Force-deflection behavior of a spring element: (A) linear; (B) nonlinear, (C) linearization.

Table 1 Equivalent masses of typical mass/inertia elements

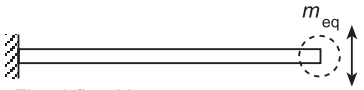
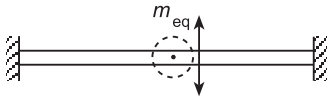
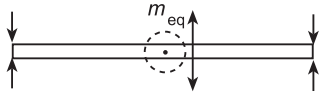
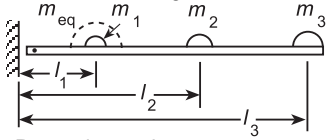
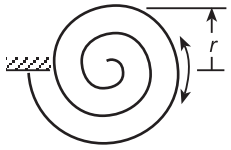
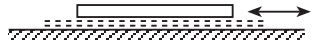
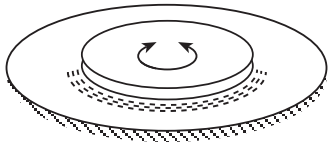
1. Cantilever beam 	$m_{eq} = \frac{m}{4}$ (m = mass of beam)
2. Fixed-fixed beam 	$m_{eq} = 0.375m$ (m = mass of beam)
3. Simply supported beam 	$m_{eq} = \frac{m}{2}$ (m = mass of beam)
4. Spring in axial motion 	$m_{eq} = \frac{m}{3}$ (m = mass of spring)
5. Masses on a hinged bar 	$m_{eq} = m_1 + \left(\frac{l_2}{l_1}\right)^2 m_2 + \left(\frac{l_3}{l_1}\right)^3 m^3$
6. Bar under torsion 	$J_{eq} = \frac{J}{3}$ (J = mass moment of inertia of beam)
7. Coil spring in torsion 	$J_{eq} = \frac{mr^2}{4}$ (m = mass of coil spring; r = outside radius)
8. Plate moving on fluid 	$m_{eq} = \frac{m}{3}$ (m = mass of fluid)
9. Piston moving in fluid 	$m_{eq} = \frac{m}{3}$ (m = mass of surrounding fluid)
10. Disk rotating on fluid 	$J_{eq} = \frac{J}{3}$ (J = mass moment of inertia of fluid)
11. Cylinder rotating in fluid 	$J_{eq} = \frac{J}{3}$ (J = mass moment of inertia of fluid)

Table 2 Spring constants of typical elastic elements

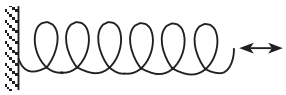
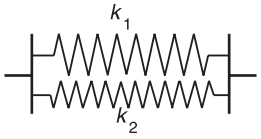
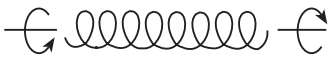
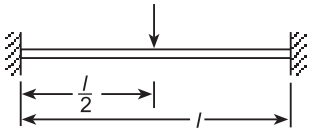
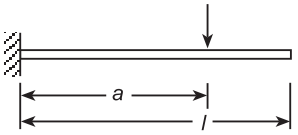
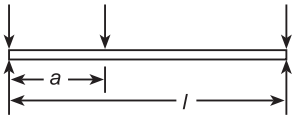
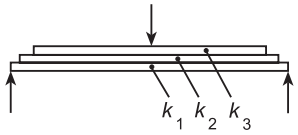
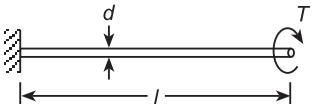
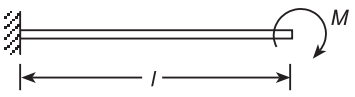
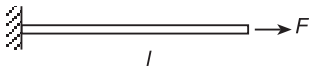
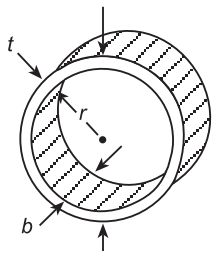
1. Spring in axial motion 	$k_{eq} = \dfrac{Gd^4}{8D^3N}$ d = wire diameter D = coil diameter G = shear modulus N = number of turns
2. Springs in series 	$k_{eq} = k_1 + k_2$
3. Springs in parallel 	$k_{eq} = \dfrac{1}{\dfrac{1}{k_1} + \dfrac{1}{k_2}}$
4. Spring in torsion 	$k_{eq} = \dfrac{Ed^4}{64DN}$
5. Fixed–fixed beam 	$k_{eq} = \dfrac{192EI}{l^3}$ E = Young's modulus I = area moment of inertia
6. Cantilever beam 	$k_{eq} = \dfrac{6EI}{a^2(3l - a)}$
7. Simply supported beam 	$k_{eq} = \dfrac{3EIl}{a^2(l - a)^2}$
8. Leaf spring 	$k_{eq} = \sum_i k_i$ k_i = spring constant of beam i
9. Bar under torsion 	$k_{t_{eq}} = \dfrac{\pi d^4 G}{32l}$ G = shear modulus
10. Cantilever beam under end moment 	$k_{eq} = \dfrac{2EI}{l^2}$
11. Bar under axial motion 	$k_{eq} = \dfrac{AE}{l}$ A = area of cross-section E = Young's modulus

Table 2 (continued)

12. Ring



$$k_{eq} = \frac{Ebt^3}{1.79r^3}$$

E = Young's modulus

13. Semicircular ring

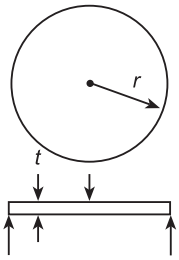


$$k_{eq} = \frac{2EI}{3\pi r^3}$$

E = Young's modulus

I = area moment of inertia

14. Simply supported circular plate



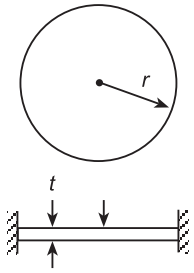
$$k_{eq} = \frac{16\pi D(1+v)}{r^2(3+v)}$$

v = Poisson's ratio

E = Young's modulus

$$D = \frac{Et^3}{12(1-v^2)}$$

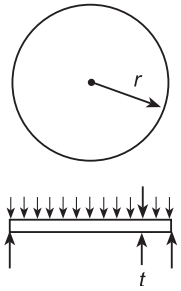
15. Clamped circular plate



$$k_{eq} = \frac{16\pi D}{r^2}$$

$$D = \frac{Et^3}{12(1-v^2)}$$

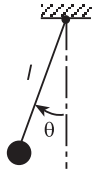
16. Simply supported circular plate



$$k_{eq} = \frac{64\pi D(1+v)}{r^2(5+v)}$$

$$D = \frac{Et^3}{12(1-v^2)}$$

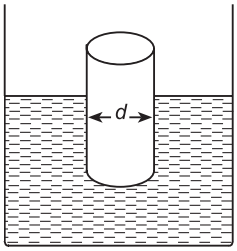
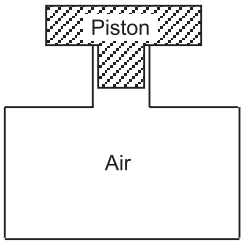
17. Simple pendulum



$$k_{eq} = \frac{mg}{l}$$

g = acceleration due to gravity

Table 2 (continued)

18. Cylinder floating in fluid 	$k_{eq} = \dfrac{\pi d^2 \gamma}{4}$ γ = unit weight of fluid
19. Piston moving in pressurized cylinder 	$k_{eq} = \dfrac{p\gamma A^2}{v}$ A = Cross-sectional area of piston v = volume of air p = pressure of air γ = adiabatic constant (1.4)

Damping Elements

A damping element is a mechanical member in which a force (F) is developed proportional to the rate of deformation ($\dot{x} = dx/dt$) it undergoes as $F = c\dot{x} = cv$, where $\dot{x} = dx/dt = v$ is the rate of change of deformation or velocity of the member and the constant of proportionality (c) is known as the damping constant. A damping element dissipates an energy (E) in time t given by:

$$E = \int_0^t Fv \, dt = \frac{1}{2} \int_0^t cv^2 \, dt \qquad [8]$$

For example, if the deformation of the damping element is simple harmonic with $x(t) = X \sin \omega t$, where X is the amplitude and ω is the angular frequency of simple harmonic motion, the energy dissipated in one cycle of motion ($t = 2\pi/\omega$) can be determined as $E = \pi c \omega X^2$. The damping constants of some representative dampers are given in **Table 3**. Although a damping element is usually assumed to be linear (**Figure 6A**) for simplicity, most practical dampers behave nonlinearly, as shown in **Figure 6B**. As in the case of a nonlinear spring, a nonlinear damper can be approximated as a linear damper around any specific rate of deformation or velocity using Taylor series approximation, as shown in **Figure 6C** with $F = cv$ where:

$$c = \frac{df}{d\tilde{v}}(\tilde{v}^*)(\tilde{v} - \tilde{v}^*) \qquad [9]$$

is the linear damping constant and $v = \tilde{v} - \tilde{v}^*$ is the net rate of deformation of the element.

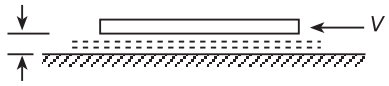
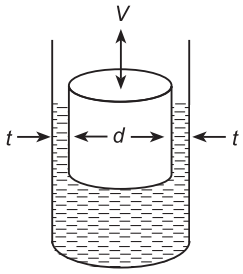
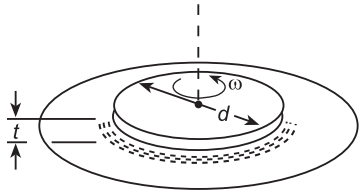
Types of Dampers

Depending on the mechanism assumed for energy dissipation, dampers can be classified as viscous, Coulomb or hysteretic dampers. In a viscous damper, the damping element is assumed to vibrate in a fluid medium such as air, water, or oil. During the motion of the element, the fluid offers resistance to the motion proportional to the shape and size of the element, the viscosity of the fluid and the velocity of motion. Viscous damping is the most commonly used damping model in practice. When two surfaces slide relative to one another, separated by a fluid, as in the case of the motion of a piston in a cylinder or the motion of a journal in a lubricated bearing, the viscous damping model can be used. When relative motion occurs between two surfaces with no or inadequate lubricant, the dry friction force developed between the surfaces causes damping. Hence this type of damping is also known as dry friction damping. In hysteretic damping, the friction developed between the internal planes of the body or structure during deformation is assumed to cause the dissipation of energy. Hence this type of damping is also known as structural, solid, or material damping.

Nomenclature

A	cross-sectional area
E	Young's modulus

Table 3 Damping constants of typical dampers

1. Plate moving on fluid 	$c_{eq} = \frac{\mu A}{t}$ A = surface area of plate μ = viscosity of fluid
2. Piston moving in a cylinder 	$c_{eq} = \frac{3\pi\mu d^3 l}{4t^3}\left(1 + \frac{2t}{d}\right)$
3. Disk rotating on a fluid 	$c_{t_{eq}} = \frac{\pi\mu d^4}{16t}$
4. Mass moving on a dry surface 	$c_{eq}7 = \frac{4\mu N}{\pi\omega X}$ μN = friction force ω = frequency X = amplitude of vibration

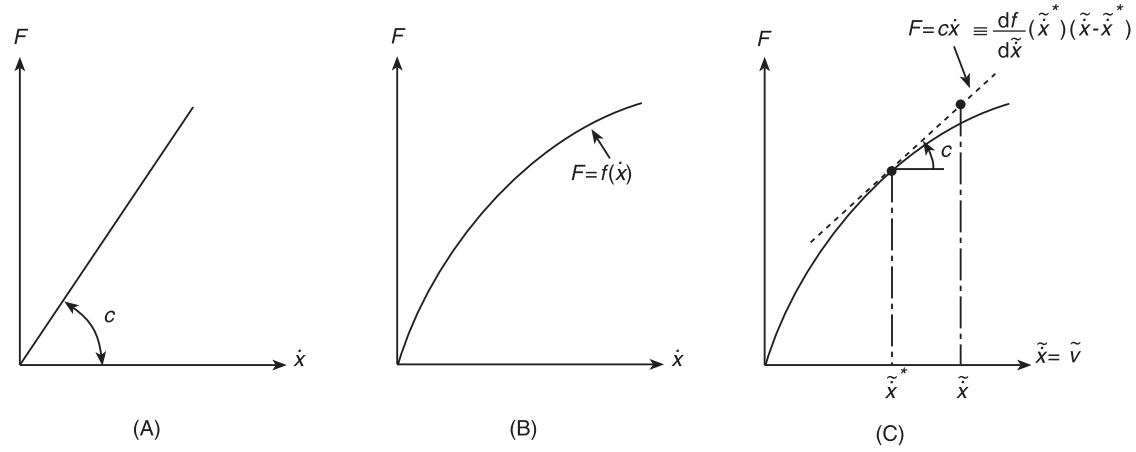


Figure 6 Force-velocity behavior of a damping element: (A) linear; (B) nonlinear; (C) linearization.

F	force
g	acceleration due to gravity
G	shear modulus
I	moment of inertia
I_0	mass moment of inertia
p	pressure of air
r	radius
v	volume of air
$\dot{x}$	velocity
$\ddot{x}$	acceleration
X	amplitude of vibration
γ	viscosity of fluid
μ	viscosity of fluid
ν	Poisson's ratio
ρ	density

See also: **Damping, active**; **Damping materials**; **Damping measurement**; **Dynamic stability**.

Further Reading

Cochin I (1980) *Analysis and Design of Dynamic Systems*. New York: Harper & Row.

Rao SS (1995) *Mechanical Vibrations*, 3rd edn. Massachusetts: Addison-Wesley.

DISKS

D J Ewins, Imperial College of Science, Technology and Medicine, London, UK

Copyright © 2001 Academic Press

doi:10.1006/rwvb.2001.0133

Introduction

Many engineering structures and machines that are prone to vibration problems contain components which can be described as 'disk-like'. Some of most common examples include:

- turbomachinery disks, including bladed disks
- gear wheels
- computer disks
- brake disks
- circular saws
- railway and other vehicle wheels
- internal baffles in chemical plants.

Although these applications are quite disparate, the relevant disk-like components all share a very well-defined set of vibration characteristics which are closely related to the vibration properties of a 'simple' disk. A 'simple' disk is defined as one which is truly axisymmetric and has a uniform (constant thickness) radial cross-section (see **Figure 1A**). It is a relatively simple matter to extrapolate from these simple-disk vibration characteristics to those of quite complex engineering disk-like structures. Consequently, it is of value to describe the vibration properties of a simple disk in some detail.

Types of 'Disk'

First, it is necessary to define more precisely the three different classes of 'disk' that are included in this article. The first of these, the 'basic' disk is a structure which is completely axisymmetric in its form and whose geometry is fully described by the two-dimensional profile of a radial cross-section (**Figure 1B**). This is the case for computer disk and most (but not all) vehicle wheels and brake disks. The second category includes the more common disk-like structure which is cyclically symmetric (or periodic) in that its geometry is defined by a sector (rather than a simple radial section) which is repeated an integer number of times in a circumferential direction (**Figure 1C**). This is the case for gear wheels, bladed disks and even, strictly speaking, circular saws. This classification also applies to wheels that have a series of holes, or scallops arranged in a circumferential pattern. Finally, there is a third category of disk which has no exact symmetry at all, and this applies to any disk which is 'mistuned', a situation which arises when there is an irregularity in the geometry, either because of damage or simply because of manufacturing tolerances (**Figure 1D**). Also, there are occasions when a disk-like structure is deliberately mistuned (or 'detuned') and made non-symmetric for a specific purpose or reason.

Modes of Vibration: Axisymmetric Disks

Figure 2 shows the essential features and notation used to describe the out-of-plane flexural vibration of a 'basic' disk. The governing equation of motion for such a plate-like structure can be simply expressed as a partial differential equation:

$$\nabla^4 w + k^4 \frac{\partial^2 w}{\partial t^2} = 0 \qquad [1]$$

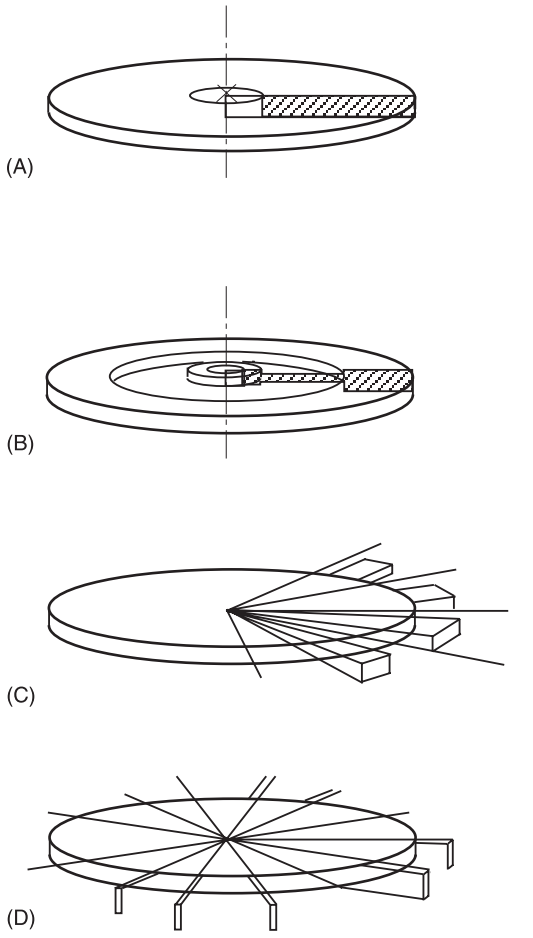


Figure 1 Basic form of disk-like structures. (A) Basic disk, (B) simple disk, (C) periodic disk, and (D) asymmetric disk.

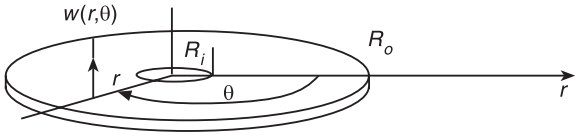


Figure 2 Essential features for disk vibration studies.

Of course, this structure, as all others, can be approximated by a discrete, finite element, type of model and for that case the governing equation of motion is the standard second-order differential matrix equation:

$$\mathbf{M}\ddot{\mathbf{x}} + \mathbf{K}\mathbf{x} = \mathbf{f}$$

The exact solution of the earlier partial differential equation (eqn [1]) is quite straightforward in the case of a simple (uniform thickness) disk and because of the relevance of the properties of this reference configuration, it is worth reporting and studying that solution, not least because it helps to check the validity of results obtained when using the conventional finite element (FE) approach in a more 'black-box' analysis.

Solution of the equation of motion for free vibration of a simple disk reveals a number of natural frequencies which occur in two types: some as single roots, or eigenvalues, and others (the majority) as double roots – pairs of modes with identical natural frequencies. The general expression for the transverse deflection, w, when the disk is vibrating in mode j is:

$$w_j(r, \theta, t) = \phi_j(r, \theta)e^{i\omega t}$$
$$\phi_j(r, \theta) = f_j(r)g_j(\theta)$$

where

$$f_j(r) = a_0 + a_1 r + a_2 r^2 + \cdots$$
$$g_j(\theta) = \cos\ n(\theta + \alpha)$$

For the special case of $n = 0$, these modes are single modes, there being just one mode with the specific natural frequency and a mode shape described by:

$$\phi_j(r, \theta) = f_j(r)$$

For all other values of n, the modes exist in pairs with mode shapes of the general form:

$$\phi j(r, \theta) = f_q(r) \cos n(\theta + \alpha)$$
$$\phi k(r, \theta) = f_q(r) \sin n(\theta + \alpha)$$

Thus, the 'typical' modal solution of vibration of a simple disk is a pair of modes, or a double mode, comprising two modes with the same natural frequency, usually denoted as $\omega_{n,s}$, which have the same radial profile and the same circumferential mode shape profile ($\cos n\theta$) but with angular orientations which differ by 90°. These circumferential variations of deflection can be seen to represent motion on the disk which create patterns of n nodal diameter (ND) lines on its surface, lying symmetrically and antisymmetrically disposed about a diameter at $\theta = \alpha$ to the origin. For obvious reasons, these modes are referred to as 'n ND modes' and a typical example is illustrated in **Figure 3A**. A feature of these modes that sometimes adds confusion is that, as the two modes of a pair have identical natural frequencies, then any combination of the stated mode shapes is also a valid mode shape. This means that any combination of a $\cos n(\theta + \alpha)$ deflection pattern and a $\sin n(\theta + \alpha)$ deflection pattern is also a valid mode shape. In practice, this means that the nodal diameters can lie

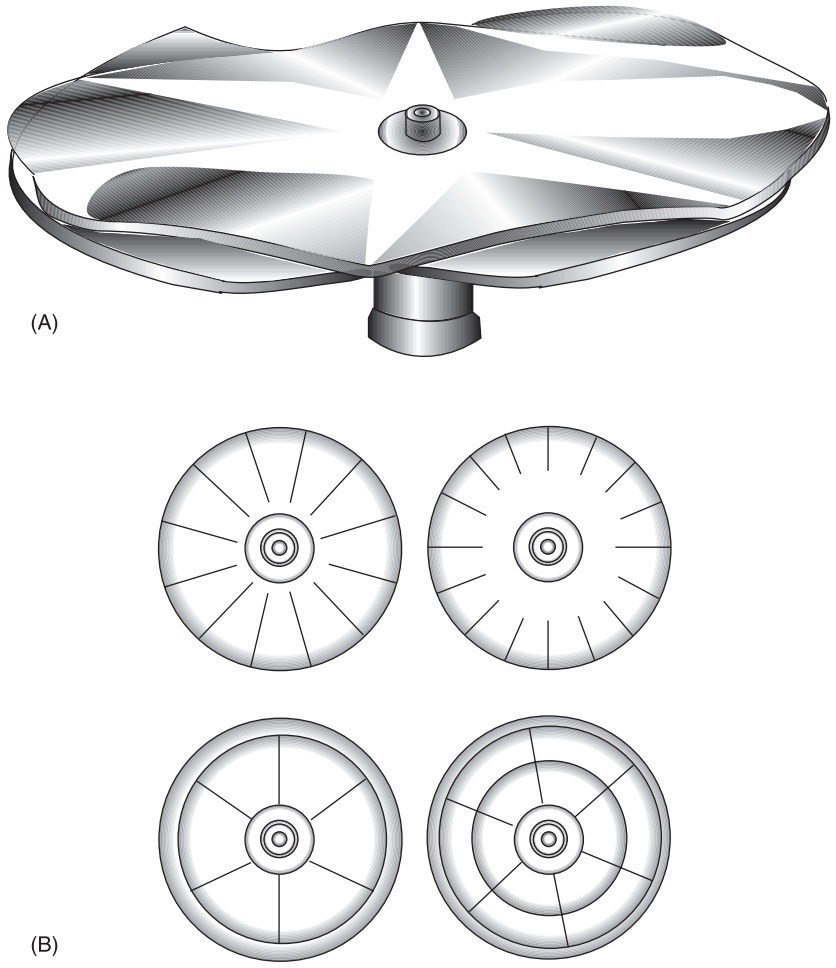


Figure 3 Typical mode shapes of a simple disk. (A) View of 3 ND mode; (B) nodal line diagrams for modes: 2, 0; 3,1; 0,1.

at any angular position, so that their orientation is 'arbitrary'.

In addition to this clear nodal diameter feature, it can be seen that there is a second element in the mode shape definition in the form of the particular solution for the radial displacement pattern, indicated by $f_q(r)$, defined from $r = R_I$ (the inner radius of the disk) to $r = R_O$, the outer radius. This function can be considered as a polynomial which will have a number, $s\,(s = 0, 1, 2, \ldots)$, of zero values, each of which indicates a radius at which there is zero amplitude of vibration. These radial nodes represent nodal circles which, when combined with the number of nodal diameters, describe the specific mode in full – mode$_{n,\,s}$ has a natural frequency of $\omega_{n,\,s}$ and a mode shape described by n nodal diameters and s nodal circles. **Figure 3B** illustrates a number of typical modes of this general type.

It is customary to display the essential modal properties of a disk-like structure by plotting the natural frequencies of the disk against the number of nodal diameters in the mode shape, and to show 'families' of modes according to the number of nodal circles: first family, modes with 0 nodal circles; second family, modes with 1 nodal circle, . . . etc. **Figure 4** shows the data for the specific case of a uniform-thickness continuous (no central hole) disk with fixed–free boundary conditions (the disk center constrained). The corresponding diagram for a disk of arbitrary cross-section will depend on the details of that profile but the general format will be the same as those shown in **Figure 3**, and the actual distribution of modal frequencies will follow the illustrated form quite closely.

It is worth mentioning two special cases amongst this array of modes. These are the modes with 0 ND, and those with 1 ND. We have already noted that modes with 0 ND are single modes which do not have the double-mode characteristic that all others have. Motion in a 0 ND mode necessarily involves

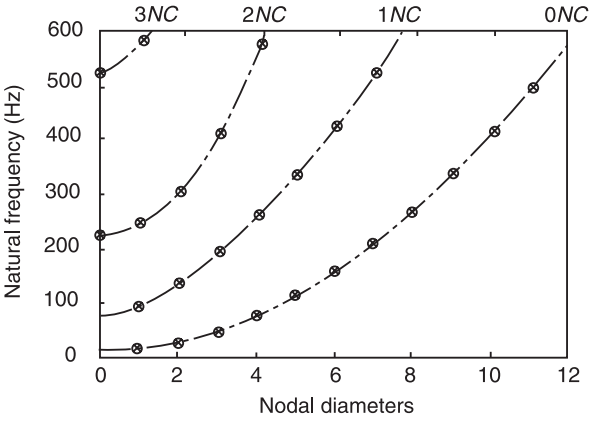


Figure 4 Natural frequencies of simple disks. Fixed (at disk center)–free boundary conditions.

movement at the center of the disk (it is not 'balanced' at the disk center) and, as a result, it involves whole-body motion of the disk, either axially or torsionally. Similarly, modes with 1 nodal diameter, while occurring in double-mode pairs, also involve motion of the disk center by virtue of their rotation about a diameter or motion along a diameter. All other modes, with 2 ND and above, share the property that they are in equilibrium at the disk center at all times. The particular consequence of the special features associated with these particular 0 and 1 ND modes is that their properties are influenced by the characteristics of the shaft and its bearings upon which the disk is mounted. Conversely, the modal properties of all modes with two or more nodal diameters, are not influenced by the shaft. We shall see later how this feature affects vibration in operating conditions.

Modes of Vibration: Cyclically Symmetric (Periodic) Disks

In many practical applications, the actual 'disk' will have a number of appendages attached to its rim, or its surface, such as gear or saw teeth, blades or vanes, and this class of disk is described as a 'cyclically symmetric' disk, differing slightly from the plain or 'simple' disk by the fact that the radial profile is no longer defined by a single cross-section. Instead, it is necessary to define the details of a sector of the disk, that being the portion of the complete 'disk' that encompasses one appendage, or period of the structure (**Figure 1C**).

For these periodic disk-like structures, no simple equation of motion, or closed-form solution, is available for the modal properties. However, we may use the features described in the preceding section for simple disks to anticipate and to understand the essential features that are found in these periodic structures.

First, it is convenient to classify and to describe the vibration modes of a periodic disk-like structure using the same notation as was used above: namely, to refer to each mode of vibration as having n nodal diameters and s nodal circles. However, if we look closely at the details of the mode shapes of these components, we find that the circumferential variation in deflection no longer displays a simple n ND pattern but, rather, comprises a series of sinusoidal components with a circumferential function of the form: $g_j(\theta) = \sum \cos q(\theta + \alpha) \sin \omega t$ where the summation over q includes the following terms: n, $N - n$; $N + n$; $2N - n$; $2N + n$; ;... and where N is the number of teeth/blades/vanes. In any one mode, it is common for one of these components to dominate and this feature leads to the justifiable use of the n ND label, even though it is a simplification. Thus there is a second grouping of the modes for this class of disk; the typical example being the group of modes which all contain the 'n ND set of diametral components'. Thus within one nodal circle family (i.e., all those modes which all have s nodal circles) there are subfamilies or groups: the modes with $1, N - 1, N + 1, 2N - 1, 2N + 1, \ldots,$ ND components being one such group; the modes with $2, N - 2, N + 2, 2N - 2, 2N + 2, \ldots,$ ND being a second group, and so on.

On a practical point: it is common practice to describe the circumferential mode shape of a disk or a bladed disk by defining the deflections at a series of P regularly spaced points around a given circumference. When this type of mode shape description is adopted, it is possible to convert such a list of amplitudes into (nodal) diametral components by performing a discrete Fourier transform on them. It will be appreciated that such a set of diametral components is restricted to contain just $P/2$ terms (higher terms are inaccessible because of aliassing). In the case of a periodic disk-like structure such as a bladed disk, it is natural to choose the number of circumferential measurement points to be equal to the number of blades, so that $P = N$. The ND description of any mode shape described in this discrete way is necessarily limited to terms up to and including $N/2$, so that components of, for example, $(N - 1)$, $(N + 1)$ cannot be included explicitly. In turn, this means that a mode which is predominantly an $(N - n)$ ND shape would register in a description based on an analysis of amplitudes shown at N regularly-spaced points around the disk as an n ND mode (see **Figure 5** for a simplified illustration).

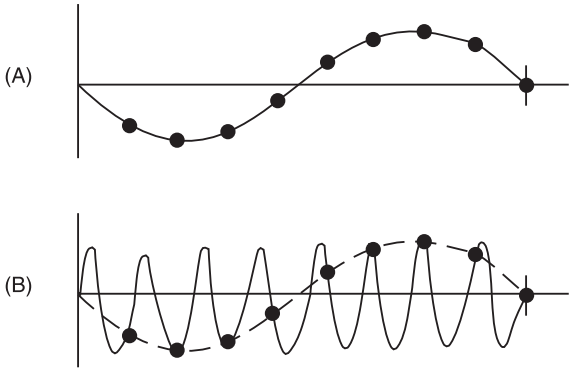


Figure 5 (A, B) Possible misinterpretation of mode shapes using discrete description.

A typical plot of the natural frequencies of a bladed disk is given in **Figure 6**, showing the presentations both when (a) the dominant ND component is used to classify the mode and (b) when the description is assumed to be limited to N discrete points around the rim (so that $N/2$ is the highest number of ND possible). In either presentation, both the similarities and the differences between these properties and those of the plain disk are clear and understandable.

It should be noted that, with just one exception, the modes of periodic disk-like structures share most of the properties of the simple disk. In particular, the 1 and higher ND modes occur in pairs: double modes with identical natural frequencies and mode shapes which are oriented orthogonally to each other so that the actual positioning of the nodal diameter lines is arbitrary. The exception is the family of modes with $N/2$ NDs: these now take the same form as modes with 0 ND and exist as single modes, rather than double modes, and have no arbitrariness in the location of the nodal lines.

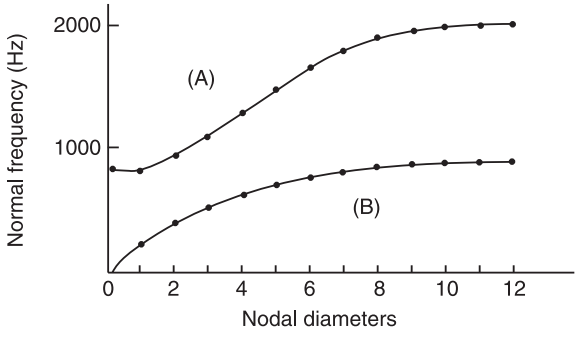


Figure 6 Natural frequency vs ND plots for cyclically symmetric (periodic) disk-like structure (bladed disk). (A) Full range of ND components; (B) restricted range of ND components (applicable to discrete mode shape descriptions).

Modes of Vibration: Asymmetric Disks

This last category of disks is intended to include those cases where, for some reason, deliberate or accidental, the disk possesses neither axisymmetry nor cyclic symmetry. This situation can arise for several reasons: the most common is the inevitable consequence of manufacturing tolerances which mean that real disks or bladed disks do not quite attain their intended symmetry and are 'mistuned' as a result. It is a well-documented fact that even a very slight loss of symmetry can have a dramatic effect on the vibration properties of disk-like structures and so it is appropriate to include a reasonable discussion of this phenomenon here. A similar end result occurs when a disk is designed to have an in-built asymmetry, such as occurs with a single hole, or other protuberance, as part of its design function, or when a deliberate break in symmetry is introduced, 'detuning', in order to take advantage of the particular features of the modified vibration properties that we shall outline below (for example, some unstable aeroelastic phenomena can be positively affected by such a loss of symmetry).

There is a marked sensitivity in some of the vibration properties of a disk to small changes in the structural details, such as mass or stiffness distributions, partly because of the existence of double modes. Mathematically, it can be shown that a small perturbation in mass or stiffness brings about a correspondingly small change in modal properties, except in cases of close modes (modes with close natural frequencies), which is exactly the situation that prevails here, especially in the cyclically symmetric case where we have not only double modes, but clusters of these double modes in certain well-defined frequency ranges.

The essential changes in the modal properties which result from a loss of symmetry in the disk (for whatever reason) are that the double modes split into pairs of distinct modes with close natural frequencies and mode shapes that are only slightly different from the original n–ND form but each of which, importantly, now have an angular orientation which is fixed relative to the disk reference (recall here that for a symmetrical disk, the double mode property means that nodal diameters can lie at any angular orientation). This result is illustrated in **Figure 7A**.

The above-mentioned pattern of behavior applies to all double modes of the disk. However, a further complication arises when two pairs of (double) modes are themselves 'close'. For example, in many bladed disk structures, we may find that the natural frequency of, say, an 8 ND mode might be at 234 Hz, while that of the 9 ND mode is at 245 Hz, etc. If, in such a case, some asymmetry or mistuning

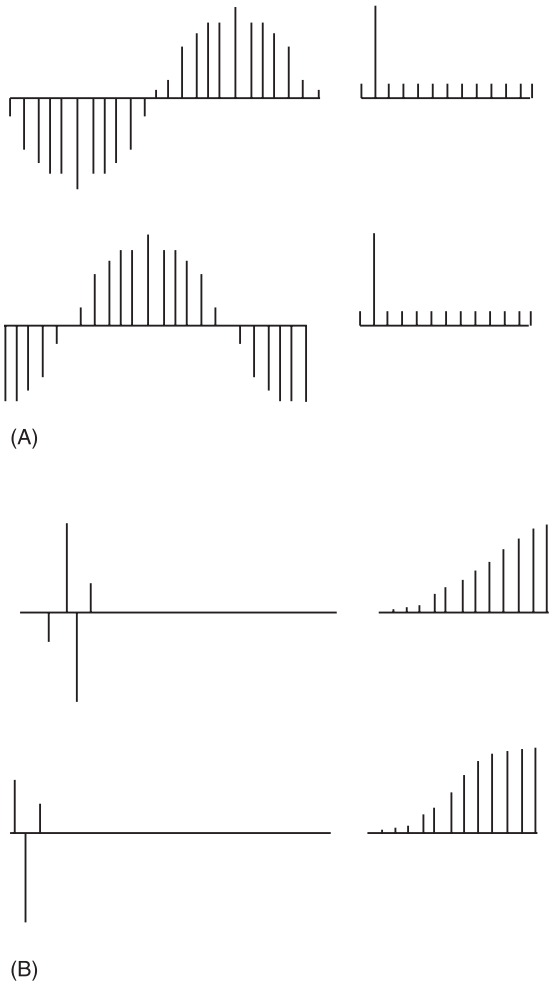


Figure 7 Sketches of mode shapes for asymmetric (mistuned) disk-like structure. (A) separated double modes of symmetric system; (B) close double modes in symmetric system.

is introduced, then the pair of 8 ND modes will split and form two distinct modes with natural frequencies at, for example, 229 Hz and 239 Hz, and at the same time the pair of 9 ND modes might slit into two modes with, say 240 Hz and 250 Hz. In such a situation, we find that the upper of the 8 ND modes of the mistuned disk (at 239 Hz) is almost at the same natural frequency of the lower of the pair of 9 ND modes (240 Hz) and this effect creates a considerable distortion in the shapes of the proximate modes, resulting in vibration modes that can no longer be described or classified as having a simple n ND form. **Figure 7B** illustrates such a situation in comparison with that which applies when the adjacent modes of the symmetric system are not close.

Modes of Vibration: Rotating Disks

It is clear from the list of examples cited at the beginning of the article that many of the disks encountered in practice will rotate and so it is appropriate to extend the discussion to include the additional features that apply in theses conditions. There are essentially two features to describe: first, the effects on the modal properties of the forces which apply under rotating conditions (mainly, those arising from centrifugal and gyroscopic effects); and secondly, the implications of the introduction of a second frame of reference which means that vibration experienced (in a rotating disk) and observed (by a stationary observer) appear to occur at different frequencies.

If we consider first the implications of centrifugal and gyroscopic (Coriolis) effects, we find that the former may cause the disk to experience and exhibit an increase in effective stiffness so that some natural frequencies may rise under rotation. The extent of this effect is generally quite small, except for very high speeds. However, there is one class of disk-like structure in which the centrifugal effect can be very pronounced, and that is the bladed disk, especially when the blades are relatively large and flexible. It is not uncommon in these structures, typically of the front stages of aircraft engine fans, for the natural frequencies of the lowest modes of the bladed disk assembly to increase to double the values which apply at rest.

The gyroscopic effects, on the other hand, apply directly to disks and to wheels, and are frequently significant factors in determining the natural frequencies of disks installed on rotors where the primary rotor dynamics properties are intimately linked with the 0 and 1 ND modes of the disk(s) which are installed. In situations where a disk is free to move about one of its diameters, incurring a 'rocking' motion, while it is rotating about its principle axis, Coriolis accelerations are generated which, in turn, cause the so-called gyroscopic forces that result in a sharp change in the vibration properties of the rotor disk system. The essence of these properties may be illustrated by reference to **Figure 8A** which shows a simple disk–rotor system, which is assumed to be free to vibrate in the two transverse directions illustrated, at the same time as spinning about its own axis. The vibration modes of this system at rest are simple: one mode where the disk moves in the horizontal (x) direction, and the other where it moves in the vertical (y) direction. Each of these modes has a distinct natural frequency according to the two stiffnesses, k_x and k_y. When the rotor spins, these two modes change quite significantly to one mode with a lower natural frequency than either of the two at-rest modes and a mode shape which is a backward-traveling orbit, plus a second mode with a higher natural frequency than either of those at rest and a mode

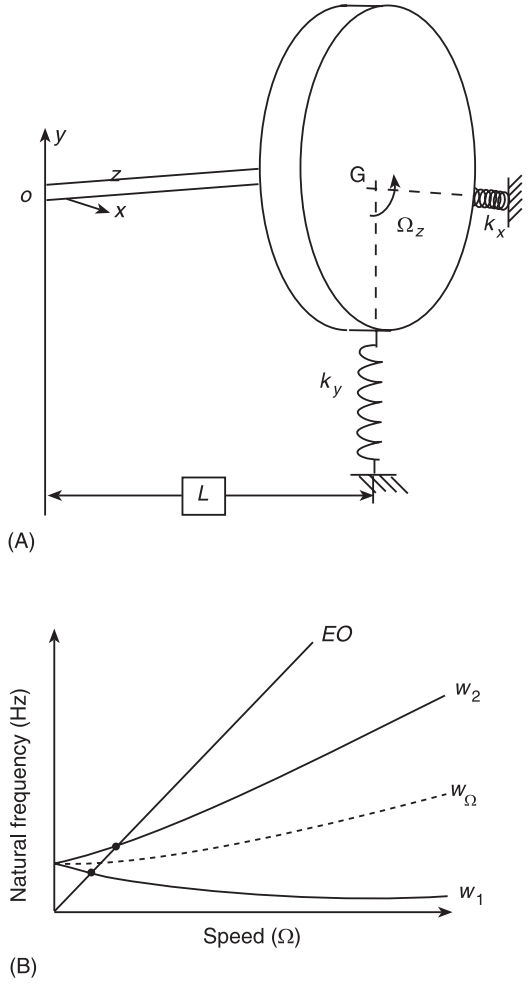


Figure 8 (A, B) Natural frequencies of a rotating disk under the influence of gyroscopic effects.

shape which is a forward-traveling orbit. The pattern of natural frequencies is shown in **Figure 8B** and this simple example serves to illustrate a phenomenon which is widely encountered in many installations of rotating disks.

Turning to the matter of frames of reference, it can be seen that if a disk is rotating (at speed Ω) at the same time as it is vibrating (at frequency ω_R, as sensed by a transducer fixed to the disk), then this vibration will be observed by a stationary transducer to be occurring at a different frequency, ω_S. In fact, the frequency that is detected by a stationary observer (such as a microphone, or noncontacting motion transducer) is found to be related to the actual frequency of vibration, the speed of rotation, and the number of nodal diameters of the deflection pattern of the vibration. The vibration frequency detected by a stationary observer, ω_S, can be related to the actual vibration behavior of the disk itself, at frequency ω_R, with a mode shape of n ND, spinning at speed, Ω, determined by: $\omega_S = \omega_R + n\Omega$. This relationship can be used to construct the frequency–speed diagram presented in **Figure 9** which shows the apparent vibration frequency (ω_S) plotted against rotation speed (Ω) for the first few modes of the rotating disk. An important application of this diagram is to indicate the rotation speeds at which a stationary source of vibration excitation with a frequency of ω_E will coincide with the apparent natural frequencies of the spinning disk. For example, **Figure 9** shows how a stationary (nonrotating) excitation at frequency ω_E might generate a resonant response in a disk mode at any of several rotation speeds, since at these indicated conditions ($\times$), the excitation is 'felt' by the disk at a frequency which coincides with one of its own natural frequencies. Of even greater interest in this respect, are the rotation speeds marked as $\circ$, as these represent speeds at which resonance might be induced in a mode of the spinning disc by a stationary and constant (i.e., static, nonoscillatory) force applied to the disk rim. These critical speeds have long been known as potentially dangerous conditions, to be avoided in the operating range of almost all machines.

Vibration Response of Disk-like Structures

Most of the important characteristics of the vibration of disk-like structures have been addressed in the preceding sections describing the modal properties. Using the standard theory of modal analysis, the response of these structures to any prescribed excitation can readily be determined using the modal properties we have described in some detail. It remains here to highlight certain features of the forced response of disks that are peculiar to this type of structural component.

It transpires that there are two types of forced response which are of special interest: firstly, that from a single point of excitation, and secondly that which results from a particular form of multipoint excitation, where the excitation force patterns travels around the disk at a steady speed. (This latter excitation is commonly encountered under rotating conditions where it is called 'engine-order excitation'.)

When a disk is excited at a single point, and when the excitation frequency coincides with the natural frequency of a mode with n NDs, the appropriate mode shape is readily observed, but almost universally with the NDs symmetrically disposed about the excitation point (**Figure 10A**). If the excitation is moved around the disk by an arbitrary angle, keeping the same radius, and the measurement repeated, it is found that the pattern of nodal lines has 'followed'

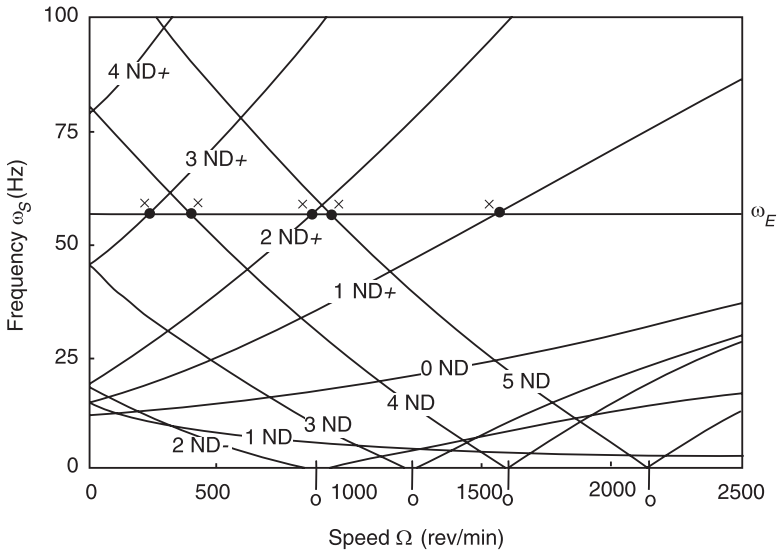


Figure 9 Apparent and actual vibration frequencies observed and experienced in a rotating vibrating disk. (–) Apparent natural frequencies as detected by stationary observer; (- - -) actual natural frequencies as experienced by rotating disk; × 'critical' speeds for stationary excitation at frequency ω_E of disk modes; ○ critical speeds for stationary static force ($\omega_E = 0$) excitation of disk modes.

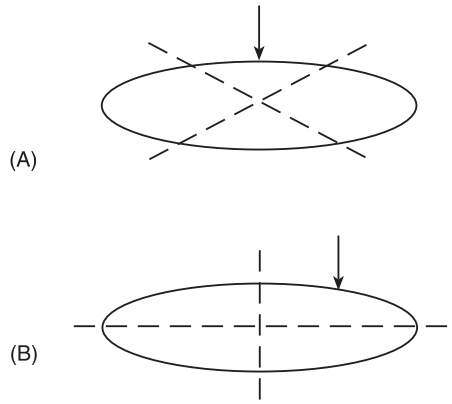


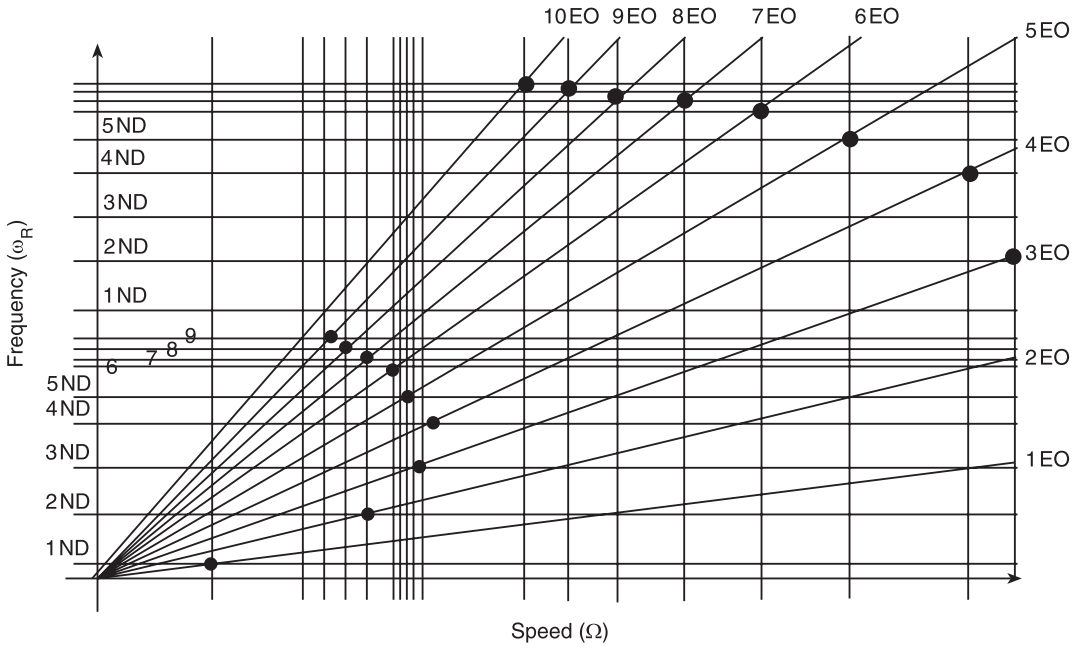
Figure 10 (A, B) Nodal diameters 'follow' point of excitation.

the point of excitation so that the nodal lines once again are set symmetrically about the point of excitation (**Figure 10B**). This phenomenon is a clear demonstration of the fact that there are two modes at this resonance frequency. If there was only one mode, then the nodal lines observed by the first excitation point would be fixed in the disk and so, when the point of excitation was moved, they would stay in the same place. The fact that they 'move' can (only) be explained if there are two modes at this natural frequency. The same measurement carried out on an asymmetric disk will reveal the existence of two modes at different (although close) natural frequencies, and will show a different nodal line pattern for each resonance. Further, these two nodal patterns will be the same for an excitation applied at the first point and then at the second point. In other words, these nodal patterns will not 'follow' the excitation.

There is a special type of excitation which occurs when a disk is rotating past a stationary (nonrotating) excitation force field. In many cases, this force field is simply a steady (static) pressure which is exerted on the disk face, although the same features arise if the force field includes a time-varying oscillating component. To illustrate the phenomena which arise, it is convenient to define the force field as:

$$F(\theta) = F_n \cos n\theta$$

In the general case, F_n may itself be time-varying, but the effects of interest can be illustrated in the case where F_n is simply a constant, static force. It can be shown that this type of excitation, which constitutes a multipoint excitation effect because the force is felt by the disk at all points simultaneously, has a selective effect on the modes of vibration of the disk with n NDs. In fact, an excitation force field of the nth-order form shown, will excite all modes of vibration of the disk that contain a component of n ND in their mode shape, and will do so at a frequency experienced by the disk of $n\Omega$. In contrast, this same excitation pattern will not excite any response in modes that do not have an n ND component in their mode shape, and this is a valuable feature in many practical situations. This type of engine-order (EO) excitation can be used to explain almost all the response phenomena encountered in the vibration of disks, rotating and stationary, found in all types of machine. **Figure 11** summarizes this phenomenon: it shows a



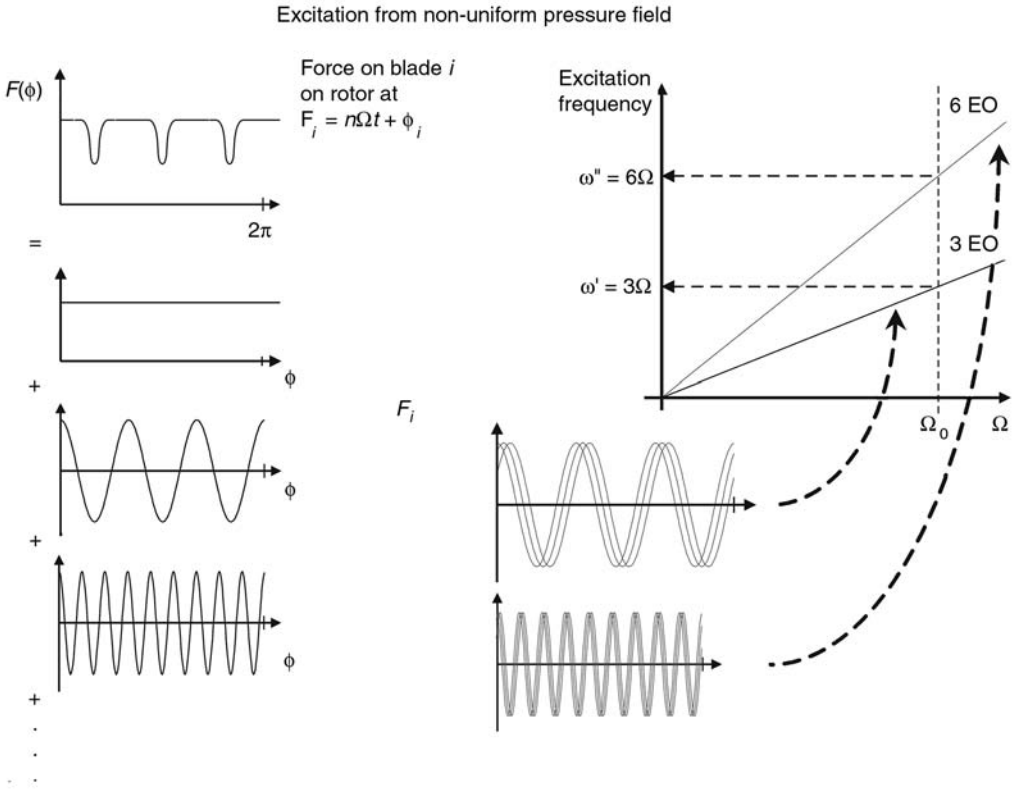


Figure 11 EO excitation of rotating disks. (A) Critical speeds indicating EO resonances, (B) explanation of the origin of multiple EO excitation components.

diagram of vibration frequency (as experienced on the rotating disk) against rotation speed, and it illustrates the regions of resonance that can be expected if there is a stationary excitation force field that includes several different orders, n. It can be seen clearly on this diagram how each EO selectively picks out the disk mode with the matching number of NDs and generates resonances accordingly. It is also clearly seen how coincidence of excitation frequencies with natural frequencies which do not satisfy the additional requirement of matching engine order and number of NDs does not lead to resonance.

It remains only to explain how there might come to be a 'stationary excitation force field that includes several orders, n'. In many machines, there are sources of vibration excitation which result from obstructions to the flow of working gas, or other features, and these are responsible for the force field, $F(\theta)$. If there is a simple, single, obstruction in the working fluid stream, at some arbitrary angular orientation, then simple Fourier analysis of this perturbation in the steady force reveals that it will be the equivalent of many harmonic components, such as F_n above.

See also: **Mode of vibration**; **Plates**; **Rotor dynamics**.

Further Reading

Leissa AW (1975) *Vibration of Plates*, NASA.

Southwell RV (1992) On the free transverse vibrations of a uniform circular disc clamped at its centre; and on the effects of rotation. *Royal Society Proceedings (London)* **101 A**, 133–153.

Tobias SA, Arnold RN (1957) The influence of dynamics imperfections on the vibrations of rotating disks. *Proceedings of the Institute of Mechanical Engineers* **171**, 669–690.

DISPLAYS OF VIBRATION PROPERTIES

M Radeş, Universitatea Politehnica Bucuresti, Bucuresti, Romania

Copyright © 2001 Academic Press

doi:10.1006/rwvb.2001.0168

Displays are valuable instruments in engineering practice, condensing large amounts of data into simple and convenient presentation formats. Examination of time histories and frequency-based spectral data, orbit analysis, and observation of the animated mode shapes and operating deflection shapes allows us to pinpoint areas and properties of interest in dynamic analysis, giving important visual insight into the way in which structures are vibrating.

Displays of Modal Data

Displays of modal data – natural frequencies, damping ratios, mode shapes, and modal participation factors – are useful in the measurement, analysis, and interpretation of vibrations.

Natural Frequency Plots

While tabular presentations of natural frequencies are sometimes sufficient, different display formats reveal more clearly the interrelation between various parameters. From a long list of possible applications, one can mention:

1. Bar plots for the comparison of measured and predicted natural frequencies. For each natural frequency, a colored bar shows the magnitude of, say, the measured value, and a white bar shows the predicted value.
2. Root-locus diagrams, showing the variation of damped natural frequencies as a function of damping (see **Theory of vibration**, Fundamentals).
3. Diagrams of variation in natural frequencies against a stiffness or a mass parameter. For rotating shafts, the critical speed map shows the variation of the undamped critical speeds as a function of an average bearing stiffness (see **Blades and bladed disks**; **Rotor dynamics**).
4. Diagrams of variation in natural frequencies of rotor-bearing systems as a function of bearing damping. **Figure 1** shows a plot of the imaginary versus the real part of eigenvalues for the first two modes of precession of a shaft-bearing system. The values on the curves give the bearing damping ratio. It is seen that the lowest mode becomes critically damped.
5. Interference diagrams: plots of natural frequencies versus a speed-related parameter, with overlaid lines of excitation frequencies (see **Rotating machinery, essential features**).
6. Campbell diagrams: plots of natural frequencies of rotating systems as a function of rotational speed. In the case of analytical data, the connection of

points is based on knowledge of the mode shapes. In the case of measured data the magnitude of response at resonance is indicated by circles, with the circle calibration factor also given on the display (not shown). Only peaks exceeding a selected threshold level may be presented (**Figure 2**). Structural resonances often appear as being excited at approximately the same frequency over a wide range of speed change.

7. For systems with hydrodynamic bearings and seals, an instability diagram can also be plotted, as a graph of the damping factor (real part of eigenvalues) versus rotational speed. The onset speed of instability is located at the lowest abscissa crossing point of any curve with the speed axis (see **Rotating machinery, essential features**).
8. Diagrams of natural frequencies of plate-like components as a function of the nodal line indices.

The last of these types of display will be discussed in more detail below.

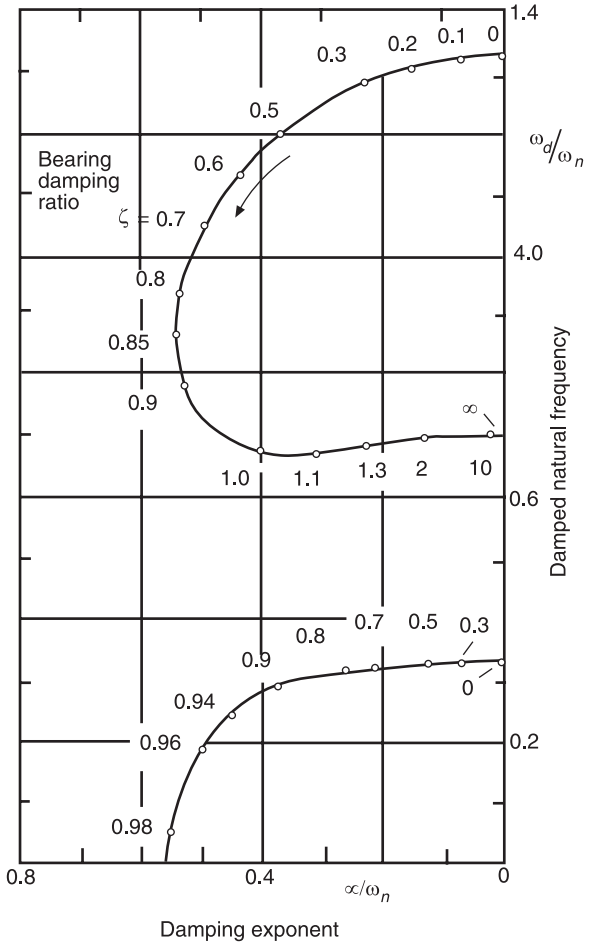


Figure 1 Lowest two damped natural frequencies of a rotor-bearing system, as a function of bearing damping.

Natural Frequencies of Plates and Beams

A systematic study of the normal vibration modes of plate-like components may be based on the analysis of their nodal lines, sometimes referred to as the Chladni figures.

For a circular plate, the basic constituent nodal lines are circles and diameters (**Figure 3A**). Each normal mode is characterized by a certain pattern, defined by the pair of indices **c**, **d**, where **c** is the number of nodal circles and **d** is the number of nodal diameters. Sometimes, a plus or minus sign is used in front of this ratio, to take into account the two possible modal forms, phase shifted with 180° or the two superimposed orthogonal modes.

The natural frequencies can be plotted against the number of nodal diameters, in families of curves, each having as a parameter the number of nodal circles. For a free circular plate, typical results are shown in **Figure 3B**.

This type of display may be useful in an experimental study, when the nodal patterns are obtained by holographic interferometry, or by sprinkling fine granular material on the surface of the plate, and observing the stationary figures formed at resonances. First, the natural frequency of each mode is plotted against its number of nodal diameters. Then, points representing modes with the same number of nodal circles are connected by continuous lines. If one of the natural frequencies has been omitted, then it can be determined as the ordinate of the point located where a mode family line intersects the vertical line corresponding to a given number of nodal diameters. Characteristic for plate-like components is the existence of physically different modes having coincident or close natural frequencies. In damped systems, two neighboring modes can combine due to the flatness of resonance responses, producing compounded modes, whose nodal pattern is no more made up of simple circles and diameters.

A diagram such as **Figure 3B** helps to identify the pairs of modes susceptible of compounding and to explain their origin. For example, consider the modes 1, 2 and 0, 5, which have almost the same frequency (**Figure 3C**). For each individual mode, the shaded areas are considered to vibrate downwards, while the unshaded areas vibrate upwards. When the two figures are superimposed, the doubly shaded areas vibrate downwards, and the unshaded areas vibrate upwards. The nodal lines will pass through the single shaded areas, where the two opposite motions cancel each other. Opposite phase combinations give rise to rotated patterns. Irregular nodal patterns, determined for propeller blades, for impellers and turbine-bladed disks, can be conveniently studied using the type of display shown in **Figure 3B**.

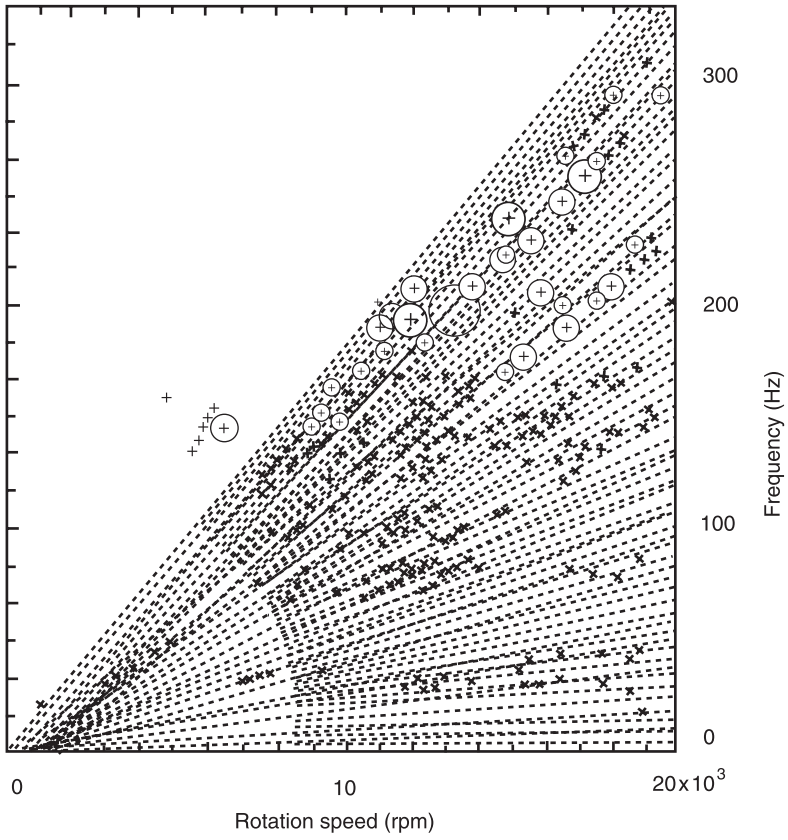


Figure 2 Three-dimensional Campbell diagram.

This display may be used to study the possible resonances of bladed disks. In a perfectly uniform system, each point on the diagram represents a pair of modes with orthogonally oriented identical modal patterns. Due to imperfections or to blade variability, in actual bladed disks the two modes separate and take on slightly shifted natural frequencies, complicating the picture. An interference diagram (see **Blades and bladed disks**) helps to locate modes with close natural frequencies being excited at the same engine speed.

Mode Shape Plots

Probably the displays most often used are those of mode shapes. While animation offers 'live' displays, showing how a structure actually moves at a natural frequency, hard-copy print-outs can contain only frozen images, i.e., pseudo-animated displays. Static (nonanimated) displays, containing zero deflection and the maximum distortion frame, are often sufficient to serve the desired goal. Three-dimensional structures may be represented in wire frame format or in solid hidden-line format.

From the wide range of applications in vibrations, several typical examples can be chosen, where the mode shape plots reveal important information, such as that described below.

1. The relative amplitude of displacement throughout the structure and the location of nodal points of real modes. **Figure 4** illustrates the lowest three planar mode shapes of a cantilever beam. For straight beams, there is a direct correlation between the mode index and the number of nodal points, a fact which helps in measurements.

   If stationary nodes are not visible on pseudoanimated displays, then the modes are not real. Complex modes exhibit nonstationary zero-displacement points, at locations that change in space periodically, at the rate of vibration frequency. These complex modes are sometimes converted into equivalent real mode shapes. The complexity of measured modes is observed using so-called compass plots (**Figure 5**), i.e., vector diagrams in which each modal vector element is represented by a line of corresponding length and inclination, emanating from the origin. The complex mode shape is then rotated through an angle equal to the mean phase angle of its entries. Finally, for lightly damped structures, the real

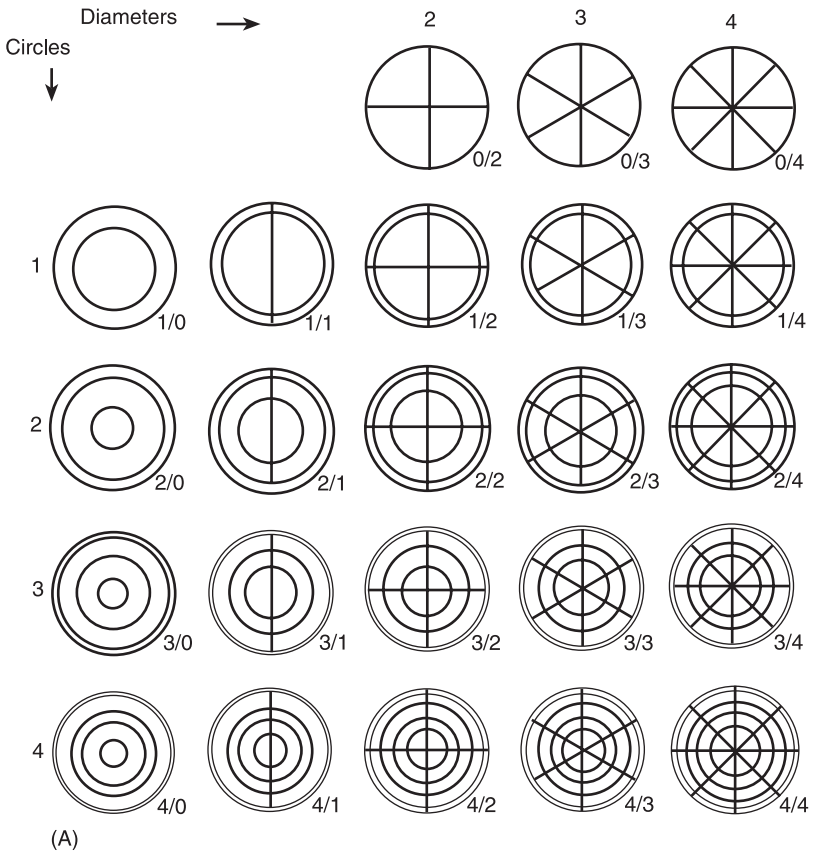


Figure 3A Natural frequencies of free circular plates: nodal patterns of natural modes of vibration.

mode is realized by taking the modulus of each complex vector element and multiplying it by the sign of its real part.

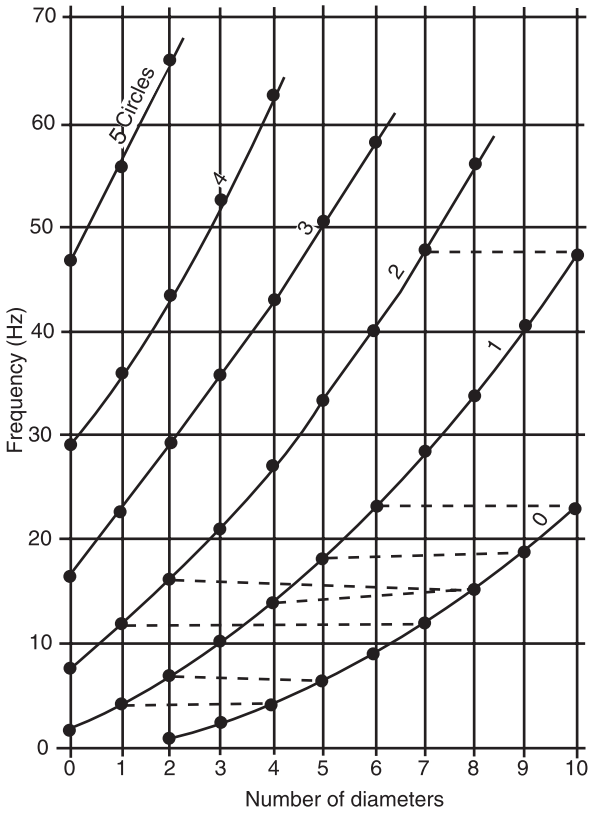
Symmetric structures possess symmetric and antisymmetric mode shapes that can be studied separately to reduce the problem order. Periodic structures can also be analyzed by being broken into constituent substructures.

2. Dynamically weak components or joints. **Figure 6** shows a simplified mode shape trace of a milling machine, for a mode identified as the main source of chatter during operation. The deviation from 90° of the lines concurrent at the joint between the working table and the vertical column indicates that the table mounting screws are responsible for the machine tool instability.

   In more detailed analyses, a wire frame model is developed to represent the geometry of the structure, connecting the instrumented points by trace links. The animated display shows the nature of measured or calculated vibration modes: rigid body, flexural, torsional, longitudinal, plate-like, or a combination of these.

   A contour map of the mode shapes of panel or shell-like structures reveals areas of large relative displacement amplitude. It may help in the selection of locations where ribs, braces, or other stiffeners can be welded in order to raise the natural frequency of the component beyond the range of excitation frequencies.

3. Combined bending and torsion, and plate vibration mode shapes. **Figure 7** illustrates the lowest 12 modes of vibration of a cantilevered planar plate structure. Modes are classified by the ratio between the number of nodal lines perpendicular to the built-in side and the number of nodal lines parallel to the built-in side, including the fixed root.
4. The existence of double modes in axially symmetric structures. **Figure 8** shows the pair of two-diameter modes of a circular plate structure, having almost coincident natural frequencies and identical mode shapes, but 45° phase-shifted in space.
5. Compound modes, consisting of both global and local modes. An eight-bay free–free planar truss can have 'pure' global modes, like the three-node bending mode shown in **Figure 9A** and composite modes, like the four-node bending mode shown in **Figure 9B**, with diagonals vibrating in the first local mode.



(B)

Figure 3B Natural frequencies of free circular plates: natural-frequency plot.

6. Whirling modes of rotor-bearing systems. **Figure 10** shows the orbits of the finite element model nodal points along a rotor, together with two spatial mode shape traces, plotted at a quarter of a rotation time interval. Because the trajectory of each point in the free damped motion is a spiral, the orbits are plotted as open ellipses, with the missing part at the end of the precession period. This helps to establish whether the whirling is forward or backward.

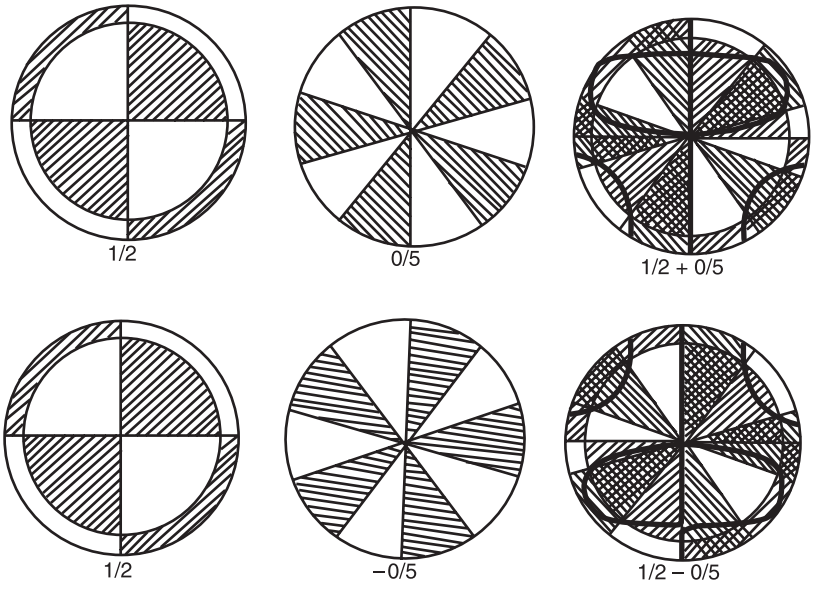
Various other kinds of display are also available, taking advantage of the graphical capabilities of the computer programs in current use. Time–domain animation, based on time history data, may be used to study transient, shock and nonlinear responses. Operation deflection shapes help to visualize the structure's motion in its normal operating conditions.

Displays of Frequency Response Data

Frequency Response Function Plots

Frequency response function (FRF) data are complex and thus there are three quantities – the frequency plus the real and imaginary parts (or modulus and phase) of the complex function – to be displayed.

The three most common graphical formats are: (1) the Bode plots (a pair of plots of modulus versus frequency and phase versus frequency); (2) the Co-Quad plots (real component versus frequency and imaginary component versus frequency); and (3) the Nyquist plots (imaginary versus real part, eventually with marks at equal frequency increments).



(C)

Figure 3C Natural frequencies of free circular plates: compounded modes.

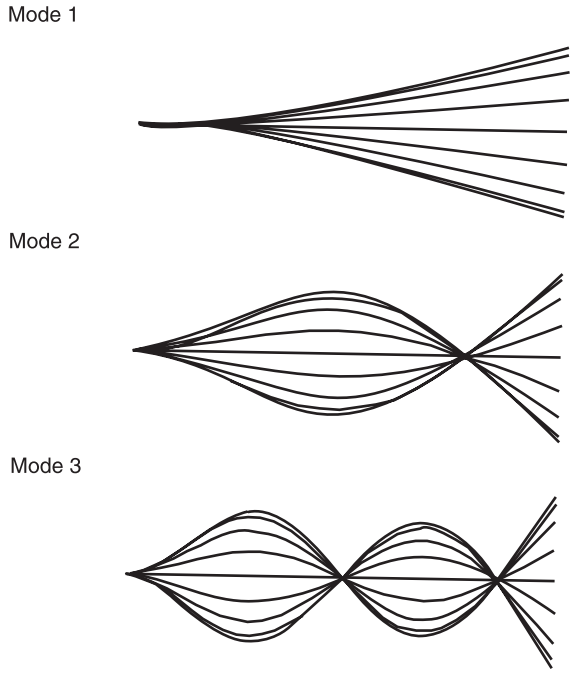


Figure 4 First three planar flexural mode shapes of a cantilever beam.

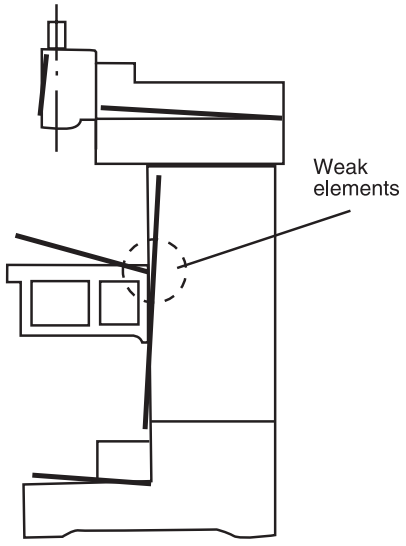


Figure 6 Mode shape trace of a milling machine showing the location of a weak area.

Plotted quantities include motion/force-type functions like receptance, mobility, and accelerance, as well as their inverses, dynamic stiffness, impedance and dynamic mass (see **Modal analysis, experimental**, Parameter extraction methods).

Scales can be linear, logarithmic, and semilogarithmic, with or without grid lines, with one or two cursors, zoom capabilities and overlay facilities.

Figure 11 shows parts of the Bode plots for the receptance FRF of a typical damped structure, with the displacement response measured at DOFs 1, 2, and 3, due to forcing applied at DOF 1. Note the logarithmic vertical scale for the magnitude plots, necessary to reveal the details at the lower levels of the response exhibited at antiresonances.

Figure 12 shows the respective plots of the real (coincident) and imaginary (quadrature) components of receptance, while the first column in **Figure 13** shows the corresponding Nyquist plots. It is seen that for lightly-damped systems with relatively well-separated natural frequencies, the response near resonances can be approximated by circular loops. For comparison, mobility and inertance plots are presented in the second and third columns of **Figure 13**, for the same FRFs. For the point receptance H_{11}, a three-dimensional plot is illustrated in **Figure 14**, together with the companion coincident, quadrature, and Nyquist plots.

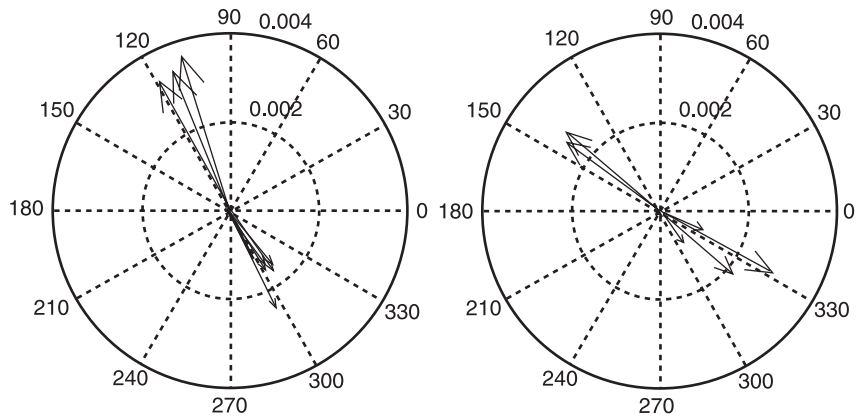


Figure 5 Compass diagrams of complex mode shapes.

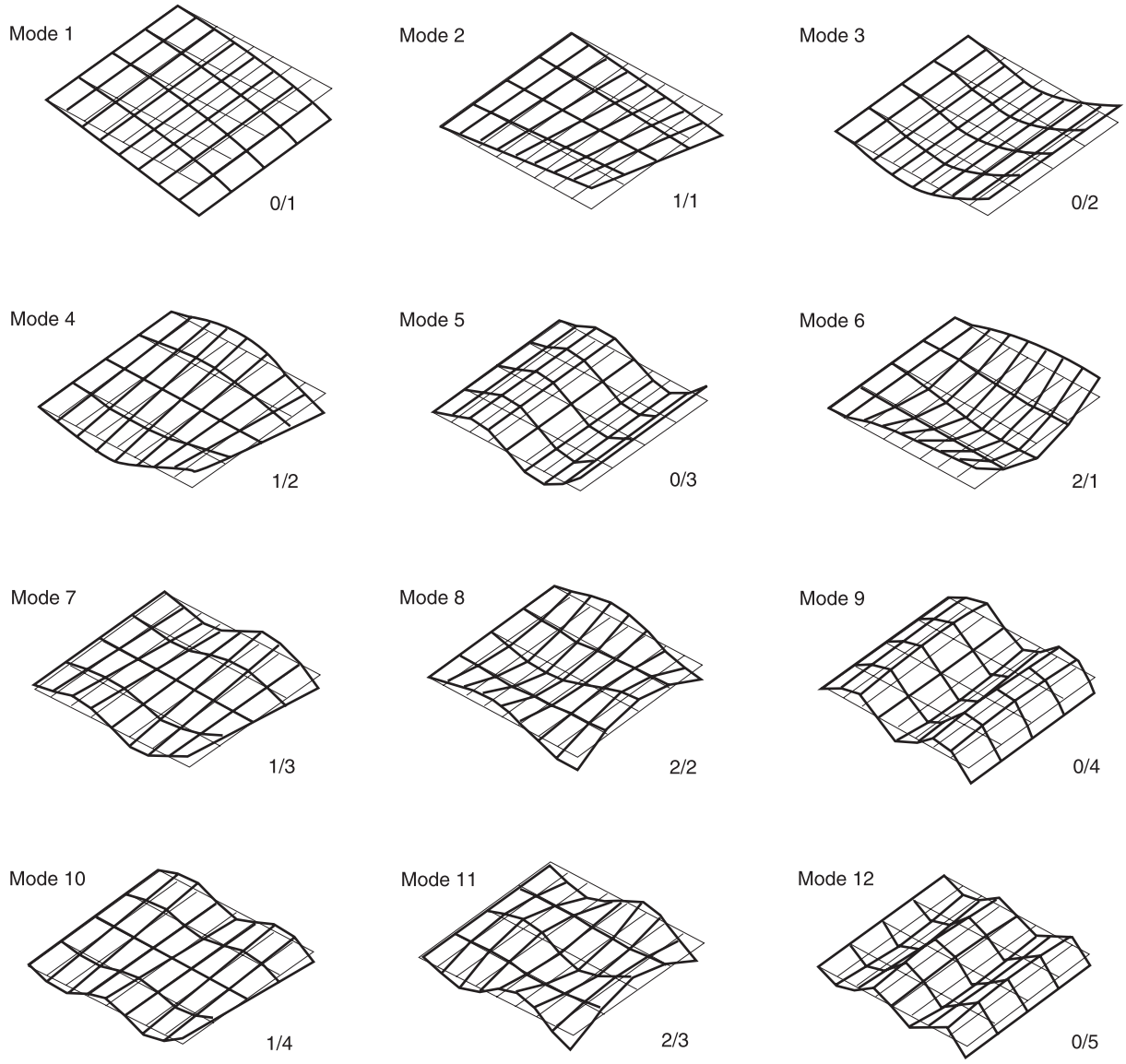


Figure 7 Mode shapes of a cantilevered planar structure.

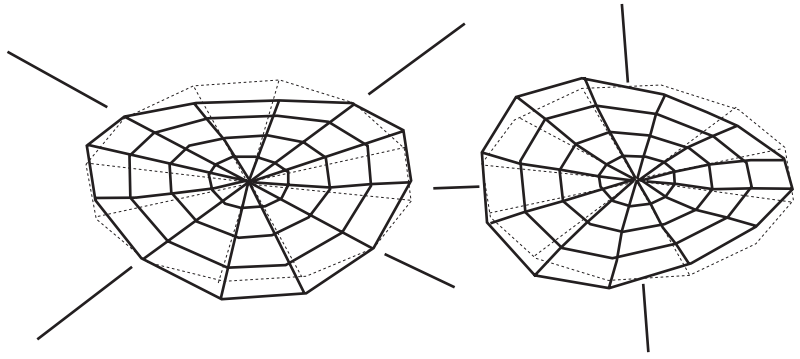


Figure 8 Two two-diameter mode shapes of a circular planar structure.

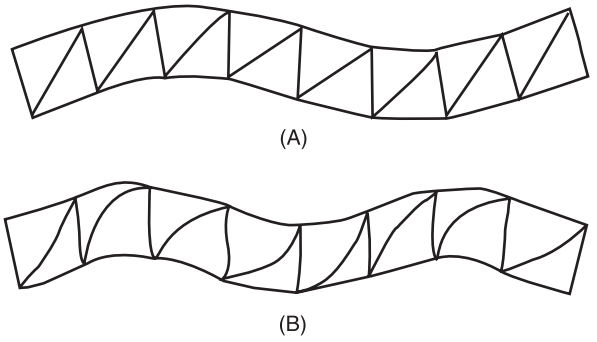


Figure 9 Free–free planar truss: (A) global mode; (B) compound mode.

Figure 15 gives a detailed presentation of the three receptance Nyquist plots calculated for a two-degrees-of-freedom (2DOF) system with low damping and relatively well-separated natural frequencies. The values on the curves give the excitation frequency in rad s^{-1}. For systems with close natural frequencies and/or higher damping, there is only one loop in the Nyquist plot for the 2DOF system.

FRF displays are distorted by nonlinearities. **Figure 16** summarizes some of the effects of nonlinear stiffness on the response plots of single-degree-of-freedom systems with hysteretic damping. Two families of curves are plotted in this case: first, the Nyquist plots, connecting points of constant excitation level, and second, the isochrones connecting points of constant excitation frequency.

Damping nonlinearity can also be recognized from the pattern of isochrones (**Figure 17**).

For rotor-bearing systems, unbalance response plots are being used to display shaft orbit-related quantities as a function of the rotational (spin) speed. Assuming elliptical orbits, **Figure 18** illustrates three graphical formats: first, a plot of major (a) and minor (b) ellipse semiaxes against speed; second, a plot of two motion components, along two mutually perpendicular directions, y and z, in a plane normal to the rotor axis, against speed; and third, a plot of the radii of the ellipse generating forward and backward circular motions, r_f and r_b, against speed.

Displays of Frequency Spectra

Autopower and cross-power spectra and coherence functions are useful data descriptors in vibration measurement and analysis.

The frequency spectra of the complex signals generated by machines are characteristic for each machine, constituting a unique set of patterns, referred to as the machine signature. Analysis of machine mechanical signatures facilitates the location of vibration sources. Observing the evolution of such signatures in time permits the evaluation of a machine's mechanical condition. By monitoring the growth of the amplitude of certain spectral

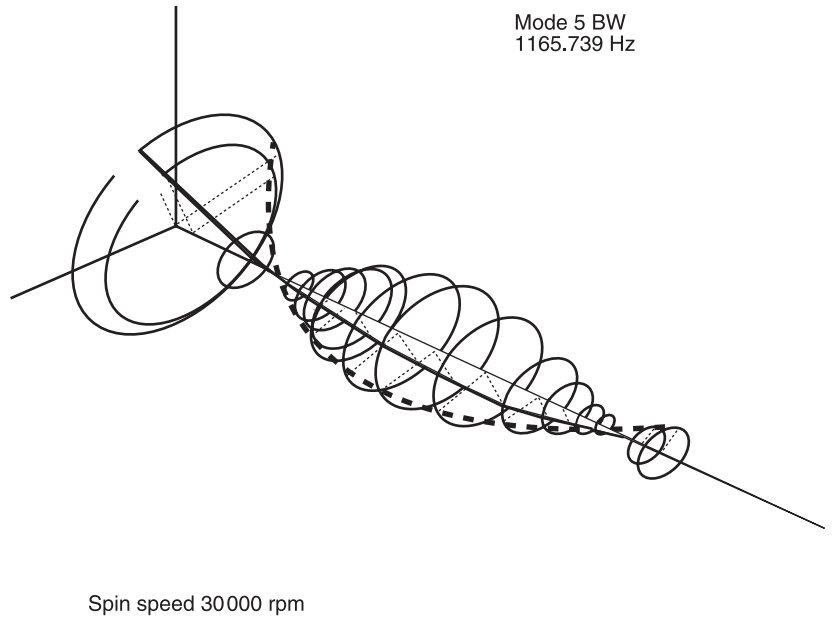


Figure 10 Whirling orbits and spatial mode shapes of a rotor-bearing system.

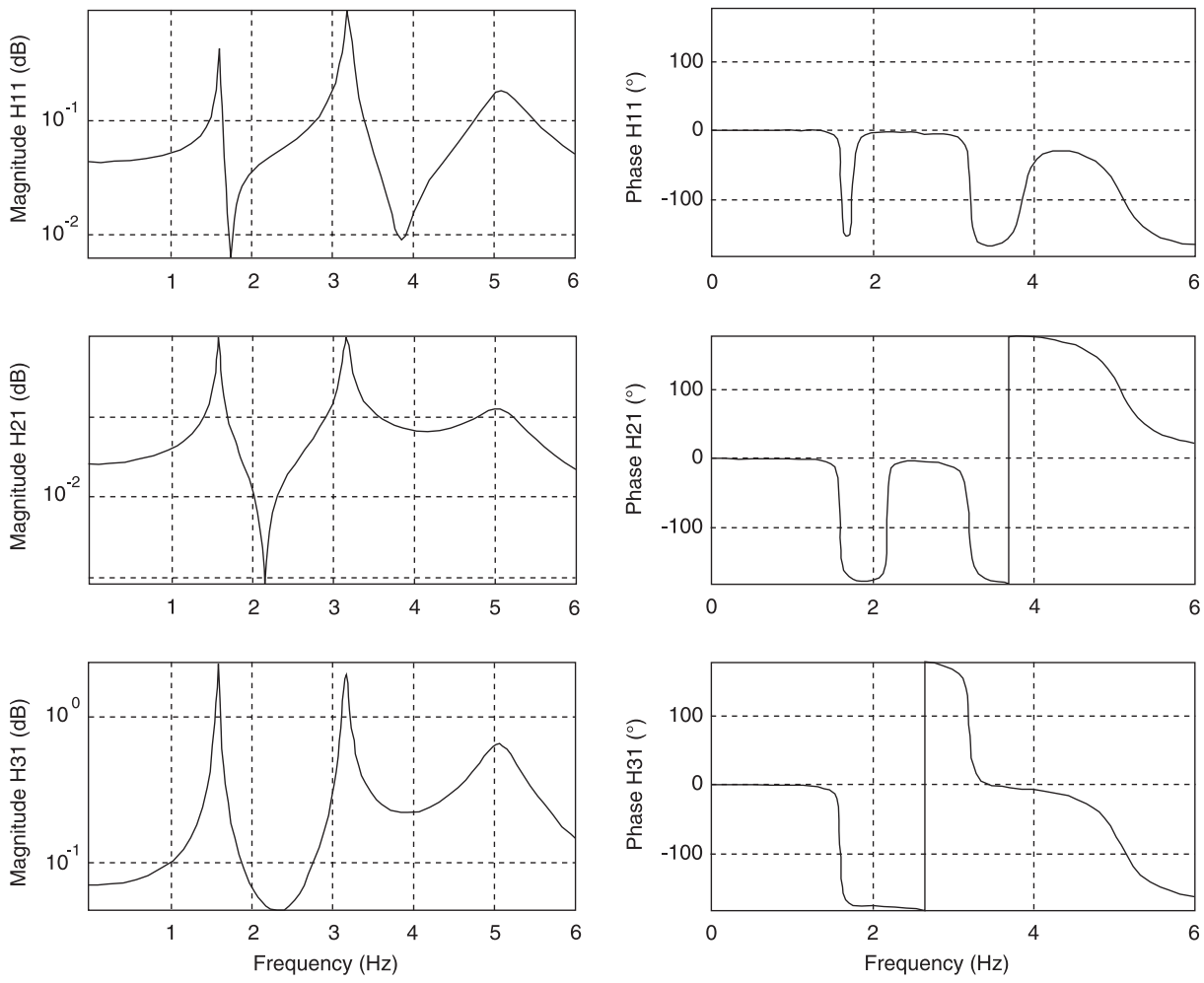


Figure 11 Plots of magnitude and phase of the receptance of a simple structure.

components, faults can be detected by correlating their frequencies to the machine operating parameters.

Spectrum plots are commonly $x - y$ plots in which the x axis represents the vibration frequency and the y axis represents amplitudes of a signal's individual frequency components.

A characteristic spectrum plot for a five-cylinder, four-stroke diesel engine is shown in **Figure 19**. The large-amplitude components $2X$ and $2\frac{1}{2}X$ are produced by the unbalanced pitching moment, and by the ignition rate, respectively. The harmonic $5X$ is produced by the unbalanced rolling moment while the $7\frac{1}{2}X$ component corresponds to the impact rate of the camshaft. The one-half-order component $\frac{1}{2}X$ is the fundamental harmonic of the gas-pressure cycle. Note that not the relative level of the spectral components but their variation in time is significant for fault diagnosis.

A series of spectrum plots can be combined into a three-dimensional presentation, where one spectrum appears slightly displaced from the other, as a function of either machine speed (cascade plot) or time (waterfall plot). **Figure 20** illustrates a cascade spectrum typical for the oil whirl and whip. Speed-related phenomena will track along a diagonal, whereas speed-independent resonance-related responses appear on lines parallel to the ordinate axis. Such a display shows changes in vibration frequencies and amplitudes. Very short time or speed increments can be chosen to see the effects of nonstationary phenomena (like subharmonic instabilities).

Model Order Indicators

Singular Value Plots

Estimation of the rank of a matrix of measured FRF data can be made using the singular value decomposition (SVD) of a composite FRF (CFRF) matrix, $[\mathbf{A}]_{N_f \times N_o N_i}$. Each column of the CFRF matrix contains elements of an individual FRF measured for

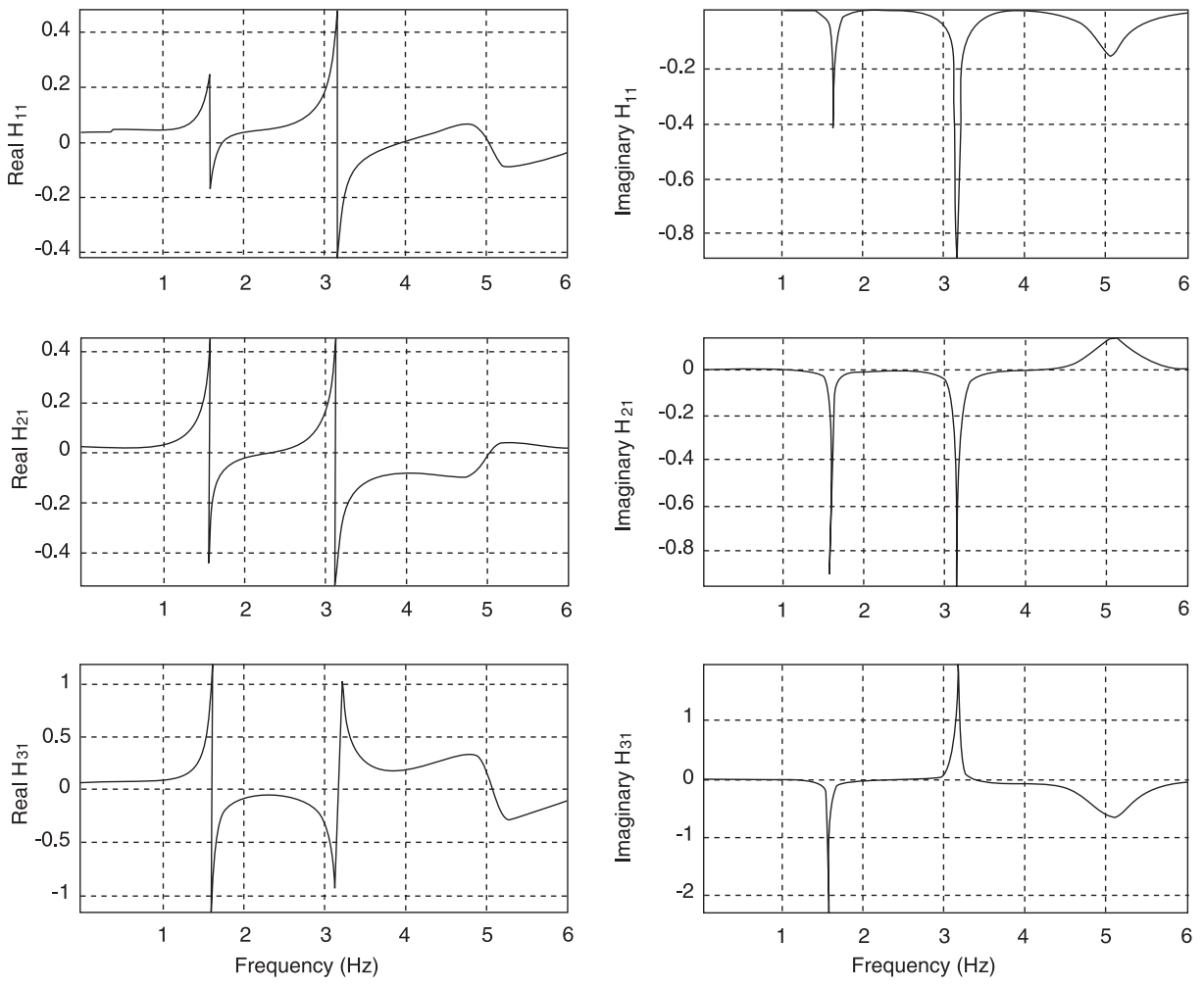


Figure 12 Plots of real and imaginary parts of the receptance of a simple structure.

given input/output location combination at all frequencies.

By performing an SVD, the CFRF matrix is decomposed into a diagonal matrix of positive singular values and two unitary matrices containing the left and right singular vectors, respectively:

$$[\mathbf{A}]_{N_f \times N_o N_i} = [\mathbf{U}]_{N_f \times N_o N_i} [\mathbf{\Sigma}]_{N_o N_i \times N_o N_i} [\mathbf{V}]^{\mathrm{H}}_{N_o N_i \times N_o N_i}$$

The singular values are indexed in descending order. If there is a gap in the singular value array then the number of significant (non-trivial) singular values can be taken as a good estimate of the number of modes that have an identifiable contribution to the system response.

In order to separate these larger singular values from the others, two kinds of plot can be used. **Figure 21A** shows the plot of magnitudes of the singular values versus their index. They are normalized to the first singular value. The sudden drop in the curve after the sixth singular value indicates a rank $N_r = 6$, i.e., that there are six dominant modes in the frequency band of data.

Figure 21B shows the related plot of the ratio of successive singular values. The distinct trough indicates the same number of probable important modes.

Mode Indicator Functions

Modal indicators are useful for estimating the effective number of modes in the frequency range of interest. Mode Indicator Functions (MIFs) are frequency-dependent scalars, calculated from an eigenvalue or singular value solution approach, involving FRF matrices. Plotted against frequency, they exhibit peaks or troughs at the natural frequencies.

The Complex Mode Indicator Function (CMIF) is a plot of the singular values of the FRF matrix

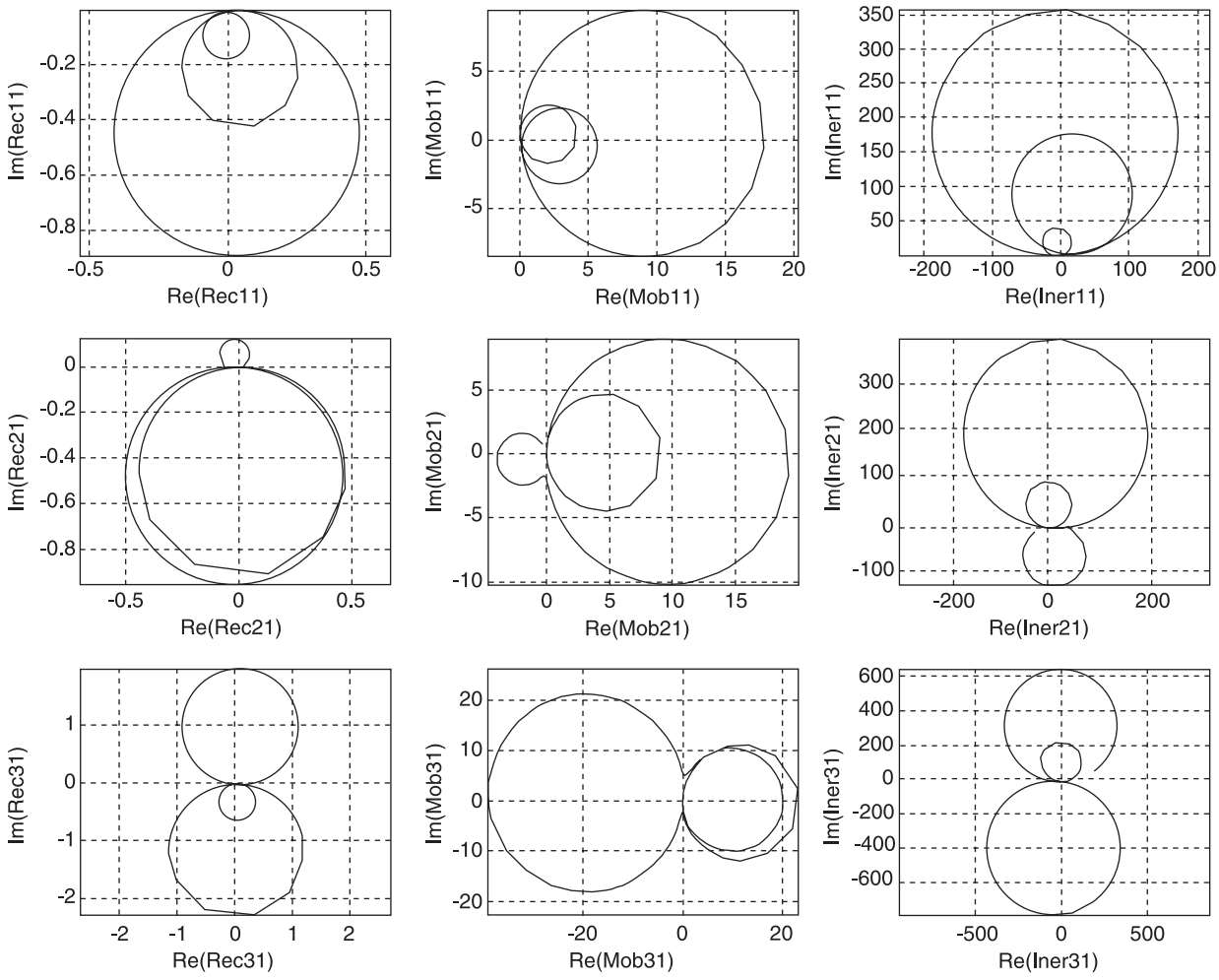


Figure 13 Nyquist plots of the receptance (Rec), mobility (Mob), and inertance (Iner) of a simple structure.

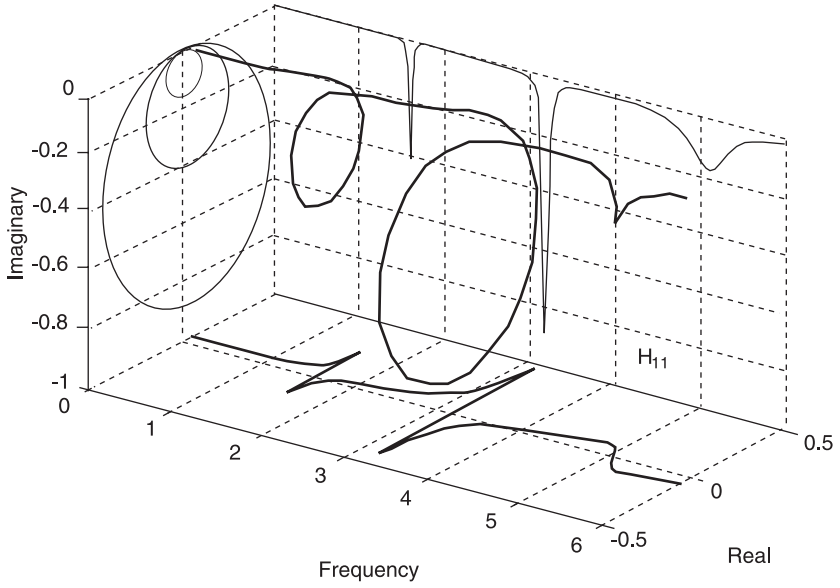


Figure 14 Three-dimensional plot of a three-mode point receptance FRF.

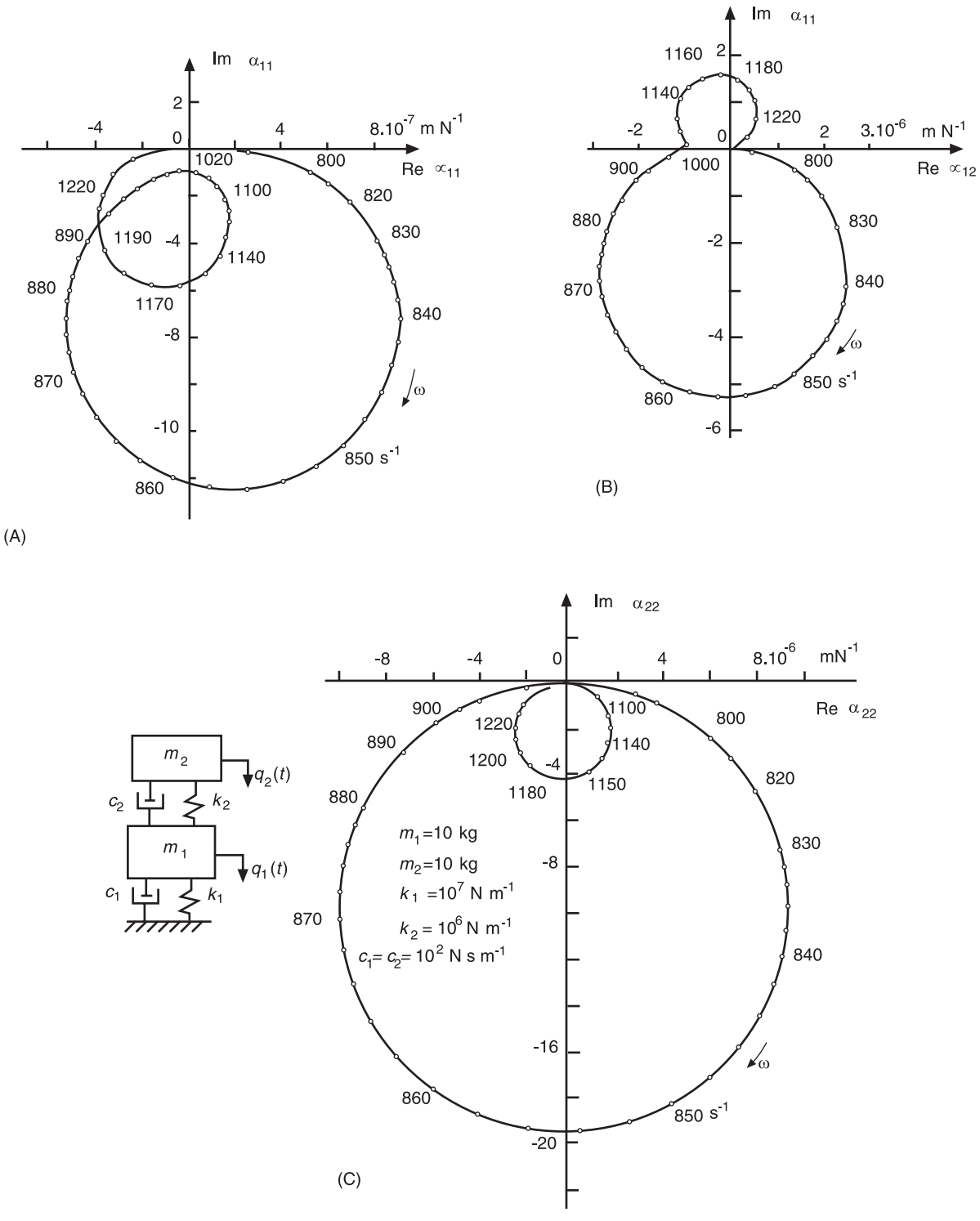


Figure 15 (A)–(C) Nyquist plots of receptances for a 2-DOF system.

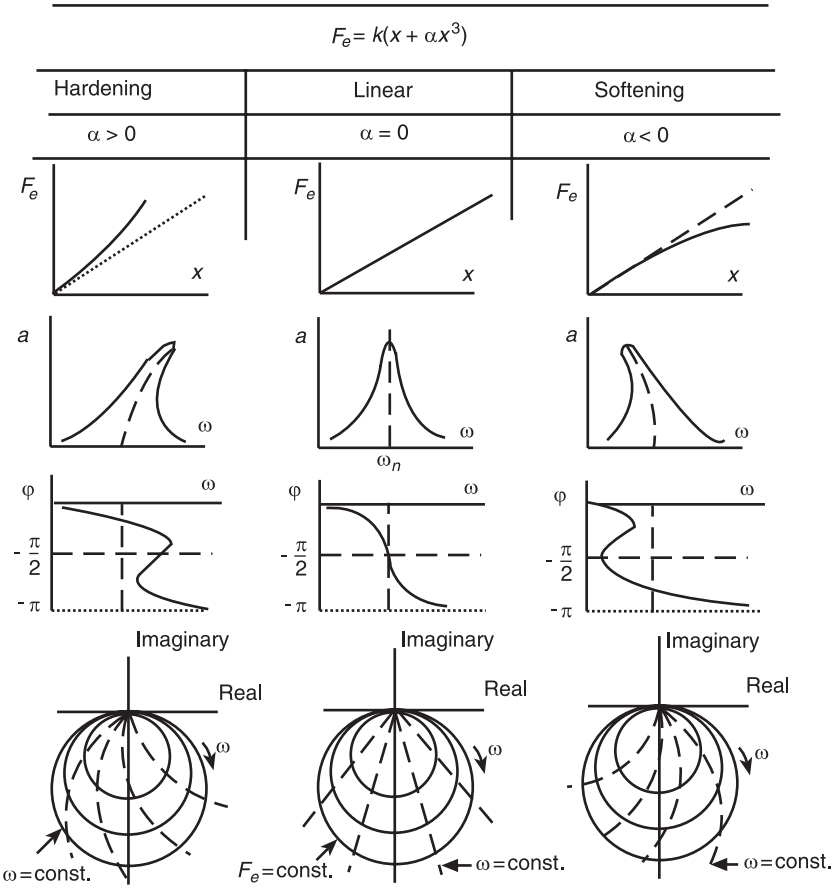


Figure 16 Effect of nonlinear stiffness on some FRF plots.

$[\mathbf{H}]_{N_o \times N_i}$, on a log magnitude scale, as a function of frequency. The number of CMIF curves is equal to the number of input reference points N_i ($N_i < N_o$). Peaks in the CMIF plot indicate the existence of modes. Multiple peaks at the same frequency indicate multiple or repeated modes.

The CMIF plot shown in **Figure 22** indicates six dominant modes of vibration, with two pairs of quasi-repeated natural frequencies at about 103 and 178 Hz.

Multivariate mode indicator function The Multivariate Mode Indicator Function (MMIF) is defined by the eigenvalues, α, of the generalized spectral problem:

$$[\mathbf{H}_R]^{\mathrm{T}}[\mathbf{H}_R]\{f\} = \alpha\Big([\mathbf{H}_R]^{\mathrm{T}}[\mathbf{H}_R] + [\mathbf{H}_I]^{\mathrm{T}}[\mathbf{H}_I]\Big)\{f\}$$

where $[\mathbf{H}_R]$ and $[\mathbf{H}_I]$ are the real and imaginary parts of the FRF matrix, respectively.

In a plot of MMIF against frequency (**Figure 23**), the undamped natural frequencies can be located by the minima of the smallest eigenvalue. Troughs in the next smallest eigenvalues indicate multiple modes.

Mode indicator function A single curve MIF calculated as:

$$\mathrm{MIF}_i = 1 - \frac{\sum_{j=1}^{N_0 N_i} |\mathrm{Re}(a_{ij})||a_{ij}|}{\sum_{j=1}^{N_0 N_i} |a_{ij}|^2}$$

where a_{ij} are the elements of the CFRF matrix **A** is shown in **Figure 24**. Apart from failing to indicate the two double modes (being a single curve mode indicator), this MIF reveals more modes than the dominant ones, performing better at the location of local modes.

The U-Mode Indicator Function (UMIF) is a plot of the left singular vectors of a composite FRF matrix in which each column contains elements of an individual FRF measured for a given input/output location combination at all frequencies, as a function of frequency. The UMIF plot calculated for the same

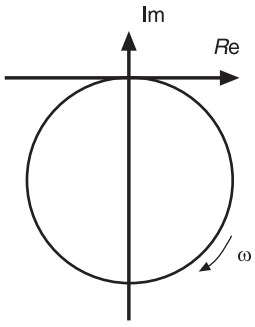
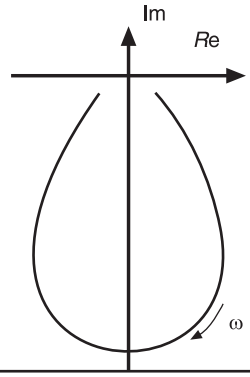
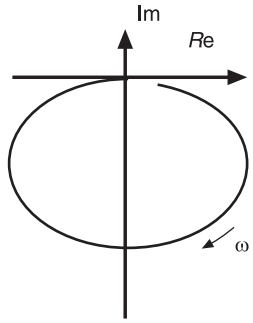
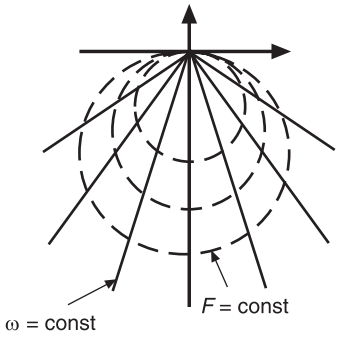
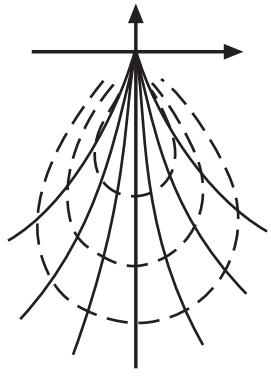
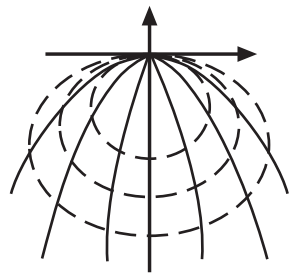
Stiffness	Linear	Linear	Linear
Damping	Hysteretic	Hysteretic and Coulomb type	Viscous quadratic
Polar plot of displacement response			
Pattern of isochrones (ω = const)			

Figure 17 Recognizing nonlinear damping from the pattern of isochrones.

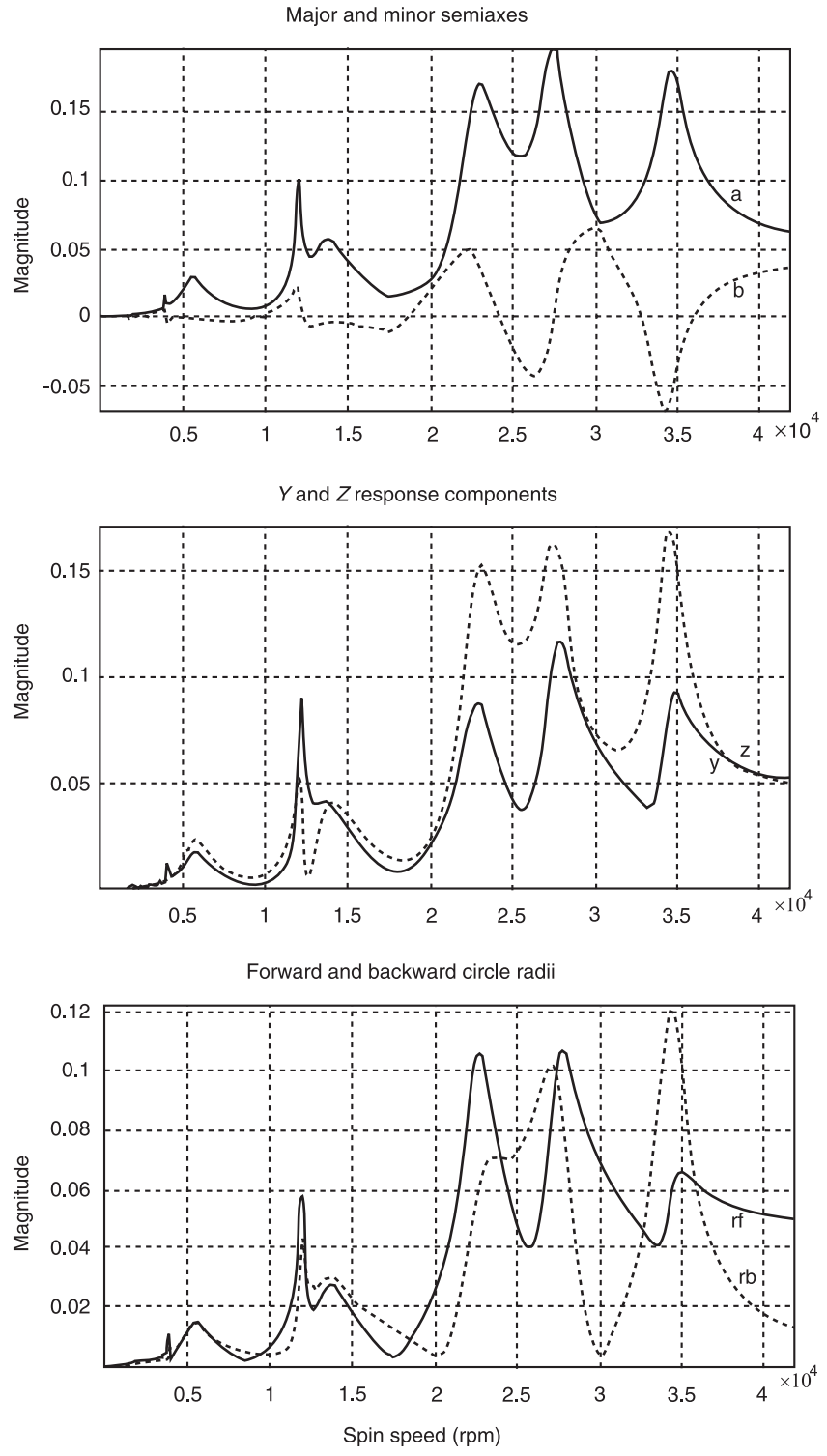


Figure 18 Typical unbalance response plots of a rotor-bearing system.

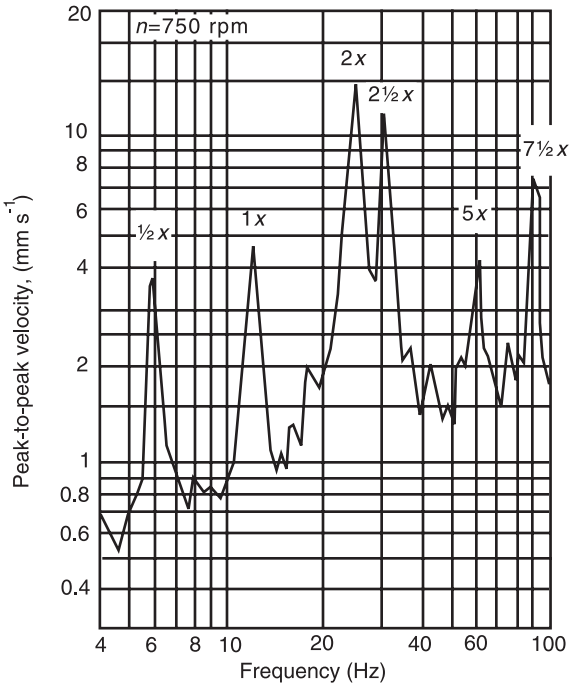


Figure 19 Spectrum plot measured on a five-cylinder, four-stroke diesel engine.

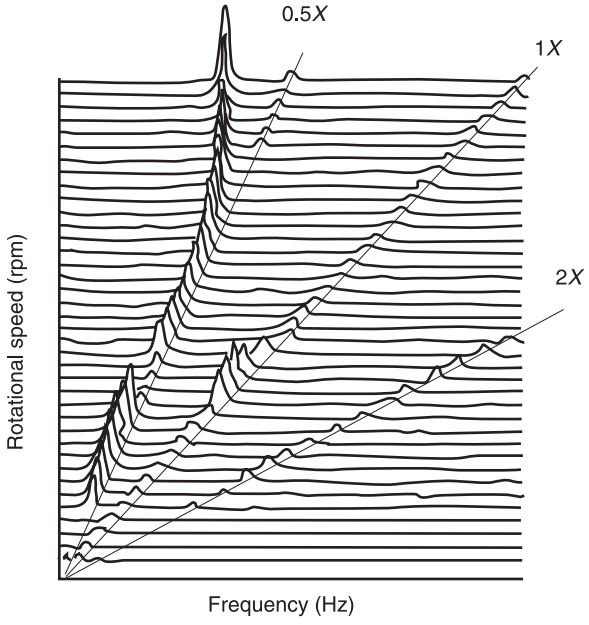


Figure 20 Cascade spectrum plot.

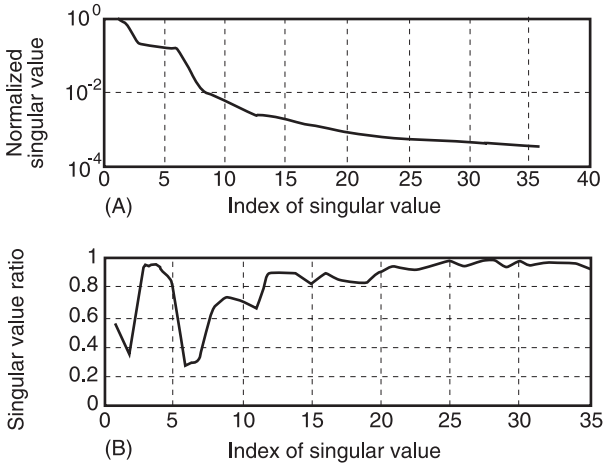


Figure 21 Singular value plots: (A) normalized magnitudes; (B) ratio of successive values.

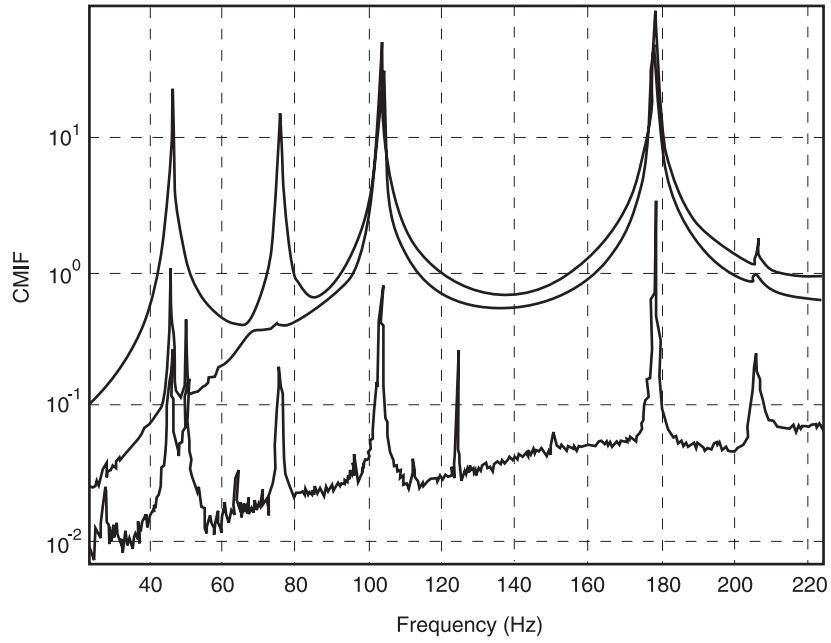


Figure 22 Complex mode indicator function plot.

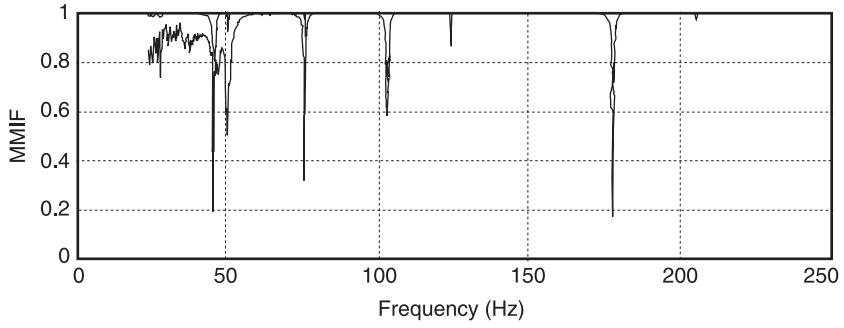


Figure 23 Multivariate mode indicator function plot.

data as the previously presented CMIF and MIF is shown in **Figure 25**. Double modes are indicated by two overlaid curves.

There are some other displays used as potential mode identifiers, like the stabilization diagram, the plot of the sum of all available FRFs, and plots of other composite functions displaying the magnitude squared or the imaginary part squared, to enhance the peaks.

Other Displays

Special displays are used to describe nonlinear vibrations and chaotic motions, like phase trajectories and phase portraits in the phase plane (velocity versus displacement) and three-dimensional orbits in the phase space (see **Nonlinear systems analysis**).

Time domain analysis displays, such as auto- and cross-correlation function plots, supplement spectrum plots in spectral analysis (see **Correlation functions**).

See also: **Blades and bladed disks**; **Correlation functions**; **Modal analysis, experimental**, Parameter extraction methods; **Nonlinear systems analysis**; **Rotating machinery, essential features**; **Rotor dynamics**; **Theory of vibration**, Fundamentals.

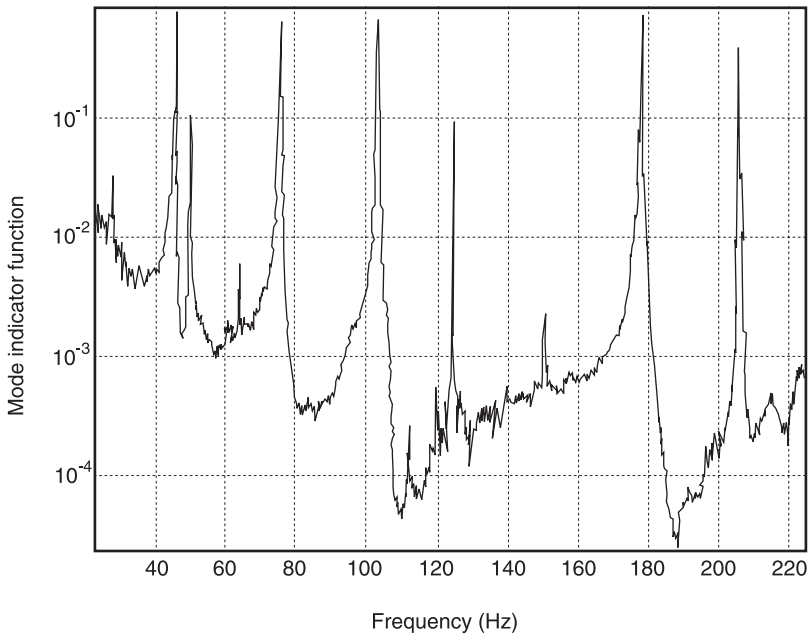


Figure 24 Mode indicator function.

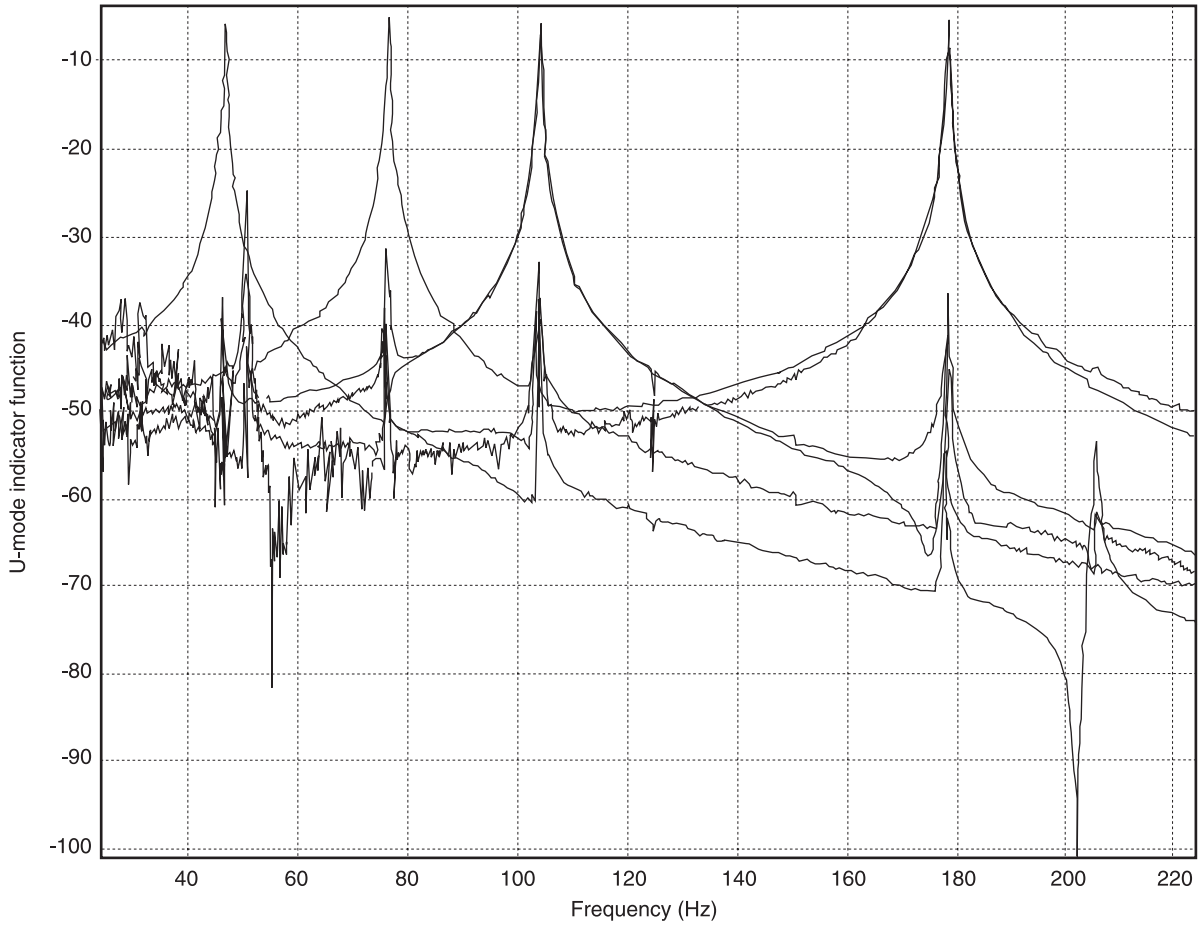


Figure 25 U-mode indicator function.

Further Reading

Buzdugan GH, Mihăilescu E and Radeş M (1986) *Vibration Measurement*. Dordrecht: Martinus Nijhoff.

Chladni EFF (1787) *Entdeckungen über die Theorie des Klanges*. Leipzig: Breitkopf und Härtel.

Ewins DJ (2000) *Modal Testing: Theory Practice and Application*. Baldock, UK: Research Studies Press.

Lord Rayleigh (Strutt JW) (1894) *The Theory of Sound*, vol. 1. London: Macmillan. (Reprinted by Dover, 1945.)

Maia NMM and Silva JMM (eds) (1997) *Theoretical and Experimental Modal Analysis*. Taunton, UK: Research Studies Press.

Morse PM (1948) *Vibration and Sound*, 2nd edn. New York: McGraw-Hill.

DISTRIBUTED SENSORS AND ACTUATORS

See **SENSORS AND ACTUATORS**

DUHAMEL METHOD

See **THEORY OF VIBRATION: DUHAMEL'S PRINCIPLE AND CONVOLUTION**

DYNAMIC STABILITY

A Steindl and H Troger, Vienna University of Technology, Vienna, Austria

Copyright © 2001 Academic Press

doi:10.1006/rwvb.2001.0047

Introduction

One of the key problems in stability theory is the loss of stability of a given stable state, for example an equilibrium or a periodic motion, of a nonlinear dynamical system under variation of a system parameter, which will be called λ. Let us consider, as a typical example, a straight vertically downhanging tube conveying fluid, clamped at the upper end and free at the lower end under a quasistatically increasing flow rate. (In general one understands by a quasistatic parameter variation that the stability behavior of the state is studied at gradually increasing but fixed values of the parameter. This is in contrast to the case of (slowly) continuously varying parameter values, on which we comment later in this article). It is well known from everyday experience, for example from hosing the garden, that for small flow rate the vertically downhanging equilibrium position is stable. However, increasing the flow rate λ it finally reaches a critical value (denoted by λ_c) for which experience shows that an oscillatory motion sets in. In the language of stability theory the originally stable state has lost stability. Now three questions are of interest:

1. What is the value of λ_c at which the loss of stability occurs?
2. What type of motion is setting in after loss of stability of the originally stable state and how is the motion changing by further increasing the parameter λ?
3. How do small changes of the system (small variations of other system parameters) affect the system's behavior?

Under mild requirements on the smoothness of the system description, it is possible to give completely satisfying answers to these questions.

The answer to the first question is supplied from the solution of a linear eigenvalue problem and has been known to engineers for a long time. The answers to the second and third questions, however, can only recently be given, in a systematic and complete way, due to strong progress achieved in the 1970s and 1980s in the field of nonlinear stability theory making use of the methods of local bifurcation theory. Here, as pioneers among many others, the names VI

Arnold, R Thom, M Golubitsky, Ph Holmes may be mentioned. Their work is based on ideas dating back to H Poincare and AA Andronov.

The basic approach to solving the problem of dynamic stability loss consists of three steps:

1. Dimension reduction: One can show that in many important practical cases after the loss of stability the behavior of a high-dimensional or even infinite-dimensional dynamical system can be analyzed by a low-dimensional bifurcation system, which can be obtained by a method of dimension reduction.
2. Normal form theory: The low-dimensional bifurcation system can be further strongly simplified by normal form theory.
3. Classification and unfolding: For bifurcations with low codimension a classification of all qualitatively different types of loss of stability is possible.

Dimension Reduction

We consider here only the loss of stability of a stable equilibrium and comment on periodic solutions later in the article.

There are many ways to perform the dimension reduction. Galerkin methods are well known to engineers. Both linear and nonlinear Galerkin methods can be used. The use of Galerkin methods is recommended if a mathematically rigorous method called the center manifold theory cannot be applied because the requirements for its application are not satisfied. In the following section we give a short explanation of center manifold theory. However, other authors who have performed the reduction by the closely related Liapunov–Schmidt method, treat the dimension reduction problem at varying levels of detail.

Idea of Dimension Reduction

It is well known from experiments and also from engineering experience that even complicated, apparently random time behavior of high-dimensional or infinite-dimensional dissipative dynamical systems can often be described by the deterministic flow on a low-dimensional (chaotic) attractor.

Hence, the first, most important, step in the analysis of the loss of stability of a certain state of a nonlinear dynamical system will always be the attempt to reduce its dimension. For certain systems this goal can be achieved without essential loss of accuracy in the description of the dynamics of the system by removing inessential degrees-of-freedom from the system.

Before indicating which calculations are necessary, let us explain first the basic idea behind dimension reduction. We consider an equilibrium u_E of an infinite-dimensional nonlinear system under quasi-static variation of a system parameter λ. Keep in mind the tube example mentioned in the introduction. For small perturbations out of the equilibrium the system behavior will be governed by its linearized equations. As long as the values of the parameter λ (the flow rate in the tube) are below a critical value λ_c, all eigenvalues of the linearized operator will have negative real parts and all modes, whose superposition represent the perturbation, will be damped and u_E will be stable. A critical value λ_c of the parameter λ will be reached when for the first time eigenvalues are located at the imaginary axis in the complex plane. The corresponding modes are mildly unstable or only slightly damped in linear theory. If the number of these modes is finite the loss of stability can be described in terms of the temporal evolution of the amplitudes of these (active) modes. Their amplitudes are governed by a set of ordinary differential equations called bifurcation equations or amplitude equations of the critical modes and they basically govern the behavior of the full system since the other (infinitely many) modes are damped out and hence do not appear in the description of the dynamics (see **Figure 1** where it can be seen that the relevant dynamics takes place on the manifold M^c, after a strong contraction of the flow towards M^c).

Center Manifold Theory

Mostly, for the application of center manifold theory the admissible variation of λ about $\lambda = \lambda_c$ is restricted to be very small and, secondly, in treating infinite-dimensional systems only a finite number of eigenvalues are allowed to cross the imaginary axis at loss of stability. However, it supplies a mathematically rigorous method of dimension reduction for both infinite- and large finite-dimensional dynamical systems.

We explain now for an n-dimensional system:

$$\dot{\mathbf{u}} = \mathbf{F}(\mathbf{u}, \lambda) \qquad [1]$$

where $\mathbf{u}, \mathbf{F} \in \Re^n$, $\lambda \in \Re^1$, which calculations must be performed. Assuming that $\mathbf{u}_E$ is an equilibrium of eqn [1], that is $\mathbf{F}(\mathbf{u}_E, \lambda) = \mathbf{0}$ we insert $\mathbf{u} = \mathbf{u}_E + \mathbf{v}$ into eqn [1] and write the dynamical system in the form:

$$\dot{\mathbf{v}} = \mathbf{A}(\lambda)\mathbf{v} + \mathbf{r}(\mathbf{v}, \lambda) \qquad [2]$$

Here $\mathbf{A}(\lambda)$ is the Jacobian which is an $n \times n$ matrix.

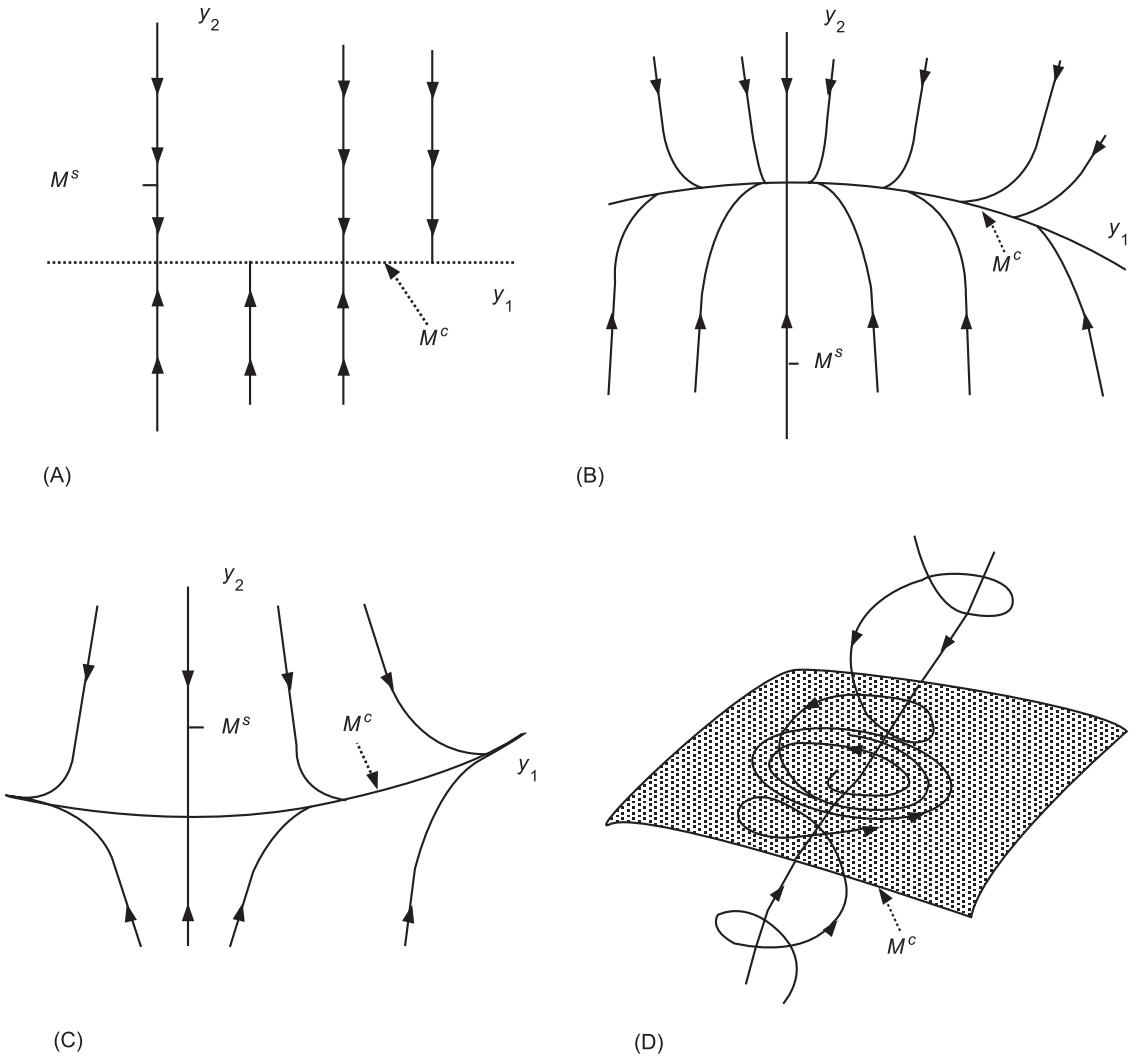


Figure 1 Center manifolds M^c and flows for eqns [7] with the coefficients $a = f = d = e = 0, b = 1$. (A) For the linear system or eqn [7]; (B) for the nonlinear system of eqn [7] $c<0$; (C) for the nonlinear system of eqn [7] for $c>0$; (D) the flow nearby and on the center manifold for a three-dimensional system after a Hopf bifurcation.

We study the loss of stability of the initially asymptotically stable equilibrium $\mathbf{u}_E$ for quasistatically increasing values of λ. At the critical parameter value $\lambda = \lambda_c$ for the first time n_c eigenvalues are located at the imaginary axis, whereas all other n_y eigenvalues are located left of the imaginary axis $(n = n_c + n_s)$. Now we introduce a change of variables $\mathbf{v} = \mathbf{Bq}$ which transforms $\mathbf{A}(\lambda_c)$ into diagonal, or if this is not possible, into Jordan form. As is well known, the transformation matrix $\mathbf{B}$ is composed by the eigenvectors or by the principal vectors of $\mathbf{A}(\lambda_c)$. Then eqn [2] takes the form:

$$\dot{\mathbf{q}} = \mathbf{B}^{-1}\mathbf{A}(\lambda_c)\mathbf{Bq} + \mathbf{B}^{-1}\mathbf{r}(\mathbf{q}, \lambda_c) = \mathbf{Jq} + \mathbf{g}(\mathbf{q}, \lambda_c)$$

which by simply rearranging the variables can be rewritten in the form:

$$\begin{aligned} \dot{\mathbf{q}}_c &= \mathbf{J}_c\mathbf{q}_c + \mathbf{g}_c(\mathbf{q}_c, \mathbf{q}_s) \\ \dot{\mathbf{q}}_s &= \mathbf{J}_s\mathbf{q}_s + \mathbf{g}_s(\mathbf{q}_c, \mathbf{q}_s) \end{aligned} \quad [3]$$

The splitting of $\mathbf{q}$ is done so that the first block of $\mathbf{J}$, called $\mathbf{J}_c$, contains the n_c eigenvalues, which all have zero real part, and all n_s eigenvalues of $\mathbf{J}_s$ have negative real part. If:

$$\mathbf{q}_s = \mathbf{h}(\mathbf{q}_c) \quad [4]$$

is an invariant manifold for the system (a manifold M is invariant, if all trajectories starting on M stay on

the manifold for all $t>t_0$) and if $\mathbf{h}$ is smooth, we call $\mathbf{h}$ a center manifold if $\mathbf{h}(\mathbf{0}) = \mathbf{h}'(\mathbf{0}) = \mathbf{0}$. Note that for the case $\mathbf{g}_c = \mathbf{g}_s = \mathbf{0}$, all solutions tend exponentially fast to solutions of $\dot{\mathbf{q}}_c = \mathbf{J}_c\mathbf{q}_c$. Hence, the linear n_c-dimensional equation on the center manifold determines the asymptotic behavior of the entire n-dimensional linear system, up to exponentially decaying terms (see **Figure 1A**). The center manifold theorem enables us to extend this argument to the case when $\mathbf{g}_c$ and $\mathbf{g}_s$ are not equal to zero and, hence, a nonlinear system is treated.

Center Manifold Theorem

1. There exists a center manifold $\mathbf{q}_s = \mathbf{h}(\mathbf{q}_c)$ for eqns [3] if $|\mathbf{q}_c|$ is sufficiently small. The behavior of eqn [3] on the center manifold is governed by the equation:

$$\dot{\mathbf{q}}_c = \mathbf{J}_c\mathbf{q}_c + \mathbf{g}_c(\mathbf{q}_c, \mathbf{h}(\mathbf{q}_c)) \qquad [5]$$

2. The zero solution of eqn [3] has exactly the same stability properties as the zero solution of eqn [5].
3. If $\mathbf{H}$: $R_c^n \to R_c^n$ is a smooth map with $\mathbf{H}(0) = \mathbf{H}'(0) = 0$ and is defined by:

$$\begin{aligned}\mathbf{P}(\mathbf{H}) := {} & \mathbf{H}'(\mathbf{q}_c)[\mathbf{J}_c\mathbf{q}_c + \mathbf{g}_c(\mathbf{q}_c, \mathbf{H}(\mathbf{q}_c))] \\ & - \mathbf{J}_s\mathbf{H}(\mathbf{q}_c) - \mathbf{g}_s(\mathbf{q}_c, \mathbf{H}(\mathbf{q}_c)) = O\big(|\mathbf{q}_c|^p\big)\end{aligned} \qquad [6]$$

then if $\mathbf{P}(\mathbf{H}) = O(|\mathbf{q}_c|^p), p > 1$, as $|\mathbf{q}_c| \to 0$, we have $|\mathbf{h}(\mathbf{q}_c) - \mathbf{H}(\mathbf{q}_c)| = O(|\mathbf{q}_c|^p)$ as $|\mathbf{q}_c| \to 0$.

Item 3 of the theorem says that it is possible to approximate the center manifold $\mathbf{h}$ by the function $\mathbf{H}$ up to terms of order $O(|\mathbf{q}_c|^p)$. This is a very important feature from the practical point of view because it allows to calculate a sufficiently accurate approximation by cutting off a Taylor series expansion.

In the infinite-dimensional case care must be taken concerning the spectrum of the linearized operator, since eqn [1] is a partial differential equation and defined on an infinite-dimensional space.

Examples We first indicate the calculations for the loss of stability of a steady state if a zero root crosses the imaginary axis and present some quantitatively drawn figures following from this calculation. Secondly, for the classical flutter instability where a complex pair of eigenvalues crosses the imaginary axis, which mathematicans call the Hopf bifurcation, the reduced system of equations and a qualitative picture is given.

Steady-state bifurcation We consider the stability problem of the zero solution of the two-dimensional system:

$$\begin{aligned}\dot{x} &= bxy + fx^3 \\ \dot{y} &= -\mu y + cx^2\end{aligned} \qquad [7]$$

which, due to the occurrence of a zero eigenvalue is a critical case in the sense of Liapunov. The linear part is already in diagonal form with eigenvalues $0, -\mu$. Hence $x = q_c$ is the critical variable describing the essential dynamics and $y = q_s$ can be eliminated by treating the stability problem. The first equation will become the equation on the center manifold from which y must be eliminated. This is done by making an *ansatz* for the approximation of the center manifold according to eqn [4] in the form:

$$y = H(x) = h_2x^2 + h_3x^3 + \ldots \qquad [8]$$

Inserting into eqn [6] we obtain up to third-order terms ($p = 3$ in eqn [6]):

$$\mu\big(h_2x^2 + h_3x^3\big) - cx^2 + O\big(x^4\big) = 0$$

Requiring that the coefficients of the second- and third-order terms vanish we obtain:

$$\mu h_2 - c = 0, \qquad \mu h_3 = 0$$

From this system we obtain the coefficients of eqn [8]:

$$h_2 = \frac{c}{\mu}, \quad h_3 = 0 \qquad [9]$$

Inserting eqn [9] into eqn [8] and eliminating y from the first equation of eqn [7] with eqn [8], the one-dimensional equation:

$$\dot{x} = b\frac{c}{\mu}x^3 + fx^3 + \ldots$$

is obtained on the center manifold according to eqn [5]. Considering now the case $\mu = 1, b = 1, f = 0$, the center manifolds for the linear and two nonlinear systems are shown in **Figure 1**. We see that the stability behavior of the origin is determined by the coefficient c of the nonlinear term occurring in the second (eliminated) equation.

Hopf bifurcation If for an infinite-dimensional system, for example the tube conveying fluid, one purely imaginary pair of roots $\pm i\omega$ crosses the imaginary

axis and all other roots have negative real parts, then this system typically can be reduced to a two-dimensional third-order system of the form:

$$\begin{aligned}\dot{q}_1 &= -\omega q_2 + a_{1,30}q_1^3 + a_{1,21}q_1^2 q_2 + a_{1,12}q_1 q_2^2 \\ &\quad + a_{1,03}q_2^3 + O\left(|\mathbf{q}|^5\right) \\ \dot{q}_2 &= -\omega q_1 + a_{2,30}q_1^3 + a_{2,21}q_1^2 q_2 + a_{2,12}q_1 q_2^2 \\ &\quad + a_{2,03}q_2^3 + O\left(|\mathbf{q}|^5\right)\end{aligned} \quad [10]$$

From the sketches shown in **Figure 1** it is intuitively clear how the inessential variables are neglected because in the phase space the flow of the full system is contracted exponentially fast to the center manifold M^c where the asymptotic behavior of the trajectories and especially the stability of the equilibrium is governed by the nonlinear terms (e.g., in eqn [7] by the term with coefficient c).

Normal Form Simplification

The low-dimensional system of amplitude equations of the critical modes or eigenvectors (eqn [5]) can still be strongly simplified by means of normal form transformation.

The basic idea is to try to annihilate the nonlinear terms in eqn [5] by a nonlinear change of variables. However, complete annihilation is only possible if a linear operator, derived below, is regular. If it is singular then those terms which are not in its range cannot be eliminated and form the nonlinear normal form. We insert the nonlinear change of coordinates $\mathbf{q}_c \to \mathbf{x}$:

$$\mathbf{q}_c = \mathbf{x} + \mathbf{n}(\mathbf{x}) \quad [11]$$

into eqn [5] and obtain:

$$(\mathbf{E} + \mathbf{n}'(\mathbf{x}))\dot{\mathbf{x}} = \mathbf{J}\mathbf{x} + \mathbf{J}\mathbf{n}(\mathbf{x}) + \mathbf{g}(\mathbf{x} + \mathbf{n}(\mathbf{x})) \quad [12]$$

Here $\mathbf{E}$ denotes the unit matrix. Writing the transformed system in the form:

$$\dot{\mathbf{x}} = \mathbf{J}\mathbf{x} + \mathbf{f}(\mathbf{x}) \quad [13]$$

the unknown function $\mathbf{n}(\mathbf{x})$ in eqn [11] should now be chosen such that the nonlinear terms $\mathbf{f}(\mathbf{x})$ in eqn [13] are as simple as possible. The most desirable situation would be to eliminate all terms in $\mathbf{f}(\mathbf{x})$. Substituting eqn [13] into eqn [12] we find for the lowest-order terms:

$$\mathbf{J}\mathbf{n}(\mathbf{x}) - \mathbf{n}'(\mathbf{x})\mathbf{J}\mathbf{x} = \mathbf{f}(\mathbf{x}) - \mathbf{g}(\mathbf{x}) + o(\mathbf{n}(\mathbf{x})) \quad [14]$$

where $o(\mathbf{n}(\mathbf{x}))$ designates terms of higher order than those included in $\mathbf{n}(\mathbf{x})$. Since we want to have $\mathbf{f} = 0$ in eqn [13], we set $\mathbf{f} = \mathbf{0}$ in eqn [14] resulting in the equation:

$$\mathbf{J}\mathbf{n}(\mathbf{x}) - \mathbf{n}'(\mathbf{x})\mathbf{J}\mathbf{x} = -\mathbf{g} \quad [15]$$

which is called the homological equation and can be solved only if $-\mathbf{g}$ lies in the image of the linear map $\mathbf{ad}_J: \mathbf{n}(\mathbf{x}) \mapsto \mathbf{J}\mathbf{n}(\mathbf{x}) - \mathbf{n}'(\mathbf{x})\mathbf{J}\mathbf{x}$ on the left-hand side, called the homological operator. The homological operator is regular if the eigenvalues of $\mathbf{J}$ are not located on the imaginary axis and in addition a resonance condition is not satisfied. Then $\mathbf{f} = \mathbf{0}$ can be achieved and the nonlinear system can be replaced by its linearization in the neighborhood of the singular point (**Figure 2**). However, in the bifurcation case, typically this requirement is not fulfilled and hence certain terms will always remain, forming the nonlinear normal form.

Examples

We present two examples. The first shows the strong reduction of complexity and the second shows an important feature of the system in normal form namely that it has an artificial symmetry.

Normal form after a Hopf bifurcation A straightforward application of the above formulas yields instead of eqn [10]:

$$\begin{aligned}\dot{x}_1 &= -\omega x_2 + A_1\left(x_1^2 + x_2^2\right)x_1 - B_1\left(x_1^2 + x_2^2\right)x_2 \\ \dot{x}_2 &= \omega x_2 + B_1\left(x_1^2 + x_2^2\right)x_1 + A_1\left(x_1^2 + x_2^2\right)x_2\end{aligned} \quad [16]$$

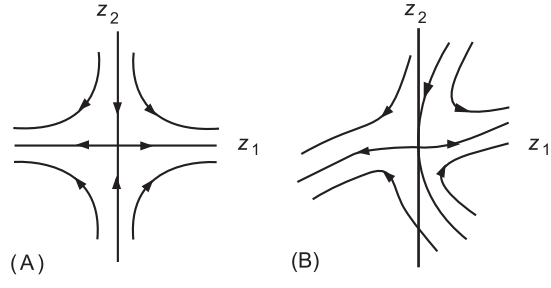


Figure 2 Near a hyperbolic point all nonlinear terms can be removed from the nonlinear system (B) by a nonlinear change of coordinates, yielding the system in normal form as a linear system (A) provided the resonance condition is not fulfilled.

where only two coefficients A_1, B_1 appear in the normal form. They are related to the eight coefficients $a_{1,\,kl}$ and $a_{2,\,kl}$ in eqn [10] by:

$$A_1 = \tfrac{3}{8}a_{1,30} + \tfrac{1}{8}a_{1,12} + \tfrac{3}{8}a_{2,21} + \tfrac{3}{8}a_{2,03}$$
$$B_1 = -\tfrac{3}{8}a_{1,03} - \tfrac{1}{8}a_{1,21} + \tfrac{1}{8}a_{2,12} + \tfrac{3}{8}a_{2,30}$$

Inserting polar coordinates $x_1 = r\cos\varphi$, $x_2 = r\sin\varphi$ into the normal form (eqn [16]) it takes the form:

$$\begin{aligned}\dot{r} &= A_1 r^3 \\ \dot{\varphi} &= \omega + B_1 r^2\end{aligned} \qquad [17]$$

Van der Pol oscillator By means of the example of the van der Pol oscillator $\ddot{x} + x = \varepsilon(1 - x^2)\dot{x}$ we show that the transformation into normal form following the approach explained before introduces an artificial rotational symmetry. Introducing the complex coordinate $z = x - \mathrm{i}\dot{x}$, one obtains a complex first-order equation $\dot{z} = (\mathrm{i}z + (\varepsilon(z - \bar{z})/2 - \varepsilon(z^3 + z^2\bar{z} - z\bar{z}^2 - \bar{z}^3)/8$. Neglecting terms of order $O(\varepsilon^2)$, the normal form reduction yields $\dot{z} = ((\varepsilon/2) + \mathrm{i})z - (\varepsilon/8)z^2\bar{z}$, which admits as solution the circular limit cycle $z = 2\exp \mathrm{i}t$. The limit cycles of the original equation and of the equation transformed into normal form are shown in **Figure 3.**

Classification and Unfolding

After dimension reduction by the center manifold theory and simplification by the normal form theory a third important step in the study of the loss of stability of a state can be made by a classification.This is made possible by the fact that there is only a very limited number of qualitatively different cases of loss of stability. This number of cases can be classified depending on the codimension of the critical systems.

The concept of codimension arises quite naturally if we not only ask for the solution of the critical system (eqn [17]) but also for all qualitatively different solutions in the family of systems to which the critical (singular) system belongs. The first question is how many parameters are necessary to make such an embedding of a singular system into a parameter family in which all qualitatively different solutions of this class are included. The minimum number of parameters necessary to form such a universally unfolded family is the codimension.

Codimension one contains two cases: first, one zero eigenvalue with quadratic nonlinear terms (eqn [7]); and secondly, one purely imaginary pair (eqn [17]), with third-order nonlinear terms. Hence for eqn [17] with one parameter a universally unfolded family can be obtained including all qualitatively possible solutions. This parametrized family has the form:

$$\begin{aligned}\dot{r} &= A_1 r^3 + ar \\ \dot{\varphi} &= \omega + B_1 r^2\end{aligned} \qquad [18]$$

where a is the unfolding parameter. The stationary solutions of eqn [18] which give the amplitude of the limit cycle oscillations with the frequency ω, which sets in after loss of stability, can be calculated from $A_1 r^3 + ar = 0$ and are presented for $A_1 < 0$ and $A_1 > 0$ in **Figure 4**. It can be clearly seen from **Figure 4** that the stability of the singular point of the system (eqn [16]) depends on whether A_1 is positive or negative, hence on the nonlinear terms. In the neighborhood of the critical parameter value the oscillation of the infinite dimensional tube conveying fluid is completely governed by eqn [18] as in **Figure 4**. Here the local parameter $a \sim \lambda - \lambda_c$ has been introduced. **Figure 4** also shows the stratification of the parameter space (here one-dimensional) into domains of qualitatively similar behavior ($a<0$ and $a>0$).

Two-parameter families (codimension 2) are also completely classified resulting in five different cases. They are best presented with the corresponding

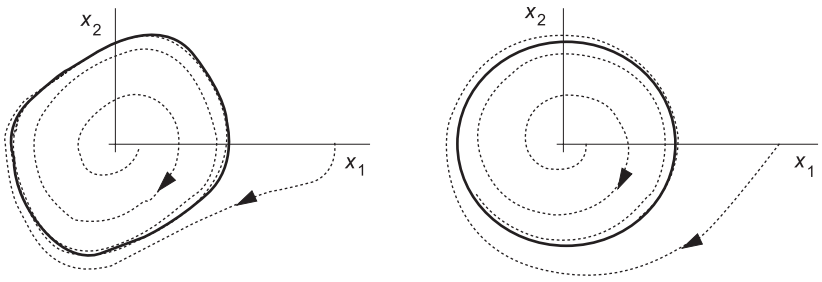


Figure 3 Solutions of the van der Pol equation and its normal form equation in the $z = x_1 - \mathrm{i}x_2$ phase plane for $\varepsilon = 0.4$, showing the artificial rotation symmetry introduced in the flow by the normal form transformation.

stratification of the two-dimensional parameter space.

Recent Developements in Bifurcation Theory

Loss of Stability of a Periodic Solution

The treatment indicated above for the loss of stability of a steady state can be extended in exactly the same way, to a periodic solution if, instead of the differential equations for the description of the system, the point mapping in the Poincare section is used. Of course, the practical calculation of the point mapping is a nontrivial step. In the point mapping the original periodic state corresponds to a fixed point and the three steps explained before can be performed again.

Continuous Parameter Variation

If the parameter variation is not quasistatical but continuous the situation is much more complicated and, in general, the onset of instability may be retarded.

Symmetric Systems

Treating systems which are equivariant under the action of a symmetry group by the methods explained before, one has to note that due to the symmetry of the system the critical eigenvalues may appear with higher multiplicity. Hence the reduced set of equations, for example eqn [10] for a Hopf bifurcation, has a higher dimension. In the case of a Hopf bifurcation for a rotationally symmetric system, instead of the two-dimensional system (eqn 10), a four-dimensional system is obtained. However, these equations must also be rotationally symmetric and hence the number of terms can be strongly reduced by checking their equivariance.

Hamiltonian Systems

Models of physical or technical systems which are governed by Hamiltonian systems are mostly found in the dynamics of space vehicles where the dissipative effects are so small that for short time periods such systems may be modelled as conservative systems. Here the basic problem arises that for Hamiltonian systems the location of the eigenvalues in the complex plane is reflectionally symmetric with respect to both the real and the imaginary axes. Hence, from the location of the eigenvalues of the linearized problem in the complex plane, a decision concerning the instability of a state can be made but a decision about its stability cannot be made because in the most favorable case all eigenvalues are located on the imaginary axis. Energy methods such as the Dirichlet method have been developed for such problems. Modern developments in connection with satellite attitude stability where conserved quantities, like angular momentum are often available, make use of energy-momentum methods which can be used to reduce the dimension of the problem.

Chaotic Dynamics

One major approach towards understanding chaotic behavior is to study the growing complexity of the dynamics due to a sequence of bifurcations by varying a parameter, starting from an equilibrium state. There is a vast literature on chaotic dynamics. An

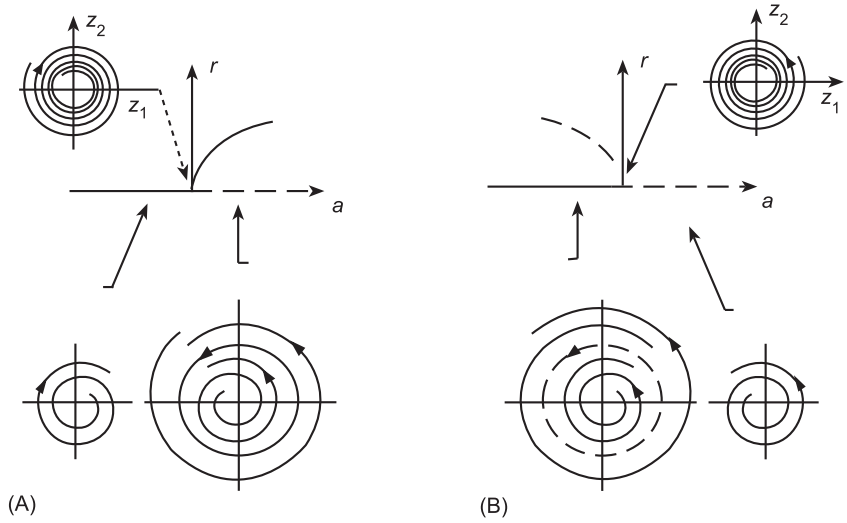


Figure 4 All possible solutions according to eqn [18] for a Hopf bifurcation. (A) A stable limit cycle is obtained for $A_1 < 0$; (B) an unstable limit cycle is obtained for $A_1 > 0$.

important possibility of having chaotic dynamics follows from global bifurcations.

Acknowledgement

This work has been supported by the Austrian Science Foundation (FWF), under project P 13131 – MAT.

See also: **Chaos**; **Nonlinear systems analysis**; **Nonlinear systems, overview**; **Theory of vibration**, Fundamentals.

Further Reading

Andronov A, Vitt A and Khaikin S (1966) *Theory of Oscillations*. New York: Addison Wesley.

Arnold VI (1983) *Geometrical Methods in the Theory of Ordinary Differential Equations*. Berlin: Springer-Verlag.

Carr, J (1981) *Applications of Centre Manifold Theory*. Applied Mathematical Sciences, vol. 35. New York: Springer-Verlag.

Glendinning P (1994) *Stability, Instability and Chaos: an Introduction to the Theory of Nonlinear Differential Equations*. London: Cambridge University Press.

Golubitsky M, Stewart I and Schaeffer D (1988) *Singularities and Groups in Bifurcation Theory II*. Applied Mathematical Sciences vol. **69**. Berlin: Springer-Verlag.

Guckenheimer J and Holmes P (1983) *Nonlinear Oscillations, Dynamical Systems, and Bifurcations of Vector Fields*. Applied Mathematical Sciences, vol. 42. Berlin: Springer-Verlag.

Hassard BD, Kazarinoff ND and Wan YH (1981) *Theory and Applications of Hopf Bifurcation*, London Mathematical Soceity Lecture Note Series, vol. 41. London: Cambridge University Press.

Holmes Ph, Lumley JL and Berkooz, G (1996) *Turbulence, Coherent Structures, Dynamical Systems and Symmetry*. London: Cambridge University Press.

Looss G and Joseph DD (1980) *Elementary Stability and Bifurcation Theory*. New York: Springer-Verlag.

Marsden J and Ratiu T (1994) *Introduction to Mechanics and Symmetry, Texts in Applied Mathematics*. New York: Springer-Verlag.

Moon FC (1987) *Chaotic Vibrations, An Introduction for Applied Scientists and Engineers*. Chichester: Wiley.

Seydel R (1994) *Practical Bifurcation and Stability Analysis*, 2nd edn. New York: Springer-Verlag.

Troger H and Steindl A (1991) *Nonlinear Stability and Bifurcation Theory. An Introduction for Engineers and Applied Scientists*. New York: Springer-Verlag.

Tufillaro NB, Tyler A and Reilly J (1992) *An Experimantal Approach to Nonlinear Dynamics and Chaos*. New York: Addison Wesley.

E

EARTHQUAKE EXCITATION AND RESPONSE OF BUILDINGS

F Naeim, John A Martin & Associates, Inc., Los Angeles, CA, USA

Copyright © 2001 Academic Press

doi:10.1006/rwvb.2001.0067

Building structures are designed to have a 'seismic capacity' that exceeds the anticipated 'seismic demand'. Capacity is a complex function of strength, stiffness and deformability conjectured by the system configuration and material properties of the structure. Given a particular building, seismic demand is controlled by what is commonly termed the 'design ground motion criteria', which may be defined in one or more of the following three distinct forms:

1. Static base shear and lateral force distribution formulas;
2. A set of 'design spectra';
3. A suite of earthquake acceleration 'time histories'.

The design ground motion may be defined in its most simple form by application of simple design base shear equations and static lateral force distribution formulas such as those embodied in a typical building code. These simple formulas are in essence, simplified interpretations of a design spectrum of certain shape and amplitude at the fundamental vibration period of the building.

For more complex analyses, the design ground motion criteria may be defined by a series of either code-specified or site-specific design spectra and rules on how to apply these spectra and how to interpret the results. If seismic design of a project requires application of dynamic time–history analysis, then an appropriate set of earthquake records have to be selected and rules have to be established on how these records are to be applied in analysis and design. The earthquake records, in this case, are needed in addition to a site-specific design spectra, and rules have to be set on how application of these records produces a demand that is consistent with the site-specific seismic hazard, which is usually summarized in the form of design spectra.

While a properly established design ground motion criteria is expected to provide a consistent expression of demand, regardless of its form, overzealous emphasis on one form over the others, without proper understanding of the strength and limitations of each form, can result in unrealistic design ground motion requirements.

Evaluation of the seismic hazard at a given site requires an estimate of likely earthquake ground motions at the site of the building. This is because: (i) sites for which a recorded earthquake ground motion is readily available are extremely rare, and (ii) even for the sites where such recordings are available, there is no guarantee that future ground motions will have the same exact characteristics of previously observed motions. Possible ground motions for a site are estimated by use of various regression analysis techniques on a selected subset of available earthquake recordings deemed proper for such estimation. The resulting mathematical formulas which provide estimates of maximum response parameters, such as peak ground acceleration or response spectral ordinates for a site are called 'predictive relations' or 'attenuation relations'. The term attenuation is used because these empirical relations in fact represent formulas for attenuation of seismic waves originating from a given source, at a given distance, through a given medium (i.e., site soil conditions). Dozens of attenuation relations have been developed and are in use today (**Table 1**).

Characteristics of Earthquake Ground Motions

The number of earthquake records available has grown rapidly during the past decade. While obtaining earthquake accelerograms was not simple up to about the mid-1980s, hundreds of earthquake records

Table 1 Typical attenuation relationships

Data source	*Relationship**	*by*
1. San Fernando earthquake February 9, 1971	$\log \text{PGA} = 190/R^{1.83}$	Donovan
2. California earthquake	$\text{PGA} = y_0/[1+(R'/h)^2)]$ where $\log y_0 = -(b+3)+0.81M-0.027M^2$ and b is a site factor	Blume
3. California and Japanese earthquakes	$\text{PGA} = 0.0051 / \text{s}\sqrt{(\text{T}_\text{G})}10^{(0.61\text{M}-\text{plogR}+0.167-1.83/\text{R})}$ where $P = 1.66+3.60/R$ and T_G is the fundamental period of the site	Kanai
4. Cloud (1963)	$\text{PGA} = 0.0069e^{1.64M}/(1.1_e^{1.1M}+R^2)$	Milne and Davenport
5. Cloud (1963)	$\text{PGA} = 1.254e^{0.8M}/(R+25)^2$	Esteva
6. U.S.C. and G.S.	$\log \text{PGA} = (6.5-2\log(R'+80))/981$	Cloud and Perez
7. 303 Instrumental Values	$\text{PGA} = 1.325e^{0.67M}/(R+25)^{1.6}$	Donovan
8. Western US records	$\text{PGA} = 0.0193e^{0.8M}/(R^2+400)$	Donovan
9. US, Japan	$\text{PGA} = 1.35e^{0.58M}/(R+25)^{1.52}$	Donovan
10. Western US records, USSR, and Iran	$\ln \text{PGA} = -3.99+1.28M-1.75\ln[R = 0.147e^{0.732M}]$ – M is the surface wave magnitude for M greater than or equal to 6, or it is the local magnitude for M less than 6.	Campbell
11. Western US records and worldwide	$\log \text{PGA} = -1.02+0.249M-\log\sqrt{(\text{R}^2+7.3^2)}-0.00255\sqrt{(\text{R}^2+7.3^2)}$	Joyner and Boore
12. Western US records and worldwide	$\log \text{PGA} = 0.49+0.23(M-6)-\log\sqrt{(\text{R}^2+8^2)}-0.0027\sqrt{(\text{R}^2+8^2)}$	Joyner and Boore
13. Western US records	$\ln \text{PGA} = \ln\alpha(M)-\beta(M)\ln(R+20)$ – M is the surface wave magnitude for M greater than or equal to 6, or it is the local magnitude for smaller M. – R is the closest distance to source for M greater than 6 and hypocentral distance for M smaller than 6. – $\alpha(M)$ and $\beta(M)$ are magnitude-dependent coefficients.	Idriss
14. Italian records	$\ln \text{PGA} = -1.562+0.306M-\log\sqrt{(\text{R}^2+5.8^2)}+0.169S$ – S is 1.0 for soft sites or 0.0 for rock.	Sabetta and Pugliese
15. Western US and worldwide (soil sites)	For M less than 6.5, $\ln \text{PGA} = -2.611+1.1M-1.75\ln(R+0.822e^{0.418M})$ For M greater than or equal to 6.5, $\ln \text{PGA} = -2.611+1.1M-1.75\ln(R+0.316e^{0.629M})$	Sadigh et al.
16. Western US and worldwide (rock sites)	For M less than 6.5, $\ln \text{PGA} = -1.406+1.1M-2.05\ln(R+1.353e^{0.406M})$ For M greater than or equal to 6.5, $\ln \text{PGA} = -1.406+1.1M-2.05\ln(R+0.579e^{0.537M})$	Sadigh et al.
17. Worldwide earthquakes	$\ln \text{PGA} = -3.512+0.904M-1.328\ln\sqrt{[\text{R}^2+(0.149e^{0.647M})^2]}$ $+(1.125-0.112\ln R-0.0957M)F+(0.440-0.171\ln R)S_{sr}$ $+(0.405-0.222\ln R)S_{hr}$ – $F = 0$ for strike-slip and normal fault earthquakes and 1 for reverse, reverse-oblique, and thrust fault earthquakes. $-S_{sr} = 1$ for soft rock and 0 for hard rock and alluvium – $S_{hr} = 1$ for hard rock and 0 for soft rock and alluvium	Campbell and Bozorgnia
18. Western North American earthquakes	$\ln \text{PGA} = b+0.527(M-6.0)-0.778\ln\sqrt{[\text{R}^2+(5.570)^2]}$ $-0.371\ln(V_s/1396)$ – where $b = -0.313$ for strike-slip earthquakes $= -0.117$ for reverse-slip earthquakes $= -0.242$ if mechanism is not specified – V_s is the average shear wave velocity of the soil in (m s^{-1}) over the upper 30 meters – The equation can be used for magnitudes of 5.5 to 7.5 and for distances not greater than 80 km	Boore et al.

* Peak ground acceleration *PGA* in *g*, source distance *R* in km, source distance *R'* in miles, local depth *h* in miles, and earthquake magnitude *M*. Refer to the relevant references for exact definitions of source distance and earthquake magnitude.

may now be screened, viewed and downloaded from the Internet or obtained at a nominal cost from various public agencies.

The characteristics of ground motion that are important for building design applications are: (i) peak ground motion (peak ground acceleration, peak ground velocity, and peak ground displacement), (ii) duration of strong motion, and (iii) frequency content. Each of these parameters influences the response of a building. Peak ground motion primarily influences the vibration amplitudes. Duration of strong motion has a pronounced effect on the severity of shaking. A ground motion with a moderate peak acceleration and a long duration may cause more damage than a ground motion with a larger acceleration and a shorter duration. There are several methods currently in use for measuring the duration of strong ground motion. These methods often use different indicators for assigning a particular duration to a given earthquake record and the user must be aware of the assumptions inherent in each method of assessing duration before using them (**Figure 1**). Frequency content strongly affects the response characteristics of a building. In a structure, ground motion is amplified the most when the frequency content of the motion and the natural frequencies of the structure are close to each other.

Earthquake ground motion is influenced by a number of factors. The most important factors are (i) earthquake magnitude, (ii) distance from the source of energy release (epicentral distance or distance from the causative fault), (iii) local soil conditions, (iv) variation in geology and propagation velocity along the travel path, and (v) earthquake source conditions and mechanism (fault type, slip rate, stress conditions, stress drop, etc.). Past earthquake records have been used to study some of these influences. While the effect of some of these parameters, such as local soil conditions and distance from the source of energy release are fairly well understood and documented, the influence of source mechanism is under investigation and the variation of geology along the travel path is complex and difficult to quantify. It should be noted that several of these influences are interrelated; consequently, it is difficult to evaluate them individually without incorporating the others.

Near-Source Effects

Recent studies have indicated that near-source ground motions contain large displacement pulses (ground displacements which are attained rapidly with a sharp peak velocity). These motions are the result of stress waves moving in the same direction as

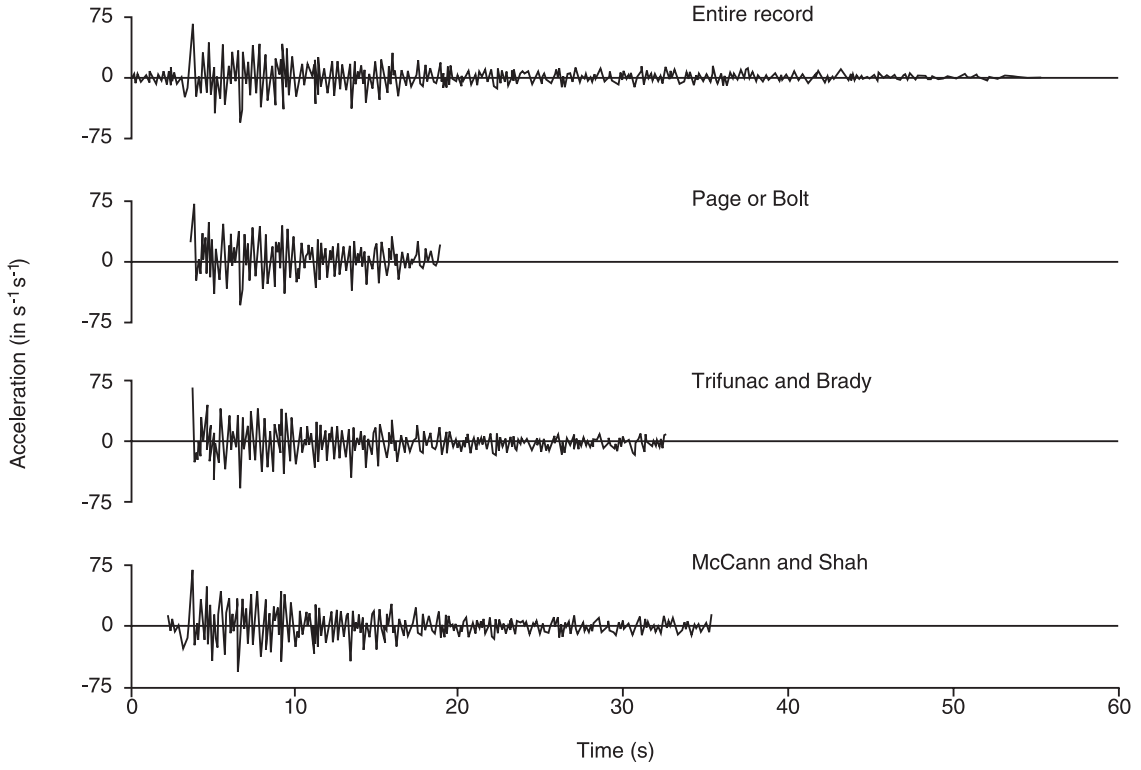


Figure 1 Comparison of strong motion duration for the S69E component of the Taft, California earthquake of 21 July, 1952 using different procedures.

the fault rupture, thereby producing a long-duration pulse. Consequently, near source earthquakes can be destructive to structures with long periods. Peak ground accelerations, velocities, and displacements from 30 records obtained within 5 km of the rupture surface, for example, have shown ground accelerations varying from 0.31 to 2.0*g* while the ground velocities ranged from 0.31 to 1.77 m s^{-1}. The peak ground displacements were as large as 2.55 m.

Figure 2 and **Figure 3** offer two examples of near-source earthquake ground motions. The first was recorded at the LADWP Rinaldi Receiving Station during the Northridge earthquake of 17 January 1994. The distance from the recording station to the

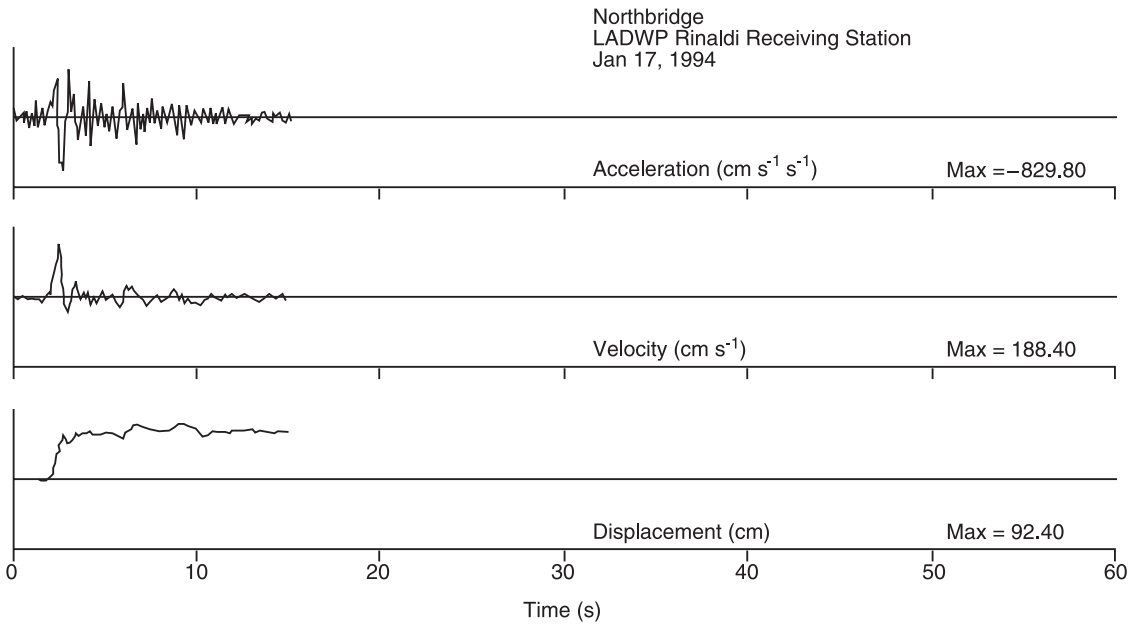


Figure 2 Ground acceleration, velocity, and displacement time-histories recorded at the LADWP Rinaldi Receiving Station during the Northridge earthquake of 17 January, 1994.

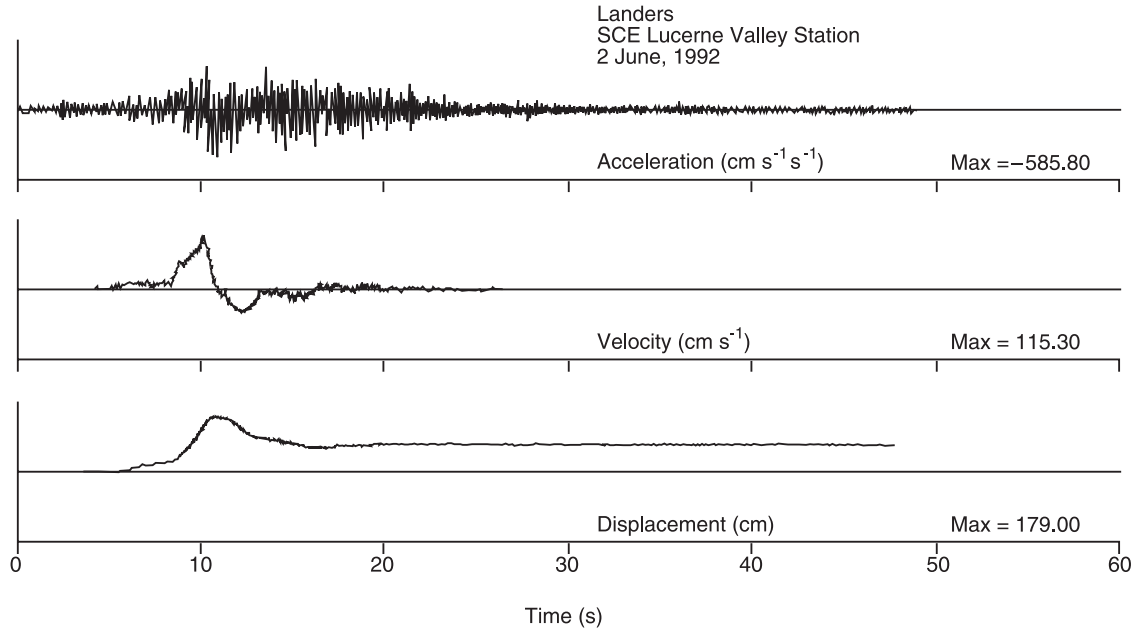


Figure 3 Ground acceleration, velocity, and displacement time-histories recorded at the SCE Lucerne Valley Station during the Landers earthquake of 28 June, 1992.

surface projection of the rupture was less than 1.0 km. The figure shows a unidirectional ground displacement that resembles a smooth step function and a velocity pulse that resembles a finite delta function. The second example, shown in **Figure 3**, was recorded at the SCE Lucerne Valley Station during the Landers earthquake of 28 June 1992. The distance from the recording station to the surface projection of the rupture was approximately 1.8 km. A positive and negative velocity pulse that resembles a single long-period harmonic motion is reflected in the figure. Near-source ground displacements similar to that shown in **Figure 3** have also been observed with a zero permanent displacement. The two figures clearly show the near-source ground displacements caused by sharp velocity pulses. Far-source ground motions, however, generally lack the pulse type motion often observed in near-source ground motions (**Figure 4**).

The frequency content of ground motion can be examined by transforming the motion from a time domain to a frequency domain through a Fourier transform. The Fourier amplitude spectrum and power spectral density, which are based on this transformation, may be used to characterize the frequency content.

Fourier Amplitude Spectrum

The finite Fourier transform $F(\omega)$ of an accelerogram $a(t)$ is obtained as:

$$F(\omega) = \int_0^T a(t)\mathrm{e}^{-\mathrm{i}\omega t}\,\mathrm{d}t, \quad i = \sqrt{(-1)} \qquad [1]$$

where T is the duration of the accelerogram. The Fourier amplitude spectrum $\mathrm{FS}(\omega)$ is defined as the square root of the sum of the squares of the real and imaginary parts of $F(\omega)$. Thus:

$$\mathrm{FS}(\omega) = \sqrt{\left\{\left[\int_0^T a(t)\sin\omega t\,\mathrm{d}t\right]^2 + \left[\int_0^T a(t)\cos\omega t\,\mathrm{d}t\right]^2\right\}} \qquad [2]$$

Since $a(t)$ has units of acceleration, $\mathrm{FS}(\omega)$ has units of velocity. The Fourier amplitude spectrum is of interest to seismologists in characterizing ground motion. **Figure 5** shows a typical Fourier amplitude spectrum for the S00E component of El Centro, the

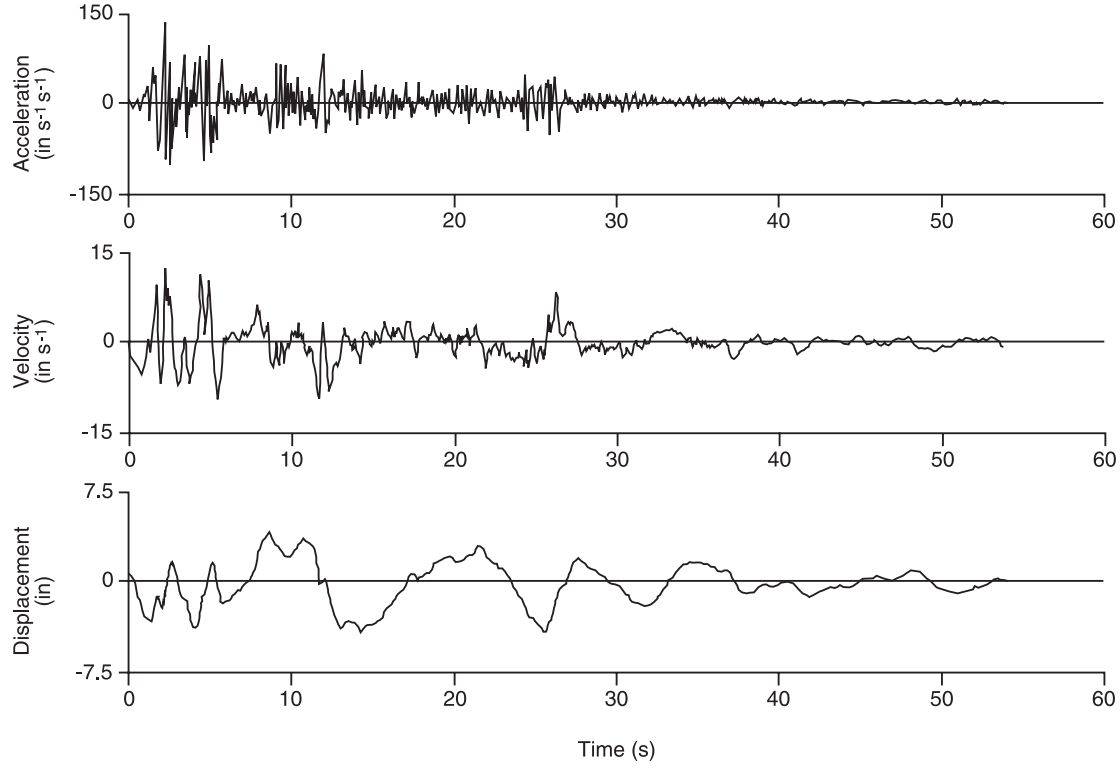


Figure 4 Corrected accelerogram and integrated velocity and displacement time-histories for the S00E coponent of El Centro, the Imperial Valley Earthquake of 18 May, 1940 is an example of an earthquake record not exhibiting near-source effects.

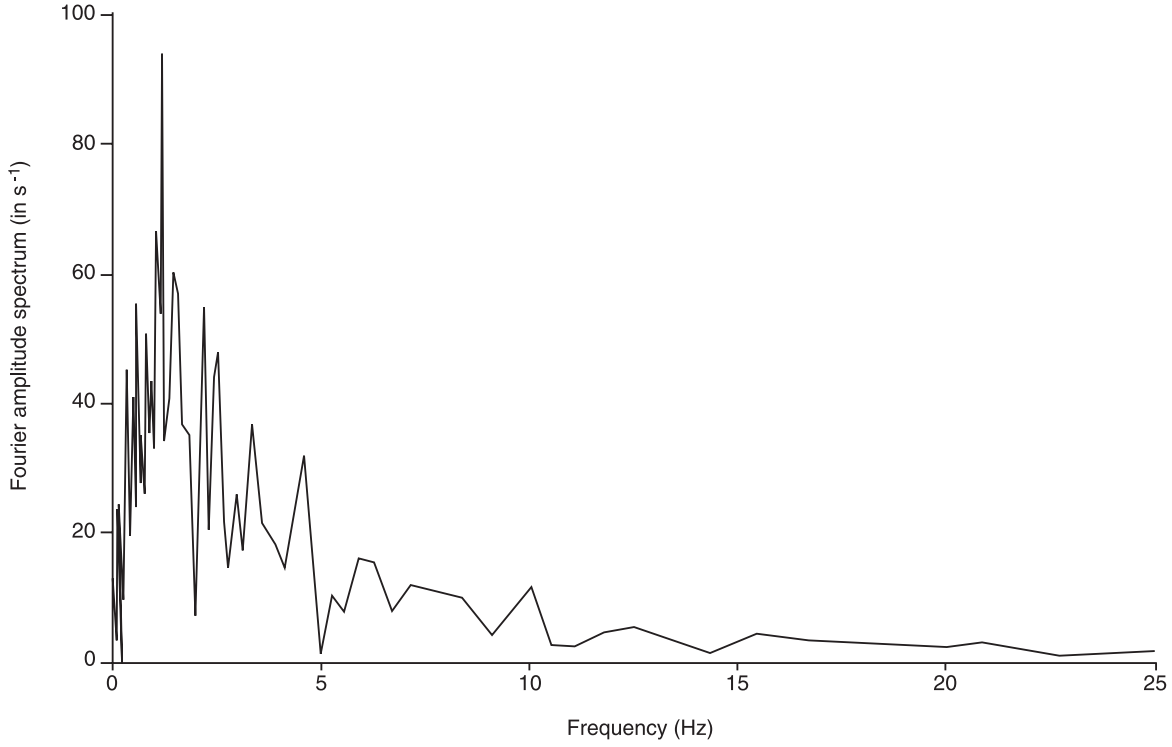


Figure 5 Fourier amplitude spectrum for the S00E component of El Centro, the Imperial Valley earthquake of 18 May, 1940.

Imperial Valley earthquake of 18 May 1940. The figure indicates that most of the energy in the accelerogram is in the frequency range 0.1–10 Hz, and that the largest amplitude is at a frequency of approximately 1.5 Hz.

It can be shown that subjecting an undamped single-degree-of-freedom (SDOF) system to a base acceleration $a(t)$, the velocity response of the system and the Fourier amplitude spectrum of the acceleration are closely related. The equation of motion of the system can be written as:

$$\ddot{x} + \omega_n^2 x = -a(t) \qquad [3]$$

in which x and $\ddot{x}$ are the relative displacement and acceleration, and ω_n is the natural frequency of the system. Using Duhamel's integral, the steady state response can be obtained as:

$$x(t) = \frac{1}{\omega_n} \int_0^t a(\tau) \sin \omega_n (t - \tau)\, dt \qquad [4]$$

The relative velocity $\dot{x}(t)$ follows directly from eqn [4] as:

$$\dot{x}(t) = \int_0^t a(\tau) \cos \omega_n (t - \tau)\, d\tau \qquad [5]$$

Eqn [5] can be expanded as:

$$\dot{x}(t) = -\left[\int_0^t a(\tau) \cos \omega_n \tau\, d\tau\right] \cos \omega_n t - \left[\int_0^t a(\tau) \sin \omega_n \tau\, d\tau\right] \sin \omega_n t \qquad [6]$$

Denoting the maximum relative velocity (spectral velocity) of a system with frequency ω by SV(ω) and assuming that it occurs at time t_v, one can write:

$$\mathrm{SV}(\omega) = \sqrt{\left\{\left[\int_0^{t_v} a(\tau) \sin \omega\tau\, d\tau\right]^2 + \left[\int_0^{t_v} a(\tau) \cos \omega\tau\, d\tau\right]^2\right\}} \qquad [7]$$

The pseudo-velocity PSV(ω) defined as the product of the natural frequency ω and the maximum relative

displacement or the spectral displacement $SD(\omega)$ is close to the maximum relative velocity. If $SD(\omega)$ occurs at t_d then:

$$PSV(\omega) = \omega SD(\omega) = \sqrt{\left\{\left[\int_0^{t_d} a(\tau)\sin\omega\tau\,d\tau\right]^2 + \left[\int_0^{t_d} a(\tau)\cos\omega\tau\,d\tau\right]^2\right\}} \quad [8]$$

Comparison of eqns [2] and [7] shows that for zero damping, the maximum relative velocity and the Fourier amplitude spectrum are equal when $t_v = T$. A similar comparison between eqns [2] and [8] reveals that the pseudo-velocity and the Fourier amplitude spectrum are equal if $t_d = T$. **Figure 6** shows a comparison between $FS(\omega)$ and $SV(\omega)$ for zero damping for the S00E component of El Centro, the Imperial Valley earthquake of 18 May 1940. The figure indicates the close relationship between the two functions. It should be noted that, in general, the ordinates of the Fourier amplitude spectrum are less than those of the undamped pseudo-velocity spectrum.

Power Spectral Density

The inverse Fourier transform of $F(\omega)$ is:

$$a(t) = \frac{1}{\pi}\int_0^{\omega_0} F(\omega)e^{i\omega t}\,d\omega \quad [9]$$

where ω_0 is the maximum frequency detected in the data (referred to as Nyquist frequency). Eqns [1] and [9] are called Fourier transform pairs. The intensity of an accelerogram is defined as:

$$I = \int_0^T a^2(t)\,dt \quad [10]$$

Based on Parseval's theorem, the intensity I can also be expressed in the frequency domain as:

$$I = \frac{1}{\pi}\int_0^{\omega_0} |F(\omega)|^2\,d\omega \quad [11]$$

The intensity per unit of time or the temporal mean square acceleration ψ^2 can be obtained by dividing eqn [10] or eqn [11] by the duration T. Therefore:

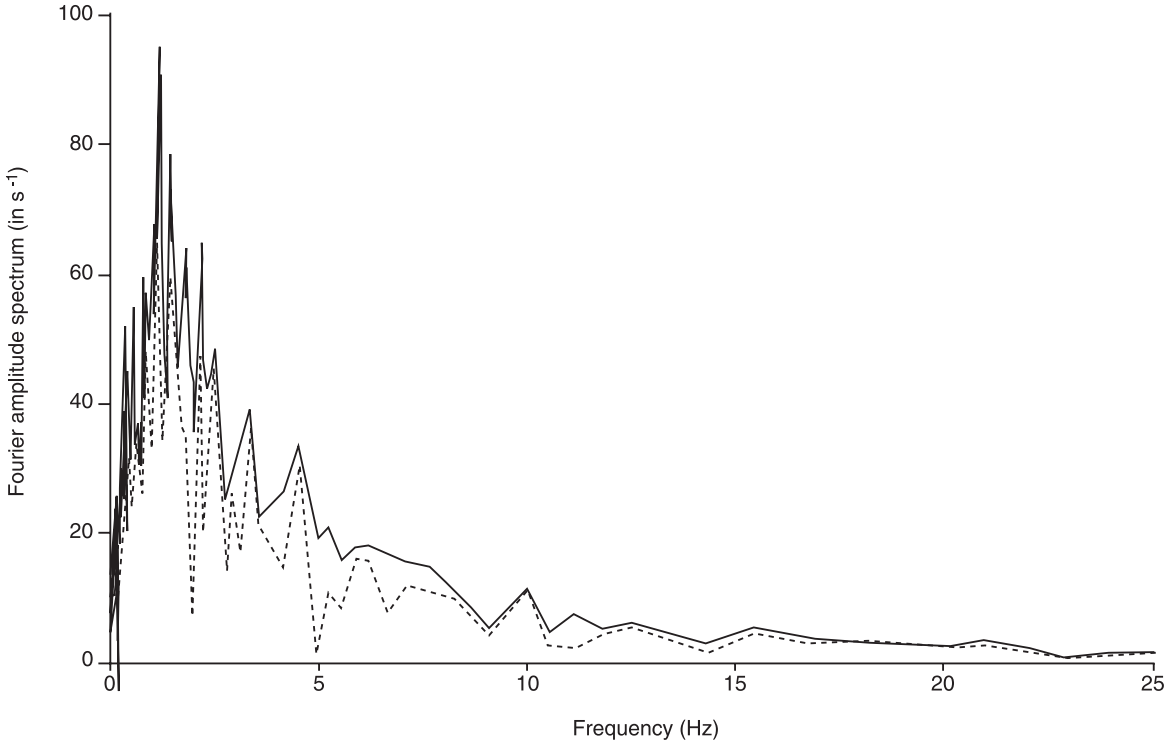


Figure 6 Comparison of Fourier amplitude spectrum (dashed line) and velocity spectrum (continuous line) for an undamped single-degree-of-freedom system for the S00E component of El Centro, the Imperial Valley earthquake of 18 May, 1940.

$$\psi^2 = \frac{1}{T}\int_0^T a^2(t)\,\mathrm{d}t = \frac{1}{\pi T}\int_0^{\omega_0} |F(\omega)|^2\,\mathrm{d}\omega \qquad [12]$$

The temporal power spectral density is defined as:

$$G(\omega) = \frac{1}{\pi T}|F(\omega)|^2 \qquad [13]$$

Combining eqns [12] and [13], the mean square acceleration can be obtained as:

$$\psi^2 = \int_0^{\omega_0} G(\omega)\,\mathrm{d}\omega \qquad [14]$$

In practice, a representative power spectral density of ground motion is computed by averaging across the temporal power spectral densities of an ensemble of N accelerograms. Therefore:

$$G(\omega) = \frac{1}{N}\sum_{i=1}^{N} G_i(\omega) \qquad [15]$$

where $G_i(\omega)$ is the power spectral density of the ith record. **Figure 7** shows a typical example of a normalized power spectral density computed for an ensemble of 161 accelerograms recorded on alluvium. Once the power spectral density of ground motion at a site is established, random vibration methods may be used to formulate probabilistic procedures for computing the response of structures. In addition, the power spectral density of ground motion may be used for other applications such as generating artificial accelerograms.

Earthquake Response of Buildings

The main cause of damage to structures during an earthquake is their response to ground motions which are input at the base. In order to evaluate the behavior of the structure under this type of loading condition, the principles of structural dynamics must be applied to determine the stresses and deflections, which are developed in the structure.

When a single-story structure, shown in **Figure 8A**, is subjected to earthquake ground motions, no external dynamic force is applied at the roof level. Instead, the system experiences an acceleration of the base. The effect of this on the idealized structure is shown in **Figure 8B** and **Figure 8C**. Summing the forces shown in **Figure 8D** results in the following equation of dynamic equilibrium:

$$f_\mathrm{i} + f_\mathrm{d} + f_\mathrm{s} = 0 \qquad [16]$$

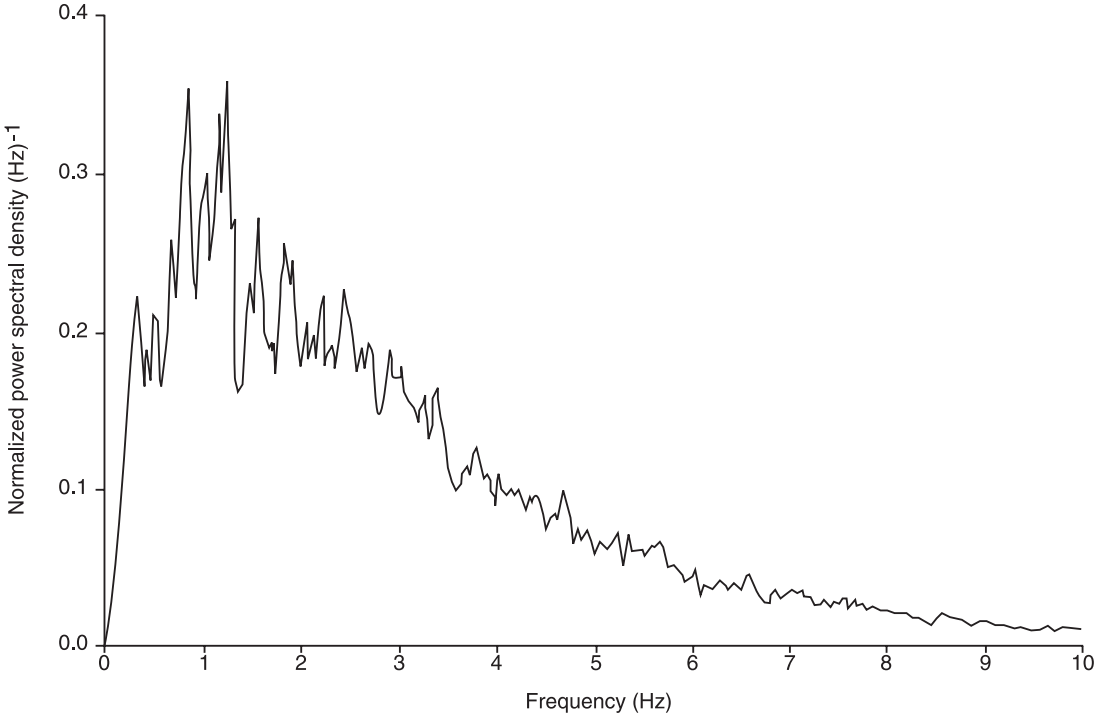


Figure 7 Normalized power spectral density of an ensemble of 161 horizontal components of accelerograms recorded on alluvium.

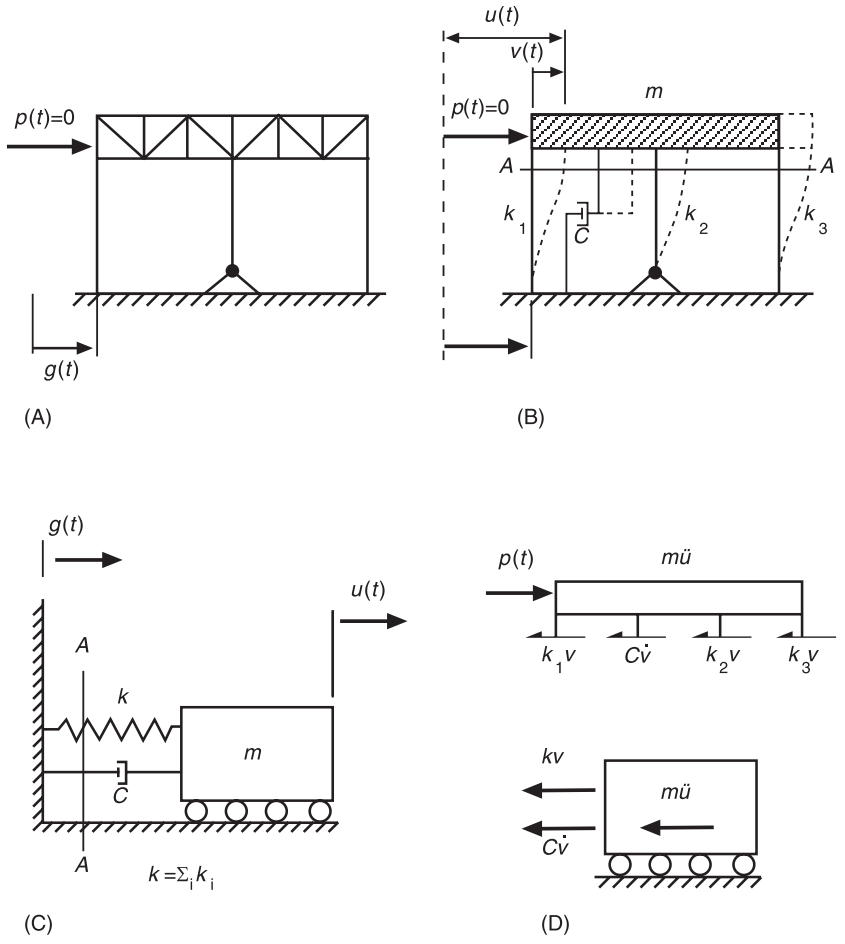


Figure 8 Single-degree-of-freedom system subjected to base motion. (A) Single story frame; (B) idealized structural system; (C) equivalent spring–mass–damper system; (D) free body diagrams, section A–A.

where $f_i =$ inertia force $= m\ddot{u}$, $f_d =$ damping (dissipative) force $= c\dot{v}$, $f_s =$ elastic restoring force $= kv$, $\ddot{u}$ is the total acceleration of the mass, and $\dot{v}$, v are the velocity and displacement of the mass relative to the base. Substituting the physical parameters for f_i, f_d and f_s in eqn [16] results in an equilibrium equation of the form:

$$m\ddot{u} + c\dot{v} + kv = 0 \qquad [17]$$

or:

$$m\ddot{v} + c\dot{v} + kv = p_e(t) \qquad [18]$$

where:

$p_e(t) =$ effective time-dependent force $= -m\ddot{g}(t)$

and:

$\ddot{v}(t) =$ acceleration of the mass relative to the base

$\ddot{g}(t) =$ acceleration of the base.

Therefore, the equation of motion for a structure subjected to a base motion is similar to that for a structure subjected to a time-dependent force if the base motion is represented as an effective time-dependent force which is equal to the product of the mass and the ground acceleration.

Earthquake Response of an Elastic SDOF System

Time–history response The response to earthquake loading can be obtained directly from the Duhamel integral as:

$$v(t) = \frac{V(t)}{\omega} = \frac{1}{\omega}\int_0^t \ddot{g}(\tau)e^{-\lambda\omega(t-\tau)} \sin \omega_d(t-\tau)\, d\tau \qquad [19]$$

where the response parameter $V(t)$ represents the velocity.

The displacement of the structure at any instant of time during the entire time history of the earthquake

under consideration can now be obtained using eqn [19]. If damping is small and the damping term can be neglected as contributing little to the equilibrium equation, the total acceleration can be approximated as:

$$\ddot{u}(t) = -\omega^2 v(t) \quad [20]$$

The effective earthquake force is then given as:

$$Q(t) = m\omega^2 v(t) \quad [21]$$

The above expression gives the value of the base shear in a single-story building at every instant of time during the earthquake time history under consideration. The overturning moment acting on the base of the building can be determined by multiplying the inertia force by the story height, h:

$$M(t) = hm\omega^2 v(t) \quad [22]$$

Response spectra Consideration of the displacements and forces at every instant of time during an earthquake time history can require considerable computational effort, even for simple structural systems. For most practical building design applications only the maximum response quantities are required. The maximum value of the displacement, as determined by eqn [19], is defined as the 'spectral displacement', S_d:

$$S_d = v(t)_{max} \quad [23]$$

As a result, the following expressions for the maximum base shear and maximum overturning moment in a SDOF system are obtained:

$$Q_{max} = m\omega^2 S_d \quad [24]$$

$$M_{max} = hm\omega^2 S_d \quad [25]$$

An examination of these equations indicates that the maximum velocity response can be approximated by multiplying the spectral displacement by the circular frequency. This response parameter is defined as the 'spectral pseudovelocity' and is expressed as:

$$S_{pv} = \omega S_d \quad [26]$$

In a similar manner, the 'spectral pseudoacceleration' is defined as:

$$S_{pa} = \omega^2 S_d \quad [27]$$

A plot of the spectral response parameter against frequency or period constitutes the 'response spectrum' for that parameter. Because the three response quantities (S_d, S_{pv}, S_{pa}) are related by the circular frequency, it is convenient to plot them on a single graph with log scales on each axis. This special type of plot is called a 'tripartite' log plot. The three response parameters for the El Centro motion are shown plotted in this manner in **Figure 9**. For a SDOF system having a given frequency (period) and given damping, the three spectral response parameters for this earthquake can be read directly from the graph.

For each earthquake record, response spectra can be constructed. Earthquakes share many common characteristics, but have their own unique attributes as well. Response spectra of earthquake records usually contain many peaks and valleys as a function of period (see **Figure 9** for example). There is no reason to believe that the spectra for future earthquakes will exhibit exactly the same peaks and valleys as previous recordings. Furthermore, the natural periods and mode shapes of building structures cannot be exactly predicted. Many uncertainties are present which include but are not limited to (i) unavoidable variations in the mass and stiffness properties of the building from those used in design, (ii) difficulties involved in establishing exact properties of site soil conditions, and (iii) inelastic response that tends to lengthen the natural period of the structure. For these reasons, it is more rational to use average curves obtained from a number of earthquake records for design purposes. These average curves, which do not reflect the sharp peaks and valleys of individual records, are also known as 'smoothed response spectra', or more commonly as 'design spectra'. While a response spectrum is an attribute of a particular ground motion, a design spectrum is not. A design spectrum is merely a definition of a criteria for structural analysis and design. A sample design spectrum chart is shown in **Figure 10**. Generally a design spectrum is generated for the standard critical damping ratio of 5% and building code specified damping adjustment factors are used to construct design spectra corresponding to other damping values. The adjustment factor, B, is defined as:

$$B = \frac{R_5}{R_x} \quad [28]$$

where R_x and R_5 are the spectral ordinates of the x% and 5% damped design spectrum at a given period, respectively. It is common to provide one adjustment value for medium to long periods of vibration, B_1 (usually calculated for the vibration period of about

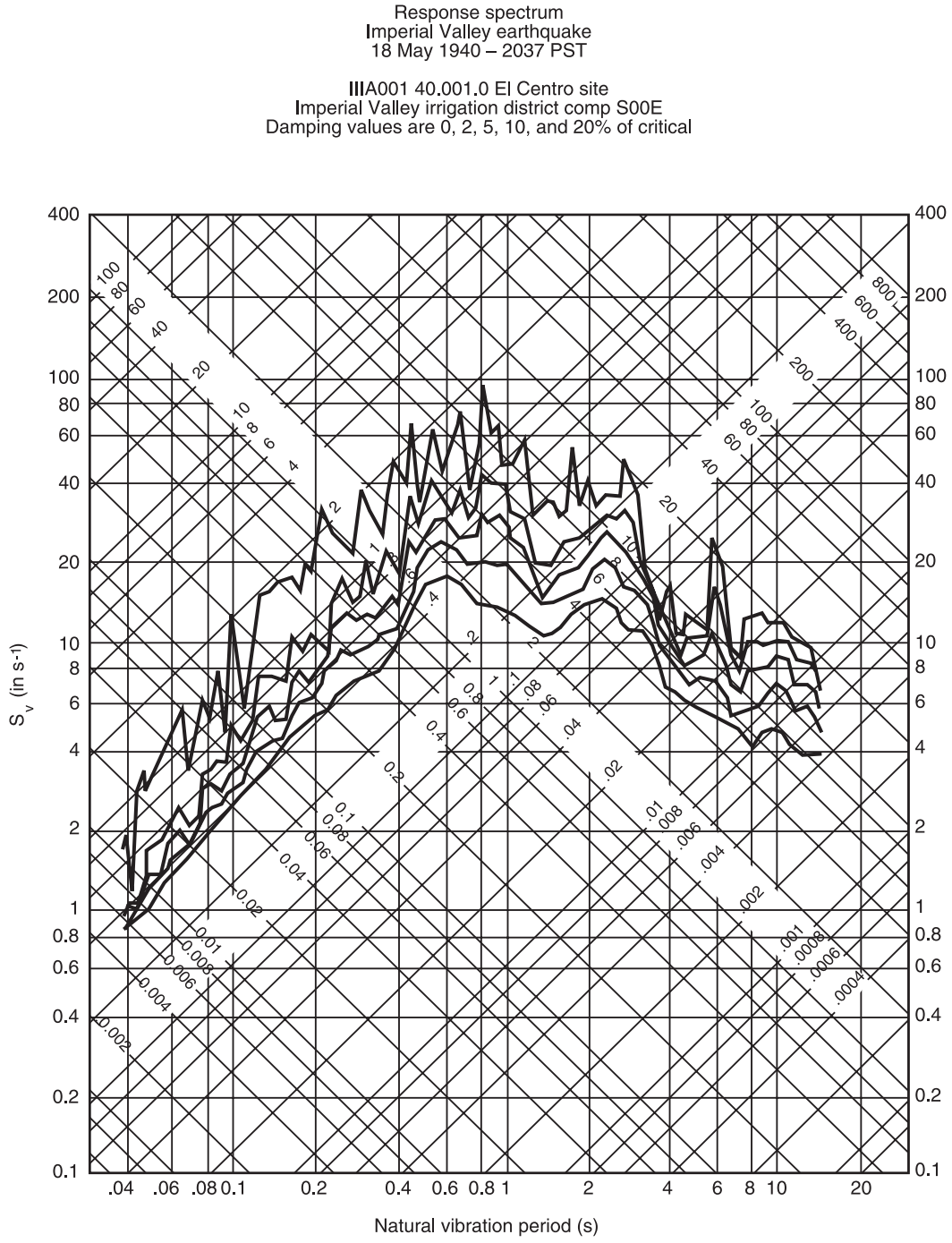


Figure 9 Typical tripartite response-spectra curves.

$1.0\,s^{-1}$) and another for short periods of vibration, B_s (usually determined for the vibration periods in the range 0.1–$0.3\,s^{-1}$). Typical values of such damping adjustment factors utilized in modern building codes are given in **Table 2**. The reader should note that these values are merely suggestive of the average values of anticipated adjustment factors and recent studies have shown that there is a wide scatter among adjustment factors obtained from various earthquake records (**Figure 11**).

Approximate Analysis of Response of Elastic MDOF Systems Using the Generalized Coordinates Method

Up to this point, the only structures which have been considered are single-story buildings which can be

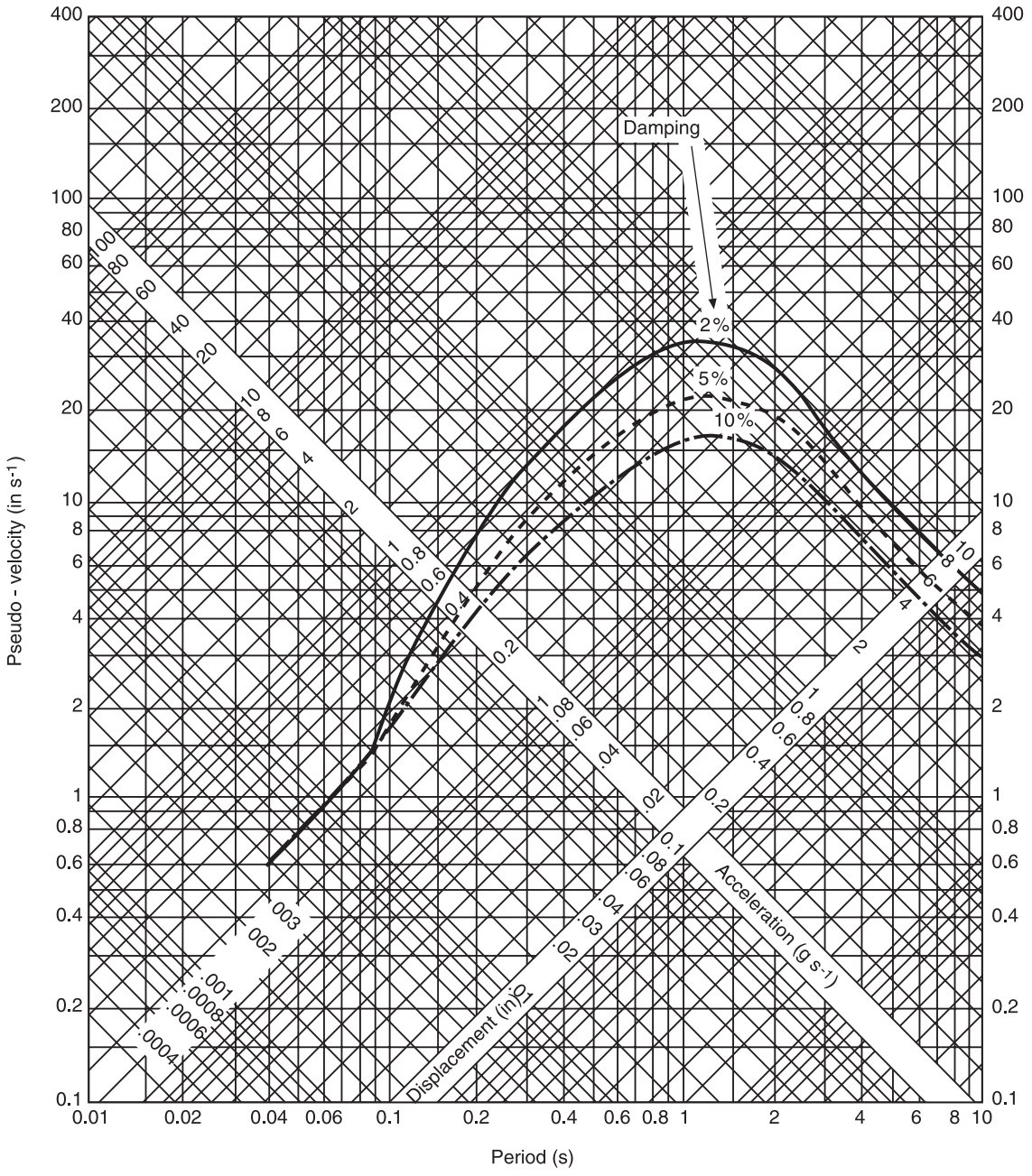


Figure 10 A sample 'smoothed' design spectra.

idealized as SDOF systems. The analysis of most structural systems requires a more complicated idealization even if the response can be represented in terms of a single degree of freedom. The generalized–coordinate approach provides means of representing the response of more complex structural systems in terms of a single, time-dependent coordinate, known as the generalized coordinate. Displacements in the structure are related to the generalized coordinate as:

$$v(x,t) = \phi(x)Y(t) \qquad [29]$$

where $Y(t)$ is the time-dependent generalized coordinate and $\phi(x)$ is a spatial shape function which relates the structural degrees of freedom, $v(x,t)$, to the generalized coordinate. For a generalized SDOF system, it is necessary to represent the restoring forces in the damping elements and the stiffness elements in terms of the relative velocity and relative displacement between the ends of the element:

$$\Delta\dot{v}(x,t) = \Delta\phi(x)\dot{Y}(t) \qquad [30]$$

Table 2 Typical building code recommended damping adjustment factors

Percent of critical damping	*Damping coefficient*	
	B_1	B_s
<2	0.8	0.8
5	1.0	1.0
10	1.2	1.3
20	1.5	1.8
30	1.7	2.3
40	1.9	2.7
>50	2.0	3.0

$$\Delta v(x,t) = \Delta\phi(x)Y(t) \qquad [31]$$

Most buildings can be idealized as a vertical cantilever, which limits the number of displacement functions that can be used to represent the horizontal displacement. Once the displacement function is selected, the structure is constrained to deform in that prescribed manner. This implies that the displacement functions must be selected carefully if a good approximation of the dynamic properties and response of the system are to be obtained.

Here, the formulation of the equation of motion in terms of a generalized coordinate will be restricted to systems which consist of an assemblage of lumped masses and discrete elements which is typical of most building structures. Lateral resistance is provided by discrete elements whose restoring force is proportional to the relative displacement between the ends of the element. Damping forces are assumed proportional to the relative velocity between the ends of the discrete damping element. The principle of virtual work in the form of virtual displacements states that if a system of forces which are in equilibrium is given a virtual displacement which is consistent with the boundary conditions, the work done is zero. Applying this principle to a SDOF system shown in **Figure 8** results in an equation of virtual work in the form:

$$f_i\,\delta v + f_d\,\delta\Delta v + f_s\,\delta\Delta v - p(t)\,\delta v = 0 \qquad [32]$$

where it is understood that $v = v(x, t)$ and that the virtual displacements applied to the damping force and the elastic restoring force, are virtual relative displacements. The virtual displacement can be expressed as:

$$\delta v(x,t) = \phi(x)\,\delta Y(t) \qquad [33]$$

and the virtual relative displacement can be written as:

$$\delta\Delta v(x,t) = \Delta\phi(x)\,\delta Y(t) \qquad [34]$$

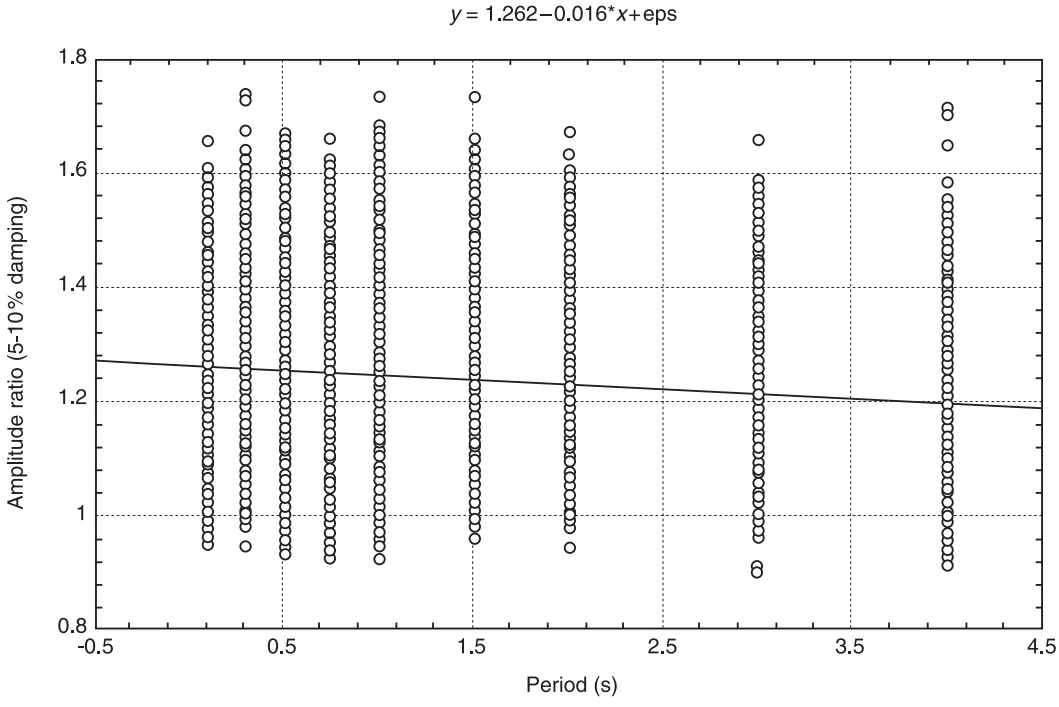


Figure 11 Individual damping adjustment factors for 10% damping as computed for 1047 distinct earthquake records (each circle represents an adjustment factor corresponding to an earthquake record at a distinct period of vibration).

where:

$$\Delta v(x,t) = \phi(x_i)Y(t) - \phi(x_j)Y(t) = \Delta\phi(x)Y(t) \quad [35]$$

The inertia, damping and elastic restoring forces can be expressed as:

$$\begin{aligned} f_{\mathrm{i}} &= m\ddot{v} = m\phi\ddot{Y} \\ f_{\mathrm{d}} &= c\Delta\dot{v} = c\Delta\phi\ddot{Y} \\ f_{\mathrm{s}} &= k\Delta v = k\Delta\phi Y \end{aligned} \quad [36]$$

resulting in the following equation of motion in terms of the generalized coordinate:

$$m^*\ddot{Y} + c^*\dot{Y} + k^*Y = p^*(t) \quad [37]$$

where m^*, c^*, k^*, and p^* are referred to as the 'generalized parameters' and are defined as:

$$\begin{aligned} m^* &= \sum\nolimits_i m_i\phi_i^2 = \text{generalized mass} \\ c^* &= \sum\nolimits_i c_i\Delta\phi_i^2 = \text{generalized damping} \\ k^* &= \sum\nolimits_i k_i\Delta\phi_i^2 = \text{generalized stiffness} \\ p^* &= \sum\nolimits_i p_i\phi_i = \text{generalized force} \end{aligned} \quad [38]$$

For a time-dependent base acceleration the generalized force becomes:

$$p^* = \ddot{g}\Gamma \quad [39]$$

where:

$$\Gamma = \sum\nolimits_i m_i\phi_i = \text{earthquake participation factor} \quad [40]$$

It is also convenient to express the generalized damping in terms of the percent of critical damping in the following manner:

$$c^* = \sum\nolimits_i c_i\Delta\phi(i)^2 = 2\lambda m^*\omega \quad [41]$$

where ω represents the circular frequency of the generalized system and is given as:

$$\omega = \sqrt{\left(\frac{k^*}{m^*}\right)} \quad [42]$$

The effect of the generalized-coordinate approach is to transform a multiple-degree-of-freedom dynamic system into an equivalent SDOF system in terms of the generalized coordinate. This transformation is shown schematically in **Figure 12**. The degree to which the response of the transformed system represents the actual system will depend upon how well the assumed displacement shape represents the dynamic displacement of the actual structure.The displacement shape depends on the aspect ratio of the structure, which is defined as the ratio of the height to the base dimension. Possible shape functions for high-rise, mid-rise, and low-rise structures are summarized in **Figure 13**. It should be noted that most building codes use the straight-line shape function which is shown for the mid-rise system. Once the dynamic response is obtained in terms of the generalized coordinate, eqn [29] must be used to determine the

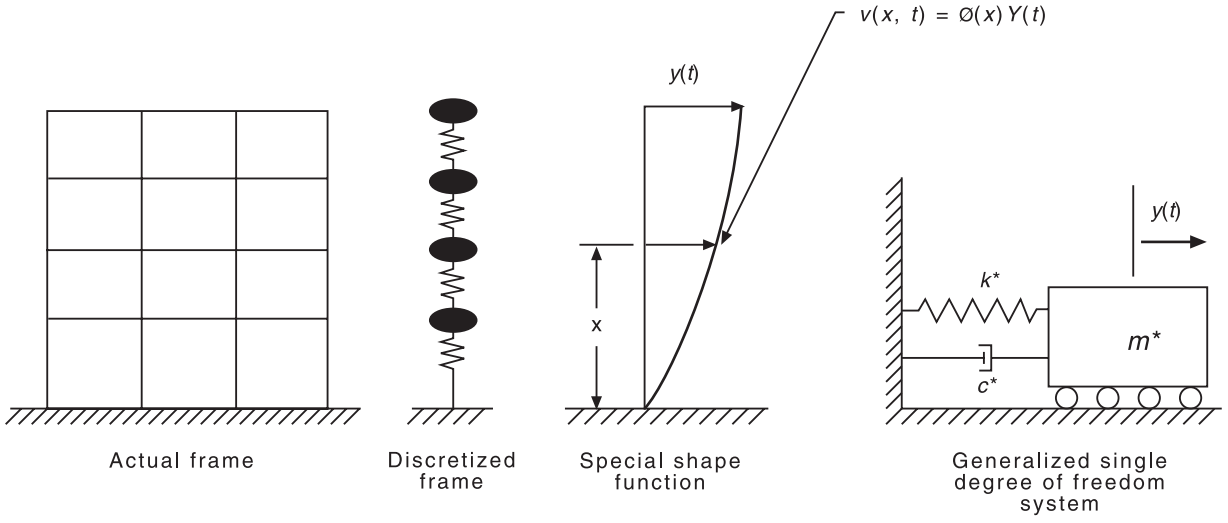


Figure 12 Generalized single-degree-of-freedom system.

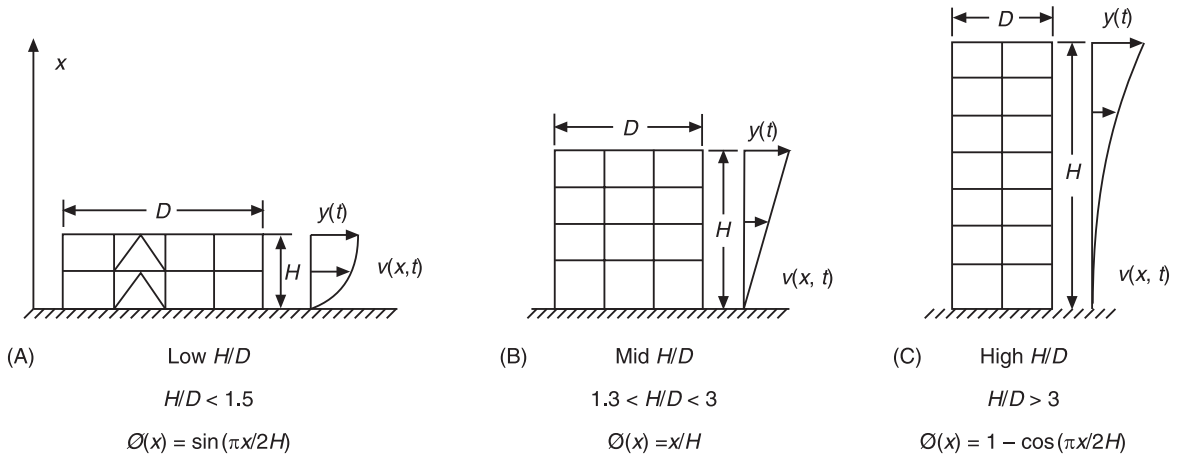


Figure 13 Possible shape functions based on aspect ratio.

displacements in the structure, and these in turn can be used to determine the forces in the individual structural elements.

In principle, any function which represents the general deflection characteristics of the building and satisfies the support conditions could be used. However, any shape other than the true vibration shape requires the addition of external constraints to maintain equilibrium. These extra constraints tend to stiffen the system and thereby increase the computed frequency. The true vibration shape will have no external constraints and therefore will have the lowest frequency of vibration. When choosing between several approximate deflected shapes, the one producing the lowest frequency is always the best approximation. A good approximation to the true vibration shape can be obtained by applying forces representing the inertia forces and letting the static deformation of the structure determine the spatial shape function.

Time–history analysis Substituting the generalized parameters into the Duhamel integral solution results in the following solution for the displacement:

$$v(x,t) = \frac{\phi(x)\Gamma V(t)}{m^*\omega} \qquad [43]$$

Therefore, the inertia force at any position x above the base can be obtained from:

$$q(x,t) = m(x)\ddot{v}(x,t) = m(x)\omega^2 v(x,t) \qquad [44]$$

or simply:

$$q(x,t) = \frac{m(x)\phi(x)\Gamma\omega V(t)}{m^*} \qquad [45]$$

The base shear is obtained by summing the distributed inertia forces over the height H of the structure:

$$Q(t) = \int q(x,t)\,\mathrm{d}x = \frac{\Gamma^2}{m^*}\omega V(t) \qquad [46]$$

The above relationships can be used to determine the displacements and forces in a generalized SDOF system at any time during the time history under consideration.

Response-spectrum analysis Using the definitions of the spectral pseudovelocity (S_{pv}) and spectral displacement (S_{d}), the maximum displacement in terms of the spectral displacement is obtained from:

$$v(x)_{\max} = \frac{\phi(x)\Gamma S_{\mathrm{d}}}{m^*} \qquad [47]$$

The forces in the system can readily be determined from the inertia forces, which can be expressed as:

$$q(x)_{\max} = m(x)\ddot{v}(x)_{\max} = m(x)\omega^2 v(x)_{\max} \qquad [48]$$

Rewriting this result in terms of the spectral pseudoacceleration (S_{pa}) results in the following:

$$q(x)_{\max} = \frac{\phi(x)m(x)\Gamma S_{\mathrm{pa}}}{m^*} \qquad [49]$$

Of considerable interest to structural engineers is the determination of the base shear. This is a key parameter in determining seismic design forces in most building codes. The base shear Q can be obtained from:

$$Q_{\max} = \frac{\Gamma^2 S_{\text{pa}}}{m^*} \quad [50]$$

It is also of interest to express the base shear in terms of the effective weight, which is defined as:

$$W^* = \frac{\left(\sum_i w_i \phi_i\right)^2}{\sum_i w_i \phi_i^2} \quad [51]$$

The expression for the maximum base shear becomes:

$$Q_{\max} = W^* S_{\text{pa}}/g \quad [52]$$

This form is similar to the basic base-shear equation used in the building codes. In the code equation, the effective weight is taken to be equal to the total dead weight W, plus a percentage of the live load for special occupancies. The seismic coefficient C is determined by a formula but is equivalent to the spectral pseudo-acceleration in terms of g. The basic code equation for base shear has the form:

$$Q_{\max} = CW \quad [53]$$

The effective earthquake force can also be determined by distributing the base shear over the story height. This distribution depends upon the displacement shape function and has the form:

$$q_i = Q_{\max} \frac{m_i \phi_i}{\Gamma} \quad [54]$$

If the shape function is taken as a straight line, the code force distribution is obtained. The overturning moment at the base of the structure can be determined by multiplying the inertia force by the corresponding story height above the base and summing over all story levels:

$$M_0 = \sum_i h_i q_i \quad [55]$$

Response of Nonlinear SDOF Systems

Many building structural systems will experience nonlinear response sometime during their life. Any moderate to strong earthquake will drive a building structure designed by conventional methods into the inelastic range, particularly in certain critical regions. A very useful numerical integration technique for problems of structural dynamics is the so-called step-by-step integration procedure. In this procedure the time history under consideration is divided into a number of small time increments Δt. During a small time step, the behavior of the structure is assumed to be linear. As nonlinear behavior occurs, the incremental stiffness is modified. In this manner, the response of the nonlinear system is approximated by a series of linear systems having a changing stiffness. The velocity and displacement computed at the end of one time interval become the initial conditions for the next time interval, and hence the process may be continued step by step.

Consider SDOF systems with properties m, c, $k(t)$ and $p(t)$, of which the applied force and the stiffness are functions of time. The stiffness is actually a function of the yield condition of the restoring force, and this in turn is a function of time. The damping coefficient may also be considered to be a function of time; however, general practice is to determine the damping characteristics for the elastic system and to keep these constant throughout the complete time history. In the inelastic range, the principle mechanism for energy dissipation is through inelastic deformation, and this is taken into account through the hysteretic behavior of the restoring force.

The numerical equation required to evaluate the nonlinear response can be developed by first considering the equation of dynamic equilibrium. Note that this equation must be satisfied at every increment of time. Considering the time at the end of a short time step, the equation of dynamic equilibrium can be written as:

$$f_{\text{i}}(t+\Delta t) + f_{\text{d}}(t+\Delta t) + f_{\text{s}}(t+\Delta t) = p(t+\Delta t) \quad [56]$$

where the forces are defined as:

$$\begin{aligned} f_{\text{i}} &= m\ddot{v}(t+\Delta t) \\ f_{\text{d}} &= c\dot{v}(t+\Delta t) \\ f_{\text{s}} &= \sum_{i=1}^{n} k_i(t)\Delta v_i(t) = r_t + k(t)\Delta v(t) \\ \Delta v(t) &= v(t+\Delta t) - v(t) \\ r_{\text{t}} &= \sum_{i=1}^{n-1} k_i(t)\Delta v_i(t) \end{aligned} \quad [57]$$

and in the case of ground accelerations:

$$p(t+\Delta t) = p_{\text{e}}(t+\Delta t) = -m\ddot{g}(t+\Delta t) \quad [58]$$

resulting in an equation of motion of the form:

$$m\ddot{v}(t+\Delta t) + c\dot{v}(t+\Delta t) + \sum k_i \Delta v_i = -m\ddot{g}(t+\Delta t) \quad [59]$$

It should be noted that the incremental stiffness is generally defined by the tangent stiffness at the beginning of the time interval:

$$k_i = \frac{\mathrm{d}f_s}{\mathrm{d}v} \qquad [60]$$

Note that these equations can also be used in a generalized SDOF system.

Many numerical integration schemes are available in the literature. The most popular direct integration schemes are: the Newmark, the Wilson-θ, and the Houbolt methods.

An important response parameter that is unique to nonlinear systems is the ductility ratio. For a SDOF system, this parameter can be defined in terms of the displacement as:

$$\mu = \frac{v(\max)}{v(\text{yield})} = 1.0 + \frac{v(\text{plastic})}{v(\text{yield})} \qquad [61]$$

As can be seen from the above equation, the ductility ratio is an indication of the amount of inelastic deformation that has occurred in the system. In the case of a SDOF system or generalized SDOF system the ductility obtained from eqn [61] usually represents the average ductility in the system. The ductility demand at certain critical regions, such as plastic hinges in critical members, may be considerably higher.

Multiple-Degree-of-Freedom (MDOF) Systems

In many structural systems it is impossible to model the dynamic response accurately in terms of a single displacement coordinate. These systems require a number of independent displacement coordinates to describe the displacement of the mass of the structure at any instant of time.

Mass and stiffness properties In order to simplify the solution it is usually assumed for building structures that the mass of the structure is lumped at the center of mass of the individual story levels. This results in a diagonal matrix of mass properties in which either the translational mass or the mass moment of inertia is located on the main diagonal:

$$\mathbf{f}_i = \begin{bmatrix} m_1 & & & & & & \\ & m_2 & & & & & \\ & & m_3 & & & & \\ & & & \cdot & & & \\ & & & & \cdot & & \\ & & & & & \cdot & \\ & & & & & & m_n \end{bmatrix} \begin{Bmatrix} v_1 \\ v_2 \\ v_3 \\ \cdot \\ \cdot \\ \cdot \\ v_n \end{Bmatrix} \qquad [62]$$

It is also convenient for building structures to develop the structural stiffness matrix in terms of the stiffness matrices of the individual story levels. The simplest idealization for a multistory building is based on the following three assumptions: (i) the floor diaphragm is rigid in its own plane; (ii) the girders are rigid relative to the columns and (iii) the columns are flexible in the horizontal directions but rigid in the vertical. If these assumptions are used, the building structure is idealized as having three dynamic degrees-of-freedom at each story level: a translational degree-of-freedom in each of two orthogonal directions, and a rotation about a vertical axis through the center of mass. If the above system is reduced to a plane frame, it will have one horizontal translational degree of freedom at each story level. The stiffness matrix for this type of structure has the tridiagonal form shown below:

$$\mathbf{f}_s = \begin{bmatrix} k_1 & -k_2 & & & & & & & \\ k_2 & k_1+k_2 & -k_3 & & & & & & \\ & -k_3 & k_2+k_3 & -k_4 & & & & & \\ & & \cdot & \cdot & \cdot & & & & \\ & & & \cdot & \cdot & \cdot & & & \\ & & & & \cdot & \cdot & \cdot & & \\ & & & & & \cdot & \cdot & -k_n & \\ & & & & & & -k_n & k_{n-1}+k_n & \end{bmatrix} \times \begin{Bmatrix} v_1 \\ v_2 \\ v_3 \\ \cdot \\ \cdot \\ \cdot \\ v_{n-1} \\ v_n \end{Bmatrix} \qquad [63]$$

For the simplest idealization, in which each story level has one translational degree-of-freedom, the stiffness terms k_i in the above equations represent the translational story stiffness of the ith story level. As the assumptions given above are relaxed to include axial deformations in the columns and flexural deformations in the girders, the stiffness term k_i in eqn [63] becomes a submatrix of stiffness terms, and the story displacement v_i becomes a subvector containing the various displacement components in the particular story level. The calculation of the stiffness coefficients for more complex structures is a standard problem of static structural analysis.

Mode shapes and frequencies The equations of motion for undamped free vibration of a MDOF system can be written in matrix form as:

$$\mathbf{M}\boldsymbol{\nu} + \mathbf{K}\boldsymbol{\nu} = \mathbf{0} \quad [64]$$

Since the motions of a system in free vibration are simple harmonic, the displacement vector can be represented as:

$$\boldsymbol{\nu} = \bar{\boldsymbol{\nu}} \sin \omega t \quad [65]$$

Differentiating twice with respect to time results in:

$$\ddot{\boldsymbol{\nu}} = -\omega^2 \boldsymbol{\nu} \quad [66]$$

Substituting eqn [66] into eqn [64] results in a form of the eigenvalue equation:

$$(\mathbf{K} - \omega^2 \mathbf{M})\boldsymbol{\nu} = \mathbf{0} \quad [67]$$

The classical solution to the above equation derives from the fact that in order for a set of homogeneous equilibrium equations to have a nontrivial solution, the determinant of the coefficient matrix must be zero:

$$\det(\mathbf{K} - \omega^2 \mathbf{M}) = \mathbf{0} \quad [68]$$

Expanding the determinant by minors results in a polynomial of degree N, which is called the frequency equation. The N roots of the polynomial represent the frequencies of the N modes of vibration. The mode having the lowest frequency (longest period) is called the first or fundamental mode. Once the frequencies are known, they can be substituted one at a time into the equilibrium eqn [67] which can then be solved for the relative amplitudes of motion for each of the displacement components in the particular mode of vibration. It should be noted that since the absolute amplitude of motion is indeterminate, $N - 1$ of the displacement components are determined in terms of one arbitrary component.

This method can be used satisfactorily for systems having a limited number of degrees-of-freedom. Programmable calculators have programs for solving the polynomial equation and for doing the matrix operations required to determine the mode shapes. However, for problems of any size, computer programs which use special numerical techniques to solve large eigenvalue systems must be used.

Equations of motion in normal coordinates Betti's reciprocal work theorem can be used to develop two orthogonality properties of vibration mode shapes which make it possible to greatly simplify the equations of motion. The first of these states that the mode shapes are orthogonal to the mass matrix and is expressed in matrix form as:

$$\boldsymbol{\phi}_n^{\mathrm{T}} \mathbf{M} \boldsymbol{\phi}_m = \mathbf{0} \quad (m \neq n) \quad [69]$$

The second property can be expressed in terms of the stiffness matrix as:

$$\boldsymbol{\phi}_n^{\mathrm{T}} \mathbf{K} \boldsymbol{\phi}_m = \mathbf{0} \quad (m \neq n) \quad [70]$$

which states that the mode shapes are orthogonal to the stiffness matrix. Although not necessarily true, for the sake of computational convenience it is further assumed that the mode shapes are also orthogonal to the damping matrix:

$$\boldsymbol{\phi}_n^{\mathrm{T}} \mathbf{C} \boldsymbol{\phi}_m = \mathbf{0} \quad (m \neq n) \quad [71]$$

Since any MDOF system having N degrees-of-freedom also has N independent vibration mode shapes, it is possible to express the displaced shape of the structure in terms of the amplitudes of these shapes by treating them as generalized coordinates (sometimes called normal coordinates). Hence the displacement at a particular location, v_i, can be obtained by summing the contributions from each mode as:

$$v_i = \sum_{n=1}^{N} \phi_{in} Y_n \quad [72]$$

In a similar manner, the complete displacement vector can be expressed as:

$$\boldsymbol{\nu} = \sum_{n=1}^{N} \boldsymbol{\phi}_n Y_n = \boldsymbol{\Phi}\mathbf{Y} \quad [73]$$

It is convenient to write the equations of motion for a MDOF system in matrix form as:

$$\mathbf{M}\ddot{\boldsymbol{\nu}} + \mathbf{C}\dot{\boldsymbol{\nu}} + \mathbf{K}\boldsymbol{\nu} = \mathbf{P}(t) \quad [74]$$

which is similar to the equation for a SDOF system. The differences arise because the mass, damping, and stiffness are now represented by matrices of coefficients representing the added degrees-of-freedom, and the acceleration, velocity, displacement, and applied load are represented by vectors containing the additional degrees-of-freedom. The equations of motion can be expressed, as well, in terms of the normal coordinates:

$$\mathbf{M\Phi\ddot{Y}} + \mathbf{C\Phi\dot{Y}} + \mathbf{K\Phi Y} = \mathbf{P}(t) \qquad [75]$$

Multiplying the above equation by the transpose of any modal vector $\boldsymbol{\phi}_n$ results in the following:

$$\boldsymbol{\phi}_n^{\mathrm{T}}\mathbf{M\Phi\ddot{Y}} + \boldsymbol{\phi}_n^{\mathrm{T}}\mathbf{C\Phi\dot{Y}} + \boldsymbol{\phi}_n^{\mathrm{T}}\mathbf{K\Phi Y} = \boldsymbol{\phi}_n^{\mathrm{T}}\mathbf{P}(t) \qquad [76]$$

Using the orthogonality conditions, this set of equations reduces to a set of independent equations of motion for a set of generalized SDOF systems in terms of the generalized properties for the nth mode shape and the normal coordinate Y_n:

$$M_n^*\ddot{Y}_n + C_n^*\dot{Y}_n + K_n^*Y = P_n^*(t) \qquad [77]$$

where the generalized properties for the nth mode are given as

$$\begin{aligned} M_n^* &= \text{generalized mass} = \boldsymbol{\phi}_n^{\mathrm{T}}\mathbf{M}\boldsymbol{\phi}_n \\ C_n^* &= \text{generalized damping} \\ &= \boldsymbol{\phi}_n^{\mathrm{T}}\mathbf{C}\boldsymbol{\phi}_n = 2\lambda_n\omega_n M_n^* \\ K_n^* &= \text{generalized stiffness} \\ &= \boldsymbol{\phi}_n^{\mathrm{T}}\mathbf{K}\boldsymbol{\phi}_n = \omega_n^2 M_n^* \\ P_n^*(t) &= \text{generalized loading} = \boldsymbol{\phi}_n^{\mathrm{T}}\mathbf{P}(t) \end{aligned} \qquad [78]$$

The above relations can be used to further simplify the equation of motion for the nth mode to the form:

$$\ddot{Y}_n + 2\lambda_n\omega_n Y_n + \omega_n^2 Y_n = \frac{P_n^*(t)}{M_n^*} \qquad [79]$$

The complete solution for the system is then obtained by superimposing the independent modal solutions. For this reason, this method is often referred to as the 'modal-superposition' method. Use of this method also leads to a significant saving in computational effort, since in most cases it will not be necessary to use all N modal responses to accurately represent the response of the structure. For most buildings, the lower modes make the primary contribution to the total response. Therefore, the response can usually be represented to sufficient accuracy in terms of a limited number of modal responses in the lower modes.

Time–history analysis As in the case of SDOF systems, for earthquake analysis the time-dependent force must be replaced with the effective loads, which are given by the product of the mass at any level, M, and the ground acceleration $g(t)$. The vector of effective loads is obtained as the product of the mass matrix and the ground acceleration:

$$P_{\mathrm{e}}(t) = \mathbf{M\Psi}\ddot{g}(t) \qquad [80]$$

where $\boldsymbol{\Psi}$ is a vector of influence coefficients of which component i represents the acceleration at displacement coordinate i due to a unit ground acceleration at the base. For the simple structural model in which the degrees-of-freedom are represented by the horizontal displacements of the story levels, the vector $\boldsymbol{\Psi}$ becomes a unity vector, **1**, since for a unit ground acceleration in the horizontal direction all degrees-of-freedom have a unit horizontal acceleration. The generalized effective load for the nth mode is given as:

$$P_{en}^*(t) = \Gamma_n g(t)$$

where:

$$\Gamma_n = \boldsymbol{\phi}_n^{\mathrm{T}}\mathbf{M\Psi} \qquad [81]$$

Resulting in the following expression for the earthquake response of the nth mode of a MDOF system:

$$\ddot{Y}_n + 2\lambda_n\omega_n\dot{Y}_n + \omega_n^2 Y_n = \varphi_n\ddot{g}(t)/M_n^* \qquad [82]$$

In a manner similar to that used for the SDOF system, the response of this mode at any time t can be obtained by the Duhamel integral expression:

$$Y_n(t) = \frac{\varphi_n V_n(t)}{M_n^*\omega_n} \qquad [83]$$

where $V_n(t)$ represents the integral:

$$V_n(t) = \int_0^t \ddot{g}(\tau)\mathrm{e}^{-\lambda_n\omega_n(t-\tau)}\sin\omega_n(t-\tau)\,\mathrm{d}\tau \qquad [84]$$

The complete displacement of the structure at any time is then obtained by superimposing the contributions of the individual modes:

$$\boldsymbol{\nu}(t) = \sum_{n=1}^{N}\boldsymbol{\phi}_n Y_n(t) = \boldsymbol{\Phi}\mathbf{Y}(t) \qquad [85]$$

The resulting earthquake forces can be determined in terms of the effective accelerations, which for each mode are given by the product of the circular frequency and the displacement amplitude of the generalized coordinate:

$$\ddot{Y}_{\mathrm{ne}}(t) = \omega_n^2 Y_n(t) = \frac{\varphi_n\omega_n V_n(t)}{M_n^*} \qquad [86]$$

The corresponding acceleration in the structure due to the nth mode is given as:

$$\ddot{\boldsymbol{\nu}}_{\mathrm{ne}}(t) = \boldsymbol{\phi}_n \ddot{Y}_{\mathrm{ne}}(t) \quad [87]$$

and the corresponding effective earthquake force is given as:

$$\mathbf{q}_n(t) = \mathbf{M}\ddot{\boldsymbol{\nu}}_n(t) = \mathbf{M}\boldsymbol{\phi}_n \omega_n \varphi_n V_n(t)/M_n^* \quad [88]$$

The total earthquake force is obtained by superimposing the individual modal forces to obtain:

$$q(t) = \sum_{n=1}^{N} q_n(t) = \mathbf{M}\boldsymbol{\Phi}\omega^2 Y(t) \quad [89]$$

The base shear can be obtained by summing the effective earthquake forces over the height of the structure:

$$Q_n(t) = \sum_{i=1}^{H} q_{in}(t) = \mathbf{1}^{\mathrm{T}}\mathbf{q}_n(t) = M_{\mathrm{en}}\omega_n V_n(t) \quad [90]$$

where $M_{\mathrm{en}} = \Gamma_n^2/M_n^*$ is the effective mass for the nth mode.The sum of the effective masses for all of the modes is equal to the total mass of the structure. This results in a means of determining the number of modal responses necessary to accurately represent the overall structural response. If the total response is to be represented in terms of a finite number of modes and if the sum of the corresponding modal masses is greater than a predefined percentage of the total mass, the number of modes considered in the analysis is adequate. If this is not the case, additional modes need to be considered. The base shear for the nth mode, can also be expressed in terms of the effective weight, W_{en}, as:

$$Q_n(t) = \frac{W_{\mathrm{en}}}{g}\omega_n V_n(t) \quad [91]$$

where:

$$W_{\mathrm{en}} = \frac{\left(\sum_{i=1}^{H} W_i \phi_{in}\right)^2}{\sum_{i=1}^{H} W_i \phi_{in}^2} \quad [92]$$

The base shear can be distributed over the height of the building with the modal earthquake forces expressed as:

$$\mathbf{q}_n^{\mathrm{T}} = \frac{\mathbf{M}\boldsymbol{\phi}_n Q_n(t)}{\Gamma_n} \quad [93]$$

Response–spectrum analysis The above equations for the response of any mode of vibration are exactly equivalent to the expressions developed for the generalized SDOF system. Therefore, the maximum response of any mode can be obtained in a manner similar to that used for the generalized SDOF system. Therefore, by analogy, the maximum modal displacement can be written as:

$$Y_n(t)_{\max} = \frac{V_n(t)_{\max}}{\omega_n} = S_{\mathrm{dn}} \quad [94]$$

and:

$$Y_{n\max} = \varphi_n S_{\mathrm{dn}}/M_n^* \quad [95]$$

The distribution of the modal displacements in the structure can be obtained by multiplying this expression by the modal vector:

$$\boldsymbol{\nu}_{n\max} = \boldsymbol{\phi}_n Y_{n\max} = \frac{\boldsymbol{\phi}_n \Gamma_n S_{\mathrm{dn}}}{M_n^*} \quad [96]$$

The maximum effective earthquake forces can be obtained from the modal accelerations as:

$$\mathbf{q}_{n\max} = \frac{\mathbf{M}\boldsymbol{\phi}_n \varphi_n S_{\mathrm{pan}}}{M_n^*} \quad [97]$$

Summing these forces over the height of the structure gives the following expression for the maximum base shear due to the nth mode:

$$Q_{n\max} = \varphi_n^2 S_{\mathrm{pan}}/M_n^* \quad [98]$$

which can also be expressed in terms of the effective weight as:

$$Q_{n\max} = W_{\mathrm{en}} S_{\mathrm{pan}}/g \quad [99]$$

where W_{en} is defined by eqn [92]. Finally, the overturning moment at the base of the building for the nth mode can be determined as:

$$M_o = \langle \mathbf{h} \rangle \mathbf{M}\boldsymbol{\phi}_n \Gamma_n S_{\mathrm{pan}}/M_n^* \quad [100]$$

where $\langle \mathbf{h} \rangle$ is a row vector of the story heights above the base.

Modal combinations Using the response spectrum method for MDOF systems, the maximum modal response is obtained for each mode of a set of modes, which are used to represent the response.

The question then arises as to how these modal maxima should be combined in order to get the best estimate of the maximum total response. The modal response equations provide accurate results only as long as they are evaluated concurrently in time. In going to the response spectrum approach, time is taken out of these equations and replaced with the modal maxima. These maximum response values for the individual modes cannot possibly occur at the same time; therefore, a means must be found to combine the modal maxima in such a way as to approximate the maximum total response. One such combination that has been used is to take the sum of the absolute values (SAV) of the modal responses. This combination can be expressed as:

$$r \leq \sum_{n=1}^{N} |r_n| \qquad [101]$$

Since this combination assumes that the maxima occur at the same time and that they also have the same sign, it produces an upper-bound estimate for the response, which is too conservative for design application. A more reasonable estimate, which is based on probability theory, can be obtained by using the square root of sum of squares (SRSS) method, which is expressed as:

$$r \approx \sqrt{\left(\sum_{n=1}^{N} r_n^2\right)} \qquad [102]$$

This method of combination has been shown to give a good approximation of the response for two-dimensional structural systems. For three-dimensional systems, it has been shown that the complete quadratic combination (CQC) method may offer a significant improvement in estimating the response of certain structural systems. The complete quadratic combination is expressed as:

$$r \approx \sqrt{\left(\sum_{i=1}^{N}\sum_{j=1}^{N} r_i p_{ij} r_j\right)} \qquad [103]$$

where for constant modal damping:

$$p_{ij} = \frac{8\lambda^2(1+\zeta)\zeta^{3/2}}{\left(1-\zeta^2\right)^2 + 4\lambda^2\zeta(1+\zeta)^2} \qquad [104]$$

and:

$$\zeta = \omega_j/\omega_i$$
$$\lambda = c/c_{\mathrm{cr}}$$

Using the SRSS method for two-dimensional systems and the CQC method for either two- or three-dimensional systems will give a good approximation to the maximum earthquake response of an elastic system without requiring a complete time history analysis. This is particularly important for purposes of design.

Nonlinear response of MDOF systems The nonlinear analysis of buildings modeled as MDOF systems closely parallels the development for SDOF systems presented earlier. However, the nonlinear dynamic time history analysis of MDOF systems is currently considered to be too complex for general use. Therefore, recent developments in the seismic evaluation of buildings have suggested a performance-based procedure which requires the determination of the demand and capacity. For more demanding investigations of building response, nonlinear dynamic analyses can be conducted.

For dynamic analysis, the loading time history is divided into a number of small time increments, whereas, in the static analysis, the lateral force is divided into a number of small force increments. During a small time or force increment, the behavior of the structure is assumed to be linear elastic. As nonlinear behavior occurs, the incremental stiffness is modified for the next time (load) increment. Hence, the response of the nonlinear system is approximated by the response of a sequential series of linear systems having varying stiffnesses.

The equations of equilibrium for a MDOF system subjected to base excitation can be written in matrix form as:

$$\mathbf{M}\ddot{\boldsymbol{\nu}} + \mathbf{C}\dot{\boldsymbol{\nu}} + \mathbf{K}\boldsymbol{\nu} = -\mathbf{M}\boldsymbol{\Psi}\ddot{g}(t) \qquad [105]$$

In the mode superposition method, the damping ratio was defined for each mode of vibration. However, this is not possible for a nonlinear system because it has no true vibration modes. A useful way to define the damping matrix for a nonlinear system is to assume that it can be represented as a linear combination of the mass and stiffness matrices of the initial elastic system:

$$\mathbf{C} = \alpha\mathbf{M} + \beta\mathbf{K} \qquad [106]$$

where α and β are scalar multipliers which may be selected so as to provide a given percentage of critical damping in any two modes of vibration of the initial

elastic system. These two multipliers can be evaluated from the expression:

$$\begin{Bmatrix} \alpha \\ \beta \end{Bmatrix} = 2 \begin{bmatrix} \omega_j & -\omega_i \\ -\dfrac{1}{\omega_j} & \dfrac{1}{\omega_i} \end{bmatrix} \frac{\omega_i \omega_j}{\omega_j^2 - \omega_i^2} \begin{Bmatrix} \lambda_i \\ \lambda_j \end{Bmatrix} \qquad [107]$$

where ω_i and ω_j are the percentage of critical damping in the two specified modes. Once the coefficients α and β are determined, the damping in the other elastic modes is obtained from the expression:

$$\lambda_k = \frac{\alpha}{2\omega_k} + \frac{\beta \omega_k}{2} \qquad [108]$$

A typical damping function which was used for the nonlinear analysis of a building is shown in **Figure 14**. Although the representation for the damping is only approximate it is justified for these types of analyses on the basis that it gives a good approximation of the damping for a range of modes of vibration and these modes can be selected to be the ones that make the major contribution to the response. Also in nonlinear dynamic analyses the dissipation of energy through inelastic deformation tends to overshadow the dissipation of energy through viscous damping. Therefore, an exact representation of damping is not as important in a nonlinear system as it is in a linear system. One should be aware of the characteristics of the damping function to insure that important components of the response are not lost. The matrix form of the numerical integration techniques illustrated before for analysis of nonlinear SDOF systems are used for response analysis of nonlinear MDOF systems. Furthermore, for building systems exhibiting local nonlinearity such as base isolated structures, techniques based on modified modal superposition techniques and Ritz vectors have also been successfully utilized.

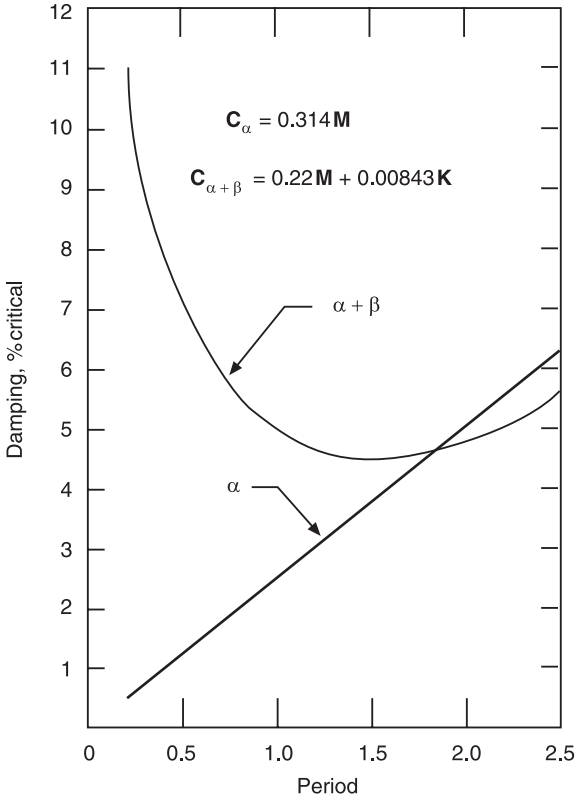


Figure 14 An example of damping functions selected for a building structure.

Acknowledgments

Substantial parts of this article were extracted from *The Seismic Design Handbook*, 2nd edition, edited by the author. The author is indebted to Professors James C. Anderson Bijan Mohraz, and Fahim Sadek whose contributions to the *Handbook* have been liberally used in development of this article. The author also wishes to express his gratitude to Kluwer Academic Publishers for granting permission to extract this material from the *Handbook*.

Nomenclature

$a(t)$	accelerogram
B	adjustment factor
$F(\omega)$	Fourier transform
$\mathrm{FS}(\omega)$	Fourier amplitude spectrum
g	acceleration
h, H	height
I	intensity
$\mathrm{PSV}(\omega)$	pseudo velocity
Q	base shear
$\mathrm{SD}(\omega)$	spectral displacement
T	duration of accelerogram
$V(t)$	velocity
W	weight

See Plates 29, 30, 31, 32.

See also: **Dynamic stability**; **Finite element methods**; **Seismic instruments, environmental factors**; **Structural dynamic modifications**.

Further Reading

Anderson JC (2001) Dynamic response of structures. In: Naeim F (ed.) *The Seismic Design Handbook*, 2nd edn. Boston, MA: Kluwer Academic Publishers.

Bathe KJ (1982) *Finite Element Procedures in Engineering Analysis*. Englewood Cliffs, NJ: Prentice-Hall.
Chopra AK (1980) *Dynamics of Structures: A Primer*. Oakland, CA: Earthquake Engineering Research Institute.
Chopra AK (2001) *Dynamics of Structures: Theory and Applications to Earthquake Engineering*, 2nd edn. Englewood Cliffs, NJ: Prentice-Hall.
Clough RW, Penzin J (1993) *Dynamics of Structures*, 2nd edn. New York: McGraw-Hill.
Hudson DE (1979) *Reading and Interpreting Strong Motion Accelerograms*. Oakland, CA: Earthquake Engineering Research Institute.
International Code Council (2000) *International Building Code 2000*. VA: Fall Church.
Mohraz B, Sadek F (2001) Earthquake ground motion and response spectra. In: Naeim F (ed.), *The Seismic Design Handbook*, 2nd edn. Boston, MA: Kluwer Academic Publishers.
Naeim F (1994) Earthquake response and design spectra. In: Paz M (ed.) *International Handbook of Earthquake Engineering*. New York: Chapman and Hall.
Naeim F, Anderson JC (1996) *Design Classification of Horizontal and Vertical Earthquake Ground Motion (1933–1994)*. Los Angeles: John A. Martin.
Naeim F, Kelly JM (1999) *Design of Seismic Isolated Structures: From Theory to Practice*. New York: John Wiley.
Naeim F, Somerville PG *Earthquake Records and Design*. Oakland, CA: Earthquake Engineering Research Institute.
Newmark NM, Hall WJ (1982) *Earthquake Spectra and Design*. Oakland, CA: Earthquake Engineering Research Institute.
Structural Engineers Association of California (1999) *Recommended Lateral Force Requirements and Commentary*, 7th edn. Sacramento, CA.
Wilson EL (1998) *Three Dimensional Static and Dynamic Analysis of Structures*. Berkeley, CA: Computers and Structures.

EIGENVALUE ANALYSIS

O Bauchau, Georgia Institute of Technology, Atlanta, GA, USA,

Copyright © 2001 Academic Press

doi:10.1006/rwvb.2001.0001

Introduction

The fundamental eigenproblem in vibration analysis writes:

$$\mathbf{K}\mathbf{u}_i = \omega_i^2 \mathbf{M}\mathbf{u}_i \qquad [1]$$

where $\mathbf{K}$ and $\mathbf{M}$ are the $n \times n$ stiffness and mass matrices, respectively; ω_i^2, $i = 1, 2 \ldots n$ the n eigenvalues of the problem; and $\mathbf{u}_i$ the corresponding eigenvectors. The stiffness and mass matrices are assumed to be symmetric and positive-definite, implying that all the eigenvalues are real and positive. In the following, it will be assumed that the eivenvalues have been ordered in ascending order, i.e., $\omega_1^2 \leq \omega_2^2 \leq \omega_3^2 \leq \ldots \leq \omega_n^2$.

The characteristic polynomial $p(\omega^2)$ associated with the eigenproblem is defined as:

$$p(\omega^2) = \det(\mathbf{K} - \omega^2 \mathbf{M}) \qquad [2]$$

It is clear that the roots of the characteristic polynomial are the eigenvalues ω_i^2.

It is well known that the eigenvectors $\mathbf{u}_1, \mathbf{u}_2 \ldots \mathbf{u}_n$ are orthogonal to each other in the spaces of both stiffness and mass matrices. It is customary to normalize the modes in the space of the mass matrix. These relationships can be expressed in a compact manner by introducing a nonsingular matrix $\mathbf{P}$, the columns of which are the normalized eigenvectors:

$$\mathbf{P} = [\mathbf{u}_1, \mathbf{u}_2 \ldots \mathbf{u}_n] \qquad [3]$$

The orthonormality relationships then write:

$$\mathbf{P}^{\mathrm{T}}\mathbf{M}\mathbf{P} = I; \quad \mathbf{P}^{\mathrm{T}}\mathbf{K}\mathbf{P} = \mathrm{diag}(\omega_i^2) \qquad [4]$$

where I is the $n \times n$ identity matrix, and $\mathrm{diag}(\omega_i^2)$ a diagonal matrix storing the eigenvalues.

The computation of the eigenvalues and corresponding eigenvectors is a fundamental problem in vibration analysis. More often than not, only the lowest eigenvalues must be extracted. Below, some relevant properties of eigenproblem are reviewed. Four classes of computational methods for the solution of eigenproblems are subsequently presented. The basic algorithms based on similarity tranformation methods and vector iteration methods are then discussed. Conclusions and recommendations are presented in the last section.

Basic Properties of Eigenproblems

Similarity Transformations

Consider a linear transformation $\mathbf{u} = \mathbf{Q}\hat{\mathbf{u}}$, where $\mathbf{Q}$ is a nonsingular matrix. Introducing this transformation into eqn [1] and premultiplying by $\mathbf{Q}^{\mathrm{T}}$ then yields:

$$\hat{\mathbf{K}}\hat{\mathbf{u}}_i = \omega_i^2 \hat{\mathbf{M}}\hat{\mathbf{u}}_i \qquad [5]$$

where $\hat{\mathbf{K}} = \mathbf{Q}^{\mathrm{T}}\mathbf{K}\mathbf{Q}$ and $\hat{\mathbf{M}} = \mathbf{Q}^{\mathrm{T}}\mathbf{M}\mathbf{Q}$. It can be readily shown that this similarity transformation does not affect the spectrum of eigenvalues. Indeed, the characteristic polynomial $\hat{p}(\omega^2)$ associated with the transformed problem is:

$$\begin{aligned}\hat{p}(\omega^2) &= \det(\hat{\mathbf{K}} - \omega^2\hat{\mathbf{M}}) \\ &= \det(\mathbf{Q}^{\mathrm{T}})\det(\mathbf{K} - \omega^2\mathbf{M})\det(\mathbf{Q}) \\ &= \det(\mathbf{Q}^{\mathrm{T}})\det(\mathbf{Q})p(\omega^2)\end{aligned} \qquad [6]$$

Since $\mathbf{Q}$ is nonsingular, $\det(\mathbf{Q}) \neq 0$, and the roots of $\hat{p}(\omega^2)$ are identical to those of $p(\omega^2)$. In summary, the similarity transformation leaves the spectrum of eigenvalues unchanged, and the eigenvectors are related through the similarity transformation $\mathbf{u}_i = \mathbf{Q}\hat{\mathbf{u}}_i$. It should be noted that the similarity transformation $\mathbf{u} = \mathbf{P}\hat{\mathbf{u}}$ leads to $\hat{\mathbf{K}} = \mathrm{diag}(\omega_i^2)$ and $\hat{\mathbf{M}} = I$, as implied by the orthonormality relationships (eqn [4]). Both mass and stiffness matrices have been transformed simultaneously to a diagonal form.

The Rayleigh Quotient

An eigenvalue of the problem can be computed by premultiplying eqn [1] by $\mathbf{u}_i^{\mathrm{T}}$, then solving to find:

$$\omega_i^2 = \frac{\mathbf{u}_i^{\mathrm{T}}\mathbf{K}\mathbf{u}_i}{\mathbf{u}_i^{\mathrm{T}}\mathbf{M}\mathbf{u}_i} \qquad [7]$$

This is not a pratical tool for computing an eigenvalue, as the knowledge of the corresponding eigenvector is required to start with. By analogy, the Rayleigh quotient is defined for an arbitrary vector $\mathbf{v}$ as:

$$\rho(\mathbf{v}) = \frac{\mathbf{v}^{\mathrm{T}}\mathbf{K}\mathbf{v}}{\mathbf{v}^{\mathrm{T}}\mathbf{M}\mathbf{v}} \qquad [8]$$

It presents the following important property, $\omega_1^2 \leq \rho(\mathbf{v}) \leq \omega_n^2$, which implies that the minimum value of the Rayleigh quotient for arbitrary choices of $\mathbf{v}$ is ω_1^2.

Consider now a vector $\mathbf{v}$ which closely approximates eigenvector $\mathbf{u}_i$, i.e., $\mathbf{v} = \mathbf{u}_i + \varepsilon\mathbf{x}$, where ε is a small number and $\mathbf{x}$ represents the discrepancy between $\mathbf{v}$ and the eigenvector $\mathbf{u}_i$. Hence, $\mathbf{x}$ has no components along $\mathbf{u}_i$ and can be expanded in terms of the remaining eigenvectors:

$$\mathbf{x} = \sum_{r=1, r\neq i}^{n} \alpha_r \mathbf{u}_r \qquad [9]$$

Using the orthogonality properties (eqn [4]), it is now readily verified that:

$$\mathbf{u}_i^{\mathrm{T}}\mathbf{K}\mathbf{x} = 0; \quad \mathbf{x}^{\mathrm{T}}\mathbf{K}\mathbf{x} = \sum_{r=1, r\neq i}^{n} \alpha_r^2 \omega_r^2 \qquad [10]$$

and similar relationships hold for the mass matrix. The Rayleigh quotient now writes:

$$\begin{aligned}\rho(\mathbf{v}) &= \frac{\mathbf{u}_i^{\mathrm{T}}\mathbf{K}\mathbf{u}_i + 2\varepsilon\mathbf{u}_i^{\mathrm{T}}\mathbf{K}\mathbf{x} + \varepsilon^2\mathbf{x}^{\mathrm{T}}\mathbf{K}\mathbf{x}}{\mathbf{u}_i^{\mathrm{T}}\mathbf{M}\mathbf{u}_i + 2\varepsilon\mathbf{u}_i^{\mathrm{T}}\mathbf{M}\mathbf{x} + \varepsilon^2\mathbf{x}^{\mathrm{T}}\mathbf{M}\mathbf{x}} \\ &= \frac{\omega_i^2 + \varepsilon^2 \sum_{r=1, r\neq i}^{n} \alpha_r^2 \omega_r^2}{1 + \varepsilon^2 \sum_{r=1, r\neq i}^{n} \alpha_r^2}\end{aligned} \qquad [11]$$

After expansion for small values of ε, we find:

$$\rho(\mathbf{v}) = \omega_i^2 + \varepsilon^2 \sum_{r=1, r\neq i}^{n} \alpha_r^2(\omega_r^2 - \omega_i^2) + O(\varepsilon^4) \qquad [12]$$

This important result shows that if a vector $\mathbf{v}$ is an approximation to eigenvector $\mathbf{u}_i$ to $O(\varepsilon)$, the corresponding Rayleigh quotient is an approximation of ω_i^2 to $O(\varepsilon^2)$. This powerful tool is used in several methods for computing eigenvalues.

Rayleigh–Ritz Analysis

Rayleigh–Ritz analysis is a general tool for obtaining approximate solutions to eigenproblem [1]. Consider a subspace $\mathbf{X}$ spanned by p Ritz vectors, $\mathbf{x}_1, \mathbf{x}_2 \ldots \mathbf{x}_p$:

$$\mathbf{X} = [\mathbf{x}_1, \mathbf{x}_2 \ldots \mathbf{x}_p] \qquad [13]$$

A vector $\mathbf{v}$ is now constrained to belong to this subspace:

$$\mathbf{v} = \mathbf{X}\,\mathbf{q} \qquad [14]$$

The choice of vector $\mathbf{v}$ within the subspace is determined by p independent quantities $q_1, q_2 \ldots q_p$, the components of $\mathbf{q}$. Since ω_1^2 is the minimum value that the Rayleigh quotient $\rho(\mathbf{v})$ can achieve for all arbitrary choice of $\mathbf{v}$, the vector $\mathbf{v}$ that best approximates $\mathbf{u}_1$ should minimize $\rho(\mathbf{v})$ with respect to all the choices of the components q_i:

$$\frac{\partial\rho(\mathbf{v})}{\partial q_i} = 0, \quad i = 1 \ldots p \qquad [15]$$

Introducing the definition of the Rayleigh quotient (eqn [8] and eqn [14]) leads to:

$$\frac{\partial}{\partial \mathbf{q}}\left(\frac{\mathbf{v}^{\mathrm{T}}\mathbf{K}\mathbf{v}}{\mathbf{v}^{\mathrm{T}}\mathbf{M}\mathbf{v}}\right)=\frac{\partial}{\partial \mathbf{q}}\left(\frac{\mathbf{q}^{\mathrm{T}}\hat{\mathbf{K}}\mathbf{q}}{\mathbf{q}^{\mathrm{T}}\hat{\mathbf{M}}\mathbf{q}}\right)=0 \qquad [16]$$

where $\hat{\mathbf{K}}=\mathbf{X}^{\mathrm{T}}\mathbf{K}\mathbf{X}$ and $\hat{\mathbf{M}}=\mathbf{X}^{\mathrm{T}}\mathbf{M}\mathbf{X}$ are $p\times p$ reduced stiffness and mass matrices, respectively. Taking the derivatives then leads to a new, reduced eigenproblem:

$$\hat{\mathbf{K}}\mathbf{q}=\left(\frac{\mathbf{q}^{\mathrm{T}}\hat{\mathbf{K}}\mathbf{q}}{\mathbf{q}^{\mathrm{T}}\hat{\mathbf{M}}\mathbf{q}}\right)\hat{\mathbf{M}}\mathbf{q}; \quad \text{or} \quad \hat{\mathbf{K}}\mathbf{q}=\hat{\omega}^2\hat{\mathbf{M}}\mathbf{q} \qquad [17]$$

In summary, the vector $\mathbf{v}$ that best approximates eigenvector $\mathbf{u}_1$ within the subspace $\mathbf{X}$ is determined by the components of $\mathbf{q}$, which are the solution of the reduced eigenproblem [17]. If ω_1^2 and $\mathbf{q}_1$ are the lowest eigenvalue and eigenvector of [17], respectively, then $\omega_1^2\approx\hat{\omega}_1^2$ and $\mathbf{u}_1\approx\mathbf{X}\mathbf{q}_1$. At first, it seems that nothing has been gained, since the solution of an eigenproblem has been replaced by that of another eigenproblem. However, it should be noted that the original eigenproblem is of size $n\times n$, whereas the reduced eigenproblem is of size $p\times p$. If $p\ll n$, it is, of course, much simpler to solve the reduced eigenproblem.

The major deficiency of the Rayleigh–Ritz approach is that little can be said about how well the solution of the reduced eigenproblem approximates that of the original eigenproblem. If an eigenvector $\mathbf{u}_k$ exactly lies in the subspace spanned by $\mathbf{X}$, the corresponding eigenvalue will be exactly recovered in the reduced eigenproblem. If the subspace $\mathbf{X}$ is chosen arbitrarily, the quality of the approximation is doubtful.

The Sturm Sequence Property

Consider the quantity $p(\mu^2)=\det(\mathbf{K}-\mu^2\mathbf{M})$ where μ^2 is not an eigenvalue. Clearly, $p(\mu^2)\neq 0$, and hence, the nonsingular matrix $\mathbf{K}-\mu^2\mathbf{M}$ can be trifactorized as:

$$\mathbf{K}-\mu^2\mathbf{M}=\mathbf{L}^{\mathrm{T}}\,\mathrm{diag}\,(d_{ii})\mathbf{L} \qquad [18]$$

where $\mathbf{L}$ is a lower triangular matrix with unit entries on the diagonal, and $\mathrm{diag}(d_{ii})$ a diagonal matrix with diagonal entries d_{ii}. The quantity $p(\mu^2)$ now becomes:

$$\begin{aligned}p(\mu^2)&=\det\left(\mathbf{L}^{\mathrm{T}}\mathrm{diag}\,(d_{ii})\mathbf{L}\right)\\&=\det\left(\mathbf{L}^{\mathrm{T}}\right)\left(\prod_{i=1}^{n}d_{ii}\right)\det(\mathbf{L})=\prod_{i=1}^{n}d_{ii}\end{aligned} \qquad [19]$$

since $\det(\mathbf{L})=1$. The following theorem will be given here without proof:

Theorem 1 In the trifactorization $\mathbf{K}-\mu^2\mathbf{M}=\mathbf{L}^{\mathrm{T}}\mathrm{diag}(d_{ii})\mathbf{L}$, the number of negative elements $d_{ii}<0$ is equal to the number of eigenvalues smaller than μ^2.

Types of Computational Methods for Eigenproblems

Computational methods for eigenvalue problems can be broken into four groups, according to the relationship used as a basis for the method:

1. Polynomial iteration methods based on the characteristic polynomial (eqn [2]).
2. Sturm sequence methods based on the properties of the trifactorization (eqn [19]).
3. Similarity transformation methods based on the properties of similarity transformations (eqn [5]).
4. Vector iteration methods based on the eigenproblem statement (eqn [1]).

The first two groups of methods do not lead to practical tools for computing eigenvalues unless n is very small. The last two groups do lead to practical algorithms (see below).

The characteristic polynomial approach replaces the computation of eigenvalues by the extraction of the roots of an nth-order polynomial. It is well known that no explicit formula exists for the computation of the roots of a polynomial for $n>4$. Hence, all computational methods for eigenvalues will be iterative in nature. All methods for finding the roots of a polynomial do apply to the computation of eigenvalues. In particular, Graeffe's root-squaring method has been used for this purpose. However, the computation of the characteristic polynomial coefficients is cumbersome, and rapidly becomes overwhelming as n increases. Most root-finding methods are not robust and cannot be recommended as a computational tool for evaluating eigenvalues when $n>10$.

The most important use of the Sturm sequence property is for *a posteriori* verification of eigenvalue extraction. Assume a number of eigenvalues, say k eigenvalues, have been identified within an interval (α^2,β^2). Let n_α and n_β be the number of negative terms in the diagonal matrix of the trifactorization of $\mathbf{K}-\alpha^2\mathbf{M}$ and $\mathbf{K}-\beta^2\mathbf{M}$, respectively. In view of theorem 1, the number of eigenvalues between α^2 and β^2 must then be $n_\beta-n_\alpha$. If $k<n_\beta-n_\alpha$, additional eigenvalues must exist in the interval. This technique is particularly useful in the presence of closely clustered eigenvalues: most eigenvalue extraction algorithms will have difficulties identifying all the eigenvalues within a cluster. Obtaining a complete picture of the dynamical behavior of a system

requires the identification all eigenvalues present within the frequency range of interest. Knowing the exact number of eigenvalues present within that interval is an important element to avoid missing some of the eigenvalues. If $k = n_\beta - n_\alpha$, all eigenvalues in the interval (α^2, β^2) have been identified. Conceptually, the Sturm sequence property could be used to extract eigenvalues using successive bisections of the interval (α^2, β^2) until a single eigenvalue has been bracketed to the desired accuracy. This method is prohibitively expensive as it requires a large number of matrix trifactorizations.

Similarity Transformation Methods

The simplest similarity transformation method for eigenvalue computation is the Jacobi method which deals with the standard eigenproblem $\mathbf{K}\mathbf{u}_i = \omega_i^2 \mathbf{u}_i$, i.e., the mass matrix is the identity matrix. Consider a similarity transformation defined by the following matrix

$$\mathbf{Q} = \begin{bmatrix} 1 & 0 & 0 & \dots & \dots & \dots & 0 \\ 0 & \ddots & \vdots & & & & \\ \vdots & & \cos\theta & \dots & -\sin\theta & & \vdots \\ & & & \ddots & & & \\ \vdots & & \sin\theta & \dots & \cos\theta & & \vdots \\ & & & & & \ddots & 0 \\ 0 & 0 & \dots & & \dots & 0 & 1 \end{bmatrix} \quad [20]$$

where the trigonometric entries appear in rows and columns i and j. It is readily verified that $\mathbf{Q}$ is an orthogonal matrix, i.e., $\mathbf{Q}^{\mathrm{T}}\mathbf{Q} = I$. The transformed stiffness matrix is $\hat{\mathbf{K}} = \mathbf{Q}^{\mathrm{T}}\mathbf{K}\mathbf{Q}$. The angle θ is arbitrary, and will be selected so as to zero the entry $\hat{K}_{ij} = (K_{jj} - K_{ii}) \sin\theta \cos\theta + K_{ij}(\cos^2\theta - \sin^2\theta)$. Solving for the angle θ then yields:

$$\tan 2\theta = \frac{2K_{ij}}{K_{ii} - K_{jj}} \quad [21]$$

In the Jacobi method, each off-diagonal entry is zeroed in turn, using the appropriate similarity transformation. It is important to note that the off-diagonal entry zeroed at a given step will be modified by the subsequent similarity transformations. Hence, the procedure must then be repeated until all off-diagonal terms are sufficiently small. At convergence, the diagonal entries of $\hat{\mathbf{K}}$ will store the eigenvalues.

To prove convergence of the method, let s_0 and s_1 be the sum of the squares of the off-diagonal terms, before and after a similarity transformation to zero the K_{ij} entry, respectively. It can be readily shown that $s_1 = s_0 - 2K_{ij}^2$. This means that s must decrease at each step, and the optimum strategy is to zero the maximum off-diagonal term at each step. This implies:

$$s_1 \leq \left(1 - \frac{2}{n(n-1)}\right) s_0 \quad [22]$$

and after k steps:

$$s_k \leq \left(1 - \frac{2}{n(n-1)}\right)^k s_0 \quad [23]$$

This relationship implies the convergence of the method when $k \to \infty$. It is possible to estimate the number of steps required to decrease s by t orders of magnitude, i.e., $s_k/s_0 \approx 10^{-t}$. From eqn [23], $k \approx tn^2$. The number of steps increases as n^2, which means that this approach will become increasingly expensive when the order of the systems increases. For instance, if $n = 100$ and $t = 12$, 120 000 similarity transformations will be required. Clearly, the Jacobi method is not a practical approach when $n > 50$.

The Jacobi method can be generalized to treat eigenproblem in the form of eqn [1]. Other similarity transformations methods are applicable to the problem at hand written as $\mathbf{D}\mathbf{u}_i = (1/\omega_i^2)\mathbf{u}_i$, where the dynamic flexibility matrix $\mathbf{D}$ is defined as $\mathbf{D} = \mathbf{K}^{-1}\mathbf{M}$. Householder's method will transform $\mathbf{D}$ into an upper Hessenberg matrix $\mathbf{H}$ through n successive similarity transformations. The QR algorithm is then very effective in extracting the eigenvalues of $\mathbf{H}$, through similarity transformations, once again.

Vector Iteration Methods

Consider an arbitrary vector $\mathbf{x}_1$ and an arbitrary frequency $\omega^2 = 1$. The inertial forces associated with this mode shape oscillating at this unit frequency are:

$$\mathbf{R}_1 = \omega^2 \mathbf{M}\mathbf{x}_1 = \mathbf{M}\mathbf{x}_1 \quad [24]$$

Since $\mathbf{x}_1$ is not an eigenvector, $\mathbf{K}\mathbf{x}_1 \neq \omega^2\mathbf{M}\mathbf{x}_1$. However, a vector $\mathbf{x}_2$ can be defined such that:

$$\mathbf{K}\mathbf{x}_2 = \omega^2 \mathbf{M}\mathbf{x}_1 \quad [25]$$

$\mathbf{x}_2$ can be readily found by solving this set of linear equations. In fact, $\mathbf{x}_2$ corresponds to the static deflection of the system under the steady loads $\mathbf{R}_1$. Intuitively, one would expect $\mathbf{x}_2$ to be a better

approximation to an eigenvector than $\mathbf{x}_1$. By induction, the following algorithm is proposed

Algorithm 1 (Inverse Iteration Method)

- Step 1 (inverse iteration): $\mathbf{K}\bar{\mathbf{x}}_{k+1} = \mathbf{M}\mathbf{x}_k$
- Step 2 (Rayleigh quotient): $\rho_{k+1} = \dfrac{\mathbf{x}_{k+1}^{\mathrm{T}}\mathbf{K}\mathbf{x}_{k+1}}{\mathbf{x}_{k+1}^{\mathrm{T}}\mathbf{M}\mathbf{x}_{k+1}}$
- Step 3 (normalization): $\mathbf{x}_{k+1} = \dfrac{\mathbf{x}_{k+1}}{\left(\mathbf{x}_{k+1}^{\mathrm{T}}\mathbf{M}\mathbf{x}_{k+1}\right)^{1/2}}$

The first step of the algorithm is the inverse iteration operation. Step 2 evaluates an approximate eigenvalue ρ_{k+1} based on the Rayleigh quotient. Finally, step 3 is a normalization step enforcing $\mathbf{x}_{k+1}^{\mathrm{T}}\mathbf{M}\mathbf{x}_{k+1}$ to prevent undue growth or decay of the norm of the vectors. As $k \to \infty \rho_{k+1} \to \omega_1^2$ and $\mathbf{x}_{k+1} \to \mathbf{u}_1$, i.e., the algorithm converges to the lowest eigenvalue and corresponding eigenvector. The proof of this claim follows.

The heart of the algorithm is the inverse iteration $\mathbf{K}\mathbf{x}_{k+1} = \mathbf{M}\mathbf{x}_k$. The similarity transformation $\mathbf{x}_k = \mathbf{P}\mathbf{z}_k$ is now applied to this inverse iteration step, which becomes:

$$\operatorname{diag}(\omega_i^2)\mathbf{z}_{k+1} = \mathbf{z}_k \qquad [26]$$

Note that this transformation is not a practical one as the exact eigenvectors of the system stored in matrix P are unknown. However, the eigenvalues are not altered by the similarity transformation, and the convergence characteristics of [26] are identical to those of algorithm 1. Eqn [26] is readily solved for $\mathbf{z}_{k+1}$, and recursive application then yields:

$$\begin{aligned}\mathbf{z}_{k+1} &= \operatorname{diag}(1/\omega_i^2)\mathbf{z}_k = \operatorname{diag}(1/\omega_i^2)^2\mathbf{z}_{k-1} \\ &= \operatorname{diag}(1/\omega_i^2)^k\mathbf{z}_1\end{aligned} \qquad [27]$$

If the arbitrary starting vector $\mathbf{z}_1^{\mathrm{T}} = [1, 1 \ldots 1]$ is selected, $\mathbf{z}_{k+1}$ becomes:

$$\mathbf{z}_{k+1} = \begin{bmatrix} (1/\omega_1^2)^k \\ (1/\omega_2^2)^k \\ (1/\omega_3^2)^k \\ \vdots \\ (1/\omega_n^2)^k \end{bmatrix} = (1/\omega_1^2)^k \begin{bmatrix} 1 \\ (\omega_1^2/\omega_2^2)^k \\ (\omega_1^2/\omega_3^2)^k \\ \vdots \\ (\omega_1^2/\omega_n^2)^k \end{bmatrix} \qquad [28]$$

Since the eigenvalues have been arranged in ascending order, $(\omega_1^2/\omega_i^2)^k \to 0$ for $i \neq 1$. It follows that $\mathbf{z}_{k+1} \to (1/\omega_1^2)^k\mathbf{e}_1$, where $\mathbf{e}_1^{\mathrm{T}} = [1, 0 \ldots 0]$. Clearly, as $k \to \infty, \mathbf{z}_{k+1}$ becomes parallel to $\mathbf{e}_1$, the eigenvector of the system corresponding to the lowest eigenvalue ω_1^2.

The convergence rate r for the eigenvector is:

$$r = \lim_{k\to\infty} \frac{\left\|\mathbf{z}_{k+1} - (1/\omega_1^2)^k\mathbf{e}_1\right\|}{\left\|\mathbf{z}_k - (1/\omega_1^2)^k\mathbf{e}_1\right\|} = \frac{\omega_1^2}{\omega_2^2} \qquad [29]$$

The convergence rate is ω_1^2/ω_2^2, the ratio of the first two eigenvalues. The eigenvalues are given by the Rayleigh quotient ρ_{k+1}:

$$\rho_{k+1} = \frac{\mathbf{z}_{k+1}^{\mathrm{T}}\mathbf{z}_k}{\mathbf{z}_{k+1}^{\mathrm{T}}\mathbf{z}_{k+1}} = \frac{(1/\omega_1^2)^{2k+1}\sum_{i=1}^{n}(\omega_1^2/\omega_i^2)^{2k+1}}{(1/\omega_1^2)^{2k+2}\sum_{i=1}^{n}(\omega_1^2/\omega_i^2)^{2k+2}} \qquad [30]$$

As $k \to \infty$, $\rho_{k+1} \to \omega_1^2$. The convergence rate is:

$$r = \lim_{k\to\infty} \frac{|\rho_{k+1} - \omega_1^2|}{|\rho_k - \omega_1^2|} = \left(\frac{\omega_1^2}{\omega_2^2}\right)^2 \qquad [31]$$

This result is consistent with the basic property of Rayleigh quotients: if an eigenvector is estimated to order ε, the corresponding eigenvalue estimated from the Rayleigh quotient will be accurate to order ε^2.

Note that if the lowest root has a multiplicity m, $\mathbf{z}_k + 1 \to (1/\omega_1^2)^k[1, 1, 1, 0 \ldots 0]$, where the unit entry is repeated m times. $\mathbf{z}_{k+1}$ is now parallel to a linear combination of $\mathbf{e}_1, \mathbf{e}_2 \ldots \mathbf{e}_m$, which are m orthogonal eigenvectors corresponding to the lowest eigenvalue of multiplicity m. In this case, the convergence rate for the eigenvector is $\omega_1^2/\omega_{m+1}^2$, the ratio of the first two distinct eigenvalues.

It is possible to give a rough estimate of the number of iterations N required to converge t digits of the lowest eigenvalue [7], i.e.:

$$\left|\frac{\rho_{N+1} - \rho_N}{\rho_N}\right| \approx 10^{-t} \qquad [32]$$

Introducing eqn [30] yields:

$$N \approx \frac{t}{\log(\omega_2/\omega_1)} \qquad [33]$$

Figure 1 shows this estimated number of iterations as a function of the ratio of the two lowest eigenvalues ω_2/ω_1, for $t = 8$. When the lowest eigenvalues are well separated, say $\omega_2/\omega_1 > 4$, a small number of iterations is required, $N < 15$. This number of iterations is independent of the order n of the system, and hence, this approach is suitable for large-order systems. This contrasts with the similarity transformation methods described previously, in which the required number of iterations increases in proportion

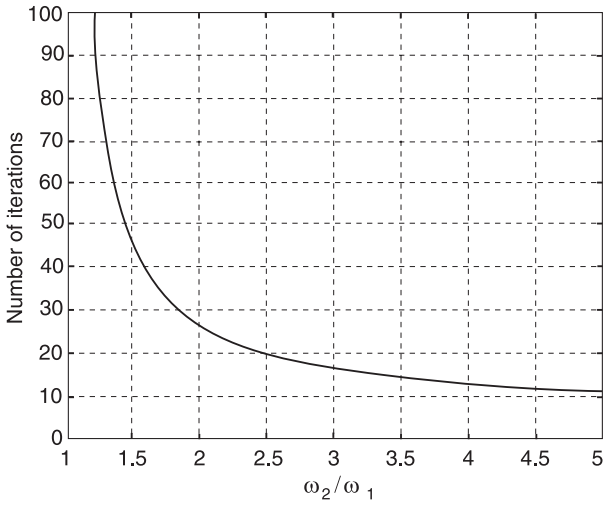


Figure 1 Convergence characteristic of the inverse iteration method.

to n^2. On the other hand, when $\omega_2/\omega_1 < 1.2$, over 100 iterations will be required to stabilize eight-digits of the eigenvalue. This means that inverse vector iteration will become increasingly ineffective in the presence of closely clustered eigenvalues. In practice, the algorithm fails to converge when $\omega_2/\omega_1 < 1.1$.

The inverse iteration technique described above presents two major deficiencies. First, it will always converge to the lowest eigenvalue for any arbitrary starting vector. Second, it performs poorly in the presence of clustered eigenvalues. In an attempt to alleviate these problems, the basic algorithm can be extended through the vector orthogonal deflation procedure which allows convergence to the higher eigenvectors. Another approach is to consider the following shifted eigenproblem:

$$(\mathbf{K} - \mu^2\mathbf{M})\mathbf{u}_i = (\omega_i^2 - \mu^2)\mathbf{M}\mathbf{u}_i \qquad [34]$$

The stiffness matrix $\mathbf{K}$ has been replaced by $\mathbf{K} - \mu^2\mathbf{M}$, and the eigenvalues ω_i^2 have all been shifted by a constant value μ^2 to $\omega_i^2 - \mu^2$. Using the same transformation as described above, the basic relationship of the shifted inverse iteration method becomes $\text{diag}(\omega_i^2 - \mu^2)\mathbf{Z}_{k+1} = \mathbf{Z}_k$, which now replaces eqn [26]. Similar arguments to those presented earlier lead to:

$$\mathbf{z}_{k+1} \rightarrow \left(\frac{1}{\omega_j^2 - \mu^2}\right)^k \mathbf{e}_j \qquad [35]$$

where ω_j^2 is the eigenvalue the closest to the shift μ^2, and $\mathbf{e}_j$ the corresponding eigenvector. The convergence rate is now:

$$r = \max_{p \neq j} \left| \frac{\omega_j^2 - \mu^2}{\omega_p^2 - \mu^2} \right| \qquad [36]$$

The shifted inverse iteration approach allows convergence to any eigenvalue ω_j^2, provided the shift μ^2 is chosen close enough to ω_j^2. Various eigenvalues can be obtained independently with adequate choices of the shift. Furthermore, choosing μ^2 very close to an eigenvalue will result in excellent convergence characteristics. In fact, if $\mu^2 = \omega_j^2$, the corresponding eigenvector is exactly recovered in one single iteration. The problem of this approach is to select the proper shift to obtain good convergence characteristics to the desired eigenvalue.

The subspace iteration method generalizes the inverse iteration approach by iterating simultaneously on a number of vectors, i.e., on a subspace of the system. Furthermore, to prevent convergence of all these vectors to the lowest eigenvector of the system, the vectors of the subspace are orthogonalized to each other at each step of the algorithm. The algorithm is as follows:

Algorithm 2 (Subspace Iteration Method)

- Step 1 (simultaneous inverse iteration): $\mathbf{K}\mathbf{X}_{k+1} = \mathbf{M}\mathbf{X}_k$
- Step 2 (Rayleigh–Ritz analysis): $\hat{\mathbf{K}}_{k+1} = \mathbf{X}_{k+1}^{\mathrm{T}}\mathbf{K}\bar{\mathbf{X}}_{k+1}; \hat{\mathbf{M}}_{k+1} = \bar{\mathbf{X}}_{k+1}^{\mathrm{T}}\mathbf{M}\bar{\mathbf{X}}_{k+1}$
- Step 3 (reduced eigenproblem solution): $\hat{\mathbf{K}}_{k+1}\mathbf{Q}_{k+1} = \hat{\mathbf{M}}_{k+1}\mathbf{Q}_{k+1}\text{diag}(\omega_{i,k+1}^2)$
- Step 4 (improved approximation): $\mathbf{X}_{k+1} = \bar{\mathbf{X}}_{k+1}\mathbf{Q}_{k+1}$

Step 1 performs the simultaneous inverse iteration on each vector of the subspace. A Rayleigh–Ritz analysis based on this subspace follows in steps 2 and 3: $\omega_{i,k}^2 + 1$ are the eigenvalues of the reduced problem and the matrix $\mathbf{Q}_{k+1}$ stores the corresponding eigenvectors. Step 4 enforces the orthogonality of the subspace in the space of the mass matrix. Indeed,

$$\begin{aligned} \mathbf{X}_{k+1}^{\mathrm{T}}\mathbf{M}\,\mathbf{X}_{k+1} &= \mathbf{Q}_{k+1}^{\mathrm{T}}\bar{\mathbf{X}}_{k+1}^{\mathrm{T}}\mathbf{M}\,\bar{\mathbf{X}}_{k+1}\mathbf{Q}_{k+1} \\ &= \mathbf{Q}_{k+1}^{\mathrm{T}}\hat{\mathbf{M}}_{k+1}\mathbf{Q}_{k+1} = I \end{aligned} \qquad [37]$$

As $k \rightarrow \infty \omega_{i,k+1}^2 \rightarrow \omega_i^2$ and $\mathbf{X}_k \rightarrow [\mathbf{u}_1, \mathbf{u}_2 \ldots \mathbf{u}_p]$. As iterations proceed, the reduced matrices $\hat{\mathbf{K}}_{k+1}$ and $\hat{\mathbf{M}}_{k+1}$ tend toward a diagonal form. Consequently, the Jacobi method described previously is ideally suited to the solution of the reduced eigenproblem. The subspace iteration method removes the deficiencies of the simple inverse iteration algorithm. The p lowest eigenvalues and corresponding eigenvectors are extracted simultaneously. Furthermore,

the convergence is not delayed if a cluster of eigenvalues is present within these p lowest eigenvalues. The Sturm sequence property, theorem 1, should be used to verify that all eigenvalues have been extracted within a certain frequency range of interest.

Conclusions and Recommendations

A large number of methods can be applied to computation of the eigenvalues and eigenvectors of dynamical systems. When the order of the system is low, say $n < 10$, polynomial iteration methods and Sturm sequence methods can be applied. As n increases these methods are not robust and rapidly become prohibitively expensive.

Similarity transformation methods can be used for larger systems, say $n < 250$. The preferred method would be Householder's method to transform the dynamic flexibility matrix to an upper Hessenberg form, followed by the QR algorithm. Once the eigenvalues have been found, the corresponding eigenvectors are evaluated by means of the shifted inverse iteration procedure. The Jacobi algorithm is only used in practice after the initial eigenproblem has been projected on to a sufficiently small subspace, such as in the subspace iteration method.

Inverse iteration is a robust method for extracting the lowest eigenvalue of large systems. The simple version of the algorithm presents two major limitations: first, it always converges to the lowest eigenvalue no matter what starting vector is selected, and second it cannot deal with closely clustered eigenvalues. The most reliable form of inverse iteration is the subspace iteration method which performs inverse iteration on a number of vectors simultaneously while keeping them orthogonal to each other.

The most efficient methods for large eigenproblems, like those generated by the finite element method, are those based on the construction of Krylov subspaces.

Nomenclature

$\mathbf{D}$	dynamic flexibility matrix
$\mathbf{H}$	Hessenberg matrix
$\mathbf{I}$	$n \times n$ identity matrix
$\mathbf{L}$	lower triangular matrix
$\mathbf{P}, \mathbf{Q}$	non-singular matrices
r	convergence rate
$\mathbf{u}_i$	eigenvector
$\mathbf{v}$	arbitrary vector
$\mathbf{X}$	subspace
$\rho(\mathbf{v})$	Rayleigh quotient

See also: **Commercial software**; **Computation for transient and impact dynamics**; **Krylov-Lanczos methods**.

Further Reading

Bathe KJ (1996) *Finite Element Procedures*. Englewood Cliffs, NJ: Prentice Hall.

Clough RW and Penzien J (1993) *Dynamics of Structures*. New York: McGraw-Hill.

Dahlquist G and Björck Å (1974) *Numerical Methods*. Englewood Cliffs, NJ: Prentice Hall.

Géradin M and Rixen D (1994) *Mechanical Vibrations: Theory and Application to Structural Dynamics*. New York: John Wiley.

Meirovitch L (1967) *Analytical Methods in Vibrations*. London: Macmillan.

Meirovitch L (1975) *Elements of Vibration Analysis*. New York: McGraw-Hill.

Wilkinson JH (1965) *The Algebraic Eigenvalue Problem*. Oxford: Clarendon Press.

ELECTRORHEOLOGICAL AND MAGNETORHEOLOGICAL FLUIDS

R Stanway, The University of Sheffield, Sheffield, UK

Copyright © 2001 Academic Press

doi:10.1006/rwvb.2001.0080

Semiactive Vibration Control

In the control of vibrations in various types of structures and machines it has long been recognized that performance benefits are available if damping levels can be optimized to suit a changing environment. It is also well established that variable damping can be implemented using a fully active vibration control strategy. However, there are severe penalties associated with the use of active control: complexity, weight, and cost are perhaps the most obvious. Consequently, in many applications it is necessary to pursue compromise solutions where control is

exercised over an essentially passive damping mechanism. This latter form of control is often referred to as semiactive, although it can be argued that the phrase 'controlled passive' provides a more accurate description.

Traditionally the control of passive damping has required the introduction of some mechanism (typically an electromechanical solenoid) which alters the flow paths in an otherwise conventional viscous dashpot arrangement. If the chosen mechanism operates through opening and closing orifices which control fluid flow, then the effective damping can be varied in stepwise fashion. An alternative approach, made possible through the development of so-called smart fluids, involves modulating the energy dissipation characteristics of a damping device through an applied electric or electromagnetic field. Not only does the use of smart fluids offer an elegant solution to the problem of controlling damping levels but the control is continuous in form, as opposed to the stepwise variations obtainable using electromechanical switching.

Smart Fluids

Composition of Smart Fluids

There are two principal classes of smart fluid which can be harnessed for use as controllable vibration dampers: electrorheological (ER) and magnetorheological (MR) fluids. ER fluids generally consist of fine semiconducting particles dispersed in a liquid medium such as silicone oil. The particles are often roughly cylindrical in shape, with diameters chosen to lie in the range 5–75 μm. The carrier liquid is usually chosen to possess a kinematic viscosity in the range 10–50 cSt. The volume fraction of the particles suspended in the liquid carrier can be as high as 50%. There are no firm guidelines as to the choice of particle size, kinematic viscosity, or volume fraction; however, the ranges quoted above have been shown to produce fluids capable of producing operational ER fluids.

In contrast, MR fluids consist of a suspension of magnetically soft particles in a carrier liquid such as mineral or silicone oil. The particle sizes quoted in the literature are generally smaller than those used in ER fluids and lie in the range 0.1–10 μm. Operational MR fluids can be produced using the values of kinematic viscosity (for the carrier liquid) and volume fraction (of particles in suspension) quoted above.

Control of Flow Properties

The smart fluids described above are of direct interest to specialists in mechanical vibration as they offer an elegant means of fabricating damping devices capable of providing continuously variable levels of force. This ability arises from the almost instantaneous and reversible change in their resistance to flow which can be induced through the application of an electric or magnetic stimulus. ER fluids will respond to the application of an electric field while MR fluids require a magnetic field. In both cases the field causes the particles to form into chain-like structures. As the field strength is increased these chains eventually bridge the electrodes, thus significantly increasing the resistance to flow.

Figure 1A shows the orientation of particles in a smart fluid in the absence of an applied electric (or magnetic) field. The formation of particle chains which follows the application of a field strength of sufficient intensity is shown in **Figure 1B.**

In macroscopic terms, the behavior of smart fluids is often likened to that of the class of materials known as Bingham plastics. The shear stress versus shear rate characteristic of an ideal Bingham plastic is shown in **Figure 2**. With reference to **Figure 2**, a Bingham plastic effectively combines the yield-type behavior of a conventional solid with the Newtonian-type behavior of a viscous fluid. In the absence of an applied electric or magnetic field, smart fluids will generally behave like a Newtonian fluid. However, as the applied field is gradually increased, so a yield stress, denoted τ_y, will be established. In any device incorporating a smart fluid this yield stress must be overcome before flow can occur.

Harnessing Smart Fluids for Vibration Control

In order to construct a controllable damping device using smart fluids it is necessary to recognize the three possible modes of operation which may be utilized. These three modes – flow, shear and squeeze – are shown in **Figure 3**.

In the flow mode of operation, **Figure 3A**, the smart fluid is contained between a pair of stationary electrodes (or poles). The term 'electrode' will be used exclusively for the remainder of this article. The resistance to flow of the fluid is controlled by varying

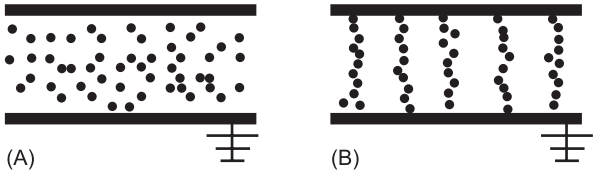


Figure 1 (A) Orientation of particles in a smart fluid in the absence of an applied electric or magnetic field. (B) Formation of particle chains following application of a field strength of sufficient intensity.

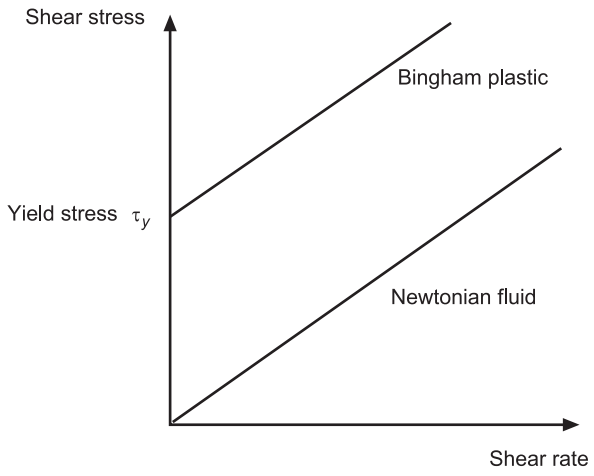


Figure 2 Shear stress versus shear rate characteristic of an ideal Bingham plastic and a Newtonian fluid.

the electric or magnetic field between the electrodes. Thus the field is used to modulate the pressure/flow characteristics of what is effectively a controllable valve. By using such a valve as a bypass, for example across a conventional hydraulic piston and cylinder arrangement, continuously variable control of the force/velocity characteristics can be obtained. Such devices are said to operate in the flow mode.

Alternatively, relative motion (either translational or rotational) can be introduced between the electrodes. Such motion places the smart fluid in shear, as illustrated in **Figure 3B**. As we have noted earlier, the shear stress/shear rate characteristics can be varied continuously through the applied field and thus we have the basis of a simple, controllable damping device, said to operate in the shear mode.

The third possibility for obtaining variable damping from smart fluids is shown in **Figure 3C**, the so-called squeeze-flow mode of operation. Here the electrodes are free to translate in a direction roughly parallel to the direction of the applied field. Consequently the smart fluid can be subjected to alternate tensile and compressive loading. Shearing of the fluid also occurs. Through this mechanism larger forces are available than with flow or shear devices but displacement levels are limited to no more than a few millimeters.

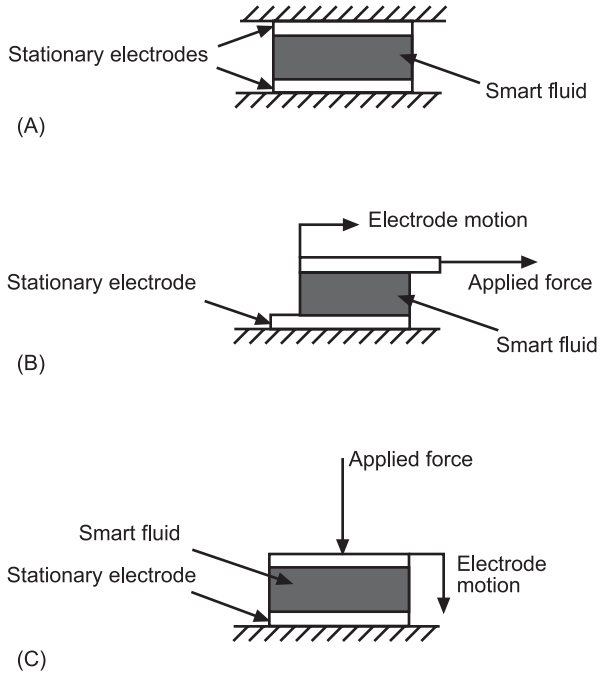


Figure 3 The three modes of operation utilized to construct a controllable damping device using smart fluids. (A) Flow, (B) shear, (C) squeeze.

Modeling Smart Fluids for Vibration Control

Macroscopic Models

At the time of writing considerable efforts are being directed towards the development of mathematical models of smart fluids. These models are predominantly macroscopic in nature and are being developed both as aids to understanding the behavior of smart fluids and to assist in the design of suitable control systems. There is insufficient space here to present a survey of the various modeling techniques which are available. However, it is helpful to present a quasi-static approach to modeling a flow-mode vibration damper and then summarize the extension of the model to account for dynamic effects in the smart field. Here the main purpose of the model is to assist us in visualizing the physical behavior of the controllable damper.

Physical Arrangement

Figure 4 shows a controllable damper where a smart valve is used as a bypass across a hydraulic piston and cylinder. Assume that the valve has a single annulus of length l containing the smart fluid. Denote the annular gap by h and note that the ratio of diameter d to gap h is so large that the valve's behavior may be modeled as similar to that of two flat plates of breadth b ($= \pi d$). The smart fluid around the hydraulic circuit has viscosity μ and density ρ. The fluid in the annulus of the valve is subjected to either an electric or magnetic field, which results in the development of a yield stress τ_y in the fluid, as shown in **Figure 2**.

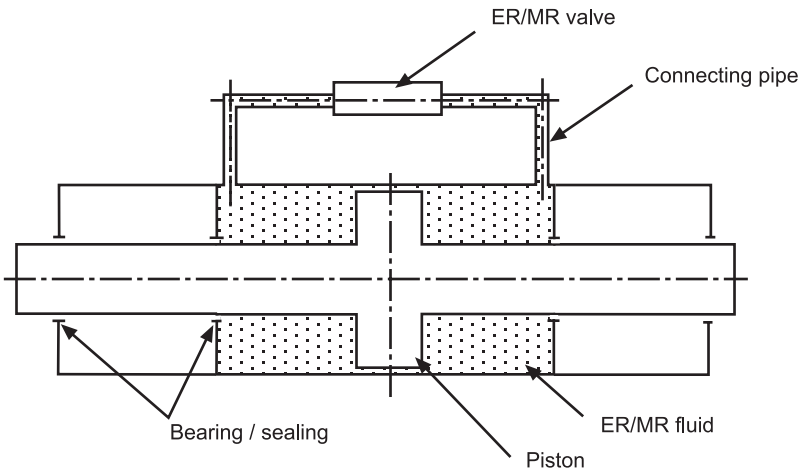


Figure 4 A controllable damper, using a smart valve as a bypass across a hydraulic piston and cylinder.

A Quasisteady Model of a Smart Control Valve

The quasisteady operation of the smart fluid control valve can be described in terms of three dimensionless parameters. If τ_w is the shear stress at the electrode surface and $\bar{u}$ is the mean velocity of flow between the electrodes then a dimensionless friction coefficient:

$$\pi_1 = \tau_w / (\rho \bar{u}^2) \qquad [1]$$

can be defined. The Reynolds number associated with the flow of fluid is defined as:

$$\pi_2 = (\rho \bar{u} h)/\mu \qquad [2]$$

Finally the influence of the electric or magnetic field on the behavior of the valve is characterized through the so-called Hedström number:

$$\pi_3 = \frac{\tau_y \rho h^2}{\mu^2} \qquad [3]$$

The three dimensionless groups defined by eqns [1]–[3] allow us to visualize the controlling influence of the applied field on ER valve performance.

It is assumed that the effective working area of the piston is A and that the piston translates within the cylinder at a steady velocity of v. This piston data allow the volume flow rate to be calculated and then given the valve dimensions l, b and h, then $\bar{u}$, the mean velocity of fluid flow through the valve can be calculated. At this stage the corresponding value of the Reynolds number, π_2, can be established.

The next step is to establish a value for the Hedström number, π_3. Initially a static value is estimated from a value of τ_y established from static tests on the smart fluid. This value is then corrected to allow for the presence of fluid flow. Given values for the dimensionless parameters π_2 and π_3, the dimensionless friction coefficient can be computed by solving the well established cubic equation for Bingham plastic flow:

$$f(\pi_1) = \pi_1^3 - \left[\frac{3}{2} + 6\frac{\pi_2}{\pi_3}\right]\left[\frac{\pi_3}{\pi_2^2}\right]\pi_1^2 + \frac{1}{2}\left[\frac{\pi_3}{\pi_2^2}\right] = 0 \qquad [4]$$

A graphical interpretation of eqn [4] is facilitated by defining a further dimensionless parameter:

$$\pi^* = \frac{\pi_1 \pi_2^2}{\pi_3} \qquad [5]$$

where $\pi* = \tau_w/\tau_y$, i.e., the ratio of shear stress at the electrode wall to the yield stress developed within the smart fluid. For flow to occur the shear stress developed at the electrode wall must obviously exceed the smart fluid's yield stress and this enables a physical interpretation of the solutions of eqn [4]. In terms of $\pi*$, eqn [4] is rewritten as:

$$f(\pi^*) = (\pi^*)^3 - \left[\frac{3}{2} + 6\left(\frac{\pi_2}{\pi_3}\right)\right](\pi^*)^3 + \frac{1}{2} = 0 \qquad [6]$$

The condition $\pi_2/\pi_3 \to 0$ represents the limiting case which distinguishes between flow occurring and the absence of flow. The condition $\pi_2/\pi_3 \to 0$ is approached by increasing the applied electric field, E, which in turn increases the Bingham yield stress,

τ_y, and thus the Hedström number, π_3. Setting $\pi_2/\pi_3 = 0$ in eqn [6] results in:

$$f(\pi^*) = (\pi^*)^3 - \frac{3}{2}(\pi^*)^2 + \frac{1}{2} = 0 \qquad [7]$$

which has only one physically meaningful solution. This solution can be found by plotting $f(\pi^*)$ vs π^*, as shown in **Figure 5**. With reference to **Figure 5**, there is a double root at $\pi^* = 1$, representing the case where the wall stress is equal to the Bingham plastic yield stress. Any reduction in π_3 will obviously cause fluid flow to occur. Two such cases are superimposed on **Figure 5**; these are for $\pi_2/\pi_3 = 0.05$ and 0.1. For all three plots, one root is clearly negative and therefore meaningless as a ratio of stresses. The double root is created when $\pi_2/\pi_3 = 0$ splits with one root increasing and the other decreasing. From the definition of $\pi^*(= \tau_w/\tau_y)$, only the root greater than unity will give rise to fluid flow and thus represents a meaningful solution.

When the wall shear stress is exactly equal to the Bingham plastic yield stress, i.e., $\tau_w = \tau_y$ and thus $\pi^* = 1$, eqn [5] defines asymptotes which represent limiting cases. **Figure 6** shows a plot of friction coefficient π_1 against Reynolds number π_2. The asymptotes for $\pi_3 = 10, 100$, and 1000 are shown. When the Bingham yield stress is reduced such that π_3 approaches zero and thus π_2/π_3 approaches infinity, then it can be shown that $\pi_1\pi_2 \rightarrow 6$, which corresponds to the well-known relationship between π_1 and π_2 for Newtonian flow between smooth flat plates. The asymptote corresponding to $\pi_1\pi_2 = 6$ is superimposed on to **Figure 6**.

Figure 6 enables the operation of the ER flow control valve to be visualized in terms of three dimensionless groups. The asymptotes on **Figure 6** illustrate the limits of operation at both low and high values of the Hedström number π_3. Perhaps most importantly, the graph shows how the Hedström number influences the mapping of the Reynolds number π_2 on to the friction coefficient π_1. Furthermore, it enables the force/velocity characteristics of a valve-controlled smart vibration damper to be predicted.

Prediction of Force/Velocity Characteristics

The force/velocity characteristics of the smart valve-controlled vibration damper (shown in **Figure 6**), under steady flow conditions, can be found using eqns [1]–[4]. The calculation is started by specifying the steady value of the piston velocity and the piston area. For a given valve configuration this enables the volume flow rate, Q, to be calculated and hence the mean velocity ($\bar{u} = Q/bh$). A numerical value for the corresponding Reynolds number follows directly from the definition in eqn [2]. For a given value of electric or magnetic field strength the yield stress, τ_y, of the smart fluid is computed and then eqn [3] gives

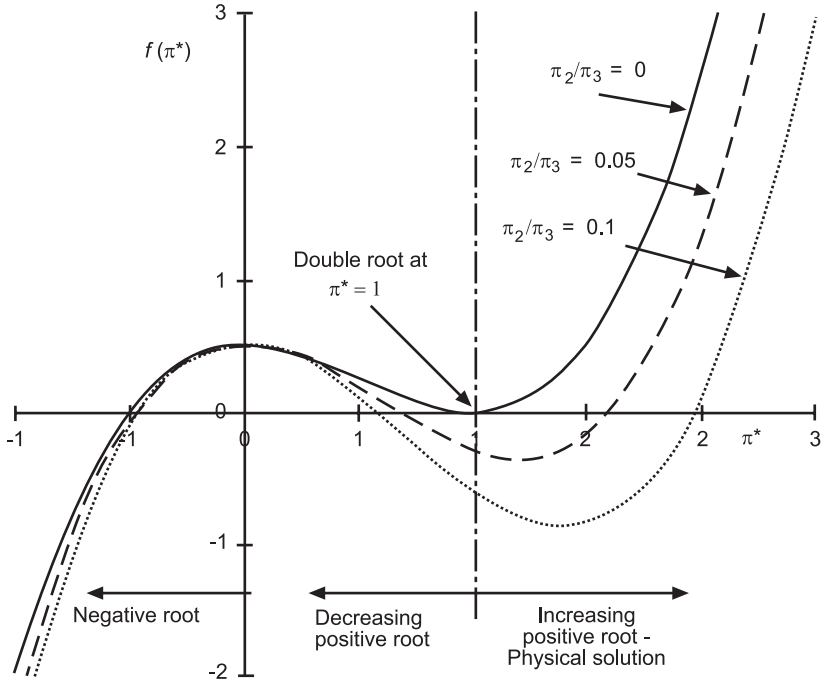


Figure 5 Plot of $f(\pi^*)$ vs π.

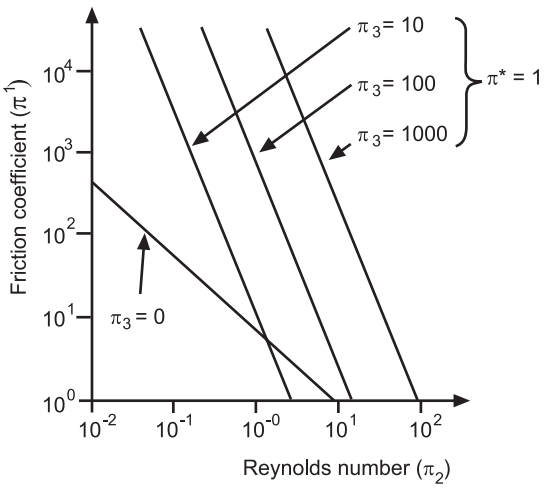


Figure 6 Plot of friction coefficient π_1 against Reynolds number π_2.

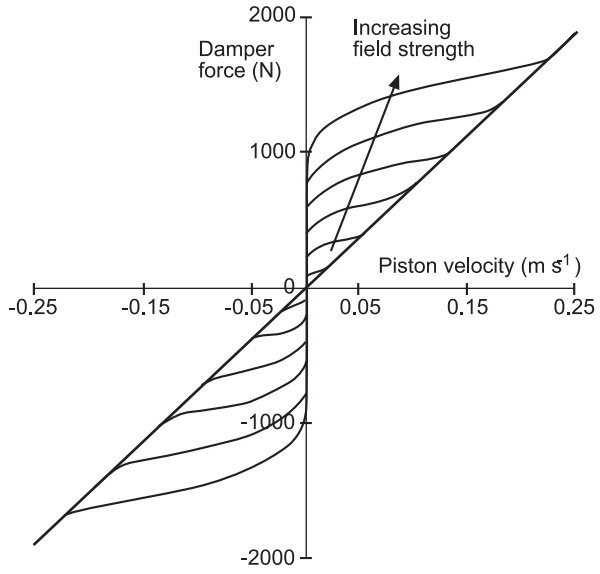


Figure 7 The general form of force/velocity characteristics.

the Hedström number, π_3. The numerical values of π_2 and π_3 are then substituted into eqn [4] and a suitable root-solving routine is applied to determine the three possible values of the friction coefficient, π_1.

The physically meaningful value of π_1 is used to calculate the pressure drop across the valve and thus across the piston. (The influence of the connecting pipes is assumed to be negligible.) The piston force follows by multiplying the pressure by the piston area. The piston force can then be plotted against the value of the piston velocity which was used to start the calculation. The procedure is repeated for the desired range of values of piston velocity so as to generate a complete set of force/velocity characteristics. The general form of the force/velocity characteristics generated in this way is illustrated in **Figure 7**.

Inclusion of Fluid Dynamic Effects

It has now been established that a quasisteady model can provide realistic predictions of a valve-controlled smart vibration damper. However, experimental studies involving excitation frequencies of (say) 1 Hz and above reveal features which cannot be accounted for by the use of quasisteady model. These features arise from the presence of dynamic effects – notably inertia and compressibility of the smart fluid – which can play a significant role in the operation of an experimental device.

A simple lumped arrangement, which has been shown capable of accounting for dynamic effects, is shown in **Figure 8**. The model is derived on the basis of a number of assumptions, specifically: the effective inertia of the smart fluid in the cylinder, connecting pipes and control valve is denoted by m; the compressibility of the fluid in the cylinder is lumped with

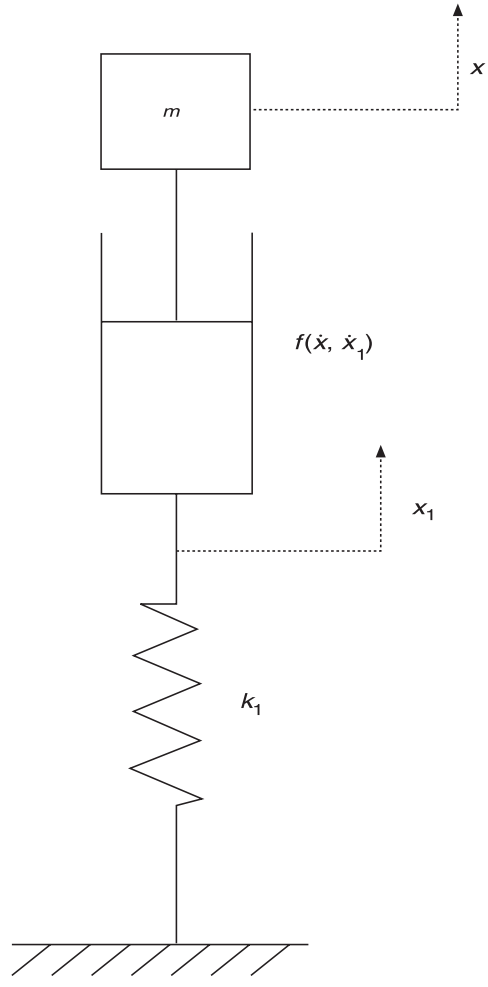


Figure 8 A simple lumped arrangement model, capable of accounting for dynamic effects.

other such effects and denoted by the spring constant k_1; and the resistance to flow is represented by a nonlinear function of velocity, $f(\dot{x}, \dot{x}_1)$, where $\dot{x}_1$ is the velocity associated with the spring element k_1.

Given these assumptions and with reference to **Figure 8**, the equations of motion are:

$$\left.\begin{aligned} m\ddot{x} + f(\dot{x}, \dot{x}_1) &= F \\ -f(\dot{x}, \dot{x}_1) + k_1 x_1 &= 0 \end{aligned}\right\} \quad [8]$$

where F is the net piston force.

Owing to the presence of the nonlinear function $f(\dot{x}, \dot{x}_1)$, the solution of eqn [8] requires the use of an iterative numerical procedure. Numerical values for the fluid inertia and stiffness can be calculated from purely theoretical considerations. However, it has been found that agreement between model predictions and experimental data is dramatically improved if the inertia and stiffness values are updated to reflect experimental observations.

At relatively low frequencies (say, up to 3 Hz) the influence of smart fluid dynamics on the force/velocity characteristics is not significant. However, above 3 Hz the dynamics play an increasingly important role. As an example, **Figure 9** shows a typical performance prediction at a mechanical excitation frequency of 10 Hz. Note the presence of the hysteresis loop due to the fluid's compressibility and the additional loops at the higher levels of force and velocity. Experimental studies involving valve-controlled smart dampers show broad agreement with the results in **Figure 9** but there is still enormous scope for improvements in modeling techniques, both to improve our basic understanding and as a basis for control system design.

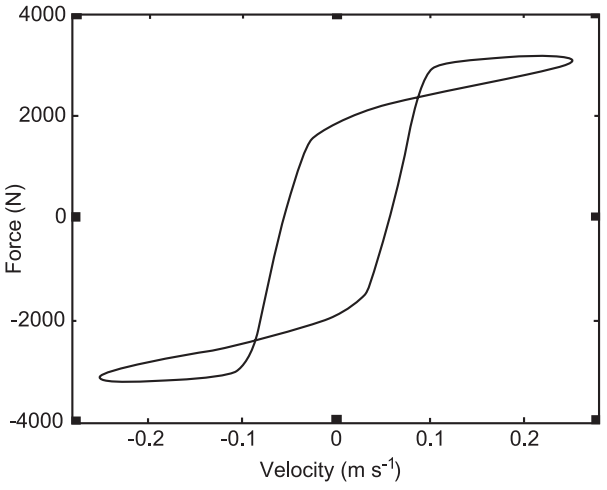


Figure 9 Typical performance prediction at a mechanical excitation.

Current Developments in Smart Fluids

Squeeze-flow Devices

Valve-controlled smart dampers, described in the previous section, are suitable for applications where substantial displacements need to be accommodated, for example, in road and rail vehicle suspension systems. However, there are many potential applications where machines and mechanisms need to be isolated from vibration but where the displacement levels are relatively small.

Squeeze-flow devices are capable of providing large force levels over small displacement ranges, say up to 5 mm. Moreover the construction of squeeze-flow devices can be extremely simple. If ER fluid is to be used, then two plane electrodes will suffice as the interface between the mechanical components and the ER fluid. Published experimental results from various sources have shown that the force levels available are more than adequate for use in, for example, automotive engine mount applications. If a MR fluid is used as the working medium then complexity and weight are increased owing to the requirement for an electromagnet to excite the MR fluid, but the resulting devices are still remarkably compact.

There are factors which, at first sight, appear to detract from the performance of squeeze-flow devices. Unlike conventional flow- and shear-mode devices, in squeeze-flow the gap between the electrodes or poles is liable to be constantly changing as a result of the applied mechanical excitation. Furthermore, placing the fluid in tension on each alternate stroke is likely to lead to cavitation and produce force levels which bear no relation to the forces produced by compression of the fluid. Fortunately there are ways to counteract problems which arise as a result of squeeze-flow operation. For example, a displacement feedback loop can be used to provide a constant electric or magnetic field irrespective of the instantaneous gap size. Also there is considerable scope for ingenuity in the design of the electrode/pole configurations: arranging for smart fluid to act on opposite faces of the moving electrode/pole serves to compensate for the asymmetry of operation between tension and compression.

Modeling and Control

Before the development of dynamic models to account for the behavior of smart fluids, static models were used, mainly for the rough sizing of components at the design stage. However, given the generally crude formulations of earlier generations of smart fluids, experimental verification was invariably essen-

tial. In the recent development of dynamic models, emphasis has been placed on the necessity to account for observed behavior and to behave robustly in the face of environmental changes. In the modeling technique described in the previous section the intention was to develop a characterization wherein the performance of industrial scale devices could be predicted on the basis of fluid data derived using laboratory-scale apparatus. The feasibility of this form of performance prediction has now been established. Taken together with the findings of various other leading groups in this field it can be stated with confidence that the modeling of smart fluids is gradually maturing. Robust models are now available which not only account for observed behavior, but also help to improve our understanding of the operation of smart fluids.

As smart fluid damping devices are developed and further applications uncovered (see later), it is reasonable to suggest the increasing effort will be directed at the development of suitable control schemes. At the time of writing it is far from clear which direction (if any) controller design will take. Various approaches to feedback control system design are currently being pursued, ranging from formal schemes which draw heavily on modern control theory to heuristic controllers designed to suit specific applications. Where the disturbance is known or can be measured then gain scheduling (or feedforward control) offers an alternative approach which is being pursued by some groups. Amongst the simpler possibilities is the use of feedback strategies to linearize the force/velocity characteristics associated with smart fluids. A configuration involving force feedback of a valve-controlled ER damper is shown in **Figure 10**. Numerical simulation studies indicated the feasibility of this approach and experimental confirmation has now been obtained for input frequencies of up to 5 Hz. Higher bandwidths may require additional ingenuity in the design of control elements.

New Areas of Application

We conclude with a brief review of new applications of ER/MR fluids which have recently been identified. In the 1970s and 1980s it was the aerospace and automotive industries which were the first to identify potential applications of smart fluids. Aerospace companies were certainly deterred from using ER fluids by the requirement to provide a high-voltage supply to excite the fluid. Now that the advent of MR fluids has obviated this requirement, investigations into aerospace applications have resumed: aircraft landing gear is an obvious target for MR dampers and the feasibility of a controllable lag mode damper in a helicopter is also being studied. In the automotive field smart dampers for vehicle suspensions and engine mounts continue to be developed. In addition, vehicle seats incorporating a smart fluid suspension have been developed to the mass production stage.

In the past 5 years there has been a significant research effort to develop smart fluids for civil engineering applications. Perhaps greatest emphasis has been placed upon the use of MR dampers to reduce the vulnerability of base-isolated structures when subjected to seismic disturbances. Considerable progress has been made in terms of device development, modeling, and the design of feedback controls. In the general structural field, research into composite beams which include a smart fluid layer has produced some exploitable results. In principle, the smart fluid layer provides controllable damping but ingenuity in the mechanical design of the beam is essential if the increase in damping forces with electric/magnetic field is to be significant.

One promising application area which has been slow to respond to the possibilities offered by smart fluids is robotics and other automated machining and assembly operations. It has been demonstrated that smart fluids form a basis for simple but versatile rotary actuators. Such actuators can provide accurate control of torque and position and can be designed in such a way as to act as a torsional vibration absorber. The large force/small displacement characteristics of squeeze-flow devices is compatible with many vibration isolation problems inherent in modern machinery, but reports on the development of industrial applications are still awaited.

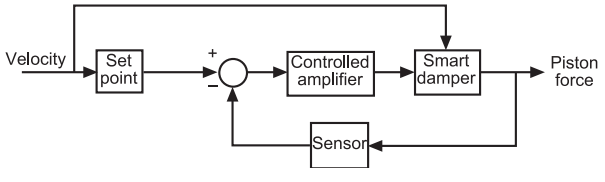


Figure 10 Force feedback of a valve-controlled ER damper.

Further Reading

Bullough WA (ed.) (1996) Electro-rheological fluids, magneto-rheological suspensions and associated technology. *Proceedings of the 5th International Conference*, 10–14 July 1995, Sheffield, UK. Singapore: World Scientific.

Culshaw B (1996) *Smart Structures and Materials*. Norwood, MA: Artech House.

Dyke SJ, Spencer BF, Sain MK, Carlson JD (1996) Modelling and control of MR dampers for seismic response reduction. *Smart Materials and Structures* 5: 565–575.

Gandhi MV, Thomson BS (1992) *Smart Materials and Structures*. London: Chapman and Hall.

Inman DJ (1989) *Vibration Control, Measurement and Stability*. Englewood Cliffs, Prentice Hall.

Jolly MR, Carlson JD, Muñoz BC (1996) A model of the behaviour of MR materials. *Smart Materials and Structures* 5: 607–614.

Kamath GM, Wereley NM (1997) Modeling the damping mechanism in electrorheological fluid based dampers. In Wolfenden A, Kinra VK (eds) *Mechanics and Mechanisms of Material Damping*, ASTM STP 1304, pp. 331–348. West Conshohocken, PA: ASTM.

Siginer DA, Dulikravich GS (1995) *Developments in Electrorheological Flows*, FED, vol. 235. New York: ASME.

Sims ND, Stanway R, Johnson AR (1999) Vibration control using smart fluids: a state-of-the-art review. *Shock and Vibration Digest* 31: 195–203.

Stanway R, Sproston JL, El-Wahed AK (1996) Applications of electrorheological fluids in vibration control: a survey. *Smart Materials and Structures* 5; 464–481.

Tzou HS, Anderson GL (1992) *Intelligent Structural Systems*. Dordrecht: Kluwer.

Wilkinson WL (1960), *Non-Newtonian Fluids*. Oxford: Pergamon Press.

ELECTROSTRICTIVE MATERIALS

K Uchino, The Pennsylvania State University, University Park, PA, USA

Copyright © 2001 Academic Press

doi:10.1006/rwvb.2001.0078

Introduction

The word electrostriction is used in a general sense to describe electric field-induced strain, and hence frequently also implies the converse piezoelectric effect. However, in solid-state theory, the converse piezoelectric effect is defined as a primary electromechanical coupling effect, i.e., the strain is proportional to the applied electric field, while electrostriction is a secondary coupling in which the strain is proportional to the square of the electric field. Thus, strictly speaking, they should be distinguished. However, the piezoelectricity of a ferroelectric which has a centrosymmetric prototype (high-temperature) phase is considered to originate from the electrostrictive interaction, and hence the two effects are related.

In this section, first the origin of piezoelectricity and electrostriction are explained microscopically and phenomenologically. Then, electrostrictive materials are described in detail, and finally their applications are introduced.

Microscopic Origins of Electrostriction

Solids, especially ceramics (inorganic materials), are relatively hard mechanically, but still expand or contract depending on the change of the state parameters. The strain (defined as the displacement ΔL/initial length L) caused by temperature change and stress is known as thermal expansion and elastic deformation. In insulating materials, the application of an electric field can also cause deformation. This is called electric field-induced strain.

Why a strain is induced by an electric field is explained herewith. For simplicity, let us consider an ionic crystal such as NaCl. **Figure 1** shows a one-dimensional rigid-ion spring model of the crystal lattice. The springs represent equivalently the cohesive force resulting from the electrostatic Coulomb energy and the quantum mechanical repulsive energy. **Figure 1B** shows the centrosymmetric case, whereas **Figure 1A** shows the more general noncentrosymmetric case. In **Figure 1B**, the springs joining the ions are all the same, whereas in **Figure 1A**, the springs joining the ions are different for the longer or shorter ionic distance, in other words, hard and soft springs existing alternately are important. Next, consider the state of the crystal lattice (**Figure 1A**) under an applied electric field. The cations are drawn in the direction of the electric field and the anions in the opposite direction, leading to the relative change in the interionic distance. Depending on the direction of the electric field, the soft spring expands or contracts more than the contraction or expansion of the hard spring, causing a strain x (i.e., unit cell length change) in proportion to the electric field E. This is the converse piezoelectric effect. When expressed as:

$$x = dE \qquad [1]$$

the proportionality constant d is called the piezoelectric constant.

On the other hand, in **Figure 1B**, the amounts of extension and contraction of the spring are nearly the

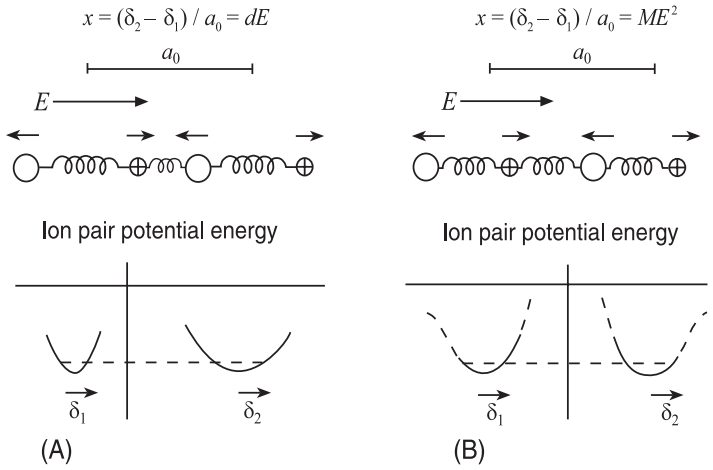


Figure 1 Microscopic explanation of (A) piezostriction and (B) electrostriction.

same, and the distance between the two cations (i.e., lattice parameter) remains almost the same, hence there is no strain. However, more precisely, ions are not connected by such idealized springs (those are called harmonic springs, in which (force F) = (spring constant k) × (displacement Δ) holds). In most cases, the springs possess anharmonicity ($F = k_1\Delta - k_2\Delta^2$), i.e., they are somewhat easy to extend, but hard to contract. Such subtle differences in displacement cause a change in the lattice parameter, producing a strain which is independent of the direction of the applied electric field, and which is an even function of the electric field. This is called the electrostrictive effect, and can be expressed as:

$$x = ME^2 \qquad [2]$$

where M is the electrostrictive constant.

Phenomenology of Electrostriction

Devonshire Theory

In a ferroelectric whose prototype phase (high-temperature paraelectric phase) is centrosymmetric and nonpiezoelectric, the piezoelectric coupling term PX is omitted and only the electrostrictive coupling term P^2X is introduced into the phenomenology (P and X are polarization and stress). This is almost accepted for discussing practical electrostrictive materials with a perovskite structure. The theories for electrostriction in ferroelectrics were formulated in the 1950s by Devonshire and Kay. Let us assume that the elastic Gibbs energy should be expanded in a one-dimensional form:

$$G_1(P, X, T) = (1/2)\alpha P^2 + (1/4)\beta P^4 + (1/6)\gamma P^6 - (1/2)sX^2 - QP^2X \qquad [3]$$

$$\alpha = (T - T_0)/\varepsilon_0 C \qquad [4]$$

where P, X, T are polarization, stress, and temperature, respectively, and s and Q are called the elastic compliance and the electrostrictive coefficient. This leads to eqns [5] and (6) for the electric field E and strain x:

$$E = (G_1/P) = \alpha P + \beta P^3 + \gamma P^5 - 2QPX \qquad [5]$$

$$x = -(G_1/X) = sX + QP^2 \qquad [6]$$

Case 1: $X = 0$ When an external is zero, the following equations are derived:

$$E = \alpha P + \beta P^3 + \gamma P^5 \qquad [7]$$

$$x = QP^2 \qquad [8]$$

$$1/\varepsilon_0\varepsilon = \alpha + 3\beta P^2 + 5\gamma P^4 \qquad [9]$$

If the external electric field is equal to zero ($E = 0$), two different states are derived:

$$P = 0 \quad \text{and} \quad P^2 = \sqrt{(\beta^2 - 4\alpha\gamma - \beta)}/2\gamma$$

1. Paraelectric phase: $P_S = 0$ or $P = \varepsilon_0\varepsilon E$ (under small E)

$$\text{Permittivity}: \quad \varepsilon = C/(T - T_0) \quad \text{(Curie} - \text{Weiss law)} \qquad [10]$$

$$\text{Electrostriction}: \quad x = Q\varepsilon_0^2\varepsilon^2E^2 \qquad [11]$$

Therefore, the previously mentioned electrostrictive coefficient M in eqn [2] is related to the electrostrictive Q coefficient through:

$$M = Q\varepsilon_0^2\varepsilon^2 \qquad [12]$$

Note that the electrostrictive M coefficient has a large temperature dependence like $\propto 1/(T - T_0)^2$, supposing that Q is almost constant.

2. Ferroelectric phase: $P_S^2 = \left(\sqrt{\beta^2 - 4\alpha\gamma} - \beta\right)/2\gamma$

or $P = P_S + \varepsilon_0\varepsilon E$ (under small E)

$$\begin{aligned} x &= Q(P_S + \varepsilon_0\varepsilon E)^2 \\ &= QP_S^2 + 2\varepsilon_0\varepsilon QP_SE + Q\varepsilon_0^2\varepsilon^2E^2 \end{aligned} \qquad [13]$$

$$\text{Spontaneous strain}: \quad x_S = QP_S^2 \qquad [14]$$

$$\text{Piezoelectric constant}: \quad d = 2\varepsilon_0\varepsilon QP_S \qquad [15]$$

Thus, we can understand that piezoelectricity in a perovskite crystal is equivalent to the electrostrictive phenomenon biased by the spontaneous polarization.

Case 2: $X \neq 0$ When a hydrostatic pressure $p(X = -p)$ is applied, the inverse permittivity is changed in proportion to p:

$$\begin{aligned} &1/\varepsilon_0\varepsilon = \alpha + 3\beta P^2 + 5\gamma P^4 + 2Qp \\ &\text{(ferroelectric state)} \\ &1/\varepsilon_0\varepsilon = \alpha + 2Qp = (T - T_0 + 2Q\varepsilon_0Cp)/(\varepsilon_0C) \\ &\text{(paraelectric state)} \end{aligned} \qquad [16]$$

Therefore, the pressure dependence of the Curie–Weiss temperature T_0 or the transition temperature T_C is derived as follows:

$$(T_0/p) = (T_C/p) = -2Q\varepsilon_0C \qquad [17]$$

In general, the ferroelectric Curie temperature is decreased with increasing hydrostatic pressure (i.e., $Q_h > 0$).

Converse Effect of Electrostriction

So far, we have discussed the electric field-induced strains, i.e., piezoelectric strain (converse piezoelectric effect, $x = dE$) and electrostriction (electrostrictive effect, $x = ME^2$). Let us consider here the converse effect, i.e., the response to the external stress, which is applicable to sensors. The direct piezoelectric effect is the increase of the spontaneous polarization by an external stress, and is expressed as:

$$\Delta P = dX \qquad [18]$$

In contrast, since the electrostrictive material does not have spontaneous polarization, it does not exhibit any charge under stress, but changes permittivity (see eqn [16]):

$$\Delta(1/\varepsilon_0\varepsilon) = 2QX \qquad [19]$$

This is the converse electrostrictive effect.

Temperature Dependence of Electrostrictive Coefficient

Several expressions for the electrostrictive coefficient Q have been given so far. From the data obtained by independent experimental methods such as:

1. electric field-induced strain in the paraelectric phase
2. spontaneous polarization and spontaneous strain (X-ray diffraction) in the ferroelectric phase
3. d constants from the field-induced strain in the ferroelectric phase or from the piezoelectric resonance
4. pressure dependence of permittivity in the paraelectric phase

nearly equal values of Q were obtained. **Figure 2** shows the temperature dependence of the electrostrictive coefficients Q_{33} and Q_{31} of the complex perovskite $Pb(Mg_{1/3}Nb_{2/3})O_3$, whose Curie temperature is near 0 °C. It is seen that there is no significant anomaly in the electrostrictive coefficient Q through the temperature range from a paraelectric to a ferroelectric phase, in which the piezoelectricity appears. Q is almost temperature-independent.

Electrostriction in Oxide Perovskites

Perovskites and Complex Perovskites

Among the practical piezoelectric/electrostrictive materials, many have the perovskite-type crystal structure ABO_3. This is because many such materials undergo a phase transition on cooling from a high-symmetry high-temperature phase (cubic paraelectric phase) to a noncentrosymmetric ferroelectric phase. Materials with a high ferroelectric transition temperature (Curie temperature) show piezoelectricity at room temperature, whereas those with a transition

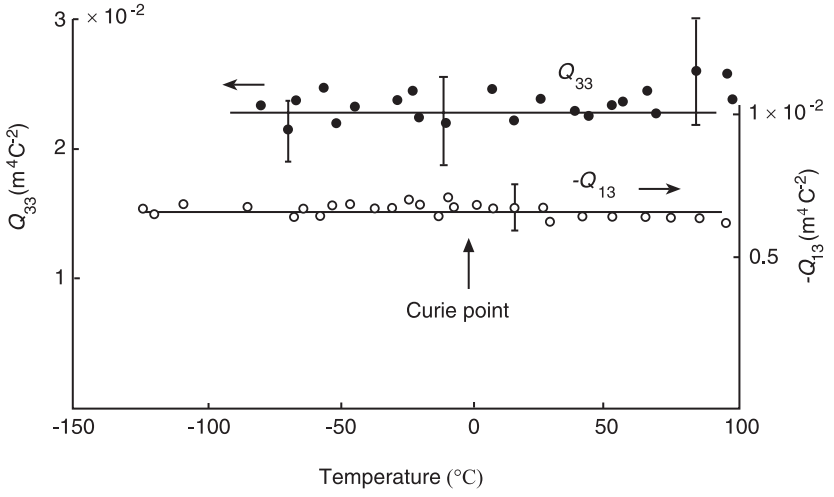


Figure 2 Temperature dependence of the electrostrictive constants Q_{33} and Q_{13} in $Pb(Mg_{1/3}Nb_{2/3})O_3$.

temperature near or below room temperature exhibit the electrostrictive effect. For the latter, at a temperature right above the Curie temperature, the electrostriction is extraordinarily large because of the large anharmonicity of the ionic potential. Besides, simple compounds such as barium titanate ($BaTiO_3$) and lead zirconate ($PbZrO_3$), solid solutions such as $A(B, B')O_3$, and complex perovskites such as $A^{2+}(B^{3+}_{1/2}B'^{5+}_{1/2})O_3$ and $A^{2+}(B^{2+}_{1/3}B'^{5+}_{2/3})O_3$ can be easily formed; such flexibility is important in materials design. **Figure 3** shows the crystal structures of the above-mentioned complex perovskites with B-site ordering. When B and B' ions are randomly distributed, the structure becomes a simple perovskite.

Electrostrictive Effect in Simple Perovskites

Yamada has summarized the electromechanical coupling constants of not only perovskite-type oxides but also tungsten bronze and $LiNbO_3$ types, which contain oxygen octahedra. Following the DiDomenico–Wemple treatment for the electrooptic effect, by expressing the electrostrictive tensor Q_{ijkl} of $LiNbO_3$ with a trigonal symmetry $3m$ in a coordinate system based on the fourfold axis of the oxygen octahedron, and making a correction for the packing density ξ by:

$$Q^P_{ijkl} = \xi^2 Q_{ijkl} \qquad [20]$$

Yamada obtained the electrostrictive coefficient Q^P normalized to a perovskite unit cell. It could be concluded that the electrostrictive coefficient Q^Ps of the simple perovskite-type oxides with one kind of B ion have nearly equal values. The average values are:

$$\begin{aligned} Q^P_{11} &= 0.10\,\mathrm{m^4\,C^{-2}} \\ Q^P_{12} &= -0.034\,\mathrm{m^4\,C^{-2}} \\ Q^P_{44} &= 0.029\,\mathrm{m^4\,C^{-2}} \end{aligned} \qquad [21]$$

Electrostrictive Effect in Complex Perovskites

Uchino *et al.* extended these investigations to complex perovskite-type oxides to obtain the electrostrictive coefficient Q_h and Curie–Weiss constant C. The results are summarized in **Table 1**. It is important to note that the magnitude of the electrostrictive coefficient does not depend on the polar state, whether it is ferroelectric, antiferroelectric, or paraelectric, but strongly depends on the crystal structure, such as whether the two kinds of B and B' ions are randomly distributed in the octahedron or ordered like $B - B' - B - B'$ (1:1 ordering). The electrostrictive coefficient Q increases with increasing degree of cation order and follows the sequence disordered, partially ordered, simple, and finally ordered-type perovskites. For the polar materials, their Curie–Weiss constants are also listed in **Table 1**, showing a completely opposite trend to the Q_h values. It was consequently found that the invariant for the complex perovskite-type oxides is not Q itself, but the product of the electrostrictive coefficient and the Curie–Weiss constant (Uchino's constant):

$$Q_h C = 3.1(\pm 0.4) \times 10^3\,\mathrm{m^4\,C^{-2}\,K} \qquad [22]$$

This QC constant rule can be understood intuitively, if we accept the assumption that the material whose dielectric constant changes easily with pressure also exhibits a large change of the dielectric constant

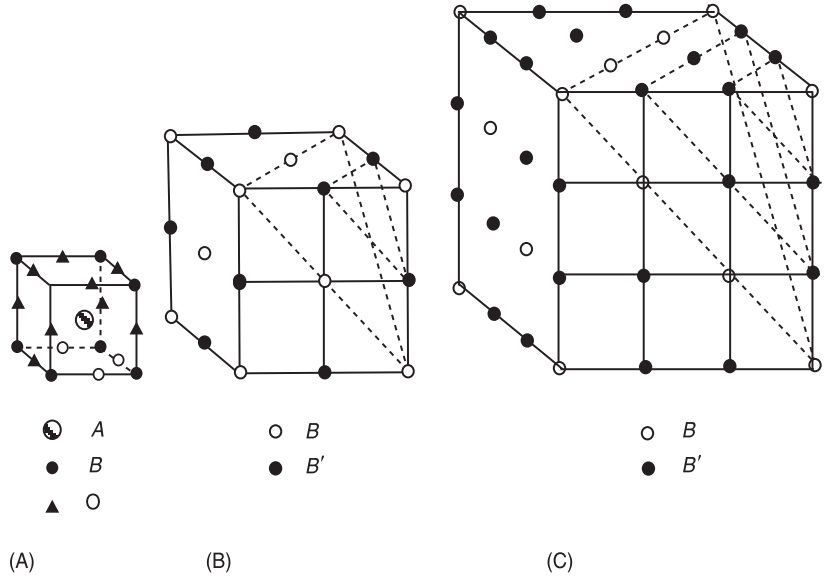


Figure 3 Complex perovskite structures with various B ion arrangements: (A) simple: ABO_3; (B) 1:1 ordered: $AB_{1/2}B'_{1/2}O_3$; (C) ordered: $AB_{1/3}B'_{2/3}O_3$.

Table 1 Electrostrictive coefficient Q_h and Curie–Weiss constant C for various perovskite crystals

Ordering	*Material*	Q_h ($\times 10^{-2} m^4 C^{-2}$)	C ($\times 10^5 K$)	$Q_h C$ ($\times 10^3 m^4 C^{-2} K$)
Ferroelectric				
Disorder	$Pb(Mg_{1/2}Nb_{2/3})O_3$	0.60	4.7	2.8
	$Pb(Zn_{1/3}Nb_{2/3})O_3$	0.66	4.7	3.1
Partial order	$Pb(Sc_{1/2}\ Ta_{1/2})O_3$	0.83	3.5	2.9
Simple	$BaTiO_3$	2.0	1.5	3.0
	$PbTiO_3$	2.2	1.7	3.7
	$SrTiO_3$	4.7	0.77	3.6
	$KTiO_3$	5.2	0.5	2.6
Antiferroelectric				
Partial order	$Pb(Fe_{2/3}U_{1/3})O_3$		2.3	
Simple	$PbZrO_3$	2.0	1.6	3.2
Order	$Pb(Ca_{1/2}W_{1/2})O_3$		1.2	
	$Pb(Mg_{1/2}\ W_{1/2})O_3$	6.2	0.42	2.6
Nonpolar				
Disorder	$(K_{3/4}Bi_{1/4})(Zn_{1/6}Nb_{5/6})O_3$	0.55–1.15		
Simple	$BaZrO_3$	2.3		

with temperature, i.e., the proportionality between the following two definitions:

$$Q_h = [\partial(1/\varepsilon)/\partial p]/2\varepsilon_0 \qquad [23]$$

$$1/C = [\partial(1/\varepsilon)/\partial T] \qquad [24]$$

Another intuitive crystallographic 'rattling ion' model has also been proposed. **Figure 4** illustrates two models of $A(B_{I\,1/2}B_{II\,1/2})O_3$ perovskite, one being ordered and the other disordered. If the rigid ion model is assumed, in the disordered lattice, the larger B_I ions locally prop open the lattice, and there is some 'rattling' space around the smaller B_{II} ion. In contrast, in the ordered lattice, the larger neighboring ions eliminate the excess space around the B_{II} ion, and the structure becomes close-packed. The close packing in an ordered arrangement, as shown in **Figure 4A**, has been confirmed by Amin *et al.* in $0.9\,Pb(Mg_{1/2}W_{1/2})O_3 - 0.1\,Pb(Mg_{1/3}Nb_{2/3})O_3$.

When an electric field is applied to the disordered perovskite, the B_{II} ions with a large 'rattling space' can easily shift without distorting the oxygen octahedron. Thus, large polarizations per unit electric field, in other words, large dielectric constants,

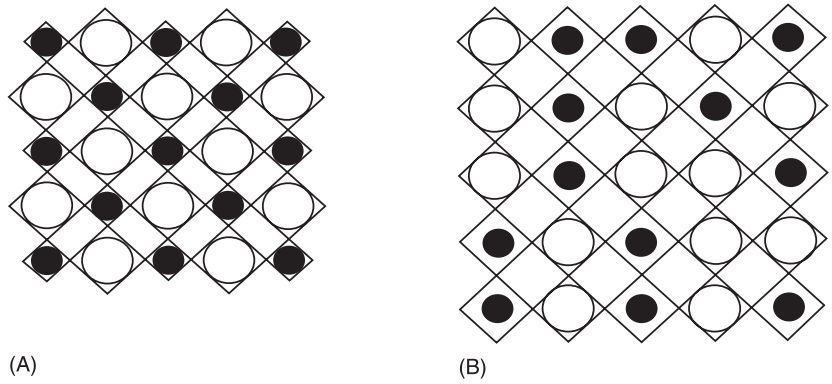


Figure 4 'Ion rattling' crystal model of $A(B_{I\,1/2}B_{II\,1/2})O_3$. (A) Ordered; (B) disordered arrangement of B_I (open circles) and B_{II} (filled circles).

Curie–Weiss constants can be expected (recall that $\varepsilon = C/(T - T_0)$). Strain per unit polarization, i.e., electrostrictive Q coefficients, are also expected to be small. In the case of the ordered arrangement, neither B_I nor B_{II} ions can shift without distorting the oxygen octahedron. Hence, small polarizations, dielectric constants and Curie–Weiss constants, and large electrostrictive Q coefficients can be expected.

Here, we summarize the empirical rules for the electrostrictive effect of perovskite-type oxides.

1. The value of the electrostrictive coefficient Q (defined as $x = QP^2$) does not depend on whether the material is ferroelectric, antiferroelectric, or nonpolar, but is greatly affected by the degree of ordering of the cation arrangement. The Q value increases in the sequence from disordered, partially ordered, then simple, and finally to ordered perovskite crystals.
2. In perovskite solid solutions with a disordered cation arrangement, the electrostrictive coefficient Q decreases with increasing phase transition diffuseness, or with increasing dielectric relaxation.
3. The product of the electrostrictive coefficient Q and the Curie–Weiss constant C is about the same for all perovskite crystals ($Q_h C = 3.1 \times 10^3\ \mathrm{m^4\ C^{-2}\ K}$).
4. The electrostrictive coefficient Q is nearly proportional to the square of the thermal expansion coefficient α.

These empirical rules lead to the following important result. Since the figure of merit of electrostriction under a certain electric field is given by $Q\varepsilon^2$ (ε: dielectric constant) or QC^2 (excluding the temperature dependence), and the product QC is constant, it is more advantageous to use the disordered perovskite ferroelectrics (relaxor ferroelectrics) which have a large Curie–Weiss constant C and hence a small electrostrictive coefficient Q than the normal ferroelectrics ($Pb(Zr,Ti)O_3$, $BaTiO_3$-based ceramics, etc.).

Electrostrictive Materials

Electrostrictive materials do not, in principle, exhibit the domain-related problems observed in piezoelectrics. A common practical ceramic system is the $Pb(Mg_{1/3}Nb_{2/3})O_3$-based compound. So-called relaxor ferroelectrics such as $Pb(Mg_{1/3}Nb_{2/3})O_3$ and $Pb(Zn_{1/3}Nb_{2/3})O_3$ have also been developed for very compact chip capacitors. The reasons why these complex perovskites have been investigated intensively for applications are their very high polarization and permittivity, and temperature-insensitive characteristics (i.e., diffuse phase transition) in comparison with the normal perovskite solid solutions.

The phase transition diffuseness in the relaxor ferroelectrics has not been satisfactorily clarified as yet. We introduce here a widely accepted microscopic composition fluctuation model which is even applicable in a macroscopically disordered structure. Considering the Känzig region (the minimum size region in order to cause a cooperative phenomenon, ferroelectricity) to be in the range of 10–100 nm, the disordered perovskite such as $Pb(Mg_{1/3}Nb_{2/3})O_3$ reveals a local fluctuation in the distribution of Mg^{2+} and Nb^{5+} ions in the B sites of the perovskite cell. **Figure 5** shows a computer simulation of the composition fluctuation in the $A(B_{I1/2}B_{II1/2})O_3$-type crystal calculated for various degrees of short-range ionic ordering. The fluctuation of the B_I/B_{II} fraction x obeys a Gaussian error distribution, which may cause Curie temperature fluctuation. HB Krause reported the existence of short-range ionic ordering in $Pb(Mg_{1/3}Nb_{2/3})O_3$ by electron microscopy. The high-resolution image revealed somewhat ordered (ion-ordered) islands in the range of 2–5 nm, each of which might have a slightly different transition temperature.

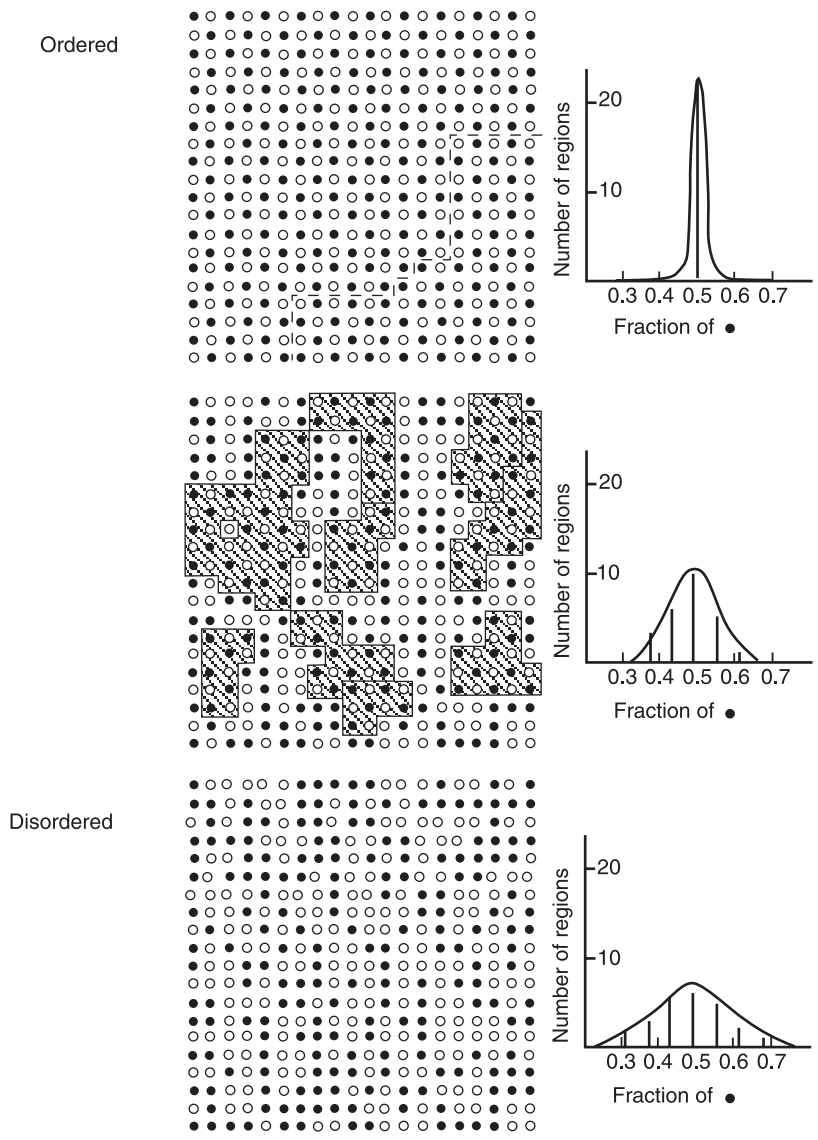


Figure 5 Computer simulation of the composition fluctuation in the $A(B_{I\,1/2}B_{II\,1/2})O_3$ type calculated for various degree of the ionic ordering (Känzig region size 4 × 4).

Another significant characteristic of these relaxor ferroelectrics is dielectric relaxation (frequency dependence of permittivity), from which their name originates. The temperature dependence of the permittivity in $Pb(Mg_{1/3}Nb_{2/3})O_3$ is plotted in **Figure 6** for various measuring frequencies. With increasing measuring frequency, the permittivity in the low-temperature (ferroelectric) phase decreases and the peak temperature near 0 °C shifts towards higher temperature; this is contrasted with the normal ferroelectrics such as $BaTiO_3$ where the peak temperature hardly changes with the frequency. The origin of this effect has been partly clarified in $Pb(Zn_{1/3}Nb_{2/3})O_3$ single crystals. **Figure 7** shows the dielectric constant and loss versus temperature for an unpoled and a poled PZN sample, respectively. The domain configurations are also inserted. The macroscopic domains were not observed in an unpoled sample even at room temperature; in which state, large dielectric relaxation and loss were observed below the Curie temperature range. Once the macrodomains were induced by an external electric field, the dielectric dispersion disappeared and the loss became very small (i.e., dielectric behavior became rather normal!) below 100 °C. Therefore, the dielectric relaxation is attributed to the microdomains generated in this material.

Thus, the PMN is easily electrically poled when an electric field is applied around the transition temperaure, and completely depoled without any remanent polarization because the domain is separated into

microdomains when the field is removed. This provides extraordinarily large apparent electrostriction, though it is a secondary phenomenon related to the electromechanical coupling ($x = ME^2$). If the phase transition temperature can be raised near room temperature, superior characteristics can be expected.

Figure 8A shows the longitudinal-induced strain curve at room temperature in such a designed material $0.9PMN - 0.1PbTiO_3$. Notice that the magnitude of the electrostriction (10^{-3}) is about the same as that of a piezoelectric PLZT under unipolar drive, as shown in **Figure 8B**. An attractive feature of this material is the near absence of hysteresis.

Other electrostrictive materials include $(Pb,Ba)(Zr,Ti)O_3$ and the PLZT systems. In order to obtain large (apparent) electrostriction, it is essential to generate ferroelectric microdomains (in the range 10 nm). It may be necessary to dope ions with a different valence or an ionic radius, or to create vacancies so as to introduce the spatial microscopic inhomogeneity in the composition.

Here, the characteristics of piezoelectric and electrostrictive ceramics are compared and summarized from a practical viewpoint:

1. Electrostrictive strain is about the same in magnitude as the piezoelectric (unipolar) strain (0.1%). Moreover, almost no hysteresis is an attractive feature.

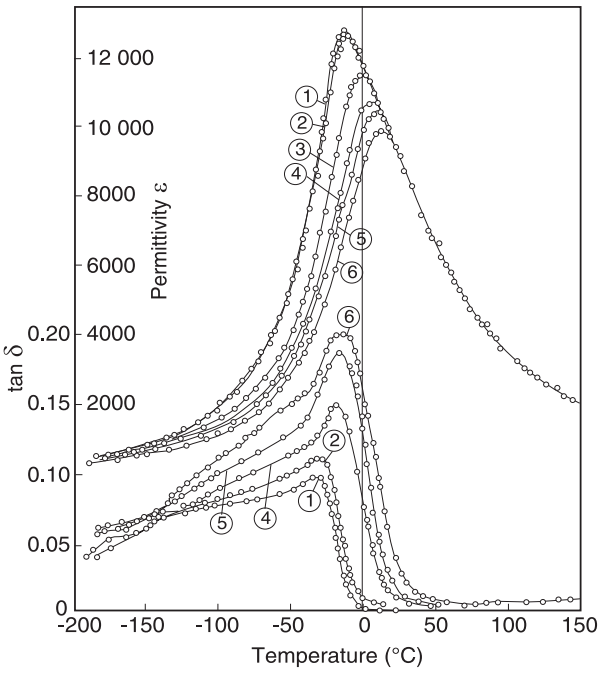


Figure 6 Temperature dependence of the permittivity in $Pb(Mg_{1/3}Nb_{2/3})O_3$ for various frequencies (kHz): (1) 0.4, (2) 1, (3) 45, (4) 450, (5) 1500, (6) 4500.

2. Piezoelectric materials require an electrical poling process, which leads to a significant aging effect due to the depoling. Electrostrictive materials do not need such pretreatment, but, require a proper DC bias field in some applications because of the nonlinear behavior.
3. Compared with piezoelectrics, electrostrictive ceramics do not deteriorate easily under severe operation conditions, such as high-temperature storage and large mechanical load.
4. Piezoelectrics are superior to electrostrictors, with regard to temperature characteristics.
5. Piezoelectrics have smaller dielectric constants than electrostrictors, and thus show faster response.

Applications of Electrostrictions

Classification of Ceramic Actuators

Piezoelectric and electrostrictive actuators may be classified into two categories, based on the type of driving voltage applied to the device and the nature of the strain induced by the voltage: first, rigid displacement devices for which the strain is induced unidirectionally along an applied DC field, and second, resonating displacement devices for which the alternating strain is excited by an AC field at the mechanical resonance frequency (ultrasonic motors). The first category can be further divided into two types: servo displacement transducers (positioners) controlled by a feedback system through a position detection signal, and pulse-drive motors operated in a simple on/off switching mode, exemplified by dot matrix printers. **Figure 9** shows the classification of ceramic actuators with respect to the drive voltage and induced displacement.

The AC resonant displacement is not directly proportional to the applied voltage, but is, instead, dependent on adjustment of the drive frequency. Although the positioning accuracy is not as high as that of the rigid displacement devices, very high speed motion due to the high frequency is an attractive feature of the ultrasonic motors. Servo displacement transducers, which use feedback voltage superimposed on the DC bias, are used as positioners for optical and precision machinery systems. In contrast, a pulse drive motor generates only on/off strains, suitable for the impact elements of dot matrix or ink jet printers.

The materials requirements for these classes of devices are somewhat different, and certain compounds will be better suited for particular applications. The ultrasonic motor, for instance, requires a very hard piezoelectric with a high mechanical quality

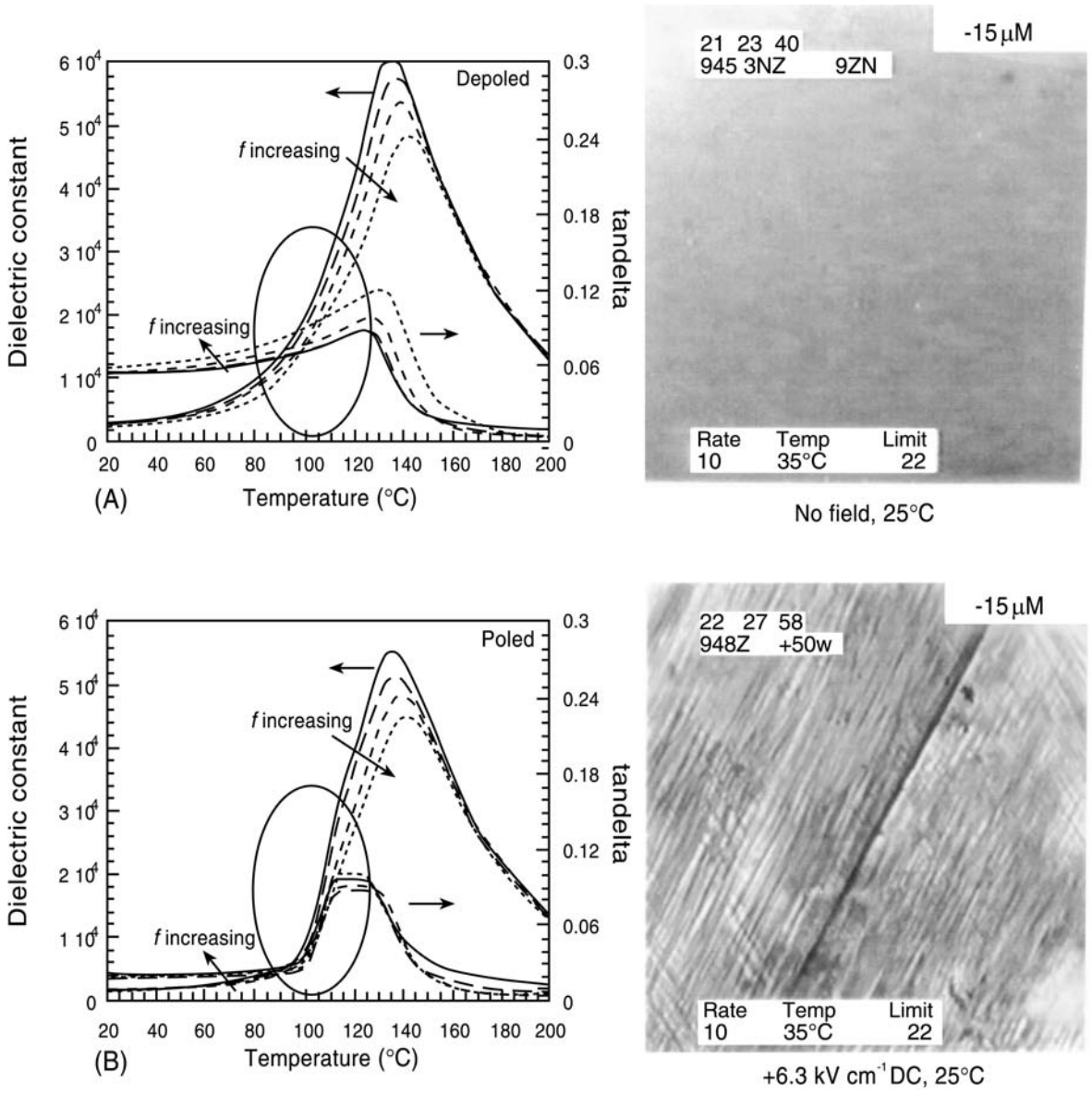


Figure 7 Dielectric constant versus temperature for a depoled (A) and a poled $Pb(Zn_{1/3}Nb_{2/3})O_3$ single crystal (B) measured along the $<111>$ axis.

factor Q, in order to minimize heat generation. The servo displacement transducer suffers most from strain hysteresis and, therefore, a PMN electrostrictor is preferred for this application. Notice that even in a feedback system the hysteresis results in a much lower response speed. The pulse-drive motor requires a low-permittivity material aiming at quick response with a limited power supply rather than a small hysteresis, so that soft PZT piezoelectrics are preferred to the high-permittivity PMN for this application.

Deformable Mirrors

Precise wave front control with as small a number of parameters as possible and compact construction is a common and basic requirement for adaptive optical systems. For example, continuous-surface deformable mirrors may be more desirable than segmented mirrors from the viewpoint of precision.

Multimorph-type deformable mirror Sato *et al.* proposed a multimorph deformable mirror, simply operated by a microcomputer. In the case of a two-dimensional multimorph deflector, the mirror surface can be deformed by changing the applied voltage distribution and the electrode pattern on each electroactive ceramic layer.

The mirror surface contour is occasionally represented by Zernike aberration polynomials in optics.

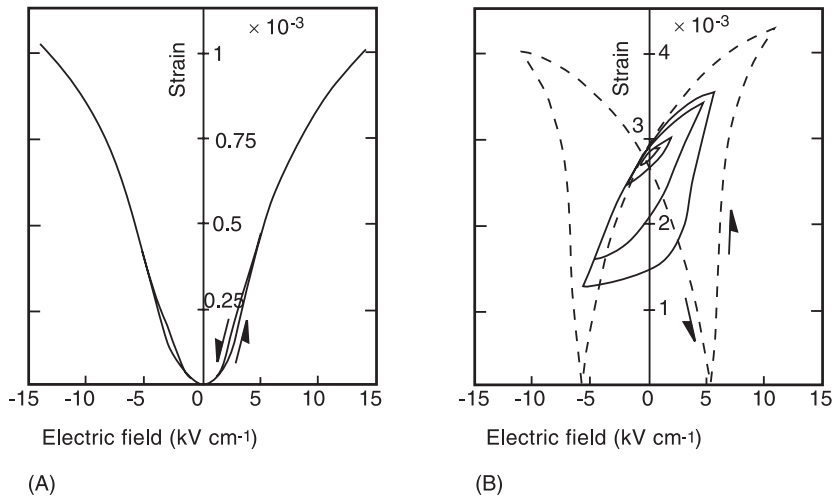


Figure 8 Field-induced strain curve in an electrostrictor $0.9Pb(Mg_{1/3}Nb_{2/3})O_3 - 0.1PbTiO_3$ (A) and in a piezoelectric PLZT 7/62/38 (B) at room temperature.

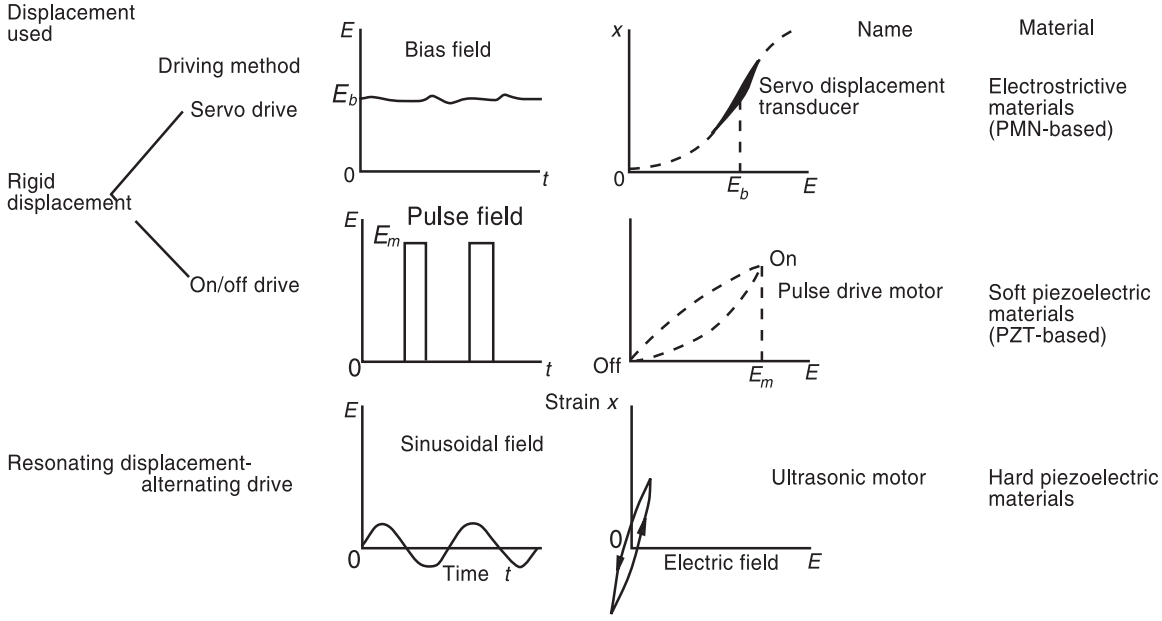


Figure 9 Classification of piezoelectric/electrostrictive actuators.

An arbitrary surface contour modulation $g(x, y)$ can be expanded as follows:

$$g(x,y) = C_r(x^2+y^2) + C_c^1 x(x^2+y^2) + C_c^2 y(x^2+y^2) + \cdots \quad [25]$$

Notice that the Zernike polynomials are orthogonal to each other, i.e., can be completely controlled independent of each other. The C_r and C_c terms are called refocusing and coma aberration, respectively. The aberration, up to the second order, can provide a clear image apparent to the human; this is analogous to the eye examination. The optometrist checks the degree of your lens, initially, then the astigmatism is corrected; no further correction will be made for human glasses.

As examples, let us consider the cases of refocusing and coma aberration. Uniform whole-area electrodes can provide a parabolic (or spherical) deformation. In the case of the coma aberration, the pattern obtained is shown in **Figure 10**, which consists of only six divisions and has the fixed ratio of supply voltages.

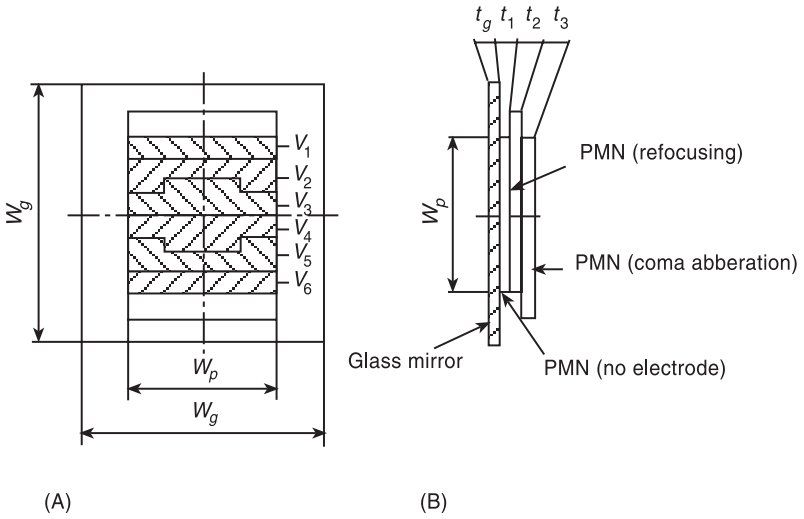


Figure 10 Two-dimensional multimorph deformable mirror with refocusing and coma aberration functions. (A) Front view; (B) cross-section.

The deflection measurement of the deformable mirror was carried out using the interferometric system with a hologram. The introduction of a hologram is to cancel the initial deformation of the deformable mirror. Typical experimental results are summarized in **Figure 11**, where the three experimentally obtained interferograms of refocusing aberration, coma aberration, and a combination of the two are compared with the corresponding ideal ones. Good agreement is seen in each case. These results demonstrate the validity of the superposition of deformations and the appropriateness of the method of producing the electrode patterns. It was also observed that the deformable mirror responds linearly up to 500 Hz for sinusoidal input voltages.

Figure 12 shows the fringe patterns observed for several applied voltages for the conventional PZT piezoelectric and PMN electrostrictive deformable mirrors. It is worth noting that, for a PZT device, a distinct hysteresis is observed optically on a cycle with rising and falling electric fields, but no discernible hysteresis is observed for the PMN device.

Hubble space telescope Fanson and Ealey have developed a space qualified active mirror called articulating fold mirror. Three articulating fold mirrors are incorporated into the optical train of the Jet Propulsion Laboratory's wide field and planetary camera-2, which was installed into the Hubble space telescope in 1993. As shown in **Figure 13**, each articulating fold mirror utilizes six PMN electrostrictive multilayer actuators to position a mirror precisely in tip and tilt in order to correct the refocusing aberration of the Hubble telescope's primary mirror.

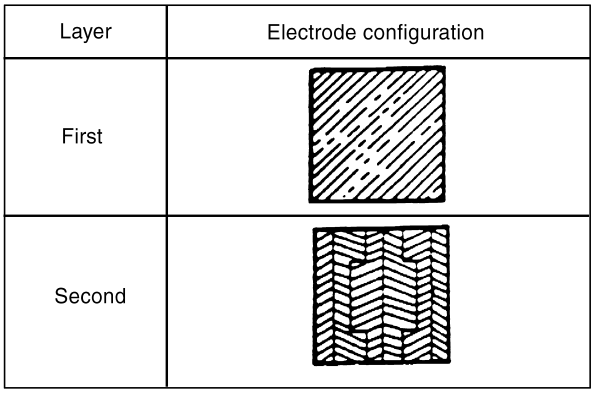
Figure 14 shows the images of the core of M100, a spiral galaxy in the Virgo cluster, before and after correction of the refocusing aberration. Both contrast and limiting magnitude have been greatly improved, restoring Hubble to its originally specified performance.

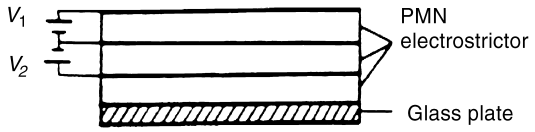
Oil-Pressure Servo Valves

For oil pressure servo systems, an electric–oil pressure combination (electrohydraulic) is necessary in order to obtain large power and quick response. Quicker response has been requested for this electrohydraulic system, and the present target is 1 kHz, which is categorized in an 'impossible' range using conventional actuation. Ikabe *et al.* simplified the valve structure by using a piezoelectric PZT flapper. However, since pulse width modulation was employed to control the device to eliminate PZT hysteresis, the flapper was always vibrated by a carrier wave, and the servo valve exhibited essential problems in high-frequency response and in durability. To overcome this problem, Ohuchi *et al.* utilized an electrostrictive PMN bimorph for the flapper instead of a piezoelectric bimorph.

Construction of oil-pressure servo valves **Figure 15** is a schematic drawing of the construction of a two-stage four-way valve, the first stage of which is operated by a PMN electrostrictive flapper. The second-stage spool is 4 mm in diameter, which is the smallest spool with a nominal flow rate of $6\,\mathrm{l\,min^{-1}}$.

An electrostrictive material 0.45 PMN–0.36 PT–0.19 BZN was utilized because of its large displacement and small hysteresis. A flapper was fabricated





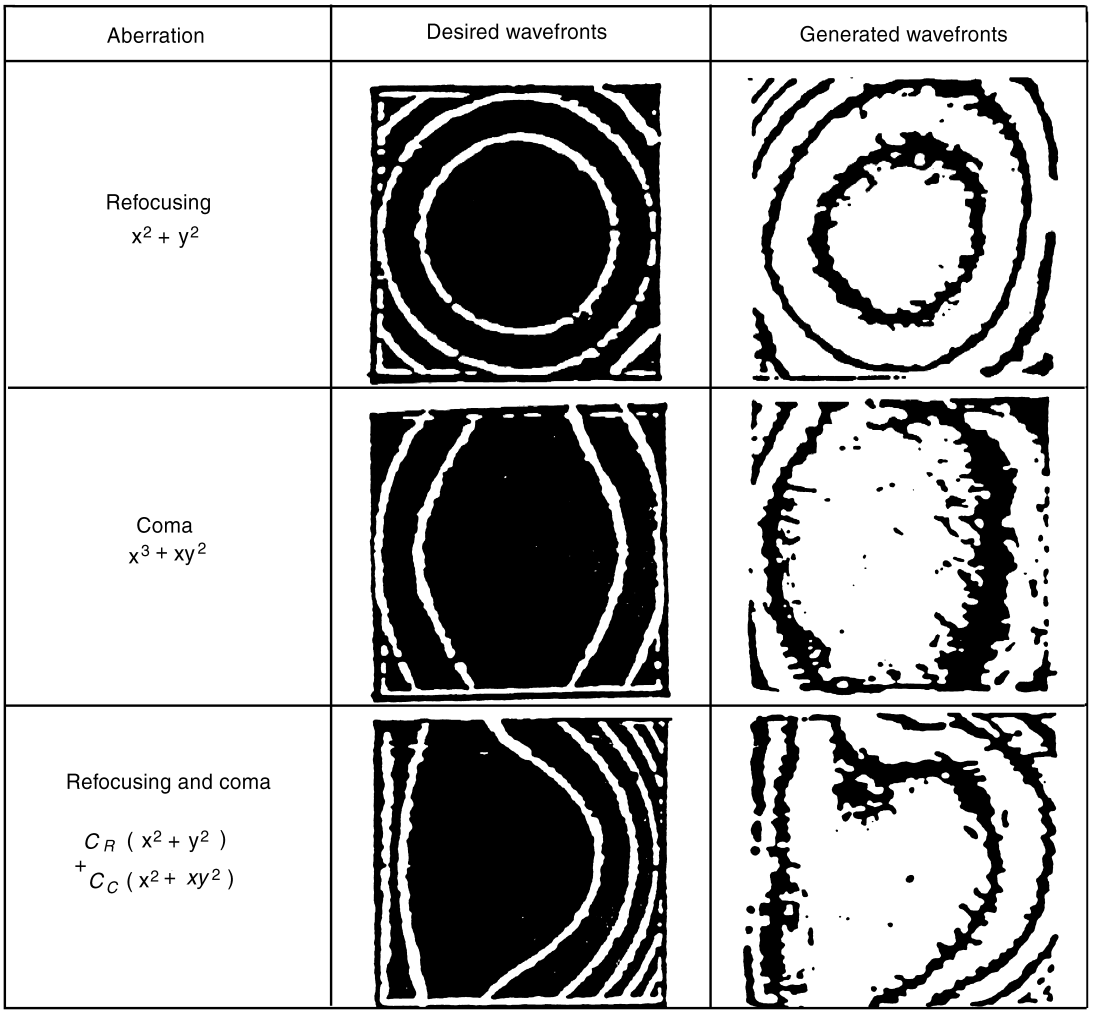


Figure 11 Interferograms showing deformation by the multilayer deformable mirror.

using a multimorph structure, in which two PMN thin plates were bonded on each side of a phospher bronze, shim (**Figure 16**). The multimorph structure increases the tip displacement, generative force, and response speed. The top and bottom electrodes and the metal shim were taken as ground, and a high voltage was applied on the electrode between the two PMN plates. The tip deflection showed a quadratic curve for the applied voltage because of the electrostriction. Thus, in order to obtain a linear relation, a push–pull driving method was adopted with a suitable DC bias electric field, which is demonstrated in **Figure 17**. Notice that the displacement hysteresis in the PMN ceramic is much smaller than in the PZT piezoelectric. The resonance frequency of this flapper in oil was about 2 kHz.

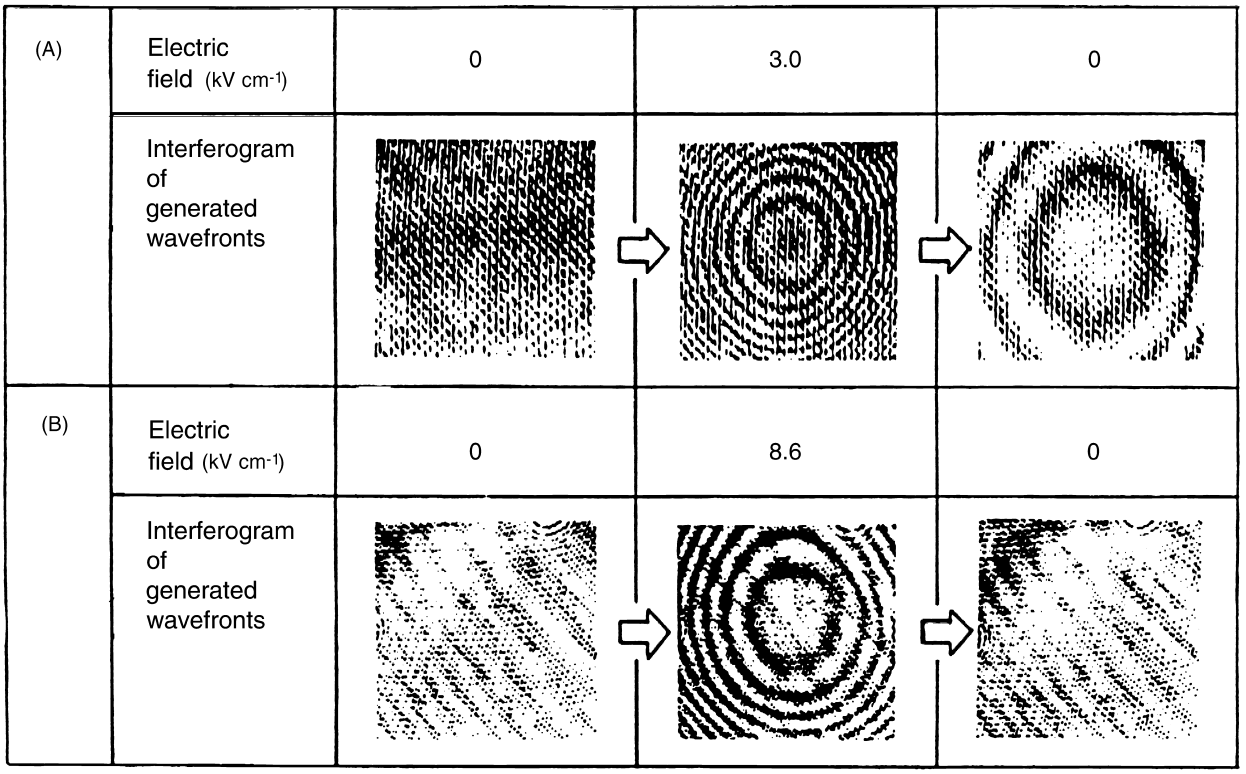


Figure 12 Comparison of function between (A) PZT and (B) PMN deformable mirrors.

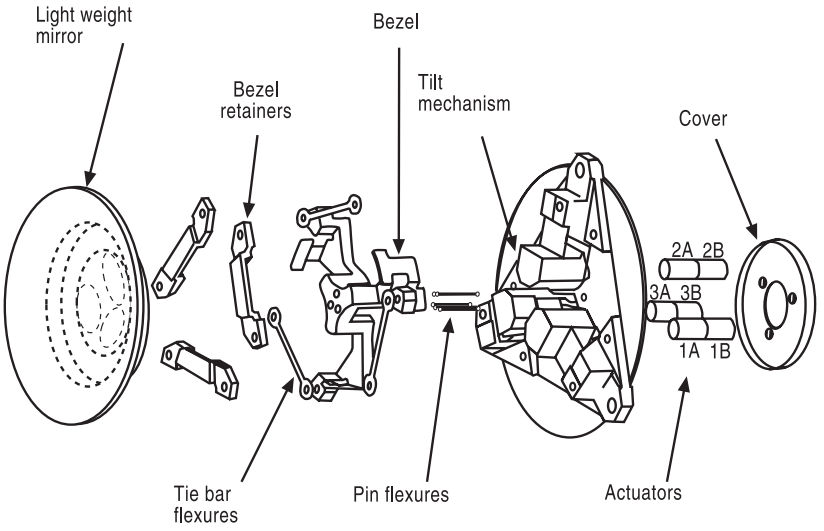


Figure 13 Articulating fold mirror using PMN actuators.

Since the conventional force feedback method has a structure connecting the flapper tip and the spool with a spring, limiting the responsivity, Ohuchi *et al*. utilized an electric feedback method. The feedback mechanism using an electric position signal corresponding to the spool position has various merits, such as easy change in feedback gain and availability of speed feedback. A compact differential transformer (50 kHz excitation) was employed to detect the spool position.

Operating characteristics of the oil-pressure servo valve **Figure 18** shows a static characteristic of the spool displacement for a reference input. The slight

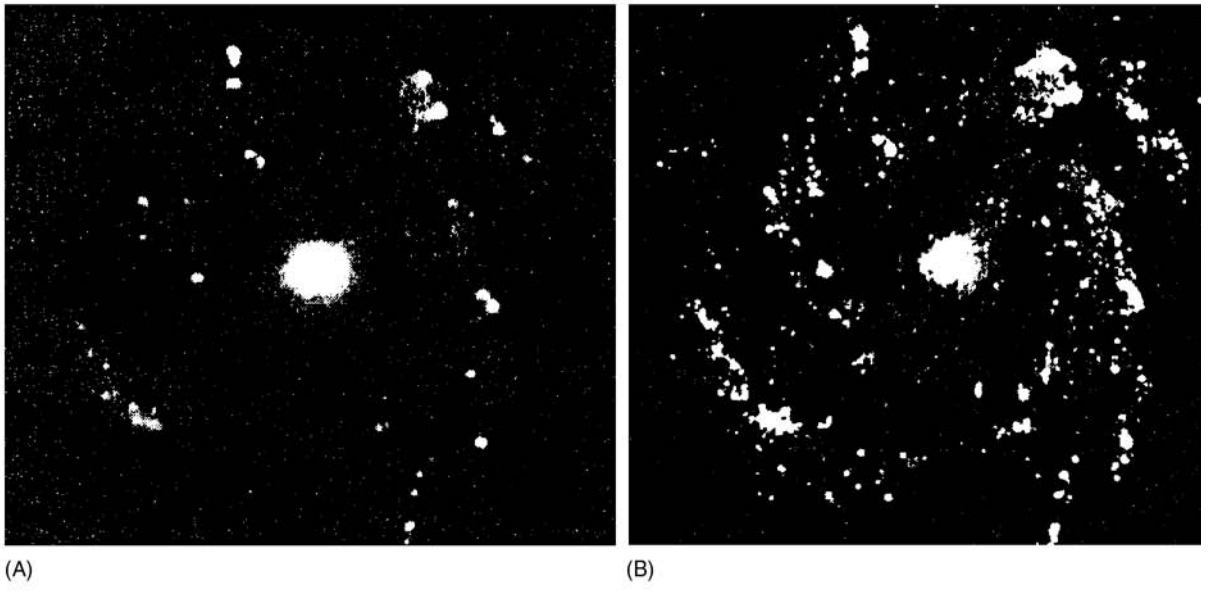


Figure 14 M100 galaxy comparison. (A) Before activation; (B) after activation of the PMN.

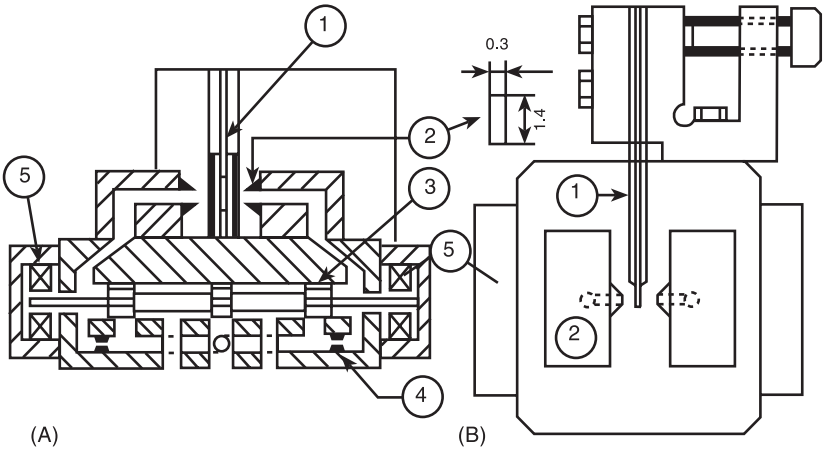


Figure 15 Construction of the oil pressure servo valve. (A) Front (section) view; (B) top view. 1, PMN-flapper; 2, nozzle; 3, spool; 4, fixed orifice; 5, spool position sensor.

hysteresis and nonlinearity observed in **Figure 17** was completely eliminated in **Figure 18** through the feedback mechanism. **Figure 19** shows a dynamic characteristic of the spool displacement. The 0 dB gain was adjusted at 10 Hz. The gain curve showed a slight peak at 1800 Hz and the 90° retardation frequency was about 1200 Hz. The maximum spool displacement at 1 kHz was $\pm$ 0.03 mm, which results in the quickest servo valve at present.

Nomenclature

d	piezoelectric constant
E	electric field
F	force
k	spring constant
M	electrostrictive constant
P	polarization
Q	electrostrictive coefficient

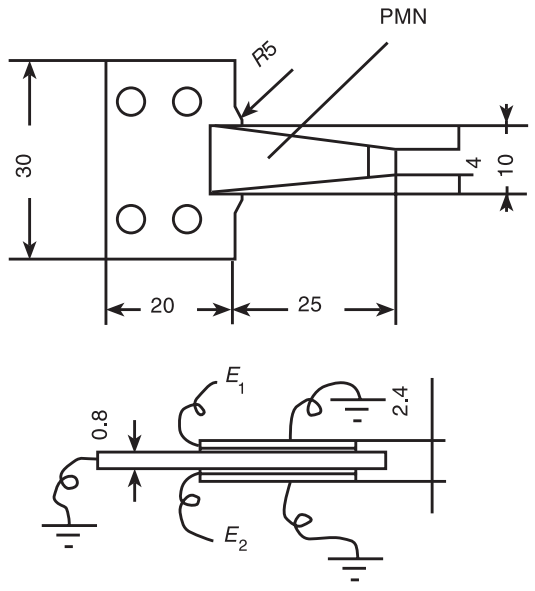


Figure 16 Multimorph electrostrictive flapper.

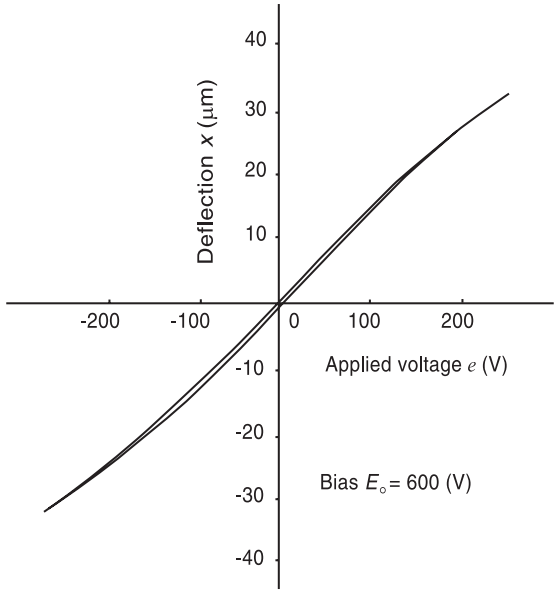


Figure 17 Push–pull drive characteristics of the electrostrictive flapper.

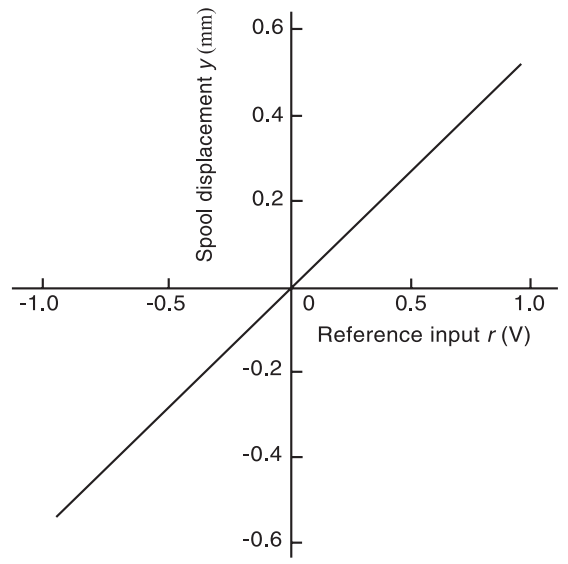


Figure 18 Static characteristics of the servo valve.

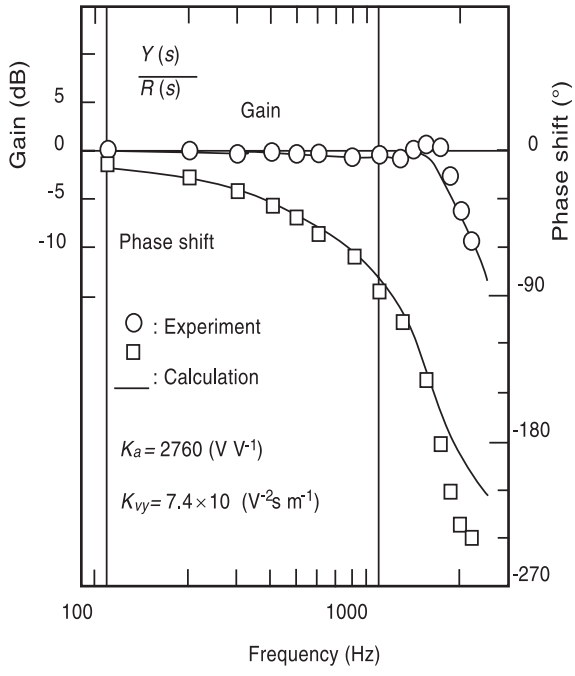


Figure 19 Normalized frequency characteristics of the servo

s	elastic compliance
T	temperature
X	stress
Δ	displacement
ε	permittivity

See also: **Actuators and smart structures**.

Further Reading

Cross LE, Jang SJ, Newnham RE, Nomura S and Uchino K (1980) Large electrostrictive effects in relaxor ferroelectrics. *Ferroelectrics* 23: 187–192.

Nomura S and Uchino K (1982) Electrostrictive effect in Pb $(Mg_{1/3}Nb_{2/3})O_3$ type materials. *Ferroelectrics* 41: 117–

132.
Uchino K (1986) Electrostrictive actuators: materials and applications. *Ceramic Bulletin* 65: 674–652.
Uchino K (1993) Ceramic actuators: principles and applications. *MRS Bulletin* XVIII: 42–48.
Uchino K (1996) *Piezoelectric Actuators and Ultrasonic Motors*. MA, USA: Kluwer Academic.
Uchino K (1999) *Ferroelectric Devices*. New York: Marcel Dekker.
Uchino K, Cross LE, Newnham RE and Nomura S (1981) Electrostrictive effects in antiferroelectric perovskites. *Journal of Applied Physics* 52: 1455–1459.
Uchino K, Nomura S, Cross LE and Newnham RE (1980) Electrostriction in perovskite crystals and its applications to transducers. *Journal of the Physics Society of Japan* 49 (suppl.B): 45–48.
Uchino K, Nomura S, Cross LE, Jang SJ and Newnham RE (1980) Electrostrictive effects in lead magnesium niobate single crystals. *Journal of Applied Physics* 51: 1142–1145.
Uchino K, Nomura S, Cross LE, Newnham RE and Jang SJ (1981) Electrostrictive effects in perovskites and its transducer applications. *Journal of Material Science* 16: 569–578.

ENVIRONMENTAL TESTING, OVERVIEW

D Smallwood, Sandia National Laboratories, Albuquerque, NM, USA

Copyright © 2001 Academic Press

doi:10.1006/rwvb.2001.0106

Environmental testing can cover a large variety of natural and artificial environments. In the context of this article, the environments are limited to mechanical vibration. Sometimes it is important to consider combinations of environments, but this is beyond the scope of this article. Environmental testing can include the exposure of test hardware to actual use environments. This is also beyond the scope of this article. Environmental testing in this article is the reproduction in the laboratory of a vibration environment that is intended to simulate a real or potential natural or use vibration environment. Some typical environments that produce significant vibration levels include: surface transportation in cars and trucks with vibration caused by irregular surfaces, air turbulence, and mechanical noise from engines, etc.; aircraft environments with vibration caused by airflow and engines; rocket environments with vibration caused by airflow, shock waves, engine noise, and stage separation; ocean environments with vibration induced by wind and waves; building vibration with motion excited by internal and external machinery, wind, and earthquakes. Structural response to mechanical shock can be considered a transient vibration and is discussed.

Environmental testing generally falls into one of four classifications: development testing, qualification testing, acceptance testing, or stress screening.

1. Development testing is intended to explore the response of the test hardware to a variety of vibration stimulations with the goal of identifying vibration characteristics of the hardware or to uncover design weaknesses of the hardware. Typically, the hardware tested is not production hardware but development hardware in various stages of development.
2. Qualification testing is used to determine if the hardware will perform satisfactorily when exposed to a representative or worst-case use environment. The purpose is to determine if the design meets a set of vibration requirements. Typically, the hardware tested is representative of production hardware, but is not hardware that will be used in the use environment. Qualification testing is typically performed with methods and levels defined in specifications.
3. Acceptance testing is used to determine if a particular set of production hardware is satisfactory for release and subsequent use by a customer. All production hardware is not necessarily subjected to acceptance testing. Some programs demand 100% acceptance testing, and some programs accept lot testing. The test methods and levels are typically defined in specifications. Sometimes the acceptance test levels are related to the qualification levels. The levels are typically lower than the qualification levels because the risk of damage to the hardware must be kept to a minimum.
4. Stress screening is a tool used to expose hardware at various stages of manufacture to vibration environment that will precipitate infant failures and

identify manufacturing defects early in the manufacturing cycle. The methods and levels are defined by the manufacturer and tailored to a specific product. The levels should not induce damage to well-manufactured hardware.

The development of environment test methods and levels can be divided into two stages. First is the identification and characterization of the environments. Second is the development of test methods that will satisfactorily simulate the environment in the laboratory.

Identification of the Use Environment

By far the most common field measurements are with accelerometers. The use of accelerometers is covered elsewhere. Much less frequently used are measurements of velocity, displacement, and force. The data from the field measurements are collected and stored for later analysis. The most versatile method is to store the raw unprocessed time histories. If the original data are stored, data-processing decisions can be changed at any time. Recently most data are sampled and stored as digital records. All the precautions associated with this process should be carefully observed (see Further Reading).

The next step is to classify the data for reduction. Data will seldom fall neatly into a classification. Judgment must be used. Sometimes data can be analyzed making several assumptions of the class, and the most appropriate reduction can be chosen after the data reduction.

The data must first be classified as random or deterministic. Loosely deterministic data are data that, if the experiment is repeated, the data will be the same. Deterministic data can be a transient, periodic, or complex nonperiodic. A transient is data that starts and ends within a few periods of the lowest natural frequency of the object being observed. Periodic data theoretically extend over all time, repeating at a regular period. In practice a signal that repeats itself and extends over many cycles of the lowest natural frequency can be treated as periodic. A periodic waveform can often be treated as a Fourier series expansion. Complex nonperiodic data is typically composed of the sum of periodic waveforms that are not harmonically related; thus the waveform does not have a period. As for periodic waveforms, the waveform must extend over a period of time that is much longer than the lowest natural period of the object being observed.

Random data are data that can be described only in statistical terms. The future time history cannot be predicted from past values except in statistical terms. The data can be stationary, which loosely means that the statistical measures are not dependent on the location in time. As for periodic data, random data theoretically extend over all time. In practice much data can be treated as stationary if the duration is much longer than the period of the lowest natural frequency of the object under study. The most common procedures used to analyze stationary random data are the autospectral densities (commonly called the power spectra density) and the cross-spectral densities. The statistical moments and probability density functions are also important parameters. These are described elsewhere in this volume. By far the most common assumption about the data is that they are normally distributed. This assumption should always be checked because much data is not normal.

If the duration of random data is too short to be treated as stationary, it must be treated as nonstationary random data. Many techniques are available to treat nonstationary data. All the techniques add complications to the analysis, and the results will be dependent on the method and parameters used. Several of these techniques are discussed elsewhere in this volume but are beyond the scope of this discussion. The most common error made in nonstationary random analysis is to ignore the uncertainty theorem. Loosely, the uncertainty states that you cannot resolve time and frequency independently. If you desire good time resolution, you will have poor frequency resolution and vice versa.

One is tempted simply to reproduce the field environment in the laboratory. If this is done, the field environment is being treated as deterministic. If a random component is present, the reproduction will not necessarily be adequate.

Data can also be a mixture of all the types. These problems are difficult to handle. Usually some attempt is made to separate the data into the component parts and each part is analyzed separately.

Periodic environments are seldom encountered in the field. Exceptions are rotating machinery measurements that often contain the fundamental and harmonics of the rotational frequency. Random environments usually treated as stationary random include: excitation from turbulent fluid flow, rocket and turbojet excited response, wind excitation, and long-term surface transportation environments. Deterministic transient environments can include some shocks and chirps (a short-duration sine sweep).

Examples of nonstationary random environments include: seismic excitation (earthquakes); pyroshock (transients in structures caused by explosive hardware, like bolt-cutters); response of structures to nonpenetrating impacts; and response to bumps and potholes in surface transportation. To the extent that

the structure is deterministic, some of these shocks are essentially the impulse response of the structure and can be partially deterministic. An example of a mixed environment is the resonant burn condition found in the response of some solid rocket motors. This environment is a mixture of a swept sinusoid with harmonics and stationary random. Another example of a mixed environment is the response of propeller-driven aircraft. This is a mixture of stationary random caused by the turbulent airflow and possibly the turboprop exhaust and the periodic blade passage frequency with harmonics.

Basic Equivalence between Field and Laboratory Dynamic Environments

The purpose of an environmental vibration test is usually to simulate a field environment. The basic requirements for the equivalence between a field and a laboratory simulation of the environment will now be considered. To simplify the discussion, only linear systems will be considered.

Assume the system under consideration is a multiple-input linear system described by N nodes (**Figure 1**). A pair of variables can describe the dynamics at each node: the external force applied at the node and a motion parameter for the node. Each node represents a degree of freedom of the structure. The force can be a translational force or a torque applied to the node. The force will be designated by the variable F. The motion variable can be a displacement, velocity, or acceleration. The motion can be translation or rotation consistent with the applied force at the node. The motion variable will be designated by the variable V. The variables are complex functions of frequency. For a sinusoidal excitation the variable represents an amplitude and phase of the sinusoid. For a transient the variable is the Fourier transform of the transient time history. For stationary random the variable is the expected value of the Fourier transform of the random signal in the sense of Bendat and Piersol (see Further Reading).

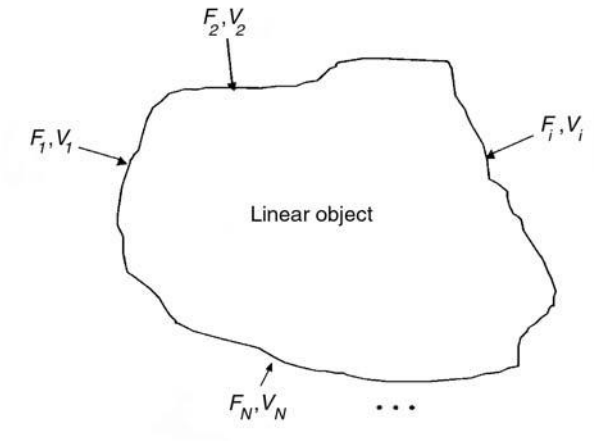


Figure 1 Multiple-input linear system.

The system can be characterized by a square matrix of impedance functions, Z.

$$\{V\} = [Z]\{F\} \quad [1a]$$

or:

$$\mathbf{V} = \mathbf{ZF} \quad [1b]$$

The system can also be represented by a matrix of admittance functions:

$$\mathbf{F} = \mathbf{YV} \quad [2]$$

where:

$$\mathbf{Y} = \mathbf{Z}^{-1} \quad [3]$$

Partition the nodes into three categories denoted by a subscript: c will indicate a control point in the laboratory test, r will indicate a response point measured in the field environment, and i will indicate an interior point that is not observed in either the test environment or in the field environment.

A superscript will be used to denote the environment in which the measurements are made: f for a field measurement and t for a test or laboratory measurement.

$$\begin{Bmatrix} V_c \\ V_r \\ V_i \end{Bmatrix} = \begin{bmatrix} Z_{cc} & Z_{cr} & Z_{ci} \\ Z_{rc} & Z_{rr} & Z_{ri} \\ Z_{ic} & Z_{ir} & Z_{ii} \end{bmatrix} \begin{Bmatrix} F_c \\ F_r \\ F_i \end{Bmatrix} \quad [4]$$

We can ask the basic question: Under what conditions can we control a test at the points c with the system mounted on a test apparatus and reproduce the motion observed at the points r in the field?

The motions in the laboratory test at the response points are given by:

$$V_r^t = [\, Z_{rc} \quad Z_{rr} \quad Z_{ri} \,] \begin{Bmatrix} F_c^t \\ F_r^t \\ F_i^t \end{Bmatrix} \quad [5]$$

For now, assume the applied forces at points other than the control points are zero in the laboratory test.

$$F_r^t = F_i^t = 0 \quad [6]$$

This is not always true: for example, the cross-axis motion at the control points is often restrained in a

vibration test. This assumption results in motions at the response points and the control points of:

$$V_r^t = Z_{rc} F_c^t \quad [7]$$

$$V_c^t = Z_{cc} F_c^t \quad [8]$$

Combining eqns [7] and [8] gives the test motions at the response points:

$$V_r^t = Z_{rc} Z_{cc}^{-1} V_c^t \quad [9]$$

The test motions at the control points are:

$$V_c^t = Z_{cc} Z_{rc}^{-1} V_r^t \quad [10]$$

The inverses must exist or a pseudoinverse must be used. If Z_{rc}^{-1} exists, the number of response points must equal the number of control points and the matrix is full-rank.

Thus, we can derive a set of control motions that will reproduce the motion at a set of response points for the conditions where a solution of eqn [10] exists.

The motions at the response points in the field are given by:

$$V_r^f = [\, Z_{rc} \quad Z_{rr} \quad Z_{ri} \,] \begin{Bmatrix} F_c^f \\ F_r^f \\ F_i^f \end{Bmatrix} \quad [11]$$

The motion at the response points in the laboratory can be made the same for the field:

$$V_r^f = V_r^t \quad [12]$$

However, this does not insure that the motion at other points on the structure will be the same for the test as for the field. To meet this requirement:

$$\begin{bmatrix} Z_{cc} & Z_{cr} & Z_{ci} \\ Z_{rc} & Z_{rr} & Z_{ri} \\ Z_{ic} & Z_{ir} & Z_{ii} \end{bmatrix} \begin{Bmatrix} F_c^t \\ 0 \\ 0 \end{Bmatrix} = \begin{bmatrix} Z_{cc} & Z_{cr} & Z_{ci} \\ Z_{rc} & Z_{rr} & Z_{ri} \\ Z_{ic} & Z_{ir} & Z_{ii} \end{bmatrix} \begin{Bmatrix} F_c^f \\ F_r^f \\ F_i^f \end{Bmatrix} \quad [13]$$

In general, the solution to all the constraints imposed above can be satisfied only if:

$$F_r^f = F_i^f = 0 \quad [14]$$

This implies that the response of the system in test is equivalent to the response in the field only if forces are applied to the system in the field at the test control points. If forces in the field environment are applied at points other than the control points, the test environment will not, in general, be equivalent to the field environment.

The conclusion of this discussion is that simulation of a field vibration environment in the laboratory is almost always imperfect. The importance of the imperfection is always a point of discussion.

Motion Control at a Single Point in a Single Direction

The motion is controlled at one point in probably more than 95% of vibration tests. The motion at the control point is assumed to move in only one direction with a force applied at the control point. Because control is at one point, the test items are usually mounted on rigid fixtures. It is usually assumed that the interface between the fixture and the test item moves as a plane in one direction. Exceptions are many, as strictly rigid fixtures are impossible to construct, and motion in one direction is difficult to achieve. Thus, in general, the laboratory test can be fully equivalent to the field test only if the force is applied to the test object in the field through the same interface used in the laboratory at the control point location. Errors caused by this simplifying assumption can vary from minor to major and are the subject of many debates.

Use of Environmental Envelopes

The development above assumes that the measured field motion is duplicated in the laboratory with all of its detail. This is rarely possible in practice. In practice, envelopes of the environment are usually used. Many times, composite envelopes of several different environments are used. The purpose of the envelope is to insure a conservative test. Consider the simple case of one response point, one control point, and where the errors caused by the failure of eqn [14] are acceptable. Eqn [9] becomes an algebraic equation:

$$V_r^t = Z_{rc} Z_{cc}^{-1} V_c^t \quad [15]$$

For the case where the test control point motion is equal to an envelope of the field control point motion:

$$\left| V_c^t \right| = V_c^{\text{envelope}} \geq \left| V_c^f \right| \quad [16]$$

Using eqn [9] with f substituted for t, eqn [16] reduces to:

$$V_r^t \geq \left| Z_{rc} Z_{cc}^{-1} V_c^f \right| = \left| V_r^f \right| \quad [17]$$

The test environment will always be larger than the field environment for this special case. If forces are applied to the test object at any location other than at the control point, we are not guaranteed that the test environment will generate responses greater than or equal to the field environment. Unfortunately, this is frequently the case. The forces in the field are often applied in a distributed manner over the test object, and motion is measured at one or a few points. The motion is enveloped, and the envelope is reproduced at the control points (usually a single point) in the laboratory with the sometimes unreasonable expectation that the laboratory test is a conservative test.

Motion in the field is seldom in one direction. Even if the motion of the control point is in a single direction, the motion of the test object in the laboratory is seldom in a single direction. A typical assumption is that the motion observed in the field can be adequately simulated with three tests in the laboratory, one in each of three orthogonal directions. At best this is a practical compromise and has little rigorous development to justify the assumption.

For those cases where eqn [17] is valid, the motions at the response points can be very much larger than the field response. The very high input impedance of shakers, coupled with large power amplifiers and modern control equipment, typically causes the overtest. The control system will attempt to maintain the motion at the control point regardless of the force required. In the field the driving point impedance of the interface looking back into the structure on which the test object is mounted limits the force. The overtest caused by a near-infinite impedance of the shaker can be alleviated through the use of force or response limiting.

As can be seen from the above discussion, practical vibration tests require many compromises. Even for a linear system, vibration testing is an imperfect science. Engineering judgment and past experience are valuable guides in picking an appropriate test.

Identification of Measurement Locations

An important consideration in gathering field information that will later be used to characterize a vibration environment is the determination of the measurement locations. Usually an attempt is made to place the measurement location in the load path of the input to the system. This is not always possible, as multiple load paths may exist or the interface between the item and its foundation is not accessible. In many cases the number of input points desired is beyond the capabilities of the data-gathering system. In this case 'typical' locations are chosen and the resulting motion is determined for a 'zone' of the structure. Care must be taken to insure the measurement is typical and not greatly influenced by local phenomena. For example, if an accelerometer is mounted on a thin plate, the motion can be dominated by the local plate resonances and not be representative of the structural response in the neighborhood.

In some cases it may be desirable to measure multiple inputs to a component or system. If this is done the phase relationships between the inputs must be preserved, as this will be of critical importance if a multiple-input test is designed.

Test Methods

Many test machines are used to generate vibration in the laboratory. Several of these are discussed in greater detail in other articles. The most common machines are electrodynamic and electrohydraulic shakers.

An electrodynamic shaker is built on the same principle as a speaker in a radio or home entertainment system. A magnet (either permanent or an electromagnet) provides a magnetic field. A coil of wire is placed in the field. When a current is passed through the coil, a force is generated. This force moves the coil and the attached structure that includes the test item.

An electrohydraulic shaker is essentially a double-acting hydraulic cylinder. Most of the energy is supplied by hydraulic fluid under pressure. A servo valve (often driven by a small electrodynamic shaker) controls the fluid flow in the hydraulic cylinder.

Vibration can also be generated by a variety of mechanical shakers. These devices have limited use today because the versatility and control of the devices are usually not as good as for electrodynamic and electrohydraulic shakers.

The testing of aerospace structures is often accomplished by placing the test item in a reverberant chamber and exposing the item to high-intensity acoustic noise. A reverberant chamber is a large chamber with hard walls and many modes of acoustic vibration. The chamber provides a diffuse acoustic field that simulates the high-intensity noise of many acoustic environments found in the aerospace industry.

Many machines generate mechanical shock, which can be considered a transient vibration. The most common of these machines are drop tables. The drop table essentially generates a specified velocity. The shock is generated when the test item impacts a stationary structure. The characteristics of the shock are determined by the design of the impacting structures, including the interface between items. The

material placed at the interface is sometimes called a shock programmer. Many other devices are used, essentially to generate a velocity. The kinetic energy is used as the energy source for the shock test. The shock produced is determined by the details of the impact between the moving structure and the stationary structure. The test item is usually mounted on the moving structure. In some cases the test item is stationary and a moving target is impacted into the test item. This is called a turn-around test. Machines used to generate the initial velocity include: rocket sleds, drop towers, cable pull-down facilities, actuators, and guns.

Pyrotechnic shock is a special category of shock that requires special care in the measurements and simulation. A discussion of pyroshock is beyond the scope of this article.

The location of control accelerometers in vibration testing requires care since vibration at high frequencies ('high' being defined here as frequencies above the first structural resonances of the test apparatus being used) is a local phenomenon. The vibration levels can vary significantly with location. The common method is to mount the control accelerometer near the location where field data were measured that defined the environment. If this is not possible, the accelerometer is usually mounted on the fixture near the test item–fixture interface.

As explained earlier, the boundary conditions for the field environment and the test greatly influence the equivalence of the simulation. It is rare that the boundary conditions of the field environment are simulated in the laboratory. Limiting is often used to reduce the conservatism of a test caused by improper boundary conditions and overly conservative test specifications. Common methods include: limiting the response at other locations than the control point, limiting the input force, limiting the current into an electrodynamic shaker, and averaging the response at several points.

Accelerated Testing

Test compression is often required to permit reasonable test times. There are several pitfalls with these methods. The methods usually use some form of Minors rule for fatigue damage. This assumes failures are related to fatigue, and the fatigue mechanism is known. Generally it is wise to keep the vibration level at or below the highest expected field environment. This will prevent unwarranted failures from peak loads. Lower levels of vibration can be accelerated with reasonable confidence by raising the level to the highest expected field environment and reducing the time.

Fixture Design

As discussed earlier, fixtures are usually designed as rigid as possible for several practical reasons. First is the previously mentioned assumption of a single control point. If the fixture is not rigid, this assumption is obviously flawed. Another major practical reason is control of the test. If the fixture, and hence a control accelerometer mounted on or near the fixture, is involved in resonant behavior with more than one participating mode, there will almost certainly be one or more frequencies at which the modal response destructively interferes and the motion will cancel. This is called an antiresonance. Very large motion of the system will result with essentially zero motion at the control point. Not only is this potentially destructive, but the control system and shaker will have great difficulty maintaining the required motion. Care must be taken to avoid placing the control accelerometer at such a location. This can usually be accomplished if the fixtures are rigid. For the same reasons the control accelerometer is often placed at the extreme end of a fixture, like a cube or slip table. The free end of a beam is free of antiresonances. If a rigid fixture is not possible, averaging or extremal (usually means control on the largest) control of several accelerometers is used to limit the motion caused by antiresonances. Locations can usually be found where the several control accelerometers do not all have antiresonances at the same frequencies. Force limiting can also be used to limit the effect of antiresonances. Fixtures can also be built with a significant amount of damping. The damping limits the depth of the antiresonances. The mass of the fixtures is also important. All the shaker moving parts, including the fixtures, must be moved, which increases the force required. Fixtures with small mass require less force from the shaker. This is contrary to the requirement for rigid fixtures. For this reason most fixtures are constructed from aluminum or magnesium that have high stiffness-to-weight ratios.

System Level Tests that Attempt to Match Field Conditions

At the system level tests are often designed to match closely the field boundary conditions and environment. Examples include:

1. Automobile road simulators. These devices can employ as many as 18 electrohydraulic actuators to simulate road conditions.
2. Automobile crash testing. Automobiles are crashed at various velocities into a variety of barriers.

3. Aerospace high-level reverberant acoustic testing. Reverberant acoustic fields can reasonably represent the environment experienced by spacecraft at launch.
4. Shipping container impact testing. Shipping container damage is often simulated by drop tests into various targets to simulate a crash environment.
5. Reentry vehicle impulse testing. Certain hostile environments can subject reentry vehicles to essentially an impulse distributed over the surface of the vehicle. Several techniques have been developed to simulate this impulse.
6. Impact testing of energy-absorbing structures. Since energy-absorbing structures are typically very nonlinear problems, the performance of energy-absorbing structures can often be tested only through the accurate simulation of the use environment.
7. Live fire testing within the Department of Defense. In live fire testing, military hardware is subjected to test conditions that simulate an actual attack as closely as possible.

Nomenclature

c	control point
f	field measurement
F	force variable
i	interior poit
r	response point
t	test measurement
V	motion variable
Z	square matrix of impedance functions

See also: **Crash**; **Environmental testing, implementation**; **Packaging**; **Standards for vibrations of machines and measurement procedures**.

Further Reading

(STD) GEVS-SE, (1990) *General Environmental Verification Specification for STS & ELV Payloads, Subsystems, and Components*, NASA Goddard Space Flight Center, Greenbelt, MD 20771, USA.

(STD) Himelblau H, Manning JE, Piersol AG, and Rubin S (1997), *Guidelines for Dynamic Environmental Criteria*, NASA.

(STD) MIL-PRE-1540 (Proposed) (1997) *Product Verification Requirements for Launch, Upper Stage, and Space Vehicles*, Aerospace Corporation.

(STD) MIL-STD-810E *Test Method Standard for Environmental Engineering Considerations and Laboratory Tests*, Methods 514.5 Vibration, 515.5 Acoustic, 516.5 Shock, 517 Pyroshock, 519.5 Gunfire, and 523.2 Vibro-Acoustic, Temperature.

(STD)MIL-S-901D, (1989) *Shock Tests, H. I. (High-Impact) Shipboard Machinery, Equipment, and Systems, Requirements For*.

Bendat JS and Piersol AG (1986) *Random Data, Analysis and Measurement Procedures*, 2nd edn. New York: Wiley.

Curtis AJ, Tinling NG and Abstein HT Jr (1971) *Selection and Performance of Vibration Tests*, SVM-8, Shock and Vibration Information Analysis Center, 2231 Crystal Drive, Suite 711, Arlington, VA 22202, USA.

Harris CM (ed.) (1996) *Shock and Vibration Handbook*, 4th edn. New York: McGraw-Hill.

Himelblau H, Piersol AG, Wise JH and Grundvig MR (1994) *Handbook for Dynamic Data Acquisition and Analysis*. IEST Recommended Practice 012.1. Mount Prospect, IL: IEST.

McConnell KG (1995) *Vibration Testing Theory and Practice*. New York: Wiley.

Pusey HC (ed.) (1996) *50 Years of Shock and Vibration Technology, SVM-15*. Arlington, VA: Shock and Vibration Information Analysis Center.

Steinberg DS (1988) *Vibration Analysis for Electronic Equipment*. New York: Wiley.

Wirsching PH, Paez TL and Ortiz K (1995) *Random Vibrations Theory and Practice*. New York: Wiley.

ENVIRONMENTAL TESTING, IMPLEMENTATION

P S Varoto, Escola de Engenharia de São Carlos, USP, São Carlos, Brasil

Copyright © 2001 Academic Press

doi:10.1006/rwvb.2001.0107

Environmental vibration testing can be defined as the process of simulating the actual or potential vibration environments experienced by a given structure or equipment. In the context of this article the word simulation is primarily related to experimental tests that are conducted in the laboratory environment in order to predict or reproduce given field vibration data. This simulation process requires the definition of suitable laboratory inputs to the structure under test and, when available, vibration data from the field environment can be used to define these inputs. In the absence of field data, as it is often the case of a new

test structure that is to be tested prior to its exposure to field conditions, a successful laboratory simulation can still be achieved under some special circumstances, as outlined below.

Three major structures are involved in the simulation process. The test item represents the structure under test that is to be attached to the vehicle in the field dynamic environment. The vehicle is the structure used to transport or simply to support the test item. In the field environment the test item is attached to the vehicle forming a combined structure. The vibration exciter is the structure employed in the laboratory environment in order to generate the required test item inputs. In the laboratory environment, the test item is attached to multiple vibration exciters in order to simulate the field conditions. A typical laboratory set-up employs a single vibration exciter, usually driven by a digital control system that is responsible for generating a prescribed input to be applied to the test item by the exciter through a test fixture. More sophisticated excitation systems employ multiple-axis exciters connected to different points on the test item.

The development of acceptable testing procedures and test specifications requires the definition of pertinent variables, as well as understanding of the physical processes which control the vibration data to be measured and how this data can be used to generate suitable test item inputs in laboratory simulations.

Multiple Input–Output Frequency Domain Relationships

Consider the linear structure shown in **Figure 1**. The input vector at the structure's qth location is represented in the frequency domain by $\mathbf{F}_q = \mathbf{F}_q(\omega)$, where ω is the excitation frequency. This input vector consists of two vectors, a force vector and a moment vector. Each input vector can be resolved in terms of the global coordinate system, as shown in **Figure 1**. Thus, the input vector at the qth location has a total of six components, three forces (F_1, F_2, and F_3) in the x, y, and z directions, and three moments (M_1, M_2, and M_3) about the x, y, and z directions, respectively.

Similarly, the structure's output response in the frequency domain at the pth location $\mathbf{X}_p = \mathbf{X}_q(\omega)$ consists of two vectors, a vector of three linear motions and a vector of three angular motions, where the structure's output motion can be given in terms of small linear and angular displacements, velocities, or accelerations. Each output vector can be resolved in terms of the global coordinate system shown in **Figure 1**. Thus, the output response vector $\mathbf{X}_p$ contains six components, three linear motions (X_1, X_2, and X_3) in the x, y, and z directions and three angular motions (X_4, X_5, and X_6) about the x, y, and z directions, respectively.

The frequency domain equations of motion for a linear structure having N degrees of freedom can be presented in the frequency domain as:

$$\mathbf{X} = \mathbf{HF} \qquad [1]$$

where $\mathbf{X} = \mathbf{X}(\omega)$ is the output motion vector, $\mathbf{F} = \mathbf{F}(\omega)$ is the input force vector, and $\mathbf{H} = \mathbf{H}(\omega)$ is the structure's frequency response function (FRF) matrix. Eqn [1] can be rewritten relating the pth output location to the qth input location:

$$\mathbf{X}_p = \mathbf{H}_{uv\,pq}\mathbf{F}_q \qquad [2]$$

Subscripts u and v range from 1 to 6 and the structure's FRF matrix (receptance, mobility, or acceleration), and hence the $\mathbf{H}_{\mathrm{uv\,pq}}$ matrix has 36 entries. Thus, between each pair of input–output points p and q on the structure, there are potentially 36 input–output relationships.

Eqn [2] can be further expanded in partitioned form as:

$$\begin{Bmatrix} \mathbf{X} \\ \Theta \end{Bmatrix}_p = \begin{bmatrix} \mathbf{H}_{FF} & \mathbf{H}_{FM} \\ \mathbf{H}_{MF} & \mathbf{H}_{MM} \end{bmatrix}_{pq} \begin{Bmatrix} \mathbf{F} \\ \mathbf{M} \end{Bmatrix}_q \qquad [3]$$

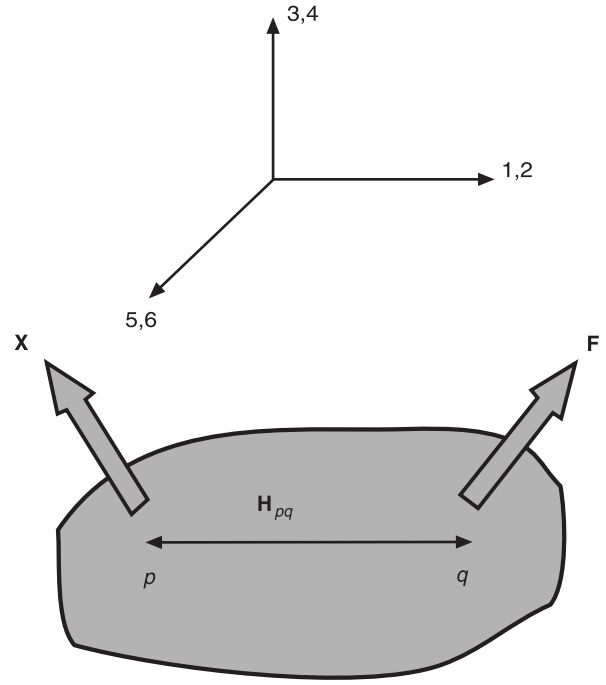


Figure 1 Structure with input and output vectors relative to coordinate system.

where $\mathbf{X} = \mathbf{X}(\omega)$ and $\Theta = \Theta(\omega)$ are 3×1 vectors containing the linear and angular output motions at the structure's pth location, respectively, and $\mathbf{F} = \mathbf{F}(\omega)$ and $\mathbf{M} = \mathbf{M}(\omega)$ are 3×1 vectors containing the forces and moments applied to the structure's qth point, respectively.

The importance of eqn [3] can be recognized by considering a situation where there is a single-axis accelerometer mounted at the pth location with its primary sensing axis oriented in the 2 direction, and a single axis force transducer mounted at the structure's qth location with its primary sensing axis oriented in the 1 direction, according to the global coordinate system shown in **Figure 1**. Thus, from eqn [3], the output acceleration at the pth location due to the excitation vector at the qth point is given as:

$$X_{2p} = H_{21}F_{1q} + H_{22}F_{2q} + H_{23}F_{3q} + H_{24}M_{1q} + H_{25}M_{2q} + H_{26}M_{3q} \quad [4]$$

where H_{uv} denotes the FRF relating the points p and q in the pq directions. Thus, from eqn [4], the output at the pth location is the sum of six terms involving linear as well as angular FRF relative to forces and moments applied at the qth location. However, in practice the sensors used to measure the input and output signals do not account for all terms involved in eqn [4]. Instead the following simpler equation is used:

$$X_p = H_{pq}F_q \quad [5]$$

and the effects of the remaining terms in eqn [4] are not accounted for.

Frequency Domain Substructuring Modeling

Most substructuring techniques consider a partition of the structure's degrees of freedom in terms of master and slaves degrees of freedom. In the context of this article, a similar concept is employed where connector (interface) points are differentiated from external (nonconnector) points by expressing eqn [1] in the following form:

$$\begin{Bmatrix} \mathbf{X}_c \\ \mathbf{X}_e \end{Bmatrix} = \begin{bmatrix} \mathbf{H}_{cc} & \mathbf{H}_{ce} \\ \mathbf{H}_{ec} & \mathbf{H}_{ee} \end{bmatrix} \begin{Bmatrix} \mathbf{F}_c \\ \mathbf{F}_e \end{Bmatrix} \quad [6]$$

Eqn [6] can be used to describe not only the input–output relationship for a single structure, but it can also be applied to any number of independent structures that are coupled at a finite number of Interface points. It is important to emphasize that interface or connector points are points on the test item where coupling occur either with the vehicle in the field or the exciter in the laboratory. External points are points on the test item that are not directly involved with the coupling process. Similarly, interface motions $\mathbf{X}_c$ occur at interface points and external motions $\mathbf{X}_e$ occur at external points. Interface forces $\mathbf{F}_c$ occur at interface points and are due to coupling effects only. The external forces vector $\mathbf{F}_e$ contains the remaining forces applied to the structure. Any excitation source due to internal forces as well as external forces applied at interface points is included in the broad definition of external forces. Eqn [6] also shows that differentiation between interface and external points requires a partition of the structure's FRF matrix into four submatrices. In this case, $\mathbf{H}_{cc}$ defines FRF relationships between interface points while $\mathbf{H}_{ee}$ defines FRF relationships for external points. The $\mathbf{H}_{ce} = \mathbf{H}_{ec}^{\mathrm{T}}$ matrix defines the FRF between interface (external) and external (interface) points.

Interface and external motions can be further expressed from eqn [6] in the following alternate form:

$$\mathbf{X}_c = \mathbf{X}_{cc} + \mathbf{X}_{ce} \quad [7]$$

$$\mathbf{X}_e = \mathbf{X}_{ec} + \mathbf{X}_{ee} \quad [8]$$

Eqns [7] and [8] show a double subscript on the terms appearing on the right-hand side. The first subscript refers to the location where the motion occurs (connector or interface and external) while the second subscript indicates the type of load that caused the motion (connector or external). Thus, $\mathbf{X}_{cc}$ contains interface motions caused by interface forces only while $\mathbf{X}_{ce}$ reflects the influence of the external loads on the interface motions. Each term on the right-hand side of eqns [7] and [8] is related to the corresponding FRF matrix, as shown in eqn [6] (e.g., $\mathbf{X}_{cc} = \mathbf{H}_{cc}\mathbf{F}_c$).

The Field Dynamic Environment

In the field dynamic environment the test item it attached to the vehicle at N_c interface points, as illustrated in **Figure 2**. The resulting field combined structure is subjected to field external forces $\mathbf{F}_e$ and $\mathbf{P}_e$ which, in turn, produces the interface forces $\mathbf{F}_c$ at the N_c interface points.

In order to get expressions for interface forces and test item motions in the field, appropriate test item field boundary conditions must be defined. In this article, a simple interface boundary condition is used, in which the interface connectors are considered to be

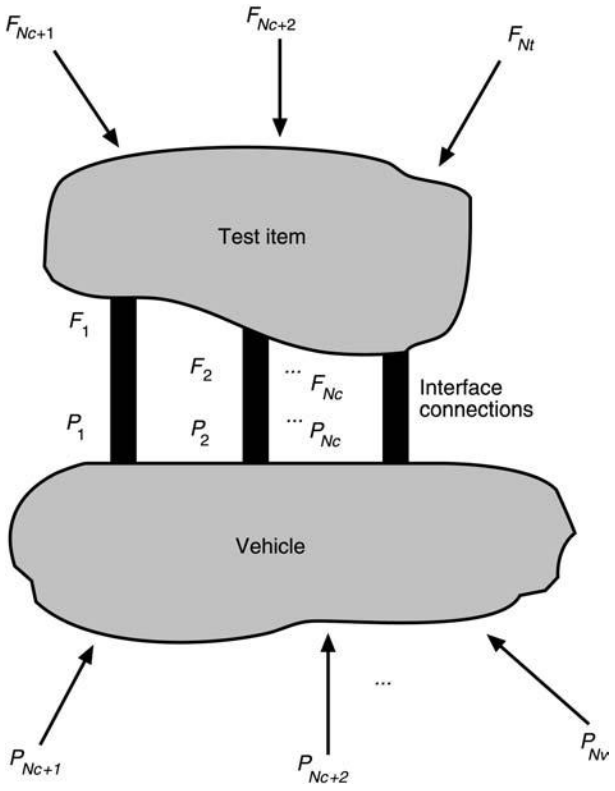


Figure 2 Test item attached to vehicle in the field environment.

part of the test item. Thus, the following relationships for compatibility of motions and equilibrium of forces can be used for interface points:

$$\mathbf{X}_c = \mathbf{Y}_c \qquad [9]$$

$$\mathbf{F}_c = -\mathbf{P}_c \qquad [10]$$

where the $N_c \times 1$ $\mathbf{X}_c$ and $\mathbf{Y}_c$ vectors contain the motions at the test item and vehicle interface points and the $N_c \times 1$ $\mathbf{F}_c$ and $\mathbf{P}_c$ vectors contain the interface forces on both structures, respectively.

Combining eqn [8] written for the test item and vehicle interface points with the equilibrium relationships shown in eqns [9] and [10] leads to the following expression for the field interface forces:

$$\mathbf{F}_c = \mathbf{TV}(\mathbf{Y}_{ce} - \mathbf{X}_{ce}) \qquad [11]$$

Each term appearing in eqn [11] can be defined as follows:

- The $N_c \times N_c$ $\mathbf{TV}$ matrix is the field interface FRF matrix. It is given as:

$$\mathbf{TV} = (\mathbf{T}_{cc} + \mathbf{V}_{cc})^{-1} \qquad [12]$$

where $\mathbf{T}_{cc}$ and $\mathbf{V}_{cc}$ are the test item and vehicle interface FRF $N_c \times N_c$ matrices.

- The $N_c \times 1$ $(\mathbf{Y}_{ce} - \mathbf{X}_{ce})$ vector is the interface relative motion vector. It is formed by the difference of two vectors, namely, the bare vehicle interface motion vector $\mathbf{Y}_{ce}$ and the test item response vector $\mathbf{X}_{ce}$. The bare vehicle interface motions correspond to the vehicle's response at interface points when the test item is not attached to it. Hence $\mathbf{Y}_{ce}$ is due to the vehicle external forces $\mathbf{P}_e$ only (**Figure 2**). The $N_c \times 1$ $\mathbf{X}_{ce}$ vector contains the test item response at interface points due to the external loads ($\mathbf{F}_e$) (nonconnector) applied to the test item.

A particular and important field environment occurs when the test item is not subjected to any field external forces, $\mathbf{F}_e = 0$, and this leads to $\mathbf{X}_{ce} = 0$. In this case, eqn [11] assumes the form:

$$\mathbf{F}_c = \mathbf{TV}\,\mathbf{Y}_{ce} \qquad [13]$$

Eqn [13] shows that, when test item field external forces are negligible, the field interface forces depend only on the test item and vehicle interface driving point and transfer FRFs ($\mathbf{TV}$) and on the bare vehicle interface motion vector $\mathbf{Y}_{ce}$. An important aspect of eqn [13] is that, in principle, one can predict what interface forces should be in cases where the test item has never been exposed to the field environment.

Eqns [11] and [13] also show that in the process of predicting the test item interface forces, the vehicle interface FRF matrix $\mathbf{V}_{cc}$ is required to evaluate the $\mathbf{TV}$ matrix, as shown in eqn [12]. This requirement raises the important issue of what field measurements should be taken when attempting to use eqns [11] and [13]? Clearly, eqns [11] and [13] show that the bare vehicle interface motion $\mathbf{Y}_{ce}$ alone is meaningless. It is vital to have information about the vehicle modal model so that $\mathbf{V}_{cc}$ can be properly accounted for in this force prediction process.

Once interface forces are obtained, they can be used to estimate the test item field motions. Substituting of eqn [11] into eqn [1] leads to the following result for the test item field motions:

$$\begin{Bmatrix} \mathbf{X}_c \\ \mathbf{X}_e \end{Bmatrix} = \begin{bmatrix} \mathbf{T}_{cc}\mathbf{TV} & -\mathbf{T}_{cc}\mathbf{TV} \\ \mathbf{T}_{ec}\mathbf{TV} & -\mathbf{T}_{ec}\mathbf{TV} \end{bmatrix} \begin{Bmatrix} \mathbf{Y}_{ce} \\ \mathbf{X}_{ce} \end{Bmatrix} + \begin{Bmatrix} \mathbf{X}_{ce} \\ \mathbf{X}_{ee} \end{Bmatrix} \qquad [14]$$

and, in the absence of field external forces, eqn [14] is rewritten as:

$$\begin{Bmatrix} \mathbf{X}_c \\ \mathbf{X}_e \end{Bmatrix} = \begin{bmatrix} \mathbf{T}_{cc}\mathbf{TV} & -\mathbf{T}_{cc}\mathbf{TV} \\ \mathbf{T}_{ec}\mathbf{TV} & -\mathbf{T}_{ec}\mathbf{TV} \end{bmatrix} \begin{Bmatrix} \mathbf{Y}_{ce} \\ \mathbf{0} \end{Bmatrix} \qquad [15]$$

As seen from eqn [15], in the absence of field external forces, the test item's field motions depend only on the bare vehicle interface motions $\mathbf{Y}_{ce}$ and on the test item and vehicle FRF matrices. Despite being a particular case of the field dynamic environment, eqn [15] represents an important case, since it often occurs in practice and offers a good chance for a successful laboratory simulation, as will be seen below.

The Laboratory Dynamic Environment

The process of simulating a given field vibration environment in the laboratory environment requires the definition of a suitable set of test item inputs. A simple laboratory test set-up consists of attaching the test item to a single vibration exciter, as shown in **Figure 3**. In this case, it is assumed that the test item is attached to the exciter at E_c connecting points.

The test item input–output relationships in the laboratory environment are defined by using the same frequency domain approach as used in the field environment, given by eqn [6]. In this case, this equation is rewritten as:

$$\begin{Bmatrix} \mathbf{U}_c \\ \mathbf{U}_e \end{Bmatrix} = \begin{bmatrix} \mathbf{T}_{cc} & \mathbf{T}_{ce} \\ \mathbf{T}_{ec} & \mathbf{T}_{ee} \end{bmatrix} \begin{Bmatrix} \mathbf{R}_c \\ \mathbf{R}_e \end{Bmatrix} \qquad [16]$$

where $\mathbf{U}_c$ and $\mathbf{U}_e$ represent the test item interface and external motions obtained in the laboratory, and $\mathbf{R}_c$ and $\mathbf{R}_e$ contain the test item interface and external laboratory inputs. It is noticed here that eqn [16] assumes that the test item's FRF matrix in the laboratory is the same as in the field.

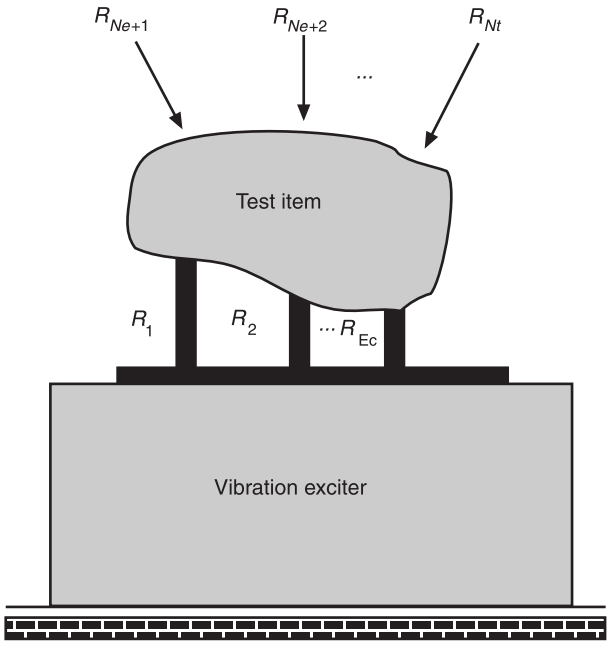


Figure 3 Test item attached to the vibration exciter in the laboratory environment.

The vibration exciter is the mechanical structure responsible for generating the test item inputs in the laboratory environment. The vibration exciter input–output relationships are given by eqn [1] rewritten as:

$$\mathbf{Z} = \mathbf{E}\,\mathbf{Q} \qquad [17]$$

where $\mathbf{Q}$ and $\mathbf{Z}$ are the exciter input and output vectors and $\mathbf{Q}$ is the exciter FRF matrix.

The same frequency domain substructuring approach will be employed in order to obtain expressions for laboratory interface forces and test item motions. Hence, the following equation is obtained for the laboratory interface forces:

$$\mathbf{R}_c = \mathbf{TE}(\mathbf{Z}_{ce} - \mathbf{U}_{ce}) \qquad [18]$$

where $\mathbf{R}_c$ is the $E_c \times 1$ vector containing the test item interface forces in the laboratory, $\mathbf{Z}_{ce}$ contains the vibration exciter bare table motions and $\mathbf{U}_{ce}$ is the test item response to external forces. The $E_c \times E_c$ $\mathbf{TE}$ matrix is the laboratory interface FRF matrix and it is defined as:

$$\mathbf{TE} = (\mathbf{T}_{cc} + \mathbf{E}_{cc})^{-1} \qquad [19]$$

As in the field, the laboratory interface forces depend on the relative motion vector $(\mathbf{Z}_{ce} - \mathbf{U}_{ce})$ between the vibration exciter and the test item interface points. In the absence of laboratory external forces acting on the test item, eqn [18] reduces to:

$$\mathbf{R}_c = \mathbf{TE}\,\mathbf{Z}_{ce} \qquad [20]$$

since $\mathbf{U}_{ce} = 0$ in this case.

Substituting eqn [18] into eqn [16] results in the following expression for the test item laboratory motions:

$$\begin{Bmatrix} \mathbf{U}_c \\ \mathbf{U}_e \end{Bmatrix} = \begin{bmatrix} \mathbf{T}_{cc}\mathbf{TE} & -\mathbf{T}_{cc}\mathbf{TE} \\ \mathbf{T}_{ec}\mathbf{TE} & -\mathbf{T}_{ec}\mathbf{TE} \end{bmatrix} \begin{Bmatrix} \mathbf{Z}_{ce} \\ \mathbf{U}_{ce} \end{Bmatrix} + \begin{Bmatrix} \mathbf{U}_{ce} \\ \mathbf{U}_{ee} \end{Bmatrix} \qquad [21]$$

When the test item is not subjected to laboratory external forces, eqn [21] reduces to:

$$\begin{Bmatrix} \mathbf{U}_c \\ \mathbf{U}_e \end{Bmatrix} = \begin{bmatrix} \mathbf{T}_{cc}\mathbf{TE} & -\mathbf{T}_{cc}\mathbf{TE} \\ \mathbf{T}_{ec}\mathbf{TE} & -\mathbf{T}_{ec}\mathbf{TE} \end{bmatrix} \begin{Bmatrix} \mathbf{Z}_{ce} \\ \mathbf{0} \end{Bmatrix} \qquad [22]$$

Thus, in the absence of external forces, the test item laboratory motions depend on the bare exciter table motion $\mathbf{Z}_{ce}$ and on the FRF matrix shown in eqn [22]. In the next section, some laboratory test scenarios are discussed in order to explore the possibilities of a successful laboratory simulation.

Test Scenarios for Laboratory Simulations

This section is primarily focused on describing some test scenarios that can be used in laboratory simulations. In each test scenario a different control strategy is employed. These scenarios differ in terms of the data used to define the test item laboratory inputs.

Test Scenario 1: Inputs from the Bare Vehicle Motions

In this case, the test item is absent from the field. The bare vehicle interface motions are used to generate a set of forces that will be applied to the test item interface forces in the laboratory environment. These forces are given as:

$$\mathbf{T}_{cc}\mathbf{R}_c = \mathbf{Y}_{ce} \qquad [23]$$

or:

$$\mathbf{R}_c = \mathbf{T}_{cc}^{-1}\mathbf{Y}_{ce} \qquad [24]$$

where $\mathbf{R}_c$ contains the test item laboratory interface forces. A comparison between eqn [24] with the true field interface force, eqn [11], reveals some important issues. First, the field interface FRF matrix $\mathbf{TV}$ in eqn [11] accounts for the vehicle interface FRF characteristics, as seen from eqn [12], while the expression for the laboratory forces accounts only for the test item interface FRFs. Second, field external force effects are properly accounted for in eqn [11] while their effects are absent from eqn [24]. Thus, it is clear that the laboratory inputs given by eqn [24] will not predict correctly the corresponding field motions, and therefore, the inputs obtained from the bare vehicle interface motions are not appropriate in this case.

However, suppose that in a specific, rather common situation found in practice, the field external force effects can be neglected. Then, eqn [13] contains the true field interface forces, since $\mathbf{X}_{ce} = 0$. If, in addition to the bare vehicle interface motion vector $\mathbf{Y}_{ce}$, the vehicle interface FRF matrix $\mathbf{V}_{cc}$ is available in the laboratory environment; then, eqn [24] could be reformulated to include the information about $\mathbf{V}_{cc}$ so that the laboratory interface forces will match the corresponding field forces.

In addition, it is impossible to meet the requirements of multiple excitation shown in eqn [24] with a single vibration exciter, except in the simplest case where the test item is attached to the vehicle at a single interface point. Thus, once the correct inputs are generated, each test item interface point must be driven by a different exciter which in turn must be controlled to generate the correct input.

Test Scenario 2: Inputs from the Combined Structure

In this test scenario it is assumed that field data are available from the combined structure. As previously shown, information about the field combined structure consists of field interface forces and motions, and the test item external forces and motions. Hence, when using field data from the combined structure in order to define the test item laboratory inputs, the following multi-input control strategies can be employed:

- Matching interface forces in the laboratory. In this case the exciters must be controlled such that:

$$\mathbf{R}_c = \mathbf{F}_c \qquad [25]$$

- Matching external forces in the laboratory. In this case the exciters must be controlled such that:

$$\mathbf{R}_e = \mathbf{F}_e \qquad [26]$$

- Matching interface motions in the laboratory. In this case the exciters are controlled such that field interface motions are matched:

$$\mathbf{U}_c = \mathbf{X}_c \qquad [27]$$

- Matching external motions in the laboratory. This test scenario requires that the exciters be controlled such that:

$$\mathbf{U}_e = \mathbf{X}_e \qquad [28]$$

Thus, several control possibilities exist when attempting to match field data from the combined structure in the laboratory environment. Although a detailed description of these test scenarios can be found in the suggested literature, a brief discussion of the force identification problem is made in the next section of this article, since it is directly related to the issue of defining suitable test item inputs.

Discussion of the Force Identification Problem in Environmental Vibration Testing

Direct measurement of the test item interface and external forces in the field environment is generally difficult for a number of reasons. In the case of interface forces, a direct measurement requires that force transducers be placed in the loads paths, which in some cases is simply impractical due to space limitations and/or design considerations.

Because of these difficulties, indirect force identification techniques became popular in modal and in vibration testing. These force identification techniques can be defined in the time or frequency domain. In particular, when the data are analyzed in the frequency domain, the pseudoinverse technique is frequently employed.

For deterministic input and output signals, the frequency pseudoinverse solution for the unknown forces from measured motions is obtained from eqn [1] as:

$$\mathbf{F} = \mathbf{H}^{+}\mathbf{X} \qquad [29]$$

where the plus symbol denotes the pseudoinverse of the test item FRF matrix $\mathbf{H}$. Since there are usually a greater number of measured motions than unknown forces, the forces are obtained by solving a least-squares problem with the pseudoinverse of matrix $\mathbf{H}$, given as:

$$\mathbf{H}^{+} = \left[\mathbf{H}^{H}\mathbf{H}\right]^{-1}\mathbf{H}^{H} \qquad [30]$$

where the superscript H denotes the Hermitian operator (complex conjugate) of the $\mathbf{H}$ matrix. Use of eqns [29] and [30] is restricted to input and output frequency spectra, that carry both magnitude and phase information.

When input and output signals are random, the input–output relationships are given by the following expression:

$$\mathbf{G}_{xx} = \mathbf{H}^{*}\mathbf{G}_{ff}\mathbf{H}^{\mathrm{T}} \qquad [31]$$

where the asterisk and T denote the complex conjugate and nonconjugate transpose of the $\mathbf{H}$ matrix, respectively. The $\mathbf{G}_{ff}$ and $\mathbf{G}_{xx}$ matrices are the input and output frequency domain spectral density matrices whose diagonal entries are the real valued input and output autospectral densities, while the off-diagonal entries are the complex valued cross-spectral densities, respectively. The solution for the unknown input spectral density matrix $\mathbf{G}_{ff}$ from eqn [31] is obtained in a least-squares sense as:

$$\mathbf{G}_{ff} = [\mathbf{H}^{+}]^{*}\mathbf{G}_{xx}[\mathbf{H}^{+}]^{\mathrm{T}} \qquad [32]$$

where, in this case, the unknown $\mathbf{G}_{ff}$ matrix is obtained in a least-squares sense from the measured $\mathbf{G}_{xx}$ matrix and the test item FRF matrix $\mathbf{H}$. The $\mathbf{G}_{xx}$ and $\mathbf{G}_{ff}$ matrices as given by eqns [31] and [32] contain the correct phase relationships required by the input and output variables since the off-diagonal cross-spectral densities are complex with real and imaginaty parts and are accounted for in both equations. Thus, proper correlation between the corresponding time variables is accounted for when using eqn [32] to solve for the unknown forces. Eqn [32] is referred to as the correlated equation.

A commonly accepted procedure when working with eqns [31] and [32] in random vibration environments is to assume that the input random forces are statistically uncorrelated. When this assumption is made, the off-diagonal input cross-spectral densities in the $\mathbf{G}_{ff}$ matrix in eqn [31] are identically zero and this equation reduces to:

$$\mathbf{G}_{xx} = \left[|\mathbf{H}|^{2}\right]\mathbf{G}_{ff} \qquad [33]$$

where $\mathbf{G}_{ff}$ and $\mathbf{G}_{xx}$ are real valued vectors containing the input and output autospectral densities, respectively. The solution for the unknown input forces is obtained from eqn [33] and is given as:

$$\mathbf{G}_{ff} = \left[|\mathbf{H}|^{2}\right]^{+}\mathbf{G}_{xx} \qquad [34]$$

Thus, eqn [33] essentially shows that, under the assumption of uncorrelated input forces the resulting motions are equally uncorrelated and the solution for the input forces in eqn [34] results in estimates of the input autospectral densities, and no information about the input cross-spectral densities is obtained. Eqn [34] is referred to as the uncorrelated equation.

The feasibility of the correlated (eqn [32]) and uncorrelated (eqn [34]) is checked in a simple experiment where a cold rolled steel beam ($92 \times 1.25 \times 1.0$ in) is suspended by flexible cords and driven by two vibration exciters. One exciter is attached to the beam's midpoint while the second exciter is attached to one of the beam's endpoints. The exciters are driven by two independently generated random signals. The input random forces are measured by piezoelectric force transducers for comparison purposes. Acceleration auto- and cross-spectral densities and the beam's FRFs are measured at four different locations, including the points of application of the input forces. Eqns [32] and [34] are used in order to predict estimates of the measured input forces.

Figure 4 shows the results for the estimated input auto- and cross-spectral densities when the correlated eqn [32] is used to solve the inverse problem. **Figure 4A** and **4B** show the estimated and measured force autospectral densities at the beam mid- and endpoint respectively. **Figure 4C** and **4D** show magnitude and phase of the estimated and measured force cross-spectral density, respectively. The estimated inputs are in good agreement with the measured input autospectral densities, except in the vicinity of certain frequencies where the estimated force is distorted when compared with the measured ones. A reasonably good result is also obtained for the cross-spectral density between the excitation signals, as seen from **Figure 4C** and **4D**.

The results for the uncorrelated eqn [34] are shown in **Figure 5**. **Figure 5A** shows the measured and estimated force autospectral density at the beam midpoint while **Figure 5B** shows the estimated force autospectral density for the beam endpoint. It is seen that the predicted values of the force at the beam endpoint presents serious distortions in comparison with the measured values. This is due to the fact that the motions are always correlated regardless of the input forces being correlated or uncorrelated. Hence, when solving for input random forces from measured motions, eqn [32] must be employed since it contains the correct phasing between the input and output variables.

See also: **Environmental testing, overview**.

Further Reading

Ewins DJ (1984) *Modal Testing: Theory and Practice*. UK: Research Studies Press.

Maia NMM and Silva J (1997) *Theoretical and Experimental Modal Analysis*. UK: Research Studies Press.

McConnell KG (1995) *Vibration Testing: Theory and Practice*. New York, NY: John Wiley.

McConnell KG and Varoto PS (1996) *A Model For Vibration Test Tailoring, Part I: Basic Definitions and Test Scenarios*. Tutorial session. XIV International Modal Analysis Conference, Dearborn, MI, pp. 1–7.

Varoto PS (1996) *The Rules for the Exchange and Analysis of Dynamic Information in Structural Vibration*. PhD dissertation, Iowa State University of Science and Technology, Ames, IA, USA.

Varoto PS and McConnell KG (1996a) *A Model For Vibration Test Tailoring, Part II: Numerically Simulated Results for a Deterministic Excitation and no External Loads*. Tutorial session. XIV International Modal Analysis Conference, Dearborn, MI, pp. 8–15.

Varoto PS and McConnell KG (1996b) *A Model For Vibration Test Tailoring, Part IV: Numerically Simulated Results for a Random Excitation*. Tutorial session. XIV

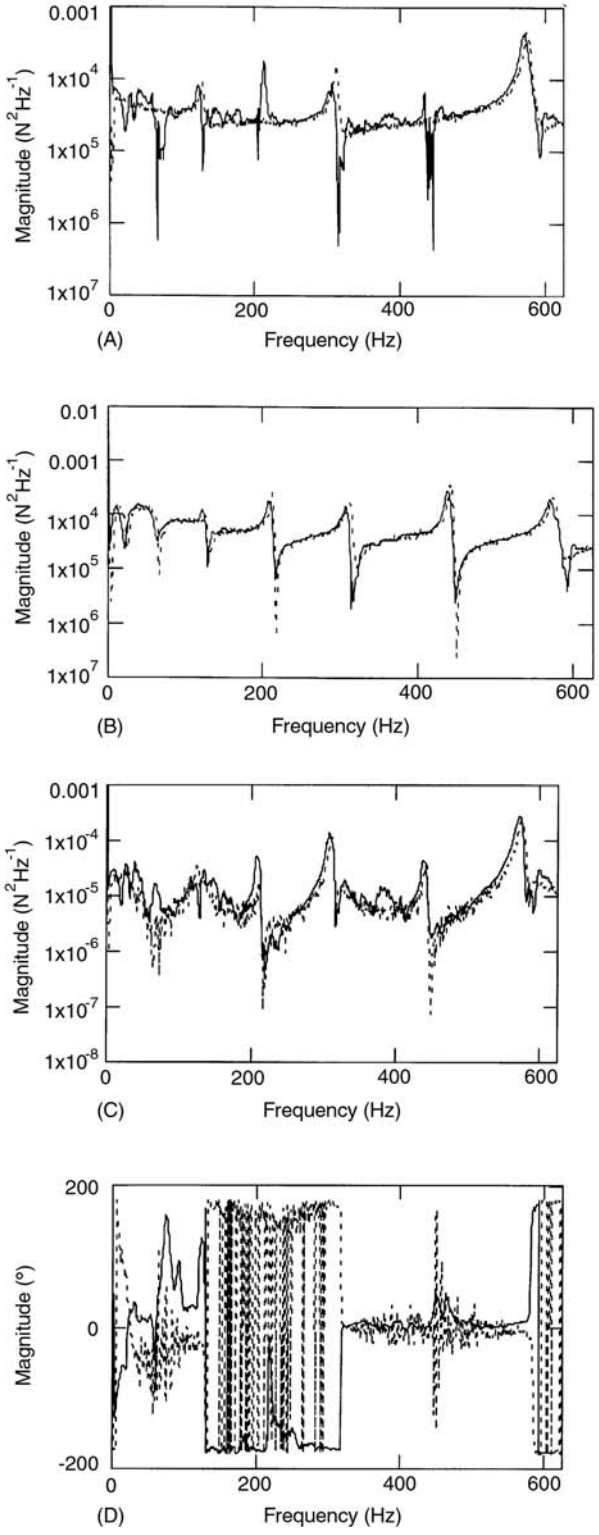


Figure 4 Estimated forces from correlated equation: (A) force autospectral density at beam midpoint; (B) force autospectral density at beam endpoint; (C) magnitude of force cross-spectral density between excitation points; (D) phase angle of force cross-spectral density between excitation points.

International Modal Analysis Conference, Dearborn, MI, pp. 31–47.

Varoto PS and McConnell KG (1996c) READI – a vibration testing model for the 21st century. *Sound and Vibration* October, 22–28.

Varoto PS and McConnell KG (1997a) Predicting random excitation forces from acceleration response measurements. In: *Proceedings of the XV International Modal Analysis Conference – IMAC,* Orlando, FL, February, pp. 1–8.

Varoto PS and McConnell KG (1997b) READI: the rules for the exchange and analysis of dynamic information in structural vibration. In: *Proceedings of the XV International Modal Analysis Conference,* Orlando, FL, pp. 1937–1944.

Varoto PS and McConnell KG (1998) *Single Point vs Multi Point Acceleration Transmissibility Concepts in Vibration Testing*. XVI International Modal Analysis Conference, Sta Barbara, CA, USA, February, pp. 734–843.

Varoto PS and McConnell KG (1999) On the identification of interface forces and motions in coupled structures. In: *Proceedings of the XVII International Modal Analysis Conference,* Orlando, FL, February, pp. 2031–2037.

Wirsching PH, Paez TL and Ortiz K (1995) *Random Vibrations: Theory and Practice*. New York: Wiley Interscience.

EQUATIONS OF MOTION

See **THEORY OF VIBRATION: EQUATIONS OF MOTION**

F

FATIGUE

M Ramulu and A S Kobayashi,
University of Washington, Seattle, WA, USA

Copyright © 2001 Academic Press

doi:10.1006/rwvb.2001.0105

Introduction

Fatigue is an ever-present problem that plagues any structure subjected to cyclic and/or variable loading. Extending fatigue cracks, which ultimately could lead to complete failure of a structure, create considerable costs in terms of time, money and lives. As an example, 75% of the United States Air Force C-141 fleet is currently flying under flight restrictions due to fatigue cracks in the wings and cockpit window frames and this problem will cost millions of dollars to correct and years to complete. The incentive to study fatigue crack propagation is thus very high. Engineers who design damage-tolerant structures, must fully understand and be able to predict the growth of fatigue cracks under service load conditions such that the structure will not fail prior to inspection or replacement.

Fatigue can be divided into two processes, namely the initiation phase and the propagation phase. The initiation phase refers to the period when a crack-free structure component develops minute cracks under sustained cyclic loading. The propagation phase is when the minute crack grows to a critical crack length under cyclic loading, and then fails. The transition from a minute to an extending crack is a subjective decision where 0.1 inch (2.5 mm) is often used in engineering design as the beginning of crack propagation. Fatigue is also categorized by the mode of driving force for crack extension, namely that of high-cycle and low-cycle fatigue. The former is generated by relatively low stresses while the latter is caused by high stresses which may exceed the yield strength of the material. Again, the division between low- and high-cycle fatigue is vague and falls between 10 and 10^5 cycles. High- and low-cycle fatigue both refer to the entire fatigue life and do not distinguish between the initiation and propagation periods. Many of the vibration-generated fatigue cracks are by nature high-cycle fatigue. Historically, high-cycle fatigue commanded the attention of early designers who found that a structure component could fail at an applied stress level as low as half of its yield strength. Low-cycle fatigue became an issue more recently with the availability of accurate tools for structural analysis, such as the finite element method, to predict critical stresses. As a result, design allowables approaching the yield strength can now be used to design efficient structure components.

In the following, a brief account of the classical theories on fatigue, i.e., high- and low-cycle fatigue, will be presented. It will be followed by a more in-depth presentation of the modern theory of fatigue crack propagation based on the linear theory of fracture mechanics.

Stress–Life Method

Theories

While fatigue of metals has been documented for over 150 years, the most quoted early research is the full-scale axle fatigue tests of Wöhler (1860). He advanced the concept of an endurance limit for the design of axles for railway rolling stock. The subsequent 100 years of development in fatigue was dominated by the 'Wöhler's diagram' or the *S–N* diagram which is a plot of the alternating stress, *S*, vs the cycle to failure, *N*. The commonly-used rotating bend specimen to establish the *S–N* diagram was a direct simulation of the rotating axle.

Figures 1 and **2** show typical *S–N* diagrams, which were generated by smoothly polished rotating bend specimens subjected to a constant moment, of 7075–T6 and 2024–T3 alloys, respectively. For a body-centered cubic material, such as steel, the *S–N* curve exhibits an endurance or fatigue limit, S_e, below which the material has an infinite life. Again, the definition of infinite life is vague with one million cycles as a commonly accepted engineering criterion. An *S–N* curve is affected by: loading factors, such as the mean stress effect; geometric factors, such as

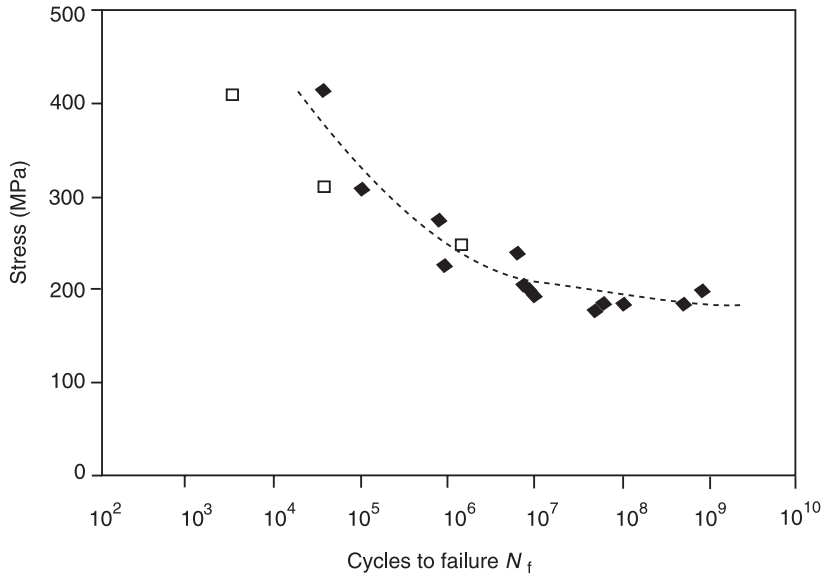


Figure 1 *S–N* curve for 7075–T6.

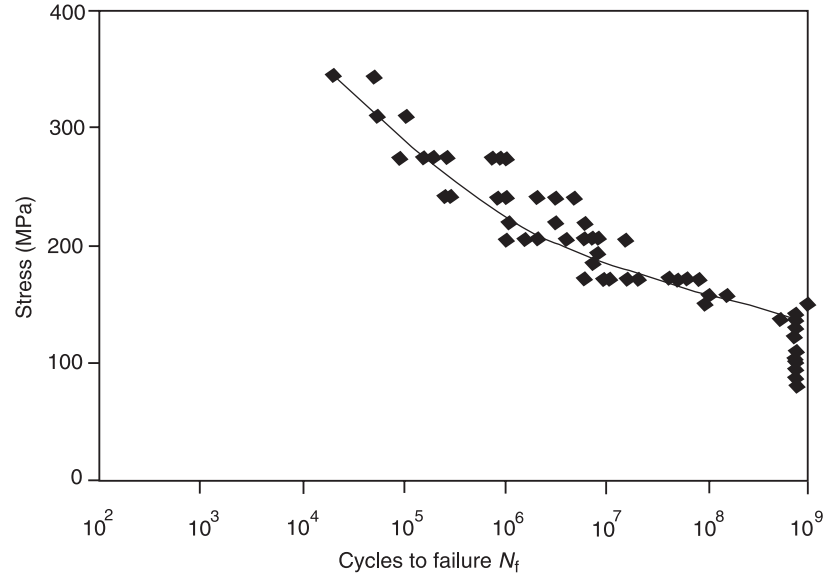


Figure 2 *S–N* curve for 2024–T3.

stress concentrations; processing factors, such as surface finish and surface treatment; and environmental factors, such as temperature and atmosphere. These factors were extensively studied and appended as modifying factors to the empirical stress–life, *S–N*, method. The empirical relations established to estimate the fatigue limit and its modification factors are summarized in **Table 1**.

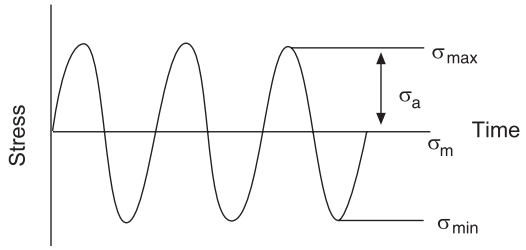
The *S–N* curve, as discussed above, addresses only the constant amplitude loading. In practice, a structure component is subjected to a complex loading history involving a multitude of variable amplitude loadings. A method, which is still widely used today, to account for the varying damage generated by different durations of different amplitude loadings is the linear damage summation method of Palmgren and Miner. This method, which is commonly known as Miner's method, is based on the hypothesis that for failure to occur:

$$\sum n_i/N_i = 1 \qquad [1]$$

where n_i is the number of cycles at stress level S_I and N_i is the fatigue life in cycles at that same level. Test data indicate that the damage summation, as represented by eqn [1], varies with the load history and that the right hand term of unity generally varies from

Table 1 Basic relations associated with stress-life approach to fatigue

Stress–life



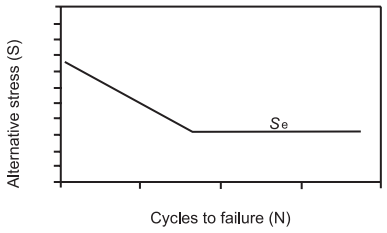
Stress range: $\Delta\sigma = \sigma_{max} - \sigma_{min}$
Stress amplitude: $\sigma_a = (\sigma_{max} - \sigma_{min})/2$
Mean stress: $\sigma_m = (\sigma_{max} + \sigma_{min})/2a$
Stress ratio: $R = (\sigma_{min})/\sigma_{max}$

Amplitude ratio: $$A = \frac{\sigma_a}{\sigma_m} = \frac{\sigma_{max} - \sigma_{min}}{\sigma_{max} + \sigma_{min}} = \frac{1 - R}{1 + R}$$

Fully reversed: $R = -1,\ A = \infty$
Zero to maximum: $R = 0,\ A = 1$
Zero to minimum: $R = \infty,\ A = -1$

Empirical method:

S–N **Curve for steel empirical relations:**



$S = 10^c N^b \quad (10^3 < N < 10^6)$

where : $c = \log_{10} \frac{(S_{1000})^2}{S_e}$

and $b = -\frac{1}{3} \log_{10} \frac{S_{1000}}{S_e}$

or $N = 10^{-c/b} S^{1/b} \quad (10^3 < N < 10^6)$

or $S = 1.62 S_u N^{-0.085}$

Mean stress correction relationships

Soderberg (1930, USA):
$$\frac{\sigma_a}{S_e} + \frac{\sigma_m}{S_y} = 1$$

Goodman (1899, England):
$$\frac{\sigma_a}{S_e} + \frac{\sigma_m}{S_u} = 1$$

Gerber (1874, Germany):
$$\frac{\sigma_a}{S_e} + \left(\frac{\sigma_m}{S_u}\right)^2 = 1$$

Morrow (1960, USA):
$$\frac{\sigma_a}{S_e} + \frac{\sigma_m}{\sigma_f} = 1$$

Notch effect

Fatigue notch factor:

$$K_f = \frac{S_e^{(\text{unnotched})}}{S_e^{(\text{notched})}}$$

Notch sensitivity factors:

$$q = \frac{K_f - 1}{K_t - 1}, \quad K_t = \frac{\sigma_{max}}{S}$$

$$K_f = 1 + \frac{K_f - 1}{1 + (a/r)}$$

$$a = \left[\frac{300}{S_u(ksi)}\right]^{1.8} \times 10^{-3} \text{ in}$$

$S_u \approx 0.5BHN$

and r is a notch root radius

$\cdot S_e = S'_e \times C_{size} \times C_{load} \times C_{sur} \times C_s \times C_T \times C_{envi}$

0.5 to 2.0 in practice. Nonlinearity has been incorporated into Miner's linear damage summation method by using $(n_i/N_i)^p$ where p is a function of the stress level. For a complex load history, the variable loadings must be reduced to a series of constant amplitude cycle events in order to be accommodated in eqn [1] or its variation. This reduction process, which is referred to as cyclic counting, includes level-crossing counting, peak counting and simple-range counting, none of which include the sequencing effect. Load sequencing effect is incorporated in the more popular rainflow counting procedure.

Application

The simple theory allows a quick estimate of the total fatigue life, initiation and propagation, of component with a long fatigue life. However, it cannot distinguish between the initiation and propagation phases.

Strain–Life Method

Theories

Fatigue loading at a high load level inevitably results in fatigue failure at a low number of cycles. For such

fatigue loading, the applied load and the stress component in the stress–life method can be replaced with an applied displacement loading and a plastic strain component, respectively, and the *S–N* diagram is replaced by a strain–life curve. Manson observed that the plastic strain–life, i.e., ε_p–N, relation can be linearized on log–log coordinates or:

$$\frac{\Delta\varepsilon_p}{2} = \varepsilon'_f(2N_f)^c \qquad [2]$$

where: $\Delta\varepsilon_p/2$ = plastic strain amplitude; $2N_f$ = reversals to failure; ε'_f = fatigue ductility coefficient; c = fatigue ductility exponent. By noting that the total strain is decomposable into elastic and plastic strains and by using the stress–plastic strain power hardening law, eqn [2] can be rewritten in terms of the total strain as:

$$\frac{\Delta\varepsilon}{2} = \frac{\sigma'_f}{E}(2N_f)^b + \varepsilon'_f(2N_f)^c \qquad [3]$$

where σ'_f is the fatigue strength coefficient, and b is the fatigue strength exponent.

Equation [3] is the basis of the strain–life method. The summary of strain–life equations are summarized in **Table 2**. The relative contributions of the elastic and the plastic strains in eqn [3] are represented graphically in **Figure 3** with schematic representations of the stabilized hysteresis loops of the cyclic stress–strain relations. The transition fatigue life, $2N_f$, which is also marked in **Figure 3**, decreases with ultimate strength of the material. The strain–life method, as represented by eqn [3], requires four empirical constants of b, c, σ'_f and ε'_f. Since these constants are obtained through curve-fitting fatigue data, a problem arises when eqn [3] is used outside the bounds of the data points.

Limited studies on one of the modifying factors, i.e., the mean stress effect, shows that at high strain levels, the cyclic plastic strains tend to cause the mean stresses to relax to zero. Miner's rule can also be used to account for the load history effect in the strain–life method by using, N, life to failure for the constant strain amplitude loading.

Application

The strain–life approach is most useful for high stress levels or at locations of high stress concentration with considerable plastic strains. Such loading results in a low propagation life and thus the strain–life approach only accounts for the crack initiation phase.

Classical Approach to Fatigue Analysis

Given the 100 years of its history, the stress–life approach to fatigue has been extensively documented in the literature. While the strain–life approach is relatively new, thirty years in the making, it is a logical extension of the stress–life approach and thus is considered as one of the two classical approaches in fatigue analysis. The vast literature on the stress and strain–life approaches is summarized in numerous text books. The classical approach

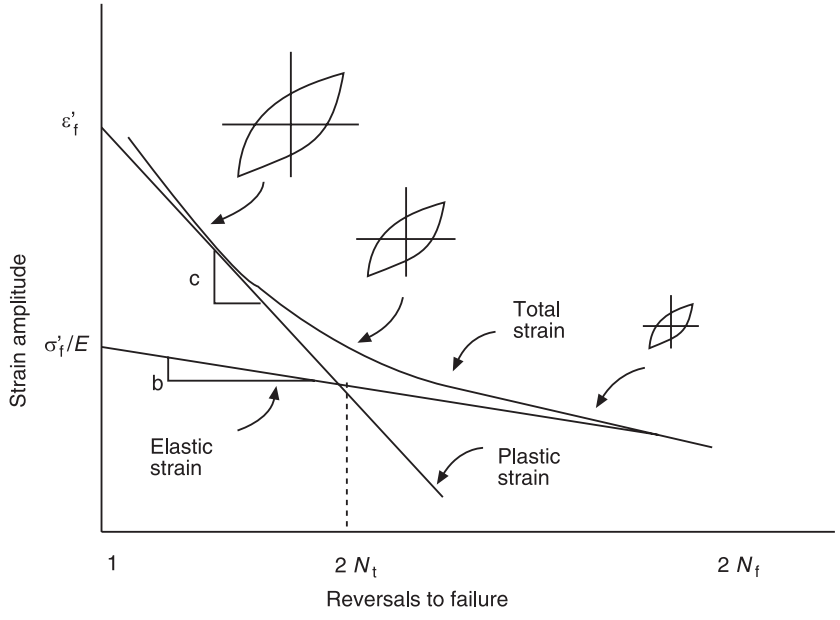


Figure 3 Strain amplitude vs number of reversals to failure.

Table 2 Basic relations associated with strain–life approach to fatigue.

Strain life:

Power relationship between stress, σ, and plastic strain, ε_p:

$$\sigma = K(\varepsilon_p)^n$$

Strain hardening exponent:

n = slope of log σ vs. log ε_p

Strength coefficient:

$$K = \frac{\sigma_f}{\varepsilon_f''}$$

Total strain = elastic strain + plastic strain:

$$\varepsilon_t = \varepsilon_e + \varepsilon_p = \frac{\sigma}{E} + \left(\frac{\sigma}{K}\right)''$$

Strain and stress amplitude:

$$\varepsilon_a = \frac{\Delta\varepsilon}{2}$$

$$\sigma_a = \frac{\Delta\sigma}{2}$$

$$\Delta\varepsilon = \Delta\varepsilon_e + \Delta\varepsilon_p$$

$$\frac{\Delta\varepsilon}{2} = \frac{\Delta\sigma}{2E} + \frac{\Delta\varepsilon_p}{2}$$

Cyclic stress – plastic strain relationship:

$$\sigma = K'(\varepsilon_p)^{n'}$$

Cyclic stress – total strain relationship:

$$\varepsilon = \frac{\sigma}{E} + \left(\frac{\sigma}{K'}\right)^{1/n'}$$

Hysteresis curve:

$$\Delta\varepsilon = \frac{\Delta\sigma}{E} + 2\left(\frac{\Delta\sigma}{2K'}\right)^{1/n'}$$

Strain – life relationship:

$$\frac{\Delta\varepsilon}{2} = \frac{\sigma_f'}{E} + (2N_f)^b + \varepsilon_f'(2N_f)^c$$

Transition life:

$$2N_t = \left(\frac{\varepsilon_f' E}{\sigma_f'}\right)^{1/(b-c)}$$

Cyclic strength coefficient:

$$K' = \frac{\sigma_f'}{(\varepsilon_f')^{n'}}$$

Cyclic strain hardening exponent:

$$n' = \frac{b}{c}$$

Mean stress effect:

Morrow (1968)

$$\frac{\Delta\varepsilon}{2} = \frac{\sigma_f - \sigma_0}{E}(2N_f)^b + \varepsilon_f'(2N_f)^c$$

Manson and Halford (1981)

$$\frac{\Delta\varepsilon}{2} = \frac{\sigma_f' - \sigma_0}{E}(2N_f)^b + \varepsilon_f'\left(\frac{\sigma_f' - \sigma_0}{\sigma_f'}\right)^{c/b}(2N_f)^c$$

Smith, Watson and Topper (SWT: 1970)

$$\sigma_{max}\frac{\Delta\varepsilon}{2} = \frac{(\sigma_f')}{E}(2N_f)^{2b} + \sigma_f'\varepsilon_f'(2N_f)^{b+c}$$

where $\sigma_{max} = \frac{\Delta\sigma}{2} + \sigma_0$

$\sigma_{max}\Delta\varepsilon \propto N_f$

Neuber relationship:

$$K_t = \sqrt{K_\sigma K_\varepsilon}$$

$$K_t^2 = \frac{\sigma\,\varepsilon}{S\,e}$$

where: K_t = stress concentration factor
K_σ = local stress concentration factor
K_ε = local strain concentration factor

Neuber relationship (nominally elastic behavior):

$$\frac{(K_t S)^2}{E} = \sigma\varepsilon$$

can be characterized by its empirical and one-dimensional analysis of a complex three-dimensional structural problem. Also, the classical approach does not discriminate between the period of crack initiation and crack propagation. While the former accounts for 90% of the fatigue life, the latter is particularly important for damage-tolerant design. The reason being, damage-tolerant design relies on the residual life estimation of a structure with a flaw(s), which includes that generated by fatigue during the initiation period. Fatigue crack initiation is governed by the anisotropic and heterogeneous microstructure of the material studied by material scientists. The role of a structural designer in damage-tolerant design is to predict the amount of crack propagation of this preexisting crack under real loading conditions.

Crack Propagation Analysis

Current fatigue crack growth studies are based on a semi-empirical correlation between the rate of crack propagation, (da/dN), and the range of the stress intensity factor, $\Delta K = K_{max} - K_{min}$. The methodology is limited to a uniaxial stress field and a single mode of fatigue crack propagation involving the opening mode or mode I crack tip deformation. Under mixed-mode, cyclic loading conditions, a fatigue crack will generally curve in the direction of a vanishing sliding mode or mode II stress intensity factor, K_{II} with mode I stress intensity factor, K_I, dominating the crack propagation rate. Mixed-mode fatigue crack propagation is also observed in the zig-zag path of a short crack which extends in the

direction of minimum resistance due to grain orientation, inclusions and other material defects in the path of crack extension. Macroscopically, however, the short crack is propagating under mode I loading. Thus this short overview of fatigue will be concerned with mode I loading only. It will be preceeded by a short presentation of the crack tip stress field from linear elastic fracture mechanics (LEFM).

Crack Tip Stress Field

The elastic stress field in the vicinity of a crack is dominated by the stress singularity and the strength of the singularity is expressed by the mode I stress intensity factor, K_{I}. The elastic stress state near the crack tip, in terms of the polar coordinates $(r,\ \theta)$ with its origin at the crack tip, is:

$$\begin{aligned}
\sigma_{rr} &= \frac{1}{\sqrt{(2\pi r)}}\cos\frac{\theta}{2} \\
&\quad \times \left[K_{\mathrm{I}}\left(1+\sin^2\frac{\theta}{2}\right)+\frac{3}{2}K_{\mathrm{II}}\sin\theta-2K_{\mathrm{II}}\tan\frac{\theta}{2}\right] \\
&\quad +\frac{T}{2}(1+\cos 2\theta) \\
\sigma_{\theta\theta} &= \frac{1}{\sqrt{(2\pi r)}}\cos\frac{\theta}{2}\left[K_{\mathrm{I}}\cos^2\frac{\theta}{2}-\frac{3}{2}K_{\mathrm{II}}\sin\theta\right] \\
&\quad +\frac{T}{2}(1+\cos 2\theta) \\
\sigma_{r\theta} &= \frac{1}{2\sqrt{(2\pi r)}}\cos\frac{\theta}{2}[K_{\mathrm{I}}\sin\theta+K_{\mathrm{II}}(3\sin\theta-1)] \\
&\quad -\frac{T}{2}\sin 2\theta
\end{aligned} \qquad [4]$$

The crack tip stresses are controlled by the mode I stress intensity factor, K_I, which is a function of the length and orientations of the crack, the magnitude and distribution of the applied load, and the dimensions of the body in which the crack is located. The second term, T, can provide better results in describing the stress field, of the order of 10%, and accounts for the shape and size of the cracked component or specimen. More important, however, is the influence of the T-stress on the stability of crack propagation path. For further details on the crack tip states of stress and displacements in an elastic solid, the readers are referred to text books on fracture mechanics. Stress intensity factors for various boundary value problems can be found in stress intensity factor handbooks.

Theories of fatigue crack propagation

Paris and Erdogn suggested that the growth of cracks resulting from cyclic applied stress may also be described by the stress intensity factor, even though the maximum stress may be much less than the critical stress. They postulated that the rate of growth per cycle of stress ($\mathrm{d}a/\mathrm{d}N$) was a function of the stress intensity range ΔK ($\Delta K = K_{\max} - K_{\min}$) as:

$$\mathrm{d}a/\mathrm{d}N = f(\Delta k) \qquad [5]$$

Figures 4 and **5** show typical $\mathrm{d}a/\mathrm{d}N$ vs ΔK curves of 7075–T6 and 2024–T3 aluminum alloys, respectively. There have been many attempts to describe the linear portion of the sigmoidally shaped fatigue crack

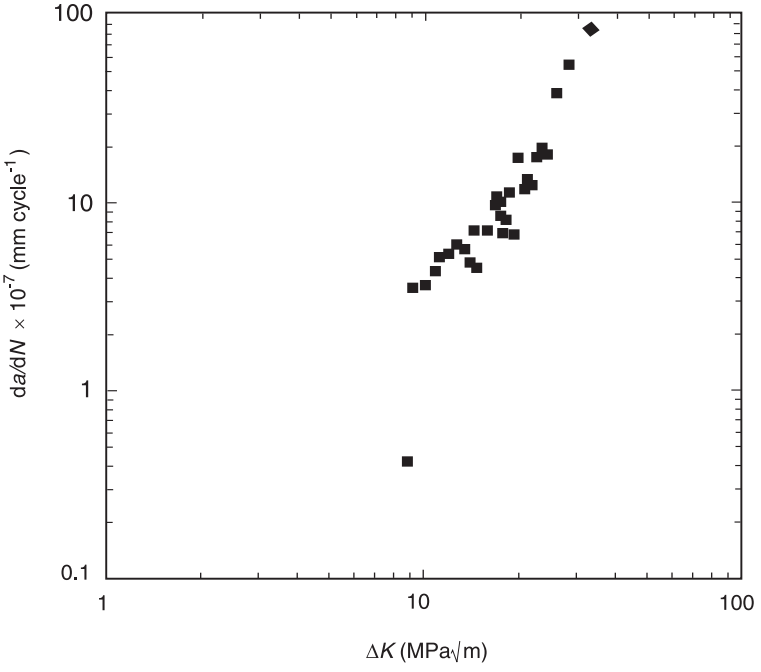


Figure 4 Fatigue crack growth rate in 7075–T6 aluminum alloy.

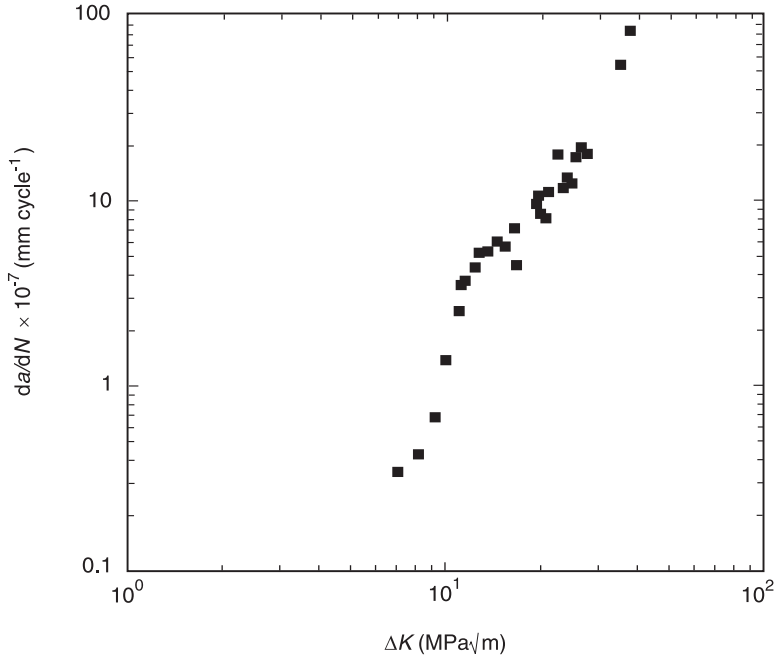


Figure 5 Fatigue crack growth rate in 2024–T3 aluminum alloy.

growth rates in these figures by semi or wholly empirical formula. The simplest explicit form of eqn [5] is:

$$da/dN = C(\Delta k)^m \qquad [6]$$

where C and m are constants. Later work suggested that C was not strictly constant but depended on such parameters as R ($R = K_{min}/K_{max}$), the fracture toughness, K_c, and the threshold stress intensity factor, ΔK_{th}. At high K values, C must depend on K_{max}, since $K_{max} = K_c$ and static failure ($da/dN = \infty$) must occur. At low values of ΔK, C must depend on ΔK_{th}, since no crack growth will occur ($da/dN = 0$) if $\Delta K < \Delta K_{th}$.

Several attempts have been made to establish empirical relationships which incorporate the effect of R and the formula most widely accepted is:

$$\frac{da}{dN} = \frac{C(\Delta K_I)^m}{[I - R]K_{Ic} - \Delta K_I} \qquad [7]$$

Other attempts have been made to incorporate the load ratio, threshold and crack closure effects on fatigue crack growth. The above description of fatigue crack growth is adequate for many practical applications where the stress range undergoes periodic or narrow band random fluctuations.

Fatigue cracks in a material under tension deviate significantly from their normal mode I growth plane under the influence of many factors. Particularly important are: the material, remote multiaxial stresses, interaction of the crack tip with microstructural inhomogeneities, variable amplitude loading in the form of overloads or the embrittling effect of an aggressive environment. Fatigue crack results have shown that the application of a negative biaxial ratio, B, where $B = \sigma_{xx}/\sigma_{yy}$, increases fatigue crack propagation rates. As B becomes more negative, the plastic zone size increases resulting in larger plastic zones and hence higher growth rates.

Even under ideal conditions for a given material, the component geometry, the crack configuration, and the remote load determine the stress field at the crack tip, and subsequently the crack growth rate and the crack path during fatigue crack growth. It should be noted that the T-stress has no influence on the stress intensity factor, K, but it does affect the crack tip plasticity. The data scatter suggests that the inclusion of the T-stress effects in fatigue cracks propagation may allow better correlation with experimental data involving the fracture path and the crack growth rate.

Crack tip plasticity is the cause of a significant difference in the crack growth rate, da/dN, generated under constant and variable amplitude loadings. A single overload, i.e., a tensile overload, during a constant amplitude fatigue test will retard the crack growth rate until the crack can grow out of the large crack tip plastic zone created by the tensile overload. Likewise, a single underload, i.e., compressive overload, will cause a momentary acceleration in the crack growth rate. The notch root radius and plasticity effect on the short fatigue crack relation is

Table 3 Fracture mechanics approach to fatigue

Fracture mechanics

$K_I = \sigma\sqrt{[\pi a f(g)]}$

where: K_I = stress intensity factor
a = crack length
W = width
$f(g)$ = geometric correction factor

At fracture:

$$K_I \rightarrow \begin{bmatrix} K_c & \text{plane stress material property} \\ K_{Ic} & \text{plane strain material property} \end{bmatrix}$$

Critical (final) crack size:

$$a_f = \frac{1}{\pi}\left[\frac{K_I}{\sigma f(g)}\right]^2$$

Plane stress and plane strain relationship:

$$K_c = K_{Ic}\left[1 + \frac{1.4}{t}\left(\frac{K_{Ic}}{\sigma_{yield}}\right)^2\right]$$

where: K_c = plane stress fracture toughness
K_{Ic} = plane strain fracture toughness
t = thickness

Stress intensity factor range, ΔK:

$\Delta K = K_{max} - K_{min} = f(g)\Delta\sigma\sqrt{\pi a}$

Number of cycles to failure:

$$N_f = \int_{a_i}^{a_f} \frac{da}{C(\Delta K)^m} = \frac{2}{(m-2)C[f(g)\Delta\sigma\sqrt{(\pi)}]^m}\left(\frac{1}{a_i^{(m-2)/2}} - \frac{1}{a_f^{(m-2)/2}}\right)$$

where:
$m \neq 2$
a_i = initial crack length
a_f = final crack length

Short crack solution

$K_{short} = 1.12K_t S\sqrt{\pi l}$

where: l = free surface crack length

Long crack solution:

$K_{long} = S\sqrt{\pi a}$

where: $a = l + D$
D = radius of circular hole

Transition crack length estimates: Smith and Miller's

$l_t = 0.13\sqrt{D\rho}$

Dawling's

$$l_t = \frac{D}{[1.12K_t/2f(2g)]^2 O1}$$

where: ρ = actual notch root radius
$f(g)$ = 1.12 = free surface correction factor

Combination approach for total life estimate

Total life = initiation life (N_I) = propagation life (N_p)

$$\underbrace{(a < l_t)}_{\substack{\text{Strain–life} \\ \text{approach}}} \qquad \underbrace{(a > l_t)}_{\substack{\text{Fracture mechanics} \\ \text{approach}}}$$

summarized in **Table 3**. Retardation in crack growth rate will prolong the life of a structure and must be incorporated in the damage tolerant design of an airplane which encounters frequent overloading through wind gusts and maneuvers. The commonly used prediction models for fatigue crack growth under variable loading are those, and their variations, of Wheeler and Willenborg.

Application

The LEFM-based fatigue crack propagation analysis is used to estimate the residual life of a structure component given a crack or crack-like defect. When combined with a nondestructive inspection technique, the propagation analysis provides the only quantitative measure of the safe-life of a cracked component. Propagation analysis cannot be used to estimate the initiation of a fatigue crack in a smoothly finished component under cyclic loading.

Acknowledgments

The authors-would like to thank Ms S. Kunaporn for her assistance in plotting the graphs, and Flow International and the Washington Technology Center for their financial support to Ramulu.

Further Reading

Fuch HO, Stephen RI (1980) *Metal Fatigue in Engineering*. Wiley-Interscience.

Manson SS (1953) *Behavior of Materials under Conditions of Thermal Stress*. NACA TN 2933.

Miner MA (1945) Cumulative damage in fatigue. *Journal of Applied Mechanics, Vol. 12, Transaction of ASME* 67: A159–A164.

Palmgren A (1924) Durability of ball bearings. *ZVDI* 68(14): 339–341.

Paris PC, Erdogan F (1963), A critical analysis of crack propagation laws. *Journal of Basic Engineering, Transaction of ASME* 85: 525–534.

Sines G and Waisman JL (1953) *Metal Fatigue*. McGraw Hill.

Suresh S (1991) *Fatigue of Materials*. London: Cambridge University Press.

Wheeler OE (1972) Spectrum loading and crack growth. *Journal of Basic Engineering, Transaction of ASME* D94(1): 181–186.

Willenborg J, Englew RM, Wood HA (1971) *A Crack Growth Retardation Model Using an Effective Stress Concept*. AFFDL TM-71-1-FBR.

Wöhler A (1860) *Zeitschrift fuer Bauwesen* 10.

Zahavi E (1996) *Fatigue Design*. CRC Press.

FE MODELS

See **DAMPING IN FE MODELS; FINITE ELEMENT METHODS**

FEEDFORWARD CONTROL OF VIBRATION

C R Fuller, Virginia Tech, Blacksburg, VA, USA

Copyright © 2001 Academic Press

doi:10.1006/rwvb.2001.0199

Over the last decade there has been much work concerned with the active control of transient vibrations of flexible structures. The great majority of this work has been concerned with feedback control of large flexible systems at relatively low frequencies. More recently, due to applications in the noise control community, there has been a rise in interest and developments of systems for feedforward control of vibration and associated sound radiation at audio frequencies and steady state excitation. These developments have also been fueled by the recent availability of powerful, cost effective, digital signal processing (DSP) chips and analog to digital and digital to analog signal converters.

The purpose of an active vibration control system is to reduce or modify the vibration of an elastic system in a desired manner by using actuators to apply variable control inputs. The types of actuators used in a control system can be broadly separated into the two types of fully active and semi-active. Fully active actuators are those which can supply mechanical power to the system to be controlled. Semi-active actuators are essentially passive devices which can store or dissipate energy. In this chapter we are only concerned with fully-active control systems and applications.

Feedforward Control

In general, feedforward control systems are used when prior knowledge related to the disturbance or excitation of the structure can be obtained. There are two main cases in which this is possible. In the first case, the excitation is deterministic and a reference signal generated from the disturbance is used to maintain synchronization of the control signal. For example, if the disturbance is a rotating machine, then the excitation will take the form of single frequencies associated with the fundamental and harmonics of the rotating out-of balance forces. In this case, a reference signal can be generated from a tachometer signal related to the machine shaft rotation. In the second case, prior knowledge of the excitation is obtained from the disturbance as it propagates through the structure. In this case, a sensor can be located on the structure, usually upstream of the control inputs, and used to generate a reference signal. In both cases the reference signal is used to generate control signals as discussed next.

The physical components of a single input–single output (SISO) feedforward control system are shown in **Figure 1**. The main components consist of a reference sensor as discussed above, an electrical feedforward controller which modifies the reference signal to obtain the control signal, a control actuator which is applied to the structure to modify its response and an error sensor which is used to monitor the system response and can be used to adapt the electrical controller. The SISO control arrangement is readily extendable to a multiple input–multiple output (MIMO) used for multiple control actuators and error sensors.

Figure 2 shows the feedforward controller arrangement in block diagram form where all the signals are represented by Laplace transforms and the system dynamics are represented by transfer functions. It is clear that the total response of the system can be expressed as:

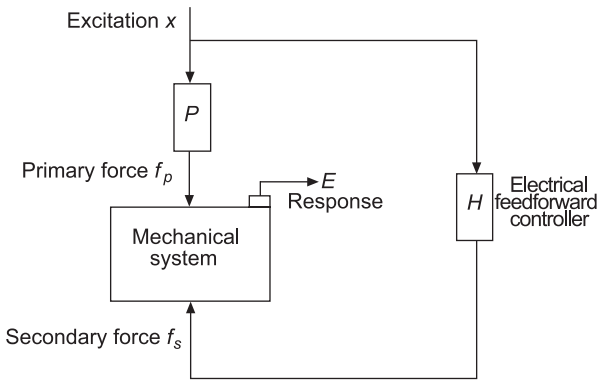


Figure 1 The components of a feedforward control system.

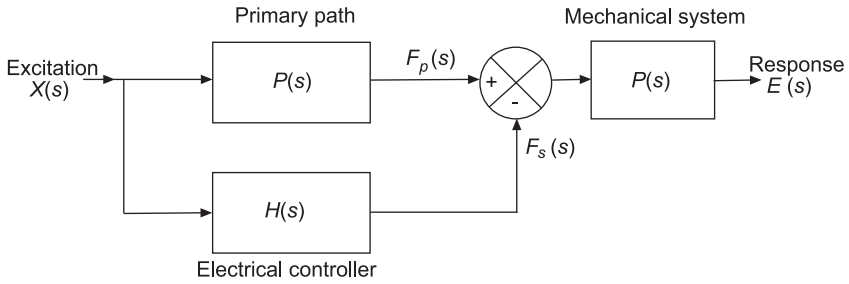


Figure 2 Equivalent block diagram of a feedforward control system.

$$E(s) = G(s)[P(s) - H(s)]X(s) \qquad [1]$$

If the objective is to drive the response of the system to zero at the point where the error sensor is located, then it is trivial to show that the optimal controller response is given by:

$$H(s) = P(s) \text{ when } E(s) = 0 \qquad [2]$$

This result physically means that the transfer function of the controller must exactly match that of the path through the structure of the disturbance to error sensor at all frequencies of interest. In theory it is possible to measure the transfer function, $P(s)$, calculate $H(s)$ and then implement it in a fixed control design. In practice there are a number of problems associated with this approach. The primary problem is that, unlike feedback systems, feedforward control arrangements require a high degree of accuracy in magnitude and phase of the control system to obtain good cancellation. If there are errors in the estimates of the system transfer functions due to noise, for example, or if the system characteristics change slightly due to environmental conditions, for example, then the performance of the fixed control approach degrades rapidly. Hence the most common implementation of feedforward controller relies on adaptive digital filters as the basis of the electrical controller whose characteristics are adapted via the error signal to achieve the required control objective. The most common digital filters used are the finite impulse response (FIR) filters due to their inherent stability.

Figure 3 shows a block diagram of a practical implementation of an adaptive digital feedforward controller. In this figure the physical structural system is not shown and the response of the structural system at the error sensor point is represented by $d(n)$. The reference signal is passed through a digital adaptive control filter $H(q)$ and then applied to the structure via the secondary path represented by $G(q)$. The reference signal $x(n)$ is used in conjunction with the error signal $e(n)$ to compute the control filter coefficients in order to (in this case) minimize the error signal. These control filter coefficients are then copied into the control filter. The most effective way to compute the optimal control filter coefficients is to take advantage of the linear nature of the system and form a control cost function by squaring the amplitude of the error signal. The resultant cost function is a quadratic function in the control filter coefficients and thus has a unique minimum. The values of the control filter coefficients that achieve this minimum are the optimal control filter parameters. In theory, as discussed above, this optimal point could be calculated by accurately measuring the system transfer functions. However, in practice, there are a number of small unknowns such as discretization effects of

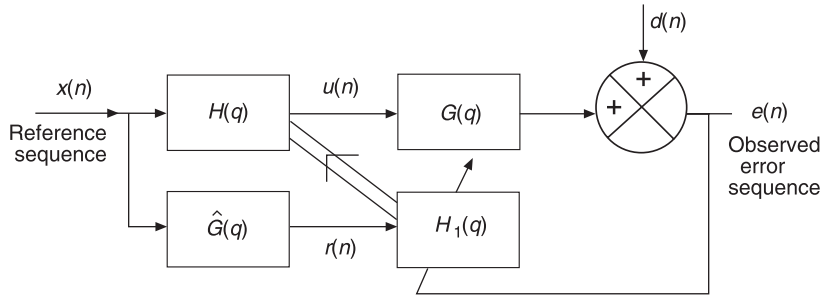


Figure 3 A block diagram of a practical implementation of the filtered-x LMS algorithm in which the normal LMS algorithm is used to update a slave filter $H_1(q)$ which is driven by the filtered reference sequence $r(n)$ obtained by passing the reference sequence $x(n)$ through an estimate $\hat{G}(q)$ of the secondary path $G(q)$. The coefficients of $H_1(q)$ are then copied into the FIR control filter $H(q)$.

the digitizing process and the finite length of the FIR filters which make this impracticable. Different methods have thus been used to find the optimum control point (minimum of the cost function). The most common method is to calculate the local gradient of the cost function at the point on its surface corresponding to the present control point and step down the gradient in an iterative process towards the minimum. In this manner, small measurement errors etc., or system changes are automatically taken care of, as the controller searches for the cost function minimum. This method is termed as an adaptive approach since the control filter coefficients are changed or adapted until the minimum (or near the minimum) is reached. Various algorithms have been developed to implement such gradient approaches. The most common and one of the most effective is know as the filtered-x adaptive LMS algorithm given below in multi-channel form for a feedforward controller in which the coefficients of an array of digital FIR filters whose inputs are K reference signals $x(n)$ and whose outputs $u(n)$ drive M control actuators to minimize the signals at L error sensors. The total number of FIR control filters is MK with I coefficients in each:

$$h_{mki}(n+1) = h_{mki}(n) - \alpha \sum_{l=1}^{L} \hat{r}_{lmk}(n) e_l(n-i) \quad [3]$$

In eqn [3] the ith coefficient of the filter driving the mth actuator is denoted h_{mki} and the time step or sample point of the digital sequence is represented by n. The equation thus represents the new (or adapted) filter coefficients at time $n+1$ in terms of the old filter coefficients at time n plus an incremental term related to the local gradient of the control cost function. This incremental term is composed of a convergence coefficient α which can be used to adjust the adaption step size and thus at the rate of convergence, e_l is the error signal of the lth error sensor and $\hat{\mathbf{r}}_{lmk}$ is the filtered reference signal obtained by passing the reference signal through an estimate of the transfer function from the mth actuator to the lth error sensor. The latter process (from which the algorithm name arises) is necessary to account for the delay from the actuator inputs to the corresponding response at the error sensor and ensure that the gradient estimate points in the correct direction. The characteristics of the fixed filters used to prefilter the reference signal are usually measured in a system identification process before the control is turned on. The most common method is to drive the control actuators without the disturbance present and use a similar adaptive LMS loop around the actuator to sensor path. On converging, the coefficients of the adaptive filters of this system identification loop can be copied over to the fixed filters for reference signal filtering. If it is not possible to turn off the disturbance or for on-line system identification, a low level white noise signal can be injected as a probe signal.

Controller performance

There are a number of parameters that effect the performance of the controller in terms of achieving the desired control condition. For the rest of this article, we will assume the desired control condition is minimization of the error signals. As discussed previously a feedforward controller is built around a reference signal which has prior information related to the response of the system to the disturbance. Since the reference signal is used to form the control signals, it is important that the response of the system at the error points be highly correlated with the reference signal. This correlation is likely to be reduced by the presence of such factors as noise on the error sensors, etc. In fact, the maximum achievable attenuation of the controller can be estimated by measuring the coherence between the reference signal and the error signal and using the following relation:

$$\text{Attenuation(dB)} = -10 \log \left(1 - \gamma_{xd}^2\right) \quad [4]$$

where γ_{xd}^2 is the measured coherence between the reference and disturbance signals.

A second important parameter is the delay in the control path, an important parameter which affects what is known as the causality of the controller. This aspect is important when a reference sensor is used to pick up information about the disturbance upstream of where the control inputs are applied. There will be a time of flight (or delay) for the disturbance field from the position of the reference sensor to the location of the control inputs. Correspondingly there will be a delay in the control path, from picking up the reference signal, passing it through the digital controller and associated antialiasing and smoothing filters to the generation of the control field in the structure at the control actuator locations. If the delay through the control path is longer than the disturbance path, then the system is acausal. If the disturbance field is random and completely unpredictable, then an acausal controller will result in no attenuation even if the coherence is unity. In essence, the control signal has arrived too late to be able to interact with the part of the random disturbance that generated the reference signal and is thus unable to affect it. The other extreme is when the disturbance is perfectly predictable, as in the case of pure sinusoidal oscillations. In this case, delay through the control path is unimportant as it does not matter if the control signal is many cycles

ahead or behind the disturbance signal, since the wave has the same predictable sinusoidal shape through the complete time axis. In this case, with unity coherence, total attenuation is possible. In practice, even random disturbances are predictable to some degree due to finite bandwidths, dynamic filtering through the system response, etc. In this case, even if the control system is acausal, some attenuation will result due to the predictability of the response. One approach to reduce loss of performance due to acausality is to increase the sampling frequency of the digitizing process, thus reducing the delay through the FIR filters, etc. However, for a constant impulse, length also increases the number of coefficients in the FIR filters, adding increased computational load to the DSP.

A third important parameter that affects controller performance is the magnitude of the convergence coefficient α used in the filtered-x algorithm. As discussed previously, larger values of α will result in larger adaption steps and faster convergence. However this adaption loop can also be viewed as a performance feedback loop in that information from the error sensors is fed back to adapt the control filters. Consequently, as in all feedback systems, instability is a significant possibility depending on feedback gain. Thus, in practice, there is a maximum value of α which can be used to adapt the control filters and still keep the control system stable. This value can be determined by the eigenvalues of the autocorrelation matrix of the filtered reference signals. The largest stable value of α is approximately given by:

$$\alpha_{\max} \approx \frac{1}{I\bar{r}^2} \qquad [5]$$

where I is the number of coefficients in the adaptive filter and $\bar{r}^2$ is the mean square value of the filtered reference signal.

A fourth important parameter is the degree of feedback of the control signal onto the reference signal. When the reference signal is generated from a correlated variable such as shaft rotation, then this is not an issue. However, if a reference sensor is located directly on the structure, then this situation may be important if there is significant control signal present in the reference signal. In this case it is necessary to measure the transfer function of the actuator-to-reference sensor feedback path. A second feedback filter is then implemented in the controller and with the same response as the feedback path. Its output is then subtracted from the detected reference signal to remove the feedback signal. As for the fixed reference signal filters, the feedback filter characteristics can be measured before the control is turned on or on-line with a low level white noise probe signal in conjunction with another adaptive LMS loop. In some applications, the degree of feedback is limited by the physics of the application. Alternatively, it is also possible in some cases to use a directional reference sensor to eliminate the response due to the control actuator.

Other factors that affect controller performance are the resolution of the FIR filters and actuator control authority. For a single sinusoid, it is only necessary to have two coefficients in each filter. However, for broadband noise for good performance, it is important to have enough coefficients to model the detail and length of the system impulse response which is excited by the disturbance. For example, a highly resonant system will require a long FIR filter to model the length of the impulse response. Likewise if the broadband disturbance excites many modes, then many coefficients with short tap delays will be needed to represent the rapidly changing nature of the impulse response of the filter. It is tempting then to use as high a sampling rate as possible in conjunction with as longer filters as possible to achieve good attenuation. However, for a MIMO system using this approach, the number of coefficients required to be adapted rises rapidly and soon reaches the computational limit of the DSP system. By superposition it can be seen that the control inputs must be capable of generating control field response levels identical to the disturbance field at the error points. In applications on structures with low mobility at low frequencies, this can place a severe requirement on the control actuators. Often the actuators are simply unable to generate enough level, particularly at low frequencies, and this limits the amount of attenuation achieved. Various forms of actuators are discussed in **Actuators and smart structures**. Likewise, in order to be controllable, the response of the system needs to be observable. Thus the performance of the controller can be limited by how well the sensors measure the variables to be controlled. Different sensors for active vibration control systems are discussed in **Active vibration suppression**.

Example Applications

In this section, three applications of feedforward control of vibration are briefly discussed. These applications were chosen to illustrate the various aspects of the controller and its physical implementation which are important or a challenge under the different arrangements. There are many other uses and applications of feedforward control of vibration and for information on these, the interested reader is referred to the list of further reading at the end of this chapter.

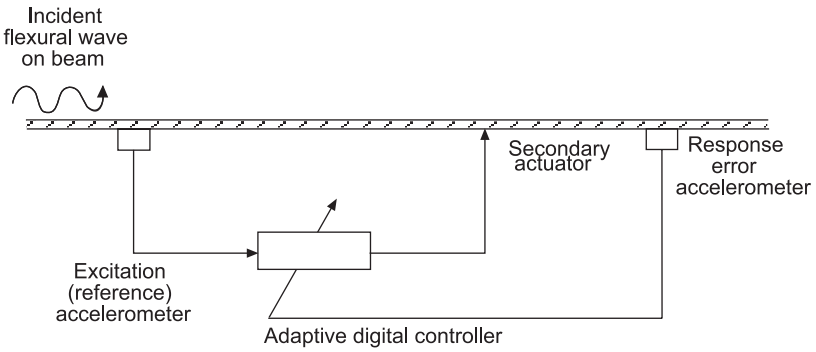


Figure 4 An adaptive system for the active control of broadband flexural disturbances on a beam.

Control of Flexural Waves in Beams

In many applications it is desired to control vibrational waves traveling down long slender structures. The struts that support a helicopter gear box are a good example. By application of feedforward control to the struts, it is possible to isolate vibrations from the gearbox traveling down the struts to the helicopter fuselage. **Figure 4** shows a schematic arrangement of a feedforward control system designed to suppress flexural waves in thin beams. In this case, the reference signal is generated by a single accelerometer located on the beam. A single control input is applied to the beam downstream of the reference sensor by an electromagnetic actuator. An error sensor is located further downstream of the beam and used to adapt the digital controller.

The beam was anechoically terminated downstream of the error sensor ensuring only positive traveling waves (to the right) occur in the system. A disturbance which generated broadband random flexural waves was applied to the left end of the beam. This example illustrates the aspects which influence the ease and difficulty of applying feedforward control. Since only flexural waves (due to the source) travel in the beam, then total vibrational reduction is theoretically possible with a SISO controller. Thus the application is relatively simple in a spatial sense and as a result has a low requirement in terms of channels of control. In this case global reductions (throughout an extended area or volume) are readily achievable with a SISO system. However, the application is complicated in the temporal sense in that the excitation is random, so causality in the control path and lengths of the FIR filters are important issues. For the controller of this example, the delay through the control path was measured to be approximately 2.4 ms. The beam used in the test was manufactured from steel with a thickness of 6 mm. Flexural waves in beams are dispersive, that is, their phase and group velocity vary with frequency (see **Beams**). At low frequencies, the waves travel relatively slowly. As the frequency is increased, the waves travel with increasing velocity. For the beam considered here, the delay through the beam from the reference sensor to the control actuator is less than the control path at 800 Hz. Furthermore, the reference sensor will not only pick up the disturbance field but also the control response traveling in the negative direction. For good performance, the resultant feedback from the control actuator must be compensated for, as discussed previously.

Figure 5 shows the attenuation achieved in experimental testing. In this case, the control paradigm used was the feedforward filtered-x with feedback removal. Note that there are large attenuations of the output of the error sensor between 200 and 800 Hz. The fall off in performance above 800 Hz is due to the control system becoming acausal as discussed previously. A measurement of the coherence between the reference and error sensor revealed that the coherence is low, below 200 Hz, due to external sources of vibration transmitted through the beam suspension system at various points. As outlined above, a low value of coherence between the reference and error signal will result in poor attenuation.

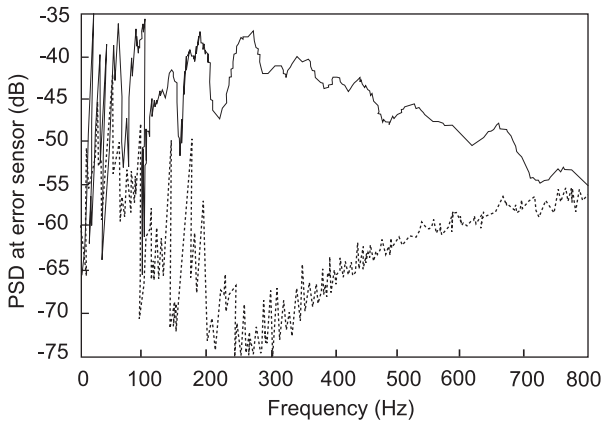


Figure 5 The power-spectral density at the response error sensor on the beam illustrated in **Figure 4** before control (— —) and after the adaptive controller has converged (- - -).

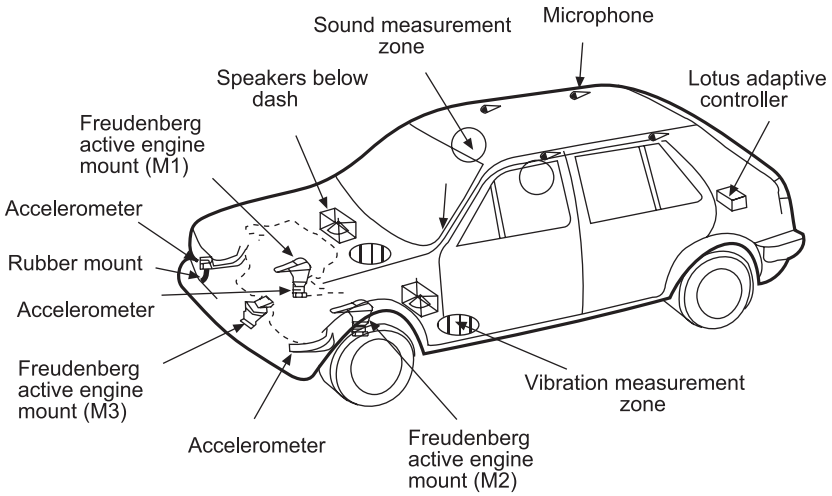


Figure 6 The installation of the active mounts in a Volkswagen Golf GTI™ 16-valve vehicle.

Isolation of Engine-Induced Vibrations in an Automobile Body

The second example discusses isolation of engine vibrations from the body structure of an automobile. Since the disturbance source is the automobile engine, the disturbance vibrations are predominantly single frequencies well correlated with the rotation of the engine crankshaft. This application is thus simplified in the temporal sense in that a reference signal can easily be generated from a crankshaft pick-up and thus feedback of control signals onto the reference sensor is not an issue. In addition, since the disturbance field is dominated by peaks at the engine harmonics, it is very predictable and thus delay and the associated causality of the control path are not issues. However, this application is complicated in the spatial sense in that there are many paths for the engine vibration to transmit through to the automobile body and the body structure is well distributed and complex. Thus, in order to achieve global reductions of the body, multiple control actuators and error sensors are needed. **Figure 6** shows a schematic arrangement of a feedforward control approach designed to control engine-induced vibrations in the body of a Volkswagen Golf GTI™ with a four-cylinder 16-valve engine. In this case the control actuators are co-located and integrated with the passive engine mounts in a device called an active engine mount. The active engine mount enables control inputs to be applied to the car in the load path of the standard rubber passive isolation mount.

Three active engine mounts are used to replace the standard passive mounts. Error sensors in the form of accelerometers were located on the chassis side of the engine mounts and two additional error sensors were located on the engine front cross member. The control algorithm used was a MIMO version of the filtered-x LMS algorithm.

Figure 7 presents the performance of the control system in vibration measurement zone shown in **Figure 6**. The results of **Figure 7** are vibration levels at the second-order (twice crankshaft speed) frequency. Significant reductions are demonstrated. In addition, the controller demonstrates the ability to adapt to a changing system. Variations in the engine speed resulted in changes in the disturbance frequencies and thus response of the vehicle at the error sensor locations. This change in dynamics will result in the minimum of the cost function moving to a new point. The adaptive controller then automatically locates

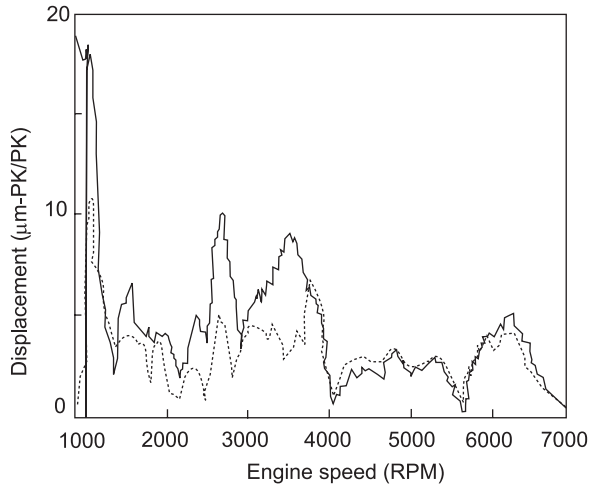


Figure 7 Experimental results illustrating the effect of active control of engine vibrations produced in the Volkswagen Golf GTI™ 16-valve vehicle shown in **Figure 6**. Three active mounts were used and the results show the displacements measured in the driver's footwell produced by second-order engine vibrations: — —, before active control; - - -, after active control.

the new minimum using the gradient search approach discussed above.

Control of Sound Radiation from Vibrating Structures

In this last example we discuss the control of sound radiation from structures. As is well known (see **Vibration generated sound: fundamentals**), vibrating structures radiated sound due to their out-of-plane motion. Thus it is possible to actively reduce the sound radiation by applying control inputs to the structure to globally minimize its vibration in what is called an active vibration control approach (AVC). However, it is also well known that, well below the structural critical frequency, certain structural modes radiate sound much more efficiently than others. For example the $(1,\ 1)$ mode of a simply supported plate is monopole like and is thus an efficient radiator. The $(2,\ 1)$ mode however is dipole like and thus is an inefficient radiator. A more efficient control strategy for minimizing structurally radiated sound is to only control the efficient radiating modes. This can be achieved by applying control actuators to the structure and using error sensors that observe the radiated sound or only the efficient structural modes. Such an approach is called active structural acoustic control (ASAC). The easiest form of error sensors for an ASAC approach is of course microphones located in the radiated far field and enough error sensors are needed to ensure global control. In some cases this is impracticable and then specially designed sensors which are located on the structure but only observe the structural vibrations that efficiently radiate sound are used. Often the sensing material is a piezoelectric material (see **Piezoelectric materials and continua**) such as the polymer PVDF which can be used as a distributed sensor. PVDF sensors for ASAC range from simple strips which only observe the odd–odd plate modes, to more sophisticated volume velocity sensors which directly observe the plate volume velocity. Other ASAC sensor approaches employ arrays of accelerometers whose outputs are processed to obtain the structural wavenumber information. Once this is obtained, only signals at wavenumber values inside the plate supersonic circle (radiating components) are used as error signals.

Figure 8 presents a schematic of an experimental ASAC system designed to minimize sound radiation from a baffled simply supported rectangular plate. The plate is excited by a point force shaker driven with a single frequency disturbance. Two piezoceramic actuators were bonded to the plate to provide active control inputs to the structure. Two different sensing arrangements were evaluated; either an array of three microphones in the radiated sound field or two PVDF strips glued across the plate in each coordinate axis. Since the PVDF strip sensors completely covered the plate in each coordinate, they only both gave outputs for the odd–odd modes $(1, 1\ 3, 1, \text{etc.})$ which were the efficient modes in terms of sound radiation. The PVDF strips thus represented a simple structural sound radiation sensor. **Figure 8** also shows the feedforward control arrangement. The reference signal was taken directly from the signal generator driving the disturbance shaker. This application is thus straightforward in a temporal sense, since causality and control feedback are not an issue. However, the application is difficult in that significant control design in terms of the location of the control actuators and error sensors

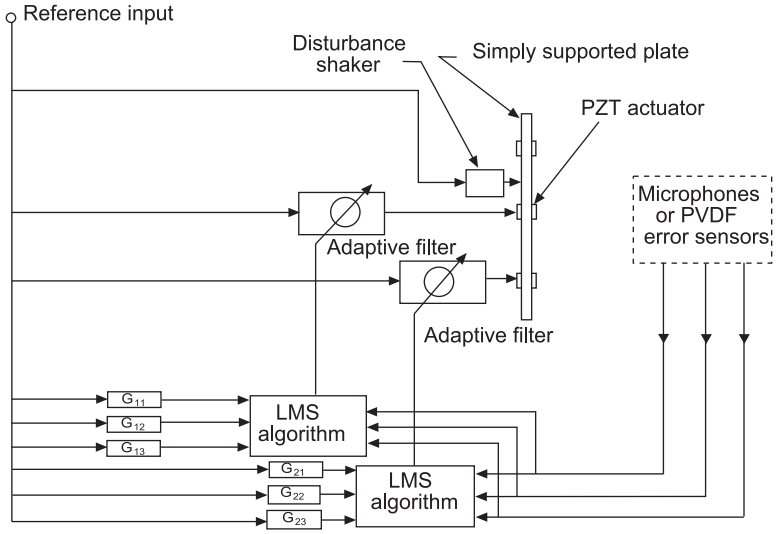


Figure 8 Schematic layout of controller and test rig for an ASAC experiment.

needs to be carried out in order to ensure global control. **Figure 8** shows the adaptive FIR filters used to derive the control signal and represents the least mean squares (LMS) algorithm used to adapt the FIR filters in block diagram form. Also shown are the fixed filters used to prefilter the reference signal before it is used in the filtered-x update equation.

Figure 9 presents experimental results for the baffled simply supported plate excited by a frequency of 349 Hz, which is near the (3,1) mode resonance. The results are the radiated sound field pressure level measured with a polar traversing microphone. When three microphones are used as error sensors, global reductions of the order of 20 dB are evident. Comparison tests using an AVC system reveal that direct control of the plate vibration requires many more control actuators to achieve the same level of global control. When the microphone error sensors are replaced with the PVDF strip structural sensors, global control is still evident but to reduced degree, since the PVDF strips are only approximate radiation sensors. The results for the PVDF sensors do however demonstrate that it is possible to integrate the sound radiation sensors directly into the structure. The resultant control system consisting of a MIMO adaptive, nonmodel based controller in conjunction with structurally integrated control actuators and sensor is part of the rapidly growing field known as smart or intelligent structures.

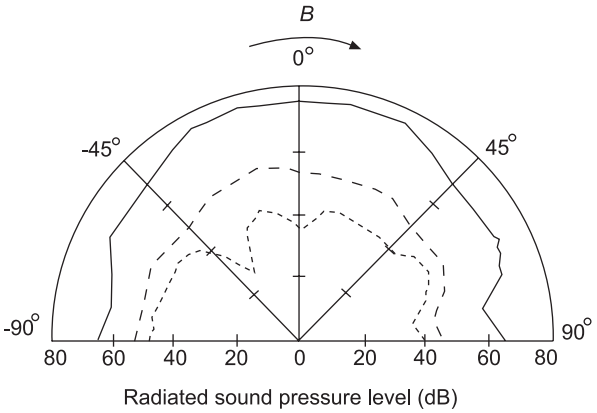


Figure 9 Measured radiation directivity, $f = 349$ Hz: — , uncontrolled; – –, controlled with two PVDF sensors; - - - - -, controlled with three error microphones.

Acknowledgement

The author gratefully acknowledges input for this chapter from Professor S. J. Elliott and P.A. Nelson of the ISVR, University of Southampton, UK.

See also: **Active vibration suppression**; **Actuators and smart structures**; **Adaptive filters**; **Beams**; **Piezoelectric materials and continua**; **Vibration generated sound**, Fundamentals.

Further Reading

Fuller CR, Elliott SJ, Nelson PA (1996) *Active Control of Vibration*. London: Academic Press.

Nelson PA, Elliott SJ (1992) *Active Control of Sound*. London: Academic Press.

FFT METHODS

See **TRANSFORM METHODS**

FILTERS

See **ADAPTIVE FILTERS; DIGITAL FILTERS; OPTIMAL FILTERS**

FINITE DIFFERENCE METHODS

S S Rao, University of Miami, Coral Gables, FL, USA

Copyright © 2001 Academic Press

doi:10.1006/rwvb.2001.0002

Introduction

The ordinary derivative of a function $f(x)$ in differential calculus is defined as:

$$\frac{\mathrm{d}f}{\mathrm{d}x} = \lim_{\Delta x \to 0} \frac{\Delta f}{\Delta x} = \lim_{\Delta x \to 0} \frac{f(x + \Delta x) - f(x)}{\Delta x} \qquad [1]$$

where $\mathrm{d}f/\mathrm{d}x$ is not a ratio of the quantities $\mathrm{d}f$ and $\mathrm{d}x$, but merely denotes the limit that the true ratio $\Delta f/\Delta x$ approaches. On the other hand, the finite difference derivative is defined as:

$$\frac{\Delta f}{\Delta x} = \frac{f(x+\Delta x) - f(x)}{\Delta x} \quad [2]$$

where $\Delta f/\Delta x$ is the ratio of the quantities (finite increments) Δf and Δx. Eqn [2], in fact, denotes the forward finite difference formula for the first derivative of f.

The equation of motion of a vibrating system is in the form of an ordinary differential equation (for a discrete system) or a partial differential equation (for a continuous system). In the finite difference method, the solution domain, over which the equation of motion is to be satisfied, is replaced by a finite number of points known as the mesh or grid points. Then the equation of motion is written at each grid point by replacing the derivatives in the equation of motion by their equivalent finite difference derivatives. This implies that the governing equation is satisfied only approximately at the grid points of the solution domain. The boundary and initial conditions are also replaced by the relevant finite difference equations. Thus the application of finite differences reduces a differential equation into a system of algebraic equations, which can be solved in a simple manner.

Finite Difference Formulas

Three types of finite difference formulas, namely, the forward, backward, and central difference formulas, can be used to approximate any derivative. We consider the derivation of all three types of formulas for the first and second derivatives in this section.

The Taylor's series expansion of the function $f(x)$ at $x + \Delta x$ is given by (**Figure 1A**):

$$f(x+\Delta x) = f(x) + \Delta x \left.\frac{df}{dx}\right|_x + \frac{1}{2}(\Delta x)^2 \left.\frac{d^2 f}{dx^2}\right|_x + \cdots \quad [3]$$

By deleting terms involving second and higher-order derivatives of function $f(x)$, eqn [3] becomes:

$$f(x+\Delta x) = f(x) + \Delta x \left.\frac{df}{dx}\right|_x \quad [4]$$

which yields the first forward difference derivative at x as:

$$\left.\frac{df}{dx}\right|_x = \frac{f(x+\Delta x) - f(x)}{\Delta x} \quad [5]$$

For the backward difference formula, we express the Taylor's series expansion of $f(x)$ at $x - \Delta x$ as (**Figure 1B**):

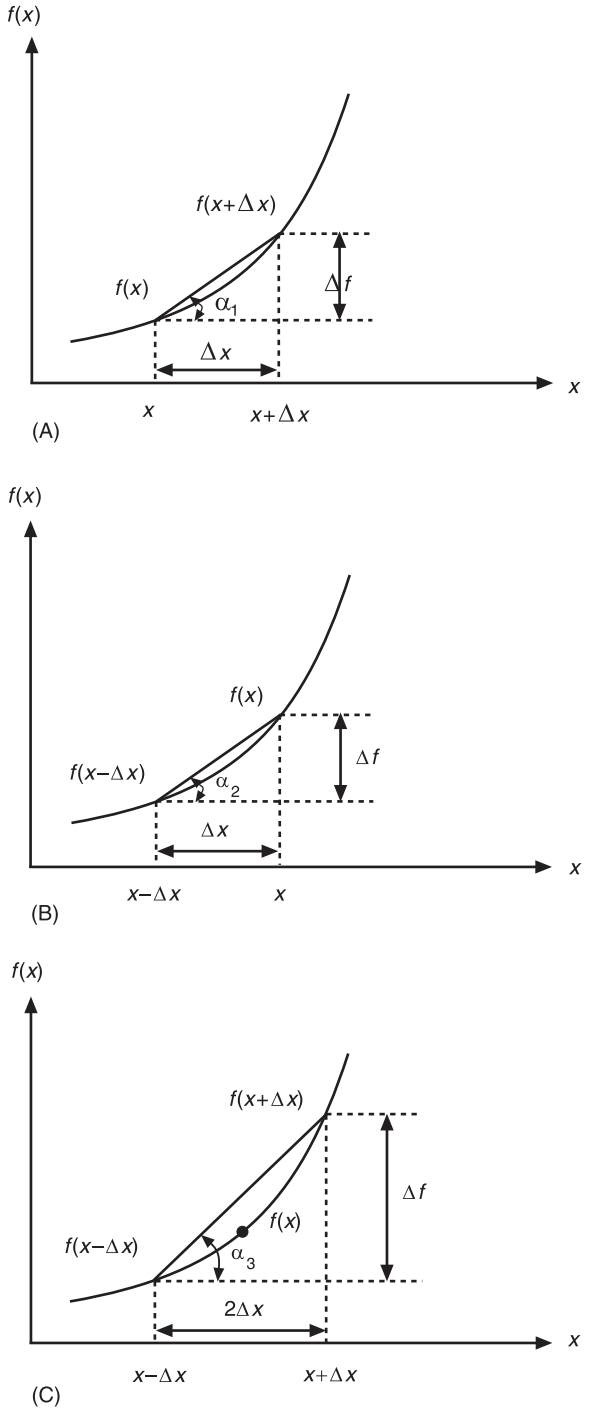


Figure 1 (A) Forward differences; (B) backward differences; (C) central differences.

$$f(x-\Delta x) = f(x) - \Delta x \left.\frac{df}{dx}\right|_x + \frac{1}{2}(\Delta x)^2 \left.\frac{d^2 f}{dx^2}\right|_x - \cdots \quad [6]$$

By retaining only the first two terms on the right-hand side, eqn [6] becomes:

$$f(x+\Delta x) = f(x) - \Delta x \left.\frac{df}{dx}\right|_x \quad [7]$$

from which the first backward difference derivative at x can be obtained as:

$$\left.\frac{df}{dx}\right|_x = \frac{f(x) - f(x-\Delta x)}{\Delta x} \quad [8]$$

To derive the central difference formula, we subtract eqn [7] from eqn [4] to obtain:

$$\begin{aligned} &f(x+\Delta x) - f(x-\Delta x) \\ &= f(x) + \Delta x \left.\frac{df}{dx}\right|_x - f(x) + \Delta x \left.\frac{df}{dx}\right|_x \end{aligned} \quad [9]$$

Rearranging eqn [9], we obtain the first central difference derivative at x as:

$$\left.\frac{df}{dx}\right|_x = \frac{f(x+\Delta x) - f(x-\Delta x)}{2\Delta x} \quad [10]$$

To derive the forward difference formula for the second derivative, we use eqn [5] for the first derivative:

$$\left.\frac{d}{dx}\left(\frac{df}{dx}\right)\right|_x = \frac{(df/dx)(x+\Delta x) - (df/dx)(x)}{2\Delta x} \quad [11]$$

with:

$$\frac{df}{dx}(x) = \frac{f(x+\Delta x) - f(x)}{\Delta x} \quad [12]$$

and:

$$\frac{df}{dx}(x+\Delta x) = \frac{f(x+2\Delta x) - f(x+\Delta x)}{\Delta x} \quad [13]$$

Using eqns [12] and [13], eqn [11] gives the forward difference formula for the second derivative as:

$$\left.\frac{d^2f}{dx^2}\right|_x = \frac{f(x+2\Delta x) - 2f(x+\Delta x) + f(x)}{(\Delta x)^2} \quad [14]$$

By proceeding in a similar manner, the backward and central formulas for the second derivative can be derived as:

$$\frac{d^2f}{dx^2}(x) = \frac{f(x) - 2f(x-\Delta x) + f(x-2\Delta x)}{(\Delta x)^2} \quad [15]$$

$$\frac{d^2f}{dx^2}(x) = \frac{f(x+\Delta x) - 2f(x) + f(x-\Delta x)}{(\Delta x)^2} \quad [16]$$

Note that eqns [14]–[16] assume that the mesh points are equally spaced along the x-axis as shown in **Figure 2**. Some of the commonly used finite difference formulas are given in **Table 1** along with the order of magnitude of the truncation error involved. Note that $f_i = f(x_i)$, $f_i' = (df/dx)(x_i)$ ... is implied in the formulas given in **Table 1**. It is possible to derive higher-accuracy finite difference formulas. A collection of higher-accuracy forward, backward, and central finite difference formulas is given in **Table 2**.

Finite Difference Operators

If the values of f are known at equally spaced points $x_i = x_0 + ih$, $i = 0, 1, 2 \ldots n$, the various finite difference formulas can be conveniently expressed using the following operators:

$$Ef(x_i) = f(x_i + h)$$
(E = shift operator)

Table 1 Common finite difference formulas

Type of approximation	*Formula*	*Truncation error*
Forward differences	$f_i' = (f_{i+1} - f_i)/(\Delta x)$	$O(\Delta x)$
	$f_i'' = (f_{i+2} - 2f_{i+1} + f_i)/(\Delta x)^2$	
	$f_i''' = (f_{i+3} - 3f_{i+2} + 3f_{i+1} - f_i)/(\Delta x)^3$	
	$f_i'''' = (f_{i+4} - 4f_{i+3} + 6f_{i+2} - 4f_{i+1} + f_i)/(\Delta x)^4$	
Backward differences	$f_i' = (f_i - f_{i-1})/(\Delta x)$	$O(\Delta x)$
	$f_i'' = (f_i - 2f_{i-1} + f_{i-2})/(\Delta x)^2$	
	$f_i''' = (f_i - 3f_{i-1} + 3f_{i-2} - f_{i-3})/(\Delta x)^3$	
	$f_i'''' = (f_i - 4f_{i-1} + 6f_{i-2} - 4f_{i-3} + f_{i-4})/(\Delta x)^4$	
Central differences	$f_i' = (f_{i+1} - f_{i-1})/(2\Delta x)$	$O(\Delta x^2)$
	$f_i'' = (f_{i+1} - 2f_i + f_{i-1})/(\Delta x)^2$	
	$f_i''' = (f_{i+2} - 2f_{i+1} + 2f_{i-1} - f_{i-2})/(2(\Delta x)^3)$	
	$f_i'''' = (f_{i+2} - 4f_{i+1} + 6f_i - 4f_{i-1} + f_{i-2})/(\Delta x)^4$	

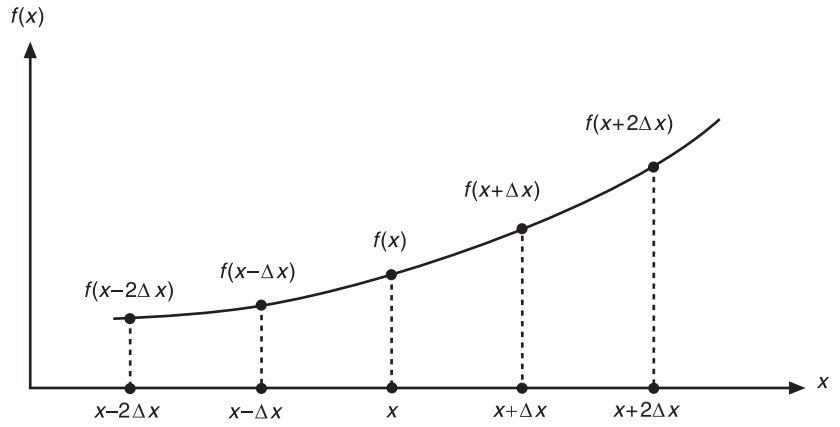


Figure 2

Table 2 Higher-order finite difference formulas

Type of formula	*Formula*	*Truncation error*
Forward differences	$f_i' = (-f_{i+2} + 4f_{i+1} - 3f_i)/(2(\Delta x))$	$O(\Delta x)^2$
	$f_i'' = (-f_{i+3} + 4f_{i+2} - 5f_{i+1} + 2f_i)/(\Delta x)^2$	
	$f_i''' = (-3f_{i+4} + 14f_{i+3} - 24f_{i+2} + 18f_{i+1} - 5f_i)/(2(\Delta x)^3)$	
	$f_i'''' = (-2f_{i+5} + 11f_{i+4} - 24f_{i+3} + 26f_{i+2} - 14f_{i+1} + 3f_i)/(\Delta x)^4$	
Backward differences	$f_i' = (3f_i - 4f_{i-1} + f_{i-2})/(2(\Delta x))$	$O(\Delta x^2)$
	$f_i'' = (2f_i - 5f_{i-1} + 4f_{i-2} - f_{i-3})/(\Delta x)^2$	
	$f_i''' = (5f_i - 18f_{i-1} + 24f_{i-2} - 14f_{i-3} + 3f_{i-4})/(2(\Delta x)^3)$	
	$f_i'''' = (3f_i - 14f_{i-1} + 26f_{i-2} - 24f_{i-3} + 11f_{i-4} - 2f_{i-5})/(\Delta x)^4$	
Central differences	$f_i' = (-f_{i+2} + 8f_{i+1} - 8f_{i-1} + f_{i-2})/(12(\Delta x))$	$O(\Delta x^4)$
	$f_i'' = (-f_{i+2} + 16f_{i+1} - 30f_i + 16f_{i-1} - f_{i-2})/(12(\Delta x)^2)$	
	$f_i''' = (-f_{i+3} + 8f_{i+2} - 13f_{i+1} + 13f_{i-1} - 8f_{i-2} + f_{i-3})/(8(\Delta x)^3)$	
	$f_i'''' = (-f_{i+3} + 12f_{i+2} - 39f_{i+1} + 56f_i - 39f_{i-1} + 12f_{i-2} - f_{i-3})/(6(\Delta x)^4)$	

$$\Delta f(x_i) = f(x_i + h) - f(x_i)$$
(Δ = forward difference operator)

$$\nabla f(x_i) = f(x_i) - f(x_i - h)$$
(∇ = backward difference operator)

$$\delta f(x_i) = f\left(x_i + \frac{h}{2}\right) - f\left(x_i - \frac{h}{2}\right)$$
(δ = central difference operator)

$$\mu f(x_i) = \frac{1}{2}\left\{f\left(x_i + \frac{h}{2}\right) + f\left(x_i - \frac{h}{2}\right)\right\}$$
(μ = averaging operator)

The repeated application of the difference operators lead to the following higher-order differences:

$$E^n f(x_i) = f(x_i + nh)$$
$$\Delta^n f(x_i) = \Delta^{n-1} f_{i+1} - \Delta^{n-1} f_i = \sum_{k=0}^{n} (-1)^k \frac{n!}{k!(n-k)!} f_{i+n-k}$$

where $f_i = f(x_i)$. The forward, backward, and central differences of various orders can be conveniently computed using **Tables 3–5**. It is to be noted that the differences $\Delta^k f_0$, $\nabla^k f_3$ and $\delta^{2k} f_2$ lie on a straight line sloping downward, upward, and horizontally, respectively, to the right. It can be verified that:

$$\Delta f_i = \nabla f_{i+1} = \delta f_{i+(1/2)}$$
$$\Delta = E - 1,\ \nabla = 1 - E^{-1},\ \delta = E^{1/2} - E^{-1/2}$$
$$\mu = \frac{1}{2}\left(E^{1/2} + E^{-1/2}\right)$$

The relationships among the various finite difference operators are indicated in **Table 6**.

Table 3 Forward difference table

x	$f(x)$	Δf	$\Delta^2 f$	$\Delta^3 f$
x_0	f_0			
		Δf_0		
x_1	f_1		$\Delta^2 f_0$	
		Δf_1		$\Delta^3 f_0$
x_2	f_2		$\Delta^2 f_1$	
		Δf_2		
x_3	f_3			

Table 4 Backward difference table

x	$f(x)$	∇f	$\nabla^2 f$	$\nabla^3 f$
x_0	f_0			
		∇f_1		
x_1	f_1		$\nabla^2 f_2$	
		∇f_2		$\nabla^3 f_3$
x_2	f_2		$\nabla^2 f_3$	
		∇f_3		
x_3	f_3			

Table 5 Central difference table

x	$f(x)$	δf	$\delta^2 f$	$\delta^3 f$	$\delta^4 f$
x_0	f_0				
		$\delta f_{1/2}$			
x_1	f_1		$\delta^2 f_1$		
		$\delta f_{3/2}$		$\delta^3 f_{3/2}$	
x_2	f_2		$\delta^2 f_2$		$\delta^4 f_2$
		$\delta f_{5/2}$		$\delta^3 f_{5/2}$	
x_3	f_3		$\delta^2 f_3$		
		$\delta f_{7/2}$			
x_4	f_4				

Single-Degree-of-Freedom System – Forward Finite Difference Method

The equation of motion of a spring-mass-damper system is given by:

$$m\frac{\mathrm{d}^2x}{\mathrm{d}t^2} + c\frac{\mathrm{d}x}{\mathrm{d}t} + kx = f(t) \qquad [17]$$

where $f(t)$ is the force applied to the mass. If the solution of eqn [17] is desired over a period of time τ, we divide the interval τ into n equal parts so that $\Delta t = h = \tau/n$ with $t_0 = 0,\ t_1 = \Delta t,\ t_2 = 2\Delta t,\ \ldots,$ $t_n = n\Delta t = \tau$. For a satisfactory solution, the time step Δt is to be selected to be smaller than a critical time step Δt_{cri}. Using forward difference formulas for the first and second derivatives, eqn [17] can be written at grid point i (time t_i) as:

$$m\left[\frac{x_{i+2} - x_{i+1} + x_i}{(\Delta t)^2}\right] + c\left[\frac{x_{i+1} - x_i}{\Delta t}\right] + kx_i = f_i \qquad [18]$$

where:

$$x_i = x(t_i = i\Delta t), \quad x_{i+1} = x(t_{i+1} = t_i + \Delta t),$$
$$x_{i+2} = x(t_{i+2} = t_i + 2\Delta t) \text{ and } f_i = f(t_i)$$

Eqn [18] can be rearranged to obtain the relationship:

$$x_{i+2} = x_{i+1}\left(1 - \frac{c}{m}\Delta t\right) + x_i\left[-1 + \frac{c}{m}\Delta t - \frac{k}{m}(\Delta t)^2\right] + \frac{(\Delta t)^2}{m}f_i \qquad [19]$$

which can be used to find x_{i+2} once x_i, x_{i+1} and f_i are known. Since the initial conditions of the system are specified as $x(t=0) = x_0 = \dot{\bar{x}}_0$ and $\mathrm{d}\dot{x}(t=0) = \mathrm{d}\dot{\bar{x}}_0$, eqn [19] cannot be used directly to start the procedure with $i = 0$. For this we apply the equation of motion at $t = 0$:

$$m\ddot{x}_0 + c\dot{x}_0 + kx_0 = f_0 \qquad [20]$$

which upon substitution of the known initial conditions, yields:

$$\ddot{x}_0 = \frac{1}{m}\left(f_0 - c\dot{\bar{x}}_0 - k\bar{x}_0\right) \qquad [21]$$

Table 6 Relationship between finite difference operators

	E	Δ	∇	δ
E	E	$\Delta + 1$	$(1-\nabla)^{-1}$	$1 + \frac{1}{2}\delta^2 + \delta\sqrt{(1 + \frac{1}{4}\delta^2)}$
Δ	$E - 1$	Δ	$(1-\nabla)^{-1} - 1$	$\frac{1}{2}\delta^2 + \delta\sqrt{(1 + \frac{1}{4}\delta^2)}$
∇	$1 - E^{-1}$	$1 - (1+\Delta)^{-1}$	∇	$-\frac{1}{2}\delta^2 + \delta\sqrt{(1 + \frac{1}{4}\delta^2)}$
δ	$E^{1/2} - E^{-1/2}$	$\Delta(1+\Delta)^{-1/2}$	$\nabla(1-\nabla)^{-1/2}$	δ
μ	$\frac{1}{2}(E^{1/2} + E^{-1/2})$	$(1 + \frac{1}{2}\Delta)(1+\Delta)^{1/2}$	$(1 - \frac{1}{2}\nabla)(1-\nabla)^{-1/2}$	$\sqrt{(1 + \frac{1}{4}\delta^2)}$

Since $\bar{\dot{x}}_0 = (x_1 - x_0)/\Delta t$, we obtain:

$$x_1 = \bar{x}_0 + \Delta t \bar{\dot{x}}_0 \qquad [22]$$

Using eqns [14], [21], and [22] we obtain:

$$\begin{aligned} \ddot{x}_0 &= \frac{1}{m}\left(f_0 - c\bar{\dot{x}}_0 - k\bar{x}_0\right) \\ &= \frac{x_2 - 2x_1 + x_0}{(\Delta t)^2} \\ &= \frac{x_2 - 2\left(\bar{x}_0 + \Delta t \bar{\dot{x}}_0\right) + \bar{x}_0}{(\Delta t)^2} \end{aligned} \qquad [23]$$

which can be rewritten as:

$$\begin{aligned} x_2 = \frac{(\Delta t)^2}{m} f_0 - \left[c\frac{(\Delta t)^2}{m} - 2\Delta t\right]\bar{\dot{x}}_0 \\ - \left[k\frac{(\Delta t)^2}{m} - 1\right]\bar{x}_0 \end{aligned} \qquad [24]$$

Once x_1 and x_2 are determined from eqns [22] and [24], eqn [19] can be used to find the displacement of the mass at grid points 3, 4 ... n.

Multidegree-of-Freedom System – Forward Difference Method

The equations of motion of a viscously damped multi-degree-of-freedom system are given by:

$$\mathbf{M}\ddot{\mathbf{x}} + \mathbf{C}\dot{\mathbf{x}} + \mathbf{K}\bar{\mathbf{x}} = \mathbf{f}(t) \qquad [25]$$

where $\mathbf{M}$, $\mathbf{C}$, and $\mathbf{K}$ are the mass, damping, and stiffness matrices, respectively. $\mathbf{f}(t)$ is the vector of forces applied to the masses and $\mathbf{x}$, $\dot{\mathbf{x}}$, and $\ddot{\mathbf{x}}$ are respectively, the vectors of displacements, velocities, and accelerations of the masses. The forward finite difference procedure for solving eqn [25] is similar to that of the single-degree-of-freedom system except that matrices and vectors are to be used in the present case.

Using the finite difference formulas:

$$\dot{\mathbf{x}}_i = \frac{\mathbf{x}_{i+1} - \mathbf{x}_i}{\Delta t} \qquad [26]$$

and:

$$\ddot{\mathbf{x}}_i = \frac{\mathbf{x}_{i+2} - 2\mathbf{x}_{i+1} + \mathbf{x}_i}{(\Delta t)^2} \qquad [27]$$

in eqn [25] we obtain:

$$\begin{aligned} \mathbf{M}\frac{1}{(\Delta t)^2}(\mathbf{x}_{i+2} - 2\mathbf{x}_{i+1} + \mathbf{x}_i) \\ + \mathbf{C}\frac{1}{\Delta t}(\mathbf{x}_{i+1} - \mathbf{x}_i) + \mathbf{K}\mathbf{x}_i = \mathbf{f}_i \end{aligned} \qquad [28]$$

Eqn [28] gives the recurrence relationship:

$$\begin{aligned} \mathbf{x}_{i+2} =& \mathbf{M}^{-1}\mathbf{f}_i + \mathbf{x}_{i+1}\left(2 - \mathbf{M}^{-1}\mathbf{C}\Delta t\right) \\ &+ \mathbf{x}_i\left(-1 + \mathbf{M}^{-1}\mathbf{C}\Delta t - \mathbf{M}^{-1}\mathbf{K}(\Delta t)^2\right) \end{aligned} \qquad [29]$$

Since eqn [29] cannot be directly used to start the procedure with $i = 0$, we use the following approach:

1. From the known initial conditions $\mathbf{x}(t=0) = \bar{\mathbf{x}}_0$ and $\dot{\mathbf{x}}(t=0) = \bar{\dot{\mathbf{x}}}_0$, we compute $\ddot{\mathbf{x}}_0$ as:

$$\ddot{\mathbf{x}}_\mathbf{0} = \mathbf{M}^{-1}\left(\mathbf{f}_0 - \mathbf{C}\bar{\dot{\mathbf{x}}} - \mathbf{K}\bar{\mathbf{x}}_0\right) \qquad [30]$$

2. Divide the interval τ into n equal parts so that:

$$\begin{aligned} &\Delta t = \frac{\tau}{n} \text{ with } t_0 = 0,\ t_1 = \Delta t, \\ &t_2 = 2\Delta t, \ldots,\ t_n = n\Delta t = \tau, \text{ and } \Delta t < \Delta t_{\text{cri}} \end{aligned}$$

3. Compute $\mathbf{x}_1$ using a relationship similar to that of eqn [22]:

$$\mathbf{x}_1 = \bar{\mathbf{x}}_0 = \Delta t\ \bar{\dot{\mathbf{x}}}_0 \qquad [31]$$

4. Determine $\mathbf{x}_2$ using an equation similar to that of eqn [24]:

$$\begin{aligned} \mathbf{x}_2 = (\Delta t)^2\mathbf{M}^{-1}\mathbf{f}_0 - \left(\mathbf{M}^{-1}\mathbf{C}(\Delta t)^2 - 2\Delta t\right)\bar{\dot{\mathbf{x}}}_0 \\ - \left(\mathbf{M}^{-1}\mathbf{K}(\Delta t)^2 - 1\right)\bar{\mathbf{x}}_\mathbf{0} \end{aligned} \qquad [32]$$

5. Set $i = 1, 2, \ldots, n-2$ in eqn [29] and compute $\mathbf{x}_3,\ \mathbf{x}_4, \ldots, \mathbf{x}_n$ recursively.

Continuous System – Central Finite Difference Method

The equations of motion of continuous systems are partial differential equations with specified boundary and initial conditions. The transverse vibration of a cable (string), longitudinal vibration of a bar (rod), and torsional vibration of a shaft (bar) are governed by the same differential equation (**Figure 3**):

$$A_1\frac{\partial^2\phi}{\partial x^2} + f(x,t) = B_1\frac{\partial^2\phi}{\partial t^2} \qquad [33]$$

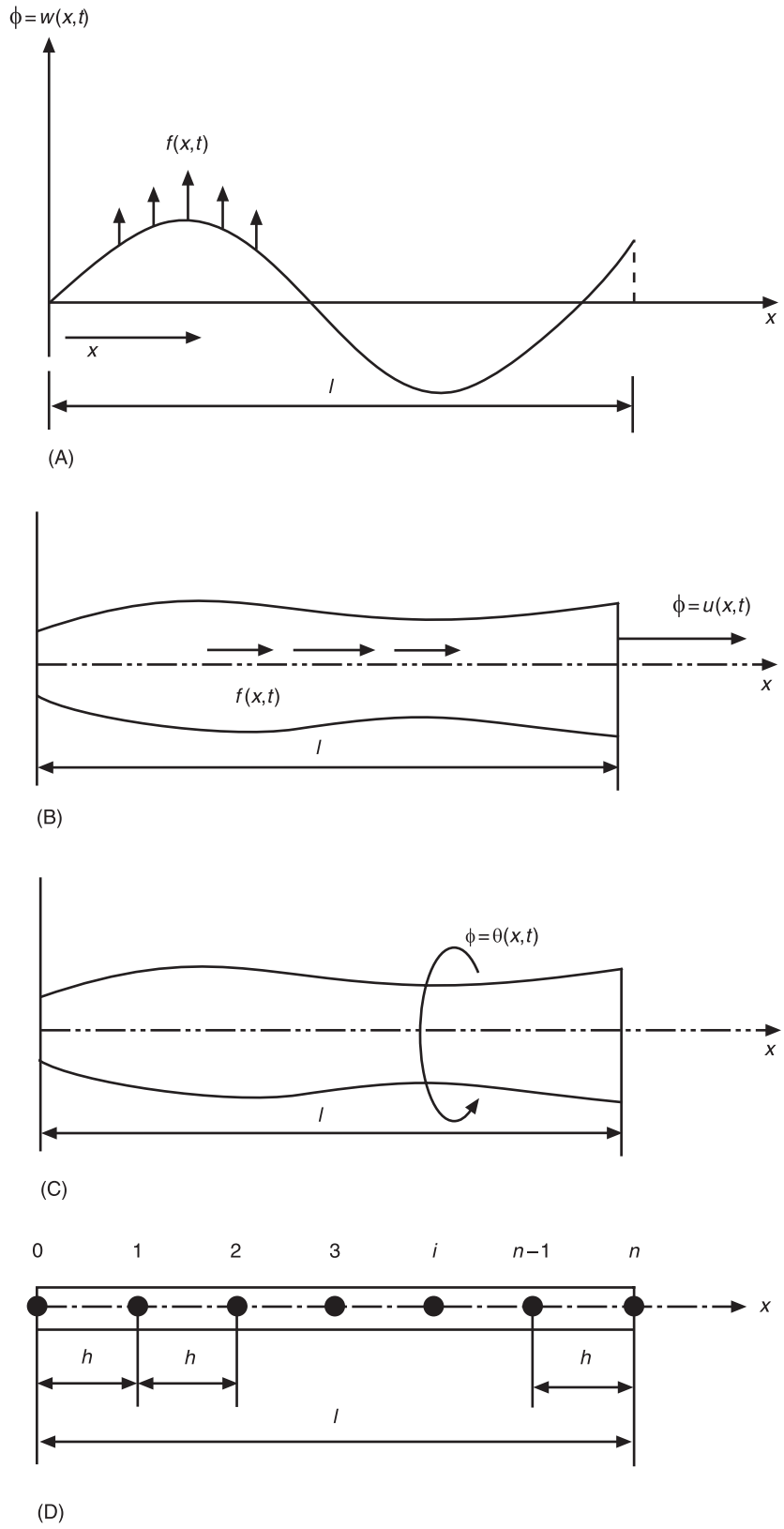


Figure 3 (A) Transverse vibration of a string; (B) longitudinal vibration of a bar; (C) torsional vibration of a shaft; (D) torsional vibration of a uniform shaft; finite difference grid.

where ϕ is the transverse deflection (in the vibration of a string), axial displacement (in the longitudinal vibration of a bar) and torsional deflection (in the case of torsional vibration of a shaft), $f(x, t)$ is the distributed force per unit length, A_1 is the tension in the string (in the case of transverse vibration of a string), axial stiffness, EA (in the case of longitudinal vibration of a bar) and torsional stiffness, GJ (in the case of torsional vibration of a shaft), and $B_1 =$ mass per unit length (in the case of transverse vibration of a string), mass per unit length, ρA (in the case of longitudinal vibration of a bar), and mass polar moment of inertia per unit length, J_0 (in the case of torsional vibration of a shaft).

For specificness, we consider the torsional vibration of a uniform shaft with governing equation:

$$GJ\frac{\partial^2\theta(x,t)}{\partial x^2} + f(x,t) = J_0\frac{\partial^2\theta(x,t)}{\partial t^2} \qquad [34]$$

where GJ is the torsional stiffness, G is the shear modulus, J is the polar moment of inertia of the cross-section, J_0 is ρJ, is the mass polar moment of inertia of the shaft per unit length, and ρ is density. For free vibration, $f(x, t) = 0$ and eqn [34] reduces to:

$$c^2\frac{\partial^2\theta}{\partial x^2} = \frac{\partial^2\theta}{\partial t^2} \qquad [35]$$

where:

$$c = \sqrt{\frac{GJ}{J_0}} = \sqrt{\frac{G}{\rho}} \qquad [36]$$

The solution of eqn [35] can be found using the method of separation of variables:

$$\theta(x, t) = U(x)\,T(t) \qquad [37]$$

where U and T are functions of only x and t, respectively. Using eqn [37] in eqn [35] leads to:

$$\frac{c^2}{U}\frac{\mathrm{d}^2U}{\mathrm{d}x^2} = \frac{1}{T}\frac{\mathrm{d}^2T}{\mathrm{d}t^2} = a = \text{constant} \qquad [38]$$

which can be rewritten as two separate equations:

$$\frac{\mathrm{d}^2U}{\mathrm{d}x^2} - \frac{a}{c^2}U = 0 \qquad [39]$$

$$\frac{\mathrm{d}^2T}{\mathrm{d}t^2} - aT = 0 \qquad [40]$$

The constant α can be proved to be a negative quantity so that $a = -\omega^2$. The solution of eqn [39] can be found using the forward finite difference method as follows.

Divide the length of the bar, l, into n equal parts as shown in **Figure 3D** so that $\Delta x = h = l/n$ and $x_i = ih$ and $U_i = U(x_i)$. Eqn [39] can be rewritten as:

$$\frac{\mathrm{d}^2U}{\mathrm{d}x^2} + \beta^2U = 0 \qquad [41]$$

with:

$$\beta^2 = \frac{\omega^2}{c^2} = \frac{\rho\omega^2}{G} \qquad [42]$$

The central difference approximation of eqn [41] at grid point i gives:

$$\frac{1}{h^2}(U_{i+1} - 2U_i + U_{i-1}) + \beta^2U_i = 0$$

or:

$$U_{i+1} - (2 - \lambda)U_i + U_{i-1} = 0 \qquad [43]$$

where:

$$\lambda = h^2\beta^2 \qquad [44]$$

The application of eqn [43] at grid points 1, 2, 3 ... $n - 1$ leads to the equations:

$$\left.\begin{array}{c} U_2 - (2-\lambda)U_1 + U_0 = 0 \\ U_3 - (2-\lambda)U_2 + U_1 = 0 \\ \cdot \\ \cdot \\ \cdot \\ U_{n-1} - (2-\lambda)U_{n-2} + U_{n-3} = 0 \\ U_n - (2-\lambda)U_{n-1} + U_{n-2} = 0 \end{array}\right\} \qquad [45]$$

which can be expressed in matrix form as:

$$\begin{bmatrix} -1 & (2-\lambda) & -1 & 0 & 0 & \cdots & 0 & 0 & 0 \\ 0 & -1 & (2-\lambda) & -1 & 0 & \cdots & 0 & 0 & 0 \\ 0 & 0 & -1 & (2-\lambda) & -1 & \cdots & 0 & 0 & 0 \\ \vdots & \vdots & \vdots & \vdots & \vdots & \ddots & \vdots & \vdots & \vdots \\ 0 & 0 & 0 & 0 & 0 & \cdots & (2-\lambda) & -1 & 0 \\ 0 & 0 & 0 & 0 & 0 & \cdots & -1 & (2-\lambda) & -1 \end{bmatrix} \begin{Bmatrix} U_0 \\ U_1 \\ U_2 \\ \vdots \\ U_{n-1} \\ U_n \end{Bmatrix} = \begin{Bmatrix} 0 \\ 0 \\ 0 \\ \vdots \\ 0 \\ 0 \end{Bmatrix} \quad [46]$$

The boundary conditions are to be applied to eqn [46]. If the shaft is fixed at $x = 0$, we set $U_0 = 0$. If the shaft is free at $x = 0$, we set $(\mathrm{d}U/\mathrm{d}x)|_0 = 0$. Using forward difference formula for $\mathrm{d}U/\mathrm{d}x$, this boundary condition becomes equivalent to setting $U_0 = U_1$. Eqn [46], after incorporating the boundary conditions, can be expressed as an eigenvalue problem. For example, when both ends of the shaft are fixed, we have $U_0 = U_n = 0$ and eqn [46] reduces to:

$$[\mathbf{A} - \lambda\,\mathbf{I}]\mathbf{U} = \mathbf{O} \quad [47]$$

where:

$$\mathbf{A} = \begin{bmatrix} 2 & -1 & 0 & 0 & \cdots & 0 & 0 & 0 \\ -1 & 2 & -1 & 0 & \cdots & 0 & 0 & 0 \\ 0 & -1 & 2 & -1 & \cdots & 0 & 0 & 0 \\ \vdots & \vdots & \vdots & \vdots & \ddots & \vdots & \vdots & \vdots \\ 0 & 0 & 0 & 0 & \cdots & -1 & 2 & -1 \\ 0 & 0 & 0 & 0 & \cdots & 0 & -1 & 2 \end{bmatrix}$$

$$\mathbf{U} = \begin{Bmatrix} U_0 \\ U_1 \\ U_2 \\ \vdots \\ U_{n-1} \\ U_n \end{Bmatrix}$$

and $\mathbf{I}$ = an identity matrix of order $n - 1$. Eqn [47] can be solved to find the natural frequencies ω and the mode shapes $\mathbf{U}$.

Finite Difference Method for Partial Differential Equations

When the field variable or the unknown function f depends on two independent variables x and y, the finite difference method can be extended easily. For this purpose, the domain of the partial differential equation is replaced by a network of points situated on a series of straight or curved lines. The network must be judiciously chosen since, by a convenient choice of the coordinate lines, considerable simplifications may be achieved based on the shape of the boundary of the domain. For simplicity, only Cartesian rectangular coordinates are considered in this section.

By drawing two sets of straight lines in the domain, parallel to the x and y axes, a network of grid points $(m,\ n)$ can be defined as shown in **Figure 4**. The value of $f(x,\ y)$ at grid point $(m,\ n)$ is assumed to be $f(x_m,\ y_n) = f_{m,\,n}$. The partial derivatives with respect to a single variable can be expressed in the same manner as if only that variable exists. The main difference is that the double subscript appears with the other variable (subscript) considered fixed. For mixed derivatives, both the subscripts vary. By using the relation:

$$\frac{\partial^{m+n} f}{\partial x^m \partial y^n} = \frac{\partial^m}{\partial x^m}\left(\frac{\partial^n f}{\partial y^n}\right) = \frac{\partial^n}{\partial y^n}\left(\frac{\partial^m f}{\partial x^m}\right) \quad [48]$$

the mixed partial derivatives of various orders can easily be evaluated. For equal intervals, the various types of derivatives can be expressed as follows (using central differences):

$$\frac{\partial f_{m,n}}{\partial x} = \frac{f_{m+1,n} - f_{m-1,n}}{2\Delta x} \quad [49]$$

$$\frac{\partial f_{m,n}}{\partial y} = \frac{f_{m,n+1} - f_{m,n-1}}{2\Delta y} \quad [50]$$

$$\frac{\partial^2 f_{m,n}}{\partial x^2} = \frac{f_{m+1,n} - 2f_{m,n} + f_{m-1,n}}{(\Delta x)^2} \quad [51]$$

$$\frac{\partial^2 f_{m,n}}{\partial y^2} = \frac{f_{m,n+1} - 2f_{m,n} + f_{m,n-1}}{(\Delta y)^2} \quad [52]$$

$$\frac{\partial^2 f_{m,n}}{\partial x \partial y} = \frac{f_{m+1,n+1} - f_{m+1,n-1} - f_{m-1,n+1} + f_{m-1,n-1}}{4\Delta x \Delta y} \quad [53]$$

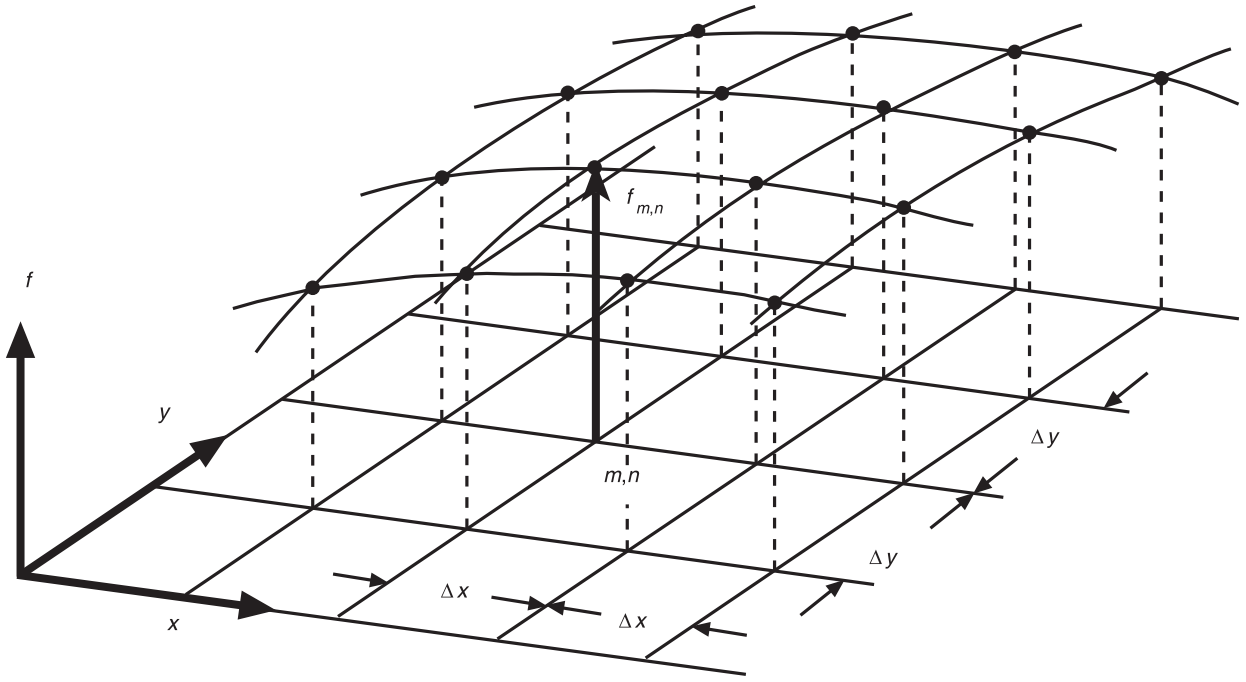


Figure 4 Finite difference grid in two-dimensional domain.

$$\frac{\partial^4 f_{m,n}}{\partial x^4} = \frac{f_{m+2,n} - 4f_{m+1,n} + 6f_{m,n} - 4f_{m-1,n} + f_{m-2,n}}{(\Delta x)^4} \quad [54]$$

$$\frac{\partial^4 f_{m,n}}{\partial y^4} = \frac{f_{m,n+2} - 4f_{m,n+1} + 6f_{m,n} - 4f_{m,n-1} + f_{m,n-2}}{(\Delta y)^4} \quad [55]$$

$$\frac{\partial^4 f_{m,n}}{\partial x^2 \partial y^2} = \frac{1}{(\Delta x)^2 (\Delta y)^2} \times \Big\{ 4f_{m,n} - 2\big(f_{m+1,n} + f_{m-1,n} + f_{m,n+1} + f_{m,n-1}\big) + f_{m+1,n+1} + f_{m+1,n-1} + f_{m-1,n+1} + f_{m-1,n-1} \Big\} \quad [56]$$

For equal intervals in both x and y directions, we have $\Delta x = \Delta y = \Delta$ and hence:

$$\Delta f_{m,n} = \left(\frac{\partial^2}{\partial x^2} + \frac{\partial^2}{\partial y^2}\right) f_{m,n} = \frac{f_{m+1,n} + f_{m-1,n} + f_{m,n+1} + f_{m,n-1} - 4f_{m,n}}{\Delta^2} \quad [57]$$

$$\Delta\Delta f_{m,n} = \left(\frac{\partial^4}{\partial x^4} + 2\frac{\partial^4}{\partial x^2 \partial y^2} + \frac{\partial^4}{\partial y^4}\right) f_{m,n} = \frac{1}{\Delta^4}\Big[20f_{m,n} - 8\big(f_{m+1,n} + f_{m-1,n} + f_{m,n+1} + f_{m,n-1}\big) + 2\big(f_{m+1,n+1} + f_{m-1,n+1} + f_{m+1,n-1} + f_{m-1,n-1}\big) + \big(f_{m+2,n} + f_{m-2,n} + f_{m,n+2} + f_{m,n-2}\big)\Big] \quad [58]$$

When the intervals along x and y directions are unequal with a constant ratio:

$$\frac{\Delta x_{m+1}}{\Delta x_m} = \alpha_x \text{ and } \frac{\Delta y_{n+1}}{\Delta y_n} = \alpha_y \quad [59]$$

we have:

$$\frac{\partial f_{m,n}}{\partial x} = \frac{f_{m+1,n} - (1 - \alpha_x^2) f_{m,n} - \alpha_x^2 f_{m-1,n}}{(1 + \alpha_x)\Delta x_m} \quad [60]$$

$$\frac{\partial f_{m,n}}{\partial y} = \frac{f_{m,n+1} - \left(1 - \alpha_y^2\right) f_{m,n} - \alpha_y^2 f_{m,n-1}}{(1 + \alpha_y)\Delta y_n} \quad [61]$$

$$\frac{\partial^2 f_{m,n}}{\partial x^2} = \frac{2}{\alpha_x(1+\alpha_x)}\left[\frac{f_{m+1,n} - (1+\alpha_x)f_{m,n} + \alpha_x f_{m-1,n}}{(\Delta x_m)^2}\right] \quad [62]$$

$$\frac{\partial^2 f_{m,n}}{\partial y^2} = \frac{2}{\alpha_y(1+\alpha_y)}\left[\frac{f_{m,n+1} - (1+\alpha_y)f_{m,n} + \alpha_y f_{m,n-1}}{(\Delta y_n)^2}\right] \quad [63]$$

$$\begin{aligned}\frac{\partial^2 f_{m,n}}{\partial x \partial y} &= \frac{\alpha_x \alpha_y}{(1+\alpha_x)(1+\alpha_y)\Delta x_m \Delta y_n} \\ &\times \left(f_{m-1,n-1} + \frac{1-\alpha_x^2}{\alpha_x^2} f_{m,n-1} - \frac{1}{\alpha_x^2} f_{m+1,n-1}\right) \\ &+ \frac{1-\alpha_y^2}{\alpha_y^2}\left(f_{m-1,n} + \frac{1-\alpha_x^2}{\alpha_x^2} f_{m,n} - \frac{1}{\alpha_x^2} f_{m+1,n}\right) \\ &\times \left[-\frac{1}{\alpha_y^2}\left(f_{m-1,n+1} + \frac{1-\alpha_x^2}{\alpha_x^2} f_{m,n+1} - \frac{1}{\alpha_x^2} f_{m+1,n+1}\right)\right]\end{aligned} \quad [64]$$

Note that by substituting $\alpha_x = \alpha_y = 1$ into eqns [60]–[64] yields eqns [49]–[53]

Nomenclature

E	shift operator
G	shear modulus
GJ	torsional stiffness
J	polar moment of inertia
δ	central difference operator
Δ	forward difference operator
∇	backward difference operator
μ	average operator
ρ	density

See also: **Continuous methods**; **Discrete elements**; **Finite difference methods**.

Further Reading

Ali R (1983) Finite difference methods in vibration analysis. *The Shock and Vibration Digest* 15: 3–7.

Constantinides A (1987) *Applied Numerical Methods with Personal Computers*. New York: McGraw-Hill.

Davis JL (1986) *Finite Difference Methods in Dynamics of Continuous Media*. New York: Macmillan.

Rao SS (1995) *Mechanical Vibrations*, 3rd edn. Reading, Mass.: Addison-Wesley.

Wah T and Calcote LR (1970) *Structural Analysis by Finite Difference Calculus*. New York: Van Nostrand Reinhold.

FINITE ELEMENT METHODS

S S Rao, University of Miami, Coral Gables, FL, USA

Copyright © 2001 Academic Press

doi:10.1006/rwvb.2001.0004

Introduction

The finite element method (FEM) is a numerical procedure that can be used for the approximate solution of complex engineering analysis problems, including structural and mechanical vibration problems. The basic concept involves replacing the actual system with several smaller pieces, each of which is assumed to behave as a continuous member, known as a finite element (FE). The FEs are assumed to be interconnected at certain points, called nodes. Since it is difficult to find the exact static displacement, eigenvalue, or transient solution of the original system under the specified conditions, a simpler solution is assumed in each FE. The idea is that, if the solutions in various FEs are assumed properly, they can be made to converge to the exact solution of the total system by reducing the sizes of the FEs. The solution of the overall system is obtained by satisfying the equilibrium equations at nodes and the compatibility of displacements between the elements. Since the method is well suited for the digital computer, several commercial software packages, such as ANSYS™ NASTRAN™ and ABAQUS™ have been developed for the FE solution of complex engineering problems.

The idea of representing a given domain as a collection of several subdomains or parts is not unique to the FEM. It is well known that ancient mathematicians estimated the value of π to accuracies of almost 40 significant digits by approximating the circumference of a circle of unit diameter by the perimeter of a polygon inscribed in the circle. In fact, by using inscribed and circumscribed polygons, lower and upper bounds can be established on the value of π. In 1941, Hrenikoff presented a framework method in which a plane solid body is represented as an assemblage of bars and beams. In 1943, Courant

introduced the concept of using piecewise-continuous functions defined over a subdomain to approximate the unknown function in the context of the St Venant torsion problem. He represented the torsion problem as an assemblage of triangular elements and used the principle of minimum potential energy for the solution. Although many features of the FEM can be found in the works of Hrenikoff and Courant, the origins of the modern-day FEM are usually attributed to Argyris and Kelsey (1954) and Turner, Clough, Martin and Topp (1956). The term 'finite element' was first used by Clough in 1960. Since its inception, the literature on the FEM and its applications has grown exponentially, and currently there are hundreds of books and numerous journals primarily devoted to the subject.

Basic Approach

Most engineering problems are governed by differential equations of the form:

$$\mathbf{A}(\boldsymbol{\phi}) = \begin{Bmatrix} A_1(\boldsymbol{\phi}) \\ A_2(\boldsymbol{\phi}) \\ . \\ . \\ . \end{Bmatrix} = \mathbf{0} \qquad [1]$$

over the domain V subject to the boundary conditions (**Figure 1**):

$$\mathbf{B}(\boldsymbol{\phi}) = \begin{Bmatrix} B_1(\boldsymbol{\phi}) \\ B_2(\boldsymbol{\phi}) \\ . \\ . \\ . \end{Bmatrix} = \mathbf{0} \qquad [2]$$

on the boundary, S, of the domain V where $\boldsymbol{\phi}$ is a vector of field variables or unknowns. In eqns [1] and [2] A_i and B_j denote linear differential operators. In the FEM, the domain is divided into several subdomains or FEs $V^{(e)}$ and an approximate solution is assumed in each subdomain as:

$$\boldsymbol{\phi}^e = \mathbf{N}\boldsymbol{\Phi}^e = \sum_{i=1}^{p} N_i \Phi_i \qquad [3]$$

where $\mathbf{N} = \{N_i\}$ is the matrix of shape functions in terms of the spatial coordinates x, y and z, $\boldsymbol{\Phi}^e$ is the vector of nodal unknowns, i.e., the vector of values of $\boldsymbol{\phi}$ at the nodes of the FE, and p is the number of nodal unknowns in the element. The nodal unknowns Φ_i are determined from equations of the type:

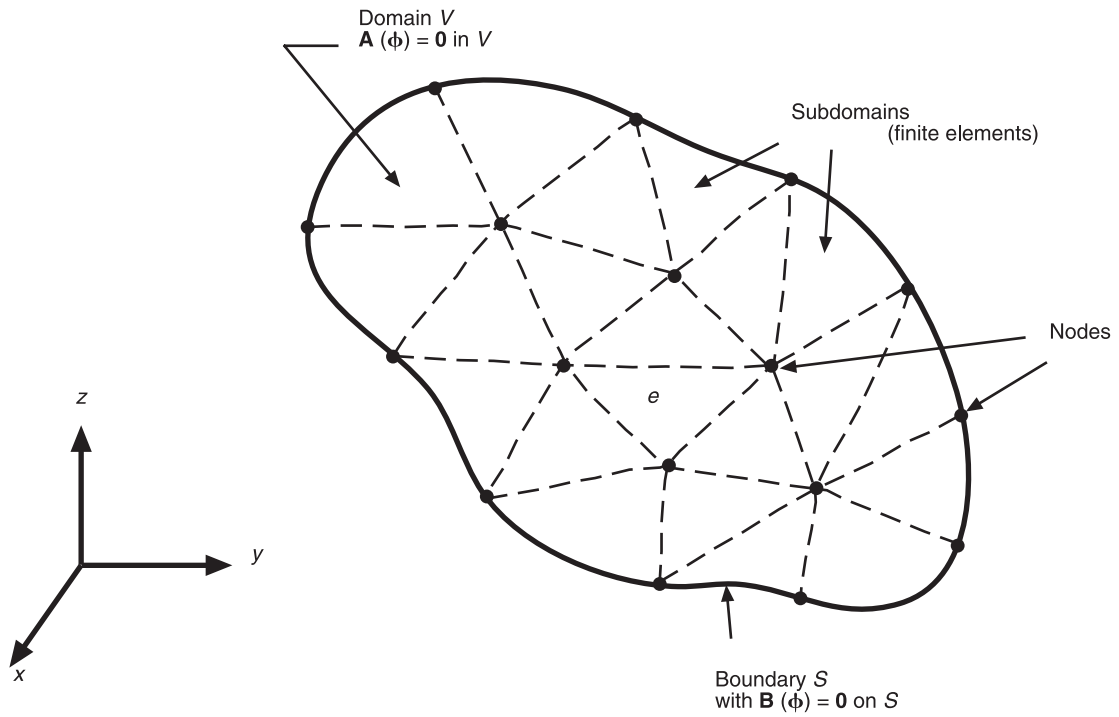


Figure 1 A domain divided into subdomains.

$$\int_V D_j(\boldsymbol{\phi})\,\mathrm{d}V + \int_S d_j(\boldsymbol{\phi})\,\mathrm{d}S = 0, \quad j = 1, 2, \ldots \quad [4]$$

where D_j and d_j are known operators or functions. Using eqn [3], eqn [4] can be expressed as:

$$\sum_{e=1}^{E} \left\{ \int_{V^{(e)}} D_j\left(\boldsymbol{\phi}^{(e)}\right)\mathrm{d}V + \int_{S^{(e)}} d_j\left(\boldsymbol{\phi}^{(e)}\right)\mathrm{d}S \right\} = 0, \quad j = 1, 2, \ldots \quad [5]$$

where E is the number of FEs in the system. Upon integration, eqn [5] leads to a set of linear algebraic equations:

$$\tilde{\mathbf{K}}\tilde{\boldsymbol{\Phi}} - \tilde{\mathbf{P}} = \tilde{\mathbf{0}} \quad [6]$$

where:

$$\tilde{\mathbf{K}} = \sum_{e=1}^{E} \mathbf{K}^{(e)} \quad [7]$$

and:

$$\tilde{\mathbf{P}} = \sum_{e=1}^{E} \mathbf{P}^{(e)} \quad [8]$$

denote the assembled characteristic matrix and characteristic vector of the system, respectively. Basically, two distinct methods can be used to derive eqn [6] from eqn [5]. The first is the variational method and the second is the weighted residual method.

Variational Approach

In the variational or Rayleigh–Ritz approach, the extremization of a functional I over the domain V is required. Let the functional I corresponding to the governing equation [1] and boundary conditions [2] be:

$$I = \int_V F\left[\boldsymbol{\phi}, \frac{\partial}{\partial x}(\boldsymbol{\phi}), \ldots\right]\mathrm{d}V + \int_S g\left[\boldsymbol{\phi}, \frac{\partial}{\partial x}(\boldsymbol{\phi}), \ldots\right]\mathrm{d}S \quad [9]$$

The field variable $\boldsymbol{\phi}$ in each element is expressed by eqn [3]. When the conditions of extremization of the functional I are used:

$$\frac{\partial I}{\partial \tilde{\boldsymbol{\Phi}}} = \begin{bmatrix} \dfrac{\partial I}{\partial \boldsymbol{\Phi}_1} \\ \dfrac{\partial I}{\partial \boldsymbol{\Phi}_2} \\ \vdots \\ \dfrac{\partial I}{\partial \boldsymbol{\Phi}_M} \end{bmatrix} = \mathbf{0} \quad [10]$$

where M is the total number of nodal unknowns in the problem or system. Since the functional I can be expressed as a summation of elemental contributions:

$$I = \sum_{e=1}^{E} I^{(e)} \quad [11]$$

and eqn [10] can be written as:

$$\frac{\partial I}{\partial \boldsymbol{\Phi}_i} = \sum_{e=1}^{E} \frac{\partial I^{(e)}}{\partial \boldsymbol{\Phi}_i} = 0; \quad i = 1, 2, \ldots, M \quad [12]$$

When I is a quadratic functional of $\boldsymbol{\phi}$ and its derivatives, the elemental equations can be found as:

$$\frac{\partial I^{(e)}}{\partial \boldsymbol{\Phi}^{(e)}} = \mathbf{K}^{(e)}\boldsymbol{\Phi}^{(e)} - \mathbf{P}^{(e)} \quad [13]$$

where $\mathbf{K}^{(e)}$ and $\mathbf{P}^{(e)}$ are the element characteristic matrix and characteristic vector (or vector of nodal actions), respectively. The overall equations of the system, eqn [12], can be rewritten as:

$$\frac{\partial I}{\partial \tilde{\boldsymbol{\Phi}}} = \tilde{\mathbf{K}}\tilde{\boldsymbol{\Phi}} - \tilde{\mathbf{P}} = \mathbf{0} \quad [14]$$

where $\tilde{\mathbf{K}}$ and $\tilde{\mathbf{P}}$ are given by eqns [7] and [8], respectively. Eqn [14] can be solved, after applying the boundary conditions, to find the nodal unknowns $\tilde{\boldsymbol{\Phi}}$. Then the field variables $\boldsymbol{\phi}$ in each element can be determined using eqn [3]. The following conditions are to be satisfied for the convergence of results as the subdivision of the domain is made finer:

1. As the element size decreases, the functions F and g of eqn [9] must tend to be single-valued and well-behaved. Thus, the shape functions $\mathbf{N}$ and nodal unknowns $\boldsymbol{\Phi}^{(e)}$ chosen must be able to represent any constant value of $\boldsymbol{\phi}$ or its derivatives present in the functional I in the limit as the element size $V^{(e)}$ decreases to zero.
2. In order to make the summation $I = \Sigma_{e=1}^{E} I^{(e)}$ valid, terms involving F and g must be insured to remain finite at interelement boundaries. This can be

achieved if the highest derivatives of the field variables $\boldsymbol{\phi}$ that occur in F and g remain finite. Thus, the element shape functions $\mathbf{N}$ are to be selected such that, at element interfaces, $\boldsymbol{\phi}$ and its derivatives, of one order less than those occurring in F and g, are continuous.

Weighted Residual Approach

Let the governing differential equation be expressed, for simplicity, as:

$$A(\phi) = b \ \text{ in } \ V \qquad [15]$$

with the boundary conditions:

$$B_j(\phi) = g_j, \quad j = 1,\ 2, \ldots,\ q \ \text{ on } \ S \qquad [16]$$

Of the various weighted residual methods, the Galerkin method is most commonly used. In the Galerkin method, an approximate solution $\tilde{\phi}$ is assumed for ϕ and the weighted residual is set to zero as:

$$\int_V \left[A\left(\tilde{\phi}\right) - b\right] f_i \, \mathrm{d}V = 0, \quad i = 1,\ 2, \ldots, n \qquad [17]$$

where f_i are trial functions used in the approximate solution ($\tilde{\phi}$):

$$\tilde{\phi} = \sum_{i=1}^{n} C_i f_j \qquad [18]$$

satisfy the boundary conditions of eqn [16]. Eqn [17] is made valid for element e as:

$$\int_{V^{(e)}} \left[A\left(\phi^{(e)}\right) - b^{(e)}\right] N_i^{(e)} \, \mathrm{d}V^{(e)} = 0 \ , \quad i = 1,\ 2, \ldots, n \qquad [19]$$

with the interpolation model taken as:

$$\phi^{(e)} = \mathbf{N}^{(e)} \boldsymbol{\Phi}^{(e)} = \sum_i N_i^{(e)} \Phi_i^{(e)} \qquad [20]$$

Comparing eqns [18] and [20], C_i and f_i can be seen to be same as $\Phi_i^{(e)}$ and $N_i^{(e)}$ respectively. Eqn [19] gives the required FE equations for a typical element. These elemental equations are to be assembled to obtain the system or overall equations.

Eigenvalue and Propagation Problems

Eigenvalue Problems

An eigenvalue problem can be stated as:

$$A\phi = \lambda B\phi \ \text{ in } \ V \qquad [21]$$

$$E_j\phi = 0, \quad j = 1,\ 2, \ldots,\ q \ \text{ on } \ S \qquad [22]$$

where A, B, and E_j are differential operators, ϕ is the field variable (or eigenfunction) and λ is the eigenvalue. By using eqns [18] and [21], the residual, R, can be expressed as:

$$R = \lambda B\tilde{\phi} - A\tilde{\phi} = \sum_{i=1}^{n} C_j\left(\lambda B f_j - A f_i\right) \qquad [23]$$

where the trial functions $f_j(x)$ satisfy the boundary conditions of eqn [22]. If the trial solution of eqn [18] contains any true eigenfunctions, then there exist sets of C_i and values of λ for which the residual R vanishes identically over the domain V. If $\tilde{\phi}(x)$ does not contain any eigenfunctions, then only approximate solutions will be obtained. In the Galerkin method, the integral of the weighted residual is set equal to zero:

$$\int_V f_i R \, \mathrm{d}V = 0, \quad i = 1,\ 2, \ldots, n \qquad [24]$$

which yields the algebraic (matrix) eigenvalue problem:

$$\mathbf{AC} = \lambda[\mathbf{B}]\mathbf{C} \qquad [25]$$

where $\mathbf{A}$ and $\mathbf{B}$ denote square symmetric matrices of size $n \times n$, given by:

$$\mathbf{A} = \mathbf{A}_{ij} = \left[\int_V f_i A f_j \, \mathrm{d}V\right] \qquad [26]$$

$$\mathbf{A} = \mathbf{B}_{ij} = \left[\int_V f_i B f_j \, \mathrm{d}V\right] \qquad [27]$$

and $\mathbf{C}$ denotes the vector of unknowns C_i, $i = 1,\ 2,\ \ldots,\ n$. The eigensolution of eqn [25] can be obtained by any of the standard methods.

Propagation Problems

A propagation problem can be expressed as:

$$A\phi = e \text{ in } V \text{ for } t > t_0 \quad [28]$$

$$B_i\phi = g_i, \ \ i = 1, 2, \ldots, k \text{ on } S \text{ for } t \geq t_0 \quad [29]$$

$$E_j\phi = h_j, \ \ j = 1, 2, \ldots, l \text{ in} V \text{ for } t = t_0 \quad [30]$$

where A, B_i and E_j are differential operators. The trial solution of the problem is taken as:

$$\tilde{\phi}(x,t) = \sum_{i=1}^{n} C_i(t) f_i(x) \quad [31]$$

where $f_i(x)$ are chosen to satisfy the boundary conditions of eqn [29]. Since eqns [28] and [30] are not satisfied by $\bar{\phi}(x, t)$, there will be two residuals, one corresponding to each of these equations. If eqn [30] gives the initial conditions explicitly as:

$$\phi(x,t) = \phi_0 \text{ at } t = 0 \quad [32]$$

the residual corresponding to the initial conditions, R_1, can be formulated as:

$$R_1 = \phi_0 - \bar{\phi}(x,0) \text{ for all } x \text{ in } V \quad [33]$$

where:

$$\tilde{\phi}(x,0) = \sum_{i=1}^{n} C_i(0) f_i(x) \quad [34]$$

Similarly, the residual corresponding to the field equation, R_2, is defined as:

$$R_2 = e - A\tilde{\phi}(x,t) \text{ for all } x \text{ in } V \quad [35]$$

In the Galerkin procedure, each of the residuals R_1 and R_2 is used to obtain:

$$\int_V f_j(x) R_1 \, dV = 0, \ \ i = 1, 2, \ldots, n \quad [36]$$

$$\int_V f_i(x) R_2 \, dV = 0, \ \ i = 1, 2, \ldots, n \quad [37]$$

Eqns [36] and [37] lead to $2n$ equations in the $2n$ unknowns $C_i(0)$ and $C_i(t)$, $i = 1, 2 \ldots n$ which can be solved either analytically or numerically.

Finite Element Equations for Solid and Structural Mechanics Problems

Static Problems

In solid mechanics problems, the nodal displacements (displacement formulation), element stresses (stress formulation), or a combination of displacements and stresses (hybrid formulation) can be chosen as the unknowns. Since the displacement formulation is most commonly used in practice; only this formulation is considered in this article. In the displacement approach, the components of displacement, u, v, and w, in an element are assumed as:

$$\mathbf{U} = \begin{Bmatrix} u(x,y,z) \\ v(x,y,z) \\ w(x,y,z) \end{Bmatrix} = \mathbf{N}\mathbf{Q}^{(e)} \quad [38]$$

where $\mathbf{Q}^{(e)}$ is the vector of nodal displacement degrees-of-freedom of the element and $\mathbf{N}$ is the matrix of shape functions. The potential energy functional of the body π_p is written as:

$$\pi_p = \sum_{e=1}^{E} \pi_p^{(e)} \quad [39]$$

where E is the number of FEs and $\pi_p^{(e)}$ is the potential energy of element e, given by:

$$\pi_p^{(e)} = \frac{1}{2} \int_{V^{(e)}} \boldsymbol{\varepsilon}^{\mathrm{T}} [\mathbf{D}] (\boldsymbol{\varepsilon} - 2\boldsymbol{\varepsilon}_0) \, dV - \int_{S_i^{(e)}} \mathbf{U}^{\mathrm{T}} \bar{\boldsymbol{\Phi}} \, dS_1 - \int_{V^{(e)}} \mathbf{U}^{\mathrm{T}} \bar{\boldsymbol{\phi}} \, dV \quad [40]$$

where $V^{(e)}$ is the volume of the element, $S_l^{(e)}$ is the portion of the surface of the element over which tractions $\bar{\boldsymbol{\Phi}}$ are prescribed, $\bar{\boldsymbol{\phi}}$ is the vector of body forces per unit volume, $\boldsymbol{\varepsilon}$ is the strain vector, and $\boldsymbol{\varepsilon}_0$ is the initial strain vector. The strain vector $\boldsymbol{\varepsilon}$ can be expressed in terms of the nodal displacement vector as:

$$\boldsymbol{\varepsilon} = \mathbf{B}\mathbf{Q}^{(e)} \quad [41]$$

where:

$$\boldsymbol{\varepsilon} = \{\varepsilon_{xx} \ \varepsilon_{yy} \ \varepsilon_{zz} \ \varepsilon_{xy} \ \varepsilon_{yz} \ \varepsilon_{zx}\}^{\mathrm{T}} \quad [42]$$

for a three-dimensional body and $\mathbf{B}$ can be expressed in terms of derivatives of $\mathbf{N}$. The corresponding stress vector $\boldsymbol{\sigma}$ can be obtained from the strain vector $\boldsymbol{\varepsilon}$ as:

$$\boldsymbol{\sigma} = \mathbf{D}(\boldsymbol{\varepsilon} - \boldsymbol{\varepsilon}_0) = \mathbf{DBQ}^{(e)} - \mathbf{D}\boldsymbol{\varepsilon}_0 \qquad [43]$$

where $\mathbf{D}$ is the elasticity matrix. The potential energy of element e can be expressed as:

$$\pi_{\mathrm{p}}^{(e)} = \frac{1}{2}\int_{V^{(e)}} \mathbf{Q}^{(e)^{\mathrm{T}}}\mathbf{B}^{\mathrm{T}}\mathbf{DBQ}^{(e)}\,\mathrm{d}V - \int_{V^{(e)}} \mathbf{Q}^{(e)^{\mathrm{T}}}\mathbf{B}^{\mathrm{T}}\mathbf{D}\varepsilon_0\,\mathrm{d}V - \int_{S_i^{(e)}} \mathbf{Q}^{(e)^{\mathrm{T}}}\mathbf{N}^{\mathrm{T}}\bar{\boldsymbol{\Phi}}\,\mathrm{d}S_1 - \int_{V^{(e)}} \mathbf{Q}^{(e)^{\mathrm{T}}}\mathbf{N}^{\mathrm{T}}\bar{\boldsymbol{\phi}}\,\mathrm{d}V \qquad [44]$$

If $\overline{\mathbf{P}}_c$ denotes the vector of nodal (concentrated) forces, the total potential energy of the body is given by:

$$\pi_p = \sum_{e=1}^{E}\pi_p^{(e)} - \tilde{\mathbf{Q}}^{(e)^{\mathrm{T}}}\tilde{\mathbf{P}}_c = \frac{1}{2}\tilde{\mathbf{Q}}^{\mathrm{T}}\mathbf{K}\tilde{\mathbf{Q}} - \tilde{\mathbf{Q}}^{\mathrm{T}}\bar{\mathbf{P}} \qquad [45]$$

where $\overline{\mathbf{Q}}$ is the vector of nodal displacements of the entire solid body. The static equilibrium configuration of the body is found from conditions of minimization of potential energy:

$$\frac{\partial \pi_p}{\partial \tilde{\mathbf{Q}}} = 0 \quad \text{or} \quad \frac{\partial \pi_p}{\partial \mathbf{Q}_i} = 0, \quad i = 1, 2, \ldots, M \qquad [46]$$

where M is the total number of nodal displacements of the body. Eqn [46] can be rewritten as:

$$\left(\sum_{e=1}^{E}\mathbf{K}^{(e)}\right) = \tilde{\mathbf{P}}_c + \sum_{e=1}^{E}\left(\mathbf{P}_i^{(e)} + \mathbf{P}_s^{(e)} + \mathbf{P}_b^{(e)}\right) = \tilde{\mathbf{P}} \qquad [47]$$

where the element stiffness matrix $\mathbf{K}^{(e)}$ and the load vectors due to initial strains, surface forces, and body forces, ($\mathbf{P}_i^{(e)}$, $\mathbf{P}_s^{(e)}$, and $\mathbf{P}_b^{(e)}$), are given by:

$$\mathbf{K}^{(e)} = \int_{V^{(e)}} \mathbf{B}^{\mathrm{T}}\mathbf{DB}\,\mathrm{d}V \qquad [48]$$

$$\mathbf{P}_i^{(e)} = \int_{V^{(e)}} \mathbf{B}^{\mathrm{T}}\mathbf{D}\varepsilon_0\,\mathrm{d}V \qquad [49]$$

$$\mathbf{P}_s^{(e)} = \int_{S_1^{(e)}} \mathbf{N}^{\mathrm{T}}\bar{\boldsymbol{\Phi}}\,\mathrm{d}S_1 \qquad [50]$$

$$\mathbf{P}_b^{(e)} = \int_{V^{(e)}} \mathbf{N}^{\mathrm{T}}\bar{\boldsymbol{\phi}}\,\mathrm{d}S_1 \qquad [51]$$

Eqn [47] can be written in a compact form as:

$$\tilde{\mathbf{K}}\tilde{\mathbf{Q}} = \tilde{\mathbf{P}} \qquad [52]$$

where $\tilde{\mathbf{K}}$ and $\tilde{\mathbf{P}}$ are the assembled or global stiffness matrix and load vector, respectively. Eqn [52] can be solved using the known boundary conditions.

Dynamic Problems

The kinetic energy of element, e, $T^{(e)}$, is given by:

$$T^{(e)} = \frac{1}{2}\int_{V^{(e)}} \rho\,\mathrm{d}\mathbf{U}^{\mathrm{T}}\,\mathrm{d}\mathbf{U}\,\mathrm{d}V \qquad [53]$$

where ρ is the density and $\mathrm{d}\mathbf{U} = \partial\mathbf{U}/\partial t$ is the vector of velocities within the element. Using eqn [38], $T^{(e)}$ can be expressed as:

$$T^{(e)} = \frac{1}{2}\int_{V^{(e)}} \mathrm{d}\mathbf{Q}^{(e)^{\mathrm{T}}}\mathbf{M}^{(e)}\,\mathrm{d}\mathbf{Q}^{(e)} \qquad [54]$$

where the element mass matrix is given by:

$$\mathbf{M}^{(e)} = \int_{V^{(e)}} \rho\mathbf{N}^{\mathrm{T}}\mathbf{N}\,\mathrm{d}V \qquad [55]$$

with $\mathrm{d}\mathbf{Q}^{(e)}$ denoting the vector of nodal velocity components of element e. The kinetic energy of the body is given by:

$$T = \sum_{e=1}^{E} T^{(e)} = \frac{1}{2}\mathrm{d}\tilde{\mathbf{Q}}^{\mathrm{T}}\tilde{\mathbf{M}}\,\mathrm{d}\tilde{\mathbf{Q}} \qquad [56]$$

where $\tilde{\mathbf{M}}$ is the assembled or global mass matrix of the body. Lagrange's equations, in the absence of damping, are given by:

$$\frac{\partial}{\partial t}\left(\frac{\partial L}{\partial \dot{Q}}\right) - \frac{\partial L}{\partial Q} = 0 \qquad [57]$$

where Q is the generalized coordinate and L is the Lagrangian given as:

$$L = \pi_p - T \qquad [58]$$

Using eqns [45] and [56], the equations of motion of the body can be found as (using $\overline{\mathbf{Q}}$ for Q in eqn [57]):

$$\tilde{\mathbf{M}}\mathrm{d}^2\tilde{\mathbf{Q}}(t) + \tilde{\mathbf{K}}\tilde{\mathbf{Q}}(t) = \tilde{\mathbf{P}}(t) \qquad [59]$$

where $\mathrm{d}^2\tilde{\mathbf{Q}}$ is the vector of nodal accelerations of the body. The simultaneous second-order differential equations (eqn [59]), can be solved using the known boundary and initial conditions.

Nonlinear Analysis for Structural Problems

In general, two types of nonlinearities can occur in a solid mechanics or structural problem. The first type, called material nonlinearity, occurs due to the nonlinearity of the stress–strain relations as in the case of nonlinear elastic and plastic or viscoelastic behavior of certain materials. It is well known that most materials are linear in a region close to the origin of the stress–strain curve, beyond which they are mostly nonlinear. Furthermore, at high temperatures, all materials soften and hence the region of linearity reduces again. The second type, known as geometric nonlinearity, occurs whenever the deflections are large enough to cause significant changes in the geometry of the structure so that the equilibrium equations must be formulated with respect to the deformed geometry.

Depending on the sources of nonlinearities, nonlinear structural problems can be divided into three categories: (i) problems involving material nonlinearities alone; (ii) problems involving geometric nonlinearities alone; and (iii) problems involving material as well as geometric nonlinearities. Due to the presence of nonlinear terms, the governing matrix equations cannot be obtained in an explicit form for a nonlinear problem and hence an iterative procedure has to be adopted to find the solution.

Basic Techniques of Nonlinear Analysis

The incremental, iterative, and mixed methods can be used to solve a nonlinear problem. The basic approach of each of these methods is considered with reference to a problem involving material nonlinearity alone. The nonlinear equilibrium equations can be written as:

$$\mathbf{KQ} = \mathbf{P} \qquad [60]$$

where the nonlinearity occurs in the stiffness matrix $\mathbf{K}$ due to the nonlinear stress–strain relation:

$$\boldsymbol{\sigma} = \mathbf{D}(\boldsymbol{\sigma})\boldsymbol{\varepsilon} \qquad [61]$$

Since the material properties are not constant, the equilibrium equations can be expressed as:

$$\mathbf{K}(\mathbf{Q}, \mathbf{P})\mathbf{Q} = \mathbf{P} \qquad [62]$$

Eqn [61] denotes a nonlinear stress–strain relation and eqn [62] indicates a nonlinear stiffness relation, as shown in **Figure 2**.

Since a new stiffness matrix has to be computed at every step of the incremental or iterative method, we need to compute the matrix $\mathbf{D}$ at the current displacement. This involves the determination of Young's modulus, E, and Poisson's ratio, v, which are functions of the state of stress within a FE for isotropic nonlinear elastic materials. For this, either the tangent modulus or secant modulus approach can be used. After finding the increment of displacements of the structure at step j, $\Delta\mathbf{Q}_j$, the corresponding increments in strains and stresses can be evaluated using the appropriate strain–displacement and stress–strain relations. For material nonlinear behavior with small displacements and strains, the strain–displacement and the stress–strain relations can be expressed as:

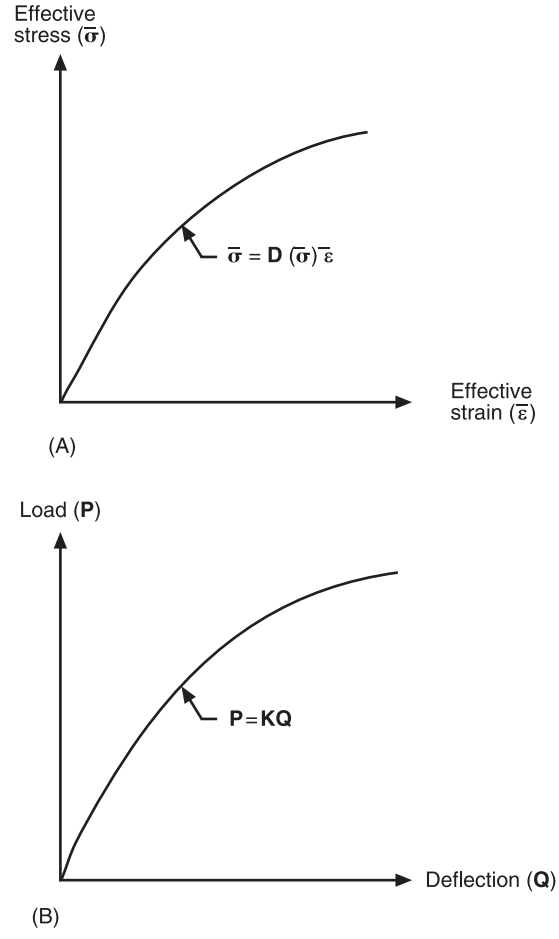


Figure 2 Nonlinear relationships. (A) Stress–strain curve; (B) load–deflection curve.

$$\Delta\boldsymbol{\varepsilon}_j = \mathbf{B}_{j-1}\Delta\mathbf{Q}_j \quad [63]$$

$$\Delta\boldsymbol{\sigma}_j = \mathbf{D}(\boldsymbol{\sigma}_{j-1})\Delta\boldsymbol{\varepsilon}_j \quad [64]$$

The total strains and stresses at the end of the jth stage may be obtained by the cumulative addition of increments as:

$$\boldsymbol{\varepsilon}_j = \sum_{i=1}^{j} \Delta\boldsymbol{\varepsilon}_j \quad [65]$$

$$\boldsymbol{\sigma}_j = \sum_{i=1}^{j} \Delta\boldsymbol{\sigma}_j \quad [66]$$

Once the states of stress and strain at the end of the jth step are found, equivalent stress–strain curve can be used to compute the appropriate moduli.

Incremental Method

The incremental method, also known as the stepwise method, is analogous to Euler and Runge–Kutta methods used to integrate systems of differential equations. The method involves the subdivision of the total load into many increments so that the total load vector $\mathbf{P}$ can be expressed as:

$$\mathbf{P} = \sum_{i=1}^{N} \Delta\mathbf{P}_i \quad [67]$$

where $\Delta\mathbf{P}_i$ indicates the ith load increment and N denotes the total number of load increments. After the application of the jth load increment, the total load applied is given by:

$$\mathbf{P}_j = \sum_{i=1}^{j} \Delta\mathbf{P}_i \quad [68]$$

so that the total load at the end of the Nth increment becomes:

$$\mathbf{P}_N \equiv \mathbf{P} = \sum_{i=1}^{N} \Delta\mathbf{P}_i \quad [69]$$

All the increments $\Delta\mathbf{P}_i$ need not be equal in magnitude but are generally taken to be the same for simplicity. If $\Delta\mathbf{Q}_i$ denotes the incremental displacement caused by the application of the incremental load $\Delta\mathbf{P}_i$, the total displacement after the application of the jth increment of load is given by:

$$\mathbf{Q}_j = \sum_{i=1}^{j} \Delta\mathbf{Q}_i \quad [70]$$

The load is applied one increment at a time and, for the purpose of computing the corresponding displacement increment, the equations are assumed to be linear during the application of that load increment. By using a constant value of the stiffness which is computed at the end of the previous increment of load, the equilibrium equations for the jth step can be expressed as:

$$\mathbf{K}_{j-1}\Delta\mathbf{Q}_j = \Delta\mathbf{P}_j, \quad j = 1, 2, \ldots, N \quad [71]$$

where:

$$\mathbf{K}_{j-1} = \mathbf{K}(\mathbf{Q}_{j-1}, \mathbf{P}_{j-1}) \quad [72]$$

The initial stiffness $\mathbf{K}_0$ is calculated from the material constants derived from the known stress–strain curve at the start of the loading. Generally the initial and subsequent stiffness matrices $\mathbf{K}_j$, $j = 0, 1, 2 \ldots N-1$, are computed using tangent moduli and hence are known as tangent stiffness matrices.

The incremental method is shown graphically in **Figure 3** for a single-degree-of-freedom system. It can be seen that the incremental method always underestimates the true displacement. The accuracy of the method can be improved using smaller increments of load. However, this involves more computational effort since a new stiffness matrix $\mathbf{K}_{j-1}$ has to be computed for each increment.

Iterative Method

The iterative method is similar to the Newton and Newton–Raphson methods used for the solution of nonlinear equations. In this method, the total load is applied to the structure in each iteration and the displacement is computed using an approximate but constant value of stiffness. Since an approximate value of stiffness is used in each iteration, equilibrium conditions may not be satisfied. Hence at the end of each iteration, the part of the total load that is not balanced is computed and used in the next iteration to calculate the additional increment of the displacement. The iterative procedure is continued until the equilibrium equations are satisfied to some tolerable degree. The equations corresponding to the jth iteration can be derived as follows. Let $\mathbf{P}$ be the total load and $\mathbf{P}_{j-1}^{(eq)}$ be the load equilibrated at the end of $j-1$th iteration. Then the unbalanced load to be applied in the jth iteration ($\mathbf{P}_j$) is given by:

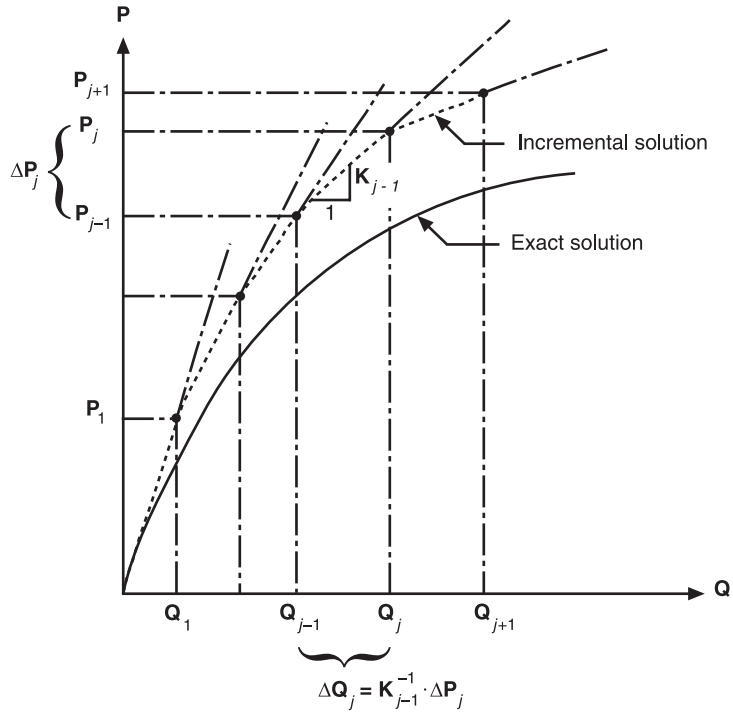


Figure 3 Incremental procedure.

$$\mathbf{P}_j = \mathbf{P} - \mathbf{P}_{j-1}^{(eq)} \quad [73]$$

The incremental displacement in the jth iteration ($\Delta\mathbf{Q}_j$) can be found by solving the linear equations:

$$\mathbf{K}_{j-1}\Delta\mathbf{Q}_j = \mathbf{P}_j \quad [74]$$

so that the total displacement at the end of jth iteration can be expressed as:

$$\mathbf{Q}_j = \mathbf{Q}_{j-1} + \Delta\mathbf{Q}_j \quad [75]$$

The stiffness to be used in the jth iteration, namely $\mathbf{K}_{j-1}$, can be computed by using the tangent modulus as in the incremental method. Thus $\mathbf{K}_{j-1}$ will be the tangent stiffness (slope of the load–deflection curve) computed at the point ($\mathbf{P}_{j-1},\ \mathbf{Q}_{j-1}$). The equilibrating load $\mathbf{P}_{j-1}^{(eq)}$ is nothing but the load necessary to maintain the displacement $\mathbf{Q}_{j-1}$ of the actual structure. It can be calculated by first finding the strains $\boldsymbol{\varepsilon}_{j-1}$ as:

$$\boldsymbol{\varepsilon}_{j-1} = \mathbf{B}\mathbf{Q}_{j-1} \quad [76]$$

and then finding the load vector $\mathbf{P}_{j-1}^{(eq)}$ from the relation:

$$\mathbf{Q}_{j-1}^{\mathrm{T}}\mathbf{P}_{j-1}^{(eq)} = \int_V \boldsymbol{\varepsilon}_{j-1}^{\mathrm{T}}\boldsymbol{\sigma}_{j-1}\,\mathrm{d}V = \mathbf{Q}_{j-1}^{\mathrm{T}}\left(\int_V \mathbf{B}^{\mathrm{T}}\mathbf{D}\boldsymbol{\varepsilon}_{j-1}\,\mathrm{d}V\right)$$

or:

$$\mathbf{P}_{j-1}^{(eq)} = \int_V \mathbf{B}^{\mathrm{T}}\mathbf{D}\boldsymbol{\varepsilon}_{j-1}\,\mathrm{d}V \quad [77]$$

The iterative procedure is shown graphically in **Figure 4**.

Mixed Method

The mixed or step-iterative method is a combination of the incremental and iterative methods. Here also the total load is divided into several increments and one increment is applied at a time. But after applying each increment of the load, equilibrium equations are satisfied by using an iterative scheme. This method is shown graphically in **Figure 5** for a single-degree-of-freedom system. It can be seen that this method leads to more accurate results at the cost of more computational effort.

Nonstructural Problems

Although the FEM was originally developed for the analysis of aircraft structures, the general nature of its

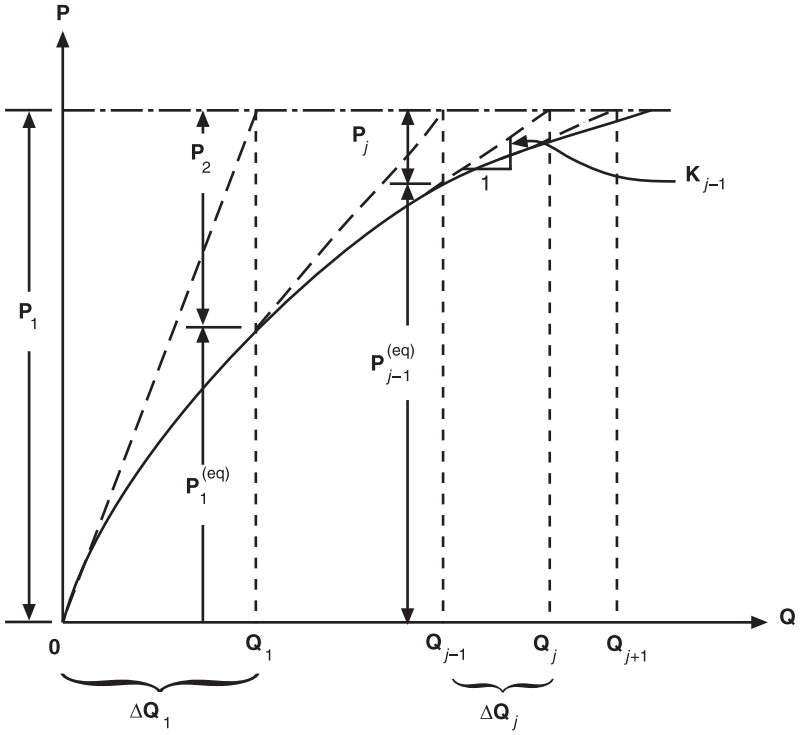


Figure 4 Iterative method.

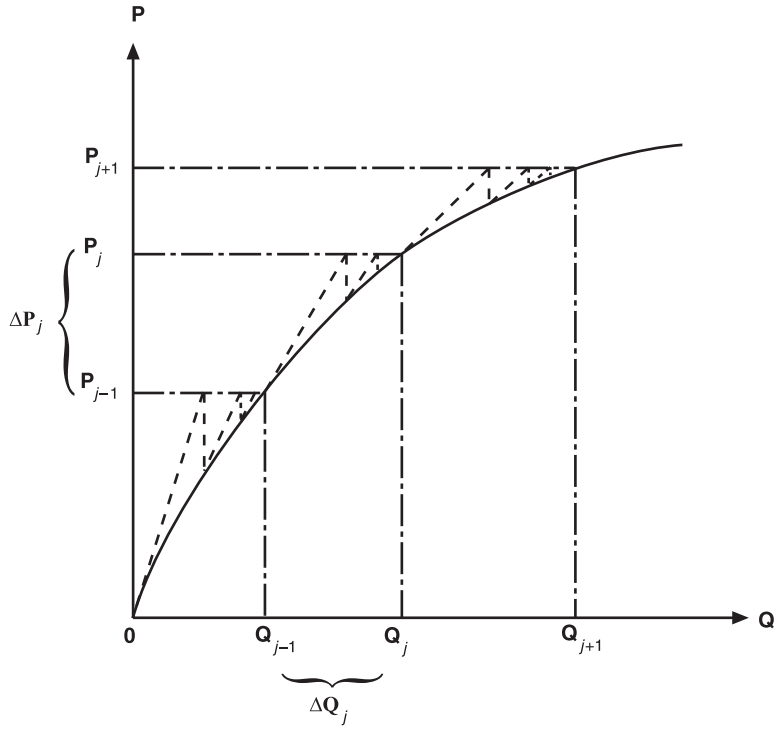


Figure 5 Mixed or step-iterative method.

theory makes it applicable to a wide variety of boundary value problems in engineering and applied mathematics. The method has been applied to all types of boundary value problems, namely, the equilibrium, eigenvalue, and propagation problems. For example, the FEM is routinely used to solve steady-state field problems governed by the quasiharmonic equation:

$$\frac{\partial}{\partial x}\left(k_x\frac{\partial\phi}{\partial x}\right)+\frac{\partial}{\partial y}\left(k_y\frac{\partial\phi}{\partial y}\right)+\frac{\partial}{\partial z}\left(k_z\frac{\partial\phi}{\partial z}\right)+c=0 \text{ in } V \quad [78]$$

subject to the Dirichlet condition:

$$\phi=\bar{\phi} \text{ on } S_1$$

and the Cauchy condition:

$$k_x\frac{\partial\phi}{\partial x}m_x+k_y\frac{\partial\phi}{\partial y}m_y+k_z\frac{\partial\phi}{\partial z}m_z+q+r\phi=0 \text{ on } S_2$$

where ϕ is the field variable, k_x, k_y, k_z, and c are functions of x, y, and z, $\bar{\phi}$ is the prescribed value of ϕ, m_x, m_y, and m_z are the direction cosines of the outward normal to the surface (S) of the domain (V) and $S=S_1+S_2$. **Table 1** gives some typical field problems and the associated significances of ϕ and other parameters of eqn [78]. As a second example, consider the Helmholtz equation:

$$\frac{\partial}{\partial x}\left(k_x\frac{\partial\phi}{\partial x}\right)+\frac{\partial}{\partial y}\left(k_y\frac{\partial\phi}{\partial y}\right)+\frac{\partial}{\partial z}\left(k_z\frac{\partial\phi}{\partial z}\right)+\lambda^2\phi=0 \quad [79]$$

with Dirichlet and Cauchy-type boundary conditions. This equation represents several physical problems, such as the vibration of a membrane, the propagation of electromagnetic waves in a waveguide, the oscillatory or seiche motion of an enclosed mass of water in a lake or harbor, and the acoustic vibrations of a body of fluid enclosed in a room or vehicle. The physical significances of k_x, k_y, k_z, ϕ, and λ for various types of problems is given in **Table 2.**

Error Analysis

There are three basic sources of error in a FE solution, as indicated below:

1. Domain approximation errors: Usually some approximation is made in modeling the physical geometry of the system. This introduces an error into the solution.
2. Quadrature and finite precision errors: The FE solution involves the evaluation of integrals numerically in the solution process. For example, in structural analysis, the integrals involved in defining the element stiffness matrices and load vectors are often evaluated numerically. Thus, a truncation error is introduced from these numerical procedures. In addition, because the computer can only maintain a finite number of significant figures, roundoff error is also introduced.
3. Approximation error: In the FEM, the exact solution u is approximated by a series of nodal values of the solution multiplied by the corresponding interpolation functions:

$$u\approx\sum_{i=1}^{n}N_iU_i \quad [80]$$

where N_i denotes the interpolation function associated with node i and U_i the value of u at node i. The majority of work in the FE error analysis has dealt with this source of error; hence only this error is considered in this section.

The error in a FE solution, E, is the difference between the exact, u, and the FE, u_h, solutions:

$$E=u-u_h \quad [81]$$

There are several ways to measure the difference or distance between the two solutions. The pointwise error is the difference of u and u_h at each point of the domain. The supmetric error is the maximum of all absolute values of the difference of u and u_h in the (one-dimensional) domain $V=(a,\ b)$:

$$\|u-u_h\|_\infty=\max_{a\le x\le b}|u(x)-u_h(x)| \quad [82]$$

It can be seen that the supmetric is a real number, whereas the pointwise error is a function. These specifications of local error are not the most convenient approaches and they can, at times, be misleading. For instance, under a point load, the local stresses will be infinite, yet the global solution may be entirely acceptable. For this reason, a norm is used to characterize the level of error in the solution. The two most common norms used are the energy norm and the L_2 norm defined as:

Energy norm:

$$\|u-u_h\|_m=\left(\int_a^b\sum_{j=0}^{M}\left|\frac{\mathrm{d}^j u}{\mathrm{d}x^j}-\frac{\mathrm{d}^j u_h}{\mathrm{d}x^j}\right|^2\mathrm{d}x\right)^{1/2} \quad [83]$$

$$L_2 \text{ norm: } \|u-u_h\|_0=\left(\int_a^b|u-u_h|^2\,\mathrm{d}x\right)^{1/2} \quad [84]$$

where $2m$ denotes the order of the differential equation. To see the origin of the energy norm, consider the generalized second-order ordinary differential equation ($m=1$):

Table 1 Typical steady-state field problems governed by eqn [78]

Physical problem	*Field variable*, ϕ	*Significance of* k_x, k_y, k_z	*c*	*Remarks*
Heat conduction	Temperature	Thermal conductivities	Rate of internal heat generation	q = boundary heat generation r = convective heat transfer coefficient
Seepage flow	Pressure	Permeability coefficients	Internal flow source	
Torsion of prismatic shafts	Stress function	1/G where G is shear modulus	$c = 2\theta$ where θ is angle of twist per unit length	
Irrotational flow of ideal fluids	Velocity potential or stream function		$c = 0$	q = boundary velocity, $r = 0$
Fluid film lubrication	Pressure	k_x and k_y are functions of film thickness and viscosity, $k_z = 0$	Net flow due to various actions	q = boundary flow
Distribution of electric potential	Electric potential (voltage)	Specific conductivities	Internal current source	q = externally applied boundary current
Electrostatic field	Electric force field intensity	Permittivities	Internal current source	
Magnetostatics	Magnetomotive force	Magnetic permeabilities	Internal magnetic field source	q = externally applied magnetic field intensity

Table 2 Typical problems governed by eqn [79]

	Physical significance of		
Problem	k_x, k_y, k_z	ϕ	λ^2
Propagation of electromagnetic waves in a waveguide filled with a dielectric material	$k_x = k_y = k_z = 1/\varepsilon_d$ where ε_d = permittivity of the dielectric	A component of the magnetic field strength vector (when transverse magnetic modes are considered)	$\lambda^2 = \omega^2\mu_0\varepsilon_0$ where ω = wave frequency, μ_0 = permeability of free space, ε_0 = permittivity of free space
Seiche motion (oscillations of an enclosed water mass in a lake or harbor)	$k_x = k_y = h$, $k_z = 0$ where h = depth from the mean water level to the lake or harbor bed	Elevation of free surface (or standing wave) measured from the mean water level	$\lambda^2 = 4\pi^2 / sgT^2$ where g = acceleration due to gravity, T = period of oscillation
Free transverse vibrations of a membrane	$k_x = k_y = k_z = 1$	Transverse displacement of the membrane	$\lambda^2 = \rho\omega^2 / T$ where ρ = mass per unit area, ω = natural frequency, T = tension (force per unit length) of membrane
Vibrations of an enclosed fluid (acoustic vibrations)	$k_x = k_y = k_z = 1$	Excess pressure above ambient pressure	$\lambda^2 = \omega^2/c^2$ where ω = wave frequency, c = wave velocity in the medium

$$Lu = \left\{ -\frac{\mathrm{d}}{\mathrm{d}x}\left[p(x)\frac{\mathrm{d}}{\mathrm{d}x}\right] + q(x)\right\}u = f \qquad [85]$$

The corresponding functional for extremization ($I(u)$) is:

$$I(u) = \frac{1}{2}\int_a^b \left\{p(u')^2 + qu^2 - 2fu\right\}\mathrm{d}x \qquad [86]$$

The energy norm is given by:

$$\|u - u_h\|_1 = \left\{\int_a^b \left\{\left(\frac{\mathrm{d}u}{\mathrm{d}x} - \frac{\mathrm{d}u_h}{\mathrm{d}x}\right)^2 + (u - u_h)^2\right\}\mathrm{d}x\right\}^{1/2} \qquad [87]$$

For structural problems, $I(u)$ denotes the potential energy which contains the same-order derivatives as the energy norm.

Error Estimation

The error estimation procedures can be grouped into two distinct types: *a priori* and *a posteriori* estimates. *A priori* error estimates are based upon the characteristics of the solution and provide qualitative information about the asymptotic rate of convergence. The classic *a priori* error estimate is given by:

$$\|u - u_h\|_m \leq ch^p,\ p = k + 1 - m > 0 \qquad [88]$$

where k is the degree of the interpolation polynomial, h is the characteristic length of an element, p is the rate of convergence, and c is a constant. Eqn [88] gives not only the rate at which the FE solution approaches the exact solution, but also indicates how one can improve the solution. We can decrease the mesh size (called h-convergence) or increase the order of the interpolation polynomial (called p-convergence). Incorporating both h- and p- convergences produces the $h - p$ convergence technique. For illustration, consider the differential equation:

$$\frac{d^2u}{dx^2} + 2 = 0; \quad 0 < x < 1 \qquad [89]$$

with:

$$u(0) = u(1) = 0 \qquad [90]$$

The exact solution of the problem is:

$$u(x) = x(1 - x) \qquad [91]$$

and the FE solutions are given by, for different number of elements, N:

$$\text{For } N = 2: \quad u_h(x) = \begin{cases} hx, & 0 \leq x \leq h \\ h^2\left(2 - \dfrac{x}{h}\right), & h \leq x \leq 2h \end{cases} \qquad [92]$$

$$\text{For } N = 3: \ u_h(x) = \begin{cases} 2hx, & 0 \leq x \leq h \\ 2h^2, & h \leq x \leq 2h \\ 2h^2\left(3 - \dfrac{x}{h}\right), & 2h \leq x \leq 3h \end{cases} \qquad [93]$$

$$\text{For } N = 4: \ u_h(x) = \begin{cases} 3hx, & 0 \leq x \leq h \\ 2h^2 + hx, & h \leq x \leq 2h \\ 6h^2 - hx, & 2h \leq x \leq 3h \\ 3h^2\left(4 - \dfrac{x}{h}\right), & 3h \leq x \leq 4h \end{cases} \qquad [94]$$

The energy and L_2 norms can be determined using $N = 2(h = 0.5)$, $N = 3(h = 0.333)$ and $N = 4(h = 0.25)$ and the results are given in **Table 3**. These results are shown plotted in **Figure 6** using a log–log scale. The slopes of the plots represent measures of the rates of convergence. The results indicate that the error in the energy and L_2 norms have different rates of convergence; the error in the energy norm is of order one lower than the error in the L_2 norm. Physically, this indicates that derivatives (stresses in structural problems) converge more slowly than the values themselves (displacements in structural problems). *A priori* estimates are adequate for determining the convergence rate of a particular FE element solution, but they lack the ability to give quantitative information about the local or global errors of the solution. If refinement of the solution is to be performed, quantitative estimates are clearly needed to determine whether refinement is needed in any given area of the computational domain. For this reason, *a posteriori* (after the solution of the problem) error estimates are developed. Many researchers have developed different estimates over the years and all the methods can be grouped into four categories: (i) dual analysis; (ii) Richardson's extrapolation; (iii) residual type of estimator; and (iv) postprocessing type of estimator.

In the dual analysis, the principles of complementary energy and potential energy are applied to obtain upper and lower bounds, respectively, on the energy of the exact solution. Since the potential and complementary energy principles are fundamentally different, two separate programs are to be used for this analysis. In addition, the solution based on complementary energy is very difficult and hence the dual analysis is not commonly used. The Richardson's extrapolation is a numerical analysis technique for estimating the error in the solution by solving the problem with two different grid sizes, provided the functional form of the solution is known. In the context of the FE method, the *a priori* analysis provides the functional form. Similar to the dual analysis, the extrapolation technique is a classic method of error estimation that has proven to be computationally very expensive in order to compete with other more efficient methods and hence is not widely used.

Table 3 *A priori* estimates of the error in the energy and L_2 norms

h	$\|e\|_0$	$\|e\|_1$
0.5	0.04564	0.2923
0.333	0.02029	0.1935
0.25	0.01141	0.1443

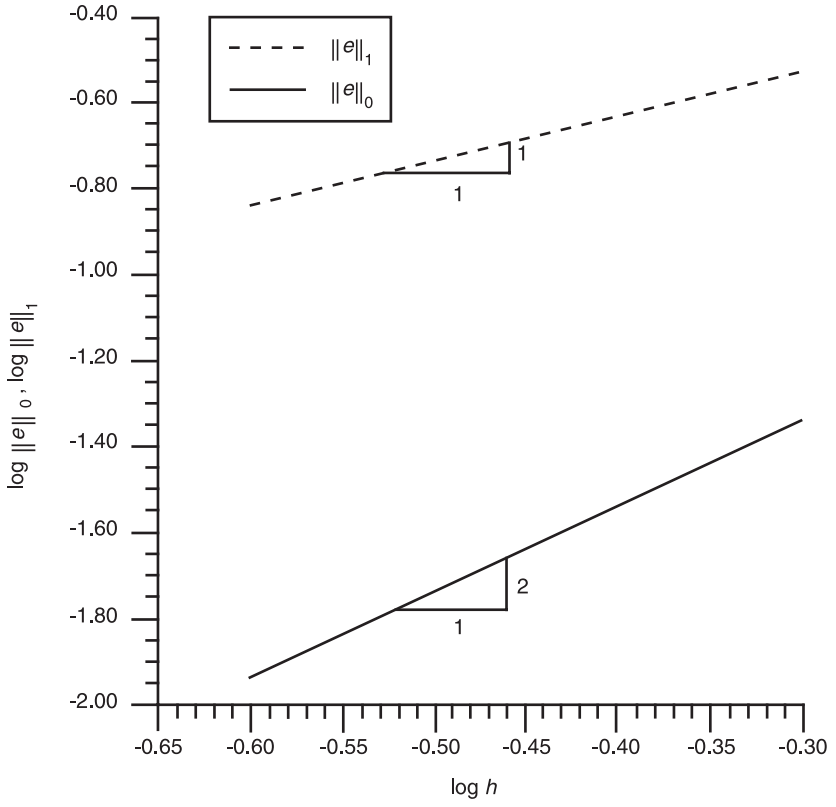


Figure 6 Energy and L_2 norms of error with mesh size.

The residual type of error estimation can be understood by considering the FE solution of the following boundary value problem, stated in operator form:

$$Au + f = 0 \qquad [95]$$

When the FE finite element solution u_h is used, eqn [95] leads to the residual R:

$$Au_h + f = R \neq 0 \qquad [96]$$

Eqn [96] shows that the residual effectively acts as a separate forcing function in the differential equation. This leads to the concept that the FE solution is the exact solution to a perturbed problem with a supplementary pseudo-force system. Subtracting eqn [96] from [95] produces:

$$Ac + R = 0 \qquad [97]$$

where $e = u - u_h$ is the error. Hence the estimation of the error in the problem amounts to finding the solution of this problem. The residual R is composed of residuals in the interior of the domain as well as residuals on the boundary. The domain residuals are determined by substituting the FE solution into the differential equation. The boundary residuals, however, are more complicated since the derivatives of u_h may not be continuous along the boundary.

For the postprocessing type of estimator, the error in the FE stress solution (obtained by differentiating the FE displacement solution) is defined as:

$$e_\sigma = \sigma - \sigma_h \qquad [98]$$

Then the error in the energy norm is computed as:

$$\|e\| = \|u - u_h\| = \left(\int_V e_\sigma^{\mathrm{T}} \mathbf{D}^{-1} e_\sigma \, \mathrm{d}V \right)^{1/2} \qquad [99]$$

where $\mathbf{D}$ is the elasticity matrix. An estimator to e_σ can be produced by replacing σ in eqn [98] by the recovered solution σ^*:

$$e_\sigma \approx e_\sigma^* = \sigma^* - \sigma_h \qquad [100]$$

where $\sigma*$ is interpolated from the nodal values using the same basis functions $\mathbf{N}$ as those used for u_h.

Nomenclature

A, B	square symmetric matrices
C	vector of unknowns
D	elasticity matrix
e	element
E	number of FEs in the system
N	matrix of shape functions
P	total load vector
Q	vector nodal displacement
R	residual
S	surface
V	domain
$\boldsymbol{\varepsilon}$	strain vector
λ	eigenvalue
ϕ	eigenfunction fluid variable
ρ	density
$\boldsymbol{\sigma}$	stress vectors

See also: **Nonlinear systems analysis**; **Nonlinear systems, overview**.

Further Reading

Argyris JH (1965) Continua and discontinua, *Proceedings, Conference on Matrix Methods in Structural Mechanics*, pp. 11–189. Oct. Ohio: Wright-Patterson AFB.

Argyris JH, Kelsey S (1954–5) Energy theorems and structural analysis. *Aircraft Engineering*, vols 26 and 27, Oct to May. (Part I by Argyris and Part II by Argyris and Kelsey).

Clough RW (1960) The finite element method in plane stress analysis. *Proceedings, Second ASCE Conference on Electronic Computation*, pp. 345–78, Sept. PA: Pittsburgh.

Courant R (1943) Variational methods for the solution of problems of equilibrium and vibrations. *Bulletin of the American Mathematical Society* 49: 1–23.

Hrenikoff A (1941) Solution of problems in elasticity by the framework method. *Transactions of the ASME, Journal of Applied Mechanics* 8: 169–75.

Kardestuncer H, Norrie DH (eds) (1987) *Finite Element Handbook*, New York: McGraw-Hill.

Noor AK (1991) Bibliography of books and monographs on finite element technology. *Applied Mechanics Reviews*, 44: 307–17.

Rao SS (1995) *Mechanical Vibrations*, 3rd edn. Reading, MA: Addison-Wesley.

Rao SS (1999) *The Finite Element Method in Engineering*, 3rd edn. Boston: Butterworth-Heinemann.

Ross CTF (1991) *Finite Element for Structural Vibrations*. London: Springer-Verlag.

Synge JL (1957) *The Hypercircle in Mathematical Physics*. London: Cambridge University Press.

Turner MJ, Clough RW, Martin HC, Topp LJ (1956) Stiffness and deflection analysis of complex structures. *Journal of the Aeronautical Sciences* 23: 805–23.

Weaver Jr W, Johnston PR (1987) *Structural Dynamics by Finite Elements*. Englewood Cliffs, NJ: Prentice Hall.

Zienkiewicz OC (1987) *The Finite Element Method*, 4th edn. London: McGraw-Hill.

Zienkiewicz OC, Cheung YK (1967) *The Finite Element Method in Structural and Continuum Mechanics*. London: McGraw-Hill.

Zienkiewicz OC, Zhu JZ (1992) The super convergent patch recovery and a posteriori error estimation. Part 1: The recovery technique, Part 2: Error estimates and adaptivity. *International Journal for Numerical Methods in Engineering*, 33: 1331–64.

FLUID/STRUCTURE INTERACTION

S I Hayek, Pennsylvania State University, University Park, PA, USA

Copyright © 2001 Academic Press

doi:10.1006/rwvb.2001.0166

The field of fluid–structure interaction involves the interaction of a vibrating elastic structure in contact with a fluid. Structures vibrating due to mechanical or fluid sources accelerate the adjoining fluid, resulting in acoustic waves being generated in the fluid, known as acoustic radiation. The other form of structure fluid interaction is the excitation of a structure to vibration due to incident acoustic waves in the adjoining fluid, known as acoustic scattering. In either case, the normal velocity of the structure is matched to the normal particle velocity in the fluid.

For an elastic structure in contact with a large acoustic medium, the acoustic medium acts as an absorber of elastic energy in the form of acoustic energy propagating away from the structure, as well as adding to the inertia of the structure.

Elastic structures such as plates and shells are generally two-dimensional in nature. In this article, representative structures, such as one- and two-dimensional plates, will be explored.

Acoustic Radiation from Line-Force Excited Isotropic Elastic Plates

Consider an infinite thin elastic plate ($x - y$ plane) coupled to a semi-infinite acoustic medium occupying the space $z \geq 0$. The plate is excited by an infinite line

force of magnitude $P_0 e^{-i\omega t}$ (force/unit length) located at $x = 0$ and directed in the same direction as w, i.e., along the positive z-axis. The equation of motion of the forced plate, the acoustic wave equation and the continuity equation are given below:

$$D\left[\nabla^4 w - \alpha^4 w\right] + p(x, z = 0) = q(x) \qquad [1]$$

$$\nabla^2 p + k^2 p = 0 \qquad [2]$$

$$w(x) = -\frac{1}{\rho\omega^2}\frac{\partial p}{\partial z}\bigg|_{z=0} \qquad [3]$$

where α is the plate wavenumber, and α^4 is defined as:

$$\alpha^4 = \frac{\rho_s h\omega^2}{D} = \frac{12\omega^2}{c_p^2 h^2} \qquad [4]$$

The driving line force can be described by $q(x) = P_0\delta(x)$, where δ represents the Dirac delta function. The pressure field of the excited plate is given by:

$$p(x, z) = \frac{\rho\alpha^4 P_0}{2\pi\rho_s h} \times \int_{-\infty}^{\infty} \frac{e^{i\left[ux + iz\sqrt{(u^2 - k^2)}\right]}}{(u^4 - \alpha^4)\sqrt{(u^2 - k^2)} + (\rho\alpha^4/\rho_s h)}\, du \qquad [5]$$

At large distances $kr \gg 1$, one can obtain an asymptotic value of the integral in [5], by the use of the stationary phase method resulting in an expression for the radiated field:

$$p(r, \theta) = P_0\sqrt{\left(\frac{k}{2\pi r}\right)} \times \frac{e^{i(kr - \pi/4)}\cos\theta}{1 - (i\rho_s kh/\rho)\left(\Omega^2 \sin^4\theta - 1\right)\cos\theta} \qquad [6]$$

where $\Omega = \omega/\omega_c$ and coincidence frequency ω_c is given by:

$$\omega_c = \frac{\sqrt{(12)}c^2}{hc_p} \qquad [7]$$

A normalized expression for the pressure given in [6], $|p\sqrt{hr}/P_0|$, is plotted in **Figure 1** for steel plates in water and in **Figure 2** for aluminum plates in water, for several values of the normalized frequency Ω.

The maximum pressure occurs at the coincidence angle θ_c for frequencies higher than the coincidence frequency:

$$\sin\theta_c = \frac{1}{\sqrt{\Omega}} \qquad \Omega \geq 1,$$

where the maximum pressure is given by:

$$p_{\max}(r, \theta_c) = P_0\sqrt{\left(\frac{k}{2\pi r}\right)}\sqrt{\left(1 - \Omega^{-1}\right)}e^{i(kr - \pi/4)} \qquad \Omega > 1 \qquad [8]$$

is plotted in **Figure 3**.

The influence of the fluid loading on the acoustic radiation from excited plates below the coincidence

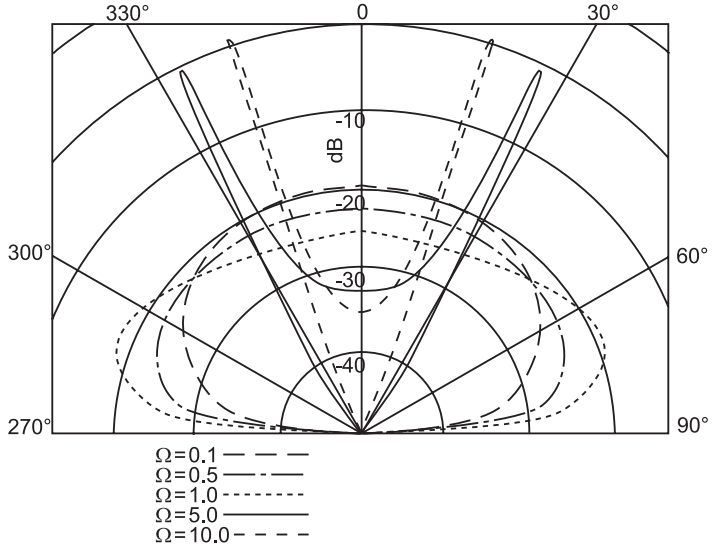


Figure 1 Normalized directivity function for line excited steel plates in water for $\Omega = 0.1-10.0$.

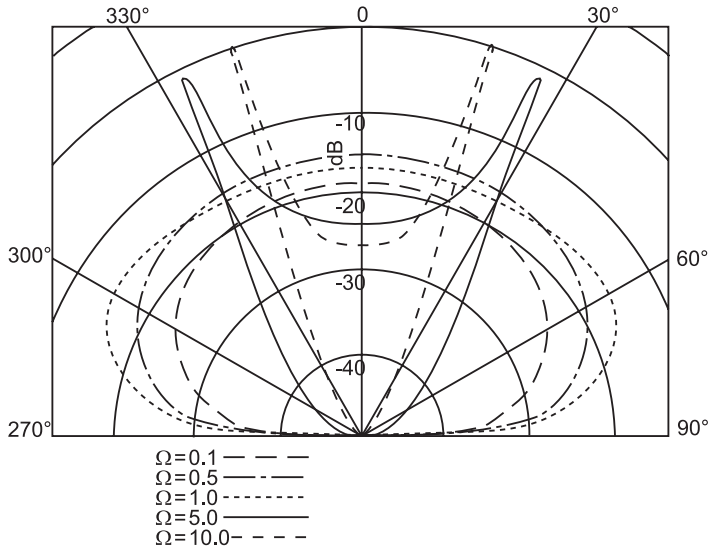


Figure 2 Normalized directivity function for line excited aluminum plates for $\Omega = 0.1-10.0$.

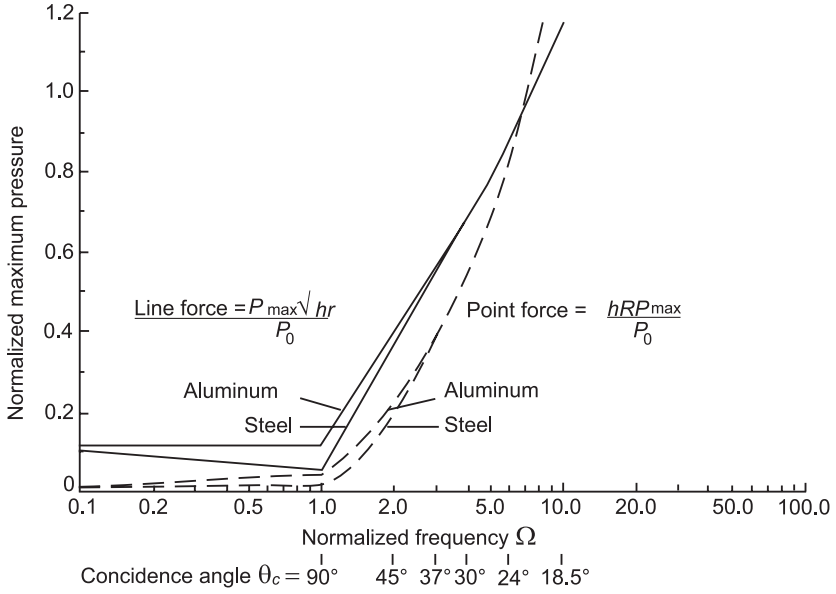


Figure 3 Normalized peak pressure at the coincidence angle for steel and aluminum plates in water excited by line or point forces.

frequency can be obtained approximately. For $\Omega < 1$ one can neglect the term $\Omega^2 \sin^2\theta$ when compared to unity, hence resulting in an approximate expression for the acoustic radiated pressure for frequencies below the coincidence frequency:

$$p \sim P_0 \sqrt{\left(\frac{k}{2\pi r}\right)} e^{i(kr-\pi/4)} \frac{-i\beta \cos\theta}{-i\beta + \cos\theta} \qquad [9]$$

where:

$$\beta = \frac{\rho c}{\rho_s h \omega} = \frac{1}{\mu \Omega}$$

represents the fluid loading parameter. The parameter μ has the following typical values for certain metals and fluids:

$$\mu = 2.6 \text{ (aluminum–water)}, \quad 150 \text{ (aluminum–air)},$$
$$7.0 \text{ (steel–water)}, \quad 450 \text{ (steel–air)}$$

Thus, the fluid loading parameter β is very small for light fluid loading and very large for heavy fluid loading.

To compute the radiated power per unit length of the driving line force, one needs to perform the integration on the radiated farfield pressure as follows:

$$N = \frac{r}{\rho c}\int_0^{\pi/2} |p|^2 \, d\theta = \frac{kP_0^2}{2\pi\rho c}\int_0^{\pi/2} \frac{\cos^2\theta \, d\theta}{1+\mu^2\Omega^2\left(\Omega^2 \sin^4\theta - 1\right)^2\cos^2\theta} \quad [10]$$

The power transmitted to a fluid unloaded plate is given by:

$$N_0 = \frac{P_0^2}{8c\rho_s h\sqrt{\Omega}} \quad [11]$$

Thus, the radiated power, referred to the input power to a fluid unloaded plate defined in eqn [11] becomes:

$$\frac{N}{N_0} = \frac{4\mu\Omega^{3/2}}{\pi}\int_0^{\pi/2} \frac{\cos^2\theta \, d\theta}{1+\mu^2\Omega^2\left(\Omega^2 \sin^4\theta - 1\right)^2\cos^2\theta} \quad [12]$$

The parameter $\mu\Omega = \beta^{-1}$ represents the effect of fluid loading. The radiated power given in eqn [12] is plotted in **Figure 4** for steel and aluminum plates in water.

An expression for the radiated power below coincidence for a general fluid loading may be obtained as follows:

$$\frac{N}{N_0} = \frac{4\mu\Omega^{3/2}}{\pi}\int_0^{\pi/2} \frac{\cos^2\theta \, d\theta}{1+\mu^2\Omega^2\cos^2\theta} = 2\beta\sqrt{(\Omega)}\left[1 - \frac{\beta}{\sqrt{(1+\beta^2)}}\right] \quad [13]$$

Above the coincidence frequency ($\Omega > 1$), the radiated acoustic pressure peaks at the coincidence angle θ_c, a fact that can be used to develop an approximate expression for the radiated power:

$$\frac{N}{N_0} \approx \frac{1}{\pi}\left\{ \arctan\left[4\mu\Omega^{3/2}\left(1-\Omega^{-1}\right)\left(1-\Omega^{-1/2}\right)\right] + \arctan\left[4\mu\Omega\left(1-\Omega^{-1}\right)\right]\right\} \quad \text{for } \Omega = 2$$
$$= 1.0 \qquad \text{for } \Omega \gg 1 \quad [14]$$

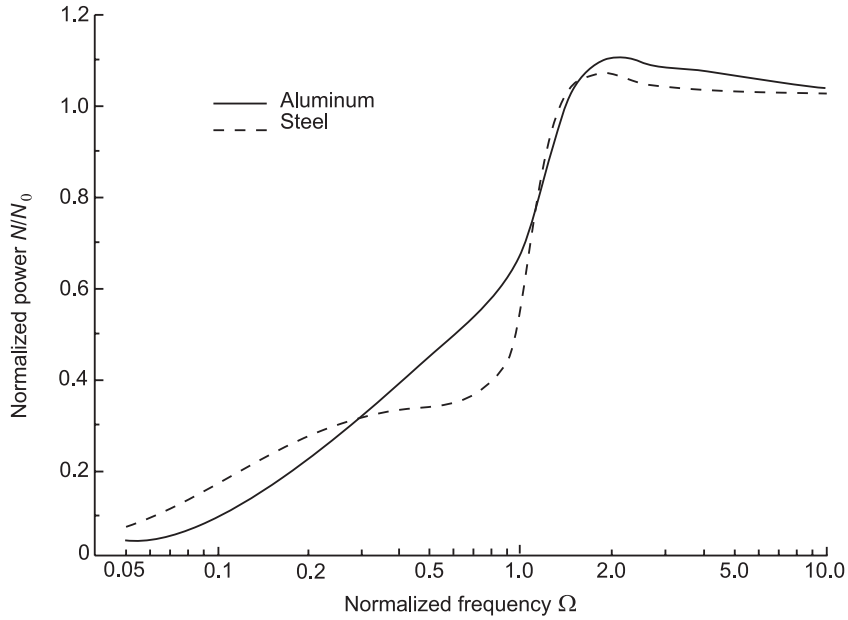


Figure 4 Normalized radiated power from line excited steel and aluminum plates in water.

Acoustic Radiation from Point-force Excited Isotropic Elastic Plates

Consider an infinite thin plate (x–y plane) coupled to a semi-infinite acoustic medium occupying the space $z \geq 0$. The plate is excited by a point force of magnitude $P_0 e^{-i\omega t}$ located at $x = 0$, $y = 0$ and directed in the same direction as w.

The radiated acoustic pressure for a point excited plate is given by:

$$p(r,z) = \frac{P_0}{2\pi}\frac{\rho\alpha^4}{\rho_s h}\int_{-\infty}^{\infty} \frac{uH_0^{(1)}(ur)e^{-z\sqrt{(u^2-k^2)}}\,du}{(u^4-\alpha^4)\sqrt{(u^2-k^2)}+(\rho\alpha^4/\rho_s h)} \quad [15]$$

Using the steepest descent method, it can be shown that an expression for the far-field pressure results in:

$$p(R,\theta) \rightarrow -\frac{iP_0 k}{2\pi}\frac{e^{ikR}}{R}\frac{\cos\theta}{1-i\mu\,\Omega\left(\Omega^2\sin^4\theta-1\right)\cos\theta} \quad [16]$$

The directivity plots for the farfield pressure, normalized to the pressure at $\theta = 0^\circ$, are shown in **Figure 5** for steel–water and in **Figure 6** for aluminum–water for various values of Ω. The maximum pressure occurs at the coincidence angle θ_c for frequencies higher than the coincidence frequency where the maximum pressure is given by:

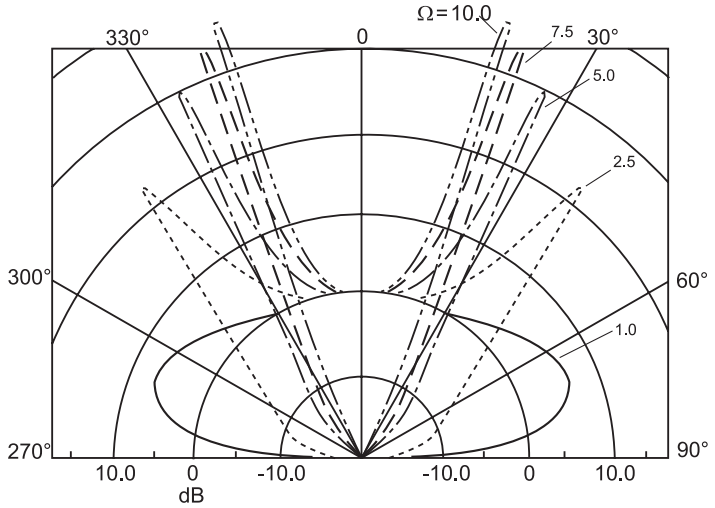


Figure 5 Normalized directivity function for a point excited steel plates in water.

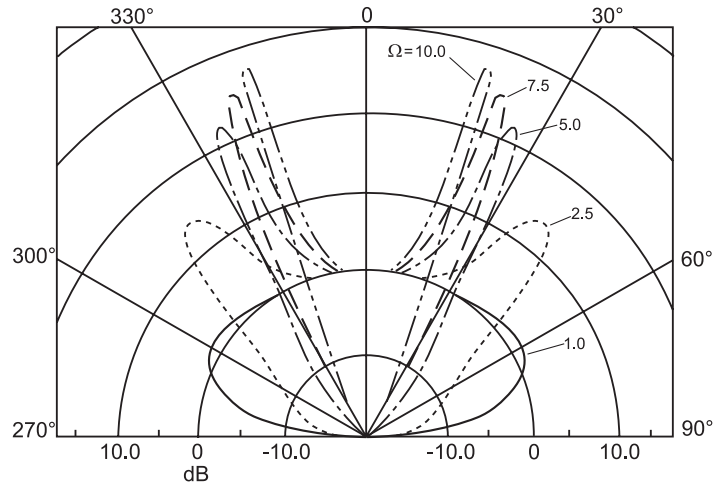


Figure 6 Normalized directivity function for a point excited aluminum plates in water.

$$p_{\max}(r,\theta_c) = -\mathrm{i}\frac{P_0 k}{2\pi}\frac{\mathrm{e}^{\mathrm{i}kR}}{R}\sqrt{(1-\Omega^{-1})} \qquad [17]$$

The maximum pressure is plotted in **Figure 3** for steel and aluminum plates in water. To compute the radiated power, one needs to perform the integration on the radiated far-field pressure as follows:

$$N = \frac{P_0^2 k^2}{4\pi\rho c}\int_0^{\pi/2} \frac{\cos^2\theta \sin\theta \,\mathrm{d}\theta}{1+\mu^2\Omega^2\left(\Omega^2\sin^4\theta - 1\right)^2\cos^2\theta} \qquad [18]$$

The power transmitted to a fluid unloaded plate due to a point force is given by:

$$N_0 = \frac{P_0^2\omega_c}{16c^2\rho_s h} \qquad [19]$$

Thus the expression for the radiated power N, referred to input power N_0 of a fluid unloaded plate becomes:

$$\frac{N}{N_0} = \frac{4\mu\,\Omega^2}{\pi}\int_0^{\pi/2} \frac{\cos^2\theta \sin\theta \,\mathrm{d}\theta}{1+\mu^2\Omega^2\left(\Omega^2\sin^4\theta - 1\right)^2\cos^2\theta} \qquad [20]$$

The radiated power, given in eqn [20] is plotted in **Figure 7** for steel and aluminum plates in water.

An expression for the radiated power below coincidence for a general fluid loading can be obtained approximately as follows:

$$\frac{N}{N_0} = \frac{4}{\pi\mu}\left(1 - \frac{1}{\mu\,\Omega}\ \arctan\ (\mu\,\Omega)\right) \qquad [21]$$

Above the coincidence frequency ($\Omega > 1$), the pressure peaks at the coincidence angle θ_c, a fact that can be exploited to obtain an approximate expression for the radiated power as:

$$\begin{aligned}\frac{N}{N_0} &= \frac{1}{\pi}\Big\{\ \arctan\ 4\mu\,\Omega^{3/2}\left(1-\Omega^{-1}\right)\left(1-\Omega^{-1/2}\right) \\ &\quad +\ \arctan\ 4\mu\,\Omega\left(1-\Omega^{-1}\right)\Big\} \quad \Omega > 1 \\ &= 1.0 \quad \text{for} \quad \Omega \gg 1\end{aligned} \qquad [22]$$

Acoustic Radiation from Point-excited Plates Accounting for Shear Deformation and Rotatory Inertia

It can be seen that the plate flexural phase velocity, as predicted by the classical Bernoulli–Euler plate theory (eqn [4]), is parabolic in the frequency, such that the flexural phase velocity became unbounded when $\omega \to \infty$. Mindlin's correction to the classical plate equation did rectify this anomaly, whereby the phase velocities in the new theory do approach the exact values predicted by the theory of elasticity. The correction to the classical plate theory becomes significant when the driving frequency is higher than twice the coincidence frequency for steel or aluminum plates submerged in water.

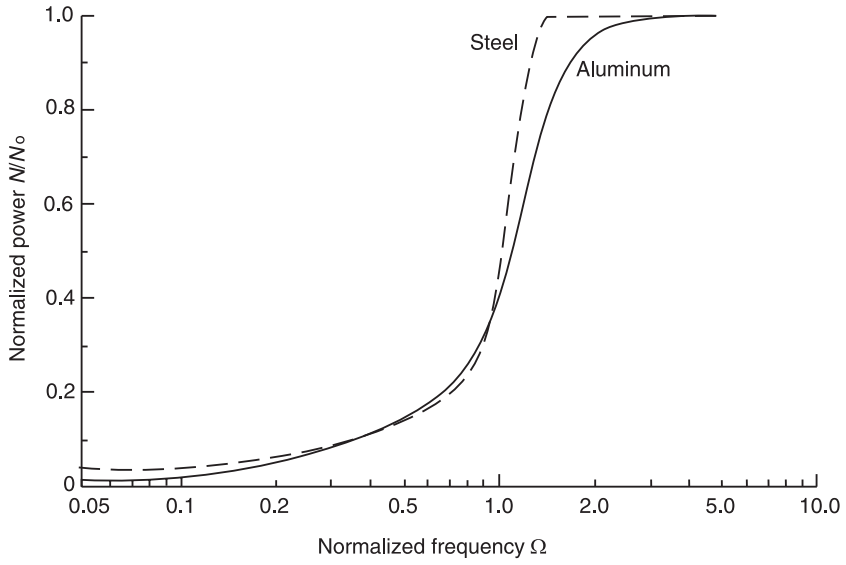


Figure 7 Normalized radiated power from point excited steel and aluminum plates in water.

Consider an infinite plate occupying the space $-\infty < x,\ y < \infty$ in contact with an infinite acoustic medium occupying the semi-infinite space $z \geqslant 0$. The plate is acted upon by a point force located at the origin. Using Mindlin's theory of deformation of plates and describing the point force P_0 and the acoustic surface pressure by $p(r,\ z = 0)$, the resulting equation of axisymmetric motion of a fluid-loaded, point-excited plate is given by:

$$\left(\nabla^2 + \frac{m}{D}S\omega^2\right)\left(D\nabla^2 + mI\omega^2\right)w(r) - m\omega^2 w(r) = \left(1 - S\nabla^2 - \frac{m}{D}SI\omega^2\right)\left[\frac{P_0}{2\pi r}\,\delta(r) - p(r, z = 0)\right] \quad [23]$$

where $S = D/hG\kappa^2$ is the shear deformation factor, $I = h^2/12$ is the rotatory inertia factor and $\kappa^2 = \pi^2/12$ is the Mindlin's shear correction factor.

Using the Hankel transform on the acoustic pressure, one obtains the solution for the pressure field:

$$p(R,\theta) = -\frac{\mathrm{i}P_0 k}{2\pi R}\mathrm{e}^{\mathrm{i}kR}\frac{\cos\theta\, L(\sin\theta,\Omega)}{L(\sin\theta,\Omega) - \mathrm{i}\mu\,\Omega\cos\theta\left\{1 - \Omega^2\left[\sin^2\theta - \left(c^2\Big/c_p^2\right)\right]\left[\sin^2\theta - \left(c^2/c_s^2\right)\right]\right\}} \quad [24]$$

where $R = \sqrt{r^2 + z^2}$

$$L(\sin\theta,\Omega) = 1 + \Omega^2\frac{c^2}{c_s^2}\left(\sin^2\theta - \frac{c^2}{c_p^2}\right)$$

$$c_s^2 = \frac{\kappa^2 E}{2(1+\upsilon)\rho_s} = \frac{\kappa^2(1-\upsilon)}{2}c_p^2 \quad < c_p^2$$

It should be noted that if $\Omega \ll 1$, then:

$$p(r,\theta) \to \frac{-\mathrm{i}P_0 k}{2\pi R}\quad \mathrm{e}^{\mathrm{i}kR}\frac{\cos\theta}{1 - \mathrm{i}\mu\,\Omega\cos\theta}\quad \Omega \ll 1 \quad [25]$$

which is the low-frequency limit of the radiated acoustic pressure of the classical Bernoulli–Euler plate.

The radiated pressure predicted by eqn [24] has two peaks. The two peaks can be identified by setting the second term in the denominator of eqn [24] to zero, resulting in two solutions for $\sin\theta_c$ given by:

$$\sin\theta_{\substack{c3\\c4}} = \left\{\frac{1}{2}\left(\frac{c^2}{c_s^2} + \frac{c^2}{c_p^2}\right) \pm \left[\frac{1}{4}\left(\frac{c^2}{c_s^2} - \frac{c^2}{c_p^2}\right)^2 + \frac{1}{\Omega^2}\right]^{1/2}\right\}^{1/2} \quad [26]$$

It can be shown that there are no real roots θ_c if the frequency is below the coincidence frequency, signifying that there are no peaks when $\Omega < 1$. It can also be shown that if:

$$\frac{2}{\Omega^2} - \frac{c^4}{c_p^2 c_s^2} > 0 \qquad \Omega > 1 \quad [27]$$

there is only one real root for the coincidence angle θ_c. The cut-off frequency up to which only one peak occurs is solved by equating eqn [27] to zero, giving $\Omega_{co} = 7.0$ for steel–water and 6.7 for aluminum–water. For frequencies above the cut-off frequency Ω_{co}, two peaks exist at two angles of coincidences θ_c predicted by eqn [26]. It is interesting to note that the classical plate theory predicts a single peak, occurring at the coincidence angles θ_c which approaches zero (towards the normal to the plate) as $\Omega \to \infty$. The high-frequency limit of the coincidence angles θ_c approach constant limits. This means that the two peaks occur at angles which approach certain values as $\Omega \to \infty$ unlike a classical plate where $\theta_c \to 0$. The limit for the two coincidence angles as $\Omega \to \infty$ are given by:

$$\begin{aligned}
\sin\theta_{c3} \to \frac{c}{c_s} \quad \theta_{c3} &= 29.9^\circ \quad \text{steel–water}\\
&= 32.8^\circ \quad \text{aluminum–water}\\
\sin\theta_{c4} \to \frac{c}{c_p} \quad \theta_{c4} &= 16.6^\circ \quad \text{steel–water}\\
&= 15.9^\circ \quad \text{aluminum–water}
\end{aligned}$$

The directivity functions for the radiated pressure for frequencies $\Omega = 0.3{-}9.0$ are plotted for steel plates in water and air in **Figure 8** and **Figure 9**, respectively. One can see that the two peaks are confined between $\theta_{c3} = 29.9^\circ$ and 90° and $\theta_{c4} = 0^\circ$ and 16.6° respectively. The radiated power of steel plates in air and water are plotted in **Figure 10**. (**Figures 8–10** are reprinted by permission of Dr. Alan Stuart, Penn State University Ph.D. thesis, 1972.)

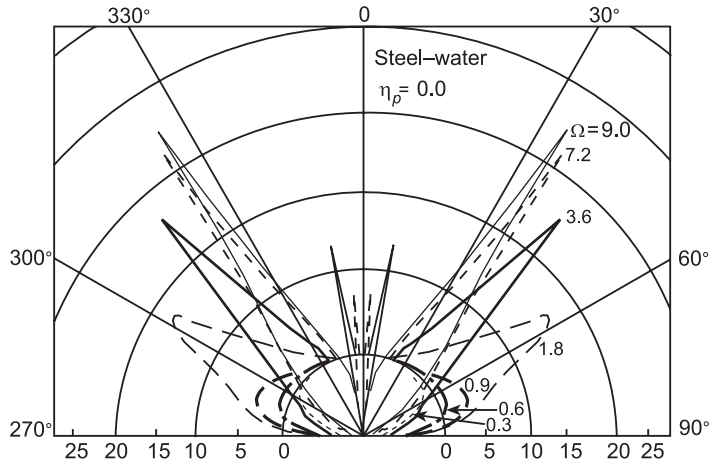


Figure 8 Normalized directivity function for a steel plate in water.

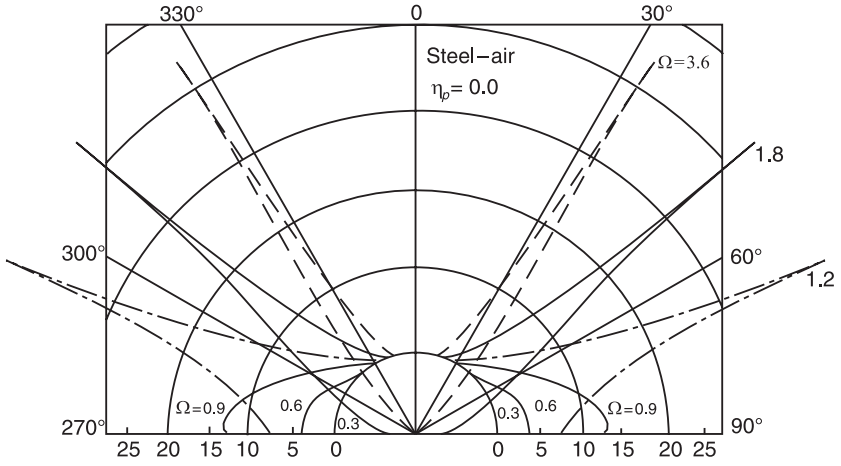


Figure 9 Normalized directivity function for a steel plate in air.

Influence of Damping on the Radiated Pressure

The influence of damping on the radiated pressure from excited infinite plates can be studied by introducing a loss factor in the representation of the Young's modulus, i.e., let $\overline{E} = E(1 + i\eta)$, η being the loss factor. One does not need to rederive the expressions for the radiated sound, it is sufficient only to introduce a complex Young's modulus in the coincidence frequency $\bar{\omega}_c$, the fluid loading term $\bar{\mu}$ and the plate speed $\bar{c}_p$. Thus for $\eta \ll 1$:

$$\begin{aligned}
\bar{c}_p &\approx c_p\left(1 + \frac{1}{2}i\eta\right) \\
\bar{\omega}_c &= \frac{\sqrt{(12)}c^2}{h\bar{c}_p} \approx \omega_c\left(1 - \frac{1}{2}i\eta\right) \\
\bar{\mu} &= \frac{\sqrt{(12)}c\rho_s}{\bar{c}_p\rho} \approx \mu\left(1 - \frac{1}{2}i\eta\right) \\
\bar{\Omega} &= \frac{\omega}{\bar{\omega}_c} \approx \Omega\left(1 + \frac{1}{2}i\eta\right) \\
\bar{\beta} &= \bar{\mu}\,\bar{\Omega} = \mu\,\Omega = \beta
\end{aligned} \qquad [28]$$

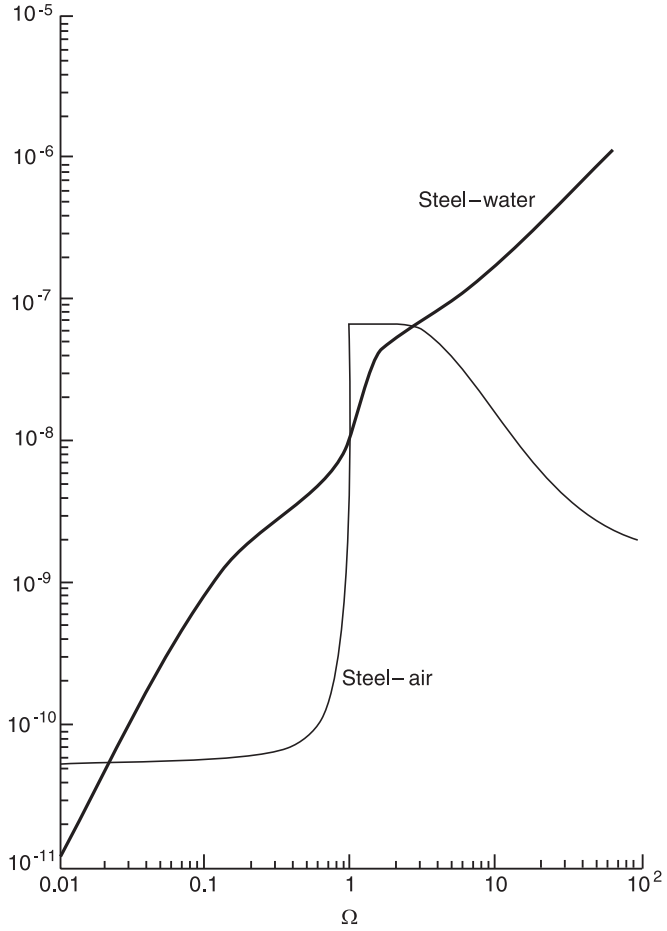


Figure 10 Normalized radiated power from point excited steel plate in water and air.

Substitution of the relationships in eqn [28] into the expressions for the radiated pressure, say eqn [16], for a point excited plate, results in a new expression as follows:

$$p(R,\theta) = -\frac{\mathrm{i}P_0 k}{2\pi}\frac{\mathrm{e}^{\mathrm{i}kR}}{R}\frac{\cos\theta}{1-\mathrm{i}\mu\Omega\cos\theta\left[\Omega^2(1+\mathrm{i}\eta)\sin^4\theta-1\right]} \qquad [29]$$

In the very low-frequency limit, $\Omega^2 < 1$, the influence of the damping is negligible. For excitation frequencies above the coincidence frequency ($\Omega > 1$), the influence of the damping on the directivity function is negligible except near the coincidence angle θ_c. The peak pressure at the coincidence angle is given by:

$$p_{\max}(R,\theta_c) = -\frac{\mathrm{i}P_0 k}{2\pi}\frac{\mathrm{e}^{\mathrm{i}kR}}{R}\frac{\sqrt{(1-\Omega^{-1})}}{1+\eta\mu\Omega\sqrt{(1-\Omega^{-1})}} \qquad [30]$$

The peak pressure is influenced greatly by the loss factor η, especially at high frequencies where $p_{\max}$ approaches:

$$p_{\max}(R,\theta_c) = -\frac{\mathrm{i}P_0 k}{2\pi}\frac{\mathrm{e}^{\mathrm{i}kR}}{R}\frac{1}{\eta\mu\Omega} \qquad \Omega \gg 1 \qquad [31]$$

The influence of the loss factor on the radiated power at high frequencies can be obtained by using eqn [29] resulting in an expression:

$$\frac{N}{N_0} \rightarrow \frac{\rho c}{\rho c + \eta\omega m} \qquad \Omega \gg 1 \qquad [32]$$

The limit given in eqn [32] can be shown to apply also to line excited isotropic plates.

Nomenclature

I	rotatory inertia factor
N	radiated power

N_0	input power of unloaded plate
P_0	line or point force
S	shear deformation factor
α	plate wavenumber
β	fluid loading parameter
ω_c	coincidence frequency
θ_c	coincidence angle
Ω_{co}	cut off frequency
η	loss factor

See also: **Noise**, Noise radiated by baffled plates; **Structure–acoustic interaction, high frequencies**; **Vibration generated sound**, Fundamentals; **Vibration generated sound**, Radiation by flexural elements.

Further Reading

Cremer L, Heckl M, Unger EE (1973) *Structure-Borne Sound*. Berlin: Springer-Verlag.

Fahy F (1985) *Sound and Structural Vibrations*. London: Academic Press.

Junger MC, Feit D (1993) Sound, structures, and their interaction. *Acoustical Society of America*. New York: American Institute of Physics.

Mindlin RD (1951) Influence of rotatory inertia and shear on flexural motion of isotropic elastic plates. *Journal of Applied Mechanics* 18: 31–38.

Skudrzyk EJ (1968) *Simple and Complex Vibratory Systems*. Pennsylvania: The Pennsylvania State University Press.

FLUTTER

J Wright, University of Manchester, Manchester, UK.

Copyright © 2001 Academic Press

doi:10.1006/rwvb.2001.0126

Introduction to Aeroelasticity

Aeroelasticity is the science of the interaction of elastic, inertia and aerodynamic forces on a structure, shown schematically in Collar's aeroelastic triangle (**Figure 1**). Aeroelasticity differs from classical vibration studies (the interaction of elastic and inertia forces) in that aerodynamic forces arise from static or dynamic deformations of the structure when in an airflow and then feed back to modify the deformation. The stiffness of the structure is usually the critical feature in determining aeroelastic effects. (However, for a control surface, the moment of the mass about the hinge line can also be very important.) Aeroelastic behavior is also influenced by thermal effects (aerothermoelasticity) and by the influence of closed-loop control feedback effects (aeroservoelasticity).

Static Aeroelasticity

Static aeroelasticity concerns the interaction between 'elastic' and 'aerodynamic' forces. A brief coverage will be given here to show how this interaction leads to 'aeroelasticity phenomena'.

For an aerodynamic surface (e.g., wing or tail), the aerodynamic force normal to the airstream (usually called lift) increases with (speed)^2 and with the angle of incidence (the angle between the surface and the flow direction) as shown in **Figure 2** for a cross-section of the surface. The lift will normally cause the surface to twist 'leading edge up' if the surface is

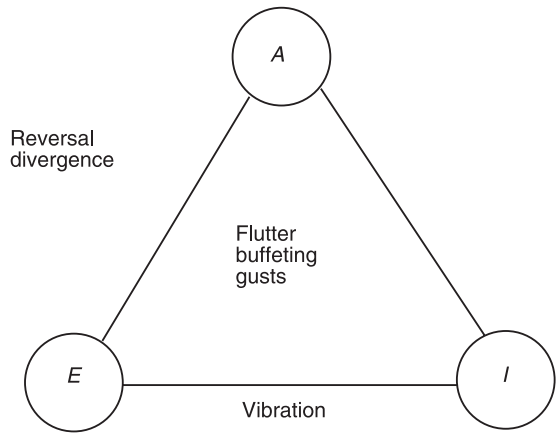


Figure 1 Collar's aeroelastic triangle. *A*, aerodynamic forces; *E*, elastic forces; *I*, inertia forces.

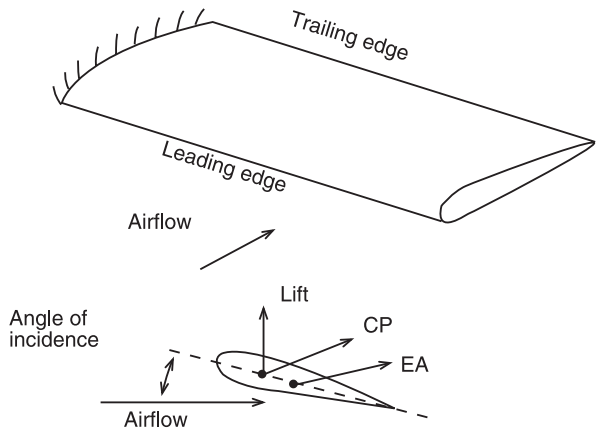


Figure 2 Aerodynamic notation. CP, center of pressure; EA, elastic axis.

flexible because the centre of pressure on the section is usually forward of the elastic axis (i.e., axis of twist) as shown in **Figure 3**. The twist causes the angle presented by the surface to the airstream to increase; therefore the aerodynamic force increases further, increases the twist further and so on until an equilibrium condition is reached.

In practice the situation is more complex; the overall flight attitude of the aircraft needs to be adjusted to compensate for the changes in lift due to surface flexibility effects so that the overall aircraft remains in equilibrium (i.e., it is 'trimmed'). Thus it is only strictly true to speak of the divergence speed for the whole aircraft, and not for a cantilevered aerodynamic surface.

At a sufficiently high speed, the 'divergence' speed, flight becomes impossible because an equilibrium condition cannot be reached; this was a critical problem in the early days of flight where wings were extremely flexible. Langley's attempt at flight, shortly before the Wright brothers' successful first flight in 1903, is thought to have failed on its catapulted launch due to wing divergence.

In practice, divergence is unlikely to occur in modern aircraft because, as the flight speed increases, it will probably become impossible to trim the aircraft as the divergence condition approaches. Also, other aeroelastic effects tend to occur at lower speeds.

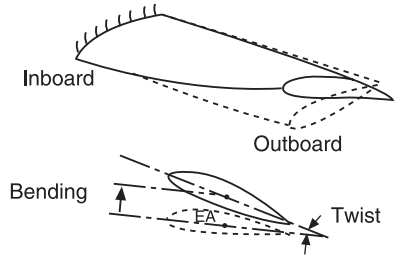


Figure 3 Aerodynamic surface deformation.

A further outcome of this static aeroelastic effect is that the spanwise lift distribution is altered by the surface twist; the overall surface centre of pressure moves outboard for an unswept and untapered surface, so altering the internal load distribution (e.g., bending moments, etc.). However, the effect of sweep-back of the surface is to move the overall centre of pressure inboard and to increase the divergence speed. On the other hand, forward sweep aggravates the divergence effect and some form of aeroelastic 'tailoring' is necessary (e.g., designing a composite wing such that it twists leading-edge down under aerodynamic load instead of leading edge up).

A different but important static aeroelastic phenomenon is the fact that the effectiveness of a trailing edge control surface decreases as speed increases. This is because the upwards control force associated with a trailing-edge down control deflection acts behind the elastic axis and causes the whole surface to twist, leading-edge down. The effect of this twist is to reduce the effectiveness of the control deflection in comparison with a rigid surface, as shown in **Figure 4**. At the so-called 'reversal' speed, the two effects are equal and the control effectiveness becomes zero.

The reversal speed for a particular surface may never be reached in practice because the aircraft will gradually become impossible to trim as the control effectiveness degrades; the control deflections will eventually reach their physical limits. However, in practice, the overall control effectiveness of any control surface may deteriorate to an unacceptable degree, especially for the outboard ailerons of a commercial aircraft; for this reason, the outboard (low speed) ailerons are often locked above a certain speed.

Dynamic Aeroelasticity

Dynamic aeroelasticity concerns the interaction between inertia, elastic, and unsteady aerodynamic forces. This dynamic problem is more complex than static aeroelasticity, since vibration of the structure is

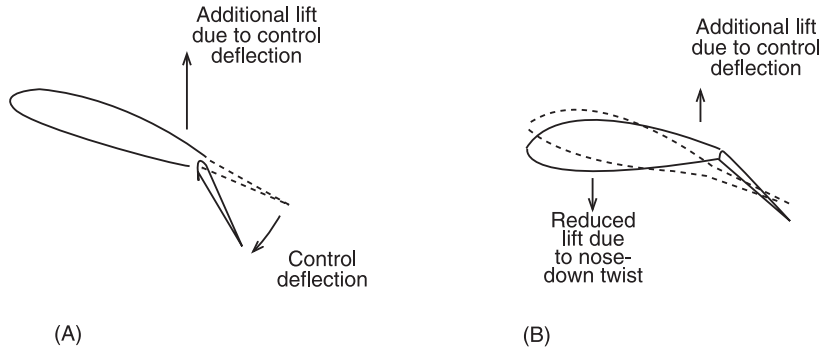


Figure 4 Control effectiveness. (A) Rigid surface; (B) flexible surface.

also involved. For aircraft applications, there are a number of different phenomena that can occur. The most important of these is flutter. Flutter is an *instability* of the aircraft (or some part of it) where, beyond the so-called 'flutter' speed, vibration of the structure increases in amplitude, theoretically without limit. Flutter can lead to the destruction of the aircraft in a very short time. It has been a major problem historically and still is today. The first known example of flutter was in 1916 when the Handley Page O/400 bomber experienced violent tail oscillations (around $\pm 45^{\circ}$). Since then, there have been many flutter incidents, some with catastrophic consequences to human life. Flutter is the main subject of this item and will be covered in more detail later on.

Other topics involving dynamic aeroelastic effects are: control surface buzz, buffeting, and the response to rapid maneuvers (e.g., pitch, roll), gusts, turbulence, store release, birdstrike, landing and taxiing, etc. These and other response-related issues are covered elsewhere (see **Aeroelastic response**).

Other Applications of Aeroelasticity

Problems of static and dynamic aeroelasticity occur not only for aircraft but also for other aerospace vehicles and even for nonaerospace structures. Helicopters and space launch vehicles suffer from similar effects, as do propeller/fan and compressor/turbine blades in aero-engines. Rotational motion of a structure leads to an even greater complexity in the dynamics and aerodynamics.

Civil engineering structures such as bridges, chimneys and transmission lines can also experience aeroelastic effects. The best known event of this type is the failure of the Tacoma Narrows bridge in 1942 due to a form of flutter (stall flutter) involving separated flow and vortex shedding. Even racing car designers need to consider aeroelastic effects for add-on wings.

Aeroelastic Flutter Model

Basic Vibration Model

In order to be able to predict dynamic aeroelastic effects such as flutter, it is essential to generate a mathematical model of the aircraft structure as a first step. Later on, aerodynamic terms will be added into the equations of motion. The basic mathematical model of the aircraft must be able to represent its vibration behavior over the frequency range of interest, typically 0–40 Hz for a large commercial aircraft, 0–60 Hz for a small commercial aircraft and 0–80 Hz for a military aircraft. Thus the model will need to yield natural frequencies and normal mode shapes up to frequencies beyond these limits.

Until the last 10 years or so, the traditional approach to determining a mathematical model for aircraft with fairly slender wings was to represent the major aircraft components (e.g., wing, front fuselage, rear fuselage, tailplane, fin) by beams that can bend and twist. Each beam is divided into several sections or elements (aligned chordwise in the case of an aerodynamic lifting surface) as shown in **Figure 5**.

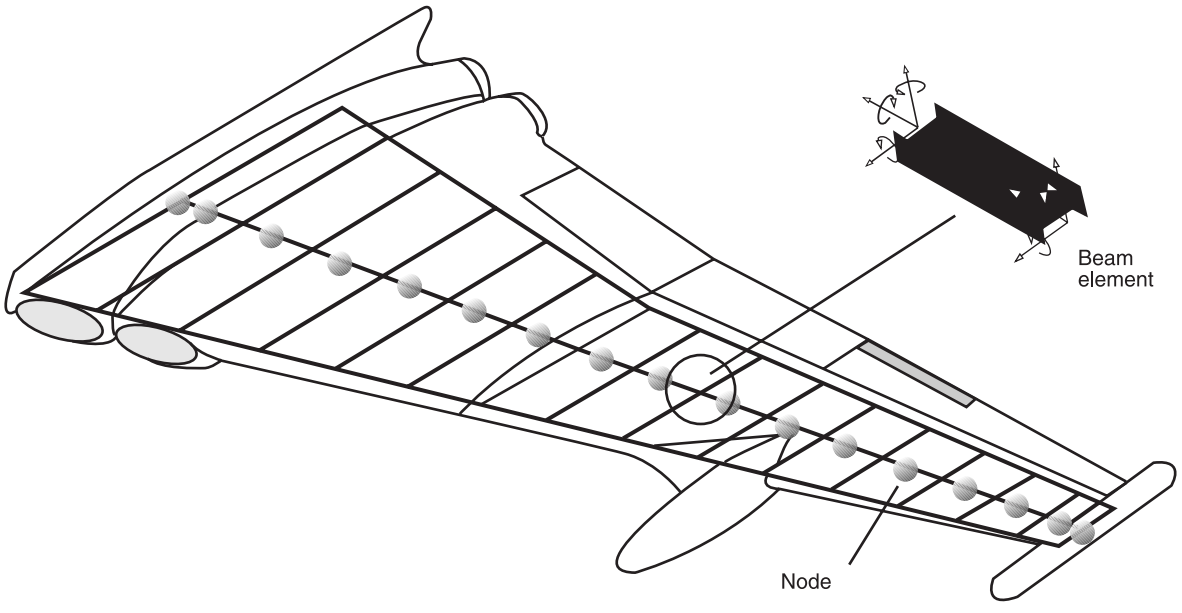


Figure 5 Representation by beam/stick elements/sections. Each beam element represents the stiffness properties of the strip of the wing (courtesy of Airbus).

The combination of such 'beams' for all parts of the aircraft is sometimes called a 'stick' or 'beam' model, as shown in **Figure 6**. Each component beam is 'cantilevered' from the point where it is connected to the adjacent component beam.The beam equations of motion expressed in terms of the displacements and rotations of each section are then set up via mass and stiffness (or flexibility) matrices and the natural frequencies and normal mode shapes are computed; these are termed the 'branch' modes for that component. The beam equations are then transformed into 'branch mode coordinates' and the resulting uncoupled model is truncated by discarding some of the modes. Branch mode coordinates are so-called 'generalized' coordinates that define the proportion of each branch mode present in the model (analogous to the common 'modal coordinates'. The branch mode models for each component are then combined into a single model and the fixed datum point is allowed freedom to move. Then the free–free (i.e., unsupported) modes of the overall aircraft can be calculated.

More recently, the finite element method has been used to set up the equations of motion for the aircraft. The whole structure, or each separate component, is meshed using a range of element types; the dynamic model is not usually as detailed in structural representation as the model used for stress analysis. **Figure 7** shows an example of a model for wing and pylons. The assembled equations of motion are of the form:

$$\mathbf{M}\ddot{\mathbf{w}} + \mathbf{K}\mathbf{w} = 0 \qquad [1]$$

Here $\mathbf{M}$ and $\mathbf{K}$ are the $(N \times N)$ mass and stiffness matrices and $\mathbf{w}$ is the $(N \times 1)$ vector of structural displacements/rotations. (Note that the stick model also yields equations of the same form.)

The first $n(\ll N)$ natural frequencies, $\omega_j (j = 1, 2 \ldots, n)$, and normal mode shapes, $\boldsymbol{\varphi}_j (j = 1, 2 \ldots, n)$, of the structure are then computed using an eigenvalue solution procedure. Typical mode shapes involve bending and twisting of the wing and fuselage, with engine and tail motion

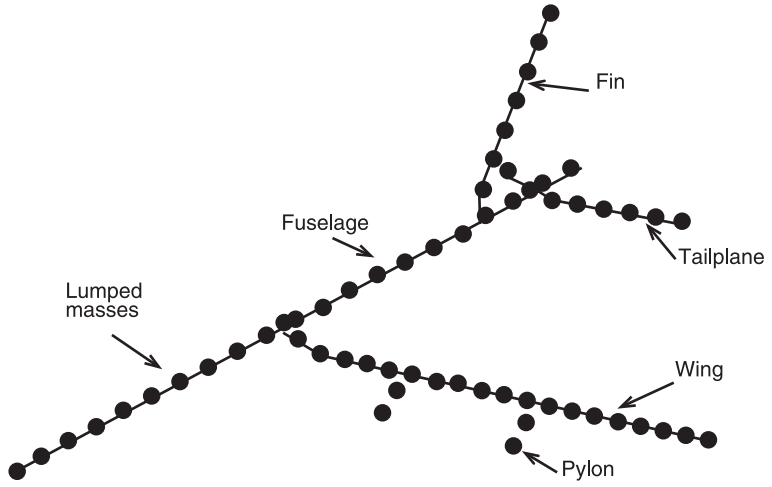


Figure 6 Aircraft 'stick' or 'beam' model (courtesy of Airbus).

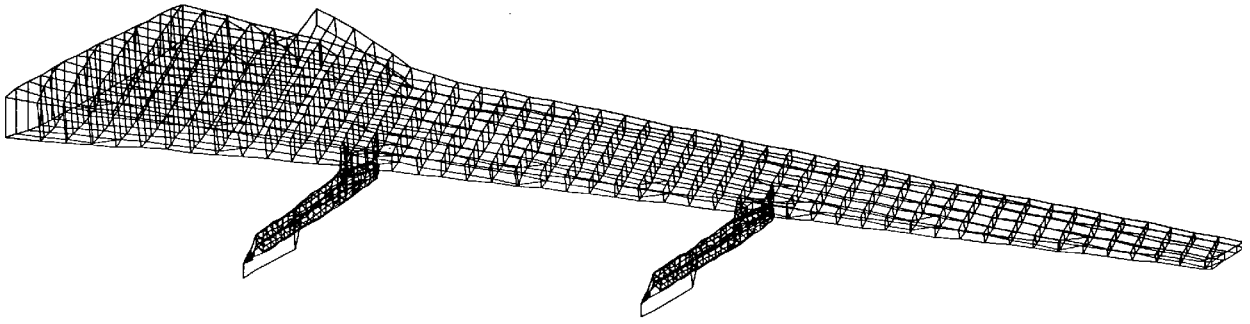


Figure 7 Finite element model for wing/pylons (courtesy of Airbus).

where relevant (**Figure 8**). Often, only half the aircraft is considered so as to exploit symmetry.

In order to reduce the number of equations used in determining aerodynamic forces and in obtaining the flutter solution, the equations are transformed to modal space using the transformation:

$$\mathbf{w} = \mathbf{\Phi q} \qquad [2]$$

Here $\mathbf{\Phi} = [\phi_1\, \phi_2 \ldots \phi_n]$ is the modal matrix and $\mathbf{q}$ is the $(n \times 1)$ vector of modal (or generalized) coordinates. If eqn [2] is substituted into [1] and the equation premultiplied by $\mathbf{\Phi}^{\mathrm{T}}$ then because of the orthogonality of modes, the final equation is:

$$\mathbf{A}\ddot{\mathbf{q}} + \mathbf{E}\mathbf{q} = \mathbf{0} \qquad [3]$$

Here $\mathbf{A} = \mathbf{\Phi}^{\mathrm{T}}\mathbf{M}\mathbf{\Phi}$ and $\mathbf{E} = \mathbf{\Phi}^{\mathrm{T}}\mathbf{K}\mathbf{\Phi}$ are the diagonal $(n \times n)$ modal (or generalized) mass and stiffness matrices.

Thus the large set of N finite element equations of motion have been reduced to a small set of n uncoupled single-degree-of-freedom equations; typically, N is of the order of n^3 and maybe only 20–40 modes are retained. Note that separate analyses are usually performed for symmetric and antisymmetric behavior of the aircraft and for different fuel and payload states.

If the finite element model was set up for a component (i.e., branch), the process would be repeated for each component and the results combined, rather like the branch mode models for the 'stick' model representation, in order to yield an equation of the form of [3]. Modeling the whole aircraft in one step would obviously lead to the same form of equation.

Unsteady Aerodynamic Model

The next phase in the process of estimating the flutter behavior of the aircraft is to introduce the aerodynamic forces that arise from the general motion of the vibrating aircraft. This is an extremely difficult task because the aerodynamic forces depend upon the history of the motion and also 'lag' behind the motion of the relevant aerodynamic surface.

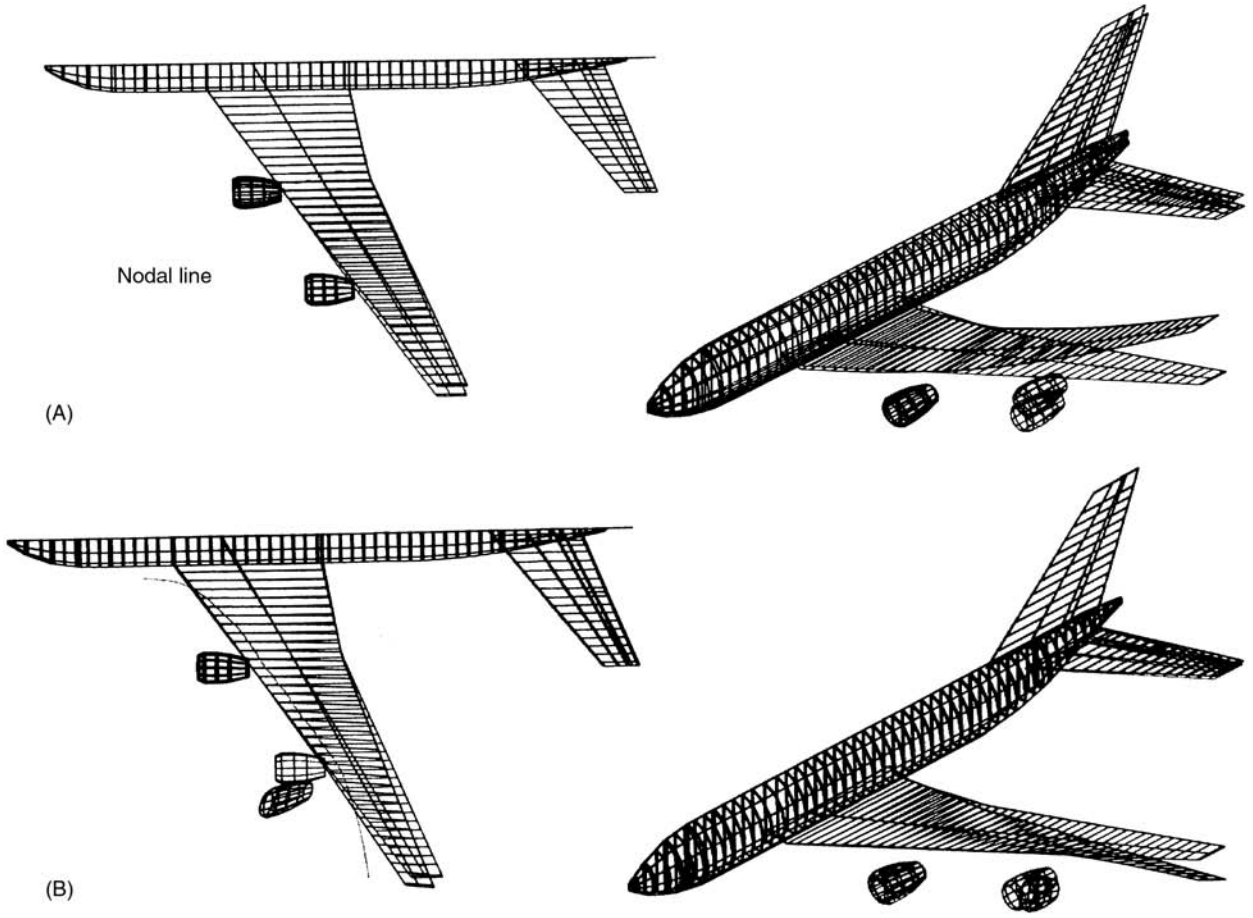


Figure 8 (A) Wing-bending mode shape; (B) wing torsion mode shape. (Courtesy of Airbus).

The ideas behind unsteady aerodynamics will be introduced in this section using the classical 2D approach, though it should be emphasized that more advanced and accurate 3D methods are used in current practice (see later).

For example, consider a 2D airfoil in an incompressible (Mach number $\ll 1$) and inviscid flow (i.e., ignoring compressibility and viscous effects) given a unit step change in the angle presented to the airstream (i.e., angle of incidence). The resulting lift force takes time to build up because the flow around the airfoil surface cannot respond instantaneously. The resulting step response function is shown in **Figure 9**.

The response is determined by the so-called Wagner function (which has the same shape as **Figure 9**). This behavior is an unsteady aerodynamic effect, as distinct from the quasisteady effect in which the force is assumed to develop instantly following any change in incidence. Given the Wagner function it would be possible to use a convolution integral to obtain the aerodynamic force due to a general pitching/heaving motion of the 2D surface. (This process is analogous to computing the response of a dynamic system by considering the input to be made up of a sequence of impulses and using the system impulse response function.) Using a strip theory approximation, in which a slender 3D wing is represented by a series of nominally independent streamwise 2D strips (see **Figure 5**), the resulting aerodynamic force on a complete vibrating wing could be estimated.

Unfortunately, such a time domain convolution representation is not convenient for determining the flutter stability of an aircraft. Instead, an approach has been developed in which the aerodynamic forces are obtained in the frequency domain by calculating the aerodynamic force due to oscillatory motion of the airfoil surface at different frequencies. In this case, the unsteady effect is manifested as a phase lag and attenuation on the harmonic aerodynamic force when it is compared to the quasisteady result, as shown in **Figure 10**. The lag and attenuation may be shown to be a nonlinear function of the nondimensional frequency parameter:

$$\nu = \frac{\omega c}{V} \qquad [4]$$

Here ω is the frequency of the oscillatory motion, c is a characteristic length (typically the airfoil chord), and V is the true airspeed. A zero frequency parameter corresponds to the quasisteady condition. The higher the frequency parameter, the larger is the lag and attenuation. Sometimes a reduced frequency, $k = \nu/2$, is employed in place of ν (US notation).

The complex Theodorsen function, $C(k)$, is essentially a frequency-domain equivalent of the time-domain Wagner function and may be expressed as:

$$C(k) = F(k) + iG(k) \qquad [5]$$

Here, i is the complex number and F, G are the real and imaginary parts as shown in **Figure 11**. The real part defines the component of force in phase with the motion whereas the imaginary part represents the out-of-phase component. Strictly, the Theodorsen function is the Fourier Transform of the response to an impulsive incidence (as opposed to a step). This

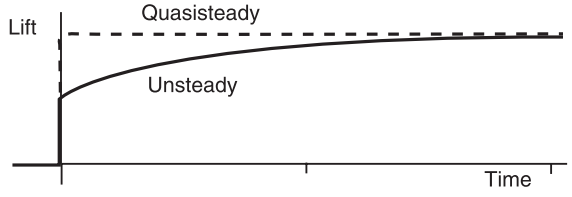


Figure 9 Change in lift following a step change in incidence.

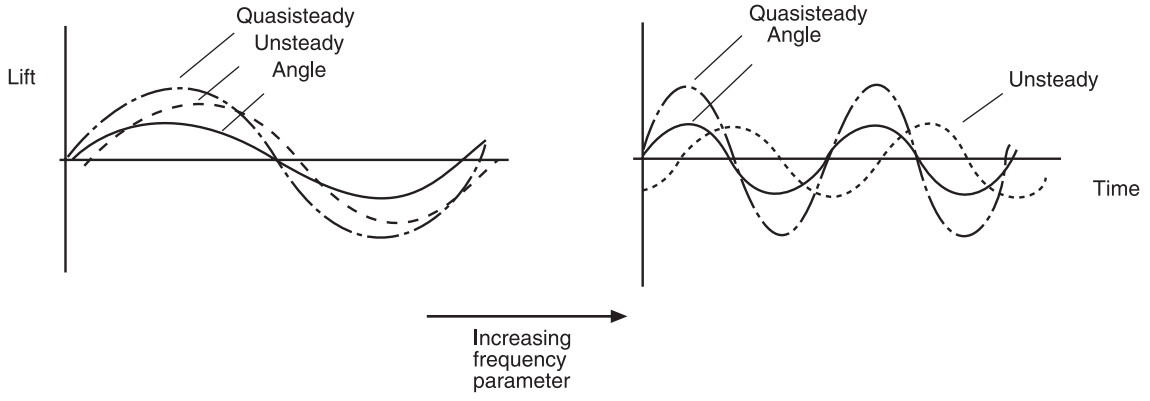


Figure 10 Variation of lift under steady-state oscillatory aerofoil motion.

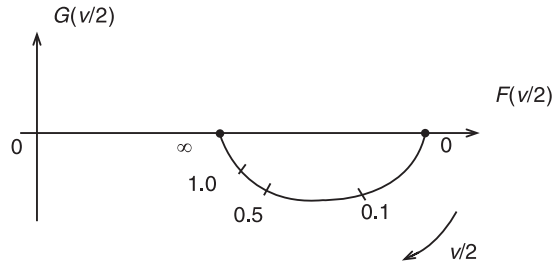


Figure 11 Theodorsen function shown in Argand diagram form.

complex function may also be regarded as a filter that converts the quasisteady aerodynamic forces into unsteady forces.

Using the Theodorsen function, the unsteady lift and pitching moment corresponding to a harmonic heave-and-pitch motion of a 2D airfoil at a single frequency may be determined. It can be shown that the lift and moment have two components, one in phase with the displacement motion (proportional to airspeed squared) and the other in phase with the velocity motion (proportional to airspeed).

Thus, using strip theory for this simple case, the distribution of lift forces and pitching moments along a slender 3D wing oscillating in one of its normal modes, may be found. Consequently, the aerodynamic modal (or generalized) forces applied in this mode, and in the other modes, may be determined. These force expressions will have terms that are proportional to modal velocity and displacement, and that are also dependent on speed and reduced frequency. It is important to emphasize that the forces determined using any other more modern 2D or 3D unsteady aerodynamic approach would lead to the same form of result.

The aerodynamic forces will add to the basic equation of motion [3]. Eventually, the flutter equation, expressed in modal coordinates, $\mathbf{q}$, for convenience, may be obtained and written as:

$$\mathbf{A}\ddot{\mathbf{q}} + (\rho V\mathbf{B} + \mathbf{D})\dot{\mathbf{q}} + \left(\rho V^2\mathbf{C} + \mathbf{E}\right)\mathbf{q} = 0 \qquad [6]$$

Here ρ is the true air density and V is the true airspeed, although some authors use an equivalent airspeed representation for eqn [6]. $\mathbf{B}$ and $\mathbf{C}$ are the aerodynamic damping and stiffness matrices (both a function of k). $\mathbf{D}$ is a structural damping matrix that is estimated based on modal damping values measured during the ground vibration test (see later).

It is important to recognize that because both the $\mathbf{B}$ and $\mathbf{C}$ matrices are derived from the Theodorsen function (or its equivalent for a more advanced method), and are dependent on reduced frequency, they are only strictly accurate at one frequency of motion. (Thus the aerodynamic representation is actually most accurate near to flutter where the motion usually becomes dominated by a single frequency.)

This whole procedure is very involved but only the classical, historical approach has been explained. In practice, compressibility (i.e., Mach number) effects will be present in the flow and surfaces may have general nonslender planforms. Strip theory is inappropriate for such analyses. Therefore, it is normal practice to use a 3D 'panel' method such as Doublet Lattice to generate the aerodynamic $\mathbf{B}$ and $\mathbf{C}$ matrices at a range of frequency parameters and Mach numbers.

Such panel methods are fairly accurate into the low transonic speed regime prior to the formation of strong shock waves. However, once shock waves are formed, the unsteady flow phenomena are even more complex and time-stepping Computational Fluid Dynamic (CFD) solution methods are currently being developed to examine the flutter behavior at flight conditions where the aerodynamics are nonlinear and flutter is very difficult to predict accurately. Although 3D compressible viscous unsteady flow codes are beginning to gain industrial acceptance, the time-domain solution is still very expensive for routine use.

Flutter Solution

Returning to the basic flutter model, in order to estimate the flutter speed, the basic stability of eqn [6] must be investigated over a range of speeds, Mach numbers and frequency parameters. The procedure is to assume a solution for the unforced motion of the form:

$$\mathbf{q}(t) = \mathbf{q}_0 e^{\lambda t} \qquad [7]$$

Here $\mathbf{q}_0$ is the amplitude and λ is the exponent that indicates stability. Upon substituting into eqn [6] and cancelling the exponential term, then:

$$\left[\lambda^2\mathbf{A} + \lambda(\rho V\mathbf{B} + \mathbf{D}) + \left(\rho V^2\mathbf{C} + \mathbf{E}\right)\right]q_0 = 0 \qquad [8]$$

This is an nth order eigenvalue problem that can be solved either directly by locating values of λ at which the determinant of the matrix is zero, or by converting the equations into first-order form and using a complex eigenvalue solver.

In either case, the eigenvalues/roots are $\sigma_j \pm \mathrm{i}\delta_j$ ($j = 1, 2, \ldots, n$). The imaginary parts, δ_j, are the frequencies at which unforced motion is possible and the real parts, σ_j, are the corresponding

decay exponents (yielding a percentage critical damping value). If $\sigma_j < 0$ (for all j) the aircraft is stable, whereas if $\sigma_j = 0$ (for any j) then sustained motion is possible and flutter will occur. If $\sigma_j > 0$ (for any j), the motion will be unstable and will grow without limit until failure or until some nonlinear effect takes over. The corresponding eigenvectors of eqn [8] are the complex modes of the flutter system, related to, but not the same as, the normal modes.

There are a number of different iterative ways of seeking to ensure that the reduced frequency used in the unsteady aerodynamics is consistent with the flutter speed and frequency calculated (so-called 'frequency matching'), i.e., that the aerodynamics are as appropriate as possible.

It is common practice to present flutter calculation results as plots of frequency and damping against speed for a particular Mach number (or altitude), any flutter speed being indicated where the damping becomes zero (**Figure 12**). The flutter speed is then obtained for a range of payload and fuel states in order to cover the whole range of possible operating conditions.

Note that the airworthiness requirements demand that flutter calculations be carried out. If the calculated flutter speed were found to be less than 1.15 times the design dive speed at any point on the operating envelope of the aircraft, then a range of design changes would be explored to try to increase the flutter speed. Various failure cases need to be investigated (i.e., hydraulic).

Flutter Phenomenon

Returning to the basic flutter phenomenon, an attempt will now be made to define it. Classical linear flutter is an instability (not a resonance or forced vibration) that involves the coupling of two or more modes or DOFs. At flutter, the unsteady aerodynamic forces associated with the motion in the modes are so phased as to do net work and extract sufficient energy from the airstream to balance that dissipated by structural damping forces; then vibration following any small disturbance will not be damped out. Above the flutter speed, the energy extracted from the air exceeds that dissipated by the structure and the vibration grows without limit.

The flutter mechanism for an aircraft can often be represented by extraction of a subset of only two or three modes from the model. This simplification can help decide which modes are controlling the flutter, what the flutter mechanism is, and therefore how the flutter speed may be increased.

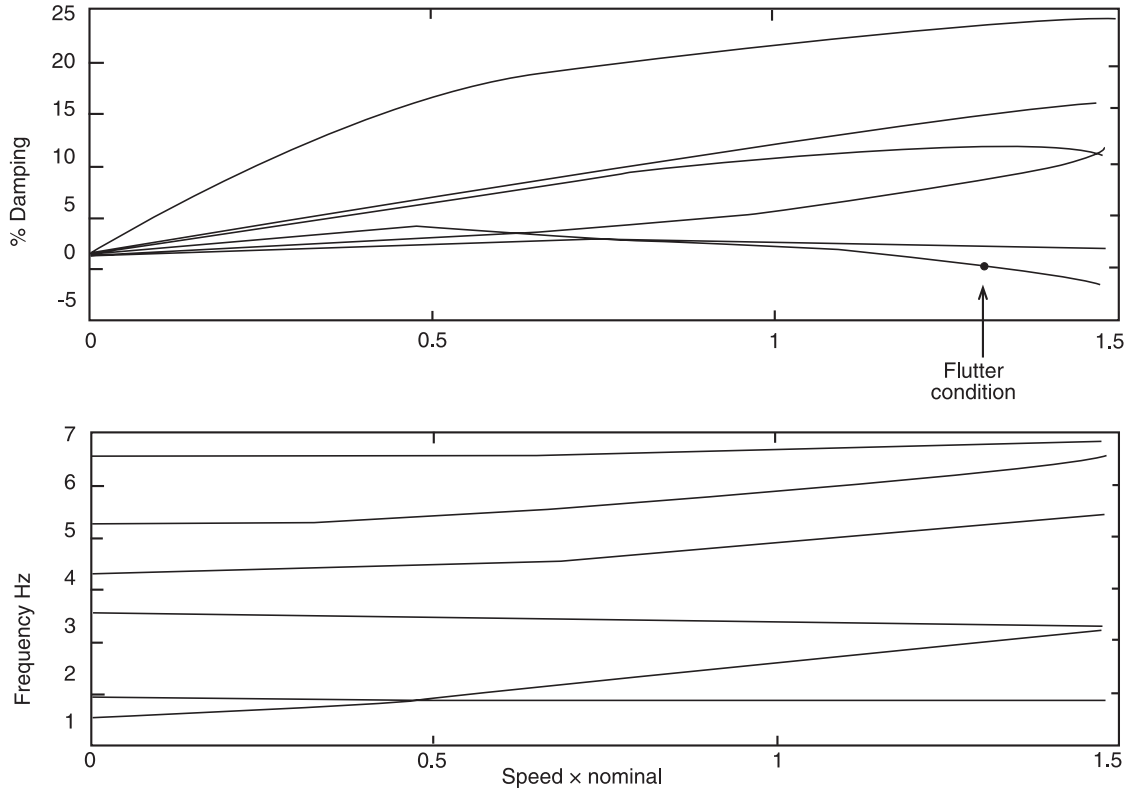


Figure 12 Sample frequency and damping variation with speed.

Binary Flutter

The textbook flutter problem is that of a 2D aerofoil allowed to pitch and heave. A variant on this 2D problem, a flapping and twisting rigid wing, has been extensively discussed elsewhere, and a number of common fallacies regarding the explanation of classical 2D flutter were highlighted.

One common fallacy in the understanding of flutter is that it occurs where two mode frequencies coalesce (i.e., have exactly the same value). Even for a 2D problem, this is only true when there is no aerodynamic damping present (i.e., $\mathbf{B} = 0$ in eqn [6]). If aerodynamic damping is present (i.e., $\mathbf{B}$ not zero), the frequencies may be close at the flutter speed but not necessarily identical. Nevertheless, the proximity of natural frequencies can be an indicator of incipient flutter and the flutter speed can usually be increased by separation of frequencies.

Bending/Torsion Flutter

The classical wing flutter involves bending and torsion of the lifting surface and is akin to the classical 2D problem. The key approach to raising the flutter speed is to increase the wing torsional stiffness. This increases the separation of the bending and torsional natural frequencies.

Control Surface Flutter

Control surface flutter typically involves wing torsion and control surface rotation. The flutter speed may be raised by an increase in the control circuit stiffness (to increase the control frequency) or by mass-balancing the control surface (to eliminate or reduce inertia coupling). It is also possible for tab flutter to occur.

Store Flutter

Store (engine or missile) flutter involves wing modes and store modes (e.g., pitch, yaw, or sway motion). The flutter may be controlled by alteration of the store attachment position and stiffness. On military aircraft, the wide range of missile configurations in use needs to be cleared for flutter and this is a time-consuming process. In addition, store flutter often involves limit cycle oscillations (LCOs) that are a nonlinear phenomenon but tend to cause more of a fatigue problem (see **Aeroelastic response**).

Tail Flutter

The tailplane can flutter in a similar way to a wing. However, because of the flexibility of the rear fuselage it is more common for flutter of the entire tail to occur, involving the tailplane and fin. T-tail flutter led to one of the classical flutter incidents in which a Victor bomber crashed in 1956 with a loss of lives.

Propeller Whirl Flutter

Propeller whirl flutter involves gyroscopic coupling between the propeller in which the propeller disc moves relative to the wing. It may be controlled by alteration of the attachment stiffness.

Stall Flutter

All the other flutter mechanisms are essentially linear in nature and need at least two modes to occur. Stall flutter, however, involves flow separation during some part of the vibration cycle and may occur for only one mode (typically wing torsion). Again this is a nonlinear phenomenon and tends to be a fatigue problem (see **Aeroelastic response**).

Validation by Test

Validation of Dynamic Model – Ground Vibration Test

An aircraft is a complex structure and many assumptions have to be made in order to develop a basic vibration model for it. In particular, it is quite possible that the stiffness at the major structural joints (e.g., wing/fuselage and wing/engine) may be incorrectly modeled and so may lead to errors in the modes and therefore in the flutter predictions.

For this reason, it is normal to perform a ground vibration test (GVT) on a prototype aircraft prior to first flight in order to validate experimentally the aircraft natural frequencies, mode shapes and modal masses. Modal damping values are also estimated. The GVT is very similar to the classical modal test in many ways.

The aircraft is supported upon a soft suspension in order that the rigid body mode natural frequencies (i.e., heave, roll, and pitch particularly) are well below the first natural frequency of the aircraft (ideally less than 10 per cent of it). This constraint is becoming more difficult to meet for very large aircraft where the first mode may be as low as 1–1.5 Hz. Typical types of aircraft suspension are as follows:

- support by elastic cords from a frame
- support on pneumatic air springs
- support on coil springs set in the ground
- support on deflated tyres

It is important to permit motion of the aircraft in the fore-and-aft and lateral directions as well as vertically but this is not always straightforward.

Several electrodynamic shakers (typically 2–6) are attached to the aircraft via stinger rods and force gauges at a number of positions. Shakers are supported

on small stiff frames or suspended by wires/elastic cords with the aim of ensuring that the natural frequency of the shaker on its support is well outside the frequency range of interest. The aircraft is instrumented with a large number of accelerometers (typically 200–1000), sufficient to allow visualization of the modes of interest.

A range of different test procedures may be employed. Firstly, using the so-called phase separation approach, the shakers are driven with independent random excitation signals and the frequency response function (FRF) matrix estimated. The FRF matrix is then curve-fitted using one of a number of system identification methods so as to yield the natural frequencies, mode shapes, damping ratios and modal masses.

Secondly, using the more traditional phase resonance approach, the estimated FRF matrix is used to generate the monophase force pattern required to excite each undamped normal mode in turn. The force pattern is then applied to the aircraft and the excitation frequency adjusted (or 'tuned') until the response has single-degree-of-freedom characteristics (90° phase between reference force and all acceleration channels). The aircraft will then be responding in a single normal mode. The mode shape and other modal characteristics can be measured directly. This approach also has the benefit of allowing nonlinear effects to be explored. The presence of friction or backlash on control surfaces, stores, etc., can be difficult to handle since the resulting measured frequencies depend upon the level of excitation employed.

Once the natural frequencies and normal mode shapes have been determined, they can be compared with the theoretical results. Various methods of updating a finite element model based on experimental results are available but they are not yet fully reliable on such a complex structure as an aircraft (see **Model updating and validating**). It is thus more common for the two sets of modes to be reconciled by adjusting key joint stiffness values. Once the match between experimental and theoretical results is considered satisfactory, most companies use this adjusted mathematical model as the basis of the final flutter calculations. It should be pointed out that many flutter calculations are performed using the theoretical model prior to the GVT results being available.

Validation by Test – Flight Flutter Testing

The degree of uncertainty in the flutter model, and particularly in the unsteady aerodynamics, means that the calculated flutter speeds will probably be inaccurate, especially in the transonic region. It is therefore essential from a safety point of view to validate the flutter behavior and to clear the flight envelope in a flight flutter test (FFT) program. This procedure is a requirement of the airworthiness authorities.

On the basis of calculations, a nominal flight envelope is cleared to permit a first flight to take place. Thereafter, the FFT program precedes every other flight test because of the critical safety issue of flutter. The basic FFT philosophy seeks to gradually extend this nominal flight envelope by assessing the flutter stability of the aircraft at progressively increasing speed and Mach number. A typical flight envelope is shown in **Figure 13**, together with typical test points.It is normal to assess the flutter stability by

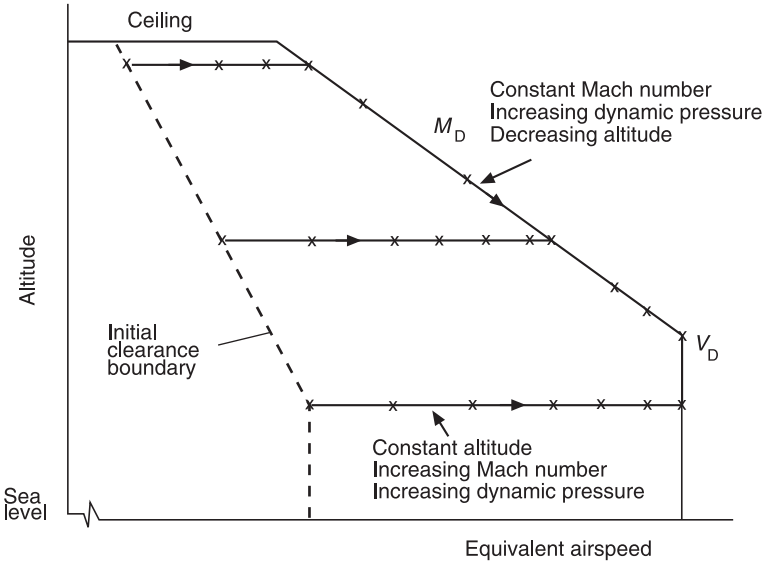


Figure 13 Sample flutter test flight envelope. x, test point.

identifying the natural frequency and damping of the complex modes of the aircraft at the test point of interest. The damping values may be compared with results from previous test points and the damping trends for each mode extrapolated to allow selection of the next test point (i.e., permitted increment in speed or Mach numbers). The test process is complete when the extrapolated damping values are still positive at a margin (typically 15 percent) above the design dive speed for each Mach number.

The procedure at each test point is to excite vibration of the aircraft over the frequency range of interest and to measure its response. A range of excitation devices can be used, namely

- control surface movement via stick/pedal input or explosive charges
- control surface movement via Flight Control System (FCS) signal
- movement of aerodynamic vane fitted to aircraft flying surface or engine/store
- inertia exciter mounted in fuselage

The aircraft response is measured using typically around 20 accelerometers, far fewer than for a GVT.

The most common excitation signals are pulse (via stick/pedal or explosive charge) and chirp (a fast frequency sweep applied as a signal to the control surface, vane or inertia exciter). Where excitation devices are available on both sides of the aircraft, then excitation is often applied in or out of phase in order to exploit symmetry and to simplify the analyses. Occasionally a random excitation signal is employed. Sometimes the response of the aircraft to natural turbulence is used (but this is not good practice). Where possible, it is preferable that the excitation signal is recorded in order to improve the identification accuracy but analysis methods are available if this is not the case.

Each excitation sequence will probably only last a maximum of 60 s because of the difficulty of holding the aircraft on condition, especially near to the limit of the flight envelope. The test may be repeated and some form of averaging employed. Sample chirp excitation and response signals are shown in **Figure 14**. Once the test is over, then the results are processed on the ground during or after the flight. FRFs are computed or alternatively the raw time data are used directly. A sample FRF is shown in **Figure 15**. A time- or frequency-domain identification algorithm is then employed in order to identify the frequency and damping values for each mode in the data. Again, this process is very similar to modal testing but the levels of noise are far more severe since turbulence (an unmeasured excitation) is exciting the aircraft during the test and the test time is limited.

A sample set of frequency and damping results plotted against speed is shown in **Figure 16**. These results are compared to the predictions from the model and some basic attempts may be made to reconcile any differences. Any flutter problem (i.e., the flutter speed from test is too low) will require urgent design action and could prove to be extremely costly.

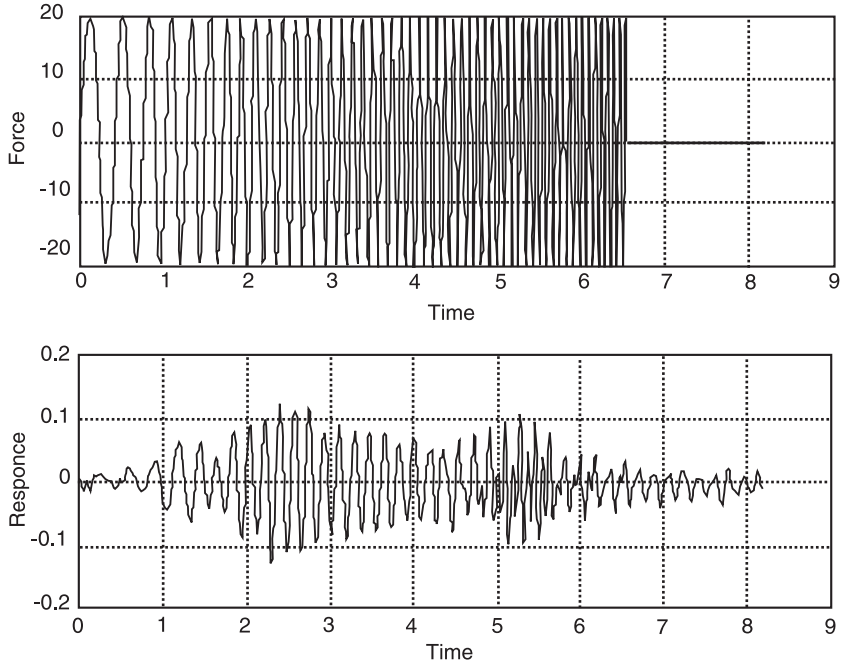


Figure 14 Chirp excitation and response time histories.

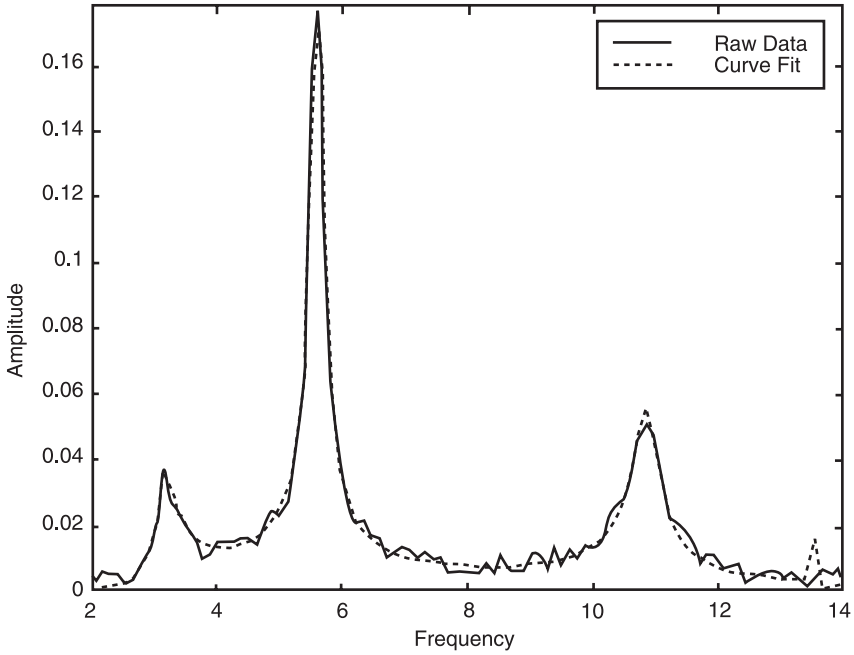


Figure 15 Sample FRF from flutter test.

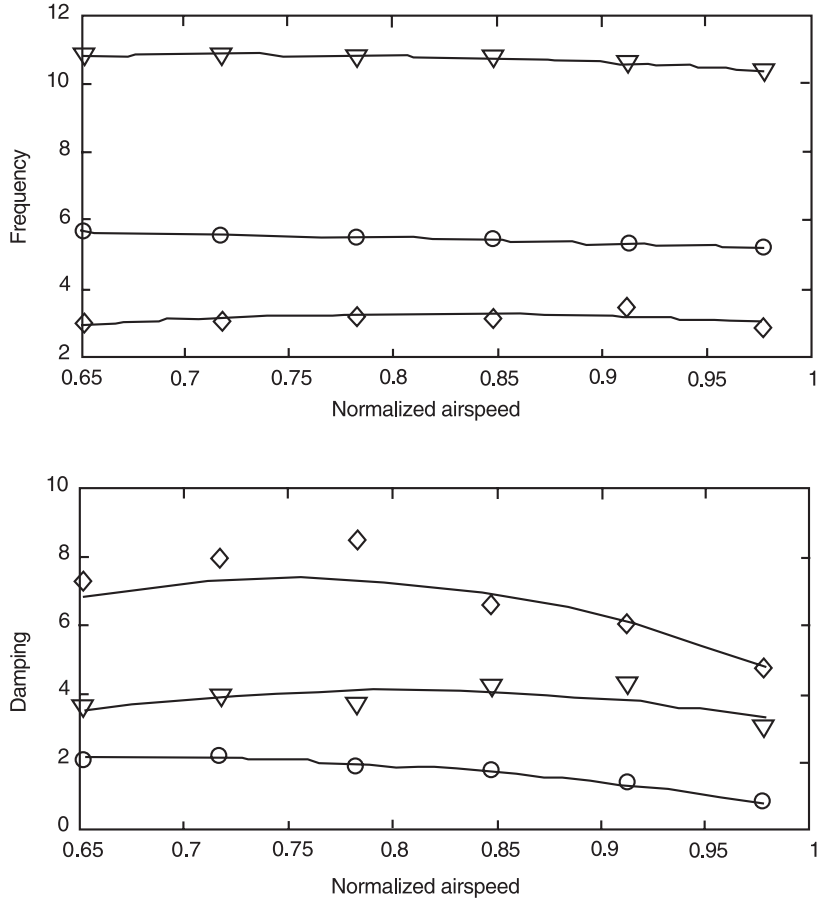


Figure 16 Sample flutter test results.

Nomenclature

$\mathbf{B}$	aerodynamic damping matrix
c	characteristic length
$\mathbf{D}$	structural damping matrix
V	true airspeed
$\mathbf{w}$	$(N \times 1)$ vector of structural displacement/rotations
ρ	air density
$\mathbf{\Phi}$	modal matrix

See also: **Aeroelastic response**; **Finite element methods**; **Flutter, active control**; **Model updating and validating**.

Further Reading

Bisplinghof RL, Ashley H, Halfman RL (1996) *Aeroelasticity*. Dover.

Collar AR (1978) *The First 50 years of Aerolasticity*. Aerospace (Royal Aeronautical Society, London), vol 5 (paper no 545).

Ewins DJ (2000) *Modal Testing*, 2nd edn. Research Studies Press.

Fung YC (1993) *An Introduction to the Theory of Aeroelasticity*. Dover.

Garrick IE, Reed III WH (1981) Historical development of aircraft flutter. *Journal of Aircraft* 18 (11).

Hancock GJ, Simpson A, Wright JR (1985) On the teaching of wing bending-torsion flutter. *Aeronautical Journal*.

Wright JR (1991) *Flight Flutter Testing*. Von Karman Institute Lecture Series.

FLUTTER, ACTIVE CONTROL

F H Gern, Virginia Polytechnic Institute and State University, Blacksburg, VA, USA

Copyright © 2001 Academic Press

doi:10.1006/rwvb.2001.0194

Introduction

One of the key factors for viable airplane design has been the avoidance of flutter throughout the flight envelope. Flutter, as an interaction between structural dynamics and unsteady aerodynamics, has been documented from the beginnings of human flight. Historically, in aircraft design, the remedy of a flutter problem resulted in an increase of structural stiffness. Other solutions included mass balancing or even modifications in aircraft geometry. In almost all cases, the mitigation of the flutter problem resulted in increased structural weight and reduced aircraft performance.

Admissible flutter boundaries for airplanes are defined by different standards for commercial and military airplanes. According to FAR Part 25, section 25.629 (1992) the flutter-free margin for commercial airplanes has to be a 15% increase in equivalent airspeed beyond the flight envelope. Flutter boundaries for military airplanes are given by military specification MIL-A-8870B (AS), and are required to be equal to a 15% increase in equivalent airspeed beyond the design limit speed envelope at both constant altitude and constant Mach number.

The increasing need for reductions in structural airframe weight, usually resulting in increased structural flexibility, has been defining the need for active flutter control to meet the afore-mentioned flutter margin requirements. For commercial airplanes, the flight envelope is restricted by air traffic regulations and passenger comfort. Here, active flutter control allows aerodynamic improvements and structural weight reduction, which are almost directly related to reduced fuel consumption and reduced direct operating costs (DOC). With the recent ultra-high-capacity aircraft concepts pursued by major airframe manufacturers, active vibration control will be a key issue to satisfy the stringent airworthiness requirements for these huge airframes. For military aircraft, the need for active flutter control is not only defined by weight savings, but also by increased performance or enhanced flight envelopes and mission profiles without structural weight penalties. Changing mission requirements during the lifespan of a military airframe may require different wing attachments and therefore cause different flutter problems. One prominent example is the wing–store flutter problem, which will be discussed in a later section.

During the past 20 years, numerous concepts have been developed to employ existing, conventional leading and trailing edge control surfaces for active flutter suppression. So far, the development and implementation of active flutter and load control systems, has been tightly coupled with the introduction of digital flight control computers (FCC) into

military and commercial flight. As an example, the Airbus A320 was designed from the beginning to have an electrical flight control system and to have an integrated gust load alleviation function (LAF) to ameliorate wing loads and vibrations resulting from sharp large-intensity discrete vertical gusts (**Figure 1**). Key issues for active flutter and vibration suppression systems involve reliability and robustness. In other words, the probability of exceeding design limit loads with an active control system shall not be greater than the probability of exceeding design limit loads on a comparable aircraft design without an active control system.

Recent research on active flutter control has employed 'smart' wing technology, where discrete control surfaces are being replaced by an actively controlled wing structure. A distributed actuation of the wing may be achieved by different means, including a wide variety of approaches from hydraulic actuators to piezoelectric materials. Together with the benefits of increased aerodynamic effectiveness, smart wing technology offers a tremendous potential towards weight reduction and increased airframe performance. As a result, smart wing technology has been under investigation by all major airframe manufacturers as well as governmental agencies like the Air Force, DARPA, and NASA.

Classical Flutter Solution and Modal Analysis

The development of active flutter control systems requires a profound understanding of the mechanisms leading to flutter instabilities. Since active flutter control involves actuation of control surfaces or of the wing structure itself, the simulation of active control systems needs to consider the influence of control surface deflections or wing deformations on the aeroservoelastic behavior of the airplane. The general dynamic behavior of an aircraft vibrating in the airflow is given by:

$$\mathbf{M}\ddot{r} + \mathbf{C}\dot{r} + \mathbf{K}r = 0 \qquad [1]$$

In eqn [1], $\mathbf{M}$ is the mass matrix containing the structural mass tensor of the airplane and the (in most cases negligible) oscillating mass of the airflow, the matrix $\mathbf{C}$ contains the viscous damping matrices obtained from structural and aerodynamic damping, and $\mathbf{K}$ is the generalized stiffness matrix containing the elastic and aerodynamic stiffness terms. Both the stiffness matrix $\mathbf{K}$ and the damping matrix $\mathbf{C}$ may depend on the actual frequency of vibration. Even for noncomplex matrices, the solution of eqn [1] generally yields complex eigenvalues and eigenvectors.

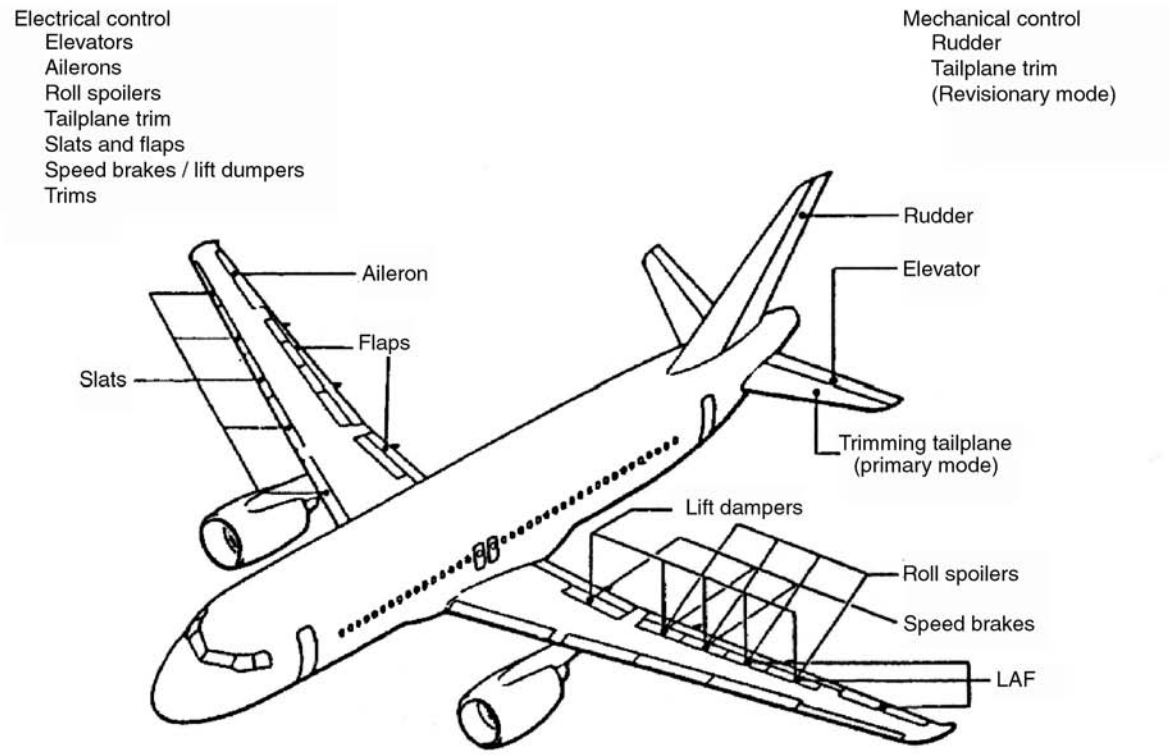


Figure 1 The Airbus A320 electrical flight control system (courtesy of the European Aeronautic Defense and Space Company (EADS) Airbus).

As a first approximation of the solution, the aerodynamic loads are neglected, yielding the natural frequencies and mode shapes of the aircraft. Using these mode shapes and frequencies as initial values, the flutter mode shapes and frequencies may be found in an iterative procedure. It should be noted that the obtained vibration parameters are only valid for the actual flight conditions, i.e., Mach number and altitude.

Since natural frequencies and mode shapes are of crucial influence on the accuracy of the obtained flutter solution, great effort has been put into their reliable prediction. In general, this is achieved via finite element analyses employing models of several thousand degrees-of-freedom (**Figure 2**). Wind-tunnel and vibrational testing of models and actual aircraft are used to verify the applied computational methods.Using the eigenvectors of the individual eigenmodes, the equation of motion of the aircraft in the airflow can be written in modal coordinates for each mode:

$$\bar{\mathbf{K}}q + \bar{\mathbf{D}}\dot{q} + \bar{\mathbf{M}}\ddot{q} + \tfrac{1}{2}\rho v^2 \mathbf{Q}(k, Ma)q = 0 \qquad [2]$$

In eqn [2], $\bar{\mathbf{K}}$ is the modal stiffness matrix, $\bar{\mathbf{D}}$ is the modal damping matrix, $\bar{\mathbf{M}}$ is the modal mass matrix, and $\mathbf{Q}$ is the matrix of the aerodynamic loads, depending on the flight Mach number Ma and the reduced frequency k.

Due to the order of magnitude of many aeroelastic problems, the solution of eqn [2] may require extensive computational efforts. However, in a modal analysis this equation is being decoupled using the eigenvalues of the system. For given flight conditions, the system matrix can be found using the complex eigenvalues, λ_F, the complex eigenvectors, ϕ_F, and their conjugate complex counterparts, λ_F^*, and ϕ_F^*. If the flutter analysis is performed in modal coordinates, the eigenvectors, ϕ_F, are automatically obtained in terms of the generalized coordinates, q_s.

Aeroservoelastic Model of the Controlled Aircraft

After the transformation:

$$\begin{bmatrix} q_s \\ \dot{q}_s \end{bmatrix} = \underbrace{\begin{bmatrix} \phi_F & \phi_F^* \\ \phi_F\lambda_F & \phi_F^*\lambda_F^* \end{bmatrix}}_{\mathbf{T}} \begin{bmatrix} q_F \\ q_F^* \end{bmatrix} \qquad [3]$$

the system matrix of the aircraft $\mathbf{A}_F$ can be expressed in terms of the flutter eigenvalues:

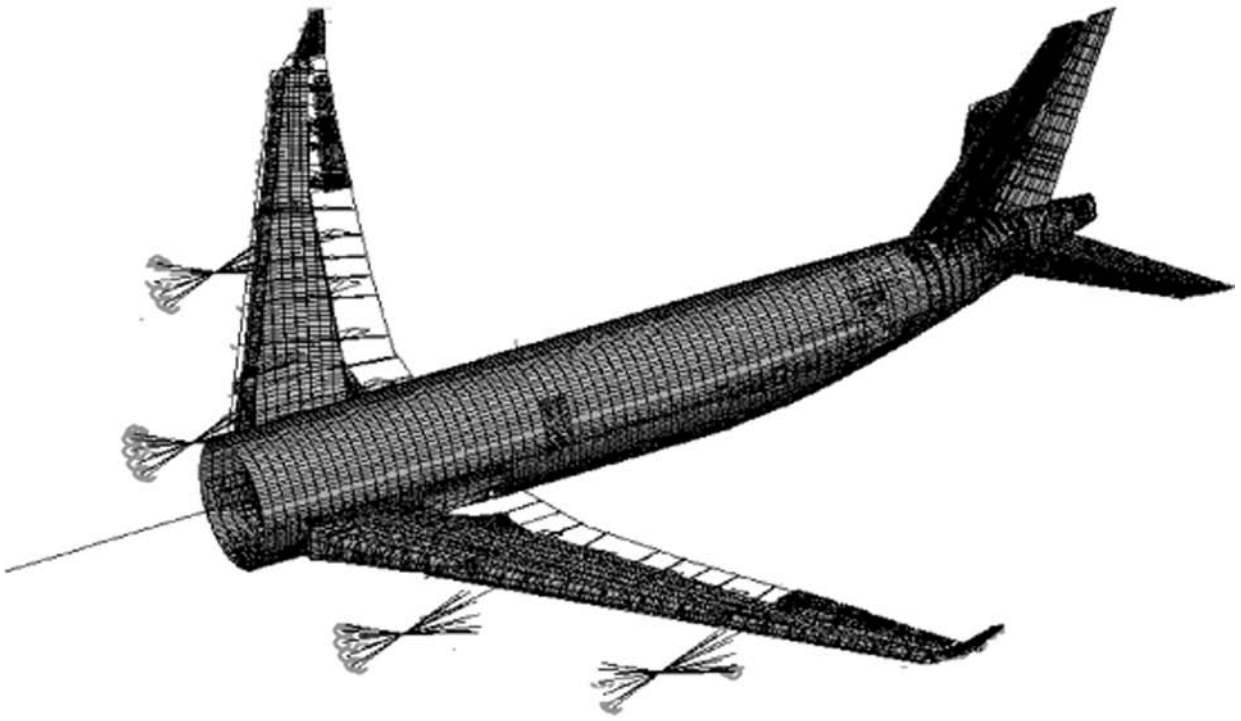


Figure 2 (See Plate 33). Finite element discretization of a commercial transport airplane (courtesy of the Institute of Flight Mechanics and Control).

$$\mathbf{A}_F = \mathbf{T}\begin{bmatrix} \lambda_F & 0 \\ 0 & \lambda_F^* \end{bmatrix}\mathbf{T}^{-1} \qquad [4]$$

with real coefficients in the matrix $\mathbf{A}_F$, which can be subdivided into four quadratic submatrices:

$$\mathbf{A}_F = \begin{bmatrix} 0 & 1 \\ a_{21} & a_{22} \end{bmatrix} \qquad [5]$$

A new form of the equation of motion of the elastic aircraft, considering disturbances and the influence of control surfaces may now be written as:

$$\begin{bmatrix} \dot{q}_s \\ \ddot{q}_s \end{bmatrix} = \begin{bmatrix} 0 & 1 \\ a_{21} & a_{22} \end{bmatrix}\begin{bmatrix} q_s \\ \dot{q}_s \end{bmatrix} + \mathbf{Bu} + \mathbf{Ff} \qquad [6]$$

In eqn [6], the vector $\mathbf{u}$ describes the control surface deflections, $\mathbf{B}$ is the matrix of the control surface influence coefficients, $\mathbf{f}$ is the disturbance vector, and $\mathbf{F}$ is the matrix containing the disturbance influence coefficients. The structural deflection vector $\mathbf{y}_F$ due to flutter vibrations is obtained via:

$$\mathbf{y} = \mathbf{C}\begin{bmatrix} q_s \\ \dot{q}_s \end{bmatrix} + \mathbf{Du} \qquad [7]$$

Here, the matrices $\mathbf{C}$ and $\mathbf{D}$ contain the geometrical parameters of the structure, relating generalized coordinates to local coordinates. A complete description of elastic aircraft vibrations requires the consideration of aeroelastic degrees-of-freedom and rigid-body degrees-of-freedom. The rigid-body motion of the structure can be incorporated by classical, nonlinear flight mechanics. As a result, the state space vector of the aeroelastic system can be expressed in the form:

$$\mathbf{x} = [x_R \quad x_A \quad \dot{x}_R \quad \dot{x}_A \quad x_C]^T \qquad [8]$$

In eqn [8], x_R are the rigid-body degrees-of-freedom and x_A are the aeroelastic degrees-of-freedom, whereas x_C describes the influence of the control surfaces. Upon reordering the vector $\mathbf{x}$, the matrix equation of the aeroelastic system can be written in the following form:

$$\begin{bmatrix} \dot{x}_R \\ \dot{x}_A \\ \ddot{x}_R \\ \ddot{x}_A \\ \dot{x}_C \end{bmatrix} = \begin{bmatrix} 0 & 0 & 1 & 0 & 0 \\ 0 & 0 & 0 & 1 & 0 \\ a_{31} & a_{32} & a_{33} & a_{34} & a_{35} \\ a_{41} & a_{42} & a_{43} & a_{44} & a_{45} \\ 0 & 0 & 0 & 0 & a_{55} \end{bmatrix}\begin{bmatrix} x_R \\ x_A \\ \dot{x}_R \\ \dot{x}_A \\ x_C \end{bmatrix} + \begin{bmatrix} 0 \\ 0 \\ 0 \\ 0 \\ b_5 \end{bmatrix}\mathbf{u} \qquad [9]$$

$$y_F = [c_1 \quad c_2 \quad c_3 \quad c_4 \quad 0]x + [0]u$$

Here y_F is the modal deflection of the individual flutter modes. Changing the order of the state space vector allows separation of aeroelastic components from rigid-body components and a new system matrix, consisting of four blocks, is obtained:

$$\begin{bmatrix} \dot{x}_R \\ \ddot{x}_R \\ \dot{x}_A \\ \ddot{x}_A \\ \dot{x}_C \end{bmatrix} = \left[\begin{array}{cc|ccc} 0 & 1 & 0 & 0 & 0 \\ a_{31} & a_{33} & a_{32} & a_{34} & a_{35} \\ \hline 0 & 0 & 0 & 1 & 0 \\ a_{41} & a_{43} & a_{42} & a_{44} & a_{45} \\ 0 & 0 & 0 & 0 & a_{55} \end{array}\right]\begin{bmatrix} x_R \\ \dot{x}_R \\ x_A \\ \dot{x}_A \\ x_C \end{bmatrix} + \begin{bmatrix} 0 \\ 0 \\ 0 \\ 0 \\ b_5 \end{bmatrix}\mathbf{u}$$

$$yF = \left[\begin{array}{cc|ccc} c_1 & c_3 & c_2 & c_4 & 0 \end{array}\right]x + [0]u \qquad [10]$$

Here, the submatrix in the upper main diagonal represents the rigid-body dynamics, whereas the submatrix in the lower main diagonal describes the aeroelastic vibration of the aircraft. The off-diagonal coupling matrices consider the influence of the rigid-body dynamics on the aeroelastic behavior and vice versa. Separation of aeroelastic states from rigid body states yields:

$$\begin{bmatrix}\dot{x}_A\\ \ddot{x}_A\\ \dot{x}_C\end{bmatrix} = \begin{bmatrix}0 & 1 & 0\\ a_{42} & a_{44} & a_{45}\\ 0 & 0 & a_{55}\end{bmatrix}\begin{bmatrix}x_A\\ \dot{x}_A\\ x_C\end{bmatrix} + \begin{bmatrix}0 & 0 & 0\\ a_{41} & a_{43} & 0\\ 0 & 0 & b_5\end{bmatrix}\begin{bmatrix}x_R\\ \dot{x}_R\\ u\end{bmatrix}$$

$$\begin{bmatrix}\ddot{x}_R\\ y_F\end{bmatrix} = \begin{bmatrix}a_{32} & a_{34} & a_{35}\\ c_2 & c_4 & 0\end{bmatrix}\begin{bmatrix}x_A\\ \dot{x}_A\\ x_C\end{bmatrix} + \begin{bmatrix}0 & 0 & 0\\ c_1 & c_3 & 0\end{bmatrix}\begin{bmatrix}x_R\\ \dot{x}_R\\ u\end{bmatrix} + \begin{bmatrix}a_{31} & a_{33}\\ 0 & 0\end{bmatrix}\begin{bmatrix}x_R\\ \dot{x}_R\end{bmatrix} \quad [11]$$

From eqn [11], it can be seen that the entire rigid-body acceleration can be separated into the aeroelastic contributions and into the ones calculated from the rigid-body model:

$$\ddot{x}_R = [a_{32} \quad a_{34} \quad a_{35}]\begin{bmatrix}x_A\\ \dot{x}_A\\ x_C\end{bmatrix} + [a_{31} \quad a_{33}]\begin{bmatrix}x_R\\ \dot{x}_R\end{bmatrix} \quad [12]$$

or, simplified:

$$\ddot{x}_R = \Delta_A\ddot{x}_R + \Delta_R\ddot{x}_R \quad [13]$$

The second term in eqn [13] can be replaced by the nonlinear flight mechanics model and becomes:

$$\Delta_R\ddot{x}_R = g(x_R, \dot{x}_R, x_A, \dot{x}_A; t) \quad [14]$$

By replacing eqns [12] and (13) into eqn [11], the system of equations simplifies to:

$$\begin{bmatrix}\Delta_A\ddot{x}_R\\ y_F\end{bmatrix} = \begin{bmatrix}a_{32} & a_{34} & a_{35}\\ c_2 & c_4 & 0\end{bmatrix}\begin{bmatrix}x_A\\ \dot{x}_A\\ x_C\end{bmatrix} + \begin{bmatrix}0 & 0 & 0\\ c_1 & c_3 & 0\end{bmatrix}\begin{bmatrix}x_R\\ \dot{x}_R\\ u\end{bmatrix} \quad [15]$$

Transfer Function of the Aircraft

For active control simulation and control system design, it proves convenient to express the aircraft dynamic behavior in terms of transfer functions. For this purpose, the complete system from eqn [15] can now be expressed as:

$$\dot{\mathbf{x}}_A = \mathbf{A}\mathbf{x}_A + \mathbf{B}\mathbf{u} \quad [16]$$

$$\mathbf{y} = \mathbf{C}\mathbf{x}_A + \mathbf{D}\mathbf{u} \quad [17]$$

where:

$$\mathbf{x}_A = [x_A, \dot{x}_A, x_C]^T$$
$$\mathbf{u} = [x_R, \dot{x}_R, u]^T$$
$$\mathbf{y} = [\Delta_A\ddot{x}_R, y_F]^T$$

The relation between the input vector $\mathbf{u}$ and the output vector $\mathbf{y}$ is now given by the transfer matrix $\mathbf{F}$:

$$\begin{bmatrix}\Delta_A\ddot{x}_R\\ y_F\end{bmatrix} = \mathbf{F}\begin{bmatrix}x_R\\ \dot{x}_R\\ u\end{bmatrix} \quad [18]$$

where:

$$\mathbf{F} = \begin{bmatrix}F_{\ddot{x},x} & F_{\ddot{x},\dot{x}} & F_{\ddot{x},u}\\ F_{y,x} & F_{y,\dot{x}} & F_{y,u}\end{bmatrix}$$

Some complex control system analyses may require solving the system in the time domain. However, for most active control purposes, it is recommended to perform a Laplace transformation at this stage, enabling one to solve the system in the frequency domain. In the frequency domain, the vector, $\dot{\mathbf{x}}_A$, becomes $\mathbf{I}.s.\mathbf{x}_A$, with $\mathbf{I}$ being a unit matrix and s being the Laplace variable. As a result, eqn [16] becomes:

$$[\mathbf{I}s - \mathbf{A}]\mathbf{x}_A = \mathbf{B}\mathbf{u} \quad [19]$$

or:

$$\mathbf{x}_A = [\mathbf{I}s - \mathbf{A}]^{-1}\mathbf{B}\mathbf{u} \quad [20]$$

$\mathbf{x}_A$ can now be eliminated by replacing it into eqn [17] and the system becomes:

$$\mathbf{y} = \underbrace{\left\{\mathbf{C}[\mathbf{I}s - \mathbf{A}]^{-1}\mathbf{B} + \mathbf{D}\right\}}_{\mathbf{F}}\mathbf{u} \quad [21]$$

With $\mathbf{F} = \{\mathbf{C}[\mathbf{I}s - \mathbf{A}]^{-1}\mathbf{B} + \mathbf{D}\}$, the relation between the input vector $\mathbf{u}$ and the output vector $\mathbf{y}$ is given by the simple expression:

$$\mathbf{y} = \mathbf{F}\mathbf{u} \qquad [22]$$

Eqn [22] allows computation of the individual transfer functions for each aeroelastic mode. To reduce further the computational effort, a modal reduction can be performed. In such a way, it is only necessary to calculate transfer functions for the modes of interest for the simulation without a significant loss of accuracy:

$$\mathbf{F}_{ij}(s) = \frac{\mathbf{y}_i(s)}{\mathbf{u}_j(s)} \qquad [23]$$

Each aeroelastic mode is now given by a broken rational transfer function in terms of the eigenvalue λ_i and the residual r_i of the considered modal form:

$$H_i = \frac{r_i}{s - \lambda_i} \qquad [24]$$

Assuming that the different modes can be superposed without mutual interaction, the flutter behavior of the aircraft can be described by the summation of all considered modes. As a result, the transfer function of the airplane can be written as:

$$H_0 = \sum_{i=1}^{n} H_i = \sum_{i=1}^{n} \frac{r_i}{s - \lambda_i} \qquad [25]$$

This representation of an aeroservoelastic system in terms of transfer functions is very convenient for the simulation and optimization of active flutter control / laws.

Active Flutter Control System Simulation

Figure 3 depicts a block diagram of a closed-loop system for active control of lateral aeroelastic vibrations. For realistic simulation of such a damping augmentation function (DAF), it is important to model all components as accurately as possible. This usually leads to highly nonlinear elements in the analysis. The feedback signal used by the flight control computer is the aeroelastic acceleration measured at selected aircraft locations. In the simulation, these accelerations are obtained by double differentiation of the aeroelastic displacements computed from the aircraft transfer function derived above (eqn [25]). To avoid saturation effects, a band-pass filter reduces the bandwidth of the processed signal to the frequency range of the employed actuators, generally in a

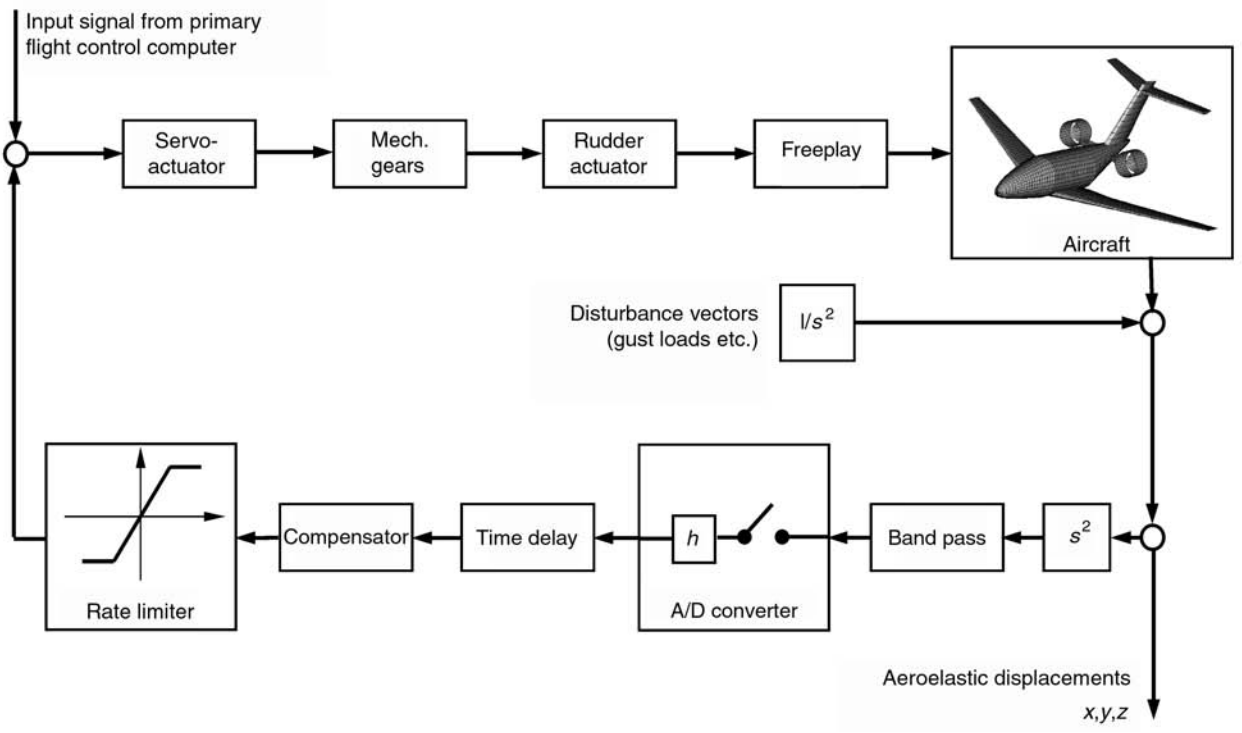


Figure 3 Block diagram of a generic active flutter control system.

spectrum within 1–5 Hz. An analog/digital converter (A/D converter) simulates digital signal processing. The time delay accounts for the processing time necessary for the flight control computer to calculate the required rudder deflection, usually 5 ms or less. A compensation filter converts the acceleration signals back into rudder commands, and a rate limiter limits the rudder deflections to 2.5° in order to avoid system instabilities due to resonance. In addition to the characteristics of servo actuators and rudder actuators (**Figure 4**), nonlinearities due to mechanic gears and freeplay are considered.

Figure 5 depicts the frequency response of an aircraft in the range from 0.5 to 10 Hz. For this purpose, a simulated excitation by the primary flight control system was increased from 0.5 to 10 Hz over a time span of 10 s. In **Figure 5A** the DAF is deactivated, i.e., the aircraft is uncontrolled. For the investigated aircraft configuration, **Figure 5A** shows excitation of a flutter critical mode in the vicinity of 2.2 Hz. Using the modal analysis procedure outlined above, this mode can be identified as mode 2 (first torsional wing mode). As a result, for excitation frequencies higher than 2.2 Hz, the aeroelastic response of the aircraft is dominated by the instability of mode 2 instead of resonance of the higher modes. **Figure 5B** depicts the system response for an activated DAF and shows the characteristic resonance of the different aeroelastic modes. However, no critical instability develops and the amplitude of the aeroelastic vibrations is much smaller throughout the entire frequency range. Note that the *y*-axis of **Figure 5B** covers a shorter amplitude range.

Wing/Store Flutter Suppression

External store carriage has long been a major design issue for advanced air combat systems and aeroelastic problems resulting from wing/store interaction have been investigated for decades. The well-known phenomenon of wing/store flutter typically occurs upon coupling of the fundamental wing-bending mode with the store-pitching mode. Throughout the 1980s, wing/store flutter was a very prominent

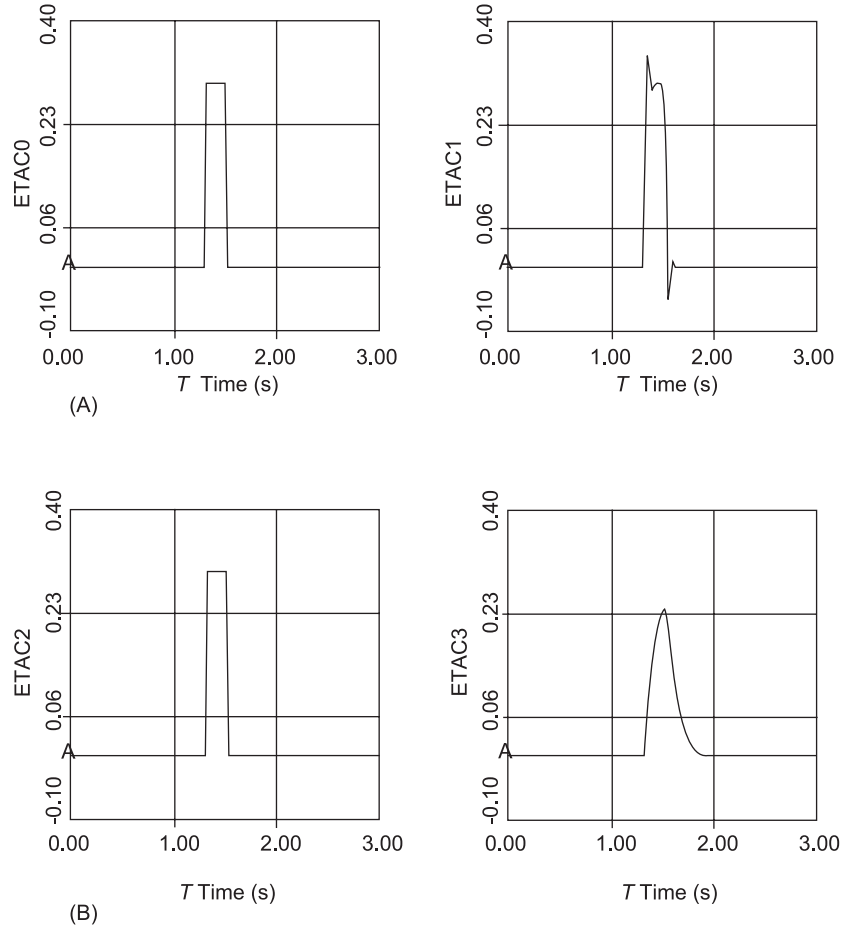


Figure 4 Response characteristics of different actuator types. (A) Yaw damper servo actuator; (B) rudder actuator; left: input signal; right: actuator response.

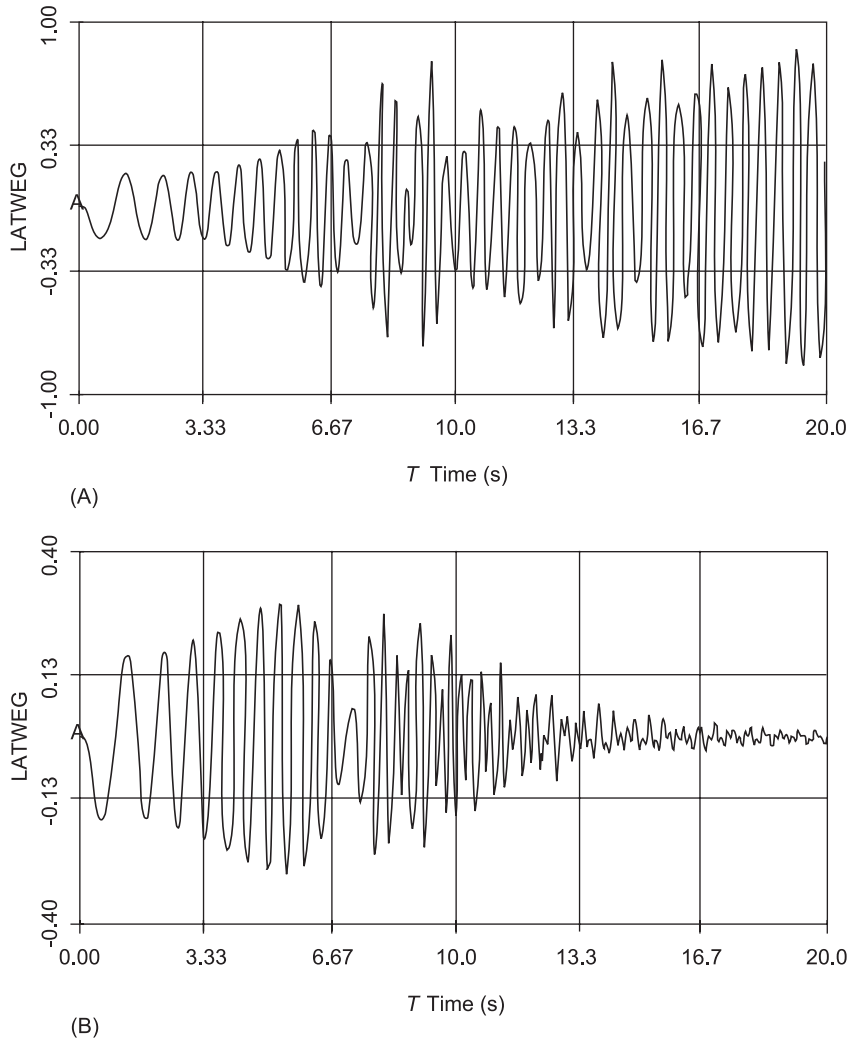


Figure 5 Frequency response of a generic commercial transport aircraft in the range from 0.5 to 10 Hz: (A) uncontrolled aircraft, (B) actively controlled aircraft with damping augmentation function. Note that the vertical scale in (A) is smaller than in (B).

research topic. However, reliable prediction of wing/store flutter has remained difficult and the appearance of the phenomena has been examined for aircraft configurations like the F-4, F-5, F-16, F-111, F/A-18, and F-15.

Since sufficient flutter data are not available in advanced design, flutter analysis is usually done after the wing is designed. For fighter and attack aircraft, due to the mere number of different store attachments, 95% of all flutter analyses are consumed by the flutter clearance for wings with external stores (**Figure 6**).

Closely related to wing/store flutter is the occurrence of limit cycle oscillations (LCO) of wings carrying external stores. The circumstances leading to LCO are various and often much more difficult to identify. From an operational point of view, although not as violent and destructive as flutter, LCO results in undesirable airframe vibration, causing premature fatigue damage and reducing the aircraft's operational lifespan. More importantly, targeting accuracy is degraded, e.g., wing-mounted missiles cannot be fired because of high levels of wing motion that prevent target lock-on. So far, there has been common agreement in the expert community that the occurrence of LCO has to involve at least one nonlinearity in the aeroelastic system. This nonlinearity may be of structural (nonlinear pylon stiffness, freeplay in the store attachment) or aerodynamic nature (shock-induced or trailing-edge flow separation). Very often, correlation between the occurrence of LCO in the nonlinear system and flutter of a linearized system has been possible. Due to their similarities in nature, wing/store flutter and LCO are generally suppressed via similar active control strategies.



Figure 6 Different external stores carried by the F/A-18 fighter aircraft (courtesy of Salamander).

Wing/Store Flutter Suppression Using Wing Control Surfaces

Two basic strategies exist to control actively wing/store flutter or external store-related LCO: the use of the wing's existing control surfaces, or the employment of active store pylons or fins. The use of existing control surfaces has been extensively investigated for many different aircraft configurations. An advantage of using existing control surfaces for active flutter control is the possibility to control store-induced flutter with already developed or modified control systems.

There is one airplane on which, most probably, more wing/store flutter investigation has been done than on any other: the General Dynamics F-16. Being designed as a very versatile multi-role fighter aircraft, the F-16 can carry literally hundreds of different store configurations. To identify a large number of critical wing/store flutter modes for the F-16, extensive flight testing at the US Air Force Seek Eagle group at Eglin AFB, Florida as well as wind-tunnel testing at NASA Langley, has been conducted. Because of the large number of critical flutter modes associated with external stores, both USAF and General Dynamics became interested in all promising flutter suppression techniques, including active flutter control. To investigate the potential of active flutter control on the F-16, General Dynamics provided a quarter-scale, full-span flutter model to NASA Langley for extensive testing in their Transonic Dynamics Tunnel (TDT) facility (**Figure 7**).

Based on NASA's experience from previous programs on Delta wing active flutter suppression, Lockheed C-5A active load alleviation, B-52 active control, and YF-17 wing/store active flutter suppression, the F-16 model became a testbed for evaluating active flutter control systems ranging from analog to complex digital adaptive concepts. Important research issues on active flutter control were the effects of asymmetry between left and right wing sensor signals and actuator command deflections, the simultaneous implementation of symmetric and antisymmetric control laws, switching of control laws above open-loop flutter, and the accurate determination of open-loop frequency response functions. After successful conventional flutter suppression wind-tunnel testing, research focused on the development and demonstration of a totally digital adaptive system with no prior knowledge of the aircraft configuration. Objectives of this research included the demonstration of digital adaptive flutter suppression for different store configurations with widely different flutter mode characteristics and flutter suppression

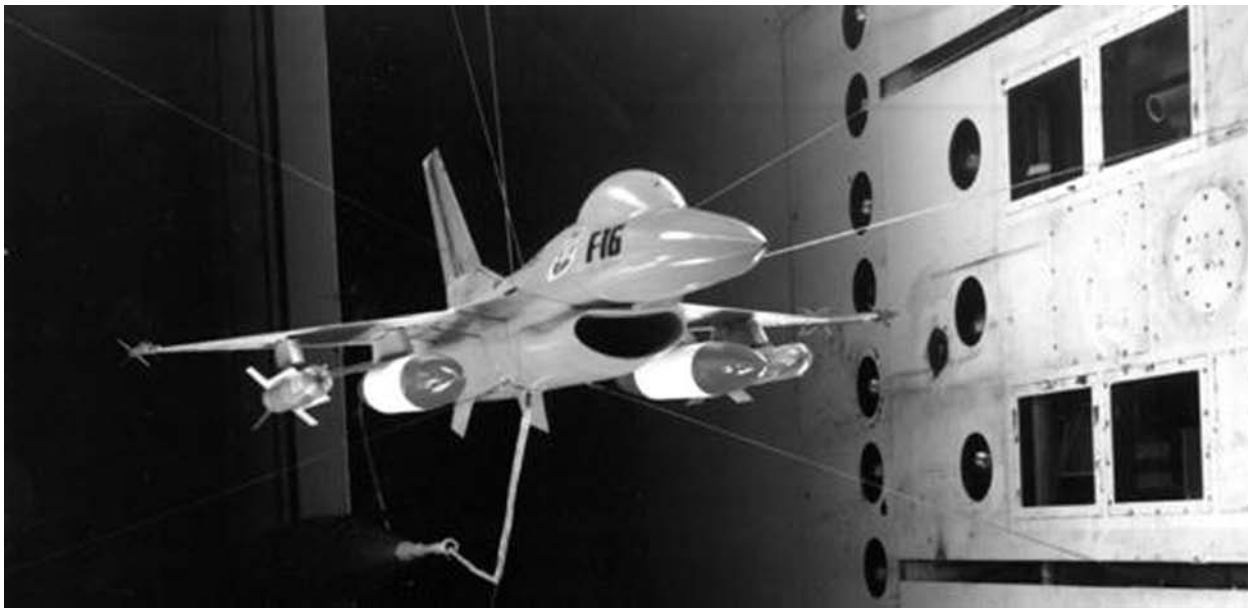


Figure 7 F-16 wind-tunnel model on the NASA Langley transonic dynamics tunnel two-cable mount system (courtesy of NASA Langley Research Center).

after the separation of a store from the wing. Significant accomplishments of the program were the use of control laws developed by the active controller as a backup analog safety system as well as the successful demonstration of adaptive control. During one test run, the adaptive controller updated the control law over 2500 times without losing control of the flutter mode (**Figure 8**).

Active Pylon Technology

Almost in time with methods relying on wing control surfaces, active store flutter control using aerodynamic surfaces on the store emerged. This approach was based on feedback signals from accelerometers at the fore-and-aft end of the store to electrohydraulic actuator-driven vanes attached to the forward part of the store. The effectiveness of these methods depended on the accurate knowledge of aerodynamic forces produced by the vanes, posing problems, especially in the transonic region, where theoretical predictions of unsteady aerodynamic coefficients are least reliable. Replacing the vanes by hydraulic actuators in the pylon to decouple the store vibration from the wing modes was limited in its practical implementation due to the actuators' inability to meet high flow-rate requirements for the control of higher frequency perturbations.

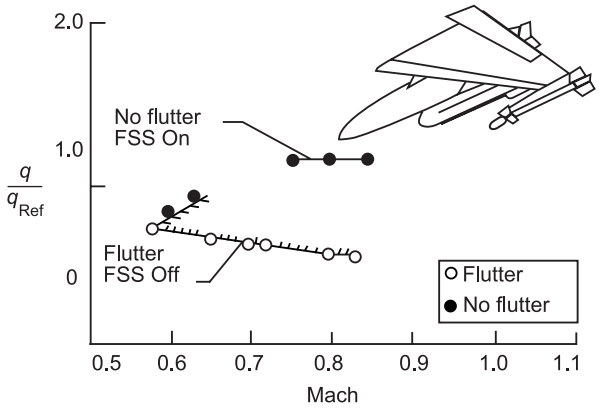


Figure 8 F-16 open and closed-loop flutter boundaries. FSS = Flutter suppression system (courtesy of NASA Langley Research Center).

Finally, a passive soft spring/damper combination was used together with a low-power active control feedback system to prevent large static deflections and maintain store alignment. This 'decoupler pylon' concept resulted in a substantial increase in flutter speed and has successfully been implemented on an F-16 aircraft. Recent developments foresee replacement of the spring/damper by stacks of piezoceramic wafer struts and robust controller design using H-infinity theory (**Figure 9**). Such an active decoupler pylon is suitable to maintain the performance characteristics of the closed-loop system in the face of uncertainties at flutter speed. It allows significant weight savings by removing all hardware required with pneumatic springs and hydraulic dashpots and benefits from the waver actuator's faster response time to input command signals.

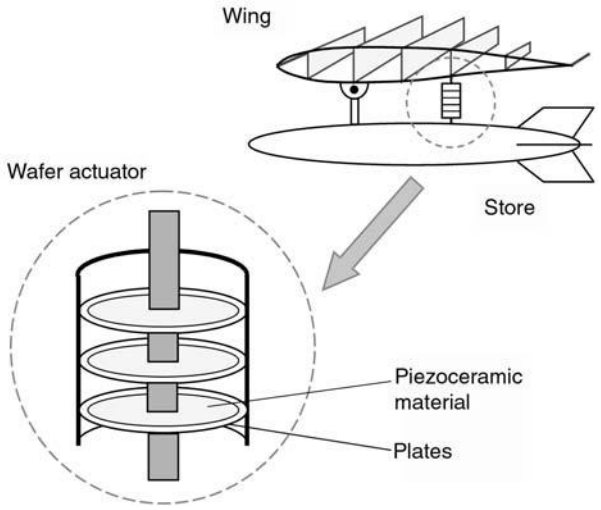


Figure 9 (See Plate 34). Active decoupler pylon with adaptive piezoceramic wafer stacks.

Smart Wing Technology

Traditionally, aircraft designers attempted to avoid aeroelastic instabilities by increasing structural stiffness. During recent years, ideas emerged considering structural flexibility as a beneficial means of controlling and enhancing the aeroelastic response of the airframe. This paradigm shift has spawned numerous research programs exploring the realization of new structural concepts for adaptive wing structures, the possibility of internal and distributed structural actuation, and the replacement of control surfaces by variable camber airfoils. Smart wing technology offers the potential of significant performance gains for both military and transport aircraft. For this reason, all major airframe manufacturers and research institutions are involved in smart wing research. Examples are the DARPA/AFRL/NASA/Northrop-Grumman Smart Wing Project and the AFRL/NASA/Boeing F/A-18 active aeroelastic wing (AAW), to name only two. The AAW concept applies to wings with multiple leading and trailing edge surfaces. Each leading and trailing edge surface will be deployed at the flight conditions where they are most effective. Trailing edge surfaces are effective at lower dynamic pressures, but lose effectiveness with increasing dynamic pressure until aeroelastic reversal occurs. A trailing edge outboard surface loses effectiveness at a lower flight speed than a trailing edge inboard surface. Leading edge outboard control surfaces become more effective as roll devices with increasing flight speed.

Due to the enormous actuation and control effort, fully actuated smart wing projects so far focused on drag reduction and improved cruise performance, or on the enhancement of static aeroelastic characteristics like roll performance. However, active flutter control using smart wing technology has been gaining considerable importance and besides theoretical efforts, several wind-tunnel experiments have been conducted. From 1991 to 1996, the Piezoelectric Aeroelastic Response Tailoring Investigation (PARTI), a cooperative effort between NASA Langley and the Massachusetts Institute of Technology, investigated analytical and experimental methods for the use of piezoelectric patch actuators for wing structural control. During the program, active flutter suppression and reduced gust loads using piezoelectric actuation on a semispan wing were demonstrated in wind-tunnel tests. Flutter dynamic pressure was increased by 12% and peak wing root bending moment due to gust loads was reduced by 75%.

The active flexible wing (AFW) research program, a joint effort of NASA and Rockwell International Corporation, investigated aeroservoelastic effects on an active flexible wing wind-tunnel model (**Figure 10**). Mathematical models developed on the basis of the AFW wind-tunnel tests resulted in successful active flutter control. Although mathematical model complexity and computing power limitations prevented attainment of real-time operation, essential test goals were met with a hot-bench simulation running at a timescale ratio no slower than 1:5. To achieve the required timescale, model reduction methods were applied to the aeroservoelastic portion of the full-order mathematical model. The reduction method was based on the internally balanced realization of a linear dynamic system. The state dimensions of the aeroservoelastic model were reduced by a factor of 2. Some results of the AFW wind-tunnel tests are illustrated in **Figure 11**.

Recent research sponsored by Air Force and DARPA investigates the possibility of removing all horizontal and vertical control surfaces on future uninhabited combat air vehicles (UCAV). Integrated flight control systems are being developed for simultaneous maneuver control and active flutter suppression using morphing airfoil sections to modify vehicle lift and drag (**Figure 12**). Such aircraft will show enhanced stealth properties and reduced radar signature, allowing deeper penetration into enemy air space without putting human pilots at risk. Important research issues are the determination of actuation energy, forces, moments, displacements, and time constants that are required of smart actuators to achieve the desired maneuverability and performance characteristics.

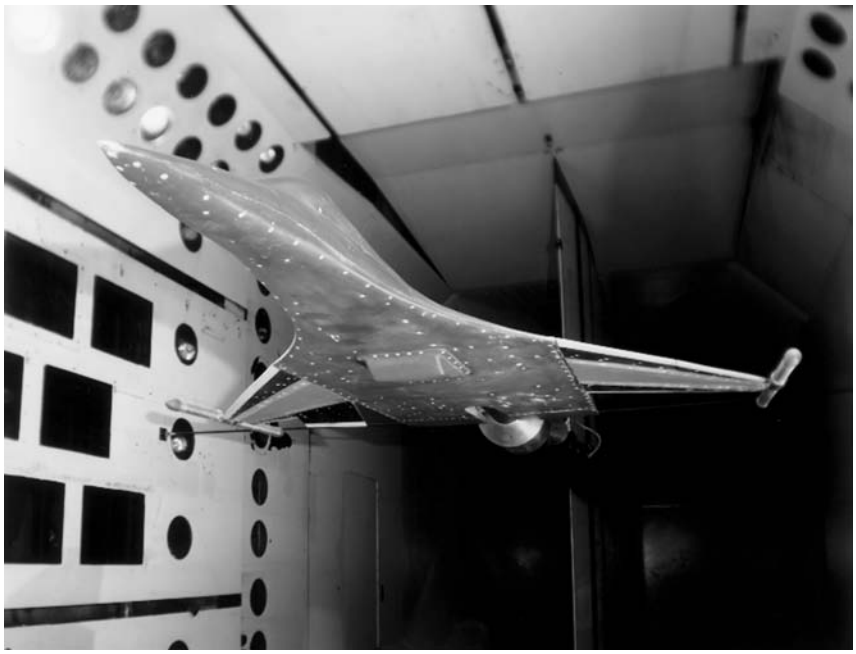


Figure 10 (See Plate 35). Active flexible wing (AFW) wind-tunnel model in the NASA Langley transonic dynamics tunnel (courtesy of NASA Langley Research Center).

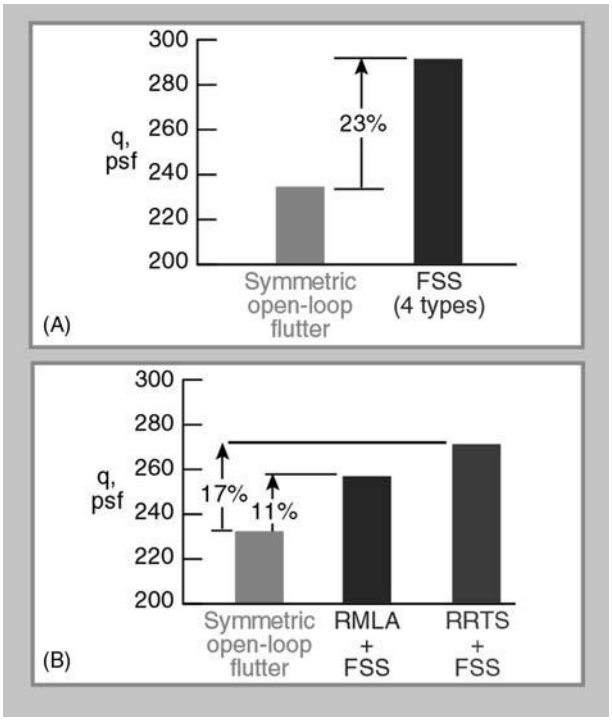


Figure 11 Active flutter control on the active flexible wing (AFW) beyond the uncontrolled flutter dynamic pressure: (A) flutter suppression only: (B) flutter suppression and roll control. FSS = flutter suppression system; RMLA = rolling maneuver load alleviation; RRTS = roll rate tracking system (courtesy of NASA Langley Research Center).

Acknowledgements

The author would like to thank the following people for providing pertinent information, picture material, and support in writing this article (in alphabetical order): Carey Buttrill (NASA Langley), Stanley R. Cole (NASA Langley), Dan Inman (Virginia Tech, CIMSS), Rakesh K. Kapania (Virginia Tech), Boyd Perry, III (NASA Langley), Jürgen Renken (EADS Airbus), Robert C. Scott (NASA Langley), Patrick Teufel (Institute of Flight Mechanics and Control), Klaus H. Well (Institute of Flight Mechanics and Control), Rudy Yurkovich (Boeing).

Nomenclature

B	matrix of control surface influence
D	modal damping matrix
f	disturbance vector
F	transfer matrix
I	unit matrix
Ma	flight Mach number
Q	aerodynamic load matrix
s	Laplace variable
u	input vector
y	output vector

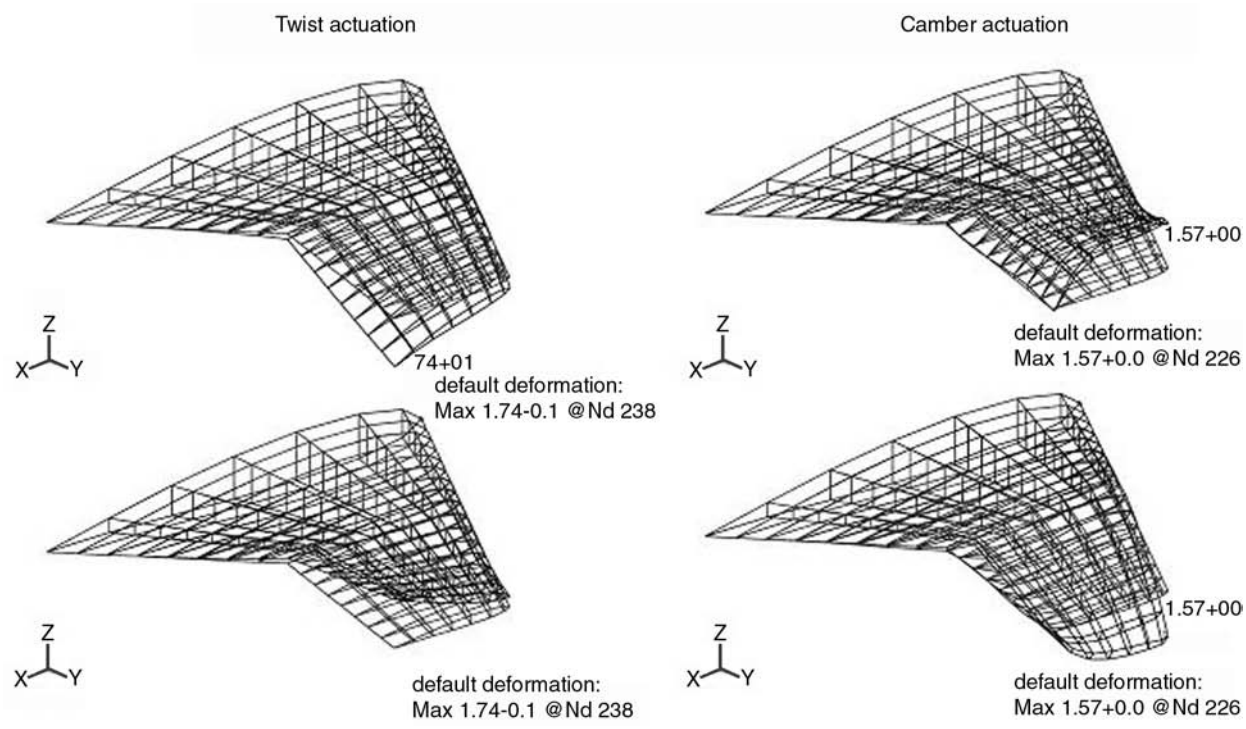


Figure 12 (see Plate 36). Finite element analysis of a smart UCAV wing with morphing airfoil sections.

See Plates 33, 34, 35, 36.

See also: **Active vibration suppression**; **Actuators and smart structures**; **Aeroelastic response**; **Damping, active**; **Fluid/structure interaction**; **Flutter**; **Modal analysis, experimental**, Basic principles; **Piezoelectric materials and continua**; **Sensors and actuators**.

Further Reading

Bisplinghoff RL, Ashley H, Halfman RL (1996) *Aeroelasticity*. Mineola, New York: Dover.

Buttrill CS, Bacon BJ, Heeg J, *et al*. (1996) *Aeroservoelastic Simulation of an Active Flexible Wing Wind-Tunnel Model*. NASA technical paper No. 3510. NASA. Hampton, VA: Langley Research Center.

FAR Part 25, Section 25.629 (1992) Aeroelastic stability requirements.

Gade PVN, Inman DJ (1999) Robust adaptive control of store release event for wings with external stores. *Journal of Guidance Control and Dynamics* 22(3) p. 408–14.

Gern FH (1991) *Nonlinear Simulation of Aeroelastic Vibrations and Active Damping Augmentation on a Transonic Commercial Transport Aircraft*, MS Thesis, Institute for Statics and Dynamics of Aerospace Structures, Stuttgart, Germany.

Gern FH, Librescu L (1999) Synergistic interaction of aeroelastic tailoring and boundary moment control on aircraft wing flutter, *Proceedings of the CEAS/AIAA/ICASE/NASA Langley International Forum on Aeroelasticity and Structural Dynamics*, June 22–25, pp. 719–733, Williamsburg, VA.

Hockenhull M (1998) Airworthiness aspects of new technologies: interaction between aircraft structural dynamics and control systems. *IME Proceedings, Part G: Journal of Aerospace Engineering*: 212:309–317.

Lomax TL (1996) *Structural Loads Analysis for Commercial Transport Aircraft: Theory and Practice*. Reston, VA: American Institute of Aeronautics and Astronautics.

Military Specification MIL-A-8870B (AS) (1987) *Airplane Strength and Rigidity Vibration, Flutter, and Divergence*. May 20, 1987.

Perry B III, Cole SR, Miller Gerald D (1995) Summary of an active flexible wing program, *Journal of Aircraft* 32: 10–15.

Perry B III, Cole SR, Miller Gerald D (1995) Summary of an active flexible wing program. *Journal of Aircraft* 32: 10–15.

Perry B III, Noll TE, Scott RC (2000) Contributions of the transonic dynamics tunnel to the testing of active control of aeroelastic response, AIAA Paper No. 2000–1769, *AIAA Dynamics Specialists Conference*, Atlanta, GA, 5–6 April.

Rivas McGowan AM, Wilkie WK, Moses RW *et al*. (1998) Aeroservoelastic and structural dynamics research on smart structures conducted at NASA Langley Research Center, *SPIE Symposium on Smart Structures and Materials, Industrial and Commercial Applications Conference*, paper no. 3326–21.

FORCED RESPONSE

N A J Lieven, Bristol University, Bristol, UK

Copyright © 2001 Academic Press

doi:10.1006/rwvb.2001.0186

Machines and structures are, by definition, required to fulfil a function. This usually involves the movement of people, fluids or materials and as such requires a force to perform these tasks. For machines or engines, a conversion of the internal energy source into motion is required which will induce a forced response in the system. Structures such as bridges and passengers in a transport system have their loads exerted externally. The consequence of a force acting on a structure can be benign; for instance, an applied static load will simply deflect the system in relation to the applied force and its stiffness. However, if the force is dynamic, or transient, and interacts adversely with the dynamic properties of the system, large amplitude vibrations will occur.

A major concern with forced vibration response is the frequency of the input force. If the frequency of the driving force in the system is in the region of a natural frequency, the response of the structure will always be greater than its static equivalent. This is the primary reason why the forced response of a driven system must be considered in the design phase of a product. A simple static load test will not reveal anything about the dynamic performance of the system under in-service loads. The reason for this is straightforward: no kinetic energy is present in the static measurement and so the influence of mass and damping is not exercised.

As with all vibration analysis, one of the primary drivers for understanding forced response is the safety and integrity of the structure. All too often the use of forced response analysis is applied retrospectively to trouble shoot large-amplitude behavior. Useful though this is, an understanding of the dynamic properties of the system coupled with the source and harmonic nature of the driving force can preempt potentially catastrophic behavior later on.

Forced Response with Harmonic Excitation

The simple model generally used to exhibit the forced response of simple viscously damped system is depicted by a mass, spring, damper model being driven by a force acting on the mass (**Figure 1**), for which the equation of motion is given by:

$$m\ddot{x} + c\dot{x} + kx = F\sin\omega t \qquad [1]$$

This conforms to the standard form of a second-order differential equation and, as such, the system will undergo simple harmonic motion. Thus, the steady-state displacement of the mass will follow the path described by $x = X\sin(\omega t - \phi)$. Note that this response includes a phase lag, ϕ, caused by the damping in the system. The effect of damping is therefore to induce the system response to lag behind the driving force.

In order to solve the equation of motion, the assumed simple harmonic response needs to be differentiated twice to derive the velocity and acceleration, respectively:

$$\begin{aligned} x &= X\sin(\omega t - \phi) \\ \dot{x} &= \omega X\cos(\omega t - \phi) = \omega X\sin(\omega t - \phi + \pi/2) \\ \ddot{x} &= -\omega^2 X\sin(\omega t - \phi) = \omega^2 X\sin(\omega t - \phi + \pi) \end{aligned} \qquad [2]$$

Thus the equation of motion becomes:

$$m\omega^2 X\sin(\omega t - \phi + \pi) + c\omega X\sin(\omega t - \phi + \pi/2) + kX\sin(\omega t - \phi) = F\sin\omega t \qquad [3]$$

If we consider each force in the system as a vector, so that the force associated with each structural component has a magnitude and a phase relative to the driving force, we can construct a vector diagram of the loads acting on the structure. This is shown in **Figure 2**.

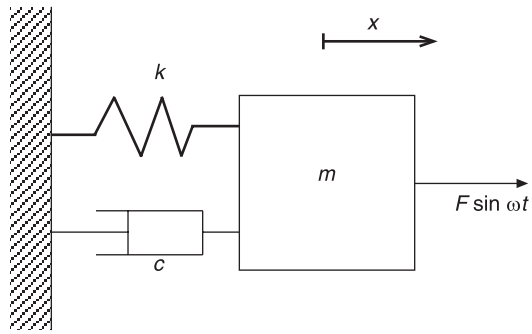


Figure 1 Single-degree-of-freedom forced response model.

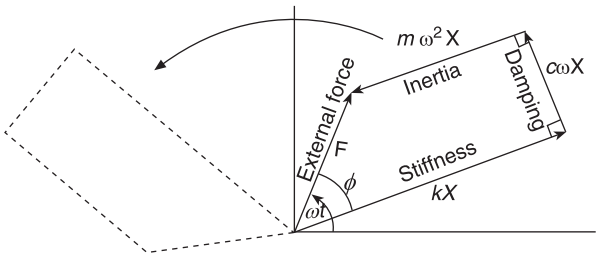


Figure 2 Vector diagram of forces.

By applying Pythagoras' theorem to the geometry of the force quadrilateral, the applied force can be related to the loads on each of the structural elements as shown in eqns [4] and [5]:

$$|F| = \sqrt{\left((kX - m\omega^2 X)^2 + (c\omega X)^2\right)} \qquad [4]$$

so:

$$\left|\frac{X}{F}\right| = \frac{1}{\sqrt{\left((k - m\omega^2)^2 + (c\omega)^2\right)}} \qquad [5]$$

The frequency response function (FRF) is defined as the ratio of the output (e.g. displacement) to the input force, so eqn [5] is the magnitude of the FRF.

From the vector diagram of forces we can also obtain the phase angle of the FRF:

$$\phi = \tan^{-1}(c\omega)/(k - m\omega^2) \qquad [6]$$

Plots of the FRF amplitude and phase are known collectively as a Bode plot (**Figures 3** and **4**).

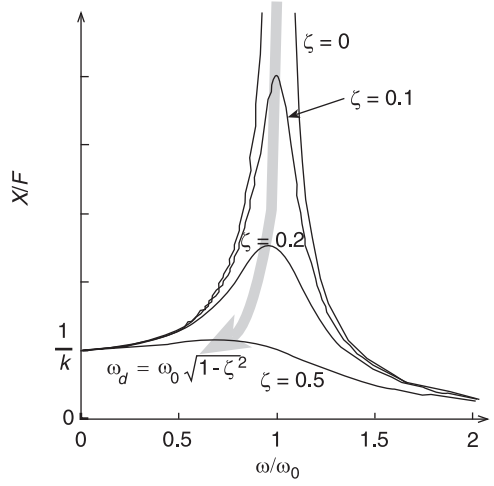


Figure 3 Magnitude of frequency response function.

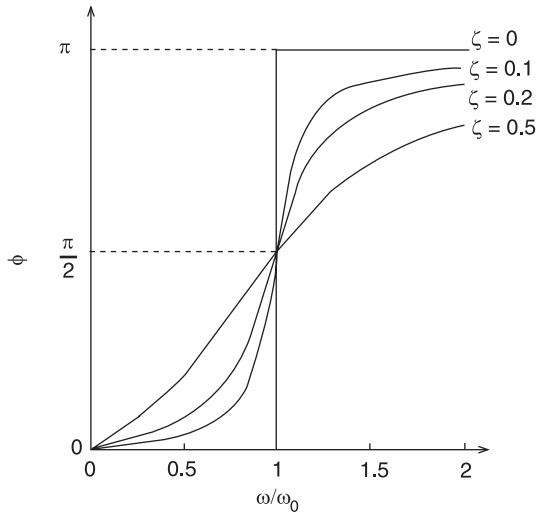


Figure 4 Phase of frequency response function.

At this point it is worth describing some of the features of the Bode plot and its significance in vibration analysis. Intuitively, it is obvious that as the damping in the system is increased the amplitude of vibration decreases. This is particularly pronounced in the region around the natural frequency ω_n. The position of maximum amplitude is defined as the resonance. Note that this does not necessarily coincide with the natural frequency as they are related by the expression $\omega_d = \omega_n\sqrt{(1-\zeta^2)^2}$ where ζ is the damping ratio. For most practical systems the inherent damping is small, less than 10%, and so effectively the damped natural frequency is assumed to be placed at the undamped natural frequency, ω_n. We should also consider the behavior both statically and at resonance and determine the ratio of these two vapor levels. This ratio is known as the Q of the system. This is simply calculated by the ratio of the dynamic response at resonance compared to the static deflection for a given force F. If we substitute the static displacement, $X_s = F/k$, in eqn [5] we obtain:

$$\frac{X}{X_s} = \frac{k}{\sqrt{\left((k - m\omega^2)^2 + (c\omega)^2\right)}} \qquad [7]$$

which is also called the dynamic magnification factor and is unity at $\omega = 0$ and $1/(2\zeta)$ at resonance.

Although this section has concentrated on the response due to forced excitation, it is also important to understand the source of the driving force. In rotating machinery for example, the excitation usually arises from a rotational out-of-balance in the engine or motor driving the system, as shown in **Figure 5**. The effect of this out-of-balance is to generate a harmonic

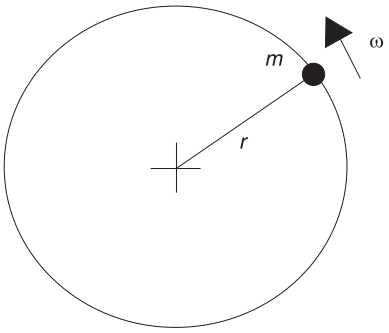


Figure 5 Rotational out of balance.

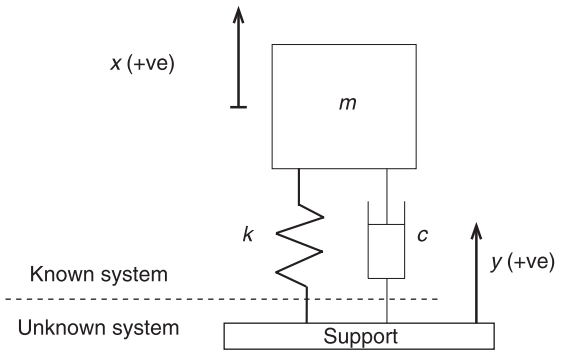


Figure 6 Base-excited structure.

force which varies according to the square of the rate of rotation of the machine i.e.:

$$F = mr\omega^2 \qquad [8]$$

Note that this form of centrifugal force differs from the simple harmonic excitation shown in eqn [1], i.e. $F\sin\omega t$ where $F = \text{const.}$, whereas the load from the centrifugal excitation will start from zero at the origin.

Base Excitation

Whilst harmonically excited forced vibrations are a source of concern, the external influence of other machines on sensitive components can be even more demanding. Many machines require a vibration-free environment to perform effectively. Typical contemporary examples include aircraft avionic systems and clean room photo-etching devices. In these applications it is essential that any vibration in the support does not interfere with the function of the machine.

In this section the mathematical description of base excited structures will be developed, followed by a brief overview of practical steps that can be taken to minimize structural response. The single-degree-of-freedom configuration presented in **Figure 6** shows the dynamic components of the system being driven by a harmonic base amplitude Y. This displacement usually arises from an external source such as a compressor or turbine. The goal here is to accept that this will remain *in situ* and its influence is to be minimized through the support structure of the machine of interest.

Thus, the net force acting on the structure is given by:

$$m\ddot{x} = -c(\dot{x} - \dot{y}) - k(x - y) \qquad [9]$$

This equation is more commonly arranged in the form:

$$m\ddot{x} + c\dot{x} + kx = c\dot{y} + ky \qquad [10]$$

Note that the system can now be considered to be a displacement and velocity input acting on the supporting spring and damper elements. This allows us to consider the device to be isolated as a single-degree-of-freedom system, even though the source of vibration is another dynamic mechanism. As before, we can now assume simple harmonic motion at the base as the solution for this second-order equation, i.e. $y = A\sin ax$. Substituting into eqn [10] gives:

$$\begin{aligned} m\ddot{x} + c\dot{x} + kx &= cA\omega\cos\omega t + kA\sin\omega t \\ &= A\sqrt{\left((c\omega)^2 + k^2\right)} \\ &\times \left(\frac{c\omega}{\sqrt{\left((c\omega)^2 + k^2\right)}}\cos\omega t + \frac{k}{\sqrt{\left((c\omega)^2 + k^2\right)}}\sin\omega t\right) \\ &= A\sqrt{\left((c\omega)^2 + k^2\right)}(\sin\alpha\cos\omega t + \cos\alpha\sin\omega t) \\ &= \sqrt{\left((c\omega)^2 + k^2\right)}A\sin(\omega t + \alpha) \end{aligned} \qquad [11]$$

Again, these forces can be displayed as a vector diagram as shown in **Figure 7**. From this the phase angle α, the lag between the base excitation and response of the system, can be observed directly:

$$\alpha = \tan^{-1}(c\omega/k) \qquad [12]$$

Hence, we can consider the loads to be acting on the system directly. This can be recognized as being equivalent to the following single-degree-of-freedom, shown in **Figure 8**.

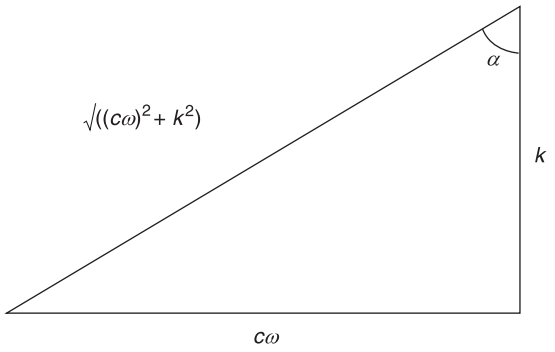


Figure 7 Vector diagram of forces.

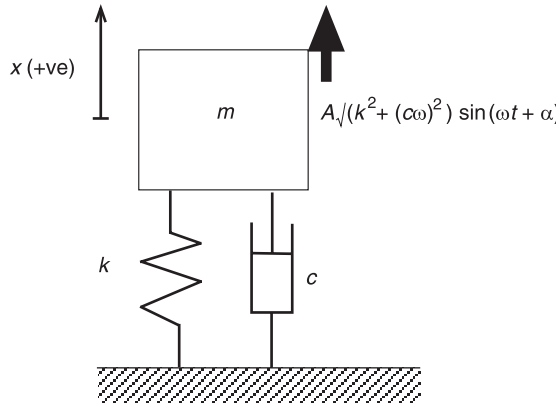


Figure 8 Equivalent single-degree-of-freedom system.

From the previous section, the solution is already known to be:

$$x(t) = X \sin(\omega t - \phi + \alpha) \qquad [13]$$

where

$$X = \frac{A\sqrt{\left(k^2 + (c\omega)^2\right)}}{\sqrt{\left((k - m\omega^2)^2 + (c\omega)^2\right)}}$$

and:

$$\phi = \tan^{-1}\left(\frac{c\omega}{k - m\omega^2}\right) \qquad [14]$$

Although transmissibility is dealt with later in a different article (see **Vibration transmission**) it is helpful to define the term here as the ratio of the amplitude of body vibration to the amplitude of the support vibration:

$$T = \frac{X}{A} = \frac{\sqrt{\left(k^2 + (c\omega)^2\right)}}{\sqrt{\left((k - m\omega^2)^2 + (c\omega)^2\right)}} \qquad [15]$$

Practical Considerations

Having derived some of the basic equations for forced response, it is worth considering their application. The influence of eqn [15] on structural dynamic design is profound. This allows vibration engineers to select the support conditions for devices which are known to be susceptible to high amplitude response. The plot of transmissibility shown in **Figure 9** clearly demonstrates the behavior around and beyond resonance.

It is no surprise that around resonance the transmissibility is high. This observation needs little explanation as the structure is being excited near its natural frequency. As with internally-excited vibration, the response in this region is suppressed by an increase in the damping. However, it is foolhardy to operate any machine in a region in which the dynamic response is greater than the displacement induced by static load. If we are to minimize the response of a structure to base excitation, the only effective course of action is to ensure the driving frequency is much higher than its natural frequency. **Figure 9** shows that excitation $\omega/\omega_n \gg \sqrt{2}$ leads to lower levels of response than the equivalent static load. This provides the key feature for vibration isolation in the case of base excitation – ensure that the natural frequency suspension is as far below the driving frequency as possible. Two courses of action are available to the engineer (presuming that the source of the excitation cannot be altered):

1. increase the mass of the system itself. For grounded structures this is often the easiest solution as additional lumped masses can be readily applied. However, aerospace structures have a minimal mass requirement and so a second solution is sought; and
2. reduce the stiffness of the support. Be warned though, the increased flexibility of the suspension makes the structure vulnerable to impact loads and to large static displacements under no load.

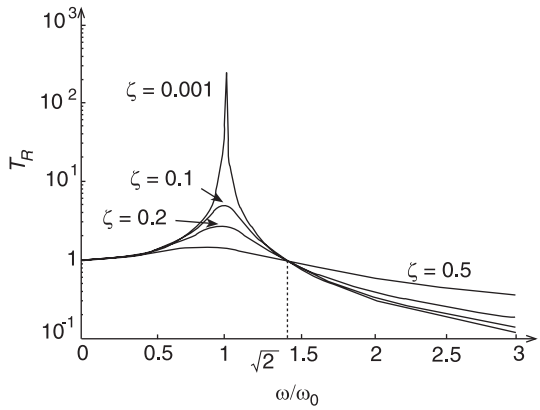


Figure 9 Transmissibility characteristics.

In either case, so long as the driving frequency is greater than $\sqrt{2}\omega_n$, it is important to ensure that the damping in the system is kept to a minimum. It can be seen from **Figure 9**, as the damping increases above this driving frequency, the response also increases.

Demonstrations of these methods are abundant in engineering structures. We only have to observe the behaviour of car engines on their mounts and washing machines: both exhibit the behaviour characteristic of vibration forced response. During start-up there is high amplitude as the rotation rate increases though the range of resonance and then dies away at high rotation rates. These simple examples reinforce the principle that little damping is included to suppress the motion around resonance. The vibration reduction is solely achieved by designing the suspension to have a natural frequency far below the driving frequency.

Nomenclature

F	force
T	transmissibility
ϕ	phase lag
ζ	damping ratio

See also **Modal analysis, experimental**, Applications; **Modal analysis, experimental**, Basic principles; **Modal analysis, experimental**, Measurement techniques; **Theory of vibration**, Fundamentals; **Vibration isolation theory**.

Further Reading

Maia NMM, Silva JMM (1997). *Theoretical and Experimental Modal Analysis*. Taunton, UK: Research Studies Press.

Thomson WT (1998) *Theory of Vibration with Applications*, 4th edn, Cheltenham UK: Stanley Thornes.

FOURIER METHODS

See **TRANSFORM METHODS**

FREE VIBRATION

See **THEORY OF VIBRATION: FUNDAMENTALS**

FRICTION DAMPING

R Ibrahim, Wayne State University, Detroit, MI, USA

Copyright © 2001 Academic Press

doi:10.1006/rwvb.2001.0017

Frictional damping is the resistance encountered by a body sliding on another surface. The work done against the friction force is dissipated in the form of heat. The energy dissipation is reflected by the measured hysteresis curve. The laws of friction are phenomenological and were formulated by Amontons in 1699 and Coulomb in 1785. Basically these laws state that: (1) the friction force is proportional to the normal load; (2) the friction force is independent of the apparent area of contact between sliding surfaces; and (3) the coefficient of static friction μ_s is greater than the coefficient of kinetic friction μ_k. The reason why the friction coefficient μ_k during sliding is often smaller than the static one μ_s may be attributed to the fact that the aspirities on one surface could jump part of the way over the gap between aspirities on the other. These laws are valid for sliding metals; however, for plastics the coefficient of friction μ_s usually decreases with increasing load as a result of the detailed way in which plastics deform. The values of the friction coefficients depend on the nature of the sliding surfaces and other factors such as relative velocity, time, and temperature.

Generally speaking, when the friction coefficient is independent of the magnitude of the sliding velocity, the friction force has a retarding effect upon the motion maintained by an external force. In this case, the friction force switches between negative and positive values depending on the sense of the sliding velocity. Under these conditions the friction force has the effect of positive damping which is associated with energy dissipation. The situation is different when the kinetic friction coefficient depends strongly on the sliding velocity and possesses a negative slope with respect to the velocity. In this case the friction gives rise to negative damping. In other words, the friction force between sliding surfaces is

greater for small relative velocities than its value for larger velocities. According to the third law of friction, the frictional force required to initiate sliding is greater than that needed to maintain the body in motion, i.e., $\mu_s > \mu_k$. In this case the friction may develop instability known as stick-slip.

Dry friction damping is used for friction base isolation as a means of passive control of structural vibration. Excellent isolation performance is achieved in conventional sliding-type systems if the friction coefficient is small, due to the reduction in transmitted ground acceleration. On the other hand, if the friction coefficient is large, the structure will be isolated only during large-amplitude loads, such as earthquakes, and the sliding system will not be activated by small to say moderate earthquakes. The basic idea behind this approach is similar to the mechanism of friction brake lining pads introduced at the intersection of frame cross-braces.

Dry friction damping arises in sliding surfaces at the boundaries of beams, plates, turbomachinery blades, and large flexible space structures. Friction in support boundaries acts as a source of energy dissipation. Moreover, the associated slip results in irregular variation of the system dynamic properties such as the natural frequency and damping coefficients. Frictional materials are usually used for power control components. These include vehicle braking systems where the kinetic energy of the vehicle is transformed into heat, friction clutches used to transmit the torque from one point and to couple the prime mover to the load, and frictional belts used to transmit power between shafts.

The case of negative friction damping will be considered in a separate section under friction-induced vibration. In this section we consider the friction only as a source of energy dissipation.

Energy Dissipation Due to Dry Friction

When the friction force is independent of the magnitude of the velocity $\dot{x}(t)$ and is opposite to the velocity direction of a sliding mass it can be represented by the expression $F_c\dot{x}/|\dot{x}|$, where F_c is the friction force amplitude and the dot denotes derivative with respect to time t. The energy dissipation due to a Coulomb friction force during one cycle is:

$$E_c = -\int_{\text{cycle}} F_c \frac{\dot{x}}{|\dot{x}|}\,dx \qquad [1]$$

If the sliding is approximated by a sinusoidal motion, i.e., $x(t) = x_0 \sin \omega t$, then the energy loss per cycle becomes:

$$E_c = -4x_0F_c \qquad [2]$$

If the Coulomb friction force were replaced by a linear viscous force given by the expression: $F_c\dot{x}/|\dot{x}|$, where $|\dot{x}|$ denotes the amplitude of the velocity, one can show that the corresponding energy loss per cycle is given by the formula:

$$E_d = -\pi x_0F_c \qquad [3]$$

It is seen that E_c is greater than E_d. Accordingly, the damping effect of a damper with a Coulomb friction is larger than that of a linear viscous dashpot. In both cases damping acts as a retarding force. The energy dissipation of both cases is represented by the area enclosed between the velocity curve and the corresponding force, as shown in **Figure 1**. Observe that the dry Coulomb friction force is a discontinuous function while the viscous damping force is a continuous one. This discontinuity in the Coulomb friction complicates the dynamic analysis since it forms a strong nonlinear term in the equation of motion.

It is not difficult to show that the equivalent viscous damping coefficient is:

$$c_{eq} = \frac{4F_c}{\pi\omega x_0} \qquad [4]$$

It is clear that the equivalent damping coefficient decreases with the amplitude of motion which reduces the effectiveness of Coulomb friction as a passive damper.

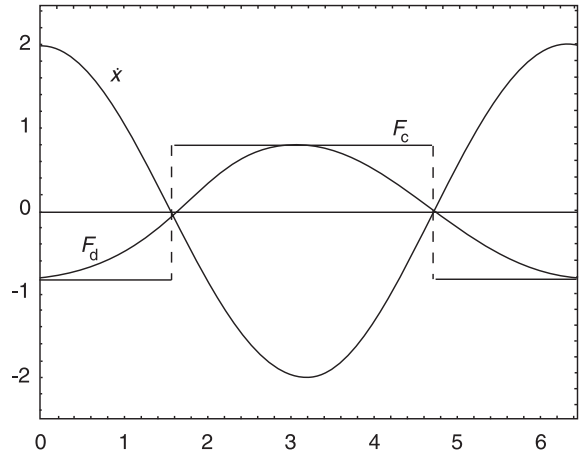


Figure 1 Velocity ($\dot{x}$), dry friction force (F_c) and viscous damping force (F_d) per cycle in harmonic motion.

Frictional Damping in Free Vibration

It is known that the free vibration of a mass-spring with a linear viscous damping possesses a constant logarithmic decrement. The logarithmic decrement is the difference in the natural logarithms of successive extreme excursions. The envelope of the free vibration record decays exponentially, as shown in **Figure 2A**. On the other hand, the free vibration of a mass-spring system with a dry friction experiences linear decay with a permanent set, as shown in **Figure 2B**. In order to understand the frictional damping in free vibration we consider the motion of the mass shown in **Figure 3**. Since the friction force acts in a direction opposite to the velocity direction, the mass m has two different free body diagrams: each is associated with one direction of the relative velocity, $\dot{x} > 0$ and $\dot{x} < 0$. The case when $\dot{x} = 0$ is very complicated where the friction force can take any value between $\pm\mu_s g$. However, we will consider the case when $\dot{x} \neq 0$.

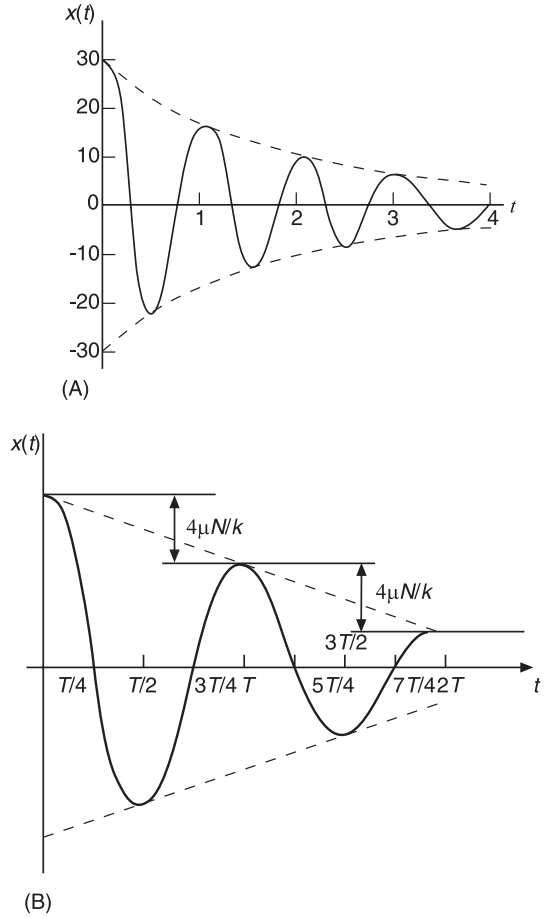


Figure 2 Time history records of free vibration in the presence of (A) viscous damping and (B) dry friction damping.

When the mass moves to the right, the equation of motion is:

$$m\ddot{x} + kx = -\mu_k N, \quad \dot{x} > 0 \qquad [5a]$$

and when it is moving to the left, the equation of motion is

$$m\ddot{x} + kx = +\mu_k N, \quad \dot{x} < 0 \qquad [5b]$$

Note that when the mass is moving to the right, the value of x varies from the lowest negative value to the maximum positive value, while when it is moving to the left it varies from the maximum positive to the minimum negative. The response of this system is described by the two linear differential eqns [5]. Such systems are referred to as bilinear. The solutions of equations [5a] and [5b] are, respectively:

$$x(t) = \mathrm{A}_1 \cos \omega_n t + \mathrm{B}_1 \sin \omega_n t - \frac{\mu_k N}{k} \quad \dot{x} > 0 \quad [6a]$$

$$x(t) = \mathrm{A}_2 \cos \omega_n t + \mathrm{B}_2 \sin \omega_n t - \frac{\mu_k N}{k} \quad \dot{x} < 0 \quad [6b]$$

where A_i and B_i are constants that depend on the initial conditions of each case, and $\omega_n = \sqrt{k/m}$. Consider the motion to be initiated by pulling the mass to the right by an initial displacement x_0 to the right with zero initial velocity. In this case the mass will move to the left and the solution [6b] is considered to determine the constants A_2 and B_2. This will give the following solution:

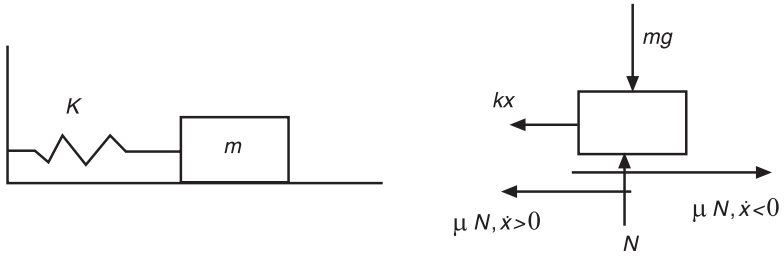


Figure 3 Schematic diagram of mass-spring system with dry Coulomb friction and the associate free-body diagram.

$$x(t) = \left(x_0 - \frac{\mu_k N}{k}\right) \cos \omega_n t + \frac{\mu_k N}{k} \quad \dot{x} < 0 \qquad [6c]$$

The motion will continue until the mass reaches zero velocity at time $t = \pi/\omega_n$, at which the displacement is:

$$x\left(\frac{\pi}{\omega_n}\right) = -x_0 + 2\frac{\mu_k N}{k}$$

The conditions at this position will be taken as initial conditions for the solution [6a] to solve for the constants A_1 and B_1 to give the following solution during the second half-period:

$$x(t) = \left(x_0 - \frac{3\mu_k N}{k}\right) \cos \omega_n t - \frac{\mu_k N}{k}, \quad \dot{x} > 0 \qquad [6d]$$

Again the mass will reach zero velocity at $t = 2\pi/\omega_n$ where its position is:

$$x\left(\frac{2\pi}{\omega_n}\right) = x_0 - 4\frac{\mu_k N}{k} \qquad [7]$$

This process of updating the initial conditions for each half-cycle will continue until the friction force exceeds the elastic restoring force, i.e., when $\mu_k N \geq kx$. The maximum amplitude is reduced in each cycle by the amount $4\mu_k N/k$. Note that because the friction damping is not part of the homogeneous side of the equation of motion, it is treated as a nonhomogeneous term. Accordingly, the natural frequency is independent of the friction force, which is different from the case of linear viscous damping.

Frictional Damping in Forced Vibration

The effect of frictional damping on the response of a single-degree-of-freedom system subjected to sinusoidal excitation can be examined by considering the equation of motion of a mass-spring system:

$$m\ddot{x} + kx + F \operatorname{sgn}(\dot{x}) = F_0 \sin(\Omega t + \varphi) \qquad [8]$$

where F_0 is the excitation force amplitude, Ω is the excitation frequency, φ is the phase angle in the excitation force, and F_c is the Coulomb friction force. The presence of Coulomb (dry) friction at the interface of sliding surfaces causes a nonlinear response of the system to the external excitation. Since the frictional force is always opposite to the motion, it must be represented by the rectangular function, as shown in **Figure 1A**. Introducing the following parameters:

$$A = F_0/k, \quad x_f = F_c/k, \quad \omega_n^2 = k/m$$

eqn [8] takes the form:

$$\ddot{x} + \omega_n^2(x - x_f) = A\omega_n^2 \sin(\Omega t + \varphi) \quad \text{for } 0 < t < \pi/\Omega, \text{ with } \dot{x} < 0 \qquad [9]$$

subject to the initial conditions:

$$\text{at} \quad t = 0, \; x = X_0, \quad \text{and } \dot{x} = 0 \qquad [10a]$$

and:

$$t = \pi/\Omega, \; x = -X_0, \quad \text{and } \dot{x} = 0 \qquad [10b]$$

With the initial condition [10a], the following general solution is obtained:

$$\begin{aligned} x(t) = & X_0 \cos \omega_n t + x_f(1 - \cos \omega_n t) \\ & + \frac{A}{1 - r^2}\left[\cos \varphi(\cos \Omega t - \cos \omega_n t)\right] \\ & + \sin \varphi(r \sin \omega_n t - \sin \Omega t) \end{aligned} \qquad [11]$$

where $r = \Omega/\omega_n$. The other two conditions [10b] are used to determine the unknown parameters X_0 and φ. This gives the following results:

$$\cos \varphi = \frac{X_0}{A}(1 - r^2)$$

and:

$$\sin \varphi = -\frac{x_f \sin(\pi/r)}{Ar(r + \cos(\pi/r))}(1 - r^2) \qquad [12a, b]$$

Eliminating φ gives:

$$X_0 = A\sqrt{\frac{1}{(1 - r^2)^2} - \left(\frac{x_f}{A}\right)^2 \left(\frac{\sin(\pi/r)}{r(1 - \cos(\pi/r))}\right)^2} \qquad [13]$$

This solution is only valid under the following conditions:

$$\frac{X_0}{x_f} \geq \frac{S}{r^2} \quad \text{for } 0 < t < \pi/\Omega \qquad [14]$$

where S is a factor which depends on the frequency ratio r and for $r > 0.5$, the value of S is almost 1. If one combines [13] with condition [14], the following bounds establish the validity of solution [13]:

$$\frac{X_0}{A} \geq 1/\sqrt{(1-r^2)^2\left[1+\left(\frac{r\sin(\pi/r)}{S(1-\cos(\pi/r))}\right)^2\right]} \qquad [15a]$$

$$\frac{X_f}{A} \leq r/\sqrt{(1-r^2)^2\left[\left(\frac{S}{r}\right)^2+\left(\frac{\sin(\pi/r)}{(1-\cos(\pi/r))}\right)^2\right]} \qquad [15b]$$

Eqn [13] represents the amplitude response for the nonstop motion. If one replaces the friction force $F\,\mathrm{sgn}(\dot{x})$ by an equivalent viscous damping force with equivalent viscous damping coefficient given by the expression

$$c_{eq} = \frac{4F}{\pi\Omega x_0} \qquad [16]$$

one can obtain the approximate well-known response amplitude based on sinusoidal motion:

$$X_0 = \frac{A}{(1-r^2)}\sqrt{1-\left(\frac{4}{\pi}\frac{x_f}{A}\right)^2} \qquad [17]$$

The approximate solution [17] is only valid for large response amplitudes. For smaller amplitudes the response becomes distorted and solution [17] is not satisfactory any more. **Figure 4** shows the amplitude frequency response for different values of friction force ratio F_c/F_0 or x_f/A. In the absence of dry friction the response is mainly governed by the resonance curve given by the first expression under the radical sign of [13] or [17]. The friction force reduces the amplitude response. However, for any friction force ratio $F_c/F_0 > \pi/4$ the response amplitude becomes infinitely large near resonance ($r \approx 1$). This means that dry friction will not bring the response amplitude into a bounded value at resonance, as in the case of linear viscous damping. The reason is that both the input energy and dissipated energy due to dry friction are linearly proportional to the response amplitude at resonance. As long as the input energy is greater than the dissipation energy, the response amplitude at resonance will grow without bound. On the other hand, the energy dissipation due to viscous damping is proportional to the square of the response amplitude, and at resonance both input energy and dissipation energy intersect at finite amplitude. This intersection brings the response amplitude at a bounded value at resonance.

The dry friction force F_c will reduce the response amplitude at frequencies different from resonance. It will also reduce the velocity of the response. A further increase of F_c will diminish the velocity to zero where the block m will stick with the surface. During each half-cycle the block will not move for a short period of time, during which the value of the friction force can take any value between $+F_c$ and $-F_c$. In order to estimate the motion with one stop where the acceleration is zero, one must establish a force balance between the excitation force, spring force and the friction force. A point-by-point calculation will lead to curves such as those indicated in **Figure 4**. Below

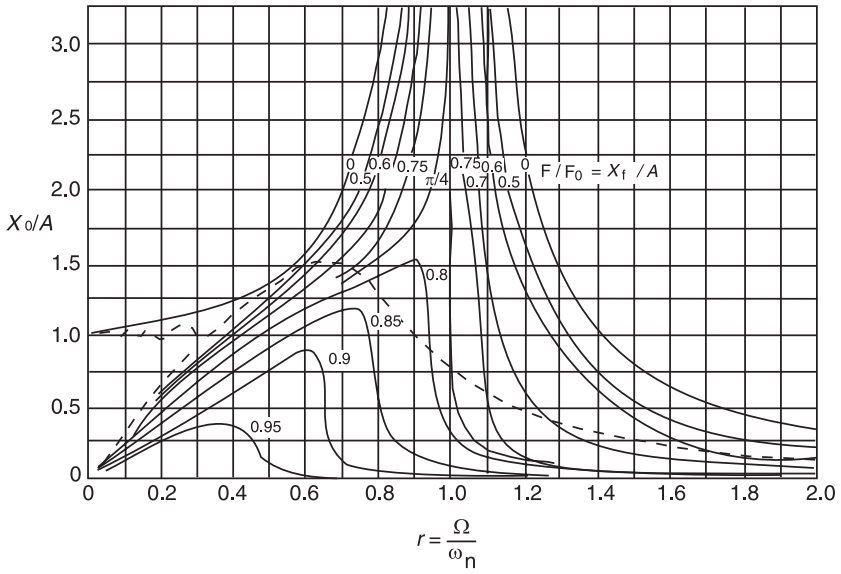


Figure 4 Amplitude–frequency response curves for different values of dry friction force ratio. The dotted curve separates between response with stops and nonstop motions. (Reproduced with permission from Den Hartog, 1931.)

the dotted curve shown in **Figure 4** the motion experiences one stop every half-cycle. The motion may also experience two stops per half-cycle in the lower left corner of **Figure 4**. Since the friction force at zero velocity can take any value between $+F_c$ and $-F_c$, the mathematical treatment is belonging to the problems of differential inclusion and differential equations with the nonsmooth right-hand side. When the friction force assumes a fixed value, the motion is governed by an ordinary differential equation of the form which can be treated as for the case of continuous nonstop motion. When the friction force can take any value ranging from $+F$ to $-F$, the system is governed by the differential inclusion of the form. Differential inclusion is encountered in problems of unilateral dynamics involving friction, contact, and impact problems. The existence and uniqueness of solutions are beyond the scope of this section.

Friction Base Isolators (FBI)

Friction base isolation systems are based on decoupling a structure from the damaging components of earthquake motion by introducing flexibility and energy absorption capacity through a system that is placed between the structure and its foundation. The performance of the base isolation systems depends on two main characteristics. These are the capability of shifting the system fundamental frequency to a lower value, which is well remote from the frequency band of most common earthquake ground motions, and the energy dissipation of the isolator. Three common types of FBI systems are employed:

1. Resilient-friction base isolators (R-FBI): this system consists of concentric layers of Teflon-coated plates that are in friction contact with each other and contain a central rubber core. A schematic diagram of this system is shown in **Figure 5A** and is described by the equation of motion:

$$\ddot{x} + 2\zeta\omega_n\dot{x} + \omega_n^2 x = \mu_k g(\mathrm{sgn}(\dot{x})) = -\ddot{U}_g \qquad [18]$$

where ζ is the damping ratio, ω_n is the undamped natural frequency of the isolator, g is the gravitational acceleration, and $\ddot{U}_g$ is the base acceleration. Under sinusoidal excitation, the response displacement and velocity are periodic but not harmonic, as shown in **Figure 6A and 6B**, respectively. The measured time history record of the friction force revealed that the static friction is constant while the kinetic friction force experience random fluctuations. The influence of the friction force on the amplitude frequency response is plotted in **Figure 6C**. It is clear that the frictional damping has a significant effect on reducing the structure displacement under sinusoidal or random base excitation.

2. The Electricité de France (EDF-FBI): this consists of a laminated (steel-reinforced) neoprene pad topped by a lead-bronze plate which is in frictional contact with a steel plate anchored to the structure. This system is shown in **Figure 5B** and is modeled by the two differential equations:

$$\ddot{x} + \mu_k g(\mathrm{sgn}(\dot{x} - \dot{y})) = -\ddot{U}_g \qquad [19a]$$

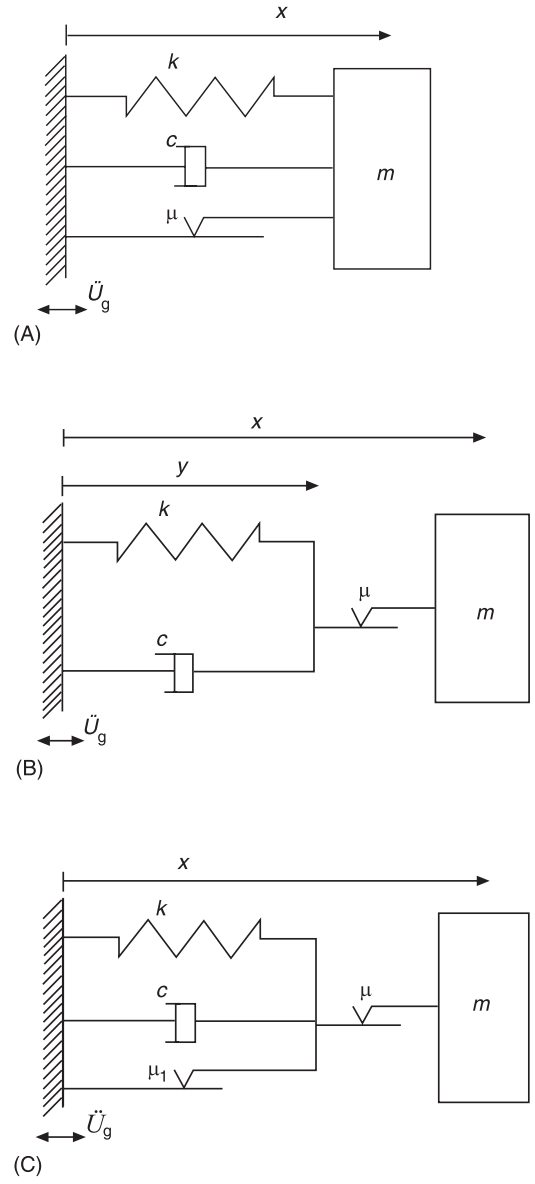


Figure 5 Schematic diagrams of friction base isolators: (A) resilient-friction base isolator (B) EDF friction base isolator; (C) sliding resilient-friction base isolator. (Reproduced with permission from Su *et al*., 1989.)

$$2\zeta\omega_n\dot{y} = \omega_n^2 y = \mu_k g(\text{sgn}(\dot{x} - \dot{y})) \qquad [19b]$$

where:

$$\text{sgn}(\dot{x} - \dot{y}) = \begin{cases} \dfrac{\ddot{U}_g + \ddot{y}}{\mu_k g} & \dot{x} = \dot{y} \quad \text{(sticking)} \\ \text{sgn}(\dot{x} - \dot{y}) & \dot{x} \neq \dot{y} \quad \text{(slipping)} \end{cases} \qquad [19c]$$

This isolator showed superiority in reducing the transmitted earthquake acceleration to the structure than the R-FBI system.

3. Sliding resilient-friction base isolator (SR-FBI): This system is a combination of the EDF and R-FBI systems with two different frictional elements, as shown in **Figure 5C**. It is modeled by the two differential equations:

$$\ddot{x} + \mu_k g(\text{sgn}(\dot{x} - \dot{y})) = -\ddot{U}_g \qquad [20a]$$

$$2\zeta\omega_n\dot{y} + \omega_n^2 y + \mu_1 g(\text{sgn}(\dot{y})) = \mu_k g(\text{sgn}(\dot{x} - \dot{y})) \qquad [20b]$$

where μ_k and μ_1 are the coefficients of friction of the upper plate and the isolator plates, respectively. This isolator exhibits greater isolation than the previous two cases.

In the absence of friction the relationship between the response amplitude and excitation amplitude is linear and passes through the origin of response–excitation plane. On the other hand, in the presence of dry friction, the dependence of the response

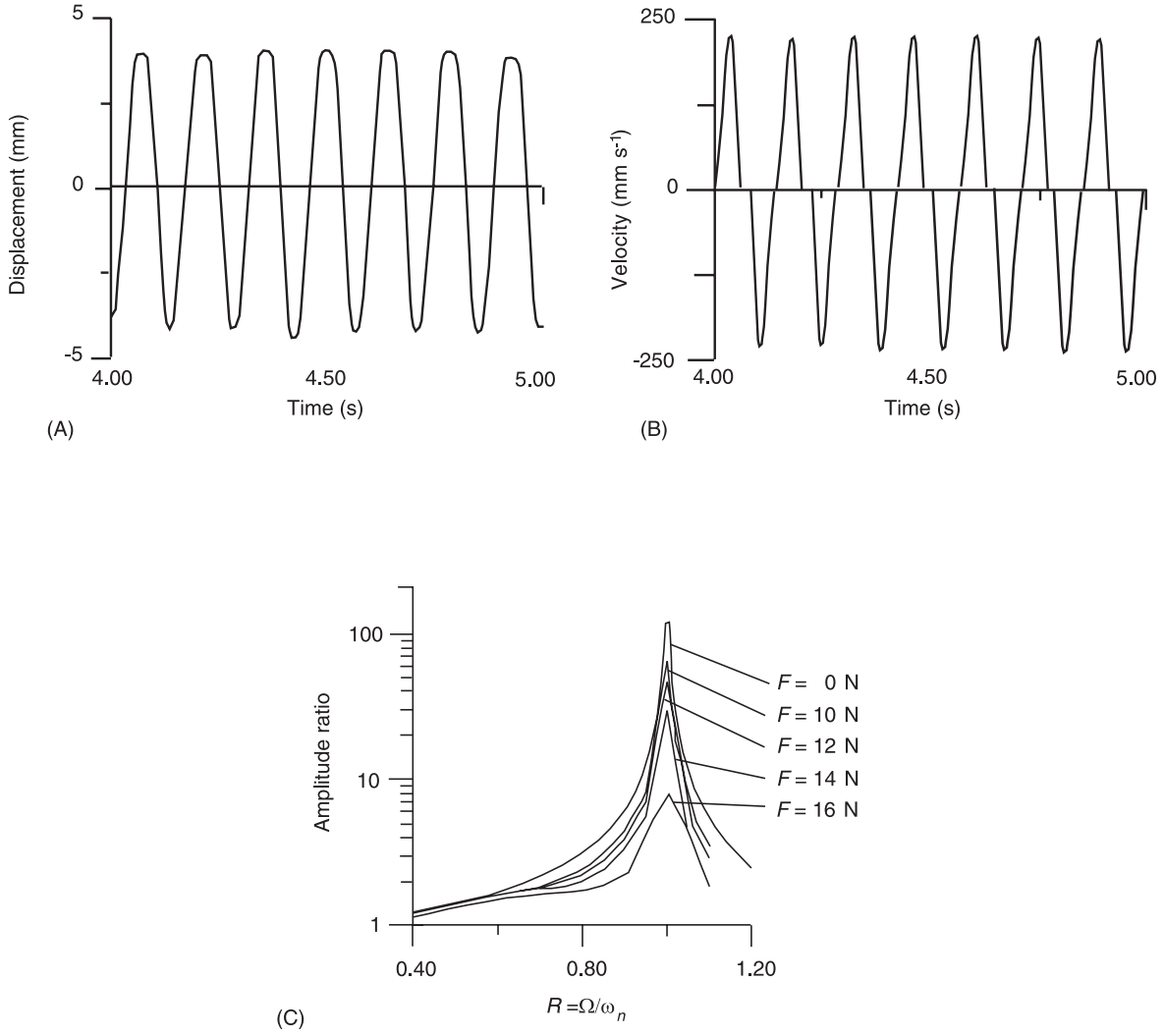


Figure 6 Response of resilient-friction base isolator under sinusoidal excitation. (A) displacement time history record; (B) velocity time history record; (C) amplitude frequency response for different values of friction force levels. (Reproduced with permission from Ibrahim *et al*., 1998.)

amplitude on the excitation amplitude usually exhibits a linear relationship for low excitation levels and becomes nonlinear for relatively higher excitation levels. Such a relationship does not pass through the origin of response–excitation plane – a feature which reveals a drift primarily caused by dry friction. Significant drop in the response amplitude takes place due to dry frictional damping of the isolation element.

Nomenclature

F_e	dry friction force
F_d	viscous damping force
g	gravitational acceleration
$\ddot{U}_g$	base acceleration
$\dot{x}$	velocity
φ	phase angle
μ_s	static friction
μ_k	kinetic friction
ξ	damping ratio
Ω	excitation frequency

See also: **Critical damping**; **Damping mounts**; **Earthquake excitation and response of buildings**; **Friction induced vibrations**; **Vibration isolation theory**.

Further Reading

Den Hartog JP (1931) forced vibrations with combined Coulomb friction and viscous friction. *ASME Transactions* **53**: 107–115.

Den Hartog JP (1985) New York: *Mechanical Vibrations*. Dover Publications.

Gueraud R, Noel-Leroux JP, Livolant M and Michalpolous AP (1985) Seismic isolation using sliding-elastomer bearing pads. *Nuclear Engineering Design* **84**: 363–377.

Ibrahim RA (1994) Friction-induced vibration, chatter, squeal, and chaos, part I: mechanics of contact and friction. *ASME Applied Mechanics Reviews* **47**(7): 209–226.

Ibrahim RA, Zielke SA and Popp K (1998) Characterization of interfacial forces in metal-to-metal contact under harmonie excitation. *Journal of Sound and Vibration* **220**: 365–377.

Kelly JM (1986) A seismic base isolation: review and bibliography. *Soil Dynamics and Earthquake Engineering* **5**: 202–216.

Mostaghel N and Khodaverdian M (1987) Response of structures supported on resilient-friction base isolators (R-FBI). *Earthquake Engineering Structural Dynamics* **15**: 379–390.

Su L, Ahmadi G and Tadjbaksh IG (1989) A comparative study of a base isolation system. *ASCE Journal of Engineering Mechanics Division* **115**: 1976–1992.

FRICTION INDUCED VIBRATIONS

R Ibrahim, Wayne State University, Detroit, MI, USA,

Copyright © 2001 Academic Press

doi:10.1006/rwvb.2001.0087

When the friction coefficient is independent of the magnitude of the sliding velocity, the friction force has the usual retarding effect with positive damping. On the other hand, when the kinetic friction coefficient depends strongly on the sliding velocity and possesses a negative slope with respect to the velocity, the friction gives rise to negative damping. In this case the friction may develop different types of instability such as stick-slip, quasiharmonic oscillation (or limit cycle), chaos, chatter, and squeal. Stick-slip oscillation is characterized by a saw-tooth displacement curve of the type shown in **Figure 1A**. The stick-slip motion is governed by static and by kinetic friction forces. The quasiharmonic motion has a near-sinusoidal displacement–time curve, as shown in **Figure 1B**. The quasiharmonic motion is initiated and maintained by the kinetic friction force. Friction phenomena of audible nature, including chatter and squeal, can take place in systems with sliding parts, and each occurs within a certain frequency band. For example, a high-frequency noise is termed squeal, and a low-frequency noise is called chatter. It appears that audible noises are generated intermittently and without any apparent order or combination. However, when their frequencies are analyzed and studied in detail, one may find that such noises are generated in combination of different frequency components.

Contact forces between sliding surfaces arise due to complex mechanisms and lead to mathematical models, which are strongly nonlinear, discontinuous, and nonsmooth. The inclusion of such nonlinearities in the equations of motion of a dynamical system can have interesting effects on the dynamic response characteristics. This nonlinearity leads to differential inclusions in the mathematical model, adding a further difficulty to the problem. Differential inclusions can be regarded as differential equations that consist of set-valued or multivalued terms. Accordingly, the existence and uniqueness of solutions are no longer guaranteed. The existence and uniqueness of solutions of problems associated with friction

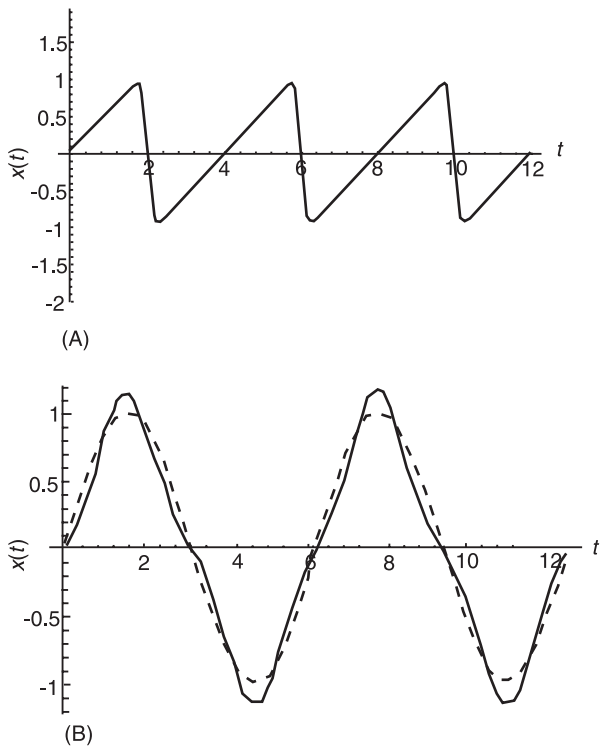


Figure 1 Typical time history records of (A) stick-slip motion and (B) quasiharmonic motion (dashed curve shows harmonic motion for comparison).

boundary conditions are beyond the scope of the present section.

Friction-induced noise is usually encountered in power control components such as vehicle braking systems, friction clutches, and frictional belts. Other applications include machine tool vibration, stern-tube water-lubricated bearings of submarines, wheel/rail squeal in mass transit systems, and machine tool vibration.

Experimental tests on a pin-on-disk-type sliding apparatus indicated that the friction force depends on the normal load for a constant sliding speed. Depending on the value of the normal load, four different friction regimes were observed. These are:

1. Steady-state friction region where the frictional force increases linearly with the normal load.
2. Nonlinear friction region in which the friction force increases nonlinearly with the normal load and the coefficient of friction is no longer constant but increases with the normal load.
3. Transient region characterized by intermittent variation of the friction force. When the mean friction force reaches a sufficiently high value, a temporary burst of self-excited vibrations occurs and the friction force falls to a low value.
4. Self-excited vibration region where the mean friction force drops to a very low value and is accompanied by high-amplitude periodic self-excited oscillations.

These four regimes are shown in **Figure 2**. The first two regimes are characterized by small-amplitude random vibrations of the slider in the tangential, normal, and torsional degrees of freedom. In the self-excited vibration regime, the normal load results in an unstable limit cycle. The source of such limit cycle is due to the presence of nonlinearity due to nonlinear contact forces and coupling between the degrees of freedom.

Mechanism of Negative Frictional Damping

In order to understand the mechanism of negative frictional damping we consider the classical example of the violin string-bow system. In moving the bow at a constant speed, v_0, in one direction the string oscillates back and forth with a smaller absolute-velocity $\dot{x}$ than that of the bow. This means that the direction of the relative velocity of the bow with respect to the string does not change. When the string is moving in the direction of the bow (in-phase), the slipping velocity $v_0 - \dot{x}$ is small and the friction force is large in order to drag the string in that direction.

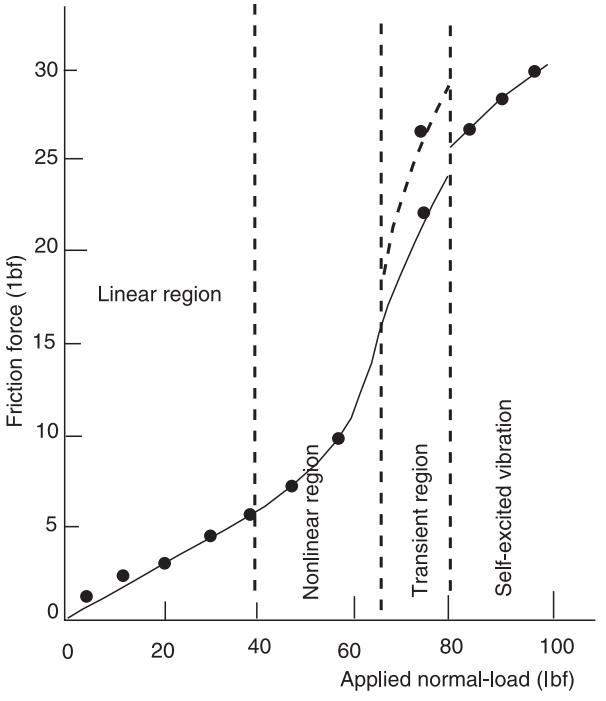


Figure 2 Dependence of the average friction force on the normal load showing four regimes. (Reproduced with permission from Dweib and D'Souza, 1990.)

However, when the string reverses its direction (out-of-phase), the relative velocity $(v_0 - (-\dot{x}))$ is the absolute summation of the bow and string velocities and is thus larger than the relative velocity when they are moving in-phase. It is obvious that the corresponding friction force is smaller than that of the out-of-phase case. Since the work done by friction force during the in-phase motion is positive and greater in magnitude than the absolute value of the work done by the smaller friction force during the out-of-phase motion friction force, the net work done by the friction force over one cycle is positive. This means that the friction imparts energy to the system rather than dissipates energy.

A simple modeling of the violin string-bow system can be represented by a mass-spring-dashpot system sliding on a moving belt at velocity v_0, as shown in **Figure 3**. The equation of motion of the mass m is:

$$m\ddot{x} + c\dot{x} + kx = F(v_0 - \dot{x}) \qquad [1]$$

where the friction force F is a function of the relative velocity $(v_0 - \dot{x})$ between the belt and the mass m. The friction force is usually obtained experimentally and a typical curve of the friction force vs the relative velocity is shown in **Figure 4** for clockwise and counterclockwise disk rotations. It is seen that the slope of the curve possesses negative slope over small values of the relative velocity. The function of the friction force can be expressed in terms of the relative velocity through a Taylor series:

$$F(v_0 - \dot{x}) \cong F(v_0) - \frac{\mathrm{d}F}{\mathrm{d}v}\dot{x} + \frac{1}{2!}\frac{\mathrm{d}^2F}{\mathrm{d}v^2}\dot{x}^2 - \frac{1}{3!}\frac{\mathrm{d}^3F}{\mathrm{d}v^3}\dot{x}^3 + \ldots \qquad [2]$$

Introducing the coordinate and time transformations:

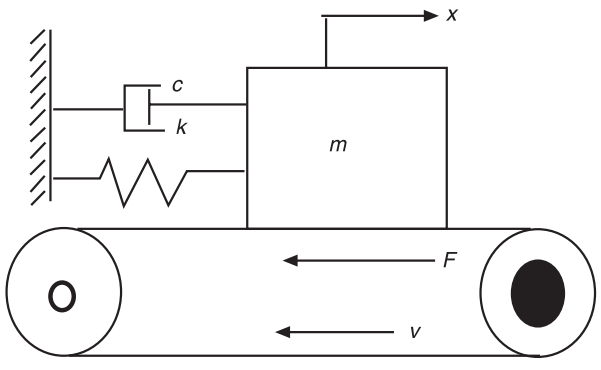


Figure 3 Schematic diagram of a mass-spring-dashpot system on a moving belt as a model of friction-induced vibration.

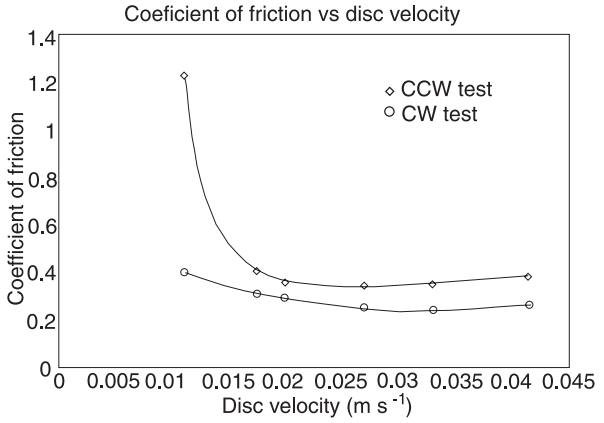


Figure 4 Typical friction–velocity curves showing regions of negative and positive slopes.

$$z = x - \frac{F(v_0)}{k}, \quad \tau = \omega_n t, \quad \zeta = \frac{c}{2m\omega_n}, \qquad \text{where} \quad \omega_n = \sqrt{k/m} \qquad [3]$$

and relation [2], eqn [1] takes the form:

$$z'' + \left(2\zeta + \frac{1}{\omega_n}\frac{\mathrm{d}F}{\mathrm{d}v}\right)z' + z = \frac{1}{2m}\frac{\mathrm{d}^2F}{\mathrm{d}v^2}z'^2 - \frac{\omega_n}{6m}\frac{\mathrm{d}^3F}{\mathrm{d}v^3}z'^3 + \ldots \qquad [4]$$

where a prime denotes differentiation with respect to the nondimensional time parameter τ. The coordinate transformation in [3] has the meaning that the coordinate z measures the displacement x minus the permanent set $F(v_0)/k$ when the motion stops.

The stability of the equilibrium position $z = 0$ of the linearized system (obtained by setting the right-hand side of eqn [4] to zero) depends on the sign of the damping coefficient:

$$\left(2\zeta + \frac{1}{\omega_n}\frac{\mathrm{d}F}{\mathrm{d}v}\right)$$

The sign of this coefficient depends mainly on the sign of the friction force slope $\mathrm{d}F/\mathrm{d}v$. If the slope is negative, then dynamic instability occurs if:

$$\left(2\zeta + \frac{1}{\omega_n}\frac{\mathrm{d}F}{\mathrm{d}v}\right) < 0$$

In other words, self-excited vibration occurs only if the inherent viscous damping coefficient c is less than the slope of the friction force. **Figure 5** shows three phase diagrams corresponding to stick-slip vibration, stable dynamic equilibrium, and a stable limit cycle.

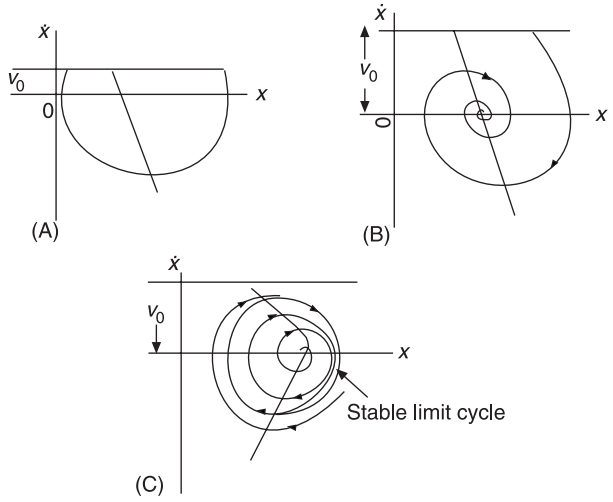


Figure 5 Phase diagrams showing (A) stick-slip, (B) stable equilibrium, and (C) limit cycle. (Reproduced with permission from Brockley and Ko, 1970.)

Limit Cycle

In order to examine the influence of nonlinear terms, eqn [4] will be written in the standard form for averaging solution:

$$z'' + z = \varepsilon(-f_1 z' + f_2 z'^2 - f_3 z'^3 + \ldots) \qquad [5]$$

where:

$$f_1 = \left(2 + \frac{1}{\zeta\omega_n}\frac{dF}{dv}\right), \quad f_2 = \frac{1}{2\zeta m}\frac{d^2 f}{dv^2}, \quad f_3 = \frac{\omega_n}{6\zeta m}\frac{d^3 F}{dv^3}$$

and $\varepsilon = \zeta$. According to the averaging method the solution is going to be very close to the harmonic oscillator motion but with slowly varying amplitude $A(\tau)$ and phase angle $\varphi(\tau)$, i.e.:

$$\begin{aligned} z(\tau) &= A(\tau)\cos\varphi(\tau), \quad \text{where } \varphi(\tau) = \tau + \vartheta(\tau) \\ z'(\tau) &= -A(\tau)\sin\varphi(\tau) \end{aligned} \qquad [6]$$

This imposes the following condition:

$$A'\cos\varphi - A\vartheta'\sin\varphi = 0 \qquad [7]$$

Substituting [6] into eqn [5] and using [7] gives the following two first-order differential equations:

$$A' = -\varepsilon\Psi(A,\varphi)\sin\varphi \qquad [8a]$$

$$A\vartheta' = -\varepsilon\Psi(A,\varphi)\cos\varphi \qquad [8b]$$

where:

$$\Psi(A,\varphi) = f_1 A\sin\varphi + f_2 A^2\sin^2\varphi + f_3 A^3\sin^3\varphi + \ldots.$$

We can take the averaging of both sides of eqns [8] over 2π. This approximation is based on the fact that, since ε is a small parameter, the amplitude A and phase ϑ are slowly varying. The averaging process yields:

$$A' = -\frac{\varepsilon}{2\pi}\int_0^{2\pi}\Psi(A,\varphi)\sin\varphi\,d\varphi = -\frac{\varepsilon A}{2}\left(f_1 + \frac{3}{4}f_3 A^2\right) \qquad [9a]$$

$$A\vartheta' = -\frac{\varepsilon}{2\pi}\int_0^{2\pi}\Psi(A,\varphi)\cos\varphi\,d\varphi = 0 \qquad [9b]$$

Eqns [9] reveal that the phase angle has constant time rate while the amplitude of the motion of mass m can have two steady-state values given by the trivial solution $A = 0$ or a nontrivial solution given by the expression:

$$A^2 = -\frac{4f_1}{3f_3} \qquad [10]$$

The amplitude is real only if $f_1 < 0$ or $f_3 < 0$. The first condition is satisfied if:

$$\left(2\zeta + \frac{1}{\omega_n}\frac{dF}{dv}\right) < 0$$

which implies that the unstable equilibrium position will end up to a limit cycle whose amplitude is given by [10]. The limit cycle is a periodic motion of an autonomous system represented in the phase diagram by an isolated closed trajectory. For a stable limit cycle, every point inside or outside the limit cycle spirals into the limit cycle. The existence of a limit cycle is a feature of friction-induced vibration. It is important to establish whether a limit cycle can exist for a certain system with dry friction. If a limit cycle exists, then asymptotic approximate techniques developed for solving nonlinear differential equations can be used.

Existence of Limit Cycle (Bendixson's Theorem)

In order to establish whether a limit cycle exists or not, consider the following nonlinear autonomous differential equation:

$$z'' + f(z)z' + g(z) = 0 \qquad [11]$$

where $f(z)$ is positive when $|z|$ is large and negative when $|z|$ is small, $g(z)$ is linear or nonlinear and is

derived from a potential field. In the absence of $f(z)$, eqn [11] describes a conservative system with periodic motion. Eqn [11] can be written in terms of the state coordinates u and v defined as:

$$\begin{aligned} u' &= v = z' = U(u,v) \\ v' &= -f(u)v - g(u) = V(u,v) \end{aligned} \quad [12]$$

Bendixson's theorem states that there are no closed paths in a simply connected domain of the phase plane on which:

$$\frac{\partial U(u,v)}{\partial u} + \frac{\partial V(u,v)}{\partial v}$$

is of one sign. This means that, if the above expression changes sign as one parameter changes, a limit cycle takes place. This condition is similar to what is known as Hopf bifurcation.

Spurr's Sprag-Slip Phenomenon

This phenomenon was developed in 1961 to explain the contact behavior for internal and external drum and disk brakes. It takes place in the form of locking a body in contact with a sliding surface followed by a slip due to a displacement of the fixed end of the body (**Figure 6**). This is known as goemetrically induced or kinematic constraint instability, which occurs even though the coefficient of friction is constant. The sprag-slip results in squeals which occur at numerous frequencies, implying nonlinearity. Sudden jumps in frequency during a single squeal are accompanied by simultaneous changes in the friction coefficient. Very occasionally, squeal depends on the magnitude of the friction coefficient, not on the friction force, and is associated with rapid oscillations in the friction coefficient. The mechanism of sprag-slip can be demonstrated by Spurr's model. The model consists of a rigid strut $O'C$ pivoted at O' and is loaded against a moving surface AB with velocity v_0, at an angle θ with an initial normal load P, as shown in **Figure 6**. The pivot at O' is mounted in a flexible support. An increase in the friction force will produce an increase in the normal load on the contact because of the geometry constraint. The increase in the normal load P_f due to the friction force can be obtained from the summation of moments about O':

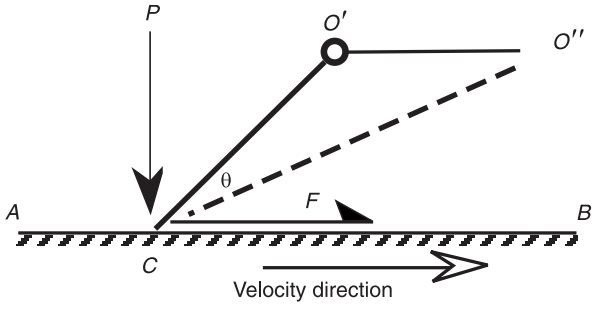


Figure 6 Sprag-slip mechanism. (Reproduced with permission from Spurr, 1961.)

$$P_f = F \tan\theta \quad [13]$$

Now introducing the definition of friction coefficient $\mu = F/\Sigma$ normal forces gives:

$$F = \frac{\mu P}{1 - \mu \tan\theta} \quad [14]$$

It is seen that the spragging angle occurs when $\mu = \cot\theta$ at which the frictional resistance F becomes infinite. If the pivot is very rigidly mounted, then F will rise to high values as $\cot\theta$ approaches μ, and eventually the strut spragged or locked and slipping becomes impossible. On the other hand, if the pivot is mounted on a flexible-support stick-slip motion will occur and not spragging. In this case the flexible support for O' can be replaced by another rigid strut $O''O'$ with a secondary pivot O. It is obvious that as long as the angle $\theta < 90^\circ$ the sprag-slip phenomenon will take place.

Experimental measurements of contact forces between a pin and disk rotating at 2 rpm exhibit different characteristics depending on whether the disk rotates clockwise or counterclockwise. Due to misalignment, the kinematic constraint takes place with clockwise rotation and the angle θ was less than 90°. However, the normal force time history record reveal irregular fluctuations, with occasional noncontact zones when the friction element loses contact with the disc surface. As the constraint force increases due to some hills on the disc surface, the normal force increases and the friction force increases as well, as shown in **Figure 7A**. The friction force record exhibits corresponding fluctuations. The plotted friction coefficient is estimated as the ratio of friction force to the normal force. One might expect this ratio to be constant over the duration of the test. However, the friction coefficient records display random fluctuations, and do not remain constant. These fluctuations may be attributed to the fact that the relative velocity is always fluctuating, and thus there is a corresponding variation in the friction coefficient. This variation is mainly due to variations of asperity heights. There is a switch in the friction force associated with a corresponding change in the relative

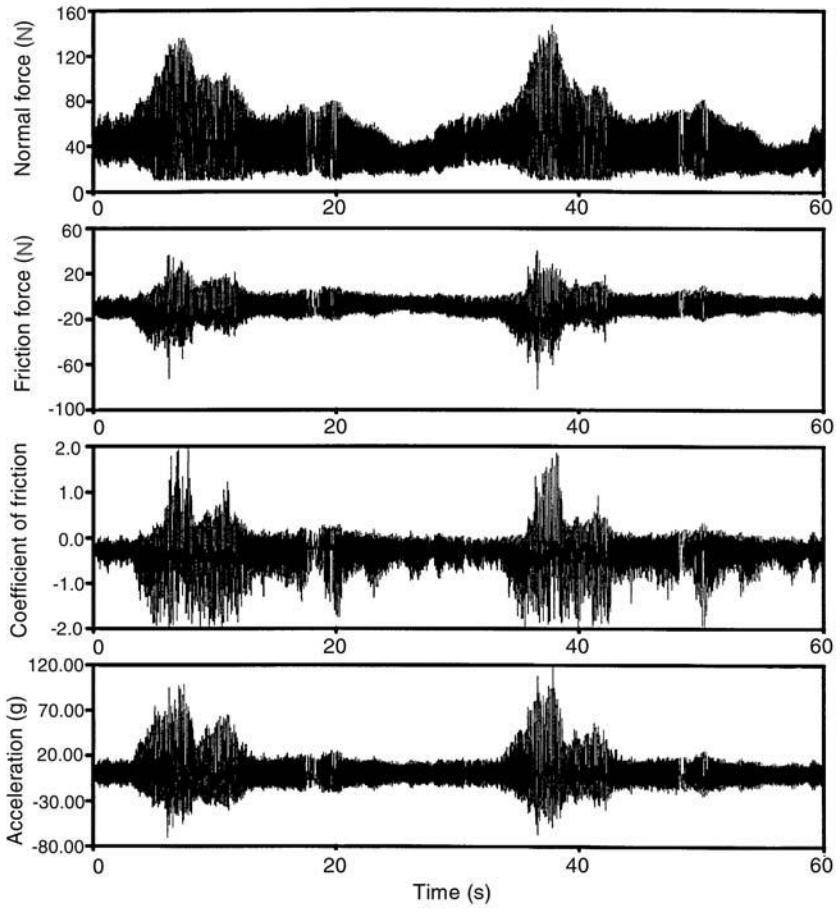


Figure 7A Time history records of normal force, friction force, friction coefficient, and friction element acceleration for the case of clockwise rotation of the disk at 2 rpm.

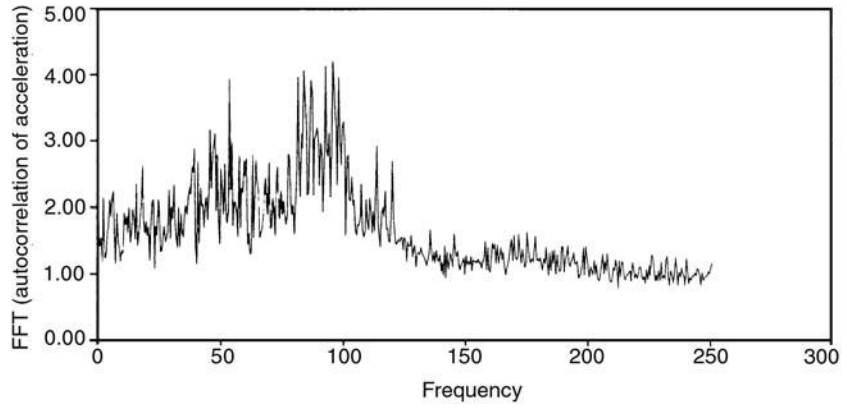


Figure 7B FFT of the friction element acceleration.

velocity direction. The acceleration of the friction element experiences also corresponding fluctuations. There is no unique peak in the acceleration frequency spectrum shown in **Figure 7B**, indicating that the natural frequency of the friction element is always changing with time. The time variation of the natural frequency is attributed to the time variation of the boundary conditions (contact forces). **Figure 7C** shows the probability density function (pdf) of the friction force which is essentially non-Gaussian. The Gaussian distribution is shown by the dashed curve for comparison.

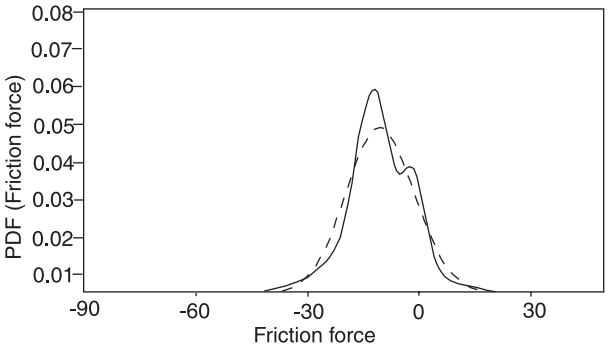


Figure 7C Probability density function of the friction force. Dashed line, Gaussian distribution.

For counterclockwise disk rotation, the angle of attack θ is greater than 90°. In this case, the constraint force is not significant and the interfacial forces experience high-frequency fluctuations over those disk zones with surface hills. In the absence of hills, the friction force is almost constant. **Figure 8A** shows time history records of normal and tangential forces, friction coefficient, and acceleration of the friction element. It is seen that the contact forces exhibit slight random fluctuations over almost half of the disk. The friction force is always positive, indicating that the relative speed does not change direction. **Figure 8B** shows the Fast Fourier Transform of the friction element acceleration. The spectrum of the friction element acceleration exhibits several peaks around 120 Hz and around 225 Hz. This means that the contact forces have significant effects on changing the frequency content of the friction element. In view of the narrow range of friction force fluctuations, its pdf curve has a peak very close to its mean value, with tails spread over a wide range. The friction pdf is still non-Gaussian, as plotted by the solid curves in **Figures 8C**. The friction pdf is seen to be significantly deviated from the Gaussian distribution indicated by dotted curves. The pdf displays more skewness with a long tail to the right. This skewness is reduced as the rpm increases, but the friction pdf is more concen-

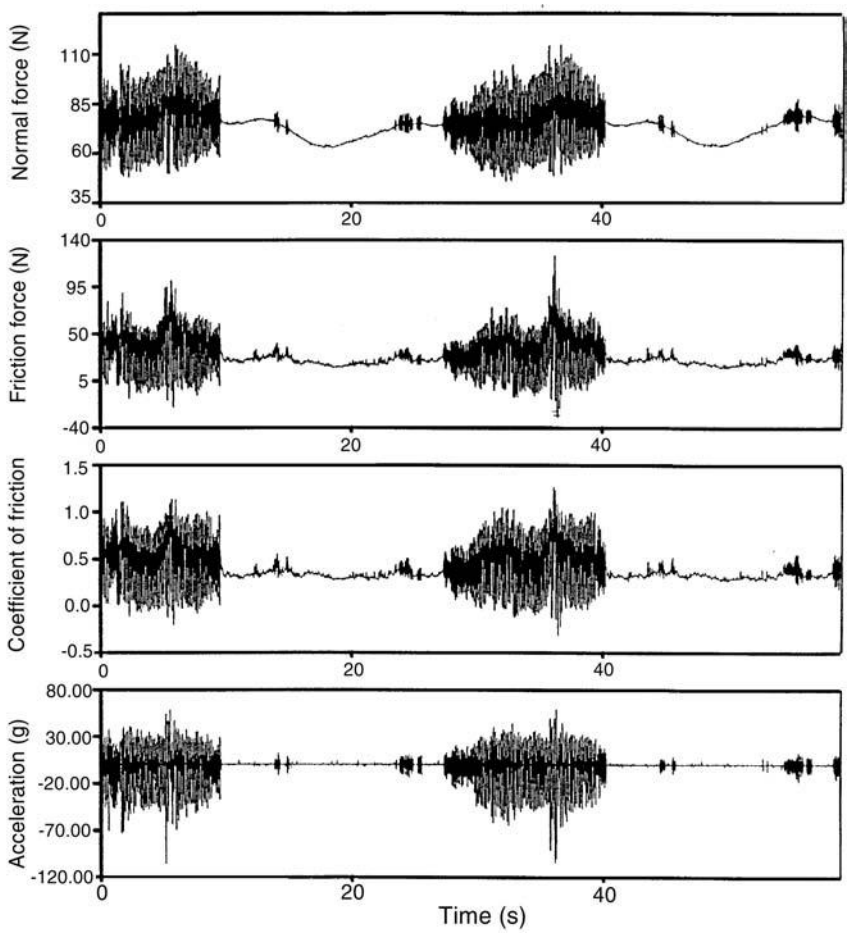


Figure 8A Time history records of normal force, friction force, friction coefficient, and friction element acceleration for the case of counter-clockwise rotation of the disk at 2 rpm.

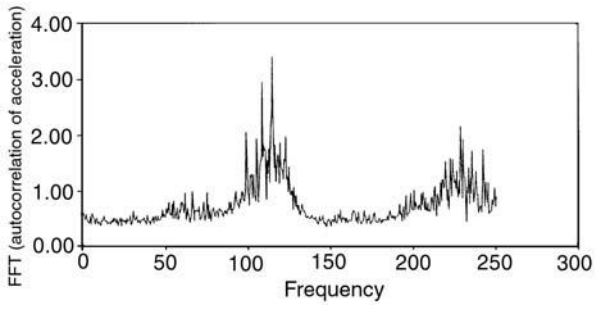


Figure 8B FFT of the friction element acceleration.

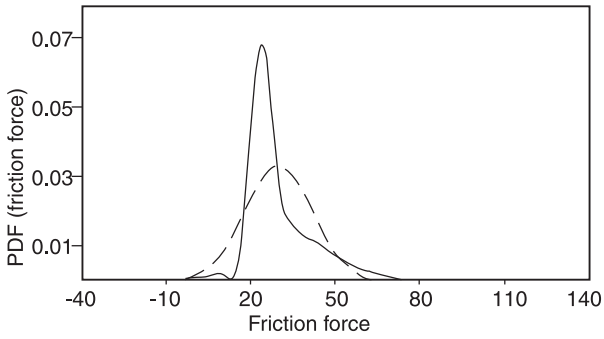


Figure 8C Probability density function of the friction force. Dashed line, Gaussian distribution.

trated at the mean value, with a peak much higher than the normal one.

Since the friction coefficient and the relative velocity vary randomly with time, the root mean square of each has been estimated for six tests running at 1 rpm through 6 rpm. The friction coefficient–velocity curves for clockwise and counterclockwise disk rotations are shown in Figure 4. It is seen that the friction–velocity curve for the counterclockwise case has higher negative slope at low values of relative speed than the clockwise case. It was observed that the instability associated with the counterclockwise case is of intermittent nature, while for the clockwise case it is of a continuous nature.

Nomenclature

A	amplitude
F	friction force
v_0	velocity

See also: **Friction damping**; **Nonlinear normal modes**; **Nonlinear system identification**; **Nonlinear system resonance phenomena**; **Nonlinear systems analysis**; **Nonlinear systems, overview**.

Further Reading

Brockley CA and Ko PL (1970) Quasi-harmonic friction-induced vibration. *ASME Journal of Lubrication Technology* 92: 550–556.

Den Hartog JP (1985), *Mechanical Vibrations*. New York: Dover Publications.

Dweib AH and D'Souza AF (1990) Self-excited vibrations induced by dry friction, part I: experimental study and part II: stability and limit cycles. *Journal of Sound and Vibration* 137: 167–175, 177–190.

Feeny B, Guran A, Hinrichs N and Popp K (1998) A historical review on dry friction and stick-slip phenomena. *ASME Applied Mechanics Reviews* 51: 321–341.

Ibrahim RA and Rivin E (eds) (1994) Friction-induced vibration. Special issue of four review articles. *ASME Applied Mechanics Reviews* 47: 209–305.

Ibrahim RA, Madhavan S, Qiao SL and Chang WK (2000) Experimental investigation of friction induced noise in disc brake systems. *International Journal of Vehicle Design* 23(3/4): 219–240.

Spurr RT (1961) A theory of brake squeal. *Proceedings of the Automotive Division, Institute of Mechanical Engineers (AD)* 1: 33–40.

Tondl A (1970) *Self-excited Vibrations*. Monograph no. 9. Bechovice: National Research Institute for Machine Design.

G

GEAR DIAGNOSTICS

C J Li, Rensselaer Polytechnic Institute, Troy, NY, USA

Copyright © 2001 Academic Press

doi:10.1006/rwvb.2001.0098

Transmitting power through gears produces vibration because gears are discrete devices having a finite number of imperfect elastic teeth. For example, when teeth mesh with each other, they are deflected tangentially and, to a lesser extent, radially. After that, the teeth spring back toward their original positions. The corresponding vibration is periodic at the meshing frequency and its harmonics. Additionally, the meshing forces excite the gear–wheel–shaft subsystem and casing.

For ordinary gears, the meshing frequency is:

$$f_m = f_s N \qquad [1]$$

where f_s is the gear speed in rps and N is the number of teeth. For a planetary gear system (**Figure 1**), the following relationship can be used:

$$\begin{aligned} &N_s f_s + N_r f_r = f_c(N_s + N_r) \\ &N_s(f_s - f_c) = N_r(f_c - f_r) \\ &\text{meshing frequency} = N_s(f_s - f_c) \end{aligned} \qquad [2]$$

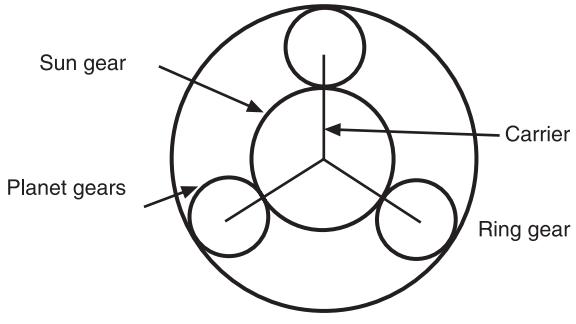


Figure 1 Planetary gear system.

where f_r, f_s, and f_c are the speed of the ring gear, sun gear, and carrier, respectively, in rps, and N_r, N_s, and N_c, are the number of teeth of the ring gear, sun gear, and carrier, respectively.

Gear Failure Modes

Gear failure modes include bending fatigue, contact fatigue, thermal fatigue, impact failure such as tooth-bending impact, tooth shear, tooth chipping, case crushing and torsional shear, also wear including abrasive wear and adhesive wear, and stress rupture.

Gear Vibration Model

Let us consider a pair of perfectly mating gears whose teeth are rigid with an exact involute profile, and are equally spaced. Such a pair of gears would exactly transmit uniform angular motion in the absence of dynamical loads and defects such as run-out, imbalance, and misalignment.

Then let us consider a pair of gears whose teeth are not rigid but are otherwise the same as the aforementioned perfect gears, meshing under a constant load at a constant speed. Since the contact stiffness varies periodically with the number of teeth in contact and with the contacting position on the tooth surface, vibration will be excited at the tooth-meshing frequency. The vibration of this pair of gears may be approximately represented in terms of the tooth-meshing frequency, f_m, and its harmonics:

$$x(t) = \sum_{k=0}^{K} X_k \cos(2\pi k f_m t + \phi_k) \qquad [3]$$

Gear defects alter the magnitude and phase of the meshing stiffness and therefore produce changes in the amplitude and phase of the vibration at meshing frequency and its harmonics as the teeth go through the meshing. In addition to changing X_i, these changes introduce the amplitude and phase-modulating functions, $a_k(t)$ and $b_k(t)$:

$$x(t) = \sum_{k=0}^{K} [1 + a_k(t)] X_k \cos [2\pi k f_m t + \phi_k + b_k(t)] \quad [4]$$

Alternatively, since $\theta = 2\pi f_s t$ and $f_m = f_s N$ for nonplanetary gears, one can also express the vibration of a gear of N teeth as:

$$x(\theta) = \sum_{k=0}^{K} [1 + a_k(\theta)] X_k \cos [kN\theta + \phi_k + b_k(\theta)] \quad [5]$$

(It would be straightforward to extend the discussion to planetary gears.) Both amplitude and frequency modulations create side-bands around the meshing frequency and its harmonics. The spacing of these side-bands is the rotating speed of the gear.

Roughly speaking, gear faults can be classified into localized ones, such as fractured teeth, that affect only a few teeth, and distributed ones such as wear that affect all the teeth. If a distributed defect has a uniform pattern in all the teeth, it would introduce virtually periodic tooth-to-tooth variations in the magnitude and phase of the meshing stiffness which, in turn, will excite a stationary response contributing to changes in meshing frequency, and its harmonics, i.e., X_k, and their side-bands. On the other hand, a nonuniform distributed fault and a localized fault would introduce variation in the meshing stiffness at gear rotating frequency which, in turn, will mostly contribute to an increase in the amplitude and phase modulations. The modulations could be smooth, as in the case of most distributed faults, or very transient, as in the case of a fractured tooth.

Gear Diagnostic Algorithms

In general, gear diagnostic algorithms can be classified into four kinds depending on what they are designed to look for. The first kind is based on time (or sometimes, spatial) domain processing such as the synchronized averaging and tooth averaging. These techniques allow a user to spot magnitude easily and, to a lesser degree, phase transients associated with a localized fault such as a fractured tooth. The second kind, such as those based on spectral and cepstral analyses, is frequency domain techniques which allow one to observe trends in energy changes in gear-meshing frequency and its harmonics and their side-bands. They are useful for something like uniform wear but less effective with nonstationary phenomena associated with localized faults. The third kind is designed to give the best of both worlds by using time–frequency analyses such as wavelet transformations (WT), the Wigner–Ville distributions (WVD), and the Choi–Williams distribution (CWD). The last kind, which outnumbers any other kind, concentrates on modulation effects that are dominant in localized faults and less so in distributed faults.

Time Domain Gear Diagnostic Algorithms

Synchronized averaging This algorithm is frequently used as a preprocessor to enhance the signal-to-noise ratio of the gear vibration. The technique consists of ensemble averaging consecutive segments of gear vibration, each one-rotation period long. It is assumed that an encoder is used to clock the sampling so that samples are taken at the same angular positions rotation after rotation. Each rotation will generate a fixed number of samples. We denote them as $x_i(n)$, where i is the rotation number and n is the sample number. The point-by-point average over M rotations can then be calculated as:

$$x_{ave}(n) = \frac{1}{M} \sum_{i=1}^{M} x_i(n) \quad [6]$$

The number of samples in each rotation should be at least five times the number of teeth to insure that adequate observation is made for each tooth mesh. M should be large enough so that a synchronized average would remain almost the same even if a larger M is used. Synchronized averaging eliminates components whose periods are not compatible with the rotating period. If an encoder is not available or practical, a once-per-revolution tachometer signal is usually required in order to carry out some kind of order tracking algorithm.

Tooth averaging In essence, this method is a synchronized averaging with a period of one tooth mesh. It takes one rotation of the gear vibration (preferably the average) and segments it into N equal-length pieces where N is the number of teeth. An average is then calculated by superimposing the N pieces and dividing the sum signal by N. The result is the average vibration of all the teeth. The difference between an individual piece and the average, which is called the residual, represents the individuality of the tooth. Naturally, a faulty tooth will stand out as having a larger error. **Figure 2** shows the result of applying tooth averaging on the synchronized average of a gear. The tooth damage severity observed optically is shown in the second figure from the top. As one can see, the level of the tooth averaging residual is consistent with the observed tooth damage.

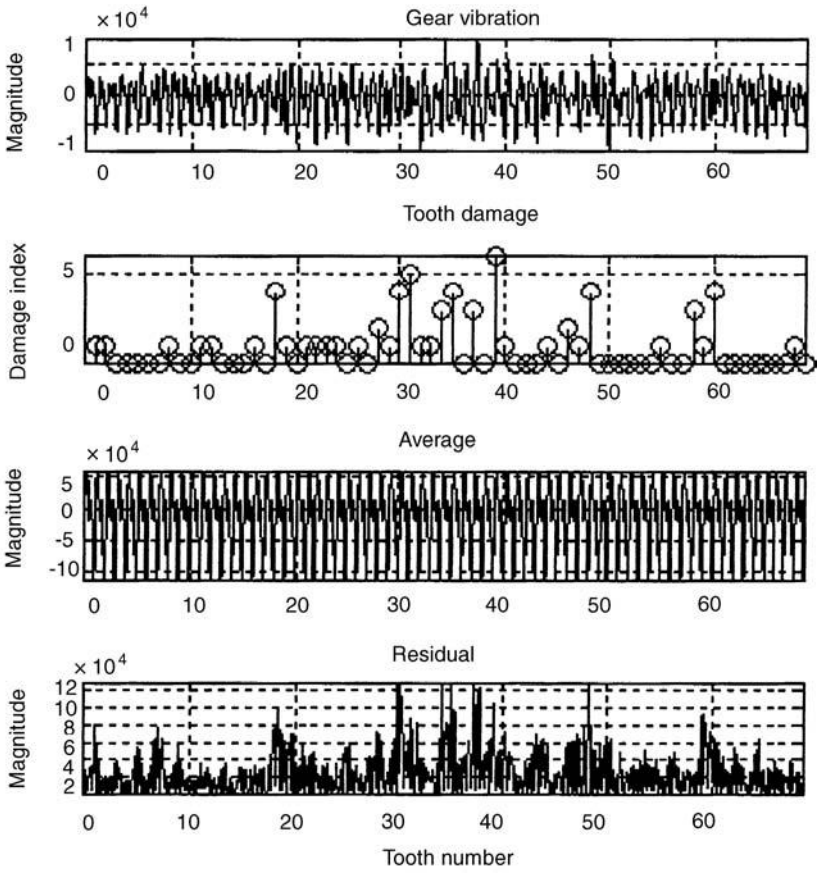


Figure 2 Tooth averaging.

Model prediction error methods This method first identifies a signal model to approximate the gear synchronized average. For example, an AutoRegressive (AR) model can be found by choosing its coefficients to minimize the discrepancy between the model and the gear vibration, usually in a residual least-squares sense. (Other models, including nonlinear AR models, could also be used.)

A model like this can be used in two ways. First, the model residual can be used to detect a tooth fault. If a tooth has a chip or crack, the vibration pattern of the faulty tooth will differ from that of the other teeth. Since most of the teeth have a normal vibration, the total residual will be minimized when the model matches this normal vibration. This means, however, that the residual at the chipped tooth will be larger in magnitude than the residual at the normal teeth, and this peak in the residual can be used to determine the location and severity of the chip.

Additionally, the model can be used to track the change of the gear vibration over time. If an adequate model is formulated at the beginning of the gear's life, later gear signals can be substituted into the model to calculate the so-called 'prediction error'. As tooth faults evolve and change the meshing dynamics, the prediction error obtained with a model formulated at the beginning of a gear's life will increase.

Frequency Domain Gear Diagnostic Algorithms

Spectral analysis Spectral analysis enables one to observe and trend energy changes in gear rotating and meshing frequencies and their harmonics, e.g., due to a uniform wear, and their side-bands to determine, e.g., if distributed faults such as run-out are present. However, practical experience has shown that it is not very effective in gear faults unless it is used after the synchronized averaging. Even for healthy gears, spectra of vibration normally contain side-bands from frequency and amplitude modulations. Gear faults usually change the magnitude and number of these side-bands. Spacing of the side-bands provides valuable diagnostic information to identify the faulty gear. The trend in the magnitude of the side-band gives some sense of severity. However, if there are multifamilies of side-bands or harmonics, it will be difficult to distinguish them in the spectra. This is why cepstral analysis is frequently preferred when gear vibration is dealt with.

Cepstral analysis The cepstrum is defined in a number of different ways, e.g.:

$$x_c(\tau) = F\left[\ \ln |X(\omega)|^2\right] \quad \text{original definition}$$
$$\text{or :}$$
$$= F^{-1}[\ \ln [X(\omega)]] \quad \text{where } X(\omega) = F(x(t)) \qquad [7]$$

The cepstrum, which is sometimes called the 'spectrum of the logarithmic power spectrum', is useful in detecting spectrum periodicity such as families of harmonics or side-bands found in the spectra of gear vibration. It reduces a whole family of side-bands or harmonics into a single cepstral line. This makes it much easier to distinguish among different families.

Time–Frequency Domain Gear Diagnostic Algorithms

Time–frequency distributions Transient vibrations due to rough meshing of faulty teeth can be revealed or accentuated with time–frequency distributions which give an account of how energy distribution over frequencies changes from one instant to the next. Examples of such distributions include the spectrogram (short-time Fourier transform), the WVD, and the CWD. **Figure 3** shows a CWD of a gear vibration and it clearly shows that tooth 37 has a rough meshing characterized by large meshing frequency and side-bands around it. The drawback of the time–frequency distributions is the higher computational cost, for the CWD in particular, compared to the time or frequency domain algorithms. Another issue is that an additional nontrivial pattern recognition step is needed if automated interpretation of these distributions is desired.

Wavelet transformation The WT can also be considered as a time–frequency distribution. However, it is not as computational costly as, say, CWD. For a continuous signal $x(t)$, the WT is defined as:

$$W_x(a,b) = \int g^{*(a,b)}(t)x(t)\ \mathrm{d}t \qquad [8]$$

where * denotes the complex conjugate and $g(t)$ represents the mother wavelet, e.g.:

$$g(t) = \exp(-\sigma t)\sin(\omega_0 t) \text{ for } t = 0 \text{ and}$$
$$g(t) = -g(-t) \text{ for } t < 0$$

and:

$$g^{(a,b)}(t) = \frac{1}{\sqrt{a}} g\left(\frac{t-b}{a}\right) \qquad [9]$$

where a is the dilation parameter which defines a baby wavelet for a given value, and b is the shifting parameter.

For a given a, carrying out the WT over a range of b is like passing the signal through a filter whose impulse response is defined by the baby wavelet. Therefore, one may consider the WT as a bank of band-pass filters defined by a number of as. The salient characteristic of the WT is that the width of the passing band of the filters is frequency-dependent. Consequently, WT can provide a good frequency resolution at the low-frequency end while maintaining good time localization at the high-frequency end.

Experimental evaluations have shown that the WT is able to detect and trend the impacts associated with faulty teeth in an experiment using spur gears and seeded faults. However, it is not clear if the WT would be effective in detecting the early stages of more graduated tooth faults (e.g., small tooth crack) in smoother operating gears such as helical gears,

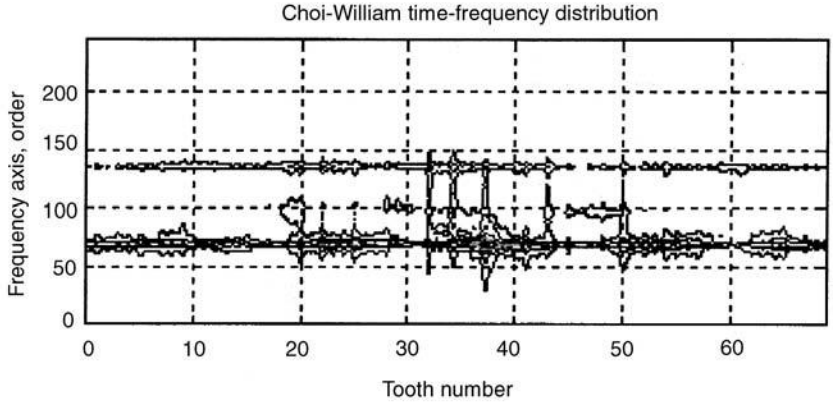


Figure 3 Choi–Williams distribution for a defective gear.

which only produce a modest amount of modulation instead of impact. The difference between WT and CWD is that the former has a better time localization of the impacts, and the latter has a better frequency resolution at high frequencies, however, at a higher computational cost.

Modulation-based Gear Diagnostic Algorithms

Side-band ratio The ratio of side-band power to tooth meshing power is expected to increase as tooth defects, such as wear or pitting, develop.

Residual Gear vibration is first band-pass-filtered around the largest meshing harmonic. The residual is then obtained by subtracting the meshing harmonic from the filtered vibration. (What is left are the side-bands.) After that, enveloping is performed on the residual. It was shown that the resulting signal is directly related to both amplitude and phase modulations which frequently accompany gear faults.

FM0, FM4, NA4, and NB4 The figures of merit are some of the best known gear condition indices. The various figures of merit, including FM0 and FM4 and the indices NA4 and NB4, were designed to detect certain kinds of gear faults from the vibration of a gear. (All of these are the fourth kind except FM0 which belongs to the first kind.) FM0 is an indicator of major faults in a gear mesh and it is defined as:

$$\mathrm{FM0} = \frac{\text{peak-to-peak}}{\text{sum of RMS of meshing harmonics}} \qquad [10]$$

When a tooth breaks, the peak-to-peak level tends to increase and thus FM0 increases. However, a single noise spike can throw it off.

FM4 indicates the amount of localized damage, such as pitting or small cracks on one or two teeth. FM4 is found by removing the tooth-meshing harmonics and their first-order side-bands from the vibration signal and taking the normalized fourth statistical moment (i.e., the normalized kurtosis) of the signal that remains (the 'difference signal'):

$$\mathrm{FM4}(M) = \frac{\frac{1}{N}\sum_{i=1}^{N}\left(d_t - \bar{d}\right)^4}{\sigma^4} \qquad [11]$$

where: d = difference signal, $\bar{d}$ = mean value of difference signal, N = total number of data points in time record, σ = standard deviation, M = current time record number in run ensemble, and i = data point number in time record.

The rationale behind FM4 is that when one or two teeth develop a defect, a peak or series of peaks appear in the difference signal, resulting in an increase in the normalized kurtosis value.

NA4 is similar to FM4, however, a residual signal is constructed by removing only meshing frequency components from the vibration signal. The fourth statistical moment is divided by the current run time averaged variance of the residual signal, resulting in the quasinormalized kurtosis given below:

$$\mathrm{NA4}(M) = \frac{\frac{1}{N}\sum_{i=1}^{N}\left(r_t - \bar{r}\right)^4}{\left\{\frac{1}{M}\sum_{j=1}^{M}\left[\frac{1}{N}\sum_{i=1}^{N}\left(r_{ij} - \bar{r}_j\right)^2\right]\right\}^2} \qquad [12]$$

where: r = residual signal, $\bar{r}$ = mean value of residual signal, and j = time record number in run ensemble.

With this quasinormalized kurtosis method, the change in the residual signal is being compared to a weighted baseline for the specific system in 'good' condition until the average of the variance itself changes.

NB4 is similar to NA4, except that it uses the envelope of the signal band-passed about the dominant meshing harmonic. The envelope is an estimation of the amplitude modulation present in the signal and is most often due to transient variations in the loading. A few damaged teeth will cause transient load fluctuations and thus the amplitude will modulate.

Some study has confirmed that NA4 and NB4 react to the onset and growth of pitting well. However, they are not as sensitive when it comes to tooth fracture.

Energy operator demodulation In the discrete form, the energy operator is defined as:

$$\Psi(x(n)) = x^2(n) - x(n+1)x(n-1) \qquad [13]$$

If the signal has the form of a simple modulated cosine wave:

$$x(n) = a(n)\cos\left(\phi(n)\right) \qquad [14]$$

then the energy operator can be shown to be related to the amplitude modulation and frequency as follows:

$$\Psi(x(n)) = a^2(n)\dot{\phi}^2(n) \qquad [15]$$

In cases where the meshing frequency or one of its harmonics dominates the gear vibration with modulations caused by defects, the energy operator can

extract the amplitude and frequency modulation. In cases where none of the meshing harmonics dominates the gear vibration, the vibration should first be band-pass-filtered about the largest meshing harmonic so that the signal can be approximated by a modulated harmonic function.

Narrow-band demodulation By assuming there is little overlap between side-bands of neighboring meshing harmonics, gear vibration is first band-pass-filtered about the largest harmonic of the gear-meshing frequency. The filtering reduces the gear vibration (eqn [4]) into the following:

$$x_k(t) = [1 + a_k(t)]X_k \cos(2\pi k f_m t + \phi_k + b_k(t)) \quad [16]$$

The Hilbert transformation is then used to compute an analytical signal:

$$c_k(t) = x_k(t) - jH(x_k(t))$$

from which the following modulation signals can be extracted:

$$\begin{aligned} ak(t) &= |c_k(t)\ |/X_k - 1 \\ bk(t) &= \arg(c_k(t)) - (2\pi k f_m t + \phi_k) \end{aligned} \quad [17]$$

Since no other harmonics are considered, knowledge of X_k and ϕ_k is not important for detecting local defects using this method; they can be set to be any convenient value.

Wide-band demodulation In the narrow-band demodulation method, gear vibration has to be band-pass-filtered so that the Hilbert transform can be used for demodulation. Much may be discarded because of the filtering. The assumption that there is little overlap between the side-bands from neighboring harmonics may also be false. On the other hand, the wide-band demodulation method employs a nonlinear programming method and a signature model to identify amplitude and phase modulation from the broad-band gear vibration containing several meshing harmonics. No band-pass filtering is needed and the interactions among side-bands of neighboring meshing harmonics are accounted for.

The algorithm has been shown to be more sensitive to gear tooth defects than narrow-band demodulation. However, it is computationally much more expensive than the narrow-band demodulation.

Cyclostationary Cyclostationary refers to the phenomenon that the statistical moments of a time series are periodic. A signal $x(t)$ is said to be cyclostationary of order n if its nth moment is a periodic function of time t. The fundamental frequency α of the periodicity is the cyclic frequency. Given a signal $x(t)$ cylostationarity of order 2 can be measured by the spectral coherence function (SCF):

$$C^{\alpha}(f) = \frac{E[(X(f - \alpha/2)X^*(f + \alpha/2))]}{\sqrt{(|S(f - \alpha/2)|)} \times \sqrt{(|S(f + \alpha/2)|)}} \quad [18]$$

where S is the power spectrum. According to the expression, SCF measures the normalized correlation between frequency lines centered about f and separated by α.

In the presence of a faulty tooth, a rough mesh occurs once per revolution and this cyclic event leads to side-bands around the gear-meshing frequency (and its harmonics) with a spacing of the gear rotating speed f_s. When the SCF is calculated with $\alpha = f_s$, or its multiple for f near a meshing harmonic, elevated levels are expected due to increased cyclostationarity with a cyclic frequency of f_s (and its multiples).

Nomenclature

f	gear speed
$g(t)$	mother wavelet
M	number of rotations
N	number of teeth of gear
r	residual system
$x(t)$	continuous signal

See Plate 37.

See also: **Averaging**; **Cepstrum**; **Diagnostics and condition monitoring, basic concepts**; **Hilbert transforms**; **Time–frequency methods**

Further Reading

Alban EL (1985) *Systematic Analysis of Gear Failures*. Metals Park, OH: American Society for Metals.

Capdessus C, Sidahmed M, Lacoume JL (2000) Cyclostationary processes: application in gear faults early diagnosis. *Mechanical Systems and Signal Processing* 14:371–385.

Choy FK, Braun MJ, Polyshchuk V *et al.* (1994) *Analytical and experimental vibration analysis of a faulty gear system*. NASA Technical Memorandum 1.15:106689.

Dalpiaz G, Rivola A, Rubine R (2000) Effectiveness and sensitivity of vibration processing techniques for local fault detection in gears. *Mechanical Systems and Signal Processing* 14:387–412.

Dousis DA (1986) Gear failure analysis in helicopter main transmissions using vibration signature analysis.

Proceedings of the 41st Meeting of the Mechanical Failures Prevention Group, Patuxent River, Maryland, October 28–30, 1986, pp. 133–144. Cambridge, UK: Cambridge University Press.

Li CJ, Limmer J, Yoo J (1996) Gear pitting and chipping assessment via model-based algorithms – a case study. In: Subramanian K (ed.) Manufacturing Science and Engineering, MED Vol. 4. *Proceedings of the Symposium on Computer Aided Diagnostics and Maintenance Methodology*, 17–22 November, Atlanta, GA, pp. 595–603. New York: ASME.

Ma J (1995) Energy operator and other demodulation approaches to gear defect detection. In: Pusey HC, Pusey SC (eds) *Proceedings of the 49th Meeting of the Society of Mechanical Failures Prevention Technology*. 18–20 April, Virginia Beach, VA, pp 127–140. Willowbrook, IL: Vibration Institute.

Ma J, Li CJ (1996) Gear defect detection through model-based wideband demodulation of vibrations. *Mechanical Systems and Signal Processing* 10:653–665.

McFadden PD, Smith JD (1985) A signal processing technique for detecting local defects in a gear from the signal average of the vibration. *Proceedings of the Institute of Mechanical Engineers* 199:287–292.

Randall RB (1982) A new method of modeling gear faults. *Journal of Mechanical Design*, 104:250–267.

Wang WJ, McFadden PD (1993) Early detection of gear failure by vibration analysis – I: calculation of the time–frequency distribution. *Mechanical Systems and Signal Processing* 7:193–203

GROUND TRANSPORTATION SYSTEMS

A K W Ahmed, Concordia University, Montreal, Quebec, Canada

Copyright © 2001 Academic Press

doi:10.1006/rwvb.2001.0165

The ground transportation systems are perhaps ideal examples of mechanical systems that encounter vibration in a wide frequency range, and present many design challenges to achieve effective attenuation of vibration and noise, while maintaining adequate handling and stability performance. Effective isolation of vibration in vehicles is vital to achieve adequate ride quality, minimal component squeaks and rattle, and to control the magnitudes of dynamic loads transmitted to the cargo and pavement when freight vehicles are involved. The design challenges primarily stem from the fact that vehicles are highly complex systems with a large number of components that undergo coupled motions, and that the safety and control performance requirements of vehicles raise conflicting design issues. Furthermore, vehicle vibrations are induced by a variety of sources including engine and drivetrain, aerodynamic forces, unbalance of tire and wheel assembly, and most importantly the dynamic interactions of the tire or track with the irregular terrain. The surface roughness of roads or terrains is known to vary widely from smooth highways to extremely rough off-road terrains. The magnitudes and predominant frequencies of the terrain-induced vehicular vibration vary with many design and operating factors, such as static and dynamic properties of tires and suspension components, inertial properties of the vehicle and vehicle speed.

The vehicle body vibration or the ride quality has been of primary concern for the vehicle engineers, irrespective of the type of ground transportation system. The enhancement of comfort performance of automobiles and passenger road and rail vehicles necessitates reduction of noise and vibration harshness. The preservation of health, safety and performance rate of operators of off-road vehicles requires the control of their terrain-induced high magnitude and low frequency vibration. In case of commercial freight vehicles, the control of vibration is vital for preservation of driver comfort and safety, cargo, and road infrastructure. The primary objective of vibration analysis of a ground transportation system is to analyze the characteristics of response vibration that the passenger and freight could be exposed to, and to enhance vibration isolation through components design. Although the road and off-road vehicles exhibit vibration along all the translational and rotational axes, the predominant vibration in most transportation systems is known to occur along the vertical axis. This section is thus limited to fundamental aspects of vertical vehicular vibration analyses, including: human sensitivity to vibration to illustrate some of the suspension design objectives; simple analytical models of different vehicles together with the methods of solution; the static and dynamic properties of major components affecting the vehicular vibration; and the description of road roughness.

Driver/Passenger Sensitivity to Vibration

Due to the subjective nature of comfort/discomfort, the ride quality associated with vehicle vibration is a highly difficult parameter to establish. Numerous studies, however, have been conducted in an attempt

to establish ride comfort limits in terms of magnitude and frequency contents of vehicular vibration. Despite some disagreements, the vibration exposure guidelines defined in the International Standards Organization documents, ISO-2631, have been widely used to assess the vehicular vibration. The earlier version of this standard, ISO-2631 (1974), provided three distinct exposure limits for assessment of whole-body vertical and horizontal vibration in the 1–80 Hz frequency range in terms of comfort, fatigue and health. **Figure 1** shows the fatigue or decreased proficiency boundaries for exposure to vertical vibration in terms of RMS acceleration as a function of third-octave band center frequency for various exposure times. (As described in the figure caption, other limits can be found from the fatigue boundary.) In its revised form, the document ISO-2631-1 (1997), different frequency-weighting filters are defined to describe human response to translational as well as rotational vibration. The standard specifies that the evaluation of vibration exposure should be made at the point of entry of vibration, namely the body–seat interface. The magnitude of vibration exposure is characterized by the overall RMS frequency-weighted acceleration, computed from:

$$\bar{a}_{\mathrm{W}} = \left[\frac{1}{T}\int_0^T a_{\mathrm{W}}^2(t)\,\mathrm{d}t\right]^{1/2}$$

where $a_{\mathrm{W}}(t)$ is the frequency-weighted acceleration at instant t, expressed in $\mathrm{m\,s^{-2}}$ or $\mathrm{rad\,s^{-2}}$. T is the duration of vibration measurement and $\bar{a}_{\mathrm{W}}$ is the overall frequency-weighted RMS acceleration. The frequency-weighting filters, W_{d} and W_{k} are defined for the assessment of effects of translational vibration on health, comfort, and perception, while weighting W_{e} is defined for assessment of rotational motions of the body. The vibration containing transient events with crest factors above nine the standard suggests the use of either running RMS method or the fourth power vibration dose value (VDV), given by:

$$\mathrm{VDV} = \left[\int_0^T a_{\mathrm{W}}^4(t)\,\mathrm{d}t\right]^{1/4}$$

The Society of Automotive Engineers' manual describes the vertical vibration comfort limits for road transportation systems on the basis of Janeway's comfort criterion. It is based on data for sinusoidal vibration of a single frequency, and the limits are specified as:

$$\begin{aligned}&\text{Peak jerk} \le 12.6\ \mathrm{m\,s^{-3}}\ \text{for}\ f \le 6\,\mathrm{Hz}\\ &\text{Peak acceleration} \le 0.33\ \mathrm{m\,s^{-2}}\ \text{for}\ 6 < f \le 20\,\mathrm{Hz}\\ &\text{Peak velocity} \le 0.0027\mathrm{m\,s^{-1}}\ \text{for}\ 20 < f \le 60\,\mathrm{Hz}\end{aligned} \qquad [1]$$

These limits can be used to establish the comfort zone in terms of peak displacement or peak acceleration response as a function of the frequency, as illustrated in **Figures 2A** and **2B**, respectively. From the above exposure limits, it is evident that the human body is most sensitive to vertical vibration in the 4–8 Hz frequency range. This can serve as one of the design requirements for the vehicle system to ensure that the vertical natural frequency of the vehicle body (sprung mass) is well below 4 Hz and that the natural frequency of the wheel assembly (unsprung mass) is well above 8 Hz. For a given vehicle, this will require a soft suspension spring, which may conflict with the requirements for handling and static ride height (static deflection). The natural frequency of the vehicle body or sprung mass usually lies between 1 and 4 Hz. The higher value generally applies to off-road and military vehicles. The natural frequency of the unsprung mass, also known as wheel hop frequency, often lies between 9 and 20 Hz. Again, the higher value generally applies to military and off-road vehicles with stiff suspensions.

The following section describes the system components that have direct influence on the vibration response characteristics of vehicles.

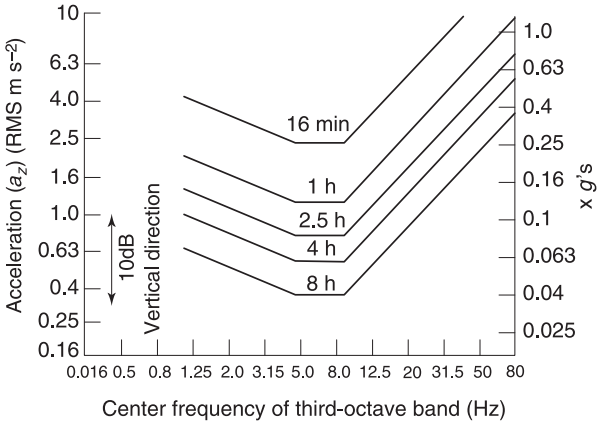


Figure 1 ISO curves for fatigue time as functions of vertical acceleration and frequency. [To obtain 'exposure limits' multiply acceleration values by 2 (6 dB higher) and to obtain the 'reduced comfort boundary' divide acceleration values by 3.15 (10 dB lower).]

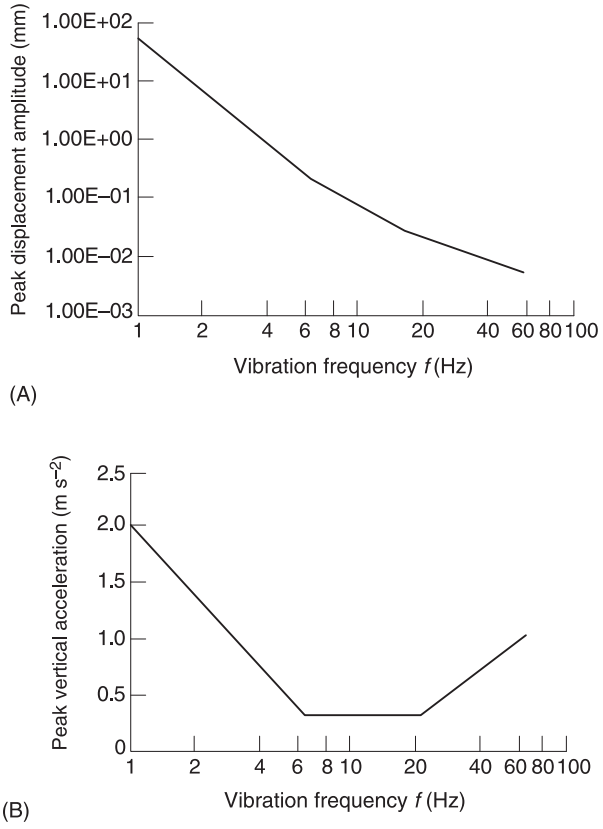


Figure 2 (A, B) Vertical vibration limits for passenger comfort proposed by Janeway.

Ground Transportation System

For the discussion in this article, ground transportation systems are grouped under road and off-road wheeled vehicles. Road vehicles include passenger cars, buses, trucks, and articulated freight vehicles. The off-road vehicles include only wheeled vehicles employed in construction, forestry, mining, agriculture and military sectors, where the terrain-induced inputs are considerably different from those of the road vehicles. The body or sprung mass of large vehicles may possess flexibility giving rise to structural vibration modes with significantly higher frequencies than those of road-induced ride vibration. For ride vibration analysis, therefore, all wheeled road and off-road vehicles can be represented by the components shown in **Figure 3**. A vast number of wheeled off-road vehicles, however, are designed with no primary suspension to achieve adequate roll stability while operating on rough terrains. The structure of the general model, shown in **Figure 3**, can be conveniently modified for off-road vehicles. The vibration response of most ground transportation systems, as shown in **Figure 3**, can be represented by seven degrees-of-freedom (DOF), namely sprung mass bounce, roll and pitch, and bounce motion of the four wheels, when independent wheel suspensions are considered. For solid beam axles, each axle is considered to possess bounce and roll DOF. For multi-axled vehicles with dual tires, all the closely spaced axles with similar tire and suspension properties are often grouped together to represent a single composite axle. For example, in case the tandem rear axles of trucks or tractors, employed in freight transport systems, the unsprung masses, suspension and tire properties of individual axles can be conveniently lumped to represent a single equivalent rear axle. At low frequencies, the vehicle body, represented by its sprung mass, moves as an integral unit supported on a suspension system consisting of spring, k_s, and damper, c_s. Each axle of the wheel assembly with associated brake hardware is represented by an unsprung mass in contact with the ground surface through tires having stiffness k_t and damping c_t. Typically the tire stiffness is 7–10 times larger than the suspension stiffness. In response to the ground roughness, the unsprung masses move as rigid bodies introducing excitation forces to the sprung mass. The motions of the sprung and unsprung masses therefore, form the primary concern for ground vehicle vibration analysis. The passengers or goods occupying the sprung mass are directly subjected to the vibrations of the sprung mass, whereas the motions of the unsprung masses determine the excitations to the sprung mass and suspension clearance (rattle space) requirements. Although the ground roughness is the primary source of vibration, the wheels unbalance, engine and power train further contribute to the overall vibration environment of a vehicle. For simplicity, one may consider one input at a time with an appropriate model to examine the influence of each input on the sprung mass vibration. Beyond this, one may also investigate the sprung mass structural vibration, resonances of selected components and subsystems, as well as the effects of operating conditions or maneuvers on vibration response (not discussed in this article).

Models for Vibration Analysis

The model selected for the purpose of vibration analysis is largely dependent on the objective of the analysis. The focus here is to illustrate simple but credible models that can be utilized for fundamental vibration analysis in terms of resonant frequencies and forced vibration response of sprung and unsprung masses. **Figure 4** and **Figure 5** illustrate schematics of various in-plane models of vehicles that have been applied to study their response to ground excitations. These models are also widely

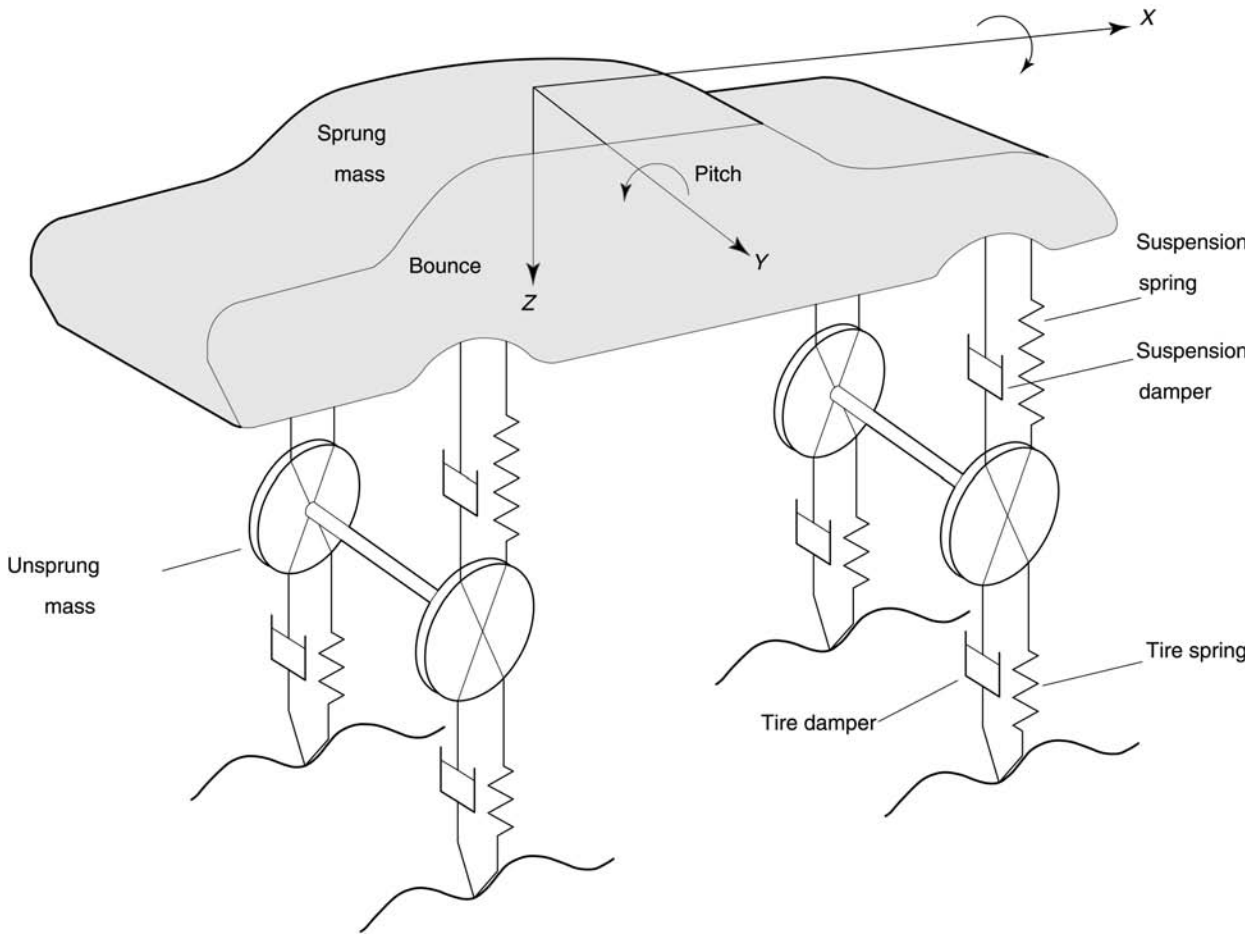


Figure 3 A seven-degree-of-freedom ride model for a ground vehicle.

used to study the suspension performance and vehicle response to self-excited vibration, such as wheel and engine unbalance.The roll motions of road vehicles with low center of mass (c.g.) height are known to be considerably smaller in magnitude. Moreover, the wheelbase of the majority of ground vehicles (longitudinal distance between centers of the front and rear axles) is significantly larger than the track width (lateral distance between wheels). The vehicular roll motions can thus be considered negligible compared to the magnitudes of vertical and pitch motions, and simplified pitch plane models, shown in **Figure 4A**, can be employed for vibration analysis. This model may be effectively used to establish the bounce and pitch motions of the sprung mass and bounce motions of the axles or wheels. In this case, m_s and I_s represent the mass and pitch mass moment of inertia of half the vehicle sprung mass. The unsprung mass and suspension properties represent one set of a wheel, tire and suspension system. The model can be further simplified to a 2-DOF pitch plane model (**Figure 4B**) to study qualitative bounce and pitch motions of the sprung mass, assuming negligible contributions due to axle and tire assembly. In this case, the road input is taken to be the same as the wheels and is suitable for estimation of the bounce and pitch natural frequencies, and associated mode shapes. This model is also considered applicable for study of off-road vehicles without the sprung suspension, where the stiffness and damping elements relate to the properties of tires alone. Similarly, a quarter-car model, shown in **Figure 4C**, is commonly utilized to evaluate vertical dynamics of the vehicle and suspension design concepts. This model can be used to estimate both sprung and unsprung mass bounce natural frequencies and dynamic rattle space. In this case, m_s is one-quarter of the sprung mass with one set of suspension and wheels.

The models that can be utilized for vibration analysis under component excitations are presented in **Figure 5**. **Figure 5A** utilizes a simplified 2-DOF pitch plane model with an engine placed on the sprung mass through a set of engine mounts. Although the engine vibrates as a rigid body with

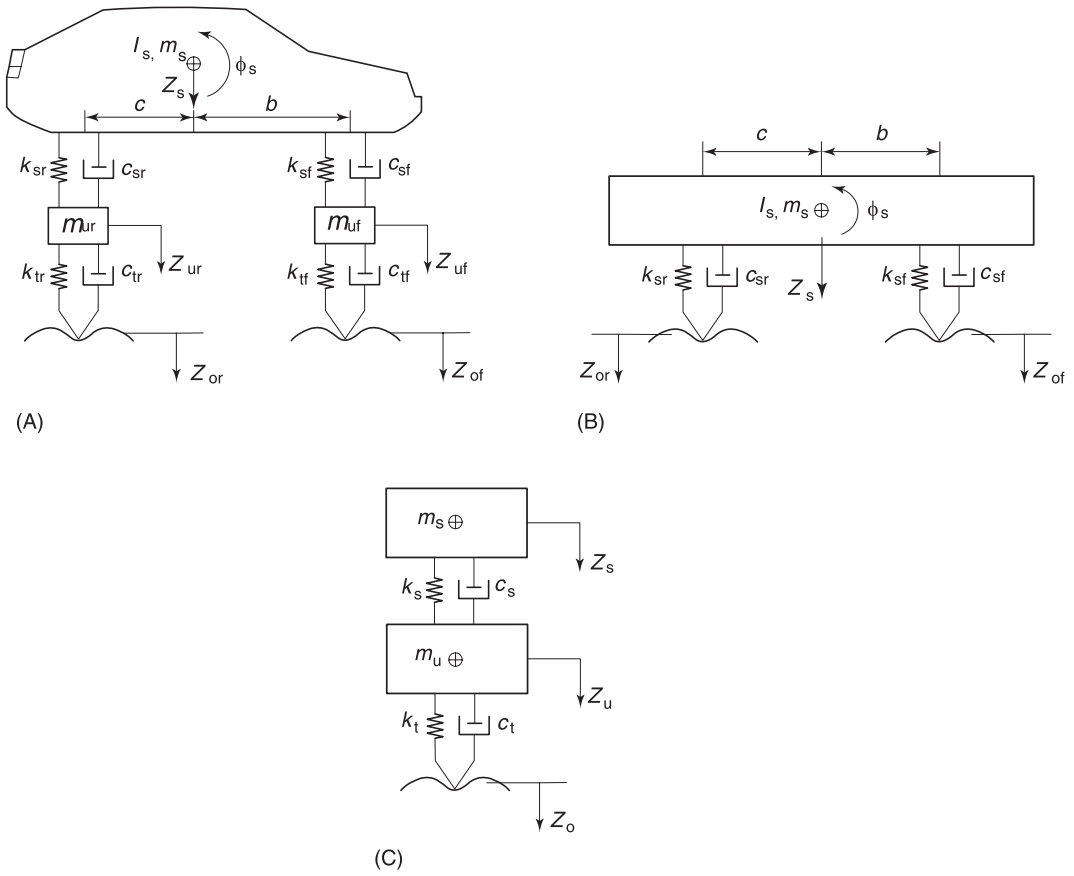


Figure 4 Ground vehicle models for vibration analysis under road excitation. (A) 4-DOF pitch plane ride model. (B) 2-DOF pitch plane ride model. (C) 2-DOF quarter-car ride model.

6-DOF, the most important component for the transversely mounted engine is the roll moment M_o. This oscillatory moment or torque occurs at the engine-firing frequency as well as at subharmonic frequencies due to cylinder-to-cylinder variation of the torque.

In this case, m_e and I_e represent the effective mass and roll mass moment of inertia of the engine, and k_e and C_e are the linear stiffness and viscous damping coefficients of the mounts. For the models presented in **Figure 4**, the engine is considered as an integral part of the sprung mass, where m_s and I_s represent the total mass and mass moment of inertia. In **Figure 5A**, m_s and I_s are the mass and pitch mass moment of inertia due to vehicle sprung mass without the engine. Although the model can be analyzed easily for simultaneous application of road and engine excitations, a smooth road is often assumed to examine the influence of engine vibration alone.

A simple 2-DOF quarter-car model, shown in **Figure 5B**, can also be effectively used to evaluate the vibration response to wheel unbalance excitations. Similar to the previous model, road excitation arising from a smooth road is often considered to study the response to predominant unbalance-induced excitation force, $F = me\,\omega^2 \sin \omega t$, where ω is the angular frequency of wheel rotation, and unbalance is represented by eccentric mass m with eccentricity e.

Analysis of Vehicle Vibration Models

The vibration response of ground vehicles to different excitations can be investigated through analysis of models presented in **Figure 4** and **Figure 5**. Three-dimensional vehicle models incorporating nonlinear properties of suspension components and tires, suspension linkages and flexible structures are also available for comprehensive analyses. The coupled differential equations of motion for the masses are derived about their respective static equilibrium using the D'Alembert's principle. The resulting equations for linear or linearized components are summarized in this section. Procedures or expressions are also

provided for obtaining frequency response, time response and natural frequencies.

4-DOF Pitch Plane Ride Model

The equations of motion relating the vertical and roll motions of the sprung mass (z_s, ϕ_s) and vertical motions of the unsprung masses (z_{u_f}, z_{u_r}) to the ground inputs encountered at front (z_{o_f}) and rear (z_{o_r}) wheels, shown in **Figure 4A**, are expressed in the following matrix form:

$$\begin{bmatrix} m_s & 0 & 0 & 0 \\ 0 & I_s & 0 & 0 \\ 0 & 0 & m_{u_f} & 0 \\ 0 & 0 & 0 & m_{u_r} \end{bmatrix} \begin{Bmatrix} \ddot{z}_s \\ \dot{\phi}_s \\ \ddot{z}_{u_f} \\ \ddot{z}_{u_r} \end{Bmatrix} + \begin{bmatrix} c_{s_f} + c_{s_r} & cc_{s_r} - bc_{s_f} & -c_{s_f} & -c_{s_r} \\ cc_{s_r} + bc_{s_f} & c^2 c_{s_r} + b^2 bc_{s_f} & bc_{s_f} & -cc_{s_r} \\ -c_{s_f} & bc_{s_f} & c_{s_f} + c_{t_f} & 0 \\ -c_{s_r} & -cc_{s_r} & 0 & c_{s_r} + c_{t_r} \end{bmatrix} \times \begin{Bmatrix} \dot{z}_s \\ \dot{\varphi}_s \\ \dot{z}_{u_f} \\ \dot{z}_{u_r} \end{Bmatrix} \quad [2]$$

$$+ \begin{bmatrix} k_{s_f} + k_{s_r} & ck_{s_r} - bk_{s_f} & -k_{s_f} & -k_{s_r} \\ ck_{s_r} - bk_{s_f} & c^2 k_{s_r} + b^2 k_{s_f} & bk_{s_f} & -ck_{s_r} \\ -k_{s_f} & bk_{sf} & k_{s_f} + k_{t_f} & 0 \\ -k_{s_r} & -ck_{s_r} & 0 & k_{s_r} + k_{t_r} \end{bmatrix} \times \begin{Bmatrix} z_s \\ \varphi_s \\ z_{u_f} \\ z_{u_r} \end{Bmatrix} = \begin{bmatrix} 0 \\ 0 \\ k_{t_f} z_{o_f} + c_{t_f} \dot{z}_{o_f} \\ k_{t_r} z_{o_r} + c_{t_r} \dot{z}_{o_r} \end{bmatrix}$$

where b and c are distances between the sprung mass c.g. and the front and rear axles, respectively. The system parameters and input are discussed under a separate section. The study of vibration response of a vehicle to ground inputs involves an analysis of the natural frequencies, damping ratios, damped free vibration characteristics and forced vibration response. For free vibration analysis, the system of equations can be expressed as:

$$\mathbf{M}\ddot{\mathbf{z}} + \mathbf{C}\dot{\mathbf{z}} + \mathbf{K}\mathbf{z} = 0 \quad [3]$$

where $\mathbf{Z}^T$ is the response vector $\{z_s\ \varphi_s\ z_{u_f}\ z_{u_r}\}$ and **M**, **C** and **K** are 4×4 mass, damping, and stiffness matrices. Using state variable approach, the equations can be rewritten in the form:

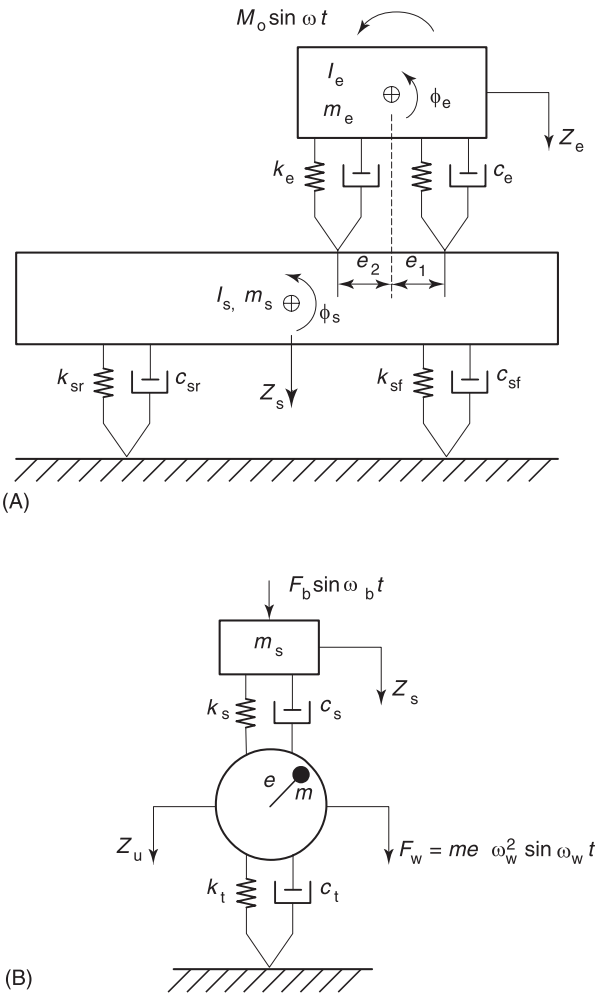


Figure 5 Ground vehicle models for vibration analysis under component excitation. (A) 4-DOF model for effect of engine vibration. (B) 2-DOF model for effect of tire unbalance and on-board source.

$$\begin{Bmatrix} \ddot{z} \\ \dot{z} \end{Bmatrix} = \begin{bmatrix} -\mathbf{M}^{-1}\mathbf{C} & -\mathbf{M}^{-1}\mathbf{K} \\ \mathbf{I} & 0 \end{bmatrix} \begin{Bmatrix} \dot{z} \\ z \end{Bmatrix} \quad [4]$$

Here the elements of the 8×8 dynamic matrix are obtained by multiplying the inverse of the mass matrix with **C** and **K** matrices. In eqn [4], **I** is an identity matrix. The eigenvalue solution of the dynamic matrix will generally yield four pairs of complex conjugates eigenvalues of the form:

$$s_i = \alpha_i \pm j\beta_i \quad [5]$$

Note that, depending on the system parameters, the eigenvalues may be real or complex; real part must be negative for the system to be stable. The vehicle systems are frequently designed with light suspension

damping and thus are expected to yield underdamped vibration behavior with complex eigenvalues. The free vibration response characteristics of the vehicle model can be obtained from the eigenvalues as follows:

Natural frequency of ith mode:

$$\omega_{n_i} = \sqrt{(\alpha_i^2 + \beta_i^2)} \quad [6]$$

Damped natural frequency of ith mode:

$$\omega_{d_i} = |\beta_i| \quad [7]$$

Damping ratio of ith mode:

$$\xi_i = \frac{-\alpha_i}{\omega_{n_i}} \quad [8]$$

In order to identify the mode associated with the ith natural frequency, the eigenvector for the ith eigenvalue may be examined. The last four elements of the 1×8 eigenvector corresponding to the ith eigenvalue will provide the relative amplitude for the four motions associated with the model. The free vibration response of the system for a given initial condition can be evaluated using:

$$\begin{aligned} z_i &= A_i e^{-\xi_i \omega_{n_i} t} \cos(\omega_{d_i} t + \phi_i) \text{ or} \\ z_i &= A_i e^{\alpha_i t} \cos(\beta_i t + \phi_i) \end{aligned} \quad [9]$$

where A_i and ϕ_i are constants to be evaluated based on the initial conditions, $z_i(0)$ and $\dot{z}_i(0)$. Substitutions of these conditions into the equations lead to:

$$A_i = \sqrt{\left\{ z_i^2(0) + \left[\frac{\alpha_i z_i(0) - \dot{z}_i(0)}{\beta_i} \right] \right\}^2} \quad [10]$$

$$\phi_i = \tan^{-1}\left[\frac{\alpha_i}{\beta_i} - \frac{\dot{z}_i(0)}{\beta_i z_i(0)} \right] \quad [11]$$

The forced harmonic response of the 4-DOF pitch plane model can be obtained by solving the four differential equations simultaneously for sinusoidal inputs defined as:

$$\begin{aligned} z_{o_f} &= z_o \sin \omega t \\ z_{o_r} &= z_o \sin \omega(t - \tau_d) \end{aligned} \quad [12]$$

where input frequence ω and time lag for rear wheels τ_d can be defined for a fixed road undulation wave length λ, forward velocity V, and wheel base L, as:

$$\omega = \frac{V}{\lambda}, \quad \text{and} \quad \tau_d = \frac{L}{V}, \text{ respectively} \quad [13]$$

For long vehicles, pitch motions may have significant influence on the bounce response at extreme ends of the vehicle. Assuming small amplitude motions, the bounce motion at a distance l_f from the c.g. towards the front can be obtained from $(z_s - l_f\phi_s)$, while at a distance l_r towards the rear is $(z_s + l_r\phi_s)$.

2-DOF Pitch Plane Model

For ground transportation systems, the natural frequencies of the sprung mass (bounce and pitch) are widely separated from the natural frequencies of the unsprung mass. This provides an opportunity to consider a 2-DOF bounce-pitch model without the unsprung masses as if they exist independently. The equations of motion derived for the 4-DOF pitch plane model, eqn [2], can be simplified by eliminating the last two rows and columns of the matrices while retaining the excitations from road at the front and rear axles. The resulting equations in the matrix form are:

$$\begin{aligned} &\begin{bmatrix} m_s & 0 \\ 0 & I_s \end{bmatrix} \begin{Bmatrix} \ddot{z}_s \\ \ddot{\phi}_s \end{Bmatrix} + \begin{bmatrix} c_{s_f} + c_{s_r} & cc_{s_r} - bc_{s_f} \\ cc_{s_r} - bc_{s_f} & c^2 c_{s_r} + b^2 c_{s_f} \end{bmatrix} \begin{Bmatrix} \dot{z}_s \\ \dot{\phi}_s \end{Bmatrix} \\ &\quad + \begin{bmatrix} k_{s_f} + k_{s_r} & ck_{s_r} - bk_{s_f} \\ ck_{s_r} - bk_{s_f} & c^2 k_{s_r} + b^2 k_{s_f} \end{bmatrix} \begin{Bmatrix} z_s \\ \phi_s \end{Bmatrix} \\ &\quad = \begin{bmatrix} k_{s_f} & k_{s_r} \\ bk_{s_f} & ck_{s_r} \end{bmatrix} \begin{Bmatrix} z_{o_f} \\ z_{o_r} \end{Bmatrix} + \begin{bmatrix} c_{s_f} & c_{s_r} \\ bc_{s_f} & cc_{s_r} \end{bmatrix} \begin{Bmatrix} \dot{z}_{o_f} \\ \dot{z}_{o_r} \end{Bmatrix} \end{aligned} \quad [14]$$

Although the same procedure for the 4-DOF model can be followed to obtain free vibration responses, a reasonable closed-form solution for steady state response can be obtained for the 2-DOF system. For inputs and response of the form $e^{j\omega t}$, steady-state responses can be expressed as:

$$z_s = \frac{z_{o_f}[A_1 - B_1\omega^2 + j(\omega C_1 - \omega^3 D_1)] + z_{o_r}[A_2 - \omega^2 B_2 + j(\omega C_2 - \omega^3 D_2)]}{(A\omega^4 - B\omega^2 + C) + j(D\omega - E\omega^3)} \quad [15]$$

$$\phi_s = \frac{z_{o_f}[-F + \omega^2 G_1 - j(\omega H - \omega^3 I_1)] + z_{o_r}[F - \omega^2 G_2 + j(\omega H - \omega^3 I_2)]}{(A\omega^4 - B\omega^2 + C) + j(D\omega - E\omega^3)} \quad [16]$$

where:

$$
\begin{aligned}
A &= m_s I_s \\
B &= m_s\left(b^2 k_{s_f} + c^2 k_{s_r}\right) + I_s\left(k_{s_f} + k_{s_r}\right) + L^2\left(c_{s_f} c_{s_r}\right) \\
C &= L^2\left(k_{s_f} k_{s_r}\right) \\
D &= L^2\left(k_{s_f} c_{s_r} + k_{s_r} c_{s_f}\right) \\
E &= m_s\left(c^2 c_{s_r} + b^2 c_{s_f}\right) + I_s\left(c_{s_f} + c_{s_r}\right) \\
L &= b + c \\
A_1 &= k_{s_f} k_{s_r}\left(c^2 + bc\right) \\
A_2 &= k_{s_f} k_{s_r}\left(b^2 + bc\right) \\
B_1 &= I_s k_{s_f} + c_{s_r} c_{s_f}\left(c^2 + bc\right) \\
B_2 &= I_s k_{s_r} + c_{s_f} c_{s_r}\left(b^2 + bc\right) \\
C_1 &= \left(k_{s_f} c_{s_r} + k_{s_r} c_{s_f}\right)\left(c^2 + bc\right) \\
C_2 &= \left(k_{s_f} c_{s_r} + k_{s_r} c_{s_f}\right)\left(b^2 + bc\right) \\
D_1 &= c_{s_f} I_s \\
D_2 &= c_{s_r} I_s \\
F &= k_{s_r} k_{s_f} L \\
G_1 &= m_s b k_{s_f} + c_{s_f} c_{s_r} L \\
G_2 &= m_s c k_{s_r} + c_{s_f} c_{s_r} L \\
H &= c_{s_r} k_{s_f} L + c_{s_f} k_{s_r} L \\
I_1 &= m_s b c_{s_f} \\
I_2 &= m_s c c_{s_r}
\end{aligned}
$$

Equations [15] and [16] are considered valid for different magnitudes of road excitations at the front (z_{o_f}) and rear axles (z_{o_r}). These equations, complex in form, can be solved to determine the steady-state response magnitude and phase. For analysis of vibration transmissibility or response gain, however, it is convenient to consider $z_{o_f} = z_{o_r} = z_o$, which represents pure bounce excitation, or $z_{o_f} = z_o = -z_{o_r}$, which implies pure pitch excitation. Substituting these into eqns [15] and [16], yields the vertical and pitch vibration transmissibility characteristics or response gains of the vehicle model.

Bounce vibration transmissibility (response gain):

$$\left|\frac{z_s}{z_o}\right| = \sqrt{\left[\frac{(M - \omega^2 N)^2 + (\omega Q - \omega^3 P)^2}{(A\omega^4 - B\omega^2 + C)^2 + (D\omega - E\omega^3)^2}\right]} \quad [17]$$

where A to E are the same as those defined after eqn [16].

For pure bounce excitation ($z_{o_f} = z_o = z_{o_r}$):

$$
\begin{aligned}
M &= k_{s_f} k_{s_r} L^2 \\
N &= I_s\left(k_{s_f} + k_{s_r}\right) + c_{s_r} c_{s_f} L^2 \\
Q &= \left(k_{s_f} c_{s_r} + k_{s_r} c_{s_f}\right) L^2 \\
P &= I_s\left(c_{s_f} + c_{s_r}\right)
\end{aligned}
$$

For pure pitch excitation ($z_{o_f} = z_o = -z_{o_r}$)

$$
\begin{aligned}
M &= k_{s_f} k_{s_r}\left(c^2 - b^2\right) \\
N &= I_s\left(k_{s_f} - k_{s_r}\right) + c_{s_r} c_{s_f}\left(c^2 - b^2\right) \\
Q &= \left(k_{s_f} c_{s_r} + k_{s_r} c_{s_f}\right)\left(c^2 - b^2\right) \\
P &= I_s\left(c_{s_f} - c_{s_r}\right)
\end{aligned}
$$

The magnitude of pitch excitation, (ϕ_o), can be expressed in terms of the wheelbase, L, as:

$$\phi_o = \tan^{-1}\frac{2z_o}{L} \quad \text{and for small angles,} \quad \phi_o = \frac{2z_o}{L}$$

Pitch transmissibility (response gain):

$$\left|\frac{\phi_s}{z_o}\right| = \sqrt{\left[\frac{(M - \omega^2 N)^2 + (\omega Q - \omega^3 P)^2}{(A\omega^4 - B\omega^2 + C)^2 + (D\omega - E\omega^3)^2}\right]} \quad [18]$$

For bounce excitation ($z_{o_f} = z_o = z_{o_r}$)

$$
\begin{aligned}
M &= 0 \\
N &= m_s\left(ck_{s_r} - bk_{s_f}\right) \\
Q &= 0 \\
P &= m_s\left(bc_{s_f} - cc_{s_r}\right)
\end{aligned}
$$

For pitch excitation ($z_{o_f} = z_o = -z_{o_r}$)

$$
\begin{aligned}
M &= 2k_{s_r} k_{s_f} L \\
N &= m_s\left(bk_{s_f} + ck_{s_r}\right) + 2c_{s_f} c_{s_r} L \\
Q &= 2c_{s_r} k_{s_f} L + 2c_{s_f} k_{s_r} L \\
P &= m_s\left(cc_{s_r} + bc_{s_f}\right)
\end{aligned}
$$

The 2-DOF pitch plane model developed above is useful for vibration analysis in the pitch plane specifically for long wheelbase ground vehicles. The vibration transmissibility characteristics or response gain of the model based upon the parameters of an urban bus are shown in **Figure 6**. **Figure 7** presents the corresponding phase response for both bounce and pitch DOF with respect to input obtained from:

$$\theta = \tan^{-1}\frac{\omega Q - \omega^3 P}{M - \omega^2 N} - \tan^{-1}\frac{\omega D - \omega^3 E}{\omega^4 A - \omega^2 B + C} \quad [19]$$

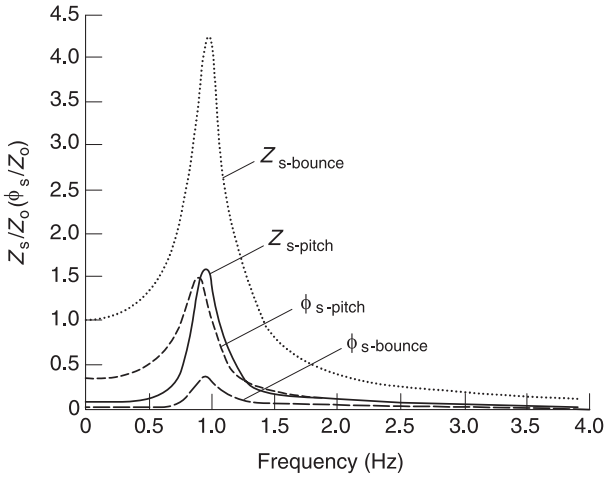


Figure 6 Bounce and pitch transmissibility (gain) under bounce and pitch excitation.

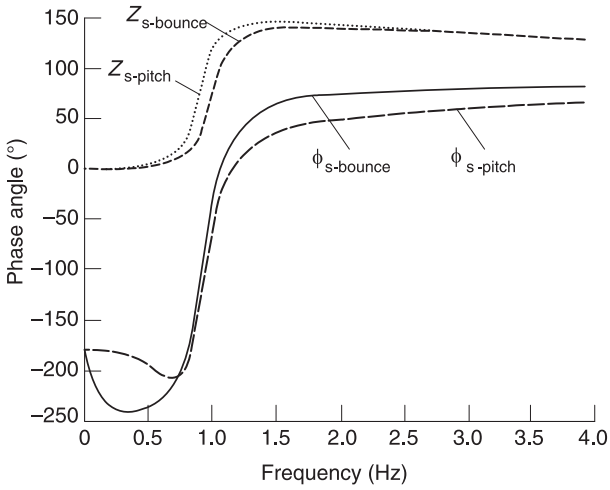


Figure 7 Phase angle of bounce and pitch response under bounce and pitch excitation.

where A, B, C, D, and E are the same as those described after eqn [16], and M, N, P, and Q are dependent on the input as described with eqns [17] and [18]. The 2-DOF pitch plane model can be simplified significantly in order to carry out an undamped free vibration analysis. Such analysis provides very important understanding of vibration modes and the coupling that exists between the modes. For undamped free vibration, equations of motion are obtained by setting $z_{o_f} = z_{o_r} = 0$, $\dot{z}_{o_f} = \dot{z}_{o_r} = 0$ and $c_{s_f} = c_{s_r} = 0$, in eqn [14] to yield:

$$\begin{bmatrix} m_s & 0 \\ 0 & I_s \end{bmatrix} \begin{Bmatrix} \ddot{z}_s \\ \dot{\phi}_s \end{Bmatrix} + \begin{bmatrix} k_{s_f} + k_{s_r} & ck_{s_r} - bk_{s_f} \\ ck_{s_r} - bk_{s_f} & c^2 k_{s_r} + b^2 k_{s_f} \end{bmatrix} \begin{Bmatrix} z_s \\ \theta_s \end{Bmatrix} = 0 \quad [20]$$

For the response of the form $e^{j\omega t}$, the equations are:

$$\begin{bmatrix} k_{s_f} + k_{s_r} - m_s\omega^2 & ck_{s_r} - bk_{s_f} \\ ck_{s_r} - bk_{s_f} & c^2 k_{s_r} + b^2 k_{s_f} - I_s\omega^2 \end{bmatrix} \begin{Bmatrix} z_s \\ \theta_s \end{Bmatrix} = 0 \quad [21]$$

The two natural frequencies can be determined by equating the determinant of the above matrix (characteristic equation) to zero. This will yield natural frequencies as:

$$\omega_{n_{1,2}}^2 = \frac{1}{2}A \pm \sqrt{\left(\frac{1}{4}A^2 - B\right)} \quad [22]$$

where:

$$A = \frac{k_{s_f} + k_{s_r}}{m_s} + \frac{c^2 k_{s_r} + b^2 k_{s_f}}{I_s}$$

$$B = \frac{\left(k_{s_f} k_{s_r}\right)(b + c)^2}{I_s m_s}$$

The mode of vibration at each of the natural frequencies or the location of oscillation centres can be determined by using:

$$\left(\frac{z_s}{\phi_s}\right)_{\omega_{n_i}} = \frac{ck_{s_r} - bk_{s_f}}{m_s\omega_{n_i}^2 - \left(k_{s_f} + k_{s_r}\right)} \quad [23]$$

Upon substitution of a natural frequency, found from eqn [22], the eqn [23] provides a ratio of bounce to pitch amplitude ($m\,rad^{-1}$). A negative value for the ratio indicates that for a positive bounce, the pitch is in the negative sense of the pitch motion shown in the model or vice versa. Typical bounce and pitch vibration modes of a ground vehicle together with their oscillation centers are shown in **Figure 8**. At the bounce natural frequency, the oscillation center lies outside the wheelbase referred to as bounce center (node 1). On the other hand, corresponding to the pitch natural frequency, the oscillation center is within the wheelbase and is referred to as the pitch center (node 2). In general, an input at the front or rear wheel will excite both the bounce and pitch motions due to coupling.The centers of oscillation, shown in the figure, have practical significance with regard to vibration behavior of the vehicle. As can be seen from eqns [20] and [21], the bounce and pitch motions will be uncoupled when $ck_{s_r} = bk_{s_f}$, indicating independent bounce and pitch motions. In this case, bounce mode

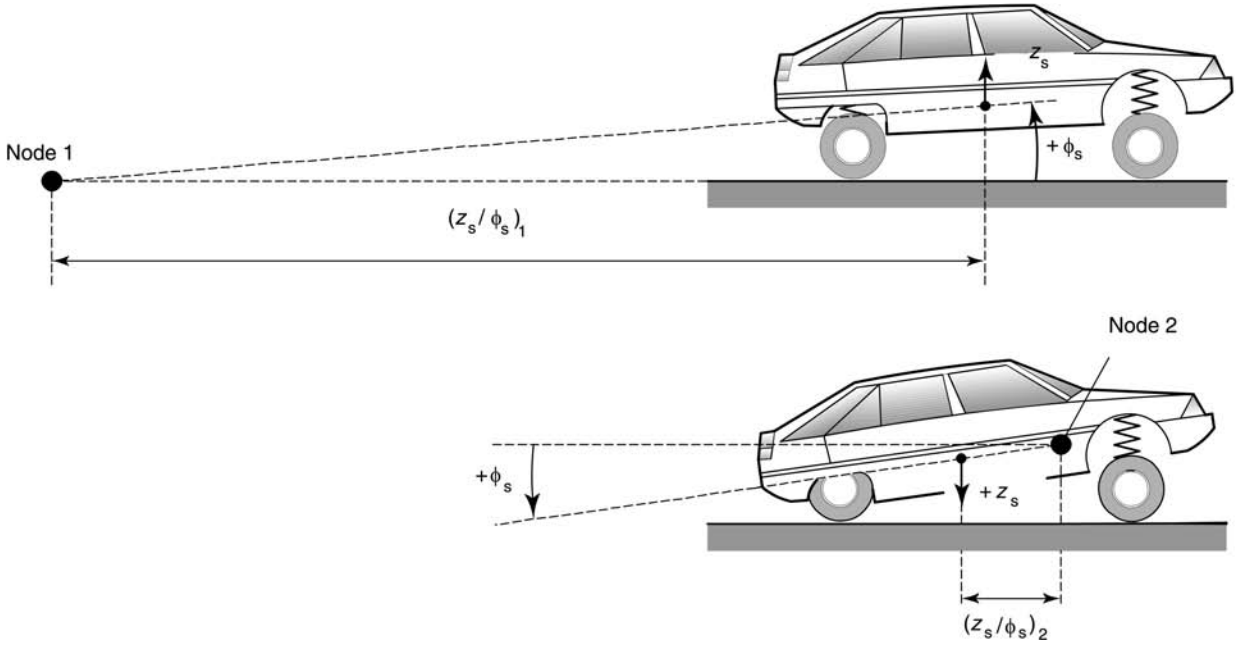


Figure 8 Modes of vibration and centers of oscillation.

center of oscillation will be at an infinite distance from the c.g., while the pitch oscillation center will be located at the c.g. Another case of interest is when parameters are selected to yield centers of oscillation [eqn 23] corresponding to natural frequencies as c and b. In this case, there is no interaction between the front and rear suspensions, and input to one axle will cause no motion at the other axle. Such conditions, however, are difficult to achieve and maintain for practical ground vehicles as they operate over wide conditions causing considerable changes in the c.g. coordinates.

2-DOF Quarter-Car Model

The most common and simple ride model that can be utilized for evaluation of sprung and unsprung mass bounce natural frequencies is the one-quarter-car model presented in **Figure 4C**. This model representing a quarter of a vehicle is widely used for studies of different suspension concepts, and vibration isolation and dynamic travel properties of the suspension. The same model, as shown in **Figure 5B**, can also be employed to study the effects of wheel unbalance and on-board force sources on the motion of unsprung and sprung masses. The equations of motion for the two masses under road excitation, wheel unbalance force (F_W) and an on-board force (F_B) that may arise from vehicle–load interactions, engine or transmission, can be written in the matrix form as:

$$\begin{bmatrix} m_s & 0 \\ 0 & m_u \end{bmatrix} \begin{Bmatrix} \ddot{z}_s \\ \ddot{z}_u \end{Bmatrix} + \begin{bmatrix} c_s & -c_s \\ -c_s & c_s + c_t \end{bmatrix} \begin{Bmatrix} \dot{z}_s \\ \dot{z}_u \end{Bmatrix} + \begin{bmatrix} k_s & -k_s \\ -k_s & k_s + k_t \end{bmatrix} \begin{Bmatrix} z_s \\ z_u \end{Bmatrix} = \begin{bmatrix} 0 \\ c_t \end{bmatrix} \dot{z}_o + \begin{bmatrix} 0 \\ k_t \end{bmatrix} z_o + \begin{bmatrix} F_B \\ F_W \end{bmatrix} \quad [24]$$

Following the approach used for the pitch plane model, the equations for the steady-state motion in the complex form is:

$$\begin{bmatrix} (k_s - m_s\omega^2) + j\omega c_s & -k_s - j\omega c_s \\ -k_s - j\omega c_s & (k_s + k_t - jm_u\omega^2) + j\omega(c_s + c_t) \end{bmatrix} \times \begin{Bmatrix} z_s \\ z_u \end{Bmatrix} = \begin{bmatrix} F_B \\ (k_t + j\omega c_t)z_o + F_W \end{bmatrix} \quad [25]$$

Considering one input at a time, the steady-state responses for harmonic road excitation of amplitude z_o are:

$$\left|\frac{z_s}{z_o}\right| = \sqrt{\left[\frac{(A_1 - B_1\omega^2)^2 + (C_1\omega)^2}{(A\omega^4 - B\omega^2 + C)^2 + (D\omega - E\omega^3)^2}\right]} \quad [26]$$

$$\left|\frac{z_u}{z_o}\right| = \sqrt{\left\{\frac{[A_1 - (B_1 + m_s k_t)\omega^2]^2 + (C_1\omega - m_s c_t \omega^3)^2}{(A\omega^4 - B\omega^2 + C)^2 + (D\omega - E\omega^3)^2}\right\}} \quad [27]$$

where ω is the frequency of road excitation, and:

$$A = m_s m_u$$
$$B = m_u k_s + c_s c_t + m_s(k_s + k_t)$$
$$C = k_s k_t$$
$$D = k_s c_t + k_t c_s$$
$$E = m_s(c_s + c_t) + m_u c_s$$
$$A_1 = k_t k_s$$
$$B_1 = c_t c_s$$
$$C_1 = D$$

The steady-state response of the sprung mass due to on-board excitation $F_B \sin \omega_B t$, can be expressed as:

$$\left|\frac{z_s}{F_B}\right| = \sqrt{\left[\frac{(k_s + k_t - m_u\omega^2)^2 + \omega^2(c_s + c_t)^2}{(A\omega^4 - B\omega^2 + C)^2 + (D\omega - E\omega^3)^2}\right]} \quad [28]$$

where ω_B is the frequency of on-board excitation.

Similarly the effect of wheel unbalance excitation $F_w \sin \omega_W t$ on the sprung and unsprung masses can be expressed as:

$$\left|\frac{z_s}{F_W}\right| = \sqrt{\left[\frac{(k_s)^2 + \omega^2 c_s^2}{(A\omega^4 - B\omega^2 + C)^2 + (D\omega - E\omega^3)^2}\right]} \quad [29]$$

$$\left|\frac{z_u}{F_W}\right| = \sqrt{\left[\frac{(k_s - m_s\omega^2)^2 + (\omega c_s)^2}{(A\omega^4 - B\omega^2 + C)^2 + (D\omega - E\omega^3)^2}\right]} \quad [30]$$

Other results of interest that may be derived from the steady-state responses include suspension travel and tire deflections. Suspension travel is a measure of relative displacement between the sprung and unsprung mass $(z_s - z_u)$. It dictates the space required to accommodate the suspension spring motion also known as rattle space. This measure can be easily obtained from eqns [26] and [27] to yield:

$$\left|\frac{z_u - z_s}{z_o}\right| = \sqrt{\left[\frac{(m_s k_t \omega^2)^2 + (m_s c_t \omega^3)^2}{(A\omega^4 - B\omega^2 + C)^2 + (D\omega - E\omega^3)^2}\right]} \quad [31]$$

Similarly, the dynamic steady-state tire deflection $(z_u - z_o)$ as a ratio of road input amplitude z_o, can be expressed using eqn [27]:

$$\left|\frac{z_u - z_o}{z_o}\right| = \sqrt{\left\{\frac{[(m_s + m_u)k_s\omega^2 - m_s m_u \omega^4]^2 + [(m_s + m_u)c_s\omega^3]^2}{(A\omega^4 - B\omega^2 + C)^2 + (D\omega - E\omega^3)^2}\right\}} \quad [32]$$

The measure and analysis of tire deflection is of significant importance to the dynamic performance of the vehicle and dynamic pavement loads. It provides insight on the possible wheel lift-off, which could have crucial implications on the vehicle performance in terms of stability, handling, traction, braking, etc. Furthermore, in this case the linear model will no longer be valid.

Various vibration performance measures discussed under the quarter-car model and represented by eqns [26]–[32] are plotted for a typical city bus in **Figure 9** and **Figure 10** to illustrate the expected trends.

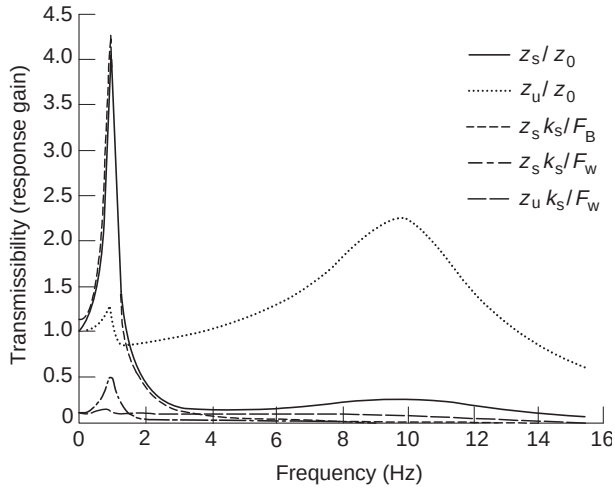


Figure 9 Sprung and unsprung mass transmissibility for various inputs (z_o, F_b, F_w)

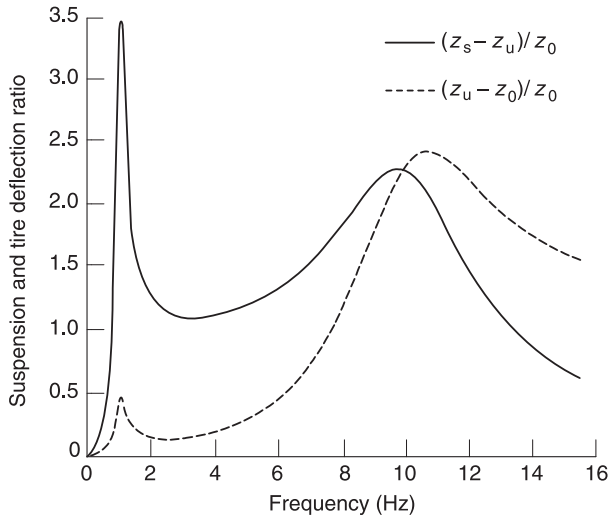


Figure 10 Suspension and tire deflection ratio.

Estimation of Ride Natural Frequencies

The quarter-car model can be simplified to estimate the natural frequencies and damping ratios associated with the vertical ride vibration. Based on the fact that sprung mass and unsprung mass natural frequencies are far apart, and the sprung mass is significantly larger than the unsprung mass, each mass can be treated as a separate independent system. Neglecting tire damping, these can be modeled as shown in **Figure 11**. Based on this sprung mass model, ride stiffness, k_{ride}, and effective unsprung stiffness, k_{u}, are defined as:

$$k_{\text{ride}} = \frac{k_{\text{t}} k_{\text{s}}}{k_{\text{t}} + k_{\text{s}}}, \quad k_{\text{u}} = k_{\text{t}} + k_{\text{s}} \qquad [33]$$

The natural frequencies can therefore be estimated from:

$$\omega_{n_{\text{s}}} = \sqrt{\left(\frac{k_{\text{ride}}}{m_{\text{s}}}\right)}, \quad \text{and} \quad \omega_{n_{\text{u}}} = \sqrt{\left(\frac{k_{\text{u}}}{m_{\text{u}}}\right)} \qquad [34]$$

The suspension-damping ratio, ξ, can be estimated from:

$$\xi = \frac{c_{\text{s}}}{2 m_{\text{s}} \omega_{\text{n}}} = \frac{c_{\text{s}}}{2\sqrt{(k_{\text{ride}} m_{\text{s}})}} \qquad [35]$$

These equations provide useful tools for preliminary selection of suspension parameters for given m_{s} and m_{u}.

Guidelines and Rules of Thumb

In view of the ride quality as determined from vibration environment of vehicles, a number of guidelines and rules of thumb have been developed for the design of suspension systems on the basis of experimental and analytical results. These are summarized below:

- In view of the human comfort, the suspension systems should be designed to achieve low vertical mode natural frequency of the sprung mass. A limiting value for this natural frequency is approximately 1 Hz to ensure adequate rattle space and it should not be greater than 1.5 Hz for passenger vehicles.
- Forces due to wheel motions and unbalance are transmitted to the sprung mass through the suspension. The unsprung mass (wheel hop) natural frequency therefore should lie outside the frequency range of vibration to which the human body is most sensitive. This implies that the vertical mode frequency of the unsprung mass should not be less than 8 Hz. On the other hand, larger frequencies will demand stiff tire affecting ride quality. A practical value for unsprung mass natural frequency is around 10 Hz.
- Pitch and bounce frequencies should be close together. The pitch motion of the sprung mass enhances the bounce motion of the body at a location away from the c.g., such as the driver location in a long wheelbase truck or bus. The bounce natural frequency less than 1.2 times the pitch frequency gives good results.
- When a vehicle goes over a bump, the front axle is subjected to the impact occurring at $\tau_{\text{d}}(L/V)$ seconds before the rear axle. This will excite the pitch resonance, which is more annoying than the vertical motion. Designing rear suspension with slightly larger ride rate than the front will introduce higher frequency of oscillation for the rear than the front. This will convert the pitch motion to a bounce motion within half a cycle after the bump is passed. Based on common operating speeds, V, and wheelbase, L, the rear suspension may be assigned 20–30 percent larger ride rate, or the c.g. should be closer to the rear axle than the front.

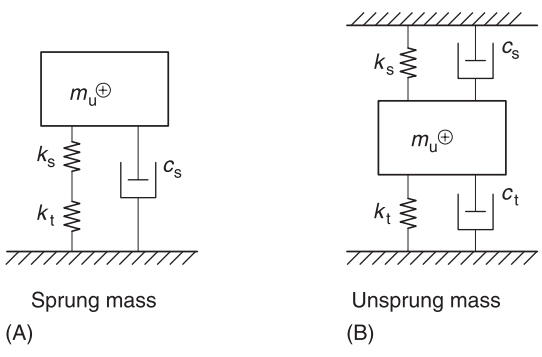


Figure 11 (A, B) Simplified quarter car model for estimation of natural frequencies.

Determination of Vehicle Model Parameters

The accuracy of vibration simulation results that can be predicted from the mathematical models are only as good as the accuracy of the system parameters. Characteristics of many elements associated with vibration analysis are strongly nonlinear. A model with linearized parameters, however, can provide good qualitative trends and comparative results. This section presents the relevant components and

their characteristics, and outlines the methodology that can be used to establish the parameters of a given ground transportation system.

Weights and Dimensions

Weights and dimensions can be established through measurement of front and rear wheel loads (W_f, W_r) as shown in **Figure 12**, and using the following relationships:

$$m_s + 2m_{uf} + 2m_{ur} = (W_f + W_r)/g = W/g \qquad [36]$$

and

$$c = \frac{W_f L}{W}, \quad b = \frac{W_r L}{W}, \quad L = b + c$$

The sprung and unsprung mass components of the total weight is difficult to determine as the mass of the suspension contributes to both masses depending on the type of suspension. As a general guideline, **Table 1** may be used to estimate the total unsprung mass as a fraction of the total vehicle mass.The total unsprung mass can then be distributed to the front and back based on the suspension system installed on the vehicle. For example, for a vehicle with Wishbones in the front and solid axle in the back, the mass distribution should be assigned as: $m_{u_f} = m_u(0.13/(0.13 + 0.26))$ and $m_{u_r} = (m_u - m_{u_f})$

Pitch mass moment of inertia, I_s, of a vehicle is a difficult parameter to estimate. Knowing the location of c.g., the moment of inertia of each section of the structure and components may be established about the c.g. of the vehicle using parallel axis theorem. There are also swing tests that can be carried out to establish I_s experimentally. In the absence of the reliable data, the following empirical relationship may be used to establish I_s within 5–20 percent accuracy for most vehicles:

$$I_s = \left[(W_f + 0.4W_r)b^2 + 0.6W_r c^2\right]/g \qquad [37]$$

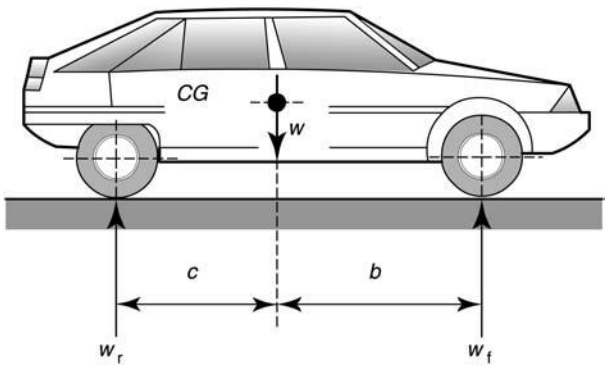


Figure 12 Location of center of gravity, c.g.

Suspension System

Suspension system components, namely spring and damper, may be highly nonlinear in character and require nonlinear analysis of vibration. For nonlinear simulation, the equations of motions presented in this chapter may be used with spring and damper forces defined by nonlinear relationships and solving the equations by numerical methods in time domain. For comparative and qualitative studies, the component characteristics may also be linearized to employ the convenience linear analytical tools.

Suspension springs Common springs used in ground transportation suspension systems include coil, leaf and air springs. Coil springs exhibit linear relationships and its stiffness can either be measured or estimated based on its design configuration or static deflection. The leaf springs exhibit hardening characteristics and hysteresis due to interleaf and bushing friction. The hardening characteristics are introduced through change of leaf length with deflection as well as auxiliary springs. Such a characteristic is useful for vehicles that may have large variation in load. A typical leaf spring characteristic is shown in **Figure 13**. The ride motions of such suspension are often small in amplitude as shown by the small inner loop. The loop for a given motion represents the damping energy dissipated by the suspension. The most important aspect of such suspension is the fact that the effective ride stiffness of the suspension may be significantly larger than the nominal stiffness under small deflections as illustrated in the figure.Air springs are gaining popularity for commercial vehicles as they exhibit hardening characteristics and provide adaptive ride height control. For commercial

Table 1 The unsprung and sprung masses as a fraction of the total vehicle weight

Suspension type	*Wishbones with coil springs*	*De Dion with coil springs*	*Swing axle with coil springs*	*Solid axle with coil springs*	*Solid axle with leaf spring*
$m_u g/W$	0.13	0.15	0.18	0.22	0.26
$m_s g/W$	0.87	0.85	0.82	0.78	0.74

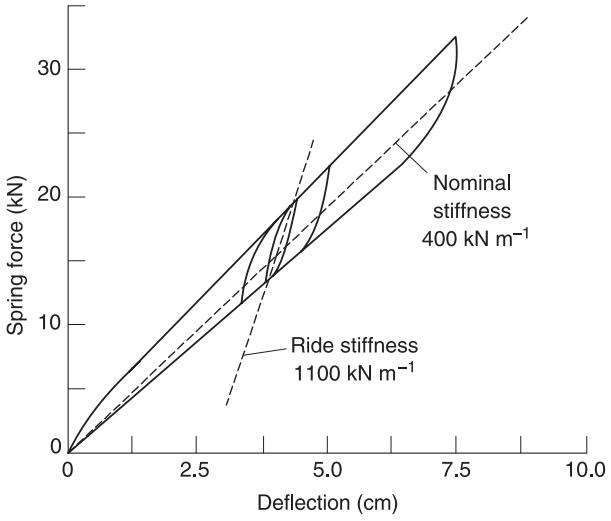


Figure 13 Loading–unloading characteristics of a leaf spring.

applications, air springs are considered most desirable to achieve improved ride quality and pavement load performance. Such a system can provide wide design parameters through variations in piston geometry. The dynamic forces developed by the air springs are related to the instantaneous relative displacements across the spring. The dynamic restoring forces are dependent on the instantaneous air pressure and effective piston area, which are related to instantaneous height of the airbag. Experimental force-deflection and effective piston area characteristics of an air spring used in urban buses for two different preloads are shown in **Figure 14** and **Figure 15**. An analytical model of the air spring can be developed based on the experimental data for given preloads.

Suspension damping Vehicle suspensions employ hydraulic dampers with blow-off and bleed-control valves to provide variable damping as a function of velocity, as well as asymmetric characteristics in

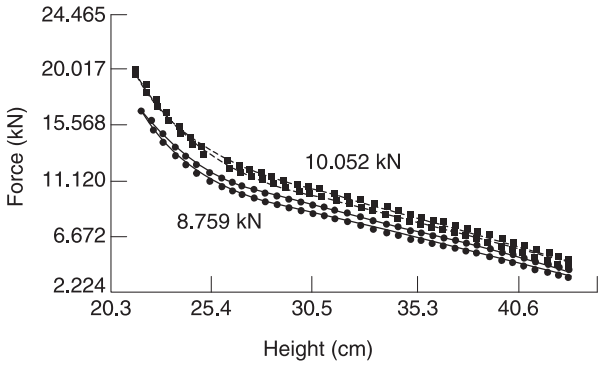


Figure 14 Force–displacement characteristics of an air spring (design height = 31.49 cm).

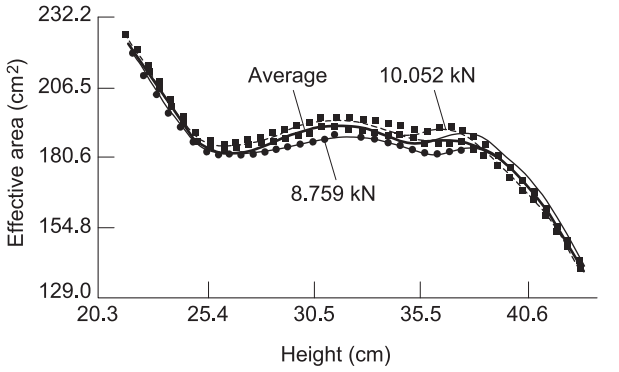


Figure 15 Effective area-displacement characteristics of an air spring (design height = 31.49 cm).

compression and rebound. Typical force–displacement and force–velocity characteristics of automotive dampers are shown in **Figure 16**. As shown, depending on the characteristics, the nonlinear force velocity relationship can be expressed by an exponent n, such that:

$$F_d = c_s \dot{z}^n \qquad [38]$$

The area enclosed within the force–deflection curve represents the energy dissipated by the damper over a cycle. An equivalent viscous damping coefficient may be determined from the experimentally derived area within the curves. The estimated damping coefficient, however, could be considered valid in the vicinity of the selected test frequency, ω, and magnitude, z, and is often referred to as local equivalent damping coefficient:

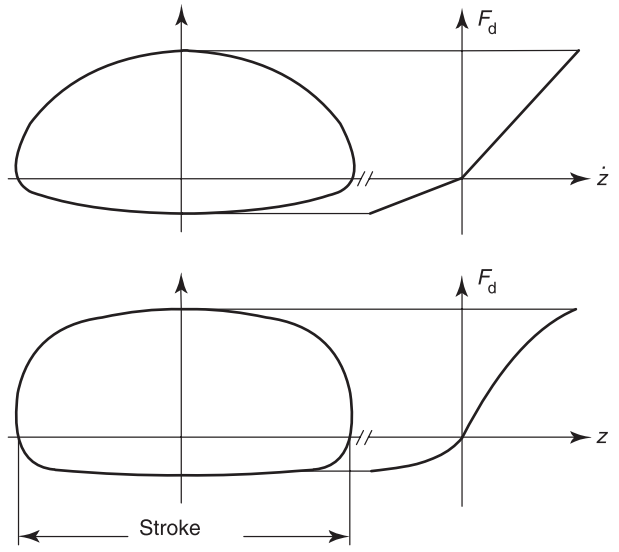


Figure 16 Typical damper force-displacement characteristics.

$$C_{eq}(\omega, z) = \frac{\text{Area}}{\pi\omega z^2} \qquad [39]$$

Since such coefficients are functions of frequency and peak displacements, an iterative process can be utilized in a linear frequency domain analysis to obtain the frequency response for given amplitude of harmonic excitations. A nonlinear damper for ground vehicle with two-stage damping characteristics can be considered to exhibit piecewise linear relations with asymmetric characteristics in compression and extension, as shown in **Figure 17**. The high value of damping at low velocities is required to control resonant oscillations, whereas low value is desirable at high velocities to achieve improved vibration isolation. The piecewise linear component may be modeled using the following relationships in a time domain analysis.

$$F_d = \begin{cases} c_1\dot{z} & 0 \le \dot{z}_1 \le \alpha_1 \\ c_3\dot{z} & \alpha_2 \le \dot{z}_1 \le 0 \\ c_1\alpha_1 + c_2(\dot{z} - \alpha_1) & \dot{z} \ge \alpha_1 \\ c_3\alpha_2 + c_4[\dot{z}_1 - \alpha_2 \text{sgn}(\dot{z}_1)] & \dot{z} \le \alpha_2 \end{cases}$$

where the 'sgn' function assumes a value of either 1 or -1 for positive and negative values of $\dot{z}$, respectively. Based on the principle of energy similarity, equivalent linear viscous damping coefficients for the three regions can be found as:

$$C_{eq}(\omega_i, z_i) = \begin{cases} 0.5(c_1+c_3) & \omega_i z_i \le \alpha_1 \\ \frac{1}{2\pi}[\pi(c_1+c_3) + \{\sin 2\omega_i t_1 - 2\omega_i t_1\}(c_1-c_2)] & \alpha_1 \le \omega_i z_i \le |\alpha_2| \\ \frac{1}{2\pi}[\pi(c_1-c_3) + \{\sin 2\omega_i t_1 - 2\omega_i t_1\}(c_1-c_2) & \\ \quad +2\pi c_4 + \{\sin 2\omega_i t_2 - 2\omega_i t_2\}(c_3 - c_4)] & \omega_i z_i \ge |\alpha_2| \end{cases} \qquad [40]$$

where:

$$\omega_1 z_i = |\dot{Z}| \quad t_1 = \frac{1}{\omega}\cos^{-1}\left[\frac{\alpha_1}{\omega z}\right]$$

and:

$$t_2 = \frac{1}{\omega}\cos^{-1}\left[\frac{|\alpha_2|}{\omega z}\right], \quad t_2 > t_1$$

Similar to eqn [38], an iterative process can be utilized in a linear frequency domain analysis to obtain the frequency response for given amplitude of harmonic excitations.

Tire Properties

For a given inflation pressure, the vertical force developed by a pneumatic tire can be considered as a linear function of the tire deflection. The stiffness coefficient of the tire, however, is a function of the inflation pressure. A simple test, known as the 'drop test' can be carried out to establish its stiffness and damping properties using the 'logarithmic decrement method'. The tire with a certain load (total mass, m) is allowed to fall freely ensuring that the tire remains in contact with the ground at all times. The decaying response signature, shown in **Figure 18**, can then be used to establish dynamic stiffness of the nonrolling tire:

$$k_t = \frac{m\omega_d^2}{1 - [\delta^2/(\delta^2 + 4\pi^2)]}$$
$$c_t = \sqrt{\left[\frac{(4m^2\omega_d^2)/(\delta^2 + 4\pi^2)}{(1-\delta^2)/(\delta^2 + 4\pi^2)}\right]} \qquad [41]$$

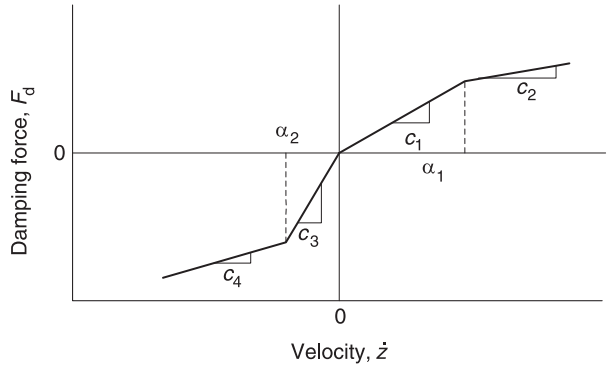


Figure 17 Characteristics of a typical nonlinear damper.

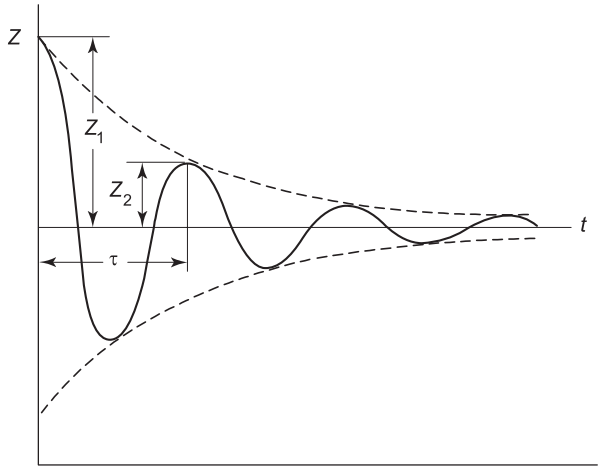


Figure 18 Response of the tire drop test.

where:

$$\omega_d = 2\pi/\tau \quad \text{and} \quad \delta = \ln(z_1/z_2)$$

The dynamic stiffness of a rolling tire may be 10–15% less than the static stiffness for typical car tires whereas for truck tires it is only about 5% less. The tire damping on the other hand reduces significantly with speed. Typical car radial tire static stiffness range between 80 and 200 kN m^{-1} for inflation pressure in the range 100–250 kPa. Truck tires at rated pressure exhibit vertical stiffness in the range 700–1000 kN m^{-1}.

A set of linearized parameters for a range of ground vehicles relevant to the vibration analyses presented in this chapter is summarized in **Table 2**. These data are collected from various sources and estimated for multiaxle vehicles by lumping axles such that the equations derived in this chapter can be used to evaluate the ride vibrations.

Road Excitations

Roughness of a road surface is described by its elevation profile along the path over which the wheels travel. For in-plane vehicle vibration models, it is assumed that the same input is applied to the left and right wheels. For harmonic motion, the road profile is assumed to be of the sinusoidal form:

$$z_{o_f} = z_o \sin\left(\frac{V}{\lambda}\right)t \qquad [42]$$

where V is the forward velocity and λ is the wavelength. For pitch plane, the rear wheel is subjected to the same input after a time delay of $\tau_d = L/V$:

$$z_{o_r} = z_o \sin\left(\frac{V}{\lambda}\right)(t - \tau_d) \qquad [43]$$

While an assumption of sinusoidal input provides highly useful results for qualitative performance and comparison of designs, they could not serve as a valid basis for studying the actual vibration behavior of the vehicle. Road profiles are highly random in nature and may include abrupt motions arising from occasional potholes or discontinuities. The road surface profiles have been characterized by their statistical properties, mostly in terms of power spectral density (PSD) of the roughness. These studies have established that the road roughness follows a nearly Gaussian distribution. A parameter, referred to as roughness index (RI) and defined as the sum of road elevations measured at specified intervals over length of 1 km, is used as a serviceability index for the roads, given by:

$$\mathrm{RI} = \frac{1}{n\Delta x}\sum_i^n |\Delta z_i| \qquad [44]$$

where n is the number of equidistant measurement points, Δz_i, is the elevation at the ith measurement location, and Δx is the measurement spacing. Based on the urban road measurements, the typical values of RI for smooth, medium, and rough roads may vary from 1.2 to 1.3, 3.2 to 3.4, and 6.4 to 6.8 respectively. The PSD of roughness properties of roads are available as a function of spatial frequency $\Omega(\mathrm{m}^{-1})$ and the trend for a range of roads are shown in **Figure 19**. The random road profiles of various highways, secondary roads and dirt roads have been measured in many studies (for more information please see Further reading).

Temporal PSD of roughness $S(\omega)$ in terms of temporal angular frequency ω for different road surfaces may be expressed as a function of vehicle speed:

$$S(\omega) = \frac{\sigma_1^2}{\pi}\left[\frac{\lambda_1 V}{\omega^2 + \lambda_1^2 V^2}\right] \qquad [45]$$

where ω denotes the angular frequency, V is vehicle speed, and λ_1, σ_1 are coefficients to fit road type. The

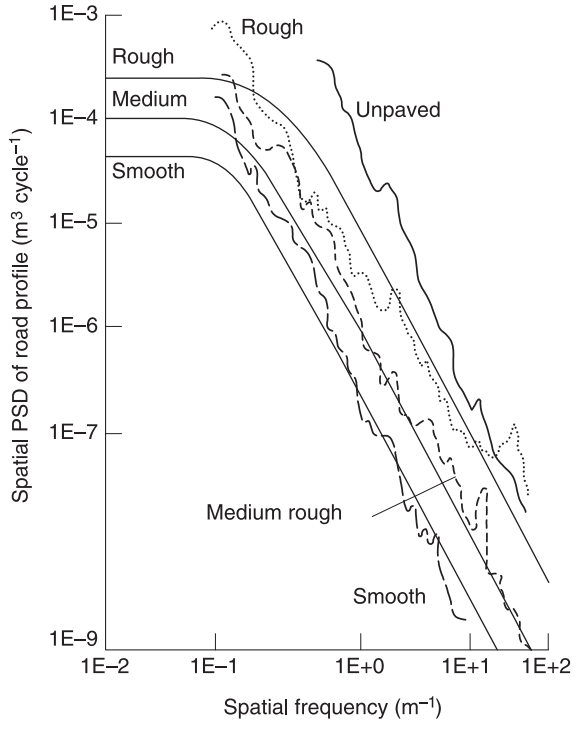


Figure 19 Spatial PSD of roughness of a range of roads and their approximation.

Table 2 Example of vehicle parameters for ride analysis

Type	*Dim* L, W, H(m)	*Total mass* (kg)	I_s(kgm^2)	b(m)	c(m)	k_{s_r}(kNm^{-1})	k_{s_f}(kNm^{-1})	C_{s_r}(kNsm^{-1})	C_{s_f}(kNsm^{-1})	k_{t_f}, k_{t_r}(kNm^{-1})	C_{t_f}, C_{t_r}(kNsm^{-1})	m_{u_r}(kg)	m_{u_f}(kg)
Small car	3.64 1.56 1.41	830	1094	0.87	1.29	17.3	25.6	1.604	2.378	150	1.5	41.2	34.2
Mid car	4.69 1.83 1.45	1150	1630	1.26	1.40	23.8	35.7	2.207	3.311	175	1.7	57	47.6
Large car	5.27 1.89 1.49	1945	4670	1.56	1.507	51.2	49.3	4.759	4.574	200	2.0	130	115
Sports car	4.25 1.9 1.16	1480	1730	1.42	1.03	44.4	32.1	4.119	2.982	200	1.0	73.4	61.2
Rigid truck	6.86	4536	12 000	2.87	0.84	366	151	27.414	11.340	809	1.5–4.0	321	133
Articulated truck	Tractor Trailer	2 000 14 000	10 000 300 000	1.5 6.0	3.65 6.20	1400 2000	350 1400	55.20 54.48	14.98 55.20	764–1024 764–1024	1.5–4.0 1.5–4.0	520 340	270 520
City Bus	12.19 2.59 3.0	15 632	175 034	3.2	2.8	70.0	60.0	2.0	3.5	922	0.8	1250	700
Highway bus	13.716 2.591 3.683	17 727	19 300	4.52	7.23	720	240	9.22	4.033	938.7	1.5–4.0	2700	3346

Data collected from various sources and estimated.
Unsprung mass and suspension properties are for each axle, tire properties are for each tire.

Table 3 Roughness parameters for typical roads

Type of road	$\lambda_1(\mathrm{m}^{-1})$	$\sigma_1(\mathrm{m})$
Asphalt (smooth)	0.30	0.0033
Concrete (medium rough)	0.40	0.0056
Concrete (rough)	0.80	0.0120

spatial PSDs $S_s(\Omega)$ in terms spatial frequency $\Omega(\mathrm{m}^{-1})$ are related to the temporal PSD and temporal frequency ω $(\mathrm{rad\,s}^{-1})$ in the following manner:

$$S(\omega) = \frac{S_s(\Omega)}{V} \quad \text{and} \quad \omega = \Omega V \qquad [46]$$

Figure 19 also presents the approximations generated by eqn [45] to demonstrate the effectiveness in representation of the PSD for different roads. The roughness parameters λ_1, σ_1 used in the computation are presented in **Table 3**. For linear analysis of response to random input, the transfer functions derived in the chapter may be applied directly as:

$$\text{Response}(\omega) = |T(\omega)|^2 S(\omega) \qquad [47]$$

where $T(\omega)$ is the transfer function or response gain derived as a function of ω. For nonlinear analysis, a synthesized or measured time history of the road input may be used with the equations of motions and solved numerically in time domain.

See Plate 38.

See also: **Absorbers, vibration**; **Active control of vehicle vibration**; **Crash**; **Tire vibrations**

Further Reading

Ahmed AKW, Rakheja S (1992) An equivalent linearization technique for the frequency response analysis of asymmetric dampers. *Journal of Sound and Vibration*, 153, 537–542.

Bastow D (1993) *Car Suspension and Handling*, Third Edition, Society of Automotive Engineers, Inc. Warrendale, PA., USA. London: Pentech Press.

Clinton A (1987) *The Mechanics of Heavy-Duty Trucks and Truck Combinations, The International Association for Vehicle Design*. The Open University, UK.

Dixon J (1999) *The Shock Absorber Handbook*, Second Edition, Society of Automotive Engineers, Inc. Warrendale, PA, USA.

Dixon JC (1991) *Tires, Suspension and Handling*. Cambridge, UK: Cambridge University Press.

Dulac A (1992) *An Investigation of Ride and Handling Performance of Passive and Combined Active-Passive-Bus-Suspension*. Thesis of Master of Applied Science, Concordia University, Montreal, Canada.

Genta G (1997) *Motor Vehicle Dynamics, Modeling and Simulation. Series on Advances in Mathematics for Applied Sciences–Vol. 43*. Singapore: World Scientific.

Gillespie DJ (1992) *Fundamentals of Vehicle Dynamics*, SAE, USA.

Rakheja S and Yang X (1999) *Urban Bus Optimal Passive Suspension Study*. Report, CONCAVE Research Centre, Concordia University, Montreal, Canada.

Reimpell J and Stoll H (1996) *The Automotive Chassis*. London: Arnold.

Thomson TW and Dahleh DM (1998) *Theory of Vibration*, 5th edn. Englewood Cliffs, NJ: Prentice-Hall.

Wong JY (1993) *Theory of Ground Vehicles*, 2nd edn. New York: Wiley.

H

HAND-TRANSMITTED VIBRATION

M J Griffin, Institute of Sound and Vibration Research, University of Southampton, Southampton, UK

Copyright © 2001 Academic Press

doi:10.1006/rwvb.2001.0083

Introduction

Hand-transmitted vibration occurs where the hands or fingers grasp or push vibrating tools or workpieces. The vibration may be produced by machines in industry, agriculture, mining, construction, and transport.

Exposure of the fingers or the hands to vibration can result in various signs and symptoms of disorder. The interrelation between the signs and symptoms is not fully understood, but five types of disorder may be identified (**Table 1**). More than one disorder can affect a person at the same time and it is possible that the presence of one disorder facilitates the appearance of another. Confusingly, the terms vibration syndrome, or hand–arm vibration syndrome (HAVS), are sometimes used to refer to an unspecified combination of one or more of the disorders listed in **Table 1**.

The development of the various disorders is dependent on the vibration characteristics, the dynamic response of the fingers or hand, individual susceptibility to damage, and other aspects of the environment.

Sources of Hand-transmitted Vibration

The vibration on tools depends on tool design and method of tool use, so it is not possible to categorize individual tool types as safe or dangerous. **Table 2** lists tools and processes that are sometimes a cause for concern. **Figure 1** shows vibration spectra measured on 24 tools that might sometimes be associated with injury.

Table 1 Five types of disorder associated with hand-transmitted vibration exposures (a combination of these disorders is sometimes referred to as the hand–arm vibration syndrome or HAVS).

Type	*Disorder*
Type A	Circulatory disorders
Type B	Bone and joint disorders
Type C	Neurological disorders
Type D	Muscle disorders
Type E	Other general disorders (e.g., central nervous system)

Effects of Hand-transmitted Vibration

Vascular Disorders

The first published cases of the condition now most commonly known as vibration-induced white finger (VWF) are generally acknowledged to have been in Italy in 1911. VWF has subsequently been reported in many widely varying occupations in which there is exposure of the fingers to vibration.

VWF is characterized by intermittent whitening (i.e., blanching) of the fingers. The finger tips are usually the first to blanch but the affected area may extend to all of one or more fingers with continued vibration exposure. Attacks of blanching are precipitated by cold and therefore usually occur in cold conditions or when handling cold objects. The blanching lasts until the fingers rewarm and vasodilation allows the return of the blood circulation. Many years of vibration exposure often occur before the first attack of blanching is noticed. Affected persons often have other signs and symptoms, such as numbness and tingling. Cyanosis and, rarely, gangrene, have also been reported. It is not yet clear to what extent these other signs and symptoms are causes of, caused by, or unrelated to, attacks of white finger.

VWF cannot be assumed to be present merely because there are attacks of blanching. It will be necessary to exclude other known causes of similar symptoms (by medical examination) and also necessary to exclude primary Raynaud's disease (also called constitutional white finger). If there is no family history of the symptoms, if the symptoms did not occur before the first significant exposure to vibration, and if the symptoms and signs are confined to areas in contact with the vibration (e.g., the fingers, not the toes, ears, etc.), they will often be assumed to indicate VWF. Diagnostic tests for VWF are not

Table 2 Some tools and processes potentially associated with vibration injuries (standards identifying type tests are indicated in parentheses)

Type of tool	*Examples of tool type*
Percussive metal-working tools	Riveting tools (ISO 8662-2) Caulking tools (ISO 8662-5) Chipping hammers (ISO 8662-2) Clinching and flanging tools (ISO 8662-10) Impact wrenches (ISO 8662-7) Impact screwdrivers (ISO 8662-7) Nut runners (ISO 8662-7) Scaling hammers Needle guns (ISO 8662-14) Nibbling machines and shears (ISO 8662-10) Swaging
Grinders and other rotary tools	Pedestal grinders Hand-held grinders (ISO 8662-4; ISO 8662-8) Hand-held sanders (ISO 8662-4; ISO 8662-8) Hand-held polishers (ISO 8662-4; ISO 8662-8) Flex-driven grinders/polishers Rotary burring tools Files
Percussive hammers and drills used in mining, demolition, road construction, and stone working	Hammer drill (ISO 8662-3) Rock drills (ISO 8662-3) Tampers and rammers (SO 8662-9) Road breakers (ISO 8662-5) Stone-working tools (ISO 8662-14)
Forest and garden machinery	Chain saws (ISO 7505) Antivibration chain saws (ISO 7505) Brush saws Mowers (ISO 5395) Hedge cutters and trimmers Barking machines Stump grinders
Other processes and tools	Nailing gun (ISO 8662-14) Stapling gun (ISO 8662-11) Pad saws (ISO 8662-12) Circular saws (ISO 8662-12) Scabblers Engraving pens Shoe-pounding-up machines Vibratory rollers Concrete vibrothickeners Concrete leveling vibrotables Motorcycle handle bars Pedestrian-controlled machines

infallible indicators of the disease, but the measurement of finger systolic blood pressure following finger cooling and the measurement of finger rewarming times following cooling can be useful.

The severity of the effects of vibration may be recorded by reference to the stage of the disorder. The staging of VWF is based on verbal statements made by the affected person. In the Stockholm Workshop staging system, the staging is influenced by both the frequency of attacks of blanching and the areas of the digits affected by blanching (**Table 3**).

A scoring system is used to record the areas of the digits affected by blanching (**Figure 2**). The scores correspond to areas of blanching on the digits commencing with the thumb. On the fingers a score of 1 is given for blanching on the distal phalanx, a score of 2 for blanching on the middle phalanx, and a score of 3 for blanching on the proximal phalanx. On the thumbs the scores are 4 for the distal phalanx and 5 for the proximal phalanx. The blanching score may be based on statements from the affected person or on the visual observations of a designated observer.

Neurological Disorders

Numbness, tingling, elevated sensory thresholds for touch, vibration, temperature and pain, and reduced nerve conduction velocity are considered to be separate effects of vibration, and not merely symptoms of VWF. A scale for reporting the extent of vibration-induced neurological effects of vibration has been proposed (**Table 4**). This staging is not currently related to the results of any specific objective test: the sensorineural stage is a subjective impression of a physician based on the statements of the affected person or the results of any available clinical or scientific testing. Neurological disorders are sometimes identified by screening tests using measures of sensory function, such as the thresholds for feeling vibration, heat, or cold in the fingers.

Table 3 Stockholm Workshop scale for the classification of vibration-induced white finger.

Stage	*Grade*	*Description*
0		No attacks
1	Mild	Occasional attacks affecting only the tips of one or more fingers
2	Moderate	Occasional attacks affecting distal and middle (rarely also proximal) phalanges of one or more fingers
3	Severe	Frequent attacks affecting all phalanges of most fingers
4	Very severe	As in stage 3, with trophic skin changes in the finger tips

If a person has stage 2 in two fingers on the left hand and stage 1 in a finger of the right hand, the condition may be reported as 2L(2)/1R(1). There is no defined means of reporting the condition of digits when this varies between digits on the same hand. The scoring system is more helpful when the extent of blanching is to be recorded.

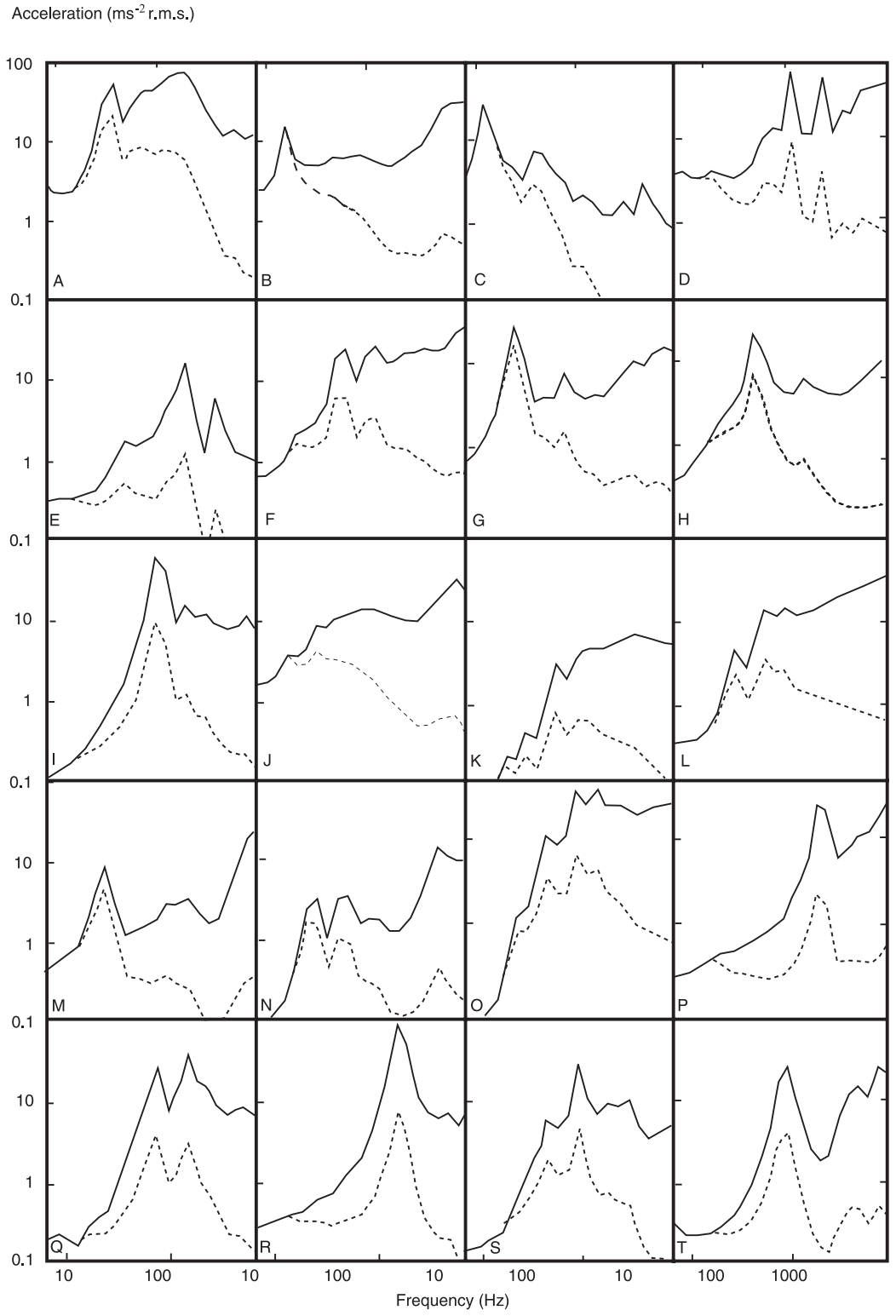


Figure 1 One-third octave band spectra on 20 powered hand tools: continuous lines, unweighted spectra; dashed lines, weighted spectra. (A) Pneumatic rock drill; (B) pneumatic road breaker; (C) petrol-driven Wacker compressing road surface after mending; (D) a nonantivibration chain saw; (E) an antivibration chain saw; (F) a pneumatic metal-chipping hammer; (G) pole scabbler; (H) needle gun; (I) random orbital sander; (J) impact wrench; (K) riveting gun; (L) dolly used with riveting gun; (M) nutrunner; (N) metal drill; (O) wire swaging; (P) etching pen; (Q) electric 9-in angle grinder; (R) pneumatic rotary file; (S) pneumatic 5-in straight grinder; (T) pneumatic 7-in vertical grinder. All spectra from the axis giving the highest weighted acceleration. (Reproduced with permission from Griffin, 1997.)

Table 4 Proposed sensorineural stages of the effects of hand-transmitted vibration

Stage	*Symptoms*
0_{sn}	Exposed to vibration but no symptoms
1_{sn}	Intermittent numbness with or without tingling
2_{sn}	Intermittent or persistent numbness, reduced sensory perception
3_{sn}	Intermittent or persistent numbness, reduced tactile discrimination, and/or manipulative dexterity

Muscular Effects

Workers exposed to hand-transmitted vibration sometimes report difficulty with their grip, including reduced dexterity, reduced grip strength, and locked grip. Muscle activity may be of great importance to tool users since a secure grip can be essential to the performance of the job and the safe control of a tool. The presence of vibration on a handle may encourage the adoption of a tighter grip than would otherwise occur and a tight grip may increase the transmission of vibration to the hand. If the chronic effects of vibration result in reduced grip, this may help to protect operators from further effects of vibration, but interfere with both work and leisure activities.

Articular Disorders

Surveys of the users of some hand-held tools have found evidence of bone and joint problems, most often among workers operating percussive tools such as those used in metal-working jobs and mining and quarrying. It is speculated that some characteristic of such tools, possibly the low-frequency shocks, is responsible. Some of the reported injuries relate to specific bones and suggest the existence of cysts, vacuoles, decalcification, or other osteolysis, degeneration, or deformity of the carpal, metacarpal, or phalangeal bones. Osteoarthrosis and olecranon spurs at the elbow, and other problems at the wrist and shoulder are also documented. There is not universal acceptance that vibration is the cause of articular problems and there is currently no dose–effect relation which predicts their occurrence. In the absence of specific information, it seems that adherence to current guidance for the prevention of VWF may provide reasonable protection.

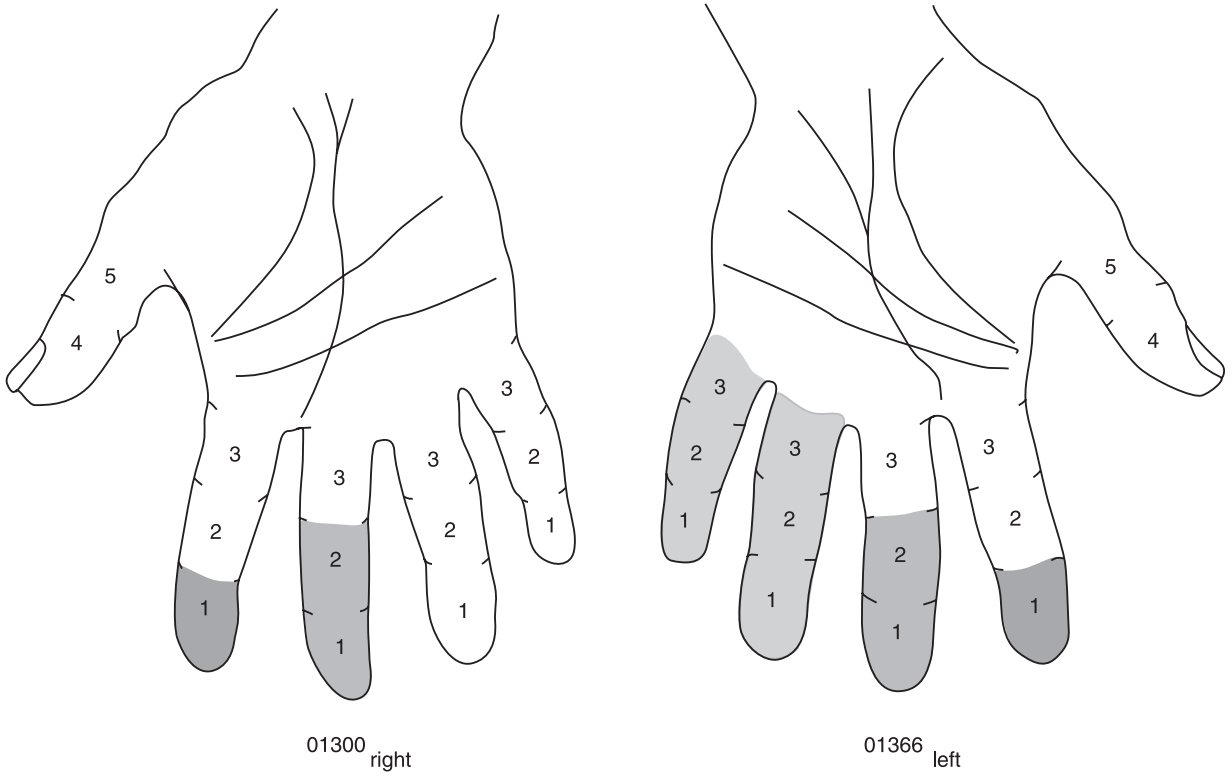


Figure 2 Method of scoring the areas of the digits affected by blanching. The blanching scores for the hands shown are 01300_{right}, 01366_{left}.

Other Effects

Hand-transmitted vibration may not only affect the fingers, hands, and arms: studies have found problems such as headaches and sleeplessness among tool users and have concluded that these symptoms are caused by hand-transmitted vibration. Although these are real problems to those affected, they are subjective effects which are not accepted as real by all researchers. Research is seeking a physiological basis for such symptoms. It currently appears reasonable to assume that the adoption of the modern guidance to prevent VWF will also provide some protection from any other effects of hand-transmitted vibration within, or distant from, the hand.

Preventive measures

Table 5 summarizes preventive measures that may be appropriate for management, tool manufacturers, technicians, physicians, and tool users. When there is reason to suspect that hand-transmitted vibration may cause injury, the vibration at tool–hand interfaces should be measured. It will then be possible to predict whether the tool or process is likely to cause injury and whether any other tool or process could give a lower vibration severity. The duration of exposure to vibration should also be quantified. Reduction of exposure duration may include the provision of breaks in exposure during the day and, if possible, prolonged periods away from vibration exposure. For any tool or process having a vibration magnitude sufficient to cause injury there should be a system to quantify and control the maximum daily duration of exposure of any individual.

Current standards imply that most commonly available gloves do not normally provide effective attenuation of the vibration on most tools. Gloves and cushioned handles may reduce the transmission of high frequencies of vibration but the standards imply that these frequencies are not usually the primary cause of disorders. Gloves may protect the hand from other forms of mechanical injury (e.g, cuts and scratches) and protect the fingers from temperature extremes. Warm hands are less likely to suffer an attack of finger blanching and some consider that maintaining warm hands while exposed to vibration may also lessen the damage caused by the vibration.

Workers who are exposed to vibration magnitudes sufficient to cause injury should be warned of the possibility of vibration injuries and educated on the ways of reducing the severity of their vibration exposures. They should be advised of the symptoms to look out for and told to seek medical attention if the symptoms appear. There should be preemployment medical screening wherever a subsequent exposure to hand-transmitted vibration may reasonably be expected to cause vibration injury. Medical supervision of each exposed person should continue throughout employment at suitable intervals, possibly annually.

Table 5 Preventive measures to consider when persons are exposed to hand-transmitted vibration

Group	*Action*
Management	Seek technical advice Seek medical advice Warn exposed persons Train exposed persons Review exposure times Policy on removal from work
Tool manufacturers	Measure tool vibration Design tools to minimize vibration Ergonomic design to reduce grip force Design to keep hands warm Provide guidance on tool maintenance Provide warning of dangerous vibration
Technical at workplace	Measure vibration exposure Provide appropriate tools Maintain tools Inform management
Medical	Preemployment screening Routine medical checks Record all signs and reported symptoms Warn workers with predisposition Advise on consequences of exposure Inform management
Tool user	Use tool properly Avoid unnecessary vibration exposure Minimize grip and push forces Check condition of tool Inform supervisor of tool problems Keep warm Wear gloves when safe to do so Minimize smoking Seek medical advice if symptoms appear Inform employer of relevant disorders

Standards for the Evaluation of Hand-transmitted Vibration

International and National Standards

International Standard 5349 employs a frequency weighting (called W_h in British Standard 6842) to quantify the severity of hand-transmitted vibration over the frequency range 8–1000 Hz (**Figure 3**). This weighting is applied to measurements of vibration

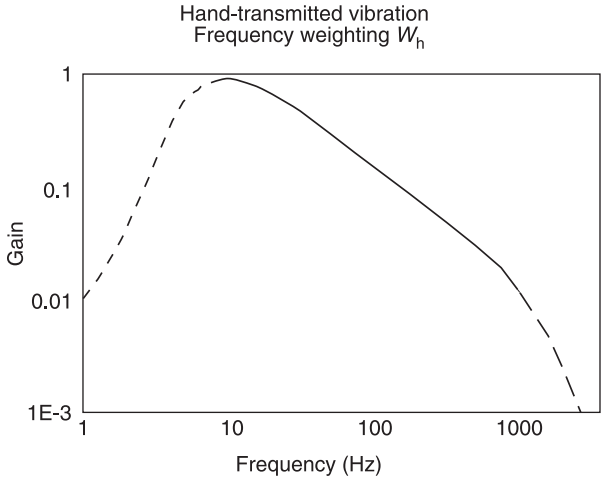


Figure 3 Frequency weighting W_h (shown here as an asymptotic weighting between 8 and 1000 Hz; when evaluating one-third octave band spectra the frequency range is specified as 6.3–1250 Hz).

acceleration in each of the three translational axes at the point of entry of vibration to the hand. Measurements of tool vibration should be obtained with representative operating conditions. The standards imply that if two tools expose the hand to vibration for the same period of time, the tool having the lowest frequency-weighted acceleration will be least likely to cause injury or disease. In **Figure 2**, the vibration spectra on 24 tools are shown before and after the application of frequency weighting W_h.

Current standards for the evaluation of hand-transmitted vibration use the concept called equal energy so that a complex exposure pattern of any duration during the day can be represented by the equivalent value for an exposure of 8 h (4 h in ISO 5349, 1986). For an exposure of duration, t, to a frequency-weighted r.m.s. acceleration, a_{hw}, the 8-h energy-equivalent acceleration, $a_{hw(eq,\,8h)}$, is given by:

$$a_{hw(eq,8h)} = a_{hw}\sqrt{(t/T_{(8)})} \qquad [1]$$

where $T_{(8)}$ is 8 h (in the same units as t). The value of $a_{hw(eq,\,8h)}$ is sometimes denoted by $A(8)$.

A relation between years of vibration exposure, E, the 4-h energy-equivalent frequency-weighted acceleration, $a_{hw(eq,\,4h)}$, and the predicted prevalence of finger blanching, C, was proposed in an Annex to International Standard 5349 (1986) (**Table 6** and **Figure 4**):

$$C = 100 \cdot \left[\frac{a_{hw(eq,4h)} \cdot E}{95}\right]^2 \qquad [2]$$

The values in **Table 6** and **Figure 4** refer to frequency-weighted acceleration (i.e., referenced to the frequency range 8–16 Hz after passing through the filter shown in **Figure 3**). British Standard 6842 (1987) offers similar guidance, but is restricted to a 10% prevalence of VWF. **Figure 5** shows how the magnitudes required for a predicted prevalence of 10% VWF after 8 years are assumed to depend on vibration frequency from 8 to 1000 Hz for exposure durations from 1 min to 8 h per day.

The frequency weighting, the time dependency and the dose–effect information used in ISO 5349 (1986) are based on less than complete information, and such information as exists has been interpolated, extrapolated, and simplified for practical convenience. Consequently, the percentage of affected persons in any group of exposed persons will not always closely match the values shown in **Table 6** or **Figures 4 and 5**. Additionally, the number of persons affected by vibration will depend on the rate at which persons enter and leave a group exposed to vibration.

EU Machinery Safety Directive

The Machinery Safety Directive of the European Community (89/392/EEC) states: machinery must be so designed and constructed that risks resulting from vibrations produced by the machinery are reduced to the lowest level, taking account of technical progress and the availability of means of reducing vibration, in particular at source. Instruction handbooks for hand-held and hand-guided machinery should specify the equivalent acceleration to which the hands or arms are subjected where this exceeds a stated value (currently a frequency-weighted acceleration of 2.5 ms^{-2} r.m.s.). The relevance of any such value will depend on the test conditions to be specified in type-testing standards (see International Standard 8662 Part 1 (1988); Table 2 provides a guide to other parts of ISO 8662). In use, many hand-held vibrating tools exceed 2.5 ms^{-2} r.m.s.

Table 6 Number of years before blanching develops in 10–50% of vibration-exposed persons according to International Standard 5349 (1986)

Weighted acceleration, $a_{hw(eq,\,4h)}$	*Percentage of population affected by finger blanching*				
(ms^{-2} r.m.s.)	10%	20%	30%	40%	50%
2	15	23	>25	>25	>25
5	6	9	11	12	14
10	3	4	5	6	7
20	1	2	2	3	3
50	<1	<1	<1	1	1

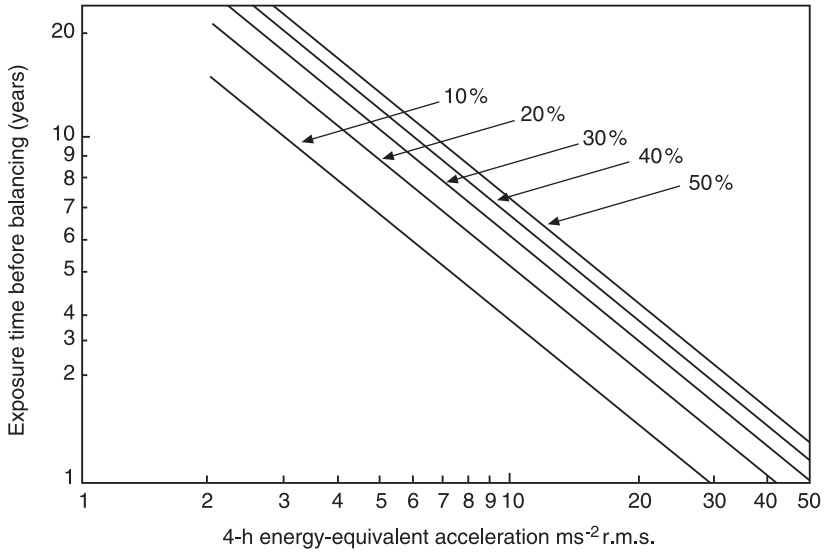


Figure 4 Years of exposure to various magnitudes of 4-h energy-equivalent frequency-weighted hand-transmitted vibration after which finger blanching in 10–50% of exposed persons should be expected according to International Standard 5349 (1986).

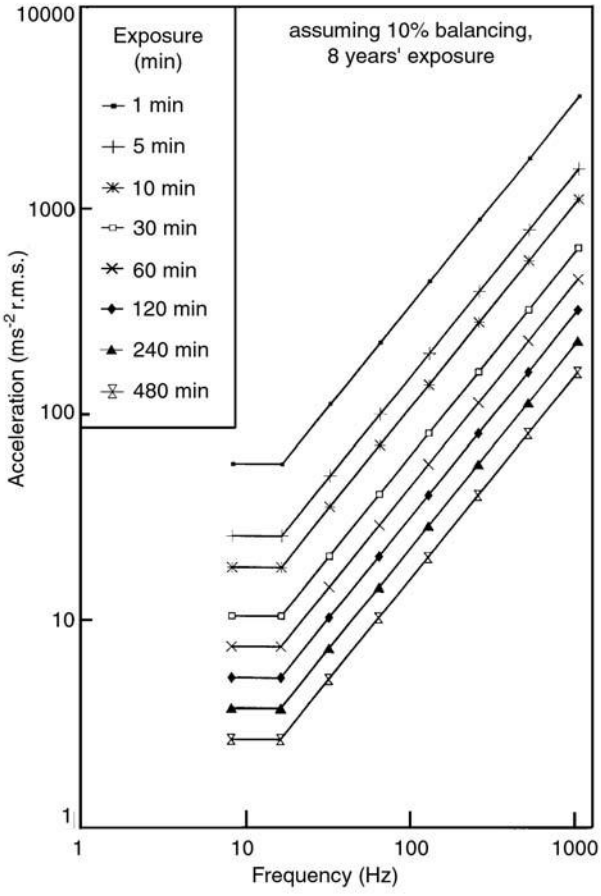


Figure 5 Acceleration magnitudes predicted to give 10% prevalence of vibration-induced white finger after 8 years for daily exposure durations from 1 min to 8 h (according to International Standard 5349, 1986).

Proposed EU Physical Agents Directive The opening principles of a proposed Council Directive on the minimum health and safety requirements regarding hand-transmitted vibration are: Taking account of technical progress and of the availability of measures to control the physical agent at source, the risks arising from exposure to the physical agent must be reduced to the lowest achievable level, with the aim of reducing exposure to below the threshold level ….

For hand-transmitted vibration, the proposed EU Directive currently identifies a threshold level ($a_{hw(eq,\ 8h)} = 1.0\,ms^{-2}$ r.m.s.), an action level ($a_{hw(eq,\ 8h)} = 2.5\,ms^{-2}$ r.m.s.), and an exposure limit value ($a_{hw(eq,\ 8h)} = 5.0\,ms^{-2}$ r.m.s.). The manner in which these 8-h equivalent magnitudes correspond to higher magnitudes at shorter durations is shown in **Figure 6**. When exposures exceed the threshold level it is proposed that workers must receive information concerning the potential risk of exposure to hand-transmitted vibration. The action level is intended to identify the conditions in which training in precautionary measures is required, an assessment of the vibration is to be made, and a program of preventive measures is to be instituted. The proposed Directive also indicates that when the action level is exceeded workers shall have the right to regular health surveillance, including routine examinations designed for the early detection of disorders caused by hand-transmitted vibration. If the exposure limit value is exceeded, health surveillance must be carried out and member states of the Community will be expected to control the harmful effects.

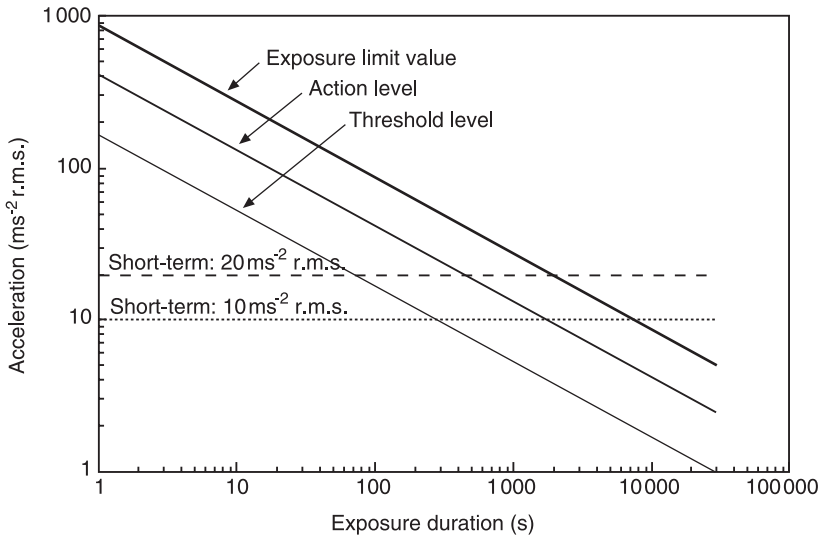


Figure 6 Threshold level, action level, and exposure limit proposed in a draft EC Directive on Physical Agents (Commission of the European Communities, 1994). In addition to these three criteria, effort shall be made to reduce the hazard when a short-term (a few minutes) equivalent acceleration exceeds $10\,ms^{-2}$ r.m.s. Exposure to a short-term (a few minutes) equivalent acceleration equal to or greater than $20\,ms^{-2}$ r.m.s. is considered a hazardous activity.

The extremely high magnitudes for short durations shown in **Figure 6** should not be considered to be representative of their safety: these high magnitudes are a consequence of the equal energy concept described above. The proposed Directive identifies exposures 'for a short-term (a few minutes) equivalent acceleration equal to or greater than $20\,ms^{-2}$' as 'activities with increased risk' which must be declared to the authority responsible. Member states would be required to ensure that appropriate measures are taken in order to control the risks associated with these activities. Equipment which transmits to the hand–arm system a short-term (a few minutes) equivalent acceleration equal to or greater than $20\,ms^{-2}$ r.m.s. must be marked. For lower magnitudes of vibration, the proposed Directive states: Where the activity involves the use of work equipment which transmits to the hand–arm system a short-term (a few minutes) equivalent acceleration exceeding $10\,ms^{-2}$, increased efforts shall be made to reduce the hazard, with priority to the use of low-vibration equipment and processes, including the revision of product design and work practice. Pending the effective implementation the duration of continuous exposure shall be reduced.

The proposed Directive is based on the root-sums-of-squares (r.s.s.) of the frequency-weighted accelerations in three axes, although an axis can be omitted if the values are less than 50% of the value in another axis at the same location. This differs from International Standard 5349 (1986) which is based on the axis having the highest weighted acceleration; however, a forthcoming revision of ISO 5349 is expected to change the evaluation method to the use of r.s.s. This proposed EU directive may be expected to be modified prior to finalization.

Nomenclature

C	prevalence of finger blanching
E	exposure
W_h	frequency weighting

See also: **Motion sickness**; **Whole-body vibration**.

Further Reading

Bovenzi M (1993). Digital arterial responsiveness to cold in healthy men, vibration white finger and primary Raynaud's phenomenon. *Scandinavian Journal of Work, Environment and Health* 19 (4): 271–276.

Brammer AJ, Taylor W and Lundborg G (1987) Sensorineural stages of the hand–arm vibration syndrome. *Scandinavian Journal of Work, Environment and Health* 13 (4): 279–283.

British Standards Institution (1987) *Measurement and Evaluation of Human Exposure to Vibration Transmitted to the Hand*. London: British Standard BS 6842.

Commission of the European Communities (1994) Amended proposal for a council directive on the minimum health and safety requirements regarding the exposure of workers to the risks arising from physical agents – individual directive in relation to article 16 of directive 89/391/EEC. *Official Journal of the European Communities* C 230, 19.8.94, 3–29.

Council of the European Communities (Brussels) (1989) On the approximation of the laws of the member states relating to machinery. Council directive (89/392/EEC). *Official Journal of the European Communities* June: 9–32.

Gemne G, Pyykko I, Taylor W and Pelmear P (1987) The Stockholm workshop scale for the classification of cold-induced Raynaud's phenomenon in the hand–arm vibration syndrome (revision of the Taylor–Pelmear scale). *Scandinavian Journal of Work, Environment and Health* 13 (4): 275–278.

Griffin MJ (1990) *Handbook of Human Vibration*. London: Academic Press.

Griffin MJ (1997) Measurement, evaluation and assessment of occupational exposures to hand-transmitted vibration. *Occupational and Environmental Medicine* 54 (2): 73–89.

Griffin MJ (1998) Evaluating the effectiveness of gloves in reducing the hazards of hand-transmitted vibration. *Occupational and Environmental Medicine* 55 (5): 340–348.

Griffin MJ, Seidel H, Bovenzi M and Benson AJ (1998) Vibration. In: Stellman JM (ed.) *Encyclopaedia of Occupational Health and Safety*, vol. 2, 4th edn. Geneva: International Labor Office, pp. 50.1–50.15.

International Organization for Standardization (1986), *Mechanical Vibration – Guidelines for the Measurement and the Assessment of Human Exposure to Hand-transmitted Vibration*. Geneva: International Standard ISO 5349.

International Organization for Standardization (1988) *Hand-held Portable Tools – Measurement of Vibration at the Handle – part 1: General*. Geneva: International Standard ISO 8662-1.

Taylor W and Pelmear PL (eds) (1975) *Vibration White Finger in Industry*. London: Academic Press.

HELICOPTER DAMPING

N M Wereley, R Snyder and R Krishnan,
University of Maryland at College Park,
College Park, MD, USA

T. Sieg, Paulstra Industries Inc., Carlsbad, CA, USA

Copyright © 2001 Academic Press

doi:10.1006/rwvb.2001.0022

The helicopter is one of the most severe vibration environments among aerospace vehicles, and vibration damping is of critical importance when enhancing aeromechanical stability and passenger comfort. The model 360 rotor hub (**Figure 1**) illustrates the typical hub configuration of an articulated rotor. The rotor blade has three degrees of freedom: (1) pitch, or rotation about the blade's longitudinal axis; (2) flap, or out-of-plane bending; and (3) lag, or in-plane bending. The need to augment damping is critical to mitigate aeromechanical instabilities, including pitch-flap, flag-lag, and ground and air resonance. Pitch-flap flutter is a modal coalescence of blade flap and torsion modes. Flap-lag flutter is an instability of primarily the lag mode, with participation from the flap mode. The flap mode is heavily damped aerodynamically, whereas the lag mode is very lightly damped. Ground resonance is a modal coalescence of the rotor lag mode with the landing gear modes of the helicopter, while the rotor is spinning up to its operational rotational frequency of 1/rev (typically 5–7.5 Hz). Air resonance is a modal coalescence of the lag mode with the rigid body modes of the helicopter while it is in high-speed forward flight. The latter three aeromechanical instabilities can be mitigated via damping augmentation, whereas pitch-flap flutter, as in fixed-wing flutter, must be mitigated in rotor design: the chordwise center of gravity must be kept at or ahead of the quarter-chord point (aerodynamic center) of the blade.

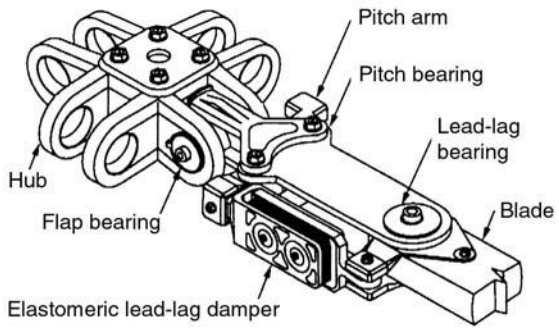


Figure 1 Rotor hub of the model 360 helicopter. Courtesy of Boeing Helicopters Inc.

In advanced rotor designs such as bearingless and hingless rotors, the lag and flap hinges, as well as the pitch bearing, are eliminated, and a flexure or flexbeam is introduced. The Comanche helicopter has such an advanced rotor (**Figure 2**). In conventional articulated rotors, ground resonance is typically mitigated using hydraulic or elastomeric dampers. Hingeless and bearingless rotors are designed to be soft in-plane rotors, which implies that the lag mode or lag/rev frequency is less than the rotor rotational or 1/rev

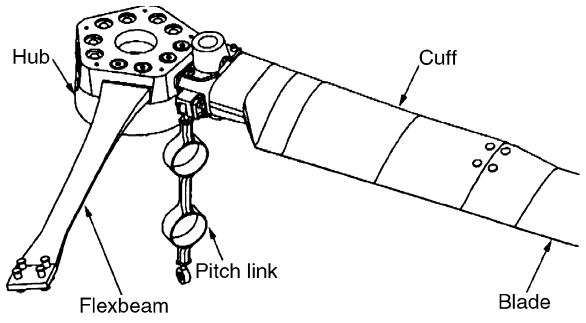


Figure 2 Wind tunnel model of the Comanche helicopter rotor hub. Courtesy of Boeing Helicopters Inc.



Figure 3 (See Plate 39). Laminated metal-elastomeric bearings for isolating transmission gear box vibrations in helicopters. Courtesy of Paulstra-Vibrachoc.

frequency. The rotor is soft in-plane due to stress considerations. As a result, elastomeric lag dampers are typically used to mitigate aeromechanical instabilities. Elastomeric dampers have some advantages: first, they have no moving parts, and second, the leakage problems that are present in hydraulic dampers are eliminated. However, a key disadvantage is that elastomeric damper behavior is nonlinear and highly dependent on frequency, temperature, and loading conditions such as preload and excitation amplitudes.

Elastomeric devices are added to the rotor hub to achieve two very different objectives: augmentation of flexibility, and augmentation of lag mode damping. Laminated metal-elastomeric bearings are used to increase the period of vibrations by softening, or introducing flexibility into, the rotor hub structures in order to isolate vibrations. Some examples of these type of bearings are shown in **Figure 3**. However, the primary focus of this article is to describe the behavior and analysis of elastomeric lag dampers used to augment stability of helicopter rotors with respect to air and ground resonance.

Damping Augmentation

The lag motion in helicopter rotors occurs at two frequencies: the lead-lag regressive frequency and the 1/rev frequency. Under these conditions, the damping in elastomers has been shown to degrade substantially at low amplitudes, thus causing undesirable limit cycle oscillations. In order to circumvent the problems associated with the elastomeric dampers, hybrid fluidic-elastomeric dampers have been used. Hybrid fluidic-elastomeric dampers use elastomers in conjunction with fluids. The fluid adds a viscous component to the energy dissipation mechanism in the dampers. Moreover, the inclusion of the fluid expands the dynamic range of forces generated by the damper. Hybrid fluidic-elastomeric lead-lag dampers were tested in a 1/6th Froude-scale rotor model and it was shown that the limit-cycle instabilities that were observed with elastomeric dampers can be substantially mitigated. A comparison between elastomeric and hybrid fluidic-elastomeric dampers shows that the former has stiffness and damping properties that are nonlinear functions of the displacement amplitude, whereas the latter exhibits relatively constant properties. Several lag dampers are shown in **Figure 4**.

The mechanical properties of lag mode dampers can vary from one damper to the next, so that they are carefully matched sets for a given rotor. Matched sets of dampers are used to minimize the impact of varying damper mechanical properties on rotor tracking conditions. The key to matching the properties of these dampers is to match their linearized damping and stiffness properties as a function of excitation amplitude, temperature, and stiffness. The methods for performing such a characterization will now be presented.

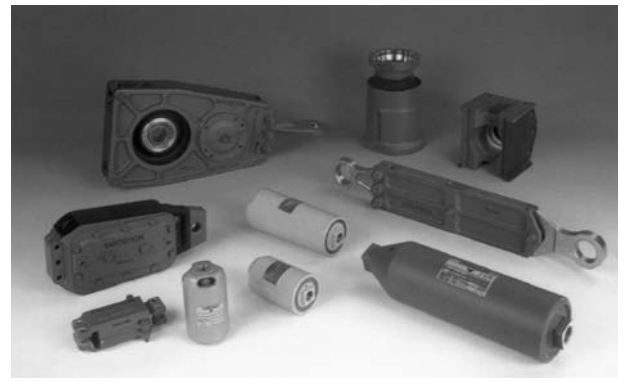


Figure 4 (See Plate 40). Lead-lag dampers are used to augment stability of helicopter rotor blade in-plane bending modes. Courtesy of Paulstra-Vibrachoc.

Example: Filled Elastomer Lag Damper

Rather than cataloging properties of various elastomers used in lag dampers, a primary objective of this article is to introduce how an elastomeric damper would be tested, characterized, and analyzed for use on a helicopter. The primary goal of such a testing program is to characterize the behavior of the damper due to steady-state sinusoidal excitation at the lag/rev frequency, and to assess the effects of the excitation at the rotor or 1/rev frequency on damping performance at the lag/rev frequency. This example is typical of what would be done for elastomeric dampers, as well as for fluidic, hybrid fluidic-elastomeric, and controllable fluid-based dampers.

Elastomeric Damper Testing

For our example, we will present the testing and characterization of double lap shear specimens incorporating Paulstra Industries material E136, which is a silicone-based filled elastomer. These specimens consist of three brass plates and a 10 mm (0.4 in) layer of damping material applied symmetrically across the center plate.

One of the important effects of a filler on viscoelastic material behavior is stress-softening. If a filled sample is stretched for the first time to 100% followed by a release in the strain and then stretched again to 200%, there is a softening in strain up to 100%, after which it continues in a manner following the first cycle. If this stress-strain is repeated in a third cycle, we can again see a softening up to 200% due to the previous strain history. This stress-softening or memory effect was first discovered by Mullins, and is called the Mullins effect. The Mullins effect was taken into account during these single-frequency tests. The material was first subjected to 300 cycles of sinusoidal excitation at 1 Hz at 5 mm (200 mil) of amplitude, which was the maximum amplitude in the chosen test matrix. All subsequent excitations were below this amplitude. During a test run, the material would be periodically excited for an amplitude of 5 mm (200 mil) at 1 Hz frequency to reinforce this memory effect. This was one of the ways in which consistency of results was ensured.

Because a viscoelastic material undergoes relaxation when subjected to loads, it requires a certain amount of time to stabilize and yield a steady value of force when a constant displacement is applied. Moreover, as an elastomeric damper is subjected to dynamic loading, the temperature of the damping material increases. This self-heating phenomenon is the result of energy dissipation via hysteresis. The temperature of the specimen can increase significantly in the first 30–50 s. Eventually, thermal equilibrium is established between the material, brass plates, and the environment. Based on preliminary tests, we concluded that, for these specimens, the dynamic relaxation, self-heating, and other unsteady effects require about 250 s to reach steady state. Data for characterization purposes were taken after the material properties had reached steady state.

The double lap shear specimens in this example were tested on a 5500 lb MTS servo-hydraulic testing machine. A schematic diagram of the system is shown in **Figure 5**.

Two types of excitation are typically studied: single-frequency sinusoidal displacement at the lag/rev frequency or a single frequency test, and the sum of two sinusoidal displacements at the lag/rev and 1/rev frequencies or a dual-frequency test.

Single-frequency testing To obtain consistent results, a sinusoidal input was applied at a given amplitude and displacement for 300 s and data were collected at the end of this period. These single-frequency tests are typically conducted at the lag/rev frequency, which was nominally $\Omega_{\text{lag}} \approx 5.0$ Hz for this example. Additional single-frequency testing is sometimes performed at the rotor rotational frequency or 1/rev, which in this case was $\Omega_1 = 7.5$ Hz. However, only sinusoidal testing at the lag/rev frequency will be

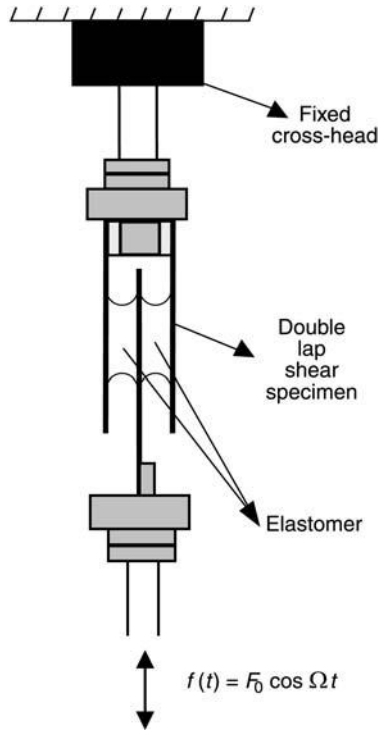


Figure 5 Schematic of MTS servo-hydraulic material testing system showing the double lap shear specimen.

considered. During each test, we measured 20 cycles of force vs displacement data and then calculated the force vs velocity hysteresis cycles for each test condition. The hysteresis cycle force and displacement data collected during each experiment were acquired on a PC-based data acquisiton system and were unavoidably noisy. However, the independent displacement variable was sinusoidal, so that a periodic Fourier series was used to eliminate, as much as possible, the effects of this noise in the input displacement signal, and the subsequent differentiations to obtain the input velocity and acceleration signals. The Fourier series expansion of the displacement was taken as:

$$x(t) = \frac{x_0}{2} + \sum_{k=1}^{\infty} \left(x_{c,k} \cos k\Omega_{\text{lag}} t + x_{s,k} \sin k\Omega_{\text{lag}} t \right) \quad [1]$$

where:

$$x_{c,k} = \frac{\Omega_{\text{lag}}}{\pi k} \int_0^{2\pi k/\Omega_{\text{lag}}} x(t) \cos k\Omega_{\text{lag}} t \, dt \quad [2]$$

$$x_{s,k} = \frac{\Omega_{\text{lag}}}{\pi k} \int_0^{2\pi k/\Omega_{\text{lag}}} x(t) \sin k\Omega_{\text{lag}} t \, dt \quad [3]$$

The bias and higher harmonics were then filtered out, and only the harmonic at the frequency of interest, Ω_{lag}, was retained, so that the displacement signal was reconstructed as:

$$x(t) = X_{c,1} \cos \Omega_{\text{lag}} t + X_{s,1} \sin \Omega_{\text{lag}} t \quad [4]$$

Calculating the velocity signal from the displacement signal using a finite difference method tends to accentuate any noise in the displacement signal. We can exploit the sinusoidal nature of the input displacement signal by differentiating the Fourier series expansion from eqn [4] to obtain:

$$\dot{x}(t) = -\Omega_{\text{lag}} X_{c,1} \sin \Omega_{\text{lag}} t + \Omega_{\text{lag}} X_{s,1} \cos \Omega_{\text{lag}} t \quad [5]$$

However, the force signal is typically not filtered because the damper response is nonlinear and it cannot be determined *a priori* exactly which harmonics contributed to damper response and/or noise. Therefore, it is typical to be conservative, and use the measured (unfiltered) force data in both characterization and model parameter identification studies.

Dual-frequency testing For the dual-frequency testing in this example, the 1/rev frequency was chosen as Ω_1 = 7.5 Hz while the lag/rev was chosen as $\Omega_{\text{lag}} = 5$ Hz. In general, a dual-frequency displacement signal has the form:

$$x(t) = X_{\text{lag}} \sin \Omega_{\text{lag}} t + X_1 \sin \Omega_1 t \quad [6]$$

The resulting signal contains the product of two harmonics $\Omega_1 + \Omega_{\text{lag}}$ and $\Omega_1 - \Omega_{\text{lag}}$. It is periodic with a period equal to the frequency corresponding to the highest common factor of these two harmonics, which in this case is $\Omega = 2.5$ Hz. The displacement signal was filtered by expanding as a Fourier series expansion of many harmonics, N, with a base frequency of $\Omega = 2.5$Hz, or:

$$x(t) = \frac{X_0}{2} + \sum_{k=1}^{n} \left(X_{c,k} \cos k\Omega t + X_{s,k} \sin k\Omega t \right) \quad [7]$$

and setting the bias term, $X_0 = 0$. In this example, the second harmonic, $2\Omega = \Omega_{\text{lag}} = 5$ Hz, and the third harmonic, $3\Omega = \Omega_1 = 7.5$ Hz, so that only the first three harmonics need to be included in the above Fourier series expansion, or $n = 3$, and noise is eliminated from the displacement. The velocity in the dual-frequency case was determined by differentiating the Fourier series expansion of the displacement signal, so in general:

$$\dot{x}(t) = \sum_{k=1}^{n} \left(-k\Omega X_{c,k} \sin k\Omega t + k\Omega X_{s,k} \cos k\Omega t \right) \quad [8]$$

Again, in this case study, $n = 3$. As in the single-frequency case, the force signal is not filtered because the damper response is nonlinear. The measured (unfiltered) force data are used directly in both the dual-frequency characterization and model parameter identification studies.

Damper Characterization: Single-frequency

Two common approaches are described for a linear characterization of the damper behavior. First, the equivalent spring stiffness and equivalent viscous damping approach is presented. This is based on first characterizing the damping force based on force vs displacement data. The damping force is subtracted from the measured damper force to obtain a residual force signal, that is used to characterize the residual spring behavior. The second approach is the calculation of the complex modulus, K^*, in which a Fourier analysis is used to characterize the in-phase

force or spring force, and the quadrature force or damper force, and hence the complex modulus.

Typical data used for such a characterization study are shown in **Figure 6,** for sinusoidal excitation at $\Omega_{lag} = 5\,Hz$, a 10% preload, for a range of amplitudes. The steady-state hysteresis cycle data are taken after stabilization of the material for a duration of 300 cycles at 1 Hz and 5 mm (200 mil) of sinusoidal excitation.

Equivalent spring stiffness and viscous damping The first characterization technique is that of equivalent spring stiffness and equivalent viscous damping. This is a standard linearization technique that can be applied to a nonlinear damper such as this elastomeric damper. Here, the damper restoring force, $f(t)$, is the sum of an equivalent spring or elastic stiffness force proportional to displacement, $f_s(t)$, and an equivalent viscous damping force proportional to velocity, $f_d(t)$:

$$f(t) = f_s(t) + f_d(t) \qquad [9]$$

where:

$$\begin{aligned} f_s(t) &= K_{eq}x(t) \\ f_d(t) &= C_{eq}\dot{x}(t) \end{aligned} \qquad [10]$$

where $x(t)$ and $\dot{x}(t)$ are the damper displacement and velocity, respectively. Here K_{eq} is the equivalent spring stiffness, and C_{eq} is the equivalent viscous damping. The equivalent viscous damping, C_{eq}, is computed by equating the energy dissipated over a cycle, E, at frequency Ω_{lag} using:

$$E = \oint F(t)\,dx = \int_0^{2\pi/\Omega_{lag}} F(t)v(t)\,dt \qquad [11]$$

and equating the dissipated energy of the nonlinear device to that of an equivalent viscous damper:

$$C_{eq} = \frac{E}{\pi\Omega_{lag}X_{lag}^2} \qquad [12]$$

where Ω_{lag} is the sinusoidal lag/rev test frequency, and X_{lag} is its amplitude. The energy dissipated over one cycle is computed using a numerical intregration technique such as the trapezoidal rule. In **Figure 7**, the hysteresis cycle is shown as the result of a sinusoidal input having nominal amplitude of $X_{lag} = 5\,mm$ (200 mil) and frequency of $\Omega_{lag} = 5\,Hz$. The damping force, $f_d(t)$, calculated as above, is plotted in **Figure 7** as a flat ellipse. The difference between the total force and the damping force is the elastic stiffness force, or:

$$f_s(t) = f(t) - f_d(t) \qquad [13]$$

This residual spring force is shown in **Figure 7**, and is characteristic of a nonlinear stiffening spring, or:

$$f_s(t) = K_1x(t) + K_3x^3(t) \qquad [14]$$

The parameters K_1 and K_3 are determined using a least mean squared error parameter optimization technique. The cost function J to be minimized in this procedure is expressed by:

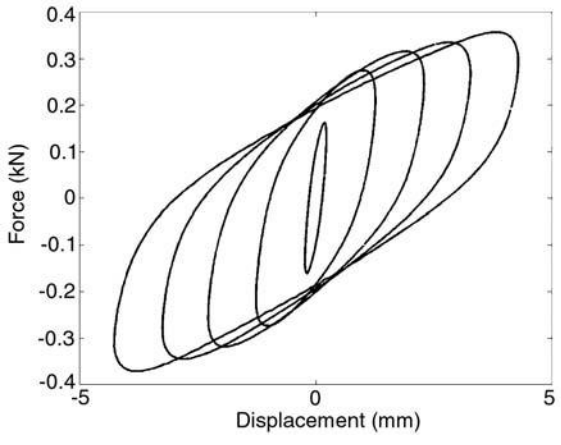


Figure 6 Hysteresis cycles for the double lap shear specimens at the lag/rev (Ω_{lag} = 5 Hz) frequency and 10% preload.

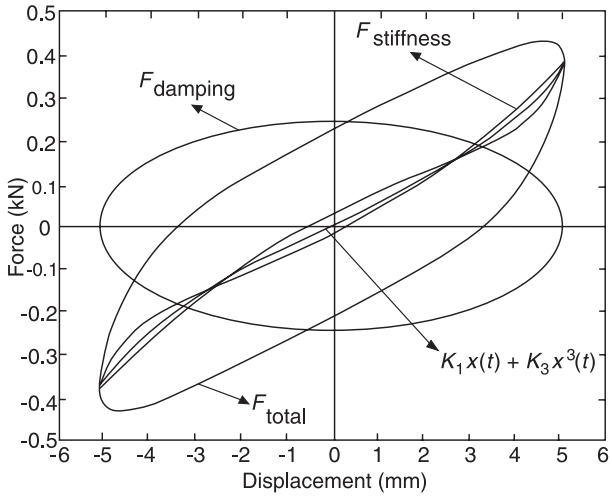


Figure 7 Contributions of the viscous damping force, and the elastic stiffness force to the total force.

$$J(K_1, K_3) = \sum_{i=1}^{m} \left(f_{s,i} - K_1 x_i - K_3 x_i^3\right)^2 \qquad [15]$$

where m is the number of datapoints taken over one period. Because the force and displacement data are sampled data with sampling period Δt, we define $x_i = x(i\Delta t)$, and $f_{s,i} = f(i\Delta t)$. The two necessary conditions that must be satisfied are:

$$\frac{\partial J}{\partial K_1} = 0 \quad \text{and} \quad \frac{\partial J}{\partial K_3} = 0 \qquad [16]$$

resulting in a solution of:

$$K_1 = \frac{1}{\Delta}(\Sigma_1\Sigma_5 - \Sigma_2\Sigma_4) \qquad [17]$$

$$K_3 = \frac{1}{\Delta}(\Sigma_2\Sigma_3 - \Sigma_1\Sigma_4) \qquad [18]$$

where:

$$\Sigma_1 = \sum_{i=1}^{m} f_{s,i} x_i \qquad [19]$$

$$\Sigma_2 = \sum_{i=1}^{m} f_{s,i} x_i^3 \qquad [20]$$

$$\Sigma_3 = \sum_{i=1}^{m} x_i^2 \qquad [21]$$

$$\Sigma_4 = \sum_{i=1}^{m} x_i^4 \qquad [22]$$

$$\Sigma_5 = \sum_{i=1}^{m} x_i^6 \qquad [23]$$

$$\Delta = \Sigma_3\Sigma_5 - \Sigma_4^2 \qquad [24]$$

The equivalent stiffness is then given by the formula:

$$K_{\text{eq}} = K_1 + \tfrac{1}{2} K_3 X_{\text{lag}}^2 \qquad [25]$$

We calculated the equivalent stiffness (**Figure 8**) and viscous damping (**Figure 9**) versus amplitude of sinusoidal excitation, ranging from 0.2 to 5 mm, using the above methods for the single frequency force vs displacement hysteresis cycle data. Clearly, both the equivalent stiffness and damping are strongly dependent on amplitude of excitation, as evidenced by the substantial decrease in these quantities as amplitude increases. The rate of change of equivalent stiffness and damping with amplitude is very large up to $X_{\text{lag}} = 2$ mm, and becomes much more gradual for amplitudes $X_{\text{lag}} > 2$ mm. In addition, comparing zero preload and 10% preload conditions at room temperature, the addition of preload tends to increase the equivalent stiffness and damping over the entire amplitude range. This effect is due to the compressive preload increasing the friction response of the filler in the elastomer. Comparing the preloaded cases at room temperature and at 50°C, an increase in temperature tends to decrease the equivalent stiffness and damping. This is a manifestation of the so-called softening effect as temperature is increased.

Complex stiffness A second approach is to characterize the complex damper stiffness, K^*, as the in-phase or storage stiffness, K', and quadrature or loss stiffness, K'', so that:

$$K^* = K' + jK'' = K'(1 + j\eta) \qquad [26]$$

where η is the loss factor. This is a common approach in the characterization of elastomeric dampers. Alternatively, is the effective or equivalent stiffness, while K''/Ω is related to the equivalent viscous damping of the damper. To determine the damper force:

$$\begin{aligned} f(t) &= F_c \cos \Omega_{\text{lag}} t + F_s \sin \Omega_{\text{lag}} t \\ &= K' x(t) + \frac{K''}{\Omega_{\text{lag}}} \dot{x}(t) \end{aligned} \qquad [27]$$

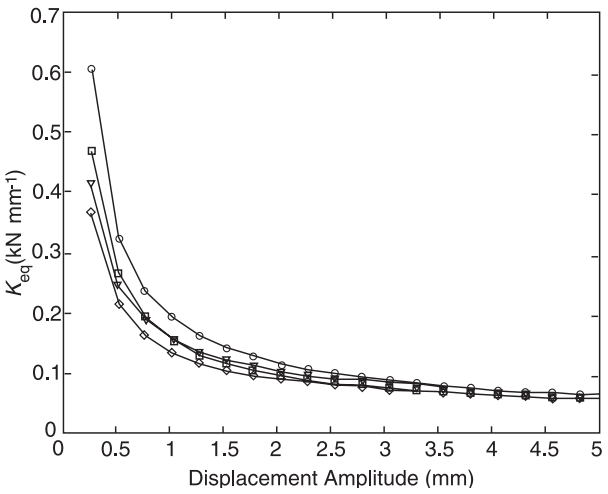


Figure 8 Single-frequency damper characterization of the equivalent elastic stiffness at Ω_{lag} = 5 Hz. Circles, preloaded; squares, zero preload; diamonds, zero preload at 50°C; triangles, preloaded at 50°C.

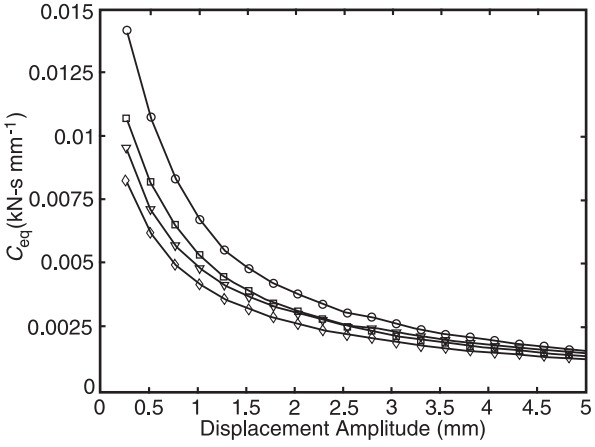


Figure 9 Single-frequency damper characterization of the equivalent viscous damping at $\Omega_{lag} = 5$ Hz. Circles, preloaded; squares, zero preload; diamonds, zero preload at 50 °C; triangles, preloaded at 50 °C.

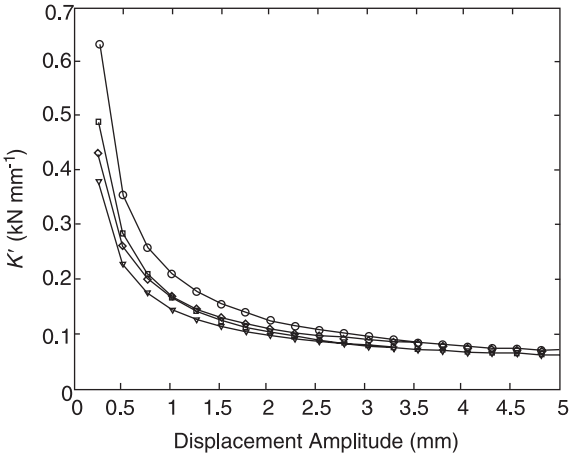


Figure 10 Single-frequency damper characterization of the stiffness at $\Omega_{lag} = 5$ Hz. Circles, preloaded; squares, zero preload; triangles, zero preload at 50 °C; diamonds, preloaded at 50 °C.

Here F_c and F_s are the cosine and sine Fourier coefficients of $f(t)$ at frequency Ω_{lag}. We assume that the displacement is sinusoidal:

$$x(t) = X_c \cos \Omega_{lag} t + X_s \sin \Omega_{lag} t \qquad [28]$$

where X_c and X_s are the cosine and sine Fourier coefficients of $x(t)$ at frequency Ω_{lag}. Substituting $x(t)$ into the force equation and equating the sine and cosine terms yields the in-phase and quadrature stiffnesses as:

$$K' = \frac{F_c X_c + F_s X_s}{X_c^2 + X_s^2}$$
$$K'' = \frac{F_c X_s - F_s X_c}{X_c^2 + X_s^2} \qquad [29]$$

In general, this calculation would be performed for a sweep in the oscillation frequency, Ω, which included Ω_{lag} in its range. In our case, we are examining only a single harmonic excitation at Ω_{lag}. The quadrature stiffness of the damper is related to the equivalent viscous damping in an approximate way by:

$$C_{eq} \approx \frac{K''}{\Omega_{lag}} \qquad [30]$$

The relation is approximate because the complex stiffness considers only the harmonic at frequency Ω_{lag}.

The results of this linear characterization are shown in **Figures 10–12**. Clearly, both the in-phase stiffness and quadrature stiffness (damping) are

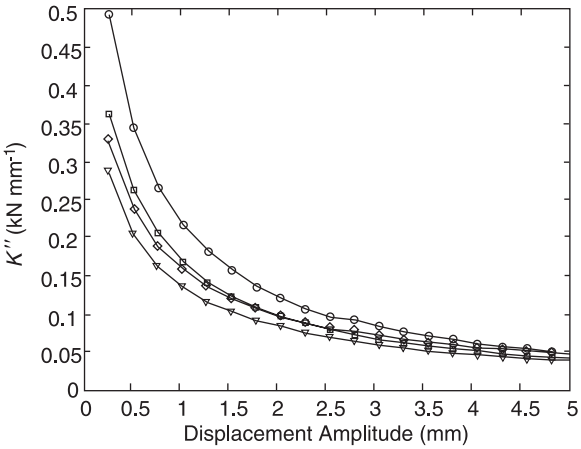


Figure 11 Single-frequency damper characterization of the damping at $\Omega_{lag} = 5$ Hz. Circles, preloaded; squares, zero preload; triangles, zero preload at 50 °C; diamonds, preloaded at 50 °C.

strongly dependent on amplitude of excitation. Again, the rate of change of these quantities with amplitude is very large up to $X_{lag} = 2$ mm, and becomes much more gradual for amplitudes $X_{lag} > 2$ mm. In addition, comparing zero preload and 10% preload conditions at room temperature, the addition of preload tends to increase the complex modulus over the entire amplitude range, which is again because the compressive preload increases the friction response of the filler in the elastomer. The softening effect as temperature is increased can be observed by comparing the preload cases at room temperature and 50°C. This comparison shows that

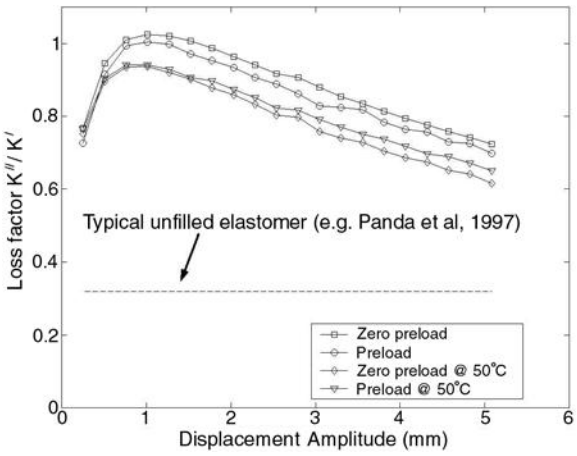


Figure 12 Single-frequency damper characterization of the loss factor at $\Omega_{lag} = 5$ Hz. Circles, preloaded; squares, zero preload; diamonds, zero preload at 50 °C; triangles, preloaded at 50 °C.

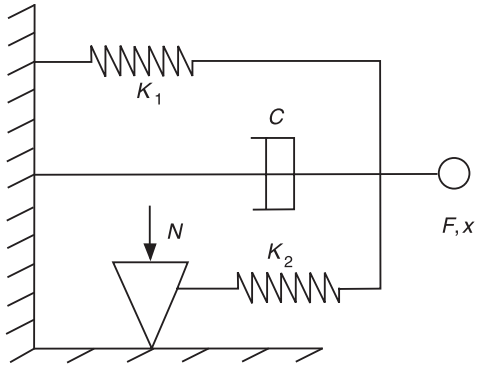


Figure 13 Schematic of the mechanisms-based stiffness-viscosity-elasto-slide analysis for the elastomeric damper.

an increase in temperature tends to decrease the complex modulus. A final useful comparison comes from the loss factor, which is the ratio of the quadrature stiffness to the in-phase stiffness, or:

$$\eta = \frac{K''}{K'} \qquad [31]$$

The loss factor, η, is a measure of the damping level relative to the stiffness, and it is desirable to have a high loss factor over a large amplitude range. The maximum value of the loss factor for this filled elastomer is as high as 1.025 for this material, which is much higher than the loss factor for elastomers used in existing dampers, which typically range from 0.4 to 0.8. A second observation is that the loss factor has its maximum effectiveness over a small amplitude range centered about an amplitude of 1 mm or, nominally, 10% shear strain, which is defined as the amplitude ($X_{lag} = 1$ mm) over the specimen thickness (10 mm or 0.4 in). These trends are fairly typical of elastomeric materials.

Single-frequency Hysteresis Modeling

The single-frequency force vs displacement hysteresis cycle data of these double lap shear specimens can be modeled using a mechanisms-based modeling approach. **Figure 13** shows a schematic of the mechanical stiffness-viscosity-elasto-slide (SVES) model used for the elastomers. The model consists of three elements: (1) a linear stiffness; (2) a nonlinear elasto-slip or triboelastic element that models the rate-independent part of the hysteresis behavior; and (3) a linear viscous damping that characterizes the rate-dependent hysteresis behavior. The model includes various physical aspects seen in elastomer hysteresis behavior, such as: (1) strong amplitude dependence of linearized coefficients; (2) linear behavior at low amplitudes; (3) mild frequency dependence; (4) deviation in hysteresis behavior from the linearized elliptical behavior near the zero-velocity points of the hysteresis cycle; and (5) presence of a rate-dependent and rate-independent part. The SVES model is typical of the class of elastomeric mechanisms-based models, in that it contains a Kelvin chain element (a spring and damper in parallel) and a triboelastic element (an elasto-slide element).

Figure 14 shows the effect of each of these mechanisms on the hysteresis cycles of the dampers. The nonlinear elasto-slip element accounts for the almost vertical drop in force near the zero-velocity region. It is modeled as a combination of a spring and Coulomb force. The slip element, which represents the friction components of the model, will be modeled such that its parameters are independent of both amplitude and frequency. The linear stiffness parameter must be modeled such that it is amplitude-dependent but frequency-independent. The linear viscous damping parameter must be modeled such that it is dependent on both the amplitude and frequency.

The linear stiffness and linear dashpot parameters give the necessary slope and area to the force vs displacement hysteresis cycle shape. The elasto-slide element represents a stiffness in the region where the velocity of the damper changes its sign and the displacement is less than a certain value $2X_s$ from the maximum amplitude. In the remaining portion of the hysteresis cycle, the elasto-slide element is equivalent to a Coulomb element. Two parameters are required to characterize the elasto-slide element completely. The linear stiffness and linear viscous damping

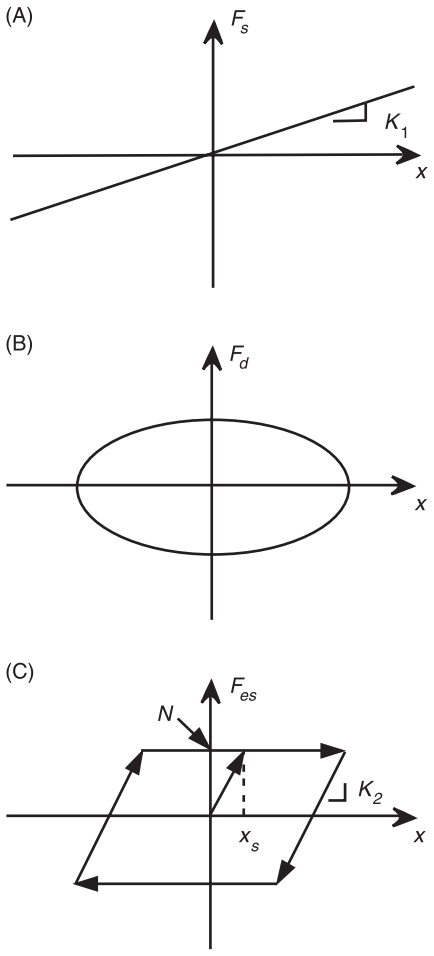


Figure 14 Mechanisms of the stiffness-viscosity-elasto-slide analysis and their influence on the shape of the force vs displacement hysteresis cycle. (A) Stiffness element; (B) damping element; (C) elasto-slide element (Lazan, 1968).

elements each require one parameter for complete characterization. Thus, the SVES model is a four-parameter model. Having established the model structure and model components, the parameters in the model need to be identified. The predicted force from the model is given by:

$$f(t) = f_s(t) + f_d(t) + f_{es}(t) \qquad [32]$$

where $f_s(t)$, $f_d(t)$ and $f_{es}(t)$ are the forces in the stiffness, viscous dashpot, and elasto-slide element at any time, t. The stiffness and damping forces are as below:

$$f_s(t) = K_1 x(t) \qquad [33]$$

$$f_d(t) = C\dot{x}(t) \qquad [34]$$

The elasto-slide element has four branches as below:

$$f_{es} = \begin{cases} -N & x = -\bar{x} & \dot{x} = 0 \\ -N + K_2(x + \bar{x}) & x < -\bar{x} + 2X_s & \dot{x} > 0 \\ N & x > -\bar{x} + 2X_s & \dot{x} > 0 \\ N & x = \bar{x} & \dot{x} = 0 \\ N + K_2(x - \bar{x}) & x > \bar{x} - 2X_s & \dot{x} < 0 \\ -N & x < \bar{x} - 2X_s & \dot{x} < 0 \end{cases} \qquad [35]$$

where $\bar{x}$ is the amplitude over the cycle, and the slide force is given by:

$$N = K_2 X_s \qquad [36]$$

The parameters N and K_2 of the elasto-slide element can be chosen *a priori* by careful observation of the force vs displacement hysteresis cycles. It was observed that, in the zero preload case, the value of the drop in force at maximum displacement was approximately 71.2 N. Hence, the Coulomb force corresponding to N was chosen to be 35.6 N. The stiffness K_2 was also fixed at 280.2 N mm^{-1}. Hence, the elasto-slide mechanism represents a Coulomb force of 35.6 N in parallel with a stiffness until the magnitude of the stiffening force becomes 35.6 N, but represents a Coulomb force of 71.2 N otherwise. This element is constant with respect to changing amplitude.

The remaining unknown parameters, K_1 and C, are estimated on the basis of minimizing the error between the predicted force, $\hat{f}$, and the measured force, f, obtained from experiments. The parameters of the model are obtained from a constrained minimization of the objective function, J, given by:

$$J(K_1, C) = \sum_{k=1}^{m} \left[\hat{f}(t_k) - f(t_k)\right]^2 \qquad [37]$$

where m is the number of data points for each hysteresis cycle. A constrained minimization was performed using design optimization tools (DOT), which uses the Broyden–Fletcher–Goldfarb–Shanno algorithm to minimize the above objective function in eqn [37]. To obtain physically meaningful results with this technique, the identified parameters are constrained to have positive values: $K_1 > 0$, and $C > 0$. The parameters K_1 and C were identified at each amplitude at the lag/rev frequency. The identified parameters are plotted versus amplitude in **Figure 15.**

Using the parameters estimated from the identification process, the force vs displacement hysteresis cycles were reconstructed. **Figure 16** shows the reconstructed hysteresis cycles for five different amplitudes at the lag/rev (5 Hz) frequency. The plots show that

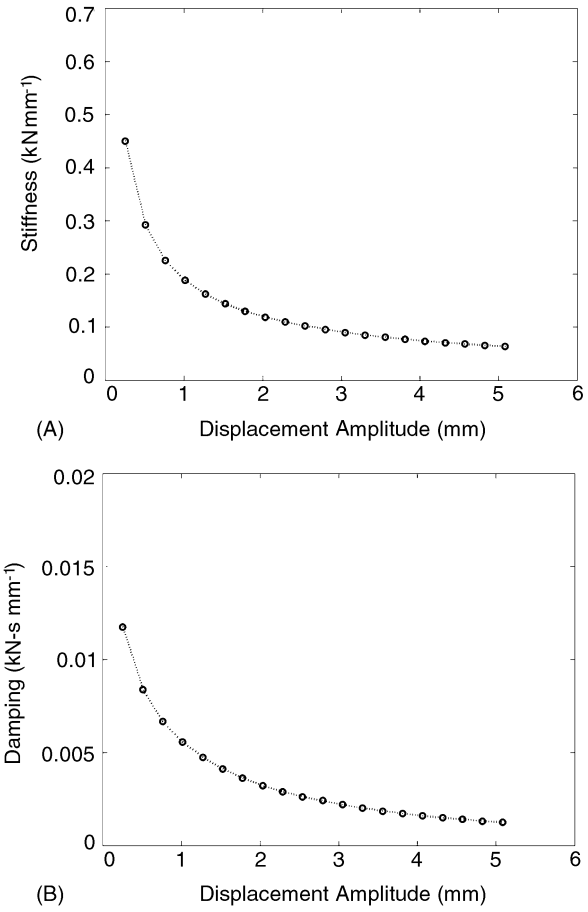


Figure 15 Identified stiffness and damping of the SVES model, assuming amplitude-independent elasto-slide element parameters, $N = 35.6$ N, and $K_2 = 280.2\,\mathrm{N\,mm^{-1}}$. (A) Stiffness parameter, K_1; (B) damping parameter, C.

the model accurately captures the hysteresis behavior of the damper.

Dual-frequency Characterization

In addition to testing the dampers at the lag/rev frequency, experiments are typically conducted at dual frequencies of the lag/rev (5 Hz) frequency and the 1/rev (7.5 Hz) rotor frequency. These tests are intended to assess the potential loss of damping at the lag/rev frequency due to dual-frequency motion. In this section, such a dual-frequency test is described, and typical test results are presented for the filled elastomer of our case study.

The dual frequency tests in our case study were carried out on an MTS servo-hydraulic testing machine with a digital control system. The range of lag/rev amplitudes is the same as for the single-frequency tests, that is, 0.25–5 mm (10–200 mil) in increments of 0.254 mm (10 mil). The 1/rev amplitudes tested were 0, 0.508, 1.524, 2.54 and 3.55 mm (0, 20, 60, 100 and 140 mil). An HP 8904A multifunction synthesizer was used to generate and sum the sinusoidal signals with the two individual frequencies. A function generator was used to have as accurate as possible the desired dual-frequency sinusoidal excitations. The force input and the displacement response were measured using the load cell and LVDT of the MTS machine, respectively, as in the single-frequency characterization tests.

To characterize the dampers under dual-frequency excitation conditions, the components of the complex stiffness $K^* = K' + jK''$ were determined at the lag/rev frequency. The stiffness, K', and damping K'' at the

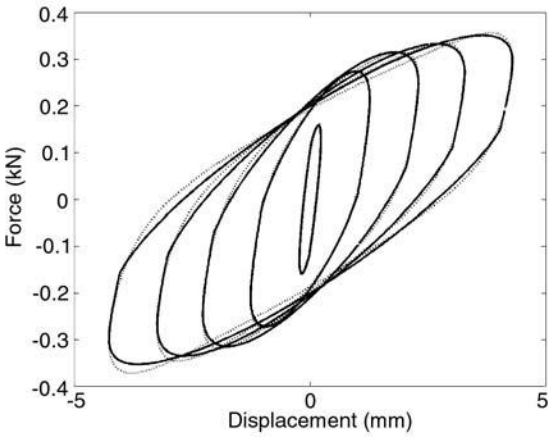


Figure 16 Validation of the mechanisms-based model at 5 Hz for different amplitudes. Continuous line, model; dashed line, experiment.

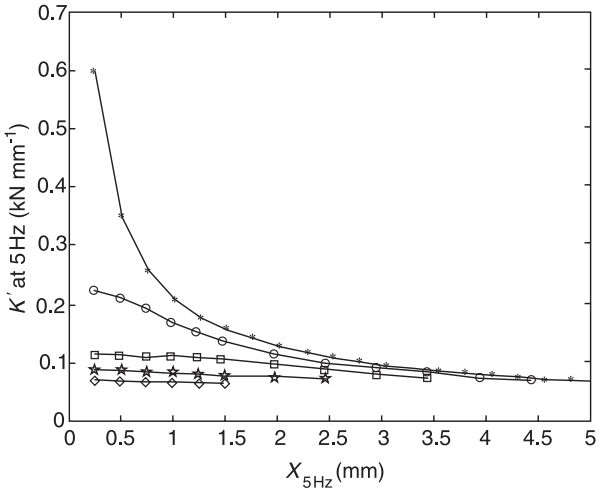


Figure 17 Dual-frequency damper characterization of stiffness at lag/rev = 5 Hz and 1/rev = 7.5 Hz. Amplitudes @ 7.5 Hz: Asterisks, 0 mm; circles, 0.508 mm (20 mil); squares, 1.524 mm (60 mil); stars, 2.54 mm (100 mil); diamonds, 3.556 mm (140 mil).

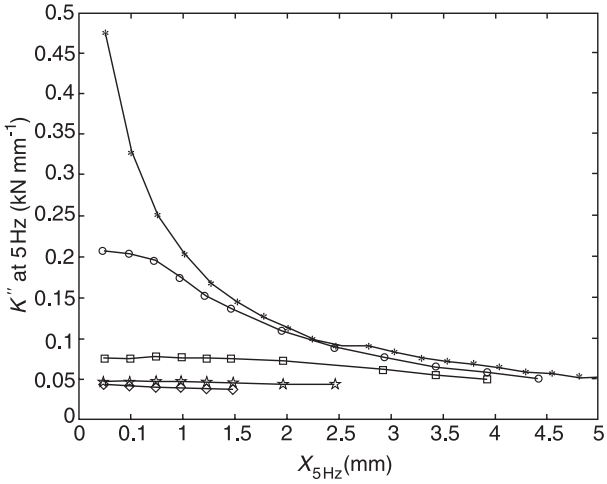


Figure 18 Dual-frequency damper characterization of the damping at lag/rev = 5 Hz and 1/rev = 7.5 Hz. Amplitudes @ 7.5 Hz: Asterisks, 0 mm; circles, 0.508 mm (20 mil); squares, 1.524 mm (60 mil); stars, 2.54 mm (100 mil); diamonds, 3.556 mm (140 mil).

lag/rev (5 Hz) frequency, shown in **Figures 17** and **18**, decrease as the 1/rev (7.5 Hz) amplitude increases. When the 1/rev (7.5 Hz) amplitude is 0.508 mm (20 mil), the reduction in stiffness and damping values is almost 50% compared to the single-frequency excitation at low 5 Hz amplitudes. The percentage reduction in these values gradually reduces with increasing amplitude of lag/rev (5 Hz) excitation and is not very significant (less than 10%) at high lag/rev (5 Hz) amplitudes. When the 1/rev (7.5 Hz) amplitude is 2.54 mm (100 mil), the stiffness and damping values at low lag/rev (5 Hz) amplitudes reduce by almost 80% and do not change substantially as the amplitude of 5 Hz excitation increases. Thus, it is clear that the 1/rev (7.5 Hz) excitation exerts a significant influence on the low-amplitude response at lag/rev (5 Hz). The elastomeric damper behavior exhibits strong nonlinearities and the nonlinearities degrade the performance of the damper. These effects of dual-frequency excitation are similar to the effects observed in other elastomeric damper studies.

Dual-frequency Hysteresis Modeling

To determine the dual frequency parameters, the Ω_{lag} (5 Hz) and $\Omega_{1/\text{rev}}$ (7.5 Hz) for each of the single frequency model parameters are used. First 10^{th} order polynomials were used to fit the behavior of the linear damping and stiffness with respect to amplitude.

Once there are polynomials for both parameters at both the Ω_{lag} (5 Hz) and $\Omega_{1/\text{rev}}$ (7.5 Hz) frequencies, the polynomials are used to determine the parameter values for each frequency at the maximum displacement for the dual frequency test case. This value will be less than sum of the two amplitudes. This is due to the testing machine and its inability to match the desired amplitude of the input signal. This problem was present for the single frequency testing, but becomes more apparent in the dual frequency testing. The problem is most visible for larger amplitude excitations, in dual frequency testing the sum of the desired amplitudes is large enough that the machine was unable to match the desired output.

Using the single frequency polynomial fits, preliminary dual frequency parameters are calculated by revaluating the parameter curve at the maximum displacement of the dual frequency test. In order to calculate the dual frequency value for each parameter the values are scaled according to the amplitude for each frequency with respect to the maximum displacement for each test case. The equation used to determine the scaling for the damping and stiffness parameters can generally be written as

$$C = C(5\,\text{Hz}, \bar{X})\frac{X_{5\,\text{Hz}}}{\bar{X}} + C(7.5\,\text{Hz}, \bar{X})\frac{X_{7.5\,\text{Hz}}}{\bar{X}}$$

The dual-frequency correlation results for two dual-frequency excitation conditions are shown in **Figures 19** and **20**. Thus, the single-frequency model can be used to predict dual-frequency behavior.

Summary of Example

This example was presented describing how an elastomeric helicopter lag damper would be characterized and modeled using a mechanisms-based approach. The typical procedures used to character-

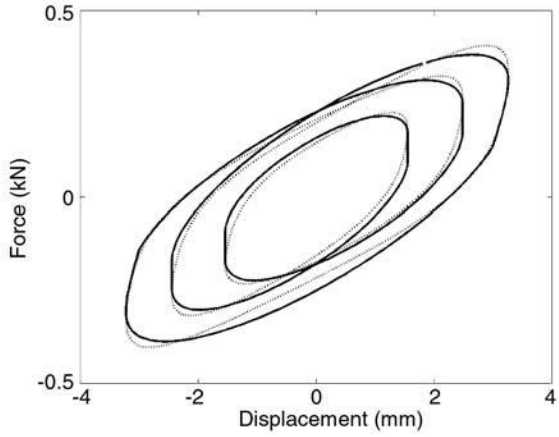


Figure 19 Dual-frequency damper analysis for 1/rev amplitude of 2.54 mm (100 mil) and lag/rev amplitude of 1 mm (40 mil). Continuous line, model; dashed line, experimental.

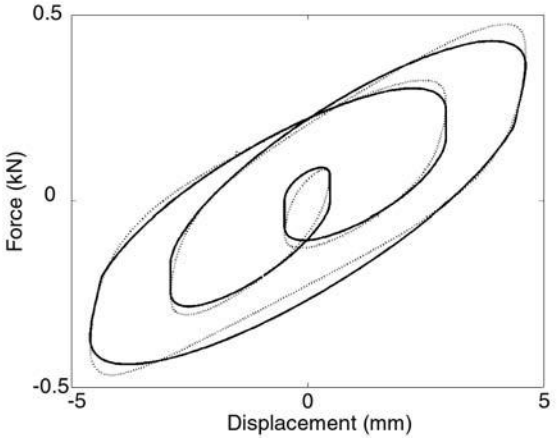


Figure 20 Dual-frequency damper analysis for 1/rev amplitude of 2.54 mm (100 mil) and lag/rev amplitude of 2.54 mm (100 mil). Continuous line, model; dashed line, experimental.

ize the steady-state behavior of elastomeric dampers under sinusoidal loading were described, including: (1) equivalent stiffness and equivalent viscous damping, and (2) complex stiffness and loss factor. The results of this linear characterization illustrated the amplitude-dependent nature of the linearized stiffness and damping. Additional effects of thermal softening, due to rising temperature, hardening due to lowering of temperature, and increases in stiffness and damping due to preload were illustrated using the linear stiffness and damping. A key component in the understanding of elastomeric helicopter lag dampers is the analysis of steady-state force response due to a sinusoidal displacement. A mechanisms-based tribo-viscoelastic analysis was outlined, specifically, the SVES analysis. Single-frequency (sinusoidal displacement at the lag mode frequency) and dual-frequency (sum of sinusoidal displacements at the lag mode frequency and the rotor rotational frequency) were analyzed. The SVES model worked well in predicting the behavior of the damper due to these classes of input displacement excitations.

Advanced Damper Concepts

New damping technologies are under development for application to the helicopter lag damping problem. Originally, hydraulic dampers were used to mitigate aeromechanical instabilities, where the damper force is proportional to the shaft velocity of the damper. However, these hydraulic dampers were prone to leakage problems. Because elastomeric dampers do not have comparable leakage problems, they were subsequently advocated for this application. The main problem, as described above, is that elastomeric damper properties are strongly dependent on amplitude and temperature. The linearized damping and stiffness of the elastomeric damper reduce substantially as amplitude is increased, or as temperature increases and the elastomer softens.

To reduce the impact of these amplitude-dependent damping and stiffness nonlinearities, hybrid fluid-elastomeric dampers have been proposed. The fluid which is passive, is used to linearize the damping and stiffness of the lag damper. As a result, the force vs displacement hysteresis cycles of these dampers are more linear, or elliptical in shape, as demonstrated for the Comanche model-scale wind tunnel damper (**Figure 21**). Using the same characterization methods described above, the equivalent viscous damping, C_{eq}, has been shown to be nearly constant as a function of excitation amplitude (**Figure 22**).

Another innovative concept is the introduction of adaptive or controllable fluids into lag dampers. Controllable fluids consist of a powder or particles dispersed in a carrier fluid. These fluids change their properties as electric field, as in electrorheological (ER) fluids, and magnetic field, as in magnetorheological (MR) fluids, is applied. This property change is manifested as a change in yield stress of the fluid, with a minimal change in plastic viscosity. This change in yield stress arises because the particles in the carrier fluid form chains, and resist shear stresses. The yield stress is the point in the shear stress versus shear rate behavior where the particle chains break or yield. This property of field-dependent yield stress can be exploited in the development of adaptive dampers.

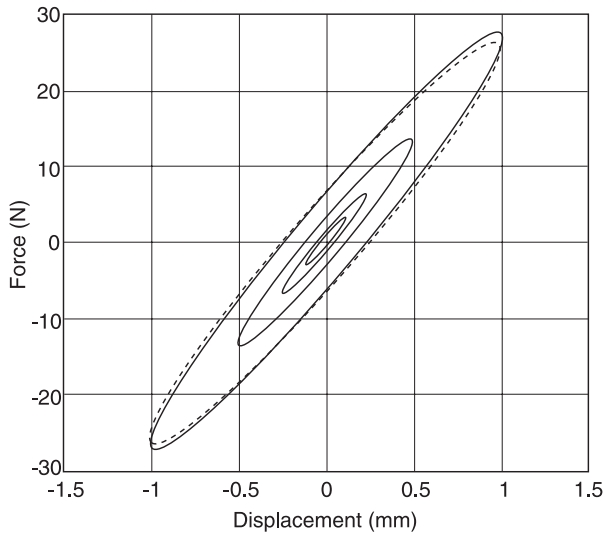


Figure 21 Force vs displacement hysteresis cycles of an elastomeric damper can be linearized via the addition of fluidic damping. Continuous line, model; dashed line, experiment.

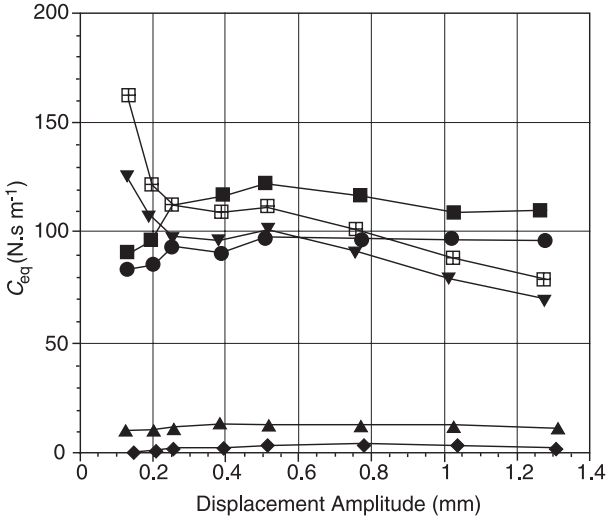


Figure 22 Linearized equivalent viscous damping constants for a pair of Comanche model-scale wind tunnel dampers under single-frequency excitation of the lag mode (in this case, 10 Hz). The MR on condition is comparable to a passive fluidic-elastomeric damper. The MR off condition has low damping. Circles, fluidlastic-zero preload; squares, fluidlastic-preloaded; diamonds, MR (off)-zero preload; triangles, MR (off)-preloaded; inverted triangles, MR (on)-zero preload; squares, MR (on)-preloaded.

To illustrate this, hybrid elastomeric MR lag dampers were fabricated for the Comanche wind tunnel model. The MR effect could be turned on and off in these dampers. The equivalent viscous damping for the MR on condition (**Figure 22**) is comparable to the fluidic-elastomeric case, however, the MR off condition has significantly reduced damping. This effect can have some interesting benefits.

Dampers must be matched sets for a given rotor so that it is balanced. However, due to manufacturing variations, dampers must be carefully matched, so that many dampers must be manufactured to achieve this matching of damper properties; that is, the properties of each damper are selected to be the same. Therefore, a damper that could adapt its properties to a fixed mechanical property specification would be of tremendous benefit. Damping augmentation is required only in certain flight regimes, which highlights the need for damping strategies that can be tailored to specific flight conditions. For example, when the helicopter is on the ground, and the rotor is spooling up to its operational rotational frequency of 1/rev, there are critical frequency ranges where the rotor can be marginally stable. Augmenting damping over these critical frequency ranges would be of benefit in increasing stability of the helicopter rotor. Also, the temperature-softening effect of elastomers can be mitigated by increasing the damping as temperature increases using an MR fluid-based damping component. Thus, controllable fluid dampers are attractive choices for augmenting lag mode damping in helicopter rotor systems.

Nomenclature

C_{eq}	equivalent viscous damping
f	measured force
$\hat{f}$	predicted force
$f(t)$	damper restoring force
K^*	damper stiffness
K'	storage stiffness
K''	loss stiffness
K_{eq}	equivalent spring stiffness
$x(t)$	damper displacement
$\Delta(t)$	sampling period

See Plates 39, 40.

See also: **Active control of vehicle vibration: Damping materials; Damping mounts**.

Further Reading

Aklonis JJ and McKnight WJ (1983) *Introduction to Polymer Viscosity*. New York: John Wiley.

Brackbill CR, Lesieutre GA, Smith EC and Govindswamy K (1996) Thermomechanical modeling of elastomeric materials. *Smart Materials and Structures* 5: 529–539.

Brackbill CR, Lesieutre GA, Smith EC and Ruehl LE (2000) Characterization and modeling of the low strain amplitude and frequency dependent behavior of elastomeric damper materials. *Journal of the American Helicopter Society* 45: 34–42.

Chopra I Perspectives in aeromechanical stability of helicopter rotors. *Vertica* 14: 457–458.

Felker FF, Lau BH, McLaughlin S and Johnson W (1987) Nonlinear behavior of an elastomeric lag damper undergoing dual-frequency motion and its effect on rotor dynamics. *Journal of the American Helicopter Society* 32: 45–53.

Gandhi F and Chopra I Analysis of bearingless main rotor aeroelasticity using an improved time domain nonlinear elastomeric damper model. *Journal of the American Helicopter Society* 41: 267–277.

Kamath GM, Wereley NM and Jolly MR Characterization of magnetorheological helicopter lag dampers. *Journal of the American Helicopter Society* 44: 234–248.

Kunz DL (1997) Influence of elastomeric damper modeling on the dynamic response of helicopter rotors. *AIAA Journal* 35: 349–354.

Lazan BJ (1968) *Damping of Materials amd Members in Structural Mechanics*. New York: Pergamon Press.

McGuire DP (1994) Fluidlastic dampers and isolators for

vibration control in helicopters. Presented at the 50th Annual Forum of American Helicopter Society, Washington D.C., May 1994.
Panda B and Mychalowycz E (1997) Aeroelastic stability wind tunnel testing with analytical correlation of the comanche bearingless main rotor. *Journal of the American Helicopter Society* 42: 207–217.

HILBERT TRANSFORMS

M Feldman, Technion-Israel Institute of Technology, Haifa, Israel

Copyright © 2001 Academic Press

doi:10.1006/rwvb.2001.0057

Introduction

The Hilbert transform (HT), as a kind of integral transformation, plays a significant role in vibration signal processing. There are two common ways it can be used. First, the HT provides a direct examination of a vibration's instantaneous attributes: frequency, phase, and amplitude. It allows rather complex systems to be analyzed in the time domain. Second, the HT can find a system's real part of transfer function from the system's imaginary part and vice versa. This allows systems to be analyzed in the frequency domain. The HT can be used as an intermediate step in more elaborate system analysis. In addition to frequency response function analysis, it is useful for hysteretic damping characterizing and nonlinear system identification.

In the field of signal processing, the HT has also stimulated some progress. The classic example of this is signal demodulation, and also signal decomposition. Today the HT is taken as a standard procedure and has long been used widely in signal processing.

The Hilbert* transformation was first introduced to signal theory by Denis Gabor. He defined a generalization of the well-known Euler formula $e^{iz} = \cos(z) + i\sin(z)$ in the form of the complex function $Y = u(t) + iv(t)$, where $v(t)$ is the HT of $u(t)$. In signal processing, when the independent variable is time, this associated complex function is known as the analytic signal and the HT $v(t)$ is called quadrature (or conjugate) function of $u(t)$. For example, the quadrature function of $\cos(t)$ is $\sin(t)$ and the corresponding analytic signal is e^{it}.

The application of the HT to the initial signal provides some additional information about amplitude, instantaneous phase, and frequency of vibrations. This information can be useful when applied to analysis of vibrational motions, including an inverse problem – the problem of vibration system identification.

*David Hilbert, born 23 January 1862 in Königsberg, Prussia (now Kaliningrad, Russia), died 14 February 1943 in Göttingen, Germany. David Hilbert was one of the world's greatest mathematicians. Hilbert contributed to many branches of mathematics, including invariants, algebraic number fields, functional analysis, integral equations, mathematical physics, and the calculus of variations. He invented the space of wave functions used in quantum mechanics.

Notation

The HT of the function $u(t)$ is defined by an integral transform:

$$H[x(t)] = \tilde{x}(t) = \pi^{-1} \int_{-\infty}^{\infty} \frac{x(\tau)}{t-\tau}\, d\tau \qquad [1]$$

Because of the possible singularity at $t = \tau$, the integral is to be considered as a Cauchy principal value. The HT is equivalent to an interesting kind of filter, in which the amplitudes of the spectral components are left unchanged, but their phases are shifted by $-\pi/2$ (**Figure 1**).

Properties of the HT

The HT of a real-valued function $x(t)$ extending from $-\infty$ to $+\infty$ is a real valued function defined by eqn [1]. Thus, $\tilde{x}(t)$ is the convolution integral of $x(t)$ with $1/\pi t$, written as $\tilde{x}(t) = x(t) \cdot 1/\pi t$. The HT of a constant is zero. The double HT (the HT of a HT) yields the original function having the opposite sign, hence

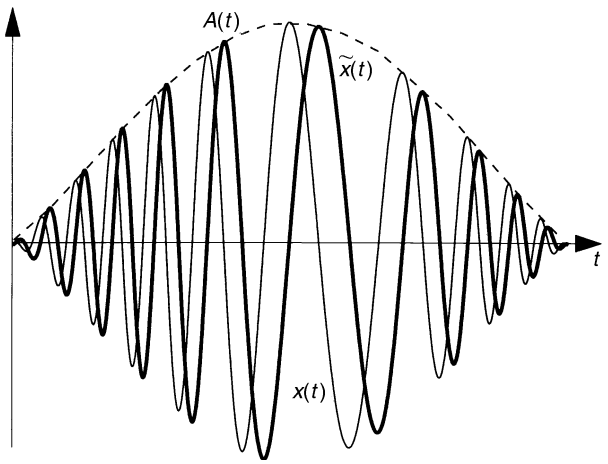


Figure 1 Real signal $x(t)$, Hilbert transform $\tilde{x}(t)$, and the signal envelope $A(t)$.

it carries out a shifting of the initial signal by $-\pi$. The power (or energy) of a signal and its HT are equal. A function and its HT are orthogonal over the infinite interval $\int_{-\infty}^{\infty} x(t)\tilde{x}(t)\mathrm{d}t = 0$.

For $n(t)$ low-pass and $x(t)$ high-pass signals with nonoverlapping spectra $H[n(t)x(t)] = n(t)\tilde{x}(t)$. More generally, the HT of the product of two arbitrary functions with overlapping spectra can be written in the form of a sum of two parts:

$$\begin{aligned} H[n(t)x(t)] &= H\{[\bar{n}(t) + n_1(t)]x(t)\} \\ &= \bar{n}(t)\tilde{x}(t) + \tilde{n}_1(t)x(t) \end{aligned}$$

where $\bar{n}(t)$ is the slow (low-pass), $n_1(t)$ is the fast (high-pass) signal component, and $\tilde{n}_1(t)$ is the HT of the fast component. The proof of the decomposition of a signal into a sum of low- and high-pass terms is based on Bedrosian's theorem for the HT of a product. For example, the HT of the cube of the harmonics $x^3 = (A\cos\varphi)^3$ is equal to $H[x^3] = H[x^2x] = A^3(3\sin\varphi + \sin 3\varphi)/4$.

Analytic Signal

The complex signal whose imaginary part is the HT of the real part is called the analytic signal. The term 'analytic' is used in the meaning of a complex function of the complex variable. When dealing with general modulated signals, it is often convenient to define the analytic signal $X(t) = x(t) + i\tilde{x}(t)$, where $\tilde{x}(t)$ is related to $x(t)$ by the HT. In order to return from a complex form of the analytic signal $X(t)$ back to the real function $x(t)$, one has to use the substitution

$$x(t) = \frac{X(t) + X^*(t)}{2}$$

where $X^*(t)$ is the complex conjugate signal of $X(t)$. The analytic signal has a one-sided spectrum of positive frequencies. The conjugate analytic signal has a one-sided spectrum of negative frequencies.

Polar Notation

According to analytic signal theory, a real vibration process $x(t)$ measured by, say, a transducer, is only one of possible projections (the real part) of some analytic signal $X(t)$. Then the second projection of the same signal (the imaginary part) $\tilde{x}(t)$ will be conjugated according to the HT. The analytic signal has a geometrical representation in the form of a phasor rotating in the complex plane, as shown in **Figure 2**.

Using the traditional representation of the analytic signal in its trigonometric or exponential form:

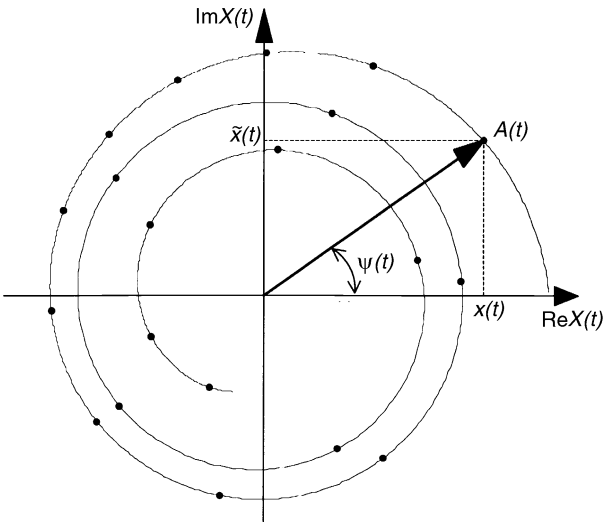


Figure 2 Analytic signal representation.

$$X(t) = |X(t)|[\cos\psi(t) + i\sin\psi(t)] = A(t)\mathrm{e}^{i\psi(t)} \quad [2]$$

one can determine its instantaneous amplitude (envelope, magnitude):

$$A(t) = |X(t)| = \sqrt{x^2(t) + \tilde{x}^2(t)} = \mathrm{e}^{\mathrm{Re}[\ln X(t)]} \quad [3]$$

and its instantaneous phase:

$$\psi(t) = \arctan\frac{\tilde{x}(t)}{x(t)} = \mathrm{Im}[\ln X(t)] \quad [4]$$

The change of coordinates from rectangular $(x, \tilde{x})$ to polar (A, ψ) gives $x(t) = A(t)\cos[\psi(t)]$, $\tilde{x}(t) = A(t)\sin[\psi(t)]$. The HT is used, almost without exception, for vibration processes with zero mean value (in the absence of a trend or DC offset). Otherwise, the instantaneous characteristics of the signal turn into fast oscillation functions and they are liable to have a much more complex configuration than the initial signal.

Instantaneous Phase

The instantaneous phase notation (eqn [4]) indicates the multibranch character of the function, as shown in **Figure 3** line 2, when the phase angle jumps between π and $-\pi$. These phase jumps can be unwrapped into a monotone function by an artificial changing of the phase values (see **Figure 3** line 1). The instantaneous relative phase shift in the case of two different real signals $x_1(t)$ and $x_2(t)$ can be estimated as the instantaneous relative phase between them according to the formula

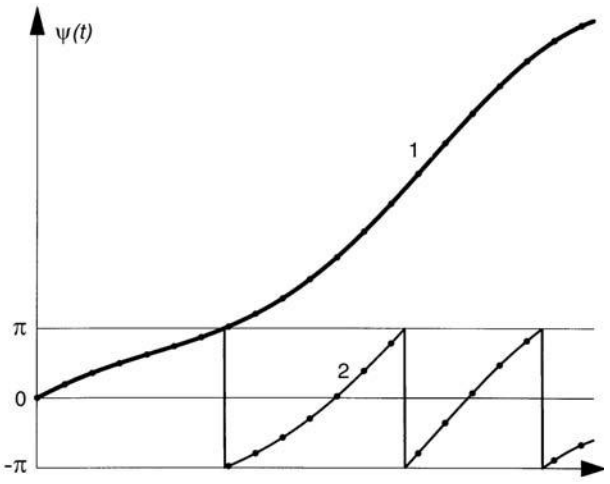


Figure 3 Instantaneous phase: 1, unwrapped; 2, wrapped.

$$\psi_2(t) - \psi_1(t) = \arctan \frac{x_1(t)\tilde{x}_2(t) - \tilde{x}_1(t)x_2(t)}{x_1(t)x_2(t) + \tilde{x}_1(t)\tilde{x}_2(t)}$$

Signal Envelope

The amplitude of the oscillation varies slowly with time, and the shape of the slow time variation is called the envelope $A(t)$ (eqn [3]). The initial signal and its envelope have common tangents at points of contact (extrema points), but the signal never crosses the envelope. The envelope often contains important information about the signal. By using the HT, the rapid oscillations can be removed from the signal to produce a direct representation of the envelope alone. For example, the impulse response of a linear single-degree-of-freedom (SDOF) system is an exponentially damped sinusoid. The envelope of the signal is determined by the decay rate.

Narrow-band vibration signals can be described with the constant carrier frequency $\psi(t) = \omega_0 t + \psi_0(t)$. Then the initial complex signal (eqn [2]) will be given by $X(t) = A_0 e^{i\psi(t)} = A_0 e^{i\psi_0(t)} e^{i\omega_0 t}$, where a new complex expression is introduced as the complex envelope $A_0 e^{j\omega_0(t)}$. The spectrum of the complex envelope can be obtained by shifting an initial signal spectrum to the left toward the origin of axes. The envelope probability density $p(A)$ is related to the signal probability density function

$$p(x) = \pi^{-1} \int_{|x|}^{\infty} \frac{p(A)\mathrm{d}A}{(A^2 - x^2)^{1/2}}$$

As an example of this relation a typical classical Gaussian (normal) form of the probability density of the random vibration which conforms to the Rayleigh probability density of the vibration envelope is shown in **Figure 4.**

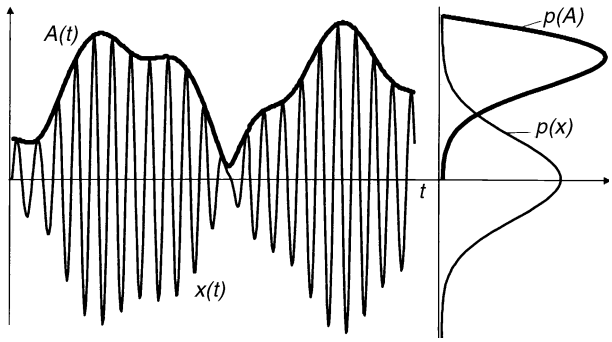


Figure 4 Random signal with envelope and their distributions.

Instantaneous Frequency

The first derivative of the instantaneous phase $\omega(t) = \dot{\psi}(t)$, called the instantaneous angular frequency, plays an important role. The angular frequency $\omega(t) = 2\pi f(t)$ has the dimension radian per second and the cycle frequency $f(t)$ has the dimension Hertz. There is a simple way to avoid the whole phase-unwrapping problem. It can be done when finding the instantaneous frequency (IF) by differentiation of the signal itself

$$\omega(t) = \frac{x(t)\tilde{x}(t) - \dot{x}(t)\tilde{x}(t)}{A^2(t)} = \mathrm{Im}\left[\frac{\dot{X}(t)}{X(t)}\right]$$

For narrow-band signals there is another alternative to the signal differentiation by direct estimation of the phase angle corresponding to the unit time shift $X(t)X^*(t + \mathrm{d}t) = [A(t) + \mathrm{d}A]e^{\omega(t)\mathrm{d}t}$, where $\omega(t)$ is the phase angle (eqn [2]), $\mathrm{d}t = 1$, and X^* is the complex conjugated signal. Thus it is seen that for narrow-band signals, small time delays may be represented as phase shifts of the complex envelope.

Naturally, for a simple monoharmonic signal, the instantaneous amplitude and frequency are constant values. In the general case, the IF of a signal is a varying function of time. Moreover, the IF of wide-band analytic signals may change sign in some time intervals. This corresponds to the change of rotation of the phasor of **Figure 2** from the counterclockwise to the clockwise direction.

Signal Time Representation

For more complicated vibration signals, the instantaneous amplitude and frequency are nonconstant; they

vary in time. While the IF is positive function, the signal itself has the same numbers of zero crossings and extrema. When the IF takes a negative value the signal has multiple extrema between successive zero crossings. It corresponds to the appearance of a complex riding wave (complicated cycle of alternating signal). Vibration signal with positive IF is considered as a monocomponent signal. A slow frequency-modulated and a random narrow-band signal are two typical different examples of the monocomponent signal. In this case the IF will not have the fast fluctuations induced by asymmetric waveforms. With this definition, the monocomponent signal in each cycle, defined by the zero crossing, involves only one mode of oscillation; no complex riding waves are allowed.

Since the IF may be considered to be the average of the signal frequency at a given time instant, it seems reasonable to inquire about the probability density function or spread at that time. Actually, the probability density function of the IF of the random normal narrow-band signal, defined by $p(\omega) = \Delta\omega_2^2/2[(\omega - \omega_{01})^2 + \Delta\omega_2^2]^{3/2}$, where ω_{01} and $\Delta\omega_2$ is the central frequency and the spectrum width parameter (see below), is spread about only one central frequency. A composition of several monocomponent signals is considered as a multicomponent signal. There exists a method to decompose the initial data into intrinsic components, for which the instantaneous frequency can be defined as positive function.

Taking into account these representations of analytic signals enables one to consider a vibration process, at any moment of time, as a quasiharmonic oscillation, amplitude- and frequency-modulated by time-varying functions $A(t)$ and $\omega(t)$: $x(t) = A(t)\cos\int_0^t \omega(t)\mathrm{d}t$. For random signals, the envelope and the IF are statistically independent functions. Thus the dynamic component of the signal is described by a variance and for such a case is given by a product of two statistically independent functions: the envelope and the fast oscillated function: $\cos[\cdot]$. The signal variance, after transformation, reduces to $\sigma_x^2 = [\sigma_A^2 + \bar{A}^2]/2$ where σ_x is the signal standard deviation, σ_A is the envelope standard deviation, and $\bar{A}$ is the envelope mean value. This means that the signal variance depends only on the envelope variation.

The instantaneous parameters are functions of time and can be estimated at any point of the vibration signal. The total number of these points which map the vibration is much greater than that of the peak points of the signal. This opens the way for averaging and for other statistical processing procedures, making vibration analysis more precise.

Signal Spectrum Representation

The normalized power spectrum ($\int_0^\infty S(\omega) = 1$) may be interpreted as a geometric figure or the probability density function of the frequency ω, and may be used to define the spectral moments. Of particular interest is the mean value of the IF. The mean value is equal to the coordinate of the center of mass of the signal spectrum $\omega_{01} = \int_0^\infty \omega S(\omega)\mathrm{d}\omega$. In some cases of vibration analysis only the positive IF values are significant, therefore the mean absolute value of the IF should be applied: $\omega_{02} = [\int_0^\infty \omega^2 S(\omega)\mathrm{d}\omega]^{1/2}$. The mean absolute value is the second-order spectral moment which corresponds to the radius of inertia of the signal spectrum. It is equal to the zero crossing of a vibration random signal. Some typical examples of the central frequency estimation based on the IF are shown in **Table 1**.

It is notable that, in the case of the SDOF vibration system, its free vibration natural frequency value $(\omega_0^2 - c^2)^{1/2} \approx \omega_0 - c^2/2\omega_0$, where c is the viscous damping, lies between these central moments of the IF (**Table 1**).

It was mentioned that the IF can take negative values that correspond to the appearance of complicated cycles of alternating load. A probabilistic prerequisite to the formation of the negative value of IF is $p[\omega(t)<0] = 0.5(1 - \omega_{01}/\omega_{02})$, from whence it follows, for example, that the probability of a negative value of the IF of random vibration of the SDOF system (**Table 1**) is proportional to the system-damping coefficient.

The IF can also be interpreted from the time–frequency distribution point of view as the average frequency at each time, because, for an unlimited number of time–frequency distributions of the analytic signal, the first conditional moment in frequency, which gives the average frequency at each time, equals the average derivative of the instantaneous phase.

There are several techniques for estimation of the spectrum bandwidth. Probably the most familiar and simplest is the half peak level width. Also, the spectrum bandwidth could be estimated as a width of a hypothetical square with the same energy and the

Table 1 The spectral central frequencies

Vibration signal	*Central frequency*	
	ω_{01}	ω_{02}
Harmonics $\cos\omega_0 t$	ω_0	ω_0
Random vibration of the system $\ddot{y}+2c\dot{y}+\omega_0^2 y$	$\omega_0 - 2c/\pi$	ω_0
Narrow-band random noise $\omega_0 - \frac{1}{2}\Delta\omega < \omega < \omega_0 + \frac{1}{2}\Delta\omega$	ω_0	$\omega_0(1+\Delta\omega^2/24\omega_0^2)$

Table 2 The spectral bandwidth

Vibration signal	*Spectral bandwidth*	
	$\Delta\omega_1$	$\Delta\omega_2$
Random vibration of the system $\ddot{y}+2c\dot{y}+\omega_0^2 y$	πc	$2(c\omega_0/\pi)^{1/2}$
Narrow-band random noise $\omega_0-\frac{1}{2}\Delta\omega<\omega<\omega_0+\frac{1}{2}\Delta\omega$	$\Delta\omega$	$\Delta\omega\frac{1}{2}\sqrt{3}/6$

peak value $\Delta\omega_1 = \int_0^\infty S(\omega)\mathrm{d}\omega/S_{\max}$. In the case of the IF analysis it is useful to introduce one more width parameter that is equal to the mean absolute value of the IF deviation from its central value $\Delta\omega_2 = [\int_0^\infty(\omega-\omega_{01})^2 S(\omega)\mathrm{d}\omega]^{1/2} = (\omega_{02}^2-\omega_{01}^2)^{1/2}$. Some typical examples of the spectral bandwidth estimation are shown in **Table 2**.

These relations between the spectral bandwidth and the central frequency enable us by convention to divide vibration signals into two groups: narrow-band ($\Delta\omega<<\omega_0$) and wide-band ($\Delta\omega>>\omega_0$) signals.

The HT and Vibration Systems

Frequency Response Function

The HT presents an interesting property for a causal function $h(t)$. The property implied by causality is that the imaginary part of the Fourier transform is completely determined by a knowledge of its real part and vice versa. If the impulse function of the linear dynamic system $h(t)$ contains no singularity at the origin, then $F(g(t)) = R(\omega) + iQ(\omega)$ is its Fourier transform, and $R(\omega)$ and $Q(\omega)$ are the HTs that satisfy the equations:

$$Q(\omega) = -\frac{1}{\pi}\int_{-\infty}^{\infty}\frac{R(\omega')}{\omega-\omega'}\,\mathrm{d}\omega',$$

$$R(\omega) = \frac{1}{\pi}\int_{-\infty}^{\infty}\frac{Q(\omega')}{\omega-\omega'}\,\mathrm{d}\omega'$$

We can associate a complex frequency response function whose real part is the function $R(\omega)$ and the imaginary part is the HT of this function. To obtain the complete function of the system, we have to apply the HT to the magnitude frequency response to obtain the phase frequency response. In other words, the real and imaginary parts of the transfer function form a Hilbert pair. Any departure from an initial linear frequency response function, i.e., distortion, can be attributed to nonlinear effects.

Hysteretic Damping

Most real materials show an energy loss per cycle with a less pronounced dependency on frequency. In fact, many materials indicate force–deformation relations that are independent of the deformation rate amplitude – so-called hysteretic relations. A known mechanical element model shows frequency-independent storage and loss moduli. This implies that the Fourier transforms of both the element force $F(\omega)$ and the element deformation $\Delta(\omega)$ satisfy $F(\omega) = k[1 + j\eta\,\mathrm{sgn}(\omega)]\Delta(\omega)$, where k is the stiffness and η is the loss factor (ratio of the loss and storage moduli of element). In this model the dissipated energy in a harmonic deformation cycle of amplitude Δ_0 is independent of the frequency of deformation $W = \pi k\eta\Delta_0^2$. Only the HT gives a correct time domain expression for the concept of linear hysteretic. This representation of the SDOF structure with linear hysteretic damping is $\ddot{y}(t) + \omega^2 y(t) + \omega^2\eta\tilde{y}(t) = 0$, where $\tilde{y}(t)$ is the HT of the deformation. This transform can be used to replace complex-valued coefficients in differential equations modeling mechanical elements.

Nonlinear System Identification

The HT method enables us to estimate instantaneous modal parameters (the natural frequency and the instantaneous damping coefficient) as functions of vibration amplitude for systems under test. The HT identification method extracts directly the backbone of a nonlinear system as a dependency between free vibration frequency and displacement amplitude and also the corresponding damping curve. This enables us to solve an inverse identification problem, namely, the problem of estimation of the initial nonlinear static elastic and damping force characteristics. Most well-known cases of nonlinearity occur in large-amplitude oscillations of elastic systems; for instance, nonlinear spring elements with hardening or softening restoring force, or nonlinear damping quadratic or cubic force.

The HT and Vibration Signals

The analytic signal method is equally applicable to deterministic and random processes, although, generally speaking, it doesn't divide them into two separate groups. Thanks to this, it enables us to investigate any oscillating time function from a general point of view. The method is also good for solving problems concerning linear and nonlinear vibration systems typical of mechanical engineering structures. It allows analysis, from the general point of view, of stationary vibrations as well as nonstationary

narrow- and/or wide-band ones. It also allows analysis of the dissipation of vibration energy, and vibration effects on machine durability.

Signal Differentiation and Integration

The analytic signal notion (eqn [2]) allows us to describe a relationship between an initial complex signal and its first derivative as

$$\dot{X} = X\left(\frac{\dot{A}}{A} + i\omega\right)$$

It is noted that all the information on the first derivative of an analytic signal is carried by the analytic signal itself (its envelope and IF). This formula defines a new notion of the instantaneous complex frequency $\Omega(t) = \alpha(t) + i\omega(t)$, where

$$\alpha(t) = \frac{\dot{A}(t)}{A(t)} = \frac{x(t)\dot{x}(t) + \tilde{x}(t)\tilde{x}(t)}{A^2(t)} = A(t)\,\mathrm{Re}\left[\frac{\dot{X}(t)}{X(t)}\right]$$

is the instantaneous radial velocity of the phasor in **Figure 2**. The second derivative of the signal takes the form

$$\ddot{Y} = X\left(\frac{\ddot{A}}{A} - \dot{\psi}^2 + 2i\frac{\dot{A}}{A}\dot{\psi} + i\ddot{\psi}\right)$$

Integration of analytic signals may be also of importance for signal processing. A complex function of a real variable t is an integral of the analytic signal if the real and the imaginary parts of the function are corresponding integrals forming a pair of the HT.

Signal Demodulation

The basic equation of frequency properties of the signal can be expressed as $\Delta\omega^2 = \sigma_\omega^2 + \sigma_{\dot{A}}^2/\sigma_A^2$ where $\Delta\omega$ is the bandwidth of the spectrum, σ_ω is the IF standard deviation, $\sigma_{\dot{A}}$ is the standard deviation of the first derivative of the envelope, and σ_A is the envelope standard deviation. The physical meaning of the basic equation is that the spectral bandwidth is described by the sum of two components: the variance of the IF and the variance of the envelope velocity. Actually, the spectral band is defined by both the frequency and the amplitude modulation. For signals which are only amplitude-modulated, the spectral bandwidth is equal to the mean square value of the velocity of the amplitude change. For signals which are only frequency-modulated, the spectral bandwidth is equal to the mean square value of the IF.

Traditional Fourier analysis simply assumes that the signal is the sum of a number of sine waves. The HT allows a complex demodulation analysis, adapted to signals of the form of a single, but perturbed sine wave. Since a vibration signal is exactly of the model that the method assumes, it is no wonder that in some cases it performs better than Fourier analysis.

Signal Decomposition

A new empirical mode decomposition method allows any complicated data set to be decomposed into a finite and often small number of intrinsic mode functions that admit well-behaved Hilbert transforms. Since the decomposition is based on the local characteristic time scale of the data, it is applicable to nonlinear and nonstationary processes.

Fatigue Estimation under Random Wide-band Loading

The HT approach can be used to count fatigue cycles in an arbitrary loading waveform. It processes a time history representing the loading condition to generate the number of cycle-counts with their corresponding amplitudes. The approach is general, is accurate within any desirable degree of accuracy, and is amenable to modern signal processing.

Hilbert Transformers

We can form the HT by designing a filter with the frequency response corresponding to the impulse response. This response is $H(\omega) = -j\,\mathrm{sgn}(\omega)$. This frequency response describes a wide-band 90° phase shifter whose positive frequencies are shifted by $-90°$ and whose negative frequencies are shifted by +90°. There are two methods for obtaining the Hilbert transformer: frequency domain and time domain. The phase shift can be implemented by a convolution filter, obtainable by the convolution theorem relating convolution to multiplication in the frequency domain.

Frequency Domain

If $x(t)$ is the real input data record of length N, then the analytic signal $X(t)$ can be obtained by: $X(t) = \mathrm{IFFT}[B(n)\cdot\mathrm{FFT}(x(t))]$ where: $B(n) = 2$, for $n = \{0, N/2 - 1\} B(n) = 0$, for $i = \{N/2, N - 1\}$. FFT is the Fourier transform and IFFT is the inverse Fourier transform. The imaginary portion of $X(t)$ contains the HT $\tilde{x}(t)$; the real portion contains the

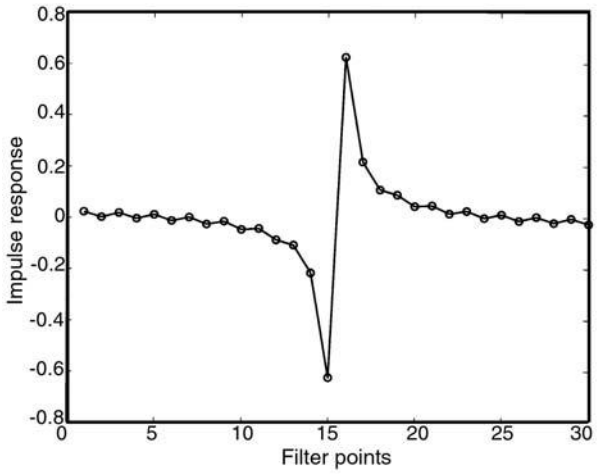


Figure 5 Length 35 Hilbert transformer.

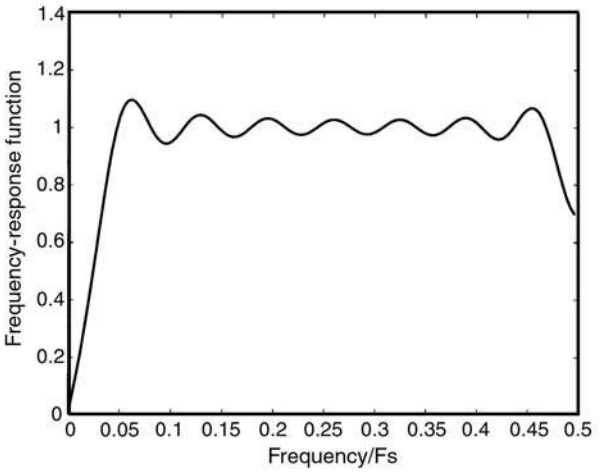


Figure 6 Frequency–response function of the Hilbert transformer.

real input signal $x(t)$. Windowing and/or zero padding may have to be used to avoid ringing.

Time Domain

The HT formulation can be used to build an approximation to an analytic signal generator by designing a finite impulse response (FIR) filter approximation to the HT operator. The analytic signal can be computed by adding the appropriately time-shifted real signal to the imaginary part generated by the Hilbert filter. Since an ideal Hilbert filter impulse response extends infinitely in both directions, approximations are necessary which yield some acceptable amplitude and phase ripples. If a type III (even impulse response length) FIR Hilbert filter is designed, then the group delay will not be a whole number of samples. The real signal will have to be resampled at the points halfway between the existing samples before it can be added to the imaginary part. This problem does not occur for type IV (odd length) Hilbert filters (**Figure 5**), but these must be designed to be band-pass, rather then high-pass (**Figure 6**). The FIR digital Hilbert transformers have the advantage of providing exactly linear phase, but at the expense of requiring a higher filter order as compared to the infinite impulse response (IIR) designs, to achieve a given negative frequency attenuation level.

See also: **Signal Integration and Differentiation**; **Signal Processing**, **Model-based Methods**; **Time–Frequency Methods**; **Transform Methods**.

Further Reading

Boashash B (ed.) (1992) *Time–Frequency Signal Analysis Methods and Applications*. Melbourne, Australia: Longman Cheshire, p. 547.

Bracewell RN (1986) *The Fourier Transform and its Applications*. New York: McGraw-Hill, p. 474.

Claerbout JF (1976) *Fundamentals of Geophysical Data Processing*. McGraw-Hill, pp. 59–62.

Feldman M (1997) Non-linear free vibration identification via the Hilbert transform. *Journal of Sound and Vibration* 208: 475–489.

Hahn SL (1996) *Hilbert Transforms in Signal Processing*. Artech House, p. 305.

Huang NE, Shen Z and Long SR (1997) New view of nonlinear water waves: the Hilbert spectrum. *Annual Review of Fluid Mechanics* 31: 417–457.

Huang NE, Shen Z, Long SR *et al.* (1998) The empirical mode decomposition and Hilbert spectrum for nonlinear and nonstationary time series analysis. *Proceedings of the Royal Society of London Series A* 454: 90395.

Inaudi JA and Kelly JM (1995) Linear hysteretic damping and the Hilbert transform. *Journal of Engineering Mechanics* 121: 626–632.

Mitra SK and Kaiser JF (1993) *Handbook for Digital Signal Processing*. Wiley-Interscience, p. 1268.

Oppenheim AV and Schafer RW (1975) *Digital Signal Processing*. Englewood Cliffs, NJ: Prentice-Hall, p. 585.

Rabiner LR and Gold B (1975) *Theory and Application of Digital Signal Processing*. Englewood Cliffs, NJ: Prentice-Hall, p. 762.

Urkowitz H (1983) *Signal Theory and Random Processes*. Dedham, MA: Artech House, p. 715.

Vainshtein and Vakman D (1983) *Frequency Separation in the Theory of Vibration and Waves* (in Russian). Moscow: Nauka, p. 288.

HUMAN RESPONSE TO VIBRATION

See **GROUND TRANSPORTATION SYSTEMS**; **HAND-TRANSMITTED VIBRATION**; **MOTION SICKNESS**; **WHOLE-BODY VIBRATION**

HYBRID CONTROL

J Tang and KW Wang, The Pennsylvania State University, University Park, PA, USA

Copyright © 2001 Academic Press

doi:10.1006/rwvb.2001.0196

Introduction

Traditionally, structural vibration control techniques have been categorized into two categories, namely, passive and active. Classical passive methods include material damping enhancement, viscoelastic dampers, frictional dampers and joints, and various vibration absorbers and isolation schemes. The advantages of the passive approach are that the devices are relatively simple and cheap, and the system will always be stable since the control is realized by energy dissipation and/or energy redistribution with no external power being added to the system. However, since it produces fixed designs, such schemes might not be optimal or even effective when the system or the operating condition changes. In addition, these schemes usually work well at the high-frequency region or within a narrow frequency range, but often have poor low-frequency performance. Due to the rapid progress in modern electronics and digital signal-processing technique, active systems with feedback/feedforward control schemes have become a viable means for vibration suppression. A typical active control system consists of the plant, actuator(s), sensor(s), and the control electronics. The vibration control is achieved by applying a secondary input to the structure, thereby modifying the system dynamic response to a desirable pattern. While active systems are generally more effective than passive methods, they have the disadvantages such as being complicated and expensive, having the potential to destabilize the system, and being sensitive to system modeling error and uncertainties.

It is clear that the passive and active vibration suppression approaches both have respective strength and weaknesses. This gives rise to the idea of active–passive hybrid vibration controls. In a hybrid system, the active and passive components are synthesized in an integrated manner such that their combined effect would be superior to that of the individual active or passive actions. If properly designed, hybrid controls could outperform the purely passive and active approaches while requiring much less control power input than active systems. Also, since energy is almost always being dissipated/redistributed by the passive components, they are much more robust and stable than the active approach. In other words, they could have the advantages of both the passive (stability, fail-safe, lower power consumption, good high-frequency performance) and active (high performance, especially in the low-frequency range, feedback/feedforward actions) schemes.

In general, the design of a hybrid vibration control system involves the selection/determination of the active and passive components. It is a natural thought first to identify the relations and performance trade-offs between the active and passive control mechanisms, and then to have the two complement each other such that a system with the best control performance and least control effort can be achieved. There are two schools of thoughts in designing a hybrid system. One is to integrate individual active and passive devices on to the host structure to synthesize a global hybrid control. The other is to design hybrid devices at a local level, such that the actuators will have self-contained active–passive hybrid actions. For both approaches, design strategies need to be developed such that the active and passive actions can be integrated in an optimal manner. A discussion of the design methodologies is presented in the following section. These strategies are generic and are not tied to specific passive control mechanisms and active control actuator/sensor selections. Lastly, some representative self-contained hybrid actuator configuration will be presented.

Design Strategies

In early time, the term hybrid control often referred to the general procedure for an integral design of the structure and its active controller. The original rationale behind this design philosophy is to take into

account the strong dynamic interaction between the structure and the controller. This concept provides the very basic foundation for synthesizing active–passive hybrid control systems. The key idea here is to treat the passive control elements as part of the structure to be synthesized, and develop the active–passive hybrid action in an integrated manner. It has been shown that the combined effect of the active and passive mechanisms can meet vibration suppression requirements that cannot be otherwise achieved by a purely active or purely passive approach alone, since the interaction between them can often be utilized to improve their individual effects.

Depending on specific applications and performance requirements, different design variables, constraints, and objective function(s) can be formulated for an active–passive hybrid system design. For example, one may define the following objective function:

$$J_a = \sigma_1 + \sigma_2 \text{ subject to } m_p \leq m_p^* \qquad [1]$$

where σ_1 and σ_2 are the measurements of structural response and control input, respectively:

$$\sigma_1 = E\left[q^{\mathrm{T}} R_1 q\right], \quad \sigma_2 = E\left[u^{\mathrm{T}} R_2 u\right] \qquad [2a, b]$$

where q is the structural response vector, u is the active control input, R_1 and R_2 are weighting matrices, m_p is the added mass of the passive control device, m_p^* is the maximum allowable value, and $E[\cdot]$ is the expected value operator.

A nested optimization process, which is essentially a simultaneous optimal control/optimization procedure, can be formulated to minimize the above objective function. For a given set of passive parameters (these could include the locations of the active, passive, and/or hybrid actuators, and the device component design and dimensions), the inner optimization loop consists of an optimal linear quadratic (LQ) control problem to determine the active control gains that minimize J_a. The outer optimization loop consists of a search for the passive parameters to minimize further the objective function J_a subject to the constraint on m_p. With this procedure, the active and passive design variables (active gains and passive parameters) are determined simultaneously through iteration between the inner and outer loop optimizations (**Figure 1**). An interesting feature of this formulation is that the inner and outer loops share the same objective function, which implies that the passive and active mechanisms directly complement or compromise with each other to reach the same goal.

Following along the similar line, one may formulate a different type of optimization procedure where the inner loop and outer loop do not share exactly the same goal. For example, a second objective function can be selected as the total added mass of the passive

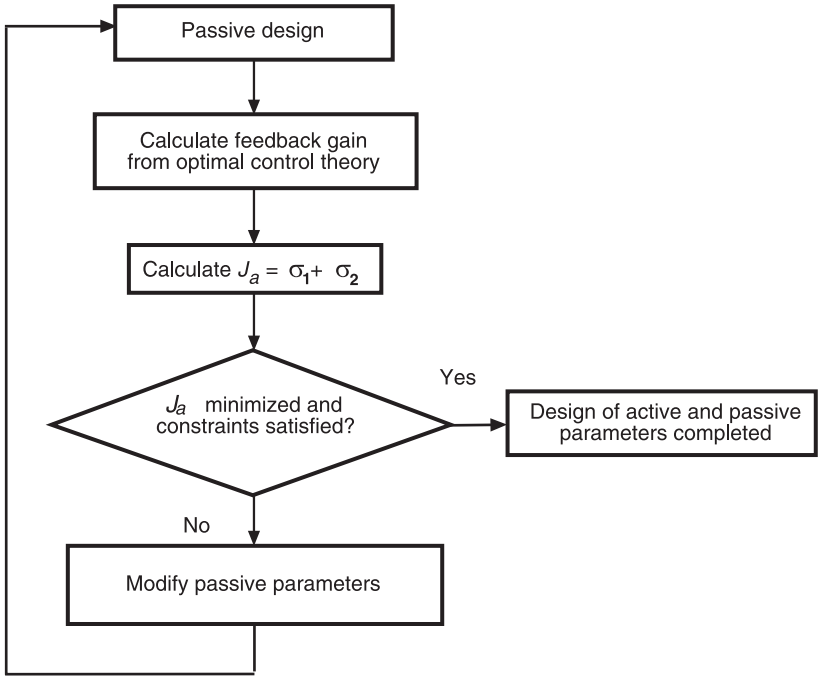


Figure 1 Simultaneous optimal control/optimization for active–passive hybrid system design. Objective function: $J_a = \sigma_1 + \sigma_2$ subject to constraint: $m_p \leq m_p^*$ (mass of passive damping treatment).

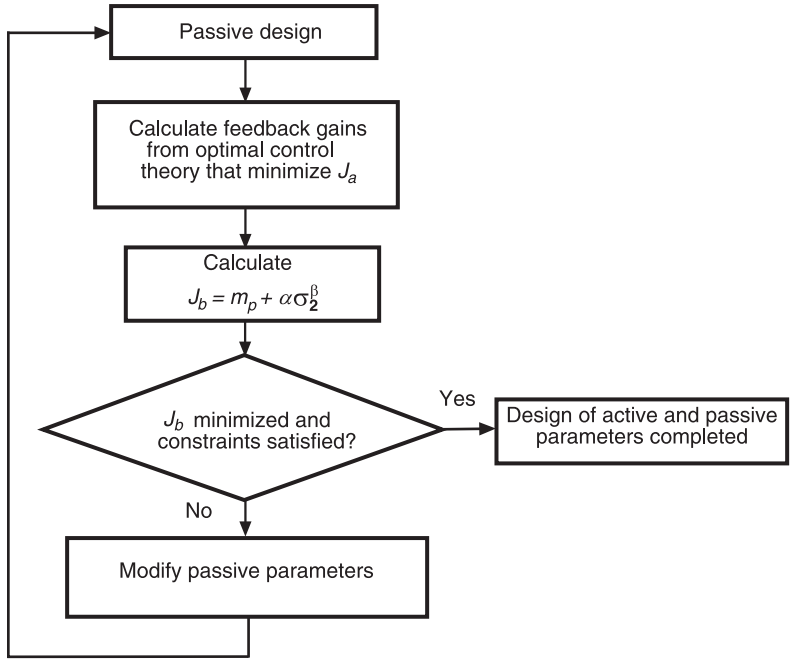


Figure 2 Integrated optimization for active–passive hybrid system design. Inner loop uses optimal control theory to minimize $J_a = \sigma_1 + \sigma_2$, and outer loop uses nonlinear programming to minimize total added mass $J_b = m_p + \alpha\sigma_2^\beta$, subject to constraint $\sigma_1 \leq \sigma_1^*$ (structural response).

control treatment and the active control hardware/power plant:

$$J_b = m_p + a\sigma_2^\beta \text{ subject to } \sigma_1 \leq \sigma_1^* \qquad [3]$$

where the mass of the active control hardware/power plant is assumed to be a linear function of σ_2^β, and σ_1^* is the maximum allowable response. An optimization procedure for minimizing J_b is illustrated in **Figure 2**, which iterates between the two loops for determining the active and passive parameters. While the inner loop still uses the linear optimal control to solve for the active control gains that minimize J_a, the outer loop now aims at minimizing the total added mass (J_b).

The above formulations both resort to the optimal control theory to determine active gains. This is preferred for applications with large number of degrees of freedom, as the well-established optimal control theory can greatly simplify the numerical calculation. On the other hand, one may use other feedback control laws to replace the optimal control theory. In that case, one can have two design options. The first option is to synthesize the active control law (which might not involve an objective function) in the inner loop. The outer loop still consists of a search for passive parameters, to minimize a design objective function, and yields certain compromise through iterations between the two loops (similar to the case shown in **Figure 2**). The second one is to fix *a priori* the active controller structure (e.g., a state-feedback or output-feedback structure) and treat the active gains and passive parameters together as design variables in an overall nonlinear programming optimization process, such that certain objective function is minimized. With this process, only one loop is needed. In general, H_2 or H_∞ norms of closed-loop transfer functions from external disturbance to structural response can be good candidates as design objectives. Still, depending on specific mission, one may use other criteria to form the objective function, such as the sensitivity of closed-loop eigenvalues (robustness), closed-loop modal damping factor, and eigenvector optimization/placement for systems with multiple inputs.

In most vibration control problems, design engineers are interested in optimizing one specific property only, and require other properties to fall within a certain range. These problems can be posed as single objective optimizations with various constraints, such as those mentioned above. A great advantage enjoyed by this kind of problem is numerical simplicity, and usually an iteration-type procedure (iteration between the passive design parameters and active control gains) suffices for solving these problems. Under certain circumstances, however, several properties might need to be simultaneously optimized to yield a successful active–passive hybrid control design. For example, one might need to minimize

the mass of passive control device and the structural response simultaneously, thus having a vector-type objective function:

$$J_c = \begin{Bmatrix} m_p \\ J_a \end{Bmatrix} \quad [4]$$

The design procedure then becomes a multiobjective or vector optimization process. Since there might exist no unique solution that would give an optimum for all the objective functions simultaneously, the concept of Pareto optimality has been found useful in this context. In a brief definition, a set of design variables is said to be Pareto-optimal if there exists no other feasible design variable set that would reduce some objective function without causing an increase in at least one objective function. A commonly used method for solving a vector optimization problem is to form a scalar objective as a weighted sum of individual objective functions. Usually, several Pareto optima exist for a multiobjective optimization problem, and by varying the relative weightings in the scalar objective one can generate an entire family of Pareto optima. It is then up to the design engineers to use additional information to make the final decision.

While in this section the optimization-based methodology is discussed as a means for active–passive hybrid control design, it should be noted that many practical designs are accomplished not completely from these analytical and numerical methods but rather based on engineering intuition. Oftentimes the design decisions come, at least partially, from experience and understanding of respective merits and limitations of the active and passive components, as well as performance tradeoffs between them in specific applications.

Active–Passive Hybrid Control Devices

In some cases, particular passive damping mechanisms/materials can be organically integrated with active control means at the local device level, which could significantly improve the overall system performance. This section presents some of the representative self-contained active–passive hybrid actuator configurations.

Proof-Mass Hybrid Actuator

The key feature of a reaction-type actuator is that the force generator acts between a proof mass and the host structure or, in other words, it creates a force by reacting against an inertial mass. A generic model of a single-degree-of-freedom structure attached with such an actuator is shown in **Figure 3A**. The equations of motion are:

$$\begin{bmatrix} M & 0 \\ 0 & m_p \end{bmatrix} \begin{Bmatrix} \ddot{x}_1 \\ \ddot{x}_2 \end{Bmatrix} + \begin{bmatrix} c_s + c_p & -c_p \\ -c_p & c_p \end{bmatrix} \begin{Bmatrix} \dot{x}_1 \\ \dot{x}_2 \end{Bmatrix} + \begin{bmatrix} K + k_p & -k_p \\ -k_p & k_p \end{bmatrix} \begin{Bmatrix} x_1 \\ x_2 \end{Bmatrix} = \begin{Bmatrix} -f_g \\ f_g \end{Bmatrix} + \begin{Bmatrix} F_m \\ 0 \end{Bmatrix} \quad [5]$$

Hereafter, M, K, and c_s denote the mass, stiffness, and damping of the main structure, m_p is the proof

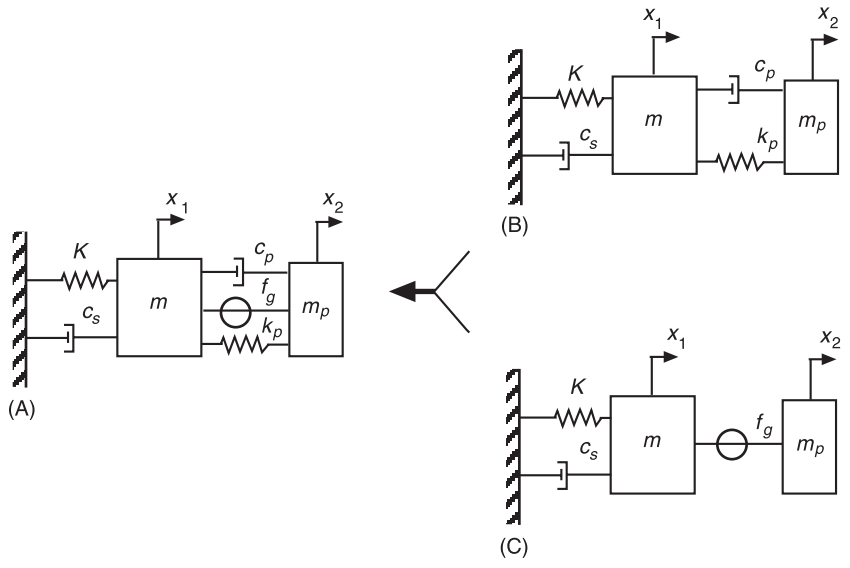


Figure 3 (A) Proof-mass hybrid actuator: design c_p, k_p, and f_g for hybrid control. (B) Tuned vibration absorber: design c_p and k_p for passive control. (C) Active control: design f_g (inherent stiffness and damping of the actuator are not shown).

mass, x_1 and x_2 are the displacements of the main structure and proof-mass, f_g is the output of the force generator, and F_m is the external disturbance. It is easy to recognize that the active and passive parameters f_g, k_p (stiffness), and c_p (damping) can be tuned together to modify the system/actuator dynamics, which gives rise to the proof-mass hybrid actuator concept. If one removes the active component, which in this case is the force generator, the remaining passive component when properly tuned can form a damped vibration absorber, as shown in **Figure 3B**, where the absorber spring-mass will transfer/store part of the kinetic energy and the damper will dissipate it. On the other hand, if one removes the passive damping mechanism, one has a purely active system, as shown in **Figure 3C**. Hereafter, a reaction-type actuator with both the passive and active control abilities is referred to as proof-mass hybrid actuator.

Under the linear system assumption, the response of a structure attached with a proof-mass hybrid actuator is the summation of that caused by the external disturbance and that caused by the control force input. The passive damping ability can be evaluated from the transfer function between the external disturbance and structural response which, in fact, is the frequency response of a system with a tuned vibration absorber. Such a frequency response function depends on the passive parameters m_p, c_p, and k_p. For broadband excitations, one method of optimizing these parameters is to minimize the maximum of the transfer function, known as the classical vibration absorber tuning (for a detailed discussion on dynamic vibration absorbers, refer to **Absorbers, active**. Moreover, in proof-mass hybrid actuator applications, the actuator dynamics can be explicitly included in the system model or even modified by selecting different passive parameters, which could have a positive effect on system performance and robustness.

An *ad hoc* method of designing the proof-mass hybrid actuator is first to select the passive parameters using the optimal passive absorber tuning results, which give the best passive damping, and then determine the active gain based on the control law used. This method obviously does not take into account the performance tradeoff between the active and passive mechanisms (this tradeoff will be illustrated in detail in a later discussion on the active–passive hybrid piezoelectric network that is analogous to the proof-mass hybrid actuator). Indeed, the passive and active parameters of a proof-mass hybrid actuator can be determined by using the simultaneous optimal control/optimization procedure outlined in the previous section. In most applications, the mass of the actuator is predetermined, and one only needs to solve for k_p and c_p as passive parameters. To simultaneously optimize the passive components and active gain, a gradient search can be performed for a range of values of the actuator's stiffness and damping. For each set of k_p and c_p, the optimal control gain is calculated from the optimal control theory. The iteration continues until the minimum objective function value is obtained.

Active–Passive Hybrid Piezoelectric Network

Because of their electromechanical coupling characteristics, piezoelectric materials have been explored extensively for both active and passive damping applications. Some of the advantages of such materials include high bandwidth, high precision, compactness, and easy integration with existing host structures to form the so-called smart structures. A piezoelectric material produces a strain when subjected to an electrical field and, conversely, produces a charge when strained mechanically (for a detailed discussion on piezoelectric material, refer to **Piezoelectric materials and continua**). For an application as shown in **Figure 4A**, under a single mode assumption, the equations of motion for the integrated system are:

$$\begin{aligned} M\ddot{q} + c_s\dot{q} + Kq + k_1Q &= F_m \\ k_2Q + k_1q &= V_a \end{aligned} \qquad [6a, b]$$

where q is the structural generalized displacement, Q the charge flowing into the patch electrodes, k_1 the electromechanical coupling coefficient, k_2 the inverse of the capacitance of the piezoelectric patch, and V_a the voltage across the piezoelectric patch.

For active control, a control voltage V_i is applied across the piezoelectric patch, thus $V_a = V_i$ and eqns [6a] and [6b] can be combined as:

$$M\ddot{q} + c_s\dot{q} + Kq - \frac{k_1^2}{k_2}q = F_m - \frac{k_1}{k_2}V_i \qquad [7]$$

The two-way electromechanical coupling exhibited by piezoelectric materials have also made them useful as passive structural dampers/absorbers. In such applications, the electrodes of the piezoelectric patch are shunted with a passive electric network that is designed to store/dissipate the electrical energy converted from mechanical energy by the piezoelectric patch. One popular scheme of passive piezoelectric network is to shunt the piezoelectric patch with a resistor and inductor. These two elements, along with the inherent capacitance of the piezoelectric patch, create a resonant RLC circuit, as shown in **Figure 4B**. The equations of motion for such system are:

$$\begin{aligned} M\ddot{q} + c_s\dot{q} + Kq + k_1Q &= F_m \\ L\ddot{Q} + R\dot{Q} + k_2Q + k_1q &= 0 \end{aligned} \qquad [8a, b]$$

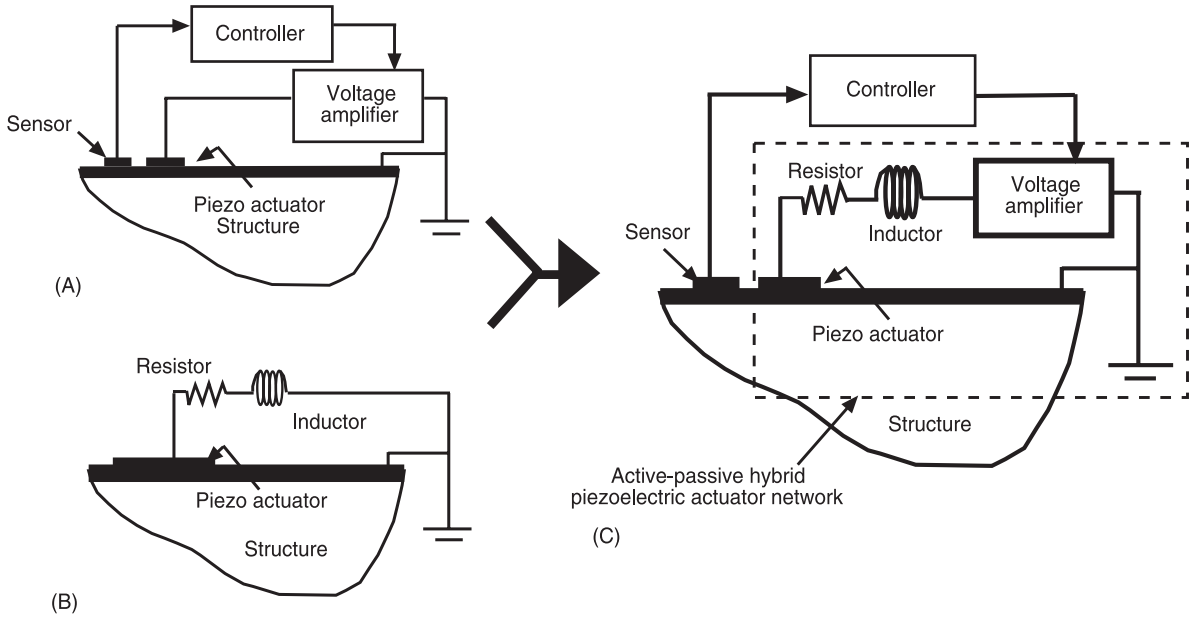


Figure 4 (A) active, (B) passive, and (C) active–passive hybrid piezoelectric controls.

where L and R are the inductance and resistance values, respectively. Clearly, this resonant piezoelectric shunt is analogous to the tuned vibration absorber shown in **Figure 3B**, except that it counters vibration strain energy instead of kinetic energy. This similarity also gives rise to the idea of combining the passive piezoelectric network and the active voltage input together to form an active–passive hybrid piezoelectric network (APPN), as shown in **Figure 4C**, which is again fundamentally analogous to the proof-mass hybrid actuator (**Figure 3C**). The equations of motion for a system integrated with the hybrid network are:

$$\begin{aligned} M\ddot{q} + c_s\dot{q} + Kq + k_1Q &= F_m \\ L\ddot{Q} + R\dot{Q} + k_2Q + k_1q &= V_i \end{aligned} \qquad [9a, b]$$

On one hand, the APPN preserves the passive damping ability of the shunt circuit. The transfer function between the external disturbance and the structural response is plotted in **Figure 5A**, where the continuous line corresponds to the result under optimal passive tuning. This optimal passive tuning is obtained from a min–max criterion similar to that of a tuned vibration absorber. On the other hand, the actuator dynamics caused by the circuit elements may improve the active control performance. Specifically, the second-order effect of the RLC circuit can greatly increase the control authority around the circuit-tuned frequency. **Figure 5B** shows the ratio between the voltage across the piezoelectric patch and the voltage applied from the driving source. One may easily conclude that an integrated APPN will have better actuation authority than the configuration with separated active and passive piezoelectric actuators, as illustrated in **Figure 6**. While the integrated and separated configurations have the same passive damping ability, the former can drive the host structure much more effectively than the latter does, which demonstrates the merit of the self-contained APPN design.

Comparing **Figure 5A** and **5B**, one can observe a performance tradeoff between the passive and active mechanisms. While the resistance in the shunt circuit is needed to provide passive damping, it tends to reduce the voltage amplification effect by dissipating a portion of the control power. To balance between these different requirements and achieve an optimal design, one may again resort to the simultaneous optimal control/optimization procedure discussed in the previous section. Parametric analyses on APPN showed that, when the weighting on control effort increases, the optimal resistance (R) and inductance (L) values using the simultaneous design would approach those derived from the passive optimization procedure. It is also shown that the optimal resistance and inductance values for the hybrid system could be quite different from those of the passive system. In general, when the demand on control performance is high, the resistance value becomes smaller to enhance the active authority amplification effect, and inductance reduces to push the actuator frequency response up to cover a wider-frequency bandwidth. The excitation bandwidth also plays an important role, as it determines to which frequency range or modes the RL values will be tuned.

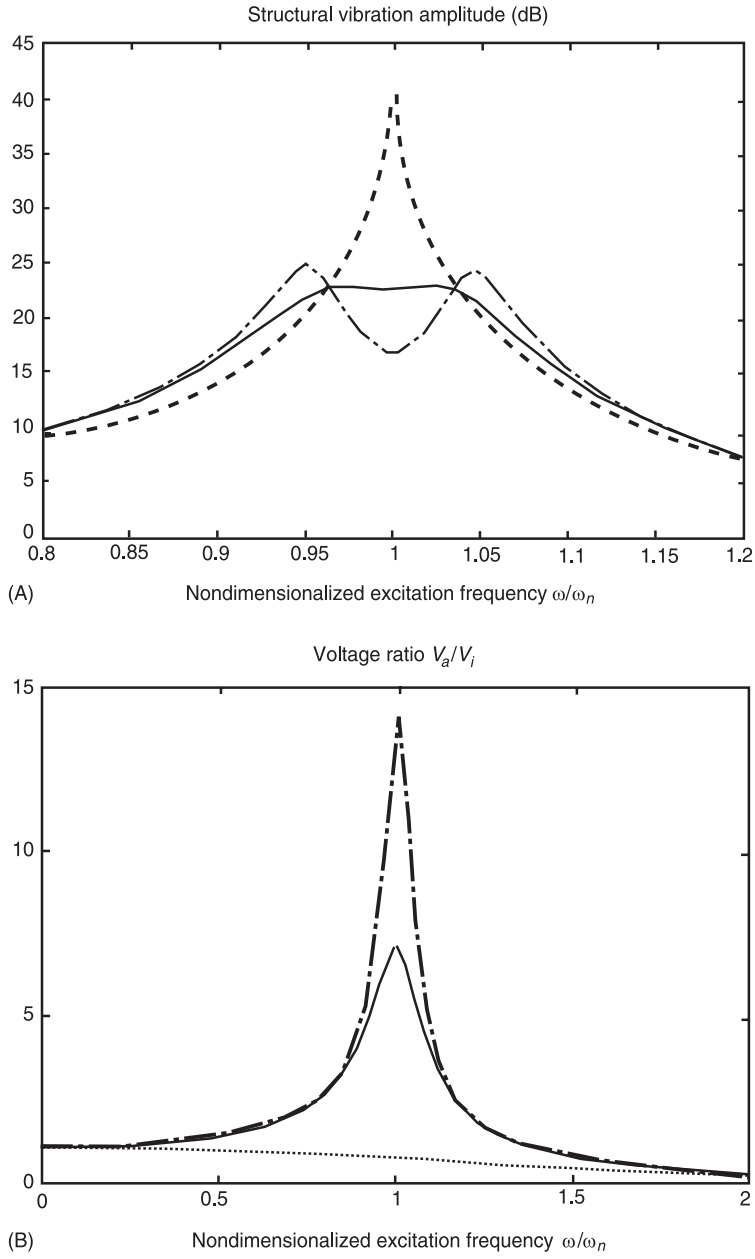


Figure 5 Results of active–passive hybrid piezoelectric network. (A) Passive damping frequency response. (B) Voltage ratio versus actuation frequency (V_a is the voltage across the piezoelectric patch, and V_i the voltage from the external voltage source). Let $\omega_n = \sqrt{K/M}$, $\omega_e = \sqrt{k_2/L}$. The nondimensional passive parameters are defined as:

$$\delta = \frac{\omega_e}{\omega_n} = \sqrt{\frac{k_2/L}{K/M}} \text{ and } r \equiv \frac{R}{k_2}\omega_m = \frac{R}{k_2}\sqrt{\frac{K}{M}}$$

Here the passive parameters are selected as: $\delta = \delta_{\text{opt}} = 1$ (optimal passive value). Continuous line, $r = r_{\text{opt}} = \sqrt{2}\left(k_1/\sqrt{Kk_2}\right)$ (optimal passive value); dots and dashes, $r = 0.5r_{\text{opt}}$; dashed line, $r = 10r_{\text{opt}}$.

Active Constrained Viscoelastic Layer

Basic active constrained layer treatments One of the popular passive damping treatments in industrial applications is to use the viscoelastic materials (VEM). VEM are elastomeric materials whose long chain molecules cause them to convert mechanical energy into heat when they are deformed. One traditional form of surface damping utilizing the viscoelastic materials is the passive constrained layer (PCL)

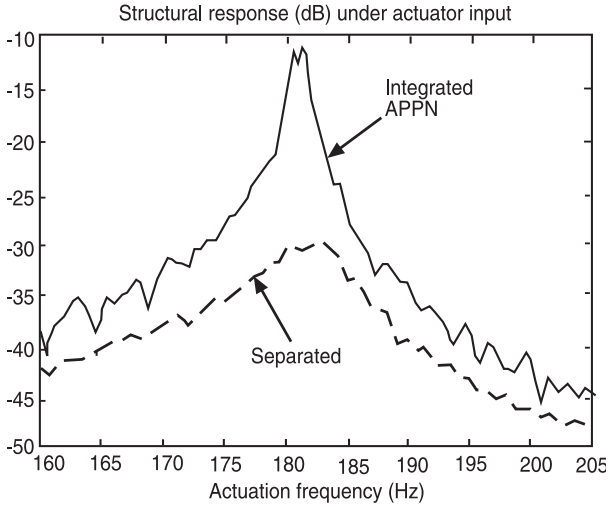


Figure 6 Experimental results on active authority comparison (open-loop structural response/actuator input) between integrated APPN and the configuration with separated active and passive actuators. The two configurations have the same passive damping ability.

treatment (**Figure 7A**), where a cover sheet is bonded on top of the viscoelastic layer to increase its shear strain under vibration, thus enhancing its passive damping ability (for detailed discussions on VEM and PCL, see **Damping materials**.

Piezoelectric materials are capable of inducing the in-plane tensile strain. Combining this in-plane actuation mechanism with the constrained layer damping, one can form another self-contained hybrid control treatment, the active constrained layer (ACL) damping. A schematic of the ACL system is shown in **Figure 7B**, where a viscoelastic layer is sandwiched in between a piezoelectric cover sheet and the vibrating host structure. The damping mechanism of ACL can be understood by considering a typical cyclic vibration motion. When the beam moves downward away from its equilibrium position, a control voltage is applied to the piezoelectric cover sheet to result in its shrinkage. This can create a shear angle in the viscoelastic layer that is larger than the angle developed by a passive constraining layer, as illustrated in **Figure 7A**. When the beam moves upward, an opposite-sign voltage is applied to the piezoelectric cover sheet to result in extension. Again, a larger shear angle than that of a passive constraining layer case can be expected. The increase of the shear deformation of the viscoelastic layer during the entire motion cycle leads to more energy dissipation. In the meantime, the tensile deformation (shrinkage during the downward half-cycle and extension during the upward half-cycle) of the piezoelectric layer produces a bending moment on the host structure that tends to

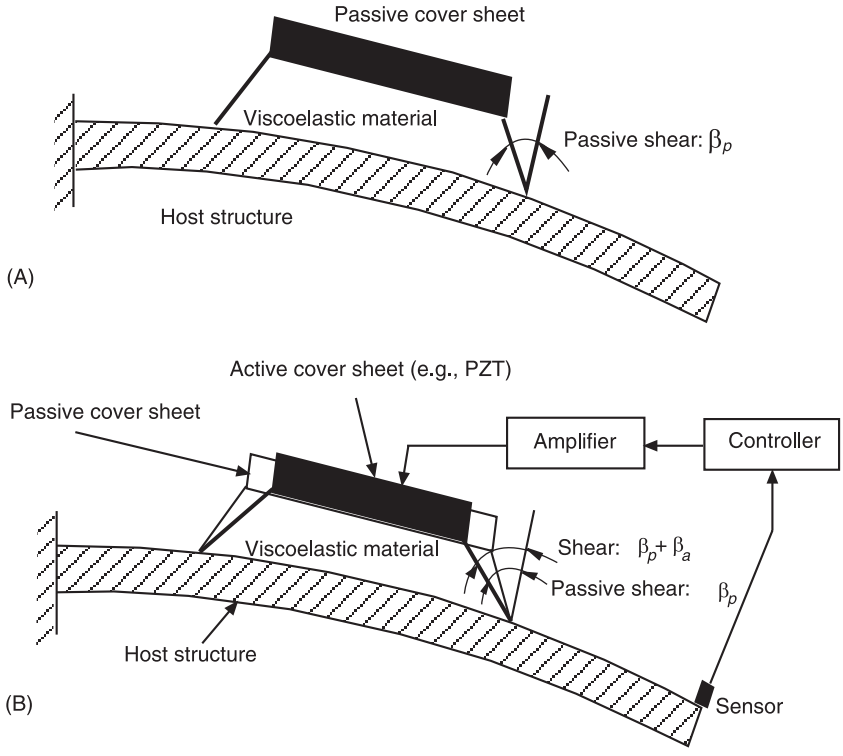


Figure 7 (A) Passive constrained layer (PCL) and (B) active constrained layer (ACL) treatments. The in-plane tensile strain induced by the piezoelectric cover sheet results in an additional shear β_a. The piezoelectric tensile deformation also creates direct active moments to bring the beam back to its original equilibrium position.

bring it back to its original equilibrium position. Therefore, ACL has a twofold vibration control mechanism, the actively enhanced passive energy dissipation and the additional active control moment.

Although straightforward in terms of its basic mechanism, the design of ACL has proven to be challenging. One major complexity is the performance tradeoffs between ACL's passive and active control abilities. While the active action of the piezoelectric constraining layer can indeed enhance the viscoelastic layer's passive damping ability, the viscoelastic material (due to its softness) will also reduce the direct active authority of the piezoelectric material. Compared with a purely active control system where the piezoelectric material is bonded directly to the host structure without the viscoelastic layer, an ACL system might require more control power while achieving less vibration reduction. That is, the passive damping enhancement of the viscoelastic material due to the piezoelectric action may not be significant enough to compensate for the active control authority loss.

The detailed tradeoffs between the active and passive actions in an ACL treatment depend on many system parameters as well as the control law employed. Some qualitative guidelines for ACL designs using linear optimal control are summarized in the following paragraphs:

- It is desirable to let the VEM loss factor be as large as possible to obtain good passive damping abilities and active–passive hybrid actions in ACL designs.
- One can categorize the VEM shear modulus into three regions: low, medium, and high. In the low shear modulus region, both the passive damping ability and active action authority are low for the ACL structure, and therefore the overall performance of the active–passive hybrid system is poor.
- To obtain large vibration reduction with high demand on performance (little concern of control effort), high active gains (high weighting on performance) are usually used. In such cases, one could select VEM with high shear modulus to achieve high active piezoelectric actions. However, the difference between the ACL and the purely active configurations might not be obvious. Another point worth noting is that, when the VEM becomes too stiff, the passive VEM damping could become ineffective, and the ACL's fail-safe ability (which is a desirable feature of such active–passive hybrid structures) could be significantly reduced.
- To achieve good vibration reduction performance under significant constraints on control effort, the active gain values are usually limited. This is the best scenario for applying ACL, where the benefits of both the passive damping and active action could be obtained. In this case, we should choose the VEM shear modulus in the medium region. Generally, this is the most useful region for ACL designs.

Enhanced active constrained layer treatments The main shortcoming of the basic ACL treatments is the active authority reduction due to the insertion of VEM. There have been recent proposals to use edge elements (boundary elements that directly connect the piezoelectric cover sheet to the host structure) to improve the active action (**Figure 8A**). Studies have shown that with sufficiently stiff edge elements, this enhanced active constrained layer (EACL) treatment can achieve more vibration suppression with less control effort than both the ACL and purely active systems. It should be noted that the selection of edge element stiffness could also introduce new tradeoff factors into the design of constrained layer treatments. In general, if closed-loop versus open-loop (without active action) damping contributions (or active versus passive action contributions) are not of concern, a properly designed symmetrical EACL with equal and stiff edge elements could achieve maximum hybrid damping for different combinations of vibration modes (host structure strain distribution) (**Figure 9**). However, an asymmetrical EACL design could provide a better mixture of active and passive damping

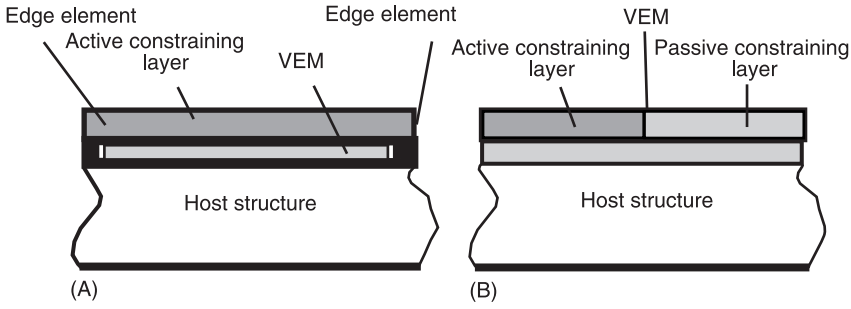


Figure 8 (A) The enhanced active constrained layer (EACL) with edge elements and (B) the hybrid constrained layer (HCL) treatment.

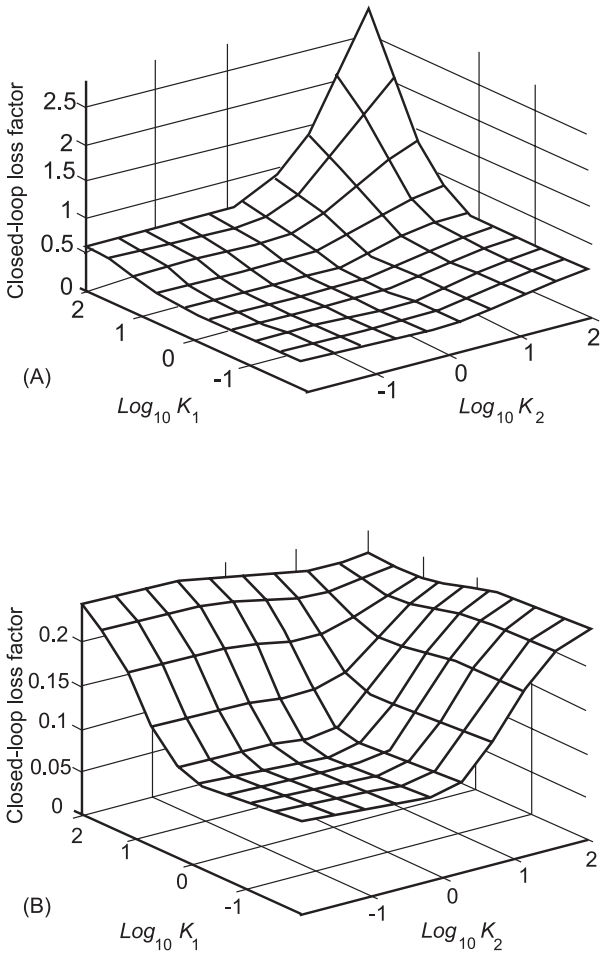


Figure 9 Closed-loop hybrid loss factor versus edge element stiffness K_1 and K_2 in EACL. (A) Constant strain field in host structure. (B) Asymmetric strain field in host structure.

(or closed-loop and open-loop damping), but could reduce the overall hybrid damping ability (**Figure 9**).

Hybrid constrained layer treatments In both the ACL and EACL treatments, the constraining layer is completely made of piezoelectric materials (e.g., lead zirconate titanate (PZT) ceramics or polyvinylidene fluoride (PVDF) polymer). PZT materials are in general much better than PVDF polymers for this purpose. Nevertheless, having a density similar to steel (relatively heavy) and a modulus close to aluminum (moderate stiffness), PZTs are not ideal as constraining materials. Due to the limited selections of active materials, it is difficult to find one with strong active action and, at the same time, good material property for constraining action. Another set of treatments recently being proposed is the HCL configuration (**Figure 8B**). In the HCL, the active segment is made of PZTs and the passive segment could use different materials under different circumstances. By selecting a passive material stiffer than PZT, the HCL could obtain higher open-loop damping than the treatment with a pure PZT cover sheet. Furthermore, it can be shown that when the active-to-passive constraining length ratio is optimally selected, the overall closed-loop damping of the HCL could also be higher than that of the configuration with a pure PZT coversheet.

Nomenclature

c	damping
$E(\cdot)$	expected value operator
K	stiffness
L	inductance
M	mass
q	structural generalized displacement
Q	charge
R	resistance
V	voltage

See also: **Active vibration suppression**; **Damping materials**; **Piezoelectric materials and continua**.

Further Reading

Lesieutre GA (1998) Vibration damping and control using shunted piezoelectric materials. *Shock and Vibration Digest* 30: 187–195.

Park CH and Baz A (1999) Vibration damping and control using active constrained layer damping: a survey. *Shock and Vibration Digest* 31: 355–364.

Tang J, Liu Y and Wang, KW (2000) Semiactive and active–passive hybrid structural damping treatments via piezoelectric materials. *Shock and Vibration Digest* 32: 189–200.

HYSTERETIC DAMPING

H T Banks and G A Pinter, North Carolina State University, Raleigh, NC, USA

Copyright © 2001 Academic Press

doi:10.1006/rwvb.2001.0018

Definition of Hysteretic Damping

Vibrational damping is associated with the dissipation of energy during mechanical vibrations/deformations of an elastic body, usually via the conversion of mechanical energy to thermal energy producing heat

in the body which is readily dissipated. Damping is most properly embodied in constitutive laws that relate a body's deformation (strain ε) or displacement to the stress σ or force associated with this deformation. These are most often given in terms of stress/strain laws $\sigma = \mathcal{F}(\varepsilon)$, the most elementary of which is Hooke's law:

$$\sigma = E\varepsilon \qquad [1]$$

where E is the material-dependent Young's modulus or modulus of elasticity. Here and throughout, we discuss concepts in a one-dimensional formulation such as occurs for example in the case of elongation of a simple uniform rod. In more general deformations one must use tensor analogs of the stress σ, the strain ε, and parameters such as the modulus of elasticity E. We shall also assume small deformations throughout so that infinitesimal strain theory can be used.

Hooke's law (which is an idealization) does not allow for dissipation, which occurs to some extent in all materials. The most widely accepted model which does is the Voigt model:

$$\sigma = E\varepsilon + C\dot{\varepsilon} \qquad [2]$$

where $\dot{\varepsilon} = \mathrm{d}\varepsilon/\mathrm{d}t$ is the strain rate. To characterize stress–strain laws, it is common to consider material behavior during cyclic loading–unloading and plot the associated stress–strain curves as given in **Figure 1** for the Voigt law.

Whenever the material behaves differently under unloading than under loading (as in the case for eqn [2] but not for eqn [1]), the material is said to be viscoelastic and to exhibit the phenomenon of hysteresis. Hysteresis is present in many materials such as filled rubber and filled rubber-like composites (often referred to as elastomers), shape memory alloys (SMAs) such as Nitinol (a nickel–titanium alloy) and CuZnAl (a copper–zinc–aluminum alloy), piezoelectrics (e.g., PZTs or lead zirconate titanates), electrostrictives (e.g., PMNs or lead magnesium niobates) and magnetostrictives (e.g., Terfenol-D, a terbium iron dysprosium alloy). The Voigt law [2] is inadequate in characterizing the hysteresis in such materials under many conditions where the hysteresis loop can be quite complex, as depicted in **Figures 2** and **3**.

A number of different modeling approaches and resulting models have been developed to describe quantitatively the various hysteretic dissipation mechanisms such as that manifested in hysteresis loops similar to those shown in **Figures 2** and **3**.

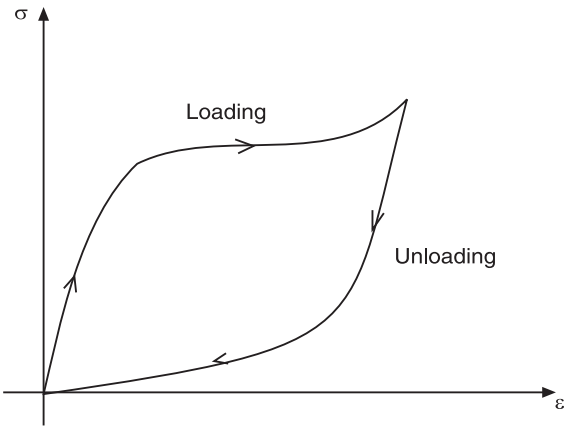


Figure 2 Loading/unloading for a shape memory alloy (SMA).

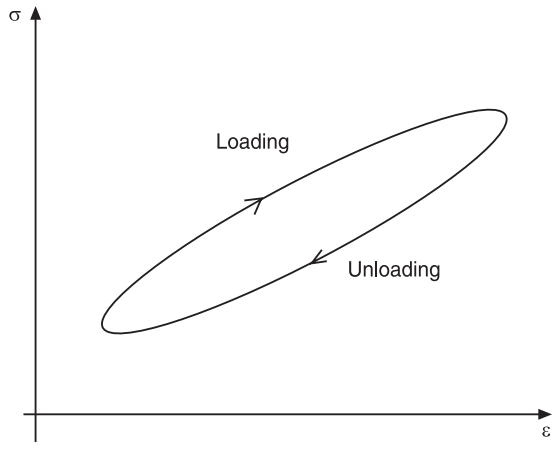


Figure 1 Loading/unloading for a Voigt material.

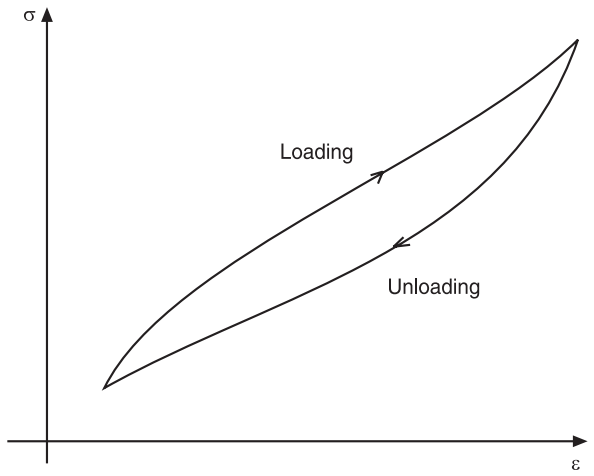


Figure 3 Loading/unloading of filled rubber.

Models for Hysteresis

The most fundamental model that correctly describes the hysteretic behavior of a number of materials is the standard linear model due to Kelvin (and therefore sometimes also referred to as the Kelvin model). This model (to be discussed below), along with a number of others, is frequently developed and analyzed in the context of the phenomena of relaxation and creep which, along with hysteresis, constitute the features of general viscoelasticity. If a viscoelastic rod is suddenly stressed (for example, with a unit step force) and held at this level of stress, the rod will continue to deform (as depicted in **Figure 4** for the Kelvin model) in a phenomenon called creep.

On the other hand, if a rod is suddenly strained (for example, with a unit step displacement) and this strain is then maintained, the resulting stress in the rod will decrease over time, as depicted for one model (the Kelvin model) in **Figure 5**. This phenomenon is called *relaxation*. While the specific shape of the creep and relaxation responses are highly dependent on the particular constitutive law chosen, the general qualitative features represented in **Figures 4** and **5** are typical.

The Kelvin or Standard Linear Model

The simplest constitutive model describing the phenomenon of hysteresis which incorporates empirically observed creep and relaxation in materials is the Kelvin or standard linear model given by:

$$\sigma + \tau_\varepsilon \dot{\sigma} = E_r(\varepsilon + \tau_\sigma \dot{\varepsilon}) \qquad [3]$$

where E_r is called the relaxed modulus of elasticity.

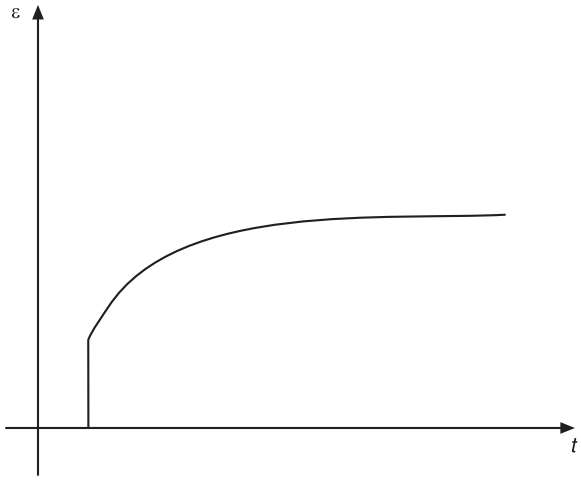


Figure 4 Standard linear model creep response.

This model can be depicted in the context of spring-dashpot analogies, as shown in **Figure 6**.

The creep solution (or creep function) $\Delta\varepsilon(t)$ of eqn [3] is the solution corresponding to step stress $\Delta\sigma$ at time $t = s$. That is, $\Delta\varepsilon(t)$ is the solution of eqn [3] corresponding to $\sigma_s(t) = H(t - s)\Delta\sigma, \sigma_{\dot{s}}(t) = \delta(t - s)\Delta\sigma$, where H is the Heaviside function and δ is the Dirac delta distribution, and is given by:

$$\Delta\varepsilon(t) = \frac{1}{E_r}\left\{1 + \left(\frac{\tau_\varepsilon}{\tau_\sigma} - 1\right)e^{-(t-s)/\tau_\sigma}\right\}H(t-s)\Delta\sigma \qquad [4]$$

For obvious reasons, τ_σ is called the constant stress relaxation time.

The relaxation solution (or relaxation function) $\Delta\sigma(t)$ of [3] is the solution corresponding to a step elongation $\varepsilon_s(t) = H(t - s)\Delta\varepsilon$, $\dot{\varepsilon}_s(t) = \delta(t - s)\Delta\varepsilon$ at time $t = s$ and is given by:

$$\Delta\sigma(t) = \frac{1}{E_r}\left\{1 + \left(\frac{\tau_\sigma}{\tau_\varepsilon} - 1\right)e^{-(t-s)/\tau_\varepsilon}\right\}H(t - s)\Delta\varepsilon \qquad [5]$$

where τ_ε is called the constant strain relaxation time.

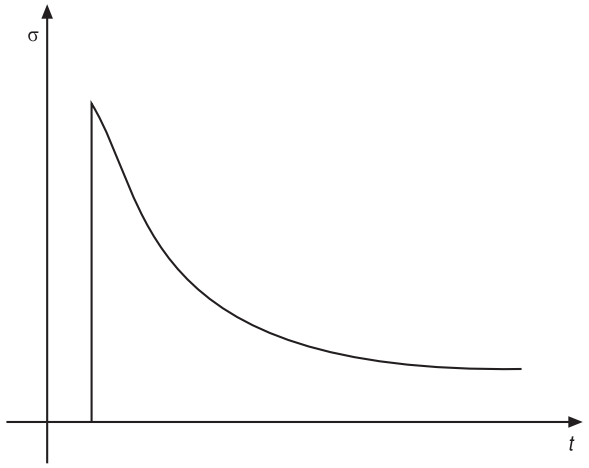


Figure 5 Standard linear model relaxation response.

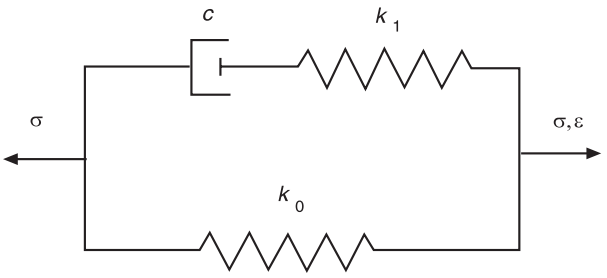


Figure 6 The Kelvin spring-dashpot model.

The Boltzmann Superposition Model

The most direct generalization of the Kelvin or standard linear model is due to Boltzmann and assumes superposition of a continuum of the relaxation solution responses to a continuum of elemental step increments in strain. The stress–strain law (in differential form) is given by:

$$\begin{aligned} d\sigma(t) &= E_0\, d\varepsilon(t) + k(t-s)\, d\varepsilon(s) \\ &= E_0\, d\varepsilon(t) + k(t-s)\dot{\varepsilon}(s)\, ds \end{aligned} \quad [6]$$

for the incremental stress at time t due to a continuum of elemental elongations $d\varepsilon(s)$ for $s \leq t$. The constant of proportionality E_0 represents the instantaneous response while the proportionality constant $k = k(t-s)$ is dependent on the length of elapsed time $t-s$ and is called the generalized relaxation function. Invoking the linear superposition hypothesis of Boltzmann and summing over the past life of the structure, one obtains (assuming $\sigma(-\infty) = 0$, $\varepsilon(-\infty) = 0$) the Boltzmann hysteretic constitutive law:

$$\sigma(t) = E_0\varepsilon(t) + \int_{-\infty}^{t} k(t-s)\frac{d\varepsilon}{ds}(s)\, ds \quad [7]$$

where E_0 represents an instantaneous modulus of elasticity and k is the relaxation response kernel. The standard linear model is a special case of the Boltzmann model with the choice $k(t-s) = E_\varepsilon e^{-(t-s)/\tau_\varepsilon}$. More general special cases that are often encountered include a generalization of the single spring-dashpot paradigm of **Figure 6** to one with multiple spring-dashpot systems in parallel, which results in the relaxation response kernel:

$$k(t-s) = \sum_{j=1}^{N} E_j e^{-(t-s)/\tau_j} \quad [8]$$

We observe that eqns [7] and [8] are equivalent to the formulation:

$$\sigma(t) = E_0\varepsilon(t) + \sum_{j=1}^{N} E_j\varepsilon_j(t) \quad [9]$$

$$\begin{aligned} &\dot{\varepsilon}_j(t) + \frac{1}{\tau_j}\varepsilon_j(t) = \dot{\varepsilon}(t) \\ &\varepsilon_j(-\infty) = 0 \quad j = 1, 2 \ldots N \end{aligned} \quad [10]$$

since the solution of eqn [10] is given by:

$$\varepsilon_j(t) = \int_{-\infty}^{t} e^{-(t-s)/\tau_j}\dot{\varepsilon}(s)\, ds \quad [11]$$

The formulation [9]–[10] is sometimes referred to as an internal variables model since the variables ε_j can be thought of as internal strains that are driven by the instantaneous strain according to eqn [10] and that contribute to the total stress via eqn [9]. Such models can be viewed as phenomenological in nature in that one does not attempt to identify any physical basis for the internal strains ε_j or they can be viewed as physical models wherein the strains ε_j are identified with specific mechanisms and/or molecules in a complex composite material with dynamics described by [10].

Generalization of the Standard Linear/Boltzmann Models

The Boltzmann model [7] is one of many generalizations of the standard linear model [3]. One such generalization due to Burger (later studied by Golla–Hughes–McTavish) is frequently encountered in the engineering literature wherein one attempts to introduce additional coordinates (essentially internal variables) into state space models to account for hysteresis. The general approach is in the frequency domain (as opposed to the time domain formulations discussed here) and employs complex modulus or loss factor data to fit rational polynomials representing the Laplace transform of hysteresis stress–strain relationships. Specifically, hysteresis is approximated by adjoining a state variable with frequency domain representation:

$$h(s) = \frac{\alpha s^2 + \beta s}{s^2 + bs + c} \quad [12]$$

This is equivalent to an internal dynamics of the form (the Burger model):

$$\ddot{\sigma} + b\dot{\sigma} + c\sigma = \alpha\ddot{\varepsilon} + \beta\dot{\varepsilon} \quad [13]$$

in the time domain, or $\hat{\sigma}\{s^2 + bs + c\} = \{\alpha s^2 + \beta s\}\hat{\varepsilon}$ in the frequency domain. This can be thought of as a direct generalization of the standard linear model [3] or can be reformulated as a generalization of internal variable/Boltzmann models such as [9]–[10] by defining generalized stress $\tilde{\sigma} = (\sigma, \dot{\sigma})$ and generalized strain $\tilde{\varepsilon} = (\varepsilon, \dot{\varepsilon}, \ddot{\varepsilon})$ vectors and writing [13] as:

$$\dot{\tilde{\sigma}} = A\tilde{\sigma} + B\tilde{\varepsilon} \quad [14]$$

so that:

$$\tilde{\sigma}(t) = \int_{-\infty}^{t} e^{A(t-\tau)} B\tilde{\varepsilon}(\tau)\, d\tau \qquad [15]$$

with:

$$A = \begin{pmatrix} 0 & 1 \\ c & b \end{pmatrix} \quad B = \begin{pmatrix} 0 & 0 & 0 \\ 0 & \beta & \alpha \end{pmatrix}$$

Nonlinear Hysteresis Models

For many materials the linear models for hysteresis discussed above are inadequate to describe experimental data. In particular, many composite materials exhibit nonlinear behavior such as that seen in **Figure 2** for SMAs and in **Figure 3** for highly filled rubbers. Biological soft tissue is also known to exhibit nonlinear hysteretic behavior.

There are several standard generalizations found in the literature in attempts to treat nonlinear behavior. The most direct one is to allow nonlinear instantaneous strain as well as nonlinear strain rate dependence in [7]. This yields models of the form:

$$\sigma(t) = f_e(\varepsilon(t)) + \int_{-\infty}^{t} k(t-s) f_v(\dot{\varepsilon}(s))\, ds \qquad [16]$$

and:

$$\sigma(t) = f_e(\varepsilon(t)) + \int_{-\infty}^{t} k(t-s) \frac{d}{ds} f_v(\varepsilon(s))\, ds \qquad [17]$$

where f_e represents the instantaneous elastic nonlinear response and f_v represents the viscoelastic nonlinear response function. This can be written in terms of internal strains similar to [9] and [10] where [8] defines k and:

$$\sigma(t) = f_e(\varepsilon(t)) + \sum_{j=1}^{N} E_j \varepsilon_j(t) \qquad [18]$$

whenever we assume linear internal dynamics of the form:

$$\dot{\varepsilon}_j(t) + \frac{1}{\tau_j}\varepsilon_j(t) = f_j(\dot{\varepsilon}(t)), \quad j = 1, 2 \ldots N \qquad [19]$$

or:

$$\dot{\varepsilon}_j(t) + \frac{1}{\tau_j}\varepsilon_j(t) = \frac{d}{dt} f_0(\varepsilon(t)), \quad j = 1, 2 \ldots N \qquad [20]$$

with $f_j = f_v$ for each j. Models of the form [18] and [20] have been successfully used to describe data for highly filled rubber such as that depicted in **Figure 3** and data involving nested hysteresis loops, as shown in **Figures 7** and **8**.

A more general nonlinear model results if one assumes different nonlinearities f_j for different j in [19] or [20]. If one assumes nonlinear internal dynamics of the form:

$$\dot{\varepsilon}_j(t) + g_j\big(\varepsilon_j(t)\big) = f_j(\dot{\varepsilon}(t)), \quad j = 1, 2 \ldots N \qquad [21]$$

in place of [19], then the model combining this with [18] cannot be written as a Boltzmann generalization in the form [16] and thus constitutes a nontrivial generalization of the Boltzmann superposition approach. A related but somewhat different generalization of the standard linear/Boltzmann approach has

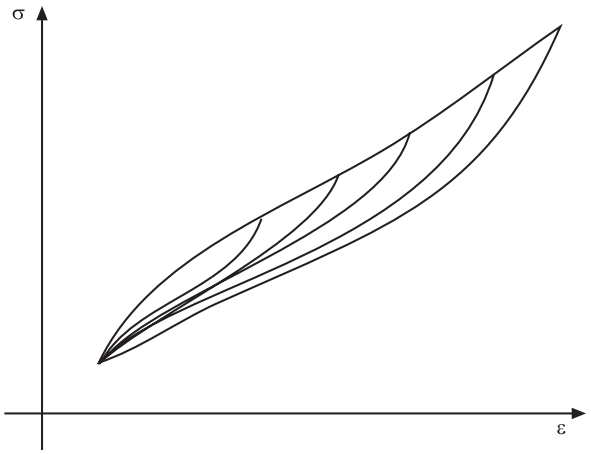


Figure 7 Complete nested hysteresis loops.

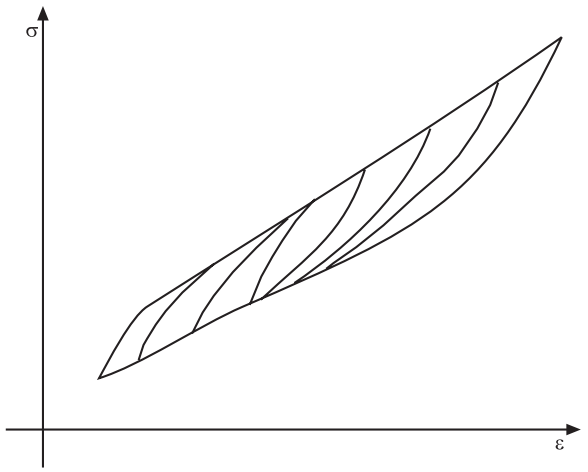


Figure 8 Incomplete nested hysteresis loops.

been used to model biological soft tissues where the hysteresis loop is independent of strain rate in a finite range of rate variation. In models due to Fung one replaces [7] by:

$$\sigma(t) = \int_{-\infty}^{t} G(t-\tau)\dot{\sigma}^{e}(\tau)\,\mathrm{d}\tau \qquad [22]$$

where σ^e is the instantaneous elastic response to a step elongation and G is a reduced relaxation kernel defined by:

$$G(t) = \{1 + c[\mathcal{E}(t/\tau_1) - \mathcal{E}(t/\tau_2)]\}/\{1 + c \ln(\tau_2/\tau_1)\} \qquad [23]$$

where:

$$\mathcal{E}(t) = \int_{t}^{\infty} \frac{\mathrm{e}^{-\tau}}{\tau}\,\mathrm{d}\tau$$

The generalized kernel G defined in eqn [23] is a decreasing function that has constant slope in the interval (τ_1, τ_2) and produces constant damping in the frequency range $\tau_1 \leq 1/\omega \leq \tau_2$. It effectively replaces the finite spectrum associated with relaxation kernels of the form given in [8] by a continuous spectrum over a finite range. The Fung model is obtained by considering a large number of Kelvin-type units as shown in **Figure 6** in series, where in each unit the springs are nonlinear functions of the elongation while the dashpots are linear functions of the tension in the springs.

The standard linear/Boltzmann models and their generalizations discussed above all entail a physics-based approach in that they are usually derived and used in connection with some (perhaps unknown) internal physics hypothesized for the viscoelastic body. There is however a large literature on purely phenomenological approaches to hysteresis wherein one attempts to approximate directly the hysteresis loops depicted in **Figures 2** and **3**. The best known of these involve Preisach models and their generalizations due to Krasnosel'skii and Pokrovskii. The approach uses ideal relay operators such as that given in **Figure 9** in parallel connections to produce hysteresis loops similar to that shown in **Figure 10**. These are then smoothed to produce a smoothed ideal relay, as depicted in **Figure 11**.

Families of these relays (which depend on 'switch points' s_1, s_2) can then be used to construct a hysteresis operator of the form:

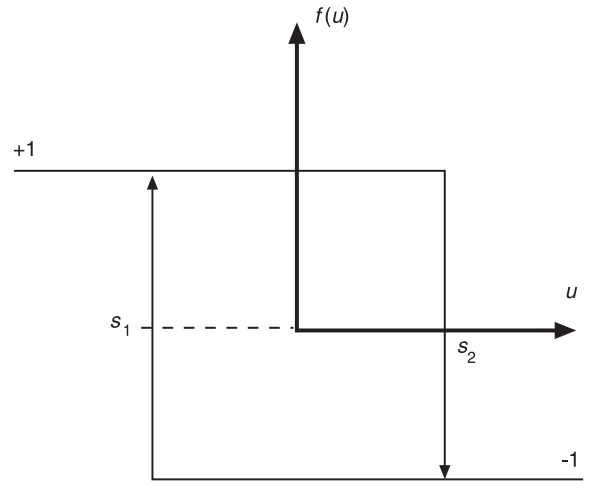


Figure 9 Ideal delayed relay operator.

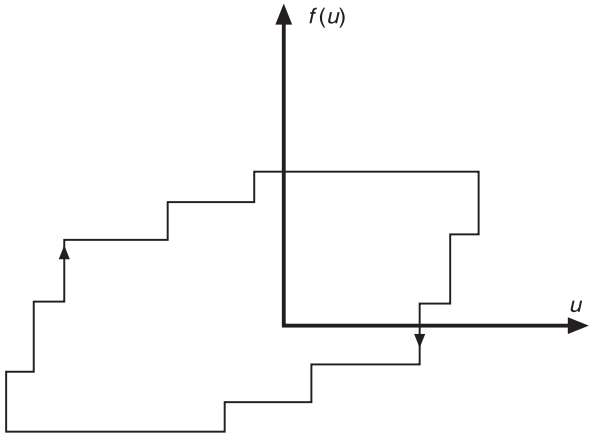


Figure 10 Parallel connection, multiple ideal relays.

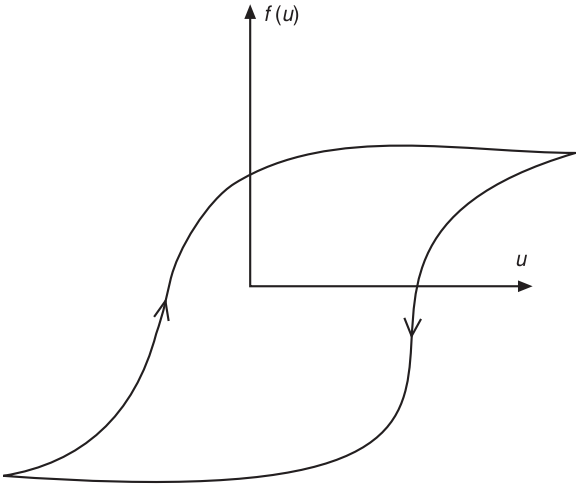


Figure 11 Smoothed ideal relay operator.

$$\sigma(t) = [P_\mu(\varepsilon, \xi)](t) = \int_{\bar{S}} [k_s(\varepsilon, \xi(s))](t)\, \mathrm{d}\mu(s) \quad [24]$$

where μ is a signed Borel measure on the closed Preisach plane $\bar{S} = \{(s_1, s_2) | s_1 \leq s_2\}$ of switches, k_s is a generalized Preisach kernel, and ξ contains initial state information. In the classical Preisach formulation, the kernel is defined in terms of linear combinations of relays as depicted in **Figure 10**, while smoothed relays as in **Figure 11** are used in the generalized Krasnosel'skii–Pokrovskii kernels. In addition to the perhaps unsatisfying aspect of being purely phenomenological, this approach has serious difficulties if used as a means to model damping in viscoelastic structures. First, there are a large number of nonphysical parameters (defining the switches and relays) that must be identified. More importantly, the resulting operator in the stress–strain relationship [24] is rate-independent and hence cannot be expected to yield adequate models to describe hysteretic damping in most viscoelastic structures which usually exhibit strong frequency (and hence rate) dependence.

Nomenclature

E	Young's modulus
G	generalized kernal
H	Heaviside function
s_1, s_2	switch points
t	time
δ	Dirac delta distribution
ε	strain
σ	stress

See also: **Viscous damping**.

Further Reading

Brokate M and Sprekels J (1996) *Hysteresis and Phase Transitions*. New York: Springer-Verlag.

Christensen RM (1982) *Theory of Viscoelasticity: An Introduction*, 2nd edn. New York: Academic Press.

Drozdov A (1998) *Viscoelastic Structures*. San Diego, CA: Academic Press.

Findley WN, Lai JS and Onaran K (1976) *Creep and Relaxation of Nonlinear Viscoelastic Materials*. Amsterdam: North-Holland.

Fung YC (1965) *Foundations of Solid Mechanics*. Englewood Cliffs, NJ: Prentice-Hall.

Fung YC (1993) *Biomechanics: Mechanical Properties of Living Tissues*, 2nd edn. New York: Springer-Verlag.

Krasnosel'skii MA and Pokrovskii AV (1989) *Systems with Hysteresis*. Berlin: Springer-Verlag.

Lakes SL (1998) *Viscoelastic Solids*. Boca Raton: CRC Press.

Mayergoyz ID (1991) *Mathematical Models of Hysteresis*. New York: Springer-Verlag.

Osiński Z (ed.) (1998) *Damping of Vibrations*. Rotterdam: A.A. Balkema.

Renardy M, Hrusa WJ and Nohel JA (1987) *Mathematical Problems in Viscoelasticity*. Harlow: Longman.

Visintin A (1994) *Differential Models of Hysteresis*. New York: Springer-Verlag.

IDENTIFICATION, FOURIER-BASED METHODS

S Braun, Technion – Israel Institute of Technology, Haifa, Israel

Copyright © 2001 Academic Press

doi:10.1006/rwvb.2001.0120

Identification of vibrating systems is in a sense the inverse of the analysis problem. In the analysis, a response is predicted based on knowledge of the system's model and the excitation (**Figure 1**). The identification extracts a model based on knowledge of an excitation and the response. It is usually based on experimentally acquired data, and measurement aspects have to be considered when performing such tasks. Identification methods thus utilize sampled data.

A major part of the identification task assumes that the vibrating system is linear, and thus draws heavily on the well-established discipline of linear system identification. As such we encounter cases of single input/single output (SISO), multiple input/single output (MISO) and multiple input/multiple output (MIMO). In this section it is mainly the SISO case that is addressed.

There are two basic types of identification methods: parametric (often referred to as model-based) and nonparametric. In the parametric methods, a model structure is assumed (or known) and the model's parameters are extracted by the identification procedure. The parameters can be mathematical, for example, the coefficients linear differential (or difference) equation. They can be physical, for example, natural frequencies and damping ratios. In general, the number of parameters identified in the parametric approach is significantly smaller than the number of points in the describing functions resulting from the nonparametric approach. In the nonparametric methods, an identifying function is sought. Examples are frequency response functions (FRFs) and impulse responses. This section deals with nonparametric frequency domain methods only.

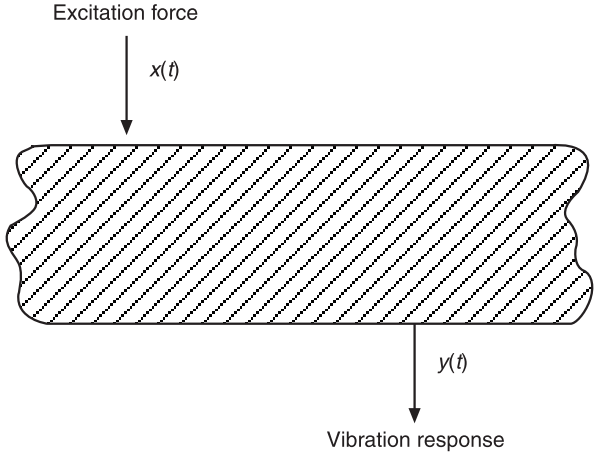


Figure 1 Identification test.

Identification methods are also categorized according to the excitation signal used. The term 'rich' is used for excitations that enable one to identify more or less the complete system characteristics. In terms of the FRF, a rich excitation would cover the frequency range of interest. Rich excitations include transients, periodic, and random functions. Harmonic excitations, usually termed sine excitations, are very powerful, but not rich. A classification according to excitation methods thus covers stepped sine testing, impulse testing (transient), random testing, periodic burst, multisine, etc. The identification procedure and characteristics may be heavily dependent on the type of excitation used.

In utilizing experimentally acquired data, the various uncertainties associated with experiments necessitate a variety of approaches to the identification task. The majority of identification approaches address uncertainties that can be modeled as additive error, usually referred to as noise, to the measured signals. The assumptions made concerning such noise can dictate the type of identification procedure to be used. A specific procedure is geared to situations where uncertainties can be modeled as white noise added to the response measurement only. Other procedures would handle noise added to the input or more general cases.

The accuracy of the results will depend heavily on the procedure, the correctness of assumptions, the type of excitation.

Frequency Domain Identification

This is a nonparametric identification. Frequency domain information is based on Fourier methods. Applying a Fourier transform to the differential equation describing the linear system results in an algebraic one.

The noiseless case: Such a case is rarely assumed, but merits fundamental consideration (**Figure 2**).

$$Y(\mathrm{i}\omega) = H(\mathrm{i}\omega)X(\mathrm{i}\omega)$$
$$H(\mathrm{i}\omega) = \frac{Y(\mathrm{i}\omega)}{X(\mathrm{i}\omega)} \qquad [1]$$

The FRF $H(\mathrm{i}\omega)$ is a complex number. For the steady-state response to a sine excitation of frequency ω, its magnitude is the gain at this frequency, and its phase is the corresponding phase shift. Bode or Nyquist plots are usually used to depict H graphically. The procedure would consist of computing the transforms of the excitations and responses and performing the division of eqn [1]. The advantage of the frequency domain approach is evident from eqn [1]: H is identified separately at each frequency. In principle, a partial identification is possible, for limited frequency ranges.

A time domain identification, the system's impulse response, can be derived similarly via the frequency domain identification. This is based on the relation between the impulse response and the FRF via an inverse Fourier transform:

$$h(t) = F^{-1}[H(\mathrm{i}\omega)] \qquad [2]$$

For a sine excitation, H is computed at a single frequency. Using a stepped sine a function, $H(\omega)$ would be computed step by step.

For a transient excitation, both the excitation and the response would be broadband, covering a range of frequencies. In contrast to the sine excitation, a complete FRF can be extracted from a single test, at least in principle. The identification can be performed as long as the absolute magnitude of $X(\omega)$ exceeds a minimum level. For too small $|X(\omega)|$ (and obviously for $|X(\omega)| = 0$) the problem is ill conditioned and the resultant H problematic. The frequency range of the identification is dictated by the richness of the excitation, i.e., by the region where excitation energy exists. Periodic rich signals can also be used. One example are periodically repeating random bursts, another example is the multisine signal, a combination of sines of different frequencies but where the sum has a periodicity of its own. The spectrum of such signals is discrete. Using eqn [1], H can again only be identified at these discrete frequencies, where $|X(\omega)|$ differs from zero.

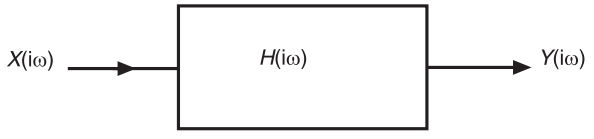


Figure 2 Frequency domain linear model.

A random excitation is also usually broadband, i.e. rich, and a complete FRF can again be identified. Owing to the statistical character of the excitation and response, the functions $X(\omega)$ and $Y(\omega)$ will have a probability distribution, which may be quite complex. The variance of spectral functions is significant, hence H as computed by eqn [1] may also have a large variance. The variance can be reduced by averaging, but some care is needed to apply this technique correctly. Averaging of separately acquired functions $X(\omega)$ and $Y(\omega)$ would be incorrect, as their expectations $E[X(\omega)]$ and $E[Y(\omega)]$ are zero. Averaging for the noiseless case would be done as:

$$\frac{1}{M}\sum_{k=1}^{M}\frac{Y_k(\mathrm{i}\omega)}{X_k(\mathrm{i}\omega)}$$

where X_k and Y_k are samples of complete frequency domain functions (Fourier transform), and M the number of sections used for averaging.

Identification with Noise-corrupted Signals

The general case, even when purely additive noise is assumed, is deceptively straightforward. For noises with given (or assumed) probability distributions, the maximum likelihood function approach can be used to estimate the 'best' FRF values. This leads to a nonlinear weighted least-squares problem, which must be solved via appropriate iterative minimization of a cost function. While appropriate commercial software packages aimed specifically at vibrating systems have been developed, this approach is not widespread in practice.

Identification for Output Additive Noise

This is probably the most popular model, even if the assumption that the noise can be modeled in such a way is not always justified (**Figure 3**):

$$Y(\mathrm{i}\omega) = H(\mathrm{i}\omega)X(\mathrm{i}\omega) + N(\mathrm{i}\omega) \qquad [3]$$

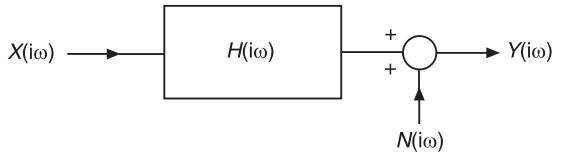


Figure 3 Additive noise at output.

While the excitation can be deterministic or random, we assume that some additive random noise exists. A 'best' identification is usually a least-squares estimate of H. This is found to be:

$$\hat{H}_1(\mathrm{i}\omega) = \frac{\Sigma X^*(\mathrm{i}\omega)Y(\mathrm{i}\omega)}{\Sigma X^*(\mathrm{i}\omega)X(\mathrm{i}\omega)} = \frac{\Sigma S_{xy}}{\Sigma S_{xx}} \qquad [4]$$

This estimator is often designated as H_1, equal to the ratio of the cross-spectrum to the auto-spectrum of the input.

According to the model described by eqn [3], the identification of $H(\mathrm{i}\omega)$ enables us to interpret $Y(\mathrm{i}\omega)$ as comprising two parts: $H(\mathrm{i}\omega)X(\mathrm{i}\omega)$, the part of the response linearly related to the excitation, and an unrelated residual. In terms of signal terminology, $Y(\mathrm{i}\omega)$ is considered to be composed of two orthogonal components. $H(\mathrm{i}\omega)X(\mathrm{i}\omega)$ is the coherent part of the response; $N(\mathrm{i}\omega)$ the residual (**Figure 4**).

A coherence function $\gamma^2(\mathrm{i}\omega)$ is then defined as:

$$\gamma^2(\mathrm{i}\omega) = \frac{\text{Coherent response power}}{\text{Total output power}} = \frac{|S_{xy}|^2}{S_{xx}S_{yy}} \qquad [5]$$
$$= 0 \leq \gamma^2 \leq 1$$

The fact that the coherence function is both bounded and normalized to 1 makes it an extremely valuable criterion for the quality of identification. A value of 1 indicates an ideal noiseless case, where all the response is linearly related (via the system's dynamics) to the excitation. A value of zero indicates a meaningless result, when there is no linear relation of any part of the response to the excitation. The coherence function thus shows the degree to which the response is linearly related to the excitation. In practice a minimum value of 0.8–0.95 is considered necessary for a mechanical identification, depending on the specific application at hand. The existence of any noise in the measurements or of additional responses to other (linearly unrelated) excitations will decrease the coherence.

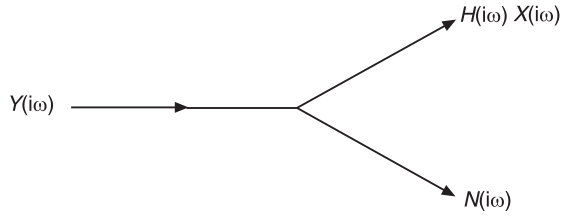


Figure 4 Response decomposition into coherent and residual components.

A coherence function less than unity may of course indicate that the basic assumption, that of testing a linear system, is not correct. Any nonlinearity existing in the system will reduce the coherence function. It should be noted that, while a nonlinearity will exhibit its presence by reducing the coherence function, the inverse does not follow: a coherence value of less than unity may be due to other causes, notwithstanding the perfectly linear system. As a final comment, we note that for a nonlinear system excited by a random input, the resultant FRF is just the best linear approximation that can be based on the measured signals.

A coherence function of unity will also result when a single pair of signals is used in eqn [4]. No residual can be computed for a least-squares estimate based on a single pair of observations.

It would be meaningless to evaluate the coherence function for purely periodic excitation and responses. Power then exists only at discrete frequencies, and the coherence between two harmonic components of equal frequency must be equal to unity.

The coherence function can be considered as the frequency domain equivalent of the normalized input/output (time domain) cross-correlation function. The advantage of identification in the frequency domain is again noticeable: the coherence function can be evaluated independently for different frequencies. The identification results can then be considered as meaningful for some frequency ranges, and unacceptable for others. The procedure is shown in **Figure 5** with the addition of the capability of computing the impulse response.

The data acquisition must be geared to the type of data at hand. For random excitation and responses, a free-running mode would be normal. For periodic signals, a triggered mode is needed, in order to avoid the randomization of the signals in the averaging process by M summations.

Identification for Input Additive Noise

The assumption that most of the additive disturbances can be modeled as occurring at the response point is not always justified. Around structural resonances, especially for cases of low damping, large responses occur with low excitation levels. The signal-to-noise ratios in data acquisition tasks will decrease when the signal level is low compared to the instrumentation

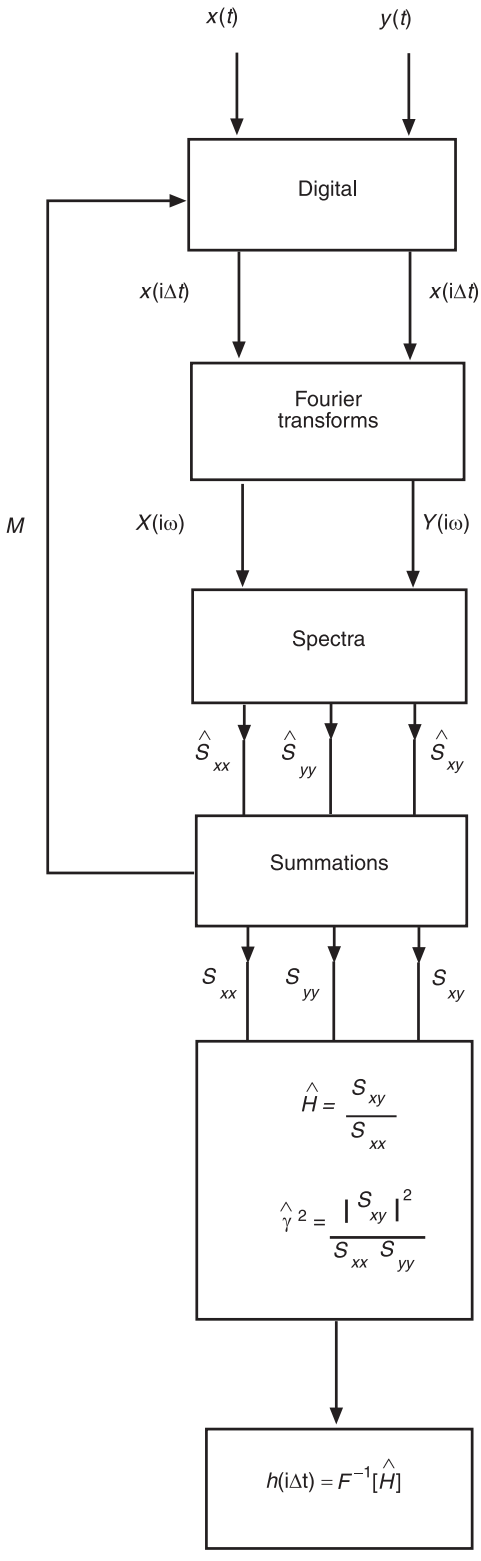


Figure 5 Identification scheme.

dynamic range. The signal-to-noise ratio in the frequency regions around resonances may thus be small, and modeling the noise as being at the input point may be justified (**Figure 6**).

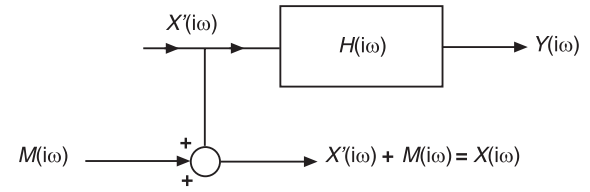


Figure 6 Additive noise at output.

$$M(\mathrm{i}\omega) = X(\mathrm{i}\omega) - \frac{Y(\mathrm{i}\omega)}{H(\mathrm{i}\omega)}$$

The least-squares solution for this model, usually known as H_2, is computed from:

$$H_2(\mathrm{i}\omega) = \frac{\Sigma Y^*(\mathrm{i}\omega)Y(\mathrm{i}\omega)}{\Sigma X^*(\mathrm{i}\omega)Y(\mathrm{i}\omega)} = \frac{\Sigma S_{yy}}{\Sigma S_{xy}} = \frac{H_1(\mathrm{i}\omega)}{\gamma^2(\mathrm{i}\omega)} \quad [6]$$

Both H_1 and H_2 can basically be computed from the same information and the general procedure of **Figure 5**. Some judgment is needed to decide on which model, and hence which estimate to use. Each of the two estimators H_1 and H_2 corresponds to different methods of noise modeling. Bias errors in the identification will occur if the estimator used does not correspond to the actual noise situation.

Sometimes the model noise to be used cannot be ascertained. Additional estimators then exist for cases where noise is modeled as additive at both the input and the output. A total least-squares estimator is one possibility. Improved least-squares methods can be used when *a priori* knowledge of the input and output RMS ratio is available. Another possibility is to average the H_1 and H_2 estimators. An estimator, usually denoted by H_v, is the geometrical mean:

$$H_v(\mathrm{i}\omega) = [H_1(\mathrm{i}\omega)\, H_2(\mathrm{i}\omega)]^{1/2}$$

Multiple Excitations/Responses

Multiple Input/Single Output Systems

For linear systems, the response is the superposition of all excitation effects (**Figure 7**):

$$\mathbf{Y} = \sum_{i=1}^{n} H_i X_i + N$$

The least-squares solution for the $(n \times 1)$ FRF is:

$$\begin{aligned} \mathbf{S}_{xy} &= \mathbf{S}_{xx}\mathbf{H} \\ \mathbf{H} &= \mathbf{S}_{xx}^{-1}\mathbf{S}_{xy} \end{aligned} \quad [7]$$

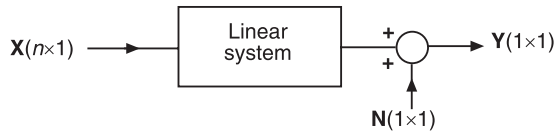


Figure 7 Multiple input/single output system.

where the dimensions of $\mathbf{S}_{xy}$ are $(n \times 1)$, of $\mathbf{S}_{xx}$ are $(n \times n)$. The elements of $\mathbf{S}_{xy}$ and $\mathbf{S}_{xx}$ are $E[X_k X_q]$ and $E[X_k Y]$, $k, q = 1 \ldots n$. This expression would not be the one to use from the computational point of view. The components of the spectral matrices are computed at all frequencies, and ill-conditioning can easily occur for some frequencies. Modern computational methods, usually incorporating the SVD, would be applied in practice to avoid the matrix inversion.

The quantitative measure of the degree of linear relation between the response and all excitations can be based on the multiple coherence function. This is again based on the ratio of the coherent output power (linearly related to all excitations) to the total output power. This scalar function can be computed via the spectral matrices. The notation is often awkward, and that used below is only one of those existing:

$$\gamma^2_{y.x} = \frac{\text{Coherent response power}}{\text{Total output power}} = \frac{\left(\mathbf{S}_{xx}^{-1}\mathbf{S}_{xy}\right)^{\mathrm{T}}\mathbf{S}_{xx}\left(\mathbf{S}_{xx}^{-1}\mathbf{S}_{xy}\right)}{\mathbf{S}_{yy}} \qquad [8]$$

A low value of the multiple coherence may be an indication that not all excitations acting on the system to be identified are monitored and measured. Matrix inversions are again avoided in practice by appropriate computational schemes.

The question whether the number of excitation monitored is appropriate can be of importance. While the mulitiple coherence functions may indicate an undetermined model, possible overdetermination has to be determined otherwise. The rank of the matrix $\mathbf{S}_{xx}$ can give an indication of the number of linearly independent excitation sources. The accepted way of rank determination is via the SVD, and this has to be computed for each frequency. For vibrating structures, such SVD functions may be heavily frequency-dependent, especially for resonating systems with narrowband spectral peaks. A simulated example is shown in **Figure 8** for a system where four responses are measured. The SVD functions indicate that only three linearly independent excitations are at hand.

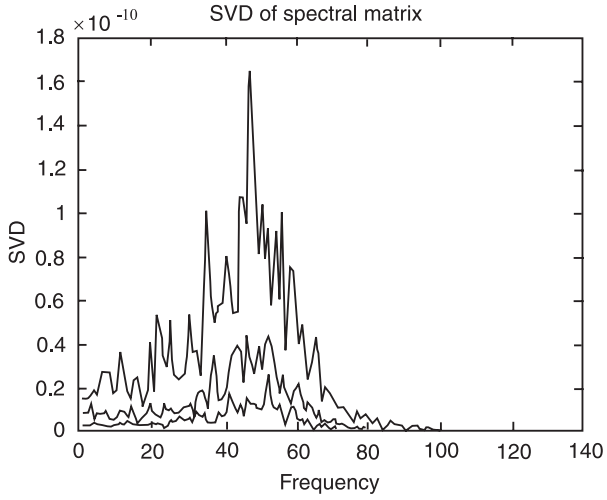


Figure 8 Singular value decomposition of spectral matrix.

Multiple Input/Multiple Output Systems

The extension from MISO leads to similar expressions. For m inputs and n outputs:

$$\mathbf{Y} = \mathbf{H}\mathbf{X}$$

with $\mathbf{Y}(n \times 1)$, $\mathbf{X}(m \times 1)$ and $\mathbf{H}(n \times m)$ (**Figure 9**). Then:

$$\mathbf{S}_{xy} = \mathbf{S}_{xx}\mathbf{H}^{\mathrm{T}}$$
$$\mathbf{H}^{\mathrm{T}} = \mathbf{S}_{xx}^{-1}\mathbf{S}_{xy} \qquad [9]$$

which is similar to eqn [7] but with dimensions $\mathbf{S}_{xy}(m \times n)$, $\mathbf{S}_{xx}(m \times m)$, $\mathbf{H}^{\mathrm{T}}(m \times n)$, where $\mathbf{H}^{\mathrm{T}}$ is Hermitian as for the elements of $\mathbf{H}$: $H_{ij} = H^x_{ji}$.

The computation of $\mathbf{H}$ will again use procedures avoiding matrix inversions. Also, specific difficulties may occur as some correlation often exists between some of the exciting forces, causing the cross-spectrum matrix to be rank-deficient.

Error Mechanisms and Their Control in the Identification Process

The general types are similar to those occurring in nonparametric spectral analysis. These are: aliasing traceable errors; bias errors; random errors; and



Figure 9 Multiple input/multiple output system.

leakage. An essential quantifier of the identification is the coherence function. Hence errors have to be considered for both the FRF and γ.

Aliasing Errors

These are due to too low a sampling frequency. They are a potential source of error in any signal-processing task, and thus also in digital indentification tasks.

Bias Errors

These are often considered as the most severe error, especially if resonance peaks in the FRF are underestimated. In spectral analysis, bias errors are due to insufficient analysis resolution. Additional mechanisms occur in the identification process.

Bias errors due to insufficient frequency resolution Most estimators, computed with the FFT, will be biased if insufficient frequency resolution is used. This resolution, Δf, must be small enough to follow local details of the estimated function. For vibrating systems local changes within resonance bandwidth have to be resolved. This bandwidth is approximately $2\xi f_n = BW$ for small damping ratios, where ξ is the damping ratio and f_n is the natural frequency, and the following is usually required:

$$\Delta f \leq \frac{1}{4} BW \qquad [10]$$

and Δf can be chosen by the parameters of the Fourier analysis.

Insufficient frequency resolution will also introduce bias errors in the coherence function. The coherence will then be underestimated. The type of window used has a significant effect on this underestimation. When a Hanning window is used, too large a Δf will cause the coherence function to exhibit sharp minima at those frequencies where H peaks, i.e., at resonances. With a rectangular window, the coherence function would show gradually decreasing values.

Bias errors due to additive noise sources These errors are a function of the noise location as well as the estimator used. For input and output noises n and m, and for noise power spectral densities S_{nn} and S_{mm}, respectively, the following results are given for the estimators $\hat{H}_1$ and $\hat{H}_2$, where H_0 is the true FRF:

$$\begin{aligned} \left|\hat{H}_1\right| &= |H_0|\left(1 + \frac{S_{mm}}{S_{xx}}\right)^{-1} \\ \left|\hat{H}_2\right| &= |H_0|\left(1 + \frac{S_{nn}}{|H_0|^2 S_{xx}}\right) \end{aligned} \qquad [11]$$

and:

$$\left|\hat{H}_1\right| < |H_0| < \left|\hat{H}_2\right|$$

These bias errors occur for the magnitude only. No bias error is introduced by the noise in the phase of the estimated FRFs.

In practice, the noise levels are dependent on the achievable signal-to-noise (S/N) ratios. For vibrating systems with small damping ratios, the input S/N decreases at resonance, where low-level excitations are used. Similarly, the output S/N decreases at antiresonances, where low response levels occur. The bias error in H_1 results in an underestimation of the maximum peaks (resonances), with those in H_2 overestimating the minima (antiresonances).

Bias due to unmonitored additional excitations Usually it is assumed that the monitored excitation $x(t)$ is responsible for the monitored output $y(t)$. In vibration tests, additional excitations may exist through unidentified paths. Should this additional excitation not be fully coherent with the monitored one, the output will not be fully coherent with the excitation, resulting in a coherence function less than unity. In addition, the FRF will be biased. For example, for H_1:

$$\hat{H}_1 = H_0\left(1 + \frac{Sx_1x_2}{Sx_2x_2}\right)$$

where x_1 is the monitored excitation and x_2 the unmonitored one. No bias error in $\hat{H}_1$ will occur if x_1 and x_2 are uncorrelated. $\hat{H}_2$ too will be biased, according to a slightly more complicated expression.

Bias due to delays between excitation and response A time delay can occur in many identification tasks. One classic example occurs in acoustic output measurements, where a propagation delay might exist for the response. Delays can also occur owing to linear-phase shifts in some part of the measurement system. A bias error will then be introduced in the identified coherence function, which will be underestimated by an amount dependent on the ratio of the time delay to that of the time duration of basic signal record (i.e., the signal to be repeated for averaging purposes).

Such a situation can sometimes be identified by noting a linear trend in the phase of the identified FRF. A 'realignment' in the form of a negative delay can then reduce or cancel this bias error.

Random Errors

These errors are due to the statistical variability of frequency domain estimates according to eqn [4] when the excitations and responses are random or include a random component. They do not occur with purely noise-free deterministic signals, either periodic or transient.

Similarly to autospectral estimates, FRF estimates based on purely random signals not only exhibit a large statistical variance but are also inconsistent, i.e., this variance does not decrease with record length, hence the need for the averaging process shown in **Figure 5**. Based on some simplifying assumptions, the normalized RMS error for the estimators have been developed as follows:

$$e\left[\hat{H}\right] = \frac{1-\gamma^2}{|\gamma|\sqrt{2M}} \qquad [12]$$

As expected, this error is inversely proportional to the square root of M, the number of records used in the averaging process. It is also dependent on the coherence function, and very large errors occur when coherence values are low and hence no strong linear relationship exists.

The use of eqn [12] is at best as a guideline, as the coherence function itself can only be estimated by the data at hand. This estimate itself is prone to statistical errors and bias as well as the random error noted.

It is usually the practice to apply windows to the data. This has the effect of increasing the correlation between adjacent spectral estimates. The number of degrees of freedom on which the FRF values are estimated increases, and hence the statistical variability decreases.

Leakage Errors

These errors, traceable to basic Fourier transform properties, occur owing to the induced periodicity of the signal spanned by the analyzed signal duration. It is usually effectively reduced by applying a window, which in this case has to be applied to both the excitation and the responses. A Hanning window is often the preferred choice for random signals. As mentioned, this also has the extra beneficial result of reducing the random errors. For periodic excitations and responses, leakage can be avoided by ascertaining that integer numbers of periods are spanned, but this necessitates a sampling frequency that must be adapted to the frequency by appropriate hardware. Otherwise, a Hanning window would be applied to this as well.

The Hanning window, centered around the analyzed signals, is not appropriate for many transient signals. A typical example would be that of exponentially decaying oscillatory responses, such as those responding to impact excitation. The S/N then decreases along with the decay.

A basic statistical approach is one giving less weight to uncertain (in this case, noisy) information. This can be achieved by using an exponential window of the form:

$$w(i\Delta T) = \exp\left(-\alpha\frac{\mathrm{i}}{n}\right) \qquad [13]$$

for the response, where α is a constant chosen so as to follow approximately the oscillating decay and n is the number of samples in the analyzing window. The modification introduced by multiplying the signal by this window is one of artificially increasing the effective damping. An appropriate correction is then necessary when damping ratios are identified from FRFs. For the case of a shock-excited single-degree-of-freedom system with natural radian frequency of ω_n, the damping ratio would be artificially increased by α/ω_n. This value must then be subtracted from any identified damping ratio.

Similarly, a rectangular window, spanning only the excitation duration (thus giving zero weight outside this span), could be used to enhance the effective S/N at the input.

Example

Some of the characteristics discussed can be seen from simulation-based results. The simulated system exhibits two resonances, separated by one antiresonance. The excitation is white. To reduce resolution attributable bias errors, the frequency spacing is approximately 1/6 of the narrowest bandwidth. The estimates are based on 10 averages, and some random errors can be seen in **Figure 10**, computed with a rectangular window. The coherence drops at the antiresonance frequency, where the coherent output is negligible. Applying a Hanning window reduces the random errors. The effect of the window on the coherence function can be seen clearly: a sharp drop at the resonance frequencies, in addition to a minimum at the antiresonant frequency (**Figure 11**).

See also: **Identification, model-based methods**; **Random vibration, basic theory**; **Spectral analysis, classical methods**; **Transform methods**; **Windows**

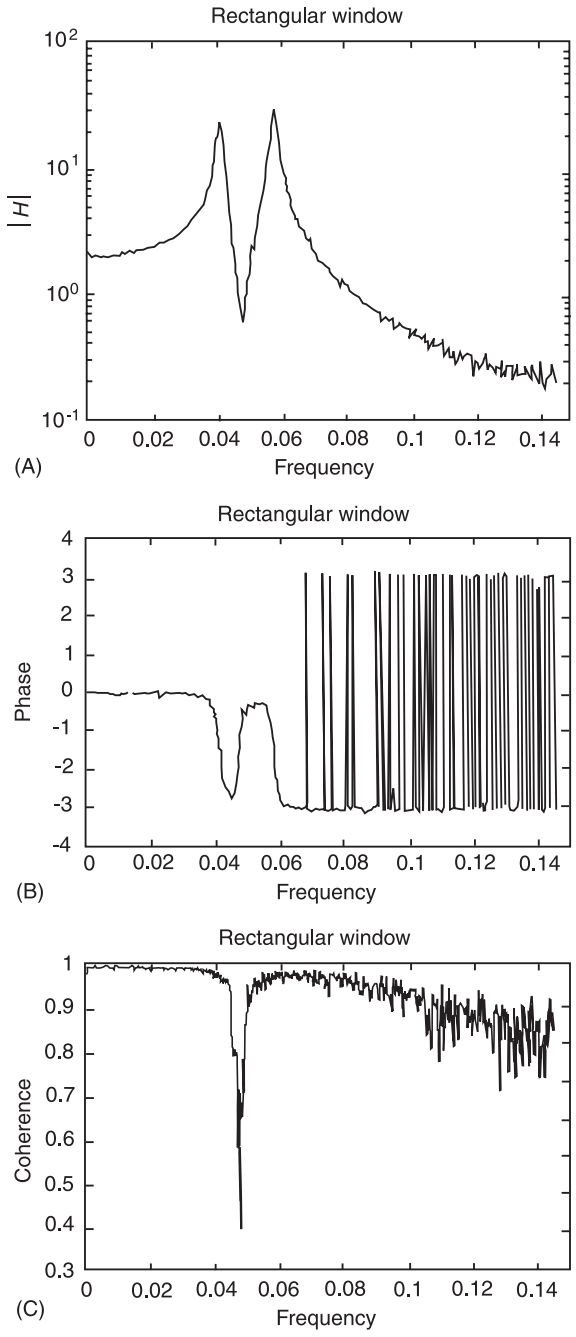


Figure 10 Identification results using a rectangular window. (A) Magnitude; (B) phase; (C) coherence function.

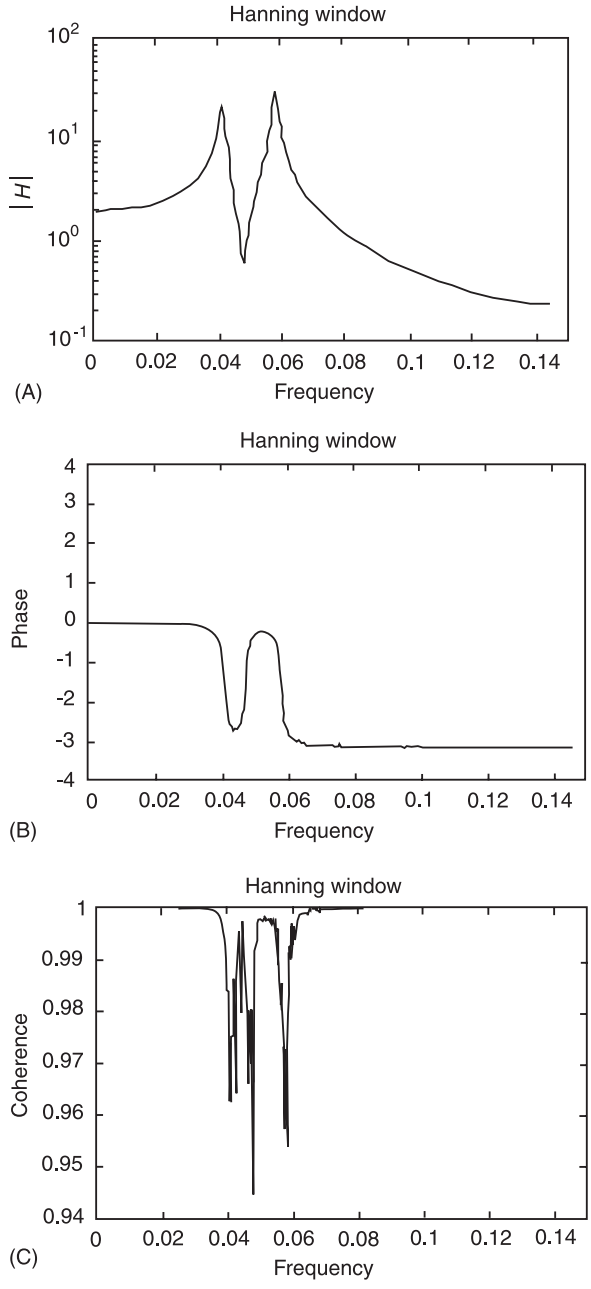


Figure 11 Identification results using a Hanning window. (A) Magnitude; (B) phase; (C) coherence function.

Further Reading

Bendat JS, Piersol AG (1986) *Random Data: Analysis, Measurement and Procedures*. New York: Wiley Interscience.

Bendat JS, Piersol AG (1993) *Engineering Applications of Correlation and Spectral Analysis*, 2nd edn. New York: John Wiley.

IDENTIFICATION, MODEL-BASED METHODS

S D Fassois, University of Patras, Patras, Greece

Copyright © 2001 Academic Press

doi:10.1006/rwvb.2001.0121

Introduction

Parametric identification of vibrating systems is the process of developing finitely parametrized models for such systems based upon measured excitation and/or response signals. Typically, the excitation is force and the response vibration displacement, velocity, or acceleration. A typical identification experiment is depicted in **Figure 1.** The structural dynamics are represented by a transfer matrix $\mathbf{G}(s)$, with s indicating the Laplace transform variable. The measurable force excitation vector is $\{\mathbf{x}(t)\}$, while the measurable vibration response vector (forced if $\mathbf{x}(t) \neq \mathbf{0}$, free if $\mathbf{x}(t) \equiv \mathbf{0}$) is $\{\mathbf{y}(t)\}$ and is assumed to be corrupted by stochastic zero-mean noise $\{\mathbf{n}(t)\}$, which is uncorrelated with $\{\mathbf{x}(t)\}$ (t indicating continuous time).

In contrast to nonparametric identification, which leads to nonparametric representations such as frequency or impulse response functions, parametric identification (also called model-based) leads to finitely parametrized models such as difference/differential equation and modal models. Such models provide important benefits due to their: (1) direct relationship with differential equation or physically significant modal representations used in engineering analysis; (2) improved accuracy and frequency resolution; (3) compactness/parsimony of representation, that is, their ability to provide complete system characterization by relatively few parameters; and (4) their suitability for analysis, prediction, fault diagnosis, and control. The price paid for these benefits includes a generally increased identification complexity and dependence of the results on the assumed model form and the estimation criterion.

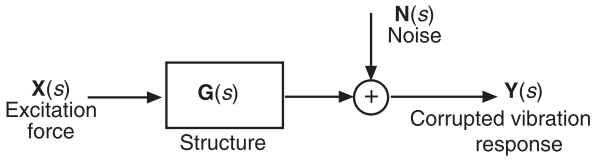


Figure 1 Typical identification experiment.

The Elements of Parametric Identification

The essential elements of any parametric identification method are:

1. the data set
2. the selected model class
3. the estimation criterion
4. the model validation procedure
5. the modal parameter extraction procedure.

The data set consists of suitable excitation and/or response signals. The model class is a selected family of models parametrized in terms of an (unknown) parameter vector $\boldsymbol{\theta}$ – for instance, the class of rational transfer function models. Upon its optimization, the estimation criterion maps the data set into a specific value of the parameter vector $\boldsymbol{\theta}$ – a common choice is the least squares criterion. The model validation procedure aims at accepting or rejecting the estimated model; in the latter case the estimation is repeated with proper modifications. Modal parameter extraction refers to the determination of the modal parameters from the estimated model and the distinction of structural from extraneous (false) modes. The general identification procedure, based upon sampled signals, is outlined in **Figure 2**.

Classification of Identification Methods

The parametric identification methods may be classified according to one of the first three of the foregoing essential elements. Hence, depending upon the type of data, they may be classified as discrete or continuous time, transient or forced response, single-input single-output (siso) or general multiple-input multiple-output (mimo). Depending upon the model class they may be classified as deterministic or stochastic, distributed or lumped parameter, linear or nonlinear, with the linear being further classified as complex exponential, polynomial (transfer function), or state space. Depending upon the estimation criterion they may be broadly classified as prediction error, least squares related, correlation, and subspace methods. Depending upon the estimator realization, they may be further classified as batch (in which the complete data record is used at once) or recursive (the data record is processed sequentially in time).

This section deals with linear, lumped parameter, and batch discrete time identification based upon sampled versions of the excitation and response signals. For simplicity the siso case is treated, although

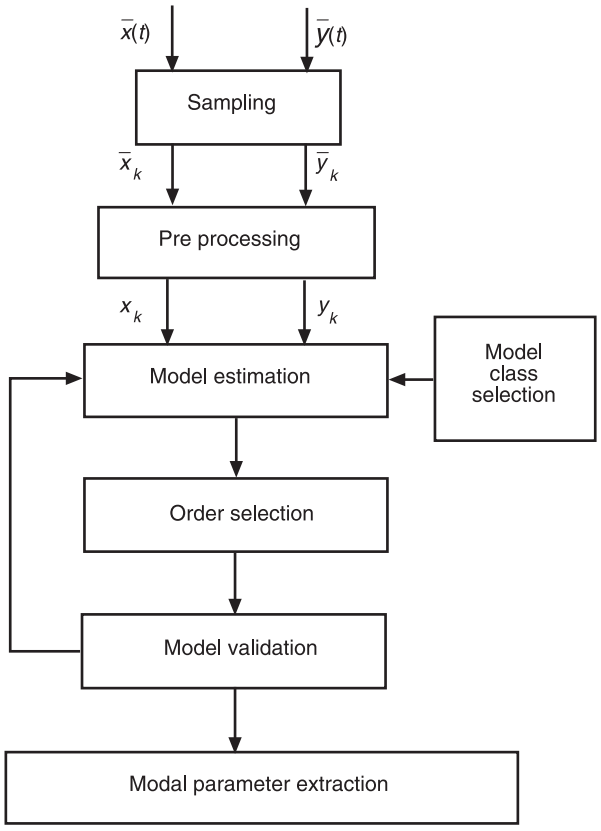


Figure 2 The general identification procedure.

the mimo case is considered within the context of the state space model class and the Eigensystem Realization Algorithm. The identified discrete time model is subsequently transformed back into the continuous time domain for modal parameter extraction.

Before embarking on our discussion of the essential elements of parametric identification methods, it is useful to note the similarity of the identification with the signal modeling problem (see the section on **Signal processing, model based methods**). The two become essentially identical when the force excitation $\{\mathbf{x}(t)\}$ is zero, or random unobservable uncorrelated (white) noise, and the noise $\{\mathbf{n}(t)\}$ is absent (**Figure 1**). Hence, the model classes used in signal modeling are either the same as those used in identification (for instance, the complex exponential model class) or suitable subsets (for instance the AutoRegressive (AR), or AutoRegressive Moving Average (ARMA) model classes). Many identification and signal modeling methods are thus closely related, as the underlying estimation theory principles are common. Yet, the presence of measured excitation in the identification problem introduces certain requirements, such as excitation richness, low cross-correlation among scalar excitations, and uncorrelatedness with the corrupting noise.

The Data Set

The siso data set consists of sampled excitation and/or noise-corrupted vibration response signals:

$$Z_0^{N-1} \stackrel{\Delta}{=} \{x_k, y_k | k = 0, 1, 2, \cdots N-1\} \qquad [1]$$

with k indicating discrete time (the corresponding analog time being $k \cdot \mathrm{d}t$, with $\mathrm{d}t$ standing for the sampling period) and N the number of data samples used in identification.

The force excitation needs to be sufficiently rich to excite the system over the frequency range (bandwidth) of interest. Written in Fourier form, it should incorporate at least as many frequencies as the order of the model to be estimated. A single harmonic excitation is, therefore, not rich, whereas a superposition of harmonic excitations, with a sufficient number of distinct frequencies, may be used. Commonly used excitations include chirp, impulsive, periodic burst, and random. In certain cases identification is based upon free response measurements, whereas, in others, the excitation is not measured (but is assumed to be uncorrelated random; see the section on **Signal processing, model based methods**).

In generating the data set to be used in identification, signal low-pass filtering and sampling, with a period satisfying the Shannon sampling theorem ($\omega_s = 2\pi/\mathrm{d}t > 2\omega_{\max}$, with $\omega_{\max}$ (rads per time unit) indicating the maximum frequency present in the analog signal), is followed by signal pre-processing (**Figure 2**). This may include further (digital) low or band-pass signal filtering, signal subsampling, scaling (so that all scalar signals assume values in a common range), and mean value removal. In case of multiple excitations it is important to ensure that the excitation forces are not collinear (linearly dependent); their mutual normalized cross-correlations should be far from absolute unity (values as close to zero as possible are recommended) in order to avoid numerical problems.

The Model Class

Time discretization of $\mathbf{G}(s)$ (**Figure 1**) leads to a discrete transfer matrix $\mathbf{G}(z)$, with z designating the z-transform variable. It is useful to note that z^{-1} is interpreted as a unit delay operator, which means that if $X(z)$ is the z-transform of $\{x_k\}$ (defined as $X(z) \stackrel{\Delta}{=} \sum_{k=0}^{\infty} x_k \cdot z^{-k}$), $z^{-1} \cdot X(z)$ is the z-transform of the delayed sequence $\{x_{k-1}\}$. Generalizing this, $z^{-l} \cdot X(z)$ is the z-transform of $\{x_{k-l}\}$. In the siso problem each scalar component (transfer function)

of $\mathbf{G}(z)$ is identified separately, with each scalar stochastic system to be identified written as:

$$\begin{aligned} Y(z) &= G(z)\cdot X(z) + N(z) \\ N(z) &= H(z)\cdot W(z) \\ Y(z) - \hat{Y}(z) &= W(z) \end{aligned} \qquad [2]$$

In these expressions $X(z)$, $Y(z)$ are the z-transforms of the sequences $\{x_k\}$, $\{y_k\}$, respectively, $N(z)$ the z-transform of $\{n_k\}$, which is a stochastic zero-mean noise generated by driving an uncorrelated (white) sequence $\{w_k\}$ (referred to as the innovations sequence and having z-transform $W(z)$) through a noise transfer function $H(z)$, and $\hat{Y}(z)$ the z-transform of $\{\hat{y}_{k/k-1}\}$, which is the sequence of the system's one-step-ahead predictions of $\{y_k\}$, each one made at the previous $(k-1)$ time instant. The first of eqns [2] represents the input–output (structural) dynamics, the second the noise dynamics, and the third indicates that the innovations sequence $\{w_k\}$ that generates the stochastic noise $\{n_k\}$ may be interpreted as the system's one-step-ahead prediction error sequence. Finally, notice that $\{n_k\}$ is assumed to be uncorrelated with the excitation $\{x_k\}$.

Letting $G(z, \boldsymbol{\theta})$, $N(z, \boldsymbol{\theta})$, and $H(z, \boldsymbol{\theta})$ represent suitable models of $G(z)$, $N(z)$, and $H(z)$, respectively, parametrized in terms of a suitable parameter vector $\boldsymbol{\theta}$, the system to be identified may be generally modeled as (compare with eqns [2]):

$$\begin{aligned} Y(z) &= G(z,\boldsymbol{\theta})\cdot X(z) + N(z,\boldsymbol{\theta}) \\ N(z,\boldsymbol{\theta}) &= H(z,\boldsymbol{\theta})\cdot E(z,\boldsymbol{\theta}) \\ Y(z) - \hat{Y}(z,\boldsymbol{\theta}) &= E(z,\boldsymbol{\theta}) \end{aligned} \qquad [3]$$

with $E(z, \boldsymbol{\theta})$, $\hat{Y}(z, \boldsymbol{\theta})$ indicating the z-transforms of $\{e_k(\boldsymbol{\theta})\}$ and $\{\hat{y}_k(\boldsymbol{\theta})\}$; the first designating the sequence of model-based one-step-ahead prediction errors (modeling $\{w_k\}$), and the second that of the model-based one-step-ahead predictions of $\{y_k\}$ (modeling $\{\hat{y}_{k/k-1}\}$). A block diagram representation of the general system and model is presented in **Figure 3**.

The various model classes, resulting from various possible parametrizations of $G(z, \boldsymbol{\theta})$ and $H(z, \boldsymbol{\theta})$, may be broadly classified as complex exponential, polynomial, and state space.

The Complex Exponential Model Class

In this case the excitation is impulsive (or zero), so that $\{y_k\}$ represents the noise-corrupted vibration impulse (or free) response which may be expressed as a sum of complex exponential functions, that is:

$$y_k = \sum_{l=1}^{n} A_l \cdot \mathrm{e}^{\mu_l k \mathrm{d}t} + e_k(\boldsymbol{\theta}) \qquad [4]$$

Obviously, $H(z, \boldsymbol{\theta}) \equiv 1$, while μ_l represents the lth continuous-time pole, $\lambda_l \triangleq \mathrm{e}^{\mu_l \mathrm{d}t}$ the corresponding discrete-time pole, A_l the amplitude of the lth vibration component, n the model order, and $\boldsymbol{\theta} \triangleq [\mu_1 \ldots \mu_n \vdots A_1 \ldots A_n]^{\mathrm{T}}$.

Polynomial Model Classes

Polynomial model classes are based upon rational transfer function representations of $G(z, \boldsymbol{\theta})$ and $H(z, \boldsymbol{\theta})$. The main such classes are:

1. The ARX (AutoRegressive with eXogenous input) model class:

$$\begin{aligned} Y(z) &= \frac{B(z,\boldsymbol{\theta})}{A(z,\boldsymbol{\theta})}\cdot X(z) + \frac{1}{A(z,\boldsymbol{\theta})}\cdot E(z,\boldsymbol{\theta}) \\ &\Rightarrow A(z,\boldsymbol{\theta})\cdot Y(z) = B(z,\boldsymbol{\theta})\cdot X(z) + E(z,\boldsymbol{\theta}) \end{aligned} \qquad [5]$$

with:

$$\begin{aligned} A(z,\boldsymbol{\theta}) &\triangleq 1 + a_1 z^{-1} + \cdots + a_{na} z^{-na} \\ B(z,\boldsymbol{\theta}) &\triangleq b_0 + b_1 z^{-1} + \cdots + b_{nb} z^{-nb} \end{aligned}$$

referred to as the AutoRegressive (AR) and eXogenous (X) polynomials, respectively, and $\boldsymbol{\theta} \triangleq [\text{ coef } A,\ \text{coef } B]^{\mathrm{T}}$. The positive integers na, nb are the AR and X orders of the model. Notice that the coefficient b_0 of $B(z, \boldsymbol{\theta})$ may be identically zero in certain cases, implying the presence of unity time delay in the input–output (structural) transfer function. The limitation of the ARX model class is that the noise transfer function is restricted to $H(z, \boldsymbol{\theta}) = 1/A(z, \boldsymbol{\theta})$.

2. The ARMAX (AutoRegressive Moving Average with eXogenous input) model class:

$$\begin{aligned} &Y(z) = \frac{B(z,\boldsymbol{\theta})}{A(z,\boldsymbol{\theta})}\cdot X(z) + \frac{C(z,\boldsymbol{\theta})}{A(z,\boldsymbol{\theta})}\cdot E(z,\boldsymbol{\theta}) \Rightarrow \\ &A(z,\boldsymbol{\theta})\cdot Y(z) = B(z,\boldsymbol{\theta})\cdot X(z) + C(z,\boldsymbol{\theta})\cdot E(z,\boldsymbol{\theta}) \end{aligned} \qquad [6]$$

in which $C(z, \boldsymbol{\theta})$ is referred to as the Moving Average (MA) polynomial (of a form similar to that of $A(z, \boldsymbol{\theta})$) and $\boldsymbol{\theta} \triangleq [\text{coef } A, \text{coef } B, \text{coef } C]^{\mathrm{T}}$. Although the noise transfer function $H(z, \boldsymbol{\theta})$ is still restricted to have common characteristic polynomial with $G(z, \boldsymbol{\theta})$, the ARMAX model class is substantially more flexible due to the incorporation of the MA polynomial in it. Yet, a high MA order (nc) may be necessary in properly capturing the noise dynamics.

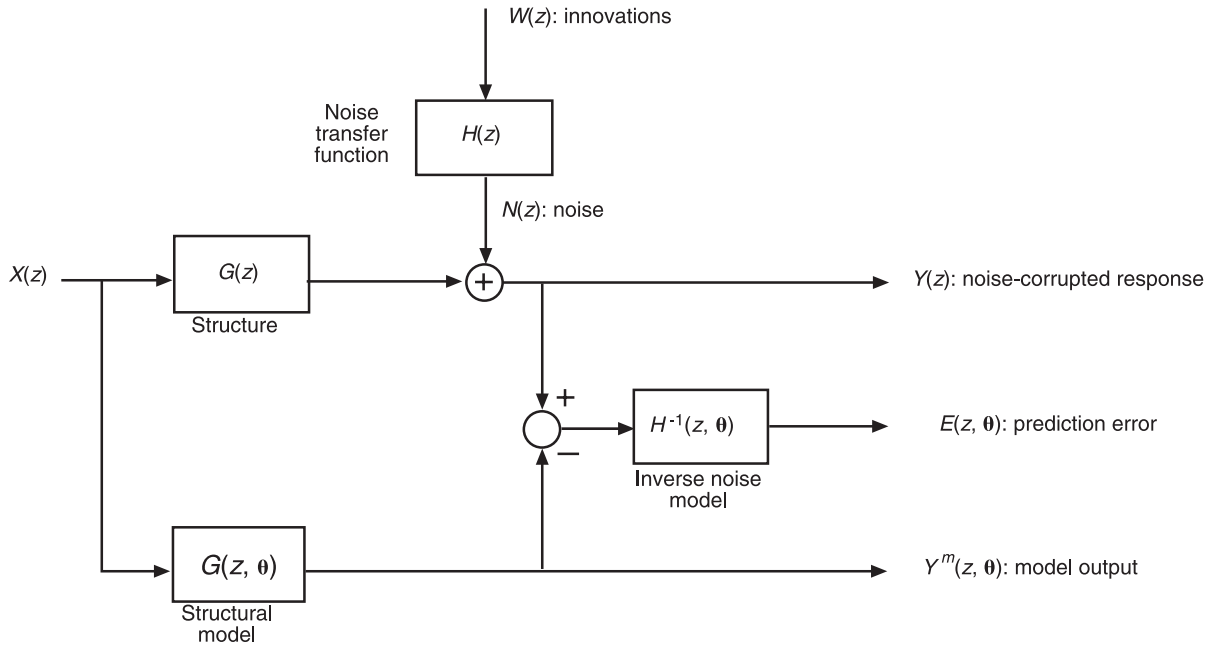


Figure 3 Block diagram representation of the general siso system and model.

3. The Box–Jenkins model class:

$$Y(z) = \frac{B(z,\boldsymbol{\theta})}{A(z,\boldsymbol{\theta})} \cdot X(z) + \frac{D(z,\boldsymbol{\theta})}{C(z,\boldsymbol{\theta})} \cdot E(z,\boldsymbol{\theta}) \quad [7]$$

in which $D(z, \boldsymbol{\theta})$ is of a form similar to that of $C(z, \boldsymbol{\theta})$, and $\boldsymbol{\theta} \triangleq [\text{coef } A, \text{ coef } B, \text{ coef } C, \text{ coef } D]^{\mathrm{T}}$. This model class offers complete decoupling between the noise and structural transfer functions.

4. The Output Error model class:

$$Y(z) = \frac{B(z,\boldsymbol{\theta})}{A(z,\boldsymbol{\theta})} \cdot X(z) + E(z,\boldsymbol{\theta}) \quad [8]$$

in which $\boldsymbol{\theta} \triangleq [\text{coef } A, \text{ coef } B]^{\mathrm{T}}$. This model class avoids modeling the noise, thus limiting its scope to the structural transfer function.

The State Space Model Class

In this case a first-order vector representation is used:

$$\begin{aligned} \mathbf{z}_{k+1} &= \mathbf{A}(\boldsymbol{\theta}) \cdot \mathbf{z}_k + \mathbf{B}(\boldsymbol{\theta}) \cdot \mathbf{x}_k + \mathbf{K}(\boldsymbol{\theta}) \cdot \mathbf{e}_k(\boldsymbol{\theta}) \\ \mathbf{y}_k &= \mathbf{C}(\boldsymbol{\theta}) \cdot \mathbf{z}_k + \mathbf{D}(\boldsymbol{\theta}) \cdot \mathbf{x}_k + \mathbf{e}_k(\boldsymbol{\theta}) \end{aligned} \quad [9]$$

in which $\mathbf{x}_k\,(r \times 1)$, $\mathbf{y}_k\,(p \times 1)$, $\mathbf{z}_k\,(n \times 1)$, and $\mathbf{e}_k(\boldsymbol{\theta})$ $(p \times 1)$ are the input, output, state, and prediction error vectors, respectively, and $\mathbf{A}$, $\mathbf{B}$, $\mathbf{C}$, $\mathbf{D}$, $\mathbf{K}$ the state, input, output, direct transmission, and Kalman gain matrices, respectively. $\boldsymbol{\theta} \triangleq [\text{col } \mathbf{A}, \text{ col } \mathbf{B}, \text{ col } \mathbf{C}, \text{ col } \mathbf{D}, \text{ col } \mathbf{K}]^{\mathrm{T}}$, with col$(\cdot)$ indicates column vector consisting of the elements of the indicated matrix. The model class [9] is known as the innovations form, and incorporates both the structural and noise dynamics. An advantage of this class is its versatility in accounting for either siso or mimo systems.

The Estimation Criterion: Identification Methods

Following the estimation criterion classification, four main families of identification methods may be distinguished:

1. Prediction Error methods
2. Least squares related methods
3. Correlation methods
4. Subspace methods

Prediction Error Methods

The Prediction Error methods postulate parameter estimation based upon minimization of a scalar function of the model-based one-step-ahead prediction error sequence $\{e_k(\boldsymbol{\theta})\}$, that is:

$$\hat{\boldsymbol{\theta}} = \arg \min_{\boldsymbol{\theta}} \frac{1}{N} \sum_{k=0}^{N-1} f(e_k(\boldsymbol{\theta})) \quad [10]$$

in which the hat denotes estimate, arg min minimizing argument, N the number of data samples (per signal) used in estimation, and $f(\cdot)$ a scalar positive function. The usual choice for $f(\cdot)$ is the quadratic:

$$f(e) = \frac{1}{2}e^2 \qquad [11]$$

whereas in certain cases a linearly filtered version of $\{e_k(\boldsymbol{\theta})\}$ is used in eqn [10]. Depending upon the selected model class, different types of Prediction Error methods are possible.

ARX models: Linear Least Squares identification The ARX model (eqn [5)] may, in the time domain, be expressed as:

$$\begin{aligned} y_k + \sum_{i=1}^{na} a_i \cdot y_{k-i} &= \sum_{i=0}^{nb} b_i \cdot x_{k-i} + e_k(\boldsymbol{\theta}) \\ \Rightarrow y_k &= \overbrace{\boldsymbol{\phi}_k^{\mathrm{T}} \cdot \boldsymbol{\theta}}^{\hat{y}_k(\boldsymbol{\theta})} + e_k(\boldsymbol{\theta}) \end{aligned} \qquad [12]$$

with:

$$\boldsymbol{\phi}_k = \left[-y_{k-1} \ldots - y_{k-na} \vdots x_k \ldots x_{k-nb} \right]^{\mathrm{T}}$$

$$\boldsymbol{\theta} = \left[a_1 \ldots a_{na} \vdots b_0 \ldots b_{nb} \right]^{\mathrm{T}}$$

Because of the linearity of the predictor $\hat{y}_k(\boldsymbol{\theta})$ with respect to the parameter vector $\boldsymbol{\theta}$ (eqn [12)], minimization of the quadratic Prediction Error (Least Squares) criterion of eqns [10]–[11] leads to the celebrated Linear Least Squares (linear regression) estimator:

$$\hat{\boldsymbol{\theta}} = \left(\frac{1}{N} \sum_{k=0}^{N-1} \boldsymbol{\phi}_k \cdot \boldsymbol{\phi}_k^{\mathrm{T}} \right)^{-1} \cdot \left(\frac{1}{N} \sum_{k=0}^{N-1} \boldsymbol{\phi}_k \cdot y_k \right) \qquad [13]$$

where the signal values outside the $[0, N-1]$ range are customarily set to zero. It is also worth observing that the quantities within the parentheses in eqn [13] are composed of sample auto- and cross-covariances of the excitation and response signals.

Assuming correct model orders, the estimator [13] converges asymptotically ($N \to \infty$) to the true parameter vector (consistency property) as long as the true system is amenable to an ARX representation, that is, the noise transfer function is $H(z) = 1/A(z)$ with the characteristic polynomial $A(z)$ being shared with the structural transfer function.

Other model structures: Prediction Error identification Because of the nonlinear dependence of the predictor $\hat{y}_k(\boldsymbol{\theta})$ on the parameter vector $\boldsymbol{\theta}$ for alternative model structures (such as the ARMAX, Box–Jenkins, Output Error, or state space), the minimization of the Prediction Error criterion of eqns [10]–[11] is a nonlinear problem lacking closed-form solution. Estimates are thus obtained via iterative numerical optimization, based upon algorithms such as the Gauss–Newton or Levenberg–Marquardt. The strong point of Prediction Error identification is its achieved (under weak conditions) consistency and asymptotic ($N \to \infty$) statistical optimality (the latter in the special case of Maximum Likelihood identification; see the third remark, below). Drawbacks include the computational complexity, the need for initial guess parameter values, the presence of local minima, and potential algorithmic instabilities.

Remarks

1. It may be shown that the prediction error estimator based upon N data samples, say $\hat{\boldsymbol{\theta}}_N$:

$$\hat{\boldsymbol{\theta}}_N \to \boldsymbol{\theta}^* \quad \text{as} \quad N \to \infty \quad (w.p.1) \qquad [14]$$

with:

$$\boldsymbol{\theta}^* \stackrel{\Delta}{=} \arg \min_{\boldsymbol{\theta}} E\{f(e_k(\boldsymbol{\theta}))\} \qquad [15]$$

with $E\{\cdot\}$ indicating statistical expectation and $w.p.1$ with probability one (consistency property). Furthermore, provided that the sequence $\{e_k(\boldsymbol{\theta}^*)\}$ is approximately white,

$$\sqrt{N} \cdot \left(\hat{\boldsymbol{\theta}}_N - \boldsymbol{\theta}^* \right) \xrightarrow{\text{dist}} \mathcal{N}(\mathbf{0}, \mathbf{P}) \quad \text{as} \quad \mathcal{N} \to \infty \qquad [16]$$

with $\mathcal{N}(\cdot, \cdot)$ designating Gaussian distribution with the indicated mean and covariance. Expression [16] indicates that the estimator converges in distribution to a random vector with mean value $\boldsymbol{\theta}^*$ and covariance matrix $\mathbf{P}$. The latter is equal to:

$$\mathbf{P} = \lambda \cdot \left[E\{\boldsymbol{\psi}_k \cdot \boldsymbol{\psi}_k^{\mathrm{T}}\} \right]^{-1} \qquad [17]$$

with:

$$\lambda \stackrel{\Delta}{=} E\{e_k^2(\boldsymbol{\theta}^*)\} \quad \boldsymbol{\psi}_k \stackrel{\Delta}{=} \frac{\mathrm{d}}{\mathrm{d}\theta} \hat{y}_k(\boldsymbol{\theta}) \Big|_{\theta=\theta^*} \qquad [18]$$

In estimating λ in eqn [18], the statistical expectation is replaced by the sample mean.

2. The quadratic Prediction Error (Least Squares) criterion of eqns [10]–[11] may be written as follows in the frequency domain:

$$V_N(\boldsymbol{\theta}) = \frac{\mathrm{d}t}{2\pi} \times \int_{-\pi/\mathrm{d}t}^{\pi/\mathrm{d}t} \frac{1}{2}\left|\frac{Y(i\omega)}{X(i\omega)} - G(i\omega,\boldsymbol{\theta})\right|^2 \cdot \left|\frac{X(i\omega)}{H(i\omega,\boldsymbol{\theta})}\right|^2 \cdot \mathrm{d}\omega \quad [19]$$

where ω represents frequency in rads per time unit, i the imaginary unit, $|\cdot|$ complex magnitude, and $X(i\omega)$, $Y(i\omega)$ the Fourier transforms (z-transforms evaluated on the unit circle) of the excitation and noise-corrupted response signals, respectively. Recognizing

$$\hat{G}(i\omega) \triangleq Y(i\omega)/X(i\omega) \quad [20]$$

as the 'customary' nonparametric (also called 'empirical') estimate of $G(i\omega)$ in the frequency domain, the quadratic Prediction Error criterion may be viewed as a criterion for the 'fitting' of $\hat{G}(i\omega)$ to the parametrized frequency response $G(i\omega,\boldsymbol{\theta})$, weighted (at each frequency) by $|X(i\omega)/H(i\omega,\boldsymbol{\theta})|^2$.

3. The selection $f(\cdot) = -\ln f_e(\cdot)$, with $f_e(\cdot)$ indicating the probability density of $e_k(\boldsymbol{\theta})$, leads to Maximum Likelihood estimation. The Maximum Likelihood estimator is asymptotically ($N\to\infty$) optimal as it achieves a minimal covariance matrix $\mathbf{P}$ (asymptotic statistical efficiency). It is also worth noting that in the Gaussian case the quadratic (equations [10]–[11]) prediction error estimator coincides with the Maximum Likelihood estimator, being thus asymptotically efficient.

Least Squares-related Methods

Least Squares related methods constitute useful alternatives to Prediction Error identification, aiming at overcoming some of its limitations at the expense of potentially reduced accuracy. Three such methods are presented: the Prony method, the Two-Stage Least Squares (2SLS) method, and the Linear Multistage (LMS) method.

The Prony method The Prony method uses free or impulse response vibration data $\{y_k\}$ $(k = 0, 1, \ldots N-1)$ to identify a complex exponential model of the form [4].

Let λ_l $(l = 1, 2, \ldots n)$ designate the discrete model poles and $C(\lambda)$ the nth order polynomial having them as its roots (characteristic polynomial). Hence:

$$C(\lambda_l) \triangleq \lambda_l^n + \sum_{i=0}^{n-1} c_i \lambda_l^i = 0 \quad (c_n \equiv 1) \quad [21]$$

Next consider the quantity:

$$y_{k+n} + \sum_{i=0}^{n-1} c_i \cdot y_{k+i} = \sum_{i=0}^{n} c_i \cdot \overbrace{\left\{\sum_{l=1}^{n} A_l \cdot \lambda_l^{k+i}\right\}}^{y_{k+i}} = \overbrace{\left\{\sum_{i=0}^{n} c_i \cdot \lambda_l^i\right\}}^{=0} \cdot \left\{\sum_{l=1}^{n} A_l \cdot \lambda_l^k\right\} = 0 \quad [22]$$

where the model expression [4] with $e_k(\boldsymbol{\theta}) \equiv 0$ (deterministic case) and $\lambda_l = \mathrm{e}^{\mu_l \mathrm{d}t}$, along with [21], were used. The resulting homogeneous difference equation implied by [22] may be rewritten as:

$$y_k = \boldsymbol{\phi}_k^{\mathrm{T}} \cdot \mathbf{c} \quad [23]$$

with:

$$\boldsymbol{\phi}_k^{\mathrm{T}} \triangleq [-y_{k-1} - y_{k-2} \ldots - y_{k-n}]^{\mathrm{T}}$$
$$\mathbf{c} \triangleq [c_{n-1}\, c_{n-2} \ldots c_0]^{\mathrm{T}}$$

Eqn [23] may be successively written for $k = n$, $n+1, \ldots N-1$ to form an overdetermined (assuming $N > 2n$) system of equations in the parameter vector $\mathbf{c}$, which may then be estimated via the Linear Least Squares estimator:

$$\hat{c} = \left(\frac{1}{\tilde{N}}\sum_{k=n}^{N-1} \phi_k \cdot \phi_k^{\mathrm{T}}\right)^{-1} \cdot \left(\frac{1}{\tilde{N}}\sum_{k=n}^{N-1} \phi_k \cdot y_k\right) \quad [24]$$

with $\tilde{N} \triangleq N - n$. Once the coefficients of the characteristic polynomial $C(\lambda)$ are available, its roots (poles) λ_l $(l = 1, 2, \ldots n)$ may be readily obtained.

For the estimation of the modal amplitudes A_l $(l = 1, 2, \ldots n)$, the Prony model (eqn [4]) is rewritten as:

$$y_k = \boldsymbol{\varphi}_k^{\mathrm{T}} \cdot \mathbf{a} + e_k(\mathbf{a}) \quad [25]$$

where $\boldsymbol{\varphi}_k \triangleq [\lambda_1^k\, \lambda_2^k \ldots \lambda_n^k]^{\mathrm{T}}$ and $\mathbf{a} \triangleq [A_1\, A_2 \ldots A_n]^{\mathrm{T}}$. Writing [25] for $k = 0, 1, 2, \ldots N-1$ defines a set of overdetermined equations in the modal amplitude vector $\mathbf{a}$, which may also be estimated via Linear Least Squares:

$$\hat{\mathbf{a}} = \left(\frac{1}{N}\sum_{k=0}^{N-1} \boldsymbol{\varphi}_k \cdot \boldsymbol{\varphi}_k^{\mathrm{T}}\right)^{-1} \cdot \left(\frac{1}{N}\sum_{k=0}^{N-1} \boldsymbol{\varphi}_k \cdot y_k\right) \quad [26]$$

When used in connection with impulse response data, the Prony method is known as the Complex Exponential method. The method's strong point is simplicity, whereas its main limitations are the assumed noise-free (deterministic) setting and the transient nature of the data which may limit the number of samples used in identification.

The Two-Stage Least Squares (2SLS) method The 2SLS method uses any type of excitation and forced response data to identify an ARMAX model of the form [6]. The method is based on the observation that the nonlinearity of the ARMAX predictor at time k, in terms of the parameter vector $\boldsymbol{\theta}$, would be overcome if the past (at times $k-1, \ldots k-nc$) model-based prediction errors were known. According to the method, these are approximately estimated via an ARX model of sufficiently high orders (ma, mb) (which constitute the method's design parameters):

$$A_{ma}(z, \boldsymbol{\theta}_m) \cdot Y(z) = B_{mb}(z, \boldsymbol{\theta}_m) \cdot X(z) + E(z, \boldsymbol{\theta}_m) \quad [27]$$

in which $\boldsymbol{\theta}_m \stackrel{\Delta}{=} [\text{coef}\, A_{ma}, \text{coef}\, B_{mb}]^{\mathrm{T}}$. Comparing this with the ARMAX model form [6], it is evident that the $A_{ma}(z)$ and $B_{mb}(z)$ polynomials attempt to approximate the transfer functions $A(z)/C(z)$ and $B(z)/C(z)$, respectively; a fact dictating high orders ma, mb, especially when the true MA polynomial has zeros close to the unit circle. The estimation of the ARX model [27] is accomplished via Linear Least Squares, from which the prediction error sequence $\{e_k(\hat{\boldsymbol{\theta}}_m)\}(k = 0, 1, 2, \ldots N-1)$ is obtained (stage 1).

Using the sequence $\{e_k(\hat{\boldsymbol{\theta}}_m)\}$, the ARMAX model form [6] is approximated as:

$$\begin{aligned} y_k + \sum_{i=1}^{na} a_i \cdot y_{k-i} &= \sum_{i=0}^{nb} b_i \cdot x_{k-i} + e_k(\boldsymbol{\theta}) \\ &+ \sum_{i=1}^{nc} c_i \cdot e_{k-i}(\hat{\boldsymbol{\theta}}_m) \\ \Rightarrow y_k &= \boldsymbol{\phi}_k^{\mathrm{T}} \cdot \boldsymbol{\theta} + e_k(\boldsymbol{\theta}) \end{aligned} \quad [28]$$

with:

$$\boldsymbol{\phi}_k \stackrel{\Delta}{=} \Big[-y_{k-1} \ldots -y_{k-na} \vdots x_k \ldots x_{k-nb} \vdots e_{k-1}(\hat{\boldsymbol{\theta}}_m) \ldots e_{k-nc}(\hat{\boldsymbol{\theta}}_m) \Big]^{\mathrm{T}}$$

$$\boldsymbol{\theta} \stackrel{\Delta}{=} \Big[a_1 \ldots a_{na} \vdots b_0 \ldots b_{nb} \vdots c_1 \ldots c_{nc} \Big]^{\mathrm{T}}$$

and the parameter vector $\boldsymbol{\theta}$ is estimated via Linear Least Squares (stage 2). The 2SLS method is simple and computationally efficient, but also suboptimal (statistically inefficient).

The Linear Multi Stage method The LMS method also identifies an ARMAX model of the form [6] based upon any type of excitation and forced response data. The method starts (stage 1) with the estimation (via Linear Least Squares) of an ARX model of the form [27] of sufficiently high orders (ma, mb; method's design parameters). It, nevertheless, subsequently relies only upon the estimated $A_{ma}(z)$ polynomial and not the prediction error sequence. Indeed, as already noted, the $A_{ma}(z)$ polynomial in [27] approximates the transfer function $A(z)/C(z)$ of the ARMAX model [6], hence:

$$\hat{A}_{ma}(z) \cdot C(z) \approx A(z) \Rightarrow \sum_{k=0}^{j} c_k \cdot (\hat{a}_{ma})_{j-k} \approx a_j \quad (j = 1, 2, \ldots) \quad [29]$$

where $(a_{ma})_0 = a_0 = c_0 = 1$, $a_j = 0$ for $j > na$, and $c_k = 0$ for $k > nc$. The c_k's $(k = 1, 2, \ldots nc)$ are then linearly estimated from nc of the above equations (those corresponding to $j = na+1, \ldots na+nc$; stage 2).

Following the initial estimation of $C(z)$, the ARMAX model form [6] is approximated as (division by the estimate $\hat{C}(z)$):

$$A(z, \boldsymbol{\vartheta}) \cdot Y^F(z, \hat{\mathbf{c}}) = B(z, \boldsymbol{\vartheta}) \cdot X^F(z, \hat{\mathbf{c}}) + E(z, \boldsymbol{\vartheta}, \hat{c}) \quad [30]$$

where:

$$Y^F(z, \hat{\mathbf{c}}) \stackrel{\Delta}{=} \hat{C}^{-1}(z) \cdot Y(z)$$
$$X^F(z, \hat{\mathbf{c}}) \stackrel{\Delta}{=} \hat{C}^{-1}(z) \cdot X(z)$$

In [30] $\boldsymbol{\vartheta} \stackrel{\Delta}{=} [\text{coef}\, A, \text{coef}\, B]^{\mathrm{T}}$ and $\mathbf{c} \stackrel{\Delta}{=} [\text{coef}\, C]^{\mathrm{T}}$. The parameter vector $\boldsymbol{\vartheta}$ is then estimated based upon the ARX model [30] and Linear Least Squares (stage 3). The MA parameter vector $\mathbf{c}$ is finally linearly reestimated from the first nc of equations [29] (those corresponding to $j = 1 \ldots nc$; stage 4). Notice that the method's last two stages may be iterated, with the ARMAX model attaining the minimal value of the criterion of eqns [10]–[11] selected as best.

The LMS maintains computational efficiency but, unlike the 2SLS, avoids the sensitive estimation of the

model-based prediction error sequence. Moreover, model and algorithmic stability (depending upon the AR and MA polynomials, respectively) may be warranted via available guaranteed stability versions.

Correlation Methods

Correlation methods are based on the observation that the prediction error $e_k(\boldsymbol{\theta})$ of a good model, being part of an uncorrelated sequence, should be uncorrelated with the past data $\{x_{k-1}, y_{k-1}, x_{k-2}, y_{k-2} \ldots\} = \mathcal{Z}_0^{k-1}$. A feasible approach for the estimation of the parameter vector $\boldsymbol{\theta}$ then is to select a vector sequence $\{\boldsymbol{\zeta}_k\}$ (sequence of correlation vectors), derived from $\mathcal{Z}_0^{k-1}$, and demand that $\boldsymbol{\zeta}_k$ be uncorrelated with $e_k(\boldsymbol{\theta})$, that is:

$$E\{\boldsymbol{\zeta}_k \cdot e_k(\boldsymbol{\theta})\} = \mathbf{0} \qquad [31]$$

or, substituting the sample mean for statistical expectation:

$$\frac{1}{N}\sum_{k=0}^{N-1} \boldsymbol{\zeta}_k \cdot e_k(\boldsymbol{\theta}) \approx \mathbf{0} \qquad [32]$$

The parameter vector $\boldsymbol{\theta}$ may thus be estimated as the vector satisfying [32]. The approach may be generalized by allowing the correlation vector to depend upon $\boldsymbol{\theta}$ as well. Also note that the dimensionality of the correlation vector needs to be at least equal to that of $\boldsymbol{\theta}$. A commonly used correlation method is presented next.

An Instrumental Variable (IV) method This method estimates a system of the form:

$$A(z) \cdot Y(z) = B(z) \cdot X(z) + N(z) \qquad [33]$$

with $N(z)$ designating the z-transform of a zero-mean, generally autocorrelated, noise sequence $\{n_k\}$, via an ARX-like model of the form (the term ARX-like signifies that the sequence $\{e_k(\boldsymbol{\theta})\}$ is not uncorrelated):

$$\begin{aligned} A(z,\boldsymbol{\theta}) \cdot Y(z) &= B(z,\boldsymbol{\theta}) \cdot X(z) + E(z,\boldsymbol{\theta}) \\ &\Rightarrow y_k = \boldsymbol{\phi}_k^{\mathrm{T}} \cdot \boldsymbol{\theta} + e_k(\boldsymbol{\theta}) \end{aligned} \qquad [34]$$

where:

$$\boldsymbol{\phi}_k = [-y_{k-1} \ldots - y_{k-na} \vdots x_k \ldots x_{k-nb}]^{\mathrm{T}}$$

$$\boldsymbol{\theta} = [a_1 \ldots a_{na} \vdots b_0 \ldots b_{nb}]^{\mathrm{T}}$$

Substituting [34] into the general criterion [32] yields:

$$\begin{aligned} &\frac{1}{N}\sum_{k=0}^{N-1} \boldsymbol{\zeta}_k \cdot (y_k - \boldsymbol{\phi}_k^{\mathrm{T}} \cdot \boldsymbol{\theta}) = \mathbf{0} \\ &\Rightarrow \hat{\boldsymbol{\theta}} = \left(\frac{1}{N}\sum_{k=0}^{N-1} \boldsymbol{\zeta}_k \cdot \boldsymbol{\phi}_k^{\mathrm{T}}\right)^{-1} \cdot \left(\frac{1}{N}\sum_{k=0}^{N-1} \boldsymbol{\zeta}_k \cdot y_k\right) \end{aligned} \qquad [35]$$

The selection of the correlation vector $\boldsymbol{\zeta}_k$ (presently instrumental variable vector) must be such that it is sufficiently well correlated with $\boldsymbol{\phi}_k$ but not influenced by the noise sequence $\{n_k\}$. Given an initial estimate, say $\hat{\boldsymbol{\theta}}_0$, of the ARX-like model [34], a reasonable way of generating the elements of $\boldsymbol{\zeta}_k$ (referred to as instruments) is:

$$\boldsymbol{\zeta}_k = [-y_{k-1}^m(\hat{\boldsymbol{\theta}}_0) \ldots - y_{k-na}^m(\hat{\boldsymbol{\theta}}_0) \vdots x_k \ldots x_{k-nb}]^{\mathrm{T}} \qquad [36]$$

with $y_k^m(\hat{\boldsymbol{\theta}}_0)$ representing the corresponding model output, that is (see also **Figure 3**):

$$A(z,\hat{\boldsymbol{\theta}}_0) \cdot Y^m(z,\hat{\boldsymbol{\theta}}_0) = B(z,\hat{\boldsymbol{\theta}}_0) \cdot X(z) \qquad [37]$$

This leads to the following iterative Instrumental Variable method: (1) obtain an initial Linear Least Squares estimate $\hat{\boldsymbol{\theta}}_0$ of the ARX-like parameter vector via expression [13]; (2) compute the sequence of instrumental variable vectors via expressions [36] and [37]; (3) obtain the Instrumental Variable estimator for $\boldsymbol{\theta}$ via expression [35]; and (4) go to the second step and iterate until the sequence of obtained estimates $\hat{\boldsymbol{\theta}}$ converges. A problem with this method is that the initial estimate $\hat{\boldsymbol{\theta}}_0$ is, due to the autocorrelation of the noise sequence $\{n_k\}$, inconsistent (asymptotically biased), and several iterations may be needed for (potential) convergence of the iterative procedure.

Subspace Methods

Subspace methods are based upon the state space model form and linear operations. In vibrating system identification the most commonly used such method is the Eigensystem Realization Algorithm (ERA).

The Eigensystem Realization Algorithm (ERA) This method utilizes a deterministic state space model form (eqn [9] with $\mathbf{e}_k(\boldsymbol{\theta}) \equiv \mathbf{0}$) and impulse vibration response data. Let $\{\mathbf{Y}_0, \mathbf{Y}_1, \ldots \mathbf{Y}_{N-1}\}$ designate the system's observed Markov parameters, with each $\mathbf{Y}_k$ $(p \times r)$ (r, p, n indicating the dimensionality of the input, output, and state vectors, respectively) being of the form:

$$\mathbf{Y}_k \stackrel{\Delta}{=} [\mathbf{y}_k^1\ \mathbf{y}_k^2\ \ldots\ \mathbf{y}_k^r] \qquad [38]$$

with $\mathbf{y}_k^i$ $(p \times 1)$ indicating the response vector (at time k) due to an impulse excitation applied at the ith input. Next, form the generalized $\alpha{\cdot}p \times \beta{\cdot}r$ Hankel matrix as:

$$\mathbf{H}[k-1] = \begin{bmatrix} \mathbf{Y}_k & \mathbf{Y}_{k+1} & \dots & \mathbf{Y}_{k+\beta-1} \\ \mathbf{Y}_{k+1} & \mathbf{Y}_{k+2} & \dots & \mathbf{Y}_{k+\beta} \\ \vdots & \vdots & & \vdots \\ \mathbf{Y}_{k+\alpha-1} & \mathbf{Y}_{k+\alpha} & \dots & \mathbf{Y}_{k+\alpha+\beta-2} \end{bmatrix} \quad [39]$$

which is of rank n, provided that $\alpha \geq n$, $\beta \geq n$ (α, β constitute the method's design parameters; their proper selection may require a number of trials).

The singular value decomposition of $\mathbf{H}[0]$ gives $(\alpha p \geq \beta r)$:

$$\mathbf{H}[0] = \mathbf{R} \cdot \mathbf{\Sigma} \cdot \mathbf{S}^{\mathrm{T}} \quad [40]$$

where $\mathbf{R}$ $(\alpha{\cdot}p \times \alpha{\cdot}p)$, $\mathbf{S}$ $(\beta{\cdot}r \times \beta{\cdot}r)$ are orthonormal matrices ($\mathbf{R}^{\mathrm{T}}\mathbf{R} = \mathbf{I}_{\alpha p}$, $\mathbf{S}^{\mathrm{T}}\mathbf{S} = \mathbf{I}_{\beta r}$, with $\mathbf{I}$ representing the identity matrix of the indicated dimensionality). The columns of $\mathbf{R}$ and $\mathbf{S}$ are the left and right singular vectors. The matrix $\mathbf{\Sigma}$ $(\alpha{\cdot}p \times \beta{\cdot}r)$ contains the system's singular values σ_i. Theoretically, an nth-order system has exactly n nonzero singular values, say $\sigma_1 \geq \sigma_2 \geq \ldots \geq \sigma_n > 0$. Thus the $\mathbf{\Sigma}$, $\mathbf{R}$, $\mathbf{S}$ matrices may be partitioned as:

$$\mathbf{\Sigma} = \begin{bmatrix} \mathbf{\Sigma}_n & \mathbf{0} \\ \mathbf{0} & \mathbf{0} \end{bmatrix} \quad \mathbf{R} = \begin{bmatrix} \mathbf{R}_n & \bar{\mathbf{R}} \end{bmatrix} \quad \mathbf{S} = \begin{bmatrix} \mathbf{S}_n & \bar{\mathbf{S}} \end{bmatrix} \quad [41]$$

with $\mathbf{\Sigma}_n \triangleq \mathrm{diag}(\sigma_1, \sigma_2 \ldots \sigma_n)$ (diag$(\cdot)$ designating diagonal matrix with the indicated elements), and $\mathbf{R}_n$, $\mathbf{S}_n$ being composed of the corresponding n columns of $\mathbf{R}$, $\mathbf{S}$, respectively.

The state space matrices may then be estimated as:

$$\hat{\mathbf{A}} = \mathbf{\Sigma}_n^{-1/2} \cdot \mathbf{R}_n^{\mathrm{T}} \cdot \mathbf{H}[1] \cdot \mathbf{S}_n \cdot \mathbf{\Sigma}_n^{-1/2} \quad [42]$$

$$\hat{\mathbf{B}} = \mathbf{\Sigma}_n^{1/2} \cdot \mathbf{S}_n^{\mathrm{T}} \cdot \mathbf{E}_r \quad [43]$$

$$\hat{\mathbf{C}} = \mathbf{E}_p^{\mathrm{T}} \cdot \mathbf{R}_n \cdot \mathbf{\Sigma}_n^{1/2} \quad [44]$$

while $\hat{\mathbf{D}} = \mathbf{Y}_0$. In the above $\mathbf{E}_p^{\mathrm{T}} \triangleq [\mathbf{I}_p\, \mathbf{0}_p \ldots \mathbf{0}_p]$, $\mathbf{E}_r^{\mathrm{T}} \triangleq [\mathbf{I}_r\, \mathbf{0}_r \ldots \mathbf{0}_r]$, with $\mathbf{0}_i$ representing a null $i \times i$ matrix.

The discrete-time eigenvalues (system poles) are estimated from the characteristic equation:

$$\det[\lambda \mathbf{I}_n - \mathbf{A}] = 0 \quad [45]$$

following the solution of which the $(\mathbf{A}, \mathbf{B}, \mathbf{C})$ matrices may be transformed to modal coordinates as $(\mathbf{\Lambda}, \mathbf{\Psi}^{-1}\mathbf{B}, \mathbf{C})$, with $\mathbf{\Lambda} \triangleq \mathrm{diag}(\lambda_1, \ldots \lambda_n)$ and $\mathbf{\Psi} \triangleq [\boldsymbol{\psi}_1 \boldsymbol{\psi}_2 \ldots \boldsymbol{\psi}_n]$ designating the corresponding eigenvector matrix. The matrix $\mathbf{\Psi}^{-1}\mathbf{B}$ provides the initial modal amplitudes (modal participation factors) and the matrix $\mathbf{C\Psi}$ the mode shapes at the sensor points.

The determination of the true structural modes (among a higher number of modes generally identified) is based upon the modal amplitude coherence (MAC). The value of the MAC for the lth eigenvalue $(l = 1, 2, \ldots n)$ is defined as the magnitude of the normalized dot product between the vectors $\bar{\mathbf{q}}_l$ and $\hat{\mathbf{q}}_l$:

$$MAC_l = \frac{\left|\bar{\mathbf{q}}_l^* \cdot \hat{\mathbf{q}}_l\right|}{\left(\left|\bar{\mathbf{q}}_l^* \cdot \bar{\mathbf{q}}_l\right| \cdot \left|\hat{\mathbf{q}}_l^* \cdot \hat{\mathbf{q}}_l\right|\right)^{1/2}} \quad [46]$$

with * indicating complex conjugate transposition. In the above $\bar{\mathbf{q}}_l$ $(\beta{\cdot}r \times 1)$ is obtained by transposing the lth row of the controllability matrix:

$$\bar{\mathbf{Q}}_{\mathrm{ctr}} = \mathbf{\Psi}^{-1} \cdot \mathbf{\Sigma}_n^{1/2} \cdot \mathbf{S}_n^{\mathrm{T}} \quad [47]$$

whereas $\hat{\mathbf{q}}_l$ $(\beta{\cdot}r \times 1)$ is obtained as:

$$\hat{\mathbf{q}}_l = \begin{bmatrix} \mathbf{b}_l^{\mathrm{T}} & \lambda_l \cdot \mathbf{b}_l^{\mathrm{T}} & \lambda_l^2 \cdot \mathbf{b}_l^{\mathrm{T}} & \cdots & \lambda_l^{\beta-1} \cdot \mathbf{b}_l^{\mathrm{T}} \end{bmatrix}^{\mathrm{T}} \quad [48]$$

with $\mathbf{b}_l$ $(r \times 1)$ being the transposed lth row of the matrix $\mathbf{\Psi}^{-1}\mathbf{B}$. MAC values are obviously confined in the interval [0, 1]. Eigenvalues (and thus corresponding modes) with values close to unity are classified as structural; otherwise as extraneous (false).

The ERA is numerically robust, but limited to impulse (or free) response data under deterministic (noise-free) conditions. Other types of data may be accommodated via an additional stage aiming at the estimation of the system's impulse response, while the presence of noise may distort the estimates and make exact order (nonzero singular value) determination difficult.

Remarks on the Methods

Despite the lack of detailed and systematic comparisons of the various identification methods with different types of vibrating systems, a few general remarks may be made. Prediction Error methods are generally considered most accurate, provided that problems related to local minima and algorithmic instabilities may be accommodated for. Least squares related and subspace methods are generally suboptimal, although their accuracy need not be far from optimality. In case of large-size (several

degree-of-freedom) problems, these may be the only viable approaches. Algorithmic and model stability may then become crucial, and schemes such as the guaranteed stability versions of the LMS method practically necessary. Correlation methods may be useful, but they may also have convergence problems and not achieve adequate accuracy.

A good strategy in practice is to use a combined procedure, in which identification (within a selected model class) is first based upon a least squares related, correlation, or subspace method, with subsequent refinement based upon a Prediction Error method. Also useful in practice (especially in low noise cases) is to identify simple ARX models via Linear Least Squares before turning to more appropriate models, such as ARMAX, output error, or state space.

Deterministic methods (such as Linear Least Squares, the Prony method, or the ERA) achieve acceptable accuracy in low noise cases. When the noise is nonnegligible, their performance generally deteriorates. In such a case significant model order overdetermination is commonly used, but the distinction of actual structural modes may become difficult. The use of stochastic methods is, then, recommended. An additional point deserving attention, especially for large-size (several degree-of-freedom) problems, is the difficulty that may be encountered with methods based on free/impulse response measurements (such as the Prony method or the ERA). This stems from the limited number of available signal samples which, in turn, limits the number of model parameters that may be estimated with acceptable accuracy.

Commercial software specifically designed for the parametric identification of vibrating systems appears limited. The MATLAB-based Structural Dynamics Toolbox by the Scientific Software Group includes some parametric identification tools. The ARTeMIS Extractor by Structural Vibration Solutions focuses on the output-only case. There is, nevertheless, a number of general-purpose packages. These include the MATLAB System Identification Toolbox by MathWorks, the MATRIXx (Xmath) System Identification (ISID) module by Integrated Systems, and the ADAPTx Automated System Identification Software by Adaptics. The MATLAB Frequency Domain System Identification Toolbox is also available for frequency domain based identification.

Model Order Selection, Validation, and Modal Parameter Extraction

Model Order Selection

Model order selection, which is theoretically related to the determination of the actual number of structural degrees of freedom, is crucial for successful identification. In reality the two issues are decoupled, as significant order overdetermination is generally necessary for accurate identification. This is especially so for deterministic methods, which rely more heavily on order overdetermination in counteracting the effects of otherwise unaccounted noise.

Identification accuracy may be evaluated in terms of quality criteria of the form:

$$V_N^1 \stackrel{\Delta}{=} \frac{1}{N}\sum_{k=0}^{N-1}\left(y_k - \hat{y}_k(\hat{\boldsymbol{\theta}})\right)^2 \qquad [49]$$

$$V_N^2 \stackrel{\Delta}{=} \frac{1}{N}\sum_{k=0}^{N-1}\left(y_k - y_k^m(\hat{\boldsymbol{\theta}})\right)^2 \qquad [50]$$

in which $\hat{y}_k(\hat{\boldsymbol{\theta}})$ represents the estimated model-based one-step-ahead prediction for time k, and $\hat{y}_k^m(\hat{\boldsymbol{\theta}})$ the model response (**Figure 3**). Both V_N^1 and V_N^2 generally decrease with increasing model order, and although they should theoretically reach a plateau as soon as the model order coincides with that of the true system, their decreasing pattern typically continues.

In order to overcome this difficulty and enable proper model order selection, a number of statistical criteria that penalize model complexity (order) as a counteraction to a decreasing quality criterion, have been introduced. Among them, well known are the Akaike Information Criterion (AIC) and the Bayesian information criterion (BIC):

$$\mathrm{AIC} \stackrel{\Delta}{=} N \cdot \ln\left[V_N^1(\hat{\boldsymbol{\theta}})\right] + 2 \cdot \dim \boldsymbol{\theta} \qquad [51]$$

$$\mathrm{BIC} \stackrel{\Delta}{=} \ln\left[V_N^1(\hat{\boldsymbol{\theta}})\right] + \dim \boldsymbol{\theta} \times \frac{\ln N}{N} \qquad [52]$$

the minimization of which indicates the optimal model order (dimensionality of the parameter vector ($\boldsymbol{\theta}$). In these expressions dim(·) stands for dimensionality of the indicated vector and ln(·) for natural logarithm. Note that these criteria may only be applied to those stochastic methods that lead to an uncorrelated prediction error (residual) sequence $\{e_k(\hat{\boldsymbol{\theta}})\}$ (thus, not to the Instrumental Variable method).

An alternative approach to model order selection is based on rank determination for an appropriate matrix, the rank of which coincides with the system order. An example of this is the Hankel matrix $\mathbf{H}[0]$ (eqn [40]) in the ERA. In practice, however, exact rank determination is often difficult due to lack of an obvious threshold.

Model order selection based upon the estimation data set $\mathcal{Z}_0^{N-1}$ should be considered tentative, with final selection following successful model validation.

Model Validation

A basic validation procedure is based upon the posterior examination of the assumptions behind the identification method used. In stochastic methods such assumptions concern the sequence of estimated prediction errors $\{e_k(\hat{\boldsymbol{\theta}})\}$, which should be (the Instrumental Variable method excluded) uncorrelated (white) and also uncorrelated with past values of the excitation.

An additional, as well as essential, validation procedure is based upon the cross-validation principle, and presumes the availability of an additional data set, referred to as the validation set. To accommodate this need, the available data are often split into estimation and validation sets, with the former used exclusively for estimation and the latter for validation. The behavior of the identified model is then examined within the validation set and model quality criteria, such as those of eqns [49] and [50], are computed. This could be done for a variety of models (and model forms), with the model behaving best selected as final.

Modal Parameter Extraction

Once an estimated model has been validated, its structural transfer function is used for modal parameter extraction. The global modal parameters are obtained as:

$$\omega_{nl} = \frac{1}{\mathrm{d}t}\sqrt{\left(\frac{\ln\left(\lambda_l \cdot \lambda_l^*\right)}{2}\right)^2 + \left(\cos^{-1}\left(\frac{\lambda_l + \lambda_l^*}{2\sqrt{\lambda_l \cdot \lambda_l^*}}\right)\right)^2} \qquad [53]$$

$$\zeta_l = \sqrt{\frac{\left[\ln\left(\lambda_l \cdot \lambda_l^*\right)\right]^2}{\left[\ln\left(\lambda_l \cdot \lambda_l^*\right)\right]^2 + 4 \cdot \left(\cos^{-1}\left(\frac{\lambda_l + \lambda_l^*}{2\sqrt{\lambda_l \cdot \lambda_l^*}}\right)\right)^2}} \qquad [54]$$

with ω_{nl} representing the lth natural frequency in rads per time unit, ζ_l the corresponding damping ratio, (λ_l, λ_l^*) the lth discrete complex conjugate eigenvalue pair, dt the sampling period, and $\ln(\cdot)$ the natural logarithm.

Mode shape determination is more complicated, requiring the selection of a particular discrete-to-continuous model transformation. The simplest such transformation is based upon the impulse invariance principle, with the lth mode shape $\boldsymbol{\phi}_l$ being then obtained as:

$$\boldsymbol{\phi}_l = \begin{bmatrix} 1 & \frac{R_{i2l}}{R_{i1l}} & \cdots & \frac{R_{iql}}{R_{i1l}} \end{bmatrix}^{\mathrm{T}} \qquad [55]$$

with q representing the estimated number of structural degrees of freedom and R_{ijl} the ijth element of the lth ($l = 1, 2, \ldots q$) residue matrix $\mathbf{R}_l$ of the estimated receptance transfer matrix $\mathbf{G}(z)$. The rest of the residue matrices are complex conjugates of the foregoing.

The distinction of structural modes A major issue in modal parameter extraction is the distinction of structural from extraneous modes, the latter being a result of the generally significant model order overdetermination that is necessary for accurate identification (overdetermination is generally higher for deterministic methods). The approaches used for this purpose include the Modal Amplitude Coherence (MAC), dispersion analysis, and frequency stabilization diagrams.

The Modal Amplitude Coherence has been already discussed within the context of ERA. The dispersion analysis methodology assesses the vibration energy associated with each mode in each identified structural transfer function (each element of $\mathbf{G}(z)$). Modes characterized by negligible dispersion (that is, contribution to the vibration energy of the transfer function response) consistently for all transfer functions in $\mathbf{G}(z)$ may be considered extraneous (or too weak to be safely identified). Mathematically, the condition for accepting an identified mode may be expressed as:

$$\|\boldsymbol{\Delta}_l\| = \left\| \left[\Delta_{ijl}\right] \right\| > \varepsilon \qquad [56]$$

with Δ_{ijl} representing the dispersion of mode l in the ijth transfer function, $\|\cdot\|$ matrix norm, and ε a selected threshold. Note that $\Delta_{ijl} \stackrel{\Delta}{=} |E_{ijl}|/E_{ij}$, with E_{ij} representing the energy of the ith vibration response due to the jth excitation, and E_{ijl} that part of E_{ij} that is associated with mode l.

Frequency stabilization diagrams represent the evolution of estimated natural frequencies with increasing model order. Their basis for structural mode distinction lies with the expectation that structural frequencies will tend to stabilize (remain invariant) as the order increases, whereas extraneous frequencies will change 'randomly' within the considered frequency range. Stabilization diagrams may indeed be useful, although the expected pattern is often distorted by phenomena such as frequency

splitting and stabilization of extraneous (noise) frequencies. In all cases, the distinction of extraneous modes may be facilitated by simultaneous examination of their associated damping ratios.

Example

Parametric identification results for a lightly damped scale aircraft skeleton structure based upon mimo experimental data ($r = 2$ random force excitations, $p = 3$ vibration acceleration responses) are presented for the frequency range of 5–75 Hz. Signal preprocessing includes signal band-pass filtering (in the aforementioned range), subsampling at $f_s \approx 205$ Hz, signal scaling, and sample mean removal. Each resulting signal is $N = 2048$ samples long.

p-dimensional ARX(na, nb) and ARMAX(na, nb, nc) models (with $A(z)$, $B(z)$, and $C(z)$ presently being polynomial matrices), which simultaneously accommodate all measured signals, are fitted to the data set. Identification is based upon the multivariate (mimo) Linear Least Squares method (ARX models) and a guaranteed stability version of the multivariate LMS method (ARMAX models). Values of the BIC criterion are, for various estimated models, presented in **Figure 4**. Minima are achieved for $na = 12$ (ARX case) and $na = 5$ (ARMAX case; notice that the criterion continues to decrease in this case). It is interesting to observe that these models are significantly overdetermined ($na = 5$ is theoretically adequate as the structure is characterized by seven modes within the considered frequency range), and also that the ARMAX models achieve uniformly better BIC values than their ARX counterparts despite the former's increased parametric complexity penalized by the BIC (see eqn [52]).

A frequency stabilization diagram is presented in **Figure 5** for ARMAX (k, k, nc) models with $k \in [5, 16]$ and nc optimally preselected. The seven structural modes (at about 6, 16, 36, two closely spaced at about 39, 44 and 61 Hz) are stabilized, and may be distinguished. It should be noted that this rather 'nice' behavior of the stabilization diagram is partly due to the adequate capturing of the noise by the ARMAX models. Similar results are obtained by dispersion analysis. Based upon them, the ARX(12,12) and ARMAX(11,11,14) models are selected.

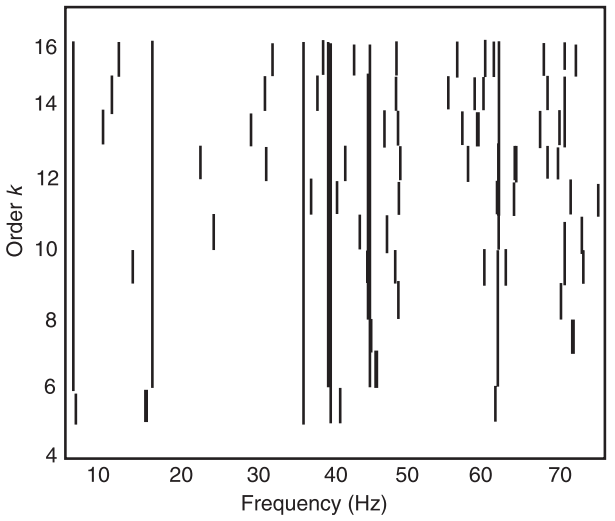


Figure 5 Frequency stabilization diagram: ARMAX (k, k, nc) models.

Model validation is partly considered in **Figure 6**, where the first measured response is compared to the ARMAX-based response. The estimates, by both the ARX and ARMAX methods, of the magnitude of the frequency response function of the transfer function $G_{11}(z)$ relating the first excitation to the first response, are presented in **Figure 7**. The two estimates are in very good agreement, clearly depicting six of the structural modes (one is evident in the neighborhood of the two closely spaced modes at ~39 Hz). In this case, owing to the low level of noise, the ARX and ARMAX results are similar; the ARMAX method mainly offers a slightly reduced model order. A comparison with classical nonparametric frequency domain identification (vector spectral analysis via

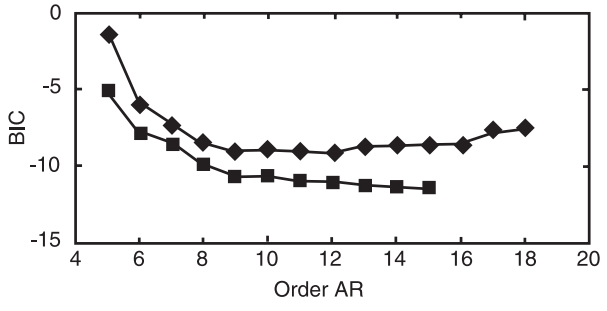


Figure 4 BIC versus AR order. Diamonds, ARX models; squares, ARMAX models.

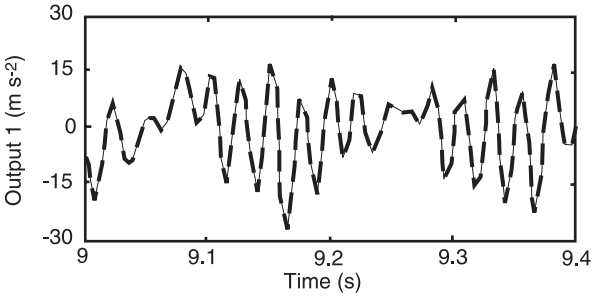


Figure 6 Actual (continuous line) and ARMAX-based (dashed line) vibration responses.

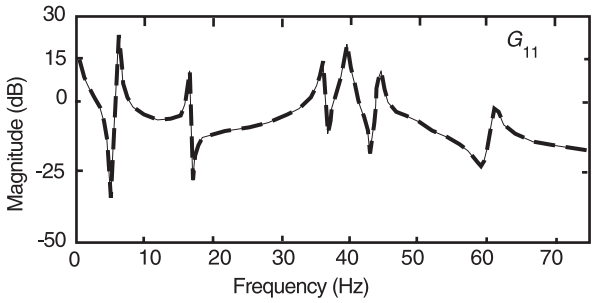


Figure 7 Estimated frequency response magnitude. Continuous line, ARX model; dashed line, ARMAX model.

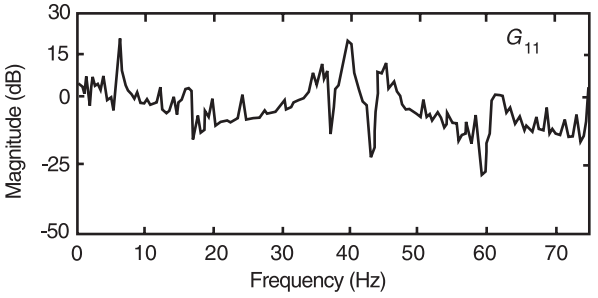


Figure 8 Estimated frequency response magnitude. Vector spectral analysis via the Blackman–Tukey method.

the Blackman–Tukey method using 512 sample long records and Hamming windowing) is made in **Figure 8**, in which the corresponding estimate of the frequency response magnitude of $G_{11}(z)$ is presented. The advantages of parametric methods in such a case, where the number of data samples is limited, are evident.

Nomenclature

x_k	sampled force excitation
y_k	sampled noise-corrupted vibration response
n_k	sampled stochastic noise
w_k	sampled white noise (optimal prediction error)
$\hat{y}_{k/k\text{-}1}$	optimal one-step-ahead prediction of y_k
n	system order
na	order of the $A(z)$ polynomial
nb	order of the $B(z)$ polynomial
nc	order of the $C(z)$ polynomial
$E\{\cdot\}$	statistical expectation
N	number of data samples (per signal)
$G(z)$	structural transfer function
$H(z)$	noise transfer function
k	discrete time corresponding to continuous time $k\cdot \mathrm{d}t$ $(k = 0,1 \ldots N-1)$
t	continuous time
$\mathrm{d}t$	sampling period
z	z-transform variable
s	Laplace transform variable
$\boldsymbol{\theta}$	model parameter vector
$\hat{y}_k(\boldsymbol{\theta})$	model-based one-step-ahead prediction of y_k
$y_k^m(\boldsymbol{\theta})$	model response
$e_k(\boldsymbol{\theta})$	model-based prediction error
$G(z,\boldsymbol{\theta})$	model of the structural transfer function
$H(z,\boldsymbol{\theta})$	model of the noise transfer function
λ_l	lth discrete pole
μ_l	lth continuous pole
ω	frequency in rads per time unit
ω_{nl}	lth natural frequency in rads per time unit
ζ_l	lth damping ratio
ϕ_l	lth mode shape

See also: **Identification, Fourier-based methods**; **Modal analysis, experimental**, Parameter extraction methods; **Model updating and validating**; **Signal processing, model based methods**

Further Reading

Box GEP, Jenkins GM and Reinsel GC (1994) *Time Series Analysis: Forecasting and Control*, 3rd edn. Englewood Cliffs, NJ: Prentice-Hall.

Braun S (1986) *Mechanical Signature Analysis: Theory and Applications*. London, UK: Academic Press.

Juang J-N (1994) *Applied System Identification*. Englewood Cliffs, NJ: Prentice-Hall.

Ljung L (1999) *System Identification: Theory for the User*. Second edition. Upper Saddle River, NJ: Prentice-Hall. PTR.

Pandit SM (1991) *Modal and Spectrum Analysis: Data Dependent Systems in State Space*. John Wiley.

Pandit SM and Wu SM (1983) *Time Series and System Analysis with Applications*. John Wiley.

Petsounis KA and Fassois SD (2001) Parametric time-domain methods for the identification of vibrating structures: a critical comparison and assessment. *Mechanical Systems and Signal Processing* (to appear).

Söderström T and Stoica P (1989) *System Identification*. Hertfordshire: Prentice-Hall.

IDENTIFICATION, NON-LINEAR SYSTEMS

See **NON-LINEAR SYSTEM IDENTIFICATION**

IMPACTS, NON-LINEAR SYSTEMS

See **VIBRO-IMPACT SYSTEMS**

IMPULSE RESPONSE FUNCTION

See **THEORY OF VIBRATION: IMPULSE RESPONSE FUNCTION**

INTENSITY

See **VIBRATION INTENSITY**

INVERSE PROBLEMS

Y M Ram, Louisiana State University, Baton Rouge, LA, USA

Copyright © 2001 Academic Press

doi:10.1006/rwvb.2001.0097

Many problems in physics, science and engineering science can be described schematically in the block diagram form shown in **Figure 1**. For example, the vector differential equation governing the motion of a linear vibrating system is given by:

$$\mathbf{M}\ddot{\mathbf{x}} + \mathbf{C}\dot{\mathbf{x}} + \mathbf{K}\mathbf{x} = \mathbf{f}(t) \qquad [1]$$

where $\mathbf{M}$, $\mathbf{C}$ and $\mathbf{K}$ are the mass, damping and stiffness matrices and $\mathbf{f}(t)$ is the vector of the external force. The block diagram takes for this case the form shown in **Figure 2**.

Problems where the system and the input are given, and the output is to be determined, are classified as direct problems. Inverse problems are those where the system is to be found based on the knowledge of the input and the output.

The algebraic eigenvalue problem plays an important role in vibration analysis. The eigenvalue problem associated with eqn [1] is to determine the poles s_i and their associated modes $\mathbf{v}_i \neq 0$ that satisfy:

$$(s_i^2\mathbf{M} + s_i\mathbf{C} + \mathbf{K})\mathbf{v}_i = \mathbf{0} \qquad [2]$$

Problems of reconstructing physical parameters appearing in the matrices $\mathbf{M}$, $\mathbf{C}$, and $\mathbf{K}$ based on partial knowledge of the poles and modes of the system are called inverse vibration problems .

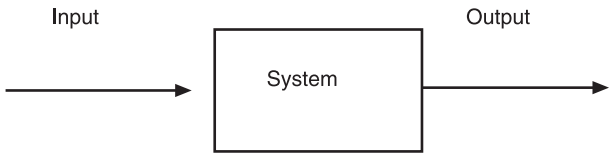


Figure 1 Input–output relation.

The Classical Problem

Perhaps the most celebrated inverse problem in vibration is that of reconstructing, using spectral data, a simply connected n-degree-of-freedom mass–spring system, such as that shown in **Figure 3A**. The eigenvalue problem associated with this system may be written in the form:

$$(\mathbf{K} - \lambda\mathbf{M})\mathbf{v} = \mathbf{0} \quad \lambda = -s^2 \qquad [3]$$

where $\mathbf{K}$ is a tridiagonal symmetric matrix:

$$\mathbf{K} = \begin{bmatrix} k_1 & -k_1 & & & & \\ -k_1 & k_1+k_2 & -k_2 & & & \\ & -k_2 & k_2+k_3 & -k_3 & & \\ & & \ddots & \ddots & \ddots & \\ & & & -k_{n-1} & k_{n-1}+k_n \end{bmatrix} \qquad [4]$$

and $\mathbf{M}$ is diagonal:

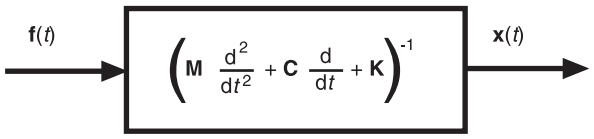


Figure 2 Block diagram for vibrating system.

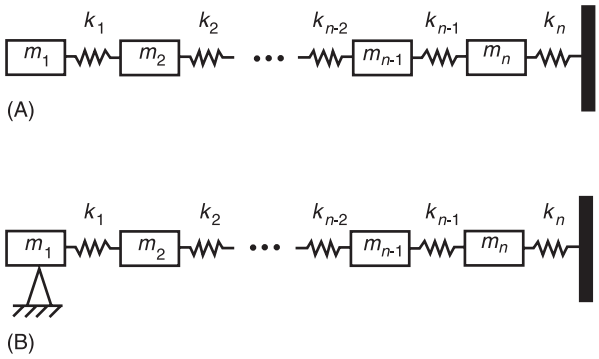


Figure 3 Mass–spring system: (A) fixed–free, and (B) fixed–fixed configuration.

$$\mathbf{M} = \text{diag}\,\{m_1 \quad m_2 \quad m_3 \quad \cdots \quad m_n\} \qquad [5]$$

This problem has n distinct positive eigenvalues which may be ordered in the form:

$$\lambda_1 < \lambda_2 < \lambda_3 < \cdots < \lambda_n \qquad [6]$$

If the mass m_1 is attached to the ground via a rigid support, as shown in **Figure 3B**, then the constrained system has $n-1$ degrees-of-freedom with the eigenvalue problem:

$$(\hat{\mathbf{K}} - \mu\hat{\mathbf{M}})\hat{\mathbf{v}} = \mathbf{0} \qquad [7]$$

where $\hat{\mathbf{K}}$ is an $(n-1)\times(n-1)$ tridiagonal symmetric matrix determined by omitting the first row and column of $\mathbf{K}$:

$$\hat{\mathbf{K}} = \begin{bmatrix} k_1+k_2 & -k_2 & & \\ -k_2 & k_2+k_3 & -k_3 & \\ & \ddots & \ddots & \ddots \\ & & -k_{n-1} & k_{n-1}+k_n \end{bmatrix} \qquad [8]$$

and similarly $\hat{\mathbf{M}}$ is a diagonal matrix obtained by removing the first row and column of $\mathbf{M}$:

$$\hat{\mathbf{M}} = \text{diag}\,\{m_2 \quad m_3 \quad \cdots \quad m_n\} \qquad [9]$$

The distinct real positive eigenvalues μ_i of this system may be numbered in an increasing order:

$$\mu_1 < \mu_2 < \cdots < \mu_{n-1} \qquad [10]$$

Knowing the total mass:

$$m_T = \sum_{i=1}^{n} m_i \qquad [11]$$

and the two sets of eigenvalues, eqns [6] and [10], the masses $m_i > 0$ and the springs $k_i > 0$, $i = 1, 2, \ldots, n$, can be determined uniquely, provided that the interlacing property:

$$\lambda_1 < \mu_1 < \lambda_2 < \mu_2 < \lambda_3 < \cdots < \mu_{n-1} < \lambda_n \qquad [12]$$

holds.

In order to show how the physical parameters of the system may be determined from the given data a matrix $\mathbf{A}$ is defined such that:

$$\mathbf{A} = \mathbf{M}^{-1/2}\mathbf{K}\mathbf{M}^{-1/2} \qquad [13]$$

where:

$$M^{-1/2} = \text{diag}\left\{\frac{1}{\sqrt{(m_1)}} \frac{1}{\sqrt{(m_2)}} \quad \cdots \quad \frac{1}{\sqrt{(m_n)}}\right\} \qquad [14]$$

The matrix $\mathbf{A}$ is symmetric tridiagonal:

$$\mathbf{A} = \begin{bmatrix} \alpha_1 & \beta_1 & & & \\ \beta_1 & \alpha_2 & \beta_2 & & \\ & \beta_2 & \alpha_3 & \beta_3 & \\ & & \ddots & \ddots & \ddots \\ & & & \beta_{n-1} & \alpha_n \end{bmatrix} \qquad [15]$$

and being congruently equivalent to the matrix pencil $\mathbf{K} - \lambda\mathbf{M}$ it has the eigenvalues given in eqn [6]. Moreover, a matrix $\hat{\mathbf{A}}$ which is formed by removing the first row and column of $\mathbf{A}$, i.e.:

$$\hat{\mathbf{A}} = \begin{bmatrix} \alpha_2 & \beta_2 & & \\ \beta_2 & \alpha_3 & \beta_3 & \\ & \ddots & \ddots & \ddots \\ & & \beta_{n-1} & \alpha_n \end{bmatrix} \qquad [16]$$

has the eigenvalues given in eqn [10].

Denote the spectral decomposition of $\mathbf{A}$ by:

$$\mathbf{A}\mathbf{V} = \mathbf{V}\mathbf{\Lambda} \qquad [17]$$

where $\mathbf{V} = [v_{ij}]$ is orthogonal:

$$\mathbf{V}^{\mathrm{T}}\mathbf{V} = \mathbf{I} \qquad [18]$$

and:

$$\mathbf{\Lambda} = \mathrm{diag}\{\lambda_1 \quad \lambda_2 \quad \cdots \quad \lambda_n\} \qquad [19]$$

Then the jth element of the first row of $\mathbf{V}$ can be determined by the eigenvalue–eigenvector relation:

$$v_{1j}^2 = \frac{\prod_{i=1}^{n-1}(\lambda_j - \mu_i)}{\prod_{\substack{i=1 \\ i\neq j}}^{n}(\lambda_j - \lambda_i)} \qquad [20]$$

The first row of eqn [17] gives the following set of equations:

$$\begin{aligned} \alpha_1 v_{11} + \beta_1 v_{21} &= \lambda_1 v_{11} \\ \alpha_1 v_{12} + \beta_1 v_{22} &= \lambda_2 v_{12} \\ &\vdots \\ \alpha_1 v_{1n} + \beta_1 v_{2n} &= \lambda_n v_{1n} \end{aligned} \qquad [21]$$

by virtue of eqn [15]. Multiplying the ith equation of eqn [21] by v_{1i} yields:

$$\begin{aligned} \alpha_1 v_{11}^2 + \beta_1 v_{11} v_{21} &= \lambda_1 v_{11}^2 \\ \alpha_1 v_{12}^2 + \beta_1 v_{12} v_{22} &= \lambda_2 v_{12}^2 \\ &\vdots \\ \alpha_1 v_{1n}^2 + \beta_1 v_{1n} v_{2n} &= \lambda_n v_{1n}^2 \end{aligned} \qquad [22]$$

Adding these equations gives:

$$\alpha_1 = \sum_{i=1}^{n} \lambda_i v_{1i}^2 \qquad [23]$$

since $\sum_{i=1}^{n} v_{1i}^2 = 1$ and $\sum_{i=1}^{n} v_{1i} v_{2i} = 0$ by virtue of the orthogonal relation given in eqn [18]. So α_1 is determined by the given data via eqns [20] and [23].

It also follows from eqn [21] that:

$$\begin{aligned} (\alpha_1 - \lambda_1)^2 v_{11}^2 &= \beta_1^2 v_{21}^2 \\ (\alpha_1 - \lambda_2)^2 v_{12}^2 &= \beta_1^2 v_{22}^2 \\ &\vdots \\ (\alpha_1 - \lambda_n)^2 v_{1n}^2 &= \beta_1^2 v_{2n}^2 \end{aligned} \qquad [24]$$

Hence adding the equations in eqn [24] and using the orthogonal relation $\sum_{i=1}^{n} v_{2i}^2 = 1$ gives:

$$\beta_1 = -\sqrt{\left(\sum_{i=1}^{n} (\alpha_1 - \lambda_i)^2 v_{1i}^2\right)} \qquad [25]$$

which determines β_1.

Knowing α_1 and β_1 the second row of the eigenvector matrix $\mathbf{V}$ can be obtained by eqn [21]. The other elements of $\mathbf{A}$, α_j and β_j, may then be determined successively for $j = 2, 3 \ldots n$ by following a similar process in which α_j and β_j are determined from the set of equations:

$$\begin{aligned} \beta_{j-1} v_{j-1,1} + \alpha_j v_{j1} + \beta_j v_{j+1,1} &= \lambda_1 v_{j1} \\ \beta_{j-1} v_{j-1,2} + \alpha_j v_{j2} + \beta_j v_{j+1,2} &= \lambda_2 v_{j2} \\ &\vdots \\ \beta_{j-1} v_{j-1,n} + \alpha_j v_{jn} + \beta_j v_{j+1,n} &= \lambda_n v_{jn} \end{aligned} \qquad [26]$$

describing the elements of the jth row of eqn [17] with $\beta_n = v_{n+1,i} = 0$. The interlacing property (eqn [12]) ensures that the diagonal elements of $\mathbf{A}$ are all positive and that $\beta_j < 0$ for $j = 1, 2, \ldots, n-1$.

After reconstructing $\mathbf{A}$ the mass and stiffness matrices can be evaluated as follows. Multiplying eqn [13] by $\mathbf{M}^{1/2}\mathbf{p}$, where:

$$\mathbf{p} = \frac{\sqrt{(m_n)}}{k_n} \begin{pmatrix} 1 \\ 1 \\ \vdots \\ 1 \end{pmatrix} \qquad [27]$$

gives:

$$\mathbf{A}\mathbf{M}^{1/2}\mathbf{p} = \mathbf{M}^{-1/2}\mathbf{K}\mathbf{p} \qquad [28]$$

Or, by virtue of eqns [4], [14] and [27]:

$$\mathbf{A}\mathbf{y} = \mathbf{e}_n \qquad [29]$$

where:

$$\mathbf{y} = \frac{\sqrt{(m_n)}}{k_n} \begin{pmatrix} \sqrt{(m_1)} \\ \sqrt{(m_2)} \\ \vdots \\ \sqrt{(m_n)} \end{pmatrix} \qquad [30]$$

and $\mathbf{e}_n$ is the nth unit vector $\mathbf{e}_n = (0 \ldots 0\ 1)^{\mathrm{T}}$. Knowing $\mathbf{A}$ the vector $\mathbf{y}$ can be determine from eqn [29]. Then:

$$\mathbf{y}^{\mathrm{T}}\mathbf{y} = \frac{m_n}{k_n^2} \sum_{i=1}^{n} m_i = \frac{m_n m_T}{k_n^2} \qquad [31]$$

implies that:

$$\frac{\sqrt{(m_n)}}{k_n} = \sqrt{\left(\frac{\mathbf{y}^{\mathrm{T}}\mathbf{y}}{m_T}\right)} \qquad [32]$$

and hence the masses m_i, $i = 1, 2 \ldots n$, are determined by eqns [30] and [32]. Knowing $\mathbf{M}$ and $\mathbf{A}$ the stiffness matrix is found by:

$$\mathbf{K} = \mathbf{M}^{1/2}\mathbf{A}\mathbf{M}^{1/2} \qquad [33]$$

which completes the reconstruction of the system.

Other Problems

One other problem that has attracted much attention is the problem of reconstructing the physical parameters m_i, k_i and d_i of a mass–spring–rod system, such as that shown in **Figure 4**. The parameters are essentially constructed from three sets of spectral data, e.g. fixed–free, fixed–fixed and fixed–simply supported configurations. This problem is associated with the reconstruction of a five-diagonal symmetric matrix. The conditions ensuring the reconstruction of a realizable system with positive parameters have been found by Gladwell and they are more involved than the simple interlacing properties.

There are several variations of the classical problem of reconstructing the mass-spring system from spectral data. Instead of fixing the left mass of **Figure 3A** a mass or spring may be attached to the free end. If a damper is attached to the free end, as shown in **Figure 5**, then m_i, k_i, and c can be reconstructed apart from a scale factor by knowing only the $2n$ (complex) poles of the damped system. This interesting result is due to K. Veselic.

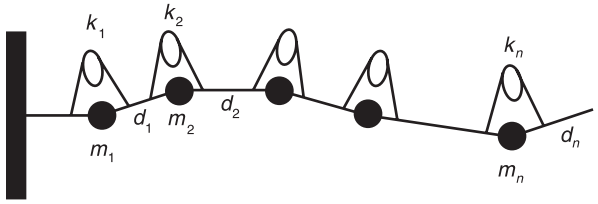


Figure 4 Mass–spring–rod system.

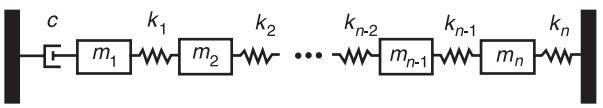


Figure 5 Vecelic's system.

Inverse mode problems are those where the reconstruction of the system is based on eigenvector and eigenvalue data. For example, the mass–spring system of **Figure 3A** may be reconstructed from two mode-shapes, one eigenvalue, and the total mass of the system. Similarly the mass–spring–rod system of **Figure 4** may be reconstructed from three eigenvectors, two eigenvalues and the total mass.

The problems mentioned so far are all finite-dimensional systems. In analogy the physical parameters of distributed parameter systems may be reconstructed from spectral and modal data. For example, the axial rigidity and density functions of a nonuniform axially vibrating rod are determined by two sets of spectral data associated with the fixed–free and fixed–fixed configurations. Alternatively two eigenfunctions, an eigenvalue and the total mass determine the rigidity and density of the rod. Many of the inverse problems associated with finite dimensional systems may be regarded as a certain discrete version of a distributed parameter problem. It should be noted, however, that since the asymptotic behavior of eigenvalues of a distributed parameter system is different from that of its related discrete model, there is no reliable way to reconstruct the physical parameters of a distributed parameter system by considering a related discrete system.

Concluding remarks

The problem of reconstructing the mass–spring system from two spectral sets and the total mass studied above is fully solved in the following sense: (1) there exists a unique realizable system, with positive masses and springs, that fits the prescribed data whenever the interlacing property eqn [12] holds, (2) there is no realizable system when the spectral data violate eqn [12], and (3) direct methods for reconstructing the system do exist.Only a few other inverse problems in vibration have been posed and fully solved in this sense. For many other inverse problems the spectral data do not allow the unique reconstruction of a realistic system. For some problems there exists a continuous family of solutions. In other problems there is a finite number of systems satisfying the given data. The necessary and sufficient conditions which allow the construction of a realistic system are not always known. For some problems there is no direct method of solution and iterative methods are used instead. Many iterative methods do not always converge.

This suggests that the subject is still in its development phase. It started with Gantmakher and Krein in 1950 with a problem similar to reconstructing the mass–spring system from spectral data. This was

highlighted by Gladwell in his monograph *Inverse Problems in Vibration* describing the state-of-the-art of knowledge, including his own major contribution in the field. It is most probable that related research will continue to be carried out in the future developing the subject further.

Nomenclature

$\mathbf{f}(t)$	vector of the external force
m	mass
$\mathbf{V}$	eigenvector matrix
μ	eigenvalue

See also: **Eigenvalue analysis**

Further Reading

Chu MT (1998) Inverse eigenvalue problems. *SIAM Review* 40: 1–39.

Gladwell GML (1986) *Inverse Problems in Vibration*. Dordrecht, The Netherlands: Martinus Nijhoff.

Gladwell GML (1986) Inverse problems in vibration. *Applied Mechanics Reviews* 39, 1013–1018.

Gladwell GML (1996) Inverse problems in vibration, II. *Applied Mechanics Reviews* 49: 25–34.

ISOLATION, ACTIVE

See **ABSORBERS, ACTIVE; ACTIVE CONTROL OF VEHICLE VIBRATION; ACTIVE ISOLATION**

ISOLATION, VIBRATION – APPLICATIONS AND CRITERIA

See **VIBRATION ISOLATION, APPLICATIONS AND CRITERIA**

ISOLATION, VIBRATION – THEORY

See **VIBRATION ISOLATION THEORY**

K

KRYLOV-LANCZOS METHODS

R R Craig Jr, The University of Texas at Austin, Austin, TX, USA

Copyright © 2001 Academic Press

doi:10.1006/rwvb.2001.0011

Introduction

This article describes structural dynamics model reduction based on Krylov vectors and Lanczos vectors. Finite element models of large or geometrically complicated structures may attain tens of thousands of degrees of freedom, or even many more. For dynamic response analyses and for control design applications it is not computationally feasible to solve such large systems of equations. Therefore, model order reduction plays an indispensable role in such analyses. Model reduction of a structural dynamics system is usually performed by the Rayleigh–Ritz method, which transforms the large-order matrix system differential equation into one of smaller order by using a projection subspace. It is indisputable that the choice of projection subspace is very important to the accuracy and computational efficiency of the reduced model. Classically, the subspace of undamped normal modes has been used for projection because it has a clear physical meaning, because it simultaneously diagonalizes both the mass matrix and the stiffness matrix, and because it preserves the system's undamped natural frequencies. This approach is called mode superposition, or the mode displacement method. However, with regard to the accuracy of a system's computed response to time-dependent excitation, various numerical studies have shown that preservation of the system natural frequencies is not necessarily the primary concern. This is particularly true if there are concentrated time-dependent loads, or if, as is usually the case, stresses are to be computed from displacements. Although mode displacement solutions may be improved by the addition of pseudostatic correction terms in a computational approach called the mode acceleration method, the methods discussed in this article produce accurate solutions in a more straightforward and efficient manner.

The Krylov vectors and Lanczos vectors discussed in this article are special types of derived Ritz vectors. Professor Ed Wilson, the originator of the method, refers to these special Ritz vectors as load-dependent Ritz vectors. The first Ritz vector (or block of vectors) corresponds to the static deflection shape(s) of the structure due to the applied load distribution(s). Inverse iteration and Gram–Schmidt orthogonalization are employed to compute additional vectors. Krylov–Lanczos model reduction methods have been found to be particularly effective in solving dynamic response problems, like response of building structures to earthquake loading. While closely related to the powerful and popular Lanczos eigensolvers, the Krylov–Lanczos procedures discussed here do not employ an eigenvector subspace; they avoid the computational expense of obtaining converged eigenvectors, and, at the same time, provide a more suitable subspace for model reduction. Thus, compared to a 'classical' mode superposition solution, the computational effort for dynamic response analysis of large structures may be reduced by a factor of three or more without compromising accuracy.

Physical Meaning of Krylov Vectors and Lanczos Vectors

The finite element model of an undamped structure may be described by:

$$\mathbf{M}\ddot{x} + \mathbf{K}x = \mathbf{F}u(t) \qquad [1]$$

where $x \in R^{n}$ is the displacement vector, $u \in R^{l}$ is the input force vector, $\mathbf{M}$ and $\mathbf{K}$ are the system mass and stiffness matrices, and $\mathbf{F}$ is the force distribution matrix. Model reduction of a structural dynamics system is usually performed by the Rayleigh–Ritz method, which employs a projection transformation of the form:

$$x = \mathbf{T}\bar{x}, \quad \bar{x} \in R^{r} \qquad [2]$$

and transforms the large-order system equation into a reduced-order model that has the form:

$$\bar{\mathbf{M}}\ddot{\bar{x}} + \bar{\mathbf{K}}\bar{x} = \bar{\mathbf{F}}\bar{u} \qquad [3]$$

In the classical Ritz transformation, the reduced system matrices and the original system matrices are related by the following expressions:

$$\bar{\mathbf{M}} = \mathbf{T}^{\mathrm{T}}\mathbf{M}\mathbf{T}, \quad \bar{\mathbf{K}} = \mathbf{T}^{\mathrm{T}}\mathbf{K}\mathbf{T}, \quad \bar{\mathbf{F}} = \mathbf{T}^{\mathrm{T}}\mathbf{F} \qquad [4]$$

The choice of the projection matrix, **T**, governs the accuracy of the reduced system. In this chapter, Krylov vectors and Lanczos vectors are used for model reduction.

Krylov Vectors and Krylov Modes

It is well known that the modes of free vibration of an n degree-of-freedom (n-DOF) finite element model of an undamped structure satisfy the algebraic eigenproblem:

$$\mathbf{K}\phi_i = \lambda_i\mathbf{M}\phi_i \quad i = 1, 2, \ldots, n \qquad [5]$$

where $\lambda_i (\equiv \omega_i^2)$ and ϕ_i are the ith eigenvalue and ith eigenvector, respectively. However, Krylov vectors and Lanczos vectors are not as well known as are eigenvectors. Note that eqn [5] is essentially an equilibrium equation relating elastic restoring forces $\mathbf{K}\phi$ to inertia forces $\omega^2\mathbf{M}\phi$, and recall that a similar equation, namely:

$$\mathbf{K}\psi_{j+1} = \mathbf{M}\psi_j \qquad [6]$$

is the basis for the inverse iteration method for computing eigenvalues and eigenvectors, assuming that **K** is nonsingular. The vector ψ in eqn [6] converges to the fundamental mode (eigenvector) or, with suitable orthogonalization with respect to lower-frequency modes, to a higher-frequency mode.

Eqn [6] states that, given a vector ψ_j, a new vector ψ_{j+1} may be generated by solving for the static deflection produced by the inertia forces associated with ψ_j, that is (symbolically):

$$\psi_{j+1} = \mathbf{K}^{-1}\mathbf{M}\psi_j \qquad [7]$$

Eqn [7] provides a basis for defining a Krylov vector subspace. Given a starting vector ψ_{K1}, the vectors ψ_{Kj} are said to form a Krylov subspace of order r, $1 \le r \le n$, given by:

$$\begin{aligned}\Psi_{Kr} &\equiv [\psi_{K1}\ \psi_{K2}\ \psi_{K3} \ldots\ \psi_{Kr}] \\ &= \left[\psi_{K1}, [\mathbf{K}^{-1}\mathbf{M}]\psi_{K1}, [\mathbf{K}^{-1}\mathbf{M}]^2\right]\psi_{K1} \\ &\quad \ldots [\mathbf{K}^{-1}\mathbf{M}]^{(r-1)}\psi_{K1}\end{aligned} \qquad [8]$$

To illustrate Krylov vectors, the Krylov sequence of eqn [8] will be obtained for the four degree-of-freedom (4-DOF) consistent-mass finite element model of the cantilever beam shown in **Figure 1**.

Figure 2 illustrates the four Krylov vectors generated from a starting vector that is the static deflection due to a unit force at DOF 1. In **Figure 2** the elements of the Krylov vectors determine the nodal displacements and rotations; standard cubic shape functions are used to determine the beam's deflection shape between nodes. The resulting Ritz functions will be referred to as Krylov modes.

Lanczos Vectors and Lanczos Modes

Lanczos vectors differ from the Krylov vectors defined in eqn [8] in that each Lanczos vector is made orthogonal to the previous two Lanczos vectors. It can be shown that this makes the present Lanczos vector (theoretically) orthogonal to *all* prior vectors. The following algorithm may be used to compute Lanczos vectors for an undamped structure. The reader should consult literature listed in the Further Reading section for other algorithms which

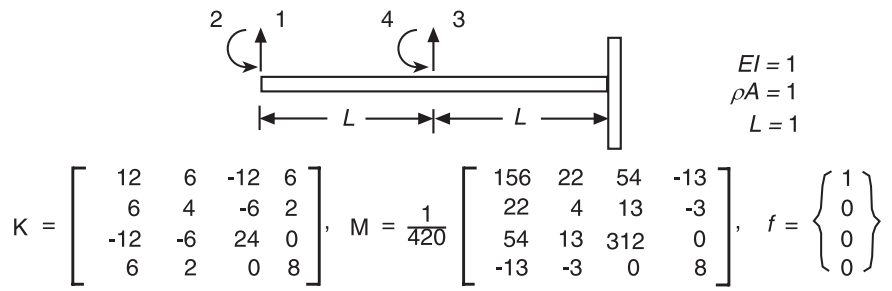


Figure 1 Four-DOF cantilever beam model.

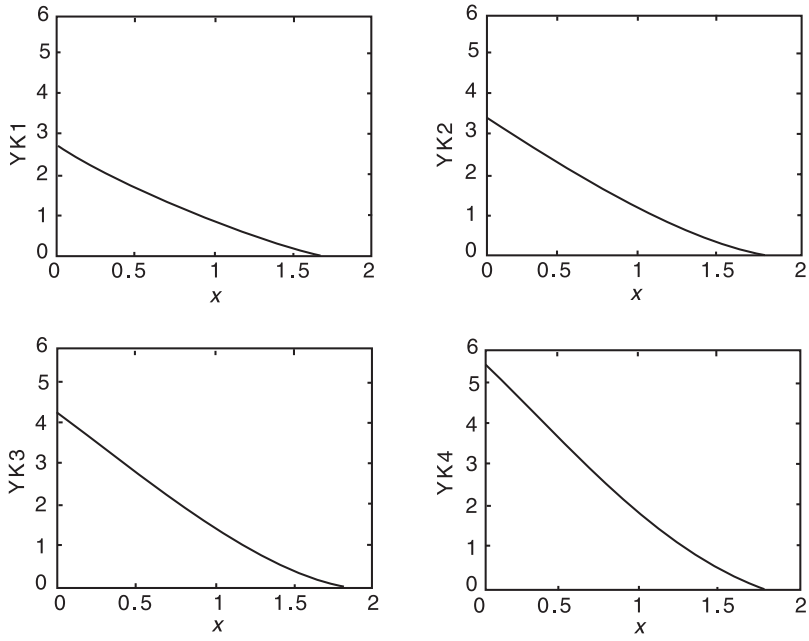


Figure 2 Four Krylov modes for the four-DOF cantilever beam.

may differ, in some details, from this algorithm. Such an alternative algorithm is described in the section on block Lanczos algorithms, below.

Algorithm 1: undamped structure; single load vector

1. *Starting vector*: As the starting vector, select the static deflection of the structure due to the load distribution vector, f. That is, solve the equation:

$$\mathbf{K}q_1 = f \qquad [a]$$

for the static deflection q_1. Mass normalize this to form the starting Lanczos vector:

$$\psi_{L1} = \frac{1}{\beta_1} q_1 \qquad [b]$$

where the normalizing factor β_1 is determined by:

$$\beta_1 = \sqrt{q_1^{\mathrm{T}} \mathbf{M} q_1} \qquad [c]$$

2. *Second Lanczos vector*: The second Lanczos vector is obtained by first solving for the static deflection of the structure subjected to inertia loading due to the first vector's deflection. In addition, there is a Gram–Schmidt orthogonalization step that removes the starting vector component. First, solve the equation:

$$\mathbf{K}\tilde{q}_2 = \mathbf{M}\psi_{L1} \qquad [d]$$

for the static deflection $\tilde{q}_2$. Then, use the Gram–Schmidt procedure to remove the ψ_{L1}-component of this iterate:

$$q_2 = \tilde{q}_2 - \alpha_1 \psi_{L1} \qquad [e]$$

where:

$$\alpha_1 = \psi_{L1}^{\mathrm{T}} \mathbf{M} \tilde{q}_2 \qquad [f]$$

Finally, mass normalize the vector q_2 to form the second Lanczos vector:

$$\psi_{L2} = \frac{1}{\beta_2} q_2 \qquad [g]$$

where the normalizing factor β_2 is determined by:

$$\beta_2 = \sqrt{q_2^{\mathrm{T}} \mathbf{M} q_2} \qquad [h]$$

3. *General Lanczos vector:* The general Lanczos vector, ψ_{Lj}, $j = 3, 4, \ldots$ is obtained by the following steps. First, solve the equation:

$$\mathbf{K}\tilde{q}_{(j+1)} = \mathbf{M}\psi_{Lj} \qquad [i]$$

for the static deflection $\tilde{q}_{(j+1)}$. Use the Gram–Schmidt procedure to remove both the $\psi_{\mathrm{L}j}$-component and the $\psi_{\mathrm{L}(j-1)}$-component of this iterate:

$$q_{(j+1)} = \tilde{q}_{(j+1)} - \alpha_j \psi_{\mathrm{L}j} - \beta_j \psi_{\mathrm{L}(j-1)} \qquad [\mathrm{j}]$$

where:

$$\alpha_j = \psi_{\mathrm{L}j}^{\mathrm{T}} \mathbf{M} \tilde{q}_{(j+1)} \qquad [\mathrm{k}]$$

and:

$$\beta_j = \psi_{\mathrm{L}(j-1)}^{\mathrm{T}} \mathbf{M} \tilde{q}_{(j+1)} \qquad [\mathrm{l}]$$

which can be shown to be just the preceeding normalizing factor. Finally, mass normalize the vector $q_{(j.+1)}$ to form the $(j+1)$-st Lanczos vector:

$$\psi_{\mathrm{L}(j+1)} = \frac{1}{\beta_{(j+1)}} q_{(j+1)} \qquad [\mathrm{m}]$$

where the normalizing factor $\beta_{(j+1)}$ is determined by:

$$\beta_{(j+1)} = \sqrt{q_{(j+1)}^{\mathrm{T}} \mathbf{M} q_{(j+1)}} \qquad [\mathrm{n}]$$

Figure 3 shows the four Lanczos modes for the cantilever beam shown in **Figure 1**. The starting vector for these is the same starting vector that was used for the set of Krylov modes.

Lanczos Coordinate Coupling; Tridiagonal Lanczos Matrix

The distinguishing feature of Lanczos algorithms is that, while one of the system matrices is diagonalized, the other system matrix is converted to tridiagonal form. Let $\Psi_{\mathrm{L}r}$ contain the first r Lanczos vectors as columns, that is, let:

$$\Psi_{\mathrm{L}r} \equiv [\psi_{\mathrm{L}1}\, \psi_{\mathrm{L}2}\, \psi_{\mathrm{L}3}\, \ldots\, \psi_{\mathrm{L}r}] \qquad [9]$$

and let the matrix $\mathbf{L}_r$, the corresponding tridiagonal matrix containing coefficients α_i and β_i, be:

$$\mathbf{L}_r = \begin{bmatrix} \alpha_1 & \beta_2 & 0 & \ldots & 0 & 0 \\ \beta_2 & \alpha_2 & \beta_3 & \ldots & 0 & 0 \\ 0 & \beta_3 & \alpha_3 & \ldots & 0 & 0 \\ \vdots & \vdots & \vdots & \ddots & \vdots & \vdots \\ 0 & 0 & 0 & \ldots & \alpha_{r-1} & \beta_r \\ 0 & 0 & 0 & \ldots & \beta_r & \alpha_r \end{bmatrix} \qquad [10]$$

which can be expressed directly in matrix form as:

$$\mathbf{L}_r = \Psi_{\mathrm{L}r}^{\mathrm{T}} \mathbf{M} \mathbf{K}^{-1} \mathbf{M} \Psi_{\mathrm{L}r} \qquad [11]$$

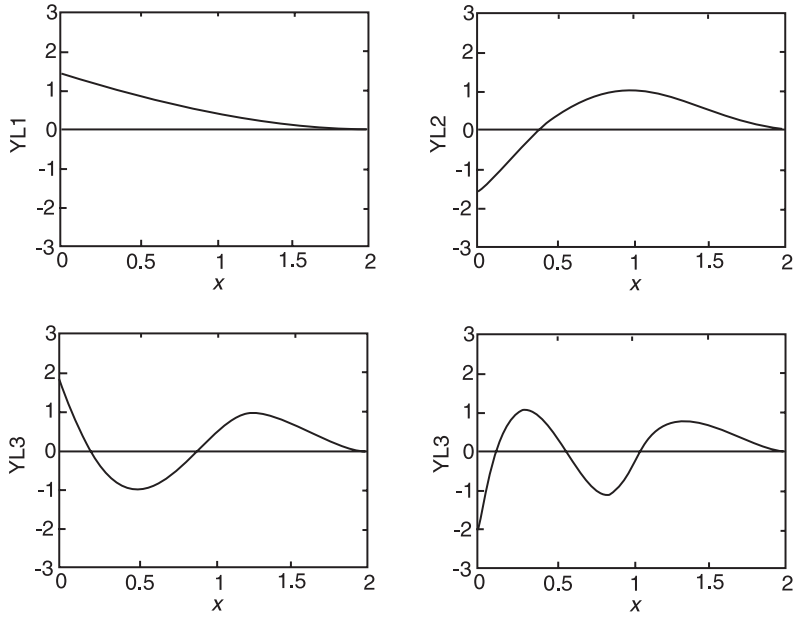


Figure 3 Four Lanczos modes for the four-DOF cantilever beam.

Because of the presence of the extra $\mathbf{K}^{-1}\mathbf{M}$ factor in eqn [11], this is not a standard Ritz transformation. However, with the Ritz-type coordinate transformation:

$$x = \Psi_{\mathrm{L}r}\bar{x}_r \qquad [12]$$

eqn [1] can be shown to reduce to the following form:

$$\begin{aligned}\Psi_{\mathrm{L}r}^{\mathrm{T}}\mathbf{M}\mathbf{K}^{-1}\mathbf{M}\Psi_{\mathrm{L}r}\ddot{\bar{\mathbf{x}}}_r(t) + \Psi_{\mathrm{L}r}^{\mathrm{T}}\mathbf{M}\Psi_{\mathrm{L}r}\bar{\mathbf{x}}_r(t) \\ = \Psi_{\mathrm{L}r}^{\mathrm{T}}\mathbf{M}\mathbf{K}^{-1}fu(t)\end{aligned} \qquad [13]$$

which reduces to the simple form:

$$L_r\ddot{\bar{x}}_r(t) + \bar{x}_r(t) = \lfloor\beta_1\ 0\ \ldots\rfloor^{\mathrm{T}}u(t) \qquad [14]$$

Note that the transformed mass matrix is the tridiagonal matrix of orthogonalization coefficients, while the transformed stiffness matrix is just the unit matrix. Also note that the only nonzero forcing term acts on the first Lanczos coordinate; the remaining coordinates are only coupled through the off-diagonal terms of the transformed mass matrix in eqn [14].

Some Properties of Lanczos Vectors

1. *Efficiency*: The efficiency of Krylov–Lanczos reduced-order models stems from the fact that the starting vector, or starting block of vectors, can be selected to span the static deflection of the structure under the given load patterns, while the higher-order terms in the sequence express the effects of inertia loads due to previous vectors in the sequence.
2. *Normalization and orthogonality*: Unlike the Krylov vectors in eqn [8], each Lanczos vector is mass orthonormalized. In 'exact arithmetic', when the $\psi_{\mathrm{L}j}$-component and the $\psi_{\mathrm{L}(j-1)}$-component have been removed from $\tilde{\mathbf{q}}_{(j+1)}$ (step j of Algorithm 1), the new Lanczos vector $\psi_{\mathrm{L}(j+1)}$ can be shown to be mass orthogonal to all previous Lanczos vectors. In practice, reorthogonalization with respect to all prior vectors may be necessary at some steps. Such computational details are discussed in the literature.
3. *Tridiagonality*: Although the coordinate transformation given in eqn [13] and based on the Lanczos vectors obtained through the use of Algorithm 1 is not a standard Ritz transformation (eqns [2]–[4]), other Lanczos algorithms do employ the standard Ritz transformation to obtain the transformed equation in the simple form of eqn [14], as will be demonstrated below. Even though the transformed equations are not completely uncoupled, as they would be if the transformation were based on eigenvectors, advantage can still be taken of the sparseness of the tridiagonal transformed mass matrix when eqn [14] is solved for dynamic response.
4. *Reduced-order models:* If Krylov vectors or Lanczos vectors are determined for an n-DOF model, but the sequence is truncated at $r<n$, the resulting subspace forms a reduced-order model of the original n-DOF system. Truncation criteria for determining an appropriate subspace order r have been presented by some authors.
5. *Block Krylov and block Lanczos algorithms*: The Krylov and Lanczos sequences can be defined for blocks of vectors, as demonstrated below.

A Block-Lanczos Algorithm for Model Reduction of Undamped Structural Systems

A block-Lanczos algorithm for an undamped structural dynamics system in input–output form will now be presented. The block format permits the force distribution matrix $\mathbf{F}$ to have more than one column. The output equation is included here to permit reduced-order modeling of the system output along with reduced-order modeling of the structure itself. Therefore, the system is described by the following system equation of motion and output equation:

$$\mathbf{M}\ddot{x} + \mathbf{K}x = \mathbf{F}u(t) \quad y = \mathbf{V}x + \mathbf{W}\dot{x} \qquad [15]$$

where $x \in R^{\mathrm{n}}$ is the displacement vector, $u \in R^{l}$ is the input force vector, $y \in R^{\mathrm{m}}$ is the output measurement vector, $\mathbf{M}$ and $\mathbf{K}$ are the system mass and stiffness matrices, $\mathbf{F}$ is the force distribution matrix, and $\mathbf{V}$ and $\mathbf{W}$ are the velocity and displacement sensor distribution matrices. The output equation is of particular interest in applications to control the flexible structures. The reduced system equation takes the form:

$$\overline{\mathbf{M}}\ddot{\bar{x}} + \overline{\mathbf{K}}\bar{x} = \overline{\mathbf{F}}u(t) \quad \bar{y} = \overline{\mathbf{V}}\bar{x} + \overline{\mathbf{W}}\dot{\bar{x}} \qquad [16]$$

with the reduced system coordinate $\bar{x}$ and the original system coordinate x related by eqn [2]. The reduced system matrices and the original system matrices are related by:

$$\begin{aligned}&\overline{\mathbf{M}} = \mathbf{T}^{\mathrm{T}}\mathbf{M}\mathbf{T}, \quad \overline{\mathbf{K}} = \mathbf{T}^{\mathrm{T}}\mathbf{K}\mathbf{T}, \quad \bar{\mathbf{F}} = \mathbf{T}^{\mathrm{T}}\bar{\mathbf{F}}, \\ &\overline{V} = \mathbf{V}\mathbf{T}, \qquad \overline{\mathbf{W}} = \mathbf{W}\mathbf{T}\end{aligned} \qquad [17]$$

The choice of the projection matrix, $\mathbf{T}$, governs the accuracy of the reduced system.

If the projection matrix $\mathbf{T}$ is formed by the set of Krylov vectors defined in eqn [18], then the reduced system has certain parameter-matching properties, which ensures that the Krylov model will faithfully represent low-frequency motion:

$$\text{span}\{\mathbf{T}\} = \text{span}\{\mathbf{T}_\text{F}\mathbf{T}_\text{V}\mathbf{T}_\text{W}\} \qquad [18]$$

The blocks of Krylov vectors contained in $\mathbf{T}_\text{F}$ can be generated by applying the simple iteration formula:

$$\mathbf{Q}_1 = \mathbf{K}^{-1}\mathbf{F}, \quad \mathbf{Q}_{i+1} = \mathbf{K}^{-1}\mathbf{M}\mathbf{Q}_i \qquad [19]$$

As noted above, Krylov vectors have a clear physical interpretation. The first block of Krylov vectors, $\mathbf{K}^{-1}\mathbf{F}$, is the system's static deflection due to the force distribution matrix, $\mathbf{F}$. The matrix $\mathbf{Q}_{i+1}$ can be interpreted as the matrix of static deflection vectors produced by the inertia force vectors associated with respective columns of $\mathbf{Q}_i$. If only the dynamic response simulation is concerned, the projection matrix $\mathbf{T}$ is simply $\mathbf{T}_\text{F}$. From an input–output point of view, $\mathbf{T}_\text{V}$, $\mathbf{T}_\text{W}$, and $\mathbf{T}_\text{F}$ are equally important. So, to construct a reduced-order model for control applications, where the input–output property is important, the following block Lanczos algorithm for generating the projection matrix $\mathbf{T}$ is given.

Algorithm 2: Undamped structural system with output equation; multiple load vectors

1. Form the starting block of vectors:
   (a) $\mathbf{Q}_0 = \mathbf{0}$
   (b) $\mathbf{R}_0 = \mathbf{K}^{-1}\tilde{\mathbf{F}}$, $\tilde{\mathbf{F}}$ = linearly-independent portion of $[\mathbf{F}\mathbf{V}^\text{T}\mathbf{W}^\text{T}]$
   (c) $\mathbf{R}_0^\text{T}\mathbf{K}\mathbf{R}_0 = \mathbf{U}_0\Sigma_0\mathbf{U}_0^\text{T}$(singular-value decomposition)
   (d) $\mathbf{Q}_1 = \mathbf{R}_0\mathbf{U}_0\Sigma_0^{-1/2}$(normalization)
2. For $j = 1, 2, \ldots, k-1$, repeat:
   (e) $\bar{\mathbf{R}}_\text{j} = \mathbf{K}^{-1}\mathbf{M}\mathbf{Q}_j$
   (f) $\mathbf{R}_j = \bar{\mathbf{R}}_j - \mathbf{Q}_j\mathbf{A}_j - \mathbf{Q}_{(j-1)}\mathbf{B}_j$ (orthogonalization)
   $\mathbf{A}_j = \mathbf{Q}_j^\text{T}\mathbf{K}\bar{\mathbf{R}}_j$, $\mathbf{B}_j = \mathbf{U}_{(j-1)}\Sigma_{(j-1)}^{1/2}$
   (g) $\mathbf{R}_j^\text{T}\mathbf{K}\mathbf{R}_j = \mathbf{U}_j\Sigma_j\mathbf{U}_j^\text{T}$(singular-value decomposition)
   (h) $\mathbf{Q}_{(j+1)} = \mathbf{R}_j\mathbf{B}_{(j+1)}^{-\text{T}} = \mathbf{R}_j\mathbf{U}_j\Sigma_j^{-1/2}$ (normalization)
3. Form the k-block projection matrix: $\mathbf{T} = [\mathbf{Q}_1\,\mathbf{Q}_2 \ldots \mathbf{Q}_k]$

In the above algorithm the $\mathbf{K}$ matrix is used as the normalization weighting matrix; in eqn [8] the $\mathbf{M}$ matrix is used. By using $\mathbf{K}$ as the normalization weighting matrix, the generated Lanczos vectors orthonormalize the $\mathbf{K}$ matrix and block-tridiagonalize the $\mathbf{M}$ matrix. Therefore, the standard Ritz method can be employed to transform the system's dynamic equation into the following form:

$$\mathbf{T}^\text{T}\mathbf{M}\mathbf{T}\ddot{\bar{x}} + \mathbf{T}^\text{T}\mathbf{K}\mathbf{T}\bar{x} = \mathbf{T}^\text{T}\mathbf{F}u \qquad [20]$$

where the transformed mass matrix $\mathbf{T}^\text{T}\mathbf{M}\mathbf{T}$ is block tridiagonal.

The vectors generated by Algorithm 2 lie in a Krylov subspace, because they are generated by the Krylov iteration formula in step (e). The algorithm is called a Lanczos algorithm because of the three-term orthogonalization scheme used in step (f). Remarks about the numerical details of Algorithm 2 and the properties of the resulting reduced-order model are discussed elsewhere in the literature.

Due to the choice of starting block of vectors in Algorithm 2, the $\mathbf{K}$-orthogonalization, and the three-term recurrence, the transformed system equation in the Lanczos coordinates has a mass matrix in block-tridiagonal form, a stiffness matrix equal to the identity matrix, and force distribution and measurement distribution matrices with nonzero elements only in the first block of each. The form of the transformed system equation is:

$$\begin{bmatrix} \times & \times & & & & & & \\ \times & \times & \times & & & & & \\ & \cdot & \cdot & \cdot & & & & \\ & & \cdot & \cdot & \cdot & & & \\ & & & \cdot & \cdot & \cdot & & \\ & & & & \times & \times & \times & \\ & & & & & \times & \times & \end{bmatrix} \ddot{\bar{x}} + \bar{x} = \begin{bmatrix} \times \\ 0 \\ \cdot \\ \cdot \\ \cdot \\ 0 \\ 0 \end{bmatrix} u \qquad [21]$$

$$y = [\times \quad 0 \quad 0 \cdots 0]\,\bar{x} + [\times \quad 0 \quad 0 \cdots 0]\,\dot{\bar{x}}$$

where $\times$ denotes the location of nonzero elements. This special form reflects the structure of a tandem system (**Figure 4**), in which only subsystem S_1 is directly controlled and measured while the remaining subsystems, S_i, $i = 2, 3, \ldots$ are excited through chained dynamic coupling. This form of the transformed system equation and output equation has a major advantage in control applications.

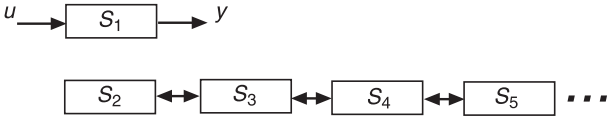


Figure 4 Structure of a tandem system.

Other Applications of Krylov Vectors and Lanczos Vectors

In addition to the two algorithms presented in this article, various authors have presented other algorithms for undamped structures. Some of these algorithms are currently available in structural dynamics finite element codes. Some of the other applications that may be found in the literature are listed below.

1. *Dynamic response of damped, linear structure*: Several authors have presented Krylov–Lanczos algorithms for analyzing the dynamic response of damped linear systems. The simplest version is for systems that have proportional viscous damping, and employs Ritz vectors for the corresponding undamped system. Iteration steps have been employed to extend this approach to handle nonproportional damping cases. In the case of nonproportional damping, Krylov–Lanczos algorithms have been proposed that are based on a transformation of the equations of motion from second-order form to first-order form. For general linear viscous damping, both one-sided and two-sided unsymmetric block-Lanczos algorithms have been presented. It has been demonstrated that much greater accuracy can be achieved than by a simple use of Ritz vectors computed for the undamped structure.
2. *Dynamic response of linear structures with nonlinear elements*: Load-dependent Ritz vectors have been used to calculate the nonlinear dynamic response of structures that have localized energy dissipation devices or that develop plastic hinges, and have also been employed for the iterative solution of other nonlinear response problems.
3. *Component mode synthesis of linear structures*: A popular approach to solving large structural dynamics problems is to divide the structure into smaller substructures and apply one of the methods of component mode synthesis. The classical component mode synthesis methods employ both normal modes of free vibration of the separate components and also various derived Ritz vectors (e.g., constraint modes or attachment modes) that improve the accuracy of dynamic response solutions. It has been shown that it is unnecessary to use component normal modes of free vibration; Krylov modes or Lanczos modes can be substituted for component normal modes without degradation of accuracy.

   Along similar lines, Lanczos modes have been employed to model the flexibility of components of multibody systems, where the governing equations are nonlinear.
4. *Feedback control design for flexible structures*: By including the output equation as well as the equation of motion, as illustrated above, it is possible to obtain reduced-order models that are very attractive for use in control system design. The benefit that accrues from the use of Lanczos vectors for model reduction is the special sparse form of the resulting Lanczos model, as illustrated in **Figure 4**, especially the sparseness of the transformed input and output distribution matrices.
5. *System identification; damage detection*: Experimental modal analysis, the standard procedure for using vibration testing to obtain an experimental model of a structure, usually seeks to obtain a 'modal model' of the structure; that is, to obtain natural frequencies, damping factors, and mode shapes (either real normal modes or complex modes). A few authors have recently proposed that vibration test data can also be used to generate a Krylov-mode or Lanczos-mode representation. Recent work has involved use of these Krylov–Lanczos vectors to assess structural damage.

Acknowledgment

The author expresses his deep indebtedness to his former student, Dr Tsu-Jeng Su, whose creativity and thorough knowledge of linear systems theory led to pioneering work in the application of Krylov–Lanczos methods to the control of flexible structures.

Nomenclature

f	load distribution vector
$\mathbf{F}$	force distribution matrix
q_1, q_2	static deflections
$\mathbf{T}$	projection matrix
$\mathbf{V}$	velocity sensor distribution matrix
$\mathbf{W}$	displacement sensor distribution
β_1, β_2	normalizing factors

See also: **Commercial software**; **Computation for transient and impact dynamics**; **Eigenvalue analysis**.

Further Reading

Arnold RR, Citerly RL, Chargin M and Galant D (1985) Application of Ritz vectors for dynamic analysis of large structures. *Computers and Structures* 21 (3): 461–467.

Clough RW and Penzien J (1993) *Dynamics of Structures*, 2nd edn. New York: McGraw-Hill.

Craig RR Jr (1981) *Structural Dynamics – An Introduction to Computer Methods*. New York: John Wiley.

Craig RR Jr (1995) Substructure methods in vibration. *Transactions of the ASME, Special 50th Anniversary Design Issue*, 117: 207–213

Craig RR Jr and Hale AH (1988) The block-Krylov component synthesis method for structural model reduction. *AIAA Journal of Guidance Control, and Dynamics* 11 (6): 562–570.

Golub FH and Van Loan CF (1996) *Matrix Computations*, 3rd edn. Baltimore, MD: Johns Hopkins University Press.

Kim H-M and Craig RR Jr (1992) Application of unsymmetric block Lanczos vectors in system identification. *International Journal of Analytical and Experimental Modal Analysis* 7 (4): 227–241.

Lanczos C (1950) An iteration method for the solution of the eigenvalue problem of linear differential and integral operators. *Journal of Research of the National Bureau of Standards* 45: 255–281.

Noor AK (1994) Recent advances and applications of reduction methods. *Applied Mechanics Reviews* 47 (5): 125–146.

Nour-Omid B and Clough RW (1984) Dynamic analysis of structures using Lanczos co-ordinates. *Earthquake Engineering and Structural Dynamics* 12: 565–577.

Su T-J and Craig RR Jr (1992a) An unsymmetric Lanczos algorithm for damped structural dynamics systems. *Proceedings of the 33rd AIAA Structures, Structural Dynamics, and Materials Conference*, pp. 2243–2252.

Su T-J and Craig RR Jr (1992b) Krylov vector methods for model reduction and control of flexible structures In: Leondes CT (ed.) *Control and Dynamic Systems – Advances in Theory and Applications*. San Diego, CA: Academic Press.

Wilson EL (1994) A complete subspace basis for a dynamic mode superposition analysis. In: *Numerical Methods in Structural Mechanics*, AMD-vol. 204, New York: ASME.

Wilson EL (1997) *Three Dimensional Dynamic Analysis of Structures*. Berkeley, CA: Computers and Structures.

Wilson EL, Yuan MW and Dickens JM (1982) Dynamic analysis by direct superposition of Ritz vectors. *Earthquake Engineering and Structural Dynamics* 10: 813–882.

L

LAGRANGE METHOD

See **BASIC PRINCIPLES; THEORY OF VIBRATION,** ENERGY METHODS

LAPLACE TRANSFORMS

See **TRANSFORM METHODS**

LASER BASED MEASUREMENTS

E P Tomasini, G M Revel and P Castellini,
Università di Ancona, Ancona, Italy

Copyright © 2001 Academic Press

doi:10.1006/rwvb.2001.0152

In recent years the techniques for the measurement and analysis of mechanical vibrations have been widely investigated because of their relevance in a large number of industrial applications. Important results have been achieved in the field of noncontact sensors by using innovative electrooptic methodologies and, in particular, those based on laser techniques.

Among the different laser-based techniques for vibration measurement (such as holography, electronic speckle pattern interferometry (ESPI), shearography, etc.), laser Doppler vibrometry (LDV) is one of the most investigated and used, mainly because of its flexibility and applicability in a wide range of testing situations.

Nonintrusive measurement techniques are advantageous with respect to traditional ones, based on the use of accelerometers, since they allow one to avoid errors due to mass loading effects, especially when testing light or small structures or highly damped nonlinear materials (like rubber); moreover, they often drastically reduce testing time and help perform remote measurements.

LDV is an interferometric technique for vibration measurements on solid bodies. This method determines the instantaneous velocity by observing the Doppler effect induced on a laser beam diffused by the object surface.

The initial studies on LDV sensors were presented in the late 1960s, and the first commercial system was introduced by DISA during the 1970s. This instrument was based on an optical heterodyne detection of Doppler shift and it was very similar to those which are available in the market at present; however, its limited sensitivity allowed measurements on only very diffusive surfaces.

During the 1980s several researches were performed in order to increase the performances of these sensors: fibre optic systems were used to improve handiness and compactness, while different alternative solutions were studied to realize specific signal analysis strategies.

It was only in the early 1990s that commercial sensors, typically fully-bulk optic systems, with the capabilities of working with higher sensitivity and signal-to-noise ratio were presented. Typical performances of actual systems are high accuracy for remote measurements (accuracy 1–2.5% root mean square of reading at a distance larger than 30 m), bandwidth up to 200 kHz, velocity range of $\pm 10\,\mathrm{m\,s^{-1}}$, resolution of about 8 nm in displacement and 0.5 $\mu\mathrm{m\,s^{-1}}$ in velocity and reduced testing time. Due to the high optical sensitivity of the last generation of sensors, the measured surface does not need to be specifically treated or prepared in advance.

The combination of an interferometer with two moving mirrors driven by galvanometric actuators makes it possible to direct the laser beam to the desired measurement points. Such an instrument, named the scanning laser Doppler vibrometer (SLDV), can quickly perform a series of velocity measurements on a grid of points over the structure under test. This particular capability, together with its noncontact nature, makes SLDV technology suited for situations where the use of accelerometers is difficult, as in the case of rotating structures. Besides, if a high number of measurements has to be taken on different points, it would be necessary to arrange an array of contact transducers, which is time-consuming and costly. In contrast, the SLDV is able to provide both spatial information and time dependence of the vibration, whereas other full-field optical techniques, including ESPI and double-pulse laser holography, supply only spatial information and have no means to control the time dependence. In addition, SLDV provides automatically calibrated velocity amplitude and phase information at each measurement point.

These new laser-based techniques have proved to be of paramount importance for overcoming problems related to vibration measurements, such as frequency range, spatial resolution, electromagnetic interference sensitivity, and for allowing measurements in harsh conditions, such as high-temperature surfaces and noisy environments, or when hard-to-reach, small, or weak objects are analyzed.

Because of their high accuracy, they are often used as a primary reference for the calibration of other sensors, like accelerometers. In addition, these techniques are effectively used in structural dynamic testing, biological and clinical diagnostics, fluid–structure interaction, online monitoring of industrial plants, acoustics, and fault detection, to cite only a few. Furthermore, the coupling of laser vibrometers and scanning systems seems to open up new possibilities, e.g., in the field of measurements in tracking mode on moving objects.

Laser Doppler Vibrometry Technique

The Doppler Effect

The laser Doppler vibrometer is a noncontact velocity transducer, based on the analysis of the Doppler effect on a laser beam emerging from a solid surface.

When a coherent radiation of frequency f (**Figure 1A**), emitted by a source S, interacts with a reflecting or diffusing moving surface P at velocity v, the radiation observed by O is affected by a Doppler shift Δf_D proportional to the surface velocity.

If, as usual (**Figure 1B**), the position of the source and of the observer are coincident (back-scatter configuration), such a frequency shift is given by:

$$\Delta f_D = \frac{2v}{\lambda} \cos\theta \qquad [1]$$

The corresponding phase shift is given by:

$$\Delta\phi = \frac{4\pi d}{\lambda} \cos\theta \qquad [2]$$

where $d(t) = \int_0^\tau v(\tau)\mathrm{d}\tau$ is the displacement of the target surface.

In general, if the target moves at a speed $v(t)$ varying in time, the phase (and frequency) difference becomes time-dependent.

The Laser Doppler Vibrometer

If a He-Ne ($\lambda = 632.8\,\mathrm{nm}$) laser is used for the measurement of a velocity of $1\,\mathrm{m\,s^{-1}}$, the frequency $f = 4.7 \times 10^{14}\,\mathrm{Hz}$ is shifted $3.16 \times 10^{6}\,\mathrm{Hz}$. A dynamic range of about 6.7×10^{-9} (164 dB) is required for detection. Under the same conditions, the phase shift observed for a displacement of 1 μm is about 6.321π.

The interferometric approach can be used in order to measure such a relatively small frequency shift and to have a reference in the phase assessment. Usually a laser beam is split in two, with one beam acting as a stationary reference (reference beam) while the other

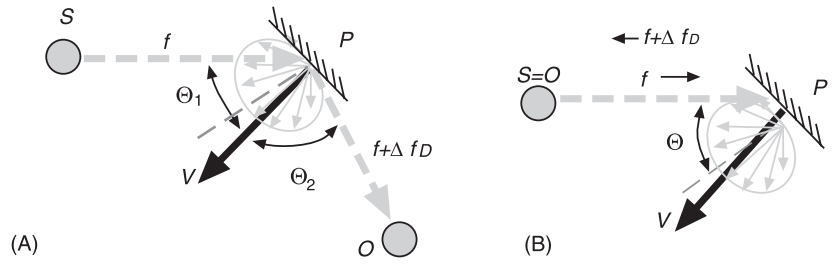


Figure 1 The Doppler effect on a scattering surface.

beam is directed to a vibrating surface (measuring beam).

If the intensity of the resulting field is measured using a photodiode with square-law response and with heterodyning efficiency ε (which is a parameter taking into account degradation of the AC current for optical distortions and misalignment and depends on intensities, coherence, and polarization, as discussed in the following paragraphs), the output signal is:

$$I(t) \propto A_m^2 + A_r^2 + 2\varepsilon A_m A_r \cos\left(2\pi \frac{2v(t)}{\lambda} \cos\theta\, t\right) = A_m^2 + A_r^2 + 2\varepsilon A_m A_r \cos\left(\frac{4\pi d(t)}{\lambda} \cos\theta\right) \quad [3]$$

where A_m, A_r are the amplitudes of electric field of light (measurement and reference). The third addendum is the only one related to displacement or velocity, therefore with an AC coupling the other components are eliminated.

When observing eqn [3] it is possible to note that the AC part of the $I(t)$ function is odd with respect to velocity and therefore the same intensity corresponds to velocities with opposite direction. Such ambiguity in the direction assessment can be eliminated in different ways depending on the optical and electronic set-up (see below).

In order to extract the information on the required component of velocity, different interferometers and different demodulation techniques can be used depending on specific requirements and applications. A review of the main instruments based on such phenomena is reported.

Basic Interferometer Configurations

The so-called single-point vibrometer, the first developed and the most diffused vibrometer, is basically an axial vibrometer, i.e., an instrument which is able to measure displacement and velocity in the direction of its optical axis.

Different interferometer configurations can be employed in such an instrument. In particular, the most widely used are the Michelson and the Mach–Zehnder interferometers.

In **Figures 2** and **3** a scheme of the different interferometers is shown.

The basic interferometer design is that of Michelson. A linearly polarized laser (usually a He-Ne oriented at 45°) beam is split by a polarizing beam-splitter, PBS2. Both reflected and transmitted beams are back-reflected along the same paths by a mirror (reference beam) and by a reflecting or scattering surface (measurement beam) on the target.

Along the optical path both beams encounter twice (before and after reflection/diffusion) a $\lambda/4$ plate. Therefore, due to the orthogonal polarization obtained, the beam splitter BS1 deviates both beams at the photodiodes where interference occurs.

If the target is moving, the optical path is continuously changing and dark and bright fringes appear to the observer.

In the Mach–Zehnder interferometer the same effect is obtained with a different optical arrangement. The first polarizing beam-splitter (PBS1) splits light (linear 45° polarized) from the source and reflected and transmitted beams run parallel to each other. A lens collects the measurement beam, interacting with the scattering surface on the target. A $\lambda/4$ plate rotates the polarization plane 90° and then the

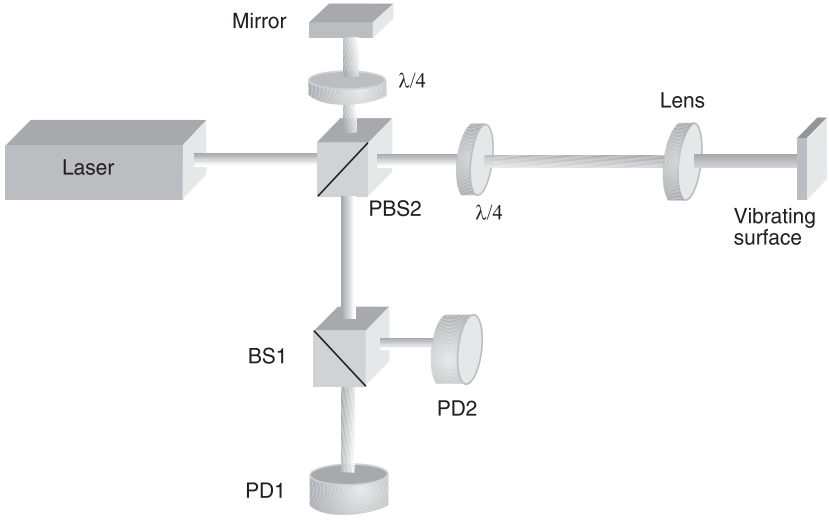


Figure 2 Scheme of a single-point vibrometer based on a Michelson interferometer.

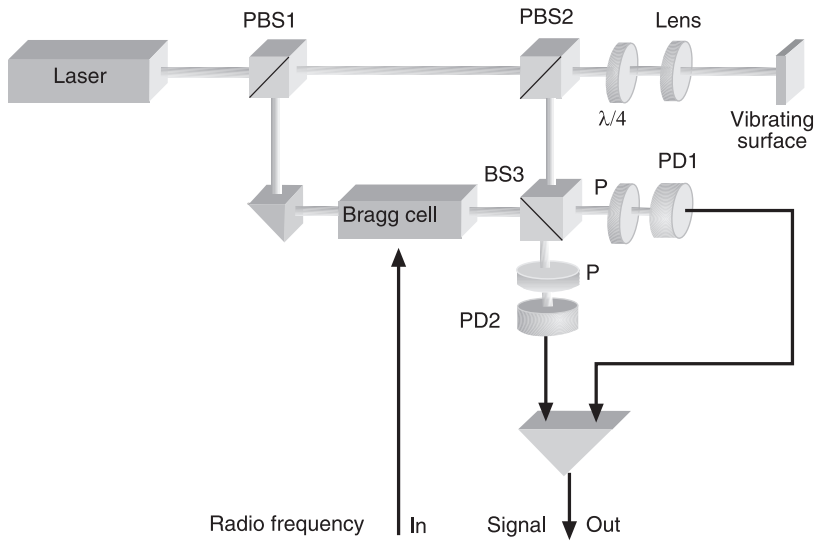


Figure 3 Scheme of a single-point vibrometer based on a Mach–Zehnder interferometer.

beam is deviated by the polarizing beam-splitters PBS2. On BS3, the measurement beam interacts with the reference beam, shifted by the Bragg cell, and it is observed by photodiodes PD1 and PD2.

In each case the observer can be composed by a single photodiode or by two photodiodes which are optically coupled by a beam-splitter (as shown in **Figure 3**). Thus it is possible to obtain two signals, corresponding to the destructive and constructive interference.

Such a solution can be used for different purposes. In particular, the Mach–Zehnder interferometer usually allows there to be two opposite signals for each interference condition. In fact, the different number of reflections in the optical path to PD1 and PD2 induces coupling of laser beams with different phases, and therefore a destructive interference on PD1 and a constructive interference on PD2 at the same time. Noises are usually not sensitive to such a phenomenon and have the same phase in both photodiodes. The difference between such signals presents a good improvement of the signal-to-noise ratio, due to common-mode noises rejection.

Frequency Shifting Devices for Direction Ambiguity Elimination and Signal-processing Scheme

As previously shown, due to the interferometer design and the sensitivity of photodiodes to light intensity, the resultant signal from photodiodes is not sensitive to the direction of the target velocity vector, and it does not allow a complete analysis of the target velocity history.

The direction ambiguity can be eliminated in different ways. An electronic approach is used with Michelson schemes, where the signal from photodiodes is at a frequency of Δf_D, fluctuating from zero to the maximum modulus of the velocity. In this case two carriers multiply sinusoidal and cosinusoidal signals (with a frequency f_{Shift}) from PD1 and PD2. The carriers, with a frequency f_c depending on the frequency range to be analyzed, are shifted 90° from each other, in order to obtain a sine and a cosine. The sum of such signals gives a modulated signal frequency, which is sensitive to velocity direction. The signal is then demodulated to obtain the velocity information.

The classical solution is the introduction of an additional modulation of the laser beam in the measurement or reference path. In fact, a modulation frequency modifies the total frequency seen by the detector, adding a virtual velocity, to:

$$\Delta f_{TOT} = \Delta f_{Shift} + \Delta f_D = \Delta f_{Shift} + \frac{2v}{\lambda} \qquad [4]$$

The resultant frequency signal depends on the velocity direction and, in particular:

$$\begin{aligned} \Delta f_{TOT} &> \Delta f_{Shift} \text{ if } v > 0 \\ \Delta f_{TOT} &< \Delta f_{Shift} \text{ if } v < 0 \end{aligned} \qquad [5]$$

Such a shift can be obtained in different ways. The most interesting seems to be acoustooptic modulators – the most used solution – and, in particular, Bragg cells.

The signal obtained from a photodiode can be processed in different ways in order to extract the information from the interference signal.

Depending on the optical arrangement of the interferometer, a heterodyne or homodyne signal is obtained. In addition the analysis strategies can be devoted to velocity or displacement assessment.

The choice between the two approaches depends on the kind of information requested and induces important effects on signal quality.

The heterodyne interference is realized when the frequency shift technique is applied to obtain velocity ambiguity resolution, as in the Mach–Zehnder. In that case, the signal from photodiodes is at frequency $f_{\text{Shift}} + f_{\text{Doppler}}$, which is usually in the range of 40 MHz.

The demodulation of such a radiofrequency signal can be performed using the same technology developed in signal transmission. For this reason radio-based chips are frequently used for this purpose, but for vibration application a more complex technique seems to be required. Therefore this demodulation is realized basically as a down-mixing of interference signal with the reference signal driving the Bragg cell. Such a signal, with a sensitivity and linearity which are optimized in several ranges of decoding, is then filtered depending on the frequency range chosen, in order to obtain the velocity signal. To this basic structure, usually smarter filtering strategies (such as amplifiers, signal conditioners, tracking filters, Butterworth filters, etc.) are added, in order to improve the signal-to-noise ratio.

In addition, the signal analysis can be devoted to displacement assessment. When a displacement d of the target surface occurs, a path length variation $2d$ in the arm of the interferometer corresponds, and the interference signal presents a phase shift (see eqn [2]), given by:

$$\Delta\phi = \frac{4\pi d}{\lambda} = 2\pi N \qquad [6]$$

For a direct evaluation of surface displacement it is sufficient to count the number N of fringes, i.e., of constructive and destructive interference, each one corresponding to a displacement of half of the wavelength λ. Digital counters usually perform this purpose.

Scanning Laser Doppler Vibrometer

The SLDV was invented in 1981, while modifying a laser Doppler sensor. An SLDV is basically a sensor equipped with a scanning device and data acquisition and processing system, where the sensor is a laser Doppler single-point vibrometer, as previously discussed.

The peculiar part of a SLDV is the scanning system that directs the laser beam by means of two moving mirrors. By adding coordinate control using scanning mirrors, a single-point vibrometer sensor can be used to scan across a surface, gathering multipoint data from large vibrating objects. A possible arrangement, which can be used to carry out the scanning, is shown in **Figure 4**.

To aim the measuring beam at specified locations, two voltages have to be applied to the galvanometric controllers (motors), so that the scanning mirrors rotate at the desired angles. This is only accurately obtained if the spatial relationship between the test structure and the SLDV system is precisely determined. In order to define uniquely a position on the test object, calibration must be performed by directing the laser spot to specified calibration points. This operation makes it necessary to use a computer in order to perform the scanning control automatically, which dramatically reduces the time required for the measurement tests.

One of the features, which turned out to be extremely helpful in calibration and application of the SLDV, was an integral video camera. This solution allows the operator to monitor the location of the laser beam on the test item (**Figure 5**) and to overlay the measured results on an image of the test item. This solution is adopted by most manufacturers of laser Doppler vibrometers. Different arrangements can be designed.

In-plane Vibrometer

The in-plane vibrometer measures the velocity component perpendicular to its optical axis and therefore

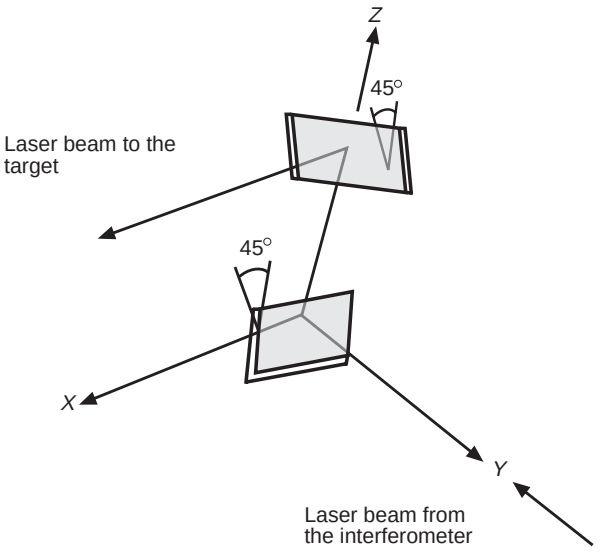


Figure 4 Scheme of a possible layout of a scanning system.

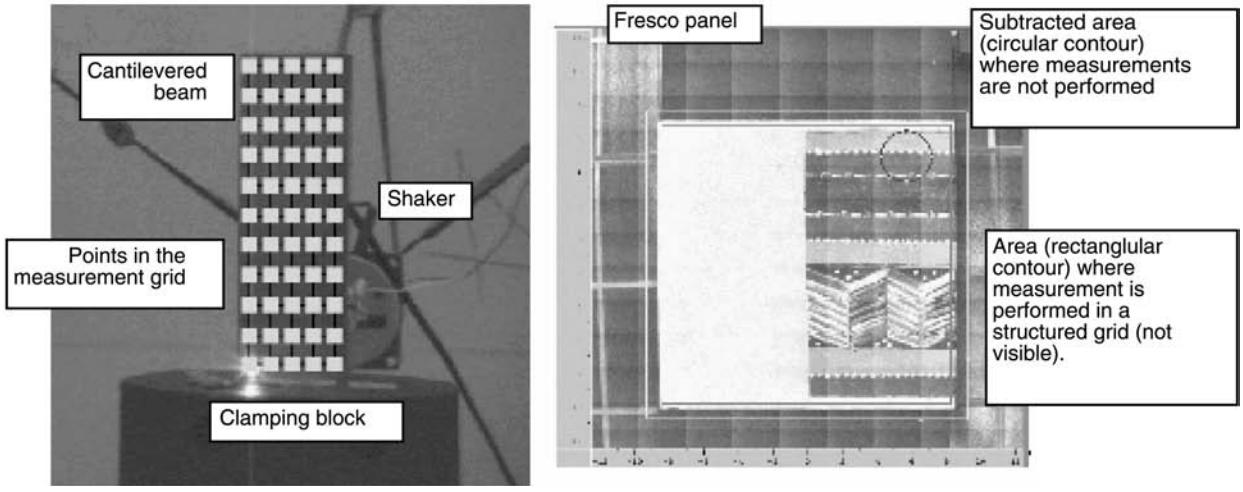


Figure 5 The measurement area in two different scanning laser Doppler vibrometer (SLDV) systems.

can be utilized to determine experimentally in-plane or tangential vibrations. Its functioning is based on the interaction between the surface roughness and the interference fringes area formed in correspondence with the intersection of two laser beams (**Figure 6**). The determination of the velocity value occurs by Doppler effect in the scattered light, which is collected by the optics to the photodetector.

If λ is the laser wavelength and θ is the angle between the two beams, the relation between the in-plane velocity v and the measured Doppler shift Δf_D is:

$$v = \frac{\lambda/2}{\sin(\theta/2)}\Delta f_D \qquad [7]$$

The measurement volume usually has an ellipsoidal shape and consists of the interference fringe area where an optical heterodyne phenomenon is produced. The introduction of a Bragg cell induces an optical frequency shift in one beam. The nonstationary fringe pattern obtained allows one to eliminate direction ambiguity. Usually a laser diode (670–690 nm, 25 mW), stabilized in temperature by a Peltier cell, is used in a back-scattering configuration. A tension signal proportional to velocity is obtained through a frequency–voltage converter.

Typical performances are a bandwidth from 0 to 10 kHz and a velocity range up to 100 m s^{-1} DC. The typical calibration accuracy is about $\pm 0.5\%$.

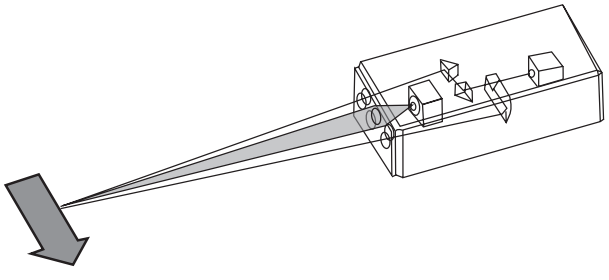


Figure 6 Optical scheme of the in-plane vibrometer.

Rotational Vibrometer

Rotational vibrometers permit the measurement of rotational speed and the analysis of torsional vibrations, also under operational conditions, with a simple and noncontact set-up. They are based on the design shown in **Figure 7** to measure the angular velocity optically.

In general, each point on the perimeter of a rotating part of any shape has a tangential velocity v_t depending on the rotational radius R and on the angular velocity ω. As shown below, it is possible to determine the angular velocity ω by measuring two parallel translational velocity components (**Figure 7**).

Two interferometers with parallel measurement beams with separation d are used and the velocity components v_A and v_B in the direction of beams are acquired. The following formula is obtained for the Doppler frequency shift in rotational vibrometers:

$$\begin{aligned} f_D &= f_{DA} + f_{DB} = \frac{2v_A}{\lambda} + \frac{2v_B}{\lambda} \\ &= \frac{2}{\lambda}\omega(r_A \cos\varphi_A + r_B \cos\varphi_B) = \frac{2}{\lambda}\omega d \end{aligned} \qquad [8]$$

which therefore only depends on the vibrometer constructive parameters (d and λ) and on the angular velocity ω.

It is evident that an additional translational motion in the direction of measurement beams, overlapping

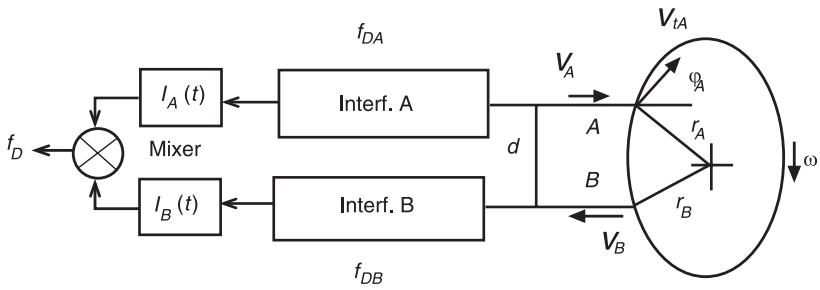


Figure 7 Scheme of the rotational vibrometer measurement principle.

both velocities v_A and v_B, has no influence on the resulting Doppler frequency. Also a vertical translation, as a motion perpendicular to the measurement beams, cannot create a measurement effect and therefore this technique seems to be basically insensitive to translational movements. It appears also to be insensitive to bending motions of the rotating object not in the plane of beams, as long as such motions do not add different velocities at the two measurement points. The only measurement requirement is that the laser beam plane must be perpendicular to the system's rotation axis. If this does not happen, only the component $\omega \cos \beta$ of the angular velocity is measured, where β is the angle between the beam plane and the shaft axis. No particular surface preparation is usually required.

Typical velocity range is from -7000 to 11 000 rpm up to 1000 rad s^{-1}. The frequency range in vibrational angle measurement is from 1 Hz to 10 kHz. The typical calibration accuracy is about $\pm$ 0.5%.

Surface Characteristic Effects: The Speckle Noise

One of the most important problems and noise sources in every kind of laser Doppler vibrometer is the effect of the speckle. The speckle is the interference image generated when a beam of coherent light interacts with a rough surface. Waves constituting the beam are diffused by the surface and interfere, generating a distribution of light intensity found by dark and bright zones, due to destructive and constructive interference. The superposition of the interference pattern with the desired light signal, containing the Doppler frequency, introduces uncertainty in the demodulation procedure, where the velocity information is carried out. The consequence of speckle noise is represented by momentarily signal drop-out (spikes) typical in a LDV output (**Figure 8**).

In general, interfering inputs due to speckle are caused by in-plane velocity components of the measurand surface: the change in the local roughness shape induces a sort of motion in the speckle pattern. There are many cases of technical interest, where it is necessary to measure the orthogonal vibration component of a surface, which is also moving tangentially (e.g., flexural vibrations of shaft and rotating disks) and therefore the study of speckle phenomena becomes important.

Interesting results in this field can be achieved using tracking filters. A tracking filter works by analyzing the instantaneous phase of the radiofrequency signal and generating a sinusoidal waveform according to the original one. The effect obtained is similar to a low-pass filter, but with a more effective result and better agreement with the input signal.

Also on the demodulated signal (i.e., the vibration velocity signal) it is possible to apply different algorithms for drop-out elimination, like the tracking filter itself; however, usually a band-pass or low-pass filter is applied. Such a simple filter allows better control of a performed test, as it is easy to set, and introduces more predictable signal-processing effect.

Applications

Due to the sensitivity, accuracy, and versatility of LDVs, different systems based on this principle are now in widespread use for a broad range of applications. In fact, these systems were applied not only in mechanics, the traditional field of application of vibration measurement techniques, but also where other techniques demonstrate important limits.

An example of those fields is represented by damage detection methods, where promising results have been found in the analysis of delaminations in frescos and composite materials. Damages in such structures are very localized and do not modify global modal properties of the object, inducing only local vibration modes: therefore, it is critical to investigate both cases by contact techniques, such as accelerometers, since they are very light, highly damped, and delicate, with important modes up to 100 kHz.

In addition, the portability of LDV systems offers a unique possibility of in-field tests, without complex

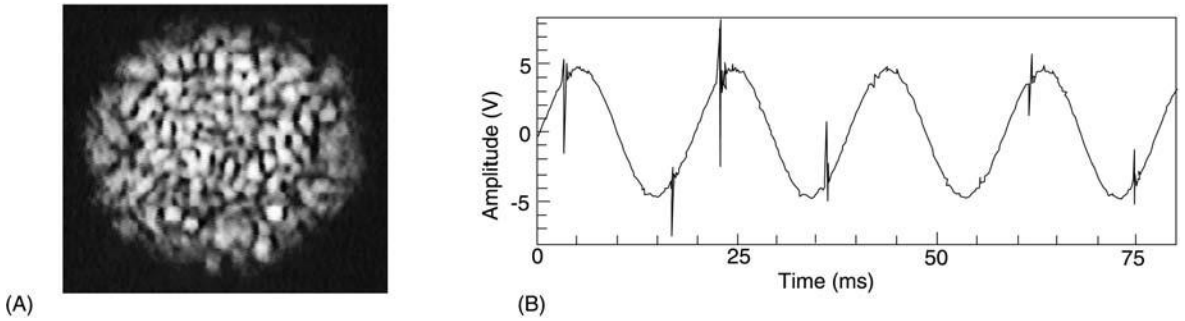


Figure 8 (A) Speckle pattern and (B) drop-out induced by optical noises in a sinusoidal velocity signal.

and costly installations, and makes it possible to operate directly where the structure is usually working or installed.

A large number of applications in the field of system identification of light or very small structures have been developed, thanks to the noncontact nature of LDV measurements. It is well known that the effects of mass loading due to accelerometers is often also significant in large or rigid structures. When mass or dimension of the measurand is comparable to those of the transducer, this effect becomes important. Interesting results have been found in the characterization of hard disk drives or in the study of tire vibrations.

The capability of SLDV to measure, quickly and in an automatic way, the velocity at a very large number of points is very useful in updating methods of the finite element model, in particular for the analysis of the high-frequency range. Furthermore, the recent availability of systems which are able to plot the measurement points on a geometrical spatially defined three-dimensional grid for modal analysis has extended this possibility. However, it has also stressed the need for accuracy when determining the relative position and orientation between laser head and test structure.

Boundary element models or superimposition methods were applied, starting from high-density data (amplitude and phase information of vibration pattern), given by SLDV in order to predict the acoustic emission of vibrating surfaces.

The versatility and ease of installation and control allow Doppler systems to be used in several industrial applications and quality control systems. In the car industry LDV has been proposed to analyze the behavior of mechanical and structural components, such as a window lift system. In quality control, laser Doppler sensors have been employed at the bench for automatic testing and selection of washing machines at the end of the production line. Data obtained during operating conditions have been analyzed using neural network algorithms.

Another interesting application is vibration measurement across a flame (e.g., in the inner surface of a burner). This is a typical case where noncontact measurement techniques are the only possible solution. In fact, because of the high temperature, conventional techniques (e.g., accelerometers, strain gauges, etc.) cannot be applied without damaging the instruments; the same restriction applies to noncontact devices which must be placed close to the measured surface (e.g., eddy current proximity sensors, etc.). Among the different noncontact remote optical measurement techniques, LDVs may be usefully employed for this application, but interactions between laser beam and flame must be carefully considered.

Finally, a field which is demonstrating an increasing interest in laser Doppler techniques is biomedical engineering, in particular for vibration measurement and analysis of different human body parts or conditions. The problems of vibration transmission from the grip of tractors or power tools to the human hand–arm system were analyzed in real case studies. Other researchers investigated problems related to bit-and-teeth structure, stressed when high rotational velocity drills or ultrasound devices are used in a dentist practice, or as a tool for evaluating degree of tooth mobility. Middle-ear ossicles and tympanic membrane vibrations in sound simulation have also been studied using laser techniques.

Other Non-Doppler Measurement Techniques

Interesting performances have also been facilitated by laser-based optical non-Doppler sensors, like optical proximity sensors and triangulation sensors.

The former, usually made up of a bundle of optic fibres from which light is emitted and received, can potentially be employed to measure vibration displacement, since they are able to detect micrometric movements to a frequency of 50 kHz. One

problem in their practical use is the need for static calibration on the surface, which will reflect the sensor's light.

Triangulation devices are displacement sensors, which cost about one-tenth of a vibrometer, with both static and dynamic performances within a range of interest for vibration analysis of mechanical systems. The triangulation sensor is based on a simple geometrical principle. A class II laser source, usually with a wavelength of 670 nm, is focused on the target surface, in points A' or A of **Figure 9**, depending on the target distance. The spot diameter is usually about 140–230 μm.

A position-sensing detector collects the light diffused by the target. Triangulation relation directly correlates the position of the spot centroid in the position-sensing detector with the distance z. The value of the distance z between the sensor and the target can be obtained by:

$$z = \frac{(OC \cdot BO \cdot \cos\gamma)}{B\prime B + BO \cdot \sin\gamma} \qquad [9]$$

where $B'B$ is the measured quantity and γ is defined as in **Figure 9**.

The typical bandwidth is from static displacement to about 60 kHz, with a range varying from ± 0.25 to ± 100 mm depending on the sensor configuration, resolution from 0.1 to 60 μm and linearity error from 2 to 600 μm.

In addition such a sensor uses laser not as a coherent source of radiation, but simply as a collimated light. Such a condition allows one to reduce the sensitivity of the sensor to noises related to phase decorrelation of the light, like the speckle effects.

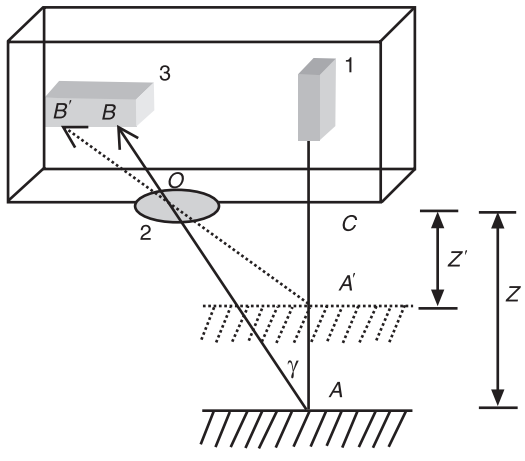


Figure 9 Elements of geometric optics for the assessment of z in a triangulation sensor: 1, laser source; 2, optics; 3, position-sensing detector.

Therefore the sensor works accurately to measure axial vibration when a tangential motion is also present: vibration measurement of a translating object with Eulerian approach becomes easier. Furthermore, triangulation is most robust to optical troubles and it is easier for the user to assess uncertainty sources.

The main problem is related to the reduced versatility of the sensor, mainly due to the fixed distance at which the sensor should work. Furthermore, since this instrument measures displacement, this quantity has reduced amplitude in the high-frequency range.

Full-field Measurement Techniques

In the field of optical techniques for vibration analysis, good alternatives to laser vibrometers, and in particular to SLDV, are two other techniques based on interferometric effect: the laser holography and ESPI.

Such techniques offer some advantages with respect to other solutions, due to their whole-field capability, i.e., the possibility to obtain noncontact information at several points at the same time. This offers an interesting opportunity to obtain static or dynamic information on the behavior of every point of the structure in a fast way. In addition, the whole-field approach gives a direct image of the vibration in test conditions (i.e., the mode shapes).

Depending on different techniques, the particular optical configuration may be different.

The measurement chain for holographic interferometry is shown in **Figure 10A**.

A pulsed laser source is used to generate a laser beam divided in two parts by a beam-splitter. The measurement arm illuminates the object, while the second arm is directly sent on the recording plate, usually composed of photographic or thermoplastic film.

The recording plate also receives the light diffused by the investigated object. Therefore, an interference image is generated on the plate, containing the information relative to the three-dimensional shape of the object. This information is received as each light wavefront, diffused by the different portions of the object surface, reaches the plate by a different optical path length and thus with a different phase. The phase depends on the spatial positions of the diffusing portions and, as a consequence, on the three-dimensional shape.

In order to extract the three-dimensional shape from the impressed plate, another step is required using the experimental set-up shown in **Figure 10B**. Here the holographic image is reconstructed by diffraction, illuminating the plate with just the reference beam. In this case the interference image, previously recorded on the plate, acts as a diffraction grid, where

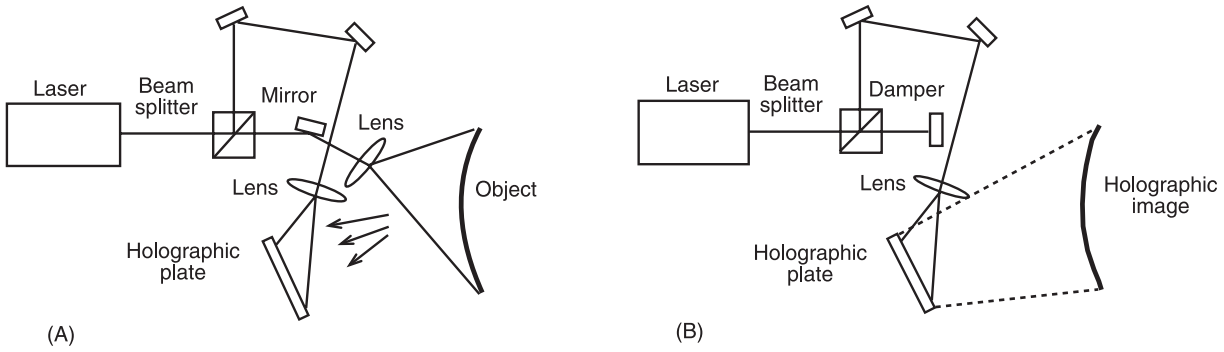


Figure 10 Scheme of system for holographic image recording (A) and reproduction (B).

the grid dimensions depend on the interference pattern. The holographic image, reconstructed where the test object was previously positioned, can be acquired using a video camera and digitally transferred to a PC.

The above measurement chain can be used for both static (shape), quasistatic (deformation) and dynamic (vibration) measurements. Two or more consecutive images of the vibrating object are recorded on the plate, where they interfere, creating a pattern which is in proportion to the variation of the object shape between the two pulses, which in practice is the mode shape. A time delay between pulses is set according to the frequency of the mode of interest, when the object must be sinusoidally excited.

Further to the multiexposure technique, time-averaging techniques can also be employed, using a longer illumination time. In this case, the result is an average of the displacement amplitude at the different points of the vibrating structure.

In order to obtain a full-field technique that is more practical, i.e. based on digital recording devices with a relatively low resolution, the ESPI has been developed in the last 10 years.

In **Figure 11** the optical arrangement of an ESPI system is shown. In the measurement chain a couple of beam-splitters are used. The first one allows one to split the beam into two arms: the measurement one, which is expanded by a lens in order to illuminate the target object, and a reference one. The reference beam is reflected by a mirror, moved by a piezo-actuator for the control of the phase, and interferes in the second beam-splitter with the light scattered by the target surface and collected by an objective. The low-aperture objective is needed to generate the speckle pattern, which can be observed by a low-resolution camera.

This set-up allows one to acquire directly the image obtained by interference between the speckle pattern and the reference wave.

A reference image is first acquired, digitized, and stored. The subsequent images of the vibrating object are acquired at different phase values and digitally compared, by subtraction, with the first one. Contiguous points, characterized by the same displacements, produce loci of black speckles that appear as fringes and can easily be observed as isodisplacement lines of the operational mode shape (as shown in **Figure 11**).

In order to improve the visibility of fringes, the phase shift method can be applied. The phase of the reference wave can be controlled by a mirror driven by a piezoelectric actuator, in such a way as to superimpose a phase shift of π to the subsequent acquired images. Subtracting the images, the common mode noise and the background light are rejected and the signal-to-noise ratio of the measurement is substantially improved. This technique can be used, together with traditional methods for signal enhancement (e.g., averaging a significant number of measurements), in order to obtain better results, in particular for automatic postprocessing based on image analysis.

This kind of system is affected by the same optical problems of laser interferometry as speckle effect, due to additional in-plane motions and surface scattering capability. However, main limits seem to be due to the need for single-frequency excitation, which reduces the in-field applicability for the measurement of operational deflection shapes, and for knowledge of the amplitude of vibration in a reference point, in order to have quantitative results.

In addition, the technological limits of employed electronics should be considered, e.g., concerning spatial resolution, but scientific improvements in this field seem to be very quick and promising.

Finally, it is interesting to compare these performances with those offered by SLDV. In fact, while the full-field techniques are based on a contemporary analysis of the whole structure, the SLDV, which is based on sequential measurements on each point of the target, allows one to improve both spatial resolution and frequency band with nonsinusoidal excitation, as in traditional modal analysis or in operating conditions. Therefore, when it is possible to excite

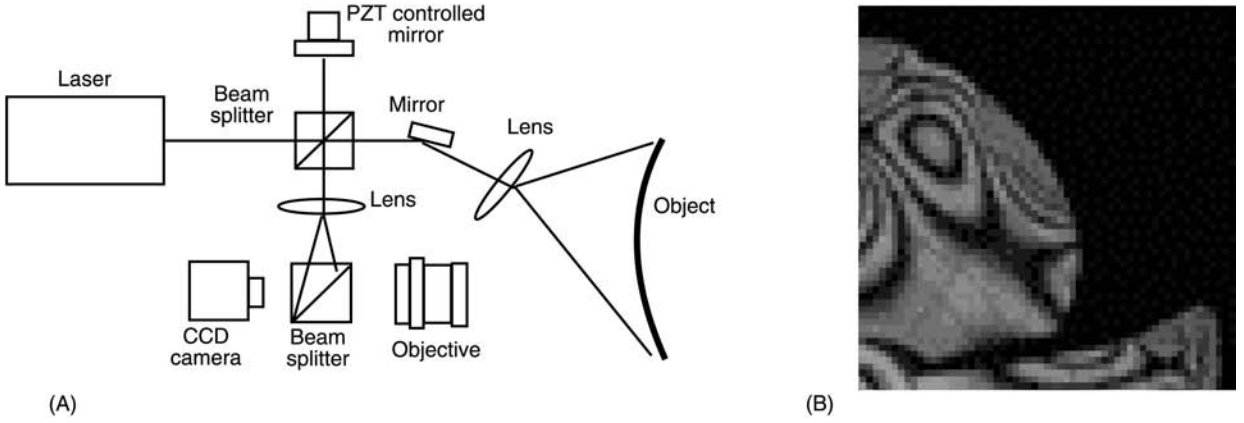


Figure 11 (A) Scheme of electronic speckle pattern interferometry (ESPI) system and (B) an example of a mode shape described by isodisplacement lines.

stationary or repeatable vibrations on the structure (as frequently happens), SLDV allows higher performances.

In contrast, in some practical problems, as in the vibration analysis for disk brake squeeze, it is quite difficult to obtain stationary and repeatable conditions or to have a reference signal for synchronous and nonsynchronous phenomena. In such cases, the whole-field techniques offer a more natural and convenient approach, obtaining direct information of the relative amplitude and phase of vibration at different points of the analyzed structure.

Nomenclature

A	amplitude
f	frequency
v	velocity
Δf_D	Doppler shift
ε	efficiency
λ	wavelength
ω	angular velocity

Further Reading

Bass M (ed.) *Handbook of Optics*, 2nd edn. CD-Rom. New York: McGraw-Hill.

Beckman P and Spizzichino A (1963) *The Scattering of Electromagnetic Waves from Rough Surfaces*, pp. 34–200. Oxford: Pergamon Press.

Born M and Wolf E (1980) *Principles of Optics*. Oxford: Pergamon.

Castellini P, Esposito E, Paone N and Tomasini EP (1998) Non-intrusive measurements of damage of frescoes paintings and icon by laser scanning vibrometer: experimental results of artificial samples and real works of art. In: *Proceedings of the 3rd International Conference of Vibration Measurement by Laser Techniques*, SPIE Vol. 3411, pp. 439–448, Ancona, Italy.

Castellini P, Giovanucci F, Nava, Mambretti G, Scalise L and Tomasini EP (1998) Vibration analysis of tire treads: a in-plane laser vibrometry approach. In: *Proceedings of the 16th International Modal Analysis Conference*, pp. 1732–1738, Santa Barbara, California.

Castellini P, Paone N and Tomasini EP (1996) The LDV as an instrument for non-intrusive diagnostic of works of art: application to fresco paintings. *Optics and Lasers in Engineering*, 25: 227–246.

Castellini P and Revel GM (1998) Damage detection and characterisation by processing of laser vibrometer measurement results: application on composite materials. In: *Proceedings of the 3rd International Conference of Vibration Measurement by Laser Techniques*, SPIE Vol. 3411, pp. 458–468.

Castellini P, Revel GM and Tomasini EP (1998) Laser Doppler vibrometry: a review of advances and applications. *Shock and Vibration Digest* 30: 443–456.

Castellini P, Revel GM, Tomasini EP, Cecconi M and Valeri F (1997) Dynamic characterisation of turbine blades: comparison between FEM and LDV results. In: *Proceedings of the 15th International Modal Analysis Conference Japan*, pp. 223–228, Tokyo, Japan.

Castellini P, Scalise L and Tomasini EP (1998) Teeth mobility measurement: a laser vibrometry approach. In: *Proceedings of the 16th International Modal Analysis Conference*, pp. 1739–1744, Santa Barbara, California.

Dändliker R and Jacquot P (1992) Holographic interferometry and speckle methods. In: Göpel W, Hesse J and Zemel JN (eds) *Sensors: A Comprehensive Survey*, vol. 6. Weinheim, Germany: VCH, pp. 589–628.

D'Emilia G, Paone N and Santolini C (1991) On the uncertainty in the estimation of modal parameters of a structure. In: *Proceedings of the Florence Modal Analysis Conference*, pp. 779–782, Firenze, Italy.

Denman M, Halliwell NA and Rothberg S (1996) Speckle noise reduction in laser vibrometry: experimental and numerical optimisation. In: *Proceedings of the 2nd International Conference of Vibration Measurement by Laser Techniques*, SPIE Vol. 2868, pp. 12–21, Ancona, Italy.

Doeblin EO (1990) *Measurement Systems: Application and Design*. Singapore: McGraw-Hill International Editions.
Drain LE (1980) *The Laser Doppler Technique*. Norwich, UK: John Wiley.
Gasparetti M, Paone N and Tomasini EP (1996) Laser Doppler techniques for the combined measurement of inlet flow and valve motion in IC engines. *Measurement Science and Technology*, 7: 576–591.
Hecht E (1987) *Optics*. Addison Wesley, USA.
Martarelli M, Revel GM and Santolini C (1998) On the use of laser Doppler vibrometry for modal analysis. In: *Proceedings of the 16th International Modal Analysis Conference*, pp. 1750–1757, Santa Barbara, California.
Paone N and Scalise L (1997) Non invasive laser measurement techniques in on-line diagnostics of house-hold appliances. In: *Proceedings of the 5th European Congress on Intelligent Techniques and Soft Computing (EUFIT)*, pp. 1738–1743, Aachen, Germany.
Revel GM and Paone N (1998) Modelling and Experimental Analysis of the Performance of a laser Doppler vibrometer used to measure surface vibrations through combusting flow. *Optics and Lasers in Engineering*, 30: 163–178.
Revel GM, Rossi GL and Tomasini EP (1996) Defects classification in loudspeaker production using laser vibrometers and neural networks. In: *Proceedings of the 3rd International Conference on Motion and Vibration Control*, pp. 211–216, Chiba, Japan.
Revel GM, Santolini C and Tomasini EP (1997) Laser Doppler vibration and acoustic intensity measurements for dynamic characterisation and noise reduction of a car window lift system. In: *Proceedings of the 15th International Modal Analysis Conference*, pp. 1636–1642, Orlando, Florida.
Revel GM and Tomasini EP (1999) Torsional vibrations: a laser vibrometry approach. *Proceedings of Vibration, Noise and Structural Dynamics '99*, Venezia, Italy, pp. 448–453.
Rossi GL and Tomasini EP (1994) Proposal of a new measurement technique for hand–arm vibration analysis. In: *Proceedings of the 1st International Conference of Vibration Measurement by Laser Techniques*, SPIE Vol. 2358, pp. 48–59, Ancona, Italy.
von Martens HJ (1994) Errors and uncertainties of interferometric measurements of linear and torsional vibrations. In: *Proceedings of 1st International Conference on Vibration Measurements by Laser Techniques: Advances and Applications*, SPIE No. 2358, pp. 2–12, Ancona, Italy.

LINEAR ALGEBRA

C Farhat, University of Colorado, Boulder, CO, USA

D Rixen, Delft University of Technology, Delft, The Netherlands

Copyright © 2001 Academic Press

doi:10.1006/rwvb.2001.0003

Solving linear systems of equations is at the heart of most computational analysis methods. In order to compute a solution accurately and fast, the method for solving those systems must be chosen according to:

- the properties of the matrix operator (i.e., symmetry, definite positiveness, singularity and sparsity)
- the size of the system (from a few unknowns up to several millions)
- the numerical conditioning of the system of equations
- its capability to efficiently handle multiple right-hand sides
- the burden of its implementation
- its ability to run on vector or parallel computers.

Although a large variety of problems encountered in practice involve symmetric definite matrices, some important cases require the solution of singular systems (e.g., analysis of floating structures), nondefinite systems (harmonic analysis or constrained systems) and nonsymmetric systems (coupled problems and nonlinear systems).

In what follows, we will assume that all matrices are real in order to outline the basic ideas in a simple manner. Nevertheless, the concepts described here can be extended to complex matrices.

Solving Nonsingular Linear Systems

Solution methods are usually classified as iterative or direct methods. Direct solvers (i.e., factorization techniques) yield an exact solution (that is up to the round-off errors due to the finite precision of computers) after a predictable number of operations. Iterative methods typically involve an evaluation of the action of the system matrix on trial vectors (matrix-vector multiplication) and yield an approximate solution whose accuracy improves as the number of iterations grows. The latter methods were devised to handle large systems at a time when powerful computers did not exist and thus, when factorization of large matrices was not an option.

Iterative schemes usually do not exhibit good robustness when applied to real-life problems. Therefore, direct solution methods have been widely favored in engineering codes. In this text, only direct methods will be discussed. Nevertheless, the reader should be aware that iterative or semi-iterative techniques have regained tremendous popularity, thanks to recent innovative algorithmic developments, to their lower storage space requirement and finally because of their natural ability to exploit efficiently vectorial and multiprocessing capabilities of modern supercomputers.

We assume that the number n of unknowns is equal to the number of equations in the system so that the linear system takes the general form:

$$\mathbf{Ax} = \mathbf{b} \text{ or } \begin{bmatrix} a_{11} & a_{12} & \dots & a_{1n} \\ a_{21} & \ddots & & \vdots \\ \vdots & & \ddots & \\ a_{n1} & \dots & & a_{nn} \end{bmatrix} \begin{bmatrix} x_1 \\ x_2 \\ \vdots \\ x_n \end{bmatrix} = \begin{bmatrix} b_1 \\ b_2 \\ \vdots \\ b_n \end{bmatrix} \quad [1]$$

We further assume that the square matrix $\mathbf{A}$ is nonsingular, which implies that a unique solution exists for $\mathbf{x}$. The case where $\mathbf{A}$ is square but singular, or rectangular will be discussed later.

Nonsymmetric Systems: the LU Factorization

The most natural method that comes to mind for solving a system as in eqn [1] consists in recasting the first equation as:

$$x_1 = \frac{1}{a_{11}}(b_1 - a_{12}x_2 \cdots - a_{1n}x_n) \quad [2]$$

so that x_1 can be eliminated from all subsequent equations by substitution of eqn [2]. Repeating the process for x_2 in the second equation and so on leads to a sequence of transformed equations, the last of which yields x_n. Substituting back the value of x_n into the transformed equation $n-1$ then yields x_{n-1} and substituting further into the transformed equations yields $x_{n-2} \dots x_1$ recursively. This procedure can also be understood as building linear combinations of the original equations so as to bring matrix $\mathbf{A}$ to an upper triangle form as follows.

Assuming that $x_1 \dots x_{k-1}$ have already been eliminated, the operator of the transformed system is as in **Figure 1**. Step k then consists in transforming equations $k+1 \dots n$ by adding a linear combination of equation k so as to zero the coefficients of x_k. Hence, if $\mathbf{U}$ and $\tilde{\mathbf{b}}$ are initially set to $\mathbf{A}$ and $\mathbf{b}$, respectively, every row i below k becomes:

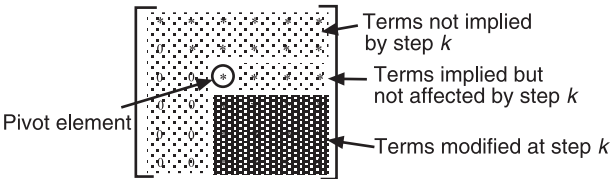


Figure 1 Gauss elimination: transforming **A** into an upper triangular form **U**.

$$u_{ij} \leftarrow u_{ij} - l_{ik}u_{kj} \quad i,j = k+1, \dots n \quad [3]$$

$$\tilde{b}_i \leftarrow \tilde{b}_i - l_{ik}\tilde{b}_k \quad [4]$$

where:

$$l_{ik} = \frac{u_{ik}}{u_{kk}} \quad [5]$$

in order to zero u_{ik}, $i = k+1 \dots n$. After $n-1$ steps, $\mathbf{U}$ is an upper triangular matrix. The solution is then found by backward substitution first for x_n, then for x_{n-1} and so on:

$$x_i = \frac{1}{u_{ii}}\left(\tilde{b}_i - \sum_{j=i+1}^{n} u_{ij}x_j\right) \quad i = n, n-1, \dots 1 \quad [6]$$

The algorithm described above is known as a Gaussian elimination and can be viewed as transforming $\mathbf{A}$ into a product of a lower triangular matrix $\mathbf{L}$ and the upper triangular matrix $\mathbf{U}$, i.e.:

$$\mathbf{A} = \mathbf{LU} \quad [7]$$

where, according to eqn [3], $\mathbf{L}$ has a unit diagonal ($l_{ii} = 1$) and its lower triangular coefficients are l_{ik} directly obtained from the elimination process. The direct solution procedure can thus be summarized as follows:

- Factorize $\mathbf{A} = \mathbf{LU}$, eqns [3] and [5], so that the system is

$$\mathbf{LUx} = \mathbf{L}\tilde{\mathbf{b}} = \mathbf{b} \quad \text{where we define} \quad \tilde{\mathbf{b}} = \mathbf{Ux} \quad [8]$$

- Solve successively the triangular systems

$$\mathbf{L}\tilde{\mathbf{b}} = \mathbf{b} \quad [9]$$

$$\mathbf{Ux} = \tilde{\mathbf{b}} \quad [10]$$

Solving eqn [9] corresponds to transforming the right-hand side as in eqn [4] and is called forward substitution whereas solving eqn [10] is a backward substitution as defined by eqn [6].

The factorization of the matrix requires of the order of $2n^3/3$ operations, while the forward and backward factorizations each involve of the order of n^2 operations. If the system must be solved for multiple right-hand sides, the factorization only needs to be performed once, and one forward and backward substitution must be performed for every right-hand side.

Example

$$\mathbf{A} = \begin{bmatrix} 1 & 2 & 3 \\ 1 & 1 & 2 \\ 1 & 0 & -1 \end{bmatrix} \xrightarrow{k=1} \underbrace{\begin{matrix} 1 \\ 1 \end{matrix}}_{l_{i1}} \begin{bmatrix} 1 & 2 & 3 \\ 0 & -1 & -1 \\ 0 & -2 & -4 \end{bmatrix}$$

$$\xrightarrow{k=2} \underbrace{2}_{l_{i2}} \begin{bmatrix} 1 & 2 & 3 \\ 0 & -1 & -1 \\ 0 & 0 & -2 \end{bmatrix}$$

$$\Rightarrow \mathbf{LU} = \begin{bmatrix} 1 & 0 & 0 \\ 1 & 1 & 0 \\ 1 & 2 & 1 \end{bmatrix} \begin{bmatrix} 1 & 2 & 3 \\ 0 & -1 & -1 \\ 0 & 0 & -2 \end{bmatrix}$$

Remarks At step k of the elimination, the diagonal element u_{kk} is called a pivot (**Figure 1**) and must be nonzero in eqn [5]. In order to have a nonzero pivot and to ensure numerical stability of the elimination, it is required to apply permutations on the rows and columns so to bring on the diagonal k the element of highest modulus of the submatrix yet to be triangularized. This procedure is called pivoting. The factorization is then expressed as:

$$\mathbf{P}_1\mathbf{A}\mathbf{P}_2 = \mathbf{LU} \qquad [11]$$

where $\mathbf{P}_1$ and $\mathbf{P}_2$ are permutation operators related to the pivoting of the rows and columns, respectively. If only the rows are reordered, the procedure is known as partial pivoting. Since permutation matrices are identity matrices with reordered rows:

$$\det(\mathbf{A}) = \pm\det(\mathbf{P}_1\mathbf{A}\mathbf{P}_2) = \pm\det(\mathbf{L})\det(\mathbf{U})$$
$$= \pm\det(\mathbf{U}) = \pm\prod_{k=1}^{n} u_{kk}$$

Therefore one is guaranteed to find a nonzero pivot if pivoting is applied and if $\mathbf{A}$ is nonsingular.

In order to minimize memory requirements, the initial matrix $\mathbf{A}$ is usually overwritten by the coefficients of $\mathbf{U}$ and $\mathbf{L}$, it being understood that the unit diagonal of $\mathbf{L}$ need not be stored.

The elimination algorithm can be rearranged in several different ways. In particular, rewriting eqn [1] in the block partitioned form:

$$\begin{bmatrix} \mathbf{A}_{11} & \mathbf{A}_{12} \\ \mathbf{A}_{21} & \mathbf{A}_{22} \end{bmatrix} \begin{bmatrix} \mathbf{x}_1 \\ \mathbf{x}_2 \end{bmatrix} = \begin{bmatrix} \mathbf{b}_1 \\ \mathbf{b}_2 \end{bmatrix} \qquad [12]$$

one can use the first set of equations to eliminate the set of unknowns $\mathbf{x}_1$ in a way similar to eqn [2], i.e.:

$$\mathbf{x}_1 = \mathbf{A}_{11}^{-1}(\mathbf{b}_1 - \mathbf{A}_{12}\mathbf{x}_2) \qquad [13]$$

where $\mathbf{A}_{11}$ is assumed to be nonsingular. Substituting eqn [13] into the partitioned form eqn [12] yields the block triangular form:

$$\begin{bmatrix} \mathbf{A}_{11} & \mathbf{A}_{12} \\ 0 & \mathbf{A}_{22} - \mathbf{A}_{21}\mathbf{A}_{11}^{-1}\mathbf{A}_{12} \end{bmatrix} \begin{bmatrix} \mathbf{x}_1 \\ \mathbf{x}_2 \end{bmatrix} = \begin{bmatrix} \mathbf{b}_1 \\ \mathbf{b}_2 - \mathbf{A}_{21}\mathbf{A}_{11}^{-1}\mathbf{b}_1 \end{bmatrix} \qquad [14]$$

This last equation should be compared to $\mathbf{U}$ in **Figure 1**. The lower diagonal block $\mathbf{A}_{22}^* = \mathbf{A}_{22} - \mathbf{A}_{21}\mathbf{A}_{11}^{-1}\mathbf{A}_{12}$ is the matrix $\mathbf{A}$ when the unknowns $\mathbf{x}_1$ have been condensed out. If $\mathbf{A}$ is a stiffness matrix, $\mathbf{A}_{22}^*$ represents the stiffness operator coupling the variables $\mathbf{x}_2$ when $\mathbf{x}_1$ are left free. To mathematicians, $\mathbf{A}_{22}^*$ is known as the Schur complement of $\mathbf{A}$ for $\mathbf{x}_2$. The blocks $\mathbf{A}_{11}^{-1}\mathbf{A}_{12}$ and $\mathbf{A}_{11}^{-1}\mathbf{b}_1$ in eqn [14] can be computed by factorizing $\mathbf{A}_{11}$ and performing forward and backward substitutions for $\mathbf{A}_{12}$ and $\mathbf{b}_1$. The factorization of $\mathbf{A}$ is then completed by factorizing $\mathbf{A}_{22}^*$. Applying this idea successively to several blocks, one can device the block LU factorization which involves mainly matrix–matrix operations and thereby renders the factorization more efficient on vector and parallel computers.

Symmetric Systems: LDL^T and Cholesky Factorization

When the system matrix is symmetric, its reduction to a triangular form can be organized so as to require only half the number of operation of the LU factorization. $\mathbf{A}$ is then factorized into the symmetric form:

$$\mathbf{A} = \mathbf{L}\mathbf{D}\mathbf{L}^{\mathrm{T}}$$

or:

$$\begin{bmatrix} a_{11} & a_{21} & a_{31} & \dots \\ a_{21} & a_{22} & a_{32} & \\ a_{31} & a_{32} & a_{33} & \\ \vdots & & & \ddots \end{bmatrix} = \begin{bmatrix} 1 & & & 0 \\ l_{21} & 1 & & \\ l_{31} & l_{32} & 1 & \\ \vdots & & & \ddots \end{bmatrix} \times \begin{bmatrix} d_{11} & d_{11}l_{21} & d_{11}l_{31} & \dots \\ & d_{22} & d_{22}l_{32} & \\ & & d_{33} & \\ 0 & & & \ddots \end{bmatrix} \quad [15]$$

where $\mathbf{L}$ is a lower triangular matrix with unit diagonal and $\mathbf{D}$ is diagonal. Obviously, comparing eqn [15] to the LU factorization, the upper triangular matrix $\mathbf{U}$ is expressed as $\mathbf{DL}^{\mathrm{T}}$ in the symmetric case. The solution $\mathbf{x}$ of eqn [1] is then found as for the LU factorization, i.e., by forward and backward substitution similar to eqns [9] and [10].

At step k of the LDL^T factorization (eqn [15]), the first $k-1$ rows of $\mathbf{L}$ and $\mathbf{D}$ are known. The coefficients of $\mathbf{L}$ on row k are recursively computed by successively identifying $a_{k1}, a_{k2} \dots a_{kk-1}$ to the right-hand side in eqn [15], and d_{kk} is then found by identifying the diagonal a_{kk}, i.e.:

step k

$$a_{kj} = d_{jj}l_{kj} + \sum_{s=1}^{j-1} l_{ks}d_{ss}l_{js} \qquad j = 1, \dots k-1$$
$$\Rightarrow l_{kj} = \frac{1}{d_{jj}}\left(a_{kj} - \sum_{s=1}^{j-1} l_{ks}d_{ss}l_{js}\right) \quad [16]$$

$$a_{kk} = d_{kk} + \sum_{s=1}^{k-1} d_{ss}l_{ks}^2$$
$$\Rightarrow d_{kk} = a_{kk} - \sum_{s=1}^{k-1} d_{ss}l_{ks}^2 \quad [17]$$

In order to reduce the number of multiplications, we can write eqns [16] and (17) in terms of the temporary variables $\tilde{l}_{kj} = d_{jj}l_{kj}$, namely:

$$\tilde{l}_{kj} = a_{kj} - \sum_{s=1}^{j-1} \tilde{l}_{ks}l_{js} \qquad j = 1, \dots k-1 \quad [18]$$

$$d_{kk} = a_{kk} - \sum_{s=1}^{k-1} \tilde{l}_{ks}l_{ks} \quad [19]$$

One can therefore determine first $\tilde{l}_{kj}$ and, after step k, determine l_{kj} by:

$$l_{kj} = \frac{\tilde{l}_{kj}}{d_{jj}} \qquad j = 1, \dots k-1 \quad [20]$$

In this form the LDL^T factorization uses approximatively half the number of operations of the LU factorization, that is $n^3/3$ operations.

Remarks As for the LU factorization, the elimination process can break down if d_{kk} becomes zero: to avoid this and to ensure numerical stability, pivoting should be applied. For the matrix to remain symmetric after pivoting, the same permutation must be applied to the row and to the columns of $\mathbf{A}$.

Since $\det(\mathbf{A}) = \det(\mathbf{L})\det(\mathbf{D})\det(\mathbf{L}) = \det(\mathbf{D}) = \Pi_{k=1}^{n} d_{kk}$, all diagonal terms d_{kk} are strictly positive if $\mathbf{A}$ is a positive definite matrix. Symmetric positive definite systems are very common, since they typically derive from quadratic energy functions which are positive and symmetric due to the very underlying physical principles. In that case, the factorization of $\mathbf{A}$ can also be given as:

$$\mathbf{A} = \mathbf{LDL}^{\mathrm{T}} = \mathbf{LD}^{1/2}\mathbf{D}^{1/2}\mathbf{L}^{\mathrm{T}} = \mathbf{CC}^{\mathrm{T}} \quad [21]$$

which is known as the Cholesky factorization. The Cholesky algorithm is similar to the LDL^{T} factorization and requires the same number of operations, but it involves computing square roots of the pivots. Note that when $\mathbf{A}$ is positive definite, all pivots are guaranteed to be strictly positive, so that in that particular case pivoting is not compulsory.

In practice, only half of $\mathbf{A}$ is stored (e.g., its lower triangular part) and $\mathbf{A}$ can be overwritten by $\mathbf{L}$ and the diagonal of $\mathbf{D}$, so that solving the system barely requires any additional memory.

As for the LU factorization, the LDL^{T} and Cholesky factorization algorithms can be re-organized in several ways. For instance the frontal method is a very popular variant for solving finite element problems.

Sparse Matrices

Discretization methods using functions defined over the entire computational domain to approximate the solution such as in the Rayleigh–Ritz or the boundary element approaches usually lead to small but full (or dense) matrices. When performing detailed analyses, the more versatile finite element or finite volume methods with fine meshes are preferred. In that case, the number of unknowns can be very large, but since the shape or flux functions are local, the connectivity between unknowns is limited to neighboring nodes so

that the system matrix is sparse. Special storage and solution techniques must then be applied in order to take advantage of sparsity.

To avoid storing zeros of a sparse matrix, one can store the index $[i, j]$ of its nonzero entries together with their values. This is the basic principle of sparse storage schemes. Special variants of the factorization algorithms sometimes called sparse solvers have been developed first, in a symbolic factorization step, the matrix coefficients that will be modified are determined, then the factorization is performed. Unfortunately, when a sparse matrix is factorized, many zero entries become nonzeros (called fill-ins) and the sparsity of the matrix is destroyed.

Renumbering schemes are usually applied to the system of equations, i.e., permutation of rows (reordering of the equations) and/or columns (renumbering of the unknowns) is performed in order to form a cluster of nonzero terms along the diagonal of the matrix (**Figure 2**). Since the factorization of the matrix corresponds to building linear combinations with previous rows, it will not introduce fill-ins above the first nonzero entry in a column so that the sparsity of the renumbered matrix will not be significantly altered during factorization.

When renumbering a symmetric matrix, the same permutation is applied to its columns and to its rows in order to preserve the symmetry. The two most commonly used renumbering schemes are Sloan's algorithm (heuristics to regroup degrees-of-freedom that are neighbors in the mesh) and the reverse Cuthill MacNeal (RCM) technique based on the minimization of the topological distance between degrees-of-freedom in the graph of the mesh connectivity.

The nonzero entries of the renumbered matrix being close to the diagonal, one can store all the entries between the skyline and the diagonal. This leads to the skyline storage technique as illustrated in **Figure 2** for a symmetric matrix: the elements of the columns between the skyline and the diagonal are stored in the one-dimensional array **a** while pointers for the position of the diagonal terms in **a** are stored separately in $\mathbf{j}_{\text{diagA}}$. Obviously, the skyline of the matrix remains unchanged when factorization is applied without pivoting. Calling b the maximum height of a column under the skyline of a symmetric matrix (commonly called the band), the number of operations required for its factorization is of the order of nb^2 operations.

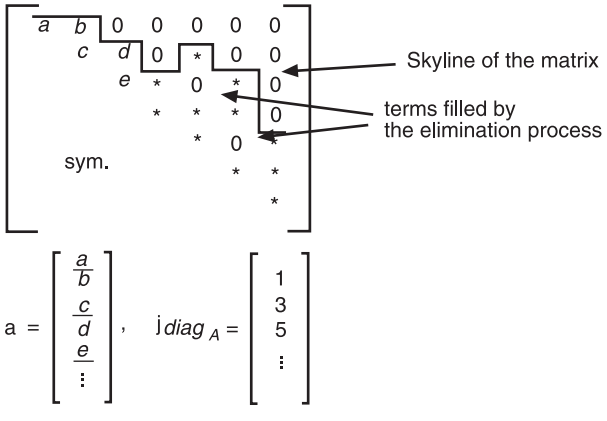


Figure 2 Skyline storage of a symmetric matrix.

Singular Systems: Nullspace, Solutions and Generalized Inverse

Singular operators are not rare in vibration analysis. For instance, the stiffness matrix of a structure having rigid-body modes is singular, namely there exists displacement modes creating no deformation energy (e.g., translations and rotations of an aircraft in flight or a satellite in orbit). We will first define the nullspace of a singular matrix and then discuss the conditions under which a solution exists for a singular system. The concept of the generalized inverse is then introduced.

Let us consider the general case of a rectangular matrix $\mathbf{A}$ of dimension $m \times n$, i.e., a system of m equations with n unknowns.

Singular Matrix and Nullspace

The set of all p independent solutions $\mathbf{r}_s$ of:

$$\mathbf{A}\mathbf{r}_s = 0 \quad s = 1, \ldots p \qquad [22]$$

forms the nullspace of $\mathbf{A}$. For a stiffness matrix, $\mathbf{r}_s$ represent the rigid-body modes if not enough boundary conditions exist to restrain the structure. Note that any linear combination of $\mathbf{r}_s$ satisfies eqn [22]. One can also define the nullspace vectors $\tilde{\mathbf{r}}_r$ of the transpose of $\mathbf{A}$ such that:

$$\mathbf{A}^{\mathrm{T}}\tilde{\mathbf{r}}_r = \mathbf{0} \quad \text{or} \quad \tilde{\mathbf{r}}_r^{\mathrm{T}}\mathbf{A} = \mathbf{0} \quad r = 1, \ldots \tilde{p} \qquad [23]$$

If p nullspace vectors $\mathbf{r}_s$ exist for $\mathbf{A}$ of dimension $m \times n$, eqn [22] indicates that only $n - p$ columns are linearly independent. Hence, the rank of $\mathbf{A}$ is $n - p$ and $\mathbf{A}$ has $n - p$ linearly independent rows. From eqn [23], the number of linearly independent rows is also $m - \tilde{p}$ and thus $m - \tilde{p} = n - p$. In particular, if $\mathbf{A}$ is square, $p = \tilde{p}$ and if furthermore $\mathbf{A}$ is symmetric, the nullspace defined by $\mathbf{r}_s$ is identical to the nullspace represented by $\tilde{\mathbf{r}}_r$.

Let us assume without loss of generality but only to simplify the notations that the system can be partitioned as:

$$\begin{bmatrix} \mathbf{A}_{11} & \mathbf{A}_{12} \\ \mathbf{A}_{21} & \mathbf{A}_{22} \end{bmatrix} \begin{bmatrix} \mathbf{x}_1 \\ \mathbf{x}_2 \end{bmatrix} = \begin{bmatrix} \mathbf{b}_1 \\ \mathbf{b}_2 \end{bmatrix} \quad [24]$$

where $\mathbf{A}_{11}$ is a nonsingular square matrix of dimension equal to the rank of $\mathbf{A}$, i.e. $\mathbf{A}_{11}$ is the largest nonsingular submatrix of $\mathbf{A}$. Since the p columns labeled 2 in eqn [24] are linearly dependent on the $n - p$ first ones, there exists a matrix $\mathbf{W}$ of dimension $(n - p) \times p$ such that:

$$\begin{bmatrix} \mathbf{A}_{12} \\ \mathbf{A}_{22} \end{bmatrix} = \begin{bmatrix} \mathbf{A}_{11} \\ \mathbf{A}_{21} \end{bmatrix} \mathbf{W} \quad [25]$$

The first set of equations in eqn [25] yields:

$$\mathbf{W} = \mathbf{A}_{11}^{-1} \mathbf{A}_{12} \quad [26]$$

and, substituting in the second set of equations in eqn [25]:

$$\mathbf{A}_{22} - \mathbf{A}_{21} \mathbf{A}_{11}^{-1} \mathbf{A}_{12} = \mathbf{0} \quad [27]$$

The left-hand side of the expression above is the system operator when $\mathbf{x}_1$ has been eliminated from the equations as indicated by eqn [14]. Hence the Gaussian elimination (LU, LDL^{T} or Cholesky factorization) would break down after $n - p$ steps since the lower diagonal block of dimension $\tilde{p} \times p$ is then zero. This is in fact an indication that the inverse of $\mathbf{A}$ does not exist. If $\mathbf{A}$ is a stiffness matrix, $\mathbf{A}_{22} - \mathbf{A}_{21} \mathbf{A}_{11}^{-1} \mathbf{A}_{12}$ is the condensed stiffness and the structure cannot be properly fixed if the degrees-of-freedom $\mathbf{x}_2$ are not restrained or, in other words, $\mathbf{x}_2$ defines a set of fixations that renders the structure statically determined. From eqn [25] we can write:

$$\begin{bmatrix} \mathbf{A}_{11} & \mathbf{A}_{12} \\ \mathbf{A}_{21} & \mathbf{A}_{22} \end{bmatrix} = \begin{bmatrix} -\mathbf{W} \\ \mathbf{I}_{p \times p} \end{bmatrix} = \mathbf{0} \quad [28]$$

where $\mathbf{I}_{p \times p}$ is the identity matrix of dimension p. Hence, the nullspace of $\mathbf{A}$ can be represented by:

$$\mathbf{R} = \begin{bmatrix} \mathbf{r}_1 & \dots & \mathbf{r}_p \end{bmatrix} = \begin{bmatrix} -\left(\mathbf{A}_{11}^{-1} \mathbf{A}_{12}\right) \\ \mathbf{I}_{p \times p} \end{bmatrix} \quad [29]$$

In the same manner, the linear dependency of the rows of $\mathbf{A}$ can be expressed by defining a matrix $\tilde{\mathbf{W}}$ of dimension $(m - \tilde{p}) \times \tilde{p}$ such that:

$$\begin{bmatrix} \mathbf{A}_{21} & \mathbf{A}_{22} \end{bmatrix} = \tilde{\mathbf{W}}^{\mathrm{T}} \begin{bmatrix} \mathbf{A}_{11} & \mathbf{A}_{12} \end{bmatrix} \quad [30]$$

or:

$$\begin{bmatrix} \mathbf{A}_{11} & \mathbf{A}_{12} \\ \mathbf{A}_{21} & \mathbf{A}_{22} \end{bmatrix}^{\mathrm{T}} \begin{bmatrix} -\tilde{\mathbf{W}} \\ \mathbf{I}_{\tilde{p} \times \tilde{p}} \end{bmatrix} = \mathbf{0} \quad [31]$$

yielding:

$$\tilde{\mathbf{R}} = \begin{bmatrix} \tilde{\mathbf{r}}_1 & \dots & \tilde{\mathbf{r}}_{\tilde{p}} \end{bmatrix} = \begin{bmatrix} -\tilde{\mathbf{W}} \\ \mathbf{I}_{\tilde{p} \times \tilde{p}} \end{bmatrix} = \begin{bmatrix} -\left(\mathbf{A}_{11}^{-\mathrm{T}} A_{21}^{\mathrm{T}}\right) \\ \mathbf{I}_{\tilde{p} \times \tilde{p}} \end{bmatrix} \quad [32]$$

Solution of Singular and Rectangular Systems

If the matrix operator of a system is square but singular or if the matrix is rectangular, the inverse of $\mathbf{A}$ cannot be defined. Nevertheless solutions to the system may exist. Indeed, let us assume that $\mathbf{b}_1$ and $\mathbf{b}_2$ exhibit the same linear dependency as the rows of $\mathbf{A}$, namely according to eqn [30]:

$$\mathbf{b}_2 = \tilde{\mathbf{W}}^{\mathrm{T}} \mathbf{b}_1 \quad [33]$$

The set of equations associated with the linearly dependent rows $[\mathbf{A}_{21}\, \mathbf{A}_{22}]$ are then redundant and the system $\mathbf{A}\mathbf{x} = \mathbf{b}$ contains only $m - \tilde{p}$ independent equations for which an infinite number of solutions exist.

Taking account of eqn [32], relation [33] is found to be equivalent to $\tilde{\mathbf{R}}^{\mathrm{T}} \mathbf{b} = \mathbf{0}$. Thus, it can be shown that a solution to the system $\mathbf{A}\mathbf{x} = \mathbf{b}$ exists if and only if $\mathbf{b}$ is orthogonal to the nullspace of $\mathbf{A}^{\mathrm{T}}$.

If $\mathbf{A}$ is a stiffness matrix, this shows that a static solution exists if and only if the applied forces are self-equilibrated with respect to the rigid-body modes. If we define the image (or range) of $\mathbf{A}$ as the set of $\mathbf{A}\mathbf{y}$ for any vector $\mathbf{y}$, it can be equivalently stated that a solution to the system $\mathbf{A}\mathbf{x} = \mathbf{b}$ exists if and only if $\mathbf{b}$ belongs to the image of $\mathbf{A}$. Indeed, by definition, if $\mathbf{b}$ belongs to the image of $\mathbf{A}$, there exists $\mathbf{y}$ such that:

$$\mathbf{A}\mathbf{x} = \mathbf{b} = \mathbf{A}\mathbf{y} \quad [34]$$

and $\mathbf{y}$ is obviously a solution for $\mathbf{x}$.

Besides, if a solution $\mathbf{x}$ exists while there exists a nullspace $\mathbf{R}$, this solution is clearly not unique since:

$$\mathbf{A}\left(\mathbf{x} + \sum_{s=1}^{p} \alpha_s \mathbf{r}_s\right) = \mathbf{A}\mathbf{x} = \mathbf{b} \quad [35]$$

for any linear combination α_s of the nullspace vectors. Hence the component of the solution lying in the nullspace is undetermined. In the context of structural mechanics, this means that if the forces are self-equilibrated, a static solution exists but the rigid-body displacements are arbitrary.

A Family of Generalized Inverses

Since, under the conditions described above, solutions $\mathbf{x}$ exist for singular systems, we can define an operator $\mathbf{A}^+$, called generalized inverse or pseudo-inverse such that a solution $\mathbf{x}$ is expressed as:

$$\mathbf{x} = \mathbf{A}^+\mathbf{b} \qquad [36]$$

Substituting the solution in the system equations, we obtain:

$$\mathbf{A}\mathbf{A}^+\mathbf{b} = \mathbf{b} \qquad [37]$$

and since $\mathbf{b}$ is in the image of $\mathbf{A}$ if a solution exists:

$$\mathbf{A}\mathbf{A}^+\mathbf{A}\mathbf{y} = \mathbf{A}\mathbf{y} \qquad [38]$$

Hence, the generalized inverse $\mathbf{A}^+$ of $\mathbf{A}$ can also be defined as an operator satisfying:

$$\mathbf{A}\mathbf{A}^+\mathbf{A} = \mathbf{A} \qquad [39]$$

which stipulates that the image of $\mathbf{A}$ is unchanged by the operator $\mathbf{A}\mathbf{A}^+$. For singular or rectangular systems, $\mathbf{A}\mathbf{A}^+$ is not the identity but has the same effect as an identity matrix when applied to the image of $\mathbf{A}$. Obviously, if $\mathbf{A}$ is square and nonsingular, $\mathbf{A}^+ = \mathbf{A}^{-1}$.

Let us point out that unless $\mathbf{A}$ is square and nonsingular, the generalized inverse satisfying eqn [39] is not unique. Indeed, calling $\mathbf{R}$ and $\tilde{\mathbf{R}}$ the nullspace of $\mathbf{A}$ and $\mathbf{A}^{\mathrm{T}}$ respectively as defined earlier, and calling $\mathbf{A}^+$ a generalized inverse satisfying eqn [39], then

$$\tilde{\mathbf{A}}^+ = \mathbf{A}^+ + \mathbf{B}\tilde{\mathbf{R}}^{\mathrm{T}} + \mathbf{R}\mathbf{C} \qquad [40]$$

also satisfies eqn [39] for any $\mathbf{B}$ and $\mathbf{C}$. Eqn [40] thus defines a family of generalized inverses. The solution obtained with $\tilde{\mathbf{A}}^+$ in eqn [40] is:

$$\mathbf{x} = \mathbf{A}^+\mathbf{b} + \mathbf{B}\tilde{\mathbf{R}}^{\mathrm{T}}(\mathbf{A}\mathbf{y}) + \mathbf{R}\mathbf{C}\mathbf{b} = \mathbf{A}^+\mathbf{b} + \mathbf{R}\mathbf{C}\mathbf{b} \qquad [41]$$

which differs from the solution $\mathbf{A}^+\mathbf{b}$ only by its rigid-body mode content.

Example Let us show that, using the block notation introduced in eqn [24], the matrix $\mathbf{A}^{[11]+}$ defined by

$$\mathbf{A}^{[11]+} = \begin{bmatrix} \mathbf{A}_{11}^{-1} & \mathbf{0} \\ \mathbf{0} & \mathbf{0} \end{bmatrix} \qquad [42]$$

is a generalized inverse, $\mathbf{A}_{11}$ being as before a square submatrix of maximum range, i.e., $\mathbf{A}_{11}$ is formed by any $n-p$ linearly independent columns and rows of $\mathbf{A}$.

To show that $\mathbf{A}^{[11]+}$ is a generalized inverse, we prove that it satisfies eqn [39] as follows:

$$\mathbf{A}\mathbf{A}^{[11]+}\mathbf{A} = \begin{bmatrix} \mathbf{A}_{11} & \mathbf{A}_{12} \\ \mathbf{A}_{21} & \mathbf{A}_{22} \end{bmatrix} \begin{bmatrix} \mathbf{A}_{11}^{-1} & \mathbf{0} \\ \mathbf{0} & \mathbf{0} \end{bmatrix} \begin{bmatrix} \mathbf{A}_{11} & \mathbf{A}_{12} \\ \mathbf{A}_{21} & \mathbf{A}_{22} \end{bmatrix} = \begin{bmatrix} \mathbf{A}_{11} & \mathbf{A}_{12} \\ \mathbf{A}_{21} & \mathbf{A}_{21}\mathbf{A}_{11}^{-1}\mathbf{A}_{12} \end{bmatrix} \qquad [43]$$

and recalling from eqn [27] that $\mathbf{A}_{21}\mathbf{A}_{11}^{-1}\mathbf{A}_{12}$ is equal to $\mathbf{A}_{22}$ concludes the proof. Another proof can be constructed by showing that $\mathbf{A}^{[11]+}\mathbf{b}$ is a solution of $\mathbf{A}\mathbf{x} = \mathbf{b}$ when $\tilde{\mathbf{R}}^{\mathrm{T}}\mathbf{b} = \mathbf{0}$. This is left to the reader.

As will be discussed later, this particular generalized inverse is of the form obtained by classical factorization techniques since it is constructed by factorizing a full-rank submatrix of $\mathbf{A}$.

Singular Value Decomposition and the Moore–Penrose Generalized Inverse

Singular Value Decomposition (SVD)

It can be shown that any matrix $\mathbf{A}$ with m rows and n columns can be decomposed as follows:

There exist $\mathbf{U}$, $\mathbf{\Sigma}$ and $\mathbf{V}$ such that:

$$\mathbf{A} = \mathbf{U}\mathbf{\Sigma}\mathbf{V}^{\mathrm{T}} \qquad [44]$$

where $\mathbf{U}$ and $\mathbf{V}$ are orthogonal matrices of dimension $m \times m$ and $n \times n$ such that:

$$\mathbf{U}^{\mathrm{T}}\mathbf{U} = \mathbf{I}_{m\times m} \quad \text{and} \quad \mathbf{V}^{\mathrm{T}}\mathbf{V} = \mathbf{I}_{n\times n} \qquad [45]$$

and where $\mathbf{\Sigma}$ is a matrix of dimension $m \times n$ whose diagonal terms are the singular values:

$$\mathbf{\Sigma} = \underbrace{\left.\begin{bmatrix} \sigma_1 & & & \\ & \ddots & & \mathbf{0} \\ & & \sigma_r & \\ & \mathbf{0} & & \mathbf{0} \end{bmatrix}\right\}_{m}}_{n} \qquad [46]$$

$r = n - p$ being the rank of $\mathbf{A}$.

From eqns [45] and [46], it is clear that the last columns of $\mathbf{U}$ and $\mathbf{V}$, respectively, store the nullspaces $\tilde{\mathbf{R}}$ and $\mathbf{R}$ of $\mathbf{A}$.

In the particular case where $\mathbf{A}$ is square and symmetric, the singular value decomposition (SVD) defined above is equivalent to the spectral expansion:

$$\mathbf{A} = [\mathbf{X}\ \ \mathbf{R}]\begin{bmatrix}\boldsymbol{\Lambda} & \mathbf{0}\\ \mathbf{0} & \mathbf{0}\end{bmatrix}\begin{bmatrix}\mathbf{X}^{\mathrm{T}}\\ \mathbf{R}^{\mathrm{T}}\end{bmatrix} = \mathbf{X}\boldsymbol{\Lambda}\mathbf{X}^{\mathrm{T}} = \sum_{k=1}^{n-p}\lambda_k x_k x_k^{\mathrm{T}} \quad [47]$$

where $\boldsymbol{\Lambda}$ is the diagonal matrix containing the nonzero eigenvalues λ_k and $\mathbf{X}$ stores the corresponding eigenvectors $\mathbf{x}_k$. Comparing eqns [47] and [44], we see that the singular values of a symmetric matrix are its nonzero eigenvalues and $\mathbf{U} = \mathbf{V} = [\mathbf{X}\ \ \mathbf{R}]$.

The Moore–Penrose Generalized Inverse

The generalized inverse of a matrix plays an important role in solving singular systems and we have shown how we can build one particular generalized inverse $\mathbf{A}^{+} = \mathbf{A}^{[11]+}$. Choosing different linear independent rows and columns in $\mathbf{A}$ to form $\mathbf{A}^{[11]+}$ in eqn [42] leads to a different generalized inverse, with a different nullspace content as shown by eqn [40].

Penrose showed in 1955 that only one generalized inverse, commonly denoted by $\mathbf{A}^{\dagger}$, satisfies the four relations:

$$\mathbf{A}\mathbf{A}^{\dagger}\mathbf{A} = \mathbf{A} \quad [48a]$$

$$\mathbf{A}^{\dagger}\mathbf{A}\mathbf{A}^{\dagger} = \mathbf{A}^{\dagger} \quad [48b]$$

$$\left(\mathbf{A}\mathbf{A}^{\dagger}\right)^{\mathrm{T}} = \mathbf{A}\mathbf{A}^{\dagger} \quad [48c]$$

$$\left(\mathbf{A}^{\dagger}\mathbf{A}\right)^{\mathrm{T}} = \mathbf{A}^{\dagger}\mathbf{A} \quad [48d]$$

known as the Penrose equations. The unique generalized inverse $\mathbf{A}^{\dagger}$ was also studied earlier by Moore and hence is known as the Moore–Penrose inverse.

The first Penrose equation [48a] is the condition introduced in the previous section to characterize the family of generalized inverses. The second Penrose equation [48b] stipulates that $\mathbf{A}$ is a generalized inverse for $\mathbf{A}^{\dagger}$. Eqns [48c] and [48d] state that $\mathbf{A}\mathbf{A}^{\dagger}$ and $\mathbf{A}^{\dagger}\mathbf{A}$ are symmetric. Note that a generalized inverse $\mathbf{A}^{[11]+}$ constructed as in eqn [42] satisfies the first and second equation, but not the last two.

Recalling the singular value decomposition, eqn [44], and defining:

$$\boldsymbol{\Sigma}^{\dagger} = \underbrace{\begin{bmatrix}1/\sigma_1 & & & \\ & \ddots & & \mathbf{0} \\ & & 1/\sigma_r & \\ & \mathbf{0} & & \mathbf{0}\end{bmatrix}}_{m}\Bigg\}\, n \quad [49]$$

the Moore–Penrose inverse of a real matrix can be written as:

$$\mathbf{A}^{\dagger} = \mathbf{V}\sum{}^{\dagger}\mathbf{U}^{\mathrm{T}} \quad [50]$$

Indeed, from eqns [44] and [45], it is straightforward to verify that eqn [50] satisfies the Penrose equations (eqn [48a] to [48d]). From eqn [50], we observe that the Moore–Penrose inverse is a generalized inverse such that if $\mathbf{R}$ and $\tilde{\mathbf{R}}$ represent the nullspace of $\mathbf{A}$ and $\mathbf{A}^{\mathrm{T}}$ respectively:

$$\mathbf{A}^{\dagger}\tilde{\mathbf{R}} = \mathbf{0} \quad \text{and} \quad \mathbf{A}^{\dagger\mathrm{T}}\mathbf{R} = \mathbf{0} \quad [51]$$

Hence, the Moore–Penrose inverse $\mathbf{A}^{\dagger}$ is characterized as having the same left and right nullspace as $\mathbf{A}^{\mathrm{T}}$. Therefore, for any generalized inverse $\mathbf{A}^{+}$, the Moore–Penrose inverse can be obtained as:

$$\mathbf{A}^{\dagger} = \mathbf{P}\mathbf{A}^{+}\tilde{\mathbf{P}} \quad [52]$$

where $\mathbf{P}$ and $\tilde{\mathbf{P}}$ are, respectively, the projectors onto the subspaces orthogonal to $\mathbf{R}$ and $\tilde{\mathbf{R}}$, respectively:

$$\mathbf{P} = \mathbf{I} - \mathbf{R}\left(\mathbf{R}^{\mathrm{T}}\mathbf{R}\right)^{-1}\mathbf{R}^{\mathrm{T}} \quad [53]$$

$$\tilde{\mathbf{P}} = \mathbf{I} - \tilde{\mathbf{R}}\left(\tilde{\mathbf{R}}^{\mathrm{T}}\tilde{\mathbf{R}}\right)^{-1}\tilde{\mathbf{R}}^{\mathrm{T}} \quad [54]$$

Note that this corresponds to defining $\mathbf{B}$ and $\mathbf{C}$ in eqn [40] of the family of generalized inverse matrices such that eqn [51] is satisfied.

In the particular case where $\mathbf{A}$ is symmetric, the SVD (eqn [50]) of the Moore–Penrose inverse becomes the classical spectral expansion:

$$\mathbf{A}^{\dagger} = \sum_{k=1}^{n-p}\frac{\mathbf{x}_k\mathbf{x}_k^{\mathrm{T}}}{\lambda_k} = \mathbf{X}\boldsymbol{\Lambda}^{-1}\mathbf{X}^{\mathrm{T}} \quad [55]$$

Comparing with the spectral expansion (eqn [47]) of $\mathbf{A}$, we observe that $\mathbf{A}^{\dagger}$ is a generalized inverse whose nullspace is equal to the nullspace of $\mathbf{A}$ and whose non-zero eigenvalues are the inverse of the nonzero eigenvalues of $\mathbf{A}$, the associated eigenvectors being identical. It can be obtained from any generalized inverse as:

$$\mathbf{A}^{\dagger} = \mathbf{P}\mathbf{A}^{+}\mathbf{P} \quad [56]$$

The role played by the Moore–Penrose inverse for the solution of linear systems and in vibration analysis in particular will be illustrated in the next sections.

Application of the Moore–Penrose Inverse

Least-squares solution When the right-hand side $\mathbf{b}$ of $\mathbf{Ax} = \mathbf{b}$ is not in the image of $\mathbf{A}$ no solution exists. In that case one can look for a solution such that the error $\mathbf{Ax} - \mathbf{b}$ is a minimum in the least squares sense, namely such that $(\mathbf{Ax} - \mathbf{b})^{\mathrm{T}}(\mathbf{Ax} - \mathbf{b})$ is a minimum. $\mathbf{x}$ is thus solution of:

$$\mathbf{A}^{\mathrm{T}}\mathbf{Ax} = \mathbf{A}^{\mathrm{T}}\mathbf{b} \qquad [57]$$

Solving the least-squares equation (eqn [57]) by a factorization technique is not recommended if the numerical conditioning of $\mathbf{A}$ is bad. Indeed, the condition number of $\mathbf{A}^{\mathrm{T}}\mathbf{A}$ is the square of the condition number of $\mathbf{A}$. An alternative consists in computing the solution to eqn [57] by the Moore–Penrose inverse as $\mathbf{x} = \mathbf{A}^{+}\,\mathbf{b}$. Indeed, using the first and third Penrose equations [48a, 48c]:

$$\begin{aligned}\mathbf{A}^{\mathrm{T}}\mathbf{A}\mathbf{A}^{\dagger}\mathbf{b} &= \mathbf{A}^{\mathrm{T}}\left(\mathbf{A}\mathbf{A}^{\dagger}\right)^{\mathrm{T}}\mathbf{b} \\ &= \left(\mathbf{A}\mathbf{A}^{\dagger}\mathbf{A}\right)^{\mathrm{T}}\mathbf{b} = \mathbf{A}^{\mathrm{T}}\mathbf{b}\end{aligned} \qquad [58]$$

If $\mathbf{A}$ has no right nullspace (i.e., $\mathbf{R} = \mathbf{0}$), the solution $\mathbf{x} = \mathbf{A}^{\dagger}\mathbf{b}$ is the unique solution of the least-squares problem. But if there exists a nullspace $\mathbf{R}$, the solution is not unique. Nevertheless, because $\mathbf{x} = \mathbf{A}^{\dagger}\mathbf{b}$ is orthogonal to $\mathbf{R}$, it is the solution of the minimal Euclidean norm.

Inverse power iterations for singular symmetric matrices If an inverse iteration scheme is used to find the eigensolutions of a singular symmetric matrix $\mathbf{A}$, the Moore–Penrose generalized inverse can be used since its spectrum is closely related to the eigenspectrum of $\mathbf{A}$ as explained above. Indeed, applying a power iteration method on:

$$\frac{\mathbf{x}}{\lambda} = \mathbf{A}^{\dagger}\mathbf{x} \qquad [59]$$

yields, according to eqn [55], the eigenvectors $\mathbf{x}_k$ associated with the lowest non-zero eigenvalues λ_k. Therefore in practice, the inverse iteration is carried out using a generalized inverse and projector $\mathbf{P}$:

$$\mathbf{x}^{i+1} = \mathbf{P}\mathbf{A}^{+}\mathbf{P}\mathbf{x}^{i} \qquad [60]$$

Note that this can also be interpreted as performing an inverse iteration with any generalized inverse and applying orthogonal deflation with respect to the nullspace $\mathbf{R}$. We observe that because $\mathbf{PP} = \mathbf{P}$, the projection of $\mathbf{x}^{i}$ is redundant.

Application of the Generalized Inverse in Vibration Analysis

We have already stressed the importance of the generalized inverse for solving static problems for structures with rigid-body modes. We now present two important applications of the Moore–Penrose inverse to computation methods in vibration analysis.

Computing Vibration Modes by Inverse Iteration in the Presence of Rigid-body Modes

Calling $\mathbf{M}$ and $\mathbf{K}$, respectively, the symmetric mass and stiffness matrices, the nonzero vibration frequencies $\omega_{(k)}$ and modes $\mathbf{x}_{(k)}$ are nontrivial solutions of the eigenproblem:

$$\mathbf{K}\mathbf{x}_{(k)} = \omega_{(k)}^{2}\mathbf{M}\mathbf{x}_{(k)} \quad k = 1, \ldots n - p \qquad [61]$$

where n is the number of degrees-of-freedom and p is the number of rigid-body modes or zero energy modes $\mathbf{r}_{(r)}$ satisfying:

$$\mathbf{K}\mathbf{r}_{(r)} = \mathbf{0} \quad k = 1, \ldots p \qquad [62]$$

It is common practice to avoid dealing with the singularity of $\mathbf{K}$ by modifying the eigenproblem (eqn [61]) either by a shifting strategy or by introducing small additional springs to fix the structure in space. There is, however, another effective and maybe more natural way to apply inverse iteration based methods to floating structures as explained below.

If $\mathbf{M}$ is nonsingular, there exists a Cholesky factorization such that $\mathbf{M} = \mathbf{C}_M\mathbf{C}_M^{\mathrm{T}}$. Therefore the eigenproblem (eqn [61]) can be put in the standard form:

$$\mathbf{C}_M^{-1}\mathbf{K}\mathbf{C}_M^{-\mathrm{T}}\mathbf{y}_{(k)} = \omega_{(k)}^{2}\mathbf{y}_{(k)}$$

where: $$\mathbf{y}_{(k)} = \mathbf{C}_M^{\mathrm{T}}\mathbf{x} \qquad [63]$$

As explained earlier, the inverse iteration can be carried out based on the Moore–Penrose inverse of $\mathbf{C}_M^{-1}\mathbf{K}\mathbf{C}_M^{-\mathrm{T}}$ as follows:

$$\mathbf{x}^{i+1} = \mathbf{P}\left(\mathbf{C}_M^{-1}\mathbf{K}\mathbf{C}_M^{-\mathrm{T}}\right)^{+}\mathbf{P}\mathbf{x}^{i} \qquad [64]$$

where:

$$\mathbf{P} = \mathbf{I} - \mathbf{V}\left(\mathbf{V}^{\mathrm{T}}\mathbf{V}\right)^{-1}\mathbf{V}^{\mathrm{T}}$$

$\mathbf{V}$ being the nullspace of $\mathbf{C}_M^{-1}\mathbf{K}\mathbf{C}_M^{-\mathrm{T}}$. If $\mathbf{R}$ stores the rigid-body modes ($\mathbf{K}\mathbf{R} = \mathbf{0}$), the nullspace $\mathbf{V}$ is represented by $\mathbf{V} = \mathbf{C}_M^{\mathrm{T}}\mathbf{R}$. We also note that $(\mathbf{C}_M^{-1}\mathbf{K}\mathbf{C}_M^{-\mathrm{T}})^{+} = \mathbf{C}_M^{\mathrm{T}}\mathbf{K}^{+}\mathbf{C}_M$. Therefore, substituting in eqn [64], the inverse iteration can be written as:

$$\begin{aligned} &\mathbf{x}^{i+1} = \mathbf{K}^{\oplus}\mathbf{M}\mathbf{x}^{i} \\ \text{where:}\quad &\mathbf{K}^{\oplus} = \mathbf{P}_M^{\mathrm{T}}\mathbf{K}^{+}\mathbf{P}_M \\ &\mathbf{P}_M = \mathbf{I} - \mathbf{M}\mathbf{R}\left(\mathbf{R}^{\mathrm{T}}\mathbf{M}\mathbf{R}\right)^{-1}\mathbf{R}^{\mathrm{T}} \end{aligned} \qquad [65]$$

This last form of the inverse iteration is used in practice since it involves using only a generalized inverse of $\mathbf{K}$ and the rigid-body modes.

Remarks The scheme described by eqn [65] iterates in a subspace orthogonal to $\mathbf{R}$ in the metric of $\mathbf{M}$, which is exactly the space of the vibration modes of nonzero frequencies. Hence, eqn [65] can also be understood as an inverse iteration with deflation of the rigid-body modes. Therefore it can be shown that:

$$\mathbf{K}^{\oplus} = \sum_{s=1}^{n-p} \frac{\mathbf{x}_{(s)}\mathbf{x}_{(s)}^{\mathrm{T}}}{\omega_{(s)}^2} \qquad [66]$$

The similarity between the spectral expansion (eqn [66]) of $\mathbf{K}^{\oplus}$ used in the inverse iteration and the spectral expansion (eqn [55]) of the Moore–Penrose inverse is noteworthy. However, $\mathbf{K}^{\oplus}$ is not a Moore–Penrose inverse: its spectral expansion is in terms of eigenmodes of the free vibration problem (eqn [61]) and not in terms of the eigenvectors of $\mathbf{K}$ itself.

As for eqn [60], the two projections are redundant because $\mathbf{P}_M\mathbf{M}\mathbf{P}_M^{\mathrm{T}} = \mathbf{P}_M\mathbf{M} = \mathbf{M}\mathbf{P}_M^{\mathrm{T}}$. Nevertheless, they are useful to prevent numerical errors which may cause rigid modes to reappear in the successive iterates.

The first projection ensures that the inertia forces $\mathbf{P}_M\mathbf{M}\mathbf{x}^i$ of iterate $\mathbf{x}^i$ are self-equilibrated so that a static solution can be found by applying $\mathbf{K}^{+}$. The second projection removes from the static solution obtained by $\mathbf{K}^{+}$ any component which does not lie in the space of the nonzero vibration modes.

Mode Acceleration Method in the Presence of Rigid-body Modes

The mode acceleration method is an improved mode superposition technique where the dynamic response computed by a truncated series of mode is corrected so that the solution exactly satisfies the quasistatic equilibrium.

Assuming, to simplify the presentation, that no damping is present, the dynamic equations are:

$$\mathbf{M}\ddot{\mathbf{x}} + \mathbf{K}\mathbf{x} = \mathbf{f}(t) \qquad [67]$$

where $\ddot{\mathbf{x}}$ represents the second-order time-derivative of $\mathbf{x}$ (i.e., the acceleration) and $\mathbf{f}$ is an external force, a function of time. In the mode acceleration method, the contributions of the high-frequency modes to the inertia forces are neglected. The solution is thus obtained by truncating the modal expansion of the dynamic response so as to include only the q first vibration modes and by correcting the response with the quasistatic contribution of the remaining modes. In the presence of rigid-body modes, assuming that the modes have been orthonormalized with respect to the mass matrix, the dynamic response is approximated by:

$$\mathbf{x} = \sum_{r=1}^{p} \alpha_r(t)\mathbf{r}_{(r)} + \sum_{k=1}^{q} \eta_k(t)\mathbf{x}_{(k)} + \sum_{s=q+1}^{n-p} \mathbf{x}_{(s)} \frac{\mathbf{x}_{(s)}^{\mathrm{T}}\mathbf{f}(t)}{\omega_{(s)}^2} \qquad [68]$$

where $\alpha_r(t)$ and $\eta_k(t)$ are the amplitudes of the rigid-body and vibration modes satisfying the normal equations:

$$\ddot{\alpha}_r = \mathbf{r}_{(r)}^{\mathrm{T}}\mathbf{f}(t) \qquad [69]$$

$$\ddot{\eta}_k + \omega_{(k)}^2\eta_k = \mathbf{x}_{(k)}^{\mathrm{T}}\mathbf{f}(t) \qquad [70]$$

The last term of eqn [68] cannot be computed as such because the modes of index higher then q are not known. Instead, we recall the spectral expansion (eqn [66]) of $\mathbf{K}^{\oplus}$ so that the mode acceleration solution is computed as:

$$\begin{aligned} \mathbf{x} = &\sum_{r=1}^{p} \alpha_r(t)\mathbf{r}_{(r)} + \sum_{k=1}^{q} \eta_k(t)\mathbf{x}_{(k)} \\ &+ \left(\mathbf{K}^{\oplus} - \sum_{s=1}^{q} \frac{\mathbf{x}_{(s)}\mathbf{x}_{(s)}^{\mathrm{T}}}{\omega_{(s)}^2}\right)\mathbf{f}(t) \end{aligned} \qquad [71]$$

Solution by Generalized Inverses and Finding the Nullspace R

Factorization of a Singular Matrix: Constructing a Generalized Inverse

If a solution exists, it can be computed using the generalized inverse $\mathbf{A}^{[11]+}$ defined in eqn [42] so that:

$$\begin{bmatrix} \mathbf{x}_1 \\ \mathbf{x}_2 \end{bmatrix} = \begin{bmatrix} \mathbf{A}_{11}^{-1} & \mathbf{0} \\ \mathbf{0} & \mathbf{0} \end{bmatrix} \begin{bmatrix} \mathbf{b}_1 \\ \mathbf{b}_2 \end{bmatrix} \quad [72]$$

namely by solving the system $\mathbf{Ax} = \mathbf{b}$ for a maximum set of independent variables and equations, i.e., $\mathbf{x}_1 = \mathbf{A}_{11}^{-1}\mathbf{b}_1$, and setting to zero the remaining unknowns $\mathbf{x}_2$.

When a factorization technique is used, it corresponds to advancing the elimination process as long as nonzero pivots exist. When factorizing a nondefinite system, pivoting must then be used and the factorization is stopped when the remaining submatrix is zero. For semidefinite matrices, pivoting is not required since zero pivots appear only when the row of the pivot is a linear combination of all preceding rows. In that case, when a zero pivot is found at step k, the corresponding unknown x_k is flagged as being part of $\mathbf{x}_2$ and the factorization is continued by skipping step k.

In structural mechanics, setting to zero the degrees of freedom $\mathbf{x}_2$ corresponds to adding fictitious links to the system to render it statically determined. Since the forces applied must be self-equilibrated for a static solution to exist if the structure is floating, applying temporary constraints for the system to be exactly statically determined does not affect the solution as far as deformations are concerned, but simply sets the rigid-body displacement of the solution.

Computing the Nullspace

Let us recall from eqn [29] that the nullspace of $\mathbf{A}$ can be computed as:

$$\mathbf{R} = \begin{bmatrix} -\left(\mathbf{A}_{11}^{-1}\mathbf{A}_{12}\right) \\ \mathbf{I} \end{bmatrix} \quad [73]$$

When a factorization technique is applied, only the nonsingular matrix $\mathbf{A}_{11}$ is factored as explained above. Hence the rigid-body modes can be found by applying forward and backward substitutions to the submatrix $\mathbf{A}_{12}$. When $\mathbf{A}$ is a stiffness matrix, eqn [73] indicates that the rigid-body modes are found by solving the system for $\mathbf{x}_1$ when setting to one a degree-of-freedom $\mathbf{x}_2$, the other $\mathbf{x}_2$ being set to zero.

Since, in order to minimize memory usage, the matrix $\mathbf{A}$ is overwritten by its factored form, $\mathbf{A}_{12}$ no longer exist after the factorization. Nevertheless, from the factorization methods described earlier it is understood that when a null pivot is found at step k, column k stores a column of $\mathbf{A}_{12}$ transformed by a forward substitution. Hence computing $\mathbf{A}_{11}^{-1}\mathbf{A}_{12}$ simply requires one to perform a backward substitution on the columns of the null pivots.

When the nullspace of a matrix is computed as a by-product of its factorization, the threshold used to detect null pivots plays an essential role in finding the null space of a matrix. Since the threshold to detect correctly the null pivots strongly depends on the conditioning of the matrix and on the machine precision, the automatic detection and computation of the nullspace as described above might yield a wrong nullspace. To circumvent this delicate problem in structural mechanics, some methods first detect rigid-body modes by geometric inspection and use that information to build the null space during the factorization in a more robust way.

Nomenclature

$\mathbf{D}$	diagonal
$\mathbf{I}$	identity matrix
$\mathbf{L}$	lower triangular matrix
$\mathbf{P}_1$, $\mathbf{P}_2$	permutation operators
$\mathbf{U}$	upper triangular matrix

See also: **Eigenvalue analysis**; **Krylov-Lanczos methods**; **Nonlinear normal modes**; **Parallel processing**

Further Reading

Bathe K-J (1996) *Finite Element Procedures*. Englewood Cliffs: Prentice Hall.

Ben-Israel A and Greville TNE (1974) *Generalized Inverse: Theory and Applications*. New York: Wiley.

Farhat C and Géradin M (1998), On the general solution by a direct method of a large-scale singular system of linear equations: application to the analysis of floating structures. *International Journal for Numerical Methods in Engineering* 41: 675–696.

Géradin M and Rixen DJ (1997) *Mechanical Vibrations, Theory and Application to Structural Dynamics*, 2nd edn. Chichester, UK: Wiley.

Golub GH and Van Loan CF (1996) *Matrix Computation*, 3rd edn. Baltimore: Johns Hopkins University Press.

Irons BM (1970), A frontal solution program for finite element analysis. *International Journal for Numerical Methods in Engineering* 2: 5–32.

Liu JWH and George A (1981), *Computer Solution of Large Sparse Positive Definite Systems*. Englewood Cliffs: Prentice Hall.

Rao CR and Mitra SK (1971) *Generalized Inverse of Matrices and its Applications*. New York: Wiley.

Saad Y (1996) *Iterative Methods for Sparse Linear Systems*. Boston: PWS Publishing Company.

Sloan SW (1989) A Fortran program for profile and wavefront reduction. *International Journal for Numerical Methods in Engineering* 28: 2651–2679.

Wilkinson JH and Reinsch C (1971) Linear algebra. In: Bauer FL *et al.* (eds.) *Handbook for Automatic Computation*, Volume II. Berlin: Springer-Verlag.

LINEAR DAMPING MATRIX METHODS

F Ma, University of California, Berkeley, CA, USA

Copyright © 2001 Academic Press

doi:10.1006/rwvb.2001.0013

Introduction

Physical systems possessing inertia and elasticity are capable of relative motion. If the motion of such systems repeats itself after a given interval of time, the motion is known as vibration. This periodic motion can be rather complex, and it may take a long time before the motion repeats itself. In addition, there are generally forces of excitation and resistance to any vibratory motion. In simple terms, the subject of vibration is the study of oscillatory motion generated by the interplay of inertia, elasticity, and impressed forces. Yet vibration manifests itself in such a great variety of ways in engineering that an understanding of this subject is a prerequisite for successful design of systems.

There are several possible starting points in the analysis of vibrating systems. As a branch in classical dynamics, vibration is amenable to the formulations of Newton, Lagrange, or Hamilton. However, in the ultimate analysis, all approaches are equivalent and may be viewed as merely a mathematical representation of energy balance. Consider the small oscillatory motion of a natural vibrating system. If the configuration of the system can be specified by n generalized coordinates $q_i\,(i = 1, 2 \ldots n)$, the Lagrange's equations of motion can be cast in the compact form:

$$\mathbf{M}\ddot{\mathbf{q}} + \mathbf{K}\mathbf{q} = \mathbf{Q} \qquad [1]$$

where $\mathbf{q} = [q_1, q_2 \ldots q_n]^{\mathrm{T}}$ is the vector of generalized coordinates and $\mathbf{Q} = [Q_1, Q_2 \ldots Q_n]^{\mathrm{T}}$ is the vector of impressed forces. The coefficients $\mathbf{M}$ and $\mathbf{K}$ are constant square matrices of order n. As an easy consequence of the Lagrangian formulation, $\mathbf{M}$ and $\mathbf{K}$ are symmetric and definite. The positive definite matrix $\mathbf{M}$ arises from system inertia and, for this reason, is called the mass matrix. The positive semidefinite matrix $\mathbf{K}$ arises from system elasticity and is called the stiffness matrix. Clearly, eqn [1] shows how system inertia, system elasticity, and impressed forces can together bring about oscillatory motion, described by the vector of system response $\mathbf{q}$.

Equivalent Viscous Damping

In engineering applications, it is customary to separate the vector of impressed forces $\mathbf{Q}$ into forces of excitation $\mathbf{f}(t)$ and resistance. Forces of excitation may be induced by unbalanced weights in rotating machinery, or they may result from natural events such as wind storms, ocean waves, or earthquakes. Characterization of the various sources of excitation is tackled in such diverse fields as machine design, wind, ocean, and earthquake engineering. In addition to excitation, there is usually some degree of friction or resistance to any vibratory motion. This type of resistance is called damping, and it may originate from air friction, Coulomb dry friction, or internal friction in materials. Energy of a system is always dissipated in damping. If damping is heavy, oscillatory motion will not occur and the system is said to be overdamped. The damping forces are regarded as viscous if they are proportional to the generalized velocities. For a viscously damped system, the impressed forces can be separated as:

$$\mathbf{Q} = \mathbf{f}(t) - \mathbf{C}\dot{\mathbf{q}} \qquad [2]$$

The matrix $\mathbf{C}$ above contains the constants of proportionality for viscous damping and is thus called the damping matrix. It is also symmetric and positive semidefinite. Strictly speaking, the assumption of viscous damping is only valid if frictional forces are generated by the laminar flow of a viscous fluid. To get an intuitive feeling of this damping mechanism, one can imagine trying to walk through treacle. A commonly used device that actually uses this mechanism is the shock absorber on an automobile. The associated dashpot device is set up to cause a piston to displace a fluid. In most engineering systems, damping is rarely plain viscous. Even fluid damping need not be viscous. Frictional forces induced by the turbulent flow of a fluid is proportional to the velocity squared. Internal damping in materials is not viscous and changes with the frequency of the excitation. In fact, there are usually more than one damping mechanisms simultaneously in play in any vibrating system.

Viscous damping has a very simple mathematical representation and is easily amenable to analysis. It would be preferable if other damping mechanisms could somehow be approximated as viscous. Indeed,

a whole array of postulations was made in the classical literature to support the approximation of damping as viscous. For instance, Lord Rayleigh used viscous damping to approximate the combined effect of air damping and internal friction in a tuning fork. It seems reasonable enough to accept that the overall damping in a sounding fork is viscous. However, to say that damping in an actual building is viscous is quite different. There are many energy-dissipating mechanisms in a vibrating building. These include friction at steel connections, opening and closing of microcracks in concrete, and friction between the structure itself and nonstructural elements such as partition walls. In fact, the various energy-dissipating mechanisms in an actual building have not been completely identified and understood.

Fortunately, extensive experimentation has been conducted in the past three decades on vibrating structures known to possess a multitude of dissipative mechanisms. Provided that the dissipative forces are small, it has been consistently observed that the system response generally looks like a viscous-type response. With this understanding, it appears reasonable to use equivalent viscous damping as an approximation of overall damping, so long as the approximation is not extended out of a suitably small range in which the various dissipative forces remain small. A common method for determining equivalent viscous damping is to equate the energy dissipated per cycle of oscillation to that due to a hypothetical viscous damper. This process generates the constants of proportionality for equivalent viscous damping. Another quantification of equivalent viscous damping is such that it will produce the same bandwidth in frequency response as obtained experimentally for an actual system. If equivalent viscous damping is indeed taken as representative, the governing equation of an n-degrees-of-freedom natural system becomes:

$$\mathbf{M}\ddot{\mathbf{q}} + \mathbf{C}\dot{\mathbf{q}} + \mathbf{K}\mathbf{q} = \mathbf{f}(t) \qquad [3]$$

This is a linear differential equation with real and constant coefficient matrices. As explained earlier, $\mathbf{M}$, $\mathbf{C}$, and $\mathbf{K}$ enjoy the properties of symmetry and definiteness. A very powerful technique for evaluating the response of viscously damped systems is modal analysis.

Undamped Vibration

The equation of motion of an undamped system, in which $\mathbf{C} = \mathbf{0}$, reduces to:

$$\mathbf{M}\ddot{\mathbf{q}} + \mathbf{K}\mathbf{q} = \mathbf{f}(t) \qquad [4]$$

In general, the above matrix differential equation is coupled. The ith component equation involves not only q_i and $\ddot{q}_i$, but also other generalized coordinates and their accelerations. If $\mathbf{M}$ is diagonal, $\ddot{q}_i$ occurs as the only acceleration in the ith component equation and the system is said to be inertially decoupled. Likewise, q_i occurs as the only displacement in the ith component equation when $\mathbf{K}$ is diagonal. The system is then said to be elastically decoupled. Should both $\mathbf{M}$ and $\mathbf{K}$ become diagonal, the entire system is decoupled. Eqn [4] may then be regarded as composing of n independent scalar equations, the solution of which is immediate. Modal analysis is a method for decoupling the equation of motion by means of a coordinate transformation. The decoupling coordinate transformation can be determined through the solution of an algebraic eigenvalue problem.

Let $\mathbf{u}$ be a column vector of order n and α be a scalar constant. If $\mathbf{q} = \mathbf{u}e^{\alpha t}$ is a homogeneous or complementary solution to eqn [4], the generalized symmetric eigenvalue problem

$$\mathbf{K}\mathbf{u} = \lambda\mathbf{M}\mathbf{u} \qquad [5]$$

must be satisfied, where $\lambda = -\alpha^2$. Eigenvalue problems of this type have been studied rather extensively in the abstract theory of matrix pencils. Owing to the properties of symmetry and definiteness of $\mathbf{M}$ and $\mathbf{K}$, there are n real and nonnegative eigenvalues λ_i. The corresponding eigenvectors $\mathbf{u}_i$ are real and orthonormal. Let the eigenvectors $\mathbf{u}_i$ be arranged as columns of a modal matrix $\mathbf{U} = [\mathbf{u}_1, \mathbf{u}_2 \ldots \mathbf{u}_n]$, and the eigenvalues λ_i as diagonal elements of a spectral matrix $\mathbf{\Lambda} = \text{diag}[\lambda_1, \lambda_2 \ldots \lambda_n]$. Then the orthonormality of the eigenvectors can be expressed in a compact form:

$$\mathbf{U}^{\mathrm{T}}\mathbf{M}\mathbf{U} = \mathbf{I} \qquad [6]$$

$$\mathbf{U}^{\mathrm{T}}\mathbf{K}\mathbf{U} = \mathbf{\Lambda} \qquad [7]$$

Utilizing the modal matrix, define a coordinate transformation $\mathbf{q} = \mathbf{U}\mathbf{p}$. Eqn [4] may now be simplified to:

$$\ddot{\mathbf{p}} + \mathbf{\Lambda}\mathbf{p} = \mathbf{U}^{\mathrm{T}}\mathbf{f}(t) \qquad [8]$$

which represents a completely decoupled system. The transformation from $\mathbf{q}$ to $\mathbf{p}$ is called the modal transformation and $\mathbf{p}$ is termed the vector of modal coordinates. Thus, an undamped system can always be decoupled by modal transformation.

Modal analysis possesses tremendous physical insight. Each positive eigenvalue λ_i of eqn [5] is the square of a natural frequency of the system. Let $\lambda_i = \omega_i^2$, where ω_i is real and positive. In free vibration at the natural frequency ω_i, various parts of the system oscillate in the same phase, passing through their equilibrium positions at the same instant of time. This form of synchronous motion of a system is called modal vibration. The eigenvector $\mathbf{u}_i$ associated with λ_i physically represents the relative amplitudes of the coordinates of a system in modal vibration. For this reason, $\mathbf{u}_i$ is also called a mode shape, or a normal mode. General free vibration of a system is simply a proper superposition of the different forms of modal vibration. Lastly, the modal transformation itself can be given a geometric interpretation. It can be thought of as a coordinate transformation that determines the principal axes of an n-dimensional ellipsoid. No wonder that modal analysis is regarded as one of the most important and intuitively appealing methods of analysis to date.

Proportional Damping

A viscously damped system is governed by eqn [3]. Upon modal transformation, the system will be decoupled inertially and elastically, in accordance with eqns [6] and [7]. Expressed in modal coordinates, eqn [3] takes the form:

$$\ddot{\mathbf{p}} + \mathbf{D}\dot{\mathbf{p}} + \mathbf{\Lambda}\mathbf{p} = \mathbf{U}^{\mathrm{T}}\mathbf{f}(t) \qquad [9]$$

where $\mathbf{D} = \mathbf{U}^{\mathrm{T}}\mathbf{C}\mathbf{U}$ is the modal damping matrix. In general, $\mathbf{D}$ will not be diagonal, and a damped system remains coupled in modal coordinates. In other words, a damped system does not usually possess the same forms of modal vibration as the undamped system. However, if:

$$\mathbf{C} = \alpha\mathbf{M} + \beta\mathbf{K} \qquad [10]$$

for some scalar constants α and β, then $\mathbf{D} = \alpha\mathbf{I} + \beta\mathbf{\Lambda}$ becomes a diagonal matrix. Eqn [9] is completely decoupled and represents n independent scalar equations. A system whose damping matrix satisfies condition [10] is said to be proportionally damped. Proportional damping was first expounded by Lord Rayleigh. It includes mass-proportional damping and stiffness-proportional damping as particular cases.

The concept of proportional damping has subsequently been extended. Express eqn [10] in the form of a series: $\mathbf{C} = \mathbf{M}(\alpha\mathbf{I} + \beta\mathbf{M}^{-1}\mathbf{K})$. It is found that the modal damping matrix $\mathbf{D}$ remains diagonal even when higher powers of $\mathbf{M}^{-1}\mathbf{K}$ are added to the series. As long as:

$$\mathbf{C} = \mathbf{M}\sum_{i=0}^{n-1} a_i(\mathbf{M}^{-1}\mathbf{K})^i \qquad [11]$$

for some constants a_i, a damped system possesses the same mode shapes as the undamped one. Note that the above series need not contain powers higher than $n-1$ because of the Cayley–Hamilton theorem in matrix analysis. Proportional damping and its power-series extension are perhaps the best known examples of damping for which modal transformation decouples the entire system. There are other forms of damping under which modal analysis remains operational.

Classical Damping

A vibrating system is said to be classically damped if $\mathbf{C}$ transforms into a modal damping matrix $\mathbf{D}$ that is diagonal. The terminology stems from the observation that a damped system is decoupled by the classical method of modal analysis only when the damping mechanism is classical. Clearly, proportional damping is a special case of classical damping. However, classical damping need not be proportional. The same can be said for the power-series extension of proportional damping. A system subjected to nonclassical damping will have a modal damping matrix $\mathbf{D}$ that is nondiagonal. Such a system is not amenable to modal analysis, and it does not possess the same normal modes as the undamped system.

A necessary and sufficient condition under which a system is classically damped is:

$$\mathbf{C}\mathbf{M}^{-1}\mathbf{K} = \mathbf{K}\mathbf{M}^{-1}\mathbf{C} \qquad [12]$$

In other words, the modal damping matrix $\mathbf{D}$ is diagonal if and only if the matrices $\mathbf{M}^{-1}\mathbf{C}$ and $\mathbf{M}^{-1}\mathbf{K}$ commute in multiplication. Condition [12] is obviously satisfied if $\mathbf{C}$ has either the form [10] or [11]. In general, there are no particular reasons why condition [12] should hold to permit modal analysis to operate. However, owing to the great convenience furnished by decoupling, engineers routinely invoke a large array of rather bold approximations to justify the use of classical damping in their analysis. The many approximations used in the postulation of classical damping may be grouped into three categories.

The first technique involves the construction of a damping matrix $\mathbf{C}$ that is classical at the outset. This approach is particularly useful for a complex system with similar damping mechanisms distributed throughout the system. An example is a multistory

building with a nearly identical floor plan and similar structural materials on each story. In contrast to the construction of $\mathbf{M}$ and $\mathbf{K}$, the damping matrix $\mathbf{C}$ for many complex structures is neither calculated from the structural dimensions nor the damping properties of the constituent structural materials. That should not be surprising since the properties of many damping mechanisms are not known precisely. It would seem impractical to try to account theoretically for the energy dissipated in mechanisms such as friction at steel connections, opening and closing of microcracks in concrete, or the friction between the structure itself and a nonstructural member such as a fireproofing partition wall. For a large and complex structure, the damping matrix $\mathbf{C}$ is usually estimated from the modal damping ratios, which are themselves estimated from available data based upon experimentation on the concerned or similar structures. If either equation [10] or [11] is incorporated as a constraint in the estimation, a classical damping matrix $\mathbf{C}$ will always be obtained. Other constraints may be used alternatively, but all such constraints must be derivable from eqn [12].

A second type of approximation that results in classical damping is simply to ignore the off-diagonal elements of the modal damping matrix. This procedure is termed the decoupling approximation in damping, and is commonly used when the off-diagonal elements of $\mathbf{D}$ are small. Many different arguments, some more appealing than others, have been given in support of the procedure. Intuitively, if the off-diagonal elements of $\mathbf{D}$ are small in magnitude, these elements would only represent second-order effect and can be ignored. Thus, the errors introduced by the decoupling approximation in damping should be small if $\mathbf{D}$ is diagonally dominant. Even when the off-diagonal elements of $\mathbf{D}$ are of the same order as the diagonal ones, the sometimes positive and sometimes negative off-diagonal elements of $\mathbf{D}$ would at least partially annihilate the influence of each other in coupling. This would lead to an overall system response that is practically the same as if the off-diagonal elements of $\mathbf{D}$ were absent.

An equally persuasive and intuitive argument may be made in the frequency domain. For many structures, the nonzero natural frequencies do not cluster around each other. Suppose the natural frequencies $\omega_i = \sqrt{\lambda_i}$ of a system are distinct and well-separated: $|\omega_i - \omega_j| \gg 1$ if $i \neq j$. Then any two normal modes of the system are relatively removed from each other in the frequency domain. For this reason, the damped system may be considered decoupled for all practical purposes. Yet another argument for decoupling approximation utilizes the response bounds of a system. Response bounds are useful in design, and decoupling approximation may sometimes be justified if it generates response bounds that are close to the exact bounds. Over the years, large-frequency separation of the normal modes or diagonal dominance of $\mathbf{D}$ have been accepted as sufficient conditions for the decoupling approximation in damping. However, examples have been constructed in recent years to show, surprisingly, that enhancing the diagonal dominance of $\mathbf{D}$ or increasing the frequency separation of the normal modes may not reduce coupling. Contrary to widely accepted beliefs, the effect of coupling can even increase over a certain range. Practically speaking, there is no objection to using the decoupling approximation in damping. Nevertheless, rigorous analysis of errors committed by such an approximation has not been reported in the literature.

A third type of approximation involves the use of indices of coupling. There are many indices of coupling, but they all quantify the extent of coupling in a damped system in some ways. Coupling indices are sometimes referred to as coupling ratios, indices of proportionality, or commutativity factors. One of the first indices thus proposed can be brought up in an intuitive way. Recall that a classically damped system must satisfy the commutativity condition [12]. Define $\mathbf{E} = \mathbf{C}\mathbf{M}^{-1}\mathbf{K} - \mathbf{K}\mathbf{M}^{-1}\mathbf{C}$. Since $\mathbf{M}$, $\mathbf{C}$, and $\mathbf{K}$ are symmetric, $\mathbf{E}^{\mathrm{T}} = -\mathbf{E}$. Thus $\mathbf{E}$ is a skew-symmetric matrix and its diagonal elements must vanish. The off-diagonal elements of $\mathbf{E}$ are numerical indicators of coupling. They are zero only if damping is classical. Let σ be the sum of magnitudes of the off-diagonal elements of $\mathbf{E}$. It is obvious that σ can be taken as an index of coupling. Many different indices of coupling have been defined, and some are defined in the frequency domain. Apparently, if appropriate coupling indices are small, a damped system may be solved by invoking the decoupling approximation in damping. If the indices are not sufficiently small, the modal damping $\mathbf{D}$ may be replaced by a selected diagonal matrix whose elements are determined through $\mathbf{D}$ and the coupling indices. In essence, a different decoupled system is substituted, and the response of the new system should resemble the original one. In practice, coupling indices that can be easily computed have rather limited applicability. Also, the errors of approximation are known to depend on the excitation, and it may be necessary to use different indices for different forms of excitation.

Further research will be needed to clarify the various issues connected with approximation by classical damping. At the present time, the tremendous conceptual and computational advantages provided by a

decoupled system often outweigh the compromises needed to impose classical damping.

Nonclassical Damping

A system is said to be nonclassically damped if it is not decoupled by classical modal analysis. A system with nonclassical damping does not possess the same normal modes of vibration as the undamped system. In general, vibrating systems are nonclassically damped. As explained in the last section, each approximation of damping as classical requires certain assumptions and has only a limited range of applicability.

The assumption of classical damping is not appropriate if a damped system is composed of two or more parts with significantly different levels of damping. Certain structure–soil systems constitute one class of examples. If a structure has very short natural periods, then the underlying soil region cannot be regarded as rigid and soil–structure interaction must be taken into account. The modal damping ratio for a soil region is typically very different from that for a structure, say 15–20% for soil as compared to 3–5% for the structure. There will be coupling between the soil and structure subsystems induced by strong soil–structure interaction. It would not be proper to assume that the structure–soil system has classical damping, even if the soil and structure subsystems can be taken as classically damped. The assumption of classical damping may also be inappropriate for structures mounted on base isolation systems, or for structures containing special energy-dissipating devices.

A variety of methods, both approximate and exact, are available for the analysis of nonclassically damped systems. For the purpose of exposition, these methods are grouped into four categories. The first technique involves the use of a truncated set of normal modes. In many systems, only the modes associated with lower frequencies contribute significantly to the response. Thus, in the solution of system [9], it would only be necessary to consider a small subset of the n coupled equations. This approximate technique can be highly efficient. However, examples have been constructed to show that such an approach can generate substantial errors in some applications.

A second type of approximate methods for treating nonclassical damping is system iteration. Express the modal damping matrix $\mathbf{D}$ as a matrix sum of its diagonal and off-diagonal elements: $\mathbf{D} = \mathbf{F} + \mathbf{G}$, where $\mathbf{F}$ is a diagonal matrix made up of the diagonal elements of $\mathbf{D}$. For a system with weakly nonclassical damping, the elements of $\mathbf{G}$ are small. An approximate solution can then be obtained through the use of matrix perturbation series. When the elements of $\mathbf{G}$ are not small compared to those of $\mathbf{F}$, a matrix iterative scheme has been devised for approximate solution. At each iteration, it is only necessary to tackle a decoupled system. An implicit assumption with any iterative method is that only a small number of iterations are required for accurate solution. However, this is not always true.

As a third approach, the simultaneous reduction of $\mathbf{M}$, $\mathbf{C}$, and $\mathbf{K}$ to certain patterned forms will be addressed. From a mathematical viewpoint, modal analysis is a method for reducing $\mathbf{M}$ and $\mathbf{K}$ to diagonal forms simultaneously. In a nonclassically damped system, modal transformation does not diagonalize the damping matrix $\mathbf{C}$. Nevertheless, it may still be possible to reduce $\mathbf{M}$, $\mathbf{C}$, and $\mathbf{K}$ to upper triangular forms by a common similarity transformation. Afterwards, the system can be solved by back-substitution. A necessary and sufficient condition for the simultaneous reduction to triangular forms is that $\mathbf{M}$, $\mathbf{C}$, and $\mathbf{K}$ generate a solvable Lie algebra. It is also possible to consider the simultaneous reduction of $\mathbf{M}$, $\mathbf{C}$, and $\mathbf{K}$ to other patterned forms. Each such conversion requires the satisfaction of certain conditions. In general, these methods of simultaneous reduction of the coefficient matrices are only applicable to a small subclass of nonclassically damped systems.

A fourth approach to nonclasssically damped systems is complex modal analysis. This is a powerful method for decoupling nonclassically damped systems in the state space. As explained in an earlier section, classical modal analysis only utilizes real modes to decouple eqn [3] when damping is classical. If damping is nonclassical, recast eqn [3] into a first-order form:

$$\mathbf{R}\dot{\mathbf{y}} + \mathbf{S}\mathbf{y} = \mathbf{g}(t) \qquad [13]$$

for which:

$$\mathbf{R} = \begin{bmatrix} \mathbf{0} & \mathbf{M} \\ \mathbf{M} & \mathbf{C} \end{bmatrix} \qquad [14]$$

$$\mathbf{S} = \begin{bmatrix} -\mathbf{M} & \mathbf{0} \\ \mathbf{0} & \mathbf{K} \end{bmatrix} \qquad [15]$$

and $\mathbf{y}^{\mathrm{T}} = [\dot{\mathbf{q}}^{\mathrm{T}}, \mathbf{q}^{\mathrm{T}}]$, $\mathbf{g}^{\mathrm{T}}(t) = [0^{\mathrm{T}}, \mathbf{f}^{\mathrm{T}}(t)]$. Although the coefficient matrices $\mathbf{R}$ and $\mathbf{S}$ are symmetric, they are no longer definite. For this reason, the associated symmetric eigenvalue problem

$$\alpha\mathbf{R}\mathbf{v} + \mathbf{S}\mathbf{v} = \mathbf{0} \qquad [16]$$

will admit complex eigenvalues α and complex eigenvectors $\mathbf{v}$. These eigenvectors are known as complex

modes, and they can still constitute a modal transformation to decouple eqn [13]. Compared to classical modal analysis, the method of complex modes is rather computationally intensive. In addition, the physical significance of various components of this exact method is not fully understood. There are alternative formulations of complex modal analysis, but they all aim at decoupling a nonclassically damped system in the state space.

The analysis of nonclassically damped systems has received a great deal of attention in recent years, due in part to the design of base-isolated structures and the use of special energy-dissipating devices in system control. As the field of vibration continues to grow, the development of new and improved techniques for nonclassical damping can certainly be anticipated.

Nomenclature

$\mathbf{D}$	modal damping matrix
$\mathbf{q}$	vector of system response
$\mathbf{u}$	column vector of order n
$\mathbf{U}$	modal matrix
α	scalar constant
$\mathbf{\Lambda}$	spectral matrix

See also: **Critical damping**; **Damping in FE models**; **Modal analysis, experimental**, Parameter extraction methods; **Viscous damping**

Further Reading

Benaroya H (1998) *Mechanical Vibration: Analysis, Uncertainties, and Control*. Upper Saddle River, NJ: Prentice Hall.

Caughey TK and O'Kelly MEJ (1965) Classical normal modes in damped linear dynamic systems. *ASME Journal of Applied Mechanics* 32: 583–588.

Chopra AK (1995) *Dynamics of Structures: Theory and Applications to Earthquake Engineering*. Englewood Cliffs, NJ: Prentice Hall.

Ewins DJ (1984) *Modal Testing: Theory and Practice*. Letchworth, Hertfordshire, UK: Research Studies Press.

Foss KA (1958) Coordinates which uncouple the equations of motion of damped linear dynamic systems. *ASME Journal of Applied Mechanics* 25: 361–364.

Inman DJ (1989) *Vibration with Control, Measurement, and Stability*. Upper Saddle River, NJ: Prentice Hall.

Meirovitch L (1997) *Principles and Techniques of Vibrations*. Upper Saddle River, NJ: Prentice Hall.

Müller PC and Schiehlen WO (1985) *Linear Vibrations*. Dordrecht, The Netherlands: Martinus Nijhoff.

Newland DE (1989) *Mechanical Vibration Analysis and Computation*. Essex, UK: Longman.

Pars LA (1965) *A Treatise on Analytical Dynamics*. London, UK: Heinemann.

Rao SS (1995) *Mechanical Vibrations*, 3rd edn. Reading, MA: Addison-Wesley.

Rayleigh JWS (1945) *The Theory of Sound*, vol. I. New York: Dover. Reprint of the 1894 edition.

Sun CT and Lu YP (1995) *Vibration Damping of Structural Elements*. Upper Saddle River, NJ: Prentice Hall.

LIQUID SLOSHING

R A Ibrahim, Wayne State University, Detroit, MI, USA

Copyright © 2001 Academic Press

doi:10.1006/rwvb.2001.0086

Sloshing means any oscillatory motion of the liquid free surface inside its container. It is created due to any disturbance to partially filled liquid containers. Depending on the excitation and container shape, the liquid free surface can experience different types of motion ranging from simple planar, nonplanar, rotational, irregular beating, symmetric, asymmetric, quasiperiodic, to chaotic. When interacting with the elastic structure of its container or its support structure, the liquid free surface can exhibit fascinating types of motion in the form of energy exchange with interacting modes. Recent studies reported complex liquid free surface motions, which occur in the presence of nonlinear resonance conditions such as internal resonance and parametric resonance conditions. One may classify liquid motion into the following categories:

1. Normal sloshing resulting from translational or pitching excitation of the liquid container.
2. Under vertical (parametric) excitation, and depending on the excitation amplitude and frequency, the liquid free surface may exhibit intermittent small oscillations, subharmonic, and chaotic oscillations.
3. Rotational (swirl) sloshing occurs at a frequency near the natural frequency of the first antisymmetric mode. The mechanism that creates rotary fluid motion is a nonlinear coupling of the fluid motion parallel with and perpendicular to the excitation plane in circular upright tanks.
4. Vortex formation during the draining of liquid from the tank.

5. Surface spray, spatial resonance, and cross-waves.
6. Dome impact due to a sudden acceleration or deceleration.
7. Low-gravity phenomena where surface tension is dominant. The liquid may be oriented randomly within the tank depending essentially upon the wetting characteristics on the tank wall.
8. Modulated free surface motion, which occurs when the liquid free surface motion interacts with the elastic support structural dynamics in the neighborhood of internal resonance conditions.

Liquid containers constitute major components in a number of dynamical systems such as aerospace vehicles, road tankers, liquefied natural gas carriers, and elevated water towers. The dynamic behavior of these systems is greatly affected by the dynamics of the liquid free surface. The basic problem of liquid sloshing involves the estimation of the liquid natural frequencies, hydrodynamic pressure distribution, forces, and moments. These parameters have a direct effect on the dynamic stability and performance of moving containers. However, under external excitation, it is important to determine the fluid free surface natural frequencies and mode shapes in order to avoid the occurrence of resonance and large sloshing amplitudes.

The problem is of great concern to civil engineers and seismologists in studying earthquake effects on large dams, oil tanks, water reservoirs, and elevated water towers. It is also important for aerospace engineers involved in the design and development of high-speed aircraft and large rockets. Near zero gravity, the liquid volume takes an arbitrary orientation and is difficult to handle. Liquid sloshing in a moving container creates a broad class of problems of practical safety importance, including tank trucks on highways, and liquid cargo in ocean-going vessels. In populated cities, gasoline and other flammable liquid tankers are prone to rollover accidents while entering and exiting highways. This is a difficult mathematical problem to solve analytically, because the dynamic boundary condition (Bernoulli's equation) at the free surface is nonlinear and the position of the free surface varies with time in a manner not known *a priori*.

Analytical solutions are limited to regular geometric tank shapes, such as cylindrical and rectangular. The nature of slosh loading in cylindrical tanks, and its prediction, is probably understood than for prismatic tanks. However, analytical techniques for predicting large-amplitude sloshing are still not fully developed. Such loads are extremely important in designing the support structure and internal components of vehicle tanks.

The liquid motion inside a tank has an infinite number of natural frequencies, but it is the lowest few modes that are most likely to be excited by the motion of a vehicle. Most studies have therefore concentrated on investigating forced harmonic oscillations near the lowest natural frequency that can be predicted by the linear theory of fluid field equations. Nonlinear effects result in the frequency of maximum response being slightly different from the natural frequency, and dependent on amplitude. These nonlinear effects include amplitude jump, parametric resonance, chaotic liquid surface motion, and nonlinear sloshing mode interaction (internal resonance among the liquid sloshing modes).

Sloshing phenomena in moving rectangular tanks can usually be described by considering only two-dimensional fluid flow. Sloshing in spherical or cylindrical tanks, however, must usually consider three-dimensional flow effects. Tanks with two-dimensional flow are divided into two classes: low and high liquid fill depths. The low fill depth case is represented by $h/a < 0.2$, where h is the still liquid depth and a is the tank width in the direction of motion. The low fill depth case is characterized by the formation of hydraulic jumps and traveling waves for excitation periods around resonance. At higher fill depths, large standing waves are usually formed in the resonance frequency range. When hydraulic jumps or traveling waves are present, extremely high impact pressures can occur on the tank walls. Impact pressures are only measured experimentally and cannot be estimated theoretically.

Liquid Free and Forced Sloshing

The theory of liquid sloshing dynamics in partially filled containers is based on developing the fluid field equations. The boundary value problem is usually solved for either the modal analysis or the response to external excitations. The general equations of motion of fluids in closed containers can be simplified by assuming that the container is rigid and impermeable. The fluid field equations in a container undergoing planar motion are obtained based on the assumption that the fluid is inviscid, incompressible, and initially irrotational. Capillary or surface tension effects are ignored in regular gravitational field. The tank may be displaced along some trajectory in space. It is convenient to refer the fluid motion to a moving coordinate system as the variables are measured by a measuring device that is moving relative to the inertial frame. The fluid equation of motion will be developed with reference to the stationary and moving coordinates, as shown in **Figure 1**. Let $O'X'Y'Z'$ be a stationary

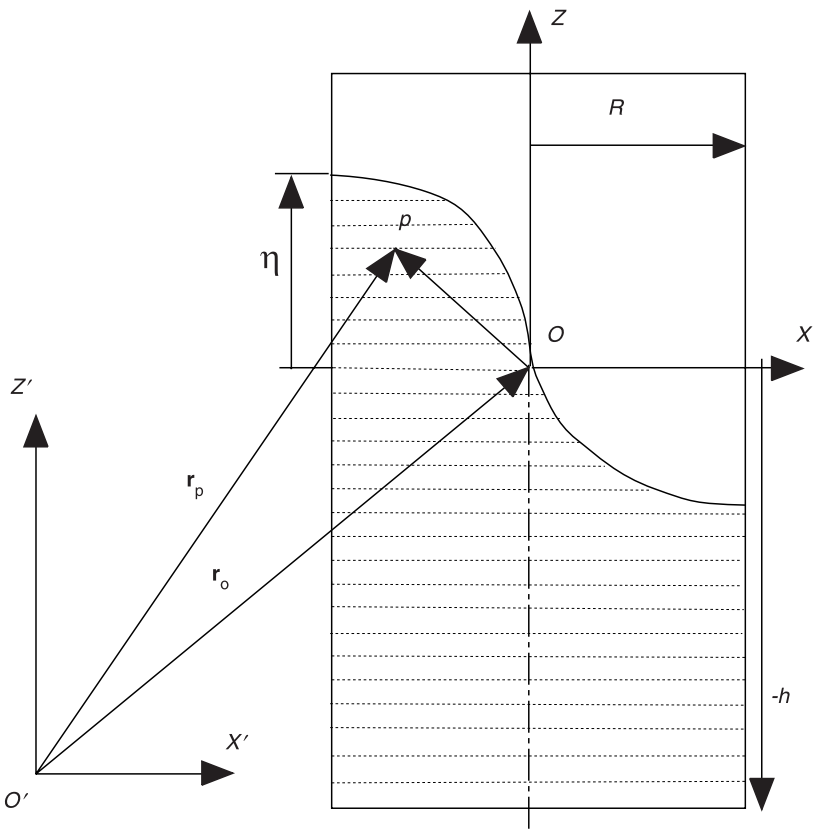


Figure 1 Fixed and moving coordinates for describing fluid particle motion.

coordinate frame in which the plane $O'X'Y'$ coincides with the undisturbed free fluid surface. For irrotational fluid motion there exists a velocity potential Φ function, whose negative gradient gives the fluid velocity, i.e.:

$$\mathbf{q} = -\boldsymbol{\nabla}\Phi \qquad [1]$$

where:

$$\boldsymbol{\nabla} = \frac{\partial}{\partial r}\mathbf{i}_r + \frac{l}{r}\frac{\partial}{\partial \theta}\mathbf{i}_\theta + \frac{\partial}{\partial z}\mathbf{i}_z$$

for cylindrical coordinates or:

$$\nabla = \frac{\partial}{\partial x}\mathbf{i} + \frac{\partial}{\partial y}\mathbf{j} + \frac{\partial}{\partial z}\mathbf{k}$$

for rectangular coordinates, and $\mathbf{q}$ is the fluid vector velocity.

Let $OXYZ$ be another coordinate frame fixed to the tank such that the OXY plane coincides with the undisturbed free surface. Let $\mathbf{V}_0$ be the velocity of the origin O relative to the fixed origin O'. The fluid particle velocity $\mathbf{q}_{\text{rel}}$ relative to the moving coordinates is given by:

$$\mathbf{q}_{\text{rel}} = \mathbf{q} - \mathbf{V}_0 = -\nabla\Phi - \mathbf{V}_0 \qquad [2]$$

The velocity potential function Φ can now be split into two functions: a disturbance potential function $\tilde{\Phi}$, which accounts for the fluid relative to the tank, and a potential function Φ_0, which defines the tank motion, i.e.:

$$\Phi = \tilde{\Phi} + \Phi_0 \qquad [3]$$

Both $\tilde{\Phi}$ and Φ_0 should satisfy Laplace's (continuity) equation:

$$\nabla^2\Phi = 0 \qquad [4]$$

The velocity of the tank:

$$\mathbf{V}_0 = \dot{X}_0\mathbf{i} + \dot{Z}_0\mathbf{k} \qquad [5a]$$

can also be expressed in terms of cylindrical coordinates as:

$$\mathbf{V}_0 = \left(\dot{X}_0 \cos\theta\right)\mathbf{i}_r - \left(\dot{X}_0 \sin\theta\right)\mathbf{i}_\theta + \dot{Z}_0\mathbf{i}_z \qquad [5b]$$

In this case, one can obtain Kelvin's equation for an unsteady flow:

$$\frac{P}{\rho} + \frac{1}{2}\left(\vec{\nabla}\tilde{\Phi}\vec{\nabla}\tilde{\Phi}\right) + \left(g + \ddot{Z}_0\right)Z + \ddot{X}_0 r\cos\theta - \frac{\partial\tilde{\Phi}}{\partial t} = 0 \qquad [6]$$

where ρ is the fluid density and g is the gravitational acceleration. Eqn [6] is the fluid field equation referred to the moving coordinate system that is moving with acceleration components $\ddot{X}_0$ and $\ddot{Z}_0$. The complete solution of eqn [4] must satisfy the relevant boundary conditions of the problem. These conditions are:

1. At the wetted rigid wall and bottom, the velocity component normal to the boundary must vanish.
2. At the free surface, the pressure is zero, which gives the dynamic free surface condition. It is obtained from eqn [6] after setting $P = 0$.
3. The kinematic free surface condition requires that the vertical velocity of a fluid particle located on the free surface should be the same as the vertical velocity of the free surface itself.

The solution of such boundary value problem for a rectangular tank is:

$$\tilde{\Phi}(X, Y, Z, t) = \sum_{m=0}^{\infty} \cdot \sum_{n=1}^{\infty} \alpha_{mn}(t) \cos\left(\frac{m\pi x}{a}\right) \times \cos\left(\frac{m\pi y}{b}\right)\cosh[k_{mn}(Z + h)] \qquad [7a]$$

where a and b are the tank width and breadth, respectively, and:

$$k_{mn} = \pi\sqrt{\frac{m^2}{a^2} + \frac{n^2}{b^2}}$$

m and n are positive integers.

For an upright circular container the velocity potential function takes the form:

$$\tilde{\Phi}(r, \theta, Z, t) = \sum_{m=0}^{\infty} \cdot \sum_{n=1}^{\infty} \alpha_{mn}(t) J_m(\lambda_{mn} r) \times \cos m\theta \frac{\cosh[\lambda_{mn}(Z + h)]}{\cosh\lambda_{mn} h} \qquad [7b]$$

where $J_m(.)$ is the Bessel function of the first kind of order m, $\lambda_{mn} = \xi_{mn}/R$ are the roots of $\partial J_m(\lambda_{mn} r)/\partial r|_{r=R} = 0$. An expression for the free surface elevation η can be written in the series form, for the rectangular tank:

$$\eta(X, Y, t) = \sum_{m=0}^{\infty} \cdot \sum_{n=1}^{\infty} A_{mn}(t) \cos\left(\frac{m\pi x}{a}\right) \cos\left(\frac{m\pi y}{b}\right) \qquad [8a]$$

and for the circular tank:

$$\eta(r, \theta, t) = \sum_{m=0}^{\infty} \cdot \sum_{n=1}^{\infty} A_{mn}(t) J_m(\lambda_{mn} r) \cos m\theta \qquad [8b]$$

The generalized coordinates α_{mn} and A_{mn} are time-dependent and obtained through satisfying the free surface conditions. Note that the time dependence of the wave height results in variation of the position of the container center of mass. Introducing the expressions (7) and (8) in the nonlinear fluid free surface boundary condition given by eqn [6] after setting $P = 0$ and the kinematic condition produces a major difficulty because of the high degree of nonlinearity of different modes. In order to get quantitative information, it appears essential to introduce approximation in the free surface equations. Note that the analysis can be significantly simplified if the fluid field equations are linearized. In this case, one can determine all dynamical parameters such as natural frequencies, mode shapes, hydrodynamic pressure, and sloshing forces and moments. Hydrodynamic pressure can be estimated in terms of the potential function using eqn [6]. The normal mode frequencies can be determined from the linearized free surface boundary condition:

$$\frac{\partial\tilde{\Phi}}{\partial t} + g\eta = 0 \qquad [9]$$

Substituting eqns [7] and [8] into [9] gives the natural frequencies, for a rectangular tank:

$$\omega_{mn}^2 = g k_{mn} \tanh(k_{mn} h) \qquad [10a]$$

and for a cylindrical container:

$$\omega_{mn}^2 = \frac{g\xi_{mn}}{R}\tanh(\xi_{mn} h/R) \qquad [10b]$$

Under forced sinusoidal excitation $\delta\cos\Omega t$ along $\theta = 0$, the total force exerted by the fluid on to the tank walls, for a circular cylindrical tank, is estimated by integrating the hydrodynamic pressure over the wetted area and the force along the x-axis is:

$$F_x(t) = M\delta\,\Omega^2 \sin\Omega t \times \left\{1 + \sum \frac{R/h}{\xi_{mn}} \frac{\Omega^2}{(\omega_{mn}^2 - \Omega^2)} \frac{2\tanh(\xi_{mn}h/R)}{(\xi_{mn}^2 - 1)}\right\} \quad [11]$$

where M is the total mass of the liquid. The liquid sloshing force given by expression [11] is accurate as long as the excitation frequency is not close to the liquid natural frequency. Near resonance, one should perform nonlinear analysis.

Parametric Sloshing

In 1831, Faraday observed that the fluid inside a glass container oscillates at one-half of the external vertical excitation frequency. Generally, the liquid free surface dynamics under parametric excitation is described by the system of Mathieu equations:

$$\frac{d^2A_{mn}}{dt^2} + 2\zeta_{mn}\omega_{mn}\frac{dA_{mn}}{dt} + \omega_{mn}^2(1 - 2Z_0\cos\Omega t)A_{mn} = 0 \quad [12a]$$

where A_{mn} is a nondimensional wave height parameter, ω_{mn} and ζ_{mn} are the sloshing mode natural frequency and damping ratio, respectively, Ω is the excitation frequency, and Z_0 is the excitation amplitude parameter. Depending on the excitation amplitude, frequency, and damping ratio the solutions of eqn [12a] can be stable or unstable. The regions of instability are given by the inequality:

$$1 - \sqrt{Z_0^2 - 4\zeta_{mn}^2\omega_{mn}^2} < \left(\frac{\Omega}{2\omega_{mn}}\right)^2 < 1 + \sqrt{Z_0^2 - 4\zeta_{mn}^2\omega_{mn}^2} \quad [12b]$$

It can be shown that if the plane free surface is unstable, the resulting motion could have frequency $k/2$ times the excitation frequency, where k is an integer. Thus, the motion might be a half-frequency subharmonic, harmonic, or superharmonic; however, experimental results usually show the half-frequency subharmonic. In most real fluids, there is sufficient damping such that the unstable regions, except the first several unstable ones, will be located completely above threshold excitation amplitude.

Eqn [12a] is adequate to predict the stability of fluid motion. However, it fails to give a unique bounded solution for the liquid response wave amplitude. In this case, it is important to include the liquid free surface nonlinearity. The modern theory of nonlinear dynamics has attracted several investigators to revisit the problem of parametric excitation of liquid in closed containers. The most interesting phenomena, including chaotic behavior, are due to internal resonance, which occurs when the ratios of natural frequencies of two or more modes of motion are near some small positive integers. In the case of a nearly square container, all the nonsymmetric modes have nearly equal natural frequencies independent of the fluid depth. The liquid free surface may be capable of exhibiting periodic and quasiperiodic standing, as well as traveling waves.

Under parametric random excitation, one can determine the stochastic stability of the liquid free surface in terms of mean square response or sample (with probability one) stability analysis. The linear stability analysis is based on the stochastic differential equation of the sloshing mode mn, i.e.:

$$a_{mn}'' + 2\zeta_{mn}a_{mn}' + \left[1 + \xi''(\tau)\right]a_{mn} = 0 \quad [13]$$

where a_{mn} is a dimensionless liquid free surface amplitude of mode mn, a prime denotes differentiation with respect to the nondimensional time parameter $\tau = \omega_{mn}t$, ω_{mn} is the natural frequency of the sloshing mode mn, ζ_{mn} is the corresponding damping ratio, and $\xi''(\tau)$ is a dimensionless vertical random acceleration of spectral density $2D$. The mean-square stability of the response of eqn [13] is given by the condition:

$$D/2\zeta_{mn} < 1 \quad [14a]$$

On the other hand, the sample stability condition is:

$$D/2\zeta_{mn} < 2 \quad [14b]$$

It was observed experimentally that the liquid free surface might follow one of the following regimes:

1. Zero liquid free surface motion, characterized by a delta Dirac function of the response probability density function. The excitation spectral density of this regime is so weak that it overcomes the liquid damping force.
2. Uncertain zero-motion of the liquid free surface, characterized by occasional small surface oscillations.
3. Partially developed (or intermittent) random liquid sloshing, characterized by the occurrence of significant liquid-free surface motion for a certain period of time which then ceases for another period of time. At higher excitation spectral density, the time period of liquid motion exceeds the time of zero motion.

4. Fully developed random sloshing. This regime exhibits continuous random liquid motion for all excitation levels, exceeding the afore-mentioned ranges. When the first symmetric sloshing mode is excited, other higher sloshing modes are excited as well. This is why the bandwidth of the symmetric mode excitation is narrow.

Equivalent mechanical models are useful in solving the complete dynamic problem of a system containing liquid. They can be incorporated in the overall dynamic analysis liquid tanks. This will be discussed in the next section.

Equivalent Mechanical Models

Experimental and analytical studies of liquid sloshing in different containers revealed that approximately the lower third of the liquid behaves essentially as a rigid mass, while most of the sloshing effects occur near the surface. This is in fact the basis upon which the idea of equivalent mechanical models are developed. A realistic representation of the liquid dynamics inside closed containers may be introduced by an equivalent mechanical system. The equivalence is taken in the sense of equal resulting forces and moments acting on the tank wall. The characteristics of the models are determined only from consideration of fluid motion in a stationary tank. Dashpot elements can also be incorporated to account for energy dissipation. The principles of constructing a mechanical model are based on satisfying the following conditions:

1. The equivalent masses and moments of inertia must be preserved.
2. The center of gravity must remain the same for small oscillations.
3. The system must possess the same modes of oscillations and produce the same damping forces.
4. The force and moment components under certain excitation of the model must be completely equivalent to that produced by the actual system.

Generally, the liquid hydrodynamic pressure in moving rigid containers is comprised of two distinct components. One component is directly proportional to the acceleration of the tank. This component is caused by part of the fluid moving in unison with the tank. The second component is known as convective pressure and experiences sloshing at the free surface. This component can be modeled by a set of mass spring-dashpot systems or by a set of pendulums. For the first liquid sloshing mode, an equivalent pendulum may be used. Three dynamic regimes are possible, as demonstrated in **Figure 2**:

1. Small oscillations, in which the fluid free surface remains planar without rotation of its nodal diameter (**Figure 2A**). This regime can be described by a linear equation for the first asymmetric sloshing mode which is equivalent to a pendulum describing small oscillations such that $\sin\theta \approx \theta$.
2. Relatively large amplitude oscillations, in which the liquid free surface experiences both nonplanar and rotational motions (**Figure 2B**). This regime is described by a differential equation with weak nonlinearity and can be analyzed using the standard perturbation techniques. The equivalent mechanical model is a simple pendulum describing relatively large motions such that $\sin\theta \approx \theta - \theta^3/3!$.
3. Strongly nonlinear motion, where the nonlinearity is mainly due to rapid-velocity changes associated

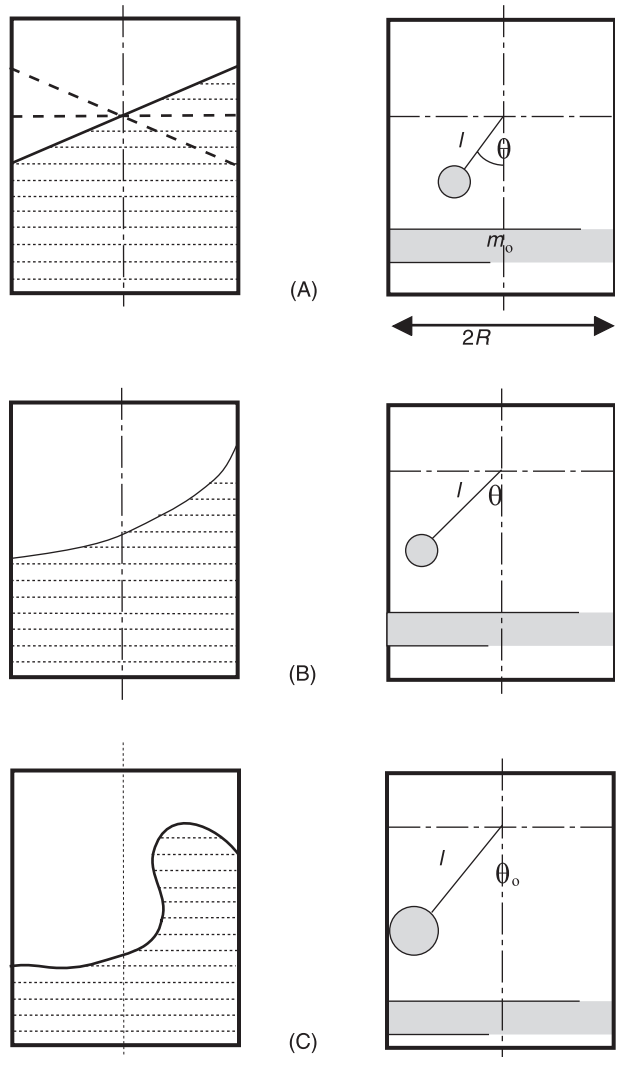


Figure 2 Regimes of liquid-free surface motion and their modeling. (A) Linear modeling; (B) weakly nonlinear modeling; (C) hydrodynamic impact modeling.

with hydrodynamic pressure impacts of the liquid motion close to the free surface (**Figure 2C**). The velocity changes of the liquid free surface are usually treated as being instantaneous (velocity jumps) and they lead to various strongly nonlinear features of the system behavior. The equivalent mechanical model of this regime is a pendulum describing impacts with the tank walls.

Expressions for the sloshing forces and moments are available for a number of simple tank shapes, such as rectangular, cylindrical, and ellipsoidal.

Model Parameters for Rectangular Tank

For a rectangular tank with cross-section dimension $a \times b$, and liquid depth h, the liquid free surface wave height $\eta(x, y)$ and natural frequencies ω_{mn} are given by the following expressions:

$$\eta(x,y) = \sum_{m=0}^{\infty}\sum_{n=0}^{\infty} A_{mn} \cos\left[\frac{m\pi}{a}x\right] \cos\left[\frac{n\pi}{b}y\right] \quad [15a]$$

$$\omega_{mn}^2 = g\pi\sqrt{\left(\frac{m^2}{a^2}+\frac{n^2}{b^2}\right)}\tanh\left(\pi\sqrt{\left(\frac{m^2}{a^2}+\frac{n^2}{b^2}\right)h}\right) \quad [15b]$$

where m and n are integers, and a and b are the tank width and breadth, respectively. For specific tank dimensions $a \times b$ the liquid natural frequencies increase with the liquid depth up to $h/a = 1$; then it becomes almost constant as the liquid depth increases.

The pendulum model For the pendulum model shown in **Figure 3**, each pendulum represents one sloshing mode. A rigidly attached mass is chosen to represent the effect of the liquid that moves in unison with the tank as a frozen mass. By comparing the expression of hydrodynamic force due to lateral excitation of the tank and the total force expression due to the system of pendulums and the rigid mass, the following model parameters are obtained:

$$\begin{aligned} m_n &= \frac{8\rho b a^2}{(2n-1)^3\pi^3}\tanh(2n-1)\frac{\pi h}{a} \\ m_0 &= \rho abh - \sum_{n=1}^{\infty} m_n \\ \ell_n &= \frac{a}{(2n-1)\pi}\coth(2n-1)\frac{\pi h}{a} \\ H_n &= \ell_n + \frac{h}{2} - \frac{2a}{(2n-1)\pi}\tanh(2n-1)\frac{\pi h}{a} \end{aligned} \quad [16]$$

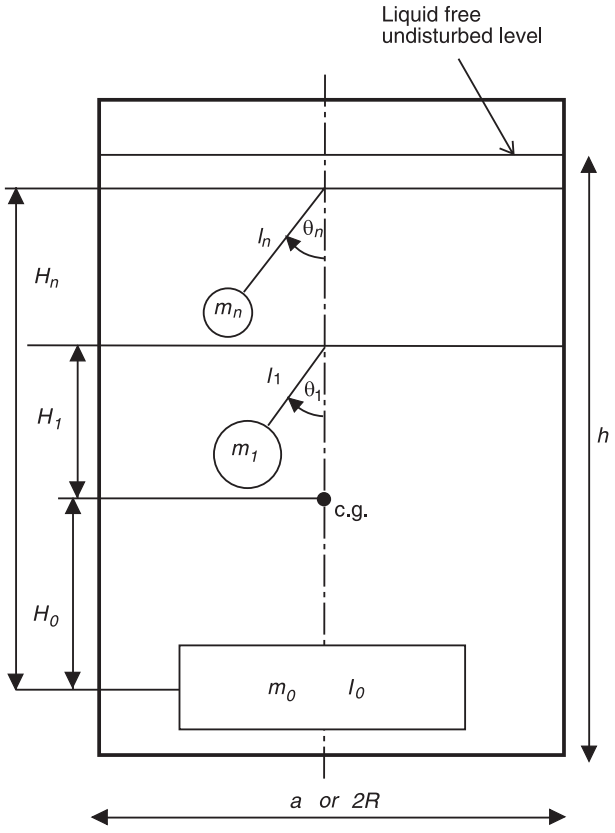


Figure 3 Pendulum equivalent modeling.

Similarly, the resulting moment about the center of mass yields the following constants.The mass moment of inertia of the frozen mass is:

$$I_0 = I_F - m_0 H_0^2 - \sum_{n=1}^{\infty} m_n (H_n - \ell_n)^2 \quad [17a]$$

I_F is the fluid mass moment of inertia given by the expression:

$$I_F = \left\{\rho abh\frac{h^2}{12} + \frac{a^2}{16} - 2a^2\sum_{n=1}^{\infty}\frac{16}{(2n-1)^4\pi^4} \times \left[1 - \frac{2a}{(2n-1)\pi h}\tanh(2n-1)\frac{\pi h}{2a}\right]\right\} \quad [17b]$$

With reference to **Figure 3**, m_n is the nth pendulum mass, and l_n represents the nth pendulum length. H_0 is the distance of the tank center of mass to the center of mass of the frozen fluid portion of mass m_n. H_n is the distance of the nth pendulum support point to the tank center of mass.

The mass spring model The parameters of mass spring equivalent model shown in **Figure 4** are:

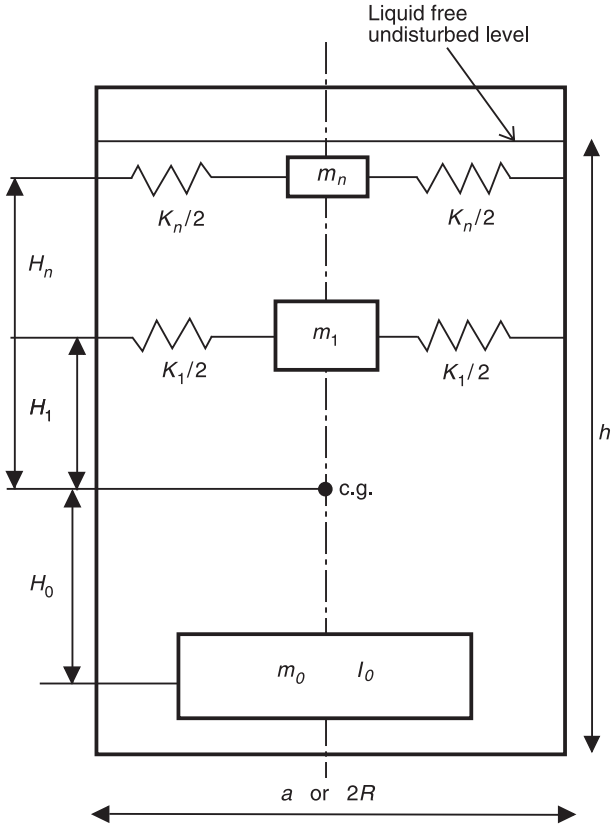


Figure 4 Mass spring equivalent modeling.

$$K_n = \frac{8\rho g a b}{\pi^2}\left(\tanh\frac{\pi(2n-1)h}{a}\right)^2$$
$$m_n = \frac{8\rho a^2 b}{\pi^2(2n-1)}\tanh\left((2n-1)\frac{\pi h}{a}\right)$$
$$m_0 = m_T - \sum_{n=1}^{\infty} m_n$$

where m_T is the total mass of the liquid:

$$H_n = \frac{h}{2} - \frac{2a}{(2n-1)\pi}\tanh\left((2n-1)\frac{\pi h}{2a}\right)$$
$$H_0 = \frac{1}{m_0}\sum_{n=1}^{\infty} m_n H_n \qquad [18]$$

for one mass spring equivalent modeling:

$$I_0 + m_0\left(H_0 - \frac{h}{2}\right)^2 + m_1\left(\frac{h}{2} - H_1\right)^2 = \frac{m_T}{12}(h^2 + a^2) \times \left[1 - \frac{4a^2}{a^2+h^2} + \frac{2.52a^3}{ha^2+h^3}\tanh 1.57\frac{h}{a}\right]$$

For n sloshing modes, the dependence of the mass moment of inertia I_0 on the fluid depth ratio h/a is shown in **Figure 5**, or given by the following discrete values:

$$I_0 + m_0 H_0^2 + \sum_{n=1}^{\infty} m_n H_0^2 = \begin{cases} 1.0 & \text{for } h/a = 0 \\ 0.45 & \text{for } h/a = 0.5 \\ 0.17 & \text{for } h/a = 1.0 \\ 0.45 & \text{for } h/a = 2.0 \end{cases} \qquad [19]$$

Model Parameters for Cylindrical Tank

The liquid free surface wave height and natural frequencies of a circular upright tank are, respectively:

$$\eta(r,\theta) = \sum_{m=0}^{\infty}\sum_{n=0}^{\infty} A_{mn}\sin(m\theta) \times \cosh(\xi_{mn}h/R)J_m(\xi_{mn}r/R) \qquad [20a]$$

$$\omega_{mn}^2 = \frac{g\xi_{mn}}{R}\tanh(\xi_{mn}h/R) \qquad [20b]$$

where R is the tank radius.

The same mechanical models shown in **Figures 3** and **4** are also applied to the cylindrical tank with radius R. With reference to **Figure 3**, and for both models the following parameters are common:

$$m_T = \pi\rho R^2 h \qquad I_{\text{rigid}} = 4m_T R^2\left[\frac{1}{12}\left(\frac{h}{2R}\right)^2 + \frac{1}{16}\right]$$

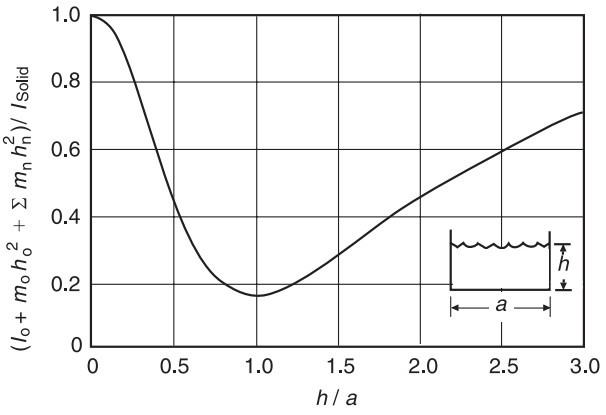


Figure 5 Ratio of effective liquid to rigid moment of inertia as function of liquid depth ratio for rectangular tanks. From Abramson HN (ed.) (1966) *The Dynamic Behavior of Liquids in Moving Containers*. SP 106. NASA.

$$I_0 + m_0 H_0^2 + m_1 (H_1 + NL_1)^2 = I_{\text{rigid}} + m_T \left(\frac{h}{2}\right) - \frac{m_T R^2}{2} \times \left[1.995 - \frac{2R}{h}\left(\frac{1.07 \cosh 1.84(h/R) - 1.07}{\sinh 1.84(h/R)}\right)\right] \quad [21]$$

The pendulum model

$$L_1 = \frac{d}{3.68} \coth 3.68 \frac{h}{d}$$

$$m_1 = m_T \left(\frac{d}{4.4h}\right) \tanh 3.68 \frac{h}{d}$$

$$m_0 = m_T - m_1 \qquad \ell_1 = -\frac{d}{7.36} \cosh 7.36 \frac{h}{d}$$

$$\ell_0 = \frac{m_T}{m_0}\left[\frac{h}{2} - \frac{d^2}{8h}\right] - (\ell_1 + L_1)\frac{m_1}{m_0} \quad [22]$$

The mass spring model

$$K_1 = m_T \left(\frac{g}{1.19h}\right)\left(\tanh 3.68 \frac{h}{d}\right)^2$$

$$m_1 = m_T \left(\frac{d}{4.4h}\right) \tanh 3.68 \frac{h}{d}$$

$$m_0 = m_T - m_1 \qquad \ell_1 = \frac{d}{3.68} \tanh 3.68 \frac{h}{d} \quad [23]$$

$$\ell_0 = \frac{m_T}{m_0}\left[\frac{h}{2} - \frac{d^2}{8h}\right] - \ell_1 \frac{m_1}{m_0}$$

$$h_0 = h_{cg} + \frac{1}{m_0}\sum_{n=1}^{\infty} (h_n + h_{cg}) m_n$$

$$h_{cg} = \frac{3L}{4}\left[\frac{(2 - h/L)^2}{3 - h/L}\right] \quad [24]$$

The mass moment of inertia of a rigid body I_{rigid}, having the same shape and mass of the liquid, is:

$$I_{\text{rigid}} = \pi \rho R^4 L \times \left\{ \frac{h^4}{R^2 L^2}\left[\frac{5 - h/L}{30} - \frac{(4 - h/L)^2}{48(3 - h/L)}\right] + \frac{h^3}{L^3}\left[\frac{1}{3} - \frac{h}{4L} + \frac{h^2}{20L^2}\right]\right\} \quad [25]$$

Since the fluid is not rigid, the above relation overestimates the mass moment of inertia of the fluid. The actual moment of inertia can be obtained by determining the ratio of the actual liquid to rigid liquid moment of inertia for a cylindrical tank having an identical fluid height and fluid mass, which is shown in **Figure 6**.

The previous models are very useful in studying the problem of linear sloshing dynamics. For nonlinear sloshing, the amplitude of motion of these elements can be extended to include the model inherent nonlinearities. The nonlinear rotational motion of the liquid free surface can be understood by studying the stability of the forced excitation of the spherical pendulum.

Damping of Liquid Sloshing

Liquid sloshing is usually associated with some energy dissipation due to the effect of boundary layers with the tank walls. Under free oscillations, the motion of the liquid free surface decays due to damping forces created by viscous boundary layers. It is necessary to measure the reduction of the peak of hydrodynamic forces during forced oscillations. The boundary layers approximation techniques can be applied to the case of standing waves where viscous dissipation in an assumed laminar boundary layer is taken to be the primary cause of damping. The analysis is in principle based on successive approximation of the vector potential function **A** such that the velocity vector is given in the Helmholtz form:

$$\mathbf{V} = -\nabla \mathbf{\Phi} + \nabla \times \mathbf{A} \quad [26]$$

where the first expression stands for the velocity component due to the irrotational flow, while the second takes into account the effect of rotational flow

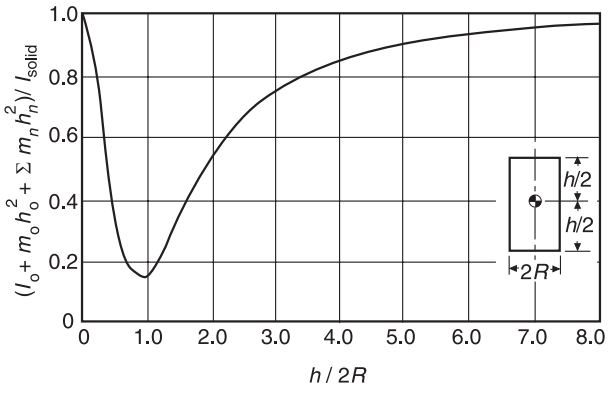


Figure 6 Ratio of effective liquid to rigid liquid moment of inertia as function of liquid depth ratio for cylindrical tasks. From Abramson HN (ed.) (1966) *The Dynamic Behavior of Liquids in Moving Containers*. SP 106. NASA.

adjacent to the walls. Note that the normal velocity at the boundaries must vanish, i.e., $-\nabla\Phi + \nabla \times \mathbf{A} = 0$. Most of the damping takes place at the rigid walls and the damping in a circular cylinder is only 18% less than that for a square tank of the same cross-sectional area. The complete analysis of liquid damping in circular cylindrical containers was developed by Case and Parkinson.

It is not difficult to measure the logarithmic decrement of the first asymmetric sloshing mode. Basically, the damping factor depends on the liquid height, liquid kinematic viscosity, and tank diameter (or tank width for rectangular cross-section). Dimensional analysis and empirical correlations showed that the damping ratio in a circular cylindrical tank is given by the empirical relationship:

$$\zeta = \frac{2.89}{\pi}\sqrt{\frac{\nu}{R^{3/2}g^{1/2}}} \times \left[1 + \frac{0.318}{\sinh\,(1.84h/R)}\left(\frac{1-(h/R)}{\cosh\,(1.84h/R)} + 1\right)\right] \quad [27a]$$

where ν is the kinematic viscosity, R is the tank radius, and g is the gravitational acceleration. For $h/R > 1$, relation [27a] takes the form:

$$\zeta = \frac{2.89}{\pi}\sqrt{\frac{\nu}{R^{3/2}g^{1/2}}} \quad [27b]$$

This relation can be generalized for other tank shapes:

$$\zeta = C_1\left(\frac{\nu}{d^{3/2}\sqrt{g}}\right)^{n_1} \quad [27c]$$

where d is the characteristic dimension of the tank, it is the width of rectangular containers, radius for cylindrical or spherical containers, or the radius of the free surface of an axisymmetric tank. The constant C_1 and the exponent n_1 take the values shown in **Table 1** for the corresponding tank geometry.

For other tank shapes it is recommended to use $C_1 \approx 1$ and $n_1 \approx 0.5$.

In order to minimize the sloshing hydrodynamic forces acting on the tank, it is desirable to suppress the liquid-sloshing amplitude. The inherent liquid viscosity in tanks without baffles will have a very limited effect in reducing the sloshing amplitude. Ring and cruciform baffles, floating lids and mats, and flexible baffles are very effective in liquid wave control. The effectiveness of damping devices should not be characterized by the amplitude decrement only. However, semiempirical relationships for the damping contributed by a flat annular ring baffle have been developed in the literature. The total damping of the fundamental antisymmetric mode is due to two main sources. The first is due to the relative motion between the liquid and the tank wall, while the second is due to the relative motion between the liquid and baffles. In considering the design of baffles, the total fluid sloshing force should not exceed a certain prescribed maximum value under all possible combinations of liquid level, tank orientation, and external tank excitation. Another important requirement is to suppress the sloshing effects throughout certain designated frequency ranges in which the liquid oscillations might reinforce the fundamental vibration mode of the vehicle. The flexible baffle might be more effective than rigid baffles for damping slosh in moving containers.

Table 1 Values of the constant C_1 and the exponent n_1 for varying tank shapes

Tank shape	C_1	n_1
Circular cylinder		
$h/R \geq 1.0$	0.79	0.5
$h/R \geq 0.5$	1.11	0.5
$h/R \geq 0.1$	3.36	0.5
Rectangular		
$h/w \geq 1$	~1.0	0.5
Spherical		
3/4 full	0.66	0.359
1/2 full	0.39	0.359
1/4 full	0.32	0.359
Upright conical	0.81	0.5

Liquid Sloshing in Road Tankers

The main problems which are of concern in the design of liquid propellant rockets include the motion of the center of mass, the vehicle attitude, and lateral bending of vehicle structure. The sloshing technology developed for space applications is not applicable to road tankers, because emphasis has been placed on frequencies and total forces as they relate to control system requirements, and, therefore, the effects of local peak impact pressure on structural requirements have not been studied to any extent. Further, the excitation amplitudes considered in space applications are too small for road vehicle simulation. In road tankers, the liquid free surface may experience large excursions for even very small motions of the container. This is an undesirable feature, which may considerably endanger the stability and maneuvering quality of the vehicle. This problem is common for fuel or cargo tanks of automotive vehicles, railroad tank cars, fuel tanks of large ships and tankers. The

study of liquid sloshing dynamics within a moving vehicle involves different types of modeling and analyses.

The forces and moments from the liquid load for harmonic oscillation steering are introduced via a mechanical model approach. Each compartment includes one rigid and one moving mass. It is speculated that liquid-carrying vehicles have more accidents than other vehicles in part because of the large movement of the liquid cargo, with the attendant forces and moments. Liquid sloshing during a highway maneuver can lead to lateral and roll instabilities, decreased controllability/maneuverability, and increased stress on tank structures.

When hydraulic jumps or traveling waves are present, extremely high impact pressures can occur on the tank walls in gasoline tankers and ship cargo tanks. The liquid sloshing can be more severe longitudinally than laterally if no transverse baffles are introduced. The longitudinal acceleration peaks are larger than the lateral ones. The liquid impact is probably much more severe to the structure for longitudinal than for lateral sloshing. The peak pressure on the end of the tank is strongly affected by the fill level and the tank length–diameter ratio. For a certain value, the pressure in the tank acted like either water hammer or an accelerated fluid column, depending on the duration of the impact relative to the pressure wave transient time.

The influence of large-amplitude liquid sloshing on the overturning and skidding stability of road tankers is very serious during dynamic maneuvers. Experimental investigations have been conducted to measure liquid sloshing force in laterally oscillated model tanks, with or without baffles and cross-walls. The effects of liquid forces on overturning and skidding tendencies were evaluated from simplified vehicle models (no roll, no yaw). The poorest lateral stability mainly arises due to a combination of two factors. The first is that the value of dynamic forces from liquid sloshing can reach twice the rigid load force. The second is that the liquid center of mass can experience large displacement, which may reach about 40 cm. The ratio between the center of mass height and effective width is often higher for heavy than for light tankers. This results in poor lateral stability and less capacity to perform escape maneuvers than for automobiles. The heavy vehicle often overturns for a less severe maneuver than what is required for skidding. In fact, poor overturning stability contributes to the skidding tendency due to lateral load transfer and nonlinear tire characteristics. The liquid impact loading is much more severe to the structure for longitudinal than for lateral sloshing.

When the steering frequency is close to the natural frequency of the liquid free surface, the liquid mass will act like a pendulum swinging with the vehicle. This will result in a distinct increase in load transfer and overturning risk factor. The overturning factor $\Re$ is defined by:

$$\Re = \left| 1 - \frac{F_l}{F_{lo}} \right| \qquad [28]$$

where F_l is the instantaneous wheel load on the left side, and F_{lo} is the static wheel load on the left side.

As $\Re \rightarrow 1$, the vehicle is close to inner wheel lift and overturning. $\Re$ depends on the lateral acceleration whose critical value, known as the overturning limit, is reached when $\Re = 1$.

If the steering frequency is greater than the natural frequency, the liquid pendulum motion will lag the tank motion. Close above resonance, this may be especially dangerous if the risk factor peak with sloshing load is close to its resonance level and therefore well above the corresponding peak for rigid loads. Above resonance the liquid will oscillate against the tank and stabilize the vehicle. Unfortunately, this stabilization is not effective in real practice because the actual high steering frequencies are very rare. Furthermore, the roll motions act like a low-pass filter, suppressing high-frequency motions in the chassis before they reach the tank.

Large liquid motion inside the tank will cause larger overturning moment due to pure displacement of the center of mass and larger overturning forces when the relative motion of the liquid is reversed by the tank wall. With reference to **Figure 7**, the side force coefficient (SC) has been defined by the expression:

$$SC = \frac{m_e a_\ell - F_v}{(m_e + m_l)g - F_z} \qquad [29]$$

where m_e is the empty vehicle mass, m_l is the liquid mass, F_y is the resultant force to the left from the liquid load, F_z is the resultant upward force from the load after subtracting the weight, and a_l is the lateral acceleration.

The overturning limits are compared for different tank partitions in **Figure 8. Figure 9** shows the side force coefficient skidding. Depending on tank cross-sectional shape, keeping the tank bottoms at the same level, the center height is more raised for the circular horizontal tank than for the elliptic tank. The overturning limit minimum value and the worst oscillation frequency are smaller for the elliptic tank than for the circular horizontal one.

Note that the liquid impact loading is not a smooth force and its treatment is not a simple task. The sloshing impact loading cannot be viewed as a single loading event since it can be repeated due to the inertia and restoring forces. Systems involving vibro impact with masses colliding with rigid or elastic barriers during their oscillations constitute a specific class of strongly nonlinear systems. The nonlinearity is mainly due to extremely rapid velocity changes during impact. These changes are usually treated as being instantaneous (velocity jumps) and they lead to various strongly nonlinear features of system behavior. If the system is linear with constant coefficients and is subjected to impact loading it will experience nonlinear behavior. Liquid pressure impacts are one of the sources of strong nonlinearity in a liquid tank system.

The liquid hydrodynamic forces can be simulated by the impact of an equivalent pendulum. The pendulum can reach the walls of the tank if its angle with the vertical axis is $\theta = \pm\theta_0$. One can phenomenologically describe the interaction between the pendulum and the tank walls with a special potential field of interaction, which is very weak in the region $|\theta| < \pm\theta_0$, but becomes fast-growing in the neighborhood of the points $|\theta| = \pm\theta_0$. For example, the desirable properties of the potential field can be provided by means of the following function of the potential energy:

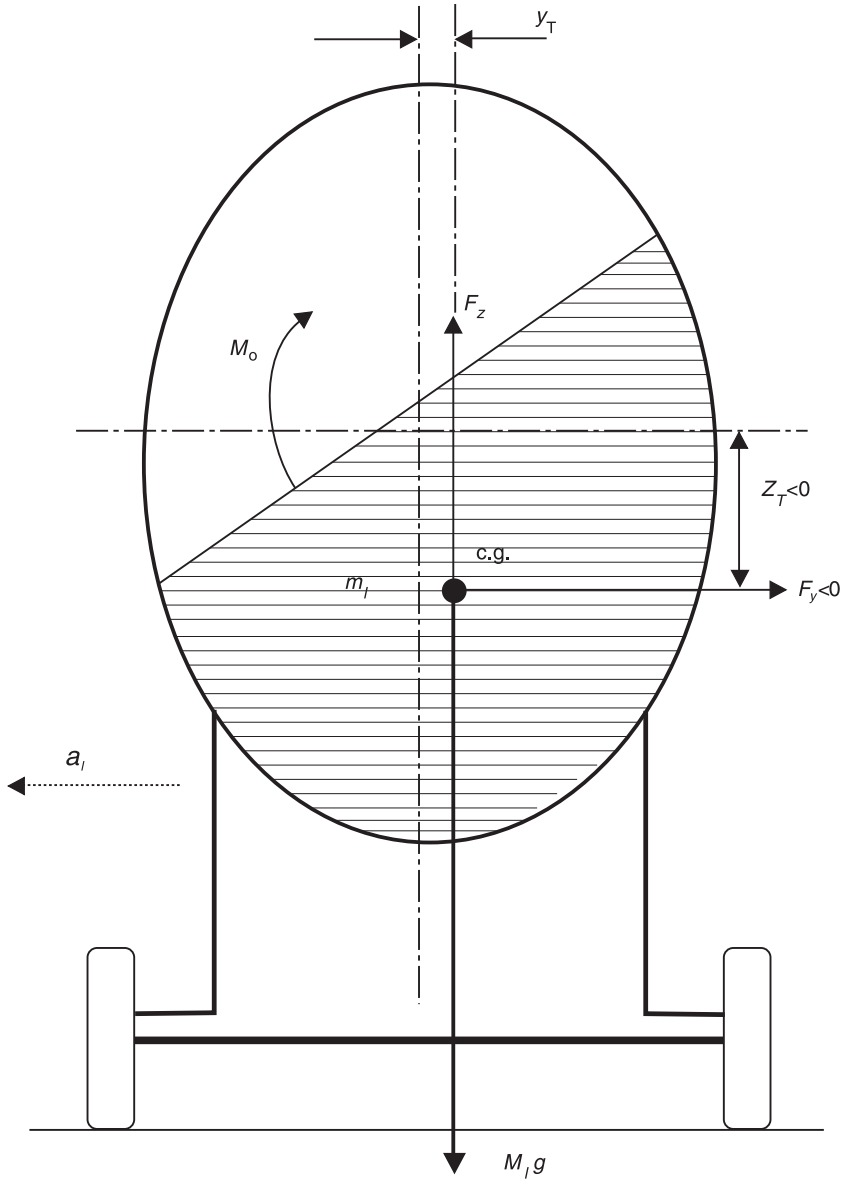


Figure 7 Schematic diagram of liquid displaced in a moving vehicle.

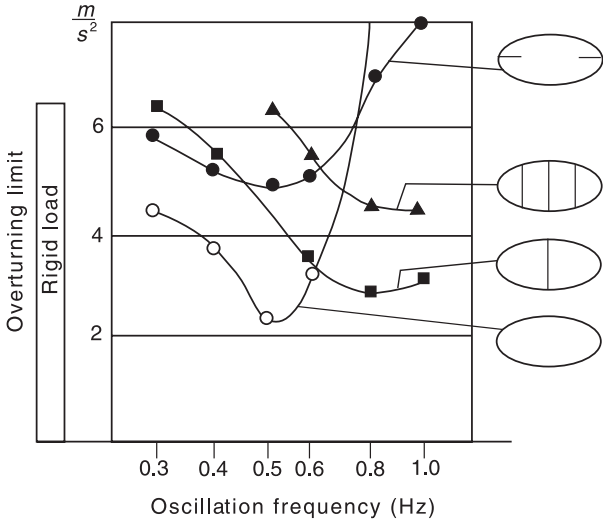


Figure 8 Dependence of overturning limits on the frequency for different tank baffles. From Strandberg (1978) *Lateral Stability of Road Tankers*, National Road and Traffic Research Institute Report 138A. Sweden, with permission.

$$\Pi_{\text{impact}} = \frac{b\theta}{2n}\left(\frac{\theta}{\theta_0}\right)^{2n} \qquad [30]$$

where $n \gg 1$ is a positive integer, and b is a positive constant parameter.

The force of interaction is:

$$F_{\text{impact}} = \frac{\mathrm{d}\Pi_{\text{impact}}(\theta)}{\mathrm{d}\theta} = b\left(\frac{\theta}{\theta_0}\right)^{2n-1} \qquad [31]$$

One has a limit of absolutely rigid bodies interaction, if $n \to \infty$. For this case, the potential energy (30) takes the square well form. If the exponent $2n - 1$ is large and finite, then the interaction field is not absolutely localized at the points $\theta = \pm\theta_0$. This means that the tank walls and the pendulum mass are not absolutely rigid, but admit a small deformation about the points of contact $\theta = \pm\theta_0$. Accordingly, a finite value of n seems more realistic than the rigid body limit; yet, the approach considered includes the rigid body limit as a particular case. **Figure 10** shows the force distribution across the tank for different values of n.

The energy dissipation of the pendulum basically results from the pendulum interaction with the container walls. This means that the dissipation is spatially localized around the points $\theta = \pm\theta_0$. The localized dissipative force will be approximated by the expression:

$$F_d = d\left(\frac{\theta}{\theta_0}\right)^{2p}\dot{\theta} \qquad [32]$$

where d is a constant coefficient, $p \gg 1$ is a positive integer (generally $p \neq n$), and a dot denotes differentiation with respect to time, t. Note that the constants b and d are determined experimentally. This modeling had been introduced into the equations of motion of a nonlinear system simulating liquid sloshing impact in tanks supported by an elastic structure.

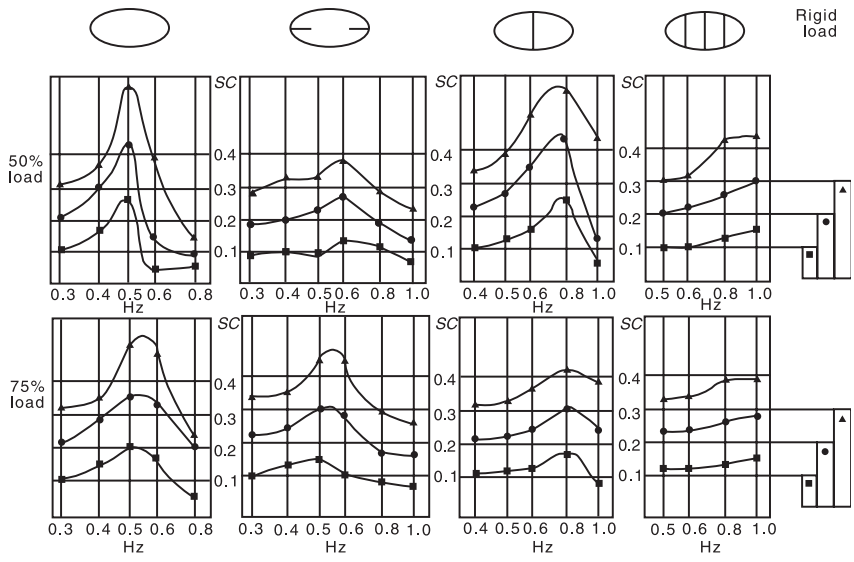


Figure 9 Side force coefficient (*SC*) as function of the oscillation frequency for different baffle settings. Later acceleration peaks: squares, 1 m s^{-2}; circles, 2 m s^{-2}; triangles, 3 m s^{-2}.

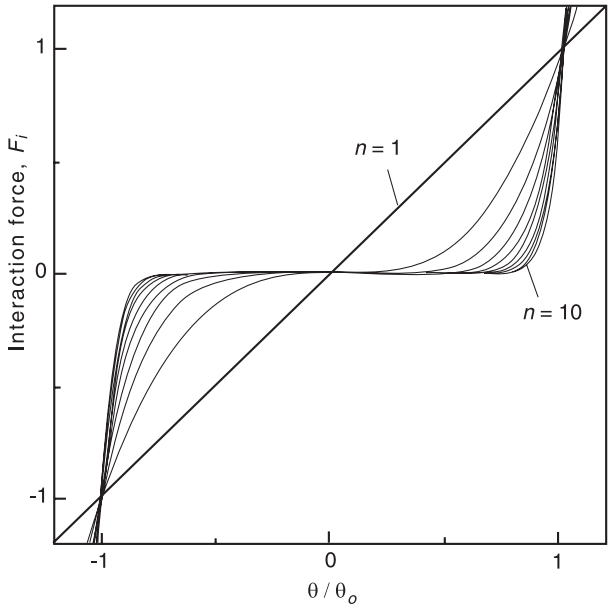


Figure 10 The force of impact between the tank walls and the pendulum for different values of the exponent n.

Sloshing under Low Gravitational Field

The liquid sloshing dynamics under microgravity involves different problems from those encountered under regular gravitational field. These problems include the reorientation of the liquid in its container and the difficulty of moving it since the body forces are almost negligible. Under microgravity, surface tension forces become predominant. The Bond number, given by the ratio of the gravitational to capillary forces, plays a major role in the liquid free surface characteristics. For very small values of the Bond number $\ll 1$, capillary forces predominate and the liquid free surface will not be any longer flat in its container, but will rise around its vertical walls. The Bond number for a cylindrical tank is defined by the expression $B_0 = \tilde{g}R^2/(\sigma/\rho)$, where $\tilde{g}$ is the equivalent gravitational acceleration (cm s^{-2}), R is the tank radius (cm), σ is the surface tension (dyn cm^{-1} or 10^{-5}N cm^{-1}), and ρ is the liquid density (g cm^{-3}). The experimental results of Salzman *et al.*, with 5 s free-fall facility, revealed that the value of the centerline liquid depth depends on the magnitude of the Bond number and the liquid volume. The maximum Bond number during a free-fall drop was 0.002, while most of free-fall drops result in Bond numbers close to 0.001. For deep liquid depth $h/R > 2$ and zero static contact angle, the following relationship was obtained empirically for the liquid first mode natural frequency ω_1:

$$\omega_1^2 = (2.6 + 1.84B_0)\frac{\sigma}{\rho R^3} \qquad [33]$$

where the constant 2.6 represents the capillary contribution to the lateral natural frequency. Eqn [33] reveals that capillary effects begin to appear for Bond numbers below about 20. The dependence of the nondimensional natural frequency $\Omega_1^2 = \omega_1^2 R^3/\beta$, where $\beta = \sigma/\rho$, on the Bond number parameter $(B_0 + 1.4)$ is plotted on a log–log graph, as shown in **Figure 11**. For shallow liquid depth $h/R < 2$ and for zero Bond number, the following relation may be used:

$$\omega_1^2 = \frac{2.6\beta}{R^3}\tanh\frac{2h}{R} \qquad [34]$$

The fundamental slosh-mode shape exhibited a similar dependence on Bond number. In the fundamental mode, the vertex of the liquid surface remains at the centerline of the cylinder and maximum displacement occurred at the cylinder wall.

The damping coefficient c was obtained in the form:

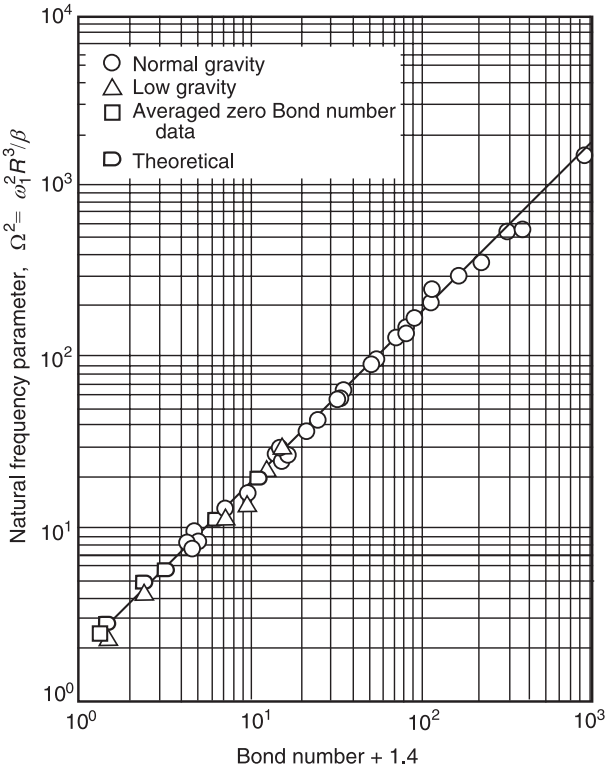


Figure 11 Dependence of liquid natural frequency of the Bond number for liquid depth ratio >2. From Salzman JA, Labus TL and Masica WJ (1967) *An Experimental Investigation of the Frequency and Viscous Damping of Liquids During Weightlessness*. TN D-4132. NASA.

$$\frac{c}{(c)_{B_0=0}} = \frac{1}{35.7} K_d (2.6 + 1.8B_0)^{1/4} \qquad [35]$$

where:

$$(c)_{B_0=0} = \frac{28.1}{2\pi} \sqrt{\frac{\mu}{\rho R^2}} \left(2.6 \frac{\sigma}{\rho R^3}\right)^{1/4}$$

is the damping coefficient at zero Bond number, K_d is an explicit function of Bond number, and μ is the liquid viscosity. The measured results showed that the normalized damping coefficient $c/(c)_{B_o} = 0$ tends to remain constant for all Bond numbers below 100. The decrease in the natural frequency compensates for the increase in the damping coefficient. For identical radii and liquids, the damping coefficient c is relatively independent of acceleration in the Bond number region from about 0 to 100.

Remarks

Liquid containers constitute major components in a number of multibody systems such as aerospace vehicles, road tankers, and liquefied natural gas carriers. Unfortunately, the basic theory of multibody dynamics does not take into account the effect of liquid sloshing loads on the overall system dynamics. Furthermore, the available multibody dynamics codes cannot handle systems with liquid containers.

There is no doubt that the modern theory of dynamics has promoted our understanding of liquid free surface motion under different types of parametric and internal resonance conditions. Finite element and boundary element algorithms have been developed to determine the hydroelastic coupling of elastic tank with the liquid free surface dynamics. The most significant contributions have dealt with the influence of sloshing loads on the stability and behavior of moving liquid tankers, ships, liquid storage subjected to earthquakes, and near zero-gravity liquid behavior.

Few attempts have considered some random excitation of liquid tanks and predicted stochastic stability boundaries under random parametric excitation. The difficulty arises when the excitation spectral density exceeds a certain level, above which other sloshing modes exist, and the liquid may experience other different regimes such as large-amplitude motion and surface disintegration. This problem may be understood by studying the stochastic bifurcation of the liquid surface motion regimes and Monte Carlo simulation of nonlinear coupled modes. The stochastic analysis needs further studies under regular and microgravitational fields in order to establish the possibility of stabilizing the free surface through a multiplicative noise.

Nomenclature

a	tank width
b	tank breadth
F	force
g	gravitational acceleration
h	liquid depth
I	inertia
M_T	total mass
$\mathbf{q}$	fluid vector velocity
R	tank radius
$\Re$	overturning factor
ν	kinematic velocity
Z_0	excitation amplitude parameter
ρ	fluid density
Ω	excitation frequency

See also: **Parametric excitation**; **Viscous damping**.

Further Reading

Abramson HN (ed.) (1966) *The Dynamic Behavior of Liquids in Moving Containers*. SP 106. NASA.

Case KM and Parkinson WC (1957) Damping of surface waves in an incompressible liquid. *Journal of Fluid Mechanics* 2:172–184.

Clark LV and Stephens DG (1967) Simulation and scaling of low-gravity slosh frequencies and damping. In: *Second ASTM, IES and AIAA Space Simulation Conference*. ASTM, pp. 43–49.

Dodge FT and Garza LR (1967) *Simulated Low-gravity Sloshing in Cylindrical Tanks Including Effects of Damping and Small Liquid Depth*. Technical Report no.5. Contract NAS8-20290, pp. 1–32. NASA.

Ibrahim RA (1985) *Parametric Random Vibration*. New York: John Wiley.

Ibrahim RA and Heinrich RT (1988) Experimental investigation of liquid sloshing under parametric random excitation. *ASME Journal of Applied Mechanics* 55: 467–473.

Ibrahim RA, Pilipchuk VN and Ikeda T (2001) Recent advances in liquid sloshing dynamics. *ASME Applied Mechanics Review* 54(2): 133–199.

Lamb H (1945) *Hydrodynamics*. Cambridge: Cambridge University Press.

Pilipchuk VN and Ibrahim RA (1997) The dynamics of a nonlinear system simulating liquid sloshing impact in moving structures. *Journal of Sound and Vibration* 205:593–615.

Salzman JA, Labus TL and Masica WJ (1967) *An Experimental Investigation of the Frequency and Viscous Damping of Liquids During Weightlessness*. TN D-4132. NASA.

Standberg L (1978) *Lateral Stability of Road Tankers*. National Road and Traffic Research Institute Report 138A. Sweden.

Thomson MM (1965) *Theoretical Hydrodynamics*. New York: MacMillan.

LOCALIZATION

C Pierre, University of Michigan, Ann Arbor, MI, USA

Copyright © 2001 Academic Press

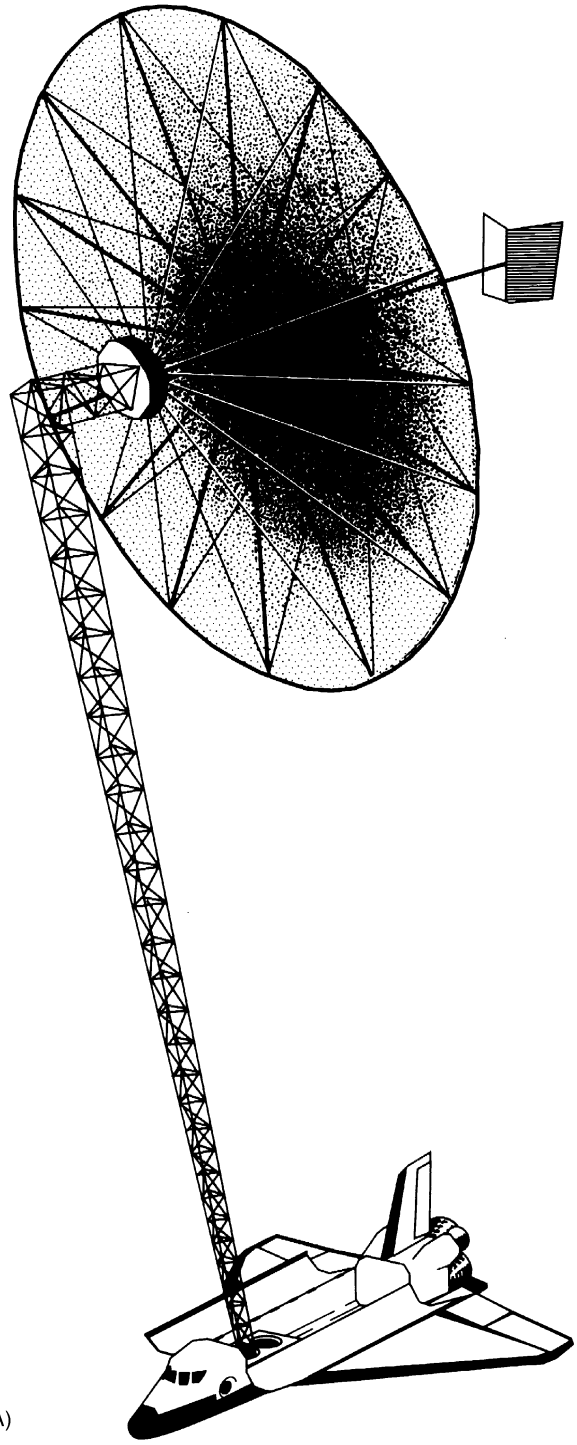
doi:10.1006/rwvb.2001.0099

Introduction

It is common practice in engineering to analyze the dynamics of periodic structures by assuming perfect regularity. A periodic system consists of an assembly of identical subsystems, or bays, repeated along one or more spatial directions, and coupled in some identical fashion. Typical examples of periodic structures are truss beams, rib antennas, and turbomachinery blade assemblies, as depicted in **Figure 1**. The analysis of these structures is considerably simplified by the assumption of perfect periodicity, essentially because this allows one to reduce the size of the problem to that of one substructure. For example, for a perfectly cyclic turbomachinery rotor such as that in **Figure 1B**, one simply needs to model a single sector of the disk, along with the corresponding attached blade, and carry out vibration analysis of this reduced model for various phase boundary conditions between adjacent sectors – a tremendous computational saving compared to a full-bladed disk analysis. In reality, however, departure from periodicity always occurs because of manufacturing and material tolerances, imperfect joints, in-service degradation, and other structural defects. These periodicity destroying irregularities, which are also referred to as disorder, or mistuning, are typically small, and one would expect their effect on dynamics of nearly periodic structures to be small as well. Nevertheless, under certain circumstances, irregularities have the potential to alter the vibrational response drastically, in a qualitative fashion, thereby resulting in a phenomenon known as normal mode localization. This is the topic of this article.

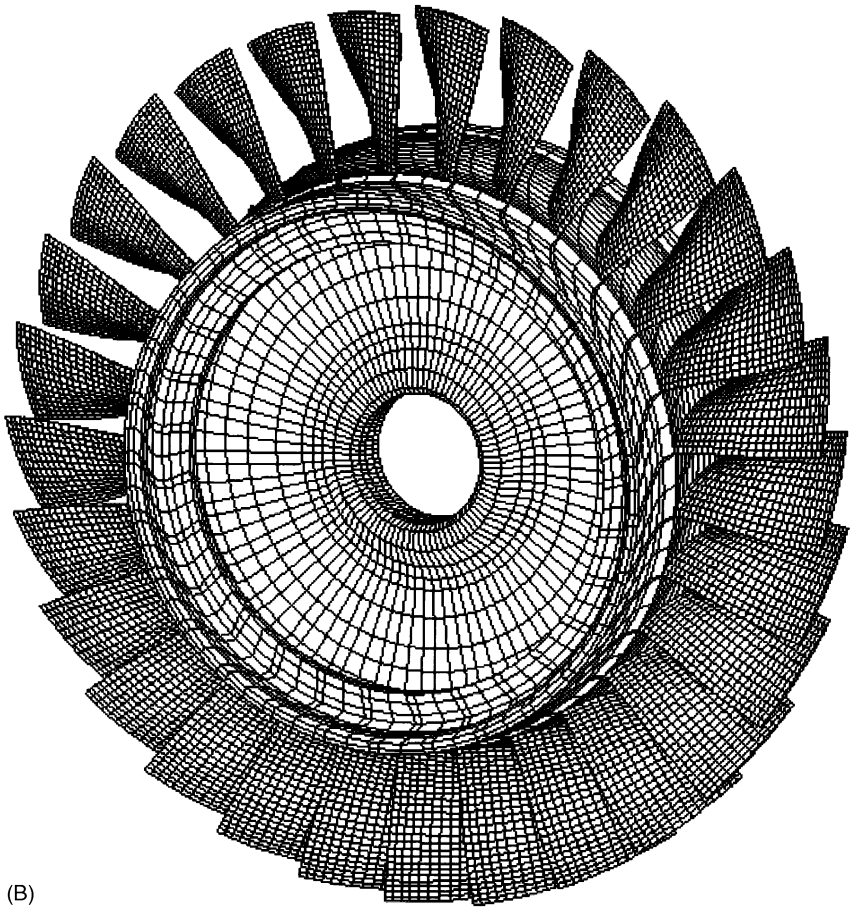
Intuitive Interpretation of Mode Localization

Consider the periodic structure shown in **Figure 2**. It consists of a one-dimensional chain of single-degree-of-freedom oscillators, coupled through identical linear springs. Note that this simple periodic structure can be generalized, at least conceptually, to one featuring periodicity in two or even three dimensions, with bays (or substructures) that possess many



(A)

Figure 1 Examples of periodic engineering structures. (A) A periodic truss beam with a cyclic radial rib antenna.



(B)

Figure 1 contd. A cyclic turbomachinery bladed disk assembly (compressor stage).

degrees-of-freedom, and with adjacent bays that are coupled through multiple coupling coordinates, thus indicating that periodic structures can be fairly complex. The structure in **Figure 2A** is said to be ordered, or tuned, if all oscillators are identical. One can easily calculate, in closed form, the linear modes of free vibration of the perfectly periodic system. These mode shapes, three of which are shown in **Figure 2B** for a 10-oscillator system, are sinusoidal in space. They feature the participation of the entire structure in the motion, and thus are referred to as extended modes. One can show that the modes of the perfectly periodic system are always extended, even for arbitrarily small, however nonzero, coupling between the oscillators. Now consider the corresponding disordered, or mistuned, structure shown in **Figure 2C**. It features slightly dissimilar oscillators with random natural frequencies. (Note that the disorder has been exaggerated in the figure; typically, unavoidable structural irregularities of a few percent or smaller are considered in engineering localization studies.) Typical modes for the disordered system are shown in **Figure 2D**. One immediately notices that the vibration modes have completely changed character with the introduction of disorder. The modes no longer extend throughout the structure as in the ordered case, but rather each mode shape primarily features the vibration of a single oscillator and a limited participation of the neighboring ones. These mode shapes are said to be spatially localized. Note how the three modes shown are localized about three different oscillators, a feature that would also hold for the other seven modes of the system.

This simple example demonstrates that the introduction of a small disorder can alter the free dynamics of a periodic structure in a fundamental, qualitative way. Clearly, the effects of disorder are not always as dramatic, but mode shapes with an arbitrary degree of localization can be obtained in the limit of vanishingly small coupling between oscillators. An intuitive explanation of this phenomenon is given below.

To explain the occurrence of the localized mode shapes depicted in **Figure 2D**, it is first useful to note that such strong localization occurs when the coupling between oscillators is small or, more accurately, when the ratio of the internal coupling strength to the disorder strength is small. Now consider the disordered system shown in **Figure 2C** in the limit of zero

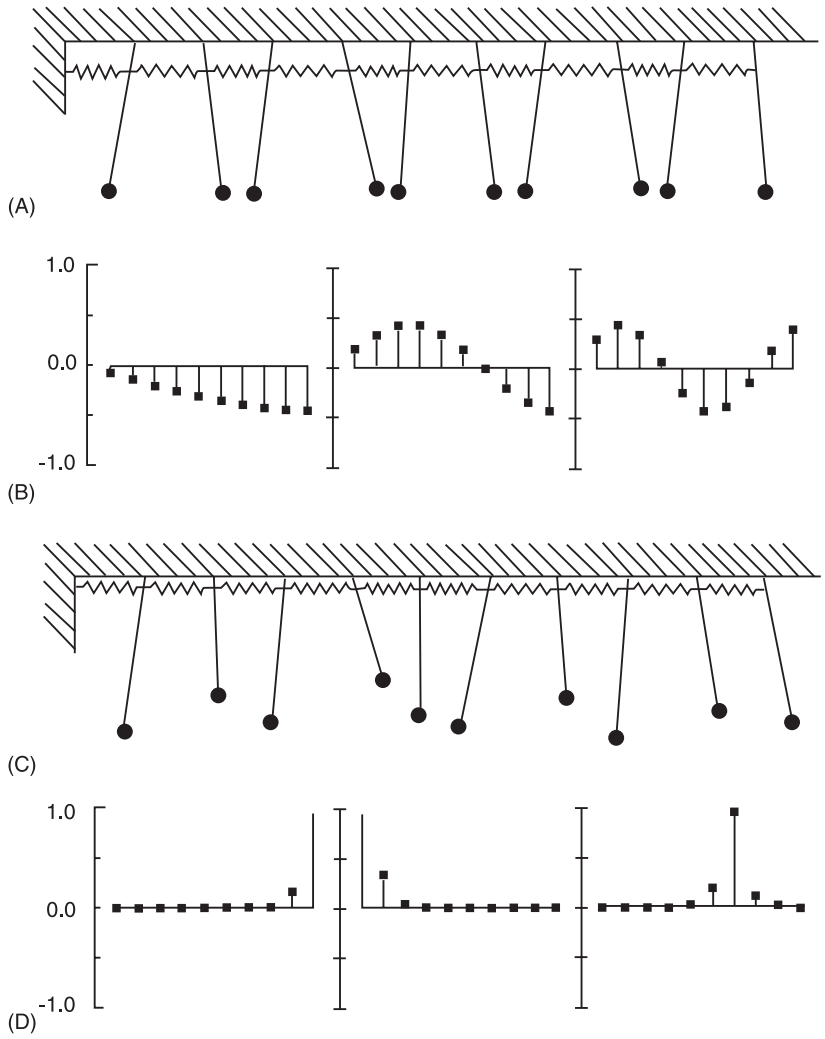


Figure 2 Mode localization for a simple chain of single-degree-of-freedom oscillators. (A) A periodic chain; (B) three extended mode shapes of the periodic chain; (C) a disordered oscillator chain; (D) three localized modes of the disordered chain.

coupling. One obtains a chain of slightly dissimilar, uncoupled oscillators (for the sake of simplicity, assume that no two oscillators have the same random natural frequency). The mode shapes of this limiting system each feature the motion of a single oscillator, with all other oscillators remaining quiescent; in mathematical terms, the associated eigenvectors are the canonical basis vectors, each with a single nonzero element and all other elements equal to zero, representing the oscillations of uncoupled oscillators. Now, if one considers a small perturbation of the uncoupled disordered system, by introducing small coupling between the oscillators, the modes of this weakly coupled system can be expected to be small perturbations of those of the uncoupled system. Thus, each mode of the weakly coupled disordered system is a perturbation of the oscillations of a single oscillator, and is precisely a localized mode such as those shown in **Figure 2D**. Therefore, by viewing not the disorder, but the small coupling as a perturbation, one can provide a physically intuitive explanation of the occurrence of localized modes, namely as perturbations of uncoupled oscillations. Paradoxically, while the localized modes now appear as entirely expected, it is the extended modes of the ordered system that seem to be anomalous. Indeed, based on the above reasoning, one would expect that for weak coupling the modes of the ordered system are also localized. However, the uncoupled ordered system features an N-fold degenerate natural frequency, where N is the number of oscillators, such that any arbitrary deflection pattern is an eigenvector. The arguments developed above for the individual uncoupled modes are invalid in the ordered case, and any amount of coupling, however small, is sufficient to remove the natural frequency degeneracy and cause a resonance among

all oscillators, yielding the extended mode shapes in **Figure 2B**. In this light, it is the ordered system with its extended modes, rather than the disordered system with its localized modes, that appears as the anomalous case.

Brief History of Localization

The mode localization phenomenon was first discovered in 1958 by P. W. Anderson in the field of solid state physics. He showed that the electron eigenstates in disordered solids may become localized, henceforth limiting metallic conduction. Since Anderson's ground-breaking work, localization has continuously excited the interest of solid state physicists, and the resulting body of research has been the precursor to the study of localization in the field of structural dynamics. Two lines of thought in solid state physics have particularly impacted vibration localization studies. In the first approach, localization in random chains is analyzed by applying Furstenberg's theorem on the limiting behavior of products of random matrices. Modeling each bay, or subsystem, of the nearly periodic system by a transfer matrix, one can represent the assembly dynamics by a product of random transfer matrices – an approach based on the traveling of waves from bay to bay. The second approach consists of a modal formulation, in which one relies on the frequency spectrum of the entire disordered chain to characterize localization. These two perspectives form the cornerstone of the study of localization in engineering structures. They differ in that the wave formulation deals with local properties (transfer matrix for each bay), while the modal method uses global information (frequency spectrum of the entire structure).

In 1982, C. H. Hodges was first to recognize that localization can occur in engineering structures and to suggest that some of the knowledge acquired by physicists could be applied to studies of structural dynamics and acoustics. Using both wave and modal arguments, Hodges discussed localization for simple periodic structural systems, such as chains of coupled oscillators and beams on randomly spaced supports. Following Hodges' pioneering work, a large number of localization studies were carried out for a variety of structural systems. In the first stage, research was mostly limited to deterministic analyses of the free vibration modes of disordered one-dimensional structures with single-degree-of-freedom bays, such as oscillator chains. In particular, various perturbation methods were developed to elucidate the underlying physical mechanisms of mode localization. Researchers then considered more complex periodic structures with multimode bays and showed that confinement effects generally increase rapidly with frequency. The occurrence of mode localization was also formally related to that of another phenomenon already known in the field of vibration, namely curve veering. It was shown that mode localization in disordered periodic structures can be predicted by the abrupt veering away of the loci of the natural frequencies when plotted against the disorder parameter.

Beginning in the late 1980s, stochastic investigations of localization were conducted, which recognized the probabilistic nature of the irregularities. The concept of the localization factor was introduced. This frequency dependent scalar characterizes the strength of localization, and is defined as the exponential spatial decay rate of the vibration amplitude along the disordered periodic structure, in an average or an asymptotic sense. It can be calculated either from the transmission of harmonic forced vibration from a local source of excitation, or from the limiting behavior of products of random bay transfer matrices. Localization factors can be approximated analytically, typically using perturbation ideas, but more accurate determinations require a numerical evaluation of the Monte Carlo type. In recent years localization factors have been determined for various periodic structures: chains of oscillators, chains of multimode systems, multispan beams, stretched strings with attached masses, truss beams, etc. These works exhibited the occurrence of two types of localization, weak or strong, depending on the internal coupling in the structure and on the frequency range. Stochastic perturbation methods, based upon modal or wave formulations, were developed for these two localization regimes. It was shown that strong localization effects are most relevant to the structural dynamicist, as they manifest themselves as rapid spatial attenuation over a few bays, whereas weak localization, though of concern to solid state physicists, affects engineering structures very little, because the small spatial attenuation rate due to localization is readily obscured by that caused by the small damping present in all structures.

In order to confirm the occurrence of localization and validate analytical and numerical findings, experiments were conducted on engineering structures beginning in the late 1980s. Simple structures were tested: a taut string with attached beads, a two-span beam, and a 12-span beam. This led to the quantitative confirmation of localization effects, both on free vibration mode shapes and on steady-state and transient forced responses, and also to the experimental estimation of localization factors. Experiments were also performed on realistic engineering structures, namely a full-scale, 12-rib, loosely coupled space antenna, and several industrial jet

engine bladed disks. The latter tests confirm that localization may take place in practical engineering situations.

The study of mode localization has recently generated intense research activity in the fields of structural dynamics and acoustics, and original contributions are being made in the areas of nonlinear periodic systems, bladed-disk assemblies, computer disk drives, and structures submerged in a fluid.

Key Localization Results

Periodic structures have characteristic properties that make much of their dynamics qualitatively the same. Thus useful results for engineering structures can be obtained from elementary models. Periodic structures are made of bays coupled through one or more coordinates, and are accordingly classified as monocoupled or multicoupled. For example, the pendulum assembly shown in **Figure 2** is monocoupled through the springs connecting adjacent oscillators. Also, a multispan beam on rigid supports is monocoupled through the bending rotation at the supports. The same beam on elastic supports is, however, bicoupled, as energy is also transmitted through the bending displacement of the supports. Finally, the bladed disk in **Figure 1B** is multicoupled, through possibly many coupling coordinates at adjacent blade-disk sectors. A periodic structure carries as many pairs of (left- and right-traveling) independent free waves as there are coupling coordinates. Alternating frequency bands in which the waves either propagate freely (passbands) or are attenuated (stopbands) correspond to each pair of harmonic waves. The number of passbands equals the number of degrees of freedom of a subsystem (which can possibly be infinite), and energy is only transmitted along the structure through the passbands. A typical passband–stopband pattern is shown in **Figure 3** for a monocoupled periodic system.

A pair of waves is characterized by a propagation constant, $\mu = \gamma + jk$, such that waves propagate according to $\exp(\pm\mu)$. The propagation constant thus accounts for the change in wave amplitude (γ) and phase (κ) at the bay interfaces. In particular, the spatial decay of the wave amplitude is governed by the real part of the propagation constant, γ, a quantity of special interest in localization. The nature of the propagation constant (real or complex) at a given frequency determines the propagation and attenuation characteristics of the corresponding wave pair at that frequency, as follows (**Figure 3**). In the frequency passbands of periodic (undamped) structures, μ is purely imaginary, thus $\gamma = 0$ and a characteristic wave propagates freely without attenuation but

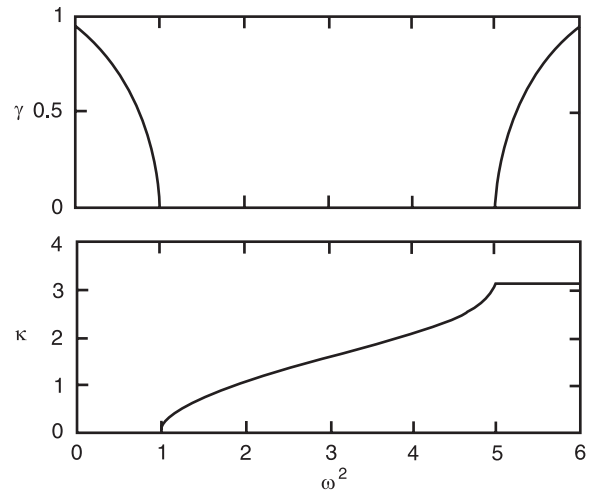


Figure 3 An illustration of stopband and passband patterns versus harmonic frequency in a periodic structure. When $\gamma = 0$, a wave propagates without amplitude attenuation, and the corresponding frequency range $[1, 5]$ defines a passband. Frequency ranges $[0, 1]$ and $[5, 6]$ define two stopbands representing waves that are attenuated with a phase change of 0 or π at each bay.

with a phase change at each bay. In the frequency stopbands, attenuation occurs and $\gamma = 0$, with a phase change of 0 or π radians per bay. In complex-bands, waves propagate with attenuation and with a phase change per bay different from 0 or π. Complex-bands require two wave pairs to exist, hence they are not present in monocoupled periodic systems. If the periodic system is damped, then the wave amplitudes decay exponentially along the system, even for frequencies in the passbands ($\gamma = 0$).

Disruption in periodicity also leads to wave attenuation at all frequencies (regardless of dissipation), because traveling waves are partly reflected by the randomized bays. In monocoupled, disordered periodic structures, when one wave impinges at the interface of two disordered, hence slightly different, bays, part of the wave amplitude is reflected and part of it is transmitted. It is this multiple scattering effect over many bays that causes the localization of waves to the region of incidence. While the spatial decay of the wave amplitude can vary greatly from bay to bay due to their random properties, the rate of spatial decay per bay is exponential asymptotically, as the number of bays tends to infinity. (Assuming spatial self-averaging, the expected value of the decay rate for a finite system is also exponential, and equivalent to the asymptotic rate for an infinite system.) For a monocoupled system, there is a single wave type, hence its spatial decay rate corresponds exactly to the spatial decay rate of the vibration amplitude. The associated exponential decay constant is known as

the localization factor. Intuitively, the localization factor can be viewed as the generalization to disordered systems of the real part of the propagation constant for ordered systems. In the disordered case, γ becomes greater than zero for all frequencies, even in the passbands of the corresponding periodic structure. As an illustration, **Figure 4** depicts one free vibration mode of a disordered 100-oscillator system, along with the corresponding decay predicted by the localization factor calculated at the mode's frequency. Note that even though the spatial amplitude decay featured by the mode is not purely exponential, it is well captured by the localization factor.

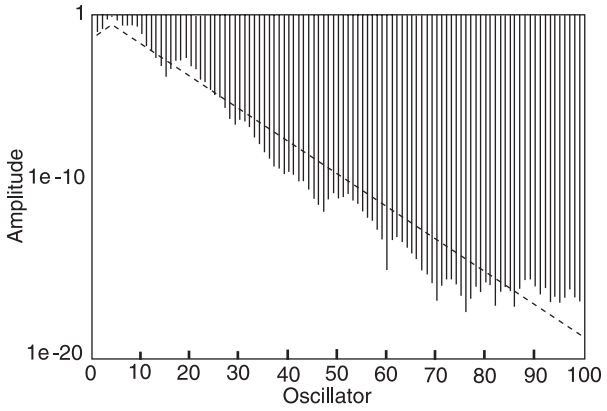


Figure 4 A localized vibration mode shape of a disordered 100-oscillator system, shown on a natural log scale to illustrate the rate of exponential decay. The decay rate predicted by the localization factor at the mode's frequency is portrayed by the slope of the line (—) superimposed on the plot.

Localization factors can be calculated by various methods: perturbation techniques, with either coupling or disorder as the perturbation parameter in strong and weak localization regimes, respectively; Monte Carlo simulations of the forced response of a finite structure to a local excitation or of the wave response of an infinite structure to an incident wave; as the largest Lyapunov exponent of the stochastic global wave transfer matrix for the disordered periodic structure. The Lyapunov exponent method combines accuracy and efficiency, and is generally the method of choice to calculate localization factors. **Figure 5** depicts the typical variation of the localization factor throughout the passband of the corresponding periodic system, obtained by various methods. Observe that γ is largest near the passband edges ($\omega^2 = 1$ and 1.4) and minimum at midpassband ($\omega^2 = 1.2$).

Similarly to damping, localization manifests itself by a spatial decay of the vibration amplitude along the structure. However, the mechanisms for localization and damping differ fundamentally. The localization phenomenon is one of energy redistribution, whereby the energy is confined, trapped by the wave-scattering disorder near the excitation source. The damping mechanism, on the other hand, dissipates energy as the vibration is transmitted through the bays without reflections.

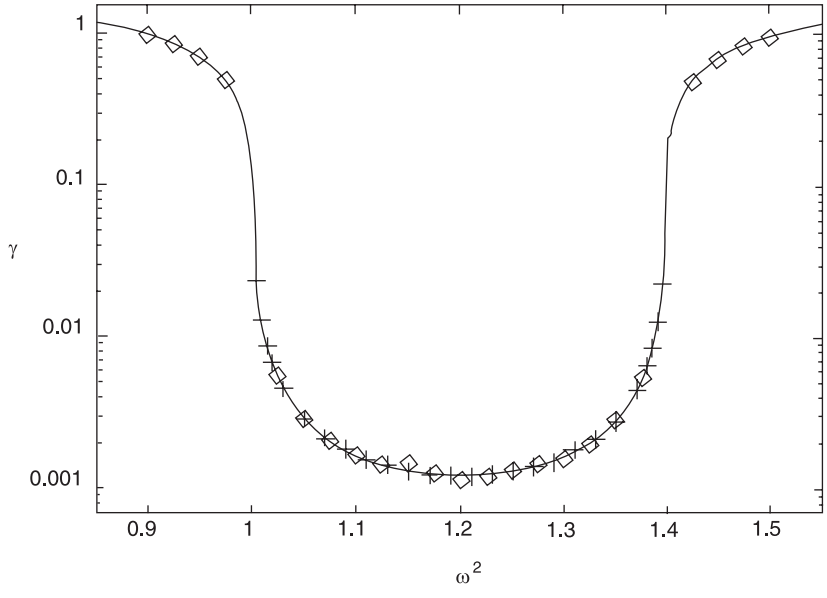


Figure 5 Localization factor for a chain of coupled oscillators, for a disorder of standard deviation $\sigma = 1\%$ and weak coupling. Results are shown for perturbation approximation (—), Lyapunov exponent using the Wolf algorithm (◇), and Monte Carlo method (+).

Localization in multicoupled systems is much more difficult to analyze, because the decay rates of the multiple wave pairs present in the structure must be considered. At any given bay, a wave type may not only be partially reflected and transmitted into waves of the same type, but into other wave types as well. The partial reflection and/or transmission of one wave type into another is referred to as wave conversion or wave interaction, because energy 'leaks' from one wave type to another, indicating that the waves are coupled. Typically, waves that are most subject to localization leak their energy to waves that are less prone to it, in an effort to sustain propagation. Multiwave localization thus exhibits a rich wave conversion mechanism caused by multiple scatterings. One way to characterize localization in multicoupled systems is to find the Lyapunov exponents of the matrix that relates the wave amplitudes at one end of the structure to the wave amplitudes at the other end – the stochastic global wave transfer matrix. The Lyapunov exponents provide a measure of the rates of amplitude decay for the various wave types. For an ordered system, the positive Lyapunov exponents simply equal the propagation constants. For a monocoupled system, the largest Lyapunov exponent is equivalent to the localization factor.

Dual to the wave properties of periodic structures are the modal properties. The natural frequencies of a finite periodic system are (almost always) found inside the frequency passbands, with N natural frequencies in each passband for an N-bay monocoupled system. The mode shapes of finite periodic structures are periodic, or extended, and feature a nonattenuated shape (**Figure 2B**). Mode shapes can be obtained from the free traveling waves of the same frequency by the phase closure principle. The localized mode shapes of disordered structures are governed, on the average, by the same exponential envelope as the free waves of same frequency, $\exp(-\gamma N)$. Obviously, this holds for a periodic structure, as $\gamma = 0$ and the mode shapes are extended.

Finite periodic structures feature closely spaced modes when the number of bays becomes large and/or the frequency passbands are narrow. This high modal density occurs because the number of natural frequencies in each passband equals the number of bays in the periodic system, and also because the passband edges characterize an infinite periodic structure and henceforth are independent of the number of bays. This property leads to another interpretation of localization, one that is based upon sensitivity arguments, as follows. Recall, from the perturbation theory for the eigenvalue problem, that the sensitivity of the mode shapes to small parameter perturbations is inversely proportional to the distance between the eigenvalues of the unperturbed structure. Considering the periodic structure to be the unperturbed system and the perturbation to be the disorder, it follows that the mode shapes of a finite periodic structure are sensitive to disorder when the number of bays is large and/or the passbands are narrow. Since narrow passbands occur when the internal coupling among the bays is small (to understand this, consider the limiting case of vanishing coupling and hence vanishing passband width for uncoupled, identical bays), it means that the mode shapes are highly sensitive to disorder for small interbay coupling. This high sensitivity of the modes is indicative of the occurrence of localization. It also follows that mode shape sensitivity increases with the number of bays and that, for a given coupling (even large), arbitrarily large sensitivity can be obtained provided the number of bays is sufficiently large. This is in agreement with the finding that localization is characterized by an exponential decay of the amplitude: for a given localization factor γ, localization becomes stronger as the number of bays in the structure increases, and even an arbitrarily small localization factor (such as one obtained for strong coupling and large passband width) can yield severe localization if the structure comprises a sufficiently large number of bays. From a sensitivity viewpoint, as the number of bays increases, the modal density – and hence the mode shape sensitivity to disorder – increases as the number of eigenvalues contained in the constant-width passband increases.

Engineering Significance of Localization

The degree of localization in a structure depends on the ratio of disorder strength to internal coupling strength and increases with this ratio. Under conditions of weak coupling between bays or, equivalently, high modal density, the effects of small disorder can be drastic. To illustrate such strong localization, consider the monocoupled assembly of component beams in **Figure 6**. **Figure 7** displays typical free

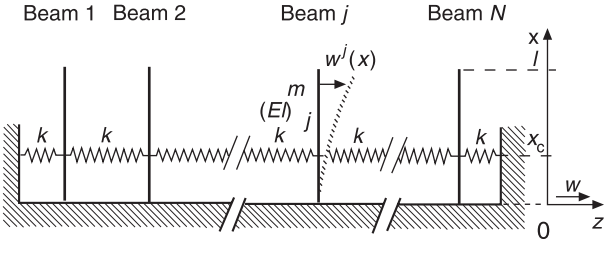


Figure 6 A monocoupled assembly of multimode component systems (cantilevered Euler–Bernoulli beams).

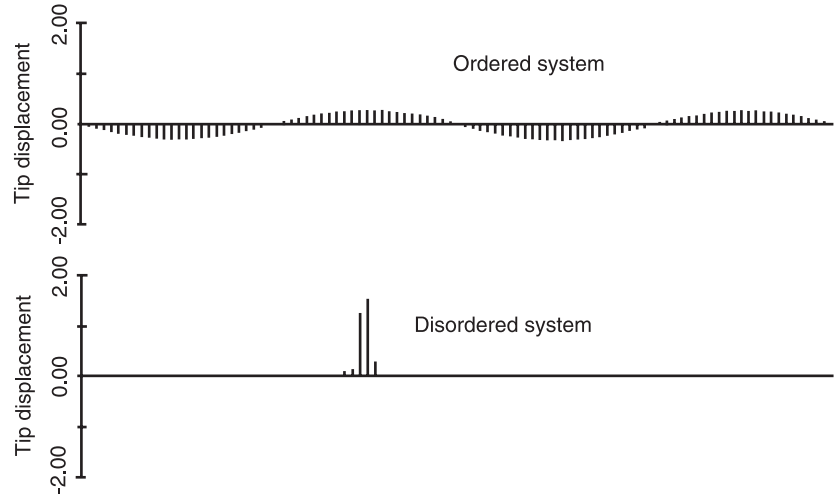


Figure 7 Fourth mode in the third passband (204th mode) for ordered and disordered assemblies of 100 cantilevered Bernoulli–Euler beams. The beams are coupled at the tip, and the coupling stiffness equals the beams' static stiffness. Tip displacements are shown. For the disordered system, the standard deviation of beam stiffness mistuning is 1%. Note the severe change from extended to localized modes.

vibration modes for an ordered assembly of 100 identical beams and a slightly disordered system. The standard deviation of disorder is on the order of typical manufacturing tolerances and the inter-beam coupling stiffness is significant. While the mode of the ordered assembly extends through the structure, the corresponding mode for the disordered assembly is localized about a few beams. Note that energy confinement also results in larger amplitudes (both modes were normalized by the same energy). Other illustrations of mode localization are shown in **Figures 8** and **9**, for a multispan beam on randomly

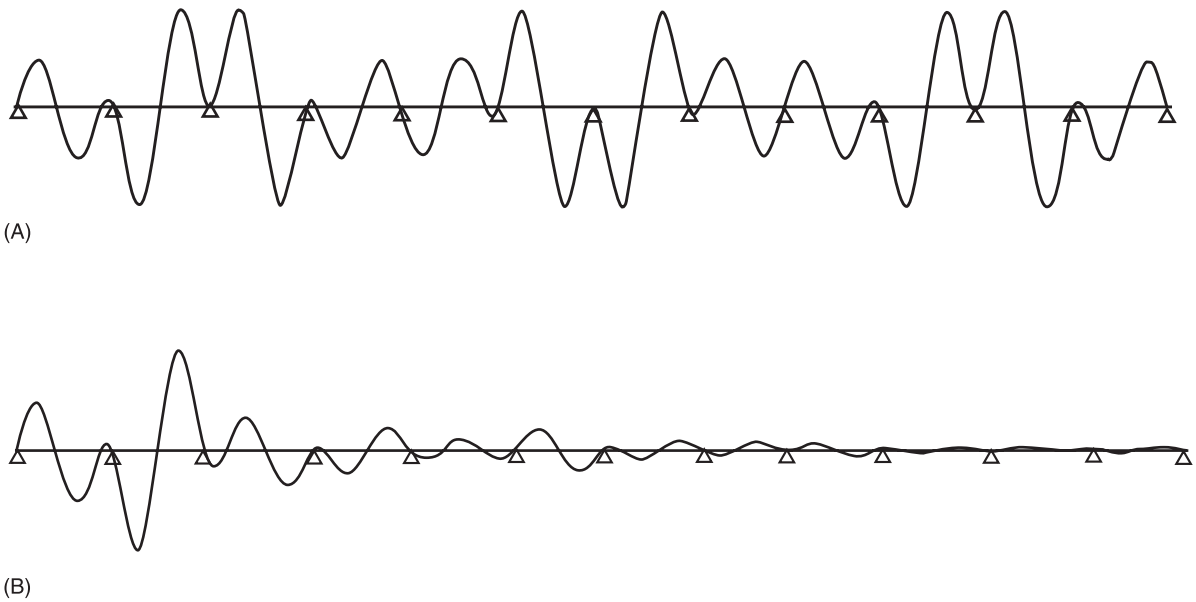


Figure 8 Modes of a multispan beam on rigid supports. (A) One extended mode of a periodic beam on equally spaced supports; (B) Mode localization in a disordered beam with slight random support spacing.

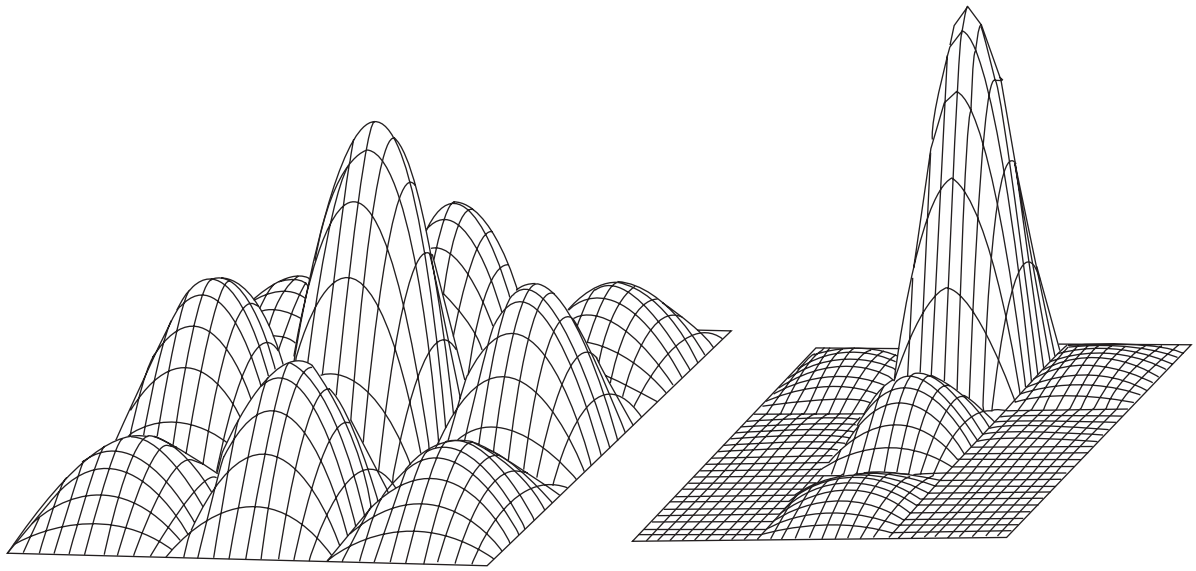


Figure 9 Mode localization in a nine-bay membrane resting on continuous lines of linear springs. (A) Ordered system; (B) disordered system. For the disordered membrane the areas of the individual bays are randomized, such that the standard deviation of support spacing is approximately 0.5%. Observe the severe localization in a single bay in (B).

spaced supports and a two-dimensional multipanel membrane resting on randomly spaced elastic line supports, respectively.

Localization can occur in a plethora of engineering structures, essentially all structures that feature spatial periodicity. An especially important class are bladed-disk assemblies such as those found in jet engines. There, the localization is induced by small blade mistuning and it can cause large increases in response amplitudes and stresses (increases of 300% are not uncommon), resulting in serious high-cycle fatigue problems. **Figures 10** and **11** illustrate forced and free response localization for bladed disks, respectively. Other structures susceptible to localization are space antennas with cyclic symmetry, truss beams in space, airframes (skin-stringer panels), laminated composites, overhead power lines, offshore jack-up structures, submarine hulls, towed-array sonars, rail road tracks, computer drives with stacked disks, etc. Thus, localization may impact virtually every engineering application in structural dynamics.

The underlying motivation for studying localization is threefold. First, through the occurrence of localization, parameter uncertainties have the potential to invalidate the predictions of commonly used deterministic modeling and analysis techniques, which reduces the effectiveness of structural models, associated control schemes, and identification techniques. For example, a control strategy based upon the erroneous extended modes of a perfectly periodic structure would be unpredictable. Also, to an experimentalist unaware of disorder effects, the spatial amplitude decay caused by localization could be easily mistaken for, and result in, an overdetermination of damping. Second, localized vibrations increase amplitudes and stresses locally and may result in severe damage. For instance, single-blade failure in turbomachinery rotors is a plausible result of blade mistuning. Third, when localization occurs, irregularities exhibit a damping-like effect that could be used as a passive control of vibration transmission. This has applications in flexible and lightly damped structures such as truss beams in space.

See Plate 41.

See also: **Nonlinear system identification**; **Random vibration, basic theory**; **Wave propagation**, Guided waves in structures; **Wave propagation**, Waves in an unbounded medium

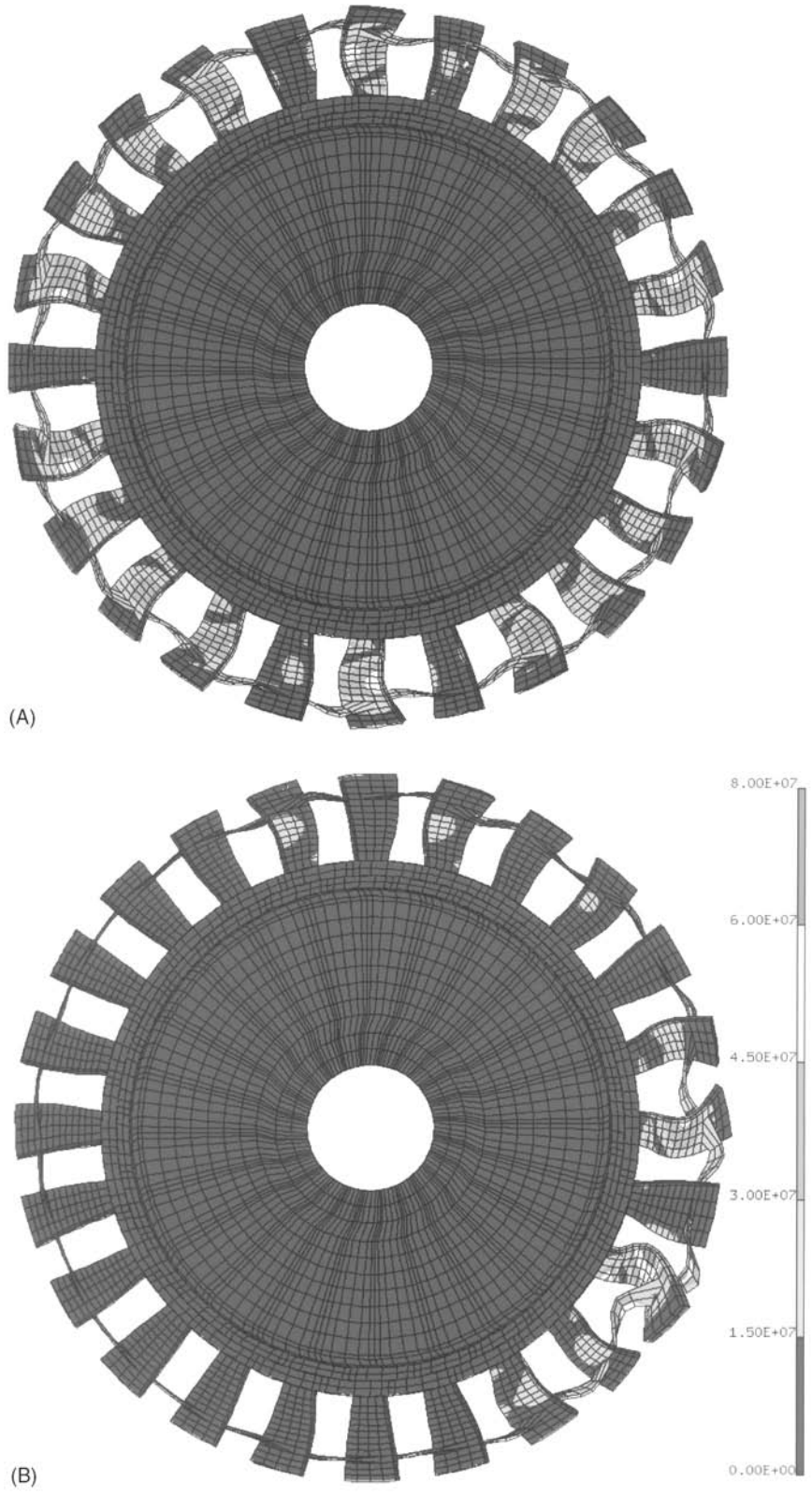


Figure 10 (See Plate 41). Forced response simulation results obtained using the finite element method. This model of a one-piece bladed disk (blisk) with continuous midspan shrouds was subject to an 'engine order 7' excitation (all blades are excited seven times per rotor revolution). (A) Extended forced response of the tuned blisk with identical blades. (B) Localized response of a blisk with slight random blade mistuning. Observe how the largest-responding blade suffers higher vibration amplitudes and stresses than any blade of the tuned system in (A).

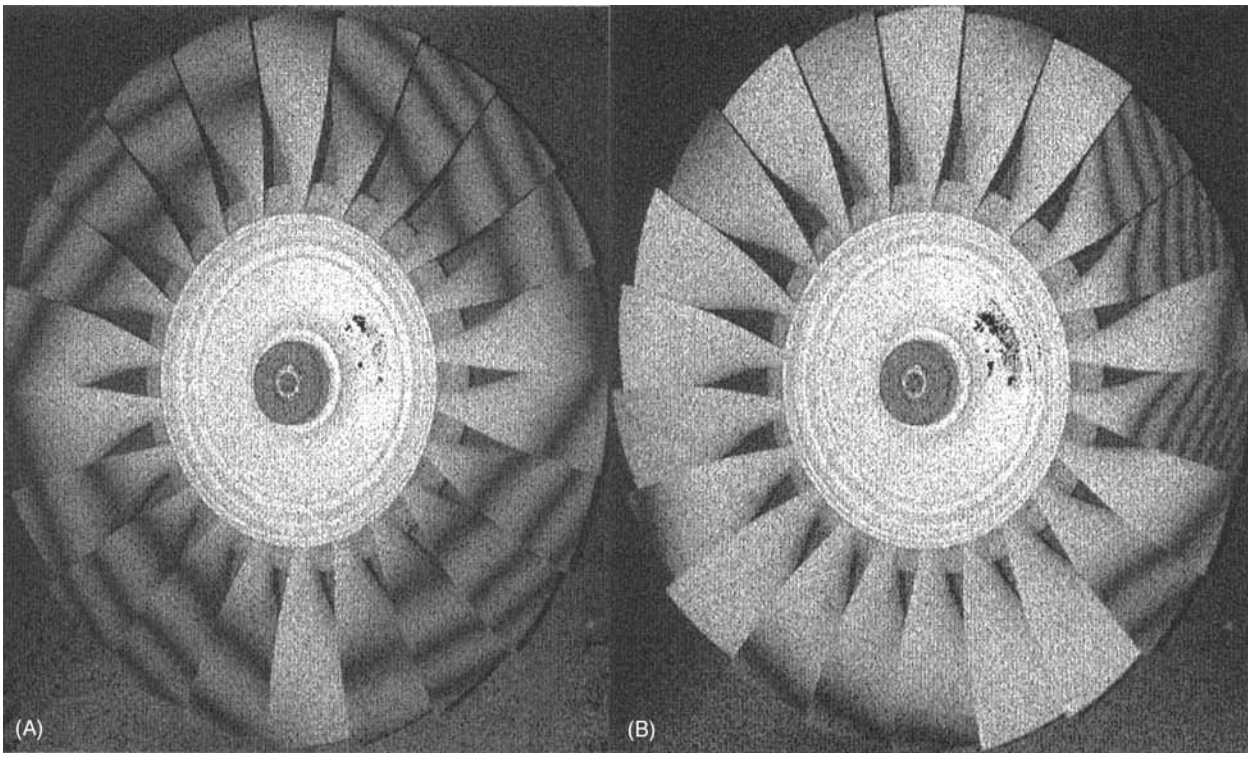


Figure 11 Normal modes of a bladed disk, measured experimentally using electronic speckle pattern interferometry. In the mode shape images, vibration is indicated by dark fringes, with each fringe corresponding to a certain level of vibration. The more fringes on a blade, the higher the vibration amplitude for that blade. (A) Extended 'two-nodal diameter' mode characteristic of a tuned bladed disk; (B) Localized mode characteristic of a mistuned system.

Further Reading

Anderson PW 1958 Absence of diffusion in certain random lattices. *Physical Review* 109: 1492–1505.

Benaroya H, Lin YK, Pierre C *et al*. (1996) Localization and the effects of irregularities in structures. *ASME Applied Mechanics Reviews* 49(2): 56–135.

Bougerol P, Lacroix J (1985) *Products of Random Matrices with Applications to Schrödinger Operators*. Boston: Birkhäuser.

Brillouin L (1953) *Wave Propagation in Periodic Structures*. New York: Dover.

Castanier MP, Pierre C (1995) Lyapunov exponents and localization phenomena in multi-coupled nearly-periodic systems. *Journal of Sound and Vibration* 183: 493–515.

Hodges CH (1982) Confinement of vibration by structural irregularity. *Journal of Sound and Vibration* 82: 411–424.

Hodges CH, Woodhouse J (1986) Theories of noise and vibration transmission in complex structures. *Reports in Progress in Physics* 49: 107–170.

Ibrahim RA (1987) Structural dynamics with parameter uncertainties. *Applied Mechanics Reviews* 40(3): 309–328.

Kissel CJ (1988) *Localization in Disordered Periodic Structures*. PhD Dissertation, Massachusetts Institute of Technology.

Pierre C (1988) Mode localization and eigenvalue loci veering phenomena in disordered structures. *Journal of Sound and Vibration* 126: 485–502.

Vakakis AF, Manevitch LI, Mikhlin YV, Pilipchuck VN, Zevin AA (1996) *Normal Modes and Localization in Nonlinear Systems*. New York: Wiley.

Wolf A, Swift JB, Swinney HL, Vastano JA (1985) Determining Lyapunov exponents from a time series. *Physica D* 16: 285–317.

Ziman JM (1979) *Models of Disorder*. Cambridge: Cambridge University Press.

M

MACHINERY, ISOLATION

See **VIBRATION ISOLATION, APPLICATIONS AND CRITERIA**

MAGNETORHEOLOGICAL FLUIDS

See **ELECTRORHEOLOGICAL AND MAGNETORHEOLOGICAL FLUIDS**

MAGNETOSTRICTIVE MATERIALS

A Flatau, National Science Foundation, Arlington, VA, USA

Copyright © 2001 Academic Press

doi:10.1006/rwvb.2001.0079

The bidirectional coupling between the magnetic and mechanical states of a magnetostrictive material provides a transduction mechanism that is used in both sensing and actuation. The current interest in the design of adaptive smart structures, coupled with the advent of materials which exhibit high sensor figures of merit such as Metglas and the so-called giant magnetostrictive materials such as Terfenol-D has led to a renewed interest in the engineering of optimized magnetostrictive transducer designs. An overview of magnetostriction and of recent sensing and vibration control applications for magnetostrictive materials is presented along with a brief discussion of some pertinent magnetostrictive device design issues. Schematics of several actuator and sensor configurations are included, as are typical experimental results.

Magnetostriction and Magnetism

Magnetostrictive materials convert magnetic energy to mechanical energy and vice versa. As a magnetostrictive material is magnetized, it strains. Conversely, as either a force or torque produces a strain in a magnetostrictive material, the material's magnetic state changes. The application of either an external magnetic field or an external stress breaks the material's internal energy balance and leads to both magnetic responses (domain wall motion, magnetization rotation, and a change in permeability) and elastic responses (strain of the material and a change in stiffness).

Magnetostriction is an inherent material property associated with electron spin and orbit orientations and molecular lattice geometries and will not degrade with time or with use. The effect is not present when a magnetostrictive material is heated above its Curie temperature; however, the effect returns fully as the material is cooled to below the Curie temperature. All ferromagnetic materials exhibit magnetostriction; however, in many materials the magnitude of the strain or shape change is too small to be of consequence. Nominal longitudinal saturation strains for various materials at room temperature are shown in **Table 1**.

Sensors are commonly based on the reciprocal magnetostrictive effects, the change in magnetization and permeability of a sample that accompanies a change in an external stress or torque. The magnetization change produced due to the application of a stress is known as either the Villari effect or the magnetomechanical effect. The magnetization

change produced due to application of a torque is known as either the inverse Wiedemann effect or the Matteuci effect.

Actuators are commonly based on the shape change that accompanies magnetization of a magnetostrictive material. The most common shape change is a change in sample length, accompanied by a change in transverse dimensions. This is known as the Joule effect (after James Prescott Joule (1818–89) for positive identification of the change in length of an iron sample) or the magnetostrictive effect. Magnetostriction can also occur as a twisting which results from a helical magnetic field, often generated by passing a current through the magnetostrictive sample. This is known as the Wiedemann effect.

At low applied magnetic field strengths, domain wall motion occurs as a consequence of the growth of domains whose magnetization is aligned favorably with respect to the applied field, at the expense of domains with magnetization opposing the field. At moderate field strengths, the magnetic moments within unfavorably oriented domains overcome the anisotropy energy and suddenly rotate (jump) into one of the crystallographic easy axes closer to the external field direction. This jump coincides with a relatively large change in strain for a small change in applied field. At moderate to high field strengths, the magnetic moments align along crystallographically easy axes lying closest to the field direction. As the field is increased further, the magnetic moments undergo coherent rotation until they reach alignment with the applied field resulting in a single-domain material and technical saturation.

Crystalline growth can be tailored or optimized so as to enhance the magnetostrictive effect in a material of a given stoichiometry. For example, in the highly magnetostrictive alloy Terfenol-D ($Tb_xDy_{1-x}Fe_y$, where $x = 0.27-0.3$ and $y = 1.92-2.0$) energy minimization is satisfied with random alignment of the magnetic domain orientations along the eight outward diagonals from the center of the molecular cubic lattice such that the bulk sample has zero (or almost zero) net magnetization. Commercially available material is grown using directional solidification techniques and patented crystallographic growth methods that lead to crystal growth and magnetic moment orientations such that jumping of magnetization between easy axes perpendicular and parallel to the sample growth direction is facilitated.

Table 1 Saturation magnetostrictions for magnetostrictive materials at 300 °K

Material	*Magnetostriction* ($\Delta L/L \times 10^{-6}$)
Fe	−9
Ni	−35
Co	−60
60% Co–40%Fe	68
60% Ni–40%Fe	25
$TbFe_2$	1753
Terfenol-D	1600
$SmFe_2$	−1560
Metglas 2605SC	40

Data produced from Restorff JB (1994) *Encyclopedia of Applied Physics*, vol. 9, pp. 229–244.

Exchanges between magnetic and mechanical energy are the primary transduction effects employed in magnetostrictive sensing and actuation applications. The two coupled linear equations given in eqns [1] and [2] model these relationships. These equations neglect temperature effects and hysteresis, and have been reduced from a three-dimensional vector form to reflect only axial behavior. These magnetostrictive equations of state are expressed in terms of mechanical parameters (strain ε, stress σ, Young's modulus at constant applied magnetic field E^H), magnetic parameters (applied magnetic field H, magnetic induction B, permeability at constant stress μ^σ), and two piezomagnetic coefficients (these are also known as magnetomechanical coefficients and as axial strain coefficients: $d_{33} = \mathrm{d}\varepsilon/\mathrm{d}H|_\sigma$, and $d^*_{33} = \mathrm{d}B/\mathrm{d}\sigma|_H$, where for small strains, these two coefficients can be shown to be equal):

$$\varepsilon = \sigma/E^H_y + \mathrm{d}H \qquad [1]$$

$$B = \mathrm{d}^*\sigma + \mu^\sigma H \qquad [2]$$

where ε and B are dependent on the externally applied quantities σ and H. The elastic modulus, permeability, and piezomagnetic coefficients can vary significantly with operating conditions. They need to be experimentally determined and are usually provided by the material manufacturer. At present, most modeling codes rely on look-up tables to capture the time-varying and load-dependent nature of these coefficients.

These equations capture the low signal, linear, coupled mechanical, and magnetic nature of magnetostriction. Eqn [1] indicates that the net strain of a magnetostrictive element is the combined response to changes in stress (Hooke's law behavior, $\varepsilon = \sigma/E$) and applied magnetic field (Joule effect magnetostriction, λ). Eqn [2] indicates the simultaneous change in the magnetic induction of the element due to change in stress (reciprocal Joule or Villari effect magnetization) and applied field. This later effect can also be

expressed as a change in permeability by writing eqn [2] in a more general form:

$$B = \mu H \qquad [3]$$

In eqn [3] the effects of stress are included in the permeability, μ. Permeability can be monitored since both B and H can be related to measurable electrical quantities as described in eqns [4] and [5].

In the early nineteenth century, Oersted discovered that a moving charge generated a magnetic field in a plane perpendicular to the direction of charge motion. Thus, a current in a conductor could be used to produce a magnetic field around the conductor. Ampere's law describes this electromagnetic relationship. For a long, thin solenoid having a number of turns N_c and a length L_c a simple expression is derived;

$$H = (N_c I)/L_c \qquad [4]$$

Placing a magnetostrictive element inside such an excitation coil (solenoid) with an impressed current I provides an efficient means of magnetizing the element and producing controlled strain and force output.

The law of electromagnetic induction (Faraday–Lenz law) describes how a magnetic flux, $\varphi = BA_c$ in area A_c, induces a potential in an electrical conductor to which it is flux-linked. In its simplest differential form, the Faraday–Lenz law is given by:

$$V = -N_c \frac{\mathrm{d}\varphi}{\mathrm{d}t} = -N_c A_c \frac{\mathrm{d}B}{\mathrm{d}t} \qquad [5]$$

where V is the induced voltage in the solenoid of constant area A_c. According to this law, a potential will be induced in any electrically conducting material that makes up the magnetic circuit.

The excitation coil described by eqn [4] can be used to generate a magnetic field in a sample spatially separated from the coil. According to Gauss's law of magnetism:

$$\nabla \cdot B = 0 \qquad [6]$$

the divergence of B is zero. This means that the magnetic flux is always conserved. Thus magnetic flux lines close, defining a magnetic circuit, and elements of the magnetic circuit through which magnetic flux flows are said to be flux-linked. This makes it possible to magnetize one component of the magnetic circuit by generating a magnetic field in another component. Based on the principle expressed by eqns [5] and [6], it is possible to measure the magnetic flux density in a magnetic circuit by the voltage induced in a flux-linked detection coil.

Transduction

Magnetostrictive materials are magnetoelastic in the sense that they do work in the process of converting between magnetic and elastic (or mechanical) energy states. However, magnetostrictive transducers are generally classified as electromechanical devices or electromagnetomechanical because their input and output are generally electrical and mechanical in nature. The conversion of magnetic energy to and from electrical and/or mechanical is transparent to the device user. A common two-port schematic appropriate for both magnetostrictive sensing and actuation devices is given in **Figure 1**. The magnetostrictive driver is represented by the center block, with the transduction coefficients T_{me} (mechanical due to electrical) and T_{em} (electrical due to mechanical), indicative of both the magnetoelastic attributes characterized by eqns [1] and [2] and the electromagnetic attributes associated with conversion between electrical and magnetic fields characterized by eqns [4] and [5].

The transduction process relating the electrical and mechanical states can be described with two coupled linear equations. These canonical equations are expressed in terms of mechanical parameters (force F, velocity v, mechanical impedance Z_m), electrical parameters (applied voltage V, current I, electrical impedance Z_e), and the two transduction coefficients:

$$V = Z_e I + T_{em} v \qquad [7]$$

$$F = T_{me} I + z_m v \qquad [8]$$

Common magnetostrictive transducer components include a magnetic circuit, a solenoid for transduction of magnetic-to-electrical energy and vice versa, mechanisms for DC magnetic and mechanical (prestress) biasing. A generic magnetostrictive device con-

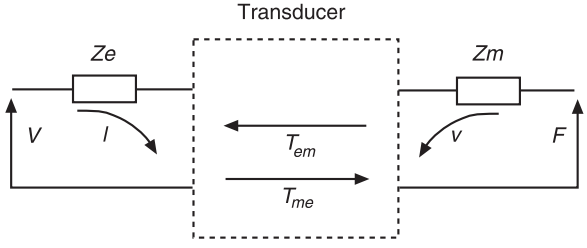


Figure 1 Two-port transducer schematic.

figuration is shown in **Figure 2**. The permanent magnet provides a DC magnetic field. The magnetic circuit passes though the magnetostrictive driver, end caps made of magnetic materials, and the permanent magnet. Belleville spring washers are used to provide an initial mechanical prestress. The solenoid can be used to provide both AC and DC magnetic fields for actuation purposes. Alternatively, for sensing applications, the change in voltage induced in the solenoid is to detect a change in strain and/or in the force applied to the device.

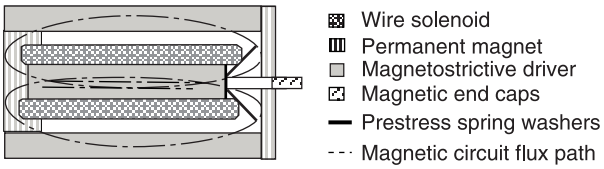


Figure 2 Components typical of a simple magnetostrictive transducer.

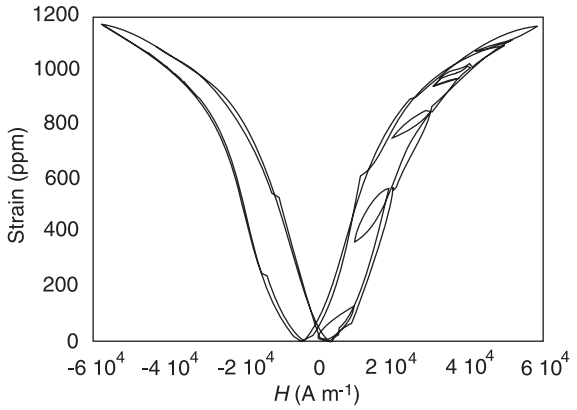


Figure 3 Strain vs applied-field major hysteresis loop and minor loops for AC fields of $\pm 5\ \mathrm{kA\,m^{-1}}$ at 0.7 Hz at DC bias levels of 5, 15, 25, 35, and 45 $\mathrm{kA\,m^{-1}}$. Device mechanical load is a prestress of 6.9 MPa.

Figure 3 depicts a major hysteresis loop from an actuator similar in design to that shown in **Figure 2**. Superimposed on the major hysteresis loop are five minor hysteresis loops collected by driving at 0.7 Hz with an applied of $\pm 5\ \mathrm{kA\,m^{-1}}$ as the DC magnetic bias was increased from 5 to 45 $\mathrm{kA\,m^{-1}}$ in increments of $10\ \mathrm{kA\,m^{-1}}$. AC operation of magnetostrictive actuators is typically achieved through the use of a DC magnetic field to provide bias operation so that it is centered about the steepest portion of the major hysteresis loop. This region is called the burst region, and the DC magnetic field amplitude required for operation about the middle of the burst region is called the critical field. All subsequent data are from magnetically biased transducers.

Figure 4 shows frequency response functions of acceleration per input current, where the change in the transducer's axial resonant frequency varies from 1350 Hz to over 2000 Hz, reflecting the effect of DC bias on the elastic modulus. The reduction in elastic modulus below that at magnetic saturation is known as the delta E effect. Note that in **Figure 4** only the axial resonant frequency of the magnetostrictive driver shifts and that the structural resonance of the device housing at 3300 Hz is not affected by the changing DC field.

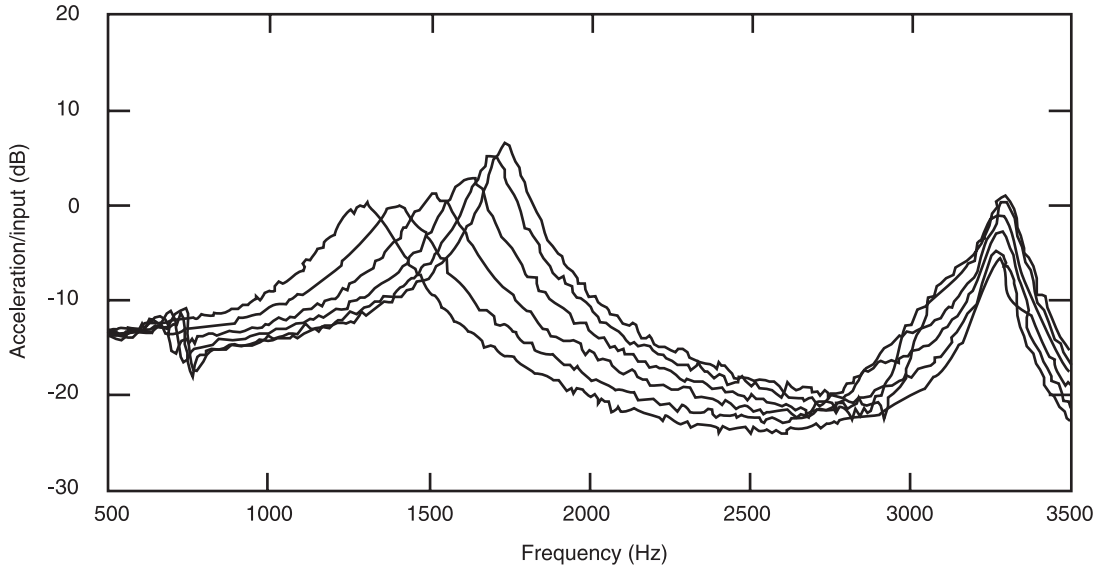


Figure 4 Acceleration per input current frequency response functions at DC bias levels of (from left to right): 20, 30, 36, 42, 50, and $60\ \mathrm{kA\,m^{-1}}$.

Figure 5 illustrates the sensitivity of major strain-applied field hysteresis loops to variations in mechanical load or prestress. While this attribute allows tailoring of devices preloaded for optimized performance under a constant load (such as acoustic source applications), this introduces a parameter that must be optimized for operation under variable load conditions which are typical of vibration control applications. Actuators using tailored magnetostrictive composite drivers can minimize device sensitivity to variations in the external load.

The upper traces in **Figures 6–8** are Bode plots of strain per applied field, strain per magnetization and magnetization per applied field, respectively. The Bode plots were obtained using a swept sinusoidal signal at a relatively low signal excitation of the device (e.g., driving the device to produce maximum strains at resonance that are less than one-third of the device full strain potential, thereby minimizing the presence of undesired harmonics). The lower traces are minor hysteresis loops of these quantities recorded at (from left to right)

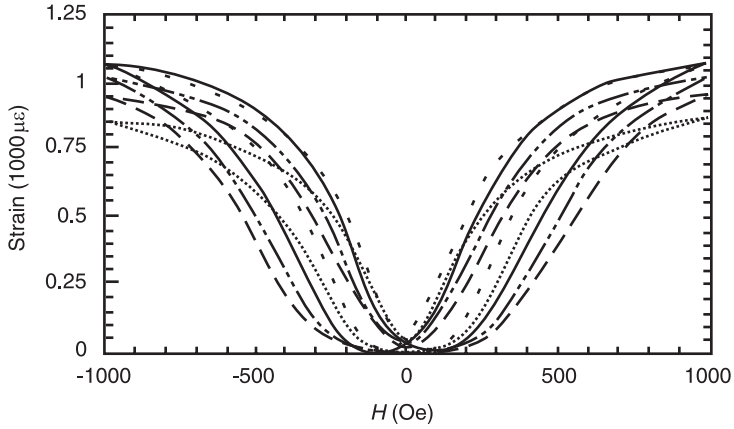


Figure 5 Strain vs applied-field major hysteresis loop corresponding to device mechanical loads of prestress: 3.5, 5.2, 6.9, 8.6 and 10.4 MPa. (– – –) 1.5 ksi; (– – – –) 1.25 ksi; (—) 1.0 ksi; (– – – – -) 0.75 ksi; (. . . . . .) 0.5 ksi.

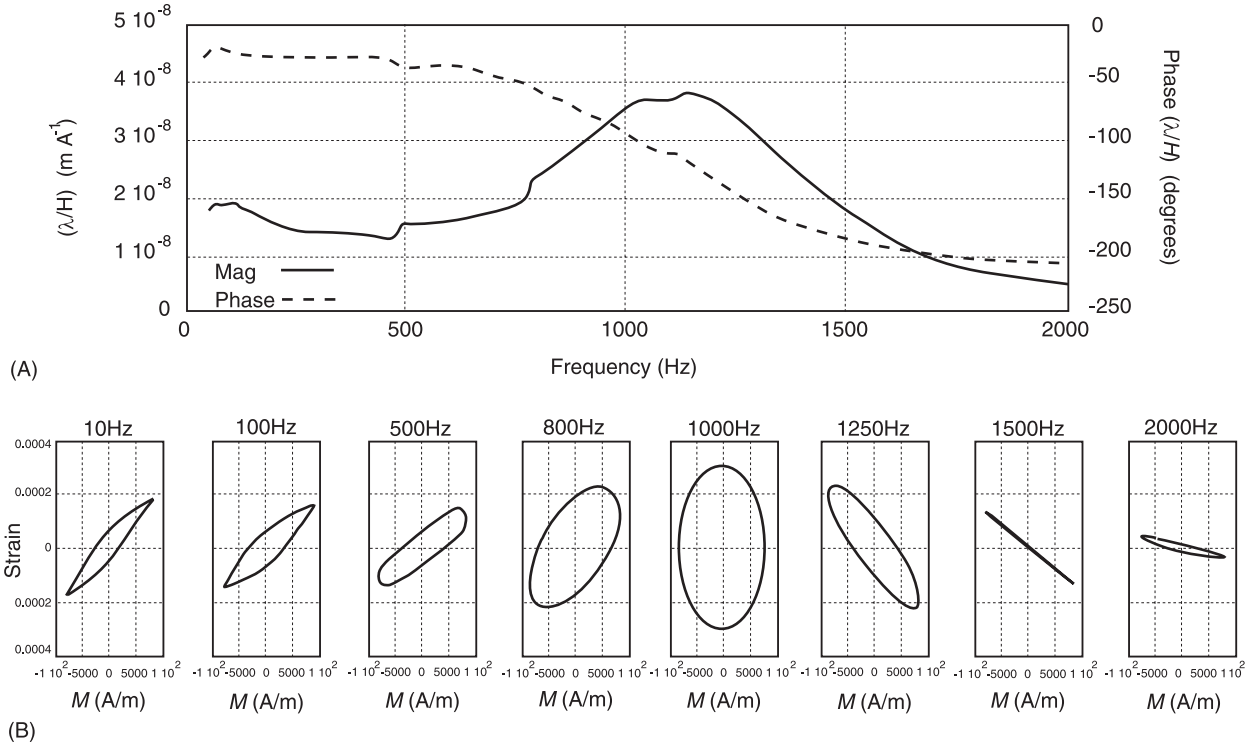


Figure 6 (A) Strain per applied magnetic field Bode plot. (B) Strain vs applied magnetic field minor loops ($\pm$400 microstrain vs $\pm$10 kA m^{-1}). From left to right, hysteresis minor loop data collected at: 10, 100, 500, 800, 1000, 1250, 1500, and 2000 Hz.

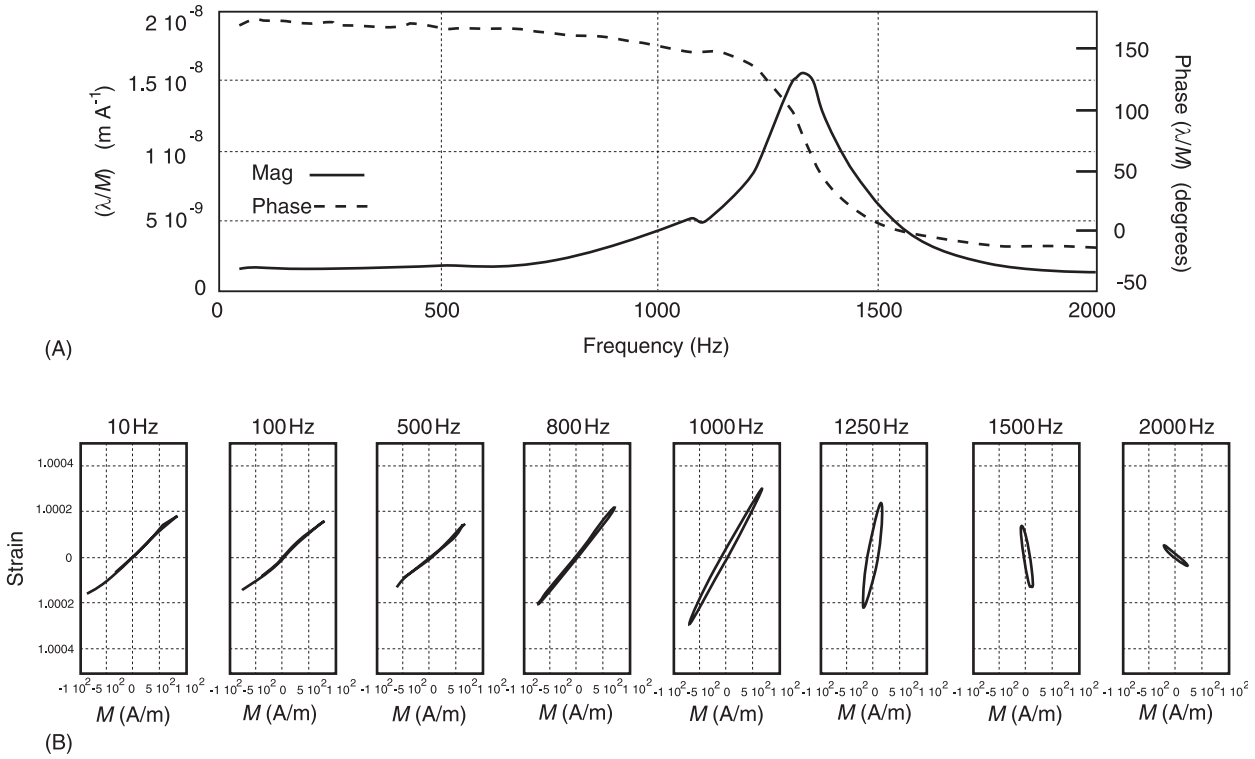


Figure 7 (A) Strain per magnetization Bode plot. (B) Strain vs magnetization minor loops ($\pm 100\,\mathrm{kA\,m^{-1}}$ vs $\pm 10\,\mathrm{kA\,m^{-1}}$). From left to right, hysteresis minor loop data collected at: 10, 100, 500, 800, 1000, 1250, 1500, and 2000 Hz.

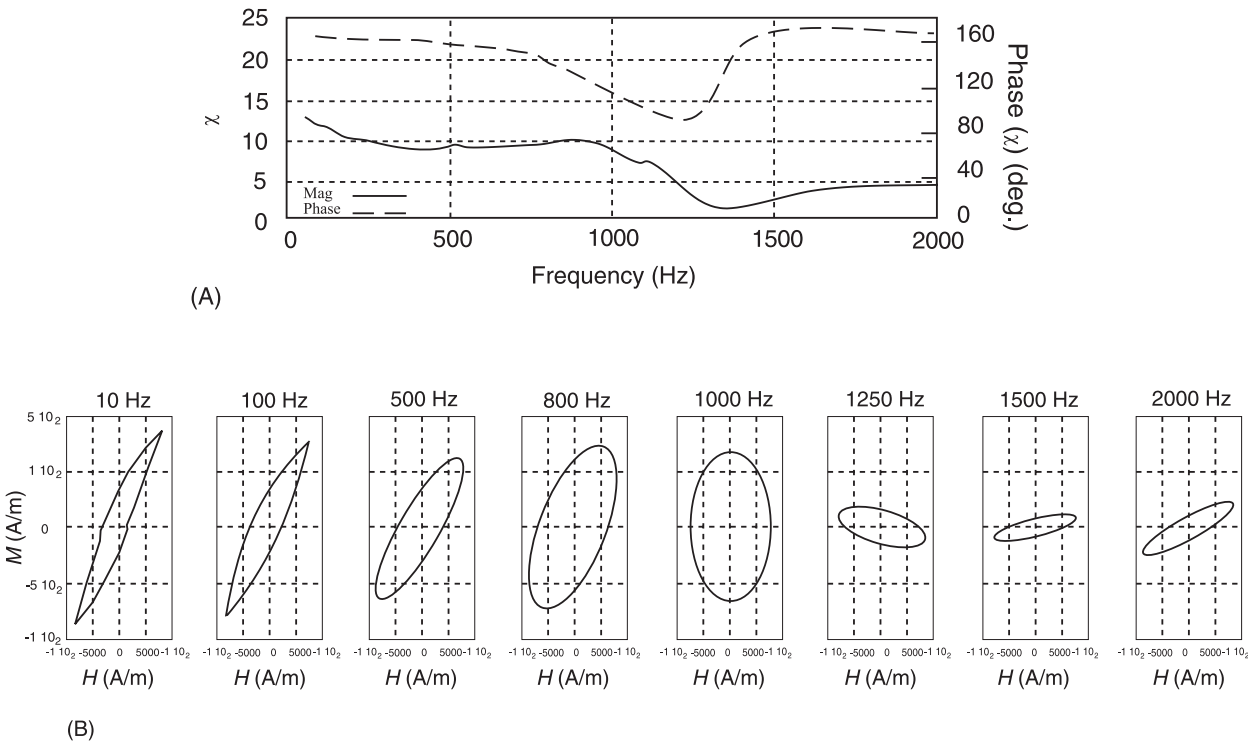


Figure 8 (A) Susceptibility (magnetization per applied field) Bode plot. (B) Susceptibility or magnetization vs applied-field minor loops (± 400 microstrain vs $\pm 100\,\mathrm{kA\,m^{-1}}$). From left to right, hysteresis minor loop data collected at: 10, 100, 500, 800, 1000, 1250, 1500, and 2000 Hz.

frequencies of 10, 100, 500, 800, 1000, 1250, 1500, and 2000 Hz.

Information on performance is used to implement calibration, input and/or output linearization, and control schemes to facilitate the optimized use of magnetostrictive devices. For example, information from **Figures 3** and **5** might be coupled to optimize the DC magnetic bias in real time to produce specified strains under varying mechanical loads. **Figure 4** demonstrates the ability to tune a system's resonant frequency in real time, which is the basis for a patent pending, tunable magnetostrictive vibration absorber design. This can be coupled with information on frequencies that minimize losses by using hysteresis loop data from **Figures 6–8** to tailor the frequency operation for the most efficient electromechanical performance. Additionally, this suggests the ability to target operating conditions for minimization of internal heating under continuous operation, which is of particular concern for ultrasonic operation.

Another significant loss factor that is associated with the transduction of electric to magnetic energy under dynamic operation is eddy currents. Eddy current power losses increase with approximately the square of frequency and thus have a significant impact on the operational bandwidth of devices. Laminations in the magnetostrictive core help to mitigate the effects of eddy currents, however, materials such as Terfenol-D are brittle and costly to laminate. Materials such as insulated magnetic particles or the silicon steels in common use in motors and power systems are suitable for the magnetic circuit components that make up the transducer housing, as they simultaneously support flux conduction and offer high resistivities. Magnetostrictive composites that use nonelectrically conducting matrix material yield reductions in eddy current losses. They have been proposed for extending device output bandwidth by an order of magnitude, from roughly 10 kHz to close to 100 kHz. Such composites offer great promise as high-frequency magnetostrictive drivers.

Actuation Configurations

Nickel was used in many of the early magnetostrictive sonar devices and is still being used in commercially available ultrasonic cleaners available from, for example, Blue Wave Ultrasonics. Other examples of magnetostrictive material use in commercial applications include Terfenol-D-based devices such as the underwater communication systems produced by Trigger Scuba, Inc., the acoustic pressure wave source (P-wave) produced by ETREMA Products, Inc. for enhancing oil well production rates, and precision micropositioners produced by Energenic, Inc.

Dynamic strains are of primary importance in low-frequency high-power transducers, namely those for sonar and underwater communications. At and near mechanical resonance, strains greater than the static saturation strain can be obtained. Three of the more common devices for sonar applications are the flextensional, the piston, and the 'ring' types of actuators. Flextensional transducers radiate acoustic energy through flexing of a shell, usually oval-shaped, caused by the longitudinal extension and contraction of a cylindrical drive motor mounted in compression inside the shell. The Tonpilz (Tonpilz is German for 'sound mushroom') transducer is a common piston-type design. The transducer has a magnetostrictive rod surrounded by a drive coil that provides AC and DC magnetic field excitation, a mechanism for prestressing the rod, a front radiating surface (piston), and a countermass. An advantage of piston-type designs over conventional flextensional transducers is that they lack parts likely to suffer fatigue-induced failure due to bending. A typical ring transducer might consist of four magnetostrictive rods that are arranged to form a square with four curved pistons that are the radiating surfaces enclosing the square and attached to the corners of the square. Monopole operation is achieved with the rods acting in unison. Dipole operation is accomplished by switching the magnetic bias on two of the rods and maintaining a constant direction on the AC magnetic field on all four rods. The interest in ring transducers during those early days was based on their ruggedness and lower cost compared to other available transducer technologies.

There is a growing interest in use of magnetostrictive devices as a source for motion and/or force, and in particular for use in conjunction with smart structures for active vibration control. These linear motor systems fall into the two general categories of piston devices and inchworm devices. An example of the performance that can be realized using magnetostrictive actuators for active vibration control is presented in **Figure 9** in which a simple analog proportion control scheme was applied to achieve significant vibration control (>33 dB at both mode 1 and 2). There are several variations on the inchworm motor concepts that move a shaft relative to the motor housing, and they all generally rely on two separate capabilities, a clamping force and a pushing force. Motors with linear shaft output rates of 20 mm s^{-1} have been designed that can develop 1000 N of force with a 200 mm stroke.

Although generic ultrasonic devices are similar to their low-frequency counterparts, e.g., they require the same components described in **Figure 2**, there are several problems associated with operation at

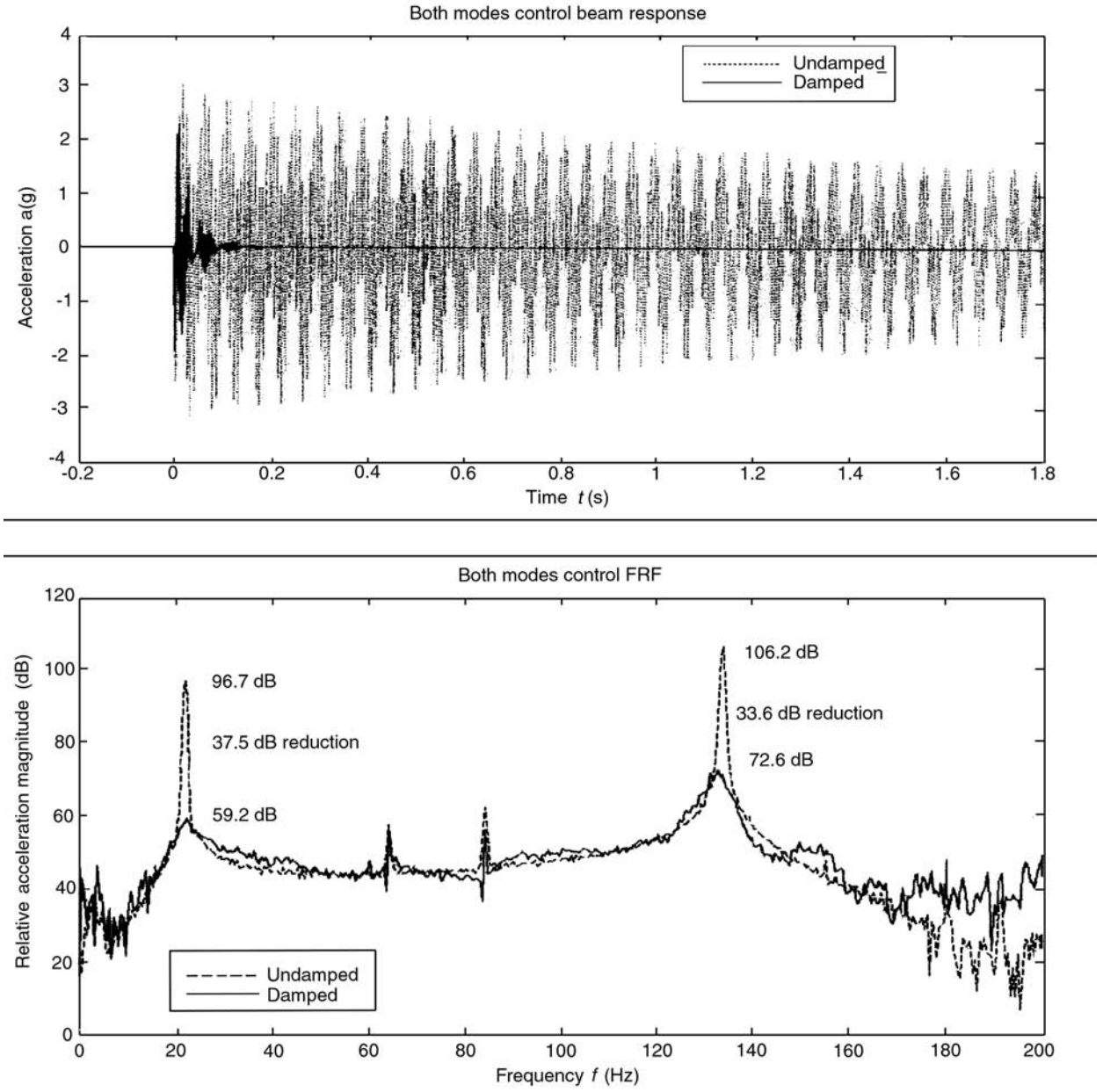


Figure 9 Magnetostrictive actuator performance for active vibration control of the transient responses of a 40 × 2 × 1 0.125-thick aluminum 'C' channel beam to impact excitation.

frequencies above 20 kHz. Hysteresis losses within a magnetostrictive driver will introduce high internal heat dissipation. Eddy currents will introduce both heat and a skin effect that effectively shields the core of the driver from an applied magnetic field. Impedance mismatches at ultrasonic frequencies make transfer of energy from the driver to the surrounding medium difficult. The use of laminated and/or composite magnetostrictive materials reduces losses associated with eddy currents. Device operation at resonance for enhanced energy output is often obtained through the use of quarter-wavelength-long drivers in conjunction with half-wavelength amplifying horns having application specific profiles.

Sensing Configurations

Magnetostrictive sensors can be classified as passive sensors, active sensors, and combined or hybrid sensors, based on how the magnetomechanical properties of the system components are used to measure the parameters of interest.

Passive sensors rely on magnetomechanical coupling to link a measurable change in the magnetostrictive material to the external property or condition of interest. For example, according to the Villari effect, the change in the magnetization of the magnetostrictive sample is correlated to an externally imposed change in stress. A coil flux-linked to the magnetostrictive sample can be used to measure changes in magnetic flux as per eqn [5]. Quantities such as external load, force, pressure, vibration, and flow rates can then be measured.

Active sensors use an internal excitation of the magnetostrictive element to facilitate some measurement of the magnetostrictive element that changes with the external property of interest. For example, an excitation coil could be used to excite the magnetostrictive sample with a known H as per eqn [4] and the detection coil used to measure B as per eqn [5]. The permeability from eqn [3] can then be monitored for changes due to an external condition. Designs that employ two coils, one to excite the magnetostrictive element and one for measurement, are known as transformer-type sensors. The most common active sensor design mentioned in the literature is the noncontact torque sensor. Many configurations employ variations on a general theme of a magnetostrictive wire, thin film, or ribbon flux-linked to a target shaft subject to a torque. The change in the magnetic induction or permeability can then be related to the torque on the specimen.

Finally, combined or hybrid sensors use a magnetostrictive element actively to excite or change another material to allow measurement of the property of interest. For example, a fiberoptic magnetic field sensor uses the change in length of a magnetostrictive element in the presence of a magnetic field (Joule effect) to change the optical path length of a fiberoptic sensor. Stress can be measured using photoelastic material, and highly accurate displacement measurements can be made with the help of a magnetostrictive guide.

Magnetostrictive transducers are particularly attractive for noncontact torque and position sensor applications. As a magnetostrictive shaft is torqued, stress develops at $\pm 45^{\circ}$ from the shaft axis, and the Villari effect produces changes in the shaft magnetization and permeability. The change in magnetization can be measured directly with a Hall probe. Alternatively, the change in permeability can be measured using a two-solenoid active technique in which an excitation solenoid is used to apply a constant magnetic field to a magnetic circuit flux-linked to the shaft and a detection solenoid monitors the torque-induced changes in the magnetic circuit permeability. These torque-induced changes can also be monitored by tracking electrical impedance function changes in flux-linked excitation and/or detection solenoids, as suggested by the data in **Figure 10**.

Several approaches exist for extending this technology to nonferromagnetic materials, by applying magnetostrictive materials directly to the surface of the rotating shafts. One technique relies on using amorphous magnetostrictive wire or ribbons that are helically wrapped around and bonded to a shaft. In another, at a high temperature the wire is exploded into fine particles which adhere strongly to the shaft.

Similarly, noncontact position sensors and force distribution sensors are available that respond to the influence of reflected signals and gaps on magnetostrictive components of a magnetic circuit (magnetostrictive waveguides and magnetostrictive delay lines, respectively). Metglas amorphous ribbons are an attractive strain sensor material because they exhibit large permeability changes in response to strain.

Velocity and force can be directly measured in a magnetostrictive transducer, as depicted in **Figure 2**, where the voltage induced in the solenoid is proportional to the velocity of the force applied to the free end of the magnetostrictive element. Similar transducers have been used as colocated sensor–actuator devices; e.g., devices that simultaneously actuate and sense. The telephone, scanning sonar, and active vibration control applications have made use of this dual operation mode. Although this can be accomplished by separating the voltage induced in the excitation solenoid via the Faraday–Lenz law from the applied (excitation) voltage, the sensed voltages is generally much smaller than that needed for actuation. Hence, it is common for a dual-mode transducer to use separate excitation and detection solenoids.

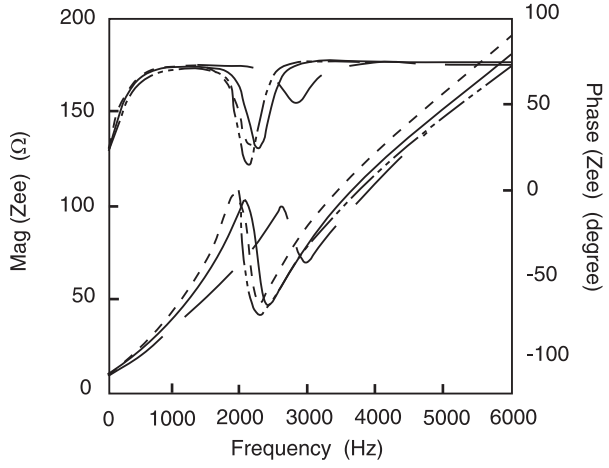


Figure 10 Sensitivity of electrical impedance functions to changes in the stress in the transducer magnetostrictive element. (Key as in **Figure 5**.)

Nomenclature

A	area
B	magnetic induction
F	force
H	magnetic field
T	current
L	length
N	number of terms
T	transduction
v	velocity
V	applied voltage
Z	impedance
ε	strain
λ	Joule effect magnetostriction
σ	stress

See also: **Actuators and smart structures**; **Electrorheological and Magnetorheological Fluids**; **Sensors and actuators**; **Transducers for absolute motion**; **Transducers for relative motion**.

Further Reading

Butler JL (1988) *Application Manual for the Design Etrema Terfenol-D. Magnetostrictive Transducers*. Ames, IA: Edge Technologies.

Calkins FT (1997) PhD dissertation, Iowa State University.

Cedell T (1995) *Magnetostrictive Materials and Selected Applications*. PhD dissertation, Lund University, Sweden.

Clark A (1980) *Magnetostrictive Rare Earth-Fe_2 Compounds, Ferromagnetic Materials*, vol.1. Amsterdam: North-Holland.

Cullity BD (1972) *Introduction to Magnetic Materials*. Reading, MA: Addison Wesley.

Dapino MJ, Calkins FT and Flatau AB (1999). In Webster JG (ed.) *Wiley Encyclopedia of Electrical and Electronics Engineering*, vol. 12, pp. 278–305. Chichester, UK: Wiley.

du Tremolet de Lacheisserie E (1993) *Magnetostriction Theory and Applications of Magnetoelasticity*. Boca Raton: CRC Press.

Fleming W (1990) Magnetostrictive torque sensors – comparison of branch, cross, and solenoidal designs. SAE Technical Paper 900264, pp. 51–78.

Hunt FV (1982) *Electroacoustics: The Analysis of Transduction, and its Historical Background*. American Institute of Physics for the Acoustical Society of America.

Jiles D (1991) *Introduction to Magnetism and Magnetic Materials*. London: Chapman and Hall.

NDRC (1946) Summary of Technical Report of Division 6. The design and construction of magnetostriction transducers, Vol. 13.

Restorff JB (1994) *Encyclopedia of Applied Physics*, vol. 9, pp. 229–244.

MATERIALS, DAMPING

See **DAMPING MATERIALS, SEISMIC INSTRUMENTS, ENVIRONMENTAL FACTORS, LASER BASED MEASUREMENTS**

MEASUREMENT

See **LASER BASED MEASUREMENTS; SEISMIC INSTRUMENTS, ENVIRONMENTAL FACTORS; STANDARDS FOR VIBRATIONS OF MACHINES AND MEASUREMENT PROCEDURES; TRANSDUCERS FOR ABSOLUTE MOTION; TRANSDUCERS FOR RELATIVE MOTION**

MEMBRANES

A W Leissa, Ohio State University, Columbus, OH, USA

Copyright © 2001 Academic Press

doi:10.1006/rwvb.2001.0132

A membrane is a structural element which is very thin in one direction compared with the other two, and is flat. In contrast with a plate, it has no bending or twisting stiffness. If a membrane is not flat, it is called a 'membrane shell' (see **Shells**). The membrane is stretched in its plane by tensile and (perhaps) shear stresses. It is these stresses which provide the restoring forces during transverse free vibrations. It is also assumed that these stresses are sufficiently large so that, if the transverse vibrational displacement (w) is kept small, the stresses will remain constant during

vibration. **Figure 1** depicts a membrane in its static equilibrium position, stretched over a boundary of arbitrary curvilinear shape. The stress (force/area) applied externally is shown as a normal stress σ_n which may vary along the boundary. In addition, a variable shear stress, which is not shown, may also act in the plane (xy) of the membrane, and tangent to its boundary. These boundary stresses cause internal normal stresses (σ_x and σ_y) and shear stress (τ_{xy}), as shown on an internal element of the membrane in **Figure 1**, which may vary with the coordinates (x and y), but not with time (t).

The equation of transverse motion of the membrane is:

$$T_x \frac{\partial^2 w}{\partial x^2} + 2T_{xy} \frac{\partial^2 w}{\partial x\, \partial y} + T_y \frac{\partial^2 w}{\partial y^2} + q = \rho h \frac{\partial^2 w}{\partial t^2} \quad [1]$$

where T_x, T_{xy}, T_y are the stress resultants (force/length) obtained by multiplying σ_x, τ_{xy} and σ_y, respectively, by the thickness (h). Transverse forcing pressure (force/area) is indicated by q, which could be present in a forced vibration situation, and ρ is the mass density/volume. In eqn [1], T_x, T_{xy}, T_y, ρ and h may each be functions of x and y, but not t.

Considering free, undamped vibrations ($q = 0$), the most widely used form of eqn [1] is the special case wherein the in-plane shear stress is zero, and the remaining tensile stress is constant and the same in all directions ($T_x = T_y = T$). In this case eqn [1] becomes:

$$T\nabla^2 w = \rho h \frac{\partial^2 w}{\partial t^2} \quad [2]$$

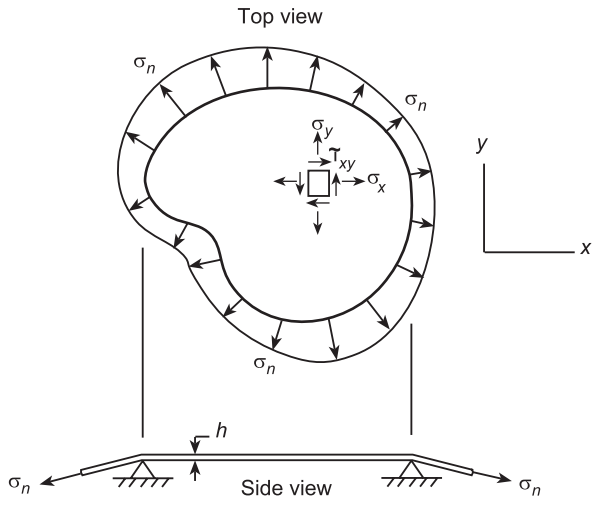


Figure 1 Membrane of arbitrary shape subjected to nonuniform tensile stress.

where $\nabla^2 = \partial^2/\partial x^2 + \partial^2/\partial y^2$ is the Laplacian differential operator.

Rectangular Membranes

Consider first a rectangular membrane with dimensions $a \times b$, stretched by uniform tension (T). Let the origin of the xy coordinate system be in one corner, so that the four edges ($x = 0, a; y = 0, b$) are fixed ($w = 0$). An exact solution for the transverse, free vibration displacement is:

$$w(x, y, t) = \sin(m\pi x/a) \sin(n\pi y/b) \sin(\omega t + \phi) \quad [3]$$

where m and n are integers, ranging from one to infinity ($m, n = 1, 2 \ldots \infty$), and ϕ is an arbitrary phase angle. It is seen that eqn [3] satisfies the boundary condition ($w = 0$) along all four edges. Substituting it into eqn [2] yields the natural frequencies (ω), which are conveniently expressed in terms of the nondimensional parameter:

$$\omega a \sqrt{\rho h/T} = \pi \left[m^2 + (a/b)^2 n^2 \right]^{1/2} \quad [4]$$

Looking at eqn [4] it is clear that the fundamental (i.e., lowest) frequency of a rectangular membrane, regardless of the aspect ratio (a/b) will be for a mode shape having one half-sine wave in each direction ($m = n = 1$). **Figure 2** shows the first nine nodal patterns of free vibration for a rectangular membrane having $a/b = 1.5$. The dashed lines are node lines ($w = 0$). The corresponding nondimensional frequencies $\omega a \sqrt{\rho h/T}$ are 5.664, 7.854, 9.935, 10.538, 11.327, 13.329, 13.421, 14.482, and 15.471, according to eqn [4]. It is seen that some frequencies may be quite close together.

One may also have two mode shapes having the same frequency. These are called 'degenerate modes'. For example, consider the square membrane ($a = b$) and its degenerate frequencies $\omega_{12} = \omega_{21}$. Because they both vibrate with the same frequency, superposition of the two mode shapes may be taken as:

$$W(x, y) = C_{12} \sin(\pi x/a) \sin(2\pi y/a) + C_{21} \sin(2\pi x/a) \sin(\pi y/a) \quad [5]$$

where C_{12} and C_{21} are arbitrary constants, determined by how the membrane is set into motion (the initial conditions). **Figure 3** shows how the node line varies with the relative magnitude (C_2/C_1) of the superimposed modes. **Figure 3** also shows some

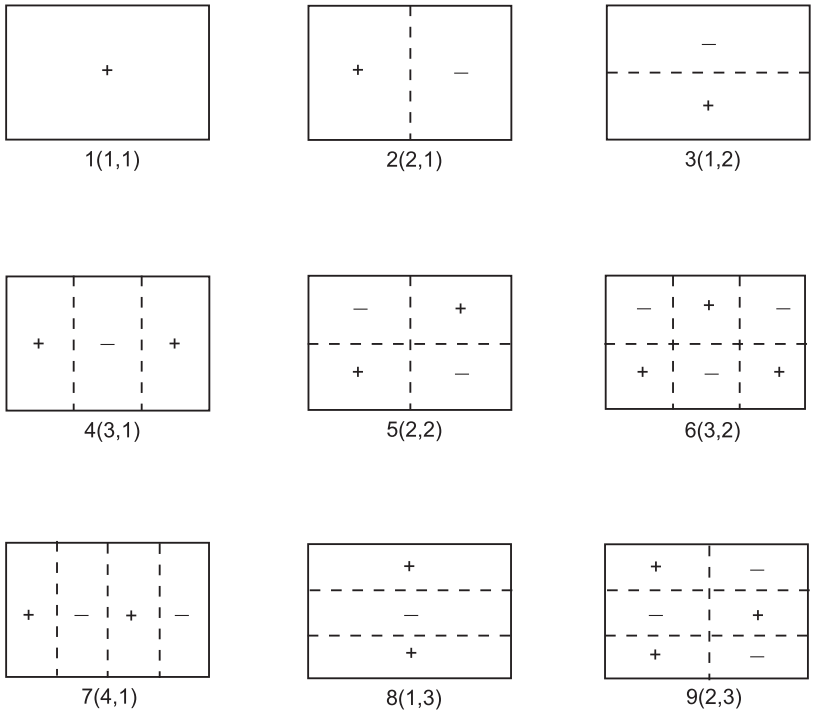


Figure 2 First nine nodal patterns of a rectangular membrane with $a/b = 1.5$.

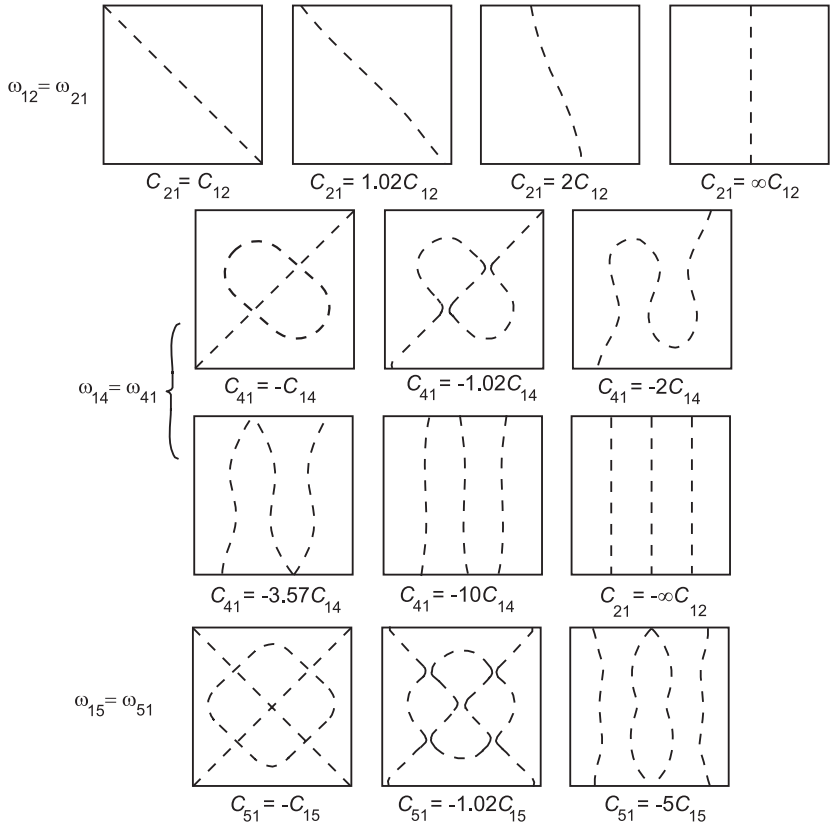


Figure 3 Some superimposed degenerate nodal patterns for square membranes.

superimposed degenerate modes for $\omega_{14} = \omega_{41}$, and for $\omega_{15} = \omega_{51}$.

Circular Membranes

For a circular membrane it is convenient to use polar coordinates, as shown in **Figure 4**. Then $\nabla^2 = \partial^2/\partial r^2 + (1/r)\partial/\partial r + (1/r^2)\partial^2/\partial\theta^2$. By separation of variables one finds the transverse displacement:

$$w(r, \theta, t) = [A_n J_n(kr) + B_n Y_n(kr)] \cos\ n\theta \sin(\omega t + \phi) \quad [6]$$

which satisfies eqn [2] exactly, where J_n and Y_n are Bessel functions of the first and second kinds, respectively, $k^2 = \omega^2 \rho h/T$, A_n and B_n are arbitrary constants, and n is an integer, beginning with zero. Because $Y_n(0) = -\infty$, it is necessary to set $B_n = 0$ to have finite displacement at the center ($r = 0$). Setting $w = 0$ along the boundary ($r = a$) results in the frequency equation:

$$J_n(ka) = 0 \quad [7]$$

The first five roots $ka = \omega a\sqrt{\rho h/T}$ of eqn [7] are given in **Table 1** for each n. Nodal patterns for the first nine frequencies of a circular membrane are shown in **Figure 5**, along with the corresponding $\omega a\sqrt{(\rho h/T)}$ It is seen that modes 1, 4, and 9 are axisymmetric ($n = 0$), having 0, 1, and 2 interior nodal circles, respectively, whereas modes 2, 3, 5, and 7 have 1, 2, 3, and 4 nodal diameters, respectively, with no interior nodal circles. Exact shapes of the vibration modes along diameters may be seen from plots of the Bessel functions $J_n(kr)$.

An annular membrane is bounded by two concentric circles, an inner one at $r = b$, and an outer one at $r = a$, with both circular boundaries being fixed and exerting uniform radial tension T (force/length). The solution (eqn [6]) of eqn [3] is again

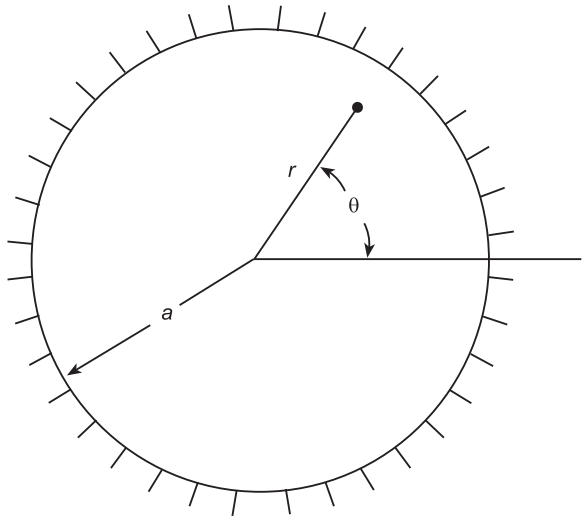


Figure 4 Circular membrane and polar coordinates.

appropriate. But both A_n and B_n are now retained, because $r = 0$ does not apply to the membrane. Setting $w = 0$ at $r = a$ and $r = b$ gives, for a nontrivial solution, the following frequency equation:

$$J_n(\lambda) Y_n\left(\frac{b}{a}\lambda\right) - J_n\left(\frac{b}{a}\lambda\right) Y_n(\lambda) = 0 \quad [8]$$

where $\lambda = ka = \omega a\sqrt{\rho h/T}$. For any desired value of b/a, all frequencies of the annular membrane are obtainable from eqn [8]. The first three frequencies (corresponding to 0, 1, and 2 interior nodal circles) are listed in **Table 2** for the $n = 0$ (axisymmetric) and $n = 1$ (one nodal diameter) modes of annular membranes having various b/a ratios, especially for $b/a < 0.5$. It is interesting to note that, as b/a approaches zero, which corresponds to a central point support, the frequency for $n = 0$ becomes the same as for the unsupported membrane (**Table 1**). This is because membranes are incapable of transmitting transversely applied concentrated forces (reactive in this situation)

Table 1 Frequencies $\omega a\sqrt{\rho h/T}$ for circular membranes.

	n (nodal diameters)					
Number of root[a]	*0*	*1*	*2*	*3*	*4*	*5*
1	2.405	3.832	5.136	6.380	7.588	8.771
2	5.520	7.016	8.417	9.761	11.065	12.339
3	8.654	10.173	11.620	13.015	14.373	15.700
4	11.792	13.324	14.796	16.223	17.616	18.980
5	14.931	16.471	17.960	19.409	20.827	22.218

[a] Number of nodal circles plus one.

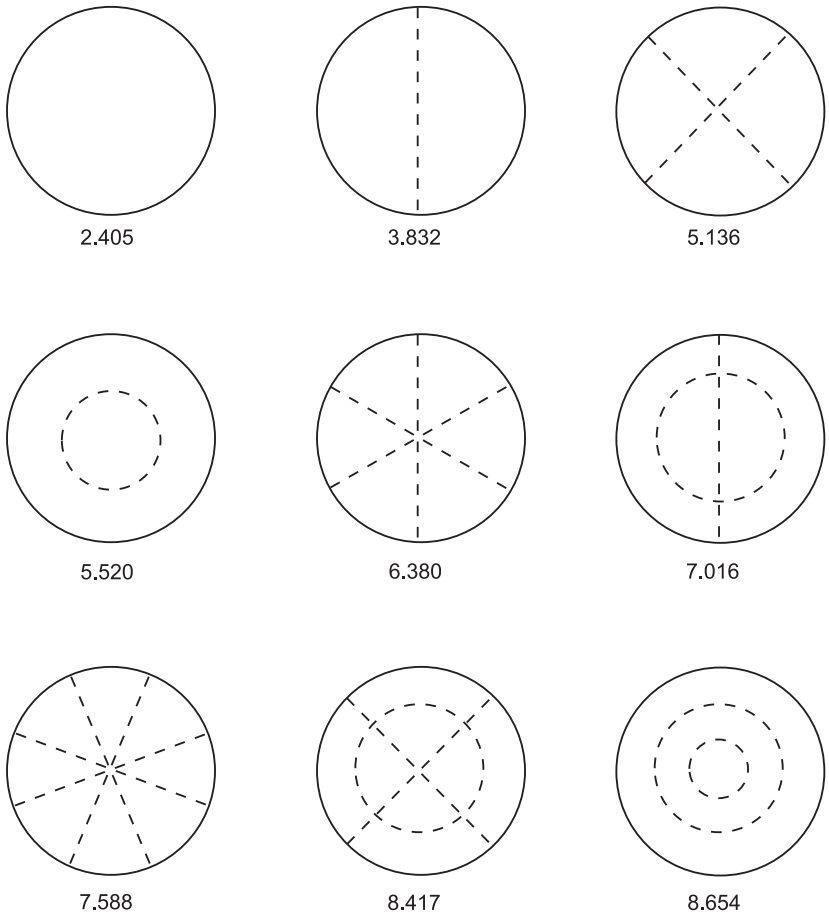


Figure 5 First nine nodal patterns of a circular membrane.

Table 2 Frequencies $\omega a\sqrt{\rho h/T}$ for annular membranes.

		Number of roots		
n	*b*/*a*	*1*	*2*	*3*
	0.80	15.698	31.411	47.121
	0.60	7.828	15.695	23.553
	0.40	5.183	10.443	15.688
0	0.20	3.816	7.786	11.732
	0.10	3.314	6.858	10.377
	0.02	2.884	6.136	9.376
	0.00	2.405	5.520	8.654
	0.80	15.738	31.431	47.134
	0.60	7.930	15.747	23.588
	0.40	5.391	10.558	15.766
1	0.20	4.236	8.055	11.927
	0.10	3.941	7.331	10.748
	0.02	3.836	7.031	10.205
	0.00	3.832	7.016	10.173

without violating the linearizing assumptions made in deriving the theory.

Other Shapes

A sectorial membrane has the shape of a sector of a circle (**Figure 6**), with a sector angle, α. The transverse displacement:

$$w(r,\theta,t) = [A_\upsilon J_\upsilon(kr) + B_\upsilon Y_\upsilon(kr)] \sin \upsilon\theta \sin(\omega t + \phi) \quad [9]$$

satisfies eqn [2]. Moreover, if noninteger values of υ are chosen such that $\upsilon = n\pi/\alpha (n = 1, 2 \ldots \infty)$, then $w = 0$ along the radial edges $\theta = 0$ and α, as desired. Setting B_υ=0 to avoid infinite displacement at $r = 0$, and $w = 0$ at $r = a$ yields:

$$J_\upsilon(ka) = 0 \quad [10]$$

Symmetric modes result from $n = 1, 3, \ldots$; antisymmetric modes from $n = 2, 4, \ldots$ For every υ there is an infinite number of nondimensional frequencies $ka = \omega a\sqrt{\rho h/T}$. Frequencies arising from half-integer orders of υ are given in **Table 3**. Results for intermediate values of $\alpha = 180^\circ$, 90°, 60°, 45°, and 36°, corresponding to integer υ, may be taken from **Table 1**. The case of $\upsilon = 1/2$, corresponding to $\alpha = 360^\circ$ in **Table 3**, yields boundaries at $\theta = 0^\circ$ and $\theta = 360^\circ$, which are the same radial line, and the case of the complete circular membrane supported along an additional single radial line is thereby represented.

Annular sectorial membranes are bounded by the circle arcs ($r = b$, $r = a$) and the two radial lines ($\theta = 0$, $\theta = \alpha$). Frequencies for arbitrary α and b/a may be found from eqn [8], replacing n by υ, where $\upsilon = n\pi/\alpha (n = 1, 2 \ldots \infty)$.

Because node lines have the same zero transverse displacement as a constrained boundary, considerable miscellaneous results for other membrane shapes

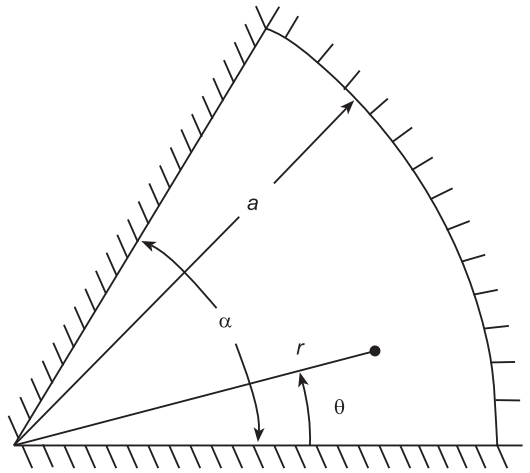


Figure 6 Sectorial membrane.

can be found by studying nodal patterns. For example **Figure 3** shows that the exact frequency for an isosceles right triangle with sides $a \times a$ is that of the (1, 2) and (2, 1) modes of a square $-\omega a\sqrt{\rho h/T} = \sqrt{5\pi}$. Considering the node lines as boundaries, **Figure 3** also shows a variety of shapes, each having straight and curvilinear lines as boundaries.

Additional information for straight-sided membranes may be obtained from published results for plates having the same configurations and all edges simply supported, using the correspondence:

$$\left(\frac{\omega_m^2 \rho h}{T}\right)^2 \sim \frac{\omega_p^2 \rho h}{D} \quad [11]$$

where the subscripts m and p correspond to membrane and plate natural frequencies, respectively (see **Plates**). Using this one can, for example, obtain the accurate frequencies for right triangular membranes of various aspect ratios (b/a) presented in **Table 4**. Corresponding nodal patterns for the second, third,

Table 3 Frequencies $\omega a\sqrt{\rho h/T}$ for sectorial membranes.

	Sector angle, α (and value of υ)					
Number of roots[a]	*360°* *(1/2)*	*120°* *(3/2)*	*72°* *(5/2)*	*51.43°* *(7/2)*	*40°* *(9/2)*	*32.73°* *(11/2)*
1	3.142	4.493	5.763	6.988	8.183	9.356
2	6.283	7.725	9.095	10.418	11.705	12.967
3	9.425	10.904	12.323	13.698	15.040	16.355

[a] Number of nodal circles plus one.

Table 4 Frequencies $\omega a\sqrt{\rho h/T}$ for right triangular membranes

	b/a					
Mode number	*1*	*1.25*	*1.5*	*2*	*2.5*	*3*
1	7.025	6.323	5.855	5.269	4.907	4.679
2	9.935	8.876	8.099	7.063	6.408	5.967
3	11.33	10.25	9.584	8.641	7.781	7.147
4	12.95	11.48	10.32	9.018	8.482	8.142

Adapted from more extensive data given in: Gorman DJ (1983) A highly accurate analytical solution for free vibration analysis of simply supported right triangular plates. *Journal of Sound and Vibration* 89: 107–118.

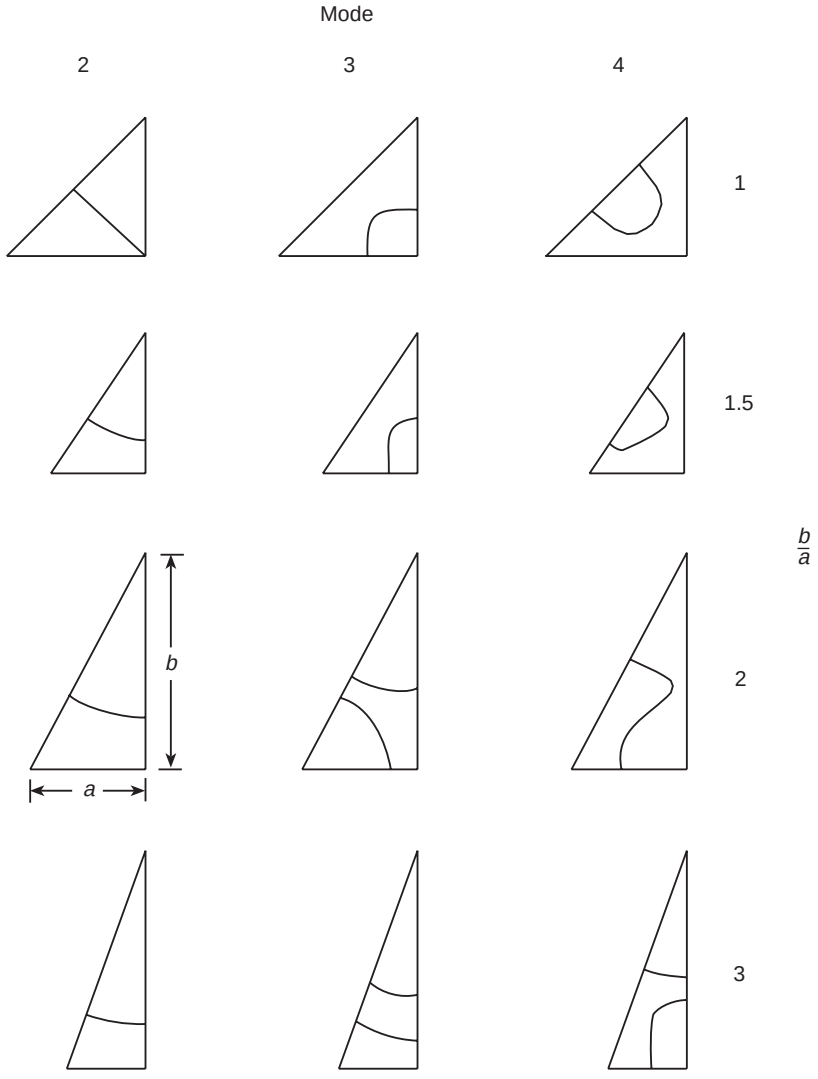


Figure 7 Nodal patterns for the second, third, and fourth modes of right triangular membranes.

Table 5 Nondimensional frequencies $\omega a\sqrt{\rho h/\sigma_x}$ for a square membrane with biaxial tension $(\sigma_y = \sigma_x)$ and additional shear stress (τ_{xy})

	Mode number						
τ_{xy}/σ_x	*1*	*2*	*3*	*4*	*5*	*6*	*7*
0.00	4.443	7.025	7.025	8.886	9.935	9.935	11.327
0.10	4.438	6.916	7.118	8.837	9.922	9.962	11.092
0.20	4.425	6.790	7.197	8.701	9.886	10.030	10.801
0.50	4.322	6.285	7.337	7.934	9.603	9.606	10.606
0.75	4.126	5.620	6.864	7.306	8.099	9.062	9.268
0.85	3.986	5.211	6.221	7.212	7.221	8.149	8.678
0.98	3.591	4.174	4.647	5.110	5.584	6.114	6.802
1	3.376	3.677	4.015	4.411	4.889	5.488	6.280

Adapted from more extensive data given in: Leissa AW, Ghamat-Rezaei A (1990). Vibration of rectangular membranes subjected to shear and nonuniform tensile stresses. *Journal of the Acoustical Society of America* 88: 231–238.

and fourth modes are exhibited in **Figure 7**. (The first modes have no interior node lines.)

Some Complicating Effects

Results for frequencies and mode shapes of free vibrations given above have all been for membranes which are initially stretched by a uniform tensile stress resultant (T) in all directions. If a rectangular membrane is subjected to different, but uniform, tensile stresses in its lengthwise and breadthwise direction $(T_x = \sigma_x h = \text{ constant}, \ T_y = \sigma_y h = \text{ constant})$, the sine wave mode shapes of eqn [3] remain valid. Substituting eqn [3] into eqn [1], with $q = 0$ and $T_{xy} = 0$, yields the exact frequencies:

$$\omega a\sqrt{\rho h/T_x} = \pi\left[m^2 + (T_y/T_x)(a/b)^2 n^2\right]^{1/2} \qquad [12]$$

If shear stress is also present then no exact solution is possible. Let σ_x, σ_y, and τ_{xy} all be constants. Reasonably accurate frequencies for a square membrane $(a/b = 1)$, with $\sigma_y = \sigma_x$ and varying amounts of additional shear stress (τ_{xy}/σ_x), were obtained by the Ritz method, and are presented in **Table 5**. For this combination of stresses, the stresses along 45° diagonal planes are principal stresses:

$$\sigma_1 = \sigma_x + \tau_{xy}, \quad \sigma_2 = \sigma_x - \tau_{xy}, \quad \tau_{12} = 0 \qquad [13]$$

as shown in **Figure 8**. As τ_{xy}/σ_x approaches unity, σ_2 becomes zero, and σ_1 becomes $2\sigma_x$. This is a special case of diagonal tension where the membrane is stretched in the direction of one of its diagonals, but is slack in the other diagonal direction. This is a limiting case, for if $\tau_{xy}/\sigma_x > 1$, σ_2 is compressive, and the membrane will buckle (wrinkle) in its initial state. Contour plots of mode shapes corresponding to some of the frequencies are shown in **Figure 9**. For $\tau_{xy}/\sigma_x = 1$, the node lines are all straight, and parallel to the direction of the applied principal stress (σ_1).

Nomenclature

h	thickness
T	uniform tension
w	transverse vibrational displacement
α	sector angle
ϕ	arbitrary phase angle

See also: **Plates**; **Shells**.

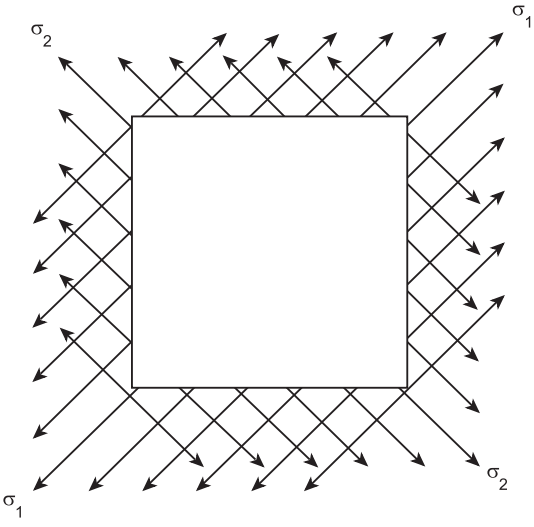


Figure 8 Biaxial diagonal tensile stresses.

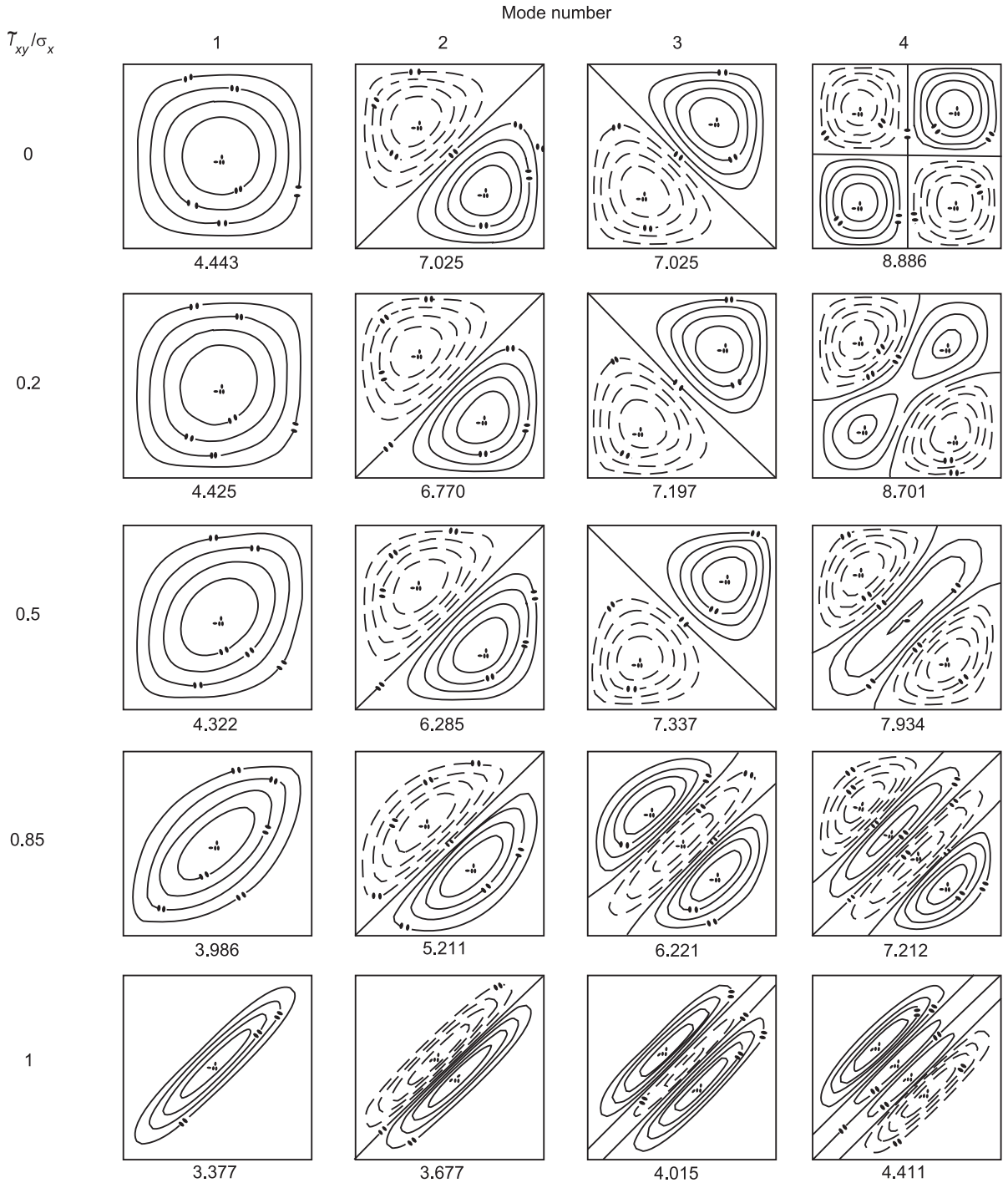


Figure 9 Mode shape nodal patterns corresponding to some of the frequencies in **Table 5**.

Further Reading

Courant R, Hilbert D (1953) *Methods of Mathematical Physics*, vol.1. New York: Wiley Interscience.

Lord Rayleigh (1945) *The Theory of Sound*, vol. 1. New York: Dover Publications (reproduction of 1877 original published by the MacMillan Co.).

Meirovitch L (1967) *Analytical Methods in Vibrations*. New York: Macmillan.

Timoshenko SP, Young DH, Weaver W (1974) *Vibration Problems in Engineering*, 4th edn. New York: Wiley.

MEMS, APPLICATIONS

I Stiharu, Concordia University, Montreal, Quebec, Canada

Copyright © 2001 Academic Press

doi:10.1006/rwvb.2001.0075

Introduction

Microelectromechanical systems (MEMS) applications have been conceived for both substitution and for new products. The decreased cost associated with very large production is directing the utilization of the microsystems into applications that require mass production. Pressure, temperature, proximity, acceleration or chemical integrated microsensors for automotive application represent a large family of substitution MEMS. Intelligent transportation systems (ITS) technology is another motor of development for new microsystems. The health care devices are also regarded as great potential applications for either substitution or new products.

The primary feature of MEMS applications is that they adequately detect and influence phenomena where microscale interactions are adjoining to macroscale effects. The small-size, low-energy consumption endorsed by high reliability, low cost, and capability to process and deliver undistorted measurement signals in a form that the user can easily exploit constitute the major strengths of MEMS. Microsensors usually do not interfere with macrophenomena, while they could track microscale events accurately. MEMS are thus capable of perceiving the nature to a much lower scale size than the normal-sized sensors do. They can be implemented in time-varying spatial microscale configurations to survey the borderline transition from micro to macro phenomena. Thus, applications of MEMS sensors in resonant structures, buckling, turbulent flow, acoustics, thermo-stress phenomena, and phase change, are befitting. The low cost of the microsensors permits allocations of much larger numbers of measurement points in systems that require synchronization of distributed response, in dynamic allocation of scarce resources systems, or in redundant control and decision management systems.

Although the great majority of the present commercially available devices are based on bulk micromachining, surface micromachined microsystems represent the desired turnout for future MEMS. The capability to integrate on the same chip when produced during the same process, the integrated circuit (IC) circuitry, and the sensing/actuating device enable applications that up to now have been unimaginable. The large number of present MEMS-based systems represent just a small fraction of the possible conceivable and unique applications that will be available in the very near future. A number of available applications involving MEMS are shown in **Table 1**. The applications listed are at various levels of development, ranging from laboratory testing to the market. Most microsystems are still related to the macroscopic perception of the world, whereas those conceived to handle the matter at miniature scale have been implemented more recently. DNA-mapping kits and bioanalysis systems on a single chip are an application that will probably soon be commercially available. However, the endowment of MEMS has become quite common, such that the acknowledgment of the microtechnology in newly developed systems is no longer publicized by the manufacturer.

The related applications of MEMS to the dynamics of mechanical systems are mostly limited at this time to those accomplished by the normal-sized sensors. Accelerometers, angular rate sensors, vibrometers, microphones, and pressure sensors, are the most common applications available at this time. There are very few MEMS devices in large-scale commercial use, other than microsensors and microvalves. However, sustained research is being carried out to accomplish fully integrated systems in one single chip. Thus, single-chip autonomous microrobot or computer hard-drive units on a single chip, implantable drug delivery systems equipped with sensors, valve, reservoir, and controller, or ion propulsion miniature systems for space application are only a few of the microsystems which have been thoroughly investigated. If the progress in accomplishing fully integrated microsystems is considered to be moderate, microelements such as new microsensors and microactuator concepts and prototypes are constantly being reported.

Mechanical Microsensors

Most MEMS mechanical sensors are alternatives for existing normal-sized sensors. Regardless of the physical quantity detected, MEMS mechanical sensors

Table 1 Potential applications of MEMS

Area of application	*Application*
Mechanical microsensors	Microaccelerometers
	Microgyroscopes
	Rate, speed, and position linear and angular sensors
	Vibration measurement systems
	Pressure, temperature, flow, gas composition sensors
Fluid control	Microvalves, smart valves
	Micropumps
	Gas/liquid chromatography
	Logic fluidic elements
	Multisensing arrays
Biomedical	Multiple microchemical test kits
	Multisensing and surgery catheters
	Drug delivery
	Cell handling
	Cell fusion
	Biomolecular handling
	Blood test integrated cell
	Multiple virus integrated test kits
Human sensing stimulation	Neural activity detection and measurement
	Tactile stimulation
	Hearing and visual aid
	Smell sensors
	Distributed arrays of multiple sensing
Microoptics	Fiberoptic alignment
	Scanning
	Modulation
	Interferometer
	Optical head
	Optomechanical integrated circuits
	Arrays of mirrors and varying-focal mirrors
Microprobing and microtesting	Atomic force microscopy probes
	Scanning tunneling microscope probes
	Near-field microscopy probes
	Tunneling probe arrays
	Microbalances
Computer/peripheral components	Magnetic, printer, compact disk head
	Laser scan
	Micromechanical memory
Integrated circuit technology	Micromanipulators, microprobes
	Micropositioners
Robotics	Microrobots
	Microteleoperators
	Mobile sensors

exhibit a larger measurement range, higher sensitivity, better linearity, and lower hysteresis. Besides, all commercially available MEMS mechanical sensors easily comply with the rule of 20% for a new product: newly developed MEMS-based products are at least 20% less expensive to build and/or perform 20% better. Many MEMS devices are developed at a cost which is 10 times less expensive and perform 10 times better than normal-sized sensors. The most significant impact of MEMS, however, arises from their applications, which in most cases cannot be realized with normal-sized systems. A multiactive linking catheter, arrayed mirror high-resolution display, or a swimming microrobot represent only a few of the research topics which are most likely to grow into commercial products which will have a large impact on our life.

The automotive industry has had most benefit from MEMS so far. The mass production of cars requires mass production of sensors, which can be made more economical and rugged through micromachining. Research reports predict a growth of the MEMS device industry to about $35 billion annually by the year 2002: more than half of this is attributed to the automotive industry. **Figure 1** illustrates the distribution of MEMS applications on the end-user industry.

Pressure and acceleration sensors have already been successfully implemented as typical MEMS commercial products. The excellent features of micromachined accelerometers enabled a tremendous impact in the improvement of car dynamics. The low mass and reduced power consumption associated with a reduced cost in microaccelerometer have facilitated the implementation of the MEMS structure in various vehicle applications, ranging from air bag deployment system to the active suspension.

Microaccelerometers

Microaccelerometers are miniature inertial masses elastically suspended on inertial frames that are rigidly connected to the body on which the acceleration should be measured. The inertial mass moves in proportion to the acceleration amplitude of the moving body. The amplitude of motion is detected and converted into an electric signal. The lower the mass of the accelerometer, the higher the natural frequency of the microaccelerometer is. Thus, the main requirement for an accelerometer could be accomplished through miniaturization. The natural frequency of microaccelerometers is often beyond 10 kHz, while their mass can be as low as 50 μg.

Such a microsystem is illustrated in **Figure 2**, as an ADXL50 micromachined accelerometer. This is a complete one-axis acceleration measurement system on a single monolithic IC. Detection of acceleration is based on inertial displacement under external acceleration of an elastically suspended mass. The fixed armatures detect both amplitude and direction of the displacement through capacitive measurement with respect to the fixed electrodes. Along with the sensing structure, the chip comprises an oscillator, reference signal circuit, preamplifier, demodulator,

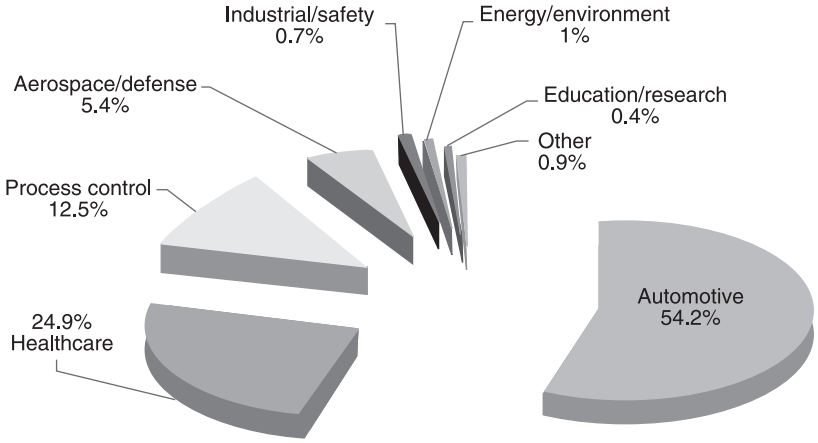


Figure 1 Applications of MEMS and end-user industries.

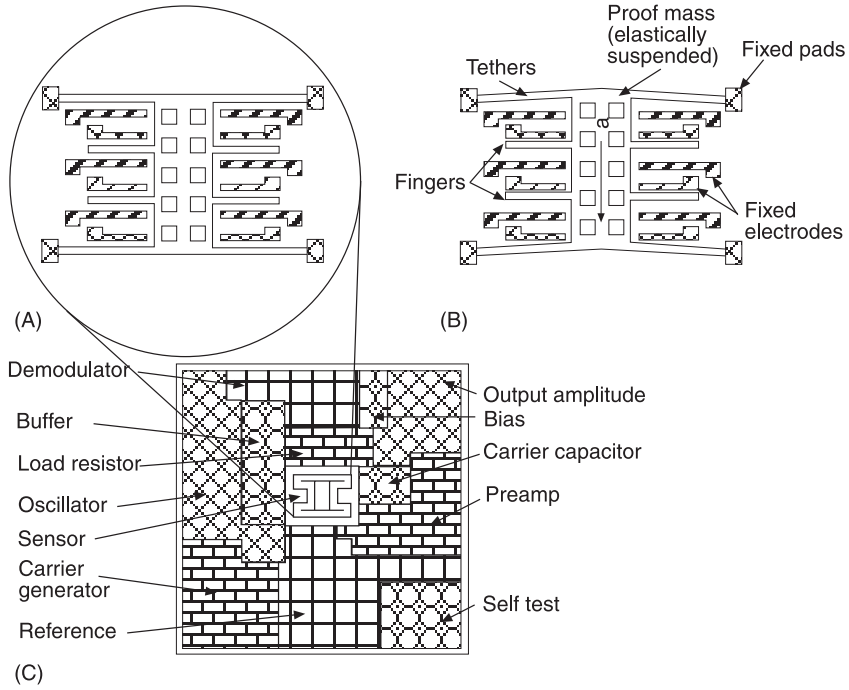


Figure 2 Schematics of the microaccelerometer ADXL50. (A) With no excitation, the proof mass rests in a balanced position. (B) Under the acceleration, the proof mass moves along with the fingers. The relative position of the fingers with respect to the fixed electrodes is related to the magnitude of the acceleration. (C) Schematic view of the entire microsystem.

bias compensation circuit, and self-test circuit. Traditionally, such microaccelerometers have been used in air bag deployment systems. However, other applications in vehicle and seat active suspensions make use of such microaccelerometers. The low cost and high reliability of MEMS represent an important driving factor in the progress of implementation of the intelligent vehicle system (IVS). This concept comprises implementation of sensors and marks, such that roads and vehicles would be able to interact and improving the traffic on congested roads. Proximity sensors, impact avoidance sensors, position and guidance sensors, and remote communication devices are essential elements in the implementation of efficient adaptive traffic schemes on highways. In the vehicle industry, many other solid-state microsystems, such as thermal, optical, magnetic, or chemical sensors, have been implemented and are intensively used. Engine management, wipers, mirrors and lights and air quality control in the car are among the best

known applications of optical and chemical sensors in vehicles. However, such sensors are semiconductor-based devices and do not exhibit any detectable mechanical dynamic outcome. The distinction between solid-state sensors and MEMS is less perceivable from the point of view of function, since most MEMS utilize one or more measurement principles used by solid-state microsensors, such as piezoresistive, magnetoresistive, piezoelectric, capacitive, and ion-sensitive field effect.

One of the most critical problems faced by MEMS is packaging. The diversity of measurands makes package standardization unfeasible for all possible types of microsensors and microsystems. **Figure 3** illustrates a standard packaging configuration that is presently used in IC. Some microsystems require sealed chips, whereas others call for access of the surrounding environment to the sensing area. In certain cases, simple sealed or perforated lids may accomplish specific requirements for specific sensors. In more complex situations, packaging issues are dealt with individually, from case to case. Thus, microactuators may require access to the plant and direct physical contact with the environment. Moreover, rotating parts need protection and lubrication. MEMS devices must also meet the milieu conditions of the application. To illustrate, **Table 2** presents the environmental conditions that a sensor used in the automotive industry must face, as prescribed by SAE J1221 and SAE J5756.

A larger potential of MEMS applications with mechanical microsensors resides in new integrated systems for innovative and emerging applications. As an example, MEMS employed in global positioning systems (GPS) create navigation systems that can provide accurate positioning on a geographic area which are sufficiently accurate to make them appropriate for the ground vehicle traffic management applications. The low cost of MEMS sensors and GPS enables the current implementation of such devices on standard consumer vehicles.

Table 2 Basic requirements for automotive sensors (SAE J1221 and SAE J5756)

Exposure to:	*Range*
Temperature	−40°C to 85°C inside the vehicle −40°C to 125°C under the hood −40°C to 150°C on the engine −40°C to 200–600°C in the exhaust and combustion areas
Mechanical shock	3000 g during assembly 50–500 g in service
Mechanical vibration	15 g, 100 Hz to 2 kHz
Chemical exposure to:	Fuel Oil Freon Humidity Salted water Exhaust gases Ethylene glycol

Since the 1980s the research on MEMS has matured tremendously. The microsystems are permanently heading towards smaller features and integration of mechanical, electrical, and control subsystems on a single chip.

Acoustic Microsensors

The acoustic sensor class exhibits considerable potential for mechanical and chemical sensing. The planar geometry configuration enables compliant fabrication of sensors using standard IC technology. The principle of detection is based on the high sensitivity of the elastic wave velocity, traveling through a resonant media while crossing an active material, which is subjected to excitation from the physical

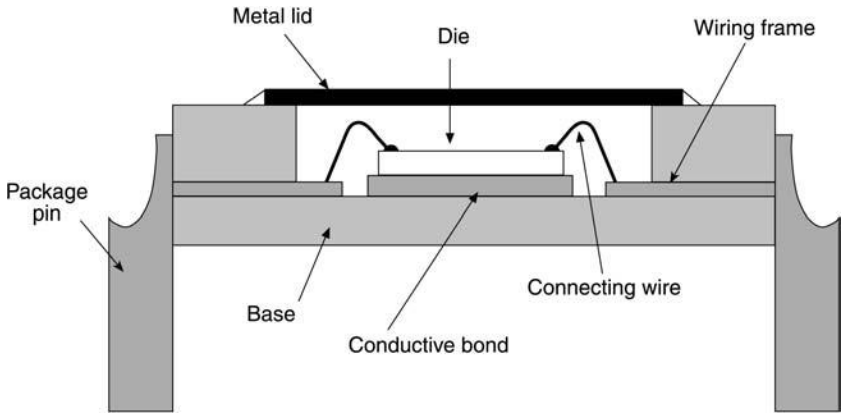


Figure 3 Standard packaging of an integrated circuit.

quantity to be measured. The acoustic wave-based sensors, such as the surface acoustic waves (SAW) and the flexural plate waves (FPW), are based on the piezoelectric properties of classes of monocrystals and ceramics. **Figure 4** illustrates the schematic configuration and functioning of an SAW sensor. One of the SAW interdigital transducers is used to excite the piezoelectric substrate of the sensor. When an electrical charge is applied to a piezoelectric structure, the structure tends to vibrate near its natural frequency or one of its harmonics. The vibration wave propagates through the substrate and travels throughout the coating, which is the active material sensitive to the quantity to be measured. The change in the active material will modify the speed of the crossing wave. The second SAW transducer detects the phase shift or amplitude modification due to the structural changes in the bulk of the sensing material. The acoustic sensors have been known since the early 1960s from their applications with large monocrystalline quartz. The piezoelectric effect can be successfully used in the miniature devices, microsensors, and microactuators. If the structure is a thin plate of mass m and thickness t, the resonance shear-mode wavelength λ (thickness is chosen such that $\lambda = t$) will be modified due to the mass change of the plate by the linear relationship:

$$\frac{\Delta m}{m} = \frac{\Delta \lambda}{\lambda}$$

Modifications to the structure of the delay line will be reflected in the signal perceived at the receiver. This information can always be related to the input excitation, which is directly related to the physical quantity to be measured. The interdigital transducer configuration is very appropriate for MEMS implementation. IC-like technologies have been used to complete monolithic piezoelectric accelerometers along the full scale ranging from 1 to 100 g. The piezoelectric substrate deposition requires some special processing which is not specific to IC processes. Among the thin film piezoelectric materials that can be implemented with IC technology are ZnO, AlN, $Pb(Zr,Ti)O_3$ (PZT), and polyvinylidene fluoride (PVDF).

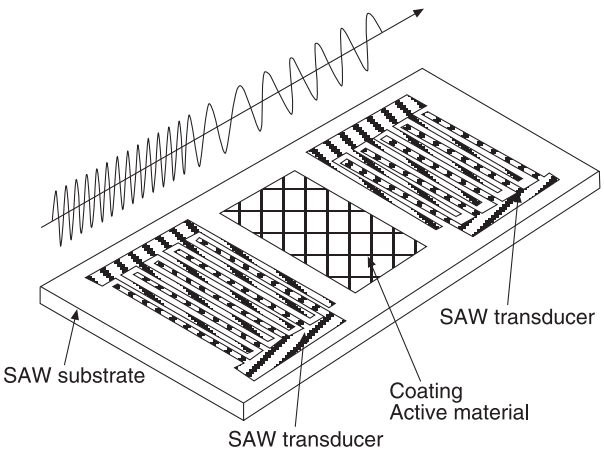


Figure 4 Schematic of a surface acoustic sensor concept. The oscillation generated by the source is changed when passing through the coating which represent the active material. The change is perceived by the surface acoustic wave (SAW) transducer, which detects the change due to the modification in the state of the active (sensing) materials.

Microactuators

Microactuators are conceived to transform various forms of energy, mostly electrical, into mechanical rotation or translation on a miniature scale.

The first electrostatic microactuators were created making use of modified surface micromachining technology in which thick polysilicon rotors actuated by side-driver electrodes were held at the center by a hollow hub. Early designs of micromotors were conceived as small replicas of normal-sized electric motors. At 500 rpm, the life of the motor would not exceed 1 h due to the substantial friction and wear on the sliding surface. Eccentrically rotating motors (wobble motors) were then created to overcome the sliding friction which would be reduced to a roll friction. Moreover, elastically suspended moving elements driven by electrostatic or magnetic fields or actuated by fluid or thermal power have been proposed. Such designs fully eliminate the contact friction.

Some other designs use the friction force between the moving and fixed parts as driving force. Such an example is represented by ciliary motion systems. Miniature actuators making use of piezoelectric, magnetostrictive, or photostrictive or phase transformation effects or thermal effects could generate larger power per mass unit efficiency factors. More creative concepts have been proposed and tremendous progress was achieved in increasing the life of the micromotor and in improving the force/torque. Interdigitated comb-like resonant structures, linear thermal actuators, shape-memory elements, or capillary force-actuated elements are among the many proposed solutions to raise the actuation force of the micromotors. In addition to modified surface machining, high-aspect ratio machining (lithografie galvanik abeforming or LIGA, and deep X-ray lithography) was used to create microactuators. **Figure 5** illustrates the concepts of micromachined actuators. Forces in the range of μN can be accomplished by single microactuators. Optical applications are most

suitable with the force range generated by single unit micromotors. **Table 3** illustrates the work per unit of volume and the frequency range of various classes of microactuators.

Certain macroscopic tasks can be performed by arrays of microactuators. Larger displacements could be achieved by multiple microactuators with synchronized motion, as illustrated in **Figure 5F**, in the case of a ciliary motion conveyer where the actuators are connected in series. Larger loads could also be supported by distributed synchronized microactuators connected in parallel. Arrays of microsensors and microactuators connected conveniently in series and parallel can produce higher forces and larger displacements and perform more complex functions than the unit microactuator. Although the energy loss in direct-driven microactuators is minimal, the undesired friction limits the type of

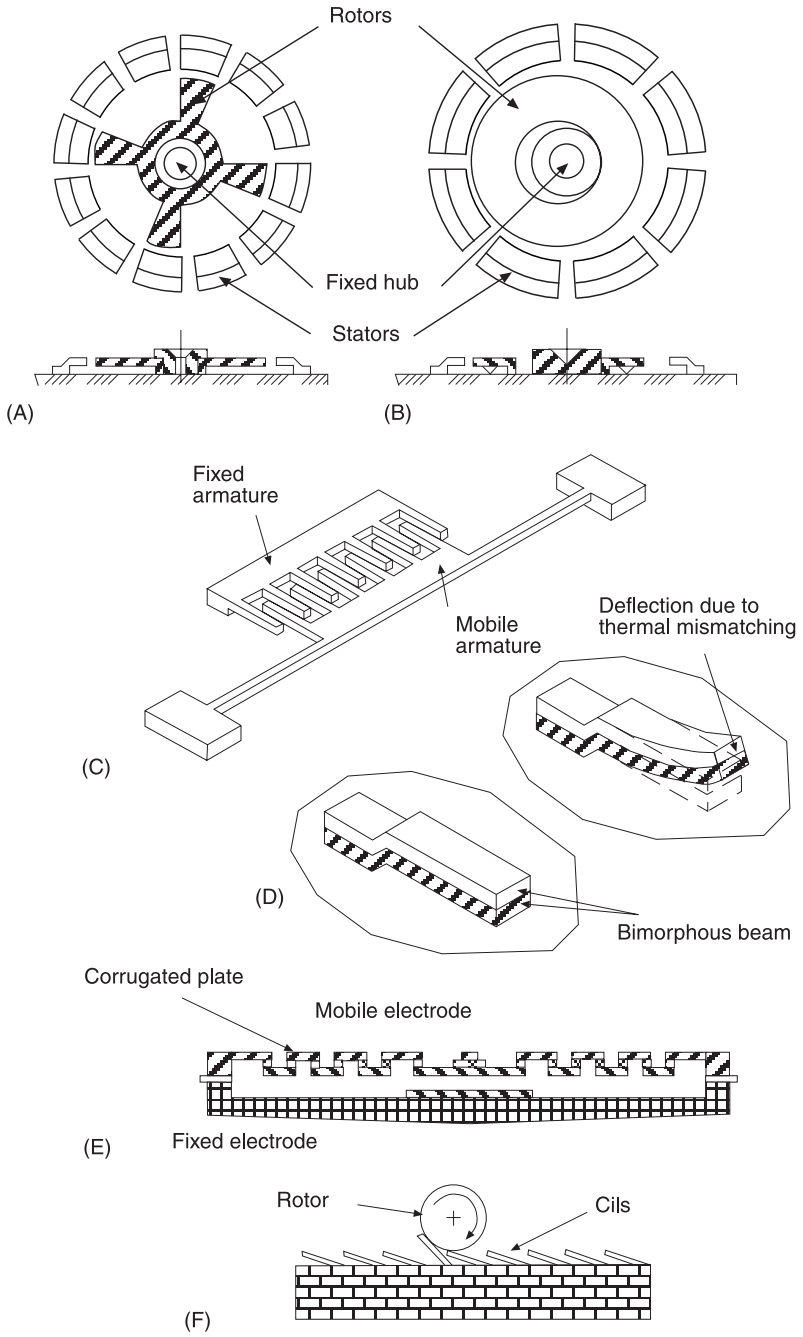


Figure 5 Microactuators. (A) Side-drive electrostatic micromotor. (B) Wobble electrostatic micromotor. (C) Comb-drive microactuator. (D) Thermal actuator (bimorphous cantilever beam). (E) Electrostatic linear microactuator. (F) Ciliary motion conveyer.

Table 3 Work per unit of volume and frequency range for selected types of microactuators

No.	*Microactuator type*	*Work/volume* ($J\,m^{-3}$)	*Frequency (Hz)*
1	Shape memory alloy (Ni-Ti)	$6 \times 10^6 - 25 \times 10^7$	10^2
2	Solid–liquid phase change	4.7×10^6	1
3	Thermal expansion	4.6×10^5	10^2
4	Electromagnetic	$1.6 \times 10^3 - 4 \times 10^5$	10^2
5	Electrostatic	$7 \times 10^2 - 1.8 \times 10^5$	10^4
6	Piezoelectric	$1.8 \times 10^2 - 1.2 \times 10^5$	10^7

transmission elements to the supported beams as linkages. Joints and gears cannot be used in microsystems due to the microscale high friction level that reduces the efficiency of the transmission to values close to zero.

Remarkable applications of microactuators to macroscopic systems have been demonstrated in the control of turbulent flow on surfaces. Augmentation of a disturbance created by a small motion of a microactuator on the surface enable formation of a vortex, which upholds the capability to control the aerodynamic macrophenomena.

Microvalves and Micropumps

MEMS applications in this group are related to fluid handling, chemical analysis, microbiology, aerodynamics, and controls. Early investigations on fluidic microdevices were directed towards the accomplishment of micropumps, microvalves, and shaped flow channels. Most devices have been accomplished through hybrid bulk and special micromachining procedures. Silicon membranes actuated by electromagnetic, electrostatic, or thermal expansion forces have been used as valves, as shown in **Figure 6**. The metallic conductor deposited on the thin membrane will move the flexing element when a current is passed through the coil. The motion can be conveniently used to obstruct one of the valve orifices. Similar structures can be used as a pump if the openings of the two orifices are synchronized. The variation of volume inside the cavity due to the motion of the membrane will induce flow from the input to the output orifices.

Fluidic elements require special packaging such that the moving element is enclosed within a specific structure. Wafer-to-wafer or glass on silicon anodic bonding is usually used to seal the fluidic elements.

Fluidic logic elements have been developed as an alternate solution to the electronic logic circuits. MEMS enable downsizing of these circuits such that full logic controllers can be built on a few square millimeters of wafer. **Figure 7** illustrates such a circuit. The flow stream switches the flow channel if the corresponding control signal is applied through the appropriate control channel.

Chemical analysis integrated systems comprising pumps, valves, sensors, and controllers are under intensive investigation.

Other Applications

Optical microsystems are among the most common applications of MEMS. Here, the mechanical load carried by the actuator is reduced to the intrinsic mass of the moving part. Besides, very performant optical cells can be built in IC technology. Micromachined high-resolution displays comprising arrays of micromirrors, each of 16 μm size, which can be tilted such that the reflected beam creating the pixel image becomes visible or invisible, integrated on metal oxide complementary circuits have been accomplished. Micromechanical optical switches and resonators, optical modulators, tunable filters, or deformable optical wave guides are also available. Applications

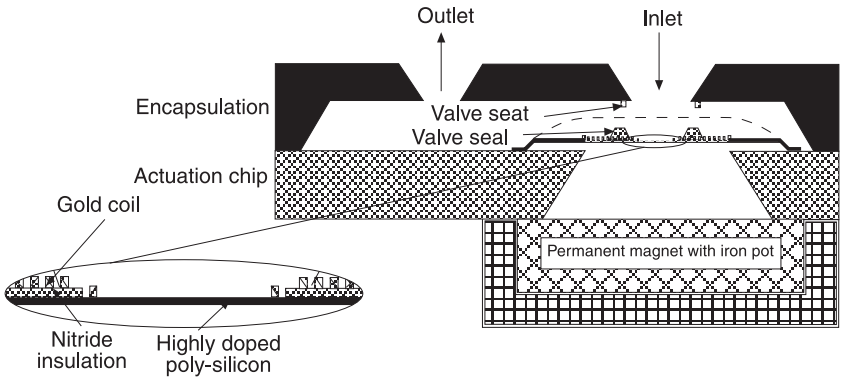


Figure 6 Scheme of a cross-section of the microvalve (actuation chip plus encapsulation and permanent magnet with iron pot).

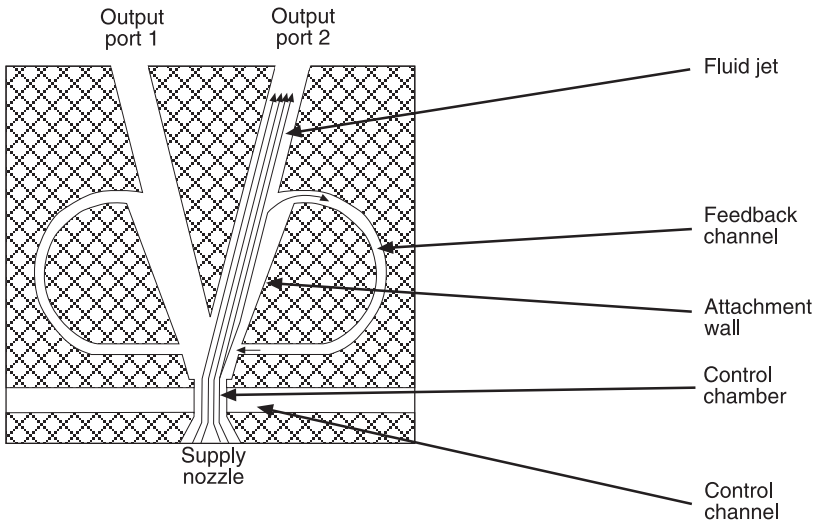


Figure 7 Schematics of a fluidic logic element.

to communications and data storage systems as well as in very high-accuracy measurement devices of the optical MEMS are quite common.

Another type of MEMS application features the investigative systems to nanoscale level of the matter. Thus, scanning tunneling or lateral force microscopy probes and arrays of probes accomplished in silicon dramatically improved the performances of the microscopes, at the same time reducing their cost. The mass of microobjects can be accurately measured, making use of simple principles such as the bending of the free end of a cantilever beam under a gravity force. **Figure 8** illustrates such a measurement system made of an array of beams conceived to measure a larger range of masses.

Biotechnology and medicine also benefit from MEMS. Catheters equipped with micropressure sensors can detect the pressure variation on a portion of an artery, which indicates the existence of clots. Research on similar catheters bearing together with pressure sensors and biochemical sensors that detect enzymes composition and concentration has been carried out. Less invasive probes for tests have been manufactured in MEMS technology and the results obtained claim more effort in developing such systems. Neural probes used to detect the electric potential generated by nerve activity have been built using a hybrid surface and bulk postprocessing of silicon. Such a microelectrode is shown in **Figure 9**. Implantable artificial organs, a microautonomous tool for minimally invasive surgery or drug delivery systems, are among the most desired MEMS due to the enormous positive impact they will have on humans' life.

The ultimate goal of the research effort in MEMS is to create useful micromachines as full systems. Successful applications make use of standard IC processes such that the microsystems could benefit from the coupling of the micromechanical components with the conditioning circuitry and controller on the same miniature unit. Besides, many original systems have been accomplished through bulk micromachining comprising anisotropic Si etching, wafer bonding, and advanced packaging. Since bulk



Figure 8 Microcantilever beam used to scale a small mass. The intrinsic interlayer stress will bend the beam. A micromass is used to bend back the beam. The new value of the deflection is directly related to the mass of the microparticle.

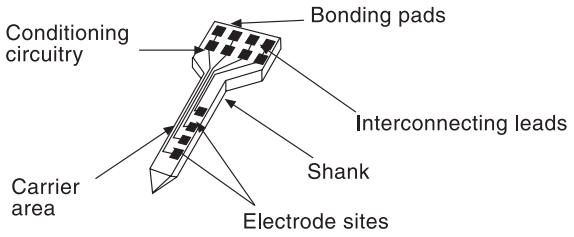


Figure 9 Neural probe.

micromachining could not enable the fabrication of the electronics on the same chip with the microstructure, the circuit is built separately and packaged on the same unit. The variance in sensitivity of the mechanical structure may range within $\pm 20\%$. Compensation is achieved through tuning of the electronic circuitry. Laser trimming as well as look-up compensation tables inscribed in EPROM circuits are compensation methods which are currently used. The low cost and high reliability of microsystems make them serious competitions to the present sensors and controllers. The capability of MEMS to investigate further into the matter of phenomena means that microtechnology has a strong future. Breakthroughs in the following five general areas are predicted to be accomplished by MEMS and MEMS technology:

1. implementation of hierarchic intelligent systems in machines which can analyze, and conclude what the decision is to be taken
2. downsizing and redundancy of systems and deeper investigation of the matter
3. biomimetics: the development of flexible, intelligent, and sensitive autonomous micromachines
4. informatics: the acquisition of information on the state of systems equipped with sensors; exchange of real-time data among interacting systems, decision taking towards the optimization of multiple system functioning
5. environment preservation: measurement, detection, cleaning

MEMS have had, and will have, a profound impact on future technology and society.

See also: **Actuators and smart structures**; **MEMS, dynamic response**; **MEMS, general properties**; **Transducers for absolute motion**.

Further Reading

Bhushan B and Gupta BK (1997) *Handbook of Tribology: Materials, Coatings, and Surface Treatments*. New York: McGraw-Hill.

Campbel SA and Lewerenz HJ (eds) (1998) *Semiconductor Micromachining*. Chichester: Wiley.

Fraden J (1993) *AIP Handbook of Modern Sensors; Physics, Design and Applications*. New York: American Institute of Physics.

Gardner JW (1994) *Microsensors; Principles and Applications*. New York: John Wiley.

Kovacs TA (1998) *Micromachined Transducers Sourcebook*. Boston: McGraw-Hill.

Lee HH (1990) *Fundamentals of Microelectronic Processing*. New York: McGraw-Hill.

Madou M (1997) *Fundamentals of Microfabrication*. New York: CRC Publishing.

Neamen DA (1992) *Semiconductor Physics and Devices; Basic Principles*. Homewood, IL: Irwin.

Ohba R (ed.) (1992) *Intelligent Sensor Technology*. Chichester: John Wiley.

Sze SM (ed.) (1994) *Semiconductor Sensors*. New York: John Wiley.

Tiller WA (1990) *The Science of Crystallization: Microscopic Interfacial Phenomena*. Cambridge, UK: Cambridge University Press.

Weste NHE and Eshraghian K (1994) *Principles of CMOS VLSI Design*. New York: Addison Wesley.

MEMS, DYNAMIC RESPONSE

I Stiharu, Concordia University, Montreal, Quebec, Canada

Copyright © 2001 Academic Press

doi:10.1006/rwvb.2001.0074

Introduction

A microstructure subjected to an input signal would respond with the same oscillation pattern of amplitude that correlates with the characteristics of the structure. Microstructures are particularly associated with high resonant frequencies. This phenomenon is mainly due to the extremely small oscillating masses of the microstructures, but it is also due to the notable influence of the electrostatic and electromagnetic fields, and the built-in interlaminar stress in the structural layers. Detecting the natural resonance frequency of a microstructure in conjunction with the appropriate operating frequency should be considered during the design process.

The dynamic response of microelectromechanical systems (MEMS) involves multiphysics interactions. The association between various physical quantities must be accurately established to evaluate the performance of a microsystem. Geometric downscaling by a factor does not necessarily mean downscaling within the same range for various physical quantities interacting at the microstructure level. For a given one-dimension downscaling factor, the mass and the moment of inertia decrease by the power of 3, the force decreases by the power of 2 and the acceleration grows by the power of 1, while the speed remains unchanged. Such dependence will definitely influence the dynamic response of a miniature structure.

From a dynamic point of view, most existing microsensors (optical, chemical, electromagnetic, temperature, and radiation) are static devices. They usually comprise both the transducer and the circuitry, which are built on the chip or packaged on the same circuit board. Under vibrations, the mechanical structure moves together with the circuitry and the chip. The stiffness of the connections is very high while the free pendent mass of the sensor is very small. Such devices can thus be considered as simple masses. Thus, for most microsystems mechanical vibration has no detectable influence on their functioning. However, the mechanical vibrations could induce quite destructive effects to the package and wire connections on the chip.

The influence of MEMS on the dynamics of the parts supporting the microsystem, on the other hand, is quite negligible. The mass of a standard 3×3 mm silicon chip does not exceed 10 mg, while the mass of a fully packaged chip does not exceed a few grams. Thus, rigid mounting of MEMS to normal-size mechanical systems would not interfere or yield a detectable influence on the overall dynamic response of the mechanical structure under most circumstances.

MEMS comprising flexing or free elements, which are free-standing structures released form the silicon chip by postprocessing, are clamped, supported, or free but constrained in their motion. Such structures are strongly affected by the oscillatory motion induced to their support or foundation. The dynamic response can be roughly modeled as a lump mass–spring–damper system fixed on a vibrating foundation, as shown in **Figure 1**. The motion along the free direction x of the swing mass of the microsystem is described by the force equilibrium equation:

$$m\ddot{x} + c(\dot{x} - \dot{x}_0) + k(x - x_0) = X_0 \sin(\omega t) \qquad [1]$$

The deflection x of the free-standing microstructure follows, after a lag, the pulse of the excitation:

$$x = A \sin(\omega t - \phi)$$

where the amplitude A and phase shift ϕ are given by:

$$A = X_0 \sqrt{\frac{k^2 + (c\omega)^2}{(k - m\omega^2)^2 + (c\omega)^2}} \qquad [2]$$

and:

$$\phi = \tan^{-1}\left(\frac{mc\omega^3}{k(k - m\omega^2) + (c\omega)^2}\right) \qquad [3]$$

The main feature related to the dynamics of MEMS is the high value of the resonant frequency, which is mainly due to the extremely low mass of the microstructure. This attribute makes them valuable measurement tools for high-frequency bandwidth vibrations in mechanical systems.

In the case of microaccelerometers, microvibrometers, atomic force probes, and microphones, the motion of the free-standing element is beneficial and regarded as the measurable input signal, so the structure must always behave in the predicted way. The motion of the free-standing element is further transformed into electric effectual signal. The dynamic behavior of the microstructure must be predicted through modeling, before such a microsystem can be accomplished. The modeling of the mechanical structure often involves fluid, thermal, and electromagnetic interactions. The electrical circuitry requires further attention, since the resonant frequency of the mechanical microstructures is in general very high. The shift in critical natural frequency makes the microsystem exhibit stronger coupling with the electronic circuitry than the

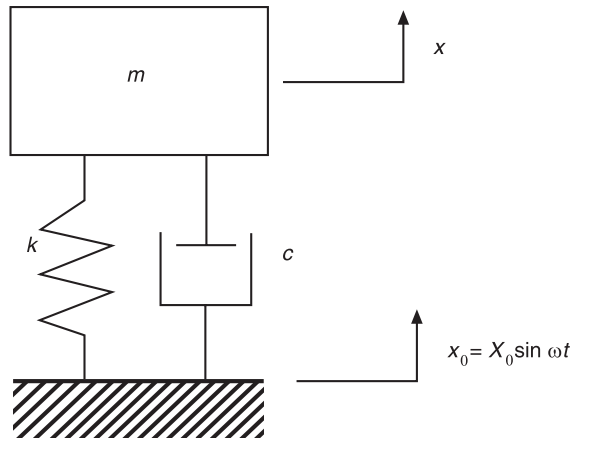


Figure 1 Lump model of damped mass elastically supported on a harmonic vibratory base.

normal-size electromechanical systems. Although MEMS are subjected to multiple physical interactions with very nonlinear effects, the lump mass model is always conceived to estimate the range of the dynamic linear response of the system.

When modeling multiple interactions among the linear physical system, it is perhaps more convenient to convert all the components to one common type of analogous system. Traditionally, all the mechanical, fluid, or thermal elements are converted to standard electrical components. The network models and the analysis methods for the electrical circuits are very popular and intuitive, such that the analysis of the analog systems is notably simplified. Furthermore, software packages can be conveniently used for the equivalent electrical network analysis.

For the normal-size world, **Table 1** gives the equivalent circuit components and signal variables among electrical, mechanical, fluid, and thermal physical quantities. The same analogy can be extended to the microworld, with some reservations due to the major influence of certain phenomena that are significant at a microscale level. However, attention is required when the figure number for the damping or stiffness or even mass is fed into the equation of the model. Moreover, it should be emphasized that microminiature systems usually exhibit noticeable nonlinearities, which should be taken into account when more accurate modeling is carried out.

Dynamic Response of MEMS

MEMS which are structured in micromechanical configurations comprising masses elastically suspended exhibit specific dynamic behavioral patterns similar to those of the normal-sized mechanical systems. The small masses associated with relatively large stiffness bring the resonant frequency of the structure in the range of kHz. However, other forces, which are associated with the processes or with the functioning principles of MEMS, may considerably influence their dynamic behavior. Two of the most significant influences, the electrostatic field and interlaminar stress, will be further discussed. A brief summary that helps to resolve the figure number of mass, stiffness, and damping for the lump model of simple MEMS structures is also given below.

Mass

Mass (the equivalent capacitance in electrical circuitry) can be evaluated assuming the geometry of the feature. However, due to the selectivity of the etchant, the initial shape of the feature may be distorted, as shown in **Figure 2**. The etchant removes the sacrificial film at a high rate but it will also etch from the structural layer to a lower extent. The inner walls of the structural film are sloped after the etching is carried out because the inner walls are gradually exposed to the etchant, whereas the external surfaces are permanently in contact with the etchant and thus uniformly etched. In certain conditions, the density of matter of the thin films is slightly smaller than that of the bulk, so the density figure number should be regarded with some caution. The equivalent mass method stands, when concentrated masses are considered along with the distributed masses.

Table 2 shows the standard formulation for the equivalent mass of cantilever and double-supported beams loaded with concentrated weight. The formulation presented in **Table 2** covers in the first iteration

Table 1 Analogous elements and variables

Electrical	*Mechanical*	*Fluid*	*Thermal*
Current (j)	Force (F)	Volume flow (q)	Heat flow (H)
Potential (V)	Speed (v)	Pressure (p)	Temperature (θ)
Resistance $R = \dfrac{\Delta V}{i}$	Mechanical resistance (damping) $\dfrac{1}{b} = \dfrac{\Delta v}{f}$	Fluid resistance $r = \dfrac{\Delta p}{q}$	Thermal resistance $R_\theta = \dfrac{\Delta \theta}{H}$
Inductance $L = \dfrac{\Delta V}{\mathrm{d}i/\mathrm{d}t}$	Mechanical resistance (spring) $\dfrac{1}{k} = \dfrac{\Delta v}{\mathrm{d}f/\mathrm{d}t}$	Fluid inertance (inertia) $L = \dfrac{\Delta p}{\mathrm{d}q/\mathrm{d}t}$	Thermal inertance — (no significance)
Capacitance $\dfrac{1}{C} = \dfrac{\Delta V}{\int i\,\mathrm{d}t}$	Mechanical capacitance (mass) $\dfrac{1}{m} = \dfrac{\Delta v}{\int f\,\mathrm{d}t}$	Fluid capacitance $\dfrac{1}{C} = \dfrac{\Delta p}{\int q\,\mathrm{d}t}$	Thermal capacitance (thermal mass) $\dfrac{1}{C} = \dfrac{\Delta \theta}{\int H\,\mathrm{d}t}$

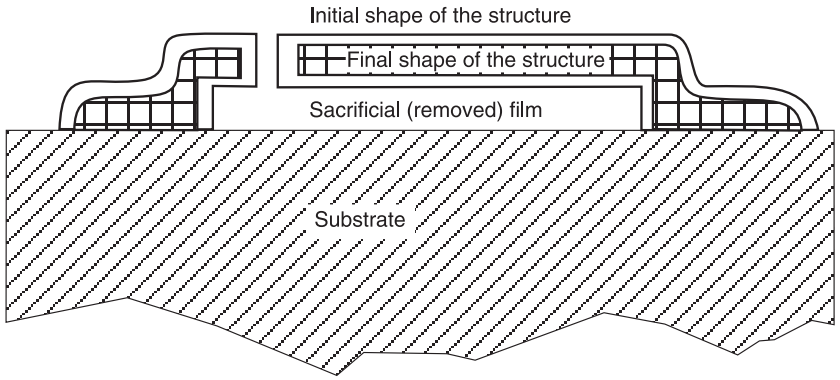
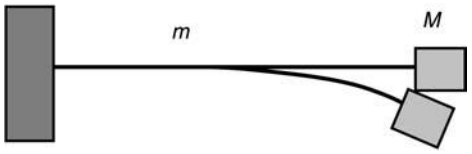
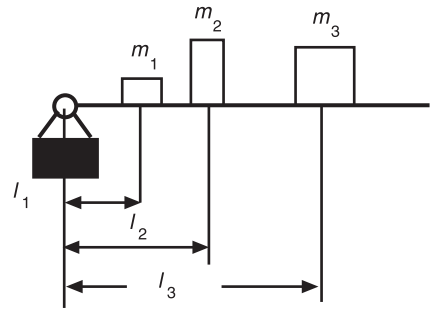
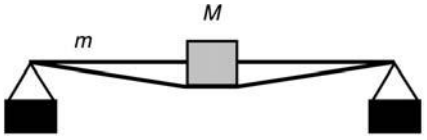


Figure 2 Cross-section through the geometry of a surface micromachined structure transformed due to the limited selectivity of the etchant.

Table 2 The equivalent mass of beams loaded with concentrated mass

	Cantilever beam of mass m carrying an end mass M	$m_{eq} = M + 0.23m$
	Cantilever beam of mass m carrying an end mass M	$m_{eq} = m_1 + \left(\frac{l_2}{l_1}\right)^2 m_2 + \left(\frac{l_3}{l_1}\right)^2 m_3$
	Simply supported beam of mass m carrying a mass M at the middle	$m_{eq} = M + 0.5m$

most of the MEMS structures, which are conceived as beams simple or double supported.

Stiffness

Stiffness (the equivalent inductance in the electrical circuit) is an essential parameter in the evaluation of the dynamic properties of microstructures. Assuming that the structures have uniform geometric features, the analogy with the helical spring can only be applied for concentrated loading. The stiffness can thus be expressed as the ratio between load and deflection:

$$k = \frac{\mathrm{d}F}{\mathrm{d}\delta} \text{ or, for single concentrated torque, } k_\theta = \frac{\mathrm{d}M}{\mathrm{d}\theta} \quad [4]$$

When the loading is uniformly distributed on a section of the structure, the equivalent loading method

may be employed to determine the equivalent stiffness. **Table 3** shows the equivalent stiffness for selected types of beams loaded with concentrated and distributed loads.

When the structure is subjected to multiple concentrated loads, the energy method is instrumental in evaluating the equivalent stiffness of the system. The strain energy in the structure is equal to the equivalent energy of a theoretical spring:

$$\sum \left[\int_l \frac{M_b^2 \mathrm{d}x}{2EI} \right] = \frac{k_{\mathrm{eq}} \delta^2}{2} \qquad [5]$$

for bending and:

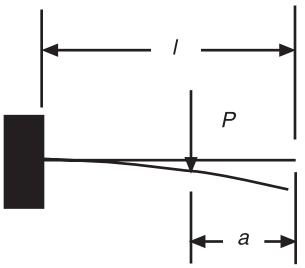
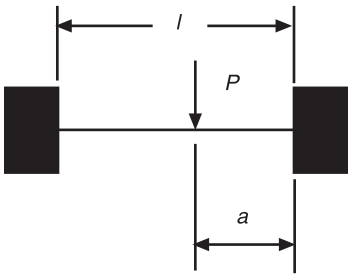
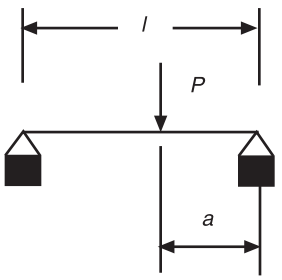
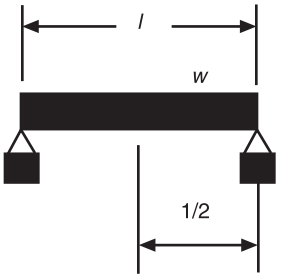
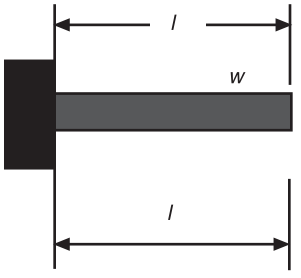
$$\sum \left[\int_l \frac{M_t^2 \mathrm{d}x}{2GI_p} \right] = \frac{k_{\theta \mathrm{eq}} \theta^2}{2} \qquad [6]$$

for torsion where M_b is the equivalent bending moment in each element of structure, M_t is the equivalent torsion moment in each element of structure, E is the Young's modulus of elasticity, G is the shear modulus of elasticity, I is the moment of inertia of the section of the structure, I_p is the polar moment of inertia of the section of the structure, K_{eq} is the equivalent bending stiffness of the structure, $K_{\theta \mathrm{eq}}$ is the equivalent torsion stiffness of the structure, δ is equivalent deflection of the structure, and θ is the equivalent torsion angle of the structure.

Damping

Damping evaluation requires the most laborious analytical effort. The small geometric size of the flexural elements and the reduced gap between the mobile and fixed part of the structure promote squeeze damping, which can reach remarkably large values of damping coefficients. Damping is critical to the performance of the microsystem throughout the frequency bandwidth of the system. Large values of squeeze film damping, which are likely to occur in MEMS, can reduce the dynamic bandwidth of the system to an unacceptable level. Damping is determined by the geometry of the gap and of the elements, as well as by the viscosity or the pressure of the surrounding fluid. Damping is of great concern for microaccelerometers and miniature microphones. The frequency response of such systems can be improved by reducing damping by configuring flow channels through the flexing or fixed elements or through low-pressure encapsulation. For laterally oscillating microstructures, like comb-like resonant structures, the dominant nature of the damping is due to Couette-type

Table 3 The equivalent stiffness of beams loaded with concentrated and distributed load

	$k = \frac{6EI}{2l^3 - 3l^2a - a^3}$
	$k = \frac{3EI(l+2a)^2}{2(l-a)^2a^3}$
	$k = \frac{48EI}{a} \cdot \left(\frac{1}{3l^2 - 4a^2} \right)$
	$k = \frac{384EI}{5l^3}$
	$k = \frac{8EI}{l^3}$

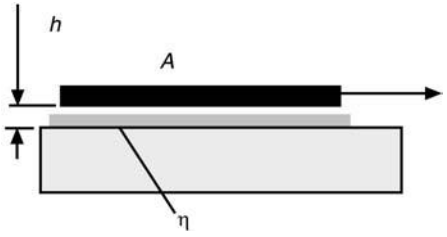
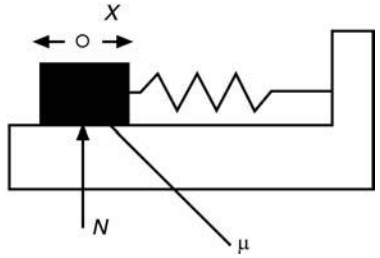
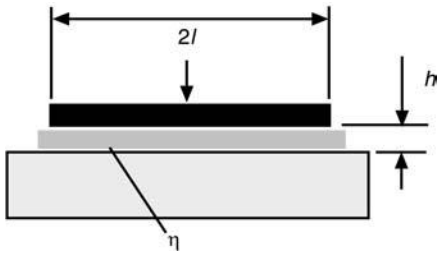
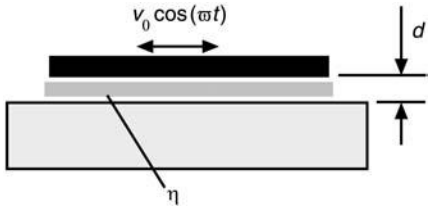
flow. **Table 4** gives the equivalent damping values for some energy dissipation arrangements. Reduced damping requires reduced pressure of the immersing fluid/gas.

Certain classes of application require very low damping. The resonant structures (piezoelectric actuators and acoustic sensors) function based on the oscillatory properties of specific active materials (quartz, $LiNbO_3$, ZnO, AlN, PZT, etc.). Low intrinsic damping properties of the material ensure that the system is more efficient through reduced energy dissipation/loss.

When damping is low, the dynamic over the static amplitude ratio at resonance, the quality factor Q, yields considerable information about the dynamic response of the system. The bandwidth of the system represents the range of frequencies for which the amplitude ratio falls beyond $Q/2$. The Q factor of a structure is associated with the ratio of the strain energy stored in the system to the energy dissipated through damping.

When the natural frequency of a more complex system is evaluated, it is more appropriate to use one of the energy methods. One of the remarkable advantages of such a method is that one can incorporate various effects of the electric and magnetic field, and capillary forces, which would otherwise be excessively difficult to incorporate in the model. Equating

Table 4 The equivalent damping for various mechanical structures

	Relative motion between parallel surfaces	$c_{eq} = \frac{\eta A}{h}$
	Vibrating mass in rigid contact with a fixed surface (Coulomb friction)	$c_{eq} = \frac{4\mu N}{\pi \omega X}$
	Squeeze film damping	$c^*_{eq} = \frac{4\eta l^3}{h^3}$ *per unit of length
	Couette-type damping	$c^*_{eq} = \frac{\pi u_0 \eta}{\omega d}$

the maximum potential energy and the kinetic energy, one can assess the influence of the external forces and fields to the natural frequency of the structure.

The Influence of the Electrostatic Field

Assume two parallel plates separated by a small gap. One plate is fixed while the other moves along the direction z normal to the two plates. The mobile plate is subjected to elastic restoring forces. The motion of the plate in the fluid filling the gap between the two plates yields a dissipative force which is proportional to the speed of the plate. The distance between the two plates is usually measured through the value of the impedance of the variable capacitor formed by the two plates. The small size of the micromechanical structures of MEMS enables the electric field which is always present to strongly influence the dynamic response of a microstructure. The energy due to the electrostatic field can be expressed by:

$$-\frac{\partial U}{\partial z} = \frac{V^2}{2}\frac{\partial C}{\partial z} \qquad [7]$$

where U represents the stored electrostatic energy, V is the voltage differential across the capacitor plates, C is the capacitance of the capacitor, and z represents the deflection of the flexible elastic armature of the capacitor.

Eqn [7] shows that enhanced displacement of the mobile armature tends to augment the intensity of the electrostatic field, reducing the gap and increasing capacitance, and this field will incline to pull the flexing element even more. The armature under the electrostatic field thus renders a larger displacement than that experienced in the absence of the electrostatic field, which could be comprehended as negative stiffening of the structure due to the existence of the electrostatic field. It must be noted that the electrostatic field, regardless the potential of the armatures, produces a weakening effect on the stiffness of the mobile plate. However, the detectable phenomenon is the attraction between the two armatures.

It has also been found that each structure exhibits a specific threshold value of static deflection due to the electrostatic force, and, if this is exceeded, the flexible armature becomes dynamical unstable. The mobile armature is perceived to be collapsing on the fixed back-plate. From the point of view of the electrical field, a threshold voltage is associated with each structure, at which pull-in and ultimately snapping occur. Usually, this condition is associated with mechanical failure of the structure, so it must be carefully avoided. The natural frequency of a plate subjected to electrostatic field will drop due to the negative stiffness effect induced by the electrostatic field. When threshold displacement is reached, the natural frequency approaches zero; this is when the balance between positive and negative stiffness is reached. The trend of the natural frequency of a double-supported plate, which is subjected to a potential difference with respect to the fixed armature, is illustrated in **Figure 3**. The natural frequency and the first few resonance frequency and mode shapes for simple stuctures are given in **Table 5**.

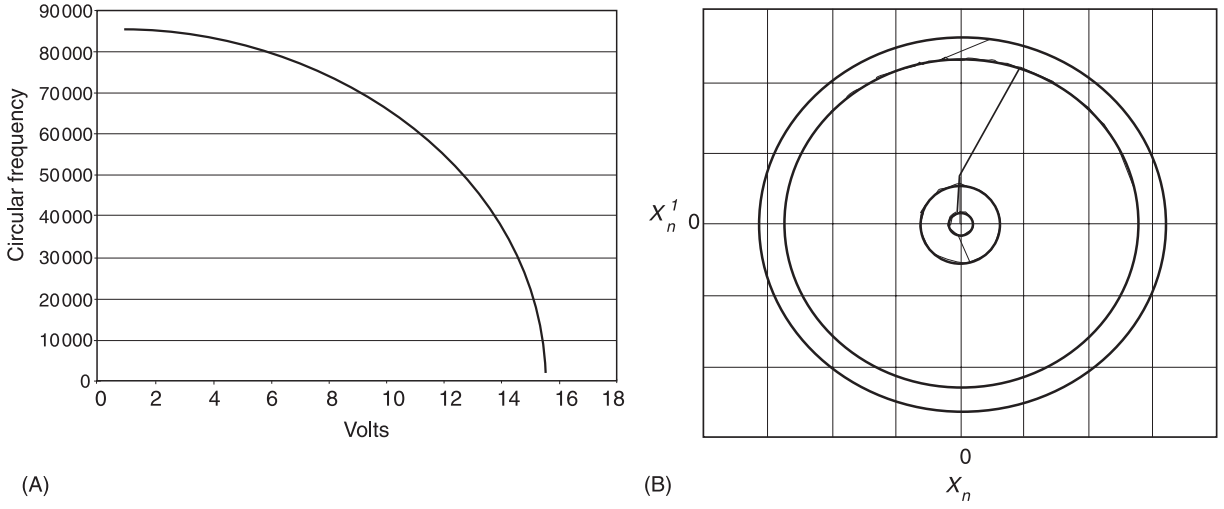
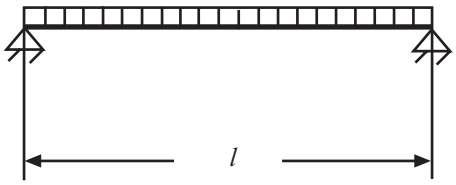


Figure 3 (A) Natural frequency of a microbeam 1000 × 1000 × 2 μm which is double-supported and subject to a variable difference of potential with respect to the fixed armature, parallel and spaced at 2 μm about the beam. The natural frequency decays such that, for voltage beyond 15 V the natural frequency of the plate is close to zero. The plate exhibit dynamic instability at even lower difference of potential, as shown in (B). (B) Phase state plot of the microbeam described in (A), subject to sinusoidal excitation and under an electric field created by 12 V potential difference between the microbeam and the fixed armature.

Table 5 The first resonance frequencies and mode shapes for simple structures.

No.	*Beam configuration*	*Natural frequencies*

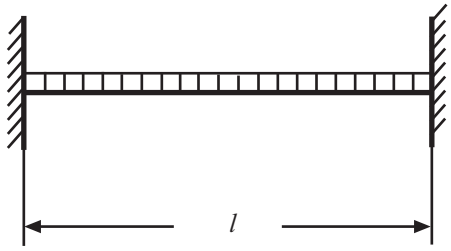
1



$$f_i = \frac{k_i}{2\pi}\sqrt{\frac{EIg}{wl^4}}$$

Mode	k_i	Nodal position/l
1	9.87	0 1
2	39.5	0 0.5 1
3	88.8	0 0.33 0.67 1
4	158	0 0.25 0.5 0.75 1
5	247	0 0.2 0.4 0.6 0.8 1

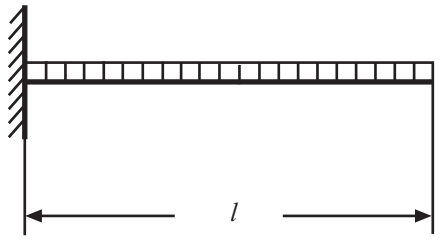
2



$$f_i = \frac{k_i}{2\pi}\sqrt{\frac{EIg}{wl^4}}$$

Mode	k_i	Nodal position/l
1	22.4	0 1
2	61.7	0 0.5 1
3	121	0 0.36 0.64 1
4	200	0 0.28 0.50 0.72 1
5	299	0 0.23 0.41 0.59 0.77 1

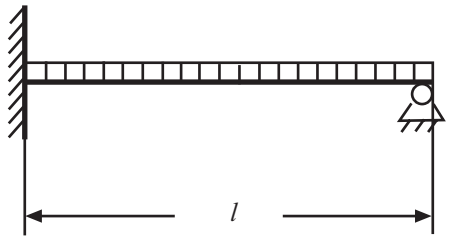
3



$$f_i = \frac{k_i}{2\pi}\sqrt{\frac{EIg}{wl^4}}$$

Mode	k_i	Nodal position/l
1	3.52	0 1
2	22	0 0.783
3	61.7	0 0.504 0.868
4	121	0 0.358 0.644 0.905
5	200	0 0.279 0.5 0.723
0.926		

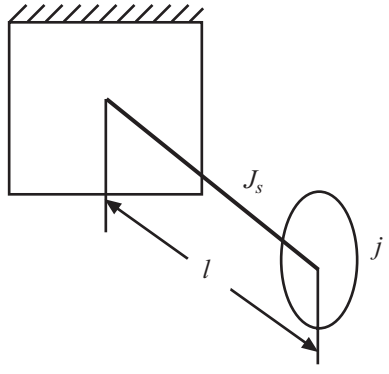
4



$$f_i = \frac{k_i}{2\pi}\sqrt{\frac{EIg}{wl^4}}$$

Mode	k_i	Nodal position/l
1	15.4	0 1
2	50.0	0 0.577 1
3	104	0 0.386 0.692 1
4	178	0 0.295 0.529 0.765 1
5	272	0 0.239 0.428 0.619 0.810
1		

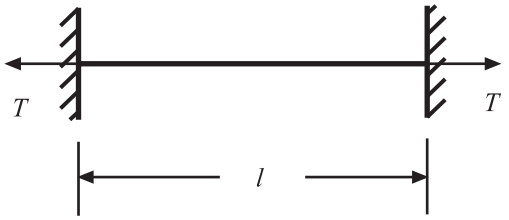
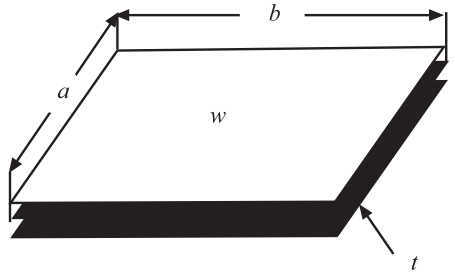
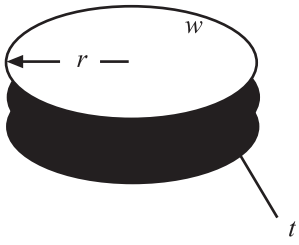
5



$$f_i = \frac{k_i}{2\pi}\sqrt{\frac{6k_i}{(j + (j_s/3))l}}$$

Mode	k_i
1	1.57
2	4.71
3	7.85

Table 5 continued.

No.	Beam configuration	Natural frequencies
6		$f_i = \frac{k_i}{2\pi}\sqrt{\frac{Tg}{wl^2}}$ Mode: 4, 5, 6; k_i: π, 2π, 3π
7		$f = \frac{k}{2\pi}\sqrt{\frac{Et^3g}{12wa^4(1-v^2)}}$ a/b: 0.9, 0.8, 0.6, 0.4, 0.2, 0; k: 10.2, 11.3, 12.6, 17.0, 27.8, 57.0
8		$f = \frac{k_i}{2\pi}\sqrt{\frac{Et^3g}{12wr^4(1-v^2)}}$ Mode: 1, 2, 3, 4; k_i: 10.2, 21.3, 34.9, 39.8

j, concentrated end-mass moment of inertia; j_s, distributed mass moment of inertia; G, shear modulus of elasticity; T, tension in string; i, the rank of the frequency; f_i, natural frequencies (Hz); k_i, constant; r, radius of the circular path; t, thickness of the plate; l, length of the beam; w, load per unit length (including beam weight); I, area moment of inertia; g, gravitational acceleration; E, Young's modulus of elasticity.

In carrying out the design of capacitive, piezoresistive, or acoustic sensors and actuators, the influence of the electrostatic field on the natural frequency decay of the structure must be carefully considered. Such analysis can be carried out using one of the energy methods (Rayleigh for natural frequency or Rayleigh–Ritz for the first few resonant frequencies). By equating the strain energy with the kinetic energy plus the electrostatic energy, the natural frequency or first few resonant frequencies can be calculated. Finite element analysis (FEA) represents another option in identifying the first few natural frequencies of a complex-shaped structure. Finite element modeling permits complex analysis of multilayered complex shape structures, including stress–strain, dynamic, thermal, or electro-magnetic loading, and even combinations of the above.

The Influence of the Interlaminar Stress

Besides the influence of the potential fields, fabrication of thin films may be responsible for the peculiar dynamic behavior of the microstructures. Thin deposited films induce either compressive or tensile stress, which is mainly due to the thermal mismatching between the substrate and the coating encountered at the low ambient temperatures after high-temperature deposition process. The residual stress may produce unwanted bending, warping, and fracture of the structures. However, the existence of the stress in

structure produces changes in the dynamic behavior of the structure. The amount of change in the dynamic properties depends mostly on the quantity of stress built into the structure. The amount of stress is strongly dependent on the parameters of the deposition process, and the values of such stress can range from a few MPa to a few GPa. The low-stressed films are almost always present when accomplishing surface micromachined structures. Certain sequences of processes and thermal treatments could lower the amount of residual stress to close to zero. The measurement of the residual stress can be carried out using experimental techniques that have been created for various stress ranges and specimen size. For full wafer measurement and stress exceeding 10 MPa, the variation of curvature yields the value of the built-in stress, as given by the relationship (Stoney):

$$\sigma_r = \frac{Et_s^2}{6(1-v)t}\left(\frac{1}{R_i} - \frac{1}{R_f}\right) \qquad [8]$$

where t_s is the thickness of the substrate, t is the thickness of the thin film, R_i is the curvature of the wafer before deposition (expected $R_i = \infty$), and R_f is the curvature of the wafer after deposition.The measurement of the large curvatures is performed with optical stress gauge machines, which can detect large radii of curvature of the substrate before and after thin film deposition.

For stress lower than 1 MPa, buckling of a subset of double-supported witness beams is used to range the compressive stress value in a narrow bandwidth. For the tensile stress, special sets of structures consisting of a ring (Guckel rings) supported by a diameter beam are used to evaluate the built-in stress between the substrate and the film. The witness test structures are made from the thin film deposited on the substrate. The two structures described above are shown in **Figure 4**. The array of structures can be contained within a certain design and the measurement consists of confronting the observation through a microscope with a table illustrating the critical stress in buckling versus the geometric dimensions of the beams. The residual stress can be evaluated out of the critical stress at buckling:

$$\sigma_r = -\frac{\pi^2 h^2 E}{3L^2} \text{ for double-supported beams} \qquad [9]$$

$$\sigma_r = -\frac{\pi^2 h^2 E}{12\zeta(R)R^2} \text{ for Guckel rings} \qquad [10]$$

where h is thickness, L is length, R is radius of the Guckel ring, and $\xi(R)$ is the function of the inner and outer diameters.

The residual stress strongly influences the vibration characteristics of the free-standing structures, which are part of MEMS. Flexing multilayered structures such as microbeams and microplates, as shown in **Figure 5**, tune their dynamic response according to the built-in residual stress. The general equation (Lagrange) describing the plate motion is:

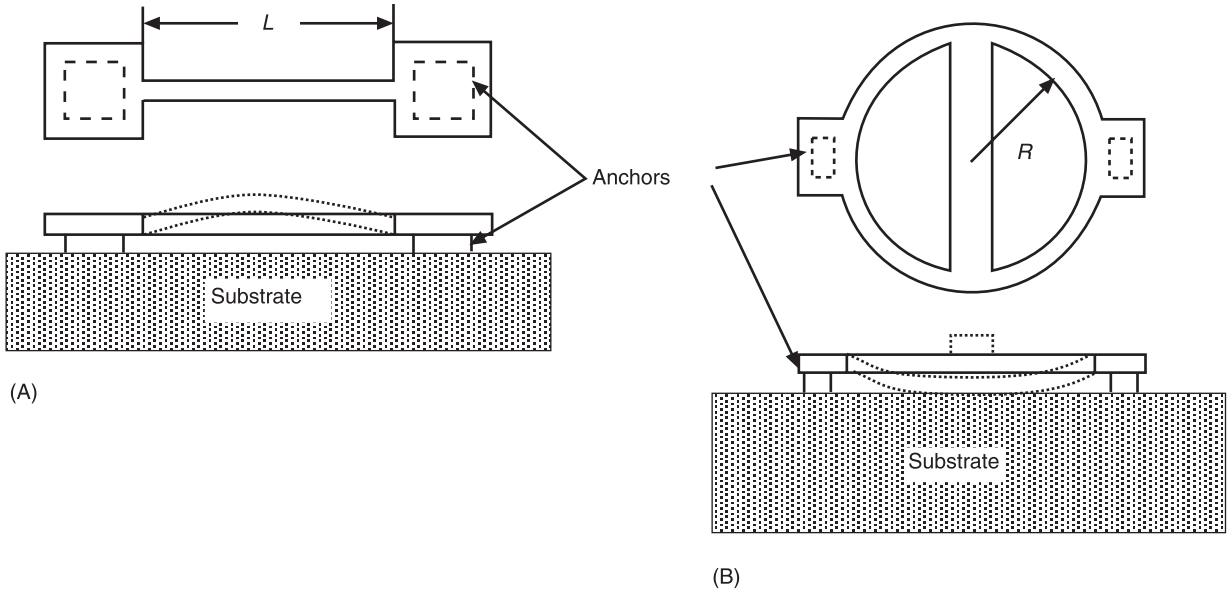


Figure 4 *In situ* structure for low residual stress measurement in thin films. (A) Double-supported beam buckles under compressive stress. (B) Gluckel ring configuration; the diameter beam buckles under the tensile stress in the ring.

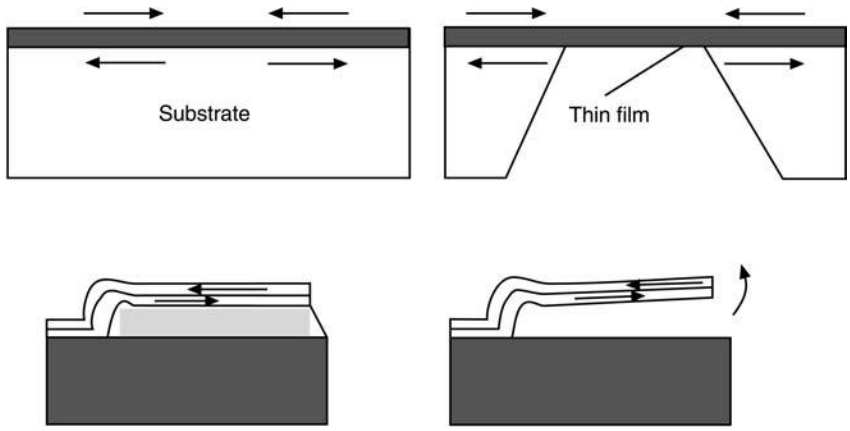


Figure 5 Mismatching stress at the thin film interface. When the substrate or the sacrificial film is etched out to reveal the microstructure, the contour stress or the built-in stress at the interface of the bimorph film will modify the static and dynamic response of the structure.

$$D\nabla^4 z + \rho\frac{\partial^2 z}{\partial t^2} = 0 \qquad [11]$$

with:

$D = \dfrac{Eh^3}{12(1-\nu^2)}$ flexural rigidity of the plate

∇^4 $\dfrac{\partial^4}{\partial x^4} + 2\dfrac{\partial^4}{\partial^2 x \partial^2 y} + \dfrac{\partial^4}{\partial y^4}$

ρ mass by surface unit

If the plate is subjected to stress, which is equivalent to the stress yielded by the contour lineal forces N_x, N_y, and N_{xy} the previous equation changes to:

$$D\nabla^4 z + \rho\frac{\partial^2 z}{\partial t^2} = N_x\frac{\partial^2 z}{\partial x^2} + 2N_{xy}\frac{\partial z}{\partial x \partial y} + N_y\frac{\partial^2 z}{\partial y^2} \qquad [12]$$

The eigenfrequencies f_i of the plate not subjected to any stress are given by:

$$f_i = \frac{1}{2\pi}\frac{\lambda_i}{a^2}\sqrt{\frac{D}{\rho}} \qquad [13]$$

The eigenvalues of the plate subjected to decoupled lineal forces N_x and N_y ($N_{xy} = 0$) are given in the form:

$$\lambda_{si}^2 = \lambda_i^2 + \frac{a^2\pi^2}{D}\left[N_y m^2 + N_x n^2\left(\frac{a}{b}\right)^2\right] \qquad [14]$$

From the above last two equations, one can identify the set of lineal forces N_x and N_y which satisfy the relationships:

$$4\rho a^2\left(f_i^2 - f_{si}\right) = N_y m^2 + N_x n^2\left(\frac{a}{b}\right)^2 \qquad [15]$$

where f_i is eigenfrequency of the unstressed plate, f_{si} is eigenfrequency of the stresses plate, a, b is dimensions of the sides of the plate, h is thickness of the plate, and m, n are mode numbers.

The last relationship can serve to solve the inverse problems, which are of practical interest. When the stress at the interface of the substrate with the thin layer is known, the shift in the vibration frequencies of a given structure can easily be predicted.

Microplates subjected to forced vibration will thus behave similarly, with the exception that their natural frequency is much higher than that of the normal-sized plates.

Annealing performed on the structures at 800–1000°C in inert gases for 2–4 h can substantially reduce residual stress. However, such treatment is too severe for the electronic circuit components and it can only be applied in the very early stages of a standard integrated circuit process, before the definition of the semiconductor junctions.

Signal Conditioning

Microsensors like any other sensors, must convert the measured physical quantity into meaningful signals. The function of the signal conditioning circuitry consists of converting the sensor output into convenient electrical signals that can be further streamed to the controller or to the data acquisition system. The output signal of the sensor should be a voltage waveform, which can be easily processed by the data acquisition circuit. The process of converting the output signal from the sensor to a voltage can be used to reduce the noise or partially to compensate

for the objective errors collected by the signal from the transducer to the conditioning circuitry.

The new generation of sensors is conceived to comprise on the same chip the signal-processing circuit, the analog to digital converter (A/D), and dedicated controllers. The resolution of the A/D can be maximized by matching the dynamic range of the input signal to the dynamic range of the data acquisition system. The source impedance of the input signal must be low, such that changes in the impedance of the data acquisition system or controller do not affect the signal. The sampling rate of the A/D must be at least twice as fast as the bandwidth of the output signal of the sensor (practically, one order of magnitude higher yields a reasonably accurate conversion).

The output signal of the sensor may include noise that must be removed before it is fed to the A/D. The noise is often associated with stray capacitance of the connection line of the circuit. The high level of integration in MEMS presents the advantage of low-level noise in the signal. However, the electrostatic of the electromagnetic fields may negatively influence the performance of the conditioning circuitry. This problem can be addressed through appropriate packaging of the integrated microsensor.

The output signal of the microsensor may not always match the required input signal of the conditioning circuitry. Thus, appropriate conversion of the signal may be required before being fed to the A/D. The conversion is carried out from voltage, current, resistance, and capacitance, to voltage. Most common conversion schemes are briefly presented below.

Voltage-to-voltage Conversion

Voltage-to-voltage conversion is required when dynamic range modifications (bandwidth reduction or impedance alteration) are necessary, when the output signal from the sensor is a voltage. The above-mentioned conversions are carried out by standard circuits. The amplifiers are used to match the output level of the sensor to the input of the data acquisition system. Some of the standard circuits, their scheme, the function carried out and their main properties are shown in **Table 6**. The output signals from the sensor can collect noise. If the frequency of the noise is off the frequency of the significant signal, the unwanted signal can be filtered out using low/high-pass filters. The filtering is usually applied before the signal is amplified. The DC component of the signal, if any, can be removed with an offset circuit.

Current-to-voltage Conversion

Current-to-voltage conversion is usually performed with an operating amplifier in an inverting configuration, since noninverting amplifiers draw very low current. This configuration scheme is most suitable with current-generating sensors. When the current output increases, the output potential increases proportionally.

Resistance-to-voltage Conversion

Resistance-to-voltage conversion is used when the sensor detects the electric resistance variation due to the input signal. Piezoresistive accelerometers, pressure sensors, or microphones are examples of such types of sensors. The resistance variation needs to be translated into standard voltage output to feed the A/DC, the data acquisition circuit, or the controller. The two basic methods to convert resistance variation to voltage output are presented below. The simplest way consists of applying a voltage to a resistor divider network made of the variable resistor R_S (the transducer) and a reference fixed resistor R_R, as shown in **Figure 6**. The voltage detected across the sensor is amplified before being converted to digital signal. The drawback of this method is that the amplifier boosts the entire voltage across the sensor, which translates through a high DC offset. Thus, the second method of converting the resistance to voltage addresses this disadvantage. The resistance bridge configuration, as shown in **Figure 7**, only amplifies the change in voltage due to the shift in the resistance of the sensor. The resistance bridge presents the advantage of zero offset, high sensitivity, and thermal compensation.

Capacitance-to-voltage Conversion

Capacitance-to-voltage conversion is used when the output from the transducer is a variation of capacitance. The capacitance-based sensing presents multiple advantages. The capacitance varies in proportion to the distance between the armatures of the capacitor. The capacitors are sensitive to the material that resides between their electrodes. The most popular methods used to convert capacitance to voltage are similar to those used to measure resistance. However, besides these methods, more innovative principles and circuits have been created. For example, the charge amplifier circuit is used to detect small capacitance variations in the *fF* range.

The voltage divider uses the variable capacitor and a reference capacitor. The circuit configuration is the same as the resistance voltage divider: the only difference is that, instead of the resistors R_S and R_R, capacitors are used. Similarly, the capacitor bridge circuit configuration looks like the resistance bridge in which resistors are replaced by capacitors.

Table 6 Standard circuits

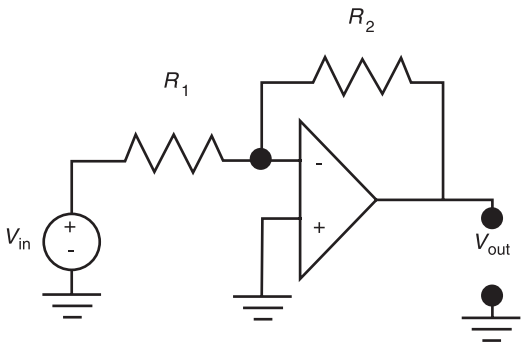
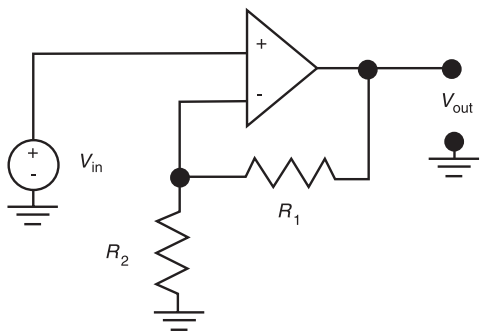
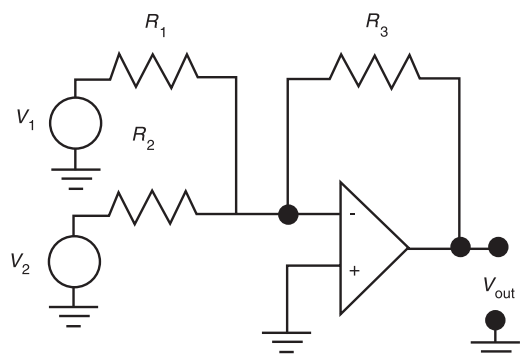
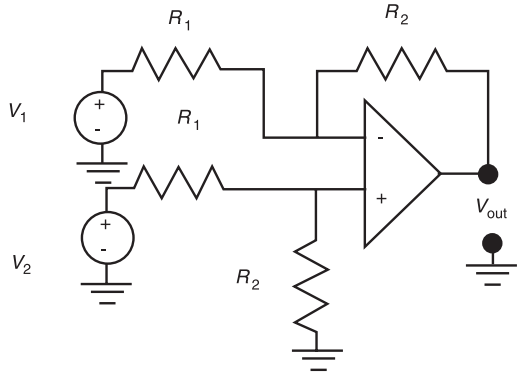
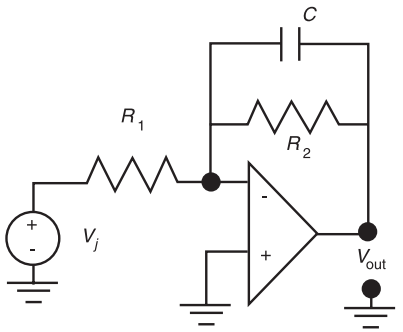
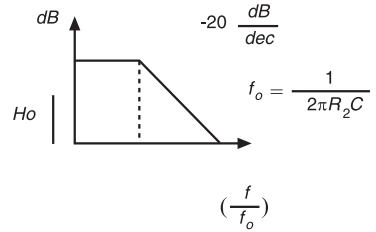
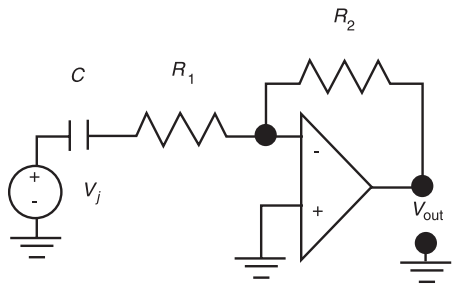
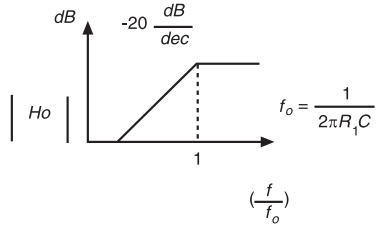
Circuit	*Scheme*	*Input–output relationship*	*Characteristics*
Amplifier inverter		$V_{out} = -\frac{R_2}{R_1} \cdot V_{in}$	Input Impedance $\sim R_1$ Output Impedance ~ 0
Amplifier noninverter		$V_{out} = \left(1 + \frac{R_1}{R_2}\right) \cdot V_{in}$	Input Impedance $\sim \infty$ Output Impedance ~ 0
Summing		$V_{out} = V_1 \frac{R_3}{R_1} + V_2 \frac{R_3}{R_2}$	Combines the output of arrays to sensors

Table 6 Continued

Circuit	*Scheme*	*Input–output relationship*	*Characteristics*
Difference		$V_{out} = (V_2 - V_1) \cdot \frac{R_2}{R_1}$	Removes unwanted DC offset
Single-pole low-pass filter		$A = -\frac{R_2}{R_1}\frac{1}{1+j(f/f_o)}$	
Single-pole high-pass filter		$A = -\frac{R_2}{R_1}\frac{j(f/f_o)}{1+j(f/f_o)}$	

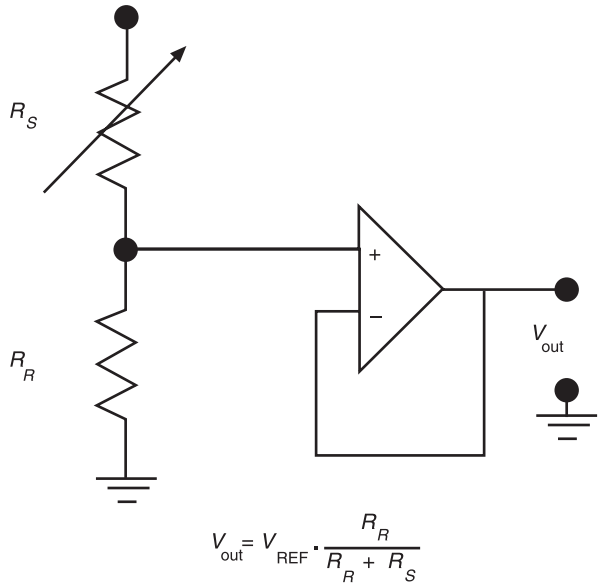


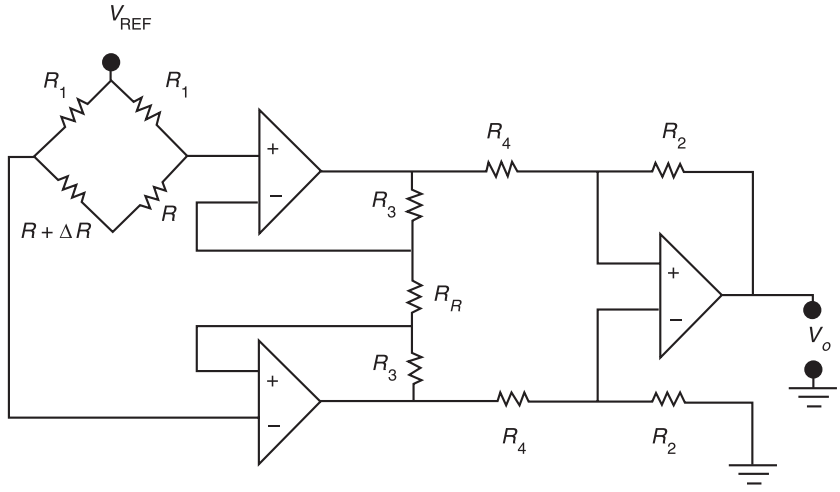
Figure 6 Resistance voltage divider measurement scheme.

The reference signal is sinusoidal, since the capacitance obstructs DC. The impedance of the capacitor is inverse in proportion to frequency. An appropriate reference frequency yields a voltage across the capacitor that is suitable for amplification. When the reference frequency is too low, the high impedance of the sensor creates high levels of noise. When the reference frequency is too high, the low impedance of the sensor allows the sensor to saturate the circuit.

The main feature of MEMS containing free-standing elements is the high natural frequency exhibited by the mechanical structure that may be strongly coupled with the electrical circuit system. MEMS perform in a very nonlinear way in dynamic characteristics. However, in a first approximation, lump mass linear models of the miniature microsystems are satisfactory. Simple formulations of the equivalent mass, stiffness, and damping are analogous with the formulations used in normal-sized systems. For a more accurate analysis of either a simple flexing structure or complex microactuators, the nonlinear phenomena must be considered and examined. They include, but are not limited to, electrostatic and electromagnetic fields, capillary forces, and interlayer mismatch stress. Analysis of the influences of nonlinear physics on the dynamics of the microstructure may be carried out using standard energy methods.

Nomenclature

A	amplitude
C	capacitance
E	Young's modulus of elasticity
g	gravitational acceleration
G	shear modulus of elasticity
h	thickness
I	inertia
L	length



$$V_o = \left(1 + 2\,\frac{R_3}{R_R}\right)\left(\frac{R_2}{R_4}\right)\frac{R}{R_1 + R}\cdot\frac{\dfrac{\Delta R}{R}}{1 + \dfrac{R}{R_1}\left(1 + \dfrac{\Delta R}{R}\right)}V_{REF}$$

Figure 7 Resistance bridge measurement scheme.

Q	quality factor
R	radius
R_R	reference fixed resistor
R_S	variable resistor
T	tension
U	electrostatic energy
V	voltage
ϕ	phase shift
ρ	mass by surface unit

See also: **Damping materials**; **Dynamic stability**; **MEMS applications**; **MEMS, general properties**; **Signal integration and differentiation**.

Further Reading

Bhushan B and Gupta BK (1997) *Handbook of Tribology: Materials, Coatings, and Surface Treatments*. New York: McGraw-Hill.

Campbel SA and Lewerenz HJ (eds) (1998) *Semiconductor Micromachining*. Chichester: Wiley.

Fraden J (1993) *AIP Handbook of Modern Sensors; Physics, Design and Applications*. New York: American Institute of Physics.

Gardner JW (1994) *Microsensors; Principles and Applications*. New York: John Wiley.

Kovacs TA (1998) *Micromachined Transducers Sourcebook*. Boston: McGraw-Hill.

Lee HH (1990) *Fundamentals of Microelectronic Processing*. New York: McGraw-Hill.

Madou M (1997) *Fundamentals of Microfabrication*. New York: CRC Publishing.

Neamen DA (1992) *Semiconductor Physics and Devices: Basic Principles*. Homewood, IL: Irwin.

Ohba R (ed.) (1992) *Intelligent Sensor Technology*. New York: John Wiley.

Sze SM (ed.) (1994) *Semiconductor Sensors*. New York: John Wiley.

Tiller WA (1990) *The Science of Crystallization: Microscopic Interfacial Phenomena*. Cambridge, UK: Cambridge University Press.

Weste NHE and Eshraghian K (1994) *Principles of CMOS VLSI Design*. New York: Addison Wesley.

MEMS, GENERAL PROPERTIES

I Stiharu, Concordia University, Montreal, Quebec, Canada

Copyright © 2001 Academic Press

doi:10.1006/rwvb.2001.0073

Introduction

MEMS, the acronym for Micro-Electro Mechanical Systems, represents an emerging technology through which miniature mechanical systems are built making use of the standard Integrated Circuits technologies on the same chip as the electronic circuitry. Micromechanical structures along with afferent electronic circuitry often perform functions with high accuracy, which cannot be accomplished by so called 'normal' sized structures. The strength of MEMS is provided through the high effectiveness of the fabrication process, which yields uniform performances for the structures at a relatively low cost, in conjunction with the low power consumption. Moreover, microstructures may probe into phenomena deeper than actual electromechanical systems do.

Microelectromechanical systems (MEMS) are miniature mechanical devices built from silicon using solid-state technology; they contain the necessary electronic circuitry built on the same chip with the mechanical structure. These devices are also known as microsystems or micromechatronic devices. Monocrystalline silicon is a very attractive mechanical material which, in addition to its enabling electrical properties, exhibits remarkable mechanical properties. The elastic modulus is close to that of steel while the specific mass is about three times lower. Silicon enables the parallel batch fabrication of microsystems, which yields higher reliability of the devices together with a dramatic drop in the fabrication cost. The concept of MEMS emerged from the need for miniaturization of the mechanical sensing elements, enabled by the anisotropic crystallographic etching properties of silicon and driven by the enormous progress made in integrated circuits (IC) technology over the last two decades. The field of MEMS has been acknowledged at the end of the 1980s, although the roots of silicon-based sensors and actuators go back to the 1970s.

MEMS are classified into two large functional classes: microsensors and microactuators. Microsensors are conceived as fully signal-conditioned transducers that provide the same function as the classic sensors along with their conditioning circuit board. Since the main functions of sensors are detection and measurement, they should interfere as little as possible with the environment, except for measured

physical quantity. Thus, the energy exchange between the environment and the microsensor should be minimized. Miniature transducers easily comply with these requirements.

Microactuators are conceived to convey energy to their surrounding environment. Their size limits tremendously their performance and thus, the area of application is mainly reduced due to their limited energy storage capability. Arrays of microsensors and microactuators together with implemented controls enable the creation of 'smart matter', which represents a natural step in the development of technology.

The first silicon-based miniature devices were produced in the early 1970s through bulk micromachining. This fabrication principle takes full advantage of batch fabrication but the minimum feature size is limited to fractions of millimeters. Besides, bulk micromachining cannot enable full implementation of the electronic circuitry with the mechanical component on the same silicon chip, using a unique processing flow. The earlier devices thus involved considerable efforts in assembling and packaging the mechanical components and the electronic conditioning circuitry. Further, the research focus has been directed towards developing a comprehensive technology to realize both the reliable electronic circuits and robust mechanical structures integrated within a single design. Attempts to fabricate mechanical devices using modified standard IC processes were successful, so that the conditioning circuitry could be included on the same chip and fabricated during the same process flow. The surface micromachining processes yield a minimum feature size in the range of micrometers. Here, superimposing several patterned layers of conducting, insulating, and transistor-forming materials to build the structural and the sacrificial configurations along with the conditioning circuitry enables the realization of MEMS structures. After the completion of both mechanical structure and electronic circuitry, a sacrificial etching is performed to release the free-standing structure without affecting the function of the electronic circuitry. This step, called postprocessing, requires highly selective etchants and a series of precautions in order to retain the integrity of the microstructure.

The feasibility of the microactuators and micromechanisms has been established through a hybrid technology that enables surface micromachined MEMS based upon thicker polysilicon as the structure and SiO_2 as sacrificial films (MUMPS).

Figure 1 illustrates the difference between bulk and surface micromachining. The bulk-micromachined structures are obtained by removing the excess from

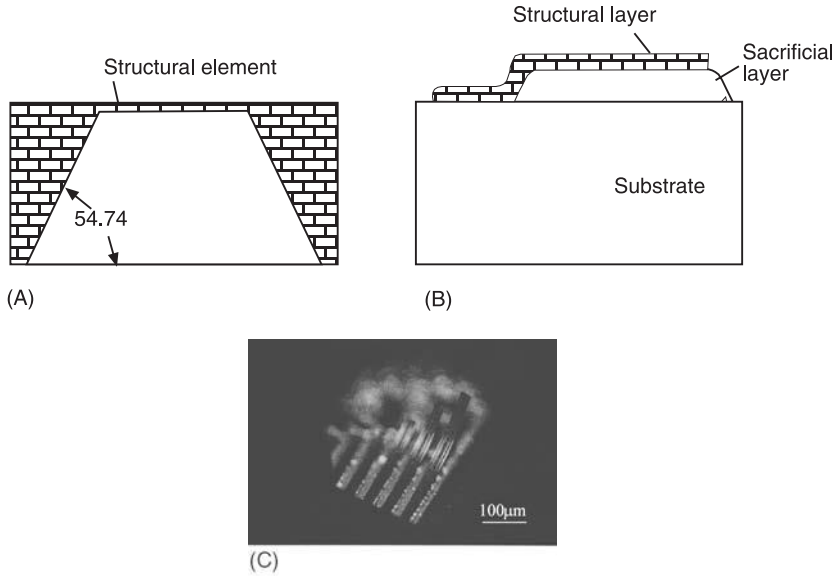


Figure 1 (A) Bulk-micromachined plate in section. The structural element is built from silicon substrate by deep crystallographic anisotropic etching. (B) Surface micromachined step-up free end beam in section. The structural element is built in the top of the sacrificial film. Postprocessing will remove the sacrificial film and release the free-standing structure. (C) Surface-micromachined microbeams released by postprocessing. Mismatching between the materials constituting the polymorphous beams induces high stress which has evolved into spectacular bending of the beam.

the substrate material, such as that shown in **Figure 1A**, through isotropic or anisotropic etching of the material. Surface micromachining yields microsystems enabled by the structural layers deposited and patterned in a specific sequence with the sacrificial layers. The sacrificial layers are removed during postprocessing and the microstructure is released as illustrated in **Figure 1B**. **Figure 1C** shows a magnified picture of a set of micromachined cantilever beams, which are released through postprocessing etching. Thermal mismatching in thin films of various materials, which constitute the beam as a composite material, induces high stresses, resulting in a dramatic bending of the free end of the beam.

Sensors and microsensors are conceived to detect and measure electrical, chemical, magnetic, mechanical, radiant, and thermal measurands. The most common physical quantities and measurands are given in **Table 1**. However, mechanical microsensors are the most interesting from the point of view of vibration. They modify mechanical measurands in electrical signals, using resistive, capacitive, inductive, piezoelectric, or other physical conversion principles.

The primary sensing element is usually a simple elastic structure such as a cantilever beam, which deflects under input measurand. This deflection, although small, is related to the input measurand, which is detected and translated into an electric signal by the built-in subminiature secondary sensing devices, such as piezoresistive, piezoelectric or capacitive elements. The rendered electric signal must be well shielded from the noise of the environment for further conversion into a meaningful indication by the conditioning circuitry. The sensitivity of the sensing element to the measured signal must be high, while sensitivity to irrelevant excitations should be as low as possible. Limitations in sensitivity are related to the measured range and the maximum permitted overloading.

The force/position feedback servosensors structure is more complex, since they comprise both microsensors and microactuators. When distorted by the input signal, the sensing element is returned to its static position by actuators, which are fed by the feedback signal. The signal used to restore the position of the element is meanwhile used for measurement, as shown in **Figure 2**. Such a design concept, although more complex, addresses issues related to overloading and hysteresis.

Implementation of the IC technology for microsystem fabrication represents a very different concept in the sensors technology. Resolutions of $0.001\text{Å}/\text{Hz}^{1/2}$ or sensitivities in the order 10^{-10} N are usual features of such microsensors. The actual achieved precision and the accuracy of MEMS sensors can improve up to one order of magnitude the performances of the classic sensors. The detected input signal can be further fed into the electronic circuitry, conveniently

Table 1 The most common measurands for microsensors

Physical quantity/ measurement principles	*Measurand*
Mechanical	Acceleration, velocity, position
Elastoelectric	Force, moment
Elastomagnetic	Stress, pressure
Thermoelastic	Strain
Thermoelectric	Mass, density
Photoelectric	Flow, flow speed
Photoelastic	Stiffness
	Viscosity
	Energy
Acoustic	Wave amplitude, wave velocity, wave phase
Elastoelectric	Polarization
Elastomagnetic	Frequency spectrum
Photoelastic	Intensity
Magnetoelectric	Energy
Thermal	Temperature
Thermoelectric	Thermal flux
Thermomagnetic	Specific heat
Thermoelastic	Thermal conductivity
Thermooptic	Thermal energy, thermal power
	Energy
Electrical	Charge, current
Magnetoelectric	Potential
Thermomagnetic	Electric field
Thermoelectric	Conductivity
Photoelectric	Permittivity
Elastoelectric	Energy
Magnetic	Magnetic field
Magnetoelectric	Magnetic flux
Elastomagnetic	Permeability
Thermomagnetic	Energy
Optical	Wave amplitude, wave velocity, wave phase
Photoelectric	Polarization
Photomagnetic	Frequency spectrum
Photoelastic	Energy
Radiation	Type
Thermoelectric	Intensity
Photoelectric	Energy
Thermooptic	
Biochemical	Composition
Physical transformation	Concentration
Chemical transformation	State
Electrochemical	
Spectroscopy	

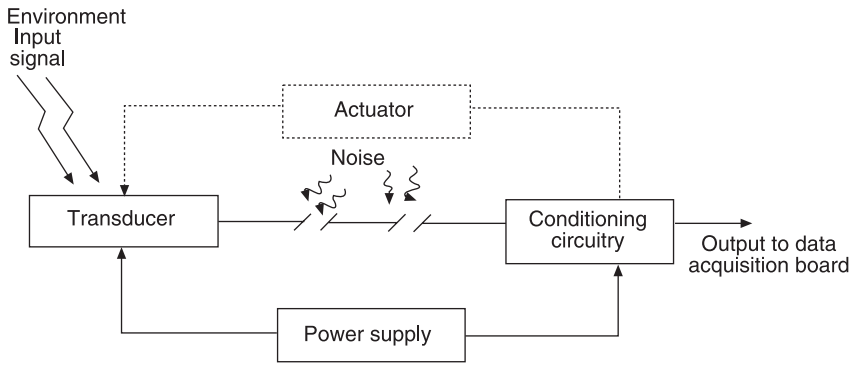


Figure 2 General configuration of a sensor. The dashed line with the feedback actuator shows the configuration of a servo sensor.

located next to the transducer, which modifies the input into a signal which matches the data acquisition system. This is usually equivalent to changing the output to a voltage. The function of the electronic circuitry extends to modifying the sensors' dynamic range to maximize accuracy, filtering the noise, and limiting the measurement spectrum.

Micromachined microactuators are conceived to convert electrostatic, electromagnetic, thermal, or fluid flow energy into mechanical rotation, translation, or oscillation. Although presently the microactuators are created for applications in which the required forces do not exceed μN range, tremendous applications in microbiology have been forecasted. Both linear and rotary microactuators have been built using bulk and surface micromachining technology, although the three-dimensional attributes of the actuators have required special technologies for high-quality vertical pattern fidelity. One main problem of the microactuators relates to the friction and wear of moving parts. The small sized pivots, the complexities associated with total control of clearances between the pivot and the bearing, and the lack of appropriate lubrication methods dramatically reduce the life of the electrostatic motor. However, IC technology has not been modified to accomplish readily assembled devices, such as hinges and articulations. Thus, the alternative technologies permit to compensate for such limitation. Elastic suspensions or levitation principles have been implemented to overcome the friction and wear in rubbing parts. Compliant mechanisms represent another option for MEMS. The compliant mechanisms allow motion through elastic deformations of one or more elements. Motion of compliant segments generally involves large-magnitude nonlinear deflections, which are difficult to predict using the linear beam theory. More accurate prediction of microstructure behavior will require multiphysics nonlinear analyses of the miniature structures. Modeling such devices is thus quite challenging. Application of the surface-micromachined compliant multistable mechanisms on microvalves and microswitches is presently under investigation.

MEMS Materials

Microsystems manufacturing (micromachining) makes use of a large variety of materials. However, only a few are used to build the structural elements. The mechanical properties of these materials are thus of prime interest for the mechanical designer of MEMS. Although the mechanical properties of bulk materials are comprehensively known, the properties of the thin deposited films are strongly dependent on the deposition process and the deposition parameters. **Table 2** provides a list of the most frequently used materials for MEMS structures together with their available relevant properties, as given in the available literature. The physical values range between broad limits, which may be attributed to excessive variations in the measurement methods employed and to the large variance in the properties of the materials. Besides, the thinly deposited films exhibit high internal compressive or tensile stresses, which may to a certain extent influence the mechanical properties of the thin structures. It has been acknowledged that the materials in thin films exhibit higher mechanical strength than the same materials in bulk state.

Apart from the mechanical properties, some materials require other special properties and conditions for the material processing, as they may not withstand subsequent processing. The active materials are specifically used to build the transducer on the measurement element, which is mostly associated with the flexing element in the mechanical microsensors. The deposition and patterning sequences rigorously

Table 2 Mechanical properties of selected materials used in MEMS processing

Material	*Thermal expansion coefficient* ($\times 10^{-6}\,^{\circ}C^{-1}$)	*Strain limit* ($\times 10^{-6}$)	*Yield strength* (*MPa*)	*E Young modulus* (*GPa*)	*Density* ($kg\,m^{-3}$)	*Hardness Knoops* (*GPa*)	*Poisson ratio*	*Thermal conductivity* ($W\,m^{-1} \times {}^{\circ}C$)
Al: film	23	2	0.124	47.2–74	2700–3500	1.3		236
Si: bulk	2.3–4.3	–	7	62–202	2330	5.3–13.1	0.22–0.278	157
Polysilicon: film		3–7	–	120–200			–	
SiO_2: film	0.41–31.9	112	8.4	46–95	2200	8.2–18	0.17	1.10–1.7
Si_3N_4: film	0.8–3.9	37	1.4	100–380	3200	34.8	0.22–0.27	9.2–30
SiC: film	4.7–5.8	–	21	302–450	3200	24.8–29.6	0.183–0.192	20.8–120
PVDF: film	6–250	–	–	2	1780			
Polymide: film	3–140	–	–	7.5–15			0.1–0.45	
Pt: film	8.9–10.2	1	–	170	21 440			73
Monosilicate glass t059: film		–	–	40–60	2250	5–7		
Diamond-like carbon (DLC)		–	–	150–800				
Au: gold	14.1–16.5	–	–	80	19 280			315

require certain standing limits for the deposited material. One should bear in mind that the same materials are used to build the IC, and thus, material selection must avoid any incompatibility problems that could jeopardize the IC performances due to the fabrication.

MEMS Fabrication Technology

MEMS fabrication mostly makes use of established IC processes. Apart from the rigid processing sequence, some new techniques have been developed and implemented to substitute for the lack of flexibility of the standard IC. They appropriately use the unconventional machining together with the standard machining processes. Thus, LIGA (deep-etch lithography, electroforming, and plastic molding), laser-assisted chemical vapor deposition (CVD), electroplating, chemical plating, and even conventional machining form the most common manufacturing techniques.

In lay terms, accomplishment of MEMS through surface micromachining is done through deposition of specific thin films (required by the IC process), patterning and etchings of the deposited material on undesired areas, followed by other successive depositions, patternings, and etchings arranged in stacks. The desired structure is thus fully completed and embedded into the consecutive layers of depositions. Postprocessing is performed to remove the sacrificial films and release the free-standing structure.

Table 3 schematically illustrates the core of the IC-for-MEMS fabrication processes. The table presents the three main processes: deposition, patterning, and the removal of sacrificial layers. These processes are subject to considerable variations in the process parameters depending upon the technology implemented. The deposition techniques have reached performance levels that enable the deposition of films with adequate mechanical and electrical properties.

Further, **Table 4** gives a list of most other common processes used to realize MEMS. As can be seen, standard machining processes are included in the list, since hybrid accomplishment of MEMS through IC and standard processes is an alternative that is still under appraisal. Some of the standard machining processes are most instrumental for packaging. Most of the standard machining processes, however, require individual manipulation of parts, which represents a bottleneck for a batch fabrication stream.

The etching process marks the postprocessing of the microstructure. Release of the free-standing structure represents a challenge, since the electronic circuitry, the contact pads, and the structure itself have to withstand the etching. The costs associated with postprocessing and packaging of MEMS often contribute to a significant increase in the cost of the MEMS. The low-cost postprocessing techniques, invariably performed outside the silicon foundry, are thus extremely desirable.

The selectivity of the etchant with respect to the passivation and structural films is of most interest in surface micromachining. **Table 5** presents the most popular etching recipes for Si, glass, Si_3N_4, Al, and Au along with the corresponding etch rates.

Table 3 Description of fabrication processes for MEMS

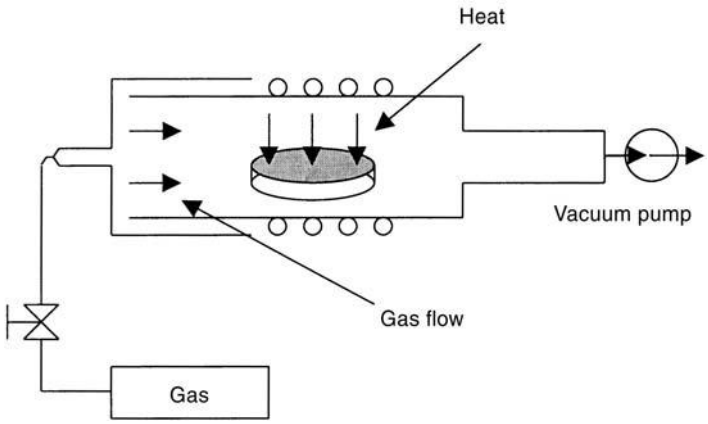
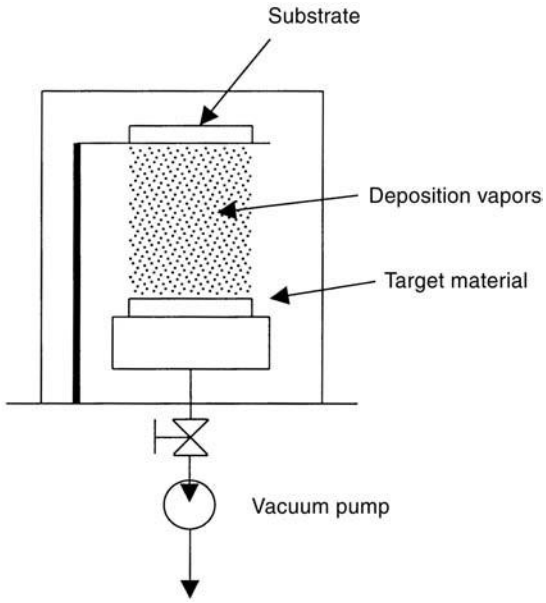
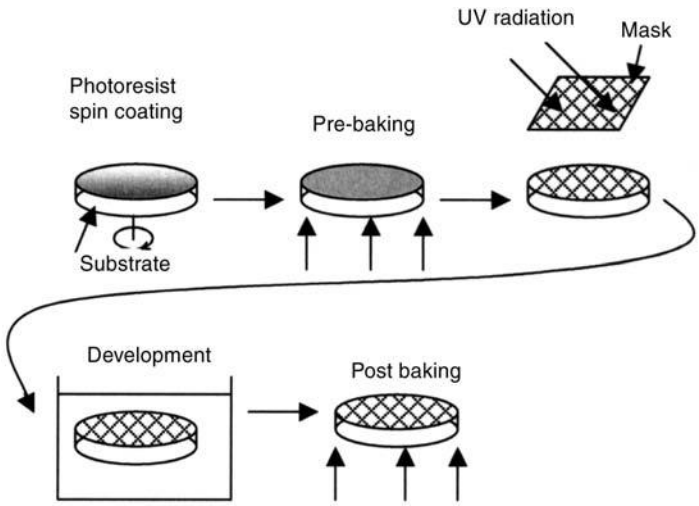
Process	*Type and method*	*Sketch*
Thin film deposition		
Uniform deposition of selected materials on the entire surface of the wafer	Chemical vapor deposition (CVD)	
	Physical vapor deposition (sputtering, vaporization)	
Lithography		
Batch printing on substrate 2-D and 3-D features on photo-sensitive polymer	UV photolithography	

Table 3 Continued

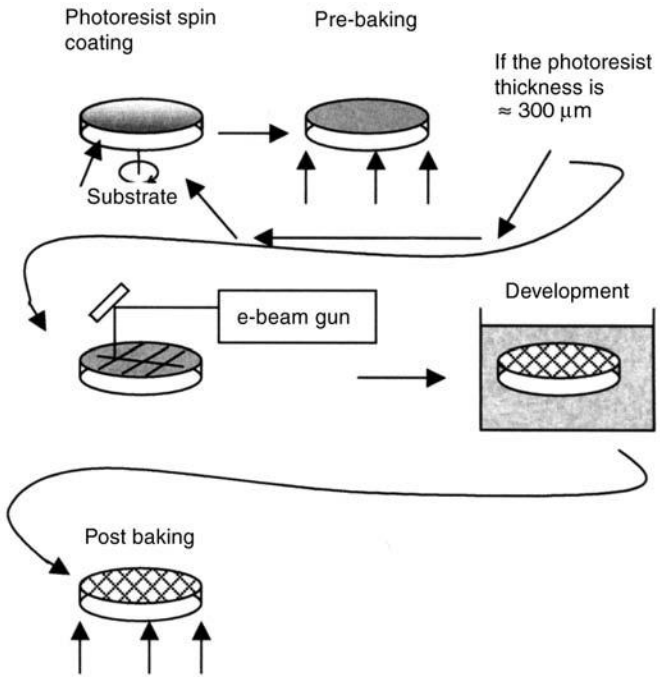
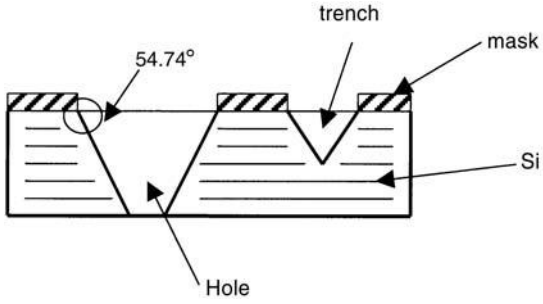
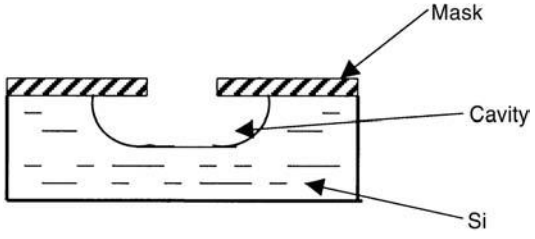
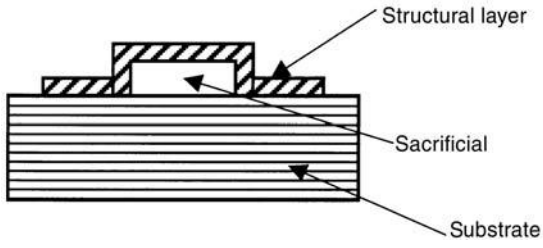
Process	*Type and method*	*Sketch*
	E-beam lithography	
Etching	Deep etching (crystallographic)	
Selective removal of undecided material from designated areas exposed to the etchant	Anisotropic – (100) silicon wafer	
	Isotropic: Si wafer	
	Thin film etching	
	Sacrificial: any material etching	

Table 4 Alternate processes used in MEMS manufacturing

Process	*Alternatives and issues*
Electroforming	Electrochemical deposition (plating): contamination
	Anodizing: contamination
	Polishing: not very productive
Surface processing	Ion implantation
	Diffusion: high temperatures
	Annealing: high temperatures
Coating	Dipping: all sides are covered
	Spinning: high process variability
	Spraying: uniformity issues
	Serigraphy: alignment
Forming	Hydro: contamination, accuracy
	Drawing: high temperature or high built-in stress
Extrusion	Direct/indirect: accuracy
Molding	High-pressure injection
	Vacuum: accuracy
	Dipping: filling
	Compression
Machining	Turning: fixture
	Milling: high forces
	Drilling: chip removal
	Sawing
	Electrochemical discharge
Finishing machining	Grinding: high forces
	Polishing: low efficiency
	Lapping: low efficiency
Microcutting	Laser: low efficiency
	Electron beam
	Electrochemical discharge: contamination, minimum size
Joining	Riveting: size (microsize riveting under investigation)
	Screwing: size
	Soldering: strength
	Brazing: high temperature
	Elastic
Bonding	Anodic: high temperature and voltage
	Thermal: high temperature
	Adhesives: limited life
Welding	Laser
	Electron beam
	Electric spot: size
	Electrochemical
Wire bonding	Ultrasonic
	Thermal: high temperature

The selectivity of the anisotropic etchant versus certain crystallographic planes is responsible for the sculpturing into silicon of V or U trenches that are conveniently used to create bulk micromachined structures. **Table 6** presents the most used silicon anisotropic etchants, typical etching temperature, etch rate, and selectivity.

The essential electrochemical etch reactions involve oxidation–reduction and dissolution of the oxidation products by complex etching agents. Both electrons and hole carriers exist at the silicon surface. Oxidation of silicon atoms takes place at the anodic sites, while the oxidant is reduced at the cathodic sites. The etching mechanism can be summarized as follows:

- Injection of holes into the semiconductor $Si + 2\oplus^{+} \rightarrow Si^{2}$
- Attachment of hydroxyl group OH^{-} to Si^{2+}, e.g. $Si^{2+} + 2(OH^{-}) \rightarrow Si(OH)_2$
- The dissociation of water $H_2O \leftrightarrow OH^{-} + H^{+}$
- Reaction of the hydrated Si with complexing agent in the solution
- Dissolution of the reacted product into etchant solution

These etching mechanisms, however, do not fully describe the crystallographic anisotropic etching of silicon, and the temperature and stress dependences or the selectivity.

More accurate etching can be carried out in reactive gases. The anisotropic etching of silicon in gas is no longer driven by the crystallographic structure. Thus, the etchant no longer follows the crystallographic direction (111), like the wet anisotropic etchants, but the cut strictly follows a perpendicular direction to the masked surface. **Figure 3** illustrates isotropic and anisotropic etching. **Table 7** gives the gas etchants for materials most commonly used in MEMS fabrication, together with specific etch rate and selectivity versus various masking materials.

MEMS Packaging

The basic considerations for MEMS packaging are:

- Connections to the chip for signal and power leads
- Means of cooling of the chip if necessary
- Mechanical structure to support and protect the chip
- Controlled-pressure environment to reduce the viscous damping of the flexing structure and provide access for the measurand to the sensing area

Satisfying all the requirements for a robust package has proven to be a very difficult task. The selected materials must possess compatible thermal coefficients of expansion, or the structure must comprise the means to release the resulting mechanical stress, and excess of heat.

Temperature changes may arise either from the chip operation or changes in the operating environment. The connections and the package should enable low noise transmission and a high-fidelity path for signals to and from the chip, and robustness of connections. Applications with specific considerations include, but are not limited to, operations in hostile environments, hybrid multichip packages,

Table 5 Wet etching solutions and etch rates for MEMS materials

Material	*Etchant solution*	*Etch rate*
Polysilicon	6 ml HF, 100 ml HNO_3, 40 ml H_2O	800 nm min^{-1}, smooth edges
	1 ml HF, 26 ml HNO_3, 33 ml CH_3COOH	150 nm min^{-1}
SiO_2	Buffered HF (BHF) (28 ml HF, 170 ml H_2O, 113 g NH_4F)	100–250 nm min^{-1} at 25°C
	1 ml BHF, 7 ml H_2O	80 nm min^{-1}
Borosilicate glass (BSG)	1 ml HF, 100 ml HNO_3, 100 ml H_2O	30 nm min^{-1} for 9 mol% B_2O_3, 5 nm min^{-1} for SiO_2
	4.4 ml HF, 100 ml HNO_3, 100 ml H_2O	75 nm min^{-1} for 9 mol% B_2O_3, 13.5 nm min^{-1} for SiO_2
Phosphosilicate glass (PSG)	Buffered HF (BHF)	550 nm min^{-1} for 8 mol% P_2O_5
	1 ml BHF, 7 ml H_2O	80 nm min^{-1}
Si_3N_4	HF	14 nm min^{-1}, CVD at 1100°C
		75 nm min^{-1}, CVD at 900°C
		100 nm min^{-1}, CVD at 800°C
	BHF	0.5–10 nm min^{-1}
	H_3PO_4	10 nm min^{-1} at 180°C
Al	4 ml H_3PO_4, 1 ml HNO_3, 4 ml CH_3COOH, 1 ml H_2O	35 nm min^{-1}, high resolution
	16–19 ml H_3PO_4, 1 ml HNO_3, 0–4 ml H_2O	150–240 nm min^{-1}, coarse
	0.1 mol $K_2Br_4O_7$, 0.51 mol KOH, 0.6 mol $K_3Fe(CN)_6$	1 μm min^{-1}, coarse
Au	3 ml HCl, 1 ml HNO_3: aqua regia	25–50 μm min^{-1}
	4 g KI, 1 g I_2, 40 ml H_2O	0.5–1 μm min^{-1}, resist mask

Table 6 Moncrystalline silicon etchants, etching rates and selectivity

Etchant	*Typical composition*	*Temperature (°C)*	*Etch rate (μm min^{-1})*	*Anisotropy (100)/(111) etch rate ratio*	*Dopant dependence*	*Masking films (etch rate of mask)*
Ethylene diamine pyrocatechol (EDP) in water	750 ml 120 g 100 ml	115	0.75	35:1	7×10^{19} cm^{-3} boron reduces etch rate by about 50	SiO_2 (0.2 nm min^{-1}) Si_3N_4 (0.01 nm min^{-1})
	750 ml 120 g 240 ml	115	1.25	35:1		
KOH in water	44 g 100 ml	85	1.4	400:1	10^{20} cm^{-3} boron reduces etch rate by about 20	Si_3N_4, SiO_2 (1.4 nm min^{-1})
KOH in isopropyl alcohol	50 g 100 ml	50	1.0	400:1		
Tetramethyl ammonium hydroxide in water (TMAH)	25 g 75 ml	85	0.6	200:1	$\geq 2 \times 10^{20}$ cm^{-3} boron reduces etch rate about 25 times	Si:SiO_2 (1000:1)
	15 g 85 ml	85	0.5	200:1		
Isotropic etchant HF HNO_3 CH_3COOH	10 ml 80 ml 30 ml 25 ml	22	0.7–3		Reduce rate by 150 for phosphorous and boron 10^{17}·cm^{-3}	SiO_2 (30 nm min^{-1})
	50 ml 25 ml	22	4			Si_3N_4 SiO_2 (70 nm min^{-1})

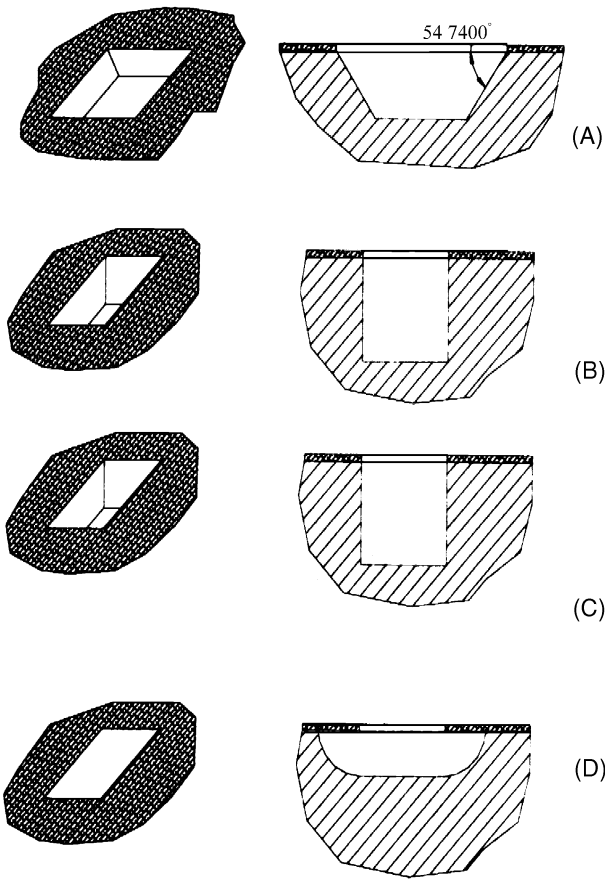


Figure 3 Section through anisotropic and isotropic etched silicon features. (A) Wet etching of (100) Si orientation; (B) wet etching of (110) Si orientation; (C) dry isotropic etching of Si; (D) isotropic etching of Si in XeF_2.

vibration control, and direct exposure of portions of the chip to outside stimuli (i.e., light, gas, pressure, and temperature).

MEMS Design

The observations on the dynamic behavior of MEMS indicate that they do not follow the pattern of similar geometric macrostructures. The design of MEMS requires a perfect knowledge of the capabilities and drawbacks of the manufacturing processes. Both bulk and surface micromachining impose specific constraints on the design that are often reflected in the geometry of the features. Both bulk and surface MEMS could be better designed using a computer-aided design (CAD) tool which are built to include the constraints of the manufacturing process. The layout design level is usually carried out on IC-compatible design tools, which enable the design of the electronic circuitry. Simulations of the dynamics of both electronic circuitry and the mechanical structure modeled as an electronic circuit help to improve the performance of the coupled electromechanical system. The simulation uses models which are created based on analogous electrical circuit elements. A comparison of the mechanical, fluid, and thermal elements with the electrical element is given in **Table 8**. It is important to note that other first-order analogs are accepted and used in simulations. The selection of analogs, however, may depend on the likeness of current and voltage used in describing the mechanical physical quantities.

Table 7 The gas etchants for materials used in MEMS, etch rate, and selectivity versus Si, SiO_2, and photoresist

Material	*Etching gas*	*Etch rate (nm min^{-1})*	*Selectivity*		
			vs silicon	*vs SiO_2*	*vs photoresist*
Si	$SF_6 + Cl_2$	100–450		80	5
Polysilicon	Cl_2	50–80		30	5
SiO_2	$CF_4 + H_2$	50	20		5
PSG	$CF_4 + H_2$	80	32		8
Al	$BCl_3 + Cl_2$	50	4	22	7

Table 8 Comparison of physical elements

	Dissipative	*Current storage*	*Potential storage*
Electric	Resistance	Inductance	Capacitance
Mechanical	Damper	Spring	Mass
Fluid	Fluid resistance	Fluid inertance	Fluid capacitance
Thermal	Thermal resistance	—	Thermal capacitance

Next Page

One of the challenges a designer has to face in modeling is to establish the figure number of the squeeze damping and the elastic constant for the continuum beam or plate element. Attempts to express analytically the equivalent stiffness of cantilever and double-supported micromachined beams have been done, but the simple analytical expressions do not always match the experimental available data. More accurate solutions are accomplished when the finite element analysis (FEA) is used in conjunction with the appropriate material data. Nonlinear characteristics of the material or nonlinear behavior of the structure can be simulated through appropriate description of the material and elements. Sufficient accuracy can be achieved by conveniently refining the mesh. A parametric design used in conjunction with multiple variable optimization algorithms can enhance the performance of the structures. Stress–strain, modal, dynamic, thermal, electromagnetic or CFD analyses can be run once a suitable model has been conceived. The output can provide essential information that may lead to improved performance of the microstructure. Some commercial codes can perform multivariable optimization, which would ease the task of the designer.

However, an overall strategy of the entire manufacturing flow, including packaging, must be planned before the analysis is carried out. Important pieces of information such as damping of the structure reside in the environment in which the structure will work and the operating temperature. Thus, the dynamic properties will strongly be influenced by the surrounding gas/fluid in which the flexing structure performs. Before the layout design is finalized, simulations of selected deposition and etching processes may be run to insure that critical features will be accomplished within the permitted tolerances.

Figure 4 illustrates the graphic output of a stress analysis performed on the section of a plate subjected to uniform pressure loading. Appropriate meshing yields the stress distribution across the thickness of the plate, which can further be used by the designer to establish the most appropriate location of the piezoresistive gauges.

After prototyping, manufacturing, and testing, the models are adjusted based on the empirical data obtained from measurements. Presently, the integrated modeling of MEMS is still in its infancy, although efforts have been made to understand and model the individual manufacturing processes, such as etching, crystal growth and physical deposition. Although not explicitly stated, it is apparent that analytical models of microstructures are also used and continuously improved, as test data become available. Modeling of electromechanical–fluid–thermal systems is thus of much interest to the designer. One of the main needs at this time is to build a good microscale data bank of parameters and material properties that can be used in the modeling and design of microsystems.

Miniaturization of mechanical systems establishes a unique momentum in both classic and emerging technologies. MEMS enables a new approach in making, running, and controlling systems and processes. Micromechanical devices and systems are essentially smaller, lighter, faster, more precise, and

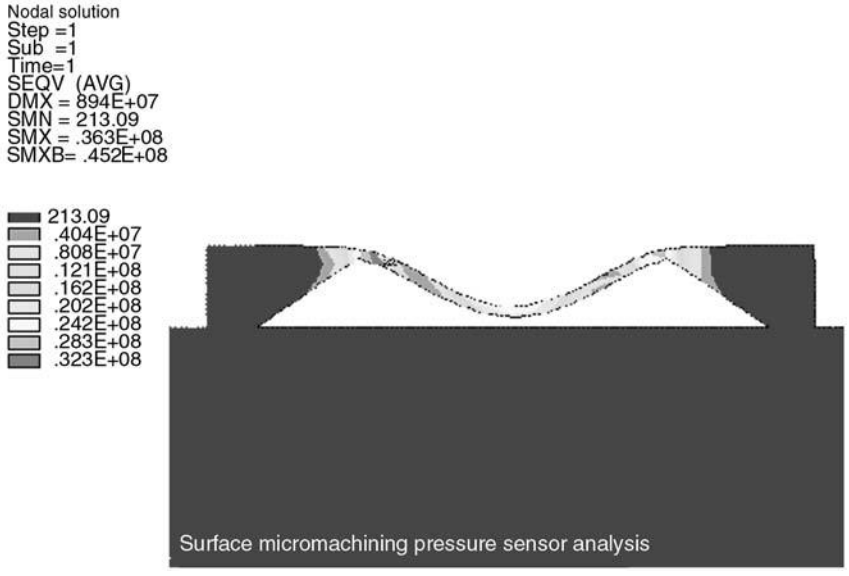


Figure 4 (see Plate 42). The output graphic file of an analysis of a silicon plate subjected to uniform distributed pressure loading.

usually less expensive than their macroscopic counterparts. The development of micromechanical systems, however, requires appropriate fabrication technologies which permit the definition of small geometry, precise dimensional control, design flexibility, interfacing with control electronics, high repeatability and reliability, high yield, and low cost.

See Plate 42.

See also: **MEMS, applications**; **MEMS, dynamic response**.

Further Reading

Bhushan B and Gupta BK (1997) *Handbook of Tribology: Materials, Coatings, and Surface Treatments*. New York: McGraw-Hill.

Campbel SA and Lewerenz HJ (eds) (1998) *Semiconductor Micromachining*. Chichester: Wiley.

Fraden J (1993) *AIP Handbook of Modern Sensors; Physics, Design and Applications*. New York: American Institute of Physics.

Gardner JW (1994) *Microsensors: Principles and Applications*. New York: John Wiley.

Kovacs TA (1998) *Micromachined Transducers Sourcebook*. Boston: McGraw-Hill.

Lee HH (1990) *Fundamentals of Microelectronic Processing*. New York: McGraw-Hill.

Madou M (1997) *Fundamentals of Microfabrication*. New York: CRC.

Neamen DA (1992) *Semiconductor Physics and Devices; Basic Principles*. Homewood, IL: Irwin.

Ohba R (ed.) (1992) *Intelligent Sensor Technology*. New York: John Wiley.

Sze SM (ed.) (1994) *Semiconductor Sensors*. John Wiley.

Tiller WA (1990) *The Science of Crystallization: Microscopic Interfacial Phenomena*. Cambridge, UK: Cambridge University Press.

Trimmer W (ed.) (1990) Micromechanics and MEMS. *Classic and Seminal Papers to IEEE PC4390-QCL*. Piscataway, NJ: IEEE.

Weste NHE and Eshraghian K (1994) *Principles of CMOS VLSI Design*. New York: Addison Wesley.

MODAL ANALYSIS, EXPERIMENTAL

Basic principles

D J Ewins, Imperial College of Science, Technology and Medicine, London, UK

Copyright © 2001 Academic Press

doi:10.1006/rwvb.2001.0026

Overview

This article introduces and explains the basic concepts of the widely-used technology which has become known as 'experimental modal analysis' or 'modal testing'. Simply put, experimental modal analysis comprises a set of experimentally-based procedures which lead to the construction of a mathematical model that can be used to describe the dynamic behavior of the test object. This model can be used on a variety of useful applications including:

1. visualization of the modes of vibration of the test structure for the purpose of gaining physical insight and an understanding of the often complex dynamic properties of real structures;
2. comparison of the actual (measured) vibration behavior of a real structure with corresponding parameters predicted from a theoretical model;
3. correcting or refining that theoretical model;
4. predicting the effects of making modifications, or predicting what modifications to introduce to change the structure's behavior;
5. predicting the behavior of structures formed by coupling two or more components together;
6. detecting damage or other changes in the integrity of a structure during its service life;
7. identification of 'unpredictable' parameters such as damping, dynamic friction effects, excitation forces from unknown sources, etc.

In effect, modal testing has been practiced for a long time but has only been formalized in the past 30 years, following the advent of computers and instrumentation capable of realizing the concepts with sufficient accuracy to warrant implementation of the ideas.

The basic sequence of steps in a modal test are:

1. measurement of the test structure's vibration response to a controlled and known excitation;
2. analysis of the resulting response functions to identify the underlying modal properties (natural frequencies and mode shapes) of the test structure;
3. construction of a mathematical model from these modal properties, suitable for the intended application.

The specific skills that are required to conduct a successful modal test include:

- a sound appreciation of the underlying theory
- measurement techniques to excite and measure the vibration response of the test structure
- signal processing techniques to define the required response function information
- data analysis methods which are capable of extracting parameters for an assumed mathematical model that can describe the observed test behavior.

Brief History of Experimental Analysis/ Modal Testing

Modal testing has been practiced at various levels for over 50 years. The earliest, and still the most common, applications of the experimental methods that are now called 'modal testing' or 'experimental modal analysis' were to validating whatever theoretical model had been constructed to predict the structure's behavior under dynamic loading conditions – usually under steady-state excitation. Nowadays, the mathematical models in question are almost always finite element models. Probably the first documented modal testing methods date back to the 1940s when engineers charged with conducting vibration tests on aircraft structures† sought to supplement the primary test data of how and when the structure would fail under dynamic loads with intermediate observations (while the test was running) of the input forces and the resulting response levels, thereby measuring the same type of frequency response functions that we use today. These early attempts to conduct what we now recognize as modal tests were frustrated by inadequacies of the transducers and signal conditioning equipment of the day and it was a full decade later before early electronic devices, and then computers, provided the means to make and to analyze adequate measurements of the essential data. In fact, it was the widespread introduction of the digital computer and development of data analysis techniques such as the fast Fourier transform (FFT) in the 1960s that heralded the real start of modern experimental modal analysis.

The 1970s saw the development and widespread use of FFT-based signal analyzers and the associated progress of the technology necessary to process the resulting measured data by extracting the coefficients in an assumed governing mathematical model. By the 1980s, experimental modal analysis was maturing to the stage where it could be used in a routine industrial context and it was during this decade that many of the powerful applications were developed: model updating; structural dynamic modification (SDM) and optimization methods as well as those for analyzing structures which comprise an assembly of different and often disparate components; and then later, damage detection, and identification of a range of quantities that are difficult, if not impossible, to describe theoretically.

More recent developments in the subject, in the 1990s, have seen progressive refinements in the primary techniques and applications, accompanied by a growing appreciation of the limitations associated by almost any experimental data in part by their inevitable imprecision but also, and more significantly, by their incompleteness, a feature brought about by the inescapable restrictions on the quantity and choice of what can be included in a given test. Bearing these effects in mind, and the trend towards the conduct of fewer and fewer tests, not least because of the resources and time they consume, there is now considerable interest and activity in refining modal test procedures and methods so as to optimize the whole process: to make careful selection of which parameters must be measured (and which are unimportant) and the accuracy that is required. By such an approach, the cost-effectiveness of modal tests can be considerably increased and their usefulness assured. These recent developments are often referred to as 'test planning' and represent a 'full circle' situation as regards the theoretical models that most modal tests are performed to validate: the subject theoretical models are often used in a numerical simulation of the proposed modal test in order to establish the optimum parameters for that test.

Basic Procedures Involved in a Modal Test

The sequence of steps that must be executed to conduct a modal test (the engineer having first thoroughly familiarized him/herself with the associated theory so that he/she can detect and explain any deviations of actual behavior from the expected and assumed characteristics of a linear, multi-degree-of-freedom system (MDOF)) are as follows:

1. set up the test structure in a mounting configuration which has been carefully selected and which can be controlled;
2. provide a means of exciting the structure into vibration in a controlable and measurable way. This may be by means of a nonattached device, such as an impact hammer or similar, or by an exciter which is connected firmly to the test structure. These exciters can generate the required

† At that time, 'vibration tests' were those conducted to simulate service loading and to determine the threshold levels that the structure could withstand before failing. They were, in effect, environmental of endurance tests.

excitation forces by several means: mechanical, electromagnetic, electrohydraulic, etc.;
3. provide a means of (transducers for) measuring the resulting response of the test structure, and to do so with the minimum of interference to the test object (often difficult to achieve);
4. provide signal processing and analysis facilities so that the required information can be extracted from the individual measured time histories yielded by the transducers. Here, it is usually necessary to convert raw measured data in the time domain into equivalent spectra in the frequency domain, as frequency domain parameters are more commonly used to describe most vibration phenomena;
5. subject the measured response function data to a subsequent analysis stage, often employing curve-fitting techniques, in order to construct a mathematical model of standard form (linear, MDOF system) whose dynamic properties most closely resemble those observed on the test structure.
6. Check that the resulting model is adequate for the intended application (before releasing the test structure).

The Essential Theory

It is important in modal testing, more so than in many experimental disciplines, that the underlying theory of both the structural dynamic behavior and the various stages of signal processing and data analysis (typically, curve-fitting) is well appreciated by those who conduct such tests. There are many situations in which poor, and even very poor, results can be obtained using perfectly adequate equipment and instrumentation because these are not being used correctly: a situation which can easily arise if the understanding of the whys and wherefores of the different techniques involved is inadequate.

Much of the necessary theory can be found in more detail in other entries in this work (see **Modal analysis, experimental**, Parameter extraction methods; **Modal analysis, experimental**, Construction of models from tests). Accordingly, here we shall simply quote some of the more important expressions and formulas and indicate some of those areas that should be mastered as necessary preparation for those aspiring to conduct successful modal tests.

Having described experimental modal analysis as the process whereby a mathematical model is constructed from test data which is capable of describing the observed behavior of the test structure, it is appropriate here to define more in detail what is meant by a mathematical model. Conventionally, there are three types of mathematical model, each of which is capable of describing the required structural dynamic behavior, but each formulating the model in a different way, based on different fundamental features.

Spatial Models

The first type of model is the spatial model which describes the distribution in space of the essential physical features of the structure – its mass or inertia, its stiffness and its damping properties. In simple terms, the spatial model is the set of mass, stiffness and damping elements which are used in describing equations of motions for the system:

$$m\ddot{x} + c\dot{x} + kx = 0$$

or

$$\mathbf{M}\mathbf{x} + \mathbf{C}\mathbf{x} + \mathbf{K}\mathbf{x} = \mathbf{f}$$

for the more representative MDOF system that is applicable to most real cases.

Modal Models

The second type of model is the modal model, which comprises the set of eigenvalues and eigenvectors – natural frequencies and mode shapes – that describe the individual 'ways' in which the structure will choose to vibrate if left to do so without any externally applied excitation, other than an initial disturbance from which it is released and allowed to vibrate. This model is defined by two matrices, $\boldsymbol{\omega}_r^2$ and $\boldsymbol{\Phi}$, containing the eigenvalues and eigenvectors, respectively.

There is a direct and algebraically simple relationship between the spatial model and the modal model which can be written for the basic undamped case as follows:

$$\boldsymbol{\Phi}^{\mathrm{T}}\mathbf{M}\boldsymbol{\Phi} = \mathbf{I}$$

and:

$$\boldsymbol{\Phi}^{\mathrm{T}}\mathbf{K}\boldsymbol{\Phi} = \bar{\boldsymbol{\omega}}_r^2$$

Response Models

The third type of model is referred to as a response model, and this consists of a set of response functions (usually but not exclusively, frequency response functions or FRFs) that relate the input/output relationships for all the degrees of freedom of the structure. The typical individual FRF from which this model is built is written as $H_{jk}(\omega)$, and is defined as the harmonic response in DOF j to a unit harmonic excitation applied in DOF k at frequency, ω. There is an important condition associated with this definition, which is that the specified excitation must be the

only excitation that is applied when the response is measured. Thus:

$$H_{jk}(\omega) = \left(\frac{X_j}{F_k}\right); \quad F_m = 0; \quad m = 1, N; \neq k$$

In fact, the complete FRF matrix, $\mathbf{H}(\omega)$, which contains the full set of individual FRFs for all j, k combinations, can be related to the preceding spatial and modal models as follows (again, shown here for the basic undamped system):

$$\mathbf{H}(\omega) = \left(\mathbf{K} - \omega^2\mathbf{M}\right)^{-1} = \mathbf{\Phi}\left[\left(\bar{\omega}_r^2 - \omega^2\right)\right]^{-1}\mathbf{\Phi}^{\mathrm{T}}$$

From this last expression, it is possible to derive a convenient expression for the individual FRF as:

$$H_{jk}(\omega) = \sum_{r=1}^{N} \frac{(\phi_{jr})(\phi_{kr})}{\bar{\omega}_r^2 - \omega^2}$$

and this is the expression which forms the basis for much of modal analysis processing methods.

See **Modal analysis, experimental**, Measurement techniques for further details of this underlying theory for experimental modal analysis.

Summary of Essential Experimental Requirements

The experimental aspects of modal testing comprise two main tasks: (i) exciting the test structure into vibration in a controled way and (ii) measuring the excitation force(s) and the resulting response(s). These tasks embrace a series of mechanical issues of excitation devices, support of the test structure, attachment of exciters and transducers plus another set of requirements concerning the signal conditioning and processing which must be applied to the transducer outputs. A sketch of a typical set-up for conducting a modal test is shown in **Figure 1**, with the major elements of the system labeled appropriately.

Support of Test Structure

The first task is to decide how to support the test structure. There are essentially two choices, free–free or grounded and the selection depends on a number of factors which are determined by the eventual application of the test results. Careful consideration must be given to these and the appropriate choice must be made.

Excitation of Test Structure

Next, it is necessary to decide whether the excitation forces should be applied by an attached exciter, or by a nonattached impact device, such as a hammer. A major advantage of the former is that much more control can be applied to the excitation levels and frequency content than is possible with an impactor. On the other hand, the very attachment of the exciter to the structure introduces the risk of interfering with the structure and changing its local stiffness or mass. Care must therefore be taken to attach the exciter in a well-controlled way. The use of a hammer exciter, or equivalent, has the advantage of being

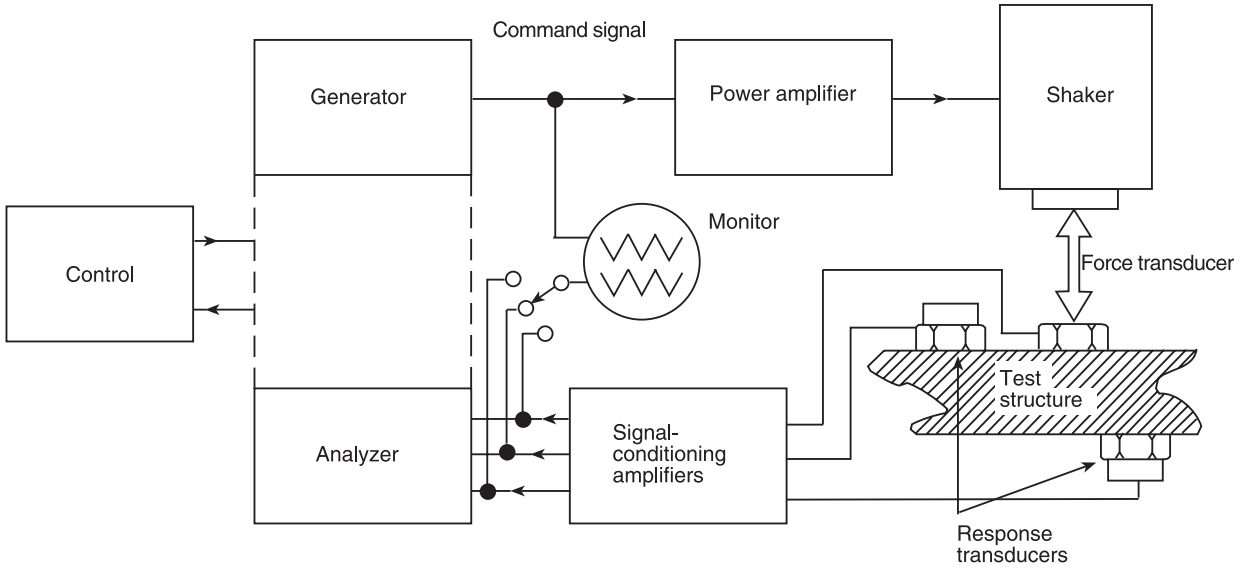


Figure 1 Typical experimental set-up for modal test.

very convenient and quick, as no attachment device is required. However, relatively little control of the excitation signal and level is possible with such an exciter and it is found that there is a relatively narrow range of structures which are well suited to impact excitation – not too lightly-damped; not too heavily damped; linear – while those outside that set can pose problems.

The structure can be excited with almost any type of signal – sinusoidal, periodic, random, transient – and essentially the same response function will be derived from each. There has been a lot of development to determine the most effective and efficient excitation signals and the choice of the one to use in each case needs careful consideration. **Figure 2** shows some of the more popular signal types.

Transducers

A wide range of transducers are available for capturing the excitation force and resulting response levels. Many of these are piezoelectric devices, simple to use and relatively free of idiosyncratic features. Such transducers are widely available to measure force and acceleration: other transducers are also available for measuring velocity responses directly, and worth a special mention are the new generation of laser Doppler vibrometers, which offer

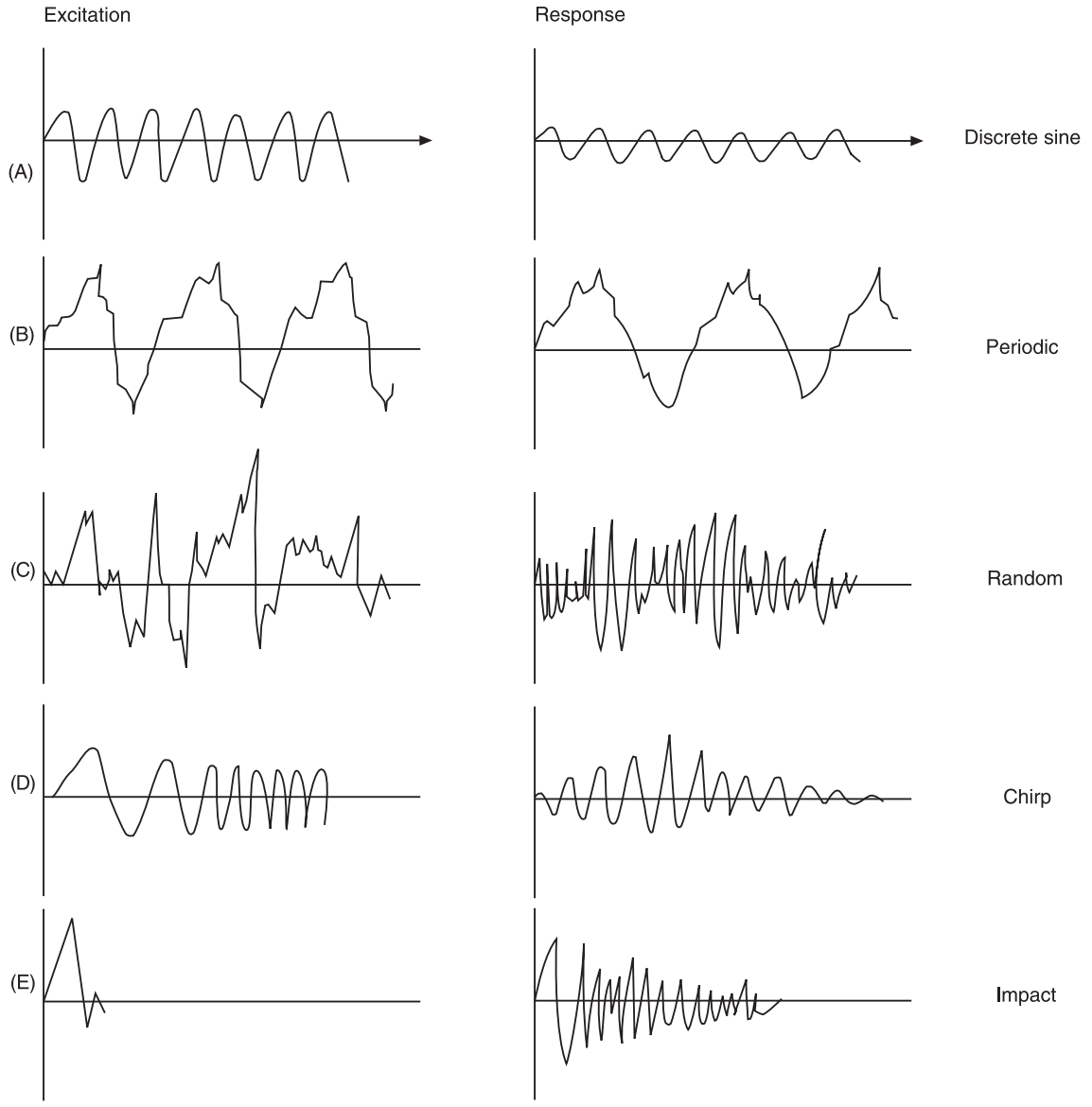


Figure 2 Popular types of excitation signal used for modal tests. (A) discrete sine; (B) periodic; (C) random; (D) transient–chirp (E) transient–impact.

advantages of being noncontacting devices, thereby minimizing interference with the behavior of the test structure.

Signal Processing

Signal processing is a major activity. It is generally required to be able to extract the individual frequency components which are present in a signal – sometimes because the original signal generating the vibration contains many components (as is the case for periodic, random or transient types of excitation), and other times because it is required to eliminate spurious components of response, introduced by noise or nonlinearities in the measuring system. These various requirements can be met with the current generation of spectrum and other frequency response analysers, often based on digital filtering and frequently employing the FFT or similar algorithms developed in the 1960s, and making signal processing very much faster than it had been hitherto. The advent of the FFT was a major development for modal testing.

The primary output from the measurement stage of a modal test consists of a series of response functions, usually – but not exclusively – FRFs, and these are yielded directly from the output of the signal processing devices (analyzers) used to treat the measured time-histories emitted from the transducers. Here, again, a thorough appreciation of the underlying theory becomes essential for the successful use of the various experimental and signal processing devices. **Figure 3** illustrates some typical signals recorded during a modal test, and the resulting FRF that is produced as the 'output' from the measurement phase of the test.

See **Modal analysis, experimental**, Measurement techniques for details of these experimental aspects of conducting a modal test.

Summary of the Analysis of Measured Response Functions

The next stage in the modal test procedure is the analysis which is applied to the measured response functions in order to reveal the properties of the mathematical model which closely describes the behavior of the measured structure.

The first part of this stage comprises a process of 'modal parameter extraction' or 'modal analysis' in which the measured response functions are scrutinized in some detail in order to determine the underlying formulas which can be used to characterize their form. This is usually achieved by using curve-fitting procedures, where the basis of each curve is a theoretically-generated formula developed for an MDOF system with, at the outset, unknown parameters. By applying curve-fitting procedures, least-squares or other criteria can be applied in order to determine the best-fit coefficients in these expressions such that a theoretically-regenerated curve can be constructed to pass through the measured data points with the minimum of discrepancy.

There are many implementations of this general procedure: some are simple methods that perform the analysis (curve-fit) on a very small part of the measured response function, such as in the vicinity of a single resonance on a single response curve, while others are more extensive, performing the same essential task on a much greater dataset, such as is provided by several response functions, each covering many resonances, in a single calculation. **Figure 4** illustrates examples of both types of analysis – the first case (A) showing the traditional 'circle-fit' approach to the analysis of a single resonance on a single curve, while the second case (B) shows the result of a multicurve, multimode simultaneous analysis of over 70 FRFs in a frequency range spanning several modes.

In each case, the essential process is the same: measured response data – usually in the form of a set of measured FRFs – are subjected to an extensive curve-fitting analysis in which the reference curves are based on the formula for response functions for an MDOF system with unknown parameters. By curve fitting, best estimates for these parameters are determined and these, in turn, yield the essential modal properties – natural frequencies, damping factors and mode shapes – of the model which has been proposed. Of course, it is important that the assumed model must be of a sufficiently general form and order such that it is possible to find values for its parameters that render it capable of representing the measured behavior. There can be a problem in achieving the desired result if, for example, the model is assumed to have only 10 DOFs when the measurements clearly reflect the behavior of a system with more modes than that. Likewise, conflicts will arise if the assumed model is linear while the measured data reflect the behavior of a structure which is noticeably nonlinear in its characteristic. In this respect, it is important to check that the results of the curve-fitting, modal analysis, process are not only the 'best-fit' results in a least squares sense, but also that they are good results. These two criteria are not automatically satisfied simultaneously.

For full details of the various methods for extracting modal parameters estimates for a structure from analysis of measured response functions, see **Modal analysis, experimental**, Parameter extraction methods.

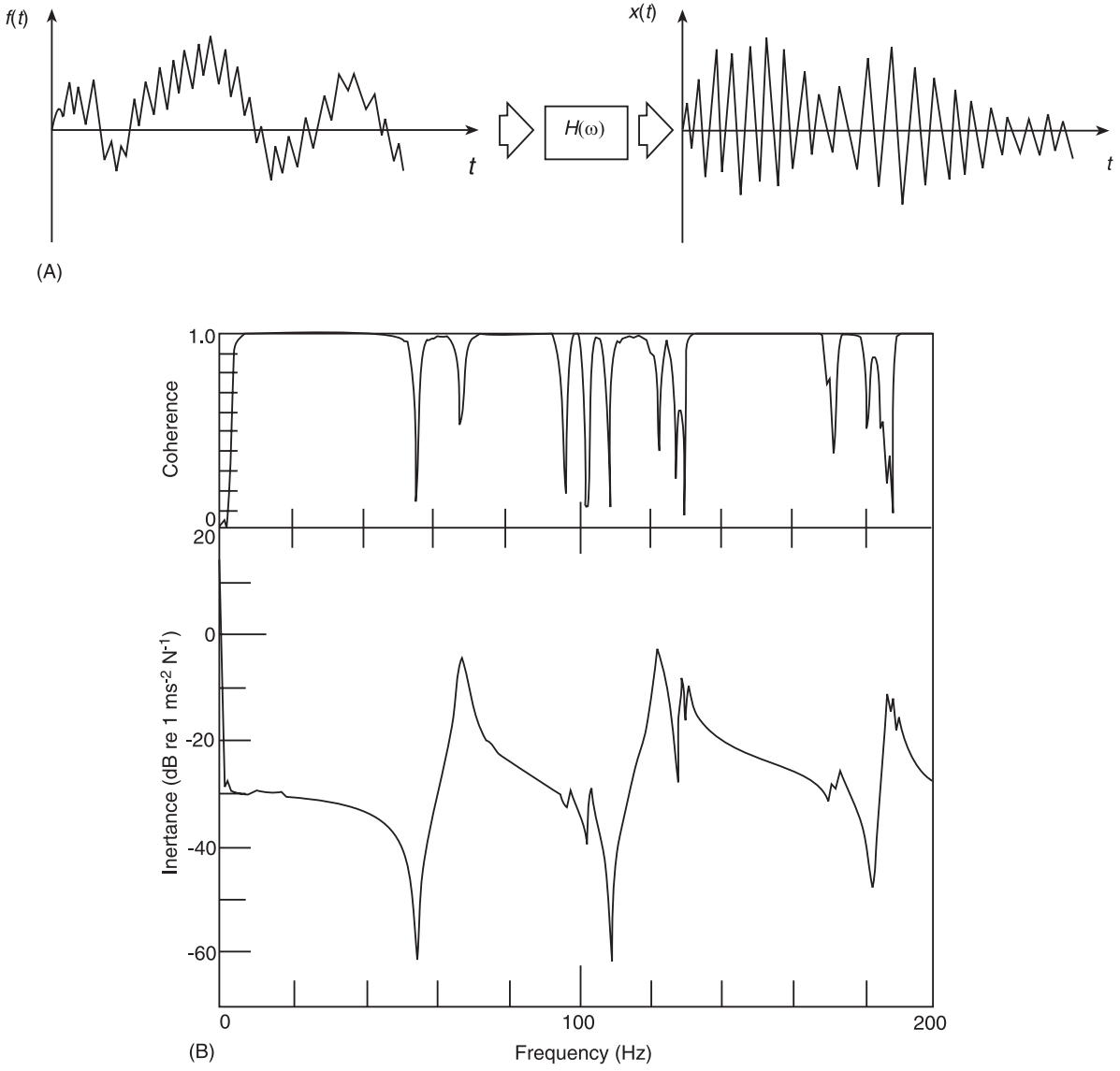


Figure 3 Typical transducer signals and frequency response function produced from modal test. (A) excitation and response signals under periodic excitation; (B) FRF produced from periodic excitation.

Construction of the Mathematical Model

The final step in the analysis of measured data is that of combining all the detailed results from the parameter extraction procedures, and using these to construct the mathematical model which is the objective of the whole exercise. In effect, once the modal parameter extraction exercise is completed, the elements for a modal model have been obtained, and a mathematical model of this type is, theoretically, available.

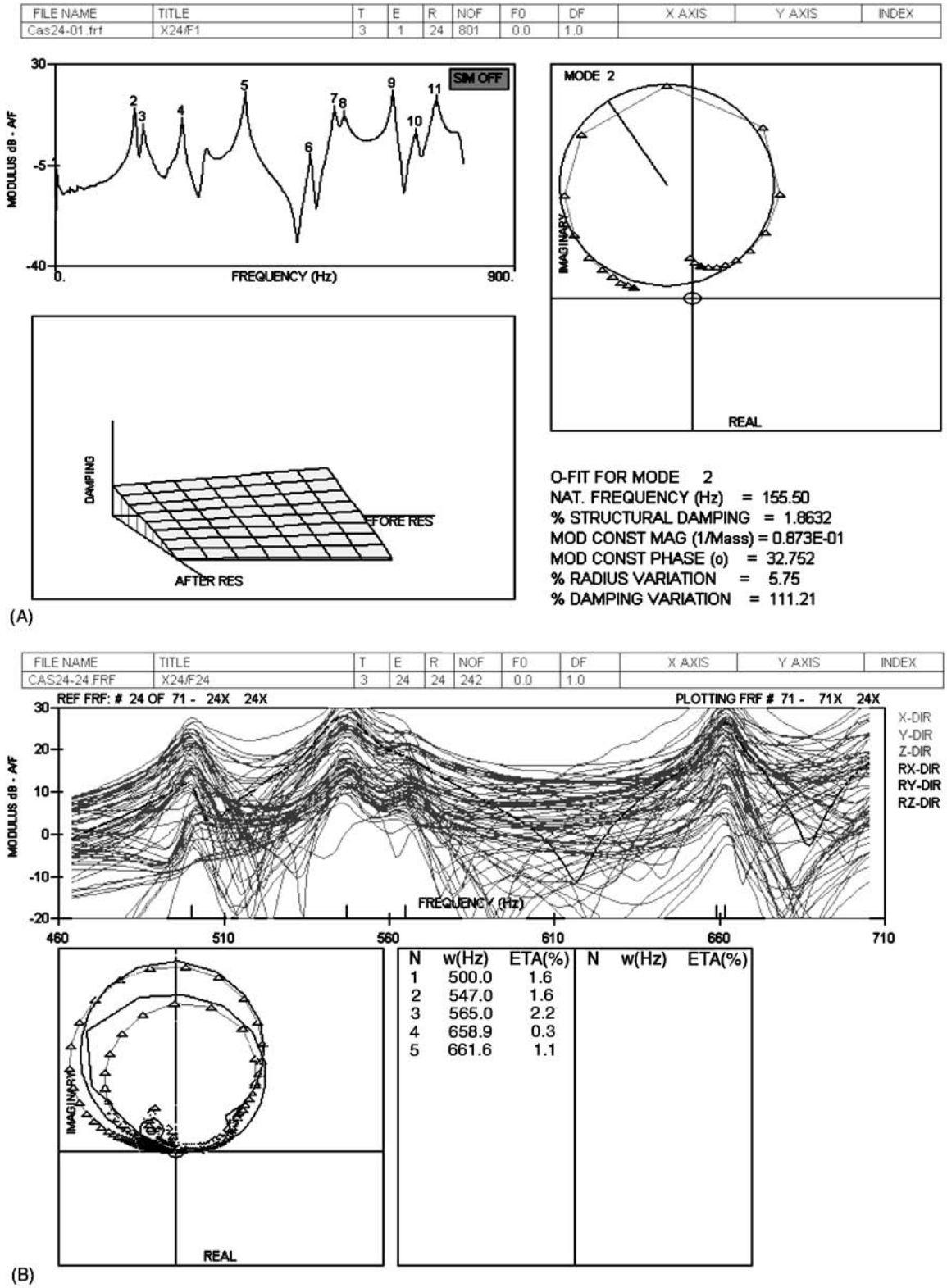


Figure 4 (See Plate 43). Example of modal analysis on measured FRF data. (A) simple, SDOF circle-fit analysis; (B) multimode; multi-DOF global analysis.

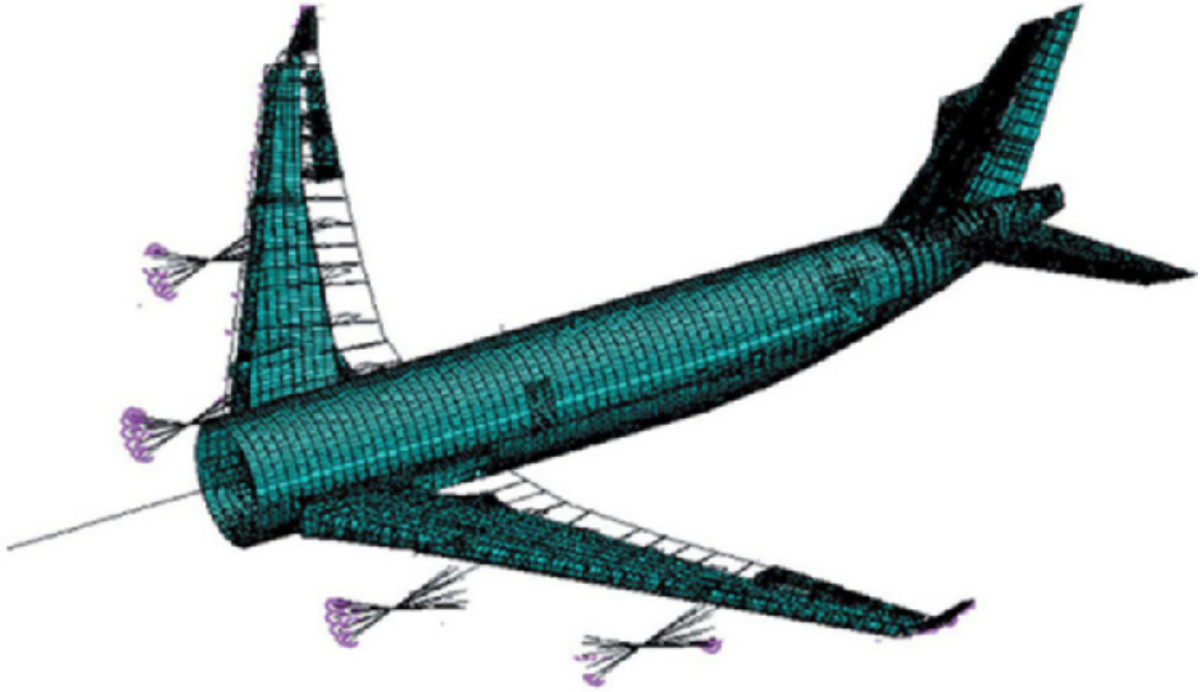


Plate 33 (above) Flutter, Active Control.
Finite element discretization of a commercial transport airplane (courtesy of the Institute of Flight Mechanics and Control).

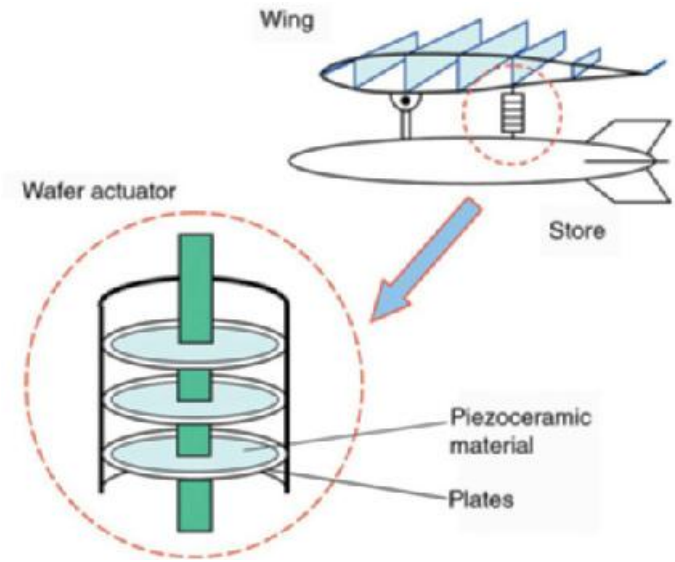
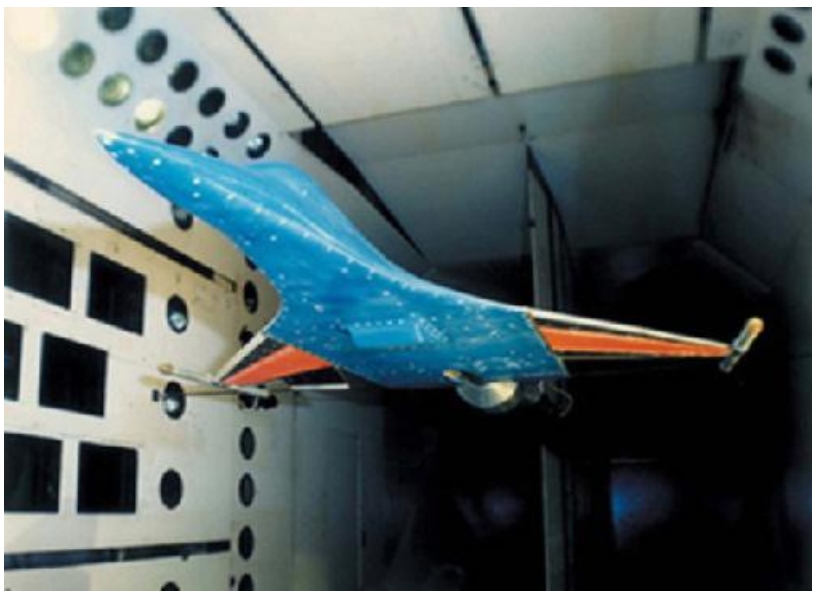


Plate 34 (right) Flutter, Active Control.
Active decoupler pylon with adaptive piezoceramic wafer stacks.

Plate 35 Flutter, Active Control.
Active flexible wing (AFW) wind-tunnel model in the NASA Langley transonic dynamics tunnel (courtesy of NASA Langley Research Center).



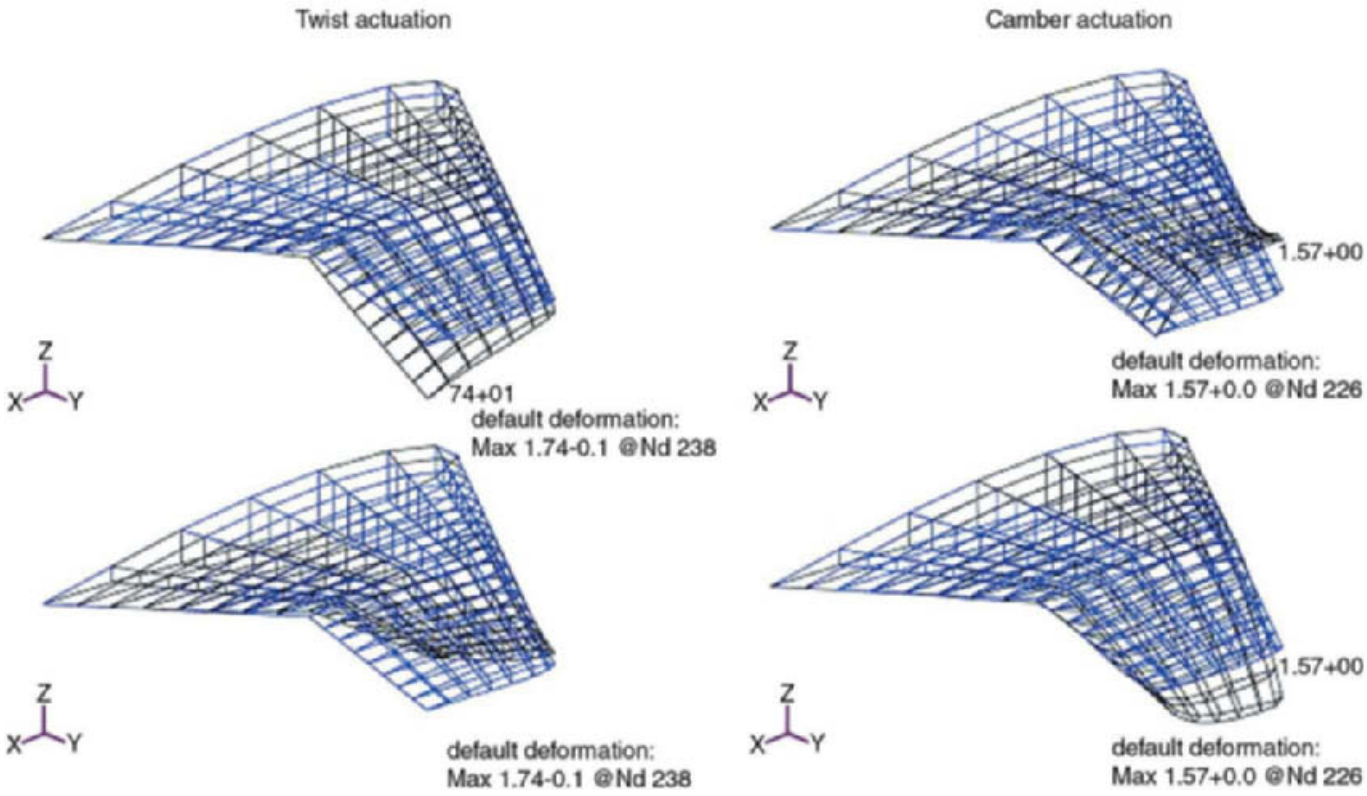


Plate 36 Flutter, Active Control. Finite element analysis of a smart UCAV wing with morphing airfoil sections.



Plate 37 Gear Diagnostics. Gear from an aircraft. Part of the transmission system in an aircraft engine. This gear consists of flywheels with teeth which transmit rotating movements between shafts. (With permission from Science Photo Library).

Plate 38 Ground Transportation Systems. A scientist at General Motors using a CRAY supercomputer to produce a computer-aided design (CAD) program to simulate the aerodynamics for a new car design. (With permission from Science Photo Library).

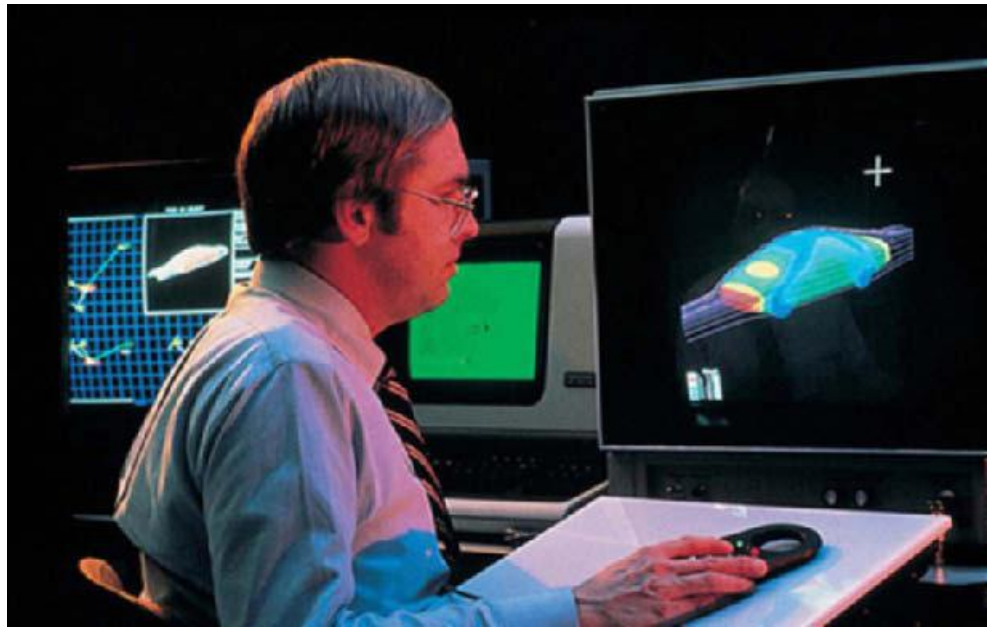


Plate 39 Helicopter Damping. Laminated metal-elastomeric bearings for isolating transmission gear box vibrations in helicopters. (Courtesy of Paulstra-Vibrachoc.)



Plate 40 Helicopter Damping. Lead-lag dampers are used to augment stability of helicopter rotor blade in-plane bending modes. (Courtesy of Paulstra-Vibrachoc.)



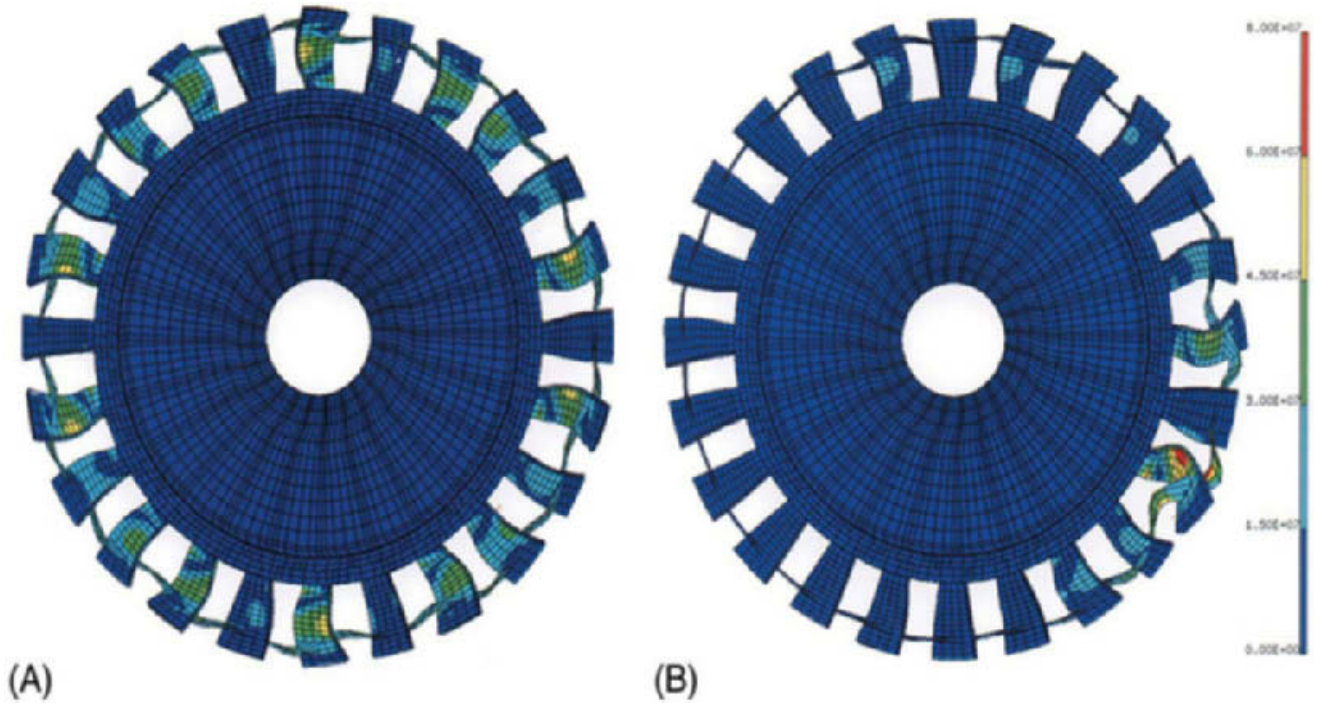


Plate 41 Localization. Forced response simulation results obtained using the finite element method. This model of a one-piece bladed disk (blisk) with continuous midspan shrouds was subject to a 'engine order 7' excitation (all blades were excited seven times per rotor revolution). (A) Extended forced response of the tuned blisk with identical blades. (B) Localized response of a blisk with a slight random blade mistuning. Observe how the largest-responding blade suffers higher vibration amplitudes and stresses than any blade of the tuned system in (A).

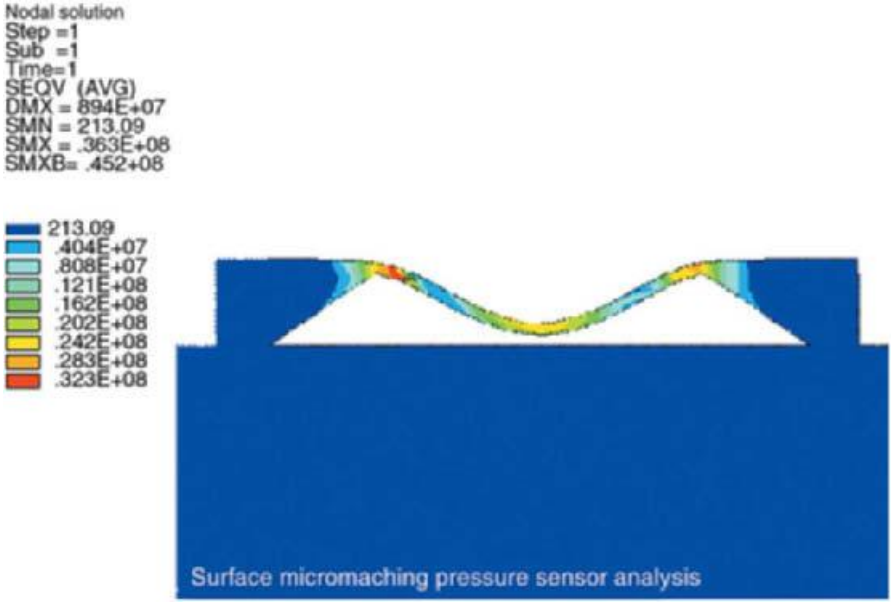


Plate 42 MEMs, General Properties. The output graphic file of an analysis of a silicon plate subjected to uniform distributed pressure loading.

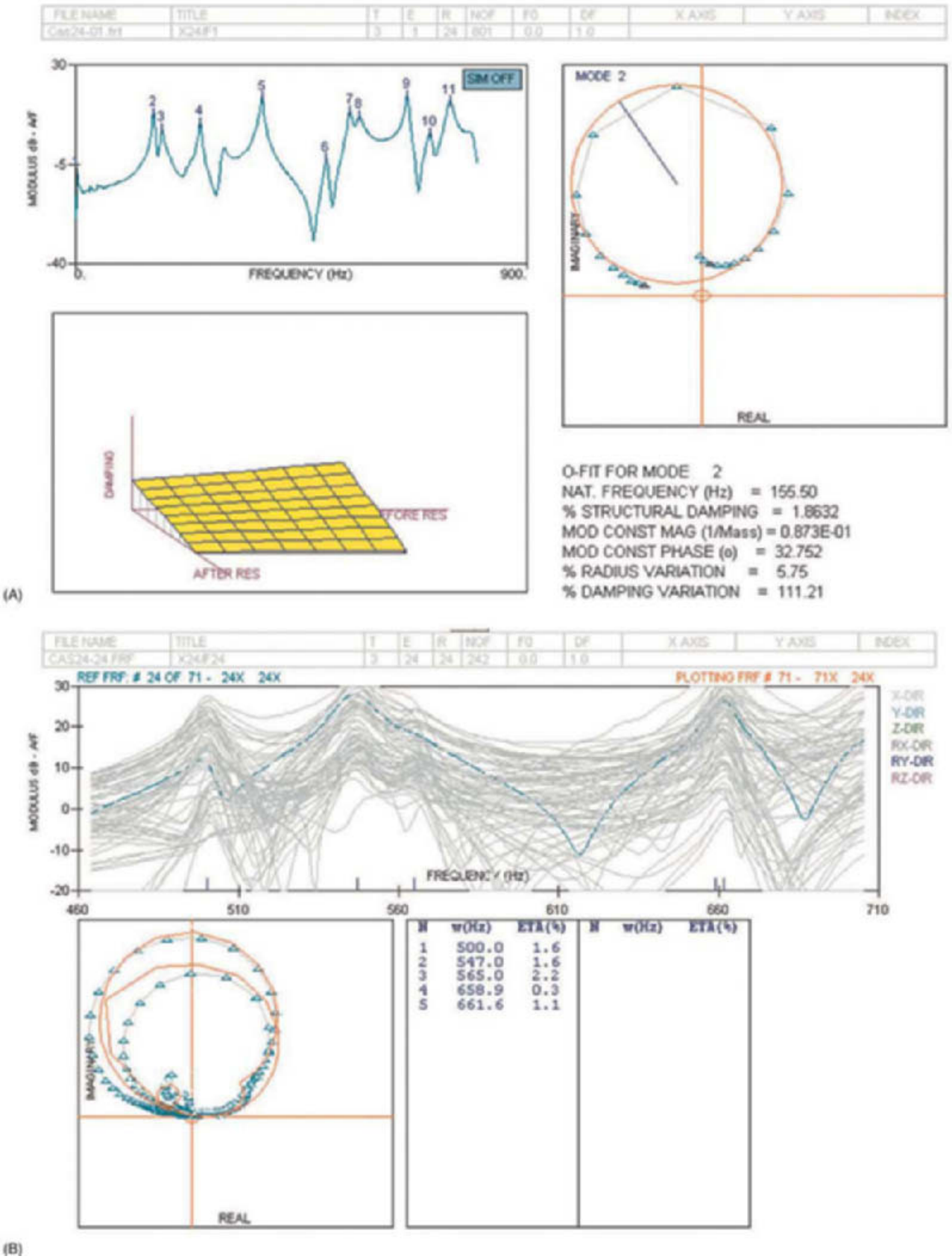


Plate 43 Modal Analysis, Experimental: Basic Principles. Example of modal analysis on measured FRF data. (A) Simple, SDOF circle-fit analysis; (B) multimode, multi-DOF global analysis.

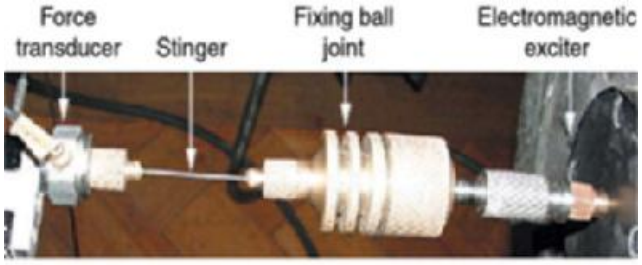


Plate 44 Modal Analysis, Experimental: Measurement Techniques. Shaker connected to test structure.



Plate 45 Modal Analysis, Experimental: Measurement Techniques. Example of multichannel FFT analyzer.

Analytical mode number	Experimental mode number									
	1	2	3	4	5	6	7	8	9	10
1	100	0	1	0	0	0	0	0	0	0
2	0	100	1	1	0	0	0	0	0	0
3	0	1	94	3	2	0	0	0	0	0
4	0	0	2	92	5	3	0	0	0	0
5	0	0	0	4	86	7	4	0	0	0
6	0	0	0	0	7	81	9	5	0	0
7	0	0	0	0	0	10	75	10	5	0
8	0	0	0	0	0	0	12	71	11	5
9	0	0	0	0	0	0	0	14	68	11
10	0	0	0	0	0	0	0	0	16	65

(A) *Modal assurance criterion (MAC) %*

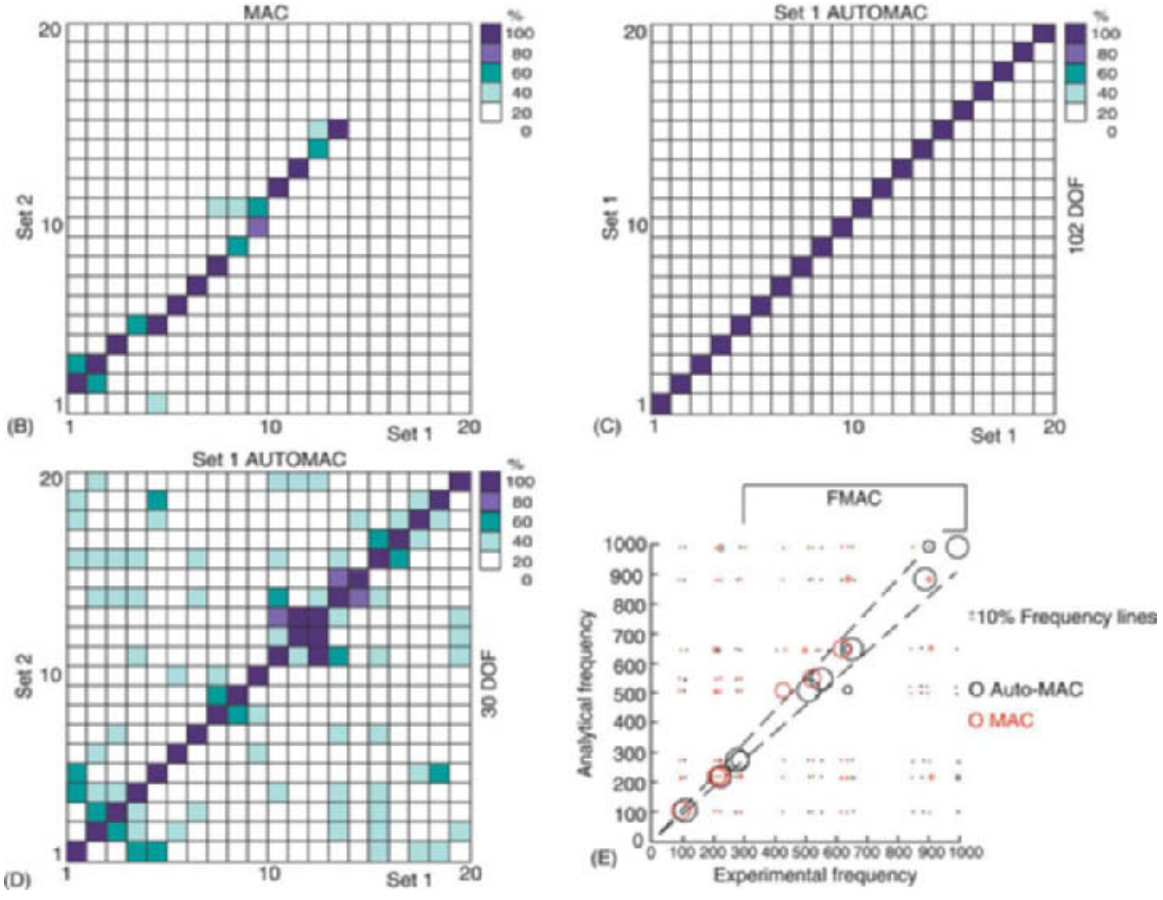


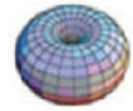
Plate 46 Modal Analysis, Experimental: Applications. Correlation of test and analysis. (A) MAC table, (B) MAC diagram, (C) AutoMAC - many DOFs, (D) AutoMAC - reduced DOFs, (E) FMAC plot.

Plate 47 Noise: Noise Radiated from Elementary Sources. Spherical harmonic functions $Y_{lm}(\theta,\phi)$ and their directivities $|Y_{lm}(\theta,\phi)|$.

i = $$Y_{00}(\theta,\phi)=\frac{1}{\sqrt{4\pi}}$$



$$Y_{11}(\theta,\phi)=-\sqrt{\frac{3}{8\pi}}\sin\theta e^{j\phi}$$

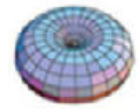


i =

$$Y_{10}(\theta,\phi)=\sqrt{\frac{3}{4\pi}}\cos\theta$$



$$Y_{22}(\theta,\phi)=\frac{1}{4}\sqrt{\frac{15}{2\pi}}\sin^2\theta e^{j2\phi}$$



i = $$Y_{21}(\theta,\phi)=-\sqrt{\frac{15}{8\pi}}\sin\theta\cos\theta e^{j\phi}$$



$$Y_{20}(\theta,\phi)=\sqrt{\frac{5}{4\pi}}\left(\frac{3}{2}\cos^2\theta-\frac{1}{2}\right)$$



Plate 48 Noise: Noise Radiated from Elementary Sources. Directivity distribution of a longitudinal and a lateral quadrupole sound radiation.

Longitudinal quadrupole



$$p(r,t)=\rho_o\omega Q(kd)^2\frac{e^{j\omega t-jkr}}{4\pi r}\sin\theta\cos\theta\sin\phi$$

Lateral quadrupole



$$p(r,t)=-j\rho_o\omega Q(kd)^2\frac{e^{j\omega t-jkr}}{4\pi r}\left[\frac{1}{3}-\sin^2\theta\sin^2\phi\right]$$

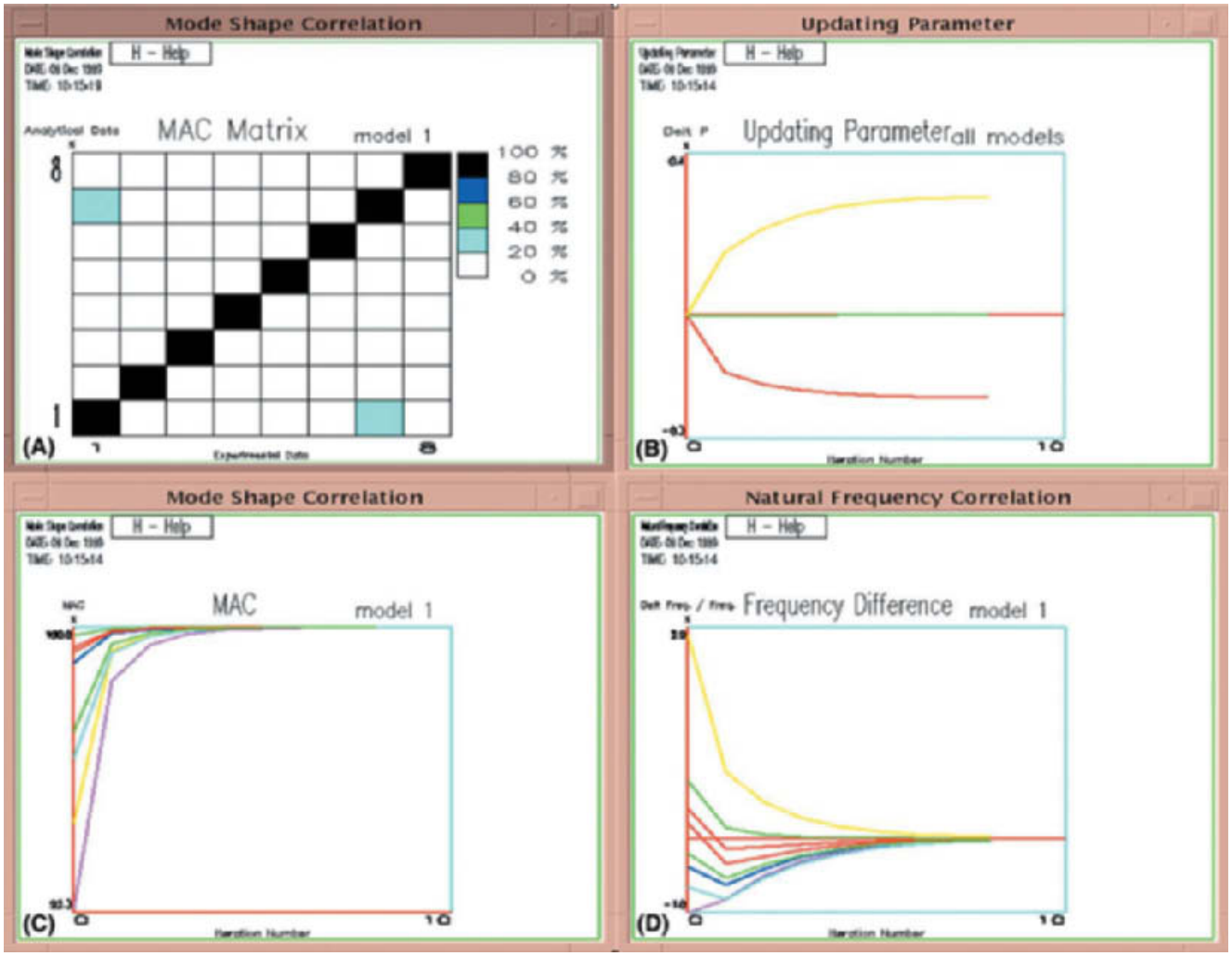
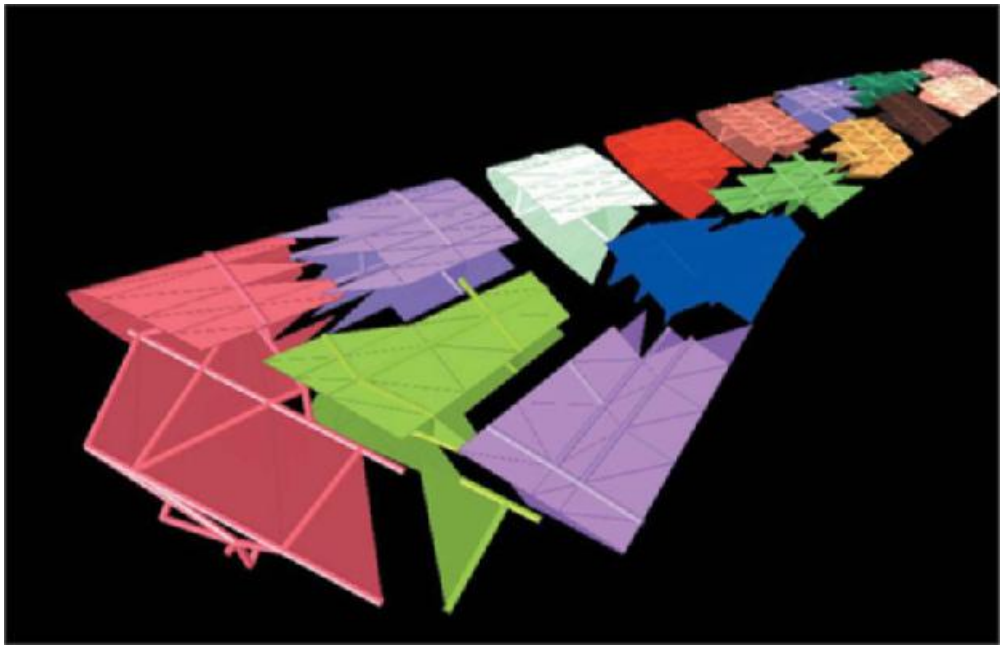


Plate 49 Modal Analysis, Experimental: Applications. Example of evolution of model updating session. (A) Current MAC matrix, (B) evolution of updated parameters, (C) evolution of MAC values for correlated model pairs, (D) evolution of natural frequency discrepancies.

Plate 50 Parallel Processing. Nonoverlapping decomposition of a finite element model. (Courtesy of the Center for Aerospace Structures, University of Colorado, Boulder, USA.)



However, there are complications that can arise in practice because of the fact that the measured data, and the resulting modal parameters that have been extracted, are not only imprecise – any measured data are liable to contain errors – but are generally incomplete. It is simply not practical to measure at all the DOFs and even less so to measure over a frequency range that captures all the modes. Thus, any model which is constructed from a practical modal test will be restricted to one which represents the behavior of only a limited number of modes and with these defined at just a small number of DOFs.

While these limitations which result from the inevitable incompleteness of the measured data are not particularly problematic when considering the modes of the structure, they can become a problem when seeking to convert the measured modal model into a spatial (mass-stiffness) model or to a response model. The equations given above which define the interrelationships between these three types of model can be seen to become inapplicable if the description in the original model is not complete – even if the data which are included are fully accurate. This presents something of a problem for some applications as several of the more popular ones really require the derived model to be in spatial or response form (see **Modal analysis, experimental**, Applications). For a full discussion of the issues which arise in constructing a suitable model from the measured and analyzed vibration data, see **Modal analysis, experimental**: Construction of models from tests.

See Plate 43.

See also: **Modal analysis, experimental**, Applications; **Modal analysis, experimental**, Construction of models from tests; **Modal analysis, experimental**, Measurement techniques; **Modal analysis, experimental**, Parameter extraction methods.

Further Reading

Dynamic Testing Agency (1993) *Handbook on Modal Testing*.

Ewins DJ (2000) *Modal Testing: Theory, Practice and Applications*. Research Studies Press.

Heylen W, Lammens S, Sas P (1998) *Modal Analysis Theory and Testing*. Belgium: Katholieke Universiteit Leuven.

Kennedy CC, Pancu CDP (1947) Use of vectors in vibration measurement and analysis. *Journal of Aeronautical Science*, 14(11).

Maia N, Silva J, He J *et al.* (1997) *Theoretical and Experimental Modal Analysis*. Research Studies Press.

McConnell KG (1995) *Vibration Testing Theory and Practice*. John Wiley.

Measurement techniques

J M M Silva, Instituto Superior Tecnico, Lisboa, Portugal

Copyright © 2001 Academic Press

doi:10.1006/rwvb.2001.0027

Introduction

The experimental determination of natural frequencies, mode shapes, and damping ratios is called experimental modal analysis and is based on vibration measurements that fall within the general designation of modal testing. The objective of this form of vibration testing is to acquire sets of frequency response functions (FRFs) that are sufficiently accurate and extensive, in both the frequency and spatial domains, to enable analysis and extraction of the dynamic properties for all the required modes of vibration of the structure. Prior knowledge of areas such as vibration analysis, instrumentation, signal processing, and modal identification, to state just a few, is required to understand modal testing.

The basic aim of modal testing is to obtain FRFs relating output vibration responses at a number of coordinates of interest, usually under the form of accelerations (or velocities, or displacements), to input vibration excitations, usually under the form of driving forces, applied at a given coordinate.

Basic Measurement System

In order to perform modal testing a number of hardware components must be available. These components may be interfaced with a host computer allowing for coordination of the operation of the overall system and enhancing the data-processing capabilities, if adequate software is available. The hardware components are schematically represented in **Figure 1**, which shows a typical set-up for a measurement system. Basically, there are three main measurement mechanisms:

- the excitation mechanism
- the sensing mechanism
- the data acquisition and processing mechanism

Adequate selection of an experimental modal analysis system is not an easy task and requires good understanding of the underlying theory.

The Excitation Mechanism

The excitation mechanism is constituted by a system which provides the input motion to the structure under analysis, generally under the form of a driving force $f(t)$ applied at a given coordinate. There are many variants for this system, their choice depending on several factors such as the desired input, accessibility, and physical properties of the test structure. Basically there are fixed exciters and non-fixed exciters.

The fixed exciter, also known as shaker, is usually an electromagnetic or electrohydraulic vibrator, driven by a power amplifier (**Figure 2**). The excitation signals, in these cases, are generated by a signal generator and can be chosen from a variety of different possibilities (stepped-sine, swept sine, impulse, random, etc.), to match the requirements of the structure under test.

This type of excitation mechanism may be easily controlled both in frequency and amplitude and therefore offers the best overall accuracy. However, it also has some disadvantages, such as the need for the exciter to be connected to the test structure. Despite the use of connecting devices (named push-rods, drive rods, or stingers) designed to reduce the attachment consequences, there are always some constraining effects and mass loading of the structure.

Conventional electromagnetic or electrohydraulic exciters vary in size and their choice depends on the structure under test. The main characteristics to take into consideration are force level, displacement level, and frequency range. The objective is for the exciter to provide inputs large enough to result in easily measured responses. The applied excitation force is commonly measured by means of a load cell (known as force transducer) which is located at the end of the stinger and is rigidly connected to the test structure (**Figure 3**).



Figure 2 Example of electromagnetic exciter and matching power amplifier.

The nonfixed exciter, known as an impulse or impact hammer, is a very popular alternative to fixed systems. It consists of a hammer with a force transducer attached to its head (**Figure 4**). The most important advantage of these excitation systems is that they do not need a signal generator and a power amplifier and nothing is attached to the structure. Hence, the excitation system does not affect the dynamics of the test structure.

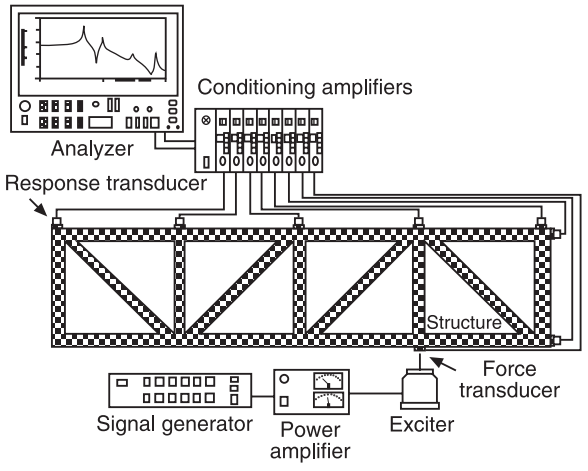


Figure 1 Typical measurement set-up.

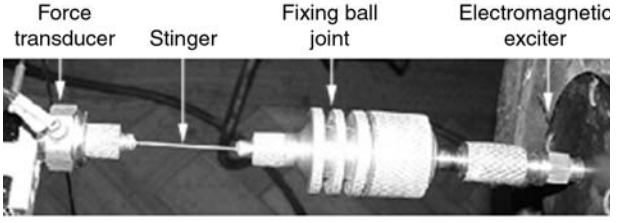


Figure 3 (see Plate 44) Shaker connected to test structure.



Figure 4 Impact hammer with force transducer and soft head.

The range of frequencies covered by a hammer depends on the hammer mass and on how hard its impacting head is (note that the mass and stiffness of the impacted structure also contribute to define this range). Furthermore, the mass and therefore the size of the hammer, together with the velocity of the impact, dictate the amplitude of the impact force. Impact hammers concentrate the total input excitation energy in a very short period of time, producing an almost flat force spectrum over a wide frequency range. Problems may arise due to local deformations and nonlinearities.

Preloading a structure and suddenly releasing it, exciting with acoustic energy (using a loudspeaker) or with a magnetic device, are other alternative nonfixed excitation possibilities. The problem with most of these cases (except in the preload/release alternative) is that the exciting force cannot be measured.

The Sensing Mechanism

The sensing mechanism is, basically, constituted by sensing devices known as transducers. There is a large variety of such devices: the most commonly used in experimental modal analysis are the piezoelectric transducers either for measuring force excitation (force transducers), as exemplified in **Figure 5**, or for measuring acceleration response (accelerometers), as exemplified in **Figure 6**. The transducers generate electrical signals that are proportional to the physical parameters one wants to measure.

Most of the time, the electrical signals generated by the transducers are not amenable to direct measurement and processing. Such a problem, which is usually related to the signals being very weak and to electric impedance mismatch, is solved by the use of conditioning amplifiers. These devices are usually considered as part of the transducers and therefore of the sensing mechanism (some transducers actually incorporate the basic conditioning electronics).

The choice of transducers is based on maximum force or maximum motion response, frequency range (which depends on the load), size (and therefore mass), and sensitivity.

Most transducers used in modal analysis have to be fixed to the structure under test and, thus, they may affect the measured dynamic response. This is especially true in the case of small lightweight structures. A common alternative is to use a contactless motion transducer, such as a laser vibrometer. This is a velocity transducer based on detection of the Doppler frequency shift of a laser beam light scattered from the moving surface.

Data Acquisition and Processing Mechanism

The basic objective of the data acquisition and processing mechanism is to measure the signals developed by the sensing mechanism, and to ascertain the magnitudes and phases of the excitation forces and responses. There are very sophisticated devices for this purpose, called analyzers, that incorporate many functions and even include the signal generation component. The most common analyzers are based on the fast Fourier transform (FFT) algorithm and provide direct measurement of the FRFs. They are known as spectrum analyzers or FFT analyzers. Basically, they convert the analog time domain signals generated by the transducers into digital-frequency domain information that can be subsequently processed with digital computers. Multichannel FFT analyzers (**Figure 7**) are a normal component of any modal analysis laboratory.

Due to the rapid development of computers, there is nowadays a tendency for the computer to replace the analyzer, provided it incorporates adequate software and a data acquisition board. More sophisticated systems are based on personal computers (PCs) or workstations with an acquisition front-end module. These solutions have the additional advantage of allowing for storage and data processing without having to go through the intermediate steps of data transfer. If based on a portable computer (lap-top), these systems may easily be carried to the test site.

The PC-based systems are usually cheap. However, one must be careful in choosing the data acquisition

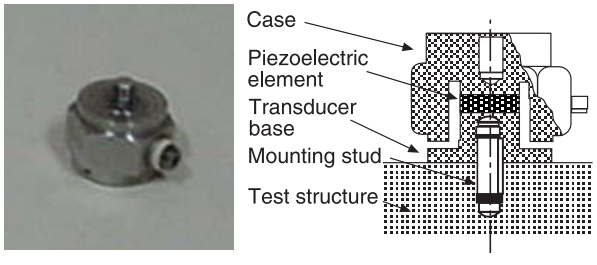


Figure 5 Example of piezoelectric force transducer and schematic representation of their cross-section.

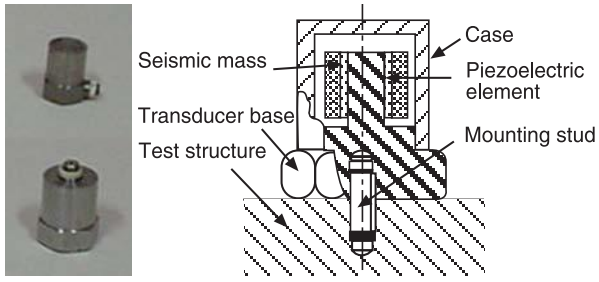


Figure 6 Example of piezoelectric accelerometers and schematic representation of their cross-section.



Figure 7 Example of multichannel FFT analyzer.

plug-in boards: Sampling rate, analog-to-digital conversion (ADC) accuracy, frequency range, filter characteristics, and zoom capabilities are some of the characteristics to take into consideration.

Understanding the principles behind signal acquisition and processing is very important for anyone involved with the use of modal analysis test equipment. The validity and accuracy of the experimental results may strongly depend on the knowledge and experience of the equipment user.

Excitation Methods and Measurement

There are various excitation signals that are commonly used in experimental modal analysis. They may be classified as single-frequency and broadband excitation signals, and each technique incorporates several different methods. Although each method has specific advantages and disadvantages, selection of a testing technique is often based (unfortunately) on the type of equipment and expertise available rather than on its suitability for a particular job.

Single-Frequency Excitation

Stepped sine and swept sine are the two types of single-frequency excitation signals commonly used.

In the stepped sine testing technique, a shaker is used to excite the structure sinusoidally at a single, precisely controlled frequency. The structure is allowed to settle under this excitation, to remove any transient effects. Steady state measurements are then made of the magnitude and phase relationship between the input force and the response at the precise excitation frequency for any desired response location. Division of the response by the force input gives the value of the FRF at that particular frequency. The excitation frequency is then changed by a small increment and the measurement process is repeated once the structure has settled at the new frequency. Thus, the FRF can be constructed for any frequency range.

One of the advantages of the stepped-sine testing technique is the large signal-to-noise ratio for all the force and response measurements. Furthermore, the input ranges for the force and response signals can be adjusted automatically for each excitation frequency point, and this allows the best possible use of the measuring equipment. This technique is especially adequate to investigate nonlinear behavior.

In the swept-sine testing technique, a shaker is used to excite the structure with a sine signal whose frequency varies slowly and continuously along the test frequency range. Sets of simultaneous measurements of the excitation signal and response signals are then taken at a given rate. The frequency of the sine signal allows a low rate of change, assuming that each set of measurements correspond to virtually steady state characteristics, i.e., that the technique sinusoidally excites the structure for each set of measurements at virtually one single frequency.

Though similar, swept sine techniques are faster than stepped sine techniques. However, since there is a continuous rate of frequency shift, accuracy is affected.

Broadband Excitation

In broadband testing, the structure is excited with a signal containing energy over a wide range of frequencies simultaneously. The time domain force and response signals are filtered, digitized and then passed through a Fourier analysis process to transform the time domain information to frequency domain spectra. By appropriate combination of the force and response spectra, the required FRFs for the structure can be derived.

Broadband excitation techniques may be classified as nonperiodic (purely random), periodic (pseudo-random, periodic random, and periodic chirp) and transient (burst random, burst chirp, and impact). Random, periodic random and impact are probably the most commonly used types of broadband excitation signals.

The pure random excitation signal is a nonperiodic stochastic signal with a Gaussian probability distribution. For a linear system, a Gaussian input will produce a Gaussian output. Since the peak-to-root mean square ratio of the output is relatively small, the random-type excitation does not cause undue problems with excitation of nonlinear structures and easily averages out noncoherent noise. However, because the force and response signals are random, a weighting function (e.g. Hanning window) must be applied to these signals before the discrete Fourier

transform (DFT) is performed, otherwise the mathematical assumptions of periodicity in the measurement time frame are invalid.

The force and response signals from the transducers contain energy at all frequencies. Because the measurement time frame is of a finite length, the Fourier analysis produces spectra that are discrete, rather than continuous, functions. Therefore, there is a 'spreading' of energy from the continuous spectra into adjacent spectral lines producing a phenomenon known as 'leakage'. The use of adequate weighting functions (windows) reduces the above-mentioned 'spreading'.

Periodic random excitation is a special form of periodic excitation, similar to pseudo-random, that has several benefits for signal processing. Although called 'random' it is not random in the true sense of the word. Within a time period equal to the analysis time frame, the signal is random, but the same signal is then repeated continuously. Usually, the signals are generated inside the data acquisition equipment in the frequency domain. The spectrum of a periodic random signal consists of discrete frequencies at integer multiples of the frequency resolution used by the DFT. Once the measurement frequency range and number of frequency lines have been selected, a flat excitation frequency spectrum may be generated by setting the magnitude of all spectral lines to the same value. The phases of the spectral components are then randomized. By use of the inverse Fourier transform (IFT), this frequency domain spectrum is transformed into the time domain to produce a random-like excitation signal in the analysis time frame. As a consequence of generating the signal in this way, it is exactly periodic in the analysis time frame, and both the force and response signals will be periodic in the analysis time frame also.

Provided that the excitation is applied to the structure more than once, so that any start-up transients have had sufficient time to decay, there is no requirement for any window function to be applied to this type of data. These signals only contain energy at the precise spectral component frequencies of the analysis and, therefore, there are no leakage problems when periodic random excitation signals are used. Furthermore, the signal-to-noise ratios for the measured force and response signals are much better than they would be with pure random excitation because there is no superfluous energy contained in the excitation.

The impact excitation is based on an input transient deterministic signal consisting of a pulse lasting for only a very small part of the sampling period. The shape, width, and amplitude of the pulse determine the frequency content of the force spectrum.

Impact excitation is usually obtained with impact hammers. The shape and amplitude of the impact signal determine the level of the force spectrum. The base-band frequency span is controlled by the width of the impact signal. The maximum frequency is inversely proportional to the width of the pulse signal.

Multipoint Testing

In tests on large complicated structures, with numerous joints and nonlinearities, the vibration energy is quickly dissipated within the structure. This may indicate that the use of multipoint testing is preferable to a series of single-point tests. By the use of multipoint excitation, the energy can be fed into the structure more uniformly than with single-point excitation and the response amplitudes at various locations can be kept much closer to those found in operation. Energy is supplied to the structure by several shakers, and so smaller and cheaper shakers can be used than would be necessary for single-point testing. Furthermore, the effects of nonlinearities, which may occur with excessive single-point forcing, can be substantially reduced. Since all the shakers are connected to the structure before the start of the test, systematic errors, resulting from repositioning the shaker during a series of single-point tests, do not occur. The influence of the shakers on the structure is not removed; it just remains constant throughout the whole of the test program. Simultaneous measurement of multiple columns of the FRF matrix means that the overall test time is shortened. There is less opportunity for structural changes (with time, temperature, or humidity) to affect the measured results.

Multipoint testing may be expensive in terms of suitable test control hardware and software that are required. Also, the process for extracting the FRFs is more complicated than for a single-input test.

The most commonly-used multiple shaker technique is known as multipoint random (MPR). For all multipoint excitation techniques, more sophisticated computer programs are necessary to extract the standard FRFs from the measured data.

To comply with the mathematical assumptions made in the analysis, it is important that the excitation inputs to the structure are purely random and uncorrelated. Although it is possible to ensure that the excitation signals driving the shakers are uncorrelated, it does not necessarily follow that the excitation force signals are uncorrelated. At the resonance frequencies, in particular, it is found that the motion of the structure tends to correlate the multiple forcing inputs. This can lead to degradation in the quality of the derived FRFs at the resonance frequencies.

Special types of multipoint excitation methods are known as 'phase resonance methods' (also known as 'tuned-sinusoidal' or 'force appropriation methods') and these rely on the ability to excite a single mode of vibration by the use of multiple shakers with independently variable force levels. All the shakers produce sinusoidal excitations at the same frequency and are either in-phase or out-of-phase with a reference source.

The excitation set-up in the 'normal mode' technique effectively cancels the damping in the structure the exciting forces are distributed such that each energy sink is canceled by a corresponding energy source and single real modes can be excited. In this condition of normal-mode vibration, the excitation frequency is the undamped natural frequency of the mode. The response at all the points on the structure is in quadrature with the excitation forces, and the structural responses relate directly to the mode shape vector.

The previous method provides the ability to measure real normal modes (for direct comparison with finite element results) and the ability to investigate nonlinear behavior. The main difficulties are the selection of excitation locations, the tuning of the force pattern, and the choice of the excitation frequency. The complete process has to be repeated for each different mode and consequently the testing time can be lengthy.

Calibration

The values measured by the test equipment represent electrical voltages and therefore it is necessary to obtain a calibration factor which translates these values into units of acceleration and force.

Though transducer manufacturers generally provide reliable calibration information, the use of their quoted sensitivities may not be accurate enough since they can change with time and environmental conditions. In addition, the transducers may have suffered some kind of damage due to rough handling or other extreme conditions and, although still working, may have lost their response linearity. Finally, the remaining units in the measurement chain (amplifiers, filters, signal conditioners, cable lengths, etc.) may change, albeit slightly, the overall sensitivity. It is therefore good practice to recalibrate the transducers before performing a test, preferably using the same measuring set-up that will be used in the test program.

Various transducer calibration techniques are available to the test engineer. The simplest and most common calibration procedure is the classical back-to-back method that compares the accelerometer to be calibrated with a reference accelerometer. This entails keeping a special reference transducer that offers a high level of linearity and stability. Another simple calibration procedure is based on the use of small hand-held calibrators that most manufacturers commercialize. In this case, the calibration is performed at one frequency only and, therefore, a flat frequency response of the transducer over the frequency band of interest is assumed.

When measuring FRF data, one is concerned with the motion/force ratio and not with the individual values of any of these quantities. This fact allows the use of a simple and straightforward technique which provides an accurate calibration of the transducers, including the influence of the remaining units of the measurement chain. The technique requires only the use of a simple rigid structure, such as a steel block, together with the equipment that is going to be used for the accelerance measurements.

For each accelerometer to be used, it is necessary to make a calibration test involving simultaneously the accelerometer and the force transducer. Applying a time-varying force to a solid block of known mass (which can be accurately measured), measuring the corresponding acceleration response, and computing the accelerance through a specified frequency range, one obtains a value in units of volt/volt which corresponds to $1/m$, where m is the mass of the block (which may include the added transducers masses). Thus, the measured accelerance will be a constant value proportional to the block mass, within a frequency range for which the block behaves as a rigid body. This calibration technique does not use the individual transducers sensitivity values and must be performed for each pair of accelerometers/force transducers.

Support Conditions

The support conditions of the structure under test are an important part of the test set-up. They must be well defined and experimentally repeatable if the results of the measurements are to reflect the properties of the structure without undue influence from the support. For test of components *in situ*, exact definition of the boundary conditions may be problematic but, nevertheless, tests should be considered to prove the repeatability of the installation. When the aim of the test is to determine the dynamic characteristics of a system under operating conditions, the test boundary conditions should be as close as possible to the operating conditions.

When testing in the laboratory, the most frequently used boundary conditions are grounded or free conditions. It is almost impossible for either of these two conditions to be achieved in practice. The most

difficult to achieve is the grounded condition as the structure will always have some movement at the grounding point (usually rotation). Free conditions are easier to achieve, although there will always be some small restraints.

For a structure to be really free, it should be suspended (floating) in the air, free in space with no holding points whatsoever. Such a situation is commonly designated as 'free–free', 'freely supported' or 'ungrounded' and is clearly impossible. However, simulation of free–free conditions can be closely approximated. It suffices to suspend or support the structure using very flexible (also designated as soft) springs so that the resonance frequencies of the mass of the structure on the stiffness of the supports or suspension devices are very low and far away from the frequency range of interest.

Pretest Decisions and Checks

Performing modal analysis tests is a time-consuming task involving qualified operators and delicate equipment. As a consequence, it is an expensive task. Thus, great care should be taken in preparing the test setups and in performing a number of checks prior to starting the real tests. All available previous knowledge about the system under test should be taken into consideration. In addition, it may be important to have accurate information about the aim of the tests, the required data, and the required accuracy of the measured data.

Parameters that must be carefully defined include, among others, the frequency range of interest, the selection of the transducer (response and excitation) locations, the selection of the suspension locations (when adequate), and the type of excitation to be used.

A large number of transducers on a structure sometimes leads to mistakes related to the correct identification of their location and values of the calibration factors when introducing the information into the analyzing system. Such mistakes may completely destroy the validity of the final measured data unless discovered in time and rectified.

Common problems that may be overlooked are related to broken leads, badly connected cables, badly attached transducers, and even pieces of equipment that are not powered (signals do show even in these cases). Careful checks will avoid most of these problems. An oscilloscope may be a valuable piece of hardware for this purpose.

Another type of verification, which is very important, is related to the efficiency of the inputs. In case of random-type excitation, the autopower spectrum of the input should be observed in order to verify if it maintains about the same level over the test frequency range, though it may be noisy. In case of impact excitation, the input autopower spectrum should be clean and flat up to the maximum frequency of interest.

Validation of Measurements

One of the problems facing the test engineer is an inability to ascertain the quality of the measured data. Throughout the complete modal test, checks should be made to assess this quality. There are several techniques in general use that can provide an indication of the quality of the measured data, e.g. repeatability, reciprocity, and coherence.

Almost always, repeatability and reciprocity checks are done by comparing sets of FRF curves to see if there are any major differences. The comparisons are made significantly easier if difference function curves (ΔFRFs) are plotted for the sets of data.

Repeatability checks are performed by repeating some measurements and comparing the results with previously measured curves. These checks assess the stability of the structural characteristics over a period of time. It is usually assumed that the structure does not change with time or as a result of the excitation itself but there are a number of practical effects, such as bolt slackening, fretting, change of temperature and humidity, etc., that can alter the characteristics of a structure.

Reciprocity checks are based on Maxwell s rule of reciprocity. The FRF matrix is symmetric and this property can be used as a check on the quality of the measured data. In fact, for a linear conservative system, the FRF measured for a force at location j and a response at location i should correspond directly to the FRF measured for a force at location i and response at location j.

Where a multiple single-input test (various separate single-input tests with the shaker located at a different position for each test). strategy is used, the reciprocity check can give an indication of shaker and accelerometer loading effects on the structure. The positions of the shaker and accelerometer are reversed in multiple single-input reciprocity checks. If the shaker and accelerometer have negligible effect on the structure, then there should be good reciprocity. If the shaker and accelerometer have a significant loading effect on the structure, then the effects in the two configurations will be different and the reciprocity check will reveal any differences between the FRFs.

Nowadays, almost all spectrum analyzers incorporate the calculation of the coherence, which is nothing but a correlation coefficient that measures the degree of consistency of all averages of the FRF evaluated by

the analyzer. A coherence equal to 1 indicates that each average is exactly the same. Low coherence values indicate a significant variance on the averages and, therefore, poor data quality. Usually, low-frequency regions and regions close to resonances and antiresonances yield low coherence values. The reason for this is poor performance of many transducers at low frequencies and low signal-to-noise ratios close to resonances and antiresonances.

See Plates 44, 45.

See also: **Modal analysis, experimental**, Applications; **Modal analysis, experimental**, Basic principles; **Modal analysis, experimental**, Construction of models from tests; **Modal analysis, experimental**, Parameter extraction methods.

Further Reading

Ewins DJ (1984) *Modal Testing: Theory and Practice*. UK: Research Studies Press.

Heylen W, Lammens S, Sas P (1998) *Modal Analysis Theory and Testing*. Belgium: KU Leuven.

Maia NMM, Silva JMM *et al.* (1997) *Theoretical and Experimental Modal Analysis*. UK: Research Studies Press.

McConnel KG (1995) *Vibration Testing: Theory and Practice*. USA: John Wiley.

Parameter extraction methods

N M M Maia, Instituto Superior Technico, Lisboa, Portugal

Copyright © 2001 Academic Press

doi:10.1006/rwvb.2001.0028

Introduction

The measurement of frequency response functions (FRFs; see **Modal analysis, experimental**, Basic principles), impulse response functions (IRFs), or simply free decay responses (either of these constitute the response model) may not be enough for the envisaged subsequent applications in modal analysis. Most of the time it is necessary to build a modal model and sometimes a spatial model (see **Modal analysis, experimental**, Construction of models from tests). The modal model comprises the so-called modal parameters, which are the natural frequencies, damping ratios, and mode shapes (amplitudes and phases). The natural frequencies and damping ratios are charateristics of the structure with its boundary constraints and are therefore related to the poles of the transfer function, whereas the modal constants, amplitudes and phases (coming from the mode shapes or vice versa) depend on the locations where the responses and forces are taken and are related to the residues of the transfer function.

Methods that estimate the modal parameters, or the poles and residues to which they are closely connected, from measured responses are called indirect methods (of system identification). They allow for the construction of the modal model. The spatial model is composed of the mass, stiffness, and damping matrices of the system. Methods that evaluate those matrices are called direct methods, as they go directly from the response model to the spatial model without computing the modal parameters.

All methods that allow for the identification of the dynamic properties (or parameters) from measurements made on a real structure or machine are called Parameter extraction methods and are the subject of this article.

Classification of Methods

There are many different methods to extract the modal parameters from measurements made on a structure. The main division between them is in the domain in which the experimental responses are treated. With respect to this, there are time-domain and frequency-domain methods. The first methods to appear, around 60 years ago, were very simple and fundamentally in the frequency domain. The main objective was to determine the resonance frequencies. At the time, modal testing was known as resonance testing.

In both time and frequency domains, there are indirect and direct methods. Within a given frequency range where measurements have been taken, there are usually various resonances. Most methods allow for the extraction of the dynamic properties taking into account all the resonances simultaneously. They are called multi-degree-of-freedom (MDOF) methods. However, there are some indirect methods in the frequency domain that can estimate the modal parameters by making a separate and progressive analysis around each resonance until the whole frequency range is covered. These are called single-degree-of-freedom (SDOF) methods.

A last classification has to do with the number of time histories (or IRFs) or FRFs that are processed at the same time. If only one FRF relating one input to one output is being analyzed, the method is called a single-input single-output one (SISO); if a method simultaneously takes data from various FRFs representing different responses due to a single input location, it is called single-input multi-output (SIMO);

when FRFs relating various outputs and inputs are considered in the analysis, the method is called multi-input multi-output (MIMO). **Figure 1** illustrates the general classification of methods.

Time-domain Methods

Within the indirect methods, probably the best known ones in the time domain are the complex exponential method, which is an SISO method, and its extended versions, the least-squares complex exponential (SIMO) and polyreference complex exponential (MIMO) methods. Also very well known are the Ibrahim time domain (SIMO) and the eigensystem realization algorithm (MIMO) methods.

Within the category of direct methods the main techniques are the autoregressive moving average (SIMO) and the direct system parameter identification (MIMO).

To understand how these methods work, a brief explanation of the complex exponential and Ibrahim time domain methods is given next.

The Complex Exponential Method

This method takes the IRF, and assumes that it can be described by a series of complex exponentials:

$$h_{jk}(t) = \sum_{r=1}^{2N} {}_rA_{jk} e^{s_r t} \qquad [1]$$

where ${}_rA_{jk}$ is the residue of mode r, related to the complex modal constant $s_r = -\omega_r\xi_r + i\omega_r\sqrt{(1-\xi_r^2)}$ and ω_r and ξ_r are the natural frequency and viscous damping ratio of mode r, respectively.

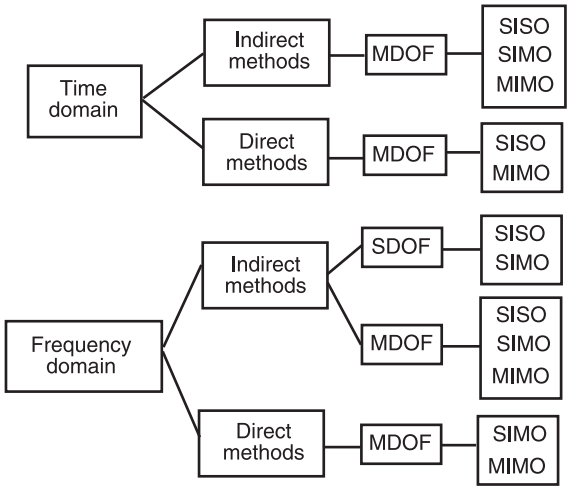


Figure 1 Classification of parameter extraction methods.

Eqn [1] is the inverse Fourier transform of the corresponding FRF:

$$H_{jk}(\omega) = \sum_{r=1}^{2N} \frac{{}_rA_{jk}}{\omega_r\xi_r + i\left(\omega - \omega_r\sqrt{\left(1-\xi_r^2\right)}\right)} \qquad [2]$$

From eqn [1], by taking L equally-spaced time intervals and simplifying the notation, one has:

$$\begin{aligned} h_0 &= h(0) = \sum_{r=1}^{2N} A_r \\ h_1 &= h(\Delta t) = \sum_{r=1}^{2N} A_r V_r \\ &\vdots \quad \vdots \quad \vdots \\ h_L &= h(L\Delta t) = \sum_{r=1}^{2N} A_r V_r^L \end{aligned} \qquad [3]$$

where A_r is an abbreviation for ${}_rA_{jk}$ and where $V_r = \exp(s_r\Delta t)$. As the roots, s_r, for an underdamped system occur in complex conjugate pairs, so also do the variables, V_r, and thus there must exist a polynomial with real coefficients, β, such that:

$$\beta_0 + \beta_1 V_r + \beta_2 V_r^2 + \cdots + \beta_L V_r^L = 0 \qquad [4]$$

It is possible to show that, for each V_r, $\sum_{i=0}^{L} \beta_i h_i = 0$. From this, taking the appropriate number of data points, the values of β can be obtained. Then, V_r are calculated from eqn [4] and so the natural frequencies and damping ratios are determined. From eqn [3], the values of the residues are easy to calculate, and from these, so are the modal constants. The above method is not iterative, and so no initial estimates for the modal parameters are necessary. The uncertainty lies in determining the correct number of participating modes. To determine that quantity, an iterative procedure is used, varying the number of assumed modes. When the error between the real measurements and the synthesized ones has a minimum, the correct number of modes is determined.

The Ibrahim Time Domain Method

This method, an example of a SIMO approach, uses free responses instead of IRFs. For a system with N DOFs, the free response of the structure at a point i and for the instant of time t_j can be expressed as a summation of the individual responses of each mode:

$$x_i(t_j) = \sum_{r=1}^{2N} \psi_{ir} e^{s_r t_j} \qquad [5]$$

where ψ_{ir} is the ith component of the complex eigenvector $\boldsymbol{\psi}_r$. Considering q response locations and L time instants leads to an expression of the type:

$$\underset{(q\times L)}{\mathbf{X}} = \underset{(q\times 2N)}{\boldsymbol{\Psi}} \underset{(2N\times L)}{\boldsymbol{\Lambda}} \qquad [6]$$

where $\boldsymbol{\Lambda}$ is composed of the various $e^{s_r t_j}$ elements. Considering a second set of L data points, shifted one interval Δt with respect to the first, it is possible to write a similar expression:

$$\underset{(q\times L)}{\hat{\mathbf{X}}} = \underset{(q\times 2N)}{\hat{\boldsymbol{\Psi}}} \underset{(2N\times L)}{\boldsymbol{\Lambda}} \qquad [7]$$

Defining $\mathbf{A_S}$ of order q such that $\mathbf{A_S}\boldsymbol{\Psi} = \hat{\boldsymbol{\Psi}}$ leads to $\mathbf{A_S}\mathbf{X} = \hat{\mathbf{X}}$, from which one can calculate $\mathbf{A_S}$. in a least-squares sense. As each vector $\hat{\boldsymbol{\psi}}_r = \boldsymbol{\psi}_r e^{s_r \Delta t}$, a standard eigenproblem is obtained:

$$\left[\mathbf{A_S} - e^{s_r \Delta t}\mathbf{I}\right]\boldsymbol{\psi}_r = \mathbf{0} \qquad [8]$$

From the eigenvalues and eigenvectors, the modal parameters are evaluted. The difficulty here is to determine the order q of the problem, as the system will have as many resonances as the number of chosen responses, q, and this is quite an arbitrary choice. If q is higher than the true number of resonances, some of the solutions of eqn [8] will not be physically meaningful, they will just be computational solutions which are a priori difficult to distinguish from the genuine ones. The quality of the results can be checked using the modal confidence factor, based on repetition of the calculations in different time interval shifts: the expected value of $\hat{\boldsymbol{\psi}}_r$ from $\hat{\boldsymbol{\psi}}_r = \boldsymbol{\psi}_r e^{s_r \Delta t}$ is then compared with the calculated value of $\hat{\boldsymbol{\psi}}_r$ in the following time interval.

Frequency-domain Methods

There are many different frequency-domain parameter extraction methods. Here, the following will be addressed: the circle-fitting method (SDOF, SISO), the rational fraction polynomial (MDOF, SISO), and the identification of structural system parameters method (MDOF, SIMO), which is a direct method.

The Circle-Fitting Method

This is one of the simplest and most popular methods in the frequency domain category. The receptance FRF of an N degree-of-freedom system with hysteretic damping is given by the following expression:

$$H_{jk}(\omega) = \sum_{r=1}^{N} \frac{{}_rC_{jk}}{\omega_r^2 - \omega^2 + i\eta_r\omega_r^2} \qquad [9]$$

where η_r and ${}_rC_{jk} = \left(C_r e^{i\phi_r}\right)_{jk}$ are the hysteretic damping loss factor and the complex modal constant associated with mode r, respectively. Expression [9] is the equivalent of eqn [2], which referred to viscous damping. In this method, each mode is treated separately and the contribution of the neighboring modes to the particular one under study is assumed to be a constant, eqn [9] is therefore approximated by:

$$H_{jk}(\omega) \approx \frac{{}_rC_{jk}}{\omega_r^2 - \omega^2 + i\eta_r\omega_r^2} + {}_rD_{jk} \qquad [10]$$

where ${}_rD_{jk}$ is a complex constant associated with mode r. It can be shown that the Nyquist plot (real part versus imaginary part) of $1/\left(\omega_r^2 - \omega^2 + i\eta_r\omega_r^2\right)$ is a circle. From eqn [10], it is clear that the multiplication by the complex constant ${}_rC_{jk}$ means a magnification or reduction of the circle radius, as well as a rotation. ${}_rD_{jk}$ corresponds to a simple translation of the whole circle.

When representing the measured data in a Nyquist plot, the complete curve will not be an exact circle around each natural frequency, but eqn [10] tells us that the curve will approach a circle around those frequencies, as illustrated in **Figure 2**.

The modal parameters associated with mode r are derived from fitting a circle to the frequency response

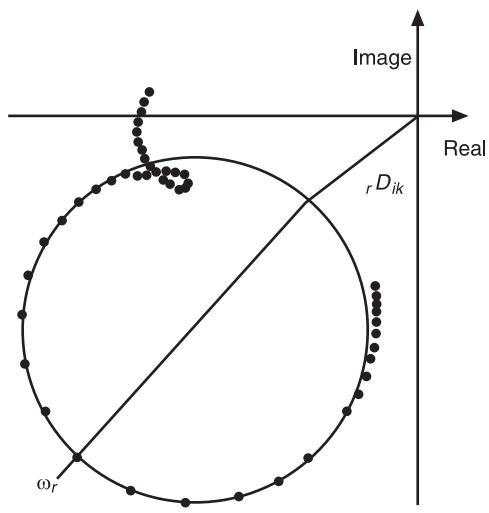


Figure 2 Nyquist plot of the receptance, showing the SDOF circle-fit approach.

curve near each natural frequency, ω_r. This objective is achieved through the use of a least-squares technique. Once the circle centre coordinates and radius are known, the natural frequency can be estimated, as it occurs where the angular frequency spacing has its highest value. The damping factor is evaluated from a generalized version of the half-power points formula. From the diameter of the circle and its position, the complex modal constant is calculated. As the process continues to the next resonance peak, the effect of the previously-identified modes is subtracted, in order to enhance the mode one is dealing with at each time.

The Rational Fraction Polynomial Method

In this method, the FRF is expressed in terms of a ratio of two polynomials (in place of the summation of simple fractions) as:

$$H(\omega) = \frac{\sum_{k=0}^{2N-1} a_k (i\omega)^k}{\sum_{k=0}^{2N} b_k (i\omega)^k} \qquad [11]$$

Defining a linearized error function between the measured FRF values and the model, and minimizing it, a linear system of equations is obtained, from which the coefficients a_k and b_k are evaluated. As such a system is usually ill-conditioned, the problem is reformulated in terms of orthogonal polynomials. Knowing the resulting coefficients, the modal parameters are retrieved. A global version of this method also exists, i.e. its SIMO version, where several FRFs are taken into account simultaneously.

The Identification of Structural System Parameters Method

This is a direct method, i.e., it provides the system matrices ($\mathbf{K}$, $\mathbf{M}$ and $\mathbf{C}$) which constitute the spatial model directly, from the response model (the FRFs), without computing the modal parameters. The general idea, common to all direct methods, is to take the dynamic equilibrium equation and write it for various frequency data points, in order to form an overdetermined system of equations, from which the system matrices are computed. Such a system will look like:

$$\begin{aligned} \left[-\omega_1^2\mathbf{M} + i\omega_1\mathbf{C} + \mathbf{K}\right]\overline{\mathbf{Y}}_1 &= \mathbf{F} \\ \left[-\omega_2^2\mathbf{M} + i\omega_2\mathbf{C} + \mathbf{K}\right]\overline{\mathbf{Y}}_2 &= \mathbf{F} \\ \vdots \qquad\qquad & \vdots \\ \left[-\omega_{\mathrm{L}}^2\mathbf{M} + i\omega_{\mathrm{L}}\mathbf{C} + \mathbf{K}\right]\overline{\mathbf{Y}}_{\mathrm{L}} &= \mathbf{F} \end{aligned} \qquad [12]$$

where $\bar{\mathbf{Y}}_i$ is the vector of complex response amplitudes, at frequency ω_i, which is the frequency data point, varying from 1 to L.

The Unified Matrix Polynomial Approach

The unified matrix polynomial approach (UMPA) is a method that shows that a considerable number of methods in both time and frequency domains are just particular cases of a more general polynomial formulation. That work helps us to understand better the similarities amongst most of the existing techniques, giving a more general panorama on the subject, and it contributes to a deeper knowledge of the philosophy of parameter extraction methods.

Methods to Check the Quality of Extracted Parameters

Almost every method has its own check for the quality of the obtained parameters. As mentioned before, in the complex exponential method, the correct number of modes is determined when the error between the measured and synthesized FRFs has a steep drop. In the Ibrahim time domain method, as already explained, the modal confidence factor is used, repeating the calculations in different time intervals. In the rational fraction polynomial method it is also usual to make the calculations taking each time a different set of data points and checking for the repeatability and variation of the results. In the identification of structural system parameters method, the singular value decomposition technique is usually employed to determine the effective number of degrees-of-freedom.

Another very popular method nowadays is the so-called stabilization chart. Some tolerance values are assigned *a priori* to each modal parameter (as a percentage) and the calculations are repeated taking each time a different number of modes. The chart then shows the progress of the results, indicating (by the display of a symbol) close to each peak which modal parameters have stabilized along the various iterations. Other methods for quality checking are the so-called mode indicator functions (MIFs) that indicate not only the number of existing modes, but also their relative incidence, by displaying the physical magnitude of each one and natural frequency. They can also detect repeated modes and are based on calculation of the singular value decomposition of the FRF matrix at each spectral line.

See also: **Modal analysis, experimental**, Applications; **Modal analysis, experimental**, Basic principles; **Modal analysis, experimental**, Construction of models from tests; **Modal analysis, experimental**, Measurement techniques.

Further Reading

Allemang RJ, Brown DL and Fladung W (1994) Modal parameter estimation: a unified matrix polynomial approach: In: *Proceedings of the 12th International Modal Analysis Conference*, I. Society for Experimental Mechanics, Honolulu, USA: pp. 501–514.

Ewins DJ (2000) *Modal Testing: Theory Practice, and Application*, 2nd edn. UK: Research Studies Press.

Maia NMM and Silva JMM *et al.* (1997) *Theoretical and Experimental Modal Analysis*. Baldock, UK: Research Studies Press.

Rades M (1979) *Metode Dinamice Pentru Identificarea Sistemelor Mecanice* (in Romenian). Bucharest, Romania: Editura Academiei Republicii Socialiste România.

Rades M (1994) A comparison of some mode indicator functions. *Mechanical Systems and Signal Processing* 8: 459–474.

Silva JMM and Maia NMM (1999) *Modal Analysis and Testing*. NATO Science Series E – Applied Sciences, vol. E-363. Dordrecht, The Netherlands: Kluwer Academic Publishers.

Construction of models from tests

N M M Maia, Instituto Superior Technico, Lisboa, Portugal

Copyright © 2001 Academic Press

doi:10.1006/rwvb.2001.0029

Introduction

Any real structure possesses an infinite number of degrees-of-freedom. In very simple cases, like a single beam of homogeneous isotropic material and constant cross-section, it is possible to derive an analytical solution enabling the calculation of all natural frequencies and mode shapes. In more general cases, such a solution cannot be found and therefore the modeling must be based either on a numerical study or on experimental tests undertaken on the real structure. In either case, it is necessary to decide on the number of degrees-of-freedom one must choose, so that the final model represents the reality as accurately as possible, i.e., the dynamic behavior of the structure under some loading conditions is well predicted when compared with its real behavior in service.

The decision on the appropriate number of degrees-of-freedom is called discretization, as we go from a continuous situation to a discrete one. Such a decision has to be balanced, taking into account the objectives of the study and also the available calculation power. For instance, to evaluate the dynamic behavior of a vehicle in order to assess the passengers' comfort, it may be irrelevant to discretize the whole structure in thousands of degrees-of-freedom. A few dozen may be enough.

Building a theoretical model of a structure based on a numerical approach, usually through a finite element discretization, is not a big problem nowadays, especially if the structure is a lightly damped one: the resulting stiffness and mass matrices are – most of the time – adequate to represent its real behavior with sufficient accuracy, at least over a limited frequency range. However, if the frequency range is considerably large, it may be important to consider more complicated theories or elements with higher complexity. In any case, a numerical model is never perfect and in general it is necessary to validate (see **Model updating and validating**) it with experimental tests and, in most situations, to correct it or update it using those tests as a reference. There are specific methods, known as updating techniques, to achieve the most correct model. The important issue here is to have accurate experimental results. The following presents some issues related to the construction of models from experimental results, and how these models relate to theoretically-derived ones.

Construction of a model from experimental results

Response Models vs Spatial Models

Let us consider a structure whose behavior can be well represented, for our application, by a four-degrees-of-freedom model as shown in **Figure 1**. It is therefore assumed that the dynamic behavior of the

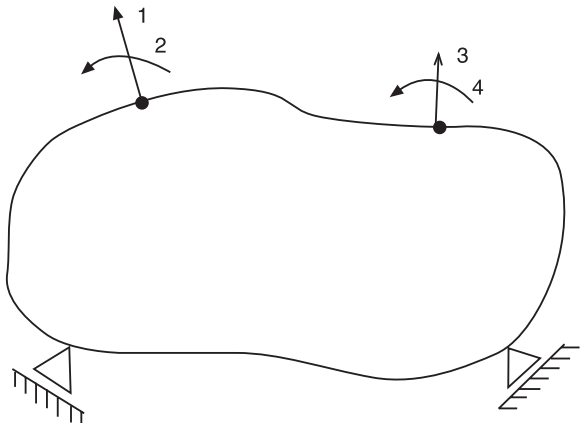


Figure 1 Real structure characterized by coordinates 1–4.

system is described with enough accuracy for our purposes using only those four-degrees-of-freedom. It is also known from the study of the single-degree-of-freedom system that the function which most conveniently reflects the behavior of that system is the particular version of the transfer function, known as a frequency response function (FRF), relating the obtained harmonic output to a given harmonic input. If F is the input, X the output and H the FRF, $X = HF$. For a system discretized by N degrees-of-freedom, the FRF properties can be contained in an $N \times N$ FRF matrix relating the amplitudes of the input and output:

$$\underset{(N\times 1)}{\mathbf{X}} = \underset{N\times N}{\mathbf{H}}\,\underset{(N\times 1)}{\mathbf{F}} \qquad [1]$$

For the example of **Figure 1**, eqn [1] turns into:

$$\begin{Bmatrix} X_1 \\ X_2 \\ X_3 \\ X_4 \end{Bmatrix} = \begin{bmatrix} H_{11} & H_{12} & H_{13} & H_{14} \\ H_{21} & H_{22} & H_{23} & H_{24} \\ H_{31} & H_{32} & H_{33} & H_{34} \\ H_{41} & H_{42} & H_{43} & H_{44} \end{bmatrix} \begin{Bmatrix} F_1 \\ F_2 \\ F_3 \\ F_4 \end{Bmatrix} \qquad [2]$$

where X_2 and X_4 are, in fact, rotational responses (angles) and F_2 and F_4 are moments.

It is worth noting that the FRF matrix is generally symmetric, due to Maxwell's reciprocity theorem, i.e., the response at degree-of-freedom (DOF) i due to an input at DOF j is equal to the response at DOF j when the same input happens at coordinate i.

The response model is available once the FRFs in $\mathbf{H}$ have been measured.

Equivalent to eqn [1] is the following inverse relationship:

$$\mathbf{F} = \mathbf{H}^{-1}\mathbf{X} \qquad [3]$$

or:

$$\mathbf{F} = \mathbf{Z}\mathbf{X} \qquad [4]$$

where $\mathbf{Z}$ is called the dynamic stiffness matrix, which for an undamped system (the damped case will be discussed later) is:

$$\mathbf{Z} = \mathbf{K} - \omega^2\mathbf{M} \qquad [5]$$

where $\mathbf{K}$ and $\mathbf{M}$ are the stiffness and mass matrices, respectively, and ω is the frequency of the applied forces. If the model is represented in terms of $\mathbf{K}$ and $\mathbf{M}$ (and of the damping matrix if this is to be considered), it is called the spatial model.

Expanding [4] in accordance to the given example, it follows that:

$$\begin{Bmatrix} F_1 \\ F_2 \\ F_3 \\ F_4 \end{Bmatrix} = \begin{bmatrix} Z_{11} & Z_{12} & Z_{13} & Z_{14} \\ Z_{21} & Z_{22} & Z_{23} & Z_{24} \\ Z_{31} & Z_{32} & Z_{33} & Z_{34} \\ Z_{41} & Z_{42} & Z_{43} & Z_{44} \end{bmatrix} \begin{Bmatrix} X_1 \\ X_2 \\ X_3 \\ X_4 \end{Bmatrix} \qquad [6]$$

Apparently, it would be easier to measure $\mathbf{Z}$ directly, from which one could evaluate $\mathbf{K}$ and $\mathbf{M}$ to obtain the spatial model directly. However, it is $\mathbf{H}$ that is measured in practice and then $\mathbf{Z}$ must be derived from: $\mathbf{Z} = \mathbf{H}^{-1}$. Let us see why this is the correct procedure to calculate $\mathbf{Z}$. First of all, it is clear that $Z_{ij} \neq H_{ij}^{-1}$; retrieving [6], the first equation is given by:

$$F_1 = Z_{11}X_1 + Z_{12}X_2 + Z_{13}X_3 + Z_{14}X_4 \qquad [7]$$

Consider, for example, the interpretation of Z_{12}. The individual dynamic stiffness coefficient, Z_{12}, is the force F_1 when $X_2 = 1$ and $X_1 = X_3 = X_4 = 0$. In theory, this is obvious, but in practice it simply cannot be achieved, as it implies that X_1, X_3 and X_4 should be blocked, something impossible to achieve in an experimental set up. In contrast, from [2], the first equation is:

$$X_1 = H_{11}F_1 + H_{12}F_2 + H_{13}F_3 + H_{14}F_4 \qquad [8]$$

It is very easy to calculate H_{12}, for example, as H_{12} equals X_1 when $F_2 = 1$ and $F_1 = F_3 = F_4 = 0$, or $H_{12} = X_1/F_2|_{F_1,\,F_3,\,F_4=0}$. Therefore, to calculate matrix $\mathbf{H}$ it is sufficient to apply a force at one point at a time, and to measure all the responses. After knowing $\mathbf{H}$, it is possible to calculate $\mathbf{Z}$ from its inverse ($\mathbf{H}^{-1}$). Note that as $\mathbf{Z}$ and $\mathbf{H}$ are both functions of frequency, and so the inverse has to be taken at each frequency point along the frequency range of interest, i.e., there will be as many inversions as frequency data points.

At this point, there is a conclusion: in practice, the system is characterized by the response model.

The Modal Model and its Relationship to the Spatial and Response Models

The undamped equilibrium equation for free vibration of an N-degree-of-freedom system leads to a generalized eigenvalue and eigenvector problem:

$$\left[\mathbf{K} - \omega^2\mathbf{M}\right]\boldsymbol{\phi} = \mathbf{0} \qquad [9]$$

This provides a set of N natural frequencies, ω_r, and N mass-normalized mode shapes, $\boldsymbol{\phi}_r$. From the orthogonality properties for mass-normalized mode shapes, it is known that:

$$\mathbf{\Phi}^{\mathrm{T}}\mathbf{M}\mathbf{\Phi} = \mathbf{I} \qquad [10a]$$

$$\mathbf{\Phi}^{\mathrm{T}}\mathbf{K}\mathbf{\Phi} = \boldsymbol{\omega}_r^2 \qquad [10b]$$

where $\mathbf{\Phi}$ is the modal matrix whose columns are the mass-normalized mode shapes and $\boldsymbol{\omega}_r^2$ is a diagonal matrix composed of the squares of the natural frequencies. When the model is characterized in terms of $\boldsymbol{\omega}_r^2$ and $\mathbf{\Phi}$, it is called the modal model. Therefore, from knowledge of $\mathbf{K}$ and $\mathbf{M}$ (the spatial model) it is possible to obtain the modal model. The opposite is also possible, as from [10a] and [10b]:

$$\mathbf{M} = \mathbf{\Phi}^{-\mathrm{T}}\mathbf{\Phi}^{-1} \qquad [11a]$$

$$\mathbf{K} = \mathbf{\Phi}^{-\mathrm{T}}\omega_r^2\mathbf{\Phi}^{-1} \qquad [11b]$$

Therefore, one can derive the modal model from the spatial model and vice-versa.

To calculate $\mathbf{Z}$ from $\mathbf{H}$ along the frequency range of interest may imply a considerable computational effort, due to the inversions referred to at the end of the previous section. An alternative approach consists of expressing $\mathbf{Z}$ in terms of the modal parameters – natural frequencies and mode shapes.

As $\mathbf{Z} = \mathbf{K} - \omega^2\mathbf{M}$, upon substitution of [11a] and [11b], it follows that:

$$\mathbf{Z} = \mathbf{\Phi}^{-\mathrm{T}}\boldsymbol{\omega}_r^2\mathbf{\Phi}^{-1} - \omega^2\mathbf{\Phi}^{-\mathrm{T}}\mathbf{\Phi}^{-1} \qquad [12]$$

or:

$$\mathbf{Z} = \mathbf{\Phi}^{-\mathrm{T}}\left(\boldsymbol{\omega}_r^2 - \boldsymbol{\omega}^{-2}\right)\mathbf{\Phi}^{-1} \qquad [13]$$

Clearly, from [13]:

$$\mathbf{H} = \mathbf{Z}^{-1} = \mathbf{\Phi}\left(\boldsymbol{\omega}_r^2 - \boldsymbol{\omega}^{-2}\right)^{-1}\mathbf{\Phi}^{\mathrm{T}} \qquad [14]$$

and one has a direct relationship between the modal and response models. Note that eqn [13] only requires the inverse of the modal matrix, which is trivial as it is diagonal. Thus, along the frequency range it is no longer necessary to invert a matrix at each frequency point.

It is now clear how the three models are interrelated. However, it is not so clear as to which model to use, when or why. **Figure 2** illustrates this point for an N-degree-of-freedom system. Note that there are two main routes. On the one hand, there is the theoretical route, where the starting point is the analytical or numerical solution, establishing the spatial model; then, through an eigensolution, the natural frequencies and mode shapes are obtained, constituting the modal model; finally, the response model may be evaluated. On the other hand, there is the experimental route, where the departure point is the response model, formed by the relevant measured FRFs; through an identification process, which is an inverse problem, the modal model is built; using the orthogonality relationships, the spatial model may be recovered.

The necessity of permutation among the three models is to bring together the theoretical and experimental results for comparison, validation or updating objectives.Although quite illustrative, **Figure 2** may look too optimistic, as one may think that everything is perfect, all models are (more or less) easily interrelated and one can readily move from one to the other in any sense. In practice, problems may arise. In what follows, some of those problems are mentioned.

Damped Systems and Complex Modes

Any real structure is dissipative. The dissipation of energy is modeled through a damping term that in most cases in structural dynamics is either the hysteretic damping model (also called structural damping: forces proportional to the displacements but in phase with velocity) or the viscous damping model (forces proportional to the velocities). If the structure is very lightly damped, then the undamped model may be a good approximation. If that is not the case, then a damping matrix must be defined, together with the stiffness and mass matrices. The equilibrium equation becomes, for the viscous damping case, as follows:

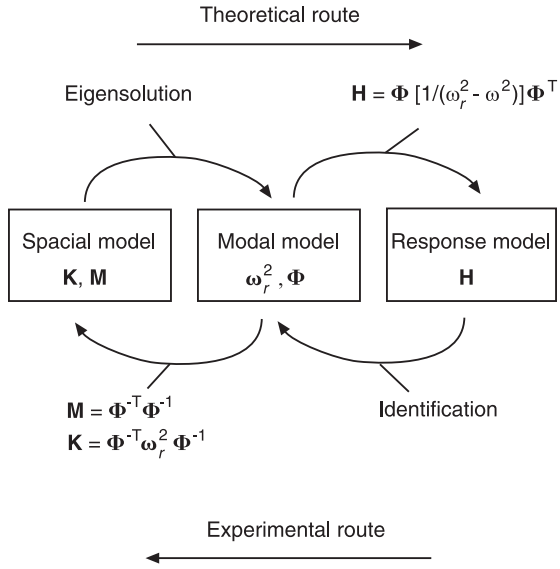


Figure 2 Interrelation among dynamic models.

$$\mathbf{M}\ddot{\mathbf{x}} + \mathbf{C}\dot{\mathbf{x}} + \mathbf{K}\mathbf{x} = \mathbf{f} \quad [15]$$

and for the hysteretic damping case, as:

$$\mathbf{M}\ddot{\mathbf{x}} + i\mathbf{D}\mathbf{x} + \mathbf{K}\mathbf{x} = \mathbf{f} \quad [16]$$

Matrices $\mathbf{M}$, $\mathbf{K}$ and $\mathbf{C}$ (or $\mathbf{D}$) now constitute the spatial model in the damped case.

Except for very special cases (for instance, if the viscous damping matrix can be defined as a linear combination of the mass and stiffness matrices), the result of the associated eigenproblem is a set of complex natural frequencies and complex mode shapes, which define in that case the modal model. Although not so easy as the undamped case, passing from the spatial to the modal model and to the response model (the theoretical route) is not a problem. The big problem in that case is how to define the damping matrix. That is why in a pure analytical or numerical approach we only have a description of the system in terms of $\mathbf{K}$ and $\mathbf{M}$, i.e., the numerical solution is the undamped one.

To model the damping, one needs to follow the experimental route where, through adequate identification methods, we are able to go from the measured response model to the modal model, with information about the natural frequencies, damping factors and complex mode shapes. For instance, in the hysteretic damping case, each FRF can be shown to relate to the modal model through the following expression:

$$H_{kj} = \sum_{r=1}^{N} \frac{\phi_{rk}\phi_{rj}}{\omega_r^2 - \omega^2 + i\eta_r\omega_r^2} \quad [17]$$

where H_{kj} is the measured FRF relating the response at coordinate k with the input force at coordinate j, N is the number of degrees-of-freedom, ϕ_{rk} and ϕ_{rj} the mode shape elements k and j of mode r (complex in general), ω_r the natural frequency and η_r the damping ratio of mode r.

The problem is that in many cases one wishes to validate the theoretical model or even to update it and on the one hand there is a set of real modes coming from the numerical solution, on the other hand a set of complex modes. This gives rise to an old problem: how to relate complex modes to real (or normal) modes? How to pass from one to the other? How to measure the complexity of the modes? The problem of having in practice considerably complex modes may be difficult to address. In some cases, linear transformations between real and complex modes are made, where the real modes are used as a basis to expand complex modes. These approximations, however, should be used with great care, as they are bound to produce erroneous or misleading results. Fortunately, in many applications, the complexity of the modes is not so high and even not genuine, i.e., it can result from other problems that have not been carefully addressed, such as the existence of aliasing, leakage, measurement noise, nonlinearity, identification errors, etc. Careful measurement procedures can significantly reduce the degree of false complexity indicated in measured mode shapes.

Turning to the issue of going from the measured response model to the modal model, we saw that eqn [17] is the kind of expression we often use as a basis for the identification of the modal properties of a system. While the damping ratios and natural frequencies are global properties of the system, i.e., they have the same values no matter which FRF H_{kj} is considered, the mode-shapes have a local nature, as each point has its own amplitude (and phase) (this is why most of the identification techniques proceed in two steps: first, the calculation of the global properties and second, the evaluation of the local ones). In the limit, we would appear to need only one FRF to obtain ω_r and η_r but all the FRFs to estimate ϕ_{rk} and ϕ_{rj}. In fact, neither of these two extremes are used. For the natural frequency and damping ratio we usually take more than just a single FRF, as variations always occur and experience advises to take a set of FRFs to obtain a kind of 'average result'. For the mode-shapes, not all the FRFs are necessary, because there are some inter-relationships that hold true and reduce the number of responses that need to be measured. If one measures a point FRF (excitation and measurement at the same DOF), say H_{kk}, the numerator of [17] becomes $(\phi_{rk})^2$ and ϕ_{rk} is therefore evaluated. Measuring a transfer FRF, H_{kj}, allows for the calculation of the product $\phi_{rk}\phi_{rk}$, known as a modal constant of mode r. As ϕ_{rk} is already known, we obtain ϕ_{rj}. As a consequence, it is not necessary anymore to measure H_{jj}, as its numerator (ϕ_{rk}^2) can now be computed. The implication of such properties of the mode-shape components, known as consistency properties, is that we only need to measure one column (or one row) of the FRF matrix $\mathbf{H}$ to obtain the whole mode-shape (or modal) matrix.

It is often recommended to measure more than a single column, to obtain some redundant data to improve our confidence in the results, especially when we suspect the existence of repeated natural frequencies. Theoretically, based on the consistency properties, we could even obtain the whole FRF matrix. For instance, for a 3×3, FRF matrix, let us suppose we measured H_{11}, H_{21} and H_{31}. Due to the symmetry of the matrix, we already know H_{12} and

H_{13}. So, we miss H_{22}, H_{23} (=H_{32}) and H_{33}. Due to the consistency properties, with H_{11} and H_{12} we could recover H_{22}; with H_{11} and H_{13}, we would obtain H_{33}; with H_{22} and H_{33}, we would obtain H_{23}.

Unfortunately, the evaluation of unmeasured FRFs based on a single column (or row) of the FRF matrix is not so straightforward as it seems, due to the incompleteness of the model in terms of frequency range, as we will see next.

Complete and Incomplete Models

To ensure clarity of exposition, the undamped case is used once more. The issue of moving to and from the different spatial, modal and response models is not the real problem, even when taking the experimental route, provided that appropriate methods are used. Probably the greatest problem of all is the incompleteness of the models obtained from the experimental tests. From the numerical solution, one has a model with N-degrees-of-freedom, which in some applications can be of the order of 10^4 or even more. Assuming that this N is representative of the behavior of the structure, the model with matrices of order N will be considered as the complete one. In contrast, from the experimental point of view, it is not usually possible to measure all the coordinate motion responses, or to apply all force excitations. Normally, only a few dozen degrees-of-freedom are measured. The system is therefore a reduced or incomplete one by comparison with the theoretical version.

Another 'source' of incompleteness is related to the measured frequency range. Only a few modes are covered and are therefore 'identifiable' from tests, in contrast with the theoretical model. To identify in an accurate way the modes within the frequency range of interest, one has to take account of the influence of the modes outside that range, the so-called low- and high-frequency residuals.

This sort of incompleteness precludes the exact evaluation of the complete FRF matrix from measurements of a single column, as explained before, since the residual mode-shapes do not verify the consistency properties. So, as in practice this is always the case, we cannot effectively reconstruct unmeasured FRFs, but can only use such properties to estimate unmeasured mode-shapes within the frequency range of interest.

If the incompleteness has only to do with the lack of measured coordinates, the relation between the modal and response models given by eqn [14] becomes:

$$\underset{(n\times n)}{\mathbf{H}} = \underset{(n\times N)}{\mathbf{\Phi}} \left(\underset{N\times N}{\boldsymbol{\omega}_r^2 - \boldsymbol{\omega}^2} \right)^{-1} \underset{(N\times n)}{\mathbf{\Phi}^{\mathrm{T}}} \qquad [18]$$

where $n < N$ is the number of measured coordinates. If the incompleteness is also in the number of modes available, say $m < N$, eqn [18] becomes:

$$\underset{(n\times n)}{\mathbf{H}} = \underset{(n\times m)}{\mathbf{\Phi}} \left(\underset{(m\times m)}{\boldsymbol{\omega}_r^2 - \boldsymbol{\omega}^2} \right)^{-1} \underset{(m\times n)}{\mathbf{\Phi}^{\mathrm{T}}} \qquad [19]$$

Note that for $\mathbf{H}$ to be of full rank the number of retained modes must be equal or larger than the number of coordinates, i.e., $m \geq n$. Inverting [18] or [19] produces a reduced stiffness matrix $\mathbf{Z}^{\mathrm{R}}$.

In the case where $n = m$, expressions [11a] and [11b] can be used to go from the modal to the spatial model, where all matrices are $n \times n$. $\mathbf{M}$ and $\mathbf{K}$ are in that case reduced mass and stiffness matrices. As already mentioned, it is often necessary to bring together the experimental and theoretical models, for validation or updating purposes, for example. As the order of magnitude of both models is very different, the comparison between the two is only possible either by a condensation of the theoretical model or by expansion of the experimental one. In either case, there are several techniques available.

For the condensation of $\mathbf{K}$ or $\mathbf{M}$, the most used method is that known as Guyan reduction: suppose one wishes to represent an N-degree-of-freedom system only through p (primary) coordinates, corresponding to the dimension of the experiments. The remaining $s\,(= N - p)$ coordinates are called secondary (or slave) and in those it is supposed that there are no applied forces. In a static case, where $\mathbf{KX} = \mathbf{F}$, $\mathbf{K}$ is partitioned so that:

$$\begin{bmatrix} \mathbf{K}_{pp} & \mathbf{K}_{ps} \\ \mathbf{K}_{sp} & \mathbf{K}_{ss} \end{bmatrix} \begin{Bmatrix} \mathbf{x}_p \\ \mathbf{x}_s \end{Bmatrix} = \begin{Bmatrix} \mathbf{f}_p \\ \mathbf{0} \end{Bmatrix} \qquad [20]$$

The objective is to obtain a condensed (or reduced) $\mathbf{K}^{\mathrm{R}}$ matrix referred to the p coordinates, i.e.,

$$\mathbf{K}^R \mathbf{x}_p = \mathbf{f}_p \qquad [21]$$

Eliminating $\mathbf{x}_s$ in [20], it follows that:

$$\mathbf{K}^R = \mathbf{K}_{pp} - \mathbf{K}_{ps}\mathbf{K}_{ss}^{-1}\mathbf{K}_{sp} \qquad [22]$$

A similar formula can be found for the reduced mass matrix.

For the expansion process, the most used technique is that known as Kidder's expansion, although several interpolation alternatives are also possible. Kidder's expansion is somehow the reverse of the Guyan reduction, although normally used together with the

mass matrix. From the partitioned free vibration equilibrium equation, it follows that:

$$\left[\left[\begin{array}{c|c}\mathbf{K}_{pp} & \mathbf{K}_{ps}\\ \hline \mathbf{K}_{sp} & \mathbf{K}_{ss}\end{array}\right] - \omega_r^2\left[\begin{array}{c|c}\mathbf{M}_{pp} & \mathbf{M}_{ps}\\ \hline \mathbf{M}_{sp} & \mathbf{M}_{ss}\end{array}\right]\right]\left\{\begin{array}{c}\boldsymbol{\phi}_p\\ \hline \boldsymbol{\phi}_s\end{array}\right\}_r = \left\{\begin{array}{c}\mathbf{0}\\ \hline \mathbf{0}\end{array}\right\} \quad [23]$$

where $(\boldsymbol{\phi}_p)_r$ are the known (measured) coordinate amplitudes and $(\boldsymbol{\phi}_s)_r$ the unmeasured ones, for each mode, r. It is possible to show that:

$$(\boldsymbol{\phi}_s)_r = -\left[\mathbf{K}_{ss} - \omega_r^2\mathbf{M}_{ss}\right]^{-1}\left[\mathbf{K}_{sp} - \omega_r^2\mathbf{M}_{sp}\right](\boldsymbol{\phi}_p)_r \quad [24]$$

Whenever trying to compare both theoretical and experimental models, several authors advise the use of expansion instead of condensation, so that most of the information in the theoretical model is preserved.

See also: **Modal analysis, experimental**, Applications; **Modal analysis, experimental**, Basic principles; **Modal analysis, experimental**, Measurement techniques; **Modal analysis, experimental**, Parameter extraction methods; **Model updating and validating**.

Further Reading

Ewins DJ (2000) *Modal Testing: Theory, Practice and Application*. UK: Research Studies Press.

Heylen W, Lammens S, Sas P (1997) *Modal Analysis Theory and Testing*. Belgium: KU Leuven.

Maia NMM, Silva JMM *et al.* (1997) *Theoretical and Experimental Modal Analysis*. UK: Research Studies Press.

McConnell KG (1995) *Vibration Testing: Theory and Practice*. New York: John Wiley.

Applications

D J Ewins, Imperial College of Science, Technology and Medicine, London, UK

Copyright © 2001 Academic Press

doi:10.1006/rwvb.2001.0030

Introduction

This final article in the series on experimental modal analysis is concerned with the applications to which the mathematical models derived from the test data are to be put. These applications fall into two categories: those which use the resulting models in a qualitative, primarily visual, way and those which use the models in a quantitative, numerical way. The first set of applications is primarily concerned with relatively practical, troubleshooting, problem-solving activities and, historically, constitutes the original purpose of most early modal tests. More recently, as the quality and reliability of the derived models have improved, several more ambitious applications have emerged in which the models are used for numerical predictions of various alternative configurations or scenarios to the test set-up. These include:

- comparisons of theoretically- and experimentally-derived models with a view to improving the analytical model (model 'validation' or 'updating');
- structural modification and optimization activities;
- structural assembly analysis;
- operating conditions response prediction and force determination; and
- measurement of dynamic properties of complex materials and structures, including for damage detection purposes.

The following sections provide an introduction to these applications, discussing the main requirements and limitations of each.

It should be noted at the outset that different applications make use of the derived mathematical model in different forms: spatial, modal or response. The troubleshooting applications generally use the derived models in their original format – as modal models. The model validation and updating applications use both modal and spatial models: modal models for the initial comparisons and spatial models at the stage when modeling errors are sought, and corrections to the original model are introduced. Structural modification and assembly applications generally rely more on response models, as do the applications concerned with operating response and excitation analysis.

Troubleshooting

In troubleshooting applications, the engineer is generally interested in obtaining visual displays of the individual modes of vibration, or even of the operating deflection shapes ('modes', but not 'normal modes'). By inspection of these mode shapes, it is often possible to develop an appreciation and physical understanding of exactly how, and why, the structure is vibrating. A skilled engineer can often diagnose troublesome vibration conditions from such a visual inspection of the structure's modes and, eventually, prescribe appropriate modifications or other corrective actions. However, all this inspection and interpretation is done in an essentially qualitative

way, and relatively few computations (if, indeed, any at all) are involved.

Theoretical Model Validation

Probably the single most practiced application of modal testing is that of validating a theoretical model using measured data. 'Validation' means checking that an already-available theoretical model (usually, a finite element model) is in fact 'valid'. By this we mean that the model is capable of predicting the actual dynamic behavior of the test structured to an acceptable accuracy. The last qualification is important because it is not realistic to expect the theoretical model to be absolutely correct.

The various phases of model validation can be listed as follows:

- Comparison
- Correlation
- Verification
- Reconciliation
- Error location or 'localization'
- Model updating or 'correction'

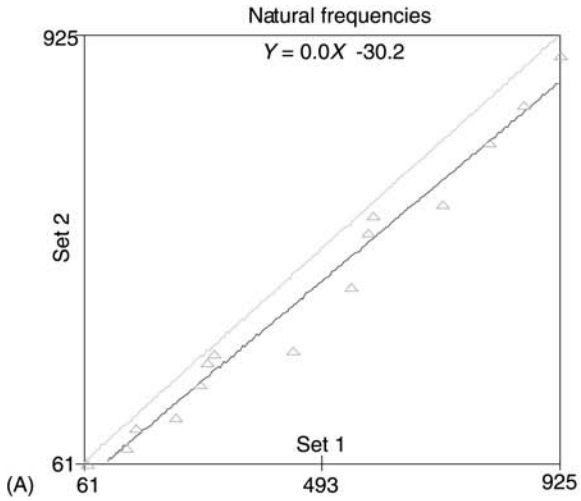
and it will be helpful to explain each of these in a few words:

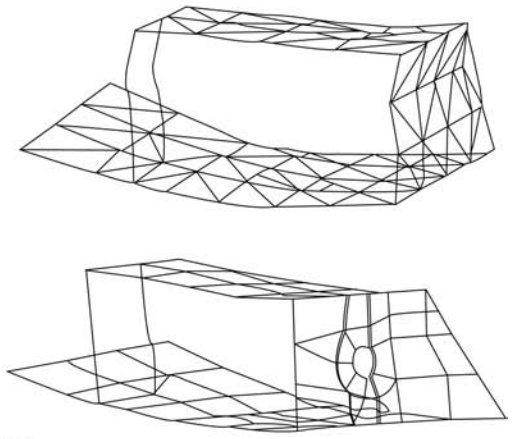
- 'Comparison' is the passive process of setting measured and predicted results side by side and observing their similarities and differences.
- 'Correlation' is the ensuing step of quantifying these differences in order to assess the extent of the comparison. A number of standard numerical indicators are widely used in this process.
- 'Verification' is a procedure which should be carried out before any attempt is made to explain and correct for the differences which have been observed between the test-derived model and its analytical counterpart. Verification is the process of determining whether a given model is capable of describing the behavior of the subject structure, if all the individual model parameters are assigned the correct values. A model may not be verified if it lacks certain features or freedoms which are present in the actual structure since, in this case, no amount of parameter correction can compensate for the errors embedded in the basic model.
- 'Reconciliation' refers to the sometime delicate task of establishing reasons for the observed differences between measurement and prediction. These differences can arise either because of inaccurate models, or because of imperfect measurements, and the necessary corrective action is, of course, different in the two cases. A third explanation is also frequently-encountered: the actual structure under test might not conform precisely to the specification (or drawings) upon which the theoretical model will have been based.
- 'Error location' is the very difficult task of establishing which elements or parts of the model contain the errors (whether these be errors in the theoretical model or in the test data). This is made difficult because of the usually heavily underdetermined nature of the analysis: there will be many more parameters with potential errors in the model than there are independent measured data from the modal test with which to locate them.
- 'Updating' is the final step in the complete validation process: it is the computation of the necessary changes to be introduced to the parameters which have been identified as containing the errors.

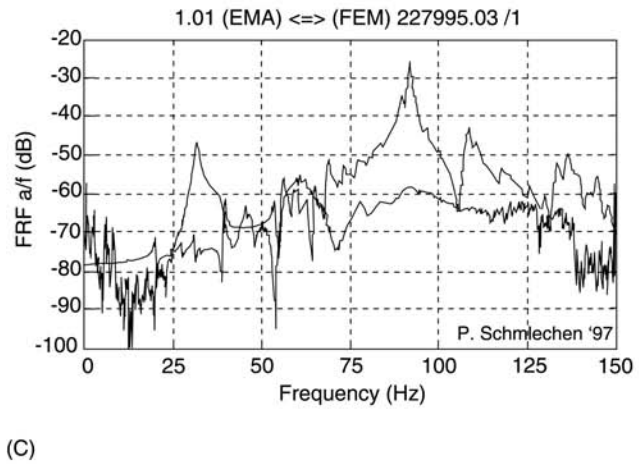
Comparison and Correlation of Vibration Properties

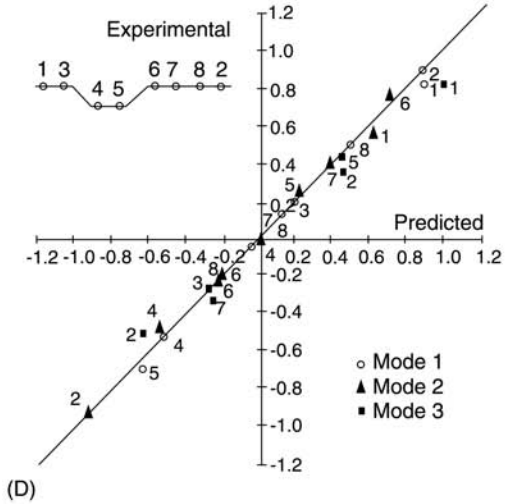
The most common form of analysis-test comparison is of the modal properties. Plots of measured vs predicted natural frequencies, such as that shown in **Figure 1A** and side-by-side comparisons of mode shapes, shown in **Figure 1B**, are fairly standard displays. It is also possible to compare measured with predicted frequency response functions (FRFs), but these are generally more difficult to interpret (**Figure 1C**). An alternative way of displaying the mode shape comparison in **Figure 1B** is to plot the values of the respective eigenvectors (the deflected mode shape display is simply one way of plotting the elements in a mode shape vector), test vs analysis, such as the example shown in **Figure 1D**.

The plot of natural frequencies in **Figure 1A** can be used to obtain a quantitative measure of the agreement between test and analysis, principally by determining the slope of the straight line drawn through the plotted points. This should be unity and any deviation in this slope, accompanied by minimal scatter of the points, suggests strongly that there is simply an error in some global property, such as modulus or density, but that the basic model is in close agreement with the measurements. If, on the other hand, the points are markedly scattered about the best-fit line, then that suggests a poor correlation between test and prediction. However, it is necessary to exercise some caution in this type of comparison: a point should only be plotted on the graph in **Figure 1A** after it has been established that the shape of the mode corresponding to the measured natural frequency matches closely that of the mode which









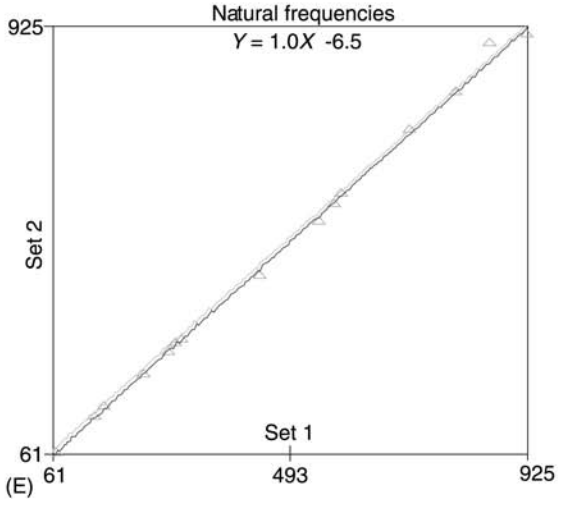


Figure 1 (A) Plot of measured vs predicted natural frequencies. (B) Measured and predicted mode shapes. (C) Measured and predicted FRFs. (D) Comparison of mode shape vectors. (E) A more reliable plot of measured vs predicted natural frequencies.

corresponds to the relevant predicted natural frequency. It is not valid to plot the natural frequency of, say, a torsion mode against a predicted natural frequency of a bending mode – just because they happen to have similar frequency values. In fact, it is essential that correlated mode pairs are identified prior to constructing a lot such as that shown in **Figure 1A** and this can only be achieved by a systematic analysis of the mode shapes of the experimental and theoretical modes.

The necessary systematic comparison between two mode shapes (such as measured vs predicted) can be made based on the plot shown in **Figure 1D** which shows the corresponding elements from the two vectors plotted one against the other. In the ideal case, all such points should lie on a straight line of slope ± 1. If they lie close to a straight line of a different slope, this indicates very similar mode shapes, but different scaling, in the two cases. From such a plot two average parameters can be extracted: the slope of the best-fit straight line drawn through the points (known as the 'modal scale factor', MSF) and the scatter of those points about that line (known as the 'mode shape correlation coefficient' or 'modal assurance criterion', MAC). The relevant formulae for these two quantities are:

$$\mathrm{MSF}(X,A) = \frac{\sum_{j=1}^{n} (\psi_X)_j (\psi_A)_j^*}{\sum_{j=1}^{n} (\psi_A)_j (\psi_A)_j^*}$$

and

$$\mathrm{MAC}(A,X) = \frac{\left|\boldsymbol{\psi}_X^{\mathrm{T}} \boldsymbol{\psi}_A\right|^2}{\left(\boldsymbol{\psi}_X^{\mathrm{T}} \boldsymbol{\psi}_X\right)\left(\boldsymbol{\psi}_A^{\mathrm{T}} \boldsymbol{\psi}_A\right)}$$

respectively. If two sets of eigenvectors are compared, say measured modes vs predicted modes, then a matrix of MAC coefficients can be produced, and can be displayed in several ways, including a table of numerical values (**Figure 2A**) or a diagram (**Figure 2B**).

From the diagram in **Figure 2B**, it can be seen that the correlated modes (those with a MAC exceeding 80%) do not correspond exactly with a direct sequential comparison. Thus the natural frequency of test mode 1 (SET 1) should not be compared numerically with the natural frequency of analysis mode 1 (SET 2) because they do not relate to the same basic mode, as determined by the shapes. The first valid comparison that can be made is between test mode 1 (SET 1) and analysis mode 2 (SET 2). Then, 2;3, 3;4, 5;5, 6;6, ... Once this pairing has been completed, the natural frequency plot can be redrawn this time making a more reliable comparison between test and analysis, see **Figure 1E**. Clearly, the earlier plot in **Figure 1A** of uncorrelated modes is misrepresentative of the true degree of correlation between test and analysis.

The MAC correlation function is widely used as the first level of quantitative comparison between two sets of modal data. The diagrams and tables shown in **Figure 2** can, however, become confused as a result of incompleteness of the measured mode shape data. To check for such problems, it is possible to compute an AUTOMAC, in which a set of eigenvectors are correlated with themselves. The result of such a computation should be a simple diagonal matrix, indicating that each mode shape vector correlates only with itself. If anything different is found, then it must be concluded that the modes are described by an insufficient number of degrees of freedom (DOFs) or points – a situation which can occur all too easily in experimental situations where the number of measured points is usually severely restricted for reasons of resource. Examples of both situations are shown in **Figures 2C** and **2D**, which show the same data plotted using 102 measured DOFs in **Figure 2C**, but only 30 DOFs in **Figure 2D**.

The most recent format for plotting all these data is shown in **Figure 2E**, in which the natural frequency plots of **Figure 1,** and the mode shape correlation in the MAC and AUTOMAC diagrams in **Figure 2,** are combined into a single plot that contains all the relevant information referred to as the FMAC.

Model Updating and Error Localization

The Basic Principle of Model Updating

Correlation constitutes the essential prerequisite for model updating, or correction. In model updating, the concern here is with the logical conclusion of comparison or correlation: namely, the discovery and correction of errors in the theoretical model (although it is also possible that the reasons for the two sets of data to differ might not always lie in the theoretical model: it is possible that certain of the measured data might contain errors). However, whether the actual errors reside in the theoretical model or in the test data, the task is essentially the same: to find the regions of the model/structure where the causes of the less-than-perfect correlation are located. Once these regions have been identified, then detailed examination of the specific data usually reveals which model contains the errors. If they are found to be in the measured data, then a partial re-test is the ideal solution, although if this is not feasible,

Analytical mode number	Experimental mode number									
	1	2	3	4	5	6	7	8	9	10
1	100	0	1	0	0	0	0	0	0	0
2	0	100	1	1	0	0	0	0	0	0
3	0	1	94	3	2	0	0	0	0	0
4	0	0	2	92	5	3	0	0	0	0
5	0	0	0	4	86	7	4	0	0	0
6	0	0	0	0	7	81	9	5	0	0
7	0	0	0	0	0	10	75	10	5	0
8	0	0	0	0	0	0	12	71	11	5
9	0	0	0	0	0	0	0	14	68	11
10	0	0	0	0	0	0	0	0	16	65

(A) *Modal assurance criterion (MAC) %*

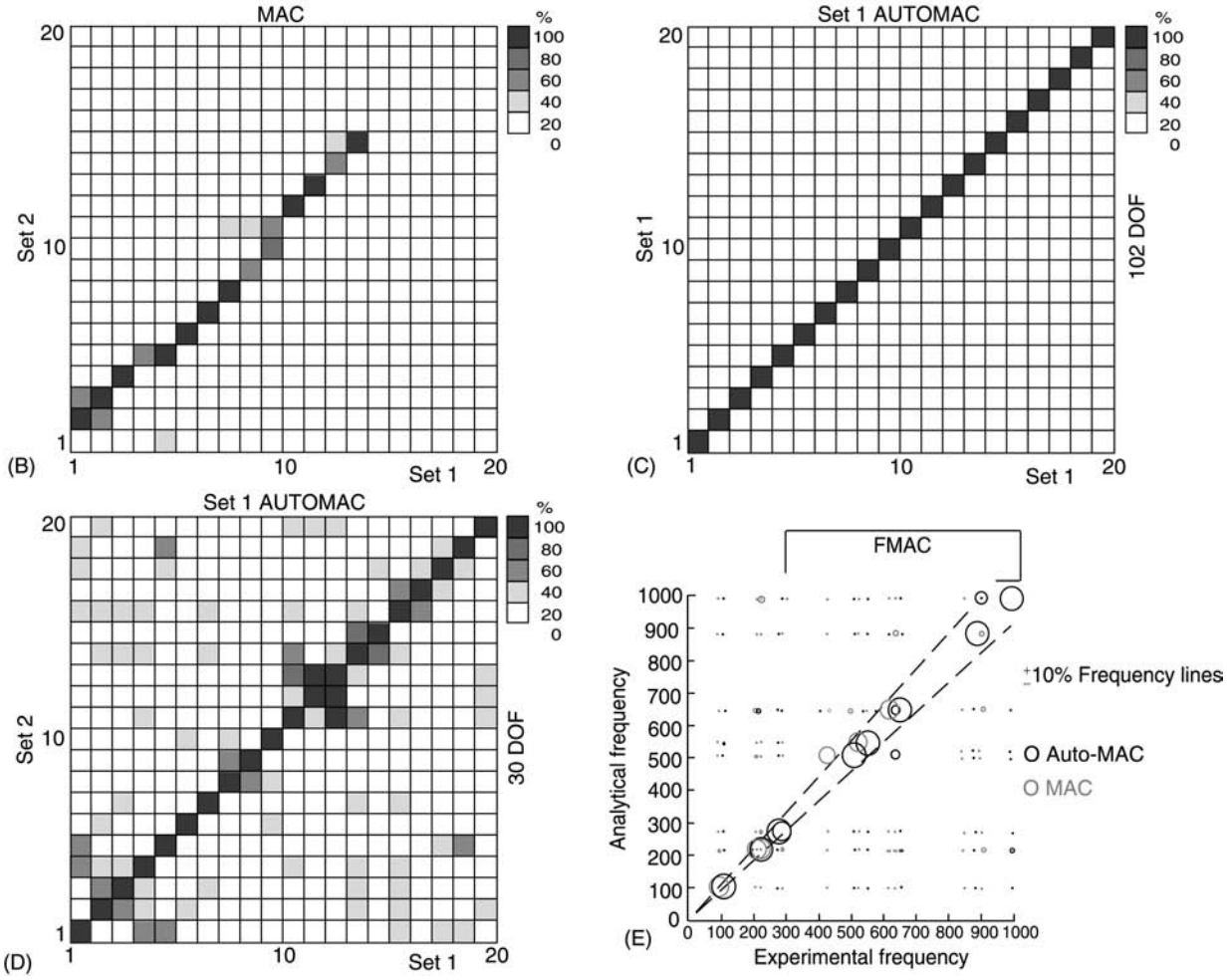


Figure 2 (See Plate 46). (A) Correlation of test and analysis. (A) MAC table; (B) MAC diagram; (C) AutoMAC – many DOFs; (D) AutoMAC – reduced DOFs; (E) FMAC plot.

then the offending data need to be eliminated from the whole validation process. If, on the other hand, the errors are believed to be contained in the theoretical model, then it is necessary to determine what adjustments to the numerical values of the critical model parameters are required in order to bring the theoretical model predictions closer into line with the measured data.

The algorithms and procedures to carry out the tasks summarized in the above paragraph are rather complex, and cannot be covered in an introductory article such as this. However, there is a complete

entry devoted to the topic of model updating and the interested reader is directed there for a more complete description (see **Model updating and validating**). This section simply discusses some of the more practical considerations.

The Processes Involved in Model Updating

Essentially, what is required in the process of updating (or 'refining', or 'correcting') a theoretical model is to identify changes that need to be made to the individual elements in the mass and stiffness coefficients in the spatial model. This is often translated into the requirement to update or correct elements in the mass and stiffness matrices which constitute the numerical representation of the spatial model.

Verification The updating task comprises one introductory and two active stages. Before embarking on an updating exercise, it is important to determine the extent to which the two models (experimental and analytical) are different as there is little point in seeking to correct for discrepancies that lie within the measurement uncertainty that must be applied to the test data. At the same time, it is also necessary to establish that the analytical model is capable of representing the measured behavior, even when numerical adjustment of its various parameters has been undertaken. In fact, satisfying this condition is by no means a foregone conclusion: if the theoretical model is too simple, and contains only a few DOFs while the actual test structure is complex and has many active DOFs, then it is clear that no amount of adjusting such a theoretical model can render it capable of replicating the behavior of a much more complicated structure. In this respect, the theoretical model which is to be updated must first be 'verified' as being intrinsically capable of describing the structure's dynamic behavior. Only then is it appropriate to search for the parameters in the model which need to be adjusted, and then to introduce the appropriate numerical changes to those parameters.

Error location Once this precondition is satisfied, the first of the two main updating tasks is to locate those regions or elements in the model which need to be adjusted. This is, in fact, the most difficult task and it is made so by the fact that the measured data that are to be used to perform this task are not only inaccurate (as are all measured data) but – and more importantly – they are generally heavily incomplete. In most modal tests on real structures, practical considerations mean that only a relatively small number of modes of vibration are measured, and these are defined at only a small number of DOFs, as compared with the total number of DOFs in the theoretical model. As a result, the error location problem is heavily underdetermined, which means that it is almost impossible to obtain a unique solution – many 'solutions' are generally found – and those which are obtained may well be ill-conditioned because of the inadequacy of the measured data.

Model adjustment Nevertheless, there are several algorithms that seek to identify the most critical of the parameters in the model and, once identified, the second task is relatively straightforward – generally using some optimization criteria, a 'best' set of individual correction factors for the identified erroneous elements can be determined. This process, also, suffers from the underdetermination feature refered to above and care must usually be exercised not to allow model parameters to be modified to a degree which cannot be justified from a physical point of view. This is very important because, in many cases, a satisfactory match between measured data and predictions from an updated model can be achieved at the expense of realism in the adjusted theoretical model. Such a situation constitutes a numerical solution, but not a reasonable one from a physical or practical viewpoint. Any updated model must be able to pass a test of 'reasonableness' in its numerical parameters.

Algorithms for Model Updating

There have been many algorithms proposed for the task of updating a theoretical model, but only two or three survive. The most popular one is an iterative one which is based on the sensitivity properties of the subject model; sensitivity to small changes in individual mass or stiffness elements in that model. **Figure 3** illustrates a typical updating session spanning some 10 iterations, showing: (a) the current degree of correlation (MAC matrix); (b) the evolution of the selected parameters being updated; (c) the evolution of the MAC values for the correlated mode pairs and (d) the discrepancies between measured and predicted natural frequencies (one of the primary indicators of agreement between two models). However, not all updating sessions are as classical as the one illustrated here.

Structural Modification and Structural Assembly Analysis

The next important application for a modal test-derived model of a structure is a family of methods which are referred to as 'modification' and 'assembly' methods. Although these two families of applications appear to be quite distinct, in fact they share the same

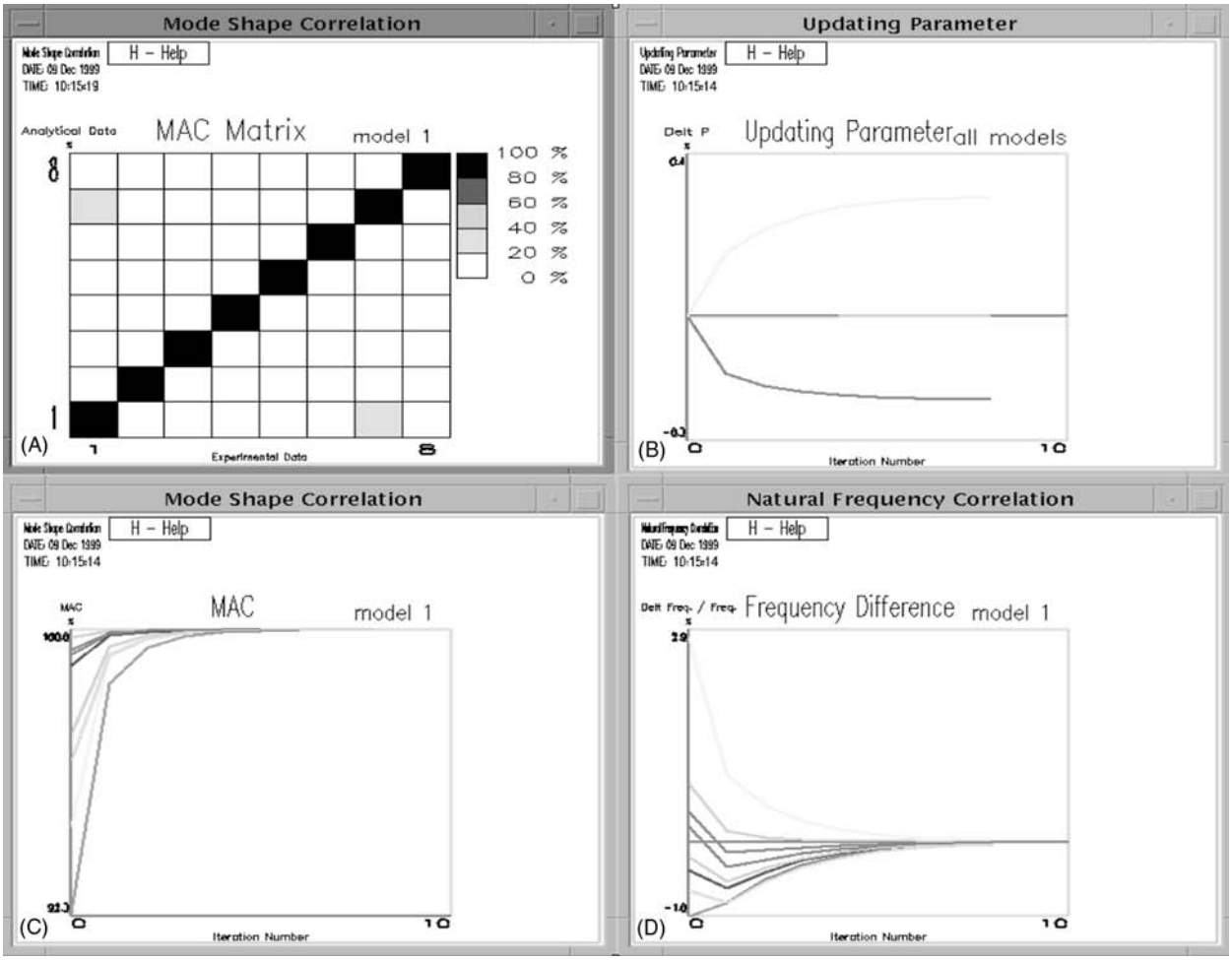


Figure 3 (See Plate 49). Example of evolution of model updating session. (A) Current MAC matrix; (B) evolution of updated parameters; (C) evolution of MAC values for correlated model pairs; (D) evolution of natural frequency discrepancies.

analytical techniques and processes. Indeed, it is quite reasonable to visualize a 'modification' as a simple case of one substructure being connected to the main test structure to form an 'assembled structure'.

The Three Specific Applications

There are three well-defined versions of this class of problem. The first – simple structural modification – seeks to answer the following question: 'if we have obtained a modal model of a particular test structure using modal testing techniques, can we readily predict (without the need for further tests) how those dynamic properties would change if a specified modification was introduced to the original test structure?'

The second application is an inverse version of the first, and can be summarized by the question: 'given a mathematical model derived from measurements on the test structure, how can we ascertain what modifications need to be made to that structure in order to change its vibration properties to some prescribed values?'

The third of these applications is more ambitious. If there are a number of components which will be combined, or coupled, to form a structural assembly, how can the dynamics of that assembly be forecast from a prior knowledge of the dynamics of each component structure individually? In other words, 'if we have a mathematical model of each separate component, (how) can we predict the dynamics of the assembly formed by coupling those components together, even before that assembly is realized physically?'

This last demand actually subsumes the first and second, and it can be seen that the generic application is structural assembly or structural coupling, and this is described pictorially in **Figure 4** which shows one component (A, with N_A DOFs) connected in a particular way to another component (B, with N_B DOFs)

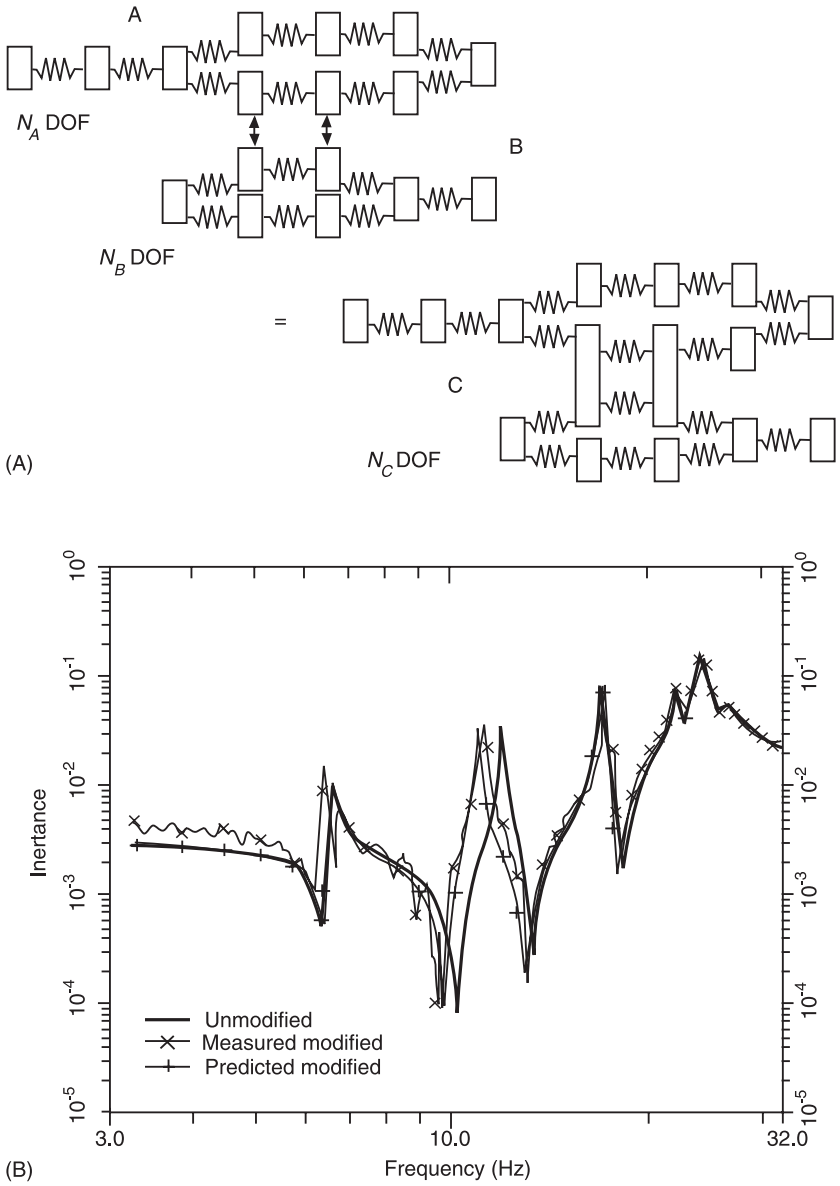


Figure 4 (A) Schematic illustration of a structural assembly formed by combining components A and B to form C; (B) practical application of structural modification.

so as to form a coupled structure, C (or structural assembly), with N_C DOFs. (It should be noted that N_C is not simply $N_A + N_B$.)

The methodology of structural assembly analysis seeks to provide a reliable prediction of the dynamic properties of the complete assembly (C) given the corresponding properties of each component individually. Thus, if we have a modal model for each of the components, A and B as separate structures, perhaps from a modal test on each, then we seek to predict the modal model for the assembly, C. Alternatively, if a response model exists for each of the component structures individually, then it may be preferred to derive a response model for the assembly. Both approaches are possible and are routinely made. Once again, a full discussion is not practical in this section, but there is a separate article on structural modification to which the reader who seeks more detail is directed (see **Structural dynamic modulations**).

It will suffice here to discuss some of the implications of using such analysis tools as can be found in that companion article in a practical situation. While the essential formulas and algorithms to undertake the required predictions are relatively simply stated, their successful implementation in practice is often difficult. This fact can be traced to the same issues as mentioned in the previous paragraphs: partly to the

imprecision but mostly to the incompleteness of the test data used to construct (limited, incomplete) models for the individual components. In this case, the incompleteness comes in two respects. First, there is the inevitable restriction to the frequency range over which tests are conducted, and modal properties are extracted. This range is usually curtailed by the structure itself because, at higher frequencies, the modes tend to become closer and closer together with the result that they eventually become indistinguishable in the response functions that are measured and analyzed to extract the required modal properties. The second restriction arises because not all the DOFs which are active in the connection interface can generally be measured, and so some are omitted from the component models, frequently with severe consequences on the resulting application. Most common amongst this category are the rotation DOFs which are notoriously difficult to measure, yet are clearly important participants in the coupled structure interactions.

As with the earlier example of model updating, care must be exercised here when seeking to exploit these advanced and potentially powerful applications in practice. Nevertheless, when such care is judiciously applied, very useful results can be obtained and considerable further testing can be avoided.

Response Prediction and Force Determination

Next, we describe two applications which are once again linked by virtue of the common underlying mathematics used in each case, even though the physical context can be quite different in the two cases.

Operating Response Levels

One obvious application of a modal-test derived model of a structure is to use that model to predict how the test structure would respond if subjected to any or many of a range of different excitations ('different' to that used for the modal test), usually referred to as 'operating' excitations, and thus to 'operating' responses. Interest might well be focussed on using the model to simulate excitations which are either multiple, and thus difficult to apply directly to the actual test piece, or at high forcing levels, thereby carrying a risk of damaging the structure. In both cases, the test-derived model can be used to make such predictions with a high degree of reliability and at a fraction of the cost that would be incurred to obtain the same results by direct testing.

The basic theory of the method can be illustrated by the specific case of single-harmonic (but multi-point) excitation, for which the equation that yields the response, $\mathbf{X}$, in terms of a specified excitation, $\mathbf{F}$, is:

$$\mathbf{X}_{n_1\times 1}e^{i\omega t} = \mathbf{H}_{n_2\times n_1}(\omega)\mathbf{F}_{n_1\times 1}e^{i\omega t}$$

The required elements in the FRF matrix, $\mathbf{H}(\omega)$, can be derived from the modal model by the familiar formula:

$$\mathbf{H}_{n_2\times n_1}(\omega) = \mathbf{\Phi}_{n_2\times m}\left(\lambda_r^2 - \omega^2\right)^{-1}_{m\times m}\mathbf{\Phi}^{T}_{m\times n_1}$$

Thus it can be seen how knowledge of the structure's modal properties can be used to predict that structure's response to an arbitrary set of harmonic excitation forces, $\mathbf{F}$, such as are experienced under service or operating conditions. Indeed, the type of response vector that has been derived here is often referred to as an operating deflection shape, or ODS. Clearly, by invoking one of several versions of Fourier analysis, the illustrated example of harmonic excitation and response can be extended to almost any type of vibration: periodic, random, transient, etc.

Determination of Unknown Excitation Forces from Measured Responses

The preceding technique of operating response analysis, based on the modal test-derived model, is generally very reliable. Care must be taken, as always, to ensure that the model used is complete enough for the task, and that means that a sufficient number of modes, m, is used so that the elements in the FRF matrix are accurate. However, the computation is generally well-conditioned.

There is an obvious extension of the foregoing approach in the form of the inverse formulation which sets out to determine the excitation force vector, which is supposed to be unknown in this application, using knowledge of the operating response levels, which can be more readily measured in a service environment than can the excitation forces.

The theoretical principle of the approach seems straightforward enough. It is the inverse of the above formula for response prediction and can be written as:

$$\mathbf{F}_{n_1\times 1}e^{i\omega t} = \mathbf{H}^{-1}_{n_1\times n_2}(\omega)\mathbf{X}_{n_{21}\times 1}e^{i\omega t}$$

However, there is an obvious problem in using this equation because of the need to invert the rectangular FRF matrix, $\mathbf{H}(\omega)$. In fact, it is necessary to use the generalized inverse to proceed with this expression, and we can write:

$$\mathbf{F}_{n_1\times 1} = \mathbf{H}^{+}_{n_1\times n_2}(\omega)\mathbf{X}_{n_{21}\times 1}$$

where the generalized inverse is defined as

$$\mathbf{H}^{+}(\omega) = \left(\mathbf{H}^{\mathrm{T}}(\omega)\mathbf{H}(\omega)\right)^{-1}\mathbf{H}^{\mathrm{T}}(\omega)$$

Although these expressions provide us with a means to solve the problem, and to determine the unknown force vector, **F**, from knowledge of the measured operating response vector, **X**, there are latent problems because of the under or overdetermination of the problem. These two conditions lead to multiple or nonunique solutions, coupled with the prospect of numerical ill-condition of the matrices involved. Needless to say, great care must be taken when implementing this innocuous formula: it may well be that an impossible solution is being sought. Experience shows that force determination is very much more difficult to apply successfully than its partner, response prediction.

Other Applications

There are a range of other applications to which the results of modal tests are being put. One recent and potentially important use is to damage detection. In this application, techniques relate to those used in model updating are employed; not for test against theory, but for test against test (generally on different occasions), where observed differences between the behaviour on day 1 and that on day N are studied for signs of structural changes that might herald incipient damage to a part of the structure. The need to 'locate' the sources for any such discrepancies becomes of paramount importance because it can be local damage that brings about these changes and it is the location of just that damage that is the primary objective of the application.

Advanced modal testing methods are also increasingly used to discover and to characterize nonlinear behavior of materials or structures. There are many situations where recourse must be made to test data in order to be able to characterize many nonmetallic materials in finite element (FE) models. Similarly, modal testing is being used more in the difficult arena of rotating machinery dynamics, where the rotation of certain components in the structure introduces significant complications of both a theoretical and a practical nature. Performing tests on rotating objects is an extremely challenging task, and the underlying theory is made significantly more complex by the loss of reciprocity, by the existence of two sets of axes and by the complicating effects such as gyroscopic and other forces.

In summary, a number of applications for modal test-derived models of structures have been discussed briefly. The first of these applications – troubleshooting – was largely of a quantitative nature, but the others are all firmly quantitative. They seek to use the test-derived model to perform computations of the effects, consequences or implications of the data that have been acquired during the modal test.

See Plates 46, 49.

See also: **Comparison of Vibration Properties**, Comparison of Modal Properties; **Comparison of Vibration Properties**, Comparison of Response Properties; **Comparison of Vibration Properties**, Comparison of Spatial Properties; **Damping measurement**; **Modal analysis, experimental**, Basic principles; **Modal analysis, experimental**, Construction of models from tests; **Modal analysis, experimental**, Measurement techniques; **Modal analysis, experimental**, Parameter extraction methods; **Model updating and validating**; **Structural dynamic modifications**.

Further Reading

Dynamic Testing Agency (1993) *Handbook on Modal Testing*.

Ewins DJ (2000) *Modal Testing: Theory, Practice and Applications*. Research Studies Press.

Heylen W, Lammens S, Sas P (1998) *Modal Analysis Theory and Testing*. Belgium Katholieke Universiteit Leuven.

Maia N, Silva J, He J *et al*. (1997) *Theoretical and Experimental Modal Analysis*. Research Studies Press.

MODE OF VIBRATION

D J Ewins, Imperial College of Science, Technology and Medicine, London, UK

Copyright © 2001 Academic Press

doi:10.1006/rwvb.2001.0062

Definition of Mode of Vibration

A mode of vibration can be defined as a way of vibrating, or a pattern of vibration, when applied to a system or structure that has several points with different amplitudes of deflection. A mode of vibration

comprises two distinct elements: first, a time variation of the vibration and, second, a spatial variation of the amplitude of the motion across the structure. The time variation defines the frequency of oscillations together with any associated rate of decay or growth. The spatial variation defines the different vibration amplitudes from one point on the structure to the next. The underlying expression that defines a vibration mode can be written as:

$$\mathbf{x}(t) = \mathbf{X}e^{st}$$

or:

$$x(y,t) = X(y)e^{st} \qquad [1]$$

depending upon whether the system is discrete, described by a finite number of specific degrees of freedom (**Figure 1A**), or continuous, in which case the motion is defined by a continuous function of position, as illustrated in **Figure 1B**. In these expressions, the coefficient s represents the time-dependent property while the vector $\mathbf{X}$ or the function $X(y)$ represents the spatial dependence of the vibration mode. Throughout this entry, it will be convenient to focus discussion on the former of these two expressions, the discrete version, as this is the one in more widespread use. However, it should be noted that all properties are common to both discrete and continuous versions.

Types of Vibration Mode

There are basically two types of vibration mode:

- free vibration modes and
- forced vibration modes

Modes of the first category, by far the more common, are sometimes called 'normal' or 'natural' modes (both names are equivalent), and those of the second category are sometimes referred to as 'operating deflection shapes'. As the names imply, these two types of mode relate to fundamentally different types of vibration. Free vibration modes describe the motion that takes place in a system that is free of any external excitation or forcing. They are therefore determined completely by the properties of the system or structure itself. Forced vibration modes, on the other hand, are influenced by the nature of the external excitation that generates the motion and are thus a reflection of both the system's parameters and the external forces.

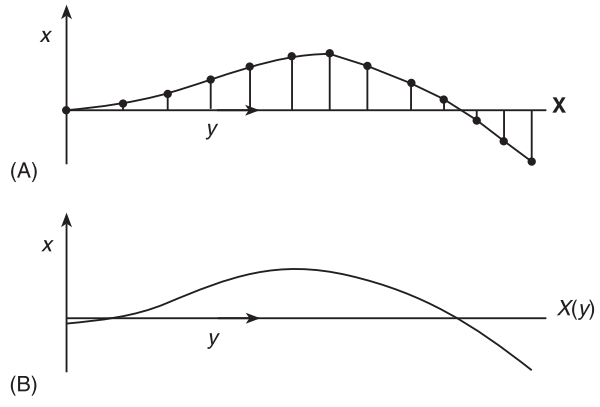


Figure 1 (A) Discrete and (B) continuous systems.

Essential Features of a Vibration Mode

The time-dependent component of a vibration mode is often referred to as the modal frequency and is represented by a complex quantity, s, appearing in the term e^{st} in the above expressions. The modal frequency is independent of spatial location of the vibration description and is called a global parameter, as a result of this feature. If s is imaginary ($s=i\omega$), then the motion is purely oscillatory at frequency ω, as illustrated by **Figure 2A**. If s is complex, then there is a combination of oscillation and exponential decay or growth, the latter alternatives following the sign of a,

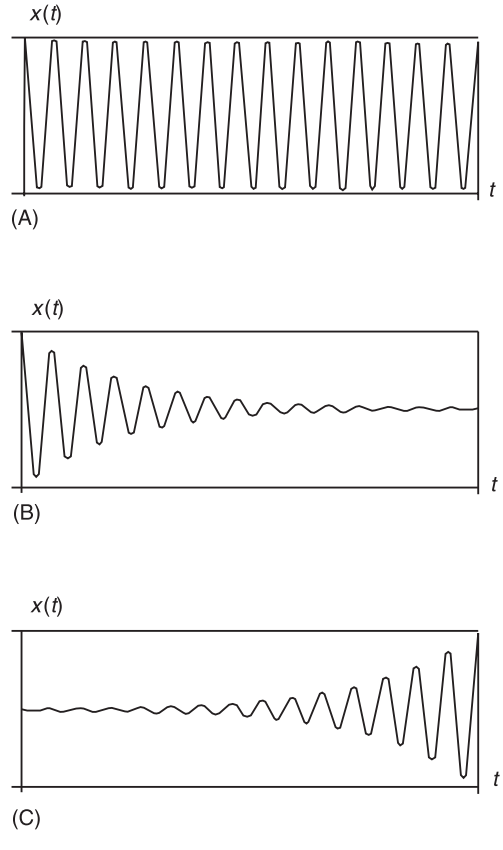


Figure 2 (A) $a = 0$; (B) $a<0$; (C) $a>0$.

the real part of s: if a is negative, then the oscillation decays and the system is stable (**Figure 2B**); if a is positive, then the oscillation grows and the system is said to be unstable (**Figure 2C**). If s is real, then the motion is nonoscillatory and consists simply of an exponential decay or growth.

The spatially-dependent component is usually referred to as the modal vector or mode shape and is represented by a vector of discrete amplitudes or by a continuous function, both of which are independent of time. The elements or coefficients that make up the mode shape may be real or complex quantities. In a real mode shape, all elements or parts of the system are vibrating exactly in or out of phase with each other. In consequence, all points reach their maximum deflections at the same instant(s) in time, and pass through their undeformed positions simultaneously. The resulting vibration is often described as constituting a standing wave as a result of the appearance of such a type of motion, and is illustrated in **Figure 3**.

In a complex mode shape, each part of the system vibrates with its own phase, which is not necessarily exactly in phase or out of phase with the other parts. As a result, each point on the structure reaches its own maximum excursion at different instants in time compared with its neighbors and, similarly, passes through its undeformed or zero position at different instants to the other points. The resulting motion in a complex mode is said to have the appearance of a traveling wave type of movement, as illustrated in **Figure 4** (although the full impact of a complex mode can only really be appreciated by viewing an animated display).

Free Vibration Modes

Origins of Free Vibration Modes

The free vibration modes represent the inherent vibration properties of the system or structure under discussion. They are usually referred to as the normal or natural modes of the structure and, although in some places a distinction may be drawn between these two different names, here they are taken as being synonymous. The normal modes are the natural modes of vibration.

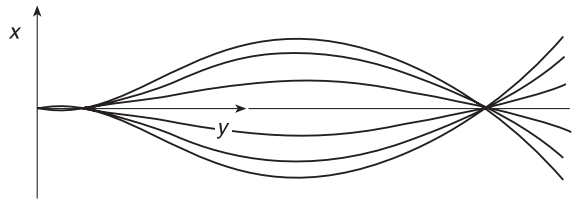


Figure 3 Standing wave (real mode).

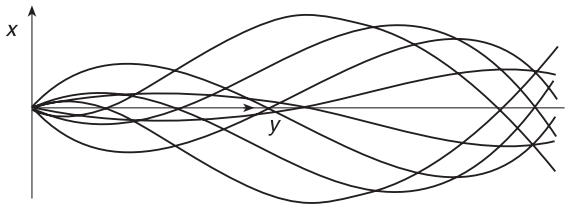


Figure 4 Traveling wave (complex mode).

The normal modes are obtained from solution of the equations of motion for the system under discussion for the case of zero external excitation, i.e., the solution to the homogeneous equations of motion. The equations of motion may be written in various forms, depending upon the exact nature of the system, and these include:

$$\begin{aligned} \mathbf{M}\ddot{\mathbf{x}} + \mathbf{K}\mathbf{x} &= \mathbf{0} \\ \mathbf{M}\ddot{\mathbf{x}} + \mathbf{C}\dot{\mathbf{x}} + \mathbf{K}\mathbf{x} &= \mathbf{0} \\ \mathbf{M}\ddot{\mathbf{x}} + (\mathbf{K} + \mathrm{i}\mathbf{D})\mathbf{x} &= \mathbf{0} \end{aligned} \qquad [2]$$

where $\mathbf{M}$, $\mathbf{C}$, $\mathbf{D}$, and $\mathbf{K}$ are the system mass, damping, and stiffness matrices, respectively. In these various cases, the solutions are

$$\begin{aligned} \mathbf{x}(t) &= \boldsymbol{\psi}_r \, \mathrm{e}^{\mathrm{i}\omega_r t} \\ \mathbf{x}(t) &= \boldsymbol{\psi}_r \, \mathrm{e}^{s_r t} \\ \mathbf{x}(t) &= \boldsymbol{\psi}_r \, \mathrm{e}^{\mathrm{i}\omega_r(1+\mathrm{i}\eta_r)t} \end{aligned} \qquad [3]$$

respectively, where ω_r and η_r are real, s_r is complex, and $\boldsymbol{\psi}_r$ may be real or complex depending upon the exact nature of the system. Thus we see that the free vibration modes can be real or complex and it is important to be able to explain and to understand the significance of the differences between the different types of mode which may be encountered in different systems.

The specific values of the modal frequency that refer to individual modes, ω_r or s_r, have a variety of different names. In some situations they are referred to as the poles or roots or characteristic values of the system equations, this term arising from the underlying mathematics. Sometimes they are referred to as the eigenvalues of the system, based on the German for characteristic value, although strictly, the eigenvalue is the square of the modal frequency. In their general form, they are complex and the two parts – real and imaginary – determine both the oscillatory and the decay/growth features of the time response of motion in that vibration mode, as previously explained. The oscillatory part is usually called the

natural frequency of the mode, while the real part contains the damping factor. In other situations, however, the whole term is referred to as the complex natural frequency, it being understood that there are two parts with the significance just defined. When analyzing undamped systems, the analysis usually delivers values of ω_r^2 directly, and these values (the squares of the natural frequencies) are then called the eigenvalues of the system.

The corresponding mode shape vectors are frequently referred to as the eigenvectors, the origin of this name being the same as that for eigenvalue. It can be seen from the solution to the equations of motion that there is an arbitrary scaling factor applicable to the mode shape vectors, $\boldsymbol{\psi}_r$, which follows from the observation that if $\boldsymbol{\psi}_r$ is a solution to the equation of motion, then so too is $A\boldsymbol{\psi}_r$, where A is a scaling factor. This means that a normal mode shape vector cannot be defined absolutely, but only as a set of relative amplitudes, or deflections, and this is an inherent feature of these properties of the free vibration modes. We shall see below that there is one particular scaling factor which it is convenient to use for further applications that refer to the mode shape vectors, but we shall leave further discussion of this point until then. This arbitrariness is not a feature that is present in forced vibration modes.

Orthogonality Properties of Normal Modes

The parameters that make up the full set of free vibration modes of a system or structure possess certain properties that are very useful for dynamic analysis in general. These are referred to as the orthogonality properties and it is appropriate to explain something of their origin and significance.

The essential orthogonality property is a relationship between the mode shape vectors of two different modes and is usually expressed in the form:

$$\boldsymbol{\psi}_q^{\mathrm{T}}\mathbf{M}\boldsymbol{\psi}_r = 0 \qquad [4a]$$

and:

$$\boldsymbol{\psi}_q^{\mathrm{T}}\mathbf{K}\boldsymbol{\psi}_r = 0 \qquad [4b]$$

There are some conditions for the validity of this relationship, the most important of which are that in this form it refers only to undamped systems and, further, that $\omega_r^2 \neq \omega_q^2$, for the two modes in question. If this latter condition is met (and the case where it is not satisfied is discussed below), then these two mode shape vectors are said to be orthogonal to each other and, provided that neither mode has the same natural frequency as any other mode in the set for that system, they are unique, save for the arbitrary scaling constant mentioned above.

If we consider the corresponding expressions where r and s are identical, we shall find both to be nonzero such that:

$$\boldsymbol{\psi}_q^{\mathrm{T}}\mathbf{M}\boldsymbol{\psi}_r = m_r \neq 0 \qquad [5a]$$

and:

$$\boldsymbol{\psi}_q^{\mathrm{T}}\mathbf{K}\boldsymbol{\psi}_r = k_r \neq 0 \qquad [5b]$$

These two quantities, m_r and k_r, are sometimes referred to as the modal mass and the modal stiffness, or generalized mass and generalized stiffness, and are related through the corresponding natural frequency by the simple relationship: $\omega_r^2 = k_r/m_r$. However, it must be noted that the modal mass and modal stiffness parameters defined in this way are not unique: they depend directly on the scaling of the mode shape vector. Nevertheless, this feature provides a means of defining a 'reference' version of the mode shape vector for each mode, by specifying a scaling factor that has a particular property of interest. It is possible to scale or multiply each mode shape vector, such as $\boldsymbol{\psi}_r$, by a constant, A_r, to create a particular (but equally valid) mode shape vector, $\boldsymbol{\phi}_r = A_r\boldsymbol{\psi}_r$, such that the modal mass is unity when computed using this new vector:

$$\boldsymbol{\phi}_q^{\mathrm{T}}\mathbf{M}\boldsymbol{\phi}_r = 1 = A_r^2\boldsymbol{\psi}_r^{\mathrm{T}}\mathbf{M}\boldsymbol{\psi}_r \qquad [6a]$$

For this scaled vector, $\boldsymbol{\phi}_r$, referred to as the mass-normalized mode shape vector for mode r, the second orthogonality expression yields the useful result that the value of the modal stiffness computed using it reverts to the eigenvalue, or square of the natural frequency:

$$\boldsymbol{\phi}_r^{\mathrm{T}}\mathbf{K}\boldsymbol{\phi}_r = \omega_r^2 \qquad [6b]$$

If the condition that $\omega_r^2 \neq \omega_q^2$ is not satisfied, and there are two modes of vibration with identical natural frequencies, then a more complicated situation exists. In such cases, it can be stated that any combination of the two mode shape vectors presented is also a valid mode shape vector; in other words, there is no unique mode shape corresponding to that particular natural frequency. However, not all such mode shape vectors (constructed from any combination of the original two) will be orthogonal to each other: only certain combinations will have this property, but these combinations will certainly exist.

If the system is damped, then the orthogonality conditions become more complex, as do the mode shape vectors and the eigenvalues themselves. In the case of structural, or hysteretic, damping, as described by the equations of motion shown in the third of equations [2], essentially the same orthogonality equations apply with the sole difference that the mode shape vectors, $\boldsymbol{\psi}_r$ or $\boldsymbol{\phi}_r$, and thus the modal mass and stiffness expressions, are now all complex quantities. In the case of general viscous damping (described by the second of equations of motion in eqn [2]), the expressions corresponding to the standard orthogonality equations in [5] are:

$$\left(s_r + s_q\right)\boldsymbol{\psi}_q^{\mathrm{T}}\mathbf{M}\boldsymbol{\psi}_r + \boldsymbol{\psi}_q^{\mathrm{T}}\mathbf{K}\boldsymbol{\psi}_r = 0$$

and: [7]

$$s_r s_q \boldsymbol{\psi}_q^{\mathrm{T}}\mathbf{M}\boldsymbol{\psi}_r - \boldsymbol{\psi}_q^{\mathrm{T}}\mathbf{K}\boldsymbol{\psi}_r = 0$$

which are clearly more complicated than the previous set.

In the most general cases, where symmetry of the system matrices cannot be assured, the situation becomes yet more complicated because the mathematics of the equations of motion gives rise to two sets of eigenvectors, the left-hand (LH) eigenvectors and the right-hand (RH) eigenvectors, only one set of which can realistically be related to mode shapes in the context discussed here. The orthogonality expressions for such cases involve a combination of LH and RH eigenvectors. Reference should be made to a detailed treatise on the mathematics of this type of case for a full description of the analysis. Suffice it to state here that all such systems possess a set of vibration modes with complex natural frequencies (roots) and complex mode shape vectors.

Real Normal Modes and Complex Normal Modes

Basically, the modal frequency (or eigenvalue) will be complex if the system contains damping of any type. As a result, all positively damped systems are expected to exhibit decaying as well as oscillatory motion. (Likewise, systems with 'negative' damping exhibit exponentially growing oscillations.)

Origins of complex mode shapes

However, when we turn our attention to the mode shapes, we find a more complicated set of rules. The mode shapes, the modal vectors $\boldsymbol{\psi}_r$, can contain real or complex elements depending on the exact nature of the damping effects. Except for the special case where all the elements in a vector have exactly the same degree of complexity (i.e., all have the same phase angle, or angles separated by 180°), modes with complex vectors are called complex modes and it is of interest to determine when such modes will exist, and the cause or interpretation of the complexity.

Visualization of complex modes can be difficult and one style of presentation is illustrated in **Figure 5**, which shows Argand diagram plots of the individual elements in three different vectors of different degrees of complexity.

If the system is undamped, so that $\mathbf{C}$ or $\mathbf{D}$ in eqn [2] is zero, then the mode shape vectors, $\boldsymbol{\psi}_r$, are all real. If the system has a particular distribution of damping such that $\mathbf{C}$ or $\mathbf{D}$ can be expressed as a linear combination of the mass and stiffness matrices, i.e., if:

$$\mathbf{C}, \mathbf{D} = \beta\mathbf{M} + \gamma\mathbf{K} \qquad [8]$$

then the system is said to be proportionally damped and it can be shown that the mode shape vectors for such a system are still real.

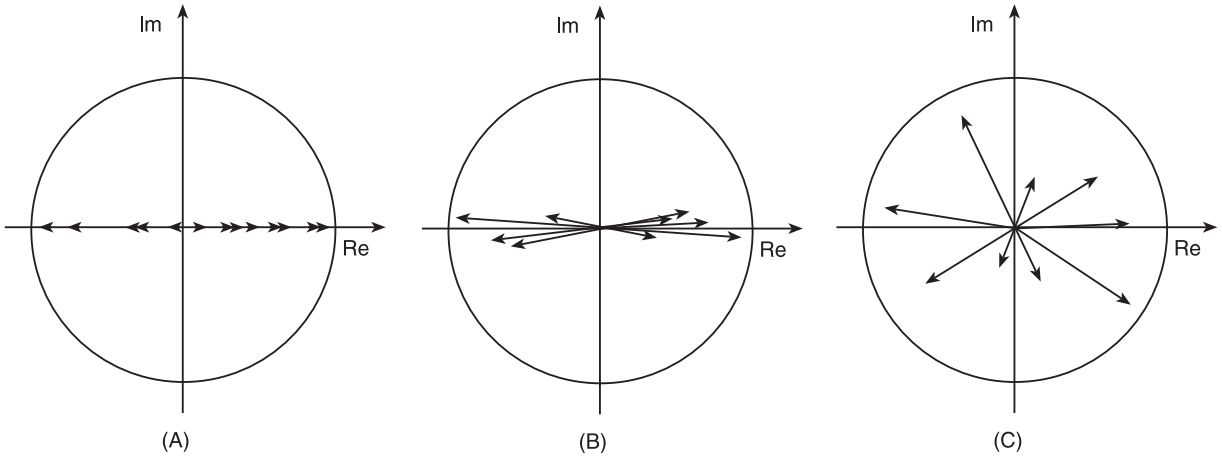


Figure 5 Plots of complex model shapes: (A) **X** is real; (B) **X** is slightly complex; (C) **X** is very complex.

If the system has damping that exhibits a more general distribution than the special case of proportional damping, so that:

$$\mathbf{C}, \mathbf{D} \neq \beta\mathbf{M} + \gamma\mathbf{K}$$

or, more generally, if: [9]

$$(\mathbf{M}^{-1}\mathbf{K})(\mathbf{M}^{-1}\mathbf{C}, \mathbf{D}) \neq (\mathbf{M}^{-1}\mathbf{C}, \mathbf{D})(\mathbf{M}^{-1}\mathbf{K})$$

then the mode shapes, $\boldsymbol{\psi}_r$, will be complex.

Complex modes can also be caused by other effects, one of the most common of which is the gyroscopic terms that exist in rotating structures. These terms, which arise from Coriolis accelerations, together with some others that are found in rotor/stator interactions in rotating machines, can have the effect of making the mode shapes complex even in situations where there is no damping. This last effect is important and can be identified as the consequence of losing the symmetry of one of the system matrices. In the case of a simple undamped rotating system with mass and stiffness properties only, the velocity-dependent matrix created by the inclusion of gyroscopic terms is skew-symmetric and it is this feature that gives rise to a system with real eigenvalues (i.e., purely oscillatory natural frequencies) and complex eigenvectors (complex mode shapes).

Extraction of real modes from complex modes

One of the topics related to complex modes is the difficulty encountered when comparing normal modes from one source (such as an FE model) with those from another (such as a modal test) when the modes in one set are real while those in the other set are complex. Although such a comparison could provide valuable information about the damping in the structure that is clearly missing from the undamped model, in fact such comparisons are usually made to validate or to correct the representation of the essential features of mass and stiffness in the simpler model. In these cases, the damping information contained in the complex normal modes is of secondary importance and so it is often required to extract the corresponding real modes (sometimes referred to as the 'undamped system normal modes') from the provided complex modes. Such a complex-to-real conversion, or 'realization' process, is in effect an attempt to remove the non-proportional damping effects from the more complete model to reveal what the vibration modes would be if these effects were absent altogether.

Several algorithms have been proposed for this task, although none is exact in the practical situation where the mode vectors are incomplete, i.e., where only a subset of the elements in the vector are known. It will be seen in the following section dealing with forced vibration modes how certain excitation patterns can be defined to bring about special mono-mode response characteristics, and this same process can be used to estimate the undamped system normal modes from a model that is described in terms of its damped normal modes, but this is the best that can be achieved for this complex-to-real transformation.

Forced Vibration Modes

The second category of vibration mode is that referred to as a forced vibration mode. As the name implies, this is the description of the pattern ('mode') of vibration present in a structure when it is subjected to external excitation forces. The term is confined to cases where the excitation itself can be represented by an expression of the form:

$$\mathbf{f}(t) = \sum_{q=1}^{Q} \mathbf{F}_q \, \mathrm{e}^{\mathrm{i}\omega_q t}$$

or: [10]

$$f(y,t) = \sum_{q=1}^{Q} F_q(y) \, \mathrm{e}^{\mathrm{i}\omega_q t}$$

which means that the set of individual excitation forces all share the same multi-harmonic time dependence, a condition that is commonplace in forced vibration but not universally the case. It is a feature of this type of excitation that there will be a steady-state response which has the form:

$$\mathbf{x}(t) = \sum_{q=1}^{Q} \mathbf{X}_q \, \mathrm{e}^{\mathrm{i}\omega_q t}$$

or: [11]

$$x(y,t) = \sum_{q=1}^{Q} X_q(y) \, \mathrm{e}^{\mathrm{i}\omega_q t}$$

Each term in the series of [11] represents a forced vibration mode for that system, and is clearly as much a function of the excitation forces as it is of the system properties. As before, it will be convenient to discuss the features of a forced vibration mode based on the first of these two variants – the discrete, rather than the continuous version – with the assurance that the same features will apply to the latter case as well. Thus we shall examine in more detail the elemental forced vibration mode form [11a], namely $\mathbf{X}_q$. This is a vector, as are the previous expressions for the free or

normal modes of the system. However, the solution to the equations of motion in this case of forced vibration yields a response vector that is unique and that harbors no undefined scaling factor, as was the case for free vibration modes. Thus, the forced vibration mode shape vector is simply $\mathbf{X}_q$, and this vector may be complex or real, depending upon the specific details of the excitation and the system. In general, it will be complex and it can be shown that this vector can be expressed in terms of the normal modes of the system using the simple modal summation, or superposition, equation:

$$\mathbf{X}_q = \sum_{r=1}^{N} \gamma_r \boldsymbol{\psi}_r \qquad [12]$$

where the coefficients, γ_r, are strongly dependent upon the frequency of the excitation relative to the natural frequencies of the system (as well as the forcing levels) and may themselves be complex. In particular, it is found that when the frequency of excitation, ω_q, approaches one of the system's natural frequencies, ω_r, then the corresponding coefficient, γ_r, becomes very large so that the forced vibration mode shape, $\mathbf{X}_q$ (also referred to as an operating deflection shape) may be heavily influenced by the normal mode shape of the nearby mode, $\boldsymbol{\psi}_r$ and thereby provide a good approximation to that free vibration mode. However, excitation at a natural frequency does not guarantee that the forced vibration mode that is generated is necessarily close to the corresponding free vibration mode shape.

For each structure, or system, there are a set of forced vibration mode shapes of special interest. These are the forced vibration modes that have the particular feature that they are real, in the sense that all the elements in each such vector have exactly the same phase as (or 180° different from) each other. These forced vibration modes have particular interest in the type of test where the objective is to excite vibration in a single (pure) mode – the so-called appropriation tests. For these tests, it is necessary to determine the vector of forces, $\mathbf{F}_q$, required to produce this mono-mode response condition, and this is achieved by finding a real (i.e., mono-phase) excitation force vector, $\hat{\mathbf{F}}_q$, which will generate a similarly mono-phase response vector, $\hat{\mathbf{X}}_q$ although the phase, θ_f, of the elements of $\hat{\mathbf{F}}_q$ and that, θ_x, of the elements of $\hat{\mathbf{X}}_q$ are not identical. It can be shown that for a given frequency of excitation there is one of these mono-phased forced vibration vectors for each mode of vibration of the structure. It can also be seen that these vectors vary with the excitation frequency. The case of greatest interest is that where the phase difference between the mono-phased force vector and the corresponding response vector $(\theta_x - \theta_f)$ is exactly 90°. At this condition, the excitation frequency, ω_q, corresponds exactly to one of the natural frequencies of the undamped version of the system in question, and the forced vibration mode, $\hat{\mathbf{X}}_q$, corresponds exactly to one of the undamped system's normal mode shape vectors which, of course, is real.

See also: **Eigenvalue analysis**; **Linear algebra**; **Modal analysis, experimental**, Basic principles; **Modal analysis, experimental**, Measurement techniques;

Further Reading

Bishop RED (1979) *Mechanics of Vibration*. Cambridge, UK: Cambridge University Press.

Bishop RED, Gladwell GML, Michaelson (1965) *The Matrix Analysis of Vibration*. Cambridge, UK: Cambridge University Press.

Ewins DJ (2001) *Modal Testing: Theory, Practice and Application*. Research Studies Press.

MODEL UPDATING AND VALIDATING

M Link, Universität Gesamthochschule Kassel, Kassel, Germany

Copyright © 2001 Academic Press

doi:10.1006/rwvb.2001.0085

Introduction

Despite the high degree of sophistication of today's structural dynamic analysis using the finite element (FE) method (see **Finite element methods**), practical applications often reveal considerable discrepancies between analytical predictions and test results. The classical way to reduce these discrepancies is to modify by trial and error the assumptions made for the mechanical idealizations and the parameters of the analytical model until the correlation of analytical predictions and experimental results satisfies practical requirements. For complex FE models, this trial-and-error approach turns out to be very

time-consuming and sometimes is simply not feasible. Some effort has therefore been spent in the development of computational procedures to update the parameters of analytical models using dynamic test data.

The FE model of an elastodynamic structure is governed by the equation of motion in the time domain in the form (see **Finite element methods**):

$$\mathbf{M}\ddot{\mathbf{y}}(t) + \mathbf{C}\dot{\mathbf{y}}(t) + \mathbf{K}\mathbf{y}(t) = \mathbf{f}(t) \qquad [1a]$$

or, after Fourier transformation (see **Transform methods**) into the frequency domain by $\mathbf{y}(\omega) = F[\mathbf{y}(t)]$ in the form:

$$\mathbf{K}\mathbf{y}(j\omega) = \mathbf{f}(j\omega) \qquad [1b]$$

where:

$$\hat{\mathbf{K}} = -\omega^2\mathbf{M} + \mathbf{K} + j\omega\mathbf{C}$$

denotes the dynamic stiffness matrix. The system matrices $\mathbf{M}$, $\mathbf{K}$, and $\mathbf{C}$ of order (N, N) represent the mass, stiffness, and viscous damping matrix. ω is the excitation frequency, $\mathbf{f}$ the excitation force vector, and $\mathbf{y}$ is the response vector (t = time, $j = \sqrt{-1}$). The solution of eqn [1b] yields the frequency response:

$$\mathbf{y}(j\omega) = \mathbf{H}(j\omega)\mathbf{f}(j\omega) \qquad [2a]$$

where $\mathbf{H}(j\omega) = \mathbf{K}^{-1}(j\omega)$ represents the frequency response function (FRF) matrix.

The undamped eigenfrequencies, ω_n, and eigenvectors, φ (also called natural frequencies and normal modes, respectively), are calculated from the undamped eigenequation (see **Eigenvalue analysis**):

$$(-\omega_n^2\mathbf{M} + \mathbf{K})\boldsymbol{\varphi} = \mathbf{0} \qquad [2b]$$

Before using such models for subsequent model updating, the user must be aware of the modeling uncertainties arising from three main sources:

1. Idealization errors resulting from the assumptions made to characterize the mechanical behavior of the physical structure. Typical errors of this type result from:
   - simplifications of the structure: for example, when a plate is treated like a beam, which may or may not be erroneous depending on the length-to-width ratio of the plate and the frequency range to be covered;
   - inaccurate assignment of mass properties, for example, when distributed masses are modeled with too few lumped masses or when an existing eccentricity of a lumped mass is disregarded;
   - when the FE formulation used neglects particular properties, for example, when the influence of transverse shear deformation or warping due to torsion in beam elements is neglected;
   - errors in the connectivity of the mesh, i.e., some elements are not connected or are connected to a wrong node;
   - erroneous modeling of boundary conditions, for example, when an elastic foundation is assumed to be rigid;
   - erroneous modeling of joints, for example, when an elastic connection is assumed to be rigid (clamped) or when an eccentricity of a beam or a plate connection possibly existing in the real structure is disregarded;
   - erroneous assumptions for the external loads;
   - erroneous geometrical shape assumptions;
   - a nonlinear structure assumed to behave linearly.
2. Discretization errors introduced by numerical methods like those inherent in the FE method, for example:
   - discretization errors when the FE mesh is too coarse (not fully converged modal data in the frequency range of interest);
   - truncation errors in order reduction methods like static condensation (see **Finite element methods**);
   - poor convergence and apparent stiffness increase due to the element's shape sensitivity (see **Finite element methods**).

   Since errors of types (1) and (2) are related to the mathematical structure of the model, they are also called model structure errors.
3. Erroneous assumptions for model parameters, for example:
   - material parameters such as Young's modulus or mass density;
   - cross-section properties of beams such as area moments of inertia;
   - shell/plate thicknesses;
   - spring stiffnesses; or
   - nonstructural masses

   The parameters can affect one element or a group of elements with the same properties, i.e., a single parameter may be assigned to a substructure.

Computational procedures for model updating are generally restricted to the correction of model parameters. When the model includes model structure

errors or when the selected correction parameters were not assigned correctly to the real source and location of the errors, then the model is called inconsistent because it is not consistent with the physics. Models of this kind may only be updated in the sense that the deviations between test and analysis are minimized. However, the parameters in this case will generally lose their physical meaning after updating. A typical result of updating such inconsistent models will be that while they may be capable of reproducing the test data they may not be useful to predict the system behavior beyond the frequency range used in the updating, or to predict the effects of structural modifications or to serve as a substructure model to be assembled into an overall structural model.

The aim of all structural analyses to predict the structural response can only be achieved if all three kinds of modeling errors are minimized with respect to the given purpose of the structural analysis. Models which fulfill these requirements are called valid models. Model quality must therefore be assessed in three steps:

- Step 1: initial assessment of idealization and numerical method errors (model structure errors) prior to parameter updating;
- Step 2: correlation of analytical model predictions and test results and selection of correction parameters; and
- Step 3: computational parameter updating and final assessment of model quality.

In this article basic procedures for computational updating of analytical model parameters are summarized. These procedures have been investigated thoroughly in the past with respect to:

- the numerical estimation techniques for solving the updating equations;
- the type of residuals formed by the test/analysis differences to be minimized;
- inconsistent assumptions related to the model structure and the parameterization in conjunction with the requirements to be posed on the initial analysis model;
- the influence of test data deficiencies resulting from incomplete test data where the number of measurement degrees-of-freedom (DOFs) is less than the number of analytical DOFs and from unavoidable random and (small) systematic measurement errors.

The residuals described here are formed by force and response equation errors, by eigenfrequency, antiresonance and mode shape errors, and by frequency response errors. An experimental frame structure is used in this article to illustrate a practical application of model updating and validating.

Mathematical Background of Parameter Identification

Parameter identification techniques aim at fitting the parameters of a given initial analytical model in such a way that the model behavior corresponds as closely as possible to the measured behavior. The parameters identified represent estimated values rather than true values since the test data are unavoidably polluted by unknown random and systematic errors. Also, the mathematical structure of the initial analysis is not unique and depends on the idealizations made by the analyst for the real structure. The method of extended weighted least-squares (LS) is summarized below since it represents the most important technique for parameter estimation.

The first step in parameter identification is the definition of a residual containing the difference between analytical and measured structural behavior, for example, the difference between analytical and measured eigenfrequencies. The weighted LS technique requires the definition of a weighting matrix, $\mathbf{W}_v$, which accounts for the importance of each individual term in the residual vector, $\boldsymbol{\varepsilon}$:

$$\boldsymbol{\varepsilon}_{\mathrm{w}} = \mathbf{W}_{\mathrm{v}}\boldsymbol{\varepsilon} = \mathbf{W}_{\mathrm{v}}(\mathbf{v}_M - \mathbf{v}(\mathbf{p})) \qquad [3]$$

where $\mathbf{v}_M$ represents the measured and $\mathbf{v}(p)$ the corresponding analytical vector which is a function of the parameter vector, $\mathbf{p} = [\ldots p_i \ldots]^{\mathrm{T}} (i = 1 \ldots n_p =$ number of correction parameters). The weighted squared sum of the residual vector yields the objective function:

$$J = \boldsymbol{\varepsilon}_{\mathrm{w}}^{\mathrm{T}}\boldsymbol{\varepsilon}_{\mathrm{w}} = \boldsymbol{\varepsilon}^{\mathrm{T}}\mathbf{W}\boldsymbol{\varepsilon} \rightarrow \min \quad \mathbf{W} = \mathbf{W}_{\mathrm{v}}^{\mathrm{T}}\mathbf{W}_{\mathrm{v}} \qquad [4]$$

whose minimization yields the unknown parameters. In general, the model vector, $\mathbf{v}$, represents a nonlinear function of the parameters resulting in a nonlinear minimization problem. One of the techniques for solving this nonlinear optimization problem is to expand the model vector into a Taylor series truncated after the linear term as follows:

$$\mathbf{v}(p) = \mathbf{v}_a + \mathbf{G}\Delta\mathbf{p} \qquad [5]$$

where $\mathbf{v}_a = \mathbf{v}|_{\mathbf{p}=\mathbf{p}_a}$ represents the model vector at the linearization point $\mathbf{p} = \mathbf{p}_a \cdot \mathbf{G} = (\partial\mathbf{v}/\partial\mathbf{p})|_{\mathbf{p}=\mathbf{p}_a}$ represents the sensitivity matrix of order (m, n_p) with

m = number of measurements and n_p = number of parameters. $\Delta\mathbf{p} = \mathbf{p} - \mathbf{p}_a$ represents the vector of the parameter changes. The index, a, denotes the linearization point. Eqn [5] introduced into eqn [3] yields the linear residual:

$$\boldsymbol{\varepsilon}_{\mathrm{w}} = \mathbf{W}_{\mathrm{v}}\boldsymbol{\varepsilon} = \mathbf{W}_{\mathrm{v}}(\mathbf{r}_a - \mathbf{G}\Delta\mathbf{p}) \qquad [6]$$

where $\mathbf{r}_a = \mathbf{v}_M - \mathbf{v}_a$ contains the residual at the linearization point. Of course, this formulation includes the special case when the model vector is a linear function of the parameters leading to a constant sensitivity matrix. The stepwise calculated minimum of the objective function with respect to the parameter changes is obtained from the derivative of the objection function, $\partial J/\partial\Delta\mathbf{p} = 0$, yielding the linear system of equations:

$$\mathbf{W}_{\mathrm{v}}\mathbf{G}\Delta\mathbf{p} = \mathbf{W}_{\mathrm{v}}\mathbf{r}_a \qquad [7]$$

with the solution:

$$\Delta\mathbf{p} = \left(\mathbf{G}^{\mathrm{T}}\mathbf{W}\mathbf{G}\right)^{-1}\mathbf{G}^{\mathrm{T}}\mathbf{W}\mathbf{r}_a = Z^{\mathrm{T}}\mathbf{r}_a \qquad [8]$$

The condition of the sensitivity matrix, $\mathbf{G}$, plays an important role in the accuracy and the uniqueness of the solution. It is clear that in the case when fewer measured data than parameters are available ($m<n_p$), eqn [7] leads to an underdetermined system whose solution is not unique. Even if a minimum norm or a minimum parameter change solution is selected, the resulting parameters will in general not retain their physical meaning. In parameter updating, the number of measurements should always be made larger than the number of parameters ($m>n_p$), which yields overdetermined equation systems. Instead of decomposing $\mathbf{G}^{\mathrm{T}}\mathbf{W}\mathbf{G}$ in eqn [8], the numerical solution of the overdetermined system [7] is preferably done via QR or singular value decomposition (see **Linear algebra**).

Assuming that the sensitivity matrix, $\mathbf{G}$, is not polluted by measurement errors, it can be shown that the statistical expectation values of the solution equal the true values. The inversion of $\mathbf{G}^{\mathrm{T}}\mathbf{W}\mathbf{G}$ in eqn [8] tends to magnify the error of the parameter estimates when the parameter sensitivities are small and when the sensitivity matrix is ill-conditioned.

The classical weighted LS method, described above, can be extended in cases where it is difficult to obtain a convergent solution because of an ill-conditioned sensitivity matrix. After introducing the linearization in eqn [5], the objective function [4] can be extended by the requirement that the parameter changes $\Delta\mathbf{p}$ shall be kept minimal:

$$J(\Delta\mathbf{p}) = \boldsymbol{\varepsilon}^{\mathrm{T}}\mathbf{W}\boldsymbol{\varepsilon} + \Delta\mathbf{p}^{\mathrm{T}}\mathbf{W}_p\Delta\mathbf{p} \;\rightarrow\; \min \qquad [9]$$

When the parameters are unbounded, the minimization [9], now with respect to the parameter changes, $\Delta\mathbf{p}$, yields the following linear problem to be solved within each iteration step, which represents the linearization point:

$$\left(\mathbf{G}^{\mathrm{T}}\mathbf{W}\mathbf{G} + \mathbf{W}_p\right)\Delta\mathbf{p} = \mathbf{G}^{\mathrm{T}}\mathbf{W}\mathbf{r}_a \qquad [10]$$

Of course, any other mathematical minimization technique could also be applied, in particular when the parameters are constrained by upper and lower bounds. Where $\mathbf{W}_p = 0$, the solution of eqn [9] represents the standard weighted LS solution; otherwise the solution is affected by the choice of the weighting matrix, $\mathbf{W}_p$.

Definition of Updating Parameters

The starting point for updating is the selection of those model parameters defining the type and location of the parameters to be updated in the equation of motion [1] of the FE elastodynamic model. In the most popular approach, the system matrices are updated by substructure matrices according to:

$$\mathbf{K} = \mathbf{K}_A + \sum_i \alpha_i\mathbf{K}_i, \quad \mathbf{M} = \mathbf{M}_A + \sum_j \beta_j\mathbf{M}_j, \quad \text{and}$$
$$\mathbf{C} = \mathbf{C}_A + \sum_k \gamma_k\mathbf{C}_k \qquad [11a-c]$$

where α_i, β_j, and γ_k denote the unknown correction (design) parameters assembled in the parameter vector $\mathbf{p}=[\ldots\alpha_i\ldots\beta_j\ldots\gamma_k\ldots]^{\mathrm{T}}$, $\mathbf{K}_A$, $\mathbf{M}_A$, $\mathbf{C}_A$ denote the analytical (initial) stiffness, mass, and damping matrices, and $\mathbf{K}_i$, $\mathbf{M}_j$, $\mathbf{C}_k$ represent the assumed correction substructure matrices (elements or element groups) defining source and location of modeling error.

The correction submatrices defined above can be related to the first derivatives of the updated matrices with respect to a physical or geometrical model parameter:

$$\mathbf{K}_i = \alpha_A\partial\mathbf{K}/\partial\alpha_i, \quad \mathbf{M}_j = \beta_A\partial\mathbf{M}/\partial\beta_j, \quad \text{and}$$
$$\mathbf{C}_k = \gamma_A\partial\mathbf{C}/\partial\gamma_k \qquad [12]$$

These derivatives are constant, as in the case of a beam element, with α representing Young's modulus

where the stiffness matrix is a linear function of the modulus. The derivatives need not be constant, as in the case when α represents the shear modulus of a Timoshenko beam where the stiffness matrix terms are nonlinear functions of the shear modulus. α_A, β_A, and γ_A denote the initial parameters used to make the parameter changes dimensionless. Other parametrizations related to generalized elements or substructures have also been reported in the literature.

The success of parameter updating is governed not only by the skill of the analyst to assume an appropriate initial analysis model but also by the ability to assume the right source and location of the erroneous parameters to be corrected.

Definition of Test/Analysis Residuals

Another important assumption the analyst has to make is the choice of residuals formed by differences in the predicted analytical and the measured behavior. In the present article we have considered the following residuals which have been applied most often in the past:

- eigenvalues and antiresonances
- mode shapes
- (weighted) input forces and
- FRF

The linearized undamped eigenvalue residuals, $\boldsymbol{\varepsilon}_\lambda$, are defined by the differences between measured (index M) and analytical undamped eigenvalues at the linearization point:

$$\boldsymbol{\varepsilon}_\lambda = \boldsymbol{\lambda}_M - \boldsymbol{\lambda} = \mathbf{r}_{\lambda a} - \mathbf{G}_\lambda \Delta\mathbf{p} \quad \left(\lambda = \omega_n^2\right) \qquad [13a]$$

where:

$$\mathbf{r}_\lambda = \boldsymbol{\lambda}_M - \boldsymbol{\lambda}_a \qquad [13b]$$

is the residual vector containing test/analysis differences of eigenvalues.

$$\mathbf{G}_\lambda = [\ldots \partial\lambda/\partial p_s \ldots] = \left[\ldots \partial\lambda/\partial\alpha_i \ldots \partial\lambda/\partial\beta_j \ldots\right]\Big|_{\alpha=\alpha_a,\beta=\beta_a} \qquad [13c]$$

is the sensitivity matrix at linearization point and $\Delta\mathbf{p} = [\ldots \Delta\alpha_i \ldots \Delta\beta_j \ldots]^{\mathrm{T}}$ is the vector of parameter changes.

If the undamped problem is considered, $\mathbf{G}_\lambda$ can be calculated by differentiation of the undamped eigenvalue eqn [2b] and by substituting the parametrization of eqns [11] or [12], which yields the sensitivity expressions:

$$\partial\lambda/\partial\alpha_i = \boldsymbol{\varphi}^{\mathrm{T}}\mathbf{K}_i\boldsymbol{\varphi} \qquad [14a]$$

and:

$$\partial\lambda/\partial\beta_j = -\lambda\boldsymbol{\varphi}^{\mathrm{T}}\mathbf{M}_j\boldsymbol{\varphi} \qquad [14b]$$

with respect to the ith stiffness and the jth mass parameter. (φ = real normal mode normalized to unit modal mass.)

Antiresonances

Antiresonances (see **Resonance and antiresonance**) may also be included in the residual. These appear as zeros in the (undamped) FRFs, thus enlarging the measured information. The zeros are calculated from the eigenvalue problem $(-\omega_a^2\mathbf{M}_{ij} + \mathbf{K}_{ij})\ \mathbf{z} = \mathbf{0}$, where the indices i and j indicate that row i and column j of the system matrices $\mathbf{M}$ and $\mathbf{K}$ are deleted. For $i = j$ (driving point FRF) the system can physically be interpreted as being grounded at DOF $i = j$, which means that the above sensitivity expressions of eqns [14a, b] can directly be applied for the grounded system matrices. It can be shown that in this case the antiresonances are located between the resonances (interlacing property).

Normal-mode Residuals

The linearized normal-mode (eigenvector) residuals, $\boldsymbol{\varepsilon}_\varphi$, are obtained from the differences of the measured and predicted modes at the reduced set of $N_M < N$ measured DOFs denoted by the index c:

$$\boldsymbol{\varepsilon}_\varphi = \boldsymbol{\varphi}_M - \boldsymbol{\varphi}_c = \mathbf{r}_{\varphi a} - \mathbf{G}_\varphi \Delta\mathbf{p} \qquad [15a]$$

where:

$$\mathbf{r}_{\varphi a} = \boldsymbol{\varphi}_M - \boldsymbol{\varphi}_{ca} \qquad [15b]$$

is the residual vector containing the test/analysis differences of the analytical modes $\boldsymbol{\varphi}_{ca} = [\boldsymbol{\varphi}_{cl} \ldots \boldsymbol{\varphi}_{cr} \ldots \boldsymbol{\varphi}_{cR}]_a$ and the corresponding measured modes, $\boldsymbol{\varphi}_M$.

$$\mathbf{G}_\varphi = [\ldots \partial\boldsymbol{\varphi}_c/\partial p_s \ldots] = \left[\ldots \partial\boldsymbol{\varphi}_c/\partial\alpha_i \ldots \partial\boldsymbol{\varphi}_c/\partial\beta_j \ldots\right]\Big|_{\alpha=\alpha_a,\beta=\beta_a} \qquad [15c]$$

denotes the sensitivity matrix at linearization point and $\Delta\mathbf{p} = [\ldots \Delta\alpha_i \ldots \Delta\beta_j \ldots]^{\mathrm{T}}$ is the vector of parameter changes.

The calculation of the mode shape sensitivity matrix involves a major numerical effort. Since the sensitivity matrices are derived from the (updated) analytical model, they do not contain measurement errors, and this is an essential prerequisite for an unbiased estimate. However, it should be kept in mind that, due to the iterative process, the sensitivity matrices depend on the parameters from the previous iteration step calculated from the noise-polluted residuals in eqns [13b] and [15b]. Another advantage stems from the fact that the mode shape residuals and the sensitivities need only to be calculated for the measured DOFs, i.e., neither the analytical model needs to be condensed nor the measured mode shapes expanded to the unmeasured DOFs. It must be noted that the modal residuals have to be formed between paired mode shapes. Most often the correct mode shape correlation is checked using the modal assurance criterion $\mathrm{MAC} = (\varphi_M^{\mathrm{T}}\varphi_A)^2/(\varphi_M^{\mathrm{T}}\varphi_M\varphi_A^{\mathrm{T}}\varphi_A)$ (see **Comparison of vibration properties: Comparison of modal properties**) which approaches unity if the measured mode, φ_M, and the analytical mode, φ_A, are fully correlated. Mode pairs with MAC values smaller than a certain threshold (for example, MAC < 0.7) should not be included in the residuals.

Input Residual

The input (or force) residual, $\boldsymbol{\varepsilon}_F$, is given by substituting the measured frequency response into the equation of motion [1b]. Since the number of measured DOFs is generally much smaller than the number of analytical DOFs, it is necessary to expand the measured vector to full model size or to condense the model order down to the number of measured DOFs by appropriate order reduction techniques (see **Finite element methods**):

$$\boldsymbol{\varepsilon}_F = \mathbf{f}_M - \hat{\mathbf{K}}_c(j\omega_M, \mathbf{p})\mathbf{y}_M \qquad [16a]$$

where:

$$\hat{\mathbf{K}}_c(j\omega_M) = \hat{\mathbf{K}}_{ca}(j\omega_M) + \sum_s p_s\mathbf{S}_{cs} \qquad [16b]$$

represents the updated dynamic stiffness matrix condensed to $N_M < N$ measured DOFs.

$$\hat{\mathbf{K}}_{ca}(j\omega_M) = -\omega_M^2\mathbf{M}_{ca} + \mathbf{K}_{ca} + j\omega_M\mathbf{C}_{ca} \qquad [16c]$$

is the condensed dynamic stiffness matrix at linearization point (index a), $p_s = \alpha_i, \beta_j$, or γ_k are the correction parameters and $\mathbf{S}_{cs} = \mathbf{K}_{ci}, \mathbf{M}_{cj}$, or $\mathbf{C}_{ck}$ are the condensed correction submatrices, $\mathbf{y}_M(j\omega_M)$ denotes the complex frequency response vector measured at c measurement DOFs and is $\mathbf{f}_M$ is the vector of measured harmonic exciter forces. If $f_{Mi} = 1$ at exciter DOF i, $\mathbf{y}_M$ represents the ith column of the measured frequency response matrix.

With eqns [16b,c] introduced, the force residual at the measured DOFs can be expressed by:

$$\boldsymbol{\varepsilon}_F = \mathbf{r}_F - \mathbf{G}_F\Delta\mathbf{p} \qquad [17a]$$

where:

$$\mathbf{r}_F = \mathbf{f}_M - \hat{\mathbf{K}}_{ca}(j\omega_M, \mathbf{p}_a)\mathbf{y}_M \qquad [17b]$$

$$\mathbf{G}_F = \left[\ldots - \omega_M^2\mathbf{M}_{cj}\mathbf{y}_m \ldots \mathbf{K}_{ci}\mathbf{y}_m \ldots j\omega_M\mathbf{C}_{ck}\mathbf{y}_M \ldots\right]_a$$

and:

$$\Delta\mathbf{p} = \left[\ldots \Delta\alpha_i \ldots \Delta\beta_j \ldots \Delta\gamma_k \ldots\right]^{\mathrm{T}} \qquad [17c]$$

denote the residual vector, the sensitivity matrix, and the vector of parameter changes, respectively. Due to the approximation errors associated with order reduction techniques and due to the pollution of the sensitivity matrix with measurement errors, the application of the input error residuals for updating large-order models is often restricted in practice.

Pseudoresponse Residual

The pseudoresponse residual, $\boldsymbol{\varepsilon}_{PR}$, is obtained from transforming the input force residual to an output residual by multiplying the force residual of eqn [16a] with the FRF matrix, $\mathbf{H}_{Ac}$, of the initial model (index A). This is equivalent to exciting the initial model by the force vector, $\boldsymbol{\varepsilon}_F$, at an arbitrary frequency ω_F.

$$\boldsymbol{\varepsilon}_{PR} = \mathbf{H}_{Ac}(\omega_F)\boldsymbol{\varepsilon}_F \qquad [18]$$

where:

$$\mathbf{H}_{Ac}(\omega_F) = \left(-\omega_F^2\mathbf{M}_{Ac} + j\omega_F\mathbf{C}_{Ac} + \mathbf{K}_{Ac}\right)^{-1} \qquad [19]$$

is the condensed FRF matrix of the initial model. $\mathbf{H}_{Ac}(\omega_F)$ can also be interpreted as a dynamic filter. The magnification of the pseudoresponse error, $\boldsymbol{\varepsilon}_{PR}$, can be controlled by exciting the initial system with the force residual vector, $\boldsymbol{\varepsilon}_F$, at a filter frequency, ω_F. The idea behind this filtering is to reduce the unfavorable influence of the measurement errors in the sensitivity matrix.

A special case is obtained by exciting the analytical system linearized at point a by the residual force

vector, $\boldsymbol{\varepsilon}_F$, at the measured excitation frequencies. In this case, the equalities $\mathbf{H}_{Ac} = \mathbf{H}_{ca}$ and $\omega_F = \omega_M$ hold which, after their introduction into eqns [18] and [17a–c], yield the pseudoresponse residuals by:

$$\boldsymbol{\varepsilon}_{PR} = \hat{\mathbf{K}}_{ca}^{-1}(\omega_F)\boldsymbol{\varepsilon}_F = \mathbf{r}_{PR} - \mathbf{G}_{PR}\Delta\mathbf{p} \qquad [20a]$$

where:

$$\mathbf{r}_{PR} = \mathbf{y}_{ca}(j\omega_M) - \mathbf{y}_M(j\omega_M) \qquad [20b]$$

is the residual response at linearization point a and:

$$\mathbf{G}_{PR} = \mathbf{H}_{ca}\left[\ldots - \omega_M^2\mathbf{M}_{cj}\mathbf{y}_M \ldots \mathbf{K}_{ci}\mathbf{y}_M \ldots j\omega_M\mathbf{C}_{ck}\mathbf{y}_M \ldots\right]_a \qquad [20c]$$

denotes the sensitivity matrix which, as the comparison with eqn [17c] shows, represents the input sensitivity matrix weighted by $\mathbf{H}_{ca}$. $\Delta\mathbf{p} = [\ldots \Delta\alpha_i \ldots \Delta\beta_j \ldots \Delta\gamma_k \ldots]^{\mathrm{T}}$ denotes the vector of parameter changes. Using the force residual and the pseudoresponse technique, bias and ill-conditioning problems must be considered.

Frequency Response Residuals

The linearized frequency response residuals are obtained from the differences of the measured and the analytical frequency response at the reduced set of $N_M < N$ measured DOFs, denoted by the index c.

$$\boldsymbol{\varepsilon}_R = \mathbf{y}_M - \mathbf{y}_c = \mathbf{r}_{Ra} - \mathbf{G}_R\Delta\mathbf{p} \qquad [21a]$$

where:

$$\mathbf{r}_{Ra} = \mathbf{y}_M(j\omega_M) - \mathbf{y}_{ca}(j\omega_A) \qquad [21b]$$

represents the residual vector containing the test/analysis differences of the frequency response at the linearization point at excitation frequency $\omega_A = \omega_M$.

$$\mathbf{G}_R = -\mathbf{H}\left[\ldots - \omega_A^2\mathbf{M}_j\mathbf{y} \ldots \mathbf{K}_i\mathbf{y} \ldots j\omega_A\mathbf{C}_k\mathbf{y} \ldots\right]\Big|_{p=p_a} \qquad [21c]$$

is the sensitivity matrix where:

$$\mathbf{H} = \left(-\omega_A^2\mathbf{M} + j\omega_A\mathbf{C} + \mathbf{K}\right)^{-1}\Big|_{p=p_a} \qquad [21d]$$

denotes the FRF matrix of the analytical model calculated at the measured DOFs at the linearization point and $\Delta\mathbf{p} = [\ldots \Delta\alpha_i \ldots \Delta\beta_j \ldots \Delta\gamma_k \ldots]^{\mathrm{T}}$ is the vector of parameter changes.

As in the case of the sensitivity matrix for the modal sensitivities, the frequency response sensitivity matrix [21c] is not directly corrupted by measurement errors allowing (approximately) unbiased parameter estimates, in contrast to the force and pseudoresponse residuals shown in eqns [17c] and [20c]. In addition, there is no need to expand the test vectors to the unmeasured DOFs. However, there is a crucial drawback in this formulation. Comparing measured and analytical frequency response functions, like that in **Figure 6** of the application example presented at the end of this article, it may be noticed that, due to the shifts of the resonance peaks caused by the mismatch of the eigenfrequencies, the test/analysis differences at a given excitation frequency become extremely large, in particular in such cases where the ordering of the test and analysis eigenfrequencies is not the same (also called mode crossing). The consequence is that the first-order theory either fails to predict the updated model response or the rate of convergence is very low unless the test/analysis deviations are very small. The problem can be avoided if the shift of the resonance peaks is considered or by updating the FRFs only at the resonance peaks taken at the analytical and experimental eigenfrequencies which are not identical due to mass and stiffness errors. The residuals in this case are the same as in eqn [21b], except that the analytical excitation frequencies, ω_A, are replaced by the analytical eigenfrequencies, ω_n, and the experimental excitation frequencies, ω_M, by the experimental eigenfrequencies, ω_{Mn}, i.e.:

$$\omega_A \Rightarrow \omega_n \text{ and } \quad \omega_M \Rightarrow \omega_{Mn} \qquad [22]$$

One advantage of FRF updating is that it includes the possibility to identify damping parameters. The FRF residuals of eqns [21] under consideration of eqn [22] could be applied directly with the damping correction parameters, $\Delta\gamma_k$, being included. However, this possibility is very restricted because the local physical damping parameterization of eqn [11c] is not available for most structural applications. This is why the modal representation of damping is widely used in practice.

Updating Modal-damping Parameters

The approach to update initial estimates of modal-damping parameters is based on the residual in eqns [21] and [22], i.e., the analytical excitation frequencies are taken at the analytical eigenfrequencies and the experimental excitation frequencies are taken at the experimental eigenfrequencies:

$$\varepsilon_\zeta = \mathbf{y}_M(\omega_{Mn}) - \mathbf{y}_c(\omega_n) = \mathbf{r}_{\zeta a} - \mathbf{G}_\zeta \Delta\boldsymbol{\zeta} \qquad [23]$$

where:

$$\mathbf{r}_{\zeta a} = \mathbf{y}_M(j\omega_{Mn}) - \mathbf{y}_{ca}(j\omega_n)$$

is the residual vector with test/analysis differences of frequency response at linearization point, $\mathbf{y}_{ca}(j\omega_n)$ is the complex frequency response vector at excitation frequency ω_n (= analytical eigenfrequency), $\mathbf{y}_M(j\omega_{Mn})$ is the frequency response vector measured at the same DOFs at experimental excitation frequency ω_{Mn} (= experimental eigenfrequency).

To calculate the sensitivity matrix of the modal damping, the response eqn [2a] is derived with respect to the viscous modal damping parameter, ζ:

$$\mathbf{G}_\zeta = [\ldots \partial\mathbf{y}(\omega_{ns})/\partial\zeta_r \ldots]_a \qquad [24]$$

($r, s = 1 \ldots R$ number of active modes $< = N =$ model order.)

Model Validation

The first step in assessing the model quality before or after computational model updating (CMU) is based on comparing analytical model predictions and test results (see **Comparison of vibration properties**, Comparison of spatial properties). Differences of test and analysis results related to eigenfrequencies, mode shapes, and FRFs most often form the basis of the initial correlation study. Of course, test data accuracy must also be checked, for example: nonlinearity, reciprocity, synthesis accuracy, weak modal excitation, mode shape spatial resolution (see **Modal analysis, experimental**, Parameter extraction methods). It should be noted that a minimum correlation quality is required for subsequent CMU to be successful. If the correlation is too poor then the test/analysis deviations cannot be assigned to the model parameters alone; model structure errors might also exist. The initial model is then said not to be consistent with the real physics. Of course, the test data might also be not accurate enough. In many practical cases of complicated industrial structures, the initial correlation requirement cannot be met. Very often such models are not yet suited for CMU and remodeling and/or retesting is required. It should be noted that CMU offers some kind of fine-tuning of the initial model which must be not too far away from the true model.

When the initial correlation requirements are met, computational updating of the model parameters may be applied. Requirements to be posed on CMU results are:

1. The updated model shall reproduce the test data used for CMU. This correlation requirement must be considered a compulsory minimum requirement which does not automatically guarantee an improvement of the prediction capabilities of the model. Therefore, the following additional checks for validating the updated model are necessary:
2. The computational iteration process should converge.
3. Parameter uniqueness and robustness checks should be satisfied with respect to the correct assignment of the location and the type of correction parameters. For example, if parameters without uncertainty are included in the parameter set then they should keep unchanged during CMU. If the assignment was not correct the correction parameter set was not consistent with the real physics.

Further validation steps include an assessment of the physical behavior of the updated model. Since a unique solution cannot be expected, the requirements must be related to the intended purpose for which the model is used, for example:

1. to predict the system behavior to types of load (input) or response (output) other than those used in the test
2. to predict the system behavior beyond the frequency range and/or at DOFs other than those used for CMU
3. to predict the effects of structural modifications and
4. to check if the model when used as a substructure within an assembled whole structure will improve the response of the whole structure model

Sometimes the consistency requirement, as defined above for the initial model idealization and the selected correction parameter set, may be relaxed if the quantity of experimental modal data is sufficient to fulfill one or more of the above requirements, for example, when the validity of the updated model is intentionally restricted to a specified frequency range. In this case, the updated model plays the role of an acceptable special-purpose model. In any case, a primary goal for the final model is to preserve the physical meaning of the parameters. In practical applications the restriction to inconsistent special-purpose models might be unavoidable and acceptable if the application requirements are met.

Illustrative Example

Figure 1 shows a sketch of a frame structure which was built and tested in the laboratory. The structure

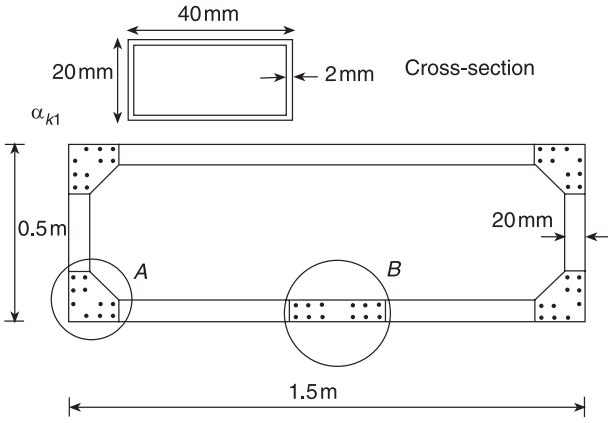


Figure 1 Frame structure, including cross-section (top).

consists of aluminum beams with hollow rectangular cross-section which were connected by bolted joints at the four corners and at the center of the lower member. The joint designs are shown in **Figure 2**. At the center joint the beams were connected at the webs only. The flanges were not connected, thus leading to a reduced bending stiffness intended to be identified by computational parameter updating.

The initial in-plane model of the frame consists of 40 beam elements as shown in **Figure 3**. The following properties have been used: Young's modulus, $E = 7 \times 10^{10}$ N m^{-2}; moment of inertia, $I = 1.4310\,\text{cm}^4$; cross-section, $A = 2.2410\,\text{cm}^2$; density, $\rho = 2700\,\text{kg m}^{-3}$; corner joint masses, $m_1 = 0.0520\,\text{kg}$ and the masses of the bolts used to fix the soft springs for the modal test under free/free boundary condition, $m_2 = 0.0318\,\text{kg}$.

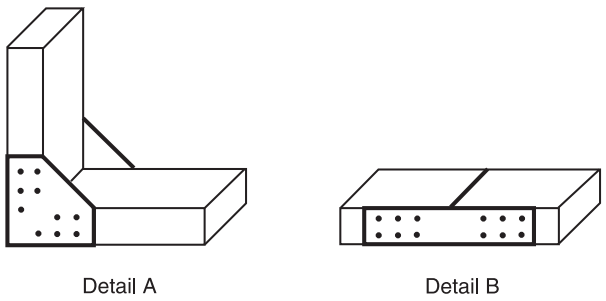


Figure 2 Joint designs.

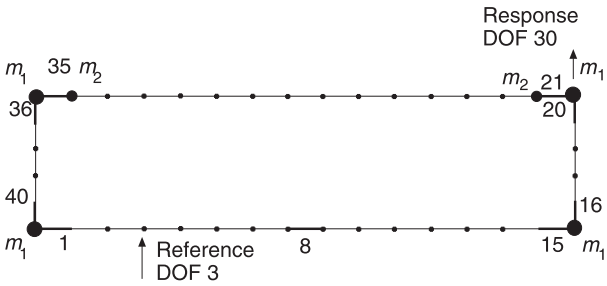


Figure 3 Frame structure, finite element model.

Experimental modal data were extracted from FRFs obtained from exciting the structure by an impulse hammer applied perpendicular to the beam axes at all the 40 FE nodes. The structure was suspended in soft springs to simulate free/free boundary conditions. **Table 1** shows a comparison of the experimental and of the initial analytical eigenfrequencies. The MAC values indicating the degree of mode shape correlation are also shown. The frequency errors are between 0.1% for the second and −6.5% for the sixth eigenfrequency. The mode shape errors are quite small, with MAC values between 99.9% for the fourth mode and 85% for the third mode. **Figure 5** shows an exploded view of the experimental mode shapes together with the modes after computational parameter updating.

During the test some slight nonlinear behavior was observed in the vicinity of the first, third, and sixth resonance belonging to the symmetrical modes, but not in the vicinity of the antisymmetric mode resonances. This was obviously caused by the nonlinear behavior of the center joint which gets high bending stress in the symmetric mode vibrations and low bending stress in the antisymmetric mode vibrations. By using the standard linear model-based modal extraction techniques, some unknown systematic errors on the experimental modal data were thus introduced.

The CMU technique was directed to identify the stiffness and mass parameters of the joints. The test/analysis differences of the first four eigenfrequencies and modes measured at 40 DOFs were minimized in the computational updating process. Three model parameters were used for updating. Parameter $p_1 \equiv \alpha_1$ refers to the correction stiffness matrix, $\mathbf{K}_1$, for the bending stiffness of element 8 (center joint), parameter $p_2 \equiv \alpha_2$ to the correction stiffness matrix, $\mathbf{K}_2$, for the bending stiffness of elements 40, 1, 15, 16, 20, 21, 35 and 36 (corner joints) and parameter $p_3 \equiv \beta_1$ refers to the correction mass matrix, $\mathbf{M}_1$, for the mass density of element 8 (center joint).

The evolution of the computational updating over the iteration steps is presented in **Figure 4** and the final results in **Table 1**. After eight iteration steps, the eigenfrequency deviations, **Figure 4A**, converged to between 0% and −1.1%. Except for mode number 3, the MAC values were better than 99% and remained nearly unchanged, whereas the MAC could be improved for mode no. 3 from 85% to 92.9%, **Figure 4C**. As mentioned before, this experimental

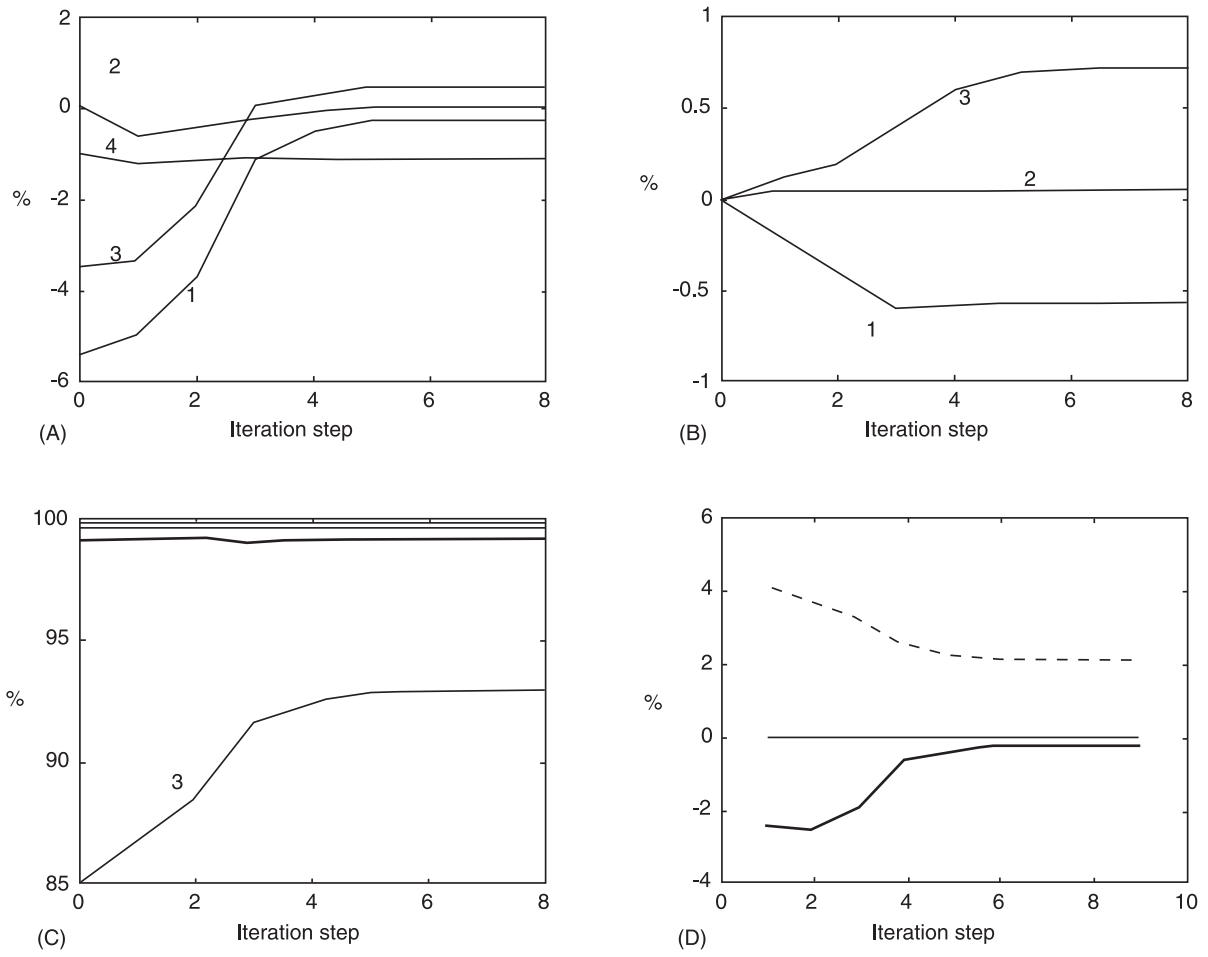


Figure 4 Evolution of updating over iteration steps. (A) Eigenfrequency deviation; (B) correction parameters; (C) modal assurance criteria (MAC) values; (D) mean frequency error: dashed line; mean (f-MAC): dotted line.

Table 1 Comparison of experimental, initial analytical, and updated modal data

No.	f_{exp} (Hz)	f_{ini} (Hz)	Error (%)	MAC (%)	f_{upd} (Hz)	Error (%)	MAC (%)
	1	2	3	4	5	6	7
1	42.56	44.98	−5.4	99.1	42.67	−0.2	99.1
2	45.20	45.16	0.1	99.5	45.18	0.0	99.5
3	73.69	76.33	−3.5	85.0	73.35	0.5	92.9
4	130.45	131.8	−1.0	99.9	131.89	−1.1	99.9
5	186.2	183.8	1.3	99.4	184.61	0.9	99.4
6	234.2	250.3	−6.5	96.6	238.52	−1.8	97.3

mode was affected by the nonlinear structural behavior. Care should be taken here to interpret a high MAC value for this mode as a model improvement. The correction parameter changes in **Figure 4B** show a decrease of 57% for the stiffness parameter, p_1, of the center joint, a small increase of about 5% for the corner joint parameter, p_2, and an increase of 72% of the mass parameter, p_3, of the center joint. These results agree well with expectations based on engineering judgment since the corner joints were stiffened by the connection plates, whereas the center joint was weakened due to the missing connection of the flanges and since the masses of the bolts and the plates were not included in the initial model.

Some of the model validation criteria described in **Motion sickness** were checked. The first two criteria

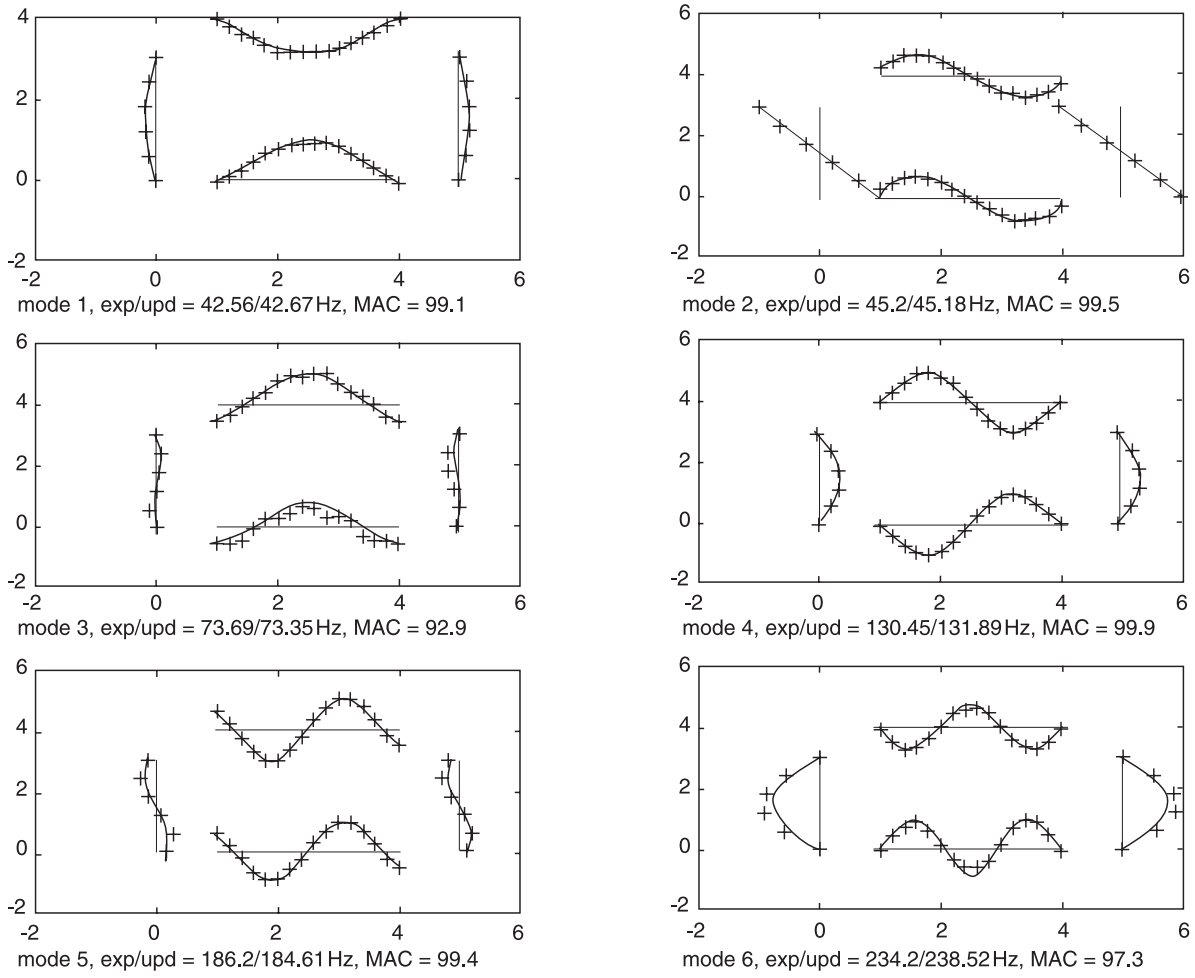


Figure 5 Comparison of experimental (+) and updated modes (—).

related to test/analysis correlation and the convergence requirement can be assessed by the results in **Figure 4**, which show a good test/analysis correlation for the modal data used for CMU. The mean frequency and MAC error converged to 0.21% and 2.1%. Since only the first four experimental frequencies and modes were used to update the capability of the updated model to predict the unused fifth and sixth experimental frequencies and modes could be used to assess the physical significance of the updated parameters (criterion number 5). The results listed in **Table 1** show that the unused fifth and sixth eigenfrequency errors were improved from 1.3% and −6.5% before updating to 0.9% and −1.8% after updating. The corresponding MAC values were also slightly improved.

Validation criterion number 4 requires to check the system behavior to other output types than those used in test. **Figure 6** shows an example for that by comparing the experimental FRF at measured response DOF number 30 with the initial and the updated model response. The improvement of the updated model response is clearly visible, even in the frequency range of the fifth and sixth unused eigenfrequencies (**Figure 6B**). The magnitude of the resonance peaks could be further improved by updating the modal damping values, which is not shown for this example, where the experimental modal damping values were used to calculate the updated model response. The uniqueness and robustness checks concerning different selections of the location and the type of correction parameters (criterion number 3) revealed only moderate differences for the three correction parameters presented here, which again supports the physical significance of the updated model.

Summary

This article summarizes current procedures for model updating and validating. At first the mathematical

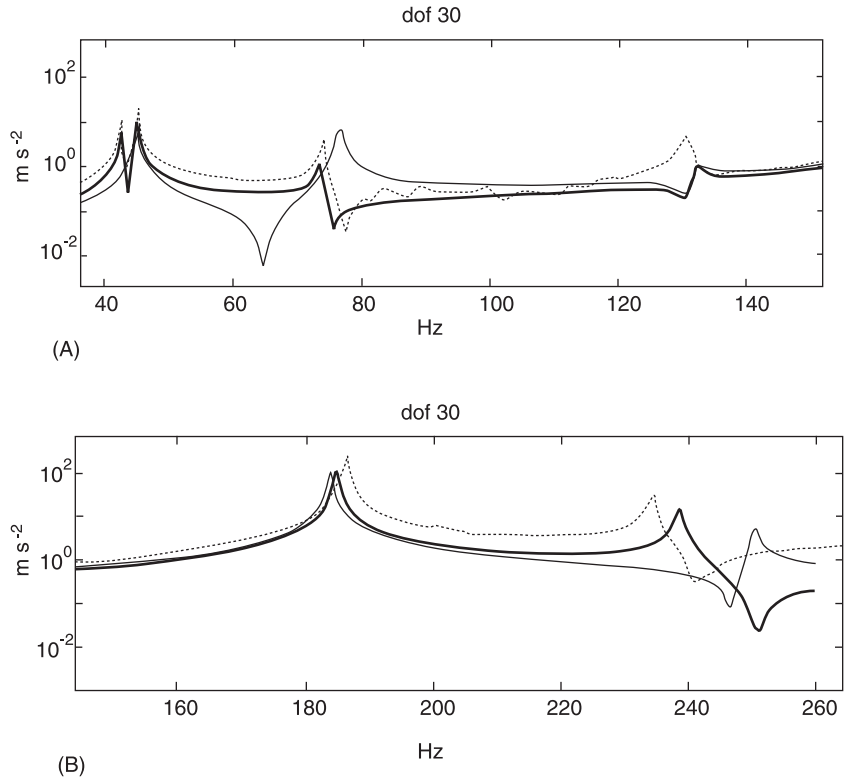


Figure 6 Comparison of experimental (. . .), initial (—) and updated frequency response functions (—). (A) Frequency range used for computational updating; (B) frequency range not used for computational updating.

background of the parameter identification is given with respect to the numerical techniques for solving the updating equations based on the iterative extended LS technique. The model parameterizations defining the type and location of the erroneous parameters are then used to construct the residuals formed by the test/analysis differences to be minimized. The residuals presented are formed by force and pseudoresponse equation errors, by eigenfrequency, antiresonance, mode shape, and by frequency response errors. The procedures permit the handling of incomplete test vectors, where the number of measured DOFs is much smaller than the number of DOFs of the analytical model. The basic steps of final model validation are discussed. Finally, an illustrative application of updating the model of a laboratory test structure is used to demonstrate some important updating and validating steps.

Nomenclature

$\mathbf{E}$	Young's modulus
$\mathbf{f}$	excitation force vector
$\mathbf{G}$	sensitivity matrix
$\mathbf{H}$	FRF matrix
I	moment of inertia
$\mathbf{p}$	parameter vector
$\mathbf{r}$	residual vector
t	time
$\mathbf{v}$	model vector
$\mathbf{W}$	weighting matrix
$\mathbf{y}$	response vector
$\boldsymbol{\varepsilon}$	residual vector
ρ	density

See also: **Comparison of vibration properties**, Comparison of modal properties; **Comparison of vibration properties**, Comparison of spatial properties; **Eigenvalue analysis**; **Finite element methods**; **Linear algebra**; **Modal analysis, experimental**, Parameter extraction methods; **Motion sickness**; **Resonance and antiresonance**; **Transform methods**.

Further Reading

Demmel JW (1997) *Applied Numerical Linear Algebra*. Philadelphia, PA: SIAM.

Friswell MJ and Mottershead JE (1995) *Finite Element Model Updating in Structural Dynamics*. Dordrecht, The Netherlands: Kluwer.

Maia NMM and Montalvao e Silva JM (eds) (1999) *Modal*

Analysis and Testing. Dordrecht, The Netherlands: Kluwer.
Natke HG (1992) *Einführung in Theorie und Praxis der Zeitreihen und Modalanalyse*. Braunschweig/Wiesbaden, Germany: Vieweg Verlag.
Natke HG, Lallement G and Cottin N (1995) Properties of various residuals within updating of mathematical models. *Inverse Problems in Engineering 1:* 329–348.
Soederstroem T and Stoica P (1989) *System Identification*. London, UK: Prentice Hall.

MODELS, DAMPING

See **DAMPING MODELS**

MODES, NON-LINEAR SYSTEMS

See **NON-LINEAR SYSTEMS MODES**

MODES, ROTATING MACHINERY

See **ROTATING MACHINERY, MODAL CHARACTERISTICS**

MONITORING

See **DIAGNOSTICS AND CONDITION MONITORING, BASIC CONCEPTS; ROTATING MACHINERY, MONITORING**

MOTION SICKNESS

M J Griffin, Institute of Sound and Vibration Research, University of Southampton, Southampton, UK

Copyright © 2001 Academic Press

doi:10.1006/rwvb.2001.0084

Introduction

Motion sickness may occur when real or illusory movements of the body or the environment lead to ambiguous inferences as to movement or orientation. Oscillations associated with motion sickness are always of very low frequency, usually below 1 Hz.

With low-frequency translational oscillation, motion on the floor and at various positions on a seat are almost identical. However, if there is low-frequency rotational motion, the translational motions will differ with position around a vehicle or vessel: they increase as the distance from the center of rotation increases. Hence, for example, there is usually more vertical oscillation at the bow and the stern of a ship than amidships. **Figure 1** illustrates the translational and rotational axes of a seated person.

The symptoms of sickness (e.g., vomiting, nausea, sweating, color changes, dizziness, headaches, and drowsiness) are normal responses to motion that are experienced by many fit and healthy people. A variety of different motions can cause motion sickness and thereby reduce the comfort and impede the activities of those afflicted, and those associated with the afflicted.

Causes of Motion Sickness

Translational and rotational oscillation, constant speed rotation about an off-vertical axis, Coriolis

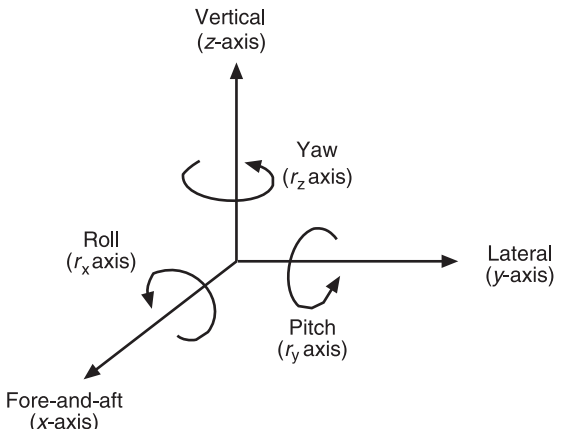


Figure 1 Axes used to report exposures of the human body to oscillation.

stimulation, movements of the visual scene, and various other stimuli producing sensations associated with movement of the body can cause sickness. Although some motions can be predicted as being more nauseogenic than others, motion sickness is neither explained nor predicted solely by the physical characteristics of motion.

Motions of the body are detected by three sensory systems: the vestibular system, the visual system, and the somatosensory system. The vestibular system is located in the inner ear and comprises the semicircular canals (sensing the rotation of the head), and the otoliths (sensing translational forces: either translational acceleration or rotation of the head relative to an acceleration field, such as the force of gravity). The eyes detect relative motion between the head and the environment, caused by either head movements (in translation or rotation) or movements of the environment, or a combination of the movements of the head and the environment. The somatosensory systems respond to force and displacement of parts of the body and give rise to sensations of body movement, or force.

In normal environments the movements of the body are detected by all three sensory systems and this leads to a sufficiently unambiguous indication of the movements of the body in space. In some other environments it is assumed that the three sensory systems give signals corresponding to different motions (or motions which are not realistic) and lead to some form of conflict. This leads to the idea of a sensory conflict theory of motion sickness in which sickness occurs when the sensory systems disagree on the motions which are occurring. However, this implies some absolute significance to sensory information, whereas the 'meaning' of the information is probably learned. This led to the sensory rearrangement theory of motion sickness which states that: all situations which provoke motion sickness are characterized by a condition of sensory rearrangement in which the motion signals transmitted by the eyes, the vestibular system and the nonvestibular proprioceptors are at variance either with one another or with what is expected from previous experience. The conflict is often considered in two categories: intermodality (between vision and the vestibular receptors) and intramodality (between the semicircular canals and the otoliths within the vestibular system). For both categories it is possible to identify several types of situation in which conflict can occur.

There is evidence that the average susceptibility to sickness among males is less than that among females, and susceptibility decreases with increased age among both males and females. However, there are larger individual differences within any group of either gender at any age: some people are easily made ill by motions that can be endured indefinitely by others. The reasons for these differences are not properly understood.

Sickness Caused by Vertical Oscillatory Motion

Motion sickness is not caused by oscillation, however violent, at frequencies much above about 1 Hz: the phenomenon arises from motions at the low frequencies associated with normal postural control of the body.

Experimental Studies

The first systematic laboratory studies of motion sickness, conducted in the 1940s with naval cadets and an elevator, investigated four different frequencies from 0.22 to 0.53 Hz and found greatest sickness at the lowest frequencies. However, moderate magnitudes of motion appeared to produce the most motion sickness and the highest magnitudes the least sickness. Other studies in the series reported an absence of a reliable effect of either temperature or time of day on sickness but a correlation between sickness and responses to a questionnaire history of motion sickness.

Studies undertaken in the 1970s exposed subjects to various magnitudes of vertical oscillation at frequencies from 0.083 to 0.7 Hz for up to 2 h with no external view. Vomiting incidence ranged from 0% to 60% with higher magnitudes of acceleration being required to generate sickness at the higher frequencies; at each frequency the vomiting incidence

increased with increasing acceleration magnitude (**Figure 2**). The frequency of maximum sensitivity to motion sickness caused by vertical acceleration was found to be 0.167 Hz. Studies of habituation with exposures on different occasions to 0.25 Hz vertical motion at 2.2 ms^{-2} r.m.s. found that motion sickness fell during five successive experimental sessions from 75% to 30%. There was evidence that after a period of 7 days without motion, susceptibility increased.

From each of the data points shown in **Figure 2** it is possible to determine the percentage of subjects vomiting per unit of acceleration; this is called normalized vomiting, expressed in percent of persons vomiting per ms^{-2} r.m.s. (**Figure 3**). This has been used to define a frequency weighting, called W_f, in various standards.

Field Studies of Vertical Oscillation

Vertical oscillation is believed to be a prime cause of motion sickness in some ships. The vertical motion of a vessel is often about 0.2 Hz and is greatly influenced by the pitch motion, so that these two motions have similar waveforms and spectra. For the same reason the lateral (y-axis) motion of a vessel is related to the roll motion (often at a slightly lower frequency than the pitch motion). The large influence of these two rotational motions results in the magnitudes of translational motions varying with position around a vessel. For a rigid vessel the rotational motions are the same at all positions. A principal effect of worsening sea conditions is an increase in the magnitudes of the motions rather than a change in their frequency. The dominant frequency of motion tends to be lower in larger vessels but the variation is not usually great (**Figure 4**). The principal vertical acceleration of most ships is close to the frequency where motion sickness sensitivity is believed to be at a maximum. Studies of the incidence of sickness aboard ships have determined dose–effect relationships between vertical oscillation and the illness and vomiting of passengers.

The incidence of sickness is not the only problem associated with low-frequency ship motion: there may be interference with activities, impairment of the performance of ship equipment, difficulty with helicopter landing operations, undesirable deck wetness and structural damage due to 'slamming'. Each of these effects requires a different method of assessing vessel motion. Additionally, the subjective response to the sense of motion, irrespective of motion sickness, can be of interest.

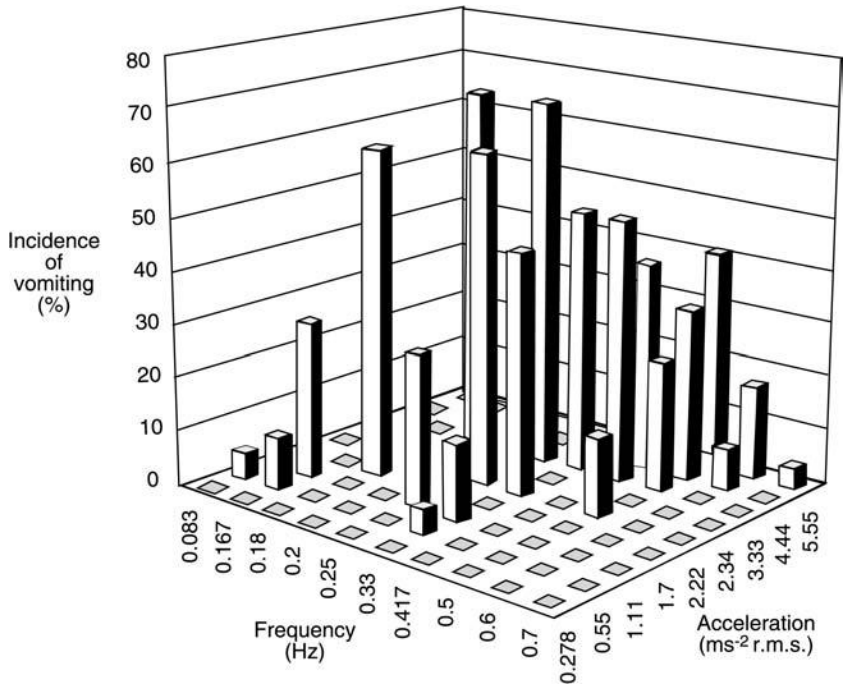


Figure 2 Incidence of vomiting associated with exposure to various magnitudes and frequencies of vertical oscillation according to McCauley *et al*. (1976). (The frequency and the magnitude axes of the figure have ordinal properties only. The percentage vomiting was 0 with 0.278 ms^{-2} r.m.s. at 0.083 Hz and at 0.167 Hz and with 1.11 ms^{-2} r.m.s. at 0.500 Hz.) (Reproduced with permission from Griffin, 1990.)

Methods of Predicting Motion Sickness from Vertical Oscillation

The various investigations of response to vertical oscillation have allowed the formulation of a frequency weighting, W_f (**Figure 3**), and the definition of a motion sickness dose value. The frequency weighting W_f reflects greatest sensitivity to acceleration in the range 0.125–0.25 Hz, with a rapid reduction in sensitivity to acceleration at higher frequencies. The dose measure based on data from laboratory studies and the development of sickness among passengers on ships is given by a squared relation between frequency-weighted acceleration, $a_{r.m.s.}$ (in ms^{-2} r.m.s.), and duration of exposure, t (in seconds):

$$\text{Motion sickness dose value (MSDV)} = a_{rms}t^{1/2}$$

The percentage of unadapted adults who are expected to vomit is given by $\frac{1}{3}$ MSDV. This relationship was derived from exposures in which up to 70% of persons vomited during exposures lasting between 20 min and 6 h.

The MSDV has been used to predict sickness on various marine craft (ships, hovercraft, and hydrofoil) in which vertical oscillation has been shown to be the prime cause of sickness. Vertical oscillation is not the principal cause of sickness in many road vehicles and some other environments: so the above expression should not be assumed to be applicable to the prediction of sickness in all environments.

Sickness Caused by Nonvertical Oscillatory Motion

Until recently, knowledge of the effects of oscillation causing sickness was primarily restricted to vertical oscillation. However, interest in the causes of sickness in road and rail transport has stimulated investigations with fore-and-aft and lateral oscillation.

Horizontal Oscillation

Studies conducted with horizontal oscillation during the 1990s have concentrated on feelings of illness rather than vomiting incidence. The results show that illness decreases with increasing frequency from about 0.2 to 0.8 Hz if the same acceleration is used at each frequency. Increases in the magnitude or the duration of horizontal oscillation appear to increase the incidence or severity of motion sickness. The direction of horizontal oscillation (fore-and-aft or lateral) has been found to have a small effect, but this may be dependent on the subject posture, especially support for the back or head.

Oscillation (or, at least, variation in acceleration) in the horizontal directions (fore-and-aft or lateral) can cause sickness in road vehicles. The effect depends on the visual field and body posture. One study, comparing three conditions (eyes open, eyes closed, and a stationary visual field achieved with a box placed over the head) found that the eyes-open condition produced the least sickness and the box-over-the-head condition produced the greatest sickness. Another study found subjects to be more sensitive when seated

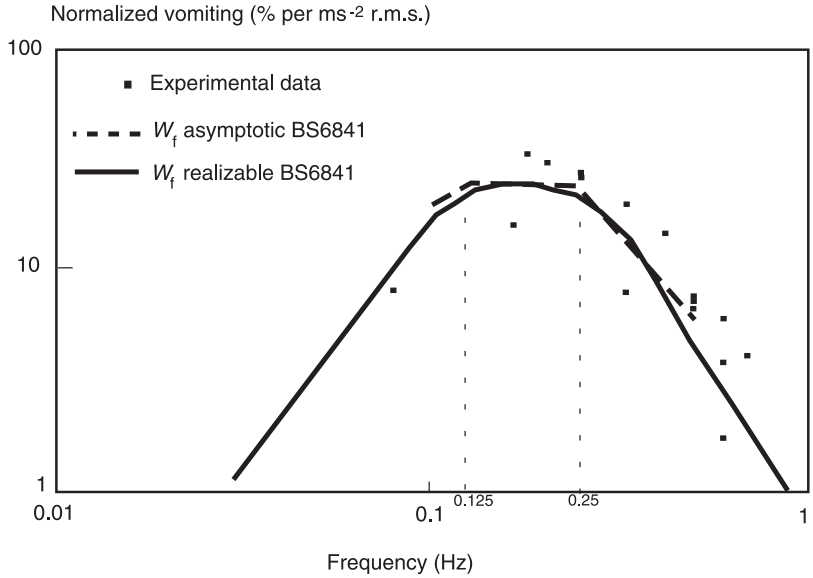


Figure 3 Effect of the frequency of vertical oscillation on the incidence of normalized vomiting during 2-h exposures compared with an asymptotic frequency weighting and the corresponding frequency weighting, W_f, defined in British Standard 6841 (1987) and ISO 2631 (1997). (Normalized vomiting is the vomiting incidence divided by the acceleration in ms^{-2} r.m.s.)

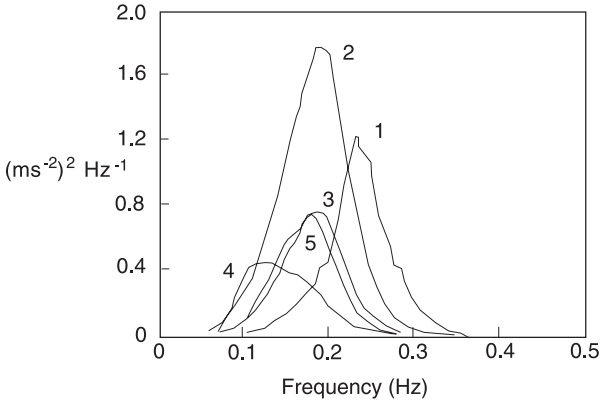


Figure 4 Average acceleration power spectral densities for vertical acceleration at central locations on five ships (resolution 0.01 Hz; based on data in Lawther and Griffin, 1988b).

facing the direction of motion than when lying along the axis of acceleration and deceleration. In road coaches, the horizontal acceleration has been shown to be correlated with the occurrence of motion sickness although, again, the effect is also influenced by the visual environment and other factors.

The concept of an MSDV (as derived from studies of sickness caused by vertical oscillation) may be satisfactory for use with horizontal oscillation, although a somewhat different frequency weighting may be required. Additionally, the frequency range for horizontal oscillation may need to be extended to frequencies below 0.1 Hz since significant acceleration can occur at such low frequencies in the horizontal direction but are less common vertically.

Rotational Oscillation

Rotational motions of the body that are sometimes associated with sickness include oscillations in roll, pitch, or yaw and constant-speed rotation when there are head movements. A consideration of the effects of rotational oscillation on sickness and on measures of translational oscillation can be complex. Rotation of the body about an earth-horizontal axis (i.e., roll or pitch for a normally seated person) alters the direction of the component of force due to gravity and will give oscillatory signals from translational accelerometers oriented along the axes of the body.

It cannot be assumed that sickness experienced in situations where there is rotational oscillation is necessarily due to the rotational acceleration: rotational oscillation causes translational oscillation at all positions other than at the center of rotation and so sickness associated with rotational oscillation could be caused by either the rotation or the translation produced by the rotation. It appears that pure roll motion at magnitudes and frequencies associated with ship motion (e.g., 0.1–0.2 Hz) is far less nauseogenic than the pure vertical oscillation often occurring on ships. For situations where there is simultaneous translation and rotation, it might be hypothesized that there could be a synergistic interaction such that roll (or pitch) oscillation may increase the effect of translational oscillation. However, the sickness caused by vertical oscillation in ships seems to be usefully predicted from the magnitudes of vertical oscillation without considering the extent of the roll or pitch motion.

With no visual field and no movement of the head, rotation of the restrained body at constant speed about an earth-vertical axis does not appear to cause sickness, but similar rotation about an earth-horizontal axis (about the *x*-, *y*-, or *z*- axis of the body) can be highly nauseogenic. Symptoms of sickness during such stimulation are reduced if there is an external view. With low-frequency rotation of a horizontal body about its *z*-axis, nausea appears to increase with increases in the rate of rotation. Constant-speed rotation about an axis only 4° off-vertical can induce nausea in susceptible subjects.

Constant-speed rotation about an earth-vertical axis can induce sickness rapidly if the head is moved in roll or pitch during the rotation. Only a few head movements may be required: this is a cross-coupled motion generating Coriolis forces and is a commonly used means of producing sickness in laboratory studies of antimotion-sickness drugs and in the desensitization of aircrew suffering from motion sickness. Similarly, in environments outside the laboratory, when there are two axes of rotation (e.g., yaw and roll) occurring simultaneously, sickness may be caused by Coriolis stimulation.

The motions of swings can also generate motion sickness. Two principal categories of swing have been used: (1) those secured so that the platform supporting the body swings as a simple pendulum and inclines under the action of the applied forces (i.e., two pole swings), and (2) parallel swings which are secured at either end so that they remain horizontal during swinging (i.e., four pole swings). The motions experienced by observers on the swing are different in the two cases and neither imparts a unidirectional translational acceleration.

See also: **Hand-transmitted vibration**; **Whole-body vibration**.

Further Reading

British Standards Institution (1987) *Measurement and Evaluation of Human Exposure to Whole-body Mechanical Vibration and Repeated Shock*. London: British Standard BS 6841.

Griffin MJ (1990) *Handbook of Human Vibration*. London: Academic Press.

Griffin MJ (1991) Physical characteristics of stimuli provoking motion sickness. In: *Motion Sickness: Significance in Aerospace Operations and Prophylaxis*. AGARD Lecture Series LS-175. Neuilly sur Seine, France: NATO, pp. 3-1–3-31.

International Organization for Standardization (1997) *Mechanical Vibration and Shock – Evaluation of Human Exposure to Whole-body Vibration – Part 1: General Requirements*. Geneva: International Standard ISO 263-1.

Lawther A and Griffin MJ (1987) Prediction of the incidence of motion sickness from the magnitude, frequency, and duration of vertical oscillation. *Journal of the Acoustical Society of America* 82 (3): 957–966.

Lawther A and Griffin MJ (1988a) A survey of the occurrence of motion sickness amongst passengers at sea. *Aviation, Space and Environmental Medicine* 59 (5): 399–406.

Lawther A and Griffin MJ (1988b) Motion sickness and motion characteristics of vessels at sea. *Ergonomics* 31 (10): 1373–1394.

McCauley ME, Royal JW, Wylie CD, O'Hanlon JF and Mackie RR (1976) Motion sickness incidence: Exploratory studies of habituation, pitch and roll and the refinement of a mathematical model. Human Factors Research Inc., Goleta, CA, USA, AD-A024 709.

Reason JT and Brand JJ (1975) *Motion Sickness*. London: Academic Press.

Turner M and Grifin MJ (1999) Motion sickness in public road transport: the effect of driver, route and vehicle. *Ergonomics* 2(12): 1646–1664.

N

NEURAL NETWORKS, DIAGNOSTIC APPLICATIONS

M Zacksenhouse, Technion - Israel Institute of Technology, Haifa 32000, Israel

Copyright © 2001 Academic Press

doi:10.1006/rwvb.2001.0151

Neural networks are adaptive data processing systems that learn from examples in a supervised mode or discover the intrinsic structure of the data in an unsupervised mode. In recent years they have emerged as a practical technology, with successful applications in pattern recognition and function approximation. These information-processing capabilities are at the core of diagnostics as further detailed here.

Diagnostic methods are generally divided into two strategies: model-based methods and feature-based methods. Feature-based methods involve pattern recognition techniques to distinguish between different patterns of features that are associated with different conditions. Model-based diagnostics (and feature-based fault trend assessment) are based on function approximation to relate the measured response to the underlying model. These general monitoring strategies are further divided here into the specific methods for which neural network techniques are applicable, as shown in **Table 1**. Each method is briefly examined in the context of neural network information processing capabilities. The appropriate neural network paradigms, the specific neural networks of choice and particular application domains are described.

Following the description of neural network applications for the different monitoring and diagnostic strategies, a critical assessment is presented, based on the relevant advantages provided by the neural network technology and the practical aspects of their successful implementation in diagnostics.

Table 1 Neural network solutions to different information processing tasks underlying system monitoring and diagnostics (see network acronym below)

Applications		*Information processing task*		
Strategy	*Method*	*Classification*	*Clustering*	*Mapping*
Model-based monitoring	Parameter updating			*MLFF *RBF
	Response prediction			*Two-sensor technique
Feature-based monitoring	Feature extraction		*ANN *SOFM	
	Fault detection	*Perceptron *MLFF		*Novelty index w/ANN
	Identification/localization	*SLFF *MLFF *MLFF with direct input–output connections	*ART *Competitive	
	Assessment (trend analysis)			*RNN *SOFM

ANN, auto-associative neural network; ART, adaptive resonance theory; BPN, back-propagation network (a MLFF trained using back propagation); MLFF, multilayer feedforward neural network; RNN, recurrent neural network; SOFM, self-organizing feature maps.

Monitoring and Diagnostic Strategies

Model Based Monitoring

Parameter updating Parameter updating involves a mapping from the space of model parameters to the space describing the response characteristics. The model might be a lumped parameter or a finite element model. The required model adjustments indicate the type and location of the fault. Model updating is also important for designing high performance control laws based on an accurate model of the system. Neural networks can learn the appropriate inverse mapping from the response characteristics to the model parameters, if the inverse mapping is unique. This is usually the case at least for small variations around the nominal model. The robustness of neural networks to noise facilitates reliable model updating even at high levels of measurement noise.

Training examples are obtained by simulating the response of the model with different sets of modified parameters. The response of the model is described in the frequency domain using frequency response functions (FRFs). However, in most cases the FRF contains a large number of points and should be further analyzed to reduce the number of inputs to the neural network. Data reduction may be based on modal analysis or on integration over frequency regions of interest.

In model updating, the neural network is used to learn the inverse mapping and to output the appropriate model changes, given the simulated response of the modified system. During operation, the network is presented with the measured response and determines the required model adjustments. In complex models, an iterative model updating may be performed on the modified model (generating new examples, re-training a new network, and re-presenting the measured vibrations) until the characteristics of the measured vibrations are close enough to those predicted by the model.

Both the multilayer neural networks (MLNN) and the radial based function (RBF) networks provide universal function approximation and are therefore suitable for model updating applications. The RBF networks, which are linear in their weights and are therefore faster to train, have been especially popular in applications of neural networks to model updating.

Response prediction In this method the neural network is trained to model the unknown and possibly nonlinear interrelationship between vibrations at different locations under normal conditions (no fault). During monitoring, the network predicts the vibrations at one location given the vibrations at another location. Significant deviations indicate that the system has undergone a significant change, which may reflect a faulty condition. A typical implementation of this scheme involves two accelerometers mounted at different locations, and a neural network that is trained to produce the vibration spectra in one sensor (desired output) given the vibration spectra at the other sensor (input pattern). In operation, the predicted spectra is compared to the measured spectra, and their mean square difference is computed as a measure of the deviation from normal operation. This two-sensor technique has been successfully demonstrated in the monitoring of check valves and pump-motor bearings.

Assuming the monitored system is linear, at least around the normal working range, the neural network learns the transfer function of the system between the two accelerometers. Faults, which modify the structure of the system, affect the transfer function, and consequently, the relationship between the vibrations at the different locations. Thus, the predicted vibrations based on the learned transfer function at normal conditions, deviates from the measured vibrations.

Feature Based Monitoring

Feature extraction Feature extraction is a critical initial step in any monitoring and fault identification system. The extracted features serve as the input to a classifier for further fault identification. Thus, feature extraction should preserve the critical information for decision-making while excluding irrelevant information that increases the computation burden. Reducing the dimension of the feature space facilitates the development of the subsequent classifier, both in terms of the number of training examples and the amount of time needed for its training.

Neural networks can learn to detect and extract significant features in the input patterns. The initial feature space is converted to a lower dimension feature space in such a way that the statistical properties and the critical similarity and differences in the original feature space are preserved. The initial feature space may include, for example, the spectrum of measured vibrations, and is usually of high dimension. Neural networks learn to generate potentially new features, which are linear or nonlinear functions of the initial features, under unsupervised learning. Two distinguished neural network approaches to feature extraction include data compression using auto-associative networks and self-organizing feature maps.

Data compression Data compression is achieved by training the neural network to learn the identity map:

Two types of neural networks, the auto-associative neural network (ANN) and the re-circulating neural network (ReNN), are commonly used for data compression.

ANNs are multilayer feedforward networks that learn the identity map. They include an input layer, one or three hidden layers and an output layer. The network is trained using supervised learning, where the target output is identical to the input pattern. By restricting the number of hidden neurons in the middle layer, the network learns to compress the input pattern in such a way that the original pattern can be reconstructed at the output layer. Thus, the middle layer provides a compressed representation of the input pattern, which preserves, as well as possible, the critical features of the input pattern. Feature extraction is achieved by presenting the input pattern to the network and reading the representation at the middle layer. The mapping from the input layer to the middle layer is linear, when there is a single hidden layer, and nonlinear, if there are more (odd number) hidden layers.

The re-circulating neural network is a four-layer auto-associative type network, which repeats the data compression process twice and compares the two results. Its basic structure is equivalent to two identical ANNs, where the output of one is the input to the next. Error signals are received from two sources: reconstruction error in the first ANN and compression-error between the two compressed representations.

Feature extraction using data compression has been applied to diagnose rolling element bearing based on the spectrum of the vibrations. The vector of activity across the hidden layer was used as the input to a subsequent neural network-based classification stage for fault identification.

Self-organizing feature maps (SOFM) Self-organizing feature maps transform the input vector of arbitrary dimension into a one- or two-dimensional discrete map, referred to as the feature map. The neurons in a one- or two-dimensional feature map are arranged in a vector or an array, respectively. A unique aspect of SOFM is the significance of the order of the neurons, which forces neighboring neurons to be mapped to similar input patterns.

The neurons in the feature map describe prototypes of the input patterns in the form of their weights. The distribution of these prototypes reflects variations in the density of the input patterns across the input space, such that a large number of neurons are assigned to dense regions of the input space. These clusters, or dense regions in the input space, are usually associated with distinguished fault-classes, so subsequent classification based on the prototypical neurons is simplified. The dimension of the feature map is determined by the dimension of the map, and is usually restricted to one or two. The number of neurons reflects the number of grid points used to cover the map. Thus, a two-dimensional feature map may be viewed as a, potentially folded, plane in the high-dimensional space determined by the inputs.

During learning, the SOFM is presented with the input patterns and learns a set of prototypical patterns in a topological order. During operation the input pattern is presented to the SOFM to determine the activity across the feature map, which identifies the close-by prototypes. This activity may then be used as input to a subsequent classifier. SOFM have been used, for example, to extract features from time–frequency representation of vibrations in order to determine the classes of transient events in machining.

Fault detection Fault detection is usually treated as a classification task involving two classes, corresponding to normal and faulty conditions. As such, fault detection is a simple case of fault identification, having only two conditions: normal and abnormal or usable and worn tool. Fault identification is described in detail in the next subsection. However, fault detection may also be achieved using a novelty measure, which signifies when the newly measured pattern is significantly different from those measured under normal operating conditions.

Novelty measure The key point in developing a novelty measure is to differentiate between significant changes and those attributed to normal fluctuations. To learn the normal range of patterns, an ANN is trained to duplicate (auto-associate) a wide range of patterns corresponding to normal operation. Discrimination power is obtained by limiting the number of neurons in the middle layer, so the network is forced to extract the significant features in the normal patterns. Once trained, the ANN is used to compute a novelty index by presenting it with a new pattern and computing the duplication error, i.e., the distance between the network output and the presented pattern.

Since the network was trained to auto-associate patterns that correspond to normal conditions, the novelty of such patterns should be small. In contrast, patterns corresponding to faulty conditions would not be duplicated well, and their novelty index would be significant. Structural fault detection with the novelty index was demonstrated using a simulated lumped-parameter structure. The input patterns, which the network learned to duplicate, were the transmissibility functions between two masses.

Fault identification Fault identification can be posed as a classification problem where the classes are the fault types. In simple gearbox transmission, for example, the faults may include specific bearing-related faults and specific gear-related faults. In a more complex gearbox, fault identification involves the localization of the fault to the particular faulty gear, bearing or shaft.

Neural networks can generate arbitrary decision regions, which may be nonconvex and disjoint. However, their ability to learn the appropriate decision regions critically depends on their size and on the number of representative training examples. The size of the neural network depends on the number of input features and on the number of output classes. Thus, only those input features that enhance separation of the fault classes should be included.

Assuming that adequate input features have been properly selected, and that there are sufficient, well-representative, examples, neural network can be trained to perform the classification task. In most cases, the training examples consist of measurements taken while a specific fault has been introduced in the system, so the fault class of the measured input feature-vector is known. Thus, it is natural to train the network in supervised mode.

Feedforward networks The networks of choice are variants of the single- (no hidden layer) or multilayer feed forward (SLFF or MLFF) neural networks (where only layers with adaptive neurons are counted). Each output neuron in a single-layer network generates a decision boundary in the form of a hyperplane. Thus, single-layer networks are appropriate only when the fault types are linearly separable. Proper feature selection may be critical in formulating the classification task in a space where the fault-classes are linearly separable. Functional link networks may be used where, based on initial analysis of the problem, specific nonlinear functions of the initial set of inputs are computed as features for the network. If the feature selection is appropriate, the classification problem may be reduced to a linearly separable problem, which can be performed by a SLFF network.

MLFF networks, even when restricted to two layers, can generate arbitrary complex decision regions by combining the decision regions generated by the neurons in the hidden layer. However, the additional hidden neurons increase the number of free parameters of the network and thus require a large number of examples for proper training.

A hybrid approach involves a multi- (specifically, two-) layer network, with additional direct connections from the input layer to the output layer. This architecture is different from standard MLFF architecture, where neurons in one layer are connected to neurons in the adjacent layer only. The direct input–output connections support gross linear separation of the input space and free the hidden neurons to form discriminating features to handle the nonlinearly separable regions.

Training may be performed with the back-propagation algorithm. However, this algorithm is known for its slow convergence. Other learning algorithms with better convergence properties, like the Levenberg–Marquart (LM) algorithm, are available.

Competitive networks Competitive networks learn in an unsupervised mode and detect clusters in the data. Their use for classification depends on associating each detected cluster with the appropriate condition class, and thus requires that the condition of each example be known (as in supervised learning). The success of the classifier depends on the extent to which the examples in each cluster are associated with the same condition. This usually requires that the number of class-dependent clusters be known ahead of time.

A family of networks that are based on the adaptive resonance theory (ART) can provide stable adaptive clustering, so that a new category (represented by a new output neuron) is generated when a new pattern does not fit any of the existing clusters. The degree of similarity that is required for inner category clustering is adjustable, using a parameter known as the vigilance parameter. The vigilance parameter can be selected to assure that clustered patterns are associated with the same condition. Thus, ART networks facilitate real-time learning during regular operation by automatically generating a new category whenever a novel input pattern is detected.

Fault assessment Fault assessment refers to the prediction of the future condition or the lifetime of a system with a deteriorating fault, so early warnings can be issued. It involves trend analysis or time series prediction, to predict the future level of the vibration indicators or the lifetime of the faulty element. Neural networks have the potential for learning nonlinear prediction, and thus for successfully forecasting machine deterioration.

Fault trend analysis Fault trend analysis is performed to detect signs of deterioration and trigger early warnings based on the predicted level of important vibration indicators. The next level of the vibration indicator is predicted, based on its current and previous levels. Trend analysis can be formulated as a mapping from a set of time-lagged indicator levels to the next indicator level. This mapping can be learned

using standard MLFF networks, where the inputs are the current and the time-lagged indicator levels and the output is the next level. However, recurrent neural networks (RNN) have better performance in time series prediction. RNN is a MLFF network with an additional feedback path from the output neuron to the input neurons. Thus, the input vector includes both the current and time-lagged indicator levels and the current and time-lagged network predictions. The feedback path provides short-term memory and makes RNN suitable for learning temporal behavior.

Lifetime trend analysis Lifetime trend analysis is targeted at estimating the lifetime of a faulty component based on several diagnostics indices. It can be formulated as a mapping from a set of features, the diagnostic indices, to the lifetime of the faulty component. Reliable lifetime estimation requires multiple indices, which usually vary nonlinearly with the state of the component. Since the functional form of the mapping is not known, its estimation involves nonparametric regression analysis, which can be performed using neural networks.

The nonparametric regression underlying lifetime trend analysis may be learned by different neural network paradigms, including the MLFF network. However, to the extent that each diagnostic index depends primarily on the lifetime of the faulty element, the lifetime is actually represented by a curve in the space defined by the indices and the lifetime. Curve-fitting involves a one-dimensional feature map where the relevant feature is the lifetime. A piecewise linear curve-fitting can be constructed using self-organizing feature maps. The location of each neuron in the one-dimensional map is determined by the weights of its connections to the underlying space. During learning, the weights are adjusted so the neurons are re-distributed along the data samples in a topological order. Their final weight-vectors determine the location and distribution of the knots of the piecewise linear fit to the curve. The direct use of SOFM for nonparametric regression analysis may result in disordered knots and a slightly modified algorithm, known as constrained topological mapping (CTM), is recommended.

Critical Assessment

Neural networks can approximate any continuous multivariate function or any high-dimension decision boundary. Moreover, they learn to perform the desired processing task from examples, without relying on any probabilistic distribution model. However, their performance depends on the structure of the network (e.g., the number of hidden neurons) and the training set. Thus, while neural networks can be powerful diagnostic tools, their development should account for their specific characteristics.

Advantages for Diagnostic Applications

Approximation power The power of neural networks to approximate general continuous functions is established by a universal approximation theorem, which guarantees the existence of a neural network, with a single hidden layer, which is capable of approximating any continuous function. Furthermore, in spaces of large dimension, neural networks offer a great advantage for function approximation over series expansion on a fixed set of functions. For neural networks, the error falls as the order of $1/M$ where M is the number of hidden units, irrespective of the dimension of the input space d. In contrast, when a fixed set of basis function is used, the error decreases as the order of $1/M^{2/d}$.

Robustness to noise Both training and testing can be successfully performed even when the examples are noisy.

High dimension feature space There is no inherent limitation on the number of features in the input to the neural network. Thus, neural network can be used in diagnostic problems that cannot be resolved, based on a single feature, but require multiple features. However, the training requirements – the burden of preparing a large set of adequate examples and the time required for training – increase with the number of input neurons. Thus, this advantage should be used wisely by including only significant features.

Generalization The trained network can interpolate and extrapolate to operate on novel inputs, which have not been included in the training examples. However, this can be done reliably only when the training examples are adequate, both in terms of their number and distribution. This important issue, known as the generalization power, has significant consequence in terms of the size of the network and the size of the training set.

In the context of classification, for example, the utility of a classifier is determined by the *probability* that a randomly selected new example is correctly classified. This unknown probability defines the generalization performance of the classifier. Given a set of training examples, the probability of correct classification can be estimated by the *frequency* of self-classification, i.e., the rate of correct classification of the training examples. The bias of this estimator is of critical importance in assuring the generalization of the network to unknown examples. In particular, if

the number of training examples is not sufficient, the network may be overtrained and achieve a high frequency of self-classification, but the generalization performance may be poor. General rules have been developed, which determine the minimum number of examples needed to train a classifier with a given number of free parameters. The number of free parameters in a neural network is the number of weights and so these rules relate the number of required examples to the size of the network.

Sensor fusion As mentioned above, neural networks can operate in a high-dimensional feature space. In particular, these features may be extracted from measurements taken by different sensors, so the network performs sensor fusion. Sensor fusion is important is a number of diagnostics applications, and in particular in tool condition monitoring, where both acoustic emission and cutting force measurements are important for determining the degree of tool wear.

Implementation Issues

Data sources Neural networks are trained and tested using a set of examples, which should be representative of the expected cases. Training examples can be collected over time as actual faults are developed, but this is usually impractical. Instead, it is customary to conduct a test program where measurements are taken under different conditions, with a healthy system and with faulty components installed. However, experiments usually produce a very limited set of examples. Even in very exhaustive test programs, only one or two examples of the same type of fault are included. Given the quasistatic nature of most faults, a test program conducted with a specific faulty element provides essentially a single example to a neural network classifier. Multiple examples would require collecting data with different faulty elements in place.

An alternative approach is to generate the training examples analytically, by running a model of the system. Acknowledging the limitations of most models, the prefered strategy is to consider only the changes in the dynamic characteristics rather than their absolute value. This approach is especially attractive in structural damage analysis, where appropriate models of the structure and the damage can be constructed.

Number of examples There are several bounds on the number of examples needed for a good generalization. A general rule for good generalization in classification tasks is that $N > (W / s\varepsilon)$, where N is the number of examples, W the number of weights and ε the permitted fraction of errors on test. This implies that the number of examples should be 10 times the number of weights to guarantee a less than 10 percent probability of error, even when the training examples were correctly classified.

The distribution of examples should reflect the actual distribution of the cases. Thus, special care should be taken when generating experimental examples. Experimental programs are usually based on running the system with known faults and measuring the vibration for an extended period of time. However, in most cases the state of the fault does not change during this period and so the relevant statistical features are not expected to change. In this case the whole test provided a single example. To produce multiple examples, multiple tests with different instances of the same type of fault, should be included.

Other considerations Practical issues for successful implementation of neural networks, which are not specific to diagnostic applications, include (i) network structure, and in particular the number of hidden neurons, (ii) normalization, and (iii) cross-validation. The reader is referred to texts on neural networks for these general issues.

See also: **Diagnostics and condition monitoring, basic concepts**; **Modal analysis, experimental**, Basic principles; **Neural networks, general principles**; **Rotating machinery, monitoring**.

Further Reading

Dellomo MR (1999) Helicopter gearbox fault detection: a neural network based approach. *J. Vib. Acoustics* 121:265–272.

Du R, Elbestawi MA, Wu SM (1995) Automated monitoring of manufacturing processes, part 1: monitoring methods, part 2: applications. *ASME J. Eng for Industry* 117:121–132; 133–141.

Haykin S (1994) *Neural Networks: A Comprehensive Foundation*. Upper Saddle River, NJ: Prentice-Hall.

Luo FL, Unbehauen R (1998) *Applied Neural Networks for Signal Processing*. Cambridge, UK: Cambridge University Press.

Patterson DW (1996) *Artificial Neural Networks Theory and Applications*. Singapore: Prentice-Hall.

Rangwala S, Dornfeld D (1990) Sensor integration using neural networks for intelligent condition monitoring. *J Eng for Industry* 112:219–228.

Simpson PK (1996) *Neural Network Applications*. New York, NY: IEEE Technology Update Series.

Sora T, Koivo HN, Koivisto H (1991) Neural networks in process fault diagnosis. *IEEE Trans Syst, Man, and Cybern*, SMC-21(4):815–825.

Tsoukalas LH, Uhrig RE (1997) *Fuzzy and Neural Approaches in Engineering*. New York, NY: John Wiley.

Zhang S, Ganesan R, Xistris GD (1996) Self-organizing neural networks for automated machinery monitoring systems. *Mech. Sys. and Sig. Proc.* 10(5):517–532.

NEURAL NETWORKS, GENERAL PRINCIPLES

B Dubuisson, La Croix Saint Ouen, France

Copyright © 2001 Academic Press

doi:10.1006/rwvb.2001.0150

Neural structures are often used in order to solve difficult nonlinear problems for which a classical solution does not give good results. No mathematical model of the world is needed. In fact, the world and the problem are represented by examples of situations.

Let us consider diagnostic problems. Given an observation on the system, one has to decide about the state of the system (normal, abnormal, etc.). Let us suppose one chooses a neural network as a solution for this decision system.

The task of the neural network is to learn a model of the world in which it is embedded and to maintain this model as sufficiently consistent with the real world in order to solve the diagnostic problem for which it has been built. For example:

1. the known world state is represented by facts;
2. observations on the system are obtained with sensors: they are noisy, with errors due to sensor noise and system imperfections. One extracts examples from these observations and these examples are used for training the network. An example is composed of an input signal and the corresponding desired output (normal state, abnormal state, ...). This set of examples represents the knowledge one has about the problem to be solved. Its quality is very important because it is the only knowledge about the diagnostic problem.

Given this set of examples the design of the neural network may proceed according to the following two phases:

1. A learning phase: an appropriate architecture is chosen for the neural network and a transfer function for each neuron. A subset of examples is used to train the network by means of a suitable algorithm.
2. A generalization phase: other examples (not used before) are tested with the preceding structure and a recognition index is computed. This index characterizes the quality of the decision system; for example, it can be an estimation of the error probability.

Neuron

A neuron is an information processing unit. A general model of a neuron is given in **Figure 1**. It can be decomposed into three parts:

1. a set of weighted inputs. To the input i is associated the weight w_i. The weight can be positive, when the associated link is said to be excitatory; if it is negative, the link is said to be inhibitory. There is a specific link associated to a threshold t; it is not an input, it has the effect of lowering the input of the activation function;
2. an adder, making a linear combination of the weighted inputs;
3. an activation function which limits the amplitude of the output either in $[-1,1]$ or $[0,1]$.

The neuron can be described with the equation:

$$y = f(u) = f\left(\sum_{j=1}^{d} w_j x_j - t\right) \qquad [1]$$

The threshold t applies an affine transformation to the output u of the linear combination. The equation can be formalized in order not to distinguish the inputs from the threshold:

$$\begin{aligned} u &= \sum_{j=0}^{d} w_j x_j \\ y &= f(u) \end{aligned} \qquad [2]$$

with:

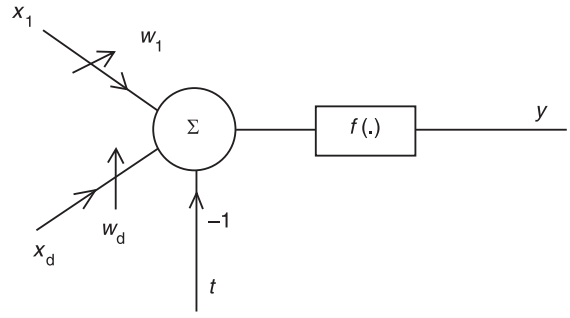


Figure 1 General model of a neuron.

$$x_0 = -1$$
$$w_0 = t \qquad [3]$$

Three types of activation functions may be distinguished:

1. A threshold function:

$$f(u) = \begin{cases} 1 & u \geq 0 \\ 0 & u < 0 \end{cases} \qquad [4]$$

   Such a neuron is called a McCulloch–Pitts neuron: its output is a binary one.
2. A piecewise linear function:

$$f(u) = \begin{cases} 1 & u \geq 1/2 \\ u & -1/2 < u < 1/2 \\ 0 & u < -1/2 \end{cases} \qquad [5]$$

   In this case, the neuron is either a linear combiner or a threshold function.
3. A sigmoid function: this function is a strictly increasing one with derivative properties. An example is the logistic function:

$$f(u) = \frac{1}{1 + \exp(-au)} \qquad [6]$$

The value a is called the slope parameter. By modifying its value, one gets different slopes. The value of the slope at the origin is $a/4$. If a approaches infinity, the sigmoid function becomes a threshold one. It is easy to introduce modifications in order that the values of the activation function be between $[-1,1]$:

for the threshold function:

$$f(u) = \begin{cases} 1 & u > 0 \\ 0 & u = 0 \\ -1 & u < 0 \end{cases} \qquad [7]$$

For the sigmoid function, the hyperbolic tangent function is used:

$$f(u) = \tanh\left(\frac{au}{2}\right) = \frac{1 - \exp(-au)}{1 + \exp(-au)} \qquad [8]$$

Network Architecture

Each architecture is associated with a learning algorithm in order to train the weights. Four architectures can be considered:

1. The single layer feedforward network: such a network is composed only of a layer: inputs are applied to all the neurons of this layer which computes the output. It is a feedforward neural network. An associative memory is an example of such a structure.
2. The multilayers network: Such a network is composed of an input layer, one or more hidden layers and a layer of output neurons. The user chooses the number of hidden layers. By adding different hidden layers, the network acquires a more extensive knowledge on the problem. Each neuron in each layer is connected to the outputs of neurons of the preceding layer. If the network has d source nodes, n_1 neurons in the first hidden layer, n_2 in the second one, q in the output layer, it is said to be a $(d; n_1; n_2; q)$ network. The network can be fully connected (each neuron in each layer is connected to every node in the adjacent forward layer) or partially connected.
3. Recurrent networks: in a recurrent network, there is at least one feedback loop. Such a structure can be complex when there are hidden neurons.
4. Lattice structures: a lattice consists of a one-dimensional or higher-dimensional array of neurons with a corresponding set of source nodes that supply the input signal to the source array. The dimension of the lattice refers to the number of the dimension of the space in which the graph lies.

Error-correction Learning

In order to train the network, one needs a set of patterns. For each pattern $\mathbf{x}_i(k)$ presented at time k to the network, one knows the desired response or target denoted $d_i(k)$. The pair composed of the input pattern $\mathbf{x}_i(k)$ and the desired response $d_i(k)$ is the example presented at time k. The set of examples is called the training set. Let $y_i(k)$ be the output of neuron i for the example k. This output is generally different from the desired response and an error signal $e_i(k)$ can be computed:

$$e_i(k) = d_i(k) - y_i(k) \qquad [9]$$

In the error-correction learning, a cost function is minimized, and is defined as the mean-squared value of the sum of squared errors:

$$J = \frac{1}{2} E\left[\sum_i e_i^2(k)\right] \qquad [10]$$

The sum is taken over all the neurons in the output layer of the network. A method of gradient descent

will be used to minimize the cost function. Because the corresponding probability laws are not known, an estimate of J is used, which is an instantaneous value $E(k)$:

$$E(k) = \frac{1}{2}\sum_i e_i^2(k) \qquad [11]$$

The network can then be optimized by minimization of $E(k)$, the variables being the weights of the network. The adjustment $\Delta w_{ij}(k)$ at iteration k is given by:

$$\Delta w_{ij}(k) = \alpha e_i(k) x_j(k) \qquad [12]$$

This rule is called the error-correction rule, with α determining the rate of learning.

Perceptron

The perceptron is the simplest architecture for a neural network (**Figure 2**). It can be used only when patterns are linearly separable. Its architecture is based on a single neuron with weighted inputs. Let $x_1, x_2, \ldots, x_d$ be the inputs of the neuron, $w_1, w_2, \ldots, w_d$, the corresponding weights. A specific 'input' consists in the threshold θ. A linear combination is computed:

$$u = \sum_{i=1}^{d} w_i x_i - \theta \qquad [13]$$

The $f(\cdot)$ function is a threshold one:

$$y = \begin{cases} 1 & u \geq 0 \\ -1 & u < 0 \end{cases} \qquad [14]$$

Consider the problem of two sets ω_1 and ω_2 of data in a d-dimensional space. Such a structure can separate them, if they are linearly separable by a plane, the equation being:

$$\sum_{i=1}^{d} w_i x_i - \theta = 0 \qquad [15]$$

The output will be (1) for data from ω_1 and (-1) for data from ω_2. Equation [15] corresponds to a perceptron architecture.

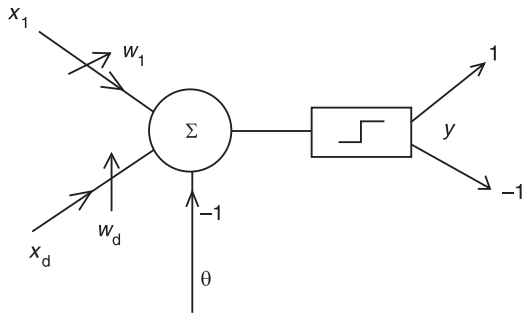


Figure 2 Perception architecture for a neural network.

Learning Algorithm

In order to explain the learning algorithm, some modifications have to be introduced in the definition of different data. In fact, the problem will be easier to understand if a $(d+1)$ component is introduced.

To define vectors $\mathbf{x}$ and $\mathbf{w}$:

$$\mathbf{x} = \begin{pmatrix} -1 \\ x_1 \\ \vdots \\ x_d \end{pmatrix} \quad \mathbf{w} = \begin{pmatrix} \theta \\ w_1 \\ \vdots \\ w_d \end{pmatrix} \qquad [16]$$

Then u is simply the inner product of $\mathbf{x}$ by $\mathbf{w}$:

$$u = \mathbf{w}^{\mathrm{T}}\mathbf{x} \qquad [17]$$

Then if two sets are linearly separables:

$$\begin{aligned} \mathbf{w}^{\mathrm{T}}\mathbf{x} \geq 0 \;&\Rightarrow\; \mathbf{x} \in \omega_1 \\ \mathbf{w}^{\mathrm{T}}\mathbf{x} < 0 \;&\Rightarrow\; \mathbf{w} \in \omega_2 \end{aligned} \qquad [18]$$

If the two sets of examples (training sets of respective size n_1 and n_2) are finite sets, they have to be modified in order to get infinite sets. The training set T is constituted by:

$$\begin{aligned} &\mathbf{x}_{11}, \mathbf{x}_{12}, \ldots, \mathbf{x}_{1n_1}\mathbf{x}_{21}, \mathbf{x}_{22}, \ldots, \ldots \mathbf{x}_{2n_2}, \mathbf{x}_{11}, \\ &\mathbf{x}_{12}, \ldots, \mathbf{x}_{1n_1}, \mathbf{x}_{21}, \mathbf{x}_{22}, \ldots \mathbf{x}_{2n_2}, \ldots \end{aligned} \qquad [19]$$

which will be written:

$$\mathbf{x}(1), \mathbf{x}(2), \ldots, \mathbf{x}(n_1), \mathbf{x}(n_1+1), \mathbf{x}(n_1+2), \ldots \qquad [20]$$

(n) means that it is the nth pattern which is presented to the perceptron.

Beginning with an initial choice $\mathbf{w}(0)$, the training algorithm is a well-known one:

1. $\mathbf{w}(n+1) = \mathbf{w}(n)$ if $\mathbf{w}^T(n)\mathbf{x}(n) > 0$ and $\mathbf{x}(n) \in \omega_1$
2. $\mathbf{w}(n+1) = \mathbf{w}(n)$ if $\mathbf{w}^T(n)\mathbf{x}(n) < 0$ and $\mathbf{x}(n) \in \omega_2$
3. $\mathbf{w}(n+1) = \mathbf{w}(n) - \alpha(n)\mathbf{x}(n)$ if $\mathbf{w}^T(n)\mathbf{x}(n) > 0$ and $\mathbf{x}(n) \in \omega_2$

4. $\mathbf{w}(n+1) = \mathbf{w}(n) + \alpha(n)\mathbf{x}(n)$ if $\mathbf{w}^T(n)\mathbf{x}(n) < 0$ and $\mathbf{x}(n) \in \omega_1$

$\alpha(n)$ is the learning parameter: it controls the adjustment applied to each weight. Usually, this parameter is a constant one and the algorithm is called a fixed increment one. The only constraint is that this parameter must be positive.

It can be easily proved that this algorithm (the weights become constant) converges in a finite number of iterations if the sets are linearly separable.

The problem with this algorithm is as follows: at some iteration, if the weights continue to be modified, one does not know if it is due to the fact that the training is not terminated or to the fact that the sets are not linearly separable.

The previous algorithm can be written in another form, which is a more general one. Using the $f(\cdot)$ definition and the $d[\mathbf{x}(n)]$:

$$d[\mathbf{x}(n)] = \begin{cases} 1 & \text{if } \mathbf{x}(n) \in \omega_1 \\ -1 & \text{if } \mathbf{x}(n) \in \omega_2 \end{cases} \quad [21]$$

$d[\mathbf{x}(n)]$ is called the desired output for input $\mathbf{x}(n)$. The algorithm is simply written:

$$\mathbf{w}(n+1) = \mathbf{w}(n) + \alpha(n)\{d[\mathbf{x}(n)] - y(n)\}\mathbf{x}(n) \quad [22]$$

It is the difference between the desired output and the observed input which is used for weight modification. It is an error-correction training algorithm.

Link with a Gaussian Classifier

The perceptron can be considered as a special case of a usual decision problem of classification between two classes in pattern recognition. Suppose there are two classes, each following a normal distribution:

$$\begin{aligned} \omega_1 &: N(\mathbf{m}_1, \boldsymbol{\Sigma}_1) \\ \omega_2 &: N(\mathbf{m}_2, \boldsymbol{\Sigma}_2) \end{aligned} \quad [23]$$

The equation of a normal distribution is:

$$f(\mathbf{x}/\omega_i) = (2\pi)^{-d/2}\det(\boldsymbol{\Sigma}_i)^{-1/2} \times \exp\left[-(\mathbf{x}-\mathbf{m}_i)^{\mathrm{T}}\boldsymbol{\Sigma}_i^{-1}(\mathbf{x}-\mathbf{m}_i)\right] \quad [24]$$

where: $\boldsymbol{\Sigma}_i$ is the covariance matrixand $\mathbf{m}_i$ is the mean vector. Consider the case where the two classes are equiprobable and have the same covariance matrix $\boldsymbol{\Sigma}$.

The decision between the two classes is based on the log-likelihood function which is the difference between the log-likelihood for class 1 and the log-likelihood for class 2. The log-likelihood for class ω_i, $l_i(\mathbf{x})$, is:

$$l_i(\mathbf{x}) = \mathbf{m}_i^{\mathrm{T}}\boldsymbol{\Sigma}^{-1}\mathbf{x} \quad [25]$$

Therefore, the log-likelihood function $l(\mathbf{x})$ is written:

$$l(\mathbf{x}) = (\mathbf{m}_1 - \mathbf{m}_2)^{\mathrm{T}}\boldsymbol{\Sigma}^{-1}\mathbf{x} - \tfrac{1}{2}\left(\mathbf{m}_1^{\mathrm{T}}\boldsymbol{\Sigma}^{-1}\mathbf{m}_1 - \mathbf{m}_2^{\mathrm{T}}\boldsymbol{\Sigma}^{-1}\mathbf{m}_2\right) \quad [26]$$

This expression is a linear function of vector $\mathbf{x}$ which can be written:

$$l(\mathbf{x}) = \mathbf{w}^{\mathrm{T}}\mathbf{x} - t \quad [27]$$

with:

$$\mathbf{w} = \boldsymbol{\Sigma}^{-1}(\mathbf{m}_1 - \mathbf{m}_2) \quad [28]$$

$$t = \tfrac{1}{2}\left(\mathbf{m}_1^{\mathrm{T}}\boldsymbol{\Sigma}^{-1}\mathbf{m}_1 - \mathbf{m}_2^{\mathrm{T}}\boldsymbol{\Sigma}^{-1}\mathbf{m}_2\right) \quad [29]$$

One recognizes the classic perceptron equation. The classification rule is the following:

$l > 0$: assign $\mathbf{x}$ to class ω_1
$l < 0$: assign $\mathbf{x}$ to class ω_2

Gaussian classifier between two classes having the same covariance matrix is analogous to a single layer perceptron.

Conclusion

Notice that the single-layer perceptron is a good solution if the sets are linearly separable. In the case it being not true, no one has any information about the solution of the algorithm. If the convergence is not reached after a finite number of iterations, it can be either because the algorithm needs more iterations or because the sets are not linearly separable.

Multilayer Network

In **Figure 3**, the structure of a fully connected multilayer network with hidden layers is indicated. Each neuron is connected with all neurons in the previous layer and with neurons in successive layers.

According to the previously described two phases, this network runs two ways:

1. usual running. An input signal is applied at the input of the network, propagates neuron by

neuron and an output signal is produced. The propagation is a forward one.
2. training running. When an input signal from the set of examples is applied to the network, an error signal is generated from the difference between the observed output and the desired one. This error is propagated backwards, layer by layer through the network. This propagation permits the learning of the weights of the network. This kind of training algorithm is called back propagation algorithm.

Back Propagation Algorithm

An error signal e_k is computed for each neuron k of the output layer at iteration n after the example n (or pattern n) has been presented. It is defined by:

$$e_k(n) = d_k(n) - y_k(n) \quad [30]$$

$d_k(n)$ is the desired output of neuron k at iteration n
$y_k(n)$ is the observed output of neuron k at iteration n

The instantaneous sum of square error is written from eqn [11]:

$$E(n) = \frac{1}{2}\sum_{k\in O} e_k^2(n) \quad [31]$$

O indicates the output layer of the network. To describe a training method, working pattern by pattern: the adjustments of the weights will be done in accordance with each observed error mean observed for each pattern. Two cases have to be considered: the first is dedicated to weight modification of neurons from the output layer, the second to weight modification of a neuron in a hidden layer.

In the first case, neuron j belongs to the output layer. The internal activity of the neuron is written:

$$u_j(n) = \sum_{i=0}^{p} w_{ji}(n)y_i(n) \quad [32]$$

where p is the total number of inputs of neuron j. Its output is:

$$y_j(n) = f\left[u_j(n)\right] \quad [33]$$

To train the weights, a gradient optimization algorithm is applied. Starting with an initial value $w_{ji}(0)$, the weight $w_{ji}(n)$ is modified at each iteration by a quantity $\Delta w_{ji}(n)$, which is deduced from the instantaneous gradient $\partial E(n)/\partial w_{ji}(n)$:

$$\frac{\partial E(n)}{\partial w_{ji}(n)} = \frac{\partial E(n)}{\partial e_j(n)}\frac{\partial e_j(n)}{\partial y_j(n)}\frac{\partial y_j(n)}{\partial u_j(n)}\frac{\partial u_j(n)}{\partial w_{ji}(n)} \quad [34]$$

It is easy to show the following results:

$$\frac{\partial E(n)}{\partial w_{ji}(n)} = -e_j(n)f'\left[u_j(n)\right]y_i(n) \quad [35]$$

The correction factor for weight $w_{ji}(n)$ is written:

$$\Delta w_{ji}(n) = \alpha e_j(n)f'\left[u_j(n)\right]y_i(n) \quad [36]$$

with α as the learning parameter. Equation [36] can be written:

$$\Delta w_{ji}(n) = \alpha\eta_j(n)y_i(n) \quad [37]$$

with

$$\eta_j(n) = e_j(n)f'\left[u_j(n)\right] \quad [38]$$

where $\eta_j(n)$ is equivalent to a local gradient.

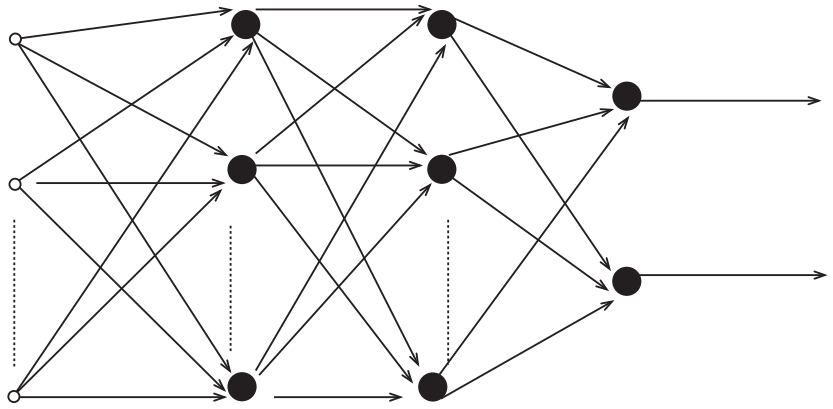


Figure 3 Structure of a fully connected multilayer network with hidden layers.

In the second case, neuron j belongs to a hidden layer if neuron j belongs to a hidden layer, it is not directly accessible. It is impossible to evaluate the $e_j(n)$, difference between the observed and the desired output because it is not known which output is desired. It is necessary to restart the computing, and the error signal for a hidden neuron has to be determined recursively from the error signals of all the neurons to which this neuron is directly connected:

$$\frac{\partial E(n)}{\partial w_{ji}(n)} = \frac{\partial E(n)}{\partial y_j(n)} \frac{\partial y_j(n)}{\partial u_j(n)} \frac{\partial u_j(n)}{\partial w_{ji}(n)} \qquad [39]$$

$$\begin{aligned} \frac{\partial E(n)}{\partial w_{ji}(n)} &= \left\{ f'\left[u_j(n)\right] \sum \eta_k(n) w_{kj}(n) \right\} y_i(n) \frac{\partial E(n)}{\partial w_{ji}(n)} \\ &= \frac{\partial E(n)}{\partial y_j(n)} f'\left[u_j(n)\right] y_i(n) \end{aligned} \qquad [40]$$

By a simple computation:

$$\frac{\partial E(n)}{\partial y_j(n)} = -\sum e_k(n) f'[u_k(n)] w_{kj}(n) \qquad [41]$$

$$\frac{\partial E(n)}{\partial y_j(n)} = -\sum \eta_k(n) w_{kj}(n) \qquad [42]$$

where $\eta_k(n)$ is based on the knowledge of the error signals, $e_k(n)$, for all the neurons belonging to the layer to the immediate right of hidden neuron, j, and are connected to this neuron.

If one uses a sigmoid activation function:

$$y_j(n) = \frac{1}{1 + \exp\left[-u_j(n)\right]} \qquad [43]$$

So:

$$y_j'(n) = \frac{\exp\left[-u_j(n)\right]}{\left\{1 + \exp\left[-u_j(n)\right]\right\}^2} = y_j'(n)\left[1 - y_j'(n)\right] \qquad [44]$$

There are two training formula according to the position of the neuron:

1. for a neuron in the output layer:

$$\eta_j(n) = \left[d_j(n) - y_j(n)\right] y_j(n)\left[1 - y_j(n)\right] \qquad [45]$$

2. for a hidden neuron:

$$\eta_j(n) = y_j(n)\left[1 - y_j(n)\right] \sum_l \eta_l(n) w_{lj}(n) \qquad [46]$$

Rate of Learning

This algorithm is an approximation to the trajectory in the weight space. The role of the training rate parameter is important: the smaller it is, the smaller will be the modifications of the weights from iteration to another one and the smoother will be the trajectory. By choosing a larger value for the training rate parameter, the network may become oscillatory.

A simple method for increasing the rate of learning and for diminishing the risk of instability is to modify the rule by including a momentum term:

$$\Delta w_{jk}(n) = \gamma w_{jk}(n-1) + \alpha \eta_j(n) y_k(n) \qquad [47]$$

where γ is positive and controls the loop introduced by using the previous modification.

Adding momentum in the algorithm may have interesting effects on the behavior of the algorithm. It can also prevent the process from finishing in a shallow local minimum of the error function.

Presentation of Patterns

An epoch is a complete presentation of the entire training set. Two ways can be used for presenting patterns:

1. each training pattern is presented singly and the parameter updating is done afterwards. This is how the algorithm has been described each time a pair $(\mathbf{x}_i, d_i)$ is presented to the network and the weights are computed according to the error detected at the output. This mode is often called the pattern mode.
2. weights updating is done after the presentation of all the training examples, that is, after an epoch. This mode is called batch mode. The estimation of the mean error is better than in the pattern mode, but the value of updating Δw_{ji} in the pattern mode is an estimate of the same quantity in the batch mode.

Stopping Criteria

In order to finish the weight adjustments, several different criteria may be used. If $\mathbf{w}^*$ is the solution corresponding to a minimum of the error function (this minimum can be local or global); for this value, the gradient vector of the error function is zero, so a criterion can be based on the computation of this vector:

1. first criterion: the norm of the gradient vector is smaller than a chosen threshold.
   Another possibility is based on the stationary property of the error function for a global or local minimum:

2. second criterion: the absolute rate of change in the average squared error per epoch is smaller than a chosen threshold.

   At last, one can use the value of the error function:
3. third criterion: the value of the error function is smaller than a chosen threshold.

Using a Multilayer Network

If we want to classify patterns coming from M classes, the output of the network may be composed of M cells. If $\mathbf{x}(n)$ is the pattern at the input at time n and $y_m(n)$ is the value of the output of the cell m, the $y_m(n)$ is one of the results of a nonlinear transformation $\mathbf{\Phi}(\cdot)$ of the input $\mathbf{x}(n)$:

$$y(n) = \mathbf{\Phi}[x(n)] \qquad [48]$$

Suppose now that the desired output is a binary one, that is:

- $d_m(n)$, desired output of cell m is equal to one when the pattern $\mathbf{x}(n)$ belongs to class m
- $d_m(n)$ is equal to zero when the pattern $\mathbf{x}(n)$ belongs to another class.

The mean-squared error J is defined by:

$$J = \frac{1}{2N}\sum_{n=1}^{N} \|d(n) - \mathbf{\Phi}[\mathbf{x}(n)]\|^2 \qquad [49]$$

If $\mathbf{w}*$ is the optimum vector minimizing J, $\mathbf{\Phi}(\mathbf{w}*, \mathbf{x})$ is a mean-squared approximation of $E[\mathbf{d}/\mathbf{x}]$. Under the choice of values of $d_m(n)$, $E[\mathbf{d}/\mathbf{x}]$ equals the *a posteriori* class probability. Therefore if $\mathbf{d}_m$ has a 1 in mth position indicating the pattern belongs to class m, $E[\mathbf{d}_m/\mathbf{x}]$ equals $Pr(\text{class } m/\mathbf{x})$.

So using classical Bayes decision theory, the rule classification is simply:

- $\mathbf{x}(n)$ is associated with class m if $\Phi_m[\mathbf{x}(n)] > \Phi_j[\mathbf{x}(n)] \quad \forall j \neq m$ where $\Phi_m[\mathbf{x}(n)]$ are the components of vector $\mathbf{\Phi}$.

So, if the network has been trained using the previous desired outputs, a new vector is classified in the class corresponding to the cell with maximum output. Notice also that the outputs may be used as a value for membership functions in fuzzy decision. Using such a decision rule, the class membership is characterized by a M-components vector $\boldsymbol{\mu}$:

$$\boldsymbol{\mu} = \begin{Bmatrix} y_1 \\ \vdots \\ y_M \end{Bmatrix} \qquad [50]$$

The only condition is the use of an activation function with values in $[0, 1]$.

Radial-basis Function Networks

Consider a multilayer network with only a hidden layer and linear outputs (**Figure 4**). The neuron k of the output layer has the weight $\mathbf{w}_k$, the neuron j of the hidden layer, the weight $\mathbf{p}_j$. The output of such a multilayer network is written:

$$y_k = \sum_j w_{kj} f(\mathbf{p}_j, \mathbf{x}) + w_{k0} \qquad [51]$$

For example, one can choose a sigmoid function:

$$g(\mathbf{p}_j, \mathbf{x}) = \frac{1}{1 + \exp\left(-\mathbf{p}_j^{\mathrm{T}}\mathbf{x}\right)} \qquad [52]$$

One can see that the expression [51] is identical to the decomposition of the value y_i on to a basis of functions. The argument of each function is the inner product between the input and a weight vector. This representation is characterized by the important number of neurons implied in the computation of the output.

Definition of Radial-basis Function (RBF) Networks

Radial-basis function networks use this property but are different in the fact that the representation is local by using local basis functions. A prototype is associated with each basis function and the value of this function is dependent on the distance between the input and this prototype.

$$g(\mathbf{p}_j, \mathbf{x}) = \phi_i(\mathbf{x}) = \phi_i(\|\mathbf{x} - \mathbf{p}_i\|) \qquad [53]$$

The functions $\phi_i()$ are maximum for $\mathbf{x} = \mathbf{p}_i$ and tend to zero when $\mathbf{x}$ tends to infinity. The most used function is the gaussian one:

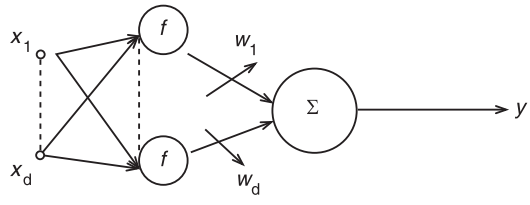


Figure 4 Multilayer network with a hidden layer and linear outputs.

Next Page

$$\phi_i(\mathbf{x}) = \exp\left[-\frac{1}{2}(\mathbf{x}-\mathbf{p}_i)^{\mathrm{T}}\boldsymbol{\Sigma}_i^{\mathrm{T}}(\mathbf{x}-\mathbf{p}_i)\right] \quad [54]$$

$\boldsymbol{\Sigma}_i$ is the covariance matrix associated with the corresponding neuron. Often, one uses a diagonal form for $\boldsymbol{\Sigma}_i$ as $\boldsymbol{\Sigma}_i = \sigma_i^2 I$. In the general case, this matrix must be positive definite. Iso-activation curves are hyper ellipsoids in a $(d-1)$ space.

Only, a small number of basis functions are implied in the computation of the output for a given input. For example, if an input is in an area far from all the prototypes, the activation of the hidden neurons will be weak. This property is very interesting for some diagnostic problems where the knowledge is incomplete.

Some problems can be solved using radial-basis architecture, which cannot be solved using classical multilayer architecture: they can detect new situations, which is impossible for multilayer networks. For example, all the outputs can be near zero for some inputs, indicating that this input does not correspond to an input used for training.

Consider a radial-basis function network with p hidden neurons, the activation function of each neuron being eqn [54]. The bias term can be put in the sum by using a specific cell with an activation function identical to one. So:

$$\begin{aligned} y_k &= \sum_{j=0}^{M} w_{kj}\phi_j(\mathbf{x}) \\ \phi_0(\mathbf{x}) &= 1 \quad \forall \mathbf{x} \end{aligned} \quad [55]$$

Let:

$$\mathbf{W} = \{w_{kj}\} \quad \boldsymbol{\Phi} = \{\phi_j\} \quad [56]$$

Therefore:

$$\mathbf{y} = \mathbf{W}\boldsymbol{\Phi} \quad [57]$$

This network, as the previous one, can also solve approximation problems.

Training of RBF networks

In order to simplify the notations, consider a network with only an output, which is called a regularization network.

Three kinds of parameters have to be determined: the prototypes $\mathbf{p}_j$, the covariance matrices $\boldsymbol{\Sigma}_j$ and the weight matrix $\mathbf{W}$. We can use also the error-correction rule, which can be implemented using a gradient-descent procedure.

To define as an instantaneous cost function:

$$E = \frac{1}{2}\sum_{i=1}^{n} e_i^2 \quad [58]$$

where n is the number of training examples, and e_i is the error signal defined by:

$$e_i = d_i - y_i \quad [59]$$

The solution is given by the following equations:

- weights

$$\begin{aligned} \frac{\partial E(n)}{\partial w_i(n)} &= \sum_{j=1}^{n} e_j(n)\phi\{[\|\mathbf{x}_j - \mathbf{p}_j(n)\|]\} \\ w_i(n+1) &= w_i(n) - \alpha_i \frac{\partial E(n)}{\partial w_i(n)} \end{aligned} \quad [60]$$

- prototypes

$$\begin{aligned} \frac{\partial E(n)}{\partial p_i(n)} &= 2w_i(n)\sum_{j=1}^{n} e_j(n)\phi'\{[\|\mathbf{x}_j - \mathbf{p}_i(n)\|]\} \\ &\quad \times \boldsymbol{\Sigma}_i^{-1}(n)[\mathbf{x}_j - \mathbf{p}_i(n)] \\ p_i(n+1) &= \mathbf{p}_i(n) - \beta\frac{\partial E(n)}{\partial \mathbf{p}_i(n)} \end{aligned} \quad [61]$$

- Covariance matrix

$$\begin{aligned} \frac{\partial E(n)}{\partial \boldsymbol{\Sigma}_i^{-1}(n)} &= -w_i(n)\sum_{j=1}^{n} e_j(n) \\ &\quad \times \phi'\{[\|\mathbf{x}_j - \mathbf{p}_i(n)\|]\}A_{ji}(n) \\ Q_{ji}(n) &= [\mathbf{x}_j - \mathbf{p}_i(n)][\mathbf{x}_i - \mathbf{p}_i(n)]^{\mathrm{T}} \\ \boldsymbol{\Sigma}_i^{-1}(n+1) &= \boldsymbol{\Sigma}_i^{-1}(n) - \gamma\frac{\partial E(n)}{\partial \boldsymbol{\Sigma}_i^{-1}(n)} \end{aligned} \quad [62]$$

Comparison of RBF and Multilayer Networks

These two kind of networks are both approximators. But there are some differences between these two kinds of architecture:

1. a multilayer network may have more than one hidden layer. The RBF network has only one.
2. in a RBF, the hidden layer is nonlinear and the output layer linear. On the other hand, all the layers in the multilayer network are nonlinear.

3. the activation function of a RBF is based on the distance between the pattern and the prototype. The activation function of a multilayer network is based on the computation of an inner product.
4. the nodes of a multilayer network have all the same activation function; it is not the case for RBF networks.
5. the approximation for a RBF network is a local one. On the contrary, multilayer networks realize global approximation in the entire space.

Using RBF Networks

For solving diagnostic problems, one has two possibilities, (i) either to train as many RBF networks as there are classes: each RBF classifies to a class. Then, the input pattern is associated with the output of the network, which is maximum. Or (ii) to train a network with as many outputs as there are classes. The input vector is then associated with the class corresponding to the maximum output. In each case, it is also possible to use fuzzy decision: the value of the output is the value of the membership function for the corresponding class. But this kind of network has another possibility, not existing for multilayer networks: when all the outputs are very small, it may indicate that the pattern comes from a class which has not been represented in the training set. So, this network can classify with an incomplete training set. Further, when there are two or more maximums in the outputs, it may indicate that the pattern may belong to more than one class. RBF network can classify with an ambiguity possibility.

Nomenclature

e	error
i	input
J	mean-squared error
$l(\mathbf{x})$	log-likelihood function
$\mathbf{m}$	mean vector
O	output layer of the network
t	threshold
T	training set
u	output
w	weight
$\mathbf{W}$	weight matrix
$\mathbf{\Sigma}$	covariance matrix

See also: **Diagnostics and condition monitoring, basic concepts**; **Neural networks, diagnostic applications**; **Nonlinear systems, overview**.

Further Reading

Bishop CM (1995) *Neural Networks for Pattern Recognition*. Oxford University Press.

Haykin S (1994) *Neural Networks. A Comprehensive Foundation*. Macmillan College.

Looney CG (1997) *Pattern Recognition using Neural Networks*. Oxford University Press.

Ripley BD (1996) *Pattern Recognition and Neural Networks*. Cambridge University Press.

Tsoukalas LH, Uhrig RE (1997) *Fuzzy and Neural Approaches in Engineering*. John Wiley.

Vapnik VN (1995) *The Nature of Statistical Learning Theory*. Springer Series in Statistics. Springer.

NOISE

Noise Radiated from Elementary Sources

M P Norton and J Pan, University of Western Australia, Nedlands, Perth, Western Australia

Copyright © 2001 Academic Press

doi:10.1006/rwvb.2001.0145

Introduction

Sound is a pressure wave that propagates through an elastic medium at some characteristic speed. It is the molecular transfer of motional energy and cannot therefore pass through a vacuum. For this wave motion to exist, the medium has to possess inertia and elasticity. Whilst vibration relates to such wave motion in structural elements, noise relates to such wave motion in fluids (gases and liquids). Two fundamental mechanisms are responsible for sound generation in typical engineering-type applications. They are:

1. the vibration of solid bodies resulting in the generation and radiation of sound energy – these sound waves are generally referred to as structure-borne sound
2. flow-induced noise resulting from pressure fluctuations induced by turbulence and unsteady flows – these sound waves are generally referred to as aerodynamic sound.

Both of the above sound generation mechanisms are associated with changes in volume velocity density due to either structural or aerodynamic excitation mechanisms. Sound pressure can also be generated through changes in force density. For instance, external electric and magnetic fields produce forces on ionized gas or plasma and are characterized as the acoustical sources of plasma waves. This article is, however, only concerned with the sound generation by the changes in the volume velocity density, specifically for the structural excitation mechanism.

With structure-borne sound, the regions of interest are generally in a fluid (usually air) at some distance from the vibrating structure. Here, the sound waves propagate through the stationary fluid (the fluid has a finite particle velocity due to the sound wave, but a zero mean velocity) from a readily identifiable source to the receiver. The region of interest does not therefore contain any sources of sound energy, i.e., the sources which generate the acoustic disturbance are external to it and can be described as boundary conditions. Classical acoustical theory (analysis of the homogeneous wave equation) can be used for the analysis of sound waves generated by these types of sources. The solution for the acoustic pressure fluctuation describes the wave field external to the source as boundary conditions. If required, the source can be accounted for in the wave field by considering the initial, time-dependent conditions.

With aerodynamic sound, the sources of sound are not so readily identifiable and the regions of interest can be either within the fluid flow itself or external to it. When the regions of interest are within the fluid flow, they contain sources of sound energy because the sources are continuously being generated or convected with the flow (e.g., turbulence, vortices, etc.). These aerodynamic sources therefore have to be included in the wave equation for any subsequent analysis of the sound waves in order that they can be correctly identified. The wave equation is now inhomogeneous (because it includes the spatially distributed source terms) and its solution is somewhat different to that of the homogeneous wave equation in that it now describes both the source and the wave fields.

The vast majority of engineering noise and vibration control relates to sources which can be readily identified, and regions of interest which are outside the source region – in these cases the homogeneous wave equation is sufficient to describe the wave field and the subsequent noise radiation provided that the boundary conditions can be specified. There are, however, instances where the inhomogeneous wave equation has to be used in place of the more familiar homogeneous wave equation. The advantage of the inhomogeneous wave equation is that it can be used for modeling noise radiation from sound sources in both situations. In this article, the noise radiated from elementary vibrational sources is derived directly from the inhomogeneous wave equation.

Sound Waves and Sound Sources

Most noise sources that are of concern to engineers (e.g., vehicles, construction equipment, industrial machinery, appliances, flow-duct systems, etc.) can be modeled in terms of simple sources. It is therefore instructive to analyze the characteristics of some of these idealized sound sources. Consider sound wave propagation through a compressible fluid of mass density ρ_o with finite volume elasticity. The combination of the fluid kinetic inertia and elastic recovery characteristics provides the two requisites for the generation and propagation of sound waves. Sound waves are described by sound pressure $p(\mathbf{r}, t)$ and particle velocity $\mathbf{v}(\mathbf{r}, t)$. The dynamic property of sound waves is characterized by:

$$\rho_o \frac{\partial \mathbf{v}}{\partial t} = -\nabla p \qquad [1]$$

and the thermal dynamic property is characterized by:

$$\frac{\partial p}{\partial t} = -P_o \gamma \nabla \cdot \mathbf{v} \qquad [2]$$

where P_o is the atmospheric pressure and γ is the ratio of specific heats. The two properties described in eqns [1] and [2] (Euler's field equations) mathematically generate the wave equation (Helmholtz equation) of sound pressure in a compressible fluid:

$$\nabla^2 p - \frac{1}{c_o^2} \frac{\partial^2 p}{\partial t^2} = 0 \qquad [3]$$

where $c_o = \sqrt{P_o \gamma / \rho_o}$ is the speed of sound.

As mentioned earlier, sound pressure may be generated through force density (force per unit volume) $\mathbf{q}_f(\mathbf{r}_o)$ and volume velocity density $q_v(\mathbf{r}_o)$ due to external excitation mechanisms, such as the out–off plane vibration of structures. With the external inputs, the Euler's field equations become:

$$\nabla p + \rho_o \frac{\partial \mathbf{v}}{\partial t} = \mathbf{q}_f(\mathbf{r}_o) \qquad [4]$$

and:

$$\frac{1}{P_o \gamma} \frac{\partial p}{\partial t} + \nabla \cdot \mathbf{v} = q_v(\mathbf{r}_o) \qquad [5]$$

which results in the inhomogeneous Helmholtz equation:

$$\nabla^2 p - \frac{1}{c_o^2}\frac{\partial^2 p}{\partial t^2} = \nabla \cdot \mathbf{q}_f(\mathbf{r}_o) - \rho_o \frac{\partial q_v(\mathbf{r}_o)}{\partial t} \qquad [6]$$

This article is concerned with the sound generation by the volume velocity density. As a result, only the second term in the right-hand side of eqn [6] is considered here.

Green's Functions and the Sound Pressure Field

The general solution to the inhomogeneous wave equation can be obtained by superposition of the acoustic fields due to simple point sources. In order to do this, a Green's function needs to be introduced. Green's functions satisfy the inhomogeneous wave equation, and if the medium surrounding the source is stationary and not restricted by any boundaries, they are commonly referred to as free-space Green's functions. The Green's function can be interpreted as the solution to the wave equation in free space for an applied unit, time-harmonic, point source, or as the solution to the wave equation in free space for a unit, impulsive, point source. An important property of the Green's function is that it is symmetrical, i.e., it remains the same when the source and the receiver positions are interchanged. This property, commonly known as reciprocity, has important applications in noise and vibration control.

The sound pressure in a free field is obtained using the Green's function technique. By solving the steady-state Green's equation:

$$\nabla^2 g(\mathbf{r}|\mathbf{r}_o) + k^2 g(\mathbf{r}|\mathbf{r}_o) = -\delta(\mathbf{r} - \mathbf{r}_o) \qquad [7]$$

the free-space Green's function is obtained as:

$$g(\mathbf{r}|\mathbf{r}_o) = \frac{1}{4\pi|\mathbf{r} - \mathbf{r}_o|}\mathrm{e}^{-jk|\mathbf{r}-\mathbf{r}_o|} \qquad [8]$$

The Green's equation and the Green's function lead to the expression of the sound pressure in free space generated by the volume velocity density of the sound source as:

$$p(\mathbf{r}, t) = j\rho_o\omega \int \frac{q_v(\mathbf{r_o})}{4\pi|\mathbf{r} - \mathbf{r_o}|}\mathrm{e}^{j\omega t - jk|\mathbf{r}-\mathbf{r}_o|}\mathrm{d}V_o \qquad [9]$$

For a confined source distribution $kr_0 \ll 1$, the sound field generated can be divided into three regions in terms of the ratio between the observation location r and the wavelength λ of the sound wave. Here:

1. for the near field: $r/\lambda \ll 1$
2. for the middle field: $r/\lambda \sim 1$
3. and, for the far field: $r/\lambda \gg 1$

In the near-field region ($kr \ll 1$), the sound pressure distribution as a function of distance r is highly dependent upon the distribution of the sound source. The sound pressure is controlled not only by the $1/r$ terms, but also by higher-order terms such as $1/r^{l+1}$ $(l = 1, 2, 3, \ldots)$. In the far-field region ($kr \gg 1$), however, the condition of $r \gg r_0$ allows for the following approximations:

$$\frac{1}{|\mathbf{r} - \mathbf{r}_o|} \cong \frac{1}{r} \qquad [10a]$$

for the amplitude in eqn [9] and:

$$|\mathbf{r} - \mathbf{r}_o| \cong r - r_o \cos\Theta \qquad [10b]$$

for the exponential term in eqn [9], where:

$$\cos\Theta = \cos\theta\cos\theta_o + \sin\theta\sin\theta_o\cos(\phi - \phi_o) \qquad [11]$$

As a result, the far-field sound pressure is:

$$p(\mathbf{r}, t) = j\rho_o\omega\frac{\mathrm{e}^{j\omega t - jkr}}{4\pi r}\int q_v(\mathbf{r_o})\mathrm{e}^{jkr_o\cos\Theta}\mathrm{d}V_o \qquad [12]$$

which is a typical radiating field with its magnitude decaying as a function of r^{-1}.

Multipole Descriptions of a Radiating Sound Field

The far-field sound radiation from a confined source can be Taylor-expanded in terms of the nondimensional size of the sound source kr_o:

$$p(\mathbf{r}, t) = j\rho_o\omega\frac{\mathrm{e}^{j\omega t - jkr}}{4\pi r} \times \sum_{l=0}^{\infty}\frac{1}{l!}\int q_v(\mathbf{r_o})(jkr_o\cos\Theta)^l\mathrm{d}V_o \qquad [13]$$

The directivity-dependent terms $(\cos\Theta)^l$ represent the far-field monopole, dipole, and quadrupole sound radiation when $l = 0,\ 1,\ 2$. This can be illustrated by expressing $(\cos\Theta)^l$ in Legendre polynomials and then in spherical harmonic functions. Using the Legendre polynomials to express $(\cos\Theta)^l$, eqn [13] becomes:

$$p(\mathbf{r},t) = j\rho_o\omega\frac{e^{j\omega t-jkr}}{4\pi r} \times \sum_{l=0}^{\infty}\int q_v(\mathbf{r_o})a_l P_l(\cos\Theta)\,dV_o \quad [14]$$

where for $kr_o \ll 1$:

$$a_0 \cong 1 \quad [15a]$$

$$a_1 \cong jkr_o \quad [15b]$$

and:

$$a_2 \cong \frac{1}{3}(jkr_o)^2 \quad [15c]$$

Using the spherical harmonic functions for the Legendre polynomials, we finally obtain the multipole expansion of the radiating sound field:

$$p(\mathbf{r},t) = j\rho_o\omega\frac{e^{j\omega t-jkr}}{r}\sum_{l=0}^{\infty}\sum_{m=-l}^{l} q_{lm}Y_{lm}(\theta,\phi) \quad [16]$$

where the coefficients of the $(l,\ m)$th-order radiating modes are:

$$q_{lm} = \frac{(-1)^m}{2l+1}\int q_v(\mathbf{r_o})(jkr_o)^l a_l Y^*_{lm}(\theta_o,\phi_o)\,dV_o \quad [17]$$

The spherical harmonic functions are defined as:

$$Y_{lm}(\theta,\phi) = \sqrt{\frac{(2l+1)}{4\pi}\frac{(l-m)!}{(l-m)!}}P_l^m(\cos\theta)e^{jm\phi} \quad [18]$$

where the $P_l^m(\cos\theta)$ are the associated Legendre polynomials and are:

$$P_l^m(x) = \frac{(-1)^m}{2^l l!}(1-x^2)^{m/2}\frac{d^{l+m}}{dx^{l+m}}(x^2-1)^l \quad [19]$$

with $x = \cos\theta$. When m is a negative number, the following relationship is used:

$$Y_{l-m}(\theta,\phi) = (-1)^m Y^*_{lm}(\theta,\phi) \quad [20]$$

In eqn [16], the monopole, dipole, and quadrupole sound radiations are represented by the fundamental radiation modes described by the spherical harmonic functions with $l = 0\,(m = 0)$, $l = 1\,(m = -1,\ 0,\ 1)$, and $l = 2\,(m = -2,\ -1,\ 0,\ 1,\ 2)$. **Table 1** shows the corresponding radiating modes and their directivities.

Monopole Sound Radiation

A monopole is a single, spherical sound source which radiates sound waves that are only a function of the radial distance, r, from the source. Some typical examples of monopole sound sources associated with vibrating structures are small electric motors, pumps, and certain types of traffic noise (at medium distances away from a single vehicle – at larger distances the source can sometimes appear to be a dipole). Aerodynamic monopole sound sources include unsteady combustion from a furnace, sirens, pulsed jets, and cavitation.

The volume velocity density of a point source with volume velocity Q at $\mathbf{r}_o = 0$ is:

$$q_v(\mathbf{r_o}) = Q\delta(\mathbf{r_o}) \quad [21]$$

With such a source distribution, the nonzero solution of eqn [17] is:

$$q_{00} = \frac{Q}{\sqrt{4\pi}} \quad [22]$$

which gives rise to the radiated monopole sound pressure:

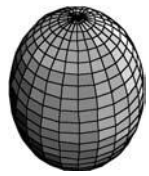
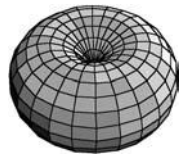
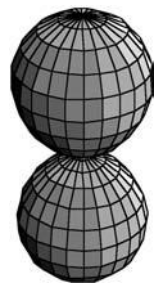
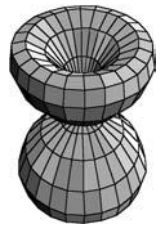
$$p(\mathbf{r},t) = \frac{j\rho_o\omega Q}{4\pi r}e^{j\omega t-jkr} \quad [23]$$

where $j\rho_0\omega Q$ is called the strength of the point source.

Dipole Sound Radiation

A dipole is a sound source model that is comprised of two monopoles in close proximity to each other. They are also of equal source strength and oscillate 180° out of phase with each other. A net fluctuating force is produced because of this out-of-phase oscillation. A dipole is thus produced by the fluctuating

Table 1 (See Plate 47). Spherical harmonic functions $Y_{lm}(\theta, \phi)$ and their directivities $|Y_{lm}(\theta, \phi)|$

$i = 0$	$Y_{00}(\theta, \phi) = \frac{1}{\sqrt{4\pi}}$	
	$Y_{11}(\theta, \phi) = -\sqrt{\frac{3}{8\pi}} \sin\theta \, e^{j\phi}$	
$i = 1$	$Y_{10}(\theta, \phi) = \sqrt{\frac{3}{4\pi}} \cos\theta$	
	$Y_{22}(\theta, \phi) = \frac{1}{4}\sqrt{\frac{15}{2\pi}} \sin^2\theta \, e^{j2\phi}$	
$i = 2$	$Y_{21}(\theta, \phi) = -\sqrt{\frac{15}{8\pi}} \sin\theta \cos\theta \, e^{j\phi}$	
	$Y_{20}(\theta, \phi) = \sqrt{\frac{5}{4\pi}}\left(\frac{3}{2}\cos^2\theta - \frac{1}{2}\right)$	

pressure forces (generated by the out-of-phase oscillations of the two monopoles in close proximity to each other) acting along the axis between the two sources.

Figure 1 shows a distribution of two point sources with equal strength but opposite phase. They are located along the Z axis, separated by a distance, d. The volume velocity density of the source is:

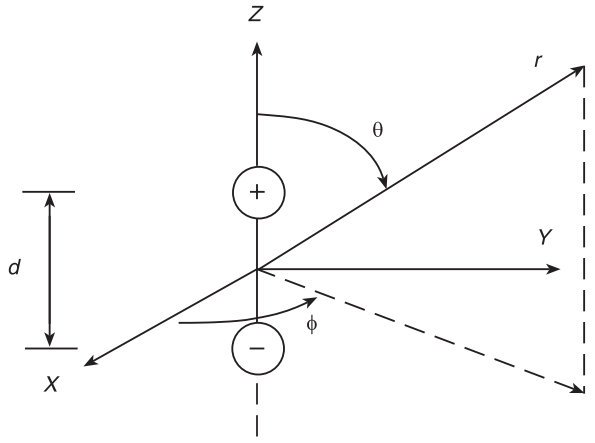


Figure 1 Spherical coordinates and a dipole sound source distribution.

$$q_v(\mathbf{r}_o) = Q\delta\left(\mathbf{r}_o - \frac{d}{2}\hat{z}\right) - Q\delta\left(\mathbf{r}_o + \frac{d}{2}\hat{z}\right) \qquad [24]$$

The nonzero term of eqn [17] is:

$$q_{10} = \frac{jQkd}{3}\sqrt{\frac{3}{4\pi}} \qquad [25]$$

Thus, the radiated sound pressure has the form:

$$\begin{aligned} p(\mathbf{r},t) &= j\rho_o\omega\frac{e^{j\omega t - jkr}}{r}q_{10}Y_{10}(\theta,\phi) \\ &= -\rho_o\omega\frac{Qkd}{4\pi r}\cos\theta\, e^{j\omega t - jkr} \end{aligned} \qquad [26]$$

which has the directivity of a dipole ($Y_{10}(\theta\phi)$).

If the source distribution is along the y-axis, as shown in **Figure 2**, the volume velocity density is:

$$q_v(\mathbf{r}_o) = Q\delta\left(\mathbf{r}_o - \frac{d}{2}\hat{y}\right) - Q\delta\left(\mathbf{r}_o + \frac{d}{2}\hat{y}\right) \qquad [27]$$

The corresponding nonzero terms from eqn [17] are:

$$q_{11} = \frac{1}{3}Qkd\sqrt{\frac{3}{8\pi}} \qquad [28a]$$

and:

$$q_{1-1} = q_{11} \qquad [28b]$$

Thus the resultant sound field is:

$$\begin{aligned} p(\mathbf{r},t) &= j\rho_o\omega\frac{e^{j\omega t - jkr}}{r}[q_{11}Y_{11}(\theta,\phi) + q_{1-1}Y_{1-1}(\theta,\phi)] \\ &= -j\rho_o\omega\frac{Qkd}{4\pi r}\sin\theta\cos\phi\, e^{j\omega t - jkr} \end{aligned} \qquad [29]$$

which also shows a dipole directivity. Note that the dumbbell radiation directivity in the y-axis is due to the superposition of two donut-shaped radiating modes ($Y_{11}(\theta\phi)$ and $Y_{1-1}(\theta\phi)$).

Quadrupole Sound Radiation

Monopoles were modeled as single oscillating spheres, and dipoles were modeled as two equal spheres oscillating out of phase. A natural extension to these acoustic source models is two dipole sources in close proximity to each other and oscillating 180° out of phase with each other. Such a sound source is called a quadrupole. Whereas a dipole has one axis (i.e., the fluctuating pressure forces act along the axis between the two sources), a quadrupole has two. The two dipoles oscillating out of phase with each other result in no net addition or subtraction of mass away from the source, and no resultant force, i.e. there is no physical mechanism available for the mass or the momentum to vary. The quadrupole does, however, apply a stress to the medium and it is this fluctuating stress that generates the sound (monopoles generate sound via fluctuating surface velocities or the addition/subtraction of mass from a source region, and dipoles generate sound via fluctuating forces). In gas flows, for instance, quadrupoles are generated by the viscous stresses within the gas.

Both longitudinal (**Figure 3A**) and lateral (**Figure 3B**) quadrupoles are also special cases of source distribution according to eqn [17]. The source distribution of a longitudinal quadrupole is

$$q_v(\mathbf{r_o}) = Q\delta(\mathbf{r_o} - d\hat{y}) - 2Q\delta(\mathbf{r_o}) + Q\delta(\mathbf{r_o} + d\hat{y}) \qquad [30]$$

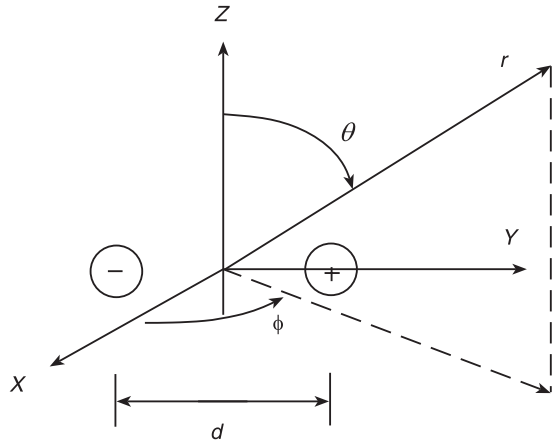


Figure 2 Dipole source distribution in the y-axis.

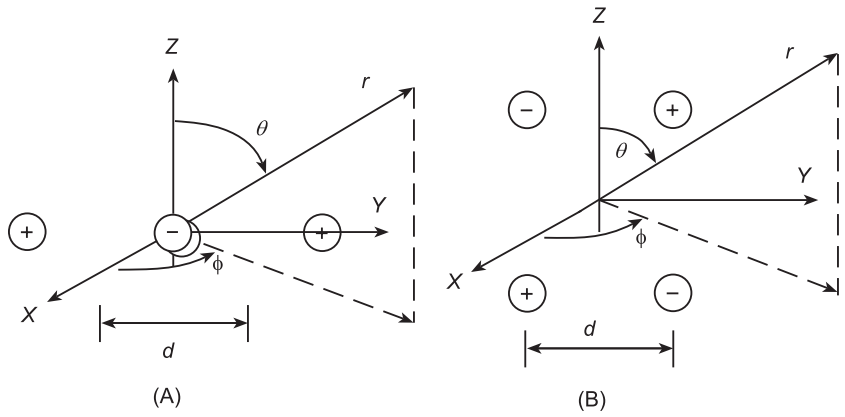


Figure 3 (A) A longitudinal quadrupole and (B) a lateral quadrupole.

whilst that of a lateral quadrupole is:

$$\begin{aligned} q_v(\mathbf{r_o}) = Q\delta\left(\mathbf{r_o} - \frac{d}{2}\hat{y} - \frac{d}{2}\hat{z}\right) \\ -\delta\left(\mathbf{r_o} + \frac{d}{2}\hat{y} - \frac{d}{2}\hat{z}\right) \\ +\delta\left(\mathbf{r_o} + \frac{d}{2}\hat{y} + \frac{d}{2}\hat{z}\right) \\ -\delta\left(\mathbf{r_o} - \frac{d}{2}\hat{y} + \frac{d}{2}\hat{z}\right) \end{aligned} \quad [31]$$

For a longitudinal quadrupole, the nonzero q_{lm} are:

$$q_{22} = -\frac{1}{30}Q(kd)^2\sqrt{\frac{15}{2\pi}} \quad [32a]$$

$$q_{2-2} = q_{22} \quad [32b]$$

and:

$$q_{20} = -\frac{1}{15}Q(kd)^2\sqrt{\frac{5}{4\pi}} \quad [32b]$$

Thus, the radiated sound pressure is:

$$\begin{aligned} p(\mathbf{r},t) &= j\rho_o\omega\frac{e^{j\omega t-jkr}}{r}\left[q_{20}Y_{20}(\theta,\phi)\right. \\ &\quad \left. + q_{2-2}Y_{2-2}(\theta,\phi) + q_{22}Y_{22}(\theta,\phi)\right] \\ &= -j\rho_o\omega Q(kd)^2\frac{e^{j\omega t-jkr}}{4\pi r}\left[1/3 - \sin^2\theta\sin^2\phi\right] \end{aligned} \quad [33]$$

The lateral quadrupole has the following nonzero q_{lm} terms:

$$q_{21} = \frac{1}{15}Q(kd)^2\sqrt{\frac{15}{8\pi}} \quad [34a]$$

and:

$$q_{2-1} = q_{21} \quad [34b]$$

which results in:

$$\begin{aligned} p(\mathbf{r},t) &= j\rho_o\omega\frac{e^{j\omega t-jkr}}{r}\left[q_{2-1}Y_{2-1}(\theta,\phi) + q_{21}Y_{21}(\theta,\phi)\right] \\ &= \rho_o\omega Q(kd)^2\frac{e^{j\omega t-jkr}}{4\pi r}\sin\theta\cos\theta\sin\phi \end{aligned} \quad [35]$$

The directivity patterns of the longitudinal and lateral quadrupole sound radiation are shown in **Table 2**.

Sound Power Radiation

The sound power radiated from a confined sound source is calculated by the far-field sound pressure and fluid particle velocity:

$$W = \frac{1}{2}\int_0^{\pi}\int_0^{2\pi}\mathrm{Re}[pv_r^*]r^2\sin\theta\,d\theta\,d\phi \quad [36]$$

where v_r is the far-field fluid particle velocity in the radial direction:

$$\begin{aligned} v_r(\mathbf{r},t) &= -\frac{1}{j\rho_o\omega}\frac{\partial p(\mathbf{r},t)}{\partial r} \\ &\cong \frac{j\rho_o\omega}{\rho_o c_o}\frac{e^{j\omega t-jkr}}{r}\sum_{l=0}^{\infty}\sum_{m=-l}^{l}q_{lm}Y_{lm}(\theta,\phi) \end{aligned} \quad [37]$$

The orthogonality of the spherical harmonic functions:

$$\int_0^{\pi}\int_0^{2\pi}Y_{l'm'}^*(\theta,\phi)Y_{lm}(\theta,\phi)\sin\theta\,d\theta\,d\phi = \delta_{l'l}\delta_{m'm} \quad [38]$$

Table 2 (See Plate 48). Directivity distribution of a longitudinal and a lateral quadrupole sound radiation

Longitudinal quadrupole radiation $p(r,t) = -j\rho_o\omega Q(kd)^2 \frac{e^{j\omega t - jkr}}{4\pi r}[\frac{1}{3} - \sin^2\theta \sin^2\phi]$	
Lateral quadrupole radiation $p(r,t) = \rho_o\omega Q(kd)^2 \frac{e^{j\omega t - jkr}}{4\pi r} \sin\theta \cos\theta \sin\phi$	

allows the multipole sound power radiation to be expressed as:

$$W = \frac{(\rho_o\omega)^2}{2\rho_o c_o} \sum_{l=0}^{\infty} \frac{(kd)^{2l}}{(2l+1)^2} \times \sum_{m=-l}^{l} \left| \int q_v(\mathbf{r}_o)(r_o/d)^l a_l Y_{lm}^*(\theta_o, \phi_o)\, \mathrm{d}V_o \right|^2 \quad [39]$$

where d may be regarded as the characteristic dimension of the sound source. It can be noted from eqn [39] that the power radiated from monopoles, dipoles, and quadrupoles is related to kd as follows:

$$W_M = \frac{(\rho_o\omega)^2}{2\rho_o c_o} \left| \int q_v(\mathbf{r}_o) Y_{00}^*(\theta_o, \phi_o)\, \mathrm{d}V_o \right|^2 \quad [40a]$$

$$W_D = \frac{(\rho_o\omega)^2}{18\rho_o c_o}(kd)^2 \times \sum_{m=-1}^{1} \left| \int q_v(\mathbf{r}_o)(r_o/d) Y_{1m}^*(\theta_o, \phi_o)\, \mathrm{d}V_o \right|^2 \quad [40b]$$

and:

$$W_Q = \frac{(\rho_o\omega)^2}{450\rho_o c_o}(kd)^4 \times \sum_{m=-2}^{2} \left| \int q_v(\mathbf{r}_o)(r_o/d)^2 Y_{2m}^*(\theta_o, \phi_o)\, \mathrm{d}V_o \right|^2 \quad [40c]$$

A comparison can be made between the sound-radiating efficiencies of monopoles, dipoles, and quadrupoles by comparing eqns [40a]–[40c]. The ratio of the sound power radiated by a dipole to that radiated by a monopole is:

$$\frac{W_D}{W_M} \sim (kd)^2 \sim \left\{\frac{d}{\lambda}\right\}^2 \quad [41a]$$

and the ratio of the sound power radiated by a quadrupole to that radiated by a monopole is:

$$\frac{W_Q}{W_M} \sim (kd)^4 \sim \left\{\frac{d}{\lambda}\right\}^4 \quad [41b]$$

It can be seen from eqns [41a] and [41b] that at low frequencies (long wavelengths), the dipole and the quadrupole are very much less efficient radiators of noise than at high frequencies (shorter wavelengths) when compared with a monopole of the same source strength. It can also be deduced that monopoles are the most efficient radiators of sound, whereas quadrupoles are the least efficient.

As mentioned previously, this chapter is primarily concerned with sound generation by the volume velocity input due to structural vibration. The relationships in eqns [40] and [41] can also be derived for aerodynamic-type sound sources via scaling relationships with flow velocity. In this instance, the sound power generated by a monopole scales with the fourth power of velocity, the sound power generated by a dipole scales with the sixth power of velocity, and the sound power generated by a quadrupole scales with the eighth power of velocity.

Superposition of Elementary Sources

Sound Radiation by a Tripole Sound Source

According to Huygens' principle, each point on a wavefront may be regarded as a source (Huygens' source) of secondary waves for the new wavefront at a later time. The strength of the Huygens' source consists of a dipole term for the pressure on the

surface of the wavefront, and a monopole term for the air particle velocity. Using the Helmholtz–Kirchhoff integral for sound pressure in a space enclosed by the wavefront surface and the surface at infinity, the radiated sound pressure by a Huygens' source at the wavefront $\mathbf{r}'$ away from a point source is:

$$p_H(r,\omega) = \frac{A'}{r}[(1+jkr') + jkr'\cos\theta]\mathrm{e}^{-jkr} \qquad [42]$$

where r is the distance from the Huygens' source to the observation point in the far field ($kr \gg 1$), θ is an angle between $\mathbf{r}'$ and $\mathbf{r}$, and A' is proportional to the sound pressure at $\mathbf{r}'$. The sound radiation directivity can be interpreted as the superposition of the sound field radiated by a dipole and a monopole mode with the dipole vector direction perpendicular to that of $\mathbf{r}'$:

$$p_H(r,\omega) = \frac{\sqrt{4\pi}A'}{r} \left[(1+jkr')Y_{00} + \frac{jkr'}{\sqrt{3}}Y_{10}\right]\mathrm{e}^{-jkr} \qquad [43]$$

Figure 4 shows the magnitude directivity of a Huygens' source for $kr' \gg 1$.

A practical tripole sound source has been invented for a limited frequency range using two loudspeakers, and is currently available. One of the loudspeakers is within an enclosure and is used as the monopole source, and the other loudspeaker is coupled with two short tubes of appropriate length at the front and rear surfaces, and is used as a dipole source. The tube diameters are the same as that of the loudspeaker.

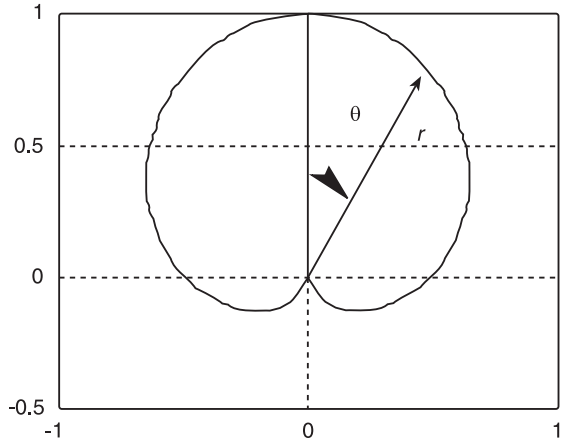


Figure 4 Magnitude directivity of a Huygens' source.

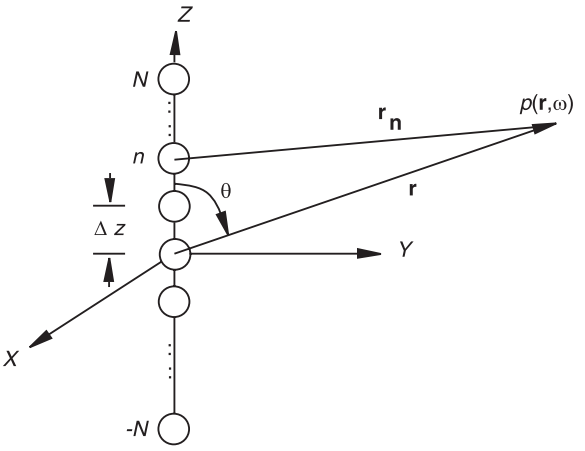


Figure 5 An array of monopole sound sources as an acoustic steering system.

Steering of Sound Beams

Consider an array of monopole sound sources with the same magnitude of volume velocity and equally spaced by Δz along the Z axis (**Figure 5**). A time delay τ may be introduced between neighboring monopoles. Thus, the total sound pressure at a far-field location due to the superposition of $2N+1$ monopole sources is:

$$p(\mathbf{r},\omega) = \sum_{n=-N}^{N} \frac{Q}{4\pi r_n}\mathrm{e}^{-jkr_n - jn\omega\tau} \qquad [44]$$

For sound pressure in the far field ($r \gg 2N\Delta z$), r_n in the denominators of eqn [44] is approximated by r and that in the exponential terms by $r - n\Delta z\cos\theta$. Thus, the far-field sound pressure radiated by the monopole array is:

$$p(\mathbf{r},\omega) = \frac{Q}{4\pi r}\mathrm{e}^{-jkr}\sum_{n=-N}^{N}\mathrm{e}^{jnk(\Delta z\cos\theta - \tau/c_o)} = \frac{Q}{4\pi r}\mathrm{e}^{-jkr}\frac{\sin\left[\frac{k(2N+1)}{2}(\Delta z\cos\theta - \tau/c_o)\right]}{\sin\left[\frac{k}{2}(\Delta z\cos\theta - \tau/c_o)\right]} \qquad [45]$$

For far-field sound radiation, the angular distribution of the sound pressure is described by the directivity index:

$$D(\theta) = \left|\frac{\sin\left[\frac{k(2N+1)}{2}(\Delta z\cos\theta - \tau/c_o)\right]}{(2N+1)\sin\left[\frac{k}{2}(\Delta z\cos\theta - \tau/c_o)\right]}\right| \qquad [46]$$

The characteristics of the directivity for $\tau = 0$ are determined by the length of the array $L = 2N\Delta z$ with

respect to the wavelength, and by the total number of monopoles $(2N + 1)$ in the array.

For N fixed, the compactness of the array length measured by kL determines the characteristics of the directivity. If $kL < 1$, the radiation of a compact monopole array gives rise to omnidirectional sound pressure. When kL increases, the sound field is characterized by major lobes with peak sound radiation. For $\tau = 0$, eqn [46] implies that the angular positions of the major lobes are:

$$\theta_m = \cos^{-1}\frac{m\lambda}{\Delta z} \qquad [47]$$

where $m = 0,\ 1,\ 2 \ldots m = 0$ corresponds to the primary major lobe, whilst $m > 0$ corresponds to the secondary major lobes. In applications where a single major lobe is required, the following condition must be satisfied:

$$\frac{\Delta z}{\lambda} < 1 \qquad [48]$$

This characteristic is illustrated in **Figure 6**, which shows the directivity indices of an array of $2N + 1 = 5$ for various values of $\Delta z/\lambda$.

When $\Delta z/\lambda < 1$, the primary major lobe becomes narrow as the total number of monopole sources increases, which is illustrated in **Figure 7** for $\Delta z/\lambda = 0.25$ and $N = 2,\ 6,\ 10$.

To steer the radiation angle of the primary major lobe, a nonzero time delay τ can be introduced. Here, the angular position of the lobe is at:

$$\theta_s = \cos^{-1}\frac{\tau}{\Delta z c_o} \qquad [49]$$

which can be varied by adjusting the time delay τ.

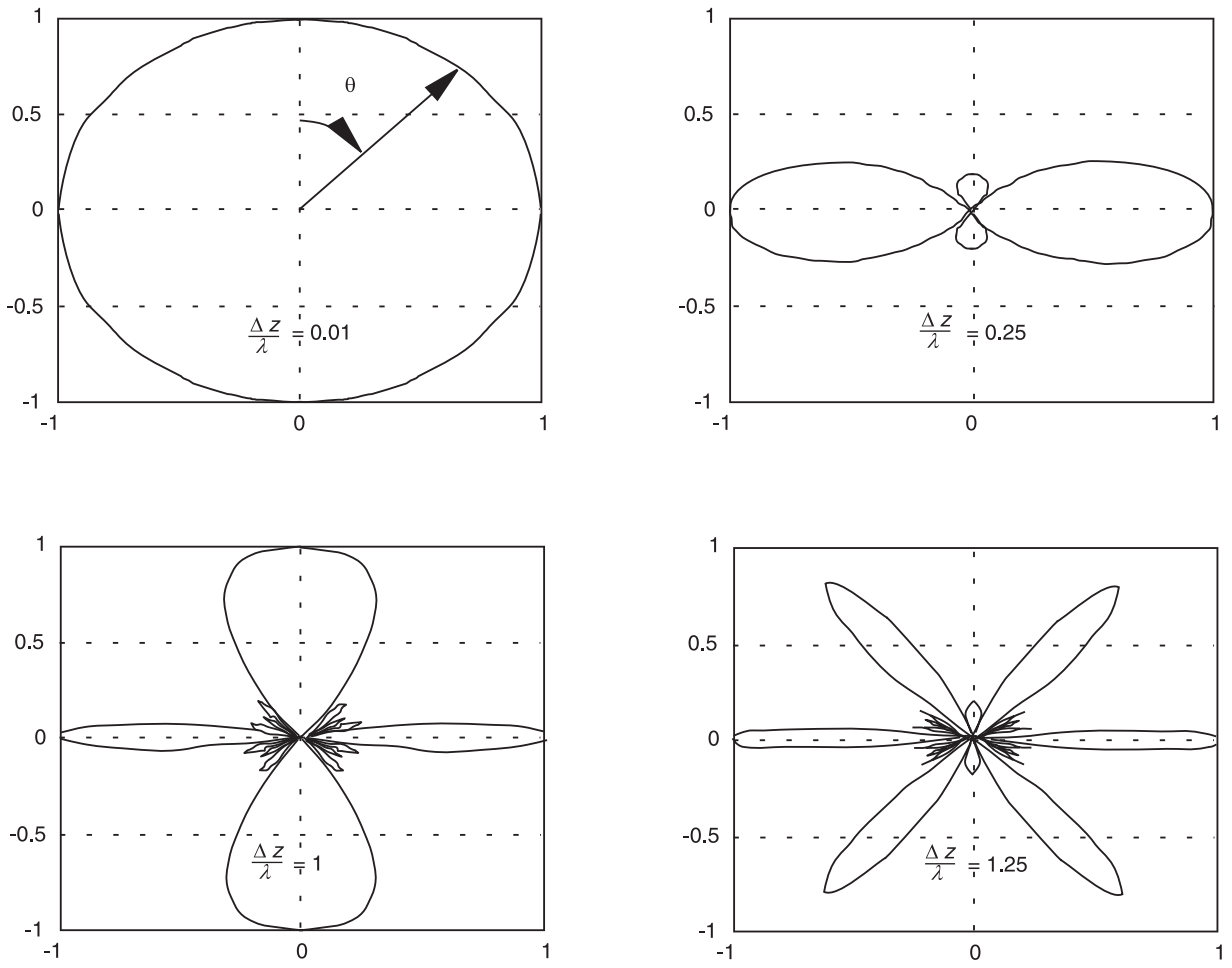


Figure 6 The directivity indices of an array of monopoles with $2N + 1 = 5$ and various $\Delta z/\lambda$.

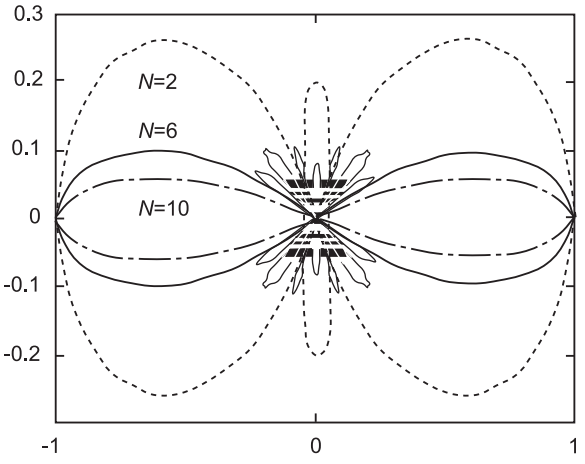


Figure 7 The primary major lobe becomes narrow as the total number of monopole sources increases ($\Delta z/\lambda = 0.25$).

Conclusions

This article has focused on the noise radiation characteristics of elementary acoustical sources. It has been limited to sound generation by the changes in the volume velocity density, specifically for structural excitation mechanisms. The noise radiation characteristics have been derived from the inhomogeneous Helmholtz equation (eqn [6]) using the Green's function and multipole expansions. Noise radiation characteristics have been quantified for the three primary sound sources (monopoles, dipoles, and quadrupoles) used in acoustic modeling. The sound power radiation characteristics of these elementary sources have also been considered together with the effects of elementary source superposition. These include the sound radiation by a tripole sound source and the effects of steering of sound beams via monopole arrays.

Nomenclature

d	distance
$p(\mathbf{r}, t)$	sound pressure
$\mathbf{v}(\mathbf{r}, t)$	particle velocity
W	power
γ	ratio of specific heats
λ	wavelength
τ	time delay

See Plates 47, 48.

See also: **Fluid/structure interaction**; **Forced response**; **Wave propagation**, Guided waves in structures.

Further Reading

Crighton DG, Dowling AP, Ffowes Williams JE, Heckl M, and Leppington FG (1992) *Modern Methods in Analytical Acoustics*. London: Springer-Verlag.

Crocker MJ (ed.) (1997) *Encyclopedia of Acoustics*. New York: John Wiley Interscience.

Morse PM and Ingard KU (1986) *Theoretical Acoustics*. New Jersey: McGraw-Hill.

Norton MP (1999) *Fundamentals of Noise and Vibration Analysis for Engineers*. Cambridge, UK: Cambridge University Press.

Parker SP (ed.) (1983) *Encyclopedia of Physics*. New York: McGraw-Hill.

Tian J and Sha JZ (1987) Secondary sources of a spatial active noise attenuation. *Proceedings Inter-Noise'87* pp. 553–556, Beijing.

Noise Radiated by Baffled Plates

M P Norton and J Pan, University of Western Australia, Nedlands, Perth, Western Australia

Copyright © 2001 Academic Press

doi:10.1006/rwvb.2001.0146

Introduction

Whilst the lumped-parameter approach to mechanical vibrations is adequate to describe mode shapes and natural frequencies, it is not suitable for relating vibrations to radiated noise. One therefore has to use the fundamental wave approach to obtain an understanding of the essential features of mechanical vibrations as they relate to sound radiation and sound transmission. These interactions between sound waves and the vibrations of elastic structures form a very important part of engineering noise and vibration control.

Because elastic structures can store energy in shear and compression, all types of waves can be sustained, i.e., compressional (longitudinal) waves, flexural (transverse or bending) waves, shear waves, and torsional waves. On the other hand, since fluids can only store energy in compression, they can only sustain compressional (longitudinal) waves. Flexural waves are the only type of structural waves that play a significant part in sound radiation and transmission. Perpendicular to the surface of the structure, the flexural wave particle velocities are capable of creating volume velocities in the fluid and this results in an

effective exchange of energy between the structure and the fluid.

Acoustic loads on arbitrary surfaces are associated with the radiated sound pressure at regions in close proximity to the surfaces. This is in addition to any mechanical excitation of the surface, which could be the primary source of vibration in the first instance. If the fluid medium is air (as is usually the case in engineering noise control), then this acoustic radiation load is generally very small and the sound pressure field at regions away from the source can be estimated from the bending wave particle velocities associated with the mechanical excitation. If, however, the fluid medium is a liquid, then the acoustic radiation load can become very significant and has to be accounted for – the radiation load modifies the forces acting on the structure, a feedback coupling between the fluid and the structure is set up, and the structure subsequently becomes fluid-loaded. This article is, however, mainly concerned with structure-borne sound in the audiofrequency range with air as the fluid medium. These conditions are often representative of typical engineering noise control problems such as sound radiation from plates, shells, and cylinders in industrial-type environments and sound transmission through building partitions.

At its most fundamental level, the radiation of sound from a vibrating boundary surface can be formulated in terms of an integral equation involving Green's functions with an imposed radiation condition, i.e., the radiation condition ensures that the integral equation for the radiated sound pressure represents outward-traveling sound waves. Green's functions were introduced in the article **Noise**, Noise radiated from elementary sources on noise radiation from elementary sources and they represent solutions to the wave equation – they can also be considered to be either frequency response functions or impulse response functions between the source and receiver. In its most general form, the integral equation is attributable to Kirchhoff, although Helmholtz modified it for single-frequency (harmonic) applications. The derivation of the integral and a discussion about the radiation condition is provided in the literature. The integral is sometimes referred to as the Kirchhoff–Helmholtz integral equation (eqn [3]). The Kirchhoff–Helmholtz integral equation relates harmonic vibrational motion of the surface to the radiated sound pressure field in the enclosed fluid. It can be interpreted as representing the sound pressure field of a vibrating surface by a distribution of volume velocity sources and forces on the surface. The velocity sources and the forces are related to normal surface velocity and surface pressure respectively. It is important to note that the surface pressure and the normal surface vibrational velocity are interrelated and not independent of each other.

For certain sound fields with simple boundary excitations, an appropriate Green's function may be constructed such that its normal derivative can be forced to be zero, thus eliminating the requirement for a knowledge of the surface pressure distributions, i.e., only a knowledge of the surface vibrational velocity is required. For complicated and three-dimensional boundary surfaces, such as truck cabins, analytical solutions are generally not possible, and the usual procedure is either to use numerical techniques to solve the integral equation, or to use experimental techniques to establish the Green's function. Rayleigh modified the Kirchhoff–Helmholtz integral equation for the specific case of a planar source located in an infinite baffle and illustrated that it is equivalent to a distribution of point sources (eqn [10]).

Sound Pressure in the Presence of Boundaries

The nature of sound fields in the presence of boundaries is described by the Helmholtz equation and the conditions of sound pressure and/or air particle velocity on the boundaries. For a steady-state sound field, the Helmholtz equation is:

$$\nabla^2 p + k^2 p = 0 \qquad [1]$$

To express the sound pressure $p(\mathbf{r}, \omega)$ due to boundary vibration and reflection, a Green's function may be constructed to satisfy the following equation:

$$\nabla^2 G(\mathbf{r}|\mathbf{r}') + k^2 G(\mathbf{r}|\mathbf{r}') = -\delta(\mathbf{r} - \mathbf{r}') \qquad [2]$$

and the relevant boundary conditions. Using eqns [1] and [2], and Green's theorem, Kirchhoff obtained the solution for sound pressure in an integral form (the Kirchhoff–Helmholtz integral):

$$p(\mathbf{r}, \omega) = \oint_S \left[G(\mathbf{r}|\mathbf{r}') \frac{\partial p}{\partial n'} - p(\mathbf{r}', \omega) \frac{\partial G(\mathbf{r}|\mathbf{r}')}{\partial n'} \right] \mathrm{d}s' \qquad [3]$$

where $\partial p / \partial n'$ represents the gradient on the boundary surface. The gradient is normal to the boundary surface and outwards positive from the volume where the sound is generated.

A special and important situation is the sound radiation from baffled plates. For this situation, the velocity of the plate in S_1 and that of the rigid baffle in S_2 (as shown in **Figure 1**) are:

$$v_B = \begin{cases} v_n(\mathbf{r}_p, \omega)e^{j\omega t} & \mathbf{r}_p = (x', y') \in S_1 \\ 0 & \mathbf{r}_p = (x', y') \in S_2 \end{cases} \quad [4]$$

Applying the Euler's field equation, the pressure gradient on the boundary surface is related to the boundary vibration velocity by:

$$\frac{\partial p}{\partial n'} = j\rho_0 \omega v_B \quad [5]$$

For such a boundary, where the pressure gradient on the surface is known, the Green's function to be constructed should satisfy:

$$\frac{\partial G(\mathbf{r}|\mathbf{r}')}{\partial n'} = 0 \quad [6]$$

at the boundary surface. Such a surface in **Figure 1** corresponds to $z = 0$. Thus, in this instance, the Green's function is selected as:

$$G(\mathbf{r}|\mathbf{r}') = \frac{1}{4\pi}\left(\frac{e^{-jkR_+}}{R_+} + \frac{e^{-jkR_-}}{R_-}\right) \quad [7]$$

where $R_+ = \sqrt{(x-x')^2 + (y-y')^2 + (z-z_+)^2}$, and $R_- = \sqrt{(x-x')^2 + (y-y')^2 + (z+z'_-)^2}$ with z'_+ and z'_- being small positive and negative perturbations in the Z direction. This Green's function has a zero gradient on the boundary $z = 0$, i.e.:

$$\frac{\partial G(\mathbf{r}|\mathbf{r}')}{\partial z'}\Big|_{z'_+, z'_- \to 0} = 0 \quad [8]$$

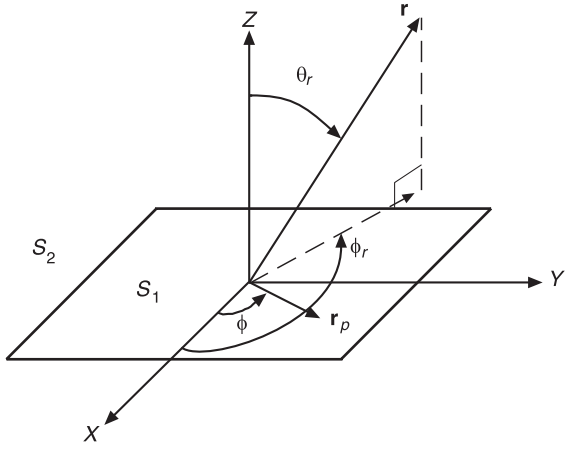


Figure 1 Coordinate system of a baffled plate.

and when the sources are limited to the boundary surface $\mathbf{r}' \to \mathbf{r}_p$, and we have:

$$G(\mathbf{r}|\mathbf{r}_p) = \frac{1}{2\pi}\frac{e^{-jkR}}{R} \quad [9]$$

where $R = |\mathbf{r} - \mathbf{r}_p| = \sqrt{(x-x')^2 + (y-y')^2 + z^2}$.

Substituting eqns [8] and [9] into the Kirchhoff–Helmholtz integral results in the Rayleigh integral for sound radiation from a baffled plate:

$$p(\mathbf{r}, \omega) = \frac{j\rho_0 \omega}{2\pi}\int_{S_1} \frac{v_n(\mathbf{r}_p, \omega)}{R} e^{-jkR}\, ds \quad [10]$$

where the time-dependent term $e^{j\omega t}$ is assumed for both sound pressure and plate velocity.

Modal Vibration of a Plate

The steady-state displacement $w(\mathbf{r}_p, \omega)$ of the flexural vibration of a thin plate of length L_x and width L_y at angular frequency ω is described as:

$$\frac{Eh^3}{12(1-\nu^2)}\nabla^4 w + j\omega C w - \rho h \omega^2 w = p_p + p_e \quad [11]$$

where E, ν, and C are respectively the Young's modulus, Poisson's ratio, and damping coefficient of the plate material, whilst ρ and h are the density and thickness of the plate. p_p is the acoustic radiation loading, and p_e is the pressure due to an external excitation. The effect of acoustic loading on a baffled plate is only important when the plate is very thin or the medium of sound radiation is significantly dense (such as water). In this chapter, the acoustic loading is assumed to be second-order and is ignored.

The plate vibrational response comprises mode shape functions ψ_{mn} and natural frequencies ω_{mn} of the (m, n)th modes. They are obtained from the solution of the eigenvalue equation:

$$\frac{Eh^2}{12\rho(1-\nu^2)}\nabla^4 \psi_{mn} = \omega_{mn}^2 \psi_{mn} \quad [12]$$

with respect to the boundary conditions of the displacement at the plate edges.

The method of modal analysis begins with the expansion of the plate displacement by the mode shape functions:

$$w(\mathbf{r}_p, \omega) = \sum_{m,n} W_{mn}\psi_{mn}(\mathbf{r}_p) \quad [13]$$

The orthogonal properties of the mode shape functions allow for the solution of the modal amplitudes of the plate displacement:

$$W_{mn} = \frac{P_{mn}}{\Lambda_{mn}\left[\rho h\left(\omega_{mn}^2 - \omega^2\right) + jC\omega\right]} \qquad [14]$$

where the modal force is:

$$P_{mn} = \int_{S_1} p_e(\mathbf{r}_p)\psi_{mn}(\mathbf{r}_p)\ \mathrm{d}s \qquad [15]$$

and:

$$\Lambda_{mn} = \int_{S_1} \psi_{mn}^2(\mathbf{r}_p)\ \mathrm{d}s \qquad [16]$$

Sound Power Associated with Plate Vibration

Far-field Approach

For the far-field condition ($r \gg \max[L_x, L_y]$), the R in the denominator of the Rayleigh integral (eqn [10]) is approximated by $R \cong r$, whilst the R in the phase term is approximated by:

$$R \cong r - |\mathbf{r}_p| \cos\Theta \qquad [17]$$

where $\cos\Theta$ is the cosine of the angle between the surface vector $\mathbf{r}_p$ and the observation vector $\mathbf{r}$ and:

$$\cos\Theta = \cos\phi \sin\theta_r \cos\phi_r + \sin\phi \sin\theta_r \sin\phi_r \qquad [18]$$

where θ_r and ϕ_r are the elevation and azimuth angles of $\mathbf{r}$, whilst ϕ is the rotation angle of $\mathbf{r}_p$ from the x-axis. As a result of these far-field approximations, the far-field sound pressure is:

$$p(\mathbf{r},\omega) = -\frac{\rho_o\omega^2}{2\pi r}\left[\sum_{m,n} W_{mn}\int_{S_1} \psi_{mn} e^{j|\mathbf{r}_p|k\cos\Theta}\,\mathrm{d}s\right] e^{-jkr} \qquad [19]$$

which is used to give the radiated sound power into the far-field:

$$W = \frac{1}{2\rho_o c_o}\int_0^{2\pi}\int_0^{\pi/2} |p(\mathbf{r},\omega)|^2 r^2 \sin\theta_r\ \mathrm{d}\theta_r\ \mathrm{d}\phi_r$$
$$= \frac{\rho_o c_o}{2}\left(\frac{k\omega}{2\pi}\right)^2 \sum_{m,n}\sum_{m',n'} W_{mn} W_{m'n'}^*$$
$$\times \int_0^{2\pi}\int_0^{\pi/2} \gamma_{mn}(\theta_r\phi_r)\gamma_{m'n'}^*(\theta_r\phi_r)\sin\theta_r\ \mathrm{d}\theta\ \mathrm{d}\phi_r \qquad [20]$$

where the modal directivity term is:

$$\gamma_{mn}(\theta_r\phi_r) = \int_{S_1} \psi_{mn}\, e^{j|\mathbf{r}_p|k\cos\Theta}\,\mathrm{d}s \qquad [21]$$

The total sound power of the plate sound radiation is usually dominated by the self-radiation terms in eqn [20] where $(m, n) = (m', n')$. Those terms with $(m, n) \neq (m', n')$ correspond to the mutual interaction of plate modes through their radiated sound.

To describe the effectiveness of sound radiation of a vibrating plate, a nondimensional ratio between the radiated power and the quadratic velocity of the plate is used. This radiation efficiency σ is defined as:

$$\sigma = \frac{W}{\rho_o c_o S_1 \omega^2 < w^2 >} \qquad [22]$$

where

$$< w^2 > = \frac{1}{2S_1}\int_{S_1} w^2\ \mathrm{d}s$$

is the space- and time-averaged quadratic displacement. The single-mode radiation efficiency can be used to study the sound power radiation in terms of the mode shape functions and the relative size of the plate with respect to the wavelength of the radiated sound (kL_x, kL_y). Here:

$$\sigma_{mn} = \left(\frac{k}{2\pi}\right)^2 \frac{\int_0^{2\pi}\int_0^{\pi/2} |\gamma_{mn}(\theta_r\phi_r)|^2 \sin\theta_r\ \mathrm{d}\theta_r\ \mathrm{d}\phi_r}{S_1 < \psi_{mn}^2 >} \qquad [23]$$

where $< \psi_{mn}^2 >$ is the square of the space-averaged mode shape function.

Near-field Approach

The sound power can also be evaluated on the surface of the plate by using the plate velocity and the sound pressure on the plate:

$$W = \frac{1}{2}\mathrm{Re}[p\dot{w}^*]_{z=0} = \frac{1}{2}\rho_o c_o \omega^2 \sum_{m,n}\sum_{m',n'} W_{mn} W^*_{m'n'} \mathrm{Re}\{Z_{mn,m'n'}\} \quad [24]$$

where $Z_{mn,\,m'n'} = \zeta_{mn,\,m'n'} + j\chi_{mn,\,m'n'}$ is the specific acoustic radiation impedance with:

$$\zeta_{mn,m'n'} = \frac{k}{2\pi}\int_{S_1}\int_{S_1} \psi_{mn}\psi_{m'n'} \frac{\sin k\left|\mathbf{r}_p - \mathbf{r}'_p\right|}{\left|\mathbf{r}_p - \mathbf{r}'_p\right|}\,\mathrm{d}s\,\mathrm{d}s' \quad [25a]$$

and:

$$\chi_{mn,m'n'} = \frac{k}{2\pi}\int_{S_1}\int_{S_1} \psi_{mn}\psi_{m'n'} \frac{\cos k\left|\mathbf{r}_p - \mathbf{r}'_p\right|}{\left|\mathbf{r}_p - \mathbf{r}'_p\right|}\,\mathrm{d}s\,\mathrm{d}s' \quad [25b]$$

Using the near-field approach, the modal sound radiation efficiency is expressed as:

$$\sigma_{mn} = \frac{\zeta_{mn,m'n'}}{S_1 < \psi^2_{mn} >}, \quad (m,n) = (m',n') \quad [26]$$

Wave Number Representation of the Radiated Sound Field

The sound radiation from a baffled plate is characterized by the sound radiation of the individual plate modes. Each mode shape function of the flexural vibration in the plate may be wave number-transformed into numerous flexural traveling waves with wave numbers k_x and k_y in the x and y directions such that:

$$\psi_{mn}(k_x,k_y) = \int_{S_1}\psi_{mn}(\mathbf{r}_p)\mathrm{e}^{-jk_x x - jk_y y}\,\mathrm{d}x\,\mathrm{d}y \quad [27]$$

The nature of the modal sound radiation can therefore be understood by the relationship between each of the traveling wave components and its induced sound field. The wave number transformation of the Helmholtz equation in semiinfinite space takes the form of:

$$P(k_x,k_y,k,z) = A\mathrm{e}^{\pm j\sqrt{k^2-k_x^2-k_y^2}z} \quad [28]$$

The sign of the exponential term is selected according to the physical conditions of sound radiation of the (k_x, k_y) traveling wave at a given k. If $k^2 > k_x^2 + k_y^2$, '$-$' is selected, as only outgoing sound pressure waves exist. If $k^2 < k_x^2 + k_y^2$, '+' has to be used, to express the sound pressure decaying exponentially with z. As the wave numbers k and $\sqrt{k_x^2+k_y^2}$ at a given frequency are inversely proportional to the phase speed, eqn [28] shows that only plate-traveling wave components with a phase speed greater than the sound speed in air radiate sound into the far field.

The amplitude of the sound pressure is determined by the boundary conditions on the plate surface:

$$A = -\rho_o\omega^2 \frac{W_{mn}\psi_{mn}(k_x,k_y)}{\pm j\sqrt{k^2-k_x^2-k_y^2}} \quad [29]$$

As a result, the wave number expression for the sound pressure radiated by the (m, n)th plate mode is:

$$p(r,\omega) = -\frac{\rho_o\omega^2 W_{mn}}{(2\pi)^2} \times \int_{-\infty}^{\infty}\int_{-\infty}^{\infty} \frac{\psi_{mn}(k_x,k_y)}{\pm j\sqrt{k^2-k_x^2-k_y^2}} \times \mathrm{e}^{jk_x x + jk_y y \pm j\sqrt{k^2-k_x^2-k_y^2}z}\,\mathrm{d}k_x\,\mathrm{d}k_y \quad [30]$$

Clearly, only those values of $\psi_{mn}(k_x, k_y)$ with $k_x^2 + k_x^2 \le k^2$ will contribute to the far-field sound pressure.

Characteristics of Sound Radiation from Baffled Plates

The preceding results of radiated sound pressure and sound power are applicable to baffled plates with arbitrary boundary conditions, provided that the orthogonal eigenfunctions of the plate vibration are available. Using the modal description of the plate vibration, the characteristics of radiation power of a vibrating baffled plate is determined by that of the self and mutual radiation of plate modes and that of the excitation of plate modes by external pressure. The self-radiation of the plate modes is described by the modal radiation efficiency σ_{mn} (as in eqns [23] and [26]). The mutual radiation terms are related to the cross-product of two different plate modes, such as:

$$\int_0^{2\pi}\int_0^{\pi/2} \gamma_{mn}(\theta_r\phi_r)\gamma^*_{m'n'}(\theta_r\phi_r)\sin\theta_r\,\mathrm{d}\theta_r\,\mathrm{d}\phi_r,$$

$$(m,n) \neq (m',n')$$

in eqn [20] and $\zeta_{mn,\,m'n'}$, $(m, n) \neq (m', n')$, in eqn [25a]. The modal amplitude W_{mn} of the plate due to external pressure is not only dependent upon the orthogonality between the distributed pressure and the plate mode (eqn [15]), but also upon whether the mode is excited at its resonance or not. A quantitative discussion of the self and mutual radiation, and the excitation of the plate mode cannot, however, proceed without information about the mode shape functions of the plate. In this article, mode shape functions for simple support plates (zero deflection and free rotation at all the edges) are used for the initial discussion. The effects of different edge conditions of the plate on the mode shape functions and the characteristics of radiated sound follow qualitatively.

If the origin of the coordinate system is at the center of a simply supported plate, the mode shape functions are:

$$\psi_{mn} = \sin\left(\frac{m\pi x}{L_x} + \frac{m\pi}{2}\right) \sin\left(\frac{n\pi x}{L_y} + \frac{n\pi}{2}\right) \qquad [31]$$

and the wave number of the (m, n)th mode is:

$$k_{mn} = \sqrt{\left(\frac{m\pi}{L_x}\right)^2 + \left(\frac{n\pi}{L_y}\right)^2} \qquad [32]$$

For such a simply supported plate, $|\gamma_{mn}(\theta_r, \phi_r)|^2$ in eqn [23] has a closed-form solution:

$$|\gamma_{mn}(\theta_r \phi_r)|^2 = \left(\frac{2L_xL_y}{mn\pi}\right)^2 \frac{[1-(-1)^m \cos\alpha][1-(-1)^n \cos\beta]}{\left[(\alpha/m\pi)^2 - 1\right]^2 \left[(\beta/n\pi)^2 - 1\right]^2} \qquad [33]$$

where $\alpha = kL_x \sin\theta_r \cos\phi_r$ and $\beta = kL_y \sin\theta_r \sin\phi_r$.

Modal Radiation Efficiency

The main features of modal radiation efficiency of simply supported plates as a function of wave number ratio k/k_{mn}, modal numbers (m, n), and phase cell area $A_{mn} = L_xL_y/mn$ can be summarized analytically. The approximate expressions of σ_{mn} for the various regions of k/k_{mn} are:

1. when $k/k_{mn} \gg 1$:

$$\sigma_{mn} \cong \frac{1}{\left[1 - (k_{mn}/k)^2\right]} \to 1 \qquad [34]$$

2. just above $k/k_{mn} = 1$, σ_{mn} has a peak, and the height of the peak increases with mode number
3. below the modal critical frequency $k/k_{mn} < 1$, when $k_n = n\pi/L_y > k$ and $k_m = m\pi/L_x < k$, and:

$$\sigma_{mn} \cong \frac{(k/k_n)^2}{kL_y} \left\{ \frac{1 + \left[(k_{mn}^2 - k^2)/k_n^2\right]}{\left[(k_{mn}^2 - k^2)/k_n^2\right]^{3/2}} \right\} \qquad [35]$$

when $k_n < k$ and $k_m > k$, k_n and L_y in eqn [35] are replaced by k_m and L_x

4. well below the modal critical frequency when $k/k_{mn} \ll 1$ and $k/k_m, k/k_n \ll 1$, but $\frac{1}{2}kL_x, \frac{1}{2}kL_y > 1$:

$$\sigma_{mn} \cong 8k^2 \frac{A_{mn}^2}{\pi^5 S_1} \qquad [36]$$

5. when $k/k_{mn} \ll 1$ with $\frac{1}{2}kL_x, \frac{1}{2}kL_y \ll 1$
   - the σ_{mn} of odd–odd modes is proportional to the square of the phase cell area and inversely proportional to the surface area of the plate such that:

$$\sigma_{mn} \cong 32k^2 \frac{A_{mn}^2}{\pi^5 S_1} \qquad [37]$$

   - for odd–even modes, the superimposed contribution of the adjacent phase cell areas (cells) gives rise to more complete cancellation of sound radiation. In this case σ_{mn} is smaller by a factor of $(kL_y)^2 (n = \text{even})$ than that of the odd–odd modes with similar phase cell area. Here:

$$\sigma_{mn} \cong \frac{8}{3}k^2 \frac{A_{mn}^2}{\pi^5 S_1} (kL_y)^2 \qquad [38]$$

     For even–odd modes (m = even), L_y in eqn [38] is replaced by L_x
   - for even–even modes, the superimposed contribution of the adjacent phase cell areas gives rise to the most complete cancellation of sound radiation. The corresponding σ_{mn} is the smallest amongst those with similar phase cell areas. Here:

$$\sigma_{mn} \cong \frac{2}{15}k^2 \frac{A_{mn}^2}{\pi^5 S_1} (kL_x)^2 (kL_y)^2 \qquad [39]$$

   - for long but narrow plates, $\frac{1}{2}kL_x > 1$, $\frac{1}{2}kL_y \ll 1$. The radiation efficiency for odd modes in the y direction is:

$$\sigma_{mn} \cong \begin{cases} 4\dfrac{kL_x}{S_1 K_n^2}, & k/k_m > 1 \\ 16k^2 \dfrac{A_{mn}^2}{\pi^5 S_1}, & k/k_m < 1 \end{cases} \quad [40]$$

and that for even modes in the y direction is:

$$\sigma_{mn} \cong \begin{cases} \dfrac{1}{3}\dfrac{kL_x}{S_1 K_n^2}(kL_y)^2, & k/k_m > 1 \\ \dfrac{4}{3}k^2 \dfrac{A_{mn}^2}{\pi^5 S_1}(kL_y)^2, & k/k_m < 1 \end{cases} \quad [41]$$

The mechanism for an odd–odd plate mode to have a dominant contribution to the sound power radiation below its modal critical frequency ($k/k_{mn} \ll 1$) is the uncancelled poles (with the same phase) of sound radiation at the plate edges (for$m = 3, 5, 7 \ldots n = 1$, or$m = 1, n = 3, 5, 7 \ldots$) and corners (for$m = 3, 5, 7 \ldots n = 3, 5, 7 \ldots$). The modal radiation efficiency of simply supported plates can be obtained by numerically integrating eqn [23]. Two typical figures of modal radiation efficiency for a baffled, simply supported square plate are shown in **Figure 2**. In addition to the general features of modal radiation as a function of modal numbers and wave number ratios, a waviness is observed in the radiation resistance curves below the modal critical frequency. The complexity of the curves increases, represented by increases in waviness, as the modal numbers increase.

The wave number analysis of the plate modal vibration below its modal critical frequency shows (see eqns [28] and [30]) that the nonzero far-field sound radiation is due to the truncation of an acoustically slow-bending wave at the plate–baffle junction. The near-field vibration also contributes to the sound radiation of a plate mode below its modal critical frequency. To illustrate the effects of boundary conditions on the far-field sound radiation, the wave number transformation of one-dimensional mode shape functions is analyzed. **Figure 3** shows the normalized amplitudes of three modes corresponding respectively to simply supported, clamped, and free boundary conditions. These three modes have similar phase cell lengths and the same number of phase cells. The amplitudes of the phase cells near the boundaries for the C–C, and F–F modes differ from that away from the boundaries because of the near-field flexural vibration. As a result, the contributions of these modes to the far-field radiation of acoustically slow sound differ, as shown in **Figure 4** for sound radiation in the acoustically slow region (e.g., $k_x/(m\pi/L) < k/(m\pi/L) = 0.5$), and the wave number components of the C–C mode have the largest value. The mode with F–F boundary conditions has the least energy in $k_x < k$.

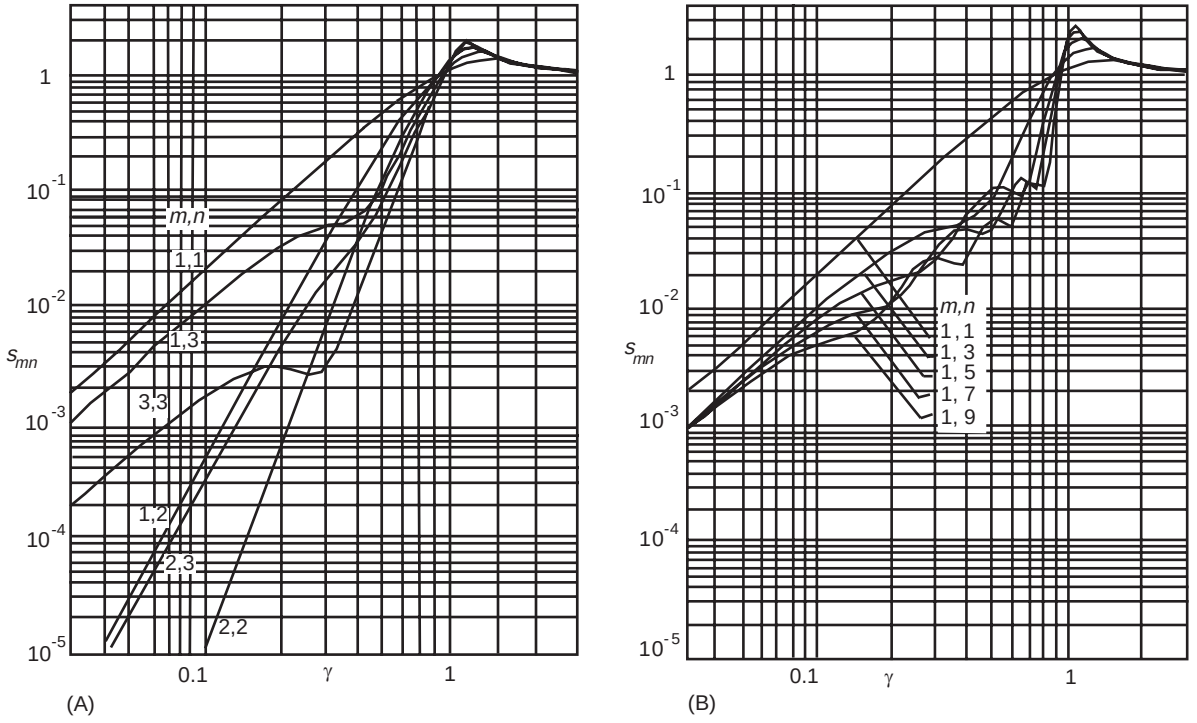


Figure 2 (A) and (B) Modal radiation efficiency of a simply supported square plate. (Note: $S_{mn} = \sigma_{mn}$, and $\gamma = k/k_{mn}$.) From Wallace (1970) with permission.

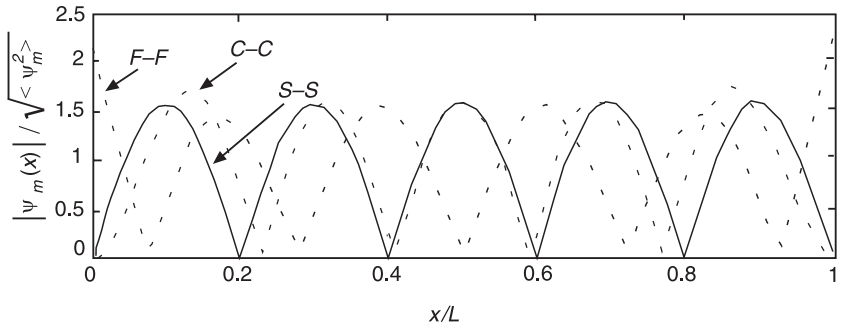


Figure 3 Normalized amplitudes of three modes corresponding respectively to simply supported (S–S), clamped (C–C), and free

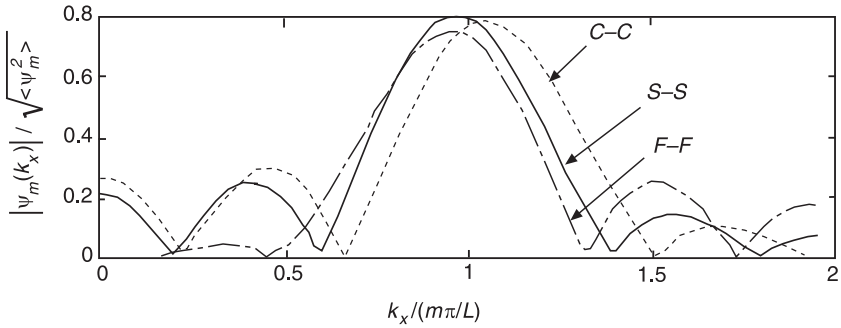


Figure 4 Normalized wave number spectrum of three modes corresponding respectively to simply supported (S–S), clamped (C–C), and free (F–F) boundary conditions.

The modal radiation efficiency of a plate with various boundary conditions has been numerically compared. The difference only occurs below the modal critical frequencies. Comparisons between simply supported plates and clamped plates show that the lower-order modes (up to the (2, 2) mode) are more efficient for the simply supported case than for the clamped case by up to 3 dB. The reverse applies for the higher-order modes.

Figure 5 shows the normalized amplitude of the three modes with only two phase cells. The corresponding wave number spectrum in **Figure 6** shows that the mode with S–S boundary conditions has the largest value in the acoustically slow region $k_x/(m\pi/L) < 0.5$.

The boundary conditions with low deflection stiffness, such as free and guided boundary conditions, provide very low radiation efficiencies for the elastic modes of the plate below the modal critical frequency. However, a plate with free or guided boundary conditions also admits rigid body motion similar to the translational and rotational motions of a piston. Sound radiation from a vibrating piston in translation or rotation demonstrates the most efficient sound radiation below the modal critical frequency. When the size of the piston is much smaller than the wavelength of sound radiation ($k_{\max}\{L_x, L_y\} \ll 1$), the approximate radiation efficiency of a vibrating piston in translation is:

$$\sigma_{pt} = \frac{1}{2\pi} k^2 L_x L_y \qquad [42]$$

and that in rotation about the y-axis is:

$$\sigma_{pr} = \frac{1}{72\pi} k^2 L_x L_y (kL_x)^2 \qquad [43]$$

Sound Power Radiated by Forced Vibration of a Baffled Plate

Sound radiation from forced vibration of a baffled plate involves the participation of multiple plate modes. As indicated in eqns [20] and [24], the radiated sound power not only depends upon the radiation characteristics of the individual plate modes and mutual interaction between the plate modes via their radiated sound, but also upon the excitation of each plate mode by the external forces.

If a plate is excited in such a way that the plate vibration field can be described as reverberant with equal distribution of the energy over all modes, the

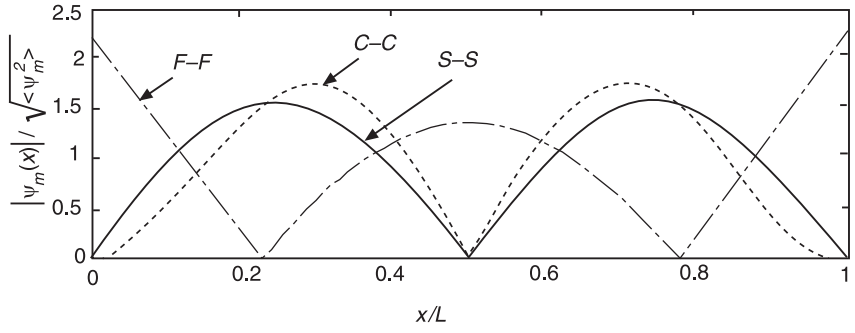


Figure 5 Normalized amplitudes of three modes corresponding respectively to simply supported (S–S), clamped (C–C), and free (F–F) boundary conditions and with two phase cells.

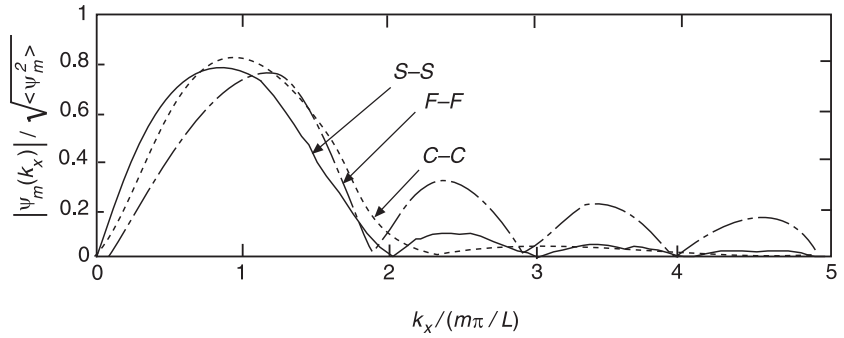


Figure 6 Normalized wave number spectrum of three modes corresponding respectively to simply supported (S–S), clamped (C–C), and free (F–F) boundary conditions and with two phase cells.

net contribution of the mutual interaction between plate modes to the total sound power may be ignored. For this case, an average radiation efficiency σ_{rad} is used to relate the sound power radiated by a plate:

$$W = \rho_o c_o S_1 \sigma_{\text{rad}} < v^2(\omega) > \qquad [44]$$

where $< v^2(\omega) >$ is the space–time average mean-square velocity of the plate at the angular frequency ω and in the frequency band $\Delta\omega$. The average radiation efficiency for a simply supported plate is:

$$\sigma_{\text{rad}} = \begin{cases} 2(\lambda_c\lambda/L_xL_y)(f/f_c)g_1(f/f_c) \\ \quad +(P\lambda_c/L_xL_y)g_2(f/f_c), & f < f_c \\ (L_x/\lambda_c)^{1/2}+(L_y/\lambda_c)^{1/2}, & f = f_c \\ (1-f/f_c)^{-1/2}, & f > f_c \end{cases} \qquad [45]$$

where $P = 2(L_x + L_y)$, $f_c = c_0^2/1.8c_L h$ is the critical frequency of an infinite plate with the same thickness h and material properties as that of the baffled plate, $c_L = \sqrt{E/\rho}$, $\lambda_c = c_o/f_c$:

$$g_1(f/f_c) = \begin{cases} (4/\pi^2)(1-2\alpha^2)/\alpha(1-\alpha^2)^{1/2}, & f < \frac{1}{2}f_c \\ 0, & f > \frac{1}{2}f_c \end{cases} \qquad [46a]$$

and:

$$g_2(f/f_c) = (2\pi)^{-2} \times \left\{(1-\alpha^2)\ln[(1+\alpha)/(1-\alpha)] + 2\alpha\right\} \Big/ (1-\alpha^2)^{3/2} \qquad [46b]$$

with $\alpha = (f/f_c)^{1/2}$. Well below the plate critical frequency:

$$\sigma_{\text{rad}} \cong \frac{4L_xL_y}{c_o^2} f^2, \quad \text{for } 0 < f < f_{11} \qquad [47]$$

The average radiation efficiency is graphically presented in **Figure 7**, where the effects of simply supported and clamped boundary conditions on σ_{rad} are incorporated.

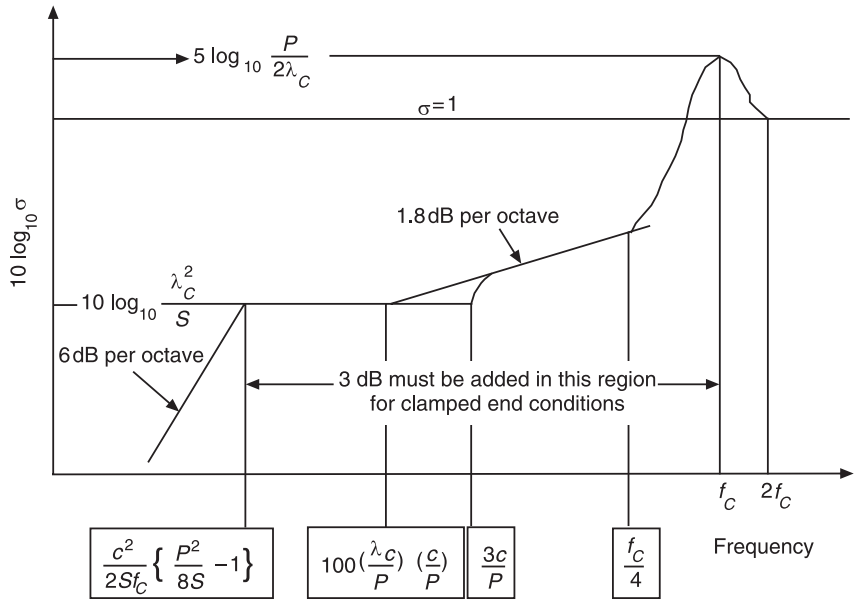


Figure 7 Average radiation efficiency of a baffled plate of perimeter $P = 2(L_x + L_y)$ and area $S = L_xL_y$ with simply supported or clamped edges. Modified with permission from Norton (1999) and Beranek (1992).

When a plate modal density is low and the frequency of sound radiation is below the critical frequency of the plate, eqns [20], [24], and [22] should be used to calculate the radiation efficiency. In this case, the total sound power produced is no longer equal to the sum of the sound powers that would be generated separately by each plate mode, and the mutual interaction of the plate modes through the radiated sound field must be taken into account. The radiated sound power is also strongly dependent, in this instance, upon the nature of the excitation force on the plate surface.

Figure 8 illustrates the radiation efficiency of a baffled plate driven by a unit point force at the center. The critical frequency of the plate is 12 kHz. The variational formulation allows calculation of free and forced plate responses for various boundary conditions, including simply supported, clamped, free, guided, and partially clamped–partially free boundary conditions.

Conclusions

In general, sound radiation from baffled plates is generated by the vibration of the various plate modes, as described by the modal radiation efficiency σ_{mn}, the mutual interaction between the modal radiation, and the degree of excitation of the plate modes by external forces. Above the modal critical frequency, the sound radiation of plate modes is effective and the mechanism of sound radiation is due to parts of the free-bending waves in the plate. In such acoustically fast regions, the boundary conditions of the plate have little effect on the radiated sound power. Below the modal critical frequency, the mechanisms of sound radiation by the plate modes are associated with the truncation of the free-bending waves at the plate–baffle junction, and the near-field plate vibration. The mode numbers, aspect ratios, and boundary conditions control both mechanisms.

Sound radiation from free-bending waves (bending waves which are not restricted by some structural discontinuity) in a structure can thus be categorized into first, modal sound radiation at any given arbitrary frequency, including nonresonant frequencies, and second, frequency band-averaged sound radiation. However, because finite structural elements always allow for the existence of natural frequencies and their associated mode shapes, when a structure is excited by a broad-band force, this results in the resonant excitation of structural modes. Hence, frequency band-averaged sound radiation is necessarily dominated by resonant structural modes, whereas modal sound radiation is not.

In practice, when structures are mechanically excited by a broad-band force, they respond in a multimode, resonant form; many natural frequencies are excited and they resonate with the applied force. In this instance it is often – but not always – the case that these resonant modes are responsible for most of the sound radiation. It is not always the case because radiation ratios of finite structures generally increase with frequency – a situation could arise where the higher-frequency, but nonresonant, modes (i.e.,

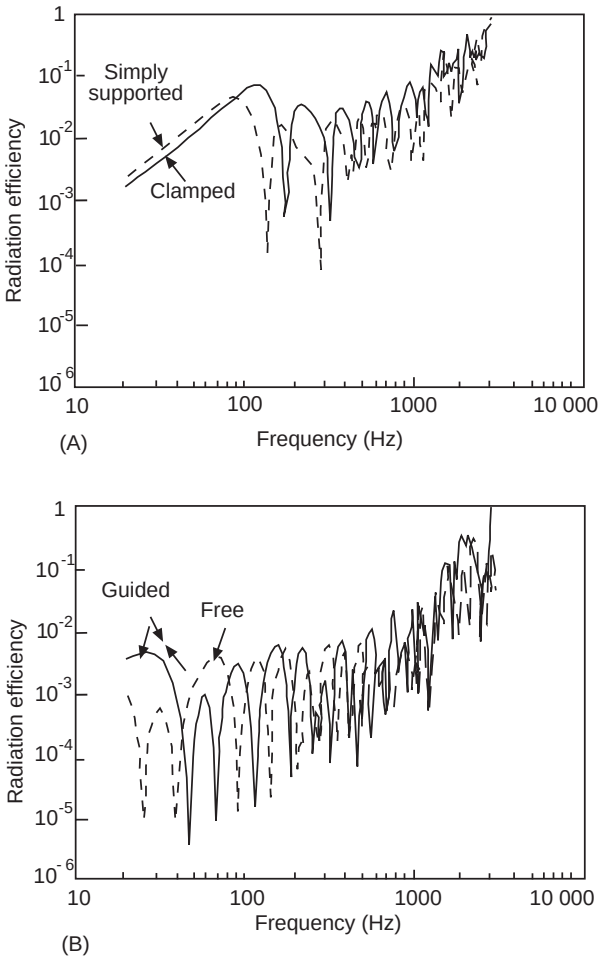


Figure 8 Radiation efficiency of a baffled plate driven by a unit point force at the center. (A) Simply supported and clamped edges; (B) free and guided edges. The plate loss factor is 0.01 and $f_c = \}12$ kHz. Reproduced with permission from Berry *et al*. (1990).

modes above the excitation frequency band) with their associated higher radiation efficiency generate more sound than the lower-frequency, but resonant, modes. Generally, however, whilst these higher-frequency modes have higher radiation efficiencies, their vibrational levels are significantly reduced because they are nonresonant; thus, the net effect is that they radiate less sound than the lower-frequency, lower-radiation-efficiency, resonant modes which are within the excitation band. Hence, as a general rule, resonant structural modes tend to dominate the sound radiation from mechanically excited structures. In practice, the mechanical excitation of plates results in most of the radiated sound being produced by resonant plate modes – the sound radiated by nonresonant forced modes tends not to be very significant.

The situation is somewhat different for acoustically excited structures. The vibrational response of finite structures to acoustic excitation (i.e., incident sound waves) is comprised of first, a forced vibrational response at the excitation frequency, and second, a vibrational response due to the excitation of the various structural natural frequencies. The former is associated with a wave that propagates through the structure at the trace wavelength of the incident sound wave. The latter is associated with the structural waves that are generated when the trace wave interacts with the boundaries; these structural waves are, in effect, free-bending waves with corresponding natural frequencies. The structural response is now both resonant and forced, and the transmission of sound through the structure (e.g., an aircraft fuselage, a partition between two rooms, or a machine cover) can be due to either one of the mechanisms or both. Thus, with acoustic excitation, it is the nonresonant forced modes, driven by the incident sound field, which match the wavelengths of the sound waves, thus transmitting sound very efficiently through the structure at frequencies below the critical frequency (but above the fundamental resonance). At frequencies above the critical frequency, both forced and resonant modes contribute to the radiated sound.

In summary, for acoustically excited plates, any sound that is radiated or transmitted (at frequencies below the critical frequency) is due to a forced response. On the other hand, for mechanically excited plates, any sound that is radiated at frequencies below the critical frequency is due to a resonant response. Above the critical frequency all the structural modes are capable of radiating sound. This conclusion is limited to regions where the bending waves are free and not restricted by structural discontinuities, i.e., regions far away from any mechanical excitation points or structural constraints such as stiffeners and joints.

When subsonic (acoustic slow) bending waves interact with a region where there are structural constraints and discontinuities (e.g., a large machine cover or an aircraft fuselage with ribs and stiffeners), reaction forces are generated on the structure. Also, there might be regions where some external mechanical excitation is transmitted to the structure via either a point or a line. Sound is radiated from regions in proximity to these various types of discontinuities. This sound is partly due to the near-field waves that are generated by the point and line reaction forces associated with some form of external mechanical excitation (a driving force) and/or any structural constraints. The other part of the sound radiation in this acoustic slow region is due to the truncation of the free-bending waves at the plate–baffle junction. This form of sound radiation from plates is produced by the uncancelled volume

velocities in regions in proximity to the structural constraint. Quite often, this sound radiation dominates over the sound radiated by the resonant corner and edge modes – the point and line forces produce sound radiation at all frequencies and not only at resonant frequencies.

Nomenclature

C	damping coefficient
E	Young's modulus
h	thickness of plate
p_e	external pressure
p_p	acoustic radiation loading
ν	Poisson's ratio
ρ	density
σ	radiation efficiency

See Plates 47, 48.

See also: **Boundary conditions**; **Eigenvalue analysis**; **Fluid/structure interaction**; **Forced response**; **Noise**, Noise radiated from elementary sources; **Plates**; **Wave propagation**, Waves in an unbounded medium.

Further Reading

Beranek LL (ed.) (1992) *Noise and Vibration Control Engineering*. New York: John Wiley.

Berry A, Guyader J and Nicolas J (1990) A general formulation for the sound radiation from rectangular, baffled plates with arbitrary boundary conditions. *Journal of the Acoustical Society of America* 88: 2792–2802.

Crocker MJ and Price AJ (1969) Sound transmission using statistical energy analysis. *Journal of Sound and Vibration* 9: 469–486.

Fahy FJ (1985) *Sound and Structural Vibration: Radiation, Transmission and Response*. Academic Press.

Junger MC and Feit D (1986) *Sound, Structures and their Interaction*. MIT Press.

Keltie RF and Peng H (1987) The effects of modal coupling on the acoustic power radiation from panels. *Journal of Vibration Acoustic. Stress and Reliability in Design, Transactions of ASME* 109: 48–54

Maidanik G (1962) Response of ribbed panels to reverberant acoustic fields. *Journal of the Acoustical Society of America* 34: 809–826

Morse PM and Ingard KU (1986) *Theoretical Acoustics*. McGraw-Hill.

Norton MP (1999) *Fundamentals of Noise and Vibration Analysis for Engineers*. Cambridge University Press.

Pan J, Snyder SD, Hansen CH and Fuller CR (1992). Active control of farfield sound radiated by a rectangular panel – a general analysis. *Journal of the Acoustical Society of America* 91: 2056–2066.

Pierce AD (1981) *Acoustics: An Introduction to its Physical Principles and Applications*. McGraw-Hill.

Skudrzyk EJ (1968) *Simple and Complex Vibratory Systems*. Pennsylvania State University Press.

Wallace CE (1970) Radiation resistance of a rectangular panel. *Journal of the Acoustical Society of America* 51: 946–952.

NONDESTRUCTIVE TESTING

Sonic

S Doebling and C Farrar, Los Alamos National Laboratory, NM, USA

Copyright © 2001 Academic Press

doi:10.1006/rwvb.2001.0138

Introduction

According to the American Society for Non-destructive Testing (ASNT), nondestructive testing (NDT) is defined as 'the examination of an object with technology that does not affect the object's future usefulness'. Sonic NDT (SNDT) refers to the examination of the integrity of a structure using dynamic response methods where the velocities of the excitation and response signals are significantly below the speed at which sound travels through the materials that compose the object. Thus, the measures that are commonly used to describe a structure's vibration behavior are also frequently used in SNDT. Distinction should be made between local SNDT, used to inspect local sections of a structure for flaws, and global SNDT, used to inspect large sections of a structure for changes in mechanical properties. Global sonic nondestructive testing (GSNDT) is the focus of this article. Common synonyms for GSNDT in

recent literature include vibration-based damage identification (or damage detection) and structural health monitoring. Structural health monitoring is also used to describe the overall measurement and analysis process whereby GSNDT is used to monitor the integrity of a structure over either continuous or discrete time intervals. This article will explain the theoretical basis for GSNDT, provide an overview of the implementation process with discussion of major issues, and provide a historical context for the application of GSNDT.

Basis of Global Sonic Nondestructive Testing

The basic philosophy of GSNDT is that the dynamic mechanical response of a structure is a function of the mechanical condition of the structure. Thus, observed changes in the dynamic response can be indicative of changes in mechanical condition. The basic approach of GSNDT is the comparison of measured vibration properties for the structure from two different measurement events to assess whether the structure has changed from its original configuration. First the structure is mechanically excited, using either an excitation that occurs in the normal operation of the structure (referred to as operating or ambient excitation) or an excitation that is introduced specifically for the purposes of identifying the dynamic response properties (referred to as forced excitation). Next, the structural response is measured using vibration instrumentation (typically accelerometers or strain gauges) and the data sets are digitized, transmitted, and stored electronically (see entry on **Modal analysis, experimental**, Measurement techniques). Features of these signals are then compared from experiments conducted at different times to assess whether damage has occurred. (Modal parameters have commonly been used, but more general types of parameters and measures have also been introduced.) Using GSNDT to assess the integrity of a structure allows the operator of the structure to follow a more cost-effective condition-based maintenance strategy (i.e., maintain the structure when necessary) rather than a time-based maintenance strategy (i.e., maintain the structure at a specific time interval no matter what condition it is in).

The following example illustrates the ability to identify changes in structural condition from changes in measured vibration properties. Consider the two degrees-of-freedom (2-DOF) vibration oscillator shown in **Figure 1**. Using the methods of standard analytical modal analysis, the free equation of motion of the system can be written as:

$$\begin{bmatrix} m & 0 \\ 0 & m \end{bmatrix} \begin{Bmatrix} \ddot{x}_1 \\ \ddot{x}_2 \end{Bmatrix} + \begin{bmatrix} 2k & -k \\ -k & 2k \end{bmatrix} \begin{Bmatrix} x_1 \\ x_2 \end{Bmatrix} = \begin{Bmatrix} 0 \\ 0 \end{Bmatrix} \quad [1]$$

Likewise, the modal frequencies, ω_n, and mode shapes, $\mathbf{U}_n$ can be written as:

$$\omega_1 = \sqrt{\frac{k}{m}} \quad \mathbf{U}_1 = \begin{Bmatrix} 1 \\ 1 \end{Bmatrix}$$
$$\omega_2 = \sqrt{\frac{3k}{m}} \quad \mathbf{U}_2 = \begin{Bmatrix} 1 \\ -1 \end{Bmatrix} \quad [2]$$

The reader will note from eqn [2] that the modal frequencies and mode shapes are functions of the mass and stiffness parameters of the system. Thus, by observing changes in these features (the modal frequencies and mode shapes), changes in the structural condition (mass and stiffness parameters) can be observed. Typically, it is assumed for practical applications that the types of damage of interest will primarily manifest as changes to the stiffness parameters while the mass parameters remain constant. Thus, for a given change in modal frequency and mode shape, information about changes to the structural stiffness parameters can be inferred.

Overview of Sonic NDT Process

The process of implementing GSNDT involves four primary steps. Each of these steps is described in detail below:

1. Operational evaluation: definition of potential damage scenarios for the system and assessment of operating conditions
2. Data acquisition and cleansing: observation of the system over a length of time using periodically spaced measurements
3. Data transformation and feature extraction; selection of parameters of interest from the data
4. Feature comparison and statistical model building: analysis of the features to determine the current mechanical state of the system

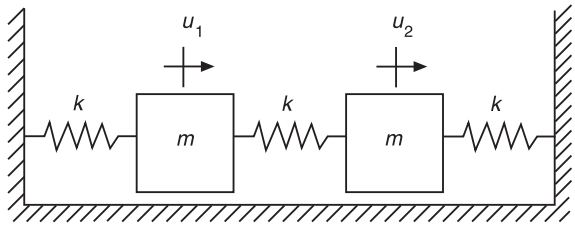


Figure 1 Two-degrees-of-freedom system.

Operational Evaluation

The first step in implementing GSNDT is operational evaluation. Operational evaluation refers to the assessment of the type of damage to be observed using GSNDT, the operational and environmental conditions under which GSNDT must be applied, the limitations which are present that will affect the GSNDT process, and the economic justification associated with GSNDT.

The first step in defining the damage that will be detected using GSNDT is to assess what level of damage is to be considered. The five levels of damage (originally presented as four levels but later modified) are:

- Level 1: Existence of damage: simple binary indication that 'something has changed'
- Level 2: Location of damage: spatial location of damage to resolution allowed by the sensor set
- Level 3: Type of damage: classification of damage into discrete typesets, usually from application-specific knowledge base
- Level 4: Magnitude of damage: usually expressed as a percentage reduction in localized stiffness
- Level 5: Prognosis of remaining useful life of structure: requires specific knowledge of the nature of the damage, damage propagation, future loading, and the level of damage tolerance possessed by the structure

It is important to define precisely what type of damage is being sought and to select the appropriate instrumentation for that damage type. Typically it is desirable to preselect a relatively small candidate set of damage locations prior to applying the GSNDT techniques. Inclusion of too many candidate damage cases creates the danger of nonuniqueness, that is, the existence of more than one damage case that creates the same change in the measured features. Because many of the GSNDT techniques are essentially inverse modeling approaches, nonuniqueness is a major source of false-positive indications of damage.

Another factor to be considered is whether or not examples of the undamaged and damaged structure are available for GSNDT. If examples of each type of damage are available, as in the case of most rotating machinery applications, then the identification of damage can be conducted in a supervised learning mode. If examples of each type of damage are not available, as in most civil engineering applications, then the identification of damage must be conducted in an unsupervised learning mode. The implication of the learning mode is explained under the section on feature comparison and statistical model building, below.

Data Acquisition and Cleansing

Sensor and excitation selection and placement The data acquisition phase of GSNDT involves selecting the types of sensors to be used, selecting the location where the sensors should be placed, determining the number of sensors to be used, and defining the data acquisition/storage/transmittal hardware. This process will be application-specific. Economic considerations will play a major role in making these decisions. Another consideration is how often the data should be collected. In some cases it may be adequate to collect data immediately before and at periodic intervals after a severe event. However, if fatigue crack growth is the failure mode of concern, it may be necessary to collect data almost continuously at relatively short time intervals.

Because data can be measured under varying conditions, the ability to normalize the data becomes very important to the GSNDT process. One of the most common procedures is to normalize the measured responses by the measured inputs. When environmental or operating condition variability is an issue, the need can arise to normalize the data in some temporal fashion to facilitate the comparison of data measured at similar times of an environmental or operational cycle. Sources of variability in the data acquisition process and with the system being monitored need to be identified and minimized to the extent possible. In general, all sources of variability cannot be eliminated. Therefore, it is necessary to make the appropriate measurements such that these sources can be statistically quantified.

Data acquisition, processing, and storage Data acquisition for GSNDT involves scaling and antialias filtering the data, converting the data to digitized samples, and storing the samples in electronic form on a magnetic or optical medium. Transmission of the data is a significant issue, because many schemes for GSNDT of large structures such as bridges and buildings require large distances (1 km and greater) between the sensor and the storage medium. Historically, long cables have been used to bring the sensor signals back to a central location for scaling, filtering, digitization, and storage. This approach has significant drawbacks as a result of signal loss and noise in the cables as well as monitoring of cable integrity. Alternatives have been proposed that use wireless systems. Some wireless systems perform a local 'clustering' of transducer signals via cables to a 'local' data acquisition system. With several of these 'local' systems across a large structure, the need to run cables along the entire structure is eliminated. Another approach is to make an integrated sensing, signal

conditioning, digitizing and storage unit, then deploy one such unit at each desired measurement point on the structure. A master unit at a centralized location queries each of the remote units via wireless connection to retrieve the data.

Data cleansing and validation Data validation is the process of deciding whether or not the data are generally acceptable and suitable for use in GSNDT. Data cleansing is the process of selectively choosing data to accept for, or reject from, the feature selection process. Filtering is a type of data cleansing where one rejects data in certain frequency bands. The data validation and cleansing process is usually based on knowledge gained by individuals directly involved with the data acquisition. Judgment of individuals based on experience and consistency across channels and data sets are some of the criteria that are commonly used. Finally, it should be noted that the process of data acquisition and cleansing is not static, but involves feedback from the feature extraction and feature comparison steps.

Data Transformation and Feature Extraction

Once the data have been acquired and validated, the process of condensing useful GSNDT information from the data begins. Usually the raw data time series are not directly indicative of changes in the structural properties. Thus, GSNDT requires the use of transforms and features to determine the state of the structure. A transform is a mathematical operation that is applied to the data to change the domain under which the data are viewed. A transform may include assumptions about the form of the data, but does not inherently add or remove information from the data. (Thus, for each transform there is also an inverse transform.) An example is the Fourier transform, which assumes that the data can be represented by superposed sinusoids, then computes the required coefficients for these sinusoids. The inverse Fourier transform returns the data back to the time domain without loss of information.

Feature extraction is the process of extracting information from the data (or a transform of the data) such that the overall quantity of data is reduced. Thus, it is through feature extraction that the GSNDT analyst seeks to reduce the (usually very large) set of raw data to the few parameters that are of interest. Note that there is a tradeoff when extracting features as information is typically lost in the process. Take, for example, the harmonic sine wave shown in **Figure 2**. It is composed of 1024 data points. However, if it is noted that the signal is simply a sine wave of amplitude 2, frequency 4 Hz, and phase 0, the 1024 data points have been reduced to three parameters, in this case without much loss of information about the signal.

Selection of the features to be identified is crucial to the GSNDT process. There are three basic characteristics of the features that must be considered:

1. Sensitivity: the feature must be relatively sensitive to the type of damage that was selected in the operational evaluation step. Also, the feature must be relatively insensitive to the measurement interference defined in the operational evaluation step.
2. Observability: the feature must be observable by the measurements defined in the data acquisition and cleansing step. In other words, the measurements obtained must contain information that the feature can be extracted from.
3. Dimensionality: it is desirable to minimize the length of the feature vector (defined as the dimensionality of the feature). In the example presented above, if the magnitudes of the individual data points had been the feature of interest, the feature vector would have dimension 1024 (or 1026 after including the starting point and spacing of the time axis). However, upon converting to the modal properties, the feature vector has dimension 3. Low dimensionality is crucial to ensuring that the multidimensional parameter spaces defined in the statistical model-building section below are well populated. (For example, in a multivariate Gaussian distribution, it is important to have low enough dimensionality such that the data set is adequate to populate the tails of the distribution.)

This so-called curse of dimensionality is demonstrated as shown in **Figure 3**. For a univariate (dimension 1) standard normal distribution, 90% of the data

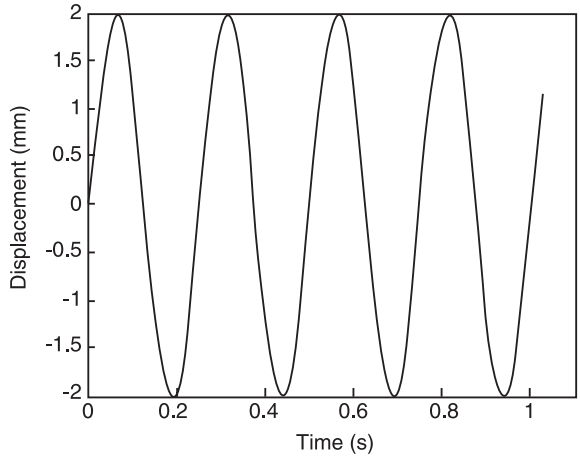


Figure 2 Sine wave for example of feature extraction.

in the distributions falls between −1.6 and +1.6. However, for a 10-dimensional standard normal distribution, less than 1% of the data falls within a distance 1.6 from the origin. Thus, a tremendous amount of data is required to describe the features accurately with so many dimensions.

Feature computation techniques can be defined as regressive or nonregressive. Regressive features are computed by curve-fitting (regression) of a parametric formula to the data or a transform of the data. Examples of regressive features are modal parameters, autoregressive moving average (ARMA) coefficients, and finite element model perturbations. Features computed directly from the data without the use of parametric curve-fitting are called nonregressive. Maximum/minimum values, root-mean-square values, and zero-crossing counts are examples of nonregressive features. In general, regressive features are more computationally intensive to extract, but are generally desirable because of the ability to incorporate an understanding of the underlying mechanics into the model.

Modal parameters are commonly used features in GSNDT because the GSNDT field grew to a great extent out of the community that practices experimental modal analysis (see **Modal analysis, experimental**, Measurement techniques). Techniques for extracting modal parameters (and for defining the data acquisition necessary to do so) are well defined and both software and hardware are available commercially. Modal parameters are determined by regression of parameters to the frequency response function or its time domain equivalent, the impulse response function.

Another issue to note is that some features are computed directly from the data or its transforms, whether by regression or not (such as modal parameters), whereas some features are themselves computed from other features. Perturbations to finite element model parameters based on regression to identified modal parameters are examples of 'features of other features'.

Nonregressive features Nonregressive features are attractive for GSNDT because they can give insight about the state of the structure without the need for detailed computations or model assumptions. Examples of nonregressive features include simple mathematical functions of the time series, such as the maximum value and the root-mean-square value. Another commonly used nonregressive feature is the comparison of the error in the frequency response function or the coherence function between the undamaged and damaged data sets. Advanced nonlinear signal-processing techniques can also be used as nonregressive features for GSNDT. Examples include higher-order spectra, beat phenomena, time–frequency transforms, and wavelet transforms.

In the rotating machinery industry, almost all GSNDT is performed using nonregressive features of the signal. Examples include the root-mean-square value of the response signal, increase of power spectral density magnitude at particular resonant frequencies, and the existence of harmonic resonances at multiples of the rotational speed. In applications where the damage can be distributed across a large spatial region (such as in civil infrastructure), nonregressive features are mainly useful for performing a quick check on the data. Detailed insight into the nature of the structural damage in such cases generally requires some sort of regression in order to bring knowledge of the underlying geometry and mechanics into the diagnosis process.

In many GSNDT applications, it is acceptable to treat the measurement set as representing the response of a purely linear system. In other situations, it may not be acceptable to assume linearity, but it is often mathematically convenient to do so anyway. For some applications, assumption of linear structural response is simply not valid. This situation occurs when the materials that compose the structure are inherently nonlinear (such as polymers or foams), or when the damage itself introduces nonlinearity. In the latter case, features that detect the onset of nonlinearity are used to conduct level 1

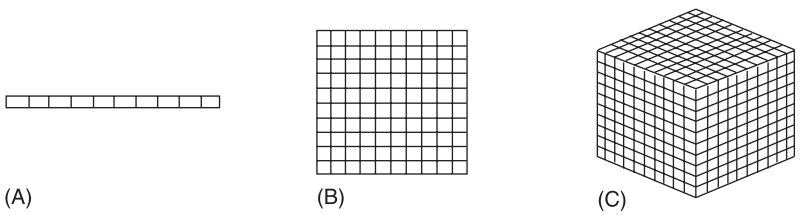


Figure 3 Illustration of the 'curse of dimensionality'. (A) 1-D: 10 bins; (B) 2-D: 100 bins; (C) 3-D: 1000 bins.

GSNDT. Changes in the coherence function and estimated probability density function can be used in this way.

Regressive features By far the most commonly used regressive feature in GSNDT applications are modal parameters, specifically the modal frequency, modal damping ratio, and mode shape. Also, functions of these features are among the most commonly used features in GSNDT. While modal parameters are typically not the best features to use for GSNDT from a sensitivity standpoint, there is widespread belief in the community that they are useful indicators of damage. Their popularity is owed to the physical insight that they provide and the large number of commercial software packages that are available to compute them.

Modal frequency is the most commonly used linear feature, followed by the mode shape and functions of the mode shape, such as mode shape curvature, bending strain energy, modal flexibility, and load-dependent Ritz vectors. Modal damping has been used for GSNDT, but due to a high level of experimental variability it tends not to be a very indicative feature. Finite element method updating (see **Finite element methods**), which was originally developed to tune linear finite element models to measured modal parameters, is also used to estimate changes in the finite element material and geometric parameters, which can be used as features in GSNDT. In the case of nonlinear response, general-purpose regression techniques include ARMA coefficients, polynomial fits, and the update of finite element method parameters using nonlinear data.

Feature Comparison and Statistical Model Building

Once features have been extracted from the data, they are compared with features extracted from previous data sets to assess whether or not structural damage has occurred. In some cases, such as rotating machinery applications, examples of 'undamaged' and 'damaged' feature sets are available, and thus the GSNDT problem reduces to classification of the measured feature into the appropriate damage set. This situation is referred to as supervised comparison. The alternative, when only undamaged feature sets or damaged feature sets are available, is referred to as unsupervised learning. In unsupervised learning, it is not possible to make a set classification, but only a hypothesis about the likelihood that the new feature is a member of the existing feature set. Feature comparison techniques can be categorized as being either deterministic (i.e., features are considered to be absolute values that are measured exactly) or statistical (i.e., features are considered to be samples from a random parent population).

Most deterministic feature comparisons are simple error comparisons (either absolute error or normalized in some way). For features such as modal frequency, the error comparison can be done for each value in the feature vector. However, for features with spatial distribution such as mode shapes, comparison metrics that reduce the aggregate comparison to a set of scalar values is desirable. An example of such a metric for mode shapes is the modal assurance criterion (MAC).

Using the results of the feature comparison to assess whether or not damage has occurred requires the definition of whether the damage identification will be unsupervised or supervised. In the case where examples of data from the damaged structure are not available, unsupervised methods must be used to detect clustering in the data and then look for outliers to the cluster to detect damage. Examples of clustering techniques include density estimation, expectation maximization, and k-means algorithms. In the case where examples of data from the damaged structure are available, supervised methods can be used to classify what damage case the current features most closely represent, or to use regression to assess the location and magnitude of damage. Examples of classification techniques include Fisher's discriminant, quadratic classification, and k-nearest neighbors. Regression techniques include linear, polynomial, and k-nearest neighbors. Neural networks can be utilized in both classification and regression techniques. The field of statistical process control also offers techniques for trending the data to track the onset of damage and predict future behavior.

Consideration of variability An important issue in the comparison of features is the variability that is present in the features as a result of factors other than structural damage. These factors can include environmental effects (such as temperature, wind, humidity, etc.), operational interference (such as acoustic loads or extraneous vibration excitations), and electrical noise. Often these effects cannot be mitigated, but the quantification of the effects is nevertheless crucial to produce a credible GSNDT result. If the effect is cyclical, observation of the feature variability over one or more complete cycles of the effect can give an approximation of the perturbation in the feature value due to this effect. Including a measure of the effect in the feature vector (such as a measurement of temperature differential or automotive traffic flow) can be an effective technique for accounting for the source of variability.

An example of the effect of temperature-induced variability in features is shown in **Figure 4**. Pictured in this figure are measurements of the first modal frequency of a bridge structure taken over a 24-h period at 2-h intervals. Superimposed are measurements of temperature differential between the eastern and western edges of the bridge. Clearly indicated is a strong variability of this feature (first modal frequency) as a function of deck temperature differential.

False-positive and false-negative indicators A key aspect of GSNDT is the elimination of false-positive and false-negative indicators from the damage diagnosis process. False-positive refers to the situation where damage is indicated when in fact none is present. False-negative refers to the situation where damage is not indicated, even though it is present. Although false-negative indicators pose the larger problem in terms of life safety, false-positive indicators are a significant issue in that they can irreparably damage the credibility of the GSNDT technique being applied or the engineer applying it. When developing or implementing a GSNDT technique on a set of data, it is important to compare two data sets from the undamaged structure under different experimental and environmental conditions to study false-positive indicators. It is also important to compare data sets from the undamaged structure and the damaged structure at various levels of damage to study false-negative indicators and to define the threshold at which damage can be detected.

GSNDT History and Applications

Early Work

It is the authors' speculation that damage or fault detection, as determined by changes in the dynamic properties or response of systems, has been practiced in a qualitative manner, using acoustic techniques, since modern human beings have used tools. More recently, this subject has received considerable attention in the technical literature and a brief summary of the developments in this technology over the last 30 years is presented below. Specific references are not cited.

The development of vibration-based damage detection technology has been closely coupled with the evolution, miniaturization, and cost reductions of fast Fourier transform (FFT) analyzers and digital computing hardware. To date, the most successful application of vibration-based damage detection technology has been for monitoring rotating machinery. The rotating machinery application has taken an almost exclusively nonregressive approach to damage detection. The detection process is based strictly on pattern recognition applied to time histories or spectra generally measured at a single point on the housing of the machinery during normal operating conditions. Often this pattern recognition is only performed in a qualitative manner. Databases have been developed that allow specific types of damage to be identified from particular features of the vibration signature. For these systems the approximate location of the damage is generally known, making a single-channel

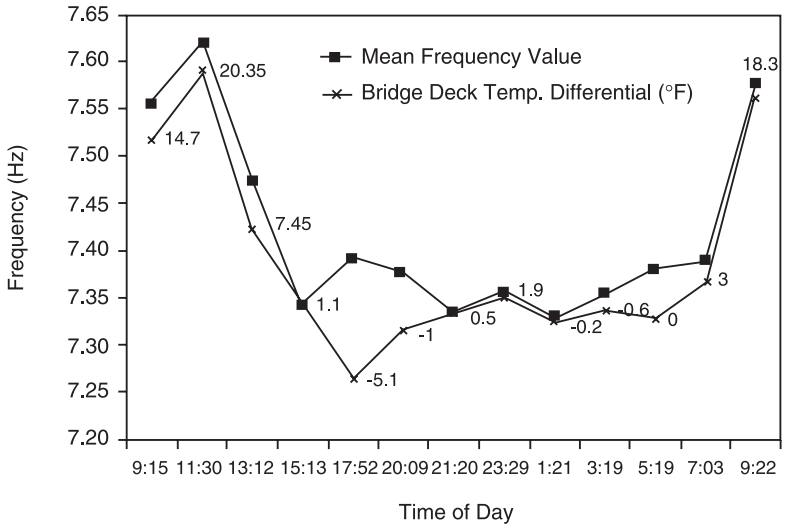


Figure 4 Example of feature variability as a function of temperature change.

FFT analyzer sufficient for most periodic monitoring activities. Typical damage that can be identified includes loose or damaged bearings, misaligned shafts, and chipped gear teeth. Today, commercial software integrated with measurement hardware is marketed to help the user systematically apply this technology to operating equipment.

During the 1970s and 1980s the oil industry made considerable efforts to develop vibration-based damage detection methods for offshore platforms. This damage detection problem is fundamentally different from that of rotating machinery because the damage location is unknown and because the majority of the structure is not readily accessible for measurement. To circumvent these difficulties, a common methodology adopted by this industry was to simulate candidate damage scenarios with numerical models, examine the changes in resonant frequencies that were produced by these simulated changes, and correlate these changes with those measured on a platform. A number of very practical problems were encountered, including measurement difficulties caused by platform machine noise, instrumentation difficulties in hostile environments, changing mass caused by marine growth and varying fluid storage levels, temporal variability of foundation conditions, and the inability of wave motion to excite higher vibration modes. These issues prevented adaptation of this technology and efforts at further developing this technology for offshore platforms were largely abandoned in the early 1980s.

Applications to Rotating Machinery

The rotating machinery application represents a mature technology where vibration-based damage detection has made the transition from a research topic to industry practice. Vibration-based damage detection for rotating machinery has been repeatedly applied with success to a variety of machinery elements such as roller bearings and gears. In the past, the greatest emphasis has been on the qualitative interpretation of vibration signatures both in the frequency and, to a lesser extent, in the time domain. Numerous summaries and reviews of this approach are available in textbook form, including detailed charts of machinery fault analysis. The approach taken has generally been to consider the detection of damage qualitatively on a fault-by-fault basis by examining acceleration signatures for the presence and growth of peaks in spectra at certain frequencies, such as multiples of shaft speed. A primary reason for this approach has been the inherent nonlinearity associated with damage in rotating machinery. Recently, more general approaches to damage detection in rotating machinery have been developed. These approaches utilize formal statistical methods to assess both the presence and level of damage on a statistical basis.

Aerospace Applications

The aerospace community began to study the use of vibration-based damage detection during the late 1970s and early 1980s in conjunction with the development of the space shuttle. This work has continued, with current applications being investigated for the National Aeronautics and Space Administration's space station and reusable launch vehicle. The shuttle modal inspection system (SMIS) was developed to identify fatigue damage in components such as control surfaces, fuselage panels, and lifting surfaces. These areas were covered with a thermal protection system, making them inaccessible and, hence, impractical for conventional local nondestructive examination methods. This system has been successful in locating damaged components that are covered by the thermal protection system. All orbiter vehicles have been periodically subjected to SMIS testing since 1987. Space station applications have primarily driven the development of experimental/analytical damage identification methods. These approaches are based on correlating analytical models of the undamaged structure with measured modal properties from both the undamaged and damaged structure. Changes in stiffness indices as assessed from the two model updates are used to locate and quantify the damage. Since the mid-1990s, studies of damage identification for composite materials have been motivated by the development of composite fuel tank for a reusable launch vehicle.

Civil Structure Applications

The civil engineering community has studied vibration-based damage assessment of bridge structures since the early 1980s. Modal properties and quantities derived from these properties, such as mode shape curvature and dynamic flexibility matrix indices, have been the primary features used to identify damage in bridge structures. Environmental and operating condition variability present significant challenges to the bridge-monitoring application. The physical size of the structure also presents many practical challenges for vibration-based damage assessment. Regulatory requirements in some eastern Asian countries, which mandate the companies that construct the bridges periodically to certify their structural health, are driving current research and commercial development of vibration-based bridge-monitoring systems.

Concluding Remarks

The field of GSNDT, while composed of well-developed technologies such as dynamic sensing, digital signal processing, modal testing, experimental modal analysis, and statistical pattern recognition, is still in its infancy. Only in the field of rotating machinery inspection has GSNDT crossed the chasm between research and application. Open research issues still exist in the areas of operational evaluation, data acquisition and cleansing, data transformation and feature extraction, and feature comparison. Nevertheless, the potential economic and societal benefits of effective GSNDT are of significant enough magnitude that research continues so that these hurdles may be overcome.

See also: **Data acquisition**; **Modal analysis, experimental**, Measurement techniques; **Model updating and validating**; **Nondestructive testing**, Ultrasonic; **Rotating machinery, monitoring**; **Transform methods**.

Further Reading

Bishop CM (1995) *Neural Networks for Pattern Recognition*. Oxford: Oxford University Press.

Braun S (1986) *Mechanical Signature Analysis – Theory and Applications*. London: Academic Press.

Craig RR Jr (1981) *Structural Dynamics: An Introduction to Computer Methods*. New York: John Wiley.

Doebling SW, Farrar CR and Prime MB (1998) A summary review of vibration-based damage identification methods. *The Shock and Vibration Digest* 30: 91–105.

Maia NMM and Silva JMM (eds) (1997) *Theoretical and Experimental Modal Analysis*. Taunton: Research Studies Press.

Mitchell JS (1993) *Introduction to Machinery Analysis and Monitoring*. Tulsa, OK: PenWel Books.

Natke HG and Czeslaw C (1997) *Model-Aided Diagnosis of Mechanical Systems*. Berlin: Springer-Verlag.

Salawu OS (1997) detection of structural damage through changes in frequency – a review. *Engineering Structures* 19: 718–723.

Ultrasonic

L W Schmerr Jr, Iowa State University, Ames, IA, USA

Copyright © 2001 Academic Press

doi:10.1006/rwvb.2001.0139

High-frequency propagating sound waves are commonly used in industry as a means for nondestructively evaluating a component for flaws. **Figure 1** shows the instrumentation of a typical ultrasonic flaw inspection setup. In such an inspection, a pulser generates very short repetitive pulses of electrical energy that are used to drive an ultrasonic transducer. A piezoelectric crystal in the transducer converts the electrical pulses into mechanical motion, producing an elastic wave which then propagates into the component and interacts with any flaws present. Waves scattered from the flaws can be received by another piezoelectric transducer and converted back to electrical signals. These received signals are amplified by the receiver section of the pulser/receiver, captured and displayed as a voltage vs time trace on a digital oscilloscope, and transferred to a computer for signal processing and data interpretation. An oscilloscope display of the flaw signals is one of the most common types of ultrasonic displays, called an A-Scan. A typical A-scan voltage vs time display is shown in **Figure 2** for a pulse–echo setup where the same transducer is used as both a transmitter and receiver. In contrast, the two-transducer setup shown in **Figure 1** is called a **pitch–catch** setup. In an A-scan display, one normally sees, in addition to the flaw signal(s), other responses from the geometry, such as the back surface reflection shown in **Figure 2,** and a large negative response at the beginning of the time trace, called the 'main bang'. This main bang signal comes from some of the electrical energy generated while the pulser is firing leaking through into the receiving section. This signal produces a 'dead zone' close to the transducer that is unusable for inspection purposes since other responses are buried in this large signal. In addition to the A-scan, there are two other commonly-used types of display in the nondestructive testing field. The B-scan, shown in **Figure 3,** uses a position sensor to measure the location (x-position) of the transducer as it moves along a linear scan path. When a signal is received from a flaw or a part of the geometry, the arrival time of this signal is used to generate a corresponding depth (z-position) from which the signal arose in the component being inspected. A response that is proportional to the amplitude of the signal received is then recorded on a computer display at these measured x- and z-positions. As the transducer moves, a complete cross-sectional display is then generated on the computer screen, as shown in **Figure 3**, producing in effect a side view of the interior of the component. Only a black and white B-scan image is shown in **Figure 3** but in practice these images may be gray-scale or color-coded.

Another type of flaw response display used in nondestructive testing is called a C-scan. In this case, a transducer is mechanically moved in a two-dimensional plane, typically in a raster-like scan as shown in **Figure 4.** Both the x- and y-coordinates of

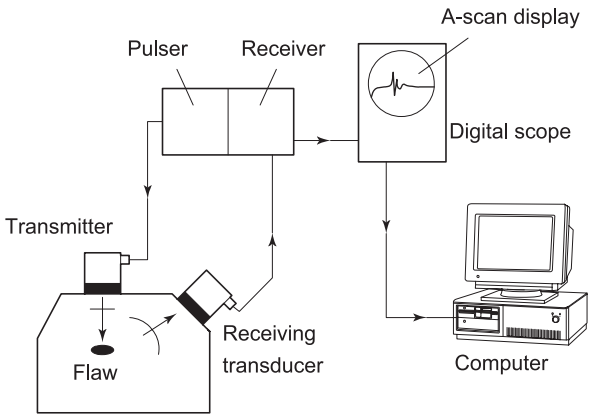


Figure 1 Components of an ultrasonic nondestructive testing measurement system.

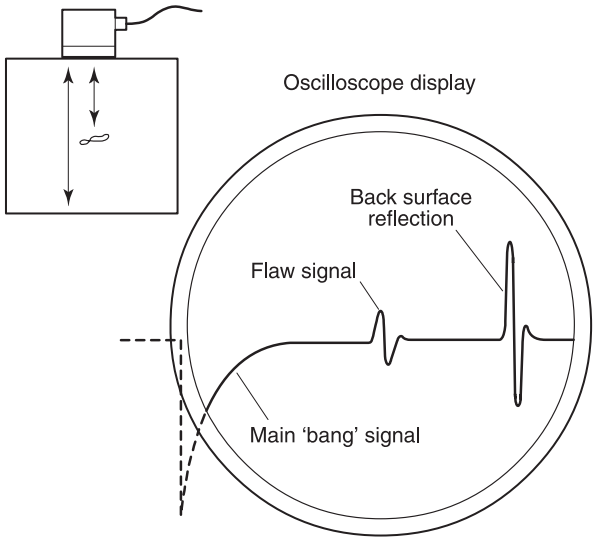


Figure 2 A-scan voltage vs time display for a simple pulse–echo inspection setup.

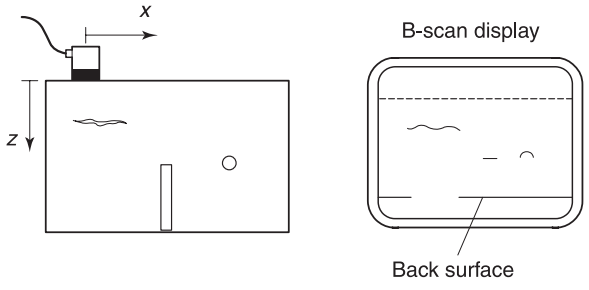


Figure 3 An ultrasonic B-scan display (one-dimensional scanning).

the transducer are measured and a response proportional to the amplitude of the signal received is recorded and displayed on a computer screen at this location, producing a two-dimensional (2-D) C-scan image as the transducer scans over the surface. In some cases, only signals received in a particular time range (corresponding to a depth range in the component being inspected) are displayed, giving a 2-D image of flaws only in a selected section of the part. If this depth range is taken as the full width of the component in the z-direction, then all the flaw responses are displayed, as shown in **Figure 4.** However, unlike the black and white image shown in **Figure 4,** the amplitude responses of many C-scans are often displayed as color-coded images on a computer screen.

Producing A-, B-, or C-scan images of flaw responses is not difficult to achieve. What is difficult is to quantitatively interpret those images in terms of flaw type, size, orientation, etc. Such interpretation requires a more detailed knowledge of the basic physics involved in the inspection process. The following se#ctions describe some of that fundamental physics, including the types of ultrasonic waves used for testing purposes (bulk waves, Rayleigh waves, plate waves), and basic wave phenomena (reflection/transmission, mode conversion, critical angles, attenuation) that are often present in ultrasonic inspections. Since ultrasonic transducers play a very important role in tests, several sections discuss the types of ultrasonic transducers commonly used in

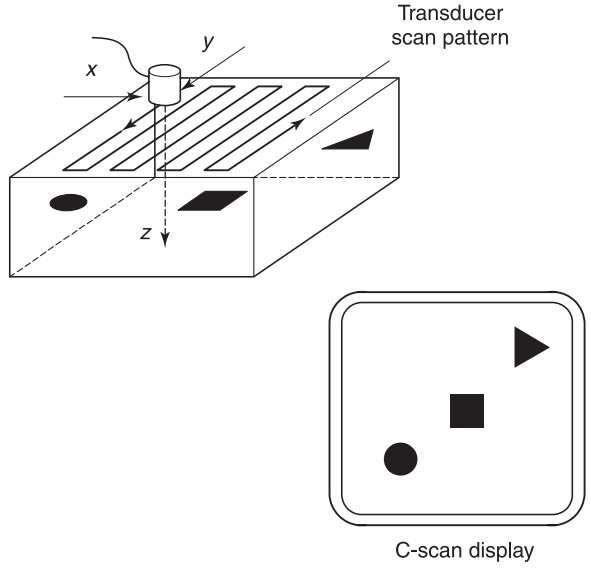


Figure 4 An ultrasonic C-scan display (two-dimensional scanning).

practice and consider the basic parameters that describe the radiated sound fields of transducers.

Ultrasonic Bulk Waves

Ultrasonic bulk waves are the type of waves most commonly used in nondestructive testing applications. The governing equations that describe bulk waves for a homogeneous, isotropic elastic solid are Navier's equations, given by:

$$G\nabla^2\mathbf{u} + \frac{E}{2(1+\upsilon)(1-2\upsilon)}\nabla(\nabla\cdot\mathbf{u}) = \rho\frac{\partial^2\mathbf{u}}{\partial t^2} \quad [1]$$

where $\mathbf{u}(\mathbf{x}, t)$ is the displacement in the solid at point $\mathbf{x}$ and time, t, ρ is the density, G is the shear modulus, and E and υ are Young's modulus and Poisson's ratio, respectively. Through the use of the Helmholtz decomposition theorem, the displacement can be expressed in terms of a scalar potential, ϕ, and a vector potential, $\boldsymbol{\psi}$, as:

$$\mathbf{u} = \nabla\phi + \nabla\times\boldsymbol{\psi} \quad [2]$$

This Helmholtz decomposition reduces Navier's equations to two separate wave equations for the potential functions given by:

$$\begin{aligned}\nabla^2\phi - \frac{1}{c_\mathrm{p}^2}\frac{\partial^2\phi}{\partial t^2} &= 0\\ \nabla^2\boldsymbol{\psi} - \frac{1}{c_\mathrm{s}^2}\frac{\partial^2\boldsymbol{\psi}}{\partial t^2} &= 0\end{aligned} \quad [3]$$

The scalar potential ϕ represents compressional waves traveling with the wave speed c_p while the vector potential $\boldsymbol{\psi}$ represents shear waves traveling with a wave speed, c_s, where:

$$\begin{aligned}c_\mathrm{p} &= \sqrt{\left[\frac{E(1-\upsilon)}{(1+\upsilon)(1-2\upsilon)\rho}\right]}\\ c_\mathrm{s} &= \sqrt{\left(\frac{G}{\rho}\right)} = \sqrt{\left[\frac{E}{2(1+\upsilon)\rho}\right]}\end{aligned} \quad [4]$$

For most structural materials the wave speed of compressional waves is approximately twice the wave speed of shear waves (see **Table 1**). Both compressional and shear waves are referred to as bulk waves since they propagate in the volume (bulk) of a solid. Compressional bulk waves are also called P-waves, pressure waves, longitudinal (L) waves, dilatational waves, or irrotational waves. Bulk shear waves are also called S-waves, transverse (T) waves, distortional waves, equivoluminal waves, or rotational waves.

Table 1 The wave speeds and densities for some common materials

Material	c_p $(\mathrm{m\,s^{-1}}\times 10^3)$	c_s $(\mathrm{m\,s^{-1}}\times 10^3)$	ρ $(\mathrm{kg\,m^{-3}}\times 10^3)$
Air	0.33	–	0.0012
Aluminum	6.42	3.04	2.70
Brass	4.70	2.10	8.64
Copper	5.01	2.27	8.93
Glass	5.64	3.28	2.24
Lucite (perspex)	2.70	1.10	1.25
Magnesium	5.77	3.05	10.0
Nickel	5.60	3.00	8.84
Nylon	2.60	1.10	1.12
Polyethylene	1.95	0.54	0.92
Steel, mild	5.90	3.20	7.90
Steel, stainless	5.80	3.10	7.83
Titanium	6.10	3.10	4.48
Water	1.48	–	1.00

An elastic solid admits plane harmonic bulk wave solutions of the form:

$$\begin{aligned}\phi &= \Phi\exp\left[ik_\mathrm{p}(x - c_\mathrm{p}t)\right]\\ \boldsymbol{\psi} &= \boldsymbol{\Psi}\exp\left[ik_\mathrm{s}(x - c_\mathrm{s}t)\right]\end{aligned} \quad [5]$$

where $k_\alpha = \omega/c_\alpha$ is the wave number for a wave of type α ($\alpha = p, s$) and ω is the circular frequency. Since both bulk wave speeds in eqn [4] are independent of frequency, harmonic wave solutions of the type given by eqn [5] represent nondispersive waves. This is strictly true, however, only if the solid is perfectly elastic so that no frequency dependent energy attenuation or dissipation mechanisms are present.

Rayleigh Waves

At a free surface of an elastic solid, waves can propagate that are confined primarily to that surface. These surface waves are called Rayleigh waves. At the stress-free plane surface ($y = 0$) of a semi-infinite elastic solid occupying the region $y \geq 0$, for example, harmonic Rayleigh waves of the form:

$$\begin{aligned}\phi &= A\exp(-\alpha y)\exp\left[ik(x - ct)\right]\\ \boldsymbol{\psi} &= B\mathbf{e}_z\exp(-\beta y)\exp\left[ik(x - ct)\right]\end{aligned} \quad [6]$$

can propagate and satisfy the stress-free surface boundary conditions if the Rayleigh wave speed, $c = c_\mathrm{R} < c_\mathrm{S}$, is a real root of the equation:

$$\left(2-\frac{c^2}{c_s^2}\right)^2-4\sqrt{\left(1-\frac{c^2}{c_p^2}\right)}\sqrt{\left(1-\frac{c^2}{c_s^2}\right)}=0 \quad [7]$$

A simple equation that gives a good fit for this root in terms of Poisson's ratio, υ, and the shear wave speed, c_s, is:

$$c_R=\frac{0.862+1.14\upsilon}{1+\upsilon}c_s \quad [8]$$

The depth of penetration of Rayleigh waves into the solid ($y\geq 0$), is controlled by the frequency. This can be seen from the expressions for the decay coefficients α, β of eqn [6] which are given by:

$$\begin{aligned}\alpha&=|k|\sqrt{\left(1-\frac{c^2}{c_p^2}\right)}\\ \beta&=|k|\sqrt{\left(1-\frac{c^2}{c_s^2}\right)}\end{aligned} \quad [9]$$

where $k=\omega/c$ is the wave number and $c=c_R$ is the wave speed of the Rayleigh wave. Although the solutions in eqn [6] are for 2-D disturbances propagating on a planar interface, similar Rayleigh waves can be propagated on the curved surfaces of 3-D geometries, allowing their use in the inspection of surface areas of a component that might not be directly accessible. Rayleigh waves are nondispersive provided that the solid behavior is perfectly elastic, and provided that the predominant wavelengths present in the propagating wave are large, relative to both the principal radii of the surface and the surface roughness.

Plate Waves

In thin geometries such as plates, potentials of the form:

$$\begin{aligned}\phi&=f(y)\exp\left[ik(x-ct)\right]\\ \boldsymbol{\psi}&=g(y)\mathbf{e}_z\exp\left[ik(x-ct)\right]\end{aligned} \quad [10]$$

can satisfy the governing equations of motion and boundary conditions of zero stress on the faces of the plate. These solutions correspond to plate waves, also called Lamb waves. It is usually convenient to consider separately the case of symmetrical extensional motions of the plate and antisymmetrical flexural motions (**Figure 5**). The wave speeds of both the extensional and flexural motions are found as roots of the equation:

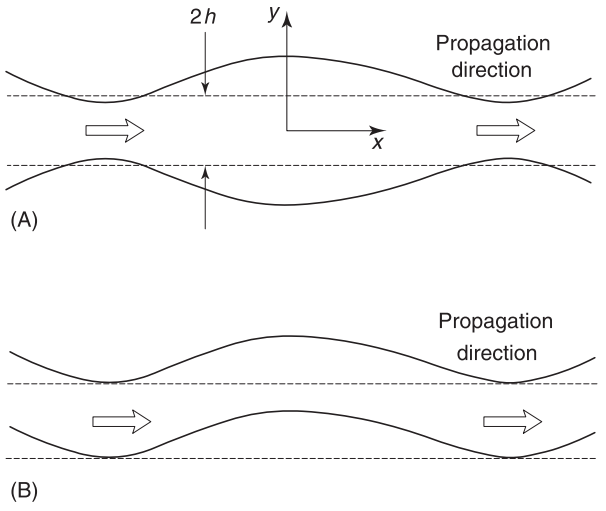


Figure 5 Displacements associated with (A) symmetrical and (B) antisymmetrical plate (Lamb) waves.

$$\frac{\tanh(\beta h)}{\tanh(\alpha h)}=\left[\frac{4k^2\alpha\beta}{\left(k^2+\beta^2\right)^2}\right]^{\pm 1} \quad [11]$$

where the plus/minus sign in eqn [11] corresponds to extensional/flexural plate waves, respectively. The thickness of the plate is $2h$ and $\alpha\beta$ are given by eqn [9] where now c is the wave speed of the plate wave. Unlike the case of Rayleigh surface waves, the wave speeds corresponding to the roots of eqn [11] are frequency-dependent so that plate waves in general are dispersive. Also, at a given frequency, there are multiple roots of eqn [11] possible, each of which corresponds to a particular plate wave 'mode'. **Figure 6** shows some of the dispersion curves for

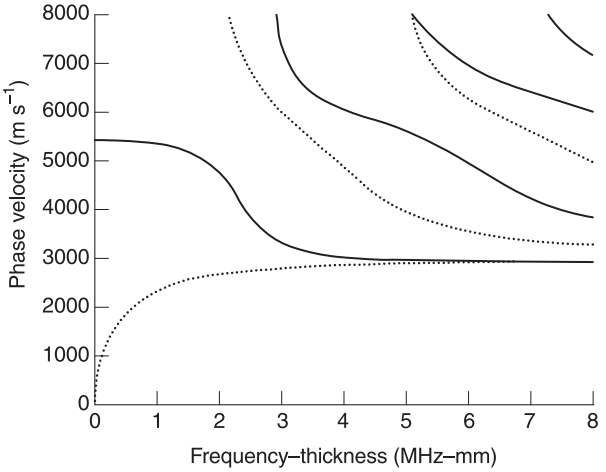


Figure 6 Phase velocity vs frequency for some of the lowest-order symmetrical (continuous lines) and antisymmetrical (dotted lines) plate Lamb waves.

various symmetrical and antisymmetrical plate wave modes. Because Lamb waves are very sensitive to changes of geometry, they are frequently used in pipe and plate inspections to detect cracks and corrosion-induced thinning and to inspect bonds in multi-layered structures.

Reflection and Refraction of Ultrasonic Waves

When an ultrasonic bulk wave of a particular type is incident on a solid interface, reflected and refracted waves of different types can be generated through the process of mode conversion. For example, in nondestructive immersion testing applications, a transducer located in a fluid generates compressional waves that then can be transmitted into an immersed solid component. An idealized model of this case is shown in **Figure 7** where the incident wave is a plane P-wave and the fluid–solid interface is planar.

The incident wave generates only a reflected plane P-wave in the fluid but both a plane P-wave and a mode-converted plane S-wave are transmitted into the solid. At oblique incidence, the directions of propagation of the reflected and transmitted waves are controlled by generalized Snell's law, given by:

$$\frac{\sin\theta_{p1}}{c_{p1}} = \frac{\sin\theta_{p2}}{c_{p2}} = \frac{\sin\theta_{s2}}{c_{s2}} \qquad [12]$$

where c_{p1}, c_{p2} are the compressional wave speeds in the fluid and solid, respectively, and c_{s2} is the shear wave speed of the solid. The polarization direction for the velocity of each wave is shown as a bold arrow in

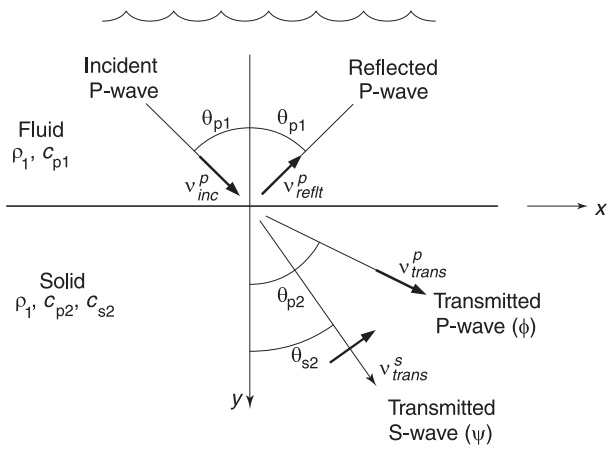


Figure 7 Reflected and transmitted plane waves at a plane fluid–solid interface due to an incident plane wave in the fluid, illustrating the process of mode conversion. Polarizations of the wave velocity vectors are shown as bold arrows.

Figure 7. Plane P-waves are longitudinally polarized along their directions of propagation while plane S-waves have a polarization in a plane perpendicular to the direction of propagation. If the polarization of an S-wave lies in a vertical plane, as is the case shown in **Figure 7**, then the S-wave is a vertically polarized (SV) wave. If the polarization is in a horizontal plane instead, then the S-wave is called a horizontally polarized (SH) wave.

The amplitudes of the reflected and transmitted waves at an interface are usually expressed as the amplitude of the incident wave multiplied by an appropriate reflection or transmission coefficient. Amplitudes can be expressed in terms of many different physical quantities (pressure, stress, velocity, displacement, energy, etc.) so that it is important to specify the physical quantity on which a particular reflection or transmission coefficient is based. For example, the reflection and transmission coefficients based on ratios of the reflected/transmitted wave velocities to the incident wave velocity at the fluid–solid interface are given by:

$$\begin{aligned} R^{PP} &\equiv \frac{v^{P}_{reflt}}{v^{P}_{inc}} = \frac{\Delta_2 - \Delta_1}{\Delta_1 + \Delta_2} \\ T^{PP} &\equiv \frac{v^{P}_{trans}}{v^{P}_{inc}} = \frac{2\cos\theta_{p1}\left[1 - 2(\sin\theta_{s2})^2\right]}{\Delta_1 + \Delta_2} \\ T^{PS} &\equiv \frac{v^{S}_{trans}}{v^{P}_{inc}} = \frac{-4\cos\theta_{p1}\cos\theta_{p2}\sin\theta_{s2}}{\Delta_1 + \Delta_2} \end{aligned} \qquad [13]$$

where:

$$\begin{aligned} \Delta_1 &= \cos\theta_{p2} \\ \Delta_2 &= \frac{\rho_2 c_{p2}}{\rho_1 c_{p1}}\left[4\left(\frac{c_{s2}}{c_{p2}}\right)^2 \sin\theta_{s2}\cos\theta_{s2}\sin\theta_{p2}\cos\theta_{p2} \right. \\ &\quad \left. + 1 - 4(\sin\theta_{s2}\cos\theta_{s2})^2\right] \end{aligned} \qquad [14]$$

Eqns [12]–[14] show that in general, these reflection and transmission coefficients are controlled by the incident angle, the wave speeds of the fluid and the solid and the acoustic impedance, Z_α, for a wave of type $\alpha(\alpha = p, s)$, defined by:

$$Z_\alpha = \rho c_\alpha \qquad [15]$$

In the SI system, the unit of Z_α is $\mathrm{kg\,m^{-2}s^{-1}} = 1$ rayl. A rayl is a very small quantity so that acoustic impe-

dance values are often quoted in terms of Mrayl $= 10^6$ rayl (**Table 2**). At normal incidence ($\theta_{p1} = 0$) eqn [13] reduces to:

$$R^{PP} = \frac{\rho_2 c_{p2} - \rho_1 c_{p1}}{\rho_1 c_{p1} + \rho_2 c_{p2}} = \frac{Z_{p2} - Z_{p1}}{Z_{p1} + Z_{p2}}$$
$$T^{PP} = \frac{2\rho_1 c_{p1}}{\rho_1 c_{p1} + \rho_2 c_{p2}} = \frac{2Z_{p1}}{Z_{p1} + Z_{p2}} \quad T^{PS} = 0 \qquad [16]$$

Equation [16] shows that there is no mode conversion at normal incidence and the reflection and transmission coefficients are controlled solely by the ratio of the compressional wave acoustic impedances of the two media.

From generalized Snell's law (eqn [12]), it follows that at oblique incidence there are two critical angles where the waves which characterize the transmission/reflection process change from the purely plane waves shown in **Figure 7**. The first of these critical angles occurs when the transmitted P-wave grazes along the interface ($\theta_{p2} = \pi/2$) which occurs at an incident angle, θ_{p1}, given by:

$$\theta_{p1} = \sin^{-1}\left(\frac{c_{p1}}{c_{p2}}\right) \qquad [17]$$

Such a critical angle always exists as long as $c_{p2} > c_{p1}$. For incident angles greater than this first critical angle, the transmitted plane P-wave disappears entirely and becomes instead an inhomogeneous wave traveling along the interface whose amplitude decays exponentially with depth from the interface. If the incident angle is increased to the point where the transmitted shear wave grazes the interface, a second critical angle, θ_{c2}, occurs where the incident angle is:

Table 2 The acoustic impedance of compressional and shear waves for some common materials

Material	Z_p (Mrayls)	Z_s (Mrayls)
Air	0.0004	–
Aluminum	17.3	8.21
Brass	40.6	18.1
Copper	44.7	20.3
Glass	12.6	7.35
Lucite (perspex)	3.11	1.27
Magnesium	57.7	30.5
Nickel	49.5	26.5
Nylon	2.91	1.23
Polyethylene	1.79	0.50
Steel, mild	46.6	25.3
Steel, stainless	45.4	24.3
Titanium	27.3	13.9
Water	1.48	–

$$\theta_{c2} = \sin^{-1}\left(\frac{c_{p1}}{c_{s2}}\right) \qquad [18]$$

This second critical angle also always can exist as long as $c_{s2} > c_{p1}$. For incident angles beyond the second critical angle, the transmitted plane shear wave also disappears and becomes an exponentially decaying inhomogeneous wave traveling along the interface. Critical angles are very important in ultrasonic nondestructive testing applications since they are used in the construction of angle beam shear wave transducers and Rayleigh wave transducers (see the section below on ultrasonic transducers).

Attenuation of Ultrasonic Waves

Navier's equations or the wave equations derived from it in terms of potentials describe the propagation in an ideal (lossless) material. However, waves in all real materials exhibit a loss of amplitude due to attenuation mechanisms such as grain scattering (also called metal 'noise'), and absorption. If the amplitude of a plane wave traveling in the x-direction in an attenuating medium is A_1 at a location x_1 and A_2 at a location $x_2 = x_1 + d$, then to account for attenuation losses we may write:

$$\frac{A_2}{A_1} = \exp\left[-\alpha(f)d\right] \qquad [19]$$

where $\alpha(f)$ is the attenuation coefficient, measured in nepers per unit length (where a neper (Np) is a dimensionless quantity). In general the attenuation coefficient will be a function of the frequency, f, of the ultrasound. For example, in water at room temperature, the attenuation has been measured as:

$$\alpha(f) = 25.3 \times 10^{-15} f^2 \quad \text{Np m}^{-1} \qquad [20]$$

where f is the frequency in Hz. Frequently, attenuation measurements are given on a decibel (dB) scale instead. Attenuation measured in terms of dB/unit length, $\alpha_{dB/l}$, can be related to the linear attenuation coefficient, α, through the relationship:

$$\alpha_{dB/l} = 8.686\alpha \qquad [21]$$

In highly attenuative materials such as rubbers or filled materials, material attenuation may also affect the wave speed in a frequency-dependent manner. These effects are called material dispersion effects to distinguish them from frequency-dependent wave

speeds arising from geometric dispersion, as found in plate waves.

Ultrasonic Transducers

One of the most common ways to generate ultrasound in ultrasonic tests is with the use of a contact P-wave transducer of the type shown in **Figure 8**. The contact transducer consists of a very thin piezo-electric crystal plate that is electroplated on both faces. Those faces are in turn connected electrically to the external input/output connector of the transducer. In some cases a small electrical network may be present for 'tuning' purposes. The front face of the plated crystal is attached to a ceramic wear plate and the back face is attached to an attenuative backing material that is used to control the vibrational characteristics of the crystal. During ultrasonic inspections, a thin fluid couplant layer is normally used between the wear plate and the part being tested to ensure good mechanical coupling of the transducer to the part. Water, oil, and glycerin are some examples of common fluid couplants used in practice. When the voltage pulse generated by the pulser excites the faces of the crystal, mechanical motion of the piezo-electric crystal is produced. Normally, the characteristics of the piezo-electric crystal plate are chosen so that this motion is generated primarily normal to the crystal faces, causing its thickness to expand and contract. This motion then launches a compressional (P)-wave through the wear plate and couplant into the adjacent material.

Contact transducers of similar construction can also be designed to launch shear waves. However, the special permanent or semi-permanent couplants required for a contact S-wave transducer prevents one from using those transducers where scanning motion of the transducer over a component is required. Instead, shear wave scanning inspections normally employ an angle beam shear wave transducer as shown in **Figure 9**. In this configuration the elements of a P-wave transducer (crystal, backing, etc.) are placed on the angled surface of a plastic wedge that is then coupled to the component with an ordinary fluid couplant. The angle of the wedge is chosen so that the first critical angle is exceeded. In this case the refracted P-wave is an inhomogeneous wave and does not propagate as a bulk wave into the component, leaving only a mode-converted bulk SV-wave propagating at an angle θ_{s2} as shown in **Figure 9**. Transducers of this same type can be used to generate Rayleigh surface waves as shown in **Figure 10**. In this case the wedge angle must be chosen so that one phase matches to the Rayleigh wave speed of the component being inspected. From generalized Snell's law, this occurs when:

$$\theta_{p1} = \sin^{-1}(c_{p1}/c_{R2}) \qquad [22]$$

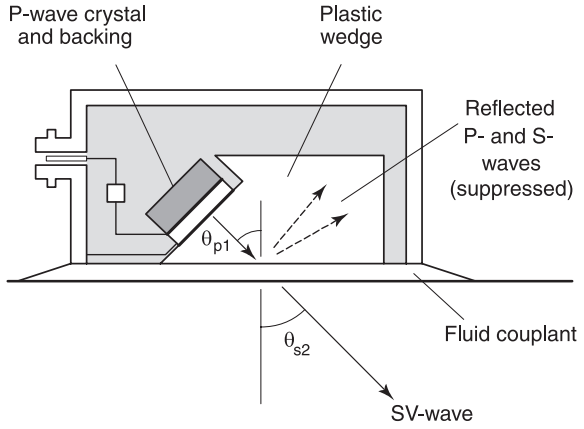


Figure 9 Elements of an angle beam shear wave transducer.

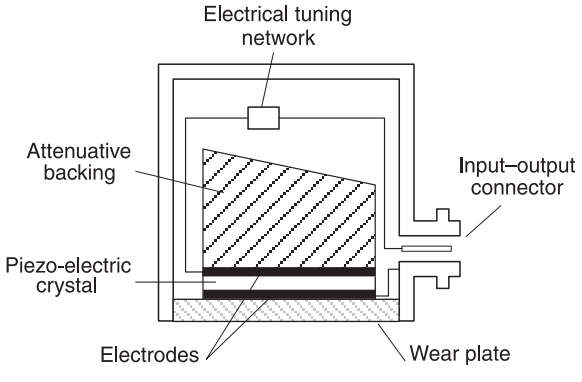


Figure 8 Elements of a contact, plane P-wave transducer.

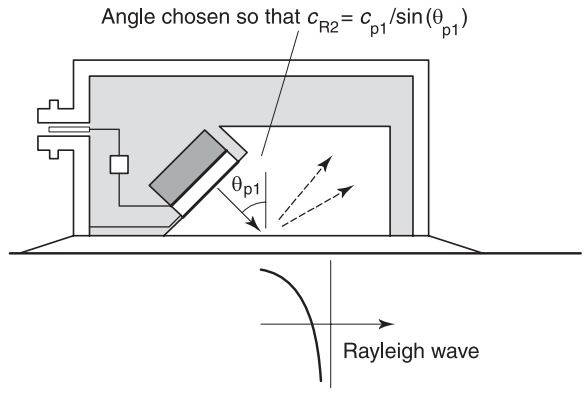


Figure 10 An angle beam transducer constructed so as to generate a Rayleigh surface wave.

where c_{p1} is the wave speed of P-waves in the plastic wedge and c_{R2} is the Rayleigh wave speed of the component.

Immersion transducers (**Figure 11**) have a construction that is very similar to that of a contact P-wave transducer. These transducers and the component to be inspected are both placed in a fluid. The transducer launches a P-wave into the fluid which propagates in the fluid and then into the component. In the immersion probe the wear plate is replaced by a facing plate, called a quarter-wave plate, that serves to improve the transmission of energy from the crystal to the water. Immersion transducers are often attached to a mechanical scanning apparatus at the end of a metal tube (called a wand) as shown in **Figure 11**.

Other types of ultrasonic piezo-electric transducer include focused transducers (**Figure 12**) and arrays (**Figure 13**). Focused transducers often employ an acoustic lens to concentrate the ultrasound at a particular depth while arrays use electronically controlled phasing of many small elemental transducers to produce both beam steering and focusing.

Devices other than piezo-electric transducers have also been used to both generate and receive ultrasound. Electromagnetic acoustic transducers (EMATS), for example, generate ultrasound through the use of eddy currents generated in an electrically conducting component interacting with a magnetic field to cause a mechanical motion of the surface of the component (**Figure 14**). In laser ultrasonics, a laser beam can be used to locally heat a small region of a surface impulsively and produce a propagating wave.

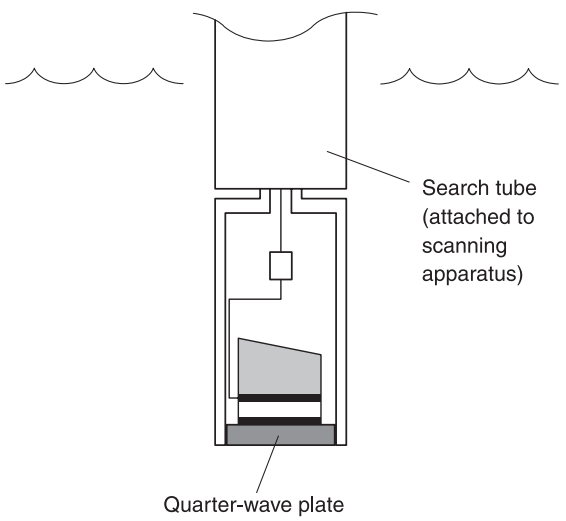


Figure 11 Elements of a plane P–wave transducer used in immersion testing.

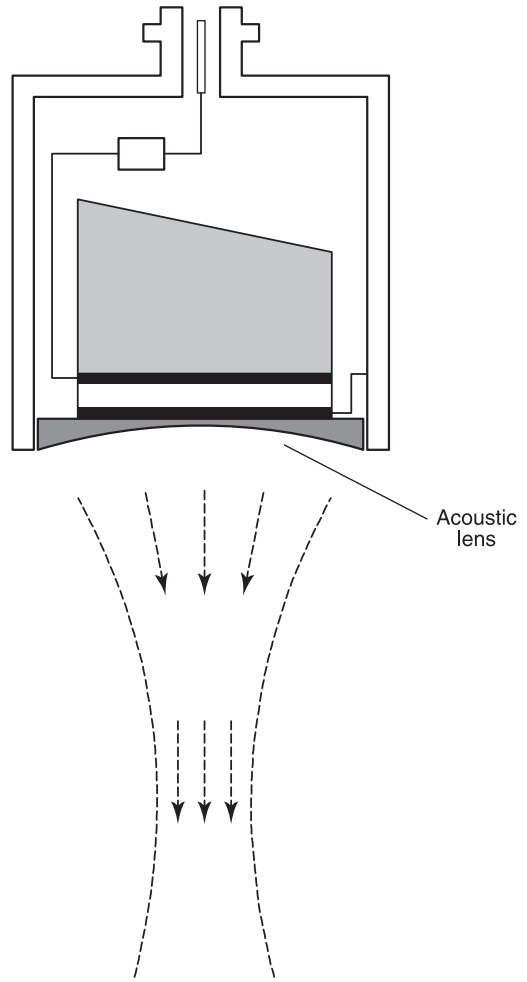


Figure 12 A focused P-wave transducer for immersion testing which uses an acoustic lens to concentrate the sound beam.

Electrostatic (capacitive), magnetostrictive and flexible polymeric transducers are also used in particular applications.

Transducer Radiated Wave Fields

The beam of sound generated by an ultrasonic transducer controls many of the important aspects of the signals received in an ultrasonic nondestructive testing measurement. Although a transducer is excited by a voltage pulse and therefore generates a short acoustical pulse of sound in the propagation medium, many of the important aspects of a transducer wave field can be studied by modeling the case when the transducer is driven by a sinusoidal input at a single frequency. One commonly used model to evaluate transducer wave fields at a single frequency is the Rayleigh–Sommerfeld integral, which models the pressure, p, generated by a planar (unfocused) trans-

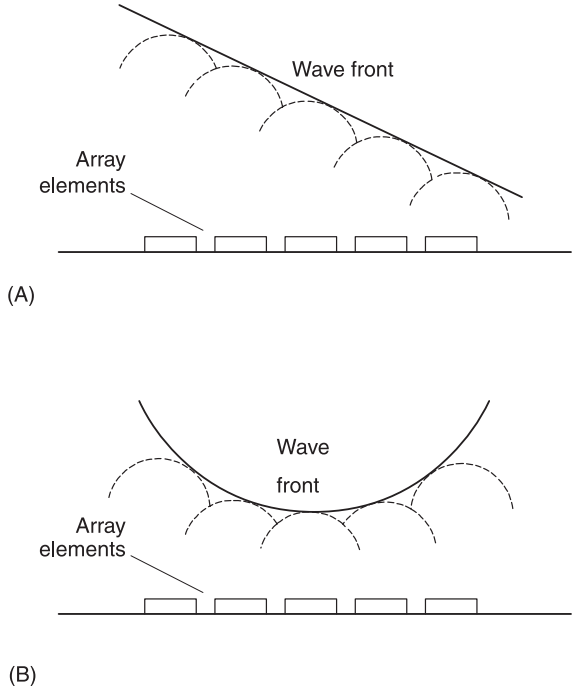


Figure 13 Elements of an array transducer where the elements are phased to produce (A) beam steering and (B) beam focussing.

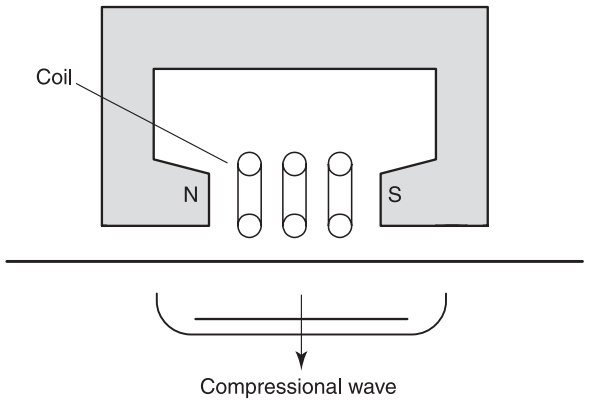


Figure 14 An electromagnetic–acoustic (EMAT) transducer for generating P-waves in an electrically conducting component.

ducer radiating into a fluid as a superposition of point sources of exp $(-i\omega t)$ time dependency acting over a planar aperture, S, of an otherwise baffled (motionless) plane (**Figure 15**). The Rayleigh–Sommerfeld integral is given by:

$$p(\mathbf{x},\omega) = \frac{-i\omega\rho}{2\pi}\int_S v(\mathbf{y},\omega)\frac{\exp(ikr)}{r}\,dS(y) \qquad [23]$$

where ρ is the density, $k = \omega/c$ is the wave number and $r = |\mathbf{x} - \mathbf{y}|$ is the distance between a point, $\mathbf{x}$, in the fluid and a point, $\mathbf{y}$, on the aperture, S, of the transducer. The velocity $v(\mathbf{y}, \omega)$ is the normal velocity field acting over the aperture, S. In general the Rayleigh–Sommerfeld integral can only be evaluated numerically but there are a number of important special cases where analytical results can be obtained.

Circular Planar Piston Transducer

If the velocity field is uniform over the entire aperture, i.e., $v(\mathbf{y}, \omega) = v_0(\omega)$, then the Rayleigh–Sommerfeld integral models the wave field of a piston transducer. For a circular piston transducer of radius a, the pressure along the central $(z-)$ axis can be found exactly in the form:

$$p(z,\omega) = \rho c v_0\{\exp(ikz) - \exp\left[ik\sqrt{(z^2 + a^2)}\right]\} \qquad [24]$$

A plot of the magnitude of this on-axis pressure is shown in **Figure 16**. It can be seen from that figure that in a region close to the transducer there are a series of maxima and nulls in the wave field while far from the transducer the pressure simply decays monotonically. The nulls are located along the axis at locations given by:

$$z_n = \frac{a^2}{2n\lambda} - \frac{n\lambda}{2} \qquad [25]$$

for the values of $n = 1, 2, 3, \ldots$, where z_n is positive. The quantity $\lambda = 2\pi/k$ is the wavelength. Similarly, the on-axis maxima of a piston transducer are located at:

$$z_m = \frac{a^2}{(2m+1)\lambda} - \frac{(2m+1)\lambda}{4} \qquad [26]$$

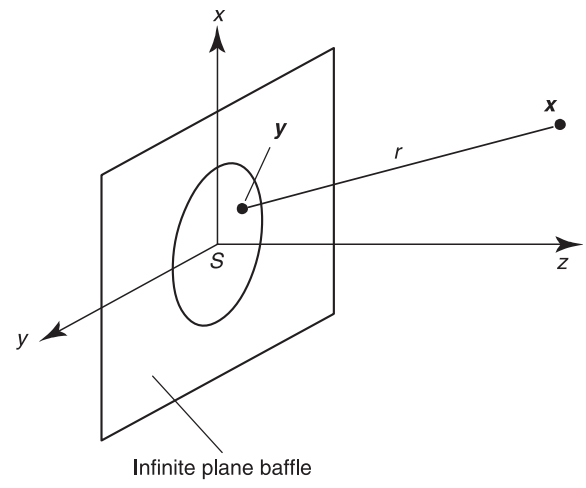


Figure 15 Plane aperture in an infinite plane baffle for modeling the waves radiated from a planar transducer into a fluid which occupies the region $z \geq 0$.

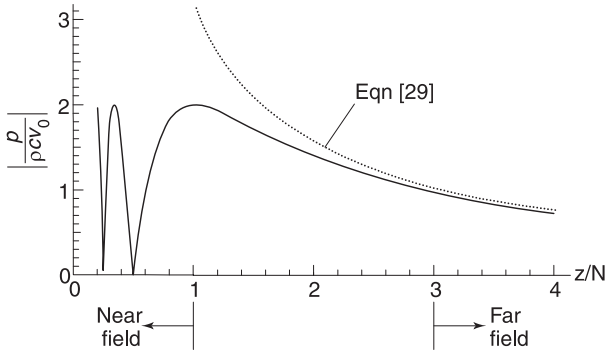


Figure 16 On-axis normalized pressure vs normalized distance for a circular, planar piston transducer ($ka = 100$), showing the near- and far-field behaviors.

for the values of $m = 0, 1, 2, \ldots$, where z_m is positive. In many ultrasonic nondestructive testing the approximate near-field distance, N, given by:

$$N = \frac{a^2}{\lambda} \qquad [27]$$

is large compared to the wavelength so that the second terms in eqns [25] and [26] can be neglected. In this case the nulls and maxima locations are given approximately by:

$$z_n \cong \frac{a^2}{2n\lambda} = \frac{N}{2n} \qquad (n = 1, 2, 3, \ldots)$$
$$z_m \cong \frac{a^2}{(2m+1)\lambda} = \frac{N}{(2m+1)} \qquad (m = 0, 1, 2, \ldots) \qquad [28]$$

As eqn [28] shows, the on-axis maximum that is the farthest from the transducer occurs for $m = 0$ at one near field distance, N, from the transducer. Distances $z < N$ are said to be in the transducer near field. Distances given approximately by $z > 3N$ are said to be in the transducer far field. In the far field the on-axis pressure is approximately given by:

$$p(z, \omega) \cong \frac{-ik\rho c v_0 a^2}{2} \frac{\exp(ikz)}{z} \qquad [29]$$

Eqn [29] shows that the pressure in the far field exhibits a $1/z$ decay, the form of which is typical of a propagating spherical wave. Thus, the far-field region is also called the spherically spreading region of the transducer (**Figure 16**). In the far field, it is also possible to analytically evaluate the Rayleigh–Sommerfeld integral for points in the transducer wave field off the z-axis (**Figure 17**). The result is:

$$p(\mathbf{x}, \omega) = -i\omega\rho v_0 a^2 \frac{\exp(ikR)}{R} \frac{J_1(k\alpha \sin\theta)}{ka \sin\theta} \qquad [30]$$

The first term in eqn [30] is just a frequency-dependent amplitude coefficient. The second term represents a spherically spreading wave, a result that is expected since the expression is for the pressure in the far field. The last term in eqn [30] represents the angular dependent amplitude term that is plotted in **Figure 18**. From **Figure 18** we see that there is typically a main lobe of the transducer radiated wave field centered around the transducer axis as well as other smaller side lobes. The first null away from the axis occurs approximately at an angle:

$$\theta_{\text{null}} \cong \frac{3.83}{ka} = \frac{0.61\lambda}{a} \qquad [31]$$

which is an expression that can be used to evaluate the angular beam spread of the transducer in the far field.

Together, the near field distance, N, and the angle, θ_{null}, define the main characteristics of a planar piston

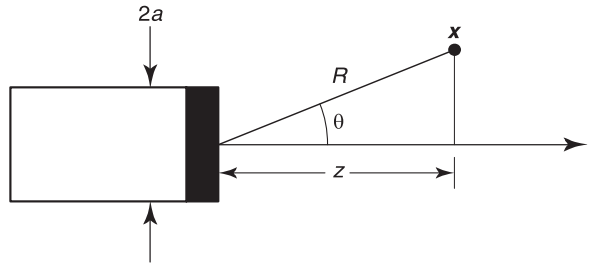


Figure 17 Geometry for defining the off-axis pressure wave field of a circular, planar piston transducer.

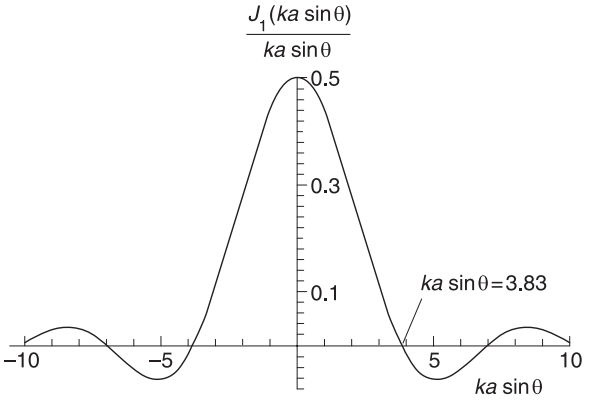


Figure 18 The far-field angular diffraction pattern for a circular, planar piston transducer showing the main lobe and side lobes of the radiated wave field.

transducer since for distances $z < N$, the beam of the transducer stays well collimated (like a flashlight beam), but with both on- and off-axis near-field variations in the pressure, while for $z > N$ the pressure in the beam simply decays monotonically and the beam spreads at an angle that can be characterized by the angle θ_{null}. This overall behavior of the transducer wave field is shown schematically in **Figure 19**.

Focused Transducer

The Rayleigh–Sommerfeld integral can also be used to model the wave field of a focused transducer if the planar aperture, S, is replaced by a curved surface aperture over which the normal velocity is specified (**Figure 20**). For a circular aperture of radius a and a spherical surface of radius R_0 the on-axis pressure can again be obtained analytically for a constant velocity (piston) transducer as:

$$p(z,\omega) = \frac{\rho c v_0}{q_0}[\exp(\mathrm{i}kz) - \exp(\mathrm{i}kr_e)] \qquad [32]$$

where $q_0 = 1 - z/R_0$, $r_e = \sqrt{\left[(z-h)^2 + a^2\right]}$, and $h = R_0 - \sqrt{(R_0^2 - a^2)}$. As seen in **Figure 21** there are again nulls and maxima in the response, with the largest maximum found at a distance somewhat less than the location of the geometric focus ($z = R_0$). The true focus distance, R_f, (where the on-axis response is the largest) is always smaller than thegeometrical focus distance, R_0, because of diffraction effects, becoming equal to R_0 only in the limit of very large frequencies (**Figure 21**). The location of the true focus can be found numerically by evaluating eqn [32]. The on-axis nulls are located at:

$$z_n = \frac{(a^2 + h^2) - n^2\lambda^2}{2h \pm 2n\lambda} \quad (n = 1, 2, 3, \ldots) \qquad [33]$$

for all values of n where $z_n > 0$. The plus sign in eqn [33] corresponds to nulls that satisfy $z_n < R_0$ and the minus sign corresponds to nulls (if they exist) for $z_n > R_0$. There is not a simple analytical expression for the location of the maxima as found in the planar piston probe case. Instead, the maxima for the focused probe must be obtained as the roots of the transcendental equation:

$$\cos(k\delta/2) = \frac{2(\delta + z)\sin(k\delta/2)}{(\delta + h)q_0 k R_0} \qquad [34]$$

where $\delta = r_e - z$. Analytical results for the off-axis pressure in the plane of the geometrical focus ($z = R_0$) can also be obtained (**Figure 22**). It is found that:

$$p(\mathbf{x},\omega) = -\mathrm{i}\omega\rho v_0 a^2 \frac{\exp(\mathrm{i}k\bar{R}_0)}{\bar{R}_0} \frac{J_1(ka\sin\theta)}{ka\sin\theta} \qquad [35]$$

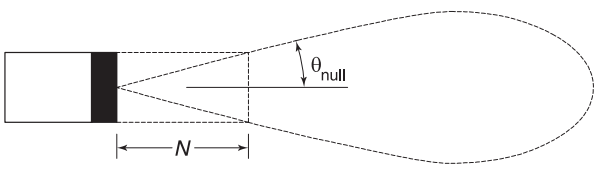


Figure 19 Characterization of the wave field of a circular, planar piston transducer by the near-field distance, N, and the angular beam spread of the main lobe, θ_{null}.

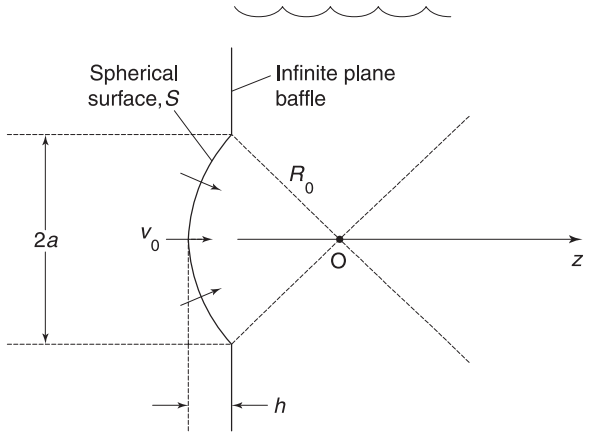


Figure 20 A spherically focused circular piston transducer modeled as a spherical aperture in an infinite plane baffle over which a normal velocity field is specified.

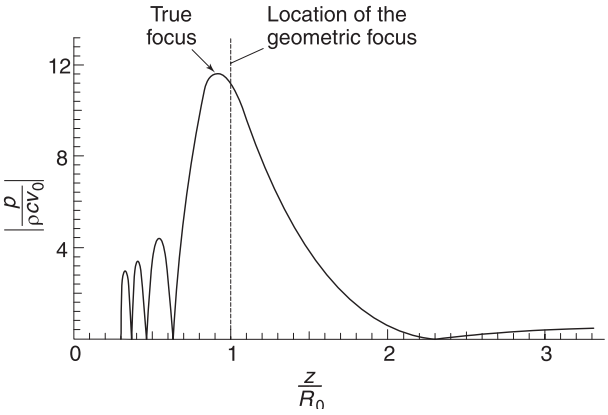


Figure 21 On-axis normalized pressure vs normalized distance for a 10 MHz, 12.7 mm diameter, 76.2 mm focal length spherically focused piston transducer radiating into water. In this case, an on-axis null exists for $z > R_0$.

which is identical in form to the far-field off-axis pressure for the planar piston probe (eqn [30]). Eqn [35] can be used to estimate the lateral spot size of the ultrasonic beam in the plane of the geometrical focus by evaluating the distance, W_f, between nulls It is found that:

$$W_f = 7.66\frac{R_0}{ka} \qquad [36]$$

One can also estimate the focal point spot size based on either a 3 dB or a 6 dB decrease of the pressure from its maximum on axis value. In those cases, the spot size estimates are:

$$W_f|_{3\,dB} = 3.20\frac{R_0}{ka}$$
$$W_f|_{6\,dB} = 4.43\frac{R_0}{ka} \qquad [37]$$

Similarly, it is desirable to have a simple estimate of the depth of focus, D_f, of the transducer, which is defined to be the axial length over which there is a specified drop off in pressure from the maximum value. One approximate depth of focus estimate is given by:

$$D_f|_{3\,dB} \cong 3.5\frac{R_0}{a}W|_{3\,dB} = 1.8\frac{R_0^2\lambda}{a^2} \qquad [38]$$

based on the assumption that the beam is highly focused. A more exact value can be obtained directly from eqn [32] by numerical means. The true focal length, R_f, the focal spot size, W_f, and the depth of focus, D_f, describe the location and size of the region over which the pressure in the focused beam is concentrated (**Figure 23**). These are the three key parameters needed when setting up an ultrasonic inspection with a focused probe.

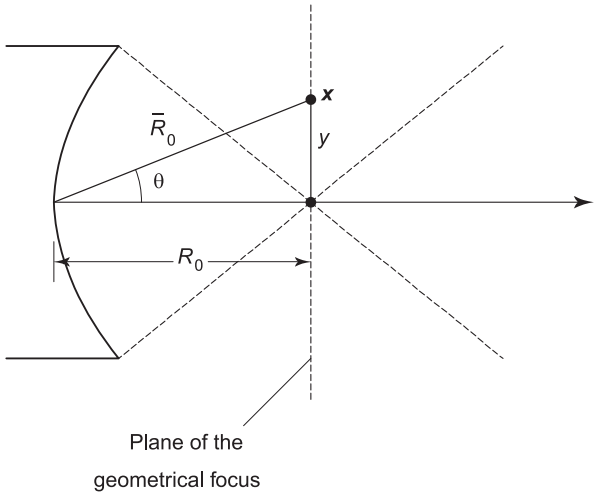


Figure 22 Geometry for defining the off-axis pressure wave field of a circular, spherically focused piston transducer in the plane of the geometrical focus.

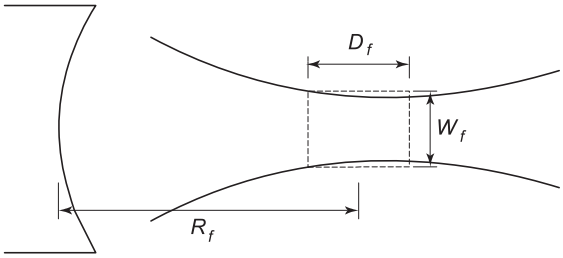


Figure 23 The three parameters that define the focussing characteristics of a circular, spherically focussed piston transducer: the location of the true focus, R_f, the lateral spot size of the beam, W_f, and the depth of focus, D_f.

Nomenclature

A	amplitude
c	wave speed
D	depth of focus
E	Young's modulus
G	shear modulus
R	true focal length
S	aperture
W	focal spot size
Z	impedance
ϕ	scalar potential
$\boldsymbol{\psi}$	vector potential
ρ	density
υ	Poisson's ratio

See also: **Nondestructive testing**, Sonic; **Ultrasonics**; **Wave propagation**, Guided waves in structures; **Wave propagation**, Interaction of waves with boundaries; **Wave propagation**, Waves in an unbounded medium.

Further Reading

Ascher RC (1997) *Ultrasonic Sensors*. Bristol: IOP.
Blitz J, Simpson G (1996) *Ultrasonic Methods of Non-Destructive Testing*. London: Chapman & Hall.
Harker AH (1988) *Elastic Waves in Solids*. Bristol: Adam Hilger.
Kino GS (1987) *Acoustic Waves: Devices, Imaging, and Analog Signal Processing*. New Jersey: Prentice-Hall.
Krautkramer J, Krautkramer H (1990) *Ultrasonic Testing*

of Materials, 4th edn. Berlin: Springer-Verlag.
Ristic VM (1983) *Principles of Acoustic Devices*. New York: John Wiley.
Rose JL (1999) *Ultrasonic Waves in Solid Media*. Cambridge: Cambridge University Press.
Schmerr LW (1998) *Fundamentals of Ultrasonic Nondestructive Evaluation – A Modeling Approach*. New York: Plenum Press.

NONLINEAR NORMAL MODES

A F Vakakis, University of Illinois, Urbana, IL, USA

Copyright © 2001 Academic Press

doi:10.1006/rwvb.2001.0046

Introduction

The concept of nonlinear normal mode (NNM) can be considered as a nonlinear extension of the linear normal mode of classical vibration theory. Although the principle of linear superposition does not apply in nonlinear theory, NNMs can be used to predict resonances of forced nonlinear systems and to study localization (spatial confinement) of vibrational energy in periodic systems. Hence, the NNM is a valuable theoretical tool for better modeling and understanding the dynamics of nonlinear oscillators. Moreover, NNMs can find additional applications in modal analysis, model reduction, and vibration and shock isolation designs.

Definition of an NNM

Engineers and physicists traditionally associate normal modes with linear vibration theory and regard them as closely related to the principle of linear superposition. Indeed, the modes of vibration of a discrete or continuous linear system can be used to express arbitrary free or forced oscillations of the system as superpositions of modal responses. On the other hand, it is a well-known result that the principle of linear superposition generally does not apply to nonlinear systems. Hence, an NNM must be carefully defined as a nonlinear extension of the classical linear normal mode, that accounts for the restrictions imposed by nonlinear theory and respects the individualistic nature of nonlinear systems. In what follows we show that the concept of 'normal mode' can be successfully extended to nonlinear theory where it finds numerous applications.

All practical engineering structures are to some extent nonlinear, the nonlinearities being kinematic, material, or geometric. For example, in rotating bladed disk assemblies, dynamic unbalances or pressure differentials due to fluid–structure interactions may excite structural resonances that lead to finite-amplitude motions where nonlinearities are strongly affecting the response. Similarly, vibrations of large-scale truss structures may be strongly influenced by clearance nonlinearities of the joints connecting individual components, or by geometric nonlinearities arising from finite deflections of oscillating structural members. In such cases the concept of NNM can be used to understand and model nonlinear dynamic phenomena that might have no counterparts in linear theory. Ignoring the nonlinear effects and using linear modes to model the dynamics, although permissible in certain cases, may lead to poor modeling and incomplete characterization of the dynamics.

An NNM can be considered as the nonlinear extension of the linear normal mode of classical vibration theory. One defines an NNM of an undamped discrete or continuous system as a synchronous periodic oscillation where all material points of the system reach their extreme values or pass through zero simultaneously. The corresponding oscillation is represented by a modal line in the configuration space of the system, which represents the synchronous oscillation. In contrast, however, to linear systems that possess straight modal lines, the modal lines of a nonlinear system can be either straight or curved. Hence, for discrete systems we define as similar NNMs those corresponding to straight modal lines in configuration space, and as nonsimilar NNMs those corresponding to curved modal lines. Nonsimilar NNMs are typical in nonlinear oscillators, whereas similar NNMs exist only under certain symmetry conditions.

As an example, consider the two-degree-of-freedom (DOF) symmetric nonlinear system of **Figure 1** with governing equations of motion given by:

$$\begin{aligned} \ddot{x}_1 + x_1 + x_1^n + K(x_1 - x_2)^n &= 0 \\ \ddot{x}_2 + x_2 + x_2^n - K(x_1 - x_2)^n &= 0 \end{aligned} \qquad [1]$$

where n is an integer and K a coupling stiffness

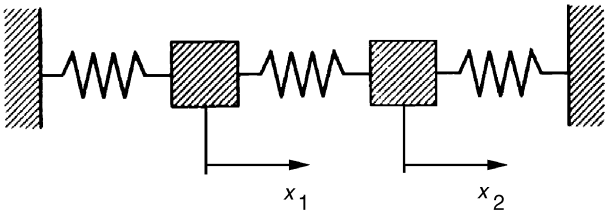


Figure 1 The two-degree-of-freedom nonlinear oscillator. Reproduced with permission from Vakakis AF (1997) Nonlinear normal modes and their applications in vibration theory: an overview. *Journal of Mechanical Systems and Signal Processing* 11: 3–22.

coefficient. This system possesses only similar NNMs, corresponding to a linear relation between the dependent variables x_1 and x_2:

$$x_2(t) = cx_1(t) \qquad [2]$$

where c is termed the modal constant. Clearly, eqn [2] represents a straight modal line in the (x_1, x_2) configuration plane of the system. Using eqn [2] we eliminate x_2 from the equations of motion (eqn [1]) as follows:

$$\begin{aligned} &\ddot{x}_1 + x_1 + [1 + K(1-c)^n]x_1^n = 0 \\ &\ddot{x}_1 + x_1 - (1/c)[K(1-c)^n + c^n]x_1^n = 0, \quad c \neq 0 \end{aligned} \qquad [3]$$

For motion on a NNM both equations [3] must provide identical solutions $x_1 = x_1(t)$, a requirement that is satisfied by matching the respective coefficients of the nonlinear terms:

$$K(1-c)^n + c^n = 1 + K(1-c)^n, \quad c \neq 0 \qquad [4]$$

The algebraic eqn [4] always possesses the solutions $c = \pm 1$, which correspond to inphase and antiphase similar NNMs. These are the only normal modes that the linear system ($n = 1$) can possess. Depending on n, the nonlinear system can have additional modes which are depicted in **Figure 2**. These additional NNMs bifurcate from the antiphase mode $c = -1$ and exist for values of the coupling parameter $K < 1/4$. Clearly, such bifurcations cannot take place in the linear system (which has as many modes as DOF), and, thus, the bifurcating NNMs are essentially nonlinear modes which cannot be regarded as analytic continuations of any linear ones. Hence, the normal modes of a nonlinear system can be more numerous than its degrees of freedom – a feature which is in contrast to linear theory. As indicated in **Figure 2**, some of the NNMs are unstable, i.e., are not maintained under small perturbations of their initial conditions. This is another exclusive feature of nonlinear modes, since linear normal modes are always neutrally stable (as are all linear periodic motions).

When the symmetry of the system of **Figure 1** is perturbed, the NNMs generally become nonsimilar. This type of NNMs is more difficult to compute, as demonstrated by the following example. We consider again eqn [1] with $n = 3$, and perturb the symmetry by adding linear coupling terms and cubic grounding terms:

$$\begin{aligned} &\ddot{x}_1 + x_1 + \nu_1 x_1^3 + k_1(x_1 - x_2) + \nu_2(x_1 - x_2)^3 = 0 \\ &\ddot{x}_2 + (1 + \alpha_1)x_2 + \nu_1(1 + \alpha_3)x_2^3 + k_1(x_2 - x_1) \\ &\quad + \nu_2(x_2 - x_1)^3 = 0 \end{aligned} \qquad [5]$$

Furthermore, we assume that weak coupling between the two masses exists, and rescale the coupling stiffness coefficients as, $k_1 = \varepsilon K_1$, $\nu_2 = \varepsilon N_2$, where ε is a small parameter, $|\varepsilon| \ll 1$. The nonsimilar NNMs of the oscillator (eqn [5]) are then sought in the form (compare with the requirement for similar NNM; eqn [2]):

$$x_2 = \hat{x}_2(x_1) \qquad [6]$$

where the modal function $\hat{x}_2(\cdot)$ governs the trajectory of the mode in the configuration plane (x_1, x_2). Asymptotic methods for analytically approximating the modal curve (eqn [6]) have been presented in the literature; they are based on perturbation expansions in terms of the small parameter ε, and will not be discussed here. In contrast to similar NNMs which do not depend on the energy of the motion, nonsimilar NNMs are energy-dependent, and the modal function (eqn [6]) depends on the specific level of the energy of oscillation. Again, the number of nonsimilar modes of a nonlinear dynamical system may exceed in number its degrees of freedom.

NNMs can also be defined for systems with damping. In this case, the NNM oscillation is not synchronous and nontrivial phase differences exist between the positional variables. Shaw and Pierre reformulated the concept of NNM for a general class of nonlinear discrete oscillators, by defining NNM invariant manifolds of the motion where the damped free oscillation takes place. The parametrization of the NNM invariant manifolds was performed by employing two independent reference positional variables, a displacement and a velocity. An extension of this invariant manifold approach to a complex framework was performed by Nayfeh and coworkers.

To demonstrate the NNM invariant manifold formulation, consider the following n-DOF oscillator:

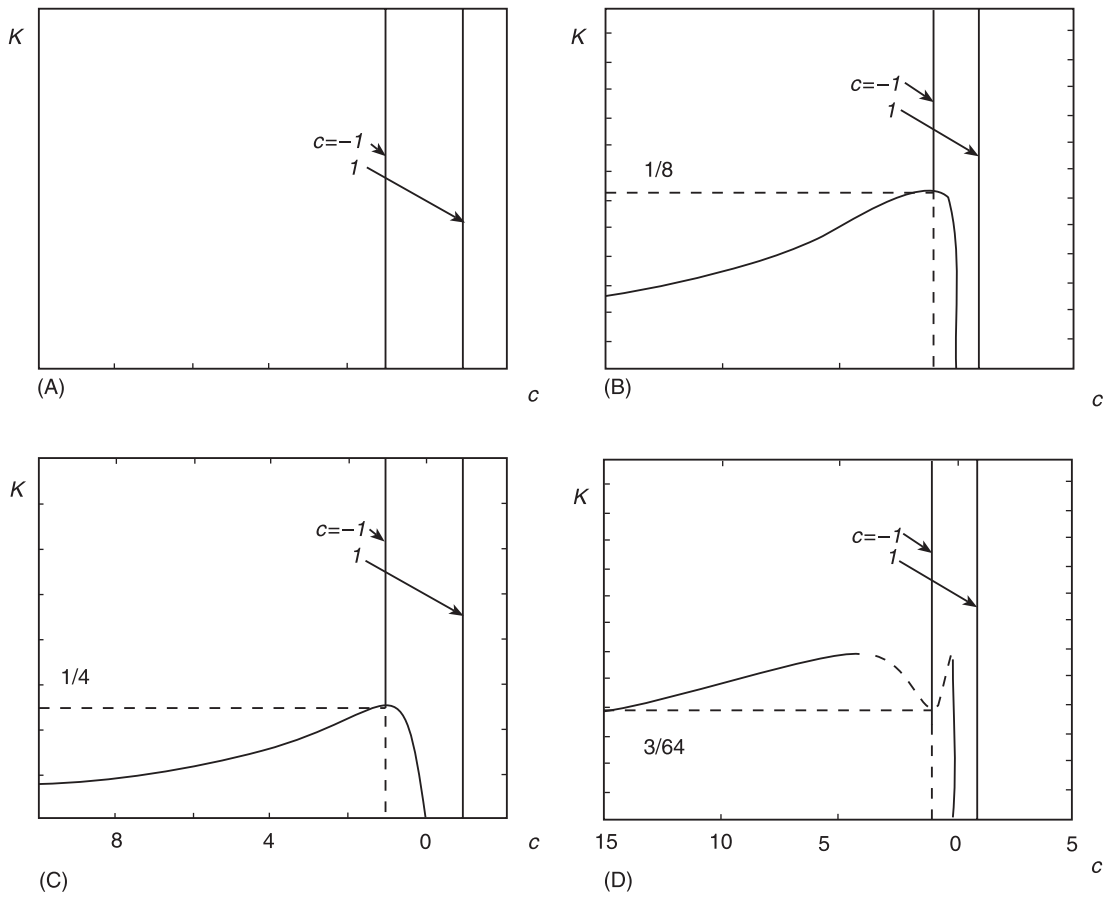


Figure 2 Nonlinear normal modes (NNMs) of the system with stiffness nonlinearities. (A) Balance of linear terms; (B) balance of fifth-order terms; (C) balance of cubic terms; (D) balance of seventh-order terms. Continuous line, stable; dashed line, unstable NNMs.

$$\ddot{x}_i + f_i(x,\ \dot{x}) = 0, \quad i = 1, 2, \ldots, n \qquad [7]$$

where $\mathbf{x}$ is an $(n\times 1)$ vector of positional variables, and $f_i(\mathbf{x}, \dot{\mathbf{x}})$ is a vector with smooth nonlinearities. Alternatively, eqn [7] is expressed in the following form:

$$\begin{aligned} \dot{x}_i &= y_i \\ \dot{y}_i &= -f_i(\mathbf{x},\ \mathbf{y}), \quad i = 1, 2, \ldots, n \end{aligned} \qquad [8]$$

An NNM of (eqn [7]) or (eqn [8]) is a free oscillation where all displacements and velocities are parametrized by a reference displacement-velocity pair, say $(x_1, y_1) \equiv (x, y)$:

$$x_i = X_i(x, y), \quad y_i = Y_i(x, y), \quad i = 1, 2, \ldots, n \qquad [9]$$

This relation defines a two-dimensional surface in the $2n$-dimensional phase space of the dynamical system which is the two-dimensional NNM invariant manifold. The NNM invariant manifold is approximated by substituting eqn [9] into eqn [8], eliminating the explicit time dependence, and solving a set of differential equations for $X_i(x, y)$ and $Y_i(x, y)$, $i = 2, \ldots, n$:

$$\begin{aligned} Y_i - \frac{\partial X_i}{\partial x} y = \frac{\partial X_i}{\partial y} f_1(x, X_2, \ldots, X_n, y, Y_2, \ldots, Y_n) \\ \frac{\partial Y_i}{\partial x} y + \frac{\partial Y_i}{\partial y} f_1(x, X_2, \ldots, X_n, y, Y_2, \ldots, Y_n) \\ = f_i(x, X_2, \ldots, X_n, y, Y_2, \ldots, Y_n), \\ i = 2, \ldots, n \end{aligned} \qquad [10]$$

Methods for solving eqn [10] have been published in the literature.

We note at this point that the previous formulations for computing NNMs are valid only in systems where no modal interactions due to internal resonances exist. When such nonlinear interactions take place, the sychronicity of the NNMs is eliminated and the ensuing periodic motion takes place in higher-

dimensional invariant manifolds. In this case, nonlinear modal interactions can be analytically studied either by performing the analysis in terms of canonical modal coordinates, or by constructing NNM invariant manifolds of higher dimensions.

Applications of NNMs in vibrations

NNMs can be used better to model and understand the nonlinear vibrations of mechanical oscillators. As mentioned earlier, a nonlinear system can possess more modes than degrees of freedom and, hence, not all NNMs can be regarded as nonlinear extensions of linear modes. Indeed, in nonlinear mechanical systems mode bifurcations may occur, generating NNMs having no analogs in linear theory. Thus, a vibration analysis based purely on linearized methods may omit certain NNMs, and result in incomplete modeling of the dynamics of the system under consideration. This indicates that extending concepts such as modal analysis or forced resonance to nonlinear systems must be performed with care. In the following sections two main applications of NNMs are discussed, namely, their influence on forced resonances and on nonlinear localization and motion confinement. Potential new applications of NNMs to vibration analysis are also discussed.

Nonlinear Forced Resonances

An important property of NNMs relates to forced resonances. It has been shown in the literature that forced nonlinear resonances occur in neighborhoods of NNMs, similarly to the resonances of classical linear theory. This fact indicates that knowledge of the structure of the normal modes of a nonlinear system can provide valuable insight on its resonances, a feature that is of importance when designing for vibration isolation. We note that, depending on its modes, a nonlinear system can possess more forced resonances than the ones predicted by a linearized approach, since a subset of the resonances can be essentially nonlinear, with no counterparts in linear theory. In such cases a 'linearization' of the system might miss certain resonances, with obvious consequences in the success of the vibration isolation design.

To illustrate better the previous points we present an example with a cyclic flexible assembly consisting of N identical uniform cantilever beams, coupled by means of linear stiffnesses (cf. **Figure 3**). Assuming beam inextensionality and finite-amplitude oscillations, nonlinear inertia and curvature terms give rise to geometric nonlinearities which affect significantly the dynamics. The governing equations of motion are of the following form:

$$\begin{aligned} &v_{itt} + v_{ixxxx} + \varepsilon c_i v_{it} \\ &\quad + \varepsilon \left\{ v_{ix}[v_{ix}v_{ixx}]_x + \frac{1}{2}\int_1^x \left[\int_0^s v_i \xi^2(\xi, t)\mathrm{d}\xi \right]_{tt} \mathrm{ds} \right\}_x \\ &\quad = -\varepsilon \frac{KL^4}{EI}\{2v_i(1/L) - v_{i-1}(1/L) - v_{i+1}(1/L)\} \\ &\qquad \times \delta(x - 1/L) + \frac{P_i(x,t)}{\varepsilon^{1/2}}, \quad i = 1, \ldots, N \end{aligned} \tag{11}$$

where K is the nonlinear coupling stiffness, c_i is the coefficient of distributed viscous damping for the ith beam, $\delta(\cdot)$ is Dirac's function, $P_i(x, t)$ is the distributed excitation applied to the ith beam, and $v_0 \equiv v_N$, $v_{N+1} \equiv v_1$ due to cyclicity. It is assumed that the coupling linear stiffnesses and viscous damping coefficients are small, $O(\varepsilon)$ quantities (with $|\varepsilon| \ll 1$), and that the beam deflections are of $O(\varepsilon^{1/2})$. It is additionally assumed that the distributed excitations $P_i(x, t)$ possess harmonic time dependence with frequency $(\omega_1 + \varepsilon\sigma)$ and identical spatial distribution to the first linearized cantilever mode of each beam:

$$\begin{aligned} P_i(x,t) &= \Phi_1(x)\cos(\omega_1 + \varepsilon\sigma)t, \\ &0 < x < 1, \quad i = 1, \ldots, N \end{aligned} \tag{12}$$

In eqn [12], $\Phi_1(x)$ is the spatial distribution and ω_1 the natural frequency of the first linearized cantilever mode of each beam. We approximate the fundamen-

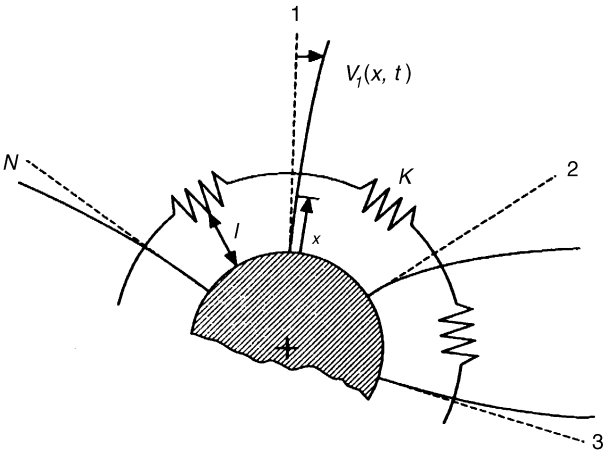


Figure 3 The cyclic assembly of N geometrically nonlinear beams. Reproduced with permission from Vakakis AF (1997) Nonlinear normal modes and their applications in vibration theory: an overview. *Journal of Mechanical Systems and Signal Processing* 11: 3–22.

tal (at the frequency of excitation) steady-state responses of the beams as:

$$v_i(x,t) = \Phi_1(x) a_i \cos\left[(\omega + \varepsilon\sigma)t + \beta_i\right] + O(\varepsilon), \quad i = 1, \ldots, N \qquad [13]$$

In **Figure 4** the resonance branches of the system with $N = 4$ beams are depicted, when harmonic excitation is applied only to beam 1. In the unforced system there are essentially nonlinear modes with no counterparts in linear theory. As a result, the nonlinear system exhibits a very complicated structure of resonances, with as many as 12 stable coexisting branches; linear theory would predict at most four resonances.

This result indicates that stiffness nonlinearities can drastically alter the topology of the steady-state response curves of a structure. This finding is especially critical in applications where precise knowledge of the resonance regimes is important for vibration isolation. Since forced resonances occur in neighborhoods of NNMs, one can optimize the topological picture if the NNMs of the unforced system before forcing is applied. This procedure can eliminate dangerous nonlinear resonances from certain frequency ranges and induce steady-state responses in other frequency domains that are beneficial to the design objectives. Hence, optimizing the structure of NNMs of the unforced system can lead to more predictable forced dynamics and improved performance of the forced system.

Nonlinear Mode Localization

NNMs provide an excellent framework for studying nonlinear mode localization in vibrating systems. Indeed, a subset of NNMs in a system can be localized, with vibration energy spatially confined to a small part of the system. This can be realized from **Figure 2** where the NNMs of the 2-DOF symmetric system of **Figure 1** are depicted. We note that as the coupling stiffness decreases (K small), there always exists a pair of NNMs with small or large values of c; these modes are stable and localize to either one of the masses the system. Similarly, considering the resonance plots of **Figure 4** for the cyclic assembly, the branch 1 of resonances is strongly localized, with the directly forced beam vibrating with considerably larger amplitude than the other beams of the assembly. This strongly localized branch exists in the neighborhood of a strongly localized NNM of the undamped unforced system, and has no counterpart in linear theory. There also exist weakly localized resonances with more than one beam oscillating with relatively large amplitudes (for example, see branches 7 and 8 in **Figure 4**).

These examples demonstrate some typical features of nonlinear mode localization, namely, that it can occur in weakly coupled, perfectly periodic systems. This is in contrast to linear-mode localization that occurs only in weakly coupled and disordered periodic systems. Hence, localization in nonlinear systems occurs even in the absence of structural disorder. Nonlinear localization can greatly influence the transient response of a structure since it can lead to passive motion confinement of disturbances generated by external forces: in a structure with localized NNMs, motions generated by external impulsive excitations remain passively confined close to the point where they are initially generated, instead of spreading through the entire structure. This passive confinement phenomenon in periodic systems is in contrast to linear theory where energy is transferred from one mass to another through the classical beat phenomenon. Hence, localized NNMs can provide a novel tool for vibration and shock isolation designs of mechanical systems, since a system whose inherent dynamics leads to motion confinement of external disturbances is more amenable to active or passive control than a system with no such dynamical properties.

Additional Applications

NNMs can find additional applications in other areas of vibration theory. Starting from modal analysis and system identification (MA-SI), the majority of currently available techniques rely on linearity, and SI methods for nonlinear systems assume weak nonlinearities and modal structures similar to that of an underlying linearized system. As shown above, even a simple 2-DOF can have more normal modes than its DOF, which shows that nonlinear MA-SI techniques should account for the possibility that certain of the sought modes have no counterparts in linear theory. In that context, NNMs coupled with nonparametric SI methods such as orthogonal mode decomposition (Karhunen–Loeve method) can provide a valuable tool for understanding the effects of structural nonlinearities on the dynamics, and for developing new nonlinear MA-SI methodologies. The need for the development of such techniques is evident when one considers that most engineering structures exhibit to some extent nonlinear behavior due, for example, to dry friction, clearances, or vibroimpacts.

As mentioned previously, NNMs provide an excellent framework for localization designs in structures. Inducing localization in a structure can be very beneficial as far as its controllability is concerned since it can lead to passive confinement of externally induced disturbances. In addition, using NNMs to study

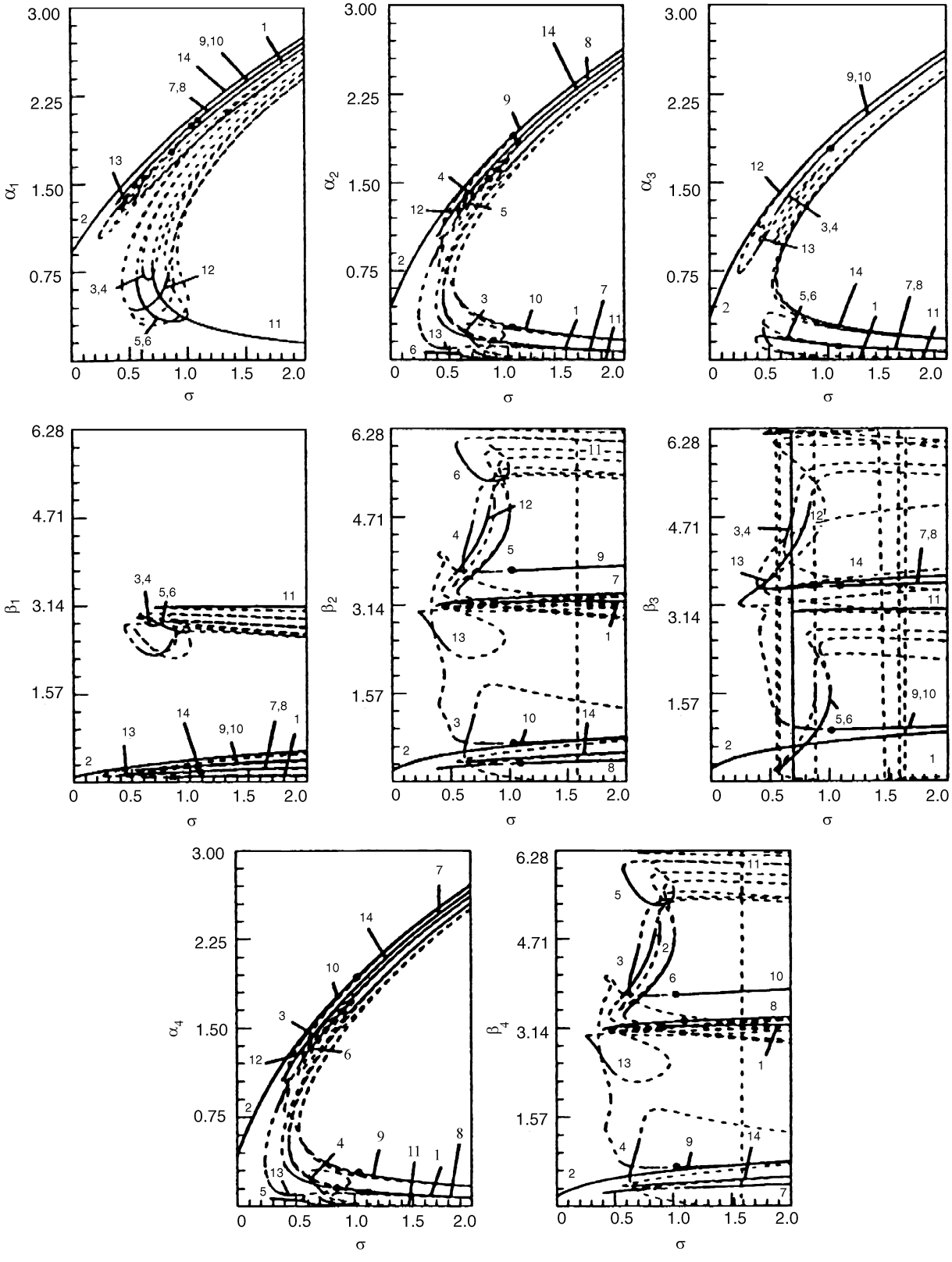


Figure 4 Fundamental resonances for $N = 4$ beams. Continuous line, stable; dashed line, unstable steady states. Reproduced with permission from Vakakis AF (1997) Nonlinear normal modes and their applications in vibration theory: an overview. *Journal of Mechanical Systems and Signal Processing* 11: 3–22.

motion confinement phenomena due to nonlinearities can be beneficial in applications where such localization phenomena are unwanted. For example, localization of vibrational energy in rotating turbine blade assemblies can be catastrophic since it may lead to failure of highly rotating blades. Understanding the mechanisms (such as structural disorder and nonlinearities) that lead to motion confinement can prevent such failures and prolong the operational life of mechanical components. To give an indication of the diverse applications that nonlinear localization has, we mention that in a recent interesting work nonlinear localization was used to explain certain dynamic phenomena in a steelpan musical instrument.

On a more theoretical level, localized NNMs can be related to certain solitary waves and solitons encountered in nonlinear partial differential equations. Hence, NNMs can provide a theoretical link between solitary waves and nonlinear localized vibrations in discrete or continuous oscillators. Of additional interest would be the development of nonlinear superposition principles that express general nonlinear transient responses as nonlinear superpositions of individual NNM responses; then a nonlinear analog to the principle of classical linear superposition of linear vibration theory could be derived.

Finally, the NNMs of elastic structures can be used as bases for Gallerkin projections that reduce the number of DOF required for vibration analysis (model reduction). In recent works it was found that a basis consisting of NNMs can capture more accurately the structural dynamics than a similar basis composed of purely linearized modes. Hence, NNMs can also be used for order reduction of nonlinear systems, and for decoupling the equations of motion of nonlinear oscillators.

Nomenclature

c	modal constant
$f_i(\mathbf{x}, \dot{\mathbf{x}})$	nonlinear coupling stiffness
x_1, x_2	dependent variables
$\mathbf{x}$	$(n \times 1)$ vector of positional variables
δ	Diracs function
$\Phi_1(x)$	spatial distribution
ω	natural frequency

See also: **Forced response**; **Localization**; **Nonlinear systems analysis**; **Nonlinear system identification**; **Nonlinear systems, overview**; **Nonlinear system resonance phenomena**; **Resonance and antiresonance**.

Further Reading

Kauderer H (1958) *Nichtlineare Mechanik*. Berlin: Springer Verlag.

Kevorkian J and Cole JD (1981) *Perturbation Methods in Applied Mathematics*. New York: Springer Verlag.

Nayfeh AH and Mook DT (1984) *Nonlinear Oscillations*. New York: Wiley.

Rosenberg RM (1966) On nonlinear vibrations of systems with many degrees of freedom. *Advances in Applied Mechanics* 9: 155–242.

Vakakis AF (1996) Nonlinear mode localization in systems governed by partial differential equations. *Applied Mechanics Reviews* 49; 87–99.

Vakakis AF (1997) Nonlinear normal modes and their applications in vibration theory: an overview. *Journal of Mechanical Systems and Signal Processing* 11; 3–22.

Vakakis AF, Manevitch LI, Mikhlin YuV, Pilipchuck VN and Zevin AA (1996) *Normal Modes and Localization in Nonlinear Systems*. New York: John Wiley.

NONLINEAR SYSTEM IDENTIFICATION

B F Feeny, Michigan State University, East Lansing, MI, USA

Copyright © 2001 Academic Press

doi:10.1006/rwvb.2001.0041

Introduction

Nonlinear system identification is the art of determining a model of a nonlinear dynamical process by combining information obtained from data with that of physical insight or *a priori* knowledge. The system to be modeled may be an experiment, a natural process, or even a large-scale computer simulation. Dynamic responses of such deterministic systems may be periodic or nonperiodic.

Nonlinear system identification is a broad subject. At the most basic level, the goal might be to merely identify how many states or modes are needed to construct a model of the system. With such information at

hand, a more detailed system identification can begin. At the more refined extreme is parametric system identification, for which the form of the differential equations of motion that model the system is known, but unknown parameters need to be identified. In between these two extremes lie techniques of nonparametric identification and nonlinear prediction, where the goal might range from revealing a nonlinear restoring force characteristic, to modeling the dynamic behavior without determining the differential equations of motion.

This article summarizes some ideas spanning this range of problems. We start with the most basic case of estimating the number of active states or modes, since in the most raw situation, this is where the analyst may start. We then discuss nonparametric identification methods, and finally, parametric system identification. There are many approaches to system identification in the literature, and we only touch on some of them. The goal here is to introduce basic ideas. Our focus is on deterministic systems, although methods are available for systems with random components. The tools discussed should enable system identification for a variety of nonlinear response regimes, be they periodic, quasiperiodic, or chaotic. Periodic responses may be more tractable for standard analyses, while nonperiodic responses tend to explore the response space and produce a large amount of information.

Estimating the Active States

When aiming for a state-space description of a vibration system, the estimation of the number of active states can be helpful in identifying low-order order models, either by reducing a high-order model, or by building a lumped-parameter model from scratch.

We can subdivide this section into two basic groups. The first group is emphasized when the modeler has access to a single time-history of data from a single observable, for example from a single sensor on the experimental rig. The second group is applicable when the analyst has access to several time histories of sensor data.

Extracting Dynamics from a Single Observable

Many of the ideas summarized here are well suited for nonperiodic data, and can be found in detail elsewhere.

The first step is to reconstruct the dynamics of the active states, i.e., to take, typically, a single sampled measurement history and view it in a higher-dimensional space, which can somehow accommodate the dynamics that generated the signal. The fully reconstructed state space can then be used for estimating a bound on the number of active states in the system.

The method of delays is the most common method for reconstructing the phase space. Suppose we have a measurement y which is essentially a smooth function of the states $\mathbf{x}$, i.e., $y = f(\mathbf{x})$, and suppose further that the measurement is sampled at a sampling interval h, generating a series producing sampled quantities y_n, with $n = 1, ..., M$. According to the method of delays, we build vectors $\mathbf{y}_n = (y_n, y_{n+l}, ..., y_{n+(d_E-1)l})$, where l is a delay index, and d_E is the dimension of $\mathbf{y}_n$. The delay time is $\tau = hl$. The psuedo vectors $\mathbf{y}_n$ can then be plotted in a d_E-dimensional space. The sequence of points $\mathbf{y}_n$ traces out a sampled curve in this pseudo phase space. This forms the reconstructed phase space, in which the next stage of data analysis and modeling can be pursued. According to Takens' embedding theorem, the dynamics in the reconstructed phase space qualitatively represent the dynamics in the true phase space for 'smooth' systems.

The method of delays can be intuitively justified by considering that the delay coordinates represent a linear transformation from coordinates that represent finite differences in time. Since mechanical systems have states which can be represented by displacements and velocities, the choice of discretized derivatives as pseudo states seems a natural one. Incidentally, derivatives of the observable have also been considered for performing reconstructions, and while this idea does produce a pseudo phase space in theory, it has the problem of noise amplification, and is not considered practical.

Practical problems associated with the method of delays are the choice of delay, and the choice of dimension d_E. If the delay is too large, and the system is chaotic, then measurement errors grow, and successive samples in the reconstructed phase space become statistically unrelated. If the delay is too small, then successive samples in the reconstructed phase space are too similar, and little information is gained. The happy medium is usually chosen by finding the delay which minimizes the average mutual information between the observable and its delay.

The choice of d_E is what we are after, as it tells us how many delay coordinates are necessary to describe the dynamics in the reconstructed space. The supposition is that this number is similar (but not exactly the same) as the number of active states. The method of false nearest neighbors (FNN) is a common choice for determining d_E. In this method, the reconstructed phase space is examined for artificial crossings of trajectories. When two trajectories cross, the phase space is too small. The first dimension for which there seems to be no trajectory

crossings is the dimension of the reconstructed space. Variations of the method have since been developed. Usually, the dimension of the reconstructed space represents an upper bound on the number of active states in the system.

Also useful is a computation of the fractal dimension, d_0. An object of dimension d_0 need be described by a maximum of $2d_0 + 1$ coordinates, which also provides a hint as to the number of delay variables needed to described the data.

Extracting Empirical Modes

If simultaneous time-histories of many sensors are available, these can be used to look for empirical modes by using proper orthogonal decomposition (or Karhunen–Loève decomposition, or principal components analysis).

Application of proper orthogonal decomposition (POD) to structures typically requires sensed dynamical quantities at M locations within the system. For this discussion, these quantities are taken to be displacements $x_1(t), x_2(t), \ldots, x_M(t)$, although other states can be used. When the displacements are sampled N times, we can form displacement-history arrays $\mathbf{x}_i = (x_i(t_1), x_i(t_2), \ldots, x_i(t_N))^{\mathrm{T}}$, for $i = 1 \ldots M$. (The means are sometimes subtracted from the displacement histories.) In performing the POD, these displacement histories are used to form an $N \times M$ ensemble matrix:

$$\mathbf{X} = [\mathbf{x}_1, \mathbf{x}_2, \cdots, \mathbf{x}_M]$$

Each row of $\mathbf{X}$ represents a point in the measurement space at a particular instant in time. The $M \times M$ correlation matrix $\mathbf{R} = (1/N)\mathbf{X}^{\mathrm{T}}\mathbf{X}$ is then formed. Since $\mathbf{R}$ is real and symmetric, its eigenvectors are orthogonal. The eigenvectors $\mathbf{v}$ of $\mathbf{R}$ are the proper orthogonal modes (POMs), and the eigenvalues λ are the proper orthogonal values (POVs).

The POMs are the principal axes of inertia of the data in the measurement space, and the POVs indicate the mean squared values of the data in the directions of the corresponding POMs. Equivalently, the POMs are the optimal distributions of signal power, and the POVs indicate the signal power associated with the corresponding POMs.

Using the POVs, the POMs can be ranked in descending order of signal power. The cumulative power is then the truncated sum of the POVs. It has been customary to say that the number of dominant, or active, modes are those of largest energy that contain, say, 99% or 99.9% of the total signal power. This is a prescription. These modes can then be used as an empirical modal basis for projecting the original large-order equations of motion to obtain a lower-order model. In linear vibrations, the POMs represent the linear normal modes only under specific circumstances.

Nonparametric Identification

In nonparametric identification, vibration behavior is modeled or predicted by means other than differential equations. Some approaches include Volterra series (or Weiner series) modeling, neural networks, and nonlinear time-series prediction, or merely the identification nonlinear stiffness characteristics.

First we mention the Volterra series approach. The response of a linear system to an input can be represented by a convolution intergral, in which the input is convolved with the impulse response function. In the Volterra series approach, this convolution integral is a first-order Volterra functional. The impulse response is the kernal. For modeling nonlinear input–output dynamics, a series of Volterra functionals is constructed, the kth term consisting of a k-fold nested convolution integral involving k delays of the input and a kth order kernal, which acts as a weighting function in the integral. In identifying the system, these kernals are to be identified, typically with a least-squares fit in the time-series response. (The time-series values of the kernals or weighting values are identified). The Weiner G-functionals, which are orthogonal functionals constructed from the Volterra functionals, can be used in place of the Volterra functionals in the system identification.

Backpropagation artificial neural networks can be applied to model discrete-time dynamics of sampled dynamic systems. The artificial neural networks are basically curve-fits to the dynamics. If input–output dynamics are written as $y_{k+1} = h(y_k, y_{k-1}, \ldots, y_{k-n_y}; u_k, u_{k-1}, \ldots, u_{nu})$ and if state-space dynamics are expressed as $x_{k+1} = f(x_k, u_k)$ and $y_{k+1} = g(x_k, u_k)$, where y_k is an output, u_k is an input, and x_k are the states, then the artificial neural network would be used to fit the functions h or f and g, i.e., the dynamics between samples, by using the arguments of the functions as inputs to the artificial neural network. In the learning process, the inputs and outputs are applied to the neural network, and a steepest descent (for example) with respect to network parameters, is used to minimize the error. The neural networks are highly nonlinear, and may have many local minima in the error. The aim would be to settle on a suitable local minimum.

The problem of identifying h in the input–output description is akin to nonlinear time-series prediction, for which the sampled output represents the time

series to be predicted. In time-series prediction, the goal is to take recent samples of an output, and predict the input for the near future. Time-series prediction can be done in the phase space reconstruction of the time series. When the reconstruction is in the appropriate dimension, as described earlier, and trajectories do not cross, then there is a unique short-time dynamical evolution for any point in the reconstructed phase space. That is, there is a well defined function that maps a given point in the phase space to its iterate, a few samples later. This function is to be identified. One way to do it is to find localized dynamics near reference trajectories in the dynamics. These localized dynamics are good within a specified distance of the reference trajectory, and are often modeled with linear functions. This can also be done by dividing the phase space into cells. Thus, when identified, the dynamics are approximated with piecewise linear maps.

The nonlinear dynamics of single-input/single-output dynamical systems and control systems can be modeled by setting up equivalent reverse multiple-input/single-output linear systems to represent the system at hand. When the system input and output are reversed, the nonlinearities can then be treated as additional correlated inputs.

Parametric Nonlinear System Identification

In this scenario, the ordinary differential equations of motion are known, and the forms of nonlinear terms are known. However, parameters in the equations of motion remain unknown and need to be identified. Among the approaches to consider in this situation are time-domain analysis, frequency-domain analysis, and bifurcation analysis.

The basic idea in time domain analysis is to take measured time histories of displacements, velocities and accelerations, and find parameters such that the equations of motion best accommodate the measured response for all time samples. This ultimately amounts to a least-squares solution with a minimized cost function based on a residual. One perspective is the direct evaluation of terms in the differential equation based on measured quantities. Here, the optimal parameters can be chosen to best balance the equation of motion at each time sample, for example by singular value decomposition. Another method is to use an analytical expression of the time response, written in terms of unknown parameters, and compare it with the measured response of the system to be identified. Then just one measurement signal is needed. Such methods have been reviewed by Stry and Mook, who in turn proposed the use of a correction term to accommodate modeling errors, which is then recast into a two-point boundary-value problem for the solution of the correction term. The correction term is then used to fit the nonlinear functions to be identified.

The idea in frequency-domain analysis is to take the Fourier transforms of the measured time histories, insert them into the differential equations of motion, and find parameter values that balance harmonics in the least-squares sense. If the system is linear in its parameters, i.e., the parameters are external coefficients on the nonlinearities in the equations of motion, then the balance equations are linear in the parameters, and a straightforward least squares solution suffices. Differentiation can be done by multiplying the transformed signal by $i\omega$. As such, for example, only measurements of displacements are needed, and velocities and accelerations can be obtained in the frequency domain. If the system response is periodic, then the Fourier coefficients can be computed by Fourier series or Fourier transforms. If the system response is chaotic, then numerous saddle-type unstable periodic orbits are 'visited' during the response. These periodic orbits can be approximately extracted and treated similarly to the way the stable periodic responses were treated, thus extending the idea to handle chaotic responses as well as stable periodic responses. The numerous periodic orbits from the chaotic response provide ample redundancy for the least-squares approximation of the parameters.

Bifurcation behavior can be exploited by finding parameters such that bifurcation events occur at the right parameter values. Bifurcations are considered to be rather sensitive to parameters, which is good for parameter identification. The bifurcation behavior is usually determined by using perturbation methods (see **Perturbation techniques for nonlinear systems**), such as multiple scales, averaging, and normal forms; to obtain analytical expressions of the bifurcation events as functions of parameters, which can then be used for the purposes of identification. In order to use bifurcations in system identification, bifurcations need to be observed experimentally. This means that the parameter space must be explored in the experiments, and parameter values for which sudden qualitative changes in the dynamical behavior must be recorded. The type of bifurcation must be recognized. As a cautionary note, bifurcation behavior is usually analyzed for steady-state, constant-parameter behavior. Experimental sweeps of parameter space really mean that the system has nonconstant, slowly varying parameters. Systems with slowly

varying parameters may have significantly different bifurcation occurrences than systems with truly constant parameters. Thus, the experimenter must be patient in the exploration of parameter space.

Conclusions

There are a range of options in nonlinear system identification, and choosing a particular method depends on the needs of the analysts, as well as the analyst's comfort with the fundamental ideas underlying a given tool.

Along with system identification should come model verification. Models can be verified by comparing responses of the model with responses of the system to be identified. If possible, it is a good idea to use data separate from those used in the identification calculation. Nonlinear system responses can be compared by characterizations of the responses, which is another subject for study. Nonlinear responses can be very sensitive to parameter errors, modeling errors, and even initial conditions. As such, validation based on responses should be performed with caution. Another possible perspective is to compare the model more directly with the system to be identified. This can be done by examining the differences in vector fields. What is meant here is that the terms in the model, say in the differential equation, approximate the flow of states in the state space. If the flow of states can be ascertained in the data, for example by finite differences of short-term sampled data, then the geometry of the phase flow can be verified. The geometry of the phase flow may turn out to be agreeable, even if the parameter sensitive and initial conditions sensitive responses seem to be off base.

In system identification there is always concern about noise and robustness, issues that we have not covered here. These issues are addressed in many of the cited references.

Nomenclature

d	delay index
d_o	fractal dimension
d_E	dimension of $\mathbf{y}_n$
$\mathbf{R}$	$M \times M$ correlation matrix
λ	eigenvalue
τ	time delay

See also: **Nonlinear systems analysis**; **Nonlinear systems, overview**; **Perturbation techniques for nonlinear systems**.

Further Reading

Abarbanel HDI, Brown R, Sidorovich JJ, Tsimring LS (1993) The analysis of observed chaotic data in physical systems. *Reviews of Modern Physics* 65: 1331–1392.

Bendat JS (1998) *Nonlinear System Techniques and Applications*. New York: Wiley.

Berkooz G, Holmes P, Lumley JL (1993) The proper orthogonal decomposition in the analysis of turbulent flows. *Annual Review of Fluid Mechanics* 25:539–575.

Billings SA (1980) Identification of nonlinear systems – a survey. *IEE Proceedings*, Pt. D 127(6): 272–285.

Guckenheimer J, Holmes PJ (1983) *Nonlinear Oscillations, Dynamical Systems, and Bifurcations of Vector Fields*. New York: Springer-Verlag.

Mohammad KS, Worden K, Tomlinson GR (1992) Direct parameter estimation in linear and nonlinear structures. *Journal of Sound and Vibration* 152:471–499.

Nayfeh AH (1985) Parametric identification of nonlinear dynamic systems. *Computers and Structures* 20(1–3):487–493.

Stry GI, Mook DJ (1992) An experimental study of nonlinear dynamic system identification. *Nonlinear Dynamics* 3:1–11.

Suykens JAK, Vandewalle JPL, De Moor BLR (1996) *Artificial Neural Networks for Modeling and Control on Nonlinear Systems*. Dordrecht: Kluwer.

Yasuda K, Kawamura S, Watanabe K (1988) Identification of nonlinear multi-degree-of-freedom systems (presentation of an identification technique). *JSME International Journal, Series III*, 31:8–14.

NONLINEAR SYSTEM RESONANCE PHENOMENA

A Bajaj and C M Krousgrill, Purdue University, West Lafayette, IN, USA

Copyright © 2001 Academic Press

doi:10.1006/rwvb.2001.0043

Introduction

Nonlinear models arise for most real systems and their presence in one form or another is generally the rule. The source of nonlinearity in structural and mechanical systems may be geometric, inertial, or

material in nature. Geometric nonlinearities typically arise from large deflections or rotations, or from other purely kinematical characteristics. Inertial nonlinearities can arise due to boundary or displacement dependent constraints. For example, when a thin elastic beam with movable supports undergoes transverse vibrations, the transverse oscillations are accompanied by small horizontal displacements of the movable end-mass. Thus, a large transverse motion of the beam leads to an axial inertial force that contributes to moments acting at the neutral axis of the beam. Examples of material nonlinearities include those arising due to nonlinear stress–strain relations, elastoplastic material behavior, etc. Other sources of nonlinearities include body forces (magnetic or electric fields), dry friction, and solid–fluid interactions.

In single-degree-of-freedom systems, the presence of nonlinear terms results in a vast variety of phenomena including: multiple periodic solutions, jumps in periodic responses, limit cycles, frequency entrainment, variation of natural frequencies with amplitude of response, subharmonic, superharmonic, combination and ultrasubharmonic resonances, period-doubling, and chaotic motions. While most of these responses are exhibited by systems subject to a single harmonic excitation, combination resonances arise only when the excitations involve more than one frequency. Many more interesting effects are generated when multiple excitations with distinct frequencies act on the system. All these types of behavior are classified as 'resonance phenomena' and arise when the linear natural frequency of the single-degree-of-freedom system and the frequencies of external or parametric excitations satisfy certain 'frequency relationships'. A large system response amplitude resulting from a small perturbation force characterizes a resonance condition. It can be explained in terms of nonzero virtual work done by the perturbing forces over a cycle of the particular mode under consideration. The simplest resonance condition is that of 'primary resonance' and it occurs when $\omega_n \approx \Omega$, where ω_n and Ω are, respectively, the linear natural frequency and the excitation frequency. In this case, the amplitude of the excitation has to be small and it is called a soft excitation. All other resonance cases arising due to external excitations involve amplitudes of excitation called hard excitations.

As an example of resonant phenomena exhibited by a single-degree-of-freedom system, consider a mathematical pendulum with a point mass attached at the end of a massless rigid rod. The rod is pinned to a support which is oscillated horizontally transverse to the gravity direction in the plane of the pendulum. In the absence of the base excitation, the pendulum rests in the bottom equilibrium position and this position is stable. When disturbed slightly, the pendulum oscillates about this static equilibrium position in its linear mode with a natural frequency determined by the length of the pendulum. When the pendulum is excited with a harmonic base displacement, the response depends on both the amplitude and the frequency of excitation. For an excitation frequency near the natural frequency, the pendulum does not need much excitation to undergo large amplitude motions. Interestingly, for frequencies below the natural frequency, there are two stable periodic motions, only one of them being large. For frequencies above the natural frequency, however, the pendulum has a unique periodic response.

We should note that if the displacement of the point of suspension of the pendulum also has a component along the vertical direction, this excitation component results in an equation of motion with time-periodic coefficients. This is an example of parametrically excited systems. For certain combinations of system and excitation parameters, these systems can exhibit parametric resonances and instabilities. These systems are considered elsewhere in the Encyclopedia and will not be addressed in this article.

Multiple-degree-of-freedom nonlinear systems can exhibit additional resonances including internal resonances and combination resonances. In an internal resonance, the system natural frequencies satisfy a certain frequency relation. In a combination resonance, both the system and excitation frequencies are involved in the frequency relation. These situations are generally called modal interactions, and they provide a mechanism for energy exchange among the modes of the system through some nonlinearity. The type of internal resonance exhibited by a system depends on the nature and degree of the nonlinearity present in it. For systems with cubic stiffness nonlinearities, an internal resonance can arise if:

$$\omega_n \approx 3\omega_m, \quad \omega_n \approx |\pm 2\omega_m \pm \omega_k| \quad \text{or} \quad \omega_n \approx |\pm \omega_m \pm \omega_k \pm \omega_l| \qquad [1]$$

where ω_n, ω_m, etc. are the linear natural frequencies of the system. When the nonlinearities in the system are quadratic, an internal resonance may additionally arise if:

$$\omega_n \approx \omega_m \quad \text{or} \quad \omega_n \approx |\pm \omega_m \pm \omega_k| \qquad [2]$$

Systems with a single harmonic excitation may exhibit a combination resonance when:

$$\Omega \approx \tfrac{1}{2}|\pm \omega_m \pm \omega_k|, \quad \Omega \approx |\pm 2\omega_m \pm \omega_k| \quad \text{or} \quad \Omega \approx |\pm \omega_m \pm \omega_k \pm \omega_l| \qquad [3]$$

and the nonlinearities are cubic. For systems with quadratic nonlinear terms, the additional possible combination resonances involve frequency relations of the form:

$$\Omega \approx |\pm \omega_m \pm \omega_k| \qquad [4]$$

When modal interactions occur due to the existence of an internal or combination resonance, modes that are not directly excited by an external forcing can also undergo large-amplitude oscillations. These motions arise, however, only when the excitation amplitude reaches a minimum critical level and a 'pitchfork' bifurcation transition occurs from a single mode to a coupled mode response. Also, these motions are predominant, that is, the energy transfer mechanism is effective, when the excitation frequency is in the vicinity of an exact resonance with a suitable system natural frequency. A further consequence of these modal interactions is the existence of complex amplitude-modulated dynamics for the system modes. These amplitude-modulated motions are similar to the well-known beating motions that arise in linear systems with two closely spaced natural frequencies.

As an example of modal interactions in multi-degree-of-freedom systems, consider the response of a stretched string to a transverse harmonic excitation. Suppose that the excitation is constrained to the vertical plane while the string can oscillate in both the vertical and horizontal planes. For small oscillations, the motions in the two orthogonal directions are uncoupled and are each governed by the wave equation. Thus, in each plane of motion, there is an infinity of natural modes of response and the associated natural frequencies. Every mode of oscillation in the vertical plane has an identical counterpart in the horizontal plane. For larger-amplitude motions, if the lowest-order nonlinearities are retained in the model, the equations of motion for the two identical modes of oscillation in the two orthogonal directions are coupled through cubic stiffness nonlinearities. Thus, the two identical modes of vibration of the string are in 'one-to-one' internal resonance. For a small harmonic forcing near a linear natural frequency of the string, the string responds harmonically in the vertical plane. Very near primary resonance, however, the response in the vertical plane becomes unstable and the string starts oscillating periodically in a three-dimensional motion. This is the well-known ballooning response of the string.

This article is focused on resonances arising in externally excited discrete dynamic systems. Quite often, these models also arise as a result of discretization of continuous models for strings, beams, rods, plates, arches, etc. Most of the analytical techniques for the study of resonance phenomena are based on constructing asymptotic or perturbation expansions for periodic and almost periodic solutions. These expansions require a small parameter, usually associated with the smallness of the nonlinearity. The asymptotic methods utilized here include the method of averaging and the method of multiple time scales. Results are described first for single-degree-of-freedom systems with quadratic and cubic nonlinearities. They are followed by some results for resonances arising in two-degree-of-freedom systems.

Resonant behavior also occurs when self-excited systems are subjected to periodic external forces or disturbances. Since the natural system itself has limit cycle motions, the external excitation frequency can interact with the self-oscillation frequency to give frequency entrainment, phase-locked motions, as well as amplitude-modulated oscillations. These motions are not discussed here.

Single-Degree-of-Freedom Systems

Consider the equation of motion for the nonlinear harmonically excited model:

$$\ddot{x} + \omega_n^2 x + 2\varepsilon\zeta\dot{x} + \varepsilon\alpha_1 x^2 + \varepsilon^2\alpha_2 x^3 = F\cos\Omega t, \quad 0 < |\varepsilon| \ll 1 \qquad [5]$$

consisting of a restoring force with linear, quadratic as well as cubic terms, and a linear velocity proportional damping. Here, ε is a small parameter usually introduced to characterize the relative order of nonlinearity and other effects in the model. Such equations frequently arise in modeling single-degree-of-freedom mechanical systems. They also arise as one-mode truncations of continuous structural systems. Here, only position-dependent restoring forces have been considered. They are usually a result of nonlinear stress–strain (or force–deflection) relations, or kinematical constraints. Nonlinear inertial terms can also be included in the model without much difficulty.

For small-amplitude motions, the response of the system can be constructed as a power series in the small parameter ε. To eliminate the presence of unbounded components in the solution (secular terms), terms that are a result of only the expansion procedure, and to develop solutions that are uniformly valid in time, many techniques have been

developed. In one popular technique, known as the method of multiple time scales, new independent time-like variables are introduced and the solution is assumed in the form:

$$x(t;\varepsilon) = x_0(T_0, T_1, \ldots) + \varepsilon x_1(T_0, T_1, \ldots) + \varepsilon^2 x_2(T_0, T_1, \ldots) + \ldots \quad [6]$$

where $T_0 = t$ is the fast time, and $T_1 = \varepsilon t$, $T_2 = \varepsilon^2 t$, ... etc., are the various slow times. The various time derivatives can be written in terms of the new independent time scales as:

$$\begin{aligned} \mathrm{d}/\mathrm{d}t &= D_0 + \varepsilon D_1 + \varepsilon^2 D_2 + \ldots, \\ \mathrm{d}^2/\mathrm{d}t^2 &= \left(D_0 + \varepsilon D_1 + \varepsilon^2 D_2 + \ldots\right)^2 \\ &= D_0^2 + 2\varepsilon D_0 D_1 + \varepsilon^2\left(2D_0 D_1 + D_1^2\right) + \ldots, \end{aligned} \quad [7]$$

where $D_n \equiv \partial/\partial T_n$. Then, substituting in eqn [5] and collecting terms of like powers in ε gives (up to second-order):

$$D_0^2 x_0 + \omega_n^2 x = F\cos\ \Omega T_0 \quad [8a]$$

$$D_0^2 x_1 + \omega_n^2 x_1 = -2D_0 D_1 x_0 - 2\zeta D_0 x_0 - \alpha_1 x_0^2 \quad [8b]$$

$$D_0^2 x_2 + \omega_n^2 x_2 = -2D_0 D_1 x_1 - 2D_0 D_2 x_0 - D_1^2 x_0 - 2\zeta D_0 x_1 - 2\zeta D_1 x_0 - 2\alpha_1 x_0 x_1 - \alpha_2 x_0^3 \quad [8c]$$

The solution of eqn [8a] is of the form:

$$x_0 = A(T_1, T_2)\mathrm{e}^{\mathrm{i}\omega_n T_0} + \Lambda \mathrm{e}^{\mathrm{i}\Omega T_0}/2 + \text{c.c.}, \quad \Lambda = F/\left(\omega_n^2 - \Omega^2\right) \quad [9]$$

where 'c.c.' indicates the complex conjugate of the preceding terms. Here, A is an arbitrary function of the slow times, and it is determined by imposing solvability requirements for the elimination of secular terms at the next level of approximation. Note that the solution (eqn [9]) contains a small-divisor term that leads to unbounded response when $\Omega \approx \omega_n$, and this is the case of primary resonance.

Primary Resonance

To develop a uniformly valid approximation to the solution when $\Omega \approx \omega_n$, the excitation force and the damping are rescaled by $F = \varepsilon^2 \hat{F}$ and $\zeta = \varepsilon\hat{\zeta}$. Clearly, there are then the corresponding changes in eqns [8a–c]. The solution (eqn [9]) at the lowest order reduces to $x_0 = A(T_1, T_2)\mathrm{e}^{\mathrm{i}\omega_n T_0} + \text{c.c.}$, where A has to be determined at the next order of approximation. The equation for the next approximation is:

$$\begin{aligned} D_0^2 x_1 + \omega_n^2 x_1 &= -2D_0 D_1 x_0 - \alpha_1 x_0^2 \\ &= -2i\omega_n D_1 A \mathrm{e}^{\mathrm{i}\omega_n T_0} - \alpha_1 A^2 \mathrm{e}^{2\mathrm{i}\omega_n T_0} - \alpha_1 A\bar{A} + \text{c.c.} \end{aligned} \quad [10]$$

For bounded solutions to exist, the resonance terms on the right-hand side of eqn [10] must vanish, that is, $D_1 A = 0$ and A does not depend on the slow time T_1. The solution for eqn [10] is then:

$$x_1 = \left(\alpha_1 A^2/3\omega_n^2\right)\mathrm{e}^{\mathrm{i}\omega_n T_0} - \left(\alpha_1/\omega_n^2\right)A\bar{A} + \text{c.c.} \quad [11]$$

where A is still an unknown variable. The equation for the second approximation is now:

$$\begin{aligned} D_0^2 x_2 + \omega_n^2 x_2 &= -2D_0(D_1 x_1 - 2D_2 x_0) - D_1^2 x_0 \\ &\quad - 2\hat{\zeta} D_0 x_0 - 2\alpha_1 x_0 x_1 - \alpha_2 x_0^3 + \hat{F}\cos\ \Omega T_0 \\ &= -\left\{2\mathrm{i}\omega_n\left(D_2 + \hat{\zeta}\right)A + \left(3\alpha_2 - 10\alpha_1^2/3\omega_n^2\right)A_2\bar{A}\right\} \\ &\quad \times \mathrm{e}^{\mathrm{i}\omega_n T_0} + \hat{F}\mathrm{e}^{\mathrm{i}\Omega T_0}/2 + \text{c.c.} + \text{NST} \end{aligned} \quad [12]$$

where NST stands for terms that do not produce any secular terms in the solution for x_2. Since $\Omega \approx \omega_n$ for primary resonance, letting $\Omega = \omega_n + \varepsilon^2\sigma$, where σ is the frequency mistuning, and eliminating terms that give rise to secular terms, gives:

$$\begin{aligned} a' &= -\hat{\zeta} a + \hat{F}\sin\gamma/(2\omega_n) \\ a\gamma' &= \sigma a - \left\{(3\alpha_2/8\omega_n) - 5\alpha_1^2/12\omega_n^3\right\}a^3 \\ &\quad + \hat{F}\cos\gamma/(2\omega_n) \end{aligned} \quad [13]$$

where $A = ae^{i\beta}/2$ and $\gamma = \sigma T_2 - \beta$. These eqns [13] are known as the amplitude equations and they determine the amplitude a and the phase β of the first term in the asymptotic expansion (eqn [6]). The two-term response of the nonlinear system is then given by:

$$x(t;\varepsilon) = a\cos\ (\omega_n t + \beta) + \varepsilon\left(\alpha_1 a^2/6\omega_n^2\right) \times \{\cos\ (2\omega_n t + 2\beta) - 3\} + \ldots \quad [14]$$

The above solution is periodic with period $2\pi/\Omega$ and contains higher harmonic components. In the presence of quadratic nonlinearities ($\alpha_1 \neq 0$), a constant term is also generated. The system thus oscillates around a nonzero mean.

For steady-state periodic solutions, we set $a' = 0, \gamma' = 0$. Then, squaring and adding the two equations in eqn [13], and eliminating the angle γ, gives the frequency–response equation

$$\sigma = \left\{(3\alpha_2/8\omega_n) - \left(5\alpha_1^2/12\omega_n^3\right)\right\}a^2 \pm \sqrt{\left(\hat{F}^2/4\omega_n^2 a^2 - \hat{\zeta}^2\right)} \qquad [15]$$

that relates the amplitude of response a to the frequency and amplitude of excitation, σ and $\hat{F}$, and the system model parameters $\hat{\zeta}$, ω_n, α_1 and α_2. Note that σ represents the deviation of the excitation frequency from the system linear natural frequency. For $\sigma > 0$, the excitation frequency is above the natural frequency and vice versa. Also note that the frequency of response is expressed as a function of the amplitude of response. This is quite different from the form conventionally utilized for frequency response functions of linear systems.

It is very instructive to study solutions of eqn [15] in various special cases. **Figures 1–6** show a representative set of response curves beginning with the response for a linear undamped ($\hat{\zeta} = 0$) system excited near primary resonance.

1. *Linear system:* The corresponding frequency–response relationship is:

$$\sigma = \pm\sqrt{\left(\hat{F}^2/4\omega_n^2 a^2 - \hat{\zeta}^2\right)} \qquad [16]$$

In the absence of damping ($\hat{\zeta} = 0$), eqn [16] reduces to $a = |\hat{F}/2\omega_n\sigma|$. As seen in **Figure 1**, the response for zero damping is unbounded at $\sigma = 0$. The response amplitude depends on the excitation amplitude $\hat{F}$. Actually, the response curves are rectangular hyperbolas in the (σa) plane. The important curves for $\hat{F} = 0$ are the line $a = 0$ and the vertical line at $\sigma = 0$. Thus, at $\sigma = 0$ the response amplitude is undefined in the free response case, whereas for any external forcing the response is unbounded.

2. *Nonlinear undamped free system:* The response amplitude a for zero damping is:

$$\sigma = \left\{(3\alpha_2/8\omega_n) - \left(5\alpha_1^2/12\omega_n^3\right)\right\}a^2 \qquad [17]$$

The response (**Figure 2**) depends on the sign of the coefficient $\alpha_e \equiv \{(3\alpha_2/8\omega_n) - (5\alpha_1^2/12\omega_n^3)\}$, which is sometimes called the effective nonlinearity. For positive values of this coefficient, the response exists only for $\sigma \geq 0$, the frequency of response is greater than the linear natural frequency ω_n, and the nonlinearity is called hardening. This sign depends on a combination of the nonlinear coefficients of the quadratic and cubic nonlinear terms. Similarly, the nonlinearity is called softening when the sign of α_e is negative so that the response exists only for $\sigma \leq 0$.

3. *Forced nonlinear undamped system:* The response amplitude in this case is:

$$\sigma = \{\alpha_e\}a^2 \pm \hat{F}/2(2\omega_n a) \qquad [18]$$

These responses for the softening and hardening nonlinearities are shown in **Figures 3** and **4** respectively. Effectively, the presence of nonlinearities bends the response curves in **Figure 1** in either a forward or a backward direction. This results in

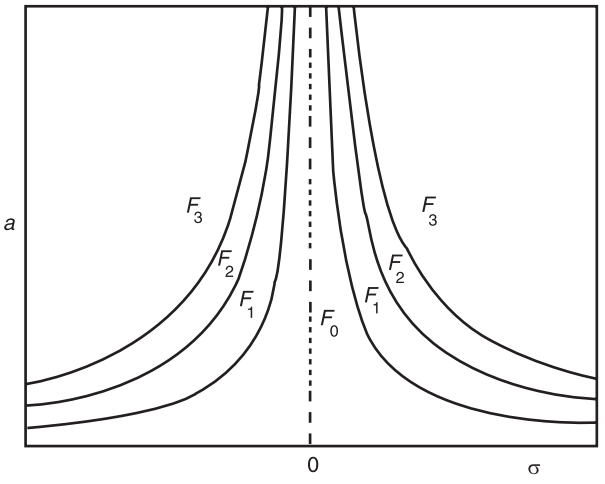


Figure 1 Response curves for the single-degree-of-freedom undamped linear system defined by eqn [16].

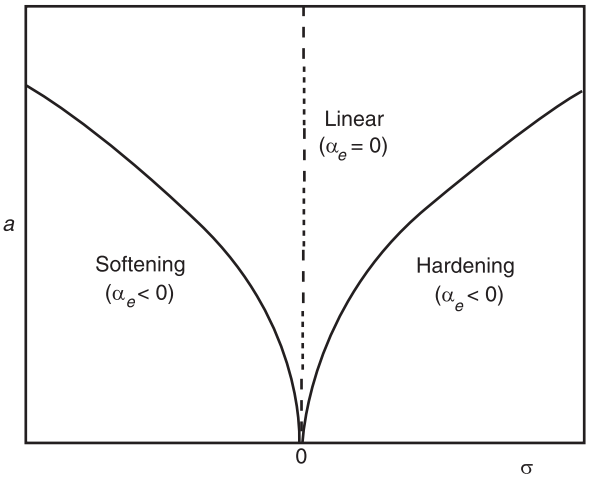


Figure 2 Free-response curves and variation of the frequency of response with amplitude for an undamped nonlinear single degree-of-freedom oscillator (eqn [17]).

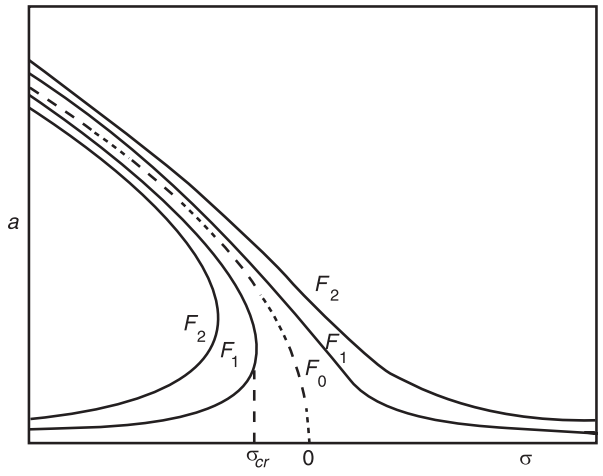


Figure 3 Response curves for resonantly excited and undamped single-degree-of-freedom nonlinear system with softening nonlinearity ($\alpha_e < 0$) (eqn [18]).

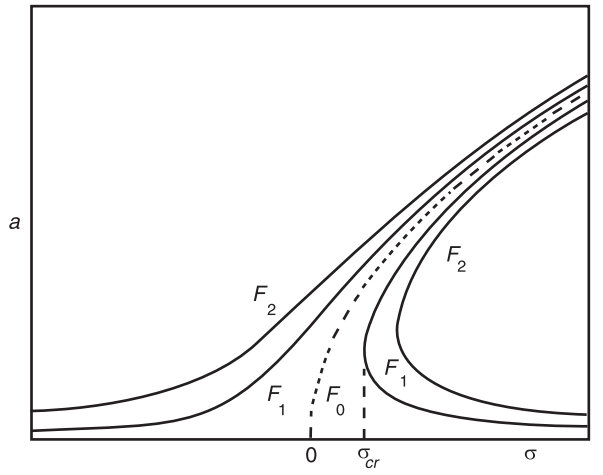


Figure 4 Response curves for resonantly excited and undamped single-degree-of-freedom nonlinear system with hardening nonlinearity ($\alpha_e > 0$) (eqn [18]).

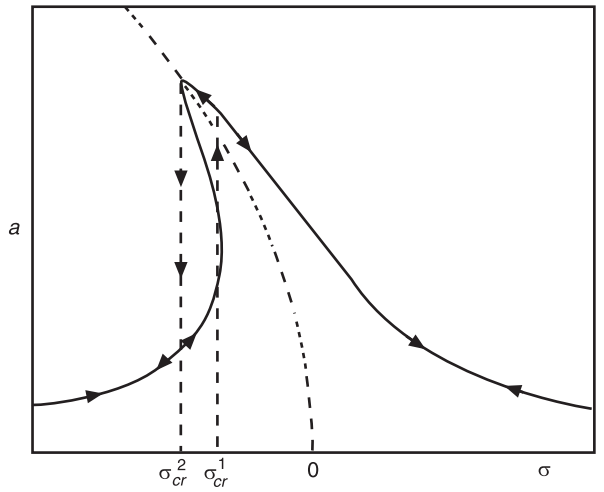


Figure 5 Response curves for resonantly excited and damped single-degree-of-freedom nonlinear system with softening nonlinearity ($\alpha_e > 0$) (eqn [15]).

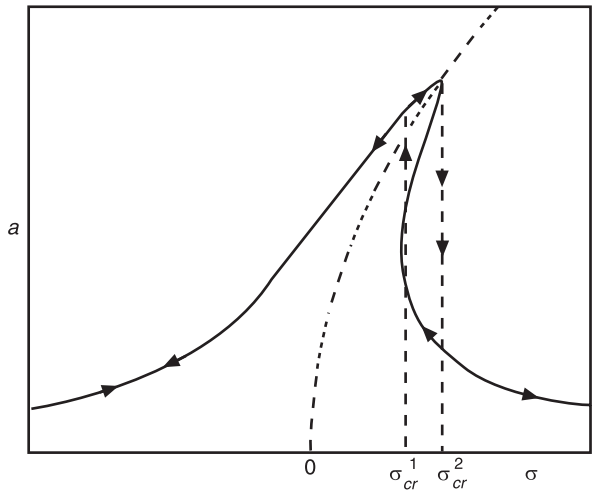


Figure 6 Response curves for resonantly excited and damped single-degree-of-freedom nonlinear system with hardening nonlinearity ($\alpha_e > 0$) (eqn [15]).

regions of frequency σ for which three distinct response amplitudes exist for the system at the same excitation frequency. For a softening nonlinearity, the three solutions region exists for frequencies below some critical value $\sigma_{cr} < 0$. Just the opposite situation arises for the hardening nonlinearity. The critical σ_{cr} is a function of the force amplitude and the nonlinearity parameters, and is a point of vertical tangency for the response curves. Furthermore, the response amplitude for the nonlinear system is finite at every excitation frequency, contrary to the linear case where the response is unbounded at exact linear resonance ($\sigma = 0$). The response of the unforced system (**Figure 2**) is shown by dotted lines in **Figures 3** and **4**. These are known as the backbone curves.

4. *Damped nonlinear system:* The response amplitudes for the two cases of softening and hardening nonlinearities are shown in **Figures 5** and **6**, respectively. Note here that the amplitude of response is bounded and there now exist two critical frequencies σ_{cr}^1 and σ_{cr}^2. Only between these two frequencies does the system have three distinct periodic responses. If the frequency of excitation is slowly changed monotonically past a critical value, the response amplitude suddenly jumps up or down. This is the classical jump phenomenon in

nonlinear vibrations. There also arises the associated hysteresis in nonlinear vibrations theory due to the different paths followed in forward and backward variations in the excitation frequency.

The stability of any of the periodic solutions, which are given by the equilibrium points of the amplitude equations, can be evaluated by a linearized analysis of these equations (eqns [13]). The characteristic equation for the linearized system, around an equilibrium point given by a root of eqn [15], is:

$$\lambda^2 + 2\hat{\zeta}\lambda + \hat{\zeta}^2 + \{\sigma - 3a^2\alpha_e\}\{\sigma - a^2\alpha_e\} = 0 \quad [19]$$

Using this equation it can be shown that, when there are three solutions of eqn [15], the middle solution is unstable with a positive and a negative eigenvalue. Furthermore, at the critical values of the frequency, σ_{cr}^1 and σ_{cr}^2, also the points of vertical tangency in the response curves, one of the roots of eqn [19] vanishes, thus indicating a saddle-node bifurcation. This essentially completes the discussion of the primary resonance case and we return to the zeroth-order solution in eqn [9] for the possibility of other resonances.

Secondary Resonances

When $\Omega \neq \omega_n$, and the excitation frequency is away from the linear natural frequency, the solution (eqn [9]) at the lowest order is uniformly valid. Now consider the equation for the next approximation, eqn [8b]. Substituting the solution (eqn [9]) into the right-hand side gives:

$$\begin{aligned} D_0^2 x_1 + \omega_n^2 x_1 = &-2\mathrm{i}\omega_n(D_1 + \zeta)A\mathrm{e}^{\mathrm{i}\omega_n T_0} - \mathrm{i}\zeta\Omega\Lambda\mathrm{e}^{\mathrm{i}\Omega T_0} \\ &- \alpha_1\Big\{A^2\mathrm{e}^{2\mathrm{i}\omega_n T_0} + \Lambda^2\mathrm{e}^{2\mathrm{i}\Omega T_0}/4 \\ &= A\Lambda\mathrm{e}^{\mathrm{i}(\omega_n+\Omega)T_0} \\ &+ A\bar{A} + A\Lambda\mathrm{e}^{\mathrm{i}(\omega_n-\Omega)T_0} + \Lambda^2/4\Big\}/ + \text{c.c.} \end{aligned} \quad [20]$$

The solution of eqn [20] contains additional secular terms when either $\Omega \approx 2\omega_n$ or $\Omega \approx \omega_n/2$. One can then proceed, as in the case of primary resonance above, and derive the amplitude equations that determine the response of the nonlinear system under appropriate resonance conditions. Since the small divisor or secular terms arise at first order, these are called secondary resonances. Secondary resonances also arise when either $\Omega \approx 3\omega_n$, or $\Omega \approx \omega_n/3$, though their appearance only becomes apparent when one considers solutions at the second-order approximation.

Subharmonic resonance of order one-half In this case, when $\Omega \approx 2\omega_n$, one assumes that:

$$\Omega = 2\omega_n + \varepsilon\sigma \quad [21]$$

where σ is the frequency mistuning away from the exact subharmonic resonance condition. Then, the two-term approximation to the solution of eqn [5] is:

$$\begin{aligned} x = &a\cos(\omega_n t + \beta) + \Lambda\cos\Omega t \\ &- \varepsilon\Big[\alpha_1\{(a^2 + \Lambda^2)/2\omega_n^2. \\ &- (a^2/6\omega_n^2)\cos(2\omega_n t + 2\beta) \\ &+ (\Lambda^2/2(\omega_n^2 - 4\Omega^2))\cos 2\Omega t \\ &- (\Lambda a/\Omega(\Omega + 2\omega_n))\cos((\omega_n + \Omega)t + \beta)\} \\ &- (2\zeta\Omega\Lambda/(\omega_n^2 - \Omega^2))\sin\Omega t\Big] + \ldots \end{aligned} \quad [22]$$

where the amplitude a and the phase β, $\beta = (\varepsilon\sigma t - \gamma + \nu)/2$, are defined by solutions of the amplitude equations:

$$\begin{aligned} a' &= -(\zeta + \alpha_1\Lambda\Gamma\sin\gamma)a \\ a\gamma' &= a\Big[\sigma - 2\alpha_1\Lambda\Gamma\cos\gamma \\ &\quad - \varepsilon\{-\zeta^2 + (3\alpha_2/2 - 5\alpha_1^2/8\omega_n^2)\Lambda^2\}/\omega_n - 2\varepsilon\alpha_e a^2\Big] \end{aligned} \quad [23]$$

Here, the constants ν and Γ are defined by the relation $2\omega_n\Gamma\mathrm{e}^{\mathrm{i}\nu} = 1 - \varepsilon(\sigma - 8\mathrm{i}\zeta/3)/2\omega_n$.

The steady-state solutions of eqns [23] define the amplitude and phase of the subharmonic component of the total response (eqn [22]), that is, with frequency $\Omega/2$. Clearly, $a = 0$ is a solution for all values of the parameters and it corresponds to the solution with frequency Ω. A linearized stability analysis for the zero solution determines its stability as a function of the system parameters. It may also be possible to find nonzero equilibrium solutions of eqns [23]. Then, the response period for the solution in eqn [22] is twice that of the excitation period. Note that because of the relation between the phase angles β and γ, and the modulo 2π nature of angular variables, there are two distinct values of β for every solution for γ and they are phase-shifted by π. Thus, for every nonzero amplitude a, there exist two subharmonic solutions that are π phase apart. No distinction is made here between these two solutions.

The important features for the subharmonic solutions are their numbers, the parameter combinations for which they arise, and the stability of the various solutions. These can be represented in the form of a bifurcation set that gives the parameter values at

which solutions change their stability. A typical bifurcation set for eqns [23], in the (σ, F) plane, is shown in **Figure 7**. In region I, the zero solution is the only solution and it is a sink (stable). Thus, no subharmonic solution exists for parameter values in this region. In region II, the zero solution is a saddle (unstable) and a nonzero solution in the form of a stable sink exists. In region III also the zero solution is stable, although there additionally exist two nonzero solutions of the amplitude equations. One of these subharmonic solutions of order one-half is a sink whereas the second solution is a saddle and unstable.

A typical frequency–response curve for a fixed excitation level is shown in **Figure 8**. The trivial solution corresponding to the solution with the period of excitation is unstable over the frequency interval $\sigma_1 < \sigma < \sigma_2$. There exist subharmonic solutions in the frequency interval $\sigma_1 < \sigma < \sigma_3$. While the subharmonic solutions are created from the zero solution at frequencies σ_1 and σ_2 via a pitchfork bifurcation, the frequency σ_3 corresponds to a turning point in the subharmonic response. In the interval $\sigma_2 < \sigma < \sigma_3$, the subharmonic solution with smaller amplitude is unstable. This figure again shows the existence of jump phenomenon and hysteresis in the response.

Superharmonic resonance of order two In this case, $2\Omega \approx \omega_n$, and one assumes that:

$$2\Omega = \omega_n + \varepsilon\sigma \qquad [24]$$

where σ is the frequency mistuning from the exact superharmonic resonance condition. Then, the two-term approximation to the solution of eqn [5] is:

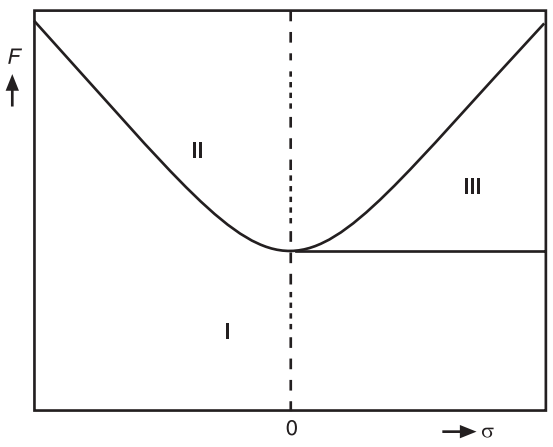


Figure 7 A typical bifurcation set in the (σ, F) plane for subharmonic response of order one-half for a single-degree-of-freedom system.

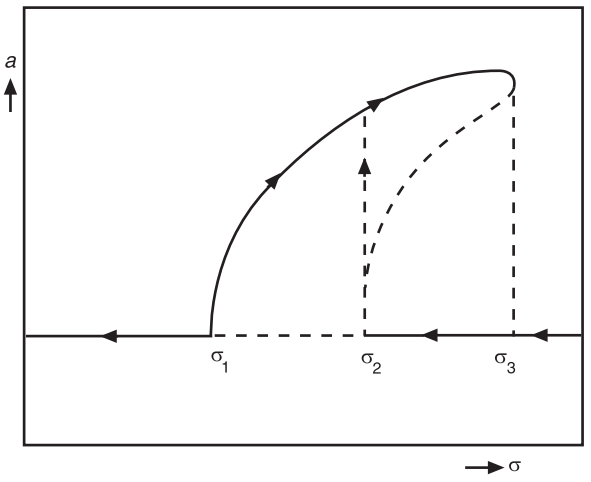


Figure 8 A representative frequency-amplitude response curve for subharmonic response of order one-half for a single-degree-of-freedom system.

$$\begin{aligned} x = {} & a\cos(\omega_n t + \beta) + \Lambda\cos\Omega t \\ & - \varepsilon\big[\alpha_1\big\{\big(a^2 + \Lambda^2\big)/2\omega_n^2 \\ & - \big(a^2/6\omega_n^2\big)\cos(2\omega_n t + 2\beta) \\ & - (\Lambda a/\Omega(\Omega - 2\omega_n))\cos((\omega_n - \Omega)t - \beta) \\ & - (\Lambda a/\Omega(\Omega + 2\omega_n))\cos((\omega_n + \Omega)t + \beta)\big\} \\ & - \big(2\zeta\Omega\Lambda/\big(\omega_n^2 - \Omega^2\big)\big)\sin\Omega t\big] + \ldots \end{aligned} \qquad [25]$$

where the amplitude a and the phase β, $\beta = (\varepsilon\sigma t - \gamma + \nu)$, are defined by the solutions of the amplitude equations:

$$\begin{aligned} a' &= -\big(\zeta a + \alpha_1\Lambda^2\Gamma\sin\gamma/4\omega_n\big) \\ a\gamma' &= a\big[\sigma - \big(\alpha_1\Lambda^2\Gamma/4\omega_n\big)\cos\gamma - \varepsilon\big\{-\zeta^2 + \big(3\alpha_2/2 \\ &\quad - 23\alpha_1^2/15\omega_n^2\big)\Lambda^2\big\}/2\omega_n - \varepsilon\alpha_e a^2\big] \end{aligned} \qquad [26]$$

Here, the constants ν and Γ are defined by the relation $\Gamma e^{i\nu} = 1 - \varepsilon(\sigma + 13i\zeta/3)/2\omega_n$.

The steady-state solutions of eqns [26] define the superharmonic solutions of order two. Note that in this case zero is not a possible equilibrium solution. Then, depending upon the strength and frequency of the external excitation, and the system parameters, eqns [26] can have one or three equilibrium solutions. The stability of these solutions is governed by the eigenvalues of the linearized system corresponding to eqns [26]. A typical set of frequency–response curves for superharmonic response of order two are shown in **Figure 9**. These curves again show the usual regions of multiple solutions, and the associated jump

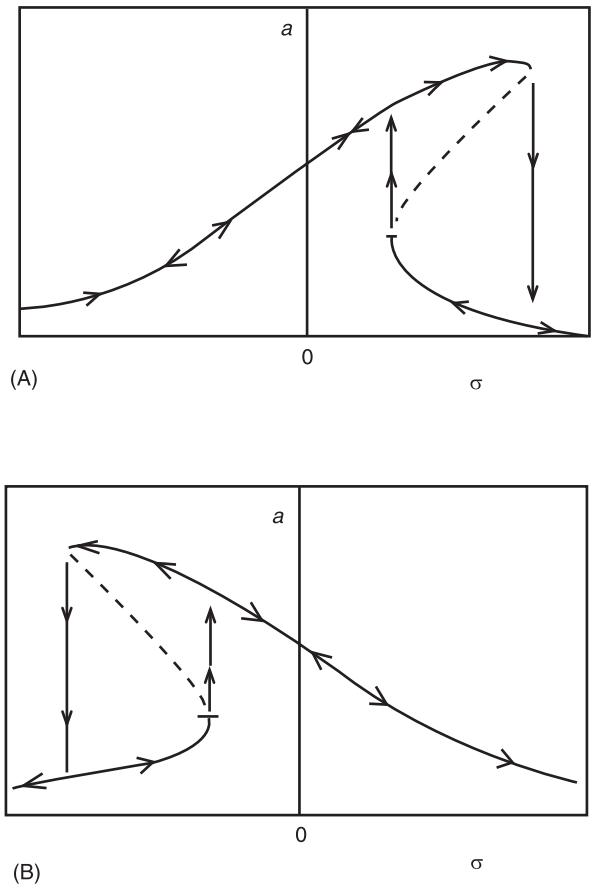


Figure 9 A representative frequency–amplitude response curve for superharmonic response of order two for a single degree-of-freedom system: (A) Hardening nonlinearity ($\alpha_e>0$); (B) softening nonlinearity ($\alpha_e<0$).

phenomenon and hysteresis. The response curves are bent forward or backward depending on the sign of the effective nonlinearity α_e.

Subharmonic resonance of order one-third When $\Omega \approx 3\omega_n$, elimination of secular terms in the solution of eqn [20] requires $D_1 A + \zeta A = 0$. Then, the solution for eqn [20] is:

$$\begin{aligned} x_1 = {} & i\zeta\Omega\Lambda e^{i\Omega T_0}/\left(\Omega^2 - \omega_n^2\right) \\ & + \alpha_1\left[\left(A^2/3\omega_n^2\right)e^{2i\omega_n T_0} - \left(4A\bar{A} + \Lambda^2\right)/4\omega_n^2\right. \\ & + \left(\Lambda^2/4\left(4\Omega^2 - \omega_n^2\right)\right)e^{2i\Omega T_0} \\ & + \left(\Lambda A/\Omega(\Omega + 2\omega_n)\right)e^{i(\Omega+\omega_n)T_0} \\ & + \left(\Lambda\bar{A}/\Omega(\Omega - 2\omega_n)\right)e^{i(\Omega-\omega_n)T_0} + \text{c.c.} \end{aligned} \quad [27]$$

Substituting this solution into eqn [8c], using $\Omega = 3\omega_n + \varepsilon\sigma$, and eliminating terms that result in secular terms, gives the amplitude equations for subharmonic oscillations of order one-third:

$$\begin{aligned} a' = {} & -\zeta a - \varepsilon\left(3\alpha_2/8\omega_n + \alpha_1^2/4\omega_n^3\right)\Lambda a^2 \sin\gamma \\ a\beta' = {} & \sigma a - \varepsilon\left[3\left\{-\zeta^2 + 3\left(\alpha_2/2 - \alpha_1^2/5\omega_n^2\right)\Lambda^2\right\}a/2\omega_n\right. \\ & + \alpha_e a^3 + \left(3\alpha_2/8\omega_n + \alpha_1^2/4\omega_n^3\right)\Lambda a^2\cos\gamma \end{aligned} \quad [28]$$

where $A = ae^{i\beta}/2$ and $\gamma = \sigma T_1 - 3\beta$. The two-term uniformly valid solution for the system response is now:

$$\begin{aligned} x = {} & a\cos\ (\omega_n t + \beta) + \Lambda\cos\ \Omega t \\ & - \varepsilon\left[\alpha_1\left\{\left(a^2 + \Lambda^2\right)/2\omega_n^2\right.\right. \\ & - \left(a^2/6\omega_n^2\right)\cos\ (2\omega_n t + 2\beta) \\ & - \left(\Lambda a/\Omega(\Omega - 2\Omega_n)\right)\cos\ ((\omega_n - \Omega)t - \beta) \\ & - \left(\Lambda a/\Omega(\Omega + 2\omega_n)\right)\cos\ ((\omega_n + \Omega)t + \beta) \\ & + \left(\Lambda^2/2\left(\omega_n^2 - 4\Omega^2\right)\right)\cos\ \Omega t\} \\ & - \left(2\zeta\Omega\Lambda/\left(\omega_n^2 - \Omega^2\right)\right)\sin\Omega t] + \ldots \end{aligned} \quad [29]$$

As was the case with the subharmonic response of order one-half, the amplitude equations for subharmonic response of order one-third also have a zero solution ($a = 0$). This implies a periodic solution with the period of the excitation. A linearized stability analysis of eqns [28] for the zero solution reveals that the zero solution, or the periodic solution at the period of excitation, is stable for all parameter values. There also exist nonzero equilibrium solutions of eqns [28] when the system and excitation parameters satisfy certain conditions. From the form of the solution in eqn [29], it can be seen that the solution then has a period which is three times that of excitation, thus implying a subharmonic solution.

Superharmonic resonance of order three When $\Omega \approx \omega_n/3$, the analysis follows steps identical to those for the case of subharmonic resonance. Introducing the appropriate mistuning, $3\Omega = \omega_n + \varepsilon\sigma$, the two-term uniformly valid response of the system is again given by eqn [29], and the amplitude and phase of the superharmonic component of the response satisfy:

$$\begin{aligned} a' = {} & -\zeta a - \varepsilon\Gamma\sin\gamma \\ a\beta' = {} & \sigma a - \varepsilon\left[\left\{-\zeta^2 + \left(3\alpha_2/2 - 53\alpha_1^2/35\omega_n^2\right)\Lambda^2\right\}a/2\omega_n\right. \\ & + \alpha_e a^3 + \Gamma\cos\gamma\Big] \end{aligned} \quad [30]$$

where $\Gamma = \{(\alpha_2 - 18\alpha_1^2/5\omega_n^2)\Lambda^3/8\omega_n\}$, and $\gamma = \sigma T_1 - \beta$. Solutions of these equations can be studied as a function of the system and excitation parameters.

This concludes the discussion of some of the important resonances that arise in harmonically excited single-degree-of-freedom nonlinear mechanical systems with quadratic and cubic stiffness, or position-dependent, nonlinearities. The nonlinearities can contribute significantly to the response of the system when the excitation frequency and the linear natural frequency of the system satisfy certain frequency relations. The most significant resonance is called the primary resonance, and it occurs when the excitation frequency is close to the system's linear natural frequency. Then, the excitation amplitude has to be $O(\varepsilon)$ and, depending on the sign of the effective stiffness, multiple periodic solutions only arise for excitation frequencies above or below the natural frequency. When the excitation frequency is nearly two or three times the natural frequency, periodic solutions at one-half or one-third of the excitation frequency can also exist in addition to the solutions at the frequency of excitation. These are the subharmonic solutions of appropriate order. When the excitation frequency is nearly one-half or one-third of the natural frequency, the periodic response at the excitation frequency also contains higher harmonics of the appropriate order, and these are the superharmonic resonances. In either of these cases, the excitation amplitude is $O(1)$ in ε.

Two-Degree-of-Freedom Systems (Quadratic Nonlinearities)

The general equations of motion for this class of system are:

$$\begin{aligned}
&\ddot{x}_1 + \omega_1^2 x_1 + \varepsilon \\
&\quad \times \left[2\zeta_1 \dot{x}_1 + \sum_{i=1}^{2}\sum_{j=1}^{2} \left\{ a_{1ij} x_i x_j + b_{1ij} \dot{x}_i \dot{x}_j + c_{1ij} x_i \ddot{x}_j \right\} \right] \\
&\quad = F_1 \cos\ (\Omega t + \tau_1) \\
&\ddot{x}_2 + \omega_2^2 x_2 + \varepsilon \\
&\quad \times \left[2\zeta_2 \dot{x}_2 + \sum_{i=1}^{2}\sum_{j=1}^{2} \left\{ a_{2ij} x_i x_j + b_{2ij} \dot{x}_i \dot{x}_j + c_{2ij} x_i \ddot{x}_j \right\} \right] \\
&\quad = F_2 \cos\ (\Omega t + \tau_2)
\end{aligned} \qquad [31]$$

Free and forced responses for many physical systems, including ships, robots, elastic pendula, beams and plates under static loadings, shallow arches, composite plates and shells, and free-surface oscillations in containers, have been described by these equations. For example, in the study of motions of a shallow arch, x_1 and x_2 represent the modal amplitudes of the lowest-frequency antisymmetric and symmetric modes, respectively. These modes and their associated linear frequencies vary as a function of the transverse load acting at the center of the arch. In the case of rigid-body motions of a ship, these coordinates represent the roll and pitch motions, respectively. In general, the pitch and roll motions are uncoupled for the linear model and the pitch frequency is higher than the frequency for roll motion. The nonlinearities couple these two motions, especially when the pitch frequency is nearly twice the roll frequency.

Periodic solutions of eqns [31] can be constructed using any number of techniques. Following the method of multiple time scales, the solution for each of the oscillators can be assumed to be of the form given in eqn [6]. Then, proceeding as for the single-degree-of-freedom system, a sequence of approximation equations similar to eqns [8] are obtained. At the zeroth-order, each oscillator has a solution in the form of eqn [9] where the complex amplitude A is determined at the next approximation by developing the appropriate solvability conditions. The solution (eqn [9]) is uniformly valid (there are no small divisor terms) unless either of the primary resonances arise, that is, Ω is near ω_1 or ω_2. In that case, only weak excitations can be considered.

In the first-order approximation, even in the absence of any excitation, small divisor terms arise when $\omega_2 \approx 2\omega_1$. In the presence of an external excitation, nonuniformity in solution arises when $2\omega_2 \approx \Omega$ (subharmonic resonance of order one-half), $\omega_1 \approx 2\Omega$ (superharmonic resonance of order two), or $\omega_1 + \omega_2 \approx \Omega$ (combination resonance of additive type). Thus, depending on the frequency relation involving the linear natural frequencies ω_1, ω_2, and the excitation frequency Ω, various resonances arise for these systems.

There is an exchange of energy between the two modes of response only when the natural frequencies satisfy the relation $\omega_2 \approx 2\omega_1$. Thus, let $\omega_2 = 2\omega_1 + \varepsilon\sigma_1$, where σ_1 is called the internal mistuning. Now, the response depends on the strength of excitation. When the excitation frequency is near either of the natural frequencies, the excitation force has to be $O(\varepsilon)$ in order for the nonlinear terms to balance the excitation. In the case of sub- or superharmonic resonances, the excitation force can be $O(1)$ in ε. Only the primary resonance cases are presented here.

Primary Resonances

Let $F_i = \varepsilon \tilde{F}_i$, $i = 1, 2$. Then, the one-term uniformly valid solution of the system given in eqn [31] is:

$$x_i(t;\varepsilon) = a_i \cos\ (\omega_i t + \beta_i) + O(\varepsilon), \quad i = 1, 2, \ldots \tag{32}$$

where the amplitude equations governing the evolution of the two amplitudes and phases, $(a_i,\ \beta_i)$, $i = 1, 2$, can be written in a unified way as:

$$\begin{aligned} a_1' &= -\zeta_1 a_1 - \Pi_1 a_1 a_2 \sin\gamma_1 + \Gamma_1 \\ a_1\beta_1' &= \Pi_1 a_1 a_2 \cos\gamma_1 + \Gamma_2 \\ a_2' &= -\zeta_2 a_2 + \Pi_2 a_1^2 \sin\gamma_1 + \Gamma_3 \\ a_2\beta_2' &= \Pi_2 a_1^2 \cos\gamma_1 + \Gamma_4 \end{aligned} \tag{33}$$

where:

$$\begin{aligned} \Pi_1 &= \Big\{(a_{112} + a_{121}) + (b_{112} + b_{121})\omega_1\omega_2 - c_{121}\omega_1^2 \\ &\quad - c_{112}\omega_2^2\Big\}/4\omega_1 \\ \Pi_2 &= \Big\{a_{211} - (b_{211} + c_{211})\omega_1^2\Big\}/4\omega_1 \\ \gamma_1 &= \varepsilon\sigma_1 t + \beta_2 - 2\beta_1 \end{aligned} \tag{34}$$

The phase angle γ_2 and the excitation terms Γ_i, $i = 1 - 4$, depend on the primary resonance condition satisfied. These terms for the two cases of interest are given below. In the absence of an external excitation, the amplitudes a_1 and a_2 of the two linear modes are coupled by the nonlinear quadratic terms. Considering eqns [31] and (34), note that only a few specific nonlinear coefficients contribute to this modal interaction. Thus, for modal interaction and internal resonance to occur, non-vanishing of the coefficients Π_1 and Π_2 is required in addition to the frequency relation. **Figure 10** depicts a representative set of time responses for the amplitude equations for the unforced system with zero damping. There is a clear interchange of energy between the two modes which depends also on the internal mistuning σ_1. Thus, the undamped system (eqns [31]) performs amplitude-modulated motions with the modulations in the two modes being out of phase. Introduction of any dissipation results in decaying oscillations. In the presence of an external excitation, there are a large variety of steady-state solutions possible for eqns [33]. These then imply constant-amplitude periodic solutions, almost periodic motions as well as chaotically modulated motions for the original equations (eqns [31]).

Primary resonance of the first mode Here the phase angle γ_2 and the excitation terms Γ_i, $i = 1{-}4$, are defined by:

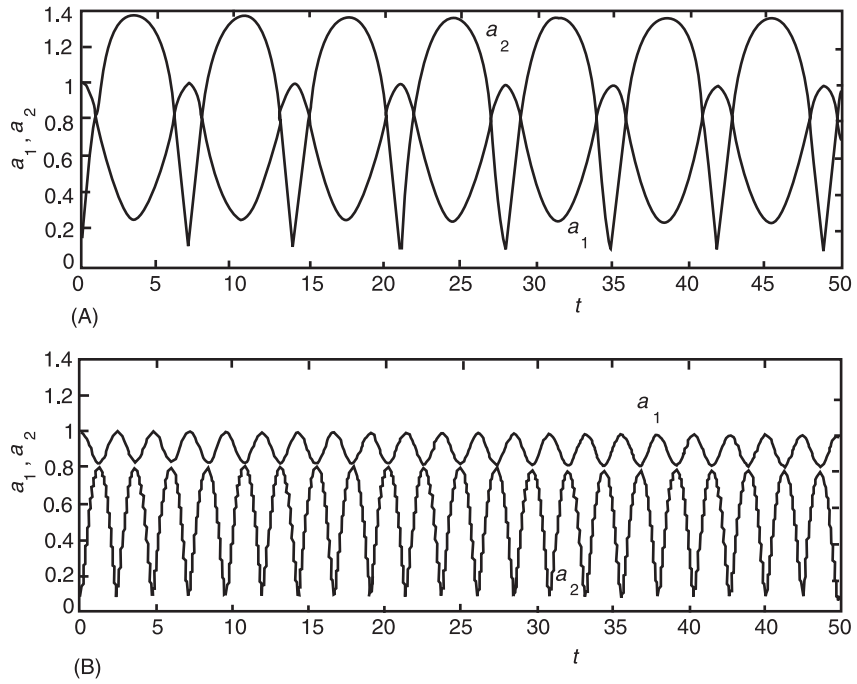


Figure 10 Free, undamped response of the amplitude equations for a two-degree-of-freedom system with quadratic nonlinearities and two-to-one internal resonance (eqns [33]): (A) Internal mistuning $\sigma_1 = 0$; (B) internal mistuning $\sigma_1 = 2.0$.

$$\gamma_2 = \varepsilon\sigma_2 t - \beta_1 + \tau_1$$
$$\Gamma_1 = \left(\tilde{F}_1/2\omega_1\right)\sin\gamma_2, \quad \Gamma_2 = -\left(\tilde{F}_2/2\omega_1\right)\cos\gamma_2,$$
$$\Gamma_3 = \Gamma_4 = 0 \qquad [35]$$

Furthermore, $\Omega = \omega_1 + \varepsilon\sigma_2$, and σ_2 is called the external mistuning. It represents the deviation of the excitation frequency from the lower of the two natural frequencies. Thus, the first or the lower natural frequency mode, is directly excited and the higher-frequency mode only obtains energy due to the nonlinear modal interaction. Also note that both modes have nonzero amplitudes of oscillation in a steady state. The steady-state solutions of eqns [34] and [35], determined by the conditions $a_i' = 0, \gamma_i' = 0, i = 1, 2$, correspond to periodic solutions of the system given in eqn [31]. Representative sets of response curves (amplitudes of solutions) for the two modes at small damping level, as a function of the excitation frequency (or external mistuning) σ_2, are shown in **Figure 11**. These curves show that the directly excited mode (a_1) has larger stable solutions except near exact resonance where the second mode extracts larger energy from the external excitation. The response curves also show the usual jump phenomenon, at least for sufficiently small damping parameters. Compared to the resonant responses in the case of a single-degree-of-freedom system, there arise additional instabilities in these response curves. They correspond to a Hopf bifurcation in the amplitude equations. Consequently, in the frequency interval near $\sigma_2 = 0$, a direct integration of eqns [33] shows limit cycle oscillations in amplitudes and phases. Thus, the coupled system given in eqns [31] executes amplitude-modulated periodic oscillations when it is excited near exact resonance and the internal mistuning is also small. These types of modulated responses have been verified in many experimental investigations. In fact, for suitable parameter combinations, eqns [33] have been shown to exhibit period-doubling bifurcations to chaotic solutions, thus implying amplitude-modulated chaos for the original oscillators.

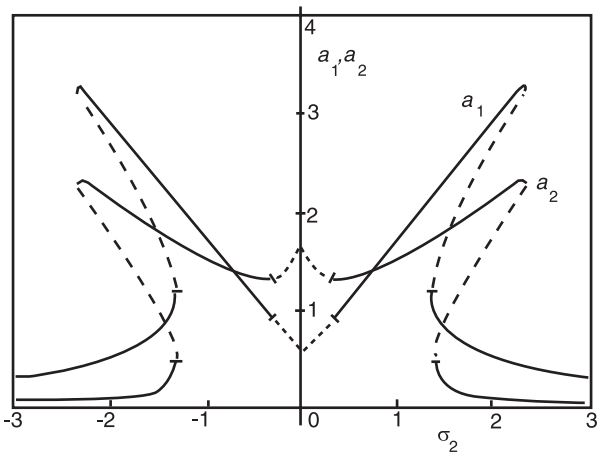


Figure 11 A representative set of frequency–response curves for a two degree-of-freedom system with quadratic nonlinearities, two-to-one internal resonance, and primary resonance of the first mode (eqns [33]).

Primary resonance of the second mode Now, the phase angle γ_2 and the excitation terms $\Gamma_i, i = 1{-}4$, are defined by:

$$\gamma_2 = \varepsilon\sigma_2 t - \beta + \tau_2$$
$$\Gamma_1 = \Gamma_2 = 0, \quad \Gamma_3 = \left(\tilde{F}_2/2\omega_2\right)\sin\gamma_2, \qquad [36]$$
$$\Gamma_4 = -\left(\tilde{F}_2/2\omega_2\right)\cos\gamma_2$$

Here, $\Omega = \omega_2 + \varepsilon\sigma_2$, and σ_2 is the external mistuning. Thus, the excitation frequency is close to the higher of the two natural frequencies. Interestingly, in this case, one steady-state solution of eqns [33] is with zero amplitude ($a_1 = 0$, $a_2 \neq 0$) for the first mode. Then, the response of the directly excited mode is like that of a linear oscillator near resonance. It is also possible to find steady-state solutions for which both $a_1 \neq 0$, $a_2 \neq 0$. In this coupled-mode solution, while the amplitude a_2 of the directly excited mode turns out to be independent of the excitation force, the amplitude of the first mode depends on it. This has been termed the saturation phenomenon, and has been suggested as a way to control passively the response amplitude of a resonantly excited system. In this sense, it is a nonlinear analog of the dynamic vibration absorber in linear vibration theory.

Representative sets of response curves depicting both the single-mode ($a_1 = 0$, $a_2 \neq 0$) and the coupled-mode ($a_1 \neq 0$, $a_2 \neq 0$) responses are shown in **Figures 12** and **13**. The single-mode solution, which is basically the linear solution, is unique. For the parameter values chosen, it loses stability by a pitchfork bifurcation to a coupled-mode equilibrium solution in some frequency interval around $\sigma_2 = 0$. For zero internal mistuning ($\sigma_1 = 0$) the coupled-mode solution branches are symmetrical around $\sigma_2 = 0$ and multiple solutions, leading to the jump phenomenon, can coexist. The amplitudes of the indirectly excited oscillator depend heavily on the damping in that mode. For very small damping in the indirectly excited oscillator ($\zeta_1 \approx 0$), the response of the directly excited oscillator (a_2) can be nearly completely suppressed. In the frequency interval

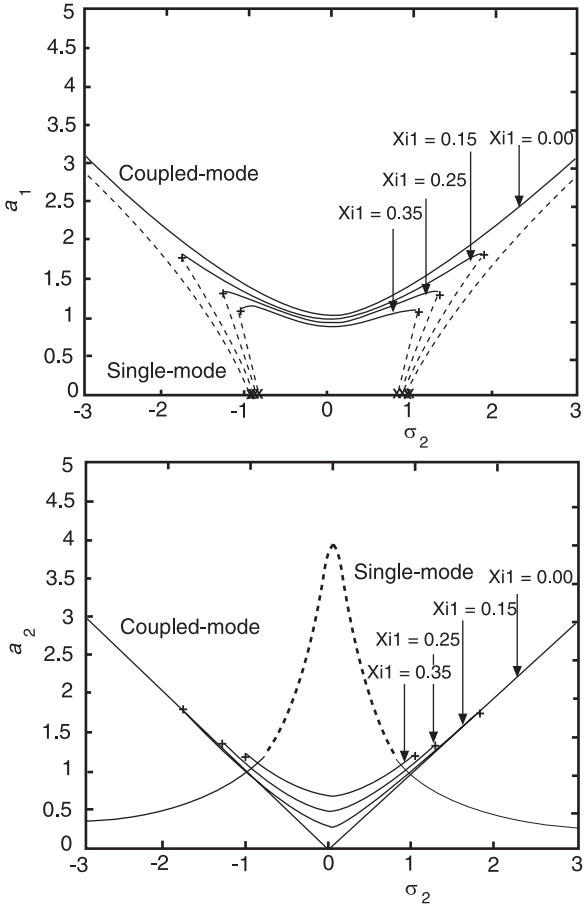


Figure 12 A representative set of frequency–response curves for a two degree-of-freedom system with quadratic nonlinearities, two-to-one internal resonance, and primary resonance of the second mode (eqns [33]); zero internal mistuning ($\sigma_1 = 0$).

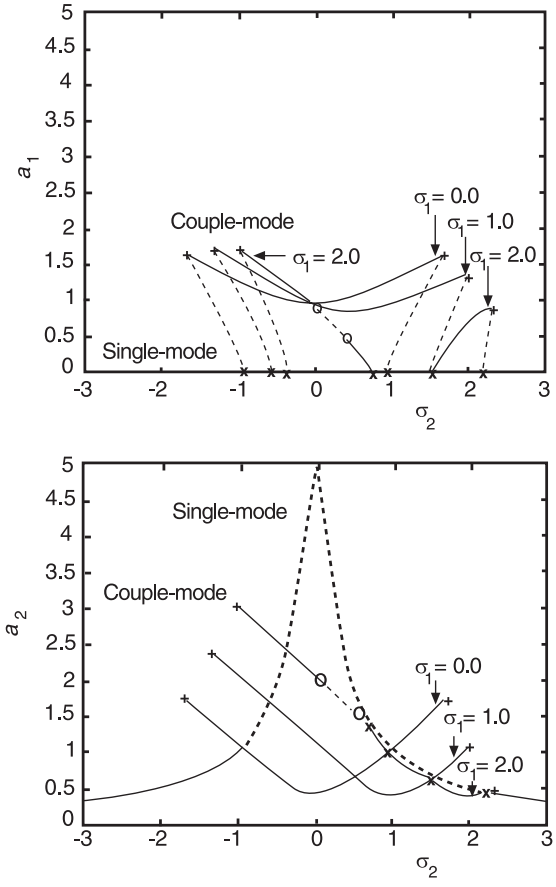


Figure 13 A representative set of frequency–response curves for a two degree-of-freedom system with quadratic nonlinearities, two-to-one internal resonance, and primary resonance of the second mode (eqns [33]); nonzero internal mistuning ($\sigma_1 \neq 0$).

where the single-mode solution is unstable, there is a unique and stable coupled-mode solution. Outside of this interval, however, multiple coupled-mode solutions arise. No Hopf bifurcation to limit cycles is possible here unless there exists a frequency mistuning between the two oscillators (**Figure 13**). For moderate values of internal mistuning σ_1, the coupled-mode solution undergoes Hopf bifurcation to a limit cycle which then leads to chaotic solutions via a period-doubling sequence (**Figure 14**). For large internal mistuning σ_1, $\sigma_1 \to \pm\infty$, the modal interaction, as expected, becomes weak and the response of the system tends toward the single-mode solution.

Two-Degree-of-Freedom Systems (Cubic Nonlinearities)

The general equations of motion for this class of structural and mechanical system are:

$$\begin{aligned}
&\ddot{x}_1 + \omega_1^2 x_1 \\
&\quad + \varepsilon\left[2\zeta_1\dot{x}_1 + \sum_{i=1}^{2}\sum_{j=1}^{2}\sum_{k=1}^{2}\left\{a_{1ijk}x_i x_j x_k\right.\right. \\
&\quad \left.\left. + b_{1ijk}x_i\dot{x}_j\dot{x}_k + c_{1ijk}x_i x_j\ddot{x}_k\right\}\right] \\
&\quad = F_1\cos\ (\Omega t) \\
&\ddot{x}_2 + \omega_2^2 x_2 \\
&\quad + \varepsilon\left[2\zeta_2\dot{x}_2 + \sum_{i=1}^{2}\sum_{j=1}^{2}\sum_{k=1}^{2}\left\{a_{2ijk}x_i x_j x_k\right.\right. \\
&\quad \left.\left. + b_{2ijk}x_i\dot{x}_j\dot{x}_k + c_{2ijk}x_i x_j\ddot{x}_k\right\}\right] \\
&\quad = F_2\cos\ (\Omega t + \tau)
\end{aligned} \qquad [37]$$

Many physical systems, including robots, elastic pendula, beams and plates, composite plates and shells,

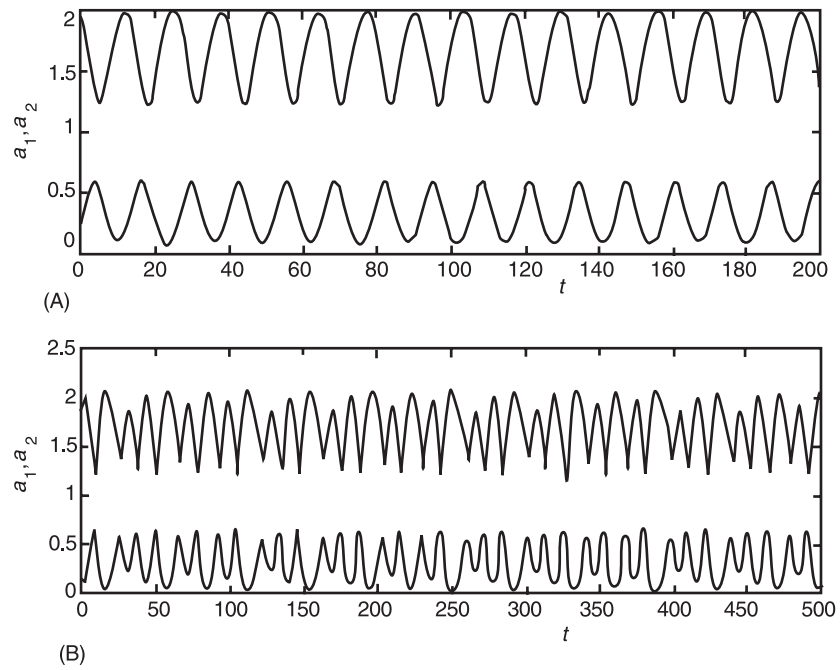


Figure 14 Typical oscillatory solutions of the amplitude equations (eqns [33]) for a two-degree-of-freedom system with quadratic nonlinearities, two-to-one internal resonance, and primary resonance of the second mode: (A) $\sigma_2 = 0.49$; (B) $\sigma_2 = 0.48$.

and free-surface oscillations in containers, have been described by these equations. Primary resonances arise in these systems when the external excitation frequency Ω is near either of the natural frequencies ω_1 or ω_2. Then, only weak excitations can be considered and the results here are limited to these cases. For this, let $F_i = \varepsilon P_i$, $i = 1, 2$. Two possible cases of internal resonance also arise, and the amplitude equations for the case of $\omega_2 \approx \omega_1$ are much more complex than the equations for the $\omega_2 \approx 3\omega_1$ case. In either case, the one-term approximate solution of the coupled system is:

$$x_n = \left\{A_n(T_1, T_2)\mathrm{e}^{\mathrm{i}\omega_n T_0} + \text{c.c.}\right\} + O(\varepsilon), \quad n = 1, 2 \qquad [38]$$

In the case when $\omega_2 \approx 3\omega_1$, the complex amplitudes for the two oscillators satisfy:

$$\begin{aligned} A_1' &= \left[\left\{\sigma_1 A_1 - 2i\nu\zeta_1 A_1 - \Pi_1 A_1^2 \bar{A}_1 - \Pi_3 A_1 A_2 \bar{A}_2\right\} + \left\{\Gamma_1 \delta_{1j} - \Pi_2 \bar{A}_1^2 A_2\right\}\right]/i\nu \\ A_2' &= \left[\left\{\sigma_2 A_2 - 6i\nu\zeta_2 A_2 - \Pi_4 A_2^2 \bar{A}_2 - \Pi_6 A_1 \bar{A}_1 A_2\right\} + \left\{\Gamma_1 \delta_{2j} - \Pi_5 A_1^3\right\}\right]/3i\nu \end{aligned} \qquad [39]$$

where $\varepsilon\sigma_1 = (\nu^2 - \omega_1^2)$, and $\varepsilon\sigma_2 = (9\nu^2 - \omega_2^2)$ are the external mistunings, δ_{ij} is the Kronecker delta, Π_i, $i = 1 - 6$ are nonlinear coefficients dependent on the system nonlinearities, and Γ_i, $i = 1, 2$, are constants related to the excitation amplitudes F_1 and F_2, respectively. The index $j = 1$ when the first oscillator is in primary resonance, and $j = 2$ when the second oscillator is in primary resonance.

For the case when $\omega_2 \approx \omega_1$, the complex amplitudes of the one-term solution are governed by:

$$\begin{aligned} A_1' &= \left[\left\{\sigma_1 A_1 - 2i\nu\zeta_1 A_1 - \Pi_1 A_1^2 \bar{A}_1 - \Pi_3 A_1 A_2 \bar{A}_2\right\} + \left\{\Gamma_1 - \Pi_2 A_1 \bar{A}_1 A_2 - \Pi_4 A_1^2 \bar{A}_2 - \Pi_5 \bar{A}_1 A_2^2 - \Pi_6 A_2^2 \bar{A}_2\right\}\right]/i\nu \\ A_2' &= \left[\left\{\sigma_2 A_2 - 2i\nu\zeta_2 A_2 - \Pi_7 A_2^2 \bar{A}_2 - \Pi_9 A_1 \bar{A}_1 A_2\right\} + \left\{\Gamma_2 - \Pi_8 A_1^2 \bar{A}_1 - \Pi_{10} A_1^2 \bar{A}_2 - \Pi_{11} A_1 A_2 \bar{A}_2 - \Pi_{12} \bar{A}_1 A_2^2\right\}\right]/i\nu \end{aligned} \qquad [40]$$

where $\varepsilon\sigma_1 = (\nu^2 - \omega_1^2)$, and $\varepsilon\sigma_2 = (\nu^2 - \omega_2^2)$ are the external mistunings, and $\Pi_i, i = 1 \ldots 12$ are coefficients determined by the system nonlinearities. Note that the terms in the first sets of parentheses in eqns [39] and [40] are identical, and represent the amplitude equations in the absence of any internal or external resonance in the system.

The amplitude equations (eqns [39] and [40]) cover a large class of structural and mechanical systems and are yet to be studied in their greatest generality, even for steady-state constant solutions representing periodic motions of the original oscillators in eqns [37]. Such a study will allow for the classification of response curves for these systems based on the system nonlinearities. In many systems, the nonlinearities arise due to the scalar potential and kinetic energy functions. Then, quite a few of the nonlinear coefficients $\Pi_i, i = 1, 2 \ldots 12$ are interdependent, thus reducing the independent nonlinear coefficients. Forms of the amplitude equations are further simplified when the system possesses certain inherent symmetries. For example, many physical systems are such that their equations of motion (eqn [37]) are invariant to the change of variables: $(x_1, x_2) \rightarrow (-x_1, x_2) \rightarrow (x_1, -x_2)$. This necessarily implies that $\Pi_2 = 0 = \Pi_5$ in eqns [39], and $\Pi_2 = 0 = \Pi_4 = \Pi_6 = \Pi_8 = \Pi_{11} = \Pi_{12}$ in eqns [40]. Physically, these are systems that possess reflection symmetry about two perpendicular axes. Examples include transverse motions of rectangular plates and nonplanar oscillations of beams with rectangular sections. Further restriction of invariance to $(x_1, x_2) \rightarrow (x_2, x_1)$ appears in the study of the response of square plates, beams with square section, orthogonal double pendula, etc. Still further simplifications result when one considers structural systems having cyclic or rotational symmetry, e.g., a stretched string, cylindrical rings and shells, circular plates, and antenna dishes.

As a final illustration of the complex dynamics arising due to the simultaneous presence of external and internal resonances, the frequency–response curves for an orthogonal double pendulum are now described. The double pendulum consists of two pendulums. The upper pendulum is attached to a point of suspension with a pin. The lower pendulum is attached with a pin at the mass point of the upper pendulum. The two pendulums have equal lengths and the particles have equal masses. The two individual pendulums oscillate in orthogonal planes that intersect along the vertical axis. The stable equilibrium position of the system corresponds to the configuration in which the two pendulums hang vertically downward. About this equilibrium position, one mode of vibration corresponds to the upper pendulum oscillating with the bottom pendulum remaining vertical. In the second mode of vibration, the upper pendulum remains stationary (vertical) and the lower pendulum oscillates. These two modes of oscillation have nearly equal natural frequencies. This leads to a one-to-one internal resonance. The excitation is in primary resonance, and is in the form of a horizontal harmonic motion of the point of suspension in the plane containing the upper pendulum. Then, the first mode of vibration is directly excited. The second mode of response is coupled to the first one only through nonlinearities in the model that arise due to geometric as well as inertial interactions.

Figures 15 and **16** show the frequency–response curves for the double pendulum. While **Figure 15** is for zero internal mistuning between the two linear modes of oscillation, **Figure 16** gives results when the upper pendulum has a slightly longer length compared to the lower pendulum. There exist stable as

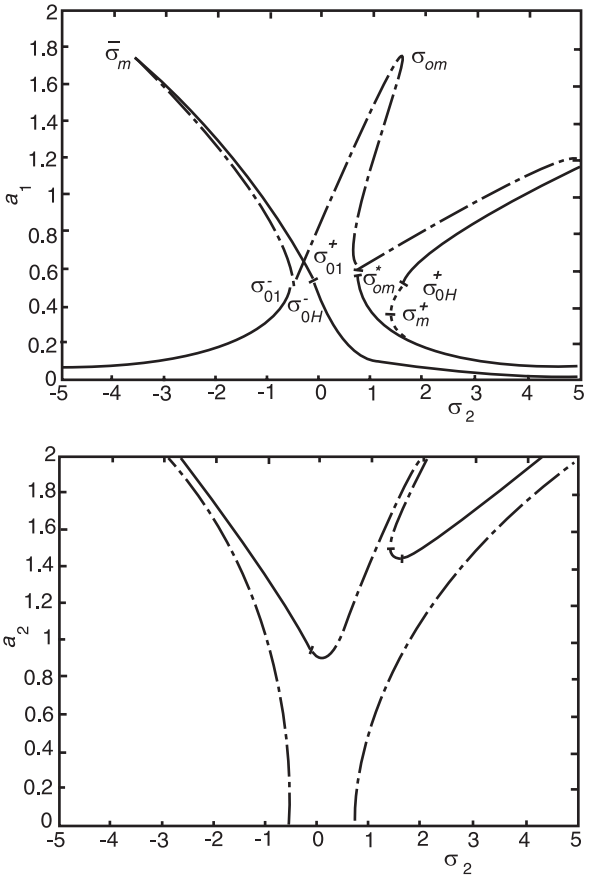


Figure 15 Frequency–response curves for an orthogonal double pendulum in primary resonance, with the two pendulums in one-to-one internal resonance; zero internal mistuning.

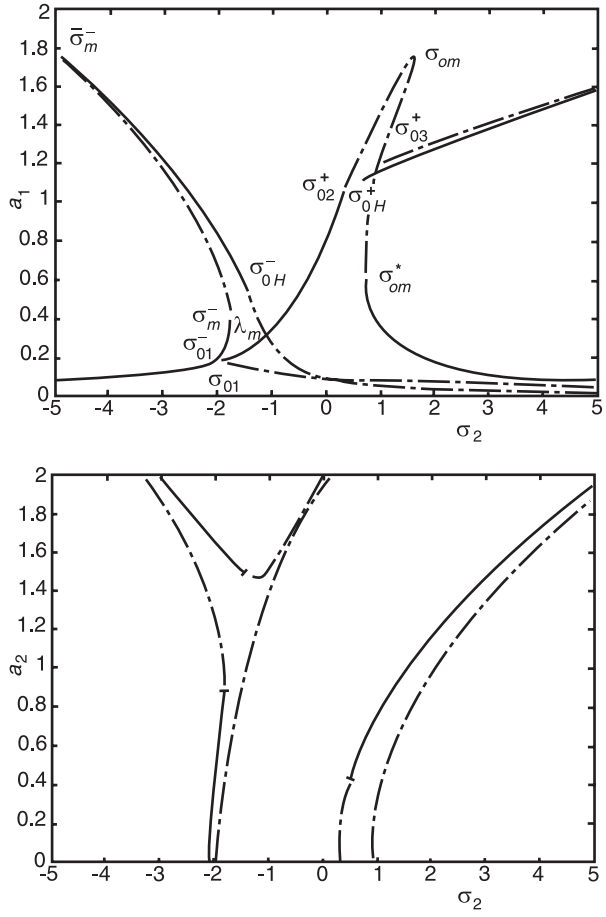


Figure 16 Frequency–response curves for an orthogonal double pendulum in primary resonance, with the two pendulums in one-to-one internal resonance; non-zero internal mistuning.

well as unstable solutions in the single-mode (lower pendulum stationary, $a_2 = 0$) with two turning points σ_{om} and σ_{om}^*. In the zero mistuning case (**Figure 15**), coupled-mode solutions (both penduli oscillating, $a_1 \neq 0, a_2 \neq 0$) arise due to a pitchfork bifurcation at excitation frequencies σ_{01}^- and σ_{01}^+. Both stable and unstable branches are also present in coupled-mode solutions indicating jumps from one branch to other as the frequency is monotonically and slowly varied. Hopf bifurcations to limit cycle oscillations, and possible transitions to chaotic solutions in couple-mode solutions, arise at frequencies σ_{0H}^- and σ_{0H}^+. The introduction of internal mistuning results in even more solution branches and additional bifurcations (**Figure 16**).

This discussion provides a glimpse into the rich variety of dynamical motions exhibited by nonlinear systems under resonant excitations. The last two decades have seen exciting developments whereby one can analytically study the origins of such complex dynamical behavior, and many of these motions have also been experimentally observed in simple structural systems.

See also: **Nonlinear systems analysis**; **Nonlinear systems, overview**; **Parametric excitation**; **Resonance and antiresonance**.

Further Reading

Bogoliubov NN and Mitropolski YA (1961) *Asymptotic Methods in the Theory of Nonlinear Oscillations*. New York: Gordon and Breach.

Cartmell MP (1990) *An Introduction to Linear, Parametric and Nonlinear Vibrations*. London: Chapman and Hall.

Ewan-Iwanowski RM (1976) *Resonance Oscillations in Mechanical Systems*. Amsterdam: Elsevier.

Hagedorn P (1981) *Nonlinear Oscillations*. Oxford: Clarendon Press.

Hale JK (1963) *Oscillations in Nonlinear Systems*. New York: McGraw Hill.

Hayashi C (1964) *Nonlinear Oscillations in Physical Systems*. New York: McGraw-Hill.

Minorsky N (1962) *Nonlinear Oscillations*. Princeton, NJ: Van Nostrand.

Nayfeh AH (1981) *Introduction to Perturbation Techniques*. New York: Wiley Interscience.

Nayfeh AH (2000) *Nonlinear Interactions: Analytical, Computational, and Experimental Methods*. New York: Wiley Interscience.

Nayfeh AH and Balachandran B (1989) Modal interactions in dynamical and structural systems. *Applied Mechanics Reviews* 42(2), part 2: S175–S201.

Nayfeh AH and Mook DT (1979) *Nonlinear Oscillations*. New York: Wiley Interscience.

Schmidt G and Tondl A (1986) *Nonlinear Vibrations*. Cambridge: Cambridge University Press.

Stoker JJ (1950) *Nonlinear Vibrations in Mechanical and Electrical Systems*. New York: Interscience Publishers.

Szemplińska-Stupnicka W (1990) *The Behavior of Nonlinear Vibrating Systems*, volume I: *Fundamental Concepts and Methods: Applications to Single-Degree-of-Freedom Systems*. Dordrecht: Kluwer.

Szemplińska-Stupnicka W (1990) *The Behavior of Nonlinear Vibrating Systems*, volume II: *Advanced Concepts and Applications to Multi-Degree-of-Freedom Systems*. Dordrecht: Kluwer.

Thomsen JJ (1997) *Vibrations and Stability: Order and Chaos*. London: McGraw-Hill.

NONLINEAR SYSTEMS, OVERVIEW

N C Perkins, University of Michigan, Ann Arbor, MI, USA

Copyright © 2001 Academic Press

doi:10.1006/rwvb.2001.0036

Introduction

Nonlinear behavior is pervasive in mechanical systems. In fact, it is fair to state that linear behavior is just an idealization of the many nonlinear phenomena that influence dynamic response. It is equally fair and important to add that assuming linear behavior quite often leads to successful estimates of dynamic response. Moreover, the analytical methods made possible through linearization form the foundation for classical vibration analysis and companion experimental methods as well; refer, for example, to entries under **Modal analysis, experimental**. Thus, the central issue is not whether a phenomenon is nonlinear or not, but rather whether the nonlinearities ultimately influence the response in any significant manner. The objective of this article is to indicate the significant ways that nonlinearities manifest themselves, and then to identify and classify their sources in mechanical systems.

Significant Effects of Nonlinearities

To appreciate immediately the effect of nonlinearities, consider the possible responses that may be exhibited by the single-degree-of-freedom system illustrated in **Figure 1A** to sustained harmonic excitation. In this example, we shall assume that the nonlinearity derives solely from the nonlinear behavior of a spring, as might be realized by either material nonlinearities or geometric nonlinearities, as discussed in the following sections. In particular, the spring-restoring force, $F(x) = k_1 x + k_3 x^3$, is a nonlinear function of the stretch x, and the stiffness of this spring, $k(x) = \mathrm{d}F/\mathrm{d}x = k_1 + 3k_3 x^2$, either monotonically decreases or increases with the stretch, depending on the sign of the ratio k_3/k_1. A spring whose stiffness decreases with stretch is said to exhibit softening behavior, while one whose stiffness increases with stretch is said to exhibit hardening behavior (refer to **Figure 1B** and examples that follow). In either case, the nonlinearity can produce motions that are qualitatively distinct from those of the approximate linear system, that is, the system for which $k_3 = 0$. (This example is classified as a damped, forced Duffing system, as discussed in the article **Analysis of nonlinear systems**.)

This fact is depicted in **Figure 1C** which shows the long-term response (the response after transients have decayed) of the approximate linear system and those possible for the nonlinear system subject to the same harmonic excitation. For the linear system, harmonic input generates a harmonic response with the very same frequency as the input. The amplitude and phase of this harmonic response are controlled by nearness to resonance, that is, how close the excitation frequency Ω is to the natural frequency $\omega_n = \sqrt{k_1/m}$ as discussed in the entry for **Resonance and antiresonance**. By contrast, the response of the nonlinear system can be periodic (harmonic as an example) or aperiodic. Among possible periodic responses are the primary resonant response (a modification of the sole resonant response of the linear system), and secondary resonant responses, including subharmonic and superharmonic resonant responses, as described in article **Resonance and antiresonance** The secondary resonant responses include response frequencies that are related to the excitation frequency by $(p/q)\Omega$, where p and q are positive integers. Among possible aperiodic responses are quasiperiodic responses (motions with periodically modulated amplitude and/or phase) and chaotic responses, as described in the article **Chaos**. In addition, multiple responses of the nonlinear system may coexist; that is, multiple solutions exist (in general) to the governing equation of motion. By contrast, solution uniqueness is guaranteed for the approximate linear system. Thus, even the prototypical single-degree-of-freedom nonlinear system illustrated here may exhibit significantly different responses than its linear counterpart. These differences become even greater with the inclusion of additional degrees-of-freedom; for example, witness the role of internal resonances as described in article **Resonance and antiresonance**. For more detailed discussions of nonlinear vibrations, see Further Reading.

With this as background, let's now proceed to classify the major types of nonlinearities and their sources in mechanical systems.

Sources of Nonlinearities

Nonlinearities arise from virtually all forces that govern the motion of mechanical systems. They may

manifest themselves in the forces contributing to system stiffness, damping, and inertia. To appreciate the many ways in which nonlinearities arise, consider a general continuum illustrated in **Figure 2**.

Let (x_1, x_2, x_3) be the components of a Cartesian triad and (u_1, u_2, u_3) be the associated components of the three-dimensional displacement field of the continuum from some reference configuration. The body occupies the three-dimensional domain D bounded by the surface B. The motion of the body, as described by the displacement components, is determined by the three momentum equations:

$$\tau_{ij,j} + f_i = \rho \ddot{u}_i \quad \text{in } D \qquad [1a]$$

and the boundary conditions:

$$\tau_{ij} n_j = T_i \text{ on } B_1 \qquad [1b]$$

$$u_i = U_i \text{ on } B_2 \qquad [1c]$$

where the index $i = 1, 2, 3$, $(\,)_{,j}$ denotes partial differentiation with respect to the independent spatial variable x_j, $\ddot{u}_i$ denotes total differentiation with respect to time (twice), and summation of repeated

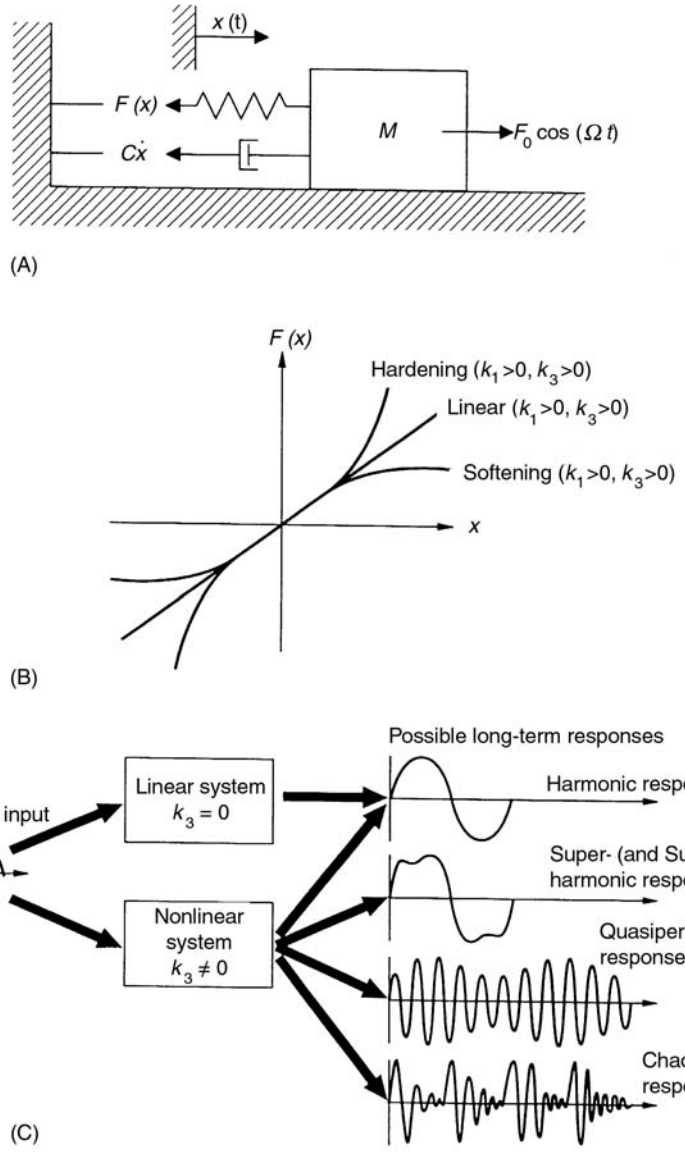


Figure 1 (A) Nonlinear single-degree-of-freedom system subject to harmonic excitation. (B) Nonlinearity derives from nonlinear elastic element that may exhibit hardening or softening behavior. (C) A comparison of possible responses of linear and nonlinear single-degree-of-freedom systems to harmonic excitation.

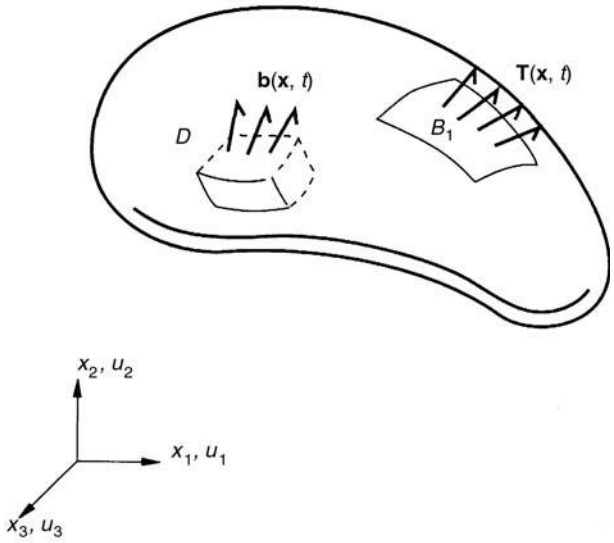


Figure 2 General continuum subject to applied body forces **b** (**x**, *t*) and surface tractions **T** (**x**, *t*).

indices is implied. Here, τ_{ij} is the (Cauchy) stress tensor, f_i are components of applied body forces, ρ is the material density, n_j are components of the unit normal vector (outward) to the boundary B_l on which tractions with components T_i are applied, and U_i denotes prescribed displacements on the remainder of the boundary B_2. This general formulation, which applies to any continuum (e.g., solids and fluids), includes all common structural elements (shells, plates, beams, etc.) as special cases and serves as a means to introduce major classes of nonlinearities.

Consider first nonlinearities introduced through the stress tensor τ_{ij}. These nonlinearities are referred to either as material nonlinearities or as geometric nonlinearities, depending upon how they arise in τ_{ij}. Material nonlinearities arise from nonlinear material laws (constitutive equations) that relate the stress tensor to the strain tensor (or derivatives thereof). By contrast, geometric nonlinearities arise from nonlinear strain–displacement relations. Thus, a linearly elastic material may exhibit nonlinear response when (finite) strain measures are used that capture the effect of geometrically large deformations. Several examples of material and geometric nonlinearities follow below. The body forces (f_i) become a source of nonlinearity whenever they are a nonlinear function of the displacement field (or derivatives thereof). Examples may include magnetic and electrostatic forces and fluid/structure interaction forces (when treated as body forces). The inertia term on the right-hand side of eqn [1a] may also introduce nonlinearities as seen in fluid mechanics (Navier–Stokes equation) where an Eulerian description of fluid motion is employed. Continuing to eqn [1b], note that the tractions T_i applied on the traction boundary may also be nonlinearly related to the displacement field (and derivatives thereof), with common examples being fluid/structure interaction forces (when treated as surface tractions), surface friction, and impact. The displacement boundary eqn [1c] may also introduce nonlinearities as, for instance, in the case of clearance problems where traction boundary conditions are suddenly replaced by displacement boundary conditions. Finally, the domain D may depend on the displacement field and thereby capture the nonlinearities that arise, for example, in fluid/structure interaction problems with free surfaces or some contact problems with deformable bodies.

Classes of Nonlinearities

Many classifications of nonlinearities are possible, with one being based upon how they enter the equations of motion, as described above. An alternative classification may be based on the mathematical forms these nonlinearities take, including analytic forms (e.g., most geometric and material nonlinearities) versus nonanalytic (nondifferentiable) forms (e.g., dry friction and impact nonlinearities). Within this article, we will describe nonlinearities associated with four major sources for mechanical systems including: (1) geometrically large motion, (2) nonlinear material behavior, (3) fluid/structure interaction, and (4) friction and impact. Each of the four major categories of nonlinearities is reviewed below.

Geometrically Large Motion

Geometrically large motions may introduce nonlinearities through inertia, damping, and stiffness terms. For the general continuum described above, geometric nonlinearities enter through the nonlinear strain–displacement relations associated with finite strain measures. For instance, consider the prototypical example of a flexible beam undergoing deformation in the plane, as depicted in **Figure 3**. Let x_1 denote the independent spatial variable along the undeformed neutral axis of the beam and let u_1 and u_2 denote the longitudinal and transverse components of the displacement field of the neutral axis. Using Kirchhoff assumptions for beam deformation, the strain of a beam element becomes:

$$\varepsilon(x_1, x_2, t) = \varepsilon_0(x_1, t) - x_2\kappa(x_1, t) \qquad [2a]$$

where:

$$\varepsilon_0(x, t) = u_{1,1} + \frac{1}{2}\left(u_{1,1}^2 + u_{2,1}^2\right) \qquad [2b]$$

represents the strain of the neutral axis and $-x_2\kappa(x_1, t)$ represents the additional strain at the level x_2 from the neutral axis due to the curvature

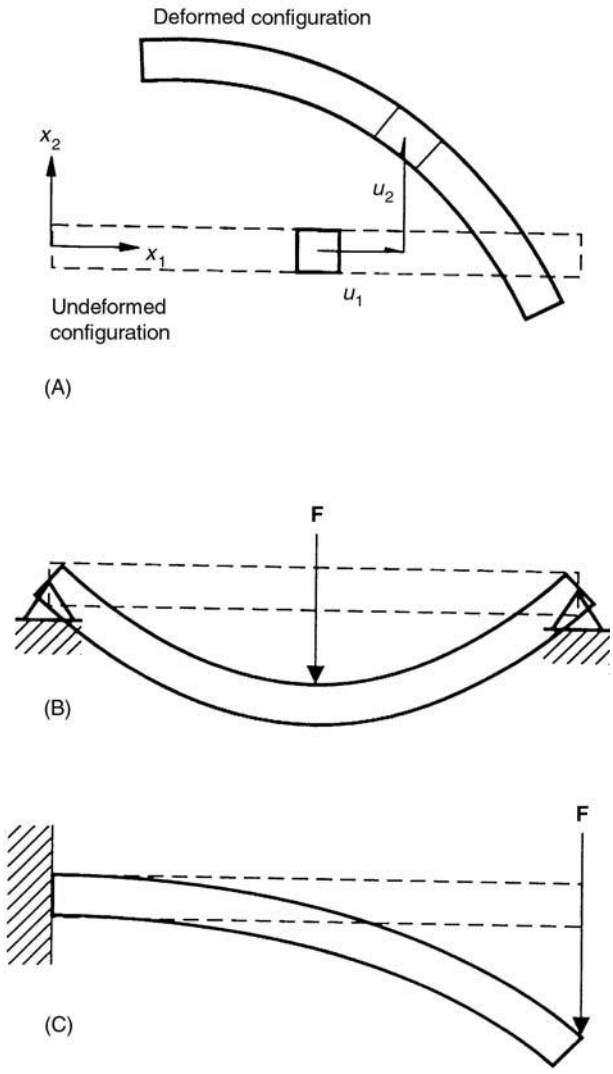


Figure 3 (A) Geometrically large planar motion of a beam as measured by the displacements $u_1(x_1, t)$ and $u_2(x_1, t)$ of the neutral axis. (B) Simply supported beam for which the dominant nonlinearity derives from the stretching of the neutral axis. (C) Cantilevered beam for which the dominant nonlinearity derives from large rotations of the beam cross-sections.

$\kappa(x_1, t)$ of the neutral axis. The curvature of the neutral axis is given by:

$$\kappa(x_1, t) = \frac{u_{2,11}}{\left(1 + u_{2,1}^2\right)^{3/2}} \qquad [2c]$$

Inspection of the strain–displacement relation, eqn [2a] with eqn [2b] and eqn [2c], reveals two sources of geometric nonlinearity for the beam. The first of these is the nonlinear strain–displacement relationship [2b] that describes the stretching of the beam neutral axis, and the second is the nonlinear curvature–displacement relationship [2c] describing large rotation of the beam cross-section. Either or both of these nonlinear mechanisms may arise in a particular application. For instance, in the case of the simply supported beam shown in **Figure 3B**, the neutral axis must stretch as the beam deflects and the dominant nonlinear mechanism in this case is associated with neutral axis stretching (eqn [2b]). By contrast, large rotation (eqn [2c]) represents the dominant nonlinear mechanism for the cantilevered beam of **Figure 3C**. Here, the beam centerline may not stretch appreciably, but the cross-sections may rotate through moderate to large angles. This effect is captured in the classical problem of the elastica; see Further Reading.

The discussion above for beams forms a special case of the general topic of the theory of rods (see Further Reading). Qualitatively similar geometrical nonlinearities arise in other structural elements, including cables, membranes, plates, and shells. For instance, von Ka'rma'n plate theory captures the nonlinearities produced by the stretching of the neutral plane of the plate in analogy to the effect modeled for the beam by eqn [2b] above. It should also be noted that the geometric nonlinearities of structural elements can exhibit hardening or softening effects or both. Consider for instance the geometric nonlinearities produced by the stretching of the centerline of a sagged flexible cable, as shown in **Figure 4A**. Note that the strain of the centerline will initially decrease (i.e., tension will decrease) if a load **F** is directed along the normal (i.e., towards the center of curvature). Thus the cable can exhibit softening behavior. By contrast, hardening behavior is immediately observed if the direction of the load is reversed (applied away from the center of curvature). Thus, the overall force–deflection behavior of the cable is asymmetric (describable by both even and odd functions of deflection), as illustrated in **Figure 4B**. This structural asymmetry is generic to all structural elements that are precurved (e.g., arches and shells).

Nonlinear Material Behavior

As discussed above, material nonlinearities may arise in eqn [1a] and eqn [1b] through the nonlinear dependence of the stress on the strain (and/or strain rate) measure. Common examples of materials that obey nonlinear material (constitutive) laws include ductile metals that yield, elastomeric materials (e.g., most rubbers), viscoleastic materials (e.g., rubbery compounds and polymers), biomaterials (membranes, skin, collagen fibers, muscle tissue), and various 'new' materials, including rheological fluids, shape memory alloys, etc. For the purpose of this overview, we shall consider two broad classes of

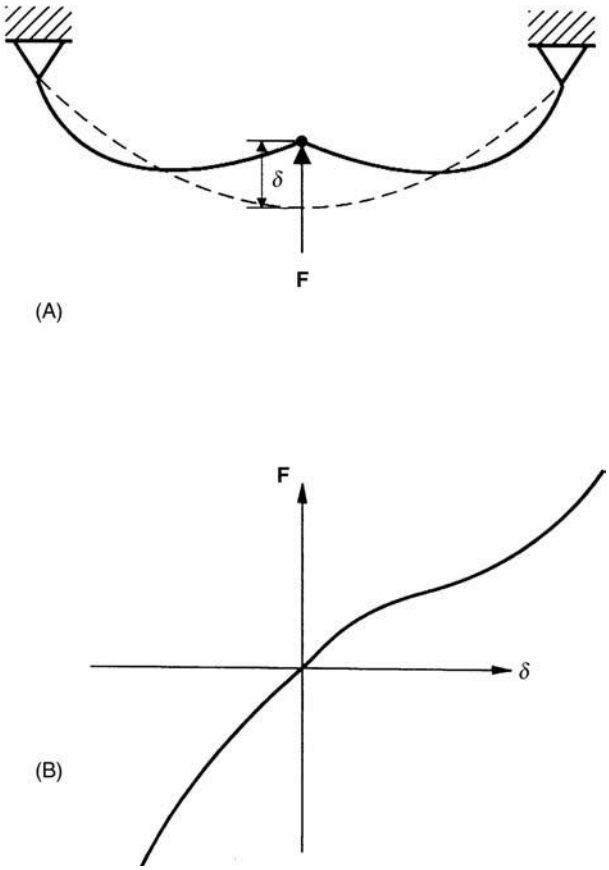


Figure 4 (A) Sagged cable subject to a central load. (B) Asymmetric force–deflection curve.

nonlinear material behavior by distinguishing materials that are dissipative from those that are not.

The nondissipative materials are nonlinearly elastic and may exhibit hardening characteristics, softening characteristics or a combination of both. As a simple example, consider the scalar constitutive law:

$$\tau = f(\varepsilon) \qquad [3a]$$

which might be expanded in a Taylor series in the strain measure ε (about a stress-free state):

$$\tau = f'(0)\varepsilon + \frac{1}{2}f''(0)\varepsilon^2 + \frac{1}{6}f'''(0)\varepsilon^3 + \cdots \qquad [3b]$$

in which $(\,)'$ denotes differentiation with respect to ε. In the expansion (eqn [3b]), the quantity $f'(0) = E$ would be identified as Young's modulus. Many nonlinearly elastic materials are 'symmetric' in their material response in that the stress changes sign when the strain changes sign (but remains the same magnitude). For these materials, eqn [3a] and eqn [3b] are odd functions of the strain (hence the coefficient $f''(0)$ would vanish in eqn [3b]). The constitutive law (eqn [3a]) or (eqn [3b]) for a typical elastomeric material might appear as shown in **Figure 5A** and exhibit an initial softening behavior for small to moderate strains followed by hardening behavior for larger strains.

Nonlinear material laws for dissipative materials include those materials exhibiting viscoelastic effects (dissipation produced by strain–rate dependency) as well as plastic effects (dissipation produced by material hysteresis). For instance, a general (scalar) model for a nonlinear viscoelastic material could be written:

$$\tau(\varepsilon, \dot{\varepsilon}) = f(\varepsilon, \dot{\varepsilon})\varepsilon + g(\varepsilon, \dot{\varepsilon})\dot{\varepsilon} \qquad [4]$$

in which the 'elastic' contribution f and the 'visco' contribution g could depend explicitly on the strain, strain rate, or both. Alternative (integral) material laws for viscoelastic materials have also been proposed that capture material memory effects. Materials exhibiting elastic–plastic behavior develop dissipation through the hysteresis loop associated

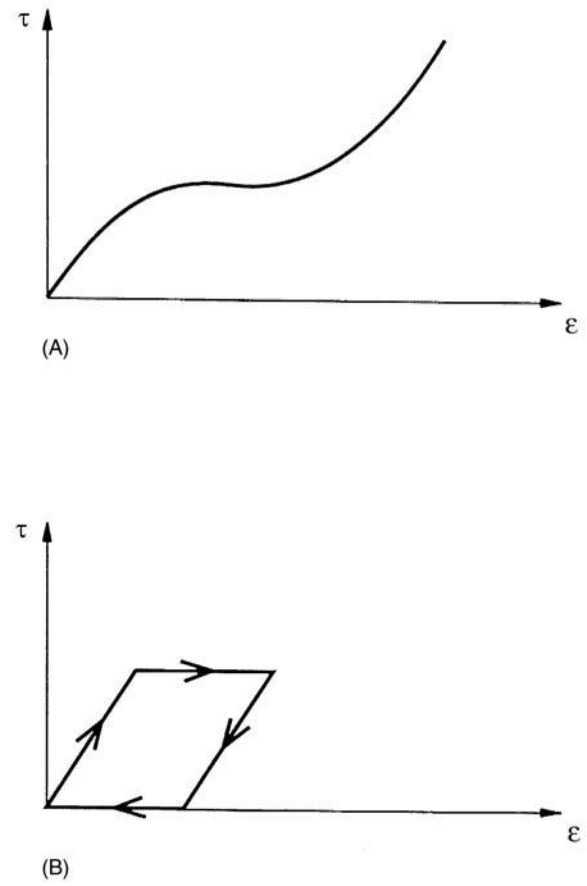


Figure 5 (A) Nonlinear stress–strain relationship for an elastomeric material, (B) nonlinear stress–strain relationship for an ideal elastic–plastic material.

with cyclical loading and unloading. For instance, consider the material law for an ideal elastic/plastic solid, as depicted in **Figure 5B**. Starting from the undeformed state, the material exhibits linearly elastic behavior up to the yield point, beyond which it exhibits ideal plastic behavior. Upon unloading, the behavior is first elastic then plastic, leading to the illustrated hysteresis loop.

Fluid/Structure Interaction

Fluids surrounding a structure exert pressure (modeled either as body forces or tractions, following the discussion above) that ultimately influence the inertia and/or damping of the structure. A survey of this topic can be found under the entry **Fluid/structure interaction**. Here, we shall focus on two common types of fluid/structure interactions that are governed by nonlinearities (recognizing that other nonlinear interactions also exist). The first example will focus on the Morison relation that accounts for the added mass and nonlinear drag imparted to a structure in a surrounding fluid (e.g., water). The second example will focus on a nonlinear wake oscillator model proposed to describe the phenomenon of vortex-induced vibrations of structures.

Consider first a body moving with some speed $\dot{x}$ in an otherwise quiescent fluid. The surrounding fluid provides both a source of added mass to the body as well as drag. These features are captured in the classical Morison relation (scalar form):

$$F_{\mathrm{f}} = C_{\mathrm{a}}\rho_{\mathrm{f}}V\ddot{x} + \frac{1}{2}C_{\mathrm{d}}\rho_{\mathrm{f}}A|\dot{x}|\dot{x} \qquad [5]$$

in which the force due to the fluid F_{f} captures the effects of added fluid mass (first term) and fluid drag (second term). Here, ρ_{f} is the fluid density, V is the volume of the body, A is the projected area of the body in the plane orthogonal to the relative motion, C_{a} is the added mass coefficient, and C_{d} is the drag coefficient. These coefficients are often determined by experiments. In employing eqn [5], it is tacitly assumed that the Reynolds number is high enough such that the drag force is proportional to the square of the relative velocity. For low Reynolds numbers in the Stokes flow regime, the drag is adequately represented as being proportional to the relative speed, rendering the drag force linear. See Further Reading for further information on this model.

The drag force modeled by the Morison relation above is strictly dissipative. However, under certain flow conditions, a slender bluff body can actually extract energy from the flow and achieve sustained vibrations. The mechanisms responsible for this behavior trace to the fluid vortices shed from the surface of the bluff body and the resulting motion is often referred to as vortex-induced vibration. Consider, for instance, the vortex-induced vibrations of the subsurface instrumentation array depicted in **Figure 6**.

While no one model for vortex-induced vibration is used exclusively, a class of nonlinear models described as wake oscillator models has received considerable attention. These phenomenological models introduce a single oscillator equation to describe the fluctuating lift forces (lift coefficient) caused by vortex shedding and invariably include several empirical coefficients that must be fit to experimental data to produce estimates of vortex-induced vibration. The wake oscillator is then coupled to a model of the structure (typically, a single-degree-of-freedom model) in forming the two equations of coupled fluid/structure interaction. For instance, let $x(t)$ denote the modal coordinate for a vibration mode of a slender structure having natural frequency ω_{n} and damping ratio ζ. Let q denote the excitation to this mode produced by vortices shed with Strouhal frequency ω_{s} (a frequency that depends on the flow velocity, the diameter of the structure, and the Strouhal number). A typical model proposed for the coupling of the vibration response $x(t)$ and the fluid lift coefficient $q(t)$ is:

$$\ddot{x} + 2\zeta\omega_{\mathrm{n}}\dot{x} + \omega_{\mathrm{n}}^2 x = \mu\omega_{\mathrm{s}}^2 q \qquad [6a]$$

$$\ddot{q} - \omega_{\mathrm{s}}G\left(C_{\mathrm{Lo}}^2 - 4q^2\right)\dot{q} + \omega_{\mathrm{s}}^2 q = \omega_{\mathrm{s}}F\dot{x} \qquad [6b]$$

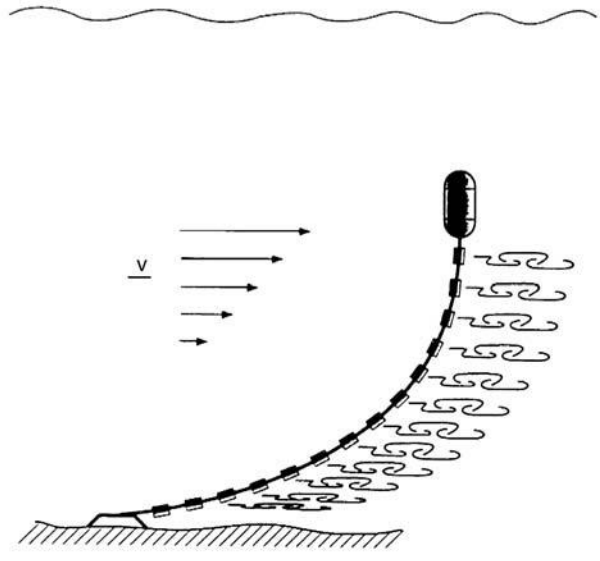


Figure 6 Fluid vortices shed may resonantly drive sustained structural vibrations as, for example, in this subsurface instrumentation array.

in which μ is a mass ratio parameter and G, C_{Lo}^2, and F are three empirically determined coefficients. While the 'structure equation' (eqn [6a]) is assumed linear, the 'fluid equation' (eqn [6b]) is of the form of a van der Pol equation with both the sign and magnitude of the damping determined by the magnitude of q. Inspection of eqn [6b] reveals that the damping is negative (energy increases) when q is small and becomes positive (energy decreases) when q is large. Thus, there is an intermediate value of q that leads to a self-sustained oscillation (a limit cycle) that drives a sustained vortex-induced vibration, as measured by x. This self-sustained vibration is governing by the coupling of eqns [6a] and [6b] and the strength of this coupling is determined by the resonance condition $\omega_{\mathrm{s}} \approx \omega_{\mathrm{n}}$. Further information on vortex-induced vibrations can be found in Further Reading.

Friction and Impact

Most of the nonlinear models discussed above are analytic (differentiable) and thus are amenable for analysis using asymptotic methods, as described in the articles **Nonlinear systems analysis** and **Perturbation techniques for nonlinear systems** under the entry Nonlinear Vibrations. Exceptions to this are the ideal elastic–plastic material law (see above) and the nonlinear drag model (see above) that are described by nonsmooth functions. The same is true of commonly used nonlinear models for friction and impact, as will be discussed here. In addition, the nonlinearities associated with friction and impact have little to do with large-amplitude motion as they are frequently exercised even for the relatively small-scale motions of mechanical assemblies. Friction and impact are also the underlying causes of squeak-and-rattle problems that remain a concern in many applications.

The study of friction has a long history, with contributions from prominent scientists including Coulomb, who proposed the classical laws for dry friction still commonly used in models of mechanical systems; refer to articles **Frictional damping** and **Friction-induced vibrations**. As an example, consider the Coulomb friction law illustrated in **Figure 7** that describes the friction force developed between two surfaces as a function of the relative (sliding) velocity. For vanishing sliding velocity, the friction force that develops is that required to maintain equilibrium and is limited by a maximum value as determined by a coefficient of static friction μ_s. Upon sliding, the friction force has a constant magnitude, as determined by a coefficient of dynamic friction μ_d. While this description is attractive because it is simple, it brings with it difficulties in analysis. This friction model renders the acceleration discontinuous in time as the friction force is a discontinuous function of the sliding velocity. Numerical and analytical methods frequently have difficulties in resolving this discontinuity.

An important nonlinear effect produced by dry friction is friction-induced vibration; refer to **Friction-induced vibrations**. These vibrations are often small-amplitude, high-frequency oscillations that produce audible tones. Friction-induced vibrations have been observed in many systems, with classic examples being the sustained vibration of the violin string due to friction from the bow and the sustained tone produced by circulating a wet finger around the perimeter of a wine glass. Other examples include the squeal of disk brakes, the screeching of railway wheels guided by rails, and the squeak of a wiper blade on a drying windshield.

Most assemblies containing moving mechanical parts have unavoidable clearances and/or backlash. Like the ideal model for friction above, ideal models representing systems with clearances and backlash are nonsmooth and may also involve impacts. Examples of mechanical systems modeled in this manner include mating gears, seating valves, seating chains, and impacting heat exchanger tubes, print hammers, pile-drivers, impulsive drills, jack-hammers, and the like.

For instance, consider a classical model for backlash represented by the system of **Figure 8A**. Here, a body (e.g., a particle) is free to move within a 'dead zone' of length d prior to contacting elastic stops. The motion of the body could be induced in many ways, one of which is through prescribing the base motion $y(t)$, as in **Figure 8A**. The simplest force/displacement model for this process would appear as a piecewise

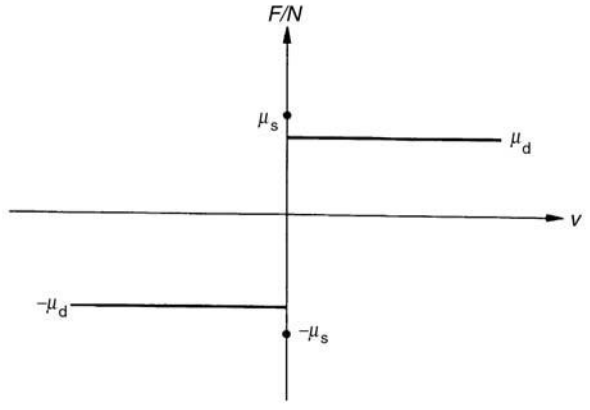


Figure 7 Classical Coulomb friction law. F and N are friction and normal forces acting between two surfaces, with v being the relative (sliding) velocity.

linear model, as illustrated in **Figure 8B**. Piecewise nonlinearities represent an important class of non-smooth nonlinearities and are frequently used as approximations for systems with clearances and backlash. A variation on this theme is an impact oscillator which can be obtained from the above example as the limiting case of infinite (contact) stop stiffness, as depicted in **Figure 8C**. The resulting motion-limiting rigid stops now form sites where impacts occur as the body rattles about in between. The simplest model for this process would be to represent the contact forces as impulses that produce discontinuities in the particle's velocity. These discontinuous changes in velocity might be modeled by introducing a coefficient of restitution for the impact process. Further discussion and examples of the nonlinearities generated by impact and clearances can be found in Further Reading.

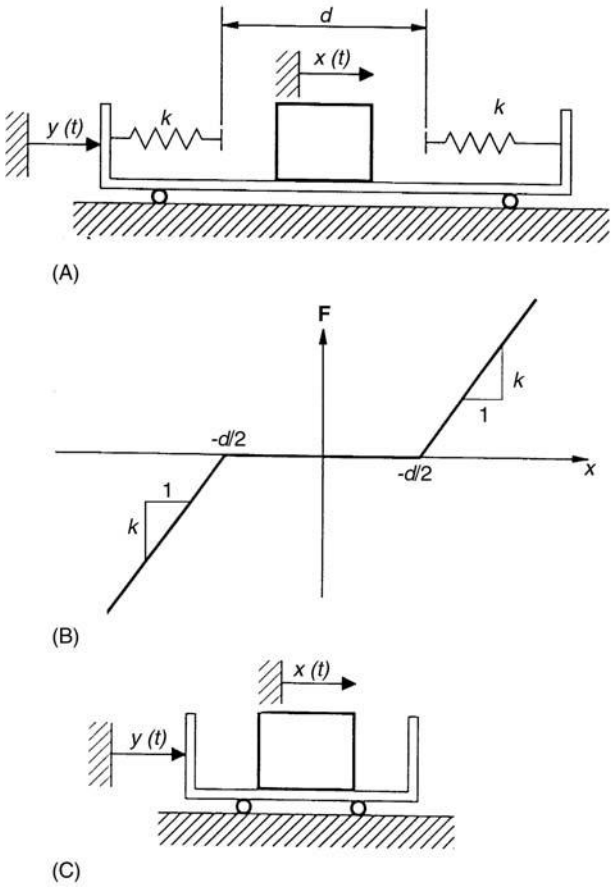


Figure 8 (A) Simple model for backlash; (B) piecewise linear model for backlash (clearance); (C) limiting case of impact oscillator.

Nomenclature

A	area
B	boundary
C_a	added mass coefficient
C_d	drag coefficient
D	three–dimensional domain
E	Young's modulus
p,q	positive integers
V	volume
ε	strain measure
μ	mass ratio parameter
ρ	density
τ_{ij}	stress tensor
Ω	excitation frequency

See also: **Chaos**; **Fluid/structure interaction**; **Friction damping**; **Friction induced vibrations**; **Modal analysis, experimental**, Basic principles; **Modal analysis, experimental**, Applications; **Modal analysis, experimental**, Construction of models from tests; **Modal analysis, experimental**, Measurement techniques; **Modal analysis, experimental**, Parameter extraction methods; **Nonlinear systems analysis**; **Nonlinear system identification**; **Nonlinear system resonance phenomena**; **Nonlinear normal modes**; **Parallel processing**; **Perturbation techniques for nonlinear systems**; **Resonance and antiresonance**; **Testing, nonlinear systems**.

Further Reading

Blevins RD (1977) *Flow-induced Vibrations*. New York: Van Nostrand Reinhold.

Clauss G, Lehmann E and Ostergaard C (1992) *Offshore Structures*, vol. 1. London: Springer-Verlag.

Dym C (1974) *Stability Theory and its Applications to Structural Mechanics*. Leyden: Noordhoff.

Feeny B, Guran A, Hinrichs N and Popp K (1998) A historical review on dry friction and stick-slip phenomena. *ASME Applied Mechanics Reviews* 51:321–341.

Hagedorn P (1988) *Non-linear Oscillations*, 2nd edn. New York: Oxford University Press.

Love AEH (1944) *A Treatise on the Mathematical Theory of Elasticity*, 4th edn. New York: Dover.

Moon FC (1992) *Chaotic and Fractal Dynamics*. New York: Wiley-Interscience.

Nayfeh AH and Mook DT (1979) *Nonlinear Oscillations*. New York: Wiley-Interscience.

Pfeiffer F and Glocker C (1996) *Multibody Dynamics with Unilateral Contacts*. New York: Wiley.

Stokker JJ (1950) *Nonlinear Vibrations in Mechanical and Electrical Systems*. New York: Wiley-Interscience.

Timoshenko SP and Geer JM (1961) *Theory of Elastic Stability*. New York: McGraw-Hill.

Wiggins S (1990) *Introduction to Applied Nonlinear Dynamics and Chaos*. New York: Springer-Verlag.

NONLINEAR SYSTEMS ANALYSIS

A Bajaj, Purdue University, West Lafayette, IN, USA

Copyright © 2001 Academic Press

doi:10.1006/rwvb.2001.0037

Nonlinear models arise for most real systems and their presence in one form or another is generally the rule. The source of nonlinearity in structural and mechanical systems may be geometric, inertial, or material in nature. In mechanical systems interacting with surroundings, forces can arise due to the interacting media (dry friction, fluid–structure interactions, impacts) or fields (magneto-elastic, acousto-elastic). The resulting nonlinear models exhibit a rich variety of phenomena of interest to scientists and engineers. Some of the well-known phenomena are: static and dynamic instabilities and buckling in structures; jump phenomenon, and sub- and super-harmonic resonances in plates and shells; flutter in wind-loaded buildings and structures; parametric instabilities in systems with pulsating loads; rattle and squeak in automotive systems; and ship capsize under wave excitation.

The equations governing the nonlinear response are usually ordinary or partial differential equations that depend on external excitations and/or parameters. Their solution can be sought with different viewpoints guided by the applications in mind. As an example, one may be interested in knowing if the system has only one equilibrium point and that it is globally stable, that is, regardless of the size of a disturbance the system returns to the equilibrium position. On the other hand, one may seek to know whether a system has some periodic solution, and if yes, how many of them exist. Thus, there arise questions of existence, uniqueness, and stability of different type of solutions a system may possess. Seeking solutions to these questions brings into play many different branches of mathematical and numerical analysis. The scope of this article is limited to the most commonly used techniques in the analysis of nonlinear vibratory systems.

Few solutions to dynamical systems, other than equilibrium points, can be obtained analytically in closed form. Thus, the investigator has to resort to analytical approximation methods or to numerical computations and simulations. In the 19th and the early part of the 20th century, the emphasis was on analytic solutions of specific nonlinear differential equations. Both convergent and asymptotic expansion techniques were developed that relied on the existence of a (small) parameter or parameters in the equations of motion. Knowing the solutions at one parameter value, techniques were developed that allowed for the prediction of behavior at neighboring parameter values. The class of solutions studied was limited to periodic solutions in periodically excited systems, and limit cycles in self-excited or autonomous systems. These techniques, where possible, were also extended to almost periodic solutions.

In recent years, motivated by the exciting developments in geometric theory of dynamical systems, the emphasis in applied dynamical systems literature has shifted to the more geometric approaches to study of solutions. These provide a global understanding of the behavior of the system in the parameter as well as phase space. The basic point of this qualitative approach is that low-order dynamical models can provide paradigms of global behavior, and these low-order models reside at the core of larger dimensional systems. There exist analytical techniques that allow for a systematic reduction of the system dimension to the bare minimum. When not possible analytically, the response of low-order models can be studied numerically. This approach has resulted in uncovering and understanding of various types of bifurcations, qualitative changes in system response as a system parameter is varied, as well as complex dynamical behaviors, including temporal and spatial chaos.

The advent of analog computers in the middle of the 20th century was critical to the early studies in complex dynamical behavior. It allowed for the exploration of responses that could not be investigated analytically. The digital computer accelerated this process of exploration and is now playing an integral part in the development of techniques for system analysis, specially for systems that are high dimensional, and those exhibiting complex behavior.

This article is focused on techniques commonly used in the analysis of various nonlinear vibratory systems. The starting point is the study of equilibria and their stability. Most of the analytical techniques for the study of resonance phenomena are based on constructing asymptotic or perturbation expansions for periodic and almost periodic solutions. The essence of these perturbation and asymptotic methods is described next. This is followed by a discussion of the techniques used in the geometric approach of applied dynamical systems theory, and some

of the essential results useful in the study of local bifurcations.

Equilibria and Stability

The simplest continuous-time, autonomous dynamical models of vibratory systems are of the form:

$$\dot{x} = f(x, p) \qquad [1]$$

where $x \in \Re^n$ is an n-dimensional real vector and $p \in \Re^m$ is an m-dimensional vector of control parameters. An equilibrium point, critical point, or singular point is defined to be a point (x_e, p_0) at which the vector field vanishes, that is, $f(x_e, p_0) = 0$. The origin of eqn [1] can be translated to the equilibrium point (x_e, p_0) to give the new system:

$$\dot{y} = \mathbf{A}y + g(y, \hat{p}) \qquad [2]$$

where $y = x - x_e$, $\hat{p} = p - p_0$, $\mathbf{A} = (\partial f/\partial x)|_{(x_e, p_0)}$, and $g(y, \hat{p}) \equiv f(x_e + y, p_0 + \hat{p}) - \mathbf{A}y$. The linearized approximation to the system (2) is given by:

$$\dot{z} = \mathbf{A}z \qquad [3]$$

Classification of Equilibrium Points

When all the eigenvalues of the constant matrix $\mathbf{A}$ have nonzero real parts, the corresponding equilibrium point (x_e, p_0) is called a hyperbolic equilibrium point. Otherwise, it is called a nonhyperbolic equilibrium point.

There are three types of equilibria: sinks, sources, and saddles. If all the eigenvalues of the matrix $\mathbf{A}$ have negative real parts, the solution $z(t, z_0)$ for any given initial condition z_0 decays to zero exponentially in time. Thus, the equilibrium $z = 0$, called a sink, is asymptotically stable. On the other hand, if all the eigenvalues of the matrix $\mathbf{A}$ have positive real parts, the solution $z(t, z_0)$ for any given initial condition z_0 grows unbounded in time, and the equilibrium $z = 0$ is called a source. A source is an unstable equilibrium. Finally, if some of the eigenvalues have positive real parts, and the rest of the eigenvalues have negative real parts, the equilibrium is unstable and is called a saddle. If all the eigenvalues of the matrix are on the imaginary axis, and at least one pair is pure imaginary and nonzero, the equilibrium is called a center. In physical systems, the equilibria as well as their stability depend on parameters. Thus, as a parameter is varied, an equilibrium may lose its stability as it changes from a sink to a center or just stable, and then to a saddle. This situation is what usually leads to a local bifurcation: creation of additional equilibria, exchange of stability in coexisting equilibria, and creation of limit cycles or periodic solutions.

The connection between the stability of an equilibrium point for the linearized approximation [3] and the nonlinear system [2] is provided by the Hartman–Grobman theorem, which implies that the equilibrium point $y = 0$ for the nonlinear system [2] is asymptotically stable if $\mathrm{Re}(\lambda_i) < 0$ for all eigenvalues of the matrix $\mathbf{A}$. The origin is unstable if $\mathrm{Re}(\lambda_i) > 0$ for one or more of the eigenvalues of $\mathbf{A}$. If some eigenvalues are with $\mathrm{Re}(\lambda_i) = 0$ and the remaining eigenvalues are in the left-half of the complex plane, no conclusion can be drawn based on the linearized system. These are called the critical cases of stability. In these cases, nonlinear terms $g(y, \hat{p})$ are essential for determining the behavior of the system. Phase portraits (a typical set of trajectories) for linearized systems with various types of equilibria in two-dimensional systems are shown in **Figure 1**. A few representative phase portraits for three-dimensional systems are given in **Figure 2**.

Stable, Unstable, and Center Eigenspaces

Suppose that the matrix $\mathbf{A}$ has n_s eigenvalues with negative real parts, n_c eigenvalues with zero real parts, and n_u eigenvalues with positive real parts. Then, as is well known, there exists a change of coordinates that transforms system [3] into:

$$\dot{u}_s = B_s u_s, \quad \dot{u}_c = B_c u_c, \quad \dot{u}_u = B_u u_u \qquad [4]$$

Furthermore, the state space of the system [3] is decomposed into a direct sum of the invariant linear spaces E^S, E^C, and E^U-corresponding to the eigenvalues with negative real parts, zero real parts, and positive real parts, respectively. These are the stable, center, and unstable eigenspaces of the linear system. They are characterized for system [4] by the conditions:

$$\begin{aligned} E^S &= \{(u_s, u_c, u_u) | u_c = 0, u_u = 0\} \\ E^C &= \{(u_s, u_c, u_u) | u_s = 0, u_u = 0\} \\ E^U &= \{(u_s, u_c, u_u) | u_s = 0, u_c = 0\} \end{aligned} \qquad [5]$$

There exists a similar decomposition of the phase space for the nonlinear system [2] in the neighborhood of the equilibrium point $y = 0$.

Local Invariant Manifolds

The stable manifold of an equilibrium point of system [2] (denoted by W^S) is the set of all initial conditions such that any solution initiated at these points asymp-

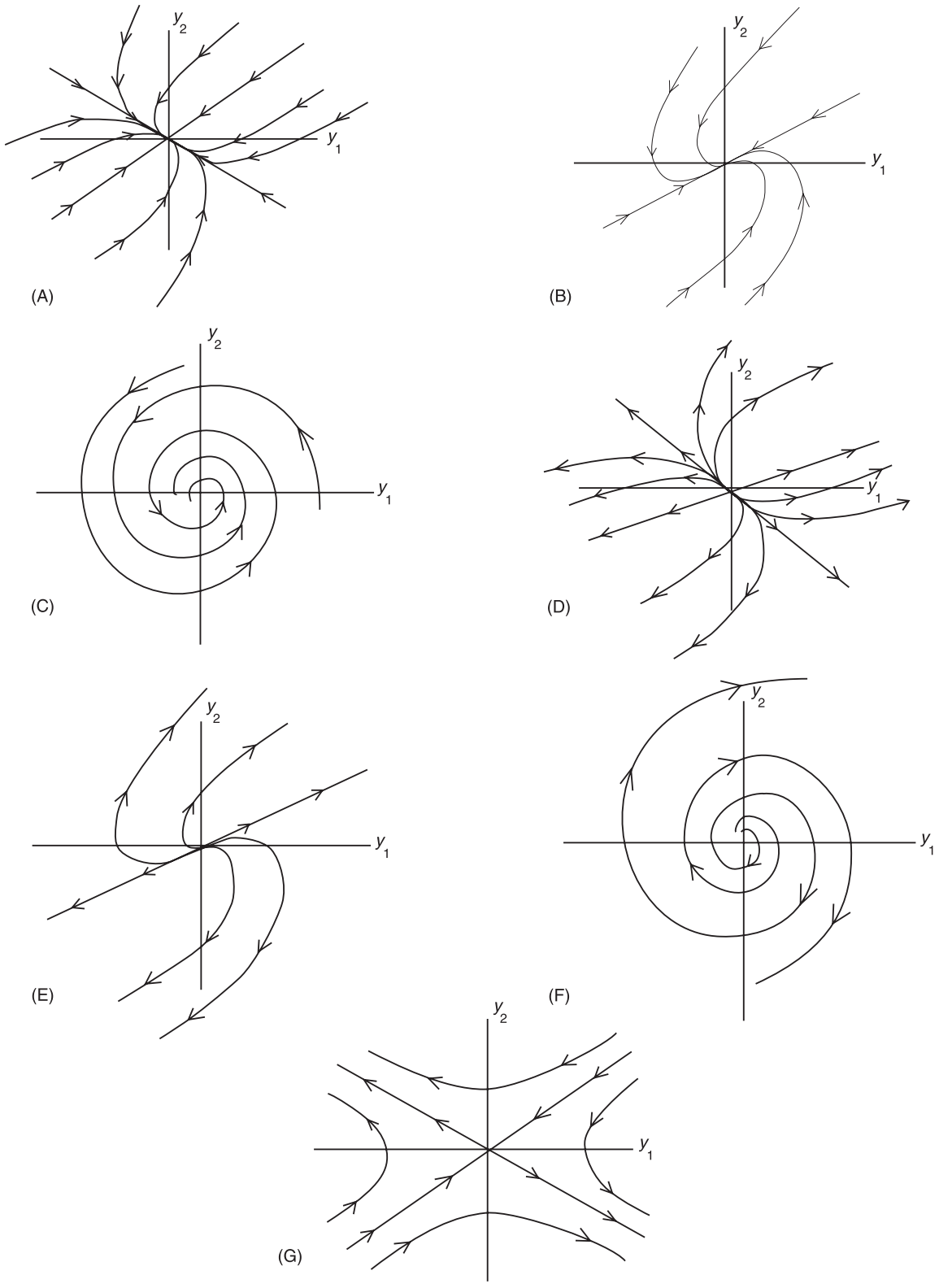


Figure 1 Various types of equilibria in two-dimensional systems: (A) sink or stable node; (B) sink or improper stable node; (C) sink or stable spiral or stable focus; (D) source or an unstable node; (E) source or an unstable improper node; (F) source or an unstable focus; (G) saddle point.

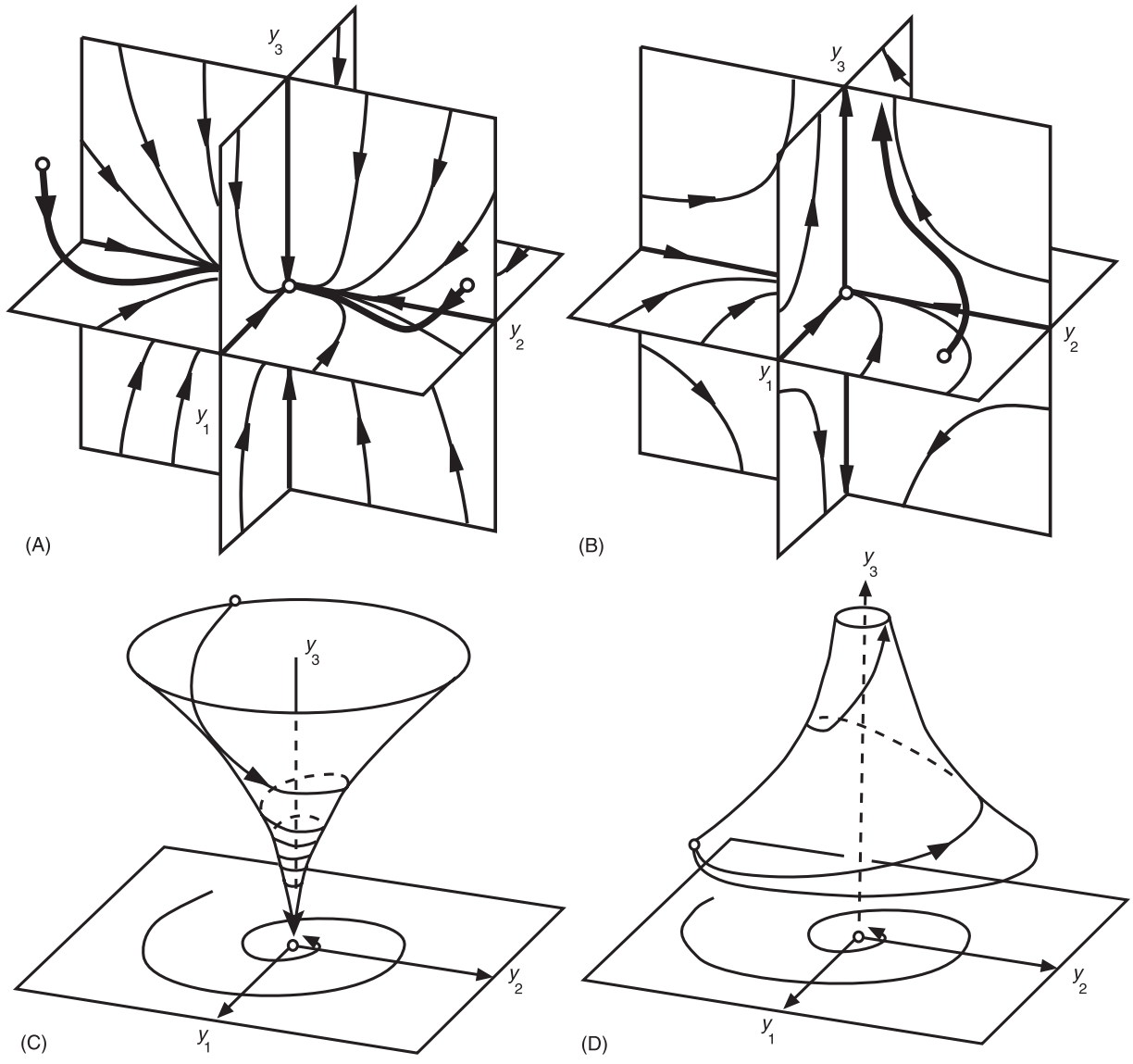


Figure 2 Examples of various types of equilibria in three-dimensional systems: (A) stable node: all eigenvalues are real and negative; (B) unstable saddle node: all eigenvalues are real, one is positive and the other two are negative; (C) stable focus: one eigenvalue is real and the other two are a complex pair, all being with negative real parts; (D) unstable saddle focus: one real positive eigenvalue and a complex pair with negative real parts.

totically approaches the equilibrium point as $t \to \infty$. Similarly, the unstable manifold of an equilibrium (denoted as W^U) is the set of all initial conditions such that solutions initiated at these points asymptotically approach the equilibrium as $t \to -\infty$. Linear eigenspaces are trivial examples of invariant manifolds for the linear system.

With these definitions in place, one can state the important stable manifold theorem: suppose that the equilibrium point $y = 0$ of [2] is a hyperbolic point and E^S and E^U are the stable and unstable manifolds of the linear system [3]. Then, there exist local stable and unstable manifolds $W^S_{\text{loc}}(0)$ and $W^U_{\text{loc}}(0)$ of the same dimension as E^S and E^U respectively (**Figure 3**). These manifolds are (respectively) tangent to E^S and E^U at the origin and are as smooth as the original function $g(y, \hat{p})$. This result provides, in the case of hyperbolic equilibrium points, a close relationship between the phase portraits of the linearized system and the original nonlinear system near the equilibrium point. The difference arises when there are eigenvalues with zero real parts, and the center eigenspace E^C comes into picture. This is treated in the section on geometric theory and bifurcation analysis.

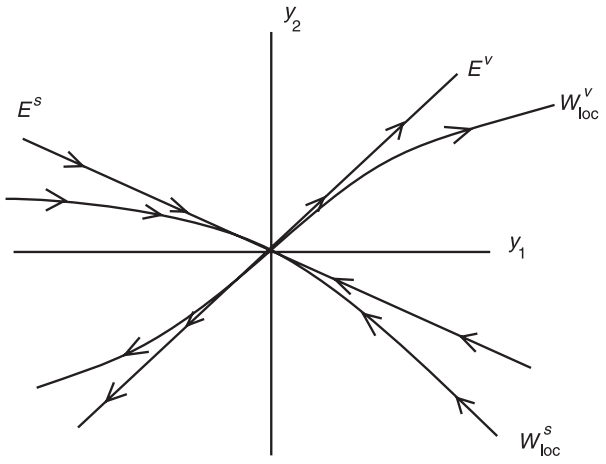


Figure 3 Local stable and unstable manifolds and linear eigenspaces near the origin.

When the eigenbasis for the linear system [3] is used to represent the nonlinear system [2], the nonlinear system takes the form:

$$\begin{aligned} \dot{u}_s &= B_s u_s + h_s(u_s, u_c, u_u) \\ \dot{u}_c &= B_c u_c + h_c(u_s, u_c, u_u) \\ \dot{u}_u &= B_u u_u + h_u(u_s, u_c, u_u) \end{aligned} \qquad [6]$$

Though linearly uncoupled, the coordinates in these equations are coupled in the nonlinear terms. Also, note that $(u_s, u_c, u_u) = (0, 0, 0)$ is an equilibrium solution. Then, the stable manifold theorem guarantees the existence of local stable and unstable invariant manifolds when $n_c = 0$, that is, when there are no center coordinates. If $u_u = H_u(u_s)$ defines the graph of the local stable manifold, it must satisfy $H_u(0) = 0$, $DH_u(0) = 0$, that is, the graph must pass through the equilibrium point and must be tangent to the stable eigenspace E^S. Similarly, if $u_s = H_s(u_u)$ defines the graph of the local unstable manifold, it must satisfy $H_s(0) = 0$, $DH_s(0) = 0$, that is, it also must pass through the equilibrium point and must be tangent to the unstable eigenspace E^U. Using the fact that $u_u = H_u(u_s)$ is an invariant for the solutions of system [6], one can easily show that the function $u_u = H_u(u_s)$ must satisfy the quasilinear partial differential equation:

$$\begin{aligned} &DH_u(u_s)[B_s u_s + h_s(u_s, H_u(u_s))] \\ &= B_u H_u(u_s) + h_u(u_s, H_u(u_s)) \end{aligned} \qquad [7]$$

In addition, the function $u_u = H_u(u_s)$ must satisfy the conditions specified at the origin. This is called the manifold condition. A similar equation must be satisfied by the graph of the unstable manifold $u_s = H_s(u_u)$. These equations can be used to construct approximations to the stable and unstable invariant manifolds.

Remarks

1. The most familiar examples of invariant manifolds are the normal modes of vibration for a linear undamped vibratory system. These characterize the free vibration response and provide a linear decomposition of the configuration space into invariant subspaces. When a system is given initial conditions consistent with a normal mode, the response of the system is a harmonic motion with the corresponding natural frequency characterizing the temporal component of the solution. In a normal mode, all components of the system vibrate in unison with a fixed-amplitude relationship among them.
2. There also exist counterparts to normal modes for nonlinear vibratory systems. The concept of a nonlinear normal mode was initially defined for conservative systems completely characterized by a potential function. Two types of nonlinear normal modes are known to exist. Similar nonlinear normal modes are modes in which the various generalized coordinates of the system vibrate with a fixed (constant) relationship among them. Nonsimilar nonlinear normal modes are the modes in which the various generalized coordinates maintain a fixed relationship on a configuration manifold.
3. Motivated by the geometric viewpoint described above, the concept of a nonlinear normal mode has also been extended to general nonlinear vibratory systems. Furthermore, techniques based on the manifold conditions have been developed to find their approximations.
4. For dynamic systems with periodic excitation, the equations of motions are of the form $\dot{x} = f(x, t, p)$, where f is 2π-periodic in t. Let there exist a 2π-periodic solution $\hat{x}(t, p)$, $\hat{x}(t + 2\pi, p) = \hat{x}(t, p)$. Then, the variational system around this solution can be written as $\dot{y} = \mathbf{A}(t, p)y + g(y, t, p)$, where the matrix $\mathbf{A}(t, p)$ and the function $g(y, t, p)$ are 2π-periodic in t. The origin $y = 0$ is now an equilibrium solution and its stability can be studied by using the nonlinear variational equation, or the linearized system $\dot{z} = \mathbf{A}(t, p)z$. The stability of the linearized system is determined by the characteristic or Floquet multipliers. Then, there is a close parallel between the concepts of stability, eigen-

spaces, and invariant manifolds for the constant coefficient systems and those for the time-periodic systems.

5. The first-order models of the type of eqn [1] arise in many nonlinear structural vibratory systems with finite degrees of freedom. They also arise as reduced-order models, obtained by an assumed-mode or Galerkin projection, for continuous structural systems having infinite-dimensional phase space. Examples include beams and columns with axial as well as thermal loads, arches with transverse loads, axially loaded plate and shell structures, wind and fluid-loaded transmission lines (cables), rotating shafts and disks, and tubes in axial or cross-flow in heat exchangers. The physical parameters of interest then turn out to be the axial and transverse loads or the fluid flow rates. So long as these parameters are constant, the models are autonomous, and one can discuss the stability of equilibrium configurations. When the parameters in the system are such that an equilibrium loses stability, phenomena like buckling and flutter arise, and local bifurcation theory, discussed later, can be used to understand the behavior of the structure close to criticality.

Perturbation and Asymptotic Techniques

There are many perturbation and asymptotic techniques available in the literature, the most prominent of them being the method of Poincaré–Lindstedt, the method of averaging, and the method of multiple time scales. Each of these techniques has associated theoretical underpinnings, and many variants on practical implementation. In this article, only the first two techniques are discussed.

Method of Poincaré

Consider the dynamic system:

$$\dot{x} = f(t, x, \varepsilon) \qquad [8]$$

where f is 2π-periodic in t, ε is a small parameter, $0 \leq \varepsilon \ll 1$, and f is smooth as a function of its arguments. Let $\phi(t,\ \xi\, t_0,\ \varepsilon)$ define a solution of eqn [8] with initial condition ξ, that is $\phi(t_0,\ \xi,\ t_0,\ \varepsilon) = \xi$. Then, a necessary and sufficient condition for $\phi(t,\ \xi,\ t_0,\ \varepsilon)$ to be a 2π-periodic solution is that:

$$\phi(t_0 + 2\pi, \xi, t_0, \varepsilon) = \xi \qquad [9]$$

The method of Poincaré for finding 2π-periodic solutions is centered around the expression [9], and the simplest analytical result can be stated in the following form.

Let $\phi(t, \xi, t_0, \varepsilon)$ with $\phi(t_0, \xi, t_0, \varepsilon) = \xi$ be a solution of eqn [8], and let $\phi(t, \xi_0, t_0, 0)$ be a 2π-periodic solution of the reduced equation $\dot{x} = f(t, x, 0)$. Let the variational equation:

$$\dot{y} = \frac{\partial f}{\partial x}(t, \phi(t, \xi_0, t_0, 0), 0)y \qquad [10]$$

corresponding to the solution $\phi(t, \xi_0, t_0, 0)$ have no characteristic multiplier $+1$. Then, there exist a constant ε^*, a function $\xi = \hat{\xi}(\varepsilon)$ with $0 \leq \varepsilon \leq \varepsilon*$ and $\xi_0 = \hat{\xi}(0)$ such that $\phi(t, \hat{\xi}, t_0, \varepsilon)$ is a 2π-periodic solution for all ε, $0 \leq \varepsilon \leq \varepsilon^*$, and this solution is unique, that is, if $\xi_1 \neq \hat{\xi}(\varepsilon)$, then $\phi(t, \xi_1, t_0, \varepsilon)$ is not a 2π-periodic solution. Furthermore, if the function $f(t, x, \varepsilon)$ is analytic in ε, so is the solution $\phi(t, \hat{\xi}, t_0, \varepsilon)$.

As an illustration, consider the weakly nonlinear oscillator:

$$\ddot{y} + \Omega^2 y = F(t) + \varepsilon f(t, y, \dot{y}, \varepsilon) \qquad [11]$$

where $F(t)$ and $f(t, y, \dot{y}, \varepsilon)$ are 2π-periodic in t and f is analytic in ε. This system in vector form, with $y_1 = y$, $y_2 = \dot{y}$, is:

$$\begin{aligned} \dot{y}_1 &= y_2 \\ \dot{y}_2 &= -\Omega^2 y_1 + F(t) + \varepsilon f(t, y_1, y_2, \varepsilon) \end{aligned} \qquad [12]$$

The associated reduced system, for $\varepsilon = 0$, is:

$$\begin{aligned} \dot{y}_1 &= y_2 \\ \dot{y}_2 &= -\Omega^2 y_1 + F(t) \end{aligned} \qquad [13]$$

Clearly, if $\Omega^2 \neq k^2$, with k an integer, the reduced system has a unique 2π-periodic solution $\psi(t)$. In case the function $F(t)$ is expressed in Fourier series as:

$$F(t) = a_0 + \sum_{n=1}^{\infty} \{a_n \cos nt + b_n \sin nt\} \qquad [14]$$

the solution of the reduced system [13] is:

$$\psi(t) = \begin{Bmatrix} a_0/\Omega^2 \\ 0 \end{Bmatrix} + \sum_{n=1}^{\infty} \frac{1}{(\Omega^2 - n^2)} \times \left[\begin{Bmatrix} a_n \\ nb_n \end{Bmatrix} \cos nt + \begin{Bmatrix} b_n \\ -na_n \end{Bmatrix} \sin nt \right] \quad [15]$$

Now, the variational equation for system [12], with $\varepsilon = 0$, is:

$$\dot{z}_1 = z_2, \quad \dot{z}_2 = -\Omega^2 z_1 \quad [16]$$

The principal matrix solution for system [16] is given by:

$$X(t,0) = \begin{bmatrix} \cos \Omega t & \sin \Omega t/\Omega \\ -\Omega \sin \Omega t & \cos \Omega t \end{bmatrix} \quad [17]$$

The corresponding characteristic multipliers satisfy the characteristic equation $\det(X(2\pi 0) - \lambda I) = 0$, or $\lambda^2 - (2 \cos 2\pi\Omega)\lambda + 1 = 0$. None of the roots of this equation equals $+1$ so long as $2 \cos 2\pi\Omega \neq 2$, or $\Omega \neq k$, where k is an integer. This implies that so long as $\Omega \neq k$, the system (12) has a unique 2π-periodic solution $y = y(t, \varepsilon)$. Furthermore, this solution is analytic in ε. Thus, the solution can be expanded in a convergent power series:

$$y(t,\varepsilon) = \sum_{n=0}^{\infty} \varepsilon^n y_n(t) \quad [18]$$

where each function $y_n(t)$ is 2π-periodic in t. This series converges for each $\varepsilon, 0 \leq \varepsilon \leq \varepsilon^*$, where ε^* is the radius of convergence.

Now, examine the case when the condition $\Omega \neq k$ is violated. Then, consider the system:

$$\ddot{y} + n^2 y = \varepsilon f(t, y, \dot{y}, \varepsilon) \quad [19]$$

where the function f is as defined above. The variational equation:

$$\ddot{z} + n^2 z = 0 \quad [20]$$

has 2π-periodic solutions. This implies that one of the corresponding characteristic multipliers is $+1$ and the condition of the above result is violated. This difficulty can be circumvented by a reformulation of the problem as an integral equation. Let $\phi(t, \xi, \varepsilon)$ be the solution vector for the system expressed in first-order form. Then, using the impulse response function for system [19] with $\varepsilon = 0$, and treating the nonlinearity as a nonhomogeneous term, the solution for the vector form of the system can be written as:

$$\begin{aligned} \phi_1(t,\xi,\varepsilon) &= \xi_1 \cos nt + \xi_2 \sin nt \\ &+ \frac{\varepsilon}{n} \int_0^t f(s, \phi_1(s,\xi,\varepsilon), \phi_2(s,\xi,\varepsilon), \varepsilon) \sin n(t-s) \mathrm{d}s \\ \phi_2(t,\xi,\varepsilon) &= -n\xi_1 \sin nt + n\xi_2 \cos nt \\ &+ \varepsilon \int_0^t f(s, \phi_1(s,\xi,\varepsilon), \phi_2(s,\xi,\varepsilon), \varepsilon) \cos n(t-s) \mathrm{d}s \end{aligned} \quad [21]$$

Now, the periodicity condition for the existence of a 2π-periodic solution requires that:

$$\begin{aligned} F_1(\xi,\varepsilon) &\equiv \phi_1(2\pi,\xi,\varepsilon) - \xi_1 = 0 \\ F_2(\xi,\varepsilon) &\equiv \phi_2(2\pi,\xi,\varepsilon) - \xi_2 = 0 \end{aligned} \quad [22]$$

Using eqn [21], the condition [22] gives:

$$\begin{aligned} F_1(\xi,\varepsilon) &= \xi_1(\cos 2\pi n - 1) + \xi_2 \sin 2\pi n \\ &+ \frac{\varepsilon}{n} \int_0^{2\pi} f(s, \phi_1(s,\xi,\varepsilon), \phi_2(s,\xi,\varepsilon), \varepsilon) \\ &\times \sin n(2\pi - s) \mathrm{d}s = 0 \\ F_2(\xi,\varepsilon) &= -n\xi_1 \sin 2\pi n + n\xi_2(\cos 2\pi n - 1) \\ &+ \varepsilon \int_0^{2\pi} f(s, \phi_1(s,\xi,\varepsilon), \phi_2(s,\xi,\varepsilon), \varepsilon) \\ &\times \cos n(2\pi - s) \mathrm{d}s = 0 \end{aligned} \quad [23]$$

Note that the development so far has not depended on n being an integer. Suppose that n is not an integer. Also, note that $\xi_1 = \xi_2 = 0, \varepsilon = 0$, is a solution of eqn [23], and the Jacobian matrix:

$$\begin{bmatrix} \dfrac{\partial F_1}{\partial \xi_1} & \dfrac{\partial F_1}{\partial \xi_2} \\ \dfrac{\partial F_2}{\partial \xi_1} & \dfrac{\partial F_2}{\partial \xi_2} \end{bmatrix} \quad [24]$$

evaluated at the solution $\xi_1 = \xi_2 = 0$, $\varepsilon = 0$, is nonsingular. Thus, the implicit function theorem implies that there exists an $\varepsilon^*, \varepsilon^* > 0$, and a function $\hat{\xi}(\varepsilon)$, $0 \le \varepsilon \le \varepsilon^*$, with $\hat{\xi}(0) = 0$, such that:

$$\begin{aligned} F_1\left(\hat{\xi}(\varepsilon), \varepsilon\right) &\equiv \phi_1\left(2\pi, \hat{\xi}(\varepsilon), \varepsilon\right) - \hat{\xi}_1(\varepsilon) = 0 \\ F_2\left(\hat{\xi}(\varepsilon), \varepsilon\right) &\equiv \phi_2\left(2\pi, \hat{\xi}(\varepsilon), \varepsilon\right) - \hat{\xi}_2(\varepsilon) = 0 \end{aligned} \quad [25]$$

The corresponding 2π-periodic solution of eqn [19] is given by $\phi(t, \hat{\xi}(\varepsilon), \varepsilon)$ such that $|\phi(t, \hat{\xi}(\varepsilon), \varepsilon)| \to 0$ as $\varepsilon \to 0$. This case is also called the nonresonant case.

The situation with n an integer is called the resonant case. Then, the first two terms on the right-hand side in eqn [23] vanish to give:

$$\begin{aligned} &F_1(\xi, \varepsilon) \\ &= \frac{\varepsilon}{n} \int_0^{2\pi} f(s, \phi_1(s, \xi, \varepsilon), \phi_2(s, \xi, \varepsilon), \varepsilon) \sin ns \, ds = 0 \\ &F_2(\xi, \varepsilon) \\ &= -\varepsilon \int_0^{2\pi} f(s, \phi_1(s, \xi, \varepsilon), \phi_2(s, \xi, \varepsilon), \varepsilon) \cos ns \, ds = 0 \end{aligned} \quad [26]$$

One can show that the implicit function theorem does not apply here and no conclusions can be made regarding the existence of a 2π-periodic solution.

The difficulty encountered can be overcome by defining new functions $G_i(\xi, \varepsilon), \equiv \varepsilon^{-1} F_i(\xi, \varepsilon)$, $i = 1, 2$. Then:

$$\begin{aligned} &G_1(\xi, \varepsilon) \\ &= \frac{1}{n} \int_0^{2\pi} f(s, \phi_1(s, \xi, \varepsilon), \phi_2(s, \xi, \varepsilon), \varepsilon) \sin ns \, ds = 0 \\ &G_2(\xi, \varepsilon) \\ &= -\int_0^{2\pi} f(s, \phi_1(s, \xi, \varepsilon), \phi_2(s, \xi, \varepsilon), \varepsilon) \cos ns \, ds = 0 \end{aligned} \quad [27]$$

and the goal is to find functions $\hat{\xi}_1(\varepsilon)$ and $\hat{\xi}_2(\varepsilon)$ that satisfy eqn [27]. When $\varepsilon = 0$, the solution $\phi(t, \xi\varepsilon)$ is given by:

$$\begin{aligned} &\begin{Bmatrix} \phi_1(t, \xi_0, 0) \\ \phi_2(t, \xi_0, 0) \end{Bmatrix} \\ &= \begin{Bmatrix} \xi_{10} \\ n\xi_{20} \end{Bmatrix} \cos nt + \begin{Bmatrix} \xi_{20} \\ -n\xi_{10} \end{Bmatrix} \sin nt \equiv \begin{Bmatrix} \phi_{10} \\ \phi_{20} \end{Bmatrix} \end{aligned} \quad [28]$$

where ξ_{10}, ξ_{20} are arbitrary. The corresponding eqn [27] reduces, for $\varepsilon = 0$, to:

$$\begin{aligned} G_1(\xi_0, 0) &= \frac{1}{n} \int_0^{2\pi} f(s, \phi_{10}, \phi_{20}, 0) \sin ns \, ds = 0 \\ G_2(\xi_0, 0) &= -\int_0^{2\pi} f(s, \phi_{10}, \phi_{20}, 0) \cos ns \, ds = 0 \end{aligned} \quad [29]$$

Given the form of solutions in [28], eqn [29] reduces to a system of nonlinear equations in the amplitudes ξ_{10} and ξ_{20}. Now, suppose that eqn [29] is satisfied by a vector ξ_0, and the associated Jacobian matrix is nonsingular. Then, from the implicit function theorem, there exists a constant $\varepsilon^* > 0$, and a function $\xi = \hat{\xi}(\varepsilon)$ for $0 \le \varepsilon \le \varepsilon^*$ with $\hat{\xi}(0) = \xi_0$, such that $G_i(\hat{\xi}(\varepsilon), \varepsilon) = \varepsilon^{-1} F_i(\hat{\xi}(\varepsilon), \varepsilon) = 0$, $i = 1, 2$. Thus, in the resonant case, the system (19) has a 2π-periodic solution $\phi(t, \hat{\xi}(\varepsilon), \varepsilon)$. In the limit, as $\varepsilon \to 0$, the 2π-periodic solution is approximated by the solution given in eqn [28].

Remarks

1. In general, the method of Poincaré can be used to prove the existence of $(2\pi m/n)$-periodic solutions to systems with 2π-periodic excitations, thus generating sub-, super-, and ultraharmonic responses. For systems with analytic nonlinearities, the solutions are analytic in the parameter ε. Thus, if one uses the power series expansion in eqn [18] as a representation of the solution, the terms in the solution can be obtained by successively solving an infinite set of linear nonhomogeneous equations. The fact that the series is uniformly convergent implies that, for a given $\varepsilon 0 \le \varepsilon \le \varepsilon^*$, the partial sum of a finite number of terms converges to the true solution as more and more terms are included. Before the advent of symbolic algebra techniques for digital computers, only a small number of terms in the series could be computed and, thus, the question of convergence of the series was not considered in most applications.

2. For a solution to be periodic, each term in the expansion [18] must be periodic. In the resonant case, when one uses the straightforward expansion, secular terms in the form of polynomials in time arise in the solution at each order of approximation. Poincaré–Lindstedt technique is one of the techniques used to remove this nonuniformity in the expansion. Thus, each successive term in the power series is obtained as a periodic function with bounded amplitude.
3. The analysis approach, described above for the nonautonomous case, can also be used to find limit cycle solutions in self-excited systems. In these systems, the period or frequency of oscillation is an additional unknown. The phase of the solution is, however, arbitrary and the process of finding limit cycles is modified by choosing one of the initial conditions to be zero. There also exist methods by which the range of small parameter ε for which the solution is convergent can be increased.
4. It is important to note that if many different periodic solutions are found to coexist for a system, the stability of each of the solutions has to be studied separately. This requires the use of linearized stability analysis using Floquet theory, as already discussed.

Method of Averaging

The method of averaging is concerned with dynamic systems of the form:

$$\dot{y} = \mathbf{A}y + \varepsilon g(y,t) + \varepsilon^2 h(y,t,\varepsilon), \quad y \in \Re^n \qquad [30]$$

where $\mathbf{A}$ is a constant real matrix with pure imaginary eigenvalues, $g(y, t)$ and $h(y, t, \varepsilon)$ are sufficiently smooth in y and 2π-periodic functions of time, and ε is a small parameter. Using the solution $y = e^{\mathbf{A}t}z$ for the system with $\varepsilon = 0$ as a transformation, the system [30] is transformed to:

$$\begin{aligned}\dot{z} &= \varepsilon e^{-\mathbf{A}t} g\left(e^{\mathbf{A}t}z, t\right) + \varepsilon^2 e^{-\mathbf{A}t} h\left(e^{\mathbf{A}t}z, t, \varepsilon\right) \\ &\equiv \varepsilon \hat{g}(z,t) + \varepsilon^2 \hat{h}(z,t,\varepsilon), \quad z \in \Re^n\end{aligned} \qquad [31]$$

where $\hat{g}(z, t)$ and $\hat{h}(z, t, \varepsilon)$ are 2π-periodic functions of time. System [31] is called the system in standard form in the method of averaging.

The idea behind the method of averaging is to seek a near-identity transformation

$$z = u + \varepsilon w(u,t) \qquad [32]$$

where $w(u, t)$ is some yet-to-be determined 2π-periodic function in time, such that the transformed system in u is simpler in some sense than the system [31]. Now, let the function $\hat{g}(z, t)$ be decomposed into its mean and oscillating parts:

$$\begin{aligned}\hat{g}(z,t) &= \overline{\hat{g}}(z) + \widetilde{\hat{g}}(z,t) \\ \overline{\hat{g}}(z) &= \frac{1}{2\pi}\int_0^{2\pi} \hat{g}(z,t)\,dt \\ \widetilde{\hat{g}}(z,t) &= \hat{g}(z,t) - \frac{1}{2\pi}\int_0^{2\pi} \hat{g}(z,t)\,dt\end{aligned} \qquad [33]$$

Then, it can be shown that with the transformation [32], the system [31] is transformed to:

$$\dot{u} = \varepsilon\left[\overline{\hat{g}}(u) + \widetilde{\hat{g}}(u,t) - \frac{\partial w}{\partial t}\right] + \varepsilon^2 h_1(u,t,\varepsilon) \qquad [34]$$

where:

$$\begin{aligned}h_1(u,t,\varepsilon) \equiv\ & D_u\overline{\hat{g}}(u)w + D_u\widetilde{\hat{g}}(u,t)w + \hat{h}(u,t,0) \\ & - D_u w\overline{\hat{g}}(u) - D_u w\widetilde{\hat{g}}(u,t) \\ & + D_u w\frac{\partial w}{\partial t} + O(\varepsilon)\end{aligned}$$

Now, let $w(u, t)$ be the 2π-periodic function that solves $\partial w/\partial t = \tilde{\hat{g}}(u, t)$. Then, eqn [34] reduces to:

$$\dot{u} = \varepsilon\overline{\hat{g}}(u) + \varepsilon^2 h_1(u,t,\varepsilon) \qquad [35]$$

This system [35] is completely equivalent to eqn [31] and, hence, to the system [30]. Dropping the second-order term in eqn [35], we get the averaged system for first-order averaging:

$$\dot{u} = \varepsilon\overline{\hat{g}}(u) \qquad [36]$$

There are many types of theorems in averaging theory. They relate steady-state as well as transient solutions of the averaged system [36] to those of the original system [35]. Here, some of the basic results for steady-state solutions are reviewed:

1. Let the averaged system [36] have a hyperbolic equilibrium solution u_0. Then, for each ε, $0 < \varepsilon < \varepsilon^*$, and some $0 < \varepsilon^* \ll 1$, there exists a 2π-periodic solution $\hat{u}(t, \varepsilon)$ of [35] that lies near u_0 and $\|\hat{u}(t, \varepsilon) - u_0\| \to 0$ as $\varepsilon \to 0$. The stability of the solution $\hat{u}(t, \varepsilon)$ is the same as that of the constant solution u_0 with respect to the averaged system [36].

2. Let the averaged system possess a limit cycle solution $u^*(\theta)$, where $u^*(\theta)$ is 2π-periodic in θ with $\theta \equiv \varepsilon\Omega t$ for some $\Omega > 0$. Then, if the limit cycle is hyperbolic, that is, all but one of the associated Floquet multipliers are away from the unit circle, for each ε, $0 < \varepsilon < \varepsilon^*$, and some $0 < \varepsilon^* \ll 1$, the solution of [35] is of the form $\hat{u}(\theta, t, \varepsilon)$. This solution lies on an integral manifold, which is a 2π-periodic surface in θ and 2π-periodic in t, lies close to the cylinder generated by the solution $u^*(\theta)$, and coincides with it as $\varepsilon \to 0$. The stability of the integral manifold is the same as that of the limit cycle for the averaged system.

As an illustration, consider the system:

$$z'' + z = \varepsilon\left[\cos\tau e_1 - \beta z'' - \alpha z' - 2|z|^2 z\right], \quad z \in \Re^2, \quad e_1 = \{1 \quad 0\}^{\mathrm{T}} \qquad [37]$$

These equations represent a two-degree-of-freedom system whose two coordinates are coupled by cubic nonlinearities. The first oscillator (z_1 coordinate) is excited by a 2π-periodic excitation. Also, the two oscillators have identical linear natural frequencies equal to 1. The parameters α and β, respectively, represent the modal damping and the linear frequency mistuning for each of the oscillators.

Since eqn [37] represents a two-degree-of-freedom system, the existence of its 2π-periodic solutions can be addressed by generalizing the method of Poincaré (as presented above), or by using the method of averaging. If the method of Poincaré is followed, it can be shown that the result is the following set of nonlinear equations:

$$G_1(\xi, \varepsilon) = G_2(\xi, \varepsilon) = G_3(\xi, \varepsilon) = G_4(\xi, \varepsilon) = 0 \qquad [38]$$

where $\xi \in \Re^4$. In the limit of $\varepsilon \to 0$, eqn [38] can be reduced to the form:

$$\begin{aligned} G_1(\xi_0, 0) &= -\alpha\xi_{10} - (\beta - 1.5E)\xi_{20} + M\xi_{30} = 0 \\ G_2(\xi_0, 0) &= -\alpha\xi_{20} - (\beta - 1.5E)\xi_{10} + M\xi_{40} + 1 = 0 \\ G_3(\xi_0, 0) &= -\alpha\xi_{30} - (\beta - 1.5E)\xi_{40} - M\xi_{10} = 0 \\ G_4(\xi_0, 0) &= -\alpha\xi_{40} - (\beta - 1.5E)\xi_{30} - M\xi_{20} = 0 \end{aligned} \qquad [39]$$

where $E = \xi_{10}^2 + \xi_{20}^2 + \xi_{30}^2 + \xi_{40}^2$ and $M = \xi_{10}\xi_{40} - \xi_{20}\xi_{30}$. Eqn [39] is a system of four simultaneous cubic equations in the constant vector $\xi_0 \in \Re^4$, and depends on the parameters α and β. If a solution can be found for these equations and the associated 4×4 Jacobian matrix is nonsingular, the Poincaré theory guarantees the existence of a constant vector $\hat{\xi}(\varepsilon) \in \Re^4$ which is a solution of eqn [38]. There is then the corresponding 2π-periodic solution of the excited coupled oscillators in eqn [37] which, in the limit of $\varepsilon \to 0$, is given by:

$$\begin{Bmatrix} \phi_1(\tau, \xi_0, 0) \\ \phi_2(\tau, \xi_0, 0) \\ \phi_3(\tau, \xi_0, 0) \\ \phi_4(\tau, \xi_0, 0) \end{Bmatrix} = \begin{Bmatrix} z_1 \\ z_1' \\ z_2 \\ z_2' \end{Bmatrix} = \begin{Bmatrix} \xi_{10} \\ \xi_{20} \\ 0 \\ 0 \end{Bmatrix} \cos\tau + \begin{Bmatrix} \xi_{20} \\ -\xi_{10} \\ 0 \\ 0 \end{Bmatrix} \sin\tau + \begin{Bmatrix} 0 \\ 0 \\ \xi_{30} \\ \xi_{40} \end{Bmatrix} \cos\tau + \begin{Bmatrix} 0 \\ 0 \\ \xi_{40} \\ -\xi_{30} \end{Bmatrix} \sin\tau \qquad [40]$$

In general, since eqn [39] is nonlinear and depends on the parameters α and β, they may have more than one real solution for a given parameter set. This would then imply the existence of that many periodic solutions of the oscillators. Furthermore, the number of these solutions may change as the parameters are varied, and this would imply bifurcations in the dynamics of the system.

If the method of averaging is used to find approximate solutions of the coupled oscillators, interestingly, the averaged equations turn out to be:

$$\dot{\xi}_1 = G_1(\xi, 0), \quad \dot{\xi}_2 = G_2(\xi, 0), \quad \dot{\xi}_3 = G_3(\xi, 0), \quad \dot{\xi}_4 = G_4(\xi, 0) \qquad [41]$$

Then, constant solutions of [41] and their stability, determined by a linearized analysis, are related to the periodic solutions of the oscillators. Since these equations depend on the parameters α and β, bifurcations from the equilibrium solutions may arise in the form of additional equilibrium solutions. Furthermore, the nonlinear autonomous system [41] can also possess periodic solutions. Some of these periodic solutions may arise as a result of loss of stability of equilibria, and subsequent bifurcations. The periodic solutions of eqn [41] are related to the invariant manifold of solutions of the oscillators. In physical terms, these invariant manifolds really correspond to amplitude and phase-modulated oscillatory motions of the oscillators. Extensions of theorems in averaging, as well as the method of Poincaré can be used to determine explicitly the periodic solutions of the averaged equations.

The methods presented above have been used extensively to study the nonlinear vibratory response

of harmonically and parametrically excited multi-degree-of-freedom as well as continuous structural systems. The systems investigated have included resonant response of beams, columns, plates, and shells with different boundary conditions. Primary, subharmonic as well as superharmonic responses have been considered. It has been seen that complex amplitude and phase-modulated motions are possible for the structural systems when the excitation frequency satisfies some resonance condition with natural frequencies of more than one degree of freedom. Examples of such situations include internal and combination resonances. Limit cycle or periodic oscillations have also been studied for systems with self-excitation. A very familiar example of such a situation is panel flutter.

Dimension Reduction and Local Bifurcations

To understand the behavior of solutions in the vicinity of an equilibrium point, one needs to study the variational system and its linearization, as discussed in the section on Equilibria and stability, above. When an equilibrium is nonhyperbolic, the behavior in its vicinity is essentially determined by the nonlinear terms. To understand this, consider the system:

$$\dot{u}_s = B_s u_s + h_s(u_s, u_c) \quad \dot{u}_c = B_c u_c + h_c(u_s, u_c) \quad [42]$$

that has n_s stable eigenvalues and n_c eigenvalues with zero real parts. Then, in the vicinity of the equilibrium point, the behavior can be studied by a reduced dimensional system with dimension n_c. This result is a consequence of the center manifold theorem.

An invariant manifold of the system (42) is called a center manifold if it can locally be represented as:

$$W^c(0) = \left\{(u_s, u_c) | u_s = H(u_c), \|u_c\| < \delta, H(0) = 0, DH(0) = 0\right\} \quad [43]$$

for δ sufficiently small. The conditions on $H(u_c)$ at $u_c = 0$ imply that the manifold is tangent to the center eigenspace E^C at the equilibrium point.

Center Manifold Theory

There are three important results in the theory.

1. The first result states that there exists a center manifold for the system [42]. The dynamics of the system on the center manifold is, for sufficiently small v, given by the n_c-dimensional system:

$$\dot{v} = B_c v + h_c(H(v), v), \quad v \in \Re^{n_c} \quad [44]$$

2. The second result states that the stability characteristics of the zero solution $(u_s, u_c) = (0, 0)$ of the system [42] are the same as those of the zero solution $v = 0$ for the system [44]. In addition, if the zero solution of [44] is stable, the solutions of [42] and [44] for small initial conditions are related, as $t \to \infty$, by:

$$\begin{aligned} u_s(t) &= H(v(t)) + O(e^{-\gamma t}) \\ u_c(t) &= v(t) + O(e^{-\gamma t}) \end{aligned} \quad [45]$$

3. The graph of the center manifold $u_s = H(u_c)$ is defined by the manifold condition:

$$\begin{aligned} &DH(u_c)[B_c u_c + h_c(H(u_c), u_c)] \\ &- B_s H(u_c) - h_s(H(u_c), u_c) = 0 \end{aligned} \quad [46]$$

The solution of this equation can be obtained up to any desired accuracy as an expansion in u_c.

When the system depends on parameters, the center manifold for the parameter-dependent system can be computed using the suspension trick where the parameters are also made state variables. Having reduced the dimension of the dynamic system to the essential minimum, further simplifications in eqn [44] can be achieved by the normal form theory.

Normal Form Theory

This generalizes the theory of normal forms for linear systems to nonlinear systems near equilibrium, and other steady-state solutions. In the case of linear systems, it is well known that there exists a linear transformation that reduces the system matrix to the Jordan canonical form (the normal form). It is the simplest form of the system matrix. The method of normal form provides a way of finding a coordinate system in which the nonlinear terms also take the simplest form. The method is local in that the form is valid in the neighborhood of a steady-state solution. Even though the transformation is nonlinear, the method relies on solving a sequence of linear problems in the appropriately defined space of polynomials.

The starting point is the nonlinear system on the center manifold (eqns [44]). Let the matrix $\mathbf{B}_c$ be in its simplest form and let the system be written as:

$$\dot{v} = \mathbf{B}_c v + F(v) = \mathbf{B}_c v + F_2(v) + F_3(v) + F_4(v) + \ldots F_{r-1}(v) + O(\|v\|^{\mathrm{r}}), \quad v \in \Re^{n_c} \tag{47}$$

where $F_i(v)$ represents the order i terms in the Taylor series expansion of $F(v)$. Now, consider the coordinate transformation:

$$v = x + X_2(x) \tag{48}$$

where $X_2(x)$ is second-order in x, and is unspecified at this stage. Substituting the near-identity transformation (48) into eqn [47] and simplifying gives:

$$\dot{x} = \mathbf{B}_c x + \mathbf{B}_c X_2(x) - DX_2(x)\mathbf{B}_c x + F_2(x) + \tilde{F}_3(x) + \ldots \tilde{F}_{r-1}(x) + O(\|x\|^{\mathrm{r}}) \tag{49}$$

Note here that the original nonlinear terms of order higher than two have been modified. In terms of order two, additional terms due to the nonlinear coordinate transformation $X_2(x)$ have appeared. Since the linear term is already the simplest, one can try to choose the function $X_2(x)$ such that the second-order terms are also the simplest possible. Thus, one needs to find solution $X_2(x)$ of the equation:

$$L_{\mathbf{B}_c}(X_2(x)) \equiv DX_2(x)B_c x - \mathbf{B}_c X_2(x) = F_2(x) \tag{50}$$

This is a linear equation with proper interpretation in the space of vector-valued monomials of degree 2. If this space is denoted by H_2, $L_{\mathbf{B}_c}(.) \equiv DX_2(x)\mathbf{B}_c x - \mathbf{B}_c X_2(x)$ is a mapping from H_2 to H_2, and H_2 can be decomposed as a direct sum $H_2 = L_{\mathbf{B}_c}(H_2) \oplus G_2$ where G_2 is space complementary to $L_{\mathbf{B}_c}(H_2)$. From standard linear algebra, if $F_2(x)$ is in the range of $L_{\mathbf{B}_c}(.)$, eqn [50] can be solved uniquely for $X_2(x)$ for every given $F_2(x)$. Then, all terms of second order are eliminated from eqn [48] and one can go on to eliminating third-order terms. Thus, the only terms that cannot be eliminated are those in the complement G_2. Interestingly, the linear operator $L_{\mathbf{B}_c}(.)$ is essentially determined by the matrix $\mathbf{B}_c$. Thus, the nonlinear terms that cannot be removed are determined by the eigenvalues of the linearized approximation. Let $F_2^r(x) \in G_2$ be the terms that cannot be eliminated. Then, eqn [47] simplifies to:

$$\dot{x} = \mathbf{B}_c x + F_2^r(x) + \tilde{F}_3(x) + \ldots \tilde{F}_{r-1}(x) + O(\|x\|^r) \tag{51}$$

This process can be continued until terms up to the desired order are simplified. Note that, as with the center manifold theory, normal form theory can also be modified to be applicable to systems with parameters.

Local Bifurcations

The simplest critical case of stability for an equilibrium point (when linearized analysis is not sufficient) arises when $n_c = 1$, that is, when an equilibrium point of a system dependent on a parameter loses stability with one eigenvalue leaving the left half of the complex plane. At the critical parameter value, the center eigenspace is one-dimensional, and a center manifold reduction results in a scalar nonlinear equation dependent on the parameter. Similarly, if the linearized system has a pure imaginary pair of eigenvalues at the critical parameter value, the center manifold is two-dimensional. Having reduced the system to the center manifold, normal form theory can be used to simplify the nonlinear terms. These simplified equations can then be used to investigate the solutions as a function of the system parameters.

The normal form equations in the various low-dimensional cases for systems with one and two parameters, and the bifurcation diagrams associated with steady-state solutions are summarized here.

Single zero eigenvalue

1. The system on the center manifold simplifies to:

$$\dot{x} = \mathbf{B}_c(p)x + F(x,p) = cpx - ax^2 + O\left(|x|^3, |p^2 x|\right) \tag{52}$$

Here c and a are model constants, and p is the variation of the parameter from its critical value. The steady-state solutions of eqn [52] are depicted in **Figure 4A**, called a bifurcation diagram. In this specific case, the bifurcation is called a transcritical bifurcation. Note that there is an exchange in stability at the critical parameter value.

2. Suppose that the simplest system, on the center manifold, is of the form:

$$\dot{x} = \mathbf{B}_c(p)x + F(x,p) = cpx - ax^3 + O\left(|x|^4, |p^2 x|\right) \tag{53}$$

The corresponding steady-state solutions up to this order are shown in the bifurcation diagram (**Figure 4B**). This type of bifurcation is called a pitchfork bifurcation.

3. Let the system on the center manifold be defined by:

$$\dot{x} = \mathbf{B}_c(p)x + F(x,p) = cp - ax^2 + O\left(|x|^3, |p|^2\right) \quad [54]$$

The associated bifurcation diagram is shown in **Figure 4C**. This type of bifurcation is called a saddle node bifurcation.

Pure imaginary pair of eigenvalues In this case, the center manifold is two-dimensional. The system on the center manifold can be simplified using the normal form theory for systems with parameters. The final system in normal form is given by:

$$\begin{aligned}\dot{x}_1 &= \alpha(p)x_1 - \omega(p)x_2 \\ &\quad + \left\{a(p)x_1 - b(p)x_2\right\}\left(x_1^2 + x_2^2\right) + O\left(|x_1|^5, |x_2|^5\right) \\ \dot{x}_2 &= \omega(p)x_1 + \alpha(p)x_2 \\ &\quad + \left\{b(p)x_1 + a(p)x_2\right\}\left(x_1^2 + x_2^2\right) + O\left(|x_1|^5, |x_2|^5\right)\end{aligned} \quad [55]$$

Here, $\alpha(0) = 0$, $(\mathrm{d}\alpha/\mathrm{d}p)(0) > 0$ and $\omega(0) \neq 0$. Also, let $a(0) \neq 0$. This implies that, at $p = 0$, the linear system is critical and the imaginary part of the critical eigenvalues is $\omega(0)$. The steady-state solutions of this system, near (0,0), can be obtained using any of the methods for finding periodic solutions. These include the method of Poincaré and the method of averaging, already discussed in this article. In polar coordinates, with $x_1 = r\cos\theta x_2 = r\sin\theta$, eqn [55] takes the form:

$$\begin{aligned}\dot{r} &= \alpha'(0)pr + a(0)r^3 + O\left(p^2 r, pr^3, r^5\right) \\ \dot{\theta} &= \omega(0) + \omega'(0)p + b(0)r^2 + O\left(p^2, pr^2, r^4\right)\end{aligned} \quad [56]$$

The final result is the Hopf bifurcation theorem which states that there exists a periodic orbit with approximate amplitude $r = \sqrt{-p\alpha'(0)/\alpha(0)}$, and frequency

$$\Omega = \omega(0) + \left\{\omega'(0) - \frac{b(0)\alpha'(0)}{a(0)}\right\}p$$

The periodic solution is supercritical (exists for $p > 0$) and asymptotically stable for $a(0) < 0$. It is unstable for $a(0) > 0$. These results are depicted in **Figure 5**.

Note that the above result regarding the existence of a bifurcating limit cycle can also be obtained using the other methods discussed. While the method of Poincaré gives the existence of a periodic solution, its stability has to be determined separately using the Floquet theory. The method of averaging, like the method of Poincaré requires the explicit introduction of a small parameter. It does, however, relate the stability of the limit cycle to the stability of the corresponding equilibrium point of the averaged equations. This makes it easier to get the complete picture, though the method is cumbersome when higher-order terms are required in the analysis. The results obtained via the use of the normal form theory

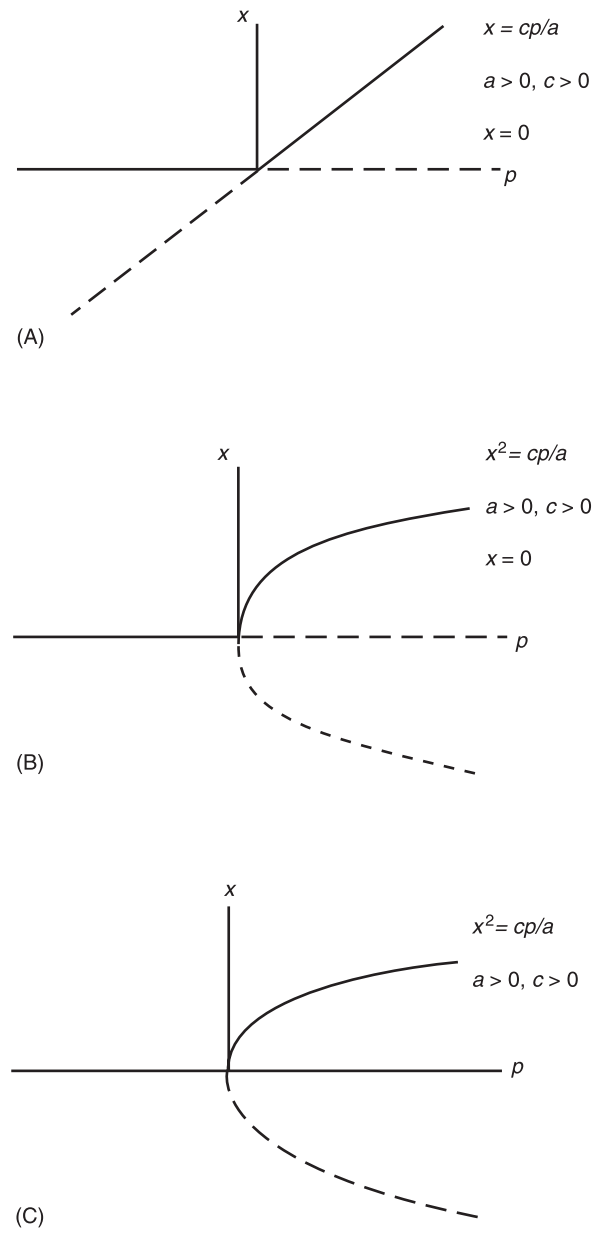


Figure 4 Local bifurcations in one-parameter systems for one zero eigenvalue; (A) transcritical bifurcation: (B) pitchfork bifurcation: (C) saddle node bifurcation.

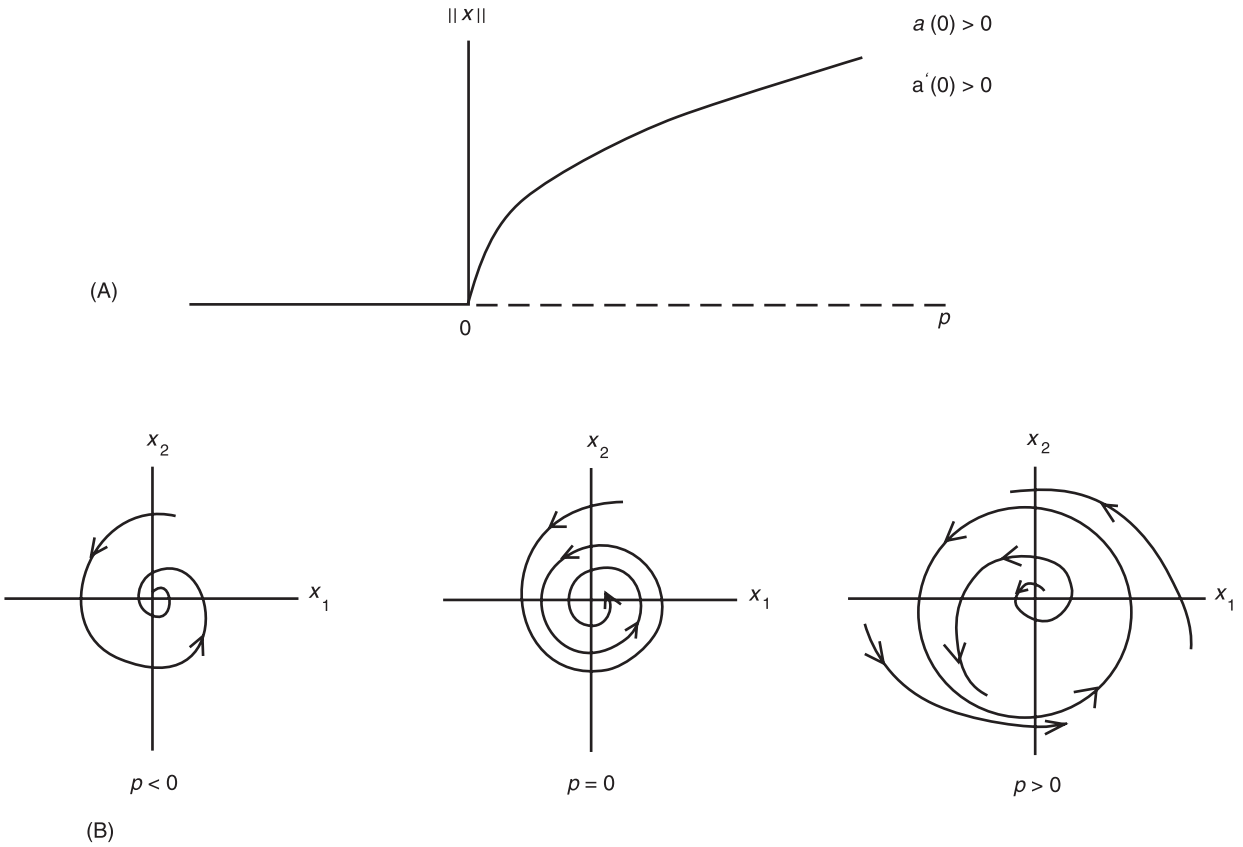


Figure 5 Hopf bifurcation to limit cycle oscillations in one-parameter system: (A) bifurcation diagram for the supercritical case; (B) phase plane for various parameter values.

do not require the explicit introduction of a small parameter, and the process is the most straightforward when even as well as odd terms are present in the original differential equations.

The results presented above are just the simplest of those available in the literature. The reader can find extensive treatments on analysis techniques and the predicted results in the literature.

See also: **Eigenvalue analysis**; **Nonlinear normal modes**; **Nonlinear system identification**; **Nonlinear systems, overview**; **Nonlinear system resonance phenomena**; **Perturbation techniques for nonlinear systems**.

Further Reading

Bogoliubov NN and Mitropolski YA (1961) *Asymptotic Methods in the Theory of Nonlinear Oscillations*. New York, NY: Gordon and Breach.

Guckenheimer J and Holmes PJ (1983) *Nonlinear Oscillations, Dynamical Systems and Bifurcations of Vector Fields*. New York, NY: Springer-Verlag.

Hale JK (1963) *Oscillations in Nonlinear Systems*. New York, NY: McGraw Hill.

Hale JK and Kocak H (1991) *Dynamics and Bifurcations*. New York, NY: Springer-Verlag.

Hayashi C (1964) *Nonlinear Oscillations in Physical Systems*. New York, NY: McGraw Hill.

Hsu CS (1987) *Cell-to-Cell Mapping*. New York, NY: Springer-Verlag.

Khalil HK (1992) *Nonlinear Systems*. New York, NY: Macmillan.

Minorsky N (1962) *Nonlinear Oscillations*. Princeton, NJ: D. Van Nostrand.

Moon FC (1993) *Chaotic and Fractal Dynamics: An Introduction for Applied Scientists and Engineers*. New York, NY: John Wiley.

Murdock JA (1991) *Perturbations: Theory and Methods*. New York, NY: Wiley Interscience.

Nayfeh AH (1973) *Perturbation Methods*. New York, NY: Wiley Interscience.

Nayfeh AH and Balachandran B (1995) *Applied Nonlinear Dynamics*. New York, NY: John Wiley.

Nayfeh AH and Mook DT (1979) *Nonlinear Oscillations*. New York, NY: Wiley Interscience.

Seydel R (1988) *From Equilibrium to Chaos: Practical*

Bifurcation and Stability Analysis. New York, NY: Springer-Verlag.

Strogatz SH (1994) *Nonlinear Dynamics and Chaos*. Reading, MA: Addison-Wesley.

Troger H and Steindl A (1991) *Nonlinear Stability and Bifurcation Theory: An Introduction for Engineers and Applied Scientist*. New York, NY: Springer-Verlag.

Vakakis AF, Manevitch LI, Mikhlin YV, Pilipchuk VN and Zevin AA (1996) *Normal Modes and Localization in Nonlinear Systems*. New York, NY: John Wiley.

Wiggins S (1988) *Global Bifurcations and Chaos: Analytical Methods*. New York, NY: Springer-Verlag.

Wiggins S (1990) *Introduction to Applied Nonlinear Dynamical Systems and Chaos*. New York, NY: Springer-Verlag.

O

OBJECT ORIENTED PROGRAMMING IN FE ANALYSIS

A Cardona, INTEC, Grupo de Technologia Mecanica, Santa Fe, Argentina

I Klapka, Université de Liège, Liège, Belgium

P Devloo, Universidade Estadual de Campinas, Campinas SP, Brazil

Copyright © 2001 Academic Press

doi:10.1006/rwvb.2001.0007

Introduction

The finite element (FE) method is currently used as an extremely valuable tool of analysis in many fields of engineering and science. Since 1960, several research teams have developed analysis software based on this method, software which has continuously grown over the years leading to powerful packages that are in use today in industry and research. However, computers and software technology have changed a lot since the days when these programs were conceived, and today provide new techniques for managing information. Also, new faster computers open the way for the solution to more complex problems, requiring in turn modern information-handling techniques. Consequently, developers are experiencing increasing difficulty, with very high costs of maintenance in keeping their software up to date. Yet, they are facing a growing demand for user-friendliness in the form of graphics, menus, and boxes.

New software technologies try to remedy the deficiencies encountered with conventional programming. In particular, 'object-oriented programming' (OOP) is currently seen as the most promising way of devising a new application.

Software Design Considerations

Research in FE software design is the result of two main observations. The first concerns the growing needs of modeling complex interaction phenomena between different physical fields. The second concerns the evolution of new computer technology which invites developers to reconsider the design of their current tools of analysis, for example, by using new language features or by proposing adapted algorithms to distribute tasks between computers connected in parallel.

The last two decades have been marked by growing computer power, allowing us to consider modeling more and more complex phenomena. Both from the point of view of model size and of the interaction between different models, management of information is always more complicated and has become a crucial issue. Achieving a correct implementation is at least as important as developing a sound basis for the formulation of the method.

Objectives

Scientific applications have usually been associated with intensive arithmetic computing and small volume of data management. However, current FE programming in a user-friendly environment requires large volumes of a variety of data:

1. to and from memory (between different zones of the program)
2. to other process or computers
3. to secondary storage (results, DB)
4. to graphic devices (display of results)

Experience with existing programs shows that large parts of the program are spent on data handling with a small amount of arithmetic (input and preprocessing, output, intermediate processing, even computation of finite element matrices), while only a small part of the program is dedicated to intensive arithmetic (algebraic linear systems solver).

Quality

Quality standards in industrial codes can be specified as follows:

- Accuracy: does the code give correct answers to correct specifications?
- Robustness: how does the code react to different conditions from those specified?
- Portability: can the code be easily implemented on different computers?
- Efficiency: is it efficient from the point of view of CPU time consumption, main and secondary storage demands, I/Os, etc.?
- Extensibility: can the code be adapted simply to follow an evolution of specifications?
- Reusability: is it possible to use parts of the code (modules) to solve a different problem?

Accuracy and robustness in a 10-year project is not so easy to assume as in a 100-line program. Besides accuracy, efficiency and extensibility priorities must also be considered as the main criteria for code design. Whenever these two features coexist, the numerical efficiency aspect must be considered first in the context of dynamics analysis. Maintainability and portability are also important issues that have to be considered.

Human Aspects

Numerous people are generally involved in the development of a large FE software. They can be grouped as follows, from the point of view of their interests and skills:

1. The final users of the code, who are interested in getting an answer to the physical problem in hand;
2. The numerical analysts, who propose new finite element methods and algorithms;
3. The programmers, seen as users of classes and methods implemented by other programmers;
4. The programmers of new classes and methods to be used by people of the previous group.

A single person may belong to more than one group. In fact, the group to which a person belongs is often determined by the task being performed at a given moment. All the groups must be taken into consideration from the very beginning of the design of a new FE program. The main concerns about software quality differ for each task, and may be described as in **Table 1**.

Object-Oriented Programming

Object-oriented methods have existed since 1960, but structured and procedural programming methods imposed themselves as being more adapted to the architecture of the new computer tool (see **Figure 1**). This was a first evolution despite the linear chaotic way of using computer technology. Today there is a tendency to invert this trend and to design software independently from the architecture of the hardware. This announces the age of maturity of the computer which is (finally) in sympathy with the human way of thinking (**Table 2**).

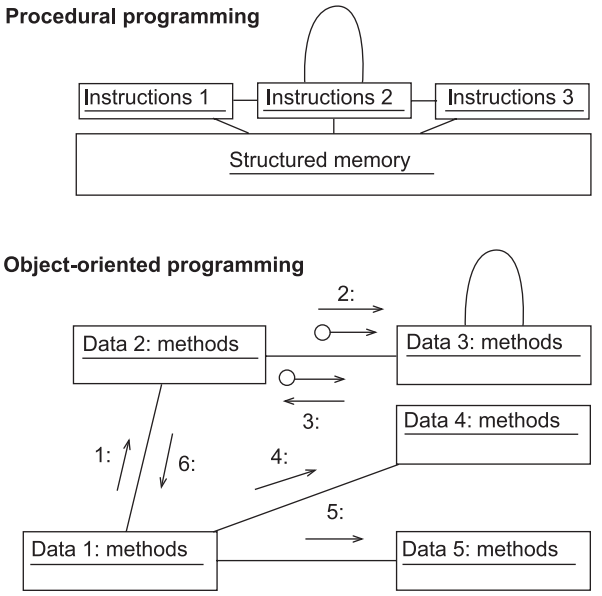


Figure 1 Procedural versus object-oriented (interaction diagram).

Table 1 Tasks

Concerned by	*1 → 2*	*2 → 3*	*3 → 4*	*4*
Accuracy	+++	+++	+++	+++
Robustness	+++	+++	+++	++
Efficiency and performance	+++	+++	+	+++
User-friendliness	+++	+	+++	0
Maintainability		+	++	+++
Reusability		0	++	+++
Extensibility	+	+++	++	+++

Table 2 The evolution of computer programming

'*Chaos*'	*Structured and procedural programming*	*Object-oriented programming*
Jumps, gotos	If-then-else	Objects
Unstructured variables	Blocks	Messages
Variables scattered throughout the program	Records	Methods
	While loops	Inheritance
		Polymorphism

A New Philosophy

The object-oriented philosophy comes from the idea that tools (methods) must be associated with the information (data) they manage. In order to do that, some new concepts have been introduced.

Classes A class defines an abstract data type. It may represent, for example, a family of objects in the real world. Classes are identified during the analysis phase of application development. A class incorporates the definition of the structure as well as the operations on the abstract data type. For example, `Element` would be defined as a class in a finite element method application. Typically, data that the system analyst would define relating to the class `Element` may include such items as localization, connected nodes, number of degrees-of-freedom, etc. Elements belonging to the collection of objects described by the class are called 'instances' of the class.

Subclasses and inheritance A subclass is subordinated to a class and has all the same elements of the class which it has inherited. Therefore, the term 'inheritance' indicates an 'is a ...' relationship between two classes. A subclass is usually of a special type and has additional data elements relating to it. For example, an `Isoparametric_Element` is an `Element` for which both positions and displacements are interpolated from nodal values.

Encapsulation In an object-oriented application, all data, functions, and services offered by a class (or subclass) are packaged together. This (independent) self-containment of classes and their functions and services (i.e., members) is called 'encapsulation'. This full modularity both greatly enhances the introduction of changes during the development phase as well as the performance of ongoing maintenance. In addition, as we will see below, encapsulation makes possible the unique 'polymorphic' capability of object-oriented applications.

Polymorphism A given function or service may be made to respond differently when performed on objects from different classes. For example, a single request to `fill_stiffness` will automatically be computed differently for a `bar` than for a `quad4` element. This is due to the fact that different calculation methods are encapsulated within subclasses `bar` and `quad4`. This unique capability of object-oriented applications to interpret the same request differently depending on the object being processed is known as polymorphism. Some languages allow polymorphism capability to be implemented either at compilation time or at running time (dynamically).

The two latter concepts may be used to get a complete data abstraction, implying for example that we can ask the elementary stiffness to a list of `Element` objects without knowing exactly what element types form each item in the list.

Analysis and Methodology

An essential factor of success in a large project is the employment of powerful analysis tools. As the complexity of systems increases, the analysis becomes even more important. Object-oriented philosophy has brought new techniques in modeling and analysis first proposed in 1991 by P. Coad and E. Yourdon (OOD) or J. Rumbaugh (OMT), then G. Booch in 1994 or with OOSE (object oriented systems engineering, Oden University). These analysis methodologies were proposed to help in the design of the architecture of an object-oriented project. Today, there is a tendency to use unified modeling language (UML) for modeling applications which fuses the concept of previously mentioned ones into a standardized modeling language, and design patterns (proposed by E. Gamma) to follow standard patterns for developing object-oriented abstractions. In design patterns, the idea is to use solutions that have been developed and evolved over time, and capture them in a succinct and easily applied form. They are broadly categorized into patterns for creational, structural, and behavioral purposes on classes or objects.

The models contain diagrams which provide a means of visualizing and manipulating the models' components and their properties. Diagrams are used to illustrate multiple views of a model and the components they represent. Several kinds of diagram can be used:

- The description of logical package uses 'class', 'object', and 'interaction diagrams'.
- The description of component package uses 'component diagrams'.
- The description of classes may use 'state diagrams'.
- The model uses the diagrams for its top-level components, its 'deployment diagram', and the diagrams contained by its logical packages and component packages. These top-level components can be classes, modules, processors, devices, and connections.

A class diagram This is a picture providing generic descriptions of possible systems. Class diagrams and object diagrams are alternate representations of object models. These representations show the typical distinction between data () and methods (), and

their attributes; public, private, protected or used for internal implementation ( ). **Figure 2** shows an example of an implementation model for classes involved in the assembling process of the FE matrices. The class `dynamic analysis` contains matrix objects M, K, eigenmodes, a vect of eigenvalues and two methods for assembling and solving the analysis. It uses a localization manager and numerical grid(s). `Matrix` objects are virtual, i.e., they are independent of any storage scheme, full matrix, sparse, skyline, or even frontal matrix. The virtual matrix 'mother' class constrains its children to implement `solve` and `product` methods and imposes a unique interface.

A state transition diagram This is used to show the state space of a given class, the event that causes a transition from one state to another, and the actions that result from a state change. Each state diagram is usually associated with one class of objects. A frequent state mechanism is implemented on matrices to manage behavior, depending on whether it is factorized or not. Another example concerns the instruction phase state of a problem (domain). It can be distinguished from its computational state, and this requires a list of degrees-of-freedom. This is represented in **Figure 3**.

Sequence diagrams and collaboration diagrams Sequence diagrams and collaboration diagrams are alternative representations of an interaction. A sequence diagram traces the execution of an interaction in time. For the FE method, one could model the elementary assembling sequence as shown in **Figure 4**. The object that has been asked to build the generalized global system will first perform equation ordering using a bandwidth optimization scheme. Then, it will ask the numerical grid object to loop over each element object to get its global localization, elementary matrices, and vectors and add its values to the global system. Then it will call a solver corresponding to the case under study. If a solver is called for time-dependent problems, one can see a similar sequence differing only by an update message sent to elements.

A deployment diagram This shows processors, devices, and connections. Each model contains a single deployment diagram which shows the connections between its processors and devices, and the allocation of its processes to processors. An example of a module which could have the ability to distribute tasks on several CPUs through a graphic workstation may have a deployment diagram as shown in **Figure 5**. The master process is controlled by mouse and

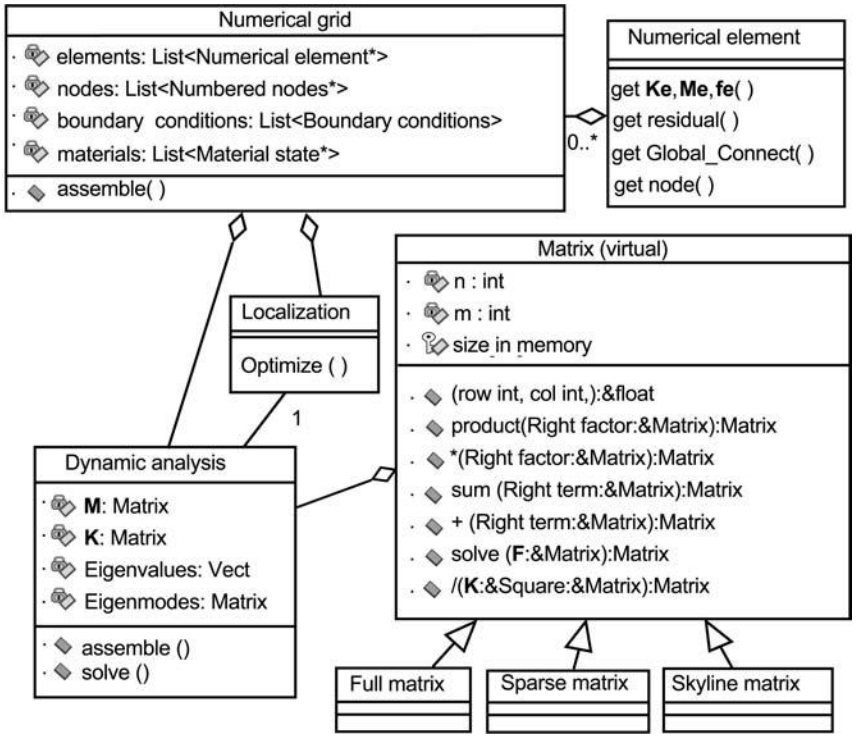


Figure 2 Class diagram for assembling process.

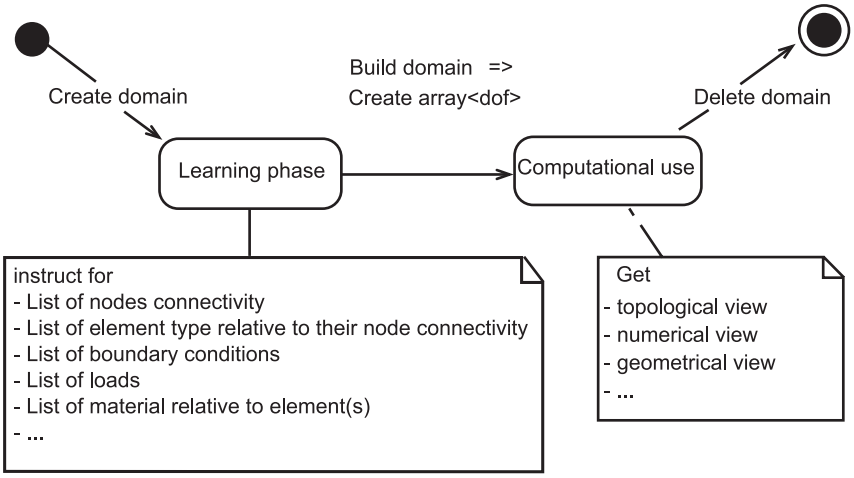


Figure 3 Domain state diagram.

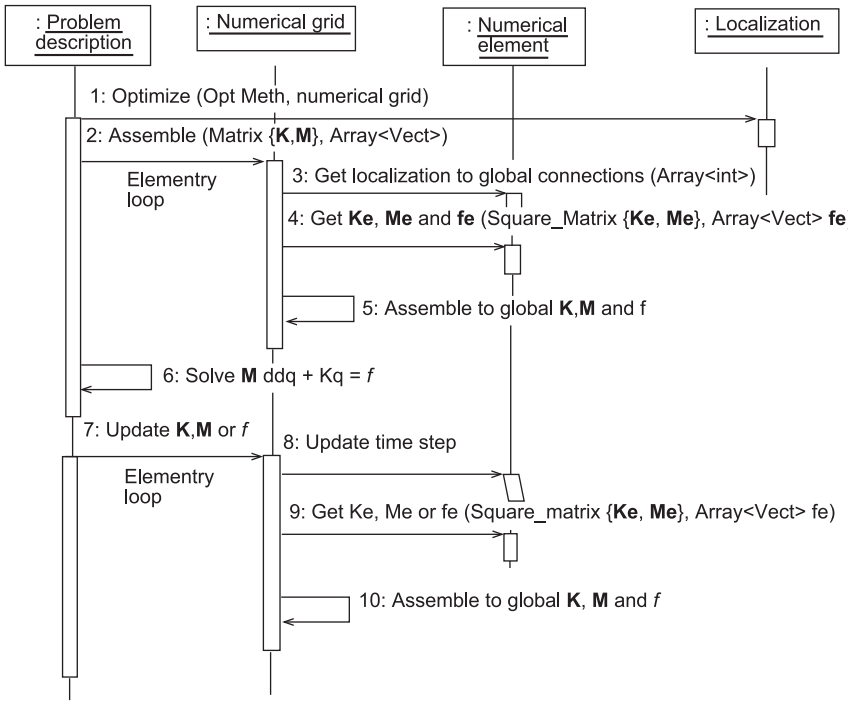


Figure 4 Sequence diagram of the assembling process.

keyboard devices. It will take benefits of other distributed memory and CPUs through a network device. A preemptive process dialogs with the master process to send graphical window output to the screen device, both accessing database on disk.

Component diagrams

These describe physical elements and their relations in the realization environment. They translate realization choices. In **Figure 6**, for example, the main process controls two tasks: communication and visualization. The first uses the OOMPI package incorporating the MPI and TCP/IP protocols. The second is split into two options depending on the nature of the visualization: 2D or 3D, each option using different graphics libraries.

The Language

Discussions on the different languages which currently propose object-oriented philosophy (OOPL)

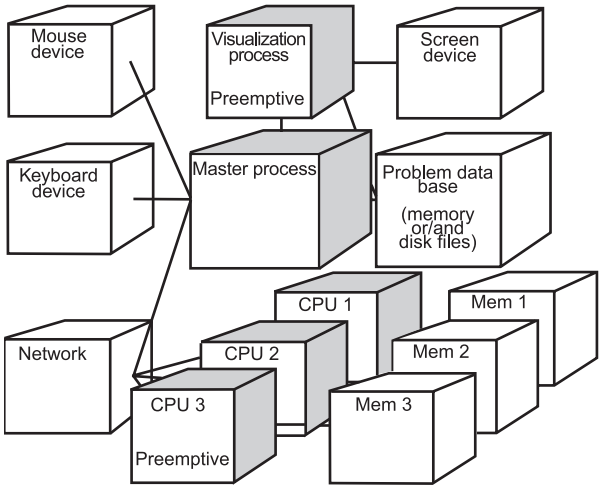


Figure 5 Example of a deployment diagram.

have been made by J. Rumbaugh and P. Coad and E. Yourdon. J. Barton gave a point of view on scientific applications. Among the many existing object-oriented languages, C++ developed by B. Stroustrup, is preferred for reasons of portability and efficiency, and because of the large number of tools available (graphical interface libraries, network tools, etc.). It revealed itself to be a language which imposes such a discipline on the programmer that it allows a single person to maintain an important code.

Several researchers, like G.W. Zeglinski and R.P.S. Han, have worked on the application of object-oriented programming techniques to the FE method in recent years. T. Zimmermann et al. used the Smalltalk programming language. Although it is considered as a pure object-oriented language, it is not used for real numerical applications for efficiency reasons. Other researchers, like B.W.R. Forde et al. and R.I. Macjkie, have presented object-oriented implementations of the FE method using object-oriented extensions of Pascal or Ada. The new standard Fortran 90 includes features which can be considered as object-oriented extensions, making this option appealing for those who are strongly involved in Fortran programming. However, it has many limitations: for instance, it does not support inheritance or dynamic polymorphism.

It is generally agreed that the C++ language – an extension to C – remains the most widespread object-oriented language for numerical computations. The success of the C++ language made usual standard C libraries to be reviewed, adapted to object-oriented philosophy, and extended with new standard tools.

Several applications of FE programming using C++ have been reported in references. In particular, A. Cardona and I. Klapka incorporated an object-oriented command line interpreter (OoFeLie) which gives the end-user direct access to the object-oriented internal architecture.

Numerical Efficiency

From a numerical efficiency point of view, it is important to understand that in C++ most of the object-oriented concepts do not extend beyond the compilation step. Only the polymorphism concept needs dynamic (during execution) binding. Historically, first versions of C++ compilers were simply translators to C, theoretically limiting efficiency to

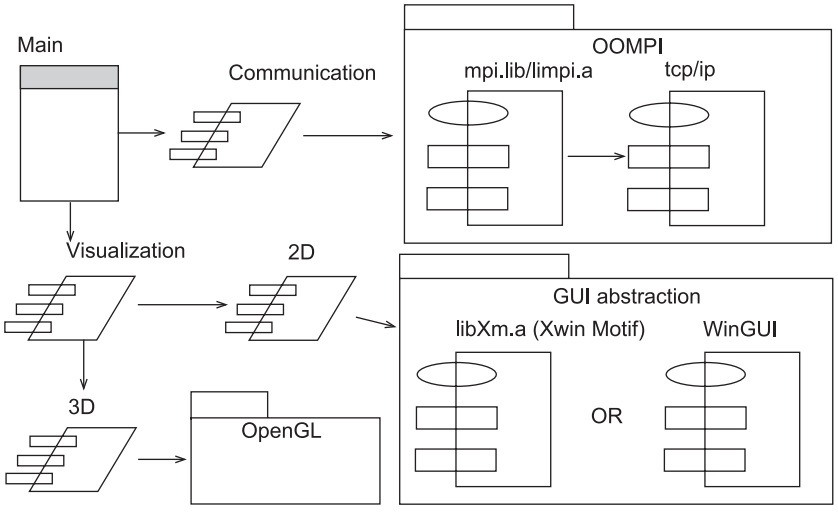


Figure 6 Component diagram.

that of C. In fact, as announced by the creator of the language, C++ is designed to be an improved C, supporting data abstraction and object-oriented philosophy. This means more concepts to be understood by the programmer and, thus, more sources of mistakes. We should bear in mind that the object-oriented philosophy must be considered as a tool, and not as a systematic obligation which could lead to make an object with each 'bit' of information.

Most of the criticisms of C++ efficiency are not valid. Practice has taught that inefficient implementation of C++ programs is the consequence of a poor understanding of the language. For example, when implementing a vector class one may be tempted to overload `operator[i]` so as to test if index `i` is inside the vector range. It may be a useful feature in some cases, but one should not expect to get Blas performance if using this operator in a vector product. It must be borne in mind that abstraction often comes with a loss of performance. Stepanov calls it the abstraction penalty and proposed a test to quantify it.

For efficiency reasons, good practice consists of limiting the nonanticipation principle proposed by Dubois-Pelerin to objects directly accessed by the end-user, or to high-level methods. This principle tries to extend the data abstraction concept to a state abstraction concept, which implies verifying the state of each data entity before using it. This idea may result in the implementation of many costly tests which may be considered unacceptable at execution time if performed with often-called functions or operators (`operator[]`, for example). This choice seems to contradict the object-oriented philosophy. However, using analysis techniques such as state diagrams, one can acquire a good knowledge about the state of the object before using it, which makes some tests unnecessary or useful only during the debugging phase of development.

Finally, the user of classes has an unavoidable responsibility; for instance, many algorithms do not need zero initialization of matrices. This is why most matrix class implementations do not initialize matrix values by default, leaving the choice to the user (e.g., Lapack++).

In terms of pure computational efficiency, J.J. Dongarra and R. Pozo obtained with the Lapack++ library (a C++ extension of the Fortran Lapack library for numerical linear algebra) exactly the same performance as with Fortran. However, the C++ implementation provided scalability, portability, flexibility, and ease of use features which were not so easy to obtain for large codes implemented in Fortran. Other researchers reported better performance than using Fortran in some cases (T. Veldhuizen, Blitz++ Consortium).

To get these results, frequent use was made of the template mechanism which allows one to define concepts (methods, algorithms) independently of the type of object being used. The main difference with the virtual inheritance mechanism consists in the fact that the connection between data and methods is made by the compiler. This implies that the compiler receives enough information to produce optimized code. This technique not only increases legibility without losing efficiency, but also allows methods to be reused without considering how data structures are implemented. The template concept is preferred to the class inheritance mechanism when implementing static polymorphism.

Numerical Solution of a Continuum Mechanics Problem

The process of solving a continuum mechanics problem customarily involves a discretization step followed by a step of finding the solution to an algebraic (discrete) problem.

Discretization allows the behavior of the continuum (e.g., space, time) to be described in terms of the behavior computed at selected points (we then talk of values computed at the degrees-of-freedom of the model). The original problem is transformed into a discrete algebraic one which can be effectively formulated and solved numerically. The components of this algebraic problem express values computed at the degrees of freedom of our model. Several kinds of algebraic problems have to be solved, depending on the problem to analyze. For instance, the continuum mechanics problem in linear statics is expressed by a boundary value problem which is transformed after discretization into a system of linear algebraic equations. When dealing with linear vibration analysis, we have to solve a linear eigenvalue problem. In nonlinear statics the problem to be solved is a system of nonlinear algebraic equations.

These algebraic problems share several characteristics unique to FE analysis. The number of equations and unknowns can be very large (e.g., it is not uncommon to talk of more than 500 000 unknowns in linear statics industrial applications). Also, the degree of coupling between unknowns is moderate to low, so that appropriate schemes to handle sparse coefficient matrices should be employed to reach maximum computational efficiency. Several strategies, specialized to FE applications, exist: e.g., the

skyline, frontal, multifrontal solution schemes. Systems of nonlinear equations range from mildly nonlinear, for which it is fairly easy to find a solution, to very ill-conditioned. There exists a large number of algorithms to solve nonlinear systems of equations in FE applications, each being adapted to a particular kind of problem. In order to get a solution to a practical industrial problem, the analyst should have a variety of algorithms at hand, and should be able to switch from one to another even while advancing along the solution path.

What has been said for systems of nonlinear equations in the preceding paragraph also applies to methods for extracting linear eigenvalues, integrating systems of ordinary differential equations, and so forth. Many specialized algorithms exist and new ones are continuously being proposed which take into account the peculiarities of these systems and of new hardware technology. Finally, it must be mentioned that, in many cases, the problem to be solved consists of a sequence (or even nesting) of algebraic problems of the kind described in the previous paragraphs. Examples of these situations can be found, for instance, in optimization, stability analysis of nonlinear structures, and dynamic stability analysis of mechanisms and structures.

Dynamic Systems

The FE method is an analysis tool for many different problems of continuum mechanics, most widely used for structural analysis. The method essentially consists of discretizing the continuum and transforming the system of partial differential equations into an algebraic problem.

Most dynamic systems can be stated directly from Hamilton's principle. Assuming the dynamic system has n state variables $\mathbf{q}_i$ and $\dot{\mathbf{q}}_i$ and m constraint equations, then the solution for a dynamic problem is a stationary value of:

$$\begin{cases} \delta \int_{t1}^{t2} (E^T - E^V - \frac{1}{2} k \phi^T \phi - \lambda^T \phi)\, \mathrm{d}t = 0 \\ \delta \mathbf{q}(t_1) = \delta \mathbf{q}(t_2) = 0 \end{cases}$$

where:

- $E^T =$ kinetic energy of the system
- $E^V =$ potential energy stored within the system
- $\phi =$ a set of constraint functions
- $k =$ value of the penalty amplification factor
- $\boldsymbol{\lambda} =$ vector of Lagrange multipliers associated with the constraint functions
- $\mathbf{q} =$ vector of state variables

Assuming that the kinetic energy, potential energy, and constraint equation depend on a vector of state variables $\mathbf{q}$ and their time derivatives $\dot{\mathbf{q}}$, the corresponding Lagrange equation takes the form:

$$\begin{cases} \left(\frac{\mathrm{d}}{\mathrm{d}t}\left(\nabla_{\dot{\mathbf{q}}}(E^T - E^V)\right) - \nabla_{\mathbf{q}}\left(E^T - E^V\right)\right)^T \\ +\left(\nabla_{\mathbf{q}}\phi\right)^T (k\phi + \boldsymbol{\lambda}) = 0 \qquad \phi = 0 \end{cases}$$

The number of equations is equal to the number of state variables plus the number of constraint functions. The first block of equations being linear in $\ddot{\mathbf{q}}_i$, the system of equations can be rewritten as:

$$\begin{cases} \mathbf{M}\ddot{\mathbf{q}} + \mathbf{f}(\mathbf{q}, \dot{\mathbf{q}}, t) = 0 \\ \phi(\mathbf{q}, \dot{\mathbf{q}}, t) = 0 \end{cases}$$

where:

$$\mathbf{M}_{ij}(\mathbf{q}, \dot{\mathbf{q}}, t) = \frac{\partial\left(E^T - E^V\right)}{\partial \dot{\mathbf{q}}_i \partial \dot{\mathbf{q}}_j}$$

and $\mathbf{f}$ include the contributions of the constraint equations.

Dynamic systems can be decomposed in components, where each component has its own kinetic energy, potential energy, dissipation rate, and/or constraints. The kinetic energy, potential energy, dissipation rate, and constraints of the complete system are obtained by summing up the corresponding values of its components. Coupling between the different components is characterized by the fact that they share state variables and constraint equations. This observation holds for systems composed of rigid bodies as well as for those resulting from the discretization of a continuum mechanics problem.

Basic Example of a Class Hierarchy

Programs applied to numerical simulation contain at least three packages: a utility package which contains vectors, lists, etc.; a mathematical/numerical package which implements different storage methods and algebra algorithms; and a physical package which instructs the numerical problem with material behavior resulting from physical models, and their integration schemes.

Tools classes The main needs are containers (tools to manage collections of user objects), memory management tools, iterators, algorithms, diagnostics, strings, and I/O tools. The standard template library (STL) proposes standard extension tools added to the C++ language itself.

Mathematical classes

Storage level Different kinds of matrix storage can be implemented with the objective of an independent-type interface. For example, a `Skyline` class inheriting from a `Moth_mat` class may be created to manage skyline array memory organization. See **Figure 7**.

Low-level computation methods In the context of the FE method, operations such as, matrix vector product, static Schur condensation and direct solver are identified as the basic matrix methods required by most algorithms. These methods can be added to the interface of the mother matrix class as member functions to allow nondependent use of children matrices in algorithms.

High-level computation methods These classes serve as 'black boxes' defining robust user interfaces to solution methods taking into account particular aspects such as, e.g., memory management, parallelism. Basic ones are:

1. `StatSyst`: base class for linear systems solvers
   (a) Direct solvers
   (b) Iterative solvers (implementations of GMRES, BiCg, BiCgStab, CGS, CG from SIAM Templates book)
2. `DynamSyst`: base class for all eigenvalue and eigenvector calculations
   (a) `Jacobi`: Jacobi method for symmetric (eventually banded) matrices
   (b) `qr`: QR method for banded matrices
   (c) `SVD`: singular value decomposition implementation
   (d) `Lanczos`: Lanczos algorithm with single iteration vector and restart, or block Lanczos algorithm
3. `Opti`: optimization functions

Physical classes The class model approximates as closely as possible the theoretical consideration on the numerical approximation of dynamical systems. A dynamic system is composed of components (elements), each of which sums its contribution to a global residual vector. An analysis class groups all components within a global dynamical system and applies Newton iterations and/or line search algorithms to anihilate the residual vector at each timestep.

The interface design to element objects must be based on the data structure needed to answer questions asked by the solvers or the results manager.

The set of physical classes is used to describe the problem under analysis and the system state. Some of the usual physical classes are:

1. `Point_state`: virtual generic class which manages physical information at a point
2. `Node_state`: virtual class, inheriting from `Point_State`, providing standard interface to access state variables at a node, including:
   (a) `Position`: coordinates of a point in Cartesian space

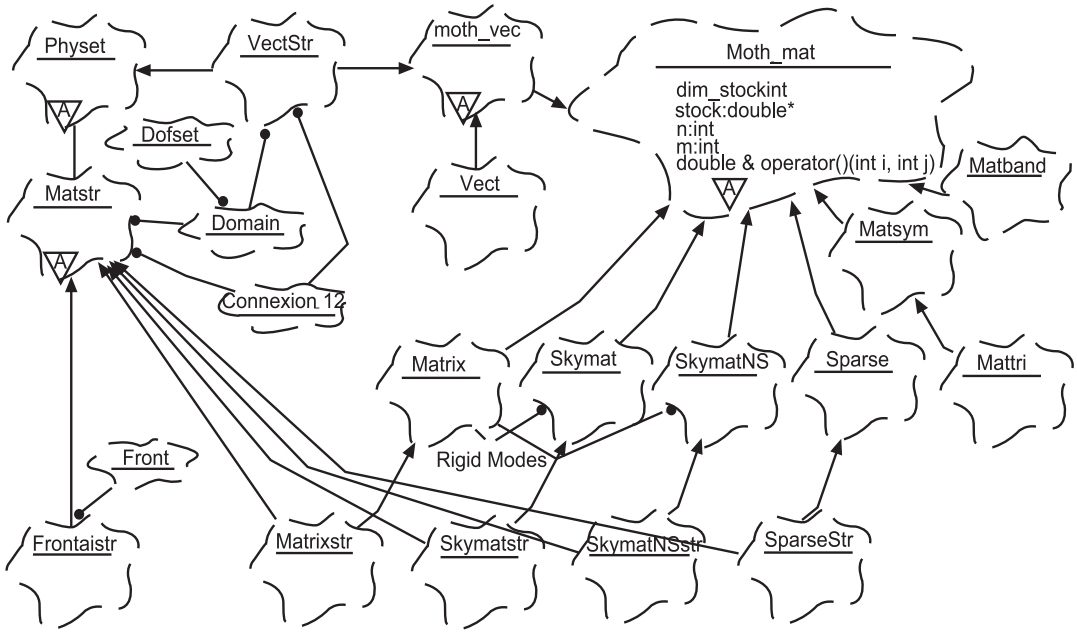


Figure 7 Hierarchy of matrix classes example in G. Booch inheritance diagram notation.

(b) `Displacement`: displacement at a point
(c) `Force`: data and methods to handle loads
(d) `Temperature`: temperature at a point

Also, time derivatives of the above are accessed through `Point_State` interface. They can be managed through STL container `List<Type>` to declare, for example, the set of Displacement as `List<Displacement>`.

- `Material`: master class for description of materials of various kinds.
- `Propelem`: master class for description of element properties
- `Fixation`: master class for information concerning boundary conditions of the model.
- `Element`: virtual master class of the FE library. It provides methods to access their attributes, and to compute the different FE arrays and tables (e.g., `fill_stiffness ()`, `fill_mass ()`, etc.).

Some of them, in nonlinear hypothesis, should use:

- `Gauss_point_state`, inheriting both from `Point_State` and `Material`, to get access to material state story information
- `Skymat_str`, inheriting from `Skymat`, adds to the matrix features the ability to manage connectivity between elements

After having the different corresponding objects and having defined the problem, the resolution scheme will first fill a `Skymat_str` Mass matrix. The matrix object will ask the `List<Element>` to fill elementary matrices `Matsym` and assemble them using connectivity given by the current `Element`. The same is done for internal and external force vectors. The difference between the two vectors is applied as a parameter of the `Skymat_str::Mass` of the solver member function. The result is stored in a `List<Displacement>`.

See also: **Dynamic stability**; **Finite element methods**

Further Reading

Ammeraal L (1991) *C++ for Programmers*. John Wiley.
Barton J, Nackman L (1994) *Scientific and Engineering C++*. Addison Wesley.
Booch G (1994) *Object Oriented Analysis and Design*. Benjamin-Cummings.
Booch G, Jacobson I, Rumbauch J (1998) *The Unified Modeling Language User Guide*. The Addison-Wesley Object Technology Series.
Breymann U (1998) *Design Components with the C++ STL*. Addison-Wesley.
Cardona A, Klapka I, Geradin M (1994) Design of a new finite element programming environment. *Engineering Computations* 11:365–81.
Cary JR, Shasharina SG, Cummings JC, Reynders JVW, Hinker PJ (1997) Comparison of C++ and Fortran 90 for object-oriented scientific programming. *Computer Physics Communications* 105:20–36.
Coad P, Yourdon E (1991) *Object-Oriented Design*. Yourdon Press Computing Series.
Devloo PRB (1994) Efficiency issues in an object-oriented programming environment. *Artificial Intelligence and Object-Oriented Approaches for Structural Engineering, Civil-Comp Press*, 147–151.
Dongarra J, Lumdsdaine A, Niu X, Pozo R, Remington X (1994) Sparse matrix libraries in C++ for high performance architectures. *Proceedings of the Second Annual Object-Oriented Numerics Conference (OON-SKI'94)*, 122–138, April 24–27.
Forde BWR, Foschi RO, Stiemer F (1990) Object-oriented finite element analysis. *Computers and Structures* 34:355–374.
Gamma E, Helm R, Johnson R, Vlissisdes J (1995) *Elements of Reusable Object-Oriented Software*. Addison-Wesley.
Klapka I, Cardona A, Géradin M (1998) An object-oriented implementation of the finite element method for coupled problems. *Revue Européenne des Eléments Finis* 7: 469–504.
Macjkie RI (1992) Object oriented programming of the finite element method. *International Journal for Numerical Methods in Engineering* 35:425–436.
Metcalf M, Reid J (1990) *Fortran 90 Explained*. Oxford: Oxford Science.
Miller GR (1991) An object-oriented approach to structural analysis and design. *Computers and Structures* 40:75–82.
Robison Arch D (1996) The abstraction penalty for small objects in C++. *POOMA'96: The Parallel Object-Oriented Methods and Applications Conference*, 28 February–1 March. Santa Fe, New Mexico.
Rodrigues Alves Filho JS, Devloo PRB (1991) Object-oriented programming in scientific computations: the beginning of a new era. *Engineering Computations* 8:81–87.
Rumbaugh J (1991) *Object Oriented Modeling and Design*.
Stroustrup B (1999) *The C++ Programming Language*, 3rd edn. Addison Wesley.
Veldhuizen T (1995) Using C++ template metaprograms. *C++ Report* 7: 36–43.
Zeglinski GW, Han RPS (1994) Object-oriented matrix classes for use in a finite element code using C++. *International Journal for Numerical Methods in Engineering* 37:3921–3937.
Zimmerman T, Dubois-Pelerin Y (1992) The object-oriented approach to finite elements: concepts and implementations. *Proceedings of the First European Conference on Numerical Methods in Engineering, Brussels*, pp. 865–70.

OPTIMAL FILTERS

S J Elliott, University of Southampton, Southampton, UK

Copyright © 2001 Academic Press

doi:10.1006/rwvb.2001.0068

Optimal filters are used to extract signals from noise and in the calculation of the optimal performance of active vibration control systems. Filters are defined to be optimal when they give the best possible performance under a given set of circumstances. The best possible performance is generally defined in terms of minimizing a least-square or H_2 cost function, since this has a physical interpretation in terms of minimizing the power of an error signal, and also leads to a linear set of equations to be solved for the optimal filter if it has a digital finite impulse response (FIR) form. It is also possible to design a filter which minimizes the maximum value of the error at any frequency, which is called minimax optimization in the signal-processing literature and H_∞ minimization in the control literature. Alternatively, the optimum parameter values could be calculated for each example of a random set of data, so the parameters are themselves random variables, and maximum *a posteriori* (MAP) or maximum likelihood (ML) estimates can then be defined.

Time Domain Formulation

We will specifically concentrate here on the optimal digital FIR filter which minimizes the mean-square (H_2) error in the prototypical electrical noise cancellation problem shown in **Figure 1**. In this figure the error signal, $e(n)$, is given by the difference between a desired signal, $d(n)$, and the reference signal, $x(n)$, filtered by an FIR filter with coefficients w_i, so that:

$$e(n) = d(n) - \sum_{i=0}^{I-1} w_i x(n-i) \qquad [1]$$

The summation over $w_i x(n-i)$ in eqn [1] can be conveniently represented as a vector inner product, such that:

$$e(n) = d(n) - \mathbf{w}^{\mathrm{T}}\mathbf{x}(n) = d(n) - \mathbf{x}^{\mathrm{T}}(n)\mathbf{w} \qquad [2\mathrm{a,b}]$$

where:

$$\mathbf{w} = [w_0 w_1 \ldots w_{I-1}]^{\mathrm{T}} \qquad [3]$$

and:

$$\mathbf{x}(n) = [x(n)x(n-1) \cdots x(n-I+1)]^{\mathrm{T}} \qquad [4]$$

The objective is to find the value of each of the filter coefficients $w_0 \ldots w_{I-1}$ which minimizes the quadratic cost function given by:

$$J = E\left[e^2(n)\right] \qquad [5]$$

where E denotes the expectation operator. If $x(n)$ were not stationary, then J, and the optimal filter coefficients, would be functions of time. We assume here that all the signals are stationary and ergodic so that the expectation is time-invariant, and can be calculated by averaging over time. The cost function given by eqn [5] is thus equal to the mean-square value of the error signal. This restricted use of the expectation operator will be assumed throughout this article.

Using eqns [2a] and [2b], the cost function can be written as:

$$J = \mathbf{w}^{\mathrm{T}}\mathbf{A}\mathbf{w} + 2\mathbf{w}^{\mathrm{T}}\mathbf{b} + c \qquad [6]$$

where:

$$\mathbf{A} = E\left[\mathbf{x}(n)\mathbf{x}^{\mathrm{T}}(n)\right] \qquad [7]$$

$$\mathbf{b} = E[\mathbf{x}(n)d(n)] \qquad [8]$$

$$c = E\left[d^2(n)\right] \qquad [9]$$

In a quadratic equation having the general form of eqn [6], the matrix $\mathbf{A}$ is known as the Hessian matrix, and in this case its elements are equal to the values of the autocorrelation function of the reference signal:

$$\mathbf{A} = \begin{bmatrix} R_{xx}(0) & R_{xx}(1) & \cdots & R_{xx}(I-1) \\ R_{xx}(1) & R_{xx}(0) & & \\ \vdots & \ddots & & \\ \vdots & & \ddots & \\ R_{xx}(I-1) & & & R_{xx}(0) \end{bmatrix} \qquad [10]$$

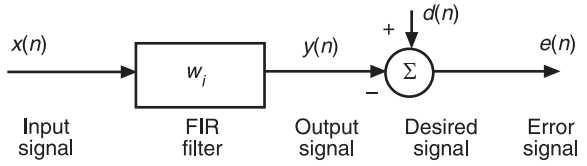


Figure 1 Model problem for the derivation of optimal FIR filter.

where $R_{xx}(m)$ is the symmetric autocorrelation function of $x(n)$, defined as:

$$R_{xx}(m) = E[x(n)x(n+m)] = R_{xx}(-m) \qquad [11]$$

in which E denotes the expectation value. Notice that the matrix $\mathbf{A}$ in eqn [10] has equal elements along each of the diagonals, i.e., it is Toeplitz.

The vector $\mathbf{b}$ has elements which are equal to the values of the cross-correlation function between the reference signal and the desired signals so that:

$$\mathbf{b} = [R_{xd}(0)R_{xd}(1) \cdots R_{xd}(I-1)]^{\mathrm{T}} \qquad [12]$$

where:

$$R_{xd}(m) = E[x(n)d(n+m)] = E[x(n-m)d(n)] \quad [13]$$

and c is a scalar constant equal to the mean-square value of the desired signal.

When written in the form of eqn [6], it is clear that the mean-square error is a quadratic function of each of the FIR filter coefficients. This quadratic function always has a minimum rather than a maximum, since J must become large and positive if any one filter coefficient takes large positive or negative values. This minimum is only unique, however, if the matrix $\mathbf{A}$ in eqn [6] is positive definite. In the case being considered here, $\mathbf{A}$ is given by eqn [7] and can either be positive definite (in which case it is also nonsingular) or positive semidefinite (in which case it is singular) depending on the spectral properties of the reference signal and the number of coefficients in the FIR filter. If there are at least half as many spectral components as filter coefficients, the reference signal is said to be persistently exciting or spectrally rich, which insures that the autocorrelation matrix given by eqn [7] is positive definite and so eqn [6] has a unique minimum. The cost function when plotted against any two coefficients will thus define a bowl-shaped performance surface or error surface, as shown in **Figure 2**.

The Wiener Filter

The value of the coefficients of the FIR filter which reduce the mean-squared error to a minimum can be found by differentiating the cost function with respect to each coefficient and setting all of the resulting derivatives to zero. It is convenient to express this differentiation using vector notation, and so we define the vector of derivatives to be:

$$\frac{\partial J}{\partial \mathbf{w}} = \left[\frac{\partial J}{\partial w_0}\frac{\partial J}{\partial w_1} \cdots \frac{\partial J}{\partial w_{I-1}}\right]^{\mathrm{T}} \qquad [14]$$

Using the definition of J in eqn [6] and the properties of vectors of derivatives, eqn [14] can be expressed as:

$$\frac{\partial J}{\partial \mathbf{w}} = 2[\mathbf{A}\mathbf{w} - \mathbf{b}] \qquad [15]$$

Assuming $x(n)$ is persistently exciting, so that $\mathbf{A}$ is not singular, the vector of optimal filter coefficients can be obtained by setting each element of [15] to zero, to give:

$$\mathbf{w}_{\mathrm{opt}} = \mathbf{A}^{-1}\mathbf{b} \qquad [16]$$

The filter which has these optimal coefficients is often called the Wiener filter after the pioneering work of Wiener in the 1940s, although the explicit solution to the discrete-time form of the problem is due to Levinson. Levinson also put forward an efficient method for solving eqn [17] which exploits the Toeplitz nature of the matrix $\mathbf{A}$, and this method is widely used in speech coding. Levinson modestly

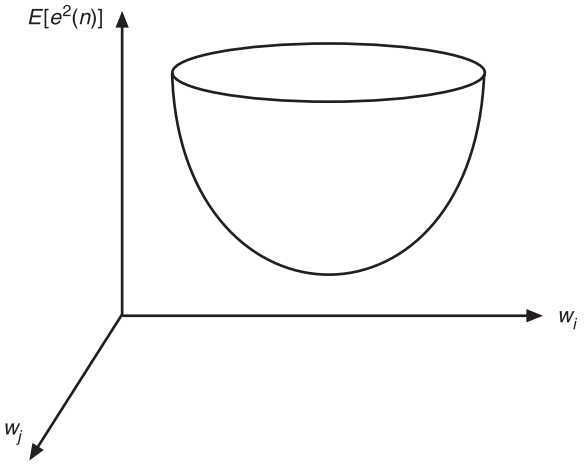


Figure 2 The quadratic error surface formed by plotting the mean square error in **Figure 1** against any two coefficients of the FIR filter.

prefaces his paper by stating that: 'A few months after Wiener's work appeared, the author, in order to facilitate computational procedure, worked out an approximate, and one might say, mathematically trivial procedure'. In fact, the discrete form of Wiener's formulation leads to an elegant matrix formulation which is very well suited to efficient numerical solution.

Using the definition of $\mathbf{A}$ and $\mathbf{b}$ in terms of the auto-and cross-correlation functions, eqn [15], for the optimal filter, can also be written as a summation of the form:

$$\sum_{i=0}^{I-1} w_i(\text{opt}) R_{xx}(k-i) R_{xd}(k) = 0 \quad \text{for} \quad 0 < k < I-1 \qquad [17]$$

This set of equations is known as the normal equations and represents a discrete form of the Wiener–Hopf equation.

The vector of cross-correlations between the I past values of the reference signal and the error signal can be written, using eqn [2b], as:

$$E[\mathbf{x}(n)e(n)] = E\left[\mathbf{x}(n)\left(d(n) - \mathbf{x}^{\mathrm{T}}(n)\mathbf{w}\right)\right] = \mathbf{b} - \mathbf{A}\mathbf{w} \qquad [18]$$

It is clear that all the elements of this vector are zero when the FIR filter is adjusted to minimize the mean-square error, as in eqn [17]. In minimizing the mean-square error, the Wiener filter thus also sets to zero the cross-correlations between the reference signal and the residual error signal over the length of the filter, which is a statement of the principle of orthogonality.

The values of the auto- and cross-correlation functions required to define the elements of $\mathbf{A}$ and $\mathbf{b}$ in eqns [7] and [8] can often be most easily estimated from measured data using the power spectral density of $x(n)$ and the cross-spectral density between $x(n)$ and $d(n)$, since the correlation function and spectral density are Fourier transform pairs. From these average properties of the reference and desired signal, the coefficients of the Wiener filter can be calculated using eqns [10], [11], and [17]. The minimum value of the mean-square error can also be obtained directly by substituting eqn [17] into eqn [6] to give:

$$J(\min) = c - \mathbf{b}^{\mathrm{T}}\mathbf{A}^{-1}\mathbf{b} \qquad [19]$$

The residual mean-square error can thus be calculated directly from the statistical properties of the reference and desired signals. This can be very useful in the early stages of a design, to help understand the trade-off between performance and filter length, for example.

Unconstrained Wiener Filter

Returning to the expression for the normal equations, eqn [17], we find that we can obtain a particularly simple expression for the frequency response of the optimal filter if we relax the assumptions that the filter must be causal and of finite length. Under these conditions the normal equations can be written as:

$$\sum_{i=-\infty}^{\infty} w_i(\text{opt}) R_{xx}(k-i) = R_{xd}(k) \quad \text{for} \quad -\infty < k < \infty \qquad [20]$$

Taking the z transform of eqn [20] allows us to express the Wiener filter in this completely unconstrained case, which is sometimes referred to as the unconstrained or two-sided Wiener filter, as:

$$W_{\text{opt}}(z) = \frac{S_{xd}(z)}{S_{xx}(z)} \qquad [21]$$

where $S_{xd}(z)$ and $S_{xx}(z)$ are the double-sided z transforms of $R_{xd}(m)$ and $R_{xx}(m)$, which can also be written as:

$$S_{xx}(z) = E\left[X\left(z^{-1}\right)X(z)\right] \qquad [22]$$

and:

$$S_{xd}(z) = E\left[X\left(z^{-1}\right)D(z)\right] \qquad [23]$$

where E denotes the expectation operator, and $X(z)$ and $D(z)$ are the z transforms of $x(n)$ and $d(n)$. In principle, the expectation operator is taken over an ensemble of signals but in practice can be taken over a series of data lengths of finite duration if the signals are stationary and ergodic. The Fourier rather than the z transform could also be taken on measured data to give estimates of the power spectral density $S_{xx}(\mathrm{e}^{\mathrm{j}\omega T})$ and cross-spectral density $S_{xd}(\mathrm{e}^{\mathrm{j}\omega T})$, in which case the Fourier transform of the optimal filter becomes:

$$W_{\text{opt}}\left(\mathrm{e}^{\mathrm{j}\omega T}\right) = \frac{S_{xd}\left(\mathrm{e}^{\mathrm{j}\omega T}\right)}{S_{xx}\left(\mathrm{e}^{\mathrm{j}\omega T}\right)} \qquad [24]$$

Causally Constrained Wiener Filter

It is easy to compute the frequency response of the optimal filter given by eqn [24], but its use could be misleading because it is not constrained to be causal, and so might be impossible to realize in a real-time system. It is also possible to calculate the frequency response of the optimum filter when it is constrained to be causal but not constrained to be of finite duration. In practice this gives an equivalent result to solving the normal equations for an FIR filter with very many coefficients and then taking the Fourier transform of the resulting impulse response. The method of deriving such a filter in the frequency domain, which is outlined below, was originally due to Bode and Shannon.

The Wiener–Hopf equation for the optimal filter when it is constrained to be causal, but not constrained to be of finite length, can be written from eqn [17] as:

$$\sum_{i=0}^{\infty} w_i(\text{opt}) R_{xx}(k-i) = R_{xd}(k) \quad \text{for} \quad -\infty < k < \infty \qquad [25]$$

We now assume the very special condition that the reference signal, $x(n)$, is given by a sequence, $v(n)$, which is completely uncorrelated from sample to sample, i.e., white noise, and also has zero mean and unit variance, so that $R_{xx}(m) = R_{vv}(m) = \delta(m)$, which equals 1 if $m = 0$ and which otherwise equals zero. Under these conditions eqn [25] has the form:

$$\sum_{i=0}^{\infty} w_i(\text{opt}:v)\delta(k-i) = R_{vd}(k) \quad \text{for} \quad -\infty < k < \infty \qquad [26]$$

and because of the sifting property of $\delta(m)$, eqn [26] is equivalent to:

$$w_k(\text{opt}:v) = R_{vd}(k) \quad \text{for} \quad 0 < k < \infty \qquad [27]$$

Thus, if the reference signal is white noise, the impulse response of the optimal causal filter is equal to the causal part of the cross-corelation function between the reference and desired signal. The z transform of the optimal filter under these conditions can be written as:

$$W_{\text{opt}:v}(z) = \{S_{vd}(z)\}_+ \qquad [28]$$

where $S_{vd}(z)$ is the z transform of the cross-corelation between $v(n)$ and $d(n)$ and $\{\cdot\}_+$ denotes the fact that the z transform of the causal part of the quantity inside the brackets has been taken, so that:

$$\{S_{vd}(z)\}_+ = Z[R_{vd}(m)U(m)] \qquad [29]$$

where Z denotes z transformation and $U(m)$ is the discrete step function which is equal to 1 for $m > 0$ and is equal to zero for $m < 0$.

In the more general case, the reference signal is not a white-noise sequence. The problem can still be reduced to that of a white-noise reference, however, by prewhitening the reference signal. Specifically, we assume that the reference signal was originally generated by passing a zero mean white-noise signal, $v(n)$, which has a variance of unity, so that its power spectral density is also unity, through a minimum-phase shaping filter, with frequency response $F(e^{j\omega T})$. If the double-sided z transform of the autocorelation function $R_{xx}(m)$, which can be written as $S_{xx}(z)$, is rational, i.e., it has a number of well-defined poles and zeros, then $S_{xx}(z)$ can be expressed in the form:

$$S_{xx}(z) = F^+(z)F^-(z) \qquad [30]$$

where $F^+(z)$ contains the poles and zeros of $S_{xx}(z)$ inside the unit circle and thus has an entirely causal and minimum phase impulse response, and $F^-(z)$ contains the poles and zeros of $S_{xx}(z)$ outside the unit circle, and thus has a noncausal impulse response. $F^+(z)$ and $F^-(z)$ are called the spectral factors of $S_{xx}(z)$.

Notice that because $R_{xx}(m)$ is symmetrical and so $S_{xx}(z) = S_{xx}(z^{-1})$, then:

$$F^-(z) = F^+(z^{-1}) \qquad [31]$$

$F^-(z)$ can thus be interpreted as having the same form of impulse response as $F^+(z)$, but reversed in time. Since we are assuming that $x(n)$ is generated by passing $v(n)$ through the shaping filter $F(e^{j\omega T})$, then in the frequency domain the power spectral density must be equal to:

$$S_{xx}(e^{j\omega T}) = F(e^{j\omega T})F^*(e^{j\omega T})S_{vv}(e^{j\omega T}) \qquad [32]$$

where * denotes complex conjugation. But $S_{vv}(e^{j\omega T})$ is equal to unity by definition and setting $z = e^{j\omega T}$ in eqn [30] and comparing this with eqn [32], we can see that the frequency response of the shaping filter and its conjugate are equal to:

$$F(e^{j\omega T}) = F^+(e^{j\omega T}), \quad F^*(e^{j\omega T}) = F^-(e^{j\omega T}) \qquad [33a, b]$$

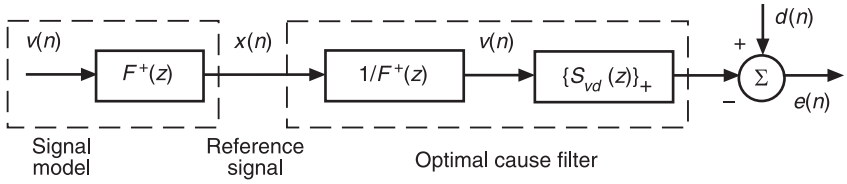


Figure 3 Signal model for the reference signal, $x(n)$, in which it assumed to be generated by passing a white-noise signal, $v(n)$, through a shaping filter, $F(z)$, and the optimal causal filter, which then takes the form of a prewhitening filter, $1/F(z)$, and the Fourier transform of the causal part of the cross-correlation function between $v(n)$ and $d(n)$, $\{S_{vd}(z)\}^{+}$.

The reference signal can also be transformed back into a white-noise signal of unit variance, $v(n)$, by passing it through the inverse of the shaping filter, which is stable since $F^{+}(z)$ is minimum phase, in which case the z transform of $v(n)$ is given by:

$$V(z) = \frac{X(z)}{F^{+}(z)} \qquad [34]$$

Thus the complete form of the z transform of the optimum causal filter is equal to:

$$W_{\text{opt}}(z) = \frac{1}{F^{+}(z)}\{S_{vd}(z)\}_{+} \qquad [35]$$

as illustrated in **Figure 3**.

Using the definition of the cross-spectral density, we can also write:

$$\begin{aligned} S_{vd}(z) &= E[V^{*}(z)D(z)] \\ &= \frac{1}{F^{-}(z)}E[X^{*}(z)D(z)] = \frac{S_{xd}(z)}{F^{-}(z)} \end{aligned} \qquad [36]$$

so that the optimal causal filter can be written in terms of the cross-spectral density between the reference and disturbance signal and the spectral factors of the reference signal's power spectral density as:

$$W_{\text{opt}}(z) = \frac{1}{F^{+}(z)}\left\{\frac{S_{xd}(z)}{F^{-}(z)}\right\}_{+} \qquad [37]$$

The frequency domain expression for the optimum causal filter can be found by letting $z = e^{j\omega T}$ in eqn [37] and noting that $F^{+}(e^{j\omega T}) = F(e^{j\omega T})$ and $F^{-}(e^{j\omega T}) = F^{*}(e^{j\omega T})$ so that:

$$W_{\text{opt}}(e^{j\omega T}) = \frac{1}{F(e^{j\omega T})}\left\{\frac{S_{xd}(e^{j\omega T})}{F^{*}(e^{j\omega T})}\right\}_{+} \qquad [38]$$

Eqn [38] can be used as the basis for the practical calculation of the optimum filter from measured data, although some care needs to be taken with the discrete frequency form of this equation for the optimal filter because of the circular nature of the discrete Fourier transform. The frequency response of the shaping filter may be calculated in practice from the measured power spectral density by using the Hilbert transform to calculate the minimum-phase component of the frequency response of a system whose magnitude is equal to $\sqrt{S_{xx}(e^{j\omega T})}$.

Both the time and frequency domain formulations of the optimal filter may be extended to the multichannel case and to the case of the feedforward and feedback controllers used in active control.

Nomenclature

$\mathbf{A}$	Hessian matrix
c	scalar constant
$d(n)$	desired signal
$e(n)$	error signal
E	expectation operator
$U(m)$	discrete step function
$v(n)$	white-noise signal
$x(n)$	reference signal

See also: **Adaptive filters**; **Digital filters**; **Signal processing, model based methods**; **Stochastic systems**

Further Reading

Clarkson PM (1993) *Optimal and Adaptive Signal Processing*. Boca Raton, FL: CRC Press.

Elliott SJ (2001) *Signal Processing for Active Control*. Academic Press.

Grimble MJ, Johnson MA (1988) *Optimal Control and Stochastic Estimation: Theory and Applications*, volume II, p. 784.

Haykin S (1996) *Adaptive Filter Theory*. 3rd edn. Englewood Cliffs, NJ: Prentice Hall.

Kailath T (1981) *Lectures on Wiener and Kalman Filtering*. Springer.

Markel JD, Gray Jr. AH (1976) *Linear Prediction of Speech*. Springer.

Orfanides SJ (1985) *Optimum Signal Processing*. New York: Macmillan.

Rabiner LR, Gold B (1975) *Theory and Application of Digital Signal Processing*. Prentice Hall.

Treichler JR, Johnson CR, Larimore MG (1987) *Theory and Design of Adaptive Filters*. John Wiley.

Widrow B, Stearns SD (1985) *Adaptive Signal Processing*. Prentice Hall.

Widrow B, Walach E (1995) *Adaptive Inverse Control*. Prentice Hall.

Wiener N (1949) *Extrapolation Interpolation and Smoothing of Stationary Time Signals*. John Wiley.

P

PACKAGING

J Marcondes, San Jose University, San Jose, CA, USA

Copyright © 2001 Academic Press

doi:10.1006/rwvb.2001.0161

Most packaging systems are designed to protect products from the hazards of the distribution environment. To properly design a packaging system, a packaging engineer needs to identify design parameters from three areas: the distribution environment, the product, and the packaging material. Among the many hazards of the distribution environment that can cause product damage, shock, vibration and compression forces are of high significance and should be addressed in design. This article covers the identification of these forces in (i) the distribution environment; (ii) the product; and (iii) the packaging materials. In addition, it also covers how this information is used to design a protective packaging system for a fragile product, and how to test the packaging system to verify that it in fact works as designed.

Information Required for Structural Packaging Design

Although many hazards exist in distribution, those indicated in **Table 1** are usually the three most used for a proper packaging design. In **Table 1**, the first column represents the nature of the hazard (shock, vibration or compression). The second column indicates the type of information that is required to identify the hazards in the distribution environment. These can be extended to the use of the product, or to moving it from one place to another anytime in its life. The third column represents the information that is required about the product. This is important because the design needs to cover only what is required by the product. Designing a package that overprotects the product is wasteful. For example, if a product can sustain without damage, drops of up to 25 cm and it is known that in distribution, drops from up to 75 cm are expected, then the protective package needs to account for the difference (50 cm). The information required for design is combined as shown in **Figure 1**. Initially, the information needs to be acquired. As seen in **Figure 1**, information about the distribution environment is used for the design of the protective packaging system as well as for the testing of the final system. Information about product

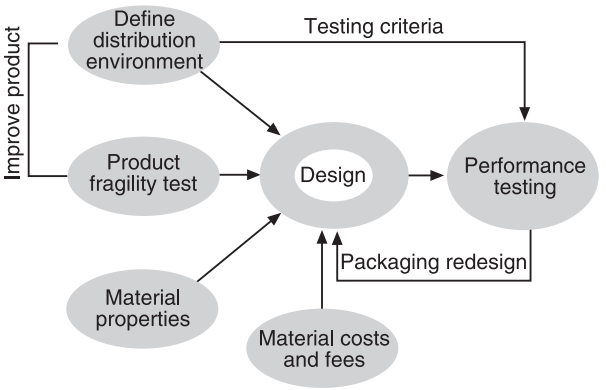


Figure 1 The structural development process for protective packaging.

Table 1 Information required for structural packaging design

Hazard	Distribution environment	Product	Packaging material
Shock	Equivalent free fall drop height	Shock fragility	Shock transmission characteristics
Vibration	Power spectrum density envelope	Resonance of components	Vibration transmission characteristics
Compression	Stacking height in storage and transport	Compression strength and creep load share allowed	Compression strength and creep

testing may be used for product improvement if the packaging development occurs in parallel with the development of the product. Packaging redesign is often necessary due to design oversights, since the procedure used for structural packaging design is rather simplified.

Obtaining Information about the Distribution Environment

Information about the distribution environment may be obtained in the following ways: (i) direct measurement and observation; (ii) applicable standards and specific industry requirements; or (iii) available literature. The most accurate way to obtain this information is by direct measurement and observation, since the conditions change with time. However, for the information to be reliable and truly representative of the distribution environment, the measurement procedure must account for all variables, which in many cases may be impractical.

Obtaining shock information about the distribution environment In essence, what a designer needs to know is the 'equivalent drop height', a quantity that represents not only free fall drops but also all other kinds of impacts a package receives in distribution (see **Shock**).

Obtaining vibration information about the distribution environment Vibration information may be obtained from the literature. It may also be measured with accelerometers and further processed using spectral analysis (**Figure 2**). Many studies have shown that the most severe levels of vibration in road transport are encountered above the rear axle of vehicles. Also, studies have shown that the vertical vibration is generally more severe than lateral or longitudinal. Most vibration data reported in the literature refer to vertical vibration. When designing packages, engineers look for significant frequencies in the spectrum. Vibration intensity, although important, is not used often in the design process. However, it is used in testing packaging and packaging systems for performance in distribution. **Table 2** shows the most significant frequencies encountered in the literature, and **Figure 3** shows a power spectrum density (PSD) for a loaded semitrailer measured when traveling at speeds between 60 and 80 km h^{-1} on a variety of pavements (in the PSD shown, the bandwidth used was 1 Hz, as in most vibration measurements for packaging applications).

Table 2 Frequency ranges of high vibration intensity for various modes

Mode	*Range* (Hz)
Reference: ASTM	
Road	4–16
Air	12–100
Rail	2–50
Reference: Other studies	
Road	2–5

Obtaining compression information about the distribution environment Compression forces are usually split into static and dynamic forces. Static forces are usually found in warehouse storage and dynamic forces in vehicles for transport. Static forces are determined by calculating the weight imposed on the lowest package in a stack. Simply, for a stack of packages with n packages, the static force is given by:

$$F_s = (n_s - 1)m_p g \quad [1]$$

In cases when the packages to be stacked are unknown, a common density of 10 lb ft^{-3} (160 kg m^{-3}) may be used to calculate the static force. In this case the static force becomes:

$$F_s = \delta_L g(H_s - H_p)L_p W_p \quad [2]$$

Dynamic force is calculated by incorporating a dynamic factor, and using the stack heights encountered in

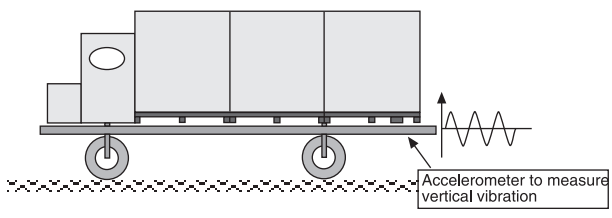


Figure 2 Measuring vibration in vehicles.

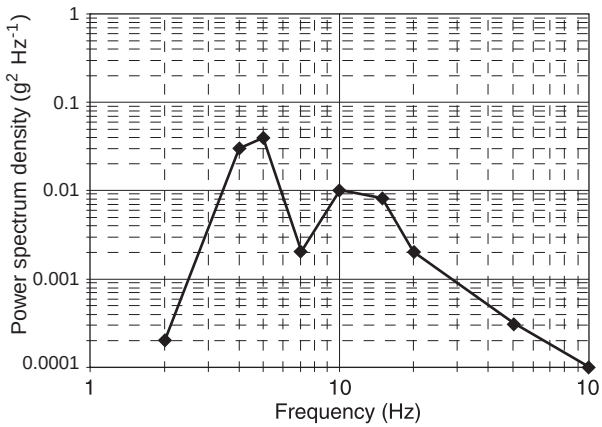


Figure 3 Random vibration spectrum for ISTA testing.

vehicles for transport. The dynamic force may be calculated by:

$$F_d = (n_t - 1)m_p g D_f \quad [3]$$

For mixed or unknown loads, the dynamic force is:

$$F_d = \delta_L g(H_t - H_p)L_p W_p D_f \quad [4]$$

The dynamic factor has been determined experimentally and is shown in **Table 3**, and is related to the intensity of vibration and the conditions of the road.

Obtaining Information about the Product

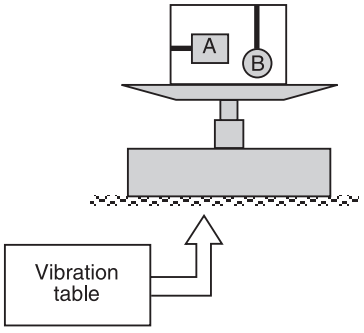
Products are tested, without any packaging, to determine their inherent ability to sustain shock, vibration and compression forces. In many cases, due to the lack of prototypes for testing, the information may be estimated, based on the properties of the components of the product. However, due to the complexity of most products, it is best to perform product-testing in order to obtain the most accurate data possible. This is important because any inaccurate information used about the product will produce a nonoptimal design, which will result either in product damage or overpackaging (often never detected).

Obtaining information about the product shock fragility Typically, one determines the ability of the product to sustain impacts without damage. This level, in acceleration units, *g*, is the 'product shock fragility' (see **Shock**).

Obtaining information about the product vibration sensitivity To obtain vibration data about the product, a prototype is placed on a vibration tester and a test is conducted to identify the resonant frequency of its components, in each of the orthogonal directions (**Figure 4**). There are basically two methods for this; resonance search using a sine sweep test, and monitored component random vibration.In the sine sweep test, components of the product are observed for resonance (visually or audibly). In the random vibration method, components need to be monitored by mounting a small accelerometer on the components, and determining the vibration transmission between product and component. The added mass of the accelerometer needs to be taken into account, using:

$$\omega_{Rc} = \omega_{Rca}(m_c + m_a/m_c)^{0.5} \quad [5]$$

Obtaining information about the product compression resistance A compression test may be used to determine the product's ability to sustain compression forces. This is done by applying orthogonal compression forces until product failure or some other predetermined limit is achieved.



	Example	
Direction	Resonance	
	Component A	Component B
Vertical	18 Hz	none
Longitudinal	25 Hz	35 Hz
Lateral	none	35 Hz

Figure 4 Product fragility – vibration sensitivity.

Table 3 Dynamic factor vs road condition and *RMS* g vertical vibration

Road surface	Smooth		Some roughness		Rough	
Typical condition	New pavements		Joints, cracks		Damaged pavement	
RMS g	0.2	0.35	0.4	0.5	0.6	0.7
D_f	2	3	4	5	7	10

Obtaining Information about the Packaging Material

Packaging material, usually expanded foams and corrugated pads, are tested to determine their ability to absorb impacts, attenuate vibration and resist compression forces. An important factor to observe is that these tests are highly influenced by ambient conditions, therefore proper conditioning is important. For most packaging applications, cushioning for vibration attenuation is not the main goal. Packages are designed for shock protection and must be verified that they do not amplify vibration in ranges that are critical for the vehicles used in transport, or for the product. **Figure 5** shows what a designer is looking for, for a frequency that either (i) has a high intensity input from the vehicle, or (ii) makes components in the product resonate. If the frequency in which either (i) or (ii) occur will make the material amplify vibration (**Figure 6**), then the design needs to be modified. **Figure 7** shows a typical effect of cushioning a product.

Obtaining shock data about packaging materials Typically, the information required is the shock transmission through the material to the product, during an impact (see **Shock**).

Obtaining vibration data about packaging materials Vibration transmission properties of packaging materials are obtained by determining the range of frequencies where vibration is amplified or attenuated (**Figures 8 and 9**). The results are presented in the form of vibration transmissibility curves, as shown in **Figure 10**. The tests used to obtain this curve are conducted using samples of the packaging material, with a specified weight on top (**Figure 8**). The assembly is subjected to vibration and the vibration transmissibility is measured between the vibration table and the weight on top of the cushion. The three lines in **Figure 10** represent: (i) the boundary between coupling and amplification; (ii) the maximum amplification, or resonance; and (iii) the boundary between amplification and attenuation.

Obtaining compression data about packaging materials Two pieces of data are needed from materials: compression resistance and creep. Compression resistance may be determined by applying a quasi-static force at a speed of approximately 12 mm min^{-1}, as most standards specify. This is used to obtain force–deflection information or modulus of elasticity of the

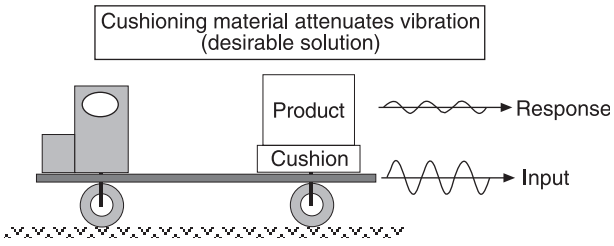


Figure 5 Vibration transmission attenuation.

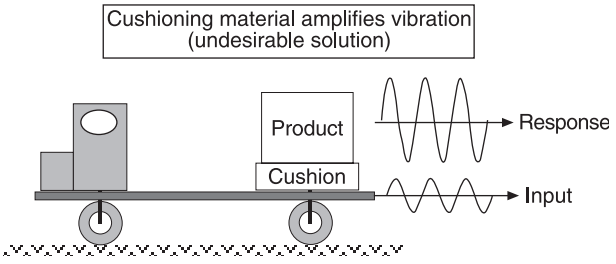


Figure 6 Vibration transmission amplification.

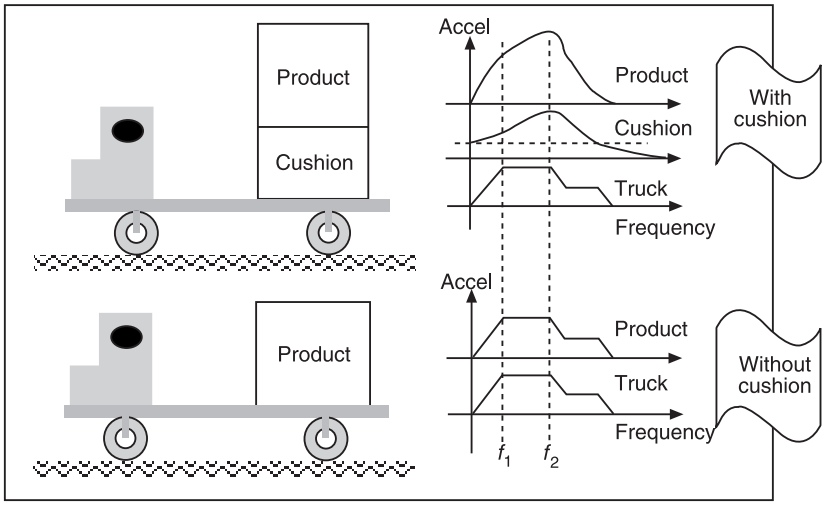


Figure 7 Vibration transmissibility – effect of cushioning a product.

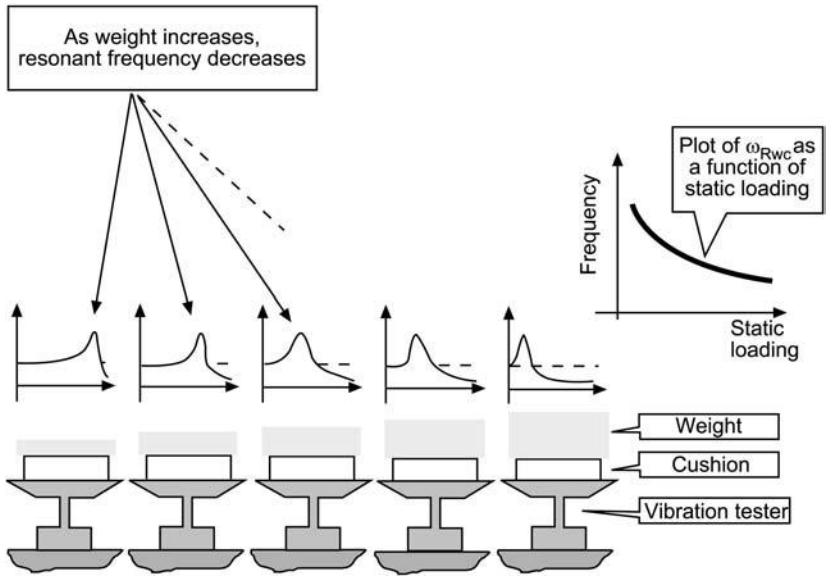


Figure 8 Building transmissibility curves.

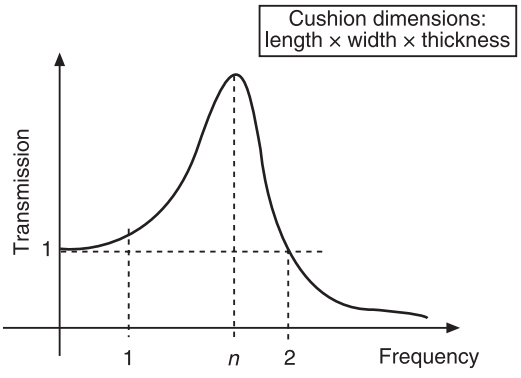


Figure 9 Data for constructing transmissibility curves.

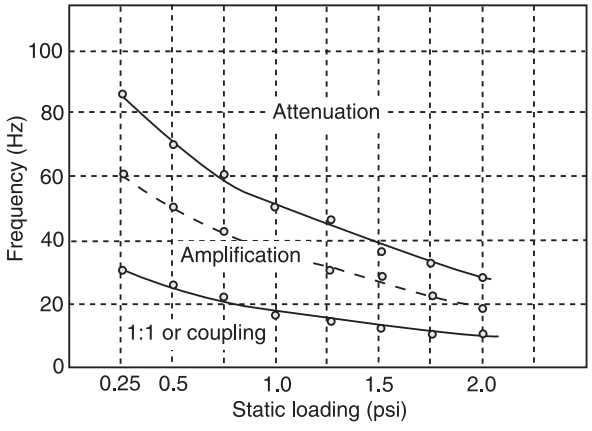


Figure 10 Vibration transmissibility curves for data in **Figure 9**.

material. Most materials have different behaviors as force is applied in different directions, so it is important to note the direction of force application. Creep data is determined by measuring slow deformation over time as a constant force is applied on the material.

Different materials have different properties. For all practical purposes, there is not such a thing as a good or bad cushioning material, neither an overall 'superior' cushioning material. What one may find is a bad design, using incorrect information. As long as a material deflects when a dynamic force is imposed on it, it should work as a cushion for product protection. In design, one is to find the range of conditions in which the material will work satisfactorily.

Packaging Design

The package is designed by combining all nine elements of data obtained (last three rows in **Table 1**). Usually the first thing to do is to determine the range of static loading (product weight over cushion bearing area) that will provide maximum product protection against impacts. Then, the material chosen is studied for vibration transmission and creep. The result must be a material configuration that works for all three factors: shock, vibration and compression. **Figures 11–13** show how the static loading is picked from cushion curves and vibration transmissibility curves and how the information is combined to determine the proper static loading for product protection. This procedure is done for each face of the product. After the static loading for each product face

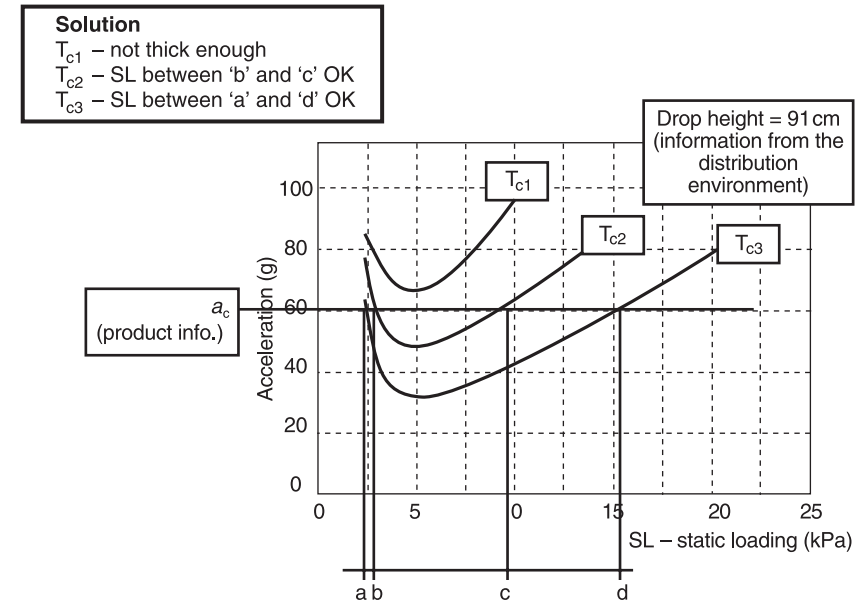


Figure 11 Selecting static loading for shock.

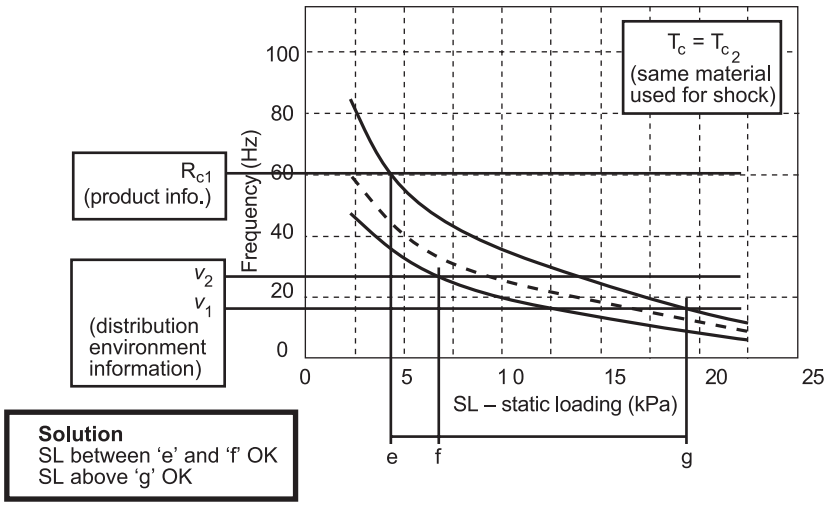


Figure 12 Selecting static loading for vibration.

is selected, as shown in **Figure 13,** the designer determines how the required cushion area is to be distributed on the product's face. At this point, care is taken that the area is distributed according to the location of the center of gravity, and that the area of individual cushion blocks are not too small compared to the cushion thickness, otherwise buckling may occur during impacts.

Packaging Testing

Packaging performance testing is a common procedure, used to determine the performance of the packaging system when subjected to tests that simulate the conditions used for design. Tests may be performed according to general standards (such as American Society for Testing and Materials, ASTM, International Safe Transit Association, ISTA, or International Standards Organization, ISO), or to specific protocols, that are generally company-specific. Most testing protocols include the following tests: free fall drop, random vibration, and compression.

There are various types of testers that may be used. The combination of testing equipment available and the knowledge about the distribution environment hazards usually define the testing protocol used. An

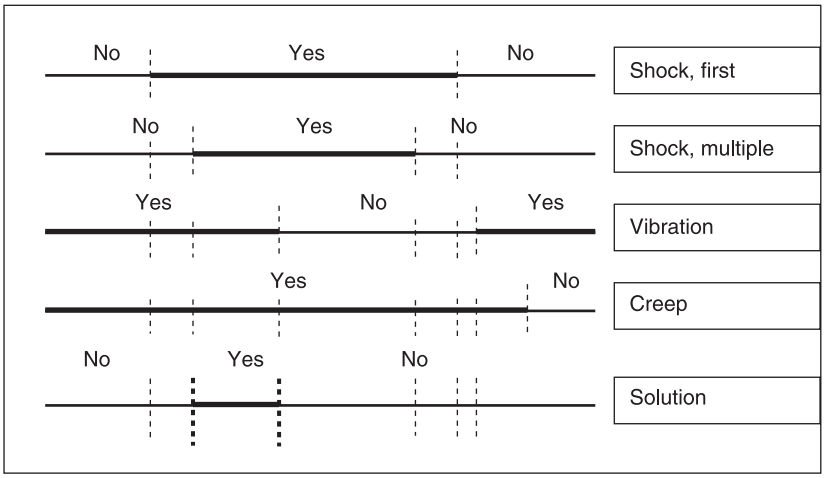


Figure 13 Choosing static loading.

important issue to be considered is the clear definition of the acceptance criteria, or damage. Sometime this is rather straightforward, but for some products it may be quite difficult to draw the line between pass and fail.

Nomenclature

a_c	product critical acceleration or shock fragility
D_f	dynamic factor
F_d	dynamic vertical force on bottom package
F_s	static vertical force on bottom package
g	acceleration of gravity
H_p	height of a package
H_s	height of a stack of identical packages in storage
H_t	height of a stack of identical packages in transport
L_p	length of a package
m_a	mass of an accelerometer
m_c	mass of a products component
m_p	mass of each of the identical packages in the stack
n_s	number of identical packages in a stack in storage
n_t	number of identical packages in a stack in transport
SL	static loading
T_c	cushion thickness
W_p	width of a package
δ_L	load density
ω_{Rc}	resonant frequency of a products component
ω_{Rca}	measured resonant frequency of a products component plus accelerometer attached to it
ω_{Rwc}	resonant frequency of a weight/cushion combination
ωv_1	lower end of a frequency range with high vibration intensity in a vehicle
ωv_2	upper end of a frequency range with high vibration intensity in a vehicle
ω_1	boundary between coupling and amplification in transmissibility curves
ω_2	boundary between amplification and attenuation in transmissibility curves

See also: **Absorbers, vibration**; **Crash**; **Environmental testing, overview**; **Shock**; **Transducers for relative motion**; **Vibration transmission**.

Further Reading

ASTM (1993) *Selected ASTM Standards on Packaging*. D-4169-93. ASTM.

Burgess G (1988) Product fragility and damage boundary theory. *Packaging Technology and Science* 1: 5–10.

Crede CE (1988) Theory of vibration isolation. In: Harris CM (ed.) *Shock and Vibration Handbook*, ch. 30. McGraw Hill.

Hatae MT (1988) Packaging. In: Harris CM (ed.) *Shock and Vibration Handbook*, ch. 41. McGraw Hill.

Marcondes J (1997) Vibration. In: Brody AL and Marsh KS (eds) *The Wiley Encyclopedia of Packaging Technology*, pp. 955–958. John Wiley.

Prather S (1998) *Determining a Dynamic Strength Reduction Factor for Regular Slotted Containers*. MS thesis, Packaging Program, San Jose State University, CA.

Singh SP, Antle JR, Burgess GJ (1992) Comparison between lateral, longitudinal and vertical vibration levels in commercial truck shipments. *Packaging Technology and Science* 5: 71–75.

PACKAGING, ELECTRONIC

See **ELECTRONIC PACKAGING**

PARALLEL PROCESSING

D Rixen, Delft University of Technology, Delft, The Netherlands

Copyright © 2001 Academic Press

doi:10.1006/rwvb.2001.0008

Introduction

To perform numerical simulations of complex systems, powerful computing systems are required. Computational speed and memory size are continuously improving thanks to breakthroughs in electronic ship technologies and to advanced computer architecture (vector instructions, RISK processors, caching ...). So-called supercomputing systems can be obtained by teaming together several computing units in order to increase the computing power and the memory that can be managed. It is not the intention of this text to review the technology of parallel computers, but it is essential to understand the architecture of such machines in order to make good use of their high-performance computing (HPC) capabilities.

Parallel computers are mainly characterized according to the following aspects:

- Granularity. Coarse grain computers have a small number of processors (e.g., 32) and are used for applications where the problem to be solved calls for multitasking with a high degree of interdependence between tasks. Fine grain supercomputers contain up to several thousands of processors and are suitable for applications involving highly independent tasks such as in neural networks.
- Memory organization. For a shared memory machine, the same memory is accessible to all the processors, meaning that a data has a single address for all processors. In distributed memory machines, every processor manages its memory locally and data are exchanged between processors by sending messages (message passing paradigm). To handle the message passing and synchronization between processors, users rely on specific instructions provided by the computer manufacturer or use standard packages such as MPI (message passing interface). It should be noted that in shared memory machines, memory is also physically distributed among the processors in order to avoid saturation of the communication network between processors and memories. But the data handling is then performed by the operating system and is transparent to the user. The advantage of shared memory machines is that it simplifies programming and ensures that a data exists only once, but the user has a better control on the data traffic in distributed memory machines.
- Interconnectivity. The topology of the network connecting all the processors and memory locations is of primordial importance to the user in order to make efficient use of the hardware. Some of the basic interconnectivity topologies are described in **Figure 1**. The computing modules are in a single box (supercomputers) or separated such as in a cluster of interconnected computers.

For some applications, it is sufficient if every processor performs the same task but on different data (single instruction/multiple data (SIMD)). For most scientific computing applications however, MIMD (multiple instructions/multiple data) computers are used.

The fundamental question in parallel computing is 'Do we compute faster if we run the job on more processors?' Parallel performance is measured by the speed-up S_p and the parallel efficiency E_p defined as:

$$S_p = t_1/t_p \quad \text{and} \quad E_p = S_p/p \qquad [1]$$

where t_1 and t_p are the time required to perform the computation on one processor and on p processors, respectively.

The parallel efficiency that can be achieved depends on the fraction f of work that must be performed sequentially. The maximum speed-up that can be obtained when increasing the number of processors used to solve a given problem is $S_p = 1/f$ and the parallel efficiency E_p goes to zero (Amdahl's law). Hence it is essential to design algorithms with a minimum fraction of sequential work. If we now assume that the size of the problem to be solved

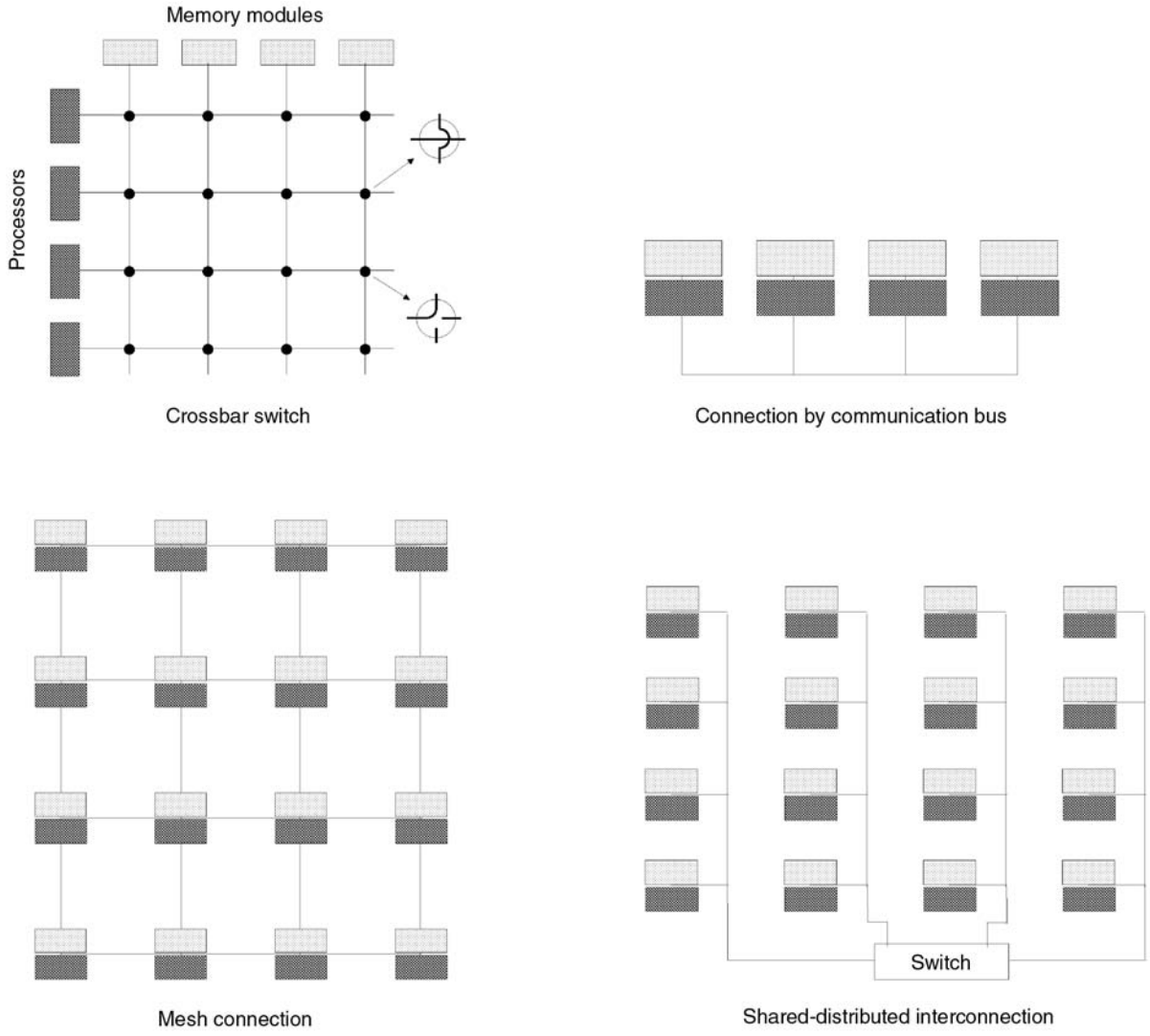


Figure 1 Network topology of parallel computers.

increases proportionally to the number of processors used (e.g. because memory size increases with the number of processors), the maximum speed-up that can be achieved tends towards $S_p = p(1 - f)$ which is a more optimistic perspective (Gustafson's model). Let us note that communication costs are not included in this simple analysis.

Reorganizing in parallel subtasks the way the final result will be computed can lead to an increase in the number of operations, hence jeopardizing the desired parallel efficiency. The property of an algorithm to incur a constant (or nearly constant) number of operations when the number of processors is increased is known as numerical scalability. Although numerical scalability is an essential property of a parallel algorithm, it will exhibit parallel scalability, i.e. deliver larger speed-up for a larger number of processors only if the communication costs and management overhead are small. Unfortunately, numerical scalability is usually obtained by transferring data among processors and thus numerical and parallel scalability are generally conflicting objectives.

Some operations can be parallelized in a straightforward manner such as multiplying and adding matrices. Indeed basic matrix operations can be distributed among processors by partitioning the matrices into blocks. Most machines are provided with a library of matrix routines optimized for the specific processor and network architecture (basic linear algebra subprograms (BLAS)). However, in engineering computations, most of the computing time is spent in solving systems of equations. Designing efficient parallel solvers is not easy and is usually problem dependent. In the next section we will discuss the different approaches advocated for building parallel solvers.

Direct and Iterative Parallel Solvers

For some special engineering problems, naturally independent tasks can be easily defined (e.g., computing the coefficients of the Fourier expansion of the solution in an axisymmetric structure or evaluating simultaneously different designs in optimization). However, in general, a single system or a sequence of nonsimultaneous systems of equations must be solved. Solving large linear systems on parallel computers has been, and still is, a challenging research field since algorithms that are highly efficient for sequential machines usually perform poorly on parallel computers. Parallel solvers can be constructed in different ways as explained next. First by re-organizing classical factorization methods and secondly by applying iterative solvers. Some of the most efficient methods, however, are found by combining direct and iterative solvers.

Direct Solvers

Consider the linear system:

$$\mathbf{K}\mathbf{u} = \mathbf{f} \qquad [2]$$

where $\mathbf{K}$ is for instance a stiffness matrix, a dynamic time-stepping operator or a tangent matrix in nonlinear analysis, and where $\mathbf{u}$ is the set of degrees of freedom (DOF). Direct solvers perform the factorization of $\mathbf{K}$ (e.g., Gaussian factorization) and forward/backward substitutions to find $\mathbf{u}$. The looping sequence on rows and columns within the factorization and substitutions can be organized in order to maximize the amount of independent (i.e., parallel) tasks. However, as the number of processors increases, the parallel efficiency becomes very poor due to the large amount of communications required by the inherently sequential factorization and substitution algorithm.

A better alternative is then to use an approach similar to multifrontal or block-LU methods. Assuming that the structure is subdivided into N_s subparts (called substructures or subdomains) as in **Figure 2**, each part $\Omega^{(s)}$ has internal DOF $\mathbf{u}_i^{(s)}$ and boundary DOF $\mathbf{u}_b^{(s)}$ on the interface. Calling $\mathbf{f}_i^{(s)}$ and $\mathbf{f}_b^{(s)}$ the forces applied on the internal and boundary DOF, the local equilibrium of a subdomain $\Omega^{(s)}$ is:

$$\begin{bmatrix} \mathbf{K}_{ii}^{(s)} & \mathbf{K}_{ib}^{(s)} \\ \mathbf{K}_{bi}^{(s)} & \mathbf{K}_{bb}^{(s)} \end{bmatrix} \begin{bmatrix} \mathbf{u}_i^{(s)} \\ \mathbf{u}_b^{(s)} \end{bmatrix} = \begin{bmatrix} \mathbf{f}_i^{(s)} \\ \mathbf{f}_b^{(s)} + \mathbf{g}^{(s)} \end{bmatrix} \qquad [3]$$

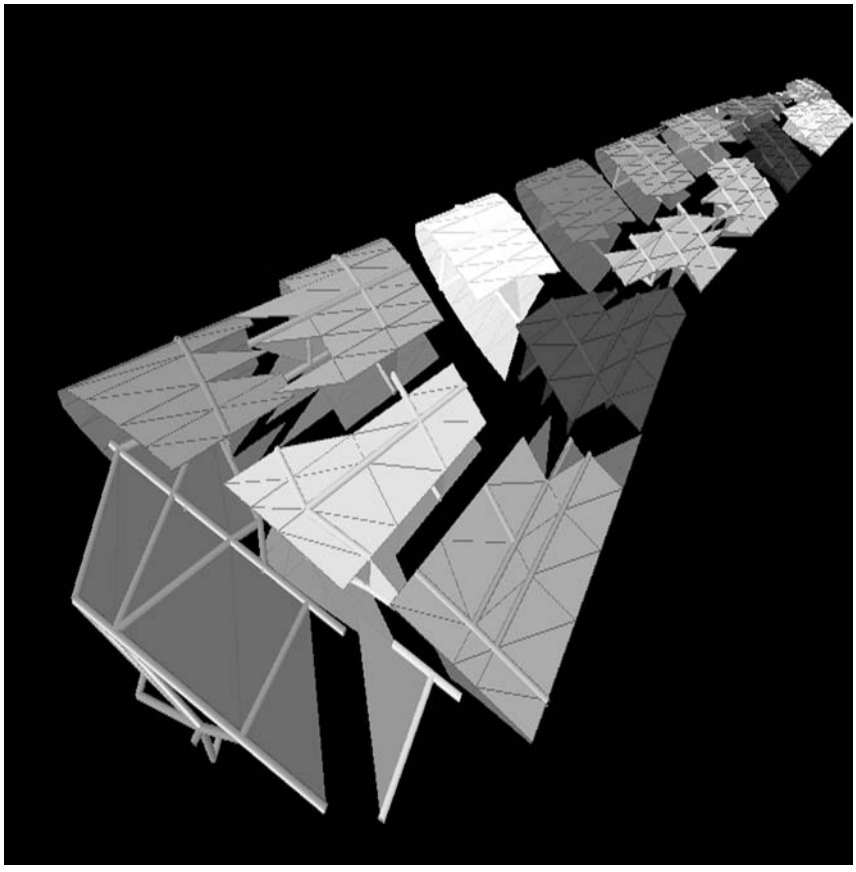


Figure 2 (See Plate 50). Nonoverlapping decomposition of a finite element model. (Courtesy of the Center for Aerospace Structures, University of Colorado, Boulder.)

where $\mathbf{g}^{(s)}$ are the connection forces to the neighboring domains. The local DOF are then identified to the global set $\mathbf{u}$ by:

$$\begin{bmatrix} \mathbf{u}_i^{(s)} \\ \mathbf{u}_b^{(s)} \end{bmatrix} = \begin{bmatrix} \mathbf{0} & \cdots & \mathbf{0} & \mathbf{I} & \mathbf{0} & \cdots & \mathbf{0} & \mathbf{L}_b^{(s)} \end{bmatrix} \begin{bmatrix} \mathbf{u}_i^{(1)} \\ \vdots \\ \mathbf{u}_i^{(N_s)} \\ \mathbf{u}_b \end{bmatrix} \quad [4]$$

or:

$$\mathbf{u}^{(s)} = \mathbf{L}^{(s)}\mathbf{u} \quad [5]$$

where $\mathbf{L}_b^{(s)}$ is a Boolean matrix expressing the assembly of the subdomains on the interface. The initial problem (eqn [2]) can now be expressed as if it results from the assembly of the substructures, namely:

$$\left(\sum_{s=1}^{N_s} \mathbf{L}^{(s)^{\mathrm{T}}} \mathbf{K}^{(s)} \mathbf{L}^{(s)} \right) \mathbf{u} = \sum_{s=1}^{N_s} \mathbf{L}^{(s)^{\mathrm{T}}} \mathbf{f}^{(s)} \quad [6]$$

or:

$$\begin{bmatrix} \mathbf{K}_{ii}^{(1)} & \mathbf{0} & \mathbf{0} & \mathbf{K}_{ib}^{(1)}\mathbf{L}_b^{(1)} \\ \mathbf{0} & \ddots & \mathbf{0} & \vdots \\ \mathbf{0} & \mathbf{0} & \mathbf{K}_{ii}^{(N_s)} & \mathbf{K}_{ib}^{(N_s)}\mathbf{L}_b^{(N_s)} \\ \mathbf{L}_b^{(1)^{\mathrm{T}}}\mathbf{K}_{bi}^{(1)} & \cdots & \mathbf{L}_b^{(N_s)^{\mathrm{T}}}\mathbf{K}_{bi}^{(N_s)} & \sum_{s=1}^{N_s} \mathbf{L}_b^{(s)^{\mathrm{T}}}\mathbf{K}_{bb}^{(s)}\mathbf{L}_b^{(s)} \end{bmatrix} \times \begin{bmatrix} \mathbf{u}_i^{(1)} \\ \vdots \\ \mathbf{u}_i^{(N_s)} \\ \mathbf{u}_b \end{bmatrix} = \begin{bmatrix} \mathbf{f}_i^{(1)} \\ \vdots \\ \mathbf{f}_i^{(N_s)} \\ \sum_{s=1}^{N_s} \mathbf{L}_b^{(s)^{\mathrm{T}}}\mathbf{f}_b^{(s)} \end{bmatrix} \quad [7]$$

This expression indicates that the internal stiffness matrices $\mathbf{K}_{ii}^{(s)}$ can be factorized independently, which is equivalent to eliminating all internal DOF to build the condensed interface problem for $\mathbf{u}_b$. Computing $\mathbf{u}_b$ then requires the factorization of the global interface operator. Thus, the decomposition should be such that the number of interface DOF is small in order to minimize the size of the global interface problem. Also the work load between processors when factorizing $\mathbf{K}_{ii}^{(s)}$ must be well balanced. This approach is efficient on a small number of processors, but it does not scale well on massively parallel computers because the condensed interface problem cannot be efficiently factorized in parallel and its size increases as the decomposition is refined, thereby putting the overall speed-up in jeopardy.

Iterative Methods

Factorization schemes are inherently sequential since they are based on Gaussian elimination where the solution is obtained for one variable after the other. In contrast, iterative solvers search for approximations of all unknowns simultaneously and involve simple matrix operations. They are thus naturally parallel. Iterative methods use only a small amount of memory space since the matrices need not be explicitly assembled or factorized. For that reason, they are commonly used in computational fluid mechanics to solve large nonlinear problems. In structural analysis, direct solvers have been favored for their robustness compared to iterative methods where fast convergence can be difficult to achieve in practice. With the advent of parallel computing however, iterative methods have gained new momentum.

Iterative solvers look for a solution in a subspace $\mathcal{V}_k = \mathrm{span}\{\mathbf{y}_1, \mathbf{y}_2, \ldots, \mathbf{y}_k\}$ where the dimension of the search space increases at every iteration. For symmetric positive-definite systems, the most effective algorithm is the conjugate gradient method. It can be interpreted as successive Rayleigh–Ritz approximations: at iteration k, find the best solution in subspace $\mathcal{V}_k$ spanning the columns of $\mathbf{Y}_k = [\mathbf{y}_1\ \mathbf{y}_2 \ldots \mathbf{y}_k]$ as:

$$\mathbf{u}_k = \mathbf{Y}_k \boldsymbol{\eta}_k \quad [8]$$

$$\left(\mathbf{Y}_k^{\mathrm{T}}\mathbf{K}\mathbf{Y}_k\right)\boldsymbol{\eta}_k = \mathbf{Y}_k^{\mathrm{T}}\mathbf{f} \quad [9]$$

In the next step $k+1$, a new search direction $\mathbf{y}_{k+1}$ related to the residual $\mathbf{r}_k = \mathbf{f} - \mathbf{K}\mathbf{u}_k$ is then added to the subspace. If the new direction $\mathbf{y}_{k+1}$ is orthogonalized with respect to the previous subspace such that $\mathbf{Y}_k\mathbf{K}\mathbf{y}_{k+1} = \mathbf{0}$, the new approximation is easily found as:

$$\begin{aligned} \mathbf{u}_{k+1} = \mathbf{Y}_{k+1}\boldsymbol{\eta}_{k+1} &= \begin{bmatrix} \mathbf{Y}_k & \mathbf{y}_{k+1} \end{bmatrix} \begin{bmatrix} \eta_k \\ \eta_{k+1} \end{bmatrix} \\ &= \mathbf{u}_k + \eta_{k+1}\mathbf{y}_{k+1} \end{aligned} \quad [10]$$

where:

$$\eta_{k+1} = \frac{\mathbf{y}_{k+1}^{\mathrm{T}}\mathbf{f}}{\mathbf{y}_{k+1}^{\mathrm{T}}\mathbf{K}\mathbf{y}_{k+1}} = \frac{\mathbf{y}_{k+1}^{\mathrm{T}}\mathbf{r}_k}{\mathbf{y}_{k+1}^{\mathrm{T}}\mathbf{K}\mathbf{y}_{k+1}} \quad [11]$$

A conjugate gradient iteration step involves simple matrix operations that can be performed for instance by BLAS routines or based on domain decomposition

as indicated by the splitting (eqn [6]). Hence iterative schemes are naturally parallel.

The iterations are stopped when the relative norm $\|\mathbf{r}_k\|/\|\mathbf{f}\|$ is below a user defined tolerance ε. For the iterations to converge quickly, the search directions $\mathbf{y}_{k+1}$ are chosen as:

$$\mathbf{y}_{k+1} = \tilde{\mathbf{K}}^{-1}\mathbf{r}_k + Y_k\boldsymbol{\beta} \qquad [12]$$

where $\tilde{\mathbf{K}}^{-1}$ is an approximation of the inverse of $\mathbf{K}$ called the preconditioner and where $\boldsymbol{\beta}$ are the coefficients of orthogonalization with respect to previous directions. Note that because of recursive orthogonality properties between conjugate gradient directions, $\mathbf{y}_{k+1}$ needs to be orthogonalized only with respect to the previous direction $\mathbf{y}_k$. Nevertheless, due to round-off errors, full re-orthogonalization is required in practice. The algorithm is summarized in **Table 1**.

For the conjugate gradient algorithm, the preconditioner $\tilde{\mathbf{K}}^{-1}$ must be symmetric positive definite and the cost of computing $\tilde{\mathbf{K}}^{-1}\mathbf{r}_k$ must be small. The convergence of the iteration is function of the condition number $\kappa(\tilde{\mathbf{K}}^{-1}\mathbf{K})$, namely the better $\tilde{\mathbf{K}}^{-1}$ approximates the inverse of $\mathbf{K}$, the better the convergence. Efficient preconditioners $\tilde{\mathbf{K}}^{-1}$ such as those obtained by incomplete factorization of $\mathbf{K}$ or by multigrid methods, are required to solve global problems and are not suitable for parallel computation with a high number of processors. Note that parallel incomplete block factorization schemes have been proposed, but their effectiveness becomes poor as the number of processors increases.

Table 1 The preconditioned conjugate gradient iteration method

$k = 0, \mathbf{u}_o = \mathbf{0}$
$\mathbf{r}_o = \mathbf{f}$
while $\|\mathbf{r}_k\| > \varepsilon\|\mathbf{f}\|$ **do**
  −Preconditioning
  $z_{k+1} = \tilde{\mathbf{K}}^{-1}\mathbf{r}_k$
  −Orthogonalization of directions−
  for $i = 1, \ldots k$ **do**
    $\beta_i = \dfrac{\mathbf{y}_i^{\mathrm{T}}\mathbf{K}\mathbf{z}_{k+1}}{\mathbf{y}_i^{\mathrm{T}}\mathbf{K}\mathbf{y}_i}$
    $\mathbf{y}_{k+1} = z_{k+1} - \beta_i\mathbf{y}_i$
  end for
  $\eta_{k+1} = \dfrac{\mathbf{y}_{k+1}^{\mathrm{T}}\mathbf{r}_k}{\mathbf{y}_{k+1}^{\mathrm{T}}\mathbf{K}\mathbf{y}_{k+1}}$
  $\mathbf{u}_{k+1} = \mathbf{u}_k + \eta_{k+1}\mathbf{y}_{k+1}$
  $\mathbf{r}_{k+1} = \mathbf{r}_k - \eta_{k+1}\mathbf{K}\mathbf{y}_{k+1}$
  $k = k+1$
end while

When using direct solvers, once the matrix has been factorized, low cost forward and backward substitutions are used to solve problems with multiple right-hand sides. This is an essential feature for instance when computing linear static solutions for multiple load cases, in inverse power iterations for eigenvalue computations and when performing implicit time-integration. For the iterative conjugate gradient method, computations performed to solve the system with the first right-hand side can be reused as follows.

Let us call $\mathbf{Y}_{k_1}$ the matrix of the search directions of the iterations for the first right-hand side $\mathbf{f}_1$, and let us assume that the results $\mathbf{K}\mathbf{Y}_{k_1}$ computed during those iterations have been stored. An initial guess for the solution relative to a second right-hand side $\mathbf{f}_2$ is then searched in the subspace $\mathbf{Y}_{k_1}$, such that:

$$\mathbf{u}_0 = \mathbf{Y}_{k_1}\boldsymbol{\eta}_0 \qquad [13]$$

$$\mathbf{r}_0 = \mathbf{f}_2 - \left(\mathbf{K}\mathbf{Y}_{k_1}\right)\boldsymbol{\eta}_0 \qquad [14]$$

where:

$$\boldsymbol{\eta}_0 = \left(\mathbf{Y}_{k_1}^{\mathrm{T}}\mathbf{K}\mathbf{Y}_{k_1}\right)^{-1}\left(\mathbf{Y}_{k_1}^{\mathrm{T}}\mathbf{f}_2\right) \qquad [15]$$

Finding this initial approximation is a low cost operation since $\mathbf{Y}_{k_1}^{\mathrm{T}}\mathbf{K}\mathbf{Y}_{k_1}$ is a diagonal matrix. Then, starting from $\mathbf{u}_0$, conjugate gradient iterations can be performed and the new search directions will be orthogonalized to all previous ones, including $\mathbf{Y}_{k_1}$. Obviously, once the number of search directions in $\mathbf{Y}$ is equal to the dimension of the system, the exact solution will be found.

Similarly to the Lanczos method, the search directions of the conjugate gradient iterations belong to the so-called Krylov space $\mathcal{K} = \text{span}\ \{\mathbf{y}_1, \mathbf{K}\mathbf{y}_1, \ldots \mathbf{K}^k\mathbf{y}_1\}$. For nonsymmetric systems, similar ideas can be used to design iterative solvers such as the biconjugate gradient algorithm and the popular generalized minimum residual (GMRES) method.

Domain Decomposition Methods and Semi-iterative solvers

Direct solvers are very robust but do not scale well on parallel computers because the factorization process and the substitutions are inherently sequential procedures. On the other hand, iterative solvers are naturally parallel but obtaining parallel scalability is difficult because efficient preconditioners are expensive and not parallel. Hence, some of the most efficient and useful parallel solvers rely on domain decomposition of the structure and use a blend of direct solvers to solve independent local problems

and iterative solvers to solve the globally coupled interface problem.

The first domain decomposition method goes back to Schwarz in 1870. The Schwarz method iterates between overlapping subdomains (i.e. where DOF in the vicinity of the interface belong to more than one partition) and is mathematically similar to the Gauss–Seidel algorithm. Most algorithms in use today consider nonoverlapping decompositions as in **Figure 2**.

In order to simplify the discussion, let us consider the case of a structure divided into two subdomains (**Figure 3**). The compatibility between the two parts can be enforced in two different ways leading to two different approaches of domain decomposition.

The Primal Schur Complement Method

The compatibility between the two parts in **Figure 3** can be enforced by stating that the boundary DOF in each subdomain are unique. Assuming that the boundary DOF $\mathbf{u}_b^{(1)}$ and $\mathbf{u}_b^{(2)}$ are numbered in the same order:

$$\mathbf{u}_b^{(1)} = \mathbf{u}_b^{(2)} = \mathbf{u}_b \qquad [16]$$

and the assembled system can be written as:

$$\begin{bmatrix} \mathbf{K}_{ii}^{(1)} & \mathbf{K}_{ib}^{(1)} & \mathbf{0} \\ \mathbf{K}_{bi}^{(1)} & \mathbf{K}_{bb}^{(1)} + \mathbf{K}_{bb}^{(2)} & \mathbf{K}_{bi}^{(2)} \\ \mathbf{0} & \mathbf{K}_{ib}^{(2)} & \mathbf{K}_{ii}^{(2)} \end{bmatrix} \begin{bmatrix} \mathbf{u}_i^{(1)} \\ \mathbf{u}_b \\ \mathbf{u}_i^{(2)} \end{bmatrix} = \begin{bmatrix} \mathbf{f}_i^{(1)} \\ \mathbf{f}_b \\ \mathbf{f}_i^{(2)} \end{bmatrix} \qquad [17]$$

Eliminating the internal DOF, we find:

$$\mathbf{u}_i^{(s)} = \mathbf{K}_{ii}^{(s)^{-1}} \left(-\mathbf{K}_{ib}^{(s)} \mathbf{u}_b + \mathbf{f}_i^{(s)} \right) \qquad [18]$$

and the following condensed interface problem is obtained:

$$\mathbf{S}_{bb} \mathbf{u}_b = \mathbf{f}_b^{(1)*} + \mathbf{f}_b^{(2)*} \qquad [19]$$

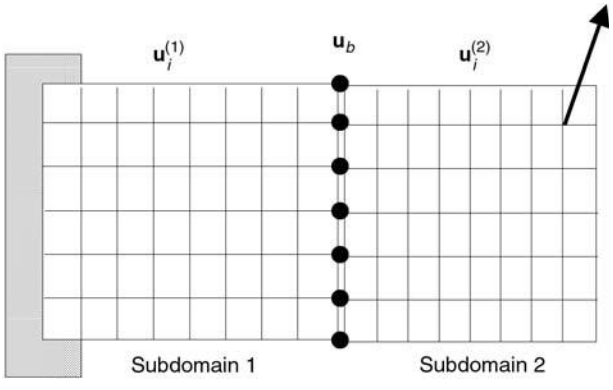


Figure 3 A simple structure partitioned into two subdomains.

where:

$$\begin{aligned} \mathbf{S}_{bb} &= \left(\mathbf{S}_{bb}^{(1)} + \mathbf{S}_{bb}^{(2)} \right) \\ \mathbf{S}_{bb}^{(s)} &= \mathbf{K}_{bb}^{(s)} - \mathbf{K}_{bi}^{(s)} \mathbf{K}_{ii}^{(s)^{-1}} \mathbf{K}_{ib}^{(s)} \\ \mathbf{f}_b^{(s)*} &= \mathbf{f}_b^{(s)} - \mathbf{K}_{bi}^{(s)} \mathbf{K}_{ii}^{(s)^{-1}} \mathbf{f}_i^{(s)} \end{aligned} \qquad [20]$$

The operators $\mathbf{S}_{bb}^{(s)}$ are the local operators condensed on the interface and correspond to the mathematical concept of Schur complements, and $\mathbf{S}_{bb}$ represents the assembled interface operator. An efficient parallel procedure based on eqn [19] then consists in factorizing the internal matrices $\mathbf{K}_{ii}^{(s)}$ independently on different processors and solving the interface problem (eqn [19]) for $\mathbf{u}_b$ iteratively.

For an approximate solution $\mathbf{u}_{b,k}$ found at iteration k, the corresponding interface forces $\mathbf{r}^{(s)} = \mathbf{f}^{(s)*} - \mathbf{S}_{bb}^{(s)} \mathbf{u}_{b,k}$ are computed on each side of the interface and assembling these forces on the interface, the interface equilibrium $\mathbf{r}_k = \mathbf{r}^{(1)} + \mathbf{r}^{(2)}$ is evaluated (see left-hand side of **Figure 4**). A correction $\Delta \mathbf{u}_{b,k+1}$ to the interface unknowns $\mathbf{u}_{b,k}$ is then estimated in the preconditioning step as follows.

The difference between $\mathbf{u}_{b,k}$ and the exact solution is $\Delta \mathbf{u}_{b,k+1} = \mathbf{S}_{bb}^{-1} \mathbf{r}_k$ which is approximated by:

$$\Delta \mathbf{u}_{b,k+1} = \frac{1}{2} \left(\mathbf{S}_{bb}^{(1)^{-1}} + \mathbf{S}_{bb}^{(2)^{-1}} \right) \frac{\mathbf{r}_k}{2} \qquad [21]$$

This correction can be computed in parallel and its mechanical interpretation is described in the right part of **Figure 4**: apply half of the residual force $\mathbf{r}_k$ on the boundary of each subdomain and compute the corresponding interface displacement $\Delta \mathbf{u}_b^{(s)} = \mathbf{S}_{bb}^{(s)^{-1}} (\mathbf{r}_k / 2)$. The correction for the interface displacement is then the average of the displacements on each side of the interface. This step involves solving local Neumann problems (force applied on the interface) and is therefore called the Neumann preconditioner.

In the expression [21] of the preconditioner, it is assumed that the local operators $\mathbf{S}_{bb}^{(s)}$ are nonsingular. When $\mathbf{K}^{(s)}$ is a stiffness matrix of a subdomain that possesses modes of zero deformation energy (rigid body modes or kinematical modes), then the associated Schur complement is singular. For instance in **Figure 3**, the right subdomain has not enough constraints on its external boundaries to prevent it from floating when it is not connected to the left subdomain. In that case, the problem of finding $\Delta \mathbf{u}_b^{(2)}$ when the force $\mathbf{r}_k/2$ is applied on its interface has a solution only if $\mathbf{r}_k/2$ is self-equilibrated. Calling $\mathbf{R}_b^{(2)}$ the matrix which columns are the restriction on

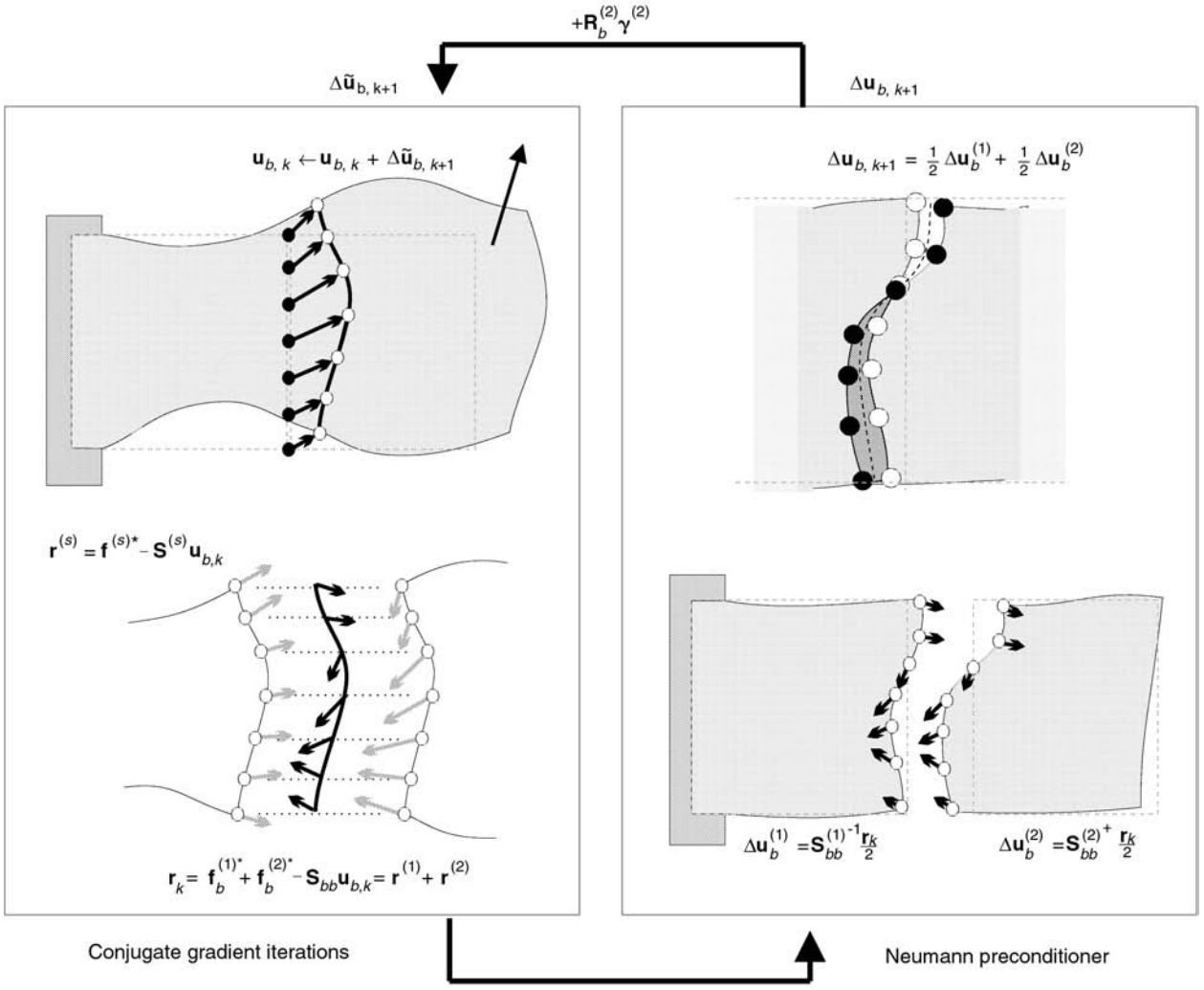


Figure 4 The balanced primal Schur complement method.

the interface of the local rigid modes (i.e., the nullspace of $\mathbf{S}_{bb}^{(2)}$):

$$\mathbf{S}_{bb}^{(2)}\Delta\mathbf{u}_b^{(2)} = \frac{\mathbf{r}_k}{2} \qquad [22]$$

has a solution only if:

$$\mathbf{R}_b^{(2)^{\mathrm{T}}}\frac{\mathbf{r}_k}{2} = 0 \qquad [23]$$

If this condition is satisfied, the Neumann preconditioning step can be written as:

$$\Delta\mathbf{u}_{b,k+1} = \frac{1}{2}\left(\mathbf{S}_{bb}^{(1)^{-1}} + \mathbf{S}_{bb}^{(2)^{+}}\right)\frac{\mathbf{r}_k}{2} \qquad [24]$$

where $\mathbf{S}_{bb}^{(2)+}$ is a generalized inverse of $\mathbf{S}_{bb}^{(2)}$. Rigid body displacements are then added to $\Delta\mathbf{u}_{b,\,k+1}$ to construct the modified correction:

$$\Delta\tilde{\mathbf{u}}_{b,k+1} = \left(\mathbf{I} - \mathbf{R}_b^{(2)}\left(\mathbf{R}_b^{(2)^{\mathrm{T}}}\mathbf{S}_{bb}\mathbf{R}_b^{(2)}\right)^{-1}\mathbf{R}_b^{(2)^{\mathrm{T}}}\mathbf{S}_{bb}\right)\Delta\mathbf{u}_{b,k+1} \qquad [25]$$

such that $\mathbf{R}_b^{(2)^{\mathrm{T}}}(\mathbf{S}_{bb}\Delta\tilde{\mathbf{u}}_{b,\,k+1}) = \mathbf{0}$ and thus, such that the next residual satisfies eqn [23].

Since the iterative solver is applied to the interface problem expressed for the primal variables $\mathbf{u}_b$, this method is known as the balanced primal Schur complement method. It is summarized in **Figure 4**.

For N_s subdomains, the method is generalized as follows. Assuming as described in eqn [4] that all local boundary DOF $\mathbf{u}_{b_{(s)}}^{(s)}$ are linked to the unique interface set by $\mathbf{u}_b^{(s)} = \mathbf{L}_b^{(s)}\mathbf{u}_b$, the interface problem (eqn [19]) can be written as:

$$\mathbf{S}_{bb}\mathbf{u}_b = \mathbf{f}_b^* \qquad [26]$$

where:

$$\mathbf{S}_{bb} = \sum_{s=1}^{N_s} \mathbf{L}_b^{(s)^{\mathrm{T}}} \mathbf{S}_{bb}^{(s)} \mathbf{L}_b^{(s)}$$

$$\mathbf{f}_b^* = \sum_{s=1}^{N_s} \mathbf{L}_b^{(s)^{\mathrm{T}}} \mathbf{f}_b^{(s)*}$$

where $\mathbf{S}_{bb}^{(s)}$ are the Schur complements of the subdomains as defined in eqn [20]. Note that this corresponds to assembling the subdomains as if they were macro-elements and is equivalent to the multifrontal form [7] where the internal DOF have been condensed out. The primal Schur complement method then consists in applying conjugate gradient iterations to solve for $\mathbf{u}_b$ in eqn [26].

Calling m_i the multiplicity of a boundary DOF (i.e., the number of subdomains connecting on the node) and calling $\mathbf{D}^{(s)}$ the diagonal matrix diag$(1/m_i)$, the Neumann preconditioner is expressed by:

$$\Delta \mathbf{u}_{b,k+1} = \left(\sum_{s=1}^{N_s} \mathbf{L}_b^{(s)^{\mathrm{T}}} \mathbf{D}^{(s)} \mathbf{S}_{bb}^{(s)^+} \mathbf{D}^{(s)} \mathbf{L}_b^{(s)} \right) \mathbf{r}_k \quad [27]$$

where $\mathbf{r}_k$ is the residual of [26] and $\mathbf{S}_{bb}^{(s)^+}$ is a generalized inverse if subdomain s is floating or, otherwise, the inverse. Calling $\mathbf{R}_b^{(s)}$ the rigid modes of subdomain s, the balancing procedure (eqn [25]) becomes:

$$\Delta \tilde{\mathbf{u}}_{b,k+1} = \Delta \mathbf{u}_{b,k+1} + \sum_{s=1}^{N_s} \bar{\mathbf{R}}_b^{(s)} \boldsymbol{\gamma}^{(s)} \quad [28]$$

where:

$$\bar{\mathbf{R}}_b^{(s)} = \mathbf{L}_b^{(s)^{\mathrm{T}}} \mathbf{D}^{(s)} \mathbf{R}_b^{(s)} \quad [29]$$

The amplitudes $\boldsymbol{\gamma}^{(s)}$ of the rigid modes are solution of the coarse grid:

$$\mathbf{S}_{RR} \begin{bmatrix} \boldsymbol{\gamma}^{(1)} \\ \vdots \\ \boldsymbol{\gamma}^{(N_s)} \end{bmatrix} = - \begin{bmatrix} \bar{\mathbf{R}}_b^{(1)^{\mathrm{T}}} \\ \vdots \\ \bar{\mathbf{R}}_b^{(N_s)^{\mathrm{T}}} \end{bmatrix} \mathbf{S}_{bb} \Delta \mathbf{u}_{b,k+1}$$

where:

$$\mathbf{S}_{RR} = \begin{bmatrix} \bar{\mathbf{R}}_b^{(1)^{\mathrm{T}}} \mathbf{S}_{bb} \bar{\mathbf{R}}_b^{(1)} & \cdots & \bar{\mathbf{R}}_b^{(1)^{\mathrm{T}}} \mathbf{S}_{bb} \bar{\mathbf{R}}_b^{(N_s)} \\ \vdots & \ddots & \vdots \\ \bar{\mathbf{R}}_b^{(N_s)^{\mathrm{T}}} \mathbf{S}_{bb} \bar{\mathbf{R}}_b^{(1)} & \cdots & \bar{\mathbf{R}}_b^{(N_s)^{\mathrm{T}}} \mathbf{S}_{bb} \bar{\mathbf{R}}_b^{(N_s)} \end{bmatrix} \quad [30]$$

The algorithm is outlined in **Table 2**. Let us note that computing the residual $\mathbf{r}_k$ and performing the preconditioning step are naturally parallel operations. The balancing step requires however solving a globally coupled system, but as shown by eqn [30], computing the amplitudes of the rigid body modes is a coarse problem of small dimension.

FETI, the Dual Schur Complement Method

In the primal Schur complement method described above, the compatibility between subdomains was enforced by assembling the interface DOF. Another approach is to introduce connecting forces in order to enforce the compatibility conditions. The interface compatibility is expressed as:

$$\sum_{s=1}^{N_s} \mathbf{B}^{(s)} \mathbf{u}^{(s)} = \mathbf{0} \quad [31]$$

where $\mathbf{B}^{(s)}$ are signed Boolean matrices. For the simple case of two subdomains (**Figure 5**):

$$\mathbf{B}^{(1)} = [\mathbf{0} \quad \mathbf{I}] \quad \text{and} \quad \mathbf{B}^{(2)} = [\mathbf{0} \quad -\mathbf{I}] \quad [32]$$

Table 2 The balanced primal Schur complement method

$k = 0$, $\mathbf{u}_{b,0} = \sum_{s=1}^{N_s} \bar{\mathbf{R}}_b^{(s)} \gamma^{(s)}$, where $\begin{bmatrix} \boldsymbol{\gamma}^{(1)} \\ \vdots \\ \boldsymbol{\gamma}^{(N_s)} \end{bmatrix} = \mathbf{S}_{RR}^{-1} \begin{bmatrix} \bar{\mathbf{R}}_b^{(1)^{\mathrm{T}}} \\ \vdots \\ \bar{\mathbf{R}}_b^{(N_s)^{\mathrm{T}}} \end{bmatrix} \mathbf{f}_b^*$

$\mathbf{r}_0 = \mathbf{f}_b^* - \mathbf{S}_{bb} \mathbf{u}_{b,0}$

while $\|\mathbf{r}_k\| > \varepsilon \|\mathbf{f}_b^*\|$ **do**

-Preconditioning-

$\Delta \mathbf{u}_{b,k+1} = \left(\sum_{s=1}^{N_s} \mathbf{L}_b^{(s)^{\mathrm{T}}} \mathbf{D}^{(s)} \mathbf{S}_{bb}^{(s)^+} \mathbf{D}^{(s)} \mathbf{L}_b^{(s)} \right) \mathbf{r}_k$

-Balancing-

$\Delta \tilde{\mathbf{u}}_{b,k+1} = \Delta \mathbf{u}_{b,k+1} + \sum_{s=1}^{N_s} \bar{\mathbf{R}}_b^{(s)} \boldsymbol{\gamma}^{(s)}$

where

$$\begin{bmatrix} \boldsymbol{\gamma}^{(1)} \\ \vdots \\ \boldsymbol{\gamma}^{(N_s)} \end{bmatrix} = -\mathbf{S}_{RR}^{-1} \begin{bmatrix} \bar{\mathbf{R}}_b^{(1)^{\mathrm{T}}} \\ \vdots \\ \bar{\mathbf{R}}_b^{(N_s)^{\mathrm{T}}} \end{bmatrix} \mathbf{S}_{bb} \Delta \mathbf{u}_{b,k+1}$$

−Orthogonalization of directions−

for $i = 1, \ldots k$ **do**

$\beta_i = \dfrac{\mathbf{y}_i^{\mathrm{T}} \mathbf{S}_{bb} \Delta \tilde{\mathbf{u}}_{b,k+1}}{\mathbf{y}_i^{\mathrm{T}} \mathbf{S}_{bb} \mathbf{y}_i}, \quad \mathbf{y}_{k+1} = \Delta \tilde{\mathbf{u}}_{b,k+1} - \beta_i \mathbf{y}_i$

end for

$\eta_{k+1} = \dfrac{\mathbf{y}_{k+1}^{\mathrm{T}} \mathbf{r}_k}{\mathbf{y}_{k+1}^{\mathrm{T}} \mathbf{S}_{bb} \mathbf{y}_{k+1}}$

$\mathbf{u}_{b,k+1} = \mathbf{u}_{b,k} + \eta_{k+1} \mathbf{y}_{k+1}$

$\mathbf{r}_{k+1} = \mathbf{r}_k - \eta_{k+1} \mathbf{S}_{bb} \mathbf{y}_{k+1}$

$k = k+1$

end while

Introducing Lagrange multipliers $\boldsymbol{\lambda}$ to enforce the compatibility constraints, the initial problem (eqn [2]) can be expressed in the equivalent form:

$$\begin{bmatrix} \mathbf{K}^{(1)} & \mathbf{0} & & \mathbf{B}^{(1)^{\mathrm{T}}} \\ \mathbf{0} & \ddots & & \vdots \\ & & \mathbf{K}^{(\mathrm{N_s})} & \mathbf{B}^{(\mathrm{N_s})^{\mathrm{T}}} \\ \mathbf{B}^{(1)} & \cdots & \mathbf{B}^{(\mathrm{N_s})} & \mathbf{0} \end{bmatrix} \begin{bmatrix} \mathbf{u}^{(1)} \\ \vdots \\ \mathbf{u}^{(N_s)} \\ \boldsymbol{\lambda} \end{bmatrix} = \begin{bmatrix} \mathbf{f}^{(1)} \\ \vdots \\ \mathbf{f}^{(N_s)} \\ \mathbf{0} \end{bmatrix} \quad [33]$$

where, as shown in **Figure 5** for the case of two subdomains, $\mathbf{B}^{(s)^{\mathrm{T}}}\boldsymbol{\lambda}$ are the connecting forces. To find the interface problem, we solve eqn [33] for the local DOF $\mathbf{u}^{(s)}$:

$$\mathbf{u}^{(s)} = \mathbf{K}^{(s)^{+}}\left(\mathbf{f}^{(s)} - \mathbf{B}^{(s)^{\mathrm{T}}}\boldsymbol{\lambda}\right) - \mathbf{R}^{(\mathrm{s})}\boldsymbol{\alpha}^{(s)} \quad [34]$$

As before, $\mathbf{K}^{(s)+}$ is the inverse of $\mathbf{K}^{(s)}$ for subdomains with no rigid modes or a generalized inverse if subdomain s is floating, in which case $\mathbf{R}^{(s)}$ are the rigid modes. The forces applied to a floating subdomain must be in self-equilibrium, namely:

$$\mathbf{R}^{(s)^{\mathrm{T}}}\left(\mathbf{f}^{(s)} - \mathbf{B}^{(s)^{\mathrm{T}}}\boldsymbol{\lambda}\right) = \mathbf{0} \quad [35]$$

Substituting in the compatibility conditions [31] the expression [34] of $\mathbf{u}^{(s)}$ in terms of $\boldsymbol{\lambda}$, and taking into account eqn [35], we find:

$$\begin{bmatrix} \mathbf{F}_I & \mathbf{G}_I \\ \mathbf{G}_I^{\mathrm{T}} & \mathbf{0} \end{bmatrix} \begin{bmatrix} \boldsymbol{\lambda} \\ \boldsymbol{\alpha} \end{bmatrix} = \begin{bmatrix} \mathbf{d} \\ \mathbf{e} \end{bmatrix} \quad [36]$$

where:

$$\mathbf{F}_I = \sum_{s=1}^{N_s} \mathbf{B}^{(s)}\mathbf{K}^{(s)^{+}}\mathbf{B}^{(s)^{\mathrm{T}}}$$

$$\mathbf{d} = \sum_{s=1}^{N_s} \mathbf{B}^{(s)}\mathbf{K}^{(s)^{+}}\mathbf{f}^{(s)}$$

$$\mathbf{G}_I = \begin{bmatrix} \mathbf{B}^{(1)}\mathbf{R}^{(1)} & \cdots & \mathbf{B}^{(N_s)}\mathbf{R}^{(N_s)} \end{bmatrix}$$

$$\boldsymbol{\alpha} = \begin{bmatrix} \boldsymbol{\alpha}^{(1)} \\ \vdots \\ \boldsymbol{\alpha}^{(N_s)} \end{bmatrix} \quad \text{and} \quad \mathbf{e} = \begin{bmatrix} \mathbf{R}^{(1)^{\mathrm{T}}}\mathbf{f}^{(1)} \\ \vdots \\ \mathbf{R}^{(N_s)^{\mathrm{T}}}\mathbf{f}^{(N_s)} \end{bmatrix}$$

$\mathbf{F}_I$ is the interface flexibility operator, $\mathbf{d}$ is the interface gap created by the applied loads, $\mathbf{G}_I$ is the restriction of the rigid modes on the interface and $\mathbf{e}$ is the default of self-equilibrium of the applied loads. The interface problem (eqn [36]) expresses that the connecting forces should be such that they fill the interface gap created by the external loads, and such that, together with the applied loads, they are in equilibrium with respect to the local rigid modes (self-equilibrium). Eqn [36] is called the dual interface problem because it is expressed in terms of the dual variables $\boldsymbol{\lambda}$ representing the interface connecting forces.

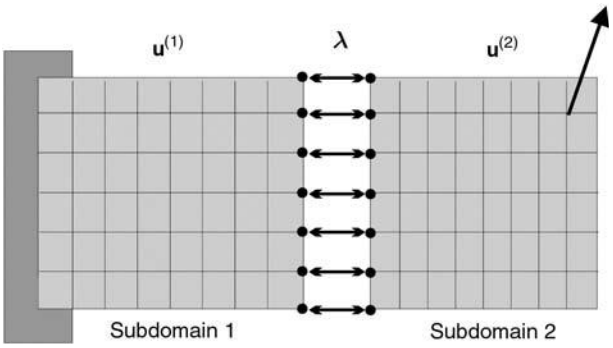


Figure 5 A structure partitioned into two subdomains: the dual approach.

In order to reduce the interface to a positive form, the Lagrange multipliers are split as:

$$\boldsymbol{\lambda} = \boldsymbol{\lambda}_0 + \mathbf{P}\bar{\boldsymbol{\lambda}} \quad [37]$$

where:

$$\mathbf{P} = \mathbf{I} - \mathbf{G}_I\left(\mathbf{G}_I^{\mathrm{T}}\mathbf{G}_I\right)^{-1}\mathbf{G}_I^{\mathrm{T}}$$

$$\boldsymbol{\lambda}_0 = \mathbf{G}_I\left(\mathbf{G}_I^{\mathrm{T}}\mathbf{G}_I\right)^{-1}\mathbf{e}$$

such that the self-equilibrium is satisfied for any $\boldsymbol{\lambda}$ and the interface problem is finally written as:

$$\left(\mathbf{P}^{\mathrm{T}}\mathbf{F}_I\mathbf{P}\right)\bar{\boldsymbol{\lambda}} = \mathbf{P}^{\mathrm{T}}(\mathbf{d} - \mathbf{F}_I\boldsymbol{\lambda}_0) \quad [38]$$

An efficient parallel solver then consists in solving the latter equation for $\boldsymbol{\lambda}$ by conjugate gradient iterations. Indeed, the projection operator $\mathbf{P}$ requires solving only a small coarse grid problem related to the rigid body modes whereas multiplication by $\mathbf{F}_I$ involves solving for $\mathbf{u}^{(s)}$ locally as in eqn [34].

For the convergence of the iterations to be rapid, a good preconditioner is found by observing that the residual $\mathbf{r}_k$ at iteration k on the dual interface problem (eqn [38]) is a compatibility gap on the interface (**Figure 6**). A good correction for $\boldsymbol{\lambda}$ in the two subdomain case is then found as follows: prescribed on both sides of the interface a displacement equal to $\mathbf{r}_k/2$ to bridge the gap. In each subdomain, compute the interface forces required to prescribe those interface displacements as $\Delta\mathbf{f}_b^{(s)} = \mathbf{S}_{bb}^{(s)}\mathbf{r}_k/2$. A good correction for $\boldsymbol{\lambda}$ is then given by the average of $\Delta\mathbf{f}_b^{(s)}$ on both sides of the interface. This mechanical description is depicted in (**Figure 6**). Since the estimation of the correction is based on solving Dirichlet problems

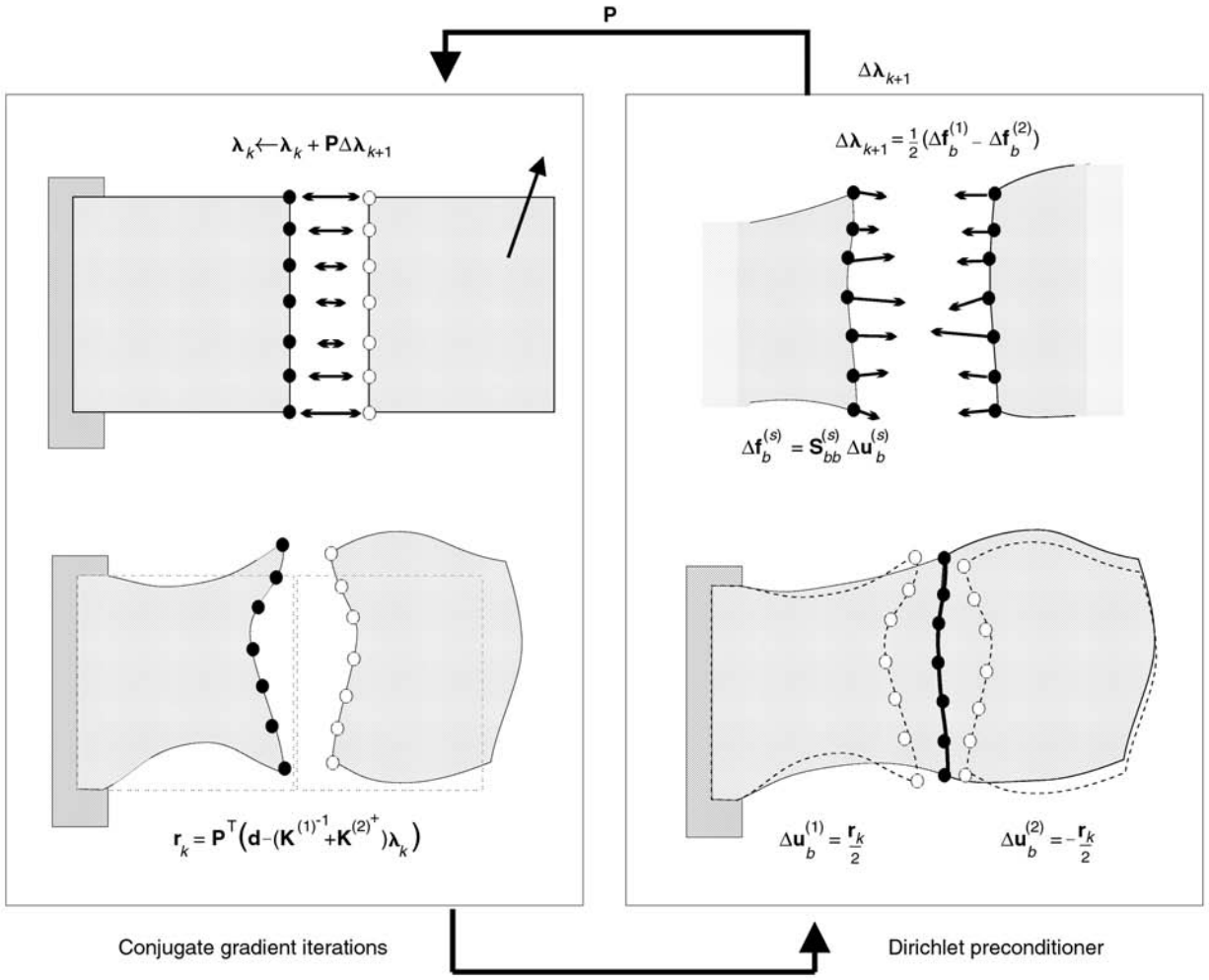


Figure 6 The FETI method.

in each subdomain (prescribed displacements on the interface), the preconditioner is called the Dirichlet preconditioner.

For N_s subdomains the Dirichlet preconditioner is expressed by:

$$\Delta\boldsymbol{\lambda}_{k+1} = \tilde{\mathbf{F}}_I^{-1}\mathbf{r}_k \qquad [39]$$

where

$$\tilde{\mathbf{F}}_I^{-1} = \sum_{s=1}^{N_s} \mathbf{B}^{(s)} \begin{bmatrix} \mathbf{0} & \mathbf{0} \\ \mathbf{0} & \mathbf{S}_{bb}^{(s)} \end{bmatrix} \mathbf{B}^{(s)^{\mathrm{T}}}$$

and where it is assumed for the sake of writing the matrix form, that the boundary DOF are numbered last in every subdomain. It is obviously a naturally parallel preconditioner since it involves solving local Dirichlet problems.

The algorithm described above is summarized in **Table 3**. Since it consists in tearing apart the domains and then 'gluing them together' by computing the interconnecting forces, this algorithm is called finite element tearing and interconnecting (FETI). The method is the dual of the primal Schur complement method and is also called the dual Schur complement method.

Note that the Dirichlet preconditioning step (eqn [39]) can be modified into a low cost variant called the lumped preconditioner:

$$\Delta\lambda_{k+1} = \left(\sum_{s=1}^{N_s} \mathbf{B}^{(s)} \begin{bmatrix} \mathbf{0} & \mathbf{0} \\ \mathbf{0} & \mathbf{K}_{bb}^{(s)} \end{bmatrix} \mathbf{B}^{(s)^{\mathrm{T}}} \right) \mathbf{r}_k \qquad [40]$$

It assumes that the internal DOF remain fixed when prescribing interface displacements. Although it yields slower convergence of the iterations on the interface problem, this low cost preconditioner is often used because it reduces the overall computing time.

Primal and Dual Schur Complement Methods in Practice

From the description of the balanced primal Schur complement method and the FETI algorithm, it is

Table 3 The FETI or Dual Schur Complement method.

$k = 0, \boldsymbol{\lambda}_0 = \mathbf{G}_l(\mathbf{G}_l^{\mathrm{T}}\mathbf{G}_l)^{-1}\mathbf{e}$
$\mathbf{r}_0 = \mathbf{P}^{\mathrm{T}}(\mathbf{d} - \mathbf{F}_l\boldsymbol{\lambda}_0)$
while $\|\mathbf{r}_k\| > \varepsilon\|\mathbf{d}\|$ do
  −Preconditioning−
  $\Delta\boldsymbol{\lambda}_{k+1} = \tilde{\mathbf{F}}_l^{-1}\mathbf{r}_k$
  −Orthogonalization of directions−
  for $i = 1, \ldots k$ do
    $\beta_i = \dfrac{\mathbf{y}_i^{\mathrm{T}}\mathbf{F}_l\Delta\boldsymbol{\lambda}_{k+1}}{\mathbf{y}_i^{\mathrm{T}}\mathbf{F}_l\mathbf{y}_i}, \quad \mathbf{y}_{k+1} = \Delta\boldsymbol{\lambda}_{k+1} - \beta_i\mathbf{y}_i$
  end for
  $\eta_{k+1} = \dfrac{\mathbf{y}_{k+1}^{\mathrm{T}}\mathbf{r}_k}{\mathbf{y}_{k+1}^{\mathrm{T}}\mathbf{F}_l\mathbf{y}_{k+1}}$
  $\boldsymbol{\lambda}_{k+1} = \boldsymbol{\lambda}_k + \eta_{k+1}\mathbf{y}_{k+1}$
  $r_{k+1} = \mathbf{P}^{\mathrm{T}}(\mathbf{r}_k - \eta_{k+1}\mathbf{F}_l\mathbf{y}_{k+1})$
  $k = k+1$
end while
$\alpha = (\mathbf{G}_l^{\mathrm{T}}\mathbf{G}_l)^{-1}\mathbf{G}_l^{\mathrm{T}}\mathbf{r}_k$
$\mathbf{u}^{(s)} = \mathbf{K}^{(s)^+}(\mathbf{f}^{(s)} - \mathbf{B}^{(s)^{\mathrm{T}}}\lambda) - \mathbf{R}^{(s)}\alpha^{(s)}$

clear that these methods are very similar. For instance, the balanced primal Schur complement iterates on an interface problem involving local Dirichlet solves and has a Neumann preconditioner, whereas the FETI algorithm iterates on a dual interface problem involving local Neumann solves and has a Dirichlet preconditioner. Moreover, the similarity between the balancing step (eqn [30]) for the primal method and the projection $\mathbf{P}$ in FETI is striking: they both define a coarse grid problem where an exact interface solution is computed in the subspace of the rigid body modes. This coarse grid can be understood as solving at every iteration a global problem where the domains are given rigid displacement modes.

The condition number of the preconditioned interface problems of both methods have been shown to be of the order of:

$$\kappa = O(1 + \log(H/h))^2 \qquad [41]$$

for regular decompositions and meshes, where H is a characteristic dimension of the domains and where h describes the characterisitc dimension of the finite elements. This result indicates that as the number of domains (i.e., H) varies or as the mesh size (i.e., h) is changed, the number of preconditioned iterations on the primal or dual interface problem will only be weakly affected. Both methods are therefore numerically scalable. Moreover, they involve local operations except for the small size coarse grids. Therefore they also exhibit good parallel scalability. It should be noted that the scalability of these methods results from the efficient preconditioners and from the fact that a coarse grid is solved at every iteration similarly to multigrid methods.

Schur complement methods have been successfully used to solve very large problems on several hundred processors. Even on one processor, using domain decomposition and Schur complement methods can speed up the computation.

Several improvement to the basic algorithms described here have been proposed for instance to handle fourth-order problems (shell structures), models with multipoint constraints, and for transient dynamics. Also, for problems where important heterogeneities are present (e.g., structures made of steel and rubber), the methods can be made efficient by changing the multiplicity scaling in the precondioners into scaling with respect to relative stiffness on the interface. A FETI-H method has been proposed to solve Helmoltz problems arising in acoustics.

To solve problems with multiple right-hand sides, the projection/re-orthogonalization technique described in the section on iterative methods can be used. For problems with several similar left-hand sides such as encountered in nonlinear solvers or in sensitivity analysis, namely when the operator $\mathbf{K}$ changes, the search directions computed for the interface problem in previous solves can be used in a preconditioning step to speed up the convergence.

Decomposing in Domains

The efficiency of domain decomposition solvers highly depends on the subdomain decomposition itself. Several issues must be taken into account when defining a decomposition of a domain, such as load balancing between processors, minimization of the number of interface unknowns and of subdomain interconnectivity, and subdomain aspect ratios.

Finding the optimum decomposition for a large system can be costly. Therefore a quasioptimum decomposition is searched for in two steps: a crude decomposition is first computed and it is then optimized according to a cost function including load balancing, interface size and subdomain aspect ratio.

Decomposition algorithm can be based on simple heuristics such as in the greedy algorithm which simply accumulates a certain number of neighboring nodes to build subdomains. They can also rely on graph partitioning methods.

See Plate 50.

See also: **Eigenvalue analysis**; **Inverse problems**; **Linear algebra**.

Further Reading

Axelsson O (1994) *Iterative Solution Methods*. Cambridge: Cambridge University Press.

Barret R, Berry MW, Chan TF, *et al.* (1993) *Templates for the Solution of Linear Systems: Building Blocks for Iterative Methods*. Philadephia: SIAM.

Bertsekas DP, Tsitsiklis JN (1989) *Parallel and Distributed Computation*. Englewood Cliffs: Prentice-Hall.

Dongarra JJ, Duff IS, Sorensen DC, van der Vorst HA (1998) *Numerical Linear Algebra for High-Performance Computers*. Philadelphia: SIAM.

Farhat C, Roux FX (1994) Implicit parallel processing in structural mechanics. *Computational Mechanics Advances*, vol. 2, no. 1, pp. 1–124. Amsterdam: North-Holland.

Hestenes HR, Stiefel E (1952) Methods of conjugate gradient for solving linear systems. *Journal of Research of the National Bureau of Standards* 49: 409–436.

Le Tallec P (1994) *Domain-decomposition Methods in Computational Mechanics*, Computational Mechanics Advances, vol. 1, no 2, pp. 121–220. Amsterdam: North Holland.

Papadrakakis M (1997) *Parallel Solution Methods in Computational Mechanics*. Chichester: Wiley.

Saad Y (1996) *Iterative Methods for Sparse Linear Systems*. Boston: PWS.

Schwarz HA (1890), *Gesammelte Mathematische Abhandlungen*. Springer, Berlin, vol. 2, pp. 133–143. (First published in *Vierteljahrsschrift der Naturforschenden Gesellschaft in Zürich* (1870) 15: 272–286).

Topping BHV (ed.) (1999) *Parallel and Distributed Processing for Computational Mechanics: Systems and Tools*. Edinburgh: Saxe-Coburg Publications.

PARAMETRIC EXCITATION

S C Sinha and A David, Auburn University, Auburn, AL, USA

Copyright © 2001 Academic Press

doi:10.1006/rwvb.2001.0038

Introduction

Excitation of a dynamic system is called parametric when the effect of the forcing appears as a coefficient of a variable in the governing equations of motion. This phenomenon leads to the family of time-varying (or nonautonomous) equations, whose coefficients are explicit functions of time. In most of the applications the nature of the explicit time dependence is periodic or can be modeled to be periodic as a good approximation to the true excitation. As a very simple example, consider a child playing on a swing. In order to drive the swing the child leans back and forth rhythmically, providing excitation that destabilizes the vertical equilibrium position of the swing. Although the excitation is not perfectly periodic, it is still a sufficiently accurate model of the motion.

Time-periodic systems play an important role in sciences and engineering, and have been the subject of investigation since 1868, when Mathieu first studied such a system, while analyzing the vibrations of an elliptical membrane. Since that time, the study of time-periodic equations has found applications in many areas such as dynamic stability of structures, circuit theory, systems and control, satellite dynamics, rotating shafts, helicopter rotor blades, quantum mechanics, and biomechanics (human or animal locomotion or modeling the function of the heart). Some physical examples are shown in **Figure 1**. In many situations modeling of these systems leads to nonlinear differential equations with periodic coefficients.

In general, it is not possible to obtain exact solutions of time-periodic nonlinear systems, except in a few very special cases. However, in most applications, it may suffice to obtain approximate solutions or information about the stability. The most natural idea is to somehow eliminate the explicit time dependence, and make the system autonomous and amenable to applications of a large number of theories developed for time-invariant systems. This is the basic motivation of point-mapping techniques, which are mainly used in stability and bifurcation theory. In the averaging method an approximate time-invariant system is constructed by averaging the equation over the period. Perturbation techniques seek approximate solutions under various conditions such as resonance, or limit cycle solutions after bifurcations, by assuming the periodic and nonlinear terms of the equation to be small perturbations of a linear time-invariant system. The Liapunov–Floquet transformation (L–F transformation) approach makes the linear part of a periodic equation time-invariant and thus retains the stability and bifurcation characteristics of the original system in the entire parameter space. The resulting equation can then be studied via standard techniques. The method of time-dependent normal form reduction aims to simplify the nonlinear equations by reducing the number of nonlinear terms to a minimum, even make them linear or time-invariant in some cases. The goal of time-periodic center manifold reduction is to reduce the dimension of the systems for the purpose of stability analysis in critical cases. These are the most current tools of analysis. In the following sections each method will be described and discussed briefly.

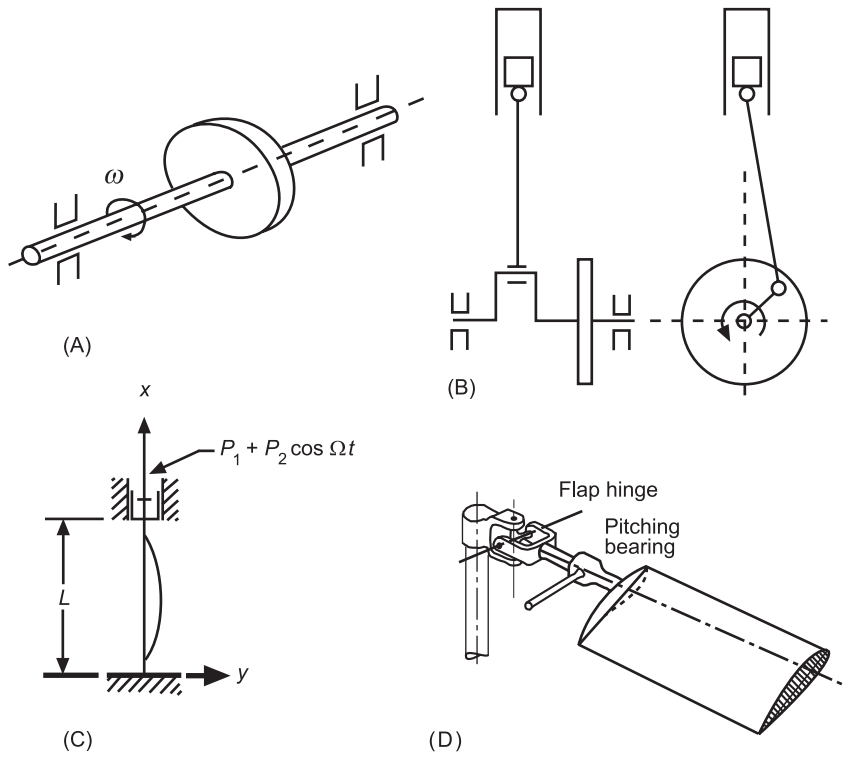


Figure 1 (A) Rotor-bearing system; (B) connecting rods; (C) periodically loaded column; (D) helicopter rotor blade.

Problem Formulation

The general form of nonlinear time-periodic systems is given by the equation:

$$\dot{x} = f(x, t) \qquad [1]$$

where x and f are n real vectors and $f(x, t) = f(x, t + T)$. T is called the principal period of the system. If we restrict ourselves to studying moderately large vibrations only, then we can expand the above equation in Taylor series about an equilibrium position or a known periodic solution of eqn [1] and obtain:

$$\dot{x} = \mathbf{A}(t)x + f_2(x, t) + \cdots + f_k(x, t) + O\left(\left|x^{k+1}\right|, t\right) \qquad [2]$$

or:

$$\dot{x} = \mathbf{A}(t)x + F(x, t) \qquad [3]$$

where $\mathbf{A}$ is an $n \times nT$-periodic matrix, and the vector functions f_i, $i = 2...k$, contain ith order monomials of x and are T-periodic in time. F is suitably defined in terms of f_i's. The index k is the highest order considered. The goal is either to predict stability and analyze bifurcations or to find the system response (most often steady-state solutions). Stability of the equilibrium position or the known periodic solution can be studied by Floquet theory if in the linear equation:

$$\dot{x} = \mathbf{A}(t)x \qquad [4]$$

matrix $\mathbf{A}$ is not critical, that is, it does not have Floquet multipliers on the unit circle. If the system is critical, a nonlinear analysis is necessary. Floquet theory is also useful for finding the response of linear time-periodic equations.

Floquet Theory

Consider the linear periodic system given by eqn [4]. Let $\Phi(t)$ denote the fundamental solution matrix or state transition matrix (STM) that contains n linearly independent solutions of eqn [4] with the initial conditions $\Phi(\mathbf{0}) = \mathbf{I}$ where $\mathbf{I}$ is the $n \times n$ unit matrix. Then the following statements hold:

1. $\Phi(t + T) = \Phi(T)\Phi(t) \quad 0 \le t \le T$ and, consequently
2. $\Phi(t + jT) = \Phi(T)^j\Phi(t)\ 0 \le t \le T, j = 2, 3 \ldots$
3. $x(t) = \Phi(t)x(0)\ t \ge 0$

These results imply that, if the solution is known for the first period, it can be constructed for all

time t. The matrix $\Phi(T)$ is called the Floquet transition matrix (FTM). The next statement considers the stability of eqn [4].

4. Let $\zeta_i (i = 1, \ldots, n)$ denote the eigenvalues of $\Phi(T)$. System (4) is asymptotically stable if all ζ_i's lie inside the unit circle of the complex plane. The system is unstable if at least one of the eigenvalues of the FTM has magnitude greater than one. The eigenvalues ζ_i are called the Floquet multipliers. The above statements briefly summarize the results of Floquet theory.

The Necessity of Nonlinear Analysis: Bifurcations and other Nonlinear Phenomena

In nonlinear systems a number of phenomena can occur which are impossible to predict from the linear analysis. Linear theory can predict the instants when a system goes through a change of stability characteristics, called bifurcation, but it cannot predict what kind of motion follows and whether or not the system is stable in critical situations. The nonlinear phenomena of time-periodic systems include cyclic bifurcations of equilibria and periodic orbits. When one Floquet multiplier of the system leaves the unit circle of the complex plane at -1, a period doubling (or flip) bifurcation occurs, the equilibrium or limit cycle changes its stability characteristic and a new limit cycle with twice the period of the original is born. When a multiplier crosses the unit cycle at $+1$, there are several possibilities, depending on the structure of the nonlinearities. Transcritical bifurcation occurs in the presence of quadratic terms, while cubic terms without any quadratics imply symmetry-breaking bifurcation. In transcritical bifurcation a stable and an unstable limit cycle (or an equilibrium point and a limit cycle) that exist together, switch their stability. Symmetry-breaking bifurcation is similar to flip bifurcation, without the doubling of the period. The cyclic-fold bifurcation, which also occurs when a multiplier becomes $+1$, is a phenomenon when a stable and an unstable cycle collide and disappear. For instance, two cyclic-fold bifurcations cause the jump phenomenon of resonance. If a pair of complex multipliers leave the unit circle, a quasiperiodic solution arises in a secondary Hopf (or Neimann–Sacker) bifurcation. The stability and bifurcation diagram is shown in **Figure 2.** Chaos can occur in these systems as well, through common routes, a series of period-doubling bifurcations or through secondary Hopf bifurcations. Intermittent chaos is also often observed. Features such as limit cycles and chaos observed in nonlinear systems have great significance in both theory and practical applications and can be treated only by means of nonlinear analysis techniques.

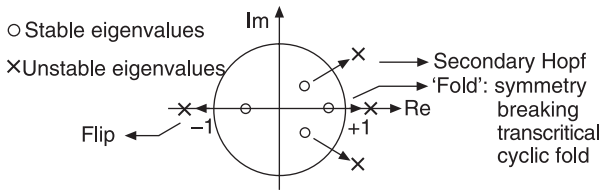


Figure 2 Stability and bifurcation diagram.

Tools of Nonlinear Analysis

Perturbation Methods

Perturbation theory has been widely used to obtain approximate solutions of many problems, in various branches of science and engineering. The basic idea is that if the problem at hand differs from a simple solvable problem only by small additional terms, then we could assume that the solutions of the two problems will be close as well. Therefore we can start from the solution of the simple problem, called the 'unperturbed problem' and try to find a series of corrections, in order to construct the solution of the original problem. The corrections are most often expressed as a power series of a small quantity called the 'perturbation parameter'. In the last step one needs to show that a few terms in the series will provide a useful approximate solution.

In the case of time-periodic nonlinear differential equations, perturbation techniques are only generally applicable if there exists a small parameter multiplying the periodic linear and nonlinear terms. Since the periodic linear terms as well as the nonlinear terms are small compared to the time-invariant linear part, the solution can be composed as slowly varying vibrations superimposed on the well-known periodic steady-state solution of the time-invariant linear system. The solution is written as a power series in terms of the small parameter. Substituting the series into the original equation and equating the coefficients of powers of the small parameter on both sides of the equations, a set of linear differential equations is obtained. These equations are solved to yield an approximate solution up to some desired power of the small parameter.

If eqn [3] can be written as:

$$\dot{x} = \mathbf{B}x + \varepsilon[A_1(t)x + F(x,t)] \qquad [5]$$

where $\mathbf{B}$ is a constant matrix, $A_1(t)$ is the periodic part of matrix $\mathbf{A}(t)$, $F(x, t)$ is an n vector containing the nonlinear terms and ε is a small parameter. Then

we seek a uniform expansion of the solution of the form:

$$x(t) = x_0(t) + \varepsilon x_1(t) + \varepsilon^2 x_2(t) + \cdots \qquad [6]$$

After substituting this expression into eqn [5] and collecting the coefficients for powers of ε, we obtain a set of linear differential equations in x_i. The equation for ε^0 is obviously given by the solution of which is $x_0 = \mathbf{\Phi}(t)a$, where a is a constant vector and $\mathbf{\Phi}(t)$ is the fundamental solution matrix of $\dot{x} = \mathbf{B}x$. Now, we let $a = a(t)$ be the modulation, an unknown function of time. An approximation of $a(t)$ can be obtained from the equation corresponding to ε^1, by eliminating the resonant (so-called the secular) terms. This elimination is necessary in all problems with excitation in order to obtain a uniform expansion. Once again, to refine the approximation further, we assume that the coefficient of $a(t)$ is an unknown function of time, to be determined from the ε^2 equation, and so on, until we obtain a 'reasonably good' approximation.

A modification of this method called the method of multiple scales makes special use of the fact that the corrections superimposed on the solution of the linear time-invariant system are relatively 'slow' vibrations with much smaller frequencies. Because of the limitation on the size of the parameter ε, however, the applicability of these methods is limited. They also seem to yield poor approximations for the locations of bifurcation points as well as for steady-state solutions in the neighborhood of bifurcations for time-periodic equations.

Averaging Method

The averaging method is based on the same basic idea as the perturbation methods. Once again, the periodic and nonlinear terms are assumed to be small compared to the constant linear part and are treated as slowly varying perturbation of the time-invariant linear equation. The solution of the nonlinear problem can be treated as a slowly varying modulation added to the solution of the time-invariant part, which can be constructed as before. The aim of averaging is to obtain an approximate solution based on these assumptions. In eqn [5] if we let $x = \mathbf{\Phi}(t)z$, then it can be transformed into the standard form:

$$\dot{z} = \varepsilon \mathbf{\Phi}^{-1}(t) g(\Phi(t)z, t) \qquad [8]$$

where $g(x, t) = \mathbf{A}_1(t)x + F(x, t)$ and the variable $z(t)$ represents the modulation. Since an exact solution of eqn [8] is not possible, the theorem of averaging allows us to construct the following averaged system:

$$\dot{\bar{z}} = \varepsilon \bar{g}(\bar{z}) \qquad [9]$$

where:

$$\bar{g}(\bar{z}) = \frac{1}{T}\int \mathbf{\Phi}^{-1}(t) g(\mathbf{\Phi}(t)z, t)\, \mathrm{d}t \qquad [10]$$

The error between $z(t)$ and $\bar{z}(t)$, can be expressed as:

$$z(t) - \bar{z}(t) = O(\varepsilon), \quad \varepsilon \to 0, \quad t \in \left[0, \frac{1}{\varepsilon}\right] \qquad [11]$$

This implies that for small ε the solution of the averaged equation is a good approximation of the solution of eqn [5], but only in a finite time interval depending on ε. Eqn [9] is a quasilinear autonomous differential equation in the slowly varying averaged coefficient $\bar{z}$. Although it is quasilinear, in general, an exact analytical solution is still not possible, except in some cases the averaged equation may become solvable in a closed form. Further simplification is possible via normal form theory and in some cases an approximate analytical solution is possible. Like the perturbation methods, the applicability of the method is limited due to the small parameter assumption.

Liapunov–Floquet transformation

According to the Liapunov–Floquet theorem, the fundamental matrix (or STM) $\mathbf{\Phi}(t)$ of eqn [4] can be written as a product of two matrices as:

$$\mathbf{\Phi}(t) = \mathbf{L}(t)\mathrm{e}^{Ct} \qquad [12]$$

where $\mathbf{L}(t)$ is T-periodic and $\mathbf{C}$ is a constant matrix, both, in general, are complex. There also exists a real factorization of the same form as eqn [12], where $\mathbf{L}(t)$ is real $2T$-periodic and $\mathbf{C}$ is a real constant matrix. $\mathbf{L}(t)$ is called the (T or $2T$-periodic) Liapunov–Floquet (LF) transformation matrix. Applying the transformation:

$$x = \mathbf{L}(t)y \qquad [13]$$

results in:

$$\dot{y} = \mathbf{C}y \qquad [14]$$

which is a dynamically equivalent autonomous form of eqn [4], either complex or real. After applying eqn [13], the nonlinear system (eqn [2]) becomes:

$$\dot{y} = \mathbf{C}y + \mathbf{L}^{-1}\left(f_2(y, t) + \cdots + f_k(y, t) + O\left(\left|y^{k+1}\right|, t\right)\right) \qquad [15]$$

Eqn [15] is dynamically equivalent to eqn [2] and it has a time-invariant linear part. This form allows one to apply the method of normal forms and/or center

manifold reduction, which can provide considerable simplifications.

However, in general, it is not possible to obtain the L–F transformation in a closed form because for this purpose one needs to compute the fundamental solution matrix $\mathbf{\Phi}(t)$ of the linear periodic differential eqn [4] (cf., eqn [12]). On the other hand, recent developments suggest that the elements of the solution matrix $\mathbf{\Phi}(t)$ can be obtained as a sum of Chebyshev polynomials to a desired accuracy. The L–F transformation $\mathbf{L}(t)$ and matrix $\mathbf{C}$ can then be obtained by a factorization of $\mathbf{\Phi}(t)$. Since $\mathbf{L}(t)$ is a periodic function of time, it can be expressed as a Fourier series.

Time-dependent Normal Form Theory

The idea of normal form reduction is to simplify nonlinear equations by eliminating as many nonlinear terms as possible, while keeping the linear part (and therefore the stability and bifurcation characteristics) unchanged. This is achieved by a series of near-identity transformations. Because $\mathbf{A}(t)$ in eqn [2] is time-dependent, a direct application of normal form theory is not possible. Therefore, first the $2T$-periodic L–F transformation is used to transform eqn [2] to a vector field where the linear part is time-invariant. Then the resulting eqn [15] can be handled by the method of 'time-dependent normal forms' (TDNF). Eqn [15] can be written in the Jordan canonical form as:

$$\dot{y} = Jy + w_2(y,t) + \cdots + w_k(y,t) + \cdots + O\left(|y|^{k+1}, t\right) \qquad [16]$$

where J is the Jordan form of the real matrix $\mathbf{C}$ and w_r's $(r = 2 \ \ldots \ k)$ are $2T$-periodic functions which contain homogeneous monomials of y of order r. Now one can construct a sequence of transformations which successively removes the nonlinear terms w_r. The transformation is of the form:

$$y = v + h_r(v,t) \qquad [17]$$

where h_r is a formal power series in v of degree r with $2T$-periodic coefficients. Applying the above change of coordinates, one can establish the conditions for eliminating each nonlinear term, and solve for h_r. These conditions are expressed in the form of a set of partial differential equations for h_r, called the homological equation. Since the coefficients of w_r and the unknown nonlinear transformation h_r can be expressed in finite Fourier series, one only needs to solve a set of algebraic equations for the coefficients of h_r, instead of solving the differential equations. Following this procedure it is not always possible to eliminate all of the nonlinear terms. The nonlinear terms corresponding to the resonance condition remain in the normal form that is the simplest possible nonlinear form of eqn [2]. In some cases it can even be linear, or, although nonlinear, completely time-invariant. In many instances, the resulting normal form equations can be analyzed analytically and the stability and bifurcation characteristics can be examined. Usually, some algebraic manipulations and/or transformation to polar coordinates render closed-form solutions for simple nonlinear equations. Thus, the solutions of the original quasilinear time-periodic equations can be obtained in the original coordinates by substituting back all the transformations, including the L–F transformation. Usually these computations are tedious due to the presence of a large number of periodic terms in eqn [16]. In order to simplify the procedure, without any significant compromise in the quality of solutions, only time-invariant terms in w_r may be retained and the periodically varying terms may be neglected. Then eqn [16] takes the form:

$$\dot{\bar{y}} = J\bar{y} + \bar{w}_2(\bar{y}) + \cdots + \bar{w}_k(\bar{y}) + O\left(|\bar{y}|^{k+1}\right) \qquad [18]$$

which is autonomous and $\bar{y}$ and $\bar{w}_r(\bar{y})$ are the approximate states and nonlinear functions, respectively. Then the solution can be obtained by application of the time-independent normal form (TINF) theory.

Time-periodic center manifold reduction

In situations where some of the eigenvalues of matrix $\mathbf{C}$ in eqn [15] are critical, the stability can be discussed in the local center manifold via the time-periodic center manifold theorem. The idea of center manifold theorem is to reduce the dimension of the system to the minimum possible, i.e., to the dimension of the invariant manifold associated with the critical eigenvalues. All 'critical' dynamics take place in this manifold. The center manifold theorem states that if the reduced system on the center manifold is stable (unstable) then the original n-dimensional system is also stable (unstable). Due to the periodic nature of eqn [2], a direct application of the center manifold theorem is not possible, but it can certainly be applied to eqn [15]. Let us assume that eqn [15] has n_1 eigenvalues that are critical and n_2 eigenvalues that have negative real parts. Then it can be rewritten in the form:

$$\begin{pmatrix} \dot{y}_c \\ \dot{y}_s \end{pmatrix} = \begin{bmatrix} J_c & 0 \\ 0 & J_s \end{bmatrix} \begin{pmatrix} y_c \\ y_s \end{pmatrix} + \begin{pmatrix} w_{c2} \\ w_{s2} \end{pmatrix} + \begin{pmatrix} w_{c3} \\ w_{s3} \end{pmatrix} + \cdots \qquad [19]$$

where the subscripts c and s represent the critical and stable vectors, respectively. At this point a nonlinear

relation is sought to decouple the nonlinear terms of the equations corresponding to the critical and stable states, in the form of:

$$y_s = h(y_c, t) \qquad [20]$$

such that $h(y_c, t)$ is a polynomial of y_c with $2T$-periodic unknown coefficients. The relation for y_s can be obtained by substituting eqn [19] into the set of n_2 equations associated with the stable eigenvalues in eqn [18]. The substitution results in a set of partial differential equations for the coefficients of h. Since these coefficients have to be periodic, we can assume a formal Fourier series form with unknown coefficients. Then the differential equations reduce to a set of linear algebraic equations for the Fourier coefficients. After solving for the coefficients, substitution of eqn [19] in eqn [18] decouples stable and critical states and hence the problem reduces to the investigation of stability of an n_1-dimensional system in the center manifold. If necessary, the center manifold equations can be simplified further by the time-dependent normal form theory as described earlier. For certain types of bifurcation they become completely time-invariant and solvable in a closed form.

Point-Mapping Techniques

For periodic systems, one could also represent the motion of the system as events in discrete time instants. The goal here is to eliminate the explicit time dependence from the equation by replacing the dynamic system as a set of difference equations sampled at period T. This process links the state of the system at the beginning of a period to the state of the system at the end of the period by a point-mapping transformation. The advantage of the discrete time approach is that by introducing this formulation, one eliminates the explicit continuous dependence on time. This feature allows, at least in principle, an easier determination of the various solutions and their stability properties. Another advantage is that difference equations are easy to simulate on digital computers. One of the main obstacles in applying point-mapping techniques to real problems is in obtaining the corresponding difference equations. In order to obtain the complete difference equation representation one has to find a solution of a nonautonomous nonlinear system of differential equations over one period. This is not possible except in a few special cases. Thus, in general, one is forced to accept an approximation to the point mapping.

Consider a nonlinear dynamic system described by eqn [1], i.e.:

$$\dot{x}(t) = f(t, x(t)) \qquad [21]$$

where x and f are real vectors and f is periodic in time with period T. The state of the system is observed at discrete instances of T units of time. The dynamic relationship between the state of the system at $t = nT$ and the state at $t = (n+1)T$ results in a set of difference equations which are independent of time. If such a relationship can be found, the discrete counterpart to the set of equations in eqn [21] can be written as:

$$x(n+1) = G(x(n)), \quad n = 1,\ 2,\ 3\ldots \qquad [22]$$

where $x(n+1)$ and $x(n)$ are the state of the system at $t = (n+1)T$ and $t = nT$, respectively. The representation of the system dynamics given by eqn [22] is called the Poincaré map. An equilibrium point or a T-periodic orbit of eqn [21] is represented as a fixed point of the map. A periodic solution of period KT consists of K distinct points $x*(j), j = 1\ \ldots\ K$, such that:

$$\begin{aligned} &x^*(m+1) = G(x^*(m)), \quad m = 1,\ 2, \ldots K-1 \\ &x^*(1) = G^K(x^*(1)) \end{aligned} \qquad [23]$$

Approximations of the map are usually obtained numerically, for example, by the Runge–Kutta method for solving systems of ordinary differential equations. By keeping track of the various coefficients, an approximation up to any desired degree can be obtained. Point-mapping methods are mostly used to study the local as well as global stability and bifurcation characteristics of a system. Unlike the perturbation and averaging methods, this technique is not restricted to systems with small parameters. The main disadvantage of this method is that the construction of the Poincaré map requires knowledge of either the exact or an approximate solution of the original problem. Further, the discretized system dynamics cannot be transformed back to the original continuous state. Computational problems may also arise as the system dimension becomes larger.

Illustrative Examples

In this section some simple examples are considered to demonstrate the application of the methods discussed above. First, consider a Mathieu equation with cubic nonlinearity in the form:

$$\begin{Bmatrix} \dot{x}_1 \\ \dot{x}_2 \end{Bmatrix} = \begin{bmatrix} 0 & 1 \\ -(\alpha + \beta\cos\omega t) & -\delta \end{bmatrix} \begin{Bmatrix} x_1 \\ x_2 \end{Bmatrix} + \begin{Bmatrix} 0 \\ -\varepsilon x_1^3 \end{Bmatrix} \qquad [24]$$

where δ, α, β, ω, and ε are the parameters of the system. Results for two sets of parameters are shown

in **Figures 3** and **4**. As seen from **Figure 3**, when $\alpha(=10)$ is much larger than $\beta(=0.2)$, then the averaging method does provide meaningful results although it is not as accurate as the two normal form methods, viz., TINF and TDNF. However, when $\alpha(=0.5)$ is small compared to $\beta(=4)$, the averaging method incorrectly predicts unbounded solution while TINF and TDNF provide very good results (**Figure 4**). As an example of the application of time-dependant center manifold reduction, the bifurcation analysis of a base-excited simple pendulum shown in **Figure 5** is considered:

$$\ddot{\theta} + d\dot{\theta} + (a + b\sin\omega t)\sin\theta = 0 \qquad [25]$$

where $a = g/L$, $b = A\omega^2/L$, and $d = c/ML^2$. Writing $\{x_1\, x_2\} = \{\theta\, \dot{\theta}\}$ and expanding $\sin\theta$ in a Taylor series about the zero equilibrium point up to the cubic terms, yields:

$$\begin{Bmatrix} \dot{x}_1 \\ \dot{x}_2 \end{Bmatrix} = \begin{bmatrix} 0 & 1 \\ -(\alpha + \beta\sin\omega t) & \alpha \end{bmatrix} \begin{Bmatrix} x_1 \\ x_2 \end{Bmatrix} + \begin{Bmatrix} 0 \\ (a + b\sin\omega t)\dfrac{x_1^3}{6} \end{Bmatrix} \qquad [26]$$

Letting a be the bifurcation parameter; for $b = 4$, $d = 0.31623$, and $\omega = 2$, the system undergoes a symmetry breaking bifurcation (one of the Floquet multipliers is $0.999999 \approx 1$, the other being 0.370292) at $a_c = 3.917787$. After applying the L–F and modal transformations, the time-dependent center manifold reduction is used to decouple the critical equation from the other. The center manifold equation is further simplified via normal form theory to yield:

$$\dot{v} = -0.4306v^3 \qquad (v \text{ is a new variable}) \qquad [27]$$

indicating that the equilibrium of the nonlinear system is asymptotically stable at the critical point. The versal deformation of eqn [27] yields the normal form of symmetry breaking bifurcation for this system as:

$$\dot{v} = \mu v - 0.4306v^3 \qquad [28]$$

where μ is the unfolding parameter. It is solvable in a closed from; the solution for the initial condition $v(0) = v_0$ being:

$$v(t) = \left(\left(\frac{1}{v_0^2} + \frac{-0.4306}{\mu}\right)e^{-2\mu t} - \frac{-0.4306}{\mu}\right)^{-1/2} \qquad [29]$$

Unlike the case of autonomous systems, here the normal form does not contain all the information

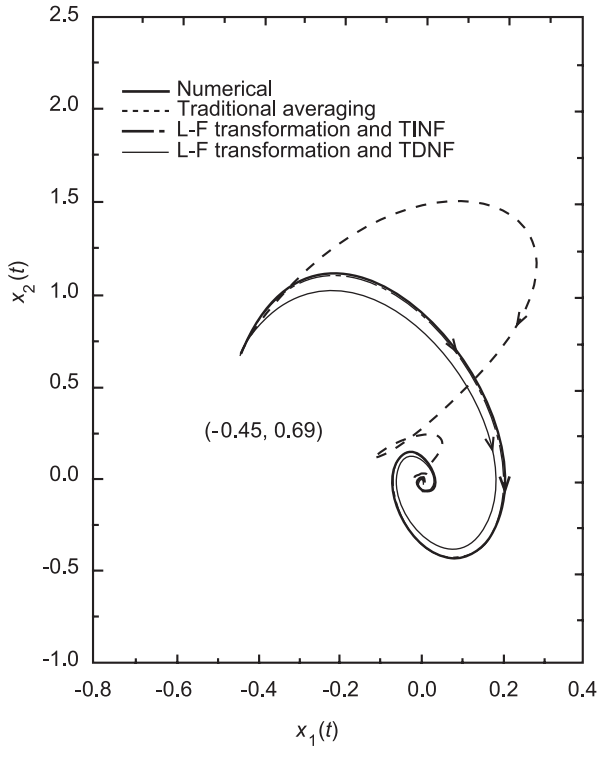


Figure 3 Solutions of Mathieu equation with cubic nonlinearity ($\alpha = 10.0$, $\beta = 0.2$, $\delta = 1.8974$, $\varepsilon = 3.0$).

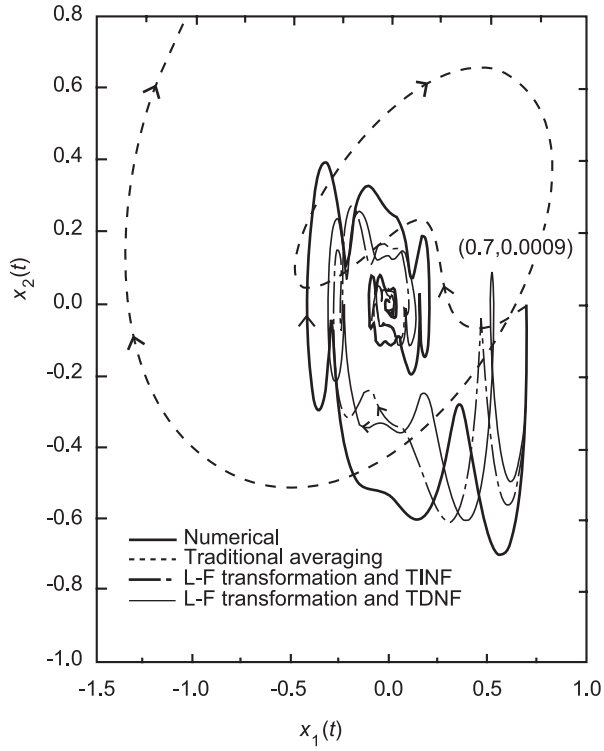


Figure 4 Solutions of Mathieu equation with cubic nonlinearity ($\alpha = 0.5$, $\beta = 4.0$, $\delta = 0.4243$, $\varepsilon = 3.0$).

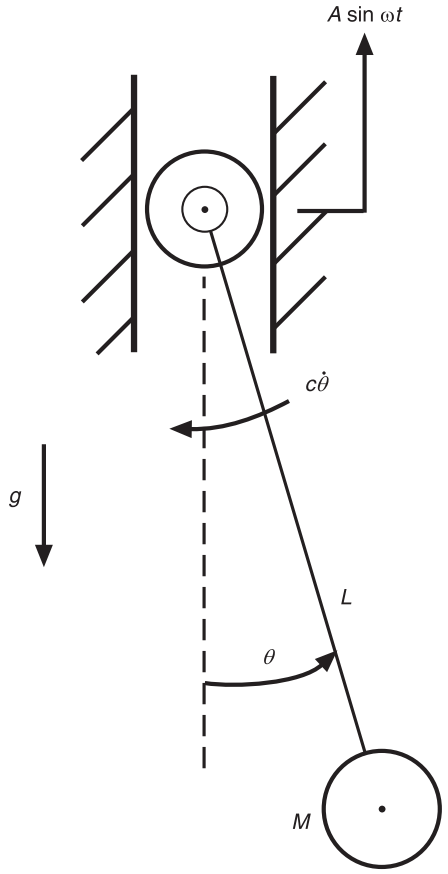


Figure 5 Base-excited simple pendulum.

about the bifurcation and the L–F transformation also plays an important role. From eqn [29] one can conclude the following about the dynamics in the neighborhood of the bifurcation. For $\mu < 0$ the $v = 0$ equilibrium is stable and there are no other limit sets in the neighborhood. For $\mu > 0$ the zero equilibrium becomes unstable and there is a stable nonzero equilibrium born. This equilibrium point becomes a stable T-periodic limit cycle in the original domain because the real L–F transformation is T-periodic in this case. So we say that the stability has been lost softly. This limit cycle is the boundary of the small attractive domain around the unstable equilibrium. By computing the amplitude of the limit cycle we have estimated the size of the stable region, and we can also estimate the rate of its growth as the bifurcation parameter goes further away from the critical value. The limit cycle is obtained by substituting the initial condition:

$$v_0 = -\left(\frac{\mu}{-0.4306}\right) \qquad [30]$$

into eqn [29] and applying the necessary transformations to yield the original state $x(t)$. However, one must establish a relationship between μ and η $(\equiv a - a_c)$ which represents the change in the bifurcation parameter a. By performing a sensitivity analysis of the Floquet transition matrix (FTM), one can obtain a relationship between μ and η. However, the FTM must be computed in a symbolic form. One can also obtain such a relationship numerically by the curve-fitting technique. Using:

$$\mu = 0.865\eta - 1.635\eta^2 \qquad [31]$$

the postbifurcation limit cycles for $\eta = 0.01$ and $\eta = 0.1$ are shown in **Figures 6A** and **B**, respectively. Numerical results are included for a comparison.

Phenomena Associated with Time-periodic Nonlinear Systems

The time-periodic nonlinear systems contain typical features of parametric excitation and other phenomena associated with nonlinear systems. The para-

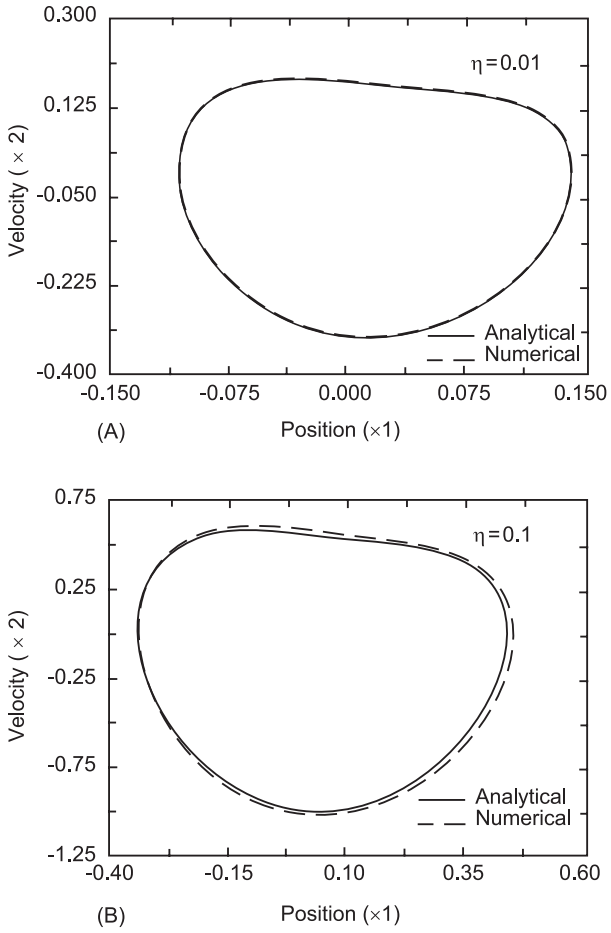


Figure 6 Postbifurcation limit cycles.

metric excitation can cause resonance which, in nonlinear systems, is associated with the jump phenomenon, the amplitude of vibration grows as the excitation frequency grows in the neighborhood of the resonant frequency, but at a certain frequency it drops suddenly, and the system vibrates with a much smaller amplitude. Near resonance another interesting feature, synchronization (or entrainment of frequencies) can also occur in these systems due to nonlinearities. The existence of limit cycles, quasiperiodic, and chaotic attractors is also observed in these systems.

These features can be analyzed by the use of the methods described above. Perturbation, averaging, point–mapping methods, and the L–F transformation with a subsequent use of normal form reduction have been employed to construct periodic, quasiperiodic, and even chaotic solutions. For bifurcation analysis, the L–F transformation combined with center manifold reduction and normal form theory appears to be very useful. The L–F transformation also appears to be a powerful tool in control of time-periodic systems. These are the current subjects of research.

Nomenclature

a	bifurcation parameter
$\mathbf{A}$	$n \times n$ T-periodic matrix
$\mathbf{B}$	constant matrix
$\mathbf{C}$	constant matrix
$\mathbf{I}$	$n \times n$ unit matrix
$\mathbf{L}(t)$	Liapunov–Floquet transformation matrix
T	principal period
$\mathbf{\Phi}(t)$	fundamental solution matrix
$\mathbf{\Phi}(T)$	Floquet transition matrix

See also: **Averaging**; **Critical damping**; **Dynamic stability**; **Nonlinear systems analysis**; **Nonlinear systems, overview**; **Perturbation techniques for nonlinear systems**.

Further Reading

Arnold VI (1988) *Geometrical Methods in the Theory of Ordinary Differential Equations*. New York: Springer-Verlag.

Arrowsmith DK, Place CM (1990) *An Introduction to Dynamical Systems*. Cambridge: Cambridge University Press.

Bogoliubov NN, Mitropolski JA (1963) *Asymptotic Methods in the Theory of Nonlinear Oscillations* (in Russian). Moscow: State Press for Physics and Mathematical Literature. (English translation: Hindustan Publishing, Delhi, India and Gordon and Breach, New York).

Chow Sh.-N, Li Ch, Wang D (1994) *Normal Forms and Bifurcations of Planar Vector Fields*. Cambridge: Cambridge University Press.

Dávid A, Sinha SC (2000) Versal deformation and local bifurcation analysis of time-periodic nonlinear systems. *Nonlinear Dynamics* 21: 317–336.

Minorsky N (1974) *Nonlinear Oscillations*. Malabar, FL: RE Krieger.

Nayfeh AH, Balachandran B (1995) *Applied Nonlinear Dynamics*. New York: Wiley.

Nayfeh AH, Mook DT (1979) *Nonlinear Oscillations*. New York: Wiley.

Sanders JA, Verhulst F (1985) *Averaging Methods in Nonlinear Dynamical Systems*. New York: Springer-Verlag.

Schmidt G, Tondl A (1986) *Nonlinear Vibrations*. Cambridge: Cambridge University Press.

Sinha, SC Pandiyan R, Bibb JS (1996) Liapunov–Floquet transformation: computation and applications to periodic systems. *Journal of Vibration and Acoustics* 118: 209–219.

Troger H, Steindl A (1991) *Nonlinear Stability and Bifurcation Theory*. New York: Springer-Verlag.

PERTURBATION TECHNIQUES FOR NONLINEAR SYSTEMS

S Shaw, Michigan State University, East Lansing, MI, USA

Copyright © 2001 Academic Press

doi:10.1006/rwvb.2001.0042

Summary

Perturbation techniques are a class of analytical methods for determining approximate solutions of nonlinear equations for which exact solutions cannot be obtained. They are useful for demonstrating,

predicting, and describing phenomena in vibrating systems that are caused by nonlinear effects. They can also be applied to nonlinear and linear systems with variable coefficients and/or complex boundary conditions where closed form exact solutions are not known. They are useful for determining solutions that are 'close' in some sense to a known solution, and provide results that are perturbations of that known solution. These approximate solutions are obtained by carrying out expansions in terms of a small parameter, where the known solution is recovered when the parameter is zero, and the higher-order terms in the expansion contain the additional information. There are a number of different types of expansions involving the (unknown) solution and, in some cases, the independent variable(s) in the problem (e.g., time). The range of physical applications of perturbation techniques covers virtually all of theoretical physics; here we provide a brief summary of topics specific to nonlinear vibrations.

Perturbation techniques complement numerical simulations, with certain advantages and disadvantages. Their primary disadvantage is that they are limited to relatively narrow, but important, classes of mathematical problems. Their distinct advantage is that they provide analytical formulas that describe the influence and role of system parameters on the response. This is very important when exploring behavior that is fundamentally different from that observed in linear systems. In fact, many of the classic problems solved by perturbation techniques play a role in nonlinear vibrations analogous to that of forced harmonic oscillators in linear vibration theory; that is, they set the framework for a wide range of applications by demonstrating fundamental behavior and show how system parameters influence that behavior.

One important class of systems where perturbation techniques are very useful are those that are weakly nonlinear. Here perturbation techniques allow one to explore phenomena that cannot be captured by linear system models: the existence of multiple stable steady state responses in a system; the existence of self-excited oscillations, i.e., responses that do not arise from an external time-dependent excitation; subharmonic and superharmonic resonances, in which the system response is dominated by a harmonic different from that of the excitation; and internal resonances, where commensurability between natural frequencies in a system can lead to energy exchange that often results in quite complex behavior. Perturbation techniques can also be applied to systems where a nonlinear solution is known at a particular set of parameter values, whereby the solution is extended to nearby parameter values, often leading to new and important responses. An example of this is the case of adding damping and periodic forcing to conservative nonlinear oscillators. The interaction of the underlying, unforced system with the excitation and dissipation can lead to a multitude of resonance conditions that are captured by such an approach. Another class of problems amenable to perturbation techniques is those in which behavior occurs on significantly different time scales. For example, one may have a stiff structure with high natural frequencies to which are attached relatively soft subsystems with relatively low frequencies. In such a case, the methods of singular perturbation can be applied in order to attack the different timescales in a systematic manner.

Many books have been written on these topics, and many more include these techniques as part of the toolbox one must have in hand when investigating nonlinear systems. There are differing philosophies about perturbation techniques, depending on whether one simply wants an answer or has a desire to understand the deeper implications of the methods and how these affect the results obtained. The book by Nayfeh is a good starting point, since it covers a wide range of problems that can be tackled using these methods, and it demonstrates the steps used in the calculations. A complementary book by Murdock, demonstrates the methods, but asks deeper questions and places the methods in a more mathematical setting where the underlying principles can be understood and explored. Perturbation analyses require careful calculations and are ideally suited for computer-assisted symbolic manipulation, such as Mathematica, MACSYMA, or Maple. Rand and Armbruster's book takes the reader on an instructive tour of some classical perturbation calculations using MACSYMA. The emphasis in many texts is on the mathematical expressions obtained, but there is an important and useful connection between these analytical techniques and topological approaches for nonlinear systems; issues that are explored in a number of books, e.g., Nayfeh and Mook, and Guckenheimer and Holmes.

A crucial step in any perturbation analysis is the identification of the small parameter and the scaling required to set the equations of interest in the proper form for application of the method. This is not always straightforward; experience, physical insight and the literature for the specific application at hand are useful aids in this regard, since the textbooks tend to focus on the mathematical steps of the analysis.

See also: **Dynamic stability**; **Nonlinear normal modes**; **Nonlinear systems analysis**; **Nonlinear system identification**; **Nonlinear systems, overview**.

Further Reading

Guckenheimer J, Holmes P (1983) *Nonlinear Oscillations, Dynamical Systems and Bifurcations of Vector Fields*. New York: Springer–Verlag.

Murdock JA (1991) *Perturbations: Theory and Methods*. New York: Wiley.

Nayfeh AH (1981) *Introduction to Perturbation Techniques*. New York: Wiley.

Nayfeh AH, Mook DT (1979) *Nonlinear Oscillations*. New York: Wiley.

Rand RH, Armbruster D (1987). *Perturbation Methods, Bifurcation Theory and Computer Algebra*. New York: Springer-Verlag.

PIEZOELECTRIC MATERIALS AND CONTINUA

H S Tzou, University of Kentucky, Lexington, KY, USA

M C Natori, Institute of Space and Astronautical Science, Kanagawa, Japan

Copyright © 2001 Academic Press

doi:10.1006/rwvb.2001.0076

Smart materials are active materials whose properties can be actively tuned and controlled via electromechanical, magnetic, electrical, temperature, and high-energy light means. Furthermore, synergistically integrating smart materials, structures, sensors, actuators, control electronics, and artificial intelligence yields an active or adaptive (lifelike) structronic (*struc*ture + elec*tronic*) system with inherent self-sensing, diagnosis, and control capabilities. These new smart structures and structronic systems could revolutionalize many engineering systems.

Piezoelectric material is one kind of smart material and piezoelectricity is an electromechanical phenomenon coupling the elastic field and the electric field (**Figure 1**). (Note that *piezo* means press in Greek.) Ever since the discovery of piezoelectric behavior by the Curie brothers (Jacques and Pierre) in 1880, this coupled electromechanical characteristic has brought a new dimension in transducer (sensor and actuator) applications. In general, a piezoelectric material responds to mechanical force/pressure and generates an electric charge/voltage, which is called the direct piezoelectric effect. Conversely, an electric charge/field applied to the material induces mechanical stresses or strains, and this is called the converse piezoelectric effect. The direct effect is usually the basis in sensor and measurement applications; the converse effect is for precision actuation and manipulation in control applications.

Piezoelectric materials have been applied to engineering applications since 1917. Recent research activities involving smart materials, smart (intelligent) structures, structronic systems, precision mechatronic systems, and microelectromechanical systems (MEMS) further renew a widespread interest in traditional piezoelectric materials and continua, elastic/piezoelectric composites, and thin-layer piezoelectric devices due to their high potentials in many advanced static and dynamic applications, e.g., aerospace/aircraft structures, robot manipulators, vibration/noise control and isolation, high-precision devices, microsensors/actuators, thin-film devices, MEMS, and microdisplacement actuation and control. This article provides an overview of the historic background, material varieties, fundamental piezoelectric theories, sensor and actuator applications, piezoelectric continua, outlook, and prospects. See also **Sensors and actuators** for distributed sensing and control applications.

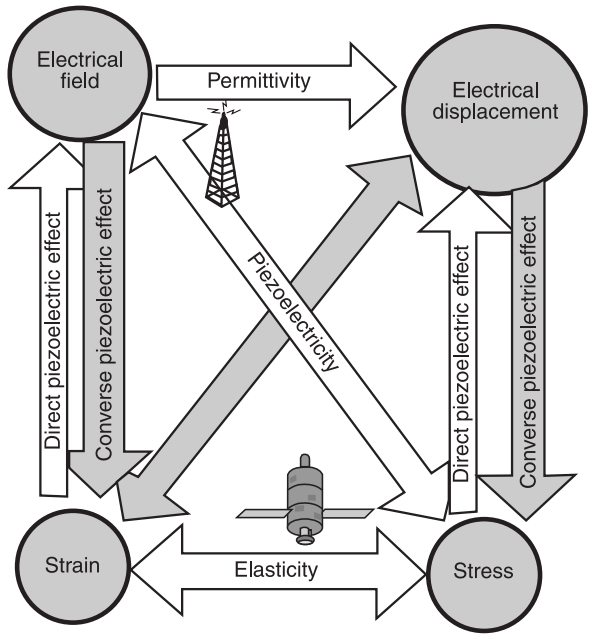


Figure 1 Piezoelectric effect.

Piezoelectric Materials

Many natural and synthetic materials exhibit piezoelectric behavior; **Table 1** summarizes popular natural and synthetic piezoelectric materials. Certain materials naturally exhibit piezoelectric behavior; however, other, especially synthetic, materials require an artificial poling process. The poling process involves applying a high electric field at an elevated temperature. The field aligns the molecular dipoles in the material and the dipoles are fixed into the aligned orientation when the material cools down while the strong field is still maintained. The poled piezoelectric material becomes anisotropic and it deforms when subject to an electric field and polarizes when subject to mechanical stress, although the original raw material was nonpiezoelectric and isotropic.

In general, synthetic materials can be fabricated into arbitrary shapes and geometries, while natural crystals usually remain in their natural formations and appearances. Accordingly, synthetic piezoelectric ceramics (e.g., lead zirconate titanate and lead lanthinum zirconate titanate) and polymers (e.g., polyvinylidene fluoride) are widely used in many sensor and actuator applications. Note that for low electric fields ($<0.1\,\mathrm{MV\,m^{-1}}$ approximately), the linear proportionality between the strain and electric field is valid. However, for higher ac fields ($>0.6\,\mathrm{MV\,m^{-1}}$ approximately), significant electromechanical hysteresis can occur as the response domain grows, which can cause servo-displacement control problems in precision piezoelectric actuator devices. These materials still have certain limitations, such as being fairly weak mechanically, and nonreproducible effects (e.g., hysteresis on the order of 10% or greater). While the range of piezoelectric applications is well documented, there are other desired applications that these materials cannot achieve effectively due to their properties, such as hysteresis, and low stroke. New high-authority materials, e.g., single crystal piezoelectric materials, are continuously being composed and evaluated. Fundamental piezoelectricity theory is presented next, followed by practical applications. Other advanced topics on piezoelectric continua are presented subsequently.

Table 1 List of common piezoelectric materials

Natural crystals	*Quartz, Rochelle salt, ammonium phosphate*
Liquid crystals	
Noncrystalline materials	Glass rubber, paraffin
Textures	Bone, wood
Synthetic piezoelectric materials	Piezoceramics Lead zirconate titanate (PZT), barium titanate, lead niobrate, lead lanthinum zirconate titanate (PLZT) Crystallines Ammonium dihydrogen phosphate, lithium sulfate Piezoelectric polymer Polyvinylidene fluoride (PVDF or PVF_2)

Linear Piezoelectricity

Linear piezoelectric theory indicates the coupling between the electric field (static coupling) and the mechanical (dynamic coupling) field (Figure 1), which is a first-order effect implying that an induced strain is proportional to the electric field and the direction of the displacement is dependent on the sign of the electric field. In this section, the linear piezoelectric theory is reviewed, and the relations among various elastic and electric constants are defined. Note that the pyroelectric effect – the temperature effect – will be discussed in a later section.

The linear piezoelectricity theory is based on a quasistatic assumption in which the electric field is balanced with the elastic field so that these two fields can be decoupled at a given time instant. The direct and converse piezoelectric effects are written as:

$$\mathbf{D} = e\mathbf{S} + \varepsilon^{\mathrm{S}}\mathbf{E} \qquad [1]$$

$$\mathbf{T} = c^{\mathrm{E}}\mathbf{S} - e^{\mathrm{t}}\mathbf{E} \qquad [2]$$

where $\mathbf{D}$ is the electric displacement vector[1]; $\mathbf{T}$ is the stress tensor (second-order); $\mathbf{S}$ is the strain tensor (second-order); $\mathbf{E}$ is the electric field vector; e is a tensor of piezoelectric stress coefficients (third-order); e^{t} is the transposed tensor of e; ε^{S} is the dielectric tensor (second-order) evaluated at constant strain; and c^{E} is the elasticity tensor (fourth-order) evaluated at constant electric field. If the piezoelectric tensor e is set to zero, eqns [1] and [2] become the conventional dielectric and Hooke's equations. Note that the stress $\mathbf{T}$ and strain $\mathbf{S}$ are represented in column vectors:

$$\mathbf{T} = [T_1\ T_2\ T_3\ T_4\ T_5\ T_6]^{\mathrm{t}} \qquad [3]$$

$$\mathbf{S} = [S_1\ S_2\ S_3\ S_4\ S_5\ S_6]^{\mathrm{t}} \qquad [4]$$

[1] IEEE piezoelectricity notation.

where the superscript t denotes the vector or matrix transpose. Subscripts 1–3 denote the normal components and 4–6 denote the shear components. The electric field **E** and the electric displacement (flux density) **D** are also written in column vectors:

$$\mathbf{E} = [E_1\ E_2\ E_3]^{\mathrm{t}} \quad [5]$$

$$\mathbf{D} = [D_1\ D_2\ D_3]^{\mathrm{t}} \quad [6]$$

Four Sets of Fundamental Equations

There are a number of ways to write the elastic, piezoelectric, and dielectric governing equations in which (1) stress and electric field, (2) strain and electric displacement, (3) strain and electric field are respectively used as dependent and/or independent variables. **Table 2** summarizes the four sets of representations, including the equations defined above.

s^{D} is the compliance matrix defined at constant dielectric displacement (note $s = c^{-1}$); d is the piezoelectric strain constant matrix; g matrix relates the open-circuit voltage at a given stress; e is the piezoelectric stress constant matrix; h matrix relates the open-circuit voltage at a given strain; β^{T} is a free dielectric impermeability matrix evaluated at constant stress and β^{T} can be obtained from the inverse of the dielectric matrix ε. The superscript T (inside the matrix) denotes the properties measured at constant stress T. (Recall that $^{\mathrm{t}}$ denotes a vector or matrix transpose and $^{-1}$ denotes the matrix inverse.). **Table 3** shows that the four piezoelectric coefficient matrices d, e, g, and h are all related. Note that an adiabatic condition ensures that no heat is added or removed from a given space or volume. The elastic constants are defined at the adiabatic conditions. The piezoelectric and dielectric constants of a piezoelectric material are defined at isothermal and adiabatic conditions. The piezoelectric material is assumed to be nonpyroelectric in this case. Again, the superscripts T, S, E, and D denote the matrix/tensor defined at constant stress, strain, electric field, and dielectric displacement, respectively.

Table 2 Four sets of piezoelectric equations

No.	Elastic relationship	Electric relationship
1	$\mathbf{T} = c^{\mathrm{D}}\mathbf{S} - h^{\mathrm{t}}\mathbf{D}$	$\mathbf{E} = -h\mathbf{S} + \beta^{\mathrm{S}}\mathbf{D}$
2	$\mathbf{T} = c^{\mathrm{E}}\mathbf{S} - e^{\mathrm{t}}\mathbf{E}$	$\mathbf{D} = e\mathbf{S} + \varepsilon^{\mathrm{S}}\mathbf{E}$
3	$\mathbf{S} = s^{\mathrm{D}}\mathbf{T} + g^{\mathrm{t}}\mathbf{D}$	$\mathbf{E} = -g\mathbf{T} + \beta^{\mathrm{T}}\mathbf{D}$
4	$\mathbf{S} = s^{\mathrm{E}}\mathbf{T} + d^{\mathrm{t}}\mathbf{E}$	$\mathbf{D} = d\mathbf{T} + \varepsilon^{\mathrm{T}}\mathbf{E}$

Table 3 Relations among elastic, piezoelectric, and dielectric constants

No.	Elastic	Piezoelectric	Dielectric
1	$s^{\mathrm{D}} = s^{\mathrm{E}} - d^{\mathrm{t}}g$	$g = \beta^{\mathrm{T}}d$	$\beta^{\mathrm{T}} = \varepsilon^{\mathrm{T}-1}$
2	$c^{\mathrm{E}} = s^{\mathrm{E}-1}$	$e = dc^{\mathrm{E}}$	$\varepsilon^{\mathrm{S}} = \varepsilon^{\mathrm{T}} - ed^{\mathrm{t}}$
3	$c^{\mathrm{D}} = c^{\mathrm{E}} - e^{\mathrm{t}}h$	$h = \beta^{\mathrm{S}}e$	$\beta^{\mathrm{S}} = \beta^{\mathrm{T}} + hg^{\mathrm{t}}$
4	$c^{\mathrm{D}} = s^{\mathrm{D}-1}$	$h = gc^{\mathrm{D}}$	$\beta^{\mathrm{S}} = \varepsilon^{\mathrm{S}-1}$

Piezothermoelasticity

Certain piezoelectric materials are also temperature-sensitive, i.e., an electric charge or voltage is generated when exposed to temperature variations. This effect is called the pyroelectric effect. (Note that *pyro* originally means fire in Greek.) When temperature influences the piezoelectricity, the fundamental piezoelectric equations need to expand to include the temperature components, e.g., pyroelectricity and thermal elasticity. Thus, the fundamental piezoelectric equations become the piezothermoelasticity equations:

$$\mathbf{T} = c\mathbf{S} - e^{\mathrm{t}}\mathbf{E} - \boldsymbol{\lambda}\theta \quad [7]$$

$$\mathbf{D} = e\mathbf{S} + \varepsilon\mathbf{E} + \mathbf{p}\theta \quad [8]$$

$$\Im = \boldsymbol{\lambda}^{\mathrm{t}}\mathbf{S} + \mathbf{p}^{\mathrm{t}}\mathbf{E} + \alpha_{\mathrm{v}}\theta \quad [9]$$

where $\boldsymbol{\lambda}$ is the thermal stress constant vector; θ is the temperature; $\mathbf{p}$ is the pyroelectric constant; $\Im$ is the thermal entropy; α_{v} is a material constant ($\alpha_{\mathrm{v}} = \rho c_{\mathrm{v}}\theta$ where ρ is the material density and c_{v} is the specific heat at constant volume).

Engineering Applications

The discovery of piezoelectricity took place in 1880; however, it wasn't until 1917 that Langevin invented the first engineering application – the depth-sounding device designed with Rochelle salt. Over the years, sophisticated piezoelectricity theories have been proposed and refined; new piezoelectric materials have been discovered or synthesized; and novel piezoelectric devices have been continuously invented and applied to a variety of engineering systems. **Table 4** summarizes a number of typical sensor and actuator applications. As discussed previously, sensor application is based on the direct piezoelectric effect; actuator application is based on the converse piezoelectric effect. A number of sample application areas are also summarized in **Table 5**. Note that these areas

Table 4 Sensor and actuator applications

Sensors	Accelerometer, pressure transducer, force transducer, noise/acoustic sensor, microphone, impact transducer, distributed sensor, orthogonal (modal) sensor, health monitoring
Actuators	Precision manipulator, pressure generator, ink/fuel injection, displacement actuator, vibration isolation, vibration and noise control, ultrasonic motors, distributed control, constrained layer damping, passive shunt damping, orthogonal (modal) actuator, self-sensing actuator, active structures, smart composites

Table 5 Sample application areas

Structures	Vibration, noise, stress, strain, health monitoring, measurements (e.g., flow, pressure, force, impact)
Machines and mechanical systems	Vibration and noise (monitoring and control), strength, stress, strain, health monitoring and diagnosis, optical systems, measurements (e.g., force, acceleration, pressure, impact, noise), rotor control
Medical and biomedical applications	Disposable sensors, ultrasonic devices, precision drives and control (e.g., scanning tunneling microscopes, manipulators)
Robotics and mechatronic systems	Precision actuation, manipulation, control, precision/micro robots, robot grippers, flexible robot control, microelectromechanical systems (MEMS), microsensor/actuator
Smart structures and structronic systems	Adaptive structures and composites, structural control, adaptive geometry and shape control, adaptive aircraft wings or helicopter blades, noise and vibration control, damage detection, health monitoring, self-sensing actuators, damage repairs, precision truss structures, positioning, aerospace structures and satellites, reinforced vehicle structures

are artificially categorized and lots of them are actually interrelated and somehow overlapped. In many cases, both sensor and actuator functions are often incorporated in these application areas. Advanced topics on (linear and nonlinear) piezoelectric shell continua and their derivatives are discussed next. For distributed sensing and vibration control of elastic continua (e.g., shells, plates, etc.) using distributed thin piezoelectric sensor/actuator layers, see **Sensors and actuators**.

Piezoelectric Continua and Advanced Theories

The Curie brothers initiated the studies of piezoelectric continua in 1880. Advances have continuously been made over the years (e.g., Mason, Cady, Mindlin, Tiersten, Sesseler, Dökmeci, Tzou, and Rogacheva). Although studies of piezoelectric shells of specific shapes have advanced in the last few decades, most of them have primarily been concerned with wave propagation (i.e., in-plane motions), electromechanics, and vibrations of specific geometries with finite and infinite dimensions, such as thin rods, plates, rings, disks, and circular cylindrical shells. Later, more advanced geometries (such as spherical shells, shells of revolution, hollow ceramic cylinders, radially polarized composite piezoceramic cylinders, piezoelectric solid cylinder guided by a thin film, and wave propagations in a piezoelectric solid cylinder of arbitrary cross-sections) were investigated. Recent development of smart structures and structronic systems reveals the need to derive a more generic linear and nonlinear piezoelectric continuum theory applicable to distributed sensors and actuators in control of elastic continua and distributed parameter systems. Accordingly, piezoelectric theories based on a generic double-curvature deep shell with triclinic or hexagonal crystal structures have been investigated. **Figure 2** illustrates a generic piezoelectric double-curvature deep shell defined in a triorthogonal coordinate system, in which α_1 and α_2 define the neutral surface and α_3 defines the normal direction; R_1 and R_2 are the radii of curvature of the α_1 and α_2 axes, respectively. Theories related to the generic shell can be, in general, applied to a number of common configurations and geometries.

Generic theories on piezoelectric shells of arbitrary shape are of importance in many applications. Theories derived based on the generic shell continuum can easily be simplified and applied to other common geometries (e.g., shells of revolution, spherical shells, conical shells, cylinders, cylindrical shells, plates, arches, rings, and beams) using four geometric parameters: two radii of curvatures (R_1 and R_2) and two Lamé parameters (A_1 and A_2). (See **Sensors and actuators** for detailed simplification procedures.) Advanced (linear and nonlinear) theories of generic (triclinic and hexagonal) piezoelectric (thin, thick,

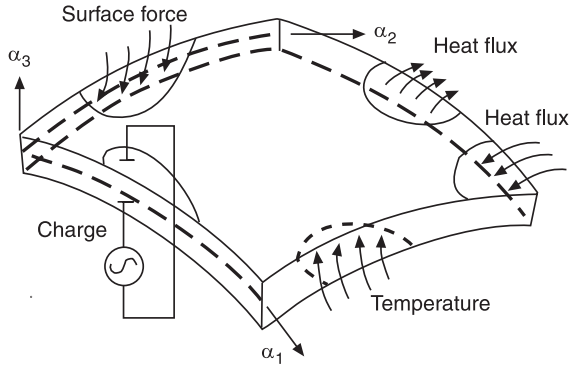


Figure 2 A generic piezothermoelastic shell continuum subjected to multifield excitations.

and composite) (deep or shallow) shells have recently been proposed. System equations coupling electric, elastic, and temperature fields are derived using the energy-based Hamilton's principle. Generic equations of mechanical motion and mechanical boundary conditions, as well as a charge equation of electrostatics and electric boundary conditions are formulated. Temperature effects to these piezoelectric shell continua are also discussed and its effects on system characteristics and sensing/control effectiveness are evaluated. These concepts are briefly outlined next.

Thermoelectromechanical system equations of a nonlinear piezothermoelastic shell continuum, i.e., the von Karman-type geometric nonlinearity, are also presented to illustrate multifield coupling (Figure 2).

Thermoelectromechanical Coupling of Nonlinear Piezoelectric Shell Continuum

Hamilton's principle is used in deriving the shell thermoelectromechanical equations and boundary conditions of the piezothermoelastic shell continuum. Hamilton's principle assumes that the energy variations over an arbitrary time period are zero. Considering all energies associated with a piezothermoelastic shell continuum subjected to mechanical, temperature, and electric inputs, one can write Hamilton's equation:

$$\delta \int_{t_0}^{t_1} \left\{ \left(\int_V \frac{1}{2}\rho \dot{U}_j \dot{U}_j \right) \mathrm{d}V - \left[\int_V \left(H(S_i, E_i, \Theta) + \Im\Theta \right) \mathrm{d}V - \int_S \left(t_j U_j - Q_j \phi \right) \mathrm{d}S \right\} \mathrm{d}t = 0 \qquad [10]$$

where ρ is the mass density; H is the electric enthalpy; t_j is the surface traction in the α_j direction; Q_j is the surface electric charge; ϕ is the electrical potential; V and S are the volume and surface of the piezothermoelastic shell continuum, respectively; and U_j and $\dot{U}_j$ are the displacement and velocity vectors. It is assumed that only the transverse electric field E_3 is considered in the analysis and a linear variation of the displacement field in the shell, i.e., $U_i = u_i + \beta_i$. Substituting all energy expressions into Hamilton's equation and imposing the thin-shell assumptions, one can derive the nonlinear piezothermoelastic shell equations and boundary conditions of the continuum.

$$-\frac{\partial(N_{11}A_2)}{\partial\alpha_1} + N_{22}\frac{\partial A_2}{\partial\alpha_1} - \frac{\partial(N_{21}A_1)}{\partial\alpha_2} - N_{12}\frac{\partial A_1}{\partial\alpha_2} - \frac{1}{R_1}\left[\frac{\partial(M_{11}A_2)}{\partial\alpha_1} - M_{22}\frac{\partial A_2}{\partial\alpha_1} + \frac{\partial(M_{21}A_1)}{\partial\alpha_2} + M_{12}\frac{\partial A_1}{\partial\alpha_2}\right] + A_1A_2\rho h\ddot{u}_1 = A_1A_2F_1 \qquad [11]$$

$$-\frac{\partial(N_{22}A_1)}{\partial\alpha_2} + N_{11}\frac{\partial A_1}{\partial\alpha_2} - \frac{\partial(N_{12}A_2)}{\partial\alpha_1} - N_{21}\frac{\partial A_2}{\partial\alpha_1} - \frac{1}{R_2}\left[\frac{\partial(M_{22}A_1)}{\partial\alpha_2} - M_{11}\frac{\partial A_1}{\partial\alpha_2} + \frac{\partial(M_{12}A_2)}{\partial\alpha_1} + M_{21}\frac{\partial A_2}{\partial\alpha_1}\right] + A_1A_2\rho h\ddot{u}_2 = A_1A_2F_2 \qquad [12]$$

$$-\frac{\partial}{\partial\alpha_1}\left[\frac{1}{A_1}\left(\frac{\partial(M_{11}A_2)}{\partial\alpha_1} - M_{22}\frac{\partial A_2}{\partial\alpha_1} + \frac{\partial(M_{21}A_1)}{\partial\alpha_2} + M_{12}\frac{\partial A_1}{\partial\alpha_2}\right)\right] - \frac{\partial}{\partial\alpha_2}\left[\frac{1}{A_2}\left(\frac{\partial(M_{22}A_1)}{\partial\alpha_2} - M_{11}\frac{\partial A_1}{\partial\alpha_2} + \frac{\partial(M_{12}A_2)}{\partial\alpha_1} + M_{21}\frac{\partial A_2}{\partial\alpha_1}\right)\right] + A_1A_2\left(\frac{N_{11}}{R_1} + \frac{N_{22}}{R_2}\right) + A_1A_2\rho h\ddot{u}_3 - \left\{\left[\frac{\partial(N_{11}A_2/A_1)}{\partial\alpha_1} + \frac{\partial N_{12}}{\partial\alpha_2}\right]\frac{\partial u_3}{\partial\alpha_1} + \left[\frac{\partial(N_{22}A_1/A_2)}{\partial\alpha_2} + \frac{\partial N_{12}}{\partial\alpha_1}\right]\frac{\partial u_3}{\partial\alpha_2} + 2N_{12}\frac{\partial^2 u_3}{\partial\alpha_1\partial\alpha_2} + N_{11}\frac{A_2}{A_1}\frac{\partial^2 u_3}{\partial\alpha_1^2} + N_{22}\frac{A_1}{A_2}\frac{\partial^2 u_3}{\partial\alpha_2^2}\right\} = A_1A_2F_3 \qquad [13]$$

where u_i is the displacement in the α_i direction; ρ is the mass density; F_i is the external input; A_1 and A_2

are the Lamé parameters; and R_1 and R_2 are the radii of curvature. Note that all terms inside the braces are contributed by the nonlinear effects, showing that the nonlinear influence on the transverse equation u_3 is significant. Also, the thermoelectromechanical equations are similar to standard shell equations. However, the force and moment expressions defined by mechanical, thermal, and electric effects are much more complicated than the conventional elastic expressions. Membrane force resultants N_{ij} and bending moments M_{ij} can be derived based on the induced strains (i.e., membrane strains s_i^0 and bending strains k_i).

$$\begin{bmatrix} N_{11} \\ N_{22} \\ N_{12} \\ M_{11} \\ M_{22} \\ M_{12} \end{bmatrix} = \begin{bmatrix} A_{11} & A_{12} & A_{16} & 0 & 0 & 0 \\ A_{12} & A_{22} & A_{26} & 0 & 0 & 0 \\ A_{16} & A_{26} & A_{66} & 0 & 0 & 0 \\ 0 & 0 & 0 & D_{11} & D_{12} & D_{16} \\ 0 & 0 & 0 & D_{12} & D_{22} & D_{26} \\ 0 & 0 & 0 & D_{16} & D_{26} & D_{66} \end{bmatrix} \begin{bmatrix} s_1^0 \\ s_2^0 \\ s_6^0 \\ k_1 \\ k_2 \\ k_6 \end{bmatrix} - \begin{bmatrix} N_{11}^{e} \\ N_{22}^{e} \\ N_{12}^{e} \\ M_{11}^{e} \\ M_{22}^{e} \\ M_{12}^{e} \end{bmatrix} - \begin{bmatrix} N_{11}^{\theta} \\ N_{22}^{\theta} \\ N_{12}^{\theta} \\ M_{11}^{\theta} \\ M_{22}^{\theta} \\ M_{12}^{\theta} \end{bmatrix} \quad [14]$$

It is observed that there are three components, mechanical, electric, and temperature, in the force/moment expressions. Superscripts e and θ respectively denote the electric and temperature components; N_{ij}^{e} and N_{ij}^{θ} are the electric- and temperature-induced forces; and M_{ij}^{e} and M_{ij}^{θ} are the electric- and temperature-induced moments, respectively. In actuator applications, these electric forces and moments are used to control the static and dynamic characteristics of shells. A_{ij} and D_{ij} are the extensional and bending stiffness constants. (Note that all zeroes in the force matrix are replaced by the coupling constants B_{ij} in a piezoelectric *composite laminated* shell. The membrane strains and bending strains are coupled by the coupling stiffness coefficients B_{ij} in the elastic force/moment resultants.) Substituting the expressions of $N_{11}, N_{22}, N_{12}, M_{11}, M_{22}, M_{12}$ into the shell equations leads to the thermoelectromechanical shell equations defined in the neutral surface displacements u_1, u_2, and u_3. The transverse shear deformation and rotatory inertia effects are not considered. The electric terms, forces and moments, can also be used in controlling the mechanical- and/or temperature-induced excitations.

Based on Hamilton's equation, one can also derive all admissible mechanical and electric boundary conditions. Admissible mechanical boundary conditions on the boundary surfaces defined by a distance α_2 and α_1 are respectively summarized in **Table 6** and **Table 7**. The superscript * denotes the boundary forces, moments, displacements, and slopes. Usually, only either the force/moment boundary conditions or the displacement/slope boundary conditions are selected for a given physical boundary condition. In addition, additional transverse shear force terms Q_{i3} are nonlinear components induced by large deformations. These force terms do not appear in the linear case. The shear stress resultants are defined as:

$$V_{12} = N_{12} + \left(\frac{M_{12}}{R_1}\right) \quad [15]$$

$$V_{21} = N_{21} + \left(\frac{M_{21}}{R_1}\right) \quad [16]$$

$$V_{13} = Q_{13} + \frac{\partial}{\partial \alpha_2}\left(\frac{M_{12}}{A_2}\right) \quad [17]$$

Table 6 Boundary conditions (α_1 axis)

	Force/moment	*Displacement*
1	$N_{11} = N_{11}^*$	$u_1 = u_1^*$
2	$M_{11} = M_{11}^*$	$\beta_1 = \beta_1^*$
3	$N_{12} + \dfrac{M_{12}}{R_2} = V_{12}^*$	$u_2 = u_2^*$
4	$Q_{13} + \dfrac{\partial}{\partial \alpha_2}\left(\dfrac{M_{12}}{A_2}\right) + \left[N_{11}\left(\dfrac{1}{A_1}\dfrac{\partial u_3}{\partial \alpha_1}\right) + N_{12}\left(\dfrac{1}{A_2}\dfrac{\partial u_3}{\partial \alpha_2}\right)\right] = V_{13}^*$	$u_3 = u_3^*$

Table 7 Boundary conditions (α_2 axis)

	Force/moment	*Displacement*
1	$N_{22} = N_{22}^*$	$u_2 = u_2^*$
2	$M_{22} = M_{22}^*$	$\beta_2 = \beta_2^*$
3	$N_{21} + \dfrac{M_{21}}{R_1} = V_{21}^*$	$u_1 = u_1^*$
4	$Q_{23} + \dfrac{\partial}{\partial \alpha_1}\left(\dfrac{M_{21}}{A_1}\right) + \left[N_{22}\left(\dfrac{1}{A_2}\dfrac{\partial u_3}{\partial \alpha_2}\right) + N_{21}\left(\dfrac{1}{A_1}\dfrac{\partial u_3}{\partial \alpha_1}\right)\right] = V_{23}^*$	$u_3 = u_3^*$

$$V_{23} = Q_{23} + \frac{\partial}{\partial \alpha_1}\left(\frac{M_{21}}{A_1}\right) \qquad [18]$$

where V_{13} and V_{23} are the Kirchhoff effective shear stress resultants of the first kind; V_{12} and V_{21} are the Kirchhoff effective shear stress resultants of the second kind. Note that all elastic-, electric-, and thermal-related terms are included in the force and moment expressions. These electric terms can be used, in conjunction with control algorithms, as control forces/moments counteracting mechanical- and temperature-induced vibrations in distributed structural control of shells. The nonlinear piezothermoelastic shell equations can be further simplified based on (1) linear approximation, (2) material simplification, and (3) geometry simplifications.

In order to assist design and application of piezoelectric devices in industry, new finite element formulations (thick and thin solid elements, shell/plate elements, and composite elements) and computer codes have been developed in recent years. Accordingly, thermoelectromechanics, vibration behavior, sensing, and control encompassing all possible directions (e.g., three translational and two rotatory coordinates) of the generic piezoelectric shell continuum (and its derived geometries) and applications to smart structures and structronic systems are further explored and evaluated. Furthermore, distributed sensor and actuator can be surface- or thickness-shaped using the modal strain functions. In this case, the shaped sensor or actuator is only sensitive to the designated natural mode (i.e., the orthogonal modal sensor or actuator) and it is insensitive to other natural modes, based on the modal orthogonality of natural modes. (See **Sensors and actuators** for details on distributed sensor and actuator applications and their related theories.)

Summary

Piezoelectricity is one of the most important electromechanical coupling phenomena successfully applied to engineering applications today. Practical applications range from micro- (e.g., MEMS and microsensors and actuators) to macrosystems (e.g., smart structures and structronic systems, aerospace structures, satellite systems, and gossamer systems) and many other applications in between (e.g., force/pressure sensors, precision actuators, robotics and mechatronic systems, and vibration/noise isolation and control). However, the performance of today's piezoelectric devices is still limited to material properties and deficiencies, e.g., nonlinearity, hysteresis effects, limited strain rates, breakdown voltages, and temperature instability, etc. These material properties need to be further improved in order to enhance future sensor/actuator performance and efficiency.

On the other hand, piezoelectricity typically represents the coupling of electric and elastic (mechanical) fields (Figure 1). Beyond the typical two-field coupling, there is a three-field coupling (temperature–electric–mechanical) and a four-field coupling (light–temperature–electric–mechanical; **Figure 3**). As the coupling complicates, the complexity of research issues increases, too. Although piezoelectricity has been around since 1880, there are still plenty of research issues that need to be addressed. Furthermore, novel applications and devices need to be continuously explored and utilized. (Note that other popular smart materials, e.g., electrostrictive materials, magnetostrictive materials, shape memory alloys, electro- and magnetorheological materials are introduced in separate articles.)

Nomenclature

A_1, A_2	Lamé parameters
c_v	specific heat at constant volume
$\mathbf{D}$	electric displacement vector
$\mathbf{E}$	electric field vector
$\mathbf{p}$	pyroelectric constant
R_1, R_2	radii of curvature
$\mathbf{S}$	strain tensor
$\mathbf{T}$	stress tensor
$\boldsymbol{\lambda}$	thermal stress constant vector
θ	temperature
ϕ	electrical potential
ρ	density
$\Im$	thermal entropy

See also: **Electrorheological and magnetorheological fluids**; **Electrostrictive materials**; **Magnetostrictive materials**; **Sensors and actuators**; **Shape memory alloys**.

Further Reading

Cady WG (1964) *Piezoelectricity*. New York: Dover.
Dökmeci MC (1983) Dynamic applications of piezoelectric

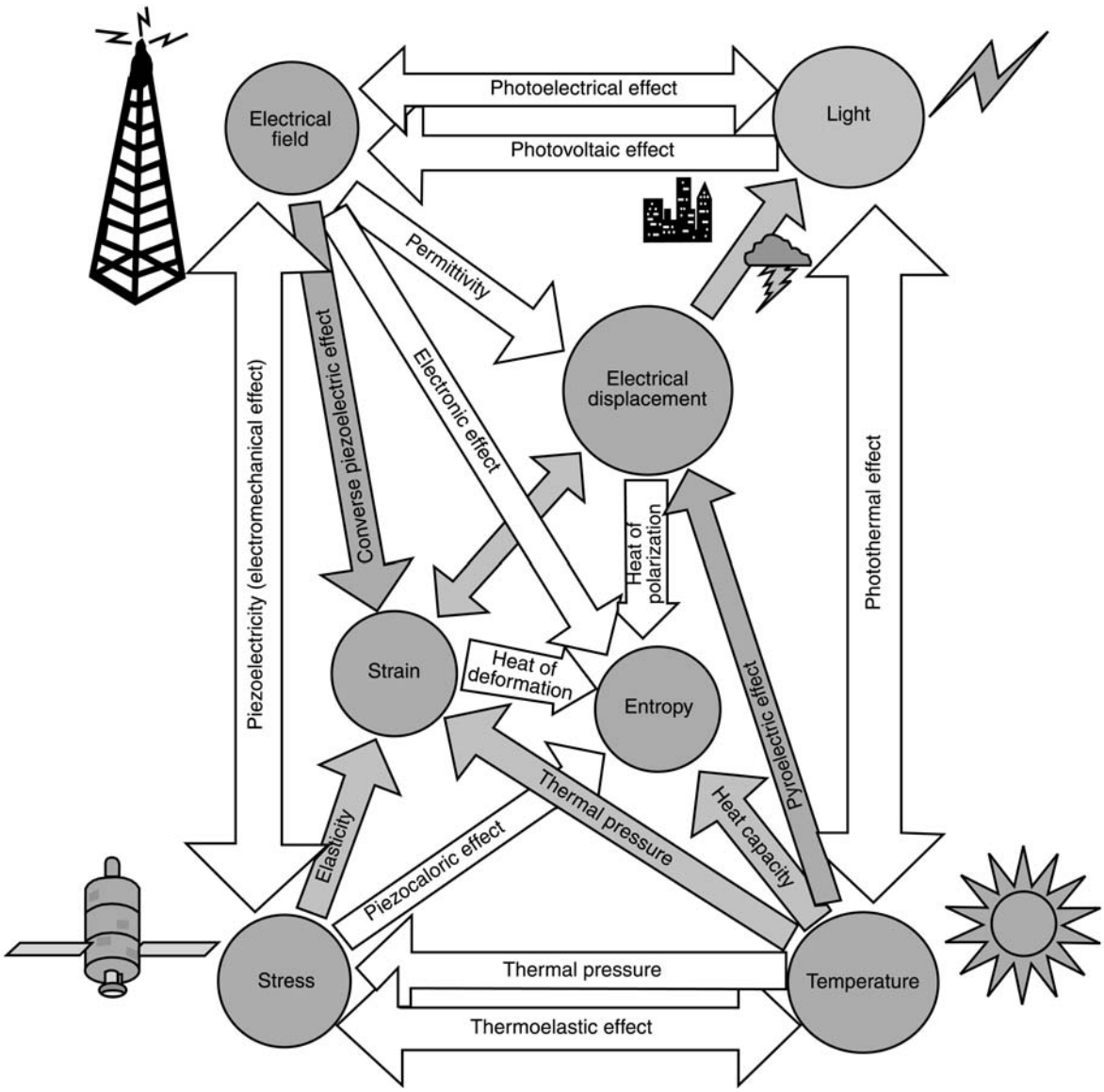


Figure 3 Four-field light–piezoelectric–thermoelastic effect.

crystals. *Shock and Vibration Digest*, 15(3): 9–22.

Guran A and Tzou HS (eds) (1998) *Structronic Systems – Smart Structures, Devices and Systems*, Vol. 1. *Materials and Structures*. Singapore: World Scientific.

Mason WP (1950) *Piezoelectric Crystals and Their Application to Ultrasonics*. New York: Nostrand.

Mason WP (1981) Piezoelectricity, its history and application. *Journal of the Acoustic Society of America* 70(6): 1561–1566.

Rogacheva NN (1994) *The Theory of Piezoelectric Shells and Plates*. Boca Raton, FL: CRC Press.

Sessler GM (1981) Piezoelectricity in polyvinylidene fluoride. *Journal of the Acoustic Society of America* 70(6): 1596–1608.

Tiersten HF (1969) *Linear Piezoelectric Plate Vibrations*. New York: Plenum.

Tzou HS (1993) *Piezoelectric Shells (Distributed Sensing and Control of Continua)*. Dordrecht: Kluwer.

Tzou HS (1998) Multi-field transducers, devices, mechatronic systems, and structronic systems with smart materials. *Shock and Vibration Digest* 30(4): 282–294.

Tzou HS and Anderson GL (eds) (1992) *Intelligent Structural Systems*. Dordrecht: Kluwer.

Tzou HS and Bergman LA (1998) *Dynamics and Control of Distributed Systems*. New York: Cambridge University Press.

Tzou HS and Fukuda T (eds) (1992) *Precision Sensors, Actuators, and Systems*. Dordrecht: Kluwer.

Tzou HS and Guran A (eds) (1998) *Structronic Systems – Smart Structures, Devices and Systems*, vol. 2. *Systems and Control*. Singapore: World Scientific.

PIPES

S S Rao, University of Miami, Coral Gables, FL, USA

Copyright © 2001 Academic Press

doi:10.1006/rwvb.2001.0136

Introduction

Pipes involving internal or external fluid flow can be found in many engineering applications such as power plants, chemical and petrochemical industries, heat exchangers, nuclear reactors, jet pumps, and hydraulic machinery. Pipes with fluid flow are subject to flow-induced vibration due to fluid pressure, turbulence in the flow and, sometimes, due to resonance with some periodicity in the flow. Four types of problems can be identified as: (i) pipes with internal fluid flow; (ii) pipes with external fluid flow; (iii) annular flow in systems of coaxial pipes, and (iv) cross-flow about arrays of tubes. Of these four types of problems, the first involving pipes with internal fluid flow is the oldest and best studied. Another classification of flow-induced vibration problems, based on the source of excitation, includes problems involving (i) extraneously induced excitation, (ii) instability induced excitation and (iii) movement-induced excitation. The extraneously induced vibration is caused by fluctuations in the flow or pressure, independently of any structural motion and flow instabilities. An example of this is the turbulence-induced excitation of a cylinder in fluid flow. The instability induced excitation is due to the instability of the flow as in the case of vortex shedding from a cylindrical structure. The movement induced excitation is a self-excited vibration as in the case of flutter of a cantilever pipe with internal fluid flow. The earliest work on the vibration of pipes conveying fluids is perhaps the experimental work of Aitken (1878). Housner was among the first to investigate the stability of a simply supported pipe conveying fluid.

Vibration of Pipes with Internal Fluid Flow

Some pipes with internal fluid flow, having different support conditions, are shown in **Figure 1**. The pipe is assumed to have an inner diameter d_i, an outer diameter d_o and Young's modulus E and the fluid is assumed to have a density ρ, pressure p and velocity v. The fluid flow imposes a pressure on the pipe walls and causes the pipe to deflect. The fluid is subject to centrifugal acceleration as it passes through the deflected pipe due to the changing curvature of the pipe. In the absence of gravity and internal damping effects, the equation of motion of the pipe can be obtained as:

$$EI\frac{\partial^4 y}{\partial x^4} + (pA - T)\frac{\partial^2 y}{\partial x^2} + m_f\left(\frac{\partial}{\partial t} + v\frac{\partial}{\partial x}\right)^2 y + m\frac{\partial^2 y}{\partial t^2} = 0 \quad [1]$$

where y is the transverse deflection of the pipe, I is the area moment of inertia of the pipe, A is the cross-sectional area of the pipe, T is the longitudinal tension in the pipe, $m_f = \rho A$ is the mass of the fluid per unit length, m is the mass of the pipe per unit length, x is the axial coordinate and t is time. If the tension in the pipe is zero and the fluid pressure is equal to the ambient pressure at the end of the pipe, $p = T = 0$ at $x = L$ and it can be shown that $pA - T = 0$ for all x. Setting $pA - T = 0$, eqn [1] gives the equation of motion for the free transverse vibration of a tension-free straight pipe carrying fluid as:

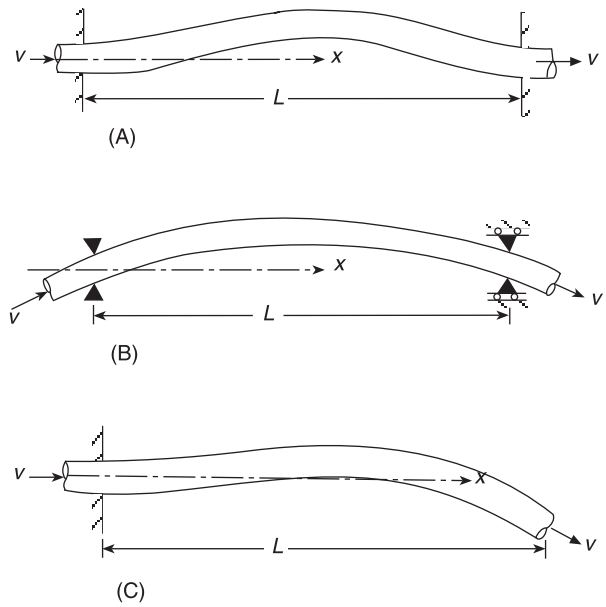


Figure 1 Pipes with internal fluid flow. (A) Clamped–clamped pipe; (B) simply supported pipe; (C) cantilever pipe.

$$EI\,\frac{\partial^4 y}{\partial x^4} + m_f v^2\,\frac{\partial^2 y}{\partial x^2} + 2m_f v\,\frac{\partial^2 y}{\partial x \partial t} + M\,\frac{\partial^2 y}{\partial t^2} = 0 \quad [2]$$

where $M = m + m_f$ is the mass per unit length of the pipe including the fluid. Note that the first and fourth terms denote the stiffness and inertia terms that are independent of the flow velocity. The third term represents Coriolis force and causes asymmetric distortion of classical mode shapes (due to the presence of the mixed derivative) and leads to flutter like instability. The second term indicates the centrifugal force due to the acceleration of fluid passing through the deformed pipe. This term is similar to an axial compression term that produces a reduction in natural frequency and ultimately buckling of the pipe. For comparison, the equation of motion of a pipe subject to an axial compressive force P at the end (without fluid) is given by:

$$EI\,\frac{\partial^4 y}{\partial x^4} + P\,\frac{\partial^2 y}{\partial x^2} + m\,\frac{\partial^2 y}{\partial t^2} = 0 \quad [3]$$

It can be seen from eqns [2] and [3] that as the velocity of the fluid, v, increases, the effective stiffness of the pipe decreases and for a sufficiently large value of v, the destabilizing centrifugal force may overcome the restoring flexural force, thereby causing divergence (or buckling).

Solution

Using the dimensionless parameters:

$$\xi = \frac{x}{L}\ ,\ \eta = \frac{y}{L}\ ,\ \tau = \left(\frac{EI}{m + m_f}\right)^{1/2}\frac{t}{L^2} \quad [4]$$

the equation of motion, eqn [2], can be expressed as:

$$\frac{\partial^4 \eta}{\partial \xi^4} + \alpha^2\,\frac{\partial^2 \eta}{\partial \xi^2} + 2\alpha\sqrt{(\beta)}\,\frac{\partial^2 \eta}{\partial \xi \partial \tau} + \frac{\partial^2 \eta}{\partial \tau^2} = 0 \quad [5]$$

where:

$$\alpha = vL\sqrt{\left(\frac{m_f}{EI}\right)}, \quad \beta = \frac{m_f}{m_f + m} \quad [6]$$

The boundary conditions for a pipe simply supported at both the ends are:

$$\eta = \frac{\partial^2 \eta}{\partial \xi^2} = 0 \text{ at } \xi = 0, \text{ and } \xi = 1 \quad [7]$$

For a cantilever pipe, the boundary conditions are:

$$\eta = \frac{\partial \eta}{\partial \xi} = 0 \text{ at } \xi = 0 \quad [8]$$

$$\frac{\partial^2 \eta}{\partial \xi^2} = \frac{\partial^3 \eta}{\partial \xi^3} 0 \text{ at } \xi = 1 \quad [9]$$

The solution of eqn [5] is assumed to be of the form:

$$\eta(\xi, \tau) = \mathrm{Re}\left[U(\xi)\mathrm{e}^{\mathrm{i}\Omega\tau}\right] \quad [10]$$

where Re denotes the real part and Ω is the nondimensional frequency, defined in terms of the circular frequency, ω, as:

$$\Omega = \omega L^2\left[\frac{m_f + m}{EI}\right]^{1/2} \quad [11]$$

In general, $\Omega = \Omega_R + i\Omega_I$ is complex [$\mathrm{i} = \sqrt{(-1)}$] and the system will be stable (unstable) if the imaginary part, Ω_I, is positive (negative). The condition, $\Omega_I = 0$, corresponds to neutral stability of the system. Eqns [5] and [10] result in:

$$\frac{\mathrm{d}^4 U}{\mathrm{d}\xi^4} + \alpha^2\,\frac{\mathrm{d}^2 U}{\mathrm{d}\xi^2} + 2\mathrm{i}\alpha\Omega\sqrt{(\beta)}\,\frac{\mathrm{d}U}{\mathrm{d}\xi} - \Omega^2 U = 0 \quad [12]$$

Using the solution:

$$U(\xi) = A\mathrm{e}^{\mathrm{i}\theta\xi} \quad [13]$$

the exponent θ is determined from:

$$\theta^4 - \alpha^2\theta^2 - 2\alpha\Omega\sqrt{(\beta)}\theta - \Omega^2 = 0 \quad [14]$$

Thus the complete solution can be expressed as:

$$\theta(\xi, \tau) = \mathrm{Re}\left(\sum_{j=1}^{4} A_j \mathrm{e}^{\mathrm{i}\theta_j\xi}\mathrm{e}^{\mathrm{i}\Omega\tau}\right) \quad [15]$$

The boundary conditions can be used to determine the constants A_j ($j = 1, 2, 3, 4$). For a simply supported pipe, eqns [7] and [15] yield:

$$\sum_{j=1}^{4} A_j = 0 \quad [16]$$

$$\sum_{j=1}^{4} \theta_j^2 A_j = 0 \quad [17]$$

$$\sum_{j=1}^{4} e^{i\theta_j} A_j = 0 \qquad [18]$$

$$\sum_{j=1}^{4} \theta_j^2 e^{i\theta_j} A_j = 0 \qquad [19]$$

Since the determinant of the coefficients of A_j in eqns [16] to [19] must vanish for a nontrivial solution of A_j, we have:

$$\begin{vmatrix} 1 & 1 & 1 & 1 \\ \theta_1^2 & \theta_2^2 & \theta_3^2 & \theta_4^2 \\ e^{i\theta_1} & e^{i\theta_2} & e^{i\theta_3} & e^{i\theta_4} \\ \theta_1^2 e^{i\theta_1} & \theta_2^2 e^{i\theta_2} & \theta_3^2 e^{i\theta_3} & \theta_4^2 e^{i\theta_4} \end{vmatrix} = 0 \qquad [20]$$

Eqn [20] must be solved to find the dynamic response of the system.

Pinned–pinned pipe For this case the characteristic equation can be derived as $\sin \alpha = 0$ with roots given by $\alpha = n\pi$. Thus the first nonzero root is $\alpha = \pi$. The critical velocity of the flow that causes buckling (v_0) is:

$$v_0 = \frac{\pi}{L}\sqrt{\left(\frac{EI}{m_f}\right)} \qquad [21]$$

By considering only the first two modes, the natural frequencies of the pipe can be determined as:

$$\left(\frac{\omega_i}{\omega_0}\right)^2 = \bar{\beta} \pm \left[\bar{\beta}^2 - 4\left(1 - \frac{v^2}{v_0^2}\right)\left(4 - \frac{v^2}{v_0^2}\right)\right]^{1/2}; \; i = 1, 2 \qquad [22]$$

where:

$$\bar{\beta} = \frac{17}{2} - \frac{v^2}{v_0^2}\left(\frac{5}{2} - \frac{128}{9\pi^2}\frac{\rho A}{M}\right) \qquad [23]$$

and ω_0 is the fundamental circular natural frequency of the pipe in the absence of fluid flow:

$$\omega_0 = \frac{\pi^2}{L^2}\left(\frac{EI}{M}\right)^{1/2} \qquad [24]$$

The mode shape corresponding to the fundamental frequency can be found as:

$$A_2 = -A_1\left[\frac{8\omega_1 L v/3\pi^2 v_0^2}{16 - 4(v^2/v_0^2) - (\omega_1^2/\omega_0^2)}\right] \qquad [25]$$

where A_1 and A_2 denote the magnitudes of the first and second modes, respectively. It is observed that for $v < v_0$, $|A_2| < 0.094A_1$ which indicates that the first sinusoidal bending mode dominates the response.

When $v = 0$ (no fluid flow), the first two natural frequencies of vibration of a pipe reduce to the natural frequencies of vibration of a rod, ω_0 and $4\omega_0$. As the fluid velocity increases, the values of natural frequencies decrease until the first frequency reduces to zero at $v = v_0$. At $v = v_0$, the force required to make the fluid conform to the deformed shape of the pipe exceeds the stiffness of the pipe and the pipe experiences divergence (buckling).

Cantilever pipe A cantilever pipe with internal fluid flow represents a nonconservative system. It can be shown that it loses stability by flutter, also known as Hopf bifurcation. This instability mechanism was first investigated by Benjamin. Qualitatively, the phenomenon can be explained as follows. The work done (ΔW) over a period of oscillation, τ, can be expressed as:

$$\Delta W = -Mv\int_0^t \left[\left(\frac{\partial y}{\partial t}\right)^2 + v\frac{\partial y}{\partial t}\frac{\partial y}{\partial x}\right]_L^0 dt \qquad [26]$$

It can be observed that if both ends of the pipe are supported, then the system will be conservative (since $\Delta W = 0$). This implies that no energy is lost or gained during the oscillatory motion. On the other hand, if one end is fixed (at $x = 0$) and the other end is free (at $x = L$), the system will be nonconservative with ΔW given by:

$$\Delta W = -Mv\int_0^t \left[\left(\frac{\partial y}{\partial t}\right)^2 + v\frac{\partial y}{\partial t}\frac{\partial y}{\partial x}\right]_L dt \qquad [27]$$

Thus for $v > 0$ and small, $\Delta W < 0$ and the free vibration is damped. However, if $v > 0$ and sufficiently large, the integral may be negative under certain conditions leading to $\Delta W > 0$. This impies that energy is extracted from the flow and free vibration is amplified which leads to a negative-damping type of instability (flutter).

For a quantitative analysis of the vibration of a cantilever pipe with internal fluid flow, the deflection is assumed as:

$$y(x,t) = \mathrm{Re}\left[U\left(\frac{x}{L}\right)e^{i\omega t}\right] \qquad [28]$$

The mode shapes of a cantilever pipe without fluid flow, $Y_i(x/L)$, are used to approximate the mode

shapes of a pipe with fluid flow, $U(x/L)$, as:

$$U\left(\frac{x}{L}\right) = \sum_{i=1}^{\infty} A_i Y_i\left(\frac{x}{L}\right) \qquad [29]$$

where:

$$Y_i\left(\frac{x}{L}\right) = \cosh(\lambda_i x) - \cos(\lambda_i x) - c_i[\sinh(\lambda_i x) - \sin(\lambda_i x)]\,; \quad i = 1, 2, \ldots \qquad [30]$$

where $\lambda_1 L = 1.875$, $\lambda_2 L = 4.694$, $\lambda_3 L = 7.855$, ..., $c_1 = 0.7341$, $c_2 = 1.0185$, $c_3 = 0.9992\ldots$. Eqns [29] and [12] yield the equation of motion of the pipe with fluid flow as:

$$\sum_{j=1}^{\infty}\left(Y_j'''' + \mathrm{i}\theta^2 Y_j'' + 2\Omega\beta^{1/2}\theta_j Y_j' - \Omega^2 Y_j\right)A_j = 0 \qquad [31]$$

By using the mode shapes of eqn [30] along with the property of orthogonality of mode shapes, the equations of motion of the pipe can be expressed in matrix form as:

$$[\mathbf{K} - \Omega^2\mathbf{I}]\mathbf{A} = \mathbf{0} \qquad [32]$$

By setting the determinant of the coefficient matrix in eqn [32] equal to zero:

$$|\mathbf{K} - \Omega^2\mathbf{I}| = 0 \qquad [33]$$

the natural frequencies of vibration of the pipe, Ω_j, can be determined. When the natural frequency Ω_j is expressed as a complex quantity, $\Omega_j = \Omega_{j\mathrm{R}} + \mathrm{i}\Omega_{j\mathrm{I}}$ where $\Omega_{j\mathrm{R}}$ can be seen to cause vibration with an exponentially decaying envelope and $\Omega_{j\mathrm{I}}$ an exponentially growing envelope. The condition $\Omega_{j\mathrm{I}} = 0$ corresponds to neutral stability. A typical stability map is shown in **Figure 2**. It can be seen that when the mass ratio (m_f/M) is approximately equal to 0.295, 0.67 and 0.88, an increase in the fluid velocity causes the pipe to lose stability; but soon regains the stability. When the fluid velocity exceeds a critical velocity, the cantilever pipe will not buckle as in the case of a pinned–pinned pipe, but oscillates like an unrestrained garden hose with a finite frequency.

Pipes with Unsteady Fluid Flow

The fluid flow was assumed to be steady in the previous section. If the flow is unsteady such that:

$$v = v_0(1 + c\sin\omega t) \qquad [34]$$

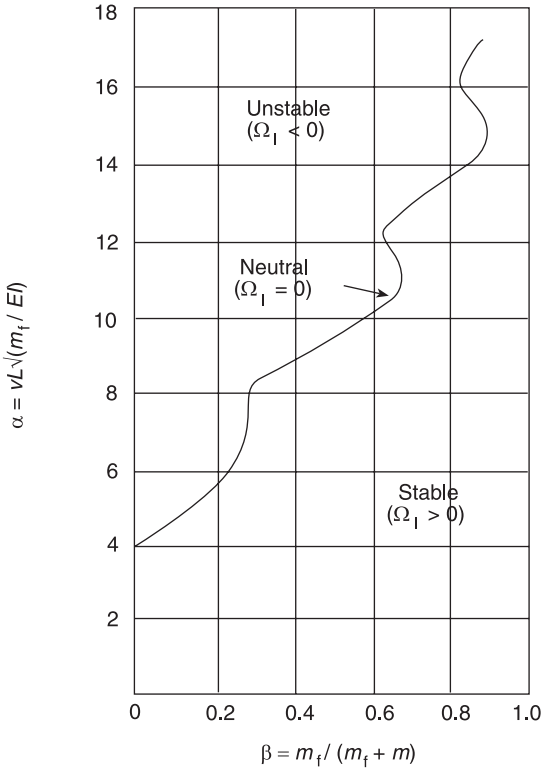


Figure 2 Typical stability map for a cantilever pipe.

where the time-dependent component involving sin ωt is superposed on the steady component, the system can experience parametric instabilities as well. Usually c is small and the parametric instabilities are similar to those of a thin column subject to an end load of the form $P = P_0(1 - c\sin\omega t)$. If the unsteady flow in the pipe is arbitrary which cannot be expressed by eqn [34], the problem needs to be solved as a stochastic stability problem.

Vibration of Pipes with External Fluid Flow

Pipes are subject to external fluid flow in heat exchangers and nuclear reactors. The forces acting on a pipe with external axial fluid flow are shown in **Figure 3**. The equations of motion of such a pipe can be expressed as:

$$EI\frac{\partial^4 y}{\partial x^4} + \rho A V^2\frac{\partial^2 y}{\partial x^2} + 2\rho A V\frac{\partial^2 y}{\partial x\partial t} - \frac{1}{2}\rho V^2 d_0 C_\mathrm{f}\left(1 + \frac{d_0}{d_\mathrm{h}}\right)(L - x)\frac{\partial^2 y}{\partial x^2} + \frac{1}{2}\rho d_0 V C_\mathrm{f}\frac{\partial y}{\partial t} + \frac{1}{2}\rho V^2 d_0 C_\mathrm{f}\left(1 + \frac{d_0}{d_\mathrm{h}}\right)\frac{\partial y}{\partial x} + M\frac{\partial^2 y}{\partial t^2} = 0 \qquad [35]$$

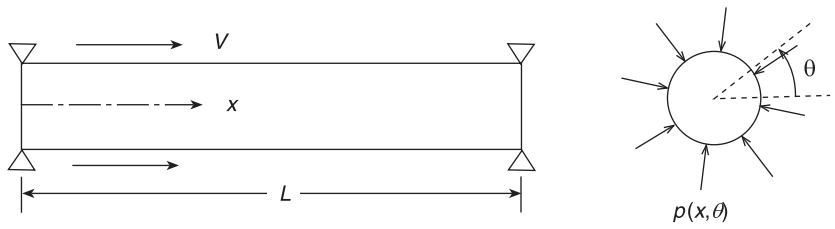


Figure 3 Pipe with external fluid flow.

where $y(x, t)$ is the transverse deflection of the pipe, V is the axial velocity of the fluid, EI is the bending stiffness of the pipe, ρ is the density of the pipe, d_0 is the outer diameter of the pipe, d_h is the hydraulic diameter = (4 × flow area/wetted perimeter), C_f is the skin friction coefficient for fluid flow over the pipe and $M = m + \rho A$ is the mass of the pipe plus external added mass of fluid per unit length. It can be observed that eqn [35] reduces to the equation of motion of a pipe with internal fluid flow, eqn [2], if $C_f = 0$ and $V = v$. This indicates that the solution for a pipe with external fluid flow will be similar to that of a pipe with internal fluid flow. It can be shown that for pipes with both ends supported, divergence can occur at low velocities and coupled mode flutter instability can take place at higher velocities of the flow. The cantilever pipes, on the other hand, can lose stability by divergence and then single mode flutter can occur at higher flow velocities of the fluid.

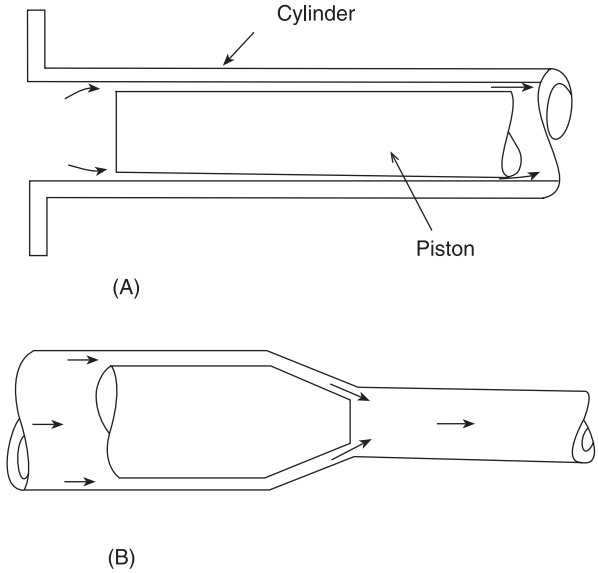


Figure 4 Annular flow due to leakage. (A) Piston and cylinder; (B) valve.

Vibration of Coaxial Pipes with Annular Fluid Flow

The problem of annular fluid flow is important in applications such as control rods in guide tubes, fuel strings in coolant channels and jet pumps, pistons and valves (**Figure 4**). The annular-flow induced instabilities are also known as leakage-flow induced instabilities since in most cases, the annular flow passage is quite narrow. Hobson (1982) is among the first to develop an analytical model for pipes with annular flow. For the sake of simplicity, Hobson considered a rigid cylindrical rod placed coaxially in a duct with fluid flow. He showed that, when one end of the rod is hinged, at sufficiently large fluid flow velocities, instability occurs through a negative damping mechanism. When coaxial pipes are considered with incompressible or compressible inviscid fluid in the annulus and in the inner pipe, the system will be conservative when both ends are supported. However, it can be shown that stability will be lost first by divergence followed by either divergence in another mode or by coupled-mode flutter at sufficiently large velocities of the fluid flow. For this system, two sets of coupled modes exist; one is the symmetric set where the deformations of the two pipes will be in phase and the other is the antisymmetric set where the deformations will be in antiphase.

Vibration of Pipes with Cross-Flow

Pipes are subject to cross-flow in many applications such as heat exchangers, steam generators and condensers. Usually one type of fluid flows inside the pipes while another type of fluid flows outside the pipes in a direction normal to the pipes. In addition, the velocity of the fluid inside the pipes will be too small to induce internal-flow induced instabilities. The external cross-flow gives rise to instabilities that are commonly known as fluidelastic instabilities. The fluidelastic instability occurs when several rows of flexible pipes, arranged in a regular geometric pattern, are subject to cross-flow. At a sufficiently large velocity of the fluid flow, the pipes in one of the first few rows will experience a sudden increase in the amplitude of vibration. If the pipes are closely spaced, the large amplitude vibration leads to impact between

pipes that can cause destructive damage. At higher flow velocities, the pipes in all rows experience fluidelastic instability. The mechanism of this instability is different from the resonance that can occur due to flow periodicities associated with a wake. The mechanics of cross-flow, in general, is more difficult compared to the other three types of flows. In a cross-flow, the flow can separate forming a wake behind each of the pipes. As such, potential flow theory cannot be used in this case.

Nomenclature

A	cross-sectional area
d	diameter
E	Young's modulus
EI	bending stiffness
I	inertia
M	mass
p	pressure
P	axial compressive force
t	time
T	tension
v	velocity
ρ	density
Ω	nondimensional frequency
ΔW	work done

See also: **Flutter**; **Flutter, active control**; **Parametric excitation**.

Further Reading

Aitken J (1878) An account of some experiments on rigidity produced by centrifugal force. *Philosophical Magazine Series V* 5: 81–105.

Benjamin TB (1961) Dynamics of a system of articulated pipes conveying fluid. I. Theory and II. Experiments. *Proceedings of the Royal Society of London Series A* 261: 457–499.

Blake W (1986) *Mechanics of Flow-Induced Sound and Vibration*. New York: Academic Press.

Blevins RD (1990) *Flow-Induced Vibration*, 2nd edn. New York: Van Nostrand Reinhold.

Gregory RW, Paidoussis MP (1966) Unstable oscillations of tubular cantilevers conveying fluid, Parts 1 and 2. *Proceedings of the Royal Society of London Series A* 293: 512–542.

Habault D (ed.) (1999) *Fluid–Structure Interactions in Acoustics*. New York: Springer-Verlag.

Hobson DE (1982) *Fluid-Elastic Instabilities Caused by Flow in an Annulus*. Proceedings of Third International Conference on Vibration of Nuclear Plant, Keswick, UK, pp. 440–463.

Housner GW (1952) Bending vibrations of a pipe line containing flowing fluid. *Journal of Applied Mechanics* 19: 205–208.

Paidoussis MP (1987) Flow-induced instabilities of cylindrical structures. *Applied Mechanics Reviews* 40(2): 163–175.

Paidoussis MP (1998) *Fluid-Structure Interactions. Slender Structures and Axial Flow*, Vol. 1. San Diego: Academic Press.

PLATES

A W Leissa, Ohio State University, Columbus, OH, USA

Copyright © 2001 Academic Press

doi:10.1006/rwvb.2001.0129

A plate is a flat structural element having a thickness which is much smaller than its lateral dimensions. An example is the rectangular plate shown in **Figure 1**, having thickness h and lateral dimensions a and b. The plate shown has two edges clamped ($x = 0$ and $y = 0$), one simply supported ($x = a$, which may be supported on knife edges, as shown, or hinged), and one free.

For a sufficiently thin plate made of linearly elastic, isotropic, homogeneous material, vibrating freely in a vacuum (i.e., neglecting the mass of its surrounding air or other media) with relatively small transverse displacement ($w < h$), the equation governing its transverse motion is:

$$D\nabla^4 w + \rho h \frac{\partial^2 w}{\partial t^2} = 0 \qquad [1]$$

where $D = Eh^3/12(1 - \upsilon^2)$ is the flexural rigidity, with E and υ being the modulus of elasticity (Young's modulus) and Poisson's ratio, respectively, of the material; ρ is its mass density per unit volume; t is time; and ∇^4 is the biharmonic differential operator, which is:

$$\begin{aligned}\nabla^4 = \nabla^2\nabla^2 &= \left(\frac{\partial^2}{\partial x^2} + \frac{\partial^2}{\partial y^2}\right)^2 \\ &= \frac{\partial^4}{\partial x^4} + 2\frac{\partial^4}{\partial x^2 \partial y^2} + \frac{\partial^4}{\partial y^4}\end{aligned} \qquad [2]$$

in rectangular coordinates.

This brief summary will focus on the natural frequencies (ω) and mode shapes of the undamped, free

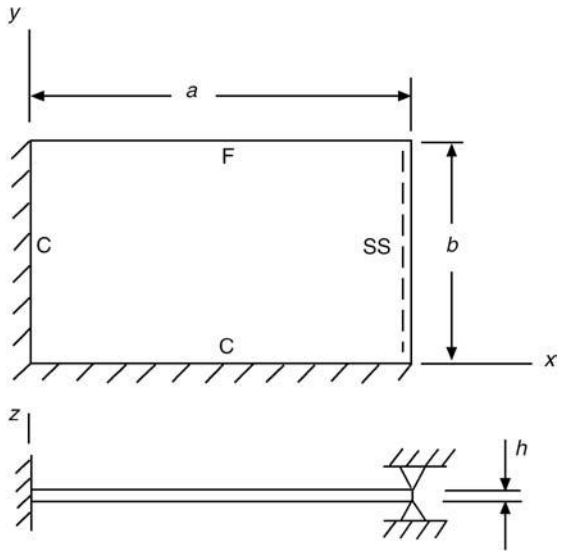


Figure 1 A clamped–clamped–simply supported–free (C–C–SS–F) rectangular plate.

vibrations, for this is typically the most important information needed in analyzing forced vibrations. That is, one needs to know the resonant frequencies of forced vibration, which are the natural frequencies, and the deformed shape of the plate at resonance, which is the corresponding free vibration mode shape. A plate may also vibrate laterally (i.e., in the x and y directions in **Figure 1**). But if the plate is thin, the frequencies of these modes are much greater than those of the transverse modes; hence, they are typically of little practical importance. Emphasis will be given to plates of rectangular and circular shape in what follows, for these are the shapes for which data are commonly needed.

Rectangular Plates

There are 21 possible, distinct combinations of edge conditions for rectangular plates. The clamped–clamped–simply supported–free (C–C–SS–F) plate shown in **Figure 1** is one of them. The edge conditions (mathematical boundary conditions) which would be satisfied for the C–C–SS–F plate are: (1) no transverse displacement or normal rotation of the clamped edges; (2) no displacement or bending moment along the simply supported edge; and (3) no bending moment or transverse shearing force along the free edge.

For six of the 21 possible combinations, exact mathematical solutions exist for the free vibration frequencies and mode shapes. These are the cases when two opposite edges (say, for example, $x = 0$ and $x = a$) are simply supported. If the plate is vibrating freely, with no damping present, then:

$$w(x, y, t) = W(x, y) \sin(\omega t + \phi) \qquad [3]$$

where $W(x, y)$ is the mode shape, a function of x and y, and ϕ is an arbitrary phase angle. When all four edges are simply supported the mode shapes are:

$$W(x, y) = \sin\frac{m\pi x}{a} \sin\frac{n\pi y}{b} \qquad [4]$$

where m and n are both integers ranging from one to infinity $(m, n = 1, 2, \ldots\infty)$. Substituting eqns [2], [3], and [4] into [1], the nondimensional frequency parameter is found:

$$\omega a^2 \sqrt{\rho h/D} = \pi^2 \left[m^2 + (a/b)^2 n^2\right] \qquad [5]$$

That is, for a plate of given dimensions (a, b, h) and material properties (ρ, E, υ) there is a doubly infinite number of free vibration frequencies (ω), corresponding to the various m and n. For the SS–SS–SS–SS plate, the mode shapes take the form of half sine waves in each direction, with the lowest frequency corresponding to one half-wave in each direction.

Consider the other five cases for which the edges $x = 0$ and $x = a$ are simply supported. Then the mode shapes take the form:

$$W(x, y) = Y(y) \sin\frac{m\pi x}{a} \qquad [6]$$

which satisfies the SS edge conditions exactly. Substituting eqn [6] into eqn [1], one finds that $Y(y)$, a function solely of y, consists of a linear combination of trigonometric and hyperbolic functions. Applying this to the two edge conditions which exist at $y = 0$ and $y = b$ yields the frequencies (eigenvalues) and mode shapes (eigenfunctions). For each m there is an infinite number of possible Y.

For the remaining 15 rectangular plates having other combinations of edge conditions, although no exact results may be found, approximate methods may be used (especially the Ritz method) to obtain free vibration frequencies and modes shapes as close to the exact ones as desired. Frequencies for all 21 cases are given in **Table 1** for square $(a/b = 1)$ and nonsquare $(a/b = 0.4$ and $2.5)$ plates. The lowest (fundamental) frequency is given for all three configurations, while for the square one the second and third lowest ones are also presented. Frequencies for the six cases having two opposite edges simply supported are shown first – they are exact to the number of digits shown. Accurate values for the other 15 cases are also given. All frequencies depend upon the Poisson's ratio (υ) of the material, because

Table 1 Nondimensional free vibration frequencies $\omega a^2\sqrt{\rho h/D}$ for rectangular plates ($\upsilon = 0.3$)

Edge conditions	a/b = *1 (square)*			a/b = *0.4*	a/b = *2.5*
	Mode 1	*Mode 2*	*Mode 3*	*Mode 1*	*Mode 1*
SS–SS–SS–SS	19.739	49.348	49.348	11.449	71.556
SS–C–SS–C	28.951	54.743	69.327	12.135	145.484
SS–C–SS–SS	23.646	51.674	58.646	11.750	103.923
SS–C–SS–F	12.687	33.065	41.702	10.189	30.628
SS–SS–SS–F	11.684	27.756	41.197	10.126	18.801
SS–F–SS–F	9.631	16.135	36.726	9.760	9.484
C–C–C–C	35.99	73.41	73.41	23.65	147.80
C–C–C–SS	31.83	63.35	71.08	23.44	107.07
C–C–C–F	24.02	40.04	63.49	22.58	37.66
C–C–SS–SS	27.06	60.54	60.79	18.85	105.31
C–C–SS–F	17.62	36.05	52.06	15.70	33.58
C–C–F–F	6.942	24.03	26.68	3.986	24.91
C–SS–C–F	23.46	35.61	63.13	22.54	28.56
C–SS–SS–F	16.86	31.14	51.63	15.65	23.07
C–SS–F–F	5.364	19.17	24.77	3.854	10.10
C–F–C–F	22.27	26.53	43.66	22.35	22.13
C–F–SS–F	15.28	20.67	39.78	15.38	15.13
C–F–F–F	3.492	8.525	21.43	3.511	3.456
SS–SS–F–F	3.369	17.41	19.37	1.320	8.251
SS–F–F–F	6.648	15.02	25.49	2.692	14.94
F–F–F–F	13.49	19.79	24.43	3.463	21.64

Adapted from more extensive data given in Leissa AW (1973) The free vibration of rectangular plates. *Journal of Sound and Vibration* 31: 257–293.

D contains υ, but the parameter $\omega a^2\sqrt{\rho h/D}$ used for **Table 1** does not depend upon υ, unless at least one edge is free. For the 15 cases in **Table 1** having at least one free edge, the frequencies shown are for $\upsilon = 0.3$, a value close to that for most commonly used metals (e.g., steel, aluminum). Comparing the data in **Table 1** for various cases it is seen that adding constraint to a vibrating system increases its frequencies, while taking it away decreases them. For example, the C–C–C–C plate has higher frequencies than the C–C–C–SS one, whereas the C–C–C–F plate has lower ones. Much experimental data can be found which agrees closely with the theoretical data given in **Table 1**. However, it is difficult to replicate a clamped edge experimentally – the stiffness of the edge-clamping fixture must be much greater than that of the plate to approximate a clamped edge adequately.

Examples of free vibration mode shapes may be seen in **Figure 2**, these being for a completely free square plate. The modes are classified as SS, SA, AS and AA, depending upon whether they are symmetric or antisymmetric with respect to the plate centerlines, and the first two are depicted for each class. The first three frequencies given in **Table 1** (13.49, 19.79, 24.43) correspond to the AA-1, SS-1, and SS-2 modes of **Figure 2**. Contour lines of equal displacement are shown in **Figure 2**, as well as the heavier nodal lines (zero displacement).

Circular Plates

A circular plate of radius a is depicted in **Figure 3**. Also shown there is a polar (r, θ) coordinate system, which is useful for dealing with circular boundaries. In polar coordinates the Laplacian differential operator (∇^2) to be used in eqn [2] is:

$$\nabla^2 = \frac{\partial^2}{\partial r^2} + \frac{1}{r}\frac{\partial}{\partial r} + \frac{1}{r^2}\frac{\partial^2}{\partial \theta^2} \qquad [7]$$

The solution form of eqn [3] may again be used for the equation of motion [1], except now $W = W(r, \theta)$, where:

$$W(r, \theta) = R(r)\cos n\theta \ (n = 0, 1, 2, \ldots \infty) \qquad [8]$$

and $R(r)$ is a function involving ordinary and modified Bessel functions. Applying the edge conditions at $r = a$ (clamped, simply supported, or free) yields an eigenvalue determinant, the roots of which are the nondimensional frequency parameters $\omega a^2\sqrt{\rho h/D}$.

Table 2 gives $\omega a^2\sqrt{\rho h/D}$ for a clamped circular plate, where n is the number of nodal diameters, and s the number of nodal circles, in the free vibration mode shape. **Figure 4** shows examples of the nodal patterns, consisting of diametral and circular node lines (i.e., lines where the transverse displacement

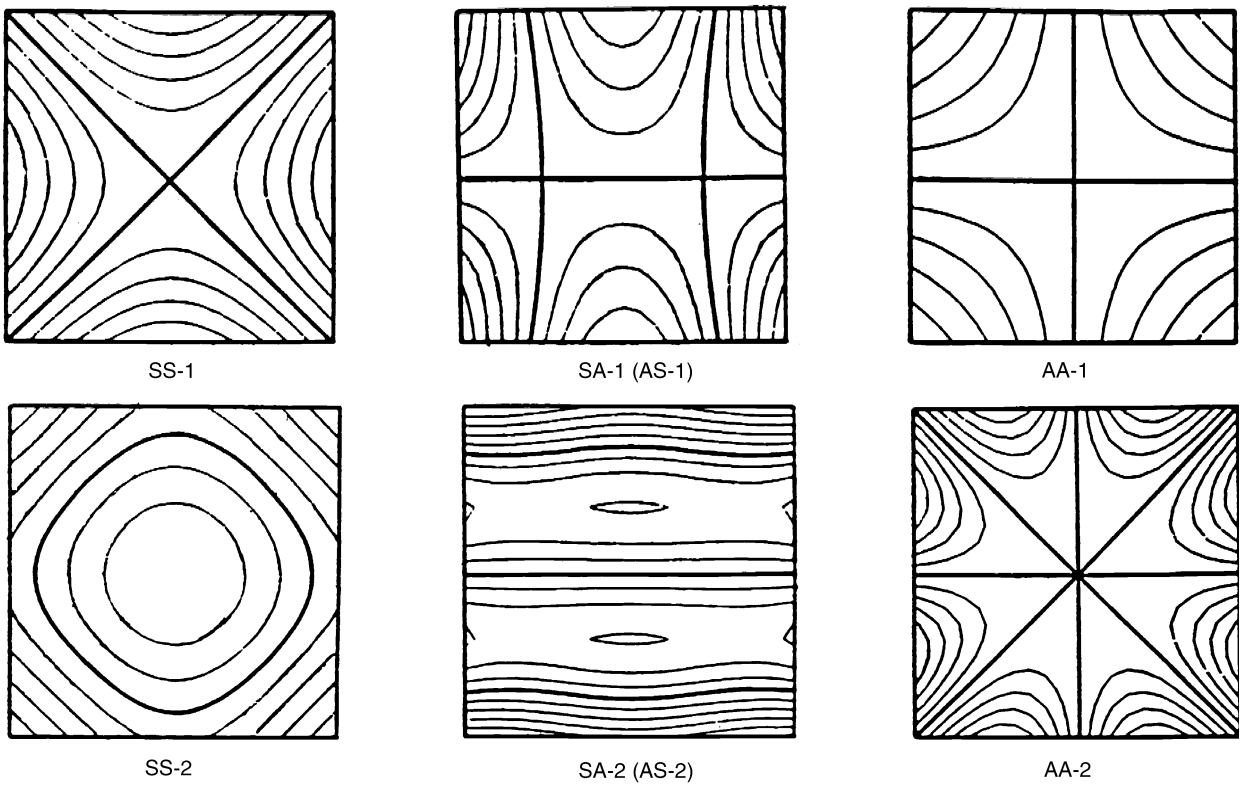


Figure 2 Contour plots of mode shapes for F–F–F–F square plates ($\nu = 0.3$).

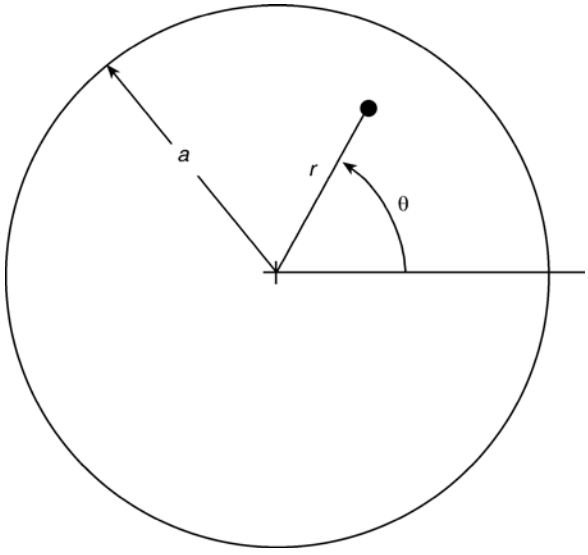


Figure 3 A circular plate.

(W) is always zero while the plate is vibrating). The plus and minus signs on the patterns are there to emphasize that, while a region on one side of a node line is moving towards the reader, on the other side it is moving away. Locations of the nodal circles, corresponding to the frequencies of **Table 2**, are listed in **Table 3**.

Table 2 Nondimensional frequencies $\omega a^2\sqrt{\rho h/D}$ for a clamped circular plate.

	s			
n	*0*	*1*	*2*	*3*
0	10.22	39.77	89.10	158.2
1	21.26	60.82	120.1	199.1
2	34.88	84.58	153.8	242.7
3	51.04	111.0	190.3	289.2
4	69.67	140.1	229.5	338.4
5	90.74	171.8	271.4	390.4

Adapted from more extensive data given in Leissa AW (1969) *Vibration of Plates*. Washington, DC: US Government Printing Office. Reprinted 1993 by The Acoustical Society of America.

For simply supported plates, the zero bending moment condition at the edge involves Poisson's ratio; therefore, $\omega a^2\sqrt{\rho h/D}$ not only contains υ within it ($D = Eh^3/12(1-\upsilon^2)$), but varies with υ. Therefore, **Table 4** for SS plates gives $\omega a^2\sqrt{\rho/Eh^2}$ which does not contain υ. These results show that changing υ may have a large effect upon the frequency.

Other Shapes

Plates may be found in an unlimited variety of shapes; for example, they may be annular, elliptical, parallel-

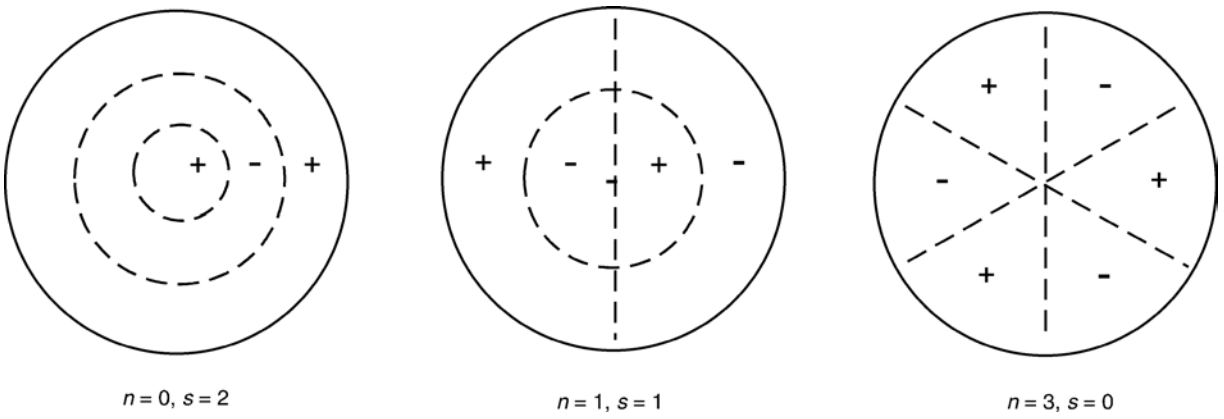


Figure 4 Examples of nodal patterns for clamped circular plates.

Table 3 Radii of interior nodal circles (r/a) for a clamped circular plate.

n	s					
	1	*2*		*3*		
0	0.379	0.583,	0.255	0.688,	0.439,	0.191
1	0.490	0.640,	0.350	0.721,	0.497,	0.272
2	0.559	0.679,	0.414	0.746,	0.540,	0.330
3	0.606	0.708,	0.462	0.765,	0.574,	0.375
4	0.641	0.730,	0.501	0.781,	0.601,	0.412
5	0.669	0.749,	0.532	0.787,	0.618,	0.439

Adapted from more extensive data given in Leissa AW (1969) *Vibration of Plates*. Washington, DC: US Government Printing Office. Reprinted 1993 by The Acoustical Society of America.

Table 4 Nondimensional frequencies $\omega a^2\sqrt{\rho/Eh^2}$ for simply supported circular plates with $\nu = 0, 0.3, 0.5$

n	ν	s			
		0	*1*	*2*	*3*
	0	1.283	8.476	21.31	39.84
0	0.3	1.493	8.994	22.44	41.86
	0.5	1.738	9.982	24.79	46.18
	0	3.897	13.90	29.57	50.95
1	0.3	4.206	14.67	31.10	53.50
	0.5	4.714	16.23	34.33	59.00
	0	7.287	20.14	38.67	62.90
2	0.3	7.751	21.22	40.64	66.03
	0.5	8.615	23.44	44.84	72.80
	0	11.43	27.20	48.60	75.68
3	0.3	12.09	28.61	51.04	79.43
	0.5	13.39	31.59	56.30	87.56

Adapted from more extensive data given in Leissa AW and Narita Y (1980) Natural frequencies of simply supported plates. *Journal of Sound and Vibration* 70: 221–229.

ogram, trapezoidal, other quadrilaterals, triangular, or polygonal. Besides the hundreds of research papers which have been published for rectangular and circular plates, presenting natural frequencies and, to a much lesser extent, mode shapes, numerous others present data for other shapes. Very few of these free vibration problems have exact solutions; approximate methods must typically be used to determine frequencies and node shapes.

Figure 5 depicts a cantilevered (C–F–F–F) parallelogram (or skew) plate with side lengths a and b. **Table 5** shows how the frequency parameter $\omega a^2\sqrt{\rho b/D}$ changes as the skew angle β increases. To obtain the accurate results shown in **Table 5** it was necessary to represent the bending and twisting moment singularities in the reentrant corner correctly.

Accurate frequencies and corresponding nodal patterns have also been obtained for completely free triangular plates by the Ritz method. A representative

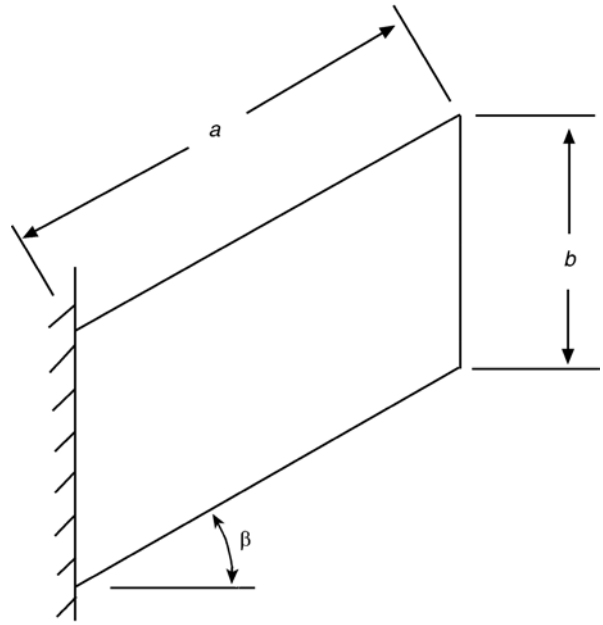


Figure 5 Cantilevered skew plate.

Table 5 Nondimensional frequencies $\omega a^2\sqrt{\rho h/D}$ for cantilevered skew plates ($\nu = 0.3$)

β	a/b	*Mode number*			
		1	*2*	*3*	*4*
	0.5	3.636	5.535	10.41	19.29
15°	1	3.583	8.697	22.23	26.33
	2	3.509	15.02	22.33	47.29
	0.5	4.057	6.252	11.24	20.12
30°	1	3.928	9.410	25.29	25.93
	2	3.718	15.86	25.07	46.84
	0.5	4.669	8.289	13.35	22.24
45°	1	4.505	11.25	29.97	31.50
	2	4.057	17.86	30.06	49.40
	0.5	5.346	14.29	19.22	27.50
60°	1	5.243	16.02	30.36	45.30
	2	4.496	21.47	39.85	56.64
	0.5	6.054	25.00	47.21	57.86
75°	1	6.024	24.82	48.75	72.64
	2	4.970	25.55	64.91	74.88

Adapted from more extensive data given in McGee OG, Leissa AW and Huang CS (1992) The free vibration of cantilevered skew plates with stress singularities. *International Journal for Numerical Methods in Engineering* 35: 409–424.

Table 6 Nondimensional frequencies $\omega a^2\sqrt{\rho h/D}$ for completely free triangular plates ($\nu = 0.3$)

c/b	a/b	*Mode number*					
		1	*2*	*3*	*4*	*5*	*6*
	0.5	7.962	16.34	28.61	38.87	45.68	63.84
-0.5	1	17.39	41.12	63.38	81.77	106.40	139.50
	0.5	6.428	14.96	17.29	28.66	30.76	36.28
0	1	19.07	29.12	45.40	49.48	72.37	84.09
	0.5	4.096	8.496	12.36	15.85	20.35	26.71
0.5	1	14.86	20.98	26.88	37.53	49.97	64.85

Adapted from more extensive data given in Leissa AW and Jaber NA (1992) Vibration of completely free plates. *International Journal of Mechanical Sciences* 34: 605–616.

triangular configuration defining the dimensions a, b and c is shown in **Figure 6**. The first six frequency parameters $\omega a^2\sqrt{\rho h/D}$ for $c/b = -0.5$ (scalene triangle), 0 (right triangle), and 0.5, and $a/b = 0.5$ and 1, are seen in **Table 6.** Corresponding nodal patterns are shown in **Figure 6**.

Complicating Effects

The plates described above may all have further complicating effects. An edge constraint may be discontinuous; for example, it may be clamped partly along an edge, and simply supported along the remainder. Then its frequencies fall between those of plates having the edge continuously clamped or continuously simply supported. Addition of a notch or crack decreases the frequencies – the mass of the system is virtually unchanged, but the plate stiffness is significantly decreased.

There are many complicating effects which result in a governing differential equation of motion being different than that of eqn [1]. Some of them relate to the material composition of the plate. The material may be anisotropic, or orthotropic (a special case of anisotropy), where the flexural rigidity (D) changes with direction. Or the material may be nonhomogeneous (i.e., having properties which vary with location in the plate). Examples of this would be: (1) a styrofoam plate with varying density and resulting variation of the modulus of elasticity (E), and (2) a layered plate. There is ever-increasing utilization of laminated composite plates, that is, plates made of layers (lamina), the layers being orthotropic. A great deal of free vibration frequency and mode shape data has been published for these kinds of plates, especially laminated composites.

If a plate is subjected to inplane tensile stresses along its edges, frequencies are increased. Conversely, inplane compressive stresses cause the frequencies to decrease. For example, consider an SS-SS-SS-SS rectangular plate subjected to uniform tensile stresses σ_x and σ_y in the x and y directions, respectively, acting along its edges. For this case the free vibration mode shapes remain those of eqn [4], whereas the frequencies may be determined from:

$$\frac{\omega^2 a^4 \rho h}{D} = \left[(m\pi)^2 + (n\pi)^2\left(\frac{a}{b}\right)^2\right]^2 + \frac{\sigma_x h a^2}{D}(m\pi)^2 + \frac{\sigma_y h a^2}{D}(n\pi)^2\left(\frac{a}{b}\right)^2 \quad [9]$$

Eqn [9] shows clearly that compressive stresses (negative σ_x and/or σ_y) cause all frequencies to decrease. Sufficiently large compressive stresses can decrease the frequencies to zero. Such an event corresponds to bifurcation buckling, with the first frequency to approach zero identifying the critical buckling stresses – when the destabilizing effects of compressive stress approach the magnitude of the stabilizing plate stiffness, the plate loses its ability to return to the flat, static equilibrium position, as required in a vibratory motion. These general statements apply to all plate configurations and edge constraints, as well as to other structural elements having bending stiffnesses (e.g., straight and curved beams, shells) or complete structures. One can determine buckling loads by plotting frequency versus loading. Shear stresses are also destabilizing (frequency-decreasing).

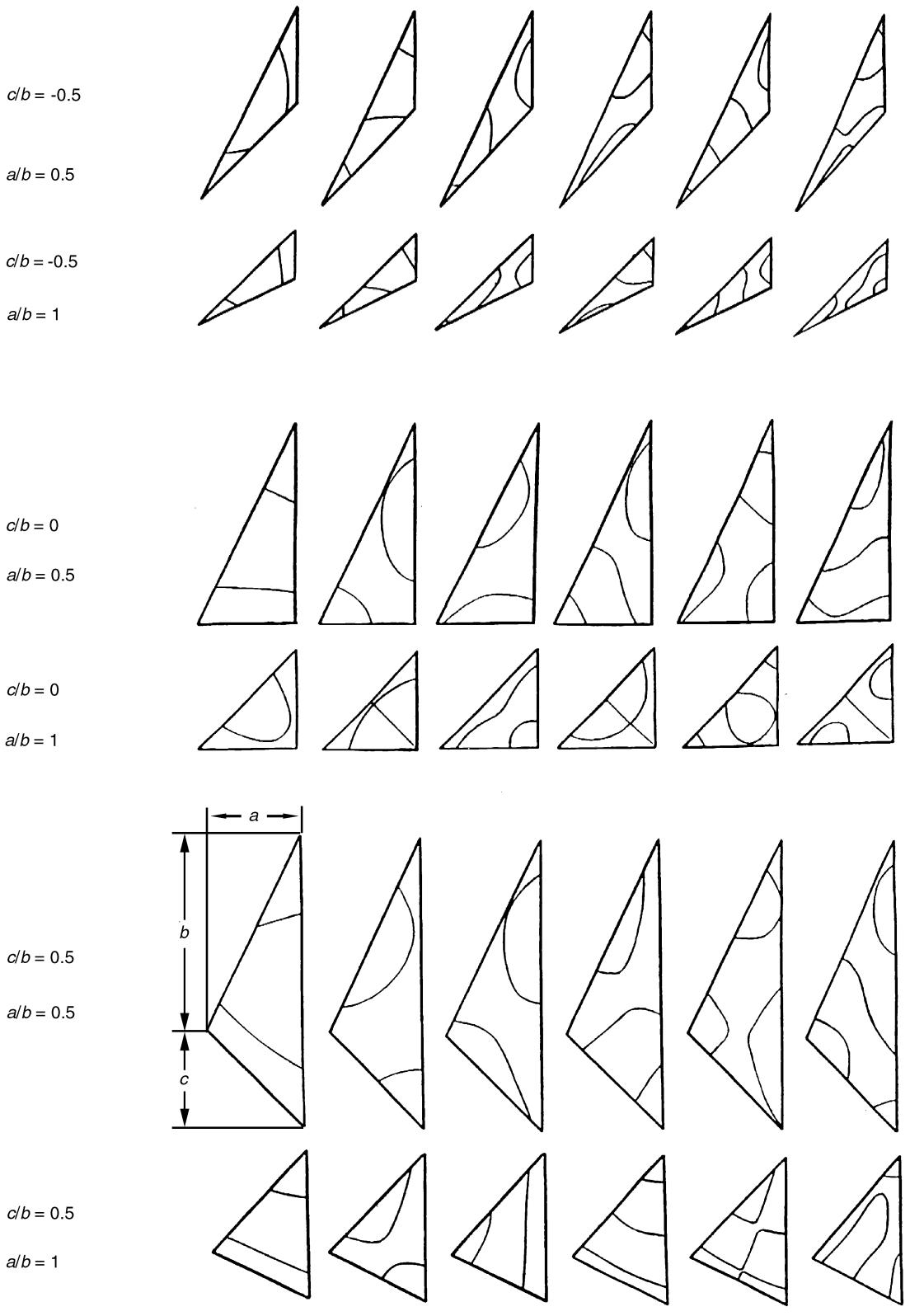


Figure 6 Triangular plates with dimensions *a*, *b*, and *c*.

If a plate has variable thickness, say $h = h(x, y)$, then not only is h a variable in eqn [1], but the first term $(D\nabla^4\omega)$ becomes considerably generalized. The resulting problem is much more difficult to solve, and approximate methods are usually used.

A plate vibrating in a fluid medium, either compressible (e.g., air), or incompressible (e.g., water), has its frequencies decreased because the vibratory plate motion requires movement of the additional mass in the surrounding medium. Liquids typically reduce the frequencies considerably because of their relatively large mass density. But a plate vibrating even in a gas may also have a significant decrease ($\sim 5\%$) in some of its frequencies. Thus, experimental frequencies (typically obtained in air) can be expected to be somewhat less than theoretical frequencies (based upon vibration in a vacuum).

Eqn [1] includes the bending flexibility of a plate, but does not include its transverse shear flexibility. Also, it considers the translational inertia, but not the rotary inertia of the plate. The theory may be generalized to include both shear deformation and rotary inertia, and both effects are found to decrease the frequencies. A widely used sixth-order theory (three boundary conditions to be satisfied along each edge) was developed by Mindlin. Both effects become more significant as the relative thickness (say, h/a, for a rectangular plate) increases, and for the higher-frequency vibration modes. Because of their relatively large shear flexibility, laminated composite plate frequencies are affected greatly.

If a plate is constrained in its plane along its edges, then frequencies will increase if the amplitude of the transverse, vibratory motion is increased. Quite a significant frequency increase ($\sim 30\%$) may be expected as the magnitude of the amplitude approaches that of the plate thickness. The increase is due to the additional stretching stiffness of the plate, which increases with amplitude (i.e., hard spring response). Generalization of eqn [1] to include this effect results in its character changing from being a linear equation to a nonlinear one.

Nomenclature

D	flexural rigidity
E	modulus of elasticity
ν	Poisson's ratio
ϕ	phase angle
ρ	density
σ	tensile stress

See also: **Disks**; **Membranes**; **Shells**; **Mode of vibration**.

Further Reading

Chia C-Y (1980) *Nonlinear Analysis of Plates*. New York: McGraw Hill.

Gorman DJ (1982) *Free Vibration Analysis of Rectangular Plates*. New York: Elsevier North Holland.

Leissa AW (1969) *Vibration of Plates*. Washington, DC: US Government Printing Office. (Reprinted 1993 by The Acoustical Society of America.)

Leissa AW (1973) The free vibration of rectangular plates. *Journal of Sound and Vibration* 31: 257–293.

Liew KM, Wang CM, Xiang Y and Kitipornchai S (1998) *Vibration of Mindlin Plates: Programming the p-Version Ritz Method*. Oxford: Elsevier.

Warburton GB (1954) The vibrations of rectangular plates. *Proceedings of the Institution of Mechanical Engineers, Series A* 168: 371–384.

R

RANDOM PROCESSES

M F Dimentberg, Worcester Polytechnic Institute, Worcester, MA, USA

Copyright © 2001 Academic Press

doi:10.1006/rwvb.2001.0122

The probabilistic approach provides perhaps the most important method of treating uncertainty in dynamic loads and material properties for engineering analyses. In particular, the theory of probability and the theory of random processes provide a description for excitation forces, that cannot be adequately described by specified deterministic functions (wind loads on buildings, wave loads on ships and offshore structures, ground motions during earthquakes). The resulting structural response is certainly random, and should be treated accordingly.

This article provides a brief outline of the fundamentals of the theory of probability and the theory of random processes. Models for random dynamic loads and excitations are described.

A complete description of a continuous random variable (RV) X is provided by its probability density function (pdf) $p_X(x) = \mathrm{d}F_X(x)/\mathrm{d}x$, $F_X(x) = \text{Prob}\{X \le x\}$ or set of moments $\langle X^n \rangle = \int_{-\infty}^{\infty} x^n p_X(x)\mathrm{d}x$, with n being positive integers (angular brackets denote probabilistic averaging). Two lowest-order moments have special names: the mean or expected value and variance of X: $m_X = \langle X \rangle, D_X = \langle (X - m_X)^2 \rangle = \langle X^2 \rangle - m_X^2 = \sigma_X^2$ where σ_X is a root mean square (RMS) value of X. The normal or Gaussian RV, with pdf:

$$p_X(x) = \left(\sigma_X \sqrt{2\pi}\right)^{-1} \exp\left[-(x - m_X)^2/\left(2\sigma_X^2\right)\right] \qquad [1]$$

is completely described by these two moments. The constant cofactor with the exponential function provides the normalization condition. Namely, the integral of the pdf within a relevant domain, the whole axis x in this case, should be equal to unity as the probability of a certain event.

Alternatively, the Fourier transform of the pdf can be used, and this is called a characteristic function of the RV:

$$\begin{aligned} f_X(u) &= \int_{-\infty}^{\infty} \exp(\mathrm{i}ux) p_X(x)\,\mathrm{d}x \\ &= \sum_m ((\mathrm{i}u)^m/m!)\langle X^m \rangle \end{aligned} \qquad [2]$$

For the pdf (eqn [1]) with $m_X = 0$:

$$f_X(u) = \left(\sigma_X \sqrt{(2\pi)}\right)^{-1} \exp\left(-\sigma^2 u^2/2\right) \qquad [3]$$

If two RVs are related deterministically as $Y = f(X)$, the pdf of Y can be expressed in terms of the pdf of X, using the condition for the same probability of events $Y \le y$ and $X \le g(y)$ or $Y \le y$ and $X \ge g(y)$, within ranges with monotonously increasing or decreasing f, respectively, where $g(y)$ is the inverse function to $f(x)$. In the case of a monotonous and single-valued $f(x)$, the relation between the pdf functions is:

$$p_Y(y) = p_X(g(y))\ |\mathrm{d}g/\mathrm{d}y| \qquad [4]$$

In particular, if X is normal RV and f is linear, then Y is also normal. Eqn [4] can simply be extended to nonmonotonous $f(x)$ using summation in the RHS over the corresponding branches of the multivalued g.

A vector RV $\mathbf{X}$ is described by joint pdf of its components X_j. The normal joint pdf is described completely by its mean vector with components m_j and covariance matrix $\mathbf{K_{XX}}$ with elements:

$$\left\langle (X_j - m_j)(X_k - m_k) \right\rangle = \left\langle X_j X_k \right\rangle - m_j m_k$$

This matrix is nonsingular, provided that there is no deterministic relation(s) between any pair of components, otherwise the selected extraneous components may be excluded by reduction to the vector of a lower dimension. The normal joint pdf of an n-dimensional vector is:

$$p_{\mathbf{X}}(\mathbf{x}) = C \exp\left[-(1/2)(\mathbf{x}-\mathbf{m}_{\mathbf{x}})^{\mathrm{T}}\mathbf{K}_{\mathbf{XX}}^{-1}(\mathbf{x}-\mathbf{m}_{\mathbf{X}})\right]$$
$$C = (2\pi)^{-n/2}|\mathbf{K}_{\mathbf{XX}}|^{-1/2}$$

In the case of a diagonal covariance matrix this expression reduces to a product of exponents, corresponding to the independent normal RVs. The possibility of diagonalization of a given covariance matrix implies that a set of linear combinations may be introduced for given correlated RVs, which are uncorrelated, and therefore independent in case of their normality.

The normality is preserved if linear transformations are applied to a vector RV. This fact makes this property particularly important, together with the notorious central limit theorem (CLT). Thus, the pdf of a sum of two independent RVs $Z = X + Y$ may be written as a convolution integral of their individual pdfs. Applying the Fourier transform to the pdfs, one can express the characteristic function of Z as a product:

$$f_Z(u) = f_X(u)f_Y(u)$$

Thus, a characteristic function of the sum:

$$S_N = N^{-1/2}\sum_{k=1}^{N} X_k$$

where X_k are independent RVs, which have an arbitrary identical pdf $p_X(x)$ with zero mean and unit standard deviation, may be reduced, using the two-term expansion in eqn [2], to the Nth power of the $f_{X/\sqrt{N}}(u)$. In the limit with $N \to \infty$ the exponent of the form (eqn [3]) is obtained for $f_{S_N}(u)$, which corresponds to the normal, or Gaussian pdf of S_N.

In its general formulation, the CLT states, that the pdf of a sum of independent RVs approaches the normal one with an increasing number of components, irrespective of the pdfs of the components, provided that none of these components is dominant.

This property provides a rationale for detecting defects in a roller bearing from its vibrational signal X. Thus, the nonsmall value of a properly scaled fourth-order moment, the so-called coefficient of excess

$$\gamma = \left\langle (X - m_X)^4 \right\rangle \Big/ \sigma_X^4 - 3 \qquad [5]$$

which should be zero for the Gaussian pdf (eqn [1]), may imply the appearance of a dominating, and therefore abnormal source of vibration (defect).

In the case of a general relation between two vector RVs, their joint pdfs are related via the relevant Jacobian of the transformation (extension of eqn [4] to a multidimensional case). In particular, if a two-dimensional vector $\mathbf{X}$ has normal zero-mean independent components with the same RMS value σ, its amplitude $A = \sqrt{(X_1^2 + X_2^2)}$ and phase $\Theta = \tan^{-1}(X_1/X_2)$ have a Rayleigh pdf and uniform pdf, respectively:

$$p_A(a) = \left(a/\sigma^2\right) \exp\left(-a/2\sigma^2\right) \qquad [6]$$

$$p_\Theta(\theta) = 1/2\pi \quad \text{for } 0 \le \theta < 2\pi \qquad [7]$$

A time-dependent RV $X(t)$ is called a random process. For its complete description a joint pdf of values at different time instants may be required in general. To make such a description practical some model of temporal variations for excitation force(s) is usually needed. The commonest one is that of a continuous normal $X(t)$, which is described completely by the (deterministic) mean value and autocorrelation function:

$$m_X(t) = \langle X(t) \rangle$$
$$R_{XX}(t_1, t_2) = \langle X(t_1)X(t_2) \rangle \qquad [8]$$

The first-order pdf of a Gaussian $X(t)$ is of the same form (eqn [1]) as for the RV, with $\sigma_X^2 = R_{XX}(t,\ t)$. The second-order joint pdf of $X_1 = X(t_1)$ and $X_2 = X(t_2)$ is a negative exponent of a positively definite quadratic form of x_1, x_2, with coefficients being defined by first-order and second-order moments (eqn [8]). Higher-order pdfs are uniquely related to the first-order and second-order ones.

Eqn [4] can be applied to a periodic signal $X(t)$, provided the time argument is selected in a random fashion, or a random phase Θ is added to it, which has a uniform pdf (eqn [7]). Thus, if:

$$X(t) = \lambda \sin(\omega t + \Theta)$$

then:

$$p_X(x) = (1/\pi)\left(\lambda^2 - x^2\right)^{-1/2} \quad \text{for } |x| \le \lambda \qquad [9]$$

and zero otherwise. The singularities, which can be seen in **Figure 1A** are typical for any periodic signal $X(t)$ with smooth peaks. Whilst these singularities may become 'smeared' for real signals due to the presence of other (nonperiodic) signals and/or noises, the observed bimodal pattern in the pdf of a vibrational signal (**Figure 1B**) may imply the presence of a certain periodicity in the signal, which usually has unimodal pdfs (**Figure 1C**). This method of detecting periodicity has an important advantage: it is relatively

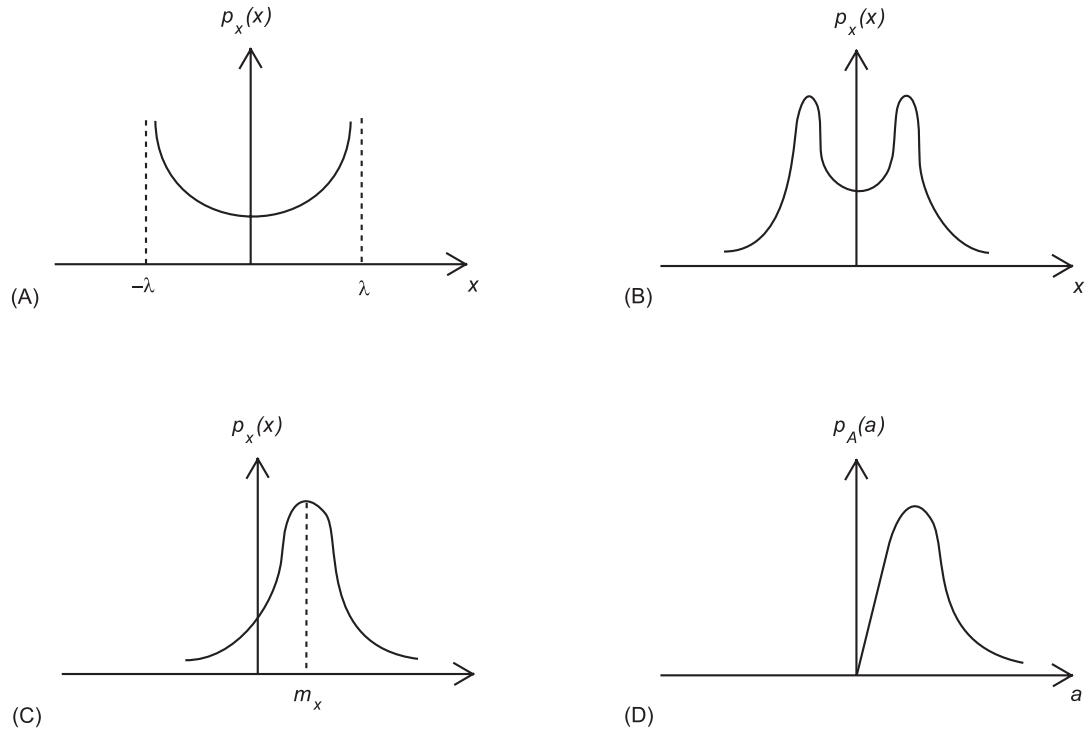


Figure 1 Specific pdfs. (A) Sinusoid with random phase; (B) bimodal; (C) unimodal; (D) Rayleigh pdf.

insensitive to temporal variations of phase. Thus, it is particularly appropriate for online detection of inherent 'mild' dynamic instability, which does not lead to an immediate failure but may still be undesirable. Such instability implies limited growth of the response with time, which is eventually restricted by some nonlinearity(ies). This results in limit-cycle vibrations, that would not be strictly periodic in the presence of external random excitation. Thus, online discrimination between subcritical and postcritical states of operation may be of interest, based on processing measured response signal(s) (heat exchanger tubes in a fluid flow and machine tool chatter).

A pair of normal processes $X(t)$, $Y(t)$ can be described by their mean values and cross-correlation function:

$$R_{XY}(t_1, t_2) = \langle X(t_1)Y(t_2)\rangle$$

Other useful models of excitation include:

- Poisson process: pulses, appearing at random instants, with an important parameter being their arrival rate.
- Periodic process with random-phase modulation, or random temporal variations of frequency. Each sinusoidal component of such a process has the strongly non-Gaussian pdf of the form given in eqn [9].

A random process is called stationary if its properties are invariant with respect to shift of time origin, and in particular, weakly stationary if only the first-order and second-order moments are considered. A weakly stationary process has a constant mean value, whereas its autocorrelation function only depends on a time shift $\tau = t_2 - t_1$. A random process may very often be regarded as a stationary one if it is generated under constant conditions, such as in the case of turbulent pressure oscillations in a steady flow.

Nonstationary excitation forces (such as those due to ground motions during earthquakes) are very often modeled by introducing deterministic temporal variations of parameters. If a random process is governed by a linear differential equation with a random RHS (as for random vibrations of systems with lumped parameters), it may be stationary provided that three following conditions are satisfied:

1. The process in the RHS, or excitation, is stationary.
2. Only the particular solution which corresponds to the steady-state response is considered. The initial conditions are 'forgotten' due to the decay of the initial transients in the (asymptotically stable) system.
3. The coefficients of the equation of motion are constant (time-invariant system).

A stationary process may also be ergodic, in which case probabilistic, or ensemble, averaging is equivalent to averaging over a single sample of sufficient length:

$$\langle * \rangle = \lim_{T\to\infty} T^{-1} \int_0^T (*)\, \mathrm{d}t$$

The additional necessary conditions for ergodicity in various moments are those of a sufficiently rapid decay of the autocorrelation function, or finite correlation time. Such conditions insure that the initial state of the process may be 'forgotten' and all its properties are reflected in a single sample. The ergodic property is particularly important for processing measured random signals.

The autocorrelation function of a stationary random process $X(t)$ has the following important properties, which are obvious from its definition: it is an even function, that is, $R_{XX}(-\tau) = R_{XX}(\tau)$, and $R_{XX}(0) \geq R_{XX}(\tau)$ for any nonzero value of τ. Yet another property, the so-called positive definiteness, guarantees (together with the two above-mentioned ones), the properties of the power spectral density (PSD) of $X(t)$, which will be introduced later.

The basic properties of the autocorrelation function are used for online evaluation of the properties of structures with traveling random waves. Thus, consider nondispersive one-dimensional waves, say, longitudinal waves in elastic rods, with a propagation speed c. Let the response signals be measured at two points, the distance between points being L. The signals may then be related by a simple delay equation: $Y(t) = X(t - \Delta)$, where $\Delta = L/c$ is the transit time of the wave between the points. The autocorrelation functions of the signals are clearly the same in this case, whereas their cross-correlation function reproduces the autocorrelation function with a time shift, equal to the transit time L/c. Thus, the sign of the shift of the absolute maximum of $R_{XY}(\tau)$ indicates the direction of propagation (from X towards Y if it is positive), whereas its magnitude may provide an estimate for the propagation speed c. Energy losses may also be estimated, from the measured reduction of the absolute peak of $R_{XY}(\tau)$ compared with that of $R_{XX}(\tau)$.

The approach may also be extended to cases of media with dispersion of waves, such as bending waves in beams, which do not have a universal propagation speed. The apparent propagation speed of a sinusoidal signal depends in this case on its frequency ω, that is $c = c(\omega)$. The above approach may then be applied separately within various frequency bands, such that c is approximately constant within each band, by band-pass filtering both signals X and Y. The procedure provides the so-called group velocity of waves, defined as:

$$c_g(\omega) = \frac{c}{1 - (\omega/c)(\mathrm{d}c/\mathrm{d}\omega)}$$

An interesting example of an actual application is online *in vivo* measurement of the pulse wave propagation speed in the human artery, which can be used to estimate the elasticity of its wall.

An important characteristic of a stationary random process is its PSD defined as a Fourier transform (FT) of the autocorrelation function:

$$\begin{aligned} S_{XX}(\omega) &= \frac{1}{2\pi} \int_{-\infty}^{\infty} R_{XX}(\tau)\, \mathrm{e}^{-\mathrm{i}\omega t}\, \mathrm{d}\tau \\ &= \lim_{T\to\infty} (\pi/T) \langle \tilde{X}(\omega, T) \tilde{X}^*(\omega, T) \rangle \\ \tilde{X}(\omega, T) &= \frac{1}{2\pi} \int_{-T}^{T} X(t)\, \mathrm{e}^{-\mathrm{i}\omega t}\, \mathrm{d}\tau \qquad [10] \\ R_{XX}(\tau) &= \int_{-\infty}^{\infty} S_{XX}(\omega)\, \mathrm{e}^{\mathrm{i}\omega t}\, \mathrm{d}\omega \end{aligned}$$

(* denotes the complex conjugate). In view of the properties of the autocorrelation function, the PSD is found to be a real, positive, and even function. It describes the continuous distribution of energy between different frequency components of the stationary random process, which is sustained but not periodic. This can be seen from the second, alternative expression for the PSD in terms of the 'direct' FT of the sample of $X(t)$. (The limit for this direct FT does not exist by itself, since its variance does not vanish with increasing sample length T.) A special case of eqn [10] for zero time shift illustrates how the mean square value of the random process, the integral of its PSD, is compiled from contributions due to different frequency components of $X(t)$.

Relations, similar to eqn [10], with the subscript XX replaced by XY, are used for a pair of processes $X(t)$ and $Y(t)$. Thus, the cross-correlation function of a pair of processes forms a FT pair with their cross-spectral density (the name autospectral density is used for a single process). The latter is complex in general, and its magnitude indicates a degree of coupling between the components of $X(t)$ and $Y(t)$ with a given frequency ω; thus its normalized version is called the coherence function.

An exponentially correlated process (with zero mean), considered as an example, has:

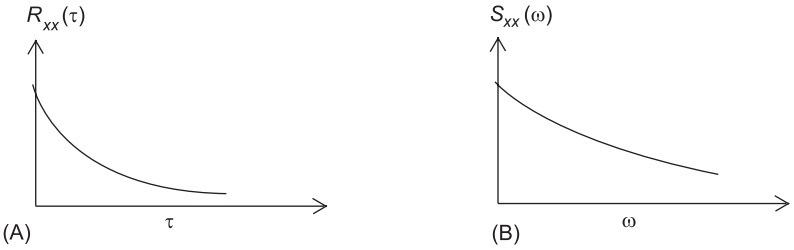


Figure 2 (A) Exponential autocorrelation function; (B) corresponding PSD.

$$R_{XX}(\tau) = \sigma_X^2 \exp(-\gamma|\tau|)$$
$$S_{XX}(\omega) = (\sigma_X^2\gamma/\pi)/(\gamma^2 + \omega^2) \quad [11]$$

Here σ_X is the RMS value of $X(t)$, and γ is seen to be a bandwidth parameter of S and also a reciprocal of the correlation time of $X(t)$, or of a characteristic decay time of R. (The autocorrelation function and PSD (eqn [11]) are illustrated in **Figure 2** within positive semiaxes of the corresponding arguments of these even functions.) The Uncertainty Principle is thereby illustrated for the correlation/spectral properties of a stationary random process.

In the limiting case: $\gamma \to \infty, \sigma_X^2/\pi\gamma = S_0 =$ const., $R_{XX}(\tau) = D\delta(\tau)$ with $D = 2\pi S_0$ and δ is the Dirac delta-function; the process $X(t)$ is called the white noise of intensity D. Its PSD is constant everywhere, implying infinite variance. Whilst such a process seems to be physically impossible, a white-noise model of excitation is used very often and is found to be very convenient for random vibration studies. The reason is that any causal system only responds to a limited range of excitation frequencies, so components of the excitation which have frequencies that are too high become irrelevant for predicting the system's response.

PSDs of a derivative and an integral of a stationary random process can be expressed in terms of the PSD of the process itself. The relevant relations are actually special cases of a general input–output relation in statistical dynamics. Namely, if $H(i\omega)$ is a transfer function, or complex frequency response from the input, or excitation $X(t)$ to output, or response $Y(t)$, then:

$$S_{YY}(\omega) = |H^2(i\omega)|S_{XX}(\omega) \quad [12]$$

provided that both $X(t)$ and $Y(t)$ are stationary. Thus, say, $S_{\dot{X}\dot{X}}(\omega) = \omega^2 S_{XX}(\omega)$. Eqn [12] is used, in particular, to generate the process $Y(t)$ with a given PSD from an available process $X(t)$ (e.g., white noise) by passing the latter through a specially designed system with the transfer function H. Such a system is called a shaping filter.

Whilst the PSD (eqn [11]) has a peak at zero frequency, a stationary random process may also, in general, have a nonzero predominant frequency. A process with a small spread of its power around the predominant, or center frequency, is called narrow-band; the half-power bandwidth is often used as an indicator of this spread, at the level where S equals half of its maximal value. Thus, the response of a lightly damped single-degree-of-freedom system to a white-noise excitation is usually narrow-band (see **Figure 3**, which has been obtained for the system with bandwidth ratio 0.02; Such a process has slowly varying amplitude and phase, which may be convenient state variables for analysis in a 'slow time', as well as the in-phase and quadrature components of the process, by using the stochastic averaging method.

For a normal, or Gaussian, random process information on its first-order and second-order moments is sufficient to establish its pdf. Thus, the probability for staying above a given level can be predicted, which in the case of a stationary process may be interpreted as a relative stay time above the level. However, in many cases of randomly vibrating structures this probability may not be sufficient by itself for an adequate description of the reliability of the structures. More complex functionals of the random structural response (e.g., stress, displacement, etc.) should be considered, depending on the possible failure mode of the structure and/or component. Three such modes are usually considered as:

- First-passage failures, such as those due to exceeding limiting stress in a brittle material or exceeding potential barrier for transition into the nondesigned state of the system ('snap-through' of a shallow arch or panel, ship capsizing).
- Failure due to damage accumulation, such as fatigue, wear.
- Failure due to stochastic (dynamic) instability.

Characteristics of the random processes, related to probabilistic analysis for the first two of the above

failure modes, are sometimes called 'excursions'. One of these, an expected crossing rate (per unit time) with positive slope of a given threshold x by a process $X(t)$ is:

$$n_+(x) = \int_0^\infty v p_{X\dot{X}}(x, v)\, \mathrm{d}v$$
$$= (2\pi)^{-1}(\sigma_V^2/\sigma_X^2)\, \exp\,(-x^2/2\sigma_X^2), \quad v = \dot{x} \qquad [13]$$

Here $p_{X\dot{X}}(x, v)$ is a joint pdf of a random process $X(t)$ and its time derivative, which is denoted by $V(t)$. The second expression in eqn [13] corresponds to the case of a stationary normal zero-mean $X(t)$, with σ_X, σ_V being the RMS values of $X(t)$ and $V(t)$, respectively (the stationary process and its time derivative are uncorrelated).

This characteristic of a random process can also be used to evaluate the pdf of local peaks, or the amplitude of stress cycles. This pdf is used in certain simple models of fatigue failure, such as that of a linear damage rule. A simplified version of such an analysis only involves moments of stress peaks, which can be obtained from the joint pdf of the process and its first two derivatives. In particular, the amplitude of a Gaussian process has a Rayleigh pdf (eqn [6]). This approach is straightforward, at least for narrow-band temporal variations of stress, with only positive peaks and negative troughs (**Figure 3**). It may also be rather accurate for relatively broad-band stress variations at high levels, where the 'irregular' peaks/troughs of stress have a very small probability, roughly speaking, for $IF > 0.5$. Here IF is a so-called irregularity factor, which is used as a quantitative measure of the PSD bandwidth for excursion calculation: $IF = \sigma_{\dot{X}}^2/(\sigma_X \sigma_{\ddot{X}})$. It can be clearly seen from the general expression (eqn [13]) and its obvious application to $V(t)$ and its derivative, that IF is the ratio of the expected number of zeros to that of peaks of $X(t)$ per unit time, and $IF = 1$ for a 'truly narrow-band' $X(t)$. For highly broadband stress variations other, more sophisticated models may be appropriate, such as the 'rainflow model'.

Consider an example of a prismatic bar in a cross-flow of fluid, which may lead to an aeroelastic instability, or divergence of the bar at a certain critical speed. In the presence of a small 'softening' nonlinearity in the lift force as a function of the twist angle, the postcritical torsion is restricted, and is governed by:

$$Y = \sqrt{(X^2 - 1)} \text{ for } X \geq 1, \quad Y = 0 \text{ for } X < 1 \qquad [14]$$

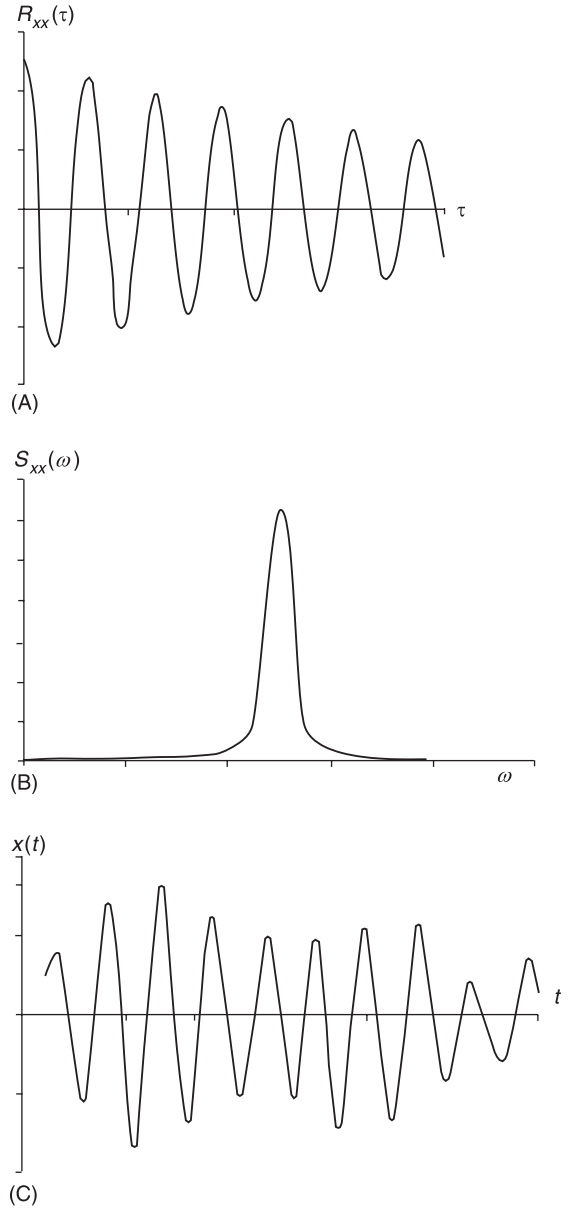


Figure 3 (A) Autocorrelation function and (B) PSD of a narrow-band process $x(t)$ (C) computer-generated with the use of a second-order shaping filter.

Here X is the ratio of the flow speed to its critical value and Y is the nondimensional stress due to aeroelastic torsion. The low-cycle fatigue due to occasional upcrossings of the flow speed $X(t)$ beyond the level $X = 1$ can be studied by direct application of eqn [4], provided that these temporal variations are slow enough to warrant use of the quasistatic relation (eqn [14]) (thereby ignoring inertia terms in the equation of the bar). In particular, if $X(t)$ is a zero-mean Gaussian process, then its amplitude, or peak

value $X_p = A$ has the Rayleigh pdf (eqn [5]). Eqn [4] is applied for this case to eqn [14], with subscript 'p' added to both X and Y in order to indicate their peak values. It results in the same but 'nonnormalized' Rayleigh pdf for peaks of nondimensional stress as:

$$p_{Y_p}(y_p) = P_D(y_p/\sigma_X^2)\ \exp\ \left(-y_p^2/2\sigma_X^2\right)$$
$$P_D = \exp\ \left(-1/2\sigma_X^2\right)$$

The 'denormalizing' factor P_D is a total probability for exceeding the critical flow speed $X = 1$ by a local peak of $X(t)$. Thus, the peak value of the stress is a combined discrete-continuous RV, with the finite probability $1 - P_D$ of a zero value, which corresponds to the subcritical state of the structure.

As for the first-passage failures, the (mean time before failure) (MBTF) $T(\mathbf{X})$ may be regarded as an important reliability characteristic for a given vector process $\mathbf{X}(t)$. This is a conditional expectation, the condition being that the crossing of the barrier should be the very first crossing. The argument $\mathbf{X}$ is the initial value of $\mathbf{X}(t)$, which is assumed to be within the safe domain. However, particularly for high threshold levels, $T(\mathbf{X})$ is frequently found to be almost independent of $\mathbf{X}$, as long as the initial value is not too close to the threshold. (This is the case, where T is very large compared with the characteristic time for reaching the stationary pdf by $\mathbf{X}(t)$ when this pdf exists.) For so-called Markov processes the function $T(\mathbf{X})$ satisfies certain deterministic partial differential equations. More general partial differential equations are also introduced in this theory for the probability of staying within the safe domain during a given time interval, as well as for higher-order moments for the time before failure (see **Stochastic systems**).

An approximate approach for predicting reliability is based on using eqn [6] for the upcrossing rate (as well as its multidimensional extensions) together with the assumption of independent upcrossings (in this case x is a threshold level). The assumption may be adequate for systems with high reliability. As long as the upcrossings are rare for large X, they may be regarded as being independent, so that the MTBF may be related directly to $n_+(x)$. For narrowband (scalar) $X(t)$ this approach may have somewhat poor convergence rate with increasing barrier height because of the high correlation time (upcrossings appear in clusters); the accuracy may be improved by applying eqn [13] to the slowly varying amplitude of $X(t)$. The PDE for T can also be studied for the amplitude of X, and it may be of the reduced dimension, even an ODE in the case of a single-degree-of-freedom system with a white-noise excitation, which can easily be integrated numerically.

Nomenclature

A	amplitude
c	propagation speed
IF	irregularity factor
$\mathbf{K_{XX}}$	covariance matrix
L	distance between points
δ	Dirac delta function
σ_X	RMS value of X
τ	time shift

See also: **Correlation functions**; **Random vibration, basic theory**; **Spectral analysis, classical methods**; **Stochastic systems**.

Further Reading

Bendat JS, Piersol AG (1986) *Random Data: Analysis Measurement and Procedures*. New York: Wiley Interscience.

Bolotin VV (1965) *Statistical Methods in Structural Mechanics*. San Francisco: Holden Day.

Cramer H, Leadbetter MR (1967) *Stationary and Related Stochastic Processes*. New York: Wiley.

Dimentberg M (1988) *Statistical Dynamics of Nonlinear and Time-Varying Systems*. Taunton, UK: Research Studies Press.

Khasminski RZ (1980) *Stochastic Stability of Differential Equations*. Norwell: Kluwer.

Lin YK (1967) *Probabilistic Theory of Structural Dynamics*. New York: McGraw Hill.

Lin YK, Cai GQ (1995) *Probabilistic Structural Dynamics*. New York: McGraw Hill.

Lutes LD, Sarkani S (1997) *Stochastic Analysis of Structural and Mechanical Vibrations*: Englewood Cliffs: Prentice Hall.

Madsen HO, Krenk S, Lind NC (1986) *Methods of Structural Safety*. Englewood Cliffs: Prentice Hall.

Papoulis A (1965) *Probability, Random Variables and Stochastic Processes*. New York: McGraw Hill.

Roberts JB, Spanos PD (1990) *Random Vibration and Statistical Linearization*. New York: Wiley.

Sobczyk K, Spencer BF (1992) *Random Fatigue*. San Diego: Academic Press.

Soong TT, Grigoriu M (1993) *Random Vibration of Mechanical and Structural Systems*. Englewood Cliffs: Prentice Hall.

Stratonovich RL (1963) *Topics in the Theory of Random Noise*, vol. 1. New York: Gordon and Breach.

Stratonovich RL (1967) *Topics in the Theory of Random Noise*, vol. 2. New York: Gordon and Breach.

Yaglom AM (1962) *An Introduction to the Theory of Stationary Random Functions*. Englewood Cliffs: Prentice Hall.

RANDOM VIBRATION

See **RANDOM VIBRATION, BASIC THEORY; RANDOM PROCESSES; STOCHASTIC SYSTEMS.**

RANDOM VIBRATION, BASIC THEORY

M F Dimentberg, Worcester Polytechnic Institute, Worcester, MA, USA

Copyright © 2001 Academic Press

doi:10.1006/rwvb.2001.0123

Whenever a vibrating system is excited by random force(s), the response is also random. Two methods are described in the following for predicting first- and second-order response moments for a given system from available data on the random excitation. Systems with lumped parameters are considered as governed by ordinary differential equations (ODEs), with random processes in their RHSs. (It goes without saying, that systems with distributed parameters may also be analyzed by the same methods, as long as they are reduced to ones with finite number of degrees-of-freedom (DOF)).

The method of moments, as described in the following, is applicable to any linear system subjected to an external random excitation. The latter may be nonstationary, whereas deterministic temporal variations of the system's parameters can also be included in the analysis (extension to the systems with randomly varying parameters is also possible, to some extent, based on another version of the method).

The other approach relies on a direct use of the basic excitation/response relation for power spectral densities (PSDs). Therefore it is only applicable to the steady-state responses of time-invariant systems to stationary excitations. (Certain extensions of the approach to nonstationary processes, based on evolutionary spectra, are known). However, it is important for qualitative insight into phenomena, particularly for interpreting measured random vibration data.

To apply the method of moments one should reduce the system's equations to the form where all excitations are white noises. This is done by introducing shaping filters for all given nonwhite excitations and adding the equations of the shaping filter(s) to those of the system itself. As long as the PSD of the white noise is constant, one should just approximate the given PSD of any excitation by the ratio of two polynomials of squared frequency, with the degree of the numerator being less than that of the denominator. This results in a squared magnitude of the filter's transfer function H, so that the shaping filter's parameters become known. For example, let the excitation $z(t)$ have a PSD with a single peak at frequency v with half-power bandwidth β. A simple possible approximation for such a PSD with a single peak is:

$$S_{zz}(\omega) = \frac{S_0}{(\omega^2 - v^2) + 4\beta^2\omega^2} \qquad [1]$$

It implies, that $z(t)$ satisfies the stochastic differential equation (SDE) $\ddot{z} + 2\beta\dot{z} + v^2 z = \varsigma(t)$, where $\varsigma(t)$ is a white noise with intensity $2\pi S_0$. This requires the introduction of one additional DOF. Thus, for example, the study of a two-degrees-of-freedom (TDOF) tuned vibration absorber for offshore applications requires a model with at least three DOFs, as long as ocean waves usually have a nonzero predominant excitation frequency, which may require the use of an additional DOF for the shaping filter.

Thus, consider the n-dimensional state vector $\mathbf{u}$ as compiled of the displacements and velocities x, v and possibly shaping filter variables z with some of their time derivatives. The basic matrix equation in the canonic form is written as:

$$\dot{\mathbf{u}} = \mathbf{A}(t)\mathbf{u} + \mathbf{F}(t) + \mathbf{B}(t)\varsigma(t) \qquad [2]$$

where $\mathbf{A}(t)$ and $\mathbf{B}(t)$ are deterministic $n \times n$ matrices, $\mathbf{F}(t)$ is an n-dimensional vector of deterministic forcing functions and $\varsigma(t)$ is an n-dimensional vector of zero-mean white noises. The latter are defined with intensity matrix $\mathbf{W}(t)$, so that $\langle \varsigma_i(t)\varsigma_j(\theta)\rangle = W_{ij}(t)\delta(t-\theta)$. Temporal variations of the excitation

intensity may be used to describe nonstationary random dynamic loads.

The response vector $\mathbf{u}(t)$ is decomposed into its mean or expected value $\mathbf{m}(t) = \langle \mathbf{u}(t) \rangle$ and zero-mean part $\mathbf{u}^0(t) = \mathbf{u}(t) - \mathbf{m}(t)$. The mean response is analyzed separately by solving the deterministic equation $\dot{\mathbf{m}} = \mathbf{A}(t)\mathbf{m} + \mathbf{F}(t)$. The correlation matrix of the zero-mean part of the response is analyzed then, namely $\mathbf{R}_{\mathbf{uu}}(t, \theta) = < \mathbf{u}^0(t)\mathbf{u}^{0\mathrm{T}}(\theta) >$. A two-step procedure is used, as based on the following pair of deterministic matrix ODEs:

$$\begin{aligned} &\dot{\mathbf{D}} = \mathbf{AD} + \mathbf{DA}^{\mathrm{T}} + \mathbf{BWB}^{\mathrm{T}} \\ &(\mathrm{d}/\mathrm{d}t)\mathbf{R}_{\mathbf{uu}}(\theta, t) = \mathbf{R}_{\mathbf{uu}}(\theta, t)\mathbf{A}^{\mathrm{T}}(t) \\ &\mathbf{R}_{\mathbf{uu}}(\theta, \theta) = \mathbf{D}(\theta) \end{aligned} \qquad [3]$$

Here $\mathbf{D}$ is clearly seen to be the variance matrix, i.e., a special version of the correlation matrix, which corresponds to a zero time shift. It is obtained by integrating the first equation (eqn [3]) for any given initial conditions at $t = 0$, uncorrelated with the excitation if they are random (whereas $\mathbf{D}(0) = 0$ if they are deterministic). Integration of the second equation (eqn [3]) can be performed then, whereas the last relation (eqn [3]) is imposed as the initial condition, which specifies a relation between $\mathbf{D}$ and $\mathbf{R}$.

As an example, consider a SDOF system with a white-noise excitation:

$$\ddot{X} + 2\alpha\dot{X} + \Omega^2 X = \varsigma(t) \qquad [4]$$

for a zero-mean white noise $\varsigma(t)$ with intensity D_ς. Rewriting eqn [4] in the form of eqn [2] with $u_1 = X$, $u_2 = \dot{X}$, the following set of three equations for variances is obtained as a scalar version of the matrix equation (eqn [3]):

$$\begin{aligned} &\dot{D}_{11} = 2D_{12}, \quad \dot{D}_{12} = D_{22} - 2\alpha D_{12} - \Omega^2 D_{11} \\ &\dot{D}_{22} = -4\alpha D_{22} - 2\Omega^2 D_{12} + D_\varsigma \end{aligned} \qquad [5]$$

This set has a simple (constant) steady-state solution, as obtained by equating the RHSs to zero:

$$D_{11} = D_\varsigma/4\alpha\Omega^2, \quad D_{12} = 0, \quad D_{22} = D_\varsigma/4\alpha \qquad [6]$$

This steady-state solution, which is clearly also stationary in this case, exists only in the presence of damping. The transient solution to eqns [5] for the undamped case ($\alpha = 0$) for zero initial conditions indicates linear growth of the mean square displacement and velocity with time:

$$D_{11}(t) = \left(D_\varsigma/2\Omega^2\right) t, \quad D_{22}(t) = D_\varsigma t/2$$

This growth may be regarded as being 'mild' compared with the case of a perfectly resonant sinusoidal excitation for an undamped SDOF system (where the linear growth is observed for the response amplitude). However, it may be regarded as unavoidable, as long as detuning from a white noise is impossible.

Applying the second matrix equation (eqn [4]), we may derive three ODEs for the autocorrelation functions, R. For the stationary response their single argument will be $\tau = t - \theta$. Denoting derivatives over this argument by primes, we obtain, in particular, the following ODE for the autocorrelation function of the displacement response $R''_{11} + 2\alpha R'_{11} + \Omega^2 R_{11} = 0$ which coincides with the equation for free vibrations. Its solution, satisfying the initial condition $R_{11}(0) = D_{11}$ is:

$$\begin{aligned} R_{11}(\tau) &= D_{11} \exp(-\alpha\tau)[\cos\omega_d\tau + (\alpha/\omega_d)\sin\omega_d\tau] \\ \omega_d &= \sqrt{\left(\Omega^2 - \alpha^2\right)}, \quad \tau > 0 \end{aligned}$$

(The other initial condition, satisfied by this expression, is also correct, since $R'_{11} = R_{12}$, and $D_{12} = 0$ according to the solution (eqn [6]).

The correlational analysis of the measured response to random excitation may be used, therefore, for an online evaluation of the system's natural frequency and damping, when free vibration testing is not possible. Measurements of excitation are not needed, as long as it can be reasonably assumed, that its PSD is broadband with respect to the system. (This may be the case, e.g., with measured flow-induced vibrations in unconfined unseparated flows.) Damping can be conveniently estimated by plotting the (supposedly exponential) envelope of the autocorrelation function in semilog coordinates and using only that range of τ where the actual plot is indeed found to be linear. (Ranges with too large and too small values of τ are very often discarded – the former because of large scatter of statistical errors, the latter because of the influence of a band-pass filter, which may be used for MDOF systems to separate a specific modal response; in view of the Uncertainty Principle, the influence of such a filter decays earlier than the autocorrelation function, provided that the filter is broadband with respect to the given mode).

Whenever the response is stationary, its PSD can be predicted in terms of the excitation PSD and relevant complex frequency response H, using the basic relation:

$$S_{XX}(\omega) = \left| H^2(i\omega) \right| S_{FF}(\omega) \qquad [7]$$

with appropriately assigned subscripts. (Excitation and response are denoted here by $F(t)$ and $X(t)$, respectively). The mean square response is then obtained by a simple integration. Very often one of the cofactors in the RHS of eqn [7] has a sharp peak at a certain frequency, which provides the dominating contribution to the mean square response (**Figure 1**). The latter may be calculated approximately by assuming the other cofactor to be constant in the vicinity of the peak. Thus, for a SDOF system (eqn [4]) with undamped natural frequency and damping factor, Ω and α, respectively (and with excitation $F(t)$ in the RHS), the mean square value of the (stationary) response $X(t)$ is found to be:

$$\langle X^2 \rangle = \int_{-\infty}^{\infty} \frac{S_{FF}(\omega)\mathrm{d}\omega}{\left(\omega^2 - \Omega^2\right)^2 + 4\alpha^2\omega^2} \cong \frac{\pi S_{FF}(\Omega)}{2\alpha\Omega^2} = \frac{D_\varsigma}{4\alpha\Omega^2} \qquad [8]$$

if $\alpha/\Omega \ll 1$. This formula clearly illustrates filtering property of a lightly damped system. Namely, the system responds to a single frequency component of the excitation only, one with the system's natural frequency. And as long as excitation components with other frequencies become irrelevant, the response is found to be the same as in the case of a white-noise excitation $\varsigma(t)$ with intensity $D_\varsigma = 2\pi S_{\mathrm{FF}}(\Omega)$ (compare with the first expression (eqn [5]). The condition for white-noise approximation for the excitation for a SDOF system is clearly seen to be that of a large excitation/system bandwidth ratio. (In the time domain it may be formulated as that of the short correlation time of the excitation compared with the system's time constant as defined by the reciprocal of its half-power bandwidth). The white-noise approximation is also seen to be adequate for predicting the mean square of velocity, but not that of the response acceleration, as long as $S_{\ddot{X}\ddot{X}}(\omega) = \omega^4 S_{XX}(\omega) \to S_{FF}(\omega),$ with $\omega \to \infty$.

The approximation (eqn [8]), which only filters a single frequency component from the excitation PSD, can be easily extended to the MDOF systems, where the excitation may be regarded as 'locally broadband' in the frequency domain, that is, broadband with respect to each modal bandwidth. Values of this PSD at the natural frequencies of various systems will then be involved.

A similar approximation, based on an asymptotic evaluation of the integral for the mean square response, can also be used in the opposite case, where the excitation $F(t)$ is narrowband with mean frequency ν, whereas $|H^2(i\omega)|$ is slowly varying in the vicinity of this frequency. The approximate expression for the contribution of this excitation into the overall response is then $\langle X^2 \rangle \cong |H^2(i\nu)/\langle F^2 \rangle$.

Eqn [8] clearly indicates the inadequacy of undamped models of the systems for predicting steady-state random vibration. This should be expected, as long as the continuous excitation spectrum always contains a frequency component, which would be the resonant one.

Another general property of random vibrations of a SDOF system is related to the influence of the bandwidth of the excitation with fixed overall level. If the mean, or center frequency of the narrowband excitation is tuned to the system's natural frequency, the spread of the excitation energy in the frequency domain leads to reduction of its resonant component and thus of the response. On the other hand, in the case of large detuning of the center excitation frequency, this spread may increase the resonant component of the excitation, thereby increasing the response level. The critical value of the detuning between these two extreme cases is of the order of the system's half-power bandwidth.

Evaluation of the response correlation function(s) is also found to be rather simple by the spectral approach, since it just requires calculating the Fourier transform of the corresponding PSDs. Thus, applying the procedure to the integrand of eqn [8] (with approximately constant PSD of $F(t)$) yields the autocorrelation function of the SDOF system's response displacement to a white-noise excitation, which is the same expression as was obtained before.

The case of systems with periodic system matrix $\mathbf{A}(t)$ deserves some special attention, as long as some important analytical solutions can be obtained by asymptotic methods. The methods may be applied either to the deterministic ODE (eqn [3]) for the variance matrix, or directly to the original stochastic equation of motion. Thus, averaging over the period can be applied to a SDOF system with periodic

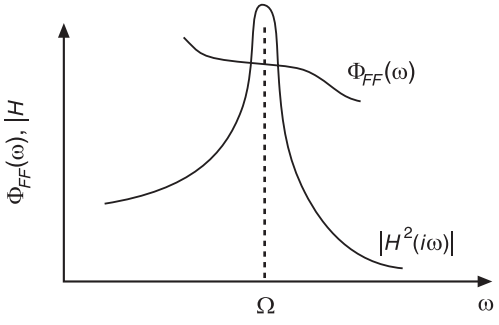


Figure 1 Broadband excitation of a lightly damped SDOF system.

parametric and external random excitation, as governed by:

$$\ddot{x} + 2\alpha\dot{x} + \Omega^2 x(1 + \lambda \sin 2\nu t) = \varsigma(t) \qquad [9]$$

By introducing slowly varying in-phase and quadrature response components $x_c(t)$, $x_s(t)$ for small α, λ, $|\nu - \Omega|$, where $x(t) = x_c(t)\cos \nu t + x_s(t)\sin \nu t$, eqn [9] may be reduced approximately to a set of two SDEs with constant parameters. Steady-state analytical solution for the second-order moments $D_{cc,\,ss} = \langle x^2_{c,\,s}\rangle D_{cs} = \langle x_c x_s\rangle$ can be obtained then, provided that $\mu < 1$, $\mu = (\lambda\Omega/4)/\sqrt{(\alpha^2 + (\nu - \Omega)^2)}$. The latter inequality is the parametric stability condition for the system (eqn [9]). The solution yields, in particular:

$$\mu = \frac{\left[(D_{cc} - D_{ss})^2 + D^2_{cs}\right]^{1/2}}{(D_{cc} + D_{ss})}$$

(thereby relating the stability margin of the system (eqn [9]) to the second-order moments of its subcritical response, which can be estimated when $x(t)$ is measured on-line. The probability density function (pdf) of the response $x(t)$ is normal if $\varsigma(t)$ has a normal pdf. Transforming in-phase and quadrature components of $x(t)$, which are also normal, to amplitude and phase, one can derive the pdfs of the latter state variables, in the same way as the pdfs (eqns [5] and [6]) were obtained in **Random processes**. The pdf of phase is found to be nonuniform, with the magnitude of its variations within $[0,\, 2\pi)$ equal to μ.

The method of moments may sometimes also be applied to systems with state-dependent random excitation(s), such as stochastic parametric excitations, provided that the linear deterministic ODEs for moments are still obtained. This generalization is based on the SDE calculus, as considered in more detail in **Stochastic systems**. Here we may just refer to the following relation for a set of SDEs for components an $n-$dimensional state space vector $\mathbf{X}$, with Gaussian white-noise excitations:

$$\text{if } \dot{X}_i = g_i(\mathbf{X})\varsigma_i(t); \quad \left\langle \varsigma_i(t)\varsigma_j(t+\tau)\right\rangle = D_{\varsigma,ij}$$
$$i,j = 1,2,\ldots,n, \text{then}$$
$$\langle g_i(\mathbf{X})\varsigma_i(t)\rangle = (1/2)\sum_{k=1}^{n}\left\langle g_k(\mathbf{X})\frac{\partial g_i(\mathbf{X})}{\partial X_k}\right\rangle D_{\varsigma,ik} \qquad [10]$$

The expected values, which appear in the RHSs of the deterministic equations for expectations of the components of state vector $\mathbf{X}$, are seen to be linear in the case of linear functions g. This provides a possibility of applying the method of moments to linear systems with white-noise parametric excitation(s). Thus, consider the SDOF system (eqn [4]) with an additional stochastic parametric excitation term $\Omega^2\xi(t)$ added to its LHS. Here $\xi(t)$ is a zero-mean Gaussian white noise with intensity D_ξ, uncorrelated with the external white noise in the RHS of eqn [4]. The corresponding additional terms in the RHSs of the second and third expressions in eqn [6] would be $\langle -\Omega^2 u_{11}\xi(t)\rangle$ and $\langle -2\Omega^2 u_{12}\xi(t)\rangle$, respectively, where $u_{ij} = X_i X_j; i,\, j = 1,\, 2$ (double subscripts for state variables are convenient here). According to the basic relation (eqn [10]), the second of these two expected values is found to be $\Omega^4 D_{11} D_\xi$ (the first one is zero). This results in the following modified solution for mean square displacement responses:

$$D_{11} = \frac{(D_\varsigma/4\alpha\Omega^2)}{1 - (\Omega^2 D_\varsigma)/4\alpha}, \quad D_{22} = \Omega^2 D_{11} \qquad [11]$$

The numerator in eqn [11] for the mean square displacement coincides with the previously obtained expression (eqn [6]) for the case of a purely external excitation. The reciprocal of the denominator may then be called a parametric amplification factor of the mean square response to external excitation. It increases monotonously with the intensity level of the parametric excitation and becomes infinite at critical value of the latter, when:

$$D_\xi = D_{\xi^{**}} = 4\alpha/\Omega^2 \qquad [12]$$

This value corresponds to a threshold for stochastic stability in the mean square of the SDOF system. Study of stochastic stability is presented in **Stochastic systems**, whereas in this article only subcritical cases are considered, i.e., those where $D_\xi < 4\alpha/\Omega^2$. It should be noted that exceeding the stability threshold (eqn [12]) does not necessarily imply infinite growth of the response itself; the stationary response pdf may exist, which would, however, have infinite variance. Of course, such a situation is impossible in the case of a purely external Gaussian excitation, where the response is also Gaussian.

A generalized version of the method of moments, based on the relations, given in eqn [10], may also be used to incorporate another model of random excitation into random vibration analyses. This is a model of periodic excitation with random temporal variations of instantaneous frequency, or random phase modulation. In its simplest version of sinusoidal

periodic excitation with white-noise phase modulation, it can be described as follows:

$$F(t) = \lambda \cos z(t), \quad \dot{z} = v + \xi(t) \qquad [13]$$

where $\xi(t)$ is a zero-mean stationary Gaussian white noise with intensity D_ξ. The PSD of the random process (eqn [13]) is:

$$S_{FF}(\omega) = \frac{\left(\lambda^2 D_\xi/2\right)\left(\omega^2 + v^2 + D_\xi^2/4\right)}{\left(v^2 + D_\xi^2/4 - \omega^2\right)^2 \omega^2 D_\xi^2} \qquad [14]$$

The parameter D_ξ describes a 'spread' of the excitation energy in the frequency domain around the expected excitation frequency v. The PSD (eqn [14]) is seen to be similar to the PSD of a filtered white noise (eqn [1]). In the case of narrow-band excitations $z(t)$ and $F(t)$ these PSDs can be made identical by equating the intensity of frequency variations to the doubled bandwidth of the shaping filter: $D_\xi = 2\beta$ for $\beta \ll v$. On the other hand, the pdf of the excitation $F(t)$ is strongly non-Gaussian (see eqn [9] of **Random processes**).

To incorporate the model (eqn [13]) into a random vibration analysis one can use the following 'autonomous' representation of the trigonometric functions:

$$F(t) = \lambda z_1, \quad \dot{z}_1 = -(v + \xi(t))z_2, \quad \dot{z}_2 = (v + \xi(t))z_1 \qquad [15]$$

The equations for second-order moments of the introduced 'trigonometric' state variables $D_{ij} = \langle u_{ij} \rangle = \langle z_i z_j \rangle$; $i,\ j = 1,\ 2$ are:

$$\begin{aligned}
\dot{D}_{11} &= -2vD_{12} - 2v\langle u_{12}\xi(t)\rangle \\
&= -2vD_{12} - D_\xi(D_{11} - D_{22}), \\
\dot{D}_{12} &= v(D_{11} - D_{22}) + \langle (u_{11} - u_{22})\xi(t)\rangle \\
&= v(D_{11} - D_{22}) - 2D_\xi D_{12} \\
\dot{D}_{22} &= 2v\dot{D}_{12} + 2v\langle u_{12}\xi(t)\rangle \\
&= 2vD_{12} + D_\xi(D_{11} - D_{22})
\end{aligned}$$

These equations for second-order moments should be supplemented with an obvious relation $\langle z_1^2 \rangle + \langle z_2^2 \rangle = 1$, and then the unique steady-state solution is $D_{11} = D_{22} = 1/2,\ D_{12} = 0$ (the last equality is a clear result of random temporal phase variations, represented by the 'damping' term with D_ξ in the second equation).

Thus, the equation of motion with a forcing function $F(t)$ is supplemented by two equations [15] and a second-order trigonometric relation. The method of moment can then be applied, based on eqn [10]. Similar (multiple) relations between trigonometric functions would be required when higher-order moments of the response are calculated; such predictions may be relevant for reliability studies as long as the response may be non-Gaussian.

Eqn [13] seems be particularly relevant for describing excitations due to traveling loads and/or traveling structures in case of an imperfect spatial periodicity of the loading pattern (and constant travel speed). It may also be appropriate in general for random excitations with relatively small variations of amplitude. The second-order moments of the response to such an excitation would be certainly the same as in case of a filtered Gaussian white-noise excitation with the same PSD. The higher-order moments may be different however, or they may not be if the normalization effect according to the central limit theorem (CLT) is present. **Figure 2** illustrates results for fourth-order response moments for a SDOF system with natural frequency and damping factor Ω and α respectively, excited by the external force (eqn [15]).

The excess factor γ of the response displacement (with negative sign) is defined in eqn [5] of **Random processes** together with expression [7] for the pdf of the sinusoid with random phase; the latter implies that the excitation $F(t)$ should have $\gamma = -1.5$. Curves of $-\gamma$ vs excitation/system bandwidth ratio D_ξ/α are presented for three different values of detuning between mean excitation frequency and system's natural frequency (and fixed α/Ω). All three curves start at the value 1.5 for the extreme case of a perfectly sinusoidal excitation (zero excitation bandwidth), and all three approach zero value for high excitation/system bandwidth ratios, which

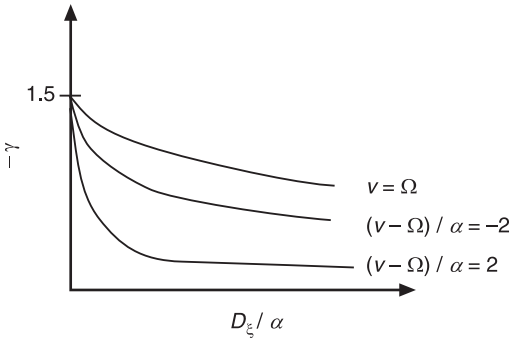


Figure 2 Excess factor of the response vs excitation/system bandwidth ratio.

correspond to the other extreme of an asymptotically normal, or Gaussian response. The convergence rate is not particularly high, with values of γ of the order 0.5 at $D_\xi/\alpha = 20$, however, all values were found to be zero up to four significant digits at $D_\xi/\alpha = 50$. The dependence of the convergence rate on detuning can also be seen. It is lowest at the exact resonance and lower for a subresonant excitation than for the post-resonant one with the same detuning.

Thus, application of the method of moments for systems with purely external narrowband excitation seems to be straightforward. It leads to some expansion of the vector of state variables. This is not the case with systems, which are subject to a narrowband parametric excitation. If the latter is described as a filtered white noise, the expanded system (with added shaping filter) will contain a (product-type) nonlinearity in the parametric excitation term. In the case of the parametric excitation of the type shown in eqn [13] a limited analytical study is possible, based on reduction of the original SDOF system by the method of stochastic averaging.

Results of the analysis of the first- and second-order moments of the response provide a complete description of the response pdf, provided that it is normal. Basically, there are two cases where the response to an external random excitation may be normal indeed (random parametric excitation can bring significant deviations from normality; this topic is studied in **Stochastic systems**:

- The excitation is normal.
- The excitation/system bandwidth ratio is large, so that the CLT may be relied upon (actual convergence rate to normality is case-dependent, of course).

If neither of these conditions is satisfied, another approach may be adopted based on the theory of Markov processes (see **Stochastic systems**).

An attempt can also be made to apply the method of moments to nonlinear systems with nonlinearities of a polynomial type. This attempt faces a basic difficulty with obtaining closed systems of equations for moments of various orders. For example, if the original SDE for $X(t)$ contains a term with X^3, the equation for $\langle X \rangle$ would contain a term with $\langle X^3 \rangle$, the equation for $\langle X^2 \rangle$ would contain a term with $\langle X^4 \rangle$, etc. The difficulty is usually resolved by adopting a certain approximate closure scheme, whereby some relation(s) are enforced between response moments of various orders. The Gaussian closure scheme is the most common one, whereby, say, relation $\langle X^4 \rangle = 3(\langle X^2 \rangle)^2$ is imposed for the case of a single variable X, which corresponds to the relation between second- and fourth-order moments of the normal pdf. General relations of this form can be used similarly for the case of a vector $\mathbf{X}$. The reasoning is that in the case of a small nonlinearity the pdf of the nonlinear system's response should not deviate much from that of a linear system. The resulting eqn [9] for variance matrix $\mathbf{D}$ is found to be nonlinear in this case.

The approach can be extended to more general nonlinearities, including those of non-smooth type, by using method of statistical linearization. The original nonlinear system is replaced approximately by the 'equivalent' linear one. The condition for equivalence is that of a minimal mean square error of such a replacement. Being applied together with some closure scheme, it leads to an 'equivalent' linear system, with parameters of the latter being functions of the (unknown) first- and second-order moments of the response. This system may be analyzed either by the method of moments, or by the spectral approach if the stationary response is studied.

Thus, a system with nonlinear stiffness and a zero-mean Gaussian white-noise excitation

$$\ddot{X} + 2\alpha\dot{X} + f(X) = \varsigma(t) \qquad [16]$$

is approximated by an 'equivalent' linear one with the same white noise $\varsigma(t)$ with intensity D_ς:

$$\ddot{X} + 2\alpha\dot{X} + \Lambda^2 X = \varsigma(t) \qquad [17]$$

(in the case of a nonlinear damping in the original system (eqn [16]) the equivalent linear damping should also be introduced). The steady-state displacement response variance of the equivalent system is:

$$\sigma^2 = \langle X^2 \rangle = D_\varsigma / 4\alpha\Lambda^2 \qquad [18]$$

Now, the condition for equivalence is found to be $\Lambda^2 = \langle Xf(X) \rangle / \langle X^2 \rangle$. Using the Gaussian closure scheme, these expected values can be obtained by averaging over the normal pdf with zero mean and a (yet unknown) variance σ^2. The resulting expression for the (response dependent) natural frequency of the equivalent linear system is then substituted into the solution (eqn [18]). An algebraic equation for the mean square response of the equivalent system (eqn [17]) is obtained in this way, which may provide a reasonable approximation to that of the original system (eqn [16]). Thus, for a system with cubic nonlinearity, where $f(X) = \Omega^2(X + \mu X^3)$, the equation is:

$$3\mu(\sigma^2)^2 + \sigma^2 - D_\varsigma / 4\alpha\Omega^2 = 0$$

and can even be solved explicitly. For a system with a set-up spring, where $f(X) = \Omega^2(X + \mu \text{sgn} X)$, the corresponding equation is found to be:

$$\sigma^2 = \left(D_\varsigma / \left(4\alpha\Omega^2\right)\right)\left[1 + (\mu/\sigma)\sqrt{(2\pi)}\right]$$

For both these examples the exact solutions by the method of Markov processes are available (see **Stochastic systems**). They show the above results to be of a reasonable accuracy even for values of the corresponding nonlinearity parameter μ which are not very small.

This success of the statistical linearization is not universal. Predictions of the response PSD are usually less accurate, as well as those of the excursions, especially at high levels, which are needed for reliability analyses. The presence of a stochastic parametric excitation also may lead to a poor accuracy of the approach, as long as significant deviations from the Gaussian response pdf may appear. A certain improvement in the resulting estimates is found to be possible sometimes through the use of other closure schemes. For example, whenever the response may be expected to be narrowband and with relatively small random variations of amplitude, another pdf would be more appropriate for establishing the desired relation between response moments of various orders – the pdf of a sinusoid with random phase. In any case, however, the accuracy of the method cannot be predicted in advance and should rely upon comparisons with benchmark results, obtained by other approaches – direct Monte-Carlo simulations or (if available) the method of Markov processes. The latter approach is considered in **Stochastic systems**. On the other hand, statistical linearization is perhaps the most general method for (nonlocal) analysis of nonlinear random vibration problems for MDOF systems.

Nomenclature

$\mathbf{A}(t)$,$\mathbf{B}(t)$	deterministic $n \times n$ matrices
$\mathbf{D}$	variance matrix
$\mathbf{F}(t)$	deterministic forcing functions
$\mathbf{m}(t)$	mean or expected value
$\mathbf{R}$	response matrix
$\mathbf{u}(t)$	response vector
$\mathbf{W}(t)$	intensity matrix
β	half-power bandwidth
ν	frequency
ς	white noise

See also: **Correlation functions**; **Random processes**; **Stochastic systems**.

Further Reading

Bendat JS, Piersol AG (1986) *Random Data: Analysis Measurement and Procedures*. New York: Wiley Interscience.

Bolotin VV (1965) *Statistical Methods in Structural Mechanics*. San Francisco: Holden Day.

Cramer H, Leadbetter MR (1967) *Stationary and Related Stochastic Processes*. New York: Wiley.

Crandall SH, Mark WD (1963) *Random Vibration in Mechanical Systems*. New York: Academic Press

Dimentberg M (1988) *Statistical Dynamics of Nonlinear and Time-Varying Systems*. Taunton, UK: Research Studies Press.

Khasminski RZ (1980) *Stochastic Stability of Differential Equations*. Norwell: Kluwer.

Lin YK (1967) *Probabilistic Theory of Structural Dynamics*. New York: McGraw Hill.

Lin YK, Cai GQ (1995) *Probabilistic Structural Dynamics*. New York: McGraw Hill.

Lutes LD, Sarkani S (1997) *Stochastic Analysis of Structural and Mechanical Vibrations*. Prentice Hall.

Madsen HO, Krenk S, Lind NC (1986) *Methods of Structural Safety*. Englewood Cliffs: Prentice Hall.

Papoulis A (1965) *Probability, Random Variables and Stochastic Processes*. New York: McGraw Hill.

Roberts JB, Spanos PD (1990) *Random Vibration and Statistical Linearization*. New York: Wiley.

Soong T, Grigoriu M (1993) *Random Vibration of Mechanical and Structural Systems*. Englewood Cliffs: Prentice Hall.

Stratonovich RL (1963) *Topics in the Theory of Random Noise,* vol. 1. New York: Gordon and Breach.

Stratonovich RL (1967) *Topics in the Theory of Random Noise,* vol. 2. New York: Gordon and Breach.

RESONANCE AND ANTIRESONANCE

M Radeş, Universitatea Politehnica Bucuresti, Bucuresti, Romania

Copyright © 2001 Academic Press

doi:10.1006/rwvb.2001.0163

Resonance vs Antiresonance

In a lightly-damped linear system, resonance occurs when the frequency of the applied harmonic excitation coincides with (or is close to) one of the natural

frequencies of the system. Resonance is a state of forced vibration. It takes place at the resonance frequency, i.e., at the frequency of excitation, which is close to one of the natural frequencies of the system.

Periodic excitation can produce resonance when the frequency of one of its harmonic components becomes equal (or close) to a natural frequency of the system. Random and frequency sweep excitations give rise to resonance when the frequency spectrum of the excitation encompasses any of a system's natural frequencies.

A swing pushed at the right time intervals exhibits resonant oscillations. Operation of soil compactors, concrete tampers, vibration conveyers, road drills, vibrating screens, and some fatigue-testing machines is often based on resonant vibrations. Resonance is produced in multiple-reed gauges and in piezoelectric accelerometers used for the detection of defects in rolling element bearings.

However, the main concern with resonance relates to its adverse effects. During operation at resonance, excessive motion (and stress) amplitudes are generated, causing structural fatigue and failure, harmful effects or discomfort to humans, and a decrease in product accuracy. The nuisance of a noisy component vibrating at resonance can be an obstacle to the sale of a car or a household appliance.

Sometimes resonance is a loosely used term. In the general acceptance, resonance is a condition whereby a minimum of excitation is required to produce a maximum of dynamic response. Resonance relates to the condition where either a maximum motion is produced by a force of constant magnitude, or a minimum force is required to maintain a given motion. The frequencies where the peak value of the forced vibration appears are referred to as resonance frequencies.

A resonance is defined by a frequency, a response (or excitation) level, and a bandwidth. Avoidance of large resonant vibration levels can be accomplished by:

1. changing the excitation frequency;
2. making stiffness and/or mass modifications to change the natural frequency;
3. increasing (or adding) damping;
4. adding a dynamic vibration absorber.

Antiresonances is a local state, in contrast to resonance, whereby a vibrating system most strongly resists being made to vibrate. It takes place at a frequency at which a maximum of force magnitude produces a minimum of motion, and is confined to specific frequencies at specific points.

Resonances occur at natural frequencies that are global properties of a vibrating system, independent of the driving point. Antiresonances are local (subsystem) properties, dependent on the driving location.

There is a clear distinction between the nodal points (or lines), that are characteristics of mode shapes, and the driving point of an antiresonance deflection shape, which is a local property of the system. Vibration nodes can be created by the mutual cancellation of a pole (natural frequency) with a zero (antiresonance).

The Grounded Mass-Spring-Damper System

Consider a mass-spring-damper grounded system subjected to a harmonic force applied to the mass (**Figure 1**). The steady-state response of the viscously-damped single-degree-of-freedom (SDOF) system is a harmonic motion of the same frequency as the excitation force, with a phase shift due to damping. The motion is describable in terms of displacement, velocity, or acceleration. The displacement amplitude, X, and the phase angle between displacement and force, φ, are functions of the forcing frequency, ω. For subcritical damping, as the excitation frequency approaches the undamped natural frequency, $\omega_r = \sqrt{k/m}$, the displacement amplitude approaches a peak value and the phase shift passes through 90° (see **Theory of vibration**, Fundamentals).

The frequency response diagram, displaying the motion amplitude versus forcing frequency for a given value of damping and constant force amplitude, exhibits a resonance peak (**Figure 1**). For viscous damping, the peak of the displacement resonance curve occurs at $\omega = \omega_r(1 - 2\zeta^2)^{1/2}$, while the phase shift is 90° at $\omega = \omega_r$. The first condition is often referred to as an amplitude resonance, while the second one is termed phase resonance. The difference in frequencies is small for lightly-damped systems.

For viscously-damped systems with a critical damping ratio $\zeta > 0.707$, the resonance peak is completely smooth. Over-critically damped systems do not exhibit resonances.

At the natural frequency $\omega = \omega_r$, the spring force balances the inertia force of the mass, and the excitation force overcomes the damping force only (**Figure 2**). There is a continuous interchange of potential and kinetic energy between the spring and the mass. The only external force that has to be applied to maintain the system vibrating is that needed to supply the energy dissipated in the damper.

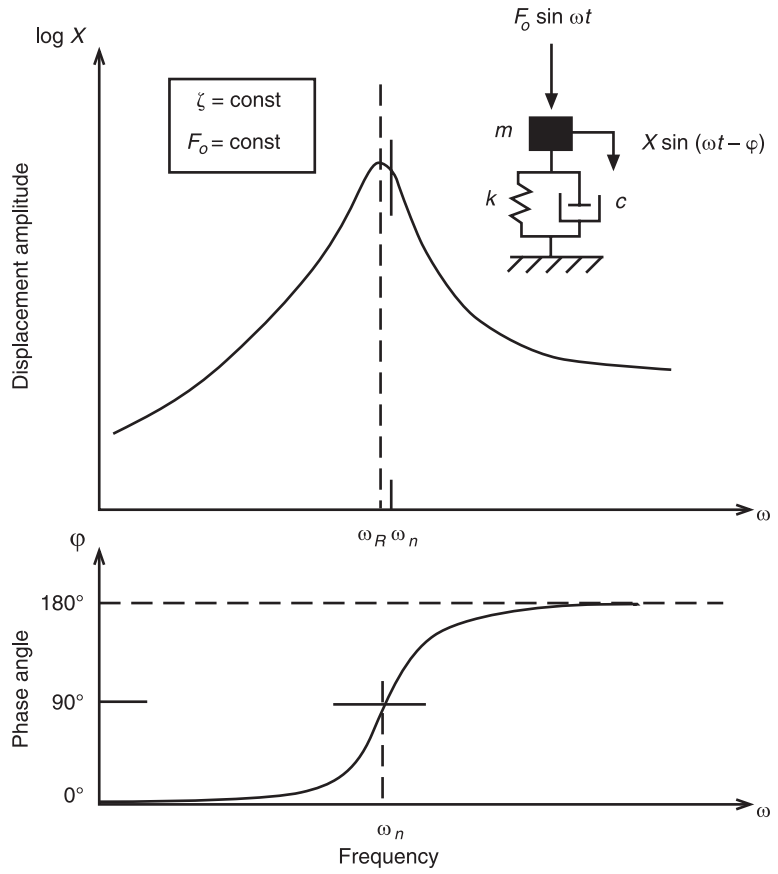


Figure 1 Resonant response of grounded single-degree-of-freedom (SDOF) system.

At resonance, the reactive energy (in spring and mass) is zero and the active energy (actually dissipated) is maximum. That is why a minimum of force is required to maintain a given displacement amplitude.

On a plot of the dynamic stiffness (force required to produce unit displacement at the driving point) versus frequency, the resonance appears as a trough.

The Ungrounded Mass-Spring-Damper System

One of the simplest systems exhibiting antiresonance is the mass-spring-damper ungrounded system, subjected to a harmonic force applied to the base. For constant force amplitude, the driving point displacement amplitude has a minimum value at antiresonance (**Figure 3**).

In the absence of damping, the antiresonance frequency of the base-excited sprung-mass system is the same as the resonance frequency of the mass-excited system grounded at the other end of the spring. The presence of light damping has a small effect upon the equality of these frequencies. The sprung-mass system can be replaced by an equivalent, frequency-dependent mass that is infinitely large for the excitation at the antiresonance frequency.

The motion transmissibility, i.e., the ratio of the mass displacement to the base displacement, is maximum at the antiresonance.

If the sprung mass is attached to a free mass at the driving point, the resulting mass-spring-mass system exhibits both a resonance and an antiresonance in the driving-point response (**Figure 4**). At resonance, a node of vibration occurs at a point somewhere along the spring. If the system is divided into two parts at this location, then each subsystem is antiresonant at this frequency, because the large force acting across the spring is producing a negligible displacement at that point.

If the sprung-mass system is attached to the mass-excited mass-spring grounded system, the former acts as a dynamic vibration absorber. When it is tuned to the driving frequency of the grounded system (i.e., its parameters are chosen so that its antiresonance

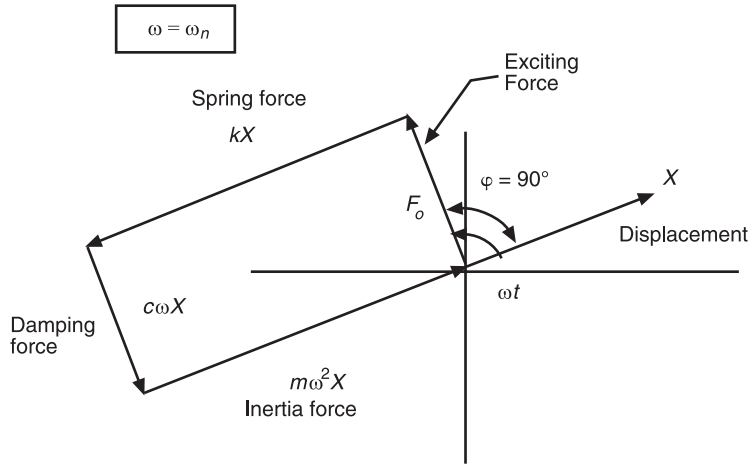


Figure 2 Force balance diagram at resonance for single-degree-of-freedom system.

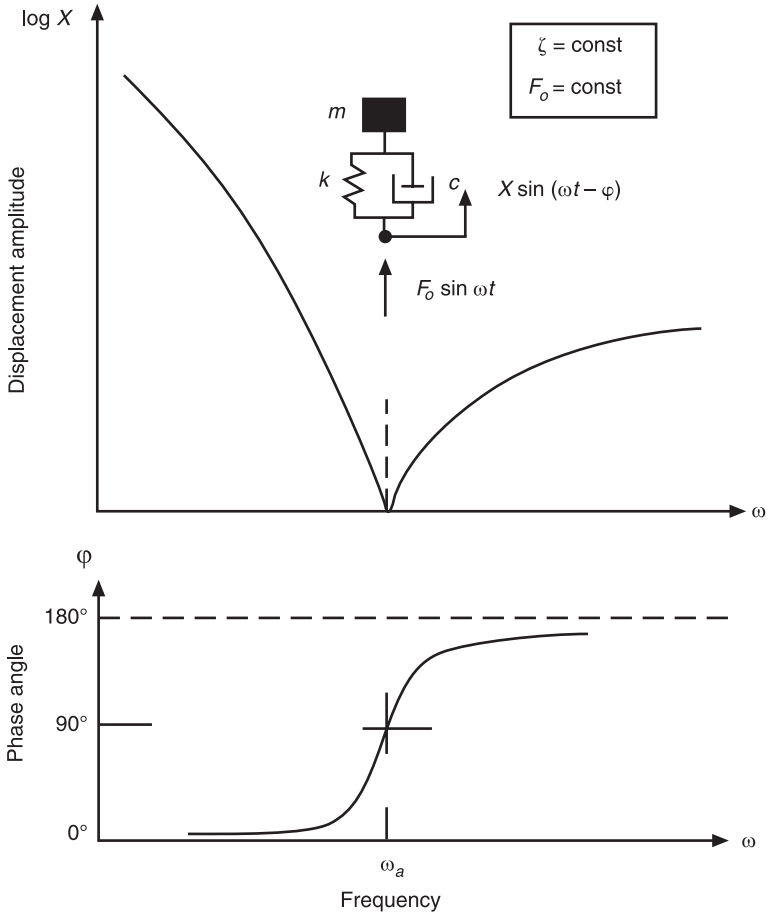


Figure 3 Antiresonant response of single-degree-of-freedom ungrounded system.

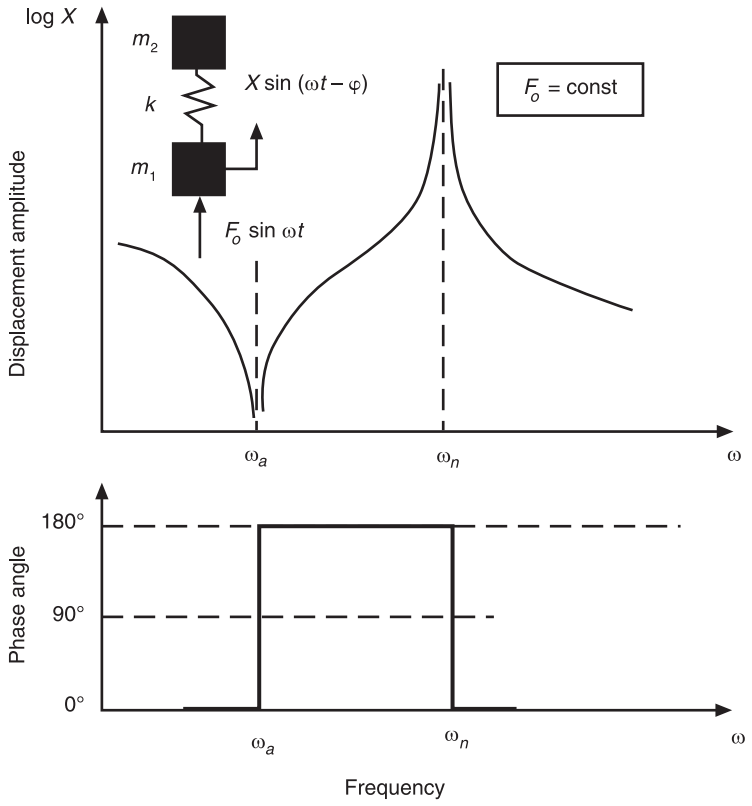


Figure 4 Frequency response of mass-spring-mass system.

frequency is equal to the frequency of the excitation force), the mass of the latter does not vibrate. The sprung mass vibrates in such a way that the spring force is equal and opposite to the excitation force. There is no net force acting on the mass of the grounded system at the antiresonance frequency of the sprung-mass subsystem.

Resonance in SDOF Systems

In the neighborhood of resonance, the response of a vibrating system can be analyzed from different points of view: the manner in which the system is made to vibrate, the physical quantities that are measured, the graphs that are plotted, and the model of damping considered.

Harmonic vs Swept-Sine Excitation

Resonance is basically defined as a forced vibration under steady-state conditions, i.e., for constant forcing frequency. In practice, the frequency of the harmonic excitation is varied, either continuously or stepwise, to determine the resonances. When the excitation frequency becomes equal to (and dwells on) a natural frequency of the system, it takes time until the steady-state response is attained. This time depends upon the damping level. The lighter the damping, the longer is the time to reach the steady-state level of vibration.

When the forcing frequency is swept through a range of frequencies in the neighborhood of the resonance frequency, the system is said to pass through the resonance. The response exhibits a resonance-like peak, sometimes followed by a beating-like response. The maximum response amplitude does not necessarily occur at the steady-state peak frequency and an additional apparent bandwidth is created.

If the sweep is upwards in frequency, the peak frequency is higher than that obtained for steady-state conditions, the peak amplitude is lower, and the bandwidth is larger. If the sweep is downwards in frequency, the peak frequency is lower, and the peak amplitude is also lower than the dwell values. The effect of sweep rate is dependent on both the system damping and the dynamic range of the instrumentation.

Viscous vs Hysteretic Damping

The peak values of the dynamic flexibility acceptance, mobility and accelerance (displacement, velocity, and acceleration per unit force amplitude) diagrams occur

at slightly different forcing frequencies (**Table 1**). While some authors call these displacement resonance frequency, velocity resonance frequency, and acceleration resonance frequency, respectively, with the tacit assumption of constant excitation level, it seems more appropriate to term them peak frequencies. For damping levels usually encountered in engineering applications, the difference between the above three resonance frequencies is negligible. The frequency corresponding to the peak is often taken as being equal to the undamped system natural frequency.

Resonance Location

For harmonic force excitation, the complex displacement amplitude can be written:

$$\overline{X} = X\,\mathrm{e}^{-i\varphi} = X_R + iX_I$$

where X is the modulus, φ the phase shift, X_R the coincident component, and X_I the quadrature component.

In plots of these quantities versus the driving frequency, resonance is located at peaks in X and X_I, and by points of maximum slope in φ and X_R. Also, at resonance, $\varphi = 90^\circ$ and $X_R = 0$.

In a Nyquist plot (X_I vs X_R), resonance occurs at the crossing of the circle with the imaginary axis (for hysteretic damping) or where the rate of change of the arc length with respect to frequency attains a local maximum.

These criteria are valid for receptances of SDOF systems with hysteretic damping. Provided that the natural frequencies are not close to each other, and that the damping is light, some of these resonance location criteria can be used to analyze single modes of multiple-degree-of-freedom (MDOF) systems during resonance testing (see **Modal analysis, experimental,** Parameter extraction methods).

If signals proportional to the force and displacement are applied to the X and Y plates of an oscilloscope, then an elliptical Lissajous figure is obtained. When the driving frequency is swept, the size and inclination of the ellipse change. At the phase resonance, when the phase shift is 90° the ellipse has vertical and horizontal minor and major axes.

Sharpness of Resonance

The sharpness or width of the magnitude frequency response diagram in the neighborhood of a resonance can be used as a measure of the amount of damping in the respective mode of vibration.

For a viscously damped SDOF system, at $\omega = \omega_r$, the dimensionless displacement amplitude (magnification factor) is $kX_{\mathrm{res}}/F_o = 1/(2\zeta)$, where F_o is the amplitude of the harmonic driving force (see **Viscous damping**).

The quality factor, Q (borrowed from electrical engineering), is defined as $Q = 1/(2\zeta)$. It is related to the width $\Delta\omega$ of the resonance diagram at the half-power points (where the power dissipated by damping is half of that dissipated at resonance) by the approximate relationship:

Table 1 Peak and trough frequencies and frequency response function magnitudes for linear single-degree-of-freedom systems

Frequency response function	Viscous damping $\zeta = \dfrac{c}{2\sqrt{km}}$		Hysteretic damping $\eta = \dfrac{h}{k}$	
	Peak frequency	Peak magnitude	Peak frequency	Peak magnitude
Dynamic flexibility	$\omega_n(1-2\zeta^2)^{1/2}$	$\dfrac{1}{k}\dfrac{1}{2\zeta(1-\zeta^2)^{1/2}}$	$\omega_n = \sqrt{k/m}$	$\dfrac{1}{\eta k} = \dfrac{1}{h}$
Mobility	$\omega_n = \sqrt{k/m}$	$\dfrac{1}{\sqrt{km}}\dfrac{1}{2\zeta} = \dfrac{1}{c}$	$\omega_n(1+\eta^2)^{1/4}$	$\dfrac{1}{\sqrt{km}}\dfrac{1}{\sqrt{2}(\sqrt{1+\eta^2}+1)}$
Accelerance	$\omega_n(1-2\zeta^2)^{-1/2}$	$\dfrac{1}{m}\dfrac{1}{2\zeta(1-\zeta^2)^{1/2}}$	$\omega_n(1+\eta^2)^{1/2}$	$\dfrac{1}{m}\left(\dfrac{1}{\eta^2}+1\right)^{1/2}$
	Trough frequency	Trough magnitude	Trough frequency	Trough magnitude
Dynamic stiffness	$\omega_n(1-2\zeta^2)^{1/2}$	$k2\zeta(1-\zeta^2)^{1/2}$	$\omega_n = \sqrt{k/m}$	$k\eta = h$
Impedance	$\omega_n = \sqrt{k/m}$	$2\zeta\sqrt{km} = c$	$\omega_n(1+\eta^2)^{1/4}$	$\sqrt{km}\sqrt{2}\left(\sqrt{1+\eta^2}-1\right)$
Apparent mass	$\omega_n(1-2\zeta^2)^{-1/2}$	$m2\zeta(1-\zeta^2)^{1/2}$	$\omega_n(1+\eta^2)^{1/2}$	$m\eta(1+\eta^2)^{-1/2}$

$$\frac{\Delta\omega}{\omega_r} = \frac{1}{Q} = 2\zeta$$

For hysteretic damping, the quality factor $Q = 1/\eta$, where η is the hysteretic damping factor (see **Hysteretic damping**).

Resonance in MDOF Systems

Resonances occur in MDOF systems having underdamped modes of vibration. Heavily damped systems do not exhibit resonances because the overdamped modes of vibration are not distinguishable.

Resonances can be defined by the imaginary parts of the poles of transfer functions. They appear as peaks in frequency response modulus plots of receptance, mobility, or accelerance, and as troughs in plots of dynamic stiffness, impedance, and apparent mass.

Resonance Testing

Resonance frequencies, levels of damping, and close approximations to the normal modes of vibration are measured by resonance testing. By exciting the system with harmonic forces (or by imposed harmonic displacements), and adjusting the driving frequency, successive modes are brought to resonance.

Frequency response data are collected and presented as a set of frequency response function (FRF) diagrams (see **Displays of vibration properties**). For lightly-damped systems with low modal density, resonance is indicated in the FRF plots by peaks of the magnitude of either modulus or the quadrature component of receptance as a function of frequency. Location at zero in-phase component or 90° phase shift gives erroneous values due to the (contribution of) off-resonant modes of vibration. Better location on the latter plots is obtained at the points of inflection.

In systems with proportional damping and low modal density, resonance is located at the frequencies of local maxima of the quadrature component of receptance FRFs. These are different from the frequencies of maximum modulus magnitude.

For systems having moderate damping and/or close modes, best resonance location is achieved on Nyquist plots, at the points where the rate of change of phase angle (and the arc length) with respect to frequency has local maxima. The resonance diameter of the approximating circles is neither coincident nor parallel to the imaginary axis. If marks are made on the plot at equal frequency increments, resonance is located at maximum spacing between successive points.

For systems with proportional damping, if the contribution of the off-resonant modes can be considered to be constant, then the resonance diameter of the circle fitted to the points around a given resonance is parallel to the imaginary axis of the Nyquist plot. It means that the peaks of the quadrature component of response versus frequency give an accurate resonance location.

Resonance search is a simpler test aiming to determine resonance frequencies alone. It is used in the pretest phase, for instance in vibration test programs, to establish the complexity of the behavior of the test object, the levels of excitation during the main test, and the degree of nonlinearity of the tested item. In modal testing, once resonances are located, one can decide whether or not to use lower sweep rates (in sine sweep) and/or larger dwell periods of time (in sine dwell) in the resonance vicinity.

Phase Resonance Method

The phase resonance testing method uses multipoint harmonic excitation, adjusted to excite a best approximation to an undamped mode of vibration at a time, at the respective phase resonance frequency.

The complication comes from the fact that at resonance, a single harmonic force cannot excite a pure undamped mode of vibration. If the structure is not too large, and if the driving frequency is equal to an undamped natural frequency, the steady-state response due to a single force is an operating deflection shape or forced mode of vibration, made of a summation of contributions from several normal modes.

Theoretically, for a system with a finite number of DOFs, it is possible to find a set of monophase (in-phase with one another) forces applied at all DOFs, capable of driving the system at resonance in a pure natural mode of vibration.

A pure mode is excited when the response and the excitation are in quadrature at each DOF or when the real part of the response vector is zero.

Indeed, at resonance, the stiffness and inertia forces oppose one another (the reactive energy being zero) and the excitation forces must balance only the damping forces. They should have the same spatial distribution as the damping forces and their work must compensate the energy dissipated by damping. The result is that the real part of the response is zero, hence the determinant, or one of the eigenvalues of the real part of the FRF matrix, vanishes. The total response is equal to the quadrature component, so that at resonance the response is in quadrature with the excitation.

If the system is excited harmonically by an array of monophased forces and the driving frequency is

adjusted, phase resonance is obtained when a monophase response is obtained with a phase shift of $\pm 90^\circ$ relative to the excitation.

However, in practice, in a test using a finite number of forces, it is impossible to achieve the pure phase resonance condition, because the damping forces are continuously distributed throughout the system. When the damping forces are in equilibrium with the applied forces at only the excitation points, a local pseudoresonance is obtained at a test natural frequency. If the number of forces is small in comparison with the total number of DOFs of a system, the quadrature condition cannot be fulfilled, and a residual phase lag occurs in the modal displacements.

In modal testing, resonances can be located using various mode indicator functions (MIFs). Because measured FRF matrices are rectangular, plots of singular values versus frequency are used to locate resonance frequencies at peaks, troughs, or zero crossings, depending on the particular type of MIF used.

Antiresonance in MDOF Systems

Antiresonances appear as deep troughs in FRF modulus plots of the type motion/force, and as peaks in FRF plots of the type force/motion.

For undamped systems, antiresonances are defined by zeros of receptance-like transfer functions. Writing the transfer function in the rational fraction form, antiresonances are defined by zeros of the numerator polynomial, while resonances are located at the zeros of the denominator polynomial.

In a driving point FRF, resonances and antiresonances alternate (Foster's reactance theorem). Between any two resonance peaks there is a deep antiresonance trough. This pattern can be used as a preliminary check of the validity for a measured driving point FRF.

In a transfer FRF, some or all antiresonances are replaced by minima (shallow troughs). While the phase of the FRF changes at both resonance and antiresonance, it does not change at minima that are not antiresonances.

The number and location of antiresonances change in FRFs plotted for different response measurement points and directions. They are found from the eigenvalues of a reduced system, obtained by deleting, from the stiffness and mass matrices, the response point column and the driving point row. Because antiresonances characterize the local behavior of a system, they can be used for detecting and localizing damage, although they are selectively sensitive to changes in system parameters.

Figure 5 is an overlay of three receptance curves calculated for three different directions at the same point of a structure. It illustrates the coincidence of resonance peaks and the different number and location of antiresonance troughs. The upper curve, where resonances and antiresonances alternate, is a drive-point receptance.

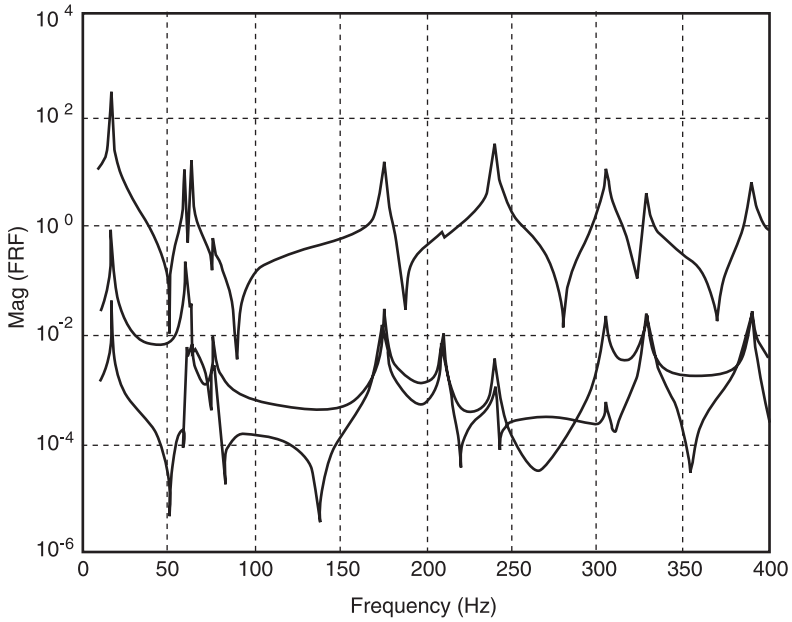


Figure 5 Receptance curves for the same location, in three different directions. FRF, frequency response functions.

Using the partial fraction expansion form of an FRF, it is seen that an antiresonance occurs between two consecutive resonances when the two resonant modes have the same sign for the modal constants. If the modal constants of the adjacent modes have opposite signs, there will be a minimum, not an antiresonance.

If a vibrating system is rigidly constrained in one DOF, the resonances of the constrained system occur at the antiresonances of the unconstrained system viewed at the location (or in the DOF) of constraint. When antiresonances of two subsystems coincide, a resonance of the combined system exists at that frequency and the respective mode has a node at the point of interconnection. As a result of a local, single-DOF, point modification, each resonance of the original system cannot be shifted farther than the adjacent antiresonance.

It is possible to create a vibration node at a given location by a so-called pole-zero cancellation, i.e., producing an antiresonance at a resonance frequency. The eigenvector of the pole (without the nodal coordinate) must be identical to the eigenvector of the zero. Also, the zero must show up in the point FRF and all the cross FRFs at the location of the node.

Isolation techniques based on the attachment of substructures at the nodal points are based on the same principle as the dynamic antiresonant vibration isolators, in which the motion of the excited body is accompanied by a reverse motion of some part of the isolating system. In the absence of damping, the internal transmitted force is zero at the antiresonance frequency, but it is small and finite when modest amounts of damping are present.

It should be remembered that absorbers, or dynamic neutralizers, are force-balancing devices attached to vibrating systems to bring the resonance peak down to its lowest possible value (see **Absorbers, vibration**). Usually, a resonance peak of the original system is transformed into an antiresonance of the modified system, by providing a reaction force that inhibits the vibration in the main system at that particular frequency. In a general treatment of dynamic neutralizers, the Frahm-type dynamic absorber can be replaced by a frequency-dependent equivalent mass (attached to the main system), which is infinitely large for the excitation at the absorber antiresonance frequency, plus a grounded damper.

Resonance in Parametric Vibrations

It was shown that, in linear systems, resonance occurs when the driving frequency and a natural frequency coincide. The term resonance is used in a wider sense in parametric vibrations, sometimes instead of the term parametric instability (see **Parametric excitation**).

When the driving frequency is an integer multiple of the natural frequency of the associated linear system, nonlinear SDOF systems described by Mathieu equations exhibit parametric instabilities, referred to as parametric resonances.

The principal parametric resonance occurs when the excitation frequency is twice the natural frequency. Parametric resonances of fractional order also exist. MDOF systems can experience parametric resonance if the driving frequency and two or more natural frequencies satisfy a linear relation with integer coefficients.

Parametric resonance is a state of vibration in which energy flows into the system from an external source at resonance, increasing the amplitude of the system's response. This energy is dependent upon both the natural frequency of the system and the frequency of the parameter variation.

During resonant vibrations and self-excited vibrations, the system vibrates at its own natural frequency. But while the former are forced vibrations, whose frequency is equal to a whole-number ratio multiple of the external driving frequency, the latter is independent of the frequency of any external stimulus.

Resonance in Nonlinear Vibrations

Various types of resonance can also occur in nonlinear systems. Of primary interest is the synchronous resonant response. It occurs when the dominant frequency component is that of the driving frequency which is close to the natural frequency of the associated linear system (see **Nonlinear system resonance phenomena**).

The amplitude–frequency diagram of an SDOF system with nonlinear stiffness, calculated using the method of harmonic balance (see Figure 16 in **Displays of vibration properties**), is bent to higher frequencies (for a hardening spring) or to lower ones (for a softening spring). Resonance is located at the crossing of the frequency response curve with the backbone or skeleton curve, corresponding to the free vibration (frequency of the free vibration as a function of its amplitude).

When the excitation amplitude is increased, the nonlinear resonant response can exhibit a so-called jump phenomenon. As a result, the amplitude and frequency of the peak response depend on the manner in which the resonance is approached. If the excitation frequency is swept through the resonance,

transient motions occur due to sudden jumps between two steady states of different amplitudes at almost the same frequency.

Subharmonic resonance occurs when the system vibrates with a frequency equal to an integral submultiple of the driving frequency. Such a condition is possible because the free motion contains higher harmonics. The driving force can do work on one of them and, apparently, the peak amplitude is excited at a frequency lower than the forcing frequency. Superharmonic resonance occurs when the driving frequency is a submultiple of the frequency of the fundamental resonance. If the multiple is not an integer, the state is an ultrasuperharmonic resonance.

MDOF systems can exhibit autoparametric or internal resonances when there is a linear relationship between some of their natural frequencies. A transfer of energy between different modes of vibration takes place in these cases.

Nomenclature

F_o	amplitude of the harmonic driving force
Q	quality factor
X	modulus
$\overline{X}$	displacement complex amplitude
φ	phase angle
ω	frequency
ζ	damping ratio

See also: **Absorbers, vibration**; **Displays of vibration properties**; **Hysteretic damping**; **Modal analysis, experimental**, Parameter extraction methods; **Nonlinear system resonance phenomena**; **Parametric excitation**; **Theory of vibration**, Fundamentals; **Viscous damping**.

Further Reading

Den Hartog JP (1985) *Mechanical Vibrations*. New York: Dover.

Foster RM (1924) A reactance theorem. *Bell Systems Technical Journal* 3: 259–267.

Friswell MI and Lees AW (1998) Resonance frequencies of damped structures. *Proceedings of the 23rd International Seminar on Modal Analysis*, pp. 243–249, Katholiche Universiteit Leuven, Belgium.

Inman DJ (1989) *Engineering Vibration*. Englewood Cliffs, NJ: Prentice Hall.

La Civita M and Sestieri A (1997) On antiresonance interpretation and energy concentration along continuous one-dimensional systems. *Proceedings of the 15th International Modal Analysis Conference*, pp. 778–784. Orlando: Society of Experimental Mechanics.

Mottershead JE and Lallement G (1999) Vibration nodes and the cancellation of poles and zeros by unit-rank modifications to structures. *Journal of Sound and Vibration* 222: 833–851.

Pietrzko SJ (1996) Resonance and antiresonance dynamic behaviour of large mechanical systems. *Proceedings of the 21st International Seminar on Modal Analysis*, pp. 1327–1335, Katholiche Universiteit Leuven, Belgium.

Salter JP (1969) *Steady-State Vibration*. Hampshire, UK: Mason.

RESONANCE, NONLINEAR SYSTEMS

See **NONLINEAR SYSTEM RESONANCE PHENOMENA**

ROBOT VIBRATIONS

W Book, Georgia Institute of Technology, Atlanta, GA, USA

Copyright © 2001 Academic Press

doi:10.1006/rwvb.2001.0070

The nature of robotic arms invites vibratory behavior while the function of robotic arms is heavily penalized by that vibration. Consequently, understanding and compensating for the tendencies of a robot to vibrate are of great importance. Robotic vehicles have less tendency to vibrate, although mounting an arm on a vehicle introduces new sources of excitation and compliance and new penalties for the simple solution to vibration, that is, adding mass to rigidize the arm structure.

A key step to understanding is modeling. Modeling the vibration of a robot arm presents difficulties not found in many other mechanical systems. The arm is often called on to operate in multiple degrees-of-freedom. The vibrations are superimposed on rigid-body motions that excite the vibrations and alter the dynamic parameters of vibration. The compliance and mass elements often comprise a variety of phenomena. Bending, torsion, and compression of structural and drive components may be combined with fluid compliance of actuators, feedback control gains, and nonlinear linkage kinematics. The excitation may arise from the rigid-body motion, contact with work pieces or the surroundings, fluctuating torque of the actuators, and motion of the base or of the payload. In spite of these complexities it is important to model arm vibration to understand how it can be improved. It is useful to consider discrete or lumped models for some arm components and distributed models for others. When the nonlinear dynamics of the arm motion become important, the distributed models typically rely on modal coordinates to represent the flexible kinematics. Frequency domain models are also helpful since they accurately represent the linear distributed behavior, but must be augmented with time domain analysis if they are to represent the nonlinear behavior. Serial link arms are generally easier to model than closed chain designs that have algebraic constraints to represent the closure of a loop in the mechanism.

There are many ways to improve the vibration response of a robotic arm. Since a robot is usually computer-controlled with many sensors and actuators already in place, active options exist that might not otherwise be considered. The first step is to understand the significance of the compliance and mass of various components. If the performance requirements are not so severe, conventional approaches to rigidize the structure and drives may suffice. If the limits of performance are pushed, active controls are a viable alternative.

When should Flexibility be Considered?

To position a robotic arm according to a computer-generated command, some form of feedback control of a joint will usually be employed. The joint actuator (typically electric or hydraulic) is under closed-loop control. The great majority of closed-loop controllers employ PID control. The design of the PID control gains is commonly based on the assumption that the system consists of a rigid inertia. This assumption is acceptable as long as the damped natural frequency of the closed-loop system ω_d (approximately its bandwidth), is less than about 10% of the natural frequency of the mechanical system with the joints clamped, ω_c. It is possible to push ω_d up to about 30% of ω_c, but with higher gains it is no longer possible to achieve adequate damping on the dominant mode of motion. A root locus diagram indicates the nature of this limitation as the position and velocity gains of the PID control are increased, as shown in **Figure 1**. The natural frequency, ω_c, is therefore a viable predictor of the importance of vibrational modes in the arm motion. In addition to natural frequency, compliance itself may be an important specification of the arm behavior. This is especially important if the placement accuracy is important with varying loads but without sensing or reprogramming of the motion that accounts for the different loads. If robot position is predicted by modeled rigid kinematic behavior as in offline programming, the rigidity may also be crucial.

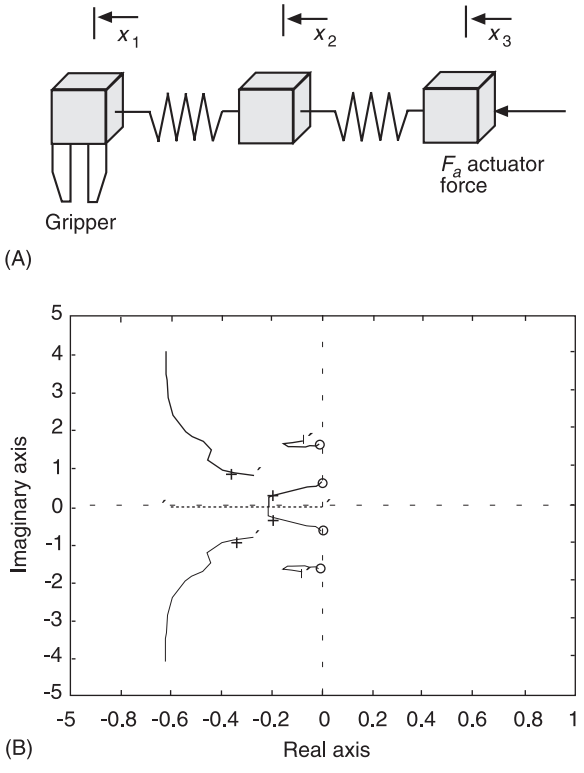


Figure 1 (A) Schematic of simple model of arm with flexibility. (B) Root locus for increasing feedback gain of position x_3. Circles are limiting root positions for infinite gains at the system natural frequencies for x_3 fixed.

When is Vibration an Important Constraint?

Vibration is one of several constraints considered when sizing structural and drive components. Other constraints include buckling stability (in various modes) and strength. If strength considerations demand a structure size that exceeds the vibrational demands, vibration is not the active constraint on design and need not be considered. A detailed analysis of this issue requires a careful model of the relevant portions of the arm system. Analysis based on general models has indicated that flexibility is most important for systems with long reach and, high accuracy, and bandwidth requirements.

To Flex or Not to Flex

When deciding how rigid to make an arm, it is important to realize the tradeoffs that are being made. Improvements often come at some consequential cost: if the alternative being considered is to move to a more rigid material, the penalty is probably the cost; if the option is to add more material to rigidize the moving structure, the penalty to be paid is added inertia, which translates to either additional motor capacity or lower speed for large movements. Large movements will slow down because, if the motor is not increased in torque, then mechanical advantage of the drive must increase and the motor will reach its limiting velocity sooner. Ultimately, in a well-designed arm, one balances small motion speed (bandwidth) that is better for a heavy rigid system, with large motion speed that is better for a light flexible system.

How to Make an Arm Less Flexible

Wise investment of structural mass and wise location of nonstructural mass is the first priority in designing a robot arm without vibration problems. It is often the case that robot joints are the source of the most compliance and are the most difficult area to rigidize. Joint compliance comes from bearings, bearing housings, shafts, and gearboxes. Closely related is the compliance of drive shafts, belts, chains, cables, fluid lines, and other power transmission devices. The length of these transmission members is determined by placement of the other actuating components, such as electric motors, reducers, and hydraulic valves. Adding structural mass to connecting beams does nothing to reduce joint and drive compliance and in fact lowers the natural frequency by increasing mass carried by proximal or inboard joints. If we observe a design where one component is effectively rigid through the investment of a substantial amount of mass, that mass would be better invested in rigidizing some other component if possible.

Vibration as a Result of Commanded Motion

Standard pick-and-place robot applications experience robot vibration most acutely when short cycle times lead to rapid deceleration and thus high jerk. The vibration may cause overshoot and thus a collision with surrounding objects or, in the desired stationary state, not following the commanded motion. The typical response is to program a delay between the completion of rapid motion and initiation of a precise motion. This increases cycle time and consequently productivity is limited.

With increasingly sophisticated control computers, improved motion profiles can be effectively generated. The simple and popular trapezoidal velocity profile which has limited acceleration but theoretically infinite jerk shown in **Figure 2A** can be replaced with a limited jerk profile, as shown in **Figure 2B**, jerk being the third derivative of position with respect to time. These profiles are compared in **Figures 2A** and **2B** where the distance traveled is the same for motions with a factor of 10 difference in the permissible jerk. The travel time is also affected. This has a profound effect on excitation of vibration, but more improvement may be needed. The use of shaping filters can again reduce vibration and can be customized to the resonances of the arm. There is a further benefit that the user can generate the initial motion profile with minimal concern for vibration, simply leaving the job to the shaping filter to clean up the motion. Shaping filters based on time delay or finite impulse response filters (impulse response and vibratory response illustrated in **Figure 3**) have the added advantage over conventional notch or low-pass filters because their response is complete after a finite and relatively short time and yet they are simple to implement on a digital controller. Motion control companies have patented some aspects of these filters.

Modeling Robot Vibration

Some aspects of modeling robot vibration are not specific to modeling any other mechanical system. We will focus here on the aspects that are somewhat unusual. Some of these aspects are:

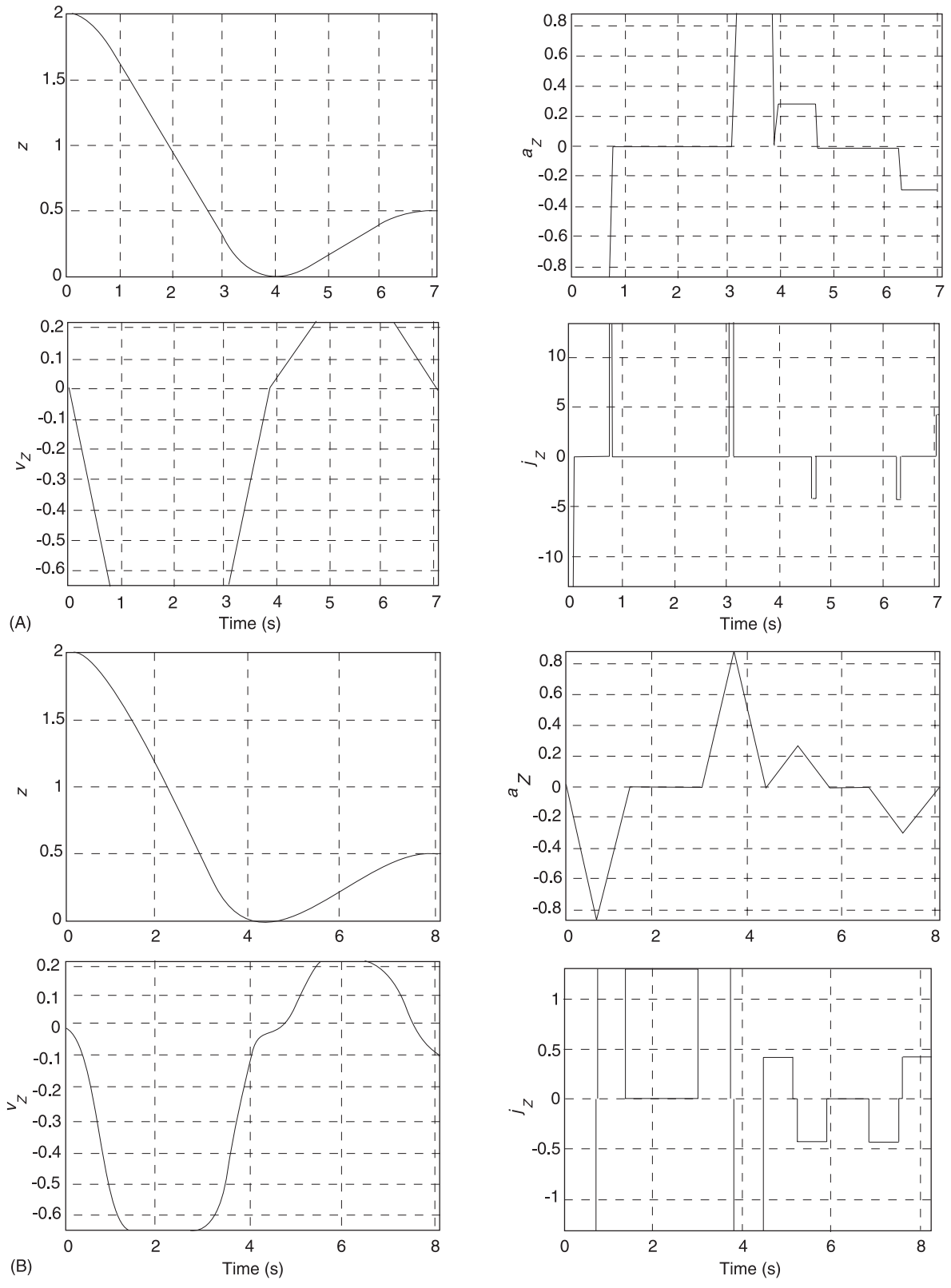


Figure 2 (A) Position (z), velocity (v_z), acceleration (a_z), and jerk (j_z) for a trajectory with limits on velocity and acceleration and very high limits on jerk. (B) As for (A) but the limits on jerk are reduced by a factor of 10. Courtesy of Ai Ping Hu, CAMotion, Inc., Atlanta, GA.

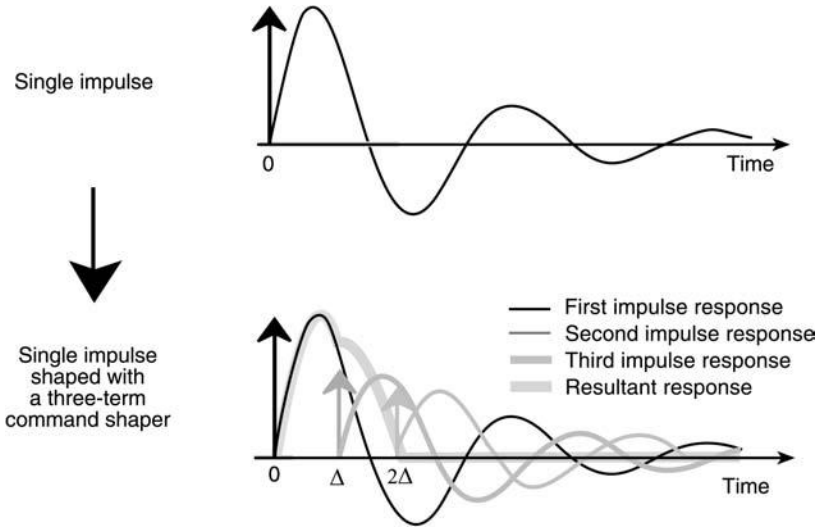


Figure 3 A time-delay command-shaper transforms a single impulse to three impulses. Optimal arbitrary time-delay filter shown. Courtesy of Sungsoo Rhim, CAMotion, Inc., Atlanta, GA.

- actuated joints
- variety of functional components (belts, shafts, bearings, motors, valves)
- variety of phenomena contributing to behavior (elastic, electromagnetic, hydraulic)
- kinematic linkages and resulting compliance and nonlinearities
- serial and/or in-parallel configuration
- the multidimensional 'rigid-body' motion

Actuated Joints

The joints are a major source of excitation when commanded to move. This leads to forced vibration. In free vibration due to initial conditions, joints pose a dilemma to the arm modeler. Is the joint free to translate or rotate when the actuators are unpowered? This is seldom the case, except possibly for direct drive arms. Direct drive joints, or joints with low friction reductions, may be back-driven to some extent, so forces imposed on the arm generate motion in the joint. The other extreme, a joint which cannot be back-driven, due to a large gear ratio and friction, is equally easy to examine since the joint is then simply a rigid connection between two links or possibly a connection with some gear compliance. The case in between the extremes is very difficult to examine. The joint motion impeded by dry or Coulomb friction behaves as a fixed connection for low-amplitude vibrations. For high-amplitude vibrations, one can treat the joint as damped by a linear viscous damping with fair accuracy. Nonlinear analysis must be applied in the vast middle ground if more precise analysis is needed. Unpowered joints are of interest primarily as a step in modeling the arm with powered joints. By modeling the free vibrations and determining the low-frequency modes, one can develop very efficient generalized coordinates for modeling a high-degree-of-freedom arm as a lower-degree-of-freedom system. This is discussed further below.

For the robot designer, the situation of greater interest is free vibration with joints powered and controlled to hold a fixed joint position. Joint friction is still an issue, much the same as for unpowered joints, discussed above. In addition, it is necessary to treat the feedback gains as if they were creating torques or forces like a physical spring (position gains) or dampers (velocity gains). The ideal equations are identical although actuator dynamics may alter the result in practice. Hydraulic actuators fed by electrohydraulic servo valves, for example, block flow from the back-driven actuator, leaving compressibility of the trapped fluid as the only compliance permitting the joint to move.

Variety of Phenomena and Components

The discussion above has already involved the reader in the variety of component types involved in robotic arm modeling. It is often possible to produce mechanical analogies of these components and phenomena. The spring analogy of position feedback control or fluid compressibility is an example.

Kinematic Linkages and Parallel/Serial Configuration

In an effort to achieve the greatest range of motion and minimize the moving mass, a combination of serial joints actuated by drive linkages is common in robot arms. **Figure 4** illustrates a popular parallel linkage design that places two actuators at the base of a planar mechanism but allows a range of motion comparable to serial actuation. In other cases the actuator near the base is connected by cables, shafts, chains, or toothed belts. These also create parallel structural paths. Vibration analysts commonly deal with parallel structural paths such as trusses, since this is a very efficient design. Such models seldom articulate over large angles, however, during the operation being analyzed. The belt compliance is lower if the load is positioned near the driving pulley than if the load is far from the driving pulley.

Parallel linkages complicate the modeling of distributed components (e.g., beams) by adding algebraic constraints to the partial differential equations. There are exact treatments for this complexity, such as adjoining the algebraic constraints to the differential equations via Lagrange multipliers. There are approximate treatments also that may incorporate these constraints in acceptable ways, as shown in **Figure 4.** For example, a parallelogram with two sides deflecting (indicated by dashed lines) experiences negligible shortening of those sides. Consequently, the motion transmitted to an outboard link driven by the parallelogram is pure translation. Point A in **Figure 4** translates to A′. This constraint simplifies the dynamic equations rather than complicates them.

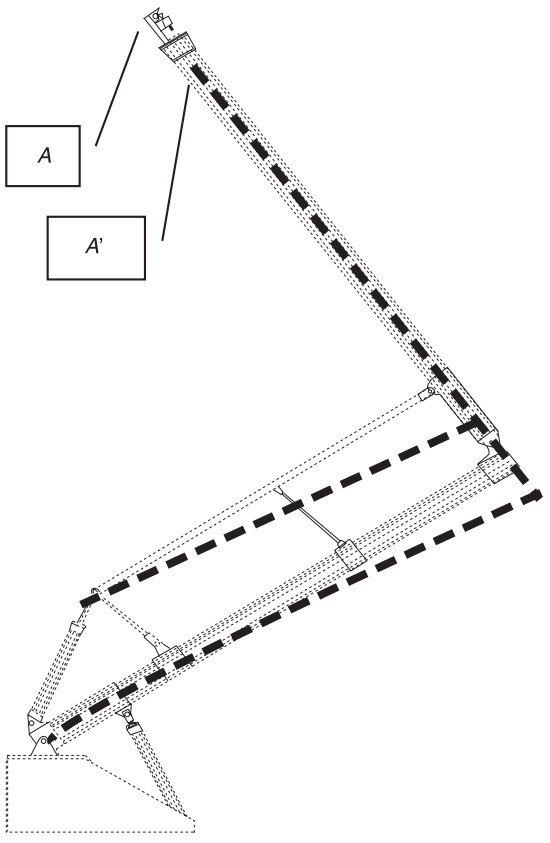


Figure 4 A flexible-link robot with parallel actuating linkage to drive outboard link. Deflection of link 1 produces no rotation on the outboard link.

Rigid-Body Motion in Multiple-Degrees-of-Freedom

Since the robot may have six or more joints to provide three positional and three rotational degrees-of-freedom, modeling the vibration as part of the full dynamic behavior is complex. Powerful numerical techniques based on finite element analysis are not usually oriented to this large motion analysis. The vibrational behavior of interest may be separately analyzed if it is sufficiently higher in frequency than the control behavior. A formal analysis based on this separation is the two time scale or singular perturbation approach. If performance of the arm is pushed higher, this separation is no longer sufficient, and the analyst must incorporate the vibrational degrees-of-freedom in the arm dynamic model. Each vibrational mode adds two system states, so the six-degree-of-freedom arm with 12 rigid states and nonlinear dynamics can easily become unmanageable for computer simulation or controller synthesis if too many modes of vibration are added.

To undertake the modeling of such a complex system is a daunting task, but it can be facilitated with symbolic manipulation software. Many analysts are familiar with Lagrange's equations and use of that method will be outlined here. A formulation known as Kane's method is also known to be suitable and may be more efficient. The technique described is suitable for chains of flexible bodies that are reasonably rigid. Because of effects known as foreshortening and centrifugal stiffening, these techniques are questionable for very large deflections and for very high rotational speeds. Lagrange's equation is given below and followed by a description of the major steps that must be followed when using that approach:

$$\frac{\mathrm{d}}{\mathrm{d}t}\left[\frac{\partial L}{\partial \dot{q}_i}\right] - \frac{\partial L}{\partial q_i} = Q_i \qquad [1]$$

where:

- $L = T - V$

- T = kinetic energy of the system
- V = potential energy of the system
- q_i = a generalized variable
- Q_i = the generalized force doing work through change in q_i

The steps in using Lagrange's equations are

1. Choose rigid-body coordinates and corresponding link boundary conditions. Two options are illustrated in **Figure 5**. The best choice depends on your purpose. For tightly controlled joints, the tangent angle rigid-body coordinate and the clamped beam boundary condition is efficient (**Figure 5A**). To determine most easily the tip position based on rigid-body coordinates alone, rigid-body angles between lines that pass through the ends of beams that are assumed to be pinned may be preferred (**Figure 5B**). **Figure 5** also shows the reference measurement consistent with a parallel linkage, as shown in **Figure 4**.

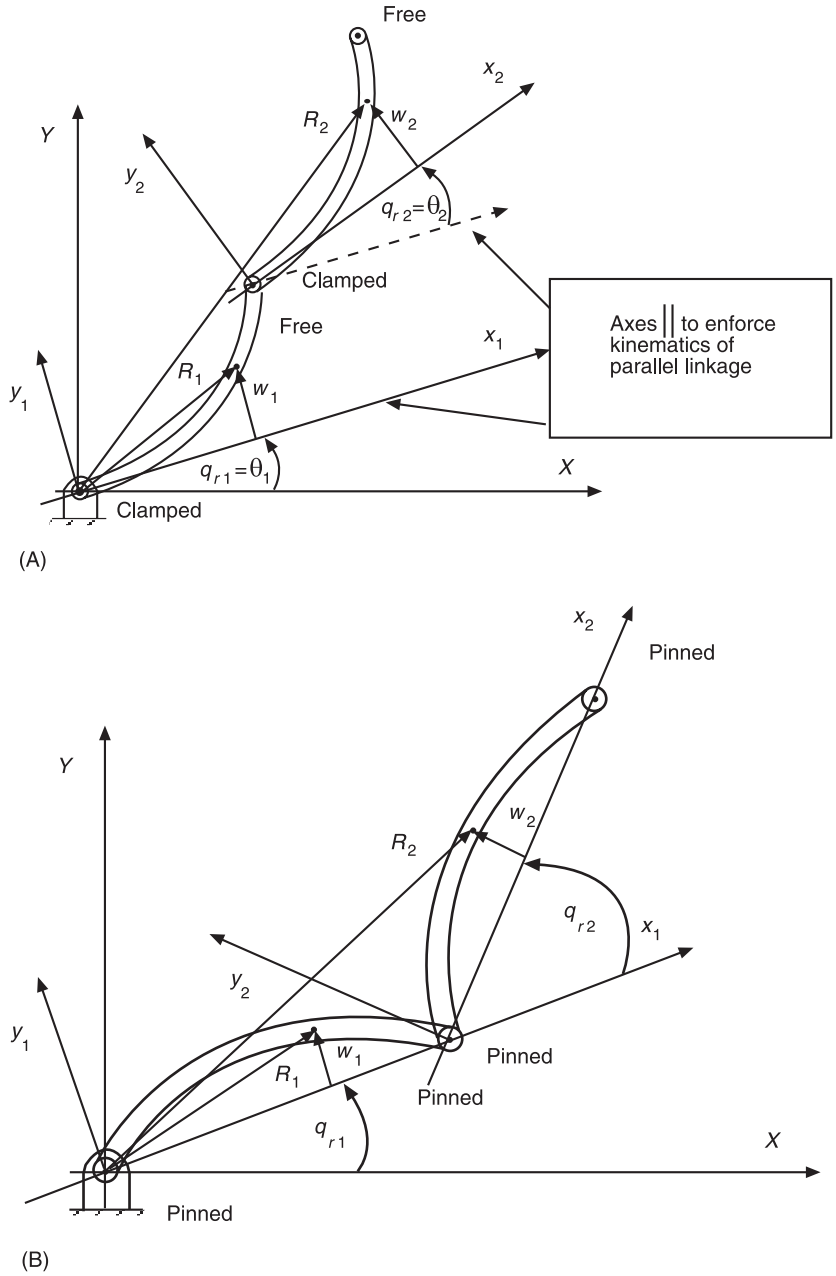


Figure 5 (A) Use of beam tangents to define 'rigid' coordinates and corresponding clamped-free boundary conditions. (B) Use of end-to-end connecting line to define 'rigid' coordinates and corresponding pinned–pinned boundary conditions.

2. Obtain basis functions (often mode shapes for assumed boundary conditions) for any components (e.g., beam-like links) that have distributed mass and compliance. As illustrated in **Figure 5**, the boundary conditions need to be consistent with the rigid-body coordinates. Finite element codes may be used for this purpose if the complex shape of the body must be incorporated.
3. Select a suitable number of basis functions for the accuracy needed
4. Combine rigid-body coordinates and basis functions into a description of the arm shape and change of shape with respect to time (velocity).
5. Formulate the kinetic energy of each component, which may involve an integral over a flexible body and hence an integral of the basis function describing shape. This ultimately leads to modal mass coefficients which reflect the choice of shape functions.
6. Formulate the potential energy consisting of gravitational, strain (of flexible bodies) and other terms (unusual). This may involve an integral over a flexible-body basis function leading to a modal stiffness coefficient.
7. Form the Lagrangian function and take appropriate derivatives.
8. Collect coefficients and simplify where possible. Identify terms that will be constant that can be replaced later with numerical values.
9. Compose the nonconservative terms consisting of joint friction, actuator forces, and torques and working forces due to contact with external objects. This term varies depending on the rigid and flexible coordinates used. It is the source of inaccuracies if complex actuator dynamics are poorly approximated.
10. Simplify if possible at each step and again at the end. Care in selecting basis functions can lead to orthogonal shapes and consequently to a large number of zero values in off-diagonal terms in the coefficients of acceleration.
11. Verify accuracy where possible with limiting cases of all types and by checking essential symmetry of mass and spring matrices. Supplement $D(q)$ with experimentally determined damping terms.

Systemization of the process listed above is crucial to accuracy. Symbolic manipulation programs are indispensable but their results should not be accepted without question either. The equations have a great deal of structure that can assist the analyst as has been noted by researchers. The final equations will have the form given in eqn [2]. The extension and use of Jacobians, popular in robotic circles, for describing the velocity is one way to do this:

$$\mathbf{M}(\mathbf{q})\ddot{\mathbf{q}} + \mathbf{D}(\mathbf{q})\dot{\mathbf{q}} + \mathbf{K}(\mathbf{q})\mathbf{q} + G(q) + H(q,\dot{q}) = \mathbf{B}(\mathbf{q})\mathbf{Q} \quad [2]$$

where:

- $\mathbf{q}$, $\dot{\mathbf{q}}$, $\ddot{\mathbf{q}}$ and $\mathbf{Q}$ are column vectors of the scalar with same symbol plus subscript
- $\mathbf{M}(\mathbf{q})$ = the inertia matrix
- $\mathbf{D}(\mathbf{q})$ = the linear damping matrix
- $\mathbf{K}(\mathbf{q})$ = the linear stiffness matrix
- $G(q)$ = the effect of gravity
- $H(q, \dot{q})$ = the nonlinear terms due to centrifugal and Coriolis forces
- $\mathbf{B}(\mathbf{q})$ = distribution matrix of generalized forces

The analyst may also consider commercial software products that are becoming increasingly powerful and accurate in approximating flexible behavior into multibody dynamic equations. Caution should be exercised in understanding that the approximations used by these products may not be suitable for an individual application.

Improving Behavior of Vibrating Robotic Arms

There exists a multitude of engineering approaches that can be used to attack a vibration problem. In many cases, a tradeoff exists and reduced vibration must be balanced against speed of operation, mass, complexity, and/or cost. This section discusses some of the strategies that have been studied and shown to be effective in practice, experiment or both.

Improved Allocation and Location of Mass

This may include adding structural material. As discussed early in this article, structural material also has mass that can harm more than help a given vibration problem. The shape of structural members is a key aspect of mass allocation. If it is possible to expand a link cross-section and place material in a beam or truss far from the bending axis of the component, the most favorable results can be obtained. Achieving the needed range of joint motion and obstacle avoidance becomes more difficult when the structure is expanded. If workspace needs are modest, a parallel-actuated design such as a 'Stewart platform' can be extremely stiff and light. Placing actuators and other massive components that do not contribute to stiffness near the base is part of this strategy, but requires compliant transmission shafts, cables, etc.

Select Improved Structural Materials

If the structure is a large part of the mass moved, as is typical, it is important to select materials with high stiffness-to-weight ratios. Many engineering materials that are lighter are also less stiff. Aluminum is one-third the weight of steel but also has one-third the elastic modulus of steel. Some composites are extremely stiff but are expensive to fabricate and join to drive structures. Do not overlook the improved damping that some materials have, particularly if there is concern for higher-frequency modes of vibration. Application of viscoelastic passive damping treatments is very effective if engineered appropriately. They should be installed with a stiff constraining layer and in appropriate segments. These treatments are similar to sound-deadening materials and may add substantial weight to a structure.

Change the Commanded Motion

The simplest version of this strategy is to slow down the motion or to wait after a move for vibration to decay. This is an unnecessary compromise of performance in most robots. Choose a velocity profile without sharp corners and filter the motion commands with shaping filters. This approach is often implemented with only minor compromise in complexity since the robot already has a computer-generated trajectory. Stability is not compromised if the command-shaping filter is outside the feedback loop. Adaptive command-shaping can be used in many cases if suitable parameters cannot be manually established.

Feedback Control and Active Vibration Damping

Even for simple feedback controllers, decisions substantially affect the vibration behavior. Very high position and velocity gains appear from a rigid analysis to give outstanding performance. However, the resulting stiff joints cannot remove vibrational energy (if the joint is back-drivable) and are more prone to excite vibrational modes (even if back-driving is not possible). This is probably the most frequent mistake relating to arm vibrational behavior. Many forms of control have been studied and shown to reduce the vibrational tendency of flexible robot arms. The need for sensors, the sensitivity to expected parameter changes and the complexity of design and implementation are all concerns to be considered before investing in one of these algorithms. With the reduced cost of sensors (e.g., accelerometers) and control computers and with the simplification possible by connecting sensors and controllers via serial networks rather than massive wire harnesses, active control of vibration is the frontier of performance enhancement.

Altered Operational Strategies

The use of a robot can be modified to reduce the tendency to vibrate greatly. Since this requires collaboration between the designer and the user, it is difficult for anyone to make this happen except in extreme cases. If large motions requiring vibration-susceptible long arms can be effectively decoupled from the small motions requiring precision that is most jeopardized by the resulting vibration, both subsystems can be optimized for their essential tasks. Studies of a bracing action show this decoupling is possible using strategies similar to a human worker. Small motions of a human are carried out, after bracing the arm on a passive support for rigidity, by the fingers and wrist, which do not have the range of motion of the arm or legs but do have more precision. To mimick this requires robots with more degrees-of-freedom and potentially of greater cost. If compared with a design to the same specifications but without the motion specialization, the cost may still be lower. Additional degrees-of-freedom for small motion can also be used as inertial dampers similar to passive dynamic vibration absorbers found in more conventional forced-vibration solutions. Tuning the motion to the vibrational frequency is accomplished by sensing the vibration and commanding small motions that absorb the vibrational energy of multiple modes in multiple directions.

See also: **Active control of vehicle vibration**; **Beams**; **Vibration generated sound**, Fundamentals.

Further Reading

Canudas deWit C, Siciliano B, Bastin G (eds) (1996) *Theory of Robot Control*. Berlin: Springer.

Fraser AR, Daniel DW (1991) *Perturbation Techniques for Flexible Manipulators*. Boston: Kluwer Academic Publishers.

Kokotovic P, Khalil HK, O'Reilly J (1986) *Singular Perturbation Methods in Control: Analysis and Design*. London: Academic Press.

Meirovitch L (1990) *Dynamics and Control of Structures*. New York: John Wiley.

Preumont A (1999) *Vibration Control of Active Structures, An Introduction*. Dordrecht: Kluwer Academic Publishers.

Rivin E (1988) *Mechanical Design of Robots*. New York: McGraw-Hill.

Sciavicco L, Siciliano B (2000) *Modeling and Control of Robot Manipulators*. New York: Springer-Verlag.

ROTATING MACHINERY

See **BALANCING; BLADES AND BLADED DISKS; ROTATING MACHINERY, ESSENTIAL FEATURES; ROTATING MACHINERY, MODAL CHARACTERISTICS; ROTATING MACHINERY, MONITORING; ROTOR DYNAMICS; ROTOR STATOR INTERACTIONS**

ROTATING MACHINERY, ESSENTIAL FEATURES

R Bigret, Drancy, France

Copyright © 2001 Academic Press

doi:10.1006/rwvb.2001.0090

Historical Background

Rotating machinery is essentially composed of a rotating part, the rotor, and a nonrotating part, the stator. Natural round forms were the inspiration for the wheel, then there followed a variety of rotating machinery. The following text reviews several developmental steps.

Two or three million years ago, the primate Australopithecus made the first tool from a sharpened stone. Left behind by glaciers, stones came hurtling down the mountainside, astounding people by their rounded form.

Some 7000 years ago the wheel and subsequently the wheelbarrow were invented. The wheel helped the Maltese people transport blocks of stone during the construction of their megaliths. The Egyptians knew about the wheel but didn't make significant use of it in building the pyramids.

The water wheel was first seen in Illyria a short time BC. In the first century AD the Chinese people were using bellows on the fires in their forges. These bellows were powered by water mills equipped with crank-connecting rod systems. The crank was introduced to the west in the 16th century, and nowadays it is used in car engines. Windmills were first turning on the plateaux of Iran in the seventh century.

In 1629 Giovanni Branca, an Italian, used a spray of steam to make a cog wheel turn, which in turn raised a power hammer, which would crush grain when released.

The Frenchman Blaise Pascal invented the Pascaline in 1642. This was a calculator using cog wheels.

Newcomen and Savary, who were English, invented an atmospheric girder-type machine to drain mines, and the water drawn up was used to irrigate the fields. Steam would set in motion a piston which moved a lever to operate a piston and pump water. In 1712, Newcomen and Savery connected the lever to a steam tap: this was the first automatic closed loop which was the forerunner of industrial cybernetics.

The Englishman James Watt's steam machine was introduced in 1767. The machine was perfected with a double-acting piston, drawer distributor, and inertia wheel which reduced the fluctuations of rotation driven by the crank-connecting rod system.

Cugnot, a French engineer, made a self-propelling machine in 1776, comprising a steam generator, piston, crank, and three wheels. In 1923 Abner Doble presented the American Beauty in San Francisco. This traveled up to $150\,\mathrm{km\,h^{-1}}$ carrying five passengers.

The first steam boat was a paddle boat, driven by the Marquis de Jouffroy d'Albans, in 1776. It was 46 m long and went upstream on the Saône. The American company Fulton built the first propellor submarine in 1798 in France.

In England Richard Trevithick built the first locomotive in a coal mine (1804) and then another one in London in 1808, to entertain a dazzled public, with the slogan 'catch me who can'. The fight was on between the road and the railway. In 1837 the first train arrived in Paris.

Between 1784 and 1884, 195 patents for steam turbines were registered with the British Patent Office, among them one from James Watt. In 1843 the Swede Scheutz built a steam turbine to operate the 'mills' of the calculator of the Englishman Babbage. Tournaire, who was French, proposed a turbine in 1853 which in turn inspired other developments. The flow of steam was studied in 1883 by the Swede Carl Gustav De Laval, who experimented with centrifugal machines at 30 000 rpm, above the first critical speed, which some people said could not

be surpassed without causing a catastrophe. For public electricity in England, the Distric Electric Lighting Company used a turbo-alternator of 75 kW built by Parsons in 1890, followed by a prototype turbine operating at 4 kW and 18 000 rpm.

De Laval and Parsons were preoccupied with significant vibration. For rotor rotation, it was necessary to introduce oil to the bearings, this occurred in 1788. Between 1883 and 1891, Beauchamp Tower was interested in this process with relation to railway bearings, and Reynolds (1884–86) studied this in England. From 1867, Newton had been using oil to reduce friction.

Newkirk in England (1924) had concerns about the compressor vibration; he studied the situation in a laboratory and dealt with strange and violent phenomena due to the oil: this was diagnosed as oil whip in 1925. It took until the 1950s to understand and name this instability, following the work of the Russian Ljapounov in 1892.

In 1901 Edmond Rateau (1863–1930), a French engineer, built turbines with 30 disks. Ljunström adopted a flow of steam perpendicular to the axis of rotation and in 1910 built a 1000 kW turbine. Rateau invented the classification of high-speed supercharging to improve fighter performance during the First World War (1914–18). This is how gas was introduced to the turbine.

The turbomachinery built in Rateau's factory in La Courneuve, near Paris, was tested there. Rateau used dimensionless classifications of rotational speed, flow, pressure, and temperature. This classification made it possible to determine machine performance away from the testing area.

These classifications result from dimensional analysis initially explained in 1822 by the mathematician and physician Joseph Fourier (1768–1830), who was well known for his series concerning on periodic signals. The Scottish physician James Clerk Maxwell (1831–79) was also interested in dimensional analysis in 1870. A theory was proposed in 1914 by Vashy and Buckingham, of England; the Englishman Reynolds (1842–1912) constructed in 1883 a classification to create order in fluid flow. Mach, an Austrian (1838–1916) introduced in 1889 the ratio between the speed of a projectile and the speed of sound, and this generated interest in fluid compressibility. The German Sommerfeld (1868–1951) set out a classification which was useful to define stiffness and damping coefficients in bearings. Strouhal associated the vortex frequencies of the American Karman (1881–1963) to the velocity of a fluid in movement and to the dimension of the body inducing it.

Dimensionless classification opened the way to universalism founded on assumptions permitting the inclusion of the unclassifiable. In Neufchatel in Switzerland a group of gas turbines, compressors, and 4 MW electrical alternators for the chemical industry had a great success in 1940, one year after the declaration of war.

At the end of the 19th century, the power of the first turbo-alternator equipped with a watt regulator was 20 kW, and its productivity was about 2%. The steam turbine became the archetype for rotating machinery.

France set a new world record in 1996 for a turbo-alternator of 1500 MW at 1500 rpm. This rotating machine can supply 15 million homes, each using 100 W.

Space shuttles use pumps supplied by gas turbines which have two small wheels, at 55 MW.

A steam turbine connected to a gas turbine can drive an alternator creating power close to 500 MW. Productivity of one single gas turbine can reach 35% at 4000–6000 rpm. The output of a car engine is about 25% maximum.

Alternators supply a large variety of systems: electrical engines, including telesurgery motors using rotating machines – these are electrical engines of 300 μm diameter rotating at 30 000 rpm.

Inside a watch, alternator rotors work at 15 000 rpm, sustained by magnetic bearings supplied by capacitors. Electrical machines were developed quickly: Oersted, who was Danish, discovered magnetic forces in 1820: Faraday, who was English, formulated the law in 1831; the Scot Maxwell set out the theory in 1864–65 and in the USA the former blacksmith Thomas Davenport built the first electrical engines to drill and turn wood around 1840. Reciprocity brought about generators and alternators once a magneto had been realized by the Frenchman Piwii in 1832. In Paris the Place de la Concorde was first illuminated in 1844, the first embryo London Underground was installed in 1863, whilst the first Paris Métro was constructed in 1900.

And what about the forces of air and wind?

As regards aviation, in 1809 Sir George Cayley connected a propellor to a gas or internal combusion engine. Was the first flight in 1890 in France by Clement Ader, or in 1903 in America the Wright brothers' attempt, which lasted 3.5 s?

Then in the 1950s the turbo-reactor made the piston engine and the crank-connecting rod system redundant: if it weren't for turbos, there would not be space travel.

The idea of the helicopter started with Leonardo da Vinci in 1483; it was developed more fully by the Frenchman Louis Bréguet in 1907, using the internal combustion engine. It was marginalized for some time, and then was developed from 1942 in the

USA. The helicopter was used by the French during the war in Algeria (1954–62) and the Americans in Korea and Vietnam (1951, 1953). The helicopter was a clever evolution in a rotation festival.

The Englishman Hales (1677–1761) is responsible for the fan. Hales was interested in gas, and in the movement of these fluids. In 1736 a fan was renewing the air in London's Chamber of Commerce, as it was in 1845 in a Brussels jail, in 1850 in the Théâtre des Variétés in Paris, and in 1857 on a convict boat traveling from Toulon to Cayenne. In mines fans were also being used. In 1890 Rateau created a new high-output fan against firedamp, using ventilation to remove the nauseating smell, heat, and cool discreetly. In 1946, the electronic numerical integrator and calculator (ENIAC), the first computer, required about 120 kW for ventilation.

So what about water?

Some 3400 years ago, water was causing a problem in iron mines in Armenia, but it was useful in Andalusia because it could be raised by the noria. The Romans used wheels with pots, which were the first pumps. In the 16th century in German mines, Agricola used suction pumps and force pumps with a crank-connecting rod system and wheels with pots, carried by men similar to squirrels in a cage. Whole towns were supplied by pumps: Nuremberg, Toledo, Gloucester, Bremen, Ausburg, London, Paris. Today the wide range of turbo-pumps and motor pumps supply the many needs of industry and life.

Hydraulic turbines naturally arrived before pumps: these turbines used the flow of falling water to rotate and Renaissance scientists, connecting a turbine and a pump, tried to create perpetual motion. Alternator power created by hydraulic tubine reached 700 MW, and even greater.

Sea tides provide so-called blue coal to tidal power stations, like that on the river Rance in France, where 24 machines have created 240 MW power since 1966. The world's water is shared by structures and dams where turbo-alternators and motor pumps are installed.

Rotating Machines: Diverse Realizations

In the beginning there was the hydraulic machine and the steam machine. The need to manipulate and transform energy led to a multitude of machines varying with electricity, technology, and computer science. Essential categories can be distinguished.

Thermal machines use two sources of heat, one hot and one cold, a petrol or fuel engine, steam or gas turbine. Thermal machines supply cars, power generators, pumps, fans, and compressors. Thus the turbine creates a category of turbo-machines: turbo supercharging engines, turbo-compressors, and turbo-fans. A turbo-reactor aids propulsion by varying the degree of fluid movement. A turbo-fan is a turbo-reactor with two flows; turbo-propulsive force drives a propellor, while turbo-bellows empower huge forges. A turbo-statoreactor combines a turbo-reactor and statoreactor using compressed air at the speed of the plane. A turbo-motor comprising a gas turbine can supply coupling for a helicopter, train, or vehicle. A turbo-generator can supply an electrical machine, while turbo-drilling drives a trepan. Turbo-pumps and turbo-alternators provide electric energy in fuel oil and coal stations and nuclear power stations. Turbo-pumps operate in satellite launchers and space shuttles. Inverse thermal machines function between a cold and a hot source: between heat pumps and refrigeration systems.

- Hydraulic machines use the flow of water or air: for example, hydraulic turbines, alternators, and pumps.
- Electric machines use electricity: examples include motor-pumps, motor-compressors, ventilation motors, motor-blowers, motor bellows, converters, motors supplying vehicle engines and various systems, such as computer disks.
- Multipliers and speed reducers with gears.

This list is not exhaustive. For example, in Paris the pump manufacturers' trade union gives its members' list as 12 full pages: pumps were used for water conveyance, baling out, and fire extinguishing. In Quebec a pump dictionary was published for use in the chemical industry and refineries running hundreds of pumps.

Vibration Availability

Some components of a rotating machine may become defective, leading to failure, and even catastrophe. A catastrophe would be measured by rotor kinetic energy ε. For a cylindrical rotor of mass m and radius R, rotating at speed Ω: $\varepsilon = \frac{1}{4} m R^2 \Omega^2$ for $m = 1000\,\text{kg}$, $R = 0.5\,\text{m}$, $\Omega = 618\,\text{rad}\,\text{s}^{-1}$ ($\rightarrow 6000\,\text{rpm}$), $\varepsilon = 2.465 \times 10^7\,\text{J}$. For a turbo-alternator rotor of 1500 MW at 1500 rpm $\varepsilon = 7.5 \times 10^9\,\text{J}$. The kinetic energy of an arrangement of 2400 trucks of 10 tonnes ($10^4\,\text{kg}$) at $90\,\text{km}\,\text{h}^{-1}$ ($25\,\text{ms}^{-1}$) it is equal to $7.5 \times 10^9\,\text{J}$.

To avoid machine downtime, the machine must be stopped for causes which require maintenance, such as assembly corrections, replacing of components, cleaning, and balancing. Machine downtime is costly, especially since halting a machine may cause

production to be canceled: this would cost 1–2 million FFr per day for a refinery, and 2–4 million FFr for a nuclear center producing electricity, not to mention client inconvenience, in the face of competition. Failure to carry out unconditional maintenance is risking material and human chaos, which cannot merely be judged by financial effects.

An optimum level between availability and unavailability, by carrying out effective maintenance, can be achieved through monitoring, analyzing conditions, such as lubricants, waste, temperature, pressure, flow, and vibratory performance. Since unbalance on a rotor cannot be canceled out, vibration is always detectable and subject to limits. Numerous other situations can be identified by descriptors derived from an analysis; their numerical values may permit diagnostics, and therefore stopping the machine or maintaining it while in use. Before the introduction of captors and systems of measurement and analysis, users would listen to bearings with a stethoscope and would see vibration with a corner placed on the edge. For the corner to remain horizontal, and supposing an harmonic variation, it is required that $mA\omega^2 > mg$, or $A\omega^2 > g$ or $v > g/\omega$ where $m =$ coin mass; $A =$ displacement amplitude; $\omega =$ displacement; $g =$ acceleration by gravity $= 9.81\,\mathrm{m\,s^{-2}}$; $v =$ amplitude of displacement speed. Where $\omega = 314\,\mathrm{rad\ \ s^{-1}}$ $(\rightarrow 3000\,\mathrm{rpm})$: $v > 31.2\,\mathrm{mm\,s^{-1}}$ $(\rightarrow 99.36\,\mu\mathrm{m})$. Such a machine is not in good order. Today, in principle, it would be subject to maintenance, and in this case balancing.

Definitions

A rotating machine (**Figure 1**) is comprised of:

- A rotor, whether its structure has symmetrical axes or not, in rotation around a rotation line; it may be formed by a shaft and added elements, such as disks, bladed disks, and cables
- A nonrotating structure comprising a stator, which also forms the envelope, bearings, whether connected or not to the stator; the stator contains elements connected to parts of the rotor, such as bladed diaphragms, diffusers, rectifiers, cables, sealing systems
- Links arranged between bearings, to insure guidance of the rotor in relation to the stator; the links use fluid, which is often oil, ball bearings and rollers, or a magnetic field; sealing systems can give rise to forces which place them in the sphere of links

A rotating machine is arranged on a receiving structure:

- connected to earth
- connected to a moving engine for transport, robotics, connected to manual use

The characteristics of the receiving structure and the elements placed between the structure and the rotating machine – the interfaces – can have a great influence on vibratory performance and on that of the supplier before use.

The Rotating Line

On the rotor radial section (**Figure 2**) the geometric center C is defined by the barycenter of the section profile. The arrangement of points C defines the rotation line (**Figure 3**) around which the rotor elements turn; the rotation line is in motion: each point describes a precession path; the rotation line is a result of flexural deformation; when the rotation line results from rotor forces, forces caused by unbalance, run outs, peaks, coaxiality faults, and performance is linear, the path is elliptical, even

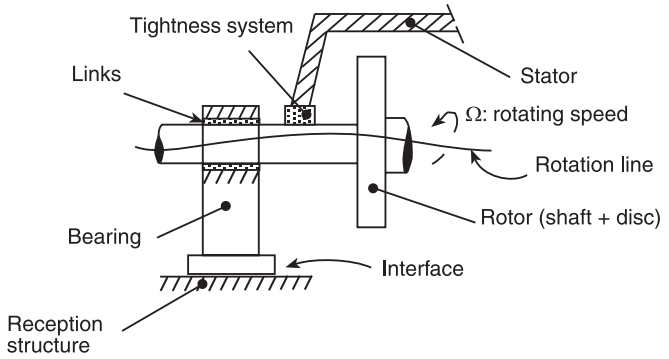


Figure 1 Rotating machine.

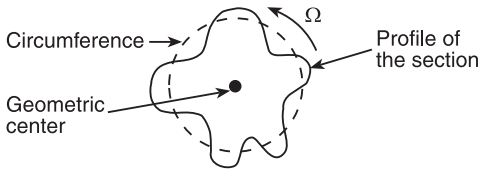


Figure 2 Radial section of a rotor.

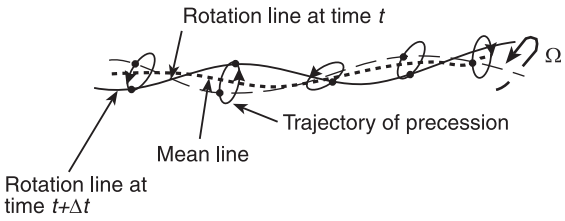


Figure 3 Rotation line.

circumferences or right-angles. On these ellipses the displacement direction of the point C may be that of speed Ω (direct precession) or inverse (inverse precession); on a rotation line the direction may be different, on either side on a rectilinear path; the direction may vary with rotation speed. When the path is not elliptical, their harmonic components are ellipses covered in the direction Ω, whether direct or inverse.

When the rotation speed is zero, the rotor is vertical, outside the force field, free, the rotation line is perpendicular; its axis is ideal for manufacturing. Such a model is classically used in theoretical studies.

The average line is fixed for a constant static condition; it is sensitive to radial forces which are not connected to speed Ω, such as the force of gravity. In a normal situation the rotation line is a result of unbalance torsion, shown in **Figure 4;** vectors *CG* rotate around *C*. Run outs are neglected (see **Bearing vibrations**). Analysis of the form of the rotation line, of the average line, and the path dimensions is one of the bases of diagnostics which makes it possible to appreciate normal or abnormal conditions of rotating machinery.

Rotor elements may vibrate around the rotation line, around vectors parallel to its axis; the rotor is then in a state of torsion, which is very characteristic of piston machines, such as petrol motors, oil motors, and compressors.

Links and Couplings

In principle, the number of links may not be less than two, in principle. In this case the static forces perpendicular to each of the two links, resulting from outside forces, are easy to determine by a classical mechanical theorem:

The sum of forces = 0
The sum of moments = 0

The rotor is in an isostatic state. When the number of links is greater than two, determining static forces perpendicular to the links involves taking into account global stiffness resulting from stiffness of the links and the receiving structure; this stiffness may be difficult to recognize. The rotor is in a hyperstatic condition.

When the rotor comprises several elements, for example, a turbine rotor and a compressor rotor, it

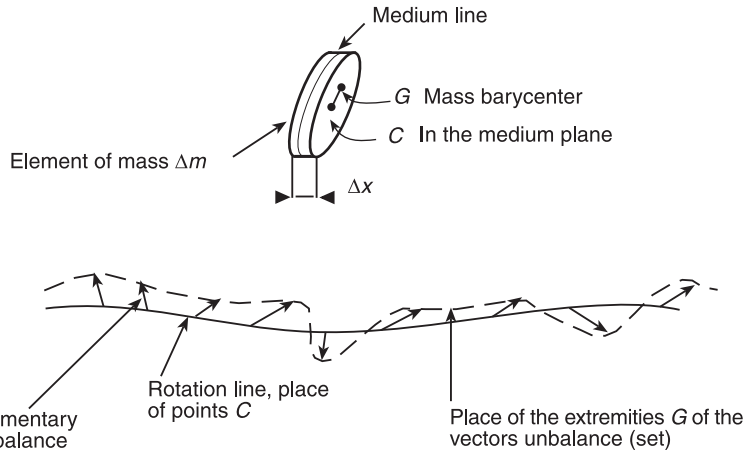


Figure 4 Elementary unbalance, $b = \Delta mCG$ and unbalance ensemble.

is possible to arrange each rotor isolated in an isostatic state, then to couple them rigidly without restraint using rigid couplings.

What is the result of forces when, for example, displacement modifies the position relative to bearings, leading to malalignment? The average rotation line is modified (see **Rotor stator interactions**).

During rotation the situation is more complex, since impedance resulting from stiffness and damping may be uncertain and variable. Such situations may lead to deterioration in the turbine caused by the compressor and, conversely, the delicate and dangerous passage of critical speed or onset of instability, defined in the article on the dynamics of rotating machinery (see **Rotor dynamics**), which may be difficult to manage when there are different manufacturers for different elements of the machine. Various types of coupling may be used, whether rigid or flexible (see **Balancing**). For rotors on ball bearings or rolling bearings, flexible couplings are useful when significant misalignment is possible in use.

See also: **Balancing**; **Bearing vibrations**; **Rotor dynamics**; **Rotor–stator interactions**;

Further Reading

Adams ML Jr (1999) *Rotating Machinery Vibration. From Analysis to Troubleshooting*. New York: Marcel Dekker.

Bigret R (1980) *Vibrations des Machines Tournantes et des Structures. [Vibrations of Rotating Machines and Structures*.] Paris: Technique et Documentation Lavoisier.

Bigret R (1997) *Stabilité des Machines Tournantes et des Systèmes. [Stability of Rotating Machines and Systems*.] Simlis, France: CETIM.

Bigret R, Feron J-L (1995) *Diagnostic, Maintenance, Disponibilité des Machines Tournantes. [Diagnostics, Maintenance, Availability of Rotating Machines*.] Paris: Masson.

Boulenger A, Pachaud S (1998) *Diagnostic Vibratoire en Maintenance Préventive. [Vibratory Diagnostics and Preventive Maintenance*.] Paris: Dunod.

Childs D (1993) *Turbomachinery Rotordynamics*. Chichester: John Wiley.

Dimentberg FM (1961) *Flexural Vibrations of Rotating Shafts*. London: Butterworths.

Frêne J, Nicolas D, Degueurce, Berthe D, Godet M (1990) *Lubrification Hydrodynamique – Paliers et Butées. [Hydrodynamic Lubrication – Bearings and Thrust*.] Paris: Eyrolles.

Gasch R, Pfützner (1975) *Rotordynamik Eine Einführung*. Berlin: Springer Verlag.

Genta G (1999) *Vibration of Structures and Machines*. Berlin: Springer Verlag.

Lalanne M, Ferraris G (1990) *Rotordynamics Prediction in Engineering*. Chichester: John Wiley.

Morel J (1992) *Vibrations des Machines et Diagnostic de leur Etat Mécanique. [Machine Vibrations and Diagnostics of their Mechanical Condition.]* Paris: Eyrolles.

Tondt A (1965) *Some Problems of Rotor Dynamics*. London: Chapman & Hall.

Vance JM (1988) *Rotordynamics of Turbomachinery*. Chichester: John Wiley.

ROTATING MACHINERY, MODAL CHARACTERISTICS

R Bigret, Drancy, France

Copyright © 2001 Academic Press

doi: 10.1006/rwvb.2001.0101

Introduction and Definitions

Dynamic characteristics of a rotating machine in planes perpendicular to the line of rotation are the result of forces, moments, and deformations caused by excitation and its components (masses, stiffness, damping) and this is expressed by modal characteristics:

- Complex eigenvalues (natural frequencies)
- Natural modes associated with natural frequencies

Natural frequencies define the temporal behavior of free responses. Natural modes describe the spatial distribution of displacements, angles, and forces. Together with excitation, forced response is expressed by a sum of modal components.

Formulations

These formulas result from the Newton–d'Alembert principle and the critical moment theorem, expressed by linear relations which make up theoretical models.

Second-order Formulation

This formulation is explained in the article on dynamics of rotating machinery (see **Rotor dynamics**). A formulation is said to be second-order if first and second derivatives of the component vector $\mathbf{u}$ are present. This formulation makes it possible to derive frequencies and natural modes, as does the study of forced response from matrix $\mathbf{S}$. It is appropriate for structures represented by symmetrical matrices. Matrices of rotating machinery, expressing gyroscopic couples, links, and sealing systems (see **Bearing vibrations**) may be asymmetric. It is then better to adapt a first-order formulation.

First-order Formulation

Dowson Duncan introduced the first-order formulation around 1960. This formulation uses second-order formulation matrices:

$$\mathbf{A}\dot{\mathbf{w}} + \mathbf{B}\mathbf{w} = \mathbf{Q} \qquad [1]$$

where:

$$\mathbf{A} = \begin{bmatrix} \mathbf{O} & \mathbf{M} \\ \mathbf{M} & \mathbf{A_v} \end{bmatrix} \qquad \mathbf{B} = \begin{bmatrix} -\mathbf{M} & \mathbf{O} \\ \mathbf{O} & \mathbf{K_d} \end{bmatrix}$$

$$\mathbf{w} = \begin{bmatrix} \dot{\mathbf{u}} \\ \mathbf{u} \end{bmatrix} \qquad \mathbf{Q}^{\mathrm{T}} = \begin{bmatrix} \mathbf{O}^{\mathrm{T}} \mathbf{S}^{\mathrm{T}} \end{bmatrix}$$

$$\mathbf{u}^{\mathrm{T}} = \{ \ldots y_l \psi_l z_l \theta_l \ldots f_{yp} f_{zp} \ldots \}^{\mathrm{T}}$$

where T is the transposition; $y_l,\ z_l$ are components of displacement from the geometric centre C_l of element l; $\psi_l,\ \theta_l$ are components of rotation around C_l of element l, $f_{yp},\ f_{zp}$ are components of forces at right-angles to section p and to links, and to sealing systems and between the elements. $\mathbf{M}$ is the mass matrix. $\mathbf{A}_v = \mathbf{A}_e + \mathbf{A}_i + \mathbf{G}$, where $\mathbf{A}_e$ is the external damping matrix; $\mathbf{A}_i$ is the internal damping matrix; $\mathbf{G}$ is the gyroscopic effects matrix. $\mathbf{K}_d = \mathbf{K} + \mathbf{K}_i$ where $\mathbf{K}$ is the rigidity matrix and $\mathbf{K}_i$ is the rigidity matrix due to internal damping.

The matrix $\mathbf{S}$ makes it possible to express forces of unbalance, moments caused by warp, forces caused by initial spurs, forces caused by coaxiality faults, harmonic forces, and spectral components of periodic forces.

Eqn [1] leads to:

$$\mathbf{M}\dot{\mathbf{u}} - \mathbf{M}\dot{\mathbf{u}} = \mathbf{O} \qquad [2]$$

$$\mathbf{M}\ddot{\mathbf{u}} + \mathbf{A_v}\dot{\mathbf{u}} + \mathbf{K}_d\mathbf{u} = \mathbf{S} \qquad [3]$$

Eqn [2] is always satisfied. Eqn [3] is presented in the article on the dynamics of rotating machinery (see **Rotor dynamics**). Eqn [1] is said to be self-attached to eqn [3].

Example: De Laval Model

Introducing components f_y and f_z of the forces which are at right-angles to the links, eqn [1] from the chapter on the dynamics of rotating machinery (see **Rotor dynamics**) is written as follows:

$$\begin{bmatrix} m & 0 & 0 & 0 & 0 & 0 \\ 0 & m & 0 & 0 & 0 & 0 \\ 0 & 0 & 0 & 0 & 0 & 0 \\ 0 & 0 & 0 & 0 & 0 & 0 \\ 0 & 0 & 0 & 0 & 0 & 0 \\ 0 & 0 & 0 & 0 & 0 & 0 \end{bmatrix} \begin{bmatrix} \ddot{y}_c \\ \ddot{z}_c \\ \ddot{y}_i \\ \ddot{z}_i \\ \ddot{f}_y \\ \ddot{f}_z \end{bmatrix}$$

$$+ \begin{bmatrix} 0 & 0 & 0 & 0 & 0 & 0 \\ 0 & 0 & 0 & 0 & 0 & 0 \\ 0 & 0 & 0 & 0 & 0 & 0 \\ 0 & 0 & 0 & 0 & 0 & 0 \\ 0 & 0 & 2f_{yy} & 2f_{yz} & 0 & 0 \\ 0 & 0 & 2f_{zy} & 2f_{zz} & 0 & 0 \end{bmatrix} \begin{bmatrix} \dot{y}_c \\ \dot{z}_c \\ \dot{y}_1 \\ \dot{z}_1 \\ \dot{f}_y \\ \dot{f}_z \end{bmatrix} \qquad [4]$$

$$+ \begin{bmatrix} k_a & 0 & -k_a & 0 & 0 & 0 \\ 0 & k_a & 0 & -k_a & 0 & 0 \\ k_a & 0 & -k_a & 0 & 1 & 0 \\ 0 & k_a & 0 & -k_a & 0 & 1 \\ 0 & 0 & 2k_{yy} & 2k_{yz} & -1 & 0 \\ 0 & 0 & 2k_{zy} & 2k_{zz} & 0 & -1 \end{bmatrix} \begin{bmatrix} y_c \\ z_c \\ y_1 \\ z_1 \\ f_y \\ f_z \end{bmatrix}$$

$$= me\Omega^2 \Re \begin{bmatrix} \exp i\Omega t \\ -i \exp i\Omega t \\ 0 \\ 0 \\ 0 \\ 0 \end{bmatrix}$$

Forces can be introduced in another way:

$$\begin{bmatrix} m & 0 & 0 & 0 & 0 & 0 \\ 0 & m & 0 & 0 & 0 & 0 \\ 0 & 0 & 0 & 0 & 0 & 0 \\ 0 & 0 & 0 & 0 & 0 & 0 \\ 0 & 0 & 0 & 0 & 0 & 0 \\ 0 & 0 & 0 & 0 & 0 & 0 \end{bmatrix} \begin{bmatrix} \ddot{y}_c \\ \ddot{z}_c \\ \ddot{y}_1 \\ \ddot{z}_1 \\ f_y \\ f_z \end{bmatrix} + \left[\begin{array}{cccc|cc} 0 & 0 & 0 & 0 & 0 & 0 \\ 0 & 0 & 0 & 0 & 0 & 0 \\ 0 & 0 & -2f_{yy} & -2f_{yz} & 0 & 0 \\ 0 & 0 & -2f_{zy} & -2f_{yy} & 0 & 0 \\ \hline 0 & 0 & 0 & 0 & -2f_{yy} & -2f_{yz} \\ 0 & 0 & 0 & 0 & -2f_{zy} & -2f_{yy} \end{array}\right] \mathbf{R}_\mathbf{f}^{-1}\mathbf{R}_\mathbf{f} \begin{bmatrix} \dot{y}_c \\ \dot{z}_c \\ \dot{y}_1 \\ \dot{z}_1 \\ \hline \dot{y}_1 \\ \dot{z}_1 \end{bmatrix}$$

$$+ \left[\begin{array}{cccc|cc} k_a & 0 & -k_a & 0 & 0 & 0 \\ 0 & k_a & 0 & -k_a & 0 & 0 \\ -k_a & 0 & k_a - 2k_{yy} & -2k_{yz} & 0 & 0 \\ 0 & -k_a & -2k_{zy}k_a & -2k_{zz} & 0 & 0 \\ \hline -k_a & 0 & 0 & 0 & k_a - 2k_{yy} & -2k_{yz} \\ 0 & -k_a & 0 & 0 & -2k_{zy} & k_a - 2k_{zz} \end{array}\right] \mathbf{R}_k^{-1}\mathbf{R}_k \begin{bmatrix} y_c \\ z_c \\ y_1 \\ z_1 \\ \hline y_1 \\ z_1 \end{bmatrix} = me\Omega^2 \Re \begin{bmatrix} \exp i\Omega t \\ -i \exp i\Omega t \\ 0 \\ 0 \\ \hline 0 \\ 0 \end{bmatrix} \quad [5]$$

where:

$$\mathbf{R}_f = \left[\begin{array}{c|cc} I & 0 & \\ \hline 0 & 2f_{yy} & 2f_{yz} \\ & 2f_{zy} & 2f_{zz} \end{array}\right],$$

$$\mathbf{R}_k = \left[\begin{array}{c|cc} I & 0 & \\ \hline 0 & 2k_{yy} & 2k_{yz} \\ & 2k_{zy} & 2k_{zz} \end{array}\right]$$

and $\Re$ = operator of the real part.

The product of $\mathbf{R}_f$ and $\mathbf{R}_k$ by $[\mathbf{y_1}\ \mathbf{z_1}]^\mathrm{T}$ leads to $[\mathbf{f_y}\ \mathbf{f_z}]e^\mathrm{T}$. These forces can also be calculated using the impedance matrix of links and $[\mathbf{y_1}\ \mathbf{z_1}]^\mathrm{T}$, $[\mathbf{y_1}\ \mathbf{z_1}]^\mathrm{T}$ determined by eqn [4] without $[\mathbf{f}_y\ \mathbf{f}_z]^\mathrm{T}$. The form of eqns [4] and [5] is identical to that of eqn [3]. It can be shown in the form of eqn [1].

Natural Frequencies

Where $\mathbf{Q} = \mathbf{O}$ and $\mathbf{u} = \mathbf{U}\exp pt$ eqn [1] leads to:

$$\mathbf{A}\begin{bmatrix} p^2\mathbf{U} \\ p\mathbf{U} \end{bmatrix} + \mathbf{B}\begin{bmatrix} p\mathbf{U} \\ \mathbf{U} \end{bmatrix} = \mathbf{O} \qquad [6]$$

$$\left[\mathbf{M}p^2 + \mathbf{A}_v p + \mathbf{K}_d\right]\mathbf{U} = \mathbf{O}$$

Complex eigenvalues:

$$p_l = \delta_l + i\omega_l$$

where $l = 1, 2, 3 \ldots$ and $i^2 = -1$ are the roots of the determinant of:

$$\mathbf{M}p^2 + \mathbf{A}_v p + \mathbf{K}_d$$

Thus:

$$\det[\mathbf{A}p + \mathbf{B}] = \mathbf{0} \qquad [7]$$

A complex eigenvalue $p_l^* = \delta_l - i\omega_l$ is always associated with p_l. For stability, $\delta_l < 0$.

Natural Modes

Natural Right and Left Modes

Right modes (associated with right eigenvectors) $\mathbf{W}_l^d$ associated with p_l are defined by:

$$[p_l\mathbf{A} + \mathbf{B}]\mathbf{W}_l^d = \mathbf{O} \qquad [8]$$

Natural left modes $\mathbf{W}_l^g$ associated with p_l are defined by:

$$\mathbf{W}_l^{g\mathrm{T}}[p_l\mathbf{A} + \mathbf{B}] = \mathbf{O}^\mathrm{T} \qquad [9]$$

so that:

$$\left[p_l \mathbf{A}^{\mathrm{T}} + \mathbf{B}^{\mathrm{T}}\right] \mathbf{W}_l^g = \mathbf{O}$$

Left modes are the right eigenvalues of a fictitious or virtual model, associated to the actual model and represented by matrices $\mathbf{A}^{\mathrm{T}}$ and $\mathbf{B}^{\mathrm{T}}$. As the second members of eqns [8] and [9] are zero, when calculating $\mathbf{W}_l^d$ and $\mathbf{W}_l^g$ it is necessary to normalize.

When $\mathbf{M}^{\mathrm{T}} = \mathbf{M}$, $\mathbf{A}_v^{\mathrm{T}} = \mathbf{A}_v$, $\mathbf{K}_d^{\mathrm{T}} = \mathbf{K}_d$; i.e., when the matrices $\mathbf{M}$, $\mathbf{A}_v$, and $\mathbf{K}_d$ are symmetrical, natural left eigenvectors are the same as the natural right eigenvectors.

Example: De Laval Model

Excluding forces and canceling the second member, eqn [4] leads to:

$$\begin{bmatrix} m & 0 & 0 & 0 \\ 0 & m & 0 & 0 \\ 0 & 0 & 0 & 0 \\ 0 & 0 & 0 & 0 \end{bmatrix} \begin{bmatrix} \ddot{y}_c \\ \ddot{z}_c \\ \ddot{y}_i \\ \ddot{z}_i \end{bmatrix} + \begin{bmatrix} 0 & 0 & 0 & 0 \\ 0 & 0 & 0 & 0 \\ 0 & 0 & -2f_{yy} & -2f_{yz} \\ 0 & 0 & -2f_{zy} & -2f_{zz} \end{bmatrix} \begin{bmatrix} \dot{y}_c \\ \dot{z}_c \\ \dot{y}_1 \\ \dot{z}_1 \end{bmatrix} + \begin{bmatrix} k_a & 0 & -k_a & 0 \\ 0 & k_a & 0 & -k_a \\ -k_a & 0 & k_a - 2k_{yy} & -2k_{yz} \\ 0 & -k_a & -2k_{zy}k_a & -2k_{zz} \end{bmatrix} \begin{bmatrix} y_c \\ z_c \\ y_1 \\ z_1 \end{bmatrix} = \mathbf{O} \quad [10]$$

If $f_{yz} = f_{zy}$ and $k_{yz} = k_{zy}$, matrices $\mathbf{A}_v$ and $\mathbf{K}_d$ are symmetrical, natural right eigenvectors are the same as those on the left. Symmetry is maintained when a different column-type of matrix is adopted, for example: $\{\mathbf{y}_c\ \mathbf{y}_1\ \mathbf{z}_1\ \mathbf{z}_c\}^{\mathrm{T}}$. In general, nonsymmetries are due to impedance of the links and gyroscopic effects.

Free Responses

Initial Conditions

Free responses are defined by initial values, at time $t = 0$, components of $\mathbf{u}$ and its speed $\dot{\mathbf{u}}$, which is connected to frequencies and natural modes by eqn [6]. The components of the natural modes are affected by the characteristics of the machine (mass, stiffness, and damping).

Example

$$\begin{aligned} u_1 &= u_{11} \exp p_1 t + u_{11}^* \exp \bar{p}_1 t \\ &\quad + u_{12} \exp p_2 t + u_{12}^* \exp \bar{p}_2 t \\ u_2 &= u_{21} \exp p_1 t + u_{21}^* \exp \bar{p}_1 t \\ &\quad + u_{22} \exp p_2 t + u_{22}^* \exp \bar{p}_2 t \end{aligned} \quad [11]$$

For $t = 0$:

$$\begin{bmatrix} u_{10} \\ u_{20} \\ \dot{u}_{10} \\ \dot{u}_{20} \end{bmatrix} = \begin{bmatrix} 1 & 1 & 1 & 1 \\ 0 & 0 & 0 & 0 \\ p_1 & p_1^* & p_2 & p_2^* \\ 0 & 0 & 0 & 0 \end{bmatrix} \begin{bmatrix} u_{11} \\ u_{11}^* \\ u_{12} \\ u_{12}^* \end{bmatrix} + \begin{bmatrix} 0 & 0 & 0 & 0 \\ 1 & 1 & 1 & 1 \\ 0 & 0 & 0 & 0 \\ p_1 & p_1^* & p_2 & p_2^* \end{bmatrix} \begin{bmatrix} u_{21} \\ u_{21}^* \\ u_{22} \\ u_{22}^* \end{bmatrix} \quad [12]$$

Relationships between natural modes are expressed by:

$$\begin{bmatrix} u_{21} \\ u_{21}^* \\ u_{22} \\ u_{22}^* \end{bmatrix} = \left[\begin{array}{c|c} \mathbf{M_1} & \mathbf{O} \\ - & - \\ \mathbf{O} & \mathbf{M_2} \end{array}\right] \begin{bmatrix} u_{11} \\ u_{11}^* \\ u_{12} \\ u_{12}^* \end{bmatrix} \quad [13]$$

Using eqns [11] and [12]:

$$\begin{bmatrix} u_{10} \\ u_{20} \\ \dot{u}_{10} \\ \dot{u}_{20} \end{bmatrix} = \begin{bmatrix} 1 & 1 & 1 & 1 \\ 0 & 0 & 0 & 0 \\ p_1 & p_1^* & p_2 & p_2^* \\ 0 & 0 & 0 & 0 \end{bmatrix} + \begin{bmatrix} 0 & 0 & 0 & 0 \\ 1 & 1 & 1 & 1 \\ 0 & 0 & 0 & 0 \\ p_1 & p_1^* & p_2 & p_2^* \end{bmatrix} \begin{bmatrix} \mathbf{M_1} & \mathbf{O} \\ \mathbf{O} & \mathbf{M_2} \end{bmatrix} \begin{bmatrix} u_{11} \\ u_{11}^* \\ u_{12} \\ u_{12}^* \end{bmatrix} \quad [14]$$

Once u_{10}, u_{20}, $\dot{u}_{10}$ and $\dot{u}_{20}$ have been imposed, eqn [14] makes it possible to calculate $[\mathbf{u}_{11}\mathbf{u}_{11}^*\mathbf{u}_{12}\mathbf{u}_{12}^*]^{\mathrm{T}}$ and eqn [13] enables the calculation of $[\mathbf{u}_{21}\mathbf{u}_{21}^*\mathbf{u}_{22}\mathbf{u}_{22}^*]^{\mathrm{T}}$.

In order for response to be carried out on $p_1 = \delta_1 + i\omega_1$, it is necessary for $U_{12} = u_{12}^* = u_{22} = u_{22}^* = 0$.

So then, according to eqn [14]:

$$\begin{bmatrix} u_{10} \\ u_{20} \\ \dot{u}_{10} \\ \dot{u}_{20} \end{bmatrix} = \mathbf{TI} \begin{bmatrix} u_{11} \\ u_{11}^* \\ 0 \\ 0 \end{bmatrix}$$

and thus:

$$\begin{bmatrix} u_{10} \\ u_{20} \end{bmatrix} = \mathbf{TI}_1 \begin{bmatrix} u_{11} \\ u_{11}^* \end{bmatrix}$$

$$\begin{bmatrix} \dot{u}_{10} \\ \dot{u}_{20} \end{bmatrix} = \mathbf{TI}_2 \begin{bmatrix} u_{11} \\ u_{11}^* \end{bmatrix} \qquad [15]$$

$$\begin{bmatrix} \dot{u}_{10} \\ \dot{u}_{20} \end{bmatrix} = \mathbf{TI}_2 [\mathbf{TI}_1]^{-1} \begin{bmatrix} u_{10} \\ u_{20} \end{bmatrix}$$

thus:

Eqn [15] shows that relations must exist between displacement and critical speed for response on p_1. Relations of the same force exist in order for free response on p_2.

When u_1 and u_2 represent displacement from the center of a rotor vortex, in a plane perpendicular to the rotation line, this center can describe a spiral in the sense of rotation Ω of the rotor (direct precession) or inversely, according to initial conditions.

Nodal Points and Zones

In certain planes the amplitude of natural modes may be zero. When $\mathbf{A}_\nu = [0]$, displacement components from the geometric centers of the sections of a rotor perpendicular to the rotation line, at frequency ω_l, when initial conditions suitable are:

$$u_k = A_k \sin(\omega_l t + \varepsilon\pi)$$

where $l = 1,\ 2 \ldots$ and $\varepsilon = \begin{cases} 0 \\ 1 \end{cases}$ and A_k depends on l.

Figure 1A shows a point of zero amplitude: a nodal point; components are canceled out simultaneously. This situation exists when $\mathbf{A}_\nu = a\mathbf{M} + b\mathbf{K}_d$, where a and b are constants. When $\mathbf{A}_\nu \neq \mathbf{0}$, around certain planes, a nodal zone may exist. **Figure 1B** shows components which do not cancel each other out simultaneously. The number of points, zones, and nodal zones increases with l.

Sensors which make it possible to measure rotor vibrations used for monitoring, protection, and diagnostics should not be installed near nodal zones which may move with rotation speed, and on which pulsations and natural modes depend.

Biorthogonality

General Relations

Natural frequencies, p, and their associated natural modes, $\mathbf{W}_0^g$ and $\mathbf{W}_0^d$, enable to define relationships of biorthogonality:

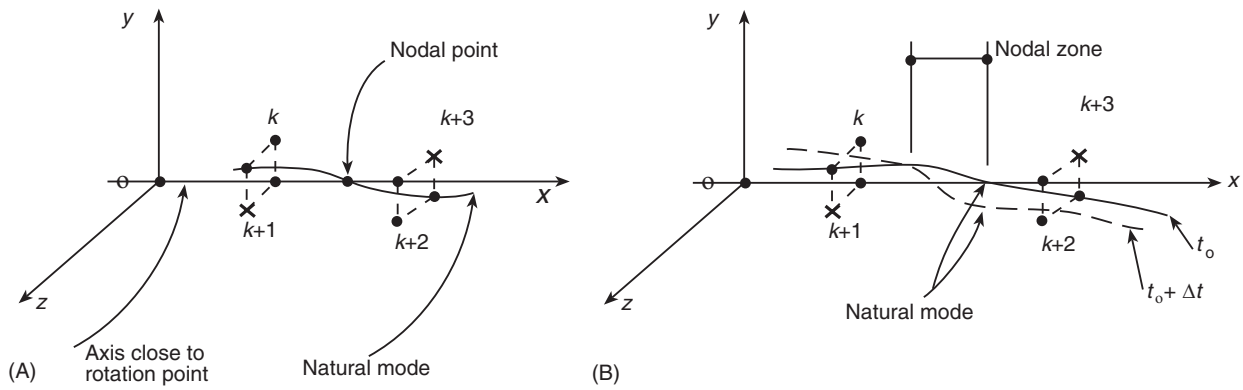


Figure 1 (A) Nodal point; (B) nodal zone.

$$\begin{aligned} U_k &= A_k \sin \omega_l t & U_k &= A_k \exp \delta_l t \sin \omega_l t \\ U_{k+1} &= A_{k+1} \sin \omega_l t & U_{k+1} &= A_{k+1} \exp \delta_l t \sin (\omega_l t + \vartheta k_{+1}) \\ U_{k+2} &= A_{k+2} \sin (\omega_l t + \pi) & U_{k+2} &= A_{k+2} \exp \delta_l t \sin (\omega_l t + \vartheta k_{+2}) \\ U_{k+3} &= A_{k+3} \sin (\omega_l t + \pi) & U_{k+3} &= A_{k+3} \exp \delta_l t \sin (\omega_l t + \vartheta k_{+3}) \end{aligned}$$

$$\mathbf{W}_s^{g\mathrm{T}}\mathbf{A}\mathbf{W}_l^d = \alpha_{sl}\delta_{sl} \qquad [16]$$

$$\mathbf{W}_s^{g}\mathbf{B}\mathbf{W}_l^d = -\alpha_{sl}p_l\delta_{sl} \qquad [17]$$

where α_{sl} = a constant linked to the standard; δ_{sl}, the Kroneker symbol = 1 if $s = l$; $\delta_{sl} = 0$ if $s \neq l$.

Eqns [16] and [17] allow us to define p_l :

$$p_l = \frac{\mathbf{W}_s^{g\mathrm{T}}\mathbf{B}\mathbf{W}_l^d}{\mathbf{W}_s^{g\mathrm{T}}\mathbf{A}\mathbf{W}_l^d}$$

This expression permits us to verify the value of p_l, which is obtained using the determinant [7].

Biorthogonality can be expressed by the second-order formulation:

$$\mathbf{u}_s^{g\mathrm{T}}[\mathbf{M}(p_s + p_l) + \mathbf{A}_v]\mathbf{u}_l^d = \alpha_{sl}\delta_{sl} \qquad [18]$$

$$\mathbf{u}_s^{g\mathrm{T}}[\mathbf{M}p_s p_l - \mathbf{K}_d]\mathbf{u}_l^d = \alpha_{sl}p_l\delta_{sl} \qquad [19]$$

Biorthogonality for $\mathbf{A}_v = a\mathbf{M} + b\mathbf{K}_d$

Eqns [18] and [19] become:

$$\mathbf{u}_s^{g\mathrm{T}}\mathbf{M}\mathbf{u}_l^d = \alpha_{sl}\frac{1 + bp_l}{a + bp_l^2 + 2p_l}\delta_{sl} \qquad [20]$$

$$\mathbf{u}_s^{g\mathrm{T}}\mathbf{K}_d\mathbf{u}_l^d = -\alpha_{sl}\frac{p_l^2 + ap_l}{a + bp_l^2 + 2p_l}\delta_{sl} \qquad [21]$$

The biorthogonality can be expressed by $\mathbf{A}_v$.

Kinetic Energy and Biorthogonality

When $\mathbf{A}_v = \mathbf{0}$ and the rotation line is an axis (**Figure 2**), limiting the description to the plane $0xy$, eqn [18] leads to:

$$[y_G + \theta l_1;\ \theta;\ \ldots\ y_G + \theta l_i\ \ldots]_l \times \begin{bmatrix} m_1 & 0\ldots & & & & \\ 0 & J_1 & & & & \\ & & \ddots & & & \\ & & & m_i & & \\ & & & & J_i & \\ & & & & & \ddots \end{bmatrix} \begin{bmatrix} y_G & + & \theta l_1 \\ & \theta & \\ y_G & + & \theta l_i \\ & \vdots & \end{bmatrix}_l = \frac{\alpha_{ll}}{2p_l}$$

$$2\varepsilon_c = my_G^2 + J\theta^2 = \frac{\alpha_{ll}}{2p_l}$$

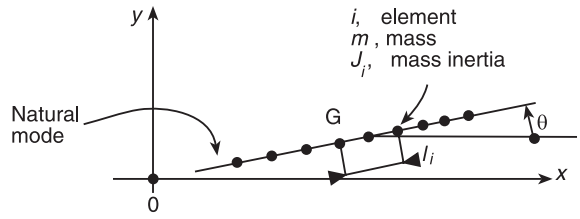


Figure 2 Rigid rotor: G, mass center of gravity.

where m is the rotor mass; J is the mass rotor inertia with relation to G; G is the mass center of gravity; ε_c is the critical energy.

For a symmetrical rotor guided by two identical links, the first natural frequency ω_1 leads to:

$$\frac{m}{2}(y_G\omega_1)^2 = \frac{\alpha_{11}\omega_1}{4i}$$

where $i^2 = -1$.

The second natural frequency ω_2 leads to:

$$\frac{J}{2}(\theta\omega_2)^2 = \frac{\alpha_{22}\omega_2}{4i}$$

These relations show that the coefficient $\alpha_{..}$ is connected to the norms of y_G and θ.

Diagonalization

Eqns [16] and [17] lead to:

$$\mathbf{G}^{\mathrm{T}}\mathbf{A}\mathbf{D} = \boldsymbol{\alpha}_{ll} \qquad [22]$$

$$\mathbf{G}^{\mathrm{T}}\mathbf{B}\mathbf{D} = -\boldsymbol{\alpha}_{ll}\mathbf{p}_l \qquad [23]$$

where $\boldsymbol{\alpha}_{ll}$ and $\boldsymbol{\alpha}_{ll}\mathbf{p}_l$ are diagonal matrices.

$\mathbf{G} = [\mathbf{W}_1^g \ldots \mathbf{W}_l^g \ldots]$ is a modal matrix of natural left eigenvalues.

$\mathbf{D} = [\mathbf{W}_1^d \ldots \mathbf{W}_l^d \ldots]$ is a modal matrix of natural right eigenvalues.

Diagonalization of the matrices $\mathbf{A}$ and $\mathbf{B}$ is possible regardless of $\mathbf{M}$, $\mathbf{A}_v$, and $\mathbf{K}_d$, which in general cannot be directly diagonalized in the same way.

Forced Responses

Base Relation

Laplace transformations, denoted as L, applied to eqn [1] lead to:

$$[\mathbf{sA}+\mathbf{B}]L\mathbf{w}=L\mathbf{Q}$$
$$L\mathbf{w}=[\mathbf{sA}+\mathbf{B}]^{-1}L\mathbf{Q}$$

The transfer function $[\mathbf{sA}+\mathbf{B}]^{-1}$ is defined by:

$$[\mathbf{sA}+\mathbf{B}]^{-1}=\mathbf{D}\left[\frac{1}{\alpha_{ll}(s-p_l)}\right]\mathbf{G}^{\mathrm{T}}$$

where $[1/\alpha_{ll}(s-p_l)]$ is a diagonal matrix.

When excitatory elements of $\mathbf{Q}$ are in harmony with the frequency Ω which is equal to rotation speed, $s=i\Omega$:

$$\mathbf{W}=\mathbf{D}\left[\frac{1}{\alpha_{ll}(i\Omega-p_l)}\right]\mathbf{G}^{\mathrm{T}}\mathbf{Q} \qquad [24]$$

where:

$$\mathbf{W}=\sum_l \frac{\mathbf{W}_l^d}{\alpha_{ll}(i\Omega-p_l)}\mathbf{W}_l^{g\mathrm{T}}\mathbf{Q}$$

This fundamental relation, once transposed, shows that excitatory elements are counterbalanced by the modal matrix of the left-hand modes.

Example

For a rotor which is affected by unbalance and an initial deflexion, defined in the article on the dynamics of rotating machinery (see **Rotor dynamics**):

$$\mathbf{Q}^{\mathrm{T}}=\{\ldots 0\ldots me\Omega^2+k_0f_0\exp i\theta_f,-i\,me\Omega^2 -ik_af_0\exp i\theta_f,-k_af_0\exp i\theta_f,ik_af_0\exp i\theta_f,\ldots 0\}^{\mathrm{T}} \qquad [25]$$

The complex number U_k, associated with displacement $u_k(u_k=|U_k|\cos(\Omega t+\varphi_k)$ where φ_k is an argument for U_k) of the geometric center of a radial section k of the rotor, is defined by eqns [24] and [25]:

$$\begin{aligned}U_k=\sum_l \frac{U_{k\,l}^d}{\alpha_{ll}(i\Omega-p_l)}&\times[U_{ql}(me\Omega^2+k_af_0\exp i\theta_f)\\&+U_{(q+1)l}^g(-i\,me\Omega^2-ik_af_0\exp i\theta_p)\\&+U_{(q+2)l}^g(-k_af_0\exp i\theta_f)\\&+U_{(q+3)l}^g(ik_af_0\exp i\theta_f)]\end{aligned} \qquad [26]$$

where $U_{kl}^d=$ component of the natural right eigenvector of section k, asociated to natural frequency p_l and $U_{0l}^g=$ component of the natural left eigenvector of section 0, linked to natural frequency p_l. The term between square brackets represents modal excitation. It contains all the excitatory terms of the rotor (unbalance, initial deflexion) considered here. Components referred to as q and $q+1$, and $q+2$ and $q+3$ are in the same radial plane.

Modal Excitation

In a general way, U_{0l}^d, U_{0l}^g, and p_l and therefore α_{ll} depend on rotation speed Ω, and in particular on the gyroscopic effects and impedance of the links and sealing systems.

Modal excitation comprises terms formed by components from the left modes (see **Rotor dynamics**):

$[U_{.l}^g-iU_{(.+1)\,l}^g][(me).\exp i\Psi.\Omega^2]$	Unbalance
$[U_{xl}^g-iU_{(x+1)l}^g][(\alpha f_0)_x\exp i\theta_x]$	Initial spur
$[U_{0l}^g-iU_{(0+1)\,l}^g]\times\left[\frac{mR^2}{4}\sqrt{V_y^2+V_z^2}\exp i(\Psi_v+\pi)\right]\Omega^2$	Thin disk

where m is the mass, R is the radius, and V_y and V_z are angles of shadow.

Modal excitation also includes terms comprising components of left modes conjugated as follows:

$$\left.\begin{array}{l}\bar{U}_{.l}^g(me).\exp i\Psi.\Omega^2\\-i\bar{U}_{(l+1)\,l}^g(me).\exp i\Psi.\Omega^2\\- - - - - - - - -\end{array}\right\} \quad \text{Unbalance}$$

Other terms may be taken into account to express unbalance of the axis.

Critical Speed

Speed at which $|U_k|$ is maximal is the critical speed. It depends on k; that is, the point and direction of observation and measurement.

Reduction to Two Terms

In certain conditions, in eqn [26] the number of sum terms can be reduced. Where there is unbalance (me) and $\delta_l\ll\omega_l;\ \omega_{l-1}\ll\omega_l\ll\omega_{l+1};\quad \omega_{l-1}\ll\Omega\ll\omega_{l+1};\ \Omega\approx\omega_l$:

$$U_k\approx\left[\frac{U_{k\,l}^d\left(U_{q\,l}^g-iU_{(q+1)l}^g\right)}{\alpha_{ll}(i\Omega-\delta_l-i\omega_l)}+\frac{\bar{U}_{k\,l}^d\left(\bar{U}_{q\,l}^g-i\bar{U}_{(q+1)l}^g\right)}{\bar{\alpha}_{ll}(i\Omega-\delta_l+i\omega_l)}\right]me\Omega^2 \qquad [27]$$

For a De Laval motor (see **Rotor dynamics**) guided by links with high levels of impedance:

$$U^g_{(k+1)l} = 0 \quad (g \to k)$$

Where $U^d_{kl} = 1,\ U^g_{kl} = -i/2m\omega$, eqn [27] leads to:

$$U_k \approx \frac{me\Omega^2}{m\left(-\Omega^2 - 2i\Omega\delta + \omega^2 + \delta^2\right)} \qquad [28]$$

Direct study of a De Laval rotor (of mass m, damping coefficient c, and stiffness k) leads to:

$$U = \frac{me\Omega^2}{-m\Omega^2 + ic\Omega + k} = \frac{e\Omega^2}{-\Omega^2 - 2i\Omega\delta + \omega^2 + \delta^2}$$
$$\delta \pm i\omega = -c/2m \pm i\sqrt{k/m - c^2/4m^2} \qquad [29]$$

are natural frequencies.

U_k obtained by modal decomposition is closely related to U which is obtained by direct study. In a general way, each term of eqn [26] represents modal participation, whose denominator is the same as that of the transfer function of a De Laval rotor.

Representation of Left Modes

Natural left modes are mathematical entities. An approximate representation results from eqn [27] where $\Omega = \omega_l$. The second neglected term and $U^g_{ql} = U^g_{(q+1)l}$.

$$U_k \approx \frac{U^d_{kl}U^g_{ql}me\Omega^2}{-\alpha_{ll}\delta_l}$$

U_k, measured for unbalance me successively disposed in planes, $q,\ q+2,\ q+4\ldots$ leads to:

$$\frac{U_{k(q+4)}}{U_{kq}} = \frac{U^g_{(q+4)l}}{U^g_{q\,l}} = \frac{U_{k(q+2)}}{U_{kq}} = \frac{U^g_{(q+2)l}}{U^g_{q\,l}}$$

The measured relations $U_{k..}/U_{kq}$ represent relationships of left modes.

Example: Left and Right Modes

A steam turbine rotor of horizontal mass 46 244 kg is guided by two identical oiled links 6960 mm apart. The mass barycenter is at equal distance from the links (**Table 1**).

Table 1 shows the ratio between natural left and right modes. The anisotropy of bearings with three lobes is not as marked as that of cylindrical bearings; the ratio A^d/A_0 are closer to 1 and the differences between the phases are smaller.

Sensitivity for Resetting

The modal characteristics of the theoretical model of rotating machinery may be compared to the modal characteristics of the physical machine it claims to represent, determined by a theoretical–experimental procedure of modal analysis. Differences can appear between the frequencies and natural modes. Updating or adjustment can make it possible to reduce these differences by modifying the numerical value of certain factors characterizing the theoretical model. Structure modifications may be applied taking into account the limits of the machine.

Table 1 Turbine rotor: natural right and left modes

Bearing ϕ 400 mm	*Natural frequencies* (rad s^{-1})		*Distance between natural right and left modes* A^d/A_0 (*amplitude at 1500 rpm*); $\theta_d - \theta_g$ (*phases: degrees*)			
	1116 rpm	*1500 rpm*	*Link 1*		*Link 2*	
			A^d/A_0	$\theta_d - \theta_g$	A^d/A_0	$\theta_d - \theta_g$
Cylindrical	$-11.75 \pm i107.7$	$-5.56 \pm i105.3$	0.98	11	0.99	11
clearance 0.2%	$-2.06 \pm i117.8$	$-2.38 \pm i115.6$	2.32	38	2.05	54
Three lobes	$-4.37 \pm i111.4$	$-1.89 \pm i109.8$	0.94	13	0.92	13
clearance 0.2%	$-1.37 \pm i119$	$-1.48 \pm i119.5$	1	8	0.91	15
Coefficient of precharge 0.5						

There are several possible methods, such as using the sensitivity coefficients S_{pq}

$$\begin{bmatrix} \Delta G_1 \\ \vdots \\ \Delta G_p \\ \vdots \end{bmatrix} = \begin{bmatrix} S_{11} & \cdots & \\ \vdots & & \cdots \\ & S_{pq} & \\ \vdots & & \end{bmatrix} \begin{bmatrix} \Delta\lambda_1 \\ \vdots \\ \Delta\lambda_q \\ \vdots \end{bmatrix} \rightarrow \mathbf{\Delta G} = \mathbf{S\Delta\lambda}$$

The matrix $\mathbf{S}$ is linked to the sensitivity.

$\Delta G_p = G_{\text{measurement}} - G_{\text{model}}$ = modal size at $\Delta\lambda = \lambda_{\text{initial}} - \lambda_{\text{corrected}}$ = mass, stiffness, and damping of the theoretical model, and $\mathbf{S}$ is used by an iterative procedure which must, if possible, lead to $\Delta G_p < \varepsilon_p$, where $p = 1,\ 2 \ldots.$ ε_p defines the model quality and it is important to fix this as a function of its application.

The sensitivity coefficient affected by natural frequency p_l is written as:

$$\frac{\delta p_l}{\delta\lambda} = \frac{-1}{\alpha_{ll}} \mathbf{W}_l^{g\mathrm{T}} \left(p_l \frac{\delta \mathbf{A}}{\delta\lambda} + \frac{\delta \mathbf{B}}{\delta\lambda} \right) \mathbf{W}_l^d$$

λ may be the mass of an element of the theoretical model. If λ is stiffness, k_p, contained in $\mathbf{B}$:

$$\frac{\delta p_l}{\delta k_p} = \frac{-1}{\alpha_{ll}} \mathbf{W}_l^{g\mathrm{T}} \frac{\delta \mathbf{B}}{\delta k_p} \mathbf{W}_l^d$$

The sensitivity coefficient affected by the natural right eigenvectors may be obtained by:

$$\frac{\delta \mathbf{W}_l^d}{\delta\lambda} = -[p_l\mathbf{A} + \mathbf{B}]^{-1} \left[\frac{\delta p_l}{\delta\lambda} \mathbf{A} + p_l \frac{\delta \mathbf{A}}{\delta\lambda} + \frac{\delta \mathbf{B}}{\delta\lambda} \right]$$

$$\frac{\delta \mathbf{W}_l^d}{\delta\lambda} = \sum_j \beta_l \lambda_j \mathbf{W}_j^d$$

where:

$$\beta_l \lambda_j = \frac{\mathbf{W}_j^{g\mathrm{T}} [\mathbf{A}] (\delta \mathbf{W}_l^d / \delta\lambda)}{\alpha_{ll}}$$

or:

$$\beta_l \lambda_j = \frac{p_l \mathbf{W}_j^g (\delta\mathbf{A}/\delta\lambda) \mathbf{W}_l^d + \mathbf{W}_l^{g\mathrm{T}} (\delta\mathbf{B}/\delta\lambda) \mathbf{W}_l^d}{\alpha_{ll} (p_j - p_l)}$$

The sensitivy coefficient affected by the left natural modes can be obtained using these formulae, defined here for the right mode, by substituting g for d:

$$\mathbf{A}^{\mathrm{T}} \text{ to } \mathbf{A} \text{ and } \mathbf{B}^{\mathrm{T}} \text{ to } \mathbf{B}$$

See also: **Balancing**; **Rotating machinery, essential features**; **Rotating machinery, monitoring**; **Rotor dynamics**.

Further Reading

Adams ML Jr (1999) *Rotating Machinery Vibration. From Analysis to Troubleshooting*. New York: Marcel Dekker.

Bigret R (1980) *Vibrations des Machines Tournantes et des Structures. [Vibrations of Rotating Machines and Structures.]* Paris: Technique et Documentation Lavoisier.

Bigret R (1997) *Stabilité des Machines Tournantes et des Systèmes. [Stability of Rotating Machines and Systems.]* Simlis, France: CETIM.

Bigret R, Feron J-L (1995) *Diagnostic, Maintenance, Disponibilité des Machines Tournantes. [Diagnostics, Maintenance, Availability of Rotating Machines.]* Paris: Masson.

Boulenger A, Pachaud S (1998) *Diagnostic Vibratoire en Maintenance Préventive. [Vibratory Diagnostics and Preventive Maintenance.]* Paris: Dunod.

Childs D (1993) *Turbomachinery Rotordynamics*. Chichester: John Wiley.

Dimentberg FM (1961) *Flexural Vibrations of Rotating Shafts*. London: Butterworths.

Frêne J, Nicolas D, Dequeurce, Berthe D, Godet M (1990) *Lubrification Hydrodynamique – Paliers et Butées. [Hydrodynamic Lubrication – Bearings and Thrust.]* Paris: Eyrolles.

Gasch R, Pfützner (1975) *Rotordynamik. Eine Einführung*. Berlin: Springer Verlag.

Genta G (1999) *Vibration of Structures and Machines*. Berlin: Springer Verlag.

Lalanne M, Ferraris G (1990) *Rotordynamics Prediction in Engineering*. Chichester: John Wiley.

Morel J (1992) *Vibrations des Machines et Diagnostic de leur Etat Mécanique. [Machine Vibrations and Diagnostics of their Mechanical Condition.]* Paris: Eyrolles.

Tondt A (1965) *Some Problems of Rotor Dynamics*. London: Chapman & Hall.

Vance JM (1988) *Rotordynamics of Turbomachinery*. Chichester: John Wiley.

ROTATING MACHINERY, MONITORING

R Bigret, Drancy, France,

Copyright © 2001 Academic Press

doi:10.1006/rwvb.2001.0096

Introduction

When rotating machinery is inoperative, this affects its associated systems and industrial complexes. In 1985, the Electric Power Research Institute estimated that 40% of stoppages at fossil-fuel stations in North America were due to rotating machinery problems, and in France the loss due to disruptions in 900-MW turboalternators was equivalent to the energy produced by a 750-MW machine. A study carried out in 1987 by the Centre Technique des Industries Mécaniques in France showed the following causes of machine failure:

1. steam turbines: rotors 50%
2. turbocompressors: rotors 30%; bearings and thrusts 26%
3. centrifugal pumps: sealing systems 44%; bearings and thrusts 24%
4. gas turbines: rotors 16%

Monitoring and protecting rotating machinery will help reduce downtime.

Monitoring, Protection, Diagnostics, and Maintenance

The noise and vibrations made by rotating machinery give a good indication of its mechanical state. Together with measurements of overall condition – temperature, pressure, flow, intensity – the indicators-features which can be drawn from an assessment of vibration will reveal degradation before there is complete failure.

Two types of feature are used:

1. Global, represented by levels within a large frequency band for monitoring and protection
2. Specific, in general within a diagnostic frequency domain

Specific features are required for diagnostics, when the value of the global features goes beyond the range fixed by the person setting the standard. The limits of this range may depend on the general condition of the machinery and knowledge acquired during operation. It may be useful to know exact quantitative values of global features even when these are obviously below the limits.

Diagnostics may lead to a maintenance operation which will reduce deterioration and prevent breakdown, catastrophe, and physical injury. Carrying out maintenance means that maximum machine availability insures maximum profit such as guaranteeing electric supply to a site and enhance reputation an important aspect in marketing and business. Machine availability is defined by the relationship between time available and time required, with numerous slight variations.

Maintenance is set out in **Figure 1**, and this cannot establish the economy of cost (direct, indirect (materials, salary, charges)) because of the uncertainty of a breakdown. The profitability of an arrangement is insured if the cost system divided by variation in the cost of unavailability is less than one.

Abnormal Situations

Feature values may go beyond the acceptable range in abnormal situations. Examples are:

- Instability
- Critical speed, when vibrations are outside the limits
- Blades being lost or destroyed
- Jammed alternator rotor bars
- Misalignments between links (bearings, rolling bearings, sealing system), each of a particular type; loss of balance caused by rotation, stator slipping, thermal anisotropy
- Coaxiality faults caused by coupling and thermal effects (slippage)
- Violent variations in the degree and phase of vibration caused, for example, by relative displacements of the elements of a rotor, or a missile release
- Friction between rotor and stator
- Friction perpendicular to the sealing systems of turbomachines and alternators
- Shocks to the rotor caused by brief rotor–stator interaction
- Problems of lubrication in the coupled elements
- Cracks in the rotor
- Loosening of rotor and stator elements
- Random variations in vibration amplitude and phase as a result of the presence of a moving foreign body in the stator

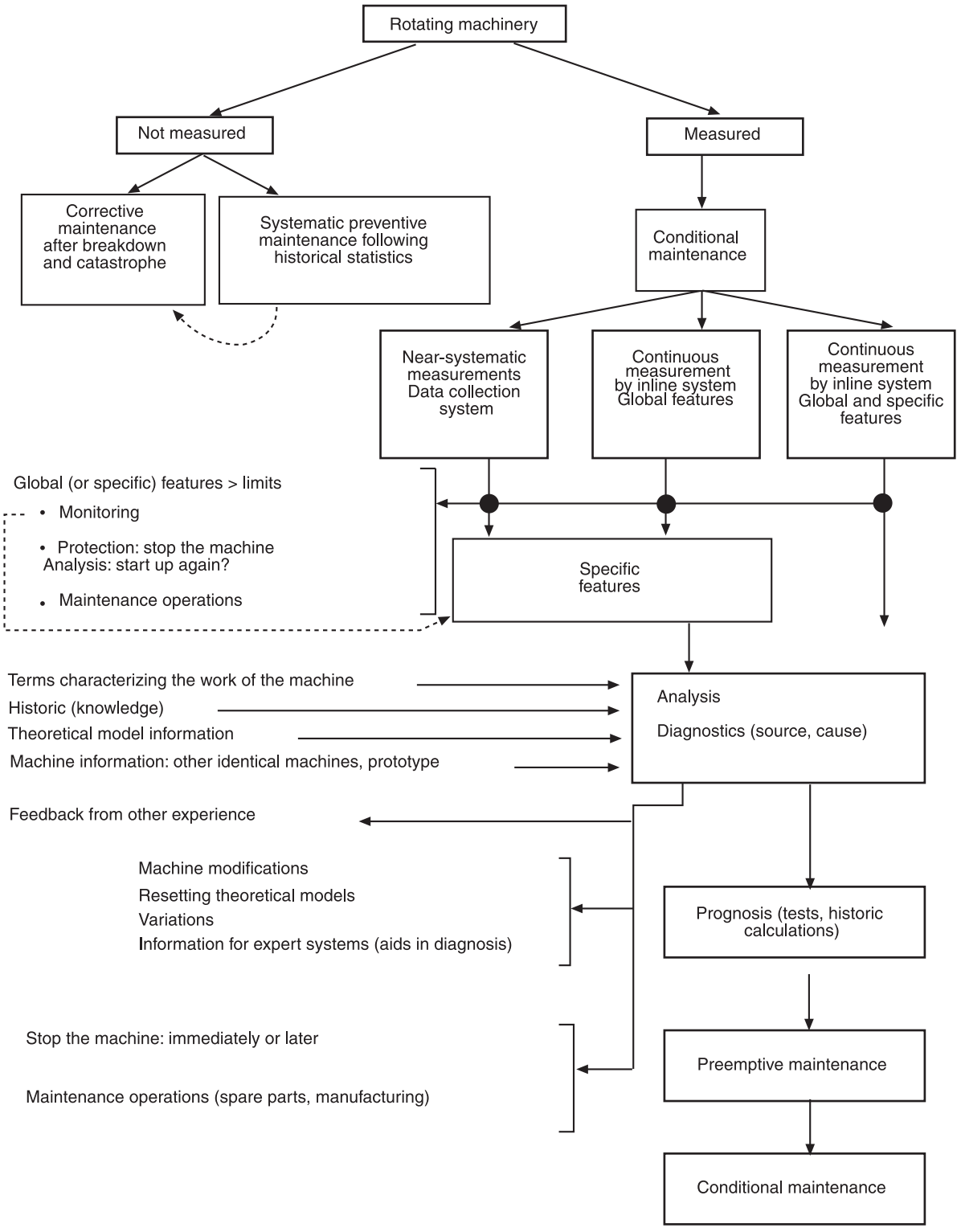


Figure 1 Maintenance.

- Blockage of ventilation circuit (alternator engine)
- Deterioration in the links, caused by fluid, bearings, magnetic field
- Deterioration in the gears
- Raised temperature in the bearings
- Unsteady torsion
- Specific states due to coupling, and deformation in the rotors

- Cavitation in the pumps
- Instability in the compressors (pumps)
- Deterioration of valves in alternating machines and variation in position of cycle phases
- Short circuits between rotor peaks in electric machines
- Electric shocks through the links generated by electrostatics resulting in pitting
- Measuring system errors

Analysis and diagnostics set in motion by abnormal situations require definitive knowledge of the technological management and maintenance policy. Theoretical models form part of this knowledge.

Measuring and Sensors

Classically, vibrations are measured using sensors which are perpendicular to the rotating elements.

- Magnetic sensors measure relative vibrations of the rotor and nonrotating structure
- Acceleration sensors measure absolute vibration of the nonrotating structure

Figure 2 shows a normal setup (see **Balancing**). Typical essential features of magnetic sensors are as follows:

- Measuring range: 0.15–2.15 to 0.9–12.9 mm
- Passband: 0–5000 Hz; 0–10 000 Hz
- Temperature range: -40°C to 220°C

The first natural frequency of the setup sensor–support–cable assembly must be more than four times the maximum frequency of interest. The sensor also measures the run-out which must be deducted from the measured value (see **Balancing**). The appropriate standard is International Standardization Organization (ISO) 7919.

Typical essential features of accelerometers are:

- With piezoelectric transducers: $5 < f < 2000$ Hz; $-200^{\circ}\text{C} < T < 650^{\circ}\text{C}$
- With piezoresistive transducers: $0.2 < f < 1000$ Hz; $-40^{\circ}\text{C} < T < 90^{\circ}\text{C}$

Different arrangements make it possible to reduce the minimum frequency and signal noise on displacement (μm) resulting from double integration of a signal. The first natural frequency of an accelerometer fixed on the structure must be four times greater than the maximum frequency of interest. Velocimeters may be used. The sensor C_r (**Figure 2**) which senses the passage of the indicator enables one to measure speed and phase difference between frequency components.

The standard ISO 10817.1 System for measuring vibrations of rotating shafts, part 1, transducers of relative and absolute signals of radial vibrations, is applied here.

The system shown in (**Figure 2**) makes it possible to make the following measurements of global vibrations: relative, and absolute for blade and rotor, in each direction, Δ and Δ'. The combination of vibrations using Δ and Δ' leads to a precession path

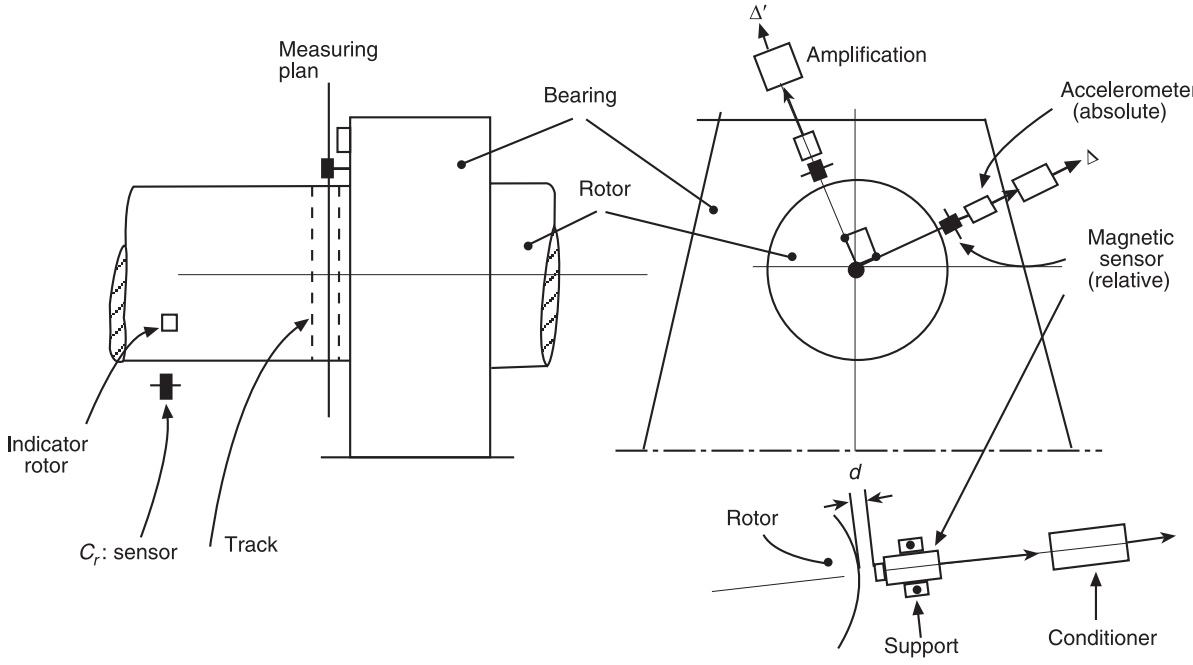


Figure 2 Normal layout of a sensor.

(**Figure 3**) called the orbit, which is relative when vibrations are relative, and absolute when rotor vibrations are absolute.

When frequency spectra contain only one component at frequency f the path is a conical ellipse, described at frequency f (for balancing $f = \Omega/2\pi$, where $\Omega =$ rotation speed). S_A (peak-to-peak) and S_B (peak-to-peak) depend on the direction of Δ and Δ'; S_{max} and S_{max} (peak-to-peak) do not depend on this factor.

Absolute bearing vibrations are generally expressed by effective values in mm s^{-1} in one direction. Temperature measured for example with thermocouples, gives additional information. Vibration in the direction of the rotor axis may also be taken into account.

Limits

Limits are set by the manufacturers, who may be inspired by the standards established by the ISO and American Petroleum Institute (API), and these limits may be modified by the machine operator. For steam turbines and turbocompressors, the API limit (S_A (peak-to-peak) or S_B (peak-to-peak)) is defined by:

$$25.4\sqrt{12\,000/N}(\text{rpm})(\mu\text{m})$$

where 25.4 μm is the peak-to-peak relative vibration for $N = 12\,000$ rpm.

In ISO standard 7919/1 (Mechanical vibrations of nonalternating machines: measurements on rotating shafts and evaluation criteria, part 1: general directives) defines four zones (**Figure 4**):

- Zone A: for machines which have recently been serviced (formula criterion)
- Zone B: normal operation
- Zone C: cannot be used for long periods (alarms go off, analytical investigations need to be made)
- Zone D: possible deterioration (possible shut down; need for protection)

Standards 7919/2–5 define the zone limits for different machine types. According to 7919/3 for industrial machines coupled at 12 000 rpm, S_{max} (peak-to-peak) = 43.8 μm as the limit of zone A for a suitable frequency band. This limit is often defined in accordance to the specific machines attached.

According to ISO7919/1, variations in levels around established values must be taken into account; standard 7919 defines the permitted range: ± 0.25 as the limit of zone B. Vibration levels may diminish when the unbalance caused by missile release is counteracted by initial unbalance.

Standard ISO 10816/1 (Mechanical vibrations: evaluation of machine vibration by measurement of nonrotating blades: part 1, general directives) defines four zones A–D for effective global levels, expressed as mm s^{-1}; the limits of the zones, which are constant between frequency f_x and $f_y > f_x$, can be reduced for $f < f_x$ and $f > f_y$: f is related to rotation speed.

Standard 10816/2–5 defines the limits of the zones for different machine types. According to 10816/3, for industrial machines of nominal power greater than 15 kW and nominal speed between 120 and 15 000 rpm measured *in situ* on rigid support (natural frequency of the machine–support $> 1.25 f_{ex}$, where $f_{ex} = f$ general rotation), the limit of zone A is equal to 2.3 mm s^{-1} RMS in a region of 10 and 1000 Hz at

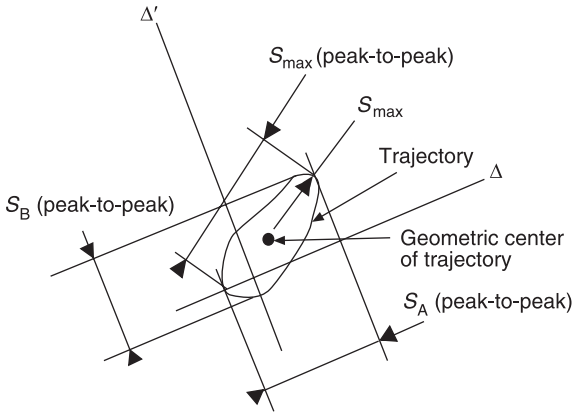


Figure 3 Precession path S measured in μm.

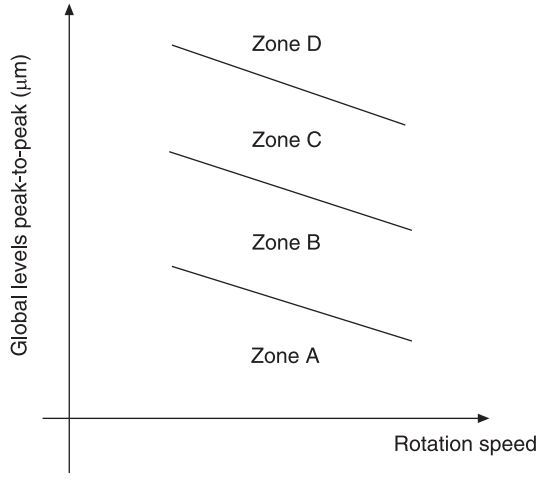


Figure 4 Zones according to ISO 7919/1. For global levels, see **Figure 3**.

speeds faster than 600 rpm. As with 7919/0, the variation in level is taken into account: ±0.25 of the limit of zone B.

Only the standard 7919/5 (hydraulic turbine) uses S_{max} and S_{max} (peak-to-peak) (see **Figure 3**) within the limits defined by 7919/0 and 10816/0 for permanent normal rates of flow. For 7919/2 (turboalternators on a radial base), an amendment published in 1998, proposes taking into account variations in flow rate at constant rotation speed (limit approaching that of zone C) and critical speed (limit approaching 1.5 times the limit of zone C). Not well defined frequencies and technological setups permit exchanges between client/user and constructor/insurer so that they can determine the limits written in the specification agreement, and revise them under certain conditions.

Standards

- ISO 11342 Methods and criteria for mechanical balancing of flexible rotors (being revised)
- ISO 10814 Machine susceptibility and sensitivity to unbalance: Normal machine speed may be close to critical speed if damping is important
- ISO 7919/0 Mechanical vibrations of nonalternating machines: Measurement and evaluation of rotating shafts
  ISO 7919/1 General directives
  ISO 7919/2 Directives on turboalternators installed on a radial base
  ISO 7919/3 Directives on coupled industrial machines
  ISO 7919/4 Directives on gas turbines
  ISO 7919/5 Hydraulic turbines
- ISO 10816/0 Mechanical vibrations: evaluation of machine vibration measured on nonrotating parts
  ISO 10816/1 General directives
  ISO 10816/2 Directives on turboalternators greater than 50 MW installed on a radial base
  ISO 10816/3 Directives on industrial machines of nominal power greater than 15 kW and nominal speed between 120 and 15 000 rpm measured *in situ*
  ISO 10816/4 Directives on gas turbine setups, with the exception of aeronautical applications
  ISO 10816/5 Directives on hydraulic machines of nominal power greater than 1 MW and nominal speed between 120 and 1800 rpm measured *in situ*
  ISO 10816/6 Alternative machines of nominal power greater than 100 MW
- AFNOR NFE 440–165 Industrial pumps. Centrifugal, spiral centrifugal, and spiral. Mechanical vibration level acceptable as regards power, speed, and flow

Online and Data Collecting Systems

Monitoring, protection, and diagnostics (**Figure 1**) can be carried out by:

- Online systems permanently connected to sensors: signals are analyzed continuously, in real time or soon after their occurrence
- Data collectors used by operators on a weekly basis: this permits immediate assessment of features and signal storage for later analysis

The two methods are comparable with regard to cause of malfunctions.

Examples of Abnormal Situations

Instability

Rotor instability may happen suddenly, in permanent or transient flow, as a result of increased rotation speed, or it may be a gradual progression. It is characterized by greater amplitude of the precession paths at frequencies which are often less than the rotation frequency.

- A permanent data-collecting system may make it possible to recognize the limit cycle by measuring the frequency. However, if a protective mechanism insures that the limit cycle automatically shuts the machine down, no information will be obtained.
- An online system receiving continuous signals (average values) and alternating signals from free-standing magnetic sensors, link fluid temperature, and other machine variables (speed, pressure, temperature, voltage) can, in both permanent and transient flow, determine the moment when the instability appeared and show average position of the rotor–stator and other variables at that precise point, to give a good diagnosis.

If the cycle limit automatically shuts the machine down because of the monitoring and protection system which is in place, such system will equally provide a great deal of information.

Variations in unbalance

Variation in unbalance is linked to an increase or decrease in vibration amplitude. Increases may cause deterioration, notably in the regions of critical speeds:

- A data-collecting system which is permanently in operation may show global variations in amplitude

as well as in amplitude component and phases. However, if a protective mechanism insures that the cycle limit automatically shuts the machine down, no information will be gained.

- An online system makes it possible to assess how vibrations have changed over time and, in particular, to detect significant changes which generally correspond to failure of rings and blades. Such a system also facilitates recognition of changes in misalignment. When an online system is in operation permanently, once the rotation speed has markedly slowed down, relative rotor movement variation in relation to the links permits the detection of coaxiality faults. When operated temporarily, recording while the machine is slowing down, when amplitude is measured, the risk of rotor–stator contact is evaluated. If the cycle limit automatically shuts the machine down because of the monitoring and protection system which is in place, this system will equally provide a great deal of information.

Faults of Ball Bearings

Uncertainty about the ball bearing lifespan may be an important factor, particularly if there is also uncertainty about the rotating forces. There are a number of software packages which provide features. Generally, ball bearings will initially deteriorate slowly, but as their condition worsens, they are quickly destroyed.

Using a data-collecting system which provides signals measured in conjunction with appropriate software, it is possible to follow the features with measurements made periodically every month or week. A suitable interval to stop and replace the parts can be established.

In this case, after measuring at time t_m, it is premature to stop the machine as long as the bearing permits it. If the machine is not stopped at time t_k, it may break down before the next measurement at time t_{k+1}, but this becomes less likely with the decrease in time between the two measurements. Availability can increase but at a higher cost of operation.

Using an online system, features are checked periodically. The frequency of checking may be small, large or even every minute. Service is then optimal and the history of deterioration is known.

Rotor Cracks

Under the effect of static and dynamic strain, a flaw will grow until it cracks apart completely. A crack causes a variety of amplitudes and phase differences of the harmonic components of vibration. The rate of change is larger, and detection of crack possible.

Vibration monitoring may be done permanently or temporarily, once the machine has slowed down.

A permanently operating online or data-collecting system using particular software makes it possible to detect the appearance of a crack. Only an online system which is able to pick up vibrations when the machine slows down can provide effective descriptors on the state of any cracks.

Coaxiality Faults

Due to the effect of a thermal spatial gradient or relative element displacements, the average rotor rotation line may move away from the normal reference line. This movement, which represents a coaxiality fault, gives rise to rotating forces which must not be confused with rotating forces from other sources, in particular as a result of unbalance.

This displacement can be assessed when rotation speed is slow, such as when the machine is started up or stopped. An online system measuring average signal values measured by sensors of relative rotor–stator displacement may make it possible to recognize misalignments. A data-collecting system is not suitable for this purpose.

Transient State of Operations

- Measuring during transient state permits to improve monitoring and protection, in particular at critical speed. Analysis of recorded signals facilitates better diagnostics and provides additional information to update theoretical models.
- Measurement in transitory state often allows satisfactory balancing (see **Balancing**).
- The article on the essential features of rotating machinery (see **Rotating machinery, essential features**) covers acquisition in transitory state. As shown, we can calculate the influence on the amplitude and phases at critical speed of damping levels ξ and of:

$$\left|\frac{d\Omega}{dt}\right| \frac{1}{\omega_0^2} = \gamma \qquad [1]$$

where $d\Omega/dt = \alpha =$ acceleration and deceleration, and $\omega_0 =$ natural radial frequency.

For large γ, the relation between the amplitude at critical speed in both permanent and transitory regimes is weak: ≈ 0.5 for $\gamma = 10^{-2}$. This property

is sometimes used to avoid contact between rotor and stator.

- The article on balancing (see **Balancing**) discusses the acquisition of fundamental components. Systems, which are generally digital, carry out the simultaneous acquisition of signals in increments of speed $\Delta\Omega$ ($\Delta\Omega \leq \Delta\Omega_{cr}/6$). The time T_a between two acquisitions may be utilized, and this enables the system to calculate features (discrete Fourier transformations), to transfer them, and to store them.

If it is accepted that $|d\Omega/dt|$ must be small in order that machine vibration may approximate the vibrations in steady state. Then errors of amplitude and component phase at rotation Ω are:

$$\varepsilon_A(\%) = 29.3\,\frac{|d\Omega/dt|}{\Delta\Omega_{cr}/T_a} \qquad [2]$$

$$\begin{aligned} Q_{3dB} &= 1/2\xi = \frac{\Omega_{cr}}{\Delta\Omega_{cr}} \\ \Delta\phi(^\circ) &= 57.5\,\frac{|d\Omega/dt|}{\Delta\Omega_{cr}/T_a} \end{aligned} \qquad [3]$$

The number of measurements between $\Omega_{cr} - \Delta\Omega_{cr}/2$ and $\Omega_{cr} + \Delta\Omega_{cr}/2$ is equal to $(57.5/\Delta\phi) + 1$.

Eqns [2] and [3] relate $|d\Omega/dt|$ and $\Delta\Omega_{cr}/T_a$ which are expressions of pressure gradients. If $|d\Omega/dt| = 0.1$, $\Delta\Omega_{cr}/T_a = 0.1 \times (80\,\text{rpm}/0.2\,\text{s}) = 40\,\text{rpm}\,\text{s}^{-1}$ from 4000 rpm to 0 in 100 s, $\varepsilon_A = 2.9\%$, and $\Delta\phi = 5.75^\circ$. The number of measurements equals 11.

When $\omega_0 = 314\,\text{rad}\,\text{s}^{-1} \approx \Omega_{cr}$ (3000 rpm), $|d\Omega/dt|/\omega_0^2 = 4.2 \times 10^{-5}$, let $|d\Omega/dt| = 4.14$, with $\xi \geq 0.02 (Q_{3dB} \leq 50)$, the transitory machine state is close to steady state. When $\omega_0 = \Omega_{cr}$, eqns [1]–[3] lead to:

$$\begin{aligned} \varepsilon_A &= 14.65\,\frac{\gamma}{\xi}\frac{T_a\varepsilon}{\Omega_{cr}} \\ \Delta\phi &= 28.75\,\frac{\gamma}{\xi}\frac{T_a\phi}{\Omega_{cr}} \end{aligned}$$

where $T_a = \max(T_{a\varepsilon},\ T_{a\phi}) > T_a$ the limit of the acquisition system. $|d\Omega/dt| \leq \gamma\Omega_{cr}^2 : \gamma$ is a function of ξ, and also the ratio of amplitude and phase shift between transitory and steady state region.

Eqns [1]–[4] address the component whose frequency is equal to rotation speed. *A priori*, Ω_{cr} and ξ can be affected by significant uncertainties; the procedure leading to $|d\Omega/dt|$ must be initialized by tests (preferably at reduced or increased speed) at different values of $|d\Omega/dt|$ and minimum T_a. These tests enable to discover the best conditions in which to acquire all the components of the spectrum which are contained in the frequency range of interest and which are necessary for monitoring, protection, and diagnostics. The discrete signals are acquired simultaneously, either in free running or sychronous mode. The noise (runout) accociated with magnetic sensor signals must be subtracted from the equation.

See also: **Balancing**; **Rotor dynamics**; **Rotating machinery, essential features**; **Rotating machinery, modal characteristics**;

Further Reading

Adams ML Jr (1999) *Rotating Machinery Vibration. From Analysis to Troubleshooting*. New York: Marcel Dekker.

Bigret R (1980) *Vibrations des Machines Tournantes et des Structures. [Vibrations of Rotating Machines and Structures.]* Paris: Technique et Documentation Lavoisier.

Bigret R (1997) *Stabilité des Machines Tournantes et des Systèmes. [Stability of Rotating Machines and Systems.]* Simlis, France: CETIM.

Bigret R, Feron J-L (1995) *Diagnostic, Maintenance, Disponibilité des Machines Tournantes. [Diagnostics, Maintenance, Availability of Rotating Machines.]* Paris: Masson.

Boulenger A, Pachaud S (1998) *Diagnostic Vibratoire en Maintenance Préventive. [Vibratory Diagnostics and Preventive Maintenance.]* Paris: Dunod.

Childs D (1993) *Turbomachinery Rotordynamics*. Chichester: John Wiley.

Dimentberg FM (1961) *Flexural Vibrations of Rotating Shafts*. London: Butterworths.

Frêne J, Nicolas D, Dequeurce, Berthe D, Godet M (1990) *Lubrification Hydrodynamique – Paliers et Butées. [Hydrodynamic Lubrication – Bearings and Thrust.]* Paris: Eyrolles.

Gasch R, Pfützner (1975) *Rotordynamik Eine Einführung*. Berlin: Springer Verlag.

Genta G (1999) *Vibration of Structures and Machines*. Berlin: Springer Verlag.

Lalanne M, Ferraris G (1990) *Rotordynamics Prediction in Engineering*. Chichester: John Wiley.

Morel J (1992) *Vibrations des Machines et Diagnostic de leur Etat Mécanique. [Machine Vibrations and Diagnostics of their Mechanical Condition.]* Paris: Eyrolles.

Tondt A (1965) *Some Problems of Rotor Dynamics*. London: Chapman & Hall.

Vance JM (1988) *Rotordynamics of Turbomachinery*. Chichester: John Wiley.

ROTOR DYNAMICS

R Bigret, Drancy, France

Copyright © 2001 Academic Press

doi: 10.1006/rwvb.2001.0091

Introduction

Rotating machinery was defined in the article **Rotating machinery, essential features**. The study of the dynamic performance of rotating machinery, which is essentially vibratory, is the subject of this article. We will follow a simple mathematical model, based on De Laval's study of the rotor.

De Laval (1845–1913) was Swedish. In 1895 Föppl used a model to demonstrate the possibility of a rotation speed which was faster than natural frequency. In 1919 Jeffcot, who was Irish, published an interesting study of a simple model which aroused the interest of other researchers.

These studies shed light on the behavior which had been observed, while mathematics enabled to quantify the phenomena.

Before reading this article, we recommend that the reader refers to the principles of vibratory mechanics which are discussed in other chapters.

From Observation to Models

In 1883 Carl Gustav De Laval's centrifuge passed a critical flexion speed to reach 30 000 rpm: in 1924–25 Newkirk, who was English, encountered a strange phenomenon, which he called oil whip.

A description of the performance of a simple machine, which is the physical model of a whole class of simple machines, provides further information. The simple machine is shown in **Figure 1**; the disk vibrations, perpendicular to the line of rotation, are measured and analyzed by a single magnetic sensor. **Figures 2** and **3** show the amplitude and frequency of the component parts:

- Maximum amplitude is at 9000 rpm close to natural frequency of the stationary rotor placed on rigid supports: 8760 cycle min^{-1}
- When the speed is increased, the frequency suddenly changes from 200 to 106 Hz and the amplitude increases: hysteresis is noted when speed is reduced

Theoretical models enable us to relate these behaviors (critical speed $N = 9000$ rpm, instability at $N \geq 12\,000$ rpm) to the characteristics of the rotor and its links.

Theoretical mathematical models help in diagnostics. They must be complemented by physical information so that adjustments can be made if necessary. Models are the building blocks from which we can create:

- A clarification of the relations between hypotheses and performance
- A review of the hypotheses
- Ideas for the analysis and investigation of complex systems
- Personal communication

De Laval's model

Formulation

In 1686–87 Newton defined the law of inertia. D'Alembert formulated it as $\overrightarrow{F} = \overrightarrow{m\gamma}$ in 1743. **Figure 4** shows De Laval's model of a rotor directed by two links. The equations of movement arise from the combined principle of Newton–d'Alembert. This can be simply expressed as a fixed Galilean referential, taking into account the isotropy of the shaft (the inflexibility which is independent of the azimuth):

$$\left.\begin{aligned}
&m\frac{\mathrm{d}^2 y_c}{\mathrm{d}t^2} + k_a(y_c - y_1) = me\Omega^2 \cos \Omega t = me\Omega^2 \,\mathrm{Re}\,(\exp i\Omega t)\\
&m\frac{\mathrm{d}^2 z_c}{\mathrm{d}t^2} + k_a(z_c - z_1) = me\Omega^2 \sin \Omega t = me\Omega^2 \,\mathrm{Re}\,(-i \exp i\Omega t)\\
&2k_{yy}y_1 + 2k_{yz}z_1 + 2f_{yy}\,\frac{\mathrm{d}y_1}{\mathrm{d}t} + 2f_{yz}\,\frac{\mathrm{d}z_1}{\mathrm{d}t} + k_a(y_c - y_1) = 0\\
&2k_{zy}y_1 + 2k_{zz}z_1 + 2f_{zy}\,\frac{\mathrm{d}y_1}{\mathrm{d}t} + 2f_{zz}\,\frac{\mathrm{d}z_1}{\mathrm{d}t} + k_a(z_c - z_1) = 0
\end{aligned}\right\} \quad [1]$$

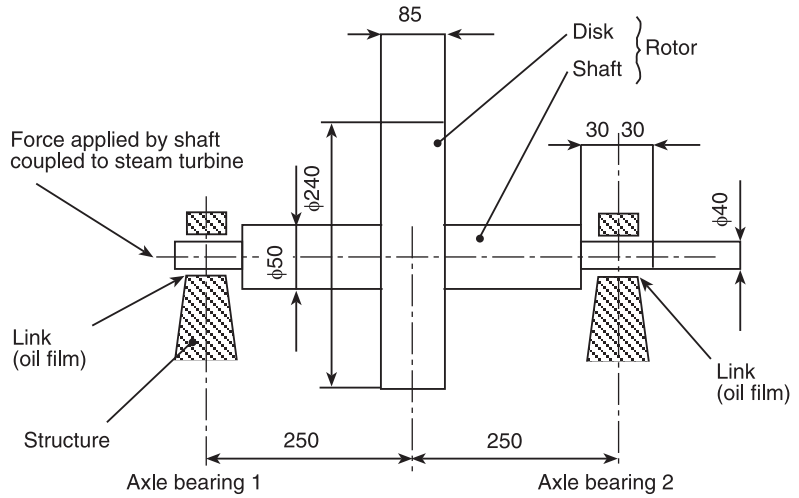


Figure 1 Arrangement of rotor, links, and structure. Connections: circular bearings; diametric clearance: 0.06μm; oil viscosity: 12 CP_o at 60°C.

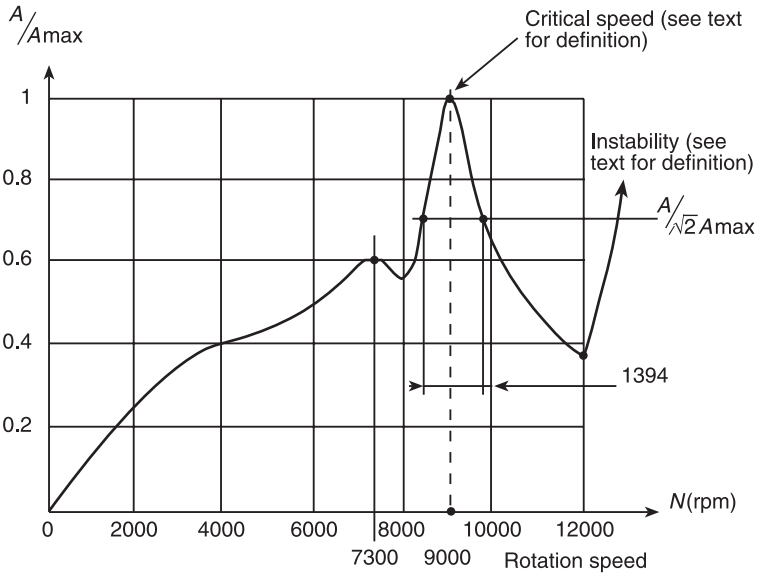


Figure 2 Amplitude of vibration displacement at right-angles to the disk as a function of rotation speed in a vertical direction. Amplification factor: $Q_{3dB} = 9000/1394 = 6.45; \xi = 0.775$.

where Re is the real part and $i^2 = -1$.

More generally, the components of centrifugal force due to $\overrightarrow{CG}$, within the referential whose notation is $C_{y_R z_R}$ are $me\Omega^2 \cos\theta_e$ and $me\Omega^2 \sin\theta_e$. This is expressed by the transformation formula $0yz$, as: $me\Omega^2 \cos(\Omega t + \theta_e)$ and $me\Omega^2 \sin(\Omega t + \theta_e)$.

When the shaft stiffnesses depend on the anisotropic azimuth, the shaft is represented by an impedance matrix which is expressed in the Galilean referential as:

$$\begin{bmatrix} \mathbf{f}_y \\ \mathbf{f}_z \end{bmatrix} = \begin{bmatrix} k'_y\cos^2(\Omega t) + k'_z\sin^2(\Omega t) + \sin(\Omega t)\cos(\Omega t)\left(k'_{yz} + k'_{zy}\right) & \sin(\Omega t)\cos(\Omega t)\left(k'_z - k'_y\right) - \sin^2(\Omega t)k'_{zy} + \cos^2(\Omega t)k'_{yz} \\ \sin(\Omega t)\cos(\Omega t)\left(k'_z - k'_y\right) - \sin^2(\Omega t)k'_{yz} + \cos^2(\Omega t)k'_{zy} & k'_y\sin^2(\Omega t) + k'_z\cos^2(\Omega t) - \sin(\Omega t)\cos(\Omega t)\left(k'_{yz} + k'_{zy}\right) \end{bmatrix} = \begin{bmatrix} \mathbf{d}_y \\ \mathbf{d}_z \end{bmatrix}$$

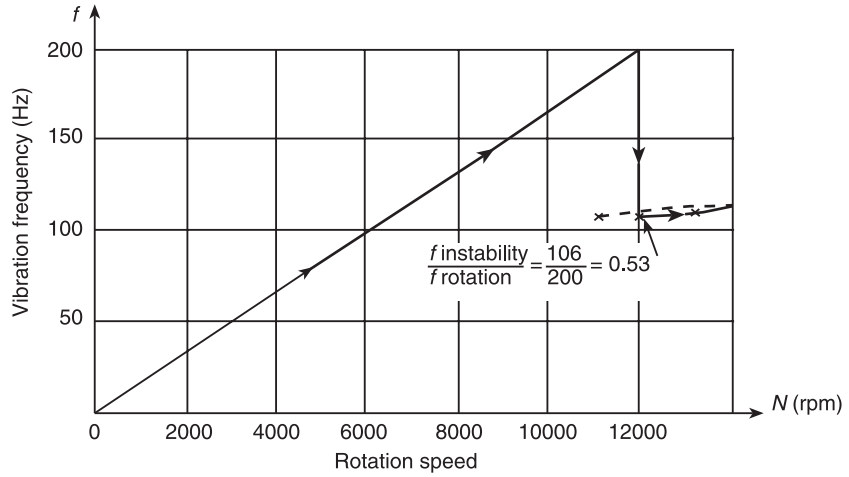


Figure 3 Fundamental vibration frequency as a function of rotation speed.

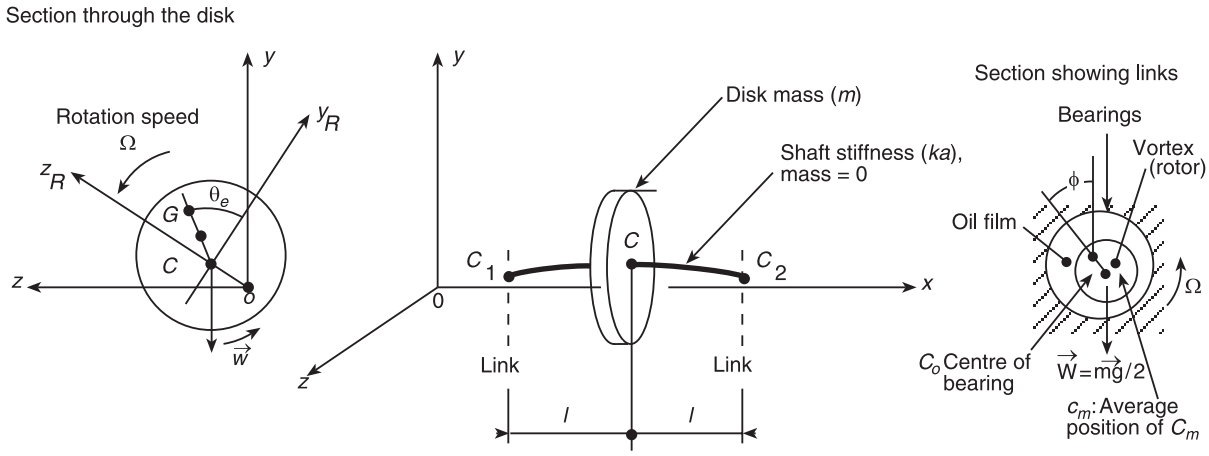


Figure 4 De Laval rotor. Model of right-angle disk. *G*, Mass of barycenter; *C*, geometric center (y_c, z_c); $\overrightarrow{CG}$, eccentricity; $|\overrightarrow{CG}| = e$; $m\overrightarrow{CG}$ = unbalance. Identical links: oil bearings, center of vortex C_1, $C_2(y_1, z_1)$. $\vec{g}$ = acceleration of gravity; $|\vec{g}| = g$.

where k_y' and k_z' are the shaft stiffness associated with the deformations d_y and d_z perpendicular to the disk, in the planes $C_{x_R y_R}$ and $C_{x_R z_R}$, k'_{yz} and k'_{zy} are coupling stiffness, and f_y and f_z are components of the force applied to the disk ($f_y/2$, $f_z/2$ perpendicular to the links).

Harmonic terms can be introduced as $2\Omega t$. They are due to nonlinearities revealing anisotropy, such as fissures, which a diagnostic method must pick up.

The linear equations given above (eqn [1]) provide a theoretical model enabling us to describe the translation movements of C and C_1 and C_2, which are identical, around the position of equilibrium due to gravity, which does not have an explicit effect. The vibrations of the shaft bearings are zero, and impedance is very high.

The links are characterized by a transfer matrix:

$$\begin{bmatrix} k_{yy} + sf_{yy} & k_{yz} + sf_{yz} \\ k_{zy} + sf_{zy} & k_{zz} + sf_{zz} \end{bmatrix} \quad [2]$$

where s is the Laplace operator, related to a frequency ω, $s = i\omega$ where $i^2 = -1$.

Refering to the transfer matrix shown in eqn [2], the impedance of displacement is called isomorphic and isochronic, where $s = i\omega$.

The stiffness, $k_{..}$, and damping coefficient, $f_{..}$, depend on the speed of rotation, Ω, and on the force $\overrightarrow{W}$ ($\vec{m}g$, for example) in the direction $0y$, which determines $\overrightarrow{C_o C_m}$ (**Figure 4**) and on the shape of the bearings (see **Balancing**).

However, the connections between a rotor and nonrotatory structure are not merely based on bearings and fluid. Sealing and magnetic systems are also contributory factors.

When cylindrical bearings of diameter $2R$, clearance to radius J, and length L are submitted to a static force W, fed by viscosity oil μ, the stiffness and damping coefficient, $|\overrightarrow{C_o C_m}| = d$ and angle ϕ (**Figure 4**) can be expressed by dimensionless values:

$$
\begin{aligned}
k_{..}\frac{J}{W} &= F_k\left(S, \frac{L}{2R}\right) = K_{..} \\
f_{..}\frac{J\Omega}{W} &= F_f\left(S, \frac{L}{2R}\right) = F_{..} \\
\frac{d}{J} &= F_d\left(S, \frac{L}{2R}\right) \\
\phi &= F_\phi\left(S, \frac{L}{2R}\right)
\end{aligned}
\qquad [3]
$$

where

$$
S = \frac{\mu\Omega}{\pi}\frac{RL}{W}\left(\frac{R}{J}\right)^2
$$

and d/J is the relative misaxiality, or eccentricity. The radial pressure on the bearings is equal to $W/2RL$, $K_{..}$ and $F_{..}$ vary with d/J.

Note that particular attention must be paid to the symbol conventions used in eqns [1] and [3].

Using the values defined in eqn [3], where $W = mg/2$, eqn [1] can be rewritten:

$$
\begin{aligned}
&\frac{d^2 y_{tr}}{d\tau^2} + y_{cr} - y_{1r} \\
&= \left(\frac{\Omega}{\omega_0}\right)^2 \cos\left(\frac{\Omega}{\omega_0}\right)\tau \\
&= \left(\frac{\Omega}{\omega_0}\right)^2 \mathrm{Re}\left[\exp i\left(\frac{\Omega}{\omega_0}\right)\tau\right]
\end{aligned}
$$

$$
\begin{aligned}
&\frac{d^2 z_{cr}}{d\tau^2} + z_{cr} - z_{1r} \\
&= \left(\frac{\Omega}{\omega_0}\right)^2 \sin\left(\frac{\Omega}{\omega_0}\right)\tau \\
&= \left(\frac{\Omega}{\omega_0}\right)^2 \mathrm{Re}\left[-i\ \exp i\left(\frac{\Omega}{\omega_0}\right)\tau\right]
\end{aligned}
\qquad [4]
$$

$$
\begin{aligned}
&2\left(k_{yy}\frac{J}{mg/2}\right)y_{1r} + 2\left(k_{yz}\frac{J}{mg/2}\right)z_{1r} \\
&+ 2\left(f_{yy}\frac{J\Omega}{mg/2}\right)\frac{\omega_0}{\Omega}\frac{dy_{1r}}{d\tau} + 2\left(f_{yz}\frac{J\Omega}{mg/2}\right)\frac{\omega_0}{\Omega}\frac{dz_{1r}}{d\tau} \\
&+ H(y_{cr} - y_{1r}) = 0
\end{aligned}
$$

$$
\begin{aligned}
&2\left(k_{zy}\frac{J}{mg/2}\right)y_{1r} + 2\left(k_{zz}\frac{J}{mg/2}\right)z_{1r} \\
&+ 2\left(f_{zy}\frac{J\Omega}{mg/2}\right)\frac{\omega_0}{\Omega}\frac{dy_{1r}}{d\tau} + 2\left(f_{zz}\frac{J\Omega}{mg/2}\right)\frac{\omega_0}{\Omega}\frac{dz_{1r}}{d\tau} \\
&+ H(z_{cr} - z_{1r}) = 0
\end{aligned}
$$

where $y_{.r} = y_{.}/e$; $z_{.r} = z_{.}/e$ (relative displacements) and $\omega_0^2 = k_a/m$; $\tau = \omega_0 t$; $H = J\omega_0^2/g$ where Hagg's number $J/\delta f$ and δf is the static rotor arrow on rigid supports with ball joints.

The terms given in brackets in the last two eqns [4] are defined in eqn [3]. Eqn [1] can be expressed by dimensionless values, taking $\Omega t = \tau$ and without introducing ω_0.

Natural Frequencies and Stability

Natural frequencies are modal characteristics of the free response. If the right-hand side of the equation is zero, and the displacements are y_0 and z_0, then the solution to eqn [4] takes the form:

$$
\begin{aligned}
y_c &= Y_c \exp p_r\tau \quad y_1 = Y_1 \exp p_r\tau \\
z_c &= Z_c \exp p_r\tau \quad z_1 = Z_1 \exp p_r\tau
\end{aligned}
\qquad [5]
$$

Incorporating eqn [5] into eqn [4] generates four equations with solutions if the determinant of the unknown terms $Y_c,\ Y_1,\ Z_c,\ Z_1$ is zero.

Development of the determinant leads to a sixth-degree equation, which relates to complex eigenvalues:

$$
pr_l = \frac{\delta_l}{\omega_0} + i\frac{\omega_l}{\omega_0} \quad l = 1, 2, 3; \quad i^2 = -1
$$

where δ_l is the growth factor (> 0) or attenuation factor (< 0), ω_l is damped natural frequency, and p_l is complex eigenvalue. $p_l = \delta_l \pm i\omega_l$ is complex eigenvalue.

Designating as ω_a, the natural frequency of the system defined by eqn [4] where $f_{oo} = 0$ (associated conversative system), $\delta_l = \omega_a\xi_l, \omega_l = \omega_a\sqrt{(1 - \xi_l^2)}$ where $\xi_l < 1$ and ξ_l is attenuation factor or level. The notation is identical to the classic notation used for the system of mass, spring, and damper at one degree of freedom.

Equation (5) permits expressing the solutions in the time domain:

$$
\begin{aligned}
y_{cl} &= Y_{cl} \exp(\delta_l + i\omega_l)t + Y_{cl}^* \exp(\delta_l - i\omega_l)t \\
y_{cl} &= \exp(\delta_l t) A y_{cl} \cos(\omega_l t + \gamma Y_{cl})
\end{aligned}
\qquad [6]
$$

z_{cl}, y_{1l} and z_{1l} are expressed by identical forms (where $\bar{u}$ is an order of u). Free response is defined by:

$$
y_c = \sum_{l=1}^{z} \exp \delta_l t A_{ycl} \cos(\omega_l t + \varphi_{cl}) \qquad [7]
$$

z_c, y_1, and z_1 are expressed by identical forms.

The amplitude $A_{.}$ and phase $\varphi_{.}$ depend on initial conditions which were imposed (see **Rotating machinery, modal characteristics**).

Following eqn [7], so that y_c, z_c, y_1, and z_1 tend towards zero when $t \to \infty$, δ_l must be less than zero, whatever the value of l. Otherwise, instability will ensue. When the logarithmic decrease $\Delta_l = -2(\pi\delta_l/\omega_l)$ is greater than one, the margin of stability is suitable.

Figure 5 shows the limits of stability of the rotor shown in **Figure 1**, guided by two cylindrical bearings characterized by the Sommerfeld number S', the Haag number H', and $L/2R = 1$. Instability can be seen $(\delta_l/\omega_o > 0)$ around $\Omega/\omega_o \approx 1.1$ at frequency $\omega_1 \approx 0.7\omega_o$. Stability is assured for $\Omega < \omega_o$ and for natural frequencies p_2 and p_3.

To clarify, the limit between stability and instability can be obtained with eqn [4] without a second member, looking for solutions of the form:

$$y_{cr} = Y_{cr} \exp p_r\tau \qquad z_{cr} = Z_{cr} \exp p_r\tau$$
$$y_{1r} = Y_{1r} \exp p_r\tau \qquad z_{1r} = Z_{1r} \exp p_r\tau$$

where

$$p_r\tau = (\delta + i\omega)t \quad = \left(\frac{\delta}{\omega_o} + \frac{i\omega}{\omega_o}\right)\tau$$

at the limit $p_r = i\omega/\omega_o$.

From the first two eqns in eqn [4]:

$$Y_{cr} = \frac{1}{1-(\omega/\omega_0)^2}\,Y_{1r} \quad Z_{cr} = \frac{1}{1-(\omega/\omega_0)^2}\,Z_{1r}$$

The two last eqns in eqn [4] lead to:

$$\left\{K_{yy} + iF_{yy}\frac{\omega}{\Omega} - \frac{H}{2}\left[1 - \frac{1}{1-(\omega/\omega_0)^2}\right]\right\}Y_{1r} + \left[K_{yz} + iF_{yz}\frac{\omega}{\Omega}\right]Z_{1r} = 0$$

$$\left[K_{zy} + iF_{zy}\frac{\omega}{\Omega}\right]Y_{1r} + \left\{K_{zz} + iF_{zz}\frac{\omega}{\Omega} - \frac{H}{2}\left[1 - \frac{1}{1-(\omega/\omega_0)^2}\right]\right\}Z_{1r} = 0$$

As for a solution to (Y_{1r}, Z_{1r}), the imaginary and complex parts of the determinant of this system must be zero:

$$M = \frac{H}{2}\frac{(\omega/\omega_0)^2}{(\omega/\omega_0)^2 - 1} = \frac{F_{yy}K_{zz} + F_{zz}K_{yy} - F_{yz}K_{zy} - F_{zy}K_{yz}}{F_{yy} + F_{zz}} \qquad [8]$$

$$(\omega/\Omega)^2 = \frac{(M - K_{zz})(M - K_{yy}) - K_{yz}K_{zy}}{F_{yy}F_{zz} - F_{yz}F_{zy}} \qquad [9]$$

with $H = J\omega_0^2/g$.

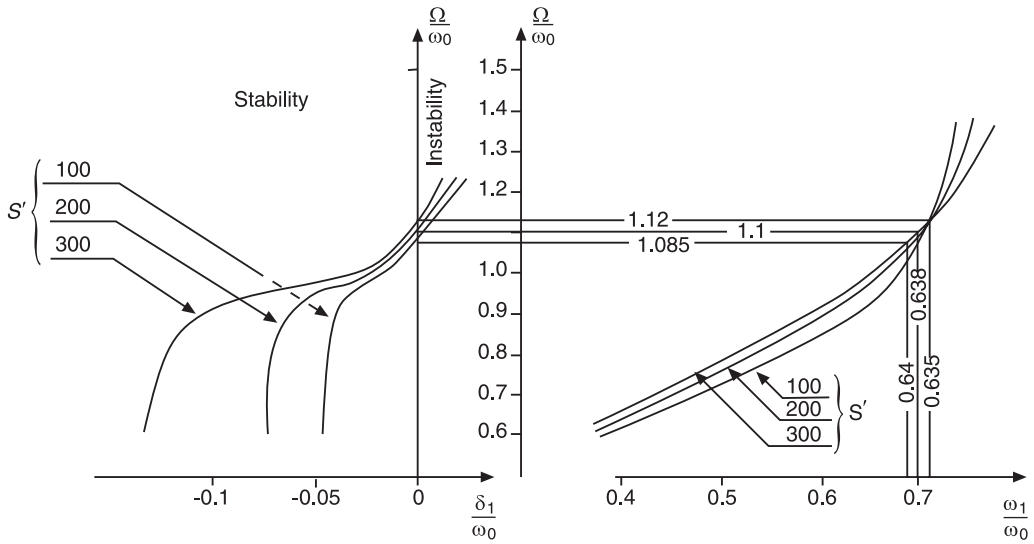


Figure 5 First natural pulsation $\delta_1 + i\omega_1$ of a rotor with oil bearings: instability. Ω: rotation (rad s^{-1}); $\omega = \sqrt{k_a/m}$; $S = \mu\Omega/[(mg/4RL)(J/R)^2] \times (30/\pi)$; Sommerfeld number, $H' = J[(30/\pi)\omega_0]^2/g = 285$; $L/2R = 1$; $g = 9.81\,\mathrm{m\,s^{-2}}$.

The frequency limit of instability is defined by eqn [8]:

$$\omega_{\text{lins}}^2 = \frac{g}{\delta_f - J/2M}$$

where M depends on $F_{..}$ and $K_{..}$ defined as a function of disaxiality and $\delta_f = mg/k_a$ is the rotor tip. The corresponding rotation speed is defined by eqn [9], where $M < 0$, frequency ω_{lins} for a flexible rotor is less than that of of a rigid rotor ($\delta_f = 0$). ω_{limit}^2 and δ_f are connected by hyperbolic law. $(\omega/\Omega)_{\text{limit}}$ only depend on $F_{..}$ and $K_{..}$, and so on S' and $L/2R$. For short cylindrical bearings ($L/2R \leq 0.5$), in 1966 Lund determined $(\omega/\Omega)_{\text{limit}}$ as a function of disaxiality d/J:

$$\begin{aligned} d/J = 0 &\rightarrow (\omega/\Omega)_{\text{limit}} = 0.5; \\ 0 \leq d/J \leq 0.58 &\rightarrow 0.5 \leq (\omega/\Omega)_{\text{limit}} \leq 0.54 \\ d/J = 0.75 &\rightarrow (\omega/\Omega)_{\text{limit}} = 0.1 \end{aligned}$$

Table 1, following Allaire and Flack, defines the stability limits of a rigid rotor (mass m, $W = mg$) on two identical bearings defined in the article on links (see **Bearing vibrations**).

The relationship between speed limits of instability for bearings with two elliptical lobes and with two asymmetric lobes is equivalent to 3.16.

Table 2 shows the stability limits of a De Laval rotor ($W = 1335\,\text{N}$) for two identical cylindrical bearings: $\mu = 0.035\,\text{N}\,\text{sm}^{-2}$; $L = 0.05\,\text{m}$; $D = 0.1\,\text{m}$; $L/D = 0.5$; clearance $= 7.5 \times 10^{-2}\,\text{mm}$; $2J/D = 1.5 \times 10^{-3}$. Limits decrease when δ_f/Cr increases.

Table 1 Limits of stability: $y = S/H_1 = 0.3$; $H_1 = \Omega\sqrt{J/g}$

Bearing	*Sommerfeld number* $S = \frac{\mu\Omega RL}{\pi W}\left(\frac{R}{J}\right)^2$	$\frac{\omega\ \text{Precession}}{\Omega\ \text{Rotation}}$	$\frac{\Omega\ \text{Rotation}}{\sqrt{J/g}}$
Two lobes (elliptical)	1.15	0.495	3.82
Three lobes	1.86	0.470	6.21
Four lobes	1.52	0.475	5.08
Two asymmetric lobes	3.62	0.361	12.07

Table 2 Limits of stability

Tip (δ_f)/ *Clearance (Cr)*	Ω_{Rotation} *(rpm)*	$\omega_{\text{Precession}}$ *(rpm)*	$\Omega_{\text{Rotation}}/\omega_{\text{Precession}}$
0 (rigid)	9530		
0.1	8730	4385	1.99
10	2090	1060	1.97

Natural Modes

Eqn [4], without a second member, in the time domain t, with frequency p_l, is written as:

$$\begin{bmatrix} p_l^2+1 & 0 & -1 & 0 \\ 0 & p_l^2+1 & 0 & -1 \\ A_1 & 0 & A_2+p_lA_3 & A_4+p_lA_5 \\ 0 & B_1 & B_2+p_lB_3 & B_4+p_lB_5 \end{bmatrix} = \begin{bmatrix} Y_{cl} \\ Z_{cl} \\ Y_{1l} \\ Z_{1l} \end{bmatrix} = \begin{bmatrix} 0 \\ 0 \\ 0 \\ 0 \end{bmatrix} \quad [10]$$

The terms $A_{.}$ and $B_{.}$ are defined by the variables of eqn [4]. Three displacements of the matrix column can be calculated using eqn [10], by fixing one of them, for example $Y_{cl} = (Y_{cl})_0 = 1$ to define the natural mode associated with p_l.

$$\begin{bmatrix} (Y_{cl})_0 & Z_{cl}^* & Y_{1l}^* & Z_{1l} \end{bmatrix}^{\text{T}}$$

where T = transposition.

Natural modes are defined by a multiplicative constant, which is taken by $(Y_{cl})_0$. The terms Z_{cl}, Y_{1l}, and Z_{1l} are generally complex. The natural mode corresponding to p_l^* is defined by:

$$\begin{Bmatrix} (Y_{cl})_0 & Z_{cl}^* & Y_{1l}^* & Z_{1l}^* \end{Bmatrix}^{\text{T}}$$

Eqn [6] is an the expression of natural modes in the spatiotemporal domain for initially imposed conditions which permit expression of natural frequency p_l, and p_l^*, by $(Y_{cl})_0$, Z_{cl}, Z_{cl}^*, Y_{1l}, Y_{1l}^*, Z_{1l}, and Z_{1l}^*.

Unbalance Response: Critical Speed

Displacement

The solution to eqn [4] takes the form:

$$u_{.r} = \text{Re}\left[U_{.r} \exp i\left(\frac{\Omega}{\omega_0}\right)\tau\right] \quad [11]$$

where $u_{.r}$: y_{cr}; z_{cr}; y_{1r}; z_{1r}. Calculations can be carried out using expressions, equally in the time domain, t:

$$\begin{bmatrix} 1-(\Omega/\omega_0)^2 & 0 & -1 & 0 \\ 0 & 1-(\Omega/\omega_0)^2 & 0 & -1 \\ C_1 & 0 & C_2+i(\Omega/\omega_0)C_3 & C_4+i(\Omega/\omega_0)C_5 \\ 0 & D_1 & D_2+i(\Omega/\omega_0)D_3 & D_4+i(\Omega/\omega_0)D_5 \end{bmatrix} \begin{bmatrix} Y_{cr} \\ Z_{cr} \\ Y_{1r} \\ Z_{1r} \end{bmatrix} = \begin{bmatrix} (\Omega/\omega_0)^2 \\ -i(\Omega/\omega_0)^2 \\ 0 \\ 0 \end{bmatrix} \quad [12]$$

The dimensionless terms $C_.$ and $D_.$ are defined by the variables given in eqn [1]. The matrix arising from eqn [12] is an impedance matrix $\mathbf{P}$. Thus:

$$[Y_{cr} \quad Z_{cr} \quad Y_{1r} \quad Z_{1r}]^{\mathrm{T}} = \mathbf{P}^{-1}\left[(\Omega/\omega_0)^2 - i(\Omega/\omega_0)^2 \quad 0 \quad 0\right]^{\mathrm{T}} \quad [13]$$

Dimensionless Y_{cr}, Z_{cr}, Y_{1r}, Z_{1r} obtained by eqn [13] are complex, of the form $V_{.r} = |V_{.r}| \exp i\varphi_r$. Thus, taken into account eqn [11]:

$$\begin{aligned} y_0/e &= y_{cr} = |Y_{cr}| \cos\left(\Omega t + \varphi_{yc}\right) \\ z_0/e &= z_{cr} = |Z_{cr}| \cos\left(\Omega t + \varphi_{zc}\right) \\ y_1/e &= y_{1r} = |Y_{1r}| \cos\left(\Omega t + \varphi_{y1}\right) \\ z_1/e &= z_{1r} = |Z_{1r}| \cos\left(\Omega t + \varphi_{z1}\right) \end{aligned} \quad [14]$$

$(\Omega/\omega_0)^2$ intervenes as a factor in each of the modules of eqn [14] which, like the phase $\varphi_.$, varies with speed by Ω/ω_0 and by the Sommerfeld number, on which depend stiffness $k_{..}$ and damping coefficients $f_{..}$, expressed by $C_1 \ldots D_5$. The amplitudes y_c, z_c, y_1, z_1 are in proportion to eccentricity and connected to unbalance, and as a result it becomes possible to reduce them by corrective unbalance which reduces e. For certain values of rotation speed Ω, the modules $|Y_{cr}|$, $|Z_{cr}|$, $|Y_{1r}|$, and $|Z_{1r}|$ are maximal. This speed is the critical speed.

When the impedance of the links is very great, the critical speed is equal to $\omega_0 = \sqrt{k_a/m}$. In the radical plane perpendicular to link 1, y_1 and z_1 (**Figure 6**) are written:

$$\begin{aligned} y_1 &= e|Y_{1r}| \cos\left(\Omega t + \varphi_{y1}\right) \\ z_1 &= e|Z_{1r}| \cos\left(\Omega t + \varphi_{z1} + \pi/2\right) \\ \left|\overrightarrow{OC_{1y}}\right| &= e|Y_{1r}| \\ \left|\overrightarrow{OC_{1z}}\right| &= e|Z_{1r}| \end{aligned} \quad [15]$$

The precession pathway C_1 is elliptical, and is even a circumference or perpendicular. The length of its axes and its angular position in the system of reference $0yz$ are defined by $e|Y_{1r}|, e|Z_{1r}|, \varphi_{y1}$, and φ_{z1}. The length of its axes does not depend on the galilean system of reference. The speed for which the length of the great axis passes by a maximum is a critical speed. Around critical speeds:

$$\frac{\mathrm{d}\left|\varphi_{z1} - \varphi_{y1}\right|}{\mathrm{d}\Omega}$$

may be large.

The precession pathways of rotor geometric centers are circumferences when the rotor is symmetrical about its axis, and the links are isotropes. These links are defined later in this article.

The direction of the course of C_1 on its pathway is identical to that of Ω when $3\pi/2 < \varphi_{z1} + \pi/2 - \varphi_{y1} < \pi/2$: direct precession is inverse when $\pi/2 < \varphi_{z1} + \pi/2 - \varphi_{y1} < 3\pi/2$.

Critical speed is not intrinsic; it depends on the variable used for its determination, unbalance, even exciters. Critical speed may be defined by the vibration of the nonrotating structure.

Critical speed identified by vibrations $y_{1\theta}$, $z_{1\theta}$ in a system of reference at angle θ of $0yz$ is such that:

$$\begin{Bmatrix} \mathbf{y_{1\theta}} \\ \mathbf{z_{1\theta}} \end{Bmatrix} = \begin{bmatrix} \cos\theta & \sin\theta \\ -\sin\theta & \cos\theta \end{bmatrix} \begin{Bmatrix} \mathbf{y_1} \\ \mathbf{z_1} \end{Bmatrix}$$

This led to different values from those identified in the system of reference $0yz$, except if the links are isotropes. The critical speed connected to the components of rotating vectors is not generally intrinsic, in contrast to those defined by maximum values of

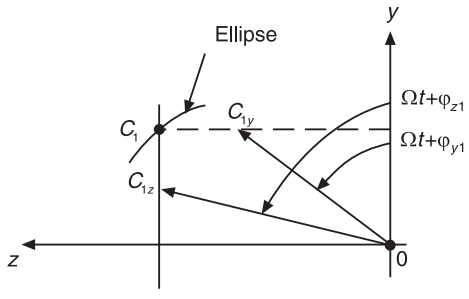


Figure 6 Rotating vectors for displacement of the center C_1 of the vertex.

length of the large elliptical axis, which is the precession pathway.

The preceding considerations are valid for C, the disk center, which in general is more difficult to access for measurements than the centers of vertices C_1 and C_2.

Generally, critical speed is the speed at which vibration amplitude is maximum. This speed is the resonance speed. The speed at which amplitude is minmal is the antiresonance speed.

Unbalance and run out associated with initial peaks, coaxiality faults, and noise on the tracks for measuring rotors (see **Balancing**; **Rotating machinery, monitoring**) can lead to antiresonance, as well as unbalance and run outs.

Forces Knowledge of y_1 and z_1, calculated by measurement, makes it possible to determine the components f_{1y} and f_{1z} of force applied by the rotor on the bearing. According to eqn [15]:

$$\begin{aligned} y_1 &= e|Y_{1r}|\,\mathrm{Re}\left[\exp i\left(\Omega t + \varphi_{y1}\right)\right] \\ z_1 &= e|Z_{1r}|\,\mathrm{Re}\left[-\exp i\left(\Omega t + \varphi_{z1}\right)\right] \end{aligned} \qquad [16]$$

In a similar way:

$$\begin{aligned} f_{1y} &= |F_{1y}|\,\mathrm{Re}\left[\exp i\left(\Omega t + \varphi_{f_{1y}}\right)\right] \\ f_{1z} &= |F_{1z}|\,\mathrm{Re}\left[\exp i\left(\Omega t + \varphi_{f_{1z}}\right)\right] \end{aligned}$$

The two last equations of eqn [1] lead to:

$$\begin{bmatrix} |F_{1y}|\exp i\varphi_{f_{1y}} \\ |F_{1z}|\exp i\varphi_{f_{1z}} \end{bmatrix} = \begin{bmatrix} 2\left(k_{yy} + i\Omega f_{yy}\right) & 2\left(k_{yz} + i\Omega f_{yz}\right) \\ 2\left(k_{zy} + i\Omega f_{zy}\right) & 2\left(k_{zz} + i\Omega f_{zz}\right) \end{bmatrix} \begin{Bmatrix} e|Y_{1r}|\exp i\varphi_{y1} \\ e|Z_{1r}|\exp i\varphi_{z1} \end{Bmatrix} \qquad [17]$$

The stiffness $k_{..}$ and damping coefficient $f_{..}$ are as calculated and confirmed by measurement, in particular that of temperature and oil, of $|\overrightarrow{C_oC_m}| = d$ and ϕ. Multiplication of the square matrix by the column matrix containing measured variables permits the determination of components of force.

As with displacement of the center C_1 (**Figure 6**), the elliptical pathway of the extremity of force can be determined in the same way as critical speed regarding this force and its components. Uncertainty regarding physical links may be caused by nonlinear behavior, which is not taken into account.

When the vibration amplitude of the bearing containing the ball bearing is significant in relation to $e|Y_{1r}|$ and $e|Z_{1r}|$, the relative vibration of the rotor journal in relation to the bearing must be substituted for y_1 and z_1.

Determining the force by measurement is preferable to determining it by calculation. These measurements, which may reduce machine reliability, are not generally performed by manufacturers.

Essentially, complex natural frequency $p_l = \delta_l + i\omega_l$, and associated complex natural modes enable to express free vibratory responses in rotor flexion, following initial imposed conditions.

In the region of linear performance or so-called small movement, stability is insured when all real parts, δ_l, of complex frequency, are negative. During instability a pseudoperiodic evolution operates on the imaginary part ω_l. Corresponding spatial configuration is seen as natural modes which, like natural frequency, depend on rotation speed. The increase in amplitude, for catastrophes, is not systematically observed in machines. Nonlinearity is observed via cycle limits of fixed amplitude which may be acceptable.

The unbalance response permits identification of critical flexion speed for which the vibration amplitude is maximum. This speed is not generally intrinsic. It partly becomes so with the length of the long axis of the elliptical pathway of precession.

The knowledge of stiffness and damping coefficients, associated with calculated or measured vibration, enable to determine force components transmitted to the bearing by the rotor, and corresponding critical speed.

Axial vibration, in the direction of the rotor axis, is acquired by measurements; they result from couplings, axial thrust, and faults, for example of misalignment. Theoretical models are difficult to establish.

The De Laval rotor model enables an interpretation of the performance of a rotating machine when the gaps between natural frequencies $\omega_{l-1}; \omega_l, \omega_{l+1}$ and attenuation factors, or development factors, $\delta_{l-1}; \delta_l, \delta_{l+1}$ are small in relation to ω. This property is a result of modal decomposition, which is defined in the article **Rotating machinery, modal characteristics**, reduced to a term whose form is identical to that of the De Laval rotor. This form makes it possible to estimate a damping factor ξ_l and amplification factor $Q_{3\mathrm{dB}} = 1/2\xi_l$ which is useful for prediction of increase in vibration on passage of a critical speed. As an example, **Figure 2** defines an amplification factor $Q_{3\mathrm{dB}} = 6.45$ and damping factor $\xi = 0.0775$. These values are appropriate.

Model with Isotropic Links

Stability

Particular impedance A liaison is istropic when the relationship between vibrations and forces in the direction of eqn [17] is independent of the system of reference.

Consider a matrix:

$$\begin{bmatrix} k + i\Omega c & c\lambda\Omega \\ -c\lambda\Omega & k + i\Omega c \end{bmatrix} \quad [18]$$

This is a matrix of isochronic transfer and impedance, representing isotropic link where k is stiffness, c is the damping coefficient, and λ is the coefficient.

$$\lambda \approx 0.5 \text{ where } \left|\overrightarrow{C_o C_m}\right| \approx 0$$
$$\lambda \approx 0.45 \text{ where } \left|\overrightarrow{C_o C_m}\right| \approx \frac{1}{2}\Delta R$$

The terms $k + i\Omega c$ express radial forces; $c\lambda\Omega$ expresses tangential forces creating coupling.

The equation of natural frequency is written:

$$(mp^2 + k_a)(-k - k_a - pc + ic\lambda\Omega) + k_a^2 = 0 \quad [19]$$

The limit between stability and instability is determined setting out $\delta = 0$ and so $p = i\omega$. Eqn [19] leads to:

$$\Omega_l^2 = \frac{k_g}{\lambda^2 m} \rightarrow \Omega_l = \frac{\omega_{og}}{\lambda} \quad \text{where} \quad \frac{1}{k_g} = \frac{1}{k_a} + \frac{1}{k} \quad [20]$$

where $\omega_{\text{ins}} = \lambda\Omega_l$ and $\omega_{og}^2 = k_g/m$; $\Omega_l =$ speed at which instability appears at frequency ω_{ins}.

Where $p = \delta + i\omega$ and $\omega = \omega_{\text{ins}} + \varepsilon; \delta$ and ε, which are small, instability is confirmed when $\Omega > \Omega_l$.

The formulae [20] show that:

- Ω_l and ω_{ins} do not depend on c
- instability arises from the coupling term $c\lambda\Omega$ which expresses a tangential force
- where $\lambda = \frac{1}{2}$, the speed limit Ω_l is equal to twice natural frequency ω_{og} of the associated conservative system ($c = 0$)
- the instability frequency ω_{ins} is equal to half rotation speed

The model defined by matrix [18] clarifies the role of coupling terms and describes the 'oil whip', which Newkirk was interested in in 1925, and which is described in many monographs. Diagnostic technicians have focused on the law $\omega_l = \Omega_l/2$, which the French call *fouettement*.

General impedance Let us consider an isotropic link. Its model is:

$$\begin{bmatrix} Z_d(\omega) & Z_c(\omega) \\ -Z_c(\omega) & Z_d(\omega) \end{bmatrix} \quad [21]$$

where $Z_d = Z_d^r + iZ_d^i$ and $Z_c = Z_c^r + iZ_c^i$ and the indices r: real and i: imaginary: $i^2 = -1$. Z_d and Z_c are functions of ω; they depend on Ω. At the limit of stability:

$$\begin{aligned} (k_a - m\omega^2)(k_a + Z_d^r + Z_c^i) - k_a^2 &= 0 \\ (k_a - m\omega^2)(Z_d^i - Z_c^r) &= 0 \end{aligned} \quad [22]$$

From which $Z_d^i = Z_c^r$ and as a result $\omega_{\text{ins}} = F(\Omega)$; substituting the first equation of eqn [22] makes it possible to calculate speed limit Ω_l, at which instability appears.

If $Z_c^r = Z_c^i = 0$, the stability limit cannot be determined. The role of coupling terms is fundamental. Within eqn [18] and eqn [21] they represent a tangential force.

A rigid rotor is defined by $k_a \rightarrow \infty$. In eqn [1] the terms $k_a(y_c - y_1)$ and $k_a(z_c - z_1)$ are replaced by forces and $y_c = y_1,\ z_c = z_1$. With the model [21] at the stability limit:

$$\begin{aligned} -m\omega^2 + Z_d^r + Z_c^i &= 0 \\ Z_d^i - Z_c^r &= 0 \end{aligned}$$

Confirming the role of Z_c as descriptive parameter.

Internal friction in the rotor In the system of reference $0\xi\eta$, in rotation at Ω, internal friction may be caused by rubber and neoprene coupling elements, at insufficient friction of a disk on a shaft. It is expressed by force component:

$$C_i \frac{d\xi_c}{dt} \qquad C_i \frac{dy_c}{dt}$$

where C_i is friction coefficient, and ξ_c and η_c are components of $\overrightarrow{OC}$.

In a galilean system of reference, this force induces a force of radial friction and tangential force. When, perpendicular to links, displacement is zero, i.e. when impedance modules are very great, performance is stable if:

$$\frac{|\Omega|}{\omega_0} < \frac{C}{C_i} + 1 \qquad [23]$$

where $\omega_0^2 = k_a/m$, C = coefficient of internal friction.

In instability frequency is equal to ω_0. Following eqn [22], the stability speed limit increases linearly with C and diminishes hyperbolically when C_i increases. In general weak hysteretic damping of materials does not bring about instability.

Tangential force When a tangential force of components $k_t y_c$ and $-k_t z_c$, where k_t is stiffness, is applied to the rotor disk on rigid links, where displacement is zero, stability is insured when:

$$-2\xi < \frac{k_t}{k_a} < 2\xi$$

where $\xi = c/2\sqrt{k_a m}$ is the damping ratio. When $\xi = 0.02$, the amplification factor is defined by $Q_{3\text{dB}} = 1/2\xi = 25$. k_t/k_a must be less than 0.04.

Response to Unbalance: Critical Speed

With the transfer matrix [18]:

$$|Y_{1r}| = |Z_{1r}| = \frac{(\Omega/\omega_0)^2}{\left|\left[1 - (\Omega/\omega_0)^2\right][\alpha + 2i\xi(1-\lambda)\Omega/\omega_0] - 1\right|}$$

where $\alpha = 1 + k/k_a$ and $\xi = c/2\sqrt{mk_a}$. Critical speed is defined by:

$$\Omega_{cr} \rightarrow \text{MAX}|Y_{1r}|$$

Substituting ξ:

$$\Omega_{cr} = \sqrt{\frac{k_a k}{k_a + k}/m}$$

m, k_a are known and Ω_{cr} is measured, k is determined.

Optimization

An important margin of stability, characterized by $\Omega_{\max} \ll \Omega_{\text{limit}}$, and weak amplitude at critical speed may need optimization in which damping plays an important role. Also, the resistance of the bearings to significant unbalance resulting from a loose element, for example a blade, and from misalignment must be taken into account.

Cycle Limits

Nonlinearities The equations of the models studied above are linear. In instability when $\delta_l > 0$, vibration amplitude tends towards infinity at ω_l. In reality, nonlinearity intervenes to limit amplitude, as long as this intervention is realized before destruction and catastrophe.

Vibration sets in on permanent cycles covering a frequency which may be close to ω_l where $\Omega > \Omega_{\text{limit}}$. Steady state may disappear when amplitude causes wear and tear. Oil whip occurs in a situation of instability at a cycle limit.

Tangential force: nonlinearity The equation of movement of a De Laval rotor subjected to nonlinear tangential force is defined by:

$$m\frac{d^2U_c}{dt^2} + b\frac{dU_c}{dt} + k_a U_c + iU_c k_t(|U_c|) = 0 \qquad [24]$$

where $U_c = y_c + iz_c$ where $i^2 = -1$ and b = friction coefficient > 0; $k_t(|U_c|)$ = stiffness; $|U_c|$ = module of U_c. A solution of the form $|U_c|\exp i\omega t$ can be assumed. Where $k_t(|U_c|)$ is defined by **Figure 7**, two permanent cycles can be seen at 1 and 2 with amplitude $|U_c|_1$ and $|U_c|_2$. These cycles are described as frequency $\sqrt{k_a/m}$ independent of rotation speed. By perturbation imposed on the rotor, cycles can be initialized. The notion of instability, in the direction of small movements, is not necessary for performance at limit cycles, which can result in chaotic performance.

Other situations may occur. To explain the observed $\omega_l = \Omega_l/2$, Newkirk and Taylor used the conservation of oil flow in a bearing shown schematically in **Figure 8**. Ignoring marginal leaks and admitting incompressible oil, it is easy to show that $\omega = \Omega/2$. Equality between ω and ω_l cannot explain friction. In contrast, precession at ω, equal to half rotation speed Ω, suggests the possibility of a different phenomenon.

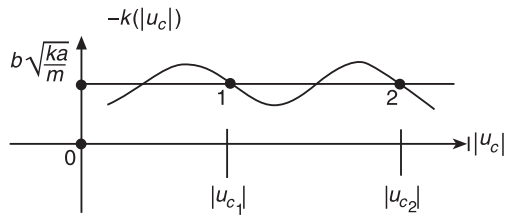


Figure 7 Stiffness of tangential force.

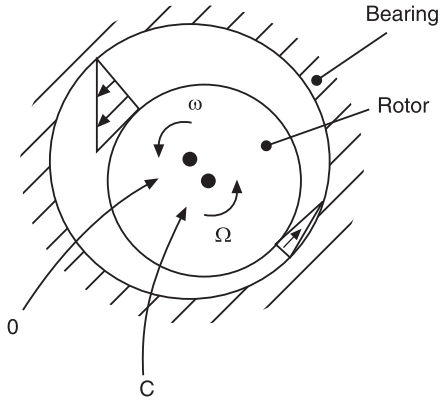


Figure 8 Movement of a whirl in a cylindrical bearing.

For an improved description, eqn [24] becomes:

$$m\,\frac{\mathrm{d}^2U_c}{\mathrm{d}t^2}+b\,\frac{\mathrm{d}U_c}{\mathrm{d}t}+k_aU_c+b_i\left[\frac{\mathrm{d}U_c}{\mathrm{d}t}-i\lambda(|U_c|)\Omega U_c\right]+\left[k_f+\psi(|U_c|)\right]U_c=0$$

$\lambda(|U_c|)\Omega$ expresses the average fluid speed in a bearing, with $\lambda=0$ for $|U_c|=$ clearance, $\lambda=\frac{1}{2}$ for $|U_c|=0$. The amplitude $|U_c|$ of cycle limit on a circumference is defined by:

$$\sqrt{\frac{1}{m}\left[\psi(|U_c|)+k_a+k_f\right]}=\frac{\Omega b_i\lambda(|U_c|)}{b+b_f}$$

Frequency ω of precession is defined by:

$$\omega=\frac{\Omega b_f\lambda(|U_c|)}{b+b_f}$$

when b is small and $\lambda=\frac{1}{2},\omega=\Omega/2$. This is a rotor.

The rotor frequency on a cycle limit is proportional to the rotation speed Ω. A different situation can be seen. The whip frequency on a cycle limit is close to the natural frequency, which is not very sensitive to Ω.

Rotor and friction can exist on the same machine. Models exist making it possible to justify the passage from one situation to another. Bently and Muszynska in 1988 used the impedance complex Z_c at the center of an elastic rotor disk guided by a link with high impedance and by a cylindrical bearing characterized by stiffness K_B, damping coefficient D, and average speed of fluid $\lambda\Omega$. The disk is subjected to a damping force which is proportional to its precession speed. K_B, D, and λ depend on the relationship d/J, of the distance d between the rotor center and the bearing center, at radial clearance J. Canceling Z_c makes it possible to calculate the precession frequency ω of rotation speed Ω. For small values of Ω rotor is evident at $\omega\approx\Omega/2.5$.

For $\omega\approx\Omega/2.7$, a transitional rate of flow appears, expressing the passage from rotor to friction at perceptably constant frequency, independent of speed. The situation varies with different numerical values of the relevant parameter.

In 1990 Grandall adopted the tangential force F_B at right-angles to each of two cylindrical bearings, defined by Robertson in 1933. Balance is expressed by equality between $2F_B$ and the sum of the forces at right-angles to the disk caused by centripetal acceleration and damping leads to $\omega\approx\Omega/2$ and $\omega=\omega_n$, which expresses rotor and friction.

Generally, mathematical models are used to attempt to explain precession observed at cycle limits for frequency in proportion to rotation speed and for frequency close to natural quasi-independent frequency of rotation speed. These states, rotor and friction, are a result of instability. They are explained by varying hypotheses with dominant role to tangential forces to explain instability and cycle limits. Bearings with oscillating runners characterized by impedance matrix, of which the coupling terms are theoretically zero, facilitate stability.

Contacts between rotor and stator have been studied using nonlinear models, which specifically show precession at $\omega\approx\Omega/2$, inscribed between chaotic performance.

Nonlinear performance, which can be approached using theoretical models formed using differential nonlinear equations, can be characterized at a rotation speed Ω by spectral frequency components $\omega_{pq}=(p/q)\Omega$ where p and q are integers.

When ω_{pq} is equal to the natural frequency ω_l, the spectral component amplitude is proportional to amplification factor $Q_{3\mathrm{dB}}=1/2\xi$ as long as gaps $\omega_{l+1}-\omega_l$ and $\omega_l-\omega_{l-1}$ are sufficient. Affecting amplitude changes at such resonance must be qualified by varying Ω, which may lead to significant variations in amplitude. It is important to change the rotation speed in order to avoid any very high amplitude variation.

Harmonic resonance permits the recognition of natural frequency which is greater than rotation speed and confirmation of lower natural frequency at rotation speed, which is encountered at machine start-up and stopping. Gyroscopic couples and link impedance generally depend on rotation speed, and so on the natural frequency. As a consequence, resonance, which is connected to natural frequency, is only defined for the corresponding speed. Nonlinearity may be caused by rotor anisotropy in the poles of electric machines, rotor cracks, coupling faults, contact between rotor and stator, stator faults,

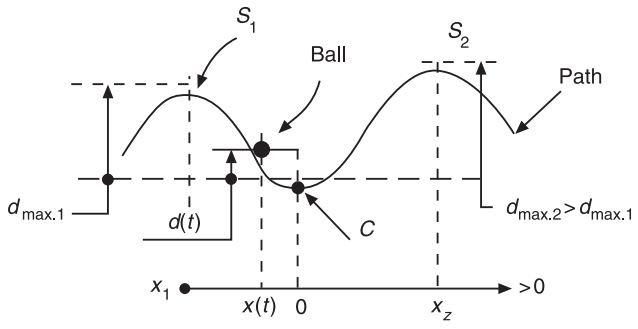


Figure 9 Path of a ball bearing.

significant rotating forces caused by unbalance and peaks, and misalignments.

Stability, Instability, and Chaos

Consider the classic situation of a ball on a track (**Figure 9**). The position of the ball subject to gravity is defined by $d(t)$. Let us take the point of equilibrium as C.

At the point t_0, $d_0 < d_{\max.1}$ defines the ball's initial position. At time t, the position is defined by $d(t)$. It is still possible to find $d_0 = \eta$, such that $d(t) \leq \varepsilon$, when ε is imposed: greater than 0 but less than $d_{\max.1}$. Equilibrium at C is stable. Around C, the stability zone is defined by $d(t) < d_{\max.1}$ where $x > x_1$ and $d(t) < d_{\max.2}$. Let the equilibrium point be S_1.

At the moment t_0, $d_0 < d_{\max.1}$ defines the ball's initial position. At time t the position is defined by $d(t)$. It is not possible to find $d_0 = \eta$ such that $d(t) \leq \varepsilon$ when $\varepsilon \geq d_{max.1}$: equilibrium at S_1 is unstable.

Instability can be seen whatever the sphere considered around S_1. The same is true around S_2. These analyses are facilitated by effecting original changes which make it possible to introduce variables which are zero at C, S_1, and S_2. Essentially, stability and instability are defined in a sphere around a point of equilibrium. If it is very small, local stability–instability is found.

These approaches are due to the definition of Ljapunov (1857–1918), a Russian mathematician who published *General Problem of the Stability of Motion* in 1892.

Consider a system possessing an entry $e(t)$ and an exit $s(t)$. Its state of equilibrium is defined by:

$$e = s = 0$$

At the moment t_0, disturbance $e(t_0) = e_0$ for $t \geq t_0$ leads to variation in $s(t)$. $e(t_0)$ and $s(t_0)$ characterize the initial state. $|s(t)|$ is compared to a value ε which is chosen, which permits one to define a quality by a constraint ($\mathrm{N\,m^{-2}}$) or displacement (μm). If $|s(t)| < \varepsilon$, the system is stable. If $|s(t)| > \varepsilon$, whatever $|e_0|$, the system is unstable. If $|s(t)| \to 0$ when $t \to \infty$, the stability is asymptotic. The checking for stability and instability uses these presentations.

Geometric approaches can be made by pathways in the plane of phase $s(t)$, $\mathrm{d}s(t)/\mathrm{d}t$. **Figure 10** defines the pathway γ_o of a permanent state and γ_p of a disturbed state; stability and instability can be checked by the distance between maximum dimensions of γ_o and γ_p which must be less than a fixed value. The geometric approach is useful for characterizing control of an engine route.

For a system represented by n variables u_i, the definition of stability and instability can be made by applying in perturbation:

$$P_0 = \left[\sum_i u_i^2(0)\right]^{1/2}$$

and observing:

$$R(t) = \left[\sum_i u_i^2(t)\right]^{1/2}$$

Stability is insured if $R(t) < \varepsilon$, asymptotic if $R(t) \to 0$, when $t \to \infty$.

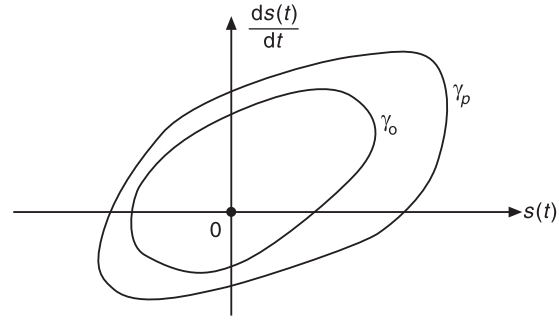


Figure 10 γ_0 = pathway of a permanent state; γ_p = pathway of a disturbed state.

Taking into account a number of values less than n may lead to different conclusions. Certain authors stability consider if it is asymptotic.

The procedure which permits determination of the state as stable or unstable may be directly linked to Ljapunov's definition, which leads to perturbation and evolution of variables u_i; such a procedure is computable. Ljapunov defined two different methods of this direct procedure.

Sensitivity to Initial Conditions (SIC): Chaos

Regarding nonlinear equations, Poincaré evoked unpredictability: 'A very small cause, which escapes us, determines considerable effect which we cannot see, and so we say that this effect is due to chance'.

In the Poincaré phase plane, 'this may happen, or else a point which is very close to the closed pathway remains very close to it, or else it goes further towards infinity, which is at times very close, or else infinite, which once it has gone into the distance remains very far away'.

Poincaré approached SIC and stability and instability without the benefits of a computer.

Lorenz, who was an American meteorologist, in 1963 proposed a system of three nonlinear deterministic and autonomous equations which represented atmospheric circulation:

$$\begin{aligned} \frac{dX}{dt} &= -\sigma X + \sigma Y \\ \frac{dY}{dt} &= rX - Y - XZ \\ \frac{dZ}{dt} &= -bZ + XY \end{aligned} \qquad [25]$$

The three states of equilibrium ($dX/dt = dY/dt = dZ/dt = 0$) are defined by:

$$\begin{aligned} X_1 &= Y_1 = Z_1 = 0 \\ X_2 &= Y_2 = -\sqrt{b(r-1)} \\ Z_2 &= r - 1 \\ X_3 &= Y_3 = \sqrt{b(r-1)} \\ Z_3 &= r - 1 \end{aligned}$$

By computing for the above, the American Lanford showed that, when $r < 1$, X, Y, and Z tend towards 0, whatever the initial conditions: this is asymptotic stability.

When $r > 1$, the appearance of convective circulation makes it possible to define instability.

Whene $r = 28$; $\sigma = 10$; $b = 8/3$, the pathways in a three-dimensional system of reference (X, Y, Z) which appear risky are in fact regular when observed over a significant period of time, and centers around two points, whatever the initial conditions.

It is possible to specify strange attractors by a determinist chaos installed around two points. In so far as dimensions of the domain containing pathways are less than fixed values, it is possible to attribute geometric stability to this state.

The pendulum makes it possible to introduce non-autonomous systems to nonlinear ones, i.e., excited systems.

The equation of the pendulum in the field of gravity, excited at right-angles to its mass element is:

$$\begin{aligned} & ml_0^2 \frac{d^2\theta}{dt^2} + c\frac{d\theta}{dt} + m\, l_0 g \sin\theta = C_e \cos \omega t \\ & \frac{d^2\theta}{d\tau^2} + \frac{c}{ml_0^2}\sqrt{\frac{g}{l_0}}\,\frac{d\theta}{d\tau} + \sin\theta = \frac{C_e}{ml_0} g \cos \frac{\omega}{\omega_0}\,\tau \end{aligned}$$

where

$$\omega/\omega_0 = 2/3; \quad \frac{C_e}{ml_0 g} = 1.5; \quad \frac{c}{(ml_0^2)}\sqrt{g/l_0} = 0.25$$

from two initial conditions ($i = 1, 2$) which are very close, such that:

$$0 < \theta_0^i < 1; \quad -1 < \left(\frac{d\theta}{dt}\right)_0^i < 0$$

the evolution of θ and of $d\theta/dt$ in the phase plane are very different and become chaotic. When:

$$\omega/\omega_0 = 2/3; \quad \frac{c}{ml_0^2}\sqrt{g/l_0} = 0.5; \quad 0.5 \le \frac{C_e}{ml_0 g} \le 1.5$$

chaos sets in around strange attractors. It is possible to attrribute this to geometric stability.

When $1.5 < C_e/ml_0 g < 0.5$, chaos is not seen. States, in forced excitation, are permanent.

When $C_e = 0$, the pendulum is autonomous and stable, towards its attractor, $\theta = 0$. Where there are small movements around the position of equilibrium $\theta = 0$, θ can be substituted for $\sin\theta$ by a Taylor series; excited or autonomous states are stable, and there is no chaos. Around the position of equilibrium, $\theta = \pi$, there is instability.

Generally, variables v and dv/dt, represented in the phase plane, are functions of time; they are checked at the moments $t_n = t_0 + n\Delta t$ (where $n = 1, 2 \ldots$; Δt:

low-value increment). When they describe the vibratory behavior of a rotating machine, it is current practice to adopt $t_{p,q} = t_0 + (p/q)\Omega/2\pi$ (where Ω = rotation speed, and p and q are integers). The function of the plane phase comprises an arrangement of points identified by $t_n(t_{p,q})$; it results from fragmentation; it is fractal. The theory of fractals, introduced in 1975 by Mandelbrot, made it possible to study specific objects.

Initial Deformation and Unbalance

At zero speed, the initial deformation characterized by its module f_0 and its angular position θ_f is defined at the center C of the De Laval rotor disk, in relation to centers C_1 and C_2 of the journal (**Figure 4**). The terms of second members of eqn [1] are:

$$\begin{aligned} &me\,\Omega^2 \cos \Omega t + k_a f_0 \cos\left(\Omega t + \theta_f\right) \\ &me\,\Omega^2 \sin \Omega t + k_a f_0 \sin\left(\Omega t + \theta_f\right) \\ &- k_a f_0 \cos\left(\Omega t + \theta_f\right) \\ &- k_a f_0 \sin\left(\Omega t + \theta_f\right) \end{aligned}$$

Generally, unbalance cannot compensate for a peak whatever the speed. There exist critical speeds and particular situations:$|Y_{cr}|$ is canceled for speed Ω_{ya}, for which $|Z_{cr}|$ does not cancel. This speed is called antiresonance. It is greater than critical speed when $f_0 \gg e$. Perpendicular to the links:

$$|Y_{1r}| = |Y_{1r}|_{y=0}$$
$$|Z_{1r}| = |Z_{1r}|_{y=0}$$

These values are independent of $k_{..}$ and $f_{..}$.

$|Z_{cr}|$ is canceled for speed Ω_{za} for which $|Y_{cr}|$ is not canceled. This speed is called antiresonance. It is greater than critical speed when $f_0 >> e$. Perpendicular to the links:

$$|Y_{1r}| = |Y_{1r}|_{z=0}$$
$$|Z_{1r}| = |Z_{1r}|_{z=0}$$

These values are independent of $k_{..}$ and $f_{..}$.

In addition, $|Y_{1r}|_{y=0} = |Z_{1r}|_{z=0}$ and $|Z_{1r}|_{y=0} = |Y_{1r}|_{z=0}$.

When links are isotropic $|Y_{cr}|$ and $|Z_{cr}|$ are canceled for the same speed Ω_{yza}. The journal centers describe a circumference of the same radius, which is independent of $k_{..}$ and $f_{..}$.

When vibrations at right-angles to links are zero (the impedance of the links is very great), and there exists damping C_a at right-angles to the disk, the pathway from the disk center C is a circumference of radius e, whatever the rotation speed, when:

$$f_0/e = 1; \quad \cos\theta_f = 2\xi_a^2 - 1 \quad \text{where } \xi_a = \frac{c_a}{2\sqrt{mk_a}}$$

When $\xi_a = 0$, $\theta_f = \pi$. When $\xi_a = 0.1$ (amplification factor $Q_{3dB} = 5$), the calculation leads to $\theta_f = 168°30$.

Coaxiality Fault

Figure 11 defines the rotor. When the rotation speed is low, centers C_1 and C_2 describe circumferences of radius $d/2$; the phase difference between $\overrightarrow{OC_1}$ and $\overrightarrow{OC_2}$ is equal to π. Therefore, whatever the speed, $e_1 = e_2$ and $\theta_G = \pi$. When:

$$tg\theta_d = \frac{e_1 + e_2 \sin\theta_G + \varepsilon d \sin\theta_d}{e_1 + e_2 \cos\theta_G + \varepsilon d \cos\theta_d}$$

when $\varepsilon = 1$, the center C_1 is fixed, at 0; the point C_2

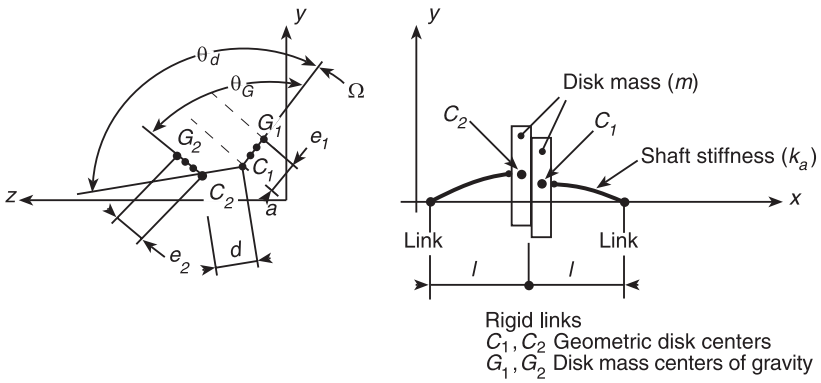


Figure 11 Coaxiality fault in a rotor.

describes a circumference of radius d. When $\varepsilon = -1$, the center C_1 is fixed, at 0; the point C_2 describes a circumference of radius d, whatever the speed. The coaxiality fault brings about antiresonance.

Gyroscopic Couple and Run Out

Formulation

Following Newton (1886–87), and d'Alembert (1743), the Swiss Euler in 1760 extended $\overrightarrow{F} = \overrightarrow{my}$ to the solid in rotation by $\overrightarrow{M_c} = I_\omega (\overrightarrow{d\omega}/dt)$ when $\overrightarrow{M_c}$ is the moment of exterior forces; I_ω is the moment of inertia in relation to the rotation axis: $\overrightarrow{\omega}$.

Figure 12 shows a De Laval rotor guided by high-impedance links (displacements $\approx$ zero from C_1 and C_2); the disk is subject to run outs characterized by angles V_z and V_y.

Within the referential $C_{x_R y_R z_R}$ the components of moments caused by run outs are small; for a thin disk:

Following $C_{y_R} : I_{x_R z_R}\Omega^2 = -(I_{x_R} - I_{z_R})V_y\Omega^2$
Following $C_{z_R} : I_{x_R y_R}\Omega^2 = -(I_{x_R} - I_{y_R})V_z\Omega^2$

Within the galilean referential:

According to $0y$:

$$[-(I_{x_R} - I_{z_R})V_y \cos \Omega t + (I_{x_R} - I_{y_R})V_z \sin\Omega t]\,\Omega^2$$

According to $0z$:

$$[-(I_{x_R} - I_{z_R})V_y \sin \Omega t + (I_{x_R} - I_{y_R})V_z \cos \Omega t]\,\Omega^2$$

In isotopy, where:

$$I_{y_R} = I_{z_R} = I_{d_R} = \frac{mR^2}{4} \quad I_{x_R} = \frac{mR^2}{2}$$

the equations of movement are:

$$\left.\begin{aligned} I_{d_R}\frac{d^2\psi_y}{dt^2} + I_{x_R}\Omega\frac{d\psi_z}{dt} + k_{ra}\psi_y \\ = \Omega^2(I_{x_R} - I_{z_R})(-V_y \cos \Omega t + V_z \sin \Omega t) \\ = \Omega^2\frac{mR^2}{4}\sqrt{V_y^2 + V_z^2}\cos(\Omega t + \psi_v + \pi) \\ I_{d_R}\frac{d^2\psi_z}{dt^2} - I_{x_R}\Omega\frac{d\psi_y}{dt} + k_{ra}\psi_z \\ = \Omega^2(I_{x_R} - I_{z_R})(-V_y \sin \Omega t + V_z \cos \Omega t) \\ = \Omega^2\frac{mR^2}{4}\sqrt{V_y^2 + V_z^2}\sin(\Omega t + \varphi_v + \pi) \end{aligned}\right\} \quad [26]$$

when k_{ra} = stiffness of shaft flexion (couple/rotation around C); ψ_y, ψ_z are rotations around parallel axes at $0y$ and $0z$:

$$\text{tg}\ \psi_v = V_z/V_y$$

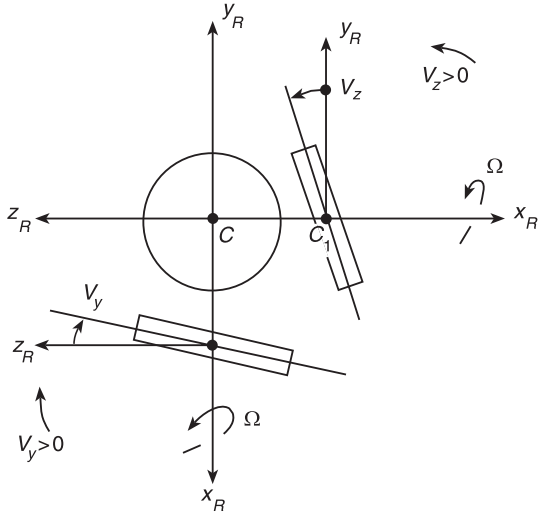
If P disks are arranged on the shaft, the angular distances $(\varphi_p/p) = 1 \ldots p-1$ between the angles representing the run outs are expressed by substituting:

$$\Omega t + \varphi_p \quad \text{for} \quad \Omega t$$

The terms

$$I_{x_R}\Omega\frac{d\psi_z}{dt} \quad \text{and} \quad -I_{x_R}\Omega\frac{d\psi_y}{dt}$$

express coupling by a moment and gyroscopic couple. In 1852, the Frenchman Foucault constructed a gyroscope to show and observe the north, after his experience at the Pantheon in Paris in 1851. The



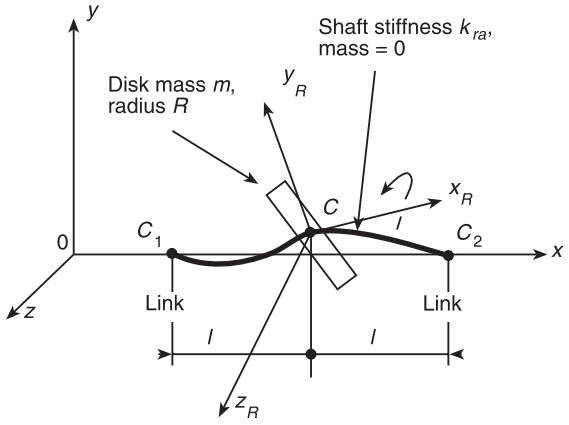


Figure 12 De Laval rotor. Model of run out disk. $C_{x_R y_R z_R}$ = referential linked to the disk; C = geometric center of the disk; moments of inertia I_{x_R}, I_{y_R}, I_{z_R} in relation to C_{x_R}, C_{y_R}, C_{z_R}; $I_{x_R z_R}$, $I_{x_R y_R}$ in relation to C_{x_R}, C_{z_R}, and C_{x_R}, C_{y_R}.

accelerations were demonstrated by the French mathematician Coriolis in 1835, and once applied to the pendulum show the earth's rotation.

Natural Frequencies

The four natural frequencies of the model defined by eqn [26] take the form $p = \delta + i\omega$. As damping is zero, $\delta = 0$ and thus:

$$\frac{2\omega.}{\omega_0} = \frac{\Omega}{\omega_0}\frac{I_{x_R}}{I_{d_R}} \pm \sqrt{\left(\frac{\Omega}{\omega_0}\right)^2\left(\frac{I_{x_R}}{I_{d_R}}\right)^2 + 4} \rightarrow \frac{\omega_1}{\omega_0}; \frac{\omega_2}{\omega_0}$$

$$\frac{2\omega_x}{\omega_0} = \frac{-\Omega}{\omega_0}\frac{I_{x_R}}{I_{d_R}} \pm \sqrt{\left(\frac{\Omega}{\omega_0}\right)^2\left(\frac{I_{x_R}}{I_{d_R}}\right)^2 + 4} \begin{cases} \rightarrow \frac{\omega_3}{\omega_0} = \frac{-\omega_1}{\omega_0} \\ \rightarrow \frac{\omega_4}{\omega_0} = \frac{-\omega_2}{\omega_0} \end{cases}$$

$$\omega_0^2 = \frac{k_{ra}}{I_{d_R}}$$

Figure 13 shows $\omega./\omega_0$ as a function of Ω/ω_0. Free movement is expressed by the vector and components ψ_y and ψ_z whose extremities describe a circumference with pulsation ω_4 (equal to $-\omega_2$) or frequency ω_1 (equal to $-\omega_3$) according to initial imposed conditions. To obtain ω_4:

$$\dot{\psi}_{y0} = -\omega_4\psi_{z0}; \quad \psi_{y0} = 0; \quad \dot{\psi}_{z0} = 0$$

or

$$\dot{\psi}_{z0} = -\omega_4\psi_{y0}; \quad \psi_{z0} = 0; \quad \dot{\psi}_{y0} = 0$$

To obtain ω_1:

$$\dot{\psi}_{y0} = -\omega_1\psi_{z0}; \quad \psi_{y0} = 0; \quad \dot{\psi}_{z0} = 0$$

or

$$\dot{\psi}_{z0} = -\omega_1\psi_{y0}; \quad \psi_{z0} = 0; \quad \dot{\psi}_{y0} = 0$$

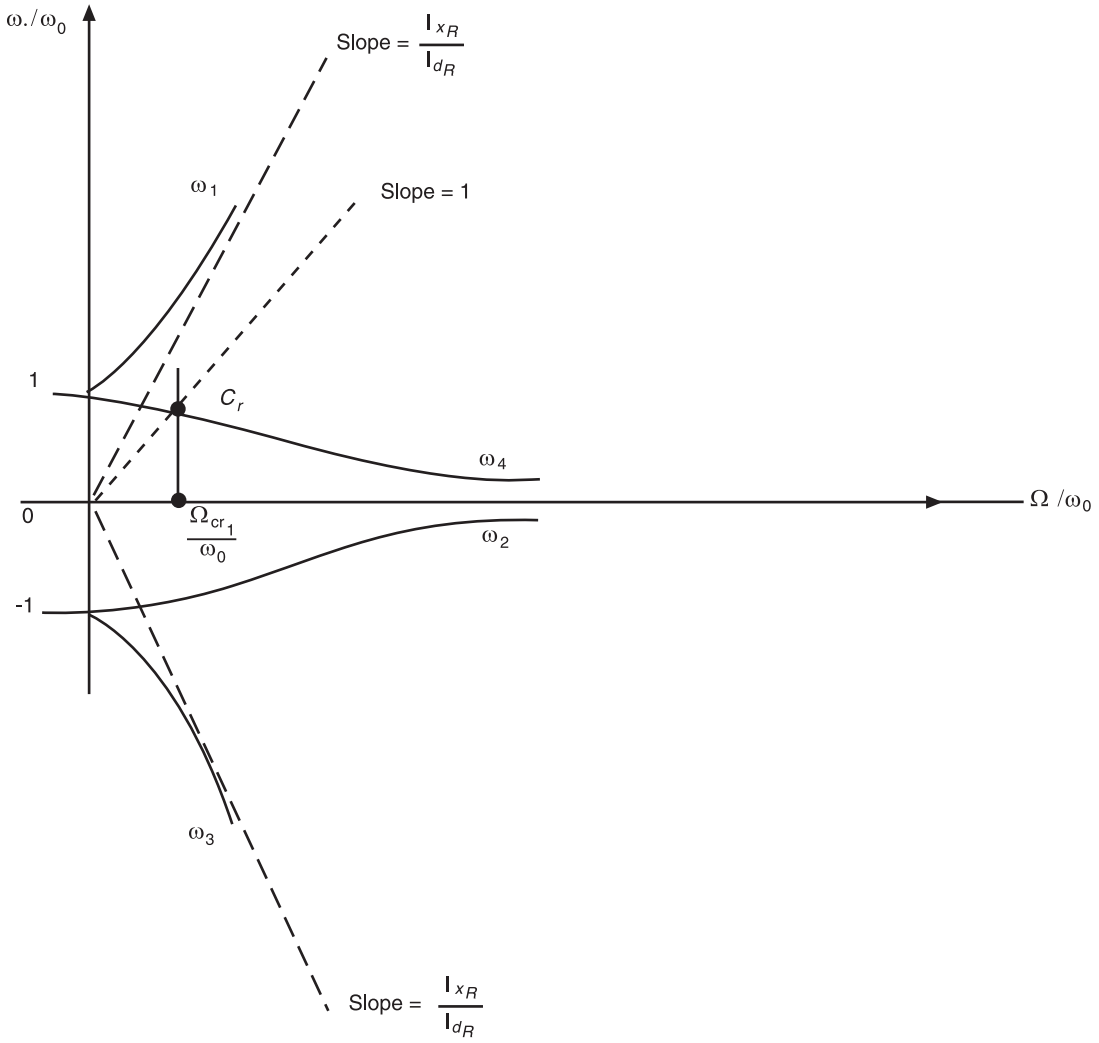


Figure 13 Natural frequencies ω_1, ω_2, ω_3, ω_4. Critical speed Ω_{cr1}.

Precession is inverse. Variation in natural frequency with Ω results from gyroscopic couple and generally, from variation in impedance of fluid links with Ω, expressed by the Sommerfeld number. Natural frequency of a free disk ($k_{ra} = 0$) subject to a damping couple of components $f\dot{\psi}_y$, $f\dot{\psi}_z$, subject to the speed Ω, are $p = -(f/I_{d_R}) \pm i(I_{x_R}/I_{d_R})\Omega$. The launched disk oscillates in translation by ψ_y and ψ_z on frequencies $(I_{x_R}/I_{d_R})\Omega$. The movement may become unstable if $f < 0$. Challenges are posed to those throwing frisbees and boomerangs: they have to find the right direction to throw whene $f > 0$ and good initial conditions to reach their goal.

Critical Speed

In eqn [26] the damping is zero. As a result, the amplitude at critical speed is infinite. The solution to eqn [26] takes the form:

$$\psi_y = \mathrm{Re}\left[A_y \exp i\Omega t\right] \quad \psi_z = \mathrm{Re}[A_z \exp i\Omega t]$$

The determinant of the equations in A_y and A_z is written as:

$$\left(k_{ra} - I_{d_R}\Omega^2\right)^2 \quad -I_{x_R}^2\Omega^4 = 0$$
$$\left(k_{ra} - I_{d_R}\Omega^2 - I_{x_R}\Omega^2\right)\left(k_{ra} - I_{d_R}\Omega^2 + I_{x_R}\Omega^2\right) = 0$$

The critical speed is defined by:

$$\frac{\Omega_{cr1}}{\omega_0} = \frac{1}{\sqrt{1 + (I_{x_R}/I_{d_R})}} \quad \frac{\Omega_{cr2}}{\omega_0} = \frac{1}{\sqrt{1 - (I_{x_R}/I_{d_R})}} \qquad [27]$$

Eqn [27] can be written as:

$$\frac{\mathrm{d}^2U_r}{\mathrm{d}\tau^2} - i\frac{I_{x_R}}{I_{d_R}}\frac{\Omega}{\omega_0} \quad \frac{\mathrm{d}U_r}{\mathrm{d}\tau} + U_r = \left(\frac{\Omega}{\omega_0}\right)^2 \frac{mR^2}{4I_{d_R}} \exp i\left(\frac{\Omega\tau}{\omega_0} + \psi_v + \pi\right) \qquad [28]$$

where:

$$U_r = \frac{\psi_y + i\psi_z}{\sqrt{V_y^2 + V_z^2}} \qquad \tau = \omega_0 t$$

To determine the critical speed:

$$U_r = U_{r1} \exp i\frac{\Omega}{\omega_0}\tau$$

In eqn [28]:

$$U_{r1} = \frac{\dfrac{mR^2}{4I_{d_R}}\left(\dfrac{\Omega}{\omega_0}\right)^2 \exp i(\psi_v + \pi)}{1 - \left(\dfrac{\Omega}{\omega_0}\right)^2 + \dfrac{I_{x_R}}{I_{d_R}}\left(\dfrac{\Omega}{\omega_0}\right)^2}$$

The value of Ω/ω_0 which cancels the denominator defines critical speed as:

$$\frac{\Omega}{\omega_0} = \frac{1}{\sqrt{1 - \dfrac{I_{x_R}}{I_{d_R}}}} \qquad [29]$$

As damping is zero, critical speed is equal to the natural frequency, $\omega_1 = \Omega_{cr}$, $\omega_2 = \Omega_{cr}$:

$$\frac{\Omega_{cr2}}{\omega_0} = \frac{1}{\sqrt{1 - \dfrac{I_{x_R}}{I_{d_R}}}} \qquad [30]$$

When $\omega_3 = \Omega_{cr}$, $\omega_4 = \Omega_{cr}$:

$$\frac{\Omega_{cr2}}{\omega_0} = \frac{1}{\sqrt{1 + \dfrac{I_{x_R}}{I_{d_R}}}} \qquad [31]$$

Formulae [27]–[31] define two critical speeds: Ω_{cr1} occurs whatever the value of I_{x_R}/I_{d_R} and Ω_{cr2} occurs if $I_{x_R}/I_{d_R} < 1$. This condition is expressed in **Figure 13**. Ω_{cr2} is only seen with drum rotors characterized by $I_{x_R}/I_{d_R} > 1$

Damping modifies the critical speed. In **Figure 13** the abscissa of the point of intersection C_r is close to critical speed. The system [26] permits calculation of amplitudes and phase difference of angles ψ_y and ψ_z as a function of Ω.

General Formulation

In a galilean referential, equations of movements of an arrangement of rotor, links, and nonrotating structure result from the principle of Newton–d'Alembert and the theorem of kinetic moment. They are written:

$$\mathbf{M}\ddot{\mathbf{u}} + \mathbf{A}_v\dot{\mathbf{u}} + \mathbf{K}_d\mathbf{u} = \mathbf{S} \qquad [32]$$

$\mathbf{M}$ = mass matrix
$\mathbf{A}_v = \mathbf{A}_e + \mathbf{A}_i + \mathbf{G}$
$\mathbf{A}_e$ = matrix of external damping
$\mathbf{A}_i$ = matrix of internal damping
$\mathbf{G}$ = matrix of gyroscopic effects

$\mathbf{K}_d = \mathbf{K} + \mathbf{K}_i$
$\mathbf{K}$ = stiffness matrix
$\mathbf{K}_i$ = stiffness matrix due to internal damping

The link impedance is expressed in $\mathbf{A}_e$ and $\mathbf{K}$; they may depend on speed Ω. The matrices defined above are square; their order is equal to number of degrees of freedom of rotor and stator elements.

$$\mathbf{U} = \left\{ \ldots y_l \quad \psi_{yl} \quad z_l \quad \psi_{zl} \ldots f_{yp} \quad f_{zp} \ldots \right\}^{\mathrm{T}}$$

y_l, z_l = displacement components of geometric center C_l of element l
ψ_{yl}, ψ_{zl} = rotation components of geometric center C_l of element l
f_{yp}, f_{zp} = force components to right-angles of section p: forces of links, sealing systems, between elements.

The matrix $\mathbf{S}$ permits expression:

- of forces caused by unbalance; for a section k associated with displacement:

$$y_k : m_k e_k \Omega^2 \cos(\Omega t + \psi_k)$$
$$z_k : m_k e_k \Omega^2 \sin(\Omega t + \psi_k)$$

- of moments due to run outs, of an element of slight thickness, of section r associated with rotation: ψ_{yr}, ψ_{zr}:

$$\psi_{yr} \rightarrow \Omega^2 (I_{x_R} - I_{z_R}) \sqrt{V y_r^2 + V z_r^2} \times \cos(\Omega t + \psi_{vr} + \pi + \varphi_r)$$
$$\psi_{zr} \rightarrow \Omega^2 (I_{x_R} - I_{y_R}) \sqrt{V y_r^2 + V z_r^2} \times \sin(\Omega t + \psi_{vr} + \pi + \varphi_r)$$

Moments of inertia $I_{..}$ are related to a system of reference $0_R x_R y_R z_R$ in rotation at Ω, around (**Figure 12**) Cx_R:

- of forces due to initial peaks, in section q
  according to $0y$: $\alpha_q f_0 \cos(\Omega t + \theta_q)$
  according to $0z$: $\alpha_q f_0 \sin(\Omega t + \theta_q)$
- of forces due to coaxiality faults
- of harmonic forces, spectral components of periodic forces

Where $\mathbf{u} = \mathbf{U} \exp pt$ and $\mathbf{S} = \mathbf{0}$, eqn [32] makes it possible to calculate complex natural frequency $p_n = \delta_n + i\omega_n$ and natural connected modes $\mathbf{U}_n$. Expressing $\mathbf{S}$ by the operator Re, solutions for frequency Ω are obtained by posing $\mathbf{U} = \mathrm{Re}[\mathbf{U} \exp j\Omega\tau]$

Particular preceding cases clarify these developments. p_n and $\mathbf{U}_n$ are modal characteristics which are discussed in the article on modal characteristics (see **Rotating machinery, modal characteristics**). Eqn [32] makes it possible to calculate the static state with $\ddot{\mathbf{u}} = \dot{\mathbf{u}} = \mathbf{0}$ and static forces in $\mathbf{S}$, in particular caused by gravity.

Computer software enables one to handle eqn [32] to derive frequency and natural modes of free states and responses to imposed forces and couples; eqn [32] may be set in the form described by Dowson Duncan, which is defined in the article **Rotating machinery, modal characteristics**. Conditions at the limits may be problematic to express; models of elasticity and volume masses must conform to physical values. In certain software, nonlinearities, for example, clearance between exterior cages of bearings and their supports may be introduced. It is important to be aware of tests and their results which make it possible to define domains where the available software give useful results.

Temporary States

A De Laval rotor on rigid links subject to a force of friction (damping factor C) is defined by a mathematical model, as shown in **Figure 4**:

$$m \frac{\mathrm{d}^2 U_c}{\mathrm{d}t^2} + c \frac{\mathrm{d}U_c}{\mathrm{d}t} + k_a U_c = me\left[\Omega^2 - i\alpha\right] \exp i\Omega t$$
$$\frac{\mathrm{d}^2 (Uc/e)}{\mathrm{d}\tau^2} + 2\xi \frac{\mathrm{d}(U_c/e)}{\mathrm{d}\tau} + \frac{U_c}{e} = \left[\left(\frac{\Omega}{\omega_0} \right)^2 - i \frac{\alpha}{\omega_0^2} \right] \exp i \left(\frac{\Omega}{\omega_0} \right) \tau \qquad [33]$$

when:

$$i^2 = -1; \quad U_c = y_c + iz_c; \quad \xi = \frac{c}{2\sqrt{k_a m}};$$
$$w_0^2 = k_a/m; \quad \tau = \omega_0 t$$

$\Omega = \Omega_0 + \alpha t; \Omega_0$ = initial speed; α = constant; > 0 for acceleration; < 0 for deceleration:

$$\frac{\Omega}{\omega_0} = \frac{\Omega_0}{\omega_0} + \frac{\alpha}{\omega_0^2} \tau$$

Eqn [33] shows that $|U_c/e|$ depends on:

$$\xi; \quad \frac{\Omega_0}{\omega_0}; \quad \gamma = \frac{\alpha}{\omega_0^2}$$

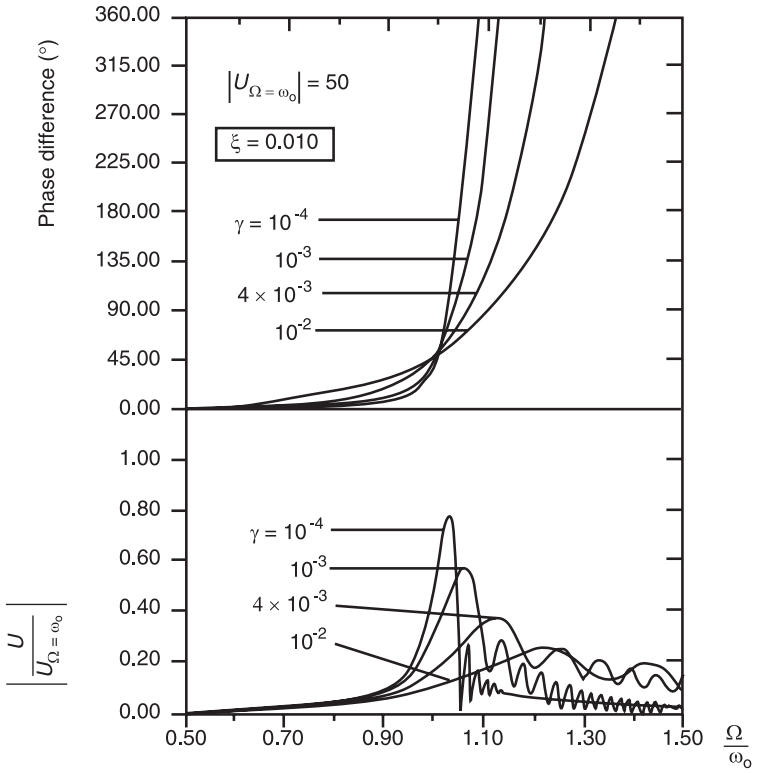


Figure 14 Increase in speed.

In a permanent state ($\alpha = 0$) where $\Omega = \omega_0$ (critical speed), $|U_c/e| = \frac{1}{2}\xi$. The solution in **Figures 14–16** is determined by numerical integration with a time increment equal to $\frac{1}{500}(2\pi/\Omega)$

For values Ω_0 close to $0.5\omega_0$ or $1.5\omega_0$, the results do not vary. $|\Omega_{\max} - \omega_0|$ increases with $|\alpha|(\Omega_{\max} \rightarrow$ maximum speed of $|U_c|)$; where $\Omega \gtrless \Omega_{\max}$, $|U_c|$ can oscillate in frequency close to the magnitude of difference between Ω and ω_0; the damping level ξ, determined by $\Delta\Omega/\Omega_{cr}(\rightarrow Q_{3\text{dB}})$ increases with $|\alpha|$.

Figures 17 and **18** define the displacement magnitude and critical speed as a function of $\alpha/\omega_0^2 = \gamma$. Where $\omega_0 = 94.2\,\text{rad}\,\text{s}^{-1}$ (900 rpm), $\xi = 0.02$ ($Q_{3\text{dB}} = 25$), $\alpha/\omega_0^2 = 2 \times 10^{-3}(\rightarrow \alpha = 17.75\,\text{rad}\,\text{s}^{-2} \rightarrow 170\,\text{rpm}\,\text{s}^{-1})$ the relation between amplitude of temporary and permanent rate of flow is close to 0.7; apparent critical speed is about 6%.

The information provided by the De Laval rotor permits to estimate the rotor performance when the gaps between critical speeds are important.

Acceleration (increase in speed) and deceleration (decrease in speed) are obtained by a couple around the rotation axis. The mathematical model comprises three equations which express equilibrium in three fixed directions: $0y$, $0z$, and $0x$, close to the axis of rotation. $|U_c/e|$ depends on:

$$\xi = \frac{c}{2\sqrt{k_a m}}$$

$$\frac{e}{r} \quad \text{with} \quad r^2 = \frac{I_{x_R}}{m}$$

where I_x is inertia in relation to the axis $\approx$ parallel to $0x$. When the initial position and speed are zero, and when:

$$\frac{C_x}{I_{x_R}\omega_0^2} = \xi = \frac{e}{r} = 0.01$$

the maximum value for $|U_c/e|$ at $\Omega \approx 1.2\ \omega_0$ is equal to 14; in a permanent rate of flow where $\Omega \approx \omega_0$ it is equal to $1/2\xi = 50$; where $\omega_0 = 100\,\text{rad}\,\text{s}^{-1}$ (critical speed $\approx$ 955 rpm), initial acceleration is equal to $10^2\,\text{rad}\,\text{s}^{-2} \rightarrow 955\,\text{rpm}\,\text{s}^{-1}$.

Torsion

The rotor shown in **Figure 19** is in permanent rotation around its axis $0x$. Each section vibrates in relation to this rotation. Between sections k and $k+1$, neglecting the axial moment of inertia, the theorem of the critical moment leads to:

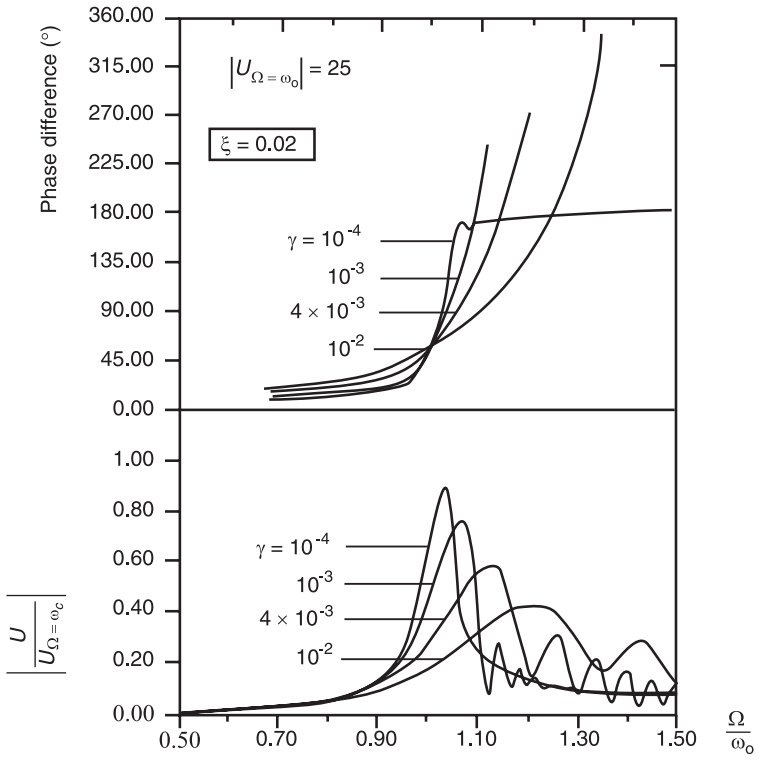


Figure 15 Increase in speed.

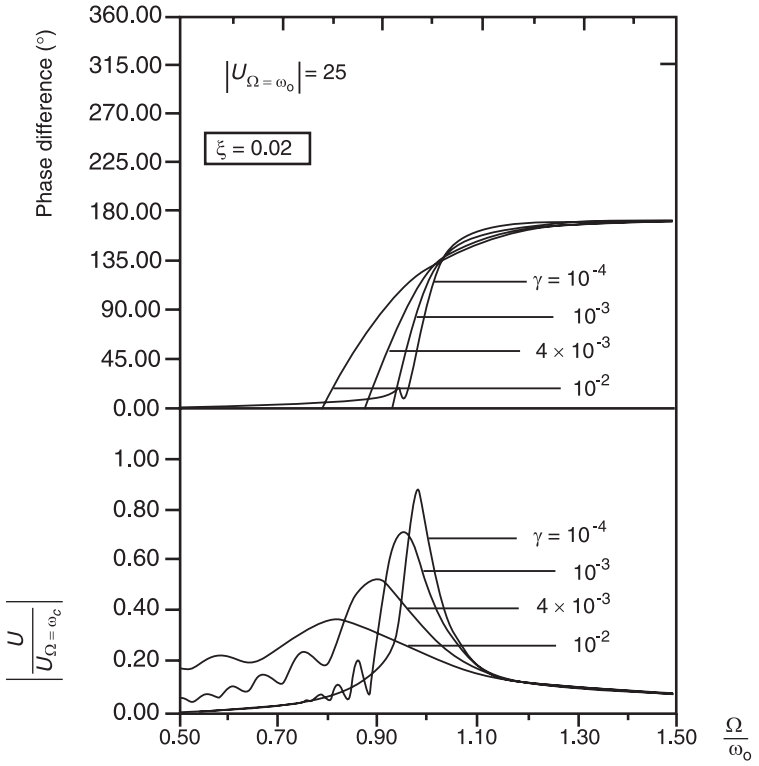


Figure 16 Decrease in speed.

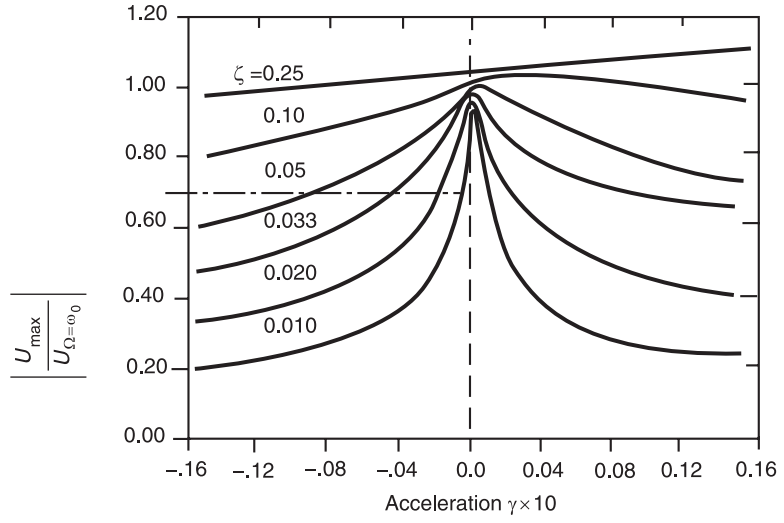


Figure 17 Displacement module U_{max} in transient state.

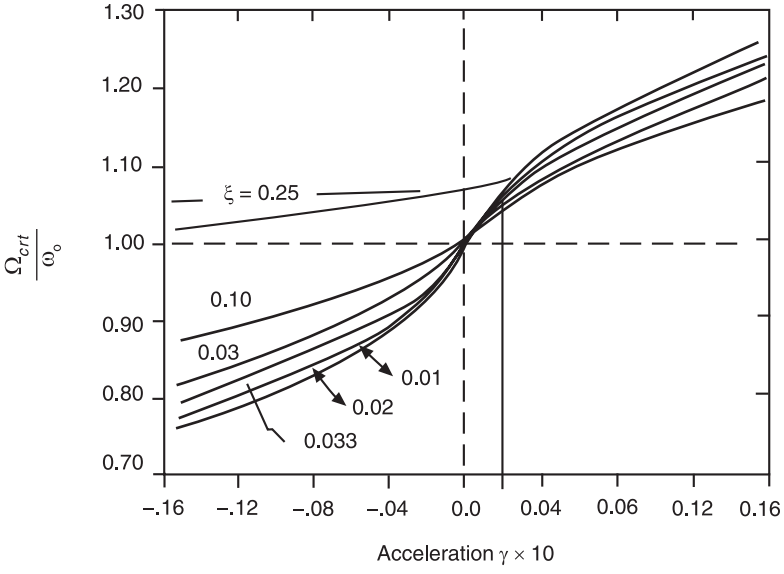


Figure 18 Critical speed Ω_{crt} in transient state.

$$c_{k+1} = c_k = (r_{k+1} - r_k)K^k_{k+1}$$

where $c_. =$ moment of torsion; $r_. =$ angle of rotation in relation to Ωt, $K^x_. =$ torsion stiffness. Between sections $k+1$ and $k+2$, admitting indeformability:

$$c_{k+2} - c_{k+1} + C_{e\,k+1} = I^{k+1}_{k+2}\frac{\mathrm{d}^2 r_{k+1}}{\mathrm{d}t^2} \qquad [34]$$

where $I^x_. =$ moment of inertia; and $C_{e.} =$ exterior moment. In a free state ($C_e = 0$) with: $c_. = C_.\exp pt$; $r_. = R_.\exp pt$ (where the dot . refers to the section index):

$$\begin{bmatrix} C_{k+1} \\ R_{k+1} \\ 1 \end{bmatrix} = \begin{bmatrix} 1 & 0 & 0 \\ \dfrac{1}{K^k_{k+1}} & 1 & 0 \\ 0 & 0 & 1 \end{bmatrix} \begin{bmatrix} C_k \\ R_k \\ 1 \end{bmatrix}$$

$$\begin{bmatrix} C_{k+2} \\ R_{k+2} \\ 1 \end{bmatrix} = \begin{bmatrix} 1 & I^{k+1}_{k+2}p^2 & 0 \\ 0 & 1 & 0 \\ 0 & 0 & 1 \end{bmatrix} \begin{bmatrix} C_{k+1} \\ R_{k+1} \\ 1 \end{bmatrix}$$

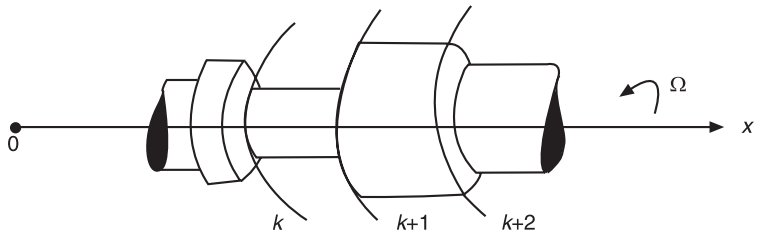


Figure 19 Turning rotor.

where:

$$\mathbf{M}_{k+1} = T_{k+1}\mathbf{M}_k; \quad \mathbf{M}_{k+2} = T_{k+2}\mathbf{M}_{k+1}$$

$T_.$ are elementary transfer matrices. Between section 0 and section N of the extremity:

$$\mathbf{M}_N = T_N T_{N-1} \ldots T_1 \mathbf{M}_0$$

After expressing two conditions at the limits $[C_. = (C_.)_l,\ R_. = (R_.)_l]$, determining the global transfer matrix $T_N\ T_{N-1} \ldots T_1$ leads to the equation with the natural frequency. Natural modes are determined more closely by matrices $T_.$. In a forced rate of flow, $c_{e.} = C_{e.}\cos(\omega t + \varphi_{e.})$ where $c_. \to C_.$; $c_{e.} \to C_{e.} \exp i\varphi_{e.}$; $r \to R$.

Eqn [34] becomes:

$$\begin{bmatrix} C_{k+2} \\ R_{k+2} \\ 1 \end{bmatrix} = \begin{bmatrix} 1 & -I_{k+2}^{k+1}\omega^2 & -C_{e.} \exp i\varphi_{e.} \\ 0 & 1 & 0 \\ 0 & 0 & 1 \end{bmatrix} \begin{bmatrix} C_{k+1} \\ R_{k+1} \\ 1 \end{bmatrix}$$

The global transfer matrix, after expressing two conditions at the limits, leads to two equations with second members which make it possible to calculate $C_.$ and $R_.$ using elementary transfer materials. Critical frequencies, or resonances, are determined by variations in ω; they must be avoided in piston machines excited by periodic forces. Other methods are used which deal with a system of N equations, in the same form as system [32].

See also: **Balancing**; **Bearing vibrations**; **Rotating machinery, essential features**; **Rotating machinery, modal characteristics**; **Rotating machinery, monitoring**; **Rotor–stator interactions**.

Further Reading

Adams ML Jr (1999) *Rotating Machinery Vibration. From Analysis to Troubleshooting*. New York: Marcel Dekker.

Bigret R (1980) *Vibrations des Machines Tournantes et des Structures. [Vibrations of Rotating Machines and Structures.]* Paris: Technique et Documentation Lavoisier.

Bigret R (1997) *Stabilité des Machines Tournantes et des Systèmes. [Stability of Rotating Machines and Systems.]* Simlis, France: CETIM.

Bigret R, Feron J-L (1995) *Diagnostic, Maintenance, Disponibilité des Machines Tournantes. [Diagnostics, Maintenance, Availability of Rotaing Machines.]* Paris: Masson.

Boulenger A, Pachaud S (1998) *Diagnostic Vibratoire en Maintenance Préventive. [Vibratory Diagnostics and Preventive Maintenance.]* Paris: Dunod.

Childs D (1993) *Turbomachinery Rotordynamics*. Chichester: John Wiley.

Dimentberg FM (1961) *Flexural Vibrations of Rotating Shafts*. London: Butterworths.

Frêne J, Nicolas D, Dequeurce, Berthe D, Godet M (1990) *Lubrification Hydrodynamique – Paliers et Butées. [Hydrodynamic Lubrication – Bearings and Thrust.]* Paris: Eyrolles.

Gasch R, Pfützner (1975) *Rotordynamik, Eine Einführung*. Berlin: Springer Verlag.

Genta G (1999) *Vibration of Structures and Machines*. Berlin: Springer Verlag.

Lalanne M, Ferraris G (1990) *Rotordynamics Prediction in Engineering*. Chichester: John Wiley.

Morel J (1992) *Vibrations des Machines et Diagnostic de leur Etat Mécanique. [Machine Vibrations and Diagnostics of their Mechanical Condition.]* Paris: Eyrolles.

Tondt A (1965) *Some Problems of Rotor Dynamics*. London: Chapman & Hall.

Vance JM (1988) *Rotordynamics of Turbomachinery*. Chichester: John Wiley.

ROTOR–STATOR INTERACTIONS

R Bigret, Drancy, France

Copyright © 2001 Academic Press

doi: 10.1006/rwvb.2001.0095

Introduction

The rotor and stator of rotating machinery are connected by elements which enable the rotor to rotate within the stator. Other links insure effective sealing. Forces and displacements are transferred by means of such elements. Forces can also be transmitted by fluids manipulated by rotors, especially turbomachine rotors, as well as by magnetic fields and coupling. These forces and displacements and their variations must guarantee constant stability, low vibratory limits, in particular at critical speed, and rotor–stator distances which are greater than fixed limits but below which the risk of contact is significant. In certain areas the rotor–stator distances are small to avoid a negative effect on the output. Contact can lead to wear and tear, deterioration, and even catastrophe. Particular behavior may be seen as limited cycles of instability or chaotic cycles.

HD Taylor, an engineer for General Electric (New York), published in 1924 *Rubbing Shafts Above and Below the Resonance (Critical Speed)*. In 1925 Thomas, a German engineer, described violent vibrations of a vertical rotor whose critical speed was greater than its nominal speed. In 1926 Newkirk published *Shaft Rubbing*, demonstrating that the speed of significant vibration was less than critical speed, and that this vibration could increase. This was termed the Newkirk effect. These studies, which attempt to explain observations using theoretical models, were the inspiration for numerous publications and research studies.

Contact as a Machine Slows Down

Example

After the alternator has been activated, when a 1000-MW turboalternator rotor slows down from 1500 rpm to ≈ 0 rpm, significant levels of vibration are seen on the bearings of a high-pressure turbine. If it is started up 15 min after being turned to 8 rpm, levels of vibration which are above the limit interrupt operation. If it is changed after 2 h, the positions of the vortices of the high-pressure turbine rotor in relation to the bearings, measured by relative magnetic captors, go from 41 to 29 μm and from 35 to 20 μm.

The height of the sealing systems at the edges of the high-pressure rotor is increased by 0.3 mm. When the machine starts up and slows down after this point, the levels of vibration are appropriate. These operations support the hypothesis of a rotor peak following anisotropic overheating, caused by contact with sealing systems.

Cycle Limited to Low Frequency and Light Contact

Figures 1 and **2** show the first harmonic of the two relative vibrations measured on-site. A so-called pseudoperiod of ≈10 h 30 min can be seen.

Using a theoretical model of the rotor–stator arrangement, as shown in **Figure 3**, an explanation for the behavior shown in **Figures 1** and **2** can be proposed. The equations for the model proposed by Kellenberger are a product of the following essential hypotheses:

- The peak at C is the sum of a mechanical peak ρ_M due to unbalance ($m_r e$) and of a thermal peak ρ_T caused by overheating provoked by rotor–stator contact. A distance of 1°C between two opposing generations of a rotor of diameter 0.5 m, of length 2 m (≈3000 kg), yields a neighboring peak of 10 μm (unbalance equivalence: 0.120 kg at 0.25 m).
- On contact the stator applies a force F_f on the rotor, where $F_f = F_R - i\mu F_R (i^2 = -1$; where μ is the coefficient of friction).
- The thermal peak $|\rho_T|$ is proportional to the temperature difference T between two generations of the rotor: $|\rho_T| = \alpha_1 T$ where:

$$\frac{\mathrm{d}|\rho_T|}{\mathrm{d}t} = \frac{\alpha_1 \alpha_3}{\alpha_2} \mu \frac{\Omega}{\omega_0} \frac{\Phi}{2} |F_R| - \frac{\alpha_4}{\alpha_2 \omega_0} |\rho_T|$$

where: $\omega_0 = \sqrt{k_r/m_r}$; $Q = \alpha_2 (\mathrm{d}T/\mathrm{d}t)\Delta t$ (heat (quantity)
$Q = Q_1 - Q_2$; $Q_1 = \alpha_3 \mu \Omega (\Phi/2)|F_R|\Delta t$ (heat quantity received by rotor with friction)
$Q_2 = \alpha_4 T \Delta t$ (heat quantity supplied by external rotor).

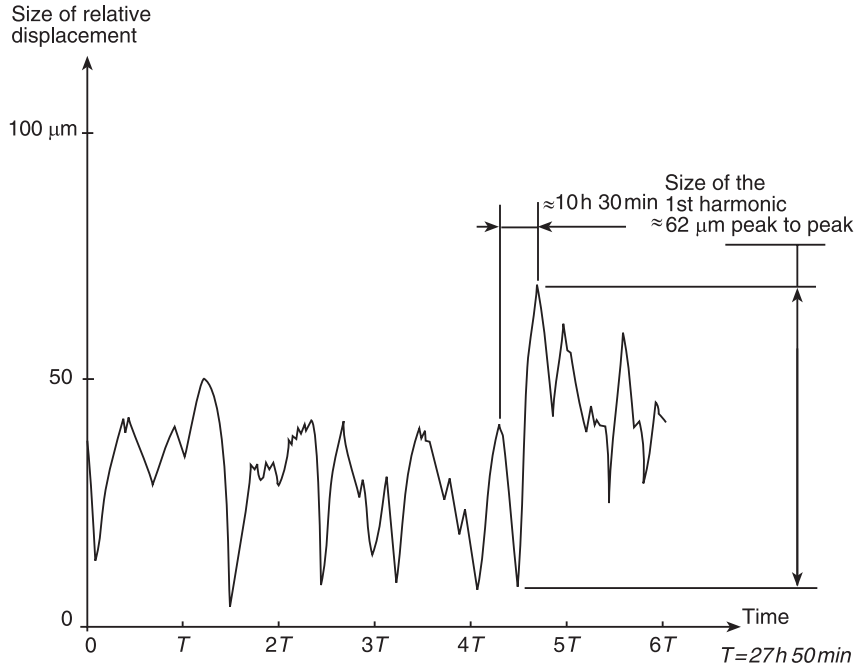


Figure 1 Size of the first harmonic (frequency = rotation speed) of relative displacement of the high-power turboalternator rotor with relation to the labyrinths of the sealing device of the low-pressure body near the alternator.

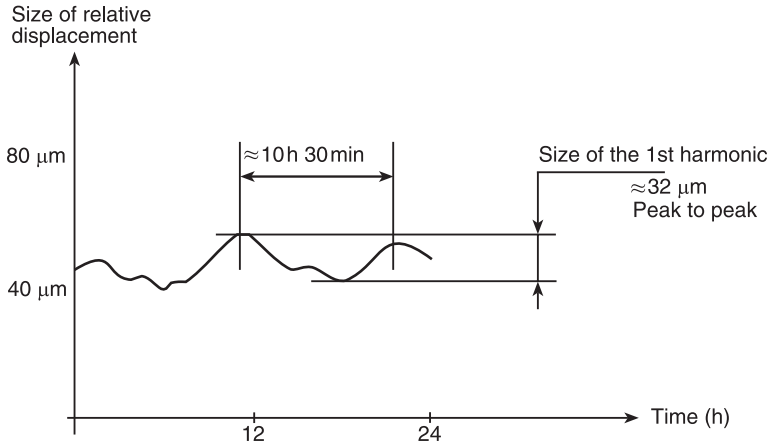


Figure 2 Size of the first harmonic (frequency = rotation speed) of relative displacement of the high-power turboalternator rotor with relation to the bearing arranged between the low-pressure body and the alternator.

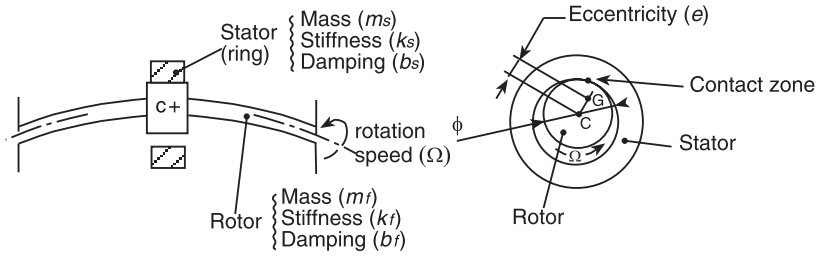


Figure 3 Rotor–stator arrangement in contact. *C*, geometric center of rotor; *G*, mass barycenter of rotor.

- ρ_M and ρ_T provoke a rotating force at rotation speed Ω.
- Balance between rotor and stator is expressed by the d'Alembert principle ($\vec{F} = \overrightarrow{m\gamma}$).

Admitting F_R, ρ_T, and $\mathrm{d}\rho_T/\mathrm{d}t$ in the same direction, so that the variations in ρ_T are slow:

$$A\frac{\mathrm{d}\rho_T}{\mathrm{d}\tau} + B\rho_T = e\left(\frac{\Omega}{\omega_0}\right)^2 \text{ where } \tau = \omega_0 t$$

$$\rho_T = e\left(\frac{\Omega}{\omega_0}\right)^2 \frac{1}{B}\left[1 - \exp\left(-\frac{B}{A}\right)\tau\right] \text{ where } \rho_T(0) = 0$$

A and B are complex numbers which depend on the characteristics of the set. It is stable if the real part of $-B/A$ is negative.

Figure 4 shows the regions of stability and instability. Instability can be seen for $\Omega/\omega_0 < 1$ (see (2) on **Figure 4**) and for $1 > \Omega/\omega_0 > 1$ (see (1) on **Figure 4**). In fact, measured observations (**Figures 1** and **2**) show the range of cycle limits due to nonlinearities excluded from theoretical models. Cycles modulate the range of the first harmonic, of which the frequency equals $\Omega/2\pi$.

In 1926, Newkirk studied the reason for instability at $\Omega/\omega_0 \ll 1$. When rotor speed Ω is less than the first critical flexion speed ($\approx \omega_0$), the phase difference φ between rotating force due to unbalance, and deformation induced by it is between 0 and $\pi/2$, close to $\pi/2$ for $\Omega = \omega_0$ (resonance). The contact between rotor and stator causes local rotor overheating and so an increase in deformation. The rotating force arising as a result of this deformation is comprised of a rotating force due to unbalance, and this force acts at the angle φ of deformation. Parallel lines to the rotor axis at the stator contact is different from that of preceeding phases. The contacts which follow are a result of the same process. They can overheat different parallel lines to the rotor axis, leading to instability.

This subject has led to a number of different studies. The results from theoretical models are similar in quality. Situations vary depending on the hypothesis. Chaos may occur.

Deterministic Contacts

The violent appearances of unbalance following rotor deterioration (broken blade, winding, crack developing) may bring about destructive contacts which require repair and analysis *a posteriori*, after machine shutdown, activated by a protection system which is sensitive to vibration.

Without immediate deterioration, contacts are seen by a transformation in vibratory states (see **Rotating machinery, modal characteristics**).

One particular study shows the influence of clearance. Carried out by Yamamoto in 1954, it

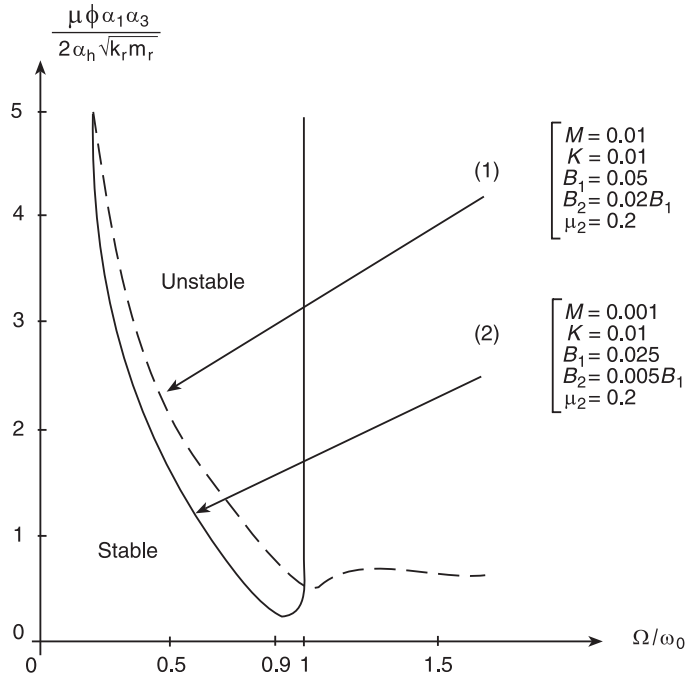


Figure 4 Regions of stability and instability. $M = m_s/m_r$, $K = k_s/k_r$, $B_1 = b_r/\sqrt{k_r/m_r}$ and $B_2 = b_s/\sqrt{k_r m_r}$.

considered a vertical De Laval rotor (not taking into account gravity) with unbalance me. The stiffness of the shaft, k_a, and the damping coefficient, c, led to $\omega_0 \approx \sqrt{k_a m}$, $\zeta = c/2\sqrt{k_a m}$. The shaft is guided by two cylindrical bearings. Clearance is represented by J. When amplitude A of vibration at rotation speed Ω is less than J, the shaft bending is zero, and the forces perpendicular to the bearings are equal to $k_c A$. When $A > J$, the shaft bending results from k_a and k_c. **Figure 5** shows a situation where, with resonance $\Omega \approx \omega_0$; $A/e \approx 1/2\zeta = 20$. This amplitude is close to that of the rotor guided by links, where $J = 0$. Orbits relating to an increase and decrease in speed are very different from each other.

In 1987 Choi and Noah and in 1991 Kim and Noah introduced radial forces to bearings; analyses carried out using a perturbation method essentially confirmed Yamamoto's results.

Theoretical models have been proposed to analyze the vibration behavior. These models comprise elastic, friction, and even damping forces. These forces are expressed by displacement of order 1 (region of linearity), and 2, 3 ... (region of nonlinearity). Other nonlinearities may be taken into consideration, particularly intermittent contacts which may produce chaos.

Malkin has shown that, in a system represented by nonlinear equations, excited at frequency Ω, resonance may occur for Ω such that:

$$u\Omega = \sum_{k=1}^{n} N_k \omega_k$$

where $u = 1, 2, 3 \ldots$; $N_k = 0, \pm 1, \pm 2 \ldots$; $\omega_k =$ natural frequency of the associated conservative linear system. This relation allows:

$$\Omega = p\omega_k (p = 1, 2, 3); \quad \Omega = \frac{\omega_k}{u}; \quad \Omega = p\frac{\omega_k}{u}$$

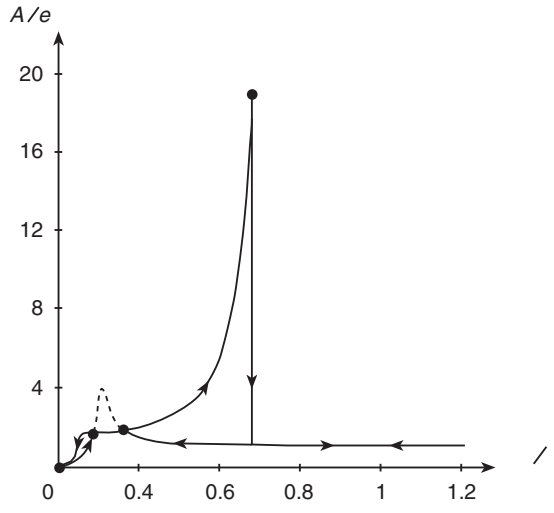


Figure 5 Size A at rotation speed Ω.
e: eccentricity; $k_c/k_a = 0.04$; $\xi = 0.025$; $J/e = 1.5$.

Example 1

A model with elastic nonlinear recall is expressed by:

$$m\frac{d^2y}{dt^2} + k_1 y + k_3 y^3 = me\Omega^2 \cos \Omega t \qquad [1]$$

This equation was formulated by Duffing in 1918 (see **Bearing vibrations**).

Research into a solution using perturbation methods ($y = y_1 + \Delta y$) leads to a Mathieu equation $(d^2u/d\tau^2) + (a - 2q \cos 2\tau)u = 0$. The terms of this equation are dimensionless: $0 < a < \infty$; $-\infty < q < \infty$. Instability appears for:

$$\Omega = \Omega_{ins} \approx \frac{1}{\sqrt{a}}\omega_0 \sqrt{1 + \frac{3k_3}{2k_1} Y_1^2} \qquad [2]$$

where $\omega_0 = \sqrt{k_1/m}$; Y_1 = amplitude where $C3 = 0$; $a = 1, 4, 9, 16 \ldots$. When $(3k_3/2k_1)Y_1^2 \approx 0$, $\Omega_{ins} \approx \omega_0/\sqrt{\alpha} = \omega_0$; $\omega_0/2$; $\omega_0/4 \ldots$. The model's forced rate of flow represented by Duffing's equation with damping expressed by $c(dy/dt)$ in eqn [1] was studied by Timoshenko and colleagues.

Around the critical speed, **Figure 6** shows the amplitude of the solution $y_1 = Y_{1T} \cos(\Omega t - \psi)$. At the point C_r, the amplitude is violently reduced (in a jump) for a weak variation of Ω according to the pathway $C_r B'$. Around the state C_r the state is unstable.

Y_{1T} is defined by:

$$\frac{3}{4}\frac{k_3}{k_1} Y_{1T}^3 = \left[\left(\frac{\Omega}{\omega_0}\right)^2 - 1\right] Y_{1T} + e\left(\frac{\Omega}{\omega_0}\right)^2 \sqrt{1 - 2\xi\left(\frac{\omega_0}{\Omega}\right)\frac{Y_{1T}}{e}} \qquad [3]$$

where

$$\xi = \frac{c}{2\sqrt{k_1 m}}$$

ψ is defined by

$$\mathrm{tg}(\psi) = \frac{2\xi\Omega/\omega_0}{1 - (\Omega/\omega_0)^2 + \frac{3}{4}\frac{k_3}{k_4} Y_{1T}^2}$$

$(Y_{1T})_{cr}$ is defined by:

$$\frac{(Y_{1T})_{cr}}{e} = \frac{1}{2\xi}\frac{\Omega_{cr}}{\omega_0}$$

$(Y_{1T})_{cr}$ and Ω_{cr} are determined using eqn [3].

When $\xi = 0$, eqn [3] leads to the equation describing the curve C_oC_r (**Figure 6**). Comparing between eqns [2] and [3] results in: $Y_1 = \sqrt{2}Y_{1T}$.

At the limit of stability, the amplitude Y_1 of movement in the linear range is greater than the amplitude y_{1T} of movement in the nonlinear range.

Free movement ($me = 0$) of the associated conservative system ($c = 0$) initialized by $y(0) = Y_m$; $dy(0)/dt = 0$, can be seen with the components of frequencies:

$$(2k+1)\omega_{lk};\ k = 0, 1, 2\ldots$$

For the first approximation, where $k = 0$:

$$\frac{3}{4}\frac{k_3}{k_1}Y_m^2 = \left(\frac{\omega_{l0}}{\omega_0}\right)^2 - 1$$

This form is identical to that of the curve C_oC_r shown in **Figure 6**. For the second approximation, where $k = 1$:

$$\frac{3}{4}\frac{k_3}{k_1}Y_m^2 - \frac{3}{128}\left(\frac{k_3}{k_1}\right)^2 Y_m^4 = \left(\frac{\omega_{l1}}{\omega_0}\right)^2 - 1$$

ω_{lk} and the amplitudes of components at frequency $(2k+1)\omega_{lk}$ are defined. For frequencies close to the resonances, severe jumps or instability can occur.

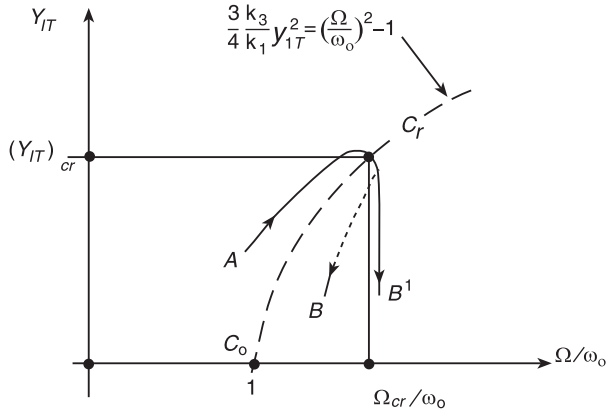


Figure 6 Critical speed where elastic force is $k_1y + k_3y^3$ (eqn [1]) and damping force $c(dy/dt)$.

Example 2

A model with periodic contact is expressed as a first approximation by:

$$m\frac{d^2Z}{dt^2} + c\frac{dZ}{dt} + k_aZ + F(t)K_0Z = 0 \qquad [4]$$

where $Z = y_c + iz_c$, and y_c and z_c are coordinates of the geometric center of the disk. K_0 is stiffness caused by the stator, which may be great in relation to k_a, shaft stiffness. For $F(t)$ a pulse train, pulse width τ_c, period $T_p = 2\pi/\omega$, ω: precessing frequency.

The term $F(t)K_0Z$ appears when the argument $Z = \beta$, where β is the average angular position in relation to the axis $0y$ of the zone of contact between rotor and stator. Decomposition of the Fourier series $F(t)$ leads to a set of equations originating from eqn [4] and pinpointed by $n = 1,\ 2\ldots$:

$$\frac{d^2Z}{d\tau_n} + c_n\frac{dZ}{d\tau_n} + (a_n + 2q_n\cos 2\tau_n)Z = 0 \qquad [5]$$

where:

$$\tau_n = \frac{n\omega}{4}\left[2t - (T_p - \tau_c)\right];\ c_n = \frac{2c}{m\omega_n}$$

$$\begin{aligned} a_n &= \left(\frac{2}{n\omega}\right)^2\frac{1}{m}\left\{k_a + K_0\left[1 - \frac{\omega}{2\pi}(T_p - \tau_c)\right]\right\} \\ &= \left(\frac{2}{n\omega}\right)^2\omega_{oc}^2 \qquad [6] \\ q_n &= \left(\frac{2}{n\omega}\right)^2\frac{K_0}{m\pi n}\sin\frac{n\omega}{2}(T_p - \tau_c) \end{aligned}$$

Eqn [5] is called Mathieu's equation with damping.

When $c = 0$, for $a_n = a = 1,\ 4,\ 9,\ 16\ldots$ and $q_n = 0$, instability (sometimes designated by parametric resonance) may be seen. When $q_n \neq 0$, the area of instability is even greater, since a_n is low, around 1, 4, 9, 16. Following eqn [5] instability may develop on frequency of precession ω, such that:

$$\omega = \frac{2}{n}\frac{1}{\sqrt{a}}\omega_{oc} \to \omega_{oc};\quad \frac{\omega_{oc}}{2};\quad \frac{\omega_{oc}}{3}\ldots$$

This relation neglects the variation of ω_{oc} with ω. For a short length of contact time $\tau_c\omega_{oc} \approx \omega_0 = \sqrt{k_a/m}$. Where $q_n = 0$, stability may be achieved. Frequency components of the precession vibrations are equal to $n\Omega$ when $a = 4,\ 16\ldots$ and $n\Omega/2$ when $a = 1,\ 9,\ 25\ldots$ when $\omega = \Omega$; $\Omega =$ rotation speed and $n = 1,\ 2,\ 3\ldots$.

When $c \neq 0$, a solution can be reached using numerical calculations. Where:

$$\frac{d^2Z}{dt^2} + (\omega_0^2 - 2q\cos 2\omega t)Z + c\frac{dZ}{dt} = 0$$

and where $\omega_0 = 0.8\,\text{rad}\,\text{s}^{-1}$, $c = 0.06(\text{s}^{-1})$ around $\omega = \omega_0,\ \omega_0/2,\ \omega_0/3,\ \omega_0/4$ the dimensions of areas of instability are less than those corresponding to $c = 0$.

Contact is caused by unbalance, which is neglected here, or by external perturbation. Transient regimes arise once the contact X has been released; contact $X+1$ is reached with initial conditions which have an influence on the behavior of the contact $X+1\ldots$ and on the behavior of the contact $X+2, X+3\ldots$. This behavior is the result of nonlinear deterministic equations under initial conditions which depend on the movements that they introduce: deterministic chaos may ensue.

Contacts and Chaos

The collision of stator and rotor may give rise to deterioration which eventually necessitates machine shutdown, or wear and tear and, with time, significant damage.

During the wear-and-tear phase, dangerous vibratory behavior may be recognized as signals in the temporal area and spectra in the frequential area. Numerous studies showed that this behavior may be typical of deterministic chaos.

With regard to rotating machinery, the De Laval rotor is widely used for studies which make it possible to discover the origins of the components whose frequencies are fractions of the rotation speed $\Omega(p/q)\Omega$, where p and q are integers) and of chaotic chance components. The situations are strongly affected by the theoretical model hypothesis and numerical values. In the article on the dynamics of rotating machinery (see **Rotor dynamics**), instability of the cycle limit of precession at a frequency which is close to half rotation frequency is explained by a nonlinear theoretical model.

The following descriptions use the work of Agnes Muszynska and Paul Goldman. The equations of movement perpendicular to the line of rotation are expressed within a fixed referential, following the Newton–d'Alembert principle ($\overrightarrow{F} = \overrightarrow{m\gamma}$).

The behavior of the disk which is in contact with the stator, either with or without friction, is computed by the following equations:

$$\begin{aligned}
&M\frac{d^2z}{dt^2} + (D + \delta D_f)\frac{dz}{dt} + Kz \\
&\quad + \delta K_f(z - c\exp i\psi) + \Delta K(x - iy) \\
&\quad + i\delta F_c(1 + a/|z|)\exp i\psi \\
&\quad = mr\Omega^2\exp i(\Omega t + \alpha) + S\exp i\gamma \\
&F_\tau = D_c\left(\frac{d\psi}{dt}|z| + \Omega a\right) \\
&\quad + f\left[D_f\frac{d|z|}{dt} + K_f(|z| - c)\right]\text{sign}\left(\frac{d\psi}{dt}|z| + \Omega a\right)
\end{aligned} \qquad [7]$$

where: $z = x + iy$; $i^2 = -1$; x and y are coordinates of the geometric center of the cylindrical disk; M is the disk mass; $2K = K_x + K_y$; $K_x,\ K_y$ is the global stiffness of the arrangement shaft and links in two perpendicular directions; isotropic shaft (stiffness independent of the azimuth): $2\Delta K = K_x - K_y$; K_f is the stator stiffness; D is the friction coefficient to the right of the disk; D_f is the friction coefficient in contact with the stator; D_c is the friction coefficient at a tangent to the rotor and stator; $mr,\ \alpha$ is the modulus and angular position of unbalance; Ω is the rotation speed which is constant for each particular value; $S,\ \gamma$ is the modulus and angular position with relation to the referential axis x of a force applied at right-angles to the disk; f is the friction coefficient; a is the disk radius; c is the radius clearance between disk and stator; ψ = arc tg y/x.

$$\delta\ (\text{Kronecker symbol}) = \begin{cases} 1 \text{ if } |z| \geq c \\ 0 \text{ if } |z| < c \end{cases} \quad |z| = \sqrt{x^2 + y^2}$$

The term $(d\psi/dt)|z| + \Omega a$ which appears in F_τ to express the speed of the point of contact between the rotor and stator; $d\psi/dt$ represents rotation speed of the precession movement of the geometric center of the disk. When $(d\psi/dt)|z| + \Omega a = 0$, the disk rolls over the stator without slipping:

$$\frac{d\psi}{dt} = \frac{-\Omega a}{c}$$

Shaft torsion is not taken into account.

Eqn [7] can be expressed by dimensionless terms in order to determine z/c as a function of Ω/ω_r where $\omega_r^2 = K_x/M$ or $\omega_r^2 = K/M$ when $K_x = K_y = K$:

$$\frac{D}{\sqrt{K_f M}};\frac{D_f}{\sqrt{K_f M}};\frac{D_c}{\sqrt{K_f M}};$$
$$\frac{K_x}{K_y};\frac{K_f}{\sqrt{K_x}};\frac{mr}{Mc};\alpha;\frac{S}{cK_y};\gamma\,\frac{a}{c};f$$

Transitory regimes at the start and end of contact are calculated using the following terms which define initial conditions:

- At the beginning of contact:

$$\left(\frac{\mathrm{d}|z|/c}{\mathrm{d}t}\right)_{-}\ ;\quad \left(\frac{\mathrm{d}\psi}{\mathrm{d}t}\right)_{-}$$

- At the end of contact:

$$\left(\frac{\mathrm{d}|z|/c}{\mathrm{d}t}\right)_{+}\ ;\quad \left(\frac{\mathrm{d}\psi}{\mathrm{d}t}\right)_{+}$$

The contact time τ_c is calculated. This makes it possible to determine the coefficient of tangential restitution:

$$K\tau = \exp\left(\frac{-aD_c\tau_c}{cM}\right)$$

which, when used with:

$$\left(\frac{\mathrm{d}\psi}{\mathrm{d}t}\right)_{-};\ \frac{a}{c};\ \frac{\Omega}{\omega_r};\ \frac{fa}{c};\ \left(\frac{\mathrm{d}|z|/c}{\mathrm{d}t}\right)_{-};\ K_n$$

enables one to determine $(\mathrm{d}\psi/\mathrm{d}t)_{+}$. The normal coefficient of restitution:

$$K_n = -\frac{\left(\frac{\mathrm{d}|z|/c}{\mathrm{d}t}\right)_{+}}{\left(\frac{\mathrm{d}|z|/c}{\mathrm{d}t}\right)_{-}}$$

is defined as a function of $\xi = D_f/2\sqrt{K_f M}$ linked to friction (D_f) with stator and with stiffness (K_f).

Calculations are carried out in numerical order with a speed increase equal to 30 rpm, after 200 revolutions to avoid temporary ratings. Signals are sampled once they have been categorized into harmonic, subharmonic, or chaotic. As an indication, **Figure 7** shows contact without friction.

The ordinates represent elongations measured at each revolution of the rotor. The procedure utilizes a stroboscope. From **Figure 7A** it can be seen that:

- where $\Omega/\omega_r \leq 2.6$, the fundamental frequency of the signal is equal to Ω; harmonic components exist: $k\Omega$ $(k = 1,\ 2\ \ldots)$
- when $2.6 \leq \Omega/\omega_r \leq 3.1$, the signal is erratic (there is chaos)
- when $3.1 \leq \Omega/\omega_r \leq 4.2$, the fundamental frequency of the signal is equal to $\Omega/2$; harmonic components exist: $k\Omega/2$
- when $4.2 \leq \Omega/\omega_r \leq 5.1$, the signal is erratic (there is chaos)
- when $5.1 \leq \Omega/\omega_r \leq 6.2$, the fundamental frequency of the signal is equal to $\Omega/3$; harmonic components exist: $k\Omega/3$

This procedure is used in **Figures 7B** and **8A–D**. The abscissa Ω/ω_r in **Figure 7A** and **8D** is the stochastic parameter. Bifurcations are seen between the chaotic zones, which are unstable and chaotic.

Figure 7B shows the maxima of the fundamental component around $\Omega/\omega_r = n$ (where $n = 1,\ 2,\ 4,\ 6$); this component frequency is always equal to Ω. Where $n = 1$, the fundamental component frequency is ω_r. When $n = 2$, the fundamental component frequency is $2\omega_r$: its period is double the rotation period: there is one oscillation for every two revolutions.

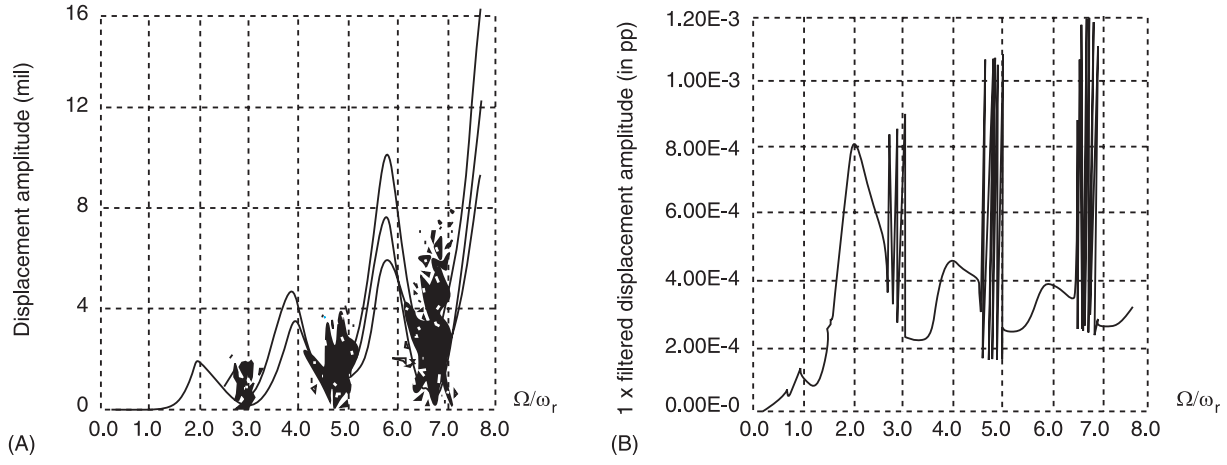


Figure 7 Contact without friction.

When $n = 4$ there is one oscillation for every four revolutions: the resonance is subharmonic. Chaotic zones appear around $\Omega/\omega_r = 3, 5, 7,$ beyond $\Omega/\omega_r \approx 2.5$.

Figure 8A–D shows contact with friction. **Figure 8A** and **B** depict chaotic zones where $\Omega/\omega_r \gtrsim 2.5$. Precession paths are shown. **Figure 8C** and **8D** shows the amplitude of the fundamental frequency components which are equal to Ω and $\Omega/2$.

Consider the De Laval rotor (shaft disk stiffness K_1 and K_2, mass M, damping coefficient D_1, force S at angle γ, and unbalance mr at 0°) guided by a link with zero perpendicular vibrations, and by a rotor of mass M_t (damping coefficient D_2) on friction (coefficient f) within a bearing (radius a, clearance c). There are small regions of speeds mainly around the rotation speed or twice where chaotic regimes may occur.

Analysis of measurements obtained on machines which have configurations like a De Laval rotor make it possible to describe, in temporal and frequential domains, forms similar to those originating from theoretical models. These theoretical models use numerical values but it is difficult to know the accuracy as related to physical values, in particular stiffness and damping coefficients at contact.

Chaos

The preceeding section discussed vibration of a De Laval rotor. Chaotic behavior may be seen here,

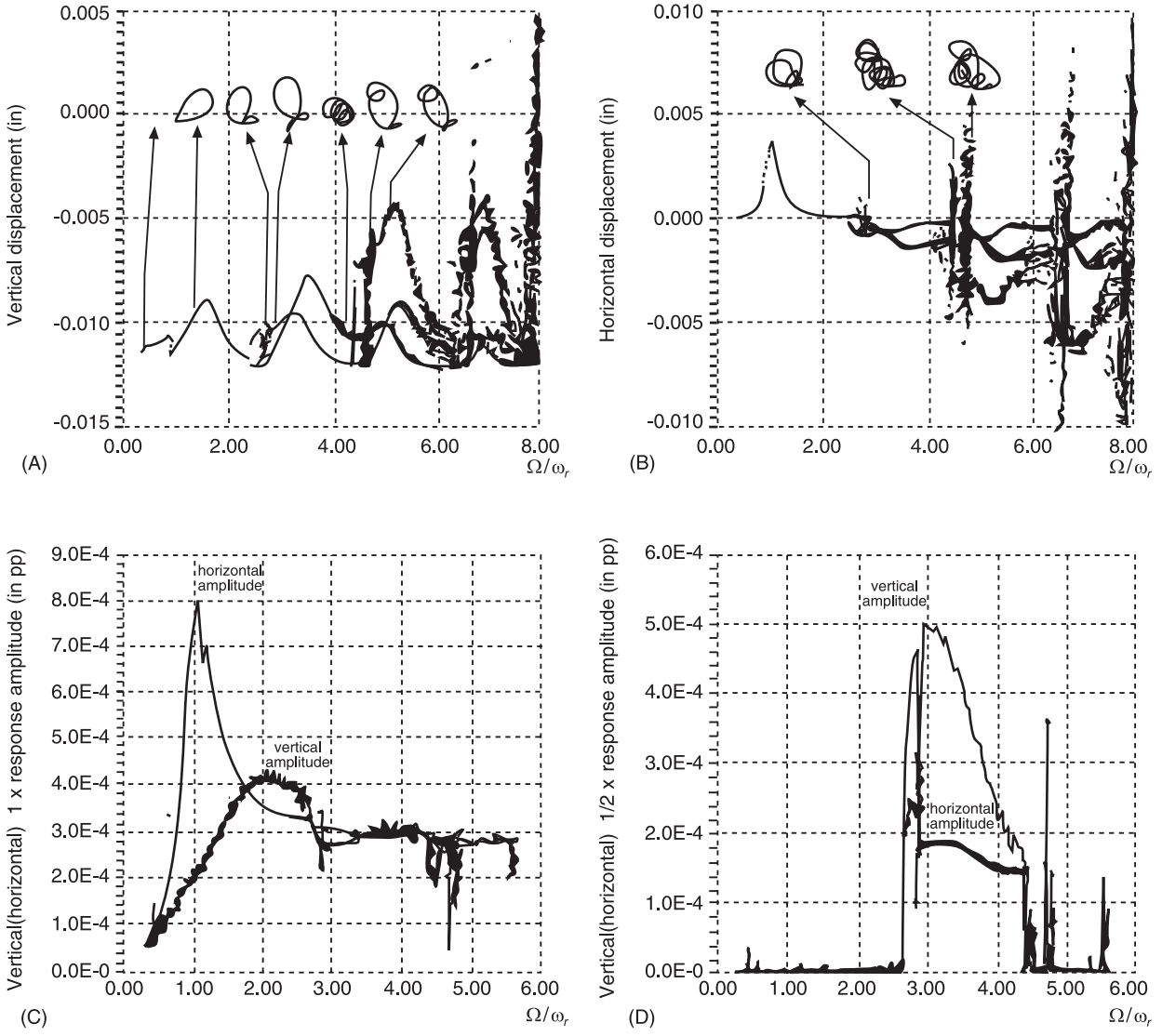


Figure 8 Contact with friction.

as well as in other systems. This section gives three such examples.

Consider a horizontal magnetic needle on a pivot, acted on by a fixed magnetic field, and a magnetic field which is turning at constant speed, at frequency f_r, around the pivot. The natural frequency of the needle in the fixed field is designated f_0. The fields are very close to the horizontal plane of the needle. For different values of f_r, the needle is strobed at frequency f_0. When only one position is determined, the needle oscillates at frequency f_0. Its movement may be described by the components of frequency kf_0, where $k = 1, 2, 3\ldots$. When two positions are determined, the needle oscillates at frequency $f_0/2$, where components are $k(f_0/2)\ldots$. At 2^n position, $k(f_0/2^n)$ components are associated.

For certain values of the stochasticity parameter f_r/f_0, erratic, chaotic behavior appears: the Fourier spectrum is continuous. The needle oscillates around the fixed field or rotating field. This behavior can be described by $f(x) = 4\lambda x(1-x)$ by an iterative process: $x_0 \rightarrow f(x_0) = x_1 \rightarrow f(x_1) = x_2 \ldots$. For $\lambda < 3/4$ measurement is characterized by one frequency; for $0.86 > \lambda > 3/4$ by two frequencies.

Consider a car driven by two persons F and H. Speed V is defined by:

$$\frac{\mathrm{d}V}{\mathrm{d}t} = aV + bV^2$$

a is defined by F, b by H at the moments $t_0 + n\tau$, where $n = 1, 2, 3\ldots$. Speed V_0 is the result of an iterative process around the higher speed limit V_l. Let us consider:

$$\frac{V_{n+1}}{V_l} = \mu\frac{V_n}{V_l}\left(1 - \frac{V_n}{V_l}\right)$$

where:

$$\mu = 1 + a\tau \qquad \frac{b\tau V_l}{1 + a\tau} = -1$$

given that:

$$a = \frac{\mu - 1}{\tau};\ b = -\frac{1}{V_l}\left(a + \frac{1}{\tau}\right)$$

μ is the stochasticity parameter; F induces acceleration when $a > 0$; H induces slowing down when $b < 0$. When $\tau = (1/100)^{\mathrm{h}}$, $V_l = 130\,\mathrm{km\,h^{-1}}$:

- when $\mu = 2$, stability is insured: $V_n/V_l = 0.5$
- when $\mu = 3.3$, speed varies between 62.4 and 107.9 km h^{-1} in a period equal to 2τ
- when $\mu = 3.7$, there is chaos when $V_{\max} = 120.25\,\mathrm{km\,h^{-1}}$
- when $\mu = 3.83$, speed varies between 21 and 65 km h^{-1} in a period equal to 4τ

Frequencies $1/2\tau$ and $1/4\tau$ can be seen.

Consider a pendulum represented by:

$$I\ddot{\theta} + c\dot{\theta} + mlg\sin\theta = 0$$

where I is the moment of inertia; c is the damping coefficient; l is the length of the cord; m is the mass; g is the acceleration of gravity; and θ is the angle with relation to vertical.

In Santiago de Compostela, in Galicia, Spain, men manipulate the pendulum:

$$l = l_0 + \Delta l\cos\omega_D t$$

As a result, the model becomes:

$$\dot{\omega} = -\frac{c}{I}\omega - \frac{ml_o g}{I}\sin\theta - \frac{mlg}{I}\Delta l\sin\theta\cos\phi$$
$$\dot{\theta} = \omega; \quad \dot{\phi} = \omega_D$$

Adopting a simplified form with direct excitation on the mass solid, m:

$$ml^2\dot{\omega} = -c\omega - mlg\sin\theta + M\cos\omega_D t$$

where $\dot{\theta} = \omega$ and $\dot{\phi} = \omega_D$:

$$\frac{\dot{\omega}}{\omega_0^2} = -\frac{c}{ml^2}\frac{\omega}{\omega_0^2} - \sin\theta + \frac{M}{ml^2\omega_0^2}\sin\frac{\omega_D\tau}{\omega_0}$$

where $\omega_0^2 = g/l$ and $\omega_0 t = \tau$:

$$\frac{\dot{\theta}}{\omega_0} = \frac{\omega}{\omega_0}; \quad \frac{\dot{\phi}}{\omega_0} = \frac{\omega_D}{\omega_0}$$

Table 1 shows the characteristics of movement of the mass solid m as a function of stochasticity parameter $M/ml^2\omega_0^2$.

Misalignment

Misalignment and Nonlinearity

Static forces on the bearings of a rotor guided by two links are the result of external forces: the system is isostatic. When the number of links is greater than two, static forces result from the relative positions of the links, from their impedance, and external forces: the system is hyperstatic. Variations in the relative

Table 1

$\frac{\omega_D}{\omega_0}=\frac{2}{3}$	$\frac{c}{ml^2\omega_D^2}=\frac{1}{2}$
$\frac{M}{ml^2\omega_D^2}$	Poincaré cup: plane $\theta,\ \dot{\theta}/\omega_0$ (strobed at ω_D)
0.9	One point: components $k\omega_D; k = 1, 2 \ldots$
1.07	Two points: components $(k/2)\omega_D$
1.15	Chaos
1.35	One point: components $k\omega_D$
1.45	Two points: components $(k/2)\omega_D$
1.47	Four points: components $(k/4)\omega_D$
1.5	Chaos

positions may come about as a result of deformation of casings and foundations through deterioration and thermal gradients.

The force perpendicular to a link helps to define the average position of the center of the vortex within a fluid bearing. Around this position the vibratory components may be described by nonlinear equations. Thus the vibration spectra has many harmonics.

Roller Bearings

The force at right-angles to a rolling link plays a part in its lifespan, which may be very short when the force is significant. **Figure 9** depicts an arrangement of rotor, roller bearings, and bearings. When there is vertical displacement, δ imposes by misalignment on the third bearing force F_r which, applied to the roller bearing, is defined by:

$$F_r = \frac{k_r/k_a}{1 + k_r/k_a}\delta k a;\ 0 < F_r < \delta k_a$$

where $k_r = 0;\ F_r = 0$ and where $k_r \to \infty;\ F_r < \delta k_a$.

This force reduces the lifespan. It may lead to the rapid destruction of the rolling bearing.

The stiffness k_a of a rotor of 1000 kg of natural frequency which is equal to $100\,\mathrm{rad\,s^{-1}} (\approx 16\,\mathrm{Hz})$ is equal to $10^4 \times 10^3 = 10^7\,\mathrm{N\,m^{-1}}$. Where $k_r = \infty$, displacement $\delta = 1\,\mathrm{mm}$ induces a force of $10^4\,\mathrm{N}$, close to its weight $(9.81 \times 10^3\,\mathrm{N})$. Flexible couplings between two rotors make it possible to reduce hyperstaticity, as well as to reduce forces within the roller bearings caused by eventual relative displacements between links and avoiding destructive nonlinearities. Thus, misalignments within the couplings may provoke their deterioration and raised vibratory levels. Couplings may also be affected by faults which require maintenance operations.

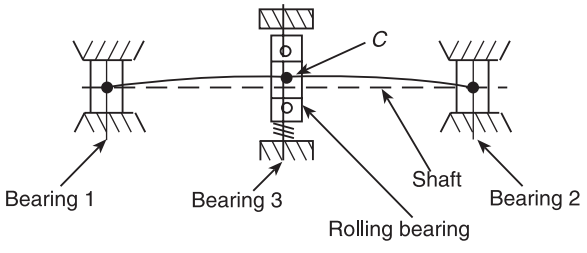


Figure 9 Rolling bearing. Shaft stiffness at $C = k_a$. Stiffness between bearing and rolling bearing k_r.

Hyperstaticity and Instability

High-power machines, in particular power generating turboalternators producing electric energy, are generally made up of horizontal rotors (high- or low-pressure, and alternators) which are rigidly coupled together. Variations in relative positions of the bearings (misalignment) which contain oil bearings cause variations in radial static forces. For a 1000-MW turboalternator operating at 1500 rpm, relative variations of forces caused by relative vertical displacements of the 1-mm bearings may be included between:

- 0 and 90% when the rotor is guided by 10 bearings
- 0 and 20% when the rotor is guided by 6 bearings

With regard to the limits of stability and amplitude at critical speed, it may be more problematic to achieve alignment with 6 bearings than with 10 bearings.

Misalignment can lead to nonlinear behavior due to squeezing of films of oil as a result of variations in amplitude at frequency rotation f_r (first harmonic) and harmonic frequencies (nf_r where $n = 2, 3 \ldots$). Equally, it may lead to instability, or whip, in limit cycles where the amplitude may be significant and dangerous. This instability may be seen when the distance betweeen the center of a vortex and the center of a cylindrical bearing is small. Variations in amplitude of the first harmonic resulting from misalignment must not be confused with those arising from variation in unbalances (see **Balancing**). Misalignment may cause contact between rotor and stator.

Example: rotor on three bearings **Figure 10** shows a rotor and bearings.

Table 2 defines rotation speed Ω_l and the limit of stability obtained by linear equations in which stiffness and damping coefficients depend on m and λ. Misalignment of 20 μm increases the speed limit of stability. A 10°C increase in temperature in the 0.2-m high bearing causes 20 μm misalignment, which increases the speed limit of stability.

Example: rotor on four bearings **Figure 11** shows an arrangement of rotor, links, and structure. **Figure 12** shows the real part δ and the imaginary part ω of the complex natural frequency $p = \delta + i\omega$ calculus (see **Rotor dynamics**). Instability can be seen where $d/J \approx 2.25 (d \approx 0.67\,\text{mm})$ at bearing 2, $d/J \approx 0.5 (d \approx 0.15\,\text{mm})$ at bearing 3. The frequency of instability is close to 130 rad s^{-1} if:

$$\Omega rl/\omega_{\text{ins}} \approx 314/130 = 2.42, \text{ where } \omega_{\text{ins}}/\Omega rl \approx 0.41$$

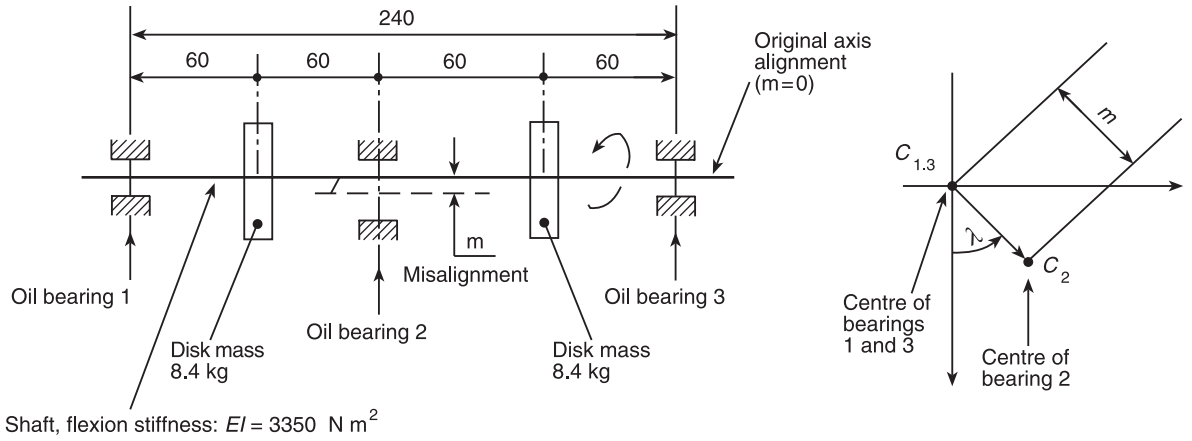
With normal alignment, where $d/J = 0$, natural frequency ω_n is close to 175 rad s^{-1}:

$\omega_{\text{ins}}/\omega_r \approx 130/175 \approx 0.74$.
Critical speed is ≈ 1670 rpm.

Table 2 Limit of stability

$m(\mu\text{m})$	λ (°)	Clearance = 25 μm	Ω_l (Hz)
0		0	~ 300
5	225	0.2	~ 230
20	110–270	0.8	360–450

In the hyperstatic rotor–stator arrangements described above, variation in speed limits of stability is caused by variation in static forces perpendicular to the bearings. This variation is a result of misalignment of the bearings subject to deformations of the stators or structures. It may arise through variation of the position of the sealant systems; and variation of the aerodynamic radial forces in the turbines, com-



Circular bearing	Diameter (mm)	Width (mm)	Radial clearance (μm)	Relative clearance	Oil viscosity (N sm^{-2} → Pa s^{-1})
1 and 3	12.5	7.5	15	2.4	0.01
2	25	15	25		

Figure 10 Rotor bearings. *E*, Young's module; *I*, diametric inertia.

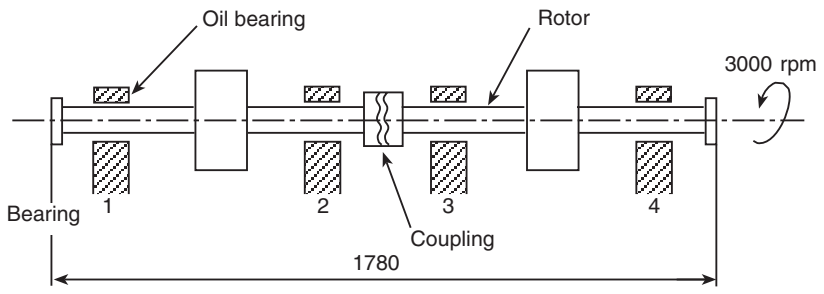


Figure 11 Arrangement of rotor–links–structure. Journal; $\phi = 50$ mm; journal breadth $\phi = 41.5$ mm; relative clearance: journal diameter/clearance = 0.006 → 6‰. Oil viscosity: 0.02 Pa s; maximum bearing charge = 150 N. From: Parszinski ZA, Kryniski K, Kirby ED (1988) Effect of bearing alignment on stability threshold and post-stability behaviour of rotor bearing systems. Institute of Mechanical Engineering.

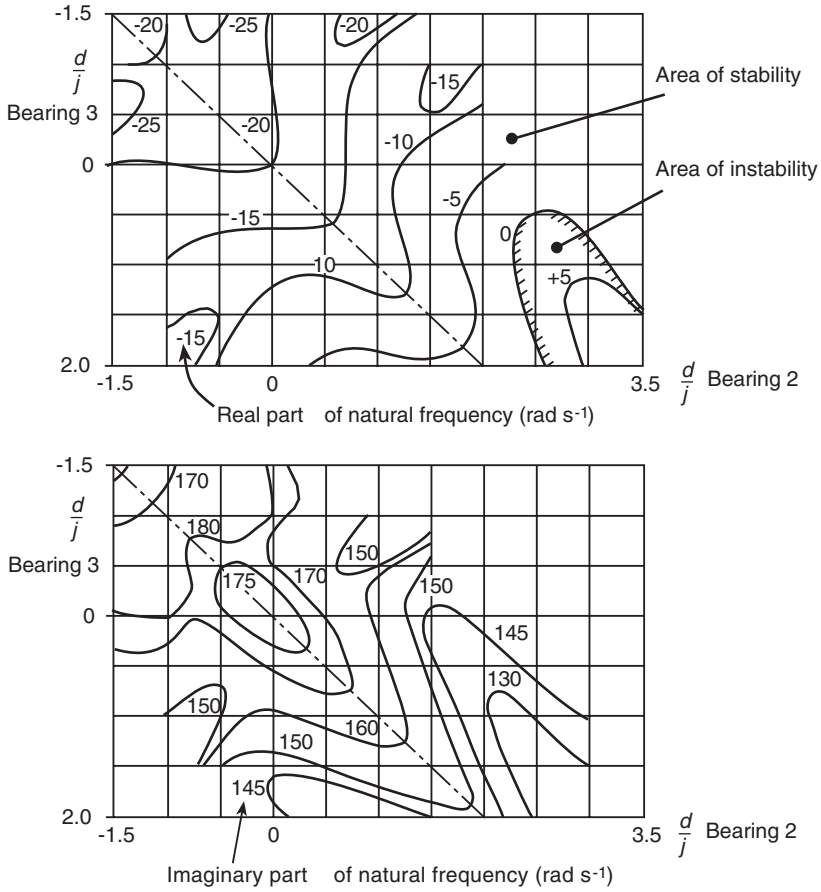


Figure 12 Complex natural frequency $p = \delta + i\omega$ where $i^2 = -1$, d = displacement, and j = clearance to diameter.

pressors, and pumps, linked to their conditions of function (flow, pressure). Temperature variation of fluid pressure supplying the bearings may also cause instability.

Deterioration in the Supports and Foundation

There may be deterioration in the metallic supports, such as cracks, or fractures of soldering or anchoring bolts, and cracks and disintegration in the concrete foundations. This may lead to critical speed or resonance in the domain of machine rotation speed, and so too vibration above fixed limits.

Seismic Excitation

A rotating machine senses earth movement through the foundation on which its base is placed. Misalignments may result, as well as seismic vibrations. As an example, the theoretical model of a De Laval rotor guided by two cylindrical bearings within a fixed referential is defined by the following equations:

$$m\,\frac{\mathrm{d}^2x}{\mathrm{d}t^2} + k(x - x_c) = -m\,\frac{\mathrm{d}^2x_m}{\mathrm{d}t^2} + mg$$

$$m\,\frac{\mathrm{d}^2y}{\mathrm{d}t^2} + k(y - y_c) = -m\,\frac{\mathrm{d}^2y_m}{\mathrm{d}t^2}$$

$$k(x - x_c) + 2F_x = 0$$

$$k(y - y_c) + 2F_y = 0$$

where x, y are displacement components from the disk center; x_c, y_c are displacement components from the journal center; x_m, y_m are displacement components from the foundation imposed on the seismic vibrations; m is the disk mass (4.4×10^4 kg); k is shaft stiffness

$$N_c = \frac{1}{2\pi}\sqrt{\frac{k}{m}} = \frac{1}{2\pi}\omega_c = 600 \text{ cycle min}^{-1}$$

g is gravity acceleration ($9.81\ \mathrm{m\,s^{-2}}$); F_x, F_y are components of force imposed on the shaft by oil bearings ($L = 331$ mm; $L/D = 0.5$; 2 clearance$/D = 0.003$; $y = 5.6 \times 10^{-3}$ Pa s); Ω is rotation speed (nominal 3600 rpm).

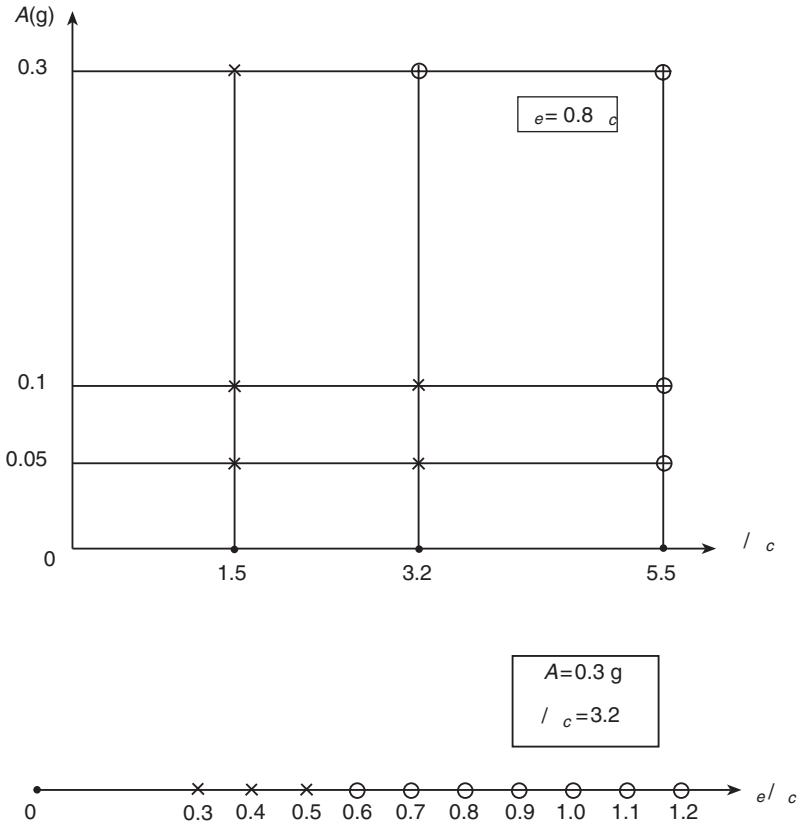


Figure 13 Earthquake upheaval. Crosses, stability; circles, instability.

Natural frequencies of the free rotor

$$\frac{d^2x_m}{dt^2} = \frac{d^2y_m}{dt^2} = 0$$

where $\Omega/\omega_c = 3.2$, are calculated modeling the bearings by stiffness and damping coefficients, or linearization.

$$i^2 = -1$$
$$p_l = \delta_l \pm i\omega_l$$
$$\delta_l/\omega_c = -0.0039;\ -0.0016;\ -5.56$$
$$\omega_l/\omega_c = 0.746;\ 0.953;\ 0.535$$

Stability is insured ($\delta_l < 0$); $\delta_l/\omega_c = 0$ (instability) where $\Omega_{\text{inst}}/\omega_c = 4.714$. When:

$$\frac{d^2x_m}{dt^2} = 0;$$
$$\frac{d^2y_m}{dt^2} = \begin{cases} A\sin\omega_c t & \text{where } 0 \le t \le 2\pi/\omega_c \\ 0 & \text{where } 0 > t > 2\pi/\omega_c \end{cases}$$

F_x and F_y are calculated using the equation and conditions at Reynolds limits (see **Bearing vibrations**). Nonlinearities are taken into account.

The equation system is solved by the Runge–Kutta-Gill method with a step equal to 0.002 s. Instability can be seen by displacement of the vortex center on cycle limits of the radius equal to the clearance. **Figure 13** shows conditions of stability and instability.

In a free state instability is seen for $N \ge N_{\text{inst}} = 4.714 \times 600 = 2828$ rpm. In a state which is disturbed by a seismic vibration of amplitude at 0.3 g and frequency $\omega_l = 0.8\omega_c = 76.4$ rad s^{-1} (480 cycle min^{-1}) instability can be seen for $N \ge N_{\text{inst}} = 3.2 \times 600 = 1920$ rpm.

See also: **Balancing**; **Bearing vibrations**; **Rotating machinery, modal characteristics**; **Rotor dynamics**.

Further Reading

Angot (1972) *Compliments de Mathématiques*. Masson.
Dimarogonas (1973) *Newkirk Effect: Thermally Induced Dynamic Instability of High Speed Rotors*. ASME paper 73 GT-26. Washington, DC: ASME.

Goldman P, Muszynska A (1995) Chaotic responses of unbalanced rotor/bearing/stator systems with looseness on rubs. In: *Chaos, Solutions and Fractals*, vol. 5, no. 9. Elsevier Science.

Goldman P, Muszynska A (1995) Rotor-to-stator. Rub-related thermal/mechanical effects in rotating machinery. In: *Chaos, Solutions and Fractals*, vol. 5, no. 9. Elsevier Science.

Kellenberger W, Wahlrab R (1981) Vibrations de la flexion sous harmoniques dans la ligne d'arbre des gros turbogroupes. *Revue Brown Boveri* 68 Switzerland

Parszinski ZA, Kryniski K, Kirby ED (1988) *Effect of Bearing Alignment on Stability Threshold and Post-stability Behaviour of Rotor Bearing Systems*. Institute of Mechanical Engineering.

Timoshenko S, Young DH, Weaver W Jr (1974) *Vibration Problems in Engineering*, 4th edn. John Wiley.

Wanda, Szempliniska, Stupnicka (1990) *The Behavior of Nonlinear Vibrating Systems*, vol. 1. Poland: Kluwer Academic.

S

SEISMIC INSTRUMENTS, ENVIRONMENTAL FACTORS

K McConnell, Iowa State University, Ames, IA, USA

Copyright © 2001 Academic Press

doi:10.1006/rwvb.2001.0104

This chapter addresses a number of user and/or environmental issues that often affect the quality of measurements. The five main issues considered here are accelerometer cross-axis sensitivity, the basic behavior of a force transducer when used in three common test environments, the effect of bending moment sensitivity, and the removal of force transducer mass loading effects on measured frequency response function (FRF) data. In addition, a list of small items from cable noise to temperature effects are reviewed. This chapter delineates effects that have been clearly identified over the past 10 years.

Cross-axis Sensitivity

Transducers are usually sensitive to the input variable in a plane perpendicular to the design sensing direction. In piezoelectric-based transducers, this cross-axis sensitivity is mainly due to contact surface irregularities between the piezoelectric crystals and their mating surfaces, while for strain gauge-based transducers it is due to slight strain gauge misalignment.

Single Accelerometer Cross-axis Sensitivity

McConnell and Han (1991) developed a model to explain cross-axis sensitivity. Consider the orientation of the effective sensing axis (S_o) relative to the designed sensing direction (z) and the xy cross-axis plane for an accelerometer, as shown in **Figure 1**. The sensitivity vector $\mathbf{S}_o$ is given by:

$$\begin{aligned}\mathbf{S}_o = &\{S_o \sin(\phi)\cos(\theta)\}\mathbf{i} \\ &+ \{S_o \sin(\phi)\sin(\theta)\}\mathbf{j} \\ &+ \{S_o \cos(\phi)\}\mathbf{k}\end{aligned} \quad [1]$$

while the corresponding transducer acceleration can be written as:

$$\mathbf{a} = a_x\mathbf{i} + a_y\mathbf{j} + a_z\mathbf{k} \quad [2]$$

The output voltage is proportional to the dot product of these two vectors, giving:

$$\begin{aligned}E_z = K\mathbf{S}_o \cdot \mathbf{a} &= (KS_o) \\ &= [\{\sin(\phi)\cos(\theta)\}a_x \\ &\quad + \{\sin(\phi)\sin(\theta)\}a_y + \cos(\phi)a_z]\end{aligned} \quad [3]$$

or:

$$E_z = S_{zx}a_x + S_{zy}a_y + S_z a_z \quad [4]$$

When the angle ϕ is small so that $\sin(\phi) < 0.06$, the sensitivities become:

$$\begin{aligned}S_{zx} &= (KS_o)\sin(\phi)\cos(\theta) \cong (KS_o\phi)\cos(\theta) \\ S_{zy} &= (KS_o)\sin(\phi)\sin(\theta) \cong (KS_o\phi)\sin(\theta) \\ S_{zz} &= (KS_o)\cos(\phi) \cong (KS_o)\end{aligned} \quad [5]$$

It is clearly evident from eqn [4] that the output signal is contaminated by the cross-axis terms. These contamination terms can be very large when the a_z acceleration component is small compared to the resultant in-plane acceleration component. For example, let $a_z = 1.0\,\mathbf{g}$ while the in-plane acceleration component is $100\,\mathbf{g}$. Then, a 5% cross-axis sensitivity gives a maximum output signal 6 **g**, an error of 6 vs 1. Hence, it is good practice to use a triaxial accelerometer in unknown acceleration situations so that potential measurement errors reveal themselves.

Triaxial Accelerometer Cross-axis Sensitivity

When eqn [4] is applied to a triaxial accelerometer, the resulting output voltage equations become:

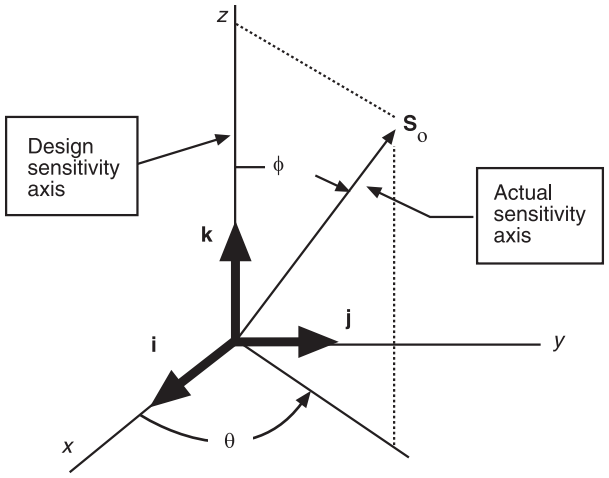


Figure 1 Orientation of design sensitivity axis and actual sensitivity axis creating cross-axis sensitivity due to *xy*-plane acceleration components. Reproduced with permission from McConnell KG and Han SB (1991) *Proceedings of the 9th International Modal Analysis Conference*, Society for Experimental Mechanics.

$$\begin{aligned} E_x &= S_{xx}a_x + S_{xy}a_y + S_{xz}a_z \\ E_y &= S_{yx}a_x + S_{yy}a_y + S_{yz}a_z \\ E_z &= S_{zx}a_x + S_{zy}a_y + S_{zz}a_z \end{aligned} \quad [6]$$

Then, dividing the pth equation by its dominant sensitivity S_{pp} in eqn [6], the result is the apparent pth acceleration b_p for $p = x$, y, and z, respectively. This gives the apparent acceleration $\mathbf{b}$ as:

$$\mathbf{b} = \boldsymbol{\varepsilon}\mathbf{a} \quad [7]$$

where $\varepsilon_{pq} = S_{pq}/S_{pp}$ is the cross-axis sensitivity ratio and $\varepsilon_{pp} = 1.0$ is the design axis sensitivity ratio. Then, the actual accelerations can be estimated from:

$$\mathbf{a} = \boldsymbol{\varepsilon}^{-1}\mathbf{b} \quad [8]$$

where $\boldsymbol{\varepsilon}^{-1}$ is the correction matrix. Most commercial triaxial accelerometers have cross-axis values of ε_{pq} limited to $\pm 5\%$, so that eqn [8] can be approximated by:

$$\begin{aligned} a_x &= +b_x - \varepsilon_{xy}b_y - \varepsilon_{xz}b_z \\ a_y &= -\varepsilon_{yx}b_x + b_y - \varepsilon_{yz}b_z \\ a_z &= -\varepsilon_{zx}b_x - \varepsilon_{zy}b_y + b_z \end{aligned} \quad [9]$$

The major difficulty with these correction schemes is that the values of ε_{pq} often change with transducer use, particularly with high levels of acceleration.

Removing Cross-axis Contamination from FRF Meassurements

It has been shown by Han and McConnell (1989, 1991) that cross-axis sensitivity can cause false mode shapes and natural frequencies to be measured when doing experimental modal analysis. These effects can be effectively removed by using eqn [9] to correct the measured FRF's, as demonstrated by their example using the free-free beam shown in **Figure 2**. Here, a triaxial accelerometer is attached at the left-hand end, the x-axis is along the beam's length, the y-axis is out of the page, and the z-axis is vertical. Node 1 is at the left end and node 24 is at the right end. The input direction S is inclined about 42° above the y-axis. The uncompensated magnitude and phase FRF data for the y-direction's first natural frequency are shown in **Figure 3** when the beam is impacted in the S direction. A false peak and valley occur at points A and B that look like a resonance condition in the y-direction. The peak at A corresponds to the beam's first natural frequency in the z-direction, while the large peak corresponds to the beam's first natural frequency in the y-direction. The data correction scheme of eqn [9] removes this false data in both magnitude and phase so that only the correct information for the y-direction remains. When wide-band data including

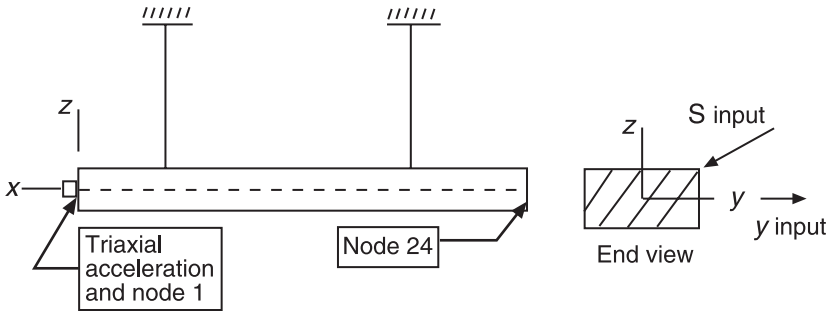


Figure 2 Free–free beam showing coordinate directions, transducer locations, and impact direction. Reproduced with permission from McConnell KG and Han SB (1991) *Proceedings of the 9th International Modal Analysis Conference*, Society for Experimental Mechanics.

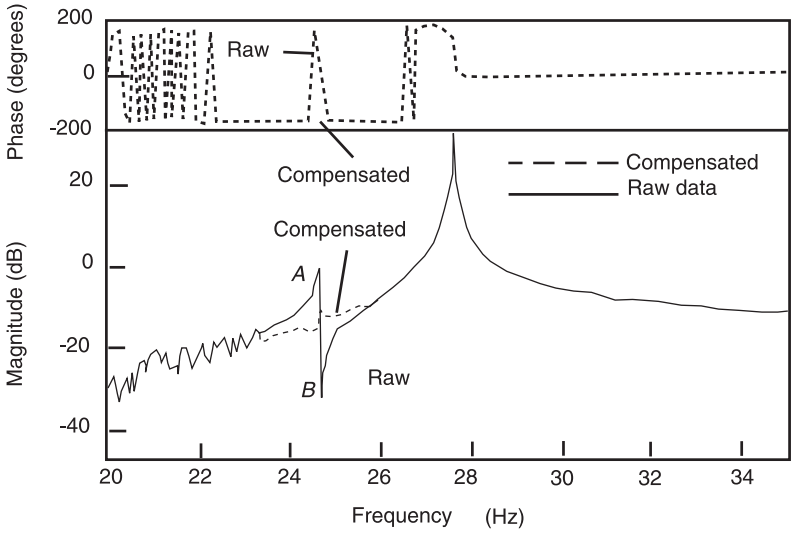


Figure 3 *y*-direction FRF accelerance magnitude and phase for *S*-direction input showing raw and compensated results where the false peak and valley are completely removed. Reproduced with permission from McConnell KG and Han SB (1991) *Proceedings of the 9th International Modal Analysis Conference*, Society for Experimental Mechanics.

the first four natural frequencies were taken and analyzed, the modal analysis program was fooled into reporting seven natural frequencies and mode shapes when there should only be four natural frequencies and mode shapes for the *y*-direction data. The presence of the three extra mode shapes caused severe distortions in the modal parameter estimates. The same modal analysis software reported the correct four natural frequencies, mode shapes, and damping estimates over the same frequency range when the cross-axis corrections were applied to the measured FRFs. It should be noted that the first two natural frequencies appeared as a single natural frequency for the first mode since the wide-band frequency analysis had a Δf that smeared these two peaks together. Consequently, it is important to measure sufficient data to determine if cross-axis signal contamination is occurring and to take appropriate action to correct the data if serious contamination is occurring.

Force Transducers

The accelerometer's main effect on measurements is its inertia, which can shift the natural frequencies of light-weight structures. However, the force transducer can and often does interact significantly with the structures under test since the transducer is connected between two different structures, one on each side. We shall explore the effects of this interaction for three different types of applications: the rigid foundation, the impact hammer, and attached between an exciter and the structure under test, as described by McConnell (1993).

Rigid Foundation

The force transducer is mounted on a rigid foundation, as shown in **Figure 4**. The mathematical model representing this situation is given by eqn [1] from **Transducers for absolute motion** as:

$$m\ddot{z} + c\dot{z} + kz = F(t) - m\ddot{x} \qquad [10]$$

where base excitation $\ddot{x}$ is zero due to the rigid foundation. In this case, the frequency domain relative motion is given by:

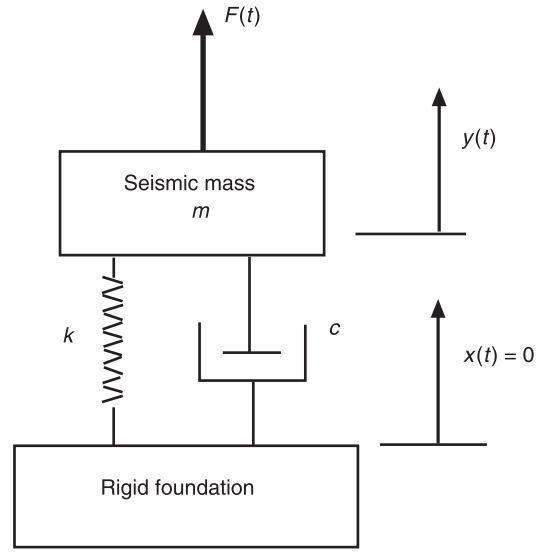


Figure 4 The force transducer mounted on a rigid foundation so that $x = 0$ and $z = y$.

$$z(\omega) = \frac{F(\omega)}{k - m\omega^2 + jc\omega} \qquad [11]$$

This is the classical single-degree-of-freedom (SDOF) model with mechanical resonance that is affected by any attachment mass that is used. This mass must be added to the instrument's seismic mass and included in the inertia parameter m. Hence, the instrument will respond within 5% of the applied force as long as the frequency of that force is $< 0.2\omega_n$.

Force Transducer Attached to a Hammer

The physical arrangement of a force transducer attached to an impact hammer is shown schematically in **Figure 5**. In this case the transducer's seismic mass is increased due to the impact head so that $m_1 = m + m_{\text{head}}$ while the base mass is increased by the hammer body mass so that $m_2 = m_{\text{base}} + m_{\text{hammer}}$. Then, using eqn [1] and noting that the base acceleration $\ddot{x}$ is the applied force divided by the total mass, the effective voltage sensitivity (S_f^*) of the hammer is related to the load cell's voltage senstity (S_f) by:

$$S_f^* = \left[\frac{m_2}{m_1 + m_2}\right] S_f \qquad [12]$$

Eqn [12] shows that the effective sensitivity is changed when either the impact head and/or the hammer body mass are changed. In most situations, the hammer body mass is much larger than the impact head mass so it is the body mass change that causes the largest change in the effective voltage sensitivity. Han and McConnell (1986) have verified eqn [12] over a broad range of mass ratios (m_2/m_1) from near unity to over 10. When dealing with very small impact hammers, the operator's hand mass can significantly contribute to mass, m_2. Hence, in these cases, the person using the hammer should be the person who calibrates it so any hand mass effects are accounted for.

Force Transducer Used with a Vibration Exciter and Stinger

The force transducer is attached directly to the structure under test (SUT) on one end and the other end is attached to a vibration exciter through a stinger, as shown in **Figure 6A**. The corresponding free body diagram (FBD) and motions are shown in **Figure 6B**. For this case, the analysis starts with eqn [2] from **Transducers for absolute motion**, which is written here in the frequency domain as:

$$(jc\omega + k)z(\omega) = F(\omega) - m\ddot{y}(\omega) \qquad [13]$$

where k, c, and m are the force transducer's parameters. In this case, the seismic mass acceleration $\ddot{y}(\omega)$ is related to the structure's driving point accelerance $A_s(\omega)$ and the interface force $F(\omega)$ by:

$$\ddot{y}(\omega) = A_s(\omega)F(\omega) \qquad [14]$$

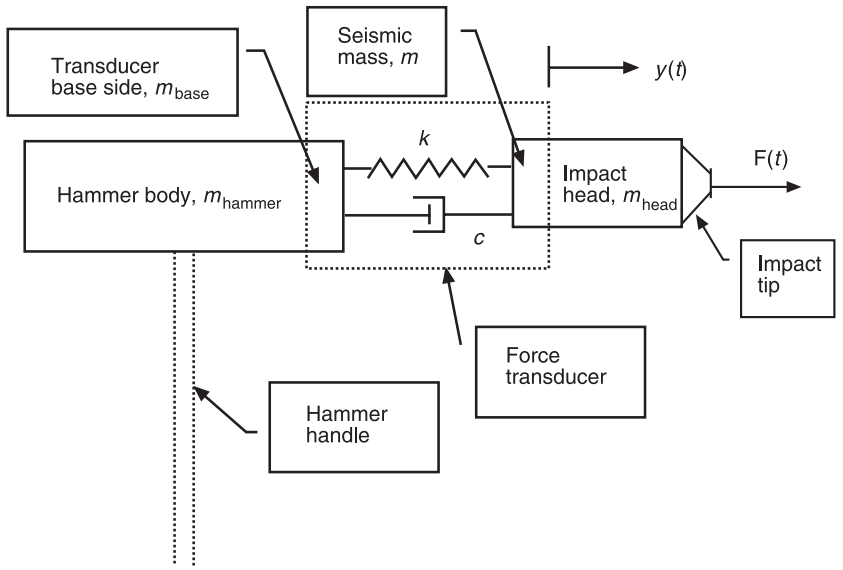


Figure 5 Schematic showing force transducer attached to an impact hammer. Note how the force transducer base and seismic masses are altered by the impact head mass and hammer body mass. Reproduced with permission from McConnell KG (1993) *Modal Analysis: The International Journal for Analytical and Experimental Modal Analysis*, Society for Experimental Mechanics.

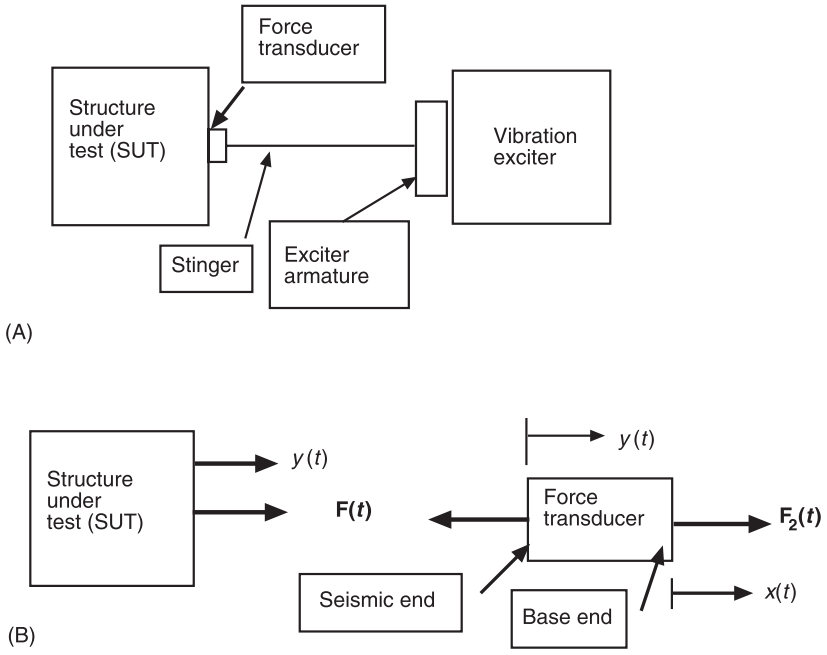


Figure 6 A force transducer is attached to a structure under test at one end and stinger connected to a vibration exciter at the other end. (A) Schematic of test arrangement; (B) FBD showing forces and motion for an ideal case without any bending moments in the stinger. Reproduced with permission from McConnell KG (1993) *Modal Analysis: The International Journal for Analytical and Experimental Modal Analysis*, Society for Experimental Mechanics.

Combining eqns [13] and (14) gives the transducer voltage as:

$$E_f(\omega) = S_f H_f(\omega)[1 - mA_s(\omega)]F(\omega) \qquad [15]$$

where the transducer's mechanical FRF $H_f(\omega)$ is given by:

$$H_f(\omega) = \frac{k}{k + jc\omega} \qquad [16]$$

Eqn [15] shows that the largest effect of the $mA_s(\omega)$ term occurs when the accelerance is most significant at the SUT's resonant conditions, the region where the SUT's dynamic behavior is of greatest interest.

In order to illustrate the nature of these errors, McConnell (1990) used a SDOF structural system with a driving point accelerance given by:

$$A_s(\omega) = \frac{-\omega^2}{k_s - m_s\omega^2 + jc_s\omega} \qquad [17]$$

where the s subscript refers to the SUT. Then, the error ratio (ER) of actual measured voltage divided by the correct measured voltage can be shown to be:

$$\frac{\widetilde{E}_f(\omega)}{E_f(\omega)} = ER = \left[\frac{k_s - m_s\omega^2 + jc_s\omega}{k_s - (m_s + m_1)\omega^2 + jc_s\omega}\right] = \left[\frac{1 - r^2 + 2j\zeta_s r}{1 - (1 + M)r^2 + 2j\zeta_s r}\right] \qquad [18]$$

where M is the mass ratio of m_l/m_s, ζ_s is the structural damping, and $r = \omega/\omega_{ns}$ is the dimensionless frequency ratio based on the SUT's natural frequency. The magnitude and phase of eqn [18] are plotted in **Figure 7** for a mass ratio $M = 0.01$ and structural damping of 0.01 in the region of the SUT's resonance. It is seen that the error ratio peaks at 1.269 just before resonance and has a minimum of 0.783 at resonance when the numerator of eqn [18] is a minimum. A rather rapidly changing phase angle is also seen to occur. This plus 27% and minus 22% change in measured force near the resonance conditions can lead to slight shifts in measured natural frequency and possibly the damping estimates when using this data for experimental modal analysis.

Bending Moment Sensitivity of Force Transducers

Force transducers have both bending moment and shear force sensitivity. This sensitivity is dependent on the direction of the shear force and bending

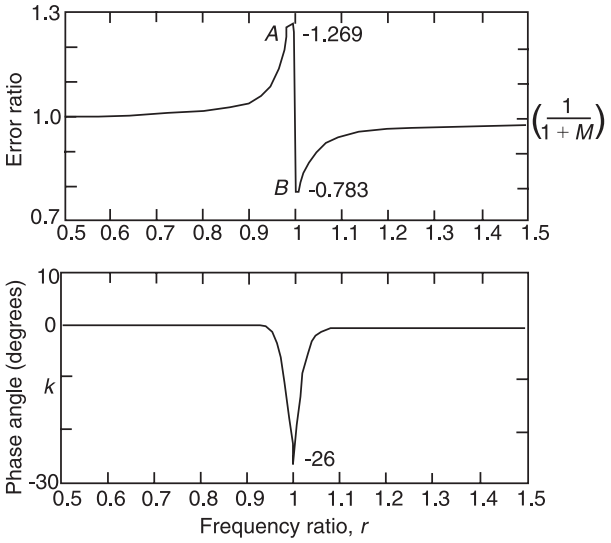


Figure 7 Magnitude and phase of error ratio as a function of dimensionless frequency ratio r for a mass ratio M of 0.01 and a structural damping ratio of 0.01. Reproduced with permission from McConnell KG (1993) *Modal Analysis: The International Journal for Analytical and Experimental Modal Analysis*, Society for Experimental Mechanics.

moment relative to the transducer. Recent research has shed some light on bending moment characteristics. This section will address both the bending moment sensitivity of a force transducer and the coupling that occurs in a transducer designed to measure a single force and two moments. Shear force sensitivity is not addressed here.

Bending Moment Sensitivity in a Single Force Transducer

The bending moment sensitivity model of a force transducer was developed by McConnell and Varoto (1993) to explain the behavior of a transducer when mounted on a nearly rigid foundation with steel bar attached as shown in **Figure 8A**. The steel bar was impacted at locations 1, 2, and 3, with the calibration results shown in **Figure 8B**. This dramatic difference in behavior led to the development of a two-degree-of-freedom (2-DOF) transducer model that involved both linear and angular transducer motions, y and θ. From these motions, they showed that the frequency domain ratio of output voltage $(E_f(\omega))$ to input force $(F_o(\omega))$ at location l from the transducer's center is given by:

$$\frac{E_f(\omega)}{F_o(\omega)} = \left\{ \frac{(S_F + lS_M)\left(1 - \alpha r_\theta^2 + j2\zeta_\theta \alpha\gamma r_\theta\right)}{\left(1 - r_y^2\right) + j2\zeta_y r_y\left(1 - r_\theta^2 + j2\zeta_\theta \gamma r_\theta\right)} \right\} \quad [19]$$

where S_F (V per unit force) and S_M (V per unit moment) are the force and bending moment sensitivities, $r_y = \omega/\omega_{ny}$ is the linear dimensionless natural frequency ratio, and $r_\theta = \omega/\omega_n$ is the angular dimensionless natural frequency ratio. The dimensionless parameters α, β, and γ are given by:

$$\alpha = \frac{\beta^2 S_F + lS_M}{\beta^2(S_F + lS_M)}$$
$$\beta = \frac{\omega_{ny}}{\omega_{n\theta}} = \frac{r_\theta}{r_y} \quad [20]$$
$$\gamma = \frac{\beta S_F + lS_M(\zeta_y \zeta_\theta)}{\beta(S_F + lS_M)}$$

For this case, $\omega_{ny} \gg \omega_{n\theta}$ so that $r_\theta \gg r_y$ and $\beta \gg 1.0$. Then, eqn [19] has several interesting features. First, at low frequencies when $r_\theta \ll 1$ and $r_y \lll 1$, the apparent force sensitivity is:

$$S_{F_a} = S_F + lS_M \quad [21]$$

which is an anticipated result. Second, two natural frequencies are involved. Third, a notch occurs whenever $\alpha r_\theta^2 = 1.0$. However, eqn [20] shows that α is either greater than unity when lS_M is negative or less than unity when lS_M is positive. Thus, this notch can occur either before or after the torsional resonance. Fourth, when $r_\theta \gg 1$, the apparent force sensitivity becomes:

$$S_{F_a} \cong \alpha(S_F + lS_M) \cong S_F + \frac{lS_M}{\beta^2} \quad [22]$$

For fairly large values of β, eqn [22] shows that the apparent sensitivity is essentially the normal force sensitivity. Eqn [19] is plotted in **Figure 9** for parameters that simulate the measured data shown in **Figure 8B**. The bending moment sensitivity S_M changes with the angular orientation of the steel bar for the transducer tested.

The One-force, Two-moment Transducer

Dong *et al.* (1998) studied the coupling that occurred in a one-force (F_z) and two-moment (M_x and M_y) transducer using the set-up shown in **Figure 10**. The plate was impacted at locations of 0, ± 30, ± 45, ± 60, ± 90, etc. degrees at radius r. The transducer force F_z and moments M_x and M_y responses and the corresponding impact force were measured. It takes three sets of measurements to obtain the cross-sensitivity matrix $\boldsymbol{\varepsilon}$. The ± 45 and ± 135 degree data are used for this purpose since these positions give the best bending moment signal-to-noise ratios. The measured moments M_{xm} and M_{ym} and force F_{zm} are corrected using $\boldsymbol{\varepsilon}$ cross-sensitivity matrix by:

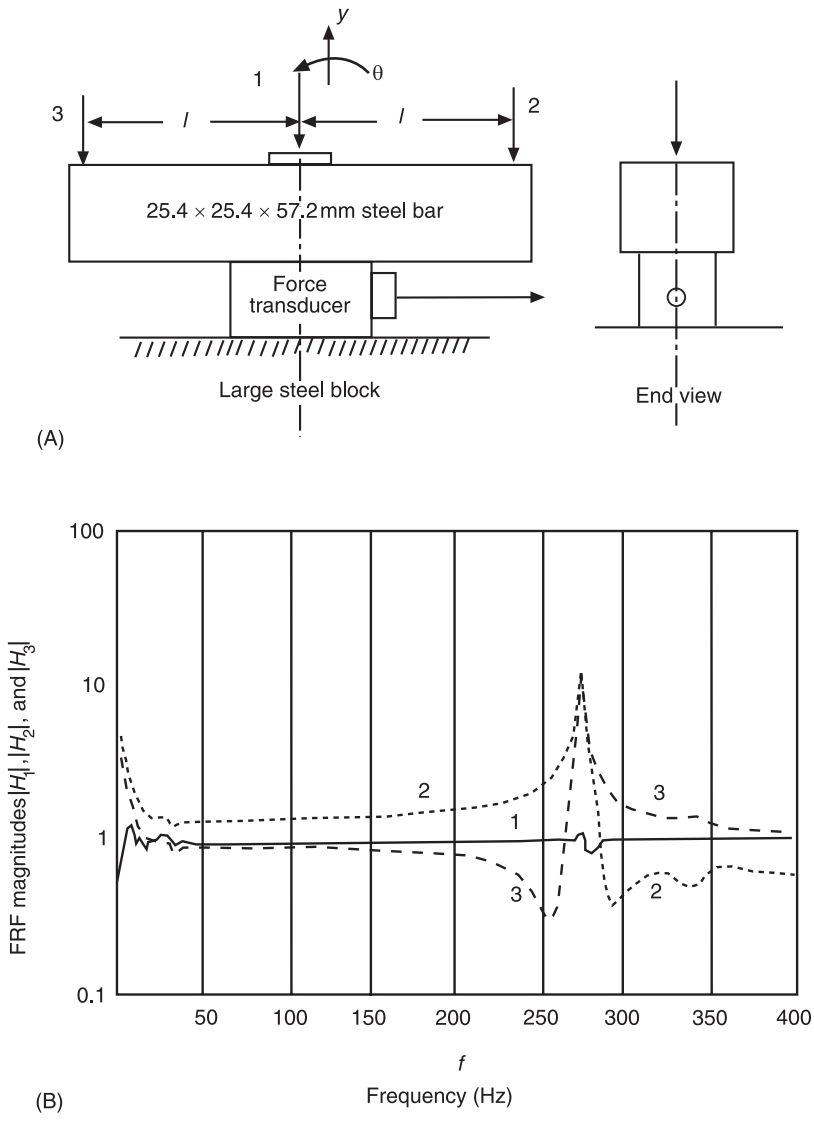


Figure 8 (A) Force transducer bending moment experimental set-up. (B) Experimental calibration FRFs showing effects of bending moments on results. Note rotational resonance at about 275 Hz. Reproduced with permission from McConnell KG and Varoto PS (1993) *Proceedings of the 11th International Modal Analysis Conference*, Society for Experimental Mechanics.

$$\begin{Bmatrix} M_{xc} \\ M_{yc} \\ F_{zc} \end{Bmatrix} = \begin{bmatrix} \varepsilon_{xx} & \varepsilon_{xy} & \varepsilon_{xz} \\ \varepsilon_{yx} & \varepsilon_{yy} & \varepsilon_{yz} \\ \varepsilon_{zx} & \varepsilon_{zy} & \varepsilon_{zz} \end{bmatrix}^{-1} \begin{Bmatrix} M_{xm} \\ M_{ym} \\ F_{zm} \end{Bmatrix} \quad [23]$$

The measured $\boldsymbol{\varepsilon}$ matrix was reported to be:

$$\boldsymbol{\varepsilon} = \begin{bmatrix} 0.9825 & 0.00971 & 1 \times 10^{-4} \\ -0.0393 & 0.9631 & 3.5 \times 10^{-4} \\ -0.4133 & 0.6555 & 0.9597 \end{bmatrix} \quad [24]$$

where the diagonal terms should be close to unity. The elements ε_{xz} and ε_{yz} are small compared to the other terms since they relate moments to forces where the instrument moment arm is very small.

Load Cell Anomaly When Loaded Through the Bolt

The transducer employed by Dong *et al*. (1998) during this test has a bolt pass though its center, as shown in **Figure 10B**. When the impact load was applied directly to the bolt, as shown in **Figures 10B** and **11A**, the sensitivity was found to be 10.58% low compared to other measurements and the manufacturer's sensitivity specification. When the plate was impacted through a loading cylinder that passed around the nut and applied the load directly to the plate, as shown in **Figure 11B**, the calibration agreed with the manufacture. An analysis of the spring and loading arrangements shown in **Figure 11A** and **11B** shows that the plate deflection per unit input force, S_{plate}, is related to the bolt deflection per unit force, S_{bolt}, by:

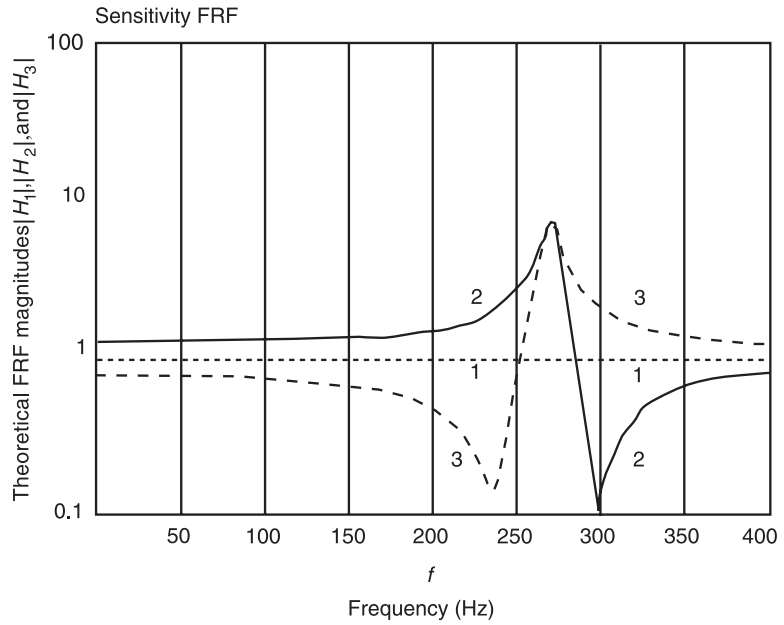


Figure 9 Plot of eqn [19] showing theoretical calibration FRFs for impacts at locations 1, 2, and 3 in **Figure 8B**. Note similarities with measured data. Reproduced with permission from McConnell KG and Varoto PS (1993) *Proceedings of the 11th International Modal Analysis Conference*, Society for Experimental Mechanics.

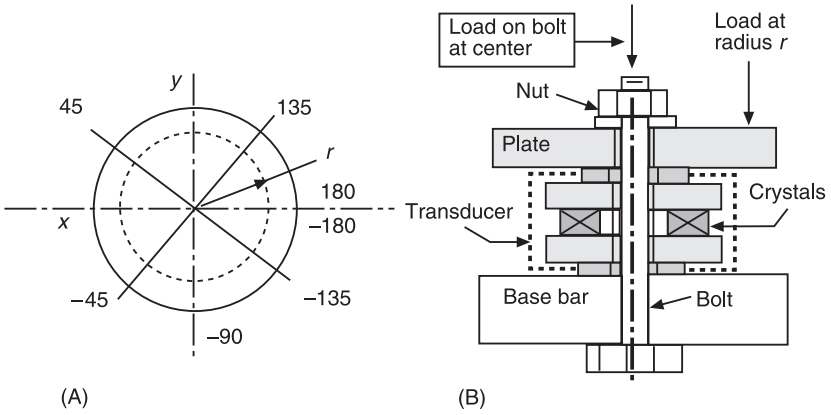


Figure 10 Two-moment, single-force load cell test set-up. (A) Top view of aluminum impact plate showing impact locations at radius *r*. (B) Cross-section showing impact plate, bolt, transducer, sensing crystals, and washer. Reproduced with permission from Dong J *et al*. (1998) *Proceedings of the 16th International Modal Analysis Conference*, Society for Experimental Mechanics.

$$S_{\text{plate}} = \left\{1 + \frac{K_{\text{bolt}}}{4K_{\text{nut}}}\right\} S_{\text{bolt}} \qquad [25]$$

where the bolt deflection per unit of force is given by:

$$S_{\text{bolt}} = \frac{1}{K_{\text{bolt}} + 4K_{\text{trans}} + (K_{\text{trans}}K_{\text{bolt}}/K_{\text{nut}})} \qquad [26]$$

The implications of eqns [25] and [26] indicate that the sensitivity supplied by the manufacturer may not be valid for the user's application since the point of loading and the bolt and nut used may be sufficiently different to cause serious errors when compared to how the manufacture calibrated the transducer.

Removing Force Transducer Mass Loading Effects from FRF Data

In **Transducers for absolute motion** and again in this article, it was observed that the measured force is contaminated by the effective seismic inertial force $m\ddot{y}$. In this section, a correction scheme is developed that removes this contamination from both the driving point $A_{pp}(\omega)$ and transfer $A_{qp}(\omega)$ accelerances where p is the driving point and q is the transfer point.

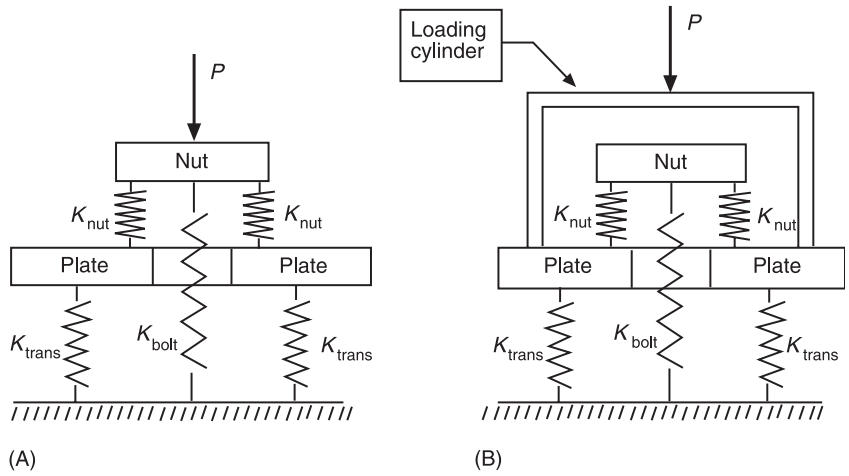


Figure 11 Model of transducer when loaded (A) through the central bolt and (B) through the plate via a loading cylinder placed around the nut. Reproduced with permission from Dong J *et al*. (1998) *Proceedings of the 16th International Modal Analysis Conference*, Society for Experimental Mechanics.

In addition, the effects of measurement system phase and magnitude on the correction scheme are reviewed.

Basic Definitions

The driving point accelerance in the frequency domain is:

$$A_{pp}(\omega) = \frac{A_p(\omega)}{F_p(\omega)} \qquad [27]$$

while the transfer accelerance in the frequency domain is:

$$A_{qp}(\omega) = \frac{A_q(\omega)}{F_p(\omega)} \qquad [28]$$

where $A_p(\omega)$ and $F_p(\omega)$ are the corresponding acceleration and force frequency spectra. The output acceleration voltage frequency spectra, $E_{a_q}(\omega)$, at point q is given by:

$$E_{a_q}(\omega) = H_{a_q}(\omega)\frac{S_{a_q}}{g}A_q(\omega) \qquad [29]$$

and the input force voltage frequency spectra, $E_{F_q}(\omega)$, at driving point p is given by:

$$F_{F_p}(\omega) = H_{F_p}(\omega)S_{F_p}\{1 + m_c A_{pp}(\omega)\}F_p(\omega) \qquad [30]$$

where $H_{a_q}(\omega)$ is the accelerometer's FRF and $H_{F_p}(\omega)$ is the force transducer's FRF. These two instrument FRFs include all mechanical, electrical, and analyzer dynamic characteristics, including the antialiasing filters. S_{a_q} and S_{F_p} are the transducer voltage sensitivities. The connector mass, m_c, includes the force transducer's seismic mass, all connection mechanism mass, and the driving point accelerometer mass.

Correcting Driving Point Accelerance

McConnell (1995) shows that the measured driving point accelerance $A^m_{pp}(\omega)$ is given by:

$$\begin{aligned} A^m_{pp}(\omega) &= \left(\frac{gS_{F_p}}{S_{ap}}\right)\left(\frac{E_{a_p}}{E_{F_p}}\right) \\ &= H_{I_{pp}}(\omega)\left(\frac{1}{1 + m_c A_{pp}(\omega)}\right)A_{pp}(\omega) \end{aligned} \qquad [31]$$

where the denominator shows the force contamination due to the $m_c A_{pp}(\omega)$ term and the instrument system FRF $H_{I_{pp}}(\omega)$ given by:

$$H_{I_{pp}}(\omega) = \frac{H_{a_p}(\omega)}{H_{F_p}(\omega)} \qquad [32]$$

The actual driving point accelerance can be obtained from eqn [31] as:

$$A_{pp}(\omega) = \frac{A^m_{pp}(\omega)}{H_{I_{pp}}(\omega) - m_c A^m_{pp}(\omega)} \qquad [33]$$

When $H_{I_{pp}}(\omega) = 1.0$, eqn [33] reduces to a very simple form of:

$$A^m_{pp}(\omega) = \frac{A^m_{pp}(\omega)}{1 - m_c A^m_{pp}(\omega)} \qquad [34]$$

Correcting the Transfer Accelerance

The measured transfer accelerance, $A^m_{qp}(\omega)$, is given by:

$$A^m_{qp}(\omega) = \left(\frac{gS_{F_p}}{S_{q_q}}\right)\left(\frac{E_{a_q}(\omega)}{E_{F_p}(\omega)}\right) = H_{I_{qp}}(\omega)\left[\frac{1}{1 + m_c A_{pp}(\omega)}\right] A_{qp}(\omega) \quad [35]$$

where $H_{I_{qp}}(\omega)$ is the instrumentation combined FRF given by:

$$H_{I_{qp}}(\omega) = \frac{H_{a_q}(\omega)}{H_{F_p}(\omega)} \quad [36]$$

The actual transfer accelerance can be obtained from eqn [35] as:

$$A_{qp}(\omega) = \left[\frac{1 + m_c A_{pp}(\omega)}{H_{I_{qp}}(\omega)}\right] A^m_{qp}(\omega) \quad [37]$$

which reduces to:

$$A_{qp}(\omega) = \left[1 + m_c A_{pp}(\omega)\right] A^m_{qp}(\omega) \quad [38]$$

when $H_{I_{qp}}(\omega) = 1.0$. It is clear that $A_{pp}(\omega)$ must be corrected first in order to correct the measured transfer accelerance.

Errors when HM_{Ipp} (ω) is Nonunity

McConnell and Hu (1993) and Hu (1991) studied the effect of $H_{I_{pp}}(\omega)$ being nonunity and developed an error expression given by:

$$\varepsilon(\omega) = \left[\frac{\left\{H_{I_{pp}}(\omega) - 1\right\}\left\{1 + m_c A_{pp}(\omega)\right\}}{1 + m_c A_{pp}(\omega)\left\{1 - H_{I_{pp}}(\omega)\right\}}\right] \times 100 \quad [39]$$

where $H_{I_{pp}}(\omega) = 1.0$ gives zero error. It was found that reasonable magnitude errors in $H_{I_{pp}}(\omega)$ created only modest errors in eqn [39]. However, positive phase shifts between data channels as defined by:

$$H_{I_{pp}}(\omega) = \mathrm{e}^{-j\theta} \quad [40]$$

caused large errors when combined with the resonance condition of a SDOF system to give:

$$\varepsilon(r) = \left[\frac{-\{1 - \cos(\theta) + j \sin(\theta)\}\{1 - (1 + M)r^2 + j2\zeta r\}}{1 - \{1 + M[1 - \cos(\theta)]\}r^2 + j2\zeta r\{1 - (Mr/2\xi) \sin(\theta)\}}\right] \times 100 \quad [41]$$

where $r = \omega/\omega_n$, $\omega_n^2 = k_s/m_s$, $M = m_c/m_s$, $\zeta = c_s/2\sqrt{k_s m_s}$. The critical angle and frequency ratio that cause the denominator to be zero are given by:

$$\theta_c \cong \left[\frac{2\zeta}{M(1 - \zeta^2 M)}\right] \quad \text{(radians)} \quad [42]$$

and:

$$r_c \cong \left[\frac{1}{1 - \zeta^2 M}\right] \quad [43]$$

When $M = 0.1$ and $\xi = 0.5\%$, the critical angle is 0.1 rad or 5.7°, a value that is within the antialiasing filter phase match between channels in some multichannel data acquisition systems. Thus, application of these correction schemes can cause very large magnitude errors near a structure's resonance, particularly for light-weight structures. Note that these errors are detectable when the correction is done in the frequency domain but are not detectable when time history signal subtraction is used in an attempt to remove the force signal contamination effects.

Transducer Calibration

Calibration is a process in which a known input is applied to an instrument and the resulting output is recorded in order to establish the transducer's input–output relationship or sensitivity over its usable frequency range. Manufacturers usually use secondary standards that are traceable to a national standard organization that uses absolute calibration methods. In this section, several practical calibration methods for accelerometers and force transducers are summarized. These methods use either secondary standards or an experimental arrangement based on Newton's second law.

Accelerometer Calibration (Back-to-back Method)

Accelerometers are often calibrated by using the back-to-back method where the accelerometer to be calibrated is mounted on a calibration standard so that both accelerometers are measuring the same mounting surface acceleration, as shown in **Figure 12A**. The calibration standard should be traceable to an absolute standard. The calibration standard is mounted on

a vibration exciter that is driven by an appropriate signal such as a chirp, pure tone sinusoid, or an impulse. Both signals are measured and compared over a range of frequencies. This is a good method to be employed in the laboratory environment, but it is cumbersome to use in the field. The hand-held calibrator shown in **Figure 12B** is convenient for verifying the sensitivity of an accelerometer in the field. This particular calibrator generates a 1.0 g rms sinusoidal acceleration at 79.6 Hz with less than 3% error for accelerometer mass under 70 g by using a feedback scheme from a built-in reference accelerometer.

Acceleration Calibration (Gravimetric Calibration Method)

Lally (1990) developed the gravimetric method, as shown in **Figure 13A**, which is a portable field type of calibration method based on Newton's second law. The accelerometer to be calibrated is mounted to a steel cylinder that falls in a guide tube and strikes an impact cushion between the force transducer and the steel cylinder. The force transducer is attached to a heavy base mass on the lower end. The output signal from each transducer is connected to either a digital oscilloscope or a frequency analyzer. This method employs two steps. First, the steel cylinder is quickly lifted off the force transducer so that an approximate step change in force signal E_{mg} is recorded as shown in **Figure 13B**. Second, the cylinder is dropped on to the force transducer and both the force and acceleration signals are recorded. If the transducers are linear and no transducer ringing occurs, then the signals plot as a straight line with slope S, as shown in **Figure 13C**, so that:

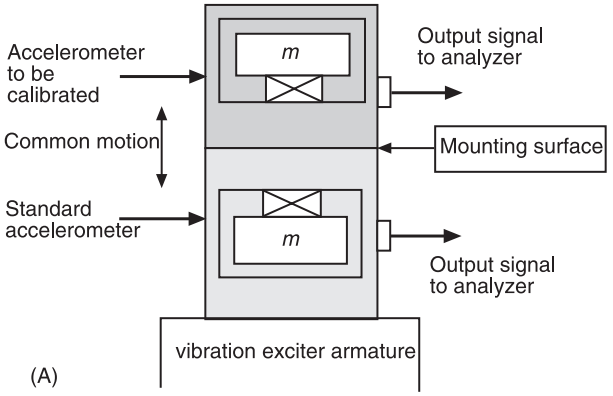




Figure 12 (A) Cross-section of accelerometers used in back-to-back calibration arrangement. (B) Photograph of a hand-held calibrator. Courtesy of PCB Piezotronics, Depew, NY.

$$S = \frac{E_a}{E_F} \qquad [44]$$

Then, the accelerometer's voltage sensitivity in units of $\mathrm{V\,g^{-1}}$ is given by:

$$S_a = SE_{mg} \qquad [45]$$

This method is dependent on the local acceleration due to gravity since E_{mg} is a measure of the local weight of the steel mass and accelerometer. Also, note that this method does not require knowledge of the force transducer voltage sensitivity, it only requires that both transducers are linear. The slope S can also be determined from a frequency analyzer where one uses the mean value of the frequency domain ratio:

$$S(\omega) = \frac{E_a(\omega)}{E_F(\omega)} \qquad [46]$$

over a range of frequencies where this ratio is essentially constant. This method requires the pulse duration to be short enough to excite the range of frequencies of interest and long enough to prevent transducer ringing.

Force Transducer Calibration (Gravimetric Method)

The force transducer can be calibrated using the gravimetric method if the weight of the steel cylinder and accelerometer assembly is determined by a weighing method that is independent of local gravity, such as a balance against a known mass or weight. Then, eqn [45] can be modified to give the force transducer sensitivity with units of volts/unit force (pound or newton) from:

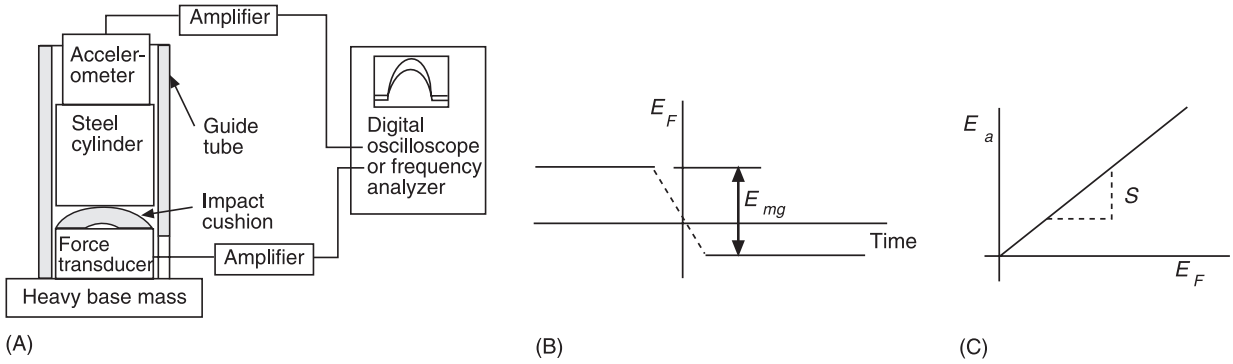


Figure 13 Gravimetric transducer calibration. (A) Test set-up; (B) first step showing static weight measurement of E_{mg};(C) second step impulse signals plotted against one another to determine slope S. Reproduced with permission from Dally JW, Riley WF and McConnell KG (1993) *Instrumentation for Engineering Measurements*. New York: John Wiley.

$$S_F + \left[\frac{S_a}{S}\right]\left[\frac{1}{mg}\right] \qquad [47]$$

$$S_F^* = \left[\frac{E_F}{E_a}\right]\left[\frac{S_a}{W_c}\right] \qquad [48]$$

where mg is the standard weight of the calibration and accelerometer mass with units of either pounds or newtons. Obviously, the accelerometer calibration must be done first so that S_a is known.

Impact Calibration of Impact Hammers and Accelerometers

This calibration method is primarily used to verify the calibration of hammer-mounted force transducers and accelerometers under field conditions using Newton's second law and the arrangement shown in **Figure 14**. The calibration mass m_c includes the accelerometer's mass and should be suspended as a pendulum using two equal length light-weight cables or strings. The effective force transducer sensitivity in volts/unit force is given by:

where the ratio of E_a/E_F can be obtained by either plotting the time histories as shown in **Figure 13C** or using the mean ratio of E_a/E_F from a frequency analyzer, as described above. It is clear that this method is essentially the same as the gravimetric method. The reader is warned that a similar method was presented at technical meetings during the 1980s where a lightweight calibration mass m_c was held by hand. These calibration results depended on the hand mass of the person doing the calibration as well as how hard that person held the calibration mass. This hand-held mass method is not recommended unless the mass exceeds 50 kg!

Environmental Factors

Transducers are purchased to make accurate measurements. The above topics have addressed some of

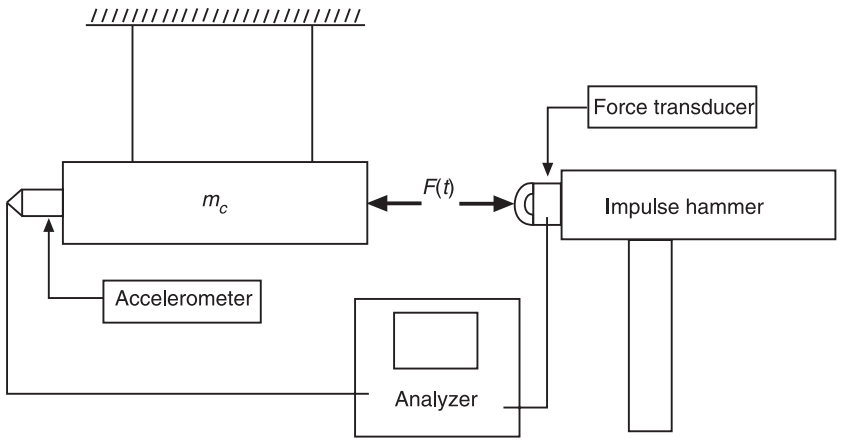


Figure 14 Schematic of calibration method either to calibrate the force transducer or to compare force and accelerometer sensitivities.

the more serious phenomena that can affect transducer performance. However, additional factors are known to affect piezoelectric transducers, such as cable noise, humidity and dirt, transducer mounting, nuclear radiation, and temperature.

Cable Noise

Three different types of cable noise effects have been identified when using charge amplifiers: electromagnetic fields, ground loops, and triboelectric effects.

Electromagnetic fields Electromagnetic fields are caused by electrical power cables carrying large currents that generate strong magnetic fields. Instrument cables should not share the same electrical conduit with these power cables. Instrument cables should be shielded in their own grounded steel conduit.

Ground loops Ground loops are due to the transducer being attached to a structure with a different electrical potential than the charge amplifier's ground so that a current flows through the cable's ground shield and causes a false signal to appear. This signal can usually be detected in frequency domain measurements such as autospectral density since ground loops usually contain line frequency and integer multiples of line frequency. However, this signal is often difficult to remove without great effort such as using an electrical isolation mounting in order to break the current flow, a task that is nearly impossible when using force transducers. However, it is often useful to ground all points of the test to a common point that is well grounded. Sometimes a building's electrical system has poor electrical grounds which causes significant ground loop-type problems.

Triboelectric effects Triboelectric effects are caused by damaged instrument cables that generate charge when the center conductor has broken free from and rubs on the insulation material to cause signals at the same frequencies as the test. The easiest way to detect this problem is to shake the instrument cable when the transducer is in a benign environment. If the cable produces significant signals, cutting the offending cable into two parts before discarding cures the problem. Then install a new undamaged cable. Note: damaged cables that are not cut into two parts and discarded have an uncanny way of showing up in other tests. The triboelectric cable-shaking check should be done at the beginning and end of each test in order to eliminate this error source. Proper mounting of cables is required to reduce cable damage.

Humidity and Dirt

Humidity and dirt can cause significant deterioration of signal quality by draining significant amounts of generated charge, particularly when using charge amplifiers. Dirty fingerprints and/or moisture on transducer connectors are a prime location for this signal contamination. The connector should be periodically cleaned using acetone or other approved cleaning agent. Using either silicone grease before assembly or covering the connection with RTV silicone rubber can reduce the connector humidity and/or moisture problem.

Mounting the Transducer

In order to work accurately, the transducer must move with the contact surface without significant relative motion. This can be achieved by using a bolted connection along with wax or waxy grease to ensure contact at high frequencies. Often it is good practice to polish the interface surface to reduce the local rough spots. A magnetic mounting is convenient to use. In this case, polishing the surface and using waxy grease will improve contact at high frequencies. Miniature accelerometers can be successfully mounted using only instrument-grade wax provided the mounting surface is clean, smooth, and the temperature is low enough. The hand-held probe is not recommended except for large structures when measuring low-frequency vibrations.

Nuclear Radiation

When using transducers in nuclear radiation fields, it is recommended that the user contact the manufacturer.

Temperature

Temperature can cause three undesirable effects. First, transducer charge sensitivity may change with temperature. Second, rapid temperature changes can cause false low-frequency signals. Third, high temperatures can cause permanent damage to piezoelectric sensing crystals when temperatures exceed about 250 °C. Once the Curie temperature is exceeded, piezoelectric crystals are permanently damaged. It is prudent to consult the manufacturers for recommendations for both low temperatures and high temperature applications.

Nomenclature

$\mathbf{a}$	transducer acceleration
$A_s(\omega)$	driving point accelerance
$\mathbf{b}$	apparent acceleration
$F(\omega)$	interface force

m_c	calibration mass
M	mass ratio
S	slope
S_o	effective sensing axis
$\mathbf{S}_o$	sensitivity vector
$\ddot{x}$	base excitation
$\ddot{y}(\omega)$	seismic mass acceleration
$\boldsymbol{\varepsilon}^{-1}$	correction matrix
ϕ, θ	angle
ζ_s	structural damping

See also: **Transducers for absolute motion**; **Transducers for relative motion**.

Further Reading

Dally JW, Riley WF, and McConnell KG (1993) *Instrumentation for Engineering Measurements*. New York, NY: Wiley.

Dong J, McConnell KG, Alfonzo M and Golovanova L (1998) Error reduction of measured impact forces and their lines of action via cross sensitivity studies. In: *Proceedings of the 16th International Modal Analysis Conference*, pp. 1099–1105. Santa Barbara, CA.

Han S and McConnell KG (1986) Effect of mass on force transducer sensitivity. *Experimental Techniques* 10: 19–22.

Han S and McConnell KG (1989) The effects of transducer cross-axis sensitivity in modal analysis. In: *Proceedings of the 7th International Modal Analysis Conference*, vol. I, pp. 505–511. Las Vegas, NV.

Han S and McConnell KG (1991) Analysis of frequency response functions affected by the coupled modes of the structure. *International Journal for Analytical and Experimental Modal Analysis* 6: 147–159.

Hu X (1991) *effects of stringer axial dynamics and mass compensation methods on experimental modal analysis*. PhD dissertation, Iowa State University, Ames, IA.

Lally RW (1990) Gravimetric calibration of accelerometers. PCB Piezotronics, Inc., 3425 Walden Ave., Depew, NY 14043–2495.

McConnell KG (1990) Errors in using force transducers. In: *Proceedings of the 8th International Modal Analysis Conference*, vol. 2, pp. 884–890. Kissimmee, FL.

McConnell KG (1993) The interaction of force transducers with their test environment. *Modal Analysis: The International Journal of Analytical and Experimental Modal Analysis* 8: 137–150.

McConnell KG (1995) *Vibration Testing Theory and Practice*, pp. 223–234. New York, NY: Wiley.

McConnell KG and Han SB (1991) A theoretical basis for cross-axis corrections in tri-axial accelerometers. In: *Proceedings of the 9th International Modal Analysis Conference*, vol. I, pp. 171–175. Florence, Italy.

McConnell KG and Hu X (1993) Why do large FRF errors result from small relative phase shifts when using force transducer mass compensations methods? In: *Proceedings of the 11th International Modal Analysis Conference*, vol. II, pp. 845–859. Kissimmee, FL.

McConnell KG and Varoto PS (1993) A model for force transducer bending moment sensitivity and response during calibration. In: *Proceedings of the 11th International Modal Analysis Conference*, vol. 1, pp. 516–521. Kissimmee, FL.

SENSORS AND ACTUATORS

H S Tzou, University of Kentucky, Lexington, KY, USA
C S Chou, National Taiwan University, Taipei, Taiwan, Republic of China

Copyright © 2001 Academic Press

doi:10.1006/rwvb.2001.0141

As discussed in the article on **Piezoelectric materials and continua**, piezoelectricity is an electromechanical phenomenon coupling the elastic field and the electric field, and it is governed by the direct piezoelectric effect and the converse piezoelectric effect. This article will discuss its advanced applications to distributed sensing and control of elastic continua (or distributed parameter systems), e.g., shells, plates, etc., based on distributed piezoelectric sensors and actuators. This synergistic integration of smart materials, sensors, actuators, and control electronics leads to a new distributed structronic (*struc*ture + elec*tronic*) system capable of self-sensing, diagnosis, and control. The fundamental background of the distributed parameter systems is introduced, followed by definitions of distributed sensors and actuators and their theories and governing equations. Application examples and design principles are presented afterwards.

Distributed Sensors and Actuators

Mass, stiffness, static and dynamic characteristics of elastic continua or structures (e.g., shells and plates) are generally distributed in nature, i.e., their properties or behaviors are functions of time and spatial coordinates. Accordingly, these systems are usually classified as distributed parameter systems (DPSs)

and they are usually modeled by partial differential equations (PDEs). In practical applications, however, due to their complexity, discretization techniques are often employed and, for convenience, the derived simplified lumped (or discrete) parameter systems (LPSs) are analyzed and evaluated. Accordingly, simplified LPS only reveals partial system characteristics of the original DPS. Similarly, sensing and control of DPS using conventional (discrete or point) sensors and actuators at spatially discrete locations also pose many technical problems, especially if they are placed at (or near) modal nodes or on nodal lines of DPSs. Eventually, these modes are neither observable nor controllable by these discrete transducers. To remedy the discrete sensor/actuator deficiencies and to observe and control the elastic DPS, spatially distributed sensors and actuators are highly desirable.

Thinly distributed piezoelectric layers are excellent candidates for distributed sensor and actuator applications, because of their distributed nature, excellent sensitivity, and easy application to elastic continua or structural DPSs. Note that distributed sensors are based on the direct piezoelectric effect and distributed actuators are based on the converse piezoelectric effect. Similar to conventional strain gauges, distributed piezoelectric sensors are strain-sensitive sensors; unlike strain gauges, their signals are rather strong and they usually do not need additional signal conditioning units. **Figure 1** illustrates two spatially distributed piezoelectric layers respectively laminated on the top and bottom surfaces of a generic deep elastic shell continuum – a generic elastic DPS. One piezoelectric layer serves as a distributed sensor and the other serves as a distributed actuator. Generic sensing and actuation theories based on the double-curvature shells are defined first, followed by applications to other geometries using four system parameters, two Lamé parameters and two radii of curvature, R_1 and R_2.

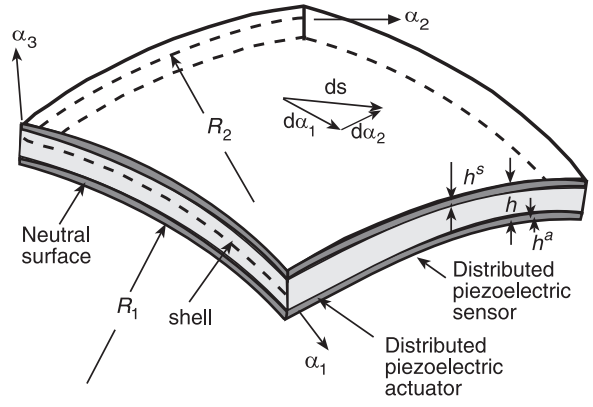


Figure 1 An elastic shell laminated with distributed piezoelectric sensor and actuator – a structronic shell system.

Distributed Sensing

As discussed previously, the distributed sensing layer responds to strain variations and generates signals due to the direct piezoelectric effect. Based on the Gaussian theory ($\nabla \mathbf{D}_i = 0$), the Maxwell equation ($\mathbf{E}_j = -\nabla \boldsymbol{\phi}$), and the direct piezoelectric effect, an open-circuit voltage ϕ^s, in the transverse direction, forms the distributed sensor layer made of hexagonal piezoelectric materials is:

$$\phi^s = (h^s/S^e) \times \int_{\alpha_1} \int_{\alpha_2} \left[h_{31}S^s_{11} + h_{32}S^s_{22} + h_{36}S^s_{12}\right] \times A_1 A_2 \, d\alpha_1 \, d\alpha_2 \quad [1]$$

where h^s is the sensor thickness; S^e is the effective sensor electrode area; h_{3i} is the piezoelectric constant indicating a signal generation in the transverse direction due to the strain in the ith direction; and S^s_{ij} is the strain on the ith surface in the jth direction. These strains are two in-plane normal strains and one shear strain. (Most current commercial materials, e.g., polyvinylidene fluoride and piezoceramics, are usually insensitive to the shear strain.) Since the sensor layer is laminated on the shell, the effective strains generating signals are the two in-plane normal strains and one in-plane shear strain. Note that the open-circuit voltage reflects the induced strains over the effective sensor area and it is averaged over the effective electrode area. Strains can be further divided into the membrane strain component s^o_i and the bending strain component k_i, i.e., $S^s_{ii} = s^o_i + \alpha_3 k_i$; these two components are expressed as follows.

Membrane Strains

$$s^o_1 = \frac{1}{A_1}\frac{\partial u_1}{\partial \alpha_1} + \frac{u_2}{A_1 A_2}\frac{\partial A_1}{\partial \alpha_2} + \frac{u_3}{R_1} + \frac{1}{2}\left(\frac{\partial u_3/\partial \alpha_1}{A_1}\right)^2 \quad [2]$$

$$s^o_2 = \frac{1}{A_2}\frac{\partial u_2}{\partial \alpha_2} + \frac{u_1}{A_1 A_2}\frac{\partial A_2}{\partial \alpha_1} + \frac{u_3}{R_2} + \frac{1}{2}\left(\frac{\partial u_3/\partial \alpha_2}{A_2}\right)^2 \quad [3]$$

$$s^o_6 = \frac{1}{A_2}\frac{\partial u_1}{\partial \alpha_2} + \frac{1}{A_1}\frac{\partial u_2}{\partial \alpha_1} - \frac{u_1}{A_1 A_2}\frac{\partial A_1}{\partial \alpha_2} - \frac{u_2}{A_1 A_2}\frac{\partial A_2}{\partial \alpha_1} + \left(\frac{1}{A_1 A_2}\frac{\partial u_3}{\partial \alpha_1}\frac{\partial u_3}{\partial \alpha_2}\right) \quad [4]$$

Bending Strains

$$k_1 = \frac{1}{A_1}\frac{\partial}{\partial \alpha_1}\left(\frac{u_1}{R_1} - \frac{1}{A_1}\frac{\partial u_3}{\partial \alpha_1}\right) + \frac{1}{A_1 A_2}\left(\frac{u_2}{R_2} - \frac{1}{A_2}\frac{\partial u_3}{\partial \alpha_2}\right)\frac{\partial A_1}{\partial \alpha_2} \quad [5]$$

$$k_2 = \frac{1}{A_2}\frac{\partial}{\partial \alpha_2}\left(\frac{u_2}{R_2} - \frac{1}{A_2}\frac{\partial u_3}{\partial \alpha_2}\right) + \frac{1}{A_1 A_2}\left(\frac{u_1}{R_1} - \frac{1}{A_1}\frac{\partial u_3}{\partial \alpha_1}\right)\frac{\partial A_2}{\partial \alpha_1} \quad [6]$$

$$k_6 = \frac{1}{A_2}\frac{\partial}{\partial \alpha_2}\left(\frac{u_1}{R_1} - \frac{1}{A_1}\frac{\partial u_3}{\partial \alpha_1}\right) + \frac{1}{A_1}\frac{\partial}{\partial \alpha_1}\left(\frac{u_2}{R_2} - \frac{1}{A_2}\frac{\partial u_3}{\partial \alpha_2}\right) - \frac{1}{A_1 A_2}\left(\frac{u_1}{R_1} - \frac{1}{A_1}\frac{\partial u_3}{\partial \alpha_1}\right)\frac{\partial A_1}{\partial \alpha_2} - \frac{1}{A_1 A_2}\left(\frac{u_2}{R_2} - \frac{1}{A_2}\frac{\partial u_3}{\partial \alpha_2}\right)\frac{\partial A_2}{\partial \alpha_1} \quad [7]$$

where u_i is the displacement in the ith direction; A_i is the Lamé parameter defined by the fundamental form; and R_i is the radius of curvature of the ith axis. Note that this definition incorporates large (nonlinear) strain generation in the distributed sensor layer. The nonlinear strain terms are the quadratic terms defined by the von Karman geometric nonlinearity in the membrane strain equations. For small (linear) deformation, these quadratic terms vanish in the membrane strains and thus the signal reflects the strains resulting from only linear vibration of the thin shell DPS. Furthermore, depending on sensor placement and geometry, the sensor layer can be solely sensitive to either membrane vibrations, bending vibrations, or a combination of both components. Taking the example of a sensor layer surface laminated on beams or flat plates, its primary strain component contributing to the sensor signal generation is the bending strain. However, when referring to a sensor laminated on the neutral surface of rings or shells, the primary strain component to the signal generation is the membrane strain. Thus, knowing what to measure on what structure is the key to sensor placement and location on distributed plate or shell systems. Furthermore, significant observation deficiency can occur when the signal generated by the positive strain is canceled out with that resulting from the negative strain in certain natural modes, especially antisymmetrical modes of symmetrical structures with symmetrical boundary conditions, e.g., simply supported beams or plates. In this case, other techniques, such as sensor segmentation or spatial (thickness or surface) shaping, can be used to alleviate the observation deficiency.

Distributed Actuation and Control

Distributed actuation and control of elastic DPSs using the distributed piezoelectric layer is based on the converse piezoelectric effect. The strain induced by a control potential ϕ^a (the converse piezoelectric effect) leads to stress (i.e., strain multiplied by Young's modulus Y_p), and then the membrane control force N_{ii}^a (**Figure 2**).

$$N_{ii}^a = d_{ii} Y_p \phi^a \quad [8]$$

Note that $d_{ii} = d_{3i}$ for the induced force resulting from a transversely applied control signal. Since the distributed actuator is surface-laminated, the control force also induces a counteracting control moment effect (M_{ii}^a) to the shell continuum.

$$M_{ii}^a = r^a d_{ii} Y_p \phi^a \quad [9]$$

where r^a is the moment arm measured from the shell neutral surface to the midplane of the distributed actuator. Accordingly, distributed actuation and control can be achieved. Previous studies have revealed that the membrane control force is important when controlling curved structures (e.g., shells and rings) and the control moment is effective in controlling zero-curvature structures (e.g., plates and beams). Furthermore, control deficiencies can also occur on antisymmetrical modes of symmetrical structures, due to cancellation of input control potential on the distributed actuator layer. Again, using segmentation and shaping (thickness or surface) techniques can alleviate the problem. **Figure 2** illustrates the control actions of the distributed piezoelectric actuator.

Following Hamilton's principle and integrating all control forces into thin shell equations yield open- or closed-loop shell system equations in the three axial directions:

$$-\frac{\partial\left(N_{11}^* A_2\right)}{\partial \alpha_1} + N_{22}^* \frac{\partial A_2}{\partial \alpha_1} - \frac{\partial(N_{21} A_1)}{\partial \alpha_2} - N_{12}\frac{\partial A_1}{\partial \alpha_2} + \frac{1}{R_1}\left[\frac{\partial\left(M_{11}^* A_2\right)}{\partial \alpha_1} - M_{22}^* \frac{\partial A_2}{\partial \alpha_1} + \frac{\partial(M_{21} A_1)}{\partial \alpha_2} + M_{12}\frac{\partial A_1}{\partial \alpha_2}\right] + A_1 A_2 \rho h \ddot{u}_1 = A_1 A_2 F_1 \quad [10]$$

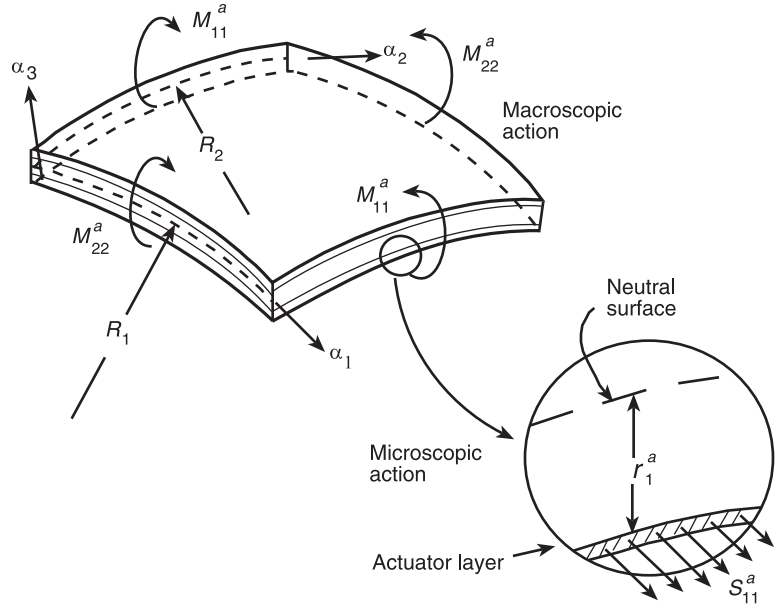


Figure 2 Distributed control induced by the distributed actuator layer.

$$
\begin{aligned}
&-\frac{\partial\left(N_{22}^{*}A_1\right)}{\partial\alpha_2}+N_{11}^{*}\frac{\partial A_1}{\partial\alpha_2}-\frac{\partial(N_{12}A_2)}{\partial\alpha_1}-N_{21}\frac{\partial A_2}{\partial\alpha_1}\\
&-\frac{1}{R_2}\left[\frac{\partial\left(M_{22}^{*}A_1\right)}{\partial\alpha_2}-M_{11}^{*}\frac{\partial A_1}{\partial\alpha_2}+\frac{\partial(M_{12}A_2)}{\partial\alpha_1}+M_{21}\frac{\partial A_2}{\partial\alpha_1}\right]\\
&+A_1A_2\rho h\ddot{u}_2=A_1A_2F_2
\end{aligned}
\qquad [11]
$$

$$
\begin{aligned}
&-\frac{\partial}{\partial\alpha_1}\left[\frac{1}{A_1}\left(\frac{\partial\left(M_{11}^{*}A_2\right)}{\partial\alpha_1}-M_{22}^{*}\frac{\partial A_2}{\partial\alpha_1}\right.\right.\\
&\left.\left.+\frac{\partial(M_{21}A_1)}{\partial\alpha_2}+M_{12}\frac{\partial A_1}{\partial\alpha_2}\right)\right]\\
&-\frac{\partial}{\partial\alpha_2}\left[\frac{1}{A_2}\left(\frac{\partial\left(M_{22}^{*}A_1\right)}{\partial\alpha_2}-M_{11}^{*}\frac{\partial A_1}{\partial\alpha_2}\right.\right.\\
&\left.\left.+\frac{\partial(M_{12}A_2)}{\partial\alpha_1}+M_{21}\frac{\partial A_2}{\partial\alpha_1}\right)\right]\\
&+A_1A_2\left(\frac{N_{11}^{*}}{R_1}+\frac{N_{22}^{*}}{R_2}\right)+A_1A_2\rho h\ddot{u}_3=A_1A_2F_3
\end{aligned}
\qquad [12]
$$

where u_i is the displacement in the α_i direction; ρ is the mass density; F_i is the external input; A_1 and A_2 are the Lamé parameters; and R_1 and R_2 are the radii of curvature. Note that the force and moment components consist of the original elastic component and the control component, i.e., $N_{ii}^{*}=N_{ii}+N_{ii}^{a}$ and $M_{ii}^{*}=M_{ii}+M_{ii}^{a}$, governed by control algorithms, which are either open-loop or closed-loop. This set of generic shell equations can be simplified to account for other geometries such that distributed sensing and control of other geometries can be investigated.

There are four geometric parameters – two Lamé parameters (A_1 and A_2) and two radii (R_1 and R_2) of curvature – required to carry out the simplification and reduction of generic shell sensing/control governing equations. Examples of various simplified geometries are shown in **Figure 3**; simplification procedures are briefly discussed below.

1. Select a coordinate system. The original generic shell continuum was defined in a tri-orthogonal curvilinear coordinate system (α_1, α_2, α_3). Depending on the given geometries (host elastic structure) and/or sensor/actuator shapes, these coordinates can be redefined to best represent the problem, e.g., $\alpha_1 = x$ and $\alpha_2 = y$ for a rectangular plate; $\alpha_1 = x$ and $\alpha_2 = \theta$ for a cylindrical shell and thin cylindrical tube shell; $\alpha_1 = \psi$ and $\alpha_2 = \theta$ for a spherical shell, etc.
2. Determine the radii of curvature. The radii of curvatures R_1 and R_2 of the two in-plane coordinate axes α_1 and α_2 can be easily observed from the coordinate system defined in step 1. For example, the radii of the x and y axes in a rectangular plate are $R_1 = \infty$ and $R_2 = \infty$. In a cylindrical shell, $R_1 = \infty$ and $R_2 = R$. In a spherical shell, the radii are $R_1 = R_2 = \mathbf{R}$.
3. Derive a fundamental form. A fundamental form represents an infinitesimal distance ds on the neutral surface of the shell continuum; the distance is the hypotenuse of a (or an approximate) right-angle triangle defined by the projected infinitesimal distances ($d\alpha_1$ and $d\alpha_2$) of the two in-plane coordinates (**Figure 1**). From the fundamental form, the two Lamé parameters A_1 and A_2

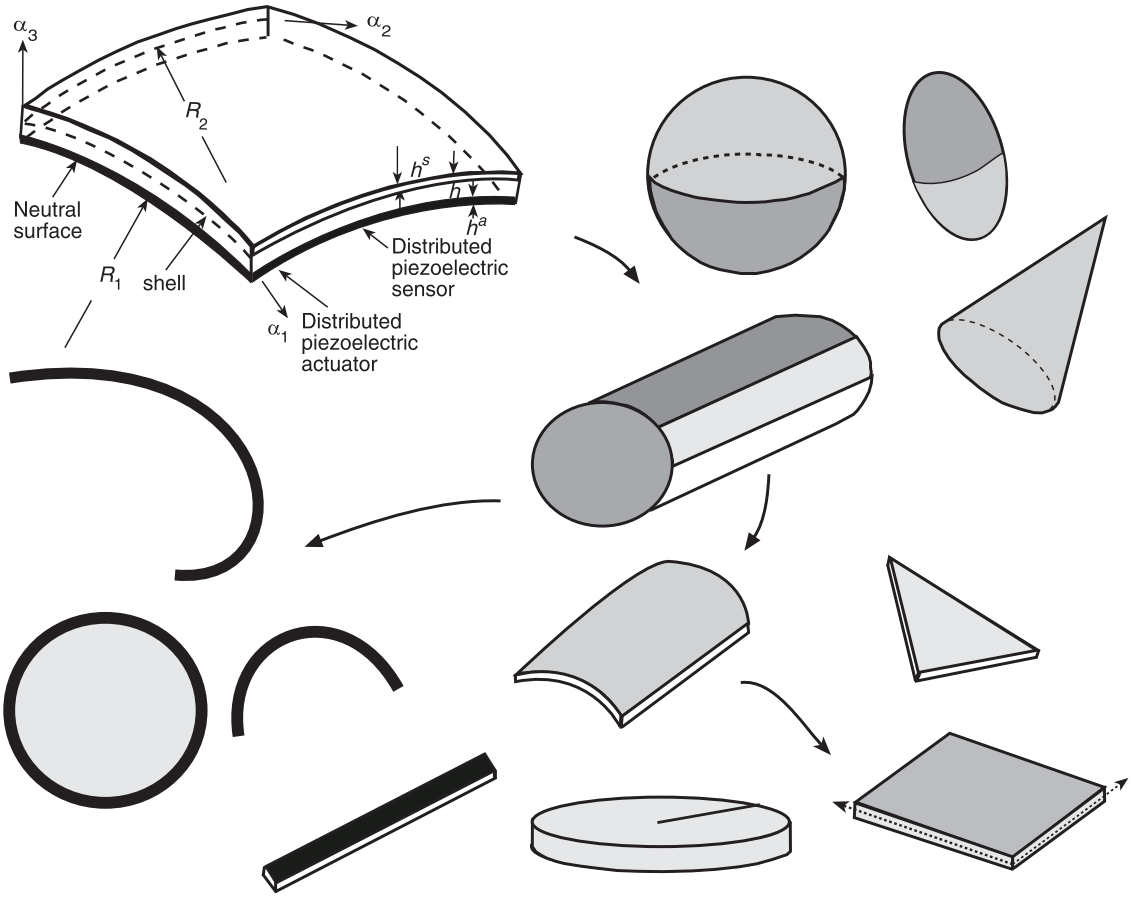


Figure 3 Applications of the distributed sensing and control of shells.

and the two selected coordinates α_1 and α_2 can be defined, i.e.,

$$(ds)^2 = (A_1)^2(d\alpha_1)^2 + (A_2)^2(d\alpha_2)^2 \qquad [13]$$

For example, the fundamental form for a rectangular plate (defined in a Cartesian coordinate system x and y) is $(ds)^2 = (1)^2(dx)^2 + (1)^2(dy)^2$, thus, the Lamé parameters are $A_1 = 1$ and $A_2 = 1$. For a cylindrical shell defined by the x and β axes, the fundamental form is $(ds)^2 = (1)^2(dx)^2 + (R)^2(d\beta)^2$, thus, $A_1 = 1$ and $A_2 = R$ (radius of the cylinder). The fundamental form defining the spherical shell is $(ds)^2 = \mathbf{R}^2(d\psi)^2 + \mathbf{R}^2\sin^2\psi(d\theta)^2$ where $\mathbf{R}$ is the radius of the spherical shell. Thus, the Lamé parameters are $A_1 = \mathbf{R}$ and $A_2 = \mathbf{R}\sin\psi$, where ψ is the meridional angle and θ is defined accordingly.

4. Simplify the shell sensor/actuator equations. By substituting the four parameters A_1, A_2, R_1, and R_2 into the generic shell sensor/actuator and/or system equations, one can easily derive the governing equations for that geometry or sensor/actuator, e.g., shells (cylindrical shells, conical shells, spherical shells, shells of revolution, etc.) or non-shell continua (rings, arches, beams, rods, etc.; **Figure 3**). (Detailed sensing/actuation and shell equations can be found in the further reading section.)

Furthermore, distributed sensors and actuates can be surface- or thickness-shaped using orthogonal functions, e.g., modal strain functions. In this case, the shaped sensor or actuator is only sensitive to the designated natural mode (i.e., the orthogonal modal sensor or actuator) and it is insensitive to other natural modes, based on the modal orthogonality of natural modes. In order to demonstrate the distributed sensor/actuator functionality and the bending/membrane effects, an example of structronic cylindrical shells is presented next.

Case Study: Sensing and Control of Structronic Cylindrical Shells

One of the important applications of distributed sensors and actuators is to evaluate detailed electromechanical sensing/control behaviors of distributed

adaptive structronic systems. Adaptive structures and structronic systems usually involve shape transformation, changing from one geometry to another, in order to achieve specific functional advantages in practical applications. A zero-curvature plate can transform to a shallow shell, a deep shell, and to a closed cylindrical shell (i.e., tube shell) when its curvature continuously changes from 0° to 360° (**Figure 4**). Usually, the bending effect dominates the plate or shallow shell dynamics; however, the membrane effect dominates the deep shell dynamics, especially for lower natural modes. (Recall that plates are defined as zero-curvature shells, i.e., radii R_1 and R_2 are infinity and the Lamé parameters A_1 and A_2 are ones.) This structronic cylindrical shell case demonstrates the utilities of distributed sensors and actuators and reveals the detailed electromechanics and functionalities, and design guideline of these devices as applied to various shell structures with different curvatures.

A cylindrical shell structronic system consists of elastic shell layers and distributed piezoelectric layers serve as distributed sensors and/or actuators (**Figure 5**). It is assumed that there is perfect bonding between the layers. Recall that the cylindrical shell is defined by the x and β axes, the fundamental form is $(\mathrm{d}s)^2 = (1)^2(\mathrm{d}x)^2 + (R)^2(\mathrm{d}\beta)^2$. Thus, the Lamé parameters are $A_1 = 1$ and $A_2 = R$ (radius of the cylinder). (Note that the sensor/actuator segmented patches laminated on the cylindrical shell can be defined by their corresponding x and β coordinates generically. When $x = L$ and $\beta = \beta^*$, it becomes a fully distributed sensor/actuator, e.g., **Figure 1**.)

Following the procedures described previously and substituting the four parameters into the generic structronic shell system equations yields the governing equations of structronic cylindrical shells:

$$-\frac{\partial N_{xx}}{\partial x} - \frac{1}{R}\frac{\partial N_{x\beta}}{\partial \beta} + \rho h \ddot{u}_1 = F_1 + \frac{\partial N^c_{xx}}{\partial x} \qquad [14]$$

$$-\frac{\partial N_{x\beta}}{\partial x} - \frac{1}{R}\frac{\partial N_{\beta\beta}}{\partial \beta} - \frac{1}{R}\left[\frac{\partial M_{x\beta}}{\partial x} + \frac{1}{R}\frac{\partial M_{\beta\beta}}{\partial \beta}\right] + \rho h \ddot{u}_2 = F_2 + \frac{1}{R}\frac{\partial N^c_{\beta\beta}}{\partial \beta} + \frac{1}{R^2}\frac{\partial M^c_{\beta\beta}}{\partial \beta} \qquad [15]$$

$$-\frac{\partial^2 M_{xx}}{\partial x^2} - \frac{2}{R}\frac{\partial^2 M_{x\beta}}{\partial x^2} - \frac{1}{R^2}\frac{\partial^2 M_{\beta\beta}}{\partial \beta^2} + \frac{N_{\beta\beta}}{R} + \rho h \ddot{u}_3 = F_3 + \frac{\partial^2 M^c_{xx}}{\partial x^2} + \frac{1}{R^2}\frac{\partial^2 M^c_{\beta\beta}}{\partial \beta^2} - \frac{N^c_{\beta\beta}}{R} \qquad [16]$$

and forces and moments are defined by $N_{ii}/M_{ii} = N^m_{ii}/M^m_{ii} + N^a_{ii}/M^a_{ii}$. As discussed previously, injecting high voltages into the distributed piezoelectric actuators induces two major control actions. One is the in-plane membrane control force(s) and the other is the out-of-plane control (bending) moment(s). In general, the control moments are essential in planar structures, e.g., plates and beams; the membrane control forces are effective to deep shells. In this study, numerical solutions are plotted to evaluate the sensing and control effectiveness.

Free Vibration Analysis

As discussed previously, adaptive structures with continuous geometry transformation have many potential applications, e.g., optical focusing, flow control, etc. Frequency variation of a continuously changing cylindrical shell (**Figures 4** and **5**) is investigated in this

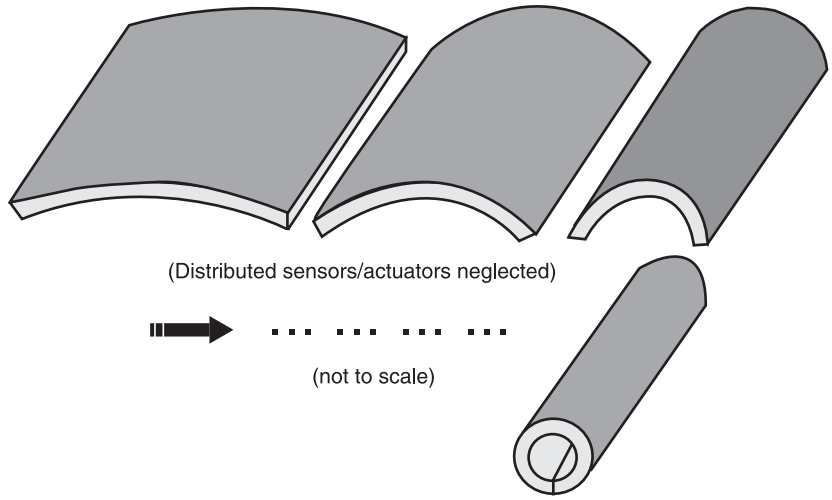


Figure 4 Shell transformation, from a shallow shell to a cylindrical.

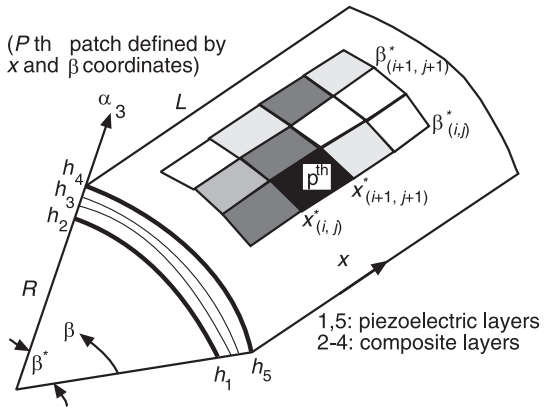


Figure 5 A cylindrical shell laminated with distributed piezoelectric layers.

section; their sensor (modal) sensitivities are presented in the next section. It is assumed that the total effective arc (circumferential) length is constant, i.e., $R\beta^* = 0.05 \times (\pi/2)m$ and the curvature angles are $\beta^* = 30^\circ\ 60^\circ\ 90^\circ\ 120^\circ\ 150^\circ$ respectively. Note that the total shell size and area remains the same; only its curvature changes, resembling geometry transformation in adaptive shells. (However, the forces inducing the changes are not considered.) Natural frequencies, i.e., (mn), where m corresponds to x and n to β, of these shells are calculated and plotted in **Figure 6**. There is a total of 16 modes for each curvature presented in the figure.

As expected, the natural frequencies of shallow shells increase as the mode number increases, and those of deep shells decrease for the first few natural modes and increase as the mode number increases when the curvature is magnified. This is due to the fact that the kinetic strain energies of lower modes are dominated by the membrane strain energies and those of higher modes are dominated by the bending strain energies. This coupling between the membrane effect and the bending effect increases as the shell curvature is magnified.

Sensor Sensitivity

Distributed sensor sensitivity can generally be divided into two components: first, the membrane sensitivity, and second, the bending sensitivity. Sensor (modal) sensitivities at various shell curvatures are presented in **Figure 7**. Recall that the bending sensitivity is important to shallow shells and plates; the membrane sensitivity is important to deep shells and shells of revolution. Accordingly, the membrane sensitivity increases when the shell curvature increases. However, the bending sensitivity remains unchanged since the moment arm never changes over the period of shell transformation. Overall, the total sensor sensitivity still increases due to the significantly increased membrane sensitivities in deep shells.

Actuator Sensitivity and Control Authority

Curvature effects to open-loop modal actuation factors and closed-loop modal damping ratios are investigated. It is assumed that the total shell size remains the same, i.e., $R\beta^* = 0.05 \times (\pi/2)m$, only the shell curvature changes, i.e., $\beta^* = 30^\circ\ 60^\circ\ 90^\circ\ 120^\circ\ 150^\circ$. Open-loop modal actuation factors, closed-loop

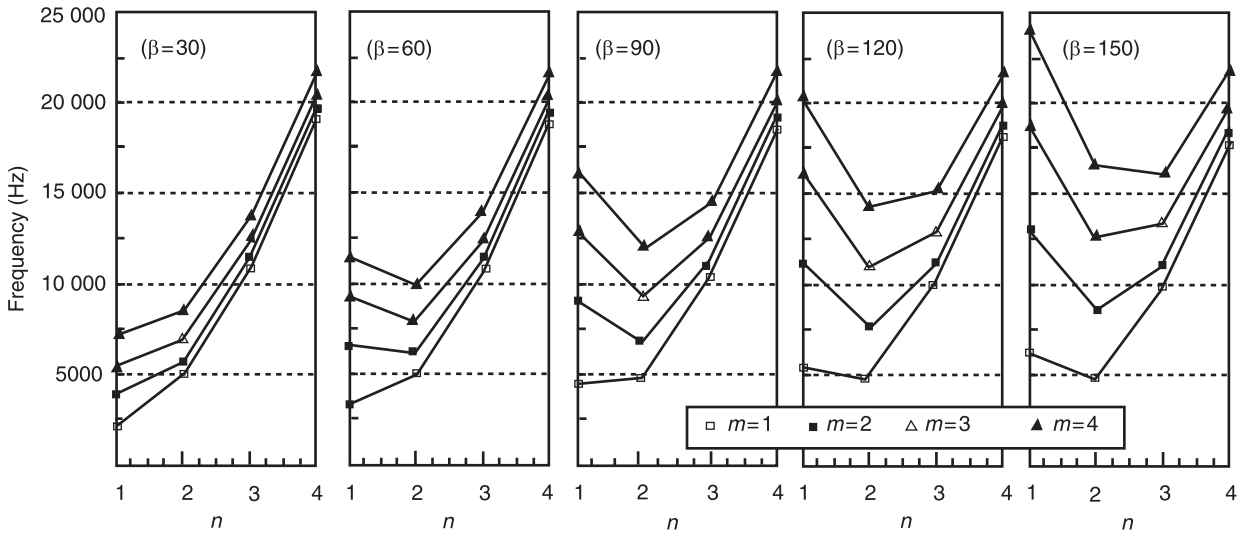


Figure 6 Frequency variations due to shell curvature changes.

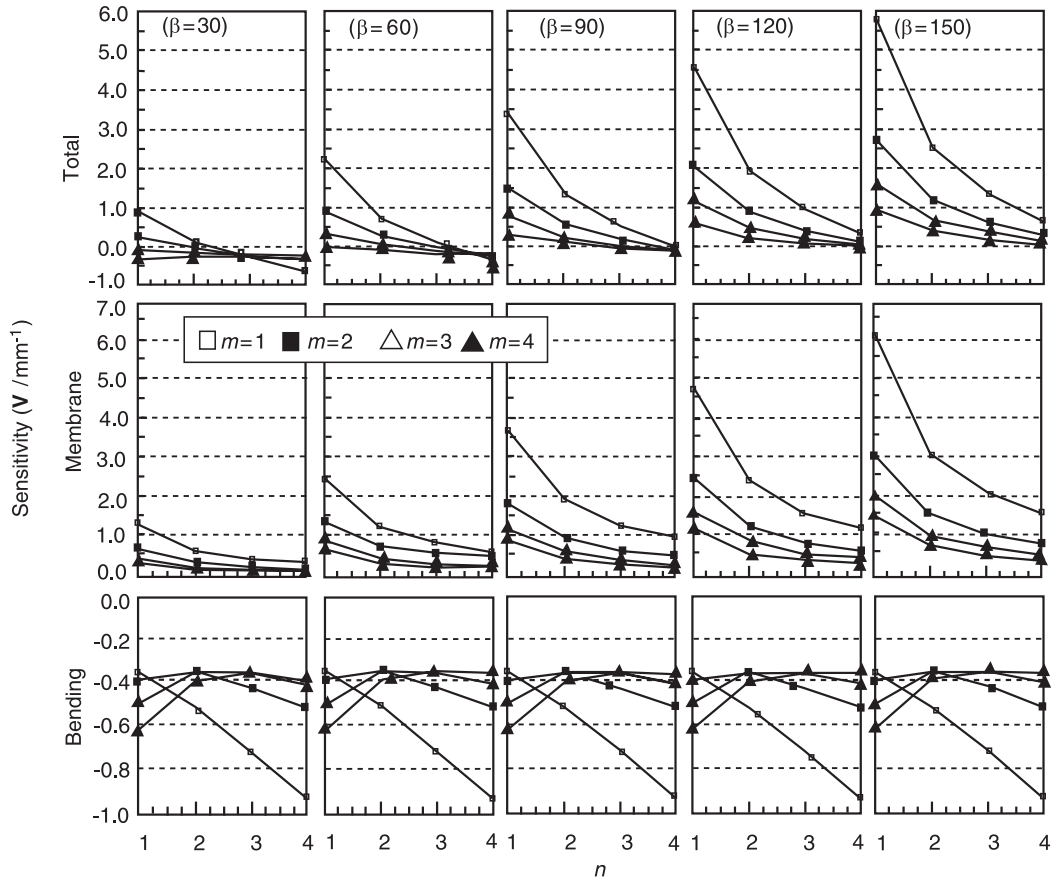


Figure 7 Sensor sensitivity and mode relationship of shells at various curvatures.

modal velocity feedback factors, and closed-loop modal damping ratios are calculated and presented in **Figures 8–10**, respectively. Note that the open-loop modal actuation factor (*mn*th) is the *mn*th modal control force magnitude per unit control voltage ($\mathrm{N\,kg^{-1}\,V^{-1}}$), which is independent of time and spatial distribution. Analytical results suggest that the membrane actuation effect increases significantly as the shell curvature increases, due to an increased membrane effect in curved shells. The bending control effect remains about the same, since the moment arm remains unchanged in **Figure 8.**

Distributed sensor sensitivity is contributed by the membrane sensitivity and the bending sensitivity respectively, related to the induced membrane and bending strains in the distributed sensor layer. In contrast, the total control effect of the distributed actuator can be divided into two control actions: the membrane control force and the control moment. Thus, ideally, it is possible to utilize the individual sensor signals, i.e., the membrane signal and the bending signal, amplify the signals, and feed them to either the membrane control action or the bending control action. Accordingly, there are four possibilities: (1) membrane signal to membrane control action (M, M); (2) membrane signal to bending control action (M, B); (3) bending signal to membrane control action (B, M); and (4) bending signal to bending control action (B, B).

Figure 9 illustrates the closed-loop velocity feedback factor and the shell curvature relationship (the modal feedback factors F_{mn} derived from the four control possibilities of the cylindrical shells at various curvatures. There are nine natural modes, $(m, n) =$ (1, 1)–(3, 3); the feedback factor of each mode (the modal feedback factor) has the above four feedback possibilities and a total effect which are plotted versus the shell curvatures from 30° to 150°. Note that the (M, B) and the (B, M) are of equal magnitude and opposite sign. Furthermore, these results clearly indicate that the membrane control action (M, M) dominates the overall control effect in deep shells; however, this effect decreases as the mode increases. The bending control action, on the other hand, dominates the control action for shallow shells and it gradually influences the total control action of higher modes for deep shells.

Examining the velocity feedback factors ($\mathbf{F}_{mn}$) is only to study further the enhanced closed-loop damping characteristics, $\zeta_{mn}^{T} = \zeta_{mn} + \mathbf{F}_{mn}/2\omega_{mn}$, among

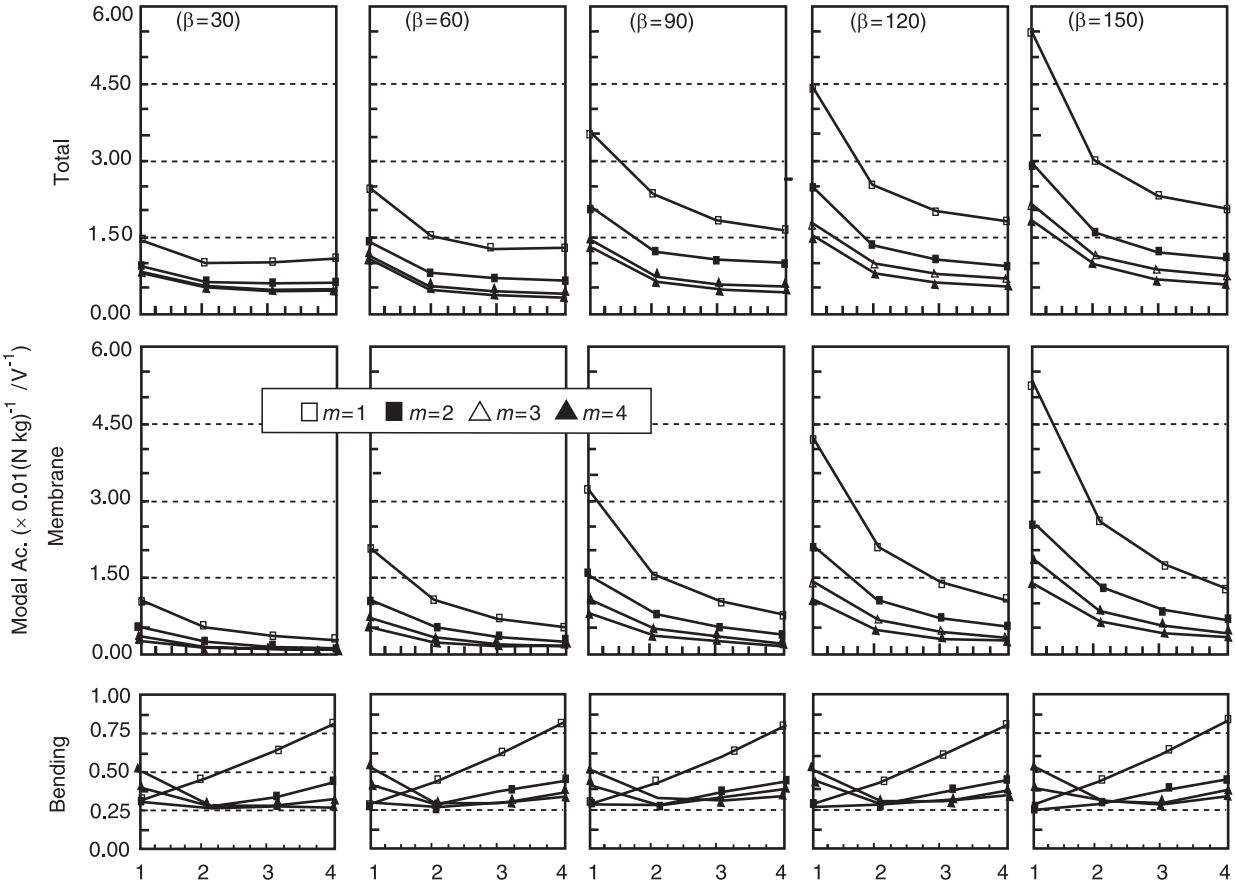


Figure 8 Modal actuation factors of shells at various curvature angles.

the four feedback possibilities, and thus to evaluate the overall closed-loop controllability of the shells with various curvatures. Inferred damping ratios of the four feedback possibilities are plotted versus various shell curvatures (**Figure 10**). Again, the membrane control effect dominates the lower natural modes as well as the total control effect in deep shells. Recall that the membrane strain energy dominates in lower natural modes of deep shells and the bending strain energy dominates in shallow or zero-curvature shells. For lower natural modes, the natural frequency of shallow shells keeps increasing, while the natural frequency of highly curved shells drops for the first few modes. This frequency variation due to the curvature changes also affects the relatively irregular variations of controlled modal damping ratios, i.e., $\zeta_{mn}^{T} = \zeta_{mn} + \mathbf{F}_{mn}/2\omega_{mn}$.

Remarks

In the recent development of smart structures and structronic systems, piezoelectric materials are widely used as sensors and actuators in sensing, actuation, and control applications. This article aims to introduce distributed sensors and actuators and their functionalities and utilities, and design guidelines applied to distributed sensing and control of elastic DPSs, precision systems, MEMS, smart structures, and structronic systems. Sensitivities, actuation factors, feedback factors, and controlled damping ratios were reported. The membrane and bending contributions to the sensor sensitivities and control effectiveness were evaluated.

Distributed sensor signal is determined by electromechanical coupling coefficients, material properties, mode numbers, locations, spatial distributions, etc. The total sensor sensitivity is contributed by two components: a membrane sensitivity and a bending sensitivity, in which the former depends on the membrane strains and the latter depends on the bending strains. Analytical results have suggested that increasing the shell curvature enhances the membrane energies while the bending energies remain identical. This can be observed in the frequency shifts of various curvatures. Consequently, the sensor membrane sensitivities significantly increase and the bending

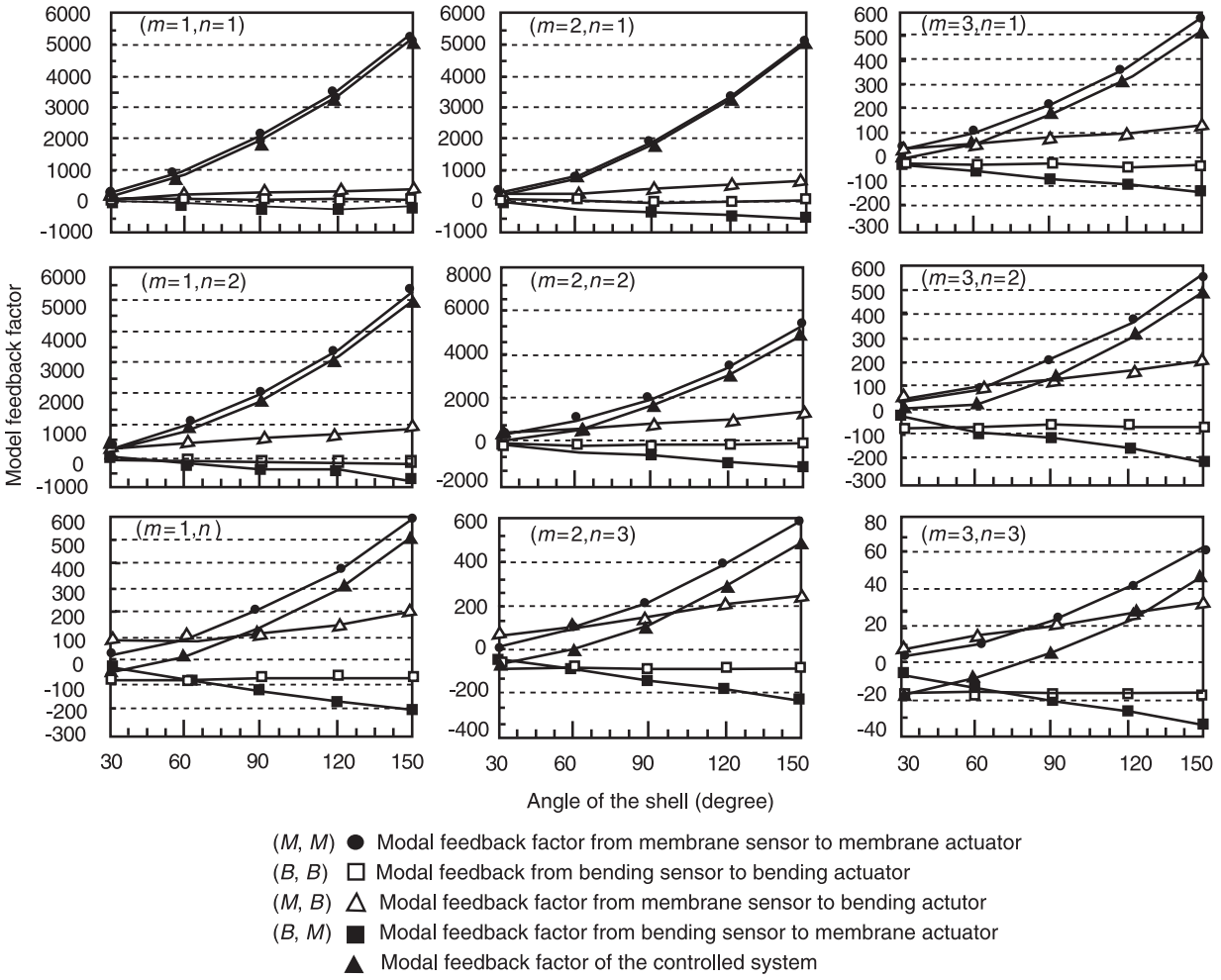


Figure 9 Modal velocity feedback factors of shells at various curvature angles.

sensitivities remain the same. The total sensitivities also increase due to a significant increase in the membrane sensitivities.

Furthermore, spatial actuation and control effectiveness of distributed actuator patches laminated on a simply supported piezoelectric laminated cylindrical shell were also studied. Modal control forces of open and closed-loop vibration control effects were respectively evaluated. Open-loop modal actuation factor and its membrane and bending components were defined. Closed-loop modal feedback factors and controlled damping ratios were presented and their membrane and bending contributions were evaluated with respect to various shell curvatures and natural modes. Analytical results suggested that the membrane control action is of importance for lower natural modes and the bending control action becomes dominating for higher natural modes in deep shells. Since the dominating control action comes from the membrane control action, the curvature increase significantly enhances the modal actuation factor and, thus, the controlled damping ratio of deep-shell structronic systems. Note that all results were evaluated based on constant piezoelectric coefficients without any hysteresis or temperature influences.

Nomenclature

A_1, A_2	Lamé parameters
$\mathbf{F}_{mn}$	velocity feedback factors
$\mathbf{R}$	radius of the spherical shell
R_1, R_2	radii of curvature
Y_p	Young's modulus
ρ	mass density

See also: **Piezoelectric materials and continua**; **Shells**.

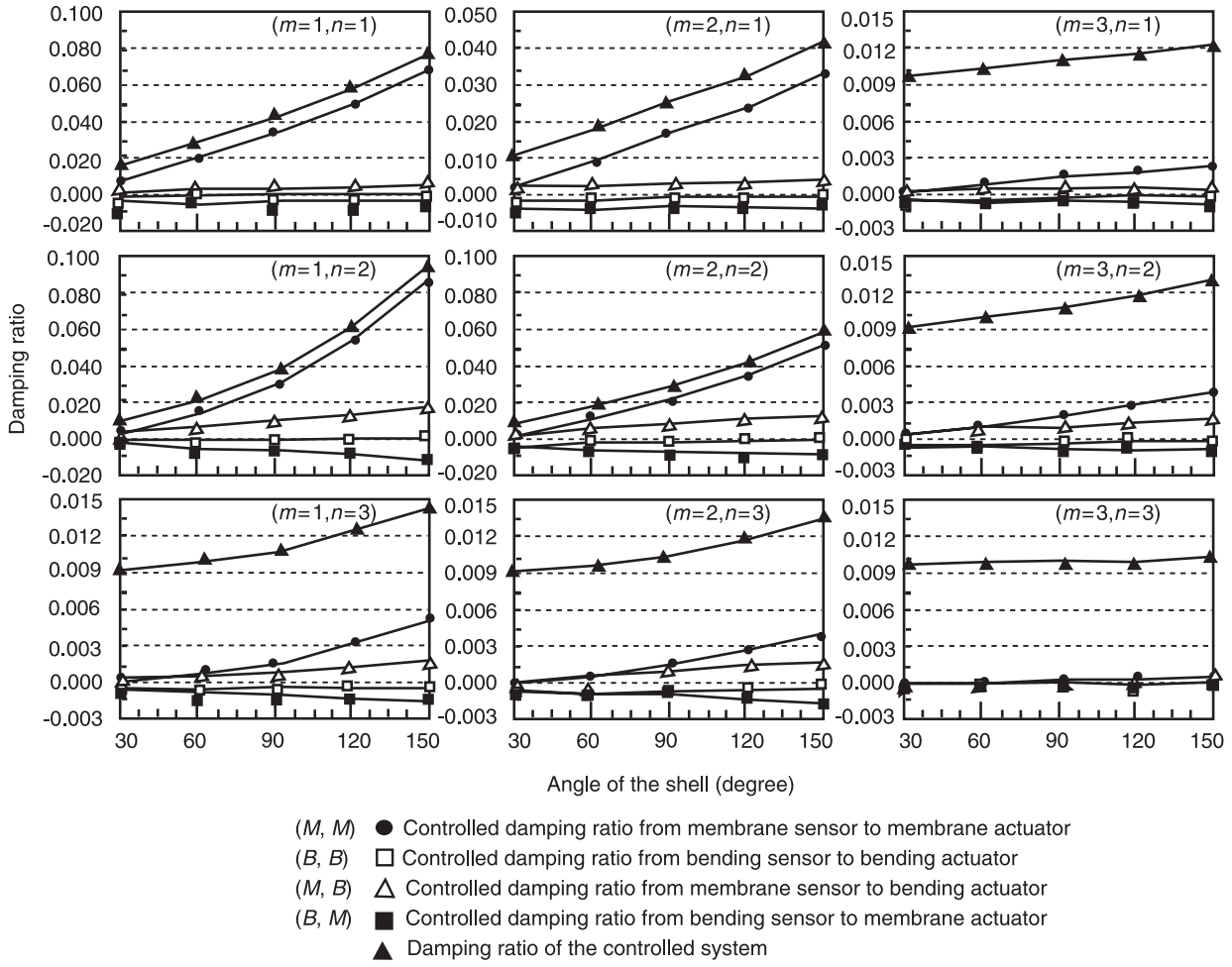


Figure 10 Controlled modal damping ratios of shells at various curvature angles.

Further Reading

Tzou HS (1993) *Piezoelectric Shells (Distributed Sensing and Control of Continua)*. Dordrecht: Kluwer.

Tzou HS and Anderson GL (eds) (1992) *Intelligent Structural Systems*. Dordrecht: Kluwer.

Tzou HS and Bergman LA (1998) *Dynamics and Control of Distributed Systems*. New York: Cambridge University Press.

Tzou HS and Guran A (eds) (1998) *Structronic Systems – Smart Structures, Devices and Systems*. Vol. 1: *Materials and Structures*. Vol. 2: *Systems and Control*. Singapore: World Scentific.

Tzou HS, Bao Y and Venkayya VB (1996) Study of segmented transducers laminated on cylindrical shells, part 1: sensor patches and part 2: actuator patches. *Journal of Sound and Vibration* 197: 207–249.

SHAPE MEMORY ALLOYS

H S Tzou, University of Kentucky, Lexington, KY, USA

A Baz, University of Maryland, College Park, MD, USA

Copyright © 2001 Academic Press

doi:10.1006/rwvb.2001.0077

Considerable attention has recently been devoted to the utilization of shape memory alloys (SMA) as an effective means of attenuating the vibration of flexible structures. Such effectiveness stems from the unique thermomechanical characteristics of the SMA. A brief description of these characteristics is

necessary to understand the principles behind the different SMA vibration control mechanisms.

Basic Properties of SMA

SMAs undergo a unique and reversible phase transformation from martensite to austenite as the temperature and/or the stress acting on the alloy are changed. **Figure 1** shows the effect of the temperature on the martensite fraction of a typical SMA. In the figure, M_s, M_f, A_s, and A_f denote the martensite start, martensite finish, austenite start, and austenite finish temperatures.

Shape Memory Effect

At temperatures below M_f, the SMA has the stress–strain characteristics shown in **Figure 2A**. Note that the SMA retains a large amount of residual strain when the stress is removed. As the temperature is increased to A_f, the strain can be completely recovered, resulting in the well-known shape memory effect.

Superelastic Effect

When the temperature is increased to above A_f, the SMA exhibits a different type of stress–strain characteristic, as shown in **Figure 2B**. In that case, the residual strains vanish and the alloy can undergo a large deformation without any significant increase in the applied stress. Such a phenomenon is known as the superelastic (pseudoelastic) effect.

Modulus of Elasticity

The effect of temperature on Young's modulus of a SMA made of nickel–titanium alloy (nitinol) is shown in **Figure 3**. Note that Young's modulus increases by almost four times as the SMA is transformed from martensite to austenite. Such changes are unique and are unlike most alloys, as the SMA becomes stiffer when heated and softer when cooled.

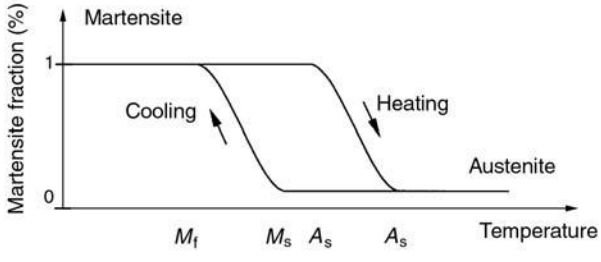


Figure 1 Effect of temperature on phase transformation of SMA.

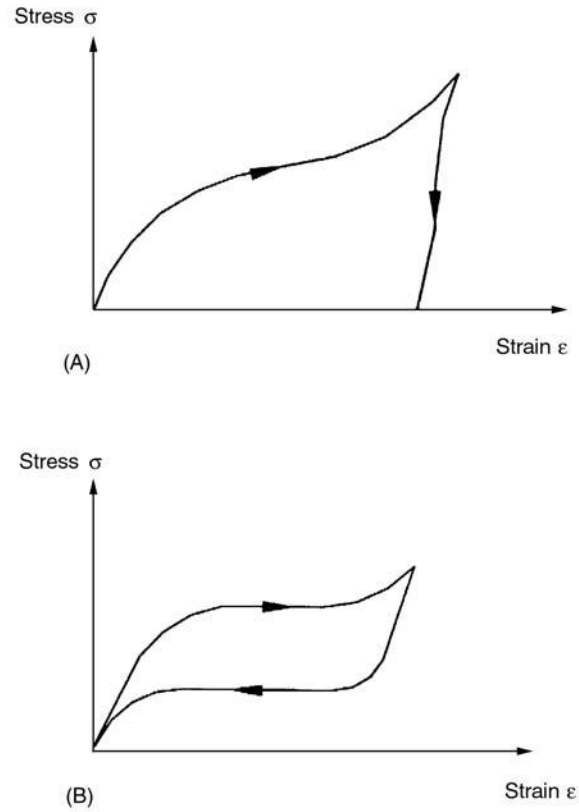


Figure 2 Stress–strain characteristics of SMA. (A) Shape memory effect; (B) superelastic effect.

Other Basic Properties

For SMA made of nitinol, typical strain recovery is about 8%. When restrained, the SMA can develop stresses in the order of 400 MPa.

Constitutive Equations

The martensitic phase transformation process of the nitinol strips is governed by the following constitutive equation:

$$(\sigma - \sigma_0) = E_s(\varepsilon - \varepsilon_0) + \Theta(T - T_0) + \Omega(\xi - \xi_0) \quad [1]$$

where σ, ε, and T denote the stress, strain, and temperature respectively. Also, E_s, Θ, and Ω define Young's modulus, the thermal expansion modulus and phase transformation modulus of nitinol. Subscript 0 correspond to the initial conditions. In eqn [1], the martensitic fraction ξ is defined as follows.

Transformation from Martensite to Austenite

$$\xi = \xi_M \, e^{[a_A(A_s - T) + b_A\sigma]} \quad [2]$$

where:

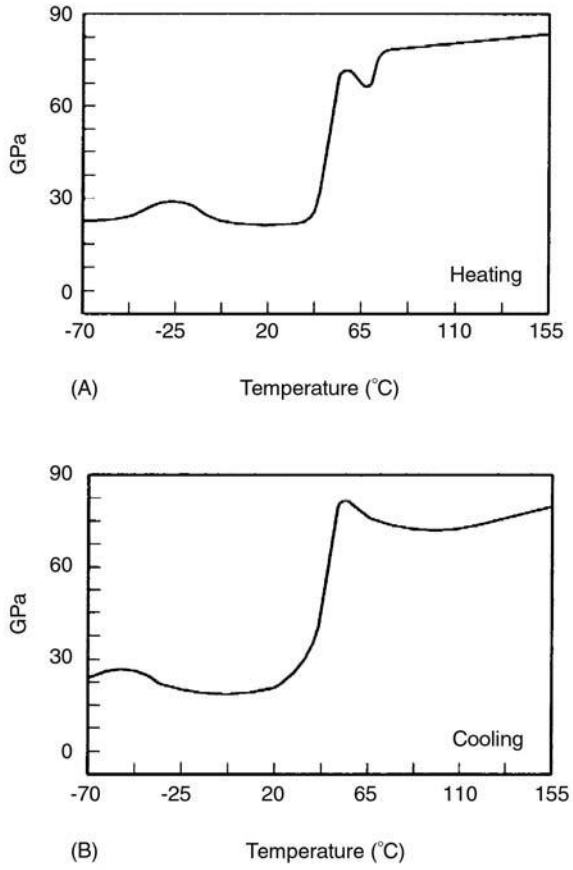


Figure 3 Typical Young's modulus of SMA (nitinol). (A) During heating; (B) during cooling.

$$a_A = \ln(0.01/\xi_M)/(A_s - A_f) \quad \text{and} \quad b_A = a_A/C \qquad [3]$$

where ξ_M, A_s, A_f, and C denote the initial martensitic fraction, austenite start temperature, austenite finish temperature, and slope of stress–transition temperature characteristics.

The domain of the transformation is defined by:

$$\ln(0.01/\xi_M)/b_A + a_A/b_A(T - A_s) \le \sigma \le a_A/b_A(T - A_s) \qquad [4]$$

Transformation from Austenite to Martensite

$$\xi = (1 - \xi_A)\left[1 - e^{[a_M(M_s - T) + b_M\sigma]}\right] \qquad [5]$$

where:

$$a_M = \ln[1 - 0.99/(1 - \xi_A)]/(M_s - M_f)$$

and:

$$b_M = a_M/C \qquad [6]$$

where ξ_A, M_s, M_f, and C denote the initial austenitic fraction, martensite start temperature, martensite finish temperature and slope of stress–transition temperature characteristics.

The domain of the transformation is defined by:

$$a_M/b_M(T - M_s) \le \sigma \le \ln[1 - 0.99/(1 - \xi_A)]/b_M + a_M/b_M(T - M_s) \qquad [7]$$

The constitutive eqns [1]–[7] can be used to determine the stress–strain–temperature characteristics of a one-dimensional SMA fiber. These relationships can be utilized to compute the recovered strain or stress of the SMA resulting from the shape memory effect as well as the energy dissipated due to the hysteresis associated with the superelastic effect.

Vibration Control Mechanisms

Based on the basic properties of the SMA, one can identify five distinct mechanisms that have been successfully utilized to control structural vibration, as outlined in **Table 1**.

There follows a brief description of these mechanisms.

Passive Damping Mechanism

In this mechanism, the inherent hysteresis characteristics of the shape memory alloy, in its superelastic form, are utilized to dissipate the vibration energy. The amount of energy dissipated is equal to the area enclosed inside the stress–strain characteristics (**Figure 4**). This passive mechanism has been successfully used to damp out the vibration of a wide variety of structures, including large structures subject to seismic excitation. In these applications, the structures are supported on springs, of one form or another, made of superelastic SMA.

Control Actuators

In this class of mechanisms, the SMA actuator takes the form of fibers or springs which are attached to

Table 1 Vibration control mechanisms of the SMA

No.	*Mechanism*	*Mode*
1	Passive damping mechanism	Passive
2	Control actuator	Active
3	Active stiffening mechanism	Active
4	Active damping augmentation	Active
5	Active impedance controller	Active

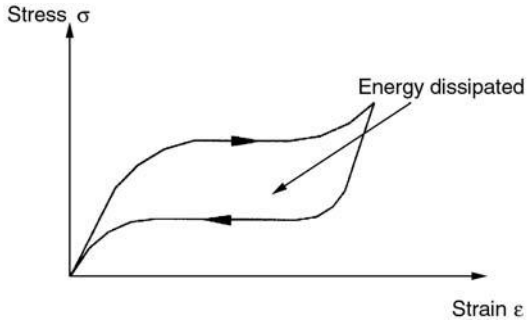


Figure 4 Hysteresis characteristics of superelastic SMA.

critical points of the vibrating structures, as shown in **Figure 5**. Usually, a pair of actuators is needed to control the vibration of the structure effectively. For example, when the vibrating beam of **Figure 5A** moves downward, the actuator A is activated thermally to counterbalance the external disturbance while actuator B remains inactive. If the motion is reversed, actuator B is activated while actuator A stays inactive. A similar arrangement is used to control the vibration of larger structures, as shown in **Figure 5B**.

Note that the need for two actuators is because most of the commonly used shape memory actuators have one-way memory, i.e., can only operate in one direction when activated and revert back to their undeflected position under the action of external load generated, for example, by a bias spring.

A block diagram of the dynamics of a structure, the SMA actuator, and the controller is shown in **Figure 6**. Simple first-order transfer functions have been considered to represent the dynamics of the SMA

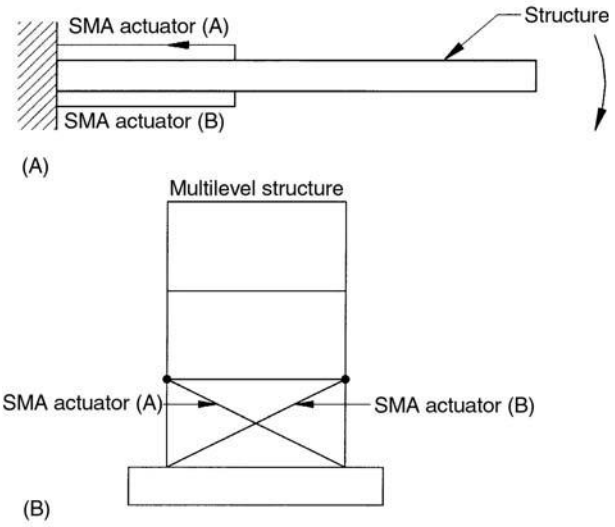


Figure 5 Use of SMA as a control actuator.

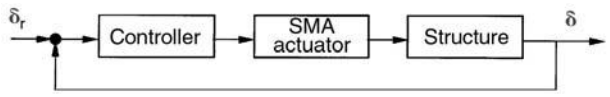


Figure 6 Block diagram of structure/SMA/control system.

actuators. With such transfer functions, classical and robust controllers, such as LQG/LTR and sliding mode controllers, have been successfully employed to control the vibration of simple beams and multilevel structures. Mathematically, the dynamics of the structure with the SMA actuator is given by:

$$\text{Structure} \quad \mathbf{M}\ddot{\delta} + \mathbf{K}\delta = \mathbf{B}\mathbf{F}_{\text{sma}} \qquad [8]$$

$$\text{Shape memory force} \quad \tau\dot{\mathbf{F}}_{\text{sma}} + \mathbf{F}_{\text{sma}} = \gamma\mathbf{V} \qquad [9]$$

$$\text{Control law} \quad \mathbf{V} = -\mathbf{G}\mathbf{C}\delta \qquad [10]$$

where $\mathbf{K}$ and $\mathbf{M}$ are the stiffness and mass matrices. Also, $\boldsymbol{\delta}$, $\mathbf{B}$ and $\mathbf{F}_{\text{sma}}$ denote the nodal deflection vector, location matrix of the actuators, and the shape memory control forces respectively. The control voltage $\mathbf{V}$ is generated using a negative feedback control law such that $\mathbf{G}$ is the control gain matrix and $\mathbf{C}$ is the measurement matrix. In eqn [9], τ denotes the time constant of the thermodynamic behavior of the SMA actuator.

Other more complex models of the SMA actuator are considered. Some of these models are extracted experimentally using classical linear and nonlinear identification methods.

Active Stiffening Mechanism

This mechanism is used extensively in shape memory composites, as shown in **Figure 7**. In the figure, a composite beam is reinforced with SMA (nitinol) fibers embedded inside sleeves placed along the neutral axes of the beam. In this arrangement, the fibers are free to move during the phase transformation process in order to avoid degradation and/or destruction of the shape memory effect which may result when the fibers are completely bonded to the composite matrix. The beam is considered to be supported

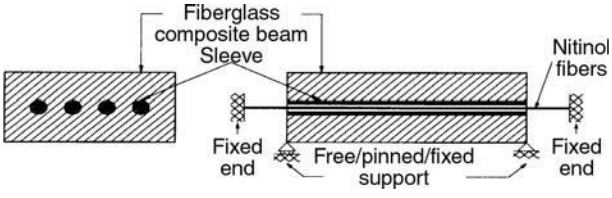


Figure 7 Typical SMA-reinforced composite beams.

on a tunable elastic foundation made of the embedded nitinol fibers. The load transfer between the matrix and the nitinol foundation, in the transverse direction, is controlled by adjusting the tension of the nitinol fibers through proper prestraining and activation of the shape memory effect.

The beam stiffness is made up of different components which include the flexural rigidity of the beam, the geometric stiffness that accounts for the axial and thermal loading, as well as the stiffness imparted by the elasticity of the nitinol fibers. Consider the nitinol-reinforced beam element shown in **Figure 8** whose length is l and is bounded by the two nodes i and j. The beam element consists of a composite with randomly oriented fibers, which is reinforced with unidirectional nitinol fibers aligned along the x-axis. In the figure, P_m, P_t, and T_t denote the axial mechanical loads, the axial thermal load, and the total tension developed by the nitinol fibers respectively. Also acting on the element are the external shear forces $V_{i,j}$ and moments $M_{i,j}$.

The stiffness matrix $\mathbf{K}_e$ of the element is obtained by using the principle of conservation of energy and equating the work done by external loads to the strain energies stored in the element. This yields the following relationships:

$$\tfrac{1}{2}\delta_e^T\mathbf{F} = \frac{1}{2}E_mI_m\int_0^1 [w'']^T[w'']dx - \tfrac{1}{2}P_n\int_0^1 [w']^T[w']dx \quad [11]$$

where δ_e and $\mathbf{F}$ denote the nodal deflection and force vectors defined by:

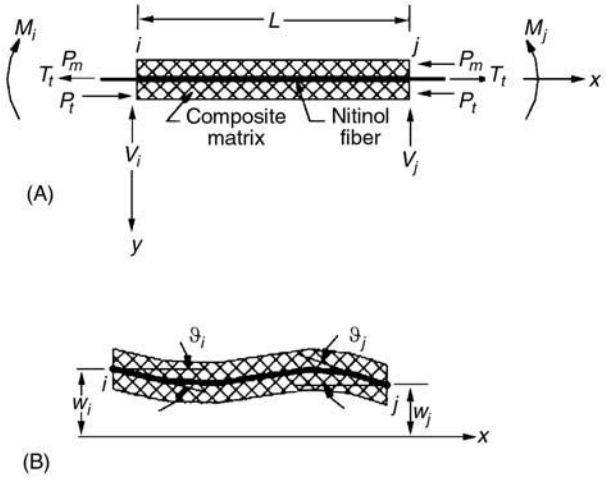


Figure 8 SMA/beam element with forces (A) and displacements (B).

$$\delta_e = \begin{bmatrix} w_i & w_i' & w_j & w_j' \end{bmatrix}^T$$

and:

$$\mathbf{F} = \begin{bmatrix} V_i & M_i & V_j & M_j \end{bmatrix}^T \quad [12]$$

with w denoting the transverse deflection and the primes representing derivatives with respect to x. Also, E_mI_m define the flexural rigidity of the beam element and P_n is the net axial force given by:

$$P_n = (P_m + P_t - T_t) \quad [13]$$

The thermal load P_t is given by:

$$P_t = \alpha\Delta\Theta E_mA_m \quad [14]$$

This thermal load is generated by changes in the temperature $\Delta\Theta$ of the element caused by the activation and deactivation of the nitinol fibers. In eqn [14], α, E_m, and A_m denote the thermal expansion coefficient of the composite, its modulus of elasticity, and cross-sectional area respectively.

Using the classical finite element formulation, the transverse deflection w and the force vector $\mathbf{F}$ are defined in terms of the nodal deflection vector $\boldsymbol{\delta}_e$ as follows:

$$w = \mathbf{A}\boldsymbol{\delta}_e \quad \text{and} \quad \mathbf{F} = \mathbf{K}_e\boldsymbol{\delta}_e \quad [15]$$

where $\mathbf{A}$ and $\mathbf{K}_e$ are an interpolating vector and the element stiffness matrix respectively.

From eqns [11] and [15], the stiffness matrix $\mathbf{K}_e$ is:

$$\mathbf{K}_e = E_mA_m\int_0^1 \mathbf{A}''^T\mathbf{A}''\,dx - P_n\int_0^1 \mathbf{A}'^T\mathbf{A}'\,dx \quad [16]$$

Eqn [16] represents the basic equation for understanding the role that the Nitinol fibers play in controlling the stiffness of the composite beam. For example, if the initial fiber tension. T_0, is high enough to counterbalance the mechanical and thermal effects (i.e., $P_n = 0$), then the beam stiffness can be maintained unchanged. For higher prestrain levels, the beam stiffness can be enhanced. Further enhancement can be achieved when the shape memory effect of the nitinol fibers is activated by heating the fibers above their phase transformation temperature. The additional phase recovery force make the net axial load P_n negative and accordingly increase the overall stiffness of the beam. The magnitude of the tension can be predicted using the constitutive equation of the SMA (eqn [1]). However, it is essential that the total tension in the nitinol fibers, i.e., the sum of the tension

due to the prestrain and the phase recovery force, must exceed the mechanical and thermal loads to compensate for the softening effect in the matrix resulting from heating the nitinol fibers inside the composite matrix.

The mass matrix $\mathbf{M}_e$ of the beam element is:

$$\mathbf{M}_e = \rho_m A_m \int_0^1 \mathbf{A}^T \mathbf{A}\, dx \qquad [17]$$

where ρ_m denotes the density of the composite beam.

The dynamic characteristics of nitinol-reinforced beams are obtained by combining the stiffness matrix $\mathbf{K}_e$ with the mass matrix $\mathbf{M}_e$ as follows:

$$\mathbf{M}_e\ddot{\boldsymbol{\delta}}_e + \mathbf{K}_e\boldsymbol{\delta}_e = \mathbf{F} \qquad [18]$$

where $\mathbf{F}$ is the external load vector.

Solution for the eigenvalues of the above equations gives the natural frequencies of the composite beam as influenced by the properties of the composite matrix and the nitinol fibers. It is important to note that these properties are influenced by the temperature distribution inside the beam which is developed by virtue of activating and deactivating the nitinol fibers.

Figure 9A shows typical changes in the first natural frequency of a beam when it is reinforced with untrained nitinol fibers which are prestrained at different levels. The changes are normalized with respect to the natural frequency of the unreinforced beam measured at 25°C, i.e., 50.1 Hz. It can be seen that the frequency of the unreinforced beam drops as the ambient temperature increases and the beam loses its elastic stability and starts to buckle when the temperature exceeds 40°C. The drop in the natural frequency of the unreinforced beam is attributed to the softening of the matrix, which is clearly demonstrated by the loss in the modulus of elasticity of the beam, as shown in **Figure 10**.

Reinforcing the beam with prestrained untrained nitinol fibers considerably increases the natural frequency of the beam. The extent of the upward shift in natural frequency increases with increased prestrain level. However, as the ambient temperature increases, he frequency shift drops in a manner similar to the characteristics of the plain unreinforced beam. Such a drop is again attributed to the softening effect of the matrix and the fact that the untrained nitinol fibers act as a static pretensioning device that produces constant tension independently of temperature. Therefore, the frequency enhancement is only generated by the reinforcement and the prestrain effects, and not by the shape memory effect.

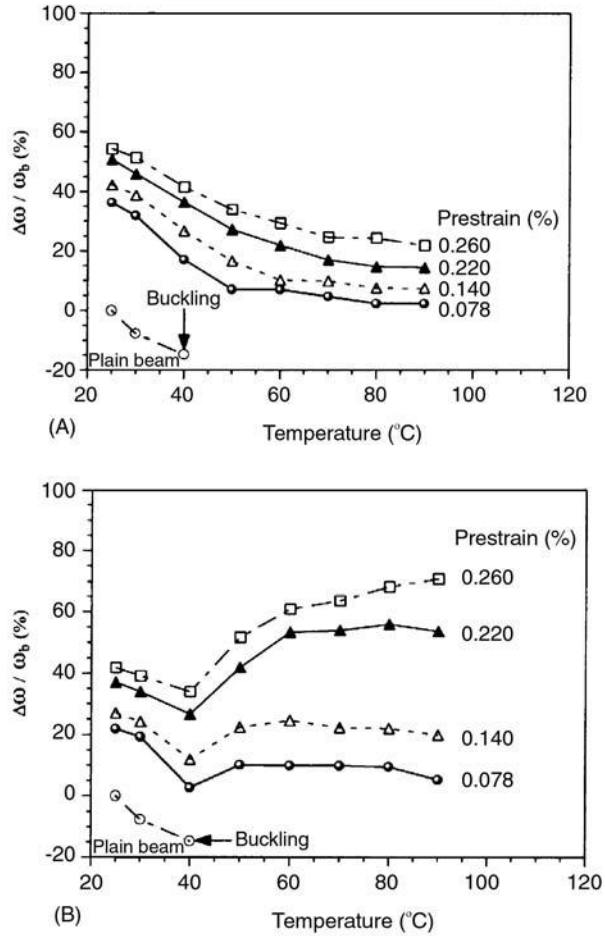


Figure 9 Effect of temperature and initial strain on enhancing first natural frequency (A) without shape memory; (B) with shape memory.

However, a greater frequency shift can be achieved by imparting the shape memory effect to the nitinol fibers. The trained fibers are inserted into the composite beam to replace the untrained set and the frequency shifts become significant, particularly at high ambient temperatures. This is clearly demonstrated in **Figure 9B**. For temperatures between room temperature and 40°C, the frequency shifts obtained are similar to those with the untrained fibers within experimental accuracy. Once the ambient temperature exceeds 50°C, i.e., the austenite phase transformation temperature of the nitinol fibers, the frequency shift characteristics changes from a gradually decaying trend to one that is gradually increasing. Such a sudden change is the result of the contribution of the phase recovery forces developed by the shape memory effect, which is illustrated in **Figure 10**.

The shape memory effect generates strain energy in the nitinol fibers to counterbalance the softening

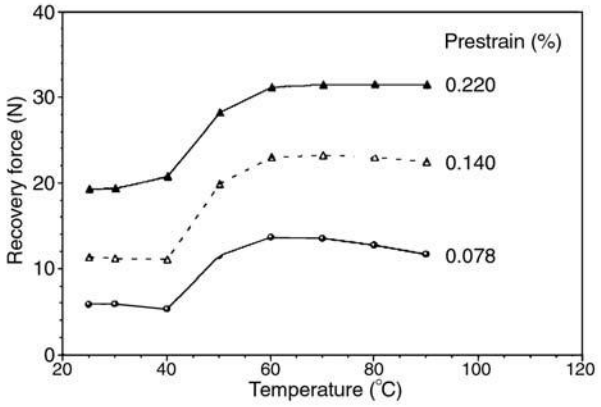


Figure 10 Young's modulus and loss factor of a typical matrix.

effect of the composite matrix with increasing temperature. As the amount of strain energy developed depends on the initial prestrain level, it can merely compensate for the softening effect to maintain the beam frequency at a near constant value which is independent of ambient temperature, as shown for a prestrain level of 0.078%. It can also increase the beam frequency as the ambient temperature increases, as indicated for prestrain levels of 0.22 and 0.26%. For a prestrain level of 0.26% and ambient temperature of 90°C, the frequency increase reaches about 70% as compared to an 18% increase when untrained fibers are used.

Active Damping Augmentation Mechanism

Using the active stiffening mechanism of the SMA composites is particularly important when the static characteristics, as the critical buckling loads, are to be controlled. But, when the dynamic response is of concern, the stiffening mechanism alone becomes ineffective in attenuating vibrations resulting from broad band excitations unless it is augmented with a controlled energy dissipation mechanism. Fortunately, SMA composites have a unique source of damping, which is built in the composite matrix itself. It is therefore possible to simultaneously utilize both the stiffening and the energy dissipation mechanisms to achieve optimal vibration attenuation over broad-frequency spectrum. The nature of interaction between the two mechanisms can easily be seen from the typical characteristics of composites shown in **Figure 11**. The displayed characteristics indicate that activation of the SMA fibers can influence both the stiffness and damping characteristics of the composite. This is attributed to the fact that the modulus of elasticity E_m of the composite beam is a complex modulus ($E_m = E'(1 + i\eta)$) whose storage modulus E' and loss factor η are controlled by the temperature and frequency.

Figure 12 shows the effect of the operating temperature and initial tension of the nitinol fibers on the first mode of vibration and the corresponding modal loss factor of a typical SMA-reinforced beam.

In **Figure 12A**, it is evident that increasing the operating temperature of the composite beam with untensioned fibers results in quick degradation of the fundamental natural frequency of the beam. This degradation quickly leads to the buckling of the beam when the temperature reaches 45 °C. But, when the nitinol fibers are tensioned to 13.34 N per fiber (3 lb per fiber), buckling is avoided even when the beam temperature is increased to 100 °C. This is due to the combined stiffening of the beam by the initial tension of the fibers and by the shape memory

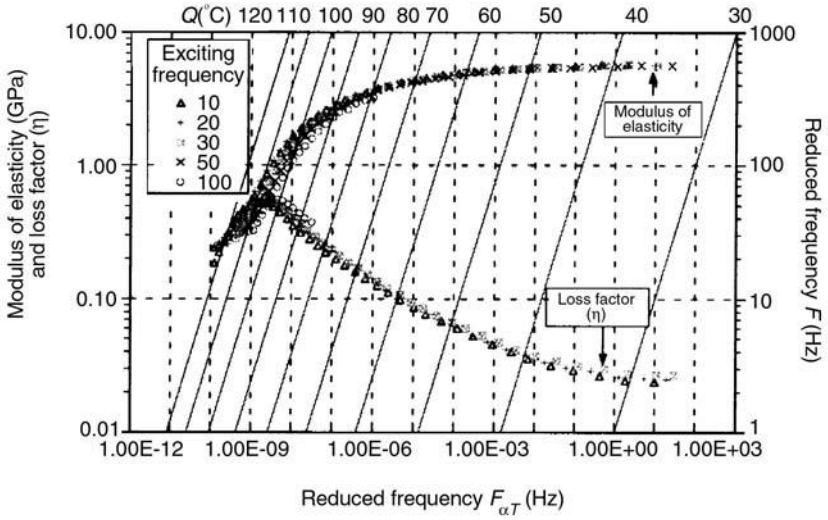


Figure 11 Phase recovery forces for different prestrains.

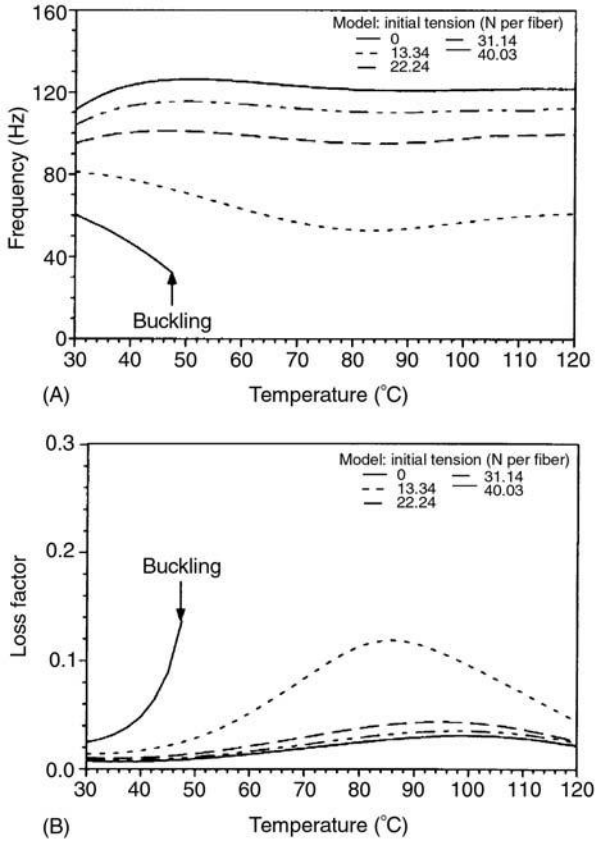


Figure 12 Effect of temperature and prestrains on frequency (A) and loss factor (B).

forces generated as the temperature is increased above the phase transformation temperature. However, the fundamental frequency still exhibits a gradual drop with increased temperature. When the initial tension of the fibers is increased to 22.24 N per fiber (i.e., 5 lb per fiber), the natural frequency is maintained almost constant over the considered temperature range. Further increase of the initial tension to 31.14 N per fiber (or 7 lb per fiber) results in a significant increase of the natural frequency with temperature followed by a plateau which is independent of temperature rise.

Figure 12B shows the modal loss factor at the first mode of vibration as a function of the operating temperature and initial tension of the nitinol fibers. It is evident that the loss factor decreases as the initial tension of the fibers is increased. This is attributed to the increased stiffness of the composite. However, for any particular tension the loss factor increases as the temperature in increased towards the glass transition temperature.

Therefore, the results displayed in **Figures 12A** and **12B** indicate that low levels of initial tensions are inadequate for compensating for the softening of the matrix. But, they are essential for increasing the loss factor. Also, operating at low temperatures will not allow for the utilization of the built-in damping capabilities of the composites. On the other hand, operating at a very high temperature will reduce not only the loss factor but also the structural stiffness. Accordingly, an optimal balance can be attained by selecting the best combination of initial tension and operating temperature in order to achieve optimal attenuation.

Optimal tuning of the initial tension and operating temperature of the nitinol fibers is determined in order to minimize the maximum amplitude of vibration of the composite beam when subjected to external excitations. Such amplitude of vibration is measured by the maximum frequency response function (FRF) $\beta_{\max}$ which is determined from:

$$\beta_{\max} = \max_{j,k,\omega} \sum_{n=1}^{N} [\phi_n(j)\phi_n(k)] / [\omega_n^2 - \omega^2 + i\eta_n\omega_n] \quad [19]$$

where $\phi_n(j)$, ω_n and η_n denote the mode shape at location j for the nth mode, the natural frequency of the nth mode, and the loss factor at the nth mode respectively. The three parameters $\phi_n(j)$, ω_n, and η_n are obtained from the solution of the eigenvalue problem of the homogeneous equation of motion of the composite beam which is given by eqn [18]. In eqn [19], ω denotes the excitation frequency of a force located at k.

Figure 13 shows the effect of the temperature and initial tension on the maximum FRF. **Figure 13A** displays a three-dimensional plot of these characteristics and **Figure 13B** shows a projection of the maximum FRF on the temperature–tension plane. It is evident that there is an optimal operating temperature for each value of the initial tension. At that temperature, the maximum FRF attains its minimum value. For example, when the initial tension is 31.14 N per fiber, the optimal operating temperature is about 92 °C. Increasing the tension beyond 31.14 N per fiber is found to produce an insignificant reduction in the maximum FRF, as can clearly be seen from **Figure 13A**.

Figure 14 shows the FRF, at beam midspan due to excitation at the same location, as a function of the excitation frequency. The figure shows the FRF for optimally tuned and activated fibers at initial tensions of 13.34 and 31.14 N per fiber respectively. For comparison purposes, the FRF of a beam with untensioned and unactivated nitinol fibers is shown in the same figure. It is evident that vibration attenuation is achieved by the activation of the nitinol fibers whether their initial tension is low (13.34 N per

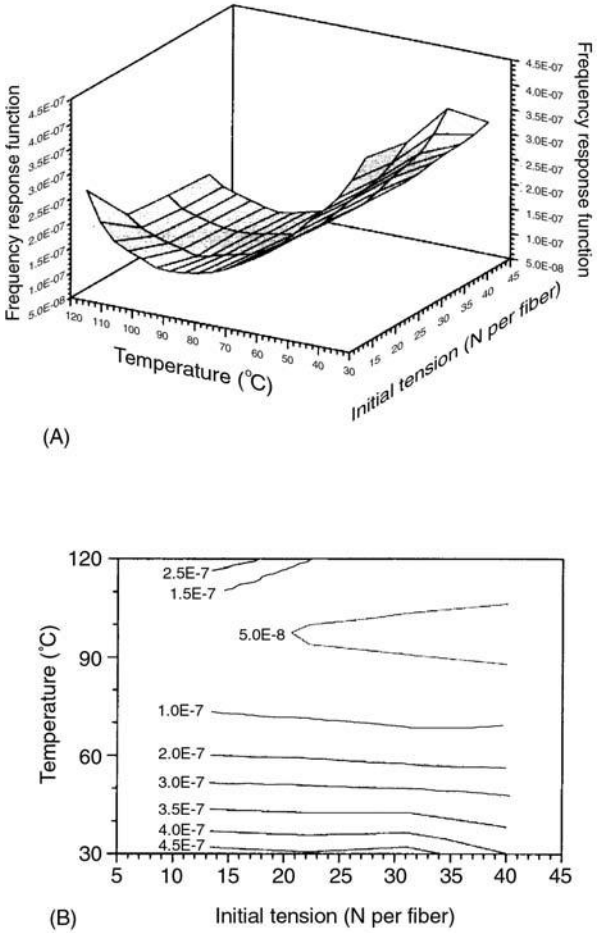


Figure 13 Effect of temperature and initial tension on frequency–response functions.

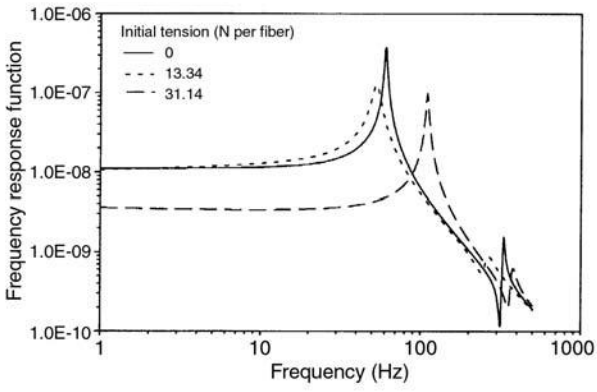


Figure 14 Effect of initial tension and excitation frequency on frequency–response function.

fiber) or high (31.14 N per fiber). In the former case, attenuation is primarily attributed to the enhanced damping which results from heating the composite matrix towards its glass transition region and not to the stiffening mechanism. This is evident as the stiffening mechanism, due to the activation of the fibers, is inadequate to compensate for the softening effect of the beam and the beam modes shift towards lower frequencies. In the latter case, when the tension is increased to 31.14 N per fiber, the attenuation is developed by the combined stiffening and damping mechanism. It is therefore more effective and higher attenuation is observed.

Active Impedance Controller

Vibration and wave propagation can also be controlled using shape memory inserts placed periodically along a structure. The inserts act as sources of impedance mismatch with tunable characteristics. Such characteristics are attributed to the unique behavior of the shape memory alloy whereby the elastic modulus of the inserts can be varied up to three to five times as the alloy undergoes a phase transformation from martensite to austenite. With such controllable capability, the inserts can introduce the proper impedance mismatch necessary to impede the wave propagation along the vibrating structures.

The propagation of waves in structures has traditionally been controlled by various passive or reactive means. For example, control can be achieved by introducing geometric and/or material discontinuities (i.e., impedance mismatch zones) along the structure in order to impede and attenuate the propagation of waves from one end of the structure to the other. Such attenuation results from the proper interaction between the incident, reflected, and transmitted waves at the discontinuity zones. The interaction is similar to that of reactive mufflers of passenger cars.

When the impedance mismatch zones are introduced periodically in a structure, very interesting wave dynamic characteristics can develop. For example, waves can be allowed to pass or stop only over selected frequency bands, called the pass and stop bands. The width of these bands can be passively controlled by proper selection of the period and nature of the impedance mismatch zones. Examples of structures with periodic impedance mismatch zones include beams, plates, and shells which are reinforced with periodic ribs and stiffeners.

Here, the structures are provided with periodic sources of impedance mismatch, which are made of shape memory inserts, as shown in **Figure 15**. When activated thermally, a phase transformation takes place, increasing Young's modulus of the inserts up to three times. With such smart inserts, the impedance can be tuned and the width of the pass and stop bands can be adjusted according to the nature of the external loading in order to reject the propagation of undesirable excitations.

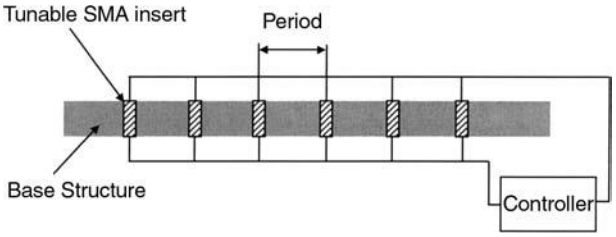


Figure 15 Periodic structures with SMA impedance mismatch zones.

Longitudinal wave propagation in composite rods with SMA inserts, as shown in **Figure 16**, is governed by the following one-dimensional equation:

$$\frac{\partial}{\partial x}\left[E(x)\cdot\frac{\partial u(x,t)}{\partial x}\right]-\rho(x)\cdot\frac{\partial^2 u(x,t)}{\partial t^2}=0 \qquad [20]$$

where $u(x, t)$ is the displacement of the rod at the longitudinal coordinate x and at time t. In eqn [1], $\rho(x)$ and $E(x)$ are respectively the density and the Young's modulus of the rod at position x. For harmonic motion of frequency ω, a solution is $u(x, t) = U(x)\cdot e^{j\omega t}$.

Under such conditions, eqn [20] reduces to the following ordinary differential equation:

$$\frac{\mathrm{d}}{\mathrm{d}x}\left[E(x)\cdot\frac{\mathrm{d}U(x)}{\mathrm{d}x}\right]+\omega^2\cdot\rho(x)\cdot\frac{\mathrm{d}^2U(x)}{\mathrm{d}t^2}=0 \qquad [21]$$

The considered composite is a rod which has periodically varying material properties and is composed of parallel, homogeneous layers, as shown in **Figure 16**. The layers are perfectly bonded along plane interfaces across which there is continuity of displacements and equilibrium of stresses. The composite rod is considered to be infinite so that the dynamics of wave propagation in its periodic layering can be studied by analyzing the behavior of its smallest physical unit, denoted as cell, whose repeated translation generates the periodic structure.

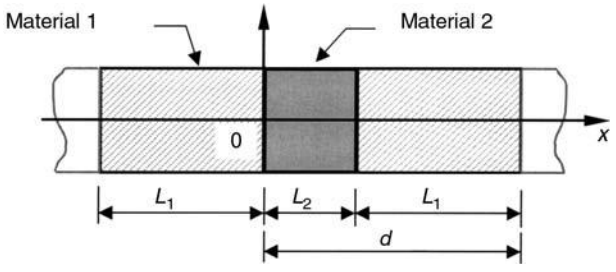


Figure 16 Geometry of a periodic composite rod with SMA inserts.

The material properties can be described by the following periodic functions of period $d = L_1 + L_2$:

$$E(x)=\begin{cases}E_1;\\ E_2\end{cases}\quad \rho(x)=\begin{cases}\rho_1 & -L_1<x<0\\ \rho_2 & 0<x<L_2\end{cases} \qquad [22]$$

Within each material, the rod can be taken as homogeneous and the wave propagation is described by the solution of the one-dimensional wave equation:

$$\frac{\mathrm{d}^2U(x)}{dx^2}+k_i^2\cdot U(x)=0;\ i=1,2 \qquad [23]$$

where $k_i=\omega\cdot\sqrt{\rho_i/E_i}=\omega/c_i=$ wave number of the ith layer with $c_i=\sqrt{E_i/\rho_i}=$ wave speed.

By applying Floquet theorem, the solution of eqn [21] can be expressed as a wave characterized by the propagation constant μ:

$$u_i(x,t)=U_i(x)\cdot e^{j\cdot(\mu\cdot x+\omega\cdot t)};\ i=1,2 \qquad [24]$$

where:

$$U_i(x)=A_i e^{j\cdot(k_i-\mu)\cdot x}+B_i e^{-j\cdot(k_i+\mu)\cdot x};\ i=1,2 \qquad [25]$$

with $i = 1$ and 2 denoting the layers defined over $-L_1 < x < 0$ and $0 < x < L_2$ respectively.

The physical meaning of the propagation coefficient μ can easily be extracted from eqn [24]. At $x = 0$, $u_i(x, t) = e^{j\mu x}u_i(0, t)$. Therefore, μ acts as an effective wave number that relates the displacements of any two points located at a distance x apart inside material i.

Hence, the nature of wave propagation inside the material depends on the value of the propagation coefficient μ. If μ is real, then the wave at $u_i(0, t)$ will propagate whereas if μ is complex, the wave will be attenuated.

The coefficients A_1, A_2, B_1, B_2 can be found by imposing the continuity at the interface $x = 0$, where both the displacement and the normal stress have to join smoothly. The other conditions required for determining the constants can be obtained by imposing the periodicity of the problem. This also yields the following characteristic equation of the composite rod:

$$\cos(\mu\cdot d)=\cos(\Omega)\cdot\cos(\Omega\cdot\tau)+\frac{1}{2}\cdot\left(\frac{\zeta^2+1}{\zeta}\right)\cdot\sin(\Omega)\cdot\sin(\Omega\cdot\tau) \qquad [26]$$

where ζ = the relative impedance of the composite:

$$\zeta = \frac{z_1}{z_2} = \frac{\sqrt{E_1 \cdot \rho_1}}{\sqrt{E_2 \cdot \rho_2}}$$

Ω = normalized frequency, $\Omega = k_1 \cdot L_1 = \omega \cdot L_1 / c_1$ and τ = ratio of the times taken by a wave to cross the layers of the composite:

$$\tau = \frac{L_2}{L_1} \cdot \sqrt{\frac{\rho_2}{\rho_1} \cdot \frac{E_1}{E_2}} = \frac{L_2}{L_1} \cdot \frac{c_1}{c_2}$$

The influence of the geometrical and physical properties of the composite on its wave propagation characteristics is demonstrated by plotting the contours of the stop and pass bands as a function of the normalized frequency Ω and $\lambda = L_1/L_2$.

The shaded areas in **Figure 17** correspond to stop bands ($|\cos(\mu \cdot d)| > 1$, i.e., μ is complex), while the white areas represent the pass-band regions ($|\cos(\mu \cdot d)| \leq 1$, i.e., μ is real). The maps are obtained for two values of the relative impedance, i.e., $\zeta = 2$ (**Figure 17A**) and $\zeta = 4$ (**Figure 17B**). Note that the increase of ζ from 2 to 4 results from the full activation of the SMA inserts. The figures indicate that the width of the stop bands varies significantly with the relative thickness λ. However, note that the width of the stop bands attains a maximum for $\lambda \cong 0.5$, as shown in **Figure 17A**. Comparison between **Figure 17A** and **17B** suggests that, a higher impedance mismatch results in a higher density of the stop bands.

Experimental demonstration of the effectiveness of the SMA in controlling the wave propagation in rods is shown in **Figure 18A**. In the figure, composite rods with three SMA inserts are excited from one end by a piezoelectric shaker and the force transmitted to the other end is monitored by a force cell. **Figure 18B** displays the transmitted force at various temperatures normalized with respect to that of the rod with unactivated inserts. Full activation of the SMA insert, when the temperature is maintained at 70°C, results in a 54% reduction in the amplitude of the transmitted force. Note that heating the entire rod/insert assembly reduces its natural frequency. This phenomenon results from the softening effect of the base structure with increased temperature. However, because of the unique characteristics of the SMA inserts, the impedance mismatch increases considerably with increased temperature. This is due to the increase of Young's modulus of the SMA with temperature whereas the inverse is true for the base structure. Generally, the amplitude of the force tends to decrease with increasing temperatures. However, when the temperature is gradually increased from 30°C to 50°C, the SMA inserts undergo a softening effect similar to that of the base structure. This contributes to the amplification of the force transmitted, as shown in **Figure 18B**. Therefore, for effective operation of the SMA inserts, it is essential to complete the phase transformation process in order to achieve maximum impedance mismatch at the interface between the inserts and the base structure.

Concluding Remarks

The use of SMA presents a viable and effective means of controlling structural vibrations. A brief summary of the basic properties of the SMA has been presented

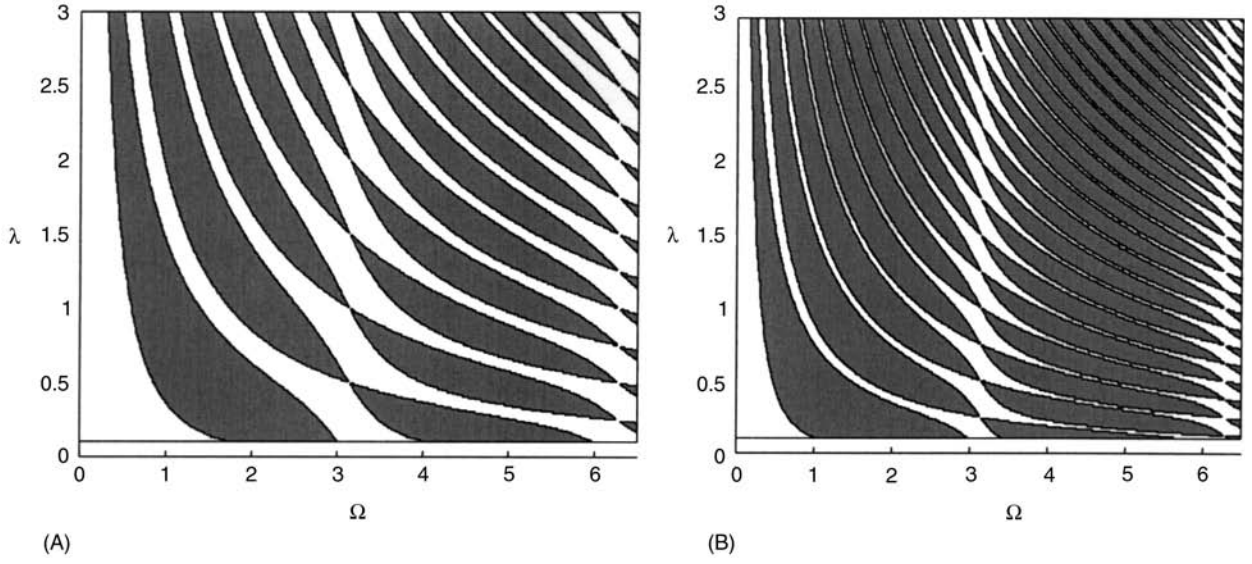


Figure 17 Effect of frequency and relative layer thickness λ on stop and pass bands ($\zeta = 2$ (A) and $\zeta = 4$ (B)).

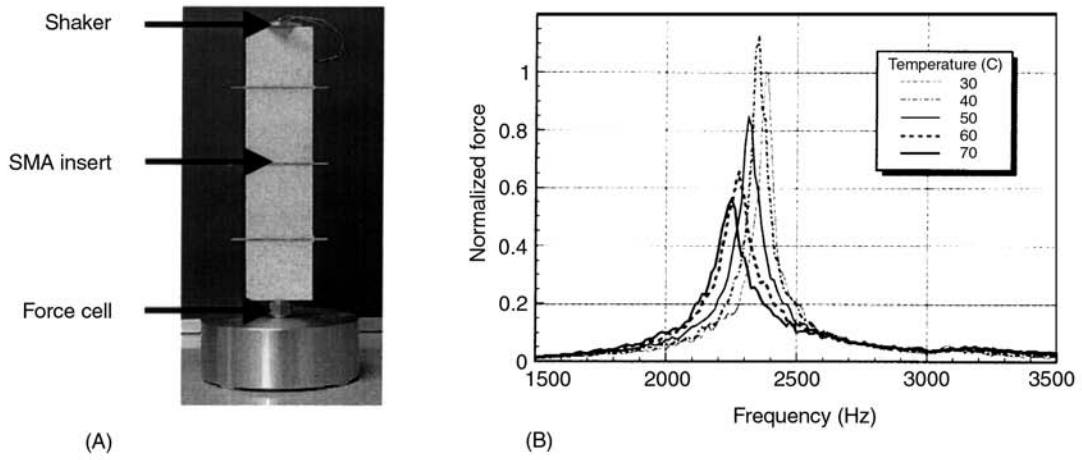


Figure 18 Experimental control of wave propagation in composite rods with three SMA inserts.

along with some of the most common mechanisms for controlling the vibration and wave propagation in simple flexible structures. Application of the SMA to other more complex structures is limited only by our imagination.

Nomenclature

A_f	austenite finish
A_s	austenite start
M_f	martensite finish
M_s	martensite start
T	temperature
σ	stress
ε	strain
ξ	martensitic fraction
$\boldsymbol{\delta}$	nodal deflection vector
ρ	density
η	loss factor

See Plate 51

See also: **Damping, active**; **Damping in FE models**; **Wave propagation**, Waves in an unbounded medium.

Further Reading

Baz A and Ro J (1994) Optimal vibration control of NITINOL-reinforced composites. *International Journal of Composite Engineering* 4: 567–576.

Baz A, Poh S, Ro J and Gilheany J (1995) Control of the natural frequencies of NITINOL-reinforced composite beams. *Journal of Sound and Vibration* 185: 175–185.

Chen T, Ruzzene M and Baz A (2000) Control of wave propagation in periodic composite rods using shape memory inserts: theory and experiments. *Journal of Vibration and Control* 6: 1065–1081.

Duerig TH, Melton KN, Stockel D and Wayman C (1990) *Engineering Aspects of Shape Memory Alloys*. London: Butterworth and Heinemann.

Funakubo H (1987) *Shape Memory Alloys*. New York: Gordon and Breach Science Publishers.

Ruzzene M and Baz A (2000) Control of wave propagation in periodic composite rods using shape memory inserts. *ASME Journal of Vibration and Acoustics* 121: 151–159.

SHELLS

W Soedel, Purdue University, West Lafayette, IN, USA

Copyright © 2001 Academic Press

doi:10.1006/rwvb.2001.0134

Curvilinear Surface Coordinates

For simplicity of formulation, it is required that coordinates are orthogonal. The coordinates are surface coordinates, with two coordinates following the reference surface which, for homogeneous and isotropic material, is halfway between the inner and outer surface, and the third coordinate is normal to the reference surface. This means that the selection of coordinates for classical geometries is dictated by the surface shape: cylindrical shells are described by cylindrical coordinates, spherical shells by spherical coordinates, and so on. For shells that are not classical shapes, orthogonal surface coordinates can be assigned by utilizing the property of surfaces that

lines of maximum and minimum curvature are orthogonal. Thus, all coordinates used in proper shell descriptions are lines of maximum and minimum curvature, with the third coordinate being normal to the surface.

To avoid having to reformulate the equations of motion of a shell each time a different orthogonal surface coordinate system is used, the equations are, in the following, expressed in a general, curvilinear form, defined by the coordinates α_1, α_2 and α_3, the Lamé parameters A_1 and A_2, and the radii of curvature in α_1 and α_2 direction, R_1 and R_2. Equations written in this form can then be easily reduced to the coordinate system being used. For example, for a circular cylindrical shell of radius a, where the lines of minimum and maximum curvature are described by cylindrical coordinates x and θ, one obtains $\alpha_1 = x$, $\alpha_2 = \theta$, $A_1 = 1$, $A_2 = a$, $R_1 = \infty$ ($1/R_1$, the curvature, = 0), and $R_2 = a$. **Table 1** gives the curvilinear coordinate terms for some of the common classical geometries (see **Figure 1**).

Love-type Equations of Motion

A set of equations that is consistent with assumptions used in the Bernoulli–Euler beam equations and the Lagrange–Kirchhoff plate equations was developed by Love and later modified in minor ways by others such as Flügge.

The assumptions are that the thickness is small relative to characteristic surface dimensions, that deflections are small, that plane sections normal to the reference surface before deflection remain plane and normal during deflection, and that deflections are small relative to the characteristic dimensions of the shell, and of course that the material follows Hooke's law.

The general equations of motion are:

$$L_1\{u_1, u_2, u_3\} + \rho h \ddot{u}_1 = q_1 \quad [1]$$

$$L_2\{u_1, u_2, u_3\} + \rho h \ddot{u}_2 = q_2 \quad [2]$$

$$L_3\{u_1, u_2, u_3\} + \rho h \ddot{u}_3 = q_3 \quad [3]$$

where:

$$L_1\{u_1, u_2, u_3\} = \frac{1}{A_1 A_2}\left[-\frac{\partial(N_{11}A_2)}{\partial\alpha_1} - \frac{\partial(N_{21}A_1)}{\partial\alpha_2} - N_{12}\frac{\partial A_1}{\partial\alpha_2} + N_{22}\frac{\partial A_2}{\partial\alpha_1} - A_1 A_2 \frac{Q_{13}}{R_1}\right] \quad [4]$$

$$L_2\{u_1, u_2, u_3\} = \frac{1}{A_1 A_2}\left[-\frac{\partial(N_{12}A_2)}{\partial\alpha_1} - \frac{\partial(N_{22}A_1)}{\partial\alpha_2} - N_{21}\frac{\partial A_2}{\partial\alpha_1} + N_{11}\frac{\partial A_1}{\partial\alpha_2} - A_1 A_2 \frac{Q_{23}}{R_2}\right] \quad [5]$$

$$L_3\{u_1, u_2, u_3\} = \frac{1}{A_1 A_2}\left[-\frac{\partial(Q_{13}A_2)}{\partial\alpha_1} - \frac{\partial(Q_{23}A_1)}{\partial\alpha_2} + A_1 A_2\left(\frac{N_{11}}{R_1} + \frac{N_{22}}{R_2}\right)\right] \quad [6]$$

and where:

$$N_{11} = K\left(\varepsilon_{11}^0 + \mu\varepsilon_{22}^0\right) \quad [7]$$

$$N_{22} = K\left(\varepsilon_{22}^0 + \mu\varepsilon_{11}^0\right) \quad [8]$$

$$N_{12} = N_{21} = \frac{K(1-\mu)}{2}\varepsilon_{12}^0 \quad [9]$$

$$M_{11} = D(k_{11} + \mu k_{22}) \quad [10]$$

$$M_{22} = D(k_{22} + \mu k_{11}) \quad [11]$$

$$M_{12} = M_{21} = \frac{D(1-\mu)}{2}k_{12} \quad [12]$$

K and D, the membrane and bending stiffnesses, characterize the resistance of the shell to deformation.

Table 1 Curvilinear coordinates

Type of shell	α_1	α_2	A_1	A_2	R_1	R_2
Shell of revolution (Figure 1A)	ϕ	θ	R_ϕ	$R_\theta \sin\phi$	R_ϕ	R_θ
Circular cylindrical shell (Figure 1B)	x	θ	1	a	∞	a
Conical shell (Figure 1C)	x	θ	1	$x \sin\alpha$	∞	$x \tan\alpha$
Spherical shell (Figure 1D)	ϕ	θ	a	$a \sin\phi$	a	a
Toriodal shell (Figure 1E)	ϕ	θ	a	$R+a \sin\phi$	a	$(R/\sin\phi)+a$

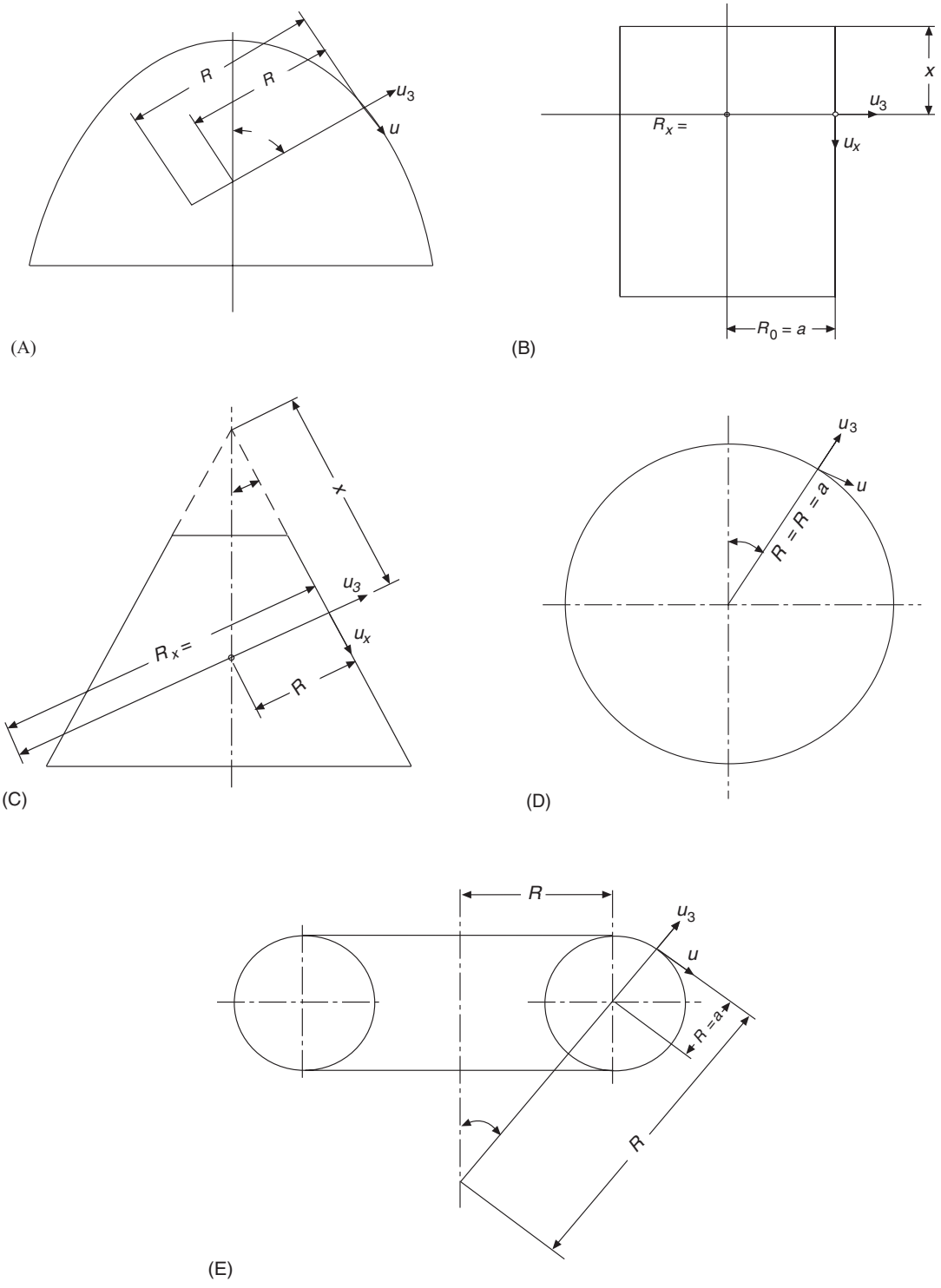


Figure 1 Examples of typical shell shapes and coordinates describing them: (A) general shell of revolution; (B) circular cylindrical shell; (C) conical shell; (D) spherical shell; (E) toroidal shell. See **Table 1** for the associated Lamé parameters and the radii of curvature expressions. The coordinate θ, in every case, is measured clockwise as viewed from below, and the displacement u_θ (not shown) is in the direction of increasing θ.

The membrane stiffness is:

$$K = \frac{Eh}{1-\mu^2} \quad [13]$$

where E is Young's modulus, h is the shell thickness and μ is Poisson's ratio. It corresponds to the term EA in the equation governing the longitudinal vibrations of a rod of cross-section A. The bending stiffness is:

$$D = \frac{Eh^3}{12(1-\mu^2)} \quad [14]$$

It corresponds to the term EI in the Bernoulli–Euler equation for a transversely vibrating beam of area moment I. The transverse shear forces per unit length are given by:

$$Q_{13} = \frac{1}{A_1A_2}\left[\frac{\partial(M_{11}A_2)}{\partial\alpha_1} + \frac{\partial(M_{21}A_1)}{\partial\alpha_2} + M_{12}\frac{\partial A_1}{\partial\alpha_2} - M_{22}\frac{\partial A_2}{\partial\alpha_1}\right] \quad [15]$$

$$Q_{23} = \frac{1}{A_1A_2}\left[\frac{\partial(M_{12}A_2)}{\partial\alpha_1} + \frac{\partial(M_{22}A_1)}{\partial\alpha_2} + M_{21}\frac{\partial A_2}{\partial\alpha_1} - M_{11}\frac{\partial A_1}{\partial\alpha_2}\right] \quad [16]$$

The membrane strains ε_{11}^0, ε_{22}^0, $\varepsilon_{12}^0 = \varepsilon_{21}^0$ and the changes of curvature k_{11}, k_{22}, $k_{12} = k_{21}$ are related to the three deflections u_1, u_2, u_3 by:

$$\varepsilon_{11}^0 = \frac{1}{A_1}\frac{\partial u_1}{\partial\alpha_1} + \frac{u_2}{A_1A_2}\frac{\partial A_1}{\partial\alpha_2} + \frac{u_3}{R_1} \quad [17]$$

$$\varepsilon_{22}^0 = \frac{1}{A_2}\frac{\partial u_2}{\partial\alpha_2} + \frac{u_1}{A_1A_2}\frac{\partial A_2}{\partial\alpha_1} + \frac{u_3}{R_2} \quad [18]$$

$$\varepsilon_{12}^0 = \varepsilon_{21}^0 = \frac{A_2}{A_1}\frac{\partial}{\partial\alpha_1}\left(\frac{u_2}{A_2}\right) + \frac{A_1}{A_2}\frac{\partial}{\partial\alpha_2}\left(\frac{u_1}{A_1}\right) \quad [19]$$

and:

$$k_{11} = \frac{1}{A_1}\frac{\partial\beta_1}{\partial\alpha_1} + \frac{\beta_2}{A_1A_2}\frac{\partial A_1}{\partial\alpha_2} \quad [20]$$

$$k_{22} = \frac{1}{A_2}\frac{\partial\beta_2}{\partial\alpha_2} + \frac{\beta_1}{A_1A_2}\frac{\partial A_2}{\partial\alpha_1} \quad [21]$$

$$k_{12} = k_{21} = \frac{A_2}{A_1}\frac{\partial}{\partial\alpha_1}\left(\frac{\beta_2}{A_2}\right) + \frac{A_1}{A_2}\frac{\partial}{\partial\alpha_2}\left(\frac{\beta_1}{A_1}\right) \quad [22]$$

where the slope changes β_1, β_2 in the α_1, α_2 directions are:

$$\beta_1 = \frac{u_1}{R_1} - \frac{1}{A_1}\frac{\partial u_3}{\partial\alpha_1} \quad [23]$$

$$\beta_2 = \frac{u_2}{R_2} - \frac{1}{A_2}\frac{\partial u_3}{\partial\alpha_2} \quad [24]$$

Boundary Conditions

Four bounding conditions have to be specified at each edge (the star superscript means 'specified'):

$$N_{nn} = N_{nn}^* \text{ or } u_n = u_n^* \quad [25]$$

$$M_{nn} = M_{nn}^* \text{ or } \beta_n = \beta_n^* \quad [26]$$

$$V_{n3} = V_{n3}^* \text{ or } u_3 = u_3^* \quad [27]$$

$$T_{nt} = T_{nt}^* \text{ or } u_t = u_t^* \quad [28]$$

where n means in normal direction to the edge, and t means in tangential direction to the edge. To resolve a problem similar to the one for free edges of plates, Kirchhoff effective shear resultants of the first and second kind are introduced:

$$V_{13} = Q_{13} + \frac{1}{A_2}\frac{\partial M_{12}}{\partial\alpha_2} \quad [29]$$

$$V_{23} = Q_{23} + \frac{1}{A_1}\frac{\partial M_{21}}{\partial\alpha_1} \quad [30]$$

and:

$$T_{12} = N_{12} + \frac{M_{12}}{R_2} \quad [31]$$

$$T_{21} = N_{21} + \frac{M_{21}}{R_1} \quad [32]$$

Note that, while $N_{12} = N_{21}$ and $M_{12} = M_{21}$, $T_{12} \neq T_{21}$ because of the different radii of curvature. Some examples of boundary conditions are given in **Table 2**, where $(-)$ means 'not defined'.

Composite Shells

For laminated and other composite shells, where the relationships between N_{11}, N_{22}, $N_{12} = N_{21}$, M_{11},

Table 2 Typical boundary conditions for Love-type equations

Edge condition	N_{nn}	M_{nn}	V_{n3}	T_{nt}	u_n	β_n	u_3	u_t
Completely clamped (welded)	(-)	(-)	(-)	(-)	0	0	0	0
Completely free	0	0	0	0	(-)	(-)	(-)	(-)
Transversely simply supported and free to slide in the tangential plane	0	0	(-)	0	(-)	(-)	0	(-)
Transversely simply supported, but not able to slide in the tangential plane	(-)	0	(-)	(-)	0	(-)	0	0

M_{22}, $M_{12} = M_{21}$ and the membrane strains ε^0_{11}, ε^0_{22}, $\varepsilon^0_{12} = \varepsilon^0_{21}$ and the bending initiated change of curvature terms k_{11}, k_{22}, $k_{12} = k_{21}$ can be expressed as:

$$\begin{Bmatrix} N_{11} \\ N_{22} \\ N_{12} \\ M_{11} \\ M_{22} \\ M_{12} \end{Bmatrix} = \begin{bmatrix} A_{11} & A_{12} & A_{13} & B_{11} & B_{12} & B_{13} \\ A_{21} & A_{22} & A_{23} & B_{21} & B_{22} & B_{23} \\ A_{31} & A_{32} & A_{33} & B_{31} & B_{32} & B_{33} \\ B_{11} & B_{12} & B_{13} & D_{11} & D_{12} & D_{13} \\ B_{21} & B_{22} & B_{23} & D_{21} & D_{22} & D_{23} \\ B_{31} & B_{32} & B_{33} & D_{31} & D_{32} & D_{33} \end{bmatrix} \begin{Bmatrix} \varepsilon^0_{11} \\ \varepsilon^0_{22} \\ \varepsilon^0_{12} \\ k_{11} \\ k_{22} \\ k_{12} \end{Bmatrix} \quad [33]$$

derived under the assumptions that plane sections normal to the reference surface before deflection remain so during deflection, the Love equations in the form of eqs [1]–[6] are still valid. The mass density per unit area, ρh, has to be viewed as a value averaged over the shell thickness.

Other Love-type Theories

The variations in use are only slightly different. The differences are, basically, that in the derivations of the Love equations, the simplification is made that $\alpha_3/R_i (i = 1, 2) \ll 1$, leading to the approximation $1/(1 + \alpha_3/R_i) \cong 1$. Theories by Novozhilov, Flügge, Byrne, Lur'ye and others either do not follow at all, or not consistently, this approximation and typically expand these types of expressions as geometric series, keeping certain higher-order terms.

Shear Deformation and Rotatory Inertia Included

In the Love-type equations of motion, deformations due to shear are not considered. Also, only the inertia effects due to the translation of mass points are included. While this is quite sufficient for thin shells and lower-mode calculations, at some point the deformations due to shear forces and the inertial resistance due to the rotation of the mass elements become important.

A theory consistent with the Timoshenko beam equation is summarized in the following. The equations of motion are:

$$L_1\{u_1, u_2, u_3, \beta_1, \beta_2\} + \rho h \ddot{u}_1 = q_1 \quad [34]$$

$$L_1\{u_1, u_2, u_3, \beta_1, \beta_2\} + \rho h \ddot{u}_2 = q_2 \quad [35]$$

$$L_3\{u_1, u_2, u_3, \beta_1, \beta_2\} + \rho h \ddot{u}_3 = q_3 \quad [36]$$

$$L_4\{u_1, u_2, u_3, \beta_1, \beta_2\} + \frac{\rho h^3}{12} \ddot{\beta}_1 = 0 \quad [37]$$

$$L_5\{u_1, u_2, u_3, \beta_1, \beta_2\} + \frac{\rho h^3}{12} \ddot{\beta}_2 = 0 \quad [38]$$

where:

$$L_1\{u_1, u_2, u_3, \beta_1, \beta_2\} = \frac{1}{A_1 A_2}\left[-\frac{\partial(N_{11} A_2)}{\partial \alpha_1} - \frac{\partial(N_{21} A_1)}{\partial \alpha_2} - N_{12}\frac{\partial A_1}{\partial \alpha_2} + N_{22}\frac{\partial A_2}{\partial \alpha_1} - A_1 A_2 \frac{k' \varepsilon_{13} G h}{R_1} \right] \quad [39]$$

$$L_2\{u_1, u_2, u_3, \beta_1, \beta_2\} = \frac{1}{A_1 A_2}\left[-\frac{\partial(N_{12} A_2)}{\partial \alpha_1} - \frac{\partial(N_{22} A_1)}{\partial \alpha_2} - N_{21}\frac{\partial A_2}{\partial \alpha_1} + N_{11}\frac{\partial A_1}{\partial \alpha_2} - A_1 A_2 \frac{k' \varepsilon_{23} G h}{R_2} \right] \quad [40]$$

$$L_3\{u_1,u_2,u_3,\beta_1,\beta_2\}=\frac{1}{A_1A_2}\left[-k'Gh\frac{\partial(\varepsilon_{13}A_2)}{\partial\alpha_1}-k'Gh\frac{\partial(\varepsilon_{23}A_1)}{\partial\alpha_2}+A_1A_2\left(\frac{N_{11}}{R_1}+\frac{N_{22}}{R_2}\right)\right] \quad [41]$$

$$L_4\{u_1,u_2,u_3,\beta_1,\beta_2\}=\frac{1}{A_1A_2}\left[-\frac{\partial(M_{11}A_2)}{\partial\alpha_1}-\frac{\partial(M_{21}A_1)}{\partial\alpha_2}-M_{12}\frac{\partial A_1}{\partial\alpha_2}+M_{22}\frac{\partial A_2}{\partial\alpha_1}+Ghk'\varepsilon_{13}A_1A_2\right] \quad [42]$$

$$L_5\{u_1,u_2,u_3,\beta_1,\beta_2\}=\frac{1}{A_1A_2}\left[-\frac{\partial(M_{12}A_2)}{\partial\alpha_1}-\frac{\partial(M_{22}A_1)}{\partial\alpha_2}-M_{21}\frac{\partial A_2}{\partial\alpha_1}+M_{11}\frac{\partial A_1}{\partial\alpha_2}+Ghk'\varepsilon_{23}A_1A_2\right] \quad [43]$$

and where:

$$\varepsilon_{13}=\frac{1}{A_1}\frac{\partial u_3}{\partial\alpha_1}-\frac{u_1}{R_1}+\beta_1 \quad [44]$$

$$\varepsilon_{23}=\frac{1}{A_2}\frac{\partial u_3}{\partial\alpha_2}-\frac{u_2}{R_2}+\beta_2 \quad [45]$$

The definitions of N_{11}, N_{22}, $N_{12}=N_{21}$, M_{11}, M_{22}, $M_{12}=M_{21}$ are the same as previously used for the Love-type equations. Note that the slope changes β_1 and β_2 are now included as two additional degrees-of-freedom of motion. It can be shown that the influence of rotatory inertia is of the same order as the influence of shear deformation. Thus, taking account of one without the other is not advisable. The value of k' is usually taken as 2/3, assuming a parabolic distribution of shear strain through the thickness of the shell.

Boundary Conditions

While these equations are more complicated than the Love-type equations, they have the advantage that they admit five boundary conditions at each edge; the use of the Kirchhoff shear equations of the first and second kind is now not necessary. The five physical conditions correspond now to five admissible boundary conditions:

$$N_{nn}=N^*_{nn}\text{ or }u_n=u^*_n \quad [46]$$

$$N_{nt}=N^*_{nt}\text{ or }u_t=u^*_t \quad [47]$$

$$Q_{n3}=Q^*_{n3}\text{ or }u_3=u^*_3 \quad [48]$$

$$M_{nn}=M^*_{nn}\text{ or }\beta_n=\beta^*_n \quad [49]$$

$$M_{nt}=M^*_{nt}\text{ or }\beta_t=\beta^*_t \quad [50]$$

This is applied in **Table 3** to the same examples used in **Table 2**. Again, n means normal to an edge and t means tangential.

The Membrane Approximation

This simplified theory is not to be confused with equations of motion of shells that are inflated membranes. It simply assumes that the resistance of certain shells to deformation is dominated by the membrane strain terms and change in curvature strain components (bending components) can be neglected. The simplification is applied to Love-type equations by setting the bending stiffness to zero:

$$D=0 \quad [51]$$

The consequence is that the Love equation operators L_1, L_2, and L_3 reduce to:

$$L_1\{u_1,u_2,u_3\}=\frac{1}{A_1A_2}\times\left[-\frac{\partial(N_{11}A_2)}{\partial\alpha_1}-\frac{\partial(N_{21}A_1)}{\partial\alpha_2}-N_{12}\frac{\partial A_1}{\partial\alpha_2}+N_{22}\frac{\partial A_2}{\partial\alpha_1}\right] \quad [52]$$

$$L_2\{u_1,u_2,u_3\}=\frac{1}{A_1A_2}\times\left[-\frac{\partial(N_{12}A_2)}{\partial\alpha_1}-\frac{\partial(N_{22}A_1)}{\partial\alpha_2}-N_{21}\frac{\partial A_2}{\partial\alpha_1}+N_{11}\frac{\partial A_1}{\partial\alpha_2}\right] \quad [53]$$

$$L_3\{u_1,u_2,u_3\}=\frac{N_{11}}{R_1}+\frac{N_{22}}{R_2} \quad [54]$$

This theory has some merit for shells that are nondevelopable, such as spherical shells and toroidal shells. It is, in general, not useful for shells that are developable, such as cylindrical and conical shells. Developable means that with a single cut, disregarding boundaries, a shell can be unfolded to a flat sheet. Cylindrical or conical shells can be cut along one coordinate and unfold. On the other hand, unfolding a spherical shell into a flat sheet is not possible. It can

Table 3 Typical boundary conditions for theory that includes shear deformation and rotatory inertia (same cases as in Table 2)

Edge condition	N_{nn}	M_{nn}	V_{n3}	T_{nt}	M_{nt}	u_n	β_n	u_3	u_t	β_t
Completely clamped (welded)	(-)	(-)	(-)	(-)	(-)	0	0	0	0	0
Completely free	0	0	0	0	0	(-)	(-)	(-)	(-)	(-)
Transversely simply supported and free to slide in the tangential plane	0	0	(-)	0	(-)	(-)	(-)	0	(-)	0
Transversely simply supported, but not able to slide in the tangential plane	(-)	0	(-)	(-)	(-)	0	(-)	0	0	0

only be approximated by multiple cuts along the meridional coordinate lines and then the unfolded shell looks like an orange peel, each segment only approximating flatness.

The Donnell–Mushtari–Vlasov Equations

This useful simplification assumes that tangential deflections can be neglected in the bending-strain (change of curvature) expressions, but not in the membrane-strain expressions. The theory is limited to transverse excitation q_3; q_1 and q_2 have to be zero. Also neglected are the transverse shear terms Q_{31}/R_1 and Q_{32}/R_2. These ratios tend to be particularly small for shallow shells. This is the reason why this theory is sometimes referred to as shallow shell theory. But it also works well for deep shells of zero or small Gaussian curvature $1/R_1R_2$, such as cylindrical and conical shells.

The resulting equations are:

$$D\nabla^4 u_3 + \nabla_K^2 \phi + \rho h \frac{\partial^2 u_3}{\partial t^2} = q_3 \qquad [55]$$

$$Eh\nabla_K^2 u_3 - \nabla^4 \phi = 0 \qquad [56]$$

where ϕ is a stress function defined such that:

$$N_{11} = \frac{1}{A_2}\frac{\partial}{\partial \alpha_2}\left(\frac{1}{A_2}\frac{\partial \phi}{\partial \alpha_2}\right) + \frac{1}{A_1^2 A_2}\frac{\partial A_2}{\partial \alpha_1}\frac{\partial \phi}{\partial \alpha_1} \qquad [57]$$

$$N_{22} = \frac{1}{A_1}\frac{\partial}{\partial \alpha_1}\left(\frac{1}{A_1}\frac{\partial \phi}{\partial \alpha_1}\right) + \frac{1}{A_1 A_2^2}\frac{\partial A_1}{\partial \alpha_2}\frac{\partial \phi}{\partial \alpha_2} \qquad [58]$$

$$N_{12} = N_{21} = -\frac{1}{A_1 A_2} \times \left(\frac{\partial^2 \phi}{\partial \alpha_1 \partial \alpha_2} - \frac{1}{A_1}\frac{\partial A_1}{\partial \alpha_2}\frac{\partial \phi}{\partial \alpha_1} - \frac{1}{A_2}\frac{\partial A_2}{\partial \alpha_1}\frac{\partial \phi}{\partial \alpha_2}\right) \qquad [59]$$

and where $\nabla^4(\cdot) = \nabla^2\nabla^2(\cdot)$ such that:

$$\nabla^2(\cdot) = \frac{1}{A_1 A_2}\left[\frac{\partial}{\partial \alpha_1}\left(\frac{A_2}{A_1}\frac{\partial(\cdot)}{\partial \alpha_1}\right) + \frac{\partial}{\partial \alpha_2}\left(\frac{A_1}{A_2}\frac{\partial(\cdot)}{\partial \alpha_2}\right)\right] \qquad [60]$$

and where:

$$\nabla_K^2(\cdot) = \frac{1}{A_1 A_2}\left\{\frac{\partial}{\partial \alpha_1}\left[\frac{1}{R_2}\frac{A_2}{A_1}\frac{\partial(\cdot)}{\partial \alpha_1}\right] + \frac{\partial}{\partial \alpha_2}\left[\frac{1}{R_1}\frac{A_1}{A_2}\frac{\partial(\cdot)}{\partial \alpha_2}\right]\right\} \qquad [61]$$

Natural Frequencies and Modes

Setting $q_1 = q_2 = q_3 = 0$ in eqns [1]–[3], for example, and separating the time variable either mathematically or by arguing physically that at each natural frequency the shell will vibrate harmonically leads to solutions of the form:

$$u_i(\alpha_1, \alpha_2, t) = U_i(\alpha_1, \alpha_2)e^{j\omega t} \qquad [62]$$

where $i = 1, 2, 3,$ and where the natural mode components $U_i(\alpha_1, \alpha_2)$ are defined by:

$$L_i\{U_1, U_2, U_3\} + \rho h \omega^2 U_i = 0 \qquad [63]$$

with boundary conditions from which time has been eliminated:

$$B_K\{U_1, U_2, U_3\} = 0 \qquad [64]$$

The next analytical step is to try to separate variables again:

$$U_i(\alpha_1, \alpha_2) = R_i(\alpha_1)S_i(\alpha_2) \qquad [65]$$

This is often not possible. In general, it can be done for certain shells of revolution. Therefore, exact analytical solutions are relatively rare. At this point, numerical methods such as the finite element method or finite difference method have to be used, or approximate methods such as the Rayleigh–Ritz

method or the Galerkin method. In the following, some examples of solutions are given.

Example: Simply Supported, Closed Circular Cylindrical Shell

Love's equations The Love equations reduce to ($\alpha_1 = x$, $\alpha_2 = \theta$, $A_1 = 1$, $A_2 = a$, $R_1 = \infty R_2 = a$):

$$\frac{\partial N_{xx}}{\partial x} + \frac{1}{a}\frac{\partial N_{x\theta}}{\partial \theta} - \rho h \frac{\partial^2 u_x}{\partial t^2} = 0 \qquad [66]$$

$$\frac{\partial N_{x\theta}}{\partial x} + \frac{1}{a}\frac{\partial N_{\theta\theta}}{\partial \theta} + \frac{Q_{\theta 3}}{a} - \rho h \frac{\partial^2 u_\theta}{\partial t^2} = 0 \qquad [67]$$

$$\frac{\partial Q_{x3}}{\partial x} + \frac{1}{a}\frac{\partial Q_{\theta 3}}{\partial \theta} - \frac{N_{\theta\theta}}{a} - \rho h \frac{\partial^2 u_3}{\partial t^2} = 0 \qquad [68]$$

For boundary conditions:

$$u_3(0,\theta,t) = 0, \quad u_3(L,\theta,t) = 0 \qquad [69]$$

$$u_\theta(0,\theta,t) = 0, \quad u_\theta(L,\theta,t) = 0 \qquad [70]$$

$$M_{xx}(0,\theta,t) = 0, \quad M_{xx}(L,\theta,t) = 0 \qquad [71]$$

$$N_{xx}(0,\theta,t) = 0, \quad N_{xx}(L,\theta,t) = 0 \qquad [72]$$

the natural frequencies are the roots of the equation:

$$\omega^6 + a_1\omega^4 + a_2\omega^2 + a_3 = 0 \qquad [73]$$

where:

$$a_1 = -\frac{1}{\rho h}(k_{11} + k_{22} + k_{33}) \qquad [74]$$

$$a_2 = \frac{1}{(\rho h)^2} \times \left(k_{11}k_{33} + k_{22}k_{33} + k_{11}k_{22} - k_{23}^2 - k_{12}^2 - k_{13}^2\right) \qquad [75]$$

$$a_3 = \frac{1}{(\rho h)^2} \times \left(k_{11}k_{23}^2 + k_{22}k_{13}^2 + k_{33}k_{12}^2 + 2k_{12}k_{23}k_{13} - k_{11}k_{22}k_{33}\right) \qquad [76]$$

and where:

$$k_{11} = K\left[\left(\frac{m\pi}{L}\right)^2 + \frac{(1-\mu)}{2}\left(\frac{n}{a}\right)^2\right] \qquad [77]$$

$$k_{12} = k_{21} = K\frac{(1+\mu)}{2}\left(\frac{m\pi}{L}\right)\left(\frac{n}{a}\right) \qquad [78]$$

$$k_{13} = k_{31} = \frac{\mu K}{a}\left(\frac{m\pi}{L}\right) \qquad [79]$$

$$k_{22} = \left(K + \frac{D}{a^2}\right)\left[\frac{(1-\mu)}{2}\left(\frac{m\pi}{L}\right)^2 + \left(\frac{n}{a}\right)^2\right] \qquad [80]$$

$$k_{23} = k_{32} = -\left(\frac{K}{a}\right)\left(\frac{n}{a}\right) - \left(\frac{D}{a}\right)\left(\frac{n}{a}\right)\left[\left(\frac{m\pi}{L}\right)^2 + \left(\frac{n}{a}\right)^2\right] \qquad [81]$$

$$k_{33} = D\left[\left(\frac{m\pi}{L}\right)^2 + \left(\frac{n}{a}\right)^2\right]^2 + \frac{K}{a^2} \qquad [82]$$

The $m = 1, 2, 3 \ldots$ and $n = 0, 1, 2, 3 \ldots$ numbers define the natural modes given by:

$$U_x(x,\theta) = A_i \cos\left(\frac{m\pi x}{L}\right)\cos n(\theta - \phi) \qquad [83]$$

$$U_\theta(x,\theta) = B_i \sin\left(\frac{m\pi x}{L}\right)\sin n(\theta - \phi) \qquad [84]$$

$$U_3(x,\theta) = C_i \sin\left(\frac{m\pi x}{L}\right)\cos n(\theta - \phi) \qquad [85]$$

where the A_i and B_i are related to the arbitrary C_i by:

$$\frac{A_i}{C_i} = \frac{k_{12}k_{23} - k_{13}\left(\rho h\omega_{imn}^2 - k_{22}\right)}{\left(\rho h\omega_{imn}^2 - k_{11}\right)\left(\rho h\omega_{imn}^2 - k_{22}\right) - k_{12}^2} \qquad [86]$$

$$\frac{B_i}{C_i} = \frac{k_{21}k_{13} - k_{23}\left(\rho h\omega_{imn}^2 - k_{11}\right)}{\left(\rho h\omega_{imn}^2 - k_{11}\right)\left(\rho h\omega_{imn}^2 - k_{22}\right) - k_{12}^2} \qquad [87]$$

For each m, n combination, there are three roots of the frequency equation, designated by $i = 1, 2, 3$. Therefore, ω_{imn} is the ith natural frequency corresponding to a particular m, n combination.

For a steel shell of $E = 20.6(10^4)\ \mathrm{N\,mm^{-2}}$, $\rho = 7.85(10^{-9})\ \mathrm{Ns^2\,mm^{-4}}$, $\mu = 0.3$, $h = 2\,\mathrm{mm}$, $a = 100\,\mathrm{mm}$, $L = 200\,\mathrm{mm}$, the natural frequencies are plotted in **Figure 2**. The ratios A_i/C_i are plotted in **Figure 3**.

These plots illustrate a phenomenon which is peculiar to many deep shells, namely that the lowest natural frequency does not correspond to the simplest natural mode, as is typically the case for rods, beams, and plates. It is therefore difficult to use the Rayleigh method because we do not know if our assumed

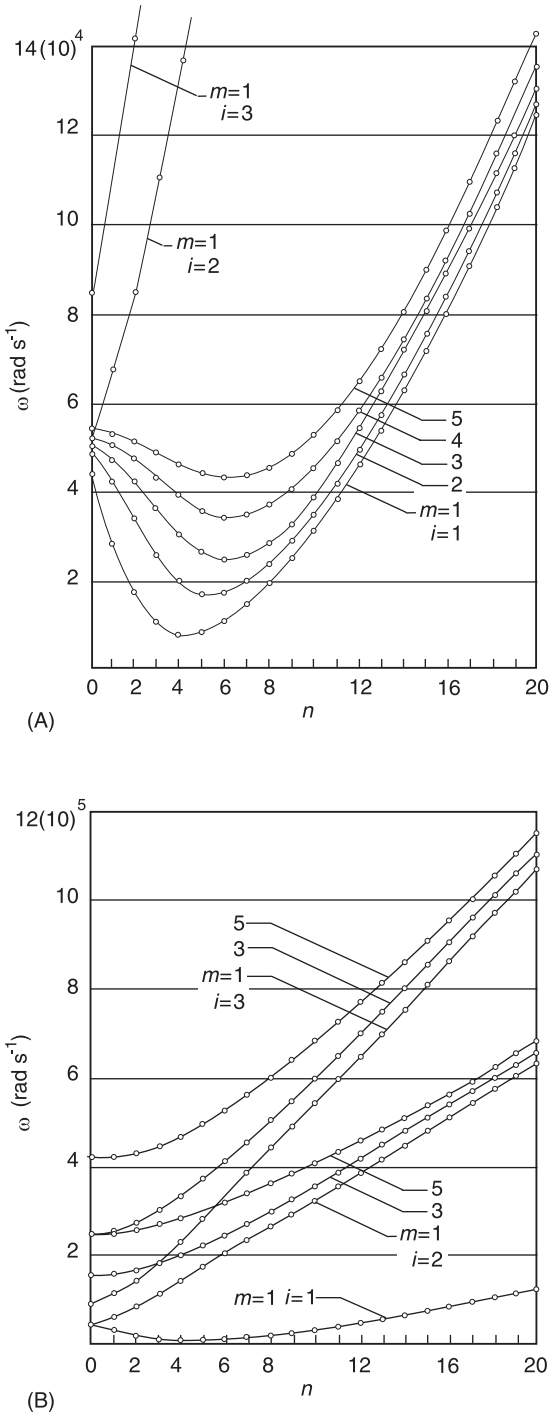


Figure 2 Natural frequencies for a typical, simply supported cylindrical shell. For each m, n combination, three natural frequencies will occur. The three sets are: (A) the lowest, transverse deflection-dominated set ($i = 1$); (B) the two higher sets ($i = 2, 3$) dominated by motion in the tangent plane – it is the same graph as (A) but at a different scale. (Reproduced with permission of the publisher from Soedel W (1993) *Vibrations of Shells and Plates*, 2nd edn. New York: Marcel Dekker.

natural mode corresponds to the lowest natural frequency. The Rayleigh-Ritz procedure has to be used with trial functions that include the natural mode corresponding to the lowest natural frequency.

Donnell–Mushtari–Vlasov equations For the same simply supported, circular cylindrical shell, we solve:

$$D\nabla^4 u_3 + \nabla_K^2 \phi + \rho h \frac{\partial^2 u_3}{\partial t^2} = 0 \qquad [88]$$

$$Eh\nabla_K^2 u_3 - \nabla^4 \phi = 0 \qquad [89]$$

where:

$$\nabla^4(\cdot) = \nabla^2\nabla^2(\cdot) = \frac{1}{a^4}\frac{\partial^4(\cdot)}{\partial\theta^4} + \frac{\partial^4(\cdot)}{\partial x^4} + \frac{2}{a^2}\frac{\partial^4(\cdot)}{\partial x^2 \partial\theta^2} \qquad [90]$$

$$\nabla_K^4(\cdot) = \frac{1}{a^2}\frac{\partial^4(\cdot)}{\partial x^4} \qquad [91]$$

The natural frequencies corresponding to the $i = 1$ natural frequencies of the Love equation solution are:

$$\omega_{mn} = \frac{1}{a}\sqrt{\xi_1 + \xi_2}\sqrt{\frac{E}{\rho}} \qquad [92]$$

where:

$$\xi_1 = \frac{(m\pi a/L)^4}{\left[(m\pi a/L)^2 + n^2\right]^2} \qquad [93]$$

$$\xi_2 = \frac{(h/a)^2}{12(1-\mu^2)}\left[\left(\frac{m\pi a}{L}\right)^2 + n^2\right]^2 \qquad [94]$$

Note that we have lost the ability to predict the higher (tangential motion-dominated) natural frequency sets $i = 2$ and 3, because of the simplifications introduced by the Donnell–Mushtari–Vlasov approach. The agreement with the $i = 1$ set is excellent, however.

Example: Closed, Spherical Shell by the Membrane Simplification

Spherical shells have nondevelopable surfaces; therefore, reasonable results can be obtained with the membrane simplification. Introducing in the general Love's equations and the other definitions $\alpha_1 = \phi, \alpha_2 = \theta, A_1 = a, A_2 = a \sin \phi, R_1 = R_2 = a$, we obtain the natural frequencies that correspond to axisymmetric natural modes ($\partial(\cdot)/\partial\theta = 0$) from:

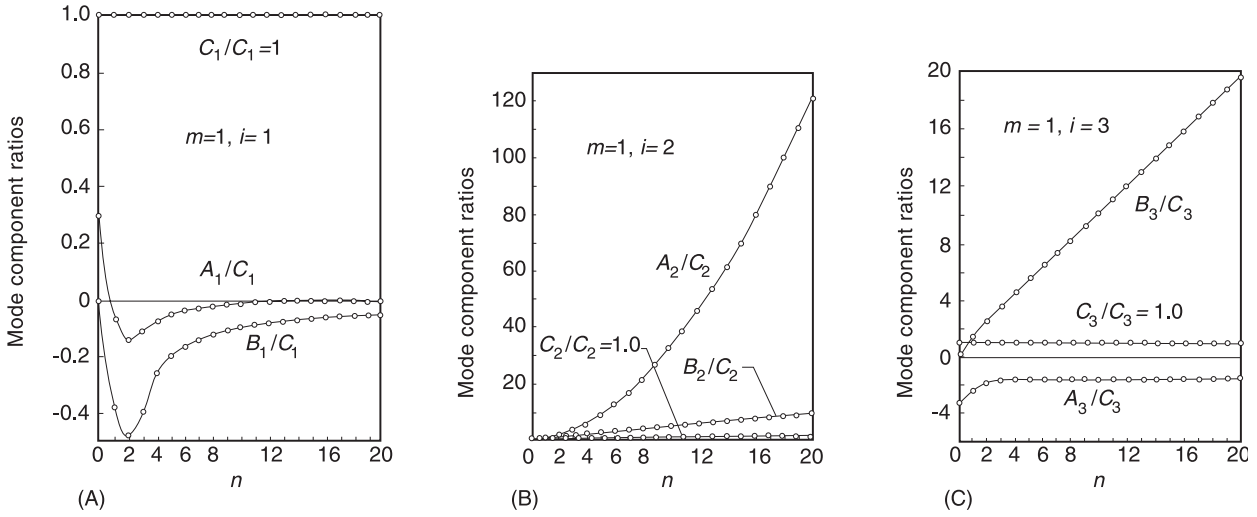


Figure 3 Mode component ratios for the natural frequencies given in **Figure 2**, to illustrate the dominance of certain components for various m, n combinations. A_i is the mode component amplitude in x direction, B_i in θ direction and C_i in transverse direction: (A) $m = 1$, $i = 1$; (B) $m = 1$, $i = 2$; (C) $m = 1$, $i = 3$. For example, (A) clearly indicates that for the $i = 1$ set, the transverse mode component dominates. (Reproduced with permission of the publisher from Soedel W (1993) *Vibrations of Shells and Plates*, 2nd edn. New York: Marcel Dekker.

$$-\frac{\partial}{\partial\phi}\left(N_{\phi\phi}\ \sin\ \phi\right)+N_{\theta\theta}\cos\phi+a\rho h\frac{\partial^2 u_\phi}{\partial t^2}\ \sin\ \phi=0 \qquad [95]$$

$$\left(N_{\phi\phi}+N_{\theta\theta}\right)+a\rho h\frac{\partial^2 u_3}{\partial t^2}=0 \qquad [96]$$

The natural frequencies are given by:

$$\omega_{n1,2}=\frac{\Omega_{n1,2}}{a}\sqrt{\frac{E}{\rho}} \qquad [97]$$

where:

$$\Omega^2_{n1,2}=\frac{1}{2(1-\mu^2)}\left[n(n+1)+1+3\mu \pm\sqrt{[n(n+1)+1+3\mu]^2-4(1-\mu^2)[n(n+1)-2]}\right] \qquad [98]$$

The natural mode components are ($i = 1, 2$):

$$U_{3i}(\phi)=\left(\frac{1+(1+\mu)\Omega^2_{ni}}{1-\Omega^2_{ni}}\right)P_n(\cos\phi) \qquad [99]$$

$$U^{(\phi)}_{\phi i}=\frac{\mathrm{d}}{\mathrm{d}\phi}P_n(\cos\phi) \qquad [100]$$

and where $P_n(\cos\phi)$ are Legendre polynomials.

Example: Approximate Solutions of Donnell–Mushtari–Vlasov Equations for Closed Circular Cylindrical Shells of General Boundary Conditions

Using the Galerkin method, assumed natural modes of the form:

$$U_3(x,\theta)=U_{3m}(x)\cos n\theta \qquad [101]$$

are used, where $U_{3m}(x)$ is the natural-mode function of a transversely vibrating beam having similar transverse boundary conditions as the circular cylindrical shell at ends $x = 0$ and $x = L$. The natural frequencies are given by:

$$\omega_{mn}=\frac{1}{a}\sqrt{\xi_1+\xi_2}\sqrt{\frac{E}{\rho}} \qquad [102]$$

where:

$$\xi_1=\frac{(\lambda_m a/L)^4}{\left[(\lambda_m a/L)^2+n^2\right]^2} \qquad [103]$$

$$\xi_2=\frac{(h/a)^2}{12(1-\mu^2)}\left[\left(\frac{\lambda_m a}{L}\right)^2+n^2\right]^2 \qquad [104]$$

and where λ_m are the roots of the corresponding beam eigenvalue problem. Examples of natural modes of beams and the corresponding values of λ_m are given in **Table 4**.

Table 4 Examples of beam functions and λ_m values to be used in eqn [102]

Boundary conditions	$U_{3m}(x)$	λ_m
Simply supported at $x = 0$ and $x = L$	$\sin(m\pi x/L)$	$m\pi/L$
Clamped at $x = 0$ and free at $x = L$	$J\left(\frac{\lambda_m x}{L}\right) - \frac{G(\lambda_m)}{F(\lambda_m)} H\left(\frac{\lambda_m x}{L}\right)$	Roots of $\cos\lambda \cosh\lambda = -1$
Clamped at $x = 0$ and $x = L$	$J\left(\frac{\lambda_m x}{L}\right) - \frac{J(\lambda_m)}{H(\lambda_m)} H\left(\frac{\lambda_m x}{L}\right)$	Roots of $\cos\lambda \cosh\lambda = 1$
Free at $x = 0$ and $x = L$	$G\left(\frac{\lambda_m x}{L}\right) - \frac{J(\lambda_m)}{H(\lambda_m)} F\left(\frac{\lambda_m x}{L}\right)$	Roots of $\cos\lambda \cosh\lambda = 1$

Note: $J(\cdot) = \cosh(\cdot) - \cos(\cdot)$, $G(\cdot) = \cosh(\cdot) + \cos(\cdot)$
$F(\cdot) = \sinh(\cdot) + \sin(\cdot)$, $H(\cdot) = \sinh(\cdot) - \sin(\cdot)$

While this equation is quite useful, it must be remembered that it is an approximate solution to an approximate theory and results have to be interpreted accordingly.

Some Extensions to the Simply Supported Circular Cylindrical Shell Formula [92]

Effect of a small curvature in x direction (barrel shell) A small curvature $1/R$ is introduced in the circular, originally cylindrical shell, in x direction. A positive $1/R$ increases all natural frequency by:

$$\omega_{Bmn}^2 = \omega_{Cmn}^2 + \left(\frac{n}{a}\right)^2 \frac{\left[n^2(a/R)^2 + 2(a/R)(m\pi a/L)^2\right]}{\left[(m\pi a/L)^2 + n^2\right]} \left(\frac{E}{\rho}\right) \quad [105]$$

where ω_{Bmn} are the new natural frequencies in radians per second, and ω_{Cmn} are the original natural frequencies as given by eqn [92]. A negative $1/R$ (negative Gaussian curvature) will decrease natural frequencies.

Effect of axial tension A uniform tension T (force per unit circumference) in axial direction increases all natural frequencies:

$$\omega_{Tmn}^2 = \omega_{Cmn}^2 + \frac{T}{\rho h}\left(\frac{m\pi}{L}\right)^2 \quad [106]$$

For negative T (compression), the natural frequencies reduce until a critical buckling state is reached.

7. Forced Vibrations

Utilizing an equivalent, distributed viscous damping model, the equations of motion to be solved are ($i = 1, 2, 3$):

$$L_i\{u_1, u_2, u_3\} - \lambda\dot{u}_i - \rho h\ddot{u}_i = -q_i \quad [107]$$

The solution is:

$$u_i(\alpha_1, \alpha_2, t) = \sum_{k=1}^{\infty} \eta_k(t) U_{ik}(\alpha_1, \alpha_2) \quad [108]$$

where, for subcritical damping ($\varsigma_k < 1$):

$$\eta_k(t) = e^{-\varsigma_k\omega_k t} \times \left\{\eta_k(0)\cos\gamma_k t + [\eta_k(0)\varsigma_k\omega_k + \dot{\eta}_k(0)]\frac{\sin\gamma_k t}{\gamma_k}\right\} + \frac{1}{\gamma_k}\int_0^t F_k(\tau) e^{-\varsigma_k\omega_k(t-\tau)} \sin\gamma_k(t-\tau)\,d\tau \quad [109]$$

where:

$$\gamma_k = \omega_k\sqrt{1-\varsigma_k^2}, \quad \varsigma_k = \lambda/(2\rho h\omega_k) \quad [110]$$

For natural modes that are damped supercritically ($\varsigma_k > 1$), the solution is:

$$\eta_k(t) = e^{-\varsigma_k\omega_k t} \left\{\eta_k(0)\cosh\varepsilon_k t + [\eta_k(0)\varsigma_k\omega_k + \dot{\eta}_k(0)]\frac{\sinh\varepsilon_k t}{\varepsilon_k}\right\} + \frac{1}{\varepsilon_k}\int_0^t F_k(\tau) e^{-\varsigma_k\omega_k(t-\tau)} \sinh\varepsilon_k(t-\tau)\,d\tau \quad [111]$$

The critical damping solution ($\varsigma_k = 1$) can be obtained from either equation by letting ς_k approach unity in the limit.

For both solutions:

$$F_k = \frac{1}{\rho h N_k} \times \int_{\alpha_2} \int_{\alpha_1} (q_1 U_{1k} + q_2 U_{2k} + q_3 U_{3k}) A_1 A_2 \, \mathrm{d}\alpha_1 \, \mathrm{d}\alpha_2 \quad [112]$$

where:

$$N_k = \int_{\alpha_2} \int_{\alpha_1} (U_{1k}^2 + U_{2k}^2 + U_{3k}^2) A_1 A_2 \, \mathrm{d}\alpha_1 \, \mathrm{d}\alpha_2 \quad [113]$$

The values $\eta_k(0)$ and $\dot{\eta}_k(0)$ are obtained from the initial conditions $u_i(\alpha_1, \alpha_2, 0)$ and $\dot{u}_i(\alpha_1, \alpha_2, 0)$ for $i = 1, 2, 3$:

$$\eta_k(0) = \frac{1}{N_k} \int_{\alpha_2} \int_{\alpha_1} \Big[u_1(\alpha_1, \alpha_2, 0) U_{1k} + u_2(\alpha_1, \alpha_2, 0) U_{2k} + u_3(\alpha_1, \alpha_2, 0) U_{3k} \Big] \times A_1 A_2 \, \mathrm{d}\alpha_1 \, \mathrm{d}\alpha_2 \quad [114]$$

$$\dot{\eta}_k(0) = \frac{1}{N_k} \int_{\alpha_2} \int_{\alpha_1} \Big[\dot{u}_1(\alpha_1, \alpha_2, 0) U_{1k} + \dot{u}_2(\alpha_1, \alpha_2, 0) U_{2k} + \dot{u}_3(\alpha_1, \alpha_2, 0) U_{3k} \Big] A_1 A_2 \, \mathrm{d}\alpha_1 \, \mathrm{d}\alpha_2 \quad [115]$$

Special Case: Steady-State Harmonic Response

The solution to a forcing of:

$$q_i(\alpha_1, \alpha_2, t) = q_i^*(\alpha_1, \alpha_2) \mathrm{e}^{\mathrm{j}\omega t} \quad [116]$$

is in steady state:

$$u_i(\alpha_1, \alpha_2, t) = \sum_{k=1}^{N} \eta_k(t) U_i(\alpha_1, \alpha_2) \quad [117]$$

where:

$$\eta_k(t) = \Lambda_k \, \mathrm{e}^{\mathrm{j}(\omega t - \phi_k)} \quad [118]$$

$$\Lambda_k = \frac{F_k^*}{\omega_k^2 \sqrt{\left[1 - (\omega/\omega_k)^2\right]^2 + 4\varsigma_k^2 (\omega/\omega_k)}} \quad [119]$$

$$\phi_k = \tan^{-1} \frac{2\varsigma_k (\omega/\omega_k)}{1 - (\omega/\omega_k)} \quad [120]$$

$$F_k^* = \frac{1}{\rho h N_k} \times \int_{\alpha_2} \int_{\alpha_1} (q_1^* U_{1k} + q_2^* U_{2k} + q_3^* U_{3k}) A_1 A_2 \, \mathrm{d}\alpha_1 \, \mathrm{d}\alpha_2 \quad [121]$$

Special Case: Response to a Point Impulse

The solution to a forcing of:

$$q_i(\alpha_1, \alpha_2, t) = \frac{M_i}{A_1 A_2} \delta(\alpha_1 - \alpha_1^*) \delta(\alpha_2 - \alpha_2^*) \delta(t - t_1) \quad [122]$$

where $\delta(\cdot)$ is the Dirac-delta function and M_i is the momentum that is transferred to the shell by the impact, is:

$$u_i(\alpha_1, \alpha_2, t) = \sum_{k=1}^{N} \eta_k(t) U_i(\alpha_1, \alpha_2) \quad [123]$$

where for $t \geq t_1$:

$$\eta_k(t) = \frac{F_k^*}{\gamma_k} \mathrm{e}^{-\varsigma_k \omega_k (t - t_1)} \sin \gamma_k (t - t_1) \quad [124]$$

and where:

$$F_k^* = \frac{1}{\rho h N_k} \Big[M_1 U_{1k}(\alpha_1^*, \alpha_2^*) + M_2 U_{2k}(\alpha_1^*, \alpha_2^*) + M_3 U_{3k}(\alpha_1^*, \alpha_2^*) \Big] \quad [125]$$

Note that the impulse response at α_1, α_2, t in i-direction ($i = 1, 2, 3$) due to a unit impulse in j-direction ($j = 1, 2, 3$) at α_1^*, α_2^*, t^* is the dynamic Green's function $G_{ij}(\alpha_1, \alpha_2, t; \alpha_1^*, \alpha_2^*, t^*)$.

Complex Modulus Model for Material Damping

For harmonic and periodic response calculations, material damping can be modeled by replacing Young's modulus E by $(1 + j\eta)E$, where η is the hysteresis loss factor. The equations of motion of the shell become ($i = 1, 2, 3$), for harmonic excitation:

$$(1 + j\eta) L_i\{u_1, u_2, u_3\} + \rho h \ddot{u}_i = +q_i^* \mathrm{e}^{\mathrm{j}\omega t} \quad [126]$$

The solution is:

$$u_i(\alpha_1, \alpha_2, t) = \sum_{k=1}^{\infty} \eta_k(t) U_{ik}(\alpha_1, \alpha_2) \quad [127]$$

where:

$$\eta_k(t) = \Lambda_k \, e^{j(\omega t - \phi_k)} \qquad [128]$$

and where:

$$\Lambda_k = \frac{F_k^x}{\omega_k^2 \sqrt{\left[1 - (\omega/\omega_k)^2\right] + \eta^2}} \qquad [129]$$

$$\phi_k = \tan^{-1} \frac{\eta}{1 - (\omega/\omega_k)^2} \qquad [130]$$

$$F_k^* = \frac{1}{\rho h N_k} \times \int_{\alpha_2} \int_{\alpha_1} (q_1^* U_{1k} + q_2^* U_{2k} + q_3^* U_{3k}) A_1 A_2 \, d\alpha_1 \, d\alpha_2 \qquad [131]$$

Nomenclature

$\alpha_1, \alpha_2, \alpha_3$	curvilinear coordinates
A_1, A_2	Lamé parameters
R_1, R_2, R	radii of curvature (m)
x, θ	cylindrical coordinates (m, rad)
a, R	radii (m)
ϕ, θ	shell of revolution, spherical, toroidal coordinates
u_1, u_2, u_3	deflections at reference surface (m)
q_1, q_2, q_3	distributed forces ($N\,m^{-2}$)
ρ	mass density ($kg\,m^{-3}$)
h	thickness (m)
N_{11}, N_{22}, N_{12}	membrane forces per length ($N\,m^{-1}$)
M_{11}, M_{22}, M_{12}	bending moments per length ($Nm\,m^{-1}$)
Q_{13}, Q_{23}	transverse shear forces per length ($N\,m^{-1}$)
K	membrane stiffness ($N\,m^{-1}$)
E	Young's modulus ($N\,m^{-3}$)
μ	Poisson's ratio
D	bending stiffness (Nm)
$\varepsilon_{11}^0, \varepsilon_{22}^0, \varepsilon_{12}^0$	membrane strains
k_{11}, k_{22}, k_{12}	curvature changes due to deflection ($1\,m^{-1}$)
β_1, β_2	slopes
V_{13}, V_{23}	Kirchhoff shear of first kind ($N\,m^{-1}$)
T_{12}, T_{21}	Kirchhoff shear of second kind ($N\,m^{-1}$)
t	time (s)
ϕ	stress function
$U_i(\alpha_1, \alpha_2)$	natural mode components (m)
L	length (m)
A_i, B_i, C_i	natural mode component amplitudes (m)
$\omega_k, \omega_{imn}, \omega_{mn}, \omega_{ni}$	natural frequencies ($rad\,s^{-1}$)
ω	forcing frequency ($rad\,s^{-1}$)
$\eta_k(t)$	modal participation factor
λ	equivalent viscous damping coefficient ($Ns\,m^{-3}$)
η	hysteresis loss factor
T	axial tension ($N\,m^{-1}$)

See also: **Boundary conditions**; **Forced response**; **Plates**.

Further Reading

Flügge W (1934) *Statik and Dynamik der Schalen*. Berlin: Springer Verlag.

Kraus H (1967) *Thin Elastic Shells*. New York: Wiley.

Leissa AW (1973) *Vibrations of Shells*, NASA SP-288. Washington, DC: US Government Printing Office.

Love AEH (1944) *A Treatise on the Mathematical Theory of Elasticity*. New York: Dover.

Novozhilov VV (1964) *The Theory of Thin Elastic Shells*. Groningen, The Netherlands: P. Noordhoff.

Soedel W (1993) *Vibrations of Shells and Plates*, 2nd edn. New York: Marcel Dekker.

Vlasov VZ (1964) *General Theory of Shells and its Applications in Engineering*. NASA TTF-99. Washington, DC: US Government Printing Office.

SHIP VIBRATIONS

W S Vorus, University of New Orleans, New Orleans, LA, USA

Copyright © 2001 Academic Press

doi:10.1006/rwvb.2001.0208

General Background

The overall dynamic response of a ship can be conveniently separated into two parts: one is the motion as a rigid body in response to a seaway; the other is the

elastic or flexural response of the hull or other structure to external or internal forces. Rigid-body motion is considered under the general subject of sea keeping and is not traditionally referred to as vibration, although the theoretical basis is of course the same.

Flexural vibration can be excited in the form of vertical and horizontal bending, torsion, and axial modes of the elastic structure of the hull girder, as well as in the form of local vibration of substructures and components. Vibration excited by the propellers has been a particularly troublesome problem, and is the principal subject to be addressed in this presentation.

A vibrating ship can be conceptually characterized as a one-dimensional beam, representing the basic hull girder, with attached sprung substructures, distributed stiffness and damping, and acted upon by distributed excitation. This characterization is depicted in **Figure 1** below.

A good platform for presenting the basic knowledge of ship vibration is the linear but general solution of the **Figure 1** model for periodic excitation.

The periodic vibratory displacement distribution $w(x, t)$ can be written as a modal series. First, for general periodic excitation, $f(x, t)$ is the Fourier series:

$$f(x,t) = \sum_{m=1}^{\infty} F_m(x) \cos(m\omega t - \beta_m) \qquad [1]$$

where ω is the fundamental frequency of the excitation and m denotes its mth harmonic, so that $m\omega$ is the mth harmonic frequency.

The vibratory displacement, $w(x, t)$, then has the general form:

$$w(x,t) = \sum_{m=1}^{\infty}\sum_{n=1}^{\infty} W_{nm}(x) \cos(m\omega t - \alpha_{nm} - \beta_m) \qquad [2]$$

with the amplitudes and phase angles:

$$W_{mn}(x) = \frac{F_{nm}/K_n}{\sqrt{\left[1-(m\omega/\omega_n)^2\right]^2 + \left[2\zeta_n(m\omega/\omega_n)^2\right]}}\psi_n(x) \qquad [3]$$

$$\alpha_{nm} = \tan^{-1}\left[\frac{2\zeta_n}{1-(m\omega/\omega_n)^2}\right] \qquad [4]$$

In eqns [3] and [4], ω_n and $\psi_n(x)$ are the nth-mode natural frequency and mode shape representing the solution to the eigenvalue problem corresponding to the undamped, unexcited system.

F_{nm} is the nth-mode, mth-harmonic modal force:

$$F_{nm} = \int_{x=0}^{L} F_m(x)\psi_n(x)\,dx \qquad [5]$$

with $F_m(x)$ from eqn [2].

The formulas [1]–[4] apply generally for any arbitrary mathematical model. The form of eqn [5], however, applies strictly to the beam model, **Figure 1**, by the integral over the beam length. More generally, the modal force is the dot-product of the excitation force vector and the mode shape vector, both of which can be multidimensional and either continuous or discrete functions of position. Any of the possible forms serve the illustrative purposes of interest here.

Likewise, in terms of the one-dimensional beam characteristics, the modal mass is:

$$M_n \equiv \int_{x=0}^{L} \mu(x)\psi_n^2(x)\,dx \qquad [6]$$

where the extension to arbitrary model dimension is considered obvious. The modal stiffness appearing directly in eqn [3] is then by:

$$K_n = \omega_n^2 M_n \qquad [7]$$

The additional requirement for the form of eqns [3] and [4] is that the damping distribution $v(x)$ indicated on **Figure 1** be proportional to either the distributions of model mass, $\mu(x)$, or stiffness, $EI(x)$; this assures that the implied orthogonality holds with the damping as well as with the mass and stiffness distributions. Then in eqns [3] and [4]:

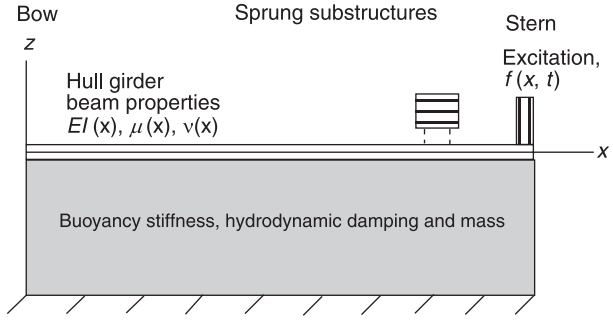


Figure 1 Ship vibration conceptual model: $EI(x)$, $\mu(x)$, $v(x)$, $f(x, t)$ distributed stiffness, mass, damping, and excitation in $x = 0 - L$.

$$\zeta_n \equiv \frac{v_n}{2M_n\omega_n} \text{ with } v_n = C_{1n}K_n + C_{2n}M_n \qquad [8]$$

with C_{1n} and C_{2n} being the required constants of proportionality, which can vary with modal order.

The form of eqns [3]–[8] is very useful for discussing, sorting out, and understanding the peculiarities of any periodic vibration, but specifically ship vibration here. The vibration displacement distribution, no matter how complex, if linear, is theoretically expressible in terms of the responses of an infinite set of single mass oscillators, by eqns [2]–[4]. The amplitudes of the oscillators are just the amplitudes of the natural mode shapes, which superimpose to produce the complete displacement distribution. Thus, the key to understanding and treating almost any vibration is the one-degree-of-freedom oscillator. All possibilities for solving or preventing a vibration problem are readily discerned from the above simple formulation. These possibilities are, in the usual order of effectiveness in dealing with ships:

1. Reduce modal excitation force amplitudes, F_{nm}, in modes where the excitation harmonic frequency is in the vicinity of the modal natural frequency. This reduces $w(x, t)$ by reducing the numerator of [3]. F_{nm} can be reduced by either reducing F_m in eqn [1] directly, or by mismatching with the modes shape distributions to result in cancellation in the integral [5]. The degree of excitability of a mode is judged by the degree to which the mode shape mismatches the force distribution in this way. Direct reduction of F_m is usually the more fruitful approach to reducing excitation, which is addressed further along.
2. Avoid resonant vibration, $\omega_n = m\omega$, in modes where F_{nm} is significant. With $\omega_n/m\omega$ in eqn [3] near unity, large amplitude in a mode with nonzero F_{nm} is opposed only by damping, which is typically quite light in structural systems. The usual approach to avoiding resonance in a mode is by changing K_n, by eqn [7]. Change in the fundamental frequency, ω, usually by change of an RPM, is also sometimes possible. If resonance is to be avoided by altering stiffness, K_n should be increased, vs decreased, because of the associated reduction to be achieved in the numerator of eqn [3].
3. Increase damping. ζ_n in eqn [3] is typically small for metal structural systems, and can be influential only very near resonances where the first term in the denominator of eqn [3] is even smaller. But if resonances can be correctly avoided, damping is a relatively noninfluential factor in the equation (which contradicts the anecdotal knowledge of most laymen on the subject). The damping contribution is also one that is hard to change much in design or postdesign corrective efforts.
4. Exploit modal cancellations. The considerations cited to this point have addressed the components of eqn [3] from a term-by-term perspective. In the lower region of the natural frequency spectrum of a complex structure such as a ship, the ω_ns are well spread apart. In this region, with small damping, the modal series, eqn [2], will be dominated by the mode with natural frequency closest to the exciting frequency. In this case, judgments can often be made on the basis of simple one-degree-of-freedom considerations by eqns [3] and [4]. On the other hand, in the higher modal spectrum of complex structures, tightly clustered modes, with small differences in natural frequency, can be encountered. Here, multiple terms participate to the same order in the modal expansion, at the harmonic exciting frequency $m\omega$ in their midst. But in view of the phase (eqn [4]) of the series terms in eqn [2], those significant modes above the exciting frequency will be out-of-phase with those below. This results in cancellation of the terms and a net vibration potentially less than that of any of the single contributing modal components. This is particularly true at locations in the system removed from the immediate region of application of the system excitation. Mode cancellation always occurs to some degree in all but very simple multi-degree-of-freedom systems, but is difficult to exploit in structural design or vibration problem rectification.

The background is now complete to review some of the more important facts and characteristics that distinguish the technology of ship vibration as a unique discipline.

Ship Vibration Excitation

Ship vibration excitation can and does occur via a myriad of sources. This includes sea waves. Sea waves excite the ship primarily at relatively low frequency, well below its flexural natural frequencies, but often in the vicinity of its rigid-body modes; these lowest natural modes correspond to the mode shapes of heave and pitch in the vertical plane. Ship vibration excitation by sea waves, which would also include transient slamming vibration involving the lower flexural modes, is probably the naval architects' most important problem, as it establishes the structural integrity of a vessel design. However, as addressed under General Background, this aspect is normally categorized as 'seakeeping', which falls outside of the traditional definition of 'ship vibration'. In the traditional view, ship vibration is flexural vibration

occurring at frequencies well above normal sea-wave encounter frequencies.

Ship vibration, in the more traditional sense, is excited, for example, by internal rotating machinery, such as pumps, compressors, engines, etc. But generally, little exists that distinguishes those shipboard applications from their land-based equivalents. In these cases the vibration is typically caused by rotating mass unbalance, for which diagnosis, treatment, and control is well established. The installation of large rotating units, such as main propulsion diesel engines, is, however, made more problematic by the fact that the shipboard mounting base is inherently less stiff than available with land-based power plants. The typical 6-cylinder low-speed marine diesel engine produces a vertical moment at twice engine RPM which can lie in the vicinity of the lower hull girder flexural natural frequencies. This potential vibration problem is usually avoided or treated by harmonic balancers installed by the engine manufacturer on the engine crank to reduce the exciting moments.

The primary distinguishing feature of ship vibration, and the aspect that makes it indeed unique, is propeller excitation. It is fact that in the majority of serious ship vibration problems, (over 80 percent), the vibration has been propeller excited. This is indeed a case of the 'tail wagging the dog'.

The fundamental exciting frequency, ω, of a propeller with N identical, symmetrically spaced blades, rotating with specified RPM, is:

$$\omega = N \times \mathrm{RPM}\left(\frac{2\pi}{60}\right) \qquad [9]$$

This fundamental is called 'blade rate' frequency. The assumption is that the propeller and shafting system are dynamically mass-balanced. Otherwise, the fundamental frequency will be 'shaft rate'. In that case the full spectrum will be composed of all multiples of the shaft RPM fundamental. But only those higher multiples corresponding to blade rate and its harmonics will be significant.

Shaft-rate vibration problems are not the usual, and are more straightforward to understand and resolve than those of propeller blade rate origin. Propeller blade rate excitation is hydrodynamically-based and involves complexities that are strictly unique to ships. For these reasons the focus here will be on the blade rate excitation components and consequences. The propeller excitation frequency spectrum of the Fourier series [1] is then established as $m\omega; m = 1, 2, 3, \ldots$, with ω by [9].

The form of [1] is specifically for a one-dimensional, one component force distribution acting at the stern-end of the ship hull beam, where the propeller is located. This is of course again an idealization to support conceptual understanding. The excitation is in reality a fully distributed unsteady vector composed of point force components acting in the propeller hub and a pressure distribution over hull surfaces in close proximity. The modal force, [5], would, in general, be the integral of the dot-product of the force and mode shape vectors over the affected stern regions of the hull, as might be conceived in a comprehensive numerical ship vibration model.

Ship Hull Wake Considerations

The forward moving hull of the ship leaves a rotational wake behind it. This wake manifests to the propeller as a 'circumferentially non-uniform' velocity distribution at radii with in the propeller blade tip circle ('propeller disc'). It is safe to say that if this wake inflow to the propeller was not circumferentially non-uniform, then propeller blade rate vibration of ships would not be, or would never have been, a problem.

It would appear to be physically clear that, if ships had perfectly uniform wakes, there would be no unsteady forces developed on the rotating propeller blades, and therefore no vibration excitation transmitted to the shafting system and hull directly from the propeller. This direct force, actually composed of both three-component force and moment vectors in the hub of the propeller, is called the 'propeller bearing' force.

The other component of the propeller excitation force system is called the 'hull surface' force, as produced by the rotating propeller blades sweeping by the hull surfaces bounding the 'stern aperture'. It is intuitively obvious that the bearing force set would be zero for a perfectly uniform wake inflow. It is not so intuitively obvious, yet true, that the hull surface force would be negligibly small and inconsequential as an exciter of ship vibration for circumferentially uniform propeller inflow. Simple fanning action of the hull by the propeller blades is not of consequence.

Locating the ship propeller in the nonuniform flow behind the ship, rather than in uniform flow in front, is superior in all respects but one. The efficiency of the propeller in the reduced average wake velocity is higher than in the higher inflow corresponding to vessel speed; the propeller can be tucked into the aperture under the stern-counter for protection; the propeller is not as subject to cyclic immersion due to vessel pitch in a seaway, as the point of rotation in pitch is near the stern, etc. Vibration does not get highest priority on the list of critical performance criteria, particularly for commercial ships, so propellers

are placed at the ship stern in the non-uniform wake of the hull.

The entire propeller blade-rate ship vibration problem is due to the circumferentially nonuniform wake in producing periodically fluctuating pressure on the propeller blades as they rotate. At set angular velocity, the velocity of the rotating blades is highest in the blade tips. Consequently, by Bernoulli's equation, the pressure is lowest there. The pressure on the blade back (forward side) is lower than on the blade face (after side). This pressure difference across the cambered blade is by design and its mean is necessary for the production of propulsive thrust. But as the blades rotate through the nonuniform wake, fluctuations in blade pressure occur with blade position. With the steadily rotating propeller, the blade back pressure is lowest as the blades traverse the high wake (low velocity) regions of the wake field, and fluctuates periodically on each blade with each propeller revolution. For typical commercial ships, the high wake regions are at the top and bottom of the propeller disc. The fluctuating blade pressure distributions integrate and sum to produce the six propeller bearing force components, all at blade rate frequency and its harmonics [1]. The blade rate (fundamental) component of 'alternating thrust' was responsible, along with resonant conditions, for a number of serious main propulsion machinery longitudinal vibration problems as the power of steam turbine plants began to increase in the 1950s and 1960s. However, it was in the 1970s that the upward evolution of ship size, speed, and power exploded propeller-induced vibration with new ships to critical levels. This was initially not very well understood technically by the international naval architecture community.

Propeller Blade Cavitation

In the mid-1970s the European model basins, in Holland and Scandinavia primarily, achieved the revelation that unsteady propeller blade, intermittent cavitation, triggered by wake nonuniformity, was the main culprit in all ship vibration trouble.

Cavitation is essentially the vaporization of water on the propeller blades due to low pressure; it is equivalent to boiling, but from low pressure rather than high temperature. As the blade backpressure drops into the vicinity of water vapor pressure (less than 1 psia), the water locally in contact with the blade backflashes to steam. Some cavitation in the blade tip regions is usually unavoidable with ship propellers and is not particularly deleterious to propulsive performance. However, its intermittency of growth and unstable collapse on the blade backs as the blades rotate through the high wake gradients can radiate very large pressure into the field (**Figure 2**). There is no dramatic effect on the propeller bearing forces, as the blades still lift effectively with the low pressure vapor on their backs, but the hull surface forces can be amplified by an order of magnitude over the noncavitating level.

The excitation series, (eqn [1]), also converges much more slowly with the involvement of intermittent cavitation. Twice and three-times blade rate frequency is clearly seen in vibration records. As a result, cavitation-induced vibration can be accompanied by extreme noise in the afterspaces of a ship.

Great strides were made in the 1970s in solving the problem of high-powered ship vibration. There was a concerted effort worldwide by laboratories, universities, shipbuilders, classification societies, owners, and others in developing the technology for controlling propeller-induced ship vibration, largely by control of propeller unsteady cavitation.

It should be stated here that the above pertains to commercial ships and perhaps some naval auxiliaries. With combatants, the problem is different. The propulsion system design is driven by quietness. Propeller cavitation is still the driver, but the measures taken to

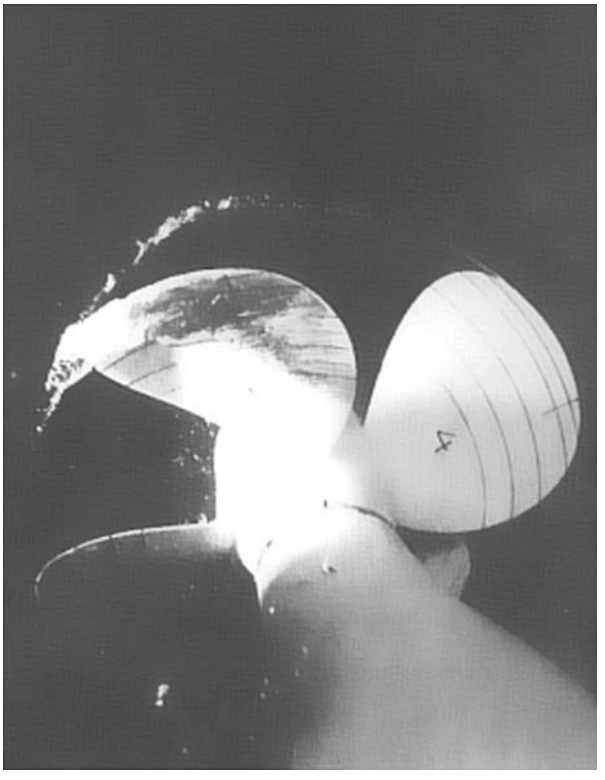


Figure 2 Propeller blade unsteady cavitation. Reprinted from *Principles of Naval Architecture* (1988), vol. 3, with the permission of the Society of Naval Architects and Marine Engineers, 601 Pavonia Ave, Jersey City, NJ 07306, USA.

achieve low noise signature, still mainly wake-smoothing, results in vessels that do not have vibration problems in the sense addressed here. For smaller, high-speed vessels, propeller-induced vibration is also not problematic as a rule. Here, wakes are naturally more uniform both because of the relative thinness of the hull viscous boundary layer, and the fact that this wake defect is swept laterally away from the propeller by the sloping sides of the typical V-shaped planing hull. Furthermore, high-speed propeller blades cavitate, or 'ventilate', more continuously around the full revolution cycle and therefore do not tend to exhibit the violent intermittency of cavity growth and collapse with in the revolution.

Propeller Blade Tip Clearance

As a final consideration with regard to propeller excitation, a great deal has been made over the years of maintaining minimum clearance between the propeller blade tips and the hull surfaces in proximity; vertical clearance of 20% of the propeller diameter is the general rule. This is also a wake-uniformity issue. The closer the blade tips to the hull surface overhead, the higher the wake gradient that the blade tips traverse. Again, unsteady blade pressure variations are the principal issue. Hull surface pressure due to diffraction of the propeller flow is a very weakly varying function of the separation distance, and not sensitive to tip clearance. Diffraction is a near-field hydrodynamics process and does not vary as the inverse of clearance, as is the case with far-field distances.

The fact that the hull wake in-flow to the propeller is the most important aspect of the problem and not the propeller itself has exacerbated the difficulty in dealing satisfactorily with propeller-induced ship vibration. The wake character is dictated by the hull lines, and the hull lines are probably the most difficult feature of the ship to alter significantly when, all too often, vibration problems have been discovered post-construction.

Resonance Effects

The attention to this point has been on the numerator of eqn [3]. We now turn to the denominator.

The full power shaft RPM of ships varies between about 80 and 150, depending on size, speed, and installed power. Propeller blade number N is almost universally either 4 or 5. This places the fundamental exciting frequency between approximately 5^+ and 12^+ Hz. Even the lower of these two limits generally lies above the frequency at which the ship hull responds as a beam; beam response, vertically, is considered to occur up to about the fifth flexural mode, which will typically lie in the range just below 5 Hz. Even in the lower flexural modes below about the fifth mode, where the ship may behave more or less one-dimensionally as a beam, the bouyancy spring implied on the **Figure 1** conceptual model is irrelevant; the beam vibrates in any of the flexural modes as free-free, statically unsupported, effectively. At the frequency level of any of the flexural beam modes, the water-added mass is significant, but is simplified physically by the fact that the flexural natural frequencies are all above the level of gravity wave generation and their outward radiation at the water surface. The water surface acts as a simple relief surface of zero transverse velocity.

As the modal order goes up, the mode shapes become increasingly more complex; one additional node is, in fact, added somewhere in the vibrating system for each successively higher mode. Above the fourth or fifth system mode, substructures have broken away from the hull girder, and are vibrating in a coupled response to the hull girder base excitation. It is at this point that modal clusters begin to develop, accompanied by mode cancellation, as discussed in the general background section, above. For a high-order mode with many nodes, adding an additional node is associated with smaller and smaller changes in the corresponding added natural frequency as the modal order advances. Because of this, resonance, where $m\omega/\omega_n = 1$ and the denominator of the nth modal component amplitude in eqn [3] is minimum, loses some significance. All the modes in the cluster are contributing at $m\omega$, leading to the canceling contributions described above. Although the formulas [1]–[8] should still hold, the hull structural system vibration response has become exceedingly complex in the range of full-power blade rate frequency and its multiples.

Damping

Damping of ship vibration, represented by ζ_n in eqn [3], is the least physically understood of the principal system parameters of mass, stiffness, damping, and excitation. In eqn [8], v_n is a small quantity composed of a myriad of even smaller components that are not rationally quantifiable. Furthermore, the modal mass for ships is very large relative to the scale of v_n. So, in eqn [8], ζ_n is viewed to be generally on the order of 1–2%. But v_n is still a large number, involving small dissipative effects integrating over large regions. Useful percentage changes in v_n would therefore be very difficult to achieve with a mind toward incorporating increased damping to prevent or eliminate ship vibration trouble.

There is some evidence that damping increases with modal order, via C_{1n} and C_{2n} in eqn [8]. This being the case, the size of the cluster-set participating in the sum at eqn [2] is then expanded because of the reduction in the amplitudes of the modes closest to the resonance, by eqn [3]. The result is even stronger mode cancellation.

Summary

The main consequence of the damping uncertainty and the mode cancellation effects that prevail in blade rate frequency excitation of ships is in the unreliable predictability of ship vibration response. Mode cancellation prediction is particularly prone to inaccuracy. It is the often encountered problem that maintaining accuracy in the net sums of large distributions of different signs (eqn [2]) requires much higher accuracy in predicting the distributions themselves.

A serious vibration problem is a 0.2–0.3 mm displacement amplitude at a blade rate frequency of, say, 10 Hz. The experience of the 1970s showed that, even with the most detailed structural dynamic math-models, this amplitude could not be predicted reliably within order of magnitude accuracy, and predictions of its distribution throughout the vessel were typically even worse. It could not be predicted to a useful level of accuracy for support of engineering/design judgments of either design adequacy or resolution alternatives.

The technology that proved effective with the prevailing problem settled as one that focused on minimizing the numerator of eqn [3], and not trying to maximize the denominator. The minimization was purely hydrodynamic, in assessing, through both experimental and analytical/numerical analysis, the technology necessary to minimize the propeller blade rate excitation force harmonic spectrum, F_m, in eqn [1].

The technology that emerged was measurement of pressure on modeled overhead surfaces in the large cavitation tunnels of the world, supported by hydrodynamic computations. Criteria was established for judging when the pressure levels predicted likely implied a ship vibration problem, or not.

With the lull in new ship design and construction worldwide, the ship vibration front was relatively quiet in 1990s. But with the need for new, more advanced ships approaching, the problem will be back. The ship design/shipbuilding community will be much better-equipped with understanding and technology for dealing with the problem the next time around than they were the last.

Nomenclature

C_{1n}, C_{2n}	constants of proportionality
$EI(x)$	stiffness
F	force
$w(x, t)$	vibratory displacement
$v(x)$	damping distribution
$\mu(x)$	model mass
ζ	damping
ω	frequency

See also: **Damping, active**; **Damping models**; **Eigenvalue analysis**; **Modal analysis, experimental**, Basic principles; **Resonance and antiresonance**.

Further Reading

Beck RF *et al*. (1989) *Motions in Waves*, ch. VIII, vol. III. *Principles of Naval Architecture*. Jersey City, NJ: SNAME.

Loeser HT (1999) *Fundamentals of Ship Acoustics*. Jersey City, NJ: SNAME.

Vorus WS (1988) *Vibration*, ch. VII, vol. II. *Principles of Naval Architecture*. Jersey City, NJ: SNAME.

SHOCK

J Marcondes, San Jose University, San Jose, CA, USA

Copyright © 2001 Academic Press

doi:10.1006/rwvb.2001.0171

This article covers mechanical shocks as they apply in product protection within a packaging system. Please refer to **Vibration Transmission** for more details on packaging design and testing. All products in distribution receive impacts, and most products are not designed to sustain the rigors of the distribution environment. Packaging is used to mitigate these impact forces and avoid damage. In **Figure 1**, notice that the use environment has a lower stress level than the transport environment. In other words, it is much more likely that a product, e.g., a television set, will

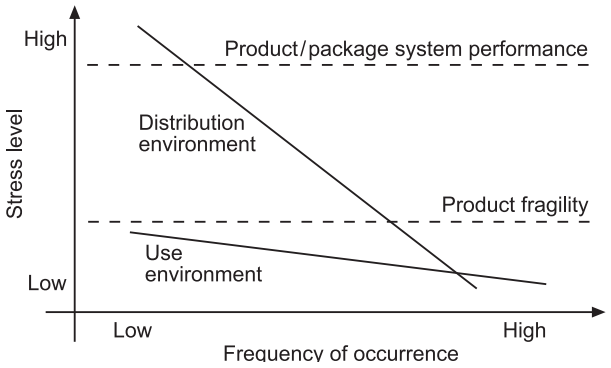


Figure 1 Distribution environment and use environment vs product and package.

be dropped from 0.5 m during distribution (now inside a package) than it will when in use (outside the package, at a user's home). Therefore, products are designed to sustain only those impacts that will most likely occur during use rather than during transport. For transport, the package can add the required ruggedness to the system to avoid damage.

Measuring Shock in the Distribution Environment

Acceleration vs time measurements are easily obtained with the use of portable, self-contained recording devices, composed of a triaxial accelerometer and memory and powered by a battery. Impact data are converted into 'equivalent free fall'. This is done to simplify the design and the testing procedure to assess package performance. Almost all impacts may be converted into an equivalent free-fall drop height. **Figure 2** shows the types of shock data typically recorded in distribution environments. These are called 'impact signatures'. Type (i), 'free fall drops', are identified by the typical intensity of 1g (acceleration of gravity) just before impact. Note that the other types of impacts do not have this characteristic. Type (ii), 'horizontal impact', shows some acceleration activity just before impact, but at a level hard to distinguish – that is because the package is sliding to the floor or ground and hits something like a wall or another stationary package. Type (iii), 'kicks', are characterized by a zero, flat line before impact – nothing is happening to the package and suddenly there is an impact – in this case, the package was stationary and something hit it. The last type, (iv) 'throw-hit-fall', is characterized by three shocks with 1g in between – this first shock is the impulse caused by a throw, usually of long duration and low intensity; the second impact is a hit on a wall, for example, and the third is the impact with the ground. These four types are not the only possible cases, but they are the most common ones. Any combination happens all the time.

These measurements may be done with a dummy package, as shown in **Figure 3**. This is a typical configuration for impact monitoring. The foam shown in the picture is used to protect the recorder and of course has an important role in the shape of the shock pulse recorded and the intensity of the impact. However, the essential information required for calculating drop height does not depend on the type of package. What accelerometers measure is the impact received by the unit in a drop, which is then converted into velocity or time of fall – neither depends on the type of package or the thickness of the foam that protects the recording unit.

Typical Results of Shock Measurements

Some results of measurements taken inside packages, like the one shown in **Figure 3**, sent by express couriers a number of times along a certain route, were used to construct the graph shown in **Figure 4**. In this figure, note that high drop heights have a low probability of occurrence, however, impacts from up to 140 cm high are normal occurrences in parcel shipments in the USA.

Calculating equivalent drop height using velocity change The equivalent drop height is obtained by measuring the impact acceleration vs time history of an impact. Two parameters may be used independently to determine the height from which the package fell, or its equivalent (drop height):

1. Velocity change of the shock pulse generated by the impact; the velocity change is the sum, in absolute values, of the impact velocity and the rebound velocity;
2. Length of time the package was under gravitational acceleration (1g)

The conversion is quite simple. The velocity change of the shock pulse (acceleration vs time) is calculated by numerically integrating the acceleration history given by:

$$\Delta v = \int a(t)\,\mathrm{d}t \qquad [1]$$

The resultant velocity change of a triaxial measurement is:

$$\Delta v_{\mathrm{R}} = \left(\Delta v_x + \Delta v_y + \Delta v_z\right)^{0.5} \qquad [2]$$

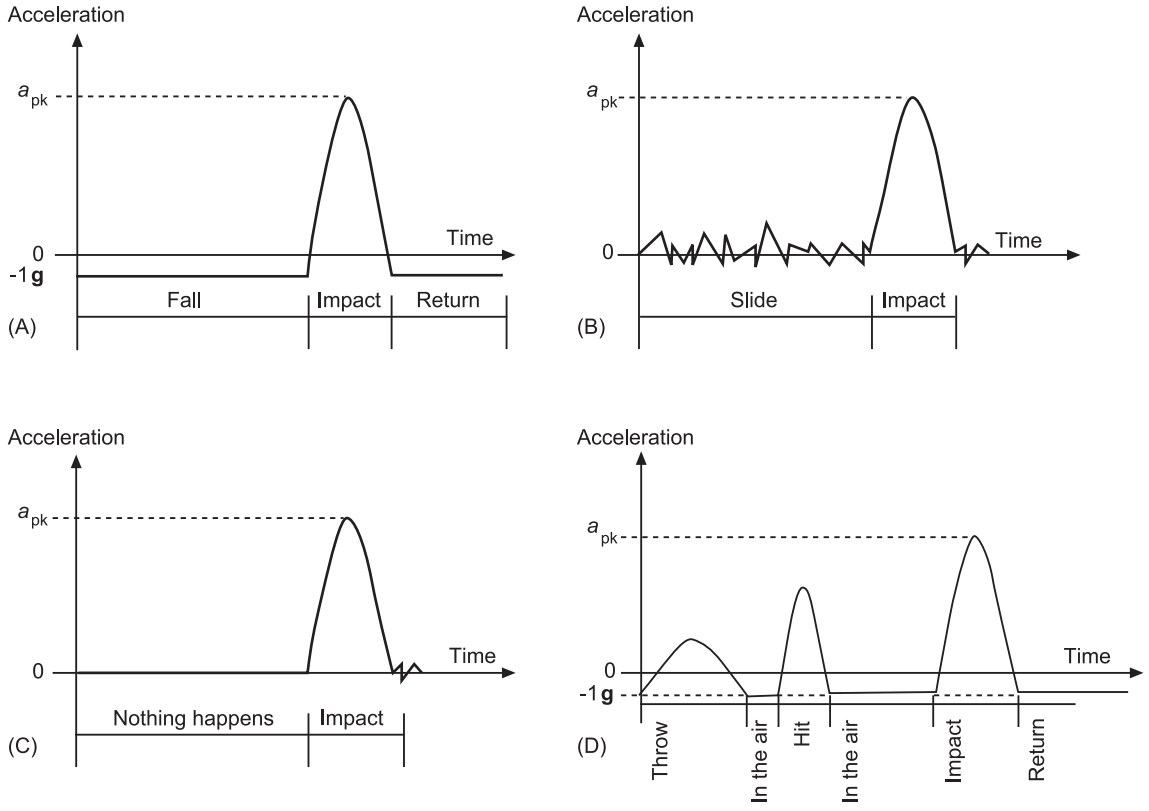


Figure 2 Typical impact signatures. (A) Free fall; (B) horizontal impact; (C) kick; (D) throw-hit-fall.

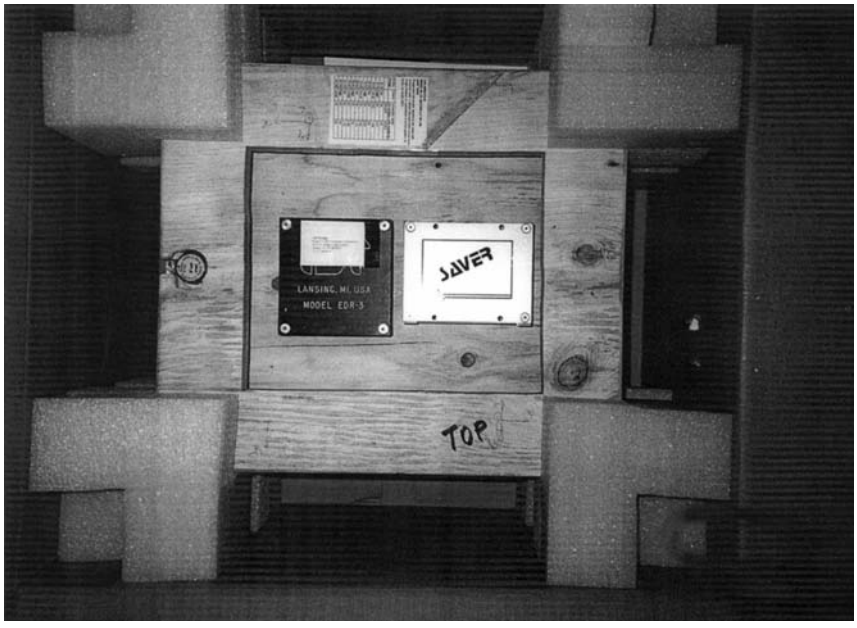


Figure 3 Monitoring the distribution environment with self-contained data acquisition instrumentation: (A) recording unit; (B) typical package configuration; (C) dummy package with the recording unit installed.

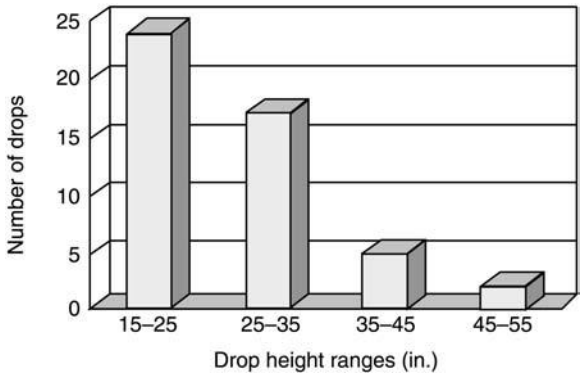


Figure 4 Drop height (equivalent), UPS + FedEx, 2nd day air, 20 lb package, San Diego–Chicago route.

where x, y, and z are the orthogonal directions of the triaxial measurements. The equivalent drop height is then given by:

$$h_{eq} = [\Delta v_R/(1+e)]^2 \Big/ (2g) \qquad [3]$$

where the values for the coefficient of restitution e are obtained by calibrating the packaging system prior to shipment. In most conditions, it varies between 0.25 and 0.75. The coefficient of restitution e is defined as the ratio between rebound velocity and impact velocity, in absolute values. The diagram in **Figure 5** shows the individual axes and a typical result of an impact, in three axes. The orientation of the axes is also used to determine the direction of the impact. A positive intensity in the x-axis indicates that the impact occurred in that direction whereas a negative intensity indicates the opposite direction. Most results show components in all three directions, which indicates that most impacts are not exactly flat on the package surfaces but on the edges or corners.

Calculating equivalent drop height using duration of fall The equivalent free-fall drop height may be estimated by measuring the time the package takes in free fall. In **Figure 2**, observe that the free-fall type (i) shows the acceleration at 1**g** level during the entire duration of the fall. The free-fall drop height may be calculated by:

$$h_{eq} = gt^2/2 \qquad [4]$$

where t is the time taken for the package to fall to the ground (friction with air is insignificant). Most recording units use these two techniques to estimate the equivalent free-fall drop. When the impact is a free fall it is easier to apply eqn [4]; however, as most drops are not free-fall, eqn [3] is used more frequently.

The impacts produced in the distribution environment need to be known by the packaging designer. The information will be essential in designing protective packages and in designing performance-testing protocol. When measurement is not possible, the designer may use commonly accepted values, or standards, which usually depend on the weight of the package.

Assessing Product Shock Fragility

A procedure recommended by ASTM D–3332 may be used to determine the shock fragility of the product. This procedure requires that an item of the product be tested on its six faces, using two series of tests, using a tester capable of producing shock pulses of controllable duration and intensity (programmable shock

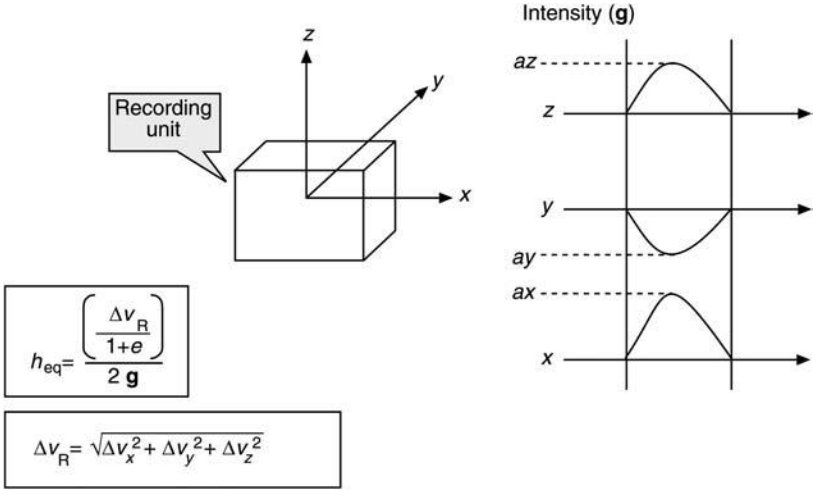


Figure 5 Impact measurement in the distribution environment.

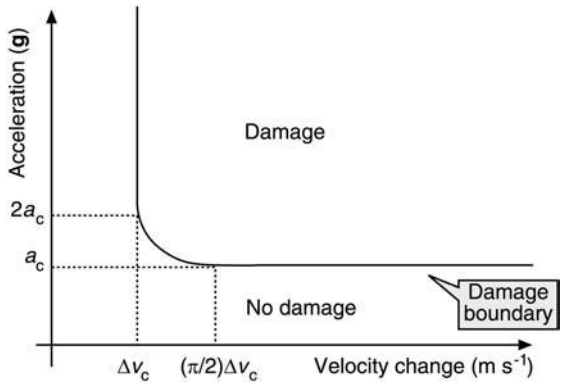


Figure 6 Product shock fragility.

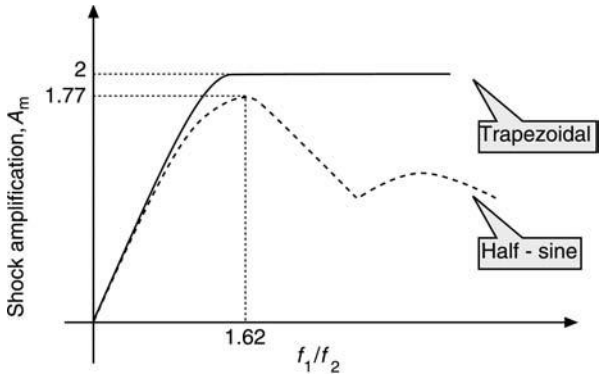


Figure 7 Shock transmission with no damping.

machine). The first series is to determine the critical velocity change of the product, Δv_c, and the second series is used to determine the critical acceleration of the product, a_c. These two parameters are then used to plot a damage boundary curve for the product, one for each product face. **Figure 6** shows a damage boundary curve for a product.

Damage Boundary Curve for a Product

The damage boundary curve indicates the level and duration of impacts, which can cause product damage. These are impacts applied to the exterior of the product, in the same fashion a package cushion would do. It may not be the same impact intensity that is received by components of the product. The method utilized to determine the critical acceleration (a_c) employs the application of a trapezoidal shock pulse. When a spring–mass system receives an impact of long duration and almost constant intensity (trapezoidal shock), the shock transmission (intensity) to the various product components is modified by the factor *Am*, which is plotted in **Figure 7**. Note that the value of *Am* depends on the ratio ω_{Rc}/ω_{Rpc}, which is the ratio between the natural frequencies of the component being considered and the frequency of the shock applied to the product.

In **Figure 8**, a model of a spring-mass system is shown to identify product and package components used to define ω_1 (m_1 and k_1) and ω_2 (m_2 and k_2).

Most package cushions impose a half-sine shock on a product during an impact. Notice in **Figure 7** that the half-sine shock usually transmits to the components of the product an impact of less intensity than the trapezoidal shock. In many instances, this procedure for testing product fragility is conservative, and this may be taken into account by designers as a safety factor.

Shock Absorption Properties of Materials

The shock absorption characteristics of packaging materials are obtained by subjecting samples of the material to a batch of impact tests. The ASTM D–1596 of D–4168 protocols may be used to obtain this information. The results of this test are often presented in the form of cushion curves. **Figure 9** shows typical shapes of the shock pulses as the weight of a product increases, all else being equal. **Figure 10**

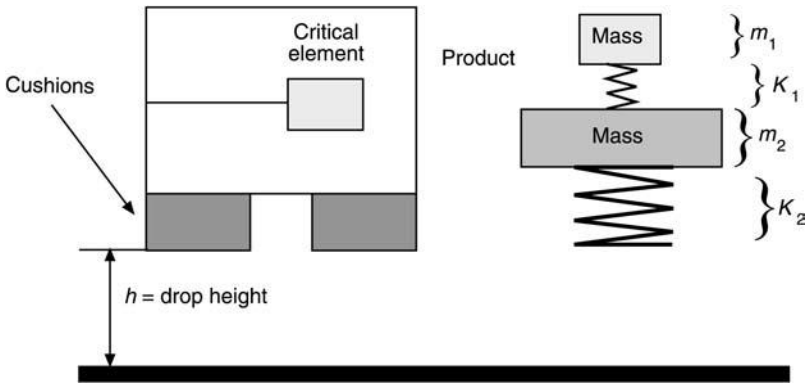


Figure 8 Physical model product package.

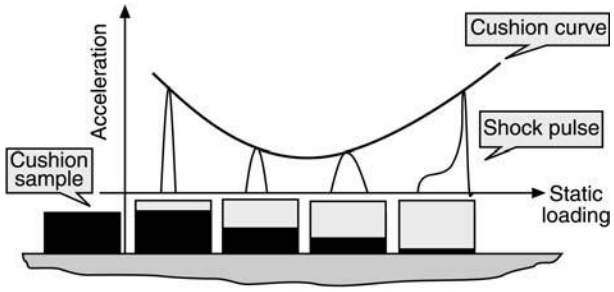


Figure 9 Plotting a cushion curve.

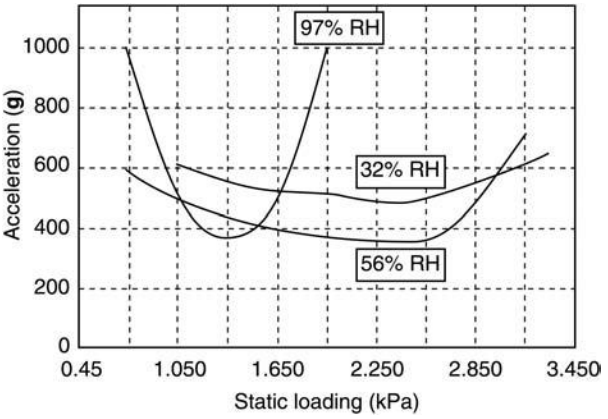


Figure 10 Cushion curves – effect of humidity, BC-flute corrugated, DH = 120 cm, first impact, 30°C. RH, relative humidity.

shows cushion curves obtained by testing double wall corrugated fiberboard (BC flute) at different conditions.

During impact, the most important property of a material is its ability to deflect. Note in **Figure 11** the relationship between cushion deflection and acceleration during a product free fall. The dynamic deflection, d_m varies according to the material being utilized. The goal in package design is to allow d_m to be as large as possible, as long as the material does not bottom out or, depending on requirements, does not crush beyond ability to recover reasonably. Most packages receive multiple impacts and the condition of the protective cushion is important; also, from the product presentation point of view, it is not a good idea to present a customer with a package that has crushed components; although the crushing occurred to protect the product, consumers do not always know that.

Interpretation of a Shock Cushion Curve

A shock cushion curve is a tool used by designers to choose a proper cushion. The curve shows peak acceleration, a_{pk} vs static loading, SL. The peak acceleration is the maximum level of shock during the impact. The static loading is the ratio between the weight of the product, $m_p g$, and the bearing area of the cushioning material, as long as the block of cushion is a rectangular block. Trapezoidal blocks and other forms that are different from rectangular blocks, often used in design, are adjusted to their equivalent rectangular block dimensions. **Figure 12** shows a cushion curve broken down into three

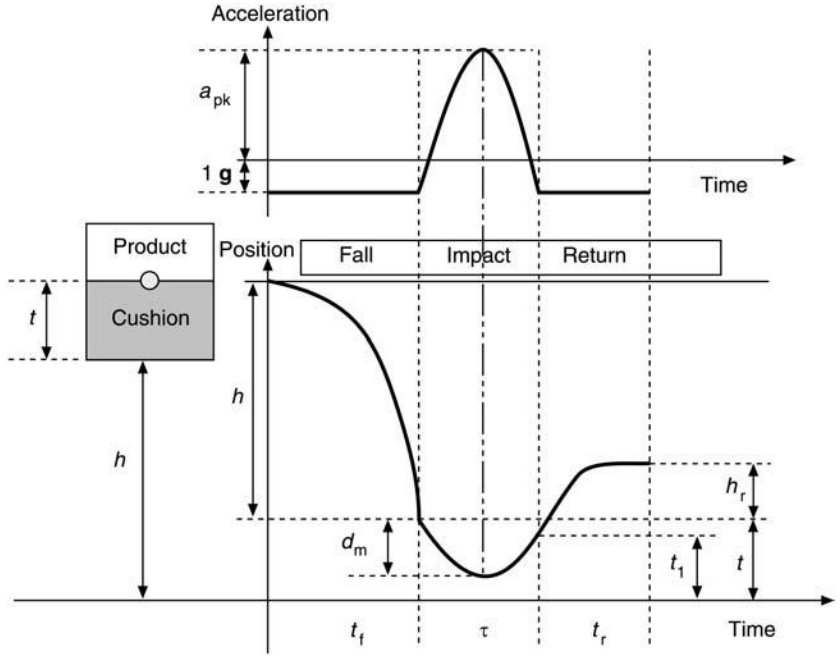


Figure 11 Impact free fall and acceleration.

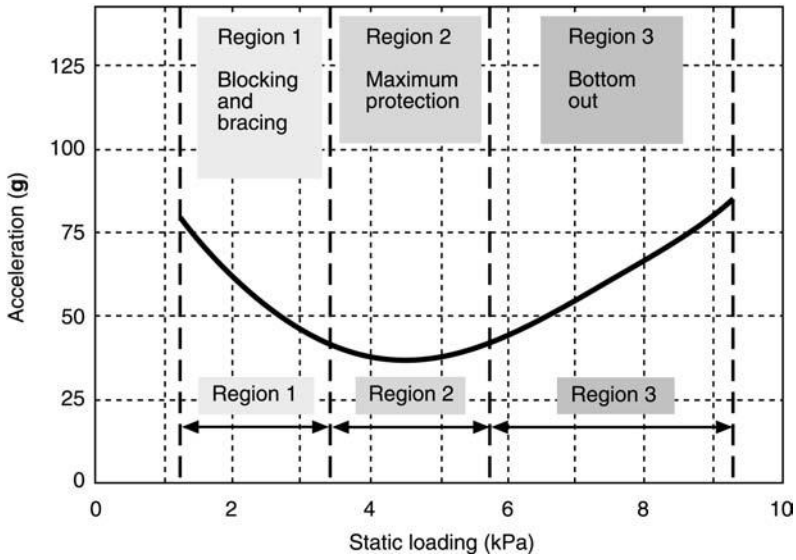


Figure 12 Typical cushion curve.

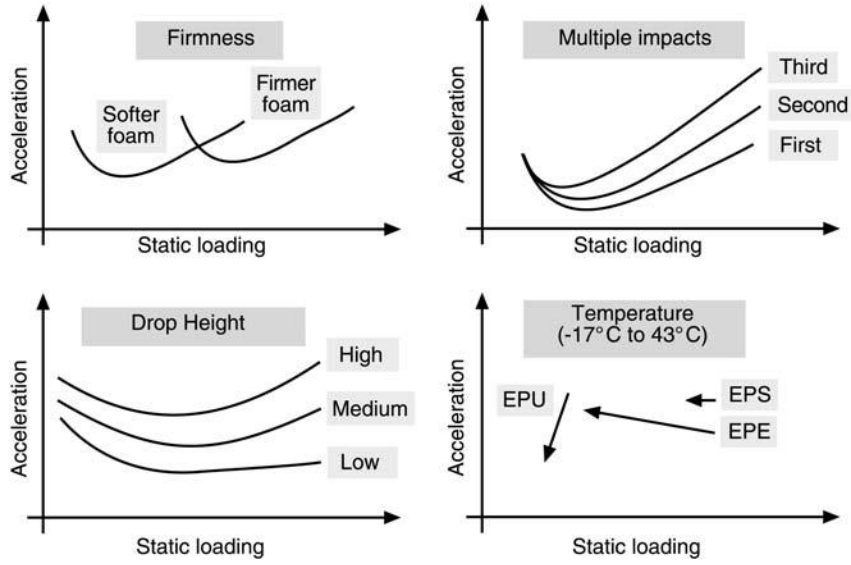


Figure 13 Effects of various parameters on cushion curves. EPE, expanded polyethylene; EPS, expanded polystyrene; EPU, expanded polyurethane.

regions. The goal is to pick a static loading that provides the best cushioning – region 2 in **Figure 12**. Factors that influence peak acceleration are shown in generic cushion curves presented in **Figure 13**. In this figure, temperature comparisons were made between expanded polyurethane, polystyrene, and polyethylene. The arrows indicate the direction that the lowest point on the curve moves in when the temperature is increased.

For applications of cushion curves in packaging design, see **Packaging**.

Nomenclature

a_c	product critical acceleration or shock fragility
a_{pk}	peak acceleration
a_x	acceleration in the x orientation

a_y	acceleration in the y orientation
a_z	acceleration in the z orientation
Am	shock amplification
d_m	dynamic deflection of a cushion
e	coefficient of restitution
$\mathbf{g}$	acceleration of gravity
H_d	free fall drop height
h_{eq}	equivalent drop height
H_r	rebound height
RH	relative humidity
SL	static loading
t_f	time of fall
t_r	time of rebound
T_c	cushion thickness
T_1	thickness after impact
τ	impact duration
ω_{Rc}	resonant frequency of a product's component
ω_{Rpc}	resonant frequency of a product/cushion combination
Δv	velocity change
Δv_c	critical velocity change of a product
Δv_R	resultant velocity change
Δv_x	velocity change in the x direction
Δv_y	velocity change in the y direction
Δv_z	velocity change in the z direction

See also: **Damping materials**; **Data acquisition**; **Digital filters**; **Environmental testing, overview**; **Packaging**; **Shock isolation systems**; **Vibro-impact systems**.

Further Reading

Burgess G (1988) Product fragility and damage boundary theory. *Packaging Technology and Science* 1: 5–10.

Hatae MT (1988) Packaging. In: Harris CM (ed.) *Shock and Vibration Handbook*, ch. 41. McGraw Hill.

Kipp W (2000) Developments in testing products for distribution. *Packaging Technology and Science* 13: 89–98.

Newton RE (1988) Theory of shock isolation. In: Harris CM (ed.) *Shock and Vibration Handbook*, ch. 31. McGraw Hill.

SHOCK ABSORBERS

See **SHOCK ISOLATION SYSTEMS**

SHOCK ISOLATION SYSTEMS

M Radeş, Universitatea Politehnica Bucuresti, Bucuresti, Romania

Copyright © 2001 Academic Press

doi:10.1006/rwvb.2001.0177

Shock isolation systems are designed for protection against high-rate input loadings from machinery excitation, transportation environments, or weapon effects. This section describes several high-performance shock isolation elements. Their design is usually based on shock disturbances expressed as motion or force-time histories. Design specifications are expressed in terms of equipment fragility levels given as acceleration response time histories or peak acceleration–frequency curves. An effective shock isolator must possess: first, a long stroke capability; second, a facility to attenuate high-frequency disturbances; and, third, a design able to control the generation and propagation of internal stress waves. These properties are not encountered in commercially available vibration isolators that have short strokes and low flexibility.

Stranded Wire Spring

A robust shock isolator is the stranded wire spring shown in **Figure 1**. The helix of the spring is wound in the opposite direction to the helix of the strands. When the spring is compressed, the strands bind together, giving rise to Coulomb friction forces between wire strands.

Ring Spring

In the ring spring, shown in **Figure 2A**, the energy is absorbed by the Coulomb friction forces between the adjoining rings. The axial spring deflection is obtained from stretching of the outer rings and compression of the inner rings. The damping force acting on the conical surfaces of the adjacent rings is proportional to the axial displacement. A typical load deflection curve is shown in **Figure 2B**. For increasing

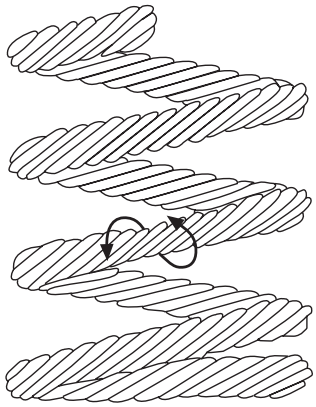


Figure 1 Stranded wire spring. From Eshleman (1970) with permission.

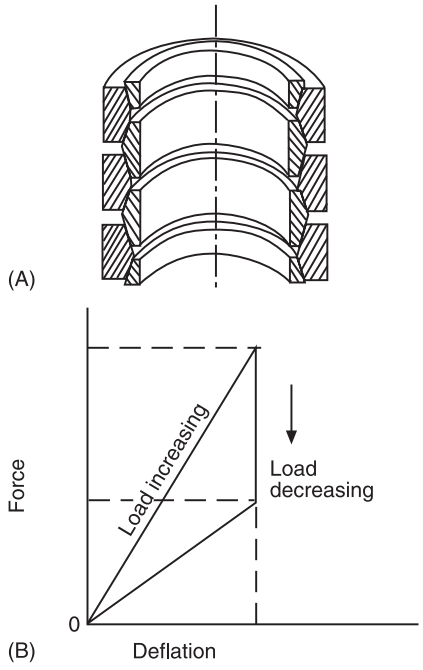


Figure 2 Ring spring. (A) Diametral section; (B) load deflection curve. From Eshleman (1972) with permission.

loads, the elastic and the friction forces act in the same direction, absorbing a large amount of energy. For decreasing loads, the friction force reverses. Part of the stored elastic energy is used to oppose the friction force. The result is a load release curve of smaller slope. The area inside these lines is a measure of the energy dissipated by the ring spring in a loading cycle. Ring springs have inherent small displacements. This drawback is alleviated by stacking rings.

Belleville Spring

The Belleville spring shown in **Figure 3** is made from washers stressed circumferentially and radially. Its nonlinear hard-to-soft spring characteristic is best suited for shock isolation. Local damping can be introduced by parallel elements or contained fluids.

Volute Spring

The volute spring (**Figure 4**) has flat steel coils wound helically to form a conical spring. The reverse-wound coils are subject to bending. The nested coils press against each other and generate friction forces to dissipate energy.

Friction Snubber

An effective shock isolation element can be made combining a helical spring in parallel with a friction snubber (**Figure 5**). The friction is produced between a liner material and the snubber wall. Preadjusting the helical spring compression, the liner material is wedged against the wall.

Solid Elastomeric Elements

Elastomeric or rubber elements work in either compression or shear. The load deflection curve is nonlinear. The nonlinearity is usually ignored for strains up to about 10%. For a compression block (**Figure 6A**), the stiffness is corrected for the effect of bulk compression. For an element in compression, provided the thickness is less than one-fourth of the least plane dimension, there should be no instability. Long strokes can be obtained by special geometrical design (**Figure 6B**).

Foam Blocks

Polyurethane foam isolation elements have large energy dissipation capacity, high stroke-to-overall-length ratio and high shock-attenuation-to-weight

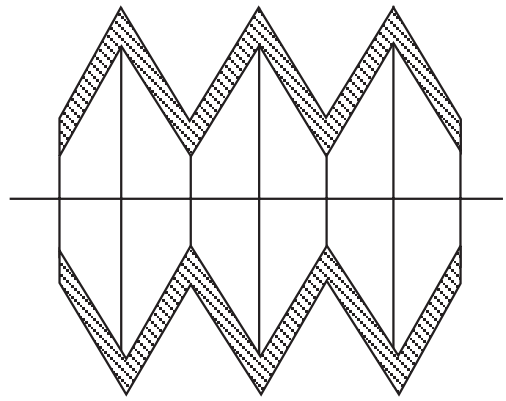


Figure 3 Belleville spring. From Eshleman (1970) with permission.

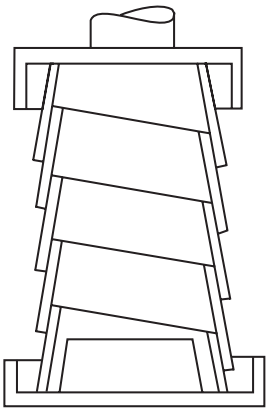


Figure 4 Volute spring. From Eshleman (1973) with permission.

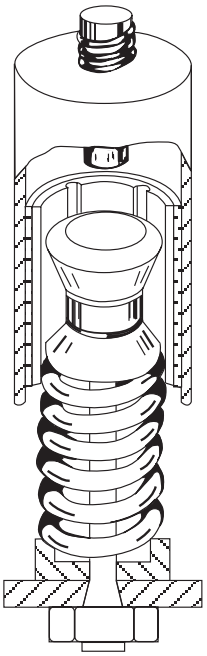


Figure 5 Friction snubber. From Eshleman (1973) with permission.

ratio. The resisting force generated by the foam isolator has two components: one is due to the nonlinear deformation of the porous structure, the other is due to the air pressure generated by the air flow produced by the distortion of the foam cell structure. The foam does not exhibit surging under high rate loading.

Liquid Spring

The liquid spring shown in **Figure 7** works on fluid compressibility. It has high damping and high wave propagation velocity. To increase the stroke, that is proportional to the volume of the constrained fluid, a fluid reservoir is added to the basic isolator.

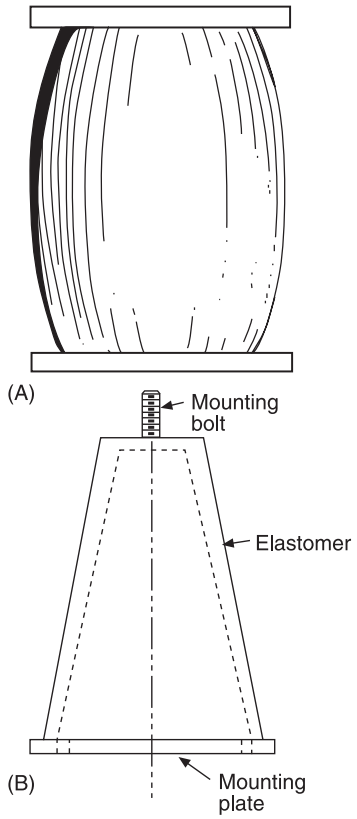


Figure 6 Solid elastomer. (A) Rubber block, from Eshleman (1973); (B) long stroke isolator, from Eshleman (1970) with permission.

Pneumatic Spring

The pneumatic spring (**Figure 8**) has similar characteristics to those of the liquid spring. Its flexibility can be adjusted by varying the air pressure. A passive

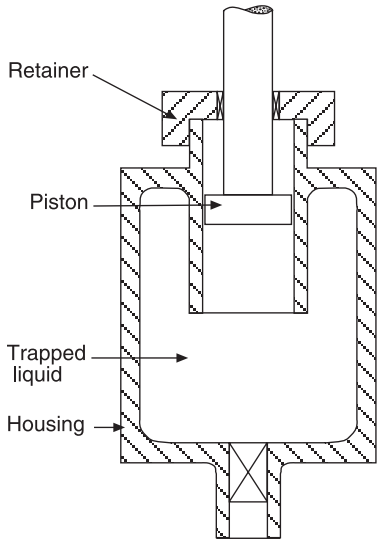


Figure 7 Liquid spring. From Eshleman (1970) with permission.

pneumatic shock isolator is shown in **Figure 9**. The transient response of the system reaches a minimum for a certa in ratio of orifice area to load area. Similar shock absorbers have been applied to the carriage return mechanism of a printer. Variable-area orifice designs have also been studied.

Active Pneumatic Isolator

A schematic diagram of an active mechanopneumatic shock isolator is shown in **Figure 10**. The use of integral displacement control reduces the steady-state relative displacement of the mass to zero.

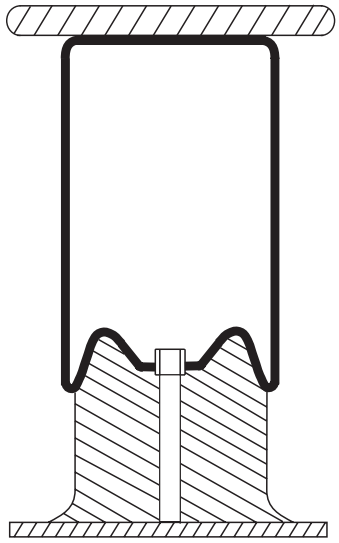


Figure 8 Pneumatic spring. From Eshleman (1970) with permission.

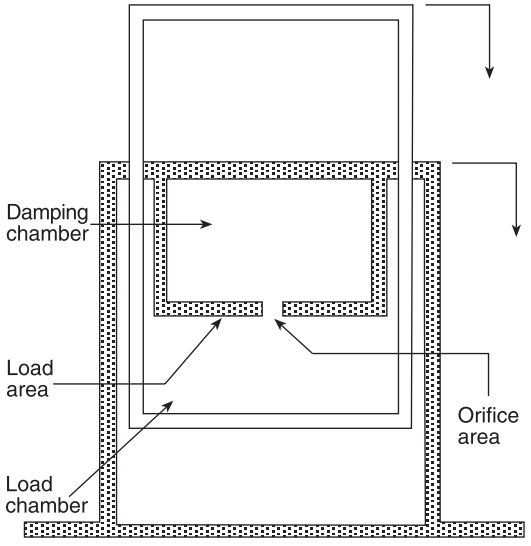


Figure 9 Passive pneumatic shock isolator. From Hundal (1980) with permission.

Semiactive Fluid Device

A fluid shock absorber with servo-controlled valving is shown in **Figure 11**. It contains a dissipative element in which the dissipation law can be modulated actively. By means of a small amount of power

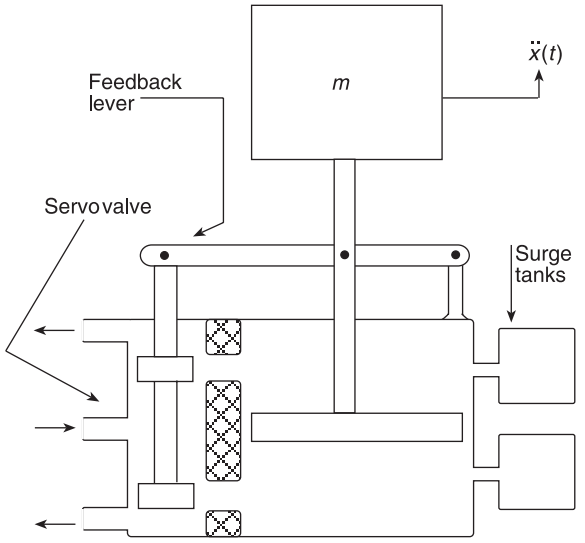


Figure 10 Active mechanopneumatic shock isolator. From Hundal (1980) with permission.

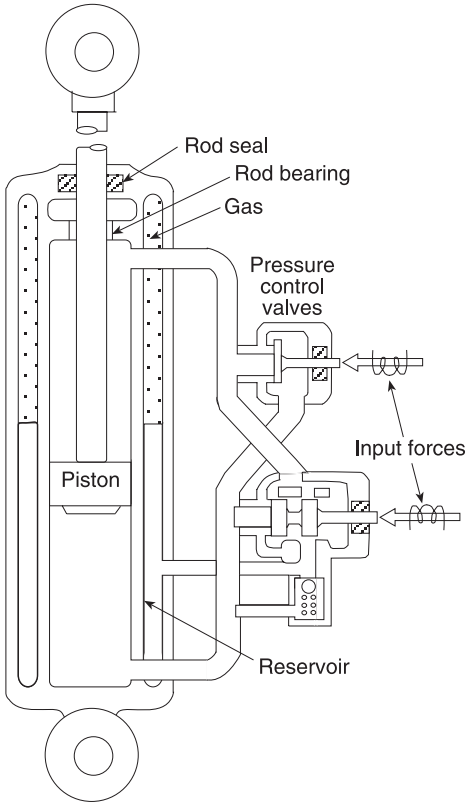


Figure 11 Electrohydraulic active shock absorber. From Karnopp (1973) with permission.

supplied to the servomechanism, a large amount of dissipated power is easily controlled.

For modeling, analysis, experimentation, and design procedures, consult the references.

See also: **Absorbers, vibration**; **Damping, active**; **Shock**; **Shock isolation systems**.

Further Reading

Eshleman RL (1970) Design of high-performance shock isolation systems. *Shock Vibration Bulletin* 41: 53–64.

Eshleman RL (1972) Dynamic response of a ring spring. *Shock Vibration Bulletin* 42: 7–14.

Eshleman RL (1973) High-performance shock isolation systems. In: *Isolation of Mechanical Vibration, Impact, and Noise*, AMD Vol. 1, pp. 221–245.

Eshleman RL, Rao PN (1969) The response of mechanical shock isolation elements to high rate input loading. *Shock Vibration Bulletin* 40: 217–234.

Fox GL, Steiner E (1972) Transient response of passive pneumatic isolators. *Shock Vibration Bulletin* 42: 85–91.

Harris CH, Crede Ch (1961) Theory of shock isolation. *Shock and Vibration Handbook*, vol. 2, chapter 31, pp. 27–31. McGraw Hill.

Hundal MS (1978) Analysis of performance of pneumatic impact absorbers. *Journal of Mechanical Des. Trans ASME* 100: 236–241.

Hundal MS (1980) Pneumatic shock absorbers and isolators. *The Shock and Vibration Digest* 12: 17–21.

Karnopp DC (1973) Active and passive isolation of random vibration. In: *Isolation of Mechanical Vibration, Impact, and Noise*, AMD Vol. 1, pp. 64–86.

Liber T, Sevin E (1966) Optimal shock isolation synthesis. *Shock Vibration Bulletin* 35; Part V.

Ruzicka JE (1969) Active vibration and shock isolation. *SAE Transactions* 77: 2872–2886.

Sevin E, Pilkey WD (1971) *Optimum Shock and Vibration Isolation*. Shock and vibration monograph no. SVM-6. Shock and Vibration Information Center, Naval Research Center, Wahington DC.

SIGNAL GENERATION MODELS FOR DIAGNOSTICS

M Sidahmed, Universite de Compiegne, Compiegne, France

G Dalpiaz, University of Bologna, Bologna, Italia

Copyright © 2001 Academic Press

doi:10.1006/rwvb.2001.0148

Introduction

Vibrations in rotating machines are due to various dynamic forces, including those due to abnormal running conditions or faults. Vibration signal generation models have been developed and make possible the identification, from measured signals, of the generating phenomena and as a consequence the faulty condition of the machine. These models allow the determination of specific characteristics or features, which can be extracted by signal processing, in order to deliver a 'diagnosis' of the machine state. These features are often termed symptoms.

Vibrations in rotating machines are due to various excitation phenomena. We use them to distinguish between mechanical, electrical, aerodynamic, and hydraulic phenomena.

Characteristics of Vibration Signals

On the Models

Most of the vibration generators are considered as the sources or excitations for which one wishes to develop a signal generation model. The existence of various models 'explaining' various phenomena in rotating machines makes vibration analysis a very powerful tool for condition monitoring and diagnosis. In fact, the models allow us to 'identify' the state of the machine from vibration measurements done with sensors which are usually fixed on the bearing casings. However, it is assumed that the transmission from the source to the measured signal is linear and not time varying. This allows us to trace any modification of the vibrations to the sources, i.e., the faults. This hypothesis implies that for any harmonic source the measured vibration will be harmonic with the same frequency content (**Figure 1**).

Models may be analytical, 'symptom'-based or statistical. Analytical models come from the kinematics and dynamic modeling and require various physical parameters which are difficult to evaluate, such as stiffness and damping. However, such models have developed in the context of modal analysis and

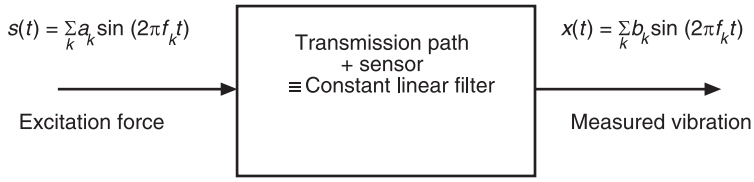


Figure 1 Linear system hypothesis.

design. Their use for vibration analysis is still under investigation. 'Symptom'-based models are more often used for condition monitoring and diagnosis. In the main they make use of the rotating machine kinematics. This allows them to determine specific frequencies that may be identified using simple frequency domain analysis. Statistical models are those that consider the signals to be random. We are generally interested in the statistical characterization (random impulse, random noise, etc.).

Vibrations of Rotating Machines

The vibrations generated by rotating machines are cyclic in nature. The frequencies of the phenomena are defined by the kinematics. A simple example, is shown in **Figure 2:** a constant speed rotating punctual mass will create a centrifugal force, and at the bearing case it creates a sinusoidal vibration with frequency equal to the rotating mass speed (linear transfer is supposed).

We will express the vibration signal measured on a rotating machine as the sum of three terms:

$$x(t) = x_r(t) + x_n(t) + b(t) \qquad [1]$$

where $x_r(t)$ is the part of the signal with cyclic frequencies which are synchronous to the fundamental shaft rotation f_r. It may have 'sinusoidal' components at frequency f_r, $2f_r$, $3f_r$,. . ., or a more complex signal such as a repetitive impact at the same frequency rate. $x_n(t)$ is similar to $x_r(t)$, in this case the cyclic frequencies are not synchronous to the fundamental f_r, and $b(t)$ is an additive noise with random characteristics.

Most of the signal generation models will 'explain' the signal in that form. This is very useful when we have to decide which signal processing technique to use for the vibration signals analysis.

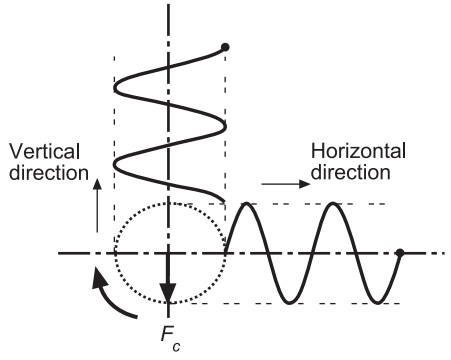


Figure 2 Sinusoidal variations in vertical and horizontal axis for a constant speed rotating force.

Vibrations of Mechanical Origin

Unbalance

Unbalance is the most common vibration generator in a rotating machine. It is due to nonsymmetrical mass distribution around the rotation axis. We consider here, only rigid rotors (rotation speed lower than the first critical speed). A rotor is well balanced if its mass center belongs to the rotation axis and if this axis is the principal axis of inertia. We distinguish between static, couple, and dynamic unbalances.

Static unbalance (**Figure 3A**) The mass center of the rotor is not on the rotation axis, this leads to the inertia force:

$$F_c = m.e.\omega_r^2 \qquad [2]$$

where ω_r is the constant rotation speed in rad s^{-1}, m is the mass of the disc in kg, and e is the distance from the mass center to the rotation axis in m.

Couple unbalance (**Figure 3B**) When the mass center does not coincide with a principal rotation axis, a couple is generated. The resulting inertia moment may be written as:

$$M = I.w_r^2 \qquad [3]$$

where I is the inertia product.

Dynamic unbalance (**Figure 3C**) This is considered for a rotor with both static and couple unbalances. We then have both an inertia force, eqn [2], and a couple moment, eqn [3]. The angle between the

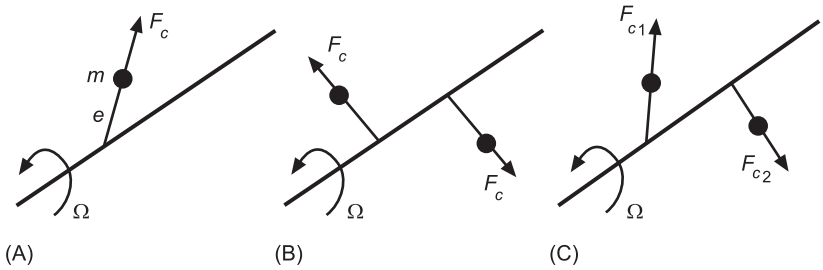


Figure 3 Forces for different kinds of unbalance. (A) Static unbalance; (B) couple unbalance; (C) dynamic unbalance.

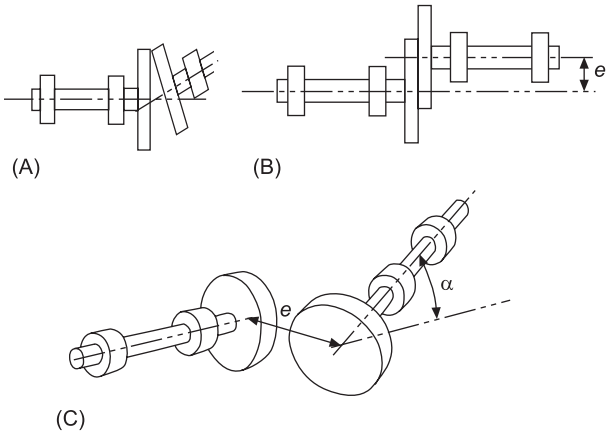


Figure 4 Types of misalignments. (A) Angular; (B) parallel; (C) both.

inertia force and the inertia moment is between $-\pi$ and $+\pi$.

Symptoms of unbalance According to eqns [2] and [3], when unbalance occurs, the measured vibrations are characterized, in the frequency domain, by a component at the rotation frequency $f_r = \omega_r/(2\pi)$. The amplitude is proportional to the amount of unbalance and to the square of the rotation speed. The phase between the vibrations on the two supporting bearings is in phase in the case of static unbalance, with π out of phase for a couple unbalance and arbitrary for a dynamic unbalance. The orbit of the rotor in the bearings, measured with two radial and orthogonal displacement sensors, exhibits a single-loop elliptical shape. Due to the transmission path, higher harmonics $((2f_r), \ldots,))$ may occur especially when the unbalance is severe.

Misalignment

Mechanical power is transmitted by coupled shafts which have to be aligned. Otherwise, significant vibrations may occur. Misalignment is a very common fault in rotating machines. The generated vibrations act on the bearings and are related to the type of misalignment (**Figure 4**), or to the type of couplings used to connect the shafts (**Figure 5**). Detailed models of the generation signals have been developed in the literature, we give only a qualitative analysis for gear couplings. **Figure 6** shows the gear coupling forces that occur when misalignment occurs. Periodic forces are caused by the friction in gear meshing and exhibit a periodicity of half of the shaft rotation period. This results in a fundamental frequency of $2f_r$.

Symptoms of misalignment The vibrations are harmonic and mainly characterized by the first harmonics of the rotation frequency f_r, i.e., $1f_r$, $2f_r$, $3f_r$, $4f_r$, ... The axial direction is, in general, more sensitive. In this direction, the measurements at each side of the coupling are in opposite phases (180°). In sleeve bearings, misalignment may also be

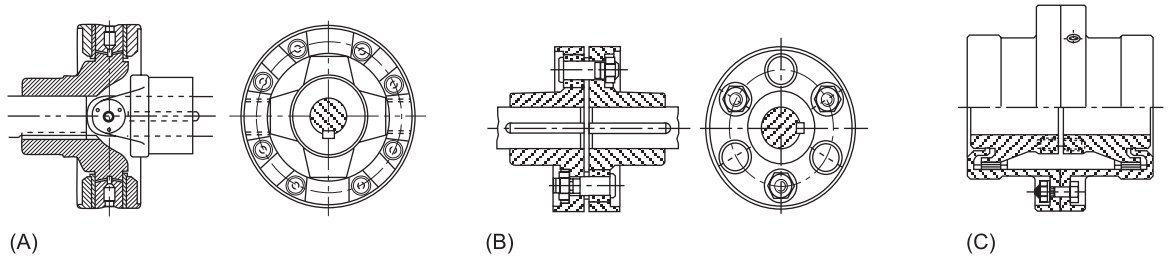


Figure 5 Types of couplings. (A) Hooke's joint; (B) elastomer coupling; (C) gear coupling.

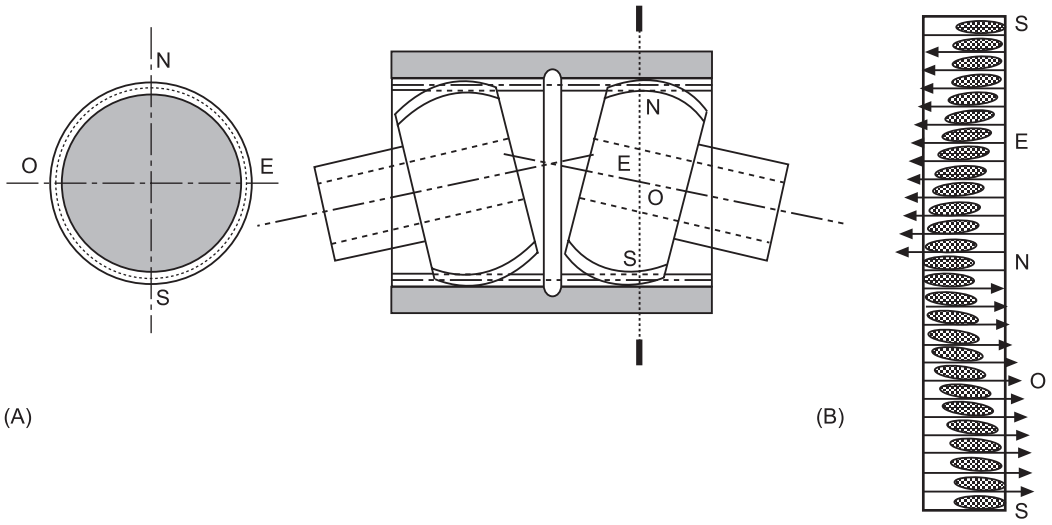


Figure 6 Friction forces acting on the teeth in misaligned gear coupling.

detected by orbit analysis, which exhibits a double loop when the $2f_r$ component is dominant. General features of the vibration due to misalignment are summarized in **Table 1** for various coupling types.

Rolling Bearing Faults

Rolling bearings are comprised of various components: the inner and outer races, the cage and the rolling elements (**Figure 7**). Vibrations are generated when the rolling bearing conditions are not perfect, i.e., surface damage, forces acting on the bearings (unbalance, misalignment, etc.). The surface damage is due to fatigue in the presence of high stresses at the contact points. More specifically, the vibrations are generated by the impacts which occur when the surface of one component strikes another surface. As the bearing rotates, the generated impulses will occur periodically. The frequencies of these impulses are uniquely determined by the location of the defect, on the inner race, outer race, or on the rolling elements (**Figure 8**). The geometry of the rolling bearing is required (**Figure 9**). The characteristic frequencies for inner race, outer race, cage and ball bearing faults are given in **Tables 2** and **3** for ball bearings with fixed and rotating outer race, respectively.

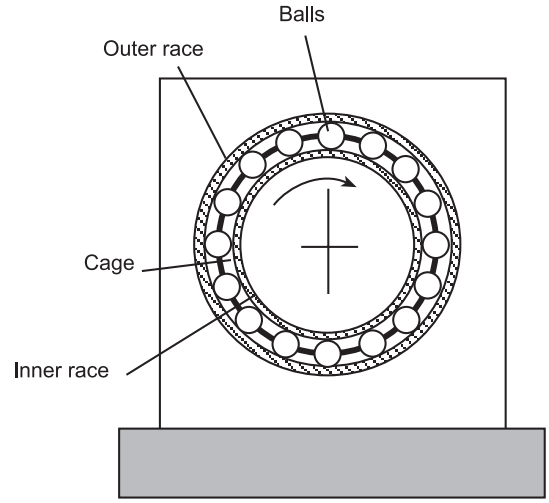


Figure 7 Rolling bearing components.

This model stating that the rolling bearing generates periodical impulses with specific frequencies is not complete. It is important to take into account first, the distribution of the load around the circumference of the bearing, which under radial load, is defined by the Stribeck equation:

Table 1 Vibration characteristics of misalignment

Coupling types	*Hooke's joint*	*Gear coupling*	*Elastomer/metallic*	*Elastomer/metallic*
Misalignment	Angular	Angular	Angular	Parallel
Direction	Radial, axial	Axial, radial	Axial	Radial
Frequency components	$2f_r$, $4f_r$, $6f_r$, ..	$2f_r$, $4f_r$, $6f_r$, ..Nf_r (N = number of teeth)	$1f_r$, $2f_r$, $3f_r$	$2f_r$, $4f_r$, $6f_r$, ..
Out of phase	180°	180°	180°	180°
Orbit	Double or more loops	Double or more loops	Double or more loops	Double or more loops

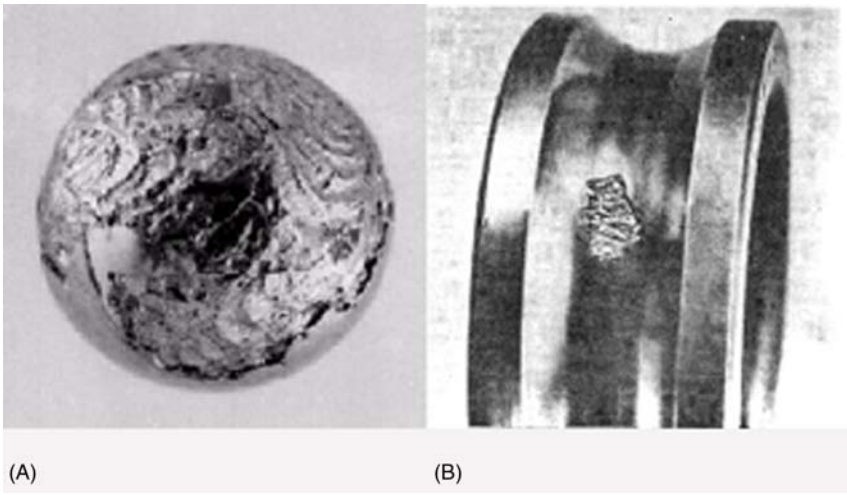


Figure 8 Rolling bearing faults. (A) Spalling on a ball; (B) spalling on inner race.

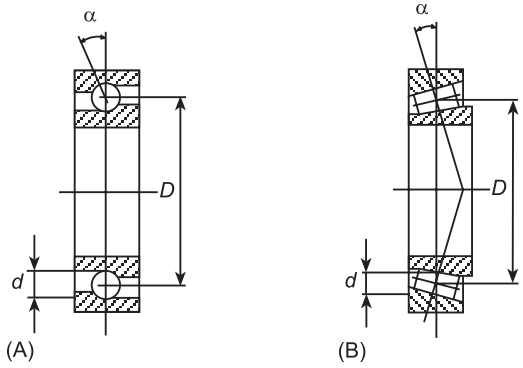


Figure 9 Rolling bearing geometry. (A) Cross-section of a ball bearing; (B) cross-section of a tapered roller bearing. $D =$ mean diameter to the center of the ball; $d =$ ball diameter; $\alpha =$ contact angle.

Table 3 Characteristic frequencies for a radial ball bearing with rotating outer race

Bearing component	*Characteristic frequencies, Hz*
Cage	$f_c = \frac{f_R}{2}\left(1 - \frac{d}{D}\cos\alpha\right) + \frac{f_{Rout}}{2}\left(1 + \frac{d}{D}\cos\alpha\right)$
Inner race	$f_i = \frac{Z}{2}\left[(f_R - f_{Rout})\left(1 + \frac{d}{D}\cos\alpha\right)\right]$
Outer race	$f_o = \frac{Z}{2}\left[(f_R - f_{Rout})\left(1 - \frac{d}{D}\cos\alpha\right)\right]$
Rolling	$f_b = \frac{1}{2}\frac{D}{d}(f_R - f_{Rout})\left[1 - \left(\frac{d}{D}\cos\alpha\right)^2\right]$

$f_R =$ shaft rotation frequency, $f_{Rout} =$ outer race rotation frequencies, $D =$ mean diameter (to the ball center), $d =$ ball diameter; $Z =$ number of rolling elements, $\alpha =$ contact angle.

Table 2 Characteristic frequencies for a radial ball bearing with fixed outer race

Bearing component	*Frequency expression*
Cage frequency (fundamental train frequency)	$FTF = f_c = \frac{f_r}{120}\left(\left(1 - \frac{d}{D}\right)\cos\alpha\right)$
Inner race frequency (Ball pass frequency of inner race)	$BPFI = f_i = \frac{f_r Z}{120}\left(\left(1 + \frac{d}{D}\right)\cos\alpha\right)$
Outer race frequency (Ball pass frequency of outer race)	$BPFO = f_o = \frac{f_r Z}{120}\left(\left(1 - \frac{d}{D}\right)\cos\alpha\right)$
Rolling element frequency (Ball spin frequency)	$BSF = f_s = \frac{f_r}{120}\frac{D}{d}\left[1 - \left(\left(\frac{d}{D}\right)\cos\alpha\right)^2\right]$

$f_r =$ shaft rotation frequency (Hz), $D =$ mean diameter (to the ball center), $d =$ diameter of balls, $Z =$ number of balls, $\alpha =$ contact angle (**Figure 10**).

$$q(\theta) = q_0[1 - \varepsilon(1 - \cos\ (\theta)]^n \qquad [4]$$

where ε controls the load distribution and θ is the angular load zone ($n = 3/2$ for ball bearings, $n = 10/9$ for roller bearings, q_0 is the maximum load value).

This results in a modulation effect for a rotating defect, i.e., ball or inner race defect. This effect is illustrated in **Figure 10**. When dynamic load is present, due to centrifugal forces, modulations are also generated for a fixed outer race defect. Secondly, the transmission from the impact to the measured vibration (bearing casing and sensor transfer function) which acts as a filter. The impacts are high-frequency dominated, they excite the system resonance localized in a high frequency band. This property is used to 'amplify' the rolling bearing impulses and is at the

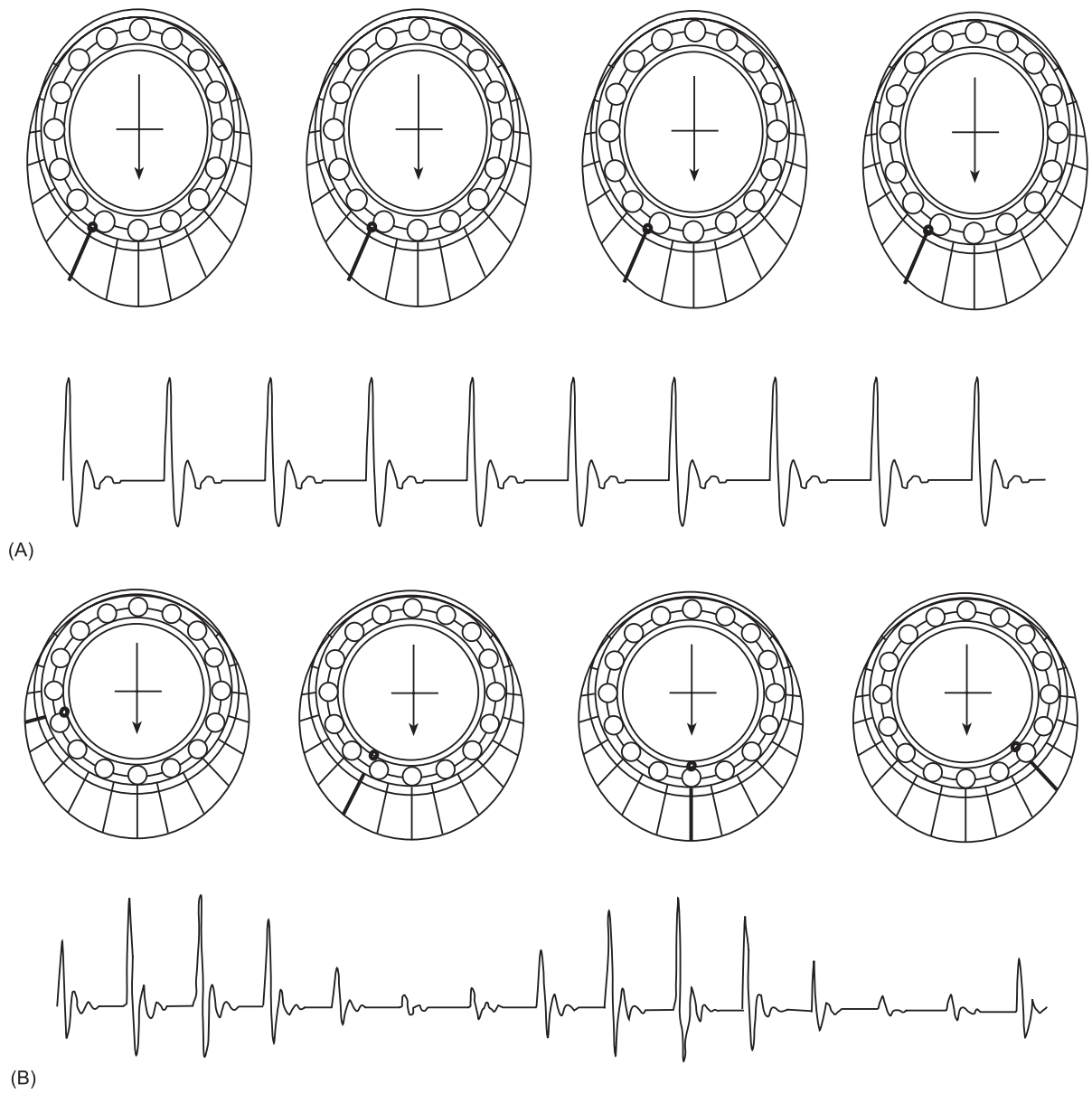


Figure 10 Rolling bearing with fixed outer race, rotating inner race and fixed load. (A) Damage in the fixed race, without modulation; (B) damage in the rotating race with load modulation.

basis of several detection techniques high-resonance frequency technique (HFRT) or the envelop demodulation technique, because of the response of a system to repetitive impulses.

Gear vibrations signal generation

Gears are important and complex mechanical elements. Different types of gears may be distinguished, some are shown in **Figure 11**. They transmit significant torques, and are subject to considerable deterioration, often with dramatic consequences. Faults may concern the teeth surface (wear, spalling, cracks) (**Figure 12**) or the wheels (eccentricity, misalignment, etc.).

The essence of the vibration generation models is, however, similar for all the gear types: the gear vibrations are produced by the impact between the teeth of the two wheels. The meshing signal is given by the deviation of the meshing point position relative to the ideal motion of a perfect gear with no load. This deviation is called the transmission error, and its components come from the deflection of the teeth due to the load and from deviations of the teeth shape from their ideal profile. Relatively simple models can be based on elementary systems composed of two gears, such as pinion/gear, planetary, etc. Taking as an example the system depicted in **Figure 13**, the model predicts, in perfect conditions

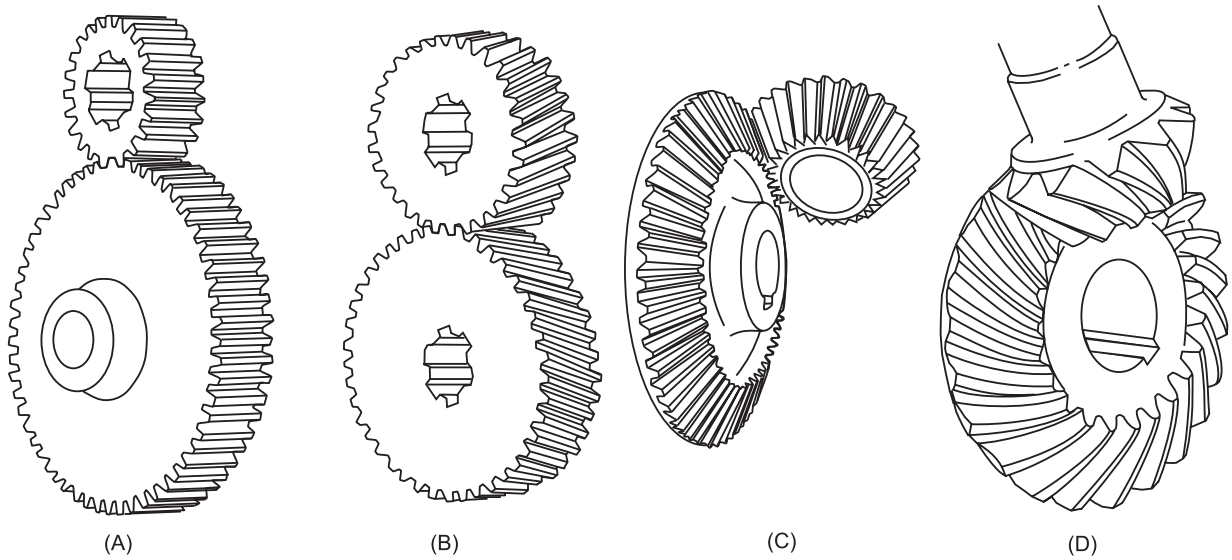


Figure 11 Various gears. (A) Spur gear; (B) helical gear; (C) bevel gear; (D) spiral bevel gear.

(perfect profile, no faults), a periodic vibration $x(t)$ given by:

$$x(t) = \sum_k x_k \ \sin \ (2\pi k f_m t + \phi_k) \qquad [5]$$

with a fundamental meshing frequency of:

$$f_m = f_{r1} n_1 = f_{r2} n_2 \qquad [6]$$

Faults occurring in a gear system will introduce time-varying torques. This will induce a multiplicative effect and obviously modulation effects. In brief, distributed effects, affecting all the teeth, (imperfect tooth profile, wear, etc.) will generate modulation at the meshing frequency, f_m. Localized defects like spalling, cracks, and obvious breakage generate repetitive impulses at the shaft's rotation frequencies f_{r1} and f_{r2}. This gives rise to amplitude or phase modulation effects at these frequencies. The simplest case would be the effect of wheel eccentricity, generating a once-per-revolution torque variation.

The amplitude, phase or combined modulation mechanisms have been noted, resulting in:

$$y(t) = \sum_k x_k[1 + a_k(t)] \ \sin \ [2\pi k f_m + \phi_k + b_k(t)] \qquad [7]$$

where $a_k(t)$ and $b_k(t)$ are, respectively, the amplitude and phase modulating functions. The modulations are basically of periodic character, and can be described by:

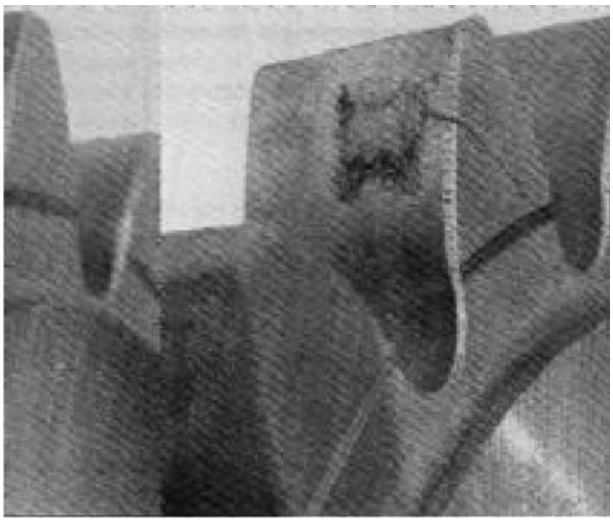
$$\begin{aligned} a_k(t) &= \sum_p a_{kp} \ \sin \ (2\pi p f_{r1} t + \alpha_{kp}) \\ &\quad + \sum_q a'_{kq} \ \sin \ (2\pi q f_{r2} t + \alpha'_{kq}) \\ b_k(t) &= \sum_p b_{kp} \ \sin \ (2\pi p f_{r1} t + \beta_{kp}) \\ &\quad + \sum_q b'_{kq} \ \sin \ (2\pi q f_{r2} t + \beta'_{kq}) \end{aligned} \qquad [8]$$

However, it should be noted that, specially for distributed faults such as spalling or cracks, the parameters $a_{ij}, b_{ij}, \alpha_{ij}$ and β_{ij} in eqns [7] and [8] are random. In the frequency domain, the models thus predict the following frequencies:

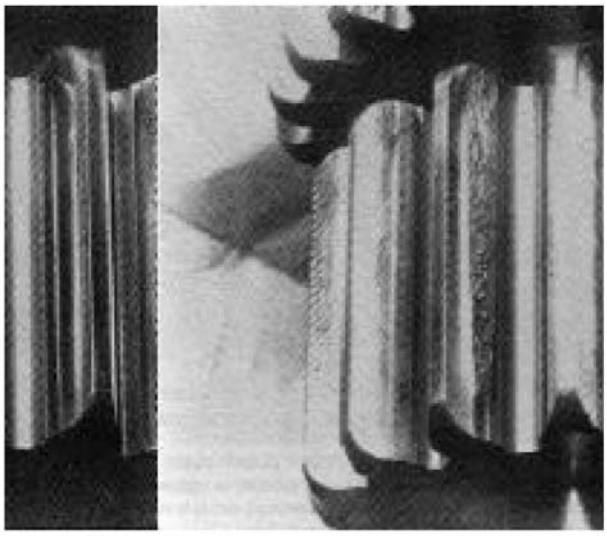
$$\begin{aligned} &k f_m \pm p f_{r1} \pm q f_{r2} \\ &\quad k = 1, 2, \ldots, K \\ &p, q = 0, 1, 2, K \end{aligned} \qquad [9]$$

This shows that the gear vibrations spectrum is rich with numerous harmonics even with a new gear set. This is due to the complexity in manufacturing these mechanical components (profile under load, teeth surface quality, etc.). Imperfect profile (specially under load) and surface quality generate these modulation effects.

The existence of complex phase and amplitude modulation may also be interpreted as a nonlinear or cyclostationary phenomenon. These models justify, for the diagnostic process, the use of more advanced signal processing techniques.



(A)



(B)

Figure 12 Teeth gear faults. (A) crack, (B) spalling.

Table 4 summarizes the time and frequency characteristics for the various type of faults that may happen in a gear system.

Other Mechanical Faults

Oil film excitation (whirl) will appear in (high speed) turbomachinery, with journal bearings. It can be described as a travelling wave in the oil film, with a speed just less than half of the shaft rotation speed $(0.43 - 0.45f_r)$.

Shaft cracks are of importance in high-power turbomachinery. This nonlinear phenomena is difficult to detect. Run-up and run-down are often used to detect these phenomena by examining the relative amplitude and phase of the first harmonics of the rotation.

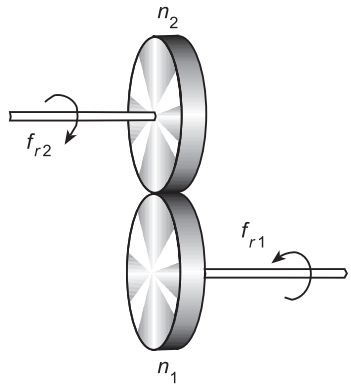


Figure 13 Pair of spur gears ($f_{r1}\, n_1 = f_{r2}\, n_2$).

Vibrations of Electric Origin

In electric machines, the electromagnetic forces give rise to vibrations. For synchronous machines, the fundamental frequency is the line frequency which is the rotation speed, and the harmonics are defined by the number of pair poles.

In asynchronous machines (induction machines), the rotation speed is just under the sector frequency (i.e., the synchronous speed), the difference being the 'slip' frequency multiplied by the number of poles. A localized fault on the rotor, say a broken bar, will produce an 'electrical unbalance' rotating at speed shaft f_r. This will generate amplitude modulation of the vibrations:

$$f_r \pm 2sf_l \qquad [10]$$

where s is the per unit slip and f_l the line frequency.

Signal generation models have been developed for the motor current. Physical models have been developed in the context of control but are also used for diagnosis.

Aerodynamic and Hydraulic Origin

Turbomachines (turbines, centrifugal pumps, fans, etc.) generate vibrations due to the excitations of the driven fluid. Clearly, for such machines harmonics forces are generated by the rotating blades (N), i.e., components at passing blade frequency (Nf_r) and harmonics are relevant. Wide-band vibrations also exit and are due to fluid turbulence and cavitation. These wide-band vibrations are high-frequency dominated. Several studies are being conducted to adapt 'specific signal processing tools' to analyze these phenomena. Wavelets are the expected candidate because of their 'fractal' nature.

Table 4 Time and frequency characteristics of faulty gear vibrations, (f_{ri} shaft rotation, f_m meshing frequency).

Types of faults	*Frequency domain*	*Time domain*	*Comments*
Eccentricity	Side bands $f_m \pm kf_{ri}$	Modulation at shaft rotation speed	New gears often exhibit these modulations
Misalignment	Increase of f_m and harmonics		
Machining effects	'Ghost' component		Frequency related to the gear manufacturing machine
Backlash	Higher gear mesh harmonics		Noisy gear
Wear	Increase f_m, harmonics and RMS value	RMS, crest value, etc.	Low evolution faults
Spalling (individual teeth)	$af_m \pm kf_{ri}$	Repetitive impacts at f_{ri}, small impacts when incipient fault	Amplitude modulation High rate evolution fault Concerns hard case hardened gears
Cracks (individual teeth)	$af_m \pm kf_{ri}$	Repetitive impacts at f_{ri}, small impacts when incipient fault	Phase and amplitude modulation High rate evolution fault
Rupture	$af_m \pm kf_{ri}$ Wide-band spectra	Repetitive high-level impacts	

Synthesis

We have showed that most of the faults occurring in rotating machines may have more or less complex underlying models. This knowledge is of importance to achieve detection and diagnosis of faults in rotating machines in order to take maintenance actions or to achieve quality control. The type of expected signal helps in the definition of the more suitable signal processing technique.

It is useful to summarize the results with tables giving the symptoms of the main faults occurring in rotating machines, classified into three categories:

- faults generating signals (that may be harmonic or impulse repetitive) with fundamental frequency synchronized to the main shaft rotation speed (**Table 5**)
- generating signals not synchronized to the rotation speed (**Table 6**)
- generating random signals (**Table 7**).

These tables clearly show that different faults may have similar symptoms. Signal processing is one way to identify the faults without any ambiguities. Knowledge-based techniques (artificial intelligence, neural networks, etc.) may be the second way.

Table 5 Excitations generating signals synchronous with the shaft rotation (f_r)

Excitations	*Main frequencies*	*Other characteristics*	*Comments*	*Direction*
Unbalance	$1f_r$	Elliptic orbit		Radial
Misalignment	$1f_r$, $2f_r$, $4f_r$, $6f_r$	Double orbit		Axial, radial
Gear system f_m meshing frequency, f_{r1}, f_{r2}	$f_m \pm nf_{ri}$	Amplitude and phase modulation Repetitive impacts for some faults	Modulation exists even in new gear	Radial and axial depends on the gear type
Pumps, fans (N = number of blades)	Nf_r and harmonics	High level	Modulation may exist	Radial, axial

Table 6 Excitations generating signals not synchronous with the shaft rotation (f_r)

Excitations	*Main frequencies*	*Other characteristics*	*Comments*	*Direction*
Oil whirl	$0.45f_r$		Journal bearing	Radial
Rolling bearings	f_b, f_i, f_o, f_c	Repetitive impacts		Axial, radial
Structural resonance	Resonance frequency		May be excited	Radial
Induction machines P = number of poles S = slip	$f_r - 2sf_l$ and harmonics	Close to the sector frequency		Radial

Table 7 Excitations generating random vibrations

Excitations	*Characteristics*	*Comments*	*Direction*
Turbulence	Wide-band	$1/f$ characteristic of the spectrum	Radial
Cavitation	High frequency	In pumps	Radial
Clearance	Random impacts		Radial, axial
Alternative machines (combustion engines compressors)	Repetitive impacts	Each impact has useful 'spectral content'	

See also: **Rotating machinery, essential features**; **Rotating machinery, modal characteristics**; **Rotating machinery, monitoring**.

Further Reading

Braun SJ (1986) *Mechanical Signature Analysis*. London: Academic Press.

Capdessus C, Sidahmed M, Lacoume JL (2000) Cyclostationary processes: applications to gear faults diagnosis. *Mechanical Systems and Signal Processing* 14(3): 371–385.

Collacot RA 1979, *Vibration Monitoring and Diagnostic*. New York: Wiley.

Ehrich FF (1992) *Handbook of Rotordynamics*. New York: McGraw-Hill.

Mark W (1978) Analysis of the vibratory excitation of gear systems: basic theory. *Journal of the Acoustic Society of America* 65(5): 1409–1430.

Mitchell JS (1981) *Machinery Analysis and Monitoring*. Tulsa: Penn Well.

Rao JS (1983) *Rotor Dynamics*. New Delhi: Wiley Eastern.

Timar PL (1989) *Noise and Vibrations of Electric Machines*. Amsterdam: Elsevier.

Wowk V (1991, 1994) *Machinery Vibration*. New York: McGraw Hill.

SIGNAL INTEGRATION AND DIFFERENTIATION

S Dyne, University of Southampton, Southampton, UK

Copyright © 2001 Academic Press

doi:10.1006/rwvb.2001.0053

The need to differentiate and integrate measured signals arises frequently in the analysis of vibration signals. For example, an accelerometer measures surface acceleration but we may be interested in surface velocity or even displacement requiring a single or double integration of the measured signal. Conversely a linear voltage differential transform (LVDT) gauge attached to a cam measures displacement directly but this would need to be differentiated once to obtain velocity and twice to obtain acceleration. This article describes the integration and differentiation of vibration signals and demonstrates the performance of algorithms for the integration and differentiation of sampled signals. Although the algorithms have been previously published widely as difference equations, Lynn and Fuerst was the inspiration for their representation as sampled signal filters and for the expressions and graphs of their performance.

Continuous vibration signals

The processes of differentiation and integration are covered by elementary calculus courses. A key result for vibration arises from the differentiation of a harmonic signal amplitude A and radian frequency ω:

$$\frac{\mathrm{d}}{\mathrm{d}t} A \cos \omega t = -A\omega \sin \omega t$$

That is, differentiation increases the amplitude of the signal by a factor ω and introduces a 90° phase shift. **Figure 1** shows a displacement signal with radian frequency $\omega = 2\ \mathrm{rad\,s^{-1}}$ together with the corresponding velocity signal. We see both the amplification factor of ω and the 90° phase shift. Similarly, for integration:

$$\int A \cos \omega t\ \mathrm{d}t = (A/\omega) \sin \omega t$$

and this reduces the amplitude by a factor ω and introduces a 90° phase shift in the opposite direction to differentiation. Note that if the frequency is given as f in Hz then the amplitude factor is $2\pi f$.

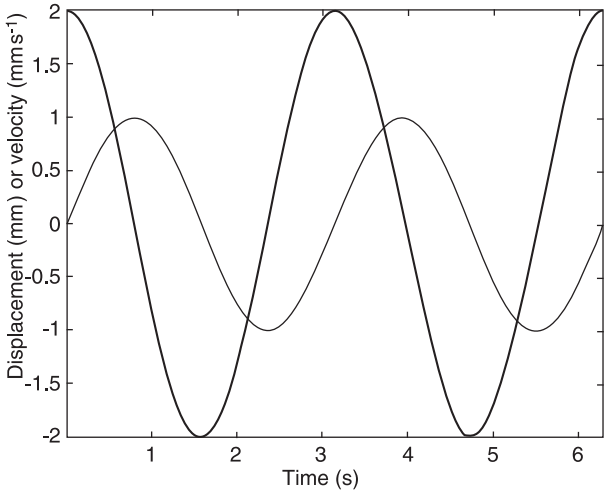


Figure 1 Harmonic displacement and corresponding velocity signal for $\omega = 2\,\text{rad}\,\text{s}^{-1}$. (–) Displacement; (**–**) velocity.

The analytical results are sometimes used directly: suppose, for example, that we wish to determine the peak velocity of a component on a machine operating at 3000 rpm and we have an accelerometer signal which reveals that the vibration is dominated by a harmonic component RMS amplitude 10 g. In this case:

$$A = 9.81 \times 10\sqrt{2} = 139\,\text{m}\,\text{s}^{-2}$$

$$\omega = 2\pi f = \frac{2\pi \times 3000}{60} = 314\,\text{rad}\,\text{s}^{-1}$$

so the peak vibration velocity level is:

$$\frac{A}{\omega} = \frac{139}{314} = 0.44\,\text{m}\,\text{s}^{-1}$$

The analytical expressions have some fairly important implications for the integration and differentiation of all vibration signals. First, since differentiation increases amplitude by a factor ω we may think of this as a process which amplifies high-frequency components (where ω is large) while attenuating low-frequency components (where ω is small) – in effect a differentiator behaves like a high-pass filter. Conversely, integration has the opposite effect. Here the amplification is greatest at low frequencies and attenuation is produced at high frequencies, so integrators act as low-pass filters. Finally, we can use the analytical results to test the performance of algorithms to compute the differentiation and integration of sampled signals which we shall explore later in this article.

At very low frequencies the integration amplification factor $1/\omega$ can become very large. Thus, any DC drift or spurious low-frequency noise in a signal will become amplified by the integration process and this may dominate the integrated signal. Consider, for example, an acceleration signal comprising a harmonic component amplitude, A but with a steady DC offset, A_0. The integrated signal is:

$$\int (A\cos\omega t + A_0)\mathrm{d}t = (A/\omega) \quad \sin \quad \omega t + A_0 t$$

The term due to the offset $A_0 t$ superimposes a ramp upon the harmonic component and for large values of t this ramp may dominate the signal. If the signal were to be integrated a second time to produce a displacement, this integrated signal would be:

$$\int \left(\frac{A}{\omega} \sin \omega t + A_0 t\right)\mathrm{d}t = \left(A/\omega^2\right)\cos\omega t + A_0 t^2$$

and the offset term has now produced a superimposed parabola $A_0 t^2$ and this can dominate the signal for even very small values for t.

For these reasons it is customary to high-pass-filter a signal to remove any low-frequency or DC offset or drift components prior to integration. Analog filters are often used for this, and the 'AC-coupled' input to signal conditioning is particularly appropriate for this application. A high-pass filter with a cut-off of 0.1–10 Hz is also suitable. It should be noted that, as the vibration signals generated by piezoelectric sensors are inherently 'AC-coupled', removal of any low-frequency components in the signal should present no particular difficulties.

An illustration of integration as a filtering operation is provided by **Figure 2** which shows the acceleration and corresponding velocity of a transient vibration. We observe that the velocity time history appears to be smoother than the acceleration time history. This is because of the low-pass filtering characteristic of the integration process between acceleration and velocity.

Sampled Signals

Differentiation

Modern signal analysis is carried out using digital computations on sampled signals. The conversion from an analog to digital signal is discussed elsewhere but a most important parameter in the conversion is the sample rate F_S and corresponding sample interval $\Delta t = 1/F_S$. We denote the sampled

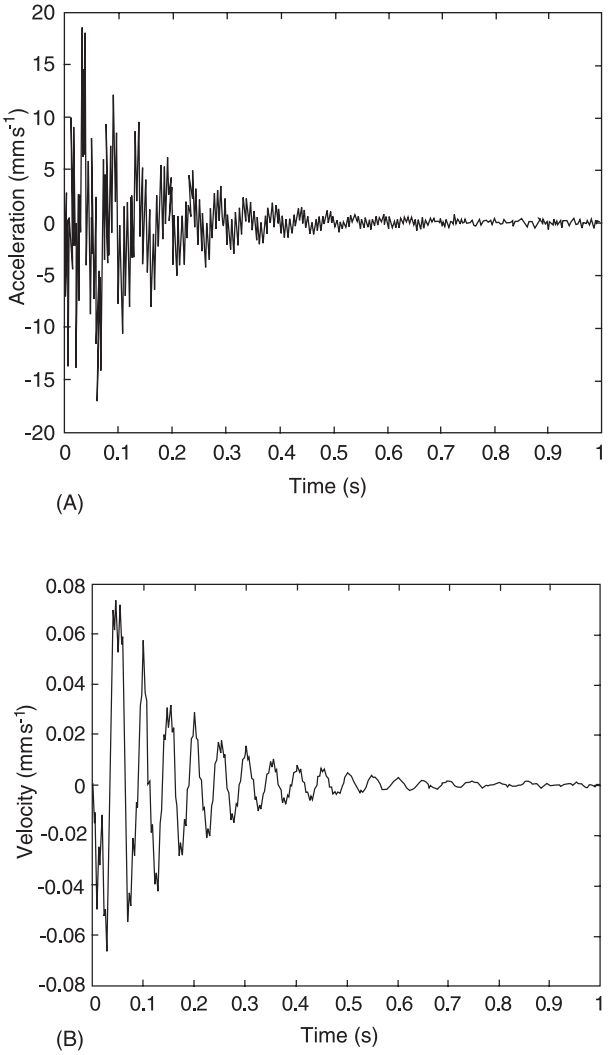


Figure 2 Comparison of transient signals. (A) Transient vibration acceleration; (B) transient vibration velocity.

values of a continuous signal $x(t)$ by the sample values $x(n)$, $n = 0, 1 \ldots N-1$.

We now consider algorithms that will differentiate and integrate a sampled input signal $x(n)$ to produce an output signal $y(n)$. Conceptually the simplest differentiator arises from the definition of differentiation as the limit of a ratio of small changes. This expresses the differential coefficient as the limit of a ratio as the small change in the independent variable (time, for vibrations) becomes infinitesimally small:

$$y = \frac{\mathrm{d}x}{\mathrm{d}t} = \lim_{\delta t \to 0} \frac{\delta x}{\delta t}$$

For the differentiation of a vibration signal, then, the differential coefficient would be the difference between two successive values divided by the sample interval:

$$y(n) = \frac{x(n) - x(n-1)}{\Delta t}$$

This differentiator is called the first-order difference approximation.

Let us now investigate how good this algorithm is compared with the ideal behavior that we discussed above. Taking the z-transform of this relation (a unit sample delay corresponds to z^{-1} so the z-transform of $x(n-1)$ is $z^{-1}X(z)$) gives:

$$Y(z) = \frac{X(z) - z^{-1}X(z)}{\Delta t} = \frac{1 - z^{-1}}{\Delta t} X(z) = H(z)X(z)$$

where: $H(z) = (1 - z^{-1}) / \Delta t$. Thus, differentiation (using this method) amounts to a filtering operation using a filter with transfer function $H(z)$. We can use tools developed for digital filters to analyze the performance of this differentiator. In particular, we obtain the frequency response function $H(\mathrm{j}\omega)$ (note that many textbooks on signal processing use a normalized frequency Ω when dealing with the frequency response characteristics of filters where $0 < \Omega < \pi$ and where the upper frequency limit of π corresponds to half the sample rate of the process $F_S/2$. The relationship between actual frequency ω and the normalized frequency Ω is $\omega = \Omega F_S = \Omega/\Delta t$) by replacing z^{-1} by $\mathrm{e}^{-\mathrm{j}\omega\Delta t}$:

$$H(\mathrm{j}\omega) = \frac{1 - \mathrm{e}^{-\mathrm{j}\omega\,\Delta t}}{\Delta t} = \frac{1 - \cos\omega\Delta t + \mathrm{j}\sin\omega\Delta t}{\Delta t}$$

The modulus of this is:

$$|H(\mathrm{j}\omega)| = \left[\frac{(1 - \cos\omega\Delta t)^2 + \sin^2\omega\Delta t}{\Delta t}\right]^{1/2} = \frac{2\sin(\omega\Delta t/2)}{\Delta t}$$

How does this compare with the ideal differentiator modulus which simply multiplies by ω? **Figure 3** shows that, for small values of ω, the filter behaves like an ideal differentiator but as ω approaches the folding frequency of πF_S the filter gain is restricted to a value of $2F_S$, so the differentiator produces lower amplitude output than is required at higher frequencies. An implication of this is that, in addition to the normal aliasing considerations, use of the integration/differentiation algorithms presented here may impose even more stringent requirements upon the sample rate F_S to achieve a given level of amplitude accuracy.

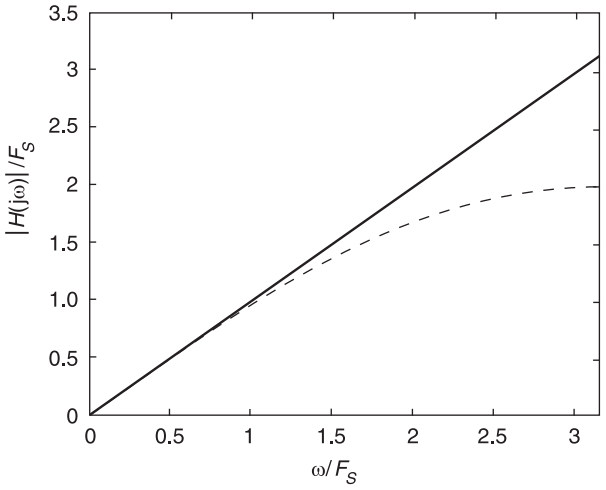


Figure 3 Comparison of the frequency response of an ideal differentiator and an algorithm based on the first-order difference approximation. (–) Ideal; (- - - -) first-order difference.

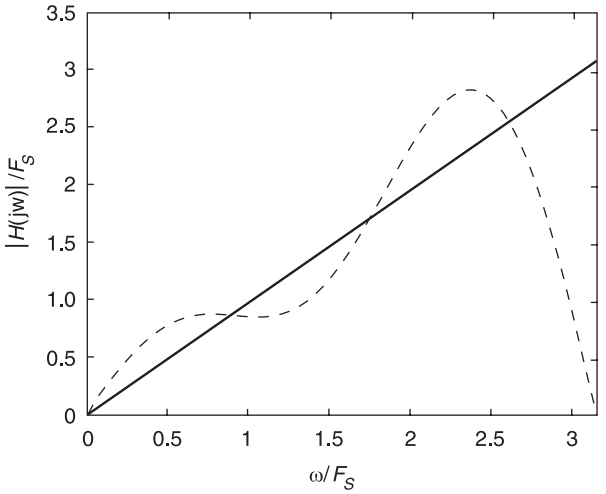


Figure 4 Comparison of an ideal differentiator and a filter designed using an improved digital algorithm. (–) Ideal; (- - - -) improved differentiator.

It can be shown in Lynn and Fuerst that a digital filter can be designed which takes the ideal differentiator modulus and phase into account. The coefficients of such a filter are:

$$h(n) = \frac{-1}{n}, \quad n = \pm 1,\ 3,\ 5 \ldots$$

$$h(n) = \frac{1}{n}, \quad n = \pm 2,\ 4,\ 6 \ldots$$

and:

$$h(0) = 0$$

This is an acausal filter, i.e., the filter responds before an input has arrived (which is obviously impractical for real-time analysis), which is antisymmetric about $n = 0$ with infinitely long 'tails'. In practice, we would restrict the filter to use finite number of points and put a delay into the filter to make it causal. So, for example, a seven-point filter would have the transfer function:

$$H(z) = \frac{2 - 3z^{-1} + 6z^{-2} - 6z^{-4} + 3z^{-5} - 2z^{-5}}{6\Delta t}$$

which corresponds to the difference equation:

$$y(n) = \Big[2x(n) - 3x(n-1) + 6x(n-2) - 6x(n-4) + 3x(n-5) - 2x(n-6)\Big]/6$$

The frequency response of this filter is shown in **Figure 4**. Note the ripples due to the truncation of the infinite series (this could be reduced by use of a window on the filter coefficients).

Many systems which implement differentiation use only the simplest first-order approximation, above, as the more refined algorithms produce only a small benefit but at the expense of considerable complexity.

Integration

We now consider the integration of sampled signals. We use as a starting point three algorithms that are often taught in a foundation course on numerical analysis for numerical integration: the running sum, the trapezium rule, and Simpson's rule.

Running Sum

The running sum amounts to finding the area under a sampled signal, assuming all sample values are held constant over the sample interval (**Figure 5A**). It is sometimes called the zero-order hold approximation.

The difference equation for a running sum is straightforward: the value of the integrated signal is the sum of the previous value and the area under the rectangle at the current point:

$$y(n) = y(n-1) + x(n) \times \Delta t$$

where signal $x(n)$ is integrated to produce $y(n)$. It can be seen that this recursive equation is actually identical to the equation for the first-order difference approximation to the differentiation with variables x and y reversed.

We can again use digital filter theory to investigate the performance of this algorithm and to compare

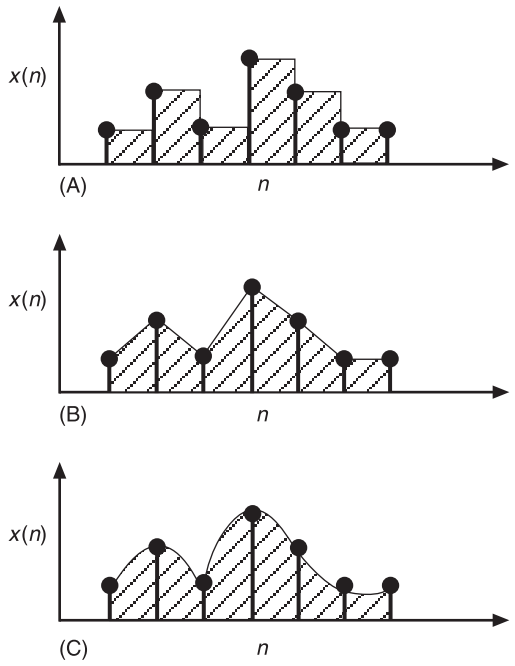


Figure 5 Integration algorithms using various interpolation methods. (A) Zero-order hold; (B) trapezium rule; (C) Simpson's rule.

this with an ideal integrator. The z-transform of the difference equation can be used to define a filter for the integration process:

$$Y(z) = z^{-1}Y(z) + \Delta X(z)$$

hence:

$$Y(z) = \frac{\Delta t}{1 - z^{-1}}X(z) = H(z)X(z)$$

where $H(z) = \Delta t/(1 - z^{-1})$ defines the filter for the running sum approximation for integration.

Trapezium Rule

For the trapezium rule we replace the zero-order hold interpolation with a straight line (or linear) interpolation between sample values (**Figure 5B**). It can be seen that the additional area to be added to the accumulated integration sum is the average of the two sample values multiplied by the sample interval so the difference equation becomes:

$$y(n) = y(n-1) + \frac{\Delta t}{2}\Big[x(n) + x(n-1)\Big]$$

This gives a trapezium rule filter transfer function:

$$H(z) = \frac{\Delta t(1 + z^{-1})}{2(1 - z^{-1})}$$

Simpson's Rule

For Simpson's rule, the interpolation between sample points is extended to quadratic segments between three sample values (**Figure 5C**) producing the difference equation:

$$y(n) = y(n-2) + \frac{\Delta t}{3}[x(n) + 4x(n-1) + x(n-2)]$$

and the corresponding filter:

$$H(z) = \frac{\Delta t(1 + 4z^{-1} + z^{-2})}{3(1 - z^{-2})}$$

Now the integrated signal is only updated for every other sample so that the integrated signal is effectively sampled at half the sample rate of the original signal. It should be noted that this can be most inconvenient for vibration signal analysis where we would generally wish to maintain the same sample rate throughout.

The performance of the three approximations is shown in **Figure 6**. The plot shows filter gain on a decibel scale (0 dB = unity gain) against frequency on a logarithmic scale up to $\omega = \pi F_S$. We have used these scales because the performance of all three algorithms is very similar for frequencies up to $\omega = F_S$. Thereafter the running sum approximation produces too much gain and the trapezium rule approximation produces too much attenuation. The Simpson's rule approximation is closer to the ideal than the other

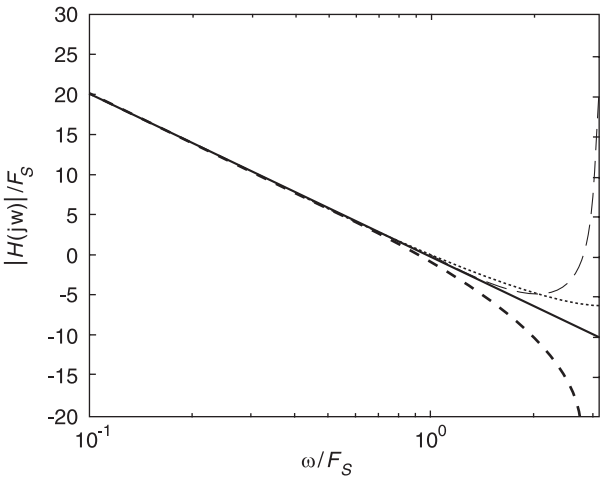


Figure 6 Comparison of the frequency response of an ideal integrator with three digital approximations. (–) Ideal; (—) Simpson's rule; (· · · ·) running sum; (- - -) trapezium rule.

approximations until about $\omega = 2.1F_S$ but then produces too much gain.

The three algorithms described above have effectively interpolated between the sampled values using polynomials of order 0, 1, and 2 but the first two methods are used most commonly for the integration of vibration signals as the improved accuracy of the third is obtained at the expense of complexity and the inconvenience of the sample rate change. There is, however, an interpolation algorithm for band-limited, sampled data, which is an improvement on any possible polynomial approximation. Indeed, Shannon's sampling theorem states that a function $x(t)$ may be expressed in terms of its sample values $x(n)$ by the relation:

$$x(t) = \sum_{n=-\infty}^{\infty} x(n\Delta t) \frac{\sin\ (\pi(t - n\Delta t)/\Delta t)}{\pi(t - n\Delta t)/\Delta t}$$

It can be shown in Dyne and Hammond that, while integration based upon this interpolation is superior to all three polynomial approximations, this is very much at the expense of simplicity and is therefore not appropriate for the majority of vibration signals.

Differentiation and Integration in the Frequency Domain

As we have seen previously, the differentiation of a harmonic signal amounts to multiplication by an angular frequency, ω, and a change of phase of 90°. Integration is a division by ω with a phase change of 90° in the opposite direction. It follows that differentiation and integration may be carried out in the frequency domain, i.e., on the spectral representation of signals, by multiplying the spectrum by $j\omega$ or dividing the spectrum by $j\omega$, respectively. So, for example, the Fourier transform of velocity can be found by multiplying the Fourier transform of displacement by $j\omega$ or by dividing the Fourier transform of the acceleration by $j\omega$.

Care needs to be exercised in the case of spectra which represent energy, or power quantities such as the power spectral density or the autospectral density formed using the product of a Fourier transform and its conjugate. For example the autospectrum of a segment of signal $x(t)$ of duration T, is the value of the product of the Fourier transform $X(f)$ and its conjugate $X^*(f)$:

$$S_{xx}(f) = \frac{X(f)X^*(f)}{T}$$

If $x(t)$ represents a velocity signal the autospectrum of the acceleration signal $y(t)$ would be:

$$S_{yy}(f) = \frac{Y(f)Y^*(f)}{T} = \omega^2 S_{xx}(f)$$

So the spectrum of the differentiated signal is found by multiplying the spectrum by ω^2 because both the Fourier transform and the conjugate take the $j\omega$ factor.

It is also worth noting that integration in the frequency domain by dividing the Fourier transform by $j\omega$ with a view to subsequent transformation back into the time domain is not straightforward and that there are pitfalls associated with the singularity at $\omega = 0$. Similarly, division of the DFT/FFT(fast Fourier transform) of an N-point sequence:

$$X(k) = \sum_{n=0}^{N-1} x(n)e^{-j2\pi nk/N}$$

by frequency $\omega_k = (2\pi kF_S)/N$, is subject to similar difficulties when subsequent transformation back into the time domain is under consideration. A pragmatic approach is often to set the value of the Fourier transform (or FFT) to zero at $0\,\mathrm{rad\,s^{-1}}$. However, while this amounts to only a single point error in the frequency domain, the error will have an impact on the whole signal following transformation back into the time domain. This method of integrating signals is therefore not recommended.

Summary

- Integration and differentiation of harmonic signals, with radian frequency ω, effectively multiply and divide the signals by a factor of $j\omega$, respectively. If the frequency is given as f in Hz then the factor is $j2\pi f$.
- For sampled signals, algorithms which approximate the effect of differentiation and integration can be implemented using difference equations and/or the equivalent digital filters.
- The frequency domain performance of differentiators/integrators can be investigated using tools developed for the interpretation of digital filters.
- The performance of the algorithms presented in this article is generally better at lower frequencies than at frequencies approaching the folding frequency $\omega = \pi F_S$ and this may have implications for the choice of F_S.
- The frequency domain characteristics can be improved by increasing the complexity of the filters but this is generally not necessary for measured vibration signals.
- Starting from the spectrum of displacement, velocity or acceleration, it is very straightforward to

derive the spectrum of any of the other quantities by multiplying by $j\omega$ to differentiate and by dividing by $j\omega$ to integrate. However, subsequent transformation back into the time domain is not recommended because of the effects of the singularity at $\omega = 0$.

See also: **Data acquisition**; **Digital filters**; **Sensors and actuators**; **Transducers for absolute motion**; **Transform methods**; **Windows**.

Further Reading

Dyne SJC, Hammond JK (1992) Integration of sampled signals. Presented at *IEE Colloquium on DSP in Instrumentation*, January London.

Kreyszig E (1979) *Advanced Engineering Mathematics*. Chichester, UK: Wiley.

Lynn P, Fuerst W (1990) *Introductory Digital Signal Processing with Computer Applications*. Chichester, UK: Wiley.

Papoulis A (1985) *Signal Analysis*. McGraw-Hill

SIGNAL PROCESSING, CEPSTRUM

See **CEPSTRUM ANALYSIS**

SIGNAL PROCESSING, MODEL BASED METHODS

S Braun, Technion – Israel Institute of Technology, Haifa, Israel

Copyright © 2001 Academic Press

doi:10.1006/rwvb.2001.0054

General

Many signal-processing techniques, which are relatively modern, extract models from measured data. In the context of vibration engineering, two major application areas utilize such techniques: signal modeling, and system identification. This article deals with signal modeling, and some applications.

Signal Modeling

Consider a signal $x(i\Delta t)$, where $i = 0, 1 \ldots n$. It may be possible to model the signal with a number of parameters p, where $p < n$. Signal modeling is thus concerned with the representation of signals in an efficient manner.

Applications of such signal models include data compression, signal prediction, classification, diagnostics and spectral analysis techniques.

It will be convenient to classify methods according to types of signal, whether random or deterministic.

Signal Models

Stochastic Models

The signal models used in vibration analysis include random process models and time series models that approximate discrete time processes encountered in practice, specifically sampled signals acquired from vibrating systems. Three major types, all of rational polynomial form in the Z-domain (see **Transform methods**), are used:

1. AR: autoregessive models
2. MA: moving average models
3. ARMA: autoregressive moving average models

One convenient point of view is to model these processes as being generated by filtering white noise by linear shift invariant filters. The following is a brief description of these three processes.

MA (moving average) process This is described as:

$$\begin{aligned} x_i &= w_i + b_1 w_{i-1} + b_2 w_{i-2} + \ldots b_q w_{i-q} \\ &= \sum_{k=0}^{q} b_k w_{i-k} x_i = \mathbf{w}^{\mathrm{T}} \mathbf{b} \end{aligned} \qquad [1]$$

with:

$$\mathbf{w} = \begin{bmatrix} w_i & w_{i-1} & \ldots & \ldots & w_{i-q} \end{bmatrix} \qquad \mathbf{b} = \begin{bmatrix} 1 & b_1 \ldots b_q \end{bmatrix}$$

In the context of linear systems, w is the system's input (white noise) and x the output. Applying a Z transform results in a transfer function:

$$X(z) = \sum_{k=0}^{q} b_k z^{-k} W(z) = B(z) W(z) \qquad [2]$$

where $B(z)$ is a rational system with q zeros – an all-zero system

AR (autoregressive) process This is described by:

$$\begin{aligned} x_i &= -a_1 x_{i-2} - a_2 x_{i-1} - \cdots a_1 x_{i-p} + w_i \\ &= -\sum_{k=1}^{p} a_k x_{i-k} + w_i \end{aligned} \quad [3]$$

This can be considered as a linear regression of x on itself, with w the residual, hence the name autoregressive.

In the Z domain:

$$X(z) = \frac{1}{1 + \sum_{k=1}^{p} a_k z^{-k}} W(z) = \frac{1}{A(z)} W(z) \quad [4]$$

where $1/A(z)$ is a rational system with p poles, i.e., an all-pole system.

ARMA (autoregressive moving average) process This is a combination of the above two processes:

$$x_i = -\sum_{k=1}^{p} a_k x_{i-k} + \sum_{k=0}^{q} b_k w_{i-k} \quad [5]$$

$$X(z) = \frac{B(z)}{A(z)} w(z) \quad [6]$$

where $B(z)/A(z)$ is a rational system with p poles and q zeroes.

Deterministic Models

These are based on equating a signal to the impulse response of a linear shift invariant filter, having a rational system function:

$$X(z) = H(z) = \frac{B(z)}{A(z)} \quad [8]$$

where $B(z)$ and $A(z)$ have q and p zeros, respectively. The matching of a given signal x_i to such an impulse response is called a Padé matching (or a Padé approximation).

This can also be stated by a time domain formulation as:

$$x_i = \sum_{k=1}^{p} c_k r_k^i$$

where r_k are the roots of the denominator of $A(z)$ and c_k are the complex coefficients of the expansion. This is similar to an original formulation (dating from 1795) created by Baron de Prony, and called the Prony model. The original model considered only the case of real roots r_k, whereas the interest in the context of vibration signals usually deals with complex roots:

$$x_i = \sum_{k=1}^{p} A_k \exp(\alpha_k + j2\pi f_k) \quad [9]$$

i.e., decaying oscillatory signals.

Modeling of Signals

The signal models are used to approximate data. Thus, the data generated by the model will approximate measured data. The sense in which the approximation is to hold has to be defined. For example, we may require that the autocorrelation (and hence the power spectral density) of the data generated by the model corresponds to that of the observed data.

The modeling task consists of two major phases. In the first one, the model's structure (or form) is defined, for example whether it is an AR or ARMA structure. This may also include the determination (or choosing) of the model's order, for example p in the AR case. In the second phase the model's parameters are found, such that the best approximation results. Obviously the criterion used must be defined, and is not necessarily unique.

The parameters themselves may have a direct physical interpretation. A synthetic model, where the parameters are purely mathematical, can still be used for the purpose of simulation and characterization. In what follows we address first the modeling of random data.

Modeling of Stochastic Signals

ARMA models From eqn [5], multiplying by x_{i-k}, we get:

$$R_x(l) = \sum_{k=1}^{p} a_k R_x(l-k) + \sum_{k=0}^{a} b_k R_{wx}(l-k) \quad [10]$$

where R are correlation functions. Let us consider x_i as the result of filtering the white noise w by a filter with impulse response h:

$$x_i = h_i \otimes w_i \quad [11]$$

Then:

$$R_x(l) + \sum_{k}^{p} a_k R_x(l-k) = \sigma_w^2 \sum_{k=0}^{q} b_k h_{k-l} = \sigma_w^2 c_k \quad [12]$$

where:

$$c_k = \sum_{k=1}^{q} b_k h_{k-l} \quad [13]$$

Thus:

$$R_x(l) + \sum_{k=1}^{p} a_k R_x(l-k) = \begin{cases} \sigma_w^2 c_k & 0 \le l \le q \\ o & l > q \end{cases} \quad [13a]$$

which for $k = 1, 2$:

$$\begin{bmatrix} R_x(0) & R_x(-1) & \cdots & R_x(-p) \\ R_x(1) & R_x(0) & & R_x(-p+1) \\ \vdots & & & \\ R_x(q) & R_x(q-1) & & R_x(q-p) \\ \cdots & \cdots & \cdots & \cdots \\ R_x(q+1) & & & R_x(q-p+1) \\ \vdots & & & \vdots \\ R_x(q+p) & & & R_x(q) \end{bmatrix} \begin{bmatrix} 1 \\ a_1 \\ \vdots \\ a_p \end{bmatrix} = \sigma_w^2 \begin{bmatrix} c_1 \cdot \\ \cdot \\ \cdot \\ \cdot \\ c_q \\ \cdots \\ \text{o} \\ \cdot \\ \text{o} \end{bmatrix} \quad [13b]$$

This is known as the Yule Walker (YW) equation.

AR models AR models are probably the most widely used models, and we will first concentrate on them.

From eqn [10], where $q = 0$, we have:

$$R_x(l) = -\sum_{k=1}^{p} a_k R_x(l-k) \quad [14a]$$

Using $k = 1, 2$, we get:

$$\begin{bmatrix} R_x(0) & R_x(-1) & \ldots R_x(-p) \\ R_x(1) & R_x(0) & \\ \vdots & & \\ R_x(p) & & \ldots R_x(0) \end{bmatrix} \begin{bmatrix} 1 \\ a_2 \\ a_2 \\ \vdots \\ a_p \end{bmatrix} = \sigma_w^2 \begin{bmatrix} 1 \\ 0 \\ \vdots \\ 0 \end{bmatrix} \quad [14b]$$

Or, in matrix notation:

$$\mathbf{Ra} = \sigma_w^2 \mathbf{I}, \quad \text{with } \mathbf{I} = [1\ 0\ 0\ 0]^{\mathrm{T}}$$

The modeling consists of computing the elements a of $\mathbf{a}$. An estimate of $\mathbf{a}$ can be solved by estimating $R(k)$ based on available data, i.e., by:

$$R(l) = E[x_k x_{k-l}] \quad [15]$$

The special symmetry noted for R is that of a Toeplitz matrix. A recursive solution, known as the Levinson–Durbin procedure, can solve this type of matrix equation in an efficient manner. Not only does it eliminate the need for a matrix inversion; at each iteration it increases the dimension of $\mathbf{a}$ (i.e., the model's order), a valuable feature when the order p has to be dealt with.

Some available procedures are based on a slightly different interpretation of the AR model (eqn [5]). This can be considered as linear prediction, where x_i is a linear combination of past observations x_{i-k}, and w is the residual or prediction error. This is a forward prediction procedure. A backward prediction can also be defined, where it is desired to predict the next earlier value, as per:

$$x_{i-p} = -b_1 x_{i-p+1} - b_2 x_{i-p+2} + \ldots w_{bi} \quad [16]$$

It can be shown that the YW equation:

$$\mathbf{Rb} = \sigma_{wb}^2 \mathbf{I} \quad [17]$$

can be used to solve $\mathbf{b}$, which minimizes the backward error w_b (in some specific sense).

Least-square estimation methods for AR modeling These are based on casting the AR prediction equations as a set of linear equations in the parameter vector $\mathbf{a}$, and minimizing the mean square of the prediction error.

From eqn [3]:

$$w_i = x_i + \sum_{k=1}^{p} a_k x_{i-k} \quad [18]$$

A matrix equation can be cast as:

$$\begin{bmatrix} w_1 \\ \vdots \\ \vdots \\ w_p \\ \vdots \\ \vdots \\ w_n \\ w_{n+1} \\ \vdots \\ \vdots \\ w_{n+p} \end{bmatrix} = \begin{bmatrix} x_0 & \dots & 0 \\ \vdots & & \vdots \\ \vdots & & \vdots \\ x_{p-1} & \dots & x_0 \\ \vdots & & \\ \vdots & & \vdots \\ x_{n-1} & \dots & x_{n-p} \\ x_n & \dots & x_{n-p+1} \\ \vdots & & \\ \vdots & & \\ x_{n+p-1} & \dots & x_n \end{bmatrix} \begin{bmatrix} a_1 \\ \vdots \\ a_p \end{bmatrix} + \begin{bmatrix} x_1 \\ \vdots \\ \vdots \\ x_p \\ \vdots \\ \vdots \\ x_n \\ x_{n+1} \\ \vdots \\ \vdots \\ x_{n+p} \end{bmatrix} \quad [19a]$$

$$\mathbf{w} = \mathbf{X}\mathbf{a} + \mathbf{x} \quad [19b]$$

With the least-squares solution:

$$\hat{\mathbf{a}} = \left(\mathbf{X}^{\mathrm{T}}\mathbf{X}\right)^{-1}\mathbf{X}^{\mathrm{T}}\mathbf{x} \quad [20]$$

The expression $\mathbf{X}^{\mathrm{T}}\mathbf{X}$ is a correlation matrix, based on observed data, and has already been encountered in eqn [13]. Correlation functions computed from data are used. In that sense it is similar to the solution of the YW equations, as computed estimators of correlation functions, and not the unknown theoretical correlation functions, are the only ones available for the solution.

Various computational schemes are available to the analyst, some of which depend on the range used. The method utilizing the range $0...n$ is called the autocorrelation method. It computes by forcing x to be zero outside the observed interval, i.e., windowing. The Toeplitz structure is however kept, enabling the use of the Levinson recursion. The range $i = n + p$ is called the covariance method. No windowing is now implied, which typically gives more accurate results, but the Toeplitz structure no longer exists. It can be shown that the autocorrelation method is equivalent to the YW method.

A modified covariance method is based on a similar approach, but minimizes the forward and backward error terms. The names are misnomers, due to historical reasons, and have no relation to the statistical functions of autocorrelation and covariance.

Another procedure, Burg's method, also minimizes the sum of squares of the forward and backward prediction errors, but uses a recursive procedure up to the pth parameter a_p, with the advantage that the resulting $A(z)$ is always stable.

Most of the above procedures are well documented and readily available in commercial as well as public domain software packages.

MA and ARMA models The ARMA model has more degrees of freedom, with a greater latitude in generating spectral shapes with sharp maxima and minima. The computational aspects are however much more complex. This is mainly due to the fact that the equations to be solved are nonlinear in the model's parameters. There exist a multitude of possible approaches, and only a few will be briefly described here.

We first start with MA models. A relatively simple approach is Durbin's method. A high-order AR model $A_p(z)$ is first fitted. A lower-order MA model $B_q(z)$ can then be obtained as:

$$A_p(z) \approx \frac{1}{B_q(z)} = \frac{1}{b_o + \sum_{k=1}^{q} b_k z^{-k}} \quad [21]$$

The two-step procedure thus consists of the following (**Figure 1**).

Fit a pth order model to the data, with a larger p than would have been used for pure AR model fitting.

Fit a qth-order model to the $B(z)$ sequence.

We turn now to ARMA modeling.

One possibility to reduce the computational complexity is applying a two-phase suboptimal procedure. First, the AR coefficients and then the MA are computed separately. In both phases a linear set of equations is solved. One typical algorithm is the following:

Fit a model via a well-established AR modeling algorithm, resulting in an approximate $A(z)$.

Apply an AR filter to the data, resulting in:

$$w(z)\frac{B(z)}{A(z)}\tilde{A}(z) \approx w(z)B(z)$$

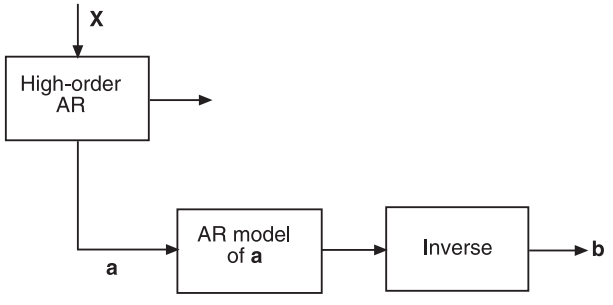


Figure 1 The Durbin moving average method. AR, autoregressive.

Fit an MA model to **wB** by an existing MA procedure (say, the Durbin logarithm). This is shown in **Figure 2**.

Simultaneous estimation of AR and MA parameter methods also exists, via iterative schemes. Basically an initial input excitation $\tilde{\mathbf{w}}$ is used. One possibility is then to identify a high-order AR model, in order to apply it as an inverse filter. Then an ARMA model is sought, such as to minimize an error between its output when driven by the assumed input **w** and the data **x**:

$$\text{Minimize } e^2\left(x - \tilde{w}\frac{B}{A}\right)^2 \qquad [22]$$

This is then linear in the coefficients a_k and b_k, and an iterative solution is readily found. Like most iterative searches for a minimum, convergence aspects need to be considered. Commercially available software for identification is often based on such iterative solutions.

Sequential methods A time-varying modeling is possible by sequential as opposed to block analysis. Techniques developed in the areas of adaptive filters can be used. As an example, let us mention the least mean square (LMS) method, where filter coefficients are updated as new data are incoming. This can be useful to track signals with relatively slow time-varying characteristics.

For the AR polynomial, the coefficients a_k will now be time-dependent. Thus, the equation will become:

$$x_i = \boldsymbol{\phi}_i^{\mathrm{T}}\mathbf{a}_i + w_i = [-x_{i-1}\cdots x_{i-p}]\mathbf{a}_i + w_i \qquad [23]$$

where the index 1 denotes the time dependency of **a**. The coefficient vector is now updated as per:

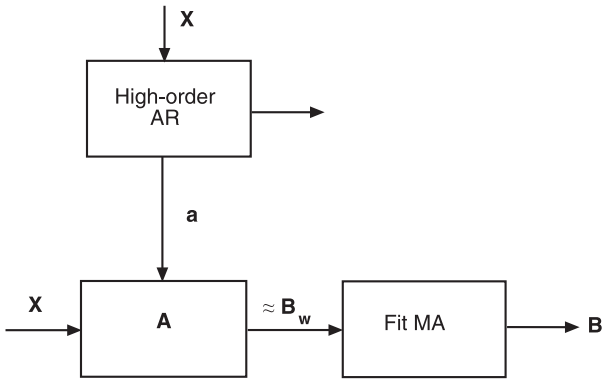


Figure 2 ARMA modeling. AR, autoregressive; MA, moving average.

$$\mathbf{a}_i = \mathbf{a}_{i-1} + \Delta\mathbf{a}_{i-1} \qquad [24a]$$

and the following updating is the LMS algorithm:

$$\Delta a_{i-1} = \mu\boldsymbol{\phi}_i(x_i - \boldsymbol{\phi}_i^{\mathrm{T}}\mathbf{a}_{i-1}) \qquad [24b]$$

where μ is the adaptive time constant which affects the adaptive performance, including its convergence. It is often suggested to use:

$$\mu = 0.01/\sigma_x \qquad [24c]$$

with σ_x the standard deviation of x. Other well-known adaptive schemes, like the RLS (recursive least square) and its various variations, are also options for the analysis of nonstationary signals.

Parametric Methods for Deterministic Signals

Model-based methods also exist for cases involving deterministic signals, such as decaying transients and harmonic signals.

Some modeling approaches attempt to approximate a signal x by an impulse response h of a linear shift time-invariant filter. In general, the transfer function of this filter is:

$$H(z) = \frac{B(z)}{A(z)} \qquad [25]$$

The coefficients of H, a_k and b_k of A and B are found by minimizing the error term:

$$\begin{aligned} \text{Minimize} \quad E &= \sum |e|^2 \\ e &= x - h \\ \frac{\partial E}{\partial a_k} &= 0 \quad k = 1, 2 \ldots p \\ \frac{\partial E}{\partial b_k} &= 0 \quad k = 1, 2 \ldots q \end{aligned} \qquad [26]$$

This results in a set of equations which are nonlinear in a and b. Direct methods of solving are thus of iterative form, such as the method of steepest descent. One other method is the iterative prefiltering method (also known as the Steiglitz–McBride method) which is available in many commercial signal-processing packages.

Indirect methods are usually simpler to solve; among these are Padé's and Prony methods.

The basic Prony method consists of modeling the signal as a sum of exponentially decaying transients.

The fact that decaying oscillating signals are accommodated can make this modeling attractive for specific vibration signals, like those of impulse response of linear vibrating systems. The original Prony procedure thus starts with:

$$x_i = \sum_{k=1}^{p} c_k \exp(s_i \Delta T) + w_i = \sum_{k=1}^{p} c_k z_k^i + w_i \quad [27a]$$

where:

$$z_k = \exp(s_i \Delta T) \quad [27b]$$

$$\begin{aligned} x_0 &= c_1 + c_2 + \ldots c_p \\ x_1 &= c_1 z_1 + c_2 z_2 + \ldots c_p z_p \\ x_2 &= c_1 z_1^2 + c_2 z_2^2 + \\ x_{p-1} &= \\ x_p &= c_1 q_1^p + \\ x_N &= c_1 z_1^N + \ldots c_N z_p^N \end{aligned} \quad [28]$$

Let z_i be the roots of the polynomial:

$$p(z) = \sum_{k=1}^{p} a_k z^k = 0 \quad [29]$$

It is simple to show that:

$$\begin{aligned} a_0 x_0 + a_1 x_1 + \ldots a_{p-1} x_{p-1} &= 0 \\ a_0 x_1 + a_1 x_2 + \ldots a_p x_p &= 0 \\ \vdots \quad & \quad \vdots \end{aligned} \quad [30]$$

We thus solve eqn [30] for the a_is. While the original Prony procedure was developed for p parameters using an equal number p of data points, a so-called overdetermined Prony procedure utilizes $N > p$ data points, and eqn [30] is in a least square sense.

The next step solves eqn [29] for z_k, using available root solvers. These are then used in eqn [28] (a Vandermonde matrix) to solve for the amplitudes c_k, again in least squares sense. The Prony method is a suboptimal procedure, computing in separate phases the parameters z_k and c_k, each one via a set of linear equations.

Another method which similarly solves separately for two sets of parameters via linear equations is often called the (modern) Prony method. Here an overdetermined set of linear equations solves $A(z)$ and $B(z)$ of eqn [25]. While the original time domain version of the Prony model is eqn [27a], it is this later Prony method which often prevails in many commercial software packages.

A comment comparing eqn [27] with fast Fourier transform analysis seems warranted. Whereas the DFT can only compute (and hence decomposes into) components of discrete frequencies of:

$$f_k = k\Delta f \quad \text{where} \quad \Delta f = \frac{1}{N\Delta T}$$

the Prony method has basis function of frequencies directly determined from the data.

Model order and overdetermination The accuracy of the parameters computed via the Prony method are highly affected by the existing signal-to-noise ratio and the model order chosen. Like all model-based methods, choosing too large a model order will result in poles which model noise terms. It is sometimes possible to estimate the signal model order via the rank of the covariance matrix of the signal (computable by a SVD decomposition).

An interesting phenomenon occurs with overdetermination of p, where p is the correct model order. In addition to generating noise-related poles, it is found that the signal-related poles will get closer to the true ones in the presence of noise. Thus it can be beneficial to choose too large a model order. The correct signal poles can be recognized by consecutively increasing the model order. Clustering of identified parameters will occur for the correct ones, while the location of the noise-related ones will be all over the parameter space.

Model-based spectral analysis

Procedure

Once a rational signal model is available, then the computation of the power spectral density is basically straightforward. For a linear system:

$$S_x(\omega) = S_w(\omega)|H(\omega)|^2 \quad [31]$$

where S_x is the power spectral density of the signal, and S_w that of the innovation process (or residual). H is the frequency response function of the signal model.

With:

$$\begin{aligned} S_w(\omega) &= S_w = \text{con} = P_w \Delta t \\ S_x(\omega) &= P_w \Delta t \left| \frac{B(\omega)}{A(\omega)} \right|^2 \end{aligned} \quad [32a]$$

where:

$$B(\omega) = B(z)|_{z=\exp(i\omega\Delta t)}$$
$$A(\omega) = A(z)|_{z=\exp(i\omega\Delta t)} \qquad [32b]$$

The power spectral density estimation thus consists of three basic steps (**Figure 3**):

- Step 1: selection of the signal model, including an appropriate order
- Step 2: estimation of the model parameters
- Step 3: insertion of the parameters into the theoretical power spectral density (equation).

The statistical properties of the estimated power spectral density depend heavily on the number of data points versus the number of model parameters. For the AR case, the result is asymptotically unbiased for large N. As parametric methods are often used in view of their improved frequency resolution, i.e., for time-limited records, such knowledge is of limited value. The variance of the estimators are roughly proportional to p/n, with p the model order.

Model or Selection

The smoothness of the PSDS function and the frequency-resolving power are strongly dependent on the model order chosen. One convenient point of view is that of data reduction, when $p + q$ parameters (plus the innovation process power) describe the characteristics of the data.

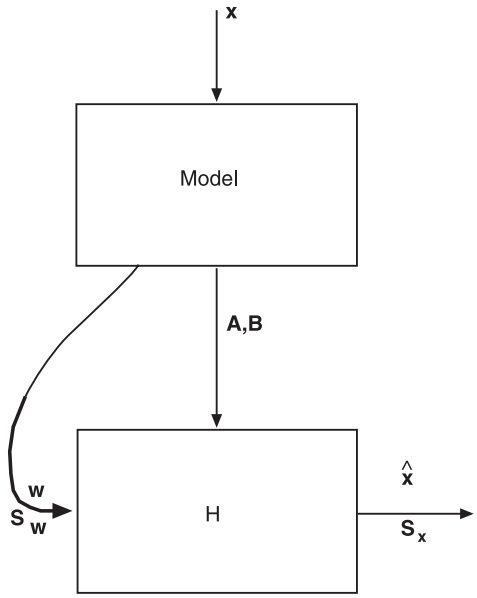


Figure 3 Model-based power spectral density.

For ARMA models, a search for reasonable orders is often an option, where the term reasonable is determined by heuristic arguments. Objective model orders, based on the minimization of specific criteria, mainly exist for AR models.

The following criteria achieve some balance between a high model order which causes a decrease in the prediction error power, and a penalty increasing with the model order.

The Final Prediction Error (FPE) Criterion

$$\mathrm{FPE}(p) = \sigma_w^2 \frac{n + (p+1)}{n - (p-1)} \qquad [33]$$

A smaller p/n ratio uses, on average, fewer data points per parameter a_k of the AR model. This results in less statistically accurate parameters. The order p minimizing FPE(p) is then used as the optimal one.

The Akaike Information Criterion (AIC)

$$\mathrm{AIC}(p) = n \ln\left(\sigma_w^2\right) + 2p \qquad [34]$$

An information theoretic function is minimized. Actually, AIC(p) and FPE(p) will be asymptotically equivalent as $n \to \infty$.

The Minimum Description Length (MDL) criterion

$$\mathrm{MDL}(p) = n \ln\left(\sigma_w^2\right) + p \ln(n) \qquad [35]$$

The penalty term $p \ln(n)$ increases with both n and p. The MDL is claimed to be consistent for increasing n.

The practical choice of p is often problematic, as no clear minimum of any criterion may be evident. A local minimum may be erroneously chosen. Often the region where a criterion plateaus is the best alternative.

An example is shown in **Figure 4**. An AR-based power spectral density is computed for an acceleration signal measured on a beam undergoing flexural vibrations. A single record of $n = 1024$ data points is available for the analysis. Increasing the model's order decreases the power spectral density's smoothness, and spurious peaks seem to occur. Lowering the model order results in smoother power spectral densities. A fast Fourier transform power spectral density (based on analyzing the same data as a single record, i.e. without any averaging) is shown for comparison.

Computing the FPE, an order of $p = 10$ seems indicated (**Figure 5**). The resulting power spectral density is shown in **Figure 4c**. This smoothed power

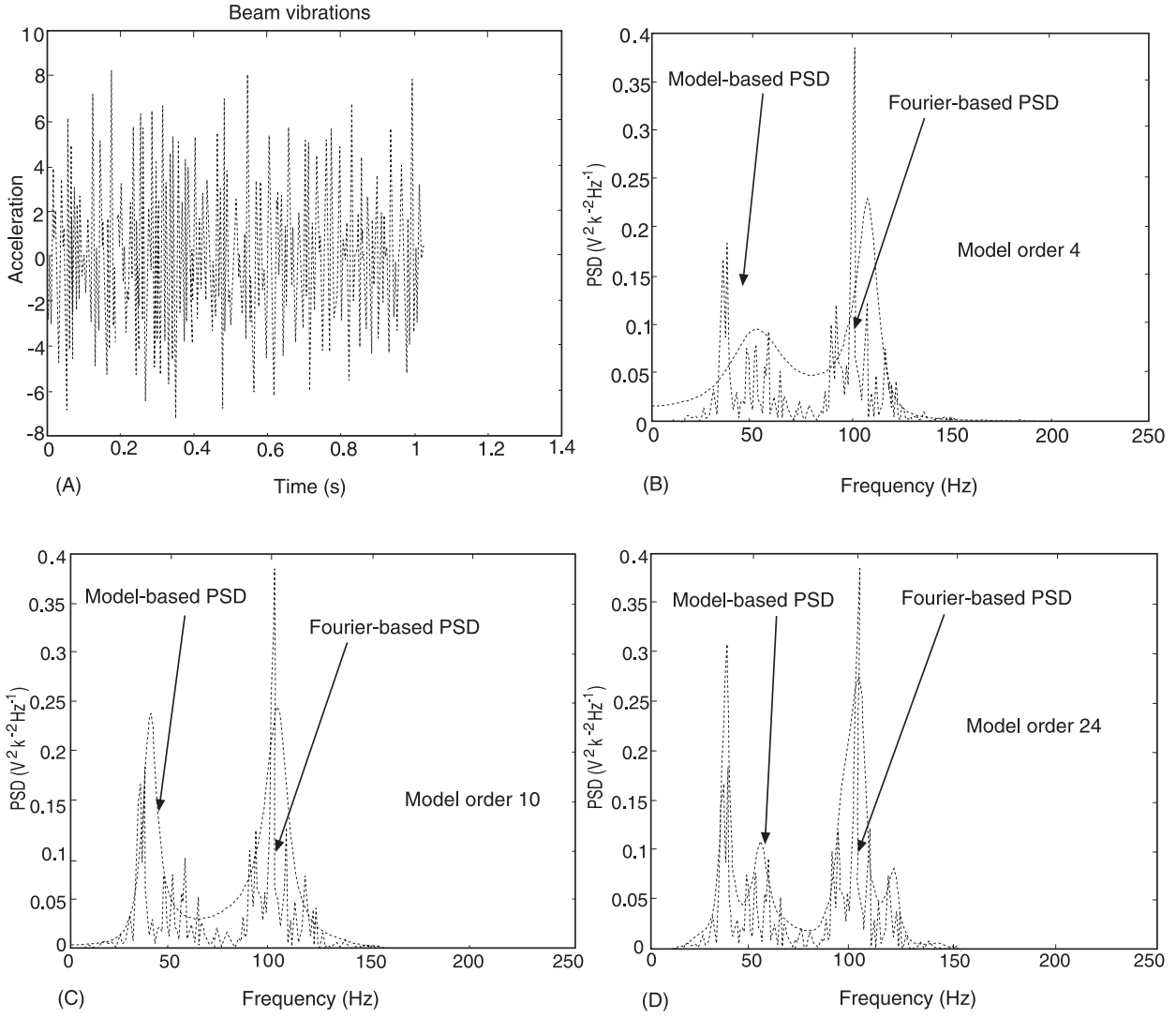


Figure 4 Fourier-based versus model-based power spectral density (PSD) of beam vibrations. (A) The time data; (B) $p = 4$; (C) $p = 10$; (D) $p = 24$.

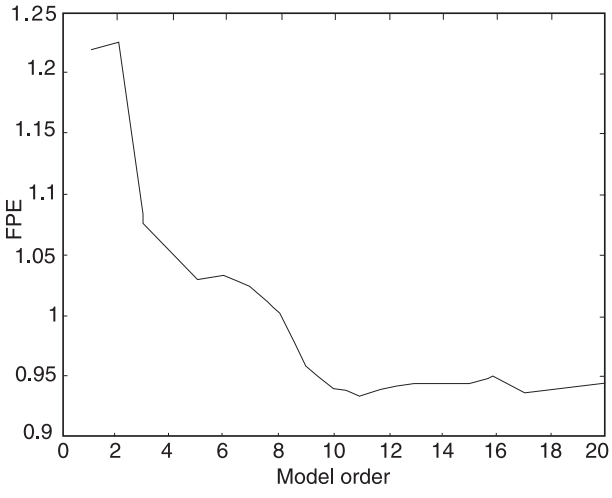


Figure 5 Akaike's criterion for beam vibration. FPE, final prediction error.

spectral density (compared to the fast Fourier transform based one) shows objective versus spurious peaks, i.e., those justified by the data (based on our model order criteria). Only additional external knowledge could indicate that additional peaks are significant.

The technique of overdetermination, already mentioned above, could also be used to identify true poles. Clustering of poles, around areas corresponding to spectral peaks, would occur while increasing the model order from 4 to 10 to 34.

Additional Analysis Methods

There exist many additional methods aimed at spectral analysis and estimation of frequencies of discrete line spectra. Only a few will be briefly mentioned, as their application to vibration signals is rare.

Subspace Methods

These are basically model-based methods aimed at estimating discrete components in the spectrum. The Pisarenko and multiple signal classification (MUSIC) are among the best known, and are aimed at estimating the frequency of line spectra. Thus they deal with signals composed of sinusoids and random components. They are based on the eigenanalysis of the correlation matrix of the observed data. For an n-point signal composed of m sinusoidal components and additive noise, the correlation space can be divided into two subspaces: a signal subspace with m eigenvectors, and a complementary subspace with $n - m$ eigenvectors. For practical situations, the largest m eigenvalues are then associated with the line spectra.

Minimum-variance Power Spectral Density

This is an adaptation of the maximum likelihood spectral analysis (hence actually a misnomer) developed for beam-forming applications. It is based on analyzing the signals by filters of unity gain, which minimize the output when a random signal is applied to them.

This is in contrast to classical spectral analysis, where the DFT filter bank (see **Transform methods**) has a constant bandwidth, independent of the signal's character. The frequency responses of the DFT filters are also less ideal, with side lobes and resulting leakage phenomenon.

Discussion

For vibration signal analysis, model-based techniques are a possible alternative to the classical, nonparametric Fourier-based ones. Some of the rationales for opting for such an approach are listed below.

1. Finite, limited data records: for the same data length, parametric methods have the potential of improved frequency resolution. If unlimited-duration signal durations are available, it is generally accepted that classical analysis performs better.
2. Again, for finite-duration data records, a smooth power spectral density is obtained. This follows from the computation of eqn [32] based on a limited number of model parameters. Using any defined criterion for model order selection, a best objective power spectral density is obtained for the given data.
3. Tracking time-dependent model parameters may be used to compute time-varying power spectral densities.
4. A model needs to be fitted to the data for the purpose of control, prediction, and diagnostics. While some models can be based on frequency domain representation, those based directly on time signals may be preferred.

In practice, the model-based spectral analysis is liable to many difficulties. The choice of model order is important. Misleading results may occur if the model chosen is not consistent with the signal generation process. For example, the best results for an ARMA process will result if an ARMA model is fitted, and the same goes for any other process. The practitioner can sometimes rely on physical insight, whenever possible. If mainly spectral peaks are anticipated (for example, for structural resonances), an all-pole (AR) model could be chosen. The AR model is also popular due to the easier computational load involved in the modeling, as a set of linear equations must be solved.

The choice of model order is perhaps the most important one in the analysis. Spurious spectral peaks occur if too large an order is chosen (i.e., overdetermination), as the contaminating noise will also be modeled.

The choice of the computational algorithm can also affect results. For example, Burg's method may result in spectral splitting, where two spectral lines occur instead of a single one. There is evidence that the modified covariance method often performs better in this respect. It also performs best when sinusoidal components exist in the data.

Where there are processes consisting of sinusoids in broad-band noise, the increased analysis resolution is a function of the signal-to-noise ratio. Thus spurious peaks have been noted. The low-frequency part of the AR spectrum can also be corrupted by DC components in the data. Like many signal-processing tasks, it may be of advantage to subtract it before any analysis is made.

Nomenclature

A, a	polynomial of denominator of transfer function
B, b	polynomial of nominator of transfer function
p, q	orders of polynomials A and B (a and b)
n	number of data points
R	correlation matrix of elements
S	power spectral density

See also: **Adaptive filters**; **Identification, model–based methods**; **Spectral analysis, classical methods**.

Further Reading

Hayes MH (1996) *Statistical Digital Signal Processing and Modeling*. New York: John Wiley.

Marple SL Jr (1987) *Digital Spectral Analysis with Applications*. Englewood Cliffs, New Jersey: Prentice Hall.

SMART MATERIALS

See **ELECTRORHEOLOGICAL AND MAGNETORHEOLOGICAL FLUIDS; ELECTROSTRICTIVE MATERIALS; MAGNETOSTRICTIVE MATERIALS; PIEZOELECTRIC MATERIALS; SHAPE MEMORY ALLOYS**

SOUND

See **VIBRATION GENERATED SOUND**, FUNDAMENTALS; **VIBRATION GENERATED SOUND**, RADIATION BY FLEXURAL ELEMENTS

SPECTRAL ANALYSIS, CLASSICAL METHODS

S Braun, Technion – Israel Institute of Technology, Haifa, Israel,

Copyright © 2001 Academic Press

doi:10.1006/rwvb.2001.0187

Rationale of frequency domain representation

The use of spectral analysis, in many areas of applications, but almost exclusively in vibration analysis, is so predominant that the rationale for using it is often ignored. The main possible reasons for this are as follows:

1. Physical insight is often easier to obtain in the frequency domain, as opposed to the original time domain description of signals and systems. The existence of periodic vibrations occurring with rotating machines is a classical example. The recognition of constant-frequency, resonance-excited signals is another one.
2. The orthogonality properties of Fourier decompositions implies that cross-products of signal components of unequal frequencies is zero. No power is contributed by such cross-products. It is thus possible to investigate independently the contribution of certain frequency regions to the total power or energy. For example, we may try to attenuate vibrations in a certain frequency band independently of other frequency regions, and different approaches could be tried for different frequency ranges.
3. Vibration patterns of diagnostic significance are often recognized more easily. Small changes, barely affecting the time signature, are often easily detected in the frequency domain representation.
4. Finally, we mention the closed-form solution for vibrating systems, often modeled as lumped linear systems, and hence described by linear differential equations. Applying a Fourier transform (or Laplace or even Z transform for discrete cases) results in sets of algebraic equations. Closed-form solutions are readily obtained, and frequency domain descriptions of signals and systems often prevail in introductory vibration textbooks (and this advantage is sometimes cited as the rationale for Fourier method).
5. While the rationale given in the previous point is of less interest to real-life situations, the closed-form solution is of practical interest, as it is often compared to experimental results. Thus, predicted signals (or system properties) are compared to those obtained experimentally, and again the patterns are often easier to interpret in the frequency domain. Examples are vibration spectra of rotating elements, and structural responses, which will be compared to those predicted analytically.

Engineering Units

Different types of frequency domain analysis can be performed, depending on the type of signals at hand, and also on the intended application, i.e., the use of the analysis results.

Some applications, mainly in the area of diagnostics, often mainly need changes to be detected. In such cases, the type of presentation and engineering units (EU) are less critical. Almost any of the prevalent spectral presentations can be used, as long as consistency is retained for comparison purposes.

For applications which require quantitative results, however, EU are of utmost importance.

Below, we address the most prevalent EU and their suitability for specific signal classes.

We thus assume that for a signal:

$$x(n) \quad n = 0, 1 \ldots N-1$$

we have computed the fast Fourier transform (FFT) (see **Transform methods**):

$$X(k) = \sum_{n=0}^{N-1} x(n) \exp\left(-j\frac{2\pi}{N}\right)^{nk} \qquad [1]$$

All signals are considered to have dimensions of voltage (V). Mechanical vibration units are readily obtained in appropriate EU when the measurement conversion units are applied.

Addressing the frequency scale, this will consist of equally spaced frequencies, with a spacing of:

$$\Delta f = 1/(N\Delta t)$$

where Δt is the sampling interval.

The time scale is thus $t = n\Delta t$, and the corresponding frequencies:

$$f(k) = k\Delta f$$

We will sometimes refer to $f(k)$ as computational (or analysis) frequencies, as opposed to actual physical ones, the reciprocal of the period of a signal. It is important to realize that the analyst has some control over the analysis frequencies (via the choice of N, or equally the signal duration), whereas the physical frequencies are independent of the analysis parameters chosen.

We now address the EU according to the type of signal analyzed.

Transients

The obvious choice is the DFT, which approximates samples of the continuous FT, given by eqn [1], which is readily computed via the FT. For EU we compute:

$$X_{\mathrm{EU}}(k\Delta f) = \Delta t\, X(k\Delta f)\ [\mathrm{V{-}s}] \qquad [2]$$

Periodic Signals

A Fourier series decomposition is indicated, at least in principle. As an example we might be interested in estimating the amplitude of the fundamental (or any specific harmonic frequency) component.

From the entry on **Transform methods** note that:

$$\begin{aligned} X &= N\, X_{\mathrm{DFS}} \\ X_{\mathrm{FS}}(f_k) &= \frac{1}{N} X(k) \quad [\mathrm{V}] \end{aligned} \qquad [3]$$

The computation equals that of the DFT, except for the factor N. The results are expressed directly in volts. A two-sided presentation (see later) is given by eqn [3].

Some aspects of the frequency scale warrant discussion. In the DFS, one period of the assumedly periodic signal is analyzed. The frequency scale:

$$f(k) = k\Delta f$$

thus shows the fundamental (at $k = 1$), second harmonic (at $k = 2$), and so forth, of a periodic signal which consists of the periodic extension of the signal section used in the FFT.

The length of the signal spanned by the analyzing window may be such that a multiple of physical periods are spanned. Let us assume that p integer periods are spanned by the signal length $N\Delta t$ being analyzed.

Denoting the number of samples in the period by M, we have:

$$T_p = M\Delta t$$

with T_p the actual period of the physical signal. Hence the total signal length:

$$N\Delta t = pM\Delta t$$

and the location of f_p on the frequency scale is:

$$\begin{aligned} k\Delta f = f_p &= 1/(M/\Delta t) \\ k &= 1/(M\,\Delta t\,\Delta f) = N/M = p \end{aligned}$$

Thus, the location index of the fundamental (physical) frequency equals M, the number of periods spanned by the signal analyzed (**Figure 1**).

It also follows that, only when an integral number of periods is spanned will the physical frequency coincide with one of the frequencies at which the DFS is computed, i.e., an integer multiple of Δf. For signals spanning a noninteger number of cycles in the analysis window, the true physical frequency will be at some intermediate location between two computed

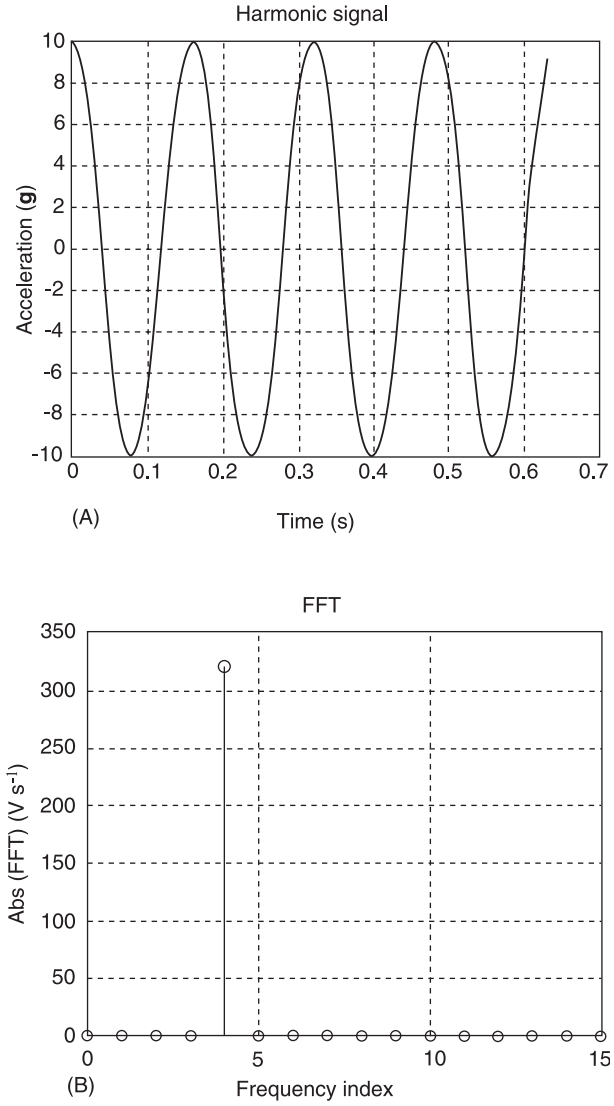


Figure 1 Harmonic signal: number of periods and frequency index. (A) Signal; (B) line spectrum.

frequencies. The magnitude, at the true frequency, is not computed.

Random Continuous Signals

Second-order statistics are used, based on the definition of the power spectral density (PSD) as the Fourier transform of the autocorrelation function (see **Correlation functions**).

We note the interpretation of the PSD (this is sometimes used as a definition) as:

$$P = \int_{-\infty}^{\infty} S(f)\,\mathrm{d}f \qquad [4]$$

which is the distribution of the power in the frequency domain. The PSD is a distribution function, and the portion of the total power contributed by the specific frequency range is given by an integration (or summation) of $S\Delta f$.

$$P_{f_1-f_2} = \int_{f_1}^{f_2} S(f)\,\mathrm{d}f \qquad [5]$$

and the units of S are $\mathrm{V}^2\,\mathrm{Hz}^{-1}$ (**Figure 2**). For digital computations, we note that for a finite N point signal, the correlation is estimated as:

$$\begin{aligned} R(m) &= \frac{1}{N}\sum x(n+m)x(n) \\ &= \frac{1}{N}x_N(m) \otimes x_N(-m) \end{aligned} \qquad [6]$$

where x_N denotes the N point signal (zero outside the interval) and $\otimes$ convolution. Applying a DFT to the convolution results in:

$$S(k) = \frac{1}{N}|X(k)|^2 \qquad [7]$$

For EU we note that a factor of Δt is needed for discrete computations of $S(\Delta f)$.

Thus, we compute the PSD via the DFT as:

$$S(k\Delta f) = \frac{\Delta t}{N}|X(k\Delta f)|^2 \qquad [8]$$

Additional Representations

As with PSD, we may define an energy spectral density for energy signals:

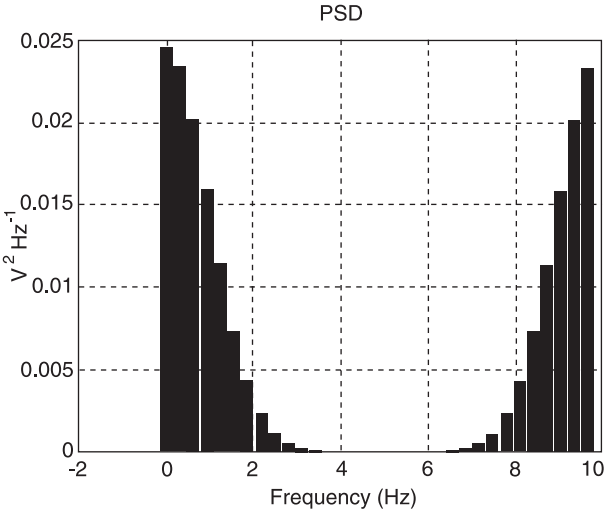


Figure 2 Power distribution in the frequency domain.

$$E = \int_{-\infty}^{\infty} S_E(f)\,\mathrm{d}f \qquad [9a]$$

with:

$$E_{f_1-f_2} = \int_{f_1}^{f_2} S_E(f)\,\mathrm{d}f \qquad [9b]$$

showing the contribution to the total energy in the band $f_1 - f_2$. These are computed as:

$$S_E(k\Delta f) = T_t S(k\Delta f) = \Delta t^2 |X(k\Delta f)|^2 \quad [\mathrm{V^2{-}s^2}] \qquad [9c]$$

We may also wish to see the power distribution as opposed to the power density distribution. This would be computed as:

$$S\Delta f = \frac{\Delta T}{N}|X(k\Delta f)|^2 \frac{1}{N\Delta t} = \frac{1}{N^2}|X(k\Delta f)|^2 \quad [\mathrm{V^2}] \qquad [10]$$

Linear (sometime called voltage)-based units are sometimes preferred over squared (power or energy)-based ones. Taking the square root of all expressions discussed so far.

It is important to realize that the original data cannot be reconstructed from power (or energy) functions in the frequency domain. This should be evident from the actual procedure, which only utilizes the magnitude of the DFT, while the phase information is ignored.

Frequency Scales, One-and Two-sided Presentations

The (computational) resolution being $\Delta f = 1/(N/\Delta t)$, the frequency scale is:

$$f(k) = k\Delta f$$

This is a two-sided presentation, involving both positive and negative frequencies. For the basic FFT algorithm, the locations:

$$k = N-1, N-2 \ldots N/2$$

correspond to negative frequencies according to:

$$X(-k) = X(N-k)$$

while $X(0)$ is the DC component (multiplied by N), and $X(N/2)$ the value at the Nyquist frequency.

A more classical presentation is often used by simple shifting (**Figure 3**).

A one-sided presentation is often preferred for engineering applications. Thus, for $X(k)$, the two-sided transform, a one-sided transform $X_1(k)$ is computed as:

$$X_1(k) = \begin{cases} X(k) & k = 0, \quad k = N/2 \\ 2X(k) & k = 1, 2 \ldots N/2 - 1 \end{cases} \qquad [11]$$

One-sided presentations for power energies are also used, for example (**Figure 4**):

$$G(k) = \begin{cases} S(k) & k = 0, \quad k = N/2 \\ 2S(k) & k = 1, 2 \ldots (N/2) - 1 \end{cases} \qquad [12]$$

For quantitative results, the EU used must be stated. This will depend on whether the signals are deterministic transients, deterministic periodic, stationary, etc. The application may also be a factor. Power units would be used for random or mixtures of deterministic and random signals. Straight DFT or alternatively EU could be used for transients. For periodic signals, the PSD, DFT or even a Fourier series decomposition X_{DFS} could be used.

The fact that all different EU are computed via the DFT (by means of the FFT algorithm) means that similarities (and sometimes equivalences) can sometimes cause confusion. The type of presentation, whether one-or two-sided, is obviously important. **Table 1** shows the different EU used, according to the type of signals.

The computational formulae contain Δt, the sampling interval. General-purpose software often includes signal-processing functions where a normalized sampling interval of $\Delta t = 1$ is assumed. Caution is thus needed when such software is used for real-case sampled signals. On the other hand, most dedicated vibration-processing software (especially operating in conjunction with data acquisition systems) will usually offer the choice of many EU and compute them automatically. Their presentation will usually be one-sided.

Performance, Errors, and Controls

Like many signal-processing tasks, the ease of employing available procedures is not enough to warrant meaningful results. The analyst must be aware of mechanisms generating uncertainties in the analysis results. Next the analyst must be acquainted with the possibilities of controlling those uncertainties. As will

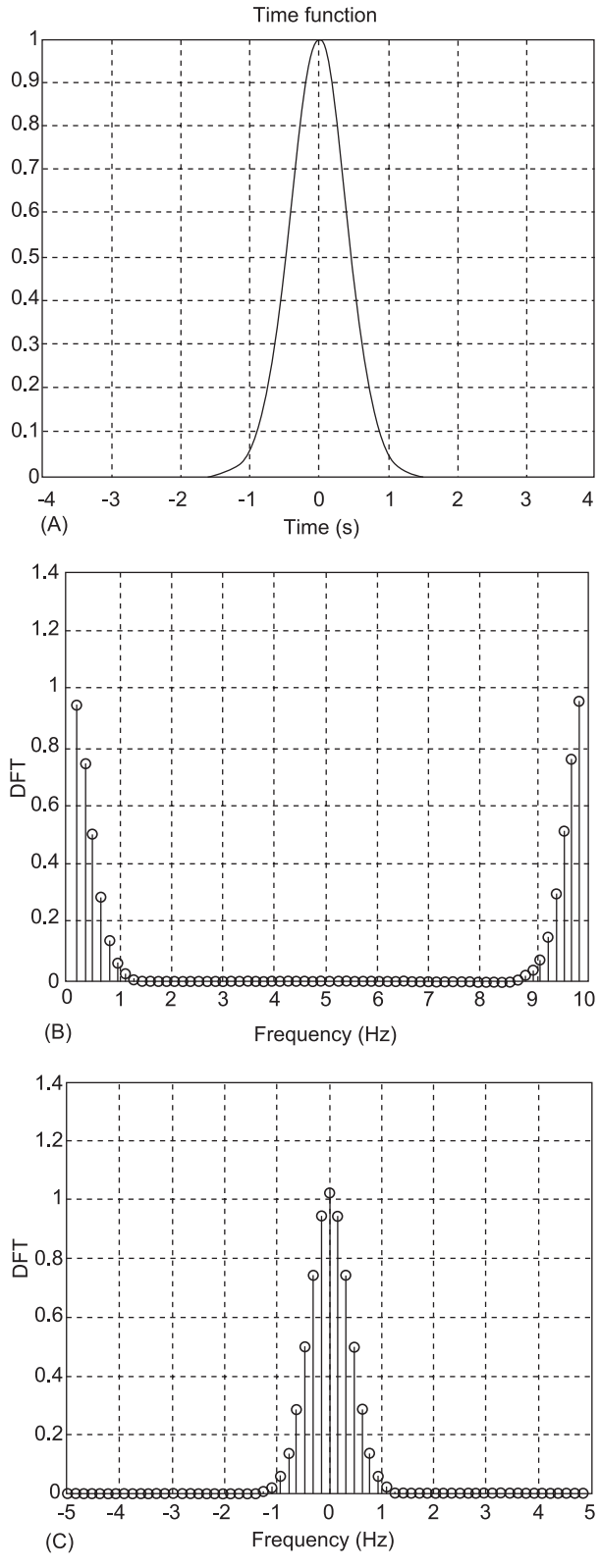


Figure 3 Frequency scale for the DFT. (A) The signal; (B) frequency index 0 to $N-1$; (C) frequency index $-N/2+1$ to $N/2$.

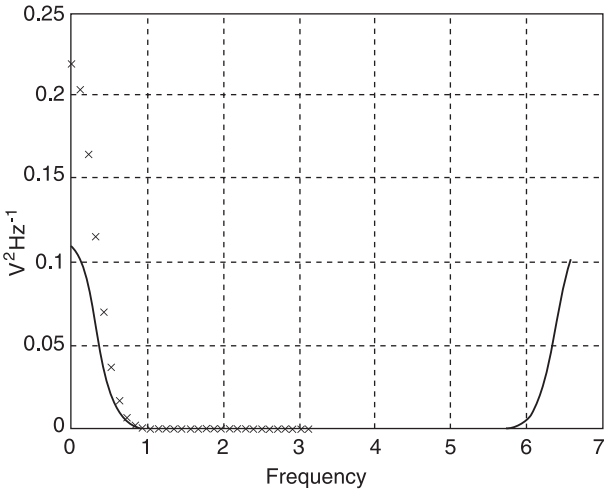


Figure 4 One and two-sided PSD. Continuous line, one-sided PSD; crosses, two-sided PSD.

become clear, these problems are of utmost importance as far as spectral analysis is concerned.

The main error mechanisms in spectral analysis can be categorized as follows:

- alias errors
- bias errors
- leakage errors
- random errors

Aliasing is related to the correct sampling of continuous signals, and hence is not addressed in the following paragraphs.

In what follows, performance aspects are tackled according to the signal's character.

Some of the errors to be controlled depend on the type of signal at hand. There is however a basic limitation to the decomposition of signals in the frequency domain, which is traceable to an uncertainty principle. This will be described first. Then errors/performances will be addressed as follows:

- transient signals
- periodic signals
- random signals

The Uncertainty Principle

The uncertainty principle describes the relationship between time duration and the frequency bandwidth of signals. The quantitative formulation depends somewhat on how the 'duration' and 'bandwidth' are defined, and more than one possibility exists for such definitions. For any reasonable definition: (time duration) $\times$ (frequency bandwidth) $> C$ where C is in the range of 1.5–3, depending on the definition. Resolving within $f_2 - f_1$ thus necessitates a duration of:

Table 1 Engineering units. Units based on $X(k) \leftrightarrow x(n) - 1$

	Computation	*EU*	*Voltage units*
FT	$\Delta t X$	V−s	
FS	X/N	V	
S(PSD)	$(\Delta t/N)\lvert X\rvert^2$	$V^2Hz^{-1} = V^2-s$	$V/\sqrt{Hz}$
S_E(ESD)	$\Delta T^2\lvert X\rvert^2$	V^2-s^2	V−s
Power in bin	$S\Delta f = (1/N^2)\lvert X\rvert^2$	V^2	
Energy in bin	$S_E\Delta f = (\Delta t/N)\lvert X\rvert^2$	V^2-s	
Total power (frequency)	$P_f = (1/N^2)\sum\lvert X\rvert^2$	V^2	
Total power (time)	$P_t = (1/N)\sum x^2$		
Total power (time)	Parseval : $\sum x^2 = (1/N)\sum\lvert X\rvert^2$	V^2	
Total energy (frequency)	$E_f = \Delta t\sum X^2$	V^2-s	
Total energy (time)	$E_t = \Delta t\sum x^2$	V^2-s	

$$T_t \geq \frac{2}{f_2 - f_1} \qquad [13]$$

The uncertainty principle is so basic that its practical implications are sometimes overlooked. Thus, given a signal length T_t, two components separated by $f_2 - f_1 = 1/T_t$ will not be separated by any signal-processing techniques (unless additional information is at hand). Another immediate conclusion is that changes in the frequency domain separated by $f_2 - f_1 < C/T_t$ are meaningless, notwithstanding the possibility of computing at sometimes closer arbitrary frequencies (see below).

For digital FFT-based computations, the frequency scale is in steps of:

$$\Delta f = 1/(N\Delta t) = 1/T_t$$

and the uncertainty principle is 'automatically' satisfied. Dedicated instrumentation sometimes have a 'zoom mode' for spectral analysis, whereby only a partial frequency range is zoomed in for analysis. High resolution is achieved if N frequency points are computed in this range. It should be clear that this can only be achieved using an appropriate data duration, and very large T_t may be needed with such a mode of operation. Specifically, if in zoom mode N frequencies are resolved in the range $f_2 - f_1$, then:

$$T_t = 1/(\Delta f) = N/(f_2 - f_1)$$

Transient Analysis and Zero Padding

We now turn to transient signals. The performance hinges on the resolving power of the analysis. As obvious from the prior section, this is limited by the signal's duration. Let us assume a signal with finite duration x/n, $i = 0, 1, 2, \ldots N_1$.

The basic frequency resolution is, assuming for the moment that a transform is computed for N_1 points:

$$\Delta f_{\text{transient}} = \frac{1}{N_1\Delta t} \qquad [14a]$$

If $N - N_1$ zeros are now appended to the signal, resulting in a total span of N points, a computational resolution of:

$$\Delta f = \frac{1}{N\Delta t} < \Delta f_{\text{transient}} \qquad [14b]$$

will be achieved. This operation, called 'zero padding' has no effect on the computed DFT, as can be noted from:

$$X(k) = \sum_{n=0}^{N_1-1} x(n)\left(\exp - j\frac{2\pi}{N}\right)^{nk} + \sum_{i=n}^{N} 0\left(\exp - j\frac{2\pi}{N}\right)^{nk} \qquad [14c]$$

and nothing is contributed to $X(k)$ by the second term.

It should be clear from the uncertainty principle that no improvement in the resolving power of the frequency function has been achieved. The fact that $X(k)$ is now computed at more closely spaced intervals is equivalent to a specific interpolation scheme in the frequency domain. (The actual-type of interpolation is outside the scope of this text.) **Figure 5** demonstrates an example of zero padding and equivalent interpolation.

Zero padding is used to comply with requirements of a specific N, often dictated by the maximum length of other signals in multichannel acquisition tasks (or compatibility with the requirements of the FFT used).

Another aspects concerns the possibility of controlling the deterioration of the signal-to-noise ratio due to additive noise. An improvement in the signal-to-noise ratio can be achieved for specific cases where *a priori* information on the signal's characteristics is at

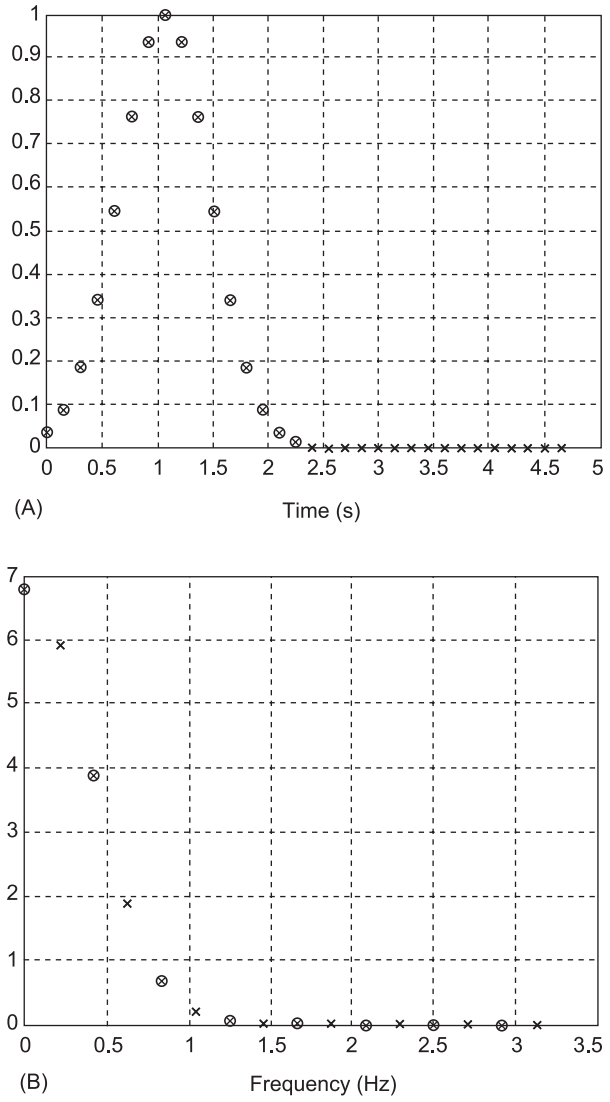


Figure 5 Zero padding. (A) Signal, time domain; (B) frequency domain. Circles, with zero padding; crosses, without zero padding.

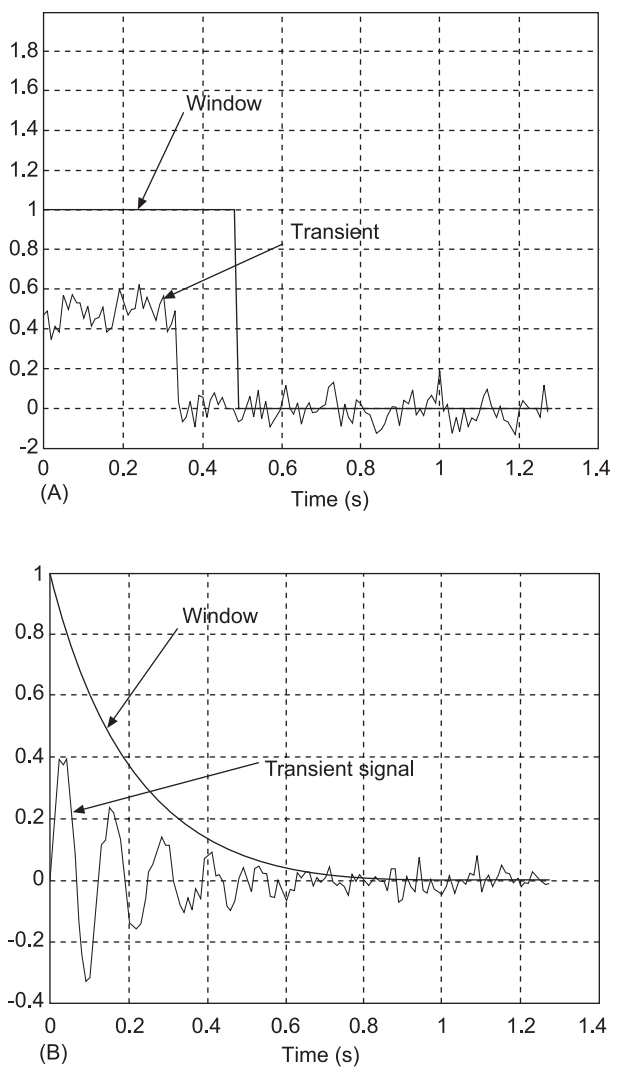


Figure 6 Specific windows for transients. (A) Time-limited signal and window; (B) decaying oscillations and exponential window.

hand. We may give less weight to signal samples with lower signal-to-noise ratio. The weighing is done by a time window function applied to the signal (see **Table 2**. Two examples are briefly described (**Figure 6**):

1. A transient limited to a small part of the analyzed time interval. A rectangular window, giving zero weight outside the signal's duration can be applied, see **Figure 6A**. The transition between 100% to zero weight should preferably be somewhat gradual.
2. A decaying oscillating signal, typical of transient response of low damped vibrating structure. An exponentially decaying window is then applied (**Figure 6B**).

Periodic Signals

In this paragraph we will often differentiate between 'physical' and computed frequencies. Only the last one can be controlled to some extent by the analyst. An error designated as leakage then occurs whenever they differ. As far as periodic signals are concerned, the analysis resolution and control of leakage are of major importance.

For periodic signals, with period T_p, the physical frequencies are:

$$k/T_p$$

whereas computed frequencies will be located at:

Table 2 Window characteristics

Window	*3 dB bandwidth*	*Secondary lobe (dB)*	*Sidelobe fall-off (dB/decade)*	*Ripple (scallop loss) (dB)*
Rectangular	$0.88\Delta f$	-13.2	20	3.92
Hanning	$1.44\Delta f$	-31.5	60	1.42
Flat top	$3.72\Delta f$	-93	0	0.01

$$k\Delta f = k/(N\Delta t)$$

As discussed before, physical and computed frequencies will only coincide when an integral number of periods are spanned by the signal analyzed.

Figure 7 shows a DFT applied to two cases: a section of a harmonic signal spanning an integral number of periods, and a nonintegral one. We note that, in the second case the computed $X(k)$ is spread over a large frequency range, in contrast to the physical signal of an actual single frequency. The effect is called leakage, as if severely affect spectral analysis. While it is often noticeable when analyzing periodic signals, it is a general effect, which exists with all types of signal.

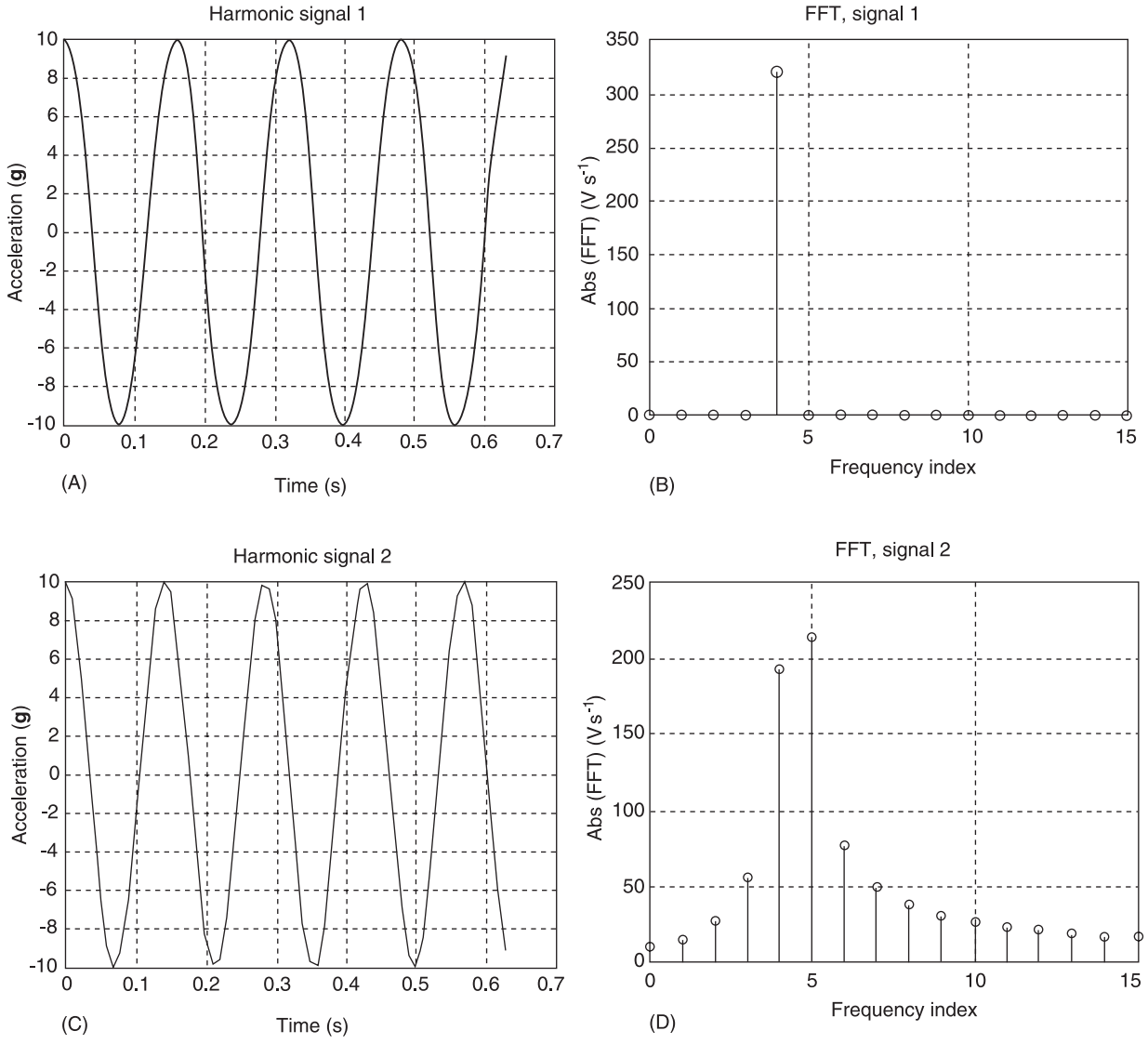


Figure 7 Example of leakage. (A) Signal 1, time domain; (B) signal 1, DFT, no leakage; (C) signal 2, time domain; (D) signal 2, DFT, leakage.

Windows One approach used to describe leakage and windows is based on imposed periodicities in DFT computations (see **Windows**). Another approach describing leakage is based on digital filtering.

Here the DFT is considered as a linear system operating on the signal. Not surprisingly, this system has characteristics of a filter bank, centered around computational frequencies. Such an approach is sometimes more intuitively appealing to the analyst (**Figure 8**). To see the DFT filtering characteristic, we note that the DFT equation can be rewritten in a matrix form as:

$$\mathbf{X} = \mathbf{W}\mathbf{x} \qquad [15a]$$

where $\mathbf{x}(N\times 1)$ and $\mathbf{X}(N\times 1)$ are the signal and DFT vectors, and $\mathbf{W}(N\times N)$ is a matrix with elements:

$$w_{nk} = \exp\left(-j\frac{2\pi}{N}\right)^{nk} \qquad [15b]$$

$$X(k) = x(0) + x(1)\exp\left(-j\frac{2\pi}{N}\right)^{n} + \ldots x(n-1)\exp\left(-j\frac{2\pi}{N}\right)^{(N-1)n} \qquad [16]$$

$X(k)$ can thus be identified as the output of a linear filter, whose unit impulse response is:

$$h_k(n) = \begin{cases} \exp\left(-j\dfrac{2\pi}{N}\right)^{(N-1-n)k} & n = 0, 1 \ldots N-1 \\ 0 & n < 0, \quad n > N \end{cases} \qquad [17a]$$

The frequency response of this filter is now found in a straightforward manner by applying a Z transform to eqn [17a] and substituting: $Z = \exp(j2\pi f\Delta t)$ This results in:

$$H_k(f) = \frac{\sin\ (\pi N f \Delta t)}{\sin\ (\pi f \Delta T - \pi k/N)} \qquad [17b]$$

The frequency response function consists of a main lobe, centered around

$$f(k) = k/(N\Delta t)$$

and side lobes of gradually decreasing magnitudes. For large N the amplitude of the first lobe is down by 13.6 dB relative to that of the main lobe (**Figure 9**).

We may thus look at the DFT as a filtering by N parallel filters H_k, centered around frequencies $f = k\Delta f$, where Δf is the frequency spacing of the DFT. (The power trough of any filter is the PSD, equal to $|X(k)|^2/N^2$.)

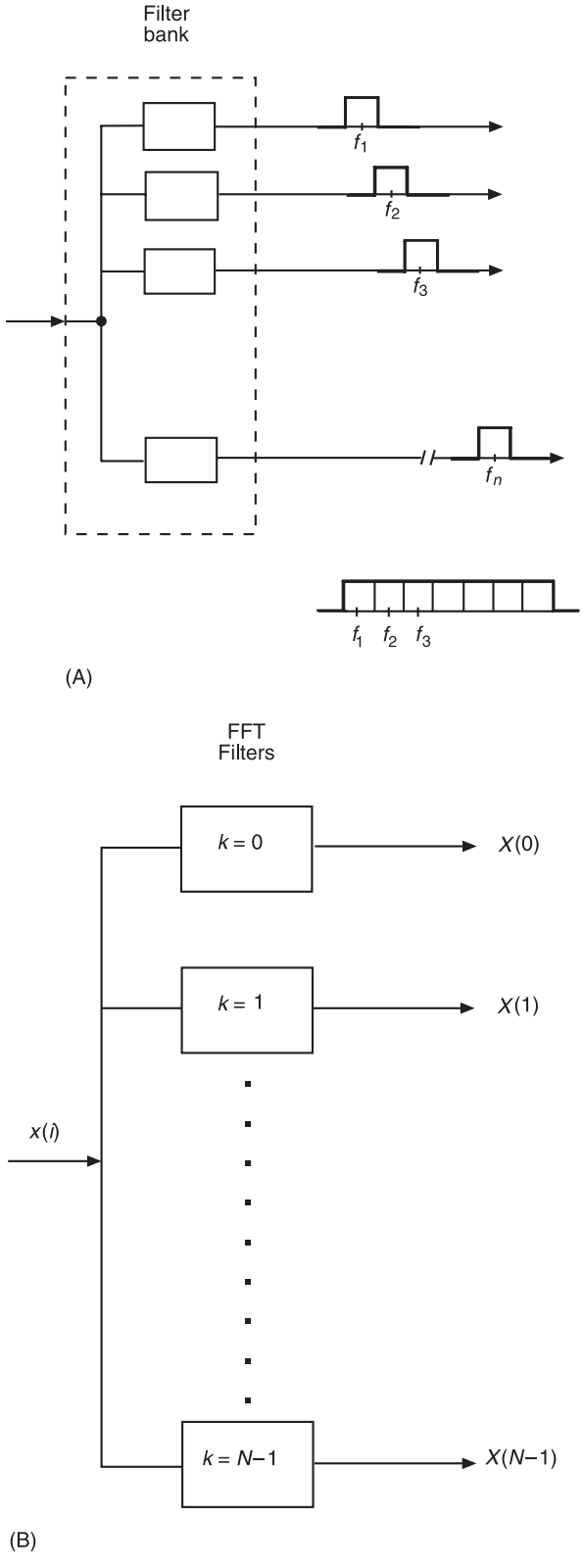


Figure 8 Filtering approach for PSD via the DFT. (A) PSD via an ideal filter bank (B) the DFT as a filter bank.

As noted above, a harmonic signal of frequency $k\Delta f$ has a period of $T_p = 1/(\Delta f)$, and the number of periods spanned by N points is:

$$N\Delta t/T_p = p = k$$

Thus, for a signal spanning exactly k periods, its physical frequency coincides computationally with the center of the main lobe of the kth filter H_k, and with zeros of all other filters, hence no leakage occurs (**Figure 9A**)

For all other cases when a noninteger number of periods are spanned, the physical frequency does not coincide with any of the computational frequencies where H_k is zero, the response of all filters will be nonzero, and leakage occurs over all frequency ranges (**Figure 9B**). The leakage, however, decreases with larger distances from the physical frequency; the attenuation is dictated by the decreasing magnitudes of the secondary lobes. We also note that increasing N will narrow the width of all lobes. This decreases the leakage; the physical frequency is now pushed to higher-order lobes for all filters except the one where it still falls in the main lobe.

To control leakage, windowing is undertaken by multiplying the time signal by the appropriate window function (see **Windows**).

$$x'(n) = w(n)x(n) \qquad [18]$$

The most frequently used window, at least for vibration signals, is the Hanning window, given by eqn [19] and shown in **Figure 10**. Other windows are used only when specific information concerning the signal's characteristics are known, and a specific window may then be of advantage.

$$w_h(n) = 0.5\left[1 - \cos\left(2\pi\frac{n}{N}\right)\right] \qquad [19]$$

Using the original signal without any weighting is equivalent to multiplying it by a rectangular window of magnitude 1. The rectangular window is thus included in any list of possible windows. Applying it implies using the original unmodified data.

A normalization is necessary, as the total energy is reduced by the windowing:

$$S'(k) = \frac{1}{\sum_k w^2(k)} S(k) \qquad [20]$$

Modifying the signal by multiplying it by a window function (eqn [18]) modifies the filtering properties of the equivalent filter (**Figure 10**). In the frequency domain, eqn [18] transforms into the convolution between the transform of the time window (called

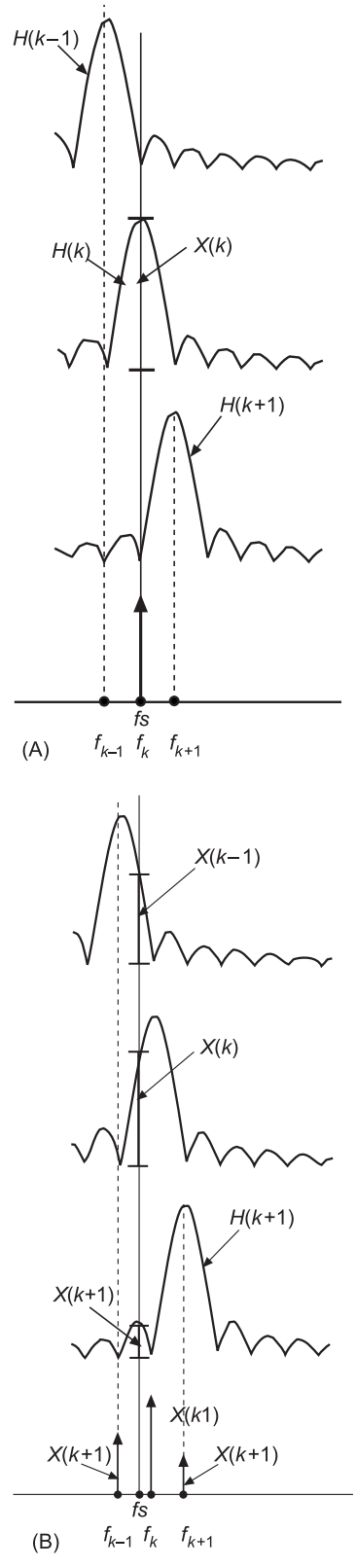
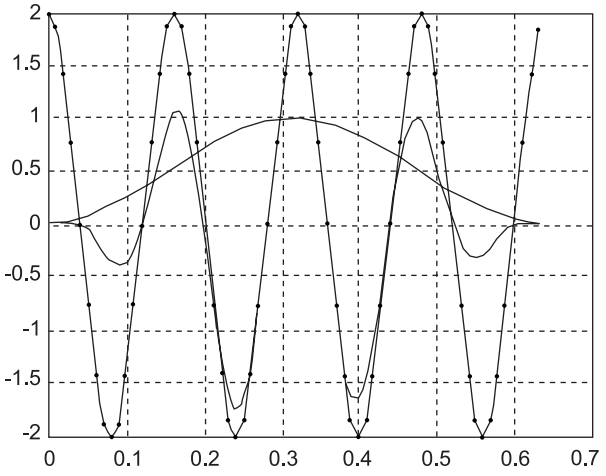


Figure 9 DFT filter bank and leakage. (A) Harmonic signal, integer number of periods; (B) harmonic signal, noninteger number of periods.



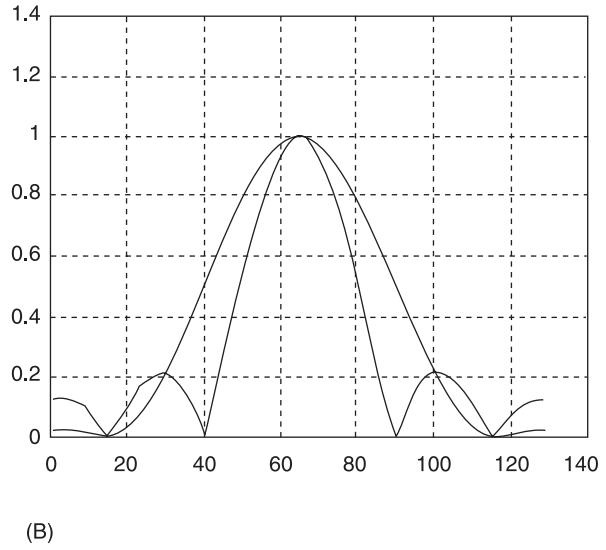


Figure 10 The use of windows and windowed signals. (A) Harmonic signal, rectangular and Hanning window; (B) filtering properties: rectangular and Hanning window.

the frequency domain window) and the transform of the signal. An equivalent filtering operation to the DFT of the windowed signal can be developed.

The effect of using a window is to modify the equivalent N filters, tuned around $k\Delta f$. The detailed derivation is beyond the scope of this text. While the main lobe is broadened, the attenuation of the secondary lobes is much sharper, and the leakage will accordingly decrease. **Table 2** summarizes the main properties of some windows.

The effect of leakage depends on the type of signal analyzed. A few examples are now addressed.

Periodic signal Leakage occurs whenever the physical frequency does not coincide with a computed version (or when a noninteger number of periods is spanned). In addition, with the signal's frequency not coinciding with the center on the main lobe of the FFT filter, the magnitude of $X(k)$ the nearest to the physical one will be attenuated. This is sometimes referred to as the scalloping loss. The maximum attenuation, occurring when the physical frequency is at $(k + 0.5)\mathrm{d}f$, at a midpoint, is 40% (corresponding to 60% attenuation in power). The use of a Hanning window will reduce the leakage as well as the scalloping loss.

For vibrations measured from rotating machinery, this can be very troublesome, as fluctuation in speeds of a few percent can cause erratic changes in peaks of $X(k)$ around rotating frequencies.

With a rectangular window, increasing N will not affect the possible scallop loss.

While the Hanning window decreases it, a special flat-top window is available which gives a very small scallop loss. It is sometimes used for rotating machinery when the effect of speed fluctuations is important. It is defined by:

$$w_{\mathrm{ft}}(n) = a_0 + 2\left[a_1 \cos 2\pi\frac{n}{N} + a_2 \cos\left(4\pi\frac{n}{N}\right) + a_3 \cos\left(6\pi\frac{n}{N}\right)\right]$$

$$a_0 = 0.9945 \quad a_1 = 0.95573$$

$$a_2 = 0.53929 \quad a_3 = 0.09158$$

Multiple components signals For a rectangular window, the minimum separable frequency increment is $2\Delta f$. When leakage exists, the leakage from a large component may mask the existence of smaller ones. We thus note one of the main effects of leakage: it is the reduction in the dynamic range. By the term dynamic range we refer to the minimum amplitude (referred to the maximum one, see par instrumentation).

Windows with much steeper secondary lobe attenuation thus improve the dynamic range significantly. They are thus often used automatically when closely spaced components exist, as for example with gear-generated signals. On the other hand we should note the increased bandwidth of the main lobe (for example, for the Hanning window it is $1.44\,\Delta f$). Thus, for very close components (of the order of $3\Delta f$), windowing would decrease the resolving power.

Random Signals

Any parameter or function describing such signals, if based on finite signals, can only be estimated. Thus, the PSD computed via eqn [8] is an estimator of the true PSD, and will be denoted by ^. The quality of this estimate is of great practical importance. The analyst

is concerned with the variance and bias of the estimate, as well as the question of consistency.

Variance Using a finite signal sequence, it is only possible to compute estimators of parameters or functions describing random data. To derive the properties of the PSD estimator, we investigate the sampling distribution of $\hat{S}$, the PSD of one random sample record (sometimes called a raw PSD):

$$E\left(\hat{S}\right) = S \qquad [20a]$$

$$\mathrm{Var}\left(\hat{S}\right) = S^2 \qquad [20b]$$

The relative random error is thus:

$$\frac{\left[\mathrm{Var}\left(\hat{S}\right)\right]^{1/2}}{S} = 1 \qquad [20c]$$

While eqn [20a] shows that the estimate is unbiased, eqn [20b] indicates a very high variability. The standard deviation of the raw PSD is 100%, making it almost meaningless. This is demonstrated by **Figure 11** showing overlays of PSDs, computed repeatedly for N points of different sections of a stationary random signal.

It should be noted that this great variability is independent of N, the data length. (The estimator is thus not consistent.)

The expected value and variance of a random variable with a probability distribution given by eqn [20] depends on ν, the number of degree of freedoms of this distribution. For the raw PSD $\nu = 2$, except for the endpoints. In the following section, we describe how to control variability. This will be equivalent to increasing the number of degrees of freedom of the estimator's distribution.

The above results, derived for white-noise Gaussian signals, is typical for the raw spectra of most random signals.

Segment averaging To reduce the variance we attempt to use averages of estimators of the raw PSD. In the method of segment averaging, estimates to be averaged are obtained from different sections of the signal.

The method is based on sectioning the signal into M non-overlapping segments:

$$x_j(n) = x(n) + (j-1)N_1] \qquad [21]$$

where $N_1 = N/M$ is the length of each segment (**Figure 12A**).

We now compute estimates $\hat{S}$ for each segment as:

$$\hat{S}_j(k) = \frac{\Delta t}{N_1}\left|X_j(k)\right|^2 \qquad [22]$$

with:

$$x_j(i) \leftrightarrow X_j(k)$$

The number of degree of freedoms of the PSD will be increased by a factor of M, assuming the raw estimates to be independent (but see below), and equal $2M$ (**Table 3**). We may consider the spectral functions $\hat{S}(k)$ as members of an ensemble of random functions whose ensemble mean is then $S(k)$. The variance of this mean decreases with M, the normalized random error now being:

$$e_r = \frac{1}{[M]^{1/2}} \qquad [23]$$

Figure 12B and **12C** shows the result of segmentation/averaging for the ensemble analysed in **Figure 11A** and **B**. Also shown is the theoretical PSD of this simulated example.

An improvement named after its developer, Welch, is based on averaging overlapping sections. This is depicted in **Figure 12D**, where $N_1 - D$ data points are overlapped, i.e., are used twice (for two segments) in the analysis. For $D = 0$, we have zero overlapping. The ratio:

$$(N_1 - D)/N_1 \cdot 100$$

is sometimes called the overlap factor (in %). M_1, the number of raw PSDs which can be averaged, are now increased.To retain the statistical independence of the raw PSDs, the segments are windowed, so as to give less weights to the overlapped points (see **Windows**). The analysis of Welch suggests an overlap of 50% in conjunction with a Hanning window, and the PSD of each section is thus modified to:

$$\hat{S}_{j(k)} = \frac{\Delta t}{N_1}\left|X_j(k)\,W(k)\right|^2 \qquad [24]$$

Table 3 summarizes the random errors for the different procedures.

Instead of a regular averaging, we may use exponential averaging to cope with time-varying situations. The PSD is then computed with a built-in fading exponentially decreasing memory.

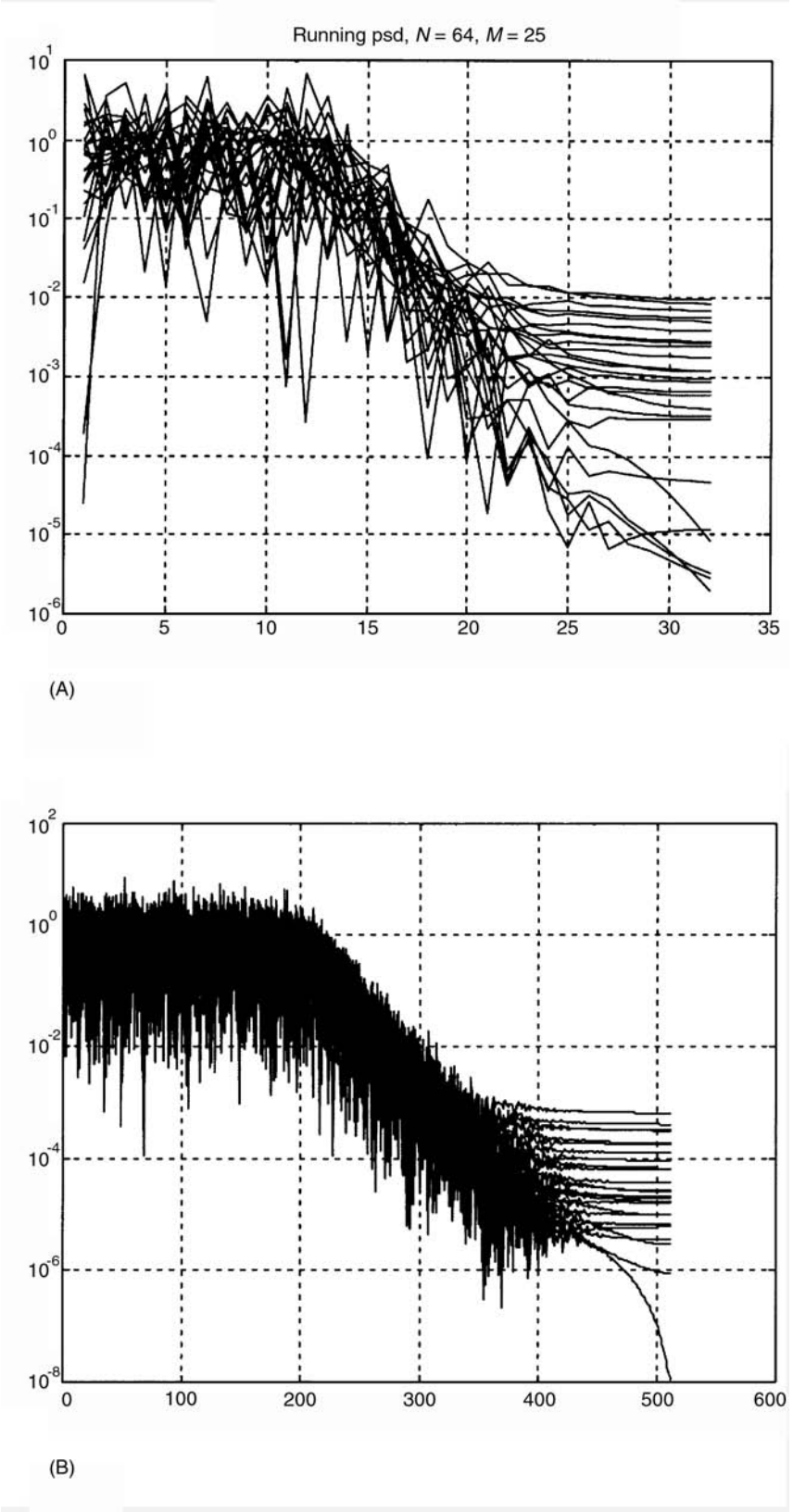


Figure 11 Running PSD. (A) 25 overlays, $N = 64$; $M = 25$; (B) 25 overlays, $N = 1024$; $M = 25$.

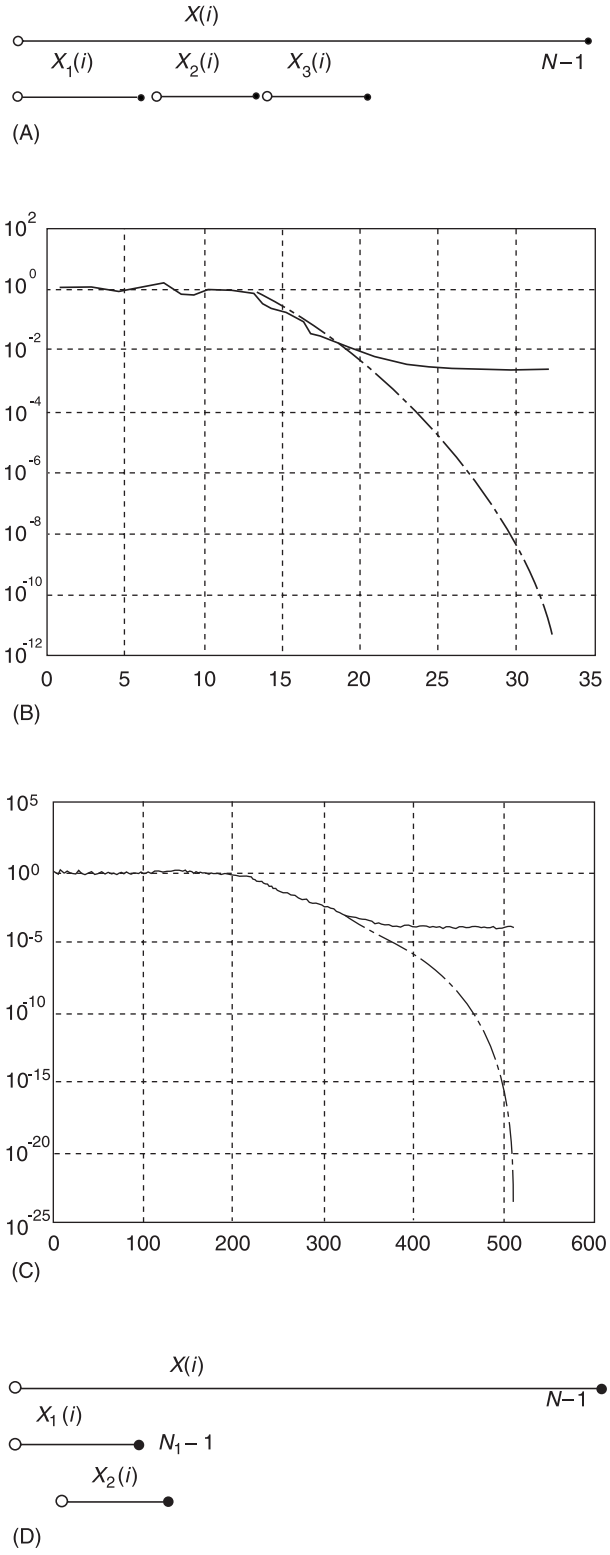


Figure 12 PSD via segmentation and averaging, (A) Segmentation; (B) 25 averages, $N = 64$, $M = 25$; averaged and theoretical PSD; (C) 25 averages, $N = 1024$, $M = 25$; averaged and theoretical PSD; (D) segmentation with overlap.

Table 3 PSD variance and overlap

Overlap	W_{rec}	W_{han}
0%	1	1
50%	0.75	0.5278
90%	0.6576	0.9307

Bias error This will occur whenever the FFT spacing is too large compared to narrow-band regions of the 'true' PSD. Our spacing Δf is the scale resolution at which we try to resolve the PSD, and some averaging within this spacing occurs for peaks much narrower than this spacing.

An approximation for the relative bias error is:

$$e_b = \frac{(\Delta f)^2}{24} S''(f) \qquad [25]$$

The second derivative appearing in eqn [25] indicates that the bias error, if not negligible, will result in underestimation of peaks (and overestimation of minima).

To avoid large bias errors, an analysis bandwidth which is much smaller than this 3 dB bandwidth is necessary. A ratio of 1:4 between those two will result in a bias error of 2%.

$$\Delta f <= 0.25\ \mathrm{BW}_{3\,\mathrm{dB}}$$

An example of bias error is shown in **Figure 13**. The PSD was computed for $M = 100$ nonoverlapping sections for both cases, i.e., with the same random error. For $N = 512$, a significant drop in the low-frequency peak of 20 Hz can be noticed, compared to the analysis results with $N = 2048$. On the other hand, the broader peak around 21 Hz is approximately unaffected by the reduced resolution. While this cannot be seen with the linear scale of **Figure 13**, an increase in the minima between the two peaks occurs when N is reduced to 512.

The difficulty is the need to estimate the true, narrowest, physical bandwidth of the PSD. Unless some bound can be based on *a priori* knowledge, a strategy is needed. One possibility is to do some testing, whereby N (and hence Δf) is gradually increased, and check when peaks become strongly underestimated. But, as will be seen from the following discussion, this could increase the variance, making the judgment more difficult.

Control of errors The random error can be controlled by the number of sections averaged. We note the diminishing return of increasing M, due to the square root relation. Thus, increasing M from 1 to

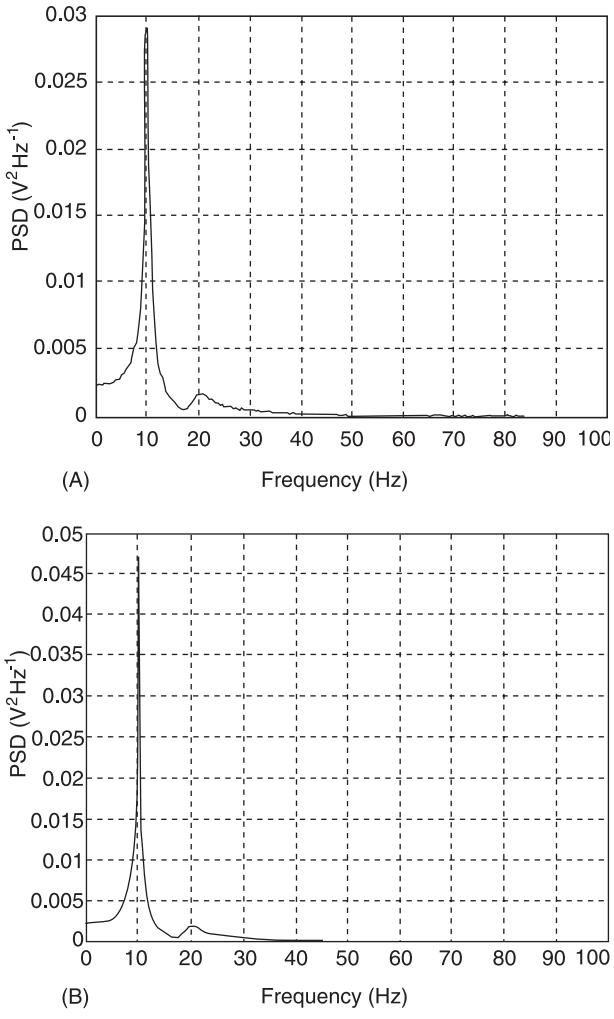


Figure 13 Bias error due to insufficient frequency resolution. (A) $\Delta f = 0.39$ Hz, $N = 512$; (B) $\Delta f = 0.098$ Hz, $N = 2048$.

100 will decrease the error by a factor of 10; a further doubling to $M = 200$ will only result in a reduction by a factor of $\sqrt{2}$.

The bias error is controlled by Δf versus the bandwidth of the signal, the controlled parameter being the number of samples per window N (the sampling interval is already fixed during data acquisition, to satisfy the required bandwidth).

We must consider two scenarios:

1. Scenario 1: the data are unlimited, and any required number of samples can be acquired. Such would be the case for rotating machinery, where the limitation would probably be the existence of a stationary vibratory regime.Specifications for analysis would be:
   - bandwidth of analysis, setting Δt during acquisition
   - frequency resolution, setting N the block length
   - Random error, setting M, the number of averages

   As an example, assume a required bandwidth of 100 Hz, analysis resolution of $\Delta f_{\text{res}} = 0.5$ Hz and a random error of 10%.

   Assuming the existence of a sampling interval of (the exact values will depend on the actual hardware used):

$$\Delta t = 1/(2f_{\max}) = 1/250 = 4\,\text{ms}$$

   The block length would be:

$$1/(\Delta t \Delta f_{\text{res}}) = 1/(0.04 \cdot 0.5) = 500$$

   and we would choose $N = 512$.

   For a random error of 10% (eq. [23]) we would choose $M = 100$.

   And the total number of samples is $NM = 512{\cdot}100 = 51\,200$, corresponding to a data duration of:

$$T_t = NM\Delta t = 208 \text{ s}$$

2. Scenario 2: assume data were acquired for 60 s, i.e., the number of data samples is $60/\Delta t = 15\,000$. As now M^*N is constant, we can only control one error, the bias via N, or the random one via M. Checking possibilities we get:
   - Case 1: random error fixed, $M = 100$, $N = 150$. Thus we may choose: $N_1 = 128$ with a resultant resolution $\Delta f = 1.95$ Hz (and the actual $M = 117$, $\varepsilon_r = 9.3\%$)
     $N_2 = 256$ with the resultant resolution of $\Delta f = 0.95$ Hz (and the actual $M = 58$, $\varepsilon_r = 13.1\%$)
   - Case 2: resolution fixed as in scenario 1: $N = 512$
     With $M = 15\,000/512 = 29$ and $\varepsilon_r = 18.6\%$
     Thus, for *a priori* fixed data length, the random error can only be balanced by the bias error.

Some practical remarks are warranted. The two scenarios show the importance of planning the analysis prior to the data acquisition; the necessary data duration can often be estimated. The question of bias versus random error is not straightforward, but many practitioners consider bias error more severe. Consider the underestimation of sharp maxima, as occurs with bias errors: this can be more troublesome than unsmooth spectra. Finally, it should be remembered that equations are asymptotic results, hence the results (as, for example, computed for the two scenarios) are only approximate.

Practice of Spectral Analysis

The analysis will depend on the type of signal at hand. Some *a priori* information will dictate the analysis and the choice of parameters.

Random Signals

The examples given above are 'classical'. Overlapped processing, usually of 50%, can also be applied, requiring a window, usually the Hanning one. For zero overlap, a rectangular window could also be adequate. If a continuous spectrum is monitored, an exponential averaging scheme will be used, enabling one to follow slow changes in spectral characteristics. Additional peak spectral values will be kept (and updated continuously) for comparison.

Periodic Signals

Purely periodic signals are a theoretical concept. Any measured data will be contaminated to some extent by noises. These usually include a random component and often deterministic ones (for example, traceable to line interfere). Thus, some averaging is usually indicated. The number of averages will depend on the signal-to-noise ratio, and for reasonable situations can be much less than for purely random signals.

The analysis parameters are an integral part of any spectral analysis results. A triggered analysis is often preferable for periodic signals. A trigger signal is often available from external devices (like a one-per-rev signal in rotating machines), but can also be obtained from the analyzed signal itself, a so-called self-trigger. In contrast to free-running analysis, temporal patterns are preserved, and the phase is not randomized. Thus, in free running analysis, a PSD would be computed, while for triggered analysis, the DFT itself could be averaged, keeping the phase information.

In dedicated data acquisition and analysis instruments, triggered data acquisition would automatically imply a triggered spectral analysis.

Windows would normally be used, generally the Hanning one, to decrease leakage and increase the dynamic range. For very close components (say, separated by $2\Delta f$), the increased bandwidth using windows has to be considered, and a rectangular window (or an increase in the analyzed data duration) is advised. Overlapped processing seems unnecessary, as it is easy to use sufficiently long signal durations, certainly in the case of rotating machines under steady-state conditions. Overlapped processing necessitates a window. The remark concerning very close components applies; overlapped processing may not enable separation).

The number of fundamental periods spanned dictates the location of the spectral line in the DFT presentation.

Transients

Only a straightforward DFT is computed. The use of a Hanning window is obviously erroneous, but special windows are often appropiate.

For repetitive transients, a triggered mode is necessary, and the analysis is performed as if a periodic signal is at hand.

A very important conclusion from the section on errors and their control is: comparisons and evaluations can sometimes be almost meaningless unless information such as analysis of Δf, degrees of freedom or estimated random error, use of window etc., is given.

Nomenclature

e_b	bias error
e_r	random error
E	energy
Δf	frequency spacing
Δt	sampling interval

See also: **Averaging**; **Correlation functions**; **Transform methods**; **Windows.**

Further Reading

Bendat JS and Piersol AG (1993) *Engineering Applications of Correlation and Spectral Analysis*, 2nd edn. New York: John Wiley.

Jenkins GM and Watts DG (1969) *Spectral Analysis and its Applications*. San Francisco: Holden Day.

SPECTRAL ANALYSIS, MODEL BASED METHODS

See **SIGNAL PROCESSING, MODEL BASED METHODS**

SPECTRAL ANALYSIS, WINDOWS

See **WINDOWS**

STABILITY

See **DYNAMIC STABILITY**

STANDARDS FOR VIBRATIONS OF MACHINES AND MEASUREMENT PROCEDURES

J Niemkiewicz, Maintenance and Diagnostic (M&D) LLC, Eddystone, PA, USA

Copyright © 2001 Academic Press

doi:10.1006/rwvb.2001.0160

Introduction

A good standard must represent a consensus of opinion among a broad spectrum of users, be simple to understand, be easy to use, and contain no ambiguities or loopholes. Any Standard must also contain vital information that leads to common measurement procedures and evaluations of data that are compared with agreed-upon criteria. Standards are intended to: (1) establish criteria for rating or classifying the performance of equipment or material; (2) provide a basis for comparison of the maintenance qualities of pieces of equipment of the same type; (3) test equipment whose continuous operation is necessary for industrial or public safety; (4) provide a basis for the selection of equipment or material; and (5) establish procedures for the calibration of equipment. Some standards establish classifications for equipment that is being rated, and indicate how measurements are to be made and how the data, so obtained, are to be analyzed. They may also indicate how the equipment is to operate during the test procedure. This paper is mainly concerned with standards related to machinery vibration and its classifications.

ISO standards are not intended to be specifications; however, equipment purchasers and users can use the applicable ISO standards for compliance when specifying machinery vibration levels or measurement procedures, either on new or in-service equipment. ISO standards, when identified as 'standards', include data that are based on the results of worldwide surveys and they usually have very specific vibration levels, zones, and measurement procedures for different types and sizes of machines. When experience and worldwide equipment manufacturer and/or user surveys cannot clearly establish accepted levels of vibration or measurement procedures, then these ISO standards are identified as 'guidelines'. These decisions are made by the responsible ISO working groups preparing the standards and are sometimes based on the ratio of normative references (requirements) or informative references (information) contained in a particular standard. In addition, at times a new document being prepared for a new class of machines will include measurement procedures that can be used as a guideline until firm acceptable performance criteria can be established.

Standards Organizations and Groups

In the field of vibration, the two recognized international organizations are the International Organization for Standardization (ISO), which is technology-oriented, and the International Electro-technical Commission (IEC), which is product-oriented. ISO and the IEC make every attempt to coordinate their respective standards activities to avoid duplication and discrepancies. These organizations also work in cooperation with national standards organizations in various countries, such as: the American National Standards Institute (ANSI) in the USA; the British Standards Institution (BSI) in the UK; the Deutches Institut für Normung (DIN) in Germany; the Austrian Standards Organization (ON); the Danish Standards Association (DS) in Denmark; Standards of Australia; and so forth.

ISO and the IEC also work with trade associations within countries that develop Standards to fit their unique requirements. For example, in the USA the American Petroleum Institute (API), the Hydraulic Institute (HI), etc., have patterned their own set of standards to satisfy their respective industry needs. These standards are established by the consensus of users, customers, and manufacturers and their use is usually voluntary.

Finally, military organizations in most countries also develop standards applicable to their special requirements for procurement and operation. There are a myriad of military standards, or specifications (MILSpecs), in the USA and many are applied to the acceptance testing of new military hardware both

prior to delivery and, in some cases, in-service acceptance testing such as for shipboard machinery. There are also MILSpecs that address vibration levels that result in airborne noise that may have an adverse affect on the close-quarter environments of military personnel. There is a current trend in the USA for military organizations to use applicable ISO standards, in lieu of MILSpecs which are becoming outdated. In fact, in line with this trend, the USA military has been encouraging the ISO/ANSI standards committees to consider the needs of the USA military when preparing ISO/ANSI standards.

Vibration standards activities in the ISO are guided by Technical Committee 108, Mechanical Vibration and Shock. Vibration standards activities in the IEC are guided by Technical Committee 50. When individual countries, trade groups or military organizations prepare their national vibration standards, most countries do so in accordance with the comparable ISO or IEC standards.

Since the IEC standards are prepared primarily by the equipment manufacturers, they are a consensus of a common ground in which these producers all agree to operate within. However, the ISO committees are a balance between the manufacturers and the users, and therefore have a more universal audience. For this reason, and the fact that it would be virtually impossible to include all of the vibration standards in existence in all of the countries, within a reasonable space and to do them justice, it has been determined that it would be most beneficial to the larger audience that this paper focuses mainly on the ISO vibration standards.

General Machinery Vibration Standards and Criteria

In the development of standards, it has been found that machinery can be subdivided into four categories for the purposes of vibration measurement and evaluation:

1. Reciprocating machinery having both rotating and reciprocation components, such as diesel engines and certain types of compressors and pumps. Vibration is usually measured on the main structure of the machine at low frequencies.
2. Rotating machinery having rigid rotors, such as certain types of electric motors, single-stage pumps, and slow-speed pumps. Vibration is usually measured on the main structure (such as on the bearing caps or pedestals) where the vibration levels are indicative of the excitation forces generated by the rotor because of unbalance, thermal bows, rubs, and other sources of excitation.
3. Rotating machinery having flexible rotors, such as large steam turbine generators, multistage pumps and compressors. The machine may be set into different modes of vibration as it accelerates through one or more critical speeds to reach its service speed. On such a machine, the vibration amplitude measured on a structure member may not be indicative of the vibration of the rotor. For example, a flexible rotor may experience very large amplitude displacements resulting in failure of the machine, even though the vibration amplitude measured on the bearing cap is very low. Therefore, it is essential to measure the vibration on the shaft directly.
4. Rotating machinery having quasirigid rotors, such as low-pressure steam turbines, axial-flow compressors, and fans. Such machinery contains a special class of flexible rotor where vibration amplitudes measured on the bearing cap are indicative of the shaft vibration.

Classification of Severity of Machine Vibration

In the classification of severity of machine vibration, the motion variable that is used (displacement, velocity, or acceleration) depends on the type of standard, the frequency range, and other factors. In classifying machinery vibration in the range 10–1000 Hz, for example, vibration velocity is normally used because it is relatively independent in this range, and thus yields a simple measure of severity for a new operating machine.

For simple harmonic motion, either peak or RMS values of the motion variable may be used. However, for machines whose motion is complex, the use of these two indices provides distinctly different results, mainly because the higher frequency harmonics are given different weights. For rotating machinery whose rotational speed is in the range of 600 to 12 000 rpm, the RMS values of the velocity amplitudes correspond most closely with vibration severity. Therefore, ISO has a special measure, vibration severity, which is defined as the highest value of the broadband RMS value of the velocity amplitude in the frequency range 10–1000 Hz, as evaluated on the structure at prescribed points (generally triaxle arrays on the bearing caps or pedestals).

Measurement Procedures

Included in the ISO standards are procedures for measuring relative shaft-to-housing signals, absolute measurements, and seismic applications as shown in

Figures 1–3. The transducers recommended and described include displacement, velocity, and acceleration. Their mounted and unmounted ranges and limits of application, magnitudes, and frequencies are also included.

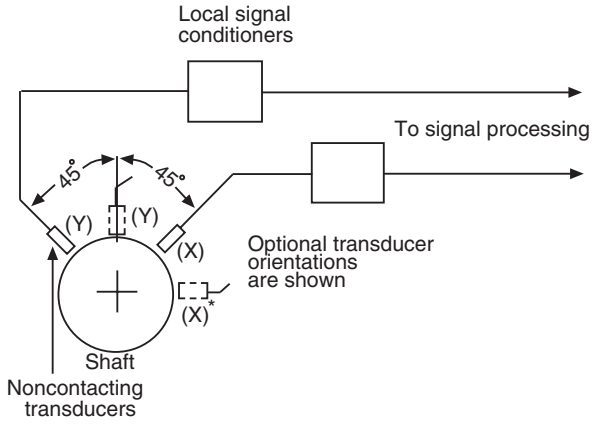


Figure 1 Schematic diagram of relative motion measurement system using non-contacting transducers.

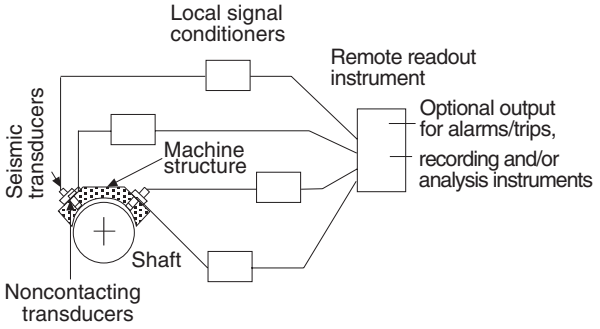


Figure 2 Schematic diagram of absolute/relative motion measurement system using a combination of noncontacting and seismic transducers.

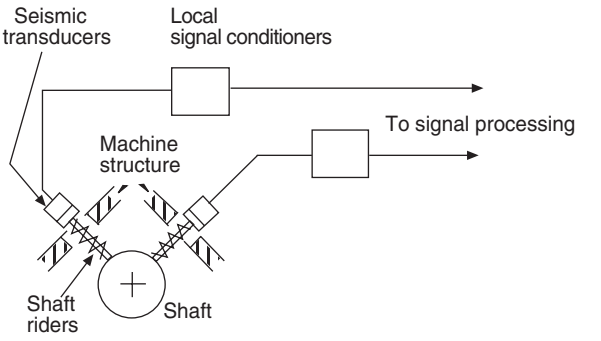


Figure 3 Schematic diagram of absolute motion measurement system using shaft-rider mechanism with seismic transducers.

Vibration Standards Summaries

The following sections contain brief descriptions of the most prominent vibration Standards, either issued or in process. The first section contains broadband measurement procedures and values, including: measurements on nonrotating parts; reciprocating machines; measurements on nonreciprocating rotating shafts; and, machines having gear units. Also considered are measurements on machines with rigid and flexible rotors. The second section contains descriptions of narrowband vibration condition monitoring standards that include spectrum analysis, trending, and diagnostics.

Broadband Vibration Standards

Early ISO vibration standards were ISO 2372, ISO 2954, and ISO 3945. These Standards have been superseded by the ISO10816 and 7917 series described in the following sections. However, these earlier standards still contain useful information.

Nonrotating Parts

ISO/10816/1; Mechanical vibration – evaluation of machine vibration by measurements on nonrotating parts, Part 1: General guidelines This provides general guidelines that describe procedures for the measurement and evaluation of vibration based on measurements made on the nonrotating parts of the machine. This is Part 1 of a series of standards that provide individual criteria for each general class of machine covered, which are unique to those machines. These criteria, which are presented in terms of both vibration magnitude and change of vibration, relate to operational monitoring and acceptance testing.

This series of standards has been written to: (1) cover the broadband frequency range of both low and high speed machines; (2) set the vibration criteria to include both the various operational zones, irrespective of whether they are increases or decreases; (3) incorporate vibration criteria through a worldwide survey; and, (4) include unique criteria and measurement procedures for specific types of machines.

The measure of vibration is broadband and the frequency range is sufficient to ensure that the particular machine is adequately covered, which depends on the type of machine under consideration. For example, the frequency range necessary to assess the integrity of a machine with rolling element bearings should include frequencies higher than those on machines with fluid film bearings.

In addition to vibration velocity measurements, which were the primary criteria in earlier Standards because they related to vibration energy, the 10816 series also includes alternate criteria such as displacement, acceleration, and peak values instead of RMS, as these criteria may be preferred for machines designed for extra low or high speed operation.

ISO/10816, Part 2: Guidelines for land-based steam turbine sets in excess of 50 MW This provides specific guidance for assigning the severity of vibrations measured on the bearings or pedestals of large steam turbine generating sets. Measurements at such specified locations reasonably characterize the overall state of vibration of these machines.

The vibration measurement system should be capable of measuring broadband vibration in $mm\,s^{-1}$ RMS over a frequency range 10–500 Hz. If, however, the instrumentation is also to be used for diagnostic purposes, or for monitoring during machine run-up or run-down, or overspeed, a wider frequency may be required.

This standard includes the vibration criteria shown in **Table 1** which is based on bearing housing/pedestal vibration velocity amplitude ($mm\,s^{-1}$, rms) for turbine generator sets exceeding 50 MW, and with nominal speeds of 1500, 1800, 3000, and 3600 rpm. The values apply to *in situ* application under steady-state conditions. Zone A represents new machines that can be operated without restriction; zone B is acceptable for long term operation; zone C represents machines that may be operated for a limited time until a suitable opportunity arises for remedial action to be taken; and, zone D is identified as a trip level as these values are considered to be of sufficient severity to cause damage.

ISO/10816, Part 3: Guidelines for coupled industrial machines with nominal power above 30 kW and nominal speeds between 120 and 15 000 rpm when measured in situ This provides specific guidance for assessing the severity of vibrations on bearings, bearing pedestals, or the housings of coupled industrial machines when measured *in situ*. This standard covers the following machines: steam turbines with power above 50 MW, compressors, industrial gas turbines with power up to 3 MW, pumps with power up to 1 MW, generators, electric motors of any type, and blowers with power greater than 300 kW.

Significant differences in design, types of bearings, and types of support structures require a division of this standard into two machinery groups, namely: (1) large machines with rated power above 300 kW, or electrical machines with shaft heights over 315 mm; and, (2) medium size machines with a rated power above 30 kW up to and including 300 kW, or electrical machines with shaft heights from 180 mm to 315 mm. The larger machines normally have sleeve bearings and the range of operating or nominal speeds is relatively broad with ranges from 120 rpm to 15 000 rpm.

Classification of the vibration severity zones for large industrial machines with rated power from 300 kW to 50 MW (Group 1) are shown in **Table 2.** Classification of the vibration severity zones for medium size industrial machines with rated power from 30 to 300 kW (Group 2) are included in **Table 3**. The zone descriptions are the same as in 10816, Part 2.

ISO/10816, Part 4: Guidelines for gas turbine driven sets excluding aircraft derivative This provides specific guidance for assessing the severity of vibrations measured on the bearing housings or pedestals of gas turbine sets.

This standard applies to heavy-duty gas turbines used in electrical and mechanical drive applications covering the power range above 3 MW, and a speed range under load between 3000 and 20 000 rpm.

Table 1 Recommended vibration velocity levels ($mm\,s^{-1}$, RMS)

Zone boundary	*Shaft rotational speed (rpm)*	
	1500–1800	*3000 or 3600*
A/B	2.8	3.8
B/C	5.3	7.5
C/D	8.5	11.8

Table 2 Severity zones for large machines (group 1)

Support class	*Zone boundary*	*Displacement (μm, RMS)*	*Velocity ($mm\,s^{-1}$RMS)*
Rigid	A/B	37	2.3
	B/C	72	4.5
	C/D	113	7.1
Flexible	A/B	56	3.5
	B/C	113	7.1
	C/D	175	11.0

Table 3 Severity zones for medium sized machines (group 2)

Support class	*Zone boundary*	*Displacement (μm, RMS)*	*Velocity ($mm\,s^{-1}$, RMS)*
Rigid	A/B	22	1.4
	B/C	45	2.8
	C/D	71	4.5
Flexible	A/B	37	2.3
	B/C	71	4.5
	C/D	113	7.1

Generally, the criteria applies to both the gas turbine and the driven equipment; however, for generators above 50 MW, the criteria of 10816, Part 2 should be used for assessing the vibration severity. For compressors in the power range from 30 to 300 kW, the criteria of 10816, Part 3 should be used for assessing vibration severity.

The evaluation of zone boundaries based on bearing housing/pedestal vibration for industrial gas turbines is given in **Table 4**. These criteria assume that the gas turbines incorporate fluid film bearings, and the vibration measurements are broadband values taken *in situ* under normal steady-state operating conditions. This standard encompasses machines which may have gears or rolling element bearings, but does not address the evaluation of the condition of those gears or bearings. The zone descriptions are the same as in 10816, Part 2.

ISO/10816, Part 5: (to be published) Guidelines for hydraulic machines with nominal power above 1 MW and nominal speeds between 120 and 1800 rpm when measured in situ This provides specific guidance for assessing the severity of vibrations measured on bearings, bearing pedestals, or housings of hydraulic machines when measured *in situ*. It applies to machine sets in hydraulic power generation, and pump plants where the hydraulic machines have speeds from 120 to 1800 rpm, shell- or shoe-type sleeve bearings, and main engine power of 1 MW or more. The position of the line shaft may be vertical, horizontal, or at an arbitrary angle between these two directions.

This Standard includes: turbines and generators, pumps, and electrical machines operating as motors, pump-turbines, and motor generators, including auxiliary equipment (e.g., starting turbines or exciters in line with the main shaft). The Standard also includes single turbines or pumps connected to generators or electric motors over gears and/or radially flexible couplings.

The recommended criteria values in mm s^{-1}, RMS vs shaft rotational speed in rpm for hydraulic machines with nominal power above 1 MW, and nominal speeds between 120 and 1800 rpm are shown in **Figure 4**. The zone descriptions are the same as in 10816, Part 2.

Table 4 Evaluation of zone boundaries based on bearing housing pedestal vibration

Shaft rotational speed (rpm)	*Zone boundary*		
	A/B	B/C	C/D
3000–20 000	4.5	9.3	14.7

ISO/10816, Part 6: Reciprocating machines with power ratings above 100 kW This establishes procedures and guidelines for the measurement and classification of mechanical vibrations of reciprocating machines. In general, this standard refers to vibration measurements made on the main structure of the machine, and the guide values are defined primarily to secure a reliable and safe operation of the machine, and to avoid problems with the auxiliary equipment mounted on the structure.

In the case of reciprocating machines, the vibrations measured on the machine main structure, and qualified according to this standard, may only give a rough idea of the stresses and vibratory states of the components within the machine itself. For example, torsional vibrations of rotating parts cannot generally be determined by measurements on the structural parts of the machine. Based on experience with similar machines, the damage that can occur when exceeding the guide values is sustained predominately by the machine-mounted components (e.g., turbochargers, heat exchangers, governors, pumps, filters, etc.), connecting elements of the machine with peripherals (e.g., pipelines), or monitoring instruments (e.g., pressure gauges, thermometers, etc.).

This standard generally applies to reciprocating piston machines mounted either rigidly or resiliently with power ratings above 100 kW. The vibration criteria for different classes of reciprocating machines are presented in **Table 5**. The class definitions are: (1) balanced opposed type rigidly mounted reciprocating gas compressors; (2) multithrow type rigidly mounted reciprocating gas compressors; (3) single-throw type rigidly mounted reciprocating gas compressors; (4) no example; (5) and (6) industrial and marine diesel engines (<2000 rpm); and, (6) and (7) industrial and marine diesel engines (>200 kW). The zone descriptions are the same as in 10816, Part 2.

Rotating Parts

ISO/7919–1, Mechanical vibration of non-reciprocating machines – measurement on rotating shafts and evaluation – Part 1: General guidelines This provides specific guidelines for vibration measurements on the rotating members of machines. Such machines generally contain flexible rotor-shaft systems. Changes in the vibration condition may be detected more decisively and more sensitively by measurements on these rotating elements. Also, machines having relatively stiff and/or heavy casings, in comparison to the rotor mass, are typical of those classes of machines for which shaft vibration measurements are frequently preferred.

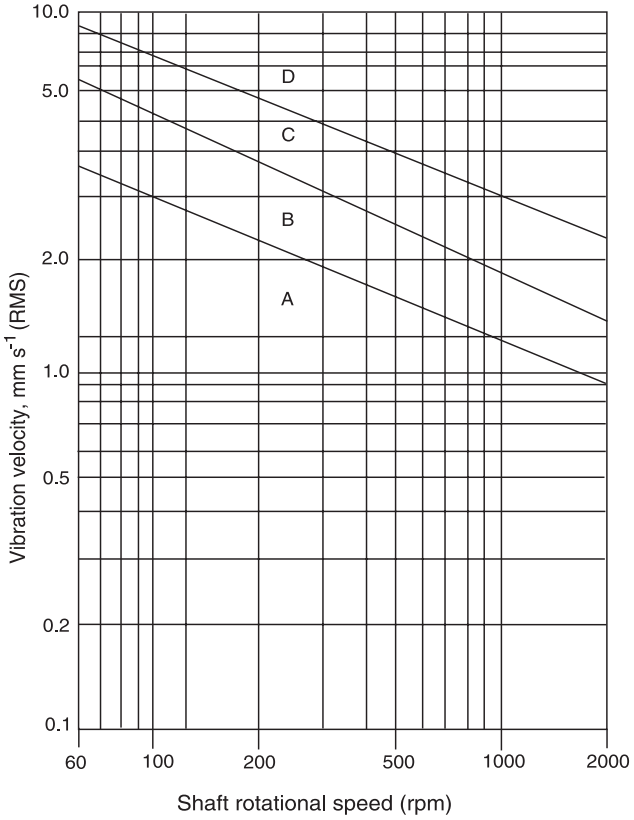


Figure 4 Recommended criteria values.

Table 5 Reciprocating machinery class definitions

Vibration severity grade	*Maximum levels of overall vibration Measured on the machine structure*			*Machine vibration classification number*						
	Displacement (μm, RMS)	*Velocity (mm s^{-1}, RMS)*	*Acceleration (m s^{-2}, RMS)*	1	2	3	4	5	6	7
1.1										
1.8	17.8	1.12	1.76							
2.8	28.3	1.78	2.79	A/B						
4.5	44.8	2.82	4.42		A/B					
7.1	71.0	4.46	7.01	C		A/B				
11	113	7.07	11.1	D	C		A/B			
18	178	11.2	17.6		D	C		A/B		
28	283	17.8	27.9			D	C		A/B	
45	448	28.2	44.2				D	C		A/B
71	710	44.6	70.1					D	C	
112	1125	70.7	111						D	C
180	1784	112	176							D

Machines such as industrial steam turbines, gas turbines, and turbocompressors, all of which have several modes of vibration in their service speed range; and, their responses due to unbalance, misalignments, thermal bows, rubs, and the unloading of bearings may be better observed by measurements on the shafts.

There are three principle factors by which the vibration level of a machine is judged, namely: (1) bearing kinetic load; (2) absolute motion of the rotor; and, (3) rotor clearance relative to the bearing. If the bearing kinetic load is of concern to ensure against bearing damage, the vibration of the shaft relative to the bearing structure should be monitored

as the overriding criteria. If the absolute motion of the shaft (a measure of rotor bending stress) or rotor-bearing clearance are of concern, the type of measurement used depends on the vibration level of the structure which supports the relative motion transducer. Hence, if the vibration level of this support structure is less than 20% of the relative shaft vibration, the absolute shaft vibration must be measured; and, if this is found to be larger than the relative shaft vibration, then this will be the more valid measurement. The rotor clearance to the bearing must be monitored to ensure against rotor seal and blading rubs which can cause rotor or blading failures.

The shaft vibrations of machines, measured close to the bearings, are evaluated on the basis of two criteria. (1) The reliable and safe running of a machine under normal operating conditions requires that the shaft vibration displacement remain below certain limits consistent with, for example, acceptable kinetic loads and adequate margins on the radial clearance envelope for the machine. Generally, this criterion is taken as the basis for the evaluation of a new machine, in the absence of any other established knowledge of the satisfactory running characteristics for a machine of that type. (2) Changes in shaft vibration displacement, even though the limits in (1) are not exceeded, may point to incipient damage or some other irregularity. Consequently, such changes relative to a reference value should not be allowed to exceed certain limits. If this reference value changes by a significant amount, and certainly if it exceeds 25% of the reference level, steps should be taken to ascertain the reasons for the change and, if necessary, appropriate action should be taken. In this context, a decision on what action to take, if any, should be made after consideration of the maximum value of vibration, and whether the machine has stabilized at a new condition.

ISO Standard 10817, Part 1 describes the sensing device (transducer), signal conditioning, attachment methods, and calibration procedures for instrumentation to measure shaft vibration.

ISO 7919, Part 2: Guidelines for large land-based steam turbine-generating sets provides the special features required for measuring shaft vibrations on the coupled rotor systems of steam turbine-generating sets for power stations, having rated speeds in the range 1500–3600 rpm, and power outputs greater than 50 MW. Evaluation criteria, based on previous experience, are presented which may be used as guidelines for assessing the vibratory conditions of such machines.

The vibration levels specified here define four quality zones for both relative and absolute shaft vibration measured at, or close to, the main load-carrying bearings, at rated speed and under steady state conditions. Higher levels of vibration can be permitted at other measuring positions and under transient conditions, such as start-up and run-down (including passing through critical speed ranges).

The recommended shaft vibration amplitude values for large steam turbine-generator sets, in micrometers peak-to-peak measured relative to the bearings, are shown in **Table 6** for relative shaft to bearing vibrations, and in **Table 7** for absolute vibrations. In both tables, zone A represents new machines that can be operated without restriction; zone B is acceptable for long-term operation; zone C represents machines that may be operated for a limited time until a suitable opportunity arises for remedial action to be taken; and, zone D is identified as a trip level as these values are considered to be of sufficient severity to cause damage.

ISO 7919, Part 3: Guidelines for coupled machines These are given for application of shaft vibration evaluation criteria measured close to the bearings under normal operating conditions. These guidelines are presented in terms of both steady running conditions, and any changes that may occur in these steady values. This standard applies to coupled industrial machines with fluid film bearings, comprising: turbocompressors, turbines, turbine-generators, and electric drives, all having maximum rated speeds in the range 1000–30 000 rpm, and powers between 30 kW and 50 MW.

Table 6 Relative shaft to bearing vibrations

	Shaft rotational frequency ($rmin^{-1}$)			
Zone boundary	1500	1800	3000	3600
	Maximum shaft relative displacement			
A	100	90	80	75
B	200	185	165	150
C	320	290	260	240

Table 7 Absolute vibrations

	Shaft rotational frequency ($rmin^{-1}$)			
Zone boundary	1500	1800	3000	3600
	Maximum shaft relative displacement			
A	120	110	100	90
B	240	220	200	180
C	385	350	320	290

The numerical values specified in **Figure 5** are not intended to serve as the only basis for acceptance specifications. In general, the vibratory condition of these machines is usually assessed by consideration of both the shaft vibration and the associated structural vibration. As a result, this Standard should be used in conjunction with 10816, Part 3. The zone descriptions of **Figure 5** are the same as in 7919, Part 2.

ISO 7919, Part 4: Guidelines for Gas-Turbines applies to industrial gas turbine sets (including those with gears) with fluid film bearings, power outputs greater than 3 MW, and shaft rotational speeds from 3000 to 30 000 rpm. Aircraft type gas turbines are excluded, since they differ fundamentally from industrial gas turbines, both in the types of bearings (rolling element), and in the stiffness and mass ratios of the rotors and support structures. Depending on the construction and mode of operation, there are three types of industrial gas turbines: (1) single-shaft constant-speed; (2) single-shaft variable-speed; and, (3) gas turbines having separate shafts for hot-gas generation and power delivery.

Guidelines are given in **Figure 6** for the application of shaft vibration criteria measured close to the bearings of industrial gas turbines under normal operating

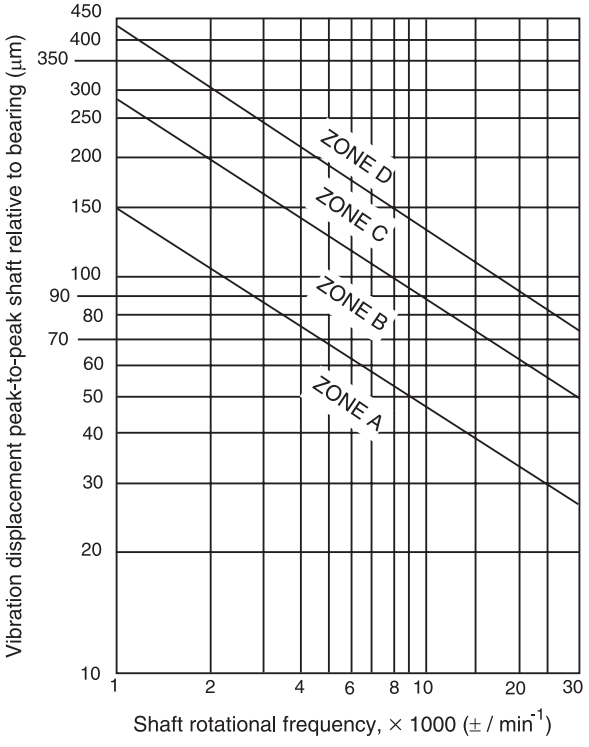


Figure 5 Recommended vibration amplitude values for coupled machines.

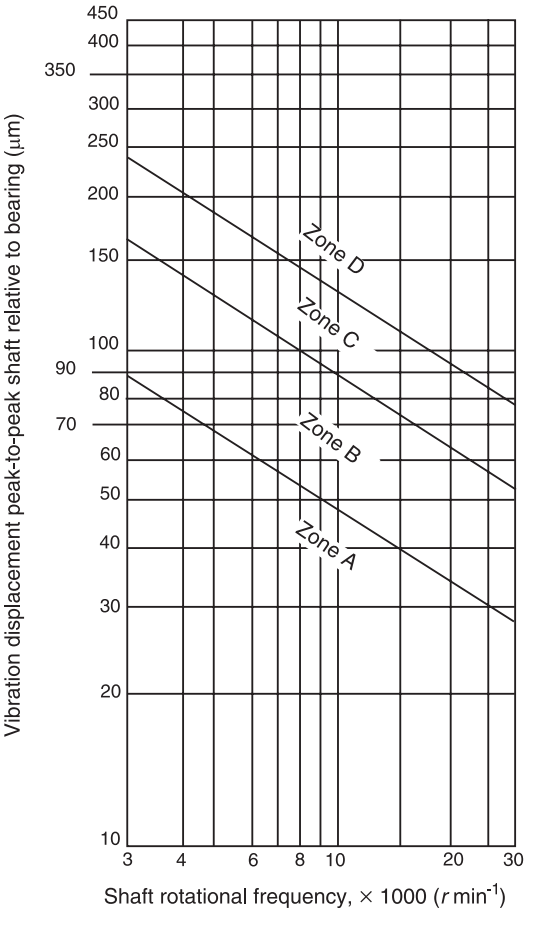


Figure 6 Recommended shaft vibration amplitudes for gas turbines.

conditions. The zone descriptions are the same as in 7919, Part 2.

ISO 7919, Part 5: Guidelines for hydraulic machine sets This lists the special features required for measuring shaft vibrations on coupled hydraulic sets. This standard applies to all types of hydraulic machines having nominal speeds between 60 and 3600 rpm, with fluid film bearings and rated powers of 1 MW or more. These machines may consist of turbines, pumps, pump-turbines, generators, motors, and motor-generators, including couplings, gears, or auxiliary equipment in the shaft line. The position of the shaft may be vertical, horizontal, or at an arbitrary angle between these two directions.

The guidelines are given for the application of shaft vibration criteria as measured close to the bearings of coupled hydraulic sets, under normal operating and steady state conditions, and any changes that may occur in these steady values. The numerical values specified in **Figure 7** present rotor displacements relative to the bearings in micrometers peak-to-peak vs shaft rotational speed in rpm. The zone descriptions are the same as in 7919, Part 2.

Gear Units

ISO 8578, Acceptance code for gears, Part 2: Determination of mechanical vibration of gear units during acceptance testing This provides a method for determining the mechanical vibration of enclosed gear units which are individually housed. This Standard applies to a gear unit under test and operating with in its design speed, load, temperature range, and lubrication specifications for acceptance testing. Two types of vibration measurements are made on gear units that operate with oil-film journal bearings: (1) shaft vibration; and (2) housing vibration.

Proximity-type transducers are usually used to measure the peak-to-peak value of the shaft's displacement relative to the housing, in the frequency range 0–500 Hz. The transducers are located as close as practical to a bearing. The measurements should be made in three orthagonal directions, one of which is parallel to the shaft axis. Only one axial transducer per shaft is necessary. The housing vibration is measured with a seismic transducer in the frequency range 10–10 000 Hz. A classification

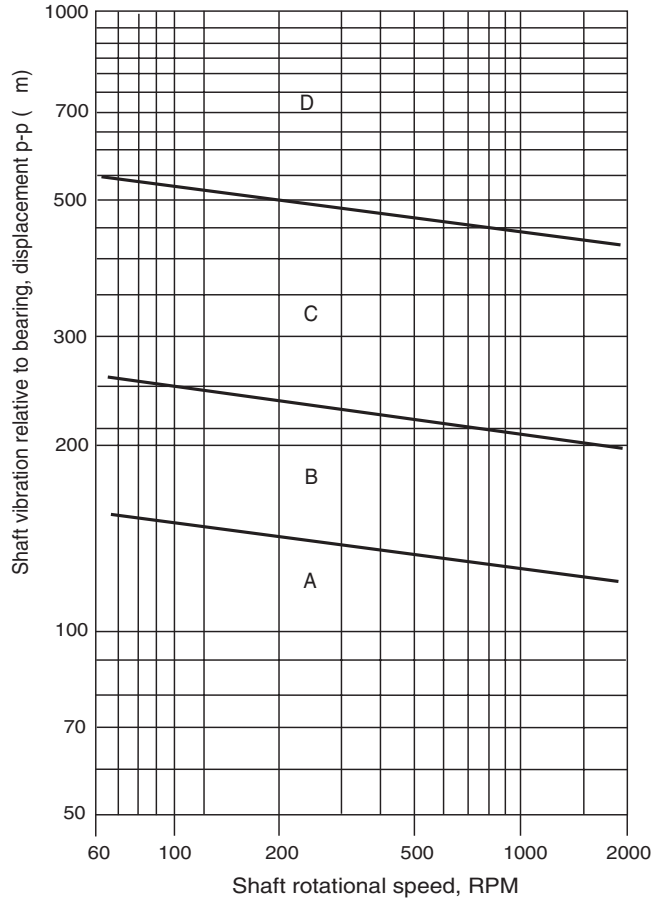


Figure 7 Recommended shaft vibration amplitudes for hydraulic machine sets.

system for gear boxes on the basis of shaft displacement and housing velocity measurements is given in **Figures 8** and **9**.

his standard also provides a subjective assessment of the acceptable vibration rating for typical applications during acceptance testing at the manufacturer's facility. The vibration of a properly manufactured gear unit will vary according to the particular design, size, and application. For example, what may be perfectly suitable for a large low-speed mill drive may not be acceptable for a precision high-speed or marine drive; and, what may be acceptable for a precision high-speed drive may be unjustifiably expensive for a low-speed drive. Therefore, care must be taken when applying a given grade as an acceptance criterion. **Figure 10** gives subjective levels of vibration for typical gear applications.

Vibration Condition Monitoring

ISO 13373–1 (to be published), Condition monitoring and diagnostics of machines – Vibration condition monitoring – Part 1: Guidelines for condition monitoring of machines This includes the general guidelines for the measurement and data collection functions necessary for the vibratory assessment of machinery vibration for condition monitoring and diagnostics. It is intended to promote consistency of the measurement procedures and practices, with concentration on rotating machines. The standard is applicable to all types of rotating machines and sizes. It also describes the types of typical monitoring systems (permanent, semipermanent, and portable); and, the various methods of data collection (continuous or periodic).

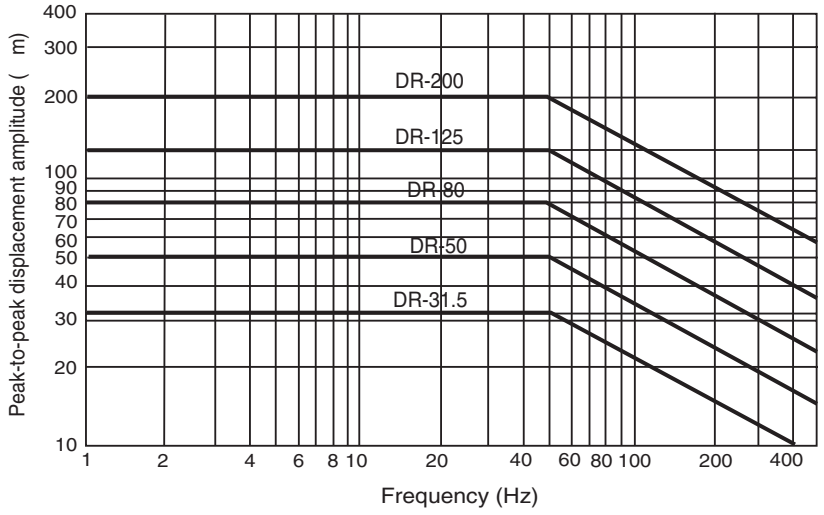


Figure 8 Gear shaft vibration amplitudes.

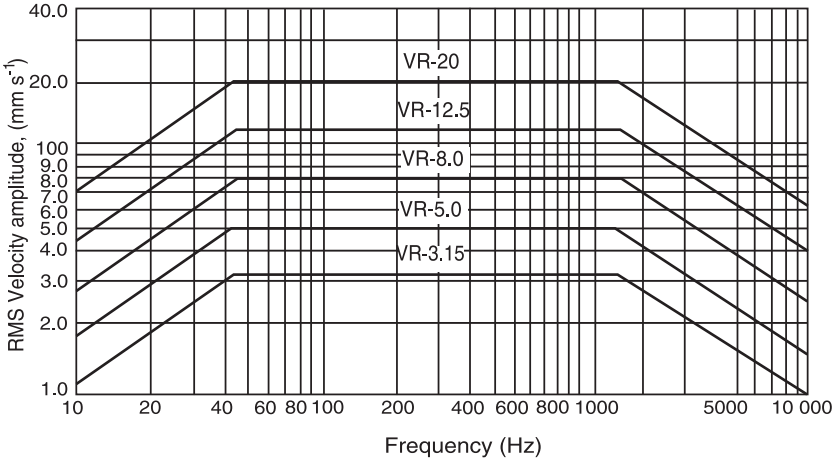


Figure 9 Gear housing vibration amplitudes.

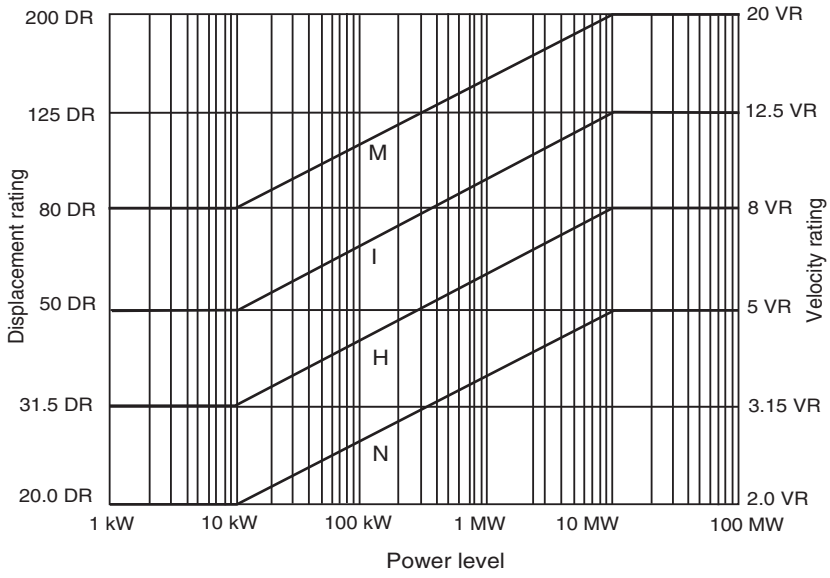


Figure 10 Subjective gear ratings.

The measurements and the transducers described are selected to provide the taking of data for recording and trending purposes (condition monitoring), and for discrete frequency analysis for the purposes of diagnostics. The trending guidelines include tracking the vibration levels and the frequencies of data collection; and, how these frequencies may change with changes in the vibration levels, and their rates of changes. A typical frequency spectrum is shown in **Figure 11** which can be used for diagnostic purposes. It can also be used for discrete frequency trending.

Recommended ranges for displacement, velocity, and acceleration transducers are specified, as well as frequency ranges of operation. **Figure 12** demonstrates the typical envelope ranges of velocity vs frequency for several type transducers.

The standard also includes guidance for transducer resonant frequency characteristics, and mounted frequency concerns.

The recommended transducer types and their locations and directions for various type machines are included in Annex A of the standard. Only p. 1 of Annex A, Table 8, is included here for information purposes. It is noted that the sizes of the machines usually indicate common construction characteristics, such as fluid film vs rolling element bearings,

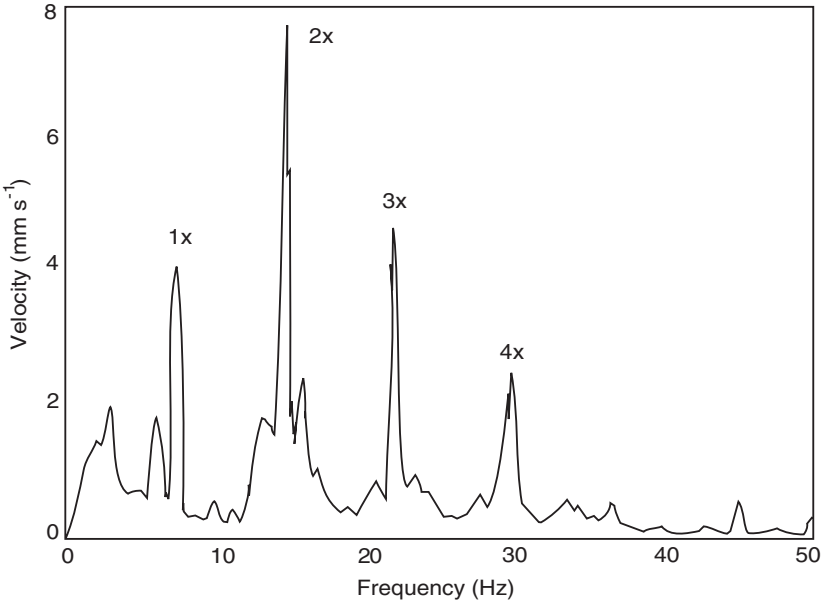


Figure 11 Frequency spectrum.

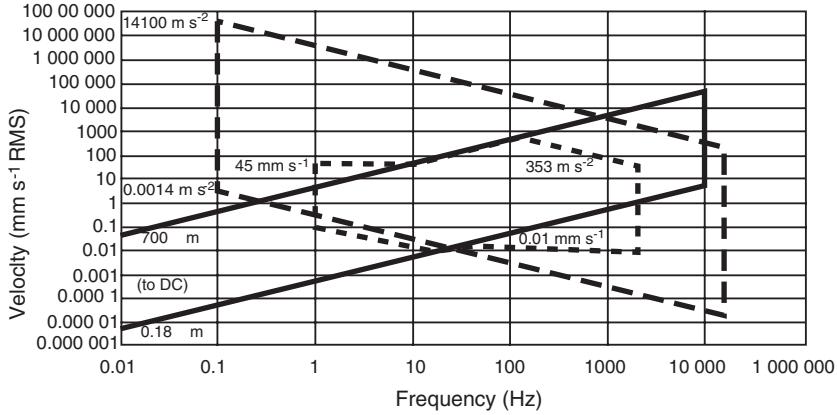


Figure 12 Dynamic ranges of various velocity transducers. (— — —) piezoelectric acceleration; (– – –) electromechanical velocity transducer; (——) eddy current proximity probe.

Table 8 Guidelines for transducer applications for various types of machine[a]

Machine type	*Evaluation parameters*	*Transducer type*	*Measurement locations*	*Direction*	*ISO standard reference*	*Notes*
Large steam turbine generator sets with fluid film bearings	Relative displacement or absolute displacement	Noncontacting transducer Noncontacting and seismic transducer combination	Shaft at each bearing	Radial ±45 deg or *X* and *Y*	7919-Part 2	*a*
Power generation	Velocity or acceleration	Velocity transducer or accelerometer	Each bearing housing	Radial *X* and *Y*	10816-Part 2	
	Shaft axial displacement	Noncontacting transducer or axial probe	Thrust collar	Axial *Z*		
	Phase reference and rpm	Eddy current/ inductive/optic-al transducer	Shaft	Radial		
Medium and small industrial steam turbines with fluid film bearings	Relative displacement	Noncontacting transducer	Shaft at each bearing	Radial±45 deg or *X* and *Y*	7919-Part 3	
	Velocity or acceleration	Velocity transducer or accelerometer	Each bearing housing and turbine housing	Radial *X* and *Y*	10816-Part 3	
Mechanical drive						
Power generation	Shaft axial displacement	Noncontacting transducer or axial probe	Thrust collar	Axial *Z*		
	Phase reference and rpm	Eddy current/ inductive/optic-al transducer	Shaft	Radial		

[a] Orthogonal measurements at ±45 deg are normally used for condition monitoring. Vertical and horizontal (*X* and *Y*) locations are acceptable alternatives.

Table 9 Most common causes of lateral vibration

Cause	*Characteristic vibration frequencies*	*Remarks*
Unbalance	1 × (once per revolution)	Changes in balance will give changes in the 1 × vector. Vibration will be highest when running speed coincides with a rotor system critical speed. Significant vibration phase change will occur when passing through critical speeds. At a fixed speed vibration levels are constant
Misalignment	1 ×, 2 ×, 3 ×	Various types and causes for misalignment are: angular, parallel, foundation movement. The axial vibration component may be as significant as the radial component, particularly for geared systems
Bearing wear	40–50% of operating speed or at first rotor critical speed	Excessive clearance due to wear, damage or improper assembly can cause bearing oil film destabilizing forces to act on the rotor
Oil film bearings		Vibration levels will be unsteady and can quickly reach high magnitudes
Rolling element bearings	Various frequencies, particularly high orders of running speed and ball pass frequencies	Vibration tends to be localized to the region of the defective bearing
		Vibration readings are usually unsteady and increase with time
Stiffness dis-symmetry (e.g., axial winding slots in generator/ motor rotors)	2 ×	Vibration peaks when a 2 × stimulus is coincident with a rotor critical speed. At a fixed rotor speed vibration levels are constant.
		Compensating grooves are used on large machines to minimize this stimulus
Bent rotor (see also thermal dis-symmetry)	1 ×, 2 ×, or higher orders	If the rotor is bent near the coupling, a high 2 × axial vibration is frequently observed. At a fixed speed, the rotor vibration levels are constant
Cracked rotor	1 ×, 2 ×, or higher harmonics	A growth in the 2 × vector is an indication that the growth of a transverse crack is getting critical. Changes in the 1 × or higher harmonic vectors can also occur
Component looseness in rotor	1 × and harmonics of running speed frequency	Vibration levels may be erratic and inconsistent between successive start-stop cycles. Sometimes subharmonic frequencies are also observed
Eccentric or noncircular bearing journals	1 × and for noncircular journals at harmonics of running speed frequency	Vibration levels can be abnormal or excessive at low rotor speeds as well as at rotor critical speeds. At a fixed rotor speed, the vibration levels are constant

and these considerations normally dictate the type(s) of transducers recommended.

Annex C of the standard provides guidance regarding the most common causes of lateral and torsional vibration. Only p. 1 of Annex C (**Table 9**) is included here for information.

ISO 13373–2 (to be published), Part 2: Processing, analysis, diagnostics, and display of data for vibration condition monitoring of machines This provides guidelines for processing vibration datain the time and frequency domains, analyzing the vibration signatures, displaying the data and applying the results of the analyses to machinery vibration diagnostics. Different techniques are described for different applications. Signal enhancement techniques and analysis methods used for the investigation of particular machine dynamic phenomenon are included. Many of these techniques can be applied to other machine types including reciprocating machines. Standard formats for the parameters that are commonly plotted for evaluation and vibration diagnostic purposes are given. These should be used for computer display screens and for hard copy presentations (line printers, laser plotters, plotters).

The signal-processing and analysis procedures applied to vibration condition monitoring are as varied as the processes to be monitored, the degree of certainty desired, the resources available, etc. A well conceived condition monitoring program will include the consideration of many factors such as process priority, criticality and complexity of the system, cost-effectiveness, probability of various failure mechanisms and identification of incipient failure indicators, etc. The standard defines the appropriate process analysis that dictates the types of data required to suitably monitor and diagnose particular types of equipment.

The standard stresses in that the vibration analyst should accumulate as much pertinent information as possible about the machine to be monitored. For example, knowing the vibration resonant frequencies from design and analytical information will provide an insight regarding the vibration frequencies anticipated, and, consequently, the frequency range that should be monitored. Also, knowing the operating conditions tells the analyst what the excitations will be. Other advantages to this pretest planning process are that it provides guidance as to what types of sensors are needed, where they should be located optimally, what kind of signal conditioning equipment is required, what types of analyses would be most appropriate, and what the relevant criteria are.

The basic signals from the displacement, velocity, and accelerometer transducers are recorded as amplitude vs time, which is the primary vibration signature, and this is termed the 'time domain'. The standard then proceeds to identify the conversion of the analog signals to the more recent techniques of digitizing the signals, which is done automatically with present-day analyzers. In this manner, analog excursions are directly converted to numerical values.

The next basic step addressed in the standard is the process of applying the FFT to the time signal to obtain a frequency spectrum of the signal, which identifies the amplitudes of the distinct repetitive frequencies that can be analyzed regarding their source(s), and this is called the 'frequency domain'. This process then leads to vibration analysis and diagnostics which can determine the machine component that is producing the dominant signal, and is therefore the likely candidate causing the machine problem.

Other factors pertaining to the signal processing in the standard include: beating, modulation, integration and differentiation, crest factor, amplifiers, filtering, dynamic range, real and imaginary, resolution, modulation, and aliasing.

The standard identifies that the discrete frequency peaks can result from a sine wave representing the fundamental frequency of a rotating shaft, or higher frequencies related to blade pass, gear mesh, or rolling element ball passing. Since these intelligent signals may be difficult to detect at times, due to noise levels or other obscuring phenomenon, the standard contains many analysis techniques that can be applied to help obtain the intelligent diagnostic information, such as: orbit analysis, Bode plots, polar plots, waterfall (cascade) plots, zoom analysis, Campbell diagram, cepstrum, kurtosis, and others.

See also: **Cepstrum analysis**; **Spectral analysis, classical methods**; **Vibration intensity**.

Further Reading

ISO 10816–1 Mechanical vibration – Evaluation of machine vibration by measurements on non-rotating parts – Part 1: General Guidelines.

ISO 10816–2 Mechanical vibration – Evaluation of machine vibration by measurements on non-rotating parts – Part 2: Large land-based steam turbine generator sets in excess of 50 MW.

ISO 10816–3 Mechanical vibration – Evaluation of machine vibration by measurements on non-rotating parts – Part 3: Industrial machines with normal power above 15 kW and nominal speeds between 120 r/m in and 15 000 r/m in when measured in situ.

ISO 10816–4 Mechanical vibration – Evaluation of machine vibration by measurements on non-rotating parts – Part 4: Gas turbine sets excluding aircraft derivatives.

ISO 10816–5, Mechanical vibration – Evaluation of machine vibration by measurements on non-rotating parts – Part 5: Machine sets in hydraulic power generating and pumping plants. (to be published).

ISO 10816–6, Mechanical vibration – Evaluation of machine vibration by measurements on non-rotating parts – Part 6: Reciprocating machines with power ratings above 100 kW.

ISO 13373–1, Condition monitoring and diagnostics of machines – Vibration condition monitoring of machines – Part 1: General Guidelines. (to be published).

ISO 13373–2, Condition monitoring and diagnostics of machines – Vibration condition monitoring of machines – Part 2: Processing, analysis and display of data. (to be published).

ISO 1925 Mechanical vibration – Balancing – Vocabulary.

ISO 2041 Vibration and shock – Vocabulary.

ISO 2372 Mechanical vibration of machines with operating speeds from 10 to 200 rps – basis for specifying evaluation standards.

ISO 2954 Mechanical vibration of rotating and reciprocating machinery – requirements for instruments for measuring vibration severity.

ISO 3945 The measurement and evaluation of vibration severity of large rotating machines, in situ; operating at speeds from 10 to 200 rps.

ISO 5348 Mechanical vibration and shock – Mechanical mounting of accelerometers.
ISO 7919–1 Mechanical vibration of non-reciprocating machines – Measurement on rotating shafts and evaluation criteria – Part 1: General Guidelines.
ISO 7919–2 Mechanical vibration of non-reciprocating machines – Measurements on rotating shafts and evaluation criteria – Part 2: Large land-based steam generator sets.
ISO 7919–3 Mechanical vibration of non-reciprocating machines – Measurements on rotating shafts and evaluation criteria – Part 3: Coupled industrial machines.
ISO 7919–4 Mechanical vibration of non-reciprocating machines – Measurements on rotating shafts and evaluation criteria – Part 4: Gas turbine sets.
ISO 7919–5, Mechanical vibration of non-reciprocating machines – Measurements on rotating shafts and evaluation criteria – Part 5: Machine sets in hydraulic power generating and pumping plants.

STOCHASTIC ANALYSIS OF NONLINEAR SYSTEMS

Y K Lin and G Q Cai, Florida Atlantic University, Boca Raton, FL, USA

Copyright © 2001 Academic Press

doi:10.1006/rwvb.2001.0044

Introduction

This article is concerned with nonlinear dynamical systems whose response to excitations is random; namely, it can only be described in terms of probability and statistics. The cause for random system response may be random excitations, random properties of the system, random initial conditions, random boundary conditions, or various combinations of the above. However, only random excitations will be considered herein, of which turbulent winds, earthquakes, rough roadways, and irregular sea waves are some examples. The system nonlinearity may result from, but not be limited to, large deformation. Specifically, governing differential equations of the following type for discrete nonlinear systems will be considered:

$$\ddot{Y}_j + \beta_j(\mathbf{Y}, \dot{\mathbf{Y}}) = \sum_k \gamma_{jk}(\mathbf{Y}, \dot{\mathbf{Y}})\xi_k(t); \quad j = 1, 2, \ldots, N \qquad [1]$$

where $\beta_j(\cdot,\cdot)$ and $\gamma_{jk}(\cdot,\cdot)$ are generally nonlinear, and $\xi_k(t)$ are stochastic processes (random functions). Letting $X_j = Y_j$ and $X_{j+N} = \dot{Y}_j$, eqns [1] may be transformed into a system of first-order equations:

$$\dot{X}_i = f_i(\mathbf{X}) + \sum_j g_{ij}(\mathbf{X})\xi_j(t); \quad i = 1, 2, \ldots, 2N \qquad [2]$$

Comparing [1] and [2]:

$$f_i = \begin{cases} X_{i+N}, & i = 1, 2, \ldots, N \\ -\beta_{i-N}(\mathbf{X}), & i = N+1, N+2, \ldots, 2N \end{cases} \qquad [3]$$

$$g_{ij} = \begin{cases} 0, & i = 1, 2, \ldots, N \\ \gamma_{i-N,j}(\mathbf{X}), & i = N+1,\ N+2, \ldots,\ 2N \end{cases} \qquad [4]$$

The form [1] or [2] suggests that the stochastic excitations $\xi_j(t)$ can be additive, or multiplicative (also known as parametric), or both. An additive excitation is one whose accompanying coefficient is merely a constant; namely, the coefficient is independent of the state $\mathbf{X}$.

Solutions to system [2] may be classified into two types: (i) the probabilistic properties of $\mathbf{X}(t)$, and (ii) the statistical properties of $\mathbf{X}(t)$. For each type, solutions may be obtained for properties at one time instant, and for joint properties at more than one time instant.

Exact Probability Solutions

Some exact solutions for the probability density of the system response $\mathbf{X}(t)$ have been obtained for system [2] when the excitation processes $\xi_j(t)$ are Gaussian white noises, to be denoted specially as $W_j(t)$, which are defined in terms of the following statistical properties:

$$E\big[W_j(t)\big] = 0 \qquad E\big[W_j(t)W_k(t+\tau)\big] = 2\pi S_{jk}\delta(\tau) \qquad [5]$$

where $E[\cdot]$ denotes an ensemble average, $\delta(\cdot)$ is the Dirac delta function, and each S_{jk} is a constant, representing the cross spectral density of $W_j(t)$ and $W_k(t)$. It represents the spectral density of $W_j(t)$ when $j = k$. Under Gaussian white-noise excitations, the response $\mathbf{X}(t)$ is a diffusive Markov vector, whose

conditional probability density $q(\mathbf{x}, t|\mathbf{x}_0, t_0)$ is governed by the following Fokker–Planck–Kolmogorov (FPK) equation:

$$\frac{\partial q}{\partial t} + \sum_i \frac{\partial}{\partial x_i}(a_i q) - \frac{1}{2}\sum_i \sum_j \frac{\partial^2}{\partial x_i \partial x_j}(b_{ij} q) = 0 \quad [6]$$

The unknown q is the transition probability density, and is treated as a function of the state variable $\mathbf{x}$ (possible value of $\mathbf{X}$) and time t, on the condition that $\mathbf{X}(t_0) = \mathbf{x}_0$, where $t_0 \leq t$. This condition is indicated specifically as $|\mathbf{x}_0, t_0$. Eqn [6] is solved under some suitable boundary conditions for the probability density, and the initial condition:

$$q(\mathbf{x}, t_0|\mathbf{x}_0, t_0) = \Pi\delta(x_i - x_{i0}) \quad [7]$$

where the x_i are components of $\mathbf{x}$, and the x_{i0} are components of $\mathbf{x}_0$. The main ingredients in eqn [6] are the coefficients a_i and b_{ij}. They are known as the first and second derivate moments, respectively, defined as:

$$a_i = \lim_{\Delta t \to 0} \frac{1}{\Delta t} E[X_i(t + \Delta t) - X_i(t)|\mathbf{X}(t) = \mathbf{x}] \quad [8]$$

$$b_{ij} = \lim_{\Delta t \to 0} \frac{1}{\Delta t} \times E\Big\{\big[X_i(t + \Delta t) - X_i(t)\big]\big[X_j(t + \Delta t) - X_j(t)\big]|\mathbf{X}(t) = \mathbf{x}\Big\} \quad [9]$$

which can be obtained from the system governing eqns [2]. Specifically:

$$a_i = f_i(\mathbf{x}) + \pi \sum_j \sum_k \sum_r K_{jr} g_{kr}(\mathbf{x}) \frac{\partial}{\partial X_k} g_{ij}(\mathbf{x}) \quad [10]$$

$$b_{ij} = 2\pi \sum_k \sum_r K_{kr} g_{ik}(\mathbf{x}) g_{jr}(\mathbf{x}) \quad [11]$$

Unfortunately, eqn [6] is difficult to solve analytically. Therefore, the special case for which the following stationary-state solution exists is considered:

$$p(\mathbf{x}) = \lim_{t - t_0 \to \infty} q(\mathbf{x}, t|\mathbf{x}_0, t_0) \quad [12]$$

The existence of the stationary probability density $p(\mathbf{x})$ requires that the boundary conditions to be imposed on eqn [6] must be such that the total probability is preserved within the domain for $\mathbf{x}$. For this special case, the stationary probability $p(\mathbf{x})$ is governed by:

$$\sum_i \frac{\partial}{\partial x_i}(a_i p) - \frac{1}{2}\sum_i \sum_j \frac{\partial^2}{\partial x_i \partial x_j}(b_{ij} p) = 0 \quad [13]$$

Equation [13] is known as the reduced FPK equation.

Solution for eqn [13] is relatively easy to obtain for the following system of nonlinear stiffness but linear damping:

$$\ddot{Y}_j + c_j \dot{Y}_j + \frac{\partial}{\partial y_j} U(\mathbf{Y}) = W_j(t); \quad j = 1, 2, \ldots, N \quad [14]$$

where $W_j(t)$ are uncorrelated Gaussian white noises; namely, $S_{ij} = 0$ if $i \neq j$. It can be seen by comparing eqns [1] and [14] that, in this case, all excitations are additive, and that the function $U(\mathbf{Y})$ represents the potential energy in the system. Under the condition:

$$\frac{c_j}{S_{jj}} = \kappa(\text{a constant}), \quad \text{for all } j \quad [15]$$

eqn [13] can be solved to yield:

$$p = C \exp\left\{-\frac{\kappa}{\pi}\left[\frac{1}{2}\sum_{j=1}^{N} x_{j+N}^2 + U(x_1, x_2, \ldots x_N)\right]\right\} \quad [16]$$

where x_j is the state variable for Y_j, x_{j+N} is the state variable for $\dot{Y}_j$, and C is a constant to be determined under the normalization condition of unit total probability. Equation [16] shows that the kinetic energies $\frac{1}{2}\dot{Y}_j^2$ of different modes are identically distributed, known as equipartioning of energy in statistical mechanics.

For more complicated cases, including nonlinear damping and/or parametric excitations, an exact solution can be found if the system belongs to a special class, called the class of generalized stationary potential. To obtain such a solution, we split both the first and second derivate moments as follows:

$$a_i = a_i^{(1)} + a_i^{(2)} \quad [17]$$

$$b_{ij} = b_{ij}^{(i)} + b_{ji}^{(j)} \qquad [18]$$

Note that the symmetry property of the second derivate moment, $b_{ij} = b_{ji}$, is maintained in eqn [18]. Equation [13] can then be replaced by:

$$\sum_i \frac{\partial}{\partial x_i}\left(a_i^{(1)}p - \sum_j \frac{\partial}{\partial x_j} b_{ij}^{(i)} p\right) + \sum_i \frac{\partial}{\partial x_i}\left(a_i^{(2)}p\right) = 0 \qquad [19]$$

Equation [19] is satisfied under the following more restrictive conditions:

$$a_i^{(1)}p - \sum_j \frac{\partial}{\partial x_j} b_{ij}^{(i)} p = 0 \qquad [20]$$

$$\sum_i \frac{\partial}{\partial x_j}\left[a_i^{(2)}p\right] = 0 \qquad [21]$$

A system is said to belong to the class of generalized stationary potential if a consistent solution p can be found which satisfies both eqns [20] and [21].

In the case of a single-degree-of-freedom system:

$$\dot{X}_1 = X_2 \qquad [22]$$

$$\dot{X}_2 = -\beta(X_1, X_2) + \gamma_k(X_1, X_2) W_k(t) \qquad [23]$$

it can be shown that the exact solution satisfying eqns [20] and [21] can be cast in the form of:

$$p = C \exp\left[-\phi(\lambda)\right] \qquad [24]$$

were ϕ, known as the probability potential, is a function of the total energy λ (to be explained shortly). This exact solution is obtainable if the β and γ_k functions in eqn [23] are related as follows:

$$\beta(x_1, x_2) = \pi x_2 \sum_i \sum_j K_{ij}\, \gamma_i(x_1, x_2)\, \gamma_j(x_1, x_2) \phi'(\lambda) - \pi \sum_i \sum_j K_{ij}\, \gamma_i(x_1, x_2) \frac{\partial \gamma_j(x_1, x_2)}{\partial x_2} + u(x_1) \qquad [25]$$

in which function $u(x_1)$ contains all the terms on the right hand side depending only on x_1, and:

$$\lambda = \frac{x_2}{2} + \int_0^{x_1} u(v)\, \mathrm{d}v = \frac{x_2}{2} + U(x_1) \qquad [26]$$

It can be seen from [25] that if all the γ_i functions are independent of x_2, then $u(x_1)$ must be the stiffness term in $\beta(x_1, x_2)$. In this case, λ represents clearly the total (kinetic plus potential) energy in the system. However, if some γ_i functions depend on x_2, then $u(x_1)$ may include terms which are not originally present in $\beta(x_1, x_2)$. In other words, the stiffness term is effectively modified due to a parametric excitation on the velocity term in the original equation of motion.

As an example, consider the following system:

$$\ddot{Y} + Y^2\left(\beta + \frac{4\alpha}{Y^2 + \dot{Y}^2}\right)\dot{Y} + [1 + W(t)Y] = 0 \qquad [27]$$

Note that only a parametric excitation $W(t)$ is present in this example. The stationary probability density of the response obtained from the above procedure is given by:

$$p(x_1, x_2) = C\left(x_1^2 + x_2^2\right)^{-2\alpha/\pi S} \exp\left[-\frac{\beta}{2\pi S}\left(x_1^2 + x_2^2\right)\right] \qquad [28]$$

where x_1 is the state variable for Y, and x_2 is the state variable for $\dot{Y}$, and where S is the spectral density of white noise $W(t)$. A nontrivial stationary probability density exists only if $S > 2\alpha/\pi$; otherwise, the stationary solution is trivial, i.e., $p(x_1, x_2) = \delta(x_1)\delta(x_2)$. When a nontrivial stationary probability density exists, its shape depends on whether $\alpha \geq 0$ or $\alpha < 0$. If $\alpha \geq 0$, the stationary probability density has a peak at $x_1 = x_2 = 0$. If $\alpha < 0$, the peak occurs on a circle $x_1^2 + x_2^2 = 4|\alpha|/\beta$, as shown in **Figure 1**, which is the stochastic analogue of a limit cycle.

Approximate Probability Solutions

It is interesting to note that rather restrictive conditions are imposed, such as eqns [15] or [25], in order to obtain an exact probability solution. Such conditions are seldom met; therefore, approximate solution techniques are important. One general scheme in obtaining approximate probability solutions makes use of the principle of weighted residuals, which will now be described.

Let the original governing equations for the system be given by:

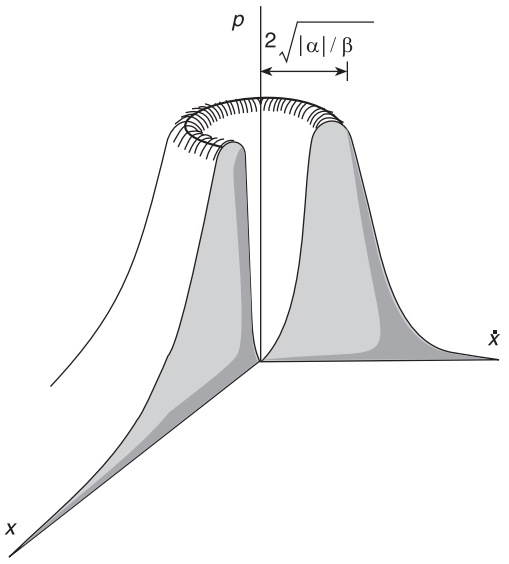


Figure 1 Stationary probability density of system [28] (with the right-front quarter removed).

$$\dot{X}_i = F_i(\mathbf{X}) + \sum_j g_{ij}(\mathbf{X}) W_j(t); \quad i = 1, 2, \ldots, N \tag{29}$$

for which an exact probability solution is presently unavailable. We wish to obtain an approximate solution by replacing eqn [29] with another set of equations:

$$\dot{X}_i = f_i(\mathbf{X}) + \sum_j g_{ij}(\mathbf{X}) W_j(t); \quad i = 1, 2, \ldots, N \tag{30}$$

which belongs to the solvable class of problems. The conditions to be satisfied in the replacement are:

$$E\left\{ \sum_i [F_i(\mathbf{X}) - f_i(\mathbf{X})]\, N_i(\mathbf{X}) \right\} = 0 \tag{31}$$

where $N_i(\mathbf{X})$ are weighting functions, and the ensemble average $E\{\ \}$ is computed on the basis of the probability density p_s for the response of the replacement system, eqn [30]. By judiciously selecting a set of $N_i(\mathbf{X})$ functions, we obtain a set of constraints from which the parameters in p_s can be determined.

One approximation scheme is well-known equivalent linearization. In this scheme, the substituting system is linear and under purely additive random excitations. It is suitable only if the nonlinearity in the original system is weak, and if no parametric excitations are present. However, the excitations need not be white noises, as long as they are Gaussian. For illustration, this scheme will now be applied to the following single-degree-of-freedom systems.

Consider:

$$\dot{X}_1 = X_2 \tag{32}$$

$$\dot{X}_2 = -\beta(X_1, X_2) + \xi(t) \tag{33}$$

where $\xi(t)$ is a stationary Gaussian process with zero mean. Let eqns [32] and [33] be replaced by a linear system:

$$\dot{X}_1 = X_2 \tag{34}$$

$$\dot{X}_2 = -c_e X_2 - k_e X_1 + \xi(t) \tag{35}$$

With two different choices $N_2(\mathbf{X}) = X_1$ and $N_2(\mathbf{X}) = X_2$ for the weighting functions, we obtain from eqn [31]:

$$E\{[\beta(X_1, X_2) - c_e X_2 - k_e X_1] X_1\} = 0 \tag{36}$$

$$E\{[\beta(X_1, X_2) - c_e X_2 - k_e X_1] X_2\} = 0 \tag{37}$$

Since $E[X_1 X_2] = 0$ in the stationary state, eqns [36] and [37] can be solved to yield:

$$k_e = \frac{E[X_1 \beta(X_1, X_2)]}{E[X_1^2]} \tag{38}$$

$$c_e = \frac{E[X_2 \beta(X_1, X_2)]}{E[X_2^2]} \tag{39}$$

The stationary solution for the substituting linear system governed by eqns [34] and [35] has the well-known Gaussian distribution, namely:

$$p(x_1, x_2) = C \exp\left[-\frac{c_e}{2\pi K} \left(x_2^2 + k_e x_1^2 \right) \right] \tag{40}$$

where K is the spectral density of $W(t)$. This probability density is now treated as an approximate solution for the original system governed by eqns [32] and [33]. From eqn [40], is obtained $E[X_1^2] = \pi K / c_e k_e$, and $E[X_2^2] = \pi K / c_e$, with which eqns [38] and [39] are reduced to:

$$E[X_1 \beta(X_1, X_2)] = \frac{\pi K}{c_e} \tag{41}$$

$$E[X_2 \beta(X_1, X_2)] = \pi K \tag{42}$$

Equations [41] and [42] are a set of nonlinear algebraic equations for the unknowns c_e and k_e. In particular, if $\beta(X_1, X_2)$ is a polynomial of X_1 and X_2, then the ensemble averages indicated on the left hand sides of these equations can be carried out analytically using the approximate probability density given in eqn [40], and in many cases c_e and k_e can be solved in closed form.

If the system is strongly nonlinear and/or parametric excitations are present, a substituting system from the solvable class of generalized stationary potential may be selected. In this case, however, the excitations are restricted to Gaussian white noises. Consider the following single-degree-of-freedom system:

$$\dot{X}_1 = X_2 \qquad [43]$$

$$\dot{X}_2 = -B(X_1, X_2) + \sum_k \eta_k(X_1, X_2) W_k(t) \qquad [44]$$

for which an exact probability solution is not available at the present time. Let this system be replaced by a solvable system within the class of generalized stationary potential:

$$\dot{X}_1 = X_2 \qquad [45]$$

$$\dot{X}_2 = -\beta(X_1, X_2) + \sum_k \eta_k(X_1, X_2) W_k(t) \qquad [46]$$

namely, $\beta(X_1, X_2)$ can be cast in the form of eqn [25]. The constraints, eqn [31], to be imposed for obtaining the approximate stationary probability density are now:

$$E\left\{\left[B(\mathbf{X}) - \pi X_2 \sum_i \sum_j K_{ij}\eta_i(\mathbf{X})\eta_j(\mathbf{X})_j\phi'(\lambda) + \pi \sum_i \sum_j K_{ij}\eta_i(\mathbf{X}) \frac{\partial \eta_j(\mathbf{X})}{\partial X_2} - u(X_1)\right] N(\mathbf{X})\right\} = 0 \qquad [47]$$

The above ensemble average is computed with the approximate probability density, eqn [24].

A physically meaningful choice for the weighting function is $N(\mathbf{X}) = X_2$. This choice implies that the average work done by the forces in $B(\mathbf{X})$ is the same as that by the forces in $\beta(\mathbf{X})$, when computed using the approximate probability density. Now, since $E[X_2 f(X_1)] = 0$ at the state of statistical stationarity for any function $f(X_1)$, only the damping components in $B(\mathbf{X})$ and $\beta(\mathbf{X})$ need to be included when evaluating the left hand side of eqn [47]. Thus, the choice of $N(X) = X_2$ is to equate the average dissipative energy of the substituting system with that of the original system; thus, the procedure has been given a physically meaningful name, 'dissipation energy balancing'. Now, using eqn [24] to compute the ensemble average in eqn [47]:

$$\begin{aligned}
&\int\int \left[B(x) - \pi x_2 \sum_i \sum_j K_{ij}\eta_i(\mathbf{x})\eta_j(\mathbf{x})\phi'(\lambda) + \pi \sum_i \sum_j K_{ij}\eta_i(\mathbf{x}) \frac{\partial \eta_j(\mathbf{x})}{\partial x_2}\right] x_2 \exp\left[-\phi(\lambda)\right] \mathrm{d}x_1 \mathrm{d}x_2 \\
&= \int_0^\infty \exp\left[-\phi(\lambda)\right] \mathrm{d}\lambda \\
&\quad \times \int_{\mu 1(\lambda)}^{\mu 2(\lambda)} \left[B(\mathbf{x}) - \pi x_2 \sum_i \sum_j K_{ij}\eta_i(\mathbf{x})\eta_j(\mathbf{x})\phi'(\lambda) + \pi \sum_i \sum_j K_{ij}\eta_i(\mathbf{x}) \frac{\partial \eta_j(\mathbf{x})}{\partial x_2}\right] \mathrm{d}x_1 = 0
\end{aligned} \qquad [48]$$

where $\mu_1(\lambda)$ and $\mu_2(\lambda)$ are two extreme values for x_1, given a total energy level λ. A sufficient condition for eqn [48] is that:

$$\int_{\mu 1(\lambda)}^{\mu 2(\lambda)} \left[B(x) - \pi x_2 \sum_i \sum_j K_{ij}\eta_i(\mathbf{x})\eta_j(\mathbf{x})\phi'(\lambda) + \pi \sum_i \sum_j K_{ij}\eta_i(\mathbf{x}) \frac{\partial \eta_j(\mathbf{x})}{\partial x_2}\right] \mathrm{d}x_1 = 0 \qquad [49]$$

Of course, when carrying out the above integration, the variable x_2 must be expressed in terms of $x_2 = \pm[2\lambda - 2U(x_1)]^{1/2}$. It is of interest to note that eqn [49] leads directly to an expression for $\phi'(\lambda)$:

$$\phi'(\lambda) = \frac{\displaystyle\int_{\mu 1(\lambda)}^{\mu 2(\lambda)} \left\{\left[\mathbf{B} + \pi \sum_i \sum_j \mathbf{K}_{ij}\eta_i \left(\partial \eta_j / \partial x_2\right)\right]_{x_2 = \sqrt{(2\lambda - 2U)}} - \left[\mathbf{B} + \pi \sum_i \sum_j K_{ij}\eta_i \left(\partial \eta_j / \partial x_2\right)\right]_{x_2 = \sqrt{(2\lambda - 2U)}}\right\} \mathrm{d}x_1}{\displaystyle\int_{\mu 1(\lambda)}^{\mu 2(\lambda)} \pi \left\{\left[x_2 \sum_i \sum_j K_{ij}\eta_i\eta_j\right]_{x_2 = \sqrt{(2\lambda - 2U)}} - \left[x^2 \sum_i \sum_j K_{ij}\eta_i\eta_j\right]_{x_2 = \sqrt{(2\lambda - 2U)}}\right\} \mathrm{d}x_1} \qquad [50]$$

The probability potential $\phi(\lambda)$ is obtained readily upon an indefinite integration on λ.

Approximate Solutions for Statistical Moments

As indicated earlier, the response $\mathbf{X}(t)$ of a dynamical system is a Markov vector if the random excitations are Gaussian white noises. In this case, the transition probability density q of $\mathbf{X}(t)$ is governed by the FPK eqn [6]. For obtaining various statistical moments of the response, it is more convenient to work with the Itô-type stochastic differential equations of the form:

$$\mathrm{d}X_i(t) = m_i(\mathbf{X}) + \sum_j \sigma_{ij}(\mathbf{X})\ \mathrm{d}B_j(t) \qquad [51]$$

where $B_j(t)$ are known as the Wiener (or Brownian motion) processes, and m_i and σ_{ij} are known as drift and diffusion coefficients, respectively, which can be determined in the same manner as the first and second derivate moments. Specifically, $m_i(\mathbf{X})$ can be obtained by replacing the state vector $\mathbf{x}$ on the right hand side of eqn [10] with the random vector $\mathbf{X}$; namely, $m_i = (a_i)_{\mathbf{x}=\mathbf{X}}$. Similarly, the (i, j) element of the product of the diffusion coefficient matrix $\boldsymbol{\Sigma}$ and its transpose $\boldsymbol{\Sigma}'$ can be obtained by replacing $\mathbf{x}$ by $\mathbf{X}$ on the right hand side of [11], namely, $(\boldsymbol{\Sigma}\boldsymbol{\Sigma}')_{ij} = (b_{ij})_{\mathbf{x}=\mathbf{X}}$.

The greatest advantage in using stochastic differential eqns [51] of the Itô type is the ease with which another Itô equation for an arbitrary scalar function $F(\mathbf{X}, t)$ can be obtained:

$$\mathrm{d}F(X,t) = \left(\frac{\partial F}{\partial t} + \sum_j m_j \frac{\partial F}{\partial X_j} + \frac{1}{2}\sum_j \sum_k \sum_l \sigma_{jl}\sigma_{kl} \frac{\partial^2 F}{\partial X_j \partial X_k}\right) \mathrm{d}t + \sum_j \sum_k \sigma_{jk} \frac{\partial F}{\partial X_j}\, dB_k(t) \qquad [52]$$

Equation [52] is known as the Itô differential rule. The applicability of this rule requires that F is differentiable with respect to t, and twice differentiable with respect to the components of $\mathbf{X}$. For the purpose of obtaining statistical moments, we let $F(\mathbf{X}, t) = X_r^{n_r} X_s^{n_s} \ldots$, where $n_r, n_s \ldots$, are nonnegative integers, and then take ensemble average of the resulting Itô equations.

As an example, consider a two-dimensional Markov vector $\mathbf{X} = \{X_1, X_2\}$. Let $F(\mathbf{X}, t) = X_1^{n_1} X_2^{n_2}$. Application of Itô differential rule yields:

$$\begin{aligned}\mathrm{d}\left(X_1^{n_1} X_2^{n_2}\right) = {} & \left\{ n_1 m_1 X_1^{n_1-1} X_2^{n_2} + n_2 m_2 X_1^{n_1} X_2^{n_2-1} \right. \\ & + \frac{1}{2}\left[n_1(n_1-1)\sum_l \sigma_{1l}\sigma_{1l} X_1^{n_1-2} X_2^{n_2} \right. \\ & + n_2(n_2-1)\sum_l \sigma_{2l}\sigma_{2l} X_1^{n_1} X_2^{n_2-2} \\ & \left.\left. + 2n_1 n_2 \sum_l \sigma_{1l}\sigma_{2l} X_1^{n_1-1} X_2^{n_2-1} \right] \right\} \mathrm{d}t \\ & + \sum_k \left(n_1 X_1^{n_1-1} X_2^{n_2} \sigma_{1k} + n_2 X_1^{n_1} X_2^{n_2-1} \sigma_{2k} \right) \mathrm{d}B_k(t)\end{aligned} \qquad [53]$$

Taking ensemble average of eqn [53], and recognizing that the ensemble average of the last term is zero, we obtain:

$$\begin{aligned}\frac{\mathrm{d}}{\mathrm{d}t} E\left[X_1^{n_1} X_2^{n_2}\right] & = n_1 E\left[m_1 X_1^{n_1-1} X_2^{n_2}\right] + n_2 E\left[m_2 X_1^{n_1} X_2^{n_2-1}\right] \\ & \quad + n_1 n_2 E\left[\sum_l \sigma_{1l}\sigma_{2l} X_1^{n_1-1} X_2^{n_2-1}\right] \\ & \quad + \frac{1}{2} n_1(n_1-1) E\left[\sum_l \sigma_{1l}\sigma_{1l} X_1^{n_1-2} X_2^{n_2}\right] \\ & \quad + \frac{1}{2} n_2(n_2-1) E\left[\sum_l \sigma_{2l}\sigma_{2l} X_1^{n_1} X_2^{n_2-2}\right]\end{aligned} \qquad [54]$$

A sequence of equations for the statistical moments can be obtained by substituting nonnegative integers for n_1 and n_2. Of course, any X_j with a negative power on the right hand side of eqn [54] should be replaced by zero.

It is of interest to note that eqn [54] is valid even when $\mathbf{X}(t)$ is still in the transient nonstationary state. When $\mathbf{X}(t)$ reaches the state of stationarity, however, eqn [54] reduces to an algebraic equation, since its left hand side reduces to zero.

Note that the drift coefficients m_j and the diffusion coefficients σ_{ij} are generally nonlinear functions of X_1 and X_2. Let such nonlinear functions be of the polynomial type. Then at least some statistical moments appearing on the right hand side of eqn [52] are of orders higher than $n_1 + n_2$. It is clear that the sequence of equations for the statistical moments so obtained constitute an infinite hierarchy; therefore, they cannot be solved exactly. Several schemes have been proposed for obtaining approximate solutions, one of which is known as Gaussian closure. In this scheme, higher statistical moments are expressed in

terms of the first- and second-order moments, using the same relationships as if they were moments of Gaussian random variables, or equivalently, neglecting those cumulants of X_1 and X_2 of an order higher than the second. In the case of additive white-noise excitations, Gaussian closure leads to the same results as would be obtained from equivalent linearization. Therefore, it is not very accurate if the system nonlinearity is strong and/or if parametric excitations are present. In principle, greater accuracy can be achieved by raising the cut-off order of the cumulants when simplifying eqn [54], as described in the general scheme called cumulant-neglect-closure. However, caution should be exercised when applying higher-order closure schemes if strong parametric excitations are present such that motion instability is a distinct possibility.

Averaging Methods

The solvability of a nonlinear stochastic system is enhanced if the dimensionality of the system can be reduced. This is accomplished with two averaging techniques, applicable under certain conditions. The first, known as stochastic averaging, is applied to systems with linear or weakly nonlinear stiffness. The method is now illustrated with the following single-degree-of-freedom-system of linear stiffness:

$$\ddot{Y} + \omega_0^2 Y = \varepsilon f(Y, \dot{Y}) + \varepsilon^{1/2} \sum_k g_k(Y, \dot{Y}) \xi_k(t) \quad [55]$$

where ε is a small parameter, indicating that the damping term is of order ε, and the random excitations $\xi_k(t)$ are of order $\varepsilon^{1/2}$. We assume that $\xi_k(t)$ are weakly stationary process, namely:

$$E[\xi_r(u)\xi_s(v)] = R_{rs}(v-u) \quad [56]$$

Note that the excitations need not be white noises. Using the transformation:

$$\begin{aligned} Y &= A(t)\cos\theta; \qquad \theta = \omega_0 t + \phi(t) \\ \dot{Y} &= -A(t)\omega_0 \sin\ \theta \end{aligned} \quad [57]$$

eqn [55] may be replaced by two first-order equations:

$$\dot{A} = -\frac{\sin\theta}{\omega_0}\left[\varepsilon f(A\cos\theta, -A\omega_0\sin\theta) + \varepsilon^{1/2}\sum_k g_k(A\cos\theta, -A\omega_0\sin\theta)\xi_k(t)\right] \quad [58]$$

$$\dot{\phi} = -\frac{\cos\theta}{\omega_0 A}\left[\varepsilon f(A\cos\theta, -A\omega_0\sin\theta) + \varepsilon^{1/2}\sum_k g_k(A\cos\theta, -A\omega_0\sin\theta)\xi_k(t)\right] \quad [59]$$

The right hand side of eqns [58] and [59] are associated only with ε and $\varepsilon^{1/2}$ terms. Physically, $A(t)$ represents the random amplitude, and $\phi(t)$ represents the random phase, and their values are nearly unchanged within a time-span $1/\varepsilon$.

Define a correlation time between random excitations $\xi_r(t)$ and $\xi_s(t)$:

$$\tau_{rs} = \frac{1}{[R_{rr}(0)R_{ss}(0)]^{1/2}} \int_{-\infty}^{0} |R_{rs}(\tau)|\, \mathrm{d}\tau \quad [60]$$

which is a measure of memory of the present $\xi_r(t)$ with respect to the past $\xi_s(t)$. If the system variables $\{A, \phi\}$ are observed at time instants at Δt apart, and if $\Delta t \gg \tau_{rs}$ for all r and s, then the observed variation of the system variables is Markov-like. However, Δt should be much smaller than ε^{-1} in order that sufficient details of the system behavior can be observed. In other words, the observed $\{A, \phi\}$ is approximately a Markov vector if $\varepsilon^{-1} \gg \tau_{rs}$ for all r and s. If this condition is satisfied, then the amplitude process may be approximated as a one-dimensional Markov process, governed by an Itô equation:

$$\mathrm{d}A = m(A)\,\mathrm{d}t + \sigma(A)\,\mathrm{d}B(t) \quad [61]$$

where the drift and diffusion coefficients $m(A)$ and $\sigma(A)$ can be obtained as follows:

$$m(A) = \varepsilon\left\langle -\frac{\sin\theta_t}{\omega_0} f(A\cos\theta_t, -A\omega_0\sin\theta_t) + \int_{-\infty}^{0} \frac{1}{\omega_0^2}\sum_k\sum_j \left\{\frac{\partial}{\partial A}[\sin\theta_t g_k(A\cos\theta_t, -A\omega_0\sin\theta_t)]\sin\theta_{t+\tau} + \frac{1}{A}\frac{\partial}{\partial\theta_t}[\sin\theta_t g_k(A\cos\theta_t, -A\omega_0\sin\theta_t)]\cos\theta_{t+\tau}\right\} g_j(A\cos\theta_{t+\tau}, -A\omega_0\cos\theta_{t+\tau}) R_{kj}(\tau)\,\mathrm{d}\tau \right\rangle \quad [62]$$

$$\sigma^2(A) = \varepsilon\left\langle \frac{1}{\omega_0^2}\sum_k \sum_j \int_{-\infty}^{\infty} \sin\theta_t \sin\theta_{t+\tau} g_k(A\cos\theta_t, -A\omega_0 \sin\theta_t) g_j(A\cos\theta_{t+\tau}, -A\omega_0\cos\theta_{t+\tau}) R_{kj}(\tau)\, \mathrm{d}\tau \right\rangle_t \quad [63]$$

in which θ_t and $\theta_{t+\tau}$ are abbreviations for $\omega_0 t + \phi(t)$ and $\omega_0(t+\tau) + \phi(t)$, respectively, and $\langle\cdot\rangle_t$ denotes a time-averaging operation:

$$\langle[\cdot]\rangle_t = \frac{\omega_0^2}{2\pi}\int_0^{2\pi/\omega_0^2} [\cdot]\, \mathrm{d}t \quad [64]$$

The validity of eqns [61] to [63] stems from the fact that the value of each correlation function $R_{kj}(\tau)$ is significant only if $|\tau| \ll \varepsilon^{-1}$, within which $A(t)$ and $\phi(t)$ can be treated as constants. Strictly speaking, eqn [61] governs the averaged amplitude over a pseudo-period $2\pi/\omega_0$, not the original amplitude.

With the knowledge of the Itô eqn [61], or equivalently, the corresponding FPK equation, one obtains the probability density of the averaged amplitude as follows:

$$p(\alpha) = \frac{C}{\sigma^2(\alpha)} \exp\left[\int \frac{2m(\alpha)}{\sigma^2(\alpha)}\, \mathrm{d}\alpha\right] \quad [65]$$

where α is the state variable for A, and C is a normalization constant. This probability density exists only if it is integrable; otherwise, the system is unstable in probability (assuming that multiplicative random excitation is present). As is well-known with deterministic excited systems, dynamic instability can occur when parametric excitations of high enough magnitudes are present. However, stability of randomly excited systems can be interpreted in more than one sense, each corresponding to one mode of convergence of a sequence of random variables.

The second averaging technique, known as quasi-conservative averaging, is applicable even when the stiffness term in the governing physical equation is strongly nonlinear. In the case of a single-degree-of-freedom system, the governing equation has the form:

$$\ddot{Y} + h(Y) = \varepsilon f(Y, \dot{Y}) + \varepsilon^{1/2}\sum_k g_k(Y, \dot{Y})\, W_k(t) \quad [66]$$

Note that the excitations are now restricted to Gaussian white noises. In this case, the total energy in the system:

$$\Lambda(t) = \frac{1}{2}\dot{Y}^2 + \int_0^Y h(u)\, \mathrm{d}u \quad [67]$$

is slowly varying, instead of the amplitude process $A(t)$. Differentiating [67] with respect to t, and combining the result with [66], we obtain:

$$\frac{\mathrm{d}}{\mathrm{d}t}\Lambda = \dot{Y}\left[\varepsilon f(Y, \dot{Y}) + \varepsilon^{1/2}\sum_k g_k(Y, \dot{Y})\, W_k(t)\right] \quad [68]$$

Equation [68] can now be converted into an Itô equation:

$$\mathrm{d}\Lambda t = m(\Lambda)\, \mathrm{d}t + \sigma(\Lambda)\, \mathrm{d}Bt \quad [69]$$

where:

$$\begin{aligned} m(\Lambda) = \varepsilon\Big\langle & \pm\{2[\Lambda - U(Y)]\}^{1/2} \\ & \times f(Y, \pm\{2[\Lambda - U(y)]\}^{1/2}) + \pi\sum_k\sum_r K_{kr}\frac{\partial}{\partial\Lambda} \\ & \times [\{2[\Lambda - U(Y)]\}^{1/2} g_k(Y, \pm\{2[\Lambda - U(Y)]\}^{1/2})] \\ & \times [\{2[\Lambda - U(Y)]\}^{1/2} g_r(Y, \pm\{2[\Lambda - U(Y)]\}^{1/2})]\Big\rangle_t \end{aligned} \quad [70]$$

$$\begin{aligned} \sigma^2(\Lambda) = \varepsilon 2\pi\sum_k\sum_r K_{kr}\Big\langle & 2\Big[\Lambda - U(Y)\Big] \\ & \times g_k\left(Y, \pm\left\{2\Big[\Lambda - U(Y)\Big]\right\}^{1/2}\right) \\ & \times g_r\left(Y, \pm\left\{2\Big[\Lambda - U(Y)\Big]\right\}^{1/2}\right)\Big\rangle_t \end{aligned} \quad [71]$$

and where the time averaging over a quasi-period is carried out equivalently in Y, namely:

$$\langle[\cdot]\rangle_t = \frac{1}{T}\int_{-A}^{A} \frac{\left([\cdot]_{\dot{Y}=\{2[\Lambda-U(Y)]\}^{1/2}} + [\cdot]_{\dot{Y}=-\{2[\Lambda-U(Y)]\}^{1/2}}\right)}{\{2[\Lambda - U(Y)]\}^{1/2}}\, \mathrm{d}Y \quad [72]$$

It may be noted that, in eqns [68] to [70], the velocity process $\dot{Y}$ has been replaced by $\pm\{2[\Lambda - U(Y)]\}^{1/2}$.

The quasi-conservative averaging technique has been extended to the case of nonwhite excitation, which is not discussed here in due to space limitation.

See also: **Correlation functions**; **Nonlinear systems, overview**; **Random processes**; **Stochastic analysis of nonlinear systems**; **Stochastic systems**.

STOCHASTIC SYSTEMS

M F Dimentberg, Worcester Polytechnic Institute, Worcester, MA, USA

Copyright © 2001 Academic Press

doi:10.1006/rwvb.2001.0124

This article describes an important approach to analysis of random vibration problems, which does not rely on the explicit convolution integral relation between response and excitation. It is based on a theory of Markov random processes and stochastic differential equation (SDE) calculus. It can be applied through reduction of the equations of motion with random excitations to the form, where all these excitations are white noises. This can be done by using shaping filters, if necessary, to obtain the extended SDE set, which may include state variable(s) of the shaping filter(s) as additional state variables.

Let a scalar process $x(t)$ be governed by SDE $\dot{x} = f(x, t) + g(x, t)\xi(t)$, where $\xi(t)$ is a stationary zero-mean normal white noise of unit intensity. Whenever the function g is not independent of x, the response is correlated with the excitation as follows:

$$\langle x(t)\xi(t)\rangle = (1/2)\left\langle \frac{\mathrm{d}g}{\mathrm{d}x}(x,t)g(x,t)\right\rangle \qquad [1]$$

Process $x(t)$ is called a diffusional Markov process, with drift and diffusion coefficients a, b, respectively, where $a = f + (1/2)g(\mathrm{d}g/\mathrm{d}x)$ and $b = g^2$. (The original SDE with added quantity [1], written in the form of differentials, is called the Ito SDE.) Eqn [1] illustrates a possibility for extending method of moments to linear systems with parametric excitation, as long as both $f(x, t)$ and $g(x, t)$ are linear in x, provided that the original excitations are white-noises. The expectation operator is applied at first to the original SDE directly, using the multidimensional counterpart of formula [1] (eqn [10] in **Random vibration, basic theory** to evaluate all relevant excitation-response correlations. This results in a linear deterministic set of equations for expected values of state variables. Thus, for a scalar case with $f(x, t) = px$, $g(x, t) = qx$, eqn [1] yields the following deterministic equation for $m(t) = \langle x(t)\rangle$: $\dot{m} = (p + q^2/2)m$. The new state variables u may be introduced then as $u_{jk} = x_j x_k$, $\dot{u}_{jk} = x_j\dot{x}_k + x_k\dot{x}_j$ for every pair of state variables. The RHSs of the given SDEs are substituted for the derivatives then, resulting in the set of SDEs for values of u. The set is linear, as long as the given set of equations for multiple state variables x contains linear functions f and g only. The expectation operator can be applied to the latter accordingly, using once again the multidimensional counterpart of eqn [1]. This results in a linear set of deterministic equations for second-order moments of the response.

The power of the Markov theory approach also lies in the possibility of analysis of the response probability density functions for systems, described by SDEs. Thus, a vector $\mathbf{X}$ diffusional Markov process, is described by vector of its drift coefficients $a_i(\mathbf{X}, t)$ and matrix of its diffusion coefficients $b_{ij}(\mathbf{X}, t)$. If the SDEs for components of $\mathbf{X}(t)$ are:

$$\begin{aligned} &X_i = f_i(\mathbf{X},t) + g_i(\mathbf{X},t)\varsigma_i(t);\ \langle \varsigma_i(t)\varsigma_j(t+\tau)\rangle \\ &\quad = D_{\varsigma,ij};\quad i,j = 1,2,\ldots,n, \\ &\text{then :} \\ &a_i(\mathbf{X},t) = f_i(\mathbf{X},t) + (1/2)\sum_{k=1}^{n} g_k(\mathbf{X},t)\frac{\partial g_i(\mathbf{X},t)}{\partial X_k}D_{\varsigma,ik} \\ &b_{ij}(\mathbf{X},t) = g_i(\mathbf{X},t)g_j(\mathbf{X},t) \end{aligned} \qquad [2]$$

and the joint pdf of these components satisfies certain partial differential equations, which would be considered somewhat later.

Linear systems with white-noise random parametric excitation(s) may become unstable due to a so-called stochastic instability. This can be seen for a SDOF system:

$$\ddot{X} + 2\alpha\dot{X} + \Omega^2 X(1 + z(t)) = 0 \qquad [3]$$

where the simplest case of excitation is one of a white noise $z(t)$ with intensity D_z. The method of moments yields a set of homogeneous deterministic ordinary differential equations (ODEs) for the response moments of a given order. Thus any one of these sets may have a zero steady-state solution, which may be either stable or unstable. The corresponding instability boundary in the response moments of the corresponding order can be predicted accordingly, using the common deterministic stability analysis. However, instability in any one of the response moments should not be regarded as 'catastrophic' for the structure (contrary to the case of common instability of deterministic systems). It simply implies, that any transients due to initial disturbances should have infinite moments of this order (and of higher orders as well). However, the response will decay eventually if the system is stable in probability. Mean square stochastic stability analysis, is used most often, i.e., one for the second-order response moments, since it usually provides the conservative boundary with respect to a 'real' or 'catastrophic' instability in probability.

For eqn [3] with a white-noise $z(t)$ the stability condition for mean square responses is found, by the method of moments, to be $D_z < D_{z**} = 4\alpha/\Omega^2$. (This stability boundary is seen to be the same as one obtained in the article **Random vibration, basic theory** from the condition of the infinite mean square response of the system [3] to an external white-noise excitation). Critical values of D_z for instability boundaries in higher-order moments are found to be higher than D_{z**}. The highest stability threshold is, however, one that corresponds to instability in probability. It is found to be $D_{z*} = 2D_{z**} = 8\alpha/\Omega^2$. Exceeding this threshold implies an unbounded growth of the response level with time. This will be illustrated later, by analyzing the stationary probability density function (pdf) of the system's (eqn [3]) response to an external white-noise excitation. The single-starred stability threshold will be seen to correspond to the normability condition of this pdf (the latter diverges at infinity if the threshold is exceeded).

Besides providing a relatively simple conservative estimate of reliability, the condition for mean square stability may also be important in yet another respect. Whilst a structure may operate safely provided it is stable in probability, its mean square instability may imply inadequacy of a linear model. In particular, online measurement results of second-order response moments should be interpreted with caution in this case, as long as these moments should be infinite if $D_{z**} < D_z < D_{z*}$ (for the linear system, eqn [3]). The measured values should therefore be strongly dependent on nonlinearity(ies) in the system.

Direct application of the method of moments to problems with nonwhite random parametric excitation is found to be impossible since an attempt to use shaping filter equation(s) to represent the excitation(s) makes the expanded system nonlinear, with product-type nonlinearity(ies). Important reduction of the underlying SDE(s) (eqn [2]) is possible, however, through the use of the stochastic averaging method, which is also very important for nonlinear systems. Namely, let the functions f and g in the RHSs be periodic in time t, with period T, and proportional to μ and $\sqrt{\mu}$, respectively, where μ is a small parameter. Then the expressions (eqn [2]) for the drift and diffusion coefficients a and b can be approximately averaged over time within the period T (with fixed 'slow' state variables X). Solution to the corresponding 'shortened' SDEs should approach the exact one with $\mu \to 0$.

Whilst the above averaging principle over explicit 'rapid' time is the same one as for deterministic systems, one specific feature of the stochastic averaging should be mentioned. The condition for white-noise excitation may be relaxed somewhat, as long as the random force with a finite correlation time leads to the same response as a 'real' white noise for a system with indefinitely increasing time constant (with $\mu \to 0$). Thus, for a quasilinear system – one with all nonlinearities and/or excitations being proportional to a small parameter – the direct excitation may usually be assumed to be broadband with respect to the system's bandwidth. Proper transformation of the original system's SDEs to those for slowly varying state variables is required, in order to have a small parameter at the RHS(s).

Consider the mean square stability of the SDOF system [3] for the case of a narrowband sinusoidal excitation with random phase modulation:

$$z(t) = \lambda \ \sin \ 2q(t), \ \dot{q} = \nu + \xi(t)$$

so that:

$$S_{zz}(\omega) = \frac{\left(\lambda^2 D_\xi/2\right)\left(\omega^2 + \nu^2 + D_\xi^2/4\right)}{\left(\nu^2 + D_\xi^2\Big/4 - \omega^2\right)^2 + \omega^2 D_\xi^2} \qquad [4]$$

with zero-mean white noise $\xi(t)$ of intensity D_ξ and small $\alpha/\Omega, \lambda$ and $\Delta = (\Omega - \nu)$. In-phase and quadrature components of the response $X(t)$ can be introduced conveniently as:

$$X(t) = X_c(t) \cos q + X_s(t) \ \sin \ q$$
$$\dot{X}(t) = \nu[-X_c(t) \ \sin \ q + X_s(t) \cos q]$$

The original equation [3] with the above excitation $z(t)$ is reduced then to a set of two SDEs for the new

state variables $X_c(t),\ X_s(t)$. The RHSs of these SDEs contain trigonometric functions of $q(t)$. After averaging over the mean period $2\pi/\nu$ these SDEs are found to be:

$$\begin{aligned}\dot{X}_c &= -(\alpha - \lambda\Omega/4)X_c - \Delta X_s - X_s\xi(t)\\ \dot{X}_s &= -(\alpha + \lambda\Omega/4)X_s + \Delta X_c + X_c\xi(t)\end{aligned} \qquad [5]$$

In the case of a perfectly periodic parametric excitation the stability boundary corresponds to the zero value of the determinant of the coefficients of the RHSs with the last terms excluded in both equations. The threshold excitation amplitude in this case is found to be:

$$\lambda_{*0}\Omega/4 = \sqrt{\left(\alpha^2 + \Delta^2\right)} \qquad [6]$$

so that the system is stable if $\lambda < \lambda_{*0}$ (the star subscript indicates the critical value of the excitation amplitude, and the additional zero subscript indicates the case of a perfect periodicity).

Three ODEs for second-order moments of the state variables $X_c(t),\ X_s(t)$ can now be derived by the method of moments. The condition for the vanishing determinant of their RHS coefficients yields the critical excitation amplitude as:

$$\lambda_* = \lambda_{*0}\left[1 + \frac{(D_\xi/\alpha)\left(\alpha^2 + \alpha D_\xi - \Delta^2/4\right)}{\alpha^2 + \alpha D_\xi + \Delta^2/4 + \Delta^2 D_\xi/4\alpha}\right]^{1/2} \qquad [7]$$

The stability boundary (eqn [7]) is seen to reduce to one for the case of perfect periodicity (eqn [6]) for vanishingly small excitation/system bandwidth ratio ($D_\xi/\alpha \to 0$). The other extreme case of a broadband random excitation, where $D_\xi/\alpha \gg 1$, is clearly seen to reduce to one with a white noise $z(t)$, of intensity $D_z = 2\pi S_{zz}(2\Omega)$: the formula $D_{z**} = 4\alpha/\Omega^2$ is obtained from eqn [7] by using eqn [4] for the PSD of $z(t)$. It can be seen, that component with frequency 2Ω, and not Ω as in case of a resonant external excitation, is filtered out by the system from the whole continuous excitation PSD, whereas all other components of the excitation do not contribute to the system's stochastic stability threshold.

Analysis of stochastic stability in probability is also possible for the system of eqns [3] and [4], based on solution for the pdf of the response phase. The resulting curve of the critical value of the parametric excitation amplitude λ_{PR} vs the excitation/system bandwidth ratio is presented in **Figure 1** (whilst this curve is calculated for a certain selected value of a relative detuning Δ/Ω, curves for other values were found to be very close to it). The ratio $\lambda_{\mathrm{PR}}/\lambda_*$ is presented in **Figure 1**, with λ_* being predicted by eqn [7]. Therefore the curve illustrates the margin, or safety factor, as provided by the threshold for mean square instability with respect to that for the 'catastrophic' instability, that is, λ_{PR}. The factor is seen to increase monotonically from unity for the case of perfect periodicity to its maximal value $\sqrt{2}$ for the 'most random' case of a broadband excitation.

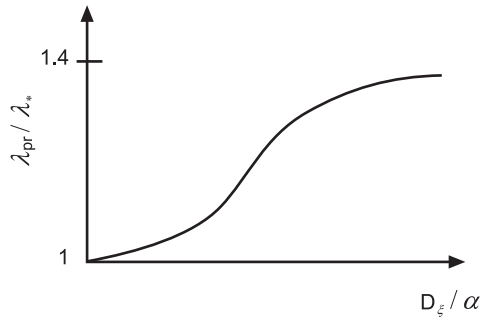


Figure 1 Ratio of stability thresholds in probability and in the mean square vs. excitation/system bandwidth ratio.

The imperfect periodicity is also seen to be stabilizing if $\Delta^2 < 4(\alpha^2 + \alpha D_\xi)$ and destabilizing otherwise. The former effect may be interpreted as being due to 'smearing' excitation energy in the frequency domain, which results in moving it away from the range of parametric resonance. However, if the initial detuning from the parametric resonance is relatively large, the above smearing brings more energy towards the resonance. This pattern is illustrated in **Figure 2**, where the generalized Ince–Strutt chart for the system of eqns [3] and (4) is shown schematically, that is, the stability boundary in the plane $\lambda\nu$. Moreover, a similar pattern is also observed for the stability boundary in probability. Of course, the above stabilization effect for large detunings exists only as long as the excitation PSD is narrow-band by itself, that is for small D_ξ/Ω; it certainly disappears, if the extreme case of a white-noise excitation is approached.

The power of the Markov theory approach lies in the possibility for analysis of response probability density functions for systems, described by SDEs. Thus, let $\mathbf{X}(t)$ be an n-dimensional vector diffusional Markov process, with drift and diffusion coefficients $a_i(\mathbf{X}, t)$ and $b_{ij}(\mathbf{X}, t)$ respectively, as defined by eqns [2]. Then its pdf $p(\mathbf{x}, t)$ satisfies the following partial differential equation, which is called the Fokker–Planck–Kolmogorov (FPK) equation:

$$\partial p/\partial t = -\sum_{i=1}^{n}\frac{\partial(a_i p)}{\partial x_i} + \frac{1}{2}\sum_{i=1}^{n}\sum_{j=1}^{n}\frac{\partial^2(b_{ij}p)}{\partial x_i\,\partial x_j} \qquad [8]$$

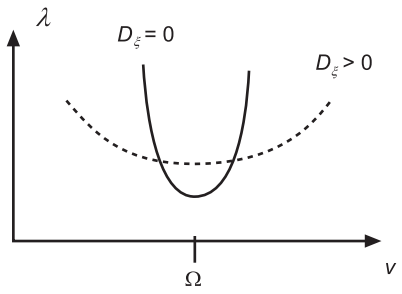


Figure 2 Generalized Ince–Strutt chart for imperfectly periodic excitation.

(small letters instead of the capital ones may be used for arguments of the deterministic function $p(\mathbf{x}, t)$, introduced for a random vector $\mathbf{X}(t)$). If the solution to this equation satisfies a deterministic initial condition of the form $p(\mathbf{x}, t) \to \delta(\mathbf{x} - \mathbf{x}_0)$ with $t \to t_0$, it is called the transition probability density. It is actually a conditional pdf $p(\mathbf{x}, t|\mathbf{x}_0, t_0)$, the condition being a given initial state $\mathbf{X}_0$. A stationary process has a pdf, which becomes independent both of time and of initial state with $t - t_0 \to \infty$, i.e. a stationary pdf $p(\mathbf{x})$. The FPK equation is usually considered within infinite domain, with boundary conditions (BCs) of proper decay at infinity; the solution also should be normable in order to qualify for being the pdf.

The transition pdf, considered as a function of $\mathbf{x}_0, t_0$, also satisfies the so-called backward Kolmogorov equation. This equation is used for first-passage-type reliability analyses. In particular, it can be used to derive the PDE for the mean time before failure (MTBF) $T(\mathbf{x})$. In a special case of a scalar $X(t)$, with time-independent-drift and diffusion coefficients a, b, the general PDE is reduced to the following ordinary differential equation

$$(b(x)/2)\left(\mathrm{d}^2T/\mathrm{d}x^2\right) + a(x)(\mathrm{d}T/\mathrm{d}x) = -1 \qquad [9]$$

The boundary conditions $T(x_1) = T(x_2) = 0$ are usually assigned at the boundaries of the safe domain x_1, x_2 in cases of constant $b(x)$ (some modifications are possible for certain special cases of $b(x)$). Here x is the initial state within the safe domain, and the above BCs simply imply zero MTBF if the system is already at its boundary. A similar zero BC at the safe boundary is assigned for the MTBF for a vector diffusional Markov process, with the multidimensional counterpart of eqn [9] being a PDE.

In many cases of systems with high reliability – particularly when all components of the matrix $\mathbf{B}$ are small – the solution $T(\mathbf{x})$ is found to be of a boundary-layer type. Namely, it is almost constant within most of the safe domain and drops to zero only within a narrow region along the boundary. The interpretation is clear: a characteristic time for reaching stationary pdf $p(\mathbf{x})$ of the $\mathbf{X}(t)$ (which is independent of the initial state) is much smaller than the MTBF.

The response vector $\mathbf{X}$ in random vibration problems should be regarded as at least an n-dimensional Markov process, where n is the total number of DOFs, since for each degree-of-freedom with a white-noise excitation both displacement and velocity are involved in the original SDE. The simplest case of an exact analytical solution to the FPK equation for random vibration problems is that of a linear system: the transition pdf of the response is found to be normal, with its vector of mean values and the correlation matrix being the same as those obtained by the method of moments.

For nonlinear systems, however, the approach faces difficulties with solving the FPK equation. The best known exact analytical solution is available for a SDOF system with a restoring force $f(X)$ and viscous damping with factor 2α, excited by a white-noise force of intensity D:

$$\begin{aligned} p(x, v) &= C \exp\left[-(4\alpha/D)H\right] \\ &= C \exp\left[-(4\alpha/D)\left(v^2/2 + U(x)\right)\right] \end{aligned} \qquad [10]$$

where:

$$v = \dot{x}, \quad \mathrm{d}U/\mathrm{d}x = f(x), \quad H = v^2/2 + U(x)$$

Here $U(x)$ is the system's potential energy, whereas H is a total energy and C is a normalizing constant. For systems with random parametric excitation, even linear ones, exact solutions to the FPK equations are very scarce.

The approximation by the stochastic averaging method is important for lightly damped systems. This averaging over the period (of the order $2\pi/\Omega$) in 'fast' time, can be made after introducing the slowly varying response amplitude (or total energy) and phase as new state variables. In the absence of any periodic excitation this results in a single first-order SDE for the amplitude in a 'slow' time. The resulting stationary FPK for the pdf of the amplitude has an analytical solution. In particular, for the linear system with combined external and parametric excitation $\varsigma(t)$ and $\xi(t)$ this solution results in:

$$\begin{aligned} p(x, v) &= \frac{(\delta - 1)\kappa^{\delta - 1}}{\left(\kappa + x^2 + v^2/\Omega^2\right)^{\delta - 1}} \\ \kappa &= 4S_{\varsigma\varsigma}(\Omega)/\left[\Omega^4 S_{\xi\xi}(2\Omega)\right] \\ \delta &= 4\alpha/\left[\pi\Omega^2 S_{\xi\xi}(2\Omega)\right] \end{aligned} \qquad [11]$$

This function is integrable, and can therefore be the joint stationary pdf of the displacement and velocity, if and only if $\delta > 1$, or $D_\xi < D_{\xi**} = 8\alpha/\Omega^2$, where $D_\xi = 2\pi S_{\xi\xi}(2\Omega)$ is the intensity of approximating parametric white noise. If the above threshold is exceeded, the integral of the stationary pdf (eqn [11)] diverges at infinity. This corresponds to the instability in the probability, which is clearly accompanied by the infinite growth of the response with time.

As $\delta \to \infty$ the solution (11) approaches a normal pdf. However, in the presence of the parametric excitation, and thus for finite values of $\delta, X(t)$ has infinite moments of order $2n$ and higher whenever $\delta \leq n + 1$. In particular, the stationary pdf of $X(t)$ with infinite variance is established if $1 < \delta < 2$. The conditions for finite subcritical response moments correspond to stability conditions in these moments, whereas the condition for the existence of the (integrable) stationary response pdf corresponds to the stochastic stability in probability. It is the latter condition that should be used in design to prevent a 'catastrophic' failure, whereas the condition for mean-square stability may be regarded as a useful conservative bound for the 'real' instability threshold.

Thus, the presence of a stochastic parametric excitation clearly amplifies the response of the structure to an external excitation, thereby reducing its reliability. This effect can clearly be seen for fatigue-type failures, as described by the linear damage accumulation rule, since the corresponding MTBF is governed by some higher-order moment of the (stress) response.

Another version of the stochastic averaging will be illustrated now, which is adequate for lightly damped systems with nonlinear restoring forces. The system is regarded as a 'quasiconservative' one, with damping and excitation forces being proportional to μ and $\sqrt{\mu}$, respectively, where μ is a small parameter. The response energy $H(t)$ is then introduced as a 'slow' state variable according to eqn [10]. The shortened SDE for this state variable is obtained by averaging over the energy-dependent period of the corresponding nonlinear conservative system.

Thus, for a SDOF system:

$$\ddot{X} + h(X, \dot{X}) + \mathrm{d}U/\mathrm{d}X = \varsigma(t) \qquad [12]$$

with zero-mean Gaussian white-noise $\varsigma(t)$ of intensity D_ς this equation is found to be (the actual integration is performed within a half-period, which is possible in view of symmetry in the absence of hysteretic nonlinearities):

$$\dot{H} = -Q(H)/T_0(H) + D_\varsigma/2 + [S(H)/T_0(H)]\varsigma_1(t)$$
$$Q(H) = \int_{x_-}^{x_+} h(x, \sqrt{(2H - 2U(x))})\,\mathrm{d}x$$
$$S(H) = \int_{x_-}^{x_+} [2H - 2U(x)]^{1/2}\,\mathrm{d}x$$
$$T_0(H) = \int_{x_-}^{x_+} [2H - 2U(x)]^{-1/2}\,\mathrm{d}x \qquad [13]$$

where $\varsigma_1(t)$ is a white noise of unit intensity, whereas x_+ and x_- are the maximal and minimal roots, respectively, of the equation $U(x) = H$. The response amplitude $A(t)$ may also be considered, which is related to the total and potential energies as $U(A) = H$. In particular, $A = \sqrt{(2H)}/\Omega$ in case of a linear restoring force, with natural frequency Ω.

The FPK equation for total energy, which corresponds to the SDE (eqn [13]), has the following stationary solution:

$$p(H) = CT_0(H) \exp\left[-\frac{2}{D\varsigma}\int_0^H \frac{Q(H')\,\mathrm{d}H'}{S(H')}\right] \qquad [14]$$

This pdf may be reduced to the exact one (eqn [10]) in the case of linear damping, where $h(x, \dot{x}) = 2\alpha\dot{x}$. A simple exponential pdf of energy is obtained in this case if the restoring force is also linear. In case of a system with linear restoring force and dry-friction damping, where $h(x, \dot{x}) = R\,\mathrm{sgn}\,\dot{x}$, the shortened SDE (eqn [13]) is found to be:

$$\dot{H} = -\left(2R\sqrt{2}/\pi\right)\sqrt{H} + D_\varsigma/2 + \sqrt{(D_\varsigma H)}\varsigma_1(t) \qquad [15]$$

and therefore:

$$p(H) = \left(\gamma^2/2\right)\exp\left(-\gamma\sqrt{H}\right), \qquad \gamma = 8R\sqrt{2}/\pi D$$

so that:

$$\langle H\rangle = 6/\gamma^2 = \left(3\pi^2/64\right)(D/R)^2$$

This case of a dry-friction damping may be of a special interest for systems with active feedback vibration control. It appears, that if the available control force is of a bounded magnitude, with R being its maximal value, the dry-friction control law $R\,\mathrm{sgn}\,\dot{X}$ is found to be the optimal one if the steady-state response energy is minimized.

Consider now a first-passage problem for a vibrating component with possibility for a first-passage failure after exceeding a certain given response energy threshold H_*. Assuming the initial energy H to be smaller than this threshold, consider an expected time T for reaching it by the system, whose dynamics is described approximately by the first-order SDE (eqn [15]). The deterministic ODE (eqn [9]) for the function $T(H)$ for this case of a linear restoring force is then:

$$(DH/2)\left(\mathrm{d}^2T/\mathrm{d}H^2\right)+ \left[D/2-\left(2R\sqrt{2}/\pi\right)\sqrt{H}\right](\mathrm{d}T/\mathrm{d}H)=-1 \quad [16]$$

The BCs for this equation are (the first one implies a finite value of T in the case $H=0$) $\mathrm{d}T/\mathrm{d}H=-2/D$ at $H=0$; $T(H_*)=0$.

Eqn [16] has a simple quadrature solution for $\mathrm{d}T/\mathrm{d}H$, which then can be integrated numerically. **Figure 3** illustrates, by a dotted line, the dependence of the MTBF, in the number of cycles to failure $N=\Omega T/2\pi$, on the nondimensional initial energy $\bar{H}=H/\langle H\rangle$. These results are compared here with those for a system with an 'equivalent' linear viscous damping, or a linear velocity feedback control (solid line). The latter had been obtained by replacing term with R in brackets in eqn [16] by $-2\alpha H$. The damping ratio α/Ω of the benchmark linear system has been calculated from the condition $D\gamma/4\alpha=\sqrt{6}$, or $\alpha/\Omega=(3/16)\pi^2\mu^2$, where $\mu^2=R^2/D_{\varsigma}\Omega$. This condition implies the same expected response energy $\langle H\rangle$, or same RMS responses of the two systems to white-noise excitation of the same intensity. It can be seen from **Figure 3**, that the system with dry-friction control should be regarded as less reliable than one with the simple linear feedback control and same RMS response level. This reduction of reliability may be interpreted as the price for the imposed bound on the control force, or for 'weak' actuators.

Another example for the application of this solution to a first-passage problem in engineering mechanics is as follows. Consider two random processes $Y(t)$ and $X(t)$,where Y is a multivalued S-shaped function of X. This inertialness relation is illustrated in **Figure 4**. The intermediate branch is shown here by a dashed line, as long as the equilibrium states are usually unstable along such decreasing branches. Therefore, the function $Y=f(X)$ is double-valued, and its upper and lower branches will be identified with subscripts U and L, respectively. Thus, two inverse functions $X=g(Y)$ will be considered: $X=g_U(Y)$ for $Y_2<Y<\infty$ and $X=g_L(Y)$ for $-\infty<Y<Y_1$. Examples of this kind of relation are: the force–displacement curve of a shallow elastic arch or thin panel with a potential 'snap-through'; the relation between the amplitude of sinusoidal excitation and that of the (almost) sinusoidal response of a SDOF with a small smooth nonlinearity in the restoring force; the vibration amplitude of a system with 'hard' self-excitation as a function of the system's parameter, which controls transitions between stable equilibrium state and the limit cycle (the lower branch is just $Y=0$ in the last example).

Consider now the following problem: find the pdf of Y if the pdf of X is known. The corresponding relation (eqn [4] of **Random processes**), which contains the inverse function $X=g(Y)$, can only be used in case of a single-valued $f(X)$. It may be generalized to the case of S-shaped $f(X)$ though, by applying the relation separately to the upper and lower branches of Y. The resulting two pdfs for two different ranges of Y are then treated as the conditional ones, each condition being that Y stays on the corresponding branch. Thus:

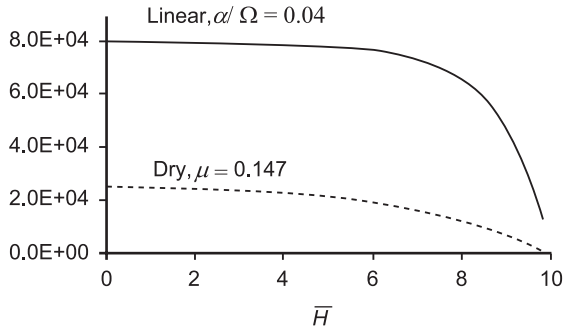


Figure 3 Expected number of cycles to failures for elastic systems with linear viscous and dry-friction damping.

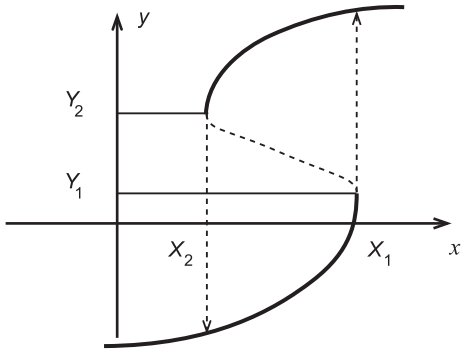


Figure 4 Multivalued function $y=f(x)$.

$$p_Y(y) = \frac{P_U \cdot p_X(g_U(y))\ |\mathrm{d}g_U/\mathrm{d}y|}{\int_{y_2}^{\infty} p_X(g_U(y))|\mathrm{d}g_U/\mathrm{d}y|\mathrm{d}y}, y > y_2$$

$$p_Y(y) = \frac{P_L \cdot p_X(g_L(y))\ |\mathrm{d}g_L/\mathrm{d}y|}{\int_{-\infty}^{y_1} p_X(g_L(y))|\mathrm{d}g_L/\mathrm{d}y|\mathrm{d}y}, y < y_1$$

$$P_U + P_L = 1$$

Here P_U and P_L are the total probabilities for staying on the upper and lower branch, respectively. Although their sum is unity, in view of a single normalization condition, nothing more can be said about the pdf of a random variable Y.

However, if $X(t)$ is a random process, the individual probabilities for $Y(t)$ staying on each of the branches can be predicted as solutions to the appropriate first-passage problems. (Note that applications to dynamic problems are possible only if $X(t)$ is slowly varying, so that the quasistatic approach is warranted.) In this case transitions between the upper and lower branches are possible, as illustrated by arrows in **Figure 4:** from lower to upper after upcrossing level x_1 by $X(t)$ and from lower to upper after downcrossing level $x_2 < x_1$, where $x_1 = g_L(y_1)$ and $x_2 = g_U(y_2)$ are the limit points of the lower and upper branches, respectively. Identifying the desired probabilities as the relative stay times of the $X(t)$ on the upper and lower branches, the ratio of these stay times may be predicted as $P_U/P_L = T_{12}/T_{21}$. Here $T_{ij}, i, j = 1, 2$ is the expected time for crossing level x_j by the process $X(t)$ if its initial value is $X = x_i$. If $X(t)$ is a scalar Markov process, the ODE for these expected times with relevant boundary conditions can simply be solved numerically.

Just one comment seems to be relevant here, on the relation between expected times for reaching and for crossing certain given level x_*. They are usually the same, if the drift coefficient of the Markov process $X(t)$ does not vanish at $X = x_*$. However, in a special case $a(x_*) = 0$ the expected time for crossing this 'potential barrier' is found to be twice as high as for reaching it. This fact is proved by asymptotic evaluation of the quadrature solution for T, and has a simple explanation: in the absence of regular forces at the potential barrier the process has equal chances for going further and for returning back.

Nomenclature

$A(t)$	response amplitude
C	normalizing constant
H	total energy
$H(t)$	response energy
$U(x)$	potential energy
Ω	natural frequency

See also: **Random processes**; **Random vibration, basic theory**.

Further Reading

Bendat JS, Piersol AG (1986) *Random Data: Analysis Measurement and Procedures*. New York: Wiley Interscience.

Bolotin VV (1965) *Statistical Methods in Structural Mechanics*. San Francisco: Holden Day.

Cramer H, Leadbetter MR (1967) *Stationary and Related Stochastic Processes*. New York: Wiley.

Dimentberg M (1988) *Statistical Dynamics of Nonlinear and Time-Varying Systems*. Taunton, UK: Research Studies Press.

Ibrahim RA (1985) *Parametric Random Vibration*. New York: Wiley.

Khasminski RZ (1980) *Stochastic Stability of Differential Equations*. Norwell: Kluwer.

Lin YK (1967) *Probabilistic Theory of Structural Dynamics*. New York: McGraw Hill.

Lin YK, Cai GQ (1995) *Probabilistic Structural Dynamics*. New York: McGraw Hill.

Lutes LD, Sarkani S (1997) *Stochastic Analysis of Structural and Mechanical Vibrations*: Englewood Cliffs: Prentice Hall.

Madsen HO, Krenk S, Lind NC (1986) *Methods of Structural Safety*. Englewood Cliffs: Prentice Hall.

Papoulis A (1965) *Probability, Random Variables and Stochastic Processes*. New York: McGraw Hill.

Roberts JB, Spanos PD (1990) *Random Vibration and Statistical Linearization*. New York: Wiley.

Soong TT, Grigoriu M (1993) *Random Vibration of Mechanical and Structural Systems*. Englewood Cliffs: Prentice Hall.

Stratonovich RL (1963) *Topics in the Theory of Random Noise*, vol. 1. New York: Gordon and Breach.

Stratonovich RL (1967) *Topics in the Theory of Random Noise*, vol. 2. New York: Gordon and Breach.

STRUCTURAL DAMPING

See **HYSTERETIC DAMPING**

STRUCTURAL DYNAMIC MODIFICATIONS

A Sestieri, Università Degli Studi di Roma, Roma, Italy

W D'Ambrogio, Università de L'Aquila, Roio Poggio, Italy

Copyright © 2001 Academic Press

doi:10.1006/rwvb.2001.0100

Aim of Structural Dynamic Modification

The possibility of changing the dynamic behavior of structures to control the vibration response or reduce the noise radiated by a vibrating system is a real challenge, particularly when these requirements are not of primary concern in the function of the structure, and significant variations to the main features of the system are not permitted.

Such control tasks can be obtained by either passive or active procedures: these last are becoming quite common because of the use of smart structures, but imply the development of control feedback that must verify important conditions of robustness and stability. Passive tools are much simpler and can accomplish surprisingly good results at a lower cost. Among them, simple structural modifications can often produce the expected goals, and by structural dynamic modification a well-known tool of modal analysis is indicated.

The enhancement of the structural or acoustic response is one of the common goals of the structural modification process. This can be related to any of the following elements: the source, the transmission path, or the receiver.

In structural dynamic modification, two problems have a particular interest: the direct problem and the inverse problem. The direct problem consists of determining the effect of established modifications on the dynamic properties, without requiring a new computation (or measurement) on the changed system. Therefore this is a 'what if' problem aimed to establish the effect of given changes on the dynamic behavior of the considered system. The inverse problem, which is more complex, tries to identify the most appropriate among many possible modifications to obtain a desired dynamic behavior. This is a typical design problem, consisting of specifying the required action to obtain an improvement of the structural or acoustic response.

Knowledge of the original system, whose dynamic behavior is amenable to modification, can derive from a theoretical analysis usually obtained from a finite element model of the system. However, in many practical situations, neither a reliable finite element database nor the modal parameters of the system are known, either because the system is too complex or because an updated finite element model is not available. In such cases, one can try to determine the system experimentally, considering it as a black box system identified through its frequency response function (FRF) matrix, from which some suitable knowledge of the structure upon which to perform modifications can eventually be obtained (see **Modal analysis, experimental**, Applications).

Since the identification of spatial parameters (mass and stiffness matrices) derived from an FRF model is a highly ill-conditioned problem, most of the work has been concentrated on modal parameters. Excluding particular situations (high modal density, strongly coupled modes), modal parameters can be identified quite efficiently in the frequency band tested, and produce useful – albeit incomplete – modal models. Once such a model is available, many structural modification algorithms can be developed and used with some advantage.

Probably due to the degree of development of modal techniques, many formulations apply to changes of modal characteristics, i.e., resonance shifts, Q-factor reduction, etc., and make use of the identified modal parameters (modal synthesis). This approach does not complete the wide field of applications that can be expected from structural modification. Among them, some concern the need to reduce the vibration behavior of particular points of the structure in a frequency band of interest, or the possibility of narrowing the rigid-body natural frequencies of a suspended system to achieve the maximum isolation efficiency. Moreover, the incomplete knowledge of the modal model identified from a continuous structure severely affects the results of structural modification analysis. A large amount of research on the subject has established the following points:

- When using modal parameters, the accuracy of the modified dynamic properties is largely affected by the quality of the modal model derived from experimental data.
- The effect of modal truncation on structural modifications is quite critical. A major role in the effectiveness of modification analysis is played by a selected number of modes rather than by the quantity of modes included in the database, and it is not possible to obtain an exact solution for structural modification when using an incomplete set of eigenvectors.

For the above reasons, in addition to modal synthesis, a frequency domain approach is also presented here. This method avoids a modal identification process and the pitfalls deriving from it. Moreover, it may handle useful applications and it permits optimal modifications for different dynamic requirements.

The modifications considered here are discrete modifications, i.e., they consist of any combination of lumped masses, stiffnesses (obtained by springs connecting two different points of the structure or one point of the structure to an external fixed point), and dampers.

Direct Problem

The data necessary to solve the direct problem are:

- the dynamic behavior of the original structure
- a knowledge of the modifications

The dynamic behavior of the original structure can be expressed:

- as a modal database, comprising natural frequencies and mode shapes (real or complex) identified by a curve-fitting of experimental data or determined from a theoretical analysis
- as an FRF database, determined experimentally or theoretically

First, the approach that uses the modal database to represent the dynamic behavior of the system is described. Next, the approach based on the frequency response function database is presented.

Let $\mathbf{M}$, $\mathbf{K}$, and $\mathbf{C}$ represent the $N \times N$ mass, stiffness, and viscous damping matrices of the original (unmodified) system: they are necessary to develop the theory, but we will find that they are not needed to solve the structural modification problem in practice. Furthermore, let $\mathbf{\Delta M}$, $\mathbf{\Delta K}$, and $\mathbf{\Delta C}$ be the matrices with entries representing mass, stiffness, and damping modifications, respectively. These matrices must have the same dimensions as $\mathbf{M}$, $\mathbf{K}$, and $\mathbf{C}$ and must contain nonzero elements only in those locations where the modifications are acting. For example, on a three degrees of freedom (3-DOF) system, a modification Δm_3 on the third mass will be represented by a 3×3 matrix, $\Delta\mathbf{M}$, whose only nonzero element is $m_{33} = \Delta m_3$. The modification consisting of a spring, Δk, between the first and third mass will be represented by the matrix:

$$\mathbf{\Delta K} = \begin{bmatrix} \Delta k & 0 & -\Delta k \\ 0 & 0 & 0 \\ -\Delta k & 0 & \Delta k \end{bmatrix}$$

Modal Database

When using the modal database, typically the case of real modes, related to an undamped or proportionally damped system, is considered. The case of a nonproportionally damped system leading to complex modes could be similarly addressed by using a state space approach. However the problem is much more intricate because the modal identification task becomes much more difficult as damping and/or modal coupling increases. Therefore, in practice the use of a complex modal database is not convenient.

Theory for real modes The equation of motion of the original system is:

$$\mathbf{M}\ddot{\mathbf{x}}_0 + \mathbf{C}\dot{\mathbf{x}}_0 + \mathbf{K}\mathbf{x}_0 = \mathbf{f} \qquad [1]$$

where proportional viscous damping $\mathbf{C} = \alpha\mathbf{M} + \beta\mathbf{K}$ is assumed.

The related undamped eigenvalue problem:

$$(\mathbf{K} - \lambda\mathbf{M})\phi = 0 \qquad [2]$$

provides N eigenvalues $\lambda_i = \omega_{ni}$ and eigenvectors (modes) ϕ_i:

$$\mathbf{\Lambda} = \begin{bmatrix} \omega_{n_1}^2 & & \\ & \ddots & \\ & & \omega_{n_N}^2 \end{bmatrix} \qquad \mathbf{\Phi} = [\phi_1 \quad \phi_2 \quad \cdots \quad \phi_m] \qquad [3]$$

that satisfy the orthonormal conditions:

$$\begin{aligned} \mathbf{\Phi}^{\mathrm{T}}\mathbf{M}\mathbf{\Phi} &= \mathbf{I} \\ \mathbf{\Phi}^{\mathrm{T}}\mathbf{K}\mathbf{\Phi} &= \mathbf{\Lambda} \\ \mathbf{\Phi}^{\mathrm{T}}\mathbf{C}\mathbf{\Phi} &= \alpha\mathbf{I} + \beta\mathbf{\Lambda} = \mathbf{\Xi} \end{aligned} \qquad [4]$$

By introducing the coordinate transformation $\mathbf{\Phi}$ from the physical space ($\mathbf{x}_0$ coordinates) to the modal space ($\mathbf{q}_0$ coordinates) in eqn [1]:

$$\mathbf{x}_0 = \mathbf{\Phi}\mathbf{q}_0 \qquad [5]$$

one obtains, after premultiplying by $\mathbf{\Phi}^{\mathrm{T}}$:

$$\mathbf{\Phi}^{\mathrm{T}}\mathbf{M}\mathbf{\Phi}\ddot{\mathbf{q}}_0 + \mathbf{\Phi}^{\mathrm{T}}\mathbf{C}\mathbf{\Phi}\dot{\mathbf{q}}_0 + \mathbf{\Phi}^{\mathrm{T}}\mathbf{K}\mathbf{\Phi}\mathbf{q}_0 = \mathbf{\Phi}^{\mathrm{T}}\mathbf{f} \qquad [6]$$

i.e., in view of the orthonormal conditions:

$$\ddot{\mathbf{q}}_0 + \Xi\dot{\mathbf{q}}_0 + \Lambda\mathbf{q}_0 = \Phi^{\mathrm{T}}\mathbf{f} \quad [7]$$

This is a system of N uncoupled equations representing the modal model of the original system.

The equation of motion of the modified structure can be written as:

$$(\mathbf{M} + \Delta\mathbf{M})\ddot{\mathbf{x}} + (\mathbf{C} + \Delta\mathbf{C})\dot{\mathbf{x}} + (\mathbf{K} + \Delta\mathbf{K})\mathbf{x} = \mathbf{f} \quad [8]$$

where it is assumed $\Delta\mathbf{C} = \alpha\Delta\mathbf{M} + \beta\Delta\mathbf{K}$ to mantain proportional damping.

If the same coordinate transformation, Φ, such that $\mathbf{x} = \Phi\mathbf{q}$ is introduced into eqn [8], one obtains after premultiplying by Φ^{T}:

$$(\mathbf{I} + \Delta\tilde{\mathbf{M}})\ddot{\mathbf{q}} + \left(\Xi + \Delta\tilde{\mathbf{C}}\right)\dot{q} + (\Lambda + \Delta\tilde{\mathbf{K}})\mathbf{q} = \Phi^{\mathrm{T}}\mathbf{f} \quad [9]$$

i.e., the equation of motion of the modified structure is written in terms of the modal coordinates of the original structure, having defined:

$$\begin{aligned} \Delta\tilde{\mathbf{M}} &= \Phi^{\mathrm{T}}\Delta\mathbf{M}\Phi \\ \Delta\tilde{\mathbf{C}} &= \Phi^{\mathrm{T}}\Delta\mathbf{C}\Phi \\ \Delta\tilde{\mathbf{K}} &= \Phi^{\mathrm{T}}\Delta\mathbf{K}\Phi \end{aligned} \quad [10]$$

Note that the above matrices are not usually diagonalized by the coordinate transformation based on the eigenvectors of the original structure.

To uncouple the equations of motion of the modified system, it is necessary to solve the undamped eigenvalue problem related to eqn [9], i.e.:

$$\left[(\Lambda + \Delta\tilde{\mathbf{K}}) - \lambda^I(\mathbf{I} + \Delta\tilde{\mathbf{M}})\right]\phi^I = 0 \quad [11]$$

It provides new eigenvalues Λ^I and eigenvectors Φ^I, for which the following orthonormal conditions hold:

$$\begin{aligned} (\Phi^I)^{\mathrm{T}}(\mathbf{I} + \Delta\tilde{\mathbf{M}})\Phi^I &= \mathbf{I} \\ (\Phi^I)^{\mathrm{T}}(\Lambda + \Delta\tilde{\mathbf{K}})\Phi^I &= \Lambda^I \\ (\Phi^I)^{\mathrm{T}}\left(\Xi + \Delta\tilde{\mathbf{C}}\right)\Phi^I &= \Xi^I \end{aligned} \quad [12]$$

Therefore, the new coordinate transformation:

$$\mathbf{q} = \Phi^I\mathbf{q}^I \quad [13]$$

from the modal space of the original system to the modal space of the modified system, yields the following uncoupled set of equations:

$$\ddot{\mathbf{q}}^I + \Xi^I\dot{\mathbf{q}}^I + \Lambda^I\mathbf{q}^{\mathbf{I}} = \Phi^{I^{\mathrm{T}}}\Phi^{\mathrm{T}}\mathbf{f} \quad [14]$$

The natural frequencies of the modified structure can be obtained from the eigenvalue matrix Λ^I, whilst the mode shapes of the modified structure are given by:

$$\Psi = \Phi\Phi^I \quad [15]$$

In fact, the transformation $\mathbf{x} = \Psi\mathbf{q}^I$ from the physical coordinates to the modal coordinates of the modified structure can be written as:

$$\mathbf{x} = \Phi\mathbf{q} = \Phi\left(\Phi^I\mathbf{q}^I\right) \quad \Rightarrow \quad \Psi = \Phi\Phi^I \quad [16]$$

and the modal matrix of the modified structure can be put in the form:

$$\Psi = [\psi_1 \quad \psi_2 \quad \cdots \quad \psi_m] \quad [17]$$

It can easily be verified from the previous relationships that $\Psi^{\mathrm{T}}(\mathbf{M} + \Delta\mathbf{M})\Psi = \mathbf{I}$, i.e., the new mode shapes are mass-normalized. Note also that the new modes are a linear combination of the modes of the original structure. In fact a given term ψ_{rs} of the matrix Ψ is:

$$\psi_{rs} = \sum_{l=1}^{N} \phi_{rl}\phi_{ls}^I \quad [18]$$

and the mode shape, i.e., a given column of Ψ, is:

$$\boldsymbol{\psi}_s = \sum_{l=1}^{N} \phi_{ls}^I\boldsymbol{\phi}_l \quad [19]$$

Notes on practical implementation Natural frequencies and mode shapes of the modified system are derived from eqn [11], which does not involve the mass, stiffness, and damping matrices, $\mathbf{M}$, $\mathbf{K}$, and $\mathbf{C}$, of the original structure. Therefore, there is no need to know these matrices in order to determine the modal parameters of the modified structure, provided that the original modal parameters are known and suitable lumped modifications involving any variation of mass, stiffness, and/or damping are established so that $\Delta\mathbf{M}$, $\Delta\mathbf{K}$ (and $\Delta\mathbf{C}$) are given.

The original modal parameters can either be derived experimentally, i.e., identified from measured FRFs, or computed theoretically from a model of the structure. In both cases, a number $m \ll N$ of modes is used in practice.

In fact, it is not possible to identify the whole set of modal parameters of a continuous system, but only those included in a given frequency bandwidth: in other words, for continuous systems, N is infinite. Even in the so-called reanalysis problem, in which an N-DOF finite element model is used, relationship (11) is only useful if the involved computation is less time-consuming than the analysis of a new finite element model. This happens when in the reanalysis a number of modes $m \ll N$ is considered.

Truncation effect If $m = N$, the modal parameters of the modified system are determined exactly, whilst they are only approximate when $m < N$ (mode truncation effect). In fact, since eqn [9] is a set of coupled equations, some coupling terms are lost by truncating it to m modes, i.e., by considering only m rows and m columns of the coefficient matrices: therefore the results obtained are only approximate.

Another way to look at the problem is to consider eqn [19]. It shows that the modified structure mode shapes are linear combinations of the mode shapes of the original system. If all N modes are considered, they represent a complete basis in the N-dimensional space, meaning that every N-dimensional vector, and therefore also all the new mode shapes, can be described by a linear combination of the vectors in the basis. In contrast, if $m < N$, the summation in eqn [19] is truncated to m terms. Therefore the vector basis is not complete and the new mode shapes are described with some error.

It has been observed that the amount of error due to mode truncation can be quite large. The following example highlights the origin of the truncation error.

In **Figure 1**, a lumped parameter system with 7 DOF is considered. The modal model of such system is shown, representing the uncoupled system [7].

In **Figure 2**, the system of **Figure 1** has been modified by adding a spring between masses 1 and 5. Since $\boldsymbol{\Delta}\tilde{\mathbf{M}} = 0$, the homogeneous problem of the modified system, written in the modal coordinates of the original system, is:

$$\ddot{\mathbf{q}} + (\boldsymbol{\Lambda} + \boldsymbol{\Delta}\tilde{\mathbf{K}})\mathbf{q} = 0 \qquad [20]$$

The model corresponding to eqn [20] is also shown in **Figure 2**. The static coupling is provided by the off-diagonal terms of $\boldsymbol{\Delta}\tilde{\mathbf{K}}$, represented by the springs interconnecting the modal masses.

The effect of truncation is shown in **Figure 3**.

If the seventh mode of the original system is neglected, the corresponding modal model is made of the first six modes only (**Figure 3** left). If the model of the modified system is expressed in the modal coordinates of the original system (**Figure 3** center), the truncation of the seventh mode does not permit accounting for the coupling terms among the first six modes and the omitted one (**Figure 3** right). These terms, the first six in the last column of the matrix $\boldsymbol{\Delta}\tilde{\mathbf{K}}$ shown in **Figure 2,** are by no means negligible with respect to those of the first six columns.

Frequency Response Function Database

The difficulty of identifying the modal parameters, especially for complex structures and/or high modal densities, and the effect of mode truncation on the structural modification problem suggest that the use of the modal database should be avoided.

Then it can be appropriate to use directly the frequency response function matrix of the structure $\mathbf{H}_0(\omega)$, experimentally determined for N DOF, thus having dimensions $N \times N$. However, the matrix $\mathbf{H}_0(\omega)$ is symmetric due to the reciprocity theorem. Consequently, the elements that must be determined are only $N \times (N + 1)/2$ (elements of the upper or lower triangular part of the matrix), instead of N^2.

It is now shown how the FRF matrix of a modified structure can be determined from knowledge of the original structure and the imposed modifications.

Using the FRF matrix, the response $\mathbf{X}_0(\omega)$ of the original structure to an external excitation $\mathbf{F}(\omega)$ is given by:

$$\mathbf{X}_0(\omega) = \mathbf{H}_0(\omega)\mathbf{F}(\omega) \qquad [21]$$

In eqn [21], $\mathbf{H}_0(\omega)$ is the FRF matrix of the original structure, whose elements can be receptances, mobilities, or inertances. Accordingly, the elements of $\mathbf{X}_0(\omega)$ are displacements, velocities, or accelerations, respectively, of the N considered DOFs, while the elements of $\mathbf{F}(\omega)$ are the forces acting on the structure at those DOFs.

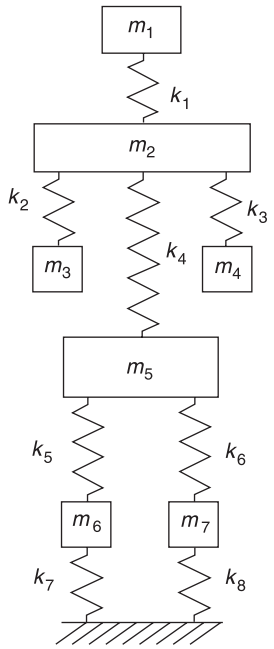
After formally introducing the impedance-like matrix of the structure $\mathbf{Z}_0(\omega) = \mathbf{H}_0^{-1}(\omega)$ the equation of motion of the original structure in the frequency domain can be written as:

$$\mathbf{F}(\omega) = \mathbf{Z}_0(\omega)\mathbf{X}_0(\omega) \qquad [22]$$

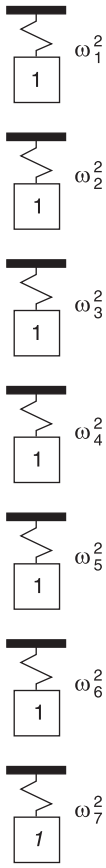
Let the modifications be described by the matrix $\Delta\mathbf{Z}(\omega)$, that can be expressed, for the dynamic stiffness as:

$$\boldsymbol{\Delta}\mathbf{Z}(\omega) = \boldsymbol{\Delta}\mathbf{K} + j\omega\boldsymbol{\Delta}\mathbf{C} - \omega^2\boldsymbol{\Delta}\mathbf{M} \qquad [23]$$

The above expression of $\boldsymbol{\Delta}\mathbf{Z}$ holds when $\mathbf{H}_0$ is a receptance matrix. For mobility or inertance matrices, $\boldsymbol{\Delta}\mathbf{Z}$ must be changed accordingly, by dividing by $j\omega$ or $-\omega^2$, respectively.



$k_1 = 5$ N m^{-1} $m_1 = 15$kg
$k_2 = 10$ N m^{-1} $m_2 = 15$kg
$k_3 = 10$ N m^{-1} $m_3 = 5$kg
$k_4 = 20$ N m^{-1} $m_4 = 5$kg
$k_5 = 10$ N m^{-1} $m_5 = 15$kg
$k_6 = 10$ N m^{-1} $m_6 = 10$kg
$k_7 = 1$ N m^{-1} $m_7 = 10$kg
$k_8 = 1$ N m^{-1}



$$\mathbf{K} = \begin{bmatrix} 5 & -5 & & & & & \\ -5 & 45 & -10 & -10 & -20 & & \\ & -10 & 10 & & & & \\ & -10 & & 10 & & & \\ & -20 & & & 40 & -10 & -10 \\ & & & & -10 & 11 & \\ & & & & -10 & & 11 \end{bmatrix}$$

$$\mathbf{\Lambda} = \begin{bmatrix} 0.16 & & & & & & \\ & 0.61 & & & & & \\ & & 0.97 & & & & \\ & & & 1.05 & & & \\ & & & & 1.41 & & \\ & & & & & 1.69 & \\ & & & & & & 2.21 \end{bmatrix}$$

$$\mathbf{M} = \begin{bmatrix} 15 & & & & & & \\ & 15 & & & & & \\ & & 5 & & & & \\ & & & 5 & & & \\ & & & & 15 & & \\ & & & & & 10 & \\ & & & & & & 10 \end{bmatrix}$$

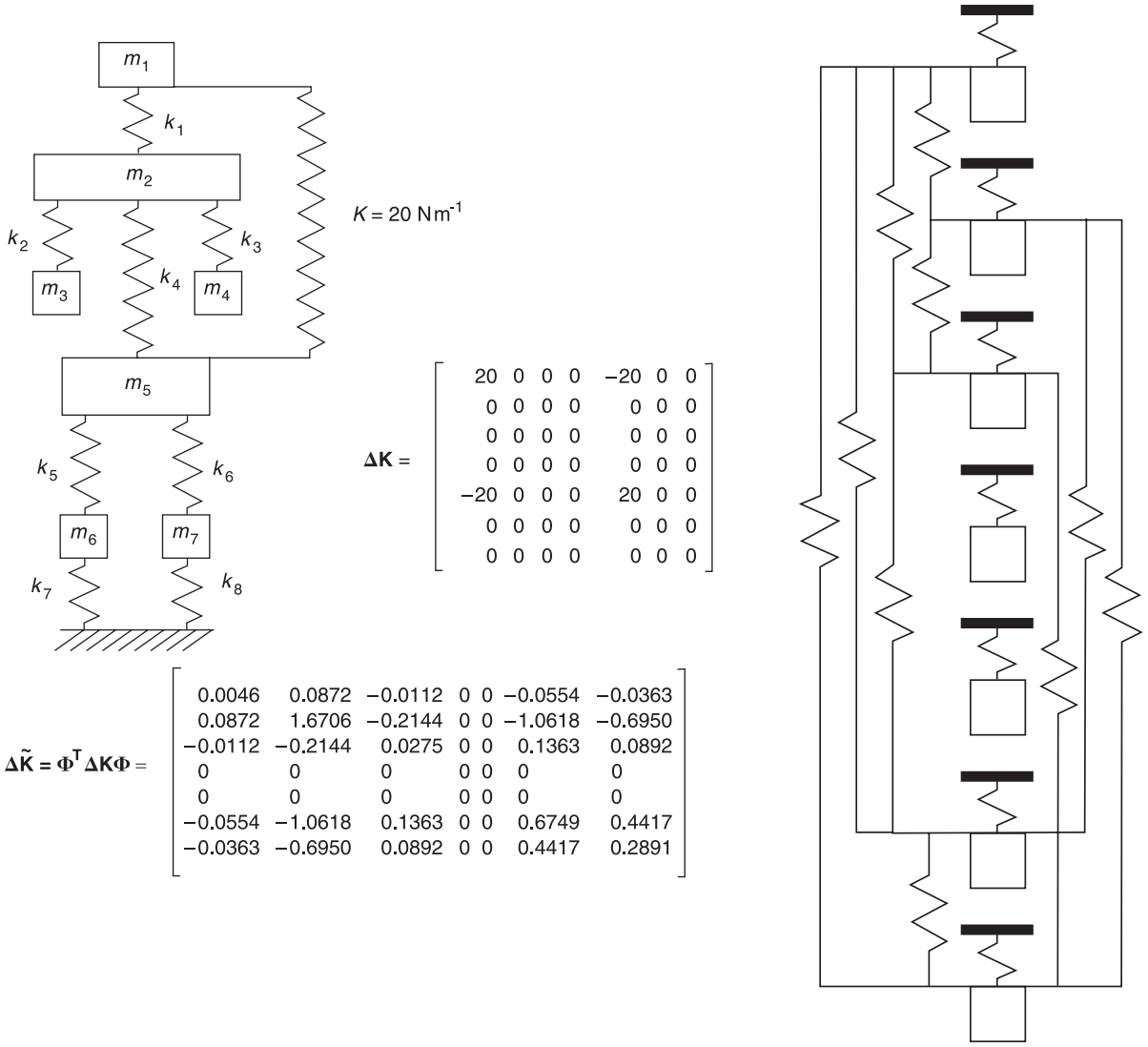
$$\mathbf{\Phi} = \begin{bmatrix} -0.127 & -0.216 & 0.059 & 0.000 & 0.000 & -0.009 & -0.014 \\ -0.118 & 0.025 & -0.107 & 0.000 & 0.000 & 0.072 & 0.188 \\ -0.119 & 0.031 & -0.201 & 0.000 & 0.316 & -0.165 & -0.130 \\ -0.119 & 0.031 & -0.201 & 0.000 & -0.316 & -0.165 & -0.130 \\ -0.112 & 0.072 & 0.022 & 0.000 & 0.000 & 0.174 & -0.134 \\ -0.104 & 0.100 & 0.135 & -0.224 & 0.000 & -0.098 & 0.035 \\ -0.104 & 0.100 & 0.135 & 0.224 & 0.000 & -0.098 & 0.035 \end{bmatrix}$$

Figure 1 7-DOF system.

Since modifications must only involve DOFs in which the $\mathbf{H}_0(\omega)$ matrix has been measured, the equation of motion of the modified structure, excited by the same forces $\mathbf{F}(\omega)$, can be written as:

$$\mathbf{F}(\omega) = [\mathbf{Z}_0(\omega) + \mathbf{\Delta Z}(\omega)]\mathbf{X}(\omega) \qquad [24]$$

in which $\mathbf{X}_0(\omega)$ is the response of the modified structure. Therefore:



$$\Delta\mathbf{K} = \begin{bmatrix} 20 & 0 & 0 & 0 & -20 & 0 & 0 \\ 0 & 0 & 0 & 0 & 0 & 0 & 0 \\ 0 & 0 & 0 & 0 & 0 & 0 & 0 \\ 0 & 0 & 0 & 0 & 0 & 0 & 0 \\ -20 & 0 & 0 & 0 & 20 & 0 & 0 \\ 0 & 0 & 0 & 0 & 0 & 0 & 0 \\ 0 & 0 & 0 & 0 & 0 & 0 & 0 \end{bmatrix}$$

$$\Delta\tilde{\mathbf{K}} = \Phi^{\mathrm{T}}\Delta\mathbf{K}\Phi = \begin{bmatrix} 0.0046 & 0.0872 & -0.0112 & 0 & 0 & -0.0554 & -0.0363 \\ 0.0872 & 1.6706 & -0.2144 & 0 & 0 & -1.0618 & -0.6950 \\ -0.0112 & -0.2144 & 0.0275 & 0 & 0 & 0.1363 & 0.0892 \\ 0 & 0 & 0 & 0 & 0 & 0 & 0 \\ 0 & 0 & 0 & 0 & 0 & 0 & 0 \\ -0.0554 & -1.0618 & 0.1363 & 0 & 0 & 0.6749 & 0.4417 \\ -0.0363 & -0.6950 & 0.0892 & 0 & 0 & 0.4417 & 0.2891 \end{bmatrix}$$

Figure 2 Modified 7-DOF system.

$$\mathbf{X}(\omega) = [\mathbf{Z}_0(\omega) + \Delta\mathbf{Z}(\omega)]^{-1}\mathbf{F}(\omega) \qquad [25]$$

Because of the relationship $\mathbf{X}(\omega) = \mathbf{H}(\omega)\mathbf{F}(\omega)$, where $\mathbf{H}(\omega)$ is the (unknown) FRF matrix of the modified structure, one has:

$$\mathbf{H}(\omega) = [\mathbf{Z}_0(\omega) + \Delta\mathbf{Z}(\omega)]^{-1} \qquad [26]$$

Recalling that the impedance-like matrix of the original structure is not practically available, one can write:

$$\mathbf{H}(\omega) = \left[\mathbf{H}_0^{-1}(\omega) + \Delta\mathbf{Z}(\omega)\right]^{-1} \qquad [27]$$

Instead of using directly eqn [27], involving two matrix inversions, it is more convenient to premultiply eqn [24] by $\mathbf{H}_0(\omega)$, thus obtaining:

$$\begin{aligned} \mathbf{H}_0(\omega)\mathbf{F}(\omega) &= \mathbf{H}_0(\omega)[\mathbf{Z}_0(\omega) + \Delta\mathbf{Z}(\omega)]\mathbf{X}(\omega) \\ &= [\mathbf{I} + \mathbf{H}_0(\omega)\Delta\mathbf{Z}(\omega)]\mathbf{X}(\omega) \end{aligned} \qquad [28]$$

in which $\mathbf{I}$ is the unit matrix. From eqn [28] one obtains:

$$\mathbf{X}(\omega) = [\mathbf{I} + \mathbf{H}_0(\omega)\Delta\mathbf{Z}(\omega)]^{-1}\mathbf{H}_0(\omega)\mathbf{F}(\omega) \qquad [29]$$

which implies:

$$\mathbf{H}(\omega) = [\mathbf{I} + \mathbf{H}_0(\omega)\Delta Z(\omega)]^{-1}\mathbf{H}_0(\omega) \qquad [30]$$

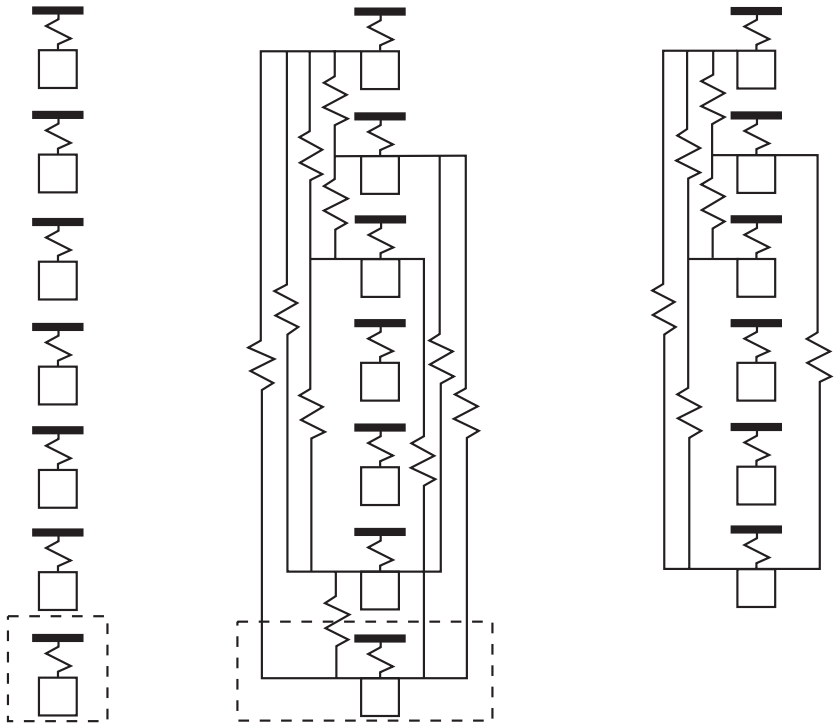


Figure 3 Truncation effect.

Eqn [30] provides the FRF matrix of the modified structure from the original FRF $\mathbf{H}_0(\omega)$ and the impedance-like matrix of the modifications $\Delta\mathbf{Z}(\omega)$: this is the prediction relationship we were looking for. With respect to eqn [27], it involves a single matrix inversion, so that it is computationally more efficient. Furthermore, it avoids the inversion of matrix $\mathbf{H}_0$, which is ill-conditioned around the resonances of the original system.

It is worth pointing out that, for a given set of modifications, the computation performed in eqn [30] must be repeated at all the frequencies of interest: these frequencies are established by the analyst among those used to determine experimentally the FRF. Since the experimental data are normally sampled at discrete time instants (and frequencies), these frequencies represent a discrete set of values.

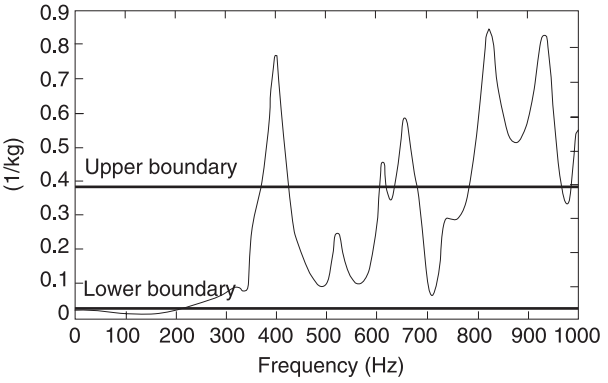


Figure 4 Establishing the wished dynamic behavior of a structure.

Inverse Problem

The inverse problem must be formulated in terms of the FRF database. In fact, it is not generally possible to establish the physical goal of an inverse problem through the modal parameters, while this is quite simple by means of the response or FRF of the system. To make this point clear, consider the case of **Figure 4**, which represents the FRF modulus of a given structure. If this response is, for any reason, unacceptable, it is quite simple to define an upper (and lower) boundary for it (e.g., those shown in the figure), and to require that the FRF of the modified structure lies within these boundaries.

In contrast, these requirements cannot be defined in terms of the modal parameters. For this reason, the FRF of the structure is generally the only practical database to formulate the inverse problem, so that the required dynamic behavior will be defined by means of parameters connected with the FRF matrix. Only the case of an FRF optimization is presented here: the possibility of extending the approach to other

response optimization is a simple exercise once the considered case is understood.

The parameters which are dependent on the structural modifications will be located in a vector $\mathbf{z}$. They can represent mass, stiffness, and/or damping modifications at or between any of the points of the measured FRF matrix, i.e., the possible modifications must be applied to points where the FRF matrix has been measured.

Definition of the Required Dynamic Behavior

The dynamic behavior of a structure may be described by means of its FRF characteristics. Through these, it is possible to determine the response of the structure when an estimate of the exciting forces is available.

In the present case, it is sufficient to examine the magnitudes of some FRFs: more precisely, the FRFs measured between the points in which the forces are supposed to act and the points where the response(s) must be controlled.

Since any element H_{ij} of the modified FRF matrix, here written as $\mathbf{H}(\mathbf{z}, \omega)$ to express that it depends on the set of modifications $\mathbf{z}$, can be determined from eqn [30], the elements amenable to optimization can be established as:

$$p_r(\mathbf{z}) = \left|H_{ij}(\mathbf{z}, \omega_k)\right| \quad \omega_k \,\varepsilon\, S_F, \quad (i,j)\varepsilon\, S_E, \quad r = 1 \ldots N_F, \quad N_P = N_F \times N_E \qquad [31]$$

where S_F is the discrete set of N_F frequencies involving the bandwidth where a modification is required to act and S_E the set of N_E pairs of indices (i, j) determining the elements of H_{ij} that must be modified.

Formulation of the Problem

The goal of the structural modification (or optimization) process, i.e., the desired dynamic behavior of a structure, can be more simply established in negative rather than in positive terms: in other words, for a given structure, it is preferable to stress what must be avoided instead of what is actually required. For example, to control the modulus of an FRF on the basis of the performance required of the system, it is rather natural to seek to avoid excessively high resonant peaks and thus to establish an upper boundary for the FRF modulus that should not be overcome; in contrast it is not natural to define a detailed behavior for the response. Therefore the conditions that are usually required are not equality conditions that would imply exact wished values, but rather inequality conditions, such as:

$$b_r^L \le p_r(\mathbf{z}) | \le b_r^U, \quad r = 1 \ldots N_P$$

where b_r^L and b_r^U are lower and upper boundaries for each $p_r(\mathbf{z}) = |H_{ij}(\mathbf{z}, \omega_k)|$.

Generally, the existence of a vector $\tilde{\mathbf{z}}$ satisfying the conditions imposed is not guaranteed. In fact, it cannot be supposed that the required behavior is physically possible, either in the absolute sense or, for more reasonable requirements, in relation to the feasible set of modifications.

In contrast, if some $\tilde{\mathbf{z}}$ which satisfies the imposed conditions does exist, in general it will not be unique, especially if the requirements imposed are expressed as inequalities. It is then necessary to establish a criterion to discriminate amongst the possible solutions and to choose consequently the most convenient of them.

The above considerations exclude the possibility of formulating the problem as the simple solution of the set of inequality equations like the ones shown above. An argument stressing the relative inconvenience of this formulation relies on the circumstance that, if one finds different solutions (e.g., when starting from different initial estimates of $\tilde{\mathbf{z}}$), the proposed scheme does not provide any criteria to choose the most appropriate of them.

A criterion to operate a comparison among different solutions can be based on considerations involving the cost of the alternative modifications. If more modification sets exist satisfying the required conditions, the preferable set would be that which costs least.

The introduction of a cost minimization condition implies a formulation of the inverse problem as a problem of mathematical programming (or optimization). To this end it is quite natural to formulate the following problem of constrained minimum:

$$\min_{\mathbf{z}} \mathrm{C}(\mathbf{z})$$

with the constraints:

$$b_r^L \le \left|H_{ij}(\mathbf{z}, \omega_k)\right| \le b_r^U \quad r = 1 \ldots N_P$$

and the technological boundaries:

$$z_i^L \le z_i \le z_i^U$$

An appropriate choice of technological boundaries avoids an impossible realization of the resulting modifications (such as springs or dampers with negative values) or just not practical (e.g., a subtraction of mass). Moreover, they can avoid modifications which

are not compatible with the system architecture, such as too-large modifications altering some important features of the system.

The solution of the optimization problem can be achieved by different methods proposed in the literature to solve nonlinear optimization problems. Among them, classical procedures that search for the steepest gradient can be used as well as new methods that make use of the genetic algorithms that have been proven to be quite robust and efficient for these kinds of problem.

Cost of Modifications

Let $C(\mathbf{z})$ be the cost associated with the modifications represented by the vector, $\mathbf{z}$. This cost would not just be the cost of the material and production: in fact, it is worth pointing out that the structure to be modified is usually already designed and, often, optimized to satisfy other requirements. Thus, any change from the original design implies *per se* a cost.

A reasonable expression for $C(\mathbf{z})$ is the following additive form, in which the cost of any elementary variable modification z_i is independent of the value of the other modifications:

$$C(\mathbf{z}) = \sum_{i=1}^{N_V} c_i(z_i)$$

Among the many possibilities for $c_i(z_i)$, two deserve particular attention:

- Constant marginal cost: in this case it is:

$$c_i(z_i) = w_i|z_i| \qquad [32]$$

  in which the cost of the ith design variable is proportional to the absolute value of the same variable through the coefficients w_i allowing one to give different weights to the different variables.
- Proportional marginal cost: in this case the cost is:

$$c_i(z_i) = w_i z_i^2 \qquad [33]$$

  in which the cost of the ith design variable is proportional to the square of the same variable through a weight coefficient w_i.

The relationship [33] is more appropriate than the constant marginal cost [32], in that it more closely satisfies the condition of not affecting too much the general architecture of the original structure. In fact, it inflicts a higher penalty to large isolated modifications than to modifications spread over several points.

Let us consider a modification consisting of adding a given mass: the expression of the constant marginal cost [32], for equal coefficients w_i, provides the same cost either when the mass is entirely concentrated in a single point or when it is split among several points. In contrast, the proportional marginal cost [33] provides a lower cost for the mass spread over several points. This is preferable because the general architecture of the system is less affected by such a solution.

Reduction of the Number of Design Variables

The solution of linear optimization problems with hundreds of variables and constraints can easily be obtained. In contrast, the solution of nonlinear optimization problems is much more complex, and only a few dozen variables and constraints can usually be considered. Therefore, before trying to solve the optimization problem, it is convenient to reduce the number of design variables, neglecting those having a small effect on the controlling parameters. This preliminary analysis of the modifications effectiveness can be performed using sensitivities.

Sensitivity analysis Using sensitivity analysis, one can determine the effectiveness of any modification in performing the required dynamic goals, through the analysis of the specific effect of any modification.

To this end, the increment of any $|H_{ij}|$ as a function of the increment of any design variable can be considered, excluding from the optimization process those modifications producing the lowest parameters' variations. Therefore, a first-order sensitivity analysis can be formulated through the derivatives:

$$\left.\frac{\partial}{\partial z_i} p_r(\mathbf{z})\right|_{z=0}$$

For application purposes, since $p_r(\mathbf{z}) = |H_{ij}(\mathbf{z}, \omega_k)|$ is frequency-dependent, it is convenient to plot the sensitivity as a function of frequency. In **Figure 5**, the derivatives of the FRF magnitude with respect to two different modifications are considered.

One can observe the fluctuations of the sensitivity between negative and positive values. Therefore it can be troublesome to establish the effectiveness of a given modification: in fact, if the goal is a reduction of the FRF modulus, the sensitivity zones higher than zero would worsen the result. However, a comparison between the two curves shows that the oscillations of one of them are higher than the other, so that one can stress that the modifications corresponding to the lower oscillations have a poor effect on the considered FRF.

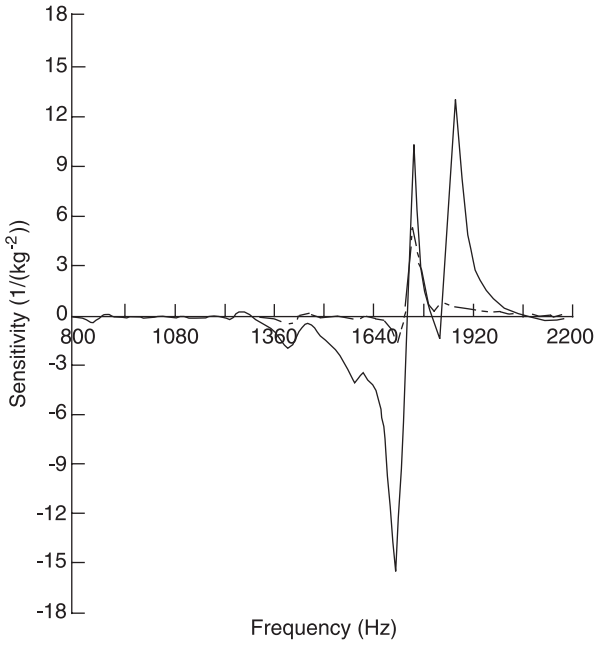


Figure 5 Example of a first-order sensitivity: derivative of the inertance FRF with respect to mass.

This suggests estimation of the potential effectiveness of a modification in the considered frequency bandwidth by its root mean square value, i.e.:

$$\left[\sum_{r=1}^{N_P}\left(\frac{\partial}{\partial z_i}p_r(\mathbf{z})\bigg|_{z=0}\right)^2\right]^{1/2} \qquad [34]$$

Applications of the Optimization Procedure

2-DOF system To clarify the approach proposed so far for the optimization problem, consider the 2-DOF system shown in **Figure 6**. Following the point of view adopted, the FRF of the system would be known experimentally whilst the physical model (**M**, **C**, and **K**) would be unknown. In the present case these matrices are known but are only used to determine the FRF matrix. From the modulus of any element of the inertance matrix (e.g., H_{12} shown in **Figure 7** (thin line) the two resonant peaks are determined at $\omega_{n1} = 364\,\mathrm{rad\,s^{-1}}$ (58 Hz) and $\omega_{n2} = 931\,\mathrm{rad\,s^{-1}}$ (148 Hz).

Let us now define a problem of structural modification with the following goal:

- It is required that the FRF modulus of the inertance H_{12}in the bandwith 55–150 Hz should have an upper boundary of $b^U = 1.2\,\mathrm{kg}^{-1}$, as shown in **Figure 7**. This requirement is imposed at discrete frequency points with a frequency step of 1 Hz. Consequently, $N_F = 96$ and $N_E = 1$, so that $N_P = 96 \times 1$.
- It is established that the admissible modifications are an increment of the mass m_2 and an increment of the stiffness k_2 between the two masses. Maximum admissible values are imposed for both variables: they are $m_2 \leq 2\,\mathrm{kg}$ and $k_2 \leq 400\,000\,\mathrm{N\,m^{-1}}$.

The parameters to control are:

$$p_k(\mathbf{z}) = |H_{12}(\mathbf{z}, \omega_k)|_{\omega_k \varepsilon [55-150]\,\mathrm{Hz}}$$

The proportional marginal cost expression is used with appropriate weights determined in such a way that the cost associated with the maximum values of m_2 and k_2 are comparable and their sum is approximately equal to 1. This implies the values $w_1 = 0.125$, associated with m_2, and $w_2 = 0.313 \times 10^{-11}$.

Consequently, the inverse problem is formulated as follows.

- Objective function:

$$C(\mathbf{z}) = \sum_{i=1}^{2} w_i z_i^2 = 0.125 m_2^2 + 0.313 \times 10^{-11} k_2^2$$

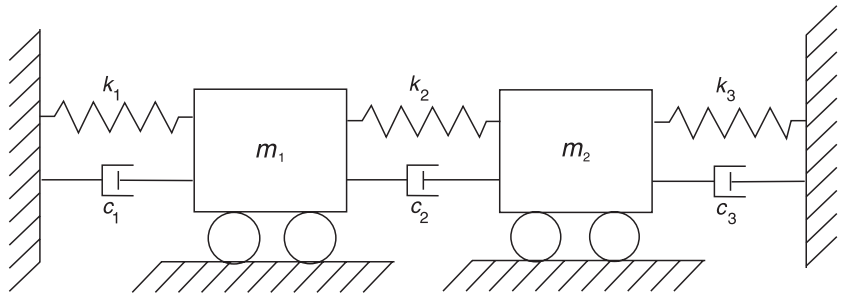


Figure 6 The 2-DOF system.

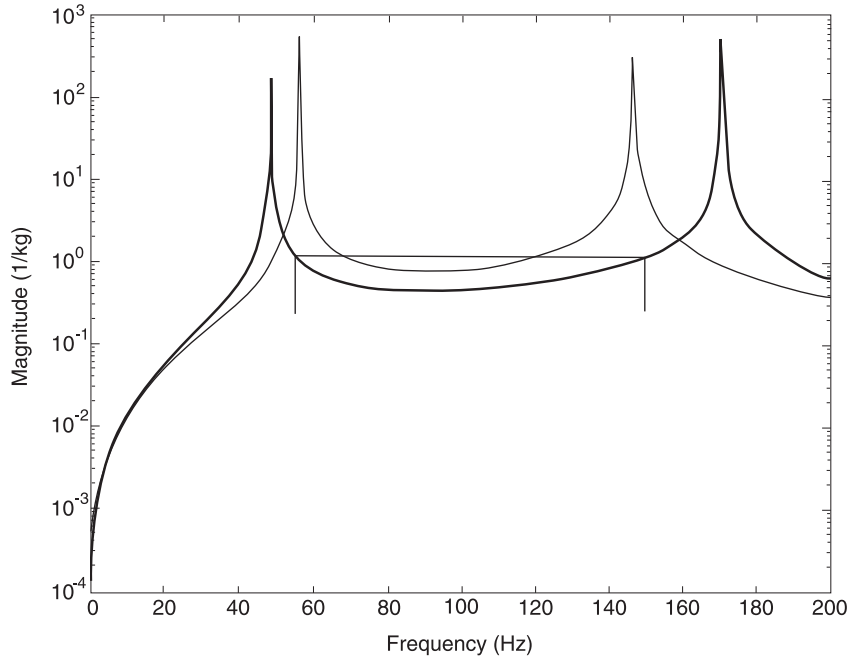


Figure 7 Modification of a 2-DOF system: original (thin line) and modified (thick line).

- Constraints:

$$p_k(m_2, k_2) = |H_{12}(m_2, k_2, \omega_k)|_{\omega_k \varepsilon [55-150]\,\mathrm{Hz}}$$
$$0 \le m_2 \le 2$$
$$0 \le k_2 \le 4 \times 10^5$$

Since the problem involves two variables only, a sensitivity analysis is not necessary.

The solution of this problem provides the two optimal values for the mass and the stiffness, i.e., $m_2 = 1\,\mathrm{kg}$ and $k_2 = 300\,000\,\mathrm{N\,m^{-1}}$. With these values the goal of the optimization problem is fully achieved, as can be observed in **Figure 7**, where the original FRF is compared with the new one (thick line), obtained after modification. It can be observed that the optimal solution implies a shift of the two natural frequencies outside the considered bandwidth.

Engine block The same approach was successfully applied to reduce the vibrations of an internal combustion engine, and thus the noise radiated by its engine block.

Practical considerations show that the engine block is the most appropriate element of the engine to modify, since it is the sole element designed with merely static criteria.

Therefore, experimental tests were performed on the block: 12 points were selected, and the FRF matrix was determined experimentally at and between these points. These were also supposed to be the points at which to locate the lumped modifications. Among them, only the positions corresponding to the journal bearings were considered not to be amenable to modifications.

In order to reduce the computation burden of the optimization algorithm and to avoid the analysis of points having a poor effect on the considered FRF, a sensitivity analysis with respect to both masses and stiffnesses was performed on the 10 points of the block. It was observed that only six points presented a significant sensitivity either to mass or stiffness variations.

The FRF to change was between the input on the journal and the response on the zone of the block which was vibrating most seriously. The frequency band of interest encompassed the range between 900 and 2000 Hz. In this frequency band, mass modifications are effective to reduce the magnitude $|H|$ of the considered FRF element.

At this point the optimization problem was formulated as follows. Find:

$$\min \sum_{i=1}^{6} (z_i)^2 \qquad [35]$$

with constraints:

$$|\mathbf{H}(\mathbf{z}, \omega)| \le b^U = 0.4\,\mathrm{kg}^{-1}$$

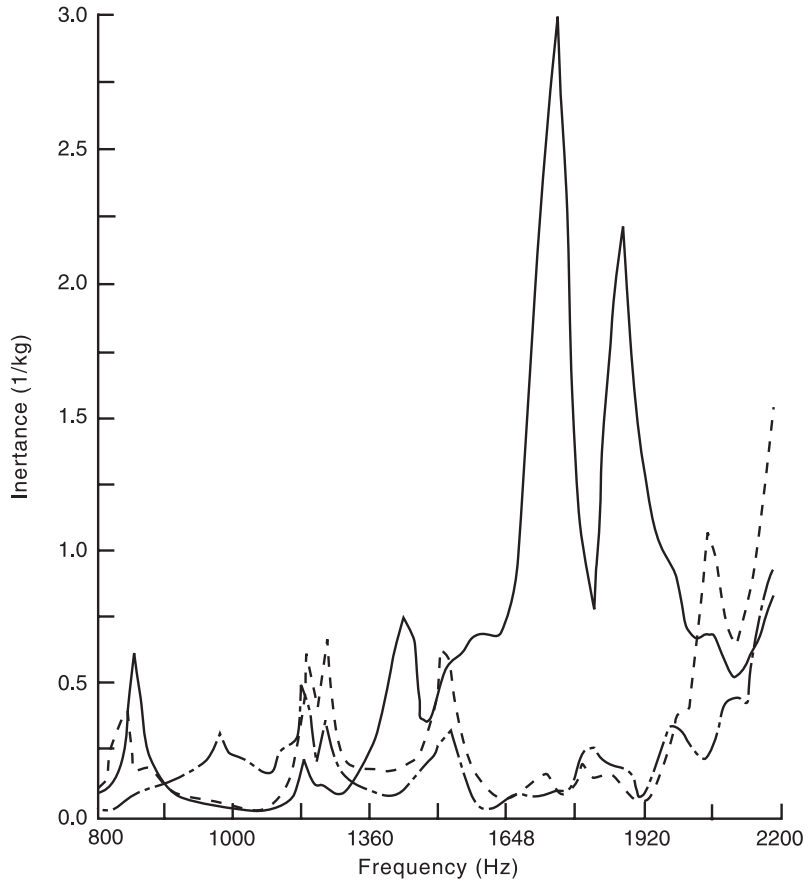


Figure 8 Modification of an engine block. Continuous line, original; dashed line, computed after modification; dots and dashes, measured after modification.

in the frequency band of interest, and boundaries:

$$z_i \geq 0$$

on the optimization variables, corresponding to mass variations only.

In order to check the computed results, the engine block, modified with the prescribed masses determined from optimization, was experimentally tested. Lumped lead masses were bolted on the established positions of the block. Of course, these masses are not the ideal masses used in the computation, so that some changes can be observed in the experimental response with respect to the theoretical one. However, the agreement between the computed modified system and the experimental one is quite satisfactory (**Figure 8**).

See also: **Active vibration suppression**; **Inverse problems**; **Identification, Fourier-based methods**; **Modal analysis, experimental**, Applications; **Modal analysis, experimental**, Basic principles; **Modal analysis, experimental**, Construction of models from tests; **Modal analysis, experimental**, Measurement techniques; **Modal analysis, experimental**, Parameter extraction methods; **Mode of vibration**.

Further Reading

Ewins DJ (2000) *Modal Testing: Theory, Practice and Application*.

Maia NMM and Silva JMM (eds) (1997) *Theoretical and Experimental Modal Analysis*. Baldock, Hertfordshire, England: Research Studies Press.

Sestieri A and D'Ambrogio W (1989) A modification method for vibration control of structures. *Mechanical Systems and Signal Processing* 3: 229–253.

STRUCTURE-ACOUSTIC INTERACTION, HIGH FREQUENCIES

A Sestieri, Università Degli Studi di Roma, Roma, Italy

Copyright © 2001 Academic Press

doi:10.1006/rwvb.2001.0154

In the previous companion paper, it was shown that the structural–acoustic interaction at high frequencies implies short acoustic wavelengths ($\lambda = c/f$) with respect to a typical dimension of the acoustic medium (cavity dimensions or distance between source and observer). Therefore, as the frequency of interest increases, the number of degrees of freedom necessary to solve numerically the problem becomes very large, so that the computational burden is more and more demanding, increasing over convenient or acceptable limits. Moreover, because of inherent uncertainties in the physical and geometrical parameters and in the boundary and joint conditions, the dynamic behavior of a complex system differs unpredictably from those of similar systems when the modal density and modal overlap are high. In this case, there is little possibility of obtaining accurate results, whatever numerical model is used: a statistical rather than a deterministic description would be more appropriate.

Consequently, the numerical solution of the high-frequency structural–acoustic interaction is much more complex than the one discussed for low frequencies, and, in fact, no approach is yet considered reliable for application at a design stage.

The interest in high-frequency problems is not recent: in 1961 a group of scientists – Noiseux, Lyon, Maidanik, Heckl, Smith, and others – met together to discuss how to predict rocket noise and vibrations of launch vehicles, and one year later Lyon and Maidanik published the first systematic work on statistical energy analysis (SEA), presenting a completely new point of view for the solution of vibroacoustic problems, able to estimate the energy flow between vibrating systems, and thus including the interaction between structures and fluids. Since then a long way has been traveled, but SEA is not yet completely accepted, even though, for its statistical character, it describes the dynamic behavior of a population of similar structures rather than a single case.

It is important to stress that, to overcome the limitations related to the large number of degrees of freedom involved, one is required to think through the high-frequency problem differently, avoiding any approach based on standard discretizations. To this aim, the techniques developed for structural–acoustic interaction at high frequencies try to use, instead of the displacement and/or acoustic pressure, a new field descriptor. Then, new governing equations must be determined, that are expected to be numerically more convenient than the original wave equations. The definition of a new descriptor implies, in general, a solution of lower informative content, but this seems to be the price to pay to solve this complex numerical problem.

In most of the developed methods, the new variable capable of describing both the sound and the structural vibrations is energy. However, the use of this variable introduces some drawbacks that will be discussed in the next sections. In the envelope method the new descriptor is a complex envelope displacement that does not have such problems.

Statistical Energy Analysis

Although recent developments have shown that SEA can be applied to different situations from those originally depicted, in that some basic assumptions seem not to be strictly necessary, SEA is supposed to be a procedure to tackle coupled problems (either fluid–structure systems or coupled structures) with broad-band excitation, capable of inducing a response characterized by several modes. In other words, SEA is a high-frequency approach for studying the interaction between highly resonant systems, as well as the interaction between resonant structures and reverberant sound fields in acoustic cavities. Unlike the deterministic methods based on partial differential equations describing wave propagation in structures and fluids, the SEA equations are simply energy flow relationships among resonant subsystems.

The traditional SEA assumptions are hereafter recalled for a better understanding of the energy relationships between coupled systems.

- The whole system is subdivided into modal groups. The modal groups (subsystems) do not necessarily coincide with a single structure that can sustain bending, longitudinal, and transverse modes, so different sets of modal groups can be generated from a single physical system.

- It is assumed that the coupling between subsystems is linear and conservative.
- The system is excited by broad-band random excitations formed by uncorrelated forces that are statistically independent (rain-on-the-roof excitation).
- It is assumed that the forces induce equipartition of energy within each modal group in a given band of frequencies.

Of course, it is not easy to establish *a priori* whether the above assumptions are satisfied for any system of interest, and this is a weak point of SEA.

Energy Flow Balance Between Two Elementary Oscillators

Together with the previous hypotheses, it is stated that any oscillator in steady-state condition stores potential and kinetic energy, and the time-average power dissipated in a frequency band (usually octave or one-third octave band) is given by:

$$P_d = \omega E \eta_d \qquad [1]$$

where E is the time-average energy (sum of potential and kinetic energies) in a frequency band, ω the mean centre frequency of the band and η_d the mean loss factor in the band. This concept is an extension of the power dissipated by a damped oscillator excited harmonically.

Moreover, it is assumed that the time-average energy flow exchange, P_{12}, between two oscillators is proportional to the difference between the total time-average energies of the individual oscillators, i.e.:

$$P_{12} = \alpha(E_1 - E_2) \qquad [2]$$

where α depends on the oscillator parameters. This basic relationship, derived rigorously by Lyon, states that the energy flows from the oscillator of higher energy content to the one of lower energy: from this point of view, this law is analogous to thermal conductivity, so that a thermal analogy can be established. Later on, Lyon and Scharton considered an array of equal oscillators, obtaining for them the same relationship.

Power Balance Between Two Modal Groups

Starting from these results, SEA tries to extend the exact relationship between two coupled oscillators to modal groups or sets of oscillators. In this attempt, the formulation becomes more insidious, making SEA somewhat muddled.

The extension to modal groups imposes that the energy flow between groups of oscillators is not severely affected by other modal groups in the system, a concept that is translated into the requirement of weak modal coupling between the modal subsystems, practically implying that the coupling between subsystems is much lower than the internal forces. Moreover, since a straightforward extension from two oscillators to a set of oscillators can be obtained in terms of vibration modes, in general eqn [2] is rewritten for any two sets of oscillators i and j by introducing the concepts of modal density n (number of modes per unit frequency) and modal energy (E/n), i.e.:

$$P_{ij} = \beta_{ij}\left(\frac{E_i}{n_i} - \frac{E_j}{n_j}\right) \qquad [3]$$

where β_{ij} is a new constant depending on the oscillator parameters and modal densities. It is worthwhile emphasizing that, in the present context, E_i is the vibrational physical energy of the ith modal group: for example, if a flexural beam generates only a modal group of bending modes, E_i is the whole flexural energy of the beam. Eqn [3] is the basic equation of SEA, stating that, in the thermal analogy, modal energy is equivalent to temperature.

Since the energy flowing away from system i to system j is similar to a dissipated power, eqn [3] is rewritten in the following form:

$$P_{ij} = \omega E_i \eta_{ij} - \omega E_j \eta_{ji} \qquad [4]$$

where the term η_{ij} is the coupling loss factor between system i and system j. By comparing eqns [3] and [4] one has the reciprocity relationship:

$$\frac{\beta_{ij}}{n_i} = \omega\eta_{ij}; \quad \frac{\beta_{ij}}{n_j} = \omega\eta_{ji} \quad \Rightarrow \quad n_i\eta_{ij} = n_j\eta_{ji} \qquad [5]$$

that can be conveniently used for determining the coupling loss factor between coupled subsystems.

To derive the power balance equations, consider now the case of **Figure 1** which represents two SEA subsystems, each characterized by numerous modes, with the first subsystem excited by an input power P_1^{in}, while $P_2^{in} = 0$. (In a practical situation the first system could be a flexurally excited plate and the second an acoustic room where the plate is suspended somewhere). It is assumed that the subsystems' energies (powers) are averaged in time.

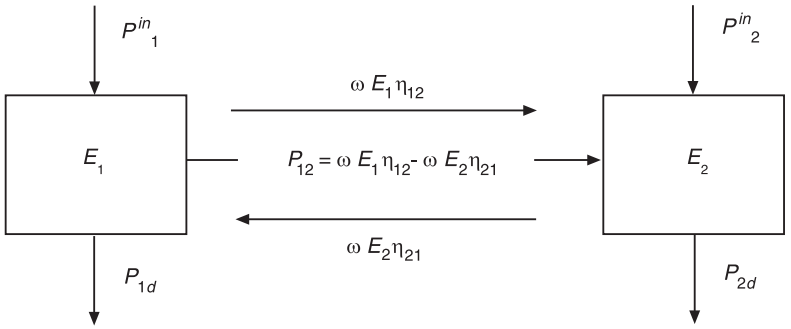


Figure 1 Energy flows between two SEA subsystems.

Using the developments of the previous section, the steady-state power balance between the two subsystems can be written as:

$$\begin{cases} P_1^{in} = \omega E_1 \eta_{d1} + \omega E_1 \eta_{12} - \omega E_2 \eta_{21} \\ 0 = \omega E_2 \eta_{d2} + \omega E_2 \eta_{21} - \omega E_1 \eta_{12} \end{cases} \quad [6]$$

This is a system with unknowns E_1 and E_2, representing the energies stored in each subsystem. From the second equation the ratio between these energies is given by:

$$\frac{E_2}{E_1} = \frac{\eta_{12}}{\eta_{d2} + \eta_{21}}$$

Note that, if $\eta_{21} \gg \eta_{d2}$, implying that the coupling loss factor is much larger than the loss factor of the second system, from the previous relationship and from eqn [5] one can derive the equality of modal energies, i.e., $E_1/n_1 = E_2/n_2$. Although it is generally difficult to fulfill exactly this condition, the equality of modal energies provides a simple estimate (upper limit) for the response of the whole system.

Extension of the Power Balance to a Set of Oscillators

Under the assumption of weak coupling, the extension of the power balance equations to multiple oscillators is straightforward. For m group of oscillators, m balance equations can be written in the form:

$$P_i^{in} = P_{d_i} + \sum_{i=1, j \neq i}^{m} P_{ij}$$

or, in matrix form, using eqn [4]:

$$\mathbf{P} = [A]\mathbf{E} \quad [7]$$

where $\mathbf{P}$ is the vector of input powers P_i^{in} and $\mathbf{E}$ is the vector of time-average energies E_i.

The off-diagonal and diagonal matrix elements are, respectively:

$$A_{ij} = -\omega n_i \eta_{ij} \quad A_{ii} = \omega n_i \left[\eta_{d_i} + \sum_{j=1, j \neq i}^{m} \eta_{ij} \right]$$

Eqn [7] can be solved for the energies $\mathbf{E}$ to yield:

$$\mathbf{E} = [A]^{-1}\mathbf{P}$$

Estimate of the Response Parameters

The balance equations provide the values of the energies stored in each modal subsystem. From them the parameters of practical interest can be determined.

For a vibrating structure, the time-average energy doubles the kinetic average energy. In fact, it is:

$$E = T + U = 2 \cdot \frac{1}{2} M < v^2 >$$

where M is the total mass of the system and $< v^2 >$ the time- and space-averaged mean-square velocity of the vibrating system. Then, one can write:

$$< v^2 > = \frac{E}{M}$$

so that the mean-square velocity of the vibrating structure is determined.

For an acoustic cavity, the quantity of interest is the mean-square pressure, averaged in time and space. The energy stored in the acoustic cavity E can be linked to the energy density: $D = < p^2 > / \rho c^2$, where ρ is air density and c the speed of sound in air. Therefore one has:

$$E = DV = \frac{< p^2 >}{\rho c^2} \quad \Rightarrow \quad < p^2 > = \frac{E}{V}\rho c^2$$

Note that the solution of any SEA problem is a unique field value for the whole modal subsystem, so that any local variable distribution along the system is lost.

In **Figure 2** the measured third-octave band average sound transmitted from an engine into an automotive compartment is compared with the sound pressure level determined by SEA, together with two curves that would represent the values $\pm 2\sigma$ (σ standard deviation) of the SEA estimate.

Comments on SEA

SEA is supposed to be a statistical approach which is capable of describing the ensemble-average response of a whole population of similar systems rather than the dynamic behavior of a single case. However, it neither determines the ensemble-average response nor provides any kind of variance. Nor is any probabilistic distribution required to solve the problem in SEA terms. Actually, SEA estimates the frequency-average value of the energy response function of archetypal subsystems over frequency intervals (Fahy); the statistical elements of SEA can be recognized in: (1) the possibility of evaluating the modal densities by general descriptors such as the area (volume) of the structural (acoustic) subsystem, without the need to define the actual boundary conditions; (2) the use, as a global descriptor, of the time-average energy that is phase-independent; and (3) the use of mean quantities averaged in space, thus smoothing away unavoidable uncertainties and space fluctuations.

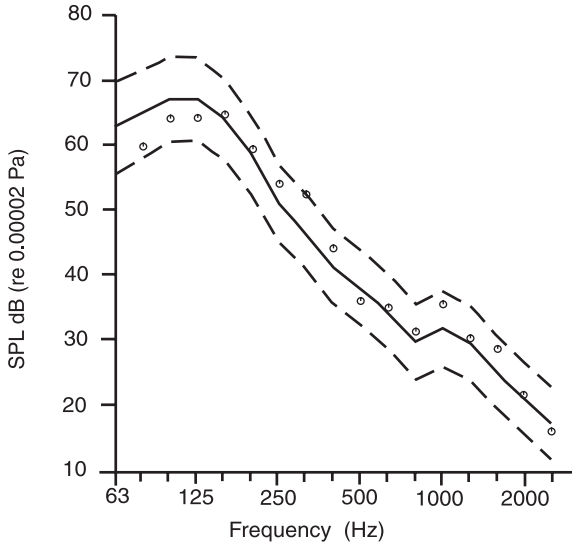


Figure 2 Sound pressure level (SPL) in an automotive compartment. Continuous line, SEA results; circles, measured results.

In this way SEA supplies an efficient and economic tool to analyze complex coupled dynamic systems, provided that its basic assumptions are verified, which is not easy to do *a priori*. However, while the balance equations are quite simple, it can be very troublesome to determine the whole set of parameters which are necessary to solve the problem in SEA terms: loss factors, coupled loss factors, modal densities, etc. Although recent developments based on the wave approach can yield most of these quantities, it is not yet easy to determine either theoretically or experimentally the large amount of input data necessary to solve a SEA problem. Moreover, the input power is never known practically (it depends on both the input excitation and the system response) and its estimate requires the development of mobility computations on equivalent infinite systems.

Finally, SEA provides results of poor informative content, represented by a space-average value on the whole domain of interest.

Notwithstanding these limitations, SEA is today the only approach which is capable of determining the solution of complex vibroacoustic problems at high frequencies, while supplying a quantitative estimate of the energy flows among the source and each subsystem. This is of paramount importance for the control engineer to perform appropriate actions, such as structural modifications on particular transmission paths.

In **Figure 3** the energy flows transmitted from the engine source to the automotive compartment through each modal subsystem are shown. It is evident that a primary action should be performed on the fire wall.

Alternative Methods to SEA

Although SEA dates from the early 1960s, it was a long journey to the 1990s when renewed interest pushed industrial and academic groups to cooperate to make SEA applicable to practical problems. In the meantime, new approaches were studied and new formulations proposed to provide valid explanations to the SEA assumptions, avoiding the uncertainties of SEA results, obtaining a local distribution rather than overall mean energy, covering the frequency gap between SEA and deterministic methods. This gap concerns the frequency bandwidth where the number of modes is too large for finite or boundary element methods but too low to yield accurate averages for SEA.

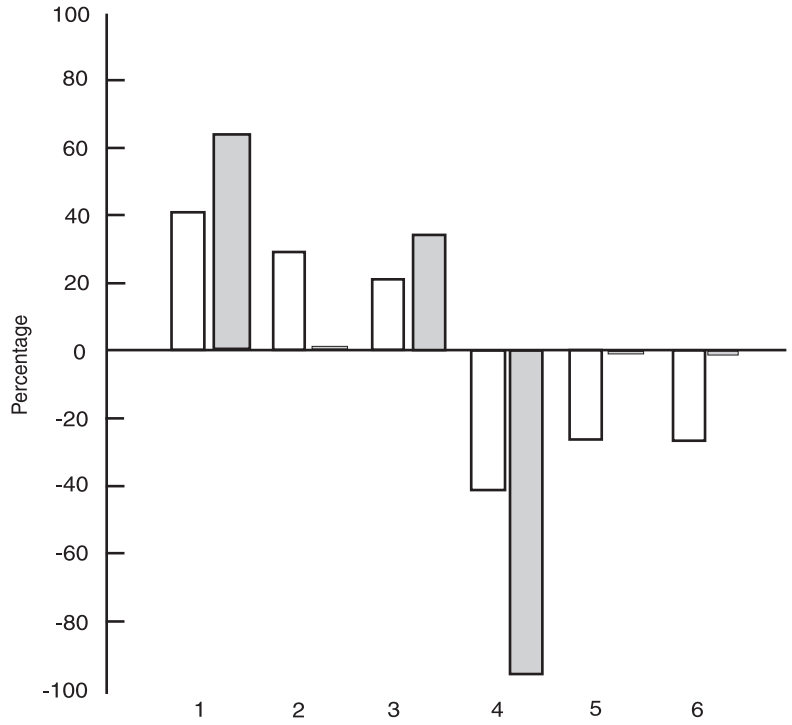


Figure 3 Energy flows into an automotive compartment. + in; − out; open columns, 63 Hz; filled columns, 2000 Hz. 1, Fire wall; 2, roof; 3, floor; 4, absorption; 5, windows; 6, other surfaces.

Among the other methods, asymptotic modal analysis (AMA) by Dowell and Kubota, wave intensity analysis (WIA) by Langley, the mean-value method by Skudrzyk, the thermal analogy methods by different groups of scientists (Nefske-Sung, Bernhard, Le Bot-Jezequel-Ichchou, etc.) and the complex envelope displacement analysis (CEDA) by Carcaterra and Sestieri deserve particular emphasis. Only some will be briefly described here.

Wave Intensity Analysis

WIA is a wave approach describing the high-frequency vibration response of elastic structures. In WIA the displacement field is regarded as a superposition of waves traveling along different directions θ, with proper amplitudes and phases. By assuming that the phase effects can be neglected, implying that the wave components are uncorrelated, the effects of resonances and anti-resonances related to the wave interactions in correspondence to in-phase and out-of-phase waves can be eliminated. From a modal point of view, this corresponds to perform modal averages on the response. When the phase dependence is eliminated, each wave is characterized by an energetic beam, corresponding to the mean energy of the traveling wave.

A power balance equation is consequently written for heading θ of each wave type j in the system that, in principle, can be solved to yield the wave energies $E_j(\theta, \omega)$. However, in WIA the problem is solved by expanding the angular dependency of the wave energy (the energy beam) into Fourier components, whose coefficients are obtained by a Galërk in procedure. In this way an algebraic linear equation is obtained that provides the unknown energies.

Langley determines a strict relationship between WIA and SEA. In fact, if the series expansion is arrested to the first term, the energy balance exactly provides the conventional SEA equations, i.e., WIA reduces to SEA, so that WIA can be considered a generalization of SEA. Moreover, the energy balance equations of WIA can be cast in the form of conventional SEA by adding nondirect coupling loss factors to circumvent the SEA assumption of diffuse vibrational field, and this can be prevented in the presence of structural joints.

Thermal Methods

Under the name thermal analogy or heat conductivity methods, a set of similar procedures have been identified. They represent an attractive alternative to SEA, able to provide a variable distribution along the structure. The thermal methods are derived by different modal and wave approaches and lead, for steady-state problems, to a parabolic equation that is much more convenient, from a numerical point of view,

than the wave equation governing any coupled problem. In fact, while the wave equation is hyperbolic and its solution is oscillatory in space with wave number increasing with the frequency of excitation, the parabolic thermal equation admits solutions exponentially decaying from the source, without oscillations. Thus, a coarse mesh can be used for the parabolic equation while a fine mesh is required for the wave equation at high frequencies.

The formal development of the thermal method was simply an extension of the SEA algebraic balance equations, which was valid for finite subsystems equipped with modes, into differential terms. Using the same relationship proposed in SEA for the dissipated power, and assuming that elemental volumes within any vibrating elastic medium exchange energy in direct proportion to their energy levels, a local energy balance equation provides:

$$\frac{\partial e}{\partial t} = -\nabla \cdot \mathbf{q} - \Pi_d$$

where e is the energy, $\mathbf{q}$ the intensity vector and Π_d the dissipated power. By the thermal assumption ($q = -\mu \,\mathrm{grad}(e)$) and considering a stationary process harmonically excited, one obtains the equation:

$$\nabla^2 E - \beta^2 E = 0 \qquad [8]$$

where E is the time-average energy.

This is analogous to the heat conductivity equation, as expected, being derived by the same SEA laws, and thus is called thermal analogy. Depending on how the problem is formulated, E is interpreted as local energy, averaged on time and on appropriate frequency bands, or as a local energy averaged in time and space.

Unlike a SEA result, the solution of this equation shows the energy variation along the system. In **Figure 4** a typical result for a damped beam is presented.

In a more recent and general procedure developed by Le Bot, Jezequel, Ichchou, and others, the thermal analogy is derived by a wave approach to describe a simplified energy propagation in dynamic systems. In this development it is assumed that no correlation exists between traveling waves. This concept is analytically formulated by assessing that the wave interference among waves propagating along different directions is negligible. Particularly it is assumed that, at high frequencies, the expected value between two wave phasors, associated with two general directions of propagation, $A(\theta_i)$ and $A(\theta_j)$, are uncorrelated, i.e.:

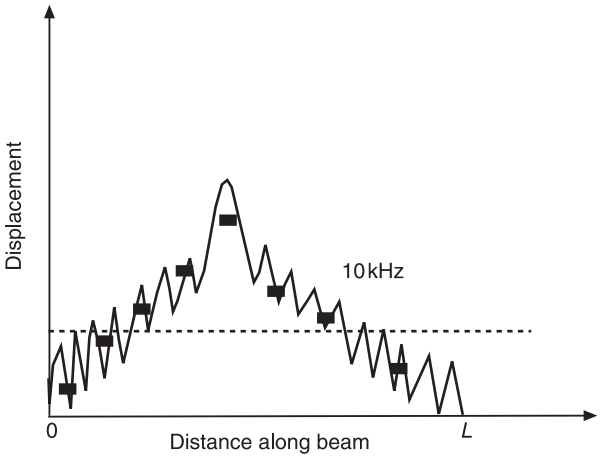


Figure 4 Comparison of a thermal analogy result (squares) with the exact (continuous line) and SEA (dashed line) solution.

$$E\{A(\theta_i)A^*(\theta_j)\} = 0$$

(E here stands for expected value). It is worthwhile pointing out that a similar assumption is introduced by Langley in developing the WIA.

Under this condition, and keeping the simplified assumptions made in the thermal analogy model, i.e.:

1. linear, elastic, dissipative system
2. steady-state conditions with harmonic excitation
3. far from singularities, evanescent waves are neglected

an energy model for symmetrical and nonsymmetrical structures is obtained. Particularly for plane waves the differential power balance equation is written as:

$$-\left(\frac{c_g^2}{\eta\omega}\right)\nabla^2 < E > + \eta\omega < E > = 0 \qquad [9]$$

where c_g is the group velocity of the plane waves, $< E >$ the time- and space-average of the energy density, and η the loss factor. One can simply verify that this equation is formally equivalent to the previous thermal equation and, consequently, presents the same numerical character. The solution of this equation is represented by a superposition of incident and reflected energies, whose amplitudes can be determined by boundary and joint energy conditions, involving energy flows that must be properly studied for any end and joint.

Several arguments have been developed in the recent literature to contrast the two derivations of the thermal analogy, and it is shown that both the simple extension of the SEA thermal laws or the possibility of neglecting the wave interference are not strictly correct. However, the results of the heat

conductivity approach are interesting and can be used as an approximate solution in many practical cases.

The Envelope Method

The envelope model tries to circumvent the theoretical limitations of the thermal methods, refusing the thermal analogy, while keeping the positive character of being independent of the frequency of excitation and providing a local description of the field variable. Since, for the envelope method standard procedures and successful applications were so far obtained for one-dimensional systems, we refer here to these simple systems.

The complex envelope displacement analysis can be achieved by a suitable transformation, through the action of an envelope operator $\mathbf{S}$ on the displacement w; that is:

$$\overleftarrow{w}(x) = \mathbf{S}[w(x)] = [w(x) + j\tilde{w}(x)]\,\mathrm{e}^{-jk_0x} \qquad [10]$$

where $\overleftarrow{w}$ represents the complex envelope displacement, j is the imaginary unit, ω_0 the exciting circular frequency, $k_0 = \omega_0/c$ the carrier wave number, and $\tilde{w}$ the Hilbert transform of the physical displacement w. The upper arrow $\leftarrow$ indicates that the envelope variable is obtained by a shift, in the space spectrum, of the analytical signal $(w + j\tilde{w})$ to the left toward the origin of wavenumbers.

By applying the envelope operator to the physical equation of motion of a general undamped structure, described by a self-adjoint differential operator $\mathbf{L}$, harmonically excited with frequency ω_0, i.e.:

$$\mathbf{L}[w(x)] + m\omega_0^2 w(x) = g(x)$$

one obtains:

$$\overleftarrow{\mathbf{L}}\left[\overleftarrow{w}(x)\right] + m\omega_0^2\overleftarrow{\omega}(x) = \overleftarrow{g}(x) = [g(x) + j\tilde{g}(x)]\,\mathrm{e}^{-j_0kx} \qquad [11]$$

This equation provides the new governing equation for the envelope displacement, that is formally identical to the equation of motion, provided that the physical displacement, the structural operator, and the external load are substituted by the corresponding envelope terms. $\overleftarrow{\mathbf{L}}$ is the new structural envelope operator defined as $\overleftarrow{\mathbf{L}} = \mathbf{SLS}^{-1}$, $\mathbf{S}^{-1}$ being the inverse envelope operator that provides the physical displacement from the complex envelope displacement, i.e.:

$$w(x) = \mathbf{S}^{-1}\left[\overleftarrow{w}\right] = \mathrm{Re}\left\{\overleftarrow{w}(x)\mathrm{e}^{jk_0x}\right\} \qquad [12]$$

Therefore, if necessary, one can recover the physical displacement, once the envelope displacement is obtained. This possibility is denied to any other method that uses the energy as field descriptor (SEA or thermal methods).

Moreover, thanks to eqn [12], the solution of the envelope equation can be obtained by using directly the boundary conditions of the physical problem. Therefore, unlike the thermal method, the boundary and joint conditions can be achieved very easily.

As an example, if one considers the equation of a longitudinal rod ($\mathbf{L} = (\partial^2/\partial x^2)$), i.e.:

$$\frac{\partial^2}{\partial x^2}w(x) + k_0^2 w(x) = g(x)$$

the second-order envelope equation is obtained:

$$\frac{\partial^2}{\partial x^2}\overleftarrow{w}(x) + 2jk_0\frac{\partial}{\partial x}\overleftarrow{w}(x) = \overleftarrow{g}(x)$$

The envelope operator provides a convenient transformation in the wave number domain. In fact, if the physical displacement is band-limited around the carrier wave number k_0 – a condition that is typically obtained for a point load or for a general uniform load, the complex envelope displacement is band-limited around the wave numbers' origin. To understand this point, consider the wave number spectrum of the physical displacement concentrated in two regions around $\pm k_0$ (**Figure 5A**). The Fourier transform of the analytic displacement $\hat{w} = (w + j\tilde{w})$ is given by:

$$\hat{W}(k) = W(k) + j\tilde{W}(k) = W(k) + \mathrm{sign}(k)\,W(k)$$

It has a spectrum with the negative contribution of $W(k)$ deleted, while the positive one is doubled (**Figure 5B**). Now, by performing the Fourier transform of the complex envelope displacement, one obtains $\overleftarrow{W}(k) = \hat{W}(k + k_0)$, implying a shift of $\hat{W}(k)$ towards the origin of wave numbers (**Figure 5C**). This situation is very convenient from a numerical point of view. In fact, the Nyquist criterion suggests that a correct sampled signal can be obtained using a sampling frequency (wave number) that doubles, at least, the maximum frequency (wave number) of the signal. While the highest wave number of the physical displacement is $k_0 + \Delta$, the highest wave number of the envelope displacement is just Δ, so that a much lower number of samples can be used for high-frequency excitation.

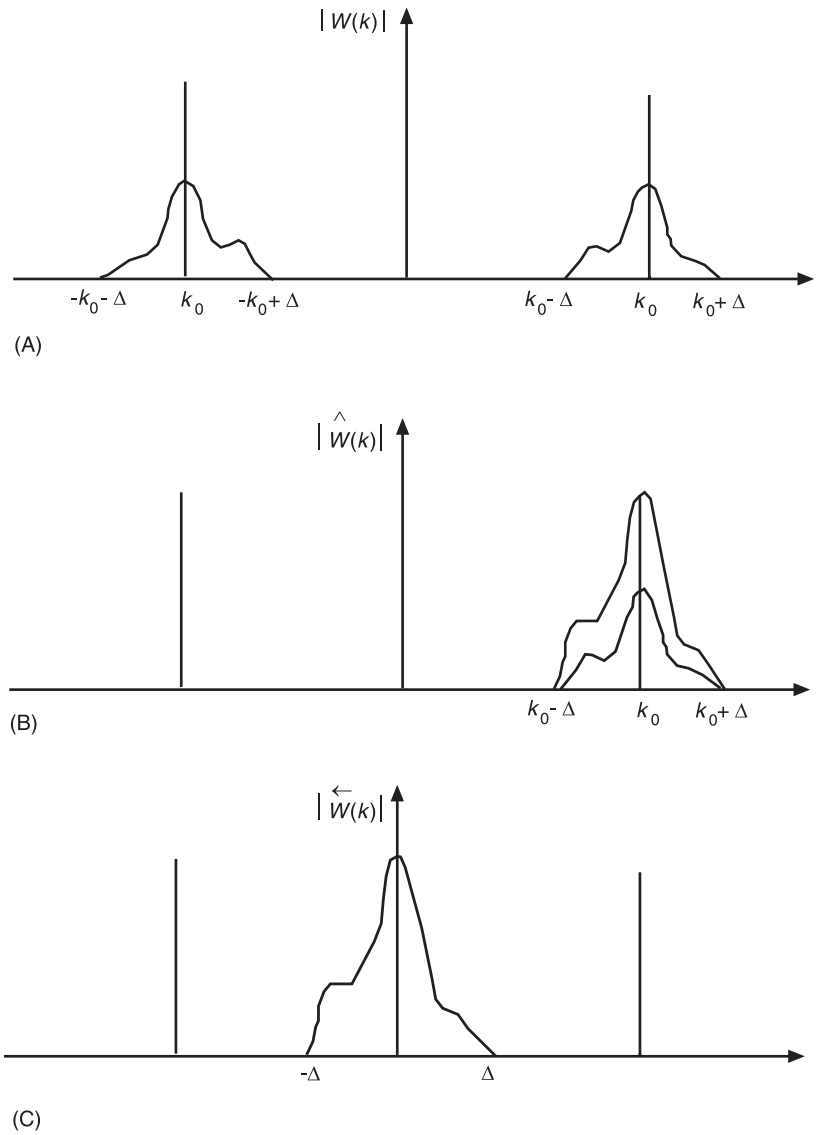


Figure 5 Fourier transform of the physical (A), analytic (B), and complex envelope displacement (C).

Therefore, the rapidly oscillating physical displacement is transformed, by the envelope operator, into a slowly oscillating solution that can be computed by a coarse number of sampled points. Moreover, due to the inverse property of the envelope operator, the physical displacement can be recovered, if required, from the envelope displacement.

Another important character of the CEDA procedure relies on the forcing term of the governing equation. Unlike in SEA or the thermal methods where the input term is the power entering the system, the input term in the envelope equation can be directly determined from the physical load, with inherent advantage.

A typical solution provided by CEDA is compared in **Figure 6** with the physical solution. In **Figure 7** the solutions of two flexural problems are presented. The cases of a beam excited by a single point force and by two point forces are respectively considered and the figure shows the comparison between the analytical and CEDA solutions, after reconstruction of the physical displacements.

Nomenclature

c	speed of sound
c_g	group velocity
e	energy
g	external load
$\hat{g}$	analytic load $g + j\tilde{g}$
$\tilde{g}$	Hilbert transform of the physical load
$\overleftarrow{g}$	complex envelope load
k	wave number
m	generalized mass density

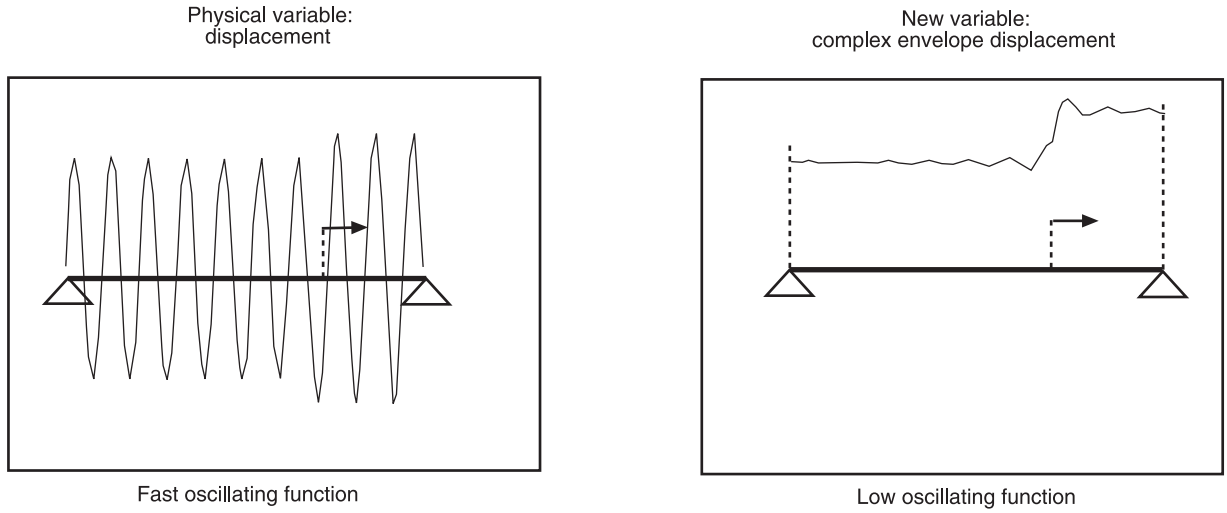


Figure 6 Physical versus CEDA solution of a wave guide.

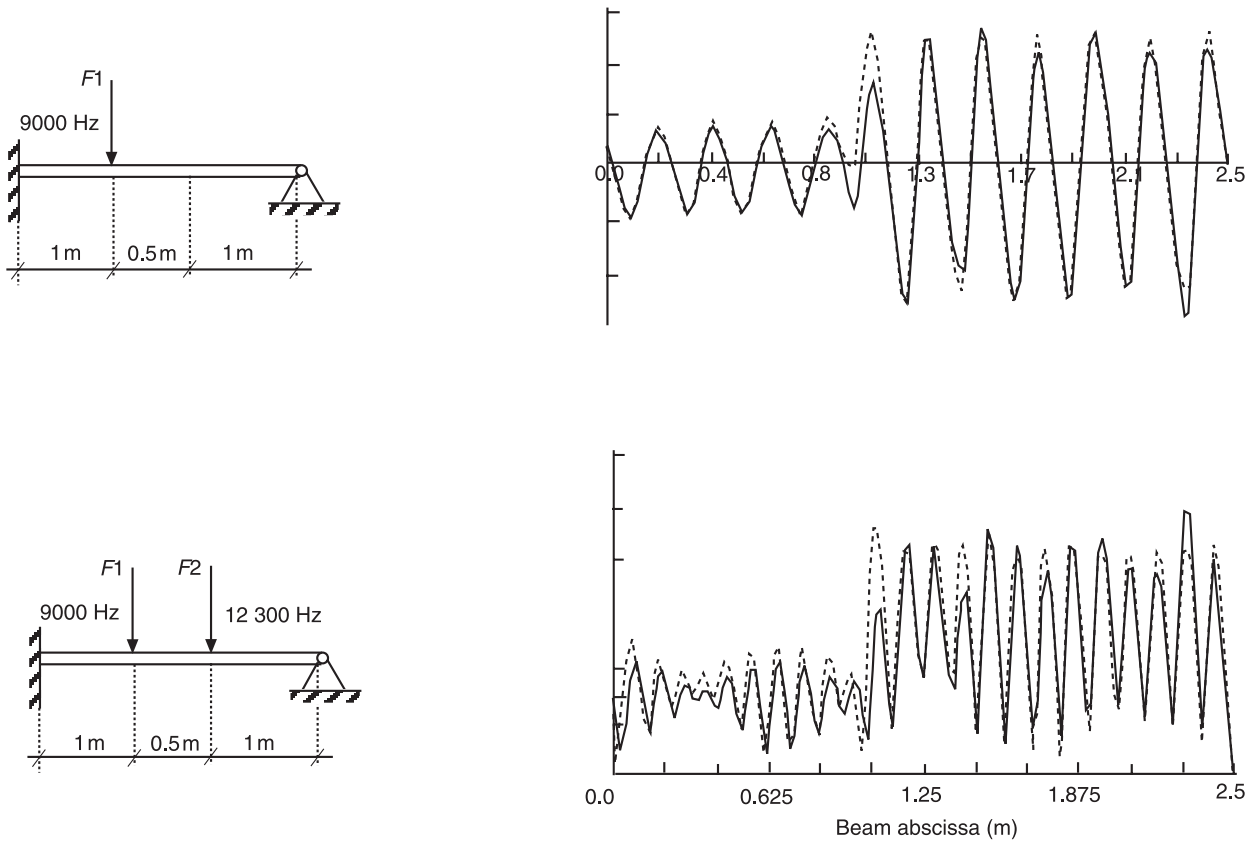


Figure 7 Comparison between the physical (solid line) and recovered solution from CEDA (dashed line) for two flexural beams.

n	modal density	w	displacement
p	acoustic pressure	$\hat{w}$	analytic displacement $w + j\tilde{w}$
$\langle p^2 \rangle$	time- and space-averaged mean square pressure	$\tilde{w}$	Hilbert transform of the physical displacement
v	velocity	$\overleftarrow{w}$	complex envelope displacement
$\langle v_2 \rangle$	time- and space-averaged mean square velocity	$\mathbf{q}$	intensity vector
		D	time-average energy density

E	time-average energy
$\underline{\mathbf{L}}$	structural operator
$\underleftarrow{\mathbf{L}}$	complex envelope of the structural operator
$\mathbf{S}$	envelope operator
P^{in}	time average input power
P_d	time-average dissipated power
P_{ij}	time-average power exchanged between subsystems i and j
T	kinetic energy
U	potential energy
M	mass of the subsystem
W	Fourier transform of the physical displacement
$\hat{W}$	Fourier transform of the analytic displacement
$\tilde{W}$	Fourier transform of the Hilbert transform
$\underleftarrow{W}$	Fourier transform of the complex envelope displacement
η_d	loss factor
η_{ij}	coupling loss factor between subsystems i and j
ω	circular frequency
ω_0	exciting circular frequency
ρ	air density

See also: **Fluid/structure interaction**; **Mode of vibration**; **Structure-acoustic interaction, low frequencies**; **Wave propagation**, Guided waves in structures; **Wave propagation**, Interaction of waves with boundaries; **Wave propagation**, Waves in an unbounded medium.

Further Reading

Cremer L, Heckl M and Ungar EE (1988) *Structure-borne Sound*. Berlin: Springer-Verlag.

Fahy FJ (1994) Statistical energy analysis: a critical overview. In: Keane AJ and Price WG (eds) *Statistical Energy Analysis. An Overview with Applications in Structural Dynamics*. Cambridge, UK: Cambridge University Press.

Lyon RH (1975) *Statistical Energy Analysis of Dynamical Systems: Theory and Applications*. Cambridge, MA: MIT Press.

Nefske DJ and Sung SH (1987) Power flow finite element analysis of dynamic systems: basic theory and application to beams. In: Hsu KH, Nefske DJ and Akay A (eds) *Statistical Energy Analysis*. New York: American Society of Mechanical Engineering.

Norton MP (1989) *Fundamentals of Noise and Vibration Analysis for Engineers*. Cambridge, UK: Cambridge University Press.

STRUCTURE-ACOUSTIC INTERACTION, LOW FREQUENCIES

A Sestieri, Università Degli Studi di Roma, Roma, Italy

Copyright © 2001 Academic Press

doi:10.1006/rwvb.2001.0153

An important effect of vibrations is that of producing sound, although sound can also be generated by other mechanisms such as density fluctuations of nonstationary flows (turbulence, jets, etc.) and heat. Depending on whether the sound is considered pleasant or not, it is called music or noise.

The subject of vibroacoustics is the interaction between structural motion and acoustic field. As such it involves a large range of frequencies, i.e., the bandwidth 20–20 000 Hz of human hearing. In dealing with vibroacoustics, where analytical solutions are generally not available, either an external or internal problem is considered and, for each, a low-, medium-, and high-frequency range is studied differently. The need for this subdivision relies on different approaches that are used for the numerical solution of each problem: the external problem is related to an infinite medium, typically characterized by fluid wave propagation, while the internal one is commonly described by acoustic eigenmodes or stationary waves. The numerical solution of an external problem is generally more demanding than an internal one if a traditional discretization of the acoustic medium is used, because it is necessary to discretize the whole region between the source and the receiver. The internal problem, especially when related to transportation vehicles, concerns relatively small cavities and, thus, a more limited number of degrees of freedom than the external problem.

With respect to frequencies, the low region involves large wavelengths ($\lambda = c/f$, where λ is the wavelength, c the speed of sound in the medium, and f the frequency considered), while the opposite is

expected for high frequencies. From a numerical point of view, large wavelengths imply a coarse discretization while short wavelengths demand fine meshes. Evidently a strict border among low, medium, and high frequencies does not exist, in that these regions are related to the ratio between the dimensions of the acoustic domain and the involved structural–acoustic wavelengths.

In this article the low-frequency problem is considered, while the companion article **Structure-acoustic interaction, high frequencies** describes the high-frequency case.

The wave and modal approaches to the problem are developed here, together with the most common numerical techniques related to them, i.e., the finite element method and the boundary integral methods. The ray approach is not considered because it cannot account for the interaction between vibrating structures and fluid, while it is frequently used for the design of large rooms, such as auditoriums and concert halls.

Acoustic Waves

The linearized wave equation, describing the propagation of small perturbations in a homogeneous, inviscid, and compressible fluid, is obtained by combining together the continuity equation, the momentum equation, and the elastic properties of the fluid. They are, respectively:

$$\frac{\partial p}{\partial t} + \rho_0 \operatorname{div} \mathbf{u} = 0$$

$$\rho_0 \frac{\partial u}{\partial t} + \operatorname{grad} p = 0$$

$$\frac{\partial p}{\partial \rho} = c^2$$

the last being valid for an adiabatic transformation, ρ is the fluid density (ρ_0 undisturbed), $\mathbf{u}$ the vector of components u_x, u_y, and u_z, representing the fluid particle velocity, p the acoustic pressure (varying with respect to the undisturbed pressure) and c, the speed of sound.

By combining together these equations one obtains the three-dimensional wave equation:

$$\nabla^2 p - \frac{1}{c^2}\frac{\partial^2 p}{\partial t^2} = 0$$

When dealing with steady-state problems, the Helmholtz equation is obtained from this by considering a harmonic time dependence of p, i.e.:

$$\nabla^2 p + k^2 p = 0 \qquad [1]$$

where $p = p(x, y, z, w)$ and $k = \omega/c$ is the fluid wave number.

The solution of the Helmholtz equation can be specified for different problems, by imposing appropriate boundary conditions. Assuming harmonic motion, the momentum equation provides directly a relationship between the pressure gradient and the fluid particle velocities: in particular the normal velocity of a vibrating surface determines the pressure gradient on the surface, due to the compatibility condition of normal velocities at the fluid–structure interface. For example, assuming the surface on the plane xz vibrating with velocity u_y, one has:

$$\left.\frac{\partial p}{\partial y}\right|_{y=0} = -j\omega\rho_0 u_y\big|_{y=0}$$

This is the type of condition used in problems of sound radiation to describe vibrating, reflecting, or absorbing surfaces. In particular, by indicating with $\mathbf{n}$ the unit normal vector outward to the surface, one has:

1. for rigid surfaces (totally reflecting):

$$\frac{\partial p}{\partial n} = 0$$

2. for vibrating surfaces with velocity v (displacement w):

$$\frac{\partial p}{\partial n} = -j\omega\rho_0 v = \rho_0 \omega^2 w$$

3. for absorbing surfaces:

$$\frac{\partial p}{\partial n} = -\frac{j\omega\rho_0 p}{Z_A}$$

where Z_A is the specific acoustic impedance of the absorbing material (which is known).

Note that $\mathbf{n}$ has a different orientation depending on whether an internal or external acoustic problem is considered (see **Figure 1**)

Interaction Between Sound Waves and Vibrating Structures

While fluids can only sustain compressional waves, solids can store energy in shear and compression.

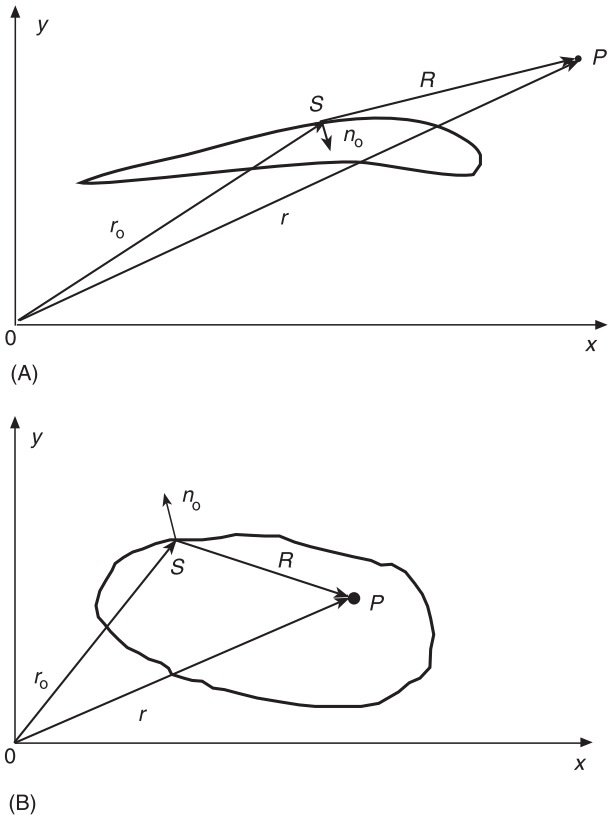


Figure 1 Source and observation points in (A) the external and (B) internal problem.

However, an effective exchange of energy between structure and fluid is only generated from structural flexural waves, because it is only in this case that the structural particle velocities are orthogonal to the direction of the fluid wave propagation.

In general, the fluid–structure interaction implies the contemporary solution of the equations governing both the structural and acoustic phenomena. In fact the (flexural) vibrating structure generates fluctuating pressures in the fluid, so that the Helmholtz equation must be solved with suitable boundary conditions specifying the motion of the vibrating surfaces. On the other hand, especially if the fluid is a liquid, the pressure produced in the fluid can significantly affect the structural motion and, in this case, a full coupled analysis is necessary, i.e., one should load the structure with the external exciting pressure and the acoustic pressure generated in the fluid.

However, if the fluid is air, as in most of structural–acoustic interaction problems, this requirement is not compulsory because the acoustic pressure is not sufficient to modify the structural motion. In this case only the effect of the vibrating surface on the acoustic medium must be considered, disregarding fluid-loading effects: therefore, first the structural problem excited by the external load is solved and then the structural solution is used as a boundary condition for the acoustic problem.

Numerical Solution of Vibroacoustic Problems

The great advantage of an analytical solution is the possibility of having a direct dependence of the solution on the physical parameters. On the other hand, in most cases an analytical solution is not available due to the complexity of geometrical, kinematic, and dynamic conditions.

The problems of practical interest in vibroacoustics can be divided into two main categories:

1. analysis of free and forced vibration of the fluid in a cavity
2. analysis of the acoustic field in an infinite medium, induced by vibrating surfaces

In any numerical analysis, the field variables that are continuous in the region of the elastic medium are represented by their values at discrete points in space (discretization), together with shape functions, providing an interpolation of the field parameters among these points.

The numerical analysis of sound fields in closed spaces (internal problem) at low frequencies is generally developed by the finite element method, as in the case of the structural problem.

For infinite regions, and often even for internal problems, the finite element method is not appropriate, and it is convenient to develop a boundary formulation that, from the Helmholtz differential equation, produces an integral equation. This equation is then solved numerically by the boundary element method or by Succi's method.

The Finite Element Method

The finite element method can be applied to any physical problem described by partial differential equations. This approach is widely described in other sections (**Finite element methods**; **Object oriented programming in FE analysis**; **Damping in FE models**). Consequently, only a brief summary will be presented here with some notes on the acoustic problem.

In the finite element method the space is divided into contiguous finite elements of appropriate shape, whose dimensions must be lower than the wavelength of the involved wave at the highest frequency of interest. At the element nodes suitable degrees of freedom are defined. They are the values of the field

variables at the nodes and, when they are needed to define the problem fully, their spatial derivatives, as in the case of the flexural vibrations of beams, where at each node both displacement and rotation must be considered.

For the analysis of structural or fluid vibrations, as well as for their interaction, the Lagrange equations are used. The potential and kinetic energies associated with each element can be expressed in terms of the nodal variables, provided that the distribution of the field variables among the nodal points is appropriately assumed. The spatial distribution of the field variables (shape functions) must be defined in a way that is simple, yet capable of satisfying continuity conditions at the nodes. Depending on the problem considered, an appropriate function is associated with each degree of freedom and put in a vector $\mathbf{f}(\mathbf{x})$ of shape functions.

For a general structure excited by a distributed load $\bar{g}$, the independent variables at each node of an element are defined and put in an element vector $\mathbf{q}_e$, so that, by means of the shape functions, one can write the general field variable (e.g., $w(\mathbf{x})$) as:

$$w(\mathbf{x}) = \mathbf{f}(\mathbf{x})^{\mathrm{T}}\mathbf{q}_e \qquad [2]$$

where $\mathbf{x} = x\mathbf{i} + y\mathbf{j} + z\mathbf{k}$.

The potential and kinetic energies of each element of the general structure are given by:

$$U_e = \frac{1}{2}\int_D \boldsymbol{\sigma}^{\mathrm{T}}\boldsymbol{\varepsilon}\,\mathrm{d}D \qquad T_e = \frac{1}{2}\int_D m(\mathbf{x})\dot{w}^2\,\mathrm{d}D$$

where $\boldsymbol{\sigma}$ and $\boldsymbol{\varepsilon}$ are the stress and strain tensors, respectively, m is the mass per unit volume of the structure and D the structural domain. Both $\boldsymbol{\sigma}$ and $\boldsymbol{\varepsilon}$ can be expressed in terms of the nodal variables by using the strain and elasticity matrices:

$$\boldsymbol{\varepsilon} = \mathbf{B}\mathbf{q}_e \qquad \boldsymbol{\sigma} = \mathbf{D}\boldsymbol{\varepsilon} = \mathbf{D}\mathbf{B}\mathbf{q}_e$$

where $\mathbf{B}$ depends on the shape functions. This permits the energies and the generalized force vector to be expressed in terms of the assumed degrees of freedom, i.e.:

$$U_e = \frac{1}{2}\mathbf{q}_e^{\mathrm{T}}\mathbf{K}_e\mathbf{q}_e \quad T_e = \frac{1}{2}\dot{\mathbf{q}}_e^{\mathrm{T}}\mathbf{M}_e\dot{\mathbf{q}}_e \quad \mathbf{F}_e = -\int_D \mathbf{f}^{\mathrm{T}}\bar{g}\,\mathrm{d}D$$

where:

$$\mathbf{K}_e = \int_D \mathbf{B}^{\mathrm{T}}\mathbf{D}\mathbf{B}\,\mathrm{d}D \qquad \mathbf{M}_e = \int_D m(\mathbf{x})\mathbf{f}\mathbf{f}^{\mathrm{T}}\mathrm{d}D$$

are the symmetric stiffness and mass matrices of the element, respectively. By means of the element matrices, the matrices of the assembled system can be determined by sum, after the definition of a dummy matrix linking together the degrees of freedom $\mathbf{q}_e$ of each element with the degrees of freedom $\mathbf{q}_s$ of the whole system, i.e.:

$$\mathbf{q}_e = \mathbf{C}_e\mathbf{q}_s$$

Therefore the potential and kinetic energies of the whole system can be written as:

$$U = \frac{1}{2}\mathbf{q}_s^{\mathrm{T}}\mathbf{K}\mathbf{q}_s \qquad T = \frac{1}{2}\dot{\mathbf{q}}_s^{\mathrm{T}}\mathbf{M}\dot{\mathbf{q}}_s$$

where $\mathbf{K}$ and $\mathbf{M}$ are the stiffness and mass matrices of the assembled system. They are respectively:

$$\mathbf{K} = \sum_{e=1}^{n}\mathbf{C}_e^{\mathrm{T}}\mathbf{K}_e\mathbf{C}_e \qquad \mathbf{M} = \sum_{e=1}^{n}\mathbf{C}_e^{\mathrm{T}}\mathbf{M}\mathbf{C}_e$$

By applying the Lagrange equation, the discretized equation of motion is obtained:

$$\mathbf{M}\ddot{\mathbf{q}}_s + \mathbf{K}\mathbf{q}_s = \mathbf{F} \qquad [3]$$

where $\mathbf{F}$ is the generalized force vector ($= \Sigma_e\mathbf{F}_e$). Finally, the geometrical boundary conditions must be imposed. Now the discrete problem can be solved by a classical modal analysis or numerical integration.

The extension of the finite element method to the acoustic (internal) problem is straightforward.

The potential and kinetic energies of an acoustic field element V_e are given by:

$$U_e = \frac{1}{2}\int_{V_e} p^2/\rho c^2\,\mathrm{d}D$$
$$T_e = \frac{1}{2}\rho_0\int_{V_e} |\mathbf{u}|^2\,\mathrm{d}D \qquad [4]$$

where p is the acoustic pressure, $p^2/\rho c^2$ the energy density, c the speed of sound, and $\mathbf{u} = u_x\mathbf{i} + u_y\mathbf{j} + u_z\mathbf{k}$ the velocity of the air particles. It is convenient to rewrite both of these energies in terms of the same field variable (either pressure or velocity). Pressure is the most suitable because it is a

scalar. Therefore, by considering a harmonic problem, T can be transformed by means of the momentum equation to yield:

$$T_e = \frac{1}{2\rho_0\omega^2}\int_{V_e}\left[\left(\frac{\partial p}{\partial x}\right)^2+\left(\frac{\partial p}{\partial y}\right)^2+\left(\frac{\partial p}{\partial z}\right)^2\right]\mathrm{d}V_e$$

From this point on, the finite element formulation of the acoustic problem follows the steps shown for the structure, leading to an equation analogous to eqn [3].

For a coupled structural–acoustic problem, the energies can be written as the sum of the energies of the whole dynamic system. However, since a full coupling is usually not necessary, the structural problem is separated from the acoustic one; the result of the structural problem is used as boundary condition for the acoustic field.

Boundary Integral Formulation for the Structural–Acoustic Problem

The Helmholtz differential equation can be transformed into an integral equation (Kirchoff–Helmholtz), with inherent advantages in solving the coupled problem.

To pass from the differential to the integral form, the Green function must be used. First we will speak about the free-space Green function leading to the boundary element formulation and then the cavity Green function leading to the Succi method.

The free-space Green function $G_\infty(r/r_0)$ for the Helmholtz equation is the solution of the equation:

$$\nabla^2 G_\infty(r/r_0) + k^2 G_\infty(r/r_0) = -\delta(r-r_0) \qquad [5]$$

satisfying the Sommerfeld condition at infinity that prevents reflected waves, because of the lack of reflecting surfaces at infinity. r and r_0 are the distances, from the origin of a reference frame, of the observer P and the source S, respectively (**Figure 1**). δ is Dirac's delta function, representing a point source in the space, located in r_0. In practice, Green's function is a particular solution of the Helmholtz equation forced by a point source. It can be demonstrated that the free-space Green function for the three-dimensional Helmholtz problem is:

$$G_\infty = \frac{1}{4\pi R}\mathrm{e}^{-jkR} \qquad [6]$$

where $R = |r - r_0|$ is the distance between source and receiver. Note that G_∞ and $\delta(r-r_0)$ are symmetric when source (r_0) and receiver (r) are interchanged.

To show the utility of the Green function, consider the Helmholtz eqn [1]. By multiplying eqn [5] by p and eqn [1] by $G_\infty(r/r_0)$, and subtracting, one obtains:

$$G_\infty(r/r_0)\nabla^2 p(r) - p(r)\nabla^2 G_\infty(r/r_0) = p(r)\delta(r-r_0)$$

By integrating on the fluid medium V, exchanging r and r_0, and recalling the symmetry property of G and δ, one has:

$$\int_V \left[G_\infty(r/r_0)\nabla_0^2 p(r_0) - p(r_0)\nabla_0^2 G_\infty(r/r_0)\right]\mathrm{d}V = \int_V p(r_0)\delta(r-r_0)\,\mathrm{d}V$$

where the subscript 0 denotes derivation with respect to the coordinates x_0, y_0 and z_0 of the source. Using Green's theorem, the first integral on the volume becomes an integral over the boundary surface of the fluid, thus:

$$p(r) = \int_{S_0}\left[G_\infty(r/r_0)\frac{\partial}{\partial n_0}p(r_0) - p(r_0)\frac{\partial}{\partial n_0}G_\infty(r/r_0)\right]\mathrm{d}S_0 \qquad [7]$$

where $r_0 \in S_0$, $r \in V$. Any possible condition on the surfaces can be stated by imposing the boundary conditions through $\partial p/\partial n$. This integral equation provides the value of the pressure $p(r)$ in any point of the fluid medium, as a function of the pressure $p(r_0)$ on the surface. n_0 is the normal outward to the surface at the source point (**Figure 1**). Since $G_\infty(r/r_0)$ is the pressure value in r produced by a point source in r_0, eqn [7] states that the pressure field in r is just the sum of the pressures produced by all the elementary sources located on the vibrating surface.

Unfortunately, the problem cannot be solved in this form because neither the surface pressure $p(r_0)$ nor the pressure at the observation point $p(r)$ is known.

To circumvent this drawback, let the observation point P tend to the surface, so that this point becomes a point on the surface. Then the problem has a single unknown, the pressure distribution on the surface $p(r_0)$, and the integral equation can be solved.

However it must be stressed that, when r tends to the surface, the integrals in eqn [7] become singular for $r \equiv r_0$. It is then necessary to determine the limit of the integrals computed on a surface that excludes a small area around the singular point. This can be done by means of the Gauss integral, and it can be shown that this yields the new equation:

$$\frac{1}{2}p(r_0) = -\int_S \left[p(r_0)\frac{\partial}{\partial n_0}\left(\frac{e^{-jkR}}{4\pi R}\right) - \frac{e^{-jkR}}{4\pi R}\frac{\partial p}{\partial n_0}\right] dS_0 \quad [8]$$

where the explicit expression [6] of the free-space Green function is written instead of G_∞.

In general, the constant that multiplies $p(r_0)$ on the left-hand side is $\beta(r_0)/4\pi$, where β is the solid angle at the point r_0. If the tangent plane exists in r_0, $\beta = 2\pi$ and the constant is just $\frac{1}{2}$ as in the considered equation.

Eqn [8] is the fundamental equation of the integral formulation. It can be solved after having determined the vibrating velocity on the surface. Once $p(r_0)$ is known, eqn [7] can be used to determine the pressure at any point of the external field, by the simple solution of an algebraic problem.

Solution of the External Problem: The Boundary Element Method

For an external problem – the case of a vibrating surface in an infinite medium – the free-space Green function must be used and eqn [8] must be solved with the boundary conditions expressed by $\partial p/\partial n = -j\omega\rho_0 v_n(r_0)$, where $v_n(r_0)$ is the normal velocity at any point of the surface, determined, for example, by a finite element method.

It is obvious that, in general, the integral eqn [8] can be tackled only numerically: the corresponding approach is called boundary element method. To this aim the vibrating surface is subdivided into surface elements of suitable dimensions, depending on the maximum frequency of analysis, as in the finite element method. The field variables can be described by appropriate shape functions: however, for the acoustic problem, a zeroth-order approximation can be used, i.e., the field variables (pressure and velocity) can be assumed constant on each element, thus obtaining a piecewise constant variation of the variables along the surface elements.

By dividing the vibrating surface in such a way, the integral equation can be substituted by the following algebraic problem:

$$p_k + \frac{1}{2\pi}\sum_{i=1}^{n} p_i \int_{S_i} \frac{\partial}{\partial n_{0_i}}\left(\frac{e^{-jkR_i}}{R_i}\right) dS_i = -\frac{1}{2\pi}\sum_{i=1}^{n} j\omega\rho_0 v_{n_i} \int_{S_i} \frac{e^{-jkR_i}}{R_i} dS_i \quad k = 1, 2, \ldots n \quad [9]$$

where the right-hand side term is known. S_i is the surface of the ith boundary element, n_{0_i} is the normal outward to the ith surface element and R_i is the distance between the kth element and any other element i of the surface (k observation point). This is now an algebraic system $n \times n$, n being the number of boundary elements, that provides the pressure value on each boundary element. This equation can be written in matrix form as follows:

$$\mathbf{p}(\omega) + \mathbf{T}(\omega)\mathbf{p}(\omega) = \mathbf{f}(\omega)$$

i.e.:

$$[\mathbf{I} + \mathbf{T}(\omega)]\mathbf{p}(\omega) = \mathbf{f}(\omega)$$

with the symbols having obvious meaning. Note that both the matrix $\mathbf{T}$ (i.e., the coefficient matrix accounting for the integrals on the left-hand side) and the vector $\mathbf{f}$ (expliciting the integrals on the right-hand side) depend on ω, which implies a recomputation of the integrals in eqn [9] every time ω changes, and this is rather time-consuming.

Solution of the Internal Problem

The internal problem implies the computation of the acoustic pressure in a cavity in which some (or all) surfaces vibrate and radiate sound inward. Only the internal field is considered. Here two different numerical approaches are possible.

The Boundary Element Method

The formulation is analogous to the external problem, and the same free-space Green function G_∞ can be used, because reflecting waves are superimposed on the outgoing waves by making explicit the corresponding boundary conditions of the cavity's surfaces. First, the problem is solved on the cavity's surface, then, the acoustic pressure in the cavity is determined as a function of the surface pressures.

However, for the internal problem, instead of using the free-space Green function, it is more convenient to use the real part of G_∞, i.e.:

$$G_R(r/r_0) = \frac{1}{4\pi R}\cos kR$$

In fact, for the internal problem the imaginary part of G_∞ is not influential, i.e., no information derives from its contribution to the integral formulation. The main advantage of this form of Green function is the following: when using G_R, the harmonic parts of G_R and its derivative:

$$\frac{\partial G_R}{\partial n} = -\frac{1}{4\pi R^2}\cos kR \cdot \cos\widehat{nR} - \frac{1}{4\pi R}\sin kR \cdot \cos\widehat{nR}$$

do not change appreciably in the integrals of eqn [9] with varying ω: therefore it is possible to carry out the harmonic parts from the integrals and compute the integrals only once. In this way, the time computation can be noticeably reduced. This choice cannot be used for G_∞ because the phases of the resulting pressure are greatly affected by this approximation.

The Succi Method

For the internal problem the possibility exists of using another form of Green function, the cavity Green function, that is obtained from eqn [3] with the boundary conditions on the cavity surfaces.

The most important difference between the acoustic pressure in a cavity and in an infinite medium is the existence, for the closed space, of acoustic modes associated with natural frequencies, as in the case of structures. They are the effect of interference between propagation waves that give rise to stationary waves. Therefore, the fluid in a cavity exhibits a resonant behavior, whose effect is that of producing a large response in correspondence to the natural acoustic frequencies.

The cavity Green function can be expressed in terms of the acoustic modes and natural frequencies (or natural wave numbers), as follows:

$$G_c(r/r_0) = \sum_n \frac{\Psi_n(r)\Psi_n(r_0)}{\Lambda_n\left(k_n^2 - k^2\right)} \qquad [10]$$

where n is the number of acoustic modes $\Psi_n(r)$, $k = \omega/c$, $k_n = \omega_n/c$ are the natural wave numbers, and Λ_n is a normalization factor for the acoustic eigenfunctions, i.e.:

$$\int_V \Psi_m(r)\Psi_n(r)\,\mathrm{d}V = \delta_{mn}\Lambda_n \qquad [11]$$

where δ_{mn} is the Kronecker delta ($\delta_{mn} = 1$ for $m = n$, $\delta_{mn} = 0$ for $m \neq n$).

If, for a cavity of any shape, we know the acoustic modes and natural wave numbers, the problem would be immediately solved because p could be obtained by series expansion of the known eigenfunctions. Unfortunately, for any complex cavity, the computation of its eigenparameters can only be achieved numerically.

Therefore, in Succi's method, the given cavity (e.g., an automobile compartment) is enclosed in a simpler cavity whose eigenfunctions are known, e.g., a rectangular volume with rigid surfaces (**Figure 2**).

The eigenfunctions of this cavity are given by:

$$\Psi_i(x,y,z) = \Psi_{nmp}(x,y,z) = \cos\frac{n\pi x}{a}\cos\frac{m\pi y}{b}\cos\frac{p\pi z}{c}$$

where Ψ_i replaces Ψ_{nmp} for the sake of simplicity.

By using the expansion theorem, we can express approximately the acoustic pressure of the automobile cabin by the eigenfunctions of the rectangular volume, i.e.:

$$p(r) = \sum_n b_n \Psi_n(r) \qquad [12]$$

Of course, depending on the shape of the cavity, the number of eigenfunctions used is generally higher (or much higher) than those which are strictly necessary if the true eigenfunctions of the cavity are used.

By this approximation, both the eigenvalue problem of the unknown cavity and the forced problem can be solved.

In practice, Succi's method is a Rayleigh–Ritz-type method where particularly simple admissible functions are used.

Eigenvalue problem for determining the eigenparameters of the complex cavity Starting from the integral eqn [7] with G_c written instead of G_∞, we wish to determine the eigenvalues and eigenfunctions of the cabin with rigid surfaces. In such a case, since $\partial p/\partial n = 0$, eqn [7] becomes:

$$p(r) = -\int_{S_0} p(r_0)\frac{\partial G_c(r/r_0)}{\partial n_0}\,\mathrm{d}S_0$$

where S_0 is the automotive surface.

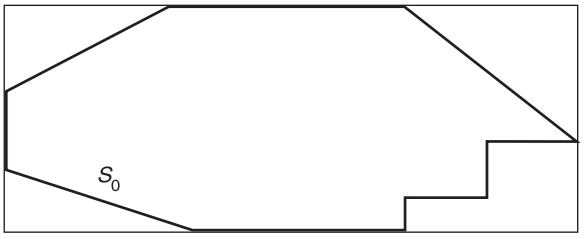


Figure 2 Automobile cabin enclosed in a rectangular volume.

By the approximation [12], this equation is transformed into the following form:

$$\sum_n b_n \Psi_n(r) = -\int_{S_0} \sum_m b_m \Psi_m(r_0) \sum_n \frac{\Psi_n(r)(\partial \Psi_n(r_0)/\partial n_0)}{\Lambda_n(k_n^2 - k^2)} \mathrm{d}S_0$$

Since r is not on the surface, $\Psi_n(r)$ can be carried out from the integral:

$$\sum_n b_n \Psi_n(r) = \sum_m \sum_n \frac{b_m \Psi_n(r)}{\Lambda_n(k^2 - k_n^2)} \int_{S_0} \Psi_m(r_0) \frac{\partial \Psi_n(r_0)}{\partial n_0} \mathrm{d}S_0$$

By computing the integral on the right-hand side (that can be put in a matrix whose elements are P_{mn}), remembering the normalization condition for the eigenmodes of the rectangular volume [11], and multiplying the previous equation by $\Psi_i(r)(i = 1, 2...n)$, one obtains, after integrating over the volume V of the rectangular cavity:

$$\Lambda_n(k^2 - k_n^2) b_n = \sum_m b_m P_{mn}$$

or, in matrix form:

$$\left[P_{mn} + \Lambda_m(k_m^2 - k^2)\delta_{mn}\right]\mathbf{b} = 0 \qquad [13]$$

In this equation the k_m are known, being the eigenvalues of the rectangular volume. k are the natural wave numbers of the automotive cabin, while $\mathbf{b}$ are the corresponding eigenvectors. Therefore, by solving this problem, the acoustic natural frequencies and the acoustic modes of the cavity are easily determined.

Forced problem In the forced problem, we assume that the cavity surface S_0 has a surface S_v harmonically vibrating with circular frequency ω, and an absorbing surface S_a (**Figure 3**). Under these conditions, eqn [7] reads:

$$p(r) = -\int_{S_0} p(r_0) \frac{\partial G_c}{\partial n_0} \mathrm{d}S - \int_{S_v} (j\omega\rho_0 v_n) G_c \, \mathrm{d}S_v - \int_{S_a} \frac{j\omega\rho p}{Z_A} p(r_0) G_c \, \mathrm{d}S_a$$

By using the approximation [12], one has:

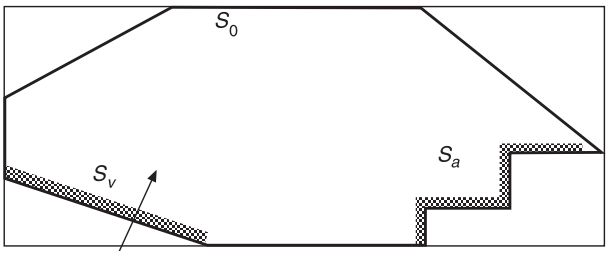


Figure 3 Automobile cabin with vibrating, absorbing, and rigid surfaces.

$$\begin{aligned}\sum_n b_n \Psi_n(r) = &-\int_{S_0} \sum_m b_m \Psi_m(r_0) \sum_n \frac{\Psi_n(r)(\partial \Psi_n(r_0)/\partial n_0)}{\Lambda_n(k_n^2 - k^2)} \mathrm{d}S \\ &- \int_{S_v} \sum_m \frac{\Psi_m(r)\Psi_m(r_0)}{\Lambda_m(k_m^2 - k^2)} (j\omega\rho_0 v_n) \, \mathrm{d}S_v \\ &- \int_{S_a} \frac{j\omega\rho_0}{Z_A} \sum_m b_m \Psi_m(r_0) \sum_n \frac{\Psi_n(r)\Psi_n(r_0)}{\Lambda_n(k_n^2 - k^2)} \mathrm{d}S_a\end{aligned}$$

i.e.:

$$\begin{aligned}\sum_n b_n \Psi_n(r) = &\sum_m \sum_n \frac{b_m \Psi_n(r)}{\Lambda_n(k^2 - k_n^2)} \\ &\times \left[\int_{S_0} \Psi_m(r_0) \frac{\partial \Psi_n(r_0)}{\partial n_0} \mathrm{d}S - \int_{S_a} \frac{j\omega\rho_0}{Z} \Psi_m(r_0)\Psi_n(r_0) \, \mathrm{d}S_a\right] \\ &- \sum_m \frac{\Psi_m(r)}{\Lambda_m(k^2 - k_m^2)} \int_{S_v} j\omega\rho_0 v_n \Psi_m(r_0) \, \mathrm{d}S\end{aligned}$$

By computing the integrals and calling them, respectively, P_{mn}, F_{mn}, and v_m, multiplying the previous equation by $\Psi_i(r)(i = 1, 2...n)$, and integrating on the volume V of the rectangular cavity, one obtains:

$$\left[P_{mn} - F_{mn} + \Lambda_m(k_m^2 - k^2)\delta_{mn}\right]\mathbf{b} = \mathbf{v} \qquad [14]$$

In this equation k_m are the natural wave numbers of the rectangular volume and are known, as well as $k = \omega/c$, the matrices $\mathbf{P}$ and $\mathbf{F}$, and the vector $\mathbf{v}$ on the right-hand side. The only unknown is vector $\mathbf{b}$, and this can be solved by inverting the equation.

When $\mathbf{b}$ is determined, the acoustic pressure p in the automobile cabin can be immediately computed using eqn [12].

Comments on the Different Numerical Approaches

In the boundary integral formulation associated with the boundary element method solution, the unknown field (the acoustic pressure in the medium) becomes the field variable in correspondence with the vibrating surface. It is obvious that, for the external problem, this yields a significantly reduced computational burden, because the number of degrees of freedom must be defined only on the surface, i.e., it is not necessary to discretize the whole fluid region, but only the vibrating surface (nonlocal discretization). In some cases, the internal problem can also be solved advantageously by this procedure: in the medium-frequency range or for large cavities, the number of degrees of freedom necessary to solve the acoustic field can become very large with respect to the structural degrees of freedom. This happens when the number of acoustic modes which are equivalent, for a cavity, to the structural modes, becomes very large.

Therefore, it can be stressed that the boundary integral formulation is convenient for external problems and for the internal case, when either the dimensions of the fluid region or the frequency of interest are quite large, that is, when the involved acoustic wavelengths ($\lambda = c/f$) become significantly smaller than the dimensions of the considered region.

However, one should always consider that the finite element formulation leads to block diagonal matrices that are very convenient to decompose, while the boundary element method introduces sparse matrices that are much more cumbersome from a numerical point of view.

With reference to the internal problem, both the boundary element method and Succi's method originate from the integral formulation. However, while the boundary element method is actually a direct method of solving integral equations (the acoustic pressure is the unknown in the integrals), Succi's method transforms the unknown pressure distribution in the integral equation into a series of known functions. From a numerical point of view this is a relevant advantage, and in most cases the computation time is noticeably reduced.

Figure 4 shows an automobile cabin, and **Figure 5** shows a comparison between a finite element method solution and Succi's method, which is presented in the bandwidth 0–200 Hz. In the same frequency range the ratio between the computer time demanded by a boundary element method solution obtained by commercial software and that required for Succi's method proved to be of the order of 6.

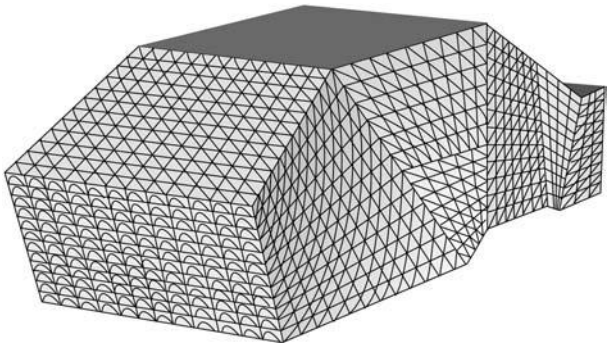


Figure 4 Automobile cabin.

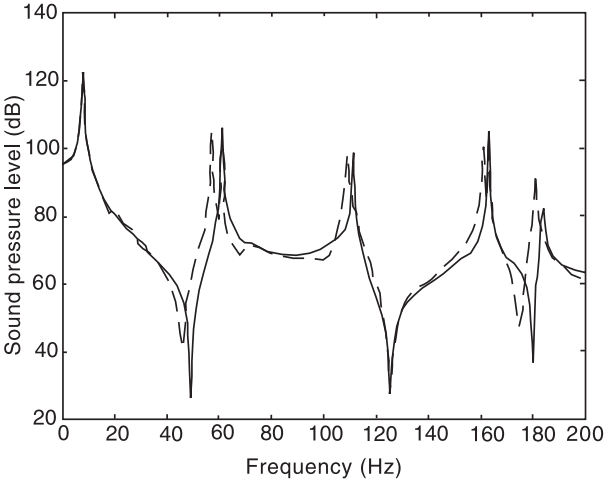


Figure 5 Sound pressure levels: comparison between finite element (continuous line) and Succi's results (dashed line).

Another advantage of Succi's method with respect to the boundary element method is represented by the possibility of determining directly, by the solution of an eigenvalue problem, the natural frequencies and acoustic eigenfunctions of a cavity.

However, it is worthwhile pointing out that the accuracy of Succi's method worsens as the cavity's shape becomes more and more dissimilar to the rectangular volume. In this case, the eigenfunctions of the rectangular volume cannot be considered an accurate basis for the solution of the cavity, and even using a high number of modes, some accuracy is lost.

Nomenclature

c	speed of sound
k	wave number
k_n	natural wavenumber
p	acoustic pressure
$\mathbf{n}$	outward unit vector normal to the surface

$\mathbf{u}$	fluid particle velocity
v	velocity of a surface point
w	displacement of a surface point
$\mathbf{q}$	vector of coordinates
r	distance of the observer from the origin
r_0	distance of the source from the origin
G	Green function
G_∞	free-space Green function
G_c	cavity Green function
G_R	real part of the free-space Green function
$\mathbf{K}$	stiffness matrix
$\mathbf{M}$	mass matrix
R	distance between source and observer
T	kinetic energy
U	potential energy
M	mass of the subsystem
δ	Dirac function
δ_{mn}	Kronecker delta
ω	circular frequency
ω_n	natural acoustic frequency
ρ	fluid density
Ψ_i	ordered acoustic mode of order i corresponding to indices mnp
Λ_n	normalization factor

See also: **Boundary element methods**; **Damping in FE models**; **Eigenvalue analysis**; **Finite element methods**; **Fluid/structure interaction**; **Object oriented programming in FE analysis**; **Modal analysis, experimental**, Basic principles; **Structure-acoustic interaction, high frequencies**; **Wave propagation**, Waves in an unbounded medium.

Further Reading

Fahy FJ (1985) *Sound and Structural Vibration: Radiation, Transmission and Response*. London: Academic Press.

Morse PM and Ingard KU (1968) *Theoretical Acoustics*. Princeton, NJ: Princeton University Press.

Pierce AD (1981) *Acoustics: An Introduction to its Physical Principles and Applications*. New York: McGraw-Hill.

Sestieri A, D'Ambrogio W, De Bernardis E (1991) On the use of different fundamental solutions for the interior acoustic problem. In: Morino L and Piva R (eds), *Boundary Integral Methods: Theory and Applications*. Heidelberg: Springer-Verlag.

SUBSTRUCTURING

See **THEORY OF VIBRATION**, SUBSTRUCTURING

SUPERPOSITION

See **THEORY OF VIBRATION**, SUPERPOSITION

SVD

See **LINEAR ALGEBRA**

T

TESTING, MODAL

See **MODAL ANALYSIS, EXPERIMENTAL: APPLICATIONS; MODAL ANALYSIS, EXPERIMENTAL: BASIC PRINCIPLES; MODAL ANALYSIS, EXPERIMENTAL: CONSTRUCTION OF MODELS FROM TESTS; MODAL ANALYSIS, EXPERIMENTAL: MEASUREMENT TECHNIQUES; MODAL ANALYSIS, EXPERIMENTAL: PARAMETER EXTRACTION METHODS**

TESTING, NONLINEAR SYSTEMS

A Haddow, Michigan State University, East Lansing, MI, USA

Copyright © 2001 Academic Press

doi:10.1006/rwvb.2001.0040

Introduction

Vibration testing of a system is usually undertaken for the purpose of parameter or system identification. If the object is linear, a great deal of information can be obtained from such tests. This is discussed elsewhere in the encyclopedia. However, when the system is nonlinear the general identification procedure is much more complicated and detailed models are often impossible to obtain. Nevertheless, it is still important to ascertain what operating conditions may lead to an unacceptable type of response. The purpose of this article is to present guidelines for testing systems that may be nonlinear and thus behave in unpredictable ways, i.e., unlike a linear system. Before embarking on this, it is important to appreciate some of the different responses that can arise on account of nonlinearities. These are presented in the next section, followed by recommendations for specific testing techniques that should be employed to guarantee that all types of responses have been found. Throughout, harmonic inputs are assumed unless otherwise stated.

Linear versus Nonlinear Response

The following subsections briefly describe some of the unusual phenomena that occur on account of nonlinearities. More details can be found in the texts cited at the end of this article.

Resonance Frequency

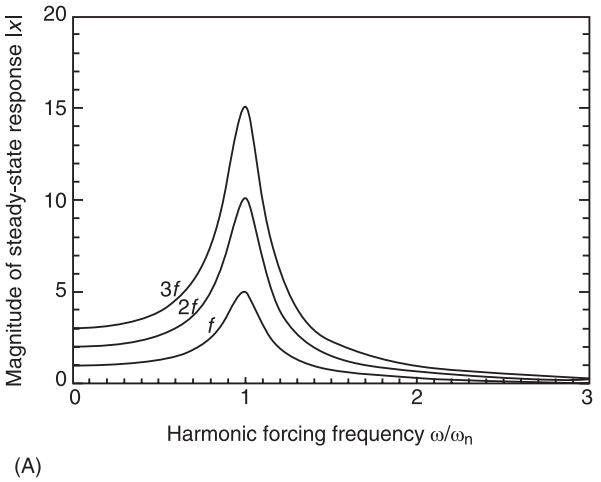
One of the most fundamental differences between linear and nonlinear systems is the dependence of the resonant frequency on the level of the response. Alternatively, this can be viewed as a dependence on the magnitude of the excitation since, normally, as the level of the excitation is increased, so is the level of the response. This behavior is represented in **Figure 1**.

Figure 1A shows a typical linear response of a one-degree-of-freedom system (1 DOF) where the steady-state response, $|x|$, linearly increases with the level of the force, f. The resonant frequency, ω_p, is essentially independent of f and is very close to the natural frequency, ω_n. In contrast, **Figure 1B** shows how a typical* nonlinear system might respond. Depending on the level of the force, the maximum response occurs at different forcing frequencies, i.e., the resonant frequency becomes a function of the level of the response.

Multiple Steady States

This type of behavior gives rise to a great deal of problems while testing nonlinear systems. In linear systems, solutions are unique, i.e., given some system that is described by linear differential equations then the solution set due to a given input term is unique.

* For this example a 'hardening' nonlinearity is shown. The description hardening refers to the stiffness term that increases or hardens as the amplitude increases. This leads to an increase in the natural frequency as the response increases.



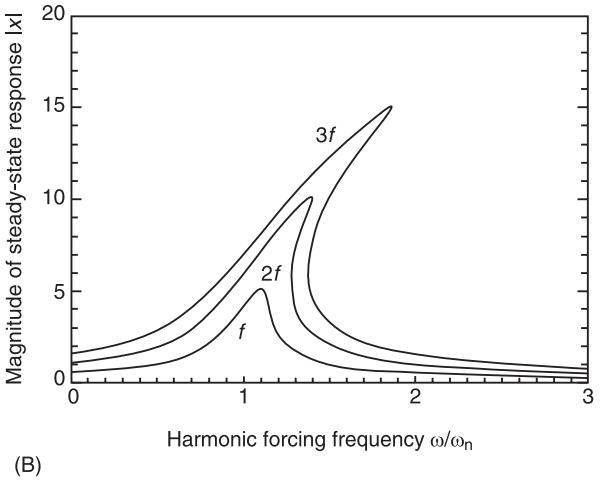


Figure 1 Frequency response for three different levels of force *f*. (A) Linear case; (B) typical nonlinear case.

However, this need not be the case in nonlinear systems. This may be more clearly understood if **Figure 1B** is redrawn for a single, constant level of force. This is shown in **Figure 2**. For any value of forcing frequency, ω, such that $\omega_a < \omega < \omega_b$, there are three possible steady-state responses. The one that is adopted is dependent on the phase relationship between the response and the force. Alternatively, this may be viewed as a dependence on the initial conditions of the problem. In addition, the midvalued solution (shown as a dashed line in **Figure 2**) is unstable and cannot be observed in practice.

Nonharmonic Response

In harmonically excited linear systems the steady-state response will always be of the same frequency as the input†. This may be almost true in some nonlinear systems where only small harmonic distortions are present, but on occasion it is quite possible to observe frequencies that are vastly different from the input term. As a general rule, if even-order nonlinearities are present they will generate even harmonics, whereas odd-order nonlinearities tend to generate odd harmonics. Moreover, the response may not be periodic at all but instead quasiperiodic or even chaotic responses may be observed. To complicate the picture further, these responses usually take a large number of forcing cycles to develop fully and are dependent on initial conditions.

† Strictly, this is limited to systems that have constant coefficients and have some damping such that transient motions decay.

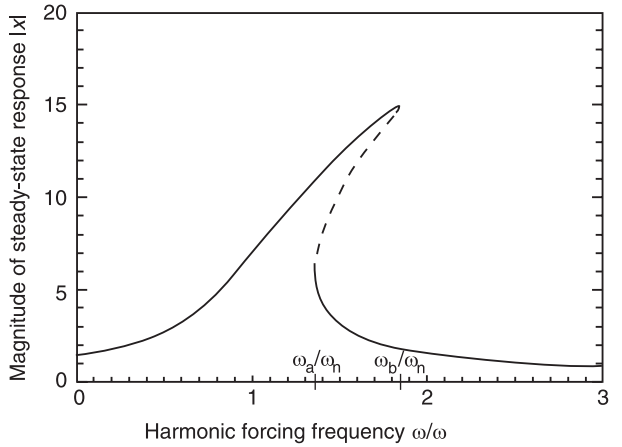


Figure 2 Typical nonlinear frequency response function. Continuous line, stable; dashed line, unstable.

Lack of Superposition

This is perhaps the key distinguishing factor between linear and nonlinear systems. Being aware of this is of great practical importance because we can no longer predict the cumulative response of a system by considering the individual components of the forcing terms. For example, 1 DOF cases exist where a two-harmonic forcing term, $f(t) = f_1 \sin \omega_1 t + f_2 \sin \omega_2 t$, can give rise to a resonant response (at the natural frequency of the system) even when ω_1 and ω_2 are well removed from that natural frequency. This is known as a combination resonance and is only one example of the type of misleading response that can occur because superposition is not valid.

Modal Interaction

Moving to systems of more than 1 DOF, additional problems are encountered when dealing with nonlinear systems. Unlike their linear counterparts where a standard eigenvalue/vector analysis can usually be used to uncouple modes, nonlinear systems typically

cannot be fully uncoupled. The practical implication of this is that modes can interact and energy can flow from one mode to others. The final response of the system might be very different from its initial behavior. The frequency content of the response can evolve in time and its final content might be vastly different from the forcing frequency. Steady-state solutions might never be attainable, with a continuing exchange of energy occurring between the modes. This is particularly true if the linear natural frequencies are, or almost are, commensurate. This condition is known as internal tuning.

Miscellaneous

Details of all of the above phenomena can be found in the texts listed in the Further Reading section at the end of this article, as can more specialized types of nonlinear behavior. Examples of this would include systems with gaps (e.g., causing rattles and chatter); friction-induced instabilities (e.g., causing brake squeal), and frequency entrapment (often observed in the run-up of rotating systems). Resonances may also arise due to time-dependent coefficients in a system's governing equation (so-called parametric resonances) and there are vast arrays of systems that exhibit chaotic responses.

While the testing procedures outlined in the next section may not give insight into why a particular response is occurring, they will uncover most of the types of the behavior listed above. Regions in the parameter space can then be mapped out indicating where resonances and other complex responses occur.

Testing Procedures

Having briefly reviewed some of the more fundamental differences between linear and nonlinear system responses we shall now detail how to modify the standard vibration-testing procedures to ensure that the true nonlinear behavior of the object is captured. In general, a slow frequency and/or force sweep is the preferred method of testing. Alternatives such as impact testing and random excitation are less desirable due to the superposition principle being inherently invalid in nonlinear systems. However, low-level impact and random inputs can be of use to determine quickly the approximate values of the (linear) natural frequencies.

The test set-up is no different whether the system is linear or nonlinear. A source of excitation, e.g., an electrodynamic shaker, is attached to the test piece by a stinger, a compliant mount, or such like. The response due to this excitation is also measured by, for example, an accelerometer, strain gauge, etc. This is shown schematically in **Figure 3**. The input and the output should be continuously monitored taking care to minimize the amount of signal preprocessing. Of course, antialiasing filters should be used if digital devices are employed, but be aware that one should sample a wide frequency bandwidth encompassing harmonics and subharmonics of the forcing frequency. This will ensure that the complete response of the system is being captured because, as previously explained, nonlinear systems often generate frequencies that are very different from the forcing frequency.

Another characteristic of nonlinear systems is that their behavior often takes a great deal of time to develop and thus, being able to observe any precursor to a change in the underlying behavior is desirable. Hence, analysis of the signals should be carried out in real time, i.e., as the test is being run. One can watch for the appearance and disappearance of harmonics and/or phase changes as they are sensitive indicators of ongoing changes and that the test needs to be continued. A two-channel fast Fourier transform (FFT) analyzer can be used for this, with displays set to show the evolution of the frequency content (akin to short-time Fourier transforms or spectrograms) or to show an orbit plot of input versus output signal. The latter is particularly useful to detect sudden changes in the phase relationship between the two signals. Some more complex types of analyses and displays can be used. For example, for very low dimensional systems Poincaré sections can be developed and for systems that contain a very wide range of frequencies and have inherent impulsive events, a wavelet-based analysis may be of use. Dimensional calculations can also be made, but all of these involve more complex processing that often has to be done offline. They give specialized information about the system, whose description is beyond the scope of this article.

We will now discuss specific test procedures that can be used to uncover a variety of nonlinear characteristics that a system may possess.

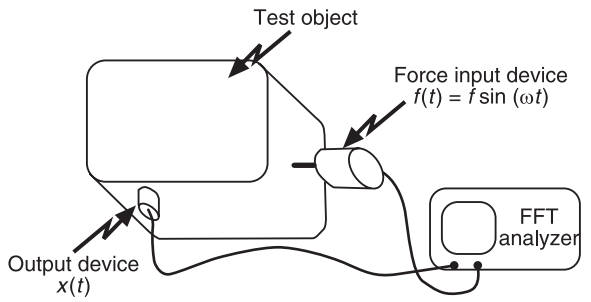


Figure 3 Typical experimental set-up.

Parameter Sweep Through Resonances

The main purpose of this test is to map out the combination of f and ω that gives rise to the largest responses in the neighborhood of a natural frequency. Closely related to this is to find regions where multiple steady states might exist and therefore jumps between different operating conditions could be observed.

One first finds the approximate values of the natural frequencies by, for example, a standard impact test, taking care to impart only a low level of excitation. One then completes a sweep of the forcing frequency, ω, by starting close to but below one of the natural frequencies and very slowly increasing ω. With reference to **Figure 2**, when ω is increased slightly above a value of ω_b, the solution will pass through a transient response and then settle to a much smaller-amplitude solution. The procedure is then reversed, starting above the natural frequency and slowly sweeping downwards. A transition, or jump, to a higher level will occur close to ω_a.

There are a number of issues one must be aware of when completing this task. Firstly, we have assumed that the nonlinearity is hardening, i.e., the peak response occurs at a forcing frequency above the linear natural frequency. The opposite may be true and so care should be taken to sweep the forcing frequency slowly in both directions from the natural frequency.

Secondly, the system may be behaving linearly and so the peak response could be exceedingly close to the linear natural frequency (see the curve labeled f in **Figure 1B** for an example of this). One can always check this by increasing the level of force, f, and see if there is a corresponding linear increase in the response. In either case, the best practice is often simultaneously to alter f and ω and carefully monitor the response for sudden changes in its behavior (also see the subsection on accelerated testing, below). If this is found, a more systematic parameter search can then be undertaken in that region.

Depending on the final application, the experimental results can be presented in a variety of ways. It is often desirable to consider the $f-\omega$ plan and divide it into regions indicating where jumps occur, where nonharmonic responses occur, etc. Results from the test to follow can also be summarized this way, quickly allowing design engineers to perceive potentially dangerous operating conditions.

Tests for Sub- and Superharmonic Resonances

In addition to testing in the neighborhood of the natural frequencies, one should also sweep through forcing frequencies that are close integer multiples and submultiples of the natural frequencies[‡]. Resonances that exist in these regions are potentially very dangerous because using conventional (linear) thinking, one only has to avoid forcing close to a natural frequency to avoid large responses. Impact and random excitation tests are unlikely to uncover these resonances since the responses take a high number of forcing cycles to develop and their domain of attraction may be small (also see the subsection on Dependence on Initial Conditions, below).

Accelerated Testing

Although it is important to sweep a parameter relatively slowly to ensure that adequate time is given for a response to develop, this can take a considerable amount of time. Moreover, many types of response may never be observed if their domain of attraction is not entered by the particular set of initial conditions that exist as the test is being run. The testing time can be accelerated by increasing the level of force above typical operating conditions and then sweeping the frequency faster. As the sweep continues there will usually be some sign of a response developing (recall that the input and output should be analyzed in real time). When this is seen, the level of force can be reduced to a more realistic level and then a detailed investigation of the existence of that solution can be made.

There is a fine art to doing this, and simultaneous changes in f and in ω may have to be made. The key is to watch for some early sign of a response growing (see the introduction to Testing Procedures, above) and then let it continue to develop while slowly reducing the level of the force. Care must be taken not to lose the response on account of changing the force level too quickly. The aim is to reduce the level of the force and simultaneously to change the forcing frequency up or down, in order to follow the solution. Of course, there is always the possibility that the response may cease to exist at the lower levels of force, regardless of the value of ω.

Different initial conditions should be tested to explore the region thoroughly for possible solutions. This is discussed in the next subsection.

Dependence on Initial Conditions

Recall that for a fixed forcing function, multiple solutions may exist. This nonuniqueness of solutions is potentially very problematic when testing, for one

‡ I.e, $\omega \approx p\omega_n$ and ω_n/p for small integer values of p. Such responses are called subharmonic and superharmonic resonances. Related to these are forcing frequencies that are linear combinations of natural frequencies in multiple DOF systems.

can never be sure that all possible solutions have been found. However, there are some general techniques that can help. If the device is small enough, one can simply hold and then release it and see if the same response returns. This should be repeated a number of times in an attempt to enter domains that will attract to different solutions. The device does not have to be brought to rest each time since the requirement is to change the phase between the forcing term and the response(s). An alternative to this is to impact the object while it is being harmonically forced and again observe if the response returns to the pre-impact level. Different levels of impact and different locations should be tested.

Mode Interaction

Modal interaction can occur when there is a simple relationship between the linear natural frequencies of a system, ω_{n_i}, $i = 1, 2, 3, \ldots$ where i denotes the ith natural frequency. Therefore, the first step in this test is to obtain a good estimate of all the linear natural frequencies. It is important to include even those lying beyond the input frequency bandwidth of interest, since energy can be transferred to modes well removed from the excitation frequency. As recommended previously, a low-level impact test is often adequate to find the natural frequencies. Once found, check for internal tuning relationships, such as $\omega_{n_i} \approx p\omega_{n_j}$ for low integer values of p ($i = 1, 2, 3 \ldots \neq j$ and $j = 1, 2, 3 \ldots \neq i$). For example, say that $\omega_{n3} \approx 2\omega_{n1}$, then a slow-frequency sweep test should be completed in the neighborhood of ω_{n3}, taking care to observe for a response growing with a frequency close to ω_{n1}. The opposite case should also be tested, i.e., sweeping through ω_{n1} and looking for a response with a frequency of ω_{n3}. One must be aware of all the previously discussed points, regarding initial conditions, sweep directions, etc. in the search for modal interaction. The procedures outlined in the subsection on Accelerated Testing can also be employed to ensure that an exhaustive search has been made. It should be noted that the responses may take many forcing cycles to develop.

The situation can readily become very complex as the number of degrees of freedom increases. The number of internal tuning conditions can quickly rise, necessitating running many tests and there may be many modes involved in a chain, or cascading effect. For example, say that $\omega_{n3} \approx 2\omega_{n1}$ and that $\omega_{n1} \approx \omega_{n4} - \omega_{n2}$, then it is possible that an excitation close to ω_{n3} will eventually cause mode 1 to grow, which in turn will eventually cause modes 4 and 2 to respond.

Concluding Remarks

Nonlinear systems are inherently difficult to test and to interpret the results correctly. Great care must be taken to avoid preconceived ideas of how the system is likely to respond, for often this would influence the type of test being run and the processing techniques employed. Time must be given for complex responses to develop and a wide range of different force, frequency, and sweep directions must be covered to ensure that all possible input regimes have been explored. Likewise, preconceived ideas about the expected type of response can lead to the introduction of inappropriate conditioning of the response signals and thus mask behaviors that may lead to incorrect classification or understanding of the system. Often commercially based testing apparatus assumes a system's linearity and thus the results generated are invalid for nonlinear systems. If one has to use a commercial test package it is good practice to check that all results are reproducible under different conditions such as sweep directions, level of excitation, and initial conditions.

Nomenclature

f	force
$\lvert x \rvert$	steady-state response
ω_p	resonant frequency

See also: **Nonlinear normal modes**; **Nonlinear systems analysis**; **Nonlinear system identification**; **Nonlinear systems, overview**; **Nonlinear system resonance phenomena**; **Parametric excitation**; **Seismic instruments, environmental factors**; **Signal processing, model based methods**; **Standards for vibrations of machines and measurement procedures**; **Testing, nonlinear systems**; **Transform methods**.

Further Reading

Berge P, Pomeau Y and Vidal C (1984) *Order Within Chaos, Towards a Deterministic Approach to Turbulence*. New York: John Wiley.

Moon FC (1987) *Chaotic Vibrations: An Introduction for Applied Scientists and Engineers*. New York: Wiley.

Nayfeh AH and Balachandran B (1995) *Applied Nonlinear Dynamics: Analytical, Computational, and Experimental Methods*. New York: Wiley Interscience.

Nayfeh AH and Mook DT (1979) *Nonlinear Oscillations*. New York: Wiley Interscience.

Thompson JMT and Stewart HB (1986) *Nonlinear Dynamics and Chaos*. New York: John Wiley.

THEORY OF VIBRATION

Fundamentals

B Yang, University of Southern California, Los Angeles, CA, USA

Copyright © 2001 Academic Press

doi:10.1006/rwvb.2001.0112

Vibrations are the oscillating motion of an object or a dynamic system about an equilibrium position. This oscillating motion can be either periodic, or nonperiodic and transient. Examples of vibrations are diverse, including the back-and-forth motion of an engine piston, the oscillations of a violin string, the fluctuations of a highway bridge with passing vehicles, and the rolling of a ship under the influence of ocean waves.

For vibrations to occur, two elements are essential: a mass or inertia element that stores kinetic energy; and a spring or elastic element that stores potential energy. The spring element provides a restoring force that continually pulls the mass toward its equilibrium position, and thus causes the oscillations of the mass. During vibrations, potential energy and kinetic energy are converted to each other as they are stored in and released from the two elements, respectively.

Vibrations of a system are initiated when energy is imparted to it. A free vibration occurs when external excitations are absent, but kinetic energy or potential energy is present initially in the system. Free vibrations of many systems are harmonic motion with periods or natural frequencies that are inherently dependent upon inertia and elastic properties. A forced vibration occurs with the application of external forces to the system. Forced vibrations can be periodic, nonperiodic, or random. Under a harmonic (sinusoidal) excitation, the response of a system becomes increasingly large if the excitation frequency is close to one of the natural frequencies of the system. This phenomenon is called resonance. Control of resonant vibrations is one important issue in design of structures and machines.

For any real vibrating system, there always exists energy dissipation in motion, which is termed damping. Damping occurs as a result of friction among moving objects, or interactions of moving objects with their surrounding environments (e.g., rough surface, air, fluids, and electromagnetic fields). Damping converts the mechanical energy in a vibrating system to other forms of energy such as heat and acoustic energy. This energy conversion process in general is irreversible. The presence of damping causes the amplitude of free vibrations to delay, and leads to the reduction in amplitude of forced vibrations. In addition, damping can be purposely introduced to suppress resonant vibrations.

Inertia, elasticity, and damping are inherent properties of vibrating systems.

Vibrations can degrade the performance and reliability of structures and machines, cause property damage, and in worst cases result in loss of human lives. Hence, vibration control is essential for proper operation of many systems. On the other hand, vibration phenomena are useful in certain devices such as musical instruments, shakers, and cardiac pacemakers. In either way, it is essential to model and analyze the behaviors of vibrating systems.

Any study of vibrations inevitably turns to dynamics, as vibration involves motion (displacement, velocity, and acceleration), forces, and inertia. Kinematics, the study of geometry of motion without reference to forces and inertia, is part of dynamics. In this article, the fundamentals of vibration theory are presented under the following headings: classification of vibrating systems; equations of motion; free vibration; forced vibration; and modal analysis. For the sake of simplicity, linear lumped systems will be mainly considered.

Classification of Vibrating Systems

There are several ways to classify vibrating systems, depending on different perspectives. In view of the distributions of inertia and elastic parameters, there are distributed parameter systems such as structures composed of flexible beams and plates, and lumped parameter systems such as systems of lumped masses, and rigid bodies. Vibrations of distributed parameter systems are described by partial differential equations, while vibrations of lumped parameters are described by ordinary differential equations. Because exact solutions of partial differential equations are difficult to obtain, distributed parameter systems are often approximated by lumped parameter models, through a procedure called discretization. In engineering practice, discretization via the finite element method is widely adopted.

From the viewpoint of energy conversion, vibrating systems are divided into two kinds: (1) conservative systems which have no damping, and no energy exchange with the surrounding environments; and (2) nonconservative systems which exchange energy with the surrounding environments via damping, gyroscopic, and circulatory forces, magnetoelectromechanical interactions, or other means. One important feature of conservative systems is the existence of normal modes of vibration, which are composed of real natural frequencies (eigenvalues) and real orthogonal mode shapes (eigenvectors). The concept of normal modes has an important position in vibration theory, and lays a foundation for the development of a useful vibration analysis technique called modal analysis.

Vibrating systems can also be categorized as linear systems whose motion is described by linear differential equations; and nonlinear systems whose motion is governed by nonlinear differential equations, due to nonlinear material and/or geometric properties of the systems. For linear systems, many well-developed methods of vibration analysis are available, as the superposition principle is valid. In the study of small oscillations, a nonlinear system can be treated as a linear one by proper linearization. However, nonlinearities must be considered when large oscillations are of concern. Physically, nonlinear systems have certain unique characteristics that linear systems lack, such as subharmonic and superharmonic resonances, parametrically excited vibrations, limit cycles, self-excited oscillations, and chaotic motion. Analysis of nonlinear vibrations is much more difficult, and still needs further development.

Vibrations become random when there are uncertainties in motion. The cause of uncertain motion may be the unpredictability of excitations, or the lack of accurate information about the physical properties of the system. Buildings under earthquake excitations and large space structures with uncertain elastic and damping parameters are two examples. Random vibrations are usually studied based on the theory of stochastic processes. Thus, vibrating systems are also classified as deterministic systems and stochastic systems.

Equations of Motion

Mathematically, the motion of a vibrating system is described by time-dependent coordinates or generalized displacements. These coordinates are governed by differential equations of motion, which are derived from basic laws of physics, like Newton's laws. Vibrating systems can be classified by the number of degrees of freedom (DOF) of motion. The number of degrees of freedom is the number of independent coordinates needed to describe motion completely.

Systems with One Degree of Freedom

The simplest vibrating system is shown in **Figure 1**, where $x(t)$ is the horizontal displacement of the mass, measured from the equilibrium position at which the spring is unstretched, and $f(t)$ is an external force. The mass does not move vertically, due to the constraint of the frictionless surface. The system has one DOF as the coordinate $x(t)$ completely describes the motion. According to Newton's second law, the motion of the spring–mass system is governed by:

$$m\ddot{x}(t) = f(t) - f_s(t) \qquad [1]$$

where $\ddot{x} = d^2x/dt^2$ is the acceleration of the mass, and f_s is the spring force which always pulls the mass towards the equilibrium position. For small oscillations, the spring force can be assumed to be proportional to the mass displacement; that is, $f_s(t) = kx$ where k is a spring coefficient or stiffness. It follows that the motion of the spring–mass system is described by the linear differential equation:

$$m\ddot{x}(t) + kx(t) = f(t) \qquad [2]$$

For large oscillations, however, the spring force may become a nonlinear function of the displacement, say $f_{NL}(x)$, which results in a nonlinear equation of motion:

$$m\ddot{x}(t) + f_{NL}(x) = f(t) \qquad [3]$$

Eqns [2] and [3] are generic of 1-DOF vibrating systems. For instance, the angular displacement θ of the shaft–disk system in **Figure 2A** is governed by the differential equation:

$$J\ddot{\theta}(t) + K\theta(t) = M_0(t) \qquad [4]$$

where M_0 is an external torque; and the swaying motion of a simple pendulum in **Figure 2B** is described by:

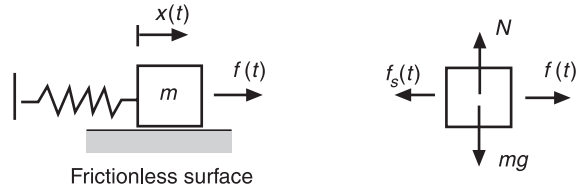


Figure 1 A spring–mass system.

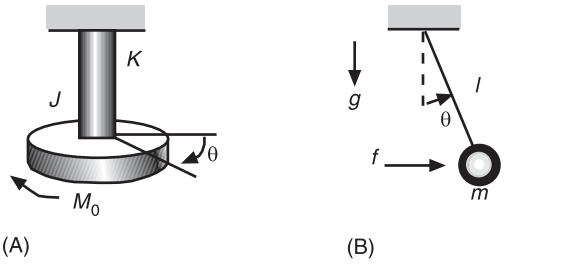


Figure 2 (A) Shaft–disk system: J, polar moment of inertia of the disk; K, torsional stiffness of the shaft. (B) Simple pendulum: g, gravitational acceleration.

$$\ddot{\theta}(t) + \frac{g}{l} \sin \theta(t) = \frac{1}{ml} f(t) \qquad [5]$$

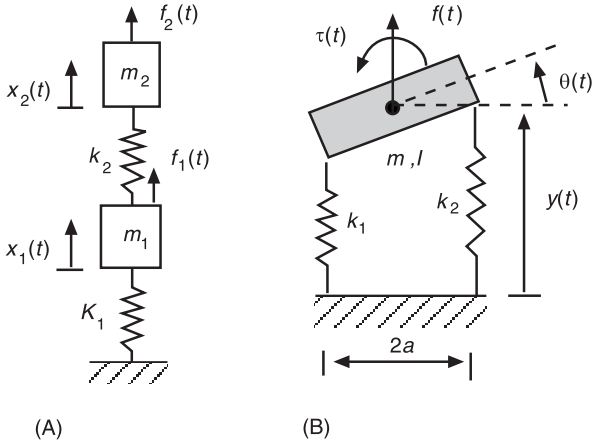


Figure 3 Two-DOF systems.

Systems with Multiple Degrees of Freedom

Many vibrating systems either have more than one mass element, or have a single mass that is in multi-dimensional motion. These systems are called multi-DOF systems because the complete description of their motion requires more than one coordinate. The motion of multi-DOF systems is governed by a set of simultaneous differential equations. As two examples, the equations of motion of the two-mass system in **Figure 3A** are of the matrix form:

$$\begin{bmatrix} m_1 & 0 \\ 0 & m_2 \end{bmatrix} \begin{pmatrix} \ddot{x}_1(t) \\ \ddot{x}_2(t) \end{pmatrix} + \begin{bmatrix} k_1 + k_2 & -k_2 \\ -k_2 & k_2 \end{bmatrix} \begin{pmatrix} x_1(t) \\ x_2(t) \end{pmatrix} = \begin{pmatrix} f_1(t) \\ f_2(t) \end{pmatrix} \qquad [6]$$

while the spring-supported rigid body in **Figure 3B**, whose motion involves both vertical translation $y(t)$ and rotation $\theta(t)$, is described by:

$$\begin{bmatrix} m & 0 \\ 0 & I \end{bmatrix} \begin{pmatrix} \ddot{y}(t) \\ \ddot{\theta}(t) \end{pmatrix} + \begin{bmatrix} k_1 + k_2 & a(k_2 - k_1) \\ a(k_2 - k_1) & a^2(k_1 + k_2) \end{bmatrix} \begin{pmatrix} y(t) \\ \theta(t) \end{pmatrix} = \begin{pmatrix} f(t) \\ \tau(t) \end{pmatrix} \qquad [7]$$

In general, the motion of an n-DOF linear vibrating system can be described by the matrix differential equation:

$$\mathbf{M}\ddot{\mathbf{x}}(t) + \mathbf{K}\mathbf{x}(t) = \mathbf{f}(t) \qquad [8]$$

where $\mathbf{M}$ and $\mathbf{K}$ are n-by-n mass and stiffness matrices, respectively, $\mathbf{x}(t)$ is a vector of n coordinates or generalized displacements, and $\mathbf{f}(t)$ is a vector of external forces. Eqn [8] can be derived by either Newton's laws or energy methods.

Distributed Parameter Systems

Eqn [8] represents lumped parameter models of vibrating systems because their mass and spring elements are concentrated at a finite number of points. For a distributed parameter system, like a flexible structure, its mass is distributed over the entire body which it occupies in space, and so are its elastic elements. Distributed parameter systems are also called infinite-dimensional systems because complete description of motion requires an infinite number of coordinates (degrees of freedom). The motion of a distributed parameter system is governed by partial differential equations like:

$$M[w_{,tt}(x,t)] + K[w(x,t)] = f(x,t) \qquad [9]$$

where $\mathbf{M}$ and $\mathbf{K}$ are mass and stiffness differential operators, respectively, x represents a point in space, $w(x,t)$ is the generalized displacement, $w_{,tt} = \partial^2 w/\partial t^2$, and $f(x,t)$ is the distribution of external forces applied to the distributed system. One example is the tensioned uniform string shown in **Figure 4A**. The transverse displacement w of the string, under a transverse load $f(x,t)$, is governed by the partial differential eqn [9] with the mass and stiffness operators given by:

$$M = \rho, \quad K = -T\,\partial^2/\partial x^2 \qquad [10]$$

where ρ and T are the linear density (mass per unit length) and tension of the string, respectively.

Eqn [9] represents a distributed model of vibrating systems. Because exact solutions of partial differential

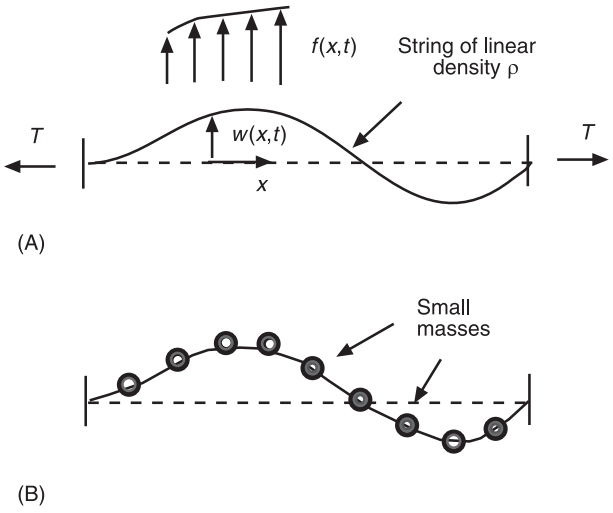


Figure 4 A string in transverse vibration: (A) distributed parameter model; (B) lumped parameter model.

equations are only available for a few simple systems, distributed vibrating systems are often approximated by lumped-parameter models. In such approximations, a vibrating continuum is treated as a finite number of elastically interconnected lumped masses (see **Figure 4B**, for instance). By certain mathematical algorithms such as the Rayleigh–Ritz method and the finite element method, the partial differential equation of motion is reduced to a set of ordinary differential equations like eqn [8]. This process is called discretization.

Besides equations of motion, a description of the vibrating systems also needs to assign initial conditions, and boundary conditions (for distributed parameter systems). A fundamental issue in vibration theory is to solve initial-boundary value problems associated with differential equations.

Free Vibration

Free vibration occurs without externally applied forces; it arises when kinetic energy or potential energy is present initially in the vibrating system. The energy input is due to initial displacements and velocities, which are also called initial disturbances.

Harmonic Motion

Free vibrations of an undamped 1-DOF system are described by the differential equation:

$$m\ddot{x}(t) + kx(t) = 0 \qquad [11]$$

with the initial conditions $x(0) = x_0$ and $\dot{x}(0) = v_0$, where x_0 and v_0 are initial displacement and velocity, respectively. The displacement is assumed as $x(t) = Ae^{\lambda t}$, which, according to eqn [11], results in the characteristic equation:

$$m\lambda^2 + k = 0 \qquad [12]$$

The roots or eigenvalues of the characteristic equation are $\lambda_1 = i\omega_n$, and $\lambda_2 = -i\omega_n, i = \sqrt{-1}$. The parameter ω_n is given by:

$$\omega_n = \sqrt{\frac{k}{m}} \qquad [13]$$

which is called the natural circular frequency of the vibrating system, of which the units are radians per second. The natural frequency depends on inertia and elastic properties of the system. The free vibration is of the form:

$$x(t) = A \sin \omega_n t + B \cos \omega_n t \qquad [14]$$

which, by the initial conditions, is determined as:

$$\begin{aligned} x(t) &= x_0 \cos \omega_n t + \frac{v_0}{\omega_n} \sin \omega_n t \\ &= A_m \sin (\omega_n t + \phi) \end{aligned} \qquad [15]$$

where the amplitude and phase angle are:

$$A_m = \sqrt{x_0^2 + \frac{v_0^2}{\omega_n^2}}, \quad \phi = \tan^{-1}\left(\frac{\omega_n x_0}{v_0}\right) \qquad [16]$$

The displacement in eqn [15] is sinusoidal, and hence is called simple harmonic motion. The period of harmonic motion (the time needed to complete a cycle of motion) is:

$$T = \frac{2\pi}{\omega_n} = \frac{1}{f_n} \qquad [17]$$

where $f_n = \omega_n/(2\pi)$ is the natural frequency of the vibrating system, in hertz (Hz). **Figure 5** shows that the harmonic motion can be viewed as the projection of a rotating vector OP of amplitude A_m and rotation speed ω_n on the vertical axis OX. Natural frequency, amplitude, and the phase angle are three major parameters of harmonic motion.

Modes of Vibration

The free vibration of an undamped multi-DOF system is described by:

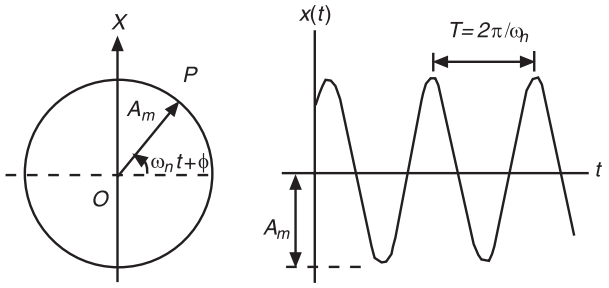


Figure 5 Simple harmonic motion.

$$\mathbf{M}\ddot{\mathbf{x}}(t) + \mathbf{K}\mathbf{x}(t) = 0 \qquad [18]$$

$$\mathbf{x}(0) = \mathbf{x_0} \quad \text{and} \quad \dot{\mathbf{x}}(0) = \mathbf{v_0} \qquad [19]$$

where the vectors $\mathbf{x}_0$ and $\mathbf{v}_0$ contain initial displacements and velocities, respectively. Extending the concept of harmonic motion, assume $x(t) = \mathbf{u}e^{i\omega t}$. According to this, eqn [18] leads to the eigenvalue problem:

$$\omega^2\mathbf{M}\mathbf{u} = \mathbf{K}\mathbf{u} \qquad [20]$$

There are n eigenvalues, $\omega_1^2, \omega_2^2 \ldots \omega_n^2$, which are the roots of the characteristic equation:

$$\det(-\omega^2\mathbf{M} + \mathbf{K}) = 0 \qquad [21]$$

The ω_k are called the natural frequencies of the system. Corresponding to ω_k, the eigenvector $\mathbf{u}_k$ describes a specific distribution of displacements, and is called mode shape. The pair $(\omega_k, \mathbf{u}_k)$ defines the kth mode of vibration of the system by:

$$\mathbf{x}_k(t) = (A_k \sin \omega_k t + B_k \cos \omega_k t)\mathbf{u}_k \qquad [22]$$

For free vibration analysis, the solution of eqn [18], is represented by a linear combination of all modes:

$$\begin{aligned}\mathbf{x}(t) &= \sum_{l=1}^{n} \mathbf{x}_l(t) \\ &= \sum_{l=1}^{n} (A_l \sin \omega_l t + B_l \cos \omega_l t)\mathbf{u}_l\end{aligned} \qquad [23]$$

where A_l and B_l are determined by the initial conditions.

The concept of modes of vibration is extremely important in the theory of vibration, and will be explained further later on.

Effects of Viscous Damping

Among the available damping models, viscous damping is most commonly used. **Figure 6** shows a viscously damped 1-DOF system, where viscous damping is indicated by a dashpot or damper. The damping force is proportional to the velocity of the mass, but opposite to the motion of the mass, i.e., $f_c(t) = c\dot{x}(t)$, where c is the damping coefficient, in $\mathrm{kg\,s^{-1}}$. The equation of motion of the damped system is:

$$m\ddot{x}(t) + c\dot{x}(t) + kx(t) = f(t) \qquad [24]$$

The characteristic equation of the damped system, obtained by assuming $x(t) = Ae^{\lambda t}$ and $f(t) = 0$ in eqn [24], is:

$$m\lambda^2 + c\lambda + k = 0 \qquad [25]$$

The roots of the characteristic equation are:

$$\lambda_{1,2} = -\xi\omega_n \pm i\sqrt{1-\xi^2}\omega_n, \quad i = \sqrt{-1} \qquad [26]$$

where $\omega_n = \sqrt{k/m}$ is called the undamped natural frequency, and $\xi = C/(2m\omega_n)$ the damping ratio.

When $0 < \xi < 1$, the roots are complex, and the free response is:

$$x(t) = e^{-\xi\omega_n t}(A \sin \omega_d t + B \cos \omega_d t) \qquad [27]$$

where $\omega_d = \sqrt{1-\xi^2}\omega_n$ is called the damped natural frequency, and A and B are determined by the initial conditions. This motion, which is oscillatory with decaying amplitude, is called underdamped vibration. In **Figure 7** the dotted curves indicate the decay in the amplitude of free vibration, which is controlled by the damping ratio ξ. This type of response is commonly seen in many vibrating systems.

When $\xi > 1$, the characteristic roots are both real and negative, and the system response is called overdamped vibration. In this case, the amplitude of free vibrations decays, without oscillatory motion:

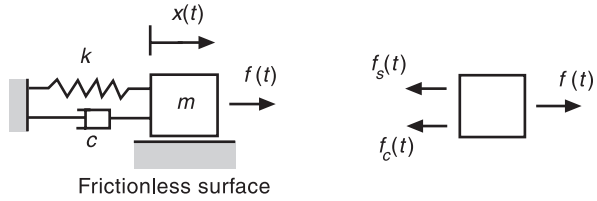


Figure 6 A 1-DOF system with viscous damping.

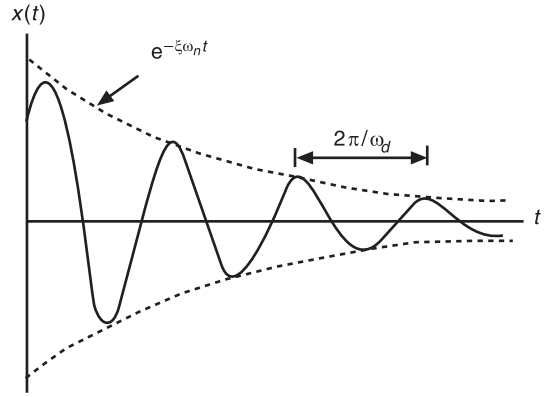


Figure 7 Free vibration of an underdamped system.

$$x(t) = e^{-\xi\omega_n t}\left(Ae^{-\beta t} + Be^{\beta t}\right), \quad \beta = \omega_n\sqrt{\xi^2 - 1} \qquad [28]$$

When $\xi = 1$, there are two repeated roots, $\lambda_1 = \lambda_2 = -\omega_n$, and the system response is:

$$x(t) = e^{-\omega_n t}(A + Bt) \qquad [29]$$

which decays without oscillation. This motion is called critically damped vibration as it is the case which separates oscillation ($0 < \xi < 1$) from non-oscillation ($\xi > 1$).

Besides decay in vibration amplitude, the effects of damping are also seen from decay in mechanical energy. The rate of change of total mechanical energy (sum of kinetic energy and potential energy) is:

$$\frac{d}{dt}\left(\tfrac{1}{2}m\dot{x}^2 + \tfrac{1}{2}kx^2\right) = -c\dot{x}^2 \qquad [30]$$

which is negative most of the time. (It is only zero at those discrete times when the displacement peaks.) Thus, the damping renders the mechanical energy decreasing continuously. If damping is absent ($c = 0$), the mechanical energy is conserved as its rate of change is zero all the time.

For a multi-DOF system with viscous damping, its motion can be described by the matrix differential equation:

$$\mathbf{M}\ddot{\mathbf{x}}(t) + \mathbf{C}\dot{\mathbf{x}}(t) + \mathbf{K}\mathbf{x}(t) = \mathbf{f}(t) \qquad [31]$$

where $\mathbf{C}$ is the damping matrix consisting of the coefficients of dampers. The concepts of free vibrations and modes of vibration presented previously can be extended here.

Forced Vibration

The motion of a vibrating system that results from externally applied forces is called forced vibration. A forced vibration often consists of two parts: transient response, which is the motion that disappears after a period of time; and steady-state response, which is the motion that remains after the transient response has disappeared.

Harmonic Excitation

Consider the motion of a damped 1-DOF system subject to a harmonically varying force:

$$m\ddot{x}(t) + c\dot{x}(t) + kx(t) = F_0 \sin \omega t \qquad [32]$$

where ω is the excitation frequency or forcing frequency. The steady-state response $x_{ss}(t)$ of the system is assumed to be sinusoidal with the same frequency, i.e.:

$$x_{ss}(t) = X_0 \sin(\omega t + \phi) \qquad [33]$$

Substitute eqn [33] into eqn [32], to find the amplitude and phase angle:

$$X_0 = \frac{F_0}{k}\frac{1}{\sqrt{(1-r^2)^2 + 4\xi^2 r^2}}, \quad \phi = \tan^{-1}\left(\frac{2\xi r}{1-r^2}\right) \qquad [34]$$

where r is the frequency ratio $r = \omega/\omega_n$, and ω_n and ξ are the undamped natural frequency and damping ratio introduced in eqn [26]. As shown in **Figure 8** and eqn [34], the amplitude of the steady-state response depends on the excitation frequency and damping ratio. For light damping, say $\xi \leq 0.1$, the amplitude approaches a maximum value as the excitation is near the undamped natural frequency ω_n. Moreover, the smaller the damping ratio, the higher the peak.

The steady-state response $x_{ss}(t)$ is a particular solution. The total solution of eqn [32] is the sum of a particular solution and the solution of the corresponding homogeneous equation. For the underdamped case ($0 < \xi < 1$) this becomes:

$$x(t) = e^{-\xi\omega_n t}(A \sin \omega_d t + B \cos \omega_d t) + X_0 \sin(\omega t + \phi) \qquad [35]$$

where A and B are determined by the initial conditions. The first term in eqn [35] is the transient response because it approaches zero for large values of t.

The response of multi-DOF systems subject to harmonic excitations can be similarly determined. To this end, consider:

$$\mathbf{M}\ddot{\mathbf{x}}(t) + \mathbf{C}\dot{\mathbf{x}}(t) + \mathbf{K}\mathbf{x}(t) = \mathbf{F_0} \sin \omega t \qquad [36]$$

By complex analysis, the excitation is the imaginary part of the exponential form $\mathbf{F}_0 e^{i\omega t}$, $i = \sqrt{-1}$. Thus, the steady-state response can be written as:

$$\mathbf{x}(t) = \mathrm{Im}\left(\mathbf{X}_0 e^{i\omega t}\right) \qquad [37]$$

where the complex vector $\mathbf{X}_0$ by eqn [36] is determined as:

$$\mathbf{X_0} = \left(-\omega^2\mathbf{M} + i\omega\mathbf{C} + \mathbf{K}\right)^{-1}\mathbf{F_0} \qquad [38]$$

The amplitudes and phase angles of the displacement parameters can be evaluated from eqns [37] and [38]. As in **Figure 8**, the amplitude can be plotted versus the excitation frequency. The difference is that the amplitude–frequency curves have multiple peaks, because there are n undamped natural frequencies from the characteristic eqn [21].

Resonance

Without damping ($\xi = 0$), the amplitude given in eqn [34] becomes infinite as the excitation frequency approaches the undamped natural frequency; see also **Figure 8**. This phenomenon of unbounded response is called resonance and $\omega = \omega_n$ is called the resonance condition. The expression given in eqn [33], however, is unable to describe the gradual growth of the amplitude. The resonant response under the harmonic excitation $F_0 \sin \omega_n t$, according to the theory of differential equations, is:

$$x(t) = \frac{F_0}{2m\omega_n} t \sin \omega_n t \qquad [39]$$

A plot of the resonant response given in **Figure 9** shows the unbounded growth of the vibration amplitude. Physically, the amplitude cannot keep growing, as the spring would be already broken.

The phenomenon of resonance is seen in general vibrating systems. Control of resonant vibrations is critical in many engineering applications. Three commonly used techniques for resonance control, among others, are: (1) passive or active damping, which reduces resonance peaks (see **Figure 8**); (2) frequency tuning, which shifts the natural frequencies away from the excitation frequencies; and (3) dynamic vibration absorption, which confines the vibration energy within an added vibrating subsystem, called vibration absorber.

Periodic Excitation

Response to arbitrary periodic excitations can be determined by extending the approach given in eqn [33]. In **Figure 10**, a general periodic forcing function $F(t)$ repeats itself in a fixed time period T (the period), such that $F(t + T) = F(t)$ for all values of t. A sinusoidal function is a periodic function, but the reverse may not be true. A periodic forcing function can be expanded in an infinite series of sinusoidal functions, called the Fourier series:

$$F(t) = \frac{a_0}{2} + \sum_{n=1}^{\infty} (a_n \cos n\omega t + b_n \sin n\omega t) \qquad [40]$$

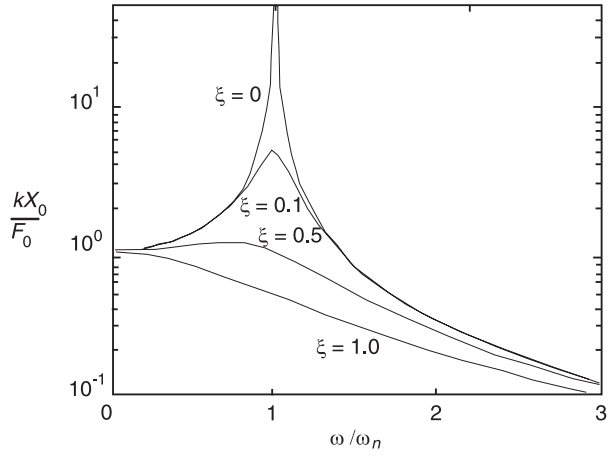


Figure 8 Amplitude of steady-state response versus frequency ratio.

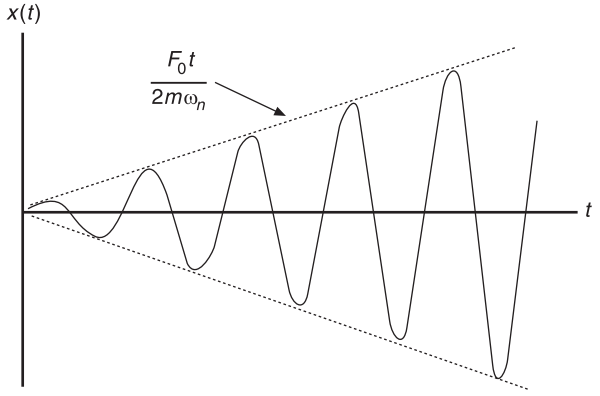


Figure 9 Resonant vibration of an undamped 1-DOF system.

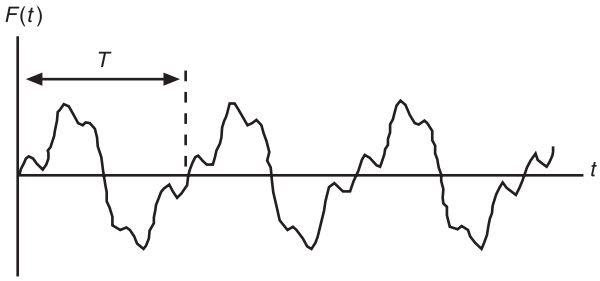


Figure 10 A periodic forcing function.

where $\omega = 2\pi/T$, and the Fourier coefficients a_n and b_n are calculated by the formulas:

$$a_n = \frac{2}{T}\int_0^T F(t)\cos n\omega t\,\mathrm{d}t, \quad n = 0, 1, 2\ldots \qquad [41]$$

$$b_n = \frac{2}{T}\int_0^T F(t)\sin n\omega t\,\mathrm{d}t, \quad n = 1, 2, 3\ldots \qquad [42]$$

Following the superposition principle, the response to a periodic excitation is the sum of the contributions of all individual harmonic components. For instance, a particular solution of eqn [24] to a periodic force can be written as:

$$x_p(t) = X_0 + \sum_{n=1}^{\infty} X_n \sin\left(n\omega t + \phi_n\right) \qquad [43]$$

It can be shown that $X_0 = a_0/(2k)$, and $X_n \sin(n\omega t + \phi_n)$ is the solution of:

$$m\ddot{x}(t) + c\dot{x}(t) + kx(t) = a_n \cos n\omega t + b_n \sin n\omega t \qquad [44]$$

which can be obtained by following eqns [33] and [34]. The total response of the system is the sum of the particular solution and the homogeneous solution accounting for the initial conditions.

The harmonic analysis given above is also applicable to multi-DOF systems. It should be pointed out that, under periodic excitations, resonance occurs if one of the natural frequencies is identical to $n\omega$ for any integer n.

Impulse Response

A common source of vibrations is the sudden application of large-magnitude, short-duration forces, such as shock and impact loads. The time history of an impact or shock load in general is difficult to measure. However, its temporal effect can be quantified. For instance, consider a damped 1-DOF system subject to an impulsive force with the time history shown in **Figure 11**, where the duration ε is arbitrarily small, i.e., $\varepsilon = 0^+$. By the impulse-momentum principle deduced from Newton's second law:

$$\begin{aligned} I_0 &= \int_0^{\varepsilon} F(t)\mathrm{d}t \\ &= m\dot{x}(\varepsilon) - m\dot{x}(0) \\ &= m\dot{x}(0^+) - mv_0 \end{aligned} \qquad [45]$$

where I_0 is the impulse of the force. This indicates that the impulsive force causes a jump in the initial velocity, $\Delta\dot{x} = \dot{x}(0^+) - \dot{x}(0) = I_0/m$. Note that $F(t) = 0$ for $t > 0^+$. Thus, the impulse-excited motion is equivalent to the free vibration problem:

$$m\ddot{x}(t) + c\dot{x}(t) + kx(t) = 0, \quad t > 0^+ \qquad [46]$$

$$x(0^+) = x_0, \quad \dot{x}(0^+) = v_0 + I_0/m \qquad [47]$$

For an underdamped system ($0 < \xi < 1$) initially at rest i.e., x_0 and v_0, its impulse response is:

$$x(t) = \frac{I_0}{m\omega_d}\mathrm{e}^{-\xi\omega_n t}\sin\omega_d t \qquad [48]$$

The above analysis is also applicable to multi-DOF systems.

Response to Arbitrary Forces

There are many solution methods for the response to arbitrary external forces, among which are convolution integral, Laplace and Fourier transforms, and modal analysis. In addition, numerical methods, such

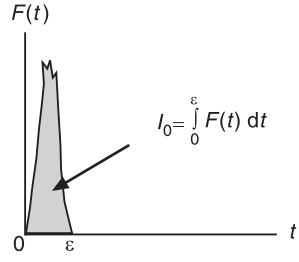


Figure 11 An impulsive force, $\varepsilon = 0^+$.

as finite difference methods and numerical integration, are often used for complex vibrating systems. For demonstrative purposes, a Laplace transform–Green's function approach is briefly discussed here.

Consider the motion of a damped multi-DOF system subject to arbitrary external and initial disturbances:

$$\begin{aligned} &\mathbf{M}\ddot{\mathbf{x}}(t) + \mathbf{C}\dot{\mathbf{x}}(t) + \mathbf{K}\mathbf{x}(t) = \mathbf{f}(t) \\ &\mathbf{x}(0) = \mathbf{x_0}, \quad \dot{\mathbf{x}}(0) = \mathbf{v_0} \end{aligned} \qquad [49]$$

Laplace transformation of eqn [49] with respect to t yields:

$$\hat{\mathbf{x}}(s) = H(s)\left\{\mathbf{M}\mathbf{v}_0 + \mathbf{C}\mathbf{x}_0 + s\mathbf{M}\mathbf{x}_0 + \hat{\mathbf{f}}(s)\right\} \qquad [50]$$

where $\hat{\mathbf{x}}(s)$ and $\hat{\mathbf{f}}(s)$ are the Laplace transforms of $\mathbf{x}(t)$ and $\mathbf{f}(t)$, respectively, s is the complex Laplace transform parameter, and $H(s) = (s^2\mathbf{M} + s\mathbf{C} + \mathbf{K})^{-1}$ is called the transfer function of the system. Inverse Laplace transform of eqn [50] gives the total response:

$$\begin{aligned} \mathbf{x}(t) = {} & G(t)(\mathbf{M}\mathbf{v_0} + \mathbf{C}\mathbf{x_0}) \\ & + \frac{\mathrm{d}}{\mathrm{d}t} G(t)\mathbf{M}\mathbf{v_0} + \int_0^t G(t-\tau)\mathbf{f}(\tau)\,\mathrm{d}\tau \end{aligned} \qquad [51]$$

where $G(t)$, the inverse Laplace transform of the transfer function $H(s)$, is called the impulse response function or Green's function of the system. Physically, the first two terms of eqn [51] represent vibration due to initial disturbances; the last term represents vibration due to external forces.

Modal Analysis

Modal analysis is a useful technique of analysis and solution for general vibrating systems. Its use depends on the existence of certain orthogonality relations among system eigenvectors (mode shapes). Orthogonality relations are used to decouple the original equations of vibration into a set of independent differential equations. The solution of those decoupled equations yields the response in a series of system eigenvectors. Solution by this technique is usually called modal expansion or eigenfunction expansion. The basic concept of modal analysis is detailed as follows.

First, consider undamped systems modeled by eqn [8]. Under the condition of symmetric mass and stiffness matrices, and the condition of distinct eigenvalues, the eigenvectors defined in eqn [20] share the orthogonality relations:

$$\mathbf{u}_k^{\mathrm{T}}\mathbf{M}\mathbf{u}_l = 0, \quad \mathbf{u}_k^{\mathrm{T}}\mathbf{K}\mathbf{u}_l = 0 \quad \text{for} \quad k \neq l \qquad [52]$$

Eigenvectors satisfying the above relations are usually called orthogonal or normal modes. The eigenvectors can be scaled or normalized such that:

$$\mathbf{u}_k^{\mathrm{T}}\mathbf{M}\mathbf{u}_k = 1 \qquad [53]$$

The orthogonality relations provide a convenient way of determining a dynamic response to arbitrary excitations. As an example, let the solution be expressed by a series of system eigenvectors:

$$\mathbf{x}(t) = \sum_{k=1}^{n} q_k(t)\{\mathbf{u}_k\} \qquad [54]$$

where the unknown time-dependent coefficients $q_k(t)$ are called modal coordinates. Eqn [54] represents a real transformation from physical coordinates to modal coordinates. Substitution of the expression [54] into eqn [8], and use of the orthogonality relations [52] and normalization condition [53], leads to n independent second-order differential equations:

$$\ddot{q}_k(t) + \omega_k^2 q_k(t) = \mathbf{u}_k^{\mathrm{T}}\mathbf{f}(t), \quad k = 1, 2, \ldots n \qquad [55]$$

which can be easily solved by many methods. With the determined $q_k(t)$, a closed-form modal expansion of the total response is given by eqn [54]. Furthermore, having solved eqn [55], the Green's function in eqn [51] is found to be:

$$G(t) = \sum_{k=1}^{n} \frac{1}{\omega_k} \sin\ \omega_k t \cdot \mathbf{u}_k^{\mathrm{T}}\mathbf{u}_k \qquad [56]$$

Next, consider the damped systems described by eqn [49]. A system is called proportionally damped if the condition:

$$\mathbf{K}\mathbf{M}^{-1}\mathbf{C} = \mathbf{C}\mathbf{M}^{-1}\mathbf{K} \qquad [57]$$

holds. Under this condition, the eigenvalues are complex, but the eigenvectors are real. More importantly, the eigenvectors are the same as those of the corresponding undamped system. Consequently, the eigenvectors enjoy the orthogonality relations given in eqn

[52]. In addition, they also satisfy:

$$\mathbf{u}_k^{\mathrm{T}}\mathbf{C}\mathbf{u}_l = 0 \quad \text{for } k \neq l \qquad [58]$$

It follows that the modal expansion, eqn [54], can be directly used to decouple eqn [49] into:

$$\ddot{q}_k(t) + 2\xi_k\omega_k\dot{q}_k(t) + \omega_k^2 q_k(t) = \mathbf{u}_k^{\mathrm{T}}\mathbf{f}(t) \qquad [59]$$

for $k = 1, 2 \ldots n$, where ξ_k is called the modal damping ratio. The response of the damped system can be obtained in closed form.

If the condition, eqn [57], is not met, the eigenvalues and eigenvectors are both complex. The system is then called nonproportionally damped. Besides nonproportional damping, complex modes are also caused by other effects such as gyroscopic forces induced by mass transport or Coriolis acceleration, and circulatory forces. These complex modes of vibration in general are not orthogonal in the sense of eqns [52] and [58]. As a result, the conventional modal expansion fails to decouple the equations of motion. In this case, complex modal analysis can be adopted. In a complex modal analysis, the original equations of vibration are cast in to a first-order state-space form with the state-space vector $z(t)$ containing displacements and velocities:

$$\mathbf{z}(t) = \begin{pmatrix} \mathbf{x}(t) \\ \dot{\mathbf{x}}(t) \end{pmatrix} \qquad [60]$$

In this form, the orthogonality relations among state-space eigenvectors can be established. Consequently, the state equation is decoupled into a set of independent first-order differential equations, and the modal expansion of the state-space vector is obtained.

Nomenclature

f_s	spring force
g	gravitational acceleration
I_0	impulse of the force
k	spring coefficient or stiffness
$\mathbf{K}$	stiffness differential operator
$\mathbf{M}$	mass differential operator
M_0	external torque
r	frequency ratio
T	tension of the string
v_0	initial velocity
x_0	initial displacement
$\ddot{x}$	acceleration of the mass
ρ	linear density
ξ_k	modal damping ratio

See also: **Absorbers, active**; **Absorbers, vibration**; **Chaos**; **Commercial software**; **Computation for transient and impact dynamics**; **Eigenvalue analysis**; **Forced response**; **Krylov-Lanczos methods**; **Modal analysis, experimental**, Basic principles; **Mode of vibration**; **Nonlinear normal modes**; **Nonlinear systems, overview**; **Resonance and antiresonance**; **Shock isolation systems**; **Testing, nonlinear systems**; **Theory of vibration**, Duhamel's Principle and convolution; **Theory of vibration**, Energy methods; **Theory of vibration**, Equations of motion; **Theory of vibration**, Impulse response function; **Theory of vibration**, Substructuring; **Theory of vibration**, Superposition; **Theory of vibration**, Variational methods; **Viscous damping**.

Further Reading

Bishop RED (1979) *Mechanics of Vibration*. Cambridge, UK: Cambridge University Press.

Dahlquist G and Björck Å *Numerical Methods*, Prentice Hall, Inc., Englewood Cliffs, New Jersey.

Goldstein H (1980) *Classical Mechanics*, 3rd edn. Massachusetts: Addison Wesley.

Harris CM (ed.) (1988) *Shock and Vibration Handbook*, 3rd edn. New York: McGraw-Hill.

Horn RA and Johnson CR (1985) *Matrix Analysis*. Cambridge, UK: Cambridge University Press.

Hughes TJR (1987) *The Finite Element Method*. Englewood Cliffs, NJ: Prentice Hall.

Huseyin K (1978) *Vibration and Stability of Multiple Parameter Systems*. Alphen aan den Rijn, The Netherlands: Sijthoff & Noordhof.

Inman DJ (1994) *Engineering Vibration*. Englewood Cliffs, NJ: Prentice Hall.

Meirovitch L (1967) *Analytical Methods in Vibrations*. New York: Macmillan.

Nayfeh AH and Mook DT (1979) *Nonlinear Oscillations*. New York: Wiley-Interscience.

Newland DE (1975) *An Introduction to Random Vibrations and Spectral Analysis*. London: Longman.

Rao SS (1995) *Mechanical Vibrations*, 3rd edn. Massachusetts: Addison Wesley.

Rayleigh JWS (1945) *The Theory of Sound*. New York: Dover.

Sun CT and Lu YP (1995) *Vibration Damping of Structural Elements*. Englewood Cliffs, NJ: Prentice Hall.

Weaver, W Jr, Timoshenko SP and Young, DH (1990) *Vibration Problems in Engineering*. John Wiley.

Superposition

M G Prasad, Stevens Institute of Technology, Hoboken, NJ, USA

Copyright © 2001 Academic Press

doi:10.1006/rwvb.2001.0109

Introduction

Linear system models are very important in vibration analysis. Linear models enable the designer to obtain a basic understanding of the component interactions in a system. Although nonlinearity exists in real systems, linear modeling and analysis are essential in most cases as they yield simpler mathematical formulation. The principle of superposition plays an extremely important role in mechanical vibrations and dynamic analysis of linear systems.

It is known generally that all physical systems are nonlinear. However, assumptions and approximations are made such that the mathematical model and the resulting equations are linear. This is done for important reasons: the solution of linear problem is feasible and provides a good insight into the system behavior. Also, the results obtained using the linear approximation are often sufficient for many engineering applications. The importance of the principle of linear superposition to vibration analysis is seen by observing some of the following ramifications of the nonvalidity of the superposition to nonlinear systems.

1. Two linearly independent solutions cannot be linearly combined to obtain the solution of a nonlinear second-order differential equation.
2. The general solution to a nonlinear system equation cannot be obtained by a summation of the free vibration and forced vibration responses. This is because of the interaction between the free and forced vibration responses.
3. The development of a convolution integral approach based on the impulse response is not valid for nonlinear systems.
4. Superposition of modes will not be valid for nonlinear systems. This is due to mode coupling.
5. The mathematical techniques, such as Fourier series and Laplace transform, cannot be used to obtain responses of nonlinear systems under combination of excitations.

Thus, it is seen that the superposition is an extremely important part of linear vibration analysis. It enables a solution of linear system models to a variety of excitations such as periodic functions, transients, modal excitations, etc. In the following section, the applications of the principle of linear superposition to wave addition, system response, convolution integral, and modal superposition are presented. It is to be noted that, although the principle of superposition is quite simple in its statement and application, it has a profound impact on all types of linear systems modeling and analysis.

Linearity and Superposition

Figure 1 shows a linear lumped system model of a single-degree-of-freedom system with mass m, spring stiffness k and viscous damping coefficient c. **Figure 2** shows a black-box model of the single-degree-of-freedom system with a harmonic input, $f(t)$, and solution, $x(t)$. The system equation is given by:

$$m(\mathrm{d}^2x/\mathrm{d}t^2) + c(\mathrm{d}x/\mathrm{d}t) + kx = f(t) \qquad [1]$$

The principle of superposition says that the harmonic motions can be combined linearly to obtain the total motion. In reference to system analysis, the total response of a linear system can be obtained by the linear combination or addition of the individual responses of the system for the corresponding individual excitations. In other words, for the linear black-box model of **Figure 2**, if $x_1(t)$ and $x_2(t)$ are the harmonic solutions, for the harmonic inputs are $f_1(t)$ and $f_2(t)$ respectively, then the total solution, as shown in **Figure 3**, is given by:

$$x(t) = x_1(t) + x_2(t) \qquad [2]$$

It is seen that, whenever linearity holds, the powerful principle of superposition can be applied effectively. Thus, superposition can also be described as that, whenever many waves pass through the same given region, their effects are simply additive. The total solution is obtained by superposition.

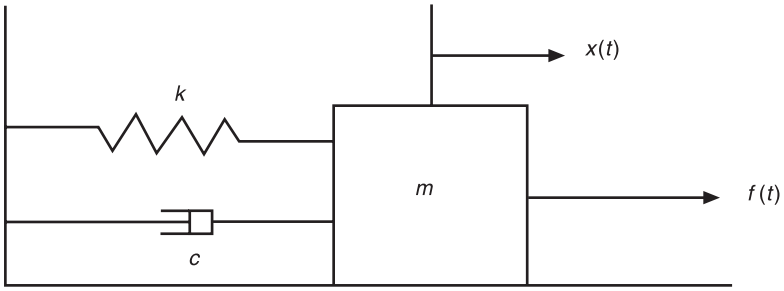


Figure 1 A single-degree-of-freedom system model.

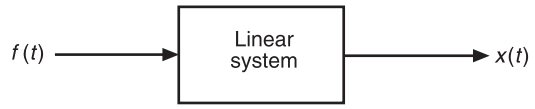


Figure 2 An input–output model of a system.

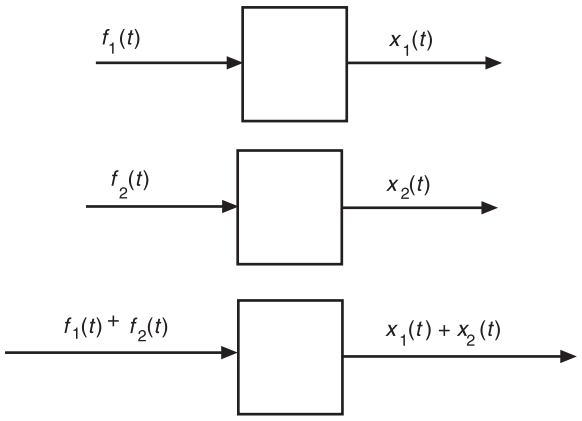


Figure 3 Principle of superposition.

To illustrate the importance of the principle of superposition, let the system shown in **Figure 3** have a nonlinear spring in place of a linear spring. Let the nonlinear spring term be $k(x + ex^2)$, where e is the nonlinearity factor. The system equation is given by:

$$m(\mathrm{d}^2x/\mathrm{d}t^2) + c(\mathrm{d}x/\mathrm{d}t) + k(x + ex^2) = f(t) \quad [3]$$

By introducing the solutions x_1 and x_2 we get:

$$m(\mathrm{d}^2x_1/\mathrm{d}t^2) + c(\mathrm{d}x_1/\mathrm{d}t) + k(x_1 + ex_1^2) = f_1(t) \quad [4]$$

$$m(\mathrm{d}^2x_2/\mathrm{d}t^2) + c(\mathrm{d}x_2/\mathrm{d}t) + k(x_2 + ex_2^2) = f_2(t) \quad [5]$$

By adding eqns [4] and (5) and then comparing them with eqn [1] we can see that the following inequality exists due to nonlinearity:

$$(x_1 + x_2)^2 \neq (x_1^2 + x_2^2) \quad [6]$$

Thus solutions x_1 and x_2 for forcing functions f_1 and f_2 respectively, cannot be added to obtain the total solutions.

Applications of Superposition

Addition of Simple Harmonic Waves

In many situations, there is a need to combine the effects of individual vibrations to obtain the superposition effect. Generally, the presence of one vibration does not alter the medium significantly such that the characteristics of the other vibrations are disturbed. Thus the total vibration is obtained by a linear superposition of individual vibrations.

Given that the two displacements have same angular frequency:

$$x_1(t) = A_1 e^{j(\omega t + \phi_1)} \quad \text{and} \quad x_2(t) = A_2 e^{j(\omega t + \phi_2)}$$

The linear superposition from eqn [2] gives:

$$Ae^{j(\omega t + \phi)} = (A_1 e^{j\phi_1} + A_2 e^{j\phi_2})e^{j\omega t} \quad [7]$$

Using phasor representation, the combined effect is shown in **Figure 4**. The real displacement is given by:

$$x(t) = A \cos(\omega t + \phi) \quad [8]$$

where:

$$A^2 = A_x^2 + A_y^2 \quad \text{and} \quad \phi = \tan^{-1}(A_y/A_x)$$
$$A_x = A_1 \cos\phi_1 + A_2 \cos\phi_2$$
$$A_y = A_1 \sin\phi_1 + A_2 \sin\phi_2$$

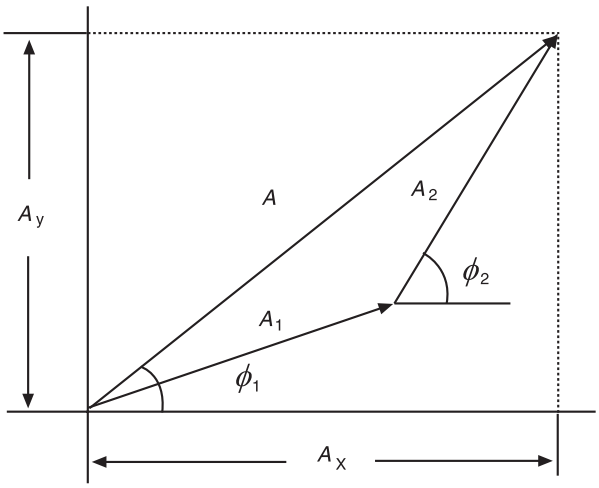


Figure 4 Superposition of two waves of same frequency.

Thus, the linear superposition of two simple harmonic vibrations of the same frequency yields another simple harmonic vibrations of the same frequency. Further, the superposition can be extended to the case where there are n number of simple harmonic vibrations of the same frequency:

$$A = \left[\left(\sum_n A_n \cos \phi_n\right)^2 + \left(\sum_n A_n \sin \phi_n\right)^2\right]^{1/2} \quad [9]$$

$$\phi = \tan^{-1}\left(\sum_n A_n \sin \phi_n \Big/ \sum_n A_n \cos \phi_n\right) \quad [10]$$

When the frequencies of the waves are not identical, then the linear superposition yields a combined solution which is dependent on the ratio of the two frequencies. If the ratio is close to unity, then the well-known beating phenomenon occurs. If the ratio is very large, then a nonperiodic solution results.

System Response

The linear equation of motion of a single-degree-of-freedom system as shown in **Figure 1** is given by:

$$m\,(\mathrm{d}^2x/\mathrm{d}t^2) + c\,(\mathrm{d}x/\mathrm{d}t) + kx = f(t) \quad [11]$$

The total response of the system eqn [6] is given by combining the solutions of the homogeneous part with $f(t) = 0$ and of the nonhomogeneous part with $f(t)$ as a given excitation function. Using the principle of superposition, the total response of the system is given by:

$$x(t) = x_\mathrm{c}(t) + x_\mathrm{p}(t) \quad [12]$$

where $x_\mathrm{c}(t)$ is the complementary solution or free response and $x_\mathrm{p}(t)$ is the particular solution or the forced response. It is to be noted that the free response $x_\mathrm{c}(t)$ depends on the initial conditions whereas the forced response is dependent on the given particular forcing function $f(t)$.

In addition it is noted that, for given different forcing functions, $f(t)$, the corresponding particular solutions, $x_\mathrm{p}(t)$, can be obtained and the total response is given by:

$$x(t) = x_\mathrm{c}(t) + x_{\mathrm{p}1}(t) + x_{\mathrm{p}2}(t) + x_{\mathrm{p}3}(t) + \cdots \quad [13]$$

In the case of $f(t)$ being a periodic forcing function, the Fourier series approach is used to express the periodic forcing function in terms of harmonic components. Then by the application of the superposition principle the total response is obtained using the individual responses for the corresponding component of the periodic forcing function.

Superposition Integral

Another important application of the superposition principle is in the case of a linear system under arbitrary excitation. When an undamped linear system is excited by a unit impulse function, then the unit impulse response is given by:

$$h(t) = (1/(m\omega_n)) \sin(\omega_n t) \quad [14]$$

Any arbitrary excitation can be considered to be a series of impulse excitations, as shown in **Figure 5**. Using an elapsed time variable, $(t - \xi)$, the unit impulse response at time $t = \xi$ is given by $h(t - \xi)$. Then the superposition principle can be used to combine these contributions for the varying amplitudes as per the given function. The response is given by:

$$x(t) = \int_0^t f(\xi)\, h(t - \xi)\, \mathrm{d}\xi \quad [15]$$

Eqn [15] is the convolution integral and is also referred to as the superposition integral.

Modal Superposition

In dealing with the linear vibrations of a continuous system, the superposition principle is very useful in evaluating the response of the system. The general solution of a wave equation is obtained by the superposition of various normal modes. A property of the normal modes is that they are linearly independent of each other. As an illustration in the case of a transverse vibration of a string, the wave equation is given by (**Figure 6**):

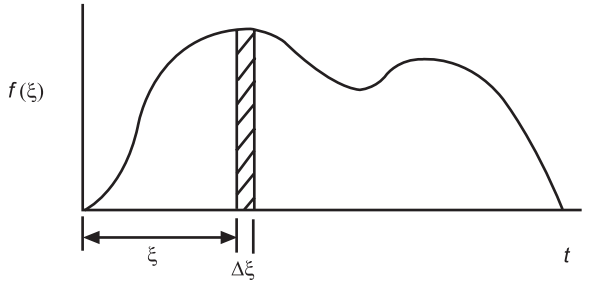


Figure 5 An arbitrary excitation.

$$c^2(\mathrm{d}^2y/\mathrm{d}x^2) = (\mathrm{d}^2y/\mathrm{d}t^2) \quad [16]$$

Then, for a prescribed boundary condition such as both ends fixed, the transverse displacements, y, at both ends are zero. Using the superposition principle, the total solution is given by:

$$y(x,t) = \sum_m y_m(x,t) \quad [17]$$

$$y(x,t) = \sum_m \sin(m\pi x/l) \times [C_n \cos(mc\pi t/L) + D_n \sin(mc\pi t/L)] \quad [18]$$

where L is the length of the string, m is the mode number, c is the wave speed, and C_n and D_n are the constants dependent on the initial conditions. Thus the principle of superposition has resulted in the total solution $y(x, t)$. **Figure 6** shows the first three modes and their superposition, which represents the net vibration of the string.

This modal superposition is based on the summation of harmonic motions that is also seen in Fourier series representation of periodic functions. To illustrate the additive effects in superposition, the following example of a square wave is presented. A square wave, $f(t)$, is given by:

$$f(t) = \begin{cases} +1 & 0 < t < T/2 \\ -1 & T/2 < t < T \end{cases} \quad [19]$$

where T is the period of the wave.

It can easily be shown that this wave is represented using the Fourier series as:

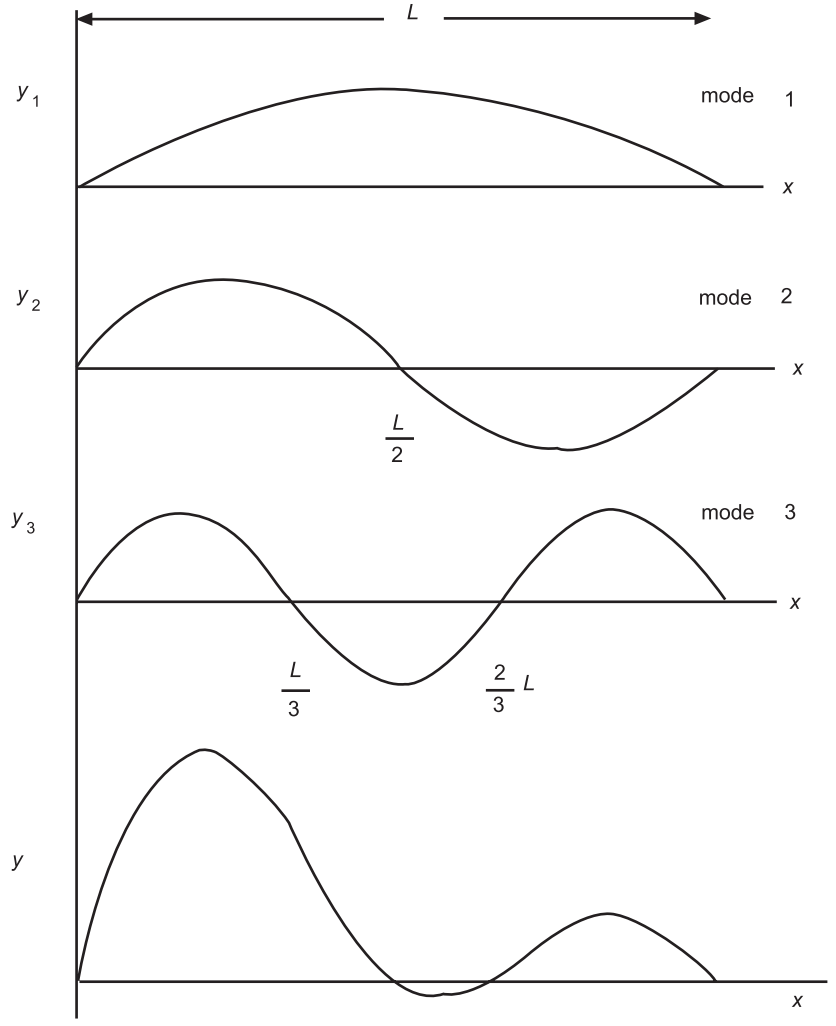


Figure 6 Three normal modes of a vibrating string.

$$f(t) = \frac{4}{\pi}\left(\sin \omega t + \frac{1}{3}\sin 3\omega t + \frac{1}{5}\sin 5\omega t + \cdots\right) \quad [20]$$

The superposition of these motions can be seen in **Figure 7**. The linear addition effect of the superposition is clearly seen as the fundamental wave transforms into a square wave. Thus, the principle of superposition can be used in both ways. This means that sinusoidal waves can be added to obtain the total solution and a periodic wave can also be represented as a summation of sinusoidal waves.

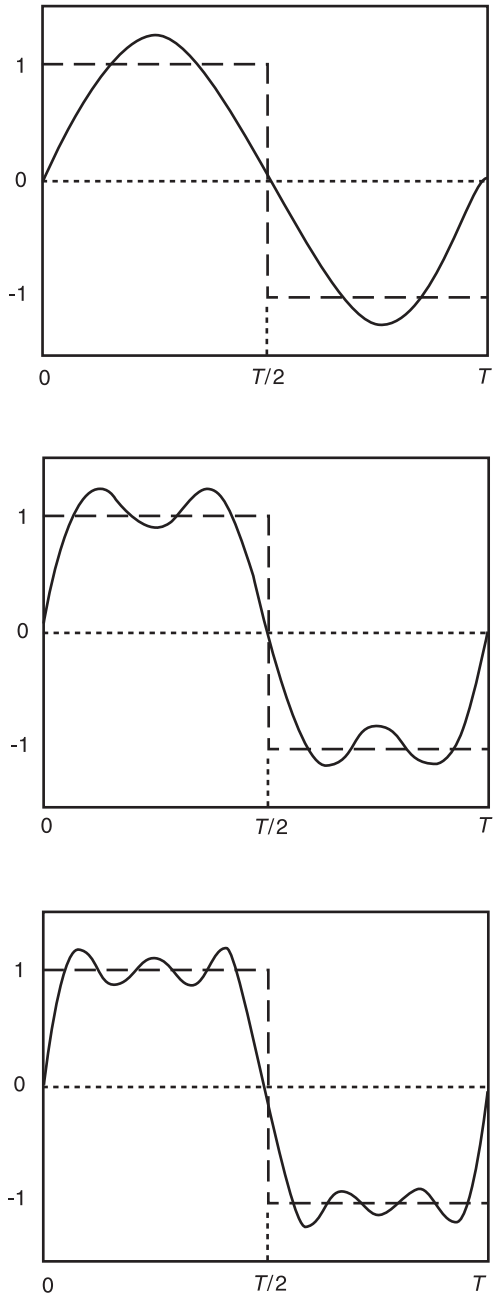


Figure 7 Summation of first three sinusoidal waves.

Conclusion

The importance of principle of superposition is seen through its many applications in linear system analysis. An understanding of the application of the principle of superposition is essential in vibration analysis of linear systems. Although most systems are nonlinear in nature, the linearization of the systems gives an insight into the system performance. Such linear analysis of systems in the presence of complex forcing functions is possible mainly due to the principle of linear superposition.

Nomenclature

c	wave speed
e	nonlinearity factor
$f(t)$	periodic forcing function
L	length of string
m	mode number
T	period of wave

See also: **Linear algebra**; **Linear damping matrix methods**; **Theory of vibration**, Fundamentals.

Further Reading

Dimarogonas AD and Haddad S (1992) *Vibrations for Engineers*. New Jersey, USA: Prentice-Hall.

Findeisen D (2000) *System Dynamics and Mechanical Vibrations: An Introduction*. Berlin, Germany: Springer-Verlag.

Hall DE (1993) *Basic Acoustics*. Florida, USA: Krieger Publishing.

Kelly SG (2000) *Fundamentals of Mechanical Vibrations*. New York, USA: McGraw-Hill.

Kinsler LE, Frey AR, Coppens AB and Sanders JV (2000) *Fundamentals of Acoustics*. New York, USA: John Wiley.

Meirovitch L (2001) *Fundamentals of Vibrations*. New York, USA: McGraw-Hill.

Rao SS (1995) *Mechanical Vibrations*. Massachusetts, USA: Addison-Wesley.

Thomson WT and Dahleh MD (1998) *Theory of Vibration with Applications*. New Jersey, USA: Prentice-Hall.

Duhamel's Principle and Convolution

G Rosenhouse, Technion - Israel Institute of Technology, Haifa, Israel

Copyright © 2001 Academic Press

doi:10.1006/rwvb.2001.0113

Duhamel's principle or convolution expresses the solution for a problem as a superposition of a set of solutions of the homogeneous wave equation and certain initial conditions. In problems that involve mechanical vibrations a force–time function that excites a system is replaced by a sequence of pulses that are represented by initial conditions at each segment of time. Now, decreasing the intervals into infinitesimal ones converts the sums into integrals, which are a special case of Duhamel's integral. This procedure allows us to obtain the aforementioned set of solutions. Finally, the total solution is obtained by superposition at any time of interest. Duhamel's principle is useful for either deterministic or random vibrations. For example, it is frequently applied in seismic analysis of structures.

About Duhamel

Jean-Marie Duhamel (1797–1872) studied at the Ecole Polytechnique. He was considered to be a remarkable teacher of mathematics. He was a professor there since 1830 for 39 years, and was elected to the Académie des Sciences in Paris in 1840. He was director of studies at the Ecole Polytechnique for the period 1848–51. In 1851 he took the chair in analysis and also became a professor at the Faculty des Science, Paris.

Duhamel worked on partial differential equations and applied his methods to acoustics, physics of harmonic overtones, rational mechanics, and heat. His acoustical studies involved vibrating strings and vibration of air in cylindrical and conical pipes. He developed a heat theory that is mathematically similar to the work of Fresnel in optics. Duhamel based his theory on the transmission of heat in crystal structures on the works of Fourier and Poisson. Duhamel's principle in partial differential equations was a consequence of his research on the distribution of heat in a solid with a variable boundary temperature.

Duhamel's Theorem: Definitions

The solution $v(x, y, z, t)$ of the boundary value problem with variable source and surface conditions is given in terms of the solution $\phi(x, y, z, t, t')$ of the boundary value problem with constant source and surface conditions by the formula:

$$v(x,y,z,t) = \frac{\partial}{\partial t}\left[\int_0^t \phi(x,y,z,t-t',t')\right] \mathrm{d}t \quad [1]$$

where (x, y, z) represents the radius vector of the point of interest in the Cartesian orthogonal spatial system of coordinates. Other equivalent coordinates systems can also be used.

A very important version of Duhamel's principle is defined as convolution. The convolution of two functions f and g is defined by $f * g$ and is given as:

$$f * g = \int_{-\infty}^{\infty} f(\tau)g(t-\tau)\,\mathrm{d}t \quad [2]$$

If the integrals involved with the convolution exist, then it is a linear operation that satisfies:

$$\begin{aligned}(f+h)*g &= f*g + h*g \\ f*(g+h) &= f*g + f*h\end{aligned} \quad [3]$$

The convolution is also commutative:

$$f * g = g * f \quad [4]$$

There are other forms of Duhamel's principle that suit the solution of problems of mechanical and electrical vibrations.

Derivation of the Convolution Theorem from Fourier Transforms

The Fourier transforms of $f(t), g(t)$ and $h(t)$ are, respectively, $F(\omega)$; $G(\omega)$, and $H(\omega)$, with ω as the radian frequency of the signals. We assume the relation $H(\omega) = F(\omega)G(\omega)$, and the aim is to find the time domain relation between the signals $f(t), g(t)$, and $h(t)$. By definition, the use of the Fourier transform yields:

$$\begin{aligned}h(t) &= \frac{1}{2\pi}\int_{-\infty}^{\infty} \left(H(\omega)\mathrm{e}^{\mathrm{i}\omega t}\right)\mathrm{d}\omega \\ &= \frac{1}{2\pi}\int_{-\infty}^{\infty} \left(F(\omega)\mathrm{G}(\omega)\mathrm{e}^{-\mathrm{i}\omega t}\right)\mathrm{d}\omega \\ &= \frac{1}{2\pi}\int_{-\infty}^{\infty} F(\omega)\left[\int_{-\infty}^{\infty} g(\tau)\mathrm{e}^{\mathrm{i}\omega t}\,\mathrm{d}\tau\right]\mathrm{e}^{\mathrm{i}\omega t}\,\mathrm{d}\omega\end{aligned} \quad [5]$$

Now, by changing the order of integration we have:

$$h(t) = \int_{-\infty}^{\infty} g(\tau)\left[\frac{1}{2\pi}\int_{-\infty}^{\infty} f(\omega)\mathrm{e}^{\mathrm{i}\omega(t-\tau)}\,\mathrm{d}\omega\right]\mathrm{d}t \quad [6]$$

Which, in turn, results in the convolution theorem:

$$h(t) = \int_{-\infty}^{\infty} g(\tau) f(t-\tau)\, \mathrm{d}u = \int_{-\infty}^{\infty} f(\tau) g(t-\tau)\, \mathrm{d}\tau = f(t) * g(t) \quad [7]$$

Because of its symmetry, a frequency domain convolution can be obtained. Using eqn [7] for the time domain, we obtain:

$$H(\omega) = \frac{1}{2\pi} \int_{-\infty}^{\infty} f(t) \left[\int_{-\infty}^{\infty} G(\Omega) \mathrm{e}^{\mathrm{i}\Omega t}\, \mathrm{d}\Omega \right] \mathrm{e}^{-\mathrm{i}\omega t}\, \mathrm{d}t = \frac{1}{2\pi} \int_{-\infty}^{\infty} G(\Omega) \left[\int_{-\infty}^{\infty} f(t) \mathrm{e}^{\mathrm{i}(\omega-\Omega)t}\, \mathrm{d}t \right] \mathrm{d}\Omega \quad [8]$$

or:

$$H(\omega) = \frac{1}{2\pi} \int_{-\infty}^{\infty} G(\Omega) F(\omega - \Omega)\, \mathrm{d}\Omega = \frac{1}{2\pi} \int_{-\infty}^{\infty} F(\Omega) G(\omega - \Omega)\, \mathrm{d}\Omega \quad [9]$$

Thus:

$$H(\omega) = \frac{1}{2\pi} F(\omega) * G(\omega) \quad [10]$$

Since Ω is generally complex, $H(\omega)$ is called the complex convolution theorem.

The Engineering Approach

The response of a mechanical system to a step function excitation or to a unit impulse can serve as a tool in the analysis of the response of a linear system to an excitation by an arbitrary function of time. This method is based on the principle of superposition that can be applied to any linear system that can be simulated by a set of linear differential equations. **Figure 1A** provides a simple illustration where a mass–spring system, with m as the mass and k as the spring constant, is vibrating in the x-direction due to an arbitrary force, $f(\tau)$. If the coefficients of the differential equations of the system are constant, it is assumed that a unit step function or a unit impulse applied at the time τ, as shown in **Figures 1B** and **1C**, respectively, yields a response $x(t)$ as a function of the elapsed time $t - \tau$ only. However, if the coefficients are functions of time this assumption is, in general, not satisfied.

The applied force $f(\tau)$ at the time τ can be split along the time axis into a sequence of step functions Δf, at each time step $\Delta\tau$, as illustrated in **Figure 1B**, by application of steps at $0, \Delta\tau, 2\Delta\tau, \ldots$. This procedure yields a finite difference approximation. A unit step function that begins at τ results in the displacement $\Phi(t-\tau)$ which depends on the properties of the system, and is defined as the indicial admittance of the system. The total displacement $x(t)$ becomes:

$$x(t) = \sum_{\tau=0}^{N(\tau=t)} \Delta f(n\Delta\tau)\Phi(t - n\Delta\tau) \quad [11]$$

If we write $\Delta f = (\Delta f/\Delta\tau)\Delta\tau$, and $n\Delta\tau = \tau$, then:

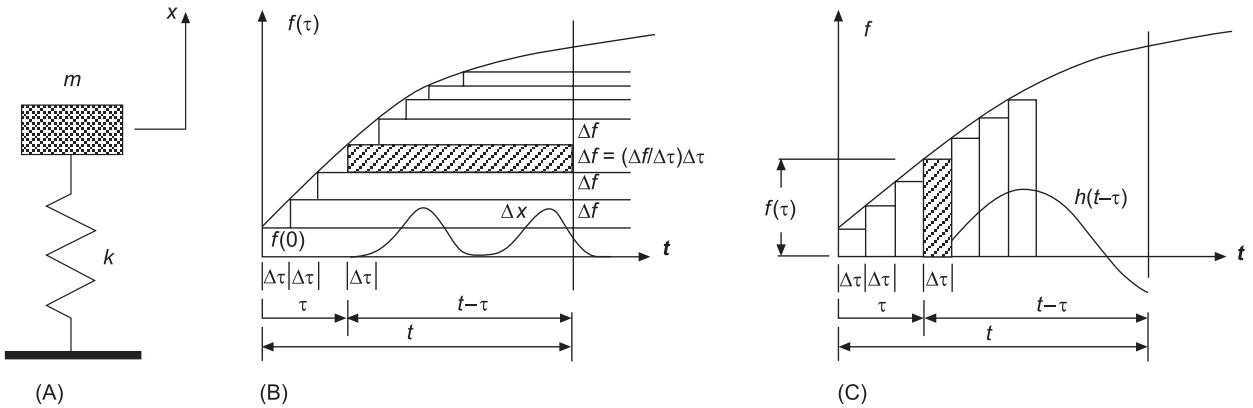


Figure 1 Schemes illustrating Duhamel's principle.

$$x(t) = \sum_{\tau=0}^{\tau=1} \frac{\Delta f}{\Delta \tau} \Phi(t-\tau)\Delta\tau \qquad [12]$$

and, in the limit:

$$x(t) = \lim_{\Delta\tau \to 0} \{x(t)\} = \int_0^1 \frac{\Delta f}{\Delta \tau} \Phi(t-\tau)\, \mathrm{d}\tau \qquad [13]$$

Eqn [13] has the form of Duhamel's integral that we have met before. By integrating by parts of eqn [13] another version of Duhamel's integral can be obtained:

$$x(t) = \int_0^t f(\tau)\Phi'(t-\tau)\, \mathrm{d}\tau \qquad [14]$$

$\Phi'(t-\tau) = h(t-\tau)$. $h(t-\tau)$ is the impulse response function (the response at t to a unit impulse at τ). This result leads to another form of solution, which collects the contributions of discrete impulses $f(\tau)\Delta t$, that exist in the interval $\tau = 0$ to $\tau = \tau$ as shown in **Figure 1C**, on the displacement $x(t)$:

$$x(t) = \sum_{\tau=0}^{\tau=t} [f(\tau)h(t-\tau)\Delta\tau] \qquad [15]$$

In the limit $\Delta\tau \to 0$, Duhamel's integral or the convolution is obtained:

$$x(t) = \int_0^t f(\tau)h(t-\tau)\, \mathrm{d}\tau \qquad [16]$$

An important feature of this approach is that the solution can be expressed in terms of the initial conditions of each step or contribution. If from **Figures 1A** and **1C** we take the impulse at τ and calculate its contribution at the time t, then from the multiplication of the impulsive force $f(\tau)$ by the increment of time Δt, we obtain the impulse $f(\tau)\Delta\tau$. The impulse equals the resulting momentum, $m\,\mathrm{d}x/\mathrm{d}\tau$. The initial conditions for the single impulse at τ are: $x(\tau) = 0$, and $\mathrm{d}x/\mathrm{d}\tau = v(\tau)$. Hence, $v(\tau) = f(\tau)\Delta\tau/m$. We remain with the homogeneous equation of motion of the mass–spring for the incremental contribution Δx of the impulse at τ to the displacement at t:

$$m\frac{\mathrm{d}^2\Delta x(t-\tau)}{\mathrm{d}(t-\tau)^2} + k\Delta x(t-\tau) = 0 \qquad [17]$$

and the last boundary conditions. Solving eqn [17] and substituting the initial conditions to find the solution constants yields:

$$\Delta x(t-\tau) = \frac{f(\tau)\Delta\tau}{m\omega_0} \sin(\omega_0(t-\tau)) \quad \omega_0 = \sqrt{\left(\frac{k}{m}\right)} \qquad [18]$$

Following eqn [16], the whole displacement of the specific problem, at t becomes:

$$\begin{aligned} x(t) &= \int_0^t f(\tau)h(t-\tau)\, \mathrm{d}\tau \\ &= \frac{1}{m\omega_0}\int_0^t f(\tau) \sin(\omega_0(t-\tau))\, \mathrm{d}\tau \end{aligned} \qquad [19]$$

The solution of the contribution $\Delta x(t-\tau)$ for the step function that begins at τ is:

$$\Delta x(t-\tau) = \frac{\Delta f(\tau)}{k}[1 - \cos(\omega_0(t-\tau))] \quad \omega_0 = \sqrt{\left(\frac{k}{m}\right)} \qquad [20]$$

and the whole displacement at t becomes:

$$x(t) = \frac{1}{k}\int_0^t \frac{\mathrm{d}f(\tau)}{\mathrm{d}\tau}[1 - \cos(\omega_0(t-\tau))]\, \mathrm{d}\tau \qquad [21]$$

Obviously eqns [19] and [21] should lead to the same result. Further development of this formulation includes the addition of damping, etc. These extensions enable us to solve more complicated problems.

In the case of a damped single-degree-of-freedom (SDOF) system, a dashpot is used where a viscous damping coefficient c, is added in parallel to the spring. The equation of motion for an impulse at τ becomes:

$$\begin{aligned} &\frac{\mathrm{d}^2\Delta x(t-\tau)}{\mathrm{d}(t-\tau)^2} + 2\beta\frac{\mathrm{d}\Delta x(t-\tau)}{\mathrm{d}(t-\tau)} + \omega_0^2\Delta x(t-\tau) \\ &\quad = \frac{f(\tau)\delta(t-\tau)}{m}\beta = \frac{c}{2m}, \quad \omega_0 = \sqrt{\left(\frac{k}{m}\right)} \end{aligned} \qquad [22]$$

and the initial conditions for the single impulse at τ are: $x(\tau) = 0$, and $\mathrm{d}x/\mathrm{d}\tau = v(\tau)$. Hence,

$v(\tau) = f(\tau)\Delta\tau/m$. Hence, for a damped SDOF system, Duhamel's integral becomes:

$$x(t) = \int_0^t f(\tau)h(t-\tau)\,\mathrm{d}\tau$$
$$= \frac{1}{m\omega}\int_0^t f(\tau)\exp\left[-\beta(t-\tau)\right]\sin\left(\omega(t-\tau)\right)\mathrm{d}\tau$$
$$\omega = \sqrt{\left(\omega_0^2 - \beta^2\right)} = \omega_0\sqrt{\left(1-\zeta^2\right)}, \quad \zeta = \beta/\omega_0 \qquad [23]$$

Eqn [16] has some other variants. For example, since all values of $f(\tau)$ at $\tau < 0$ are zero, and the integral from $\tau = -\infty$ to $\tau = t$ is zero, the limits of the integral can be extended to this range. Moreover, since the response function $h(t-\tau)$ for $\tau < t$ is zero (these impulses do not exist so far), the time limits can be extended to the interval $(-\infty\infty)$ without changing the result of eqn [16]:

$$x(t) = \int_{-\infty}^{\infty} f(\tau)h(t-\tau)\,\mathrm{d}\tau = f * h \qquad t \in R \qquad [24]$$

The Discrete Time Convolution

Whenever the right-hand side of eqn [17] exists, the discrete time convolution of the discrete time signals becomes:

$$\{f * h\}(t) = \sum_{m=-\infty}^{\infty} f[m]h[n-m] \quad n \in Z \qquad [25]$$

Hence, a discrete time convolution is an operator acting on a pair of discrete time signals f and h, resulting in a discrete time signal $f*h$, the value of which at the time n is $\{f * h\}[n]$.

The circular convolution of a finite duration discrete time signal, $\{x[n], y[n]; 0 \le n \le N-1\}$, is:

$$\{f \otimes h\}[n]$$
$$= \sum_{m=0}^{N-1} f[m]h[(n-m) \bmod N] \quad 0 \le n \le N-1 \qquad [26]$$

This is an operator acting on a pair of N-dimensional vectors f and h, which yields an N-dimensional vector $f \otimes h$, and its nth component is $\{f \otimes h\}[n]$.

See also: **Earthquake excitation and response of buildings**; **Forced response**; **Theory of vibration**, Energy methods; **Theory of vibration**, Equations of motion; **Theory of vibration**, Fundamentals; **Theory of vibration**, Superposition.

Further Reading

Karman T, Biot MA (1940 *Mathematical Methods in Engineering*, pp. 403–405. New York: McGraw Hill.

Energy Methods

S S Rao, University of Miami, Coral Gables, FL, USA

Copyright © 2001 Academic Press

doi:10.1006/rwvb.2001.0115

Introduction

Energy methods can be used to find the solution of solid mechanics problems without having to solve the governing differential equations. The foundations of energy methods can be traced to the concepts of work, potential energy, and kinetic energy that were introduced by Huygens, Leibniz, Bernoulli, and Lagrange. The energy principles of mechanics are sufficiently general to allow Newton's second law to be deduced from them. The principle of virtual work, first presented by Jean Bernoulli, leads to the principle of minimum potential energy. The principle of complementary energy can be derived from the principle of virtual work by means of Legendre transformation. The principle of minimum complementary energy can be considered as the generalization of Castigliano's theorem. The principle of virtual work, coupled with the concept of inertia force, as presented by D'Alembert, can be used to derive the Hamilton's principle. Lagrange equations of motion can be obtained directly from the Hamilton's principle.

Newton's second law of motion, Lagrange equations, or Hamilton's principle can be used to derive the equations governing the dynamics of rigid bodies as well as vibrating systems. For the solution of equations of motion of a vibrating system, exact methods of solving ordinary and partial differential equations can be used. These methods can only be used for simple systems with simple boundary and initial conditions. Useful approximate solution methods, based on variational principles and energy methods, were devised by Rayleigh, Ritz, Galerkin, and

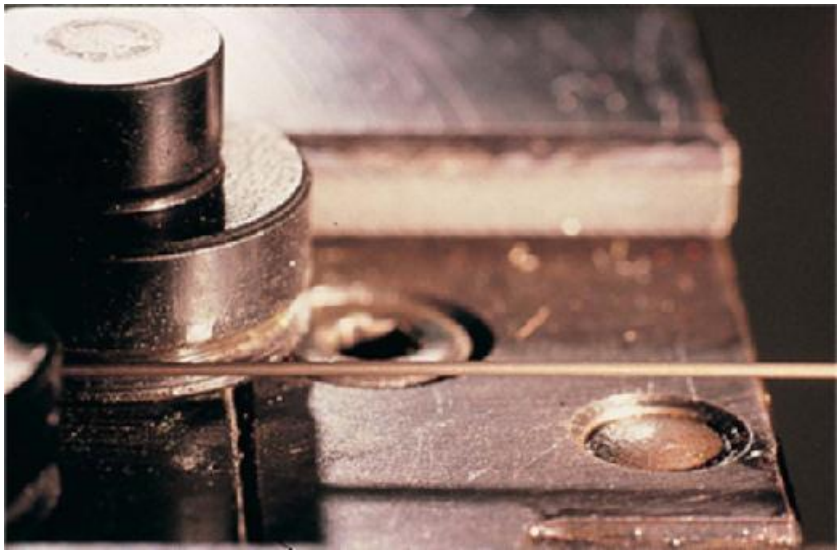


Plate 51 Shape Memory Alloys. Memory metal. Close-up view of a wire of memory metal being 'educated' by being bent around a spindle. Memory metals are alloys of nickel, titanium and aluminium or copper. Once manufactured in a certain shape the metal may be deformed with little effort, but will regain its shape upon gentle heating. The heat makes the metal plastic, allowing it to return to the structural arrangement in which it was made (its minimum energy configuration). Repeated bending of the metal, each time to the same position, alters the original structure permanently and 'educates' it to a new shape. (With permission from Science Photo Library).

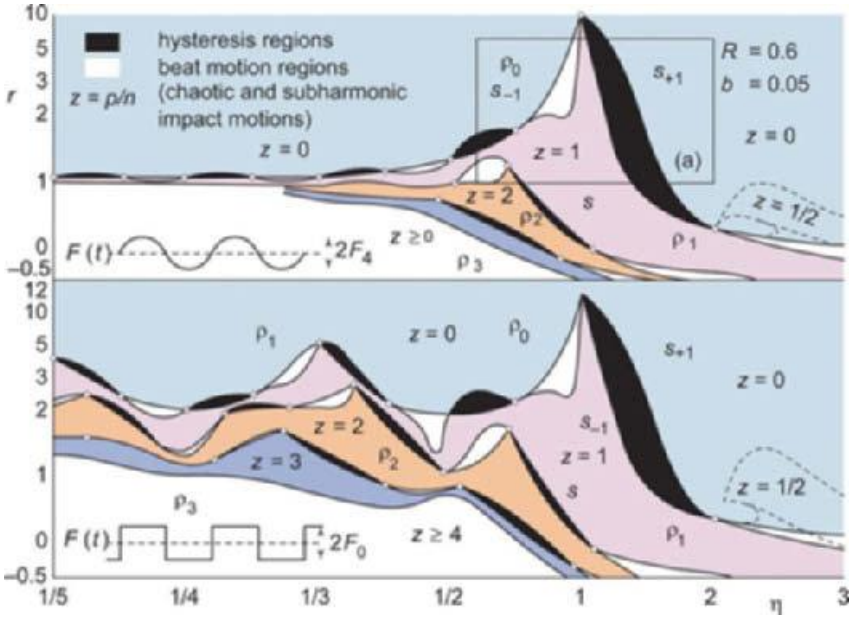


Plate 52 (left) Vibro-Impact Systems. Regions of stability and existence of impact motions for the periodic harmonic and rectangular excitations.

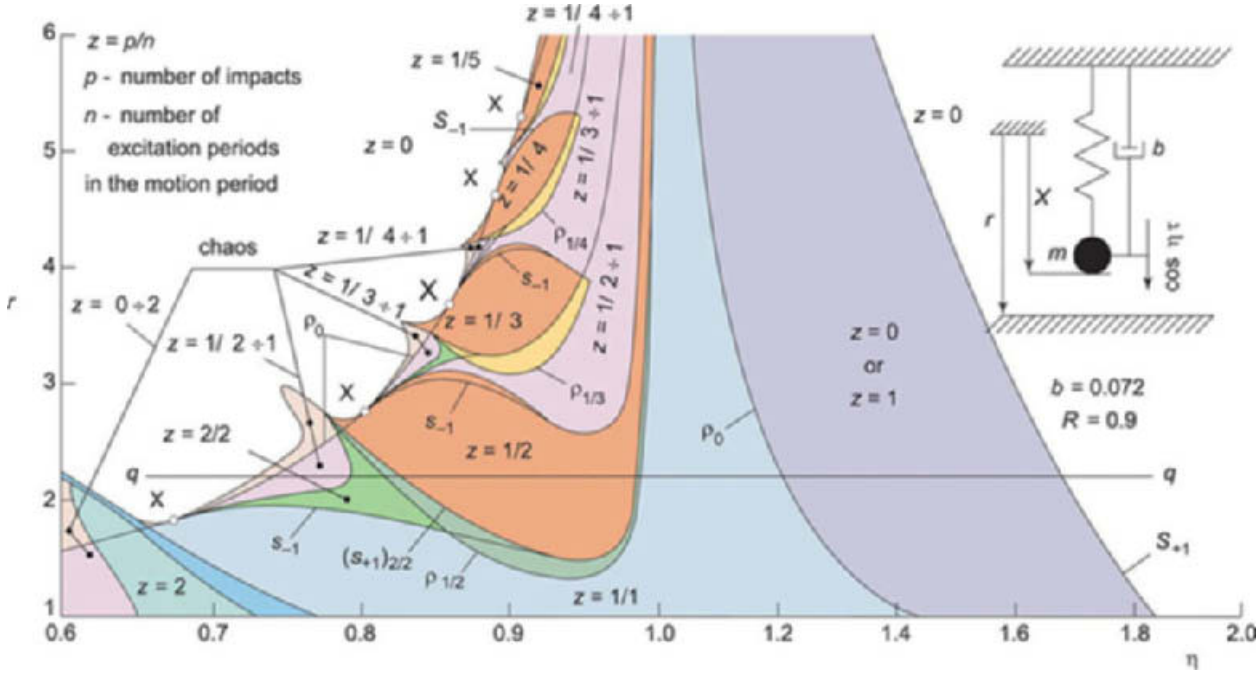


Plate 53 (below) Vibro-Impact Systems. Regions of periodic and chaotic impact motions near the resonance of the linear oscillator.

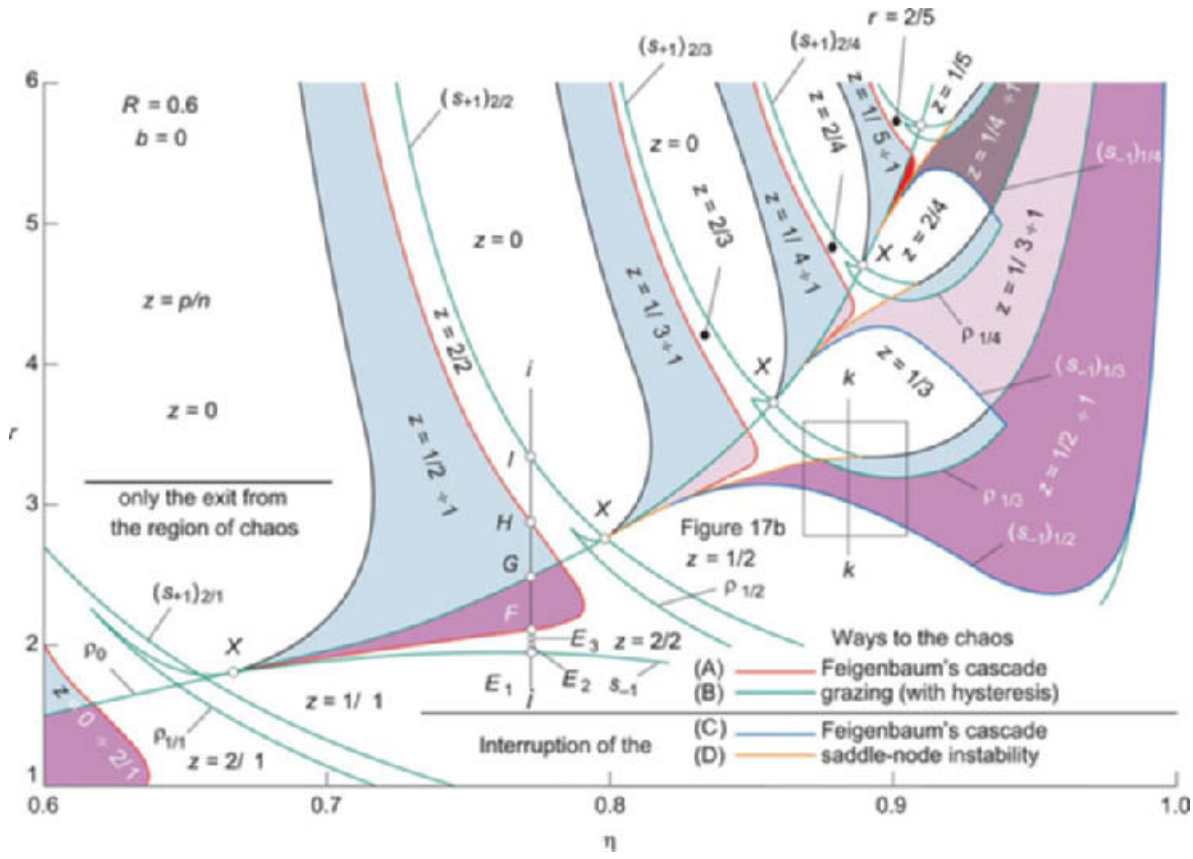
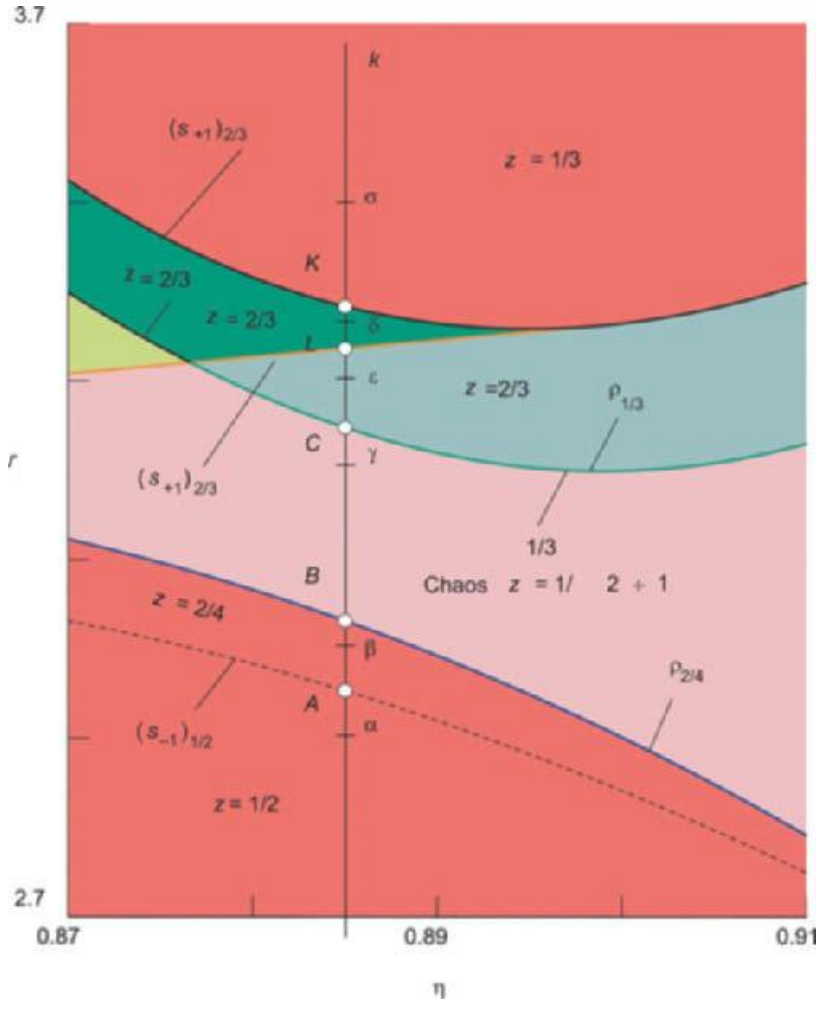


Plate 54 (above) Vibro-Impact Systems.
Regions of chaotic impact motions and classification of their boundaries (four types of way into and from chaos and one type of exit from chaos).

Plate 55 (right) Vibro-Impact Systems.
Regions of periodic and chaotic impact motions in enlarged rectangular subregion of Plate 54.



others. Approximate solutions, based on numerical analysis, such as finite difference and finite element methods have also been developed. This article deals with the approximate methods based on energy principles. These methods include the Rayleigh's method and the Rayleigh–Ritz method.

Rayleigh's Method for Discrete Systems

The Rayleigh's method is useful to find an approximate value of the fundamental natural frequency of a vibrating system. The method makes use of energy expression and does not require either the differential equation of motion of the system or its solution. Rayleigh's method can be stated as follows:

> The frequency of vibration of a conservative system vibrating about an equilibrium position has a stationary value in the neighborhood of a natural mode. This stationary value, in fact, is a minimum value in the neighborhood of the fundamental natural mode.

Although Rayleigh's method is more useful for continuous than for discrete systems, the method is described for both in this article.

To derive an expression for the approximate value of the first natural frequency of a multi-degree-of-freedom (discrete) system according to Rayleigh's method, let the displacement $x_i(t)$ of mass m_i be of the form:

$$x_i(t) = X_i \sin \omega t \qquad [1]$$

where X_i is the amplitude and ω is the frequency. The displacements of all the n masses of the system can be expressed as a vector as:

$$\bar{\mathbf{x}}(t) = \bar{\mathbf{X}} \sin \omega t \qquad [2]$$

where:

$$\bar{\mathbf{x}}(t) = \begin{Bmatrix} x_1(t) \\ x_2(t) \\ \vdots \\ x_n(t) \end{Bmatrix} \quad \text{and} \quad \bar{\mathbf{X}} = \begin{Bmatrix} X_1 \\ X_2 \\ \vdots \\ X_n \end{Bmatrix}$$

The kinetic energy of the system can be written as:

$$T(t) = \frac{1}{2}\dot{\bar{\mathbf{x}}}(t)^{\mathrm{T}}\mathbf{M}\dot{\bar{\mathbf{x}}}(t) \qquad [3]$$

and the potential (strain) energy in the form:

$$U(t) = \frac{1}{2}\mathbf{x}(t)^{\mathrm{T}}\mathbf{K}\mathbf{x}(t) \qquad [4]$$

where $\dot{\bar{\mathbf{x}}}(t) = (\mathrm{d}/\mathrm{d}x)(\mathbf{x}(t))$ is the vector of velocities of the masses:

$$\dot{\bar{\mathbf{x}}}(t) = \begin{Bmatrix} \dot{x}_1(t) \\ \dot{x}_2(t) \\ \vdots \\ \dot{x}_n(t) \end{Bmatrix}$$

$\mathbf{M}$ is the mass matrix and $\mathbf{K}$ is the stiffness matrix of the system. Using eqn [2], the kinetic and potential energies can be expressed as:

$$T(t) = \frac{1}{2}\mathbf{X}^{\mathrm{T}}\mathbf{M}\mathbf{X}\omega^{\mathbf{2}} \cos^{2}\omega t \qquad [5]$$

$$U(t) = \frac{1}{2}\mathbf{X}^{\mathrm{T}}\mathbf{K}\mathbf{X} \sin^{2}\omega t \qquad [6]$$

When the system is conservative, the maximum kinetic energy is equal to the maximum potential energy:

$$T_{\max} = U_{\max} \qquad [7]$$

Using eqns [5] and [6], eqn [7] can be rewritten as:

$$\frac{1}{2}\mathbf{X}^{\mathrm{T}}\mathbf{M}\mathbf{X}\omega^{2} = \frac{1}{2}\mathbf{X}^{\mathrm{T}}\mathbf{K}\mathbf{X} \qquad [8]$$

which yields the frequency of vibration as:

$$R = \omega^{2} = \frac{\mathbf{X}^{\mathrm{T}}\mathbf{K}\mathbf{X}}{\mathbf{X}^{\mathrm{T}}\mathbf{M}\mathbf{X}} \qquad [9]$$

The expression on the right-hand side of eqn [9] is known as Rayleigh's quotient or Rayleigh's function.

Eqn [9] can be used to find an approximate value of the fundamental natural frequency of a system. The procedure involves selecting an arbitrary trial vector $\mathbf{X}$ to represent the fundamental natural mode. The substitution of the trial vector into eqn [9] yields an approximate value of the fundamental natural frequency. Because of the stationary property of the Rayleigh's quotient, a very good estimate of the fundamental natural frequency can be found even when the trial vector deviates greatly from the exact mode (eigenvector). Naturally, a better value of the fundamental natural frequency can be obtained when the trial vector resembles the first eigenvector more closely.

Stationarity of Rayleigh's quotient

The Rayleigh's quotient is stationary when the vector $\mathbf{X}$ is in the neighborhood of an eigenvector $\mathbf{X}^{(r)}$. To prove this, let the arbitrary vector $\mathbf{X}$ be expressed as a linear combination of the normal modes of the system, $\mathbf{X}^{(i)}$, as:

$$\mathbf{X} = a_1\mathbf{X}^{(1)} + a_2\mathbf{X}^{(2)} + \cdots \qquad [10]$$

where a_1, a_2 ... are constants. Using eqn [10], the numerator and denominator of the Rayleigh's quotient can be expressed as:

$$\mathbf{X}^{\mathrm{T}}\mathbf{K}\mathbf{X} = a_1^2\mathbf{X}^{(1)\mathrm{T}}\mathbf{K}\mathbf{X}^{(1)} + a_2^2\mathbf{X}^{(2)\mathrm{T}}\mathbf{K}\mathbf{X}^{(2)} + \cdots \qquad [11]$$

$$\mathbf{X}^{\mathrm{T}}\mathbf{M}\mathbf{X} = a_1^2\mathbf{X}^{(1)\mathrm{T}}\mathbf{M}\mathbf{X}^{(1)} + a_2^2\mathbf{X}^{(2)\mathrm{T}}\mathbf{M}\mathbf{X}^{(2)} + \cdots \qquad [12]$$

Note that the mixed terms of the form $a_ia_j\mathbf{X}^{(i)\mathrm{T}}\mathbf{K}\mathbf{X}^{j}$ and $a_ia_j\mathbf{X}^{(i)\mathrm{T}}\mathbf{M}\mathbf{X}^{(j)}$, are zero due to the orthogonality property of eigenvectors. The eigenvectors also satisfy the relation:

$$\mathbf{X}^{(i)\mathrm{T}}\mathbf{K}\mathbf{X}^{(i)} = \omega_i^2\mathbf{X}^{(i)\mathrm{T}}\mathbf{M}\mathbf{X}^{(i)} \qquad [13]$$

Using eqns [11]–[13], eqn [9] can be written as:

$$R(\mathbf{X}) = \omega^2 = \frac{a_1^2\omega_1^2\mathbf{X}^{(1)\mathrm{T}}\mathbf{M}\mathbf{X}^{(1)} + a_2^2\omega_2^2\mathbf{X}^{(2)\mathrm{T}}\mathbf{M}\mathbf{X}^{(2)} + \cdots}{a_1^2\mathbf{X}^{(1)\mathrm{T}}\mathbf{M}\mathbf{X}^{(1)} + a_2^2\mathbf{X}^{(2)\mathrm{T}}\mathbf{M}\mathbf{X}^{(2)} + \cdots} \qquad [14]$$

If the eigenvectors are M-orthogonalized;

$$\mathbf{X}^{(i)\mathrm{T}}\mathbf{M}\mathbf{X}^{(j)} = 1 \qquad [15]$$

and eqn [14] reduces to:

$$R(\mathbf{X}) = \omega^2 = \frac{a_1^2\omega_1^2 + a_2^2\omega_2^2 + \cdots}{a_1^2 + a_2^2 + \cdots} \qquad [16]$$

If $\mathbf{X}$ differs from the eigenvector $\mathbf{X}^{(r)}$ by a small amount, the constant a_r, will be much larger than all other constants $a_i (i \neq r)$. Hence eqn [16] can be expressed as:

$$R(\mathbf{X}) = \frac{a_r^2\omega_r^2 + a_r^2\sum_{\substack{i=1,2,\ldots \\ i\neq r}}(a_i/a_r)^2\omega_i^2}{a_r^2 + a_r^2\sum_{\substack{i=1,2,\ldots \\ i\neq r}}(a_i/a_r)^2} \qquad [17]$$

Since $|a_i/a_r| = \varepsilon_i \leq 1$ where ε_i, is a small number for all $i \neq r$, eqn [17] yields:

$$R(\mathbf{X}) = \omega_r^2\{1 + O(\varepsilon^2)\} \qquad [18]$$

with $O(\varepsilon^2)$ denoting a function of ε of the second order. Eqn [18] implies that if the arbitrary vector $\mathbf{X}$ differs from the true eigenvector $\mathbf{X}^{(r)}$ by a small quantity of the first order, $R(\mathbf{X})$ differs from the eigenvalue ω_r^2 by a small quantity of the second order. This shows that the Rayleigh's quotient is stationary in the neighborhood of an eigenvector.

Minimum Value of $R(\mathbf{X})$

The stationary value can be shown to be a minimum in the neighborhood of the fundamental mode, $\mathbf{X}^{(1)}$. To investigate this property, rewrite eqn [17] with $r = 1$:

$$R(\mathbf{X}) = \frac{\omega_1^2 + \sum_{i=2,3,\ldots}(a_i/a_1)^2\omega_i^2}{1 + \sum_{i=2,3,\ldots}(a_i/a_1)^2} \cong \omega_1^2 + \sum_{i=2,3,\ldots}(\omega_i^2 - \omega_1^2)\varepsilon_i^2 \qquad [19]$$

In view of the fact that $\omega_i^2 < \omega_l^2$ for $i = 2,\ 3, \ldots$, eqn [19] leads to:

$$R(\mathbf{X}) \geq \omega_1^2 \qquad [20]$$

which indicates that Rayleigh's quotient is never lower than the first eigenvalue, ω_l^2.

Application – Free Vibration of a Rod Carrying an End Mass

The natural frequency of longitudinal vibration of a rod carrying an end mass (**Figure 1**) is considered. The axial displacement of the cross-section of the rod (under a static load) is assumed to vary linearly along the length of the rod, as shown in **Figure 1B**. The amplitude of vibration is also assumed to vary linearly, as shown in **Figure 1B**. If x_0 denotes the amplitude of the rod at $z = L$, the amplitude of vibration (x) of the cross-section at z can be expressed as:

$$x = \frac{x_0 z}{L} \qquad [a]$$

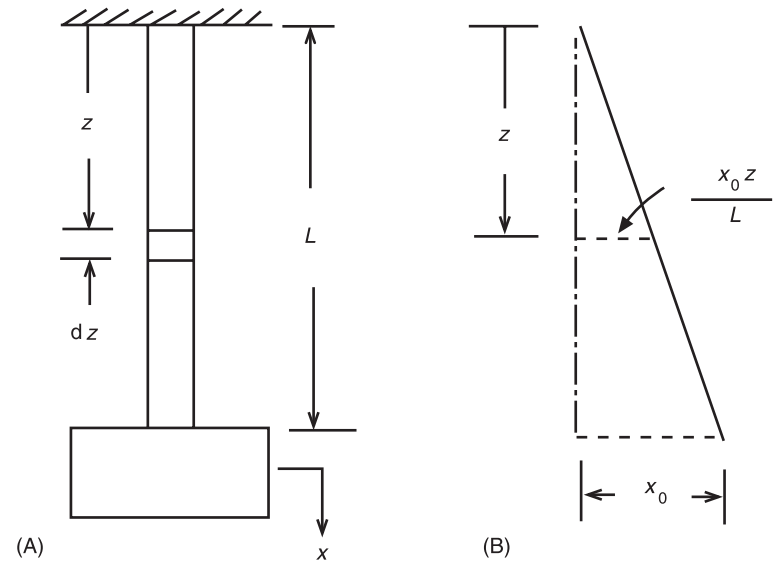


Figure 1 A rod carrying an end mass. (A) System; (B) variation of axial displacement.

When the natural frequency of vibration is ω_n, the maximum velocity of the cross-section is given by:

$$x\omega_n = \frac{x_0 z}{L}\omega_n \qquad [b]$$

The maximum kinetic energy of an element of the rod of length dz can be expressed as:

$$dT = \frac{1}{2}(\rho\, dz)\left(\frac{x_0 z \omega_n}{L}\right)^2 \qquad [c]$$

where ρ is the mass of rod per unit length and $\rho\, dz$ is the mass of the element of length dz. The maximum kinetic energy of the system (rod and the end mass) can be determined as:

$$\begin{aligned} T_{max} &= \frac{1}{2}M(x_0\omega_n)^2 + \frac{1}{2}\int_0^L \rho\left(\frac{x_0 z}{L}\right)^2 \omega_n^2\, dz \\ &= \frac{1}{2}\left(M + \frac{m_0}{3}\right)x_0^2\omega_n^2 \end{aligned} \qquad [d]$$

where $m_0 = \rho L$ is the mass of the rod. The maximum strain energy of the system can be expressed as:

$$U_{max} = \frac{1}{2}kx_0^2 \qquad [e]$$

where $k = (AE)/L$ is the axial stiffness, A = cross-sectional area, and E = Young's modulus of the rod. Equating T_{max} and U_{max}, we find that the natural frequency of vibration of the system is:

$$\begin{aligned} \omega_n &= \left(\frac{k}{m_{eq}}\right)^{1/2} = \left[\frac{k}{M + (m_0/3)}\right]^{1/2} \\ &= \left\{\frac{AE}{L(M + (m_0/3))}\right\}^{1/2} \end{aligned} \qquad [f]$$

where $m_{eq} = M + (m_0/3)$ is the equivalent mass of the system. Eqn [f] shows that one-third of the mass of the rod is to be added to the attached mass to find the equivalent mass of the system.

Application – Natural Frequency of Vibration of a Three-Degree-of-Freedom System

The natural frequency of vibration of the three degree-of-freedom spring-mass system shown in **Figure 2** is considered. The strain energy of the system can be expressed as:

$$\begin{aligned} U &= \frac{1}{2}k_1x_1^2 + \frac{1}{2}k_2(x_2 - x_1)^2 + \frac{1}{2}k_3(x_3 - x_2)^2 \\ &= \frac{k}{2}\left(3x_1^2 + 5x_2^2 + 3x_3^2 - 4x_1x_2 - 6x_2x_3\right) \end{aligned} \qquad [a]$$

The kinetic energy of the system is given by:

$$\begin{aligned} T &= \frac{1}{2}m_1\dot{x}_1^2 + \frac{1}{2}m_2\dot{x}_2^2 + \frac{1}{2}m_3\dot{x}_3^2 \\ &= \frac{m}{2}\left(\dot{x}_1^2 + 2\dot{x}_2^2 + 3\dot{x}_3^2\right) \end{aligned} \qquad [b]$$

For free vibration, harmonic motion at frequency ω_n, is assumed as:

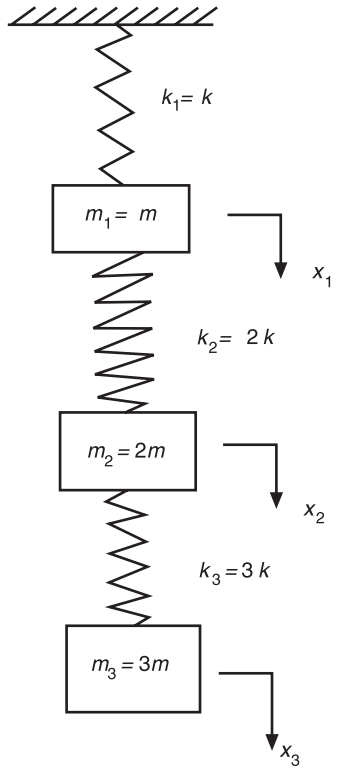


Figure 2 A three-degree-of-freedom spring–mass system.

$$x_i(t) = X_i \cos \omega_n t, \quad i = 1, 2, 3 \qquad [c]$$

so that:

$$\dot{x}_i = -\omega_n X_i \sin \omega_n t, \quad i = 1, 2, 3 \qquad [d]$$

Substituting eqns [c] and [d] into eqns [a] and [b] yields:

$$U = \frac{k}{2}\left(3X_1^2 + 5X_2^2 + 3X_3^2 - 4X_1X_2 - 6X_2X_3\right)\cos^2\omega_n t \qquad [e]$$

$$T = \frac{m\omega_n^2}{2}\left(X_1^2 + 2X_2^2 + 3X_3^2\right)\sin^2\omega_n t \qquad [f]$$

Thus, the maximum potential energy (equal to maximum strain energy in the absence of external forces) and maximum kinetic energy are given by:

$$U_{\max} = \frac{k}{2}\left(3X_1^2 + 5X_2^2 + 3X_3^2 - 4X_1X_2 - 6X_2X_3\right) \qquad [g]$$

$$T_{\max} = \frac{m\omega_n^2}{2}\left(X_1^2 + 2X_2^2 + 3X_3^2\right) \qquad [h]$$

By assuming the mode shape as:

$$\begin{Bmatrix} X_1 \\ X_2 \\ X_3 \end{Bmatrix} = \begin{Bmatrix} 1 \\ 2 \\ 3 \end{Bmatrix} X_1 \qquad [i]$$

where X_1 is the amplitude of vibration of the first mass, the maximum potential and kinetic energies can be expressed as:

$$U_{\max} = 3kX_1^2, \quad T_{\max} = 18\,mX_1^2\omega_n^2 \qquad [j]$$

By setting $T_{\max} = U_{\max}$, the natural frequency of vibration can be found as:

$$\omega_n^2 = \frac{k}{6m} = 0.166667\frac{k}{m} \qquad [k]$$

The exact value of the natural frequency is given by:

$$\omega_n^2 = 0.113992\frac{k}{m} \qquad [l]$$

Rayleigh's Method for Continuous Systems

The eigenvalue problem of a continuous (distributed) system can be expressed, in general terms, as:

$$L(\phi) = \lambda M(\phi) \qquad [21]$$

where $L(\phi)$ and $M(\phi)$ are linear homogeneous differential operators of orders p and q, respectively, with $p < q$ and p and q even numbers, λ is the eigenvalue and ϕ is the field variable such as displacement. Eqn [21] is to be satisfied over the domain of the system (D) and $\phi(D)$ denotes the distribution of ϕ over D. If λ_r represents an eigenvalue and ϕ_r the corresponding eigenfunction is:

$$L(\phi_r) = \lambda_r M(\phi_r) \qquad [22]$$

The multiplication of eqn [22] by ϕ_r and integration over the domain D gives:

$$\lambda_r = \frac{\int_D \phi_r L(\phi_r) \mathrm{d}D}{\int_D \phi_r M(\phi_r) \mathrm{d}D} = \frac{\bar{N}(\phi_r)}{\bar{D}(\phi_r)} \qquad [23]$$

where the numerator, $\bar{N}(\phi_r)$, can be shown to be proportional to the strain energy of mode r and the denominator, $\bar{D}(\phi_r)$ can be shown to be proportional to the kinetic energy of mode r. Both $\bar{N}(\phi_r)$ and $\bar{D}(\phi_r)$ are functions of the eigenfunction ϕ_r, and are positive for a positive definite system. Eqn [23] is called the Rayleigh's quotient. The explicit expressions for the Rayleigh's quotient are given below for a few simple cases.

Longitudinal Vibration of a Thin Bar

The equation of motion governing the longitudinal vibration of a thin bar is given by:

$$\frac{\partial}{\partial x}\left(EA\frac{\partial u}{\partial x}\right) = \rho A \frac{\partial^2 u}{\partial t^2} \qquad [24]$$

where E = Young's modulus, $A(x)$ = area of cross-section, ρ = density, and $u(x, t)$ = longitudinal displacement. For harmonic motion:

$$u(x,t) = \phi(x) \sin \omega t \qquad [25]$$

and eqn [24] becomes:

$$\frac{\mathrm{d}}{\mathrm{d}x}\left(EA\frac{\mathrm{d}\phi}{\mathrm{d}x}\right) = -\rho A \omega^2 \phi$$

or:

$$[EA\phi'(x)]' = -\rho A \omega^2 \phi(x) \qquad [26]$$

where a prime denotes differentiation with respect to x.

For rth mode, eqn [26] gives:

$$\left[EA\phi_r'(x)\right]' = -\rho A \omega_r^2 \phi_r(x) \qquad [27]$$

Multiplying eqn [27] by $\phi_r(x)$ and integrating over the length of the bar (L) leads to:

$$\int_0^L \left[EA\phi_r'(x)\right]' \phi_r(x)\, \mathrm{d}x = -\omega_r^2 \int_0^L \rho A(x) \phi_r^2(x)\, \mathrm{d}x \qquad [28]$$

Integrating the left-hand side integral of eqn [28] by parts results in:

$$EA\phi_r'(x)\phi_r(x)\big|_0^L - \int_0^L EA\left[\phi_r'(x)\right]\mathrm{d}x = -\omega_r^2 \int_0^L \rho A[\phi_r(x)]^2\, \mathrm{d}x \qquad [29]$$

Eqn [29] can be rewritten as:

$$R = \omega_r^2 = \frac{\int_0^L EA\left[\phi_r'(x)\right]^2 \mathrm{d}x - EA\phi_r(x)\phi_r'(x)\big|_0^L}{\int_0^L \rho A[\phi_r(x)]^2\, \mathrm{d}x} \qquad [30]$$

For simple boundary conditions such as free ends ($\phi_r' = 0$) and fixed ends ($\phi_r = 0$), eqn [30] reduces to:

$$R = \omega_r^2 = \frac{\int_0^L EA\left[\phi_r'(x)\right]^2 \mathrm{d}x}{\int_0^L \rho A[\phi_r(x)]^2\, \mathrm{d}x} \qquad [31]$$

The expressions on the right-hand side of eqns [30] and [31] denote Rayleigh's quotients.

Note that eqn [31] can also be derived from potential and kinetic energy expressions. The potential or strain energy of a bar is given by:

$$U(t) = \frac{1}{2}\int_0^L EA\left[\frac{\partial u(x,t)}{\partial x}\right]^2 \mathrm{d}x \qquad [32]$$

and the kinetic energy by:

$$T(t) = \frac{1}{2}\int_0^L \rho A\left[\frac{\partial u(x,t)}{\partial t}\right]^2 \mathrm{d}x \qquad [33]$$

Using $u(x, t) = \phi(x)\sin \omega t$, eqns [32] and [33] can be expressed as:

$$U(t) = \frac{1}{2}\sin^2\omega t \int_0^L EA\left[\frac{\mathrm{d}\phi(x)}{\mathrm{d}x}\right]^2 \mathrm{d}x \qquad [34]$$

$$T(t) = \frac{1}{2}\omega^2\cos^2\omega t \int_0^L \rho A[\phi(x)]^2 \,\mathrm{d}x \qquad [35]$$

Equation $U_{\max}$ to $T_{\max}$ results in eqn [31].

Application – Longitudinal Vibration of a Tapered Rod

Consider the longitudinal vibration of a linearly tapered fixed-free rod shown in **Figure 3**. The area of cross-section of the rod is given by:

$$A(x) = A_0\left(1 - \frac{x}{L}\right) \qquad [a]$$

where A_0 denotes the area at the root ($x = 0$). The maximum strain energy of the rod can be expressed as:

$$U_{\max} = \frac{1}{2}\int_0^L EA(x)\left[\phi_r'(x)\right]^2 \mathrm{d}x \qquad [b]$$

where $\phi_r(x)$ is the deflection (mode) shape that satisfies the fixed boundary condition. Let $\phi_r(x)$ be assumed as:

$$\phi_r(x) = \sin\frac{\pi x}{2L} \qquad [c]$$

so that:

$$\phi_r'(x) = \frac{\pi}{2L}\cos\frac{\pi x}{2L} \qquad [d]$$

and:

$$U_{\max} = \frac{1}{2}\int_0^L EA_0\left(1 - \frac{x}{L}\right)\left(\frac{\pi}{2L}\right)^2\cos^2\left(\frac{\pi x}{2L}\right)\mathrm{d}x = \frac{EA_0}{8L}\left(1 + \frac{\pi^2}{4}\right) \qquad [e]$$

The maximum kinetic energy of the rod, during harmonic vibration at frequency ω_{n}, can be determined as:

$$T_{\max} = \frac{\omega_{\mathrm{n}}^2}{2}\int_0^L \rho A(x)\phi_r^2(x)\,\mathrm{d}x \qquad [f]$$

where ρ is the density of the rod. Using eqn [c], we obtain:

$$T_{\max} = \frac{\rho\omega_{\mathrm{n}}^2}{2}\int_0^L A_0\left(1 - \frac{x}{L}\right)\sin^2\frac{\pi x}{2L}\,\mathrm{d}x = \frac{\rho A_0 L\omega_{\mathrm{n}}^2}{8}\left(1 - \frac{4}{\pi^2}\right) \qquad [g]$$

By setting $T_{\max} = V_{\max}$, we obtain:

$$\frac{\rho A_0 L\omega_{\mathrm{n}}^2}{8}\left(1 - \frac{4}{\pi^2}\right) = \frac{EA_0}{8L}\left(1 + \frac{\pi^2}{4}\right) \qquad [h]$$

from which:

$$\omega_{\mathrm{n}}^2 = \frac{E\pi^2}{4\rho L^2}\left(\frac{4 + \pi^2}{\pi^2 - 4}\right) = 5.830356\frac{E}{\rho L^2} \qquad [i]$$

This yields the natural frequency of vibration as:

$$\omega_{\mathrm{n}} = 2.414613\sqrt{\frac{E}{\rho L^2}} \qquad [j]$$

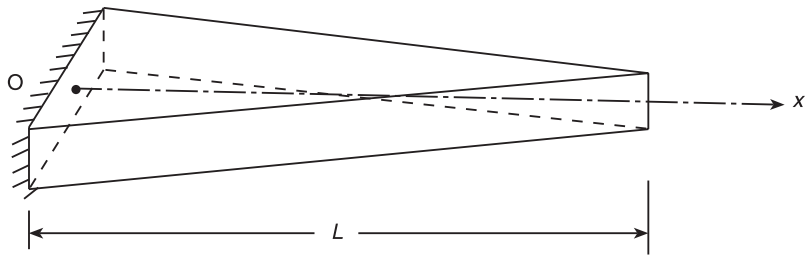


Figure 3 A tapered fixed-free rod.

Transverse Vibration of a String

The equation governing the transverse vibration of a string is given by:

$$\frac{\partial}{\partial x}\left[T(x)\frac{\partial w}{\partial x}\right] = m(x)\ \frac{\partial^2 w}{\partial t^2} \qquad [36]$$

where $T(x)$ is the tension in the string, $m(x)$ is the mass per unit length of string and $w(x, t)$ is the transverse displacement. The Rayleigh's quotient corresponding to eqn [36] is given by:

$$R = \omega_r^2 = \frac{\int_0^L T\left[\phi_r'(x)\right]^2 \mathrm{d}x}{\int_0^L m[\phi_r(x)]^2 \mathrm{d}x} \qquad [37]$$

where L is the length of the string, $w(x, t)$ is the $\phi(x)\sin\omega t$ and rth mode is assumed.

Torsional Vibration of a Shaft

The torsional vibration of a shaft is governed by the equation of motion:

$$\frac{\partial}{\partial x}\left[GJ\frac{\partial\theta(x,t)}{\partial x}\right] = J_0\ \frac{\partial^2\theta(x,t)}{\partial t^2} \qquad [38]$$

where $GJ(x)$ is the torsional stiffness, G is the shear modulus, $J(x)$ is the polar moment of inertia of the cross-section (for circular sections), $J_0(x)$ is the mass polar moment of inertia is the ρJ for shafts with uniform cross-section, and $\theta(x,\ t)$ is the angular displacement is $\phi(x)\sin\omega t$ for harmonic motion with frequency ω. The Rayleigh's quotient corresponding to eqn [38] is given by:

$$R = \omega_r^2 = \frac{\int_0^L GJ(x)\left[\phi_r'(x)\right]^2 \mathrm{d}x}{\int_0^L J_0[\phi_r(x)]^2 \mathrm{d}x} \qquad [39]$$

where L is the length of the shaft.

Transverse Vibration of a Thin Beam

The equation of motion governing the bending vibration of thin beams is given by:

$$\frac{\partial^2}{\partial x^2}\left[EI(x)\frac{\partial^2 w(x,t)}{\partial x^2}\right] = -\rho A(x)\ \frac{\partial^2 w(x,t)}{\partial t^2} \qquad [40]$$

where E is Young's modulus, $I(x)$ is the area moment of inertia of cross-section, ρ is the density, $A(X)$ is the area of cross-section and $w(x, t)$ is the transverse displacement. When harmonic motion is assumed, $w(x,\ t) = \phi(x)\sin\omega t$, eqn [40] leads to (for rth mode):

$$R = \omega_r^2 = \frac{\int_0^L EI(x)\left[\phi_r''(x)\right]^2 \mathrm{d}x + \left\{\left[EI(x)\phi_r''(x)\right]'\phi_r(x) - EI(x)\phi''(x)\phi_r'(x)\right\}_0^L}{\int_0^L \rho A(x)[\phi_r(x)]^2 \mathrm{d}x} \qquad [41]$$

where L is the length of the beam. For common boundary conditions such as fixed end ($\phi_r = 0$, $\phi_r' = 0$), pinned end ($\phi_r = 0$, $\phi_r'' = 0$) and free end ($\phi_r'' = 0$, $(EI(x)\phi_r''(x))' = 0$, eqn [41] reduces to:

$$R = \omega_r^2 = \frac{\int_0^L EI(x)\left[\phi_r''(x)\right]^2 \mathrm{d}x}{\int_0^L \rho A(x)[\phi_r(x)]^2 \mathrm{d}x} \qquad [42]$$

The expression on the right-hand sides of eqns [41] and [42] are called Rayleigh's quotients.

Application – Transverse Vibration of a Beam with Central Mass

Consider a uniform beam of mass m per unit length and bending stiffness EI, fixed at both ends and carrying a central mass, as shown in **Figure 4**. The transverse deflection of the beam during free vibration is assumed to be similar to the static deflection shape of a uniform fixed-fixed beam subject to a concentrated load at the middle:

$$\phi_r(x) = \frac{c}{48EI}\left(3Lx^2 - 4x^3\right), \quad 0 \le x \le \frac{L}{2} \qquad [a]$$

where c is a constant, denoting the magnitude of the load applied at the middle of the beam. The maximum strain energy of the beam can be found as:

$$\begin{aligned} U_{\max} &= 2\left(\frac{EI}{2}\right)\int_0^{L/2}\left(\frac{\mathrm{d}^2\phi_r}{\mathrm{d}x^2}\right)^2 \mathrm{d}x \\ &= EI\int_0^{L/2}\left[\frac{c}{8EI}(L - 4x)\right]^2 \mathrm{d}x = \frac{c^2L^3}{384EI} \end{aligned} \qquad [b]$$

The maximum kinetic energy of the beam and the central mass M_0 can be found as:

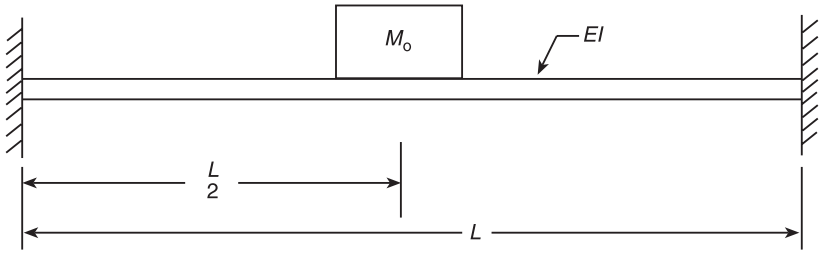


Figure 4 A fixed–fixed beam with a central mass.

$$T_{\max} = 2\left(\frac{m}{2}\right)\int_0^{L/2}\{\phi_r\omega_n\}^2 dx + \frac{M_0}{2}(\phi_r)^2_{\max}\omega_n^2$$
$$= m\omega_n^2\int_0^{L/2}\left[\frac{c}{48EI}(3Lx^2 - 4x^3)\right]^2 dx + \frac{M_0}{2}\omega_n^2\phi_r^2\left(x = \frac{L}{2}\right)$$
$$= m\omega_n^2\left(\frac{c}{48EI}\right)^2 L^7\left(\frac{13}{1120}\right) + \frac{M_0\omega_n^2}{2}\left(\frac{c}{48EI}\right)^2\frac{L^2}{16} \quad [c]$$

Using the relation $T_{\max} = U_{\max}$, we obtain:

$$\omega_n^2 = \frac{192EI}{L^3\left(\frac{13}{35}m_0 + M_0\right)} \quad [d]$$

where m_0 denotes the mass of the beam.

Transverse Vibration of a Thin Plate

The equation governing the vibration of a thin rectangular plate is given by:

$$\frac{\partial^4 w}{\partial x^4} - 2\frac{\partial^4 w}{\partial x^2\partial y^2} + \frac{\partial^4 w}{\partial y^4} + \frac{m}{D}\frac{\partial^2 w}{\partial t^2} = 0 \quad [a]$$

where $w = w(x, y, t)$ is the transverse deflection, D is the flexural rigidity given by:

$$D = \frac{Eh^3}{12(1 - \nu^2)} \quad [b]$$

with E is Young's modulus, ν is Poisson's ratio, h is the thickness of the plate and m is the mass of the plate per unit area. The strain and kinetic energies of the plate are given by:

$$U = \frac{1}{2}\iint_A D\left\{\left(\frac{\partial^2 w}{\partial x^2} + \frac{\partial^2 w}{\partial y^2}\right)^2 - 2(1 - \nu)\left[\frac{\partial^2 w}{\partial x^2}\frac{\partial^2 w}{\partial y^2} - \left(\frac{\partial^2 w}{\partial x\,\partial y}\right)^2\right]\right\} dx\,dy \quad [c]$$

$$T = \frac{1}{2}\iint_A m\left(\frac{\partial w}{\partial t}\right)^2 dx\,dy \quad [d]$$

where A is the area of the plate. By assuming harmonic motion in rth mode as:

$$w(x, y, t) = \phi_r(x)\sin\omega_r t \quad [e]$$

the Rayleigh's quotient can be expressed as:

$$R = \omega_r^2 = \frac{\bar{N}}{\bar{D}} \quad [f]$$

where $\bar{N}$ and $\bar{D}$ are given by:

$$\bar{N} = \iint_A D\left\{\left(\phi_{r,xx} + \phi_{r,yy}\right)^2 - 2(1 - \nu)\left[\phi_{r,xy}^2 - \phi_{r,xx}\phi_{r,yy}\right]\right\} dx\,dy \quad [g]$$

$$\bar{D} = \iint_A m\,\phi_r^2\,dx\,dy \quad [h]$$

where

$$\phi_{r,xx} = \frac{\partial^2\phi_r}{\partial x^2}, \quad \phi_{r,yy} = \frac{\partial^2\phi_r}{\partial y^2}, \quad \phi_{r,xy} = \frac{\partial^2\phi_r}{\partial x\,\partial y}$$

A simpler expression can be derived for the approximate natural frequency of transverse vibration of

plates. By considering the plate to be composed of several lumped masses with associated effective spring constants, the natural frequency of vibration in rth mode can be expressed as:

$$\omega_r^2 \approx \frac{g \iint_A \alpha(x,y)\phi_r(x,y)\,dx\,dy}{\iint_A \alpha(x,y)\phi_r^2(x,y)\,dx\,dy} \quad [i]$$

where $\alpha(x, y)$ is the weight of the plate per unit area, g is the gravitational acceleration and $\phi_r(x, y)$ is the deflection (mode) shape of the plate during vibration. Eqn [i] is known as the modified Rayleigh's quotient or Morley's formula.

Application – Transverse Vibration of a Square Plate

Let the dimensions of the plate be $a \times a$ (**Figure 5**) and the deflection shape be assumed to be the static deflection shape of the plate under uniformly distributed load as:

$$\phi_r(x,y) = c \sin\frac{\pi x}{a} \sin\frac{\pi y}{a} \quad [a]$$

where:

$$c = 0.00416\frac{p_0 a^4}{D} = 0.00416\frac{mga^4}{D} \quad [b]$$

with $p_0 = mg$ is the distributed load (self weight). Substitution of eqn [a] into eqn [i] of the section on Transverse vibration of a thin plate yields:

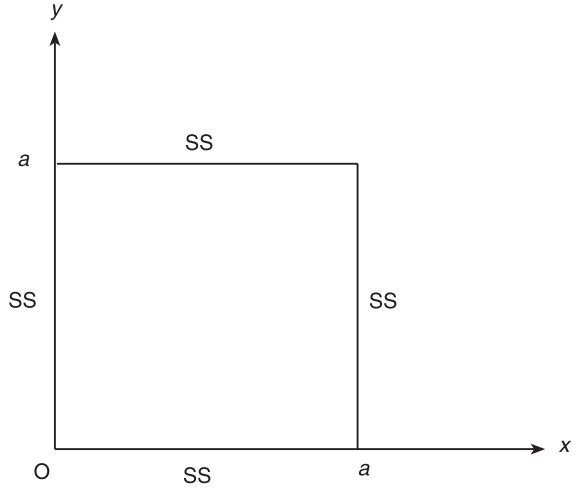


Figure 5 A simply supported square plate. SS = simple support.

$$\omega_r^2 = \frac{g}{c}\left\{\frac{\int_0^a \int_0^a \sin(\pi x/a)\sin(\pi y/a)\,dx\,dy}{\int_0^a \int_0^a \sin^2(\pi x/a)\sin^2(\pi y/a)\,dx\,dy}\right\} = \frac{16g}{c\pi^2} \quad [c]$$

and hence the frequency of vibration is given by:

$$\omega_r = \frac{19.722}{a^2}\sqrt{\frac{D}{m}} \quad [d]$$

The exact natural frequency of the plate in the fundamental mode is given by:

$$\omega_1 = \frac{19.74}{a^2}\sqrt{\frac{D}{m}} \quad [e]$$

Minimum Value of Rayleigh's Quotient

The Rayleigh's quotient gives an approximate value of the fundamental natural frequency that is higher than the exact value. To show this, let an arbitrary eigenfunction, $\bar{\phi}(x)$, be given by a linear combination of the exact eigenfunctions, $\phi_i(x)$, as:

$$\bar{\phi}(x) = a_1\phi_1(x) + a_2\phi_2(x) + \cdots = \sum_{i=1}^{\infty} a_i\phi_i(x) \quad [43]$$

where a_1, a_2 ... are constants. For specificness, consider the Rayleigh's quotient corresponding to the transverse vibration of a thin beam, eqn [42], using eqn [43] for $\phi_r(x)$:

$$R = \frac{\int_0^L EI(x)\left(\bar{\phi}''(x)\right)^2 dx}{\int_0^L \rho A(x)\left(\bar{\phi}(x)\right)^2 dx} = \frac{\int_0^L EI(x)\left(\sum_{i=1}^{\infty} a_i\bar{\phi}''(x)\right)^2 dx}{\int_0^L \rho A(x)\left(\sum_{i=1}^{\infty} a_i\bar{\phi}(x)\right)^2 dx} \quad [44]$$

The orthogonality of eigenfunctions leads to the following relation (from eqn [42]):

$$R = \frac{\sum_{i=1}^{\infty} k_i a_i^2}{\sum_{i=1}^{\infty} m_i a_i^2} \quad [45]$$

where k_i and m_i denote modal stiffness and modal mass, respectively, in mode i:

$$k_i = \int_0^L EI(x)\left(\phi_i''(x)\right)^2 dx \quad [46]$$

$$m_i = \int_0^L \rho A(x)(\phi_i(x))^2 \, \mathrm{d}x \qquad [47]$$

with:

$$a_i^2 k_i = a_i^2 \omega_i^2 m_i \qquad [48]$$

Thus eqn [45] can be rewritten as:

$$R = \frac{\sum_{i=1}^{\infty} a_i^2 \omega_i^2 m_i}{\sum_{i=1}^{\infty} a_i^2 m_i} \qquad [49]$$

since $\omega_1 < \omega_2 < \ldots$, eqn [49] implies that:

$$\begin{aligned} R &= \frac{\omega_1^2 a_1^2 m_1 + \omega_1^2 (\omega_2/\omega_1)^2 a_2^2 m_2 + \cdots}{a_1^2 m_1 + a_2^2 m_2 + \cdots} \\ &\geq \frac{\omega_1^2 a_1^2 m_1 + \omega_1^2 a_2^2 m_2 + \cdots}{a_1^2 m_1 + a_2^2 m_2 + \cdots} = \omega_1^2 \end{aligned} \qquad [50]$$

Eqn [50] indicates that the Rayleigh's quotient attains a minimum at the fundamental frequency and any assumed mode shape (eigenfunction) yields an approximate natural frequency that is higher than the exact fundamental frequency.

Rayleigh–Ritz Method

The Rayleigh quotient is defined as:

$$R = \frac{\bar{N}(\phi)}{\bar{D}(\phi)} \qquad [51]$$

where ϕ is the eigenfunction. A trial (or approximate) solution $\bar{\phi}(x)$ is chosen for $\phi(x)$ as:

$$\bar{\phi}(x) = \sum_{i=1}^{n} a_i f_i(x) \qquad [52]$$

where a_i are constants, $f_i(x)$ are trial functions satisfying only the essential boundary conditions and n is the number of terms considered in $\bar{\phi}(x)$. The functions $f_i(x)$ are called admissible functions and may not satisfy the natural or free boundary conditions. Basically, by assuming the solution as indicated by eqn [52], the continuous (or infinitely many-degrees-of-freedom) system is approximated by an n-degrees-of-freedom system. When eqn [52] is substituted into eqn [51], one obtains:

$$R = \frac{\bar{N}\left[\sum_{i=1}^{n} a_i f_i(x)\right]}{\bar{D}\left[\sum_{i=1}^{n} a_i f_i(x)\right]} \qquad [53]$$

Considering R as a function of the unknown constants $a_1, a_2 \ldots a_n$, the conditions for the stationariness of R can be stated as:

$$\frac{\partial R}{\partial a_i} = 0, \quad i = 1, 2, \ldots, n$$

or:

$$\left[\frac{\bar{D}(\partial \bar{N}/\partial a_i) - \bar{N}(\partial \bar{D}/\partial a_i)}{\bar{D}^2}\right] = 0, \quad i = 1, 2, \ldots, n \qquad [54]$$

which can be rearranged as:

$$R = \frac{\bar{N}}{\bar{D}} = \frac{(\partial \bar{N}/\partial a_i)}{(\partial \bar{D}/\partial a_i)}, \quad i = 1, 2, \ldots, n \qquad [55]$$

Eqn [55] yields a set of n equations of the type:

$$\frac{\partial \bar{N}}{\partial a_i} = \lambda_i \frac{\partial \bar{D}}{\partial a_i}, \quad i = 1, 2, \ldots, n \qquad [56]$$

since the Rayleigh's quotient gives the (approximate) value of the eigenvalue, λ_i. Eqn [56] represents an algebraic eigenvalue problem which can be solved using any of the standard techniques.

The correspondence between eqn [56] and the algebraic eigenvalue problem can be shown by expressing the numerator and denominator of the Rayleigh's quotient of eqn [53], more generally, as:

$$\bar{N}\left[\underline{\phi}(x)\right] = \int_V \underline{\phi}(x) L\left[\underline{\phi}(x)\right] \mathrm{d}V \qquad [57]$$

$$\bar{D}\left[\underline{\phi}(x)\right] = \int_V \underline{\phi}(x) M\left[\underline{\phi}(x)\right] \mathrm{d}V \qquad [58]$$

where V is the volume of the body and $L[\,]$ and $M[\,]$ are the differential operators used in the definition of the eigenvalue problem of the system:

$$L[w] = \lambda M[w] \qquad [59]$$

For example, the eigenvalue problem corresponding to the longitudinal vibration of a rod is given by:

$$\frac{\mathrm{d}}{\mathrm{d}x}\left(EA(x)\frac{\mathrm{d}w(x)}{\mathrm{d}x}\right) = \lambda m(x)w(x) \qquad [60]$$

where $m(x)$ is the mass per unit length of the rod. In this case, the expressions of $L[\ ]$ and $M[\ ]$ can be identified (from eqn [60]) as:

$$L[w] = \frac{\mathrm{d}}{\mathrm{d}x}\left[EA(x)\frac{\mathrm{d}w}{\mathrm{d}x}\right] \qquad [61]$$

$$M[w] = \rho A(x)w(x) \qquad [62]$$

When n terms are used in the assumed solution, eqn [52], eqns [61] and [62] can be used to define the stiffness and mass coefficients as follows:

$$k_{ij} = \int_V f_i L[f_j]\ \mathrm{d}V; \qquad i,j = 1,2,\ldots,n \qquad [63]$$

$$m_{ij} = \int_V f_i M[f_j]\ \mathrm{d}V; \qquad i,j = 1,2,\ldots,n \qquad [64]$$

Thus the numerator and denominator of eqn [53] can be expressed as:

$$\begin{aligned}\bar{N} &= \int_V \sum_{i=1}^{n} a_i f_i L\left[\sum_{j=1}^{n} a_j f_j\right]\mathrm{d}V \\ &= \sum_{i=1}^{n}\sum_{j=1}^{n} a_i a_j \int_V f_i L[f_j]\ \mathrm{d}V \\ &= \sum_{i=1}^{n}\sum_{j=1}^{n} a_i a_j k_{ij}\end{aligned} \qquad [65]$$

$$\begin{aligned}\bar{D} &= \int_V \sum_{i=1}^{n} a_i f_i M\left[\sum_{j=1}^{n} a_j f_j\right]\mathrm{d}V \\ &= \sum_{i=1}^{n}\sum_{j=1}^{n} \int_V f_i M[f_j]\ \mathrm{d}V \\ &= \sum_{i=1}^{n}\sum_{j=1}^{n} a_i a_j m_{ij}\end{aligned} \qquad [66]$$

Using eqns [65] and [66], eqn [56] can be written, in equivalent form, as:

$$\sum_{j=1}^{n}\left(k_{ij} - \lambda m_{ij}\right)a_j = 0; \qquad i = 1,2,\ldots,n \qquad [67]$$

In matrix form, eqn [67] becomes:

$$(\mathbf{k} - \lambda\,\mathbf{m})\mathbf{a} = \mathbf{0} \qquad [68]$$

where:

$$\mathbf{a} = \begin{Bmatrix} a_1 \\ a_2 \\ \cdot \\ \cdot \\ \cdot \\ a_n \end{Bmatrix} \qquad [69]$$

$\mathbf{k} = k_{ij}$ and $\mathbf{m} = m_{ij}$. Equation [67] or [68] defines an algebraic eigenvalue problem.

Application – Longitudinal Vibration of a Tapered Rod

The natural frequencies of longitudinal vibration of the tapered rod shown in **Figure 3** is considered using a three-term solution as:

$$\underline{\phi}(x) = \sum_{i=1}^{3} a_i f_i(x) \qquad [a]$$

with:

$$f_1(x) = \sin\frac{\pi x}{2L} \qquad [b]$$

$$f_2(x) = \sin\frac{3\pi x}{2L} \qquad [c]$$

$$f_3(x) = \sin\frac{5\pi x}{2L} \qquad [d]$$

where each of the functions $f_i(x)$ satisfies the fixed boundary condition of the problem. Since the area of cross-section of the rod varies as:

$$A(x) = A_0\left(1 - \frac{x}{L}\right) \qquad [e]$$

the operators $L[\ ]$ and $M[\ ]$ can be expressed, from eqns [61] and [62], as:

$$L[\,] = EA_0\left\{\frac{1}{L}\frac{\mathrm{d}}{\mathrm{d}x} - \left(1 - \frac{x}{L}\right)\frac{\mathrm{d}^2}{\mathrm{d}x^2}\right\}[\ ] \qquad [f]$$

$$M[\,] = \rho A_0\left(1 - \frac{x}{L}\right)[\ ] \qquad [g]$$

Substituting eqns [a] to [g] into eqns [63] and [64], we obtain the matrices $\mathbf{k}$ and $\mathbf{m}$ as:

$$\mathbf{k} = \begin{bmatrix} k_{11} & k_{12} & k_{13} \\ k_{21} & k_{22} & k_{23} \\ k_{31} & k_{32} & k_{33} \end{bmatrix}$$

$$= \frac{EA_0}{4L} \begin{bmatrix} \left(1+\frac{\pi^2}{4}\right) & 3 & \frac{5}{9} \\ 3 & \left(1+\frac{9\pi^2}{4}\right) & 15 \\ \frac{5}{9} & 15 & \left(1+\frac{25\pi^2}{4}\right) \end{bmatrix} \quad [h]$$

$$\mathbf{m} = \begin{bmatrix} m_{11} & m_{12} & m_{13} \\ m_{21} & m_{22} & m_{23} \\ m_{31} & m_{32} & m_{33} \end{bmatrix}$$

$$= \frac{\rho A_0 L}{4} \begin{bmatrix} \left(1-\frac{4}{\pi^2}\right) & \frac{4}{\pi^2} & -\frac{4}{9\pi^2} \\ \frac{4}{\pi^2} & \left(1-\frac{4}{9\pi^2}\right) & \frac{4}{\pi^2} \\ -\frac{4}{9\pi^2} & \frac{4}{\pi^2} & \left(1-\frac{4}{25\pi^2}\right) \end{bmatrix} \quad [i]$$

The solution of the eigenvalue problem:

$$\mathbf{ka} = \lambda\,\mathbf{ma} \quad [j]$$

gives the eigenvalues of the rod as:

$$\lambda_1 = \omega_1^2 = 5.7837\frac{E}{\rho L^2} \quad [k]$$

$$\lambda_2 = \omega_2^2 = 30.4878\frac{E}{\rho L^2} \quad [l]$$

$$\lambda_3 = \omega_3^2 = 75.0751\frac{E}{\rho L^2} \quad [m]$$

Energy Methods in Finite Element Analysis

Virtual Work Principle

The virtual work principle can be stated as:

$$\int_V \delta\boldsymbol{\varepsilon}^{\mathrm{T}}\boldsymbol{\sigma}\,\mathrm{d}V - \int_V \delta\mathbf{u}^{\mathrm{T}}\bar{\mathbf{B}}\,\mathrm{d}V - \int_{S_t} \delta\mathbf{u}^{\mathrm{T}}\bar{\mathbf{t}}\,\mathrm{d}S = 0 \quad [70]$$

where $\boldsymbol{\sigma}$ is the vector of stresses, $\bar{\mathbf{B}}$ is the vector of body forces, $\bar{\mathbf{t}}$ is the vector of prescribed forces or tractions on the surface S_t of the body, V is the volume of the body, $\delta\boldsymbol{\varepsilon}$ is the vector of virtual strains, and $\delta\mathbf{u}$ is the vector of virtual displacements that are compatible and consistent with the specified boundary conditions. The virtual work principle can be described as follows. Let an elastic body subject to the forces $\bar{\mathbf{B}}$ and $\bar{\mathbf{t}}$ be in equilibrium. Let the body be given virtual displacements $\delta\mathbf{u}$, corresponding to the forces $\bar{\mathbf{B}}$ and $\bar{\mathbf{t}}$, that are geometrically compatible with the constraints. If $\delta\boldsymbol{\varepsilon}$ is the virtual strain vector due to the virtual displacements, then the stress vector must satisfy eqn [70]. Here the forces $\bar{\mathbf{B}}$, $\bar{\mathbf{t}}$ and $\boldsymbol{\sigma}$ are statically compatible and $\delta\mathbf{u}$ and $\delta\varepsilon$ are geometrically compatible.

Principle of Minimum Total Potential Energy

When $\boldsymbol{\sigma}$ is expressed as $\boldsymbol{\sigma}(\boldsymbol{\varepsilon})$ and $\boldsymbol{\varepsilon}$ as $\mathbf{Bu}$ where $\mathbf{B}$ is an appropriate differential operator matrix, then a strain energy function, U, exists such that:

$$\delta U = \int_V \delta\boldsymbol{\varepsilon}^{\mathrm{T}}\boldsymbol{\sigma}\,\mathrm{d}V \quad [71]$$

and the virtual work principle will be equivalent to the minimum total potential energy principle. The total potential energy, (π_{p}), is given by:

$$\pi_{\mathrm{p}} = U(\boldsymbol{\varepsilon}) + W(\mathbf{u}) \quad [72]$$

with:

$$W = -\int_V \mathbf{u}^{\mathrm{T}}\bar{\mathrm{B}}\,\mathrm{d}V - \int_{S_t} \mathbf{u}^{\mathrm{T}}\bar{\mathbf{t}}\,\mathrm{d}S \quad [73]$$

and hence eqn [70] is equivalent to $\delta\pi_{\mathrm{p}} = 0$. In words, the principle of minimum total potential energy can be stated as follows. Of all the admissible displacement fields that are consistent with the prescribed boundary conditions, the one that minimizes the potential energy also satisfies the conditions of equilibrium. Thus, by minimizing the potential energy, we can satisfy the equilibrium equations of the body.

Principle of Minimum Total Complementary Energy

Let $\delta\boldsymbol{\sigma}$ be the virtual stress vector satisfying equilibrium with both the body forces and tractions on S_t set to zero. By equating the sum of internal and external virtual work to zero, we have:

$$\int_V \delta\boldsymbol{\sigma}^{\mathrm{T}}\boldsymbol{\varepsilon}\,\mathrm{d}V - \int_{S_u} \delta\mathbf{t}^{\mathrm{T}}\bar{\mathbf{u}}\,\mathrm{d}S = 0 \qquad [74]$$

where $\bar{\mathbf{u}}$ denotes the vector of prescribed displacements on the boundary S_u and $\delta\mathbf{t} = [E]\ \delta\boldsymbol{\sigma}$ is the vector of virtual tractions with $[E]$ defining the boundary tractions in terms of stresses. Eqn [74] assures that the boundary displacements on S_u and strains are compatible. Then a complementary strain energy function, U_c, exists such that:

$$\delta U_c = \int_V \delta\,\boldsymbol{\sigma}^{\mathrm{T}}\boldsymbol{\varepsilon}\,\mathrm{d}V \qquad [75]$$

By defining the total complementary energy, π_c, as:

$$\pi_c = U_c(\boldsymbol{\sigma}) - \int_{S_\mathrm{u}} \mathbf{t}^{\mathrm{T}}\bar{\mathbf{u}}\,\mathrm{d}S \equiv U_c + W_c \qquad [76]$$

Eqn [74] is equivalent to $\delta\pi_c = 0$, which is called the principle of minimum total complementary energy. In words, the principle of minimum total complementary energy can be stated as follows. Of all the admissible stress states that satisfy the equations of equilibrium with the given applied loads, the one that minimizes the total complementary energy satisfies the prescribed boundary conditions of displacement.

Hu–Washizu Stationary Principle

The strains are assumed to be related to the displacements as:

$$\boldsymbol{\varepsilon} = \mathbf{B}\mathbf{u} \text{ in } V \qquad [77]$$

and the displacements at the boundary are assumed to satisfy the prescribed values as:

$$\mathbf{u} - \bar{\mathbf{u}} = \mathbf{0} \text{ on } S_u \qquad [78]$$

in defining the potential energy π_p in eqn [72]. By relaxing these constraints, we can define a new function, π_hw, as:

$$\pi_\mathrm{hw} = \pi_\mathrm{p} - \int_V \boldsymbol{\lambda}_1^{\mathrm{T}}(\varepsilon - \mathbf{B}\mathbf{u})\,\mathrm{d}V - \int_{S_\mathrm{u}} \boldsymbol{\lambda}_2^{\mathrm{T}}(\mathbf{u} - \bar{\mathbf{u}})\,\mathrm{d}S \qquad [79]$$

where $\boldsymbol{\lambda}_1$ and $\boldsymbol{\lambda}_2$ are Lagrange multipliers defined in V and S_u, respectively. By varying each quantity in eqn [79] independently, we can write:

$$\begin{aligned}\delta\pi_\mathrm{hw} = \delta\pi_\mathrm{p} &- \int_V \delta\boldsymbol{\lambda}_1^{\mathrm{T}}(\boldsymbol{\varepsilon} - \mathbf{B}\mathbf{u})\,\mathrm{d}V \\ &- \int_V \boldsymbol{\lambda}_1^{\mathrm{T}}(\delta\boldsymbol{\varepsilon} - \mathbf{B}\delta\mathbf{u})\,\mathrm{d}V \\ &- \int_{S_\mathrm{u}} \delta\boldsymbol{\lambda}_2^{\mathrm{T}}(\mathbf{u} - \bar{\mathbf{u}})\,\mathrm{d}S - \int_{S_\mathrm{u}} \boldsymbol{\lambda}_2^{\mathrm{T}}\delta\mathbf{u}\,\mathrm{d}S = 0\end{aligned} \qquad [80]$$

Using the relation:

$$\int_V \boldsymbol{\lambda}_1^{\mathrm{T}}\mathbf{B}\delta\mathbf{u}\,\mathrm{d}V = -\int_V \delta\mathbf{u}^{\mathrm{T}}\mathbf{B}^{\mathrm{T}}\boldsymbol{\lambda}_1\,\mathrm{d}V + \int_s \delta\mathbf{u}^{\mathrm{T}}[E]\boldsymbol{\lambda}_1\,\mathrm{d}S \qquad [81]$$

where $[E]$ is an operator that gives boundary tractions in terms of stresses and using the variation of π_p given in eqn [72], eqn [80] can be rewritten as:

$$\begin{aligned}&\int_V \delta\boldsymbol{\varepsilon}^{\mathrm{T}}(\boldsymbol{\sigma}(\boldsymbol{\varepsilon}) - \boldsymbol{\lambda}_1)\,\mathrm{d}V - \int_V \delta\mathbf{u}\left(\mathbf{B}^{\mathrm{T}}\boldsymbol{\lambda}_1 + \bar{\mathbf{B}}\right)\mathrm{d}V \\ &+ \int_{S_\mathrm{l}} \delta\mathbf{u}^{\mathrm{T}}([E]\boldsymbol{\lambda}_1 - \bar{\mathbf{t}})\,\mathrm{d}S \\ &+ \int_{S_\mathrm{u}} \delta\mathbf{u}^{\mathrm{T}}([E]\boldsymbol{\lambda}_1 - \boldsymbol{\lambda}_2)\,\mathrm{d}S - \int_V \delta\boldsymbol{\lambda}_1^{\mathrm{T}}(\boldsymbol{\varepsilon} - \mathbf{B}\mathbf{u})\,\mathrm{d}V \\ &- \int_{S_\mathrm{u}} \delta\boldsymbol{\lambda}_2^{\mathrm{T}}(\mathbf{u} - \bar{\mathbf{u}})\,\mathrm{d}S = 0\end{aligned} \qquad [82]$$

As eqn [82] is true for any variation, we find that the various terms yield the relations:

$$\begin{aligned}&\boldsymbol{\lambda}_1 = \boldsymbol{\sigma}, \quad \mathbf{B}^{\mathrm{T}}\boldsymbol{\lambda}_1 + \bar{\mathbf{B}} = \mathbf{0}\,, \quad [E]\boldsymbol{\lambda}_1 = \bar{\mathbf{t}} \\ &[E]\boldsymbol{\lambda}_1 = \boldsymbol{\lambda}_2\,, \quad \boldsymbol{\varepsilon} = \mathbf{B}\mathbf{u}\,, \quad \mathbf{u} = \bar{\mathbf{u}}\end{aligned} \qquad [83]$$

Noting that the Lagrange multipliers are given by $\boldsymbol{\lambda}_1 = \boldsymbol{\sigma}$, and $\boldsymbol{\lambda}_2 = \bar{\mathbf{t}}$, the variational principle can be stated as:

$$\delta\pi_\mathrm{hw} = 0 \qquad [84]$$

with:

$$\pi_\mathrm{hw} = \pi_\mathrm{p}(\boldsymbol{\varepsilon}, \mathbf{u}) - \int_V \boldsymbol{\sigma}^{\mathrm{T}}(\boldsymbol{\varepsilon} - \mathbf{B}\mathbf{u})\,\mathrm{d}V - \int_{S_\mathrm{u}} \mathbf{t}^{\mathrm{T}}(\mathbf{u} - \bar{\mathbf{u}})\,\mathrm{d}S \qquad [85]$$

This is known as the Hu–Washizu stationary principle.

Finite Element Equations

The finite element equations can be derived using any of the energy principles. For example, the use of the principle of minimum total potential energy results in the following finite element equations:

$$\mathbf{KQ} = \mathbf{P} \tag{86}$$

where $\mathbf{K}$ is the stiffness matrix, $\mathbf{Q}$ is the nodal displacement vector and $\mathbf{P}$ is the nodal load vector of the body or assemblage of finite elements given by:

$$\mathbf{K} = \sum_{e=1}^{n} \mathbf{K}^{(e)} \tag{87}$$

$$\mathbf{K}^{(e)} = \int_{V^{(e)}} \mathbf{B}^{\mathrm{T}}\mathbf{D}\mathbf{B}\, \mathrm{d}V \tag{88}$$

$$\mathbf{P} = \sum_{e=1}^{n} \left(\mathbf{P}_{\mathrm{i}}^{(e)} + \mathbf{P}_{\mathrm{t}}^{(e)} + \mathbf{P}_{\mathrm{b}}^{(e)}\right) + \mathbf{P}_{\mathrm{c}} \tag{89}$$

Here $\mathbf{K}^{(e)}$ is the element stiffness matrix of element e, n is the total number of finite elements in the body, $\mathbf{D}$ is the elasticity matrix, $\mathbf{P}_{\mathrm{i}}^{(e)}$, $\mathbf{P}_{\mathrm{t}}^{(e)}$, $\mathbf{P}_{\mathrm{b}}^{(e)}$ are the load vectors of element e due to initial strains, tractions, body forces, respectively, $\mathbf{P}_{\mathrm{c}}$ is the vector of concentrated loads at the nodes of the body, and $[\mathbf{N}]$ is the matrix of shape functions used for the variation of displacement within the element e. The element load vectors are given by:

$$\mathbf{P}_{\mathrm{i}}^{(e)} = \int_{V^{(e)}} \mathbf{B}^{\mathbf{T}}\mathbf{D}\varepsilon_0\, \mathrm{d}V \tag{90}$$

$$\mathbf{P}_{\mathrm{t}}^{(e)} = \int_{S_{\mathrm{t}}^{(e)}} \mathbf{N}^{\mathrm{T}}\bar{\mathbf{t}}\, \mathrm{d}S \tag{91}$$

$$\mathbf{P}_{\mathrm{b}}^{(e)} = \int_{V^{(e)}} \mathbf{N}^{\mathrm{T}}\bar{\mathbf{B}}\, \mathrm{d}V \tag{92}$$

Variational Formulations in Dynamics

The variational formulations are useful to describe motion of a system over an arbitrary period of time. D'Alembert's principle states that:

$$\delta W_I = \left(\mathbf{F}_k - \dot{\mathbf{B}}_k\right) \cdot \delta\mathbf{r}_k = 0\,, \qquad k = 1, 2, \ldots, N \tag{93}$$

where δW_I is the virtual work done on mass particle k, $\delta\mathbf{r}_k$ is a kinematically admissible virtual displacement (with time held fixed), $\mathbf{F}_k$ is a force acting on mass k, $-\dot{\mathbf{B}}_k$ is the D'Alembert's inertial force ($\mathbf{B}$ is the linear momentum), and N is the number of mass particles.

Hamilton's Principle

The integral of D'Alembert's virtual work expression over an arbitrary period of time is:

$$\int_{t_1}^{t_2} \left(\mathbf{F}_k - \dot{\mathbf{B}}_k\right) \cdot \delta\mathbf{r}_k\, \mathrm{d}t = 0 \tag{94}$$

When the virtual displacement vanishes at times t_1 and t_2 and the applied forces possess a potential energy function V, eqn [94] reduces to:

$$\int_{t_1}^{t_2} \delta(T^* - V)\, \mathrm{d}t = \delta\pi_{\mathrm{H}} = 0 \tag{95}$$

where:

$$\pi_{\mathrm{H}} = \int_{t_1}^{t_2} L\, \mathrm{d}t \tag{96}$$

$$L = T^* - V \tag{97}$$

and T^* is the complementary kinetic energy. In Newtonian mechanics, T^* will be same as T, the kinetic energy of the system. Eqn [95] is known as Hamilton's principle and states that 'among all kinematically possible motions in the interval t_1 to t_2, the actual one is characterized by the stationary condition of the functional π_{H}'. The stationary conditions of π_{H} yield the equations of motion of the system.

Complementary Hamilton's Principle

The complementary form of Hamilton's principle can be stated as:

$$\int_{t_1}^{t_2} \delta(T - V^*)\, \mathrm{d}t = \delta\pi_T = 0 \tag{98}$$

where:

$$\pi_T = \int_{t_1}^{t_2} L^* \, \mathrm{d}t \qquad [99]$$

$$L^* = T - V^* \qquad [100]$$

and T is the kinetic energy and V^* is the complementary potential energy of the system. In words, the complementary form of Hamilton's principle can be stated as 'amongst all possible equilibrating motions in the interval t_1 to t_2, the actual one is characterized by the stationary condition of the functional π_T'. The stationary conditions of π_T yield the conditions of compatibility.

Lagrange's Equations

The Lagrange's equations can be stated as:

$$\frac{\mathrm{d}}{\mathrm{d}t}\left(\frac{\partial L}{\partial \dot{q}_i}\right) - \frac{\partial L}{\partial q_i} = 0, \qquad i = 1, 2, \ldots, N \qquad [101]$$

where $L = T^* - V$ is the Lagrangian, q_i is the generalized displacement and $\dot{q}_i$ is the generalized velocity. In addition to the forces that possess a potential, where generalized forces Q_i (that are not derivable from a potential function) act on the system, then the Lagrange's equations are given by:

$$\frac{\mathrm{d}}{\mathrm{d}t}\left(\frac{\partial L}{\partial \dot{q}_i}\right) - \frac{\partial L}{\partial q_i} = Q_i, \qquad i = 1, 2, \ldots, N \qquad [102]$$

Complementary Lagrange's Equations

The complementary form of Lagrange's equations is given by:

$$\frac{\mathrm{d}}{\mathrm{d}t}\left(\frac{\partial L^*}{\partial \dot{s}_i}\right) - \frac{\partial L^*}{\partial s_i} = S_i, \qquad i = 1, 2, \ldots, N \qquad [103]$$

where $L^* = T - V^*$ is the complementary Lagrangian, s_i is the generalized impulse, and S_i is the generalized velocity.

Principle of Least Action

Although the interval of time t_1 to t_2 is arbitrarily in Hamilton's principle, the limits t_1 and t_2 are fixed. Thus time is held fixed during the variation of the coordinates q_i. The principle of least action can be used when t_1 and t_2 are not fixed:

$$\Delta \int_{t_1}^{t_2} (T + T^*) \, \mathrm{d}t = 0 \qquad [104]$$

In words, the principle of least action states that 'amongst all possible motions of conservative systems between any two prescribed configurations, the actual motion will be such as to render the functional in eqn [104] an extremum'.

Using the principle of conservation of energy, $T + V = E =$ constant, the principle of least action can also be expressed as:

$$\Delta \int_{t_1}^{t_2} (L + E) \, \mathrm{d}t = 0 \qquad [105]$$

where:

$$L = T^* - V \qquad [106]$$

Nomenclature

A	cross-sectional area
$\mathbf{B}$	vector of body forces
D	domain; flexural rigidity
$\mathbf{D}$	elasticity matrix
E	Young's modulus
EI	bending stiffness
g	gravitational acceleration
G	shear modulus
$GJ(x)$	torsional stiffness
h	thickness
I	inertia
$J(x)$	polar moment of inertia
L	length
M_o	mass of the beam
$\mathbf{N}$	matrix of shape functions
$\mathbf{P}$	nodal load vector
$\mathbf{Q}$	nodal displacement vector
S	surface
$\mathbf{t}$	vector of tractions
T	kinetic energy
$T(x)$	tension in the string
$\bar{\mathbf{u}}$	vector of displacement
$u(x,t)$	longitudinal displacement
$U(t)$	potential (strain) energy
V	volume
$w(x,t)$	transverse displacement
X_i	amplitude
$\mathbf{X}$	arbitrary vector
v	Poisson's ratio
λ	eigenvalue

ϕ	eigenfunction
ρ	mass of rod; density
$\boldsymbol{\sigma}$	vector of stresses

See also: **Discrete elements**; **Eigenvalue analysis**; **Finite difference methods**; **Finite element methods**; **Theory of vibration**, Variational methods.

Further Reading

James ML, Smith GM, Wolford JC, Whaley PW (1989) *Vibration of Mechanical and Structural Systems*. New York: Harper & Row.

Langhaar HL (1962) *Energy Methods in Applied Mechanics*. New York: John Wiley.

Meirovitch L (1967) *Analytical Methods in Vibrations*. New York: Macmillan.

Rao SS (1995) *Mechanical Vibrations*, 3rd edn. Reading, MA: Addison-Wesley.

Rao SS (1999) *The Finite Element Method in Engineering*. 3rd edn. Boston: Butterworth-Heinemann.

Szilard R (1974) *Theory and Analysis of Plates: Classical and Numerical Methods*. Englewood Cliffs, NJ: Prentice-Hall.

Tabarrok B, Rimrott FPJ (1994) *Variational Methods and Complementary Formulations in Dynamics*. Dordrecht, The Netherlands: Kluwer Academic Publishers.

Tedesco JW, McDougal WG, Ross CA (1999) *Structural Dynamics: Theory and Applications*. Menlo Park, CA: Addison-Wesley.

Zienkiewicz OC (1977) *The Finite Element Method*, 3rd edn. London: McGraw-Hill.

Equations of Motion

J Wickert, Carnegie Mellon University, Pittsburgh, PA, USA

Copyright © 2001 Academic Press

doi:10.1006/rwvb.2001.0116

Introduction

Early procedural steps taken in the mathematical analysis of a mechanical vibration problem include: (1) modeling, in which the essentials of a physical system are extracted to produce an idealized model amenable to solution; (2) choosing appropriate coordinates which uniquely describe the system's configuration; and (3) obtaining one or more equations which describe vibration of the modeled system. The resulting equation(s) of motion (EOM) are ordinary or partial differential equations that govern the manner in which displacements of the system evolve with time. They are used extensively in subsequent analysis and computation in order to predict transient response, steady-state forced vibration, natural frequencies, and mode shapes.

EOM are derived through the application of physical laws and such methods of dynamics as Newton's laws of motion, Lagrange's equation, and Hamilton's principle. For discrete systems, the EOM take the form of ordinary differential equations, while partial differential equations in one or more independent spatial coordinates govern continuous or distributed-parameter models. The mass, stiffness, and damping properties of the model can be constant or time-dependent, and they appear in the EOM as parameters or coefficients of the coordinates and their derivatives. The external forces or torques which are applied to the system in order to excite vibration render the EOM inhomogeneous.

This article presents a brief exposition of EOM, their derivation, mathematical structure, and properties for the illustrative cases of discrete systems having one or more degrees-of-freedom and prototypical models of continuous systems.

Single-degree-of-freedom Models

In the simplest case, a mechanical system can be modeled using methods of lumped parameter analysis whereby motion is described fully by only one time-dependent coordinate. Such a system is termed a 1-degree-of-freedom (DOF) vibration model. Although the transient or steady-state vibration of the system could, in fact, be rather complicated, only one translational or rotational coordinate is presumed necessary to specify within acceptable bounds of accuracy the configuration of the system at any instant. When more than one coordinate becomes necessary, the discrete system is said to have multiple degrees-of-freedom. **Figure 1A** illustrates the prototypical vibration model having lumped mass m, stiffness k, and damping c elements, in addition to the concentrated external force $F(t)$. The parameters m, c, and k are generally interpreted as being effective values that represent combinations of other, multiple, interconnected components. An example in that regard is several springs that are connected in series and/or parallel connections so as to form a single element of equivalent stiffness k.

In order to obtain the equation of motion, the free-body diagram of the inertia element is drawn as indicated in **Figure 1B**, and Newton's second law of motion, $\mathbf{f} = m\mathbf{a}$, for a particle is applied, wherein $\mathbf{f}$

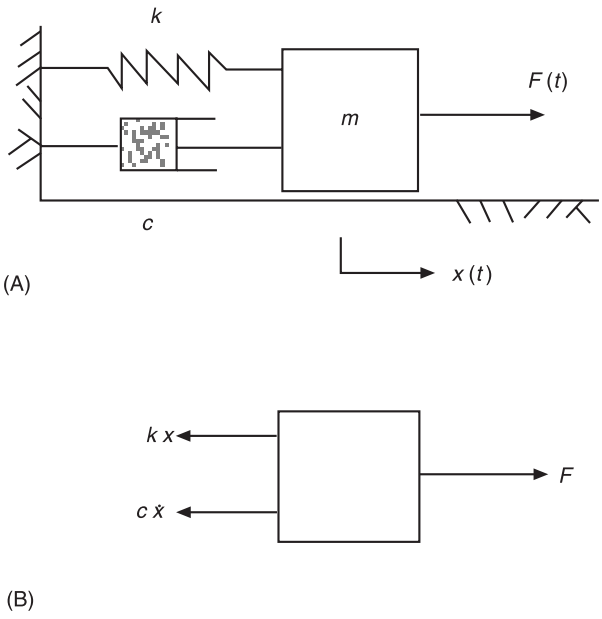


Figure 1 (A) Single-degree-of-freedom vibration model for a particle in translation. (B) Free-body diagram of the inertia element.

represents the resultant force vector, and **a** is the particle's absolute acceleration. With displacement measured by the coordinate $x(t)$, the particle's velocity and acceleration are denoted $v = \mathrm{d}x/\mathrm{d}t = \dot{x}$, and $a = \mathrm{d}^2x/\mathrm{d}t^2 = \ddot{x}$, respectively. The dot-superscript notation is used conventionally in vibration engineering to denote derivatives taken with respect to time.

With the positive sign convention directed rightward in **Figure 1**, application of the second law provides $-kx - c\dot{x} + F = m\ddot{x}$. In its standard form, the EOM is written with all terms involving displacement, velocity, and acceleration on one side, with one or more forcing terms grouped on the other. The final form of the equation of motion becomes:

$$m\ddot{x} + c\dot{x} + kx = F(t) \qquad [1]$$

which is a second-order, linear, inhomogeneous, ordinary differential equation having constant coefficients. The solution is found subject to the initial conditions on displacement $x(0) = x_0$ and velocity $\dot{x}(0) = v_0$ as evaluated at $t = 0$. By convention, the EOM is also written:

$$\ddot{x} + 2\zeta\omega_n\dot{x} + \omega_n^2 x = \frac{F(t)}{m} \qquad [2]$$

in terms of the parameters:

$$\omega_n = \sqrt{\frac{k}{m}} \quad \text{and} \quad \zeta = \frac{c}{2\sqrt{mk}} \qquad [3]$$

which are the undamped, circular, natural frequency (in units radians per second) and the dimensionless damping ratio.

An analogous procedure is applied to rotational systems, the only distinction being that the principle of angular momentum balance is invoked instead of the second law. The precise form taken by the balance law differs depending on whether it is resolved about a point O fixed in space, the mass center G of a rigid body, or an arbitrary point P; either method, when properly applied, will result in a valid equation of motion.

When rotational vibration $\theta(t)$ occurs about a fixed point, for instance, $M_0 = J_0\ddot{\theta}$ where M_0 is the resultant moment, J_0 is the mass moment of inertia, and $\ddot{\theta}$ denotes the angular acceleration. For illustration, in **Figure 2A**, the rigid-body pendulum has centroid located distance L from the support, and oscillation occurs under the restoring influence of gravity g alone. Reactions O_x and O_y produce no moment about the support, and the equation of motion becomes $J_O\ddot{\theta} + mgL\sin\theta = 0$. Due to the explicit presence of the transcendental function, the equation of motion as derived is nonlinear and therefore is valid for arbitrarily large angles of rotation, including multiple clockwise or counterclockwise circulations of the pendulum about O. For the more common circumstance of 'small' amplitude motion, the equation of motion is linearized about its stable, trivial, equilibrium point by using the Taylor series expansion $\sin\theta \sim \theta - \theta^3/6 + \ldots$, and subsequently retaining only the first-order term. The desired linear EOM then becomes $J_0\ddot{\theta} + mgL\theta = 0$ in the standard form of eqn [1]. The rigid body undergoes free vibration

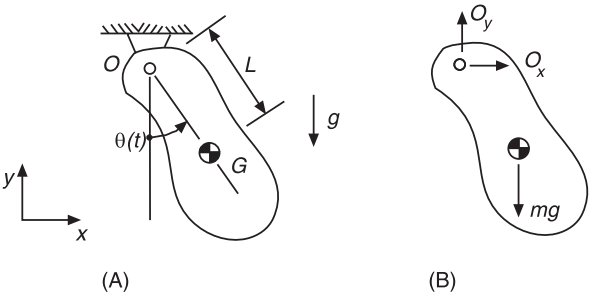


Figure 2 Rotational oscillation of a rigid-body pendulum.

since its equation of motion is homogeneous. In a straightforward application of some practical utility, with both the mass m and offset distance L known, a measurement of the natural frequency can be used to determine the rigid body's mass moment of inertia.

Two or More Degrees-of-freedom Models

For a discrete system that requires more than one coordinate to describe fully its configuration, a system of ordinary differential equations, one written for each coordinate or inertia element, arises. With N such coordinates, the system's overall mass, damping, and stiffness characteristics are embodied by matrices of dimension $N \times N$. Likewise, the translational and/or rotational displacements of individual inertia elements are collected to form an N-dimensional vector, as is also the case for any externally imposed forces or moments that may be present.

In the most general case, the system's matrices will be full, with off-diagonal elements describing the degree of coupling, if any, that exists between the various coordinates. When the mass matrix is not diagonal, for instance, the system is said to be inertially coupled; analogous terminology is applied should off-diagonal elements be present in the damping or stiffness matrices. Such coupling and interaction among the multiple equations of motion is precisely what complicates vibration analysis relative to that seen for a 1-DOF model. By proper choice of coordinates, however, coupling can be reduced, transformed, and even eliminated altogether when modal coordinates are invoked. The latter opportunity motivates the study of normal modes, and provides the emphasis given to them throughout vibration engineering.

In the lumped parameter system of **Figure 3A**, two masses vibrate with responses $x_1(t)$ and $x_2(t)$ under action of the impressed forces $F_1(t)$ and $F_2(t)$ and the indicated stiffness and damping elements. To establish the equations of motion, the second law is applied to m_1 and m_2 individually using the free-body diagrams of **Figure 3B**, providing:

$$m_1\ddot{x}_1 + (c_1 + c_2)\dot{x}_1 - c_2\dot{x}_2 + (k_1 + k_2)x_1 - k_2x_2 = F_1(t) \quad [4]$$

$$m_2\ddot{x}_2 - c_2\dot{x}_1 + c_2\dot{x}_2 - k_2x_1 + k_2x_2 = F_2(t) \quad [5]$$

The EOM are then conveniently written in the matrix vector form:

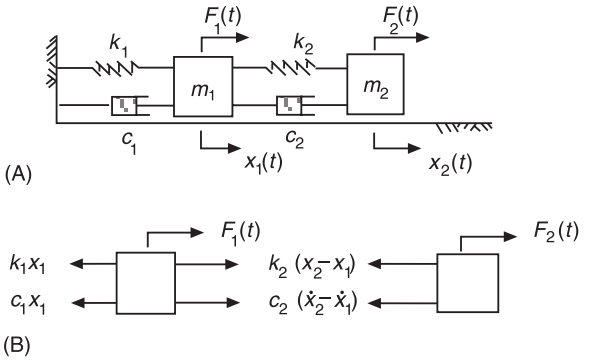


Figure 3 (A) Two-degrees-of-freedom vibration model. (B) Free-body diagrams of the inertia elements.

$$\begin{bmatrix} m_1 & 0 \\ 0 & m_2 \end{bmatrix} \begin{Bmatrix} \ddot{x}_1 \\ \ddot{x}_2 \end{Bmatrix} + \begin{bmatrix} c_1+c_2 & -c_2 \\ -c_2 & c_2 \end{bmatrix} \begin{Bmatrix} \dot{x}_1 \\ \dot{x}_2 \end{Bmatrix} + \begin{bmatrix} k_1+k_2 & -k_2 \\ -k_2 & k_2 \end{bmatrix} \begin{Bmatrix} x_1 \\ x_2 \end{Bmatrix} = \begin{Bmatrix} F_1(t) \\ F_2(t) \end{Bmatrix} \quad [6]$$

where coupling is present in both damping and stiffness.

More generally, for an N-degrees-of-freedom system subjected to viscous damping forces, the equations of motion will take the form:

$$\mathbf{M}\ddot{\mathbf{x}} + \mathbf{C}\dot{\mathbf{x}} + \mathbf{K}\mathbf{x} = \mathbf{F}(t) \quad [7]$$

where $\mathbf{M}$, $\mathbf{C}$, and $\mathbf{K}$ are the mass, stiffness, and damping matrices, and $\mathbf{x}(t)$ and $\mathbf{F}(t)$ are the state and excitation vectors. Solutions are found subject to the initial conditions $\mathbf{x}(0) = \mathbf{x}_0$ and $\dot{\mathbf{x}}(0) = \mathbf{v}_0$.

The precise nature of coupling that arises in the system matrices changes depending on the coordinates that are chosen to describe vibration. In **Figure 4**, a rigid bar is supported by springs having differing stiffness k_1 and k_2, and the centroid G is offset from the bar's geometric center. In the first choice of coordinates, translation x of the mass center and rotation θ are used to describe small-amplitude motion, and the equations of motion are:

$$\begin{bmatrix} m & 0 \\ 0 & J_G \end{bmatrix} \begin{Bmatrix} \ddot{x} \\ \ddot{\theta} \end{Bmatrix} + \begin{bmatrix} k_1+k_2 & k_2L_2 - k_1L_1 \\ k_2L_2 - k_1L_1 & k_1L_1^2+k_2L_2^2 \end{bmatrix} \begin{Bmatrix} x \\ \theta \end{Bmatrix} = \begin{Bmatrix} 0 \\ 0 \end{Bmatrix} \quad [8]$$

where m and J_G are the bar's mass and mass moment of inertia about G, respectively. There is no inertial coupling, and the EOM couple statically in stiffness

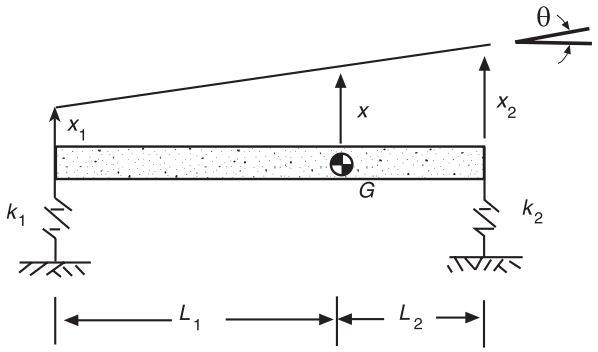


Figure 4 Rigid body with motion described alternatively by (x, θ) or by (x_1, x_2).

through the off-diagonal elements of **K**. With the special parameter values satisfying $k_1L_1 - k_2L_2 = 0$, translational and pitch motions as described by x and θ fully decouple; vibration in that case can be analyzed as if two uncoupled single DOF systems were being treated in parallel. Alternatively, when displacements x_1 and x_2 of the bar's two ends are chosen as coordinates, the equations of motion take the form:

$$\frac{1}{(L_1+L_2)^2}\begin{bmatrix} mL_2^2+J_G & mL_1L_2-J_G \\ mL_1L_2-J_G & mL_1^2+J_G \end{bmatrix}\begin{Bmatrix} \ddot{x}_1 \\ \ddot{x}_2 \end{Bmatrix} + \begin{bmatrix} k_1 & 0 \\ 0 & k_2 \end{bmatrix}\begin{Bmatrix} x_1 \\ x_2 \end{Bmatrix} = \begin{Bmatrix} 0 \\ 0 \end{Bmatrix} \quad [9]$$

and the system suffers only inertial coupling. Modal analysis, in short, involves a coordinate transformation which simultaneously decouples both system matrices.

In physical modeling and deriving equations of motion, numerical values for the mass and stiffness parameters can typically be obtained through straightforward analyses or experiments, and they are therefore generally known to within an acceptable level of accuracy. Further, within the context of a conservative mechanical system vibrating about a position of stable equilibrium, substantial theoretical justification exists for the mass and stiffness matrices being symmetric and positive definite, a result which underlies the calculation of normal modes, natural frequencies, and orthogonality among the modes. However, to the degree that a wide variety of energy dissipation mechanisms exists, including internal material damping, friction, sound radiation, and vibration transmission at joints and connections to other structures, damping models, and numerical values for viscous damping coefficients in particular, are less well-developed. Beyond issues of mathematical convenience and certain restricted cases of laminar fluid flow through a slot or an orifice, there is somewhat less justification for the introduction of the viscous damping matrix **C** in an equation of motion.

In certain practical applications, while damping in its various embodiments is recognized as being an important attribute of the system at hand, it will generally not be easily modeled in terms of damping coefficients. In such circumstances and when the effects of damping are judged to be 'light', damping is conventionally ignored insofar as deriving the equations of motion is concerned, so that the EOM are written in terms of **M** and **K** only. Vibration analysis proceeds with the calculation of natural frequencies and normal modes, on to decoupling of the EOM through modal analysis, at which point dissipation is incorporated within the context of modal damping. In short, an effective damping ratio for each mode, rather than for each physical coordinate as was present in the original model, is introduced with a numerical value determined through appropriate measurements.

The EOM for multiple-degrees-of-freedom systems can also be derived by using the Lagrangian approach of analytical dyamics, which is viewed often as a preferred technique when complicating factors of geometry, kinematics, or modeling are present. Written in terms of the scalar kinetic T and potential U energy functions, Lagrange's equation for each DOF $k = 1, 2, \ldots N$ is:

$$\frac{\mathrm{d}}{\mathrm{d}t}\left(\frac{\partial L}{\partial \dot{q}_k}\right) - \frac{\partial L}{\partial q_k} = Q_k(t) \quad [10]$$

in terms of the Lagrangian function $L = T - U$, the generalized coordinates, $q_k(t)$, and the generalized forces $Q_k(t)$.

Continuous System Models

Although discrete models of mechanical systems are often readily established and can be useful intuitive and predictive tools, in some applications and particularly at moderate or higher frequencies, they are inherently limited by the level of approximation made by lumping mass, stiffness, and damping properties into a relatively small number of elements. To the extent that in all real systems, physical properties are not concentrated at discrete points, the class of continuous or distributed-parameter vibration models provides more accurate structural representations. The higher level of model fidelity, however, is realized

at the expense of EOM having multiple independent variables, both spatial and temporal, and which are commensurately more complicated than their discrete counterparts. The EOM of continuous systems are partial differential equations that govern motion within an elastic body's interior, and they are solved subject to initial conditions in time as well as boundary conditions in space.

A seemingly direct, but primitive, method for deriving the EOM of a continuous system involves approximating it by one that contains a finite number of discrete particles, and then examining the form taken by the EOM as the number of particles becomes large, namely, as the continuous limit is approached. For instance, should more discrete mass, stiffness, and damping elements be added to the configuration of **Figure 3**, the serial chain would behave in a manner representative of a rod undergoing longitudinal vibration. For that reason, a continuous system can be viewed conceptually as one having infinite degrees-of-freedom, whereby the set of N functions which describe the discrete system's vibration is replaced by a single continuous function as evaluated over a continuum of positions and instants.

While indeed pedagogically useful, such a viewpoint suffers from lack of generality, and so it is not used commonly in practice. The more systematic technique by which to obtain the EOM and boundary conditions is to isolate an infinitesimal element from the body, apply an appropriate constitutive law so as to relate restoring forces or moments to translational or rotational displacements, and invoke Newton's second law or the angular momentum balance principle to a free-body diagram of the element. Specifically, the approach for continuous system vibration models comprises the following major steps:

- Choose coordinates to describe motion of the system and, in particular, an infinitesimal element isolated from it.
- Determine the restoring force/moment-displacement, or stress-strain, relation using an appropriate model applied from strength of materials or elasticity theories.
- Apply force or moment balance principles over the interior of the body to obtain the equation of motion.
- Apply force or moment balance principles over the structure's periphery to obtain the boundary conditions.

In a manner analogous to the utility of Lagrange's equation in analyzing discrete systems, more sophisticated approaches are available for deriving the EOM of continuous systems, including treatments of three-dimensional vibration, continuum mechanics, and elastic-wave propagation. For structures having coupling between motions, complicated kinematics, or certain constitutive properties, application of the extended Hamilton's principle:

$$\int_{t_1}^{t_2} (\delta T - \delta U + \delta W_{\mathrm{NC}})\, \mathrm{d}t = 0 \qquad [11]$$

from the field of analytical dynamics can be a preferred starting point in deriving the EOM and boundary conditions. Here T and U are expressions for the kinetic and potential energies, δ denotes variation, and δW_{NC} is the nonconservative virtual work.

Rod, String, and Shaft Vibration

A simple model of continuous system vibration, and one which enjoys significant practical application, describes longitudinal motion of a rod wherein material particles oscillate in a direction aligned with the rod's axis. The resulting deformation includes local tension and compression, which can be viewed within the context of propagation and superposition of tension and compression waves. **Figure 5A** illustrates the geometry in which the rod is fixed to a rigid support at its end $x = 0$, free at the other end $x = L$, and excited by the distributed force-per-unit-length $f(x, t)$ directed along the rod's axis. Motion is measured by $u(x, t)$, a function of longitudinal position and time.

In the strength of materials theory for uniaxial tension and compression, the rod deforms with axial stiffness $EA(x)$, where E and A denote local values of the elastic modulus and cross-sectional area, and the product is not necessarily constant. With reference to the free-body diagram of **Figure 5B**, the internal elastic force within the rod at any point is $EAu_{,x}$, where the comma-subscript notation is used

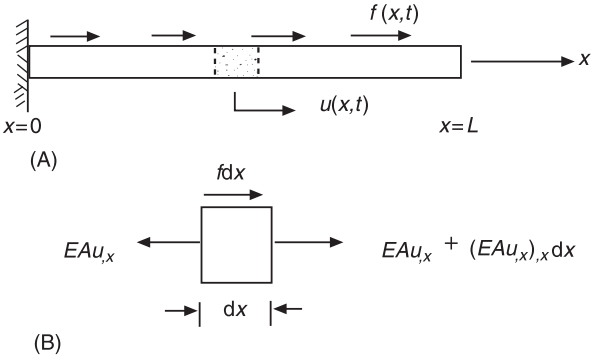


Figure 5 (A) Longitudinal vibration of an elastic rod. (B) Free-body diagram of an infinitesimal element isolated from the rod's interior.

conventionally to indicate a partial derivative, which in this case is taken with respect to x. Application of Newton's second law to the element provides:

$$(\rho A \mathrm{d}x)u_{,tt} = -EAu_{,x} + \left(EAu_{,x} + (EAu_{,x})_{,x}\mathrm{d}x\right) + f\mathrm{d}x \qquad [12]$$

where ρ is the material's volumetric density, and the internal force within the rod has already been expanded in a Taylor series about $x = 0$. The equation of motion becomes:

$$\rho A u_{,tt} - (EAu_{,x})_{,x} = f(x,t) \qquad [13]$$

which is solved subject to initial conditions on displacement u and velocity $u_{,t}$ at time $t = 0$, as well as boundary conditions that are applied to u and/or $u_{,x}$ at $x = 0$ and L.

Various boundary conditions are possible and admissible depending on the manner in which the rod is supported. One condition must be applied at each end of the rod. In the presence of a built-in support at either end, for instance, the displacement at that point vanishes. Should an end of the rod be free, the tension or compression internal to the rod would likewise vanish at that point, providing the condition $EAu_{,x} = 0$. In cases involving interactions at the boundary between the rod and other components modeled as ideal discrete elements, the appropriate expression for the boundary condition is derived by constructing the free-body diagram of an isolated boundary element, as suggested by the examples given in **Figure 6**.

When no external forces act on the rod, and the density, cross-sectional area, and elastic modulus do not vary along its length, the EOM assumes the form:

$$u_{,tt} - c^2 u_{,xx} = 0 \qquad [14]$$

of the standard-wave equation, where $c = \sqrt{E/\rho}$ is the speed at which tension and compression waves propagate. The wave equation enjoys a rich history in the theory of vibration, and it describes a variety of physical phenomena beyond longitudinal rod vibration. With appropriate substitutions, the wave equation also describes the transverse vibration of a pretensioned flexible string, and the torsional vibration of an elastic shaft – analogies which are outlined further in **Figure 7**.

Beam Vibration

A beam is defined as a structural member that is long relative to its cross-sectional dimensions, and that executes small amplitude motion v in the direction transverse to its axis, as illustrated in **Figure 8A**. The most elementary and widely used treatment of beam deformation is attributed to Euler and Bernoulli, and it specifies that the beam's rotary inertia and deformation in shear are each negligible. Those assumptions are relaxed in the Timoshenko beam model, which offers higher-order accuracy at the expense of additional analytical complexity.

In the free-body diagram of **Figure 8B** for an element that has been isolated from the beam, the internal shear V and bending moment M are expanded in Taylor series about $x = 0$, and their gradients across the element dx produce imbalances in force or moment necessary to generate the requisite acceleration and vibration. With EI denoting the beam's flexural rigidity, subject to the standard restrictions implicit in the linear moment curvature $M = EIv_{,xx}$ and shear $V = -(EIv_{,xx})_{,x}$ relationships invoked from the strength of materials theory, the equation of motion for transverse bending vibration of the beam becomes:

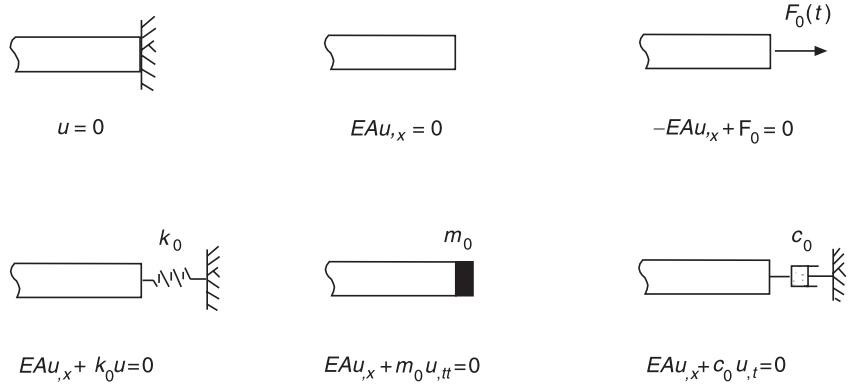


Figure 6 Examples of boundary conditions applied to the longitudinal vibration of an elastic rod, as evaluated on the right-hand end of the rod.

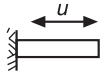
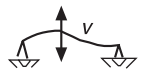
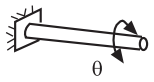
System		Motion	Equation of Motion	Wave Speed, c
Rod		Axial $u(x,t)$	$\rho A u_{,tt} - EA u_{,xx} = 0$	$\sqrt{E/\rho}$
String		Transverse $v(x,t)$	$\rho A_{,tt} - P v_{,xx} = 0$	$\sqrt{P/\rho A}$
Shaft		Torsional $\theta(x,t)$	$I\theta_{,tt} - JG\theta_{,xx} = 0$	$\sqrt{JG/I}$

Figure 7 Analogies between the longitudinal vibration of a rod, transverse vibration of a string, and torsional vibration of a shaft, for cases in which the models' properties are lengthwise constant. In the string model, P denotes the pre-tension. In the shaft model, JG is the torsional rigidity, and I is the polar moment of inertia per unit-length of the shaft.

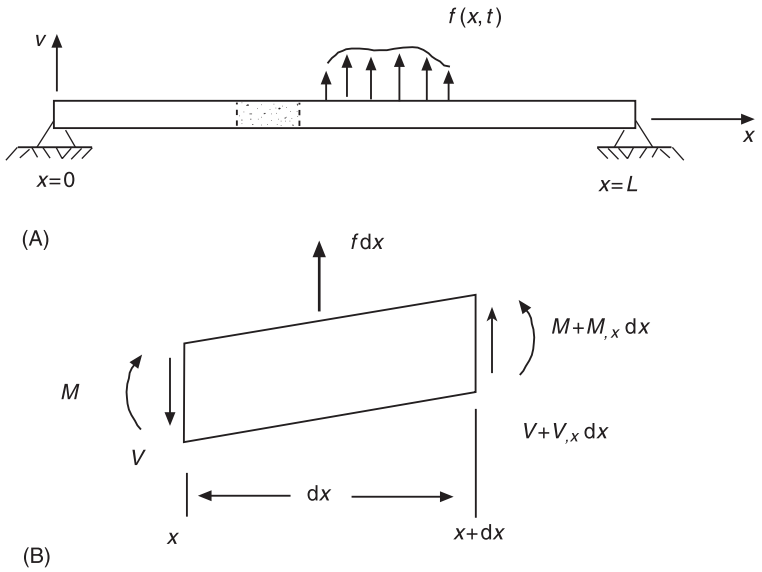


Figure 8 (A) Transverse bending vibration of a beam. (B) Free-body diagram of an infinitesimal interior element.

$$\rho A v_{,tt} + (EIv_{,xx})_{,xx} = f(x,t) \qquad [15]$$

where $f(x,t)$ is the transverse force-per-unit-length. The EOM is a linear partial differential equation and, because it is fourth-order, it is necessary to specify two conditions at each point on the beam's boundary.

Specifically, either kinematic conditions on displacement or slope, or force conditions on shear or moment, can be imposed in accordance with specific restrictions on the combinations of conditions that are allowable. For a simply supported beam, the boundary conditions become $v = 0$ and $EIv_{,xx} = 0$. Conversely, the set of conditions $v_{,x} = 0$ and $EIv_{,xx} = 0$ at the same point cannot be physically realized and is therefore inadmissible. For a clamped-free beam, the kinematic conditions $v = v_{,x} = 0$ are specified at $x = 0$, with vanishing shear and moment at $x = L$ through $EIv_{,xx} = (EIv_{,xx})_{,x} = 0$. Those conditions and others are briefly outlined in **Figure 9**.

Membrane and Plate Vibration

Membranes and plates are two-dimensional structures that vibrate in the direction transverse to their equilibrium plane. A membrane has negligible

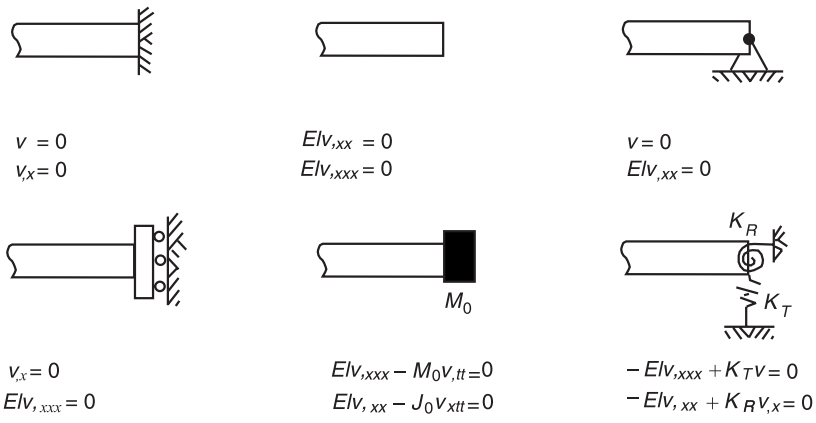


Figure 9 Examples of boundary conditions for lateral bending vibration of a beam, as evaluated on its right-hand end.

bending rigidity and derives restoring stiffness from its initial pretension; a plate, on the other hand, develops curvature-related bending stress as it deforms. In that sense, the more elementary string and beam models are interpreted as being one-dimensional realizations of membranes and plates, respectively.

For a membrane, the equation of motion in rectangular coordinates (x, y) is:

$$\rho h v_{,tt} - \left(N_x v_{,xx} + N_y v_{,yy}\right) = f(x,t) \qquad [16]$$

where h is the material's thickness, N_x and N_y are the initial tensions-per-unit-length resolved along the coordinate directions, and $f(x, t)$ denotes the transverse force applied per unit of the membrane's surface area. When the tension field is isotropic, $N_x = N_y = N_0$, the EOM takes on its standard form:

$$\rho h v_{,tt} - N_0 \nabla^2 v = f(x,t) \qquad [17]$$

in terms of the Laplacian operator in either Cartesian coordinates:

$$\nabla^2 = \frac{\partial^2}{\partial x^2} + \frac{\partial^2}{\partial y^2} \qquad [18]$$

or polar coordinates (r, θ):

$$\nabla^2 = \frac{\partial^2}{\partial r^2} + \frac{1}{r}\frac{\partial}{\partial r} + \frac{1}{r^2}\frac{\partial^2}{\partial \theta^2} \qquad [19]$$

The most straightforward boundary conditions that can be considered are the constrained $v = 0$ and free $v_{,n} = 0$ cases, the latter of which requires vanishing slope in the direction normal to the membrane's boundary, namely, a directional derivative. Along a free edge of constant x, for instance, the condition becomes $v_{,x} = 0$. Other conditions which account for coupling between the membrane and discrete inertia, stiffness, or damping elements on the boundary are treated by application of appropriate balance laws to infinitesimal elements of the membrane isolated in a free-body diagram.

In the case of a plate's bending vibration, the EOM is:

$$\rho h v_{,tt} + D\nabla^4 v = f(x,t) \qquad [20]$$

in terms of the biharmonic operator $\nabla^4 = (\nabla^2)^2$. The plate's stiffness parameter, analogous to the familiar flexural rigidity from the strength of materials theory for beam deformation, is defined:

$$D = \frac{Eh^3}{12(1-\nu^2)} \qquad [21]$$

in terms of the plate's thickness h, elastic modulus E, and Poisson ratio ν. Because the equation of motion is fourth-order, two conditions must be specified at each point on the plate's boundary. Those conditions are expressed in terms of requirements on the displacement, slope, bending moment, or equivalent shear force along the plate's edges.

Special-interest Topics

Other topics which are related to the derivation, structure, and properties of the equations of motion for discrete and continuous systems, but which are

not discussed in this section for reasons of brevity, include:

- Gyroscopic systems where small-amplitude vibration occurs in the presence of a steady superposed motion. Applications include the vibration of rotating disks and shafts, and such translating media as power transmission belts and sheet metal webs.
- Nonconservative forces, including the follower-type loading of the classical Beck or Pflüger problem in the field of dynamic stability, which render the stiffness matrix nonsymmetric.
- Parametric excitation which is present when a parameter in a vibration model, such as rotation speed or tension, is time-dependent and, in particular, periodic.
- Nonlinear systems wherein motion is of sufficiently large amplitude that nonlinear terms must be retained in the equations of motion, complicating their analysis and solution.
- Discretization in which a continuous system model is systematically reduced to an equivalent, potentially high-DOF, discrete model. Local or global techniques such as finite element, Galerkin, and Ritz comprise a powerful class of methods available for developing accurate approximate solutions to the EOM.
- Linear operators for mass, damping, and stiffness effects which are a mathematical formalism facilitating the analysis of continuous system vibration, particularly with respect to modal analysis.

Nomenclature

A	cross-sectional area
E	elastic modulus
$\mathbf{F}(t)$	excitation vector
G	centroid
T	kinetic energy
U	potential energy
$\mathbf{x}(t)$	state vector velocity
δ	variation
$\theta(t)$	rotational vibration
$\ddot{\theta}$	angular acceleration
ρ	density
∇	Laplacian operator

See also: **Beams**; **Discrete elements**; **Linear damping matrix methods**; **Membranes**; **Modal analysis, experimental**, Basic principles; **Nonlinear systems, overview**; **Parametric excitation**; **Plates**; **Theory of vibration**, Duhamel's Principle and convolution; **Theory of vibration**, Energy methods; **Theory of vibration**, Fundamentals; **Theory of vibration**, Impulse response function; **Theory of vibration**, Substructuring; **Theory of vibration**, Superposition; **Theory of vibration**, Variational methods.

Further Reading

Bishop RED and Johnson DC (1979) *The Mechanics of Vibration*. Cambridge: Cambridge University Press.

Greenwodd DT (1988) *Principles of Dynamics*, 2nd edn. New Jersey: Prentice-Hall.

Leissa A (1993) *Vibration of Plates*. New York: Acoustical Society of America.

Pars LA (1979) *A Treatise on Analytical Dynamics*. Woodbridge, CN: Ox Bow Press.

Thomson WT and Dahleh MD (1998) *Theory of Vibration with Applications*. New Jersey: Prentice-Hall.

Timoshenko SP and Woinowsky-Krieger S (1970) *Theory of Plates and Shells*. Singapore: McGraw-Hill.

Substructuring

M Sunar, King Fahd University of Petroleum and Minerals, Dhahran, Saudi Arabia

Copyright © 2001 Academic Press

doi:10.1006/rwvb.2001.0117

Substructuring is usually carried out for a vibrating structure, which is large in order. The substructuring can result in substantial savings in computations. The goal in substructuring is to reduce the order of the structure without changing many vibrational characteristics of the remainder. The truncation can be done on those coordinates whose effects are relatively insignificant in vibrations of the structure. Furthermore, if various substructures are analyzed by different people, assembling them by the use of substructuring methods may be very beneficial to predict the complete structural behavior. Among many substructuring methods, three basic ones are considered here: the Rayleigh–Ritz and Guyan reduction methods, and component mode synthesis.

The Rayleigh–Ritz Method

The Rayleigh–Ritz method is used to estimate eigenvalues and eigenvectors (eigenfunctions) of a discrete (continuous) vibrating structure on its reduced-order model. The difficulty with this method lies in the selection of Ritz basis vectors. The rate of convergence of the eigenproblem solution largely depends on the choice of these basis vectors. Guyan reduction

method and component mode synthesis discussed in the following sections are basically Rayleigh–Ritz methods with certain Ritz basis vectors (see **Basic principles**).

Guyan Reduction Method

Static Condensation

Static condensation method can be used to reduce the order of the vibrating structure for approximating its eigenvalues and eigenvectors. The structure is usually discretized using the finite element procedure, which may yield a mass matrix with some zero diagonal elements due to the usage of lumped mass matrix. The method is applied to the structure to reduce its order on the degrees-of-freedom (DOF) corresponding to these zero diagonal elements.

Consider the eigenproblem for the whole (full-order) structure:

$$\mathbf{K}\phi = \lambda \mathbf{M}\phi \qquad [1]$$

Assume that some lumping is done on $\mathbf{M}$ and the problem is written in the partitioned form as:

$$\begin{bmatrix} \mathbf{K}_{AA} & \mathbf{K}_{AB} \\ \mathbf{K}_{BA} & \mathbf{K}_{BB} \end{bmatrix} \begin{bmatrix} \phi_A \\ \phi_B \end{bmatrix} = \lambda \begin{bmatrix} \mathbf{0} & \mathbf{0} \\ \mathbf{0} & \mathbf{M}_{BB} \end{bmatrix} \begin{bmatrix} \phi_A \\ \phi_B \end{bmatrix} \qquad [2]$$

The following relation can be written from eqn [2]:

$$\mathbf{K}_{AA}\boldsymbol{\phi}_A + \mathbf{K}_{AB}\boldsymbol{\phi}_B = \mathbf{0} \qquad [3]$$

and hence:

$$\boldsymbol{\phi}_A = -\mathbf{K}_{\mathrm{AA}}^{-1}\mathbf{K}_{AB}\boldsymbol{\phi}_B \qquad [4]$$

Substituting $\boldsymbol{\phi}_{\mathrm{A}}$ in eqn [2] yields:

$$\mathbf{K}_B\boldsymbol{\phi}_B = \lambda \mathbf{M}_{BB}\boldsymbol{\phi}_B \qquad [5]$$

where:

$$\mathbf{K}_B = \mathbf{K}_{BB} - \mathbf{K}_{BA}\mathbf{K}_{\mathrm{AA}}^{-1}\mathbf{K}_{AB} \qquad [6]$$

It can be shown that the static condensation method is a Rayleigh–Ritz method with Ritz basis vectors given as:

$$\boldsymbol{\Psi} = \mathbf{K}^{-1}\mathbf{F} \qquad [7]$$

where $\mathbf{F}$ is defined as:

$$\mathbf{F} = \begin{bmatrix} \mathbf{0} \\ \mathbf{I}_{BB} \end{bmatrix} \qquad [8]$$

General Method

The finite element model of the structure yields undamped equations of motion (EOM) of the form:

$$\mathbf{M}\ddot{x} + \mathbf{K}x = \mathbf{f} \qquad [9]$$

Consider any lth substructure of the structure (**Figure 1**) whose EOM are written in the partitioned form as:

$$\begin{bmatrix} \mathbf{M}_{AA} & \mathbf{M}_{AB} \\ \mathbf{M}_{BA} & \mathbf{M}_{BB} \end{bmatrix}_l \begin{bmatrix} \ddot{\mathbf{x}}_A \\ \ddot{\mathbf{x}}_B \end{bmatrix}_l + \begin{bmatrix} \mathbf{K}_{AA} & \mathbf{K}_{AB} \\ \mathbf{K}_{BA} & \mathbf{K}_{BB} \end{bmatrix}_l \begin{bmatrix} \mathbf{x}_A \\ \mathbf{x}_B \end{bmatrix}_l = \begin{bmatrix} \mathbf{f}_A \\ \mathbf{f}_B \end{bmatrix}_l \qquad [10]$$

where the subscript A denotes the DOF to be condensed (slave DOF) and B represents the DOF to be retained (master DOF). The above equation can be expressed as:

$$\begin{bmatrix} \mathbf{K}_{AA} - \mathbf{M}_{AA}\omega^2 & \mathbf{K}_{AB} - \mathbf{M}_{AB}\omega^2 \\ \mathbf{K}_{BA} - \mathbf{M}_{BA}\omega^2 & \mathbf{K}_{BB} - \mathbf{M}_{BB}\omega^2 \end{bmatrix}_l \begin{bmatrix} \mathbf{u}_A \\ \mathbf{u}_B \end{bmatrix}_l = \begin{bmatrix} \bar{\mathbf{f}}_A \\ \bar{\mathbf{f}}_B \end{bmatrix}_l \qquad [11]$$

Eqn [11] is due to the fact that if a force in the form of:

$$f = \sum_{j=1}^{r} \bar{f}_j \mathrm{e}^{\mathrm{i}\omega_j t} \qquad [12]$$

is applied, then the substructural response can be written as:

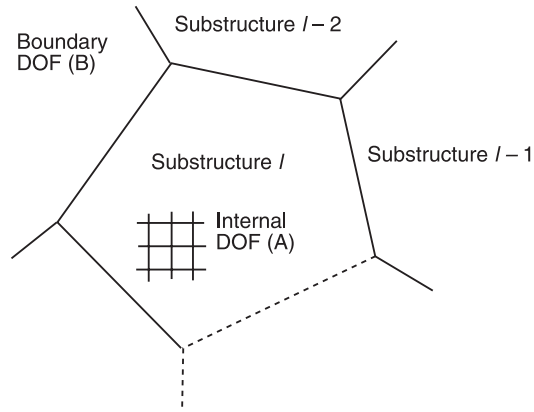


Figure 1 A typical lth substructure.

$$u = \sum_{j=1}^{r} u_j e^{i\omega_j t} \qquad [13]$$

The assumption of no applied force at the slave DOF ($\bar{\mathbf{f}}_A = 0$) yields:

$$\left[\mathbf{K}_{AA} - \mathbf{M}_{AA}\omega^2\right]_l \mathbf{u}_{Al} + \left[\mathbf{K}_{AB} - \mathbf{M}_{AB}\omega^2\right]_l \mathbf{u}_{Bl} = 0 \qquad [14]$$

which can be used to condense the slave DOF as:

$$\mathbf{u}_{Al} = -\left[\mathbf{K}_{AA} - \mathbf{M}_{AA}\omega^2\right]_l^{-1} \left[\mathbf{K}_{AB} - \mathbf{M}_{AB}\omega^2\right]_l \mathbf{u}_{Bl} \qquad [15]$$

Equation (15) can be approximated as:

$$\mathbf{u}_{Al} = -\mathbf{K}_{AAl}^{-1}\left[\mathbf{I} + \mathbf{M}_{AA}\mathbf{K}_{AA}^{-1}\omega^2\right]_l \left[\mathbf{K}_{AB} - \mathbf{M}_{AB}\omega^2\right]_l \mathbf{u}_{Bl} \qquad [16]$$

which is further approximated by:

$$\mathbf{u}_{Al} = -\mathbf{K}_{AAl}^{-1}\mathbf{K}_{ABl}\mathbf{u}_{Bl} \qquad [17]$$

For the approximation in eqn [17] to be justified, coefficients of ω^2 must be small. In other words, entries of $\mathbf{M}_{AA}$ and $\mathbf{M}_{AB}$ must be much smaller than those of $\mathbf{K}_{AA}$ and $\mathbf{K}_{AB}$. This means low mass and high stiffness for the areas of slave DOF. Eqn [17] can also be justified if ω is taken to be nearly zero. This implies that the frequencies of the applied force are small compared to the natural frequencies of the structure. From eqn [17], slave nodal displacements are also condensed as:

$$\mathbf{x}_{Al} = -\mathbf{K}_{AAl}^{-1}\mathbf{K}_{ABl}\mathbf{x}_{Bl} \qquad [18]$$

The nodal displacement vector is now written as:

$$\mathbf{x}_l = \begin{bmatrix} \mathbf{x}_A \\ \mathbf{x}_B \end{bmatrix}_l = \mathbf{T}_{ABl}\mathbf{x}_{Bl} \qquad [19]$$

The transformation matrix $\mathbf{T}_{ABl}$ in the above equation is given by:

$$\mathbf{T}_{ABl} = \begin{bmatrix} -\mathbf{K}_{AA}^{-1}\mathbf{K}_{AB} \\ \mathbf{I}_{BB} \end{bmatrix}_l \qquad [20]$$

Substituting eqn [19] in eqn [10] and premultiplying the resulting equation by $\mathbf{T}_{ABl}^{\mathrm{T}}$ yield:

$$\mathbf{M}_l^*\ddot{\mathbf{x}}_{Bl} + \mathbf{K}_l^*\mathbf{x}_{Bl} = \mathbf{f}_l^* \qquad [21]$$

where:

$$\begin{aligned} \mathbf{M}_l^* &= \mathbf{T}_{ABl}^{\mathrm{T}}\mathbf{M}_l\mathbf{T}_{ABl} \\ \mathbf{K}_l^* &= \mathbf{T}_{ABl}^{\mathrm{T}}\mathbf{K}_l\mathbf{T}_{ABl} \\ \mathbf{f}_l^* &= \mathbf{T}_{ABl}^{\mathrm{T}}\mathbf{f}_l \end{aligned} \qquad [22]$$

The EOM for the whole structure can be written as:

$$\mathbf{M}^*\ddot{\mathbf{x}}_B + \mathbf{K}^*\mathbf{x}_B = \mathbf{f}^* \qquad [23]$$

where:

$$\begin{aligned} \mathbf{x}_B &= \sum_{l=1}^{n} \mathbf{x}_{Bl}, \quad \mathbf{f}^* = \sum_{l=1}^{n} \mathbf{f}_l^* \\ \mathbf{M}^* &= \sum_{l=1}^{n} \mathbf{M}_l^*, \quad \mathbf{K}^* = \sum_{l=1}^{n} \mathbf{K}_l^* \end{aligned} \qquad [24]$$

The summations in eqn [24] must be comformable. The EOM of the reduced-order structure given by eqn [23] are solved for $\mathbf{x}_B$. Thereafter, $\mathbf{x}_{Al}$ for each substructure is recovered from eqn [18].

Component Mode Synthesis

In the constraint mode method of the component mode synthesis, vibrational mode shapes and general nodal displacements at the boundary are included for the lth substructure. The vibrational mode shapes are normal modes of the substructure with totally constrained boundary DOF. On the other hand, the boundary displacements occur due to successive generalized unit displacements at boundary DOF, while all other boundary DOF are totally constrained.

The component mode synthesis relates the internal displacements to the vibrational mode shapes and boundary displacements for the lth substructure shown in **Figure 1**. This relation is given by:

$$\mathbf{x}_{Al} = \boldsymbol{\phi}_l\mathbf{x}_{Ml} - \mathbf{K}_{AAl}^{-1}\mathbf{K}_{ABl}\mathbf{x}_{Bl} \qquad [25]$$

The generalized displacement vector $\mathbf{x}_l$ for the lth substructure can be expressed as:

$$\mathbf{x}_l = \begin{bmatrix} \mathbf{x}_A \\ \mathbf{x}_B \end{bmatrix}_l = \mathbf{T}_l \begin{bmatrix} \mathbf{x}_M \\ \mathbf{x}_B \end{bmatrix}_l = \mathbf{T}_l\mathbf{x}_l^* \qquad [26]$$

where:

$$\mathbf{T}_l = \begin{bmatrix} \boldsymbol{\phi} & -\mathbf{K}_{AA}^{-1}\mathbf{K}_{AB} \\ \mathbf{0} & I_{BB} \end{bmatrix}_l \qquad [27]$$

The generalized displacement vector $\mathbf{x}_l$ in eqn [26] couples modal coordinates with boundary displacements. The original EOM for the lth substructure are assumed as:

$$\mathbf{M}_l\ddot{\mathbf{x}}_l + \mathbf{K}_l\mathbf{x}_l = \mathbf{f}_l \qquad [28]$$

The order of this equation is reduced by substituting eqn [27] and premultiplying the resulting equation by $\mathbf{T}_l^{\mathrm{T}}$. The reduced-order EOM are now expressed as:

$$\mathbf{M}_l^*\ddot{\mathbf{x}}_l^* + \mathbf{K}_l^*\mathbf{x}_l^* = \mathbf{f}_l^* \qquad [29]$$

where:

$$\begin{aligned} \mathbf{M}_l^* &= \mathbf{T}_l^{\mathrm{T}}\mathbf{M}_l\mathbf{T}_l \\ \mathbf{K}_l^* &= \mathbf{T}_l^{\mathrm{T}}\mathbf{K}_l\mathbf{T}_l \\ \mathbf{f}_l^* &= \mathbf{T}_l^*\mathbf{f}_l \end{aligned} \qquad [30]$$

The reduced-order EOM for the whole structure are given by:

$$\mathbf{M}^*\ddot{\mathbf{x}}^* + \mathbf{K}^*\mathbf{x}^* = \mathbf{f}^* \qquad [31]$$

where $\mathbf{M}^*, \mathbf{K}^*$ and $\mathbf{f}^*$ are found via comformable summations as in eqn [24]. Eqn [31] for the reduced-order structure can be solved for $\mathbf{x}^*$. Thereafter, $\mathbf{x}_A$ for each substructure is computed from eqn [25].

The component mode synthesis is also a Rayleigh–Ritz method. The Ritz basis vectors are found as in eqn [7], where $\mathbf{F}$ now contains eigenvectors due to the inclusion of vibrational mode shapes. $\mathbf{F}$ is given by:

$$\mathbf{F} = \begin{bmatrix} \vdots & \cdots & \vdots & \cdots \\ \boldsymbol{\phi}_{l-1} & \cdots & \mathbf{0} & \cdots \\ \mathbf{0} & \cdots & \mathbf{I}_{l-1,l} & \cdots \\ \boldsymbol{\phi}_l & \cdots & \mathbf{0} & \cdots \\ \mathbf{0} & \cdots & \mathbf{0} & \cdots \\ \vdots & \cdots & \vdots & \cdots \\ \boldsymbol{\phi}_n & \cdots & \mathbf{0} & \cdots \end{bmatrix} \qquad [32]$$

Nomenclature

$\overline{f}_j$	magnitude of jth force component
$\mathbf{I}$	identity matrix
n	number of substrictures in structure
u_j	magnitude of jth component of structural response
$\mathbf{x}_A$	nodal vector of internal generalized displacements
$\mathbf{x}_B$	nodal vector of generalized displacements at boundary
$\mathbf{x}_M$	vector of modal coordinates
ϕ	eigenvector
λ	eigenvalue

See also: **Basic principles**; **Theory of vibration**, Energy methods; **Theory of vibration**, Equations of motion; **Theory of vibration**, Fundamentals; **Theory of vibration**, Variational methods.

Further Reading

Bathe K–J (1982) *Finite Element Procedures in Engineering Analysis*. New Jersey, USA: Prentice-Hall.

Craig RR (1981) *Structural Dynamics*. New York, USA: Wiley.

Meirovitch L (1980) *Computational Methods in Structural Dynamics*. Maryland, USA: Sijthoff and Noordhoff.

Weaver W Jr, Johnston PR (1987) *Structural Dynamics by Finite Elements*. New Jersey, USA: Prentice-Hall.

Impulse Response Function

R K Kapania, Virginia Polytechnic Institute & State University, Blacksburg, VA, USA

Copyright © 2001 Academic Press

doi:10.1006/rwvb.2001.0118

Response of structures to short-duration loads (i.e., the time duration of the external force is much shorter than the time period), is of great interest to a designer. Especially important is the limiting case of these loads, the loads whose time duration approaches zero but their total impulse, area under the force–time curve, stays finite. This happens because the response of a structure to such a load plays an important role both in describing the system and in acting as a building block towards finding the response of the system to any arbitrary excitation. Here we will describe the methods to determine the impulse response function, defined as the response of a single-degree-of-freedom spring-mass-damper system with zero initial displacement and velocity to a unit impulse.

The governing equation of a single-degree-of-freedom system of mass m, stiffness k, damping c, and subjected to an external force $f(t)$ is given as:

$$m\ddot{x} + c\dot{x} + kx = f(t) \qquad [1]$$

where x denotes the displacement from the static equilibrium, and a dot denotes the derivative with respect to t.

Mathematically, the impulse applied at a given time $t = \tau$ is described using Dirac's delta function, and is represented as $\delta(t - \tau)$. Dirac's delta function belongs to a class of functions called generalized functions. To understand this function, consider a uniform force $f(t)$ acting at $t = \tau$ over duration $\Delta\tau$ such that the area under the curve, termed impulse I and given as $I = f\Delta\tau$, remains unity. Now, as the value of the load duration $\Delta\tau$ is reduced, the value of the force f will increase so that the product $f\Delta\tau$ remains unity (**Figure 1**). As $\Delta\tau$ approaches zero, the force f approaches infinity, but the area under the force–time curve remains unity. This function, with value approaching infinity and acting over a vanishingly small time (the independent variable) is called Dirac's delta function. This function, denoted by $\delta(t)$, has the following important properties:

$$\int_{-\infty}^{\infty} \delta(t - \tau)\, \mathrm{d}t = 1 \qquad [2]$$

$$\int_{-\infty}^{\infty} g(t)\delta(t - \tau)\, \mathrm{d}t = g(\tau) \qquad [3]$$

Here $g(t)$ is an arbitrary function of time.

Consider the single degree of freedom system of eqn [1], and subjected to an impulse of magnitude I at $t = 0$. The governing equation then becomes:

$$m\ddot{x} + c\dot{x} + kx = I\delta(t) \qquad [4]$$

Dividing both sides of the above equation by the mass m, we obtain:

$$\ddot{x} + 2\zeta\omega_n\dot{x} + \omega_n^2 x = v_{imp}\delta(t) \qquad [5]$$

where $\omega_n = \sqrt{(k/m)}$ is the natural frequency of the system in radians per second, $\zeta = c/c_c$ is the damping ratio with $c_c = 2\sqrt{(km)}$; $v_{imp} = I/m$. Note that c_c is called critical damping. Physically v_{imp} is the change in the velocity of a mass m when subjected to an impulse $I\delta(t)$.

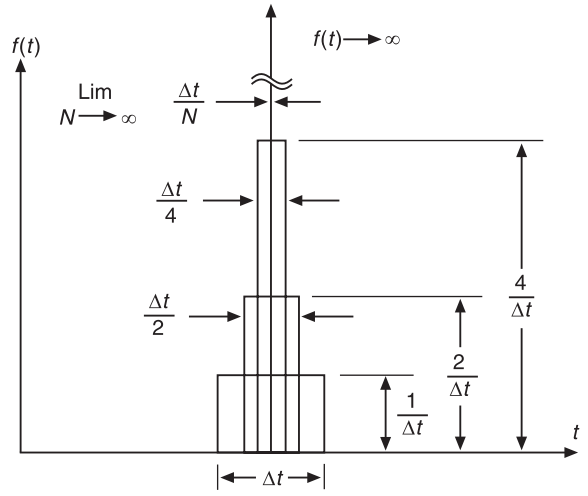


Figure 1 Dirac's delta function. The area under the load–time duration remains unity.

The response of the system to a unit impulse, termed the impulse response function, is represented as $h(t)$. It is the solution of the above equation with $v_{imp} = 1/m$ and initial conditions $x(0) = \dot{x}(0) = 0$, i.e. both initial velocity and initial displacement are zero. In terms of $h(t)$, the above equation becomes:

$$\ddot{h} + 2\zeta\omega_n\dot{h} + \omega_n^2 h = \frac{1}{m}\delta(t)$$
$$h(0) = 0; \quad \text{and} \quad \dot{h}(0) = 0 \qquad [6]$$

A number of methods can be used to obtain $h(t)$. Here, we present two classical methods: first, the Laplace transformation method; and second the Fourier series and integral method. Both methods are extensively used in determining the response of a system to an arbitrary excitation.

Laplace Transformation Method

The Laplace transform of a function $g(t)$, written as $G(s)$ is defined as:

$$G(s) = L[g(t)] = \int_0^{\infty} \mathrm{e}^{-st} g(t)\, \mathrm{d}t \qquad [7]$$

The function $g(t)$ is defined for $t < 0$ and s is a complex variable. It is assumed that the function $g(t)$ is such that the above integral exists. The Laplace transform is a linear operator, i.e.:

$$L[ag(t) + br(t)] = aL[g(t)] + bL[r(t)]$$
$$= aG(s) + bR(s) \qquad [8]$$

Here a and b are constants, and g and r both are functions of t. Other properties of importance to us here are:

$$\begin{aligned} L[\dot{g}(t)] &= sG(s) - g(0) \\ L[\ddot{g}(t)] &= s^2G(s) - sg(0) - \dot{g}(0) \end{aligned} \quad [9]$$

Knowing the Laplace transform of a function, the original function is obtained by taking the inverse Laplace transform:

$$g(t) = L^{-1}[G(s)] = \frac{1}{2\pi i}\int_{\gamma-i\infty}^{\gamma+i\infty} G(s)\,e^{st}\,ds \quad [10]$$

Here $i = \sqrt{(-1)}$. Often tables of Laplace transform pairs, widely available in many books on engineering or operational mathematics, are used to obtain the Laplace transform of a function of interest. Tables are also used to obtain the inverse transform. Determining the inverse Laplace transform of a function, not given in the tables of Laplace transform pairs, may be a rather difficult task.

Laplace transform of some functions that are important in the theory of vibrations are given in **Table 1**.

The impulse response function $h(t)$ can now be obtained by taking the Laplace transform of both sides of eqn [6]:

$$\begin{aligned} s^2H(s) - sh(0) - \dot{h}(0) \\ + 2\zeta\omega_n(sH(s) - h(0)) + \omega_n^2H(s) = \frac{1}{m} \end{aligned} \quad [11]$$

Substituting $h(0) = 0$, and $\dot{h}(0) = 0$, and combining all the coefficients of $H(s)$, we obtain:

$$(s^2 + 2\zeta\omega_n s + \omega_n^2)H(s) = \frac{1}{m} \quad [12]$$

Note that the function $H(s)$ is called the transfer function for the given system and it represents the ratio of the output of the system to the input to the system in the Laplace domain. It is given as:

$$H(s) = \frac{1}{m(s^2 + 2\zeta\omega_n s + \omega_n^2)} \quad [13]$$

The impulse response function $h(t)$ is obtained by taking the inverse Laplace transform of $H(s)$, i.e. $h(t) = L^{-1}[H(s)]$. We can obtain the inverse transform of $H(s)$ by using partial fractions. To that end, we need to factor the denominator, i.e. represent the denominator in the form $(s - s_1)(s - s_2)$, where s_1 and s_2, the two roots of the quadratic equation, $s^2 + 2\zeta\omega_n s + w_n^2 = 0$, are called the poles of the transfer function.

The poles, s_1, and s_2 are given as:

$$s_{1,2} = -\zeta\omega_n \pm \omega_n\sqrt{(\zeta^2 - 1)} \quad [14]$$

Thus, the nature of the poles depends upon the value of the nondimensional damping parameter ζ. The two roots would be complex and distinct if $\zeta < 1$ (underdamped case), equal and real negative if $\zeta = 1$ (critically damped), and distinct and real negative if $\zeta < 1$ (overdamped). These three cases lead to three completely distinct type of systems as is shown in the following.

Underdamped case ($\zeta < 1$): The two, complex, poles are:

$$s_{1,2} = -\zeta\omega_n \pm i\omega_n\sqrt{(1 - \zeta^2)} = -\zeta\omega_n \pm i\omega_d \quad [15]$$

where $\omega_d = \omega_n\sqrt{(1 - \zeta^2)}$ is the so-called damped natural frequency. The transfer function in terms of the partial fractions is given as:

$$\frac{1}{m(s^2 + 2\zeta\omega_n s + \omega_n^2)} = \frac{1}{m}\left[\frac{A}{s - s_1} + \frac{B}{s - s_2}\right] \quad [16]$$

Table 1 Laplace transform of some functions that are important in the theory of vibrations

$L[\delta(t-\tau)] = e^{-\tau s}$	$L[\sin \omega t] = \dfrac{\omega}{s^2 + \omega^2}$
$L[u(t)] = \dfrac{1}{s}$	$L[\cosh \omega t] = \dfrac{s}{s^2 - \omega^2}$
$L[t^n] = \dfrac{n!}{s^{n+1}} \quad n = 0, 1, 2, \ldots$	$L[\sinh \omega t] = \dfrac{\omega}{s^2 - \omega^2}$
$L[e^{at}] = \dfrac{1}{(s - a)}$	$L[e^{at}\cos \omega t] = \dfrac{s - a}{(s - a)^2 + \omega^2}$
$L\left[\int_0^t g(\tau)d\tau\right] = \dfrac{1}{s}G(s)$	$L[e^{at}\sin \omega t] = \dfrac{\omega}{(s - a)^2 + \omega^2}$
$L[e^{at}g(t)] = G(s-a)$	$L[e^{at}\cosh \omega t] = \dfrac{s - a}{(s - a)^2 - \omega^2}$
$L[\cos \omega t] = \dfrac{s}{s^2 + \omega^2}$	$L[e^{at}\sinh \omega t] = \dfrac{\omega}{(s - a)^2 - \omega^2}$

Multiplying both sides by the denominator in the above equation, we obtain:

$$A(s - s_2) + B(s - s_1) = 1 \qquad [17]$$

Substituting $s = s_1$ and $s = s_2$, respectively, we obtain:

$$A = -B = \frac{1}{(s_1 - s_2)} = \frac{1}{2\mathrm{i}\omega_d} = -\frac{\mathrm{i}}{2\omega_d} \qquad [18]$$

The impulse response function, for the underdamped case, is thus given as:

$$\begin{aligned} h(t) &= L^{-1}H(s), \quad t > 0 \\ &= \frac{-\mathrm{i}}{2m\omega_d} L^{-1}\left[\frac{1}{s - s_1} - \frac{1}{s - s_2}\right] \end{aligned}$$

Recalling $L^{-1}[1/(s-a)] = \mathrm{e}^{at}$, and $s_{1,2} = -\zeta\omega_n \pm \mathrm{i}\omega_d$, we obtain:

$$\begin{aligned} h(t) &= \frac{-\mathrm{i}}{2m\omega_d}\left[\mathrm{e}^{s_1 t} - \mathrm{e}^{s_2 t}\right] \\ &= \frac{-\mathrm{i}}{2m\omega_d}\mathrm{e}^{-\zeta\omega_n t}\left[\mathrm{e}^{\mathrm{i}\omega_d t} - \mathrm{e}^{-\mathrm{i}\omega_d t}\right] \qquad [19] \\ &= \frac{1}{m\omega_d}\mathrm{e}^{-\zeta\omega_n t}[\sin\omega_d t], \quad t > 0 \end{aligned}$$

Here we have made use of the Euler formula $\mathrm{e}^{\mathrm{i}\theta} = \cos\theta + \mathrm{i}\sin\theta$. Note that the impulse function for the underdamped case, because of the two poles being complex conjugate for this case, is oscillatory in nature. This is shown in **Figure 2A**.

Critically damped case ($\zeta = 1$): Both the roots are equal $s_{1,2} = -\omega_n$. The impulse response function is given as:

$$h(t) = L^{-1}\left[\frac{1}{m(s + \omega_n)^2}\right] = \frac{t\mathrm{e}^{-\omega_n t}}{m}, \quad t > 0 \qquad [20]$$

Overdamped case ($\zeta < 1$): Both the roots are distinct and are given as: $s_{1,2} = -\zeta\omega_n \pm \omega_n\sqrt{(\zeta^2 - 1)} = -\zeta\omega_n \pm \omega_d^*$. The impulse response function becomes:

$$\begin{aligned} h(t) &= L^{-1}\left[\frac{1}{m(s - s_1)(s - s_2)}\right] \\ &= \frac{1}{m\omega_d^*}\mathrm{e}^{-\zeta\omega_n t}\left[\sin h\omega_d^* t\right], \quad t > 0 \end{aligned} \qquad [21]$$

where $\omega_d^* = \omega_n\sqrt{(\zeta^2 - 1)}$. Note that the impulse response function for the critical and overdamped case are nonoscillatory in nature. This can be seen in **Figure 2B**. In both **Figures 2A and 2B**, the plot of nondimensional displacement $m\omega_n h(t)/I$ is given as a function of nondimensional time $\omega_n t$. Observe that as the value of the damping is increased from the critical value, the value of the nondimensional peak amplitude decreases but the time it takes for the response to die down increases.

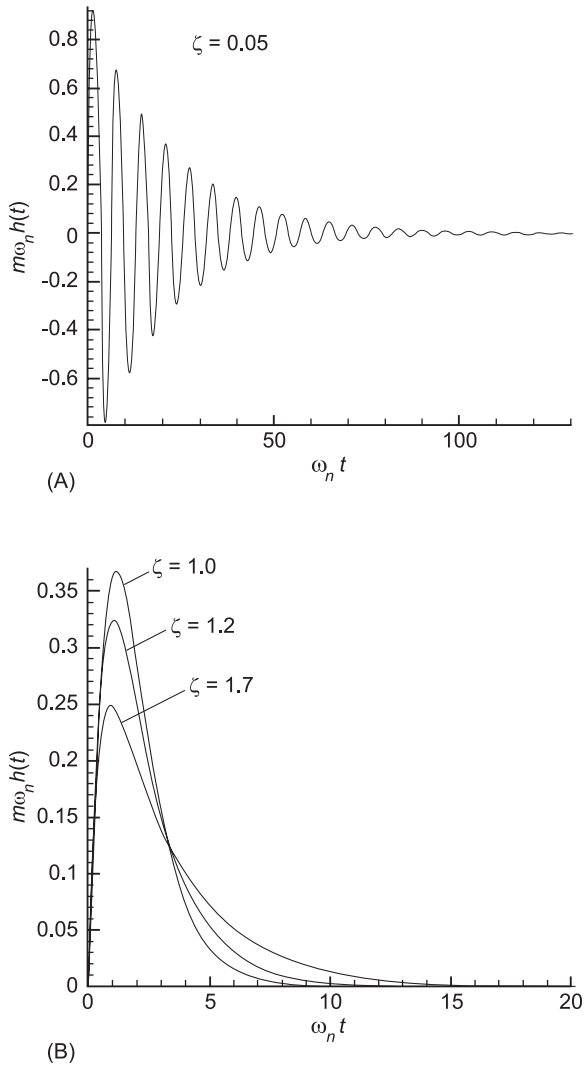


Figure 2 Nondimensional response of a single-degree-of-freedom spring-mass-damper system of mass m, and natural frequency ω_n, to an impulse I applied at $t = 0$ for different values of nondimensional damping (ζ). (A) underdamped systems ($\zeta < 1$); (B) critically ($\zeta = 1$) and overdamped systems ($\zeta > 1$). Note that the impulse response function $h(t)$ is simply $x(t)/I$.

Response to Initial Conditions

In the preceding section, we obtained the response of a dynamic system to a unit impulse by treating it as a special forcing function applied at $t = 0$. Since the effect of applying a unit impulse is to impart a sudden velocity $v_{imp} = 1/m$ at $t = 0$, the impulse response function can also be obtained by studying the response of the system under an initial velocity $\dot{x}(0) = 1/m$ but keeping both the force $f(t)$ and the initial displacement x_0 equal to zero. In this section, we present the response of a second-order system under the influence of nonzero initial conditions: $x(0) = x_0$, and $\dot{x}(0) = v_0$. The impulse response function can then be obtained by substituting $x_0 = 0$, and $v_0 = 1/m$. The response under these initial conditions, in the absence of $f(t)$, can be obtained by taking the Laplace transform of both sides of eqn [1]:

$$s^2X(s) - sx(0) - \dot{x}(0) + 2\zeta\omega_n(sX(s) - x(0)) + \omega_n^2X(s) = 0 \quad [22]$$

The Laplace transform, $X(s)$, of the desired response becomes

$$X(s) = \frac{sx_0 + v_0 + 2\zeta\omega_n x_0}{s^2 + 2\zeta\omega_n s + \omega_n^2} \quad [23]$$

The response $x(t)$ is obtained using inverse Laplace transform by keeping in mind that three distinct cases (underdamped, critically damped, and overdamped) arise, depending on the value of the nondimensional damping parameter ζ.

The response for the three cases, obtained using inverse Laplace transform (see **Table 1**), is given as

Underdamped case

$$x(t) = e^{-\zeta\omega_n t}\left[x_0 \cos \omega_d t + \frac{(v_0 + \zeta\omega_n x_0)}{\omega_d} \sin \omega_d t\right] \quad [24]$$

Critically damped case

$$x(t) = e^{-\omega_n t}[x_0 + (v_0 + \omega_n x_0)t] \quad [25]$$

Overdamped case

$$x(t) = e^{-\zeta\omega_n t}\left[x_0 \cos \omega_d^* t + \frac{(v_0 + \zeta\omega_n x_0)}{\omega_d^*} \sinh \omega_d^* t\right] \quad [26]$$

For the special case of $x_0 = 0$ and $v_0 = 1/m$, all the three equations reduce to the respective expressions for the impulse response function given in eqns [19]–[21], respectively.

Most of the systems of practical interest are underdamped systems where the nondimensional damping factor ζ is of the order of 0.02–0.05. The response due to the initial conditions (as was also seen for the case of the impulse response function in **Figures 2A and 2B**) are oscillatory in nature only for the underdamped case.

Fourier Series and Transform

For many practical cases, we are interested in finding the response of the system to external excitation, such as buildings subjected to wind and earthquake loads, an aircraft wing subjected to gusts, an automobile on uneven pavements and so on. The impulse response function derived above can be used to obtain the response of any system to any external excitation, say $f(t)$. The response can be written as a sum of a complementary solution and a particular solution:

$$x(t) = x_c(t) + x_p(t) \quad [27]$$

The complementary part x_c is the solution of the governing equation with the right-hand side equal to zero, the so-called homogeneous equation, as was done in the previous section on determining the response of the solution to initial conditions. The complementary part with arbitrary constants, due to the presence of $e^{-\zeta\omega_n t}$ term, is transitory in nature and approaches zero as t increases. While determining the response due to loads that are of longer duration, the complementary solution is often ignored and emphasis is placed only on the particular solution $x_p(t)$. This part of the solution, which does not have any arbitrary constants, can be obtained using the convolution (Duhamel's) integral:

$$x_p(t) = (f * h)(t) = \int_0^t f(\tau)h(t - \tau)\, d\tau \quad [28]$$

Performing the above integral, at times, may be quite a difficult task, especially when the forcing function $f(t)$ is not a simple function. Numerical and transform methods, Laplace and Fourier, are used in such cases. Using transform methods we can transform the above integral into an algebraic product which is easy to compute. Then, the solution in the time domain is obtained by performing the inverse transform. In previous years, the Laplace transform was the transform of choice for many engineers. However, its use is limited to only those functions whose Laplace transform is easy to obtain and also the inverse transform of the product $[H(s)F(s)]$ is easily available. Moreover, determining the Laplace transform of a function and determining the response as function in time by performing inverse Laplace transformation does not lend itself easily to the tremendous power of a modern digital computer. It should, however, be mentioned that the availability of symbolic manipulators like Mathematica and MAPLE has considerably improved our ability to obtain inverse Laplace transform. (Caution: an effective way to compute inverse Laplace transforms of long or complex expressions in Mathematica is to first produce the partial fraction expansion in the Laplace domain and then to take the inverse of each resulting term separately. Also, it has been our experience that if inverse Laplace transforms of long expressions are taken without first performing the partial fraction expansion, one may get incorrect results.)

It is because of its ability in using the power of modern computers that the Fourier transform has gained a widespread popularity for determining the system response as well as in determining the system model using experimental methods. Moreover, since the Fourier transform works in the frequency domain, it provides an additional advantage: the system parameters for many systems of practical interest can be described easier in the frequency domain than in the time domain.

To understand the use of Fourier transform in vibration theory it is important to understand the use of Fourier sine and cosine series in expressing periodic, not necessarily harmonic, functions, and to understand an extension of these series for aperiodic functions, called Fourier integrals.

The Fourier series for a function $f(t)$ of period $2T$ can be written as:

$$f(t) = \frac{a_0}{2} + \sum_{k=1}^{\infty} a_k \cos \omega_k t + \sum_{k=1}^{\infty} b_k \sin \omega_k t, \qquad \omega_k = \left(\frac{2\pi}{2T}\right) k \qquad [29]$$

In general, one only needs few terms in the series to achieve a good accuracy with respect to the given function. Here ω_k, called harmonics, are the discrete frequencies, and the Fourier coeficients a_k and b_k in eqn [29] are given by:

$$a_k = \frac{1}{T} \int_{-T}^{T} f(t) \cos \omega_k t \, \mathrm{d}t \quad k = 0, 1, 2 \ldots$$
$$b_k = \frac{1}{T} \int_{-T}^{T} f(t) \sin \omega_k t \, \mathrm{d}t \quad k = 1, 2, 3 \ldots \qquad [30]$$

Note that the coefficients a_k vanish for odd functions $[f(t) = -f(-t)]$ and the coefficients b_k vanish for even functions $[f(t) = f(-t)]$. The Fourier series converges to $f(t)$ for all t if $f(t)$ is continuous for $(0 \le t \le 2T)$, and converges to $[f(t^+) + f(t^-)]/2$ if there is a discontinuity at t. It can be shown that the coefficients obtained by eqn [30] yield the best approximation for a given number of terms used in the Fourier expansion. That is, for a given number of terms used in the Fourier series, the square of the error between the function and its Fourier representation is a minimum if the coefficients given by eqn [30] are used in eqn [29]. This implies that the accuracy of the Fourier series can only be improved by adding additional terms in the Fourier series.

In vibration theory, especially in experimental structural dynamics, a complex representation is often used. It can be shown that for a periodic function $f(t)$, the Fourier representation in terms of complex exponential harmonic function, $\mathrm{e}^{\mathrm{i}\omega_k t}$ can be written as:

$$f(t) = \frac{1}{2\pi} \sum_{k=-\infty}^{k=\infty} \bar{f}(\omega_k) \mathrm{e}^{\mathrm{i}\omega_k t} \Delta\omega \qquad [31]$$

where, $\Delta\omega$, the difference between two consecutive discrete frequencies ω_k and ω_{k+1} is given as:

$$\Delta\omega = \omega_{k+1} - \omega_k = \frac{2\pi}{2T} \qquad [32]$$

In eqn [31], $\bar{f}(\omega_k)$ is given as:

$$\bar{f}(\omega_k) = \int_{-T}^{T} f(t) \, \mathrm{e}^{-\mathrm{i}\omega_k t} \, \mathrm{d}t \qquad [33]$$

Note that in the complex representation, the integer k varies from $-\infty$ to $+\infty$. The negative frequencies are thus also included. But this representation is convenient in extending the notion of Fourier series to Fourier transform as described below.

The Fourier series described above can be used to represent an aperiodic function, since such a function can be considered as a periodic function with the period $2T$ approaching ∞. For this case, $\Delta\omega \to 0$. Thus, instead of a discrete representation in the frequency domain, one gets a continuous variation over ω. The Fourier series, in eqn [31], becomes an integral, called the Fourier integral, as given below:

$$f(t) = \frac{1}{2\pi} \int_{-\infty}^{\infty} \bar{f}(\omega) e^{i\omega t} \, d\omega \qquad [34]$$

In the above equation, $\bar{f}(\omega)$ is given as:

$$\bar{f}(\omega) = \int_{-\infty}^{\infty} f(t) e^{-i\omega t} \, dt \qquad [35]$$

Functions $f(t)$ and $\bar{f}(\omega)$ are considered to form a transform pair, the Fourier transform pair. Note that, in some references on Fourier transform, the factor 2π, seen here in the denominator of eqn [34] may be placed in the denominator of eqn [35] instead and still in some other sources it may be placed as $\sqrt{(2\pi)}$ in the denominator of both eqns [34] and [35]. Also note that, unlike the case here, some references define eqn [34] as the Fourier transform and eqn [35] as the inverse Fourier transform whereas in other references the names of the two equations are reversed.

As is the case for the Laplace transform, the Fourier transform, denoted as $F[.(t)]$, is a linear operation:

$$\begin{aligned} F[ag(t) + br(t)] &= aF[g(t)] + bF[r(t)] \\ &= aG(\omega) + bR(\omega) \end{aligned} \qquad [36]$$

Also, as is the case for Laplace transform, the Fourier transform of a convolution integral in the time domain becomes an algebraic product of the respective transforms in the frequency domain. That is:

$$\begin{aligned} F[(g * h)(t)] &= F\left[\int_0^t g(\tau) h(t-\tau) \, d\tau\right] \\ &= F[g(t)]F[h(t)] \\ &= G(\omega)H(\omega) \end{aligned} \qquad [37]$$

where $G(\omega)$ is the Fourier transform of $g(t)$ and $H(\omega)$ is the Fourier transform of $h(t)$ as defined by eqn [35]. To obtain $(g*h)(t)$ from $G(\omega)H(\omega)$, one needs to apply the inverse Fourier transform given by eqn [34]. That is:

$$\begin{aligned} (g * h)(t) &= F^{-1}[G(\omega)H(\omega)] \\ &= \frac{1}{2\pi} \int_{-\infty}^{\infty} G(\omega)H(\omega) e^{i\omega t} \, d\omega \end{aligned} \qquad [38]$$

The transfer function in the frequency domain $H(\omega)$ is the Fourier transform of the impulse response function. For the underdamped case the result obtained by, using eqns [34] and [19], is given as:

$$\begin{aligned} H(\omega) &= \int_{-\infty}^{\infty} h(t) e^{-i\omega t} \, dt \\ &= \frac{1}{m\omega_d} \int_0^{\infty} e^{-\zeta\omega_n t} [\sin \omega_d t] e^{-i\omega t} \, dt \end{aligned} \qquad [39]$$

Here we have used the fact that $h(t) = 0$ for $t \leq 0$. The integral on the right-hand side of this equation can be easily obtained as:

$$\begin{aligned} H(\omega) &= \frac{1}{m(\omega_n^2 + 2i\zeta\omega\omega_n - \omega^2)} \\ &= \frac{1}{k}\left[\frac{(1-\beta^2) - i(2\zeta\beta)}{(1-\beta^2)^2 + (2\zeta\beta)^2}\right] \end{aligned} \qquad [40]$$

where $\beta = (\omega/\omega_n)$. It is interesting to note that the transfer function in the frequency domain is the same as the steady-state (i.e. the transient part of the response containing $e^{-\zeta\omega_n t}$ term has died down) response of the system to a harmonic exponential excitation of unit amplitude and excitation frequency ω (i.e. $f(t) = e^{i\omega t}$ in eqn [1]) and is called the frequency response function (FRF). The frequency of the steady-state response will be the same as that of the excitation. The complex nature of $H(\omega)$ implies that there exists a phase difference (ϕ) between the harmonic excitation and the resulting harmonic steady-state response. This steady-state response, $x_{ss}(\omega)$, is given as:

$$\begin{aligned} x_{ss}(\omega) &= H(\omega)e^{i\omega t} = |H(\omega)|e^{i(\omega t - \phi)} \\ &= \frac{1}{k}\left[\frac{1}{(1-\beta^2)^2 + (2\zeta\beta)^2}\right]^{1/2} e^{i(\omega t - \phi)} \end{aligned} \qquad [41]$$

Here ϕ represents the phase difference between the harmonic excitation and the resulting steady-state response. This phase angle is given as:

$$\phi = \tan^{-1}\left[(2\zeta\beta)/(1-\beta^2)\right]$$

Also, since $1/k$ represents the response of the system under a unit static force, the term inside the square brackets in eqn [40] can be considered as the magnification of the static response if the unit load is instead applied in a harmonic manner with frequency ω. The term, inside the square brackets, is called the magnification factor. In some references, the transfer function (or the FRF) given above is denoted as $H(\mathrm{i}\omega)$.

The impulse response function can be obtained by taking the inverse Fourier transform of $H(\omega)$ as shown in the following:

$$h(t) = F^{-1}[H(\omega)] = \frac{1}{2\pi}\int_{-\infty}^{\infty} \frac{1}{m\left(\omega_n^2 + 2\mathrm{i}\zeta\omega\omega_n - \omega^2\right)} \mathrm{e}^{\mathrm{i}\omega t}\, \mathrm{d}\omega \qquad [42]$$

The integral on the right of the preceding equation can be performed by using Cauchy's relation, namely:

$$\oint_C \frac{f(z)}{(z - z_0)}\, \mathrm{d}z = 2\pi\mathrm{i}\, f(z_0)$$

Here C is any simple closed path around z_0 which is traversed in the anticlockwise direction and $f(z)$ is analytic within C. To apply this relation to the integral in eqn [42], consider the following integral, obtained by replacing ω with z, a complex variable, in eqn [42]:

$$I_c = \frac{1}{2\pi m}\oint_C \frac{\mathrm{e}^{\mathrm{i}zt}}{\left(\omega_n^2 + 2\mathrm{i}\,\zeta z\omega_n - z^2\right)}\, \mathrm{d}z \qquad [43]$$

Consider the path C to be the upper half plane, i.e., a semicircle of radius r as $r \to \infty$ (**Figure 3**).

Realizing that the denominator in the integrand in eqn [43] when equated to zero has two complex roots: $z_{1,2} = \mathrm{i}\zeta\omega_n \pm \omega_d$, the integral becomes:

$$\begin{aligned} I_c &= -\frac{1}{2\pi m}\oint_C \frac{\mathrm{e}^{\mathrm{i}zt}}{2\omega_d(z - \mathrm{i}\,\zeta\omega_n - \omega_d)}\, \mathrm{d}z \\ &\quad + \frac{1}{2\pi m}\oint_C \frac{\mathrm{e}^{\mathrm{i}zt}}{2\omega_d(z - \mathrm{i}\,\zeta\omega_n + \omega_d)}\, \mathrm{d}z \\ &= \left(\frac{2\pi i}{4\pi m\omega_d}\right)\left[-\mathrm{e}^{\mathrm{i}(\mathrm{i}\zeta\omega_n + \omega_d)t} + \mathrm{e}^{\mathrm{i}(\mathrm{i}\zeta\omega_n - \omega_d)t}\right] \\ &= \frac{1}{m\omega_d}\mathrm{e}^{-\zeta\omega_n t}[\sin\omega_d t] \end{aligned} \qquad [44]$$

The integral in eqn [43] can also be written, by splitting the contour C in two parts: the real axis ($z = \omega$) and the semicircular arc (denoted as S) of radius r with $r \to \infty$; as:

$$\begin{aligned} I_c &= \frac{1}{2\pi m}\int_{-\infty}^{\infty} \frac{\mathrm{e}^{\mathrm{i}\omega t}}{\left(\omega_n^2 + 2\mathrm{i}\,\zeta\omega\omega_n - \omega^2\right)}\, \mathrm{d}\omega \\ &\quad + \frac{1}{2\pi m}\int_S \frac{\mathrm{e}^{\mathrm{i}zt}}{\left(\omega_n^2 + 2\mathrm{i}\,\zeta z\omega_n - z^2\right)}\, \mathrm{d}z \end{aligned} \qquad [45]$$

The second integral on the right-hand side of the above integral approaches zero as the integrand contains z^2 term in the denominator. Comparing eqns [44] and [45], we obtain the impulse response function to be given as:

$$h(t) = \frac{1}{m\omega_d}\mathrm{e}^{-\zeta\omega_n t}[\sin\omega_d t] \qquad [46]$$

The transfer function in the frequency domain (or the FRF) $H(\omega)$ and the impulse response function $h(t)$ thus form a Fourier transform pair.

In determining the impulse response function, the inverse Fourier transform was performed using an analytical approach that used the so-called Cauchy relation (or contour integral) to perform the improper integral. Such an approach is limited only to simple functions for which such integrals can be easily obtained either using Cauchy's relation or from the tables of Fourier and inverse Fourier transform (similar to the case for the Laplace transform). However, the Fourier transform, using its discretized version, can be performed numerically for all sorts of functions using the fast Fourier transform (FFT).

Fast Fourier Transform

Let f_n represent the value of a function at a discrete point $t_n = n\Delta t$ where $\Delta t = 2T/N$, N being the total number of discrete points in the time period $2T$ or the time-history duration. Similarly $\bar{f}_m$ represents the Fourier coefficient corresponding to the mth discrete frequency ω_m given as $\omega_m = 2\pi m/(2T)$. Values of f_n and $\bar{f}_m$ are given as:

$$\begin{aligned} f_n &= \frac{1}{N}\sum_{m=0}^{N-1} \bar{f}_m \exp\left[\mathrm{i}(2\pi mn/N)\right] \\ n &= 0, 1, 2, 3 \ldots, N-1 \\ \bar{f}_m &= \sum_{n=0}^{N-1} f_n \exp\left[\mathrm{i}(2\pi mn/N)\right] \\ m &= 0, 1, 2, 3 \ldots, N-1 \end{aligned} \qquad [47]$$

The preceding set of equations constitutes the discrete Fourier transform (DFT) pair and can easily be computed. However, if the computations are done using these equations in a direct manner, a transform will take N^2 complex multiplications. A fast method to evaluate the DFT was proposed by Cooley and Tukey. This algorithm called the fast Fourier transform (FFT), needs only $O(N\log_2 N)$ complex multiplications if $N = 2^\gamma$, where γ is an integer. This results in a substantial reduction in computational time. For example, for $N = 1024 = 2^{10}$, the direct evaluation to calculate the Fourier transform will take $1024^2 = 1\,048\,576$ complex multiplications. On the other hand, one requires only $O(10\,240)$ multiplications if FFT is employed, around 1% of the effort required otherwise.

To understand the logic behind FFT, let us consider any one of the two equations in eqn [47], say the second one. It can be rewritten as:

$$\bar{f}_m = \sum_{n=0}^{N-1} f_n \exp\left[-\mathrm{i}(2\pi mn/N)\right] = \sum_{n=0}^{N-1} f_n W^{mn} \qquad [48]$$
$$m = 0, 1, 2, 3 \ldots, N-1$$

Here $W = \exp[-\mathrm{i}(2\pi/N)]$. The FFT is based on the fact that $W^0 = W^N = W^{2N} = \ldots = 1$, and $W^{N+m} = W^m$. As a result, for a given value of $\gamma (N = 2^\gamma)$, the DFT can be performed in γ stages. This is easily understood for $N = 4$ (i.e. $\gamma = 2$). For this case, eqn [48], becomes:

$$\begin{Bmatrix} \bar{f}_0 \\ \bar{f}_1 \\ \bar{f}_2 \\ \bar{f}_3 \end{Bmatrix} = \begin{bmatrix} W^0 & W^0 & W^0 & W^0 \\ W^0 & W^1 & W^2 & W^3 \\ W^0 & W^2 & W^4 & W^6 \\ W^0 & W^3 & W^6 & W^9 \end{bmatrix} \begin{Bmatrix} f_0 \\ f_1 \\ f_2 \\ f_3 \end{Bmatrix} \qquad [49]$$

Obviously a straightforward matrix-vector multiplication will take 4^2 complex multiplications. If, however, we make use of the fact that $W^0 = W^4 = 1$ and $W^6 = W^2$, etc., we can reduce the number of multiplications to eight by performing the above multiplication in two $(= \gamma)$ stages. In the first stage, using N complex multiplications, we calculate an intermediatory vector $\mathbf{g}$ whose components are given as:

$$g_0 = f_0 + W^0 f_2$$
$$g_1 = f_1 + W^0 f_3$$
$$g_2 = W^2 f_2 + f_0$$
$$g_3 = W^2 f_3 + f_1$$

In the second (γth or last) stage, also the last stage for $N = 4$ case, we calculate the DFT, once again using N complex multiplications, as:

$$\bar{f}_0 = g_0 + W^0 g_1$$
$$\bar{f}_2 = W^2 g_1 + g_0$$
$$\bar{f}_1 = g_2 + W^1 g_3$$
$$\bar{f}_3 = W^3 g_3 + g_2$$

Note that the values of $\bar{f}$ are scrambled. The same approach can be easily implemented for other values of γ. For example, for $N = 8 (\gamma = 3)$ we will require three stages and each stage will have eight complex multiplications.

The computer programs capable of performing FFT are readily available. For example, the commercially available packages Mathematica and MATLAB both contain commands for obtaining the FFT.

Nomenclature

C	closed path
f	force
I	impulse
v	velocity
$X(s)$	Laplace transform
$\delta(t)$	Dirac's delta function
ϕ	phase angle
ζ	damping factor

See also: **Critical damping**; **Transform methods**.

Further Reading

Clough RW, Penzien, J (1993) *Dynamics of Structures*, 2nd edn. New York: McGraw Hill.

Cooley JW, Tukey JW (1965) An algorithm for the machine calculation of complex Fourier series. *Mathematics of Computation* 19(90): 297–301.

Craig RR (1981) *Structural Dynamics, An Introduction to Computer Methods*. New York: Wiley.

Gerald CF, Wheatley PO (1989) *Applied Numerical Analysis*, 4th edn. Reading, MA: Addison Wesley.

Inman DJ (1996) *Engineering Vibration*. Englewood Cliffs: Prentice Hall.

Kelly SG (1993) *Fundamentals of Mechanical Vibrations*. New York: McGraw Hill.

Kreyszig E (1993) *Advanced Engineering Mathematics*, 7th edn. New York: Wiley.

Meirovitch L (1997) *Principles and Techniques of Vibrations*. Upper Saddle River: Prentice Hall.

Rao, SS (1995) *Mechanical Vibrations*, 3rd edn. Reading, MA: Addison Wesley.

Variational Methods

S S Rao, University of Miami, Coral Gables, FL, USA

Copyright © 2001 Academic Press

doi:10.1006/rwvb.2001.0119

Introduction

Vibration problems can be formulated either according to vectorial dynamics, based on the concepts of force and momentum, or to variational dynamics, based on the concepts of kinetic energy and work done by the forces. In vectorial dynamics, Newton's laws are used directly to derive the equations of motion. In variational dynamics, the conditions of extremization of a functional are used to derive the equations of motion of a system. Whereas Newton is considered by most people to be the originator of vectorial dynamics, Leibniz is considered by some and John Bernoulli and/or d'Alembert by others as the originator of variational dynamics. In solid mechanics, the principles of minimum potential energy, minimum complementary energy, and stationary Reissner energy can be used to formulate statics problems while the Hamilton's principle can be used to formulate dynamics problems. All these principles represent variational approaches that can also be used to formulate the finite element equations. Hamilton's principle can be considered to be rooted in the concept that nature will insure efficiency as a system moves freely from one configuration to another. Of all possible paths a system might traverse, that chosen by nature will always be one that minimizes a quantity that can be called action. In Hamilton's principle, the action is the integral of the Lagrangian from time t_1 to t_2, where these two times are arbitrary. When calculus of variations is used, the necessary conditions for the minimum of this action result in Lagrange's equations.

The variational approaches have the following advantages:

1. The forces that do no work, such as forces of constraint on masses, need not be considered.
2. The accelerations of masses need not be considered; only velocities are needed.
3. The mathematical operations are to be performed on scalars, not on vectors, in deriving the equations of motion.

This article presents the basic ideas of calculus of variations followed by the description of different variational principles of solid mechanics and the application of Hamilton's principle in the formulation of the equations of motion of a variety of discrete and continuous vibrating systems.

Calculus of Variations

The calculus of variations deals with the determination of extrema (maxima and minima) or stationary values of functionals. The basic problem in variational calculus is to find the function $\phi(x)$ which makes the integral functional:

$$I = \int_{x_1}^{x_2} F(x, \phi, \phi_x)\, \mathrm{d}x \qquad [1]$$

stationary. Here, x is the independent variable and $\phi_x = \mathrm{d}\phi/\mathrm{d}x$ and as the condition for the stationariness of I, the variation of I is set equal to zero so that:

$$\delta I = \int_{x_1}^{x_2} \left(\frac{\partial F}{\partial x}\delta\phi + \frac{\partial F}{\partial \phi_x}\delta\phi_x \right) \mathrm{d}x = \int_{x_1}^{x_2} \delta F\, \mathrm{d}x = 0 \qquad [2]$$

The mathematical manipulation of eqn [2] leads to the governing differential equation of the system, known as Euler or Euler–Lagrange equation, as well as the boundary conditions. The rules of variation used in the manipulation of eqn [2] are summarized in **Table 1**. The Euler–Lagrange equation and the boundary conditions corresponding to eqn [2] can be expressed as:

$$\frac{\partial F}{\partial \phi} - \frac{\mathrm{d}}{\mathrm{d}x}\left(\frac{\partial F}{\partial \phi_x}\right) = 0, \quad x_1 < x < x_2 \qquad [3]$$

$$\frac{\partial F}{\partial \phi_x}\delta\phi\Big|_{x_1}^{x_2} = 0 \qquad [4]$$

When the function F is defined as $F(x, \phi, \phi_x, \phi_{xx})$ where $\phi_{xx} = \partial^2\phi/\partial x^2$, the Euler–Lagrange equation and the boundary conditions are given by:

$$\frac{\partial F}{\partial \phi} - \frac{\mathrm{d}}{\mathrm{d}x}\left(\frac{\partial F}{\partial \phi_x}\right) + \frac{\mathrm{d}^2}{\mathrm{d}x^2}\left(\frac{\partial F}{\partial \phi_{xx}}\right) = 0, \quad x_1 < x < x_2 \qquad [5]$$

Table 1 Rules of variation

$$\delta(\phi_1 \pm \phi_2) = \delta\phi_1 \pm \delta\phi_2$$

$$\delta(\phi_1\phi_2) = \phi_2\delta\phi_1 + \phi_1\delta\phi_2$$

$$\delta(\phi^n) = n\phi^{n-1}\delta\phi$$

$$\delta\left(\frac{\phi_1}{\phi_2}\right) = \frac{\phi_2\delta\phi_1 - \phi_1\delta\phi_2}{\phi_2^2}$$

$$\delta\left(\frac{\mathrm{d}\phi}{\mathrm{d}t}\right) = \frac{\mathrm{d}}{\mathrm{d}t}(\delta\phi)$$

$$\delta\left(\frac{\partial\phi}{\partial t}\right) = \frac{\partial}{\partial t}(\delta\phi)$$

$$\delta f(\phi) = \frac{\mathrm{d}f(\phi)}{\mathrm{d}\phi}\delta\phi$$

$$\delta f(\dot{\phi}) = \frac{\mathrm{d}f(\dot{\phi})}{\mathrm{d}\dot{\phi}}\delta\dot{\phi}, \quad \dot{\phi} = \frac{\mathrm{d}\phi}{\mathrm{d}t}$$

$$\delta f(\phi, \dot{\phi}) = \frac{\partial f(\phi, \dot{\phi})}{\partial\phi}\delta\phi + \frac{\partial f(\phi, \dot{\phi})}{\partial\dot{\phi}}\delta\dot{\phi}$$

$$\delta[f(\phi_1, \phi_2, \ldots, \phi_n)] = \sum_{j=1}^{n}\frac{\partial f}{\partial\phi_j}\delta\phi_j$$

$$\delta\int_{t_1}^{t_2} f(\phi)\,\mathrm{d}t = \int_{t_1}^{t_2}\delta f(\phi)\,\mathrm{d}t$$

$$\delta\int_{t_1}^{t_2} f(\phi)\,\mathrm{d}x = \int_{t_1}^{t_2}\delta f(\phi)\,\mathrm{d}x$$

$$\delta\int_{0}^{\phi} f(\theta)\,\mathrm{d}\theta = f(\phi)\,\mathrm{d}\phi$$

$$\left[\frac{\partial F}{\partial\phi_x} - \frac{\mathrm{d}}{\mathrm{d}x}\left(\frac{\partial F}{\partial\phi_{xx}}\right)\right]\delta\phi\Big|_{x_1}^{x_2} = 0 \qquad [6]$$

$$\frac{\partial F}{\partial\phi_{xx}}\delta\phi_x\Big|_{x_1}^{x_2} = 0 \qquad [7]$$

When several dependent variables are involved as:

$$I = \int_{x_1}^{x_2}(Fx, \phi_1, \ldots, \phi_n, (\phi_1)_x, \ldots, (\phi_n)_x, (\phi_1)_{xx}, \ldots, (\phi_n)_{xx})\,\mathrm{d}x \qquad [8]$$

where $(\phi_i)_x = \partial\phi_i/\partial x$ and $(\phi_i)_{xx} = \partial^2\phi_i/\partial x^2$, the Euler–Lagrange equation can be expressed as:

$$\frac{\mathrm{d}^2}{\mathrm{d}x^2}\left(\frac{\partial F}{(\partial\phi_i)_{xx}}\right) - \frac{\mathrm{d}}{\mathrm{d}x}\left(\frac{\partial F}{\partial(\phi_i)_x}\right) + \frac{\partial F}{\partial\phi_i} = 0, \quad x_1 < x < x_2, \quad i = 1, 2, \ldots, n \qquad [9]$$

If the integrand involves derivatives of higher order than the second order as:

$$I = \int_{x_1}^{x_2} F\left(x, \phi_i, \phi_i^{(1)}, \phi_i^{(2)}, \ldots, \phi_i^{(n)}\right)\mathrm{d}x \qquad [10]$$

where $\phi_i^{(j)} = \mathrm{d}^j\phi_i/\mathrm{d}x^j$, $i = 1, 2...n$, then the corresponding Euler–Lagrange equations are given by:

$$\sum_{j=0}^{n}(-1)^{n-j}\frac{\mathrm{d}^{n-j}}{\mathrm{d}x^{n-j}}\left(\frac{\partial F}{\partial\phi_i^{(n-j)}}\right) = 0, \quad x_1 < x < x_2, \quad i = 1, 2, \ldots, n \qquad [11]$$

If the functional I is defined in terms of several independent variables and one dependent variable as:

$$I = \iiint_V F\left(x, y, z, \phi, \phi_x, \phi_y, \phi_z\right)\mathrm{d}V \qquad [12]$$

where $\phi_x = \partial\phi/\partial x$, $\phi_y = \partial\phi/\partial y$ and $\phi_z = \partial\phi/\partial z$, the Euler–Lagrange equation can be obtained as:

$$\frac{\partial F}{\partial\phi} - \frac{\partial}{\partial x}\left(\frac{\partial F}{\partial\phi_x}\right) - \frac{\partial}{\partial y}\left(\frac{\partial F}{\partial\phi_y}\right) - \frac{\partial}{\partial z}\left(\frac{\partial F}{\partial\phi_z}\right) = 0 \qquad [13]$$

Some variational problems, known as isoperimetric problems, involve auxiliary constraints:

$$\text{Extremize } I = \int_{x_1}^{x_2} F(x, \phi, \phi_x)\,\mathrm{d}x \qquad [14]$$

subject to the condition that $\phi(x)$ also satisfy the equation:

$$J = \int_{x_1}^{x_2} G(x, \phi, \phi_x)\,\mathrm{d}x = \text{known constant} \qquad [15]$$

Using the technique of Lagrange multipliers, the Euler–Lagrange equation corresponding to the constrained variational problem can be expressed as:

$$\frac{\partial F_s}{\partial\phi} - \frac{\mathrm{d}}{\mathrm{d}x}\left(\frac{\partial F_s}{\partial\phi_x}\right) = 0, \quad x_1 < x < x_2 \qquad [16]$$

where $F_s = F + \lambda G$ and λ is the Lagrange multiplier whose value is chosen so that eqn [15] is satisfied.

When potential energy, U, is used as the functional, I, eqn [2] yields the principle of minimum potential

energy. The principles of minimum potential energy, minimum complementary energy, and Reissner energy are used to formulate the problems in solid mechanics, that is, to derive the governing differential equations and the boundary conditions. When the Lagrangian function, L, is used as the functional, I, eqn [2] yields the governing equations of motion and the boundary conditions of the system. The corresponding variational principle, in this case, is called Hamilton's principle. Hamilton's principle is an integral principle that considers the entire motion of the system between two instants of time t_1 and t_2. This permits the treatment of a dynamics problem in terms of a scalar integral. A specific advantage of this formulation is that it is invariant with respect to the coordinate system used. All the variational methods of static and dynamic problems are discussed in this article.

Variational Methods in Solid Mechanics

Principle of Minimum Potential Energy

The potential energy of an elastic body, U, is defined as:

$$U = \pi - W_p \qquad [17]$$

where π is the strain energy and W_p is the work done on the body by the external forces. The principle of minimum potential energy can be stated as follows: 'Of all possible displacement states (u, v, and w) a body can assume which satisfy compatibility and specified kinematic or displacement boundary conditions, the state which satisfies the equilibrium equations makes the potential energy assume a minimum value'. If the potential energy is expressed in terms of the displacement components u, v, and w, the principle of minimum potential energy gives, at the equilibrium state:

$$\delta U(u,v,w) = \delta\pi(u,v,w) - \delta W_p(u,v,w) = 0 \qquad [18]$$

It is important to note that the variation is taken with respect to the displacements in eqn [18] while the forces and stresses are assumed to be constant. The strain energy of a linear elastic body is given by:

$$\pi = \frac{1}{2}\iiint_V \boldsymbol{\varepsilon}^T\boldsymbol{\sigma}\, dV \qquad [19]$$

where $\boldsymbol{\varepsilon}$ is the strain vector, $\boldsymbol{\sigma}$ is the stress vector, V is the volume of the body and the superscript T denotes the transpose. By expressing the stress–strain relations as:

$$\boldsymbol{\sigma} = \mathbf{D}\boldsymbol{\varepsilon} \qquad [20]$$

where $\mathbf{D}$ is the elasticity matrix, the strain energy can be expressed (in the absence of initial strains) as:

$$\pi = \frac{1}{2}\iiint_V \boldsymbol{\varepsilon}^T\mathbf{D}\boldsymbol{\varepsilon}\, dV \qquad [21]$$

If initial strains are present, with the initial strain vector $\boldsymbol{\varepsilon}_0$, the strain energy of the body is given by:

$$\pi = \frac{1}{2}\iiint_V \boldsymbol{\varepsilon}^T\mathbf{D}\boldsymbol{\varepsilon}\, dV - \iiint_V \boldsymbol{\varepsilon}^T\mathbf{D}\boldsymbol{\varepsilon}_0\, dV \qquad [22]$$

The work done by the external forces is given by:

$$W_p = \iiint_V \left(\bar{\phi}_x u + \bar{\phi}_y v + \bar{\phi}_z w\right) dV + \iint_{S_1} \left(\bar{\Phi}_x u + \bar{\Phi}_y v + \bar{\Phi}_z w\right) dS_1 \qquad [23]$$

where S_1 is the surface of the body on which surface forces (tractions) are prescribed. By denoting the known body force vector, $\bar{\boldsymbol{\phi}}$, the prescribed surface force (traction) vector, $\bar{\boldsymbol{\Phi}}$ and the displacement vector, $\mathbf{u}$, as:

$$\bar{\boldsymbol{\phi}} = \begin{Bmatrix} \bar{\phi}_x \\ \bar{\phi}_y \\ \bar{\phi}_z \end{Bmatrix}, \quad \bar{\boldsymbol{\Phi}} = \begin{Bmatrix} \bar{\Phi}_x \\ \bar{\Phi}_y \\ \bar{\Phi}_z \end{Bmatrix}, \quad \mathbf{u} = \begin{Bmatrix} u \\ v \\ w \end{Bmatrix}$$

Equation [23] can be rewritten as:

$$W_p = \iiint_V \bar{\boldsymbol{\phi}}^T\mathbf{u}\, dV + \iint_{S_1} \bar{\boldsymbol{\Phi}}^T\mathbf{u}\, dS_1 \qquad [24]$$

Using eqns [22] and [24] the potential energy of the body can be expressed as:

$$U(u,v,w) = \frac{1}{2}\iiint_V \boldsymbol{\varepsilon}^T\mathbf{D}(\boldsymbol{\varepsilon} - 2\boldsymbol{\varepsilon}_0)\, dV - \iiint_V \bar{\boldsymbol{\phi}}^T\mathbf{u}\, dV - \iint_{S_1} \bar{\boldsymbol{\Phi}}^T\mathbf{u}\, dS_1 \qquad [25]$$

As stated above, the displacement field $\mathbf{u}(x, y, z)$ that minimizes U and satisfies all the boundary conditions is the one that satisfies the equilibrium equations. If the principle of minimum potential energy is used, we minimize the functional U and the resulting equations denote the equilibrium equations while the compatibility conditions are identically satisfied.

Principle of Minimum Complementary Energy

The complementary energy of an elastic body (U_c) is defined as:

U_c = complementary strain energy in terms of stresses (π) – work done by the applied loads during stress changes ($\bar{W}_p$)

The principle of minimum complementary energy can be stated as follows: 'Of all possible stress states which satisfy the equilibrium equations and the stress boundary conditions, the state which satisfies the compatibility conditions will make the complementary energy assume a minimum value'. By expressing the complementary energy U_c in terms of the stresses σ_{ij}, the principle of minimum complementary energy gives, for compatibility:

$$\delta U_c(\sigma_{xx}, \sigma_{yy}, \ldots, \sigma_{zx}) = \delta\bar{\pi}(\sigma_{xx}, \sigma_{yy}, \ldots, \sigma_{zx}) - \delta\bar{W}_p(\sigma_{xx}, \sigma_{yy}, \ldots, \sigma_{zx}) = 0 \quad [26]$$

It is to be noted that variation is taken with respect to stress components in eqn [26] while the displacements are assumed to be constant. The complementary strain energy of a linear elastic body can be expressed as:

$$\bar{\pi} = \frac{1}{2}\iiint_V \boldsymbol{\sigma}^T\boldsymbol{\varepsilon}\, dV \quad [27]$$

The complementary strain energy can be written, in the presence of known initial strains $\boldsymbol{\varepsilon}_0$, as:

$$\bar{\pi} = \frac{1}{2}\iiint_V \boldsymbol{\sigma}^T(\mathbf{C}\boldsymbol{\sigma} + 2\boldsymbol{\varepsilon}_0)\, dV \quad [28]$$

where the strain–stress relations are assumed to be of the form:

$$\boldsymbol{\varepsilon} = \mathbf{C}\boldsymbol{\sigma} \quad [29]$$

The work done by the applied loads during stress change, also known as the complementary work, is given by:

$$\bar{W}_p = \iint_{S_2} \left(\phi_x\bar{u} + \phi_y\bar{v} + \phi_z\bar{w}\right) dS_2 = \iint_{S_2} \boldsymbol{\Phi}^T\bar{\mathbf{u}}\, dS_2 \quad [30]$$

where S_2 is the part of the surface of the body on which the values of displacements are prescribed as:

$$\bar{\mathbf{u}} = \begin{Bmatrix} \bar{u} \\ \bar{v} \\ \bar{w} \end{Bmatrix}$$

Eqns [28] and (30) can be used to express the complementary energy of the body as:

$$U_c(\sigma_{xx}, \sigma_{yy}, \ldots, \sigma_{zx}) = \frac{1}{2}\iiint_V \boldsymbol{\sigma}^T(\mathbf{C}\boldsymbol{\sigma} + 2\boldsymbol{\varepsilon}_0)\, dV - \iint_{S_2} \boldsymbol{\sigma}^T\bar{\mathbf{u}}\, dS_2 \quad [31]$$

If the principle of minimum complementary energy is used, we minimize the functional U_c and the resulting equations denote the compatibility equations while the equilibrium equations are identically satisfied.

Principle of Stationary Reissner Energy

In the principle of minimum potential energy, we expressed the potential energy, U, in terms of displacements and permitted variations of u, v, and w. Similarly, in the case of the principle of minimum complementary energy, we expressed the complementary energy, U_c, in terms of stresses and permitted variations of σ_{xx}, σ_{yy} ... σ_{zx}. In the present case, we express Reissner energy, U_r, in terms of both displacements and stresses and permit variations with respect to both displacements and stresses. The Reissner energy for a linearly elastic body is defined as: $U_r = \iiint_V$ {(internal stresses) × (strains expressed in terms of displacements) − complementary strain energy in terms of stresses} dV − work done by applied forces

$$\begin{aligned}
&= \iiint_V \left\{ \left[\sigma_{xx}\frac{\partial u}{\partial x} + \sigma_{yy}\frac{\partial v}{\partial y} + \cdots \right.\right. \\
&\left.\left. + \sigma_{zx}\left(\frac{\partial w}{\partial x} + \frac{\partial u}{\partial z}\right)\right] - \bar{\pi} \right\} dV \\
&- \iiint_V \left(\bar{\phi}_x u + \bar{\phi}_y v + \bar{\phi}_z w\right) dV \\
&- \iint_{S_1} \left(\bar{\Phi}_x u + \bar{\Phi}_y v + \bar{\Phi}_z w\right) dS_1 \\
&- \iint_{S_2} \left[(u - \bar{u})\Phi_x + (v - \bar{v})\Phi_y + (w - \bar{w})\Phi_z\right] dS_2 \\
&= \iiint_V \left[\boldsymbol{\sigma}^T\boldsymbol{\varepsilon} - \frac{1}{2}\boldsymbol{\sigma}^T\mathbf{C}\boldsymbol{\sigma} - \bar{\boldsymbol{\Phi}}^T\mathbf{u}\right] dV \\
&- \iint_{S_1} \mathbf{u}^T\bar{\boldsymbol{\Phi}}\, dS_1 - \iint_{S_2} (\mathbf{u} - \bar{\mathbf{u}})^T\bar{\boldsymbol{\Phi}}\, dS_2
\end{aligned} \quad [32]$$

The variation of U_r is set equal to zero by considering variations in both displacements and stresses:

$$\delta U_r = \sum \frac{\partial U_r}{\partial \sigma_{ij}} \delta \sigma_{ij} + \left(\frac{\partial U_r}{\partial u} \delta u + \frac{\partial U_r}{\partial v} \delta v + \frac{\partial U_r}{\partial w} \delta w \right) = 0 \quad [33]$$

The first term on the right-hand side of eqn [33] gives the stress–displacement relations while the second term gives the equilibrium equations and the boundary conditions. The principle of stationary Reissner energy can be stated in words as follows: 'Of all possible stress and displacement states the body can have, the particular set which makes the Reissner energy stationary gives the correct stress–displacement and equilibrium equations along with the boundary conditions'.

Hamilton's Principle

The variational principle that can be used for dynamic problems is called the Hamilton's principle. According to this principle, the variation of the functional is taken with respect to time. The functional, similar to U, U_c, and U_r, used in Hamilton's principle is called the Lagrangian (L) and is defined as follows:

$$L = T - U = \text{kinetic energy} - \text{potential energy} \quad [34]$$

The kinetic energy of the body, T, can be expressed as:

$$T = \frac{1}{2} \iiint_V \rho \dot{\mathbf{u}}^T \dot{\mathbf{u}} \, dV \quad [35]$$

where ρ is the density of the material and $\dot{\mathbf{u}}$ is the vector of velocity components at any point in the body:

$$\dot{\mathbf{u}} = \begin{Bmatrix} \dot{u} \\ \dot{v} \\ \dot{w} \end{Bmatrix}$$

Thus, the Lagrangian can be written as:

$$L = \frac{1}{2} \iiint_V (\rho \dot{\mathbf{u}}^T \dot{\mathbf{u}} - \boldsymbol{\varepsilon}^T \mathbf{D} \boldsymbol{\varepsilon} + 2\mathbf{u}^T \bar{\boldsymbol{\phi}}) \, dV + \iint_{S_1} \mathbf{u}^T \bar{\boldsymbol{\Phi}} \, dS_1 \quad [36]$$

Hamilton's principle can be stated in words as follows:

> Of all possible time histories of displacement states which satisfy the compatibility equations and the constraints or the kinematic boundary conditions and which also satisfy the conditions at initial and final times (t_1 and t_2), the history corresponding to the actual solution makes the Lagrangian functional a minimum.

Hamilton's principle can thus be expressed as:

$$\delta \int_{t_1}^{t_2} L \, dt = 0 \quad [37]$$

Generalized Hamilton's Principle

The generalized Hamilton's principle can be stated as follows:

$$\delta \int_{t_1}^{t_2} L \, dt = \delta \int_{t_1}^{t_2} (T - \pi + W) \, dt = 0 \quad [38]$$

where T is the kinetic energy, π is the strain energy, W is the work done by external forces, and $L = T - \pi + W$ is called the generalized Lagrangian function. The expressions of T, π and W are given by:

$$T = \iiint_V \frac{1}{2} \rho \dot{u}_i \dot{u}_i \, dV \quad [39]$$

where u_i is the ith component of displacement, $\dot{u}_i$ is the ith component of velocity and ρ is the density:

$$\pi = \iiint_V \left[\sigma_{ij} \left(\gamma_{ij} - \varepsilon_{ij} \right) + \pi_0 \right] dV, \quad i,j = 1,2,3 \quad [40]$$

where σ_{ij} are the components of stress vector, γ_{ij} are the expressions of strain in terms of the derivatives of u_i, ε_{ij} are the components of the strain vector, and π_0 is the the initial strain energy function:

$$W = \iiint_V \phi_i u_i \, dV + \iint_{S_1} \bar{\Phi}_i u_i \, dS_1 + \iint_{S_2} \Phi_i (u_i - \bar{u}_i) \, dS_2 \quad [41]$$

where ϕ_i is the ith component of body force, Φ_i is the ith component of surface tractions, a bar over a

symbol denotes a prescribed quantity, S_2 is part of the surface of the body on which displacements are prescribed and S_1 is part of the surface of the body on which surface tractions are prescribed. Note that Cartesian tensor notations and summation convention for repeated indices is used in eqns [39]–[41]. In addition, eqn [38] has the same form as in the ordinary Hamilton's principle, but π and W are now different. When variations of the displacements, strains, and stresses are taken independently, we obtain:

$$\delta \int_{t_1}^{t_2} T \, dt = \iiint_V \rho \dot{u}_i \delta u_i \, dV \Big|_{t_1}^{t_2} - \int_{t_1}^{t_2} dt \iiint_V \rho \ddot{u}_i \delta u_i \, dV \quad [42]$$

$$\delta \int_{t_1}^{t_2} \pi \, dt = \int_{t_1}^{t_2} dt \iiint_V \left[\sigma_{ij} \delta \gamma_{ij} + \left(\gamma_{ij} - \varepsilon_{ij} \right) \delta \sigma_{ij} - \left(\sigma_{ij} - \frac{\partial \pi_0}{\partial \varepsilon_{ij}} \right) \delta \varepsilon_{ij} \right] dV \quad [43]$$

$$\delta \int_{t_1}^{t_2} W \, dt = \int_{t_1}^{t_2} \left[\iiint_V \phi_i \delta u_i \, dV + \iint_{S_1} \bar{\Phi}_i \delta u_i \, dS_1 + \iint_{S_2} (u_i - \bar{u}_i) \delta \Phi_i \, dS_2 \right] dt \quad [44]$$

Since γ_{ij} are functions of the first derivatives of u_i, we can obtain:

$$\iiint_V \sigma_{ij} \delta \varepsilon_{ij} \, dV = \iint_{S_1} \frac{1}{2} \left[\sigma_{ij} \left(\frac{\partial \gamma_{ij}}{\partial e_{mn}} + \frac{\partial \gamma_{ij}}{\partial \omega_{mn}} \right) v_n \delta_{1m} + \cdots \right] dS_1 \quad [45]$$

where $\gamma_{ij} = \gamma_{ij}(e_{mn}, \omega_{mn})$ for a general nonlinear problem $(m, n = 1, 2, 3)$ with:

$$e_{mn} = \frac{1}{2} \left(u_{m,n} + u_{n,m} \right) \quad [46]$$

$$\omega_{mn} = \frac{1}{2} \left(u_{m,n} - u_{n,m} \right) \quad [47]$$

with $u_{mn} = \partial u_m / \partial x_n$, $x_1 = x$, $x_2 = y$, $x_3 = z$, $v_n = \cos(vn)$ = direction cosine and δ_{lm} = Kronecker delta. Using eqns [42]–[45], eqn [38] can be rewritten as:

$$\begin{aligned} &\int_{t_1}^{t_2} dt \iiint_V \left\{ \frac{1}{2} \left[\sigma_{ij} \left(\frac{\partial \gamma_{ij}}{\partial e_{mn}} + \frac{\partial \gamma_{ij}}{\partial \omega_{mn}} \right) \right]_{,n} \delta_{1m} \right. \\ &\left. + \frac{1}{2} \left[\sigma_{ij} \left(\frac{\partial \gamma_{ij}}{\partial e_{mn}} - \frac{\partial \gamma_{ij}}{\partial \omega_{mn}} \right) \right]_{,m} \delta_{1n} + \phi_1 - \rho \ddot{u}_1 \right\} \delta u_1 \, dV \\ &- \int_{t_1}^{t_2} dt \iint_{S_1} \left[\frac{1}{2} \sigma_{ij} \left(\frac{\partial \gamma_{ij}}{\partial e_{mn}} + \frac{\partial \gamma_{ij}}{\partial \omega_{mn}} \right) v_n \delta_{1m} \right. \\ &\left. + \frac{1}{2} \sigma_{ij} \left(\frac{\partial \gamma_{ij}}{\partial e_{mn}} + \frac{\partial \gamma_{ij}}{\partial \omega_{mn}} \right) v_m \delta_{1n} - \bar{\Phi}_1 \right] \delta u_1 \, dS_1 \\ &+ \int_{t_1}^{t_2} dt \iiint_V \left(\sigma_{ij} - \frac{\partial \pi_0}{\partial \varepsilon_{ij}} \right) \delta \varepsilon_{ij} \, dV \\ &- \int_{t_1}^{t_2} dt \iiint_V \left(\gamma_{ij} - \varepsilon_{ij} \right) \delta \sigma_{ij} \, dV \\ &+ \int_{t_1}^{t_2} dt \iint_{S_2} (u_i - \bar{u}_i) \delta \Phi_i \, dS_2 \, dt = 0 \end{aligned} \quad [48]$$

Since the variations δu_i, $\delta \sigma_{ij}$, and $\delta \varepsilon_{ij}$ are arbitrary throughout the volume of the body (V), δu_i is arbitrary on S_1 and $\delta \Phi_i$ is arbitrary on S_2, their coefficients in the five integrands in eqn [48] must be zero independently. This gives the stress equations of motion, traction boundary conditions, stress–strain relations, strain–displacement relations, and displacement boundary conditions. These equations constitute the complete set of equations (and are valid for large elastic deflections also). The generalized Hamilton's principle can be stated in words as follows:

> The displacements, strains and stresses, which, over the time interval t_1 to t_2, satisfy the stress equations of motion and the stress–strain–displacement relations throughout the body, the traction boundary conditions on S_1 and the displacement boundary conditions on S_2, are determined by setting the variation of the time integral of the generalized Lagrangian function equal to zero, provided that the variations of the displacements, strains and stresses are taken independently and simultaneously, and the variations of displacements vanish at t_1 and t_2 throughout the body

and the variations of displacements and tractions satisfy the prescribed boundary conditions.

Applications – Continuous Systems

Equation of Motion of a Uniform Bar under Axial Load

The derivation of the equation governing the longitudinal motion of a uniform bar is considered to illustrate the application of Hamilton's principle.

Strain energy, U To derive a general expression for the strain energy of the bar, consider the bar to be of variable cross-section under an axial load as shown in **Figure 1**. If $u(x, t)$ denotes the axial displacement of the cross-section at x, an element of length dx will assume a value of $dx + (\partial u / \partial x)dx$ due to axial deformation under the axial load F (**Figure 1B**). The elongation of the element dx is given by $\delta(dx) = (\partial u / \partial x)dx$ and hence the strain at point x can be expressed as:

$$\varepsilon = \frac{\delta(dx)}{dx} = \frac{\partial u(x,t)}{\partial x}$$

The stress induced (σ) can be expressed, using Hooke's law, as:

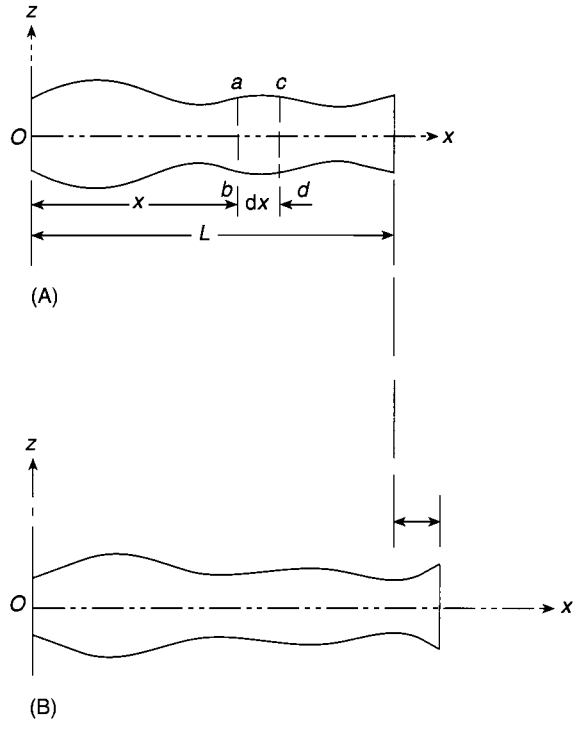


Figure 1AB Longitudinal vibration of a bar. (A) Before deformation; (B) after deformation.

$$\sigma = E\,\varepsilon = E\frac{\partial u(x,t)}{\partial x}$$

where E is the Young's modulus of the bar. The strain energy associated with the element dx (of volume $A\,dx$) can be expressed as:

$$dU = \left(\frac{1}{2}\sigma\varepsilon\right)A = \frac{1}{2}EA\left(\frac{\partial u}{\partial x}\right)^2$$

where $A = A(x)$ denotes the cross-section area of the bar at x. Thus the strain energy of the bar can be expressed as:

$$U = \int_{x=0}^{L} dU\,dx = \frac{1}{2}\int_0^L EA(x)\left[\frac{\partial u(x,t)}{\partial x}\right]^2 dx \quad [a]$$

where L is the length of the bar.

Kinetic energy, T The kinetic energy of the bar with variable cross-section can be expressed as:

$$T = \frac{1}{2}\int_0^L m(x)\left[\frac{\partial u(x,t)}{\partial t}\right]^2 dx \quad [b]$$

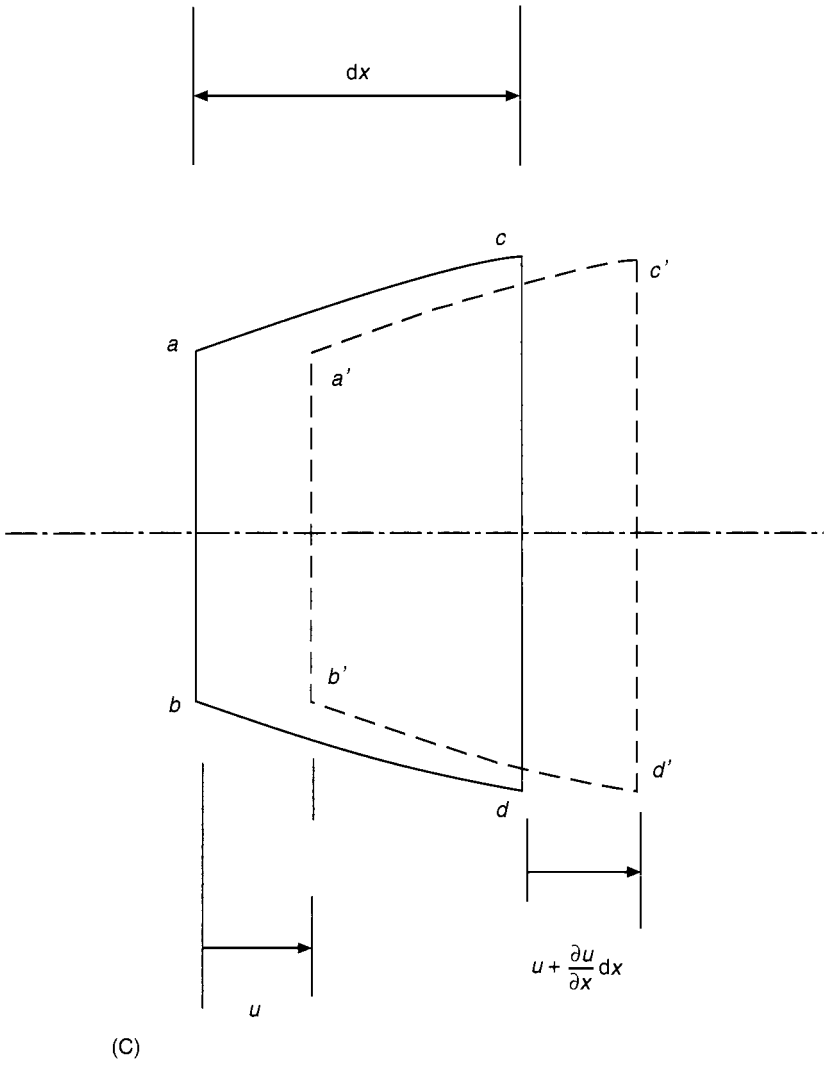
where $m(x) = \rho A(x)$ is the mass per unit length of the bar and ρ is the density of the bar. By using eqns [a] and [b], the Hamilton's principle can be used to obtain:

$$\begin{aligned}&\delta\int_{t_1}^{t_2}(T-U)\,dt\\ &= \delta\int_{t_1}^{t_2}\left[\frac{1}{2}\int_0^L m\left[\frac{\partial u}{\partial t}\right]^2 dx - \frac{1}{2}\int_0^L EA\left[\frac{\partial u}{\partial x}\right]^2 dx\right]dt\\ &= 0\end{aligned} \quad [c]$$

By carrying out the variation operation, the various terms of eqn [c] can be rewritten, noting that δ and $\partial/\partial t$ as well as δ and $\partial/\partial x$ are commutative, as:

$$\begin{aligned}&\delta\int_{t_1}^{t_2}\left[\frac{1}{2}\int_0^L m\left(\frac{\partial u}{\partial t}\right)^2 dx\right]dt\\ &= -\int_{t_1}^{t_2}\int_0^L m\frac{\partial^2 u}{\partial t^2}\delta u\,dx\,dt\end{aligned} \quad [d]$$

assuming that u is prescribed at t_1 and t_2 so that $\delta u = 0$ at t_1 and t_2. Similarly:



(C)

Figure 1C An element of bar.

$$\delta \int_{t_1}^{t_2} \left[\frac{1}{2} \int_0^L EA \left(\frac{\partial u}{\partial x} \right)^2 dx \right] dt = \int_{t_1}^{t_2} \left[EA \frac{\partial u}{\partial x} \delta u \Big|_0^L - \int_0^L \frac{\partial}{\partial x} \left(EA \frac{\partial u}{\partial x} \right) \delta u \, dx \right] dt \quad [e]$$

Thus eqn [c] becomes:

$$\int_{t_1}^{t_2} \left\{ \int_0^L \left[\frac{\partial}{\partial x} \left(EA \frac{\partial u}{\partial x} \right) - m \frac{\partial^2 u}{\partial t^2} \right] \delta u \, dx - \left(EA \frac{\partial u}{\partial x} \right) \delta u \Big|_{t_1}^{t_2} \right\} dt = 0 \quad [f]$$

Assuming that $\delta u = 0$ at $x = 0$ and $x = L$, and δu is arbitrary in $0 < x < L$, eqn [f] requires that:

$$\frac{\partial}{\partial x} \left(EA \frac{\partial u}{\partial x} \right) - m \frac{\partial^2 u}{\partial t^2} = 0, \quad 0 < x < L \quad [g]$$

and:

$$\left(EA \frac{\partial u}{\partial x} \right) \delta u = 0 \quad \text{at} \quad x = 0 \quad \text{and} \quad x = L \quad [h]$$

Thus the Hamilton's principle yields eqn [g], which denotes the equation of motion of the bar, and eqn [h], which indicates the boundary conditions.

The boundary conditions require that either $EA(\partial u / \partial x) = 0$ (stress $= 0$) or $\delta u = 0$ ($u =$ specified) at $x = 0$ and $x = L$.

Transverse Vibration of a Timoshenko Beam

Consider an element of a thick beam in bending as shown in **Figure 2B**. For a thick beam, when the effects of shear deformation and rotatory (or rotary) inertia are considered, the theory is known as the Timoshenko beam theory. The deflection of the beam at any point x is caused by bending as well as shear deformation. The slope of the deflected center line of the beam, $\partial w / \partial x$, can be expressed as:

$$\frac{\partial w(x,t)}{\partial x} = \phi(x,t) + \gamma(x,t) \qquad [a]$$

where $\phi(x, t)$ = angular rotation due to bending and $\gamma(x, t)$ = angular rotation due to shear deformation. The bending moment (M) and shear force (V) at x are given by:

$$M(x,t) = EI(x)\frac{\partial \phi(x,t)}{\partial x} \qquad [b]$$

$$V(x,t) = kA(x)G\beta(x,t) \qquad [c]$$

where E is Young's modulus, $I(x)$ is the moment of inertia of the cross-section, $A(x)$ is the area of cross-

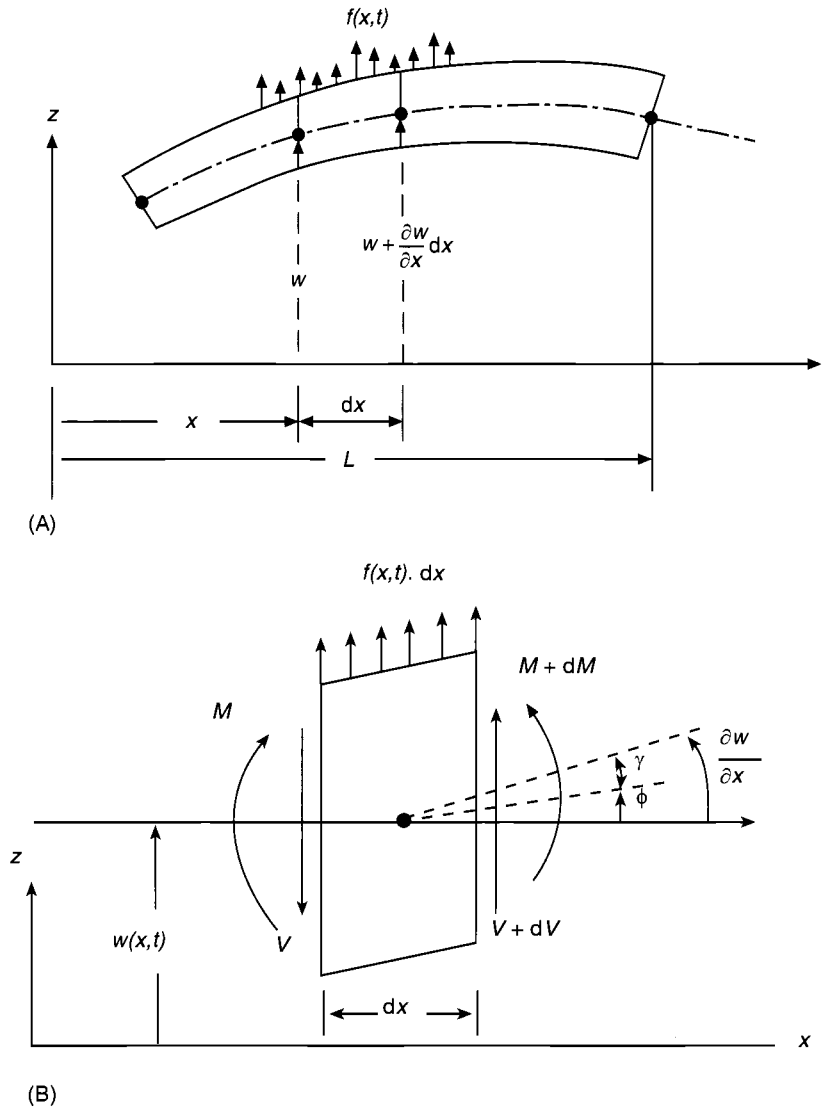


Figure 2 A nonuniform thick beam in bending. (A) Deformed configuration; (B) free-body diagram of an element of beam.

section of the beam and k is a constant whose value depends on the shape of the cross-section of the beam.

Strain energy, U The strain energy of the beam is composed of energies due to bending and shear deformation:

$$\begin{aligned} U(t) &= \frac{1}{2}\int_0^L M\frac{\partial\phi}{\partial x}\,dx + \frac{1}{2}\int_0^L V\gamma\,dx \\ &= \frac{1}{2}\int_0^L EI(x)\left[\frac{\partial\phi(x,t)}{\partial x}\right]^2 dx \\ &\quad + \frac{1}{2}\int_0^L kGA(x)\left[\frac{\partial w(x,t)}{\partial x} - \phi(x,t)\right]^2 dx \end{aligned} \qquad [d]$$

Kinetic energy, T The kinetic energy of the beam due to translational and rotational motions can be expressed as:

$$\begin{aligned} T(t) &= \frac{1}{2}\int_0^L m(x)\left[\frac{\partial w(x,t)}{\partial t}\right]^2 dx \\ &\quad + \frac{1}{2}\int_0^L J(x)\left[\frac{\partial\gamma(x,t)}{\partial t}\right]^2 dx \end{aligned} \qquad [e]$$

where $m(x) = \rho A(x)$ is the mass per unit length of the beam, ρ is density, $A(x)$ is the area of cross-section of the beam and $J(x) = \rho I(x)$ is the mass moment of inertia of the beam per unit length.

Virtual work of nonconservative forces, δW The virtual work of the applied distributed force, $f(x, t)$, is given by:

$$\delta W(t) = \int_0^L f(x,t)\delta w(x,t)\,dx \qquad [f]$$

Noting that the order of integrations with respect to t and x can be interchanged and the operators δ and d/dx or δ and d/dt are commutative, the variations of U and T can be written as:

$$\begin{aligned} \delta U &= \delta\int_{t_1}^{t_2}\int_0^L EI\left(\frac{\partial\phi}{\partial x}\right)^2 dx\,dt + \delta\int_{t_1}^{t_2}\int_0^L kGA\gamma^2\,dx\,dt \\ &= \int_{t_1}^{t_2}\left[EI\frac{\partial\phi}{\partial x}\delta\phi\Big|_0^L - \int_0^L \frac{\partial}{\partial x}\left(EI\frac{\partial\phi}{\partial x}\right)\delta\phi\,dx\,dt\right. \\ &\quad + kGA\left(\frac{\partial w}{\partial x} - \phi\right)\delta w\Big|_0^L \\ &\quad - \int_0^L \frac{\partial}{\partial x}\left[kGA\left(\frac{\partial w}{\partial x} - \phi\right)\right]\delta w\,dx \\ &\quad \left. - \int_0^L kGA\left(\frac{\partial w}{\partial x} - \phi\right)\delta\phi\,dx\right] dt \end{aligned} \qquad [g]$$

$$\begin{aligned} \delta T &= \delta\int_{t_1}^{t_2}\left[\frac{1}{2}\int_0^L m\left(\frac{\partial w}{\partial t}\right)^2 dx + \frac{1}{2}\int_0^L J\left(\frac{\partial\gamma}{\partial t}\right)^2 dx\right] dt \\ &= -\int_0^L\left[\int_{t_1}^{t_2}\frac{\partial}{\partial t}\left(m\frac{\partial w}{\partial t}\right)\delta w\,dt\right] dx \\ &\quad - \int_0^L\left[\int_{t_1}^{t_2}\frac{\partial}{\partial t}\left(J\frac{\partial\gamma}{\partial t}\right)\delta\gamma\,dt\right] dx \end{aligned} \qquad [h]$$

Using eqns [f], [g], and [h], the Hamilton's principle can be stated as:

$$\begin{aligned} &\int_{t_1}^{t_2}\left\{-\int_0^L m\frac{\partial^2 w}{\partial t^2}\delta w\,dx - \int_0^L J\frac{\partial^2\phi}{\partial t^2}\delta\phi\,dx\right. \\ &\quad - \left(EI\frac{\partial\phi}{\partial x}\right)\delta\phi\Big|_0^L + \int_0^L \frac{\partial}{\partial x}\left(EI\frac{\partial\phi}{\partial x}\right)\delta\phi\,dx \\ &\quad - \left[KGA\left(\frac{\partial w}{\partial x} - \phi\right)\right]\delta w\Big|_0^L \\ &\quad + \int_0^L \frac{\partial}{\partial x}\left[kGA\left(\frac{\partial w}{\partial x} - \phi\right)\right]\delta w\,dx \\ &\quad \left. + \int_0^L kGA\left(\frac{\partial w}{\partial x} - \phi\right)\delta\phi\,dx + \int_0^L f\delta w\,dx\right\} dt \\ &= \int_{t_1}^{t_2}\left\{\int_0^L\left\{\frac{\partial}{\partial x}\left[kGA\left(\frac{\partial w}{\partial x} - \phi\right)\right]\right.\right. \\ &\quad \left.\left. - m\frac{\partial^2 w}{\partial t^2} + f\right\}\delta w\,dx + \int_0^L\left\{\left[\frac{\partial}{\partial x}\left(EI\frac{\partial\phi}{\partial x}\right)\right.\right.\right. \end{aligned}$$

$$+ kGA\left(\frac{\partial w}{\partial x} - \phi\right)\Big] - J\frac{\partial^2 \phi}{\partial t^2}\Big\}\delta\phi \, dx$$
$$- \left(EI\frac{\partial \phi}{\partial x}\right)\delta\phi\Big|_0^L - kGA\left(\frac{\partial w}{\partial x} - \phi\right)\delta w\Big|_0^L\Big\} \, dt = 0 \qquad [i]$$

Assuming that the virtual displacements, δw and $\delta\phi$, to be zero, at $x = 0$ and $x = L$, and arbitrary in $0 < x < L$, eqn [i] leads to:

$$\frac{\partial}{\partial x}\left\{kGA\left(\frac{\partial w}{\partial x} - \phi\right)\right\} - m\frac{\partial^2 w}{\partial t^2} + f = 0, 0 < x < L \qquad [j]$$

$$\frac{\partial}{\partial x}\left(EI\frac{\partial \phi}{\partial x}\right) + kGA\left(\frac{\partial w}{\partial x} - \phi\right) - J\frac{\partial^2 \phi}{\partial t^2} = 0, \quad 0 < x < L \qquad [k]$$

$$\left(EI\frac{\partial \phi}{\partial x}\right)\delta\phi\Big|_0^L = 0 \qquad [l]$$

$$kGA\left(\frac{\partial w}{\partial x} - \phi\right)\delta w\Big|_0^L = 0 \qquad [m]$$

Eqns [j] and [k] denote the equations of motion for the transverse and shear motions of the beam, respectively, and eqns [l] and [m] represent the boundary conditions. Eqn [l] requires that either $EI(\partial\phi/\partial x) = 0$ or $\delta\phi = 0$ at $x = 0$ and $x = L$. Similarly, eqn [m] requires that either $kGA[(\partial w/\partial x) - \phi] = 0$ or $\delta w = 0$ at $x = 0$ and $x = L$. Eqns [l] and [m] can be seen to be satisfied for the following common boundary conditions:

- Clamped (fixed) end: w = transverse deflection $= 0$, ϕ = bending slope $= 0$
- Hinged (pinned) end: w = transverse deflection $= 0$, $M = EI(\partial\phi/\partial x)$ = bending moment $= 0$
- Free end: $M = EI(\partial\phi/\partial x)$ = bending moment $= 0$, $V = kGA[(\partial w/\partial x) - \phi]$ = shear force $= 0$

Coupled Twist-bending Vibrations of Circular Rings

Figure 3 shows an element of a ring along with the sign convention used for the forces and moments. The slope of the transverse deflection curve can be written as:

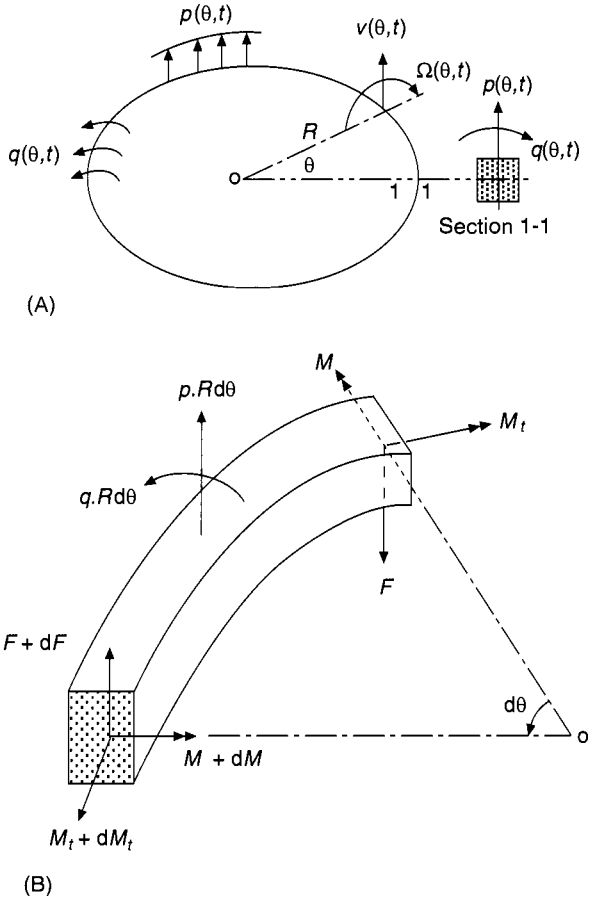


Figure 3 An element of circular ring.

$$\frac{1}{R}\frac{\partial v}{\partial \theta} = \alpha + \beta \qquad [a]$$

where R is the radius of the undeformed center line of the ring, v is the transverse deflection, θ is the angular coordinate, α is the slope of the deflection curve when the shearing force is neglected, and β is the angle of shear at the neutral axis in the same cross-section. The transverse shearing force, F, is given by:

$$F = kAG\beta \qquad [b]$$

where k is a numerical factor used to account for the variation of β through the cross-section, and is a constant for any given cross-section, A is the area of cross-section and G is the shear modulus. The moment–displacement relations, with a consideration for the shear deformation effect, can be expressed as:

$$M = \frac{EI}{R}\left(\Omega - \frac{\partial \alpha}{\partial \theta}\right) \qquad [c]$$

$$M_t = \frac{C}{R}\left(\alpha + \frac{\partial \Omega}{\partial \theta}\right) \qquad [d]$$

where M is the bending moment about a radial axis, M_t is the torsional moment about the tangential axis, E is the Young's modulus, I is the moment of inertia of the cross-section about a radial axis, C is the torsional stiffness, and Ω is the angular deformation of the cross-section of the ring. The strain and kinetic energies of a ring segment can be written as:

$$U = \int_0^{\phi} \left\{ \frac{EI}{2R^2}\left(\Omega - \frac{\partial \alpha}{\partial \theta}\right)^2 + \frac{C}{2R^2}\left(\alpha + \frac{\partial \Omega}{\partial \theta}\right)^2 + \frac{kAG}{2}\beta^2 - pv - q\Omega \right\} R \, d\theta \qquad [e]$$

$$T = \int_0^{\phi} \frac{m}{2}\left\{ \left(\frac{\partial v}{\partial t}\right)^2 + \frac{I}{A}\left(\frac{\partial \alpha}{\partial t}\right)^2 + \frac{J}{A}\left(\frac{\partial \Omega}{\partial t}\right)^2 \right\} R \, d\theta \qquad [f]$$

where ϕ is the angle subtended by the ring segment at the center, p is the distributed transverse load acting through the shear center, q is the distributed twisting moment acting about the shear center, m is the mass per unit length, and J is the polar moment of inertia of the cross-section of the ring. When the expressions for U and T are used, the Hamilton's principle results in the following equations:

$$\frac{\partial}{\partial \theta}\left[kAG\left(\frac{I}{R}\frac{\partial v}{\partial \theta} - \alpha\right)\right] + Rp - \frac{\gamma AR}{g}\frac{\partial^2 v}{\partial t^2} = 0 \qquad [g]$$

$$\frac{\partial}{\partial \theta}\left[\frac{EI}{R}\left(\Omega - \frac{\partial \alpha}{\partial \theta}\right)\right] - kAGR\left(\frac{I}{R}\frac{\partial v}{\partial \theta} - \alpha\right) + \frac{C}{R}\left(\alpha + \frac{\partial \Omega}{\partial \theta}\right) + \frac{\gamma IR}{g}\frac{\partial^2 \alpha}{\partial t^2} = 0 \qquad [h]$$

$$\frac{\partial}{\partial \theta}\left[\frac{C}{R}\left(\alpha + \frac{\partial \Omega}{\partial \theta}\right)\right] - \frac{EI}{R}\left(\Omega - \frac{\partial \alpha}{\partial \theta}\right) + Rq - \frac{\gamma JR}{g}\frac{\partial^2 \Omega}{\partial t^2} = 0 \qquad [i]$$

$$kAG\left(\frac{I}{R}\frac{\partial v}{\partial \theta} - \alpha\right)\delta v\Big|_0^{\phi} = 0 \qquad [j]$$

$$\frac{EI}{R}\left(\Omega - \frac{\partial \alpha}{\partial \theta}\right)\delta \alpha\Big|_0^{\phi} = 0 \qquad [k]$$

$$\frac{C}{R}\left(\alpha + \frac{\partial \Omega}{\partial \theta}\right)\delta \Omega\Big|_0^{\phi} = 0 \qquad [l]$$

Eqns [g], [h], and [i] denote the equations of motion corresponding to the variables v, α, and Ω and eqns [j], [k], and [l] represent the boundary conditions which are satisfied for any combination of the pinned, free, and fixed end conditions.

Hamilton's Principle for Discrete Systems

Consider a system of N mass particles. Let a particle of mass m_i be acted upon by a system of external and constraint forces with resultants $\mathbf{F}_i$ and $\mathbf{f}_i$, respectively. If the system is in equilibrium, the resultant force is zero and the work done over a virtual displacement, $\delta \mathbf{r}_i$, must be zero, that is:

$$\delta W_i = (\mathbf{F}_i + \mathbf{f}_i) \cdot \delta \mathbf{r}_i = 0 \qquad [49]$$

The constraint forces, usually, do not perform any work since the displacements do not have any components in the direction of the constraint forces. Thus, for the system of all N particles, the total virtual work can be expressed as:

$$\delta W = \sum_{i=1}^{N} \delta W_i = \sum_{i=1}^{N} \mathbf{F}_i \cdot \delta \mathbf{r}_i = 0 \qquad [50]$$

D'Alembert's principle states that a particle of mass m_i subject to an unbalanced force $\mathbf{F}_i$ can be considered to be in equilibrium with the inertia force, $m_i\ddot{\mathbf{r}}_i$, so that:

$$m_i\ddot{\mathbf{r}}_i - \mathbf{F}_i = 0 \qquad [51]$$

where $\ddot{\mathbf{r}}_i$ is the acceleration of the particle. Thus, for N particles, the virtual work expression, in conjunction with d'Alembert's principle, can be stated as:

$$\sum_{i=1}^{N} (m_i\ddot{\mathbf{r}}_i - \mathbf{F}_i) \cdot \delta \mathbf{r}_i = 0 \qquad [52]$$

with:

$$\sum_{i=1}^{N} \mathbf{F}_i \cdot \delta \mathbf{r}_i = \delta W \qquad [53]$$

denoting the virtual work done by the applied forces. The time derivative of $\dot{\mathbf{r}}_i.\delta\mathbf{r}_i$ yields:

$$\frac{\mathrm{d}}{\mathrm{d}t}(\dot{\mathbf{r}}_i \cdot \delta \mathbf{r}_i) = \ddot{\mathbf{r}}_i \cdot \delta \mathbf{r}_i + \dot{\mathbf{r}}_i \cdot \delta \dot{\mathbf{r}}_i = \ddot{\mathbf{r}}_i \cdot \delta \mathbf{r}_i + \delta\left(\frac{1}{2}\dot{\mathbf{r}}_i \cdot \dot{\mathbf{r}}_i\right) \qquad [54]$$

which can be rewritten as:

$$\ddot{\mathbf{r}}_i \cdot \delta \mathbf{r}_i = \frac{\mathrm{d}}{\mathrm{d}t}(\dot{\mathbf{r}}_i \cdot \delta \mathbf{r}_i) - \delta\left(\frac{1}{2}\dot{\mathbf{r}}_i \cdot \dot{\mathbf{r}}_i\right) \qquad [55]$$

By multiplying eqn [55] by m_i and summing over all the masses gives:

$$\begin{aligned}\sum_{i=1}^{N} m_i \ddot{\mathbf{r}}_i \cdot \delta \mathbf{r}_i &= \sum_{i=1}^{N} m_i \frac{\mathrm{d}}{\mathrm{d}t}(\dot{\mathbf{r}}_i \cdot \delta \mathbf{r}_i) - \delta \sum_{i=1}^{N} \frac{1}{2} m_i (\dot{\mathbf{r}}_i \cdot \dot{\mathbf{r}}_i) \\ &= \sum_{i=1}^{N} m_i \frac{\mathrm{d}}{\mathrm{d}t}(\dot{\mathbf{r}}_i \cdot \delta \mathbf{r}_i) - \delta T\end{aligned} \qquad [56]$$

where T denotes the kinetic energy of the system. Using eqns [53] and [56], eqn [52] can be expressed as:

$$\delta T + \delta W = \sum_{i=1}^{N} m_i \frac{\mathrm{d}}{\mathrm{d}t}(\dot{\mathbf{r}}_i \cdot \delta \mathbf{r}_i) \qquad [57]$$

Let the system of mass particles be defined in terms of n generalized coordinates. Then the configuration of the system at any instant is defined by the values of the generalized coordinates which define a point in the n-dimensional configuration space. When the configuration of the system changes with time, the various configurations define points which yield a path, which can be called the true path of the system in the configuration space. At any specific instant, if a small variation in the position of the ith mass, $\delta\mathbf{r}_i$, with no associated change in time ($\delta t = 0$), is considered, we obtain another path, known as the varied path of the system. The true and varied paths of the system are shown in **Figure 4**. If the true and varied paths are assumed to coincide at two instants t_1 and t_2, we have:

$$\delta \mathbf{r}_i = 0 \quad \text{at} \quad t = t_1 \quad \text{and} \quad t = t_2 \qquad [58]$$

The multiplication of eqn [57] by $\mathrm{d}t$ and integration from t_1 to t_2 yields:

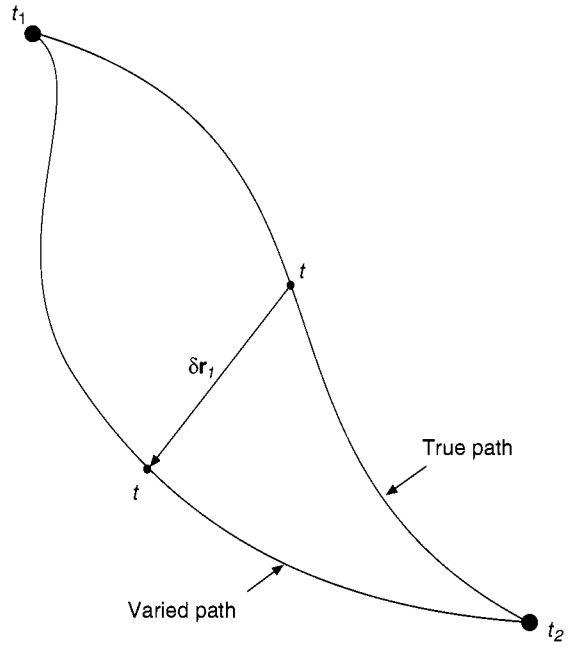


Figure 4 True and varied paths of the system.

$$\begin{aligned}\int_{t_1}^{t_2} \delta(T + W)\,\mathrm{d}t &= \int_{t_1}^{t_2} \sum_{i=1}^{N} m_i \frac{\mathrm{d}}{\mathrm{d}t}(\dot{\mathbf{r}}_i \cdot \delta \mathbf{r}_i)\,\mathrm{d}t \\ &= \sum_{i=1}^{N} \int_{t_1}^{t_2} m_i \frac{\mathrm{d}}{\mathrm{d}t}(\dot{\mathbf{r}}_i \cdot \delta \mathbf{r}_i)\,\mathrm{d}t = \sum_{i=1}^{N} m_i \dot{\mathbf{r}}_i \cdot \delta \mathbf{r}_i \Big|_{t_1}^{t_2}\end{aligned} \qquad [59]$$

Since $\delta\mathbf{r}_i = 0$ at t_1 and t_2 (eqn [58]), eqn [59] reduces to:

$$\delta \int_{t_1}^{t_2} (T + W)\,\mathrm{d}t = 0 \qquad [60]$$

In the particular case where the forces are conservative, the virtual work is equal to the negative of the variation in the potential energy of the system (δU) so that:

$$\delta W = -\delta U \qquad [61]$$

and hence eqn [60] can be rewritten as:

$$\delta \int_{t_1}^{t_2} L\,\mathrm{d}t = 0 \qquad [62]$$

where L is called the Lagrangian and is defined as:

$$L = T - U \qquad [63]$$

Eqn [62] denotes the mathematical statement of Hamilton's principle which can be stated in words as follows:

> Of all possible paths that the system can assume between the instants of time t_1 and t_2, the path that makes the value of the integral $\int_{t_1}^{t_2} L \, dt$ stationary represents the true or actual path provided that the initial and final configurations of the system are prescribed.

The stationary value is actually a minimum. Eqn [62] can be considered as the generalized Hamilton's principle where W denotes the virtual work due to conservative and nonconservative forces. Hamilton's principle is often written as:

$$\delta \int_{t_1}^{t_2} (T - U) \, dt + \int_{t_1}^{t_2} \delta W_{nc} \, dt = 0 \qquad [64]$$

where U is the potential energy, which includes both strain energy and the potential of any conservative external forces, and δW_{nc} is the virtual work done by the nonconservative forces acting on the system. As can be seen from eqns [60] and [62], Hamilton's principle reduces the problems of dynamics to the study of a scalar integral that does not depend on the coordinates used. Note that Hamilton's principle yields merely the equations of motion of the system but not the solution of the dynamics problem.

Applications – Discrete Systems

Single-degree-of-freedom System

The derivation of the differential equation of motion of a single-degree-of-freedom system, shown in **Figure 5**, is considered to illustrate the application of Hamilton's principle to discrete systems. The kinetic and strain energies of the system are given by:

$$T = \frac{1}{2} m\dot{x}^2 \qquad [a]$$

$$U = \frac{1}{2} kx^2 \qquad [b]$$

The virtual work corresponding to the applied force $F(t)$ and the damping (nonconservative) force $c\dot{x}$ is given by:

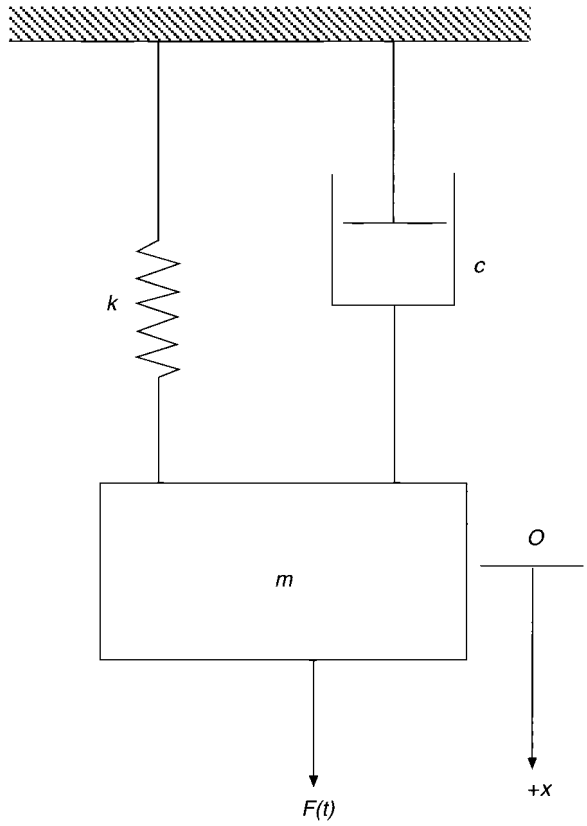


Figure 5 A single-degree-of-freedom system.

$$\delta W_{nc} = F(t)\delta x - c\dot{x}\delta x \qquad [c]$$

The application of Hamilton's principle yields:

$$\delta \int_{t_1}^{t_2} (T - U) \, dt + \int_{t_1}^{t_2} \delta W_{nc} \, dt = 0 \qquad [d]$$

with T, U, and δW_{nc} given by eqns [a], [b] and [c], respectively. The first term of eqn [d] can be rewritten as:

$$\delta \int_{t_1}^{t_2} \left(\frac{1}{2} m\dot{x}^2 - \frac{1}{2} kx^2 \right) dt = \int_{t_1}^{t_2} (m\dot{x}\,\delta\dot{x} - kx\,\delta x) \, dt \qquad [e]$$

The integration of the first term on the right-hand side of eqn [e] by parts results in:

$$\delta \int_{t_1}^{t_2} (T - U) \, dt = m\dot{x}\,\delta x\Big|_{t_1}^{t_2} - \int_{t_1}^{t_2} (m\ddot{x}\,\delta x + kx\,\delta x) \, dt \qquad [f]$$

Assuming that x is prescribed at t_1 and t_2, eqn [f] gives:

$$\int_{t_1}^{t_2} (m\ddot{x} + kx - F(t) + c\dot{x})\delta x \, dt = 0 \qquad [g]$$

Since δx is arbitrary, eqn [g] leads to the desired equation of motion of the system:

$$m\ddot{x} + c\dot{x} + kx = F(t) \qquad [h]$$

Two-degree-of-freedom System

Next, the two-degree-of-freedom system, shown in **Figure 6**, is considered. The kinetic and strain energies of the system can be expressed as:

$$T = \frac{1}{2}m_1\dot{x}_1^2 + \frac{1}{2}m_2\dot{x}_2^2 \qquad [a]$$

$$U = \frac{1}{2}k_1x_1^2 + \frac{1}{2}k_2(x_2 - x_1)^2 \qquad [b]$$

The virtual work associated with the applied forces and the damping (nonconservative) forces can be written as:

$$\begin{aligned}\delta W_{nc} = {} & F_1(t)\delta x_1 + F_2\delta x_2 - c_1\dot{x}_1\delta x_1 \\ & - c_2(\dot{x}_2 - \dot{x}_1)\delta(x_2 - x_1)\end{aligned} \qquad [c]$$

The variations of the time integrals of T and U are given by:

$$\begin{aligned}\delta\int_{t_1}^{t_2} T \, dt &= \delta\int_{t_1}^{t_2} \left(\frac{1}{2}m_1\dot{x}_1^2 + \frac{1}{2}m_2\dot{x}_2^2\right) dt \\ &= \int_{t_1}^{t_2} (m_1\dot{x}_1\delta\dot{x}_1 + m_2\dot{x}_2\delta\dot{x}_2) \, dt\end{aligned} \qquad [d]$$

$$\begin{aligned}\delta\int_{t_1}^{t_2} U \, dt &= \delta\int_{t_1}^{t_2} \left[\frac{1}{2}k_1x_1^2 + \frac{1}{2}k_2(x_2 - x_1)^2\right] dt \\ &= \int_{t_1}^{t_2} [k_1x_1\delta x_1 + k_2(x_2 - x_1)\delta(x_2 - x_1)] \, dt\end{aligned} \qquad [e]$$

By using integration by parts, eqn [d] can be rewritten as:

$$\delta\int_{t_1}^{t_2} T \, dt = \int_{t_1}^{t_2} (-m_1\ddot{x}_1\delta x_1 - m_2\ddot{x}_2\delta x_2) \, dt \qquad [f]$$

Hamilton's principle can be expressed as:

$$\delta\int_{t_1}^{t_2} (T - U) \, dt + \int_{t_1}^{t_2} \delta W_{nc} \, dt = 0 \qquad [g]$$

which, in view of eqns [c]–[f], becomes:

$$\begin{aligned}&-\int_{t_1}^{t_2} \{[m_1\ddot{x}_1 + (k_1 + k_2)x_1 - k_2x_2]\delta x_1 \\ &+ (m2\ddot{x}_2 + k_2x_2 - k_2x_1)\delta x_2\} \, dt \\ &+ \int_{t_1}^{t_2} [F_1(t)\delta x_1 + F_2(t)\delta x_2 - c_1\dot{x}_1\delta x_1 \\ &- c_2(\dot{x}_2 - \dot{x}_1)\delta(x_2 - x_1)] \, dt = 0\end{aligned} \qquad [h]$$

Assuming that x_1 and x_2 are independent coordinates, eqn [h] yields the equations of motion of the system as:

$$\begin{aligned}m_1\ddot{x}_1 + (c_1 + c_2)\dot{x}_1 - c_2\dot{x}_2 \\ + (k_1 + k_2)x_1 - k_2x_2 = F_1(t)\end{aligned} \qquad [i]$$

$$m_2\ddot{x}_2 + c_2\dot{x}_2 - c_2\dot{x}_1 + k_2x_2 - k_2x_1 = F_2(t) \qquad [j]$$

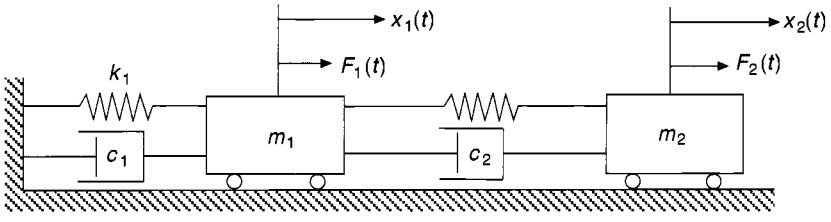


Figure 6 A two-degree-of-freedom system.

Nomenclature

A	area of cross–section of a bar
C	torsional stiffness
c,c_i	damping constant
$\mathbf{C}$	matrix relating strain and stress vectors
$\mathbf{D}$	elasticity matrix
E	Young's modulus
$F(t),F_i(t)$	external force
F	function
$\mathbf{F}_i$	ith external force
$\mathbf{f}_i$	ith constraint force
G	function; shear modulus
I	area moment of inertia of a bar; integral function
J	integral function; mass moment of inertia of a rod per unit length
k	shear coefficient
k_i,k	stiffness
L	Lagrangian; length of a bar
M	bending moment
M_t	torsional moment
m	mass for unit length of a bar; mass
m_i	ith mass
N	number of masses
n	number of dependent variables
p,q	distributed loads
R	radius of a ring
$\mathbf{r}_i$	ith radial vector
$\ddot{\mathbf{r}}_i$	ith acceleration vector
S_1	surface on which tractions are prescribed
S_2	surface on which displacements are prescribed
T	kinetic energy
t	time
U	potential energy
U_c	complementary energy
U_r	Reissner energy
u,v,w	displacements along x,y,z axes
$\mathbf{u}$	vector of displacement components
u_i	ith displacement component
$\bar{\mathbf{u}}_i$	ith prescribed displacement component
V	volume of a body (or domain of a system); shear force
W, W_p	work done by external forces
$\overline{W}_p$	work done by the applied loads during stress changes
W_{nc}	work done by nonconservative forces
x,y,z	Cartesian coordinates
x_1, x_2	initial and final values of x
α,β	slopes
δ	variation operator
$\delta\mathbf{r}_i$	ith virtual displacement vector
λ	Lagrange multiplier
π	strain energy
ρ	density
σ_{xx}, σ_{yy}...	
$\sigma_{xy}...\sigma_{ij}$...	stress components
$\boldsymbol{\sigma}$	stress vector
ϕ	function of x; dependent variable; angular rotation
ϕ_x	first derivative of ϕ with respect to x
ϕ_{xx}	second derivative of ϕ with respect to x
Φ_i	ith component of body force
$\bar{\phi}_x,\bar{\phi}_y,\bar{\phi}_z$	body force per unit volume along x,y,z axes
$\bar{\boldsymbol{\Phi}}$	vector of prescribed body forces
Φ_x,Φ_y,Φ_z	surface traction along x,y,z axes
$\overline{\Phi}_i$	ith component of surface traction
$\overline{\Phi}_x,\overline{\Phi}_y,\overline{\Phi}_z$	prescribed surface forces (tractions)
$\bar{\boldsymbol{\Phi}}$	vector of prescribed surface forces (tractions)
θ	angular coordinate
δ_{ij}	Kronecker delta
γ	angular rotation due to shear deformation
γ_{ij}	strain component in terms of derivatives of u_i
ε_{ij}	strain component
$\boldsymbol{\varepsilon}$	strain vector
$\boldsymbol{\varepsilon}_0$	initial strain vector
$\boldsymbol{\Omega}$	angular deformation
$(\ )^T$	transpose of ( )

See also: **Finite element methods**; **Theory of vibration**, Equations of motion; **Theory of vibration**, Fundamentals; **Theory of vibration**, Impulse response function.

Further Reading

Meirovitch L (1967) *Analytical Methods in Vibrations*. New York: Macmillan.

Moiseiwitsch BL (1966) *Variational Principles*. London: Interscience John Wiley.

Rao SS (1971) Effects of transverse shear and rotatory inertia on the coupled twist-bending vibrations of circular rings. *Journal of Sound and Vibration* 16: 551–566.

Rao SS (1989) *The Finite Element Method in Engineering*, 2nd edn. Oxford: Pergamon Press.

Rao SS (1995) *Mechanical Vibrations*, 3rd edn. Reading, MA: Addison-Wesley.

Schechter RS (1967) *The Variational Method in Engineering*. New York: McGraw-Hill.

Shabana AA (1997) *Vibration of Discrete and Continuous Systems*, 2nd edn. New York: Springer.

Tabarrok B, Rimrott FPJ (1994) *Variational Methods and Complementary Formulations in Dynamics*. Dordrecht: Kluwer Academic Publishers.

Timoshenko S, Young DH, Weaver Jr. W (1974) *Vibration Problems in Engineering*, 4th edn, New York: John Wiley.
Timoshenko SP (1921) On the correction for shear of the differential equation for transverse vibration of prismatic bars. *Philosophical Magazine* 41: 744–746.
Williams Jr. JH (1996) *Fundamentals of Applied Dynamics*. New York: Wiley.
Yu Y-Y (1996) *Vibrations of Elastic Plates*. New York: Springer-Verlag.

TIME–FREQUENCY METHODS

P White, Institute of Sound and Vibration Research (ISVR), University of Southampton, Southampton, UK

Copyright © 2001 Academic Press

doi:10.1006/rwvb.2001.0056

Introduction

The principles of frequency analysis have found wide application in many areas of vibration analysis. Using these techniques one represents a time domain signal as a function of frequency. A frequency domain representation allows one to observe readily which are the important frequencies within a signal. Such a representation gives incomplete information when the signal under analysis is nonstationary, i.e., when the signal's spectrum varies as a function of time. A more complete representation of such signals is provided by time–frequency methods, which seek to represent a signal's energy as a function of time and frequency simultaneously.

This article begins with a discussion of conventional spectral analysis techniques, then proceeds to introduce the principles of bilinear time–frequency methods.

Fourier Analysis

The use of Fourier methods for analysing signals is one of the most familiar signal-processing techniques. The basis of Fourier methods is the transform pair:

$$X(f) = \int_{-\infty}^{\infty} x(t)\mathrm{e}^{-2\pi ift}\mathrm{d}t \qquad [1a]$$

$$x(t) = \int_{-\infty}^{\infty} X(f)\mathrm{e}^{2\pi ift}\mathrm{d}f \qquad [1b]$$

where $x(t)$ is the signal, nominally in the time domain, and $X(f)$ is its Fourier transform, and f is the frequency variable. The interpretation of eqn [1b] is that a signal can be constructed by forming a weighted sum of complex exponentials, the weighting function being the signal's Fourier transform, as given by eqn [1a]. The Fourier transform is a linear operation, so that the Fourier transform of $x(t) = c_1a(t) + c_2b(t)$ is given by:

$$c_1A(f) + c_2B(f)$$

where $A(f)$ and $B(f)$ are the Fourier transforms of $a(t)$ and $b(t)$ respectively. It is important to realize that the exponentials in eqn [1b] are defined over the entire time axis, i.e., for $-\infty < t < \infty$, which makes them inefficient tools for decomposing signals with a finite duration. So that, for example, if the signal is such that $x(t) = 0$ for $|t| < T/2$ then the Fourier decomposition requires many frequency components to represent the signal accurately. It is this basic shortcoming of the Fourier transform that leads to effects such as side lobes and spectral leakage.

In many cases one chooses to work, not with the complete Fourier transform, but only to consider its squared magnitude, which here we refer to as the signal's spectrum. (The term spectrum can have a variety of meanings but herein it is taken to represent $|X(f)|^2$.) One reason for concentrating on the spectrum is because the spectrum is invariant to time shifts in the signal, so that the spectrum of $x(t-\tau)$ is identical to the spectrum of $x(t)$. This shift invariance arises because in computing the spectrum, the phase of the Fourier transform is discarded and it is this phase which conveys information about the temporal location of signal components.

The spectrum is sufficient to represent the signal's energy distribution over frequency, in the sense that one can express the energy in the frequency band (f_1, f_2) as:

$$\int_{f_1}^{f_2} |X(f)|^2\mathrm{d}f$$

The spectrum is a bilinear transform, so that the transform relates to the signal through a quadratic

function. Hence, unlike the Fourier transform, the spectrum does not obey a superposition principle; specifically, the spectrum of $x(t) = c_1 a(t) + c_2 b(t)$ is given by:

$$|X(f)|^2 = c_1^2|A(f)|^2 + c_2^2|B(f)|^2 + 2c_1c_2\mathrm{Re}\{A(f)B(f)^*\} \quad [2]$$

where the asterisk denotes complex conjugation. The third term on the right-hand side of eqn [2] is an interaction term arising as a consequence of the squaring operation. This interaction term will be only be significant if there are frequency bands where $A(f)$ and $B(f)$ are both large. The interaction term will be small if the two components occupy different frequency bands.

In summary, the Fourier transform, which is a linear signal representation, contains information about the location of signal components in time, encoded, predominantly, in its phase. It is difficult to interpret this phase information directly. The spectrum, which is a bilinear signal representation, contains no information about the absolute location of a signal, but is easily interpreted. The goal of time–frequency methods is to construct signal representations that concisely represent (nonstationary) signals, allowing the user to identify rapidly which frequency components are present in a signal at a particular time and how each component evolves with time.

Time–Frequency Methods

The Wigner–Ville Distribution

Conventionally, time–frequency methods are classified into linear and bilinear methods; the linear representations preserve phase information, whilst bilinear representations dispense with phase information. This distinction is very closely allied to that drawn above between the Fourier transform and the spectrum. This discussion will concentrate on the more widely used bilinear time–frequency methods.

Considering the signal spectrum, $|X(f)|^2$, one can readily show the following familiar result (the Weiner–Khintchine theorem):

$$\begin{aligned} |X(f)|^2 &= \int_{-\infty}^{\infty}\int_{-\infty}^{\infty} x(u)^* x(v) \mathrm{e}^{-2\pi i f(u-v)}\,\mathrm{d}u\,\mathrm{d}v \\ &= \int_{-\infty}^{\infty} r(\tau)\,\mathrm{e}^{-2\pi i f\tau}\,\mathrm{d}\tau \end{aligned} \quad [3]$$

where $r(\tau)$ is the instantaneous correlation function which may be defined as:

$$\begin{aligned} r(\tau) &= \int_{-\infty}^{\infty} x(t-\tau)^* x(t)\,\mathrm{d}t \\ &= \int_{-\infty}^{\infty} x(t-\tau/2)^* x(t+\tau/2)\,\mathrm{d}t \end{aligned}$$

An alternative formulation of eqn [3] is obtained by reordering the integrals to read:

$$\begin{aligned} |X(f)|^2 &= \int_{-\infty}^{\infty}\left\{\int_{-\infty}^{\infty} x(t-\tau/2)^* x(t+\tau/2)\mathrm{e}^{-2\pi i f\tau}\mathrm{d}\tau\right\}\mathrm{d}t \\ &= \int_{-\infty}^{\infty} W(t,f)\,\mathrm{d}t \end{aligned} \quad [4]$$

where $W(t, f)$ is the notation adopted to represent the term in the braces, i.e.:

$$W(t,f) = \int_{-\infty}^{\infty} x(t-\tau/2)^* x(t+\tau/2)\mathrm{e}^{-2\pi i f\tau}\mathrm{d}\tau \quad [5]$$

This function is in fact the central distribution to the class of bilinear time-frequency representations and is called the Wigner–Ville distribution (WVD). The spectrum can be thought of as the time-integrated WVD. Note that, whilst the spectrum is assuredly nonnegative, the same is not true for the WVD; indeed, it is almost always the case that the WVD of a signal is negative for some values of t and f. It is also elementary to show that:

$$\begin{aligned} &|x(t)|^2 \\ &= \int_{-\infty}^{\infty}\left\{\int_{-\infty}^{\infty} x(t-\tau/2)^* x(t+\tau/2)\mathrm{e}^{-2\pi i f\tau}\mathrm{d}f\right\}\mathrm{d}t \\ &= \int_{-\infty}^{\infty} W(t,f)\,\mathrm{d}f \end{aligned}$$

so that the frequency-integrated WVD is the instantaneous energy. Hence, the function $W(t, f)$ may be considered as a fundamental way of representing a signal's energy as a function of time and frequency.

The signal enters the WVD through a quadratic operation (see eqn [5]) and so is a bilinear transform. This means that it inevitably generates interaction terms; the WVD of $x(t) = c_1 a(t) + c_2 b(t)$ is given by:

$$W_x(t,f) = c_1^2 W_a(t,f) + c_2^2 W_b(t,f) + 2c_1c_2\mathrm{Re}\{W_{a,b}(t,f)\}$$

where the subscript in the notation for the WVD is (temporarily) used to indicate the signal used to compute the WVD. The function $W_{a,b}(t,f)$ is a cross-Wigner–Ville distribution (CWVD), defined as:

$$W_{a,b}(t,f) = \int_{-\infty}^{\infty} a(t-\tau/2)^* b(t+\tau/2)\mathrm{e}^{-2\pi i f\tau}\mathrm{d}\tau$$

Whilst interaction terms in the spectrum (see eqn [2]) are small, assuming the two signals are separated in frequency, the same is not true for interaction terms in the WVD. In general, the CWVD is of the same magnitude as the WVD, leading to significant interaction terms in the WVD, regardless of whether the signal components occupy the same frequency band. The CWVD is an oscillatory function, the rate of oscillation increasing as the separation between components increases.

Briefly consider where the interaction terms make their greatest contributions. In the case of the spectrum the interaction terms are largest at frequencies where the signals' spectra are large. For the WVD the interaction terms are largest midway (in the time–frequency plane) between two components. Consequently there is the possibility of interaction terms being confused with true signal components.

The WVD arises as a natural technique for representing the energy of a signal as a function of time and frequency. However, there are two basic problems that act as limitations on the interpretation of the WVD as a decomposition of a signal's energy. The first is that the WVD will (almost certainly) be negative for some values of t and f, causing obvious problems with interpreting $W(t,f)$ as the energy in a signal at that time and frequency. The second problem is that the interaction terms in the WVD are of a significant magnitude and further they appear in regions of the time–frequency plane away from the true signal components. The result is that the interaction terms can make the appearance of the WVD rather confused and can be misleading. The central theme of much work in time–frequency analysis has centered on reducing the effect of the interaction terms whilst maintaining many of the positive aspects of the WVD.

To illustrate the behavior of WVD, consider an example signal consisting of the sum of two components. The first component is a 100-Hz sine wave windowed using a Gaussian modulating function. The second component, windowed in the same manner, is a sinusoid whose frequency increases linearly with time, starting at 100 Hz and finishing at 400 Hz. **Figure 1A** and **1B** shows the WVDs computed for the individual components. (The plots of time–frequency representations in this chapter use a logarithmic gray scale, with dark colors representing large values. Negative points are not displayed, nor are values 30 dB less than the largest value in the distribution.) Note that resolution of WVD is the same for the tone and the swept sinusoid. It is a fundamental property of the WVD that its resolution, for a linearly swept sinusoid, is independent of the sweep rate. **Figure 1C** shows the WVD of the sum of these two signals. The interaction terms are those elements shown in **Figure 1C** that are not present in either of **Figure 1A** or **1B**. These interaction terms can be seen to oscillate, with the rate of oscillation increasing as the signal components separate in frequency.

Reduction of the Interaction Terms

The oscillatory nature of the interaction terms is the key to their reduction. The classical method to reduce interaction terms is to low-pass filter the WVD in the time–frequency plane. The result is a new time–frequency distribution, $P(t,f)$, defined below:

$$P(t,f) = \int_{-\infty}^{\infty}\int_{-\infty}^{\infty} W(\tau,\nu)\Phi(t-\tau,f-\nu)\,\mathrm{d}\tau\,\mathrm{d}\nu \quad [6]$$

The $\Phi(t,f)$ is referred to as the kernel function. The set of time–frequency distributions generated using eqn [6] is referred to as Cohen's class. For example if the kernel function is selected as $\Phi(t,f) = \delta(t)$, where $\delta(t)$ is the Dirac delta function, then $P(t,f) = |X(f)|^2$, that is to say that the time–frequency distribution degenerates to the signal's spectrum, in which case the interaction terms are small, as discussed above. In general, one seeks to select a kernel function that, like the above example, suppresses cross-terms whilst maintaining time and frequency information.

To suppress interaction terms effectively the kernel function should have the form of a low-pass filter, so that its double Fourier transform is a two-dimensional function that is large at the origin and decays away from there. The two-dimensional Fourier transform of $\Phi(t,f)$ is denoted $\phi(\theta,\tau)$, so that:

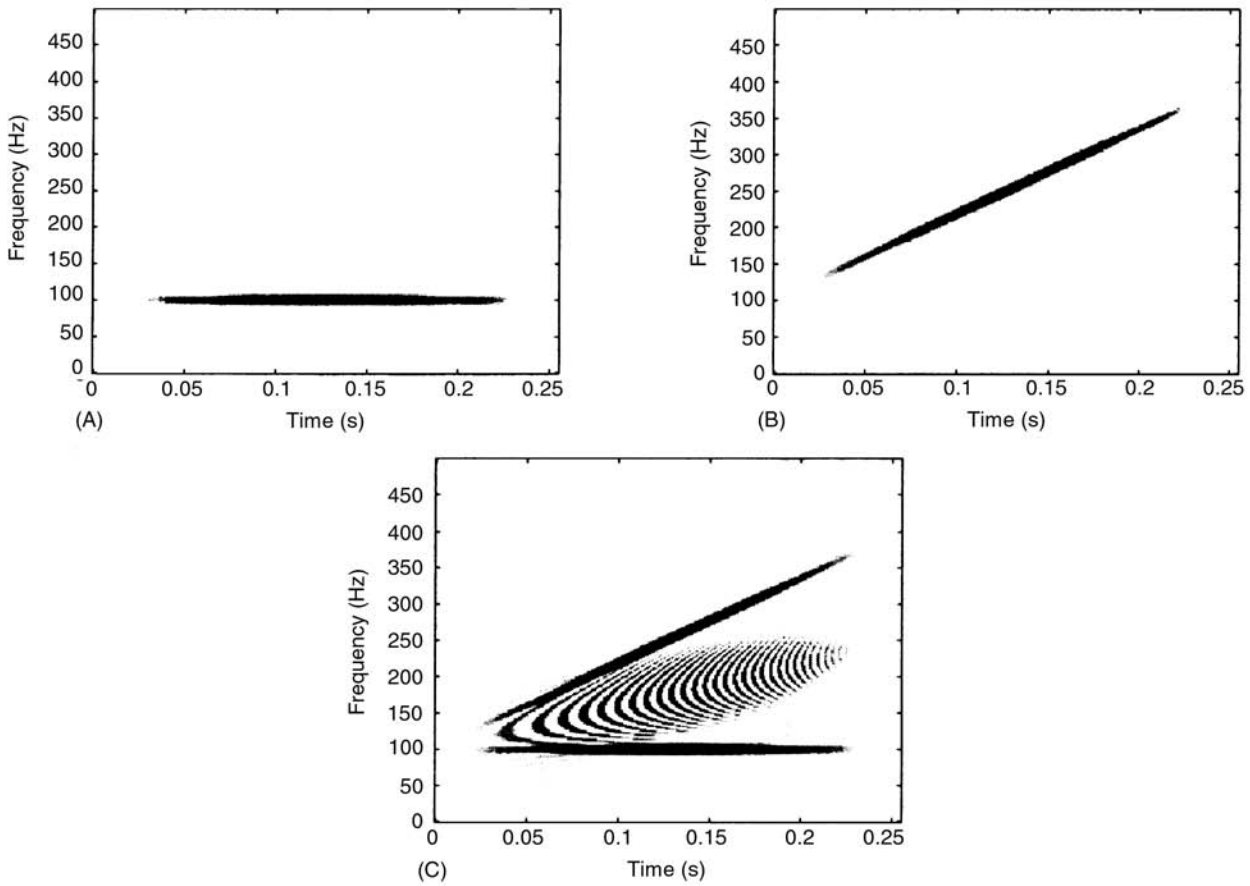


Figure 1 Wigner–Ville distributions of (A) tonal signal; (B) linearly swept sinusoid; and (C) sum of (A) and (B).

$$\phi(\theta,\tau) = \int_{-\infty}^{\infty}\int_{-\infty}^{\infty} \Phi(t,f)\mathrm{e}^{-2\pi i(\theta t + f\tau)}\mathrm{d}t\,\mathrm{d}f$$

The low-pass nature of the kernel will serve to attenuate the oscillatory interaction terms but will also smear the desirable signal components; this smearing results in a loss of resolution. Consequently, the choice of kernel function involves a tradeoff between the degree of attenuation of the interaction terms and loss of resolution.

Kernel Design

Unless care is taken the smoothing operation (eqn [6]) will destroy some of the desirable properties of the WVD. For example, the marginal properties, eqns [4] and [5], do not generally hold for members of Cohen's class. To overcome this it is possible to derive conditions that the kernel must satisfy in order that the distribution has specified properties. For example, it can be shown that if the kernel is such that:

$$\phi(0,\tau) = \phi(\theta,0) = 1 \quad \text{for all } \tau \text{ and } \theta \qquad [7]$$

then the distribution $P(t, f)$ will be such that:

$$\int_{-\infty}^{\infty} P(t,f)\mathrm{d}f = |x(t)|^2 \text{ and } \int_{-\infty}^{\infty} P(t,f)\mathrm{d}t = |X(f)|^2 \qquad [8]$$

i.e., the new distribution, like the WVD, will satisfy the marginal conditions.

The Spectrogram

One important example of a distribution that is a member of Cohen's class is obtained by using a kernel function satisfying:

$$\Phi(t,f) = W_h(t,f) = \int_{-\infty}^{\infty} h(t-\tau/2)^* h(t+\tau/2)\mathrm{e}^{-2\pi i f\tau}\mathrm{d}\tau$$

where $h(t)$ is an arbitrary function. By substitution of this kernel into eqn [4], and performing some manipulations one can show that:

$$P(t,f) = \left| \int_{-\infty}^{\infty} h(t-\tau)x(\tau)\mathrm{e}^{-2\pi i f\tau}\mathrm{d}\tau \right|^2 \qquad [9]$$

This distribution has the property of being nonnegative, a condition required if $P(t, f)$ is to be interpreted as an energy distribution. The distribution defined in eqn [9] is probably the most widely used time–frequency distribution, namely the spectrogram, and will be denoted $S(t, f)$. The spectrogram is the squared modulus of the short-term Fourier transform (STFT) (for more details, see **Transforms, wavelets**). Whilst formally there are no restrictions that are placed upon the function $h(t)$, in practice it is chosen as a windowing function, i.e., a function which is nonnegative, symmetrical, unimodal, and of finite duration. In this case the product $h(t-\tau)x(\tau)$ (considered as a function of τ) is a windowed version of the signal localized about the point t. Hence, the spectrogram is the spectrum of the signal localized about t. This represents one natural extension of the Fourier transform (spectrum) for the case of nonstationary signals. The spectrogram has a long history and remains the most widely used time–frequency distribution. As such, it is often the benchmark against which other distributions are judged. This role arises largely for historical reasons; from a theoretical standpoint the only remarkable property that the spectrogram possesses is that it is guaranteed to be nonnegative.

When using the spectrogram the choice of the duration of the windowing function $h(t)$ must be made. This critically affects the appearance of the spectrogram – a fact that betrays the *ad hoc* nature of the spectrogram. If a short-duration windowing function is used then the spectrogram is able to resolve short-duration events well, but its frequency resolution is poor. When longer windows are used, then the frequency resolution is improved, but at the expense of temporal resolution. This is a fundamental limitation of the spectrogram.

The spectrogram is constructed by concatenating spectra, so the interaction terms in the spectrogram share the properties of the interaction terms appearing in the spectrum. Specifically, the interaction terms are at their largest when the signal components are large. This is a consequence of the fact that the kernel function is an aggressive low-pass filter, which is very effective at suppressing the interaction terms but also results in a great loss of resolution. As will be shown, other members of Cohen's class allow one to reduce the level of interaction term suppression, with the benefit of increasing resolution.

Other Examples of Cohen's Class of Distributions

A range of time–frequency methods have been proposed that fall under the auspices of Cohen's class. Two of the most widely considered are outlined below, with the intention of giving a flavor of the available techniques.

The Choi–Williams distribution (CWD) uses a kernel function of the form:

$$\phi(\theta,\tau) = \mathrm{e}^{-\theta^2\tau^2/\sigma}$$

The parameter $\sigma(<0)$ is selected by the user and controls the rate of decay of $\phi(\theta\tau)$, i.e., the bandwidth of the low-pass filter, and controls the degree of interaction term suppression. This kernel function is designed so that it satisfies the condition [7] and so the resulting distribution satisfies the marginal conditions [8]. In general, the CWD is negative for some times t at some frequencies f, so it cannot be regarded as a true energy distribution. Whilst the CWD has smaller interaction terms than the WVD, this reduction is far from complete. The CWD is particularly poor at reducing interaction terms between signal elements that occur simultaneously or at different times but within the same frequency band.

Consider a signal that is zero for all times prior to time t_0 and after time t_1. One condition that can be specified is that the time–frequency distribution should be zero for values of $t \notin [t_0, t_1]$; this is referred to as the weak finite support property. Most members of Cohen's class do not satisfy this condition, including the CWD and spectrogram. One method that is specifically designed to satisfy the weak finite support property is referred to as a cone kernel distribution (CKD). This is a Cohen's class distribution that uses a kernel function of the form:

$$\phi(\theta,\tau) = g(\tau)|\tau|\frac{\sin a\theta\tau}{a\theta\tau}$$

where a is a user-selected parameter (often taken as $\frac{1}{2}$) and $g(\cdot)$ is a user-defined function (often taken as unity, i.e. $g(\tau) = 1$). This distribution, like the CWD, suppresses cross-terms whilst maintaining a specified property (in this case, the weak finite support property).

The CKD does not satisfy the marginal properties. Indeed, the weak finite support and marginal properties are incompatible; that is, if a kernel is designed to

satisfy one condition, then the other condition is necessarily violated.

It is often the case when designing a kernel that to achieve one set of properties then a second set of properties is lost. This is further illustrated if one considers the problem of designing a kernel that yields a nonnegative time–frequency representation. This condition is necessary if one wishes to interpret a time–frequency representation as representing a signal's energy as a function of time and frequency. But one can show that, for a distribution to be nonnegative for all signals, it must be a spectrogram, which does not satisfy the marginal constraints or the finite support property. This is a fundamental limit to time–frequency distributions within Cohen's class, namely that they can never yield distributions that are both positive and satisfy other desirable properties.

Figure 2 shows the results of applying a spectrogram, CWD, and CKD to the test signal, the WVD of which is shown in **Figure 1C**. The spectrogram, shown in **Figure 2A**, exhibits no visible interaction terms; however the resolution of the swept component is poor. (The window for the spectrogram was a Gaussian, with a root mean square duration of 12 ms. This was deemed to produce the most visually appealing results.) By contrast, in the CWD the interaction terms are large (**Figure 2B**), but the resolution of the two individual components is only slightly worse than that seen in the WVD (**Figure 1C**). For this example the most visually satisfying result is given by the CKD. The interaction terms are only noticeable when the two signal components are close, and there is little loss of resolution.

Whilst Cohen's class encompasses a great many of the distributions detailed in the literature, it does not cover all of them. This section briefly discusses some of the other methods that are not members of Cohen's class.

Cohen's class deals with signal representations that are bilinear (quadratic). There are linear representations, such as the STFT, and the wavelet transform.

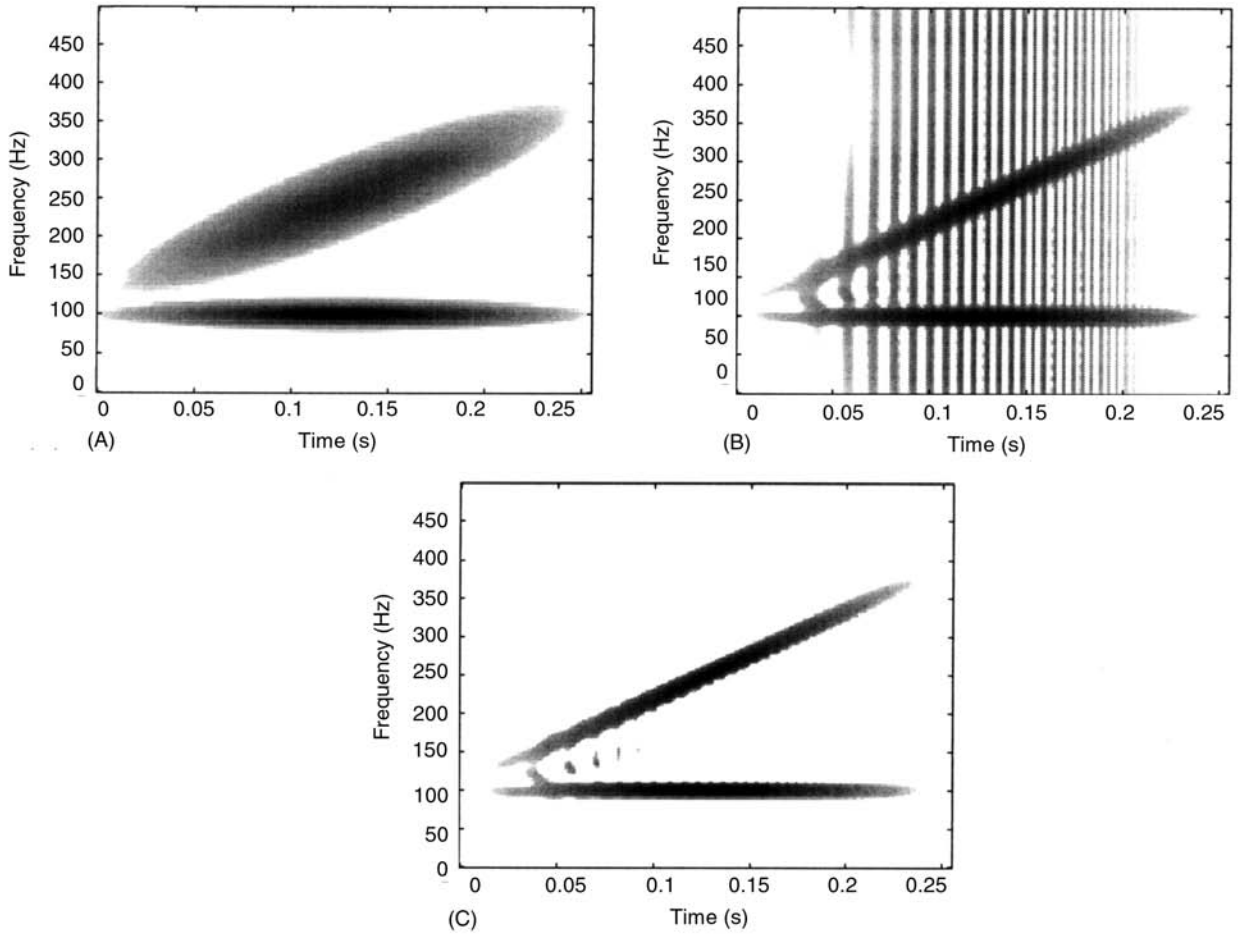


Figure 2 Various bilinear distributions for the test signal. (A) Spectrogram; (B) Choi-Williams distribution; (C) cone kernel distribution.

The linear representations obey the principle of superposition and so exhibit no interaction terms. However, the linear representations generate complex valued distributions, which are usually examined via their modulus and phase. The squared modulus of a linear representation is bilinear, e.g., as already stated, the squared modulus of the STFT is the spectrogram. Several methods are based on manipulating linear distributions. These methods are capable of giving good performance for certain classes of signals.

There also exist a variety of methods that adjust (adapt) the kernel function to suit the data set being considered.

Applications

There are many vibration-based applications to which time–frequency analysis can be applied. Here the results from two data sets will be briefly discussed so as to provide a realistic indication of the performance of the methods discussed above. The application is the analysis of frequency response measurements. It will be shown how the use of time–frequency methods allows one to glean information from structural response data that is often overlooked by considering either an impulse response function or a frequency response function (FRF).

Impulse Response Data

This section presents results from data collected using two experimental set-ups, shown in **Figure 3**. The first experiment was designed to yield simple signals that allow one to characterize a beam's dispersive behavior. The second experiment is a more realistic measurement that produces a more complex response, from which the aim is still to obtain information about the dispersive nature of the beam.

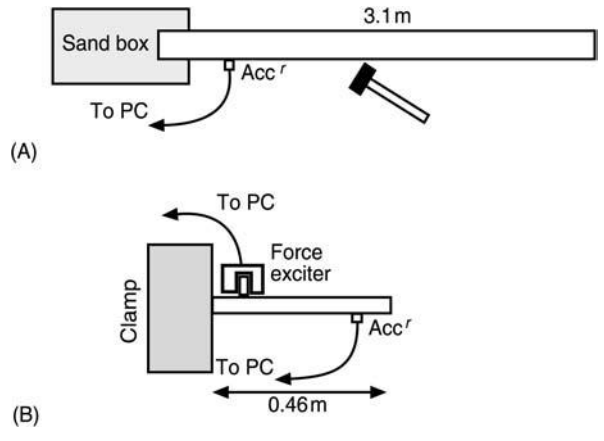


Figure 3 Experimental configurations.

The first experiment employed a simply supported beam, one end of which was embedded in sand to create a semianechoic termination. The other end was free. Response data were collected by exciting the beam with an impulse and measuring acceleration at a single point. The semianechoic termination reduced reflections: from one end such that the measured acceleration predominantly contains only two reflections, the direct signal and the signal reflected from the free end. This signal is depicted in **Figure 4**. The two reflections can be clearly distinguished, having epochs at approximately 0.004 and 0.01 s.

The first component arrives after traveling a short distance along the beam, whereas the second component arrives having traveled to the free end and been reflected back to the measuring point. This difference in path lengths for the two paths gives rise to different amounts of dispersion in the two components; the second component is more disperse than the first. Evidence for this can be observed in **Figure 4**, where the second component is significantly longer in duration than the first.

Figure 5 shows various time–frequency distributions computed for this signal. In the spectrogram (**Figure 5A**), one can readily identify the two components as distinct loci in the time–frequency plane. The first component, starting at approximately 0.004 s, is approximately vertical above 1000 Hz, but its behavior below that frequency is obscured by the poor resolution of the spectrogram. The second component, starting at approximately 0.01 s, is clearly curved, the curvature being due to dispersion, ensuring that the lower-frequency components arrive at the measurement site after the higher frequencies. From the WVD (shown in **Figure 5B**), one can more confidently define the time–frequency curves describing each component, although there are a large number

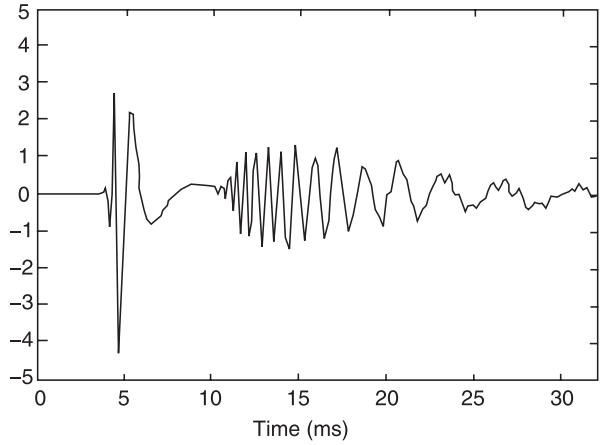


Figure 4 Impulse response data from beam with a semianechoic termination.

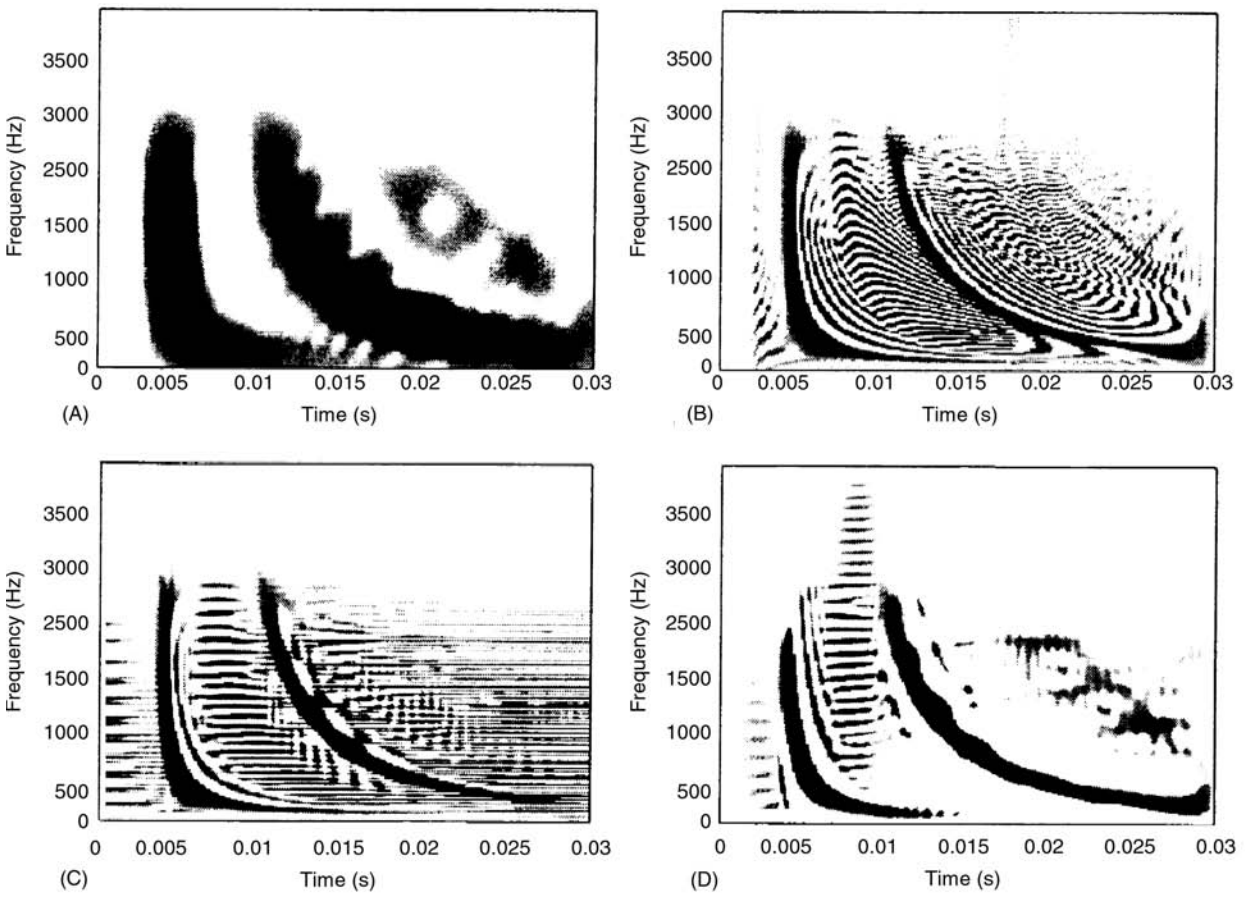


Figure 5 Bilinear time–frequency representations for data shown in **Figure 3**. (A) Spectrogram; (B) WWD; (C) CWD; (D) CKD.

of interaction terms present. In the CWD (shown in **Figure 5C**), these interaction terms are slightly reduced, with little loss of resolution. Finally, in the CKD (**Figure 5D**), the interaction terms are more heavily reduced, leaving the time–frequency curves as dominant features, but the loss of resolution required to achieve this is evident.

The second data set was collected by exciting a cantilever beam, near its root, and measuring the acceleration signal near its tip. The excitation used was band-limited white noise force input. These data were used to estimate the transfer function (inertance) between the excitation point and the measurement point using the classical $H_1(f)$ estimator. This transfer function was then used to compute the impulse response function, shown in **Figure 6**.

The impulse response of the beam contains many more components. It consists of an initial propagation delay, due to the finite time required for a disturbance to reach the measurement point from the excitation site. However, the character of wave propagation in the beam is such that high frequencies travel faster than low frequencies, i.e., the beam is dispersive. Thus, one anticipates that the onset of each mode of vibration in the beam should be different, with the high-frequency modes being excited before the low-frequency modes. Such a phenomenon cannot be observed by examining either the impulse response or the FRF directly. This example demonstrates that evidence for such a phenomenon can be obtained from the time–frequency representation.

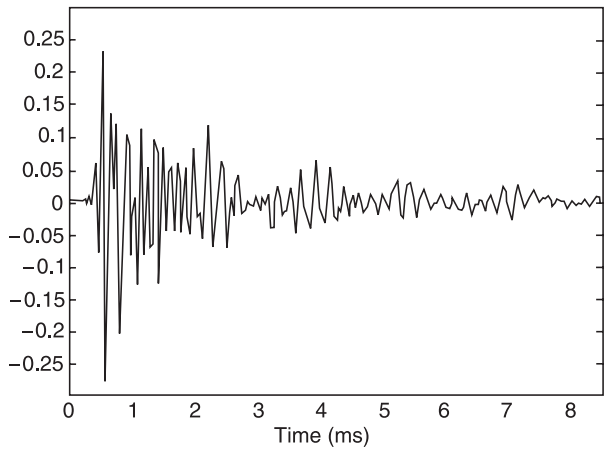


Figure 6 Impulse response data from cantilever beam.

Various time–frequency representations for a cantilever beam signal are shown in **Figure 7**. This signal contains many more components and so represents a difficult processing challenge. The spectrogram (**Figure 7A**) shows some structure. The frequency band centered near 4 kHz shows significant energy and there is evidence of packets of energy arriving at regular intervals. These packets of energy relate to the reflections arriving at measurement points. A similar effect can be seen in the frequency band near 8 kHz. The WVD, depicted in **Figure 7B**, is dominated by interaction terms and the signal details are almost completely obscured. In the CWD (**Figure 7C**), the interaction terms are reduced but the representation remains confused. The CKD (**Figure 7D**) conveys greater information about the signal. In the 4 kHz band the dispersion in the individual energy packets can be seen to exhibit its own dispersive character, with later arrivals exhibiting more dispersion than the earlier arrivals. In the higher-frequency band, near 8 kHz, the individual energy packets are smeared into a single component.

Summary

Time–frequency methods offer a convenient technique for representing the spectral content of a signal when that content varies as a function of time, i.e., when the signal is nonstationary. Basing a representation on the decomposition of a signal's energy naturally leads to a bilinear (quadratic) representation. Such representations are characterized by the fact that the distributions commonly exhibit interaction terms that are located in counterintuitive locations in the time–frequency plane. These interaction terms can be reduced by the application of a two-dimensional filter. The reduction of interaction terms in this manner necessarily leads to a loss of resolution, but can be controlled so that some of the desirable properties of the original distribution are maintained.

By careful choice of the time–frequency representation one can obtain signal representations in which the underlying character of the signal is revealed.

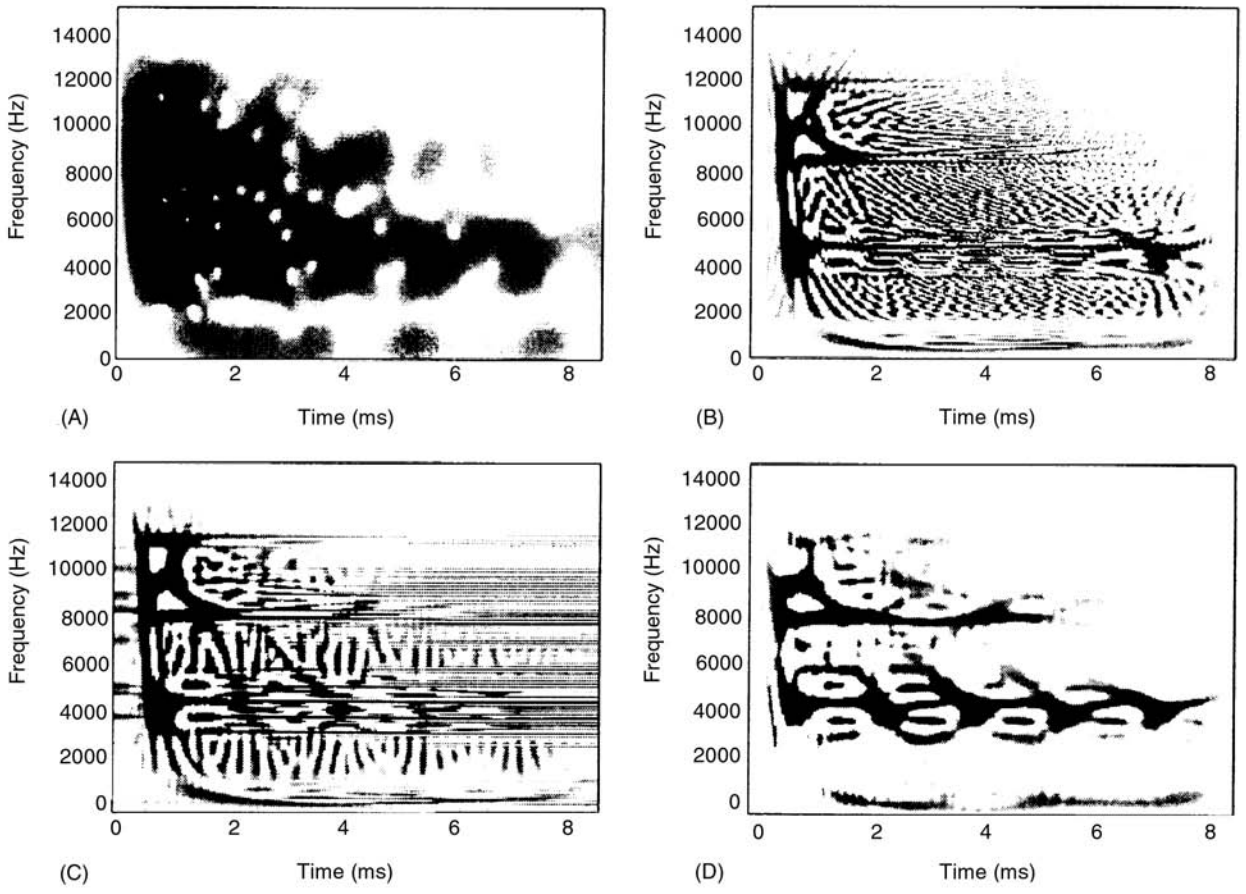


Figure 7 Various time–frequency representations computed for data shown in **Figure 5**. (A) Spectrogram; (B) WWD; (C) CWD; (D) CKD.

Nomenclature

$A(f)$	Fourier transform of $a(t)$
$B(f)$	Fourier transform of $b(t)$
f	frequency variable
$h(t)$	arbitrary function
$P(t, f)$	time-frequency distribution
$r(\tau)$	instantaneous correlation function
$S(t, f)$	spectrogram
$x(t)$	signal
$X(f)$	Fourier transform of $x(t)$
$\|X(f)\|^2$	signal spectrum
$\delta(t)$	Dirac delta function
$\Phi(t, f)$	kernel function

See also: **Transform methods**;

Further Reading

Auger F and Flandrin P (1995) improving the readability of time–frequency and time-scale representations by the reassignment method. *IEEE Transactions on Signal Processing* 43: 1068–1089.

Baraniuk R and Jones D (1993) A signal-dependant time–frequency representation: optimal kernel design. *IEEE Transactions on Signal Processing* 41: 1589–1602.

Choi HI and Williams WJ (1989) improved time–frequency representation of multicomponent signals using exponential kernels. *IEEE Transactions on Acoustics Speech and Signal Processing* 37:862–871.

Cohen L (1995) *Time–Frequency Analysis*. New Jersey: Prentice-Hall.

Delprat N, Escudié B, Guillemain P, Kronland-Martinet R, Tchamitchian P and Torrésani B (1992) Asymptotic wavelet and Gabor analysis: extraction of instantaneous frequencies. *IEEE Transactions on Information Theory* 38: 644–664.

Flandrin P (1998) *Time–Frequency/Time-Scale Analysis*. San Diego: Academic Press.

Gabor D (1946) Theory of communication. *Journal of the IEE* 93: 429–457.

Hammond JK (ed.) (1997) Special issue on time–frequency analysis. *Mechanical Systems and Signal Processing* 11.

Hammond JK and White PR (1996) The analysis of nonstationary signals using time frequency methods. *Journal of Sound and Vibration* 190: 419–447.

Hlawatch F and Bourdeaux-Bartels G (1992) Linear and quadratic time–frequency representations. *IEEE Signal Processing Magazine* 9: 21–66.

Khalili N and Hammond JK (1993) The application of cepstral techniques for the determination of reflection coefficients for dispersive systems: part I. Theory and numerical result. Part II. Comparison between theory and experiment. *Mechanical Systems and Signal Processing* 7: 425–449.

Loughlin P, Pitton J and Atlas L (1994) Construction of positive time–frequency distributions. *IEEE Transactions on Signal Processing* 42: 2697–2705.

Wang WJ and McFadden PD (1993) Early detection of gear failure by vibration analysis – I and II. Calculation of the time–frequency distribution. *Mechanical Systems and Signal Processing* 17: 193–203.

White PR and Lopes DM (2000) Time–frequency methods for analyzing structural response data. In: *Proceedings of the International Conference on Acoustics Speech and Signal Processing*, Istanbul, June 2000, pp. 3878–3881.

White RG and Walker J (eds) (1982) *Noise and Vibration*. London: Ellis Horwood.

Zhao Y, Atlas LE and Marks RJ (1990). The use of cone shaped kernel functions for generalized time–frequency representations of non-stationary signals. *IEEE Transactions on Acoustics Speech and Signal Processing* 38: 1084–1091.

TIRE VIBRATIONS

G D Shteinhauz and L T Charek, The Goodyear Tire Rubber Company, Akron, OH, USA

Copyright © 2001 Academic Press

doi:10.1006/rwvb.2001.0069

Introduction

Tire vibration is an oscillatory motion of the whole tire of its parts with respect to a neutral (mounted and loaded) position on a vehicle or a test rig. Tires are the only parts of the vehicle that connect it to the road, providing support, isolation, traction, braking, and steering. Each one of these functions involves developing, responding to, and transferring forces and moments between the road and the vehicle. Slow-changing or static forces, like vehicle weight, preload the tire, while fast-changing or dynamic forces, like road impacts or sudden braking, cause tire vibration.

In this article we discuss pneumatic tires, which are used on passenger cars, trucks, bicycles, tractors, and off-the-road vehicles. The common feature of these tires is that when installed on the wheel, they form a cavity containing a pressurized gas (mostly air). The pressurized gas preloads and stiffens the tire structure, while still maintaining enough flexibility to create a footprint on the road, which makes it

possible to carry the vehicle's load, while being able to develop and transfer the control forces and moments.

On passenger cars and trucks, the tire-wheel assembly is connected to the vehicle body through components of suspension, steering, and driving systems. The suspension system consists of springs, dampers, bushings, and connecting rods to isolate the vehicle further from the road disturbances. Bicycles, tractors, and off-the-road vehicles frequently do not have separate suspension systems, and tires function also as the suspension. **Figure 1** shows a schematic of the tire and suspension on a vehicle.

Tire vibration may be caused by: (i) road irregularities, e.g. texture, potholes, bumps; (ii) control actions of drivers, e.g. steering, accelerating, and braking; and (iii) tire-wheel assembly characteristics, e.g., nonuniformity, tread pattern, and imbalance, In response to excitation, tires vibrate with the whole vehicle in the frequency range of 0.5–3 Hz, tires vibrate with the suspension and steering systems at 10–30 Hz, and tires vibrate as a flexible body on a relatively rigid wheel at 30–300 Hz. To these we can add vibration of tire parts, such as tread lugs at 1000–4000 Hz, and vibration of the air in the cavity, starting from 150–200 Hz, depending on tire size.

Tire vibration response can be described as a combination of its natural modes, each with its own frequency, shape, and damping. Tire vibration cannot be avoided: the tire is supposed to flex along with the suspension, isolating the vehicle from the road, but the vibration can and should be controlled, to assure the optimal performance of a given vehicle. Tire vibration may be controlled by design or by changing tire boundary and operating conditions.

Tire vibrations are studied by testing and modeling of both free and constrained tire-wheel assemblies on special test rigs, as well as on vehicles. Knowledge of tire vibration characteristics is important in predicting, evaluating, and modifying tire features to obtain the desired on-vehicle performance.

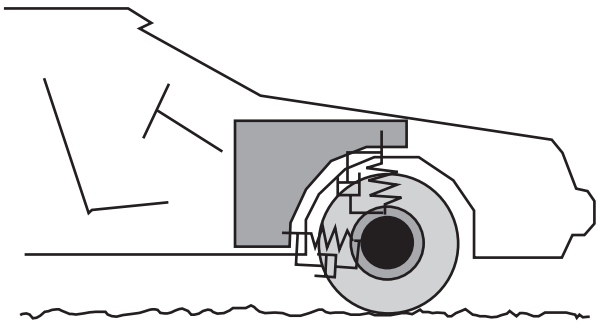


Figure 1 Tire, wheel, and suspension on vehicle.

Sources of Tire Vibration

The main sources of tire vibration are road irregularities, tire-wheel assembly imbalance, and tire-wheel nonuniformity. Drivers' inputs of accelerating, braking, and steering are of secondary importance.

Road Irregularities

Road irregularities can be continuous or discrete. The continuous ones relate to the texture and waviness of the road surface. The discrete ones are bumps, potholes, seams, and patches. The amplitudes and frequency content of the road-related excitation largely depend on the geometry of the road irregularities and the speed of the tire. In general, the waviness of the road will produce low-frequency (below 20 Hz) excitation, the surface texture will produce higher-frequency (above 100 Hz) continuous random excitation, and transient events will produce wide-band (0–2000 Hz) excitation.

Tire–Wheel Imbalance

A tire–wheel assembly can have imbalance, as a result of uneven mass or inertia distribution with respect to the assembly's center of mass (static imbalance) or axis of rotation (dynamic imbalance). Static imbalance will create centrifugal forces in vertical and longitudinal directions of the vehicle, while dynamic imbalance will create aligning and overturning moments with respect to the vertical and longitdinal axes. Frequency of imbalance-related excitation is once per revolution of the tire–wheel assembly, and it depends on vehicle speed and effective rolling radius of tire At 60 mph for passenger tires, the frequency of imbalance-related vibration may vary from 8 to 12 Hz, depending on the tire size.

Tire–Wheel Nonuniformity

Both the tire and the wheel can slow geometrical nonuniformity or run-out. A tire can also have stiffness variation, tread periodicity, and global and local mass irregularities. The tire–wheel nonuniformity produces periodic excitation, synchronous with the tire rotation in vertical, longitudinal, and lateral directions, as well as three moments about the vertical, longitudinal, and lateral axes. Nouniformity-related excitation consists of harmonic components whose frequencies are multiples of the tire rotation frequency. Harmonics 1–10 typically produce tactile vibration, while higher harmonics related to tread periodicity can produce audible vibration.

Driver Inputs

Driver inputs that excite tire vibrations are accelerating the vehicle, braking, and steering maneuvers. Amplitude levels and frequency content of these inputs largely depend on the vehicle speed, and the severity of the driver's actions. Sudden accelerating and braking can produce excitation frequencies up to 200 Hz, while steering maneuvers can produce much lower excitation up to 4 Hz.

Tire–Vehicle Dynamics System

Tire Functions and Construction

Functionally, the tire is the only component that connects the vehicle to the road, providing support, traction, braking, and steering, and serving as a cushion against road irregularities. In passenger cars and trucks, the tire is a part of the vehicle suspension system. In tractors and off-the-road vehicles, the tire is the suspension.

Geometrically, the tire is a toroidal shell, attached to a relatively rigid wheel and stiffened by inflation pressure in the tire's inner cavity.

Physically, the tire is a complex engineering product. The main functional components of a tire are shown in **Figure 2**. Steel cable beads anchor the tire to the rim. an inner liner of rubber holds the pressurized gas in the cavity. Flexible sidewalls of fabric and rubber provide the cushion for a comfortable ride. Belts of high tensile strength maintain a flat footprint for good traction, braking, handling, and treadwear. Finally, a rubber tread provides firm contact with the road.

Dynamically the tire is a flexible, nonstretchable ring on an elastic foundation. The inertial properties of a tire are dominated by mass distribution of the tread and belts. Its stiffness is controlled by inflation pressure, but is also influenced by the load, tire shape, material properties, and design. Tire damping is a combination of two mechanisms: viscous and hysteretic. Both the stiffness and damping of a tire depend on inflation pressure, load, and speed. A tire also acts as a nonlinear spring, softening with increased amplitudes but stiffening with increased frequency of excitation.

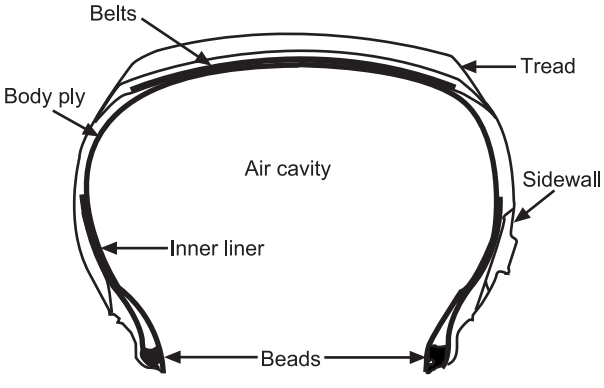


Figure 2 Main functional components of the tire.

Vehicle and Suspension System

In its simples form, the vehicle can be thought of as a rigid body on a suspension comprising a mass, spring, and damper. The tire can then be attached to a vehicle model as a mass and spring. In this fundamental approach, the tire/vehicle system exhibits four main rigid-body, or sprung-mass modes of vibration, and two suspension or unsprung-mass modes. The vehicle modes of bounce, pitch, roll, and yaw are shown in **Figure 3A**. With the exception of the yaw mode, the tire's contribution and participation in the rigid body modes is minimal, since its stiffness acts in series with the much softer suspension spring. However, in the case of the suspension modes, wheel hop and axle tramp, **Figure 3B**, the tire's mass and stiffness are key factors influencing the frequency of the suspension modes.

As the depth of study into tire/vehicle vibration increases, this simple representation must be replaced with more rigorous models in which the flexibility of the vehicle body/frame and local vehicle modes are included. **Table 1** shows frequency ranges of the main tire-related vibration modes of a typical front-wheel-drive vehicle.

The frequencies of modes are typical for an independent front suspension, and may be different for the rear suspension, but the main point to make here is: there is a group of modes of the suspension system and tire in the range 10–100 Hz. These modes cannot be eliminated, but vibration response, resulting from a combination of these modes, can be reduced by adding damping to the system, or by shifting the modal frequencies by stiffness or inertia changes.

Table 1 Tire-related vibration modes of a typical front-wheel-drive vehicle

Vibration mode	*Frequency range (Hz)*
Vehicle, bounce	1–1.2
Vehicle, pitch	1.2–1.5
Vehicle, roll	1.5–2.0
Vertical hop of suspension	12–16
Fore–Aft of suspension	14–22
Yaw of suspension	20–30
Tire on wheel first fore–aft	30–45
Tire vertical	65–100
Tire second fore–aft	75–110

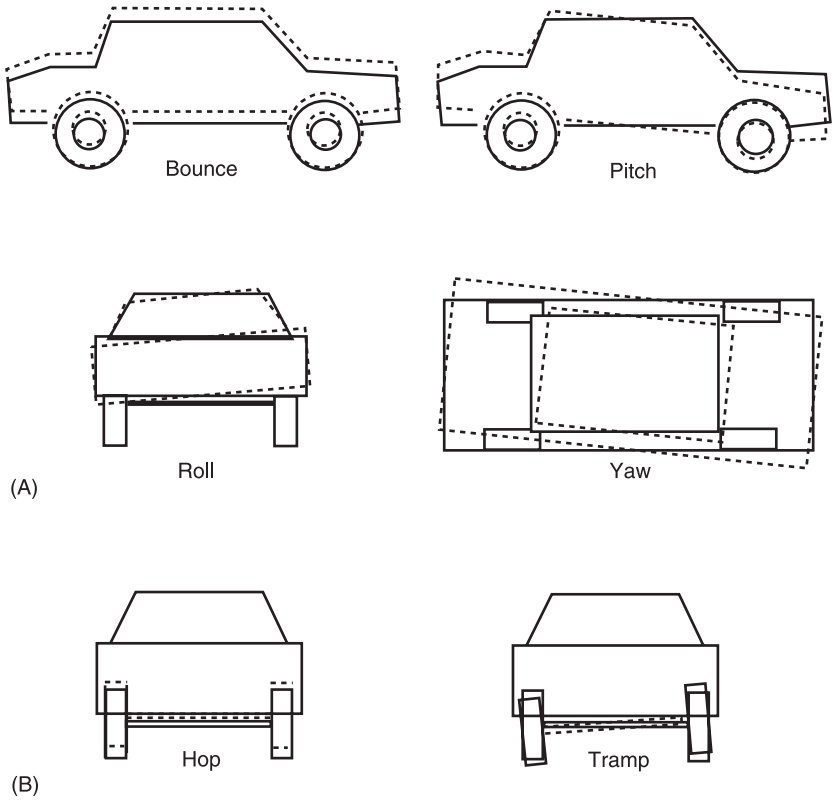


Figure 3 (A) Vehicle modes (sprung mass). (B) Suspension modes (unsprung mass).

In practice, not only is it necessary to separate tire-suspension modes from each other, but also from the modes of other vehicle components, which may be excited during vehicle operation.

Tire and Wheel System

In its simplest form, the tire and wheel assembly can be thought of as a mass on a spring attached to the ground in the vertical direction. This simple one-dimensional model is often used as a first-cut for predicting the fundamental suspension and rigid-body vehicle modes. However, as the frequency of interest increases, more detail is needed about the tire and wheel assembly.

The stiffness of the tire in the lateral and longitudinal directions must also be known and is usually obtained from tests. Tire stiffness in these two directions is found to be more sensitive to speed than is the vertical spring rate. The build-up of a cornering force as the tire rolls provides additional lateral stiffness and must be included in vehicle handling models.

For investigations involving vehicle ride, the lumped mass and spring representation of the tire is limited to frequency responses below 30 Hz. About these primary vehicle and suspension frequencies the vibration of the tire is controlled by its mass and stiffness distribution. In other words, the tire has to be represented as a flexible ring on an elastic foundation.

Tire Vibration Responses

Tire vibration responses include vibrations of the tire with the whole vehicle (0.5–3 Hz), tire vibrations with the vehicle's suspension and steering systems (10–30 Hz), and tire vibrations within the tire–wheel assembly itself (30–300 Hz). Special cases include vibrations of tread lugs, and air cavity resonance.

At the lower frequencies, 0.5–3 Hz, a tire vibrates as a spring and damper, participating in the vehicle's bounce, pitch, roll, and yaw motions. A Tire vibrates with the suspension and steering system in the range 10–30 Hz, participating in the vertical wheel hop, axle tramp, fore–aft, lateral, and steer modes. As a part of the tire-wheel assembly, the tire vibrates as a flexible ring, made up of the tread and belt package, elastically connected to the wheel and the road. The ring modes progress from the predominantly rigid body below 100 Hz, when the ring moves relative to the wheel in vertical, torsion, fore–aft, and steer directions, to the elastic modes above 100 Hz, where peaks and valleys are formed around the tire's circumference and across the tire's meridian.

Vibration modes of tires are characteristic displacement patterns, described by modal frequency, damping ratio, and mode shape. Each mode shape is the result of two waves traveling in opposite directions around the circumference of the tire and interfering with each other. In lab studies, the source of these waves might be a shaker attached to the treadband.

By adjusting the frequency of the shaker, the wavelength of the travelling wave can be changed. When the wavelength, or an integer number of wavelengths matches the circumference of the tire, reinforcement occurs at the excitation point and the vibration pattern amplifies. The interference of the two opposing traveling waves results in the creation of a stationary mode shape pattern.

In practice, typical vibration response is a combination of several modes, but depending on excitation, some modes can dominate the response. Vibration modes of tires are influenced by the following conditions: tire-road contact (free or loaded), wheel axle mount (free, pinned, or fixed), and operating parameters (inflation pressure, load, and speed).

Vehicle Rigid-body Modes (0.5–3 Hz)

The tire flexes as a part of the vehicle corner spring, while the vehicle body is bouncing, pitching, rolling, and yawing. In most of these modes of vehicle vibration, the tire and the suspension spring work in series, and the resulting effective stiffness of the vehicle corner is calculated as follows:

$$k_e = \frac{k_s k_t}{k_s + k_t} \quad [1]$$

where:

k_e = the effective stiffness of the vehicle corner
k_s = the stiffness of the vehicle suspension
k_t = the stiffness of the tire

Dividing by the tire stiffness K_t, and remembering that the tire is 5–10 times stiffer than the suspension, shows that K_e is dominated by the suspension spring stiffness:

$$k_e = \frac{k_s}{1 + k_s/k_t} \quad [2]$$

The frequencies of vehicle rigid-body modes depend on the vehicle's inertia, location of its center of mass, and the positions of the wheel centers. For example, the pitch mode frequency f_p of a vehicle can be calculated as:

$$f_p = \frac{1}{2\pi}\sqrt{\frac{k_{ef}a^2 + k_{er}b^2}{I}} \quad [3]$$

where:

k_{ef} = effective front stiffness
k_{er} = effective rear stiffness
a = the distance from the front axle to the vehicle's center of mass
b = the distance from the rear axle to the vehicle's center of mass
I = the moment of inertia of the vehicle body with respect to the lateral axis crossing the center of mass.

Tire–Suspension Mods (10–30 Hz)

The tire, wheel, brake, attached elements of the driving and steering systems (unsprung mass), vibrate between the ground and the vehicle body (sprung mass). The tire and suspension spring work in parallel, and the tire, which is 5–10 times stiffer than the suspension spring, dominates the process. The frequency of the resulting wheel hop vibration is calculated by the following formula:

$$f_{hop} = \frac{1}{2\pi}\sqrt{\frac{k_t + k_s}{m_u}} \quad [4]$$

where:

k_t = the spring rate of tire
k_s = the spring rate of suspension
m_u = the unsprung mass

Rigid Ring Modes (>100 Hz)

The lowest-frequency tire modes are descriptively called rigid ring modes. These generally display a rigid-body motion of the belt-tread ring with respect to the wheel. These modes usually occur below 100 Hz. They represent translation and rotation with respect to the three axes and are named in accordance: first Vertical, first Lateral, first Steer and first Torsional (**Figure 4**).

Because of the global nature of the tire movement about the wheel, these rigid ring modes produce a significant force at the wheel. A spectrum of road data in **Figure 5** shows peak spindle responses at the frequencies of two suspension modes (wheel hop and fore–aft) and two rigid ring modes (torsional and vertical).

Flexible Ring Modes (>100 Hz)

The next group of tire modes typically occurs above 100 Hz. They involve bending of the tread band in the

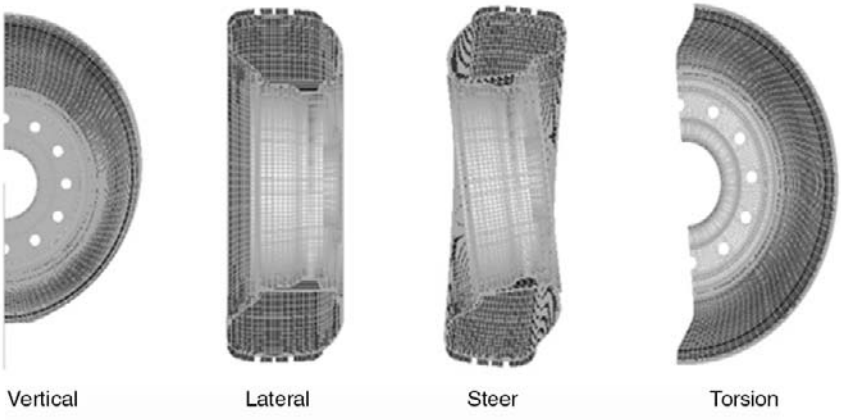


Figure 4 Rigid ring tire modes.

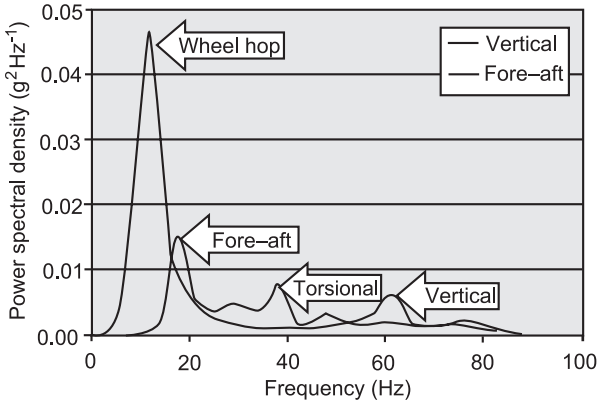


Figure 5 Vibration spectra of vehicle road response.

radial direction producing a series of peaks and valleys around the tire. Some of these modes are shown in **Figure 6**, and are identified by the number of full wavelengths around the tire. The lobe count increases by one approximately every 20-30 Hz, thus at 300 Hz, the tire will have as many as 10 or more lobes around the tread band.

The frequency of these modes can be found from the following general equation of a flexible ring on an elastic foundation, derived from the classical wave equation:

$$EI\frac{\partial^4\xi}{\partial x^4} - N\frac{\partial^2\xi}{\partial x^2} + k\xi = -m\frac{\partial^2\xi}{\partial t^2} \qquad [5]$$

where:

ξ = the deflection of the ring vibration
x = the independent circumference coordinate
t = the time
EI = the bending stiffness of the ring
N = the axial preloading
k = the stiffness of the elastic foundation
m = the mass per unit length of the ring

Solving the wave eqn [5] we obtain the formula for the natural frequencies f_n of the elastic ring, as follows:

$$f_n = \frac{1}{2\pi R^2}\sqrt{\frac{EI\,n^4 + N\,R^2n^2 + kR^4}{m}} \qquad [6]$$

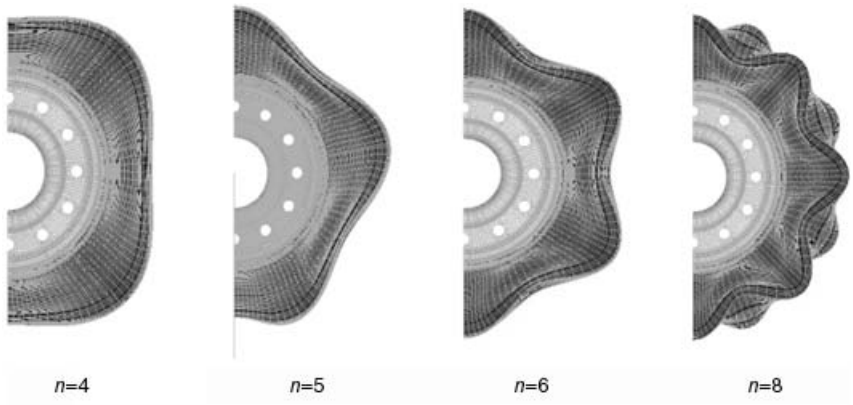


Figure 6 Flexible ring modes of tire.

where:

n = the mode number
R = the radius of the ring

Tire flexible ring modes are not significantly affected by the wheel boundary condition since they are symmetric about the wheel, resulting in little or no involvement of the wheel in the mode shapes. Because of this, flexible ring modes do not significantly amplify the road vibration transmitted to the vehicle as do the rigid ring modes. The frequencies of the rigid ring modes can be approximated from eqn [6], using the wave number $n = 0$.

While flexible ring modes may not significantly influence spindle vibration, they can impact the noise radiation pattern. Acoustic holography can be used to measure the noise radiation pattern of tires, as shown in **Figure 7A**. This noise radiation has the same pattern as the corresponding flexible ring mode, as measured by laser Doppler vibrometer, as shown in **Figure 7B**. In general, as the mode number increases, the radiation efficiency decreases, making flexible ring modes less important to tire noise radiation at higher frequencies.

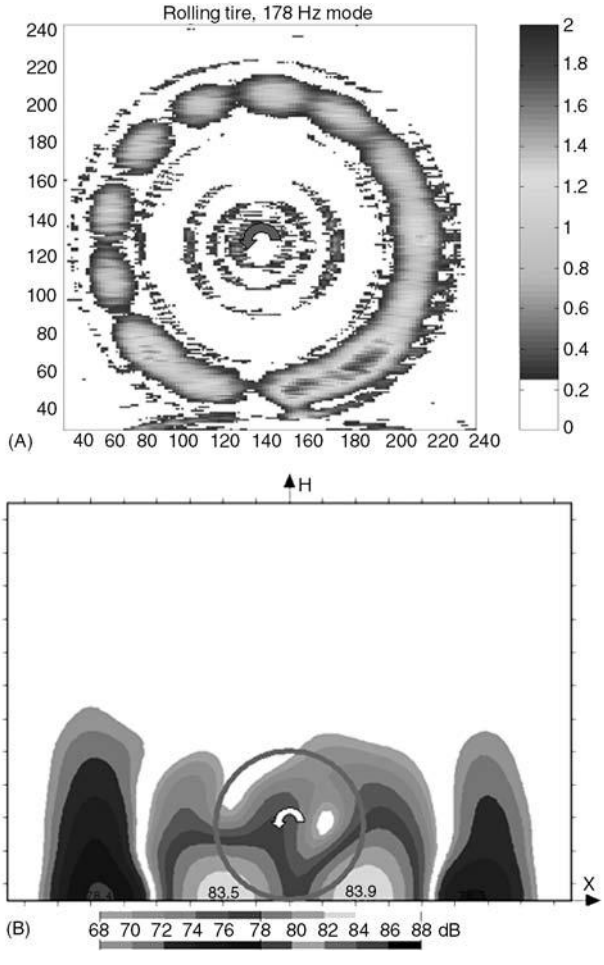


Figure 7 (A) Surface vibration map of a rolling tire. (B) Hologram of tire noise radiation.

Cross-sectional (Bead-to-Bead) Modes (>100 Hz)

As vibration frequency increases above 100 Hz, the tire begins to act as a flexible membrane in the cross-sectional (meridian) plane in addition to the circumferential (equatorial) plane. This produces a series of peaks and valleys across the tire. A few of these modes are shown in **Figure 8**, and are identified by the number of half-wavelengths from bead to bead. The half-wavelength count, m, increases by one approximately every 100 Hz. Thus at 1000 Hz, the tire may have 10 or more half-wavelengths in its cross-section.

These cross-sectional modes, sometimes referred to as meridian modes, can influence the amount of vibration transmitted to the wheel. This is demonstrated in the sample of road data in **Figure 9**, where the peaks of 10, 350, 500, and 800 Hz are related to the $m = 3$, 5, 7, and 9 modes. Above 1100 Hz, the meridian modes lose their effect on noise generation.

First acoustic Cavity Mode (200–250 Hz)

The pressurized gas inside the tire not only provides the stiffness for the ring and cross-section modes, it also acts at the medium for the propagation of acoustic waves in the internal chamber of the tire–wheel assembly. This tire cavity can be thought of as an organ pipe wrapped into a circle. The length of this organ pipe can be approximated using the radius of the tire at mid-sidewall.

The frequency of the first tire acoustic cavity mode can be estimated using a basic equation of the fundamental frequency of the standing wave in the organ pipe, as follows:

$$f_c = \frac{c}{L_c} = \frac{c}{2\pi R_c} \qquad [7]$$

where:

c = the speed of sound in the tire cavity gas
L_c = the effective length of the tire cavity
R_c = the effective radius of the tire cavity

The first acoustic cavity mode is typically in the range of 200–250 Hz, depending on the size of the tire. These acoustic modes are identified by the number of wavelengths around the tire. This wavelength count increases by one approximately every 200 Hz.

Because of the global and nonsymmetric nature of the first vertical and fore–aft acoustic cavity modes,

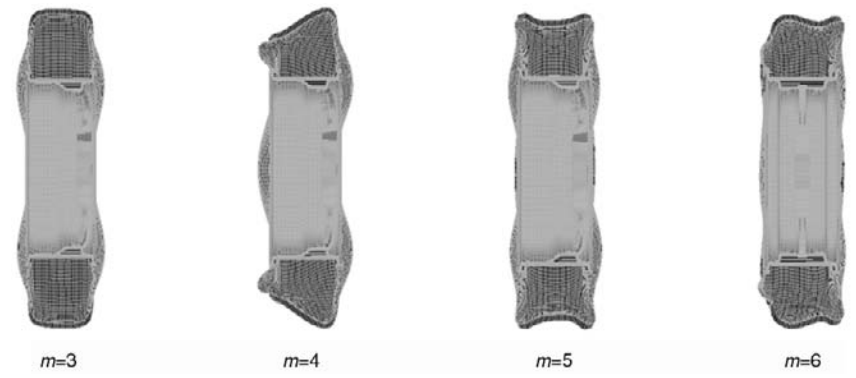


Figure 8 Meridian vibration modes of tire.

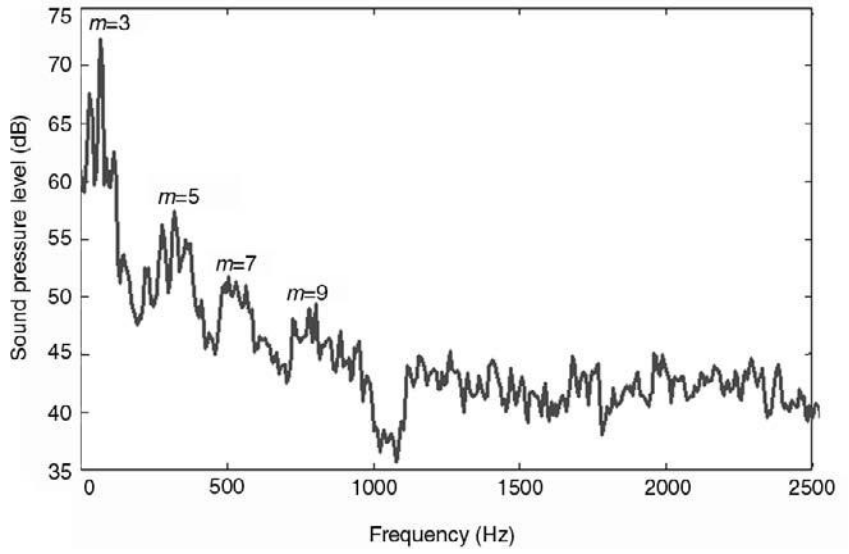


Figure 9 Contribution of vibration modes to tire noise.

these modes can produce significant spindle response, as seen in the lightly damped peaks around 230 Hz in **Figure 10**. This may be amplified if the air cavity mode is close to the wheel rocking mode, resulting in a highly tonal noise entering the vehicle cabin. The frequency of these peaks can be shifted by changing the gas in the tire, e.g., from air to helium.

Standing Wave

One interesting and potentially destructive tire vibration is the standing wave. This phenomenon can occur at high-speed operation of the loaded tire if the speed of the tire matches the speed of a displacement wave propagation in the tire (recall tire mode shapes are the result of traveling waves). At this critical speed, the footprint deflection serves to reinforce the mode shape, whose traveling wave speed matches that of the tire.

To help understand this, think of a string being excited laterally at one end. A wave can be observed traveling along the string. If an observer was able to slide a finger along the string just behind the wave, at the exact same speed as the traveling wave, he could in effect help push the wave along the string. If he goes slower or faster than the wave speed, he will destructively interfere with the traveling wave.

In the same way, the loaded spinning tire can be thought of as a stationary tire with the footprint traveling around it. When the speed of the footprint matches the speed of a traveling vibration wave, it will reinforce it. The result can be a standing wave at the trailing edge of the footprint.

The standing wave speed can be calculated for each mode number using the following equation:

$$v_n = \lambda f = \frac{2\pi R}{n} f \qquad [8]$$

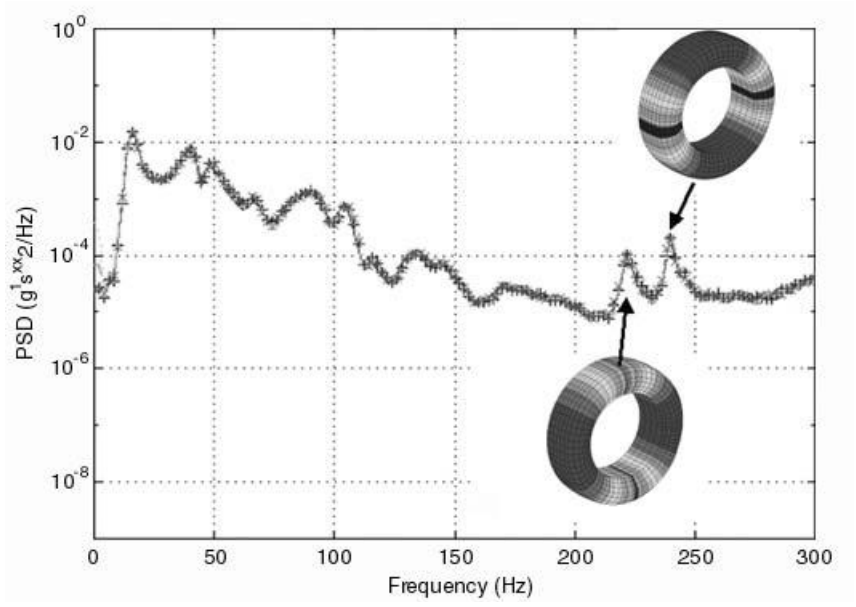


Figure 10 Acoustic cavity components of spindle vibration.

where:

v_n = the wave speed for mode n
R = the radius of the tire
λ = the wavelength
f = the frequency of mode n from eqn [6]

Applying this equation for $n = 1, 2, 3, \ldots$ the slowest wave speed analytically is found to correspond to $n = 7 - 9$.

Experimentally, standing waves typically have a wavelength similar to that of the seventh to ninth ring mode. Tests on a loaded, rolling tire confirm that these tire ring modes typically have the lowest wave speeds and are the first ones to be matched by the 'traveling' footprint as tire speed is increased. The effects of reaching the critical speed and forming the standing wave are a sharp increase in rolling resistance, overheating of the tire, and even possible tire failure. This is why, based on the lowest critical speed, each tire has a maximum speed of operation, which should not be exceeded by the driver.

Table 2 summarizes vibration modes of a topical passenger tire, including mode descriptions frequencies, and related negative effects on passenger comfort, or tire.

Influence of Design and Operating Conditions on Tire Vibration Frequencies

While all tires have the same general mode shapes as described in the previous section, natural frequencies are determined by the tire design and applied operating conditions. Tire design includes both physical dimensions and internal construction. Operating conditions include load, inflation, and speed as well as boundary conditions at the spindle and footprint. Modal frequency studies conducted over a wide range of tires have established general trends on how each of these factors shifts the frequency of tire modes. Some of these trends follow.

Physical Dimensions: Size and Shape

Typically, increasing the size of a tire will lower its modal frequencies. There are two reasons for this: (i) a larger tire will likely have more mass, thus lowering its natural frequency, and (ii) a larger tire will have a longer wavelength for a given mode shape, which for

Table 2 Typical passenger tire vibration modes, and their effect

Vibration mode	*Frequency (Hz)*	*Possible effect*
Suspension/tire first vertical	12–16	Ride discomfort described as shake
Suspension/tire first fore–aft	14–22	Ride discomfort described as shake
Tire second fore–aft	30–45	Tactile vibration and audible rumble
Tire second vertical	65–100	Tactile vibration
Tire third fore–aft	75–100	Tactile vibration
Tire ring modes	100–1000	Increased noise radiation
Tire first cavity	200–250	Tonal interior noise
Meridian plane modes	100, 350, 500 ...	Interior noise and vibration
Standing wave	7–9th ring mode	Increased rolling resistance, reduced durability

a constant traveling wave speed, means a lower frequency. In addition to size, the tire cross-sectional shape or aspect ratio of section height to width also affects tire frequencies. Lowering the tire profile typically increases modal frequencies due to a reduction of mass and an increase in stiffness from the shorter sidewall.

Tire Construction

Without getting into the details of tire construction, there are some major components in a tire that can be adjusted to shift modal frequencies. Changing the body cord angle will shift the frequencies of most torsion and vertical-type modes, while having minimal effect on lateral modes. Increasing the number of body or belt plies also will increase frequencies, since their stiffening effect outweighs their mass effect. Because there are as many as 100 components in a tire, the designer has numerous design options to facilitate shifting specific tire modal frequencies as a means of optimizing the tire to a specific vehicle. The rule of thumb for this tuning process is to avoid the coincidence of tire modes with those of the vehicle.

Operating Conditions: Inflation, Load, and Speed

While tire design can be used to shift the modal frequencies of a tire, a far greater influence on modal frequencies have the tire's operating conditions. Tire inflation pressure has the highest influence on the modal frequencies. Increased inflation pressure can increase modal frequencies roughly 1–2 Hz lbf in^{-2}. The only exception to this is the first steer mode of the tire, which reduces in frequency with increase in inflation due to shortening of the footprint length.

Increased tire load typically has a stiffening effect on a tire, causing frequencies to increase slightly. The increased footprint length also reduces the free circumference of the tire, resulting in a shorter wavelength (higher frequency) for mode shapes involving the tread band.

Interestingly, speed has an effect on modal frequencies at the onset of tire rolling, whereby modal frequencies typically drop 5–10% compared to the nonrolling tire. A further increase in speed has a stiffening effect, which shifts the tire frequencies higher.

Boundary Conditions

The natural frequencies of a tire are also influenced by the boundary conditions at the axle and at the footprint. If the axle is rigid, which is often the case for lab test fixtures, the frequencies of the tire will be higher than when the tire is mounted on a compliant spindle such as on a car. Additional modes are also introduced with the added degrees-of-freedom of the vehicle's spindle.

The presence of the footprint will also dramatically change the modal frequencies of the tire. As with increased load, when the tire is placed in contact with the ground, the free circumference length of the tire is reduced. This results in shorter wavelength mode shapes, which mean higher frequency if one assumes constant wave speed. All these factors and their effect on tire modal frequencies need to be understood in order to predict the tire road performance from the lab data.

Putting Tire Vibration Knowledge into Practice

In addition to its roles of providing support for the vehicle and directional control for the driver, the tire also serves to isolate the vehicle and driver from the irregularities of the road. Road inputs excite a variety of tire, spindle, and vehicle responses. The goal of the tire design is to minimize these vibrations. This can best be achieved by knowing what the natural frequencies of the tire and vehicle are, how they are affected by the boundary and operating conditions on the car, and then minimizing the interaction or coupling of the tire modes with those of the car.

Determining Tire Natural Frequencies

Two approaches are available for identifying the natural frequencies of a tire: experimental measurement and analytical modeling. The experimental measurement can be as simple as hitting an unloaded, mounted tire with an instrumented hammer and measuring its response, or it can be as complex as exciting the loaded, rolling tire on a test fixture and measuring spindle and/or surface vibrations. Peak responses in these frequency response functions identify the modal frequencies. The mode shape associated with each frequency can be identified through modal survey techniques. The effects of boundary and operating conditions on these frequencies can then be used to determine from the lab data how the tire will perform on the vehicle.

The second approach for identifying tire natural frequencies is analytical modeling. Like testing, tire models can be as simple as a mass on a spring, or can be as complex as a finite element model using thousands of degrees-of-freedom to represent the detailed construction of the tire. Accurate performance predictions typically require the use of the finite element model approach. The results from these complex models are put into an efficient 'modal model', and are attached to a vehicle model to predict ride performance. Much research is underway to improve the accuracy of these models and their computational efficiency.

Minimizing Tire/Vehicle System Vibration

Once the vibration properties of the tire are known through experimental or analytical means, the critical and final step is to minimize vehicle vibration by optimizing the combined tire–vehicle system. This optimization is guided by the simple rule of separating the tire modes from the vehicle modes. When natural frequencies of the tire match those of the vehicle, mode coupling occurs and the response is magnified beyond that of the individual components.

For this reason, the fundamental car modes are generally grouped below the frequencies of the suspension modes. Front suspension mode frequencies are designed to be slightly different from those of the rear suspension. Tire modes, particularly those below 100 Hz, are shifted to avoid coincidence with natural frequencies of the steering wheel, passenger compartment cavity, frame, and body/roof panels.

Due to the complex interactions of the tire and vehicle, which are also affected by the boundary conditions at the spindle and the operating conditions encountered, this optimization process is a combined effort of the tire and vehicle engineers. This article has covered only the tire vibration side of the information and the equations used by the tire engineer in this tuning process. Similar information is required on the vehicle side to achieve a successful match of the tire and vehicle systems.

Nomenclature

c	speed of sound
f	frequency
EI	bending stiffness
I	inertia
k	stiffness
L	length
M	mass
R	radius
t	time
λ	wavelength
ξ	deflection

See also: **Absorbers, active**; **Absorbers, vibration**; **Damping mounts**; **Ground transportation systems**; **Object oriented programming in FE analysis**; **Viscous damping**.

Further Reading

Clark SK (1975) *Mechanics of Pneumatic Tires*. Washington, DC: US Department of Transportation, NHTSA.

Gong S, Savkoor AR, Pacejka HB (1993) *The Influence of Boundary Conditions on the Vibration Transmission Properties of Tires*. SAE Paper 931280.

Potts GR and Csora TT (1975) Tire vibration studies: the state of the art. *Tire Science and Technology*, 3: 196–210.

Richards TR (1985) Modal analysis of tires relevant to vehicle system dynamics. *Proceedings of the 3rd International Modal Analysis Conference*, Orlando, Florida, USA.

Zegelaar PWA (1998) *The Dynamic Response of Tyres to Brake Torque Variations and Road Unevennesses*. Delft, the Netherlands: Delft University of Technology.

TOOL WEAR MONITORING

M Sidahmed, Université de Technologie de Compiègne, Compiègne, France

Copyright © 2001 Academic Press

doi:10.1006/rwvb.2001.0071

Controlled numerical center (CNC) machine tools in flexible manufacturing require the machining equipment to operate without human involvement. Online monitoring is then of importance to avoid machine unavailability and loss of product quality. Tool wear monitoring is a major factor in ensuring the quality of the machined products. Worn tools produce poor quality surfaces. Tool breakage can result in catastrophic failures resulting in significant down times and loss of productivity. Real-time and online systems process monitoring would improve the production considerably. A tremendous amount of work has been carried out, in order to develop reliable tool wear monitoring systems for various cutting processes (turning, drilling, and milling). Monitoring and diagnosis systems for industrial purposes have been available commercially since 1990, but they are still not widespread because they are often limited to specific machines and operating conditions.

The problem is made difficult by the physical complexity of the cutting process, the variable running conditions, and industrial constraints such as the online requirement or the costs of the sensors and monitoring systems.

Research and development has been carried out in various areas, discussed below.

Sensor Technology

We may distinguish two kinds of sensor technology that have been proposed to measure physical parameters useful for tool wear monitoring: first, direct methods which include: optical, radioactive and other methods, deliver a direct measure of the wear. They suffer from the difficulty of carrying out these techniques during the cutting operation. Secondly, indirect methods use sensors delivering signals related to the tool wear via signal processing or data analysis. 'Symptoms' related to the tool breakage or wear need to be determined. Several physical parameters have been used.

- Acoustic emission uses the fact that deformation, material removal, and the stress in the metal that occurs during the cutting operation generates acoustic waves at high frequencies (100 kHz to a few MHz) that may be amplified by specific piezoelectric sensors. Experience has shown good results when dealing with tool breakage. Wear monitoring is more difficult, even with advanced data analysis techniques.
- Force measurement is best related to the physical phenomena tool wear. Many researchers have investigated the dynamics of the cutting process, especially the relationship between components of the cutting forces and tool wear. This has led to various monitoring techniques, including model-based methods (observer methods), in order to separate the effects of the cutting operation from the effects of wear. Force measurement is, however, complex to implement, especially on machines that have already been built.
- Vibrations are increasingly used when associated with advanced signal processing techniques. The cutting process generates forces, and indeed vibrations, that may be measured more easily than the forces with nonintrusive sensors. Models associated with the operating conditions (feed, and depth of cut) are slightly more difficult to derive.
- Spindle currents and power were found to be sensitive to the torque variations and then to the cutting process (force variations) and finally to the tool wear.

Data Analysis Techniques

Various methods have been applied with varying success. Most of the methods used in the diagnostics of rotating machines may be applied for tool wear monitoring. The main problems are due to the changing of operating conditions inherent in the machine tools. To overcome these problems, pattern recognition analysis techniques are used (neural networks, fuzzy diagnostic techniques). Signal properties involve the response of structures (including sensors) whose dynamic properties are not easy to predict. They are excited by periodic (sometimes intermittent as in milling) forces. Their spectral content is therefore quite complex.

Physical Modeling

Research is continuing on dynamic modeling of the cutting process. Progress in automatic control and diagnostic techniques allows us to deal with complex nonlinear models. The interest in such an approach is to be able to derive monitoring systems which take account of the operating conditions directly connected to the machine tool controller. The vibration process to be modeled is different from the one geared to the dynamic properties of the machine tool structure. There the possibility of instability (known as chatter) is of interest.

See also: **Data acquisition**; **Diagnostics and condition monitoring, basic concepts**; **Model updating and validating**; **Neural networks, diagnostic applications**; **Signal processing, model based methods**.

Further Reading

Braun S, Lenz E (1986) *Machine-tool Monitoring, Mechanical Signature Analysis*. London: Academic Press.

Dan L, Mathew J (1990) Tool wear and failure monitoring techniques for turning – a review. *International Journal of Machine Tools Manufacturing* 30(4).

Dimla JR, Lister PM, Leighton NJ (1997) Neural network solutions to the tool condition monitoring problem in metal cutting: a critical review. *International Journal of Machine Tools Manufacturing* 37(9): 1219–1241.

Jaume D, Verge M, Rault A (1990) A model based diagnostics in machine tool: application to the milling cutting process. *Annals of the CIRP* 39(1): 443–446.

Oraby SE, Hayhurst DR (1991) Development of models for tool wear force relationships in metal cutting. *International Journal of Mechanical Sciences* 33(2): 125–138.

Park JJ, Ulsoy AG (1993) On-line flank wear estimation using an adaptive observer and computer vision, Part 1: theory. *ASME Journal of Engineering for Industry* 115: 30–36.

Tansel IN, McLaughlin C (1993) Detection of tool breakage in milling operation – 1 the time series approach. *International Journal of Machine Tools Manufacturing* 33(4): 545–558.

Tansel IN, McLaughlin C (1993) Detection of tool breakage in milling operation – 2 the neural network approach. *International Journal of Machine Tools Manufacturing* 33(4).

Tlusty J, McNeil P (1975) Dynamics of cutting forces in end milling. *Annals of the CIRP* 24(1): 21–25.

TRANSDUCERS FOR ABSOLUTE MOTION

K G McConnell, Iowa State University, Ames, IA, USA

Copyright © 2001 Academic Press

doi:10.1006/rwvb.2001.0103

Often it is inconvenient to measure motion and/or forces relative to a fixed reference, for the fixed reference may not be available, as in the case of vibration and forces in a rocket launch vehicle. This need to measure these quantities without a fixed reference has led to the development of seismic instruments. The general model and parameters that govern the mechanical behavior of these instruments are presented first. Then, this model is extended to describe the behavior of seismic displacement transducers, velocity transducers, acceleration transducers, and force and pressure transducers. The fact that force and pressure transducers respond to external vibration as well as force and/or pressure is often overlooked both in practice and in the literature. In this entry, force and pressure transducers are classified as seismic instruments so that this potential sensitivity to vibration motion is clear for all users.

General Model

The general elements of the two-degree-of-freedom model that make up a seismic instrument are shown in **Figure 1**. There is a seismic mass, m, a base mass, m_b, an external force, $F(t)$, that is applied to the seismic mass, and an external force, $F_b(t)$, that is applied to the base mass. The instrument is constructed so that the seismic mass motion, $y(t)$, and the base mass motion, $x(t)$, are different due to the instrument's structural stiffness, k, and damping, c.

The free-body diagram in **Figure 2** shows the forces that act on the seismic mass when it is assumed that $y > x$ and $\dot{y} > \dot{x}$. Newton's second law gives the differential equation of motion for the seismic mass in two different forms:

$$m\ddot{z} + c\dot{z} + kz = f(t) - m\ddot{x} \qquad [1]$$

and:

$$c\dot{z} + kz = f(t) - m\ddot{y} \qquad [2]$$

where $z = y - x$ and its derivatives represent the relative motion between the seismic mass and the base. It is clear that the relative motion is dependent on the type of excitation relative to the transducer characteristics. In eqn [1], the external force is altered by the seismic mass inertia force due to base acceleration ($m\ddot{x}$), while in eqn [2] the external force is altered by the seismic mass inertia force due to seismic mass acceleration ($m\ddot{y}$). These two equations will be used to develop the behavior of each type of seismic sensor.

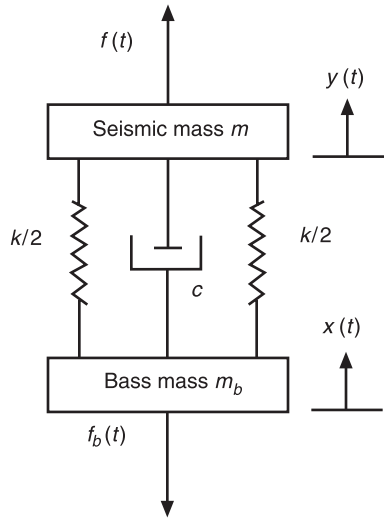


Figure 1 Two-degree-of-freedom model of a seismic-type instrument showing main transducer elements of spring, damper, masses, and coordinates. Reproduced with permission from Dally JW, Riley WF and McConnell KG (1993) *Instrumentation for Engineering Measurements*, 2nd edn. New York: John Wiley.

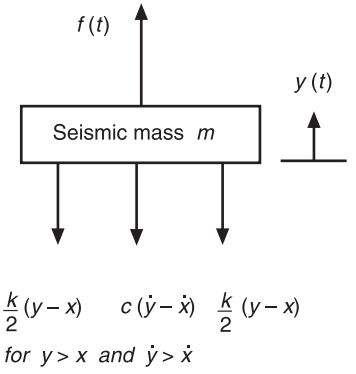


Figure 2 Free-body diagram of the seismic mass. Reproduced with permission From Dally JW, Riley WF and McConnell KG (1993) *Instrumentation for Engineering Measurements*, 2nd edn. New York: John Wiley.

Seismic Displacement Sensor

Eqn [1] is used to describe the behavior of a seismic displacement sensor when the external force, $f(t)$, is assumed to be zero. This is generally true since the seismic mass is covered to protect it from all external forces, with the exception of gravity force, mg. For illustration purposes, assume that the base motion is sinusoidal and given by:

$$x = X_o e^{j\omega t},\ \dot{x} = j\omega X_o e^{j\omega t},\ \text{and}\ \ddot{x} = -\omega^2 X_o e^{j\omega t} \quad [3]$$

where X_o is the magnitude of the base motion and $j = \sqrt{-1}$. For sinusoidal excitations, the responses will be harmonic with values dependent on frequency ω. Hence, in the following equations, the frequency ω (or the normalized frequency r) will be mixed with time domain expressions to indicate that the time domain responses depend on their frequency content. The corresponding relative motion, $z(t)$, at frequency ω becomes:

$$z(t) = Z_o e^{j\omega t} \qquad Z_o(\omega) = H(\omega) X_o(\omega) \qquad [4]$$

where $H(\omega)$ is the transducer's mechanical frequency response function (FRF) that is given by:

$$H(\omega) = \frac{m\omega^2}{k - m\omega^2 + jc\omega} \qquad [5]$$

$H(\omega)$ is seen to alter both the magnitude and phase of the relative motion, $z(t)$, compared to the input base motion, $x(t)$, at each frequency ω. $H(\omega)$ can be written in a dimensionless form as:

$$H(r) = \frac{r^2}{1 - r^2 + j2\zeta r} = \frac{r^2}{\sqrt{(1 - r^2)^2 + (2\zeta r)^2}} e^{-j\phi} \qquad [6]$$

where $\omega_n = \sqrt{k/m}$ is the natural frequency, $\zeta = c/2\sqrt{km}$ is the dimensionless damping ratio, $r = \omega/\omega_n$ is the dimensionless frequency ratio, and $\tan(\phi) = (2\zeta r)/(1 - r^2)$ is the phase angle of the output motion $z(t)$ relative to the input motion $x(t)$.

The magnitude and phase from eqn [6] are plotted in **Figure 3** for three values of damping ratio ζ (0.05, 0.50, and 0.650). It is clear from the magnitude plot

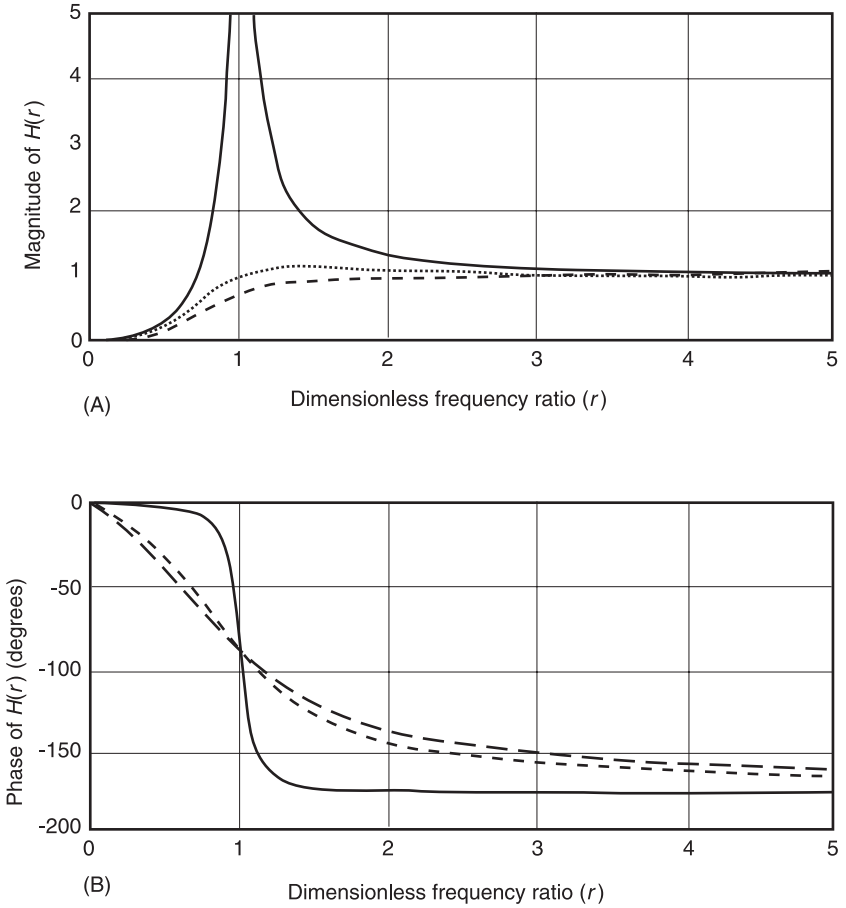


Figure 3 (A) Magnitude and (B) phase vs dimensionless frequency ratio frequency response function $H(r)$ for a displacement-type of seismic transducer for three damping ratios of 0.05 (continuous line), 0.50 (dotted line), and 0.65 (dashed line).

that the frequency ratio must be greater than 2 if the magnitude is to be reasonably correct. It is also clear that a damping ratio of approximately 0.650 gives the best magnitude results. The phase plot shows that the lightly damped curve gives the most correct phase angles at the lower frequencies while the more heavily damped response will have significant phase errors for frequency ratios approaching a value of 5. The physical meaning of these curves is that the seismic displacement transducer works by having the seismic mass essentially remain stationary while the base moves back and forth relative to it. This means that the relative motion z is the same as the base motion. The conditions required are that $r \ll 1$ and the phase angle $\phi \approx 180$ deg . To achieve this goal, the instrument must have a low natural frequency, soft springs, a large seismic mass, and a large rattle space for the relative motion. The sensor used to measure the relative motion is usually either a strain gauge or a linear voltage differential transformer. All of these requirements lead to a relatively large and massive transducer that is severely limited by the lowest frequency that can be measured.

Seismic Velocity Transducers

The seismic velocity transducer is the same as a seismic displacement transducer except that the sensing element is a velocity-sensitive electromagnetic sensor. Then, the time derivative of eqn [4] gives:

$$\dot{z}(t) = j\omega Z_o e^{j\omega t}$$
$$j\omega Z_o = H(\omega)(j\omega X_o) = H(\omega)\dot{x}(t) \qquad [7]$$

where $H(\omega)$ is the same as given by eqn [6] above. It is clear that if $r \gg 1$ and $\phi \approx 180^\circ$, then eqn [7] shows that $\dot{z}(t) \approx -\dot{x}(t)$. The seismic velocity transducer suffers from the same large size and mass as the seismic displacement transducer.

Seismic Accelerometer

The seismic accelerometer has the same transducer model given by eqn [4], which can be rewritten as:

$$z(t) = \frac{-m(-\omega^2 X_o)}{k - m\omega^2 + jc\omega} e^{j\omega t} = H_a(\omega) a_o e^{j\omega t}$$
$$= \left[\frac{H_a(r)}{\omega_n^2}\right] a_o e^{j\omega t} \qquad [8]$$

where $a_o = \omega^2 X_o$ is the magnitude of the sinusoidal acceleration. The accelerometer's mechanical FRF, $H_a(\omega)$, has two main parts: $1/\omega_n^2$ and $H_a(r)$. The $1/\omega_n^2$ term shows how the relative motion, z, decreases with increasing natural frequency so that high natural frequency shock accelerometers ($f_n \approx 200$ kHz) have approximately 10 times lower sensitivity than general-purpose accelerometers ($f_n \approx 60$ kHz). Hence, the general rule is that higher natural frequency accelerometers are significantly less sensitive than lower natural frequency accelerometers of approximately the same physical size.

The accelerometer's mechanical FRF, $H_a(r)$, is given by:

$$H_a(r) = \frac{1}{1 - r^2 + j2\zeta r} \qquad [9]$$

where the dimensionless frequency ratio r and damping ratio ζ are defined above. The magnitude and phase characteristics of eqn [9] are shown in **Figure 4**. It is seen that the magnitude and phase are nearly constant at unity and 0° for values of $r < 0.20$ for the case of lightest damping. The maximum magnitude error is about 5% when $r = 0.20$ in this case. When the damping is about 0.650, the phase shift is nearly linear with frequency for values of $r < 1.0$ and the magnitude is nearly unity ($\pm 5\%$) up to $r = 0.72$. Often a great deal of fuss is made over this fact that 65–70% damping gives the best FRF. The problem with this concept is that it is difficult to achieve the required amount of damping that is basically temperature-independent and add little to the mass of the transducer. It is desirable to have a very high natural frequency with small damping since the usable frequency range is about 0.20 of the natural frequency. This means that the spring must be very stiff and the seismic mass must be small. In this frequency range, eqn [8] shows that the output motion z is related to the acceleration by:

$$z(t) = \frac{-ma(t)}{k} = \frac{-a(t)}{\omega_n^2} \qquad [10]$$

Eqn [10] clearly shows that the relative motion is directly dependent on the inertia force divided by the transducer's spring constant, k. These terms combine to show that sensitivity decreases with the square of the natural frequency, ω_n.

Seismic Force Transducers

Seismic force transducers are governed by eqns [1] and [2] where it is desired to measure the external force, $f(t)$, that acts on the seismic mass, m. It is clear from these two equations that the relative motion, $z(t)$, depends on both inputs, $f(t)$, and an inertial force term. These inertial terms depend on the seismic mass m and either the seismic acceleration $\ddot{y}$ or the base acceleration $\ddot{x}$. The seismic mass, m, often depends on the force transducer application since

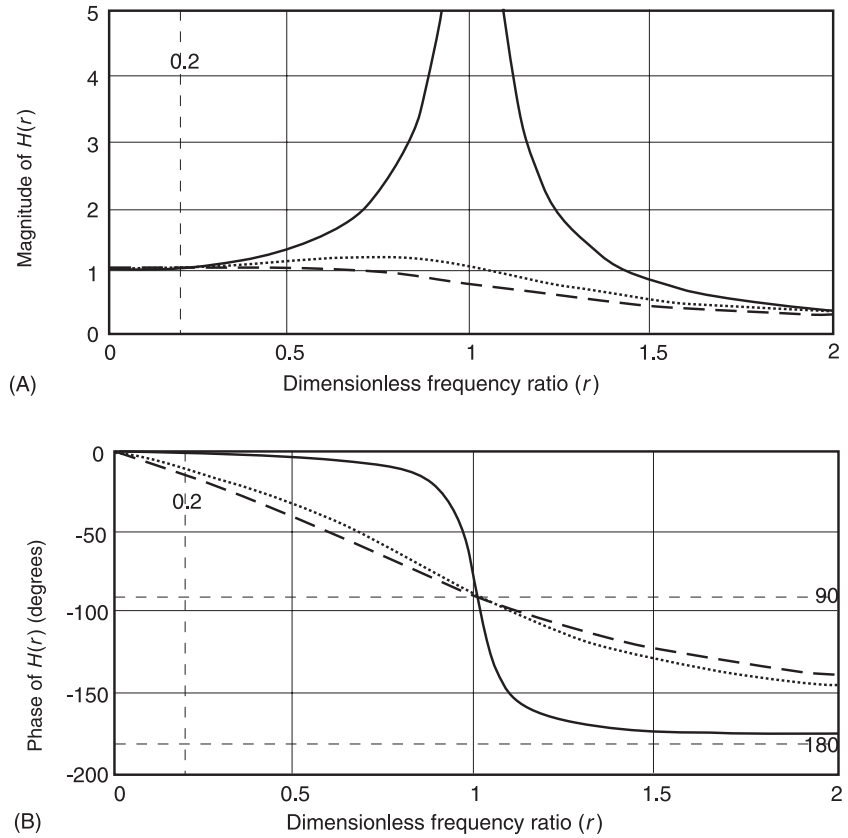


Figure 4 Accelerometer and force transducer mechanical FRF showing (A) magnitude and (B) phase characteristics as a function of dimensionless frequency ratio r for dimensionless damping ratios of 0.05 (continuous line), 0.50 (dotted line), and 0.65 (dashed line).

mounting bolts and mounting hardware are often used. Consequently, this inertial force contamination term can vary from application to application. Eqn [1] also shows that the transducer has a resonance similar to that of accelerometers, as shown in **Figure 4.** Hence, force transducers are limited to about 0.20 of the transducer's natural frequency as installed since the natural frequency is affected by a change in seismic mass that occurs in many applications. Eqn [2] shows that the transducer actually measures the difference between the applied force and the inertial force; i.e., $f(t) - m\ddot{y}$. Hence, signal contamination is always present and is most important when dealing with light-weight structures.

Pressure Transducers

The pressure transducer has the same mechanical model as the force transducer when $f(t)$ is replaced by $\{Ap(t)\}$ where A is the effective area and $p(t)$ is the pressure time history. In this case the seismic mass also includes some of the contact fluid so this sensor's dynamic characteristics are application-dependent where there is little fluid inertial effect with gases and significant fluid inertial effects with liquids.

Typical Sensors

Three different sensors – capacitive, piezoelectric, and strain gauge – are used to measure the relative motion, z, in accelerometers. The most common sensor used in accelerometers and force and pressure transducers is the piezoelectric type since it provides for good sensitivity, small size, high stiffness and natural frequency, and stable sensitivity. These sensors can be used over a wide range of temperatures as well as nuclear radiation environments. Manufacturers should be consulted about uses in extreme temperature and nuclear radiation applications. The second most popular sensor is the strain gauge that is used for accelerometers, force transducers, and pressure transducers. The capacitve sensor is used primarily in accelerometers and microphone-type pressure transducers.

Piezoelectric Sensor Model

The piezoelectric sensor is commonly used in accelerometers, pressure, and force transducers since it provides for good sensitivity, small size, high stiffness and natural frequency, and stable sensitivity. This

article is concerned with the piezoelectric sensor, its general characteristics that are of interest to the user, and the types of circuits that are commonly employed with this sensor.

General Model

Piezoelectric material occurs naturally in the form of quartz and is also made synthetically by shocking certain ceramic materials. It is used in two different basic designs, as shown in **Figure 5**. The compression design in **Figure 5A** is used in both load cells and accelerometers where the crystal is cut so that it generates an electrical charge when exposed to a change in compressive strain. This design is sensitive to base strains. The shear design is shown in **Figure 5B**, where the crystal is cut so that it generates an electrical charge when it is under shear strain deformation. In either design, the amount of charge generated, q, with units of picocoulombs, is directly proportional to the amount of relative motion, z, between the crystal's support ends so that:

$$q = S_z z \qquad [11]$$

where S_z is the displacement charge sensitivity with units of pcb/unit displacement.When the relative motion solution to eqn [1] is substituted into eqn [11], we obtain the steady-state frequency domain solution for each frequency ω to be given by:

$$\begin{aligned} q(\omega) &= \frac{S_z}{k}\left[\frac{F(\omega) - m\ddot{X}(\omega)}{1 - r^2 + j2\zeta r}\right] \\ &= H(r)\left[S_{qf}F(\omega) - S_{qa}A(\omega)\right] \end{aligned} \qquad [12]$$

where:

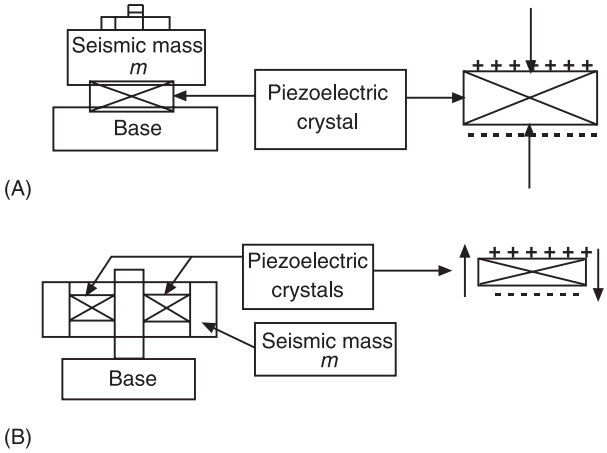


Figure 5 Basic piezoelectric transducer design. (A) Compression design used in both force transducers and accelerometers; (B) shear design, used only in accelerometers.

$$S_{qf} = \frac{S_z}{k} \qquad [13]$$

is the force charge sensitivity in pcb/unit of force

$$S_{qa} = \frac{mg}{k}S_z \qquad [14]$$

is the acceleration charge sensitivity in pcb/g

$$A(\omega) = \frac{\ddot{X}(\omega)}{g} \qquad [15]$$

is the base acceleration in g's

$$H(r) = \frac{1}{1 - r^2 + j2\zeta r} \qquad [16]$$

is the transducer's mechanical FRF, r is the dimensionless frequency ratio (ω/ω_n) and ζ is the dimensionless damping ratio. Eqns [11] and [12] clearly show how the mechanical force $F(\omega)$ and base acceleration $A(\omega)$ are converted into an electrical charge. Now, it is required to show how the charge is measured.

Basic Charge Circuit

The basic charge generator circuit is shown in **Figure 6** where the charge generator is shown as a q in a circle. Piezoelectric crystals have very high internal resistance which have little effect on system performance so that no internal resistor is shown. The piezoelectric sensor has capacitance C_t, the connecting cable has capacitance C_c, and the amplifier has input capacitance C_a. These three capacitance are in parallel so that the equivalent circuit consists of the charge generator and a single capacitance of C that is given by:

$$C = C_t + C_c + C_a \qquad [17]$$

This circuit is connected to three different types of amplifiers that are called voltage follower, charge amplifier, and built-in voltage follower.

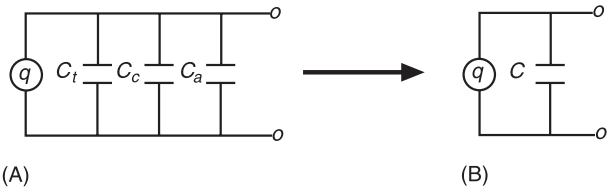


Figure 6 Equivalent piezoelectric sensor circuit showing (A) all capacitors and (B) reduced equivalent circuit where q is the charge generator.

Voltage Follower

The voltage follower is modeled as shown in **Figure 7A** by using an operational amplifier (called an op-amp) connected in the voltage follower mode where the output is connected to the negative input (−). This circuit presents a very high input impedance to the charge generated. Usually resistor R has a large value and is connected in parallel with the capacitor C to give a specific input resistance on the order of 10–100 MΩ. The differential equation governing this circuit is given by:

$$\dot{e}_o + \frac{e_o}{RC} = \frac{\dot{q}}{C} = \frac{S_q}{C} H(r)\left[\dot{f} \text{ or } \dot{a}\right] \qquad [18]$$

for either a force transducer or an accelerometer. It is clear from eqn [18] that the corresponding voltage sensitivities are given by:

$$S_f = \frac{S_{qf}}{C} \quad \text{and} \quad S_a = \frac{S_{qa}}{C} \qquad [19]$$

The steady-state solution to eqn [18] in the frequency domain is given by:

$$E_o(\omega) = \left[S_f \text{ or } S_a\right] H(r)\left[\frac{jRC\omega}{1 + jRC\omega}\right][F(\omega) \text{ or } A(\omega)] \qquad [20]$$

where $j = \sqrt{-1}$. The transducer's mechanical characteristics are contained in $H(r)$ and its low-frequency $(jRC\omega)$ electrical characteristics are contained in the bracketed term. The voltage sensitivity (S_f or S_a) and the RC time constant are dependent on cable capacitance C_c in this type of circuit. The RC time constant controls the low-frequency response, as shown in **Figure 7B** and **7C**, where the magnitude and the phase are plotted as a function of $RC\omega$. In

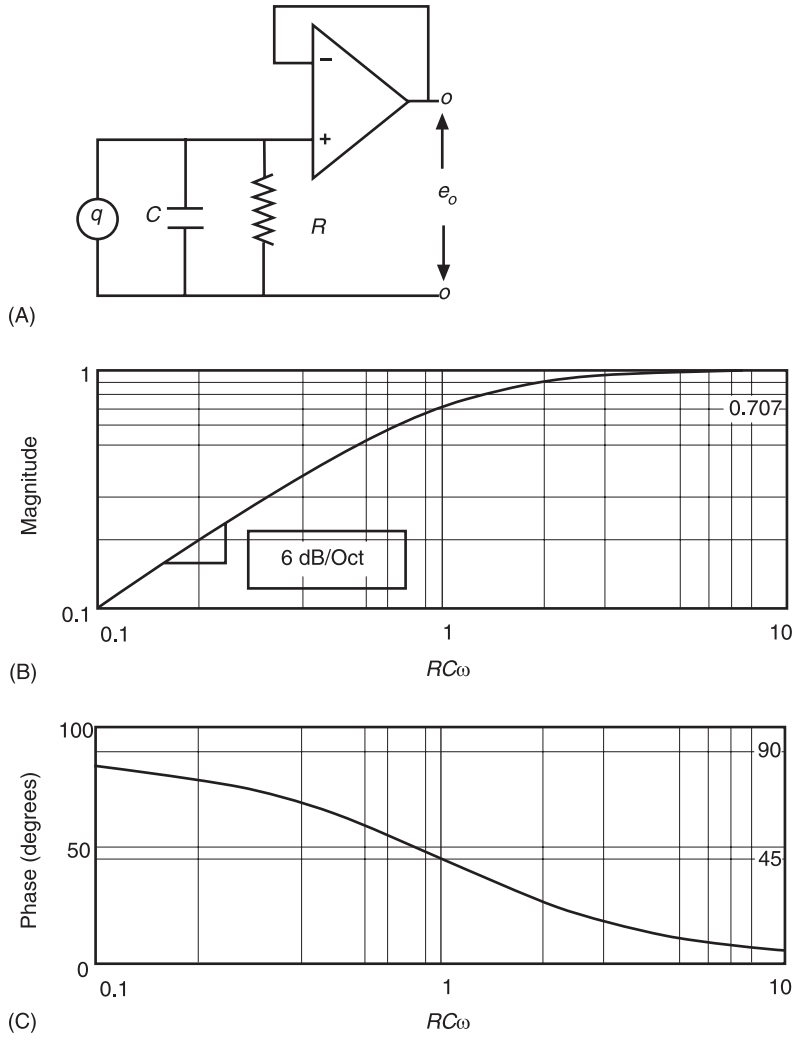


Figure 7 Voltage follower-type piczoelectric circuit (A) and low-frequency characteristics (B) magnitude and (C) phase as a function of $RC\omega$.

Figure 7B, the magnitude is attenuated with a slope of 6 dB/octave below $RC\omega = 0.5$, is down 30% and has a phase shift of 45° when $RC\omega = 1.0$. When $RC\omega = 5.0$, the attenuation is 2% and the phase shift is 11.3°. Hence, the time constant variation between data channels can cause both absolute and relative measurement errors (in magnitude and/or phase) at frequencies below $RC\omega = 10$ depending on the measurement situation.

Charge Amplifier

The charge amplifier was developed to overcome some of the problems associated with the voltage follower, such as sensitivity and low-frequency performance being dependent on cable capacitance. Charge amplifier characteristics are modeled by using two operational amplifiers, as shown in **Figure 8**. The transducer and its connecting cable are modeled as a charge generator q and total capacitance C. The first op-amp has both capacitance C_f and resistance R_f feedback components. The second op-amp is a voltage inverter with gain of $(1/\lambda)$. The equivalent capacitance controlling this circuit is given by:

$$C_{eq} = C_f\left[1 + \frac{C}{C_f G}\right] \qquad [21]$$

where G is the open-loop gain of the first op-amp. Since this gain is on the order of 100 000 or more, it is evident that the effective capacitance is the feedback capacitance so long as C is less than a specified amount for each feedback capacitance, C_f. For this instrument, the voltage sensitivity is given by:

$$S_v = \frac{S_q}{\lambda C_f} = \frac{S_q^*}{C_f} \qquad [22]$$

where it is clear that the voltage sensitivity can have standardized values like 10 mV g^{-1} or 100 mV N^{-1}

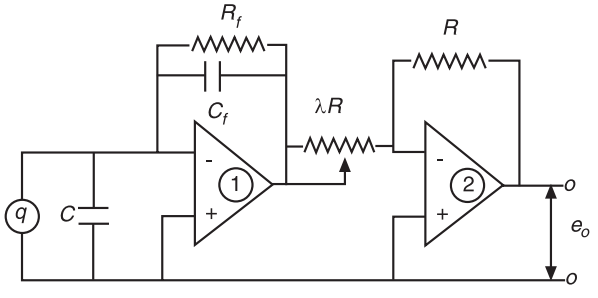


Figure 8 Charge amplifier model using two op-amps. Reproduced with permission from Dally JW, Riley WF and McConnell KG (1993) *Instrumentation for Engineering Measurements*, 2nd edn. New York: John Wiley.

when the value of λ is adjusted to be numerically equal to the actual transducer sensitivity, S_q. The charge amplifier has several advantages, such as:

- The time constant is controlled by the charge amp's feedback elements $R_f C_f$ that are independent of the transducer capacitance.
- Charge and voltage sensitivities can be standardized by use of the gain, λ.
- A wide range of voltage and time constants are available by changing the feedback capacitance, C_f.

Built-in Voltage Follower

The built-in voltage follower can be modeled as shown in **Figure 9A**. The voltage follower, capacitance, C, and resistance, R, are built into the transducer itself. The voltage follower's output is coupled through capacitance, C_1, to the data-recording device with input resistance R_1. Analysis of this circuit shows that there are two time constants, $T = RC$ and $T_1 = R_1 C_1$, where $T(R \text{ and } C)$ and C_1 are fixed by the instrument manufacturer while T_1 is determined by the user, since R_1 is dependent on the recording instrument employed. For this case, the input–output frequency domain solution is given by:

$$E_o(\omega) = \frac{S_q}{C} H(r)\left[\frac{jRC\omega}{1 + jRC\omega}\right]\left[\frac{jR_1C_1\omega}{1 + jR_1C_1\omega}\right] \times \{F(\omega) \text{ or } A(\omega)\} \qquad [23]$$

where it is evident that two different time constants, the mechanical response function, $H(r)$, the transducer's charge sensitivity, S_q, and the internal capacitance, C, are involved in describing its dynamic behavior. The effect of dual time constants is shown in the magnitude vs $RC\omega$ in **Figure 9B** and phase vs $RC\omega$ in **Figure 9C** when $T_1 = 10T$. In this case, the magnitude has a slope of 12 dB/oct below $RC\omega = 0.1$, and a slope of 6 dB/octave above $RC\omega$ above 0.1. As the values of $RC\omega$ approach unity, the curve begins to match the curves for a single time constant system. The magnitude and phase values for both a single and double time constant system ($T_1 = 10T$) are compared in **Table 1**. In this table, it is seen that 3% magnitude error occurs around $RC\omega = 4.0$ while a 2% magnitude error occurs around $RC\omega = 5.0$. The error is about 0.5% at $RC\omega = 10.0$.

Strain Gauge and Capacitance Sensors

The strain gauge type of sensor is often used in accelerometers, pressure transducers, and force transducers while the capacitive sensors are often used in

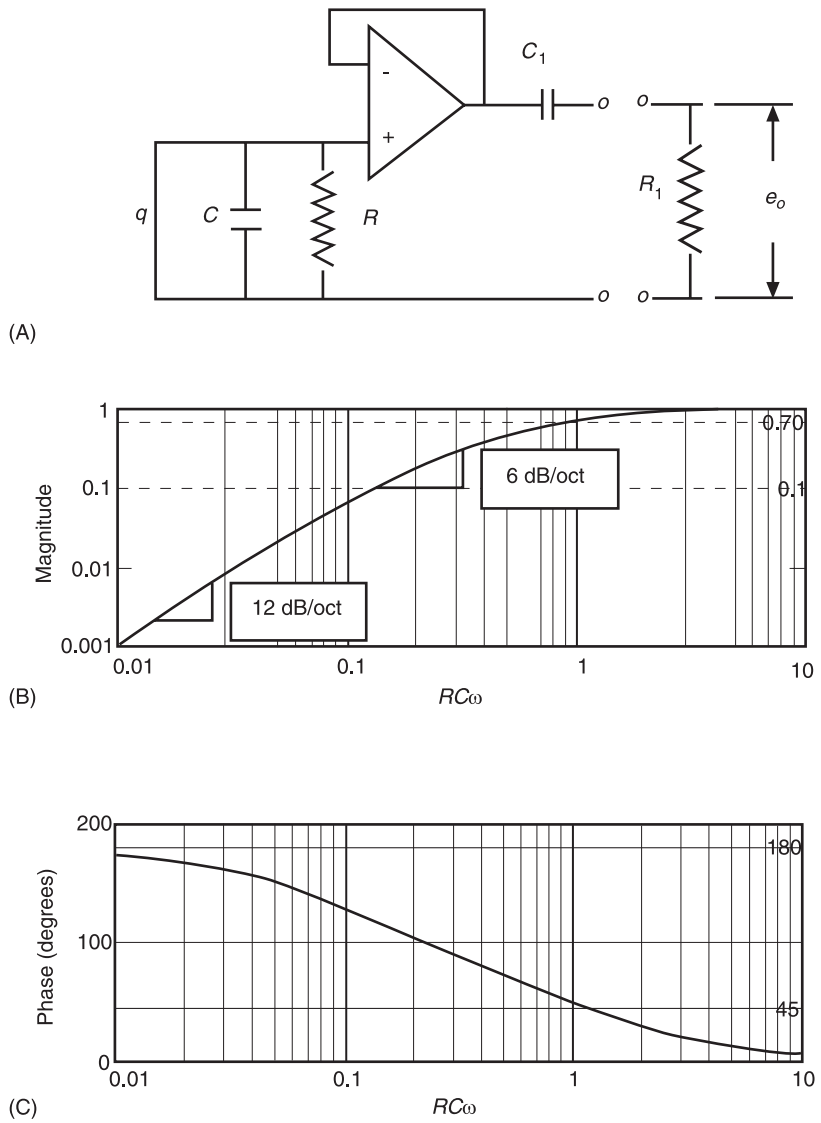


Figure 9 Built-in voltage follower circuit (A) and low-frequency characteristics (B) magnitude and (C) phase as a function of $RC\omega$. Reproduced with permission from Dally J W, Riley W F and McConnell K G (1993) *Instrumentation for Engineering Measurements*, 2nd edn. New York: John Wiley.

microphones, pressure transducers, and some accelerometers. In this section, the primary characteristics of these sensors are reviewed.

General Strain Gauge Model

The strain gauge is based on the linear variation of resistance in a wire or metal film with strain. This linear variation is called the gauge factor or gauge sensitivity, S_g and is defined as:

$$S_g = \frac{\Delta R/R}{\varepsilon} \qquad [24]$$

where R is the nominal gauge resistance, ΔR is the change in resistance, and ε is the material strain. The gauge factor ranges from 2 to 4 for common strain gauge alloys.

Wheatstone bridge The constant-voltage Wheatstone bridge is shown in **Figure 10** and consists of four resistors, R_1, R_2, R_3, and R_4, a DC supply voltage, E_s that is connected between nodes A and C, and an output voltage, e_o between nodes B and D. This bridge is said to be balanced when the output voltage, e_o, is zero. This balanced condition requires that:

$$R_1R_3 = R_2R_4 \qquad [25]$$

Consider the case when each resistor changes by an amount of ΔR_1, ΔR_2, ΔR_3, and ΔR_4, respectively.

Table 1 Comparison of low-frequency characteristics for single and dual time constant systems when $T_1 = 10T$

	Single time constant		*Dual time constants* $T_1 = 10T$	
$RC\omega$	*Magnitude*	*Phase* (°)	*Magnitude*	*Phase* (°)
0.1	0.0995	84.3	0.0704	129
1.0	0.707	45.0	0.704	50.7
4.0	0.970	14.0	0.970	15.5
5.0	0.981	11.3	0.980	12.5
10.0	0.995	5.71	0.995	6.28

Then the change in the output voltage e_o is given by:

$$\Delta e_o = \frac{r}{(1+r)^2}\left[\frac{\Delta R_1}{R_1} - \frac{\Delta R_2}{R_2} + \frac{\Delta R_3}{R_3} - \frac{\Delta R_4}{R_4}\right] E_s \quad [26]$$

where $r = R_2/R_1$. In a typical transducer application, four active gauges with equal resistances are employed so that $r = 1.0$. It is important to note that the Wheatstone bridge has good temperature compensation when the gauges are temperature-compensated. In addition, the ΔRs due to temperature are seen to cancel out in eqn [26] if each gauge has the same ΔR_T due to change in temperature. The output voltage can be given in terms of the individual gauge strains if it is assumed that each gauge has the same gauge factor, S_g, so that:

$$\frac{\Delta e_o}{E_s} = \frac{S_g}{4}[\varepsilon_1 - \varepsilon_2 + \varepsilon_3 - \varepsilon_4] = \frac{S_g}{4}[\eta\varepsilon] \quad [27]$$

where η usually ranges from 2 to 4 dependent on the transducer design in placing the strain gauges and assuming that the strain measured in each gauge is in proportion to ε, the largest strain measured. The overall transducer sensitivity is obtained when it is assumed that the strain ε is proportional to the transducer's relative motion z from eqn [8]. Then, the frequency domain output voltage becomes:

$$\begin{aligned}\frac{\Delta e_o(\omega)}{E_s} &= \frac{S_g}{4}H(r)\left[K_f F(\omega) \text{ or } K_a A(\omega)\right] \\ &= H(r)\left[S_f F(\omega) \text{ or } S_a A(\omega)\right]\end{aligned} \quad [28]$$

where the K_xs are the transducer's structural proportionality constants and $H(r)$ is the transducer's mechanical FRF. The voltage sensitivity units are usually (mV/volt/unit force) for S_f and (mV/volt/unit acceleration) for S_a. The values of these sensitivities is very small and the excitation voltage, E_s, is limited by strain gauge heat dissipation to be on the order of 1–10 V. Consequently, the transducer must be connected to an amplifier with considerable gain on the order of 1000 or more in order to have an acceptable signal level for recording purposes. These strain gauge amplifiers usually have DC or zero-frequency response. However, the user is warned that most data-recording devices from oscilloscopes to digital data acquisition systems can be either DC- or AC-coupled. When AC-coupled, the low-frequency behavior is identical to that of the piezoelectric transducer with a single RC time constant. Hence, the user must be aware of how the instrumentation system is set up when dealing with low (usually below 10 Hz) frequencies.

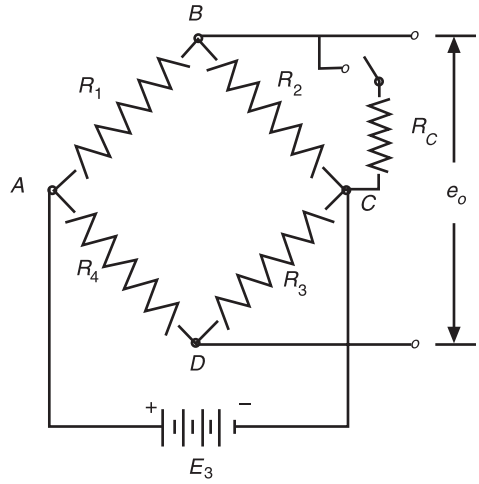


Figure 10 Basic elements of a Wheatstone bridge circuit for strain gauge sensors used in force and acceleration transducers. Reproduced with permission from Dally JW, Riley WF and McConnell KG (1993) *Instrumentation for Engineering Measurements*, 2nd edn. New York: John Wiley.

Calibration The calibration of a strain gauge-based sensor is achieved by switching the calibration resistor, R_c, between points B and C of the bridge. This resistance causes a change in resistance in arm R_2 that is given by:

$$\frac{\Delta R_2}{R_2} = S_g\varepsilon_c = \frac{-R_2}{R_2 + R_c} \approx \frac{-R_2}{R_c} \quad [29]$$

where R_c is usually much larger than R_2. This resistance change is related to the strain sensed by strain gauge. Once the transducer's voltage sensitivity, S_v, is established through direct calibration against a standard, then a standard precision resistance of, say, 250 kΩ can be used to simulate a given calibration force, F_c, or calibration acceleration, a_c. Through this means, the variations in excitation voltage and amplifier gain are automatically accounted for.

The Capacitive Sensor

The basic geometric arrangement for the capacitive sensor is shown in **Figure 11**, where the surface motion to be measured is grounded, the sensor is located a distance h from the surface of interest, the sensor has a diameter d, and is connected to appropriate electronic circuits. The capacitance, C, in picofarads (pf) for this geometry where $h < d/4$ is given by:

$$C = \frac{kKA}{h} \qquad [30]$$

where $A = \pi d^2/4$ is the sensor's area, K is the dielectric constant (1.0 for air), and k depends on units used (0.225 for in and 0.00885 for mm). The electrical impedance Z for a capacitor is given by:

$$Z = \frac{1}{jC\omega} \qquad [31]$$

where ω is the frequency applied to the capacitance sensor by the sensing electronics. It can be shown that the sensor sensitivity can be expressed in terms of the ratio of the change in impedance Z to the change in position h so that:

$$S = \frac{\Delta Z}{\Delta h} = \left|\frac{1}{Ch\omega}\right| = \left|\frac{1}{kKA\omega}\right| \qquad [32]$$

This sensitivity is limited to $h < d/4$ and the temperature range of 40–1600°F (40–870°C) when the gap medium is air. Then, an impedance bridge type of circuit is used to measure the change in capacitance with gap motion, h.

Measuring Angular Accelerations

Often the angular motion of a structure is of interest. In situations with very low frequencies and significant amplitudes of motion, the angle can be measured using potentiometer-type devices. Only since the mid-1980s has a successful single-unit angular accelerometer been developed. In this section, two different methods of measuring angular acceleration are discussed.

Two-accelerometer Method

The arrangement for the two-accelerometer method is shown in **Figure 12A**, where two accelerometers are attached $2l$ apart on a rigid bar. From the kinematics diagram of **Figure 12B** and the concept of rigid-body

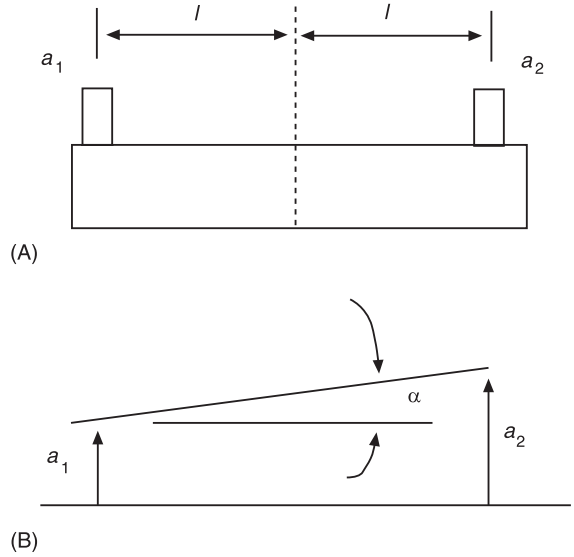


Figure 12 (A) Two accelerometers mounted on a rigid bar and (B) acceleration kinematics diagram showing geometric relationship between linear and angular acceleration.

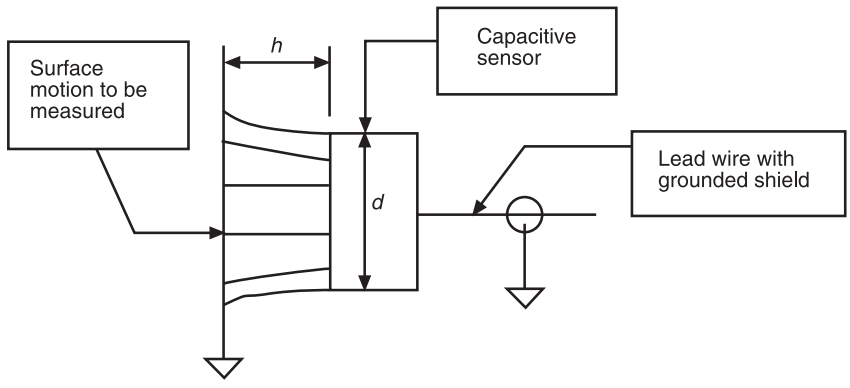


Figure 11 Schematic of capacitive sensor. Reproduced with permission from Dally JW, Riley WF and McConnell KG (1993) *Instrumentation for Engineering Measurements*, 2nd edn. New York: John Wiley.

relative acceleration, the frequency domain angular acceleration $\alpha(\omega)$ is given by:

$$\begin{aligned}\alpha(\omega) &= \left[\frac{1}{2l}\right][A_2(\omega) - A_1(\omega)] \\ &= \left[\frac{1}{2l}\right]\left[\frac{E_2(\omega)}{S_2H_2(\omega)} - \frac{E_1(\omega)}{S_1H_1(\omega)}\right]\end{aligned} \quad [33]$$

where S_1 and S_2 are the transducer voltage sensitivities, $H_1(\omega)$ and $H_2(\omega)$ are the transducer input–output FRFs that include both mechanical and electrical characteristics, and $E_1(\omega)$ and $E_2(\omega)$ are the measured voltages in the frequency domain. It is clear from eqn [33] that the two accelerometers must be carefully matched in magnitude and phase at each frequency of interest. This matching of dynamic characteristics at low frequencies can be a serious problem unless careful attention is paid to matching time constants. Even when the transducers are carefully calibrated and matched, the subtraction of two large signals can easily lead to significant signal noise dependent on the signal-processing methods employed. The successful application of these concepts is no easy matter.

Combined Linear and Angular Accelerometer

A schematic of the combined linear and angular accelerometer is shown in **Figure 13.** This unit consists of two piezoelectric beams called 1 and 2 and mounted on a center post. The center of the beam is the common connection through the center post, while each surface connection is labeled *A*, *B*, etc. When the base has a linear acceleration of a_y, as shown in **Figure 13A**, the top sides *A* and *B* of beams 1 and 2 have a positive charge generated while the bottom sides *C* and *D* have a negative charge generated as shown. When the base has an angular acceleration α_z, as shown in **Figure 13B**, beam 1 has a negative charge on side *A* and a positive charge on side *C* while beam 2 has a positive charge on side *B* and a negative charge on side *D*. It can be shown that the frequency domain output voltage for beam 1 is given by:

$$E_1(\omega) = H_1(\omega)\left[S_{1y}A_y(\omega) - S_{1z}\alpha_z(\omega)\right] \quad [34]$$

and for beam 2 is given by:

$$E_2(\omega) = H_2(\omega)\left[S_{2y}A_y(\omega) + S_{2z}\alpha_z(\omega)\right] \quad [35]$$

Eqns [34] and (35) show that addition should give the linear acceleration while subtraction of E_1 from E_2 should give the angular acceleration, provided that certain terms cancel out. The addition gives:

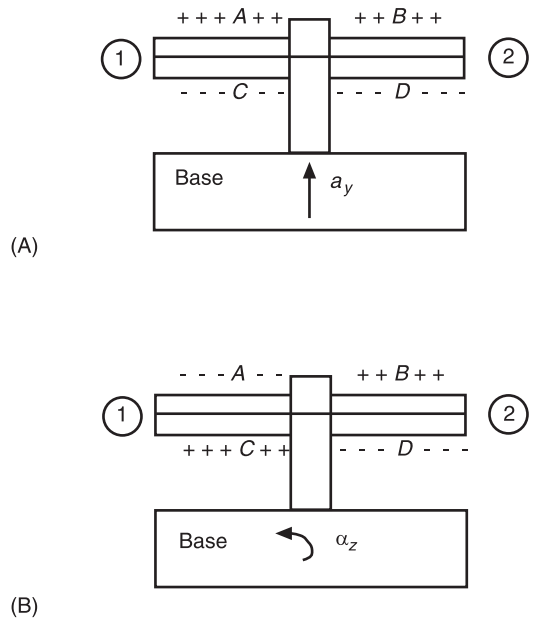


Figure 13 Schematic of combined linear and angular accelerometer using two piezo-beams. (A) Charge generated for positive linear acceleration a_y. (B) Charge generated for positive angular acceleration, α_z. Reproduced with permission from Dally JW, Riley WF and McConnell KG (1993) *Instrumentation for Engineering Measurements*, 2nd edn., New York: John Wiley.

$$\begin{aligned}E_a &= \left[H_1S_{1y} + H_2S_{2y}\right]A_y + [H_2S_{2z} - H_1S_{1z}]\alpha_z \\ &\cong S_aA_y\end{aligned} \quad [36]$$

while subtraction gives:

$$\begin{aligned}E_a &= \left[H_2S_{2y} - H_1S_{1y}\right]A_y + [H_2S_{2z} + H_1S_{1z}]\alpha_z \\ &\cong S_a\alpha_z\end{aligned} \quad [37]$$

if it is assumed that H_1 and H_2 are unity. Eqn [4] is valid so long as $(H_2S_{2z} - H_1S_{1z} = 0)$ and $(H_1S_{1y} + H_2S_{2y} = S_a)$. Similarly, eqn [37] is valid so long as $(H_1S_{1y} - H_2S_{2y} = 0)$ and $H_2S_{2z} + H_1S_{1z} = S_z)$. In both cases, the desired signal comes from terms that are additive while there is a need to balance out the subtractive terms in order to make the transducer work properly over a broad range of frequencies. This is why the addition and subtraction interface electronics must be matched to the transducer and are not interchangeable with other linear angular accelerometer units. These transducers are very efficient when both linear and angular motion must be measured at the same point. In addition, the mass of these units is low compared to using two accelerometers and a rigid bar.

Servo Accelerometers

These are force-balance transducers that incorporate a feedback control circuit, as shown in **Figure 14**. A

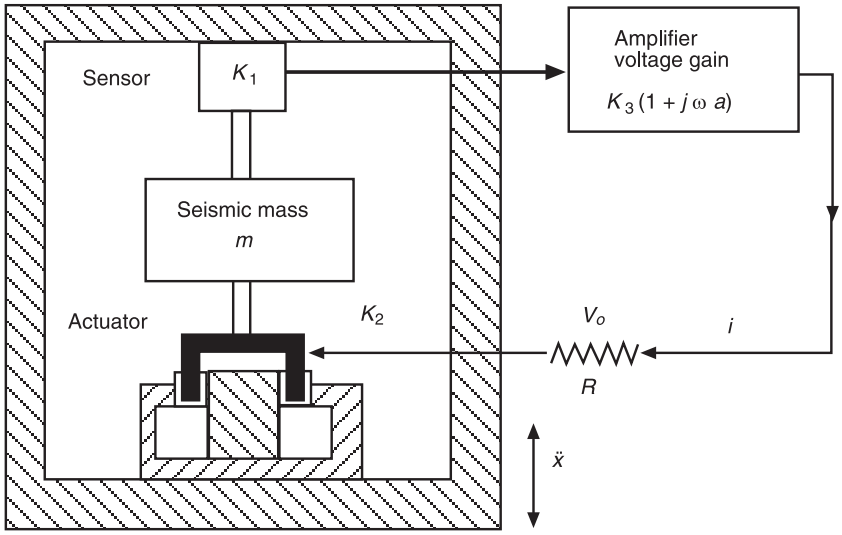


Figure 14 Schematic of servo accelerometer showing main elements of seismic mass, relative motion sensor, amplifier, and electromagnetic force actuator.

balancing force is applied to the seismic mass, m, via the electromagnetic actuator in order to maintain near-zero relative motion, z. The balance force is directly proportional to current i and is measured as a voltage drop, V_o, across resistor R, as shown. The relative motion z is measured with sensitivity $K_1(\mathrm{V\,m^{-1}})$, the electromagnetic actuator has force sensitivity $K_2(\mathrm{N\,A^{-1}})$, and the amplifier has a voltage gain of $K_3(\mathrm{V\,V^{-1}})$. The actuator back electromotive force sensitivity is also $K_2(\mathrm{V/m\,s^{-1}})$. These transducers usually have a mechanical spring with stiffness k and some mechanical damping, c. The transducer's input–output FRF is given by:

$$H_a(\omega) = \frac{V_o(\omega)}{\ddot{X}(\omega)} = \frac{K + jb\omega}{K_2\omega_n^2}\left[\frac{1}{1 - r^2 + 2\zeta r}\right] \qquad [38]$$

where:

$$b = Ka + K_2^2 \qquad [39]$$

with units of (N ohm s $\mathrm{m^{-1}}$) is due to the feedforward time constant a and the force actuator's electromagnetic constants, K_2:

$$K = K_1K_2K_3 \qquad [40]$$

is the system overall electrical stiffness (N ohm $\mathrm{m^{-1}}$):

$$r = \frac{\omega}{\omega_n} \qquad [41]$$

is the dimensionless frequency ratio:

$$\omega_n = \left[\frac{k + K/R}{m}\right]^{1/2} \qquad [42]$$

is the transducer's natural frequency, and:

$$\zeta = \frac{c + K_2^2/R + Ka/R}{2m\omega_n} \qquad [43]$$

is the dimensionless damping ratio. It is clear that the mechanical stiffness, k, and damping, c, are not critical and can be zero since the electrical parameters can be used to control the operating characteristics. While the servo accelerometer is more complicated, massive, and larger than the other types, it has the advantages of very high sensitivities and resolution on the order of micro-g's, very linear behavior, and small cross-axis sensitivity. They are well suited for making low-level acceleration measurements in the DC to 100 Hz frequency range.

Transient Response

Transient signals often contain a broad range of frequencies. Consider the two 10 ms pulses shown in **Figure 15A**. The magnitude of the transient frequency spectra for each pulse is shown in **Figure 15B**. While both pulses have the same time duration, it is seen that they have dramatically different frequency content. Both pulses have significant low-frequency components since the pulse part of the time history is only positive and the signal is zero elsewhere. This means that the measurement system must be able to measure these low frequencies, which is a problem for

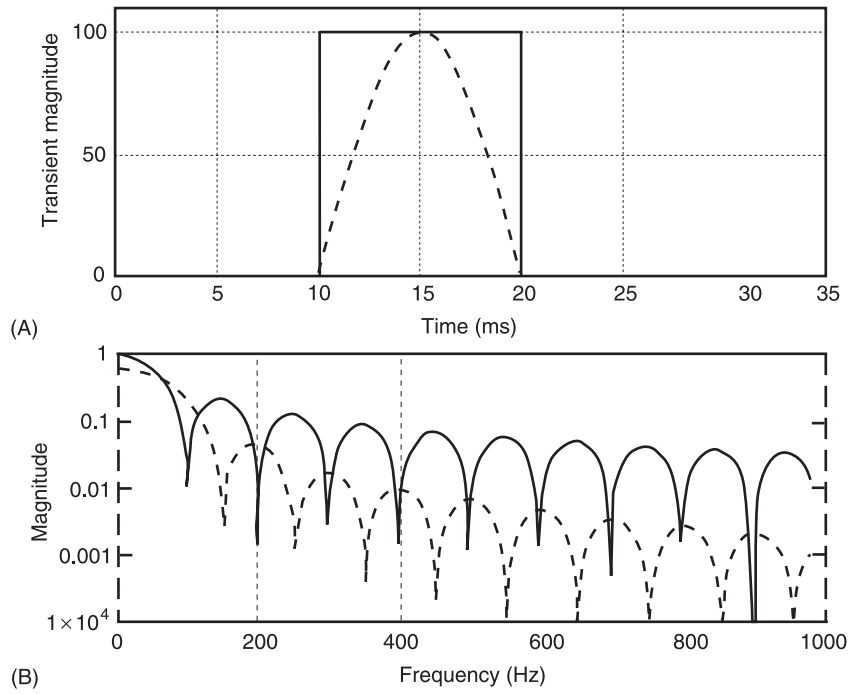


Figure 15 (A) Continuous line: square and dashed line: half-sine transient time histories, and (B) their corresponding transient frequency spectra to illustrate different frequency content in a 10 ms pulse.

the piezoelectric type of sensors as well as the AC coupling feature of many recording instruments. The square pulse has significant frequency components above 1 kHz while the half-sine has frequency components that are less than 1% of the maximum low-frequency value at 1 kHz. Consequently, the step type of pulse requires a much higher transducer natural frequency if there is to be a faithful reproduction of the input. We shall examine the electrical and natural frequency limits on making transient measurements in this section.

Mechanical Response

The mechanical limits can be easily understood by examining the response to a ramp hold-type of transient, as shown in **Figure 16A**, where the ramp duration is t_o s and the step height is a_o. The mechanical response to this ramp is broken down into two parts, one during the ramp and one after the ramp height is achieved. The undamped transducer response is used here since the resulting errors are conservative. The undamped relative motion during the ramp is given by:

$$\frac{z}{z_o} = \frac{t}{t_o} - \frac{\sin(\omega_n t)}{\omega_n t_o} \qquad [44]$$

for $0 < t < t_o$ where z_o is the reference motion for the transient input of a_o. For $t > t_o$, the response is given by:

$$\begin{aligned} \frac{z}{z_o} &= 1 - \left[\frac{\sin(\omega_n t) - \sin(\omega_n (t - t_o))}{\omega_n t_o}\right] \\ &= 1 - \frac{D \sin(\omega_n (t - \beta))}{\omega_n t_o} \end{aligned} \qquad [45]$$

where the magnitude for the oscillations about the hold position is given by:

$$D = \sqrt{2(1 - \cos(\omega_n t_o))} \qquad [46]$$

and the shift angle β is given by:

$$\tan(\beta) = \frac{\sin(\omega_n t_o)}{\{1 - \cos(\omega_n t_o)\}} \qquad [47]$$

The first term of eqn [44] is a linear ramp while the second term shows an oscillation about this linear ramp with an amplitude of $1/(\omega_n t_o)$. The maximum error at time t_o is $\sin(\omega_n t_o)/(\omega_n t_o)$. Whenever $(\omega_n t_o)$ is a multiple of π the error is zero at time t_o. However, from eqn [46], it is seen that $D = 0$ only when $(\omega_n t_o)$ is an even multiple of π. As a general rule, the transducer

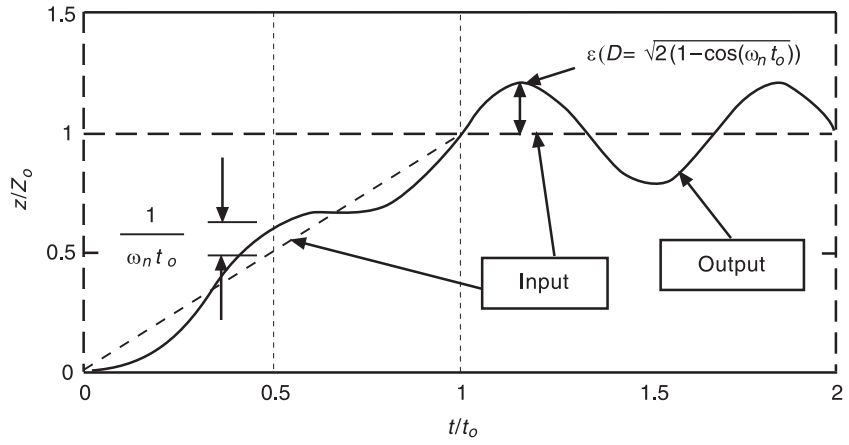


Figure 16 Input and response to ramp hold-type of transient when $t_o = 1.5T$. Reproduced with permission from Dally JW, Riley WF and McConnell KG (1993) *Instrumentation for Engineering Measurements*, 2nd edn. New York: John Wiley.

will reasonably match the ramp-type signal with little overshoot if the ramp duration is $t_o < 5T$, where T is the transducer's mechanical natural period. If this rule is applied to the half-sine pulse shown in **Figure 15A** where the ramp time is 5.0 ms, then the transducer's natural frequency should be greater than 1.0 kHz. **Figure 15B** shows that the frequency components above 1.0 kHz are less than 0.1% of the largest frequency components near 0 Hz. Now consider the limiting case when $(\omega_n t_o \cong 0)$ in eqns [46] and [47] so that $D \cong (\omega_n t_o)$ and $\beta \cong \pi/2$. Then eqn [45] gives the response as:

$$\frac{z}{z_o} = 1 - \cos(\omega_n t) \qquad [48]$$

which is the well-known undamped step response function that shows traditional transducer ringing at the transducer's natural frequency. Hence, whenever the transducer's natural frequency shows up in the measurement, the transient ramp is too steep or sharp for the transducer to respond and describe that ramp. Use of the $t_o = 5T$ rule prevents this from happening for either rapid increases or decreases in the measured variable.

RC Time Constant Effects

The RC time constant effects for the rectangular pulse are shown in **Figure 17**. The rectangular transient pulse $x(t)$ can be represented by two step functions $u(t)$ separated by t_1 as:

$$x(t) = u(t - t_o) - u(t - t_o - t_1) \qquad [49]$$

where the first pulse begins at time t_o and the second unit step begins at $(t_o + t_1)$. The solution to this input is given by:

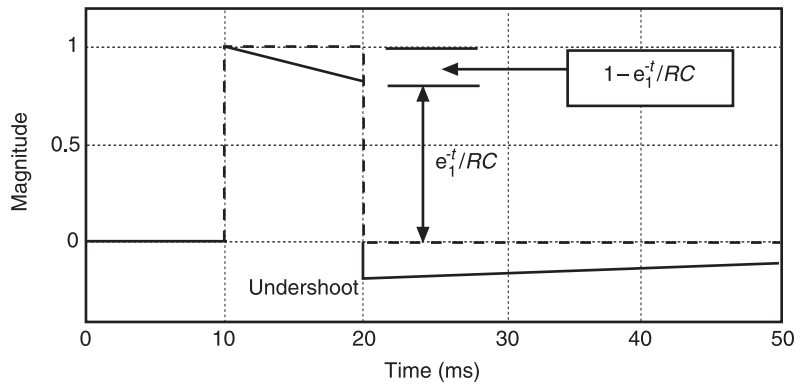


Figure 17 Electrical response of a piezoelectric sensor to a square pulse of duration $t_1 = 10.0$ ms and $RC = 50$ ms. Continuous line, response; dashed line, square input. (Reproduced with permission from Dally JW, Riley WF, and McConnell KG (1993), *Instrumentation for Engineering Measurements*, 2nd edn. New York: John Wiley.

$$z(t) = u(t - t_o)e^{-(t-t_o)/RC} - u(t - t_o - t_1)e^{-(t-t_o-t_1)/RC} \quad [50]$$

and is shown in **Figure 17**. We see that both magnitude of the top and undershoot errors at the pulse's end is given by:

$$\text{Error} = 1 - e^{-t_1/RC} \approx \frac{t_1}{RC} \quad [51]$$

for small values of the ratio of (t_1/RC). This ratio is 0.20 for the case illustrated, which is about the limit of the accuracy of eqn [51]. The presence of significant undershoot indicates that the RC time constant is too small for the duration of the transient being measured. **Table 2** gives some guidance for the required time constant for three different transient shapes. The built-in voltage follower-type of piezoelectric sensor has dual time constants. It can be shown that the effective time constant T_e for this case is given by:

$$T_e = \frac{T_1 T_2}{T_1 + T_2} \quad [52]$$

It is obvious from eqn [52] that, when the larger time constant is greater than 10 times the smaller time constant, the smaller time constant controls the low-frequency characteristics as far as transient measurements are concerned.

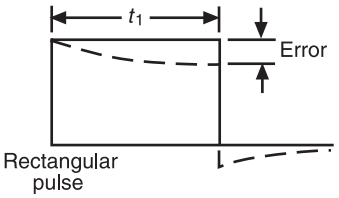
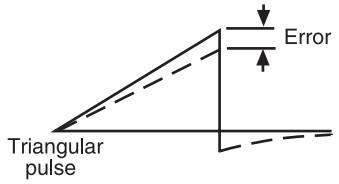
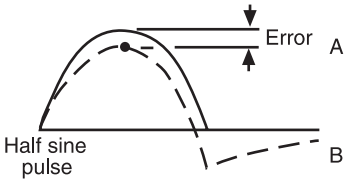
Typical Accelerometer and Force Transducer Characteristics

The previous sections have delineated the mechanical and electrical characteristics of accelerometers and force transducers as separate items. In this section, we present some typical overall characteristics for these transducers when connected to either a charge amplifier or a built-in voltage follower-type of amplifier. In addition to the characteristics shown here, there are models designed to work in cryogenic and high-temperature applications. These characteristics are typical for either shear or compression design. Contact specific vendors for additional information. Several web addresses are provided for the convenience of the reader.

Accelerometers

Accelerometers for use with charge amplifiers are given in **Table 3**, while those supplied with built-in

Table 2 Time-constant requirements to limit error

		Time constant		
Pulse shape		*2% Error*	*5% Error*	*10% Error*
		$50t_1$	$20t_1$	$10t_1$
		$25t_1$	$10t_1$	$5t_1$
	A (peak)	$16t_1$	$6t_1$	$3t_1$
	B (undershoot)	$31t_1$	$12t_1$	$6t_1$

Reproduced with permission from Dally JW, Riley WF and McConnell KG (1993) *Instrumentation for Engineering Measurements*, 2nd edn. New York: John Wiley.

Table 3 Piezoelectric accelerometers for use with charge amplifiers

Quantity	*Units*	*High-frequency shock*	*General purpose*	*High sensitivity*
Charge sensitivity	Pcb/m s^{-2}	0.27	1.0	100.0
Frequency range ($\pm$ 5%)[a]	Hz	1–20 000	1–12 000	1–2000
Resonant frequency	kHz	80	45	8
Amplitude range	$\pm$ m s^{-2} pk	10 000	10 000	5000
Mechanical shock limits	$\pm$ m s^{-2} pk	50 000	30 000	10 000
Temperature range	°C	-55 to +260	-55 to +260	-55 to +288
Transverse sensitivity	%	<5	<3	<3
Mass	grams	4.8	11	120

Adapted from Endevco Corporation product catalog 1999.
[a] Low-frequency response is controlled by the charge amplifier time constant.

voltage followers are given in **Table 4.** The general trend is for high-sensitivity transducers to have more mass and lower natural frequencies when compared to the general-purpose and high-frequency (shock) type of accelerometers. The damping is generally low (0.5–5%) for these piezoelectric-based transducers.

The characteristics of several piezoresistive accelerometers are given in **Table 5.** The same general trends for sensitivity, transducer mass, and natural frequency are observed. There are two major differences. First, the frequency response goes to DC (0 Hz) on the low end of the frequency scale. Second, there is a significant amount of damping for two of the transducers.

Force Transducers

Force transducer characteristics are shown in **Table 6** for general purpose, impact, and force ring types. The three transducers shown in **Table 5** are quite similar in terms of characteristics. The reader should be aware that the force ring type of transducer sensitivity can depend on bolt size and material as well as how the load is transmitted to the load cell. In addition, there are penetrating force transducers, force links, and press monitoring types of transducers As a general rule, all of these transducers use the basic compression design: a design that is usually sensitive to base strains and bending moments. Consequently, the user needs to be aware that signal contamination is possible if either significant bending moments or base strains are present in a given application.

Useful Web Addresses

1. Bruel & Kjaer: www.bkhome.com
2. Endevco Corporation: www.endevco.com
3. Kistler Instruments, Inc.: www.kistler.com
4. Pcb Piezotronics, Inc.: www.pcb.com

Nomenclature

a	acceleration
A	area
c	damping
C	capacitance
d	diameter
$F(t)$	external force
G	gain
h	distance

Table 4 Built-in voltage follower-type of piezoelectric accelerometer

Quantity	*Units*	*High-frequency shock*	*General purpose*	*High sensitivity*
Volt sensitivity	mV m s^{-2}	1.02	1.02	51.0
Frequency range ($\pm$ 5%)[a]	Hz	1–10 000	1–7000	1–2000
Resonant frequency	kHz	>70	>38	>14
Amplitude range	$\pm$ m s^{-2} pk	4905	4905	98
Mechanical shock limits	$\pm$ m s^{-2} pk	98 100	98 100	39 240
Temperature range	°C	-54 to +121	-54 to +121	-54 to +121
Transverse sensitivity	%	<5	<5	<5
Internal time constant	s	>0.5	>0.5	>0.5
Mass	grams	1.5	10	32

Adapted from PCB Piezotronics product catalog SSG-601C.
[a] Low frequency response is affected by time constant of the instruments connected to output terminals as well as the internal time constant.

Table 5 Typical piezoresistive accelerometer characteristics

Quantity	*Units*	*High-frequency shock*	*General purpose*	*High sensitivity*
Volt sensitivity[a]	$\mu V/m\,s^{-2}$	0.1	25	2500
Frequency range ($\pm$ 5%)	Hz	DC to 150 000	DC to 3000	DC to 500
Resonant frequency	kHz	1200	10	1.4
Amplitude range	$\pm\ m\,s^{-2}$ pk	2 000 000	20 000	200
Mechanical shock limits	$\pm\ m\,s^{-2}$ pk	2 000 000	50 000	20 000
Temperature range	°C	-34 to +66	-18 to +93	-18 to +66
Transverse sensitivity	%	<5	<3	<5
Damping ratio ζ	%	xxx	70.7	70.7
Mass	grams	1.5	28	6.0

Adapted from Endevco Corporation product catalog 1999.
[a] Excitation voltage 10.0 V DC.

Table 6 Typical force transducer characteristics

Quantity	*Units*	*General purpose*	*Impact*	*Force rings*[a]
Sensitivity:[b] voltage	$mV\ kN^{-1}$	225	225	112
Sensitivity:[b] charge	$Pcb\ kN^{-1}$	4500	4050	5050
Capacitance	pF	12	12	20
Load range: comp	kN	22.2	22.2	44.5
Load range: tens		2.22	Max comp 44.2	Max comp 66.7
Resonant frequency[c]	kHz	70	70	65
Rise time	μs	10	10	10
Internal time constant	s	>2000	>2000	>2000
Stiffness	$kN\ \mu m^{-1}$	1.75	17.5	5080
Temperature range	°C	-54 to +121	-54 to +121	-54 to +121
Mass	grams	25	14	20

Adapted from PCB Piezotronics product catalog FSG-605B.
[a] Sensitivity is affected by bolt used as well as load path, so that mounting must be done according to manufacturer's recommendations. For novel application, the user must verify transducer sensitivity as used.
[b] Low-frequency response is affected by the instruments connected to the transducer.
[c] Measured mounted on a large mass but unloaded.

k stiffness
K dielectric constant
m seismic mass
$p(t)$ pressure time history
q charge generator
R resistance
S sensitivity
T time constant
z relative motion
Z electrical impedance
β shift angle
ϕ phase angle
ζ damping ratio
ω frequency

See also: **Seismic instruments, environmental factors**; **Signal integration and differentiation**; **Transducers for relative motion**.

Further Reading

Brindley K (1988) *Sensors and Transducers*. London: Heinemann.
Change ND (1994) *General Guide to ICP Instrumentation*. Depew, NY: PCB Piezotronics.
Dally JW, Riley WF and McConnell KG (1993) *Instrumentation for Engineering Measurements*. New York, NY: Wiley.
Foster RL and Wnuk SP Jr (1985) *High Temperature Capacitive Sensing*. Durham, NC: Instrument Society of America, pp. 245–252.
Kobayashi AS (ed.) (1987) *Handbook on Experimental Mechanics*. Englewood Cliffs, NJ: Prentice-Hall.
McConnell KG (1995) *Vibration Testing Theory and Practice*. New York, NY: Wiley.
Pennington D (1965) *Piezoelectric Accelerometer Manual*. San Juan Capistrano, CA: Endevco.

TRANSDUCERS FOR RELATIVE MOTION

G E Maddux, Tipp City, OH, USA

K G McConnell, Iowa State University, Ames, IA, USA

Copyright © 2001 Academic Press

doi:10.1006/rwvb.2001.0102

General Considerations

We need to consider what we mean by fixed references. Transducers measure the relative motion between two objects or surfaces in sensing motion. Consider the situation shown in **Figure 1**. Here, we want to measure the motion of surface or object 2 relative to surface or object 1. Let the absolute fixed reference position of the base be x_1 and surface 2 be x_2. The sensor measures the position of surface 2 relative to surface or object 1. Hence, from the geometry of **Figure 1** we have:

$$x_2 = x_1 + x_{2/1} \quad [1]$$

which can be rearranged to give relative motion as:

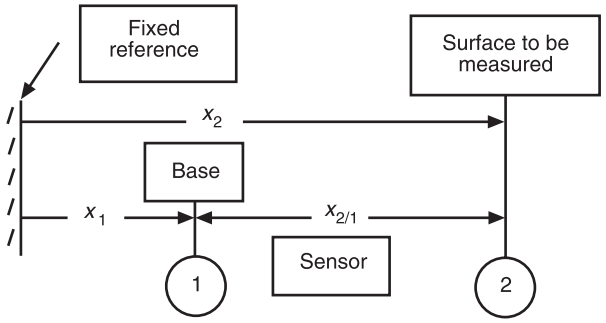


Figure 1 Geometry showing sensor placement relative to surface to be measured, 2, and instrument base position, 1, relative to the fixed reference position.

$$x_{2/1} = x_2 - x_1 \quad [2]$$

If x_1 is a constant, then the changes in the relative motion, $x_{2/1}$, will be the same as the changes in the absolute motion, x_2. While this is a very simple concept, it is often overlooked when applying sensors with fixed references, since it can happen that x_1 is not constant due to vibration of the sensor support. Unfortunately, the sensor measures only the relative motion $x_{2/1}$ and cannot distinguish whether x_1 or x_2 is the source of the signal.

This article is concerned with displacement and velocity sensors that are designed to measure motion with respect to a fixed reference. These sensors include four different displacement sensors and two different velocity transducers. The displacement sensors are capacitive, eddy current types, linear voltage differential transformer (LVDT), and strain gauges. The velocity sensors are electromagnetic and laser.

The articles **Transducers for absolute motion** and **Seismic instruments, environmental factors** deal with seismic instruments that make displacement, velocity, acceleration, and force measurements without a fixed reference. In all cases, the concept of relative motion between a base and the moving surface, as outlined in **Figure 1**, is used.

Displacement Sensors

Capacitive Displacement Sensors

A capacitive sensor has two plate or flat surfaces, called sensor head and target plate, as shown in **Figure 2**. These two surfaces are separated by an air gap of thickness x to form the two sides of a flat plate capacitor with capacitance C given by:

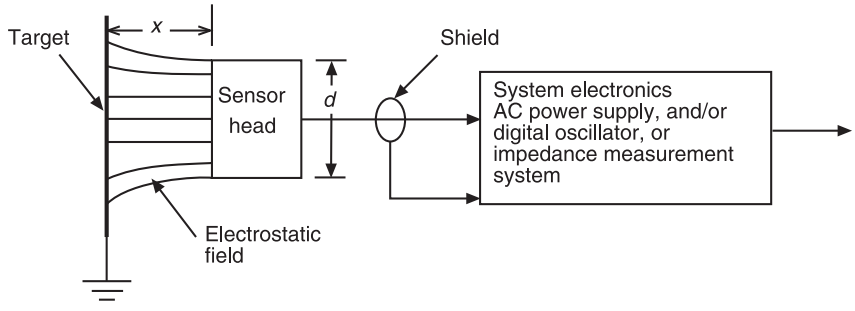


Figure 2 Capacitor sensor without guard ring where electrostatic field edge effects distort linear range. Note that either the target or the sensor head must be fixed.

$$C = \frac{kKA}{x} \quad [3]$$

where C is the capacitance in picofarads (pF), A is the sensor area ($\pi d^2/4$) for a circular plate of diameter d, K is the relative dielectric constant for the gap medium (unity for air), and k is the proportionality constant: 0.00885 for mm dimensions, or 0.225 for inch dimensions.When there is relative motion between the head and the target by an amount of Δx, the new capacitance is given by:

$$\Delta C + C = \frac{kKA}{x + \Delta x} \quad [4]$$

From eqn [4], we find that the change in capacitance divided by the original capacitance gives:

$$\frac{\Delta C}{C} = -\frac{\Delta x/x}{1 + \Delta x/x} \quad [5]$$

The impedance Z due to capacitance is given by:

$$Z = \frac{1}{\mathrm{j}C\omega} \quad [6]$$

where $\mathrm{j} = \sqrt{-1}$ and ω is the AC power supply frequency driving the electric field. Then, if we divide the change in impedance ΔZ by the original impedance Z, we obtain:

$$\frac{\Delta Z}{Z} = \frac{\Delta x}{x} \quad [7]$$

when eqns [3], [4], and [6] are used with eqn [5]. Eqn [7] shows that the change in impedance is directly proportional to the change in position. Hence, from eqn [7], the capacitive sensor sensitivity S (ohm mm^{-1} or ohm in^{-1}) becomes:

$$S = \frac{\Delta Z}{\Delta x} = \left|\frac{Z}{x}\right| = \left|\frac{1}{\omega kKA}\right| \quad [8]$$

For a given gap medium, this sensitivity is seen to depend on plate area A and power supply excitation frequency ω. We would like to make both area A and frequency ω as small as possible in order to improve sensitivity. While eqn [8] implies a linear relationship, experience shows that the transducer is linear so long as $0 < x < d/4$ for a circular sensor head, as shown in **Figure 2**.

However, if a guard ring is employed, as shown in **Figure 3**, the range of linearity is doubled so that $0 < x < d/2$. Hence, there is a practical tradeoff of limits that must be satisfied on transducer size versus the displacement to be measured. Similarly, the lowest value of the excitation frequency ω is limited by the frequency of the displacement that is to be measured. The sensitivity stability requires ω to be constant so that a digital oscillator is often used. Several different types of electronic circuits are used to implement eqn [8] that range from DC and AC-type circuits to tuned capacitive-inductive circuit to build an FM oscillator-type circuit where the frequency is controlled by the sensor capacitance and a fixed inductance.

Capacitance sensors have a number of advantages. First, it can be used with nearly any material with a resistivity less than 100 $\Omega\,\mathrm{cm}^{-2}$. Second, it can withstand large shock loads in the order of 5000 **g**. Third, it is noncontacting. Fourth, it can be used over a wide range of temperatures that range from 20°C to 870°C (68°F to 1600°F) when air is the gaseous medium between plates.

Eddy Current Sensors

Eddy current probes are noncontacting displacement sensors used extensively as gap detectors. Eddy currents are local electric currents induced in the

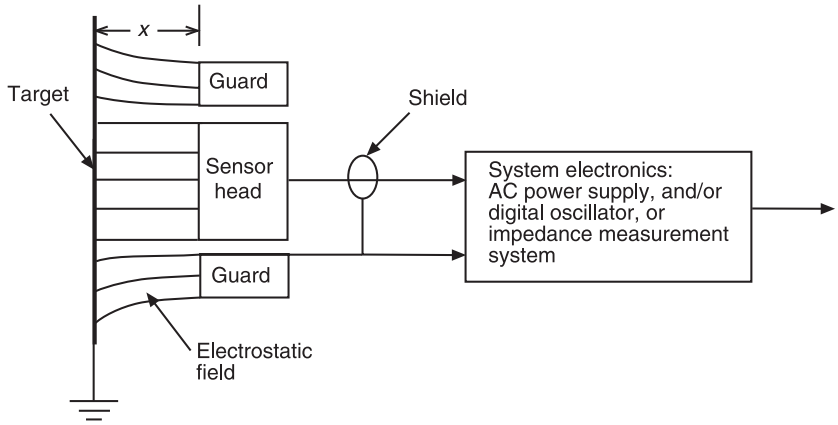


Figure 3 Capacitor sensor with guard ring to improve linearity range.

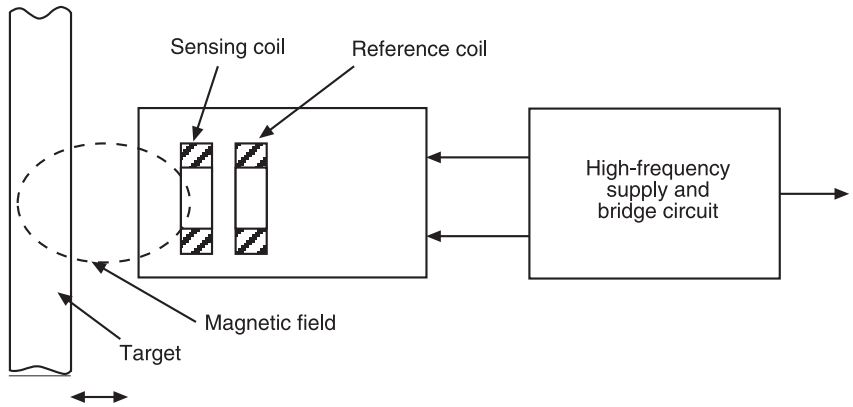


Figure 4 Schematic of eddy current sensor.

conducting target material by a time-varying magnetic field, as shown in **Figure 4.** The eddy currents generate an opposing magnetic field, resulting in a change in the induction of the sensing coil inductance. This inductance change is then measured by appropriate instrumentation.

For high-frequency excitation (say, of the order of MHz), the eddy currents are mostly at the surface of the target. Highly conductive materials like gold, copper, and aluminum are the most sensitive. Nonconducting targets can then be monitored if a metal foil is attached to it.

The sensor can be calibrated within specific tolerances to be linear in the generating range, typically from 80 μm to 1 mm. The sensitivity itself is material-dependent; unless this sensitivity is known for the specific material at hand, calibration will be necessary.

Rotating shaft vibrations are often monitored with such sensors, as shown in **Figure 5**. Many large rotating machines have built-in eddy current sensors that monitor the relative shaft-bearing vibrations in order to determine machine health.

Linear Variable Differential Transformer (LVDT)

The LVDT is well suited to measure displacements that range from $\pm$ 0.00001 in ($\pm$ 0.000254 mm) in a $\pm$ 0.050 in ($\pm$ 1.25 mm) full-scale LVDT to $\pm$ 10.0 in ($\pm$ 254 mm) full-scale in a large-displacement LVDT. The construction of a LVDT is shown in **Figure 6** where there are three coils wound around a common cylindrical core. The center coil is called the primary winding and is driven by a sinusoidal voltage. The other two coils are called secondary windings and are connected in series so that their voltages add to zero when the coupling core is at the null or balanced position. When the core is displaced in one direction or the other relative to its neutral or null, or central position, a phase-sensitive linear voltage is generated when within the linear range of the instrument. The core is usually made from a uniformly dense nickel–iron alloy that is carefully annealed to obtain excellent magnetic permeability.

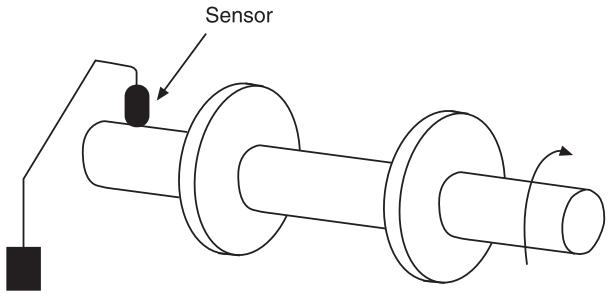


Figure 5 Schematic of eddy current sensor monitoring a rotating shaft.

The LVDT has a number of distinct features due to its principles of operation and construction. When the core is properly supported, there is no friction between the sensing elements. This makes the LVDT an excellent choice for creep or low-friction type of testing. The mechanical life is controlled by the core support system so it can have an infinite fatigue life if properly designed. The magnetic sensing circuit gives a theoretical infinite resolution characteristic that is only limited by the readout electronics. This infinite resolution is enhanced by the essentially frictionless response. The null repeatability is extremely stable due to the stability of the magnetic coupling principle that is employed. This null position is most affected by temperature changes that cause thermal expansion or contraction to occur. This high stability makes the LVDT ideal for use with high-gain closed-loop control systems. Finally, the input and output circuits are electrically isolated from one another so that excitation ground and signal ground are totally independent from one another.

The sensitivity of the LVDT depends on the excitation voltage, the resistance of the secondary windings, and the circuits connected to these windings, and the

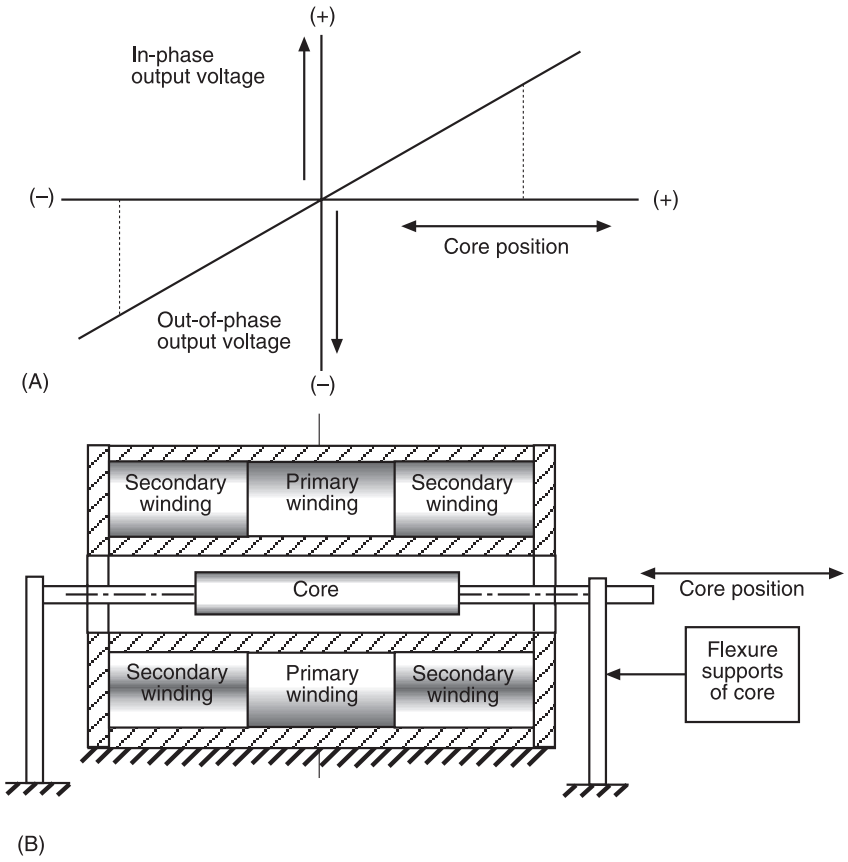


Figure 6 (A) Output voltage vs core position of linear variable differential transformer (LVDT). (B) Cross-section of LVDT showing primary winding, secondary windings, and core position.

frequency of excitation. These sensitivities are usually given in terms of $mV\,in^{-1}\,V^{-1}$ of excitation (or $mV\,mm^{-1}\,V^{-1}$ of excitation) at a specified frequency and amplifier impedance.

A modern development of the LVDT is called DCDT where all electronics such as the excitation voltage and signal demodulator are built into the transducer case. The DCDT simply requires a DC voltage like +7 or +14 V to be applied to the input terminals. The demodulator output voltage is proportional to the displacement and can be connected directly to the data-recording system as long as the data-recording input impedance is greater than a certain minimum resistance. In these cases, the sensitivity is then given simply as $mV\,in^{-1}$ or $mV\,mm^{-1}$. **Table 1** gives some typical characteristics.

Velocity

Electromagnetic Sensors

The electromagnetic sensor measures the relative velocity between the base side and the moving side by using Lenz's law. Typical construction is shown in **Figure 7**, where a wire coil is wound around a carrier structure that slips over the magnetic core in the gap between the core and the outside magnetic circuit. This construction is identical to audio speakers and even light-weight head phones. Lenz's law relates the

Table 1 Typical LVDT and DCDT specifications:

(A) AC (LVDT) excitation 3.0 V_{rms} at 2.4 kHz

Nominal range		*Sensitivity*	
(in)	(mm)	$((mV)\,V^{-1}\,in^{-1})$	$((mV)\,V^{-1}\,mm^{-1})$
± 0.050	± 1.25	5.80	230
± 0.125	± 3.0	4.20	165
± 5.00	± 125	0.14	5.50
± 10.0	± 250	0.070	2.80

(B) DC excitation (DCDT)

Nominal range		*Sensitivity*	
(in)	(mm)	$((mV)\,V^{-1}\,in^{-1})$	$((mV)\,V^{-1}\,mm^{-1})$
± 0.050	± 1.25	200	8.00
± 0.125	± 3.0	80.0	3.20
± 5.00	± 125	2.0	0.080
± 10.0	± 250	1.0	0.040

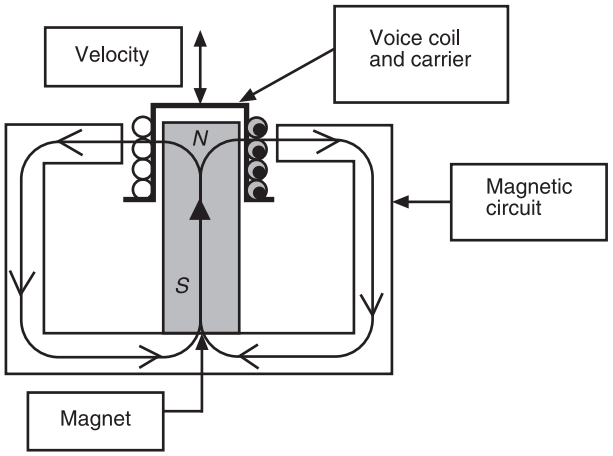


Figure 7 Cross-section of an electromagnetic sensor showing magnet and voice coil elements.

voltage generated (sometimes called back electromotive force or bemf) to the magnetic field strength B by:

$$E = (B\lambda n)v = K_v v \qquad [9]$$

where $B = \mathrm{d}\phi/\mathrm{d}x$ = field strength, ϕ is the field flux, λ is the coil length per coil, n is the number of coils, K_v is the instrument's voltage sensitivity, and v is the coil velocity.

The electromagnetic sensing circuit is shown in **Figure 8** where there is a voltage generator described by eqn [9], the sensing coil's inductance, L, and resistance, R_c, recording instrument's input impedance, R, which is usually only a resistance, and current i. The output voltage is E_o that appears across the recording instrument's input resistance, R. The differential equation describing this circuit is given by:

$$E_o = K_v v = \frac{L}{R}\dot{E} + (1+\beta)E_o \qquad [10]$$

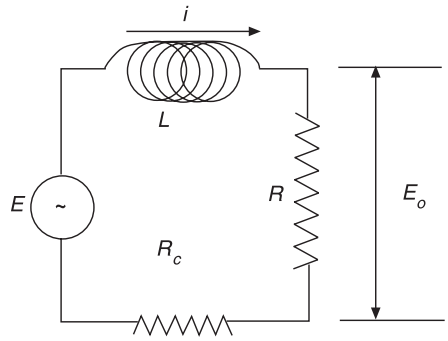


Figure 8 Equivalent electromagnetic sensor showing voltage generator, voice coil inductance, L, and resistance, R_c, instrument input resistance, R, output voltage, E_o, and circuit current, i.

where $\beta = R_c/R$ is the circuit resistance ratio. Since R_c is usually on the order of a few ohms and R should be on the order of 100 kΩ, the value of β is very small and can be neglected. Then, when the velocity is sinusoidal and is given by $v = v_0 e^{j\omega t}$, the corresponding transducer frequency response function becomes:

$$\frac{E_o}{S_v v_o} = \frac{1}{1 + j\omega T} \qquad [11]$$

where $T = (L/R)$ is the transducer's time constant and S_v is the voltage sensitivity in volts or mV per unit of velocity. It is evident that $K_v = S_v$ when β is small. **Figure 9** shows a plot of a typical frequency response function of an electromagnetic sensor, as described by eqn [11]. The time constant, T, is assumed to be equal to 0.001 s in this case. It is seen that there is little magnitude or phase error in the measured signal so long as $\omega < 100.0\,\mathrm{rad\,s^{-1}}$. Between $100 < \omega < 1000\,\mathrm{rad\,s^{-1}}$, it is seen that the magnitude is reduced and the phase angle changes dramatically. In fact, the magnitude is reduced by 3 dB (0.707) and the phase shift is 45° when $\omega = 1000\,\mathrm{rad\,s^{-1}}$. The

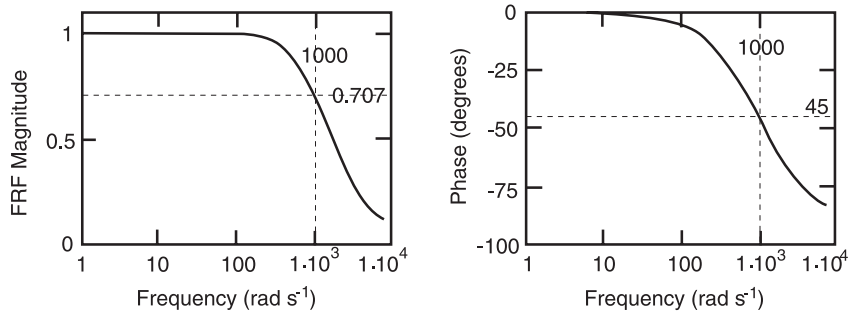


Figure 9 Magnitude and phase of typical electromagnetic sensor as function of frequency ω when the transducer time constant $T = 0.001$ s.

ability of this ideal instrument to measure velocities with frequency content above 1000 rad s^{-1}, is generally unacceptable. Hence, it is important for the user to be aware of transducer frequency limitations; particularly with this instrument, since the user is the one who selects the value of R when the instrument is connected to the recording instrument.

The Laser Doppler Vibrometer

The device used most often for measuring the velocity of a vibrating object with respect to a fixed reference system is the laser Doppler vibrometer (LDV). An outgrowth of the laser Doppler velocimeter used for gas and fluid flow measurement, it has undergone significant development in the past few years and is marketed in many countries around the world. This success is due in part to improved electrooptic technologies and to the implementation of the personal computer or workstation. The LDV is also popular because it is easy to use. One merely points the LDV laser beam at a location where a vibration measurement is required and the data can be viewed immediately and recorded for additional processing later.

Computer-controlled optical scanning and data acquisition provide for the beam to be directed rapidly at an array of locations on a structure vibrating at resonance, pausing at each for a few milliseconds to take and store data and then graphically display the mode shape on a monitor. The scanning laser Doppler vibrometer (SLDV) can capture and display a complicated resonant mode shape in seconds that would require the use of thousands of accelerometers and lengthy data processing to duplicate. The SLDV can be used for objects ranging from a few square millimeters up to several square meters.

Operating Principles

The LDV is made possible by the coherent properties of laser light. **Figure 10A** shows one complete cycle of a HeNe beam with amplitude (A_0) and wavelength (λ) of 0.6328 μm. With the speed of light (c) being approximately 300×10^6 m s^{-1}, the frequency, λ/c, is about 4.74×10^{14} Hz $(2.98 \times 10^{15}$ rad $s^{-1})$. If two coherent beams, each of amplitude A_0 are combined, the resulting waveform will have twice the amplitude (**Figure 10B**). If one of the beams is shifted in phase (ϕ) by π rad before combination, the two beams will cancel each other out (**Figure 10C**). All optical detectors produce a signal that is proportional to intensity, which is the square of the amplitude (**Figure 10D**).

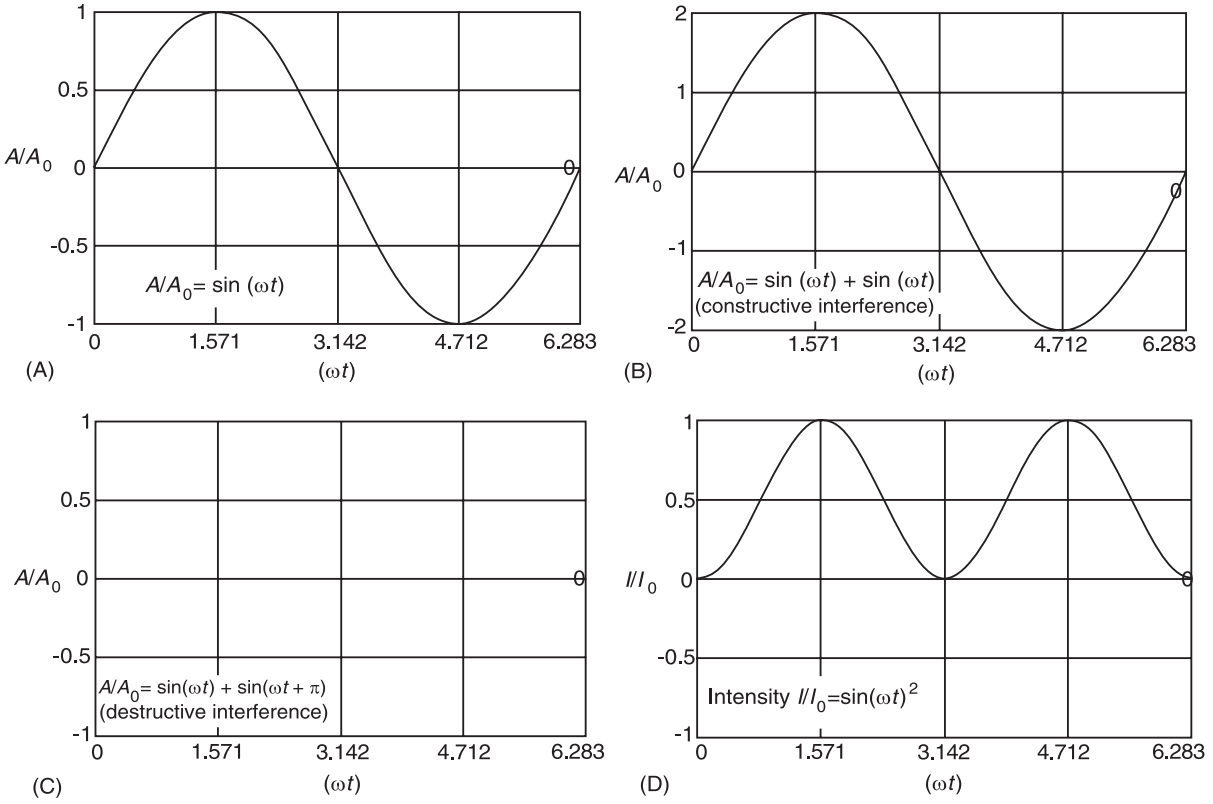


Figure 10 (A) Output from HeNe laser. (B) Superposition of two coherent beams. (C) Superposition of two completely out-of-phase coherent beams. (D) Result of using a square law detector.

One type of LDV uses a version of the Michelson interferometer (**Figure 11**). The laser light beam is divided into two beams by beam splitter (BS). One beam travels to the vibrating object, returns back along the same path, and is reflected downward by the splitter. Since it contains information about the vibrating surface, it is known as the signal beam. The other, called the reference beam, passes to a stationary mirror, is reflected downward, and is combined with the signal beam. Any change between reference and signal beam path lengths will cause an interference that is observed as a change in intensity at the detector. Each time the point on the structure moves an amount equal to half the wavelength of the laser light used, the intensity will undergo one full cycle from light to dark to light. The frequency of this fluctuation, f_D, is called the Doppler frequency and is related to the velocity, v, of the point on the structure by:

$$f_D = 2v/\lambda \qquad [12]$$

where λ is the wavelength of the laser light. If the structure is moving at a constant velocity of $1\,m\,s^{-1}$ and a HeNe laser is used ($\lambda = 0.6328\,\mu m$), $f_D = 3.174$ MHz. Since the frequency of the reference beam is 4.74×10^8 MHz, this is a very small increase (or decrease, depending upon the direction of the velocity) to detect. Since the best frequency measurement capability of even the newest detectors is less than 10^3 MHz, some additional approach is required.

When the shifted frequency is combined with the reference frequency, a time-dependent interference or beat frequency results which, when reaching the photodetector, produces an output signal that contains observable information about the velocity, v. Unfortunately, because detectors measure intensity instead of amplitude, they do not discriminate between positive and negative velocities. If the structure is vibrating, this signal is frequency-modulated. In some LDV designs a technique called homodyning is used to decode the information in the combined signal and reference beams. This method uses electronic processing and is usually performed outside the interferometer loop.

Optical Heterodyning

Another solution to the problem of velocity sign is to introduce a slight frequency shift in the reference beam using an electrooptic device such as a Bragg cell. To do this, a different type of interferometer, a modified Mach–Zender configuration, is used (**Figure 12**). The Bragg cell is inserted in the reference beam leg. The Doppler frequency generation is the same as with the Michelson interferometer. The Bragg cell produces a known frequency shift in the reference beam, such that the combined reference and object beam contains three frequencies: the original reference, the Doppler signal beam, and the Bragg cell frequency. When there is no vibration present, the output of the detector is a steady function of the Bragg cell frequency. When vibration is present, it is sensed as a frequency modulation of that signal. The output from the detector is electronically demodulated in a variety of ways, depending upon the manufacturer, to produce an output voltage that is proportional to the instantaneous velocity of the structure. The introduction of the constant frequency shift is called heterodyning.

A thorough mathematical treatment of the above processes is beyond the scope of this article and the reader is referred to current symposia papers, manufacturers' literature and the Further reading section for greater detail.

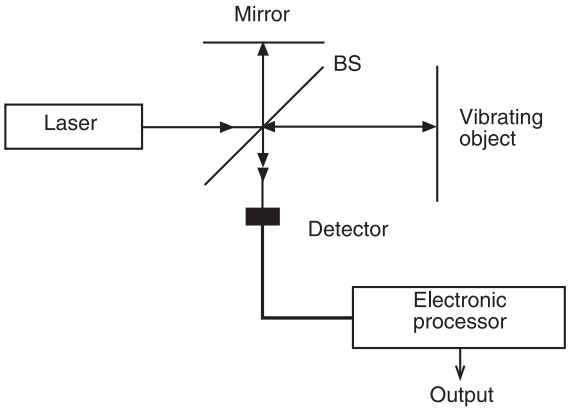


Figure 11 Michelson interferometer configuration. BS, beam splitter.

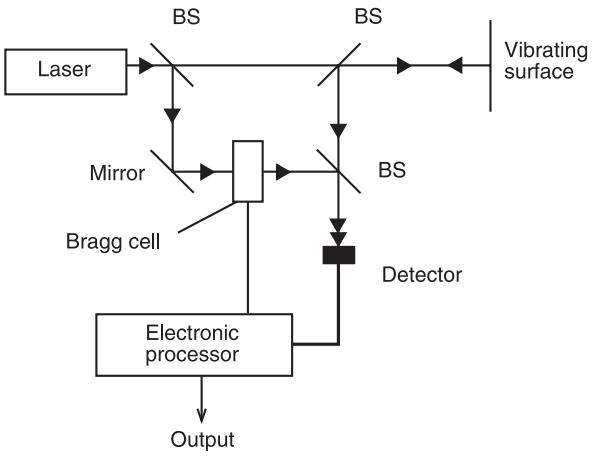


Figure 12 Modified Mach–Zender interferometer. BS, beam splitter.

Choosing an LDV

When choosing which of the many commercial LDVs to use, there are some technical factors that need to be considered.

Surface effects Unlike conventional interferometers, the LDV relies on focusing the interrogating beam to a point so that the return beam, which is actually a radiating speckle field due to diffraction effects at the surface, completely fills the aperture of the detector with as few speckles as possible. In practice, surfaces will range from nearly specular (mirror-like) to totally diffuse. Some LDV systems are very tolerant of variations in surface conditions, while others require the use of retroreflective coatings to provide usable signals. If vibration is to be measured at high temperatures, this becomes an important consideration, since the surface may undergo physical changes that affect the return signal. Most high-temperature metals require no surface treatment below 1800°C. High-temperature composite materials have been tested up to 800 °C using ceramic beads as a retroreflecting coating.

Effect of coherence Some LDVs must be located no more than a few centimeters from the vibrating structure; others have been used as far away as 200 m. When a multimode laser is used in an LDV, it is usually recommended that the vibrating structure be located at some integer multiple of the laser cavity length away to improve the quality of the data.

Filter effect Most commercial LDVs use some form of electronic filtering to optimize the quality of the output signal. If the user is interested in measuring not only the velocity of the structure but also its vibrational phase, the manufacturers' specifications must be closely examined. It is also an important consideration when measuring the response to broadband random excitation.

Operating Range

Figure 13 represents one way that the useful range of an LDV is displayed, showing the limits for velocity, displacement, frequency, and acceleration. This illustration is not for any particular LDV but is indicative of what is found in the manufacturers' literature.

Environmental Considerations

If measurements are made using the LDV in the presence of sound pressure levels greater than 130 dB, consideration must be given to designing an

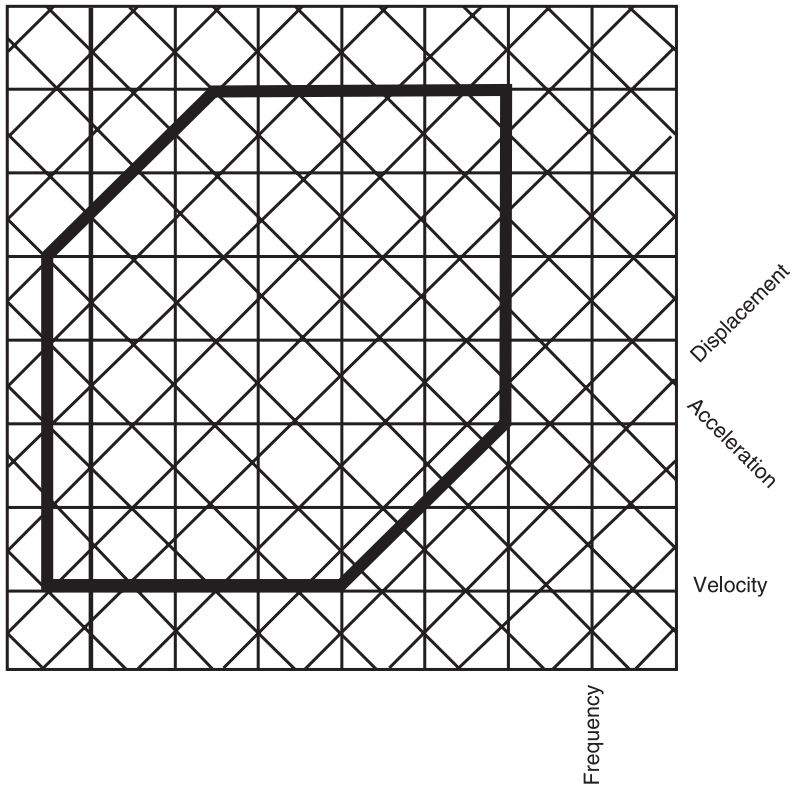


Figure 13 Usable range chart.

acoustic shield for the instrumentation. Since this is not a common use of the LDV, there is very little information available from the manufacturers as to what is a safe level.

Other LDV Devices

Some LDVs have two measurement beams, so that the difference in velocity between two moving points can be measured.

The previous discussions have been related to measuring the velocity normal to a surface. There are commercial LDVs designed specifically for measuring the velocity of rotating bodies and in-plane vibrations.

Diode lasers and fiberoptic interferometers are being incorporated into commercially available systems.

Nomenclature

A	sensor area
B	field strength
C	capacitance
d	diameter
k	proportionality constant
K	relative dielectric constant
L	inductance
R	resistance
S	sensor sensitivity
v	velocity
Z	impedance
ϕ	field flux
λ	wavelength
ω	frequency

See also: **Laser based measurements**; **Seismic instruments, environmental factors**; **Sensors and actuators**; **Transducers for absolute motion**.

Further Reading

Dally JW, Riley WF and McConnell KG (1993) *Instrumentation for Engineering Measurements*. New York, NY: Wiley.

Drain LE (1980) *The Laser Doppler Technique*. London: John Wiley.

Herceg EE (1976) *Handbook of Measurement and Control*. Pennsauken, NJ: Schaevitz Engineering. Web address: www.shaevitz.com

Kobayashi AS. (ed.) (1987) *Handbook on Experimental Mechanics*. Englewood Cliffs, NJ: Prentice-Hall.

Tomasini EP (ed.) (1996) *Second International Conference on Vibration Measurements by Laser Techniques: Advances and Applications*. Ancona, Italy: AIVELA (Associazione Italiana Velocimetria Laser).

TRANSFORM METHODS

S Braun, Technion – Israel Institute of Technology, Haifa, Israel

Copyright © 2001 Academic Press

doi:10.1006/rwvb.2001.0158

General

Mathematical transforms are main tools of disciplines dealing with signal and system. Analysis (and synthesis) in the transform domain complements the one of time domain, and often has specific advantages.

The existence of (direct) transforms as well as of their inverse enables to switch back and forth between both domains. The information in both domains is thus equivalent, even if the type of presentation is markedly different.

The transform relation is here denoted by a double arrow. A capital letter (L for Laplace, Z for Z-transform and F for Fourier) shows the transform at hand, and a superscript of $[\ ]^{-1}$ denotes the inverse transform. Upper case letters will be used for transforms domains, and lower case letters for the time domain. For example, for the Laplace transform:

$$X(s) = L[x(t)]$$
$$x(t) = L^{-1}[X(s)]$$
$$x(t) \longleftrightarrow X(s)$$

Some transforms are geared to continuous signals and systems, for instance the Laplace and Fourier transforms; others, like the Z-transform and discrete Fourier transform are geared to discrete ones.

The dynamics of linear, lumped parameter, continuous systems are modeled by linear differential equations, those of discrete systems by difference equations. The response of such systems to an excitation signal is given (with zero initial conditions) by the convolution of the input and the system's impulse response. One important property of these transforms relates to the operation of convolution: the transform of the convolution equals the product of the transforms. Applying the transform then results in a set of algebraic equations, as opposed to differential or difference ones. Analytical solution then necessitates the solving of algebraic equations. This is one reason why transform methods prevail in many theoretically oriented texts.

Another aspect is that of computability. The possibility of computing Fourier transform numerically via the efficient fast Fourier transform (FFT) algorithm has practically revolutionized signal processing. Fourier methods thus are central to spectral analysis and system identification tasks in the area of vibration engineering.

In what follows, some general aspects of Laplace, Z and Fourier transforms are given. A more detailed exposition of Fourier methods follows. This includes Fourier series and integral transforms, the discrete Fourier transform and the FFT algorithm.

The Laplace Transform

These are given by:

$$X(s) = \int_{-\infty}^{\infty} x(t) \exp(-st)\, \mathrm{d}t \qquad [1a]$$

and

$$x(t) = \frac{1}{2\pi j} \int_{\sigma-j\infty}^{\sigma+j\infty} X(s) \exp(st)\, \mathrm{d}s \qquad [1b]$$

$$s = \sigma + j\omega$$

The integral will converge for the majority of signals typical of engineering applications, but not necessarily for all of them. Associated with the transforms is a region of convergence (ROC). It is only with such an association that an inverse transform can be defined uniquely.

A unilateral transform is used for causal signals, usually encountered in vibration engineering:

$$X(s) = \int_{0}^{\infty} x(t) \exp(-st)\, \mathrm{d}t \qquad [2]$$

Properties

Some important properties of the Laplace transform are given below. Given that $x(t) \leftrightarrow X(s)$:

- Linearity:

$$a_1 x_1(t) + a_2 x_2(t) \longleftrightarrow a_1 X_1(s) + a_2 X_2(s) \qquad [3a]$$

and generally:

$$L\left[\sum_i a_i x_i(t)\right] \longleftrightarrow \sum_i a_i L[x_i(t)] \qquad [3b]$$

- Time shift:

$$x(t - t_0) \longleftrightarrow \exp(-st_0) X(s) \qquad [4]$$

- Scaling:

$$x(at) \longleftrightarrow \frac{1}{|a|} X\left(\frac{s}{a}\right) \qquad [5]$$

- Differentiation:

$$\frac{\mathrm{d}^n}{\mathrm{d}t^n} x(t) \longleftrightarrow s^n X(s) + \sum_{i=1}^{n} s^{i-1} \frac{\mathrm{d}^{n-i}}{\mathrm{d}t^{n-i}} x(t)|_{t=0^+} \qquad [6]$$

- Integration:

$$\int_{-\infty}^{t} x(\tau)\, \mathrm{d}\tau \longleftrightarrow \frac{X(s)}{s} + \frac{1}{s} \int_{-\infty}^{0^+} x(\tau)\, \mathrm{d}\tau \qquad [7]$$

- Convolution:

$$x_1(t) \otimes x_2(t) \longleftrightarrow X_1(s) X_2(s) \qquad [8]$$

- Multiplication:

$$x_1(t) x_2(t) \longleftrightarrow X_1(s) \otimes X_2(s) \qquad [9]$$

One important application concerns the solving of linear differential equations of the type:

$$\sum_{k=0}^{N} a_k \frac{\mathrm{d}^k}{\mathrm{d}t^k} y(t) = \sum_{k=0}^{M} b_k \frac{\mathrm{d}^k}{\mathrm{d}t^k} x(t) \qquad [10]$$

Applying the laws of linearity and differentiation (eqns [3] and [6]) with zero initial conditions results in:

$$\sum_{k=0}^{N} a_k s^k Y(s) = \sum_{k=0}^{M} b_k s^k X(s) \qquad [11]$$

The resulting algebraic equation is often easy to solve for analytical cases with closed form solutions.

The important notion of a 'transfer function' can now be defined as:

$$H(s) = \frac{Y(s)}{X(s)} = \frac{\sum_{k=0}^{M} b_k s^k}{\sum_{k=0}^{N} a_k s^k} = \frac{B(s)}{A(s)} \qquad [12]$$

Another characterization of systems is via their impulse response. Mathematically this is the response to a Dirac function $\delta(t)$. It is straightforward to show that:

$$L[\delta(t)] = 1 \qquad [13]$$

And hence the response:

$$Y(s) = H(s) \qquad [14a]$$

$$h(t) = y(t) = L^{-1}[H(s)] \qquad [14b]$$

An additional description of the system is that of the zero/poles. The transfer function $H(s)$ of many physical systems is described by a ratio of rational polynomials in s. The values of s for which the nominator equals zero are then the zeros of the system. Those at which the denominator equals zero are the poles:

$$\begin{aligned} A(s) &= \prod_{k=1}^{N} (s - z_k) \\ B(s) &= b_m \prod_{k=1}^{M} (s - p_k) \\ H(s) &= \frac{B(s)}{A(s)} \end{aligned} \qquad [15]$$

As will be presented later, the frequency response function (FRF) of a system is given by:

$$H(\mathrm{j}\omega) = H(s)\big|_{s=\mathrm{j}\omega} \qquad [16]$$

i.e., by evaluating H on the $s = \sigma + \mathrm{j}\omega$ contour.

Inversion of the Laplace Transform

While the general expression [1] necessitates an integration in the complex plane, simpler techniques often suffice. Tables of Laplace transforms can obviously be used for many cases. One important case concerns transfer functions where the nominator and denominator of $H(s)$ are rationale polynomials in the variable s. Inversion can then be done by fraction expansion using the method of residuals:

$$X(s) = \frac{B(s)}{A(s)} = \sum_{k=1}^{N} \frac{A_k}{s - p_k} \qquad [17]$$

and the transform of each component can be shown to equal:

$$\frac{A_k}{s - p_k} \longleftrightarrow A_k \exp(p_k t) \qquad [18]$$

The decomposition by the residual, a standard method well-documented in any mathematical text on Laplace transform, is slightly more complicated for the case of multiple poles.

Example We analyze a classic single-degree-of-freedom (SDOF), second-order system, composed of a mass, spring and damper (**Figure 1A**):

$$x(t) \longleftrightarrow X(s)$$

Applying the Laplace transform and assuming zero initial conditions:

$$ms^2 X(s) + csX(s) + kX(s) = P(s)$$

The transfer function:

$$\begin{aligned} H(s) &= \frac{X(s)}{P(s)} \\ &= \frac{1/m}{s^2 + (c/m)s + (k/m)} = \frac{1/m}{s^2 + 2\zeta\omega_\mathrm{n} s + \omega_\mathrm{n}^2} \end{aligned}$$

with $\omega_\mathrm{n} = (k/m)^{1/2}$ the undamped natural frequency in rad s^{-1}:

$$\zeta = \frac{c}{2(mk)^{1/2}} \text{ the damping ratio}$$

The system poles:

$$s^2 + 2\zeta\omega_n + \omega_n^2 = 0$$
$$s_{1,2} = -\zeta\omega_n \pm j\omega_n\left(1-\zeta^2\right)^{1/2} = -\zeta\omega_n \pm j\,\omega_d$$

with ω_d the damped natural frequency.

The impulse response: Rearranging $H(s)$, and looking at Laplace transform tables:

$$h(t) = L^{-1}[H(s)] = L^{-1}\left[\frac{1}{m\omega_d}\frac{w_d}{(s+\zeta\omega_n)^2+\omega_d^2}\right]$$
$$= \frac{1}{m\omega_d}\exp(-\zeta\omega_n t)\sin(\omega_d t)$$

The frequency response function:

$$H(j\omega) = H(s)_{s=j\omega} = \frac{1/m}{\omega_n^2 - \omega^2 + j2\zeta\omega\omega_n}$$

A specific numerical example, with $m = 0.1\,\text{kg}$, $k = 1000\,\text{N m}^{-1}$ and $c = 1\,\text{N s m}^{-1}$ is shown in **Figure 1** (where the frequency is in Hz). The corresponding natural undamped frequency is $f_0 = 19.5\,\text{Hz}$, $\zeta = 5$ percent, and the poles $-5.0000 \pm j99.8749$.

Z-transforms

This is given by:

$$X(z) = \sum_{n=-\infty}^{\infty} x(n)z^{-n} \qquad [19a]$$

$$x(n) = \frac{1}{2\pi j}\int X(z)z^{n-1}\,dz \qquad [19b]$$

The integral will converge for certain regions of the complex variable z. Associated with the transform (19) is an ROC. It is only with such an association that an inverse transform can be defined uniquely.

A unilateral transform is often used for causal signals:

$$X(z) = \sum_{n=0}^{\infty} x(n)z^{-n} \qquad [20]$$

Properties

Some important properties of the Z transform are given below:

- Linearity:

$$\left.\begin{array}{l} a_1x_1(n) + a_2x_2(n) \leftrightarrow a_1X_1(z) + a_2X_2(z) \\ Z\left[\sum_i a_ix_i(n)\right] = \sum_i a_iZ[x_i(n)] \end{array}\right\} \qquad [21]$$

- Time shift (for the unilateral case, eqn [20]):

$$x(n-n_0) \leftrightarrow z^{-n_0}X(z) \qquad [22]$$

- Time reversal:

$$x(-n) = X(1/z) \qquad [23]$$

- Convolution:

$$x_1(n) \otimes x_2(n) \leftrightarrow X_1(z)X(z) \qquad [24]$$

One important application concerns the solving of linear difference equations of the type:

$$\sum_{k=0}^{N} a_k y(n-k) = \sum_{k=0}^{M} b_k x(n-k) \qquad [25]$$

Applying the laws of linearity and time shift (eqns [21] and [22]) results in:

$$\sum_{k=0}^{N} a_k z^{-k} Y(z) = \sum_{k=0}^{M} b_k z^{-k} X(z) \qquad [26]$$

The resulting algebraic equation is often easy to solve for analytical cases with closed form solutions.

The important notion of a discrete transfer function can now be defined as:

$$H(z) = \frac{Y(z)}{X(z)} = \frac{\sum_{l=0}^{M} b_k z^{-k}}{\sum_{k=0}^{N} a_k z^{-k}} \qquad [27]$$

which is of course a linear time invariant system.

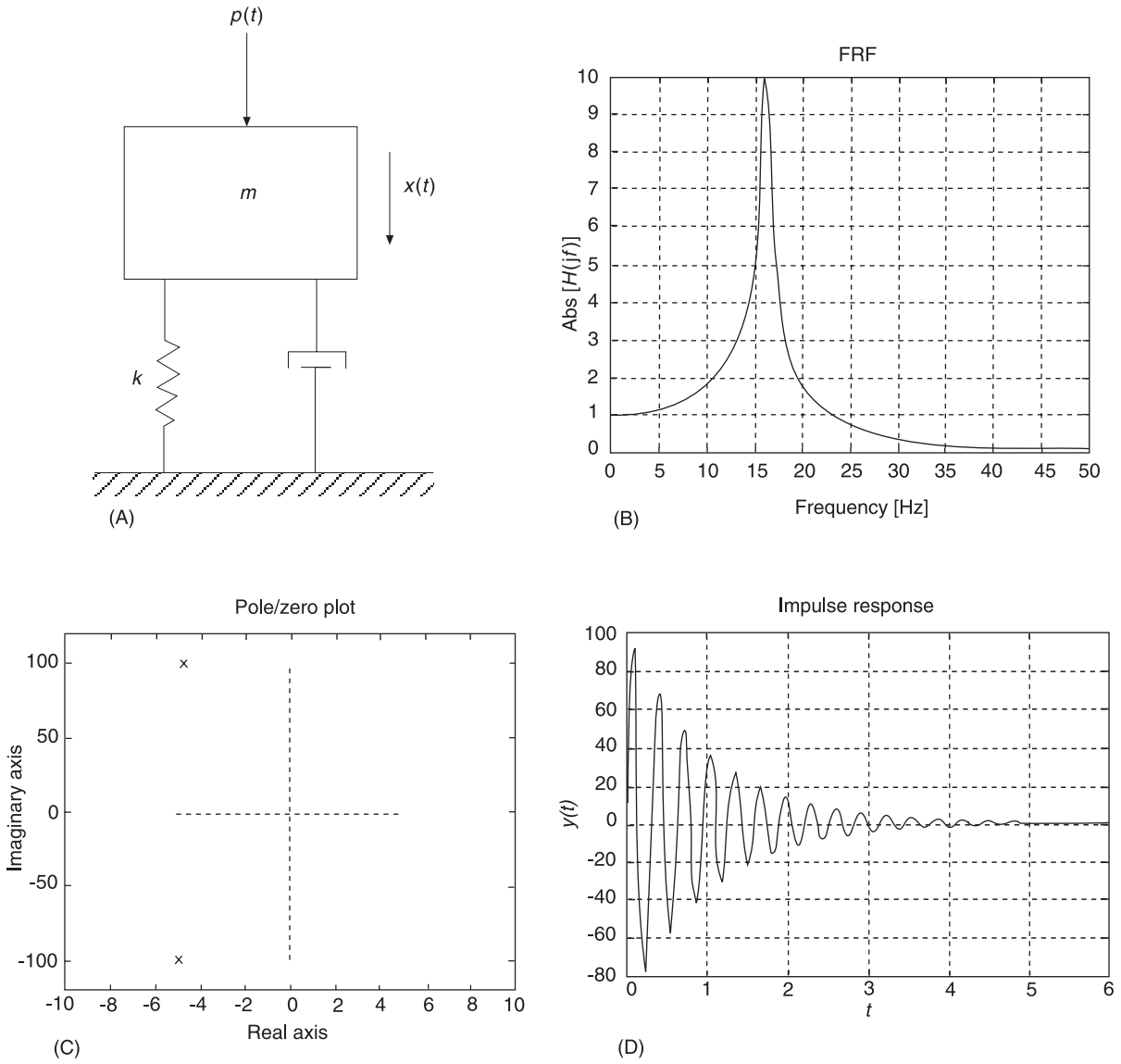


Figure 1 (A) Mass–spring–damper system. (B) Frequency response function (FRF). (C) Pole/zero plot (only poles exist). (D) Impulse response.

Another characterization of systems is via their impulse response. Mathematically, this is the response to a Dirac function $[\delta(n)]$. It is straightforward to show that:

$$Z[\delta(n)] = 1 \qquad [28]$$

And hence the response:

$$X(z) = H(z)Z[\delta(t)] = H(z)$$
$$x(n) = h(n) = Z^{-1}[H(z)] \qquad [29]$$

An additional description of the system is that of the zero/poles. The transfer function $H(z)$ of many linear time-invariant systems that is described by a ratio of rational polynomials in z. The values of z for which the nominator and denominator equals zero, are then z_k, the zeros and p_k, poles of the system:

$$H(z) = b_m \frac{\prod_{k=j}^{M}(z - z_k)}{\prod_{k=1}^{N}(z - p_k)} \qquad [30]$$

The frequency response of a discrete system is given by:

$$H(\mathrm{j}\phi) = H(z)\big|_{z=\mathrm{j}\phi} \qquad [31a]$$

$$\phi = \omega\,\Delta t \quad H(\mathrm{j}\,\omega) = H(z)\big|_{z=\exp(\mathrm{j}\omega\,\Delta t)} \qquad [31b]$$

i.e., evaluating $H(z)$ on the $z = \exp(\mathrm{j}\omega\Delta t)$ contour, with Δt the sampling interval. Note that this FRF is a continuous function of the frequency. It is also periodic with $2\pi/\Delta t$.

Inversion

While the general expression [19] necessitates an integration in the complex plane, simpler techniques often suffice. One important case concerns transfer functions where the nominator and denominator of $H(z)$ are rational polynomials is the variable z. Inversion can then be done by fraction expansion by the method of residuals:

$$X(z) = \sum_{k=1}^{N} \frac{A_k}{1 - p_k z^{-1}} \qquad [32]$$

and the transform (for the causal case) of each component can be shown to equal:

$$\frac{A_k}{1 - p_k z^{-1}} \leftrightarrow A_k z_k^n u(n) \qquad [33]$$

where $u(n)$ is the unit step function.

Comparing the descriptions of continuous and discrete systems, we can observe the similar types of descriptions available, namely transfer functions, impulse responses, poles/zeros and FRFs.

Example The following recursive difference equation simulates a SDOF system having $f_n = 40\,\mathrm{Hz}$:

$$y(n) = b_0 x(n) + b_1 x(n-1) + b_2 x(n-2) - a_1 y(n-1) - a_2 y(n-2)$$

with:

$$a_1 = -1.7217, \quad a_2 = 0.938,$$
$$b_0 = 0.0580, \quad b_1 = 0.1161, \quad b_2 = 0.0580$$

Applying a Z transform and solving the algebraic equations for:

$$H(z) = \frac{Y(z)}{X(z)}$$

results in:

$$H(z) = \frac{0.058 + 0.1161z^{-1} + 0.058z^{-2}}{1 + 1.7217z^{-1} - 0.9538z^{-1}}$$

Zeros and poles are computed by equating numerator and numerator polynomials to zero:

$$z_k = -1 \pm \mathrm{j}(0)$$
$$p_k = 0.8608 \pm \mathrm{j}0.4613$$

For data sampled at intervals of $\Delta t = 5\,\mathrm{ms}$, the FRF is:

$$H(z)_{z=\mathrm{j}\omega\Delta t} = \frac{0.058(\mathrm{j}\omega\,\Delta t)^2 + 0.1161(\mathrm{j}\omega\,\Delta t) + 0.058}{(\mathrm{j}\omega\,\Delta t)^2 + 1.7217(\mathrm{j}\omega\,\Delta t) + 0.9538}$$

and the results (with frequency in Hz) are shown in **Figure 2**.

Fourier Transforms

These have similarities to the Laplace transform, evaluated for the special case of:

$$s = \mathrm{j}\omega$$

$$x(t) \leftrightarrow X(\mathrm{j}\omega)$$

$$X(\mathrm{j}\omega) = \int_{-\infty}^{\infty} x(t)\,\exp(-\mathrm{j}\omega t)\,dt \qquad [34a]$$

$$x(t) = \int_{-\infty}^{\infty} X(\mathrm{j}\omega)\,\exp(-\mathrm{j}\omega t)\,dt \qquad [34b]$$

The transform is complex, and often presented in polar form via a modulus and phase:

$$X(\mathrm{j}\omega) = |X(\mathrm{j}\omega)|\underline{/\phi(\omega)} \qquad [34c]$$

The convergence thus may not always exist for cases where the Laplace one does. Some signals may not satisfy the requirement of being absolutely square integrable, i.e.,

$$\int_{-\infty}^{\infty} \left|x^2(t)\,\mathrm{d}t\right| < \infty$$

For some signals, the use of impulses in the Fourier transform may have to be used to enable its use in actual problems. In spite of this limitation, the

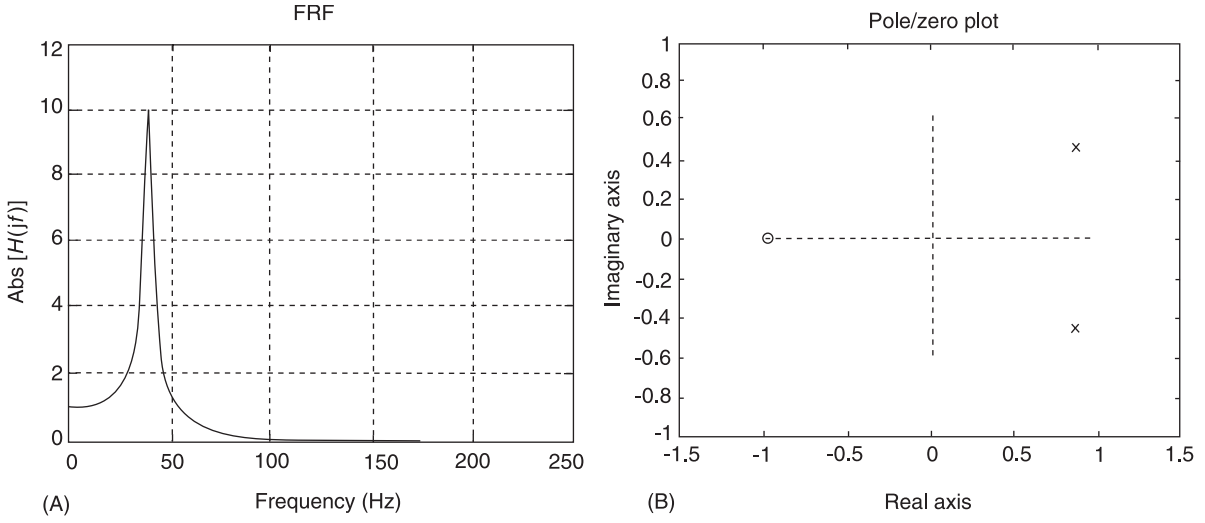


Figure 2 (A) Discrete system–FRF. (B) Pole/zero plot.

Fourier transform is widely used in signal and system analysis. One of its most appealing aspects is the physical interpretation of the domain transform: the time domain signals are transformed to the frequency domain. The frequency 'content' of a signal is an intuitively appealing description in many engineering applications.

Another advantage is the availability of efficient computational procedures. These are based on the FFT, a cornerstone of today's signal processing.

Thus signal and system analysis draws consistently on methods based on the Fourier transform. The actual tool used depends on the signal characteristics. The following describes the various existing Fourier tools in some detail, the tools used for specific signal types being:

- >Fourier transform (FT) (sometimes called the Fourier integral transform, and sometimes Fourier integral) – for continuous aperiodic (transient) signals;
- Fourier series (FS) – for continuous periodic signal;
- discrete Fourier series (DFS) – for discrete periodic signals;
- discrete Fourier transform (DFT) – for discrete aperiodic signals.

Fourier Transform

These were given by [34]. The frequency in Hz is sometimes preferred as a variable, resulting in:

$$X(f) = \int_{-\infty}^{\infty} x(t)\,\exp\,(-\mathrm{j}2\pi ft)\,\mathrm{d}t \qquad [35]$$

- Linearity:

$$a_1x_1(t) + a_2x_2(t) \leftrightarrow a_1X_1(\mathrm{j}\omega) + a_2X_2(\mathrm{j}\omega)$$
$$F\left[\sum_i a_ix_i(t)\right] = \sum_i a_iF[x_i(t)] \qquad [36]$$

- Time shift:

$$F[x(t-t_0)] = \exp\,(-\mathrm{j}\omega t_0)X(\mathrm{j}\omega) \qquad [37]$$

- Scaling:

$$F[x(at)] = \frac{1}{|a|}F\left[X\left(\mathrm{j}\frac{\omega}{a}\right)\right] \qquad [38]$$

- Differentiation:

$$F\left[\frac{\mathrm{d}}{\mathrm{d}t}x(t)\right] = \mathrm{j}\omega X(\mathrm{j}\omega) \qquad [39]$$

- Integration:

$$F\left[\int_{-\infty}^{t} x(t)\,\mathrm{d}t\right] = \frac{1}{\mathrm{j}\omega}X(\mathrm{j}\omega) \qquad [40]$$

- Convolution:

$$F[x_1(t) \otimes x_2(t)] = X_1(\mathrm{j}\omega)X_2(\mathrm{j}\omega) \qquad [41]$$

- Products, modulation:

$$F[x_1(t)x_2(t)] = X_1(j\omega) \otimes X_2(j\omega) \qquad [42]$$

- Parseval's law:

$$\int_{-\infty}^{\infty} |x(t)|^2 \, dt = \frac{1}{2\pi} \int_{-\infty}^{\infty} |X(j\omega)|^2 \, d\omega = \int_{-\infty}^{\infty} |X(f)|^2 \, df \qquad [43]$$

The energy is invariant under the FT, and can be computed in either domain.

The properties are similar to those of the Laplace transform, but physical insight can be gained. Practical implications often follow and some of these are now addressed.

Linearity The superposition indicated by [36] implies that the contribution to each frequency range may be investigated independently for each signal component.

Time shift A pure delay does not affect the modulus of the transform. The phase however is shifted proportionally to the frequency.

Differentiation/Integration These operations weigh the modulus of the transform proportionally or inversely to the frequency (with a positive or negative 90° shift in phase).

Scaling This property has important practical implications. Compressing a signal in the time domain ($a > 1$) results in a spread in the frequency domain, and vice versa. Short impulses thus occupy a wide frequency range. Time duration and bandwidth (BW) are thus inversely proportional.

The duration in the time domain, T_{DUR}, and spread in the frequency domain BW, can be defined in various ways. One possibility is through a normalized second moment as:

$$T_{DUR} = \left[\frac{\int_{-\infty}^{\infty} t^2 x^2(t) \, dt}{\int_{-\infty}^{\infty} x^2(t)} \right]^{1/2} \qquad [44a]$$

$$BW = \left[\frac{\int_{-\infty}^{\infty} \omega^2 |X(j\omega)|^2 d\omega}{\int_{-\infty}^{\infty} |X(j\omega)|^2 d\omega} \right]^{1/2} \qquad [44b]$$

but the inverse relation between these two remains for other possible definitions.

Example We will take a Gaussian signal, for which the closed-form expression will result in:

$$x(t) = K_1 \exp\left(-\frac{t^2}{2\sigma^2}\right) \leftrightarrow K_2 \exp\left(-\frac{\sigma^2\omega^2}{2}\right) \qquad [45]$$

where K_1 and K_2 are chosen so as to satisfy Parseval's law.

To see the effect of compressing the time duration, using $\sigma = 1$, we use the scaling property [38], the results being shown in **Figure 3** (for $a = 1$ and $a = 3$). The implication is of utmost practicality: the shorter the transient, the wider the frequency bandwidth of the signal.

By analogy with eqns [10]–[14], a differential equation will be transformed to an algebraic one by application of a FT. Eqn [10] will be transformed to

$$\sum_{k=0}^{N} a_k (j\omega)^k Y(j\omega) = \sum_{k=0}^{M} b_k (j\omega)^k X(j\omega)$$
$$H(j\omega) = \frac{\sum_{k=0}^{M} b_k (j\omega)^k}{\sum_{k=0}^{N} a_k (j\omega)^k} \qquad [46a]$$

which could also have been obtained directly by substituting $s = j\omega$ into $H(s)$, eqn [12]. Obviously we also have:

$$h(t) \leftrightarrow H(j\omega)$$
$$h(t) = F^{-1}[H(j\omega)] \qquad [46b]$$

A convenient interpretation of $H(j\omega)$ is that of a system gain. Exciting a linear system by an harmonic input of frequency ω_1, will result in an harmonic output with the same frequency (in the steady state condition). The gain will be $H(j\omega_1)$, and the phase shift the phase of $H(j\omega_1)$.

Real time signals In most engineering applications, time signals will be real. This results in some symmetries in the FT. Intuitively it should be obvious that only when some symmetries in the frequency domain exist will the imaginary parts of eqn [34b] cancel. Specifically we have:

$$X(-j\omega) = X^*(j\omega) \qquad [47]$$

where * stands for the complex conjugate.

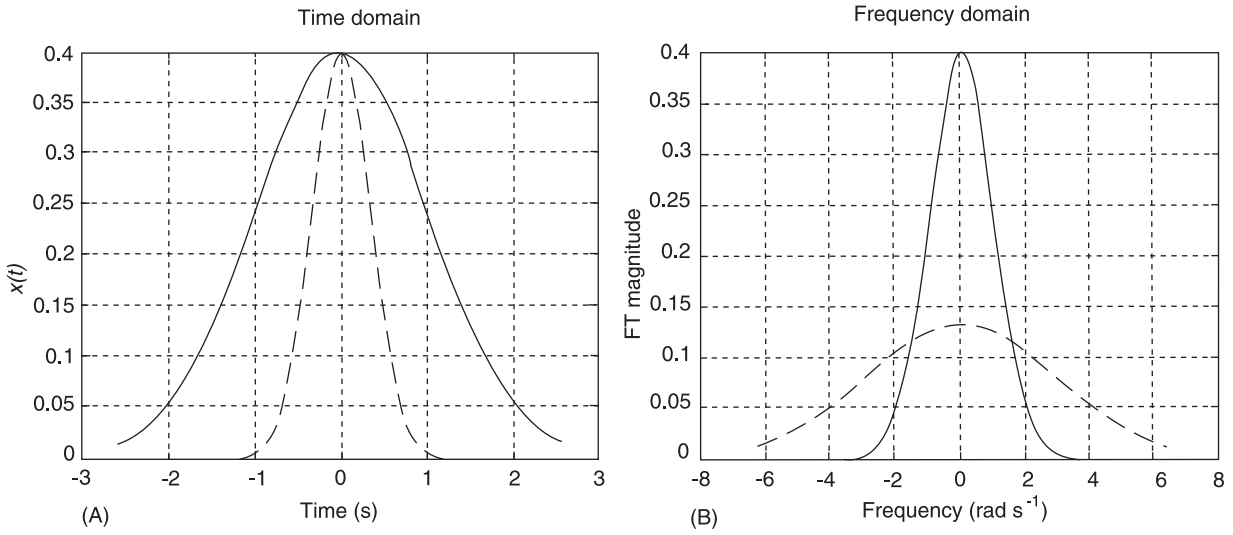


Figure 3 (A) Time domain. (—) original, (- - -) compressed. (B) Frequency domain. (—) original, (- - -) compressed.

We finally address the transform of periodic signals. Impulses in the transform are needed in such cases:

$$x(t) = x\left(t + T_\mathrm{p}\right) \quad \omega_0 = \frac{1}{T\mathrm{p}}$$
$$X(\mathrm{j}\omega) = 2\pi \sum_k X(k)\delta(\omega - \omega_0) \qquad [48]$$

indicating that the contribution in the frequency domain is concentrated at discrete frequencies.

Fourier Series

A perodic signal:

$$x(t) = x\left(t + T_\mathrm{p}\right)$$

can be decomposed into a Fourier series:

$$x(t) = \sum_{k=-\infty}^{\infty} C(k) \exp\left(\mathrm{j}2\pi k f_0 t\right), \; f_0 = \frac{1}{T_\mathrm{p}} \qquad [49a]$$

$$C(k) = \frac{1}{T_\mathrm{p}} \int_{T_\mathrm{p}}^{x} x(t) \exp\left(-\mathrm{j}2\pi k f_0 t\right) \mathrm{d}t \qquad [49b]$$

A Fourier series synthesis is obviously possible, generating a periodic signal by the superposition of harmonic components. Borrowing terms from music theory, $k = 1$ defines the fundamental component, while higher k values define the harmonics. If a truncated series is used, a minimization of the mean square error between the signal and the summation is achieved.

The series will converge if:

$$\frac{1}{T_\mathrm{p}} \int_{T_\mathrm{p}} |x(t)|^2 < \infty \qquad [50]$$

except at discontinuities where overshoots and oscillations may occur. Equations [49] show a two-sided decomposition. The use of negative indices, and hence negative frequencies, is mainly a mathematical convenience, resulting in a compact presentation (and also closer to the FT representation). A one-sided presentation is also possible.

Symmetries in $C(k)$ exist for $x(t)$ a real signal, namely:

$$C(-k) = C^*(k) \qquad [51]$$

Figure 4 shows the first few terms of a Fourier series and the partial sums for a square wave signal. The convergence can already be noticed, as well as the overshoot and oscillations around the discontinuities.

Discrete Fourier Series

Computational schemes can only be applied to discrete signals, and the continuous signals acquired by measurements are thus digitized.

The DFS is the Fourier tool suitable for decomposing discrete periodic signals of the form:

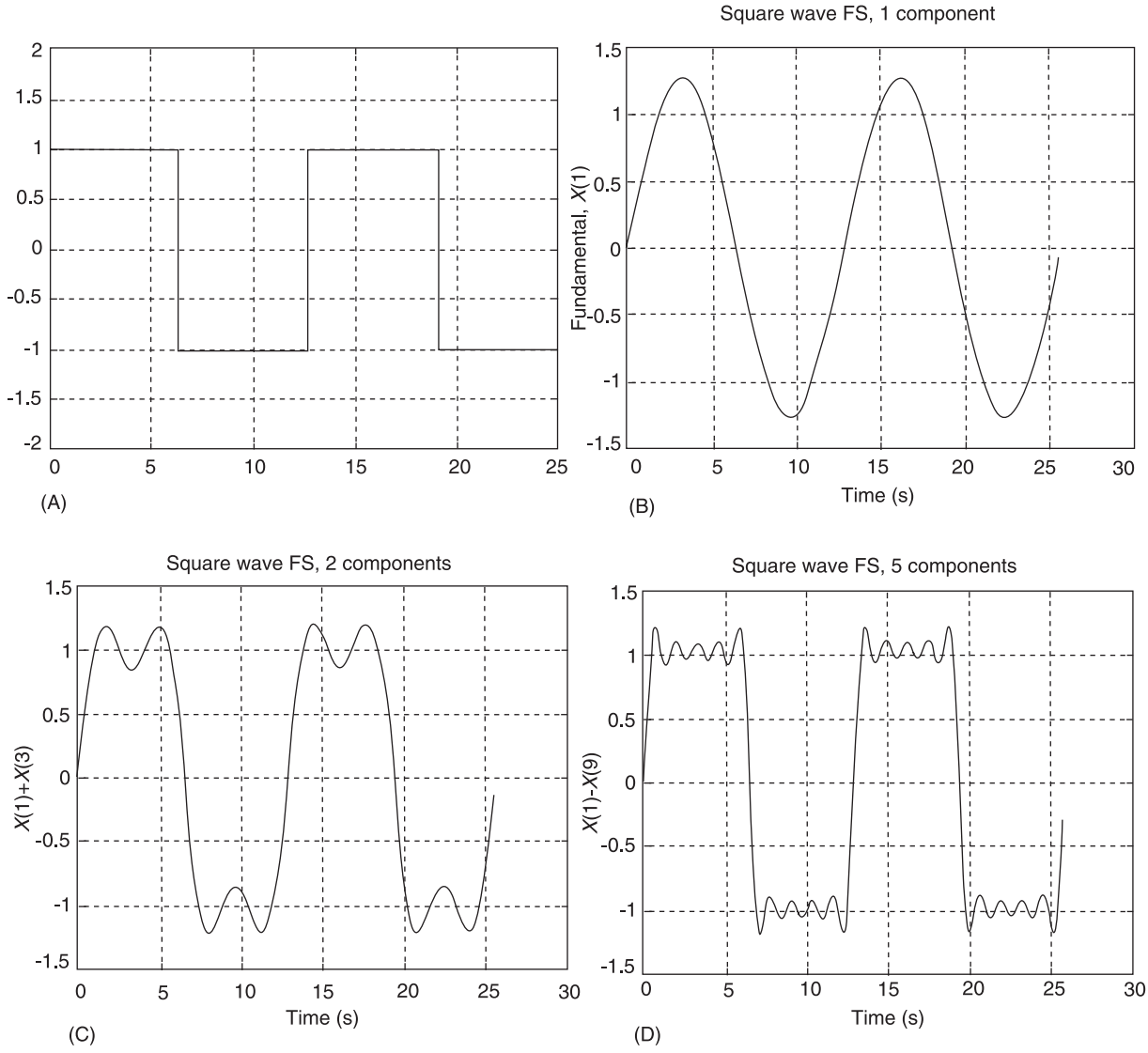


Figure 4 (A) Periodic signal (square). (B) Fundamental Fourier series component. (C) First three Fourier series components (second zero). (D) First nine components Fourier series components.

$$x(n) = x(n+N) \qquad [52a]$$

The decomposition is:

$$x(n) = \sum_k X_{\mathrm{DFS}}(k) \exp\,(\mathrm{j}2\pi k f_0 n); \quad f_0 = \frac{1}{N} \qquad [52b]$$

with:

$$X_{\mathrm{DFS}}(k) = \frac{1}{N}\sum_N x(n) \exp\,(-\mathrm{j}2\pi f_0 n) \qquad [52c]$$

We note that the transform given by eqns [52] can be manipulated in a computer, giving exact results.

The FS is a decomposition suitable for continuous periodic signal, the DFS for discrete periodic ones. The discretization however imposes a periodicity in the frequency domain (**Figure 5**), and it is easy to show that:

$$X_{\mathrm{DFS}}(k) = X_{\mathrm{DFS}}(k+N) \qquad [53]$$

and the sum [52c] is computed over N points. The transform described next is actually the one usually computed. The DFS itself, if computed, will be based on the DFT (see below, eqn [57]).

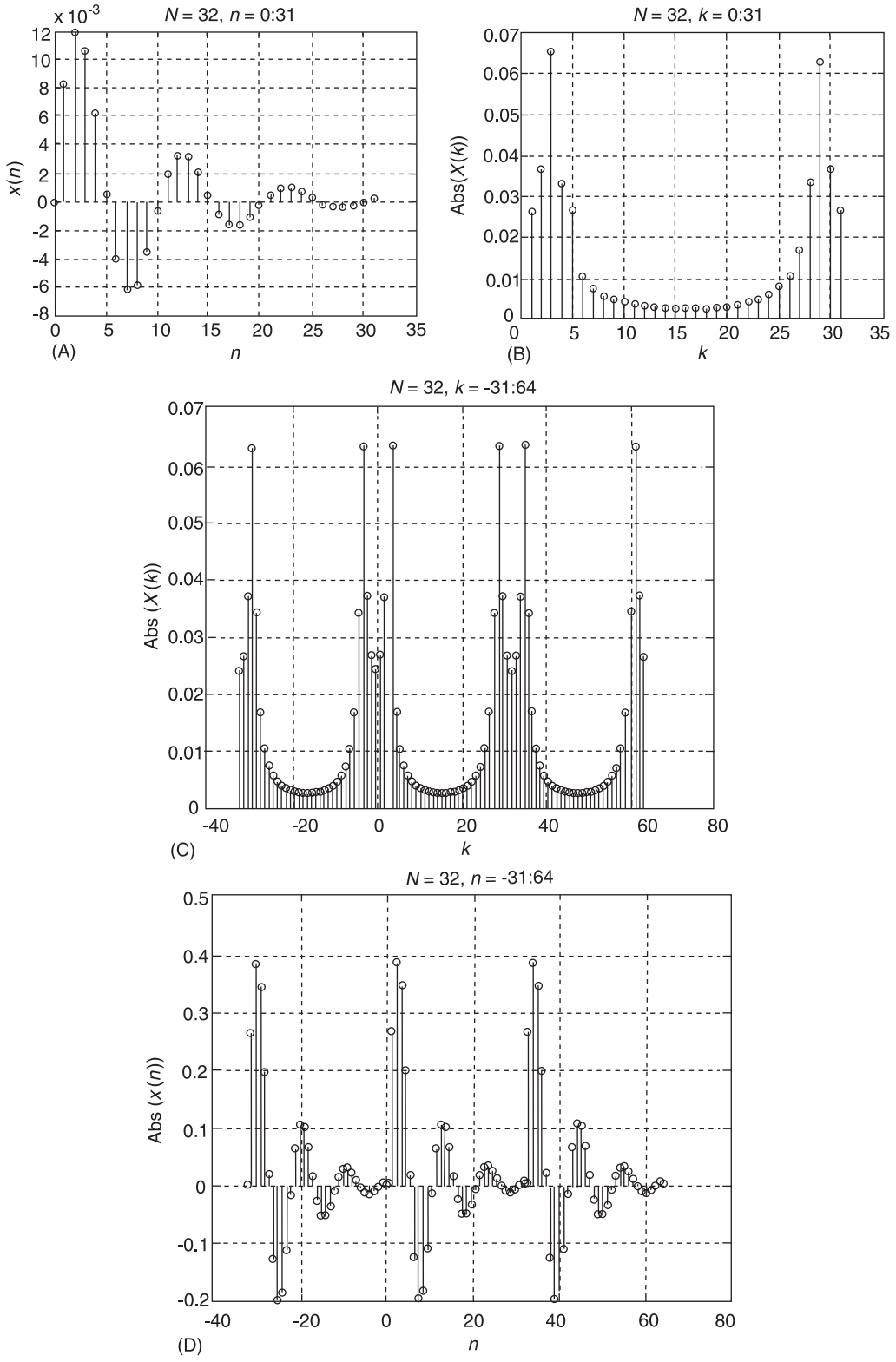


Figure 5 (A) Discrete periodic time domain sequence, single period. (B) Discrete Fourier series. (C) Discrete periodic time domain sequence. (D) Discrete Fourier series, periodic extension.

The Discrete Fourier Transform

This is the actual transformation computed in the majority of Fourier-based signal processing methods.

It is actually a transformation from one N point (complex) sequence into another N point (complex) sequence in another domain:

$$\left.\begin{aligned} X(k) &= \sum_{n=0}^{N-1} x(n) \exp\left(-\mathrm{j}(2\pi/N)nk\right) \\ x(n) &= \tfrac{1}{N} \sum_{k=0}^{N-1} X(k) \exp\left(\mathrm{j}(2\pi/N)nk\right) \end{aligned}\right\} \quad [54]$$

and in the majority of applications n and k would be time and frequency indices. It is often convenient to look at (54) as an approximation of the continuous FT with the following:

$$\begin{aligned} &\mathrm{d}t \to \Delta t = 1 \\ &\mathrm{d}f \to \Delta f \\ &f \to k\Delta f \\ &t = i\Delta t \\ &\int \to \sum \\ &\Delta f = \frac{1}{N\Delta t} \end{aligned} \quad [55]$$

where Δf and Δt are the discrete frequency and time steps, Δt being dictated by the sampling frequency. The transformation, like most signal processing basic expressions, is normalized with $\Delta t = 1$, and the frequency range then being $-\frac{1}{2} + \frac{1}{2}$. Equation [54] is the one implemented in standard signal processing software routines.

For a discrete transform approximating the FT and finite Δt to retain engineering units, EU, we modify [54] to:

$$\left.\begin{aligned} X(k\Delta f) &= \Delta t \sum_{n=0}^{N-1} x(n) \exp\left(-\mathrm{j}(2\pi/N)nk\right) \\ x(\mathrm{i}\Delta t) &= \frac{1}{N\Delta t} \sum_{k=0}^{N-1} X(k\Delta f) \exp\left(\mathrm{j}(2\pi/N)nk\right) \end{aligned}\right\} \quad [56]$$

where Δt is the sampling interval and Δf the computational frequency step (eqn [55]). The expression [56] would be implemented only in dedicated (usually commercial) instrumentation/analysers. The approximation to the FT deteriorates when aliasing occurs due to too large Δt.

When extending the indices n and k in [55] beyond N points, a periodicity in N will be noticed. Except for a factor of N, we may interpret [54] as 'the transform between one period of a periodically sequence $x(n)$ to one period of a periodically sequence $X(k)$', i.e., those described by the DFS. Thus we also have the relation:

$$X(k) = NX_{\mathrm{DFS}} \quad [57]$$

The implied peridicity in $X(k)$ enables us to give additional interpretation to the indices k and n:

$$\left.\begin{aligned} X(-k) &= X(N-k) \\ x(-n) &= x(N-n) \end{aligned}\right\} \quad [58]$$

and the region of $k = N/2 + 1, \ldots, N-1$ can be interpreted as one of negative frequencies.

Two more specific indices have a special interpretation:

For $k = 0$, eqn [54] shows that:

$$X(k) = \sum_{n=0}^{N-1} x(n) \quad [59]$$

except for a factor of N, this is the average (or DC component) of $x(n)$:

$$X_{DC} = \frac{1}{N} \sum_{n=0}^{N-1} x(n) \quad [60]$$

which is intuitively obvious as the zero frequency component is one of DC.

For $k = N/2$, we have a frequency of:

$$f = k\Delta f = \frac{N}{2} \frac{1}{N\Delta t} = \frac{1}{2\Delta t} = f_{\mathrm{NYQUIST}} \quad [61]$$

which corresponds to the Nyquist frequency (see **Data acquisition**), the maximum frequency range compatible with the sampling process.

While [54] is a transformation between two complex sequences, signals acquired are usually real. This imposes symmetries on $X(k)$ as:

$$X(-k) = X^*(k) \quad [62]$$

Figure 6, showing absolute value of $X(k)$ of a real signal, summarizes the above properties. We note the interpretation of a negative frequency region as well as the symmetries. The more conventional way of presenting positive and negative frequency region is shown in **Figure 6C**, which can be easily obtained from **Figure 6B** by a shifting operation.

Parseval's law of equal energies in the time and frequency domain holds (eqn [63]):

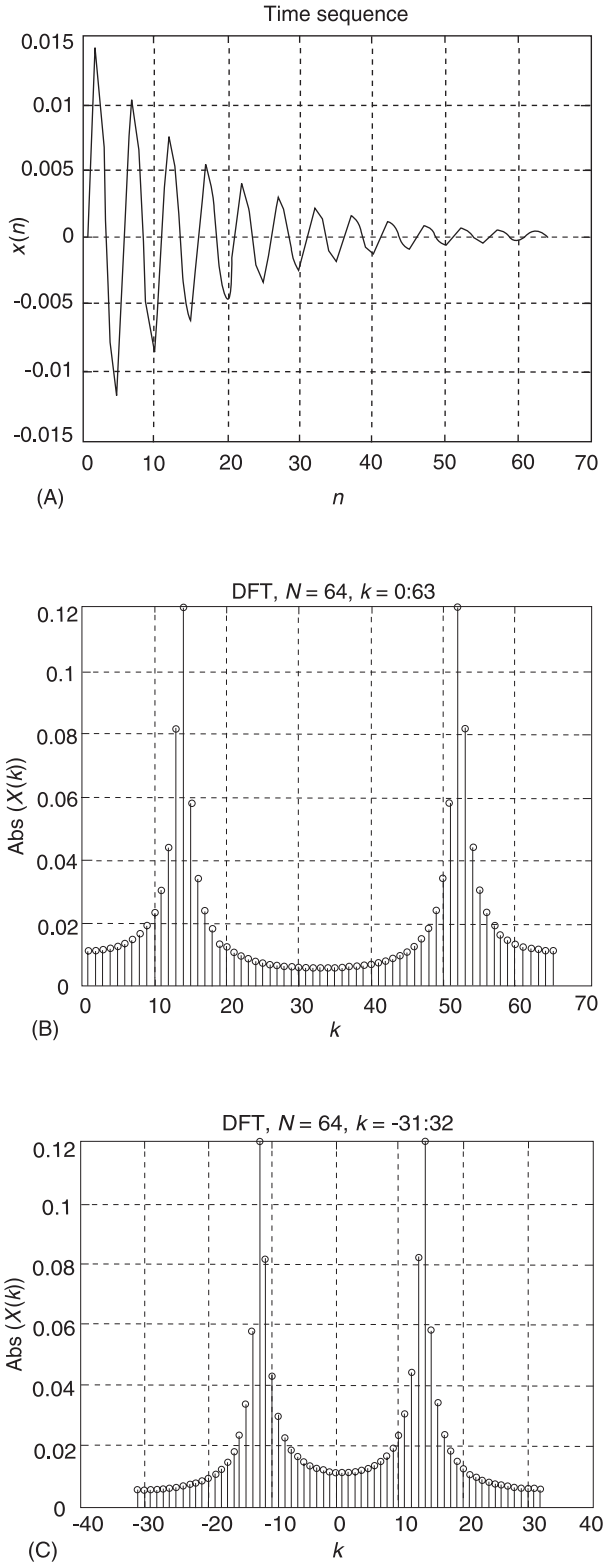


Figure 6 (A) Discrete time signal. (B) DFT. (C) DFT, negative frequencies shifted to left half plane.

$$\sum_n x^2(n) = \frac{1}{N}\sum_k |X(k)|^2 \qquad [63]$$

The Fast Fourier Transform (FFT)

This is an extremely efficient algorithm for the computation of the DFT (and its inverse). The name FFT has in many aspects become synonymous with that of the DFT, and the literature often refers to phrases like 'presented is the FFT of . . .'. The FFT takes advantage of symmetries involved in the DFT computations, to achieve efficiency.

The name FFT actually refers to a large family of algorithms, each one geared to different situations. For vibration signals, we would use a FFT from a real sequence (in time) to a complex one (in frequency). Complex-to-complex algorithms are also available.

The length N of the sequences to be transformed will affect the efficiency. For small (PC and commercial analyser) machines, a power of 2 length is usually preferred (and the only one available in the dedicated analyzers). The term 'Radix M' is sometime used, and 'Radix 2' FFT hence refers to an algorithm where the number of analyzed points is:

$$2^M \quad \text{where } M \text{ is an integer} \qquad [64]$$

i.e., $N = 32, 64, 128, \ldots$, but Radix 8 FFTs are sometimes used by practitioners.

As a result of possible requirements on the number of samples N, various computing variations are sometimes built into commercial software. Zeros are sometimes appended to the sequence in order to achieve a length of a power of 2. We note that the appending of zeros will not affect the result of the summation for $X(k)$ as per:

$$X(k) = \sum_0^{n1-1} x(n)\exp\left(-\mathrm{j}\frac{2\pi}{N}\right)^{nk} + \sum_{n1}^{N} 0\exp\left(-\mathrm{j}\frac{2\pi}{N}\right)^{nk} \qquad [65]$$

Sometimes a straight DFT computation (with the loss of efficiency) may be performed for arbitrary length sequences.

The implementation for an inverse DFT is very similar to that of the forward FFT, and is usually available in all FFT packages. Some algorithms will ignore the factor of N preceding [54b]. Sometimes a factor of $(1/N)^{1/2}$ premultiplies both [54a] and [54b]. It is thus important to check the exact computation performed by any available algorithm.

The computational complexity for the DFT can be ascertained from equation [54]: N complex operations are needed for the computation of a single $X(k)$, and for N values of k, this requires N^2 operations. In

this context 'complex operation' refers to a complex product and summation). The number of operations for a Radix 2 FFT of N points is approximately $N\log_2(N)$. The seemingly modest improvement is deceiving. As an example, with $N = 2^{13} = 8192$, the saving would be:

$$N^2/N\log_2(N) = 2^{26}/(13 \times 2^{13}) = 630$$

Many analyses necessitate the computations of hundreds of FFTs, with a tremendous saving. Actually it is only the availability of the FFT algorithm which has made modern signal processing (and, obviously, Fourier-based methods) practical.

The FFT in its present form was published in the 1970s, but some of the ideas can already be found in the works of Gauss.The constraint on the block size N limits to some extent use of an exact pre-determined frequency spacing

Example Let us assume data acquisition with a sampling interval of $\Delta t = 4$ ms, and two scenarios.

Scenario 1 The desired frequency resolution (spacing) is $\Delta f = 1$ Hz. Then:

$$N \to \frac{1/\Delta t}{\Delta f} = 250$$

We thus will choose N=256 with a resulting actual resolution of $\Delta f = 0.98$.

Scenario 2 The desired frequency resolution is 0.6 Hz. Then:

$$N \to \frac{1/\Delta t}{\Delta f} = \frac{250}{0.6} = 417$$

and two choices for N can be taken, with different resulting frequency resolutions:

$$N_1 = 256, \quad \Delta f_1 = 0.98,$$
$$N_2 = 512, \quad \Delta f_2 = 0.49$$

The first choice results in a resolution less than required. The second one results in a resolution better than required, but at the expense of an increase in computational effort.

See also: **Data acquisition**; **Signal integration and differentiation**; **Transforms, wavelets**.

Further Reading

Haykin S, Van Veen B (1999) *Signals and Systems*. New York: John Wiley.

Papoulis A (1962) *The Fourier Integral and its Applications*. New York: McGraw Hill.

Pollock DSG (1999) *A Handbook of Time Series Analysis, Signal Processing and Dynamics*. London: Academic Press.

TRANSFORMS, HILBERT

See **HILBERT TRANSFORMS**

TRANSFORMS, WAVELETS

P White, Institute of Sound and Vibration Research (ISVR), University of Southampton, Southampton, UK

Copyright © 2001 Academic Press

doi:10.1006/rwvb.2001.0157

Introduction

Many signals encountered in the field of vibration analysis can be modeled as nonstationary. One natural tool for the study of such signals is to employ time–frequency methods (see **Transform methods**). An alternative, but complementary, approach is to exploit time-scale methods based on the wavelet transform (WT). A WT seeks to represent a signal, fundamentally, as a function of time and scale, rather than time and frequency. In most applications one can directly relate scale to frequency and hence the WT can be considered as a form of time–frequency representation.

The WT can be regarded in many equivalent ways. It can be viewed as a transform method allowing one to represent a signal in terms of elementary functions. The nature of the decomposition allows one to zoom in on discontinuities in the signal. This allows one to regard the WT as a form of multiresolution analysis, whilst the WT also offers the opportunity to implement filter banks with perfect reconstruction properties. This article will predominantly address wavelets from the transform perspective, since this represents the most appropriate standpoint for most vibration-based applications.

The WT is closely related to the short-time (term) Fourier transform (STFT). Indeed, these two transforms share a common mathematical framework. This chapter begins with a discussion of the STFT and then outlines the principles behind the continuous WT (CWT). The issues associated with sampling these representations within the transform domain are then discussed, leading to a discussion of the discrete WT.

The Short-time Fourier Transform

The STFT is an extension of the Fourier transform to the case where a signal is nonstationary, i.e., its spectral characteristics vary as a function of time. The STFT is computed by windowing the signal at various times and Fourier-transforming the resulting product. The STFT, $S(t, f)$, can be defined in several fashions (all are equivalent to within a constant phase factor). The definition used herein is:

$$\begin{aligned} S(t,f) &= \int x(\tau)w(t-\tau)^* e^{2\pi i f(t-\tau)} d\tau \\ &= \int x(t-\tau)w(\tau)^* e^{2\pi i f\tau} d\tau \end{aligned} \quad [1]$$

where $w(t)$ is a windowing function, f represents frequency and * denotes complex conjugation (note that the windowing function is commonly real-valued, in which case the conjugation is obsolete). The STFT is a complex valued function. When inspecting the STFT it is often the squared magnitude of the STFT that is presented, which is termed the spectrogram (see **Transform methods**).

The form of the spectrogram/STFT critically depends on the choice of the duration of the windowing function $w(t)$. If a window with a long duration is used then the STFT will fail to resolve short-duration events, whereas if a short-duration window is used, the STFT will fail to adequately resolve narrow-band components. This is a direct consequence of the time–frequency uncertainty principle that states that there is a lower limit to the product of a signal's duration and its bandwidth. This implies that, for a given duration, one cannot construct a signal whose bandwidth is arbitrarily small. A consequence of this is that one cannot select $w(t)$ such that the STFT possesses good time and frequency resolution simultaneously. This forces the user to trade off time resolution against frequency resolution.

The following discusses an example that illustrates the practical implications of this tradeoff. The signal to be analysed is described by:

$$\begin{aligned} x(n) = &\ \sin(2\pi n/11) + 5\delta(n) \\ & n \in [-512, 512] \end{aligned}$$

where $\delta(n)$ is the Kronecker delta function, $\delta(n) = 1$ when $n = 0$ and $\delta(n) = 0$ for $n \neq 0$. **Figure 1A** shows this signal in the time domain. A good time–frequency representation of this signal contains a single horizontal and a single vertical line. The horizontal line, representing the narrow-band component, should be centered at a normalized frequency of 0.09, whilst the vertical line, representing the impulse, should be located at $n = 0$. **Figure 1B** shows a spectrogram computed with a window of root mean square duration 6.6 samples. This relatively short window generates a distribution in which the impulsive component is well resolved; however, the tonal signal is spread in frequency. **Figure 1C** shows a spectrogram computed using a window of duration 14.8 samples. This window causes both lines to smear somewhat. Finally, **Figure 1D** shows the results of applying a spectrogram using a window of duration 33 samples. This longer window causes considerable spreading of the impulse, but the tonal contribution becomes more concentrated about the correct frequency.

This example illustrates how the results using a STFT/spectrogram vary with the choice of windowing function. It also highlights that it may be difficult to select a window duration that is suited to all components in a signal.

In the following we consider how the STFT of a signal is affected by two basic operations on a signal. To aid this discussion, the notation for the STFT is extended slightly such that $S_x(t, f)$ is used to denote explicitly the STFT of $x(t)$.

Time Shifts

Consider $y(t)$ formed by delaying $x(t)$, specifically, $y(t) = x(t - \tau_0)$, then the STFTs of these two signals are related via:

$$S_y(t,f) = S_x(t-\tau_0, f)$$

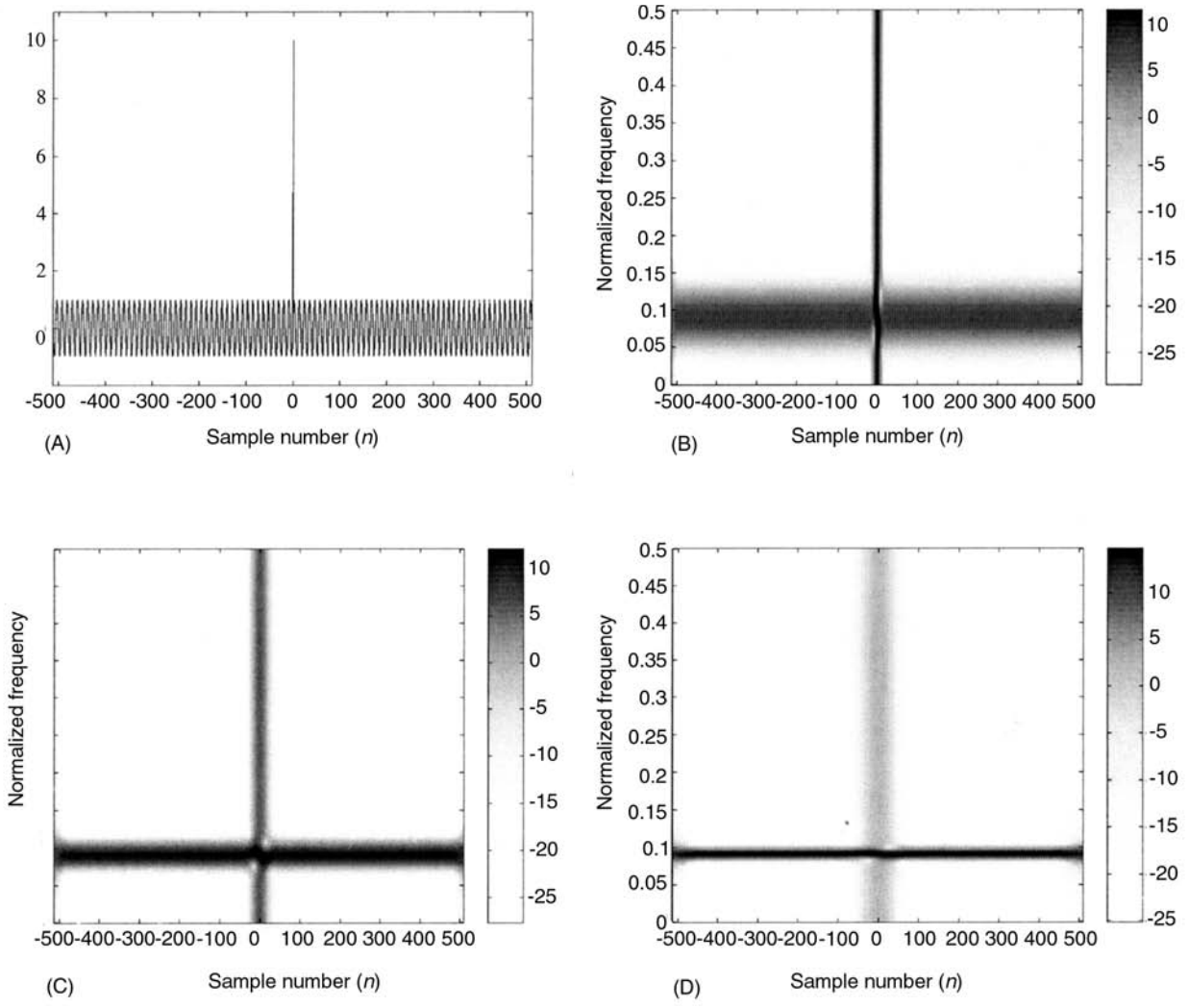


Figure 1 Examples of spectrograms. (A) Test signal; (B) spectrogram, $\sigma = 6.6$; (C) spectrogram, $\sigma = 14.8$; (D) spectrogram, $\sigma = 33.0$.

That is to say, delaying the signal merely translates the STFT along the time axis.

Frequency Shifts

Consider $y(t)$ formed by shifting $x(t)$ in frequency, by modulating it with a complex exponential, so that $y(t) = x(t)e^{2\pi i f_0 t}$, then the STFTs of these two signals are related via:

$$\begin{aligned} S_y(t,f) &= e^{2\pi i f_0 t} S_x(t, f - f_0) \Rightarrow |S_y(t,f)| \\ &= |S_x(t, f - f_0)| \end{aligned}$$

Thus, the act of frequency shifting a signal translates the STFT along the frequency axis, with the inclusion of a linear-phase term. However, the magnitude of the STFT (and hence the spectrogram) translates exactly along the frequency axis.

The above two properties of the STFT indicate how it copes in an intuitively appealing manner with the operations of time and frequency shifts.

Let us continue to consider the form of the STFT. Eqn [1] can be regarded as a set of inner products with time-shifted versions of the function $\Psi_s(t, f)$, so that:

$$S(t,f) = \int x(\tau)\Psi_s^*(t - \tau, f)\, d\tau \qquad [2]$$

where the function $\Psi_s(t, f)$ is a complex exponential multiplied by the function $w(t)$, i.e.:

$$\Psi_s(t,f) = w(t)e^{-2\pi i f t} \qquad [3]$$

The analyzing operation [2] loses considerable potency if no inverse operation exists, that is, if one

cannot recover the original data from the transform domain representation. A general inversion relation for the STFT is:

$$x(t) = \frac{1}{C_{w,\tilde{w}}} \iint S(t,f)\Gamma_s(t-\tau,f)\,\mathrm{d}f\,\mathrm{d}\tau \qquad [4]$$

where, $\Gamma_s(t,f)$ and $C_{w,\tilde{w}}$ are defined as:

$$\Gamma_s(t,f) = \tilde{w}(t)\mathrm{e}^{-2\pi ift} \qquad [5]$$

$$C_{w,\tilde{w}} = \int w^*(t)\tilde{w}(-t)\,\mathrm{d}t \qquad [6]$$

where $\tilde{w}(t)$ is a second windowing function. In view of eqn [4], the STFT can be regarded as a decomposition of the signal $x(t)$ in terms of the functions $\Gamma_s(t-\tau f)$. Indeed, one can regard the standard Fourier transform as a special case of the STFT in which $w(t) = 1$ and $\tilde{w}(t) = \delta(t)$ (where $\delta(t)$ is the Dirac delta function). In which case $C_{w,\tilde{w}} = 1$, the basis functions, $\Gamma_s(t,f)$, become the complex exponentials and $S(t,f)$ is independent of time t.

The only formal condition for the inversion formula [4] to exist is that $C_{w,\tilde{w}}$ be nonzero. There is, somewhat surprisingly, no requirement that the two functions $w(t)$ and $\tilde{\mathrm{w}}(t)$ be the same, but this restriction is often imposed and we shall concentrate on this case here, so that $\Psi_s(t,f) = \Gamma_s(t,f)$.

Whilst the choice of the function $w(t)$ is mathematically only restricted to functions that satisfy (6), with $w(t) = \tilde{w}(t)$, it is convenient to select these functions as windowing functions, so they are centered at the origin of the time–frequency plane and are well localized in both domains. Assuming $w(t)$ is selected in accordance with the above, then the spectrogram at t_0 and f_0, i.e., $|S(t_0, f_0)|^2$, reflects the energy of the signal close to frequency f_0 and time t_0.

The spectrogram can also be interpreted as a filtering operation, by realizing that eqn [4] represents a convolution between the signal $x(t)$ and $\Psi_s(t,f)$. Hence $|S(t_0, f_0)|^2$ can be interpreted as the instantaneous energy of the output of a filter whose impulse response is given by [3] with $f = f_0$. One can evaluate the spectrogram by employing a bank of filters, each filter having an impulse response that is a frequency-shifted version of $w(t)$. Each filter in such a bank has the same bandwidth, but different quality factors (Q-factors). **Figure 2** shows the impulse responses for various center frequencies, assuming that the windowing function has the form of a Gaussian function:

$$w(t) = \mathrm{e}^{-t^2/2\sigma^2}$$

The user-defined parameter σ controls the signal's duration. **Figure 2** emphasizes that neither the duration nor the bandwidth of the basis functions depend on the center frequency.

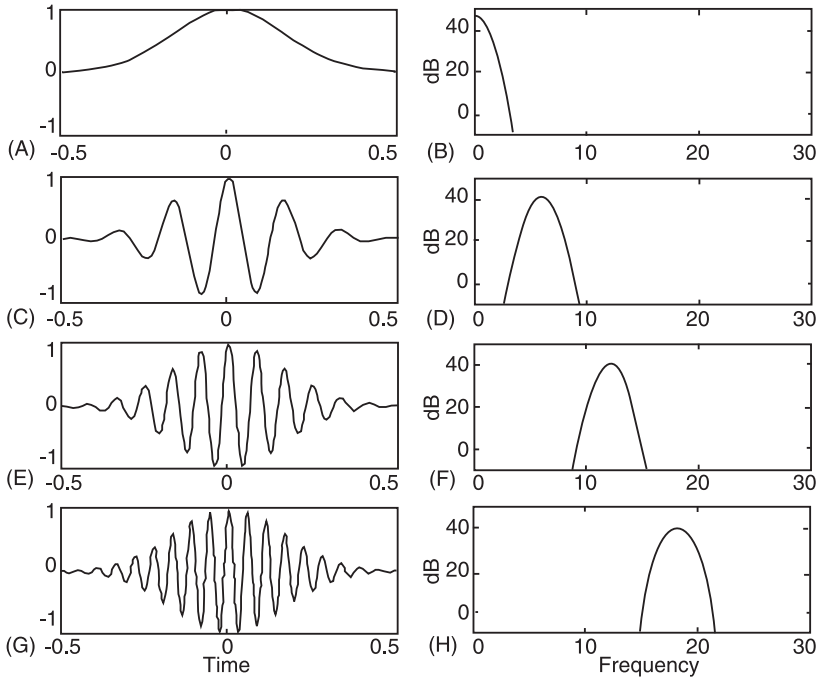


Figure 2 Basis functions for the short-time Fourier transforms.

The Continuous Wavelet Transform

The STFT is based on the operations of time and frequency shifts; the basis functions for the decomposition are time- and frequency-shifted versions of $w(t)$; see eqns [4] and [5]. The CWT is an alternative, but related, decomposition based upon the operations of time shifts and scalings. The CWT is defined as:

$$w(t,a) = \frac{1}{\sqrt{a}} \int g^*\left(\frac{t-\tau}{a}\right) x(\tau)\, \mathrm{d}\tau \qquad [7]$$

The parameter a represents scale, here assumed to be positive, and is closely allied to frequency. The CWT is, in general, a complex valued function and it is often the squared magnitude of the CWT that is considered; the squared magnitude of the CWT is dubbed the scalogram.

Like the STFT, the CWT satisfies two basic invariance properties. These are discussed below, and we temporally adopt a subscript in the notation for the WT to indicate the signal being analyzed.

Time Shifts

If $y(t)$ is formed by delaying $x(t)$, specifically, $y(t) = x(t - \tau_0)$, then the CWT of $y(t)$ satisfies:

$$W_y(t,a) = W_x(t-\tau, a)$$

Hence the effect of delaying the input signal is to shift the time axis of the CWT.

Scale Changes

If $y(t)$ is a scaled version of $x(t)$ such that, $y(t) = x(t/a_0)$, then the CWT of $y(t)$ is given by:

$$W_y(t,a) = a_0 W_x(t/a_0, a_0 a) \quad a_0 > 0$$

Thus, the effect of scaling the signal is to rescale the time axis of the CWT and to shift its center scale. The rescaling in time is necessary to account for the fact that the duration of $y(t)$ will be different to that of $x(t)$. Rescaling the time signal also introduces a multiplicative constant into the CWT which is of little practical importance.

The basic form of the CWT can, like the STFT, be expressed as a series of inner products. Eqn [7] can be expressed in the same form as eqn [2], namely:

$$W(t,a) = \int x(\tau) \Psi_w^*(t-\tau, a)\, \mathrm{d}\tau \quad a > 0 \qquad [8]$$

where:

$$\Psi_w(t,a) = \frac{1}{\sqrt{a}} g\left(\frac{t}{a}\right) \qquad [9]$$

The functions $\Psi_w(t,a)$ are scaled versions of the function $g(t)$; the leading factor of $a^{-1/2}$ is included to ensure that the energy of $\Psi_w(t,a)$ is invariant to the choice of a. The general inversion formula for the CWT is given by:

$$x(t) = \frac{1}{C_{g,\tilde{g}}} \iint W(\tau,a) \Gamma_w(t-\tau, a) \frac{\mathrm{d}a\mathrm{d}t}{|a|^2} \qquad [10]$$

where:

$$\Gamma_w(t,a) = \frac{1}{\sqrt{a}} \tilde{g}\left(\frac{t}{a}\right) \qquad [11]$$

$$C_{g,q} = \int G(f) \tilde{G}(f)^* \frac{\mathrm{d}f}{|f|} \qquad [12]$$

where $G(f)$ and $\tilde{G}(f)$ are the Fourier transforms of $g(t)$ and $\tilde{g}(t)$ respectively. The inversion (10) is valid as long as $C_{g,\tilde{g}}$ is nonzero. As with the STFT, it is common to select $\tilde{g}(t) = g(t)$, a convention that will be adhered to here. In which case, one can regard the CWT as a decomposition of a signal with respect to the functions $\Psi_w(t,a) = \Gamma_w(t,a)$.

It is informative to consider how the elementary functions, $\Psi_w(t,a)$, vary with the scale parameter a. Large values of a correspond to stretched (dilated) versions of the basic function $g(t)$, whilst small values relate to compressed (contracted) versions of $g(t)$. The function $g(t)$ is referred to as the mother wavelet. The term wavelet arises because the condition [12] equates, for most reasonable choices of function, to constraining $g(t)$ to be zero mean, ensuring that it must contain some oscillations, i.e., waves. **Figure 3** shows four examples of the basis functions for the CWT, using a modulated Gaussian windowing function and mother wavelet:

$$g(t) = \mathrm{e}^{-t^2} \mathrm{e}^{2\pi i f_o t}$$

The above mother wavelet is generally referred to as the Morlet wavelet, where f_0 is a user-defined parameter. From **Figure 3** one can see that the duration of the basis functions reduces, and the bandwidth increases, for the high-frequency components (small values of a). This is in contrast to the STFT basis functions (**Figure 2**) whose shape changes with frequency (the number of oscillations in the elementary functions increases with frequency) but the duration of the STFT basis functions is constant. This different

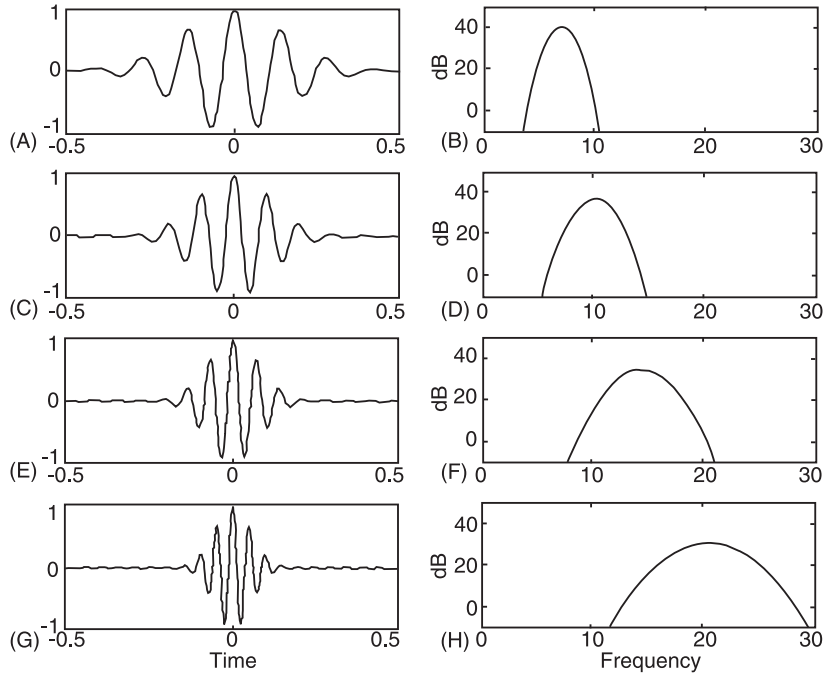


Figure 3 Basis functions for the continuous wavelet transforms.

behavior of the STFT and CWT basis functions gives rise to the different characteristics of the two methods.

As the CWT basis functions reduce in duration, their bandwidth necessarily increases. A consequence of this is that both the temporal and frequency resolution of the CWT vary with a. Specifically at small scales (high frequencies) the basis functions are short in duration and have wide bandwidths, leading to good temporal resolution but poor frequency resolution, whereas at large scales (low frequencies) the basis functions are long in duration and have narrow bandwidths, leading to poor temporal resolution but good frequency resolution.

The link between scale and frequency becomes explicit if one considers mother wavelets of the following form:

$$g(t) = w(t)\mathrm{e}^{2\pi i f_o t} \qquad [13]$$

where, as before, $w(t)$ is a windowing function, i.e., a nonoscillating function. The elementary functions for the CWT can then be expressed as:

$$\Psi_w(t,a) = w(t/a)\mathrm{e}^{2\pi i (f_o/a)t}$$

In this form it is apparent that a particular value of a corresponds to frequency f according to:

$$f = f_o/a$$

Under these conditions the CWT can be truly regarded as a time–frequency representation. As discussed, the CWT has nonuniform resolution over the time-frequency plane, in contrast to the STFT where the resolution is uniform.

Like the STFT, the CWT can be interpreted as the output of a filter bank. This observation can be drawn from [8] that represents a series of convolutions. The filter bank implied by a CWT uses filters that do not have constant bandwidth but instead have constant percentage bandwidths (constant Q). Such a filter bank has a constant number of filters within an octave, for example a third-octave filter bank uses three filters to span each octave.

Figure 4 shows the CWT computed for the test signal shown in **Figure 1A**. The good-frequency resolution of the CWT at low frequencies ensures that the tonal component is well resolved, whilst the impulse, which contains all frequencies, is well localized (in time) within the high-frequency region. As has been demonstrated, the STFT cannot well resolve both components of this signal simultaneously. The best that can be achieved by the STFT is a compromise, such as that seen in **Figure 1C**.

The variable resolution of the CWT is well matched to the signal in the first example, allowing good resolution of both components simultaneously. This variable resolution is a fundamental difference between the CWT and the STFT. However, it should be emphasized that the CWT is subject to the same

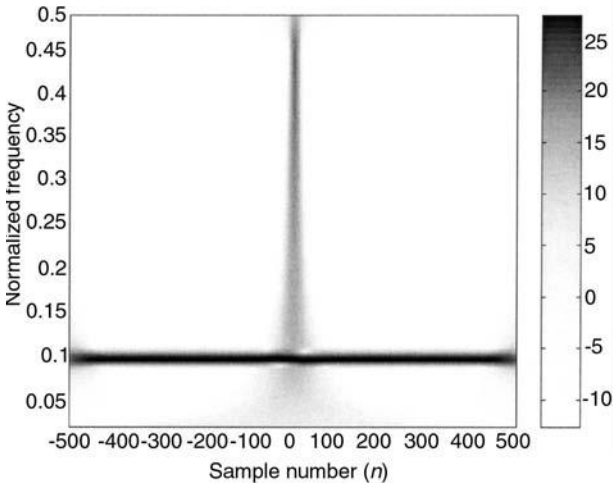


Figure 4 Continuous wavelet transform of test signal depicted in Figure 1A.

fundamental resolution limitations as the STFT, namely the uncertainty principle. One cannot reasonably claim that the CWT has better resolution than the STFT in any meaningful sense; it merely trades time and frequency resolution in a different manner to the STFT.

The CWT, computed for a second test signal, is depicted in **Figure 5**. The signal analyzed in this case is:

$$x(n) = \sin(2\pi n 4/11) + 5\delta(n)$$
$$n \in [-512, 512]$$

This second signal is the same as the original test signal, except that the narrow-band component has a much higher center frequency. **Figure 5** shows the CWT computed using the same parameters used to compute the distribution shown in **Figure 4**. The tonal component exists in a frequency band where the CWT's frequency resolution is poor. The impulse's major contribution lies in the lower-frequency bands, where the temporal resolution is comparatively poor. Consequently, for this signal the CWT is poorly matched to the signal's character and the resulting distribution is a relatively poor representation of the signal.

The two examples in **Figures 4** and **5** emphasize that the CWT is not a panacea, but for signals of suitable types the CWT offers definite advantages over the STFT. It is apparent that if a signal contains long-duration, low-frequency components, in conjunction with short-duration, high-frequency components, then the CWT is an advantageous tool. Many naturally occurring signals containing the high-frequency components decay more rapidly than the low frequencies, in which case the CWT should be considered.

Sampling of Distributions

The STFT and CWT, as presented so far, are formulated in terms of continuous functions. They represent mappings of a one-dimensional continuous signal into a two-dimensional continuous domain. A practical algorithm for implementation on a digital computer must define a transformation that maps a sampled time series to a series of points in the two-dimensional space. There are two distinct sampling issues to be addressed. The first relates to the fact that the signal to be analyzed is sampled. The second considers the effect of evaluating the distributions on a discrete set of points, i.e., the sampling of the distributions.

The issues associated with the fact that the signal is sampled rather than continuous mirror those issues encountered when considering the interrelationship between the Fourier transforms of sampled and unsampled time-series. Specifically, if one assumes that there is no aliasing introduced by the sampling process, then the distributions can be discretized in a direct manner and the results so obtained agree in the frequency range 0 to $f_s/2$ (f_s being the sampling frequency).

The operation of sampling the distributions in two-dimensional space (time–frequency or time-scale) introduces a raft of new theoretical considerations. The points at which the distributions are evaluated are called the sampling grid (or lattice). The issues associated with this sampling process for the STFT and CWT are subtly different and two different forms of grid are used. In the following sections we shall continue to assume a continuous time signal, $x(t)$,

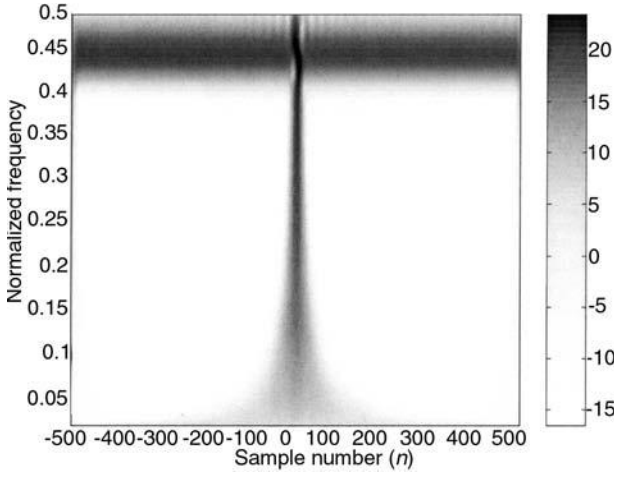


Figure 5 Continuous wavelet transform of second test signal.

and concentrate on the problems associated with sampling the distributions.

Sampling the STFT

When sampling the STFT it is conventional to use a regular sampling grid, i.e., a grid in which the sampling intervals in time and frequency are constant. This reflects the fact that the STFT has constant resolution in the time–frequency plane. Use of such a regular grid leads to the sampled STFT, $S(n, k)$, being defined as:

$$\begin{aligned} S(n,k) &= S(t,f)|_{t=n\Delta t, f=k\Delta f} \\ &= \int x(\tau) w(\tau - n\Delta t) \mathrm{e}^{-2\pi i(\tau - n\Delta t)k\Delta f} \mathrm{d}\tau \\ &= \int x(\tau) \Psi_{n,k}(\tau)^* \mathrm{d}\tau \\ \Psi_{n,k}(\tau) &= w(t - n\Delta t)\mathrm{e}^{2\pi i(t - n\Delta t)k\Delta f} \end{aligned}$$

where Δt and Δf are the sampling intervals in time and frequency respectively; the appropriate sampling grid is illustrated in **Figure 6A**. The functions $\Psi_{n,k}(t)$ form a set of functions referenced by the double index n, k.

It is natural to question whether one can continue to recover the original time series from the sampled STFT, $S(n, k)$. It is unsurprising to learn that, for fine grids, i.e., grids for which Δt and Δf are small, then signal reconstruction is possible. Clearly, if one can reconstruct a signal from a sampled STFT, then the STFT represents the signal and one can be reassured that there has been no loss of information in the transformation.

One can show that for reconstruction to be possible then the grid must be such that:

$$\Delta t \Delta f \leq 1$$

An obvious implication of this is that the coarsest possible grid that can be used to sample an STFT without losing information is one for which $\Delta t \Delta f = 1$: such grids are referred to as Von Neumann grids. These grids are attractive since they capture the full information contained within a signal with no redundancy. One subclass of such representations occurs when the windowing function and grid are selected so that the functions $\Psi_{n,k}(t)$ are orthonormal, so that:

$$\begin{aligned} \int \Psi_{n,p}(t)\Psi_{m,q}(t)^* \mathrm{d}t &= 1 \quad m = n \quad \text{and} \quad p = q \\ &= 0 \quad \text{elsewhere} \end{aligned}$$

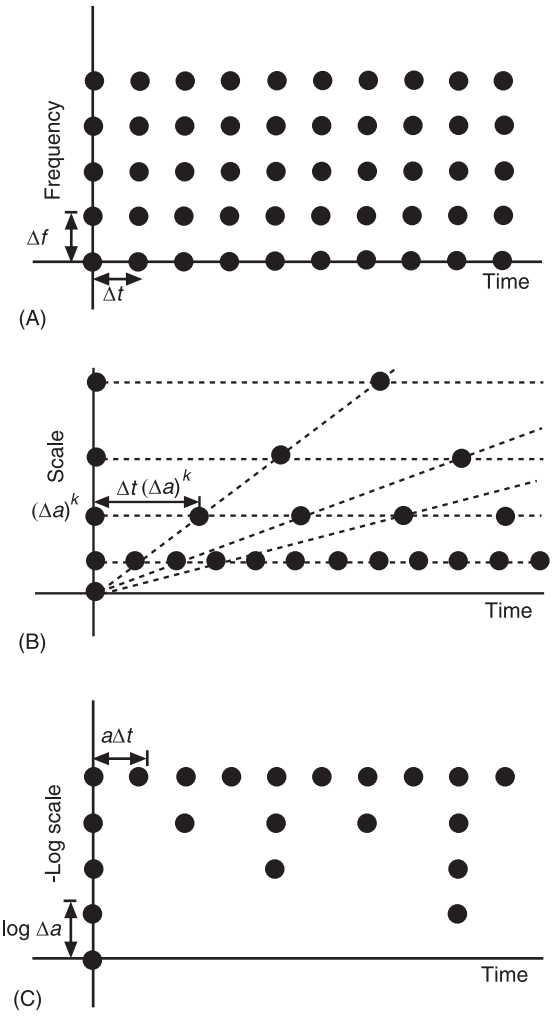


Figure 6 Sampling grids for (A) short-time Fourier transform; (B) continuous wavelet transform; (C) continuous wavelet transform grid plotted with an inverted logarithmic scale axis.

In which case one can readily show that:

$$x(t) = \sum_k \sum_n S(n,k)\Psi_{n,k}(t)$$

This formula readily allows one to interpret the sampled STFT values as the coefficients of an expansion of the signal in terms of the functions $\Psi_{n,k}(t)$. It is necessary to employ a Von Neumann grid to obtain an orthonormal decomposition. The condition of orthonormality can be relaxed using the concept of a frame, which provides the appropriate framework for analyzing such decompositions.

There is a fundamental limitation encountered when using the STFT. If a Von Neumann grid is used to sample a STFT, then the Balian–Low theorem

states that the window $w(t)$ must be poorly localized in either time or frequency. This implies that nonredundant STFT representations are incapable of yielding good simultaneous time–frequency localization. This point can be illustrated through a simple example.

Consider the STFT computed using a rectangular window, $w(t)$, with no overlapping, so that $\Delta t = T$, where T is the window's duration. The Fourier transform of the data within each window is evaluated using a sampling interval $\Delta f = 1/T$. For a digital signal, $x(n)$, this is trivial to implement using a fast Fourier transform. Clearly, this scheme employs a Von Neumann grid since $\Delta t \Delta f = 1$ and the basis functions $\Psi_{n,k}(t)$ can be shown to be orthonormal. The window $w(t)$ does have good time-localizing properties (since it has finite support), but its Fourier transform, which is a sinc function, decays very slowly in frequency and (mathematically at least) fails to give good frequency localization. This is one example that verifies the Balian–Low theorem.

Sampling the CWT

To implement a CWT, one again needs to sample it on a grid. However, in this case it is conventional to select a nonuniform grid structure. The sampling scheme almost universally employed is:

$$a_k = (\Delta a)^k \quad t_{n,k} = n\Delta t a_k = n\Delta t (\Delta a)^k$$

where Δa is the geometric scale increment and Δt is the time increment at scale $a = 1$. This scheme ensures that there are a fixed number of scales in each octave, referred to as voices. The fact that at each scale (frequency) the temporal resolution is different means that it is appropriate to adopt a scale-dependent time increment. The time increments become smaller at higher frequencies (smaller values of a). Such a sampling grid is depicted in **Figure 6B**. Note that the points on this grid lie on lines that pass through the origin, reflecting the affine nature of the transformation. **Figure 6C** depicts the same grid, but using an inverted logarithmic axis to represent scale. Such an axis is akin to a logarithmic frequency axis; this allows one to interpret the way in which the sampling occurs in the time–frequency plane.

Using such a grid, the discretized form of the CWT is:

$$W(n,k) = W(t,a)|_{a=a_k, t=t_{n,k}} = \frac{1}{(\Delta a)^{k/2}} \int g^* \left(n\Delta t - \frac{t}{(\Delta a)^k} \right) x(\tau)\, \mathrm{d}\tau$$

Like the STFT, the sampled CWT can be inverted, assuming that a sufficiently fine grid is used. However, unlike the STFT, there is no absolute limit on the values of Δa and Δt. This is in part a consequence of the fact that the base scale used to define the mother wavelet, i.e., the scale that corresponds to $a = 1$, is selected arbitrarily. This problem can be overcome by specifying the original scale of the mother wavelet. Even under these conditions there still remains no equivalent of a Von Neumann grid, i.e., a grid size that demarks the boundary between grids upon which reconstruction can and cannot occur.

The most significant theoretical advantage offered by WTs over the STFT is the fact that one can construct nonredundant wavelet transforms that are truly localized in time and frequency. (Recall that the Balian–Low theorem precludes the possibility of such STFT representations.) These nonredundant representations usually employ grids in which $\Delta a = 2$ and $\Delta t = 1$, termed a dyadic grid, with the mother wavelet scaled to suit the user.

Discrete Wavelet Transforms

A discrete wavelet transform (DWT) is, normally, defined as a nonredundant sampled CWT. The DWT aims to represent a discrete time series, $x(n)$, as a set of (wavelet) coefficients. These coefficients are sampled from a CWT, usually in a manner to yield an orthogonal (or biorthogonal) set of basis functions. There is a wealth of DWT formulations, with differing characteristics. In this section attention is restricted to the case of orthogonal wavelets with finite support.

The use of orthogonal bases ensures that the representation is nonredundant. In general, the use of orthogonal representations leads to simple algorithms for both reconstruction and decomposition. Efficient DWT algorithms exist that require computational loads that are often less than that needed to implement a fast Fourier transform.

There are several equivalent viewpoints from which the DWT can be regarded. Here we choose to discuss the DWT through the concept of a filter bank. A pair of finite impulse response (FIR) filters, with L coefficients, are defined. One of these filters is a high-pass filter, whilst the second is low-pass; both filters cut on/off at half the sampling frequency. The DWT can be defined using these filters and applying them recursively. The filters are first applied to the input time series to yield low-pass and high-pass components, $x_1(n)$ and $x_2(n)$ respectively:

$$x_1(n) = \sum_{k=0}^{L-1} c_k x(n-k)$$

$$x_2(n) = \sum_{k=0}^{L-1} d_k x(n-k)$$

where c_k and d_k are the coefficients of the low-pass and high-pass filters. It is normal to construct the high-pass filter based on the low-pass filter, which is commonly achieved using the alternating flip scheme, so that the two sets of filter coefficients are related through:

$$d_k = (-1)^k c_{L-k}$$

The output of both filters is half the bandwidth of the input sequence, such that $x_1(n)$ occupies the lower frequency range and $x_2(n)$ the upper band. The outputs of each of the filters is half the original bandwidth of $x(n)$, so that these two time series contain redundant information. One can subsample the two filter outputs to half the original sampling rate. The subsampling is achieved by discarding alternate samples in each sequence. Such a resampling means that both signals once again occupy the full bandwidth. Because of the imperfect design of the two FIR filters, the action of resampling introduces aliasing to both components.

To counter the artefacts introduced by aliasing, one can design the two filters so that the two aliasing effects cancel. If the filters are designed to ensure that aliasing cancellation occurs, then it is possible to reconstruct the original signal from the two subsampled sequences. The recovery of the original input sequence from the two subsampled sequences is realized by up-sampling the two subsampled signals, filtering them, and then summing the two components. For an orthogonal WT, using FIR filters, the synthesis filters are the same as those used for decomposition, but with the impulse responses reversed in time. The process of decomposing a signal into two subsampled sequences and then reconstructing the original signal is depicted in **Figure 7A**. Throughout **Figure 7** the symbols 2 and 2 are used to denote up and down sampling and $H_1(z)$ and $H_2(z)$ are the transfer functions of the low-pass and high-pass decomposition filters respectively, with $H_3(z)$ and $H_4(z)$ being the transfer functions of the corresponding synthesis filters.

The scheme shown in **Figure 7A** represents the basic building block of a wavelet filter bank. These elements are applied in a tree structure. Having applied the filtering and subsampling to the original time series to generate low- and high-frequency components, the operation can then be repeated on either of the new components. Most commonly one decomposes only the low-frequency (large-scale) component. This form of scheme is depicted in **Figure 7B**.

Every stage of the decomposition of the input sequence results in two sequences, each of which is half the length of the original sequence. Hence each stage of the decomposition preserves the total number of data points. The final result of the decomposition, indicated on the right side of **Figure 7B**, consists of N wavelet coefficients, which are a representation of the original N point input sequence (N is assumed here to be a power of 2). The N wavelet coefficients comprise $N/2$ coefficients at the smallest scale, $N/4$ coefficients at the next scale, etc. and at the largest scale there are two single values. If one considers the total number of coefficients required, namely $N/2, N/4 \ldots 2, 1$ and 1 additional coefficient then it is straightforward to show that this gives an overall total of N coefficients.

Reconstruction of the time series from the wavelet coefficients proceeds using the reverse of the decomposition procedure. This reconstruction is illustrated in **Figure 7C**. At each stage two signals are upsampled, filtered, and then summed.

The above derivation of the DWT hides the basis functions that are used in the DWT. These functions are completely specified by the choice of FIR filters. In fact, the basis functions are the solution of a dilation equation, the coefficients of which are the filter coefficients. The solutions of these dilation equations may have undesirable properties, for example, they may be fractal. In a reasonable decomposition one would like these orthogonal basis functions to be well behaved, at least being smooth to some extent. This effectively imposes additional constraints to the filter design procedure.

The basis functions that result from the design operation may be rather unnatural-looking (for example, they cannot, in general, be expressed in the form of eqn [13]), but do have powerful mathematical properties. **Figure 8** shows three examples of such basis functions for a common class of DWT. This family of wavelets is known as the Daubechies wavelets. The three wavelets shown correspond to different choices of filter length L. The higher-order filters also correspond to basis functions that are more smooth, so they decay more rapidly in the frequency domain. The Daubechies wavelets are designed to have compact support, so, in the time domain, they are zero outside a finite region. The frequency domain representations for these basis functions show that the basis functions are essentially band-pass in character, but they possess relatively

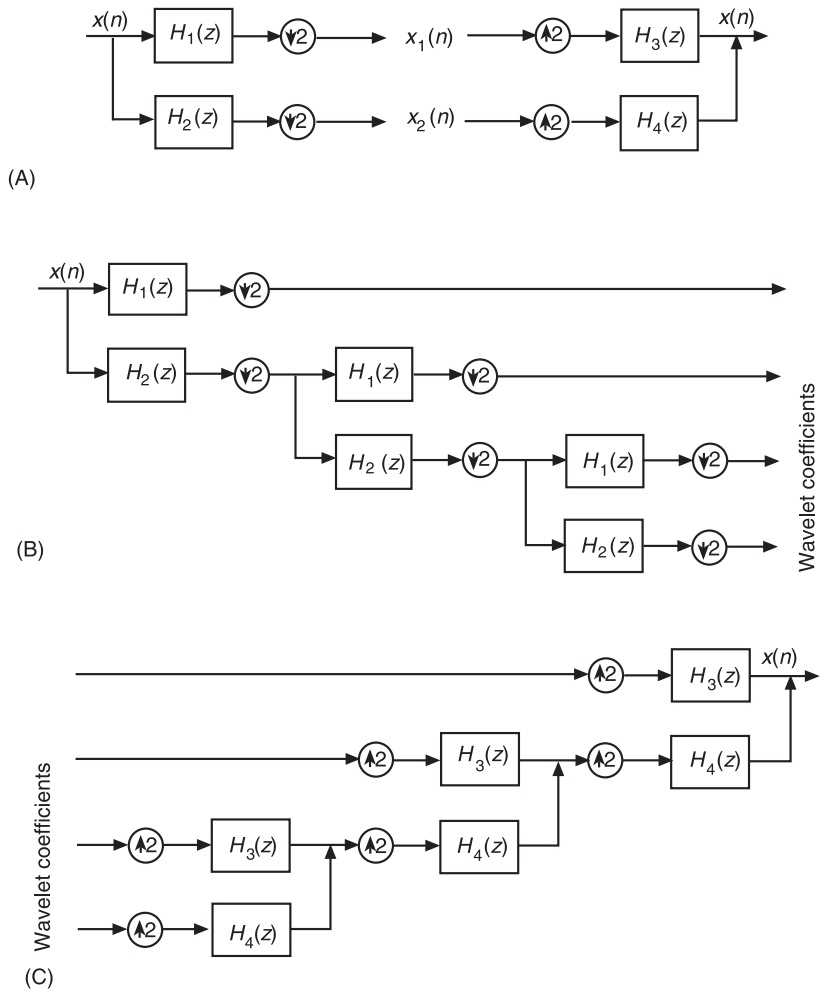


Figure 7 Filter bank implementation of a wavelet transform.

large sidelobes. This reflects the fact that the wavelet functions are designed to satisfy conditions that relate to regularity rather than classical filter design criteria.

Comparison of DWTs and CWTs

The choice of which of the two basic classes of wavelet transform to use is critically application-dependent. The critical difference between the two approaches is that the DWT is nonredundant. It completely represents the time series $x(n)$ using only as many coefficients as were present in the original signal. The CWT, as defined by eqn [7], is a continuous representation. However, it is conventional to use the term CWT to describe wavelet representations computed using a fine grid, so that the WT is greatly oversampled. (We avoid considering cases where the WT is mildly oversampled and neither of the terms DWT or CWT is really appropriate.) In this section the term CWT is understood to refer to such oversampled WTs, in which case the DWT has the obvious advantage of using a representation that employs the minimum number of coefficients, resulting in large computational savings over the CWT. Further, it is intuitively appropriate to employ such a minimalist representation of a signal when considering data compression applications.

This computational advantage is gained at some cost. The DWT fails to retain some of the most attractive properties of the CWT, namely its invariance to time and scale shifts, as described above. The loss of these two properties is a direct consequence of the sampling of the CWT that is undertaken to form the DWT. Indeed, the appearance of a lack of shift invariance similarly occurs when one samples the STFT. In both cases these invariances are lost as a result of the coarseness of the sampling of the representation relative to the sampling of the original time series. So, the loss of shift invariance is not a function of the underlying transform but is a consequence of one's choice of using a nonredundant representation.

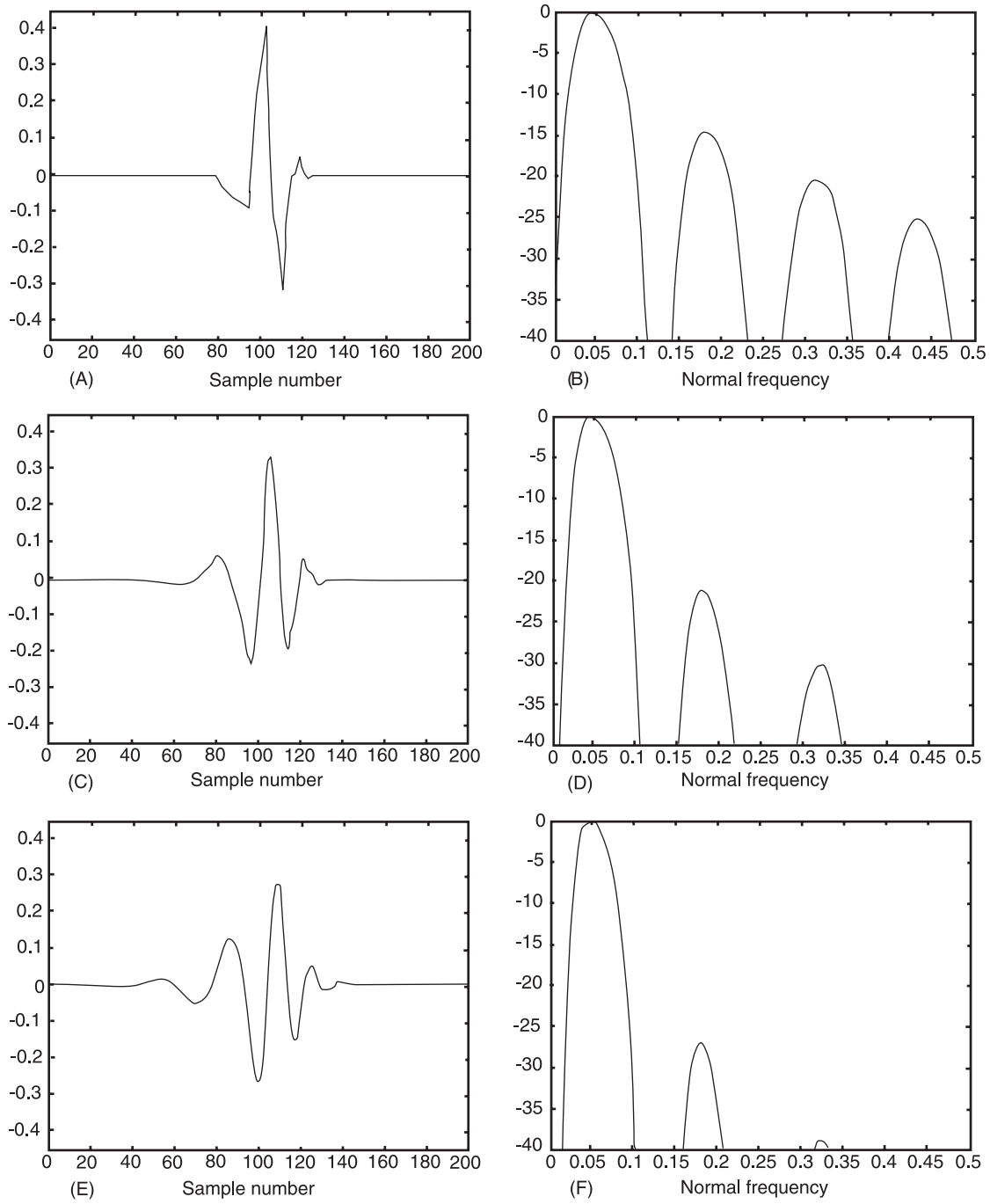


Figure 8 Examples of basis functions used in discrete wavelet transforms. (A), (C), and (E) Daubechies wavelets in the time domain using $L = 4, 8,$ and 12 respectively. (B), (D), and (F) Daubechies wavelets in the frequency domain using $L = 4, 8,$ and 12 respectively.

Figures 9 and **10** illustrate lack of shift invariance in the DWT for a simple signal, specifically a cosine wave modulated by a Gaussian window. In both these figures the DWTs, shown in the right-hand frames, are displayed using the same convention. Time is depicted on the horizontal axis. The vertical axis is linear in scale. Large scales (low frequencies) are depicted towards the bottom of the graph and are given small arguments. For each scale the same number of time points are shown (128 in this case), even though there are fewer different coefficients at the larger scales. For example, at scale 1 there

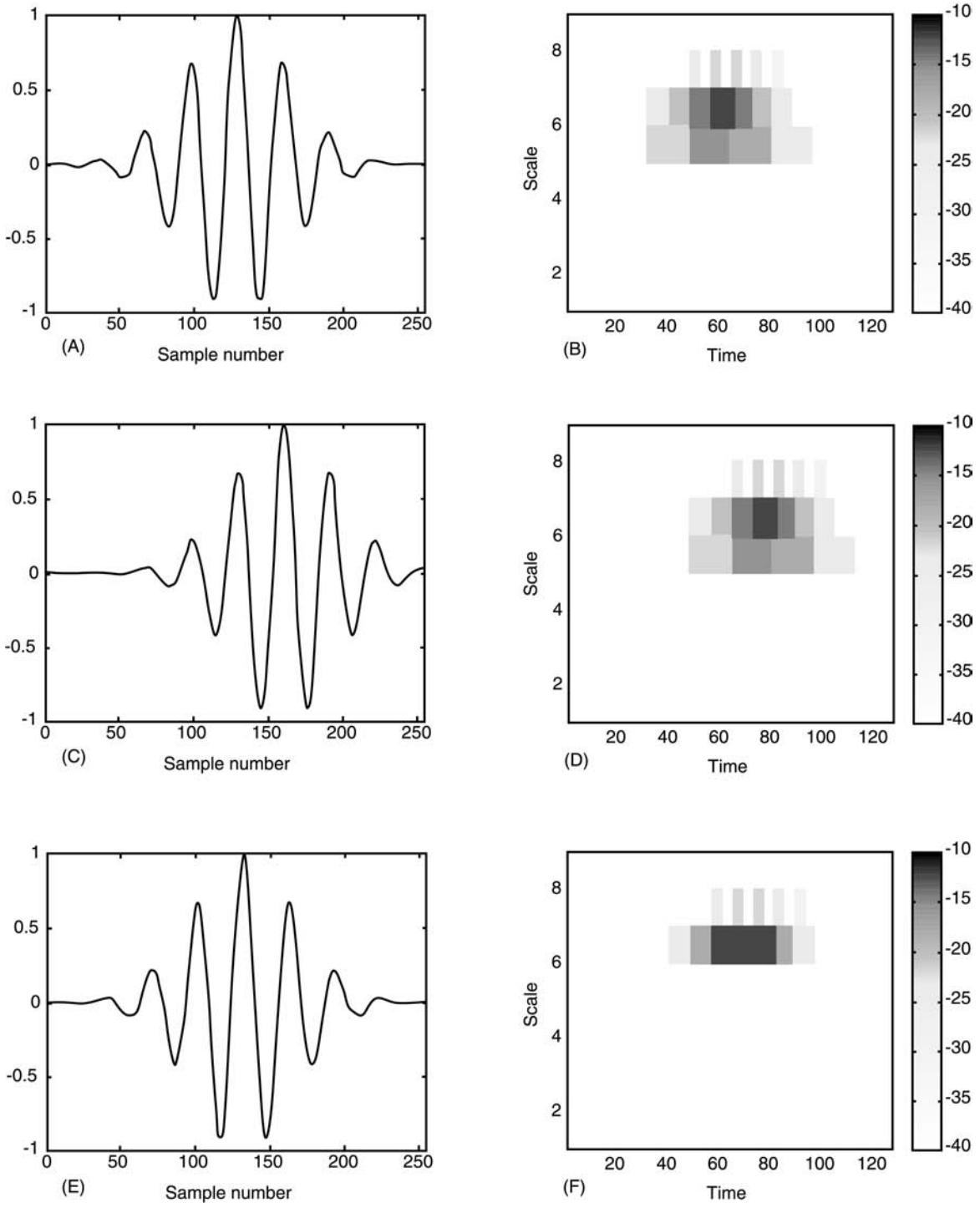


Figure 9 Discrete wavelet transform (DWT) of a Gaussian pulse with various time shifts. (A) Time series of the Gaussian pulse; (B) DWT of signal in (A); (C) Gaussian pulse shifted by 32 samples; (D) DWT of signal in (C); (E) Gaussian pulse shifted by four samples; (F) DWT of signal in (E).

is only one coefficient. To generate the DWT plots this value is repeated 128 times, at scale 2 there are two values, each repeated 64 times. The values plotted are the absolute values of the DWT coefficients on a logarithmic scale. Throughout these examples a Daubechies wavelet based on a filter of length 4 is used.

Figure 9A shows the time series of the Gaussian pulse. Its DWT, **Figure 9B**, shows that the majority of the energy in this signal is in scales 5 and 6 and

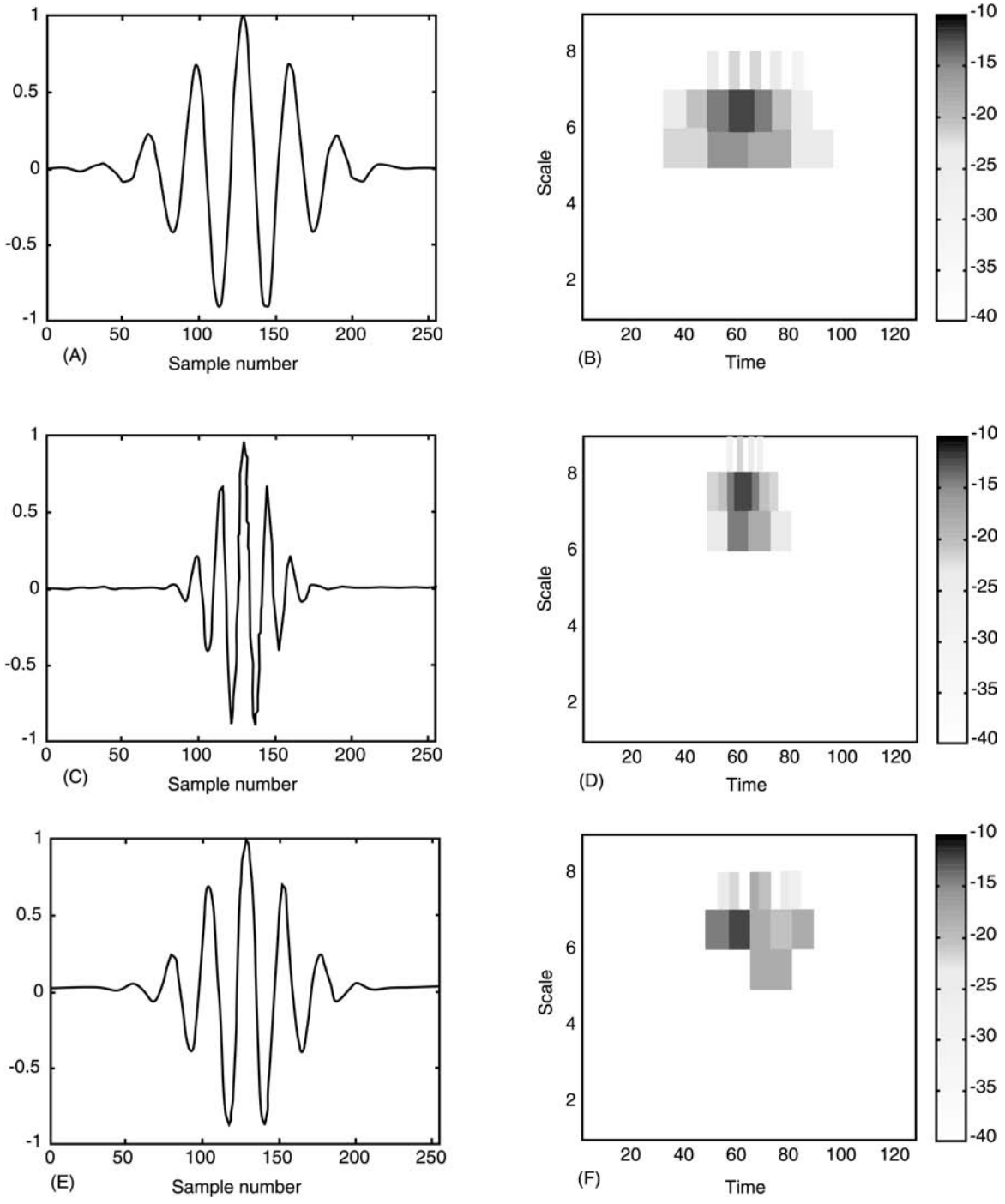


Figure 10 Discrete wavelet transform (DWT) of a Gaussian pulse with various scale shifts. (A) Time series of the Gaussian pulse; (B) DWT of signal in (A); (C) Gaussian pulse compressed by a factor of 2; (D) DWT of signal in (C); (E) Gaussian pulse compressed by a factor of $2^{1/3}$; (F) DWT of signal in (E).

centered close to 64 samples on the time axis. **Figure 9C** shows this signal shifted by 32 samples in time. The DWT coefficients correspondingly shift, as can be seen in **Figure 9D**. The two representations shown in **Figure 9B** and **9D** behave according to intuition; specifically a shift time in the signal results in a shift in time of the DWT coefficients. This result is fortuitous and only comes about through careful selection of the time shift. If one shifts the time signal by four samples, as shown in **Figure 9E**, the DWT, **Figure 9F**, changes significantly; almost all of the energy vanishes from scale 5. The two DWTs in

Figure 9B and **9D** give the impression of having arisen from very different signals, rather than two signals that are translated versions of each other. This variability in the DWT coefficients with respect to the origin of a signal makes them difficult to use for the purposes of signal interpretation.

A similar effect arises when one considers signals that are related to each other in scale. This is shown in **Figure 10**. The top two frames are identical to those in **Figure 9**. **Figure 10C** shows the effect of compressing the signal by a factor of 2. The corresponding DWT coefficients shift up one level scale, as shown in **Figure 10D**. The manner in which these plots are constructed tends to make the DWTs look more disparate than is appropriate. The coefficients shown in **Figures 10B** and **10D** are the same but they are only translated up one scale bin. **Figure 10E** shows the effect of compressing by $2^{1/3}$ (a third octave); like the time shifts, this serves to alter the character of the DWT coefficients rather than only to shift them.

The lack of shift invariance in the DWT is due to the fact that it is a CWT computed on a coarse grid. Using a finer grid results in a WT that is more robust to shifts in time and/or scale. To avoid the problem of shift invariance in time, one can implement the DWT but omit the subsampling operations. This results in a representation which is nonredundant, there being as many coefficients for each scale as there is in the original time series. Such schemes are still poorly suited for the purposes of signal interpretation. Their sampling time is as fine as is possible, but their sampling in scale is maximally coarse. It is better to construct a WT in which the oversampling occurs in both time and scale, rather than in only one domain; such a scheme is a CWT.

If the user opts to use a WT that is nonredundant, using a grid that is finer than a dyadic grid, then there seems little advantage to using DWT basis functions. One should select a mother wavelet that in some sense matches the signal being analyzed, or in the absence of such *a priori* knowledge one should use a wavelet that is well localized in the time-scale plane. This leads one commonly to use a Morlet wavelet which satisfies the uncertainty principle: which is the wavelet with the smallest area in the time–frequency plane.

Results

To illustrate the performance of WTs we present an analysis of structural response data. The data set used represents the impulse response of a beam with a semianechoic termination at one end; for details of the experimental procedure see Transforms: Time-Frequency. **Figure 11** shows the time series to be analyzed; this consists of two distinct wave packets: the first corresponding to the arrival of energy without reflection, the second derives from energy reflected from the beam's free end. The second pulse, having travelled further that the first, undergoes a greater degree of dispersion.

Figure 12 shows various representations of this signal. In each case the parameters defining the representations have been selected so that the results produce the most visually appealing representation. The scalogram (the squared magnitude of the CWT) is depicted in **Figure 7A**. The two pulses are clearly discernible and individual characteristics can be seen. For comparison the spectrogram (the squared magnitude of the STFT) is plotted in **Figure 7B**. For this signal the CWT and STFT are relatively similar. The greater temporal resolution at high frequencies offered by the CWT allows one to identify more accurately the onset of each component, whereas the loss of temporal resolution in the CWT at low frequencies makes it harder to distinguish the frequency laws for each component below, say, 1 kHz. **Figure 7C** shows the DWT computed using a 6 coefficient Daubechies wavelet. This figure is plotted using the convention used in **Figures 9** and **10**, except that the vertical axis is transformed to represent frequency rather than scale. A comparison of **Figures 7A** and **7C** shows that DWT produces plots in which the underlying dynamics of a system are not revealed as clearly as the CWT.

Conclusion

The CWT and STFT offer complementary approaches to the decomposition of a signal. The CWT is based on the operations of time shifts and

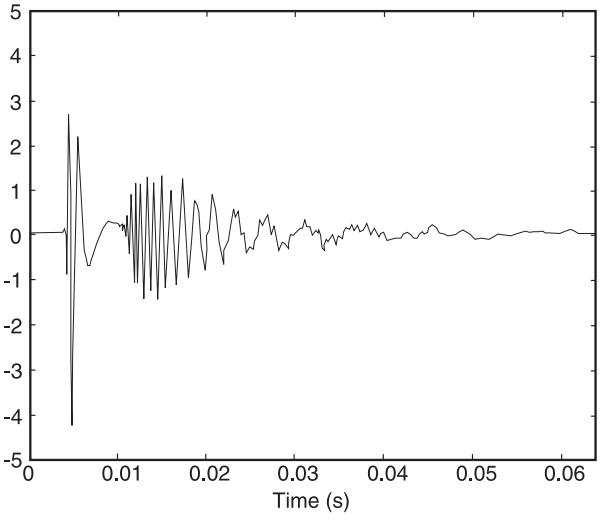


Figure 11 Beam impulse response data.

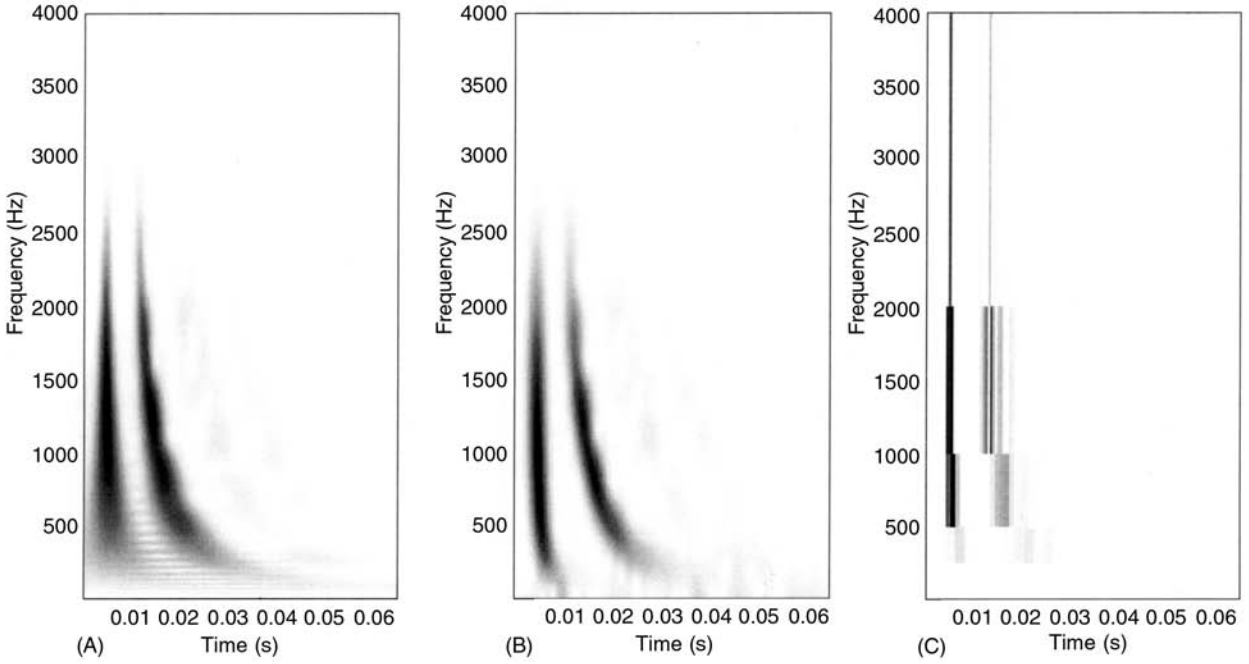


Figure 12 Time scale and time frequency representations for beam impulse response data. (A) Continuous wavelet transform; (B) short-time frequency transformation; (C) discrete wavelet transform.

temporal scalings, whilst the STFT exploits time and frequency shifts. The essential difference between the two approaches is that the time and frequency resolution in the STFT is uniform in the time–frequency plane. This is in contrast to the CWT. The CWT exploits variable resolution, has good temporal resolution in the high-frequency bands and good frequency resolution in the low-frequency bands. This makes them well suited to many classes of naturally occurring signals.

The DWT offers a nonredundant representation, which is not intended for visual inspection. It is a powerful and efficient tool in many applications, e.g., signal compression. However, its nonredundant nature makes it poorly suited to applications where one seeks to represent a signal in a manner that clearly exposes its underlying nonstationary structure.

Nomenclature

a	scale
f	frequency
f_s	sampling frequency
$G(f)$	Fourier transform of $g(t)$
$\tilde{G}(f)$	Fourier transform of $\tilde{g}(t)$
$S(t, f)$	Short-time Fourier transform
$x(t)$	continuous time signal
$w(t)$	windowing function
$\delta(n)$	Kronecker delta function
Δf	sampling intervals in frequency
Δt	sampling intervals in time

See also: **Spectral analysis, classical methods**; **Time–frequency methods**; **Transform methods**.

Further Reading

Chui CK (1992) *An Introduction to Wavelets*. Boston: Academic Press.

Daubechies I (1988) Orthonormal bases of compactly supported wavelets. *Communications on Pure and Applied Mathematics* 41: 909–996.

Daubechies I (1990) The wavelet transform, time-frequency localisation and signal analysis. *IEEE Transactions on Information Theory* 36: 961–1005.

Daubechies I (1991) The wavelet transform: a method of time-frequency localization. In: Haykin S (ed.) *Advances in Spectrum Analysis and Array Processing*, vol. 1. Prentice-Hall.

Daubechies I (1993) Orthonormal bases of compactly supported wavelets II. Variations on a theme. *SIAM Journal of Mathematical Analysis* 24: 499–519.

Daubechies I, Grossman A and Meyer Y (1986) Painless non-orthogonal expansions. *Journal of Mathematical Physics* 27: 1271–1283.

Gabor D (1946) Theory of communication. *Journal of the IEE* 93: 429–457.

Heil CE and Walnut DF (1989) Continuous and discrete wavelet transforms. *SIAM Review* 31: 628–666.

Kaiser G (1994) *A Friendly Guide to Wavelets*. Boston: Birkhauser.
Mallat SG (1989) A theory for multiresolution signal decomposition: the wavelet representation. *IEEE Transactions on Pattern Analysis and Machine Intelligence* 11: 674–693.
Papoulis A (1984) *Signal Analysis*. New York: McGraw-Hill.
Strang G (1989) Wavelets and dilation equations: a brief introduction. *SIAM Review* 31: 614–627.
Strang G and Nguyen T (1996) *Wavelets and Filter Banks*. Wellesley, MA: Cambridge Press.
Wickerhauser MV (1994) *Adapted Wavelet Analysis from Theory to Software*. St Louis: IEEE Press.

TRANSMISSION

See **VIBRATION TRANSMISSION**

TRANSPORTATION SYSTEMS

See **GROUND TRANSPORTATION SYSTEMS**

U

ULTRASONICS

M J S Lowe, Imperial College of Science, Technology and Medicine, London, UK

Copyright © 2001 Academic Press

doi:10.1006/rwvb.2001.0143

Definition of Ultrasonics

Ultrasonics is a name given to various specific topics in which the properties of ultrasound are exploited. Ultrasound is simply sound whose frequency is too high to be heard by the human ear, that is to say the frequency is above *c* 20 kHz. At the top end of the scale, ultrasound is used at frequencies up to several GHz. Ultrasound waves are characterized by elastic oscillations of the material in which they travel, that is, they are essentially traveling vibrations. This entry gives a brief introduction to the physics of ultrasound, and the concepts underlying some of its applications in fields of engineering.

Essential Features of Ultrasound

Sound travels in the form of a wave, involving the elastic straining of the material in which it travels, so the properties of the sound depend on the properties of the material. In the simple case of sound traveling in air, or indeed in any gas or fluid, the air is compressed and dilated as the wave passes through; the properties of the wave then depend on the compression stiffness and the density of the air. Elastic waves also travel in solid materials, in which case they are still commonly known by the names sound or ultrasound. Two different possible forms may propagate in solids. There are compression (or longitudinal) waves, which are essentially the same as those in gases or fluids, but there are also shear (or transverse) waves, in which the volume of the material does not change; instead the motion is at right angles to the direction of propagation and consists of shear deformation of the material (see **Wave propogation**, Waves in an unbounded medium). In brief, the velocities of the waves in elastic materials are given by, in a fluid or gas:

$$C_{\mathrm{L}} = \text{ compression wave speed } = \left(\frac{K}{\rho}\right)^{1/2} \quad [1]$$

in a solid:

$$C_{\mathrm{L}} = \text{ compression wave speed } = \left[\frac{E(1-v)}{\rho(1+v)(1-2v)}\right]^{1/2} \quad [2]$$

$$C_{\mathrm{S}} = \text{ shear wave speed } = \left[\frac{E}{2\rho(1+v)}\right]^{1/2} \quad [3]$$

where K is the bulk stiffness modulus of the fluid or gas, ρ is the density, E is Young's modulus, and v is Poisson's ratio. The velocities of sound wave propagation in a material are thus properties of the material, and in these relationships it can be seen that there is no variation of the velocities with frequency. Values of the acoustic properties for some materials are given in **Table 1**.

The propagation of a sound wave is described by a harmonic function, usually expressed as a complex exponential. For example, the particle displacement, u, the particle velocity, v, and the pressure, σ, of a compression wave traveling in the X direction can be described by:

$$u_X = A\mathrm{e}^{\mathrm{i}(kx-\omega t)} \quad [4]$$

$$v_X = \mathrm{i}\omega u_X \quad [5]$$

$$\sigma_{XX} = \mathrm{i}\omega C\rho u_X = C\rho v_X \quad [6]$$

A is the displacement amplitude of the wave, C is the wave velocity and k is the wavenumber, defined as:

$$k = \frac{\omega}{C} = \frac{2\pi}{\lambda}$$

and:

Table 1 Acoustic properties of some fluid and solid materials

Material name	*Density (kg m^{-3})*	*Longitudinal velocity (m s^{-1})*	*Shear velocity (m s^{-1})*
Air	1.21	343	–
Castor oil	971	1474	–
Kerosene	822	1319	–
Mercury	13550	1391	–
Motor car oil	870	1740	–
Water at 20°C	998.2	1478	–
Water at 50°C	988	1522	–
Aluminum	2700	6320	3130
Brass	8400	4400	2200
Concrete	2200	3900–4700	2300
Copper	8900	4700	2260
Epoxy resin	1100–1250	2400–2900	1100
Glass (crown)	2500	5660	3420
Glass (flint)	3600	4260	2560
Gold	19300	3240	1200
Ice	900	3980	1990
Lead	11400	2160	700
Nylon	1100	2200	1100
Paraffin wax	830	2200	
Perspex (acrylic resin)	1180	2730	1430
Polyethylene (MD)	950	2300	950
Quartz	2600	5570	3520
Rock	2500 (typical)	2500–4400	1500–2500
Rubber (soft)	900	1480	
Silver	10500	3600	1590
Steel	7800	5960	3260
Tin	7300	3320	1670
Titanium	4460	6060	3230
Tungsten	19100	5460	2620
Zinc	7100	4170	2410

Data from Krautkramer and Krautkramer (1983), Auld (1990), and Kaye and Laby (1995).

$$\lambda = \text{wavelength} = \frac{C}{\text{Freq(Hz)}} = \frac{2\pi C}{\omega} \qquad [7]$$

The complex exponent in eqn [4] describes the characteristic space–time harmonic nature of the wave: the wave varies sinusoidally in both distance and time. Eqn [6] shows that, for a given amplitude of the particle displacement, the pressure in the wave increases linearly with the frequency, ω. Therefore when comparing low-frequency and high-frequency waves, one may think of the former as being displacement-dominated and the latter as being pressure-dominated. The relationships between the displacement, velocity, and pressure also include the material constants ρ and C; their product, ρC, often appears in wave theory and is known as the acoustic impedance, conventionally represented by the symbol Z. Solid materials have two acoustic impedances, one for compression waves and one for shear waves, although references often give only one value, that for the compression waves.

The wavelengths of ultrasonic waves cover an enormous range. At the low-frequency end of the scale, 20 kHz, the wavelength in air is 17 mm, and in steel the wavelength of longitudinal waves is 300 mm. At 1 GHz, the wavelength in steel is just 6 μm.

Sound waves carry energy along their direction of propagation, and in the case of elastic waves the energy is transported at the same velocity as the wave. The energy transmission is often expressed by the intensity of the wave. The intensity is the quantity of energy which is propagated per second per unit cross-sectional area, where the cross-section is taken normal to the direction of propagation. The intensity is:

$$I = \overline{\sigma}_{XX}\overline{v}_X = \frac{\rho C \overline{v}_X^2}{2} = \frac{\overline{\sigma}_{XX}^2}{2\rho C} \qquad [8]$$

in which the overscore denotes the root mean square (RMS) value of the quantity. Thus, the propagation of the energy is determined by the acoustic impedance and the square of the particle velocity or stress.

Ultrasound waves are affected on arrival at any discontinuity of the material, including any change of the material properties of the medium. For example, they partially reflect and partially transmit at an

interface between two materials. The relative strengths of the reflected and transmitted components depend on the acoustic impedances of the two materials. If there are voids in a material, or there are small inclusions of another material, then the ultrasound is again partially reflected and partially transmitted and is also in general scattered in other directions. These properties are exploited in ultrasonic nondestructive testing (NDT) for the detection of voids and cracks (see **Wave propagation**, Interaction of waves with boundaries).

The assumption that the material is perfectly elastic is not strictly correct. All materials exhibit some sound-attenuating properties, including absorption (hysteresis) and scattering from small inhomogeneities. However, this assumption is practically realistic for many engineering materials; the attenuation effects are usually sufficiently small that they can be ignored in the calculation of the propagation and interaction phenomena. When the attenuation is significant, then it can fundamentally affect the nature of the propagation. For example, the velocity of a material may then be frequency-dependent (this is called dispersion), and the energy may be propagated at a different speed from that of the wave fronts.

Ultrasound in Engineering

Ultrasound is used in very many devices and applications in engineering. The following paragraphs give summary descriptions of some of the topics and concepts which are employed.

Nondestructive Testing

The principle of ultrasonic NDT is to transmit a wave signal into a structure, and then to detect defects by receiving and examining subsequent signals. A common configuration ('pulse-echo') is to position a transducer on one side of the structure, to transmit a signal into the structure, and then to receive reflections using the same transducer. If defects are present, then sound is reflected from the defects. Most ultrasonic testing is done using compression waves, although there are techniques which use shear waves and others which use structure-guided waves. An important example of the use of shear waves is the inspection of welds: in this, a shear wave is projected at an oblique angle into the material in order to detect cracks which are aligned normal to the surface; these would not be seen by a wave which was projected normal to the surface of the material. Ultrasonic NDT is very widely used; it is very sensitive to defects whilst being totally insensitive to the parts of the structure which are remote from the test location and to the support conditions.

Imaging

Ultrasound reflection or transmission measurements are used for imaging in a number of application areas. In NDT, two-dimensional maps, or C-scans are created by scanning a transducer in a raster sequence over an area of a structure. The intensity of the reflected or transmitted signal at each location is used to set the color on the image, thereby producing a map of any defective areas. Tomographic three-dimensional images, constructed by processing multiple transmitted signals, may also be generated, but this is rarely done in NDT. Ultrasound scanning is of course a routine procedure in medical diagnostic imaging, using advanced signal-processing procedures to enhance the contrast and resolution. Another area of imaging is acoustic microscopy. The acoustic microscope uses a sharply focused transducer, both sending and receiving the signal, operating at high frequencies (from 100 MHz to more than 1 GHz) to scan the surface of an object. The scans can reveal detailed information about the surface and the material just below the surface.

Cleaning

Ultrasonic cleaners use high-power ultrasound to remove grease and dirt from the surfaces of materials. It is not difficult, particularly at the low-frequency end of the ultrasonic range, to generate ultrasonic waves whose oscillating pressure is sufficiently large to create cavitation in a fluid. The growth and collapse of cavities occurs very rapidly, during which time enormous local pressure transients take place. Applied next to a surface, these have the effect of dislodging the dirt and, indeed, if sustained, can damage the material itself.

Measurement of Material Properties

The speed of ultrasonic waves can be used to make accurate measurements of the elastic properties of a material. The compression modulus of a fluid, the elastic modulus, and Poisson's ratio of an isotropic solid, can all be determined using eqns [1]–[3], once the ultrasonic velocity has been measured. Anisotropic materials are characterized by larger numbers of elastic constants, and these can be extracted from measurements of the velocity in different directions. Measurements of attenuation can be used to quantify the characteristics of an absorbing or scattering medium, such as the viscosity of a fluid and the size and distribution statistics of particles in suspension in a fluid.

Electronic Devices

Ultrasound has been used in electronic components for many years. Initial devices provided a delay to a signal simply by propagating ultrasound from a transmitter to a receiver along a short length of a solid rod. This exploited the fact that the ultrasound velocity is very much smaller than that of electrical signals. Surface acoustic wave (SAW) devices were developed in the 1960s to perform more complex operations such as filtering and hardware signal processing and are now very widely used. In these devices, the wave is guided along the surface of a piezoelectric material. The wave is excited by multiple parallel thin 'finger' electrodes which are attached to the surface; the distance between them is matched to the desired wavelength of the wave. A similar pattern of electrodes is used at the receiver location. These devices use waves with frequencies of up to several GHz.

Modifying Chemical Reactions and Processes

High-power ultrasound has many applications in modifying or enhancing chemical reactions and material production processes. It can be used to heat a material in which there are viscous losses; some of the energy is transformed from the ultrasound into heat. The heat source can be localized by using a transducer which focuses a beam at a specific location. Attenuating ultrasonic waves also introduces a steady force, and thus a net motion of a fluid, through the phenomenon of 'streaming'. Similarly, particles suspended in a viscous fluid are set into net motion by ultrasonic waves. Furthermore, the motion of the particles varies according to their size. Cavitation, as mentioned earlier, is quite easy to induce using ultrasound, and involves very large localized pressures. Thus ultrasound may be used to perform functions such as: increasing the speed of chemical reactions, degasing fluids, and dispersing or coagulating materials in suspensions.

Ultrasonic Cutting and Welding

As discussed in the previous paragraph, ultrasound waves carry energy and so can be used to heat a material. If very-high-power waves are generated, and the transduction is designed to focus the sound on a particular location of a material, then it is possible to increase the local temperature very significantly, and even to melt the material. Ultrasonic cutting and welding of materials are achieved using this principle. The transformation of the energy from the wave to heat requires some means of loss in the material, such as hysteretic damping, and so the applications of the technique are particular to those materials which have suitable properties. The main applications of ultrasonic cutting and welding are with plastics, as these have the helpful properties of high damping and relatively low melting temperature.

Acoustic Emission

When a structure is loaded towards its limit strength, it may emit acoustic signals through the mechanisms of microcracking or rubbing. Acoustic emission is the name given to the techniques which detect these emissions and so can be used to determine the state of distress of the structure. Acoustic emission signals are generally associated with discrete events and so are short-time signals. The frequencies of these signals are quite broad-band; in practice the frequency range between 100 kHz and 1 MHz has been found to be the most applicable. A typical, and popular, application of acoustic emission is to the proof-testing of pressure vessels. A set of transducers is attached to the vessel, then their signals are monitored while the pressure in the vessel is increased. The initiation of any cracking is then indicated by the emitted signals before the pressure is large enough to accumulate any significant damage. The location of the sound sources can be estimated by comparing the arrival times of signals at different receivers.

Generation of Ultrasound

Transducers for the generation of ultrasound most commonly use piezoelectric materials to convert an electrical signal into the mechanical motion. **Figure 1** shows a section through a typical ultrasonic NDT transducer, designed to excite longitudinal waves. An electrical signal is supplied as a voltage across the thickness of a piezoelectric disk which then vibrates. The first through-thickness vibration mode of the disk excites waves in the fluid or structure in front of the transducer. Thus, the center frequency of operation of the transducer can be controlled by the selection of the thickness of the disk. Damping material behind the disk absorbs the backward-traveling waves and also damps the resonance of the disk. The damping enables the transducer to produce waves which are short in time and so wide in frequency bandwidth. Transducers usually have a durable material, known as a wear plate, which is attached to the front of the piezoelectric disk for protection. The transducer may also act as a receiver, in which case it simply works in reverse: the incoming waves excite motion in the piezoelectric disk which then generates an electrical signal. The two most popular choices of the material for the piezoelectric disk are the ceramic lead zirconate titanate (PZT) and the polymer polyvinylidene

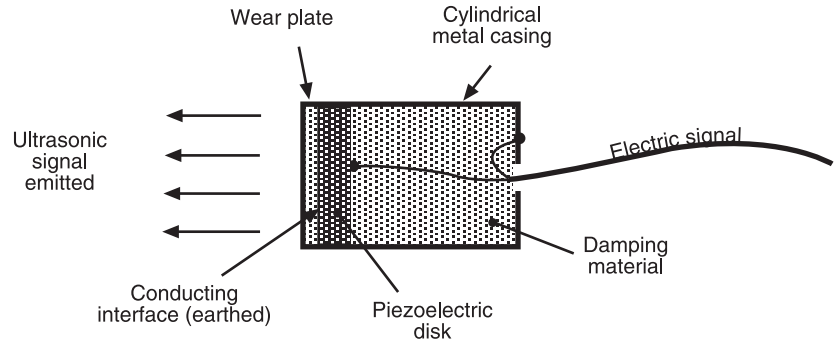


Figure 1 Section through a piezoelectric transducer.

fluoride (PVDF). Piezoelectric transducers may be used throughout the ultrasonic frequency range.

Although piezoelectric transducers are the most common, there are some alternative types in use. Electromechanical transducers which use a moving coil, similar to a loudspeaker, can generate waves with large amplitudes, but their maximum frequency is limited to some tens of kHz. Electromagnetic EMAT transducers generate wave motion directly in a conducting material. An alternating current is passed through a coil which is in close proximity to the body and within a static magnetic field. Either or both of the phenomena of Lorenz forces and magnetostriction then introduce an alternating stress field in the body. Although the electromechanical coupling of these transducers is not strong, they have the advantage that they do not need direct contact with the body and so can be used for example on dirty surfaces. They are used mostly in the frequency range from some hundreds of kHz to a few MHz. Finally, lasers may be used to generate and detect ultrasound. Sound is generated using a relatively powerful source, either by inducing a cyclic thermoelastic strain (by locally heating the material), or by spalling small quantities of the material from the surface, thereby initiating a transient reaction force. Detection of displacements at the surface of a body requires only a low-power laser interferometer. Lasers have very wide bandwidths and have the advantage that the transduction is contactless.

Nomenclature

A	amplitude
C	wave velocity
E	Young's modulus
k	wavenumber
K	stiffness
u	particle displacement
v	particle velocity
Z	acoustic impedance
λ	wavelength
ν	Poisson's ratio
ρ	density
σ	pressure
ω	frequency

See also: **Nondestructive testing**, Sonic; **Nondestructive testing**, Ultrasonic; **Wave propagation**, Guided waves in structures; **Wave propagation**, Interaction of waves with boundaries; **Wave propagation**, Waves in an unbounded medium.

Further Reading

Auld BA (1990) *Acoustic Waves and Fields in Solids*, 2nd edn. Florida. Robert E Kreiger.

Gooberman GL (1968) *Ultrasonics: Theory and Applications*. London: The English Universities Press.

Kaye GWC, Laby TH (1995) *Tables of Physical and Chemical Constants*, 16th edn. Essex: Longman.

Kolsky H (1963) *Stress Waves in Solids*. New York: Dover Publications.

Krautkramer J, Krautkramer H (1983) *Ultrasonic Testing of Materials*. Berlin: Springer-Verlag.

Leighton TG (1994) *The Acoustic Bubble*. London: Academic Press.

Miller RK (1987) *Non-destructive Testing Handbook*. American Society for Non-Destructive Testing.

Rose JL (1999) *Ultrasonic Waves in Solid Media*. Cambridge: Cambridge University Press.

ULTRASONICS, NONDESTRUCTIVE TESTING

See **NONDESTRUCTIVE TESTING: Ultrasonic**

V

VARIATIONAL METHODS

See **THEORY OF VIBRATION: VARIATIONAL METHODS**

VEHICLES, ACTIVE VIBRATION CONTROL

See **ACTIVE CONTROL OF VEHICLE VIBRATION**

VIBRATION ABSORBERS

See **ABSORBERS, VIBRATION**

VIBRATION GENERATED SOUND

Fundamentals

M P Norton and S J Drew, The University of Western Australia, Western Australia, Australia

Copyright © 2001 Academic Press

doi:10.1006/rwvb.2001.0207

Introduction

Vibration generated sound occurs when vibration waves in a solid elastic medium couple to a compressible fluid in contact with the solid. Normally, the fluid is a gas (e.g., air), although it can be a liquid (e.g., water). This and the subsequent chapter on sound radiation from. flexible structures are concerned with the generation of sound waves in gases such as air, by vibrating rigid and flexible solid bodies, respectively; these are caused to vibrate by mechanically (or electromechanically) applied forces or structurally transmitted vibration.

Sound transmission through panels, enclosures and shells occurs when pressure waves are incident on a mechanical body (e.g., a wall panel or pipe wall), resulting in the transmission and radiation of sound by the body (this is not covered here). Sound may also be generated by the fluid flow over a solid body, e.g., vortex shedding. However, flow-induced sound generation is not caused by mechanically applied forces and is also not discussed here. Vibration generated sound in fluids such as water involves significant fluid loading imposed on the structure by the fluid (see **Vibration generated sound**, Radiation by flexural elements). Sound radiated from elementary sources, baffled plates, sound transmission, fluid-structure interaction and structure–acoustic interaction are covered in other articles in this encyclopedia (see **Structure-acoustic interaction, high frequencies**).

Vibration generated sound may be either undesirable (i.e., 'noise') or desirable (e.g., a stereo speaker). The desirability or otherwise of a particular sound may be one of perception; except in cases where the sound is destructive, in which case it is always undesirable (e.g., when it causes hearing damage). However, the physics of the generation of sound by a vibrating body is the same for both intrusive (i.e., 'noise') sources and useful sound sources. In the engineering context, vibration generated sound is mostly concerned with the reduction of undesirable noise levels and this is reflected in the emphasis here. The two articles on vibration generated sound cover the two main mechanisms of mechanical vibration generated sound radiation.

Sound generated by the motion of inflexible solid bodies in air Sources covered are a baffled piston, finite monopole (i.e., a 'breathing' sphere) and a finite dipole (i.e., an oscillating sphere). These all have surface normal vibration velocities that are in-phase at every point. Oscillatory and impulsive sound generation by rigid bodies are both discussed in this article and have fundamentally different mechanisms. Sound generated by elementary point sources (generally used for sound propagation modeling) is discussed in a separate article.

Sound generated by the vibration of flexible solid structures in air Sound radiation by flexible structures is significantly more complex than rigid body sound radiation. Flexible sources have surface normal vibration velocities that are not in-phase at every point on the surface. Classical theory describing sound generation in air caused by the vibration of flexible plate and shell structures, is well established. Analytical and numerical solutions and experimental data are available for many configurations (e.g., flat plates, cylinders). Detailed derivations of the governing equations are available. A limited number of key concepts and equations are presented in the next article on vibration generated sound, along with published experimental data. Analytical procedures for the prediction of noise radiation from baffled plates are discussed in a separate article (see **Noise: Noise radiated by baffled plates**).

Basic Theory

Impedance and Sound Radiation

Mechanical vibration of solid bodies (i.e., structures) requires the application of dynamic forces to the body. With the exception of fluid and flow-induced forces and electromagnetic forces, a mechanical connection exists between the force applicator and the structure. In some cases the forces are transmitted from a remote source, via structural vibration. Sound radiation requires that the structure applies dynamic forces to the surrounding fluid medium. The surrounding fluid may also apply a fluid loading to the structure. If the fluid medium is a gas, the fluid loading effect is negligible (i.e., the dynamic forces applied to the structure by the gas are negligible). Overall, energy is transfered from the force applicator to the structure and from the structure to the surrounding fluid.

This transmission of energy and radiation of vibration generated sound involves impedances within the system. An impedance is defined as the (complex) ratio of an applied dynamic force (or pressure) to a resulting dynamic velocity (or volume velocity). All three terms are complex.

Consider a dynamic mechanical force, $\mathbf{f}_m(x, t)$, that causes a solid body (i.e., structure) to vibrate with a vibration velocity, $\mathbf{v}_m(x, t)$. The vibrating body radiates sound into the surrounding fluid, with particle velocity, $\mathbf{u}_m(x, t)$, and sound pressure, $p(x, t)$.

Mechanical impedance If the vibrating body is in a vacuum, $\mathbf{z}_m$ is the mechanical impedance of the structure. It is a property of the structure only. In practice, mechanical impedance is normally measured in air, because the *in vacuo* and in-air mechanical impedances are not very different.

Radiation impedance If the vibrating body is surrounded by a fluid, the fluid applies an acoustic pressure force in response to the surface vibration. The acoustic radiation impedance is defined to be dimensionally consistent with mechanical impedance (i.e., because it is a mechanical impedance):

$$\mathbf{z}_r = \frac{\mathbf{f}_p}{\mathbf{v}_m} = (R_r + iX_r) \qquad [1]$$

Table 1 Mechanical and acoustic impedances

Impedance	*Force/Pressure*	*Velocity*	*Equation*	*Units*
Mechanical	Mechanical force	Surface velocity	$\mathbf{z}_m = \mathbf{f}_m/\mathbf{v}_m$	$N\,s\,m^{-1}$ (mks mechanical ohms)
Radiation impedance	Sound pressure force at surface (over area A)	Surface velocity	$\mathbf{z}_r = PA/\mathbf{v}_m$	$N\,s\,m^{-1}$
Specific acoustic impedance	Sound pressure	Particle velocity	$\mathbf{z}_{sa} = p/\mathbf{u}$	$N\,s\,m^{-3}$ (mks rayls)
Acoustic impedance	Sound pressure	Volume velocity	$\mathbf{z}_a = p/(\mathbf{u}A)$	$N\,s\,m^{-5}$ (mks acoustical ohms)
Characteristic resistance			$\rho_o c$	$N\,s\,m^{-3}$ (mks rayls)

Adapted from Bies DA, Hansen CH (1996) *Engineering Noise Control – Theory and Practice*, 2nd edn. Spon E & FN, London: Chapman and Hall.

where $\mathbf{f}_p$ is the acoustic pressure force, R_r is the radiation resistance and X_r is the radiation reactance. Since the fluid particles in contact with the solid must have the same velocity as the solid surface (i.e., $\mathbf{v}_m = \mathbf{u}_{r=0}$):

$$\mathbf{z}_r = \frac{pA}{\mathbf{v}_m} = \frac{pA}{\mathbf{u}_{r=0}} = \frac{\mathbf{f}_p}{\mathbf{u}_{r=0}} \qquad [2]$$

and:

$$\mathbf{u}_{r=0} = \frac{\mathbf{f}_m}{(\mathbf{z}_m + \mathbf{z}_r)} \qquad [3]$$

Specific acoustic impedance Specific acoustic impedance is the ratio of the acoustic pressure fluctuations in the fluid to the associated acoustic particle velocity in the fluid:

$$\mathbf{z}_{sa} = \frac{p}{\mathbf{u}} = (R_{sa} + iX_{sa}) = \frac{\mathbf{z}_r}{A} \qquad [4]$$

In the region close to a vibrating structure (i.e., the acoustic near field), the specific acoustic impedance is complex, with specific acoustic resistance (R_{sa}) and specific acoustic reactance (X_{sa}) components. At sufficient distance from the structure (i.e., in the acoustic far field), the acoustic resistance dominates and the acoustic reactance becomes negligible ($X_{sa} \approx 0$). At large distances, all sound sources approximate a spherical source. At very large distances, wavefront curvature becomes negligible and all waves approach plane wave propagation, with a characteristic acoustic impedance (resistance) of the fluid of $\rho_0 c$.

Acoustic impedance Acoustic impedance at a given surface (area A) is the ratio of the acoustic pressure averaged over that surface to the associated acoustic velocity through the surface.

Sound Radiation from a Baffled Piston

One of the classical problems in acoustics is the sound radiation from a vibrating circular piston mounted in an infinite baffle. It is a good example of vibration generated sound, with which to illustrate several important concepts. The analysis assumes that all parts of the piston surface are vibrating with exactly the same amplitude and phase. The piston is rigid and vibrates only in the direction of its central axis.

Acoustic near field and impedance The mechanical and acoustic impedances of any vibrating sound source are determined at the surface of the solid, which is the interface between the solid and the surrounding fluid. This interface is in the acoustic near field. The combined mechanical and acoustic radiation impedances give the total impedance. For the baffled circular piston of radius a, mass m, stiffness k_p, damping c_v and wavenumber k ($k = \omega/c$):

$$\mathbf{z}_m = c_v + i\left[m\omega - (k_p/\omega)\right] \qquad [5]$$

$$\mathbf{z}_r = \rho_0 c(\pi a^2)\left[R_p(2ka) + iX_p(2ka)\right] \qquad [6]$$

$$R_p(x) = \left[\frac{x^2}{(2.4)} - \frac{x^4}{(2.4^2.6)} + \frac{x^6}{(2.4^2.6^2.8)} - \cdots\right]$$

$$X_p(x) = (4/\pi)\left[\frac{x}{(3)} - \frac{x^3}{(3^2.5)} + \frac{x^5}{(3^2.5^2.7)} - \cdots\right]$$

$$\mathbf{z}_{total} = (\mathbf{z}_m + \mathbf{z}_r) = \frac{\mathbf{f}_{piston}}{\mathbf{v}_{piston}} \qquad [7]$$

For the baffled piston, the impedances are known. Piston velocity is calculated from the known mechanical force applied to the piston and the known mechanical impedance. Piston velocity and radiation impedance are then used to determine the radiated sound field (e.g., sound power). For many engineering structural sound sources, it is not practical to determine the applied mechanical force or mechanical impedance. However, it is not necessary to know them, in order to determine useful information about the radiated sound field. A single lineal structural vibration velocity term is sufficient to describe the radiation of vibration generated sound from a vibrating solid body. It is the space (—) and time ($\langle\,\rangle$) averaged RMS surface normal velocity ($\langle\underline{v}_{rms}\rangle$), i.e., the component of surface vibration velocity that is normal to the surface at every point.

If the surface normal vibration velocity and the radiation impedance of the vibrating structure are both known, then the sound radiation can be determined from:

$$\mathbf{f}_p = \mathbf{z}_r \cdot \mathbf{v}_m \qquad [8]$$

Radiation impedance for a baffled piston is shown in **Figure 1**. It is complex and varies with distance from the piston. The resistive (real) part of the radiation impedance is due to the radiated sound pressure. The reactive (imaginary) part of the radiation impedance is a fluid loading term, due to the fluid in close proximity to the piston. Fluid loading is significant when the fluid is a liquid. The primary effect of significant fluid loading is to reduce the vibration velocity of the piston and thus reduce the sound power radiated. Fluid loading is usually negligible

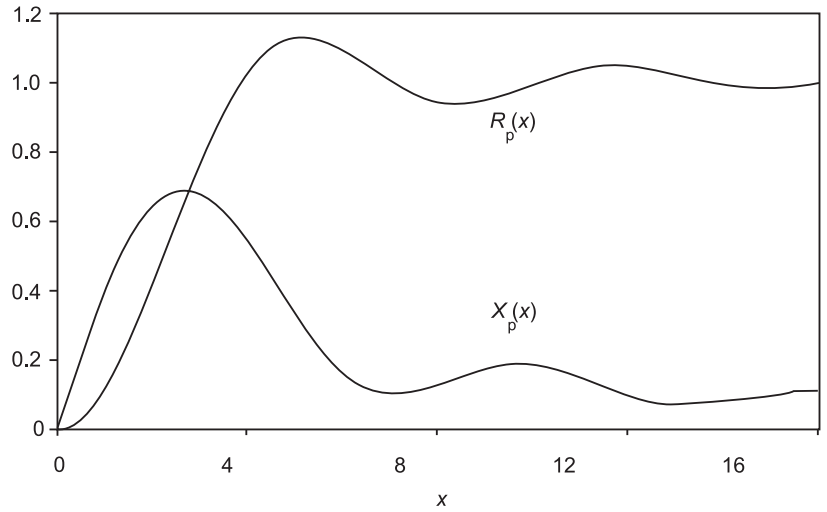


Figure 1 Radiation impedance functions for a circular piston ($x = 2ka$). Used with permission from Norton MP (1999).

for sound radiation in air, except for very thin structures.

Acoustic far field and sound power Sound is radiated into the half-space in 'front' of the piston. If the circumference of the piston is much larger than the acoustic wavelength in the surrounding air (i.e., $ka \gg 1$), then the particle velocity of the air in contact with the piston is equal to the surface normal vibration velocity of the piston surface (i.e., $\mathbf{v}_m = \mathbf{u}_{r=0}$). For a rigid piston of surface area S, the radiated sound power (force times velocity) is:

$$\Pi_{\text{piston}} = \rho_0 c S \left\langle \underline{v}^2_{\text{piston}} \right\rangle \qquad [9]$$

Note that the far-field radiation resistance of the piston in air is unity ($X_{r \gg a} = 1$). This result illustrates the general case:

For a body vibrating in air, the radiated sound power is determined by, the averaged surface normal vibration velocity and the (far-field) radiation resistance.

Radiation Ratio

The radiation ratio, σ, of an arbitrary structure is defined as the sound power radiated by the structure into half space (i.e., one side of the structure) divided by the sound power radiated by a large piston with the same surface area and vibrating with the same RMS velocity as the structure:

$$\sigma_r = \frac{\Pi}{(\rho_0 c S \langle \underline{v}^2 \rangle)} \qquad [10]$$

where Π is the sound power, S is the radiating surface area of the vibrating body and $\langle \underline{v}^2 \rangle$ is the space and time averaged mean-square surface normal velocity. In logarithmic form:

$$\begin{aligned} 10 \log_{10} \sigma_r = & 10 \log_{10} \Pi - 10 \log_{10} \langle \underline{v}^2 \rangle \\ & - 10 \log_{10} S - 146 \end{aligned} \qquad [11]$$

Radiation ratio is a frequency dependant property of the structure and surrounding fluid. It may be thought of as the real part of the frequency response function between the radiated sound and the structural vibration velocity. Mathematically, it is the nondimensional far-field component of the radiation resistance. Thus the radiation ratio curve has the same shape as the radiation resistance curve (**Figure 1**), because:

$$\sigma_r = \frac{R_r}{(\rho_0 c S)} = \frac{\text{Re}(\mathbf{z}_r)}{(\rho_0 c S)} \qquad [12]$$

If the radiation ratio of a real engineering structure is known (or can be estimated) and the surface normal vibration velocity of that structure can be measured, then the vibration generated sound power radiation can be determined. Typically, an accelerometer and FFT analyzer are used to measure the RMS (time) averaged velocity measurements (spectra) at several locations on a structure. These velocity spectra are then averaged together, producing a single time- and space-averaged velocity spectrum.

For a large rigid piston (i.e., $ka \gg 1$), $\sigma_r = 1$ (note: $\sigma_r < 1$ for $ka < 1$!). Sometimes, the radiation ratio is referred to as the sound radiation efficiency (or index)

where the radiation efficiency of a large, rigid piston is 100 percent. However, since it is possible for flexible structures to have $\sigma_r > 1$, the term radiation ratio is used in this article.

Sound Radiation from Compact Engineering Sources

This section considers the sound radiation by three-dimensional 'compact' solid bodies, where the largest body dimension is typically not more than twice the size of the smallest body dimension. Sound radiation from such bodies is typically modeled as sound radiation from a vibrating sphere with a volume equal to the actual body volume. Continuous sound radiation and impact noise are both considered.

'Point monopoles' are idealized, spherically radiating acoustic sources with a zero radius. 'Point dipoles' are represented as a pair of oppositely phased point monopoles placed a small distance apart. 'Point quadrupoles' consist of a pair of equally spaced point dipoles. These idealized point sources are discussed in the article on **Noise: Noise radiated from elementary sources**. They are not the most appropriate source models to use for vibration generated sound source modeling.

In this article, only finite monopoles and dipoles are considered (**Table 2**). A spherical oscillator is a fundamental sound source. A uniformly pulsating sphere is a 'finite monopole'. A rigid, vibrating sphere is a 'finite dipole'. A distorting sphere (with particular surface velocity profiles) can represent either a 'finite longitudinal quadrupole' or a 'finite lateral quadrupole'. Combinations of spherical oscillators can be used to model real-world sound sources provided that: (i) the source is compact, so that the size of the source is small compared to the wavelength of the radiated sound, and (ii) the source is sufficiently far away from the receiver, such that the sound waves reaching the receiver are approximately spherical.

Continuous Sound Radiation

Vibration and noise radiation may be deterministic (e.g., harmonic, periodic) or nondeterministic (e.g., nonperiodic, random, etc.). Total vibration of any solid body (i.e., structure) is the summation of two parts:

1. At higher frequencies (i.e., at the first natural frequency and above), the body shape distorts due to flexural vibration and the surface vibration velocity at all points may not be in-phase. Flexible-body sound generation is covered in a subsequent chapter.
2. Rigid-body motion occurs below the first flexural natural frequency of the structure. The whole body vibrates as a single object and the surface vibration velocity at all points is in phase. Vibration may occur for any of the three lineal ($V_1,\ V_2,\ V_3$) and three rotational ($\theta_1,\ \theta_2,\ \theta_3$) degrees-of-freedom.

It was shown earlier that rigid-body lineal vibration of a baffled piston is an efficient sound generator. Air particles in contact with the piston are forced to move in-phase with it. Energy is transmitted to the gas, and planar sound waves are radiated from the piston. In the general case, the surface vibration at any location on a solid object has two components, one normal to the surface and one tangential to the surface. It is the surface normal vibration component that causes sound radiation, by compressing and expanding the air in contact with it. The tangential vibration velocity component cannot cause compression and rarefaction of the air and therefore does not generate sound.

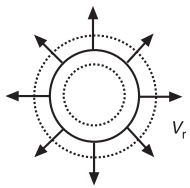
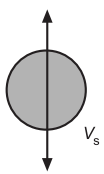
Rotational vibration of a rigid sphere results in zero normal-to-surface vibration velocity, and therefore does not radiate sound. Rotational rigid-body vibration can only radiate sound if the body is sufficiently 'nonspherical' (i.e., it has some sharp corners), so that there is significant resulting surface normal velocity at some points on the surface. However, the surface normal vibration velocity is not in-phase at all points. This chapter includes only cases where $\theta_1 = \theta_2 = \theta_3 = 0$ and sound generated by rotational vibration is not considered.

Sound radiation for two particular cases of in-phase solid body vibration of a sphere is considered here. These are the two main cases of practical importance; (i) finite, monopole-type spherical sound sources, and (ii) finite, dipole-type sound sources. Vibration generated sound radiation from many 'compact' engineering sound sources can be satisfactorily modeled as either a finite spherical monopole or as a finite spherical dipole. Finite quadrupoles are not commonly used for modeling vibrating sound sources.

Radiation ratios for compact bodies are a function of the nondimensional parameter $ka = 2\pi a/\lambda$ (acoustic wavelength λ), as shown by the formulae for σ_r in **Table 2**. This parameter (ka) maps the number of sound waves corresponding to a characteristic dimension of the body (e.g., spherical circumference $= 2\pi a$).

Finite spherical monopole An ideal finite monopole consists of a 'breathing sphere', with whole body pulsations that are normal to the body surface. A

Table 2 Compact sound sources

Source	*Picture*	*Radiation impedance*	*Radiation ratio*	*Sound power*
Finite spherical monopole ('breathing' sphere)		$z_{rM} = \dfrac{\rho_0 c(4\pi a^2)\{k^2a^2 + ika\}}{(1 + k^2a^2)}$	$\sigma_{rM} = \dfrac{k^2a^2}{(1 + k^2a^2)}$	$\Pi_M = \left\{\dfrac{k^2a^2}{1 + k^2a^2}\right\}\rho_0 c(4\pi a^2)v_{rrms}^2$
or		Acoustic wavenumber $k = \dfrac{2\pi f}{c}$		
Small pulsating body (a = radius or volume$^{1/3}$)				Note: $\langle \underline{v}^2 \rangle = v_{r,\,rms}^2$
		Frequency $= f$(Hz)		
Finite spherical dipole (vibrating rigid sphere)		$z_{rD} = \dfrac{\rho_0 c(4\pi a^2)\left[k^4a^4 + i(2 + k^2a^2)(ka)\right]}{(4 + k^4a^4)}$	$\sigma_{rD} = \dfrac{k^4a^4}{(4 + k^4a^4)}$	$\Pi_D = \left\{\dfrac{k^4a^4}{4 + k^4a^4}\right\}\rho_0 c(4\pi a^2)\left(\dfrac{v_{s\,rms}^2}{3}\right)$
or				
Small oscillating rigid body				Note: $\langle \underline{v}^2 \rangle = v_{s,\,rms}^2/3$

Adapted from Beranek LL, Ver IL (eds) (1992) *Noise and Vibration Control Engineering – Principles and Applications*. New York: John Wiley.

monopole has uniform directivity and radiates sound in a spherical pattern. Compact, vibrating engineering sources (i.e., $a = \text{volume}^{1/3}$) may be satisfactorily approximated as a finite monopole at the frequencies of interest if:

1. The source is 'compact', i.e., small compared to the acoustic wavelength ($a \ll \lambda$).
2. The sound radiation approximates that of a uniform spherical radiator. This applies if the observer is located at large distances from the source ($r \gg \lambda$) and if the source directivity is reasonably uniform.
3. The amplitude and/or direction of the mechanical forces are reasonably constant with time.

Resistive and reactive components of radiation impedance for a finite spherical monopole are shown in **Figure 2**, as a function of distance from the source. Source directivity is uniform (spherical). Radiation ratio is plotted against nondimensional parameter *ka* in **Figure 3**, and against frequency (for various source sizes) in **Figure 4**.

Finite spherical dipole An ideal finite dipole consists of a rigid sphere, oscillating about the mean position (along a single axis). The sphere has no volume change and no distortion of shape. A dipole has nonuniform directivity, shown in **Figure 5**. A pair of impacting cylinders radiates sound in a dipole-like manner (**Figure 6**). Vibrating engineering sources may be satisfactorily approximated as a finite dipole at the frequencies of interest if:

1. The source is 'compact', i.e., small compared to the acoustic wavelength ($a \ll \lambda$).
2. The source directivity approximates that of a dipole radiator. This is the case if the source directivity is significantly higher along one axis than on the perpendicular axis.
3. The amplitude and/or direction of the mechanical forces vary significantly with time.

Resistive and reactive components of radiation impedance for a finite spherical dipole are shown in **Figure 7**, as a function of distance from the source. Radiation ratio is plotted against (ka) in **Figure 8**, and against frequency and source size in **Figure 9**.

Impact Noise

Consider a fast moving solid object hitting a steel plate structure. Sound is generated by two different mechanisms. Rapid deceleration of the fast moving rigid body results in lost energy that is radiated as

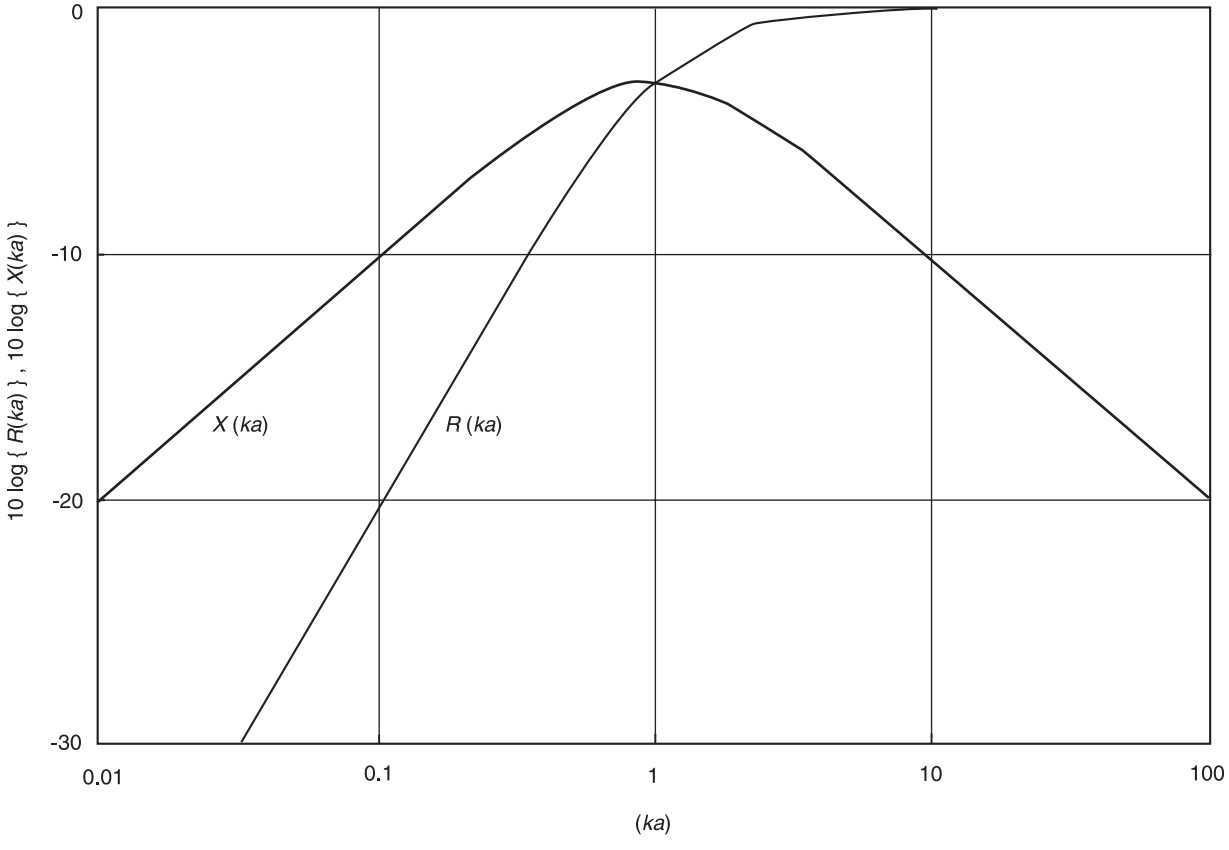


Figure 2 Radiation impedance functions for a finite spherical monopole.

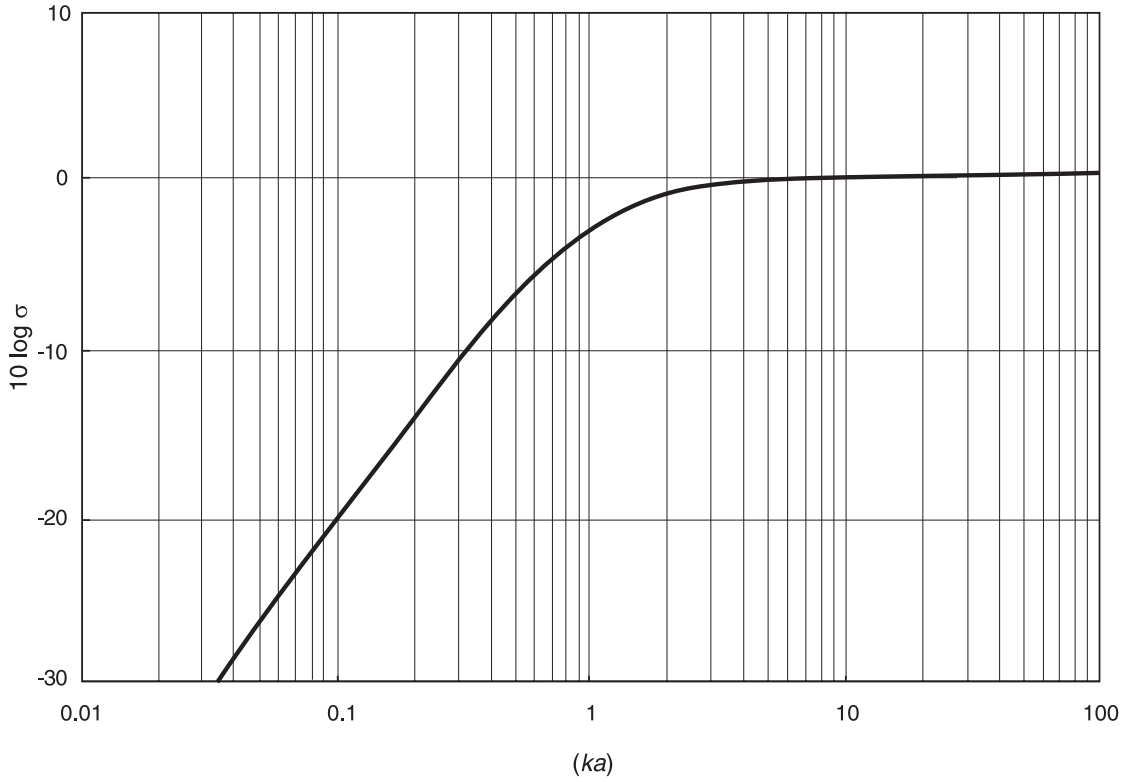


Figure 3 Radiation ratio for a finite spherical monopole.

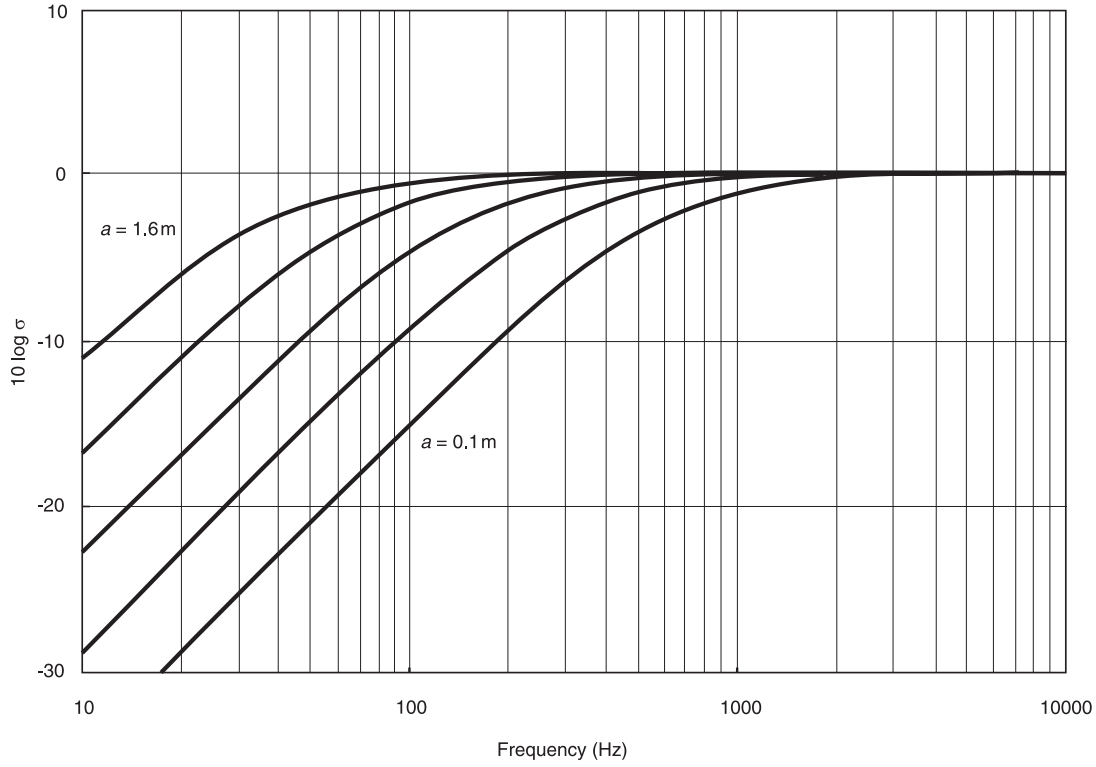


Figure 4 Radiation ratio for finite monopole-like sources (of radius $a = 0.1\,\text{m},\ 0.2\,\text{m},\ 0.4\,\text{m},\ 0.8\,\text{m}$ and $1.6\,\text{m}$).

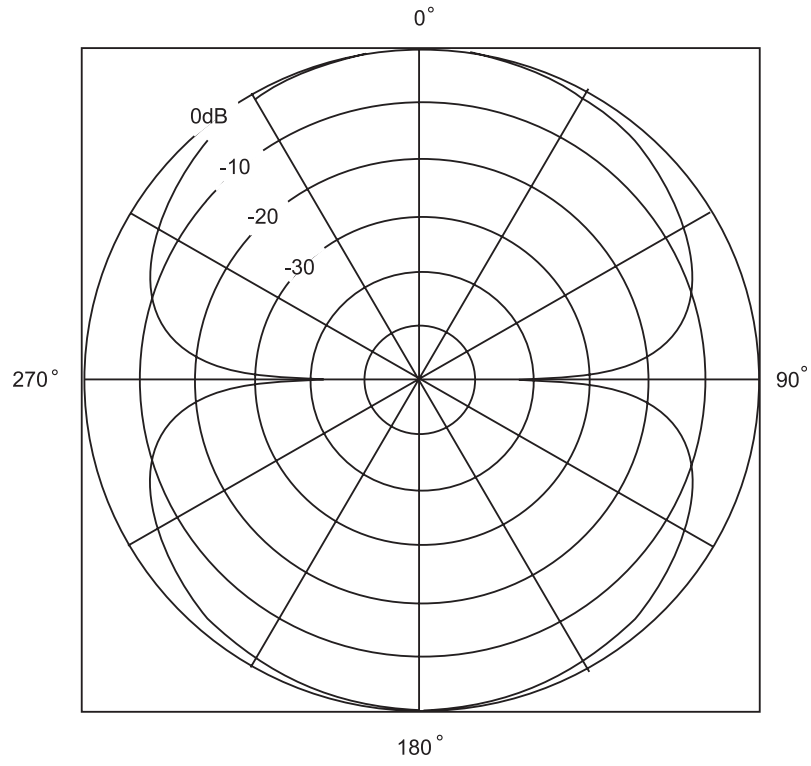


Figure 5 Directivity of a finite spherical dipole. Used with permission from Reynolds DD (1981).

sound. This is called 'acceleration noise' (Π_{accn}). Decaying vibration of the flexible steel structure results in additional sound radiation, known as 'ringing noise' (Π_{vib}). Both mechanisms are included in this article, as the forces are applied mechanically. Acceleration noise is also covered in this section. Ringing noise is covered in the article on **Vibration generated sound: Radiation by flexural elements**.

Impact noise generated by a rigid body in motion hitting another solid body, is considered to be a special case of vibration generated sound. It may be classified as 'motion-generated noise' and is included for consistency with impact noise generated by flexible structures. Flexible structures radiate noise when impulsive or transient mechanical forces are applied to them, as can rigid bodies, although the mechanism of noise generation is quite different.

Consider a solid spherical body of mass m moving with a velocity v_0, through a nonviscous fluid (e.g., air). Consider also a virtual mass of fluid equal to half of that displaced by the sphere. This virtual mass has kinetic energy. If the sphere was slowly brought to rest, most of the fluid kinetic energy would be returned to the body and very little would be released as sound energy. If the sphere was brought to rest immediately, the fluid kinetic energy would be dissipated immediately, primarily as radiated sound energy. This is refered to as acceleration noise (or deceleration noise).

Some results of measured noise radiation from impacting steel spheres and cylinders are shown in **Table 3**. There are three noise generation mechanisms; (i) acceleration noise, (ii) ringing noise due to longitudinal waves (vibration), and (iii) ringing noise due to flexural (bending) waves. Acceleration noise is dominant for the two spheres. For the cylinders, flexural ringing noise radiation is dominant.

The acceleration noise efficiency, μ_{accn}, is defined as the impact noise energy radiated by a moving body (mass m, volume V) divided by the impact noise energy that would be radiated if two equal bodies (m, V) were brought to rest immediately upon impact. Based on experimental data, Richards concluded that:

$$\mu_{accn} = 0.7 \quad \text{for } \delta < 1 \qquad [13]$$

and:

$$\mu_{accn} = \frac{0.7}{\delta^{3.2}} \quad \text{for } \delta > 1 \qquad [14]$$

where:

$$\delta = \frac{ct_0}{\sqrt[3]{(V)}} \qquad [15]$$

The impact duration is t_0 seconds and the nondimensional contact time, δ, is the number of typical body

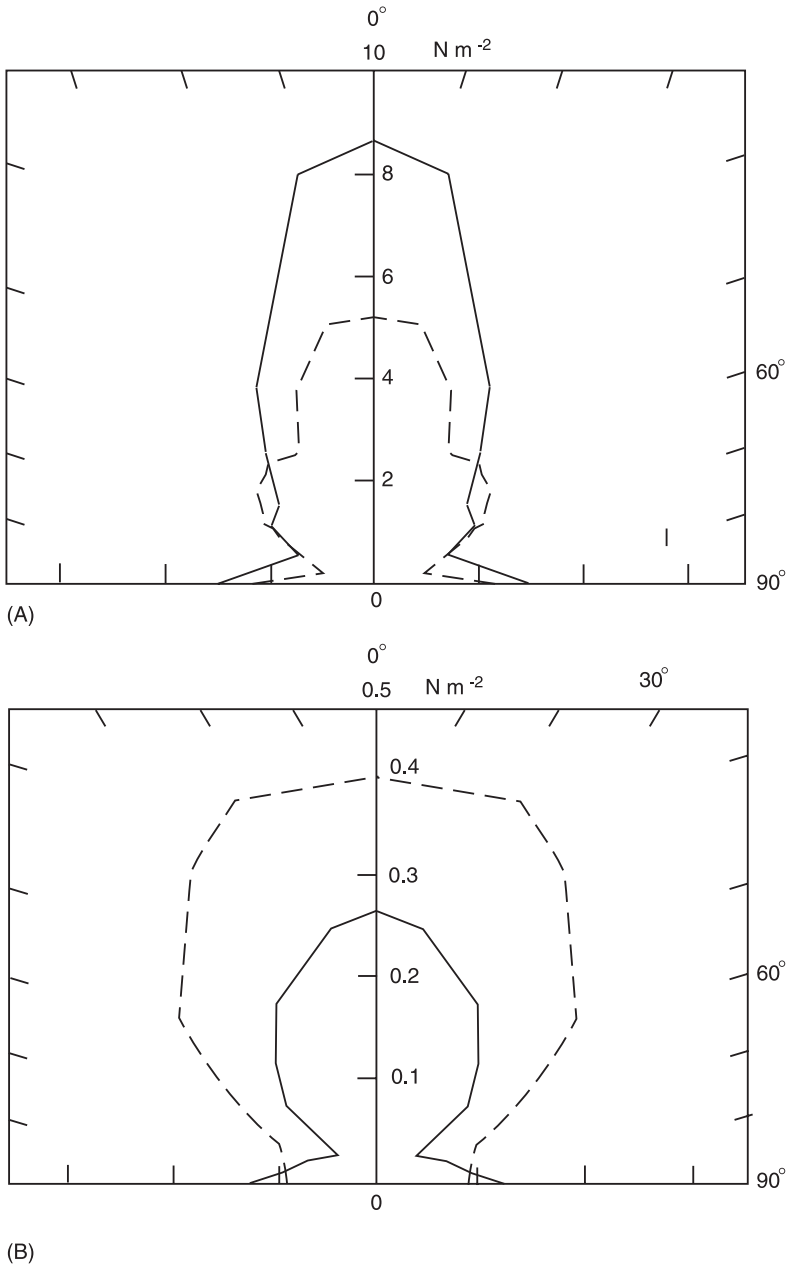


Figure 6 Directivity of two impacting steel cylinders. (A) Hard impact; (B) soft impact. Used with permission from Richards EJ (1982).

dimensions traveled by the sound wave during the deceleration process.

For two impacting solid spheres or for a solid sphere hitting a ground plane and coming to rest, an equivalent impact radiation ratio (**Figure 10**) can be determined based on the velocity just before impact, v_0, and the nondimensional impact duration, δ:

$$\sigma_{\text{accn}} = \left[\frac{1}{288\pi}\right]^{1/3} \frac{\mu_{\text{accn}}}{\delta} \approx \frac{\mu_{\text{accn}}}{10\delta} \qquad [16]$$

In practical engineering situations, the acceleration noise (sound power) can be estimated by measuring the initial velocity, v_0, and impact duration, t_0, and finding σ_{accn} from **Figure 10**. The peak radiated sound power for the impact is then given by:

$$\Pi_{\text{accn}} = \sigma_{\text{accn}} \rho_0 c S \langle v_0^2 \rangle \qquad [17]$$

Summary and Conclusions

This chapter summarizes the fundamentals of vibration generated sound with particular reference to

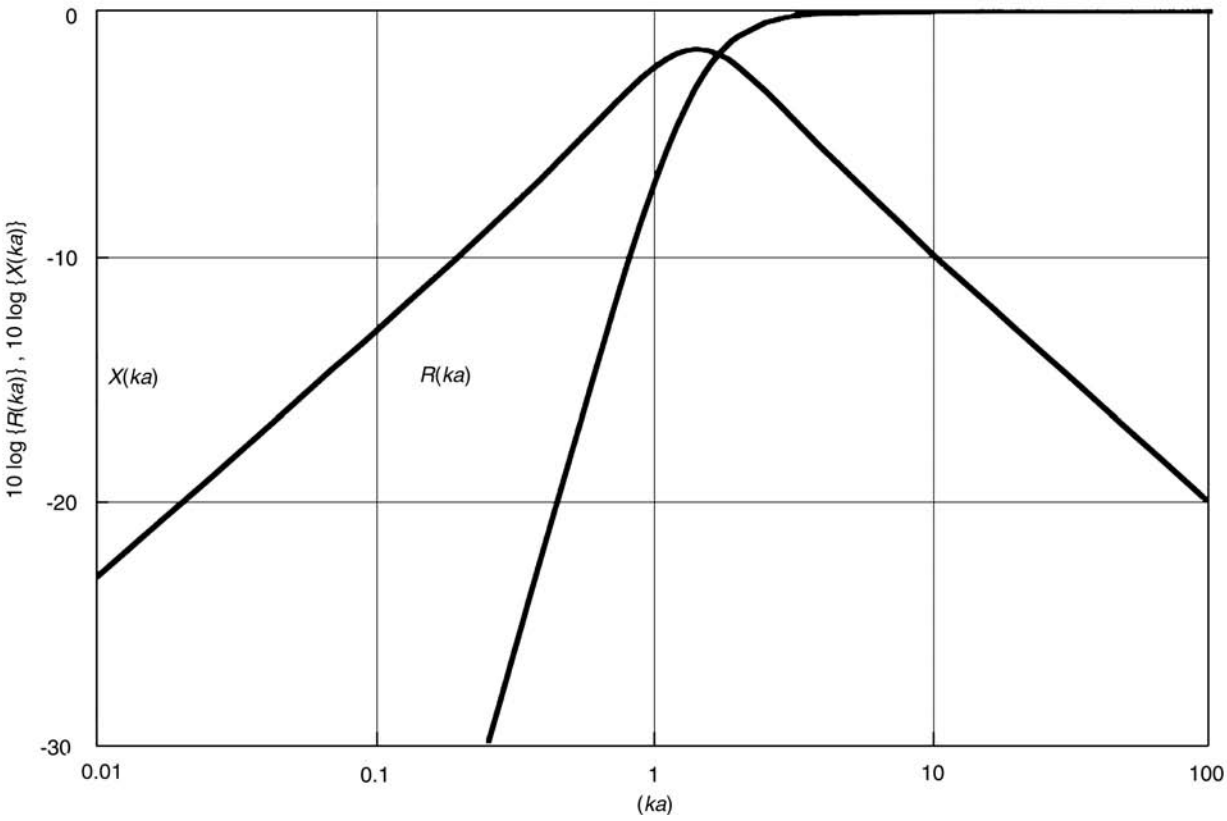


Figure 7 Radiation impedance functions for a finite spherical dipole.

Table 3 Solid body acceleration (Π_{accn}) and ringing (Π_{Vib}) noise

Impacting bodies	*Ringing mode*	*Frequency* (kHz)	Π_{vib}/Π_{accn} (nearest 0.5 dB)
102 mm diameter steel spheres	Fundamental	26	−9 dB
152 mm diameter by 305 mm long steel cylinders	Fundamental longitudinal	7.9	−4.5 dB
	Fundamental flexural	4.9	+11 dB
102 mm diameter by 305 mm long steel cylinders	Fundamental longitudinal	8.4	−1 dB
	Fundamental flexural	4.0	+25 dB
76 mm diameter by 305 mm long steel cylinders	Fundamental longitudinal	8.5	+1.5 dB
	Fundamental flexural	3.2	+21 dB

Adapted from Richards EJ (1982) Noise from industrial machines. In: White RG, Walker JG (eds) *Noise and Vibration*, Ch. 22. Chichester, England: Ellis Horwood Limited.

compact engineering sources. A clear distinction is made with elementary point sources (**Noise: Noise radiated from elementary sources**), the latter being more appropriate for sound propagation modeling. Compact sound source models with finite dimensions (as compared with point sources) are more appropriate for vibration generated sound at locations both in the near and far field but at regions in proximity to the sources such that the finite sizes of the sources are relevant. Examples include electric motors, hand tools, pumps, vacuum cleaners, gearboxes, punch presses, industrial forges (hammers and anvils), diesel engines, etc.

The chapter discusses the differences between the various types of impedances (mechanical, radiation, specific acoustic, acoustic, characteristic) and develops the concept of radiation ratios. This concept is very important in vibration generated sound as the radiation ratio is the link between vibration and radiated sound. Radiation ratios are presented in this article for compact 'inflexible' solid bodies such as finite monopoles and finite dipoles. The issue of

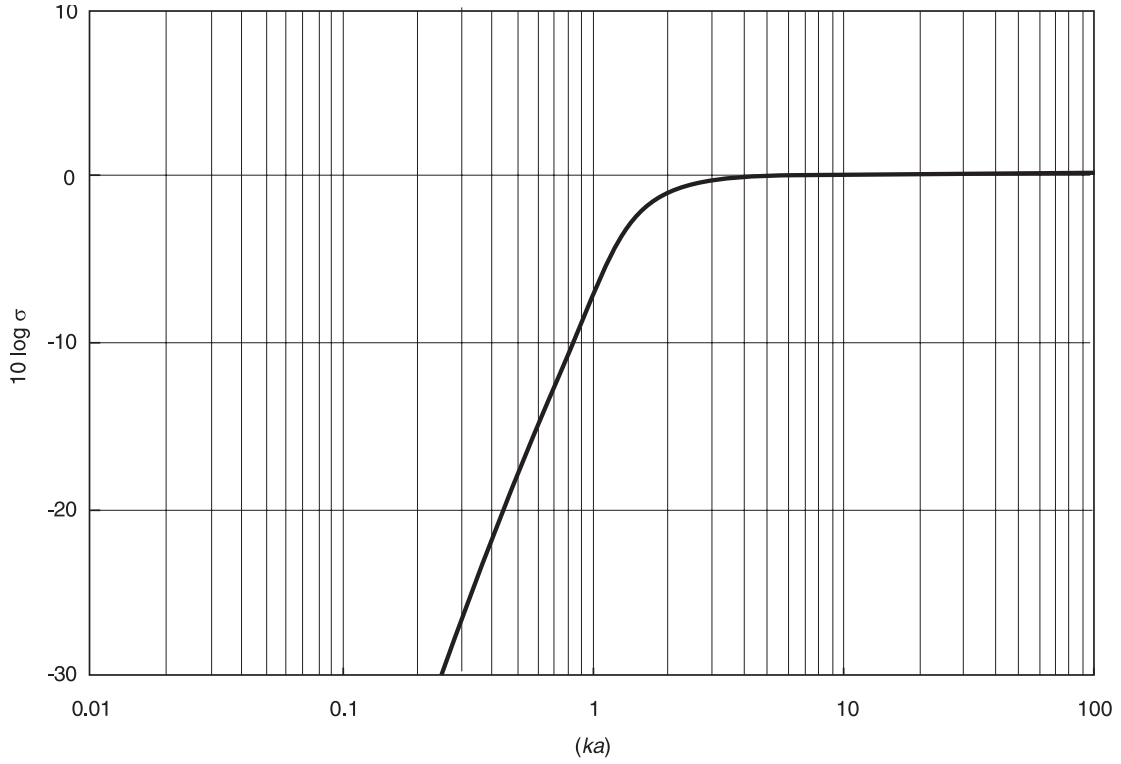


Figure 8 Radiation ratio for a finite spherical dipole.

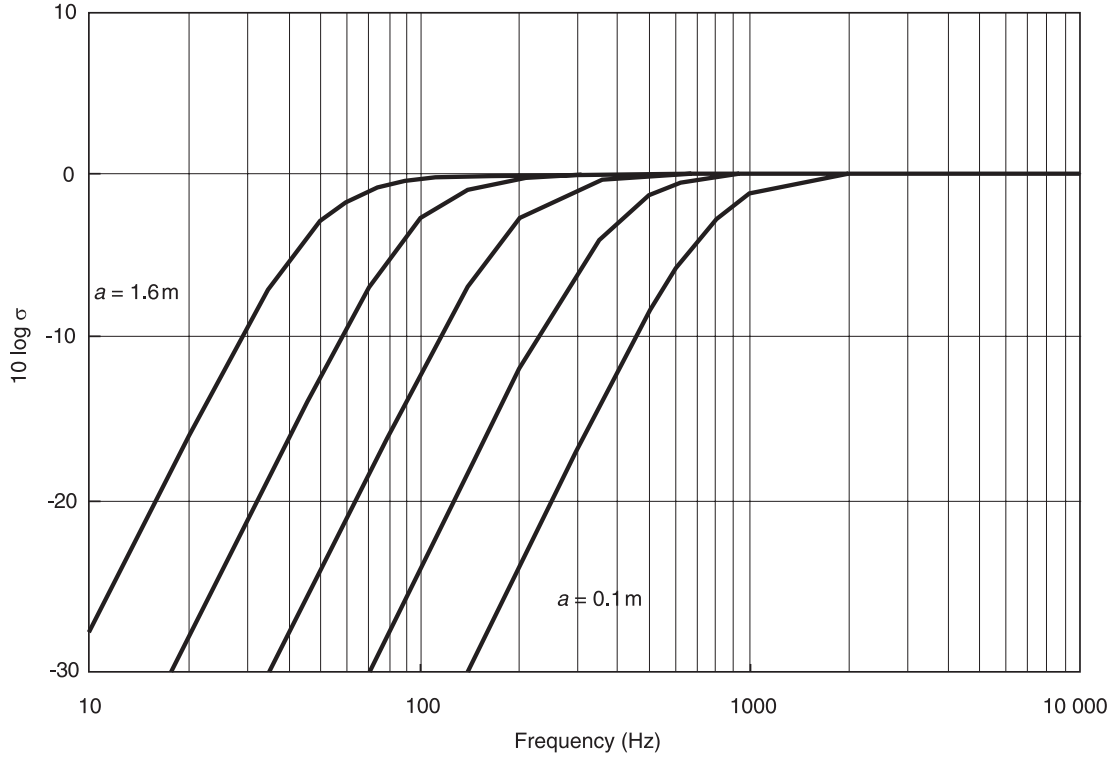


Figure 9 Radiation ratio for finite dipole-like sources (of radius $a = 0.1$ m, 0.2 m, 0.4 m, 0.8 m and 1.6 m).

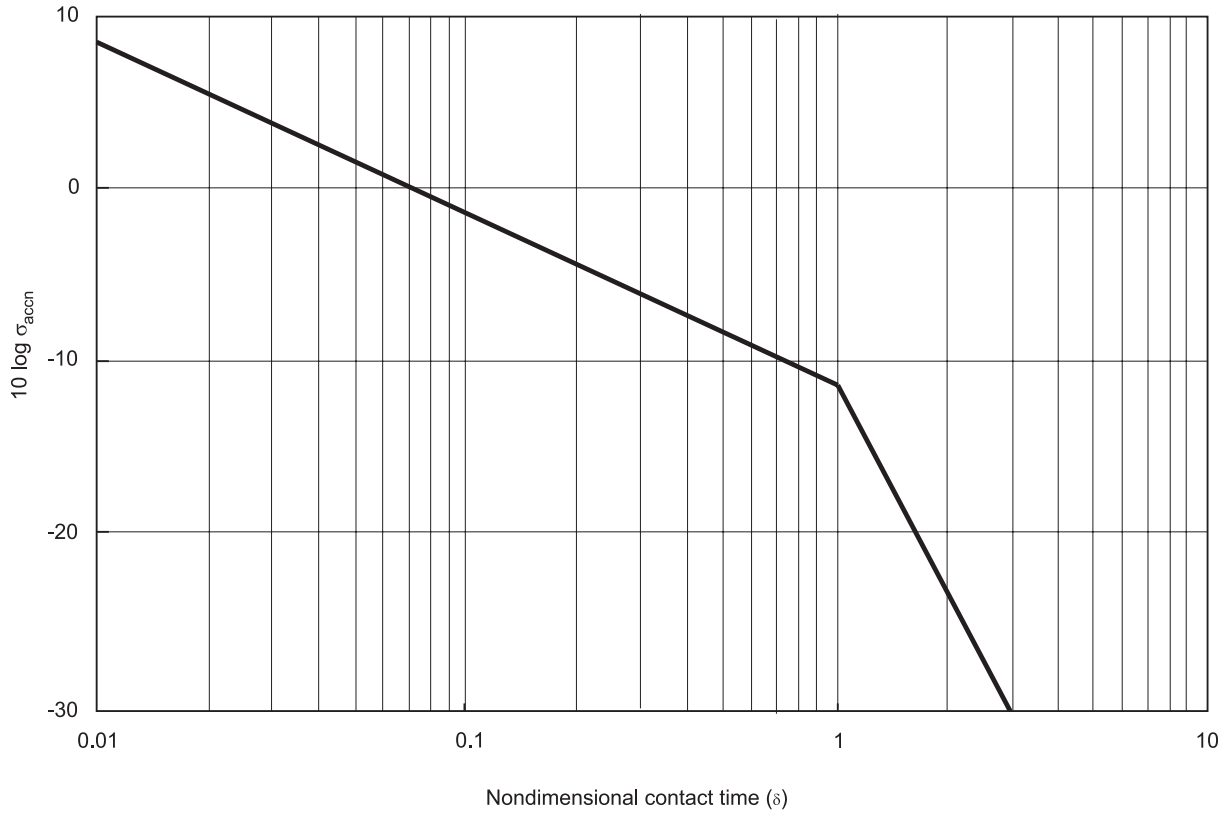


Figure 10 Radiation ratio for rigid body impact (acceleration) noise.

continuous sound radiation and impact noise is discussed and radiation ratios for solid-body impact processes are also presented. Radiation ratios for plates, shells and other flexible structures are presented in a subsequent article (**Vibration generated sound: Radiation by flexural elements**).

Nomenclature

a	radius
A	area
c	damping
$\mathbf{f}$	force
k	stiffness
m	mass
R	resistance
S	surface area
v	velocity
V	volume
X	reactance
π	sound power

See also: **Dynamic stability**; **Fluid/structure interaction**; **Noise**, Noise radiated from elementary sources; **Structure-acoustic interaction, high frequencies**; **Vibration generated sound**, Radiation by flexural elements; **Vibro-impact systems**.

Further Reading

Beranek LL, Ver IL (Eds) (1992) *Noise and Vibration Control Engineering – Principles and Applications*. New York: John Wiley

Bies DA, Hansen CH (1996) *Engineering Noise Control – Theory and Practice*, 2nd edn. Spon E and FN, London: Chapman and Hall.

Cremer L, Heckl M, Ungar EE (1988) *Structure-Borne Sound – Structural Vibrations and Sound Radiation at Audio Frequencies*, 2nd edn. Berlin: Springer-Verlag.

Fahy F (1985) *Sound and Structural Vibration – Radiation. Transmission and Response*. London: Academic Press, Harcourt Brace Jovanovich.

Norton MP (1999) *Fundamentals of Noise and Vibration Analysis for Engineers*. Cambridge University Press.

Reynolds DD (1981) *Engineering Principles of Acoustics – Noise and Vibration Control*. Boston: Allyn and Bacon.

Richards EJ (1982) Noise from industrial machines. In: White RG, Walker JG (eds) *Noise and Vibration*, Ch. 22. Chichester, England: Ellis Horwood Limited.

Smith PW Jr, Lyon RH (1965) *NASA Contractor Report. NASA CR-160. Sound and Structural Vibration*. Cambridge, MA: Bolt, Beranek and Newman.

Radiation by flexural elements

M P Norton and S J Drew, The University of Western Australia, Nedlands, Australia

Copyright © 2001 Academic Press

doi:10.1006/rwvb.2001.0209

Introduction

This article is concerned with vibration generated sound radiated from flexible structures, and not from rigid bodies (rigid-body sound radiation occurs because the whole body moves and forces the surrounding fluid to move with it). As a general rule, whilst rigid-body sound radiation from compact engineering sources occurs at lower frequencies, vibration generated sound from plates, shells and other flexible structures occurs at higher frequencies.

One of the lower flexural natural frequencies of a structure may be a 'breathing mode', where the surface vibration velocity at all points are in-phase. In this special case of flexural vibration, the shape of the body does not change (although the size does). Generally, however, flexural waves distort the shape of the structure's surface.

The theoretical basis for modal sound radiation from simply supported baffled flexible plates is presented in a separate article in this encyclopedia (see **Vibration generated sound: Fundamentals**). The theoretical basis for forced vibration (of simply supported and clamped rectangular baffled flexible plates) is also briefly discussed there. This article deals with the key concepts of band-averaged resonant and forced vibration generated sound in plates and shells, and a range of published data on radiation ratios of flexible engineering-type structures is presented. As for compact engineering sources (rigid-body sound radiation), the radiation ratio concept is very important for flexible structure vibration generated sound, as it is the link between vibration and the associated radiated sound.

Basic Theory

As for compact solid bodies, radiation ratios are used to quantify the sound power radiated by flexible structures typically used in engineering applications. However, the radiation ratio for a given flexible structure is different for different forms of vibration excitation. For example, mechanical excitation of a plate produces a different radiation ratio than does flow/acoustic excitation (**Figure 1**). In this section, we consider only mechanical excitation of finite structures. Mechanical and acoustic excitations are both considered in the next section.

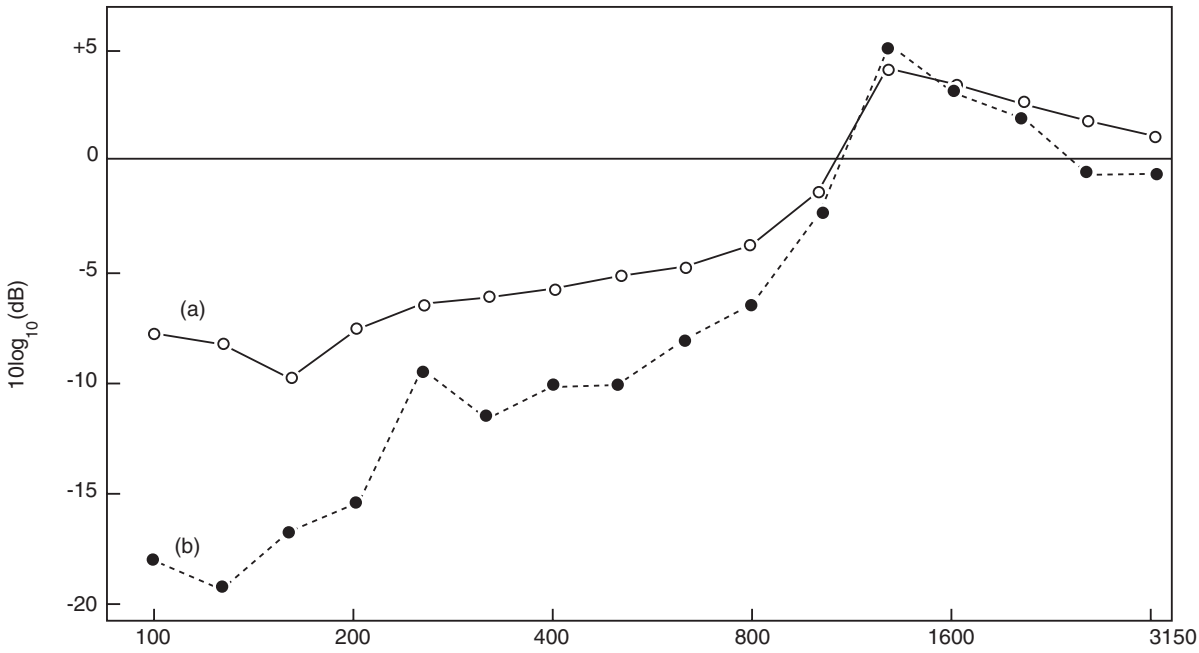


Figure 1 Steel plate radiation ratio for airborne and mechanical excitation ($h = 10\,\text{mm}$, $f_c \approx 1.25\,\text{kHz}$). Reproduced with permission from Macadam JA (1976) The measurement of sound radiation from room surfaces in lightweight buildings. *Applied Acoustics* 9: 103–118.

The classical analysis of sound radiation from flexible vibrating bodies is based on three main foundations.

1. *The governing equations for the vibration of thin-walled plates and shells*
   Resonant vibration may be interpreted as discrete modes and their natural frequencies or as the equivalent propagating waves. Structures respond differently to different forms of forced excitation – only mechanical excitation is considered here. For example, the two-dimensional bending (flexural) wave equation for transverse vibrations of a thin rectangular plate is:

$$\rho_s \frac{\partial^2 u_p}{\partial t^2} + \left(\frac{Eh^3}{12(1-\nu^2)}\right) \times \left\{\frac{\partial^4 u_p}{\partial x^4} + \frac{2\partial^4 u_p}{\partial x^2 \partial y^2} + \frac{\partial^4 u_p}{\partial y^4}\right\} = 0 \quad [1]$$

   where the mass/unit area $= \rho_s$, Poisson's ratio $= \nu$, Young's modulus $= E$, the plate thickness $= h$, and the transverse plate displacement $= u_p(x, y, t)$. Supplementary equations are given in **Table 1**.
2. *The linear, homogenous acoustic wave equation for sound waves in air*:

$$\nabla^2 p - \left(\frac{1}{c^2}\right)\frac{\partial^2 u}{\partial t^2} = 0 \quad [2]$$

   where the acoustic pressure is p, the particle displacement is u and the speed of sound in air is c.
3. *The Kirchoff–Helmholtz integral equation*
   This relates the harmonic surface vibration of an arbitrarily shaped body, to the radiated sound pressure in the surrounding fluid:

$$\mathbf{p}(\vec{\mathbf{r}}) = \int_S \{\mathbf{p}(\vec{\mathbf{r}}_0)\frac{\partial \mathbf{G}_\omega(\vec{\mathbf{r}}, \omega/\vec{\mathbf{r}}_0, \omega)}{\partial \vec{\mathbf{n}}} + i\omega\rho_0 \vec{\mathbf{u}}_n(\vec{r}_0) G_\omega(\vec{r}, \omega/\vec{r}_0, \omega)\}\, \mathrm{d}\vec{S} \quad [3]$$

   where $\vec{n}$ is the unit normal vector, $\vec{r}$ and $\vec{r}_0$ the position vectors for the receiver and a point on the surface of the vibrating body, respectively, $\mathbf{p}(\vec{r})$ is the surface pressure on the structure, and $i\omega\vec{\mathbf{u}}_n(\vec{r}_0)$ is the surface normal vibration acceleration.

Wave propagation Two classical examples of sound radiation by flexible structures are for finite flat plates and finite circular cylinders. Plate and cylinder sound radiation have been extensively studied and analytical, numerical and experimental results are readily available. Basic theory for these two cases is summarized later in this section. First, some useful concepts are outlined below.

Mechanical vibrations can be considered as the net effect of a number of sinusoidal waves propagating within the structure as a function of time and space. For any simple harmonic wave the circular frequency (ω) describes the phase change per unit increase of time. By analogy, a wavenumber is defined as the phase change per unit increase of distance. The wave propagates with a phase velocity, c_{ph}, so named because an observer travelling in the direction of wave propagation at this speed sees no change of phase (for a single frequency sinusoid). The wavenumber is:

$$k = \frac{\omega}{c_{ph}} = \frac{2\pi f}{c_{ph}} = \frac{2\pi}{\lambda} \quad \left(\mathrm{m}^{-1}\right) \quad [4]$$

where f is the frequency in Hertz and λ is the wavelength in meters.

Table 2 summarizes the seven types of waves that propagate in solids. The dispersion relationship (**Figure 2**) indicates whether or not a nonsinusoidal wave will propagate without change in spatial form (it will if $k \propto \omega$). Flexural waves are dispersive, i.e., the bending wave speed (c_{ph}) is a function of frequency. Other wave types have significantly higher phase velocities than bending waves and are nondispersive (i.e., have constant wavespeed).

Sound radiation from a structure into a fluid requires that a structural wave in the solid causes sufficient particle displacements normal to the surface of the structure. Quasilongitudinal and pure bending waves are the only two structural wave types that result in any normal-to-surface vibration. These waves propagate through the solid in a direction parallel with the surface, but generate vibration displacements in the direction normal to the surface. The requirements for effective energy transfer between the structure (source) and the surrounding fluid mean that only bending waves are of practical importance. Only this type of structural wave causes significant transverse displacement of the solid surface and will transfer acoustic energy to the surrounding fluid if impedance matching occurs.

Quasilongitudinal waves have very fast wave velocities (e.g., $c_{ph} \approx 5200\,\mathrm{m\,s^{-1}}$ for steel) compared to sound waves in air ($c \approx 345\,\mathrm{m\,s^{-1}}$) and are therefore high impedance waves. Bending wave velocities in solids are typically much lower than the quasilongitudinal wave velocities. In acoustic terms, bending waves are low-impedance waves and efficient sound radiation is possible. The other six wave types are

Table 1 Vibration of a thin rectangular plate

Quasilongitudinal wave velocity (thin plate)

$$c_{Lp} = \left\{\frac{E}{\rho(1-v^2)}\right\}^{1/2}$$

Bending wave velocity (thin plate)

$$c_B = \omega^{1/2}\left\{\frac{Eh^3}{12(1-v^2)\rho_s}\right\}^{1/4} = \left\{1.8c_{Lp}hf\right\}^{1/2}$$

Bending wavenumber (2D vector) $\mathbf{k}_B = \mathbf{k}_x + \mathbf{k}_y$ where $k_B^2 = k_x^2 + k_y^2$
Critical frequency

$$f_c = \left\{\frac{c^2}{1.8c_{Lp}h}\right\}\text{Hz}$$

Normal modes of vibration for a simply supported thin rectangular plate, where L_x and L_y are the x and y plate dimensions.
Natural frequencies

$$f_{m,n} = (1.8c_{Lp}h)\left\{\left(\frac{m}{2L_x}\right)^2 + \left(\frac{n}{2L_y}\right)^2\right\}\text{Hz}$$

with directional wavenumbers

$$k_x = \left(\frac{m\pi}{L_x}\right) \text{ for } m = 1,2,3,\ldots \text{ and } k_y = \left(\frac{n\pi}{L_y}\right) \text{ for } n = 1,2,3,\ldots$$

where m and n are the number of half-waves in the x- and y-directions.

Normal modes of vibration for a thin rectangular plate with clamped end conditions

$$f_{m,n_C} = (1.8c_{Lp}h)\left\{\left(\frac{(2m+1)}{2L_x}\right)^2 + \left(\frac{(2n+1)}{2L_y}\right)\right\}\text{Hz}$$

with directional wavenumbers

$$k_{x_C} = \left(\frac{(2m+1)\pi}{L_x}\right) \text{ for } m = 1,2,3,\ldots \text{ and } k_{y_C} = \left(\frac{(2n+1)\pi}{L_y}\right) \text{ for } n = 1,2,3,\ldots$$

where $(2m+1)$ and $(2n+1)$ are the number of half-waves in the x- and y-directions.

high impedance waves. The form of the wave equation for bending waves is also different to the other wave types, as illustrated below.

Quasilongitudinal vibrations of rods and bars This is a second-order partial differential equation with a nondispersive wavespeed:

$$\frac{\partial^2 u_r}{\partial x^2} = \left(\frac{1}{c_{Lr}^2}\right)\left\{\frac{\partial^2 u_r}{\partial t^2}\right\} \qquad [5]$$

where $c_{L_r}^2 = E/\rho$.

Transverse bending vibrations of beams (Euler equation) This is a fourth-order partial differential equation with a wave velocity that increases with frequency. The physical reason is that bending waves are a combination of shear and longitudinal waves.

$$\frac{\partial^2 u_b}{\partial t^2} + a^2\left\{\frac{\partial^2 u_b}{\partial x^2}\right\} = 0 \qquad [6]$$

where $a^2 = EI/\rho_L$, $\rho_L = \text{mass/unit length}$, $k_B^4 = (\rho_L/EI)\omega^2$ and $c_B = \omega/k_B = \left(1.8c_{Lp}hf\right)^{1/2}$.

Table 2 Structural wave types

Wave type	*Description*
Pure longitudinal waves	Particle displacement only in direction of wave propagation. Occur in large solid volumes
Quasilongitudinal waves	Particle displacements not purely in direction of wave propagation. Occur in solids with 'thin' cross-section
Torsional waves	Shear wave generated in beams by moment excitation
Transverse plane waves	Exist in solid bodies due to shear stresses. Same wave velocity as torsional waves
Pure bending waves	Exist when the bending wavelength is large compared to the cross-sectional area (i.e., large solids).
Corrected bending waves	Includes the effects of rotary inertia and shear deformation (for smaller structures)
Rayleigh waves	Surface waves with amplitude decreasing below the surface (e.g., ocean). Occur in large, thick structures

Adapted from Norton (1999).

Thin Rectangular Flat Plate

Table 1 presents formulas for bending wave motion in a finite thin rectangular plate. Consider an undamped uniform plate in contact with air and mechanically driven to carry a plane, bending wave of constant amplitude and propagation speed, c_{ph} (**Figure 3**). Wavenumbers are vector quantities, so that:

$$k_B = \frac{\omega}{c_{ph}} = \frac{2\pi}{\lambda_B} \qquad \text{in the } x \text{ direction, for the plate} \qquad [7a]$$

$$k = \frac{\omega}{c} = \frac{2\pi}{\lambda} \qquad \text{for the acoustic wave} \qquad [7b]$$

$$\lambda = \lambda_B \sin\theta \qquad [7c]$$

where θ is the acoustic propagation angle.

Resonant two-dimensional vibration of a rectangular flat plate involves vibration modes that are represented by a single point in wavenumber space (**Figure 4**), with wavenumbers:

$$k_{m,n} = \frac{2\pi}{\lambda_{m,n}} = \left\{ \left(\frac{m\pi}{L_x}\right)^2 + \left(\frac{n\pi}{L_y}\right)^2 \right\} \qquad [8]$$

Critical frequency For sound radiation, the most important parameter is the ratio of the structural wavelength compared to the acoustic wavelength at the same frequency. The critical frequency (f_c) relates the ratio of acoustic and structural wavenumbers (and wavelengths) to frequency regions of efficient and inefficient sound radiation. The critical frequency (f_c) occurs when the structural and acoustic wavelengths are equal (i.e., $\lambda_B = \lambda$ and $f_c = f$). One of three conditions can occur at any given frequency:

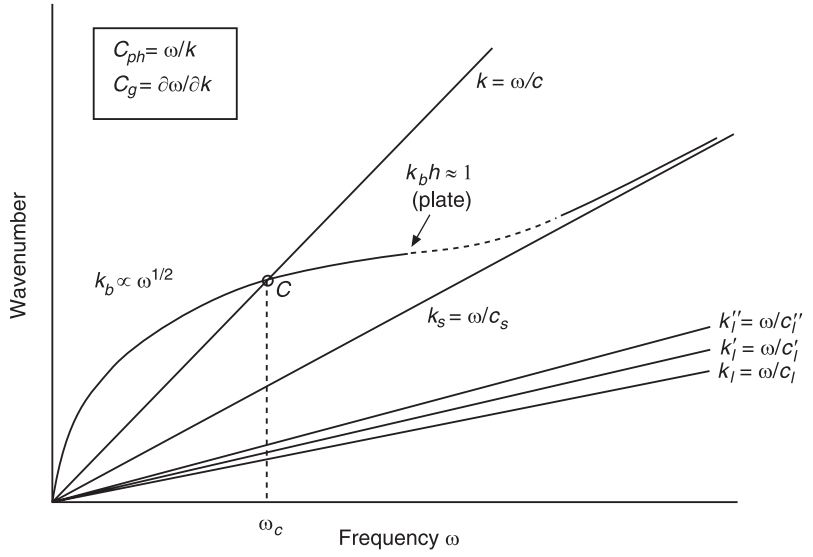


Figure 2 Dispersion curves for structural and acoustic waves. (Reproduced with permission from Fahy, 1985.)

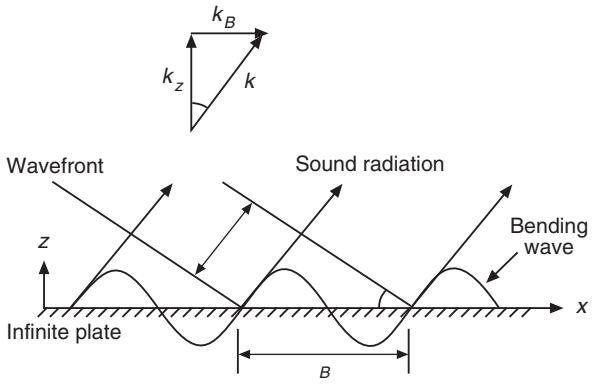


Figure 3 Sound radiation from a flat plate. (Adapted from Norton, 1999.)

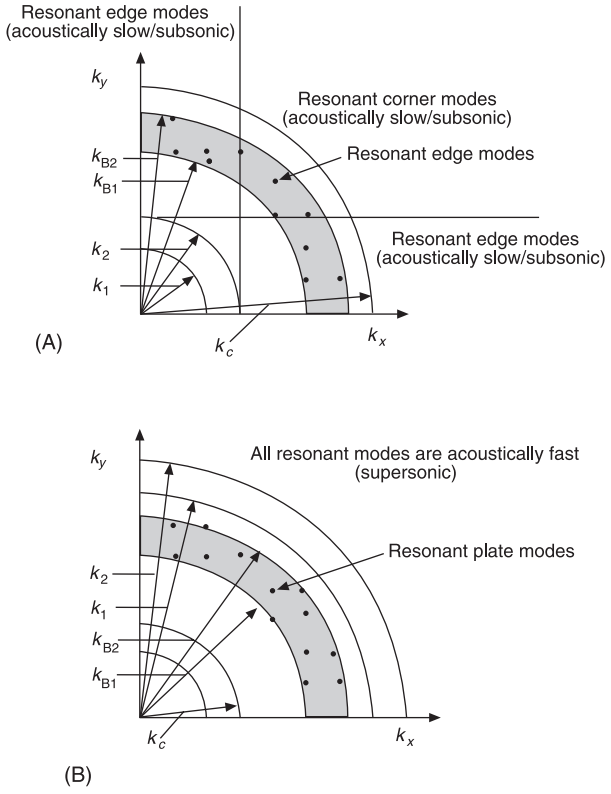


Figure 4 Flat plate wavenumber diagrams. (A) Acoustically slow plate modes ($k_{m,n} < k_C$), (B) acoustically fast plate modes ($k_{m,n} > k_C$). (Reproduced with permission from Norton, 1999.)

1. $f < f_c$ or $\lambda_B/\lambda < 1$ (equivalently, $c_{ph} < c,\ \lambda_B < \lambda,\ k < k_B$).
   In this case the wave impedance (and k_z) is imaginary. Ideally (i.e., for an infinite structure), no net acoustic energy is radiated. In practice, for finite structures the sound radiation is poor and is generated by the edges and corners. This is referred to as 'subsonic' or 'acoustically slow' (AS) sound radiation, since the structural wavespeed is lower than the acoustic wavespeed.
2. $f = f_c$ or $\lambda_B/\lambda = 1$ (equivalently, $c_{ph} = c,\ \lambda_B = \lambda,\ k = k_B$).
   This is the condition for maximum efficiency of acoustic radiation because the structural and acoustic wave speeds, wavelengths and frequencies are equal.
3. $f > f_c$ or $\lambda_B/\lambda > 1$ (equivalently, $c_{ph} > c,\ \lambda_B > \lambda,\ k > k_B$).
   At a given frequency, when the structural wavenumber is smaller than the corresponding acoustic wavenumber, net acoustic energy is radiated into the surrounding fluid by the plate. This is referred to as supersonic or 'acoustically fast' (AF) sound radiation (**Figure 5**).

Thin Circular Cylinders

A distinction is drawn between large diameter 'thin shells' and thicker walled, smaller diameter 'pipes'. This section is applicable to thin cylinders in which cross-sectional distortion is important to the vibration response and sound radiation. Thick-walled pipes and beams are covered in the next section.

Thin Cylinder Vibration

Important parameters for thin cylinders are included in **Table 3**. Vibration modes for a cylinder (**Figure 6**) are characterized by their circumferential (n) and axial (m) orders, and corresponding wavenumbers (**Table 4**). Alternatively, cylinder vibration may be interpreted in terms of propagating waves. Three

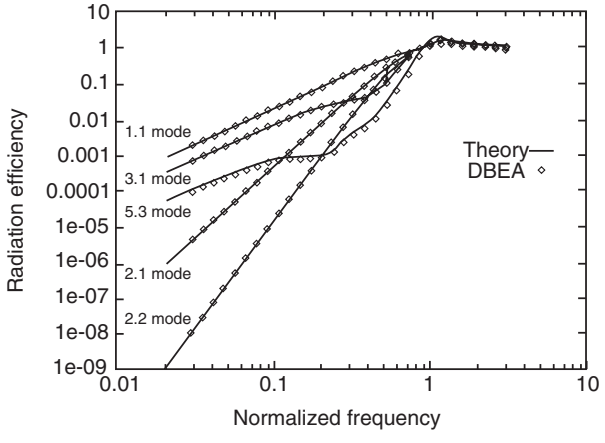


Figure 5 Radiation ratio for the low numbered modes of a square panel.(–) Theory, (o) discrete boundary element analysis. (Reproduced with permission from Gardner BK, Bolton JS, Raveendra ST, Ulahopoulos N (1996) Radiation efficiency calculations for verification of boundary element codes. *Noise Control Engineering Journal* 44(5): 215–223.)

Table 3 Parameters for a simply supported thin cylinder

Parameter	*Formula*
Quasilongitudinal (plate) wave velocity	C_{Lp} (see **Table 1**)
Poisson's ratio	v
Cylinder dimensions	Thickness h, mean radius a_m and length L
Ring frequency ($m = 0,\ n = 0$)	$f_R = (c_{Lp}/2\pi a_m)\text{Hz}$
Critical frequency	Same as for a flat plate
	$f_c = (c^2/1.8c_{Lp}h)\text{Hz}$
Ratio of ring and critical frequencies	f_R/f_c
Nondimensional frequency	$v_f = f/f_R$
Nondimensional natural frequencies ($n \geq 1$)	$v_{m,n}^2 = \beta^2 K^4 + \left\{\dfrac{(1-v^2)K_m^2}{K^4}\right\}$
Dimensional natural frequencies ($n \geq 1$) (approximate)	$f_{m,n}^2 = \left(\dfrac{c_{Lp}}{2\pi a_m}\right)^2 \left\{\beta^2 K^4 + \dfrac{(1-v^2)K_m^2}{K^4}\right\}\text{Hz}^2$
Nondimensional thickness	$\beta = \left(\dfrac{1}{\sqrt{(12)}}\right)\left(\dfrac{h}{a_m}\right)$
K_m (m = number of axial half-waves)	$K_m = k_m a_m = (m\pi/L)a_m$
K_n (n = number of full circumferential waves)	$K_n = k_n a_m = n$
K	$K^2 = K_m^2 + K_n^2$
Nondimensional axial wavenumber parameter	$k_a = k_m a_m \sqrt{\beta}$
Nondimensional circumferential wavenumber parameter	$k_c = k_n a_m \sqrt{\beta}$

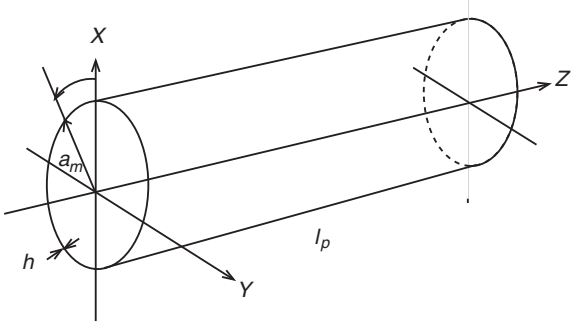


Figure 6 Thin cylinder geometry (after Szechenyi, 1971).

classes of waves may exist for a given circumferential order n, each with different ratios of axial, tangential and radial displacements. Shell curvature gives rise to tangential and axial membrane stresses when radial displacement occurs, coupling the three displacements. When considering acoustic radiation from cylinders, it is only necessary to consider the flexural wave class, for which radial displacement dominates. Cylinder flexural waves form axially propagating helical wave pairs, with the axial wavenumber k_z and circumferential wavenumbers, $\pm k_s$.

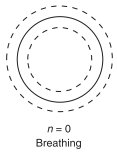
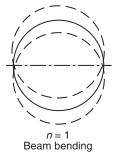
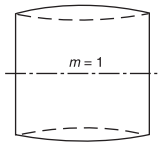
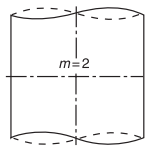
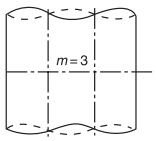
Waves of circumferential order n have a 'cutoff' frequency at $k_z = 0$ (i.e., $\lambda_z = \infty$) and cannot propagate freely below this frequency. The most important cutoff frequency is that of the $n = 0$ 'breathing' mode, referred to as the ring frequency, f_R. At this frequency, radial hooplike resonance occurs. The ring frequency separates regions in which shell curvature is more and less important. Above the ring frequency, the vibration and sound radiation properties become increasingly like that of a flat plate. Below the ring frequency, the effect of curvature and membrane strain means that phase speeds of flexural waves of low n can be supersonic at frequencies below the flat plate critical frequency (f_c). Formulas for the nondimensional cutoff frequencies are given in **Table 3**.

Modal natural frequencies and wavenumbers are constrained by the dispersion relationship for a cylindrical shell. One such approximate relationship for $n > 1$ is given by:

$$v_{m,n}^2 = \beta^2 K^4 + \left\{\frac{(1-v^2)K_m^2}{K^4}\right\} \qquad [9]$$

where supplementary formulas are given in **Table 3**. For a small number of the lower mode orders, errors in the prediction of natural frequencies exist (up to 50%). However, the equation is sufficiently accurate for most applications. **Figure 7** is the non-dimensional wavenumber diagram for circular cylinders. The

Table 4 Vibration modes for a simply supported thin cylinder

Wave	*Order*	*Description*	*Wavenumber*
Circumferential modes	$n = 0,\ 1,\ 2,\ \ldots$	Number of full circumferential wavelengths	
$n = 0$ 	$n = 0$	Peristaltic (breathing) mode	$k_{s0} = 0$ $\lambda_{s0} = \infty$
$n = 1$ 	$n = 1$	Beam bending	$k_s = 1/a_m$ $\lambda_s = 2\pi a_m$
$n = 2$ 	$n = 2$	Ovalling	$k_s = 2/a_m$ $\lambda_s = \pi a_m$
	$n = 3,\ 4,\ \ldots$	Higher order modes	$k_s = n/a_m$ $\lambda_s = (2\pi a)/n$
Axial modes	$m = 0,\ 1,\ 2,\ \ldots$	Number of axial half-wavelengths	
$m = 0$ 	$m = 0$	Waves cannot propagate axially	$k_{z0} = 0$ $\lambda_{z0} = \infty$
$m = 1$ 	$m = 1$	Waves can propagate axially	$k_{z1} = \pi/L$ $\lambda_{z1} = 2L$
$m = 2$ 	$m = 2$	Waves can propagate axially	$k_{z2} = 2\pi/L$ $\lambda_{z2} = L$
	$m = 3,\ 4,\ \ldots$	Waves can propagate axially	$k_z = m\pi/L$ $\lambda_z = 2L/m$
Propagating helical waves	$m = 1,\ 2,\ \ldots$ $n = 0,\ 1,\ 2,\ \ldots$	$k_{m,n}^2 = \left(\frac{m\pi}{L}\right)^2 + \left(\frac{n}{a_m}\right)^2$	

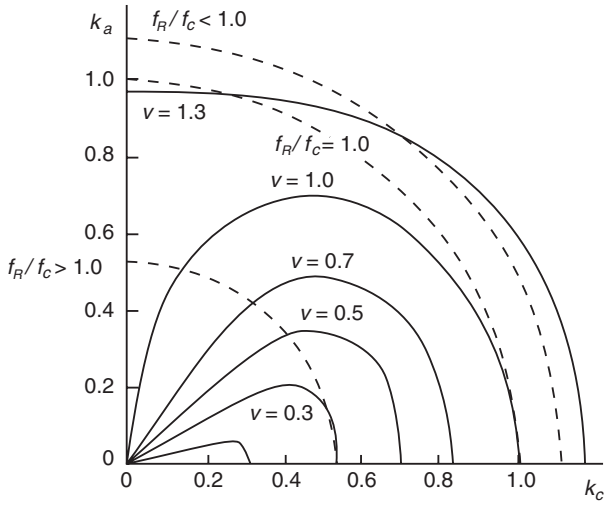


Figure 7 Nondimensional wavenumber diagram for simply supported circular cylinder with superimposed acoustic loci (for external sound radiation). (–) Constant frequency structural wavenumber loci, (- - -) critical frequency acoustic wavenumber curves (for various f_R/f_c ratios). (Adapted from Szechenyi, 1971.)

membrane effect on wave speed is seen in the bending of constant frequency loci toward the origin, particularly below the ring frequency ($v_f = f/f_R = 1$). An equivalent flat plate has circular loci.

Thin Cylinder Sound Radiation

Cylinders vibrate in response to some exciting force and this vibration will contain all the frequency components present in the excitation. The level of induced vibration and the consequent acoustic radiation depend on the type of excitation and the relative importance of resonant and nonresonant forced response. Preferential excitation of certain classes of modes may occur, where the exciting forces have a particular spatial structure or coupling constraint (such as for internal flow/acoustic excitation). The following discussion is relevant to multimode resonant vibration of cylinders in response to broadband mechanical excitation forces.

External sound radiation by a cylinder has no acoustic–structural coupling constraints other than the requirement that the acoustic wavenumber ($k = \omega/c$) must be greater than the structural wavenumber, for effective radiation. There are three relevant structural wave numbers (k_s, k_z and $k_{m,n}$). Cylinder modes are classified into two groups:

1. 'AF' (supersonic) modes ($k^2 \geq k_{m,n}^2$) are efficient sound radiators, with:

$$\sigma_{r\alpha} = \left\{1 - \left(\frac{k_{m,n}}{k}\right)^2\right\}^{1/2} \qquad [10]$$

For increasing dissimilarity between $k_{m,n}^2$ and k^2, this rapidly converges to unity and thus it may be assumed that $\sigma_{r\alpha} = 1$ for AF modes.

2. 'AS' (subsonic) modes ($k^2 < k_{m,n}^2$) are inefficient sound radiators, with two subclasses
   1. $k_z < k$, $k_s > k$ (not relevant to the $n = 0$ mode), with $\sigma_{r\beta} \approx 0$
   2. $k_z > k$, $k_s < k$ which are 'edge' modes (**Figure 8**) with $\sigma_{r\beta} \ll 1$.

An appreciation of AF and AS modes may be obtained from **Figure 7**. Acoustically fast modes lie inside the circular arc of the acoustic loci. This diagram illustrates the importance of the ratio of ring to critical frequency (f_R/f_c) on acoustic radiation:

1. $f_R < f_c$
   The 'unwinding' of the structural constant frequency loci at $v \approx 1$ causes shell waves to become subsonic between f_R and f_c and become supersonic above the critical frequency. The radiation behavior for $f > f_R$ is characteristic of a flat plate. This generally applies to large diameter thin cylinders (**Figure 9**).
2. $f_R > f_c$
   Above the critical frequency, all modes are supersonic. This generally applies to industrial pipes.

Radiation Ratios of Engineering Noise Sources

Flat Plates

Band average radiation ratios Radiation ratios for individual plate and cylinder modes were presented in the previous section. In practice, average 'band' or 'modal' radiation radios are more useful and are calculated for specified frequency ranges (e.g., for 1/3 octave bands). A number of modes will have natural frequencies in the frequency range and will contribute to the sound radiation. The analysis is based on the assumption of equipartition of vibration energy for all resonant modes within each frequency band.

This assumption is reasonably valid for mechanical excitation. However, for mechanical excitation there will be an additional contribution from the region of the plate close to the point of excitation. Resonant vibration of a flexible plate results in resonant sound radiation from the plate. This resonant sound radiation is controlled by the radiation ratio. Forced vibration of a small region near the excitation point results in additional forced sound power radiation, not controlled by the radiation ratio.

Acoustic coupling and excitation results in the selective vibration and sound radiation mainly from

efficiently radiating vibration modes. The vibration response of a flexible structure (e.g., plate, pipe) to flow/acoustic excitation will result in radiation ratios significantly different to those obtained for mechanical excitation. This is a crucial issue and was illustrated in **Figure 1** for a steel plate. The main difference between the radiation ratios for mechanically and acoustically excited plates occurs below the critical frequency. This difference occurs because of the different contributions from subsonic modes ($\sigma_r < 1$) and supersonic modes ($\sigma_r \approx 1$). Above the critical frequency, all modes are supersonic. Below the critical frequency, sound radiation from 'edge' and 'corner' modes predominates, particularly the edge modes. Thus, plate radiation ratios are also influenced by the plate boundary conditions (e.g., free, simply supported, clamped, baffled or unbaffled).

Radiation ratio formulas for mechanically excited square and rectangular flat plates (for sensible plate dimensions) are included in **Table 5**. These are based on formulas for a simply supported plate with an additional term for clamped edges. Alternative formulas are also available. Material parameters for common engineering materials are included in **Table 6**. Plate critical frequencies are plotted against plate thickness in **Figure 10** for several materials.

Radiation ratio charts (**Figures 11–13**) prepared by Richards *et al*. (1979) (based on the formulas of Smith and Lyon (1965)), can also be used for square or rectangular plates of various thickness and surface area. Alternative design charts are those of Ver and Holmer (1971) (**Figure 14**: see **Noise: Noise radiated by baffled plates**) and the nondimensional chart of Bies and Hansen (1996) (**Figure 15**). **Figure 16** shows a comparison between the formulas in **Table 5** and the Ver and Holmer approach and some experimental results. Various experimental data are presented in **Figures 17–23**.

Cylindrical Shells and Cylindrical Bars

Cylinders may be broadly classified as 'thick'- and 'thin'-walled, depending on the ratio of the wall thickness to the cylinder radius. High-pressure industrial pipes have thick walls whereas thin cylinders are more representative of structures such as air-conditioning ducts or an aircraft fuselage. This is reflected in the ratio of the critical and ring frequencies, since:

$$\frac{f_c}{f_R} = \text{constant} \times \left(\frac{\text{cylinder mean radius}}{\text{cylinder wall thickness}}\right) \qquad [11]$$

Thick cylinders have lower critical frequencies than thin cylinders and for the same radius, have lower ratios of f_c/f_R than thin-walled cylinders.

A cylindrical shell may be thought of as a rectangular plate, that has been rolled into a circular cylinder and the edges joined together. The wall thickness of a 'shell' is much smaller than the radius (i.e.,

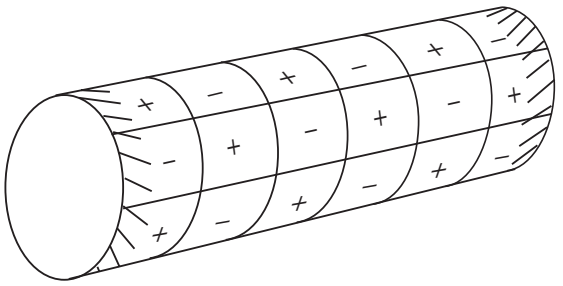


Figure 8 Cylinder 'edge mode' radiation (after Fahy, 1985).

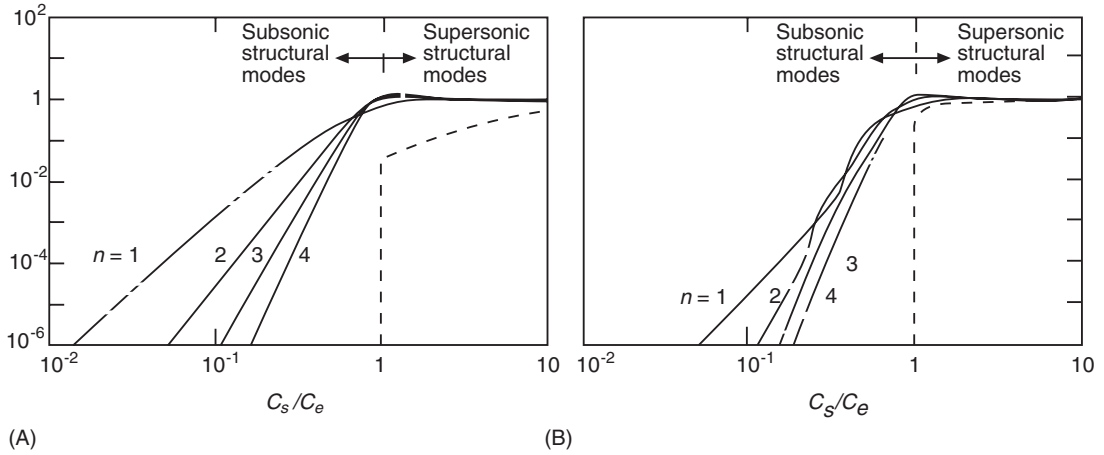


Figure 9 Radiation ratios for selected low-numbered modes of a thin cylinder. (A) $m = 1$, (B) $m = 10$ (Reproduced with permission from Norton, 1999.)

$h \ll a_m$). In the limit, a cylinder with very thick walls and relatively small radius radiates sound in the same manner as a solid circular bar. Cylinder radiation ratios vary depending on several parameters; including the type of excitation (e.g., mechanical or flow/acoustic) and cylinder dimensions (i.e., wall thickness, pipe radius, and length). In principle, there are three types of (external) radiation ratios for cylindrical shells. Formulas for the three 'shell' cases and for solid bar radiation are included in **Table 7**.

In general, the sound radiation from a mechanically vibrating cylinder may include components due to all four mechanisms, complicating the analysis. In this case, the radiation ratio to be used should correspond to the dominant type of excitation and response at the frequencies of interest.

Type 1: Uniformly radiating (pulsating) cylindrical shell The nondimensional radiation ratio for a long, uniformly radiating (pulsating) cylinder radiating into air is presented in **Figure 24A**. **Figure 24B** provides dimensional curves for a range of cylinder diameters.

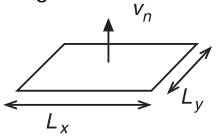
This type of sound radiation is typical of long runs of industrial pipe with a forced internal pressure pulsation, such as from a reciprocating compressor. There is no flexure (bending) along the length of the pipe. In practice, if the measured sound radiation from a long, industrial pipe run is reasonably constant (both around the circumference of the pipe and along its length), then **Figure 24** provides a reasonable upper estimate of the radiation ratio.

There is an analogy between the vibration and sound radiation characteristics of a finite monopole (i.e., the pulsating sphere in **Table 2**) and a uniformly pulsating pipe (**Table 7**). Both radiate sound uniformly, the sphere around its circumference, the cylinder around its circumference and along its length.

Type 2: Oscillating thick-walled pipe or solid circular bar Sound radiation from long vibrating cylinders with small radii and very thick walls approaches that of a vibrating solid bar or rod. Nondimensional and dimensional graphs of the radiation ratio for a long, oscillating solid bar radiating into air, are presented in **Figure 25A** and in **Figure 25B**. Some experimental data are included in **Figure 25C**.

This type of sound radiation is typical of runs of small diameter, heavy industrial pipe or solid bars that vibrate as a rigid body. The radiation from an oscillating solid bar or small radius cylinder with

Table 5 Radiation ratios for rectangular flat plates

Source	*Supplementary equations*	Radiation ratio
Thin rectangular plate supporting free bending waves Plate surrounded by a rigid baffle  	Frequency $= f$ Hz Critical frequency $= f_c$ Hz(Table 3) Speed of sound in air $= c$ Critical wavelength $= \lambda_c = c/f_c$ Surface area (one side) $= S = L_x L_y$ Perimeter $= P = 2(L_x + L_y)$ $L_{\max} = \max(L_x, L_y)$ $L_{\min} = \min(L_x, L_y)$ $\alpha^2 = f/f_c$ Sound power $\Pi = \sigma_r \rho_o c (L_x, L_y) \langle v^2 \rangle$ $\langle v^2 \rangle =$ space and time averaged $v^2_{n,\mathrm{RMS}}$	$\sigma_r = \begin{cases} (\sigma_{rc} + \sigma_{re}) \times C_1, & f \le 0.7 f_c \\ 0.45(P/\lambda_c)^{1/2}(L_{\min}/L_{\max})^{1/4}, & f = f_c \\ (1 - (f_c/f))^{-1/2} = (\alpha^2/(\alpha^2 - 1))^{1/2}, & f \ge 1.3 f_c \end{cases}$ where $\sigma_{rc} = \left(\frac{8}{\pi^4}\right)\left(\frac{\lambda_c^2}{S}\right)\left\{\begin{array}{ll} \left(\frac{(1-2\alpha^2)}{\alpha(1-\alpha^2)^{1/2}}\right), & f < 0.5 f_c \\ 0, & f > 0.5 f_c \end{array}\right\}$ $\sigma_{re} = \left(\frac{1}{4\pi^2}\right)\left(\frac{P\lambda_c}{S}\right)\left\{\frac{(1-\alpha^2)\ \ln((1+\alpha)/(1-\alpha))}{(1-\alpha^2)^{3/2}}\right\}$ $C_1 = \left\{\begin{array}{l} 1, \text{ for simply supported edges} \\ \alpha^2 \exp(10\lambda_c/P) \text{ for clamped edges} \end{array}\right\}$
Thick rectangular plate supporting free bending waves	$\lambda = c/f$ $f_b = f_c + (5c/P)$	$\sigma_r = \begin{cases} 0.45\sqrt{(P/\lambda)}, & f \le f_b \\ 1, & f \gg f_b \end{cases}$ $\sigma_r = \sigma_{rF}$ where
Finite square plate Oblique incidence, plane sound wave excitation	$\phi =$ incidence angle (deg) $A_1 = (0.8)^{(\phi/90)}/2$ $\chi = 1 - (0.34\phi/90)$ $k = 2\pi/\lambda = 2\pi f/c$	$\sigma_{rF} = \min\left\{\begin{array}{l} A_1(k/2)\sqrt{S} \\ \frac{1}{\cos\phi} \end{array}\right\}$ for $(0.1\lambda^2) < S < (0.4\lambda^2)$ $\sigma_{rF} = \min\left\{\begin{array}{l} (0.5)^{(\phi/90)}\sqrt{(k/2)\sqrt{S}} \\ 1/\cos\phi \end{array}\right\}$ for $S > (0.4\lambda^2)$
Diffuse sound field excitation		$\sigma_r = 0.5[0.2 + \ln(k\sqrt{S})]$ for $(k\sqrt{S}) > 1$

Adapted from Beranek and Ver (1992).

Table 6 Material properties* and phase speeds

Material	*Young's modulus* $E(\mathrm{N\,m^{-2}})$	*Density* $\rho(\mathrm{kg\,m^{-3}})$	*Poisson's ratio* c_l	$c_l\ (\mathrm{m\,s^{-1}})$	$c_l'\ (\mathrm{m\,s^{-1}})$	$c_l''\ (\mathrm{m\,s^{-1}})$	$c_s\ (\mathrm{m\,s^{-1}})$
Steel	2.0×10^{11}	7.8×10^{3}	0.28	5900	5270	5060	3160
Aluminium	7.1×10^{10}	2.7×10^{3}	0.33	6240	5434	5130	3145
Brass	10.0×10^{10}	8.5×10^{3}	0.36	4450	3677	3430	2080
Copper	12.5×10^{10}	8.9×10^{3}	0.35	4750	4000	3750	2280
Glass	6.0×10^{10}	2.4×10^{3}	0.24	5430	5151	5000	3175
Concrete							
light	3.8×10^{9}	1.3×10^{3}				1700	
dense	2.6×10^{10}	2.3×10^{3}				3360	
porous	2.0×10^{9}	6.0×10^{2}				1820	
Rubber							
hard	2.3×10^{9}	1.1×10^{3}	0.4	2120	1582	1450	867
soft	5.0×10^{6}	9.5×10^{2}	0.5			70	40
Brick	1.6×10^{10}	$1.9–2.2 \times 10^{3}$				2800	
Sand, dry	3.0×10^{7}	1.5×10^{3}				140	
Plaster	7.0×10^{9}	1.2×10^{3}				2420	
Chipboard†	4.6×10^{9}	6.5×10^{2}				2660	
Perspex‡	5.6×10^{9}	1.2×10^{3}	0.4	3162	2357	2160	1291
Plywood†	5.4×10^{9}	6.0×10^{2}				3000	
Cork	–	$1.2–2.4 \times 10^{2}$				430	
Asbestos cement	2.8×10^{10}	2.0×10^{3}				3700	

c_l, 'pure' longitudinal wave speed (in an infinite solid);
c_l', quasi-longitudinal wave speed in a plate; c_l'', quasi-longitudinal wave speed in a bar; c_s, transfer shear wave speed.
* Mean values from various sources.
† Temperature sensitive.
‡ Greatly variable from specimen to specimen. Reproduced with permission from Fahy (1985)

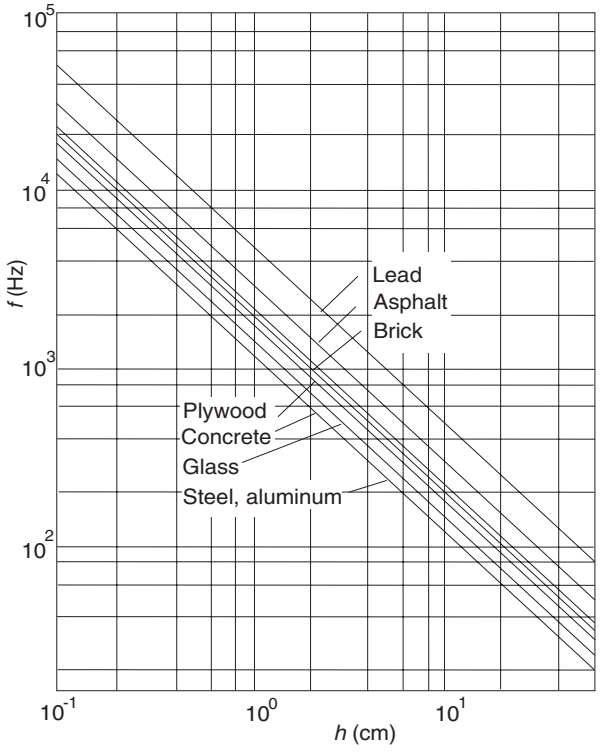


Figure 10 Flat plate critical frequencies for sound radiation into air. (Reproduced with permission from Cremer, Heckl and Ungar, 1988.)

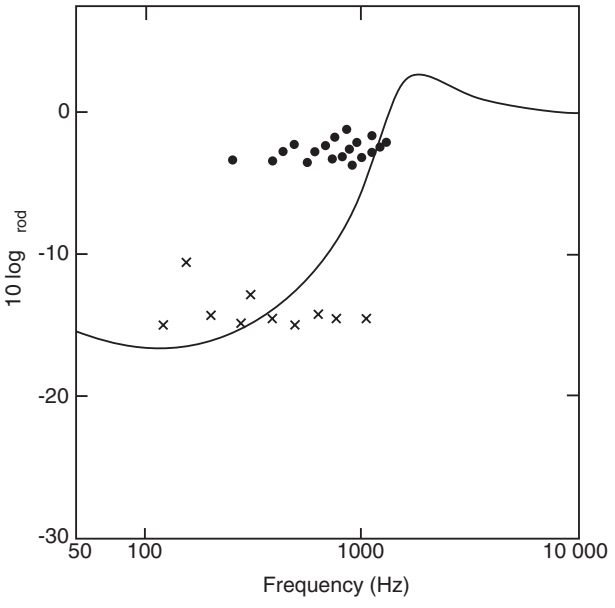


Figure 11 Theoretical radiation ratio of a $1\,\mathrm{m} \times 1\,\mathrm{m} \times 6\,\mathrm{mm}$ square plate for resonant (mechanical) excitation. (Reproduced with permission from Richards, Westcott and Jeyapalan, 1979 (based on Smith and Lyon, 1965).)

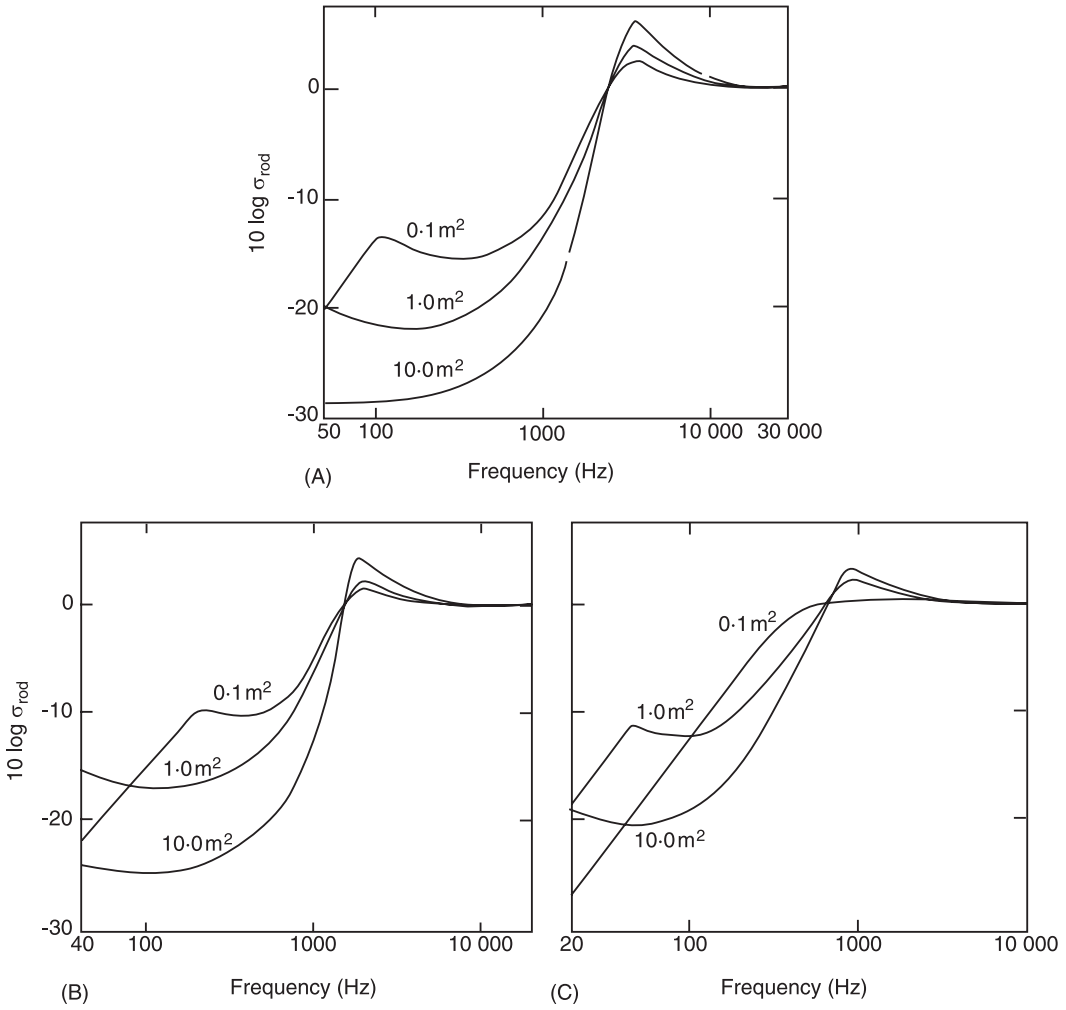


Figure 12 Theoretical radiation ratios for simply supported square steel plates of thickness (A) 3.17 mm, (B) 6.35 mm, (C) 12.7 mm. (Reproduced with permission from Richards, Westcott and Jeyapalan, 1979.)

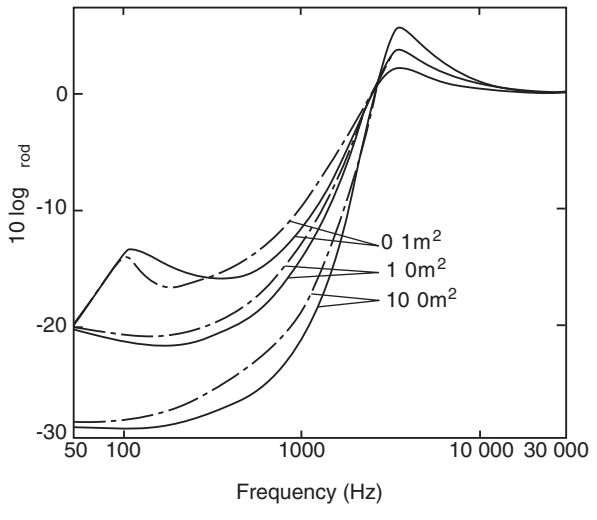


Figure 13 Theoretical radiation ratios for 3.17 mm thick, simply supported square and rectangular steel plates. (Reproduced with permission from Richards, Westcott and Jeyapalan, 1979.)

thick walls is analogous to a finite dipole, with a pronounced directivity in the plane of its cross-section (**Table 7** of this article and **Table 2** of **Noise: Noise radiated from elementary sources**).

Type 3: Forced peristaltic motion of a cylindrical shell Nonisotropic cylinders have nonuniform wall thickness (or some other nonuniformity) around the circumference or along the length of the cylinder. Forced vibration of the cylinder wall (e.g. due to internal pressure pulsations) results in a nonuniform vibration velocity pattern and sound radiation. The mechanism of sound radiation is similar to a uniformly radiating cylindrical shell (i.e., Type 1), but is complicated by the anisotropy of the cylinder wall. This is a specialized topic and interested readers are referred to the literature.

A reasonable engineering estimation for forced peristaltic sound radiation is to use the radiation

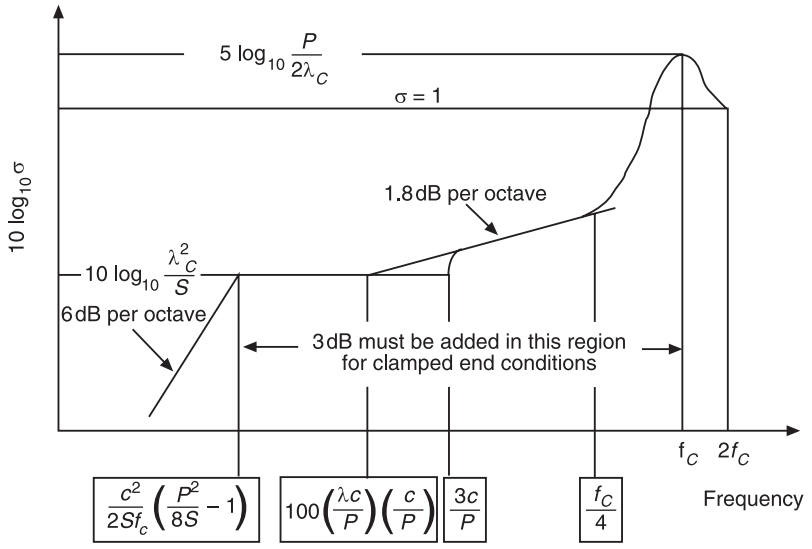


Figure 14 Radiation ratio design curve of Ver and Holmer (1971) for broadband mechanical excitation of flat plates. Perimeter P, (single sided) surface area S and critical wavelength λ_c. (Reproduced with permission from Norton, 1999.)

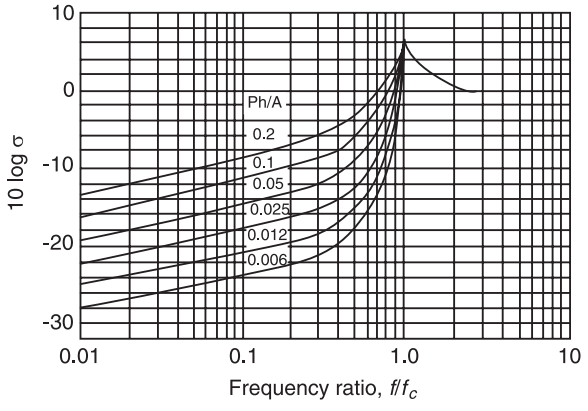


Figure 15 Theoretical radiation ratios for steel and aluminum flat plates. Perimeter P, (single sided) surface area A, octave band center frequency f and plate critical frequency f_c. (Reproduced with permission from Bies and Hansen, 1996.)

ratio for a uniformly pulsating cylindrical shell (i.e., Type 1).

Type 4: Resonant flexural vibration of a cylindrical shell Thin-walled cylinders, including low pressure piping, air-conditioning ducts and similar structures are likely to radiate sound due to resonant structural vibration. This is particularly the case where excitation of the cylinder wall occurs over a wide frequency range. Third-octave band radiation ratios of thin cylinders for mechanical excitation have been estimated (**Figure 26A**) based on the following assumptions:

1. Equipartition of vibration energy for all resonant modes within each band
2. Supersonic modes have $\sigma_{r\alpha} = 1$ and subsonic modes have $\sigma_{r\beta} = 0$
3. No nonresonant contribution to vibration response and sound radiation
4. All structural modes will radiate sound externally.

These four assumptions are reasonably valid for mechanical excitation. They are all invalid for acoustic/flow excitation because of the nature of acoustic–structural coupling.

Alternative radiation ratio charts for point excited tubes radiating into air and water, for a range of pipe radius to wall thickness (a_m/h) values have been calculated (**Figure 26B**).

Various experimental cylinder radiation ratio data for mechanical excitation are presented in **Figures 27–30**.

Type 5: Coupled flexural vibration of a cylindrical shell Various experimental cylinder radiation ratio data for flow/acoustic excitation are presented in **Figures 31–33**.

Beams and structures

The radiation ratios for elliptic beams, I-beams and a frame made from square box section tubes; including various approximate models and experimental radiation ratio measurements have been investigated. A selection of results is presented in **Figures 34–37**.

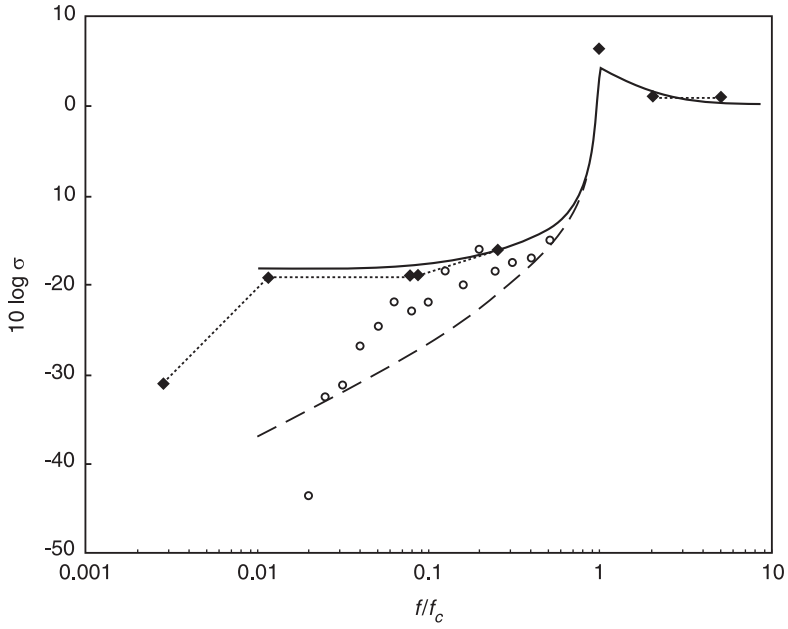


Figure 16 Comparison of theoretical and measured radiation ratios for a mechanically excited, simply supported thin steel plate (300 mm x 300 mm x 1.22 mm). (–) Theory (simply supported), (- - -) theory (clamped edges), (. . .) theory (Ver and Holmer (1971), (o) measured (Pierri RA (1977) Study of a dynamic absorber for reducing the vibration and noise radiation of plate-like structures. MSc thesis, University of Southampton).

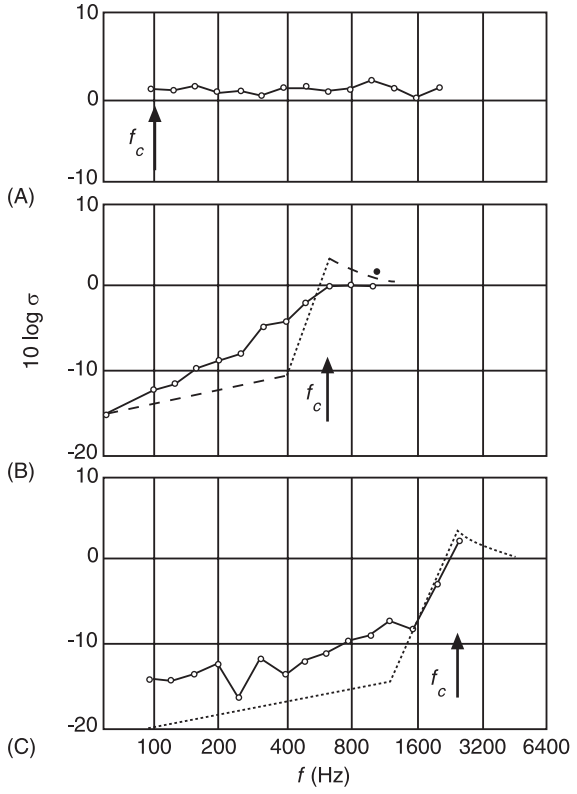


Figure 17 Measured radiation ratios of lightly damped, mechanically excited flat plates (A) 240 mm thick brick wall of area 12 m^2, (B) 4 m^2 of 70 mm thick light concrete, (C) 13 mm thick plasterboard wall, divided into 0.8 m^2 panels by lath gridwork. (Reproduced with permission from Cremer, Heckl and Ungar, 1988.)

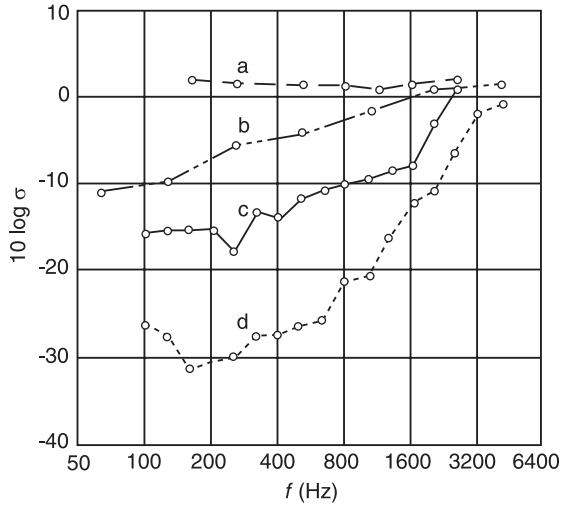


Figure 18 Measured radiation ratios of (*a*) 140 mm thick concrete ceiling, (*b*) diesel engine blocks, (*c*) 13 mm thick plasterboard wall with lath gridwork, (*d*) steel pipe of 720 mm diameter and 1.3 mm wall thickness. (Reproduced with permission from Cremer, Heckl and Ungar, 1988.)

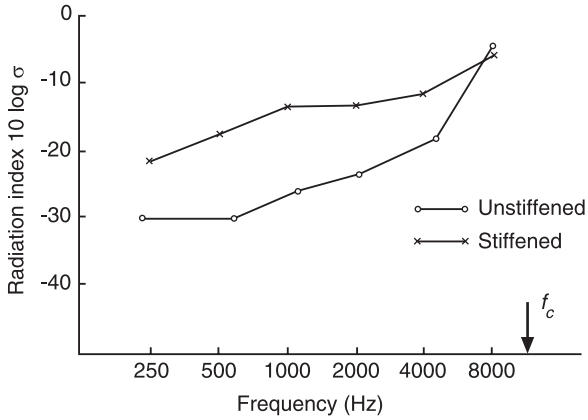


Figure 19 Measured radiation ratios of a stiffened and unstiffened model boiler casing structure. (Reproduced with permission from Fahy, 1985.)

Summary

This article summarizes the fundamentals of vibration generated sound with particular reference to flexible structures. The basic theory presented includes the governing equations for thin-walled plate and shell vibration, the linear, homogeneous acoustic wave equation, and the Kirchoff–Helmholtz integral equation. The various types of wave propagation are summarized and compared for 'acoustic efficiency'. It is demonstrated that low impedance waves dominate vibration generated sound from flexible structures. Published radiation ratio data is summarized for a wide range of practical configurations appropriate for engineering applications.

Flexible structures covered include thin rectangular flat plates, thin cylinder vibration, thin cylinder sound radiation, band averaged response of flat plates, uniform pulsating cylinders, oscillating thick-walled pipes or bars, forced peristaltic motion of shells, resonant flexural vibration of shells, coupled flexural vibration of shells, elliptic beams, I-beams, and frames.

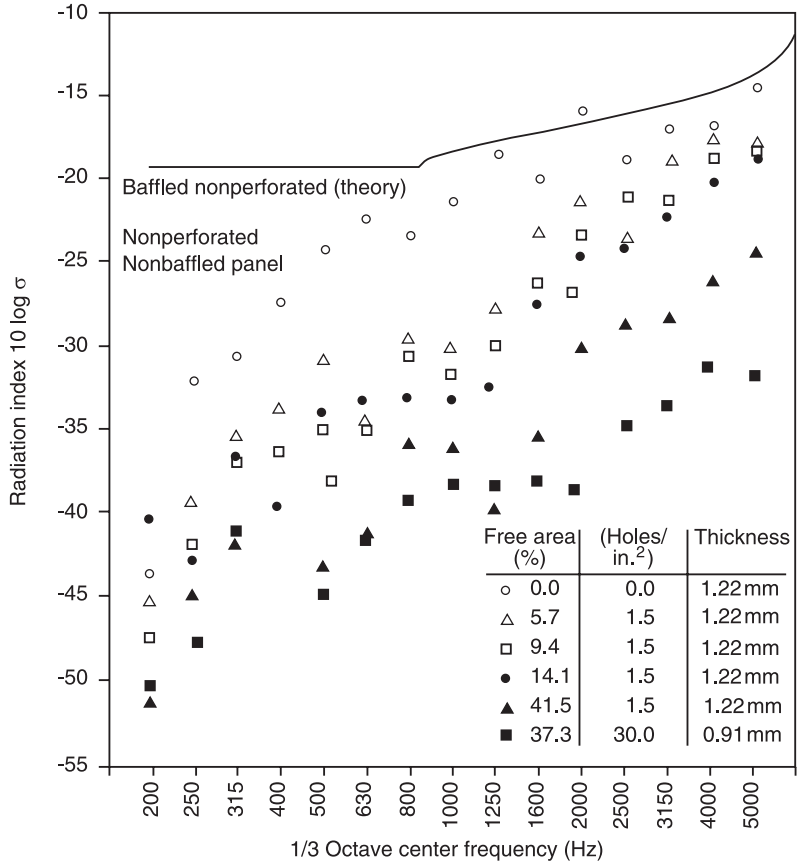


Figure 20 Measured radiation ratios of 1 mm thick perforated panels. Reproduced with permission from Fahy (1985).

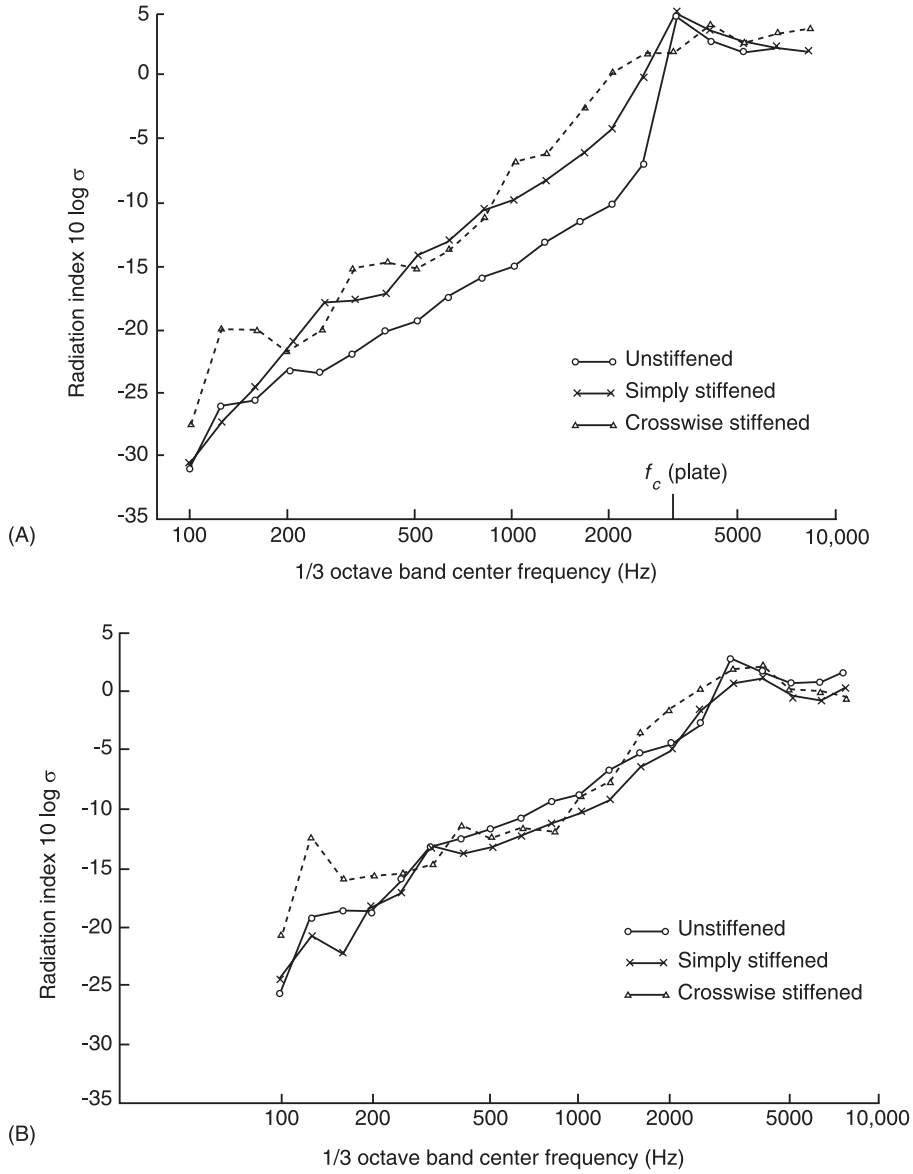


Figure 21 Measured radiation ratios of unstiffened and stiffened plates for (A) point mechanical excitation and (B) diffuse sound field excitation. (Reproduced with permission from Fahy, 1985.)

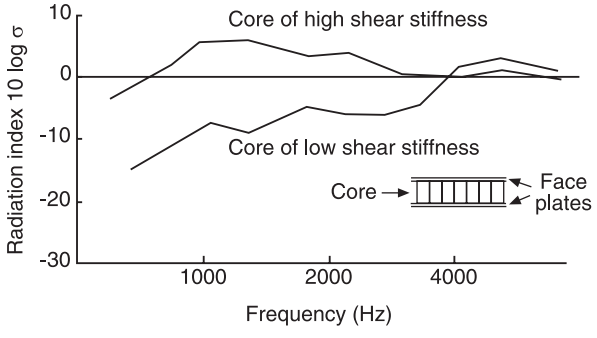
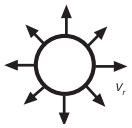
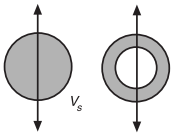
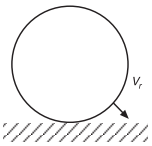


Figure 22 Measured radiation ratios of honeycomb sandwich panels. (Reproduced with permission from Fahy, 1985.)

As for compact engineering sources (rigid-body sound radiation), this article clearly illustrates that the radiation ratio is a very important parameter in vibration generated sound, as it is the link between vibration and the associated radiated sound. Knowledge of the radiation ratio of a structure allows for the prediction of vibration generated sound from measured or predicted vibration levels. The radiation ratio is thus a useful engineering design tool for noise and vibration control optimization studies.

Table 7 Radiation ratios for cylindrical shells and bars

Source	*Supplementary equations*	*Radiation ratio and sound power*
Uniformly pulsating pipe (Type 1) 	Mean radius $= a_m$ Wall thickness $= h$ Length $= L$ $k = 2\pi f/c$ $\langle v^2 \rangle$ = space, time averaged $v^2_{r,\mathrm{RMS}}$	$\sigma_r = 2/\left\{\pi k a_m \lvert \mathrm{H}_1(k a_m)\rvert^2\right\}$ where H_1 = Hankel function of second kind, order one See Figure 24 (radiation ratio graphs) Sound power $\Pi = \sigma_r \rho_o c[2\pi(a_m + (h/2))L]\langle v^2 \rangle$
Oscillating solid bar or thick walled, small diameter pipe (Type 2) 	Outside radius $= a_{ext}$ Length $= L$ $\langle v^2 \rangle$ = space, time averaged v^2_{RMS} $\langle v^2 \rangle \approx v^2_{s,\mathrm{RMS}}/3$	$\sigma_r = 2/\left\{\pi k a_{ext} \lvert \mathrm{H}_1'(k a_{ext})\rvert^2\right\}$ where H_1' = first derivative of H_1 in respect of its argument See Figure 25 (radiation ratio graphs) Sound power $\Pi = \sigma_r \rho_o c[2\pi a_{ext} L]\langle v^2 \rangle$
Forced peristaltic motion (Type 3)		See Further Reading list or Use Type 1
Resonant flexural vibration of a thin, large diameter cylindrical shell (Type 4) 	Mean radius $= a_m$ Wall thickness $= h$ Length $= L$ See Tables 3 and 4	Sound power $\Pi = \sigma_r \rho_o c[2\pi(a_m + (h/2))L]\langle v^2 \rangle$ See Figures 26 – 30 (radiation ratio graphs and experimental data)
Acoustic/flow excitation of flexural vibration of a thin, large diameter cylindrical shell (Type 5)	Mean radius $= a_m$ Wall thickness $= h$ Length $= L$ See Tables 3 and 4	Sound power $\Pi = \sigma_r \rho_o c[2\pi(a_m + (h/2))L]\langle v^2 \rangle$ See Figures 31 – 33 (experimental data)

Adapted from Beranek and Ver (1992) and Richards *et al*. (1979).

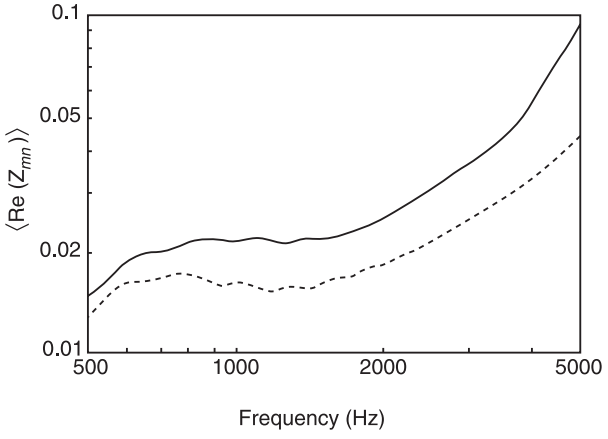


Figure 23 Predicted radiation ratios of aircraft fuselage panels on landing, (–) with flow, (- - -) without flow. (Reproduced from Graham WR (1998) The effect of mean flow on the radiation efficiency of rectangular plates. *Proceedings of the Royal Society of London Series A – Mathematical Physical and Engineering Sciences* 454(1968): 111–137.)

Nomenclature

a_m	mean radius
c	speed of sound in air
E	Young's modulus
f	frequency
h	thickness
L	length
p	acoustic pressure
P	perimeter
S	surface area
u	particle displacement
$<v^2>$	space, time averaged
ν	Poisson's ratio
λ	wavelength
θ	acoustic propagation angle
ϕ	incidence angle

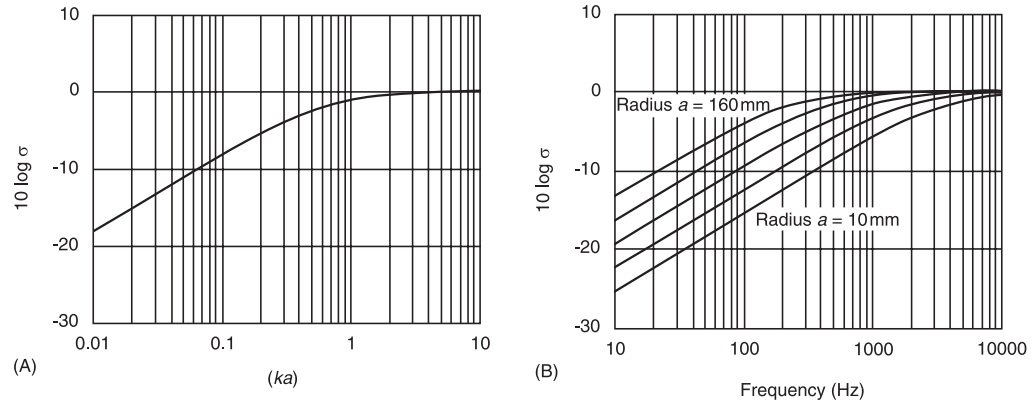


Figure 24 Radiation ratios for uniformly pulsating cylindrical shells. (A) Theoretical nondimensional, (B) theoretical dimensional. Pipe mean radius $a = 10$ mm, 20 mm, 40 mm, 80 mm and 160 mm (Type 1 after Richards, Westcott and Jeyapalan, 1979).

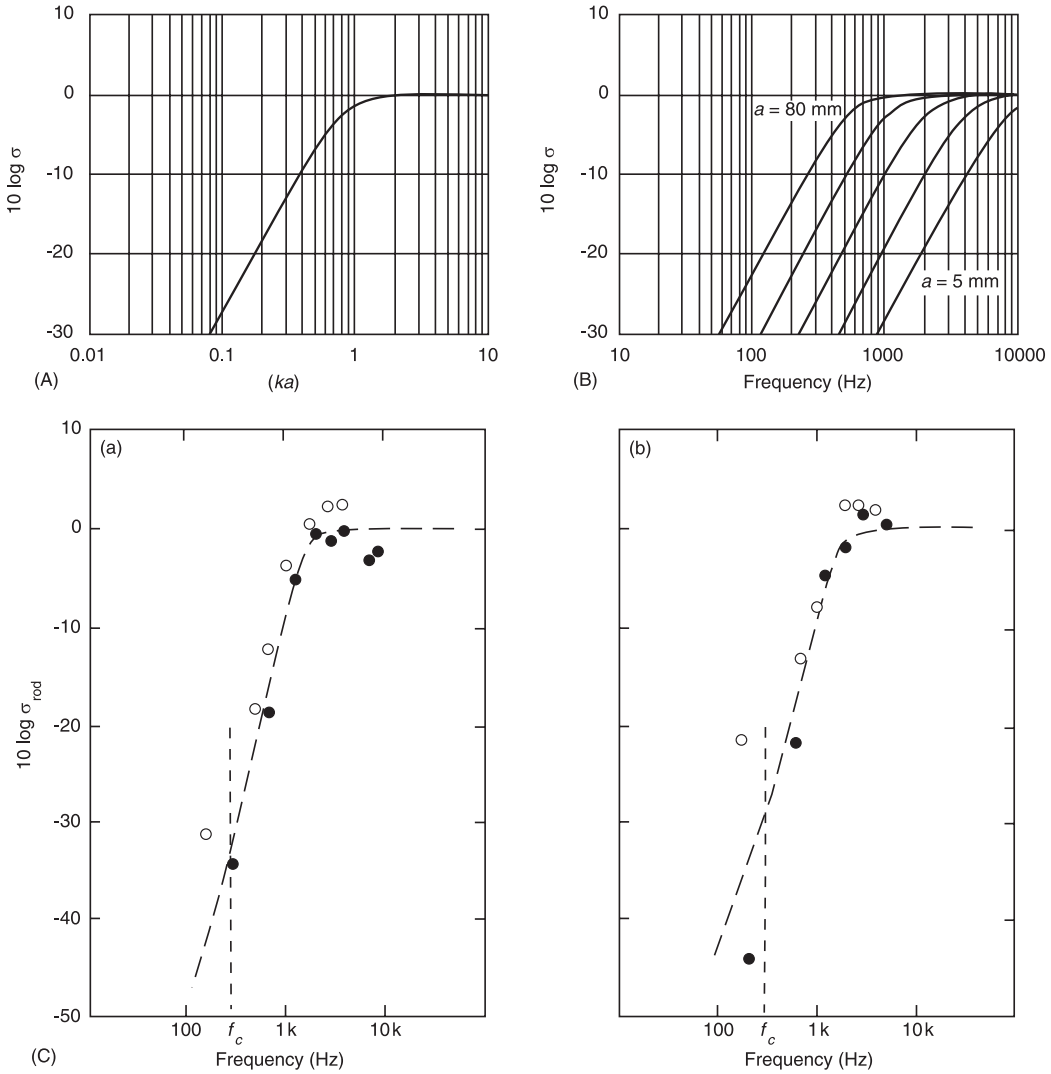


Figure 25 (A) Theoretical nondimensional radiation ratio for an oscillating cylindrical bar or very thick walled cylinder. (B) Theoretical dimensional radiation ratio for oscillating cylindrical bars or very thick walled cylinders. Outside radius $a = 5$ mm, 10 mm, 20 mm, 40 mm and 80 mm. (C) Measured radiation ratio for oscillating cylindrical bars. (a) 2 m long $\times$ 51 mm diameter, (b) 1 mm length $\times$ 51 mm diameter, (•) straight bar, (o) with 90° bend. (Type 2) (Reproduced with permission from Richards, Westcott and Jeyapalan 1979).

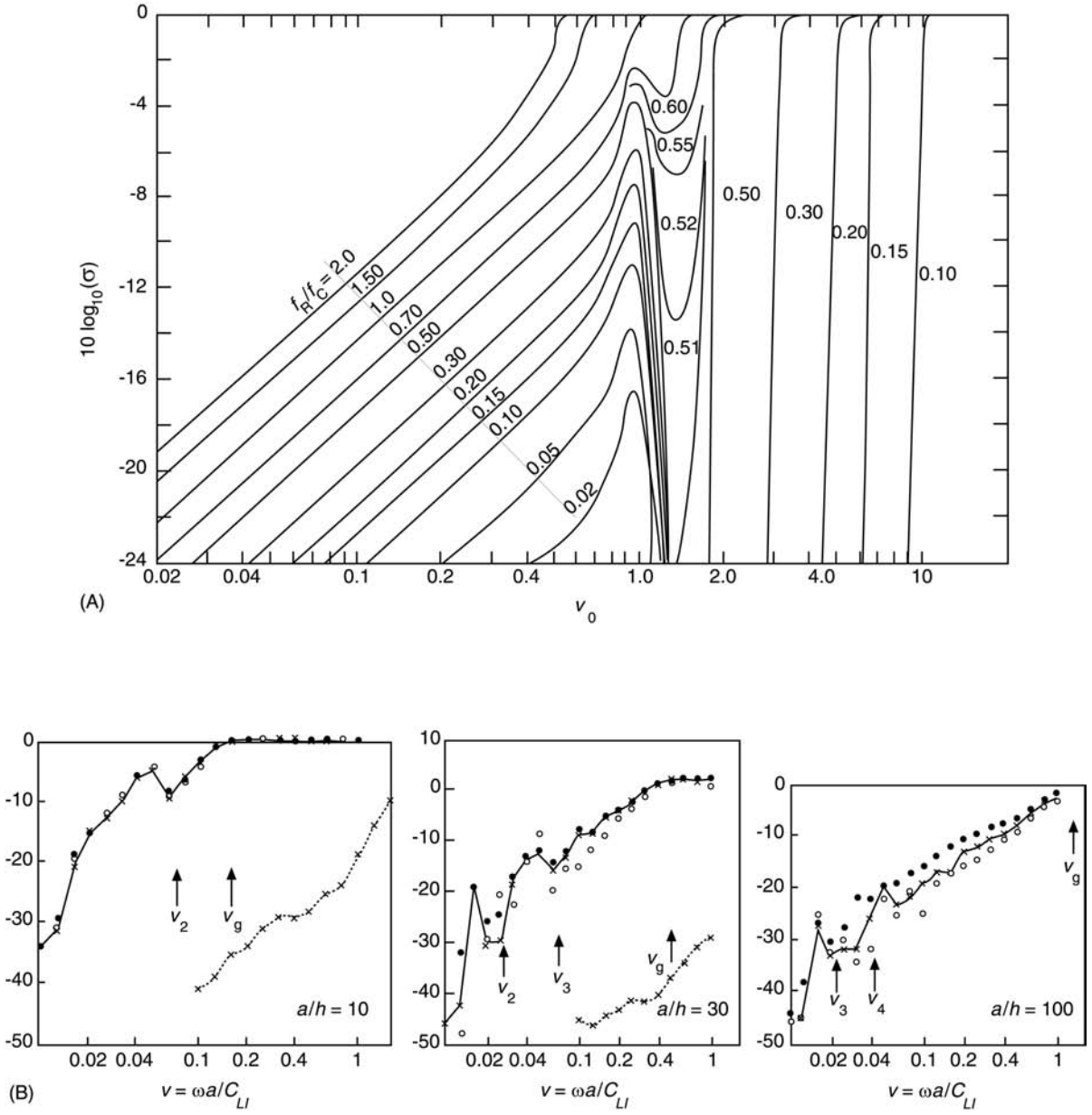


Figure 26 Calculated modal average radiation ratio (1/3 octave bands) for thin-walled, large diameter cylindrical shells in air (Type 4). (B) Theoretical radiation ratios for circular cylinders in air and water (Type 4). ((A) is reproduced with permission from Szechenyi, 1971. (B) is reproduced with permission from Cremer, Heckl and Ungar, 1988.)

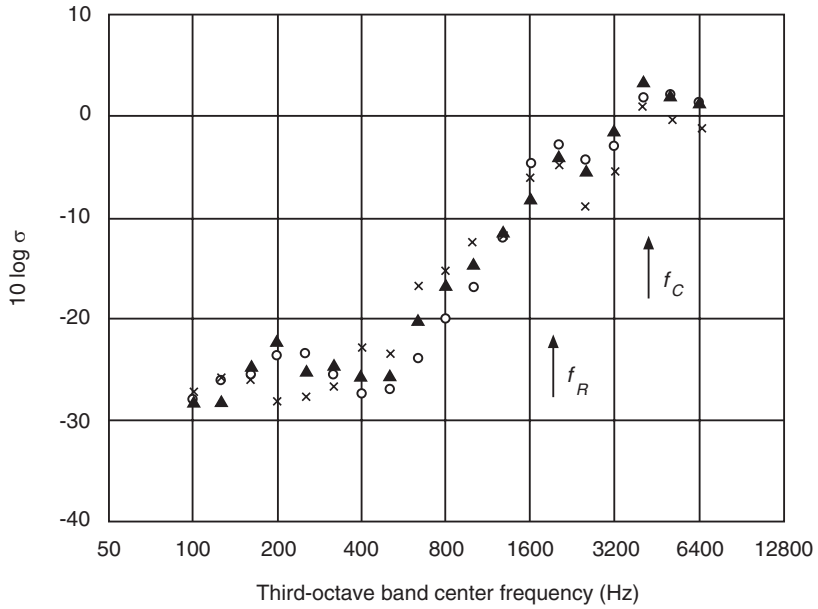


Figure 27 Measured radiation ratio for a mechanically excited, large diameter circular cylinder in air (Type 4). (o) Free ends, (▲) flanged ends, (x) three ring flanges. Diameter = 914 mm, length = 610 mm, thickness = 3.175 mm (Reproduced with permission from Manning JE and Maidanik G (1964) Radiation properties of cylindrical shells. *The Journal of the Acoustical Society of America* 36(9): 1691–1698.)

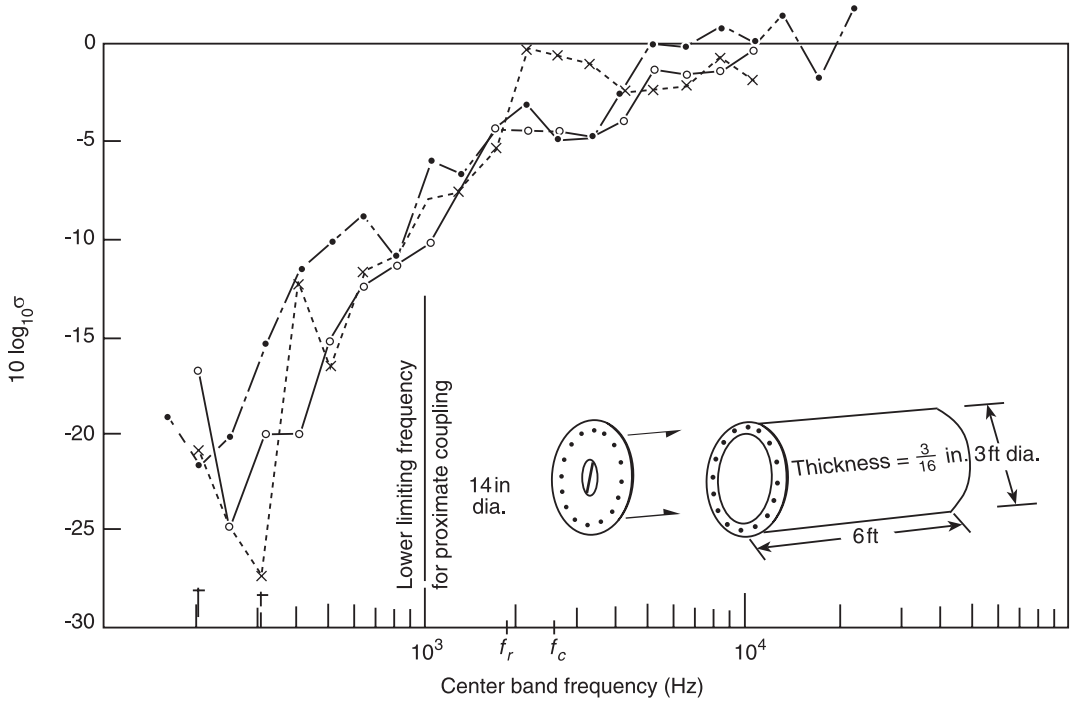


Figure 28 Measured radiation ratio (1/3 octave bands) for a large diameter circular cylinder in air (Type 4). Diameter = 914 mm, length = 1830 mm, thickness = 4.76 mm. (●) Open cylinder; (o) partially closed cylinder (flow excitation); (x) partially closed cylinder (point excitation). (Reproduced with permission from Fahy FJ (1969) Vibration of containing structures by sound in the contained fluid. *Journal of Sound and Vibration* 10(3): 490–512.)

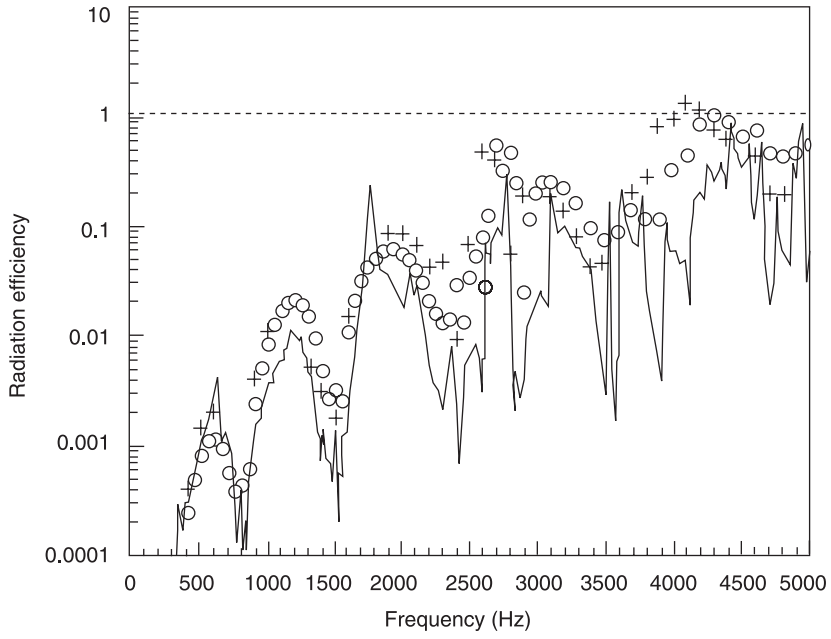


Figure 29 Measured and calculated radiation ratios of a circular cylinder in air (Type 4). Diameter = 127 mm, length = 200 mm, thickness = 1.6 mm. (–) measured, (o) boundary element method, (+) theory. (Reproduced with permission from Wang C and Lai CS (2000) The sound radiation efficiency of finite length acoustically thick circular cylindrical shells under mechanical excitation I: Theoretical analysis. *Journal of Sound and Vibration* 232(2): 431–447.)

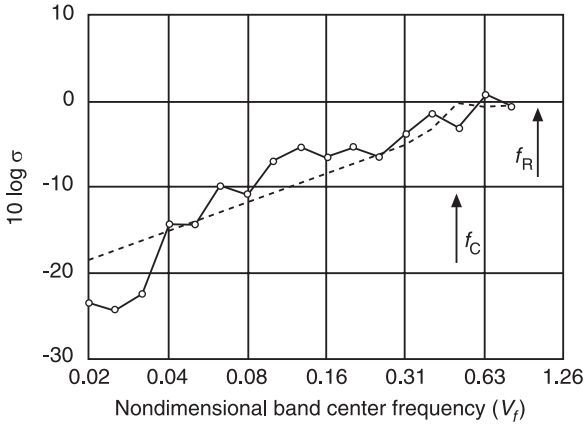


Figure 30 Measured and calculated 1/3 octave band radiation ratios of a mechanically excited circular cylinder in air (Type 4). (-o-), measured, (- - -) Szechenyi, 1971. Diameter = 64.5 mm, length = 3050 mm, thickness = 1.1 mm. (Reproduced with permission from Drew SJ (1986) Machinery noise – The external radiation ratios of cylinders. Honours thesis, University of Western Australia.)

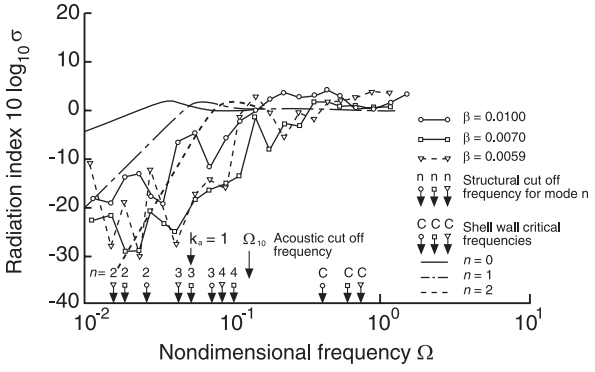


Figure 31 Measured radiation ratios of steel pipes for internal sound field excitation (Type 5). (Reproduced with permission from Rennison DC (1977) The vibrational response of, and the acoustical radiation from, thin walled pipes. PhD thesis, University of Adelaide, and from Fahy, 1985.)

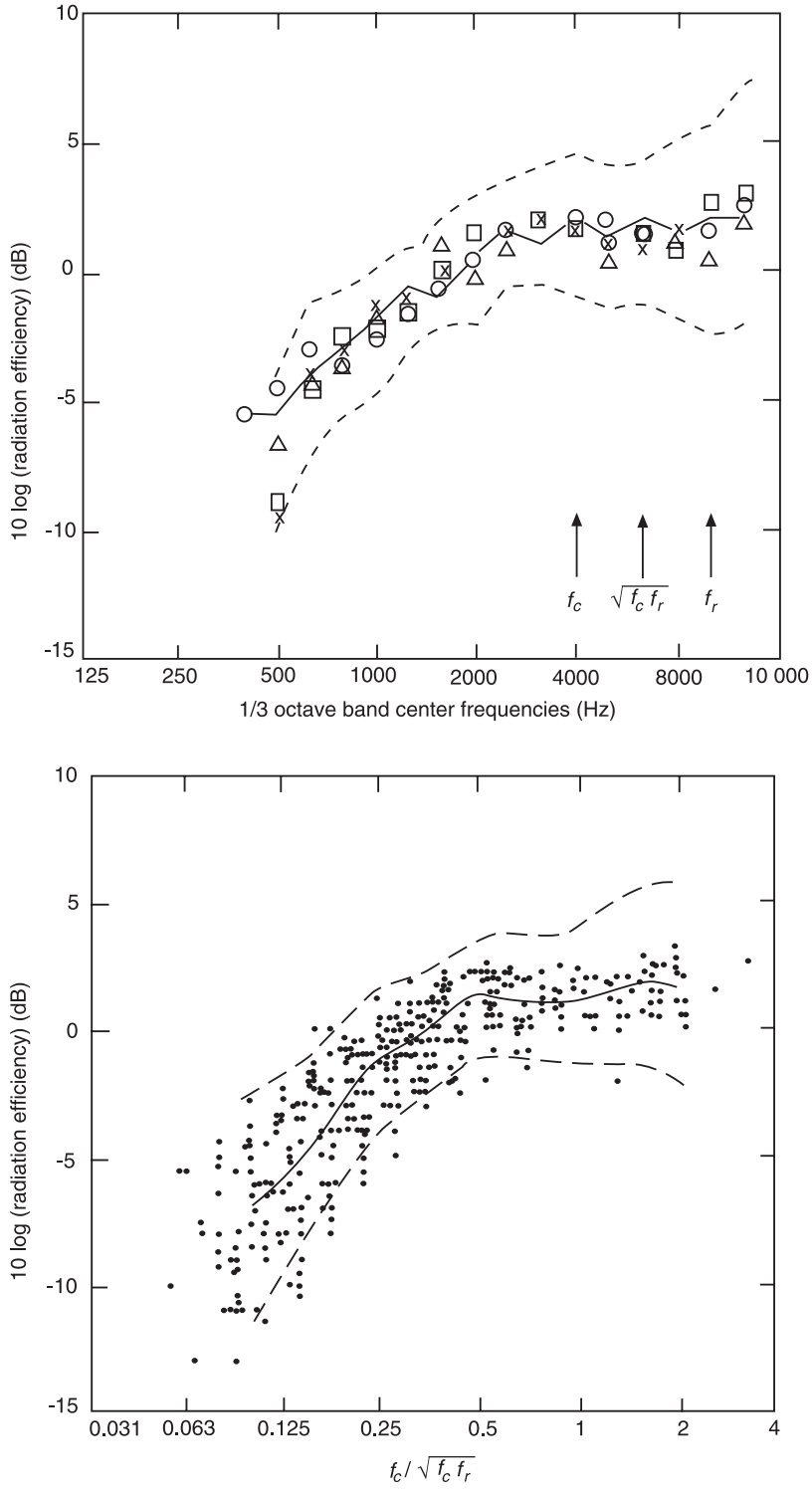


Figure 32 Measured radiation ratios of a circular cylinder in air for flow/acoustic excitation (Type 5). Diameter = 64.5 mm, length = 3050 mm, thickness = 1.1 mm. (A) (–) No flow, (o) 30 $m\,s^{-1}$ flow, (Δ) 60 $m\,s^{-1}$ flow, (◇) 90 $m\,s^{-1}$ flow, (x) 120 $m\,s^{-1}$ flow, (- - -) ±2 standard deviation error bounds. (B) (–) mean of all data, (- - -) ±2 standard deviation error bounds. (Reproduced with permission from Holmer CI and Heymann FJ (1980) Transmission of sound through pipe walls in the presence of flow. *Journal of Sound and Vibration* 70(2): 275–301.)

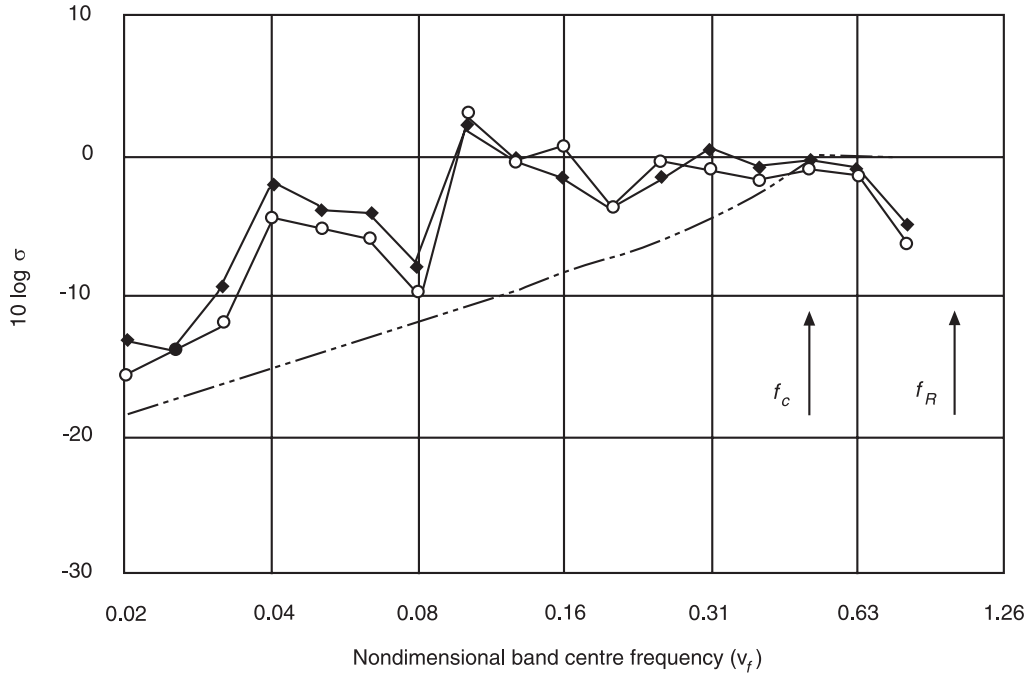


Figure 33 Measured 1/3 octave band radiation ratios for a flow/acoustically excited circular cylinder in air (Type 5). Diameter = 64.5 mm, length = 3050 mm, thickness = 1.1 mm (-o-) measured for flow/acoustic excitation (1), (-•-) measured for flow/acoustic excitation (2), (-..-) Theory (Szechenyi, 1971) for mechanical excitation. (Reproduced with permission from Drew SJ (1986) Machinery noise – the external radiation ratios of cylinders. Honours Thesis, University of Western Australia.)

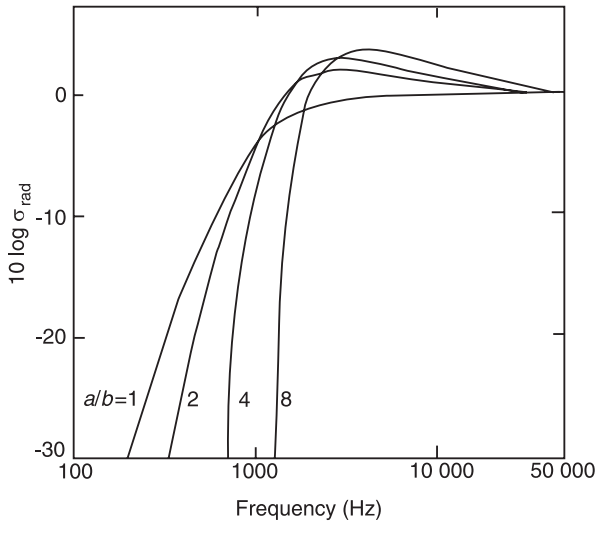


Figure 34 Calculated radiation ratios for elliptical cylinders with different aspect ratios but constant major axis of 80 mm (2*a*). (Reproduced from Richards, Westcott and Jeyapalan, 1979.)

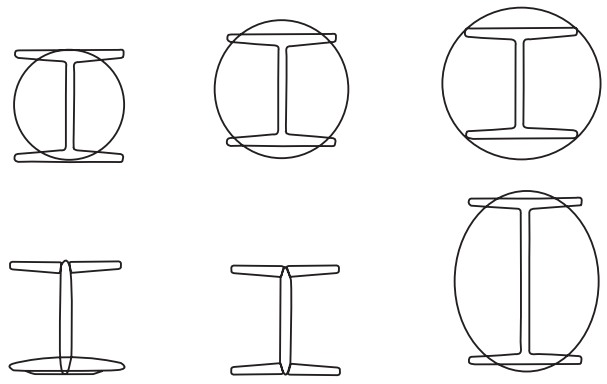


Figure 35 Models for predicting the radiation ratios of I-beams. (Reproduced with permission from Richards, Westcott and Jeyapalan, 1979.)

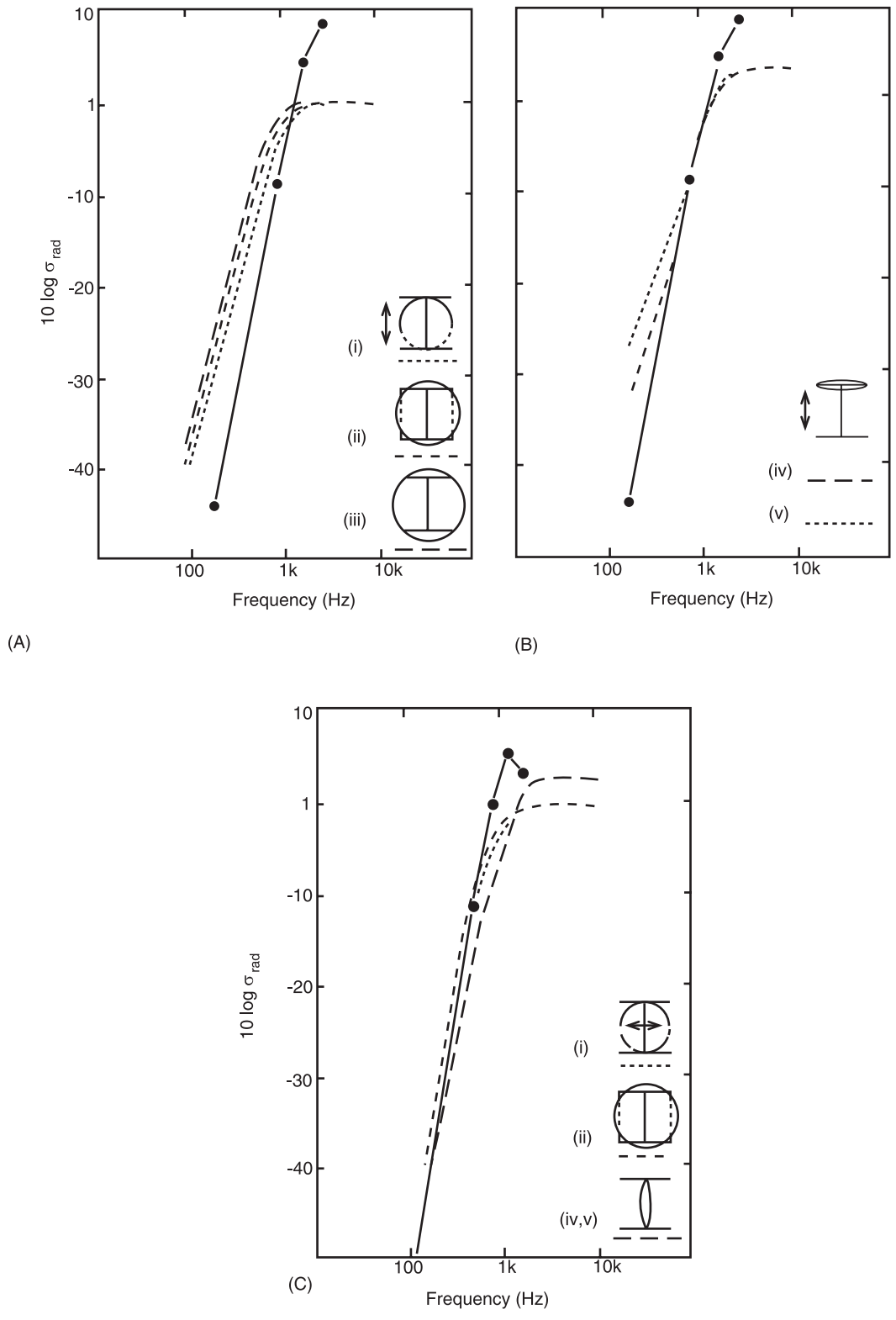


Figure 36 Measured radiation ratios for I-beams, compared to various cylindrical and elliptical models. (Reproduced with permission from Richards, Westcott and Jeyapalan, 1979.)

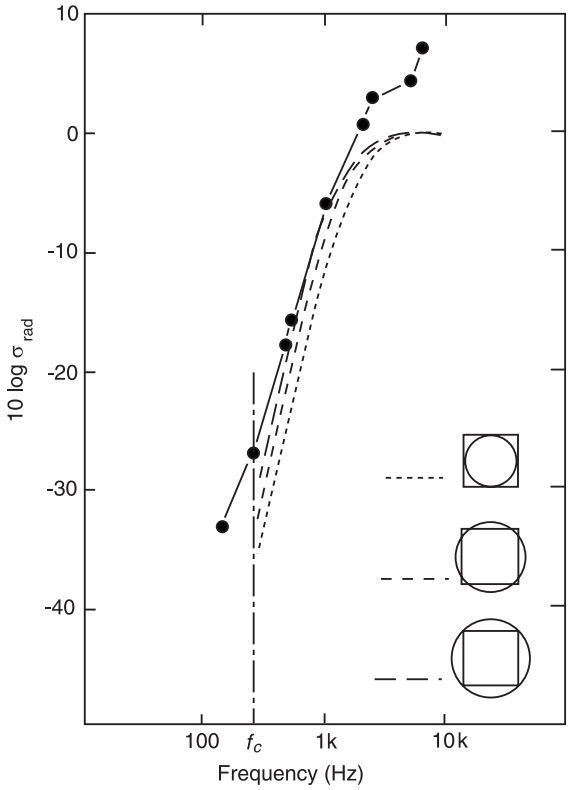


Figure 37 Measured radiation ratio of a 700 mm × 700 mm square steel frame made of 48 mm square box section compared to theoretical curves for three cylindrical models. (Reproduced with permission from Richards, Westcott and Jeyapalan, 1979.)

See also: **Noise**, Noise radiated by baffled plates; **Noise**, Noise radiated from elementary sources; **Vibration generated sound**, Fundamentals.

Further Reading

Beranek LL, Ver IL (eds) (1992) *Noise and Vibration Control Engineering – Principles and Applications*. New York: Wiley.

Bies DA, Hansen CH (1996) *Engineering Noise Control – Theory and Practice*, 2nd edn. London: E & FN Spon.

Cremer L, Heckl M, Ungar EE (1988) *Structure-borne Sound – Structural Vibrations and Sound Radiation at Audio Frequencies*, 2nd edn. Berlin: Springer-Verlag.

Crocker MJ, Price AJ (1969) Sound transmission using statistical energy analysis. *Journal of Sound and Vibration* 9(3): 469–486.

Fahy F (1985) *Sound and Structural Vibration – Radiation. Transmission and Response*. London: Academic Press.

Leppington FG, Broadbent EG, Heron KH (1982) The acoustic radiation efficiency of rectangular panels. *Proceedings of the Royal Society of London, Series A – Mathematical Physical & Engineering Sciences*, 382: 245–271.

Maidanik G (1962) Response of ribbed panels to reverberant acoustic fields. *Journal of the Acoustical Society of America* 34: 809.

Norton MP (1999) *Fundamentals of Noise and Vibration Analysis for Engineers*. London: Cambridge University Press.

Richards EJ (1982) Noise from industrial machines. In White RG and Walker JG (eds) *Noise and Vibration*, ch. 22. Chichester, UK: Ellis Horwood.

Richards EJ, Westcott ME, Jeyapalan RK (1979) On the prediction of impact noise, II: Ringing noise. *Journal of Sound and Vibration* 65(3): 419–451.

Smith PW Jr, Lyon RH (1965) NASA Contractor Report. NASA CR-160. Sound and Structural Vibration. Cambridge, MA: Bolt, Beranek and Newman Inc.

Szechenyi E (1971) Modal densities and radiation efficiencies of unstiffened cylinders using statistical methods. *Journal of Sound and Vibration* 19(1): 65–81.

Ver IL, Holmer CI (1971) In Beranek LL (ed.) *Noise and Vibration Control*, 287–296. New York: McGraw Hill.

VIBRATION INTENSITY

S I Hayek, Pennsylvania State University, University Park, PA, USA

Copyright © 2001 Academic Press

doi:10.1006/rwvb.2001.0169

Introduction

The instantaneous vibration structural intensity (VSI) is defined as the vibration mechanical power passing through a unit cross-sectional area of a structure. It is defined as the stress traction vector $\mathbf{t}$ at the surface of the cross-section times the projected particle velocity at the same cross-section, i.e.:

$$\mathbf{I}(x, y, z, t) = \mathbf{t} \cdot \mathbf{v} \qquad [1]$$

To clarify the concepts involved in this definition, and the physical interpretation of VSI, a one-dimensional elastic structural model is presented first.

Consider an infinite elastic bar of a cross-section $A(x)$ undergoing longitudinal vibration $u(x,\ t)$, with ρ and E being the constant density and Young's modulus, respectively. The net total mechanical power flow out of the surfaces of an element of length $\mathrm{d}x$ at stations x and $x + \mathrm{d}x$ with total cross-sectional forces $F(x)$ and $F(x + \mathrm{d}x)$ due to deformation of the element is given by:

$$\frac{\partial \mathbf{I}(x,t)}{\partial x} = -\frac{\partial}{\partial x}\left[F(x,t)\frac{\partial u}{\partial t}(x,t)\right]$$

Since $F(x) = EA(\partial u/\partial x)$, then the net outflow of mechanical power is:

$$\frac{\partial \mathbf{I}(x,t)}{\partial x} = -\frac{\partial}{\partial x}\left[EA\frac{\partial u}{\partial x}\frac{\partial u}{\partial t}\right] \qquad [2]$$

The equation of motion for an elastic rod is given as:

$$\frac{\partial}{\partial x}\left(A\frac{\partial u}{\partial x}\right) = \frac{1}{c^2}A\frac{\partial^2 u}{\partial t^2} - \frac{q(x,t)}{E} \qquad [3]$$

with $c = \sqrt{E}/\rho$ being both the phase and group velocity for the bar. The potential and kinetic energy densities, U and K, for the cross-section are given by, respectively:

$$U = \frac{1}{2}EA\left(\frac{\partial u}{\partial x}\right)^2$$
$$K = \frac{1}{2}\rho A\left(\frac{\partial u}{\partial t}\right)^2$$

The total energy density e is thus given by:

$$e = U + K$$

Differentiating e partially with time and substituting the equation of motion into the resulting expression one obtains the balance law for VSI.

$$\frac{\partial \mathbf{I}}{\partial x} = -\frac{\partial e}{\partial t} + \pi \qquad [4]$$

where $\pi(x,\ t)$ is the externally injected mechanical power into the element by a distributed force $q(x,\ t)$, i.e.:

$$\pi(x,t) = q(x,t)\frac{\partial u}{\partial t}(x,t)$$

Consider a free propagating longitudinal wave in an infinite undamped rod, propagating in the positive x-direction, where the longitudinal displacement is given by:

$$u(x,t) = u_0 \cos\,(kx - \omega t)$$

with u_0 being the amplitude. The instantaneous energy density e and VSI are, respectively:

$$e = k^2 EAu_0^2 \sin^2(kx - \omega t)$$
$$I = -EA\frac{\partial u}{\partial t}\frac{\partial u}{\partial x} = ck^2 EAu_0^2 \sin^2(kx - \omega t)$$

thus $I(x,\ t) = ce(x,\ t)$.

Generally, this is not true for other vibrational fields. The time- and space-averaged instantaneous $\bar{I}$ and $\bar{e}$ are:

$$\bar{\mathbf{I}} = \langle I\rangle_{x,t} = \frac{1}{2}EAu_0^2 k^2 c$$
$$\bar{e} = \langle e\rangle_{x,t} = \frac{1}{2}EAu_0^2 k^2$$

Both $\bar{I}$ and $\bar{e}$ are always positive, and $\bar{I} = c\bar{e}$.

One should note that c is the group velocity for a longitudinal wave propagating in an elastic rod. The instantaneous VSI fluctuates in time. Examining:

$$\frac{I(x,t)}{\bar{I}} = 2\sin^2(kx - \omega t) = 1 - \cos\ 2(kx - \omega t)$$

shows that $I(x,\ t)$ is always positive, with a mean-flow component and a time varying component whose frequency is 2ω, i.e., twice the frequency of the propagating wave. Furthermore, the instantaneous VSI fluctuates between 0 and 2 every half-wavelength. This indicates that the mechanical power flow fluctuates about a mean value $\bar{I}$.

For a standing wave field, such as that given by two waves propagating in opposite directions, the total displacement field is given by:

$$u(x,t) = \frac{1}{2}u_0[\cos\,(kx - \omega t) + \cos\,(kx + \omega t)]$$
$$= u_0 \cos kx \cos \omega t$$

Here the instantaneous $I(x,\ t)$ and $e(x,\ t)$ are given by:

$$I(x,t) = -\frac{1}{4}EAk^2cu_0^2 \sin(2kx)\sin(2\omega t)$$
$$e(x,t) = \frac{1}{4}EAk^2u_0^2[1-\cos(2\omega t)\cos(2kx)]$$

Note that the $I \neq ce$. The time- and space-averaged value of VSI and e are

$$\bar{I} = 0 \quad \bar{e} = \frac{1}{4}EAk^2u_0^2$$

This means that for standing wave fields in undamped rods, the net flow of energy is zero.

Complex Vibration Intensity

Frequently, the displacement, velocity and internal stress fields are represented by complex functions. To accommodate such formulation, one can derive the expressions for the VSI in terms of these complex representations. Since $I = -F\dot{u}$, then let:

$$F(x,t) = \mathrm{Re}\left[\hat{F}(x)\mathrm{e}^{-i\omega t}\right]$$
$$u(x,t) = \mathrm{Re}\left[\hat{U}(x)\mathrm{e}^{-i\omega t}\right]$$

If one defines a complex VSI as:

$$\hat{I}(x) = \frac{1}{2}\left(\hat{F}\,\mathrm{e}^{-i\omega t}\right)\left(-i\omega\hat{U}(x)\,\mathrm{e}^{-i\omega t}\right)^* = \frac{i\omega}{2}\hat{F}(x)\hat{U}^*(x) \quad [5]$$

$$\hat{I} = I_a + iI_r \quad [6]$$

where the starred quantities are the complex conjugates, then one can show that the VSI can be given by:

$$I(x,t) = \mathrm{Re}\left\{\hat{I}(x)[1+\exp(-2i\omega t)]\right\} \quad [7]$$

The real part of $\hat{I}$, I_a, is known as the active intensity and is the VSI defined as $I(x,\ t)$ and given earlier as the net power flow. The imaginary part of $\hat{I}$, I_r, is known as the reactive intensity, which represents the inertial power flowing in opposite direction within one cycle and whose time average is zero. Henceforth, using complex representation of the forces and velocities, the VSI is given by:

$$\langle I(x,t)\rangle_t = I_a = \frac{1}{2}\mathrm{Re}[F\dot{u}^*] \quad [8]$$

Waves in Elastic Media

The instantaneous VSI vector $\mathbf{I}(x,\ y,\ z,\ t)$ is defined as the mechanical power passing through a unit cross-sectional area of an elastic solid and is defined by:

$$\mathbf{I}(x,y,z,t) = \boldsymbol{\sigma}\cdot\dot{\mathbf{u}} \quad [9]$$

where $\boldsymbol{\sigma}$ is the stress dyadic at a cross-sectional area and $\dot{\mathbf{u}}$ is the particle velocity at the same cross-section. The dot denotes partial differentiation wrt time t. VSI is a function of location and time.

The mechanical power, (also known as the 'active intensity' is defined as the real part of the time-averaged instantaneous intensity, $\mathbf{I}(t)$, i.e.:

$$\mathbf{I}_a = \langle\mathbf{I}(t)\rangle_{\text{time average}} = \frac{1}{2}\mathrm{Re}(\boldsymbol{\sigma}\cdot\dot{\mathbf{u}}^*) \quad [10]$$

Consider elastic waves propagating in an elastic solid. The stress–strain relation is given by;

$$\sigma_{ij} = G\left[\frac{2\nu}{1-2\nu}\varepsilon_{kk}\delta_{ij} + 2\varepsilon_{ij}\right] \quad [11]$$

where:

$$\varepsilon_{kk} = \varepsilon_{11} + \varepsilon_{22} + \varepsilon_{33}$$

G is the shear modulus, ν is the Poisson's ratio and the strain tensor is defined by:

$$\varepsilon_{ij} = \frac{1}{2}\left[\frac{\partial u_i}{\partial x_j} + \frac{\partial u_j}{\partial x_i}\right] \quad i,j = 1,2,3$$

resulting in stress–displacement relations given by:

$$\sigma_{ij} = G\left[\frac{2\nu}{1-2\nu}\frac{\partial u_k}{\partial x_k}\delta_{ij} + \frac{\partial u_i}{\partial x_j} + \frac{\partial u_j}{\partial x_i}\right] \quad [12]$$

where $u_i,\ i = 1,\ 2,\ 3$ are the three Cartesian components of the displacement vector, and:

$$\frac{\partial u_k}{\partial x_k} = \frac{\partial u_1}{\partial x_1} + \frac{\partial u_2}{\partial x_2} + \frac{\partial u_3}{\partial x_3}$$

where:

$$\delta_{ij} = \text{Kronecker delta} = 1 \text{ if } i = j, \text{ and } = 0 \text{ if } i \neq j$$

The potential energy density U, the kinetic energy density T, and the energy density e are given by:

$$U = \frac{1}{2}\sum_{i=1}^{3}\sum_{j=1}^{3}\sigma_{ij}\varepsilon_{ij} \quad [13]$$

$$T = \frac{\rho}{2}\sum_{i=1}^{3}\frac{\partial u_i}{\partial t}\frac{\partial u_i}{\partial t} \quad [14]$$

$$e = T + U \quad [15]$$

where ρ is the density. The VSI at a cross-section whose normal is $\mathbf{n}$ is defined as:

$$\frac{\partial e}{\partial t} = -\mathbf{I}\cdot\mathbf{n}$$

The total energy in a solid whose volume is V is the volume integral of e, $e_{\mathrm{T}} = \int_v e\,\mathrm{d}V$. The time derivative of the total energy is the integral of the normal component of the VSI on the surface S enclosing V is:

$$\frac{\partial e_T}{\partial t} = -\int_s \mathbf{I}\cdot\mathbf{n}\,\mathrm{dS} = -\int_s \mathbf{I}\cdot\,\mathrm{dS}$$

These result in the VSI vector:

$$\mathbf{I} = I_x\mathbf{i} + I_y\mathbf{j} + I_z\mathbf{k}$$

where each component is expressed by:

$$\begin{aligned} I_x &= -\sigma_{xx}\dot{u}_x - \sigma_{xy}\dot{u}_y - \sigma_{xz}\dot{u}_z \\ I_y &= -\sigma_{yx}\dot{u}_x - \sigma_{yy}\dot{u}_y - \sigma_{yz}\dot{u}_z \\ I_z &= -\sigma_{zx}\dot{u}_x - \sigma_{zy}\dot{u}_y - \sigma_{zz}\dot{u}_z \end{aligned} \quad [16]$$

or more explicitly in terms of the displacement vector in Cartesian coordinates:

$$I_i = -G\left[\frac{2\nu}{1-2\nu}\frac{\partial u_k}{\partial x_k}\dot{u}_j\delta_{ij} + \frac{\partial u_i}{\partial x_j}\dot{u}_j + \frac{\partial u_j}{\partial x_i}\dot{u}_j\right] \quad [17]$$
$$i = 1,\ 2,\ 3$$

Similar expressions can also be written for cylindrical and spherical coordinates, respectively.
In cylindrical coordinates, $\dot{\mathbf{u}} = (\dot{u}_r,\ \dot{u}_\theta,\ \dot{u}_\phi)$:

$$\begin{aligned} I_r &= -\sigma_{rr}\dot{u}_r - \sigma_{r\phi}\dot{u}_\phi - \sigma_{rz}\dot{u}_z \\ I_\phi &= -\sigma_{\phi r}\dot{u}_r - \sigma_{\phi\phi}\dot{u}_\phi - \sigma_{\phi z}\dot{u}_z \\ I_z &= -\sigma_{zr}\dot{u}_r - \sigma_{z\phi}\dot{u}_\phi - \sigma_{zz}\dot{u}_z \end{aligned} \quad [18]$$

In spherical coordinates, $\dot{\mathbf{u}} = (\dot{u}_r,\ \dot{u}_\theta,\ \dot{u}_\phi)$:

$$\begin{aligned} I_r &= -\sigma_{rr}\dot{u}_r - \sigma_{r\theta}\dot{u}_\theta - \sigma_{r\phi}\dot{u}_\phi \\ I_\theta &= -\sigma_{\theta r}\dot{u}_r - \sigma_{\theta\theta}\dot{u}_\theta - \sigma_{\theta\phi}\dot{u}_\phi \\ I_\phi &= -\sigma_{\phi r}\dot{u}_r - \sigma_{\phi\theta}\dot{u}_\theta - \sigma_{\phi\phi}\dot{u}_\phi \end{aligned} \quad [19]$$

The energy propagates at the group velocity defined by:

$$\mathbf{c}_g = \frac{\mathbf{I}}{e}$$

Longitudinal Waves in Elastic Bars

For longitudinal waves in an elastic bar of a variable cross-section $A(x)$, the displacement field is given by $u_1 = u(x)$ and $u_2 = u_3 = 0$ so that stress and strain tensors reduce to:

$$\varepsilon_{xx} = \frac{\partial u}{\partial x} \quad \sigma_{xx} = E\frac{\partial u}{\partial x}$$

These result in an expression for the VSI:

$$I_x = -E\frac{\partial u}{\partial x}\dot{u}$$

and for the total VSI through the cross-section $A(x)$ is:

$$I = \int_A I_x\,\mathrm{d}A = -EA\frac{\partial u}{\partial x}\dot{u} \quad [20]$$

Flexural Waves in Beams (Bernoulli–Euler Theory)

For flexural waves in an elastic beam, the displacement vector is defined by:

$$u_1 = -z\frac{\partial w}{\partial x} \quad u_3 = w \quad u_2 = 0$$
$$-h/2 < z < h/2$$

with the transverse displacement being $w = w(x)$. The stresses become:

$$\begin{aligned} \sigma_{xx} &= E\frac{\partial u}{\partial x} = -Ez\frac{\partial^2 w}{\partial x^2} \\ \sigma_{xz} &= \frac{3}{2}\bar{\sigma}_{xz}\left[1 - \frac{4z^2}{h^2}\right] = -\frac{h^2}{8}E\frac{\partial^3 w}{\partial x^3}\left[1 - \frac{4z^2}{h^2}\right] \end{aligned}$$

The only component of the VSI is the x-component, which can be expressed by:

$$I_x(x,y,z) = -\sigma_{xx}\dot{u} - \sigma_{xz}\dot{w}$$

The total VSI is thus given by:

$$\begin{aligned} I &= \iint_{-b/2}^{b/2} I_x(x,y,z)\,\mathrm{d}z\,\mathrm{d}y \\ &= -B\left\{\frac{\partial^2 w}{\partial x^2}\frac{\partial^2 \dot{w}}{\partial x}\right\} + B\left\{\frac{\partial^3 w}{\partial x^3}\dot{w}\right\} \end{aligned} \quad [21]$$

where $B = Eh^3b/12$ is the bending rigidity. The first term of eqn [21] is due to the moment and the second term is due to shear.

Flexural Waves in Beams (Timoshenko Theory)

Timoshenko improved the Bernoulli–Euler theory for flexure in beams by introducing shear deformation and rotatory inertia. The displacement vector is given by:

$$u_1 = -z\phi \quad u_3 = w \quad u_2 = 0$$

The potential and kinetic energy densities are thus given, respectively, by:

$$U = \frac{1}{2}GAK\left(\frac{\partial w}{\partial x} - \phi\right)^2 + \frac{1}{2}B\left(\frac{\partial \phi}{\partial x}\right)^2$$

$$T = \frac{1}{2}\rho A\dot{w}^2 + \frac{1}{2}\rho I\dot{\phi}^2$$

where the K is the shear correction factor given for two cross-sections:

$$\begin{aligned} K &= 0.833 \text{ rectangular cross-section} \\ &= 1.111 \text{ circular cross-section} \\ &= \pi^2/12 \text{ Mindlin factor} \end{aligned}$$

The total VSI for the cross-section becomes:

$$I = GAK\left(\phi - \frac{\partial w}{\partial x}\right)\dot{w} - B\frac{\partial \phi}{\partial x}\dot{\phi} \quad [22]$$

The first term in eqn [22] is due to shear and the second term is due to moment.

Flexural Waves in Elastic Plates (Classical or Kirchoff Theory)

The displacement vector for a uniform thickness plate is given by:

$$u_1 = u = z\frac{\partial w}{\partial x}$$

$$u_2 = v = z\frac{\partial w}{\partial y}$$

$$u_3 = w(x,y)$$

Substitution of these into the stress–displacement equations results in the total VSI for the cross-section as follows:

$$\begin{aligned} I_x = B'\Bigg[&-\left(\frac{\partial^2 w}{\partial x^2} + \nu\frac{\partial^2 w}{\partial y^2}\right)\frac{\partial \dot{w}}{\partial x} - (1-\nu)\frac{\partial^2 w}{\partial x \partial y}\frac{\partial \dot{w}}{\partial y} \\ &+ \left(\frac{\partial^3 w}{\partial x^3} + \frac{\partial^3 w}{\partial x \partial y^2}\right)\dot{w}\Bigg] \end{aligned} \quad [23]$$

$$\begin{aligned} I_y = B'\Bigg[&-\left(\frac{\partial^2 w}{\partial y^2} + \nu\frac{\partial^2 w}{\partial x^2}\right)\frac{\partial \dot{w}}{\partial y} - (1-\nu)\frac{\partial^2 w}{\partial x \partial y}\frac{\partial \dot{w}}{\partial x} \\ &+ \left(\frac{\partial^3 w}{\partial x^2 \partial y} + \frac{\partial^3 w}{\partial y^3}\right)\dot{w}\Bigg] \end{aligned} \quad [24]$$

The first two terms of eqns [23] and [24] are due to bending and twisting moments, and the third term is due to shear.

The VSI written in terms of cylindrical coordinates can be written in terms of the transverse displacement $u(r,\ \theta)$

$$\begin{aligned} I_r = \frac{1}{2}B'\Bigg\{&\frac{\partial}{\partial r}(\Delta u)\frac{\partial u}{\partial t} \\ &- \left[\frac{\partial^2 u}{\partial r^2} + \nu\left(\frac{1}{r}\frac{\partial u}{\partial r} + \frac{1}{r^2}\frac{\partial^2 u}{\partial \theta^2}\right)\right]\frac{\partial^2 u}{\partial t \partial r} \\ &- (1-\nu)\left(\frac{1}{r}\frac{\partial^2 u}{\partial r \partial \theta} - \frac{1}{r^2}\frac{\partial u}{\partial \theta}\right)\frac{1}{r}\frac{\partial^2 u}{\partial \theta \partial t}\Bigg\} \end{aligned} \quad [25]$$

$$\begin{aligned} I_\theta = \frac{1}{2}B'\Bigg[&\frac{1}{r}\frac{\partial}{\partial \theta}(\Delta u)\frac{\partial u}{\partial t} - \left(\frac{1}{r}\frac{\partial u}{\partial r} + \frac{1}{r^2}\frac{\partial^2 u}{\partial r^2}\right)\frac{\partial^2 u}{\partial t \partial \theta} \\ &-(1-\nu)\left(\frac{1}{r}\frac{\partial^2 u}{\partial r \partial \theta} - \frac{1}{r^2}\frac{\partial u}{\partial t}\right)\frac{1}{r}\frac{\partial^2 u}{\partial r \partial t}\Bigg] \end{aligned} \quad [26]$$

where:

$$\Delta = \text{Laplacian} = \frac{\partial^2}{\partial x^2} + \frac{\partial^2}{\partial y^2}$$

$$B' = Eh^3/12(1-\nu^2)$$

Extensional and Flexural Waves in Elastic Plates (Mindlin Theory)

The Mindlin plate theory allows for the correction of the classical Kirchoff plate bending theory by the addition of shear deformation and rotatory inertia. Including the extensional components, it assumes that the displacement vector is given by:

$$u_1 = u(x,y,z) = U(x,y) + z\phi_x(x,y)$$
$$u_2 = v(x,y,z) = V(x,y) + z\phi_y(x,y)$$
$$u_3 = w(x,y)$$

The stresses are thus given in terms of displacements as:

$$\sigma_{xx} = \frac{E}{1-\nu^2}\left[\frac{\partial u}{\partial x} + \nu\frac{\partial v}{\partial y}\right]$$
$$\sigma_{yy} = \frac{E}{1-\nu^2}\left[\frac{\partial v}{\partial y} + \nu\frac{\partial u}{\partial x}\right]$$
$$\sigma_{xz} = G\left[\frac{\partial w}{\partial x} + \frac{\partial u}{\partial z}\right] = G\left[\phi_x + \frac{\partial w}{\partial x}\right]$$
$$\sigma_{yz} = G\left[\frac{\partial w}{\partial y} + \frac{\partial v}{\partial z}\right] = G\left[\phi_y + \frac{\partial w}{\partial y}\right]$$

The VSI and total VSI are given by:

$$\hat{I}_x(x,y,z) = -\sigma_{xx}\dot{u} - \sigma_{xy}\dot{v} - \sigma_{xz}\dot{w}$$
$$I_x(x,y) = \int_{-h/2}^{h/2} \hat{I}\,dz$$

The x-component of the total VSI vector has extensional and flexural components as $I_x = I_{xe} + I_{xb}$ where the x-component of the extensional and flexural total VSI is given by, respectively:

$$I_{xe} = -\frac{Eh}{1-\nu^2}\left[\frac{\partial u}{\partial x} + \nu\frac{\partial V}{\partial y}\right]\dot{U} - G\left[\frac{\partial U}{\partial y} + \frac{\partial V}{\partial x}\right]\dot{U} \quad [27]$$

$$I_{xb} = -\sigma_{xz}h\dot{w} - B'\left\{\left(\frac{\partial \phi_x}{\partial x} + \nu\frac{\partial \phi_y}{\partial y}\right)\dot{\phi}_x + (1-\nu)\left(\frac{\partial \phi_x}{\partial y} + \nu\frac{\partial \phi_y}{\partial x}\right)\dot{\phi}_y\right\} \quad [28]$$

For I_y, exchange $U \leftrightarrow V$, $\phi_x \leftrightarrow \phi_y$ and $x \leftrightarrow y$.

Elastic Waves in Cylindrical Shells

For wave propagation in an elastic cylindrical shell of thickness, h, and radius, a, the displacement vector has the components:

$$u(z,s) = \text{axial},$$
$$v(z,s) = \text{circumferential},$$
$$w(z,s) = \text{radial}$$

where z is the axial, and $s = a\theta$ is the circumferential coordinate.

The total VSI in the z- and s-directions are given by:

$$I_z = -\frac{Eh}{1-\nu^2}\left[\frac{\partial u}{\partial z}\dot{u} + \nu\frac{\partial v}{\partial s}\dot{v}\right] - Gh\left[\frac{\partial u}{\partial s}\dot{v} + \frac{\partial v}{\partial z}\dot{u}\right] - B'\left[\left(\frac{\partial^2 w}{\partial z^2} + \nu\frac{\partial^2 w}{\partial s^2}\right)\frac{\partial \dot{w}}{\partial z} - \left(\frac{\partial \Delta w}{\partial z} - \frac{1}{c_1^2}\frac{\partial \ddot{w}}{\partial z}\right)\dot{w}\right] - \frac{Gh^3}{6}\frac{\partial^2 w}{\partial s \partial z}\frac{\partial \dot{w}}{\partial s} - \frac{Eh}{1-\nu^2}\frac{\nu}{a}\left[w\dot{u} + \frac{h^2}{6a}w\frac{\partial \dot{w}}{\partial s}\right] - \frac{Gh^3}{12a}\left[\frac{\partial u}{\partial s}\frac{\partial \dot{w}}{\partial s} - \frac{\partial^2 u}{\partial s^2}\dot{w}\right] \quad [29]$$

$$I_s = -\frac{Eh}{1-\nu^2}\left[\frac{\partial v}{\partial s}\dot{v} + \nu\frac{\partial u}{\partial z}\dot{u}\right] - Gh\left[\frac{\partial v}{\partial z}\dot{u} + \frac{\partial u}{\partial s}\dot{v}\right] - B'\left[\left(\frac{\partial^2 w}{\partial s^2} + \nu\frac{\partial^2 w}{\partial z^2}\right)\frac{\partial \dot{w}}{\partial s} - \left(\frac{\partial \Delta w}{\partial s} - \frac{1}{c_1^2}\frac{\partial \ddot{w}}{\partial s}\right)\dot{w}\right] - \frac{Gh^3}{6}\frac{\partial^2 w}{\partial s \partial z}\frac{\partial \dot{w}}{\partial z} - \frac{Eh}{1-\nu^2}\frac{\nu}{a}\left[w\dot{v} + \frac{h^2}{6a}w\frac{\partial \dot{w}}{\partial s}\right] - \frac{Gh^3}{12a}\left[\frac{\partial v}{\partial z}\frac{\partial \dot{w}}{\partial z} - \frac{\partial^2 v}{\partial z^2}\dot{w}\right] \quad [30]$$

Applications

Semi-infinite Elastic Rod

Consider a semi-infinite elastic rod excited by a point force F_0 at $x = \xi$ and fixed at the end $x = 0$. The longitudinal displacement $u(x)$ is given by:

$$\hat{u}(x) = -F_0 \frac{e^{ik\xi}}{kEA} \sin\ (kx) \quad x < \xi$$
$$= -F_0 \frac{e^{ikx}}{kEA} \sin\ (k\xi) \quad x < \xi$$

then $I_a = 0, \quad 0 < x < \xi$

$$= \frac{F_0^2}{2} \frac{c}{AE} \sin k\xi \quad x > \xi$$

This shows that the vibration intensity is zero for $x < \xi$, since the vibration field is a standing wave. For $x > \xi$, the VSI is always positive, i.e., net power flow for all x. It fluctuates between 0 and a maximum $F_0^2 c/2AE$ due to the constructive and destructive interference of the two propagating waves one from source at $x = \xi$ and one from its image at $x = -\xi$.

Semi-infinite Beam

Consider a semi-infinite beam in flexure, free at end $x = 0$, is acted upon by a point force F_0 at $x = 0$. The complex form of the transverse displacement $u(x)$ is given by:

$$\hat{u} = -(1-i) \frac{F_0}{2EIk^3} \left[e^{ikx} + e^{-kx} \right]$$

One can show that the complex VSI is given by:

$$\hat{I} = \frac{\omega F_0^2}{EIk^3} \left[1 + i\sqrt{2}\, e^{-kx} \sin \left(kx - \frac{\pi}{4} \right) \right]$$

where

$$k^4 = \frac{EI}{\rho A}$$

then $\bar{I} = I_a = \omega F_0^2 / EIk^3$ is the active intensity and is a constant. The reactive intensity:

$$I_r = \frac{\omega F_0^2}{EIk^3} \sqrt{2}\, e^{-kx} \sin \left(kx - \frac{\pi}{4} \right)$$

is due to the near-field effect of the force boundary conditions at the end $x = 0$ and inertia terms.

Infinite Beam

Consider an infinite elastic beam in flexure acted upon by a point force at $x = 0$. The transverse displacement $u(x)$ is given by:

$$\hat{u}(x) = -\frac{F_0}{4EIk^3} \left[i\, e^{-ikx} + e^{-kx} \right] \quad x > 0$$

The time averaged VSI is given by:

$$\bar{I} = I_a = \frac{\omega F_0^2}{16EIk^3}$$

Finite Beam with Complex Absorbent Termination

Consider a finite beam of length L with a free end at $x = 0$, is terminated by a complex impedance termination such that the reflection coefficient $R = |R| \exp(i\theta)$. The response to a point force F_0 at $x = 0$ results in the transverse displacement field:

$$\hat{u} = \frac{iF_0[R \exp\,(2ikL) \exp\,(-ikx) + \exp\,(ikx) + (1 + R \exp\,(2ikL)) \exp\,(-kx)]}{EIk^3[(1-i) - (1+i)R \exp\,(2ikL)]}$$

The complex VSI is then given by:

$$\hat{I} = \frac{\omega F_0^2}{Elk^3} \times \left\{ \frac{1 - |R|^2 + i \exp\,(-kx) \left[\left(1 + |R|^2 \right) (\sin(kx) - \cos(kx)) - |R| \cos(\theta + k(2L - x)) + \sin(\theta + k(2L - x)) \right]}{1 + |R|^2 + 2|R| \sin(\theta + 2kL)} \right\}$$

Thus, the net power flow, i.e. active intensity is:

$$I_a = \bar{I} = \frac{\omega F_0^2}{Elk^3} \frac{1 - |R|^2}{1 + |R|^2 + 2|R| \sin\,(\theta + 2kL)}$$

The reactive intensity, the imaginary part of $\hat{I}$, is due primarily to inertial terms and the nearfield effects of the boundary conditions. Note that if the termination has a perfect reflection coefficient, i.e., $R = \pm 1$, then the vibration field represents a standing wave and hence $I_a = 0$. Also note that if $R = 0$, there is no reflection representing a totally absorbent end, the beam behaves as if it is a semi-infinite beam.

Infinite Plate

Consider an infinite thin elastic plate acted upon by a point force F_0 at the center. The axisymmetric displacement field $w(r)$ is given by (Hayek):

$$\hat{w}(r) = -\frac{F_0}{8Dk^2}\left[iH_0^{(1)}(kr) - \frac{2}{\pi}K_0(kr)\right]$$

where H and K are the Hankel and modified Bessel functions, respectively. The farfield radial component of the active VSI vector is (Piaud and Nicholas):

$$\left(\hat{I}_a\right)_{\text{radial}} = \frac{\omega F_0^2}{32\pi Dk^2 r}$$

The other component of the active VSI vector, i.e., the tangential component vanishes due to the symmetry of the point force.

Nomenclature

B, B'	bending stiffness
e	energy density
E	Young's modulus
F_0	point force
G	shear modulus
I_a	active intensity
I_r	reactive intensity
$\mathbf{I}(x, y, z, t)$	instantaneous intensity
K	shear correction factor
$\mathbf{t}$	stress traction vector
T	kinetic energy density
$\mathbf{u}$	displacement vector
U	potential energy density
V	volume
v	Poisson's ratio
ρ	density
$\boldsymbol{\sigma}$	stress dyadic

See also: **Beams**; **Plates**; **Shells**.

Further Reading

Doi K, Hayek SI (1994) Active control of structural intensity in thin plate. *Proceedings of the Second International Conference on Motion and Vibration Control*, 30 August–3 September Yokohama, Japan: 371–376.

Hayek SI (2000) *Advanced Mathematical Methods in Science and Engineering*. New York: Marcel Dekker.

Hayek SI, Nam M, Sommerfeldt SD (1995) Power flow in a plate with an attached point damper. *Proceedings of Internoise '95*, 10–12 July, Newport Beach, CA: 615–620.

Hayek SI, Perchersky MJ, Suen BC (1990) Measurement and analysis of near and far field structural intensity by scanning laser vibrometry. *Proceedings of the Third International Congress on Intensity Techniques*, 27–29 August, Senlis, France: 281–288.

Heckl M (1990) Waves, intensities, and powers in structures? *Proceedings of the Third International Congress on Intensity Techniques*, 27–29 August, Senlis, France: 13–20.

Nam M, Hayek SI, Sommerfeldt SD (1995) Active control of structural intensity in connected structures. *Proceedings of Active '95*, 6–8 July, Newport Beach, CA: 209–220.

Noiseux DU (1969) Measurement of power flow in uniform beams and plates. *Journal of the Acoustical Society of America* 47: 238–247.

Pavic G (1976) Measurement of structure-borne wave intensity, Part I: formulation of method. *Journal of Sound and Vibration* 49(2): 221–230.

Piaud JB, Nicholas J. (1986) Relationship between vibrational and acoustic intensity for an infinite plate. *Journal of the Acoustical Society of America* 80(4): 1114–1121.

Romano, AJ, Abraham PB, Williams EG (1990) A Poynting vector formulation for thin shells and plates, and its applications to structural intensity analysis and source localization. Part I theory. *Journal of the Acoustical Society of America* 87(3): 1166–1175.

Schwenk AE, Sommerfeldt SD, Hayek SI (1994) Adaptive control of structural intensity associated with bending waves in a beam. *Journal of the Acoustical Society of America* 96(5): 2826–2835.

Zhang Y, Mann JA (1996) Measuring the structural intensity and force distribution in plates. *Journal of the Acoustical Society of America* 99(1): 345–353.

VIBRATION ISOLATION THEORY

E Rivin, Wayne State University, Detroit, MI, USA

Copyright © 2001 Academic Press

doi:10.1006/rwvb.2001.0179

Vibration isolation is one of the vibration control techniques where the source of vibration excitation and the object to be protected are separated by an auxiliary system comprising special devices called vibration isolators or vibration isolating mounts.

The effect of vibration isolation amounts to weakening of dynamic coupling between the source and the object thus reducing transmission of unwanted vibration excitation to the object. The weakening of the dynamic coupling may also cause effects such as: increasing static displacements between the source and the object, increasing low-frequency and transient relative displacements between the source and the object, and increases of size, weight, and cost of the installation. Thus, in many cases a multiparameter optimization is required to provide an acceptable vibration reduction effect while satisfying other constraints.

Vibration isolation is, probably, the most widely-used approach for vibration protection, the other ones being design approaches such as reduction of vibration excitation at the source, changes of masses and/or stiffnesses of the structural components, use of dynamic vibration absorbers, etc.

Vibration isolation devices have to comply with many constraints. Examples include: a need to install highly vibration-sensitive equipment in light and low-stiffness structures; exposure of elastomeric passive vibration control elements or electronic active vibration control elements to high temperatures (e.g., in engine compartments of vehicles); and space restrictions on vibration control devices. With few exceptions, commercially-available passive vibration isolation devices have not changed much during the last 30–50 years. The new developments, such as hydromounts, active mounts, etc., are not as reliable and are much more expensive then the passive mounts, and they are used where their unique performance characteristics justify living with their shortcomings. Their shortcomings are often overlooked and their advantages are often overhyped by clever promotion and they are often used in systems where less expensive, more reliable, and more compact passive isolators could be used, provided that they are properly selected.

Vibration isolation is a very broad area, including isolation of stationary equipment and measuring instruments, both vibration-sensitive and vibration-producing; isolation of vibration-and shock-sensitive electronic boards; isolation of engines and other parts of surface, underwater, and flying vehicles.

The 'classic' principles of vibration isolation described in textbooks and handbooks are often not applicable to real-life circumstances because of the dynamic complexity of the isolated objects, supporting structures, excitations, and vibration isolators. Detailed dynamic analysis/modeling of each practical case using available software packages would result in huge expense in both time and money. Even more importantly, the modeling is often impossible because the input data on structures and excitations are not available with the required accuracy. However, an in-depth understanding of typical groups of vibration isolation problems allows us to formulate general approaches to typical cases of vibration isolation which result in near-optimal performance without the need for complex individual studies. This article addresses the characteristics of basic real-life vibration isolation systems.

Dynamic Properties of Vibration Isolation Systems

A vibration isolation system comprises three subsystems: the object being isolated, the supporting surface (floor, foundation), and the vibration isolators (mounts) placed between them. Depending on circumstances, the object must be protected from the objectionable vibratory motions of the supporting surface, or the supporting surface must be protected from the dynamic loads generated within the object. In some cases both tasks have to be addressed simultaneously. Each of the three subsystems represents a distributed dynamic system with an infinite number of degrees-of-freedom, which have to be considered at high frequencies. However, in many practical cases, the effectiveness of vibration isolation is especially critical in the low frequency range, about 5–100 Hz. Since only the lowest structural modes of the object and of the supporting structure are positioned in this frequency range, the higher modes can be neglected and both the object and the supporting structure can be considered as ideal rigid bodies.

Usually the mass of the flexible element of each isolator is a small fraction of the mass of the object being isolated, so it can be neglected at low frequencies and the isolator can be considered as a massless spring. At higher frequencies, wave resonances in the flexible element have to be considered (see below).

A correct design of the vibration isolation system results in its effective performance (adequate isolation) with maximum stiffness of the isolators, i.e., maximum stability of the system.

Inertia and Geometric Properties of Typical Isolated Objects

Inertia and geometric properties of the isolated object (mass, moments/radii of inertia, position of the center of mass/gravity (CG), directions of principal axes of inertia) significantly influence the dynamic characteristics of the vibration isolation system. Determining these parameters for a real-life object such as a heavy machine or an engine requires a substantial

experimental and/or analytical effort, which can be justified only in special cases. However, typical objects such as machines, engines, etc. demonstrate some generic trends related to their inertia and geometric properties.

Often, the natural coordinate frame is that in which the axis Z is vertical and the axes X, Y are in a horizontal plane. For example, rotational axes of rotors in rotary machines are either vertical (centrifuges, separators, machine tools with vertical spindles, etc.) or horizontal (fans, compressors, turbines, lathes, machining centers with horizontal spindles, etc.). Similarly located are massive reciprocating parts (rams of forging hammers, tables and carriages of machine tools and coordinate measuring machines (CMMs), etc.). In vibration-producing machines dynamic loads are vertical (crank presses, etc.) or horizontal (cold headers, reversing tables and gantries of surface grinders and CMMs, etc.). Vibration-sensitive machines usually have their maximum sensitivity axes in a horizontal plane, while the maximum amplitudes of floor vibration are usually in the vertical direction.

Even if there are no axes of symmetry, the principal axes of inertia are quasiparallel to the structural axes. Usually, the principal axes of inertia deviate from the axes of the natural coordinate frame by not more than 8°–10°. For a planar system, the centrifugal moment of inertia ('product of inertia') in the coordinate frame X', Y' inclined at angle α to the principal coordinate frame X, Y is $I_{x'y'} = \frac{1}{2}(I_x - I_y)\sin 2\alpha$. For $\alpha = 10^\circ$, $\sin 2\alpha = 0.34$. Thus, in the worst case when the magnitude of one of the principal moments of inertia I_x, I_y is significantly larger that the other, $I_{x'y'}$ is less than 0.17 of the larger principal moment of inertia. Often, magnitudes of the principal moments of inertia are relatively close to each other, thus magnitudes of the products of inertia are even less significant. In the first approximation, for the machine-like objects whose design axes are close to axes X, Y, Z of the natural coordinate frames, the centrifugal moments (products) of inertia are $I_{xy} \approx I_{xz} \approx I_{yz} \approx 0$.

There are some general trends related to mass distribution in typical machine-like structures, which are similar to a tri-axial ellipsoid. The radii of inertia for a tri-axial ellipsoid are $\rho_i = \sqrt{\left[\frac{1}{20}\left(H_j^2 + H_k^2\right)\right]}$, where H are diameters of the ellipsoid, and i, j, k are cyclically assigned meanings of x, y, z designating the directions of the axes. The radii of inertia of a machine or a machine-like unit can thus be calculated with errors not exceeding 10–15% if H designates the overall sizes of the unit in the respective directions.

Basic Characteristics of Elastic Mounts (Vibration Isolators)

The elastic mount (isolator) is a volumetric elastic (flexible) component having two terminals or surfaces for connecting with the isolated object and with the supporting surface. Unless special restraints are employed, the flexible element develops resistance to motion between the terminals in all translational and angular directions. In the low frequency range, usually of the greatest importance for vibration isolation, the flexible element can be considered as massless. Vibration transmissibility at high frequencies can be significantly affected by wave resonances in the body of the flexible element (see below) and the mass of the flexible element has to be considered.

The flexible elements develop resistance to motion (forces) between the terminals. This resistance is dependent on the magnitude and direction of the relative displacement between the terminals as characterized by the stiffness parameters, and on the magnitude and direction of their relative velocity, as characterized by the damping parameters. In cases when the flexible elements are represented by metal (usually, steel) springs, their damping is negligibly low and is frequently enhanced by specially designed dampers.

In a general case, the application of a force to the flexible element results in its deformation in a different direction from the direction of the force. In an arbitrary coordinate frame, whose origin coincides with the elastic center of the flexible element (see below), the elastic properties of a linear flexible element can be described by 36 stiffness constants k_{ij} where the first subscript indicates the direction of the forcing factor (force or moment), and the second subscript indicates the direction of the displacement (linear or angular) caused by this forcing factor. Three 'proper' translation stiffness constants k_{xx}, k_{yy}, k_{zz} describe deformations of the flexible elements in the directions of the coordinate axes from forces acting along the same axes. Six 'cross' translational stiffness constants k_{xy}, k_{xz}, k_{yx}, k_{yz}, k_{zx}, k_{zy} describe the translational deformations of the flexible element in the directions of the coordinate axes from forces acting along other axes; three 'proper' angular stiffness constants $k_{\alpha\alpha}$, $k_{\beta\beta}$, $k_{\gamma\gamma}$ describe the angular deformations of the flexible element about axes X, Y, Z, respectively, caused by the moments about the same axes. Six 'cross' angular stiffness constants, $k_{\alpha\beta}$, $k_{\alpha\gamma}$, $k_{\beta\alpha}$, $k_{\beta\gamma}$, $k_{\gamma\alpha}$, $k_{\gamma\beta}$, describe the angular deformations about one axis caused by moments about another axis. Another 18 'cross' stiffness coefficients represent translational–angular interactions, e.g., $k_{x\alpha}$, $k_{\alpha x}$, $k_{y\gamma}$, $k_{\gamma y}$, etc. The

stiffness constants have reciprocity properties; $k_{xy} = k_{yx}$; $k_{xz} = k_{zx}$; ... $k_{\alpha\beta} = k_{\beta\alpha}$; $k_{\alpha\gamma} = k_{\gamma\alpha}$...; etc. Directions of the deformation and of the forcing factor causing this deformation coincide only when the force or the moment is directed along (or about) one of the principal elastic axes. Any axis of symmetry is a principal elastic axis. The principal elastic axes are orthogonal to each other and intersect in the elastic center of the flexible element which defines the position of the element in the mathematical model of the system. This position is used in the equations of motion for the system. In a coordinate frame having its origin at the elastic center, translational/rotational cross stiffness constants vanish. In the principal coordinate frame of the flexible element all 'cross' stiffness constants vanish, $k_{ij} = 0$.

The overwhelming majority of the real-life vibration isolators have flexible elements with at least one axis of symmetry or one, more frequently two or more, planes of symmetry. Their dimensions are usually much smaller than the dimensions of the isolated object and/or distances between the isolators. Because of this, assuming that the elastic center of the flexible element is located in its geometrical or mass center is an acceptable approximation.

The angular stiffness of the isolation system is an important parameter. When all isolators are located in one (e.g., horizontal) plane, the angular stiffness of the installation about a horizontal axis is determined by the vertical stiffness of the isolators combined with distances between them, and by angular stiffness constants of the isolators. For a beam on two isolators with vertical, angular stiffnesses k_{z_1}, k_{z_2}, k_{α_1}, k_{α_2}, respectively, and distances between the CG and isolators a_1, a_2, respectively, the total angular stiffness is $k_\alpha^1 = (k_{\alpha_1} + k_{\alpha_2}) + (k_{z_1}a_1^2 + k_{z_2}a_2^2)$. Unless a high angular stiffness is specially designed into the isolator, the first bracket is usually negligible in comparison with the second bracket for the overwhelming majority of practical vibration isolation systems.

Usually, it is assumed that the damping constants of isolators are proportional to their stiffness constants. While it is very convenient analytically, it is not correct. First, this statement can be used only if the isolators have viscous (linear) damping. The overwhelming majority of isolators have elastomeric, wire-mesh, and other elements with nonlinear damping characteristics (e.g., dependent on vibration amplitude which is different for different isolators under the same object and for different directions for the same isolator). Also, their damping constants in various directions can vary in totally different ways from stiffness.

Elastically Supported Solid Object; Dynamic Coupling

In the general case the object is supported by an arbitrary number of arbitrarily located elastic mounts, characterized by all proper and cross-stiffness coefficients and by the corresponding damping coefficients. The system is excited by multiple forcing factors whose set can be resolved into three force components F_x, F_y, F_z, and three moment components M_x, M_y, M_z, as well as by the foundation motion acting on elastic mounts (translational motion components x_f, y_f, z_f and angular motion components α_f, β_f, γ_f). Six equations of motion can be written considering these parameters, which fully describe this six-degrees-of-freedom system. These equations show that all coordinates are dynamically coupled, or that any coordinate component of the external force or moment, as well as any coordinate component of translational or angular motion of the foundation is causing displacements of the object in all coordinate directions. Also, any coordinate component of translational or angular motion of the installed object is causing forces/moments to and displacements of the foundation in all coordinate directions. Such global coupling is not desirable, neither for performance in many important cases, nor for computational synthesis/optimization of the system.

In some cases of vibration isolation, it is required that the highest natural frequency should be below the range of frequencies of the objectionable external excitations, regardless of their directions. If there is a strong coupling between all six natural vibratory modes of the isolation system, it leads to a need to shift all natural frequencies down, thus using very low stiffness isolators and potentially causing instability of the system. This is true for both vibration sensitive objects and for vibration-producing objects. The computational analysis of such globally cross-coupled system becomes very complex and involved, partly due to the fact that the spectral characteristics of all excitations have to be identified and entered into the model.

One of the most effective ways of improving the performance of a vibration isolation system is by eliminating or, at least, reducing the dynamic intermodal coupling in the system. This simplifies computing the natural frequencies of the system and makes the influences of various design parameters on the natural frequencies and modes more transparent. Also, it makes possible or, at least, simplifies bringing natural frequencies closer together (by some reduction of higher frequencies and some increase of lower frequencies) without a significant reduction of isolator stiffness constants. Finally, it may improve

the performance when the coupling between specific vibratory modes is undesirable.

Means for alleviation/elimination of intramodal coupling can be devised by analyzing the equations of motion. While the general equations are written for the natural coordinate frame, but with arbitrary attitudes of the isolators, with the exception of a special case of inclined mounts below, the isolators, usually having planes of symmetry, are placed in such a way that their principal axes are parallel to the natural coordinate axes. Also, angular stiffnesses of isolators as well as the products of inertia can usually be neglected. For vibration isolating installation of stationary machinery (as well as for many units of mobile machinery) all isolators (mounts) are situated in one horizontal plane, or:

$$a_{z_i} = \text{const} \qquad [1]$$

If, in addition:

$$\sum_i k_{z_i} a_{x_i} = 0, \ \sum_i k_{z_i} a_{y_i} = 0 \qquad [2]$$

then vertical (z) vibration of the system is not coupled with motions in other translational or rotational coordinates. If also:

$$\sum_i k_{x_i} a_{y_i} = 0, \ \sum_i k_{y_i} a_{x_i} = 0 \qquad [3]$$

then vibrations along and about axis Z (coordinates z and γ) are uncoupled. These conditions are satisfied if the ratios of $\eta_x = k_x/k_z$, $\eta_y = k_y/k_z$ are constant for all isolators. If also:

$$\sum_i k_{z_i} a_{x_i} a_{y_i} = 0 \qquad [4]$$

then the system of equations of motion is separated into two independent equations corresponding to coordinates z and γ, and two pairs of coupled equations in the $x - z$ plane ($x - \beta$), and in the $y - z$ plane ($y - \alpha$). The last condition is satisfied if the object has at least one plane of symmetry. A further reduction of coupling is achieved if the plane of location of the isolators contains the CG or:

$$a_{z_i} = 0 \qquad [5]$$

In this case, vibratory motions along all coordinates are independent (uncoupled). The last condition can be realized if the object is isolated not directly but is attached to a massive 'inertia block' allowing the CG position to shift. The inertia block can be then placed on isolators at the new CG level. In some cases, the isolators can be supported by special brackets at the CG level even without the inertia block. The same effect can be achieved by using inclined isolators in the $x - z$ and/or $y - z$ planes (see below). Coordinates x and/or y can also be uncoupled if the angular stiffness values of the isolators in the α and/or β directions, neglected before, are made very high, e.g., by using guideways in these directions; in this case angular vibrations are simply prevented from developing.

The most interesting are vibratory motions within the plane of symmetry, comprising coupled vibratory motions in two linear and one angular coordinates. A study of such a system ($x - z - \beta$) concluded that natural frequencies of a planar vibration isolation system are only weakly dependent on compliance with eqn [2]. They are largely determined by the value of η_x. When the decoupling condition (eqn [2]) is satisfied, the excitation force in the x-direction excites the rocking (horizontal–angular) vibration with resonances at natural frequencies $f_{x\beta}$ and $f_{\beta x}$ but does not excite vibration in the z-direction. When eqn [2] is not satisfied, the third resonance of the rocking vibration appears at the frequency f_z (vertical natural frequency) and intensive vertical (z) vibration of the object develops. With two mounts 1 and 2, amplitude of this vibration at $k_{z1}a_{x1}/k_{z2}a_{x2} = 1.2$ is $0.35/6.7 \approx 0.05$ of the maximum resonance amplitude of the rocking vibration; at $k_{z1}a_{x1}/k_{z2}a_{x2} = 1.7$ it is $0.95/8 \approx 0.12$ of the maximum rocking amplitude; and at $k_{z1}a_{x1}/k_{z2}a_{x2} = 2.5$ it is $1.6/6.5 \approx 0.25$ (it is assumed that $k_{x1}/k_{x2} = k_{z1}/k_{z2} = k_1/k_2$). The results are analogous in cases when the excitation force or motion is vertical. Such coupling, where the excitation in one direction causes a significant response in the perpendicular direction is undesirable in many cases of vibration isolation. Often, precision equipment units are two-to-three times more sensitive to horizontal than to vertical floor vibrations, whereas the vertical vibration amplitudes are 1.5–2 times greater than horizontal. Conservatively, the resonance amplitude of horizontal vibrations of the unit due to vertical excitation should not exceed $1/(2)(3) \approx 0.16$ of the resonant amplitude of vertical vibrations. This implies a maximum permissible asymmetry factor $k_{z1}a_{x1}/k_{z2}a_{x2} \leq 2.0$.

The natural frequencies of the coupled rocking vibrations in relation to the vertical natural frequency f_z (see eqn [10] below) are:

$$\frac{f_{x\beta}}{f_z}, \frac{f_{x\beta}}{f_z} = \frac{1}{\sqrt{2}}\sqrt{\left(\frac{\sum k_x}{\sum k_z}\left(1+\frac{a_z^2}{\rho_y^2}\right)+\frac{a_x^2}{\rho_y^2}\right) \mp \sqrt{\left(\left[\frac{\sum k_x}{\sum k_z}\left(1+\frac{a_z^2}{\rho_y^2}\right)+\frac{a_x^2}{\rho_y^2}\right]^2 - 4\frac{\sum k_x}{\sum k_z}\frac{a_x^2}{\rho_y^2}\right)}} \quad [6]$$

where $\rho_y = \sqrt{(I_y/m)}$ is the radius of inertia of the object about the y-axis, and a_z is the distance from the CG to the plane of the isolator locations.

Considering general trends of mass distribution and magnitudes of $a_{x,y}/a_z$ in typical machines, the following simplified formula provides the lower natural frequencies of rocking vibrations in two vertical coordinate planes within 5–10% for variation of parameters in the ranges $0.25 \le \eta \le 4$ and $0 \le a_{z,y}/a_z \le 1$:

$$f_{x\beta}, f_{y\alpha} \cong f_z\sqrt{\left(0.9/\left[\eta_{x,y} + \left(a_{x,y}/a_z\right)^2\right]\right)} \quad [7]$$

This expression does not contain the radii of inertia $\rho_{x,y}$ of the object. It allows us to quickly calculate the required stiffness ratio of the vibration isolators for a given installation if the required natural frequencies are specified. A similar expression can be written for $f_{y\alpha}$.

The natural frequency of the torsional vibration about the vertical axis is:

$$f_\gamma = \frac{1}{2\pi}\sqrt{\left(\frac{k_\gamma}{I_z}\right)} \approx \frac{1}{2\pi}\sqrt{\left(\frac{k_r(a^2+b^2)}{M\frac{1}{5}(a^2+b^2)}\right)} = \frac{1}{2\pi}\sqrt{\left(\frac{4k_z}{\eta}\frac{5}{M}\right)} = f_z\sqrt{\left(\frac{5}{\eta}\right)} \quad [8]$$

The most natural way to comply with eqn [2] is to find the object weight W distribution between the mounting points and to use isolators whose stiffness constants k_{z_i} are proportional to the fraction W_i of the total weight acting on the corresponding ith mounting point:

$$k_{z_i} = AR_i,\ A = \text{const} \quad [9]$$

If each k_{z_i} in eqn [2] is replaced by W_i, it becomes an identity since distances a_x, a_y are measured from the CG. This condition can be satisfied either by constant stiffness isolators; or, by so-called 'constant natural frequency' (CNF) isolators, whose axial (vertical) stiffness in the rated load range is proportional to the axial (weight) load on the isolator.

If constant stiffness isolators are used, the total vertical (z direction) stiffness Σk_{z_i} of all isolators is determined by the desired natural frequency in the z direction:

$$f_z \approx \frac{1}{2\pi}\sqrt{\frac{\sum k_{z_i}}{M}} \quad [10]$$

For selecting individual isolators, the weight distribution between the mounting points should be known and then isolators having stiffness constants proportional to the weight loads at the mounting points should be used. The position of the CG in the horizontal plane can be determined experimentally or by a calculation using detailed design drawings. Usually, the CG position is determined by an 'expert judgment' by the user, with at least $\pm 10-15\%$ error. For objects having heavy moving parts (tables, gantries, etc.) or changeable components, the position of the CG, can shift in addition to the above error. The weight distribution (vertical reactions at the mounting points) with known CG position can be uniquely calculated only for a statically determined case (three-point 'kinematic mounting'). The weight distribution in statically indeterminate cases requires additional conditions to be known or assumed. For the assumption that the mounting surfaces of both the object and the base/floor/foundation are rigid (or, at least, much more rigid than the isolators) and flat, and the floor surface horizontal, in the first approximation all reactions are identical. Unevenness (deviations from flatness) of the mounting surfaces, not negligible in comparison with the average mount deformation, or reduced stiffness of at least one mounting surface in at least one area lead to uneven deformations of the mounts, and to changing load distribution. Conservatively, variation of weight distribution between the mounting points can be at least $\pm 35\%$. Commercial vibration isolators cannot be selected in accordance with the established/assumed weight distribution since they have a ratio of the stiffness constant between the adjacent mounts in the line of about 1.6 (on average). Hardness of rubber in elastomeric isolators varies within ± 5 Durometer units ($\pm 17\%$ stiffness variation).

With all these uncertainties, the scatter of stiffness-to-weight ratios of the isolators selected in accordance with the calculated/assumed weight distribution is $\pm 1.15 \times 1.35 \times 1.6 \times 1.17 = \pm 2.9$ times, which is equivalent to asymmetry factor $k_{z1}a_z a_{x1}/k_{z2}a_{x2} = 2.9 \gg 2$, see above. It results in excessive intramodal coupling.

CNF vibration isolators have a special nonlinear load–deflection characteristic so that their stiffness values in all directions are proportional to the load in the direction of its main axis (weight load). In the commercially realized CNF vibration isolators, deviation from this proportionality does not usually exceed $\pm 10-15\%$. It has been shown that the tolerance on the rubber hardness does not influence noticeably the CNF characteristic. Thus, the use of CNF isolators satisfies the decoupling condition (eqn [2]) with the scatter not exceeding $\pm 1.1-1.15$ times. This provides an adequate decoupling. The nonlinear load–deflection characteristic of CNF vibration isolators may create undesirable nonlinear vibratory effects such as excitation of sub- or superharmonic vibration, but such effects are not significant due to relatively low vibration amplitudes in typical vibration isolation systems, especially when damping in the isolators is not very low.

Vibration Isolation System with Inclined Mounts

The complete decoupling between horizontal and angular (about perpendicular horizontal axis) vibrations can be desirable to create conditions for independent variation of the corresponding natural frequencies in order to make them closer to each other, etc. Such a decoupling in a system having one plane of symmetry can be achieved by placing the vibration isolators in the horizontal plane passing through the CG, but such design is not always easy to realize. Another approach is by using vibration isolators with inclined principal stiffness axes ('inclined mounts'). **Figure 1** shows such system in the $x-z$ plane; a similar arrangement can be also realized in the $y-z$ plane. The origin of the coordinate frame coincides with the 'stiffness center' (a force passing through this point causes a purely translational displacement of the installed object, without angular displacements). The moment about the stiffness center causes a pure rotational motion, without any translational displacement. The principal elastic axes of the isolators p, r are inclined relative to the coordinate axes; stiffness coefficients of the isolators in directions p, r are k_p, k_r, respectively.

Decoupling of the coupled rocking (horizontal–angular) vibratory modes can be achieved by selection of the inclination angle of isolators at which the elastic center coincides with the CG. Then the resultant of the elastic reactions, acting on the object from the isolators when the object is displaced in the x-direction, is passing through the CG. Also, the resultant of the elastic reactions at a rotation of the object is a moment about the CG. The decoupling condition is $\varepsilon = 0$ or:

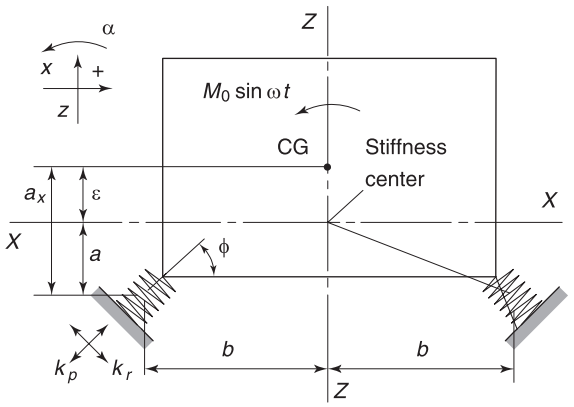


Figure 1 Vibration isolation system with inclined mounts.

$$\frac{k_r}{k_p} = \frac{(a_x/a_z) + \cot \varphi}{(a_x/a_z) - \tan \varphi} \qquad [11]$$

When this is satisfied, the natural frequency of the translational vibration is $\omega_{x\beta} = \omega_x$, and the natural frequency of angular vibration is:

$$\omega_{\beta x} = \omega_x \lambda_1 = \omega_\beta = \frac{a_x}{\rho_y} \sqrt{\left(\frac{4k_z}{m} \frac{1}{\cos^2 \varphi + (k_r/k_p) \sin^2 \varphi} \right)} \qquad [12]$$

A disadvantage of using inclined vibration isolators is the need for individual selection of the required inclination angle for each object, unless it is done for a mass produced object, e.g., for a car engine. Also, such 'geometric' decoupling does not provide for the complete decoupling if the mass distribution within the object may vary, e.g. due to the presence of moving components or the changing weight of the workpiece for machine tools. If the vibration is excited by stopping/reversal of a moving heavy mass, the complete decoupling would be realized only if the resultant of the dynamic forces passes through the CG. Otherwise, the dynamic exertion can be presented as a combination of a force passing through the CG and a moment, thus causing simultaneous translational and angular vibrations ('coupling by excitation forces').

Dynamics of Single-degree-of-freedom Vibration Isolation System

The object can be vibration-sensitive and in need of protection from steady and/or transient vibrations

transmitted from some vibration-producing objects via the base. In other cases, the object is a source of steady vibrations or shocks whose transmission to the base/foundation as dynamic or vibratory forces should be prevented or reduced. Some objects are vibration-sensitive during their working process while generating objectionable dynamic loads during their auxiliary motions (e.g., a precision surface grinder with a heavy reciprocating table or an internal combustion engine in a car, which produces undesirable dynamic inputs to the occupants but has to be protected from intense vibration transmitted from the road). Thus, transmission of vibratory forces and/or displacements (or accelerations) both from the object to the base and in the opposite direction may be of interest. It depends on correlations between the spectral components of the dynamic inputs to the system and the natural frequencies and natural modes of the vibration isolation system, as well as on the stiffness constants of the isolators, on the effective masses of the object and the base and, last but not least, on the character and magnitudes of damping in the isolators. When the dynamic characteristics of the subsystems have to be considered in more detail, e.g. when wave resonances in the isolators as well as several natural modes of the object/base have to be considered, the subsystems cease to be 'lumped parameters' and can be characterized by their impedances.

A single-degree-of-freedom (SDOF), uni-axial vibration isolation system is a convenient model to clarify the basic dynamic effects of vibration isolation installations. This system comprises: object to be isolated (mass m); flexible connectors (vibration isolator); base/foundation, mass m_f. Usually, $m_f \gg m$, or at least $m_f > m$. The vibration isolator can deform only in one direction. Five typical modifications of the dynamic model are shown in **Figure 2**. In **Figure 2A** the isolator is represented by a parallel connection of an elastic element (stiffness k) and a viscous damper whose resistance F_v to the relative motion x between its terminals is proportional to the relative velocity, $F_v = c(\dot{x}_1 - \dot{x}_2)$, where c is the damping coefficient. A pure viscous damper is a convenient idealization for analytical purposes but in most cases not a realistic element. The isolator in **Figure 2B** combines elastic properties (stiffness k) and energy dissipation properties of a hysteretic type (material damping), whereas the relative energy dissipation ψ (and logarithmic decrement δ) does not depend on the vibration frequency ω. Such hysteretic damping can be represented by a linear (viscous) damper with a variable damping coefficient, $c_h = c(\omega) = \psi/2\pi\omega$. Hysteretic damping is characteristic for elastomers (rubbers), wire mesh, etc.

Figures 2C and D show two embodiments of so-called 'relaxation' suspension: a parallel connection of elastic element k and viscous damper c in series with another elastic element $k_1 = Nk$, **Figure 2C**; a series connection of a damped isolator $k' - c'$ and an undamped isolator $k'' = Nk'$, **Figure 2D**. In **Figure 2E** the isolator is split into two elements with stiffness values k_1 and k_2 and an intermediate mass is placed between them (see below).

In applications with large vibration amplitudes (e.g., vehicle suspensions) isolators with Coulomb friction dampers are sometimes used.

The isolation systems shown in **Figure 2** can be characterized by absolute and relative transmissibilities. The absolute transmissibility is the degree of reduction of the dynamic force or vibratory motion provided by the isolation system. For dynamic force generated inside the object, transmissibility μ_F is a ratio of the force amplitude F_f transmitted to the foundation to the amplitude F of the excitation force. For vibratory motion of the foundation, transmissibility μ_x is the ratio of the vibration amplitude of the

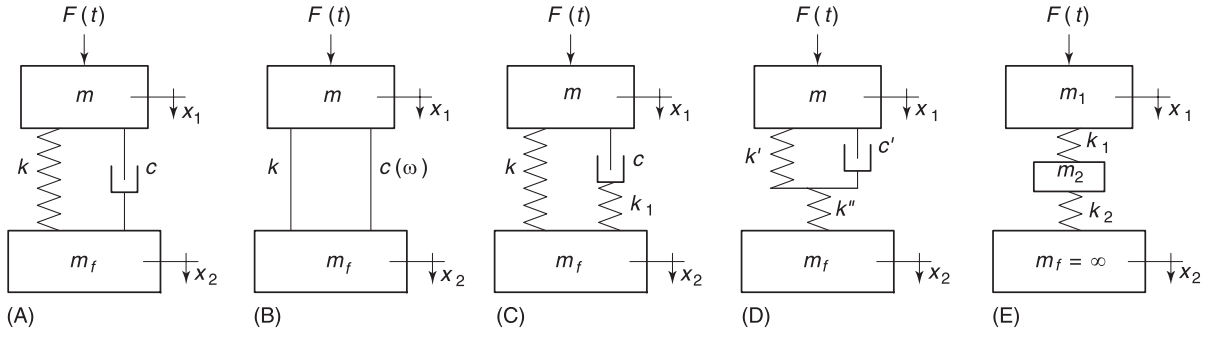


Figure 2 Typical models of general uni-axial vibration isolation system; (A) isolator with linear stiffness k and viscous damper c; (B) isolator combining stiffness k and hysteretic damping; (C,D) 'relaxation' isolators; (E) isolator with intermediate mass.

object x_1 of the foundation x_2. The relative transmissibility μ_{rel} is the ratio of the amplitude of the vibration between the object and the foundation $x_1 - x_2$ (i.e., amplitude of deformation of the flexible element) to x_2.

Isolator with Viscous Damping (Figure 2A)

For **Figure 2A**, the absolute force transmissibility coefficient is:

$$\mu_F = \frac{|F_f|}{|F|} = \frac{m_f}{m+m_f}\sqrt{\left(\frac{1+\left(2\zeta\frac{\omega}{\omega_n}\right)^2}{\left(1-\frac{\omega^2}{\omega_n^2}\right)^2+\left(2\zeta\frac{\omega}{\omega_n}\right)^2}\right)} = \frac{m_f}{m+m_f}\sqrt{\left(\frac{1+\left(\frac{\delta}{\pi}\frac{\omega}{\omega_n}\right)^2}{\left(1-\frac{\omega^2}{\omega_n^2}\right)^2+\left(\frac{\delta}{\pi}\frac{\omega}{\omega_n}\right)^2}\right)} \quad [13]$$

The absolute displacement transmissibility for 'kinematic excitation' from the foundation is:

$$\mu_x = \frac{|x_1|}{|x_2|} = \sqrt{\left(\frac{1+\left(2\zeta\frac{\omega}{\omega_n}\right)^2}{\left(1-\frac{m+m_f}{m_f}\frac{\omega^2}{\omega_n^2}\right)^2+\left(2\zeta\frac{\omega}{\omega_n}\right)^2}\right)} = \sqrt{\left(\frac{1+\left(\frac{\delta}{\pi}\frac{\omega}{\omega_n}\right)^2}{\left(1-\frac{m+m_f}{m_f}\frac{\omega^2}{\omega_n^2}\right)^2+\left(\frac{\delta}{\pi}\frac{\omega}{\omega_n}\right)^2}\right)} \quad [14]$$

Here:

$$\omega_n = \sqrt{\left(\frac{k'(m+m_f)}{mm_f}\right)}$$

is the angular natural frequency, $\zeta = c/c_{cr}$:

$$\delta = \frac{2\pi(c/c_{cr})}{\sqrt{\left[1-(c/c_{cr})^2\right]}} \approx \frac{\pi c}{\omega_n\left[mm_f/(m+m_f)\right]} \quad [15]$$

is the log decrement; $\mu_F = \mu_x = \mu$ only for an infinitely large foundation ($m_f = \infty$).

The relative transmissibility is:

$$\mu_{rel} = \frac{|x_1 - x_2|}{|x_2|} = \frac{\frac{m+m_f}{m_f}\frac{\omega^2}{\omega_n^2}}{\sqrt{\left(\left(1-\frac{m+m_f}{m}\frac{\omega^2}{\omega_n^2}\right)^2\right)+\left(2\zeta\frac{\omega}{\omega_n}\right)^2}} = \frac{\frac{m+m_f}{m_f}\frac{\omega^2}{\omega_n^2}}{\sqrt{\left(\left(1-\frac{m+m_f}{m}\frac{\omega^2}{\omega_n^2}\right)^2\right)+\left(\frac{\delta}{\pi}\frac{\omega}{\omega_n}\right)}} \quad [16]$$

Figure 3 shows $\mu(\omega/\omega_n)$ at $m_f = \infty$ and at various damping levels. The absolute transmissibility μ_F, $\mu_x < 1$ only at the frequency ratio $\omega/\omega_n > \sqrt{2} \cong 1.4$, or vibration isolation (reduction of vibration transmission) begins only at relatively high frequencies. With increasing damping, transmissibility in the isolation zone deteriorates. However, the relative transmissibility μ_{rel} is always decreasing with increasing damping (**Figure 4**).

Isolator with Internal (Hysteresis) Damping (Figure 2B)

The log decrement δ in systems with an isolator made from rubber, wire-mesh, etc. does not depend on natural frequency as in eqn [15] but usually has milder and more complicated dependence on frequency than in viscous damping systems and, in many cases, depends on vibration amplitude. For many materials frequently used for vibration isolation, such as rubber blends, in the first approximation the frequency and amplitude dependencies of δ can usually be neglected for a narrow frequency range, up to $\sim 50-100$ Hz and small vibration amplitudes. There are many ways of expressing the elastodamping characteristics of such materials. A widely used format of 'complex stiffness' is based on the fact that the deformation of such materials has a phase delay β (rad) relative to the stress causing this deformation. Thus the deformation is comprised of two components: elastic (in phase with the stress) and viscous, lagging stress by 90° ($\pi/2$ rad), or directed along the imaginary axis. In such notation, the total complex stiffness of an element is:

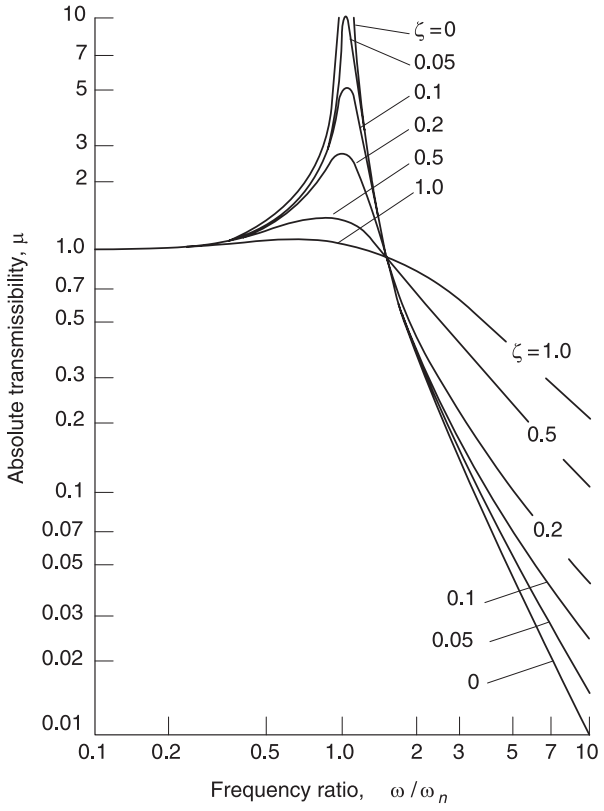


Figure 3 Absolute transmissibility of the system in **Figure 2A** for $m_f = \infty$.

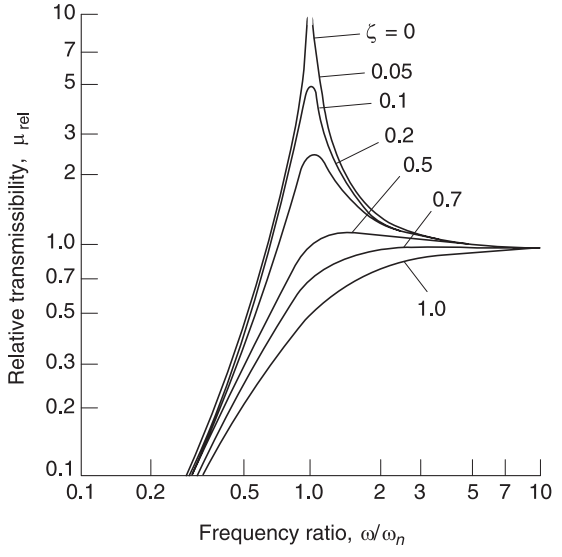


Figure 4 Relative transmissibility of the system in **Figure 2A** for $m_f = \infty$.

$$k = k' + jk'' = k'(1 + j\tan\beta) \qquad [17]$$

Neglecting the amplitude and frequency dependencies of k' and k'':

$$\mu_F = \frac{|F_f|}{|F|} = \frac{m_f}{m + m_f}\sqrt{\left(\frac{1+\tan^2\beta}{\left(1-\dfrac{\omega^2}{\omega_n^2}\right)^2+\tan^2\beta}\right)} = \frac{m_f}{m + m_f}\sqrt{\left(\frac{1+\dfrac{\delta^2}{\pi^2}}{\left(1-\dfrac{\omega^2}{\omega_n^2}\right)^2+\dfrac{\delta^2}{\pi^2}}\right)} \qquad [18]$$

and:

$$\mu_x = \frac{|x_1|}{|x_2|} = \sqrt{\left(\frac{1+\dfrac{\delta^2}{\pi^2}}{\left(1-\dfrac{m+m_f}{m_f}\dfrac{\omega^2}{\omega_n^2}\right)^2+\dfrac{\delta^2}{\pi^2}}\right)} \qquad [19]$$

$$\mu_{rel} = \frac{|x_1 - x_2|}{|x_2|} = \frac{\dfrac{m+m_f}{m_f}\dfrac{\omega^2}{\omega_n^2}}{\sqrt{\left(1-\dfrac{m+m_f}{m}\dfrac{\omega^2}{\omega_n^2}\right)^2+\dfrac{\delta^2}{\pi^2}}} \qquad [20]$$

Due to the absence of frequency-dependent terms in the numerators under the square root sign in eqns [18] and [19], their high frequency transmissibility for systems with damping is significantly reduced, thus improving the vibration isolation without deterioration in the resonance behavior. In real systems the improvement is less pronounced due to the mentioned frequency dependencies of k' and k'', but the improvement is still significant. **Figure 5** shows $\mu_F = \mu_x$ for $m_f = \infty$ and various rubber blends having different values of δ and different stiffness dependencies on the frequency. Plot 1 is for an isolator made from natural rubber without carbon black filler; it has low damping ($\delta = 0.07$) and negligible frequency dependencies below 50 Hz. Plot 2 is for an isolator made from natural rubber with 50 parts by weight of carbon black ($\delta = 0.31$) while plot 2′ is for a 'virtual' isolator with viscous damping and the same damping at the resonance (5 Hz). Plot 3 is for highly damped Thiocol RD rubber ($\delta = 1.55$ at resonance frequency 5 Hz and monotonously increasing with frequency, with three-fold increase between 1 and 50 Hz), while the plot 3′ is for a 'virtual' viscous damping isolator with the same damping at the resonance (5 Hz). In the isolation zone $\omega/\omega_n > 1.4$, the damping increase has

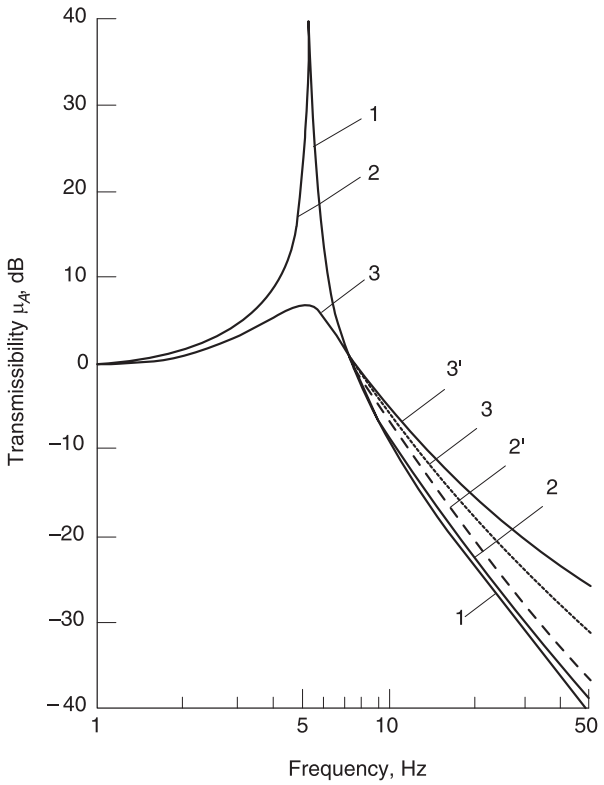


Figure 5 Absolute transmissibility of the system in **Figure 2B** for $m_f = \infty$ and isolator made of various rubber blends considering frequency dependencies of their stiffness and damping. (1) Unfilled natural rubber; (2) natural rubber filled with 50% ppw HAF carbon black; (3) Thiocol RD; (2′) isolator with viscous damping having same μ_{res} as(2); (3′) same for (3).

much less effect of isolation deterioration than in **Figure 3**.

'Relaxation' Isolation Systems with Viscous Damping (Figure 2C and D)

The two systems are equivalent if:

$$k = \left(\frac{N}{N+1}\right)k';\ c = \left(\frac{N}{N+1}\right)^2 c' \qquad [21]$$

The absolute and relative transmissibilities are:

$$\mu_x = \mu_F = \sqrt{\left(\frac{1+4\left(\frac{N+1}{N}\right)^2\zeta^2\frac{\omega^2}{\omega_n^2}}{\left(1-\frac{\omega^2}{\omega_n^2}\right)^2+\frac{4}{N^2}\zeta^2\frac{\omega^2}{\omega_n^2}\left(N+1-\frac{\omega^2}{\omega_n^2}\right)^2}\right)} \qquad [22]$$

$$\mu_{rel} = \sqrt{\left(\frac{\frac{\omega^2}{\omega_n^2}+\frac{4}{N^2}\zeta^2\frac{\omega^6}{\omega_n^6}}{\left(1-\frac{\omega^2}{\omega_n^2}\right)^2+\frac{4}{N^2}\zeta^2\frac{\omega^2}{\omega_n^2}\left(N+1-\frac{\omega^2}{\omega_n^2}\right)^2}\right)} \qquad [23]$$

where $\omega_n = \sqrt{(k/m)}$ is the natural frequency of the system in **Figure 2C** where $c = 0$; $c_{cr} = 2\sqrt{(km)}$; $\zeta = c/c_{cr}$. **Figure 6** compares μ_F, μ_x for a rigidly connected viscous damper (**Figure 2A** or **Figure 2C** at $N = \infty$) and an elastically connected viscous damper (**Figure 2C**) for $\zeta = 0.2$. Transmissibility of the latter at high frequencies (isolation zone) decreases much faster with increasing frequency ω than for the former (at 12 dB per octave vs 6 dB per octave), but at the price of an increased resonance amplification factor. For $c = 0$, the mass m is supported only by the main spring k, and μ_F, μ_x are the same as for the system in **Figure 2A**. When $c = \infty$, the transmissibility function is the same as for the case $c = 0$ but with the natural frequency

$$\omega_n' = \omega_\infty = \sqrt{\left(\frac{k+k_1}{m}\right)} = \omega_n\sqrt{(N+1)} \qquad [24]$$

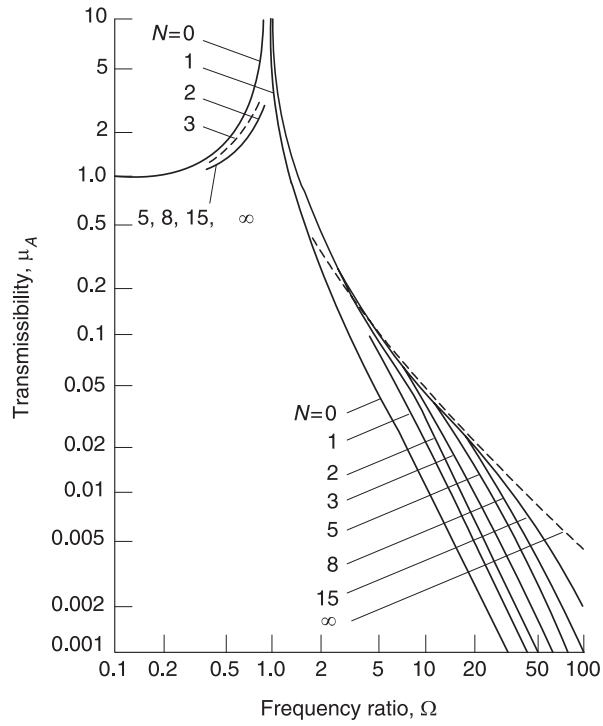


Figure 6 Absolute transmissibilities of uni-axial systems in **Figure 2C** with rigidly ($N = \infty$) and elastically connected viscous damper; $\zeta = 0.2$.

An intermediate value of c, producing the minimum resonance amplification is called the optimum damping. At high excitation frequencies, μ_F, μ_x for any values of c approach μ for $c = \infty$. and the absolute transmissibility at high frequencies is inversely proportional to the excitation frequency.

The transmissibility μ_{res} as a function of ζ and N is plotted in **Figure 7**. For $\zeta <\sim 0.1$, μ_{res} is weakly dependent on N, but at larger ζ, N determines the maximum μ_{res}. The minimum μ_{res} for a given N corresponds to the optimum damping situation. The resonance frequency ratios are different for absolute (abs) and relative (rel) transmissibility:

$$\left(\frac{\omega_{res}}{\omega'_n}\right)_{abs} = \sqrt{\left(\frac{2(N+1)}{N+2}\right)} \qquad [25]$$

$$\left(\frac{\omega_{res}}{\omega'_n}\right)_{rel} = \sqrt{\left(\frac{n+2}{2}\right)} \qquad [26]$$

The optimum (minimum) resonance amplification for both absolute and relative motion is:

$$(\mu_{res})_{opt} = 1 + 2/N \qquad [27]$$

The damping ratios producing the minimum (optimum) μ values expressed by eqn [27] are:

$$(\zeta_{opt})_{abs} = \frac{N}{4(N+1)}\sqrt{(2(N+2))} \qquad [28]$$

$$(\zeta_{opt})_{rel} = \frac{N}{\sqrt{(2(N+1)(N+2))}} \qquad [29]$$

Transmissibilities $\mu_{F,x}$ and μ_{rel} at optimum ζ are shown in **Figures 8** and **9**. For low N (soft damper attachment) the μ_{res} is large, but high frequency isolation is good (low $\mu_{F,x}$). On the other hand, large N (stiff damper attachment) reduces μ_{res}, but leads to deterioration of isolation efficiency. For μ_{rel} the influence of N variation is significant only at resonance.

Vibration Isolator with Intermediate Mass (Figure 2E)

Such isolators provide an improved transmissibility function in the high frequency range due to influence of the inertia force interacting with vibratory motions of elastic elements k_1, k_2. The natural frequencies are:

$$\omega_{1,2} = \omega_{p1}\sqrt{\left(A \pm \sqrt{\left(A^2 - \frac{\omega_{p2}^2}{\omega_{p1}^2}\right)}\right)} \qquad [30]$$

where:

$$A = \frac{1}{2}\left(\frac{\omega_{p2}^2}{\omega_{p1}^2} + 1 + \frac{k_2}{k_1}\right)$$

and:

$$\omega_{p1} = \sqrt{\left(\frac{k_1 + k_2}{m_2}\right)}$$

$$\omega_{p2} = \sqrt{\left(\frac{k_1 k_2}{k_1 + k_2}\frac{1}{m_1}\right)}$$

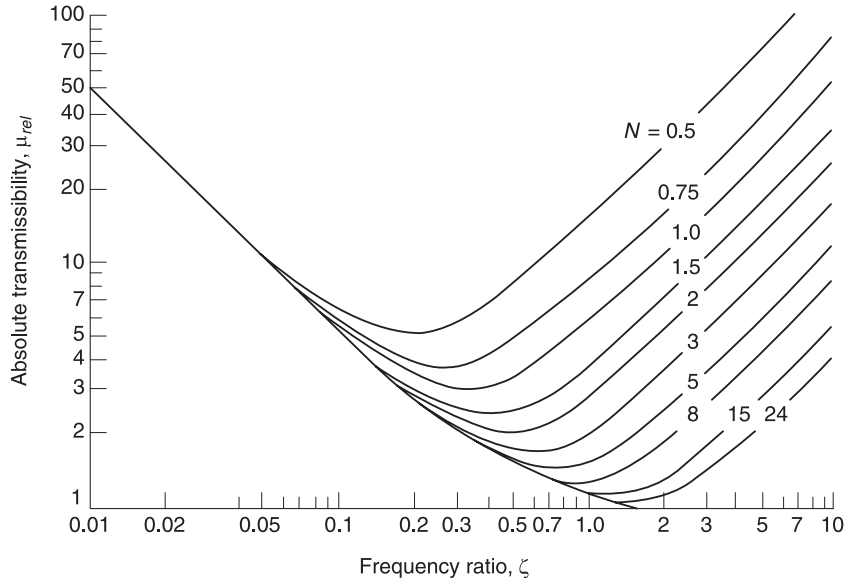


Figure 7 Transmissibility at resonance μ_{res} of the system in **Figure 2C** vs stiffness ratio N and damping ratio ζ.

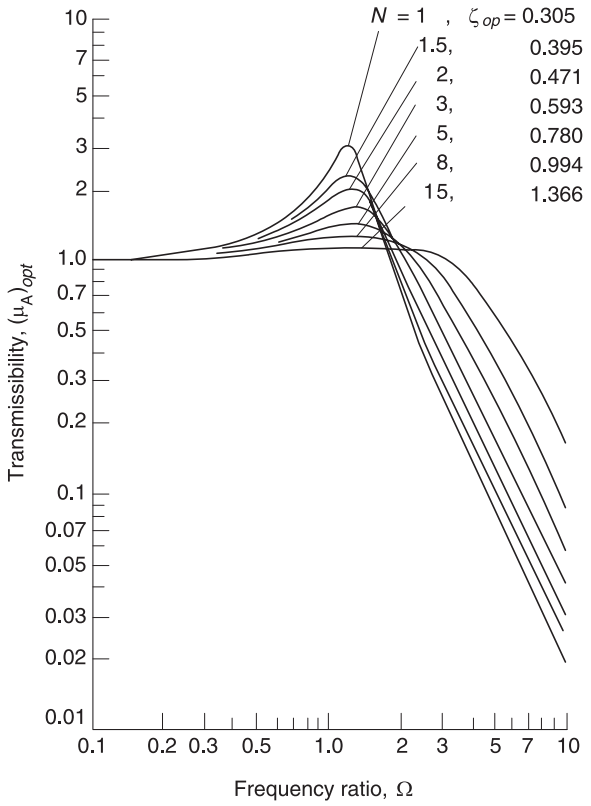


Figure 8 Absolute transmissibility of the system in **Figure 2C** at optimum damping ratios.

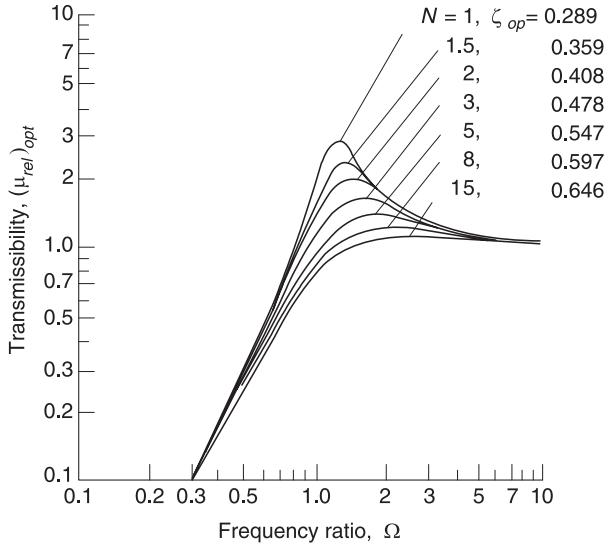


Figure 9 Relative transmissibility of the system in **Figure 2C** at optimum damping ratios.

are partial natural frequencies representing the subsystems in which m_2 is removed and m_1 is fixed, respectively. The natural frequency ω_1 (for 'minus' sign) is lower than both ω_{p1} and ω_{p2}, while ω_2 (for the 'plus' sign) is greater than both ω_{p1} and ω_{p2}. Both force and absolute displacement transmissibility (not considering damping) is given by:

$$\mu = \frac{1}{\frac{\omega_{p1}^2}{\omega_{p2}^2}\left(\frac{\omega}{\omega_{p1}}\right)^4 - \left[1 + \left(1 + \frac{k_2}{k_1}\right)\frac{\omega_{p1}^2}{\omega_{p2}^2}\right]\left(\frac{\omega}{\omega_{p1}}\right)^2 + 1} \quad [31]$$

For the excitation frequency $\omega \gg \omega_{p1}, \omega_{p2}$, $\mu \to \left((\omega_{p1}\omega_{p2})/\omega^2\right)^2$, or at high ω, μ decreases as the fourth power of the excitation frequency (**Figure 10**), while for isolators without an intermediate mass, it decreases only as the second power of ω. The price is high transmissibility at two natural frequencies ω_1 and ω_2, rather than at one resonance frequency for a simple isolator system. The ratio ω_2/ω_1 is a minimum:

$$\frac{\omega_2}{\omega_1} = \frac{1 + \sqrt{(1+\beta)}}{\sqrt{\beta}} \quad [32]$$

when the stiffness ratio $\alpha = k_2/k_1 = 1 + \beta$, where $\beta = m_2/m_1$. At high frequencies and $\beta \leq 0.5$:

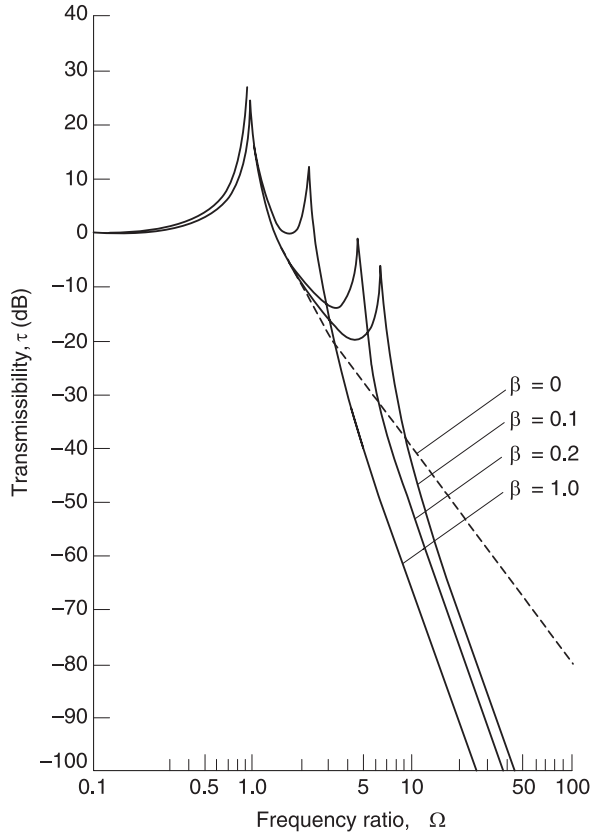


Figure 10 Transmissibility of uni-axial isolation system with intermediate mass m_2 as a function of $\beta = m_2/m_1$

$$\mu_F = \frac{\left(1 + \left(\delta^2/\pi^2\right)\right)(2+\beta)^2}{\beta(1+\beta)\Omega^4} \approx \frac{4\left(1 + \left(\delta^2/\pi^2\right)\right)}{\beta\Omega^4} \qquad [33]$$

or the transmissibility is inversely proportional to the size of the intermediate mass m_2.

The advantage of introducing the intermediate mass for high frequency transmissibility begins at quite high values of ω for masses that are not too small. For $\beta = 0.1$, the transmissibility advantage starts at a frequency that is about ten times higher than the natural frequency of the base system (without the intermediate mass). A small intermediate mass may be integrated into a vibration isolator design (**Figure 11**).

If n intermediate masses connected by spring elements are used, instead of one, then high frequency transmissibility decline at the rate of $1/\Omega^{2(n+1)}$ is realized, but with $n+1$ resonances. The starting frequency of the fast decline in transmissibility is also shifting towards higher frequencies with each added mass.

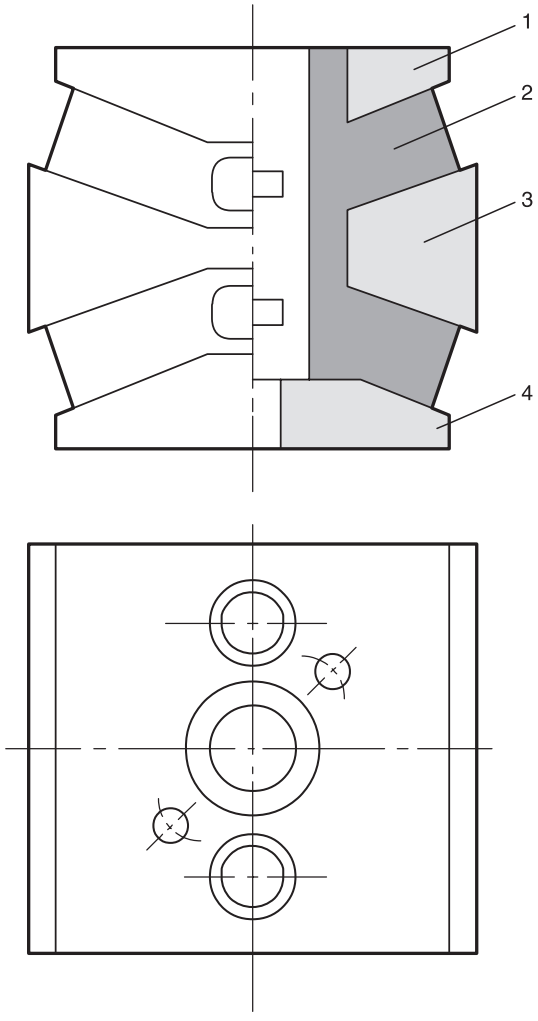


Figure 11 Intermediate mass integrated into vibration isolator; (1), (4) upper, lower base; (2) rubber flexible element; (3) intermediate mass.

SDOF System with Motion Transformation

Relaxation systems and intermediate mass isolators (see below) improve the performance of the basic SDOF system at high frequencies by having steeper declines of transmissibility at frequencies $\omega \gg \omega_n = 2\pi f_n$. Reducing high-frequency transmissibility by reducing the natural frequency is unrealistic for isolation along the z-axis since a low natural frequency f_z is associated with low stiffness and large deflections of isolators under the weight of the supported objects. Large deflections make the system unstable, especially when the object is light and the absolute stiffness of the isolators is low. Instability associated with low natural frequencies/low stiffness of isolators in the horizontal x-, y-directions is a much lesser problem than for the vertical direction. To reduce the natural frequency in a passive system, the mass of the object should be artificially enlarged by installing it on an 'inertia block' so that the stiffness of the isolator can be proportionally increased and stability improved.

By using relatively high stiffness springs and light objects, low vertical (or horizontal) natural frequencies can be realized by motion transformation systems (**Figure 12**). Object 1 (mass m), is attached to isolator (spring) 2 (stiffness k), damper 3 (c), and a motion transformer composed of flywheel/nut 4 which has same axial displacements as object 1 and is supported for rotation in relation to object 1 by thrust bearings 5. Flywheel 4 is engaged with screw 6 attached to the vibrating foundation 7. The presence of the motion transformer results in the generation of additional dynamic forces caused by the inertia of the flywheel/nut 4.

When object 1 is moving in the axial direction, flywheel 4 is forced to rotate. Axial force from the object to the flywheel should overcome inertia torque from the flywheel, $T = I\ddot{\phi}$, where ϕ is the rotational angle of the flywheel and $\ddot{\phi}$ is its angular acceleration. The resulting axial force is:

$$P = T/r \tan(\alpha \pm \gamma) = \frac{I\ddot{\phi}}{r \tan(\alpha \pm \gamma)} \qquad [34]$$

and the natural frequency of this system is:

$$f_n = \frac{1}{2\pi}\sqrt{\left(\frac{k}{m + (I/(r^2\tan^2\alpha))}\right)} \qquad [35]$$

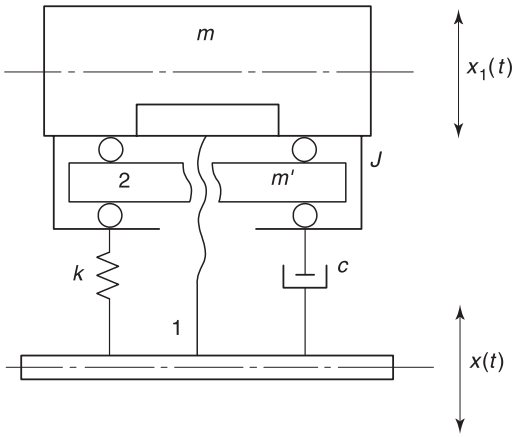


Figure 12 Vibration isolation system with motion transformation.

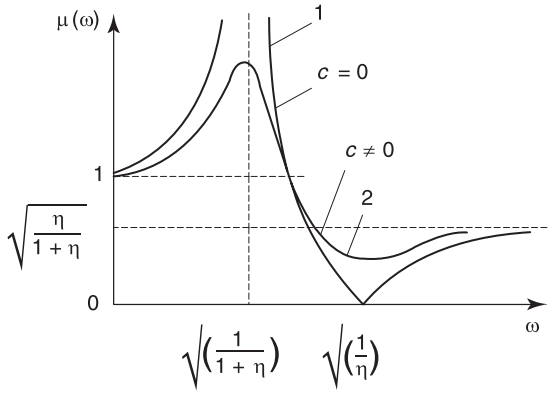


Figure 13 Transmissibility of system in **Figure 12** for $m' = m/3$ and various damping. 1, $c = 0$; 2, $c > 0$; 3, disengaged motion transformer ($m' = 0$).

where I is the moment of inertia of the flywheel, α is the helix angle of the thread, r is the median radius of the thread, γ is the friction angle (friction coefficient in the thread is $f = \tan\gamma$) and its sign depends on direction of sliding in the thread ('minus' – towards equilibrium position, 'plus' – from the equilibrium position). The value of f_n can be very low while k is quite large. Transmissibility of the system is:

$$\mu = \frac{|x|}{|x_1|} = \sqrt{\left(\frac{(1-\eta\Omega^2)^2+4n^2\Omega^2}{[1-(1+\eta^2)\Omega]^2+4n^2\Omega^2}\right)} \qquad [36]$$

or:

$$|\mu| = \frac{|1-\eta\Omega^2|}{|1-(1+\eta)\Omega^2|} \qquad [37]$$

at $c = n = 0$. Here $\omega_0^2 = 2\pi f_0^2 = k/m$ (ω_0 is the natural frequency of the system without a motion transformer); $\Omega = \omega/\omega_0; c/m = 2n; \eta = m'/m$.

Figure 13 shows plots of $\mu(\Omega)$ for $\eta = 0.33$. When $c = n = 0$ (line 1), the system has sharp resonance at $\Omega_1^2 = 1/(1_\eta)$, and transmissibility becomes zero at $\Omega_2^2 = 1/\eta$. Thus, the natural frequency is lower than for the system without the motion transformation (line 3) and also there is a 'dynamic absorption' of vibration at the frequency ratio Ω_2. The latter effect is rather unusual for a SDOF system. With increasing frequency ratio from Ω_2 to $\Omega = \infty$, transmissibility is approaching the asymptote

$$\mu = \eta(1+\eta) \qquad [38]$$

For $c > 0$, the resonance peak is reduced and the full vibration absorption does not develop (line 2). Relatively small values of η allow a noticeable reduction of the natural frequency and a significant reduction of transmissibility μ across the frequency range, starting from low frequencies.

Vibration Isolation System under Random Excitation

For random vibratory excitation, at each moment the magnitudes of its parameters, such as displacement, velocity, and acceleration are unpredictable. Such excitations are generated, for example, when a vehicle is moving along the road, due to the action of the road asperities on its wheels, due to variations of gas dynamic processes in jet or rocket engines, due to exertions from various processing equipment units on the shop floor, etc. The time history of a single occurrence (realization) of a random (stochastic) vibratory process is unpredictable. However, if the process is repeated under the same conditions, it is possible to forecast a probability that the value of a certain parameter of the process would be within a certain range. Vibration isolation systems usually connect mechanical structures. The mechanical structures of both the supporting surface (foundation) and the object can be described as multidegree-of-freedom dynamic systems acting as filters, thus enhancing some and suppressing other components of the random excitation. As a result, the random vibratory processes usually have some pronounced spectral components whose amplitudes and phases may vary as random variables. Such a process can be described as narrowband random vibration mixed with less intensive broadband random vibration. The vibration isolation system also serves as a powerful filter.

Envelopes of spectral power density (SPD), $S(\omega)$, are specified for testing critical equipment units subjected to random vibration. For example, computers

and sensitive instruments for military applications should be tested for $S(\omega) = 0.1\,g^2/Hz$ in the frequency range 10–2000 Hz with the root mean square value $\sqrt{(\bar{x}^2)} = 14\,g\,RMS$. For vibration isolation of precision equipment it is convenient, instead of specifying the envelope of $S(\omega)$, to specify an envelope of maximum floor displacement amplitudes in the potential installation sites for the equipment, or specify envelopes of the floor vibratory velocities for various classes of buildings designed to house precision equipment.

The effectiveness of vibration isolation from random vibration inputs is judged by the mean-square acceleration density on the object being protected while excited by the random vibratory input within the required envelope of $S(\omega)$. The capabilities of the vibration isolation system are limited since the use of soft (more effective) isolators results in greater deflections of the isolators and thus, excursions of the object being protected. The allowable excursions are often limited by packaging conditions.

The SPD of the output signal for the absolute acceleration of the object is:

$$S(\omega)_{out} = S(\omega)_{in}|H(\omega)|^2 \qquad [39]$$

where $H(\omega)$ is the transfer function of the system. The mean square of the output signal can be expressed via the mean square value of the input signal as:

$$\bar{y}^2 = \int_0^\infty S(\omega)_{out}\,d\omega = \int_0^\infty S(\omega)_{in}|H(\omega)|^2 d\omega \qquad [40]$$

The SPD for the relative displacement between the object and the base for the acceleration excitation from the base is:

$$S(\omega)_{rel} = \frac{1}{\omega^4}|\mu_{rel}(j\omega)|^2 S(\omega)_{in} \qquad [41]$$

Information on the range of displacements of isolators caused by the narrowband relative vibrations, is important for designing/packaging of vibration isolation systems. For low-damping systems ($\zeta \ll 1$) the mean-square of relative displacements is:

$$\bar{x}^2_{rel} = S(\omega)_{in}\int_0^\infty |\mu_{rel}|^2 d\omega = \frac{\pi}{4\zeta}\frac{S(\omega)_{in}}{\omega_n^3} \qquad [42]$$

Vibration Isolation System under Impulse Excitation

In many cases, impulse excitations are more dangerous than steady vibrations. Frequently, it is more difficult to evaluate the response of a system to pulse excitations because interaction of both forced motions and free vibration of the system excited by the impulse should be considered. While for each specific case the response can be computed, it is desirable to have some general criteria for designing isolation systems for impulse excitations, as well as quick 'first approximation' techniques. This can be accomplished by using the so-called 'shock spectrum' or 'response spectrum' approach.

The response spectrum is a graphical presentation of a selected quantity in the response process with reference to a quantity in the excitation process plotted as a function of a ratio between the natural period of the responding system and a significant time measure in the excitation pulse. **Figure 14A** gives the response time history of a SDOF system without damping to a typical versed-sine pulse, while **Figure 14B** gives the 'response spectrum' for this excitation and for the 'decaying sine wave' pulse for the SDOF system. All plots in **Figure 14** are for relative values $\xi(t)/\xi_p$ and $A = v(t)/\xi_p$, where ξ_p is the maximum pulse height, $\xi(t)$ is the pulse height as function of t, $v(t)$ is the height of the response process as function of t, and A is the pulse response spectrum; T is the natural period of the dynamic system acted upon by the pulse, and τ is the pulse duration. Both parameters should represent the same parameters of the dynamic system (e.g., ξ can be the displacement pulse coming from the foundation m_f in **Figure 2A**, then v is the forced displacement of mass m, or ξ is the impulse of force acting on mass m, then v is the force transmitted to the foundation mass m_f). Plots in **Figure 14** are computed for $m_f = \infty$; if m_f is finite, then the response is:

$$A_f = \frac{m_f}{m + m_f}A \qquad [43]$$

In the first approximation the first (and the most intense) part of the time history of the response can be approximated as a verse-sine pulse for many shapes of the excitation pulse, especially if $\tau_p \ll T_n$. The duration τ_r of this response pulse can be determined from **Figure 15**. This approximation is useful for evaluating propagation of pulses across the isolation system since usually only the peak value of the response and shape and duration of its first pulse are of interest More accurate analysis can be performed

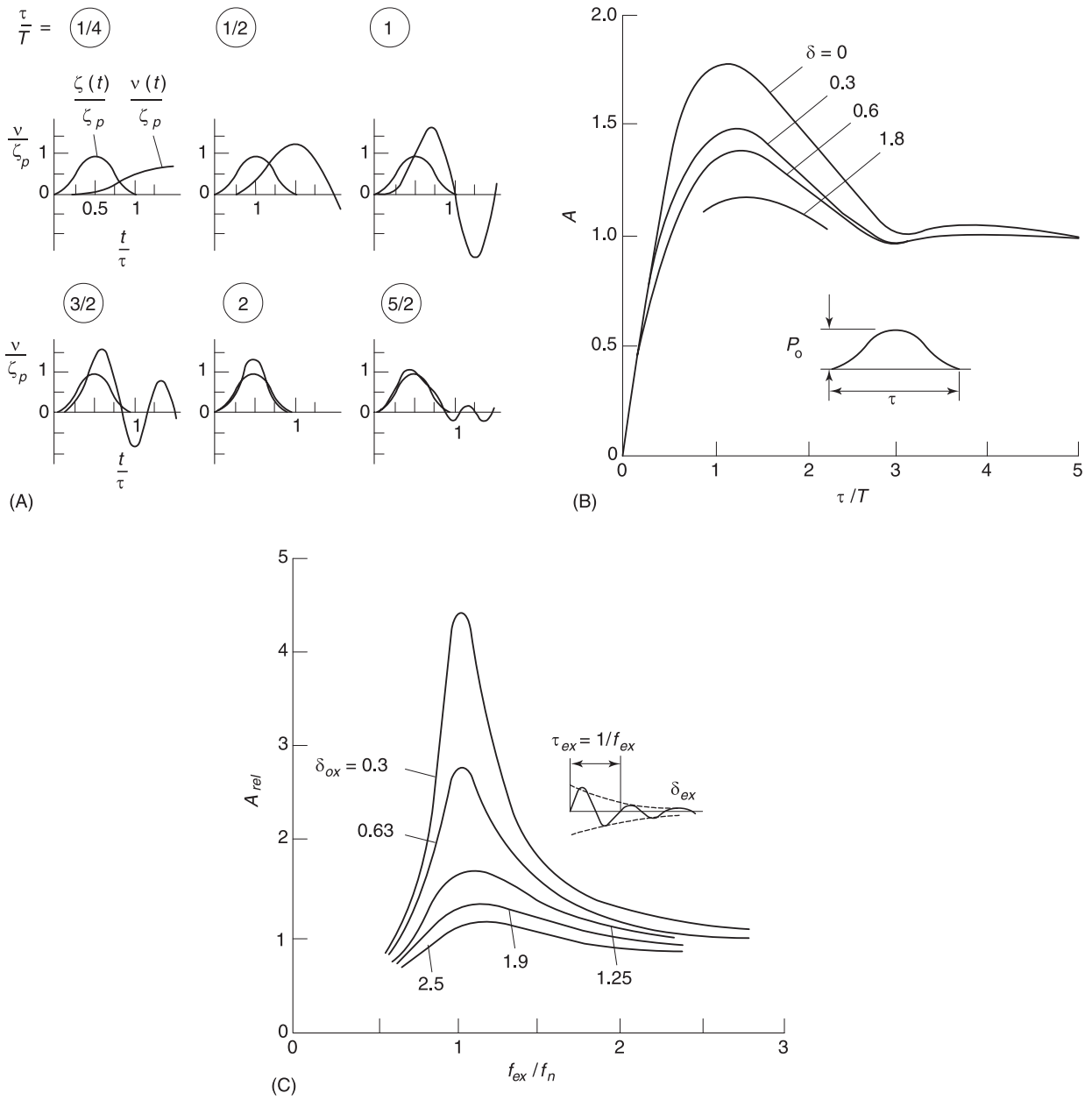


Figure 14 Response of SDOF system to various pulse excitations. (A) Time histories of response to versed-sine pulse; (B) absolute response 'shock' spectra of a SDOF system to versed-sine pulse; (C) same for decaying sinusoid pulse.

by calculating spectral content of the pulse excitation functions and its propagation within the dynamic system.

For undamped systems, shock spectra for half-sine (A_1) and versed sine (A_2) pulses can be expressed analytically as:

$$A_1 = \frac{(T_n/\tau_p)\cos(\pi\tau_p/T_n)}{(T_n/2\tau_p)^2 - 1} \qquad [44]$$

$$A_2 = \frac{\sin(\pi\tau_p/T_n)}{1-(\tau_p/T_n)^2} \qquad [45]$$

For $\tau_p \ll T_n$ (e.g., the typical case for vibration isolation of forging hammers):

$$A_1 \cong \frac{4\tau_p}{T_n}\cos\frac{\pi\tau_p}{T_n} \qquad [46]$$

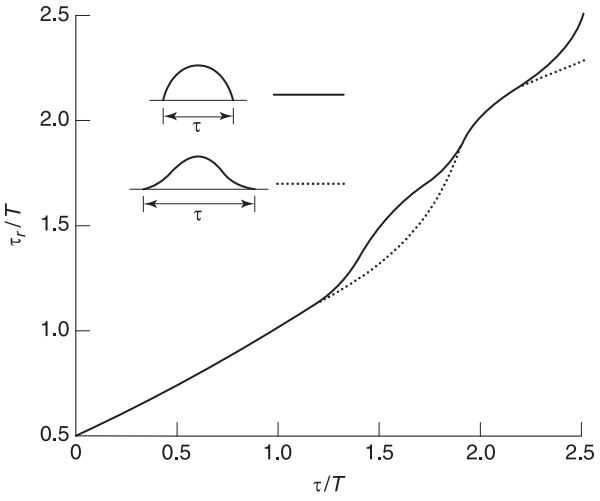


Figure 15 Duration τ_r of the response versed-sine pulse to half-sine and versed-sine excitation pulses (duration τ).

$$A_2 \cong \pi\tau_p/T_n \qquad [47]$$

The presence of damping in the dynamic system under pulse excitation results, first of all, in fast decaying of the response at $t > \tau$, and in some, not very significant, reduction of the peak value of the response function. Within $\sim 5\%$, the influence of damping on the shock spectrum values for the half-sine and verse-sine pulses can be expressed as:

$$A_d \cong A_0(1 - 0.14\delta) \qquad [48]$$

where A_d is shock spectrum value considering damping, and A_0 is the shock spectrum value without considering damping.

Nonlinearity in Vibration Isolation Systems

Nonlinearity in vibration isolation systems, like in other dynamic systems, is usually pronounced at large vibration amplitudes. However, steady vibration amplitudes in vibration isolation systems for stationary objects (production and measuring machines, internal combustion engines), as well as for aggregates on surface and air vehicles are usually much smaller than their static deformations. Thus, in most cases consideration of specifically nonlinear effects does not add much to the results of dynamic analysis performed in a linear approximation. Still, in some cases nonlinear effects have to be considered, such as: vibration isolation systems that can be subjected to high-level incidental intense impulse excitations may require snubbers introducing highly nonlinear process; use of nonlinear isolators with low damping may result in such nonlinear effects as subharmonic resonances; an additional intermodal coupling may develop in the isolation system due to nonlinear effects.

Here 'nonlinearity' is used to indicate a nonlinear character of the load–deflection characteristic of isolators ('static nonlinearity'). Other types of nonlinearity are dependencies of effective stiffness and damping of isolators on amplitude and frequency of vibration. The amplitude and frequency dependency can be a property of material of the flexible element, or it can be due to use of Coulomb friction connections in the isolator designs. The amplitude and frequency dependencies of both stiffness and damping are typical properties of elastomeric and plastic materials frequently used in vibration isolator designs. All types of such 'dynamic nonlinearities' can be pronounced and important in any amplitude ranges.

Snubbers in vibration isolation systems are, in addition to attenuation of deterministic vibratory forces, required to withstand severe incidental shocks. The typical case relates to the installation of a compressor producing near-harmonic excitation at 60 Hz. It should be attenuated 15-fold to protect adjacent precision instruments, thus requiring a low natural frequency ($f_n \cong 15$ Hz) and low damping isolation system. The system should also tolerate severe environmental shocks (a saw-tooth acceleration pulse with magnitude 50 g and duration 18 ms) and white-noise vibration input with 16.6 g RMS acceleration in the 0–2000 Hz range. For a conventional vibration system to survive such test conditions, it has to allow for unacceptably large deflections of the elastic element (spring). The proposed approach is to allow only such dynamic deflections of the isolation springs, which are adequate for performing the main task – protection of precision instruments. To accommodate the severe test conditions, the suspended object (compressor) comes in contact with relatively stiff and highly damped snubbers. Consequently, at high intensity excitations, the system is much stiffer and becomes a highly nonlinear vibro-impact system. The best dynamic quality of such system is at the minimum of a criterion:

$$\Pi = \dot{X}\ddot{X} = V^2\Psi(\zeta) \qquad [48]$$

where $\dot{X}$ and $\ddot{X}$ are, respectively, the maximum velocity, acceleration of the object after impacting (and rebounding from) the snubber with velocity V, and $\Psi(\zeta)$ is the function of damping in the snubber which reaches its minimum when its damping ratio is $\zeta \cong 0.8$ (loss factor $\tan\beta \cong 0.4$, log decrement $\delta \cong 1.25$).

The most widely used vibration isolators with static nonlinearity are CNF isolators. Since the stiffness of such isolators varies in a very broad range with changing loads, they are 'self-snubbing' and provide for the same or better performance as the snubbers described in the above paragraph. Another interesting feature of nonlinear isolators is the fact that at large vibration amplitudes across such an isolator, the amplitude–frequency characteristic of the isolation system 'bends'. This effect leads to some reduction of resonance amplitudes without adding damping to the system.

On the other hand, at high excitation amplitudes development of subharmonic vibrations in systems with nonlinear, e.g., CNF, elastic connectors is possible. Development of subharmonic regimes may result in deterioration of isolation effectiveness, especially for high frequency excitations. Subharmonic vibrations have been observed in vibration isolation systems with low damping CNF vibration isolators (based on conical springs). It is known, however, that subharmonic vibrations cannot develop if the damping in the system exceeds a certain critical value depending on the character and degree of nonlinearity and excitation amplitude.

Nonlinearity in the vibration isolators may lead to development of intermodal coupling in the system for which the decoupling conditions discussed above are satisfied. A study of the effects of the degree of cubic nonlinearity:

$$F_z = a\left(z + \varepsilon z^3\right) \qquad [49]$$

as well as vibration amplitudes on the coupling has been carried out by Henry and Tobias. If a linear planar isolation system $z - \beta(a_z = 0)$ is decoupled, the minimum amplitude $Z_{\min}$ of the z-direction vibration that excites rocking (β-direction) vibration in this system, is determined by the degree of nonlinearity (parameter ε), as well as by closeness between the natural frequencies f_z and f_θ:

$$f_\theta z_{\min} = \frac{1}{\sqrt{\varepsilon}}\sqrt{\left(\frac{4}{3}\frac{1 - n_{\beta z}^2}{3n_{\beta z}^2 - 1}\right)} \qquad [50]$$

where $n_{\beta z} = f_\beta / f_z$ is a so-called 'tuning factor' characterizing the closeness of the natural frequencies.

Wave Effects in Vibration Isolators

Expressions for transmissibility in the SDOF vibration isolation systems above were derived assuming that the isolator can be represented by a massless spring. Real-life isolators, made of metal and of other materials have some mass. As a result, wave effects may develop at high frequencies of transmitted vibrations whereas the dimensions of the isolators become commensurate with multiples of the half-wavelengths of the elastic waves passing through the flexible elements of the isolators. **Figure 16** shows the transmissibility for two SDOF systems with low damped rubber flexible elements (one in shear and one in compression) and for one system with the steel spring, having even lower damping as well as much greater weight. There are intense high frequency peaks resulting in deterioration of transmissibility in the high frequency range. For the rubber cylinder in compression, the fundamental natural frequency is $f_n = 30\,\text{Hz}$ and the high frequency peak at $f'_n = 500\,\text{Hz}$, $(f'_n/f_n > 16)$, and $\sim 47\,\text{dB}$ below the fundamental peak. For the rubber isolator in shear, $f_n = 26\,\text{Hz}$, $f'_n = 850\,\text{Hz}$ $(f'_n/f_n = 33)$, the difference in resonance peak heights $\sim 60\,\text{dB}$. However, for the steel spring there are numerous high frequency resonances in the shown frequency range, with $f_n = 15\,\text{Hz}$, a first high frequency peak at $f'_n = 83\,\text{Hz}$ $(f'_n/f_n = 5.5)$ and only 16 dB below the fundamental resonance peak.

High frequency wave resonances in vibration isolators develop at frequencies:

$$\omega_i = i\pi\omega_0\sqrt{\gamma} \qquad [51]$$

where ω_0 is the fundamental natural frequency, $i = 1, 2, 3\ldots$ is the sequential number of the resonance, and $\gamma = M/M_f = M/\rho Al$ is the mass ratio between the mass M of the supported object associated with the flexible element, M_f is the total mass of the flexible element (ρ is its density, A is the cross-sectional area, l is the length).Transmissibility at the first high frequency resonance is:

$$\mu' = \frac{0.2}{\tan\beta}\frac{M_f}{M} = \frac{0.2}{\gamma\tan\beta} \qquad [52]$$

Thus both the positioning and the intensity of the high frequency resonances caused by standing waves in the isolator are determined by the mass ratio between the isolator and the supported object and by damping in the isolator. If the high frequency transmissibility is of importance, steel springs are not the best choice. Rubber has about seven times lower density ρ than steel, and rubber isolators can be made very small for given natural frequency and load-carrying capacity.

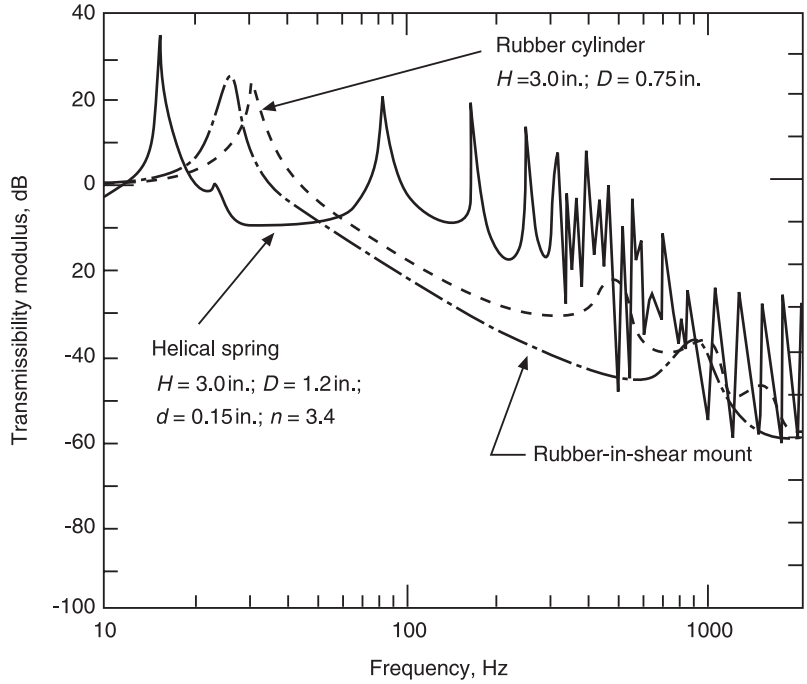


Figure 16 Transmissibility in a broad frequency range of a uniaxial vibration isolation system with isolator having rubber element in compression; rubber element in shear; and steel spring.

Nomenclature

c	damping coefficient
f	frequency
F	force
I	moment of inertia
k	stiffness constant
m	mass
M	moment
r	radius
T	torque
V	velocity
W	weight
μ	transmissibility
γ	friction angle

See also: **Dynamic stability**; **Forced response**; **Vibration isolation, applications and criteria**; **Wave propagation**, Guided waves in structures.

Further Reading

Babitsky VI, Veprik AM (1998) Universal bumpered vibration isolator for severe environment. *Journal of Sound and Vibration* 218: 269–292.

Eliseev SV (1978) *Structural Theory of Vibration Protection Systems*. Moscow: Nauka (in Russian).

Harrison M, Sykes OA, Martin M (1952) Wave effects in isolation mounts. *Journal of the Acoustical Society of America* 24: 62–71.

Henry R, Tobias SA (1959) Instability and steady-state coupled motions in vibration isolating suspensions. *Journal of Mechanical Engineering Science* 1: 19–29.

Himelblau H, Rubin, Sh (1988) Vibration of a resiliently supported rigid body, In Harris C (ed.) *Shock and Vibration Handbook*, 3rd edn. New York: McGraw Hill.

Jacobsen LS, Ayre RS (1958) *Engineering Vibrations*. New York: McGraw Hill.

Jarausch R (1965) Hammer, Fundament und Umgebung als Schwingungsystem. *Maschinenmarkt* 71: 27–38 (in German).

Miles JW, Thomson WT (1988) Statistical concepts in vibration. In Harris C (ed.) *Shock and Vibration Handbook*, 3rd edn. New York: McGraw Hill.

Rivin EI (1979) Principles and criteria of vibration isolation of machinery. *ASME Journal of Mechanical Design* 101: 682–692

Rivin EI (1985) Passive engine mounts – Directions for future development. *SAE Transactions* pp. 3.582–3.592

Ruzicka JE, Cavanaugh RD (1958) New method for vibration isolation. *Machine Design* Oct. 16, pp. 114–121

Snowdon JC (1979) *Handbook of Vibration and Noise Control*. US Department of the Navy, Report TM 79-75.

U.S. Department of Defense (1988) Environmental test methods. Military Standard MIL-STD-810E.

Veprik AM, Babitsky VI, Pundak N, Riabzev SV (2000) Vibration protection for linear split Stirling cryogenic cooler of airborne infrared application. *Shock and Vibration* 4:363–381.

VIBRATION ISOLATION, APPLICATIONS AND CRITERIA

E Rivin, Wayne State University, Detroit, MI, USA

Copyright © 2001 Academic Press

doi:10.1006/rwvb.2001.0181

Design of an optimal vibration isolation system is a complex problem due to the diversity of the requirements for the isolation of various objects in need of vibration isolation. Additional difficulties arise from the variety of working regimes and the internal configurations of some objects (such as cutting regimes in machine tools, position variations of heavy tables or gantries on machine tools and coordinate measuring machines (CMMs), etc.), as well as a variety of environmental conditions (dynamic characteristics of floor and foundation structures, presence of vibration producing and/or vibration sensitive equipment in the vicinity, etc.). While the development of special requirements for unique objects is warranted, a more appropriate way in many cases is to formulate generic criteria for four groups of similar objects:

1. Vibration-sensitive devices (precision machine tools, CMMs, electronic devices). The main goal of vibration isolation is to ensure that relative vibration in the 'working' or other critical area does not exceed permissible limits under given external and internal excitations.
2. Vibration-producing machines and devices (impact-generating machines, unbalanced rotors, reciprocating mechanisms). The main goal is to reduce intensity of dynamic exertions transmitted from the object to the supporting structure (foundation, floor, etc.).
3. General-purpose machinery and equipment, neither very sensitive to external vibratory exertions nor producing excessive dynamic forces (e.g., machine tools of ordinary precision). The main goals are to protect the object from accidental intense external shocks and vibrations; to protect the environment and adjacent precision devices, from occasional disturbances caused by the object (e.g., chatter or stick-slip vibrations); to reduce dynamic loads in bearings; to reduce noise and general vibration levels; to facilitate installation by eliminating the need to fasten or grout the objects to the floor.
4. Objects installed on nonrigid structures (upper levels of buildings, ships and surface vehicles, etc). Both internal and external dynamic excitations may be amplified due to the low dynamic stiffness of the supporting load-carrying structures. Thus, even small exciters produce severe vibrations of the supporting structures, creating the need for protection not only for precision but even for ordinary general-purpose objects.

The normal performance of the object should not be disturbed by vibration isolation, e.g., due to static instability or rocking motion of the isolated object or due to loss of required structural rigidity.

This classification is not absolute. A surface grinder or a CMM needs to be protected from floor vibrations, but reversals of heavy tables/gantries may produce intense dynamic loads disturbing nearby precision devices.

Isolation of Vibration-sensitive Objects

Sensitivity to external vibrations does not necessarily increase with increasing requirements for accuracy, since improvements in the accuracy of precision devices are usually accompanied by better designs.

Ambient Vibrations

Vibrations affecting vibration-sensitive devices can be transmitted from the supporting structures or through the air. Vibration isolators are usually intended to reduce the vibrations transmitted from the supporting structures. Floor vibrations are excited by the vibratory motions of nearby processing machines, motors, transformers, etc., by moving trains, trucks, carts, dollies, cranes, etc. For ultraprecision facilities, microseismic motions of the ground should be also considered. Structural vibrations of vehicles are due to engine excitations and to road disturbances (for surface vehicles). The character and levels of floor vibrations depend not only on the excitation, but also on the vibration-filtering effects of the dynamic system consisting of the soil, foundations, flooring, and other structural components of the building.

Floor vibrations are usually made up of a multitude of spectral components with randomly varying amplitudes and represent a nonstationary and nonergodic random process. The use of fast Fourier transform (FFT) spectrum analyzers in such conditions may give distorted results and smear the important difference between steady or quasisteady vibrations (when the amplitude of a harmonic component does not change significantly during 3–5 periods of vibratory motion) and transient vibrations with fast changing amplitudes. Envelopes of points representing absolute maximums at various frequencies of ground level floor vibration for manufacturing plants can be summarized as constant amplitudes of $\sim 3\,\mu$m in the frequency range 3–30 Hz for vertical vibrations and 25–30% less in a narrower frequency range of 2–20 Hz for horizontal vibrations. Outside these frequency ranges the amplitudes are much smaller. Vibrations on higher floors are $\sim 1.5-3$ times more intense. The intensity of impulsive vibrations can be characterized by 30–60 μm magnitudes and 0.02–0.1 s duration of the versed-sine pulses.

The intensity of floor vibrations in precision manufacturing facilities (e.g., microelectronics) is usually much lower. Vertical vibrations for three typical clean room floors indicate that maximum displacement amplitudes do not exceed 0.05μm. **Figure 1** shows generic vibration criterion (VC) curves by BBN Co. (Boston, MA, USA), frequently used to specify the vibration levels for newly constructed precision facilities. The displacement amplitudes are shown for critical points in **Figure 1**. The selection of a particular VC and/or isolation system specifications makes a significant impact on the overall cost of the facility.

The most stringent ambient vibration parameters for electronic equipment are specified by military standards. Electronic devices must withstand without loss of performance a 'white noise' excitation with power spectral density of acceleration $S(\omega) = 0.1\,\mathrm{g\,Hz^{-1}}$ in the frequency range 10–2000 Hz.

Detrimental Effects of Vibration

Many connections in precision devices are frictional joints tightened by bolts or by other means. One of the detrimental effects of vibrations is the destabilization of dimensional chains. Elements of these chains (e.g., guideways, screws, and clamps) are fastened in elastically strained conditions maintained by static friction forces. Vibratory variations of contact pressures and of friction forces in the joints lead to relaxation of the elastic strains and to possible 'jumps' in the dimensional chains. Such jumps may produce steps in machined surfaces, changes in dimensions within a batch of automatically machined parts, misalignments in optical systems, etc. Vibration-caused 'jumps' at joints of mounting systems (wedges, jack-screws) may lead to structural misalignments and deformations resulting in chatter, reduced accuracy, increased wear, etc.

Ambient vibrations may induce relative motions between the critical components of the device, such as between the cutting or measuring tool and the

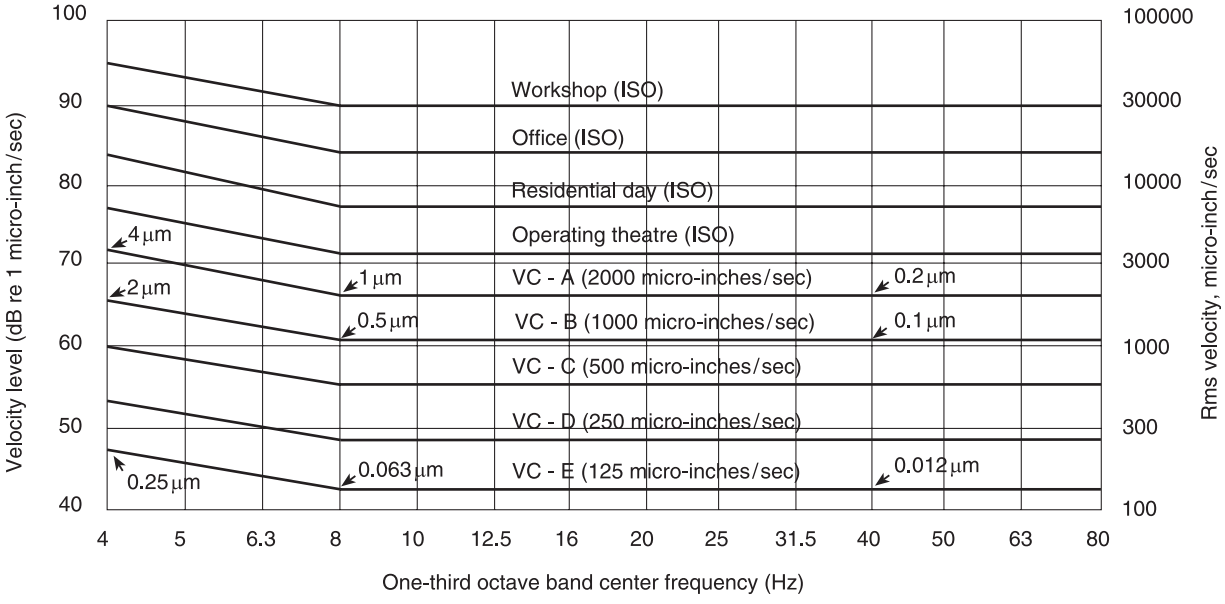


Figure 1 BBN floor vibration criteria for installation of precision equipment.

workpiece. These motions may cause waviness of the machined surface, out-of-roundness, erroneous measurement results, oscillatory misalignments between optical components, signal variations in proximity sensors, and deterioration in surface finish. Impulsive vibrations can lead to momentary misalignments, to erroneous measurements if occurring during the measurement process, and to local variations in the depth of cut (dents on the machined surfaces).

Model of Vibration Transmission

Ambient vibrations excite relative vibrations in the working (cutting/measurement) zone or in the joints comprising the dimensional set-up chain. Usually, these effects are only significant at the fundamental (seldom also at the second) natural frequency of the dynamic system. Often, the higher natural frequencies lie considerably above the frequency range of significant excitation amplitudes. The first natural frequency for grinders is between 30 and 70 Hz, the second natural frequency lies between 100 and 150 Hz, the range of greatly reduced floor amplitudes. While more intense high frequency vibrations are observed on the supporting structures of vehicles (spacecraft, aircraft, surface vehicles), the vibration-sensitive on-board devices usually have higher natural frequencies. **Figure 2** shows vibration sensitivity curves for precision 'projection aligner' used in the production of electronic circuits. The minima on these plots represent structural natural frequencies of the devices. It can be seen that the lowest natural frequencies are between 10 and 30 Hz, and many of the higher natural frequencies lie between 30 and 70 Hz. At the higher frequencies, vibrations of floor/supporting structures usually undergo much higher attenuation by vibration isolation systems.

The dynamics of vibration transmission from the supporting structure into the working zone of a precision device can be approximated by three uncoupled two-mass systems, such as the one in **Figure 3**, one for each coordinate direction of the floor vibrations. Masses and springs in **Figure 3** represent generalized inertias and stiffnesses of the unit, their values may be different for each coordinate direction. Here M_b represents the mass of the frame (bed) of the object; M_u is the mass of its upper structure (e.g., tool head or measuring head); k_m and c_m represent equivalent stiffness and damping of the internal structural components and joints; and k_v, c_v are the stiffness and damping, respectively, of the mounting devices (e.g., jacks or vibration isolators).

The effect of vibrations on an object may be described in terms of the ratio of the generalized relative displacement amplitude X_{grel} between masses M_u and M_b to the displacement amplitude X_b of the frame M_b. This ratio is given as:

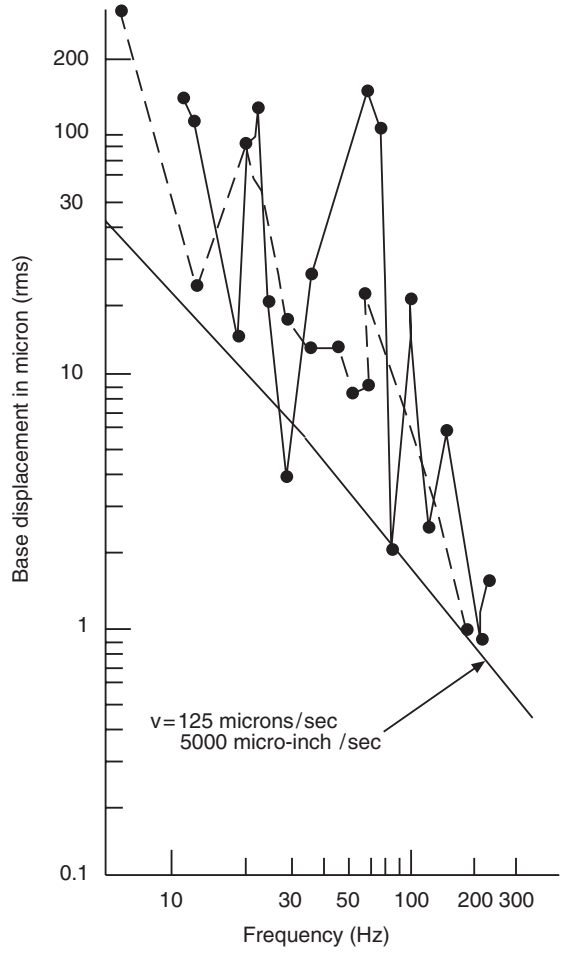


Figure 2 Vibration sensitivity for projection aligner Perkin-Elmer Microlign Mod. 341 for 0.1 μm image motion; (–) vertical floor vibration, (- - -) horizontal floor vibration.

$$\frac{X_{grel}}{X_b} = -\frac{(f^2/f_m^2)}{\sqrt{\left([1-(f^2/f_m^2)]^2+[M_b/(M_u+M_b)](\delta_m^2 f^2/\pi^2 f_m^2)\right)}} = \mu_{rel} \quad [1]$$

where f is the frequency of interest, $f_m = (1/2\pi)\sqrt{(k_m/M_u)}$ is the (partial) resonance frequency of the upper structure, and δ_m is the log decrement of that system.

The actual relative displacement in the working area of the object is proportional to X_{grel}:

$$X_{rel} = \gamma X_{grel} \quad [2]$$

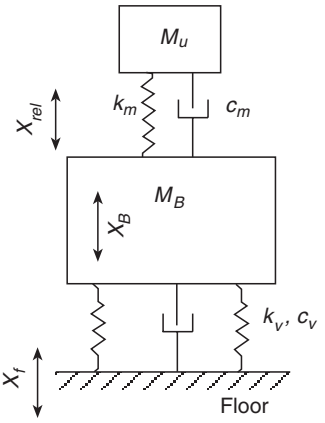


Figure 3 Two-mass dynamic model for vibration sensitivity of precision object in one principal direction.

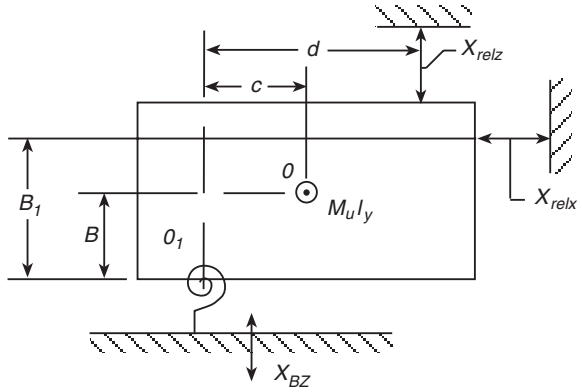


Figure 4 Dynamic model for influence of design parameters on relative vibration in working zone.

and the proportionality design constant γ depends on geometry of the device. For example, for an upper structure represented by the model shown in **Figure 4**:

$$\gamma_{zx} = \frac{M_u b_1 c}{I_{O1}} = \frac{b_1 c}{\rho_y^2 + b^2 + c^2} \qquad [3]$$

$$\gamma_{zz} = \frac{M_u c d}{I_{O1}} = \frac{cd}{\rho_y^2 + b^2 + c^2} \qquad [4]$$

The first subscript on γ refers to the direction of the bed/frame vibration, and the second to the direction of motion of the upper structure relative to the bed; I_{o1} is its mass moment of inertia about the actual axis of rotation; and ρ_y is the radius of gyration about the principal y-axis. The dimensions b, b_1, c, and d, as indicated in **Figure 4**, are measured from the center of gravity (CG) O_1. The constant γ depends on the set up of the object, particularly on the position of the upper structure with respect to the bed. In **Figure 4**, the upper structure is attached by a torsional spring having infinite vertical stiffness. This is typical for structural designs of machine tools and measuring systems (guideways have high translational stiffness perpendicular to the motion direction, but significant angular deformations). Sensitivity of horizontal displacements in the work zone to vertical vibrations of the bed (y_{zx}) can be reduced by reducing structural (design) dimensions c and b, by reducing overhang, or by adding counterweights to the back side of the structure. The sensitivity of vertical displacements in the work zone to vertical vibrations of the bed (y_{zz}) can be reduced by reducing the design dimensions c and d.

Similar machines may have very different (by one to two orders of magnitude) sensitivities to vibrations of their beds due to design differences.

The transmissibility, $X_{grel}/X_b = \mu_{rel}(f)$, from eqn [1] is a measure of the vibration sensitivity of the object as a function of the frequency f, and does not depend on the object's mounting, only on its design (structural natural frequency f_m and masses M_b, M_u). To obtain a ratio between the amplitudes of the relative vibrations within the working zone of the object and amplitudes of the floor vibrations, X_{rel}/X_b should be multiplied by the ratio of the bed vibration amplitudes to the floor vibration amplitudes (transmissibility of the mounting/isolation system), assuming that the dynamic coupling between the object structure and the vibration isolation system is weak, and that these systems can be considered to be independent. This assumption is justified since in most practical cases natural frequencies of the isolated bed in the three coordinate directions f_{vx}, f_{vy}, and f_{vz}, are considerably lower than the structural natural frequencies f_m, and the mass of the bed M_b is usually much larger than the mass of the upper structure M_u.

Principles and Criteria of Vibration Isolation

If a precision object is exposed to ambient vibrations characterized by a reasonably constant amplitude vibratory displacement, velocity, or acceleration in a certain frequency range, a resonance in the vibration isolation system is often inevitable. Accordingly, if the isolators have higher damping, natural frequencies of the isolation system (thus, stiffness values of the isolators) can be increased. The isolation system should satisfy the inequality:

$$\Phi_p^2 = f_v^2/\delta_v < \frac{\Delta_o f^2}{\pi X_f \mu_f} \qquad [5]$$

where:

$$\Phi_p = \frac{f_v}{\sqrt{\delta_v}} = \frac{\sqrt{(k_v/(M_b + M_u))}}{\delta_v} \qquad [6]$$

is the vibration isolation criterion for vibration-sensitive objects. The criterion Φ_p should be used instead of the natural frequency. It indicates that improvement in isolation can be achieved either by reducing the natural frequency f_v or by increasing the isolation damping δ_v. Such criteria can be specified for each coordinate direction of the isolation system. In eqns [5] and [6] k_v is the stiffness of the isolators, Δ_o, is the allowable vibration amplitude in the work zone, X_f is the maximum amplitude of the ambient vibration (same units, e.g., displacement or acceleration), and μ_f is the transmissibility from the object frame to the work zone at an arbitrary frequency, f.

Testing of numerous commercially produced vibration isolators for machinery and recommendations on their use based on a vast practical experience has shown that the recommendations are in good agreement with eqns [5] and [6].

The vibration isolation criterion eqn [6] also allows for a meaningful selection of resilient materials for vibration isolators. Both stiffness and damping of such materials usually depend upon amplitude a and frequency f of vibrations. The stiffness can be expressed as:

$$k = K_{dyn}(a, f)k_{st} \qquad [7]$$

where k_{st} is the static stiffness of the isolator and K_{dyn} is the dynamic stiffness coefficient. Substitution of eqn [7] into eqn [6] yields

$$\Phi_p = \sqrt{\left(\frac{k_{st}}{M_b + M_u}\right)}\sqrt{\left(\frac{K_{dyn}(a, f)}{\delta_v(a, f)}\right)} \qquad [8]$$

The static stiffness k_{st} of isolators for a given Φ_p can be increased (thus improving the stability of the isolated machine) by reducing K_{dyn}/δ_v. Since both K_{dyn} and δ_v depend upon frequency and, especially, the amplitude of vibrations, their ratio depends on material characteristics and vibration parameters. Optimum materials for vibration isolators for low ambient vibration amplitudes are very different from those for high amplitudes. Thus, wire-mesh and felt are more appropriate for high amplitudes, some rubber blends are preferable for smaller amplitudes, others for greater amplitudes.

The values of Φ_p for the three coordinate directions can be calculated using experimentally determined μ_f and given values for X_f and Δ_o. Then, using δ_v values for the selected isolators, the required natural frequencies in all three directions f_x, f_y, f_z can be calculated. Values of the permissible relative amplitudes Δ_o are chosen to correspond to one-half of the specified precision of the part being machined on a given machine tool. Values of the natural frequency ratios f_{vx}/f_{vz}, and f_{vy}/f_{vz} can be used to determine the required stiffness ratios of isolators in horizontal and vertical directions using the expression given in **Vibration isolation theory**. The results of the calculation of these parameters have been validated by the author by the successful installation of many thousands of precision machine tools.

Example If the vibration sensitivity $\mu(f)$ of a precision object is known (for example from the experimentally obtained plots as shown in **Figure 2**), then eqn [5] can be used to specify the vibration isolation parameters. For the case of **Figure 2**, $\Delta_o = 0.1\mu$m is specified. **Table 1** gives the values of $\mu(f)$ calculated for critical points from the plots in **Figure 2** for vertical and horizontal directions, respectively. **Table 1** also contains values of Φ_p calculated for these points using eqn [5] and assuming that for vertical direction $X_f(f) = \text{const.} = 3.0\ \mu$m for frequencies in the range

Table 1 Vibration isolation synthesis for **Figure 2**

Vertical direction (Y-axis)									
f, Hz	11	12	20	25	30	32	41	70	80
$\mu(f)$	0.0083	0.010	0.087	0.0091	0.056	0.303	0.05	0.0077	0.010
Φ_1, Hz	4.51	12.3	7.0	26.9	13.0	6.3	22.5	128	137
Φ_2, Hz	12.9	36.6	26.9	116	61	29.7	106	601	644
Horizontal direction (X-axis)									
f, Hz	7	12	22	65	70	100	140	210	
$\mu(f)$	0.0033	0.05	0.0125	0.071	0.090	0.090	0.056	1.25	
Φ_1, Hz	13.7	6.05	22.3	49.6	49.2	84	176	68.6	
Φ_2, Hz	23.1	37.5	78	174	172	294	616	240	

3–30 Hz and $X_f(f) = 3.0\ (30/f)\ \mu$m for frequencies $f > 30$ Hz; for the horizontal direction $X_f(f) =$ const. $= 2.5\ \mu$m for frequencies of 2–20 Hz, and $X_f(f) = 2.5(20/f)\ \mu$m for frequencies $f > 20$ Hz. The values of Φ_{p2} were calculated using floor vibration levels corresponding to line VC-B in **Figure 1** (both for vertical and horizontal directions). Values of Φ_{p1} are given only for comparison, since high precision microelectronic production equipment is never used in conventional plant facilities, only in specially designed buildings complying with some of VC curves.

It can be seen from **Table 1A** that the lowest value of Φ_{p1} for vertical direction is 4.51 Hz. If vibration isolators with medium damping $\delta_v = 0.6$ are used, then from eqn [6] the required vertical natural frequency $f_v = 4.51\sqrt{(0.6)} = 3.04$ Hz. However, if isolators made of rubber with high damping $\delta_v = 1.2$ are used, then $f_v = 5.0$ Hz, which can be realized by passive isolators. Much stiffer isolators can be used to comply with values of Φ_{p2}, which represent floor conditions at microelectronics industry installations.

A similar situation is seen in **Table 1B**, however, realization of natural frequencies corresponding to Φ_{p1}(4.7 Hz for $\delta_v = 0.6$, 6.63 Hz for $\delta_v = 1.2$) in horizontal directions with passive isolators does not present any difficulty; even much lower values can easily be realized. Use of Φ_{p2} gives even more latitude in selecting isolator parameters.

In some cases, isolation from short duration (impulsive or shock) motions of the floor or other supporting structure is required. Such excitations are less troublesome due to their short durations. Accordingly, the permissible peak relative displacement Δ_{op} in response to floor shocks can be taken to be ~ 3 times the value of Δ_o permissible for steady-state vibrations. For an object subjected to shock excitation the shock spectrum approach (see **Vibration isolation theory**) can be used to obtain:

$$\Delta_p = A_{rel} a_b \gamma = A_1 A_{rel} \gamma a_f \qquad [9]$$

where a_b denotes the peak displacement of the bed caused by shock motion of the floor with displacement magnitude a_f, A_l represents the shock spectrum corresponding to a versed-sine pulse acting on the vibration isolation system, and A_{rel} represents the shock spectrum for relative displacement in the work area corresponding to a versed-sine motion of the bed (**Figure 5**).

If γ and Δ_{op} are known, as well as the pulse magnitude a_f and duration τ_f (e.g., from **Vibration isolation theory**), then the values of the natural frequency f_{vp} of the isolation system that are necessary

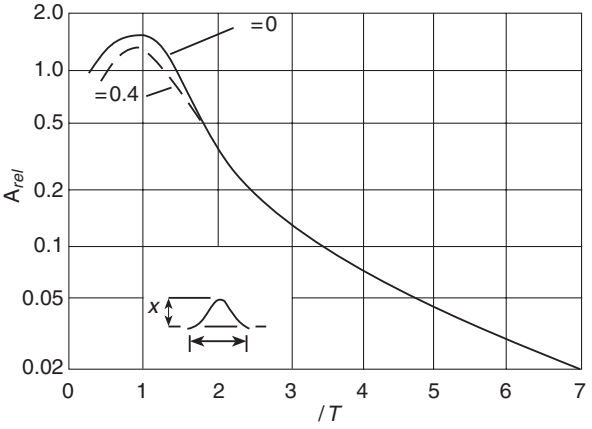


Figure 5 Maximum response amplitudes (shock spectrum) of generalized relative displacements in working zone for versed-sine pulse-motion of frame (t – pulse duration, T – natural period of object structure).

for adequate isolation may be determined from the foregoing expression by trial and error. The isolator damping has less effect on transmission of shocks than of steady motions. Values of f_{vp} for the z-direction that have been determined in this manner have been given elsewhere for a number of precision machine tools. These values are close to the natural frequency values f_v that are necessary with $\delta_v = 0.5$ to provide sufficient isolation of steady-state vertical vibration according to the Φ_{pz} criterion. This correlation holds for machine tools with very different and diverse design structures, it can be extrapolated to other precision devices. However, modern ultrahigh-precision equipment is always installed far from sources of intensive impulsive loads, and 30–60 μm displacement magnitudes of floor motions would never occur in the controlled environment facilities for high-precision equipment.

Vibration Isolation Systems

Required parameters of vibration isolation systems for various units of precision equipment are usually calculated with the assumption that there is no dynamic coupling between the vertical and horizontal vibrations of the object. However (see **Vibration isolation theory**), use of conventional constant-stiffness vibration isolators results in strong coupling of vibratory processes in various directions. This coupling can be caused by substantially nonuniform mass distribution in typical objects, difficulties in determining the CG positions and calculating weight distribution between the mounting points, large differences in nominal stiffnesses between sequential models of vibration isolators in a given isolator design line, and large deviations of the stiffness values from the

nominal values due to manufacturing tolerances. The undesirable coupling problem can be alleviated considerably by use of constant natural frequency (CNF) isolators, in which stiffness in both vertical and horizontal directions is proportional to the weight load on the isolator. Use of such isolators results in a system with very low degree of coupling between vertical and horizontal coordinates without the need to determine the CG position, to calculate the weight load distribution between the mounting points, etc. Such isolators also have a significantly reduced sensitivity to manufacturing tolerances. The effect of using CNF isolators is illustrated by **Figure 6** which shows the frequency response of relative displacements between the grinding wheel and the table of a surface grinder caused by vertical floor vibrations of 5 μm amplitude in the 7–38 Hz range. Use of CNF isolators providing a 20 Hz natural frequency in the vertical (z) direction resulted in much better isolation than the best constant-stiffness isolators with a much lower 15 Hz natural frequency in the z-direction. The difference between vertical natural frequencies of 15 and 20 Hz is equivalent to approximately doubling the isolator stiffness for $f_{vz} = 20$ Hz.

Side Issues for Vibration-isolated Precision Equipment

Vibration isolation using passive isolators results in a reduced stiffness of the connection between the isolated object and the supporting structure (foundation). This can lead to rocking motions of the object if it contains internal massive moving units (e.g., tables in surface grinders, gantries in CMMs), and to reduction of the effective rigidity of the equipment frame not structurally tied to the rigid foundation. These issues may be important for any device installed on flexible mounts, but are especially important for vibration sensitive precision devices.

The rocking motion of isolated precision machines may become objectionable if it does not settle until the next cycle of operation (next grinding pass on a surface grinder or next measurement event on CMM) and low frequency but intense rocking vibrations are transmitted into the working zone. The rocking may be reduced by installing the machine rigidly on massive foundation blocks and placing vibration isolation means under these blocks. This approach is expensive and time consuming for installation and, especially, for relocation of the object/machine. Often the direction of maximum vibration sensitivity is at a right angle to that of the internal excitation, and use of anisotropic isolators with optimized stiffness ratios can be beneficial. A higher stiffness of the isolators in the direction of internal excitation reduces the amplitudes and increases the frequency of the rocking motion. The latter leads to faster decaying of the rocking motion. Increased distances between isolators in the direction of the internal excitations reduce the angular motion component (associated with large amplitudes of motion) and increase the translational component, thus significantly improving the stability of the object. The increased distances between isolators can be achieved by installing isolators under a plate or rails attached to the frame/bed of the object. Increased damping of the vibration isolators reduces the settling time, especially in the direction of the rocking motion.

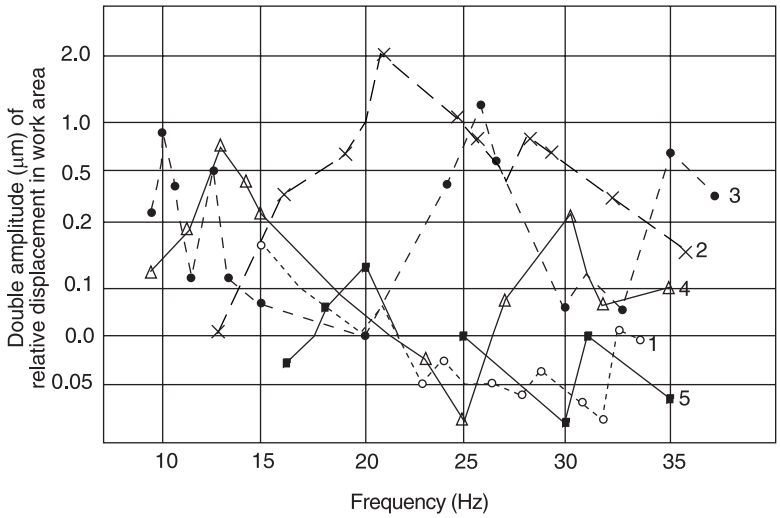


Figure 6 Amplitudes of relative motion in working area (between grinding wheel and table) of 3B71 surface grinder excited by 5 μm amplitude floor vibration for the machine installed on various isolators: (1) rubber-metal CNF isolators, $f_{vz} = 20$ Hz; (2) steel wedges, $f_{vz} = 27$ Hz; (3) wire-mesh isolators, $f_{vz} = 25$ Hz; (4) plastic pads, $f_{vz} = 30$ Hz; (5) rubber-metal isolators, $f_{vz} = 15$ Hz.

Usually, smaller precision devices do not require the addition of a foundation to enhance the rigidity of their frames, whereas larger devices (e.g., machine tools weighing over 10 t) usually do, unless they are specially designed to be mounted on three supporting points. For machines of intermediate weight (5–10 t), judicious placement of the vibration isolation mounts using the 'Bessel's points' principle may reduce static deflections of the frame, thus effectively making it act as if it were more rigid. Another way of stiffening the frames of precision equipment units is to attach them to rigid plates or specially designed rigidizing frames.

Isolation Requirements for Vibration-producing Objects

Objects Producing Single Frequency Excitations

A frequency ratio $f/f_{vz} = 4-5$ is usually recommended for isolation of objects generating a single frequency (f) dynamic force (e.g. created by rotating unbalanced parts), where f_{vz} is the vertical natural frequency of the isolation system. This brings a 15–25 times reduction of transmission of the vertical component of the dynamic force, but f_{vz} can become rather low, such as $f_{vz} = 5-6$ Hz for rotors with a rotational speed of 1500 rpm, 3–4 Hz at 900 rpm, and therefore steel-spring isolators are frequently used. They have low damping and poor performance in a high-frequency range, $f > \sim 10 f_{vz}$, thus high frequency excitations due to inaccuracies of bearings, clearances, etc., are not attenuated and may be amplified.

The frequency ratio can be reduced by considering the transmissibility in all of the modes of the isolation systems. The critical cases are ones where the largest components of the dynamic force are vertical. Horizontal force components are easier to isolate since low natural frequencies of horizontal (and/or rocking) vibrations are not associated with the instability of the isolated object, unless the vertical natural frequency is low. Objects containing horizontal (or inclined) unbalanced rotors are usually associated with generation of intense vertical dynamic forces.

Two principal force components are z, component (F_z), and x, component (F_x). The transmissibility for F_z is determined by the natural frequency f_{vz}, and for F_x, by the natural frequency $f_{x\beta}$ of the lower rocking mode.

The transmissibility for an oscillatory torque T_y is mostly determined by the higher rocking mode $f_{\beta x}$. For a z-axis rotor the correspondence is: $F_x - f_{x\beta}$; $F_y - f_{y\alpha}$; where the oscillatory torque is f_γ. Modal coupling is not considered.

The effectiveness of vibration isolation depends on attenuation of all dynamic force and torque components. Orthogonal components of the dynamic forces are phase-shifted by $\pi/2$. If for a z-axis rotor F_o is the centrifugal force amplitude, then:

$$\begin{aligned} F_x &= F_o \sin 2\pi ft \\ F_y &= F_o \sin(2\pi ft - \pi/2) \\ F'_x &= F'_{xo} \sin 2\pi ft \\ F'_y &= F'_{yo} \sin(2\pi ft - \pi/2) \end{aligned} \qquad [10]$$

$$\mu_{F_x} = F'_{x_o} \Big/ F_o; \qquad \mu_{F_y} = F'_{y_o} \Big/ F_o$$
$$\mu_F = \frac{\sqrt{\left(\left(F'_{x_o} \sin 2\pi ft\right)^2 + \left(F'_{y_o} \cos 2\pi ft\right)^2\right)}}{F_o} \qquad [11]$$

Here ($'$) denotes components on the output side of vibration isolators; μ_{F_x} and μ_{F_y} are transmissibilities along the respective axes; and μ_F is the overall force transmissibility. The amplitude of the trigonometrical expression $(A \sin \phi)^2 + (B \cos \phi)^2$ is equal to $\max(A^2,\ B^2)$, and the overall transmissibility is:

$$\mu_F = \frac{\max\left(F'_{x_o}, F'_{y_o}\right)}{F} = \max\left(\mu_{F_x}, \mu_{F_y}\right) \qquad [12]$$

The effectiveness of vibration isolation is determined by the transmissibility in the highest mode for force. Usually, only one significant factor (force or torque) is present, thus transmissibility in only one mode can be considered. If both factors are present, then the 'effective transmissibility' μ, or their weighted average can be used. For the z-axis and y-axis rotors:

$$\begin{aligned} \mu_z &= \tfrac{1}{2}(W_F \mu_F + W_T \mu_T) \\ &= \tfrac{1}{2}\left[W_F \max\left(\mu_{F_x}, \mu_{F_y}\right) + W_T \max\left(\mu_{T_x}, \mu_{T_y}\right)\right] \end{aligned} \qquad [13]$$

$$\mu_y = \tfrac{1}{2}\left[W_F \max\left(\mu_{F_z}, \mu_{F_x}\right) + W_T \max\left(\mu_{T_z}, \mu_{T_y}\right)\right] \qquad [14]$$

where weighting factors $W_F W_T = 2$. In general, transmission of torque is less dangerous. With widely

spaced isolators the forces creating the output torque are small, with narrow spaced isolators action of the torque on the supporting structure is local. Thus, $W_F = 2W_T$ can be assumed. Eqns [13] and [14] are conservative since reactions of the isolators due to forces and torques should be added up as vector quantities.

Example Validation on a vertical-axis hammer crusher ($f = 12\,\text{Hz}$; $f_{x\beta} = f_{y\alpha} = 1.66\,\text{Hz}$; $f_{\beta x} = 3.5\,\text{Hz}$; $f_{\alpha y} = 4.0\,\text{Hz}$, and $\mu_{F_x} = 0.02$; $\mu_{T_x} = 0.093$; $\mu_{T_y} = 0.125$). From eqn [13] with $W_F = 2W_F = 1.33$, we obtain $\mu = 0.042$. By measuring floor vibrations with and without isolators, we obtained $\mu = 0.0355$.

From eqns [13] and [14], the necessary natural frequencies can be determined for a required attenuation μ. Typical values for vibration isolation systems for machinery are: $\eta_{x,y} = k_z/k_{x,y} = 4.0$; $f_{x\beta}$, $f_{y\alpha} = 0.45 f_z$; $f_{\beta y}$, $f_{\alpha x} = 1.2 f_z$; $f_\gamma = 1.15\, f_z$. For these values and the required $\mu = 0.20$ (five times attenuation, which is adequate in most cases), the necessary frequency ratios are: from eqn [13] for z-axis rotors $f/f_z > \sim 2.0$; from eqn [14] for x-axis rotors $f/f_z > \sim 2.6$.

Objects Producing Polyharmonic Excitations

Isolation of polyharmonic dynamic forces depends on the spectral content of the excitation, absolute values of the lowest frequencies of dangerous components, dynamic characteristics of the structures and equipment to be protected, etc. When inertia blocks and highly damped isolators (with internal damping which does not significantly impair postresonant transmissibility) are used, resonance (not of the most dangerous spectral component) could be a permissible working regime.

Objects Producing Conservative Impact Excitations

Typical objects are stamping presses. Reaction moments generated by the production pulse loads excite the lower rocking mode in the x–z plane. Stamping presses generate 'versed-sine' pulses. Typical working conditions of crank presses generate pulses with duration $\tau = \sim 0.1 t_c$ for automatic operation and $\tau = \sim 0.05 t_c$ for manual operation (single strokes). Here t_c is the time of one working cycle (one crank revolution). The nominal pulse duration for synthesis of the vibration isolation system is calculated for $n_{\max}$, the maximum rate of strikes-per-minute (spm):

$$\tau_{\text{nom}} = 0.1(60/n_{\max}) = 6/n_{\max} \qquad [15]$$

With the press rigidly attached to the floor, the lower rocking modes are at $f_{x\beta}$, $f_{y\alpha} = 15$–$25\,\text{Hz}$. For presses with $n_{\max} = 60$–$200\,\text{spm}$, dynamic loads to the floor may be amplified by a transmissibility factor 1.2–1.5, in accordance with the 'shock spectrum' for the versed-sine pulse; see **Vibration isolation theory**. Sometimes, presses are fastened to inertia (foundation) blocks whose mass is about equal to the press mass. This reduces the dynamic pulse transmission to the environment by $\sim 50\%$, thus the transmissibility factor is about $\mu = 0.6$–0.75. The required degree of attenuation of the pulse magnitude by vibration isolation is $\mu = 0.5$ since installation of the press on vibration isolators would attenuate the most objectionable high frequency components of the pulse much more than the magnitude of the pulse. For damping in the isolators $\delta_\nu = 0.6$, the required rocking natural frequency:

$$f_\nu = f_{x\beta} = n_{\max}/30(\,\text{Hz}) \qquad [16]$$

For high CG/narrow base presses an intense rocking of the machine can occur. It can be corrected by extending distance between mounts in the rocking direction by mounting the press on a frame or rails.

Some production machines (cold heading machines, injection molding machines, etc.) generate intensive dynamic loads of the conservative nature in a horizontal direction. Such machines have heavy reversing masses generating large horizontal inertia forces in addition to conservative pulses associated with the production process. This may result in intense rocking of the machine on vibration isolators. Reduction of the undesirable rocking can be achieved by increasing vertical stiffness of the isolators.

Objects Generating Pulses of Inertial Nature

Forging hammers and casting mold conditioning machines are the most hazardous industrial sources of vibration. Hammers are installed on massive foundation blocks supported by compliant steel springs. Damping is provided by viscous friction units or large rubber cubes, but is usually low, $\delta = 0.2$–0.3. Oak beams or reinforced rubber belting pads under the anvil are the first stage of vibration isolation. **Figure 7** is a schematic model for an isolated forging hammer; m represents the mass of dropping tup with the upper die, m_2 is the anvil, $m_3 = m_3' + m_3''$ represents frame m_3' attached to foundation block m_3'', m_4 is the foundation box.

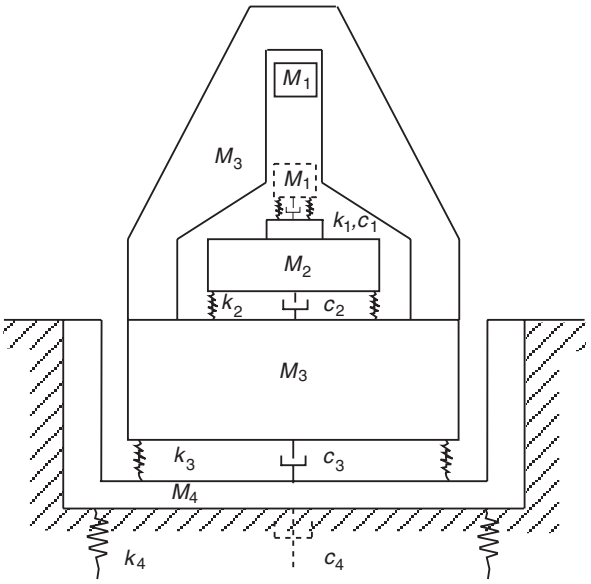


Figure 7 Dynamic model of forging hammer isolation system.

The stiffness and damping, respectively, of the die-billet subsystem are $k_1,\ c_1$; of the first isolation stage between the anvil and the foundation block $k_2,\ c_2$; of main isolators $k_3,\ c_3$; and the effective stiffness and damping coefficients for the surrounding soil are $k_4,\ c_4$. Partial natural frequencies for typical vibration isolated hammers are: for $m_2 - k_2 - m_3,\ \sim 50$ Hz; for $m_3 - k_3 - m_4$, between 2 and 7 Hz; for the foundation box–soil subsystem $m_4 - k_4$ and usually $f_{n4} = 15 - 20$ Hz.

The impact pulse in forging hammers is a half-sine pulse; its magnitude P_o and duration τ_p depend on the billet material, its temperature, design and the size of the die. For the worst case (impact of the upper die against the lower die without billet material inside) the pulse parameters are given in **Table 2**.

Analysis of the propagation of the impact pulse through the system in **Figure 7** resulted in the transmissibility expression:

$$\frac{P_{3\max}}{P_{o\max}} \cong 6.9\sqrt{\left(\frac{m_3 m_4^2}{(m_3+m_4)(m_1+m_2+m_3)(m_1+m_2+m_3+m_4)}\right)\tau_{p1} f_n} \qquad [17]$$

where $P_{3\max}$ is the magnitude of the force pulse transmitted to the foundation box, and the fundamental natural frequency of the isolated hammer is:

$$\begin{aligned} f_n &= \frac{1}{2\pi}\sqrt{\left(\frac{k_3(m_1+m_2+m_3+m_4)}{(m_1+m_2+m_3)m_4}\right)} \\ &= f_{n_3}\sqrt{\left(\frac{(m_1+m_2+m_3+m_4)m_3}{(m_1+m_2+m_3)(m_3+m_4)}\right)} \end{aligned} \qquad [18]$$

Thus, for the short pulse excitation the transmitted force $P_{3\max}$ is proportional to the natural frequency of the isolation system, while in cases of isolation of steady (e.g., sinusoidal) vibrations the transmitted force is proportional to the second power of the natural frequency. However, in the latter case the vibration transmitted to the supporting structure is at the excitation frequency, while for the pulse excitation the transmitted vibration has a less hazardous low frequency equal to the natural frequency of the main isolation system. Within the assumed approximations, the effectiveness does not directly depend on the stiffness k_2 of the auxiliary isolation system.

The amplitude of the foundation box is approximately equal to its static deflection under $P_{3\max}$, since $f_n = 2{-}7$ Hz is substantially lower than the natural frequency f_{n4}. The soil stiffness k_4 is nonlinear; the effective stiffness k_4 can be calculated as:

$$k_4 = 4\pi^2 f_{n4}^2 m_4 \qquad [19]$$

Table 2 Impact pulse parameters for forging hammers

Dropping mass (tup + upper die), $m_1,\ t$	1	2	3	5	5.5	10	15	20
Pulse duration, τ_{p1}, ms	1.0	1.26	1.44	1.69	1.75	2.07	2.45	2.64
Load magnitude, P_o, kN	1925	2830	3700	5130	5500	7500	10890	12400

The amplitude of soil vibration in the first approximation is:

$$a_s = \frac{P_{3\max}}{k_4} = \frac{P_{3\max}}{4\pi^2 f_{n4}^2 m_4} = 0.17\sqrt{\left(\frac{m_3 m_4^2}{(m_3+m_4)(m_1+m_2+m_3)(m_1+m_2+m_3+m_4)}\right)\frac{\tau_{p1} f_n}{f_{n4}^2}} \quad [20]$$

Example For a hammer with $m_1 = 5000\,\text{kg} = 5\,\text{t}$, $m_2 = 20m_1$, $m_3 = 60m_1$, $m_4 = 40m_1$, $\tau_{pl} = 0.0017\,\text{s}$, $f_n = 4.5\,\text{Hz}$, $P_{o\max} = 5.1 \times 10^6\,\text{N}$, from eqn [17] $P_{3\max} = 0.0165 P_{o\max} = 0.083 \times 10^6\,\text{N}$. From eqn [20], $a_s = 2.3 \times 10^{-4}\,\text{m}$. The measured amplitude of the foundation box vibration was $a_s = 1.8 \times 10^{-4}\,\text{m}$. The discrepancy ($\sim 24\%$) is due to: less severe impact conditions during the test (a billet was forged rather than rigid dies coimpacted); damping c_2, c_3, c_4, as well as the nonlinearity of soil behavior were not considered in the analysis; etc.

The fundamental natural frequencies of industrial and residential buildings (2–4 Hz) are in the range of the natural frequencies of the spring-isolated foundations, thus quasiresonant amplification of building vibrations may occur due to slow decay of soil vibrations resulting from one hammer blow.

The increased damping in both anvil and main isolators would reduce (but not very significantly), the transmissibility described by eqn [17]. In addition, the increased damping accelerates decaying of the foundation vibrations and thus reduces adverse vibration effects on humans, on precision equipment, and on structures. Considering both effects, the principal parameter of the vibration isolation system for an object generating inertial pulses, such as forging hammers, becomes not its main natural frequency f_n, but a shock isolation criterion:

$$\Phi_{sh} = \frac{f_n}{\delta^{0.25}} \quad [21]$$

Increasing damping in both main and anvil isolators to $\delta = 1-1.25$ allows us to increase the natural frequency of the vibration isolation system by a factor of ~ 1.5, from $f_n = 2-6\,\text{Hz}$ to $3-9\,\text{Hz}$ with the same isolation effectiveness. Stiffer springs and/or reduced mass m_3 of the foundation block can be used without degrading the system stability but significantly cutting costs. These conclusions were validated by testing a 0.75 t hammer on the foundation block supported by rubber isolating mats ($f_n = 7\,\text{Hz}$, $\delta = 0.8$). The system performance was satisfactory, similar to the performance of spring-suspended foundations having lower natural frequencies.

General Purpose Machinery and Equipment

Selection of the isolation system parameters for this large and diversified group is influenced by the dynamic stability and vibration level of the machine, and dynamic loads in the joints (especially bearings).

Influence of Mounting Conditions on Dynamic Stability

Working processes in production machinery, especially the cutting processes, may, in effect, introduce negative damping into the structure. When the total damping balance in the system machine/production process becomes negative, chatter appears. Fastening the machine bed by stiff mounts to a rigid foundation improves the dynamic stiffness of the machine structure and its chatter resistance. Compliant mounts (vibration isolators) may not have such an effect. The influence of natural frequency and damping of the isolation system on the dynamic stability of the production process can be analyzed by considering the dynamic coupling in the system. If the dynamic stability of a machine is sensitive to mounting conditions, their effect is determined by the magnitude of the dynamic stability criterion:

$$\Phi_{ds} = f_v^3 \delta_v \quad [22]$$

This criterion states that a small reduction of the natural frequency of the mounting or vibration isolation system can only be compensated by a substantial increase in damping of the mounting system.

Vibration isolators influence the chatter resistance of a machine tool only when its structural stiffness k_m and/or structural damping δ_m are low, or other structural or process features are not optimal. Stiff machine tools are usually not noticeably influenced by mounting conditions. Sensitivity to the mounting condition may change as a result of changing its internal configuration (position of the tool carriage in a lathe, position of the gantry on a plano-milling machine, etc.).

Example The dynamic stability criterion (eqn [22]) was validated by extensive tests performed on a

medium-sized lathe. Chatter resistance (the maximum depth of cut without chatter $t_{\lim}$), was measured with different sets of mounts, both all-metal jack mountings and CNF isolators with rubber flexible elements, providing various natural frequencies and degrees of damping of the installation/vibration isolation system. **Figure 8** shows that the values of t_{lim} for different mounting conditions are closely correlated with values of Φ_{ds}.

Vibration Levels of General Purpose Machines

Vibrations with the natural frequencies of the mounting system may interfere with the normal performance of general purpose machines. A real machine has a multitude of vibration sources acting in different directions and with different frequencies; the dynamic characteristics of the floors and other supporting building structures may also affect the vibration levels. While nonexcessive vibration levels may not be detrimental for performance, they may cause annoyance and discomfort to operators. Though only an experimental selection of isolators is reliable, the semi-qualitative analytical criteria listed below can be useful.

The most common vibration source is centrifugal forces from rotating unbalanced components, such as gears, pulleys, flanges, etc. The amplitude of the centrifugal force is proportional to the second power of the rotational frequency f. However, tolerances on the unbalance values become stricter for higher f. Allowable F_{cf} is proportional to $f^{0.5}$ for rotors of electric motors; to $f^{0.5}$ for grinding wheels; to $f^{0.5} - f^{-0.5}$ for unbalanced blanks for machining

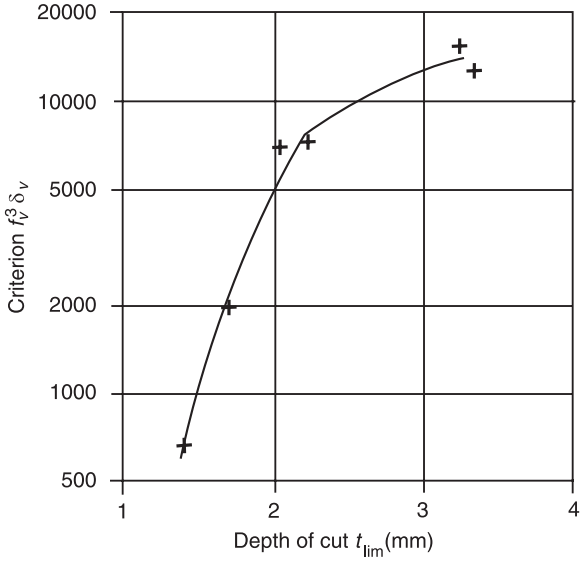


Figure 8 Maximum stable depth of cut $t_{\lim}$ vs criterion $f_v^3 \delta_v$.

on lathes, such as forgings, castings, etc. It can be assumed that the rated amplitudes of the centrifugal forces do not depend on frequency. This is often true for other sources of machine vibrations. The most pronounced spectral amplitudes of vibratory displacement for several types of machine tools, determined during idling and averaged over an ensemble can be considered as frequency independent in the 10–100 Hz range. Thus, resonances in the system 'machine on its mounts' are very probable for both rigid and soft mounting elements. The maximum amplitudes of relative displacement in the working area with the above assumptions do not depend on the natural frequency of the isolation system, but only on its damping which could be considered as a vibration level criterion:

$$\Phi_{vl} = \delta_v \qquad [23]$$

Often the vibratory velocity level is considered as an indicator of the machine vibration status. An equally hazardous or annoying action of vibration on personnel corresponds to an equal vibratory velocity level at frequencies higher than 2–8 Hz (International Standard, ISO 2631). Comparison of alternative mounting systems can be performed by the vibratory velocity level criterion:

$$\Phi_{vv} = f_v \delta_v \qquad [24]$$

Thus, to reduce the vibratory velocity level of an isolated object, increase of the natural frequency and of damping have similar effects.

Influence of Vibration Isolation on Bearing Loads

In many cases the useful life of bearings inside the machine installed on vibration isolators is lengthened. Dynamic loads acting on bearings are due mainly to the centrifugal force from the supported unbalanced rotor. While the main effect of vibration isolation is reduction of transmission of the unbalanced force $F(t)$ to the foundation, the secondary effect of vibration isolation is change of dynamic load $R(t) = R_o \cos \omega t$ in the bearing. The influence of the isolators on the dynamic load amplitude R_o can be expressed as the influence function:

$$W = (R_o)_v / (R_o)_r \qquad [25]$$

where $(R_o)_v$ is the dynamic load amplitude in the bearings of the isolated object comprising the rotor, and $(R_o)_r$ is the same for the rigidly installed object. In a broad frequency range, both force transmissibility $\mu_F < 1$, and $W < 1$, thus vibration isolation is accompanied by reduction of dynamic loads in bearings.

Figure 9 shows μ_F and W vs the frequency ratio f/f_v where f_v is the natural frequency of the vibration isolation system, for a case of light rotor $(M_1/M_2 = 0.1)$, **Figure 9A**, and for a case of heavy rotor $(M_1/M_2 = 1.0)$, **Figure 9B**. Here M_1 is the mass of the rotor, M_2 is the mass of the machine, k_1 is the stiffness of the bearing; k_2 is the stiffness of the isolators. The stiffness ratio for both cases is $k_1/k_2 = 10$ and the damping ratios for both the rotor subsystem $M_1 - k_1 - M_2$ and for the vibration isolation subsystem $M_2 - k_2$, are $\zeta_1 = \zeta_2 = 0.005$. The frequency ranges within which both μ_F and $W < 1$ are quite broad.

Influence of Vibration Isolation on Noise

Vibration isolation reduces the transmission of high frequency vibrations across structures and thus should result in reduction of noise in spaces which are adjacent to an isolated vibration-producing device, but separated from this device by structural partitions. An example of such transmission reduction is illustrated in **Figure 10**. It is less obvious what happens in the near-field at the device itself. **Figure 10** shows that noise level at the device may decrease or increase. Noise levels measured at a stamping press sometimes are reduced when the press is installed on vibration isolation mounts.

A noticeable noise reduction results if the majority of production machinery in a shop is installed on vibration isolators, most probably due to reduction of floor-radiated noise. In a shop with ten operating lathes, the sound pressure level reduction was 2 dB(A) (87.5 dB(A) for vibration isolated machines vs 89.5 dB(A) for rigidly installed machines) after rigid attachment to the floor (cement grouting) was replaced by installation on CNF isolators, $f_{vz} = \sim 20$ Hz. Even more significant, 4–5 dB(A) reduction was measured in the most annoying high frequency range.

Vibration Isolated Objects Installed on Nonrigid Supporting Structures

Stationary (e.g., production and measuring) equipment is usually attached by vibration isolators to rigid supporting structures (foundation plates, individual foundation blocks). However, in some cases both vibration-sensitive and vibration-producing devices are installed on nonrigid structures, such as floors over the basement or on higher floors of multistory buildings. This is always the case for objects installed

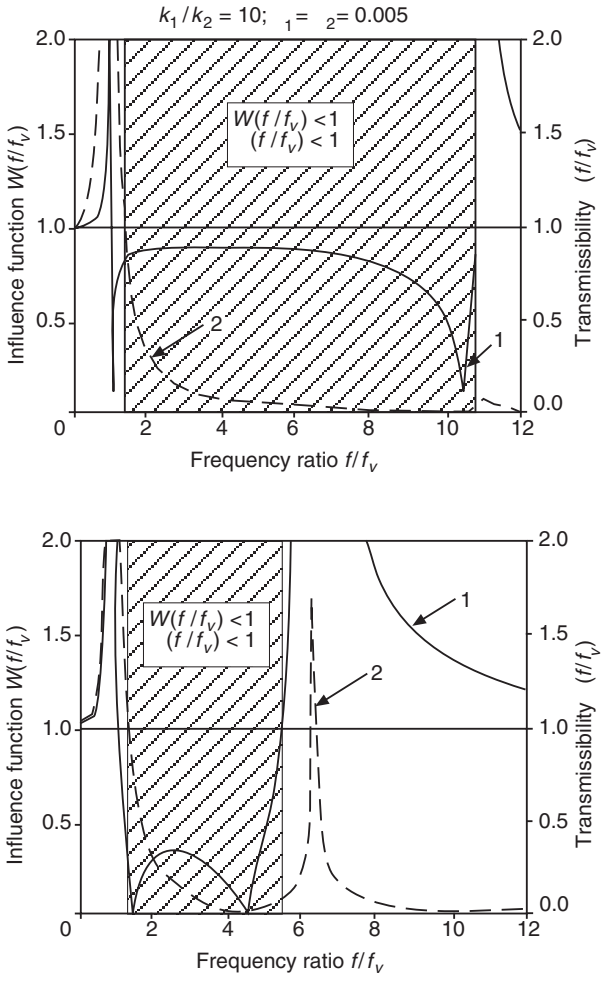


Figure 9 Frequency dependence of influence function W (1) and transmissibility μ_F (2). (A) light rotor $(M_1/M_2 = 0.1)$; (B) heavy rotor $(M_1/M_2 = 1.0)$.

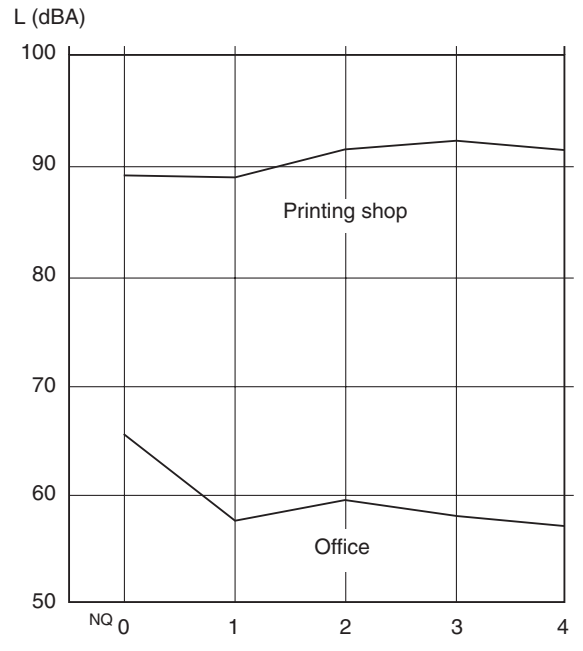


Figure 10 Noise level readings vs mounting conditions for knife-type paper folding machine on the second floor; the office is at the ground floor underneath the machine.

on vehicles, such as car engines, machinery on surface and underwater ships, aircraft, etc.

This problem can be analyzed by modeling the dynamic characteristics of the isolated object, the supporting structure, and the impedances of the vibration isolators. In most cases, the mass of the isolated object is substantially greater than the 'effective mass' of the supporting structure significantly involved in the vibratory process associated with the object. On the other hand, the effective stiffness of the supporting structure in the vicinity of the object is substantially greater than the stiffness values of the isolators. Thus, the main influence of the nonrigid supporting structure is usually modification (usually reduction) of the effective damping in the system. The situation may be significantly different in the high (acoustical) frequency range where the supporting structure, the isolated object, and the isolators (considered as distributed parameters system with corresponding high frequency resonances) are interacting dynamically. The system 'car engine–engine mounts' has been analyzed for the case of rigid foundation and for the case of actual supporting conditions on the low-stiffness vehicle sub-frame. **Figure 11** shows force transmissibility for a rigid foundation and for the actual 'flexible' supporting structure. The lines are similar; the resonance peaks of transmissibility are at the same frequencies (engine rpm) in both cases. Some peaks have increased height (reduced damping), some have reduced height (increased damping), and one peak is the same for both cases.

Some general considerations for vibration isolation of objects on nonrigid structures, based on analyses of simple models can be formulated as follows:

Installation of vibration-sensitive devices The upper floor vibration levels are usually 1.25–1.7 times higher than those of the ground floor, thus the vibration isolation criterion Φ_p from eqn [6] should be 1.4–1.7 times less than it would be for the same device on the ground floor. Since a corresponding reduction of natural frequency may create instability or excessive rocking motions, the proper approach is to increase damping while not significantly reducing isolator stiffness.

Installation of a vibration producing or a general purpose machine The response of the nonrigid supporting structure to excitation is amplified because of its small damping. Use of compliant isolators may lead to instability or to excessive rocking motions. But since the effective mass of the floor 'attached' to the installed machine is $\sim$1.5–2.5 times less than the mass of the machine (for floor structures made of prestressed concrete plates). Thus, the dynamic characteristics, especially damping, of the floor structure can be controlled by using highly damped isolators. It is possible to increase the effective damping of the floor (or other nonrigid supporting structure, such as vehicle structure) 2.5–4 fold and thus correspondingly reduce its sensitivity to external excitations.

Experimental Selection of Isolators

The above criteria do not consider the dynamic data of the floor; specific features of machine vibrations in different modes of the isolation system; dynamics of the machine itself and isolators in a high-frequency range; the real character of exciting forces; various

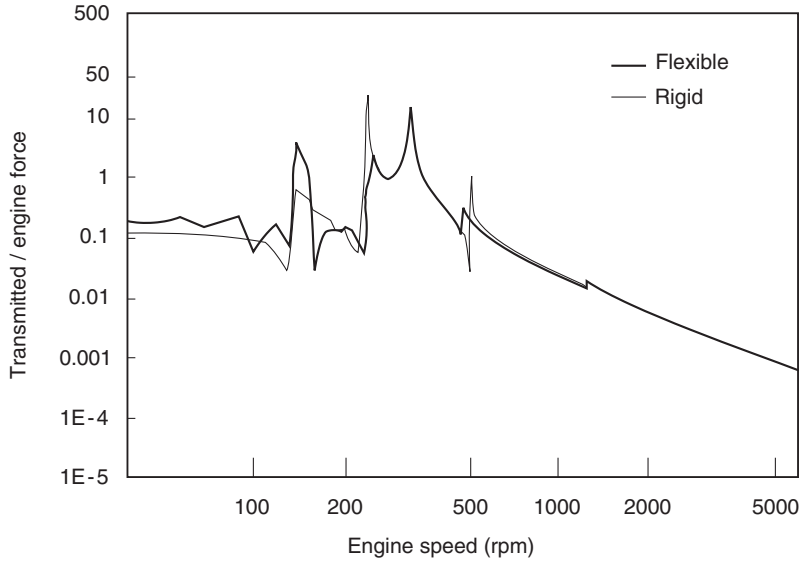


Figure 11 Transmissibility for rigid and flexible foundation models for engine mounted in vehicle (at transmission mount location).

regimes of machine performance, etc. The selection of isolators that consider these factors could provide substantial advantages. However, an analytical approach for individual objects seems to be impractical. The best way is to compare several alternatives of the machine installation, with specific reference to the specified requirements, when each alternative is characterized by a single-rated parameter (selection criterion). Since reinstallations of the objects, especially large ones, is a time- and labor-consuming procedure, variable-stiffness isolators can be useful.

When the object to be vibration isolated is used in different modes of operation (e.g., a machine tool with many spindle and feed speeds, a car engine operating in a broad rpm range), a 'common sense' approach can be used, or the selection criterion can be:

$$B_\Sigma = \alpha_1\beta_1 B_1 + \cdots + \alpha_i\beta_i B_i + \cdots \qquad [26]$$

where B_i is the selection criterion for the ith mode of operation, α_i is the weighting factor assigned to the ith mode, and β_i is a fraction of full working time during which the device is used in the ith mode of operation.

Example The 'common sense' selection of vibration isolators was applied for a knife-type folding machine installed on the second floor of the printing shop. The goal was to reduce noise transmission from the machine into the office room downstairs. **Figure 10** gives noise level readings in dBA in the office and in the printing shop for the machine on metal jack mounts (#0) and on rubber mounts providing different f_v (26 Hz – #1; 20 Hz – #; 16 Hz – #3; 10 Hz – #4). Unexpectedly, the #1 alternative (the stiffest isolators) was judged optimal (it gave the same noise level in the office as for #4 isolators, but lower noise in the printing shop and less rocking of the machine).

Nomenclature

f	frequency
F	force
I	inertia
M	mass
O_1	center of gravity
T	torque
W	weighting factor
X	amplitude
δ_m	log decrement
δ_v	isolation damping
τ	duration

See also: **Transform methods**; **Vibration isolation theory**; **Vibration transmission**.

Further Reading

Golec Z, Cempel C (1990) Machine vibroisolation and dynamic loads of bearings. *Mechanical Systems and Signal Processing* 4(5): 367–375.

Gordon CG (1991) Generic criteria for vibration-sensitive equipment. *In Vibration Control in Microelectronics, Optics and Metrology, SPIE Proceedings*, vol. 1610.

Kim J-H, Lee J-M (2000) Elastic foundation effects on the dynamic response of engine mount systems. *Proceedings of the Institution for Mechanical Engineers* Part D, 214: 45–53.

Rivin EI (1965) Review of vibration insulation mountings. *Machines and Tooling*, 8, 37–46.

Rivin EI (1974) How methods of installation affect the vibration resistance of machine tools. *Machines and Tooling* 45 (11): 25–27.

Rivin EI (1979) Principles and criteria of vibration isolation of production machinery. *Transactions of the ASME, Journal of Mechanical Design* 101 (4): 682–692.

Rivin EI (1985) Passive engine mounts – directions for future development. *SAE Transactions*, pp. 3.582–3.592.

Rivin EI (1987) Evaluation of vibration isolation systems for forging hammers. In *Vibration Isolation of Heavy Structures*. London: Institute of Acoustics, pp. 91–97

Rivin EI (1995) Vibration isolation of precision equipment. *Precision Engineering* 17: 41–56.

Rivin EI (1999) *Stiffness and Damping in Mechanical Design*. New York: Marcel Dekker.

Snowdon JC (1979) *Handbook of Vibration and Noise Control*, Report TM 79–75 U.S. Department of the Navy.

U.S. Department of Defense (1988) MIL-STD-810E, Military Standard: Environmental Test Methods.

Ungar EE, Sturz DH, Amick CH (1990) Vibration control design of high technology facilities. *Sound and Vibration* 8: 20–27.

Veprik AM, Babitsky VI, Pundak N, Riabzev SV (2000) Vibration protection for linear stirling cryogenic cooler of airborne infrared application. *Shock and Vibration* 7:363–387

VIBRATION PROPERTIES, COMPARISON

See **COMPARISON OF VIBRATION PROPERTIES: COMPARISON OF MODAL PROPERTIES; COMPARISON OF VIBRATION PROPERTIES: COMPARISON OF RESPONSE PROPERTIES; COMPARISON OF VIBRATION PROPERTIES: COMPARISON OF SPATIAL PROPERTIES**

VIBRATION TRANSMISSION

S I Hayek, Pennsylvania State University, University Park, PA, USA

Copyright © 2001 Academic Press

doi:10.1006/rwvb.2001.0167

Introduction

The propagation of vibration in complex connected structures transmits and reflects elastic waves at junctions between different structural members of that structure. These junctions represent structural discontinuities, be it a geometrical change of shape, a change in the type of the element, a change in the cross-sectional area, density or elasticity, or changes introduced externally such as blocking masses, elastic springs, and boundary conditions.

Since these changes at a junction will cause reflection and transmission of the incident waves at that junction, part of the incident vibration mechanical power is transmitted through, giving rise to attenuation of vibrational power across that junction. In this section, the reflection or transmission coefficients will be presented for structural members undergoing longitudinal, torsional or flexural vibration.

Longitudinal Vibration

Change of Cross-section

Consider an infinite elastic bar or plate, $\infty < x < \infty$, whose density, Young's modulus, Poisson's ratio and cross-section are ρ_1, E_1, v_1, and A_1, for $x < 0$ and ρ_2, E_2, v_2, and A_2 for $x > 0$. An incident longitudinal wave traveling in the $x < 0$ region in the positive x direction impinges at the junction $x = 0$ and causes a reflected wave in the $x < 0$ region and a transmitted wave in the $x > 0$ region. Defining the impedance for sections $x < 0$ or $x > 0$ as Z_1 and Z_2, respectively:

$$Z_1 = A_1' \sqrt{(\rho_1 E_1')} \qquad [1]$$

and

$$Z_2 = A_2' \sqrt{(\rho_2 E_2')}$$

where $E' = E$ for beams and $E' = E/(1 - v^2)$ for plates and $A' = A$ for beams and $A' = h$ for plates, then the transmission and reflection coefficients α_r and α_t, respectively, are given by:

$$\alpha_r = \frac{Z_1 - Z_2}{Z_1 + Z_2} \qquad [2]$$

$$\alpha_t = \frac{2Z_1}{Z_1 + Z_2} \qquad [3]$$

Since the vibrational power is proportional to the impedance and the velocity squared, the reflection and transmission efficiencies τ_r and τ_t are given by:

$$\tau_r = |\alpha_r|^2 \qquad [4]$$

$$\tau_t = \frac{Z_2}{Z_1} |\alpha_t|^2 \qquad [5]$$

Note that the reflected and transmitted efficiencies add up to unity. The formulae given in eqns [3] and [5] represent the transmission loss factors for changes due to density, elasticity or cross-sectional area.

Blocking Mass on an Infinite Bar

Consider a blocking mass M attached to an infinite uniform bar at $x = 0$, the reflection and transmission coefficients are:

$$\alpha_r = \frac{i\omega M/2Z}{1 + i\omega M/2Z} \qquad [6]$$

$$\alpha_t = \frac{1}{1 + i\omega M/2Z} \qquad [7]$$

$$\tau_r = \frac{\omega^2 M^2/4Z^2}{1 + \omega^2 M^2/4Z^2} \qquad [8]$$

$$\tau_t = \frac{1}{1 + \omega^2 M^2/4Z^2} \qquad [9]$$

where $Z = A' \sqrt{(\rho E')}$

Torsional Vibrations

Since torsional wave propagation in elastic torsion members obeys the same wave equation as longitudinal vibrations, one could rewrite the formulae, eqns [2]–[5], for torsional vibration reflection and transmission across a junction by redefining the impedances. Let ρG and J represent the density, shear modulus and cross-sectional polar moment of inertia

of a circular torsional member, respectively, then define the moment impedances as:

$$Z_1 = J_1\sqrt{(\rho_1 G_1)}$$

and

$$Z_2 = J_2\sqrt{(\rho_2 G_2)}$$

The reflection and transmission coefficients then are given by eqns [2]–[5]. If the cross-section is rectangular, the polar moment of inertia must be modified.

Flexural Vibrations

The reflection and transmission coefficients for flexural waves in two semi-infinite beams ($x < 0$ or $x > 0$) joined at the junction $x = 0$ can be evaluated for an incident bending wave traveling in the $x < 0$ region in the positive x direction. The bending waves reflected or transmitted at $x = 0$ have a propagating component and an exponentially decaying near-field component. Thus, there is a near-field and far-field reflection and transmission coefficients. For flexural waves in beams and plates, let the flexural wave number k and flexural wave speed c be given by:

$$k^4 = \frac{\rho A'\omega^2}{D'} \qquad [10]$$

$$c^4 = \frac{\rho D'\omega^2}{A'} \qquad [11]$$

where the cross-sectional area:

$$\begin{aligned} A' &= A \text{ for beams} \\ &= h \text{ for plates} \end{aligned}$$

and the bending stiffness:

$$\begin{aligned} D' &= EI \text{ for beams} \\ &= Eh^3/12\left(1-\nu^2\right) \text{ for plates} \end{aligned}$$

and where A and I are the cross-sectional area and moment of inertia of a beam, and h is the thickness of a plate. Define the radius of gyration 'r' of a cross-section as:

$$\begin{aligned} r^2 &= I/A \text{ for a beam} \\ &= \tfrac{1}{12}h^2 \text{ for a plate} \end{aligned}$$

Define a nondimensional wavenumber:

$$\bar{k} = \sqrt{(12)}kr \qquad [12]$$

Define a nondimensional linear spring of stiffness K by:

$$\bar{\beta} = \frac{K}{\rho c^2} \qquad [13]$$

Define a nondimensional helical spring of rotational stiffness γ by:

$$\bar{\alpha} = \frac{\gamma}{\rho A\sqrt{(12)}rc^2} \qquad [14]$$

Define a nondimensional blocking mass M by

$$\bar{\mu} = \frac{M}{\sqrt{(12)}\rho \mathrm{A}r} \qquad [15]$$

Change of Cross-section

Consider two semi-infinite uniform beams (plates) joined at $x = 0$, each having cross-sectional area A, moment of inertia I, Young's modulus E, and Poisson's ratio v. The near-field reflection α_{nr} and transmission α_{nt} coefficients are defined as the reflected or transmitted amplitude at $x = 0$, respectively:

$$\alpha_{\mathrm{nr}} = \frac{\zeta\left(1-\eta^2\right) - 2\mathrm{i}\zeta(1-\eta) + 2\left(1-\zeta^2\right)\eta}{\zeta(1+\eta)^2 + 2\eta\left(1+\zeta^2\right)} \qquad [16]$$

$$\alpha_{\mathrm{nt}} = \frac{2(1+\zeta)(1+\eta) - 2\mathrm{i}(\zeta+\mathrm{i})(1-\eta)}{\zeta(1+\eta)^2 + 2\eta\left(1+\zeta^2\right)} \qquad [17]$$

and the far-field reflection and transmission coefficients α_{fr} and α_{ft} are given by:

$$\alpha_{\mathrm{fr}} = \frac{2\eta\left(1-\zeta^2\right) - \mathrm{i}\zeta(1-\eta)^2}{\zeta(1+\eta)^2 + 2\eta\left(1+\zeta^2\right)} \qquad [18]$$

$$\alpha_{\mathrm{ft}} = \frac{2(1+\zeta)(1+\eta)}{\zeta(1+\eta)^2 + 2\eta\left(1+\zeta^2\right)} \qquad [19]$$

where:

$$\zeta^4 = \frac{\rho_2 A_2' D_1'}{\rho_1 A_1' D_2'} \qquad [20]$$

and:

$$\eta^2 = \frac{\rho_2 A_2' D_2'}{\rho_1 A_1' D_1'} \qquad [21]$$

The reflection and transmission efficiencies can be computed from:

$$\tau_{\mathrm{r}} = |\alpha_{\mathrm{fr}}|^2 \qquad [22]$$

$$\tau_t = 1 - |\alpha_{fr}|^2 \qquad [23]$$

Infinite Beam on Simple Support

Consider a uniform infinite beam (plate) with a simple support at $x = 0$. The conditions at support point are that the slopes and moments are continuous and the displacement is zero. The near-field and far-field reflection and transmission coefficients are given by:

$$\alpha_{nr} = -1$$
$$\alpha_{nt} = 0$$
$$\alpha_{fr} = -\frac{1+i}{2}$$
$$\alpha_{ft} = -\frac{1-i}{2}$$
$$\tau_r = \tfrac{1}{2}$$
$$\tau_t = \tfrac{1}{2}$$

Two Semi-Infinite Beams Joined by a Hinge

Consider two semi-infinite uniform and identical beams (plates) joined at $x = 0$ by a hinge such that the displacements and shears are continuous but the moments are zero at $x = 0$. The near-field and far-field reflection and transmission coefficients are:

$$\alpha_{nr} = -i$$
$$\alpha_{nt} = 1 - i$$
$$\alpha_{fr} = -\frac{1+i}{2}$$
$$\alpha_{ft} = -\frac{1-i}{2}$$
$$\tau_r = \tfrac{1}{2}$$
$$\tau_t = \tfrac{1}{2}$$

Infinite Beam with a Sliding Support

Consider an infinite uniform beam (plate) where a sliding support exists at $x = 0$ such that the displacements and shears are continuous but the slopes are zero. The near-field and far-field reflection and transmission coefficients are:

$$\alpha_{nr} = 0$$
$$\alpha_{nt} = 1$$
$$\alpha_{fr} = \frac{1-i}{2}$$
$$\alpha_{ft} = \frac{1+i}{2}$$
$$\tau_r = \tfrac{1}{2}$$
$$\tau_t = \tfrac{1}{2}$$

Two Semi-Infinite Beams Joined by a Hinge and Helical Spring

Consider two semi-infinite beams (plates) joined by a hinge and connected through a helical spring of rotational stiffness γ at $x = 0$. Here the displacements, moments and shears are continuous at $x = 0$ and the moment is given by the helical spring stiffness times the difference of the slopes of the two beams at $x = 0$:

$$\alpha_{nr} = -\frac{1+i}{1-i(1+4\bar{k}\bar{\alpha})} \qquad [24]$$

$$\alpha_{nt} = -\frac{2i(1+2\bar{k}\bar{\alpha})}{1-i(1+4\bar{k}\bar{\alpha})} \qquad [25]$$

$$\alpha_{fr} = -\frac{1}{1-i(1+4\bar{k}\bar{\alpha})} \qquad [26]$$

$$\alpha_{ft} = -\frac{i(1+4\bar{k}\bar{\alpha})}{1-i(1+4\bar{k}\bar{\alpha})} \qquad [27]$$

$$\tau_r = \frac{1}{1+(1+4\bar{k}\bar{\alpha})^2} \qquad [28]$$

$$\tau_t = \frac{(1+4\bar{k}\bar{\alpha})^2}{1+(1+4\bar{k}\bar{\alpha})^2} \qquad [29]$$

Plots of $|\alpha_{fr}||\alpha_{ft}||\alpha_{nr}|$, and $|\alpha_{nt}|$ in dB scale are shown in **Figures 1–4**, respectively, vs non-dimensional wave number $\bar{k}$ for various values of the nondimensional helical spring stiffness $\bar{\alpha} = 0.1,\ 1,\ 10$, and 100.

An Infinite Beam Resting on a Linear Spring

Consider a uniform infinite beam (plate) resting on a linear spring at $x = 0$ of linear stiffness K:

$$\alpha_{nr} = -\frac{(1-i)\bar{\beta}/\bar{k}}{\bar{\beta}/\bar{k} - i(\bar{\beta}/\bar{k}+4)} \qquad [30]$$

$$\alpha_{nt} = -\frac{4i}{\bar{\beta}/\bar{k} - i(\bar{\beta}/\bar{k}+4)} \qquad [31]$$

$$\alpha_{fr} = -\frac{\bar{\beta}/\bar{k}}{\bar{\beta}/\bar{k} - i(\bar{\beta}/\bar{k}+4)} \qquad [32]$$

$$\alpha_{ft} = -\frac{i(\bar{\beta}/\bar{k}+4)}{\bar{\beta}/\bar{k} - i(\bar{\beta}/\bar{k}+4)} \qquad [33]$$

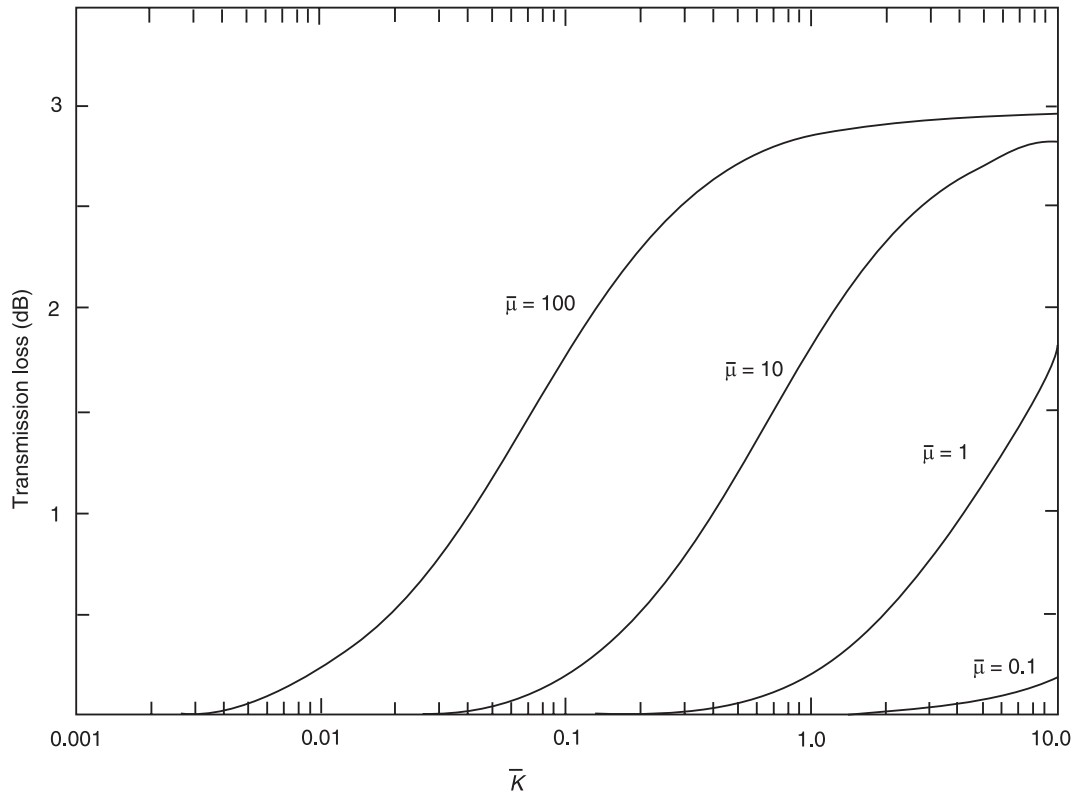


Figure 1 Far-field reflection coefficient for hinge with helical spring.

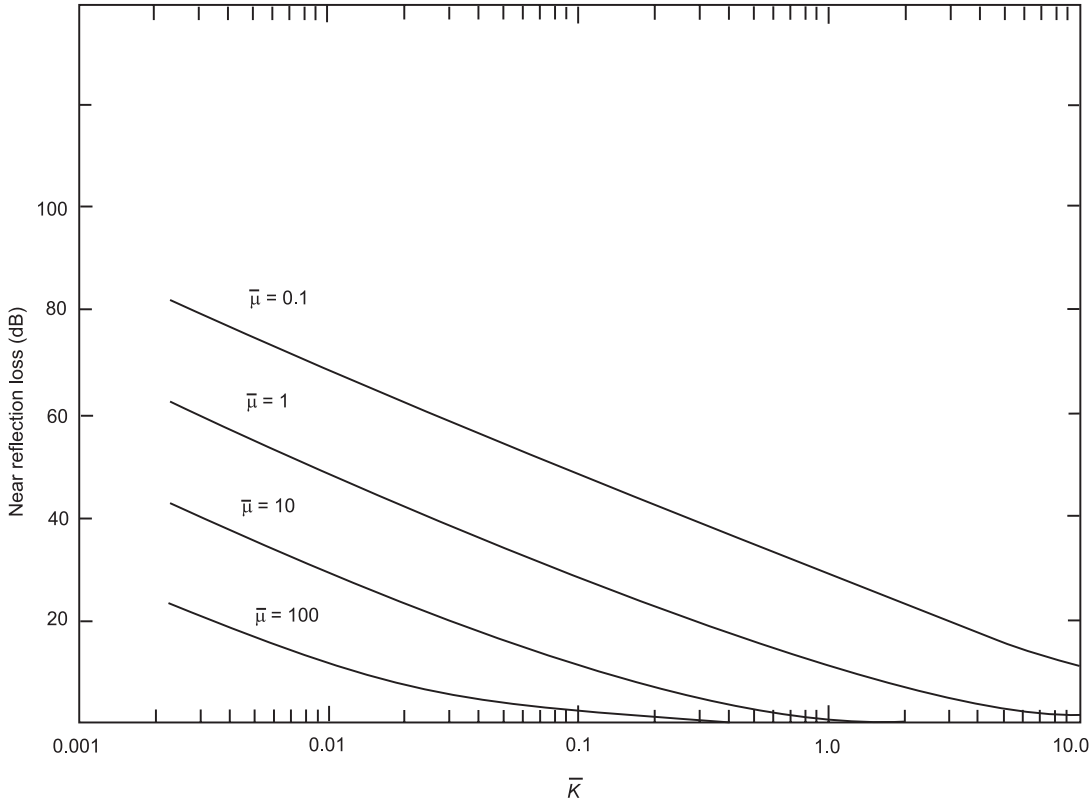


Figure 2 Far-field transmission coefficient for hinge with helical spring.

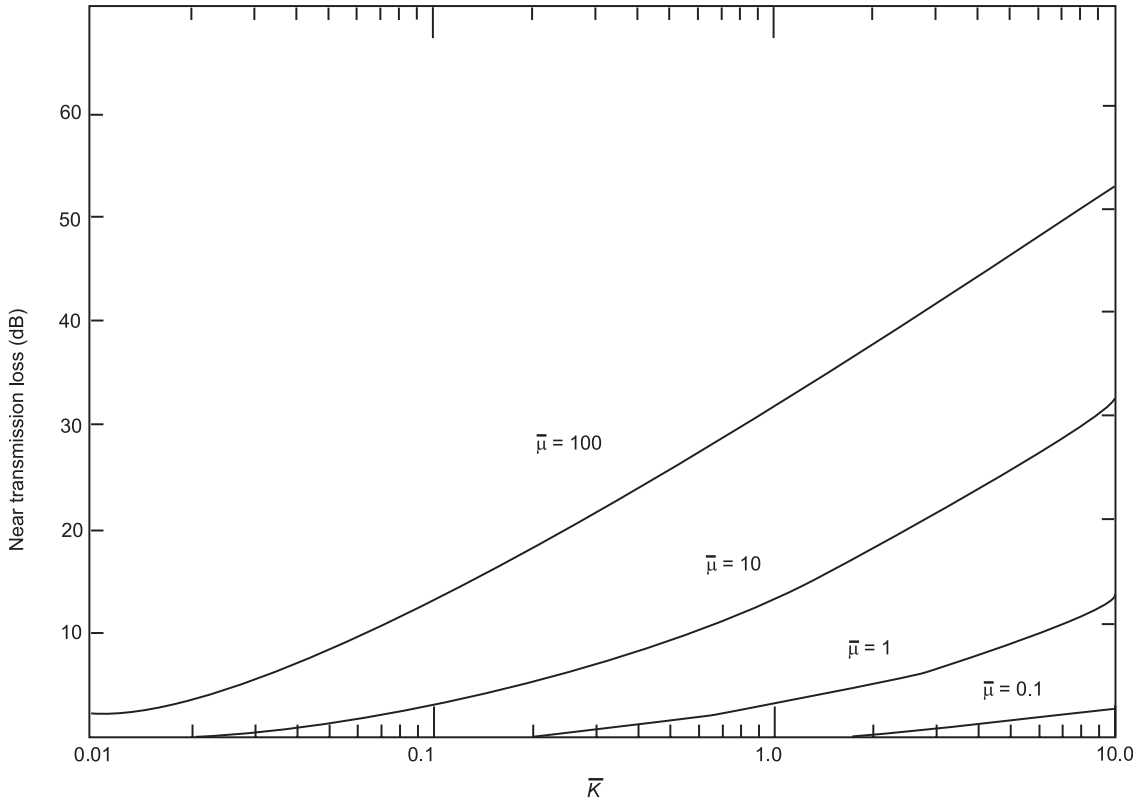


Figure 3 Near-field reflection coefficient for hinge with helical spring.

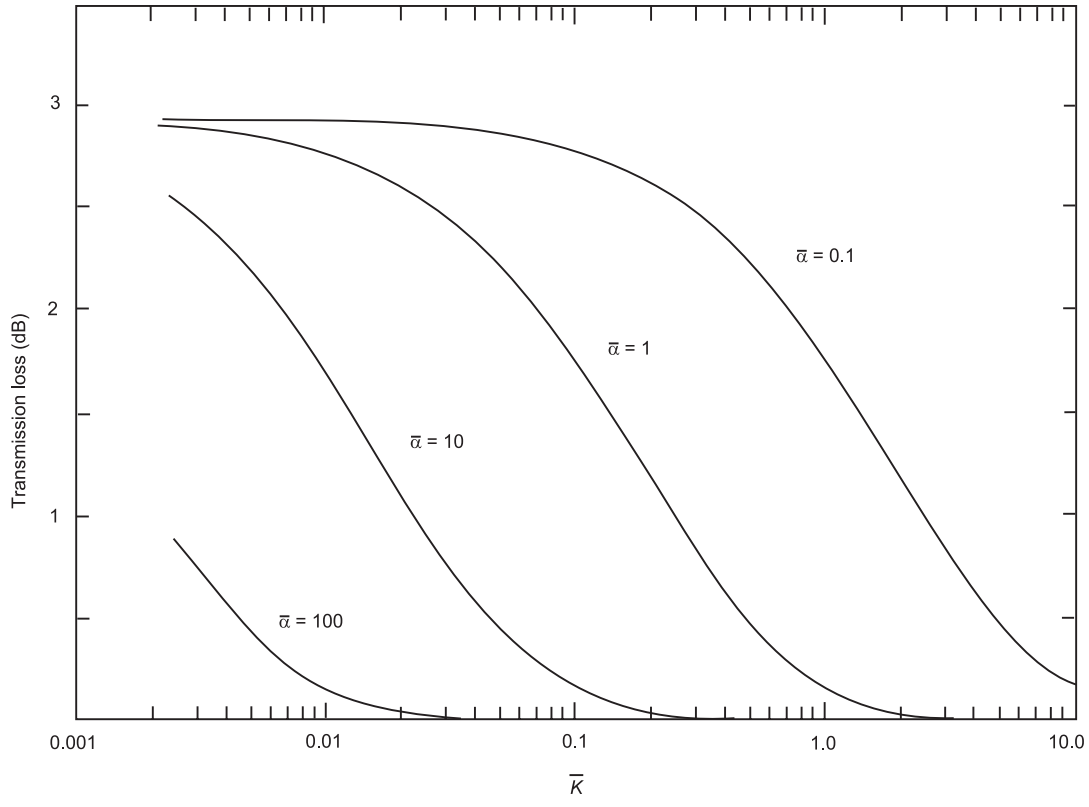


Figure 4 Near-field transmission coefficient for hinge with helical spring.

$$\tau_r = \frac{\left(\bar{\beta}/\bar{k}\right)^2}{\left(\bar{\beta}/\bar{k}\right)^2 + \left(\bar{\beta}/\bar{k} + 4\right)^2} \quad [34]$$

$$\tau_t = \frac{\left(\bar{\beta}/\bar{k} + 4\right)^2}{\left(\bar{\beta}/\bar{k}\right)^2 + \left(\bar{\beta}/\bar{k} + 4\right)^2} \quad [35]$$

Plots of $|\alpha_{fr}|, |\alpha_{ft}|, |\alpha_{nr}|$, and $|\alpha_{nt}|$ are shown in **Figures 5–8**, respectively, vs nondimensional wave number $\bar{k}$ for various values of the nondimensional spring stiffness $\bar{\beta} = 0.1$, 1, 10, and 100.

Infinite Beam with a Blocking Mass

Consider an infinite uniform beam (plate) with a blocking mass (line mass) M located at $x = 0$:

$$\alpha_{nr} = -\frac{(1 - i)\bar{\mu}\bar{k}}{\bar{\mu}\bar{k} - i\left(\bar{\mu}\bar{k} + 4\right)} \quad [36]$$

$$\alpha_{nt} = -\frac{4i}{\bar{\mu}\bar{k} - i\left(\bar{\mu}\bar{k} + 4\right)} \quad [37]$$

$$\alpha_{fr} = -\frac{\bar{\mu}\bar{k}}{\bar{\mu}\bar{k} - i\left(\bar{\mu}\bar{k} + 4\right)} \quad [38]$$

$$\alpha_{ft} = -\frac{i\left(\bar{\mu}\bar{k} + 4\right)}{\bar{\mu}\bar{k} - i\left(\bar{\mu}\bar{k} + 4\right)} \quad [39]$$

$$\tau_r = \frac{\left(\bar{\mu}\bar{k}\right)^2}{\left(\bar{\mu}\bar{k}\right)^2 + \left(\bar{\mu}\bar{k} + 4\right)^2} \quad [40]$$

$$\tau_t = \frac{\left(\bar{\mu}\bar{k} + 4\right)^2}{\left(\bar{\mu}\bar{k}\right)^2 + \left(\bar{\mu}\bar{k} + 4\right)^2} \quad [41]$$

Plots of $|\alpha_{fr}|$, $|\alpha_{ft}|$, $|\alpha_{nr}|$, and $|\alpha_{nt}|$ are shown in **Figures 9–12**, respectively vs nondimensional wave-number $\bar{k}$ for values of nondimensional mass $\bar{\mu} = 0.1,\ 1,\ 10$, and 100.

Nomenclature

A	cross-sectional area
c	flexural wave speed
E	Young's modulus
G	shear modulus
h	thickness of plate
I	moment of inertia
J	cross-sectional polar moment of inertia

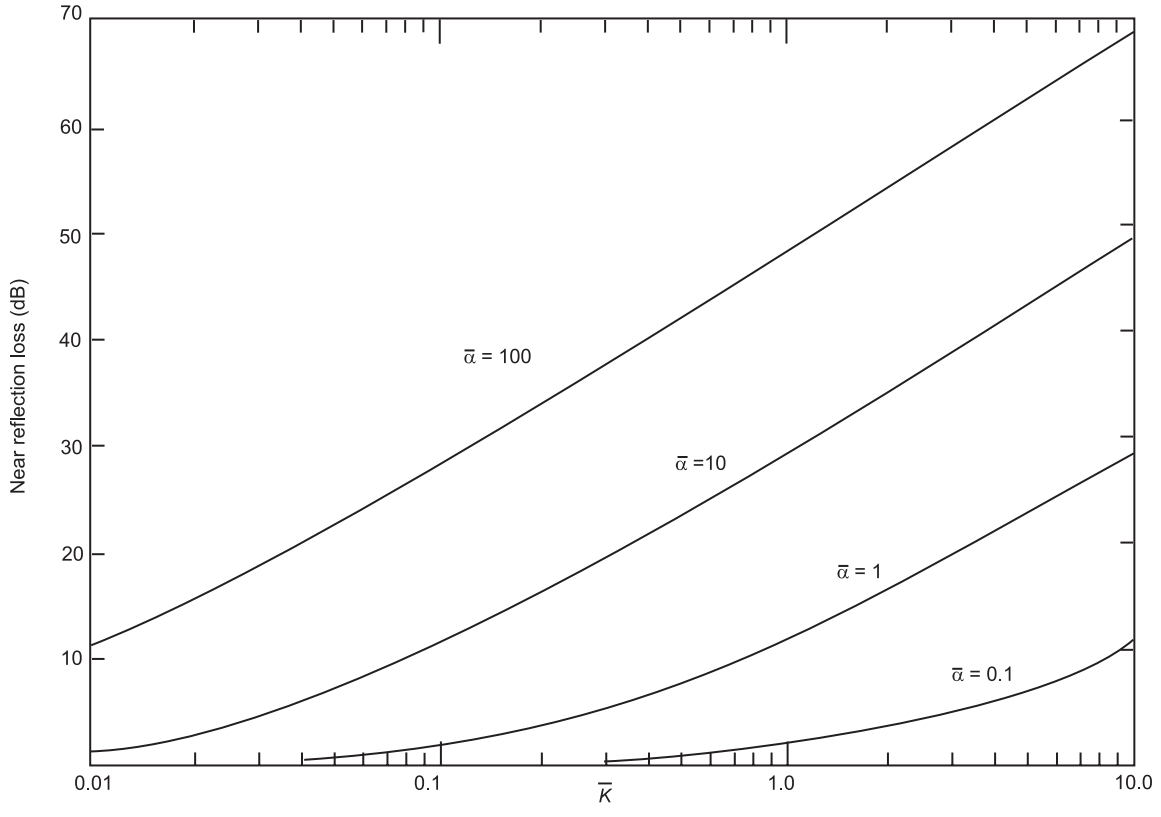


Figure 5 Far-field reflection coefficient for linear elastic spring.

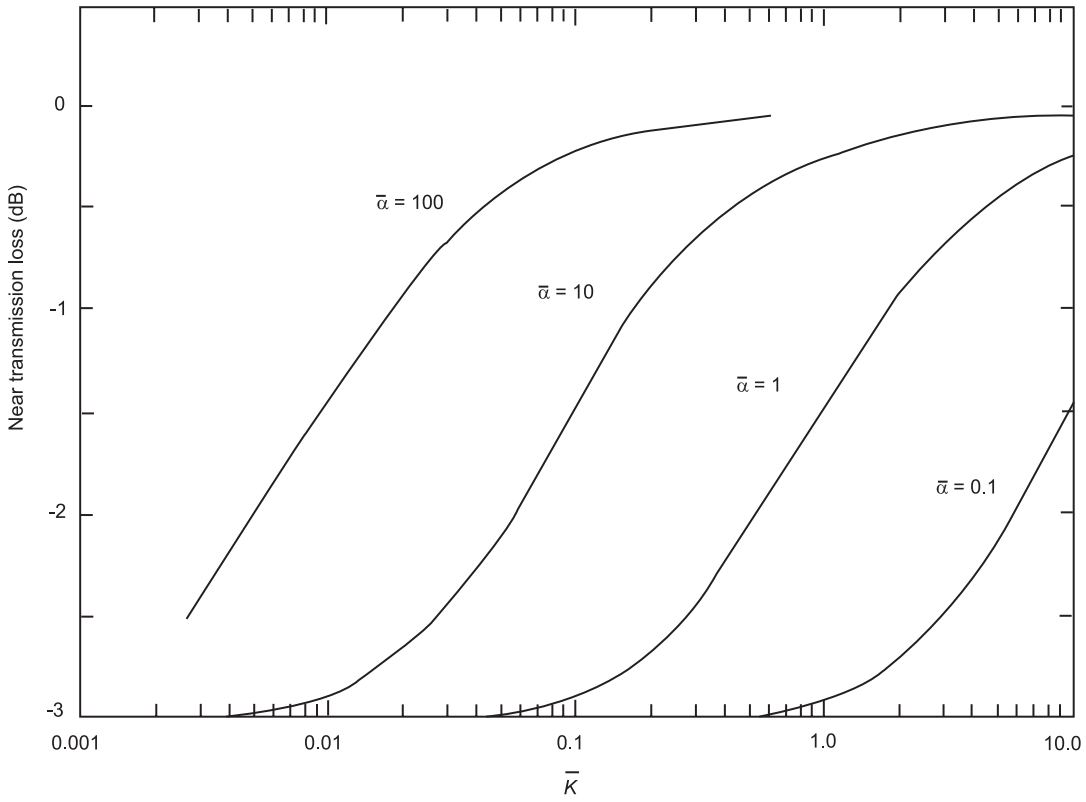


Figure 6 Far-field transmission coefficient for linear elastic spring.

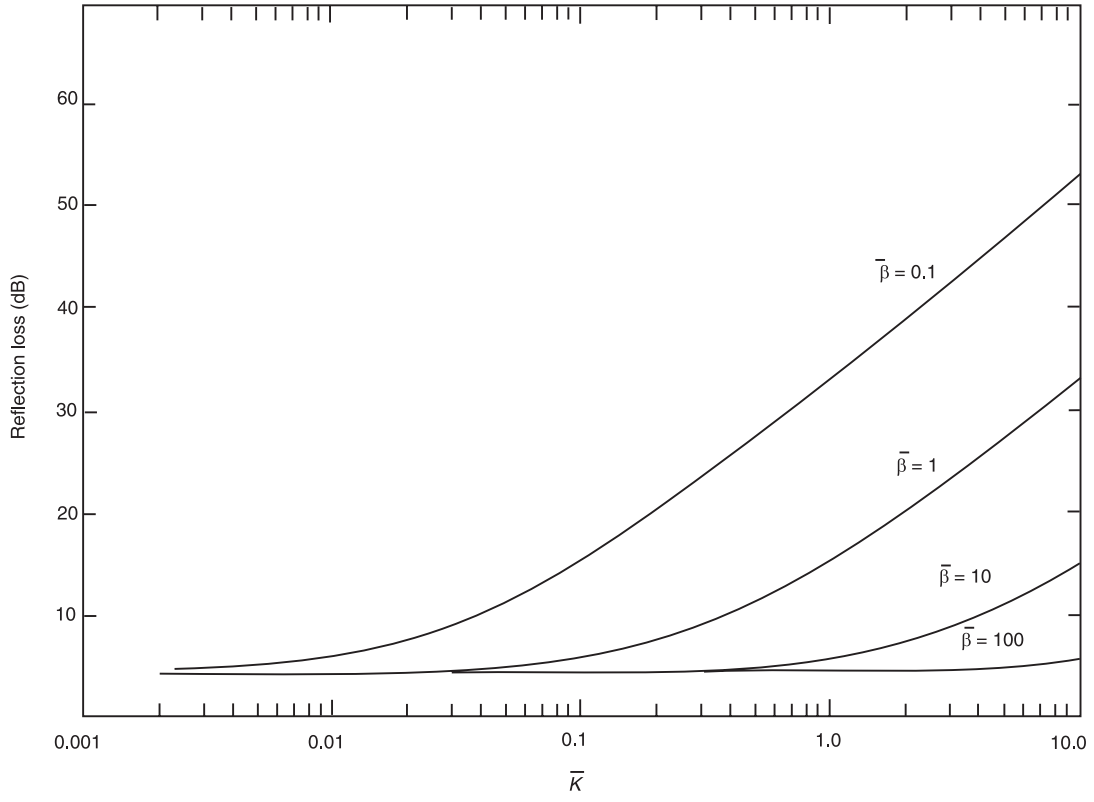


Figure 7 Near-field reflection coefficient for linear elastic spring.

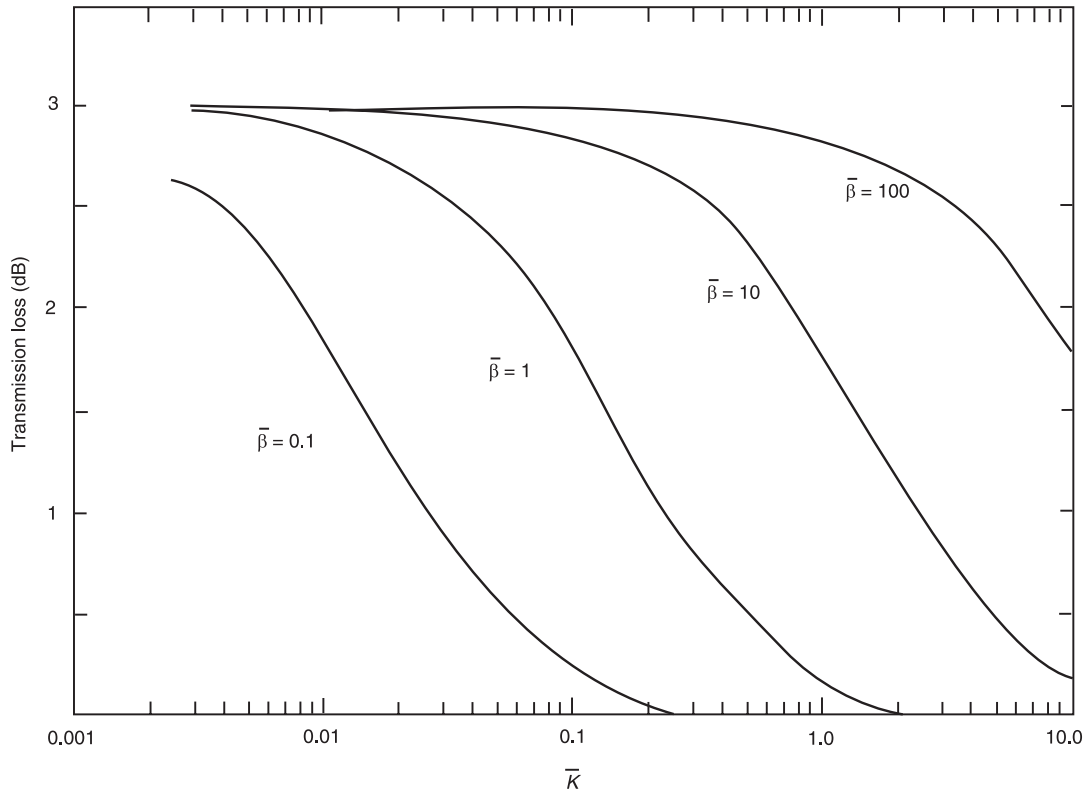


Figure 8 Near-field transmission coefficient for linear elastic spring.

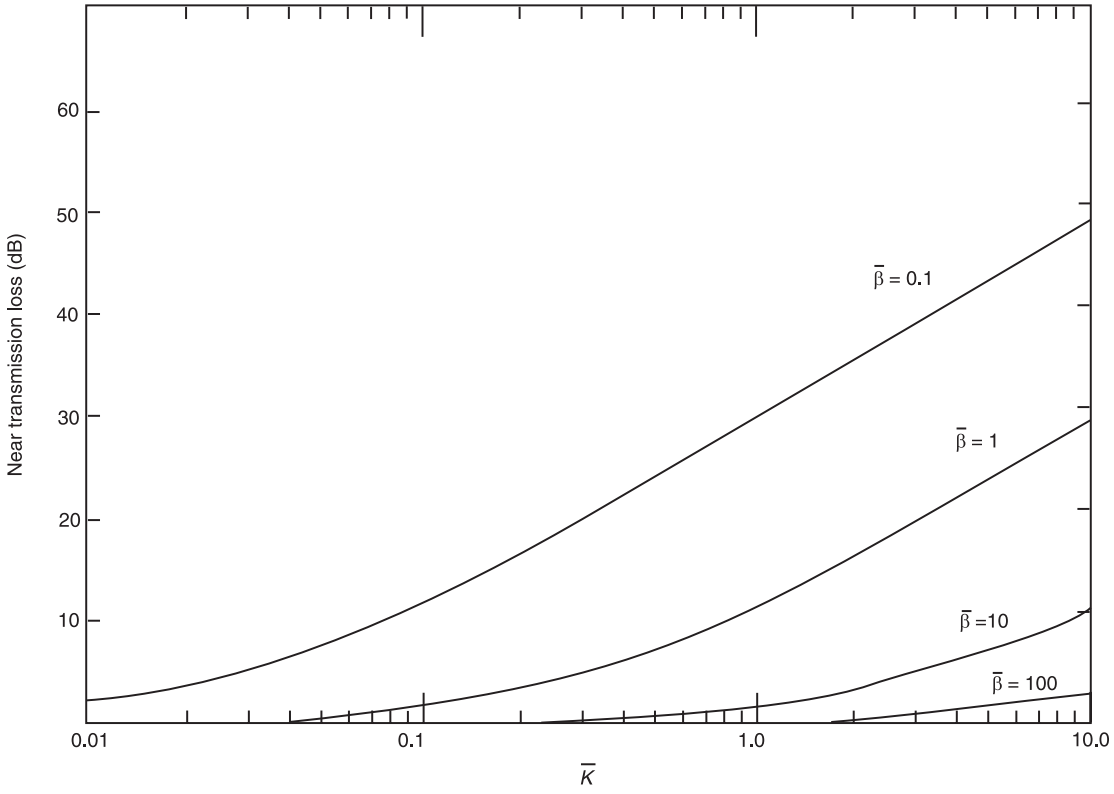


Figure 9 Far-field reflection coefficient for blocking mass.

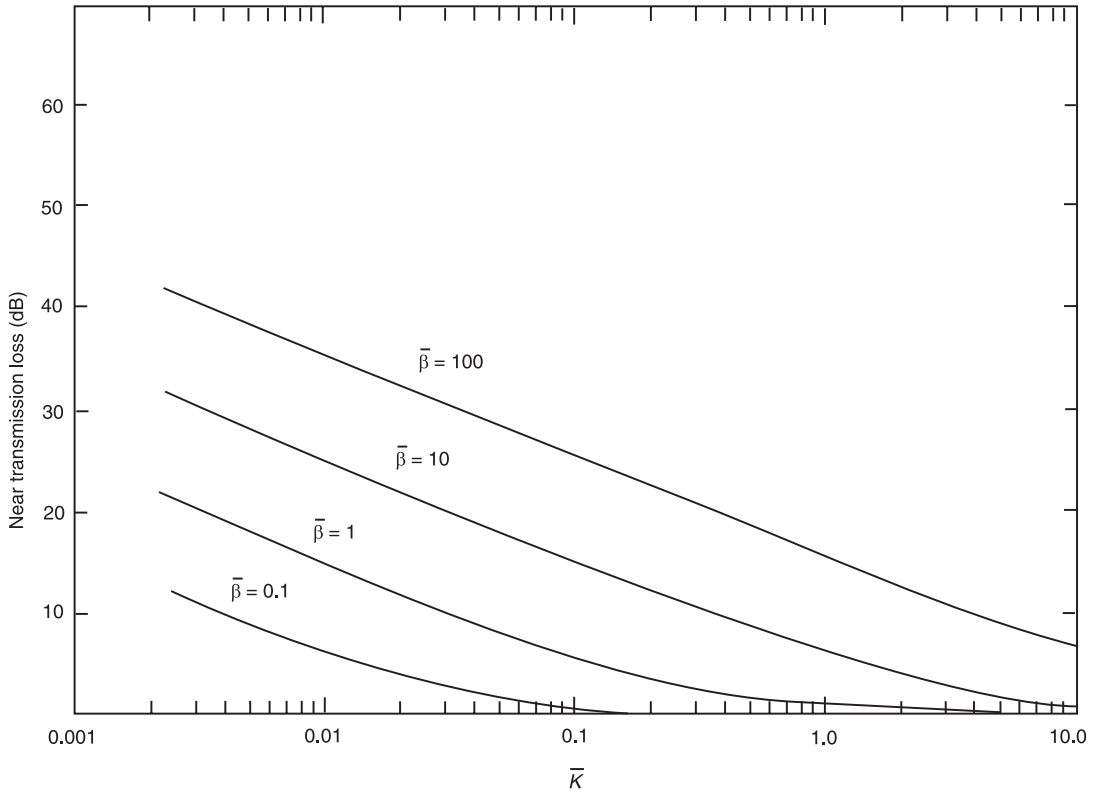


Figure 10 Far-field transmission coefficient for blocking mass.

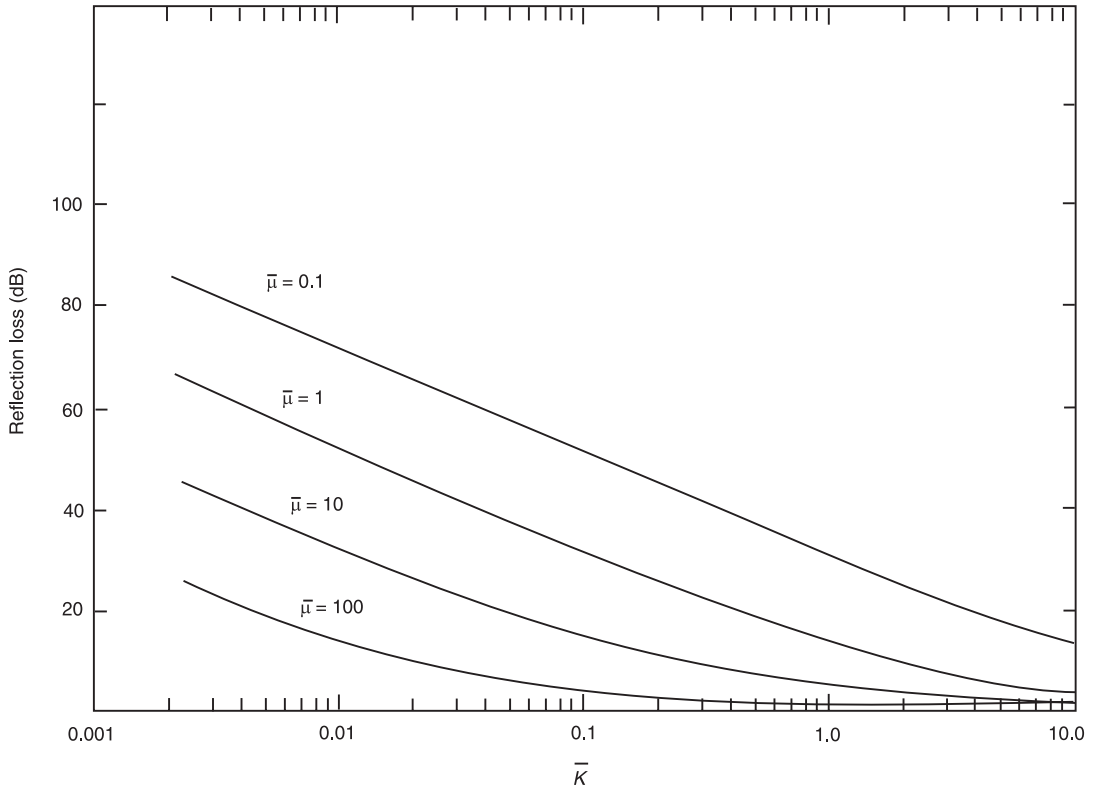


Figure 11 Near-field reflection coefficient for blocking mass.

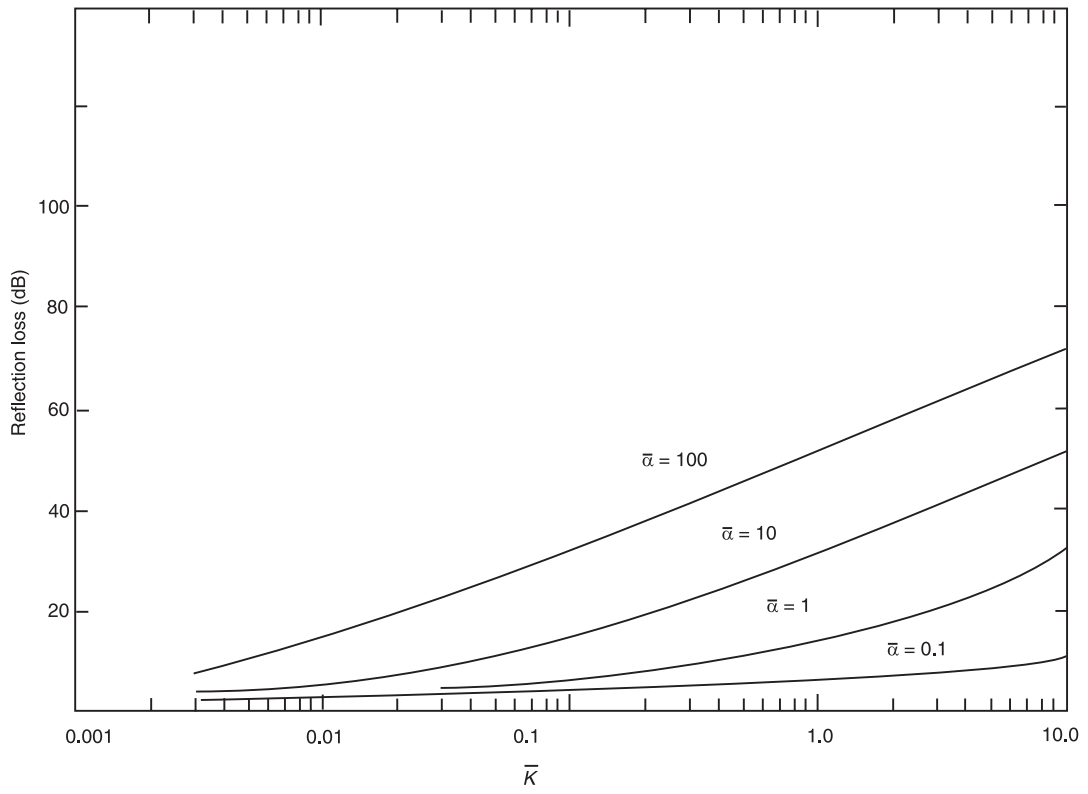


Figure 12 Near-field transmission coefficient for blocking mass.

k	flexural wave number
$\bar{k}$	nondimensional wave number
K	stiffness
M	blocking mass
Z	impedance
αr	reflection coefficient
αt	transmissions coefficient
γ	rotational stiffness
$\bar{\mu}$	nondimensional mass
ν	Poisson's ratio
ρ	density

See also: **Structure-acoustic interaction, high frequencies**; **Structure-acoustic interaction, low frequencies**; **Wave propagation**, Waves in an unbounded medium.

Further Reading

Cremer L, Heckl M, Unger EE (1973) *Structure-borne Sound*, New York: Springer-Verlag.

Graff KF (1975) *Wave Motion in Elastic Solids*, Columbus, OH: Ohio State University Press.

Skudrzyk EJ (1968) *Simple and Complex Vibratory Systems*. University Park, PA: Pennsylvania State University Press.

VIBRO-IMPACT SYSTEMS

F Peterka, Academy of Sciences of the Czech Republic, Prague, The Czech Republic

Copyright © 2001 Academic Press

doi:10.1006/rwvb.2001.0045

The motion of mechanical systems with impacts is strongly nonlinear due to sudden changes of the system parameters and the motion quantities, when the impacts of moving bodies appear. Impacts influence the system behavior so expressively, that the weak nonlinearities, acting on the system during the impactless motion, can often be neglected. Such systems are thought of as piecewise linear or systems with discontinuities.

The simplest motion with impacts can be studied using mechanical models shown in **Figures 1B** and **1C**. The mechanical oscillator in **Figure 1A** is

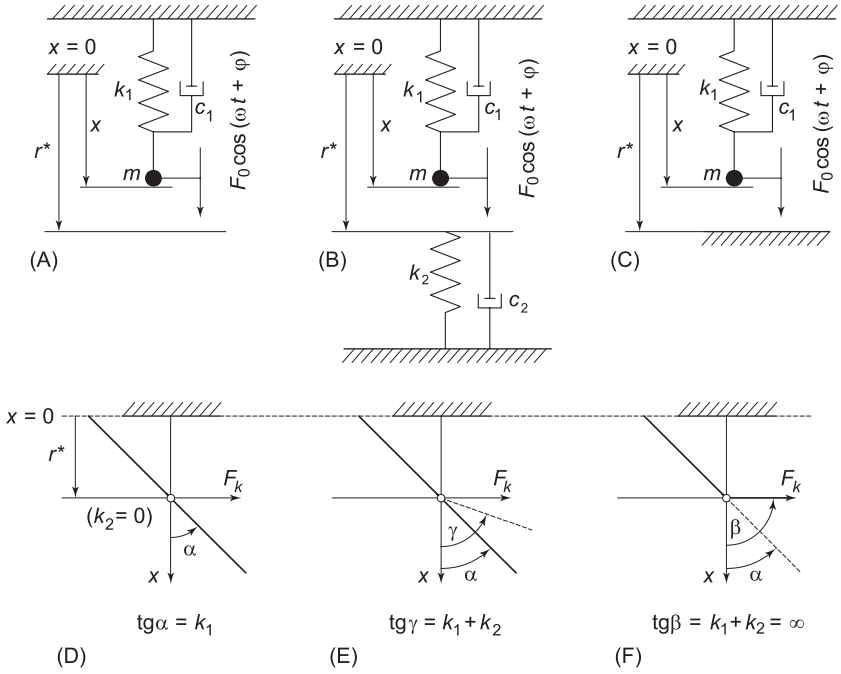


Figure 1 Schemes of linear and nonlinear oscillators.

composed from the mass element m, which is suspended on the stiffness element k_1, the spring force–deflection diagram $F_k(x)$ of which is shown in **Figure 1D**. The motion is excited by the periodic force of amplitude F_0 and damped by a linear damping element c_1. **Figure 1B** shows the mechanical model of the oscillator with soft impacts. When the displacement x of mass m exceeds the static clearance r^*, then elements k_2 and c_2 will influence the oscillator motion. They represent the elastic and damping contact forces of impacting bodies. There exist many linear, piecewise linear and non-linear models of soft impacts. The linear force–displacement characteristics $F_k(x)$ – the Kelvin–Voigt model – is in **Figure 1E**. When stiffness k_2 increases to infinity (**Figure 1F**), then the classic impact oscillator (**Figure 1C**) is obtained. It corresponds to the motion with hard impacts of the body against the rigid stop. Such motion can be described by the elementary Newton theory of direct and centric impact. Direct means that bodies move before the impact along a straight line and centric means that the resulting normal contact forces act on the straight line, connecting the centroids of impacting bodies. The duration of impact is assumed negligibly short and the change of velocity of body and the energy loss at impact can be expressed by restitution coefficient:

$$R = -\frac{v_+}{v_-} \qquad [1]$$

where v_+ and v_- are after-impact and before-impact velocities of body m, respectively. The interval $0 \le R \le 1$ embraces impacts from absolutely plastic ($R = 0$) to absolutely elastic ($R = 1$).

When Newton's impact of two bodies arises (**Figure 2**), then after-impact velocities v_{1+} and v_{2+} can be expressed in the form:

$$\begin{aligned} v_{1+} &= v_p - \frac{m_2}{m_1 + m_2} R v_{rel-} \\ v_{2+} &= v_p + \frac{m_1}{m_1 + m_2} R v_{rel-} \end{aligned} \qquad [2]$$

where $v_p = (m_1 v_{1-} + m_2 v_{2-})/(m_1 + m_2)$ is the the velocity of bodies after the plastic impact, $v_{rel-} = v_{1-} - v_{2-}$ is the the relative velocity of bodies just before the impact. Equation [2] follows from the assumption of fixing the momentum of bodies during the impact:

$$m_1 v_{1-} + m_2 v_{2-} = m_1 v_{1+} + m_2 v_{2+} \qquad [3]$$

and from the definition of restitution coefficient:

$$R = -(v_{1+} - v_{2+})/(v_{1-} - v_{2-}) \qquad [4]$$

The kinetic energy E_i lost at impact is determined by formula:

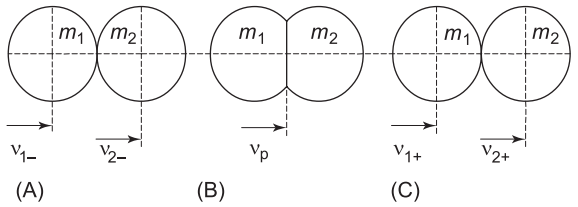


Figure 2 Direct and centric impact of two bodies: (A) state just before impact; (B) state at the instant of maximum deformation of bodies at impact; (C) state just after impact.

$$E_i = \frac{1}{2}\frac{m_1 m_2}{m_1 + m_2}\left(1 - R^2\right)v_{\text{rel}-}^2 \qquad [5]$$

and it changes into:

$$E_i = \frac{1}{2}m\left(1 - R^2\right)v_-^2 \qquad [6]$$

for the single impact oscillator (**Figure 1C**), when $m_1 = m$, $m_2 = \infty$, $v_{1-} = v_-$ and $v_2 = 0$.

Selected Examples of Vibro-impact Systems

Impacts accompany the vibration of many types of machines and devices. They are important in the forming, drilling, compaction, milling, crashing, vibration damping or control of motion, etc. They can be also undesirable, e.g., in mechanisms with clearances, where they increase the noise and the mechanical stress by impact impulses. Such impacts decrease the reliability and durability of machines and they can cause serious failures.

Examples of mechanical schemes of vibro-impact systems are shown in the following figures (**Figures 3–8**).

Complex impact interactions can appear in vibratory systems. The study of the systems behavior is based on the selection of a proper model of vibro-impact system and on its theoretical, simulation and experimental investigation.

Fundamental problems of the vibro-impact systems dynamics will be explained on the dynamical analysis of the single impact oscillator with one-degree-of-freedom.

Dynamics of the Single Impact Oscillator

The Existence Boundary of Impactless Periodic Motion (Grazing Bifurcation)

The first step in the investigation of the dynamics of impact oscillators is the determination of a boundary, beyond which the impactless motion cannot exist, because the bodies begin to touch the stops or the other moving bodies and impacts should appear. This boundary is named the *existence boundary* or the *grazing bifurcation boundary*. It is the most important condition, which limits the existence of not only impactless motion but generally the existence of every periodic impact motion.

The impactless motion of the oscillator (**Figure 1C**) is described by the ordinary differential equation:

$$m\frac{\mathrm{d}^2x}{\mathrm{d}t^2} + c_1\frac{\mathrm{d}x}{\mathrm{d}t} + k_1 x = F_0\cos\left(\omega t + \varphi\right) \qquad [7]$$

Its solution is:

$$x(t) = \mathrm{e}^{-b\Omega t}A\cos\left(\Omega_{\mathrm{d}}t + \psi\right) + \rho_0 x_{\mathrm{st}}\cos\left(\omega t + \varphi - \alpha\right) \qquad [8]$$

$$v(t) = \mathrm{d}x/\mathrm{d}t \qquad [9]$$

where: $b = c_1/2\sqrt{(k_1 m)}$ is dimensionless damping, $\Omega = \sqrt{(k_1/m)}$ is angular frequency of undamped free vibration, $\Omega_{\mathrm{d}} = \Omega\sqrt{(1 - b^2)}$ is the angular frequency of damped free vibration, A, ψ are the integration constants depending on initial conditions $x(0)$ and $v(0)$, $\rho_0 = 1/\sqrt{\left[\left(1 - \eta^2\right)^2 + (2b\eta)^2\right]}$ is the dimensionless amplitude of forced vibration, $\eta = \omega/\Omega$ is the dimensionless excitation frequency, $x_{\mathrm{st}} = F_0/k_1$ is static displacement, and $\alpha = \arctan\left[2b\eta/\left(1 - \eta^2\right)\right]$ is the phase shift between excitation force and forced vibration.

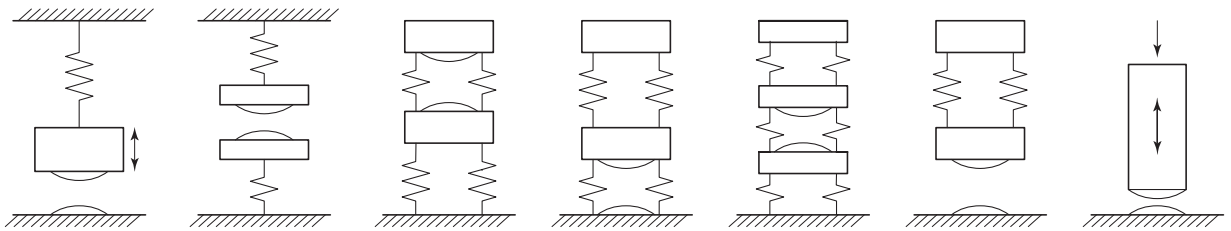


Figure 3 Impact oscillators, forming machines, crushers, automatic power nailers or pile drivers.

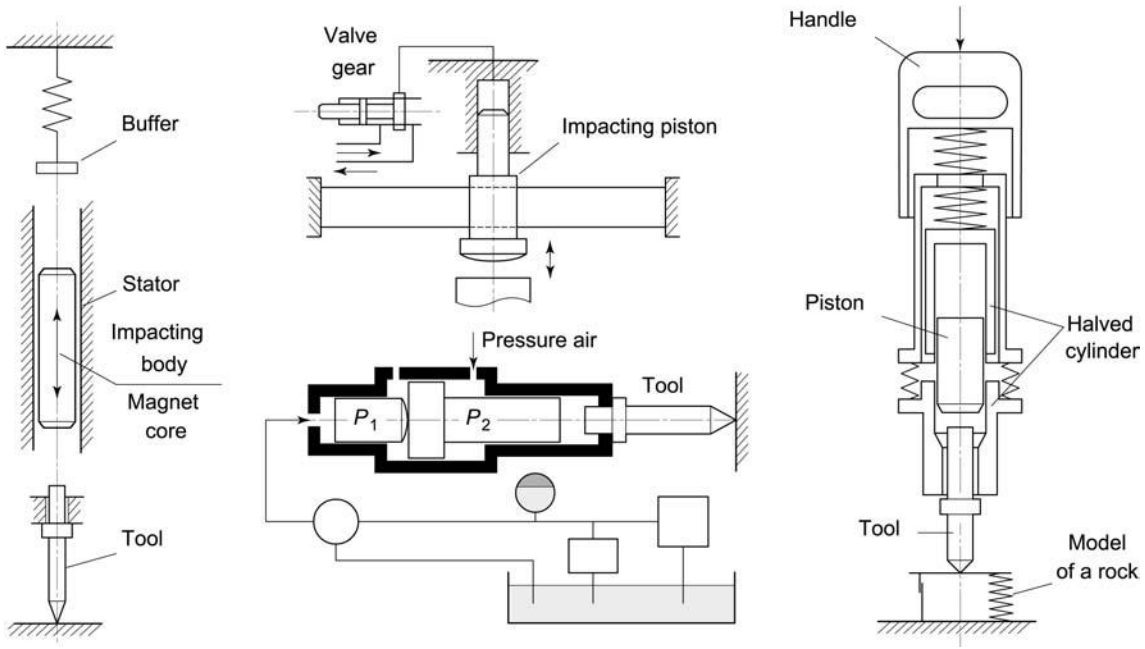


Figure 4 Electrical, hydraulic, and pneumatic power.

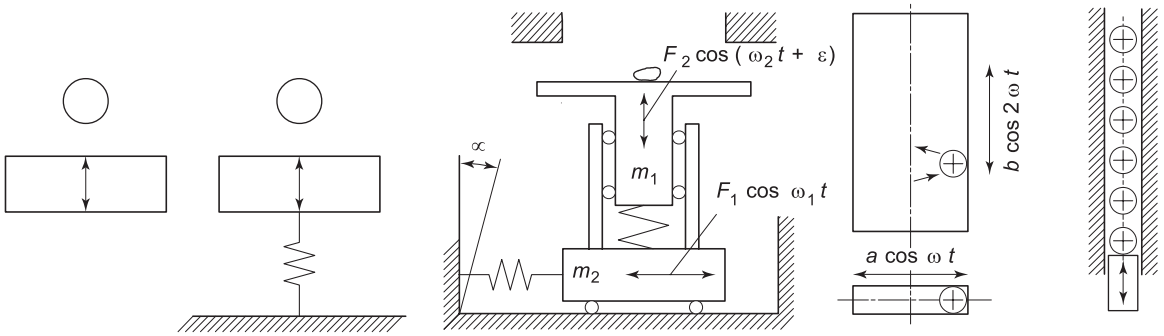


Figure 5 Vibrating platforms and conveyers.

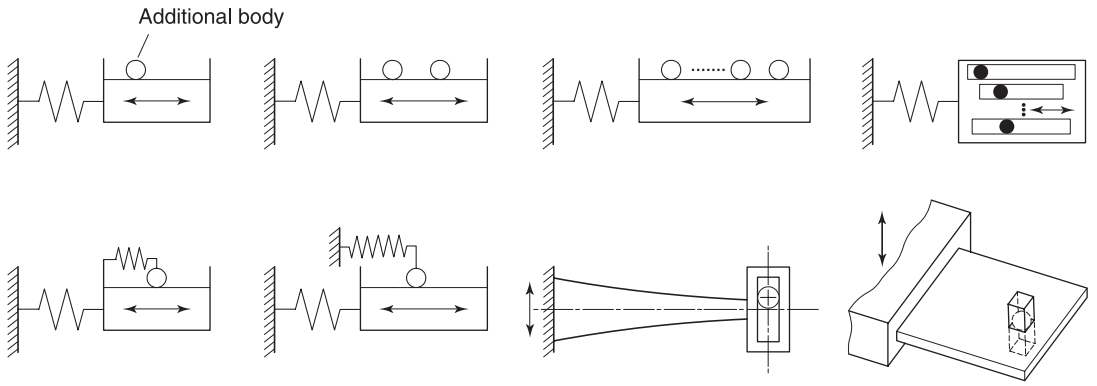


Figure 6 Impact dampers.

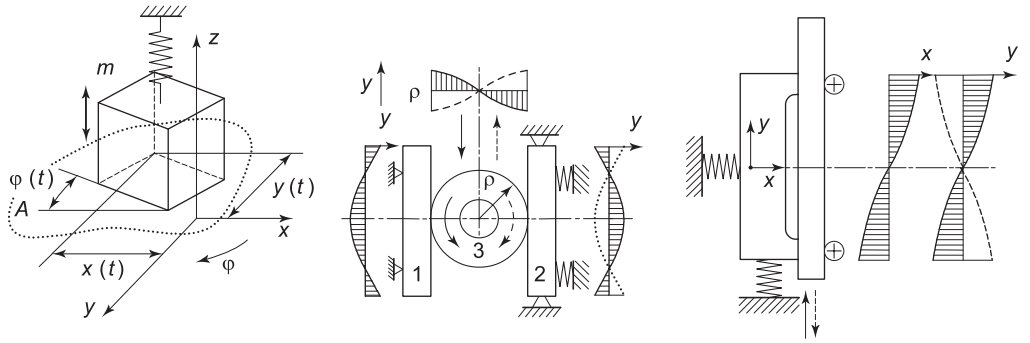


Figure 7 Vibrations with piezo-electric elements and oblique impacts.

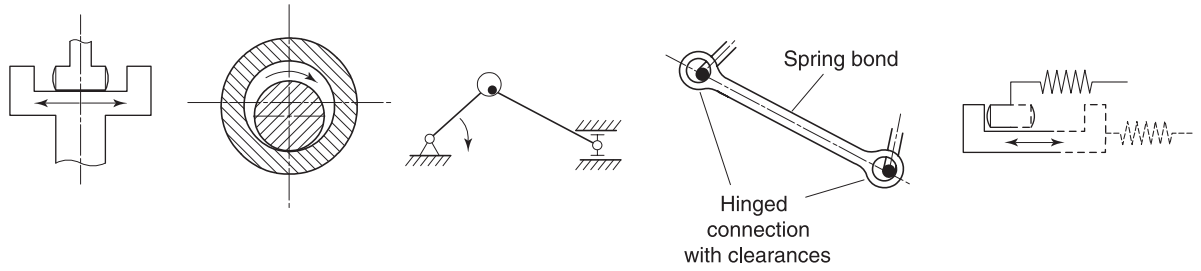


Figure 8 Mechanisms with clearances, forks, bearings, journals, and gearing.

Figure 9 shows the frequency amplitude characteristics $\rho_0(\eta)$ of the impactless motion for damping $b = 0.05$. This curve represents the grazing bifurcation boundary, where the moving body begins periodically to touch the stop (see **Figure 10**, where $X = x/x_{st}$ and V are the dimensionless displacement and velocity, respectively).

When condition:

$$0 < r < \rho_0 \qquad [10]$$

($r = r^*/x_{st}$ is the dimensionless static clearance) is met, then impactless motion ends its existence and some impact motion should appear.

The negative clearance r represents a state, when body m is prestressed to the stop in the static position by the force:

$$F_p = |r|F_0 \qquad [11]$$

When the prestress force $F_p < F_0$, then body m repeatedly disconnects from the stop and the impacts subsequently will arise. The impact motion should therefore appear in the region of the necessary onset of an impact motion (see dark region in **Figure 9**):

$$\rho_p < r < \rho_0 \qquad [12]$$

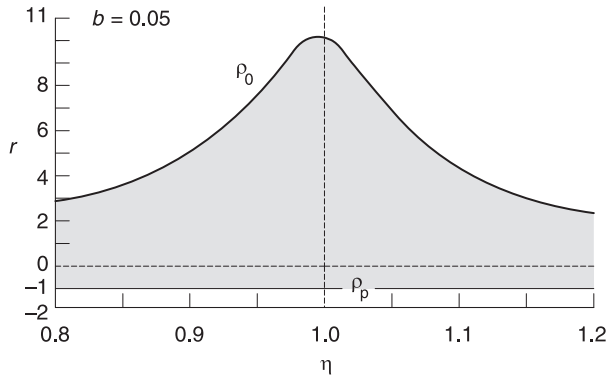


Figure 9 Region of necessary onset of an impact motion.

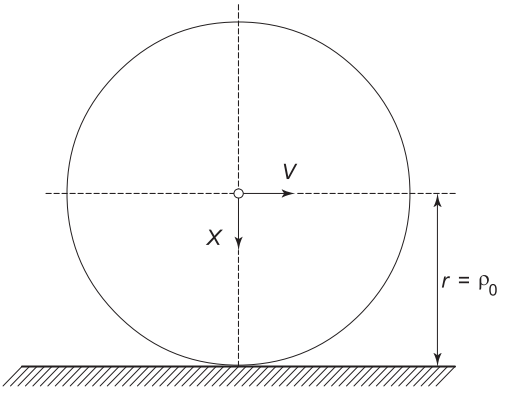


Figure 10 Phase trajectory of impactless motion on the grazing bifurcation boundary.

On boundary $r_p = -1$ the body m begins to disconnect during the decrease of prestress force F_p.

Every impact introduces new initial motion conditions and the two-dimensional set of these conditions makes possible a large variety of excited impact motions. Nevertheless steady-state vibro-impact motions can exist also outside region [12], but they should be called forth, e.g. by special motion initial conditions, by a change of system parameters, etc.

Classification of Impact Motions

The response of the impact oscillator on a periodic excitation is periodic or chaotic. Periodic motions are definitely characterized by quantity:

$$z = p/n \qquad [13]$$

where p is the number of impacts and n is the number of excitation periods $T = 2\pi/\omega$ in one period of motion. This quantity also characterizes chaotic impact motions and it refers to the mean value of impacts related to one period T.

Figure 11 introduces several series of motions classified according to quantity z for harmonic and periodic rectangular excitation forces $F(t)$. **Figure 11A** shows the first four motions of fundamental series $z = 0, 1, 2, 3, \ldots$. Motions repeat with the excitation period $T(n = 1)$ and they differ by the number $p = 0, 1, 2, 3,$ of impacts. The impactless motion $(z = 0)$ belongs to this series. Series in **Figures 11B** and **11C** show periodic subharmonic impact motions. Their period is the integer multiple of $T(n > 1)$. The first series (in **Figure 11B**) is typical by one impact $(p = 1)$, which repeats after $n = 2, 3, 4, 5, \ldots$ periods T. In the second series (in **Figure 11C**) repeat $p = 1, 3, 5, 7, \ldots$ impacts with period $2T(n = 2)$. **Figure 11D** shows the series $z = 1/2 - 1;\ 1/3 - 1;\ 1/4 - 1; 1/5 - 1, \ldots$ of chaotic impact motions.

Chaotic impact motion is the unpredictable state of the impact oscillator in the range of a strange attracting set. This set can be imagined, e.g., as a special configuration in the phase space of the system, the dimension of which is less then the dimension of the phase space.

Regions of Existence and Stability of Impact Motions

Every periodic impact motion has a region of existence and stability in the space of the system parameters. There are two important parameters η and r of the impact oscillator and regions of impact motions will be illustrated in the plane $(\eta \times r)$.

Examples of regions are shown in **Figure 12** for two periodic excitation forces $F(t)$ and for constant restitution coefficient $R = 0.6$ and linear damping $b = 0.05$. The region of each fundamental periodic motion $(n = 1;\ z = 0, 1, 2, 3)$ is bounded from below by the existence (grazing bifurcation) boundary $(\rho_0, \rho_1, \rho_2, \rho_3)$. This boundary appears at every periodic impact motion, when impactless loop of the motion phase trajectory begins to touch the stop and a new impact should arise.

Regions of impact motions $z = 1, 2, 3$ are bounded from above by stability boundaries s. Stability boundaries s and existence boundaries ρ of neighboring periodic motions (e.g., $z = 0$ and $z = 1$ or $z = 1$ and $z = 2$, etc.) mutually intersect and create two types of transition regions. They are named as hysteresis and beat-motion regions and they are illustrated as black and white regions, respectively, in **Figure 12**. Points of intersection of boundaries divide the stability boundaries s on two different parts, s_{+1}, which corresponds to the saddle-mode bifurcation and s_{-1}, which corresponds to the period-doubling bifurcation. Both neighbor periodic motions can exist in hysteresis regions, because the two-fold response of the system exists. Beat-motion regions contain subregions of periodic subharmonic and chaotic impact motions, because the fundamental z motion cannot exist and the neighbor $(z + 1)$ motion is not stable there. Values z of impact motions in beat-motion regions are in the interval $\langle z,\ z + 1\rangle$ and $n > 1$.

The configuration of mentioned subregions inside the beat-motion region is shown in more detail in **Figure 13**, which is section (a) of **Figure 12**.

It follows from **Figure 12** that the structure of impact-motion regions is independent of the type of periodic excitation. Regions which correspond to the rectangular excitation, differ from regions for the harmonic excitation only quantitatively. The rectangular exciting force can be supplemented by the series of odd subharmonics, so subharmonic resonances of order 1/3 and 1/5 appear in **Figure 12**.

Regions of Subharmonic and Impact Motions

Fundamental $z = 1$ impact motion loses its stability on boundary s_{-1} (**Figure 13**) and changes into $z = 2/2$ motion after period doubling bifurcation. One impact in the motion period $2T$ disappears on the saddle-node stability boundary $(s_1)_{2/2}$ and subharmonic $z = 1/2$ impact motion stabilizes. This motion transits into $z = 1$ or $z = 2/2$ impact motion on the grazing bifurcation boundary $\rho_{1/2}$. It means that between boundaries $(s_1)_{2/2}$ and $\rho_{1/2}$ exists the hysteresis region of neighbor motions $z = 1/2$ and $z = 2/2$ or $z = 1$.

Subharmonic motions $z = 1/2$, $z = 1/3$, $z = 1/4$, ... lose their stability, with increasing clearance r, on

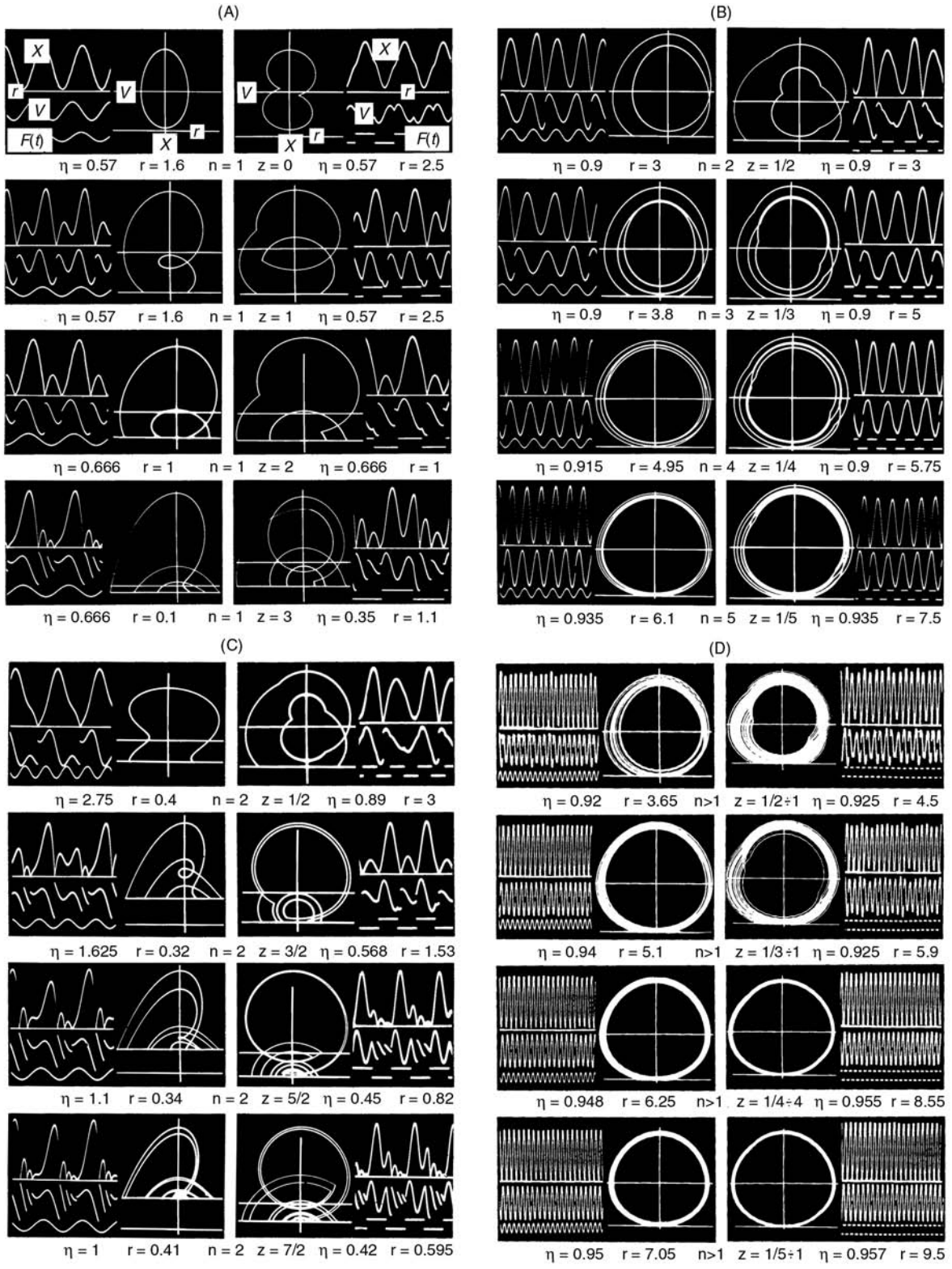


Figure 11 Examples of periodic and chaotic impact motions.

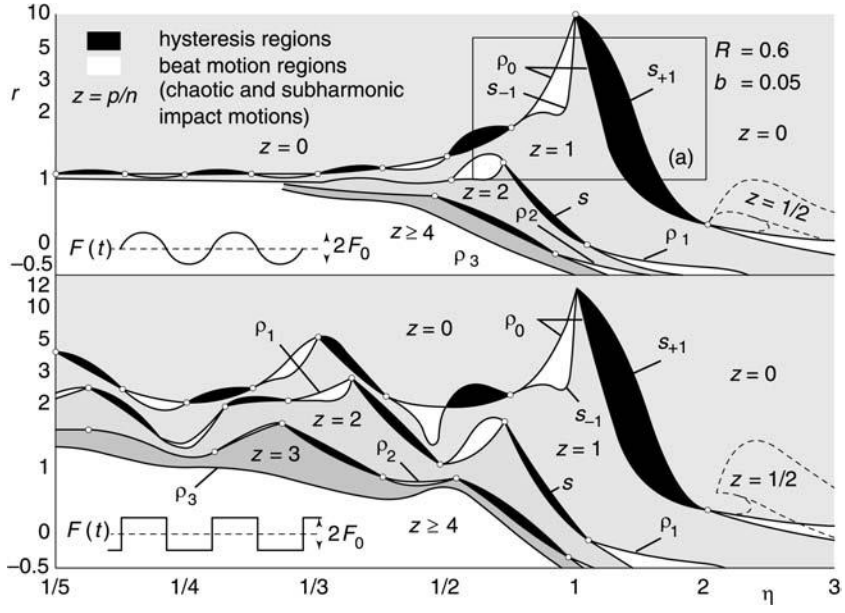


Figure 12 (see plate 52). Regions of stability and existence of impact motions for the periodic harmonic and rectangular excitations.

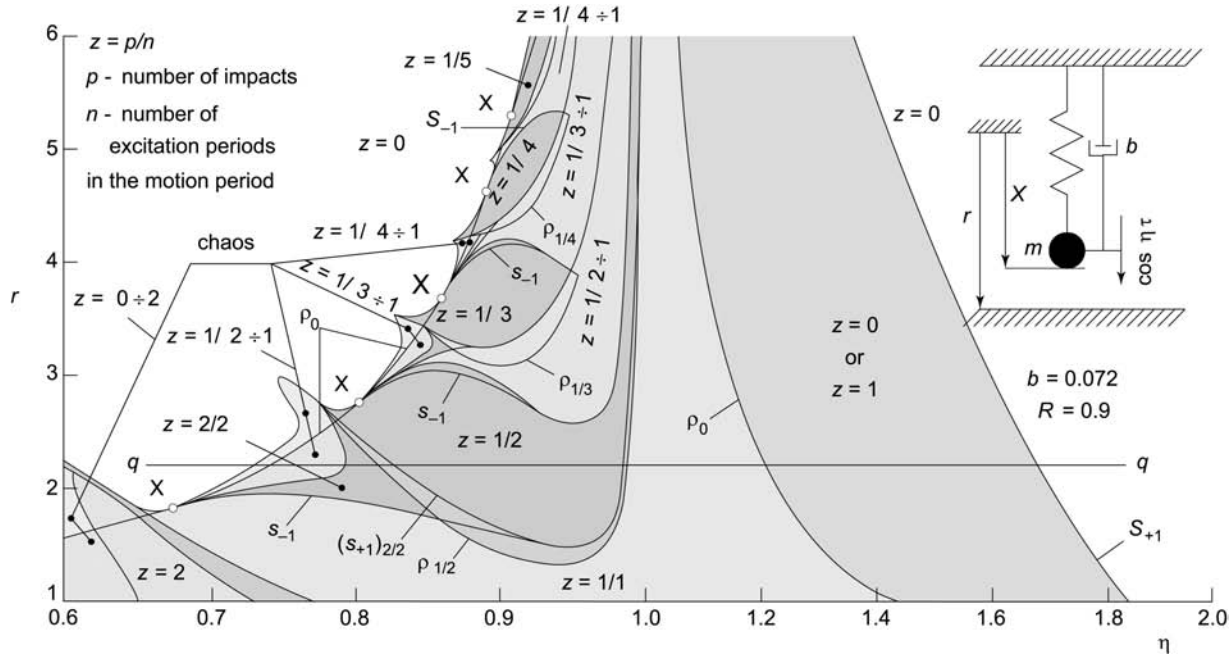


Figure 13 (see plate 53). Regions of periodic and chaotic impact motions near the resonance of the linear oscillator.

period doubling bifurcation boundaries s_{-1} and then they transit into regions of chaotic impact motions $z = 1/2 - 1$, $z = 1/3 - 1$, $z = 1/4 - 1$, ... Hysteresis regions exist also between subharmonic motions $z = 1/3,\ 1/4,\ 1/5,\ \ldots$, and chaotic motions $z = 1/2 - 1$, $z = 1/3 - 1$, $z = 1/4 - 1$, ..., (see dark blue subregions in **Figure 13**). Hysteresis regions are also salients of beat-motion regions into the region of impactless motion $z = 0$, over the boundary ρ_0, but their magnitude decreases with increasing damping b.

Similar configuration of regions of subharmonic and chaotic impact motions exist in beat-motion regions between neighboring z and $z+1$ ($z = 0,\ 1,\ 2,\ 3,\ \ldots$) periodic motions.

Bifurcation Diagrams

The useful tools for qualitative and quantitative evaluation of impact motions are bifurcation diagrams. They display the selected samples of motion, when system parameters are changed. One example is shown in **Figure 14**. Every before-impact velocity V_- and minimum displacement X_m, evaluated in every excitation period T, is plotted, while parameters η, r are changed along line q in **Figure 13**. Arrows along bifurcation diagrams express the direction of frequency η change. Diagrams expressive explain the system behavior, when line q crosses different bifurcation boundaries in **Figure 13**.

Quantity $z = p/n$ can be directly determined according to the number of branches of diagrams $V_-(\eta)$ and $X_m(\eta)$ for certain periodic impact motions.

Exact Theoretical Solution of Periodic $z = 1/n$ Impact Motions and their Local Stability

The theoretical solution of periodic impact motions can be obtained in the explicit form only for the simplest mechanical systems and simple regimes of motion. The procedure will be shown on the example of the impact oscillator in **Figure 1C**, without the damping element c_1. The scheme of the series of periodic motions $z = 1/n$ is shown in **Figure 15**.

The solution of motion differential eqn [7] for $b = 0$ is:

$$\begin{aligned} x &= A\cos(\Omega t + \psi) + \rho_0 x_{st}\cos(\omega t + \varphi) \\ v &= -A\Omega\sin(\Omega t + \psi) - \rho_0 x_{st}\omega\sin(\omega t + \varphi) \end{aligned} \quad [14]$$

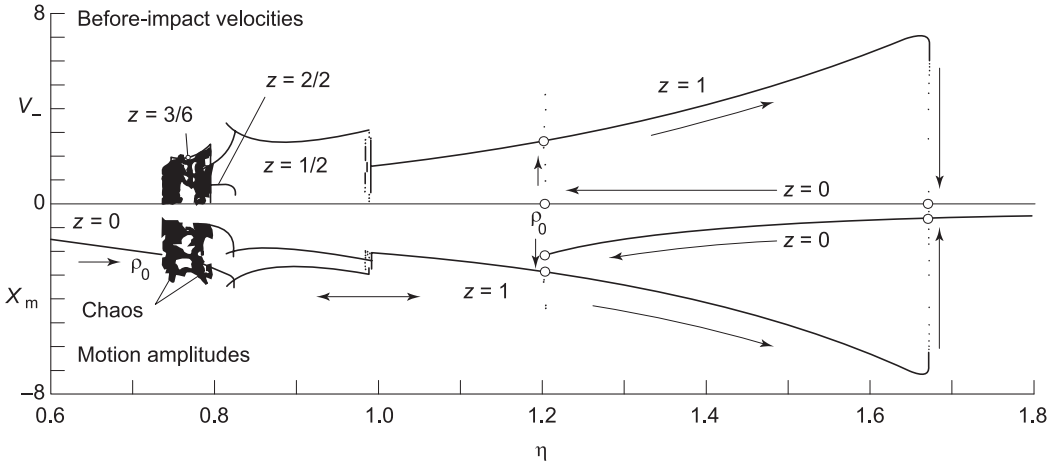


Figure 14 Bifurcation diagrams along line q in **Figure 13**.

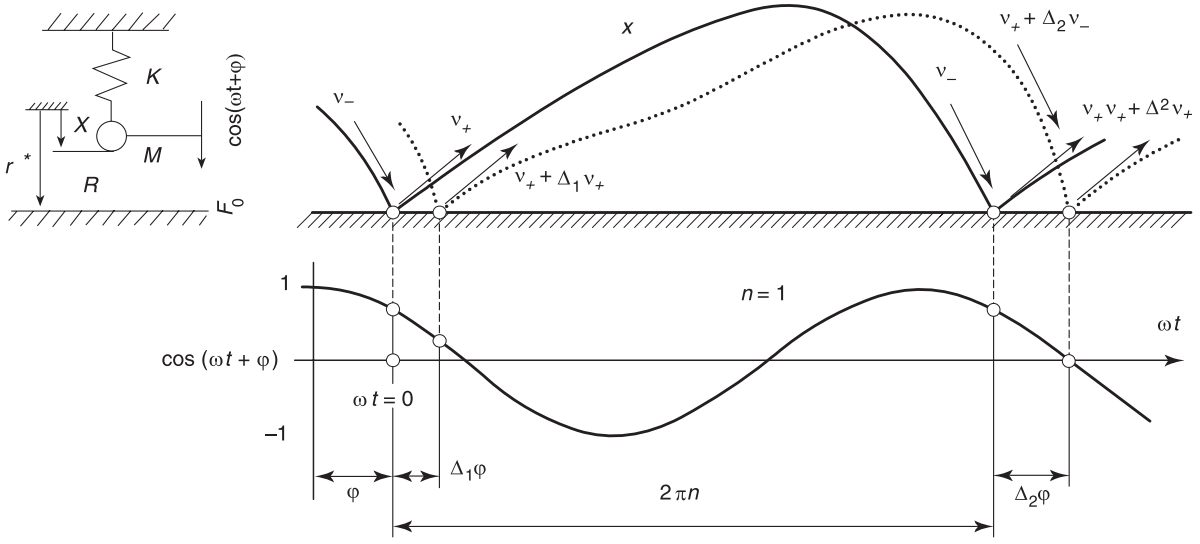


Figure 15 Scheme of periodic $1/n$ impact motions ($n = 1, 2, 3, 4 \ldots$) of the impact oscillator and their perturbation.

where constants A, ψ of the general solution – free vibration – depend on the motion initial conditions and the particular solution – forced vibration – has the dimensionless amplitude:

$$\rho_0 = \frac{1}{|1-\eta^2|} \qquad [15]$$

and it is the grazing bifurcation boundary of the impactless motion.

Periodicity Conditions

The solution of periodic $z = 1/n$-impact motions in their motion period $nT\,(0 < t < 2\pi n/\omega)$ is derived from the periodicity conditions (**Figure 15**):

$$\begin{aligned} x(0) &= x(2\pi n/\omega) = r^*, \\ v_+ &= v(0) = -Rv(2\pi n/\omega) = -Rv_- \end{aligned} \qquad [16]$$

in the form (14), where:

$$\psi = -\frac{\pi n}{\eta} = -\alpha, \qquad A = \frac{1+R}{1-R}\eta\, B\frac{\sin\varphi}{\sin\alpha} \qquad [17]$$

$$[\cos\varphi]_{\mathrm{I,II}} = \frac{-1}{B(1+K^2)}\left\{r \pm K\sqrt{[B^2(1+K^2) - r^{*2}]}\right\} \qquad [18]$$

$$[\sin\varphi]_{\mathrm{I,II}} = \frac{1}{B(1+K^2)}\left\{-rK \pm \sqrt{[B^2(1+K^2) - r^{*2}]}\right\}$$
$$B = \frac{1}{1-\eta^2}x_{\mathrm{st}}, \qquad K = \frac{1+R}{1-R}\eta\ \mathrm{cotg}\ \alpha \qquad [19]$$

The before-impact velocity v_- depends on system parameters according to equation:

$$v_- = \Omega x_{\mathrm{st}}\frac{2}{1-R}\frac{\eta}{\eta^2-1}\sin\varphi \qquad [20]$$

Impenetrability Conditions

There exist two different solutions, *I*, *II*, of the assumed periodic impact motions, $z = 1/n$. These solutions should be verified by the impenetrability conditions:

$$v_- = v(2\pi n/\omega) \geq 0$$

and

$$x(t) < r^*\ (\text{for } 0 < t < 2\pi n/\omega) \qquad [21]$$

which express the conditions of physical validity of theoretical results. A limit case:

$$x(t) = r^* \qquad [22]$$

which appears between periodic impacts, corresponds to the grazing-bifurcation boundaries $\rho_{1/n}$ of these periodic impact motions (**Figures 12** and **13**). These boundaries cannot be derived in explicit form. They should be found numerically, using simulation or experimentally.

Stability Conditions

A periodic impact motion should also satisfy the stability conditions. The stability analysis is based on the assumption that small initial motion perturbations Δ_1 of the system at the instant of the periodic impact (see **Figure 15**) will develop at next l impacts according to the relation:

$$\Delta_l = \gamma^l\Delta_1 \qquad [23]$$

The stability condition is expressed in the form:

$$|\gamma| < 1 \qquad [24]$$

Stability boundaries correspond to the condition:

$$|\gamma| = 1 \qquad [25]$$

The quantity γ depends on system parameters and it is the solution of the second-order characteristic equation, the roots of which are generally complex. Two types of stability boundaries, s_{+1}, and, s_{-1}, can be distinguished according to the real value of quantity γ on the unit circle [25]:

values of γ	absolute value of the stability boundary	stability conditions	
1) $\gamma = 1$	$s_{+1} = \rho_0\sqrt{(1+K^2)}$	$r < s_{+1}$ (for $K < 0$) and $r > -s_{+1}$ (for $K > 0$)	[26]
2) $\gamma = -1$	$s_{-1} = \rho_0\dfrac{\lvert V-1-K^2\rvert}{\sqrt{\left[(V-1)^2+K^2\right]}}$	$r > -s_{-1}$ (for $K < 0$) and $r < s_{-1}$ (for $K > 0$)	[27]

where:

$$V = \frac{2(1+R^2)}{(1-R)^2 \sin^2\alpha}$$

Summary of Theoretical Analysis

Resulting regions of the existence and stability of assumed $z = 1/n$-impact motions in the plane of system parameters r, η are hatched in **Figure 16** and they correspond to the solution I of the periodic impact motions (see signs + in eqns [18] and [19]). They are bounded by stability boundaries s_{+1}, s_{-1}, which link up at points X and by grazing bifurcation boundaries ρ.

The bifurcation boundaries s_{+1} and s_{-1} have the following simplified mathematical expression:

1. The motion disturbances Δ at the successive impacts begin to increase on the stability boundary s_{+1} with the same polarity (γ=1 in eqn [26]). This process leads to the jump change from the unstable $z = 1/n$ impact motion to the impactless or another impact motion and it corresponds to the saddle-node bifurcation boundary.
2. The motion disturbances Δ begin to increase on the stability boundary s_{-1} and their sign alternates ($\gamma = -1$ in eqn [27]). This process stabilizes in the near limit cycle, which period is double. Stability boundary s_{-1} corresponds to the period-doubling bifurcation boundary.

Point X are also points of boundaries ρ_0 and $-\rho_0$ (**Figure 16**) for $K = 0$, as follows from eqns [26] and [27]. Quantity $K(\eta)$ is a tangential function (19), which divides the frequency interval $0 \le \eta \le \infty$ on nl ($n = 1, 2, 3, \ldots$ $l = 0, 1, 2, 3, \ldots$) subintervals, which boundaries are determined by frequencies $\eta = n/l$, where $K = \pm\infty$. Corresponding points $X(K = 0)$ have coordinates $\eta = n/(l + 1/2)$.

Resulting regions of stability and existence of $z = 1/n$ impact motions create infinite series of regions $n = 1, 2, 3, 4, \ldots,$ in every l frequency subintervals η for fundamental impact motion $n = 1$, which are denoted by dot-and-dash lines in **Figure 16**.

The transition from impactless ($z = 0$) motion into the neighbor $z = 1/n$ impact motion is never continuous and stable, except singular points X of grazing bifurcation boundary ρ_0. Both neighboring motions

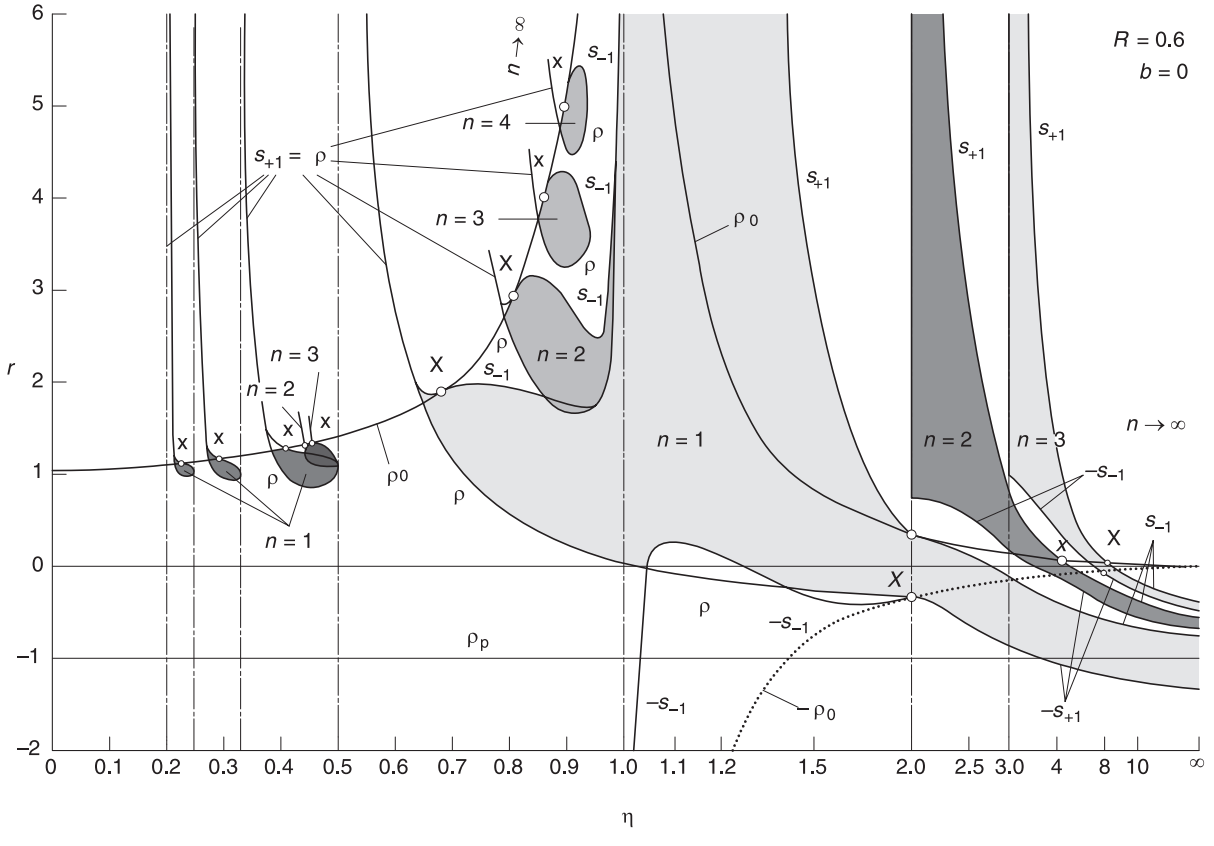


Figure 16 Resulting regions of existence and stability of $1/n$ impact motions obtained by the theoretical analysis.

are identical and both motions are stable in the neighborhood of these points. The impactless motion with the periodic touches of mass m and the rigid stop is identical with the $z = 1/n$ impact motion, the before-impact velocity V_- of which degenerates into zero (**Figure 10**).

It follows from **Figure 16**, that $z = 1/n$ impact motions are stable and can exist outside the region [12] of the necessary onset of an impact motion (see region between boundaries ρ_0 and ρ_p). They are named hysteresis regions of impact motions into the region of the impactless motion. Assumed $z = 1/n$ impact motions do not describe impact regimes in remaining white regions inside the region [12], where impact motion should appear. The simulation of the system motion and physical experiments have explained, that in these regions exist more complex periodic and chaotic impact motions (see the description of **Figures 12 and 13**).

Figure 16 expresses results of the simplified analytical solutions of periodic $z = 1/n$ impact motions. It describes only partially the behavior of impact oscillators, as it follows from the comparison of regions $z = 1/n$ in **Figures 13** and **16**. Forms of comparable regions, especially hysteresis regions, are influenced by different values of damping b of the impactless motion.

Four Ways from Periodic Motions into the Chaos

A special question of the dynamics of vibro-impact systems is the better understanding of chaotic motion and reasons of their appearance, so called ways into the chaos. Four different kinds of change from periodic into chaotic motions for the impact oscillator have been found. They will be explained using **Figure 17A**, where color regions of chaotic impact motion are shown for the system without viscous damping ($b = 0$). Four types of color boundaries of the chaotic motion regions correspond to four different ways into chaos and black segments of boundaries express only output from the chaos into periodic motions. The motion on boundaries of chaotic motion regions will be explained in more detail by bifurcation diagrams, time histories and phase trajectories of motion, when parameters η, r will change

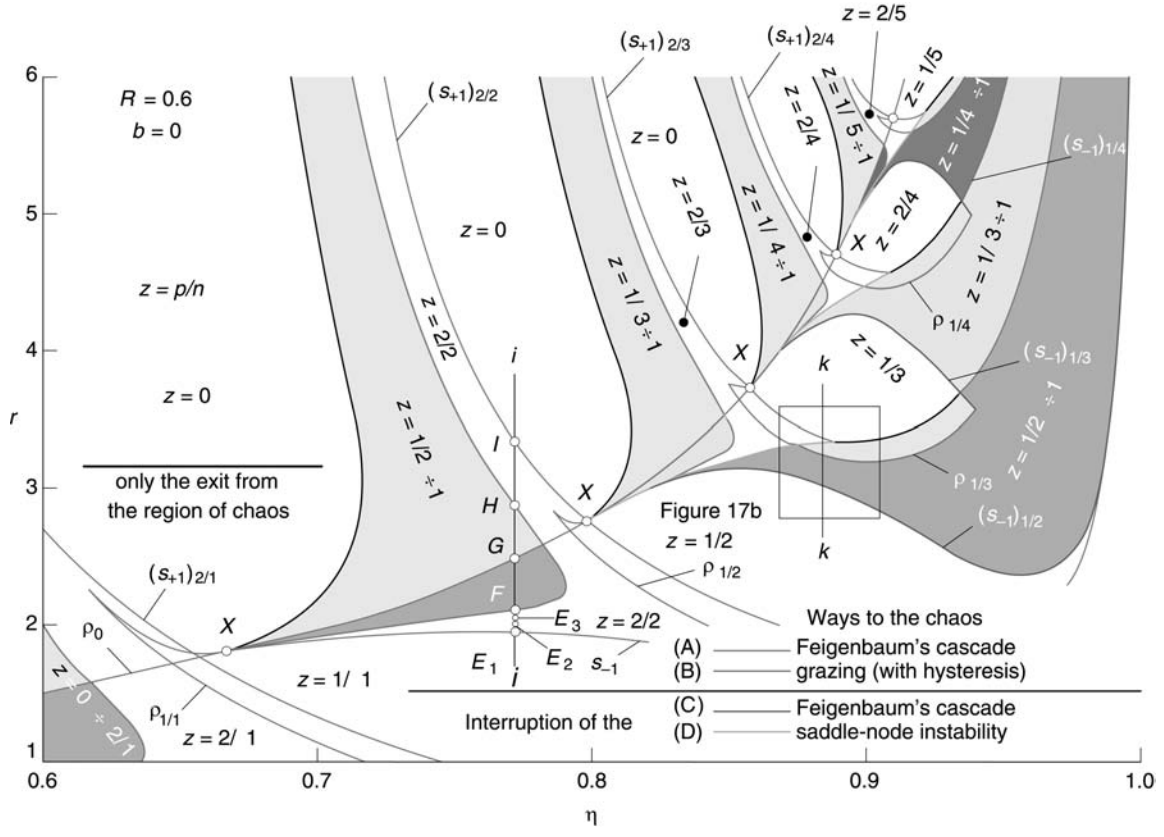


Figure 17A (see plate 54). Regions of chaotic impact motions and classification of their boundaries (four types of way into and from chaos and one type of exit from chaos).

along lines i, k crossing the boundaries. Ways to chaos are characterized in **Table 1**.

Feigenbaum's Cascade of Period Doublings

Line i ($\eta = 0.77$) in **Figure 17A** crosses the red boundary of chaotic motion $z = 1/2 - 1$ in points F, H. Bifurcation diagrams $X_m(r)$, $V_-(r)$ are shown in **Figure 18** and typical phase trajectories of the system motion in clearances (A) to (H) are shown in **Figure 19**. Fundamental $z = 1$ impact motion (**Figure 19A**) loses the stability in point E_1 ($r = 1.95$) on boundary s_{-1} and the $z = 2/2$ impact motion (**Figure 19B**) stabilizes. Next splitting appears in point E_2 ($r = 2.07$), when $z = 4/4$ impact motion (**Figure 19C**) begins to exist. The cascade of splitting or motion period doubling continues (see, e.g., point E_3 ($r = 2.1$) in **Figure 17A** for $z = 8/8$ motion – **Figure 19D**) and ends in point F, where it changes into the chaos (**Figure 19E**).

Typical features of this way into the chaos are:

1. reversible changes of the system motion, without hysteresis phenomena,
2. constant values z during the way into the chaos (e.g., $z = 1,\ 2/2,\ 4/4,\ 8/8,\ \ldots$); it means that no impact vanishes or appears in corresponding excitation periods T.

When system parameters penetrate more deeply into the region of chaotic impact motion, then impacts can vanish in some period T and number z decreases (e.g., motion $z = 1/2 - 1$ in **Figure 19G**). There exist also 'windows' of more complex periodic impact motions inside the region of chaotic motions (e.g., $z = 3/5,\ 4/5$ motions in **Figure 18** and **Figure 19F**).

The inverse Feigenbaum's cascade appears with further increase of clearance r over the point H in **Figures 17 and 18**, but this cascade is not complete, because $z = 2/2$ motion loses its stability in point I on stability boundary $(s_1)_{2/2}$ and impactless motion stabilizes after the jump transition process.

Jump Transition into the Chaos on Segments of Grazing Bifurcation Boundaries Exhibiting Hysteresis Phenomena

When clearance r decreases along line i in **Figure 17A**, then impactless motion changes suddenly into the chaotic impact motion in point G on the green segment of grazing bifurcation boundary ρ_0 (bifurcation diagrams with decreasing clearance r are represented by light grey in **Figures 18** and **20**).

Point G is placed inside the region $z = 1/2 - 1$ of the chaotic motion, so the return into the impactless motion is possible with remarkable hysteresis. The system motion has similar character along all green segments beginning in points X on boundary ρ_0 (**Figure 17A**).

Two Types of Interruption of the Instability Development of Subharmonic Impact Motions, Caused by Additional Impacts

Special ways into the chaos have been found for the series of $z = 1/n$, $z = 2/2n$ and $z = 2/(n+1)$ of subharmonic impact motions ($n \geq 2$). They will be explained using the quasistationary change of clearance r along line k ($\eta = 0.885$) in **Figure 17B** and by bifurcation diagrams in **Figure 20**.

Figure 17B is the enlarged rectangular segment of **Figure 17A** and line k crosses regions of periodic $z = 1/2; 1/3,\ 2/4,\ 2/3$ impact motions and the region of the chaotic $z = 1/2 - 1$ impact motion.

Interruption of Feigenbaum's Cascade

When clearance r increases, line k crosses the stability boundary $(s_{-1})_{1/2}$ of $z = 1/2$ impact motion (**Figure 21A**) in point A (**Figure 17B**) and motion changes to $z = 2/4$ impact motion (**Figure 21B**). The splitting of phase trajectories (extremes **1, 2, 3**, split into extremes **1a, 1b, 2a, 2b, 3a, 3b** in **Figure 21**) increases up to point B on grazing bifurcation boundary $\rho_{2/4}$ (**Figure 17B**), where impactless loop **3b** begins to touch the stop and the additional impact should appear. Additional impact turns the system motion towards the state, which corresponds to the nonsplitted motion (**Figure 21A**), i.e., it eliminates the splitting. The nonsplitted motion is unstable, so the splitting increases and an additional impact appears again. The system is continuously in transition processes between the depression and development of the splitting. The motion of the impact oscillator is chaotic (see dark area in **Figure 21C**), because the intensity and the instant of additional impact are unpredictable.

Table 1 Summary of characteristic features of different ways into the chaos

The way into chaos	*Bifurcations*	*Hysteresis phenomena*	*Quantity z*
A – Feigenbaum's cascade of period doublings	Period doublings cascade	Absent	is constant
B – Segments of grazing bifurcation boundaries	Grazing	Exist	increases
C – Interruption of development of Feigenbaum's cascade	Period doublings and grazing	Absent	increases
D – Interruption of saddle-node instability development	Saddle-node	Absent	decreases

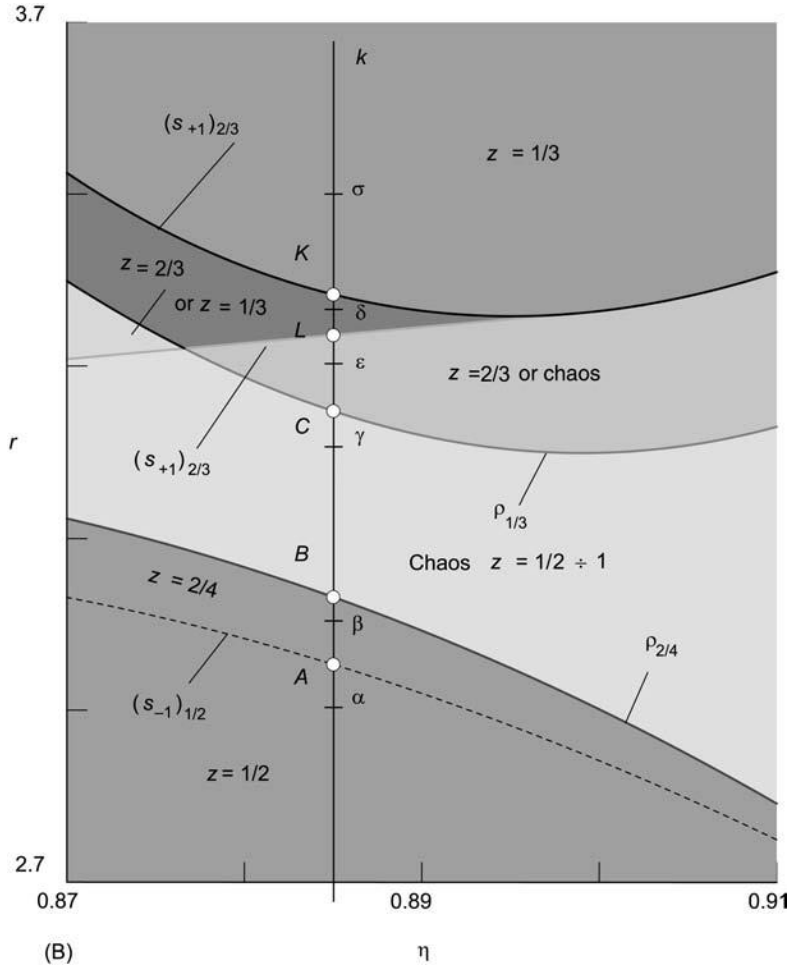


Figure 17B (see plate 55). Regions of periodic and chaotic impact motions in enlarged rectangular subregion of **Figure 17A**.

When the impenetrability condition [21] is omitted for previously impactless loops **3b** of phase trajectories of $z = 2/2n$ impact motions, then the splitting of motions can increase over the level of the stop (**Figure 21C**) and the Feigenbaum cascade is not interrupted.

This way into chaos is typical by the increase of quantity z of the chaotic motion (e.g., $z = 2/4 \rightarrow z = 1/2 - 1$) due to the additional impacts. The transition cross the grazing bifurcation boundaries $\rho_{2/2n}$ is reversible, without hysteresis phenomena.

Interruption of the Saddle-node Instability Development

Periodic $z = 2/3$ impact motion (see points δ in **Figures 17B, 20 and 21D**) loses its stability in points K, L, which are both points of saddle-node bifurcation boundaries $(s_{+1})_{2/3}$ (**Figure 17B**). The weaker of two periodic impact (point v in **Figure 21D** and curve v in **Figure 20**) vanishes in point K and the system stabilizes by the jump into $z = 1/3$ impact motion (**Figure 21F**). On the other hand, the stronger impact (point μ in **Figure 21D** and curve μ in **Figure 20**) weakens and vanishes and the weaker strengthens near point L and $z = 1/3$ impact motion (**Figure 21F**) stabilizes. This change can be accomplished, only when an additional impact is omitted. It appears at the end of this process on previously impactless loops of $z = 2/3$ motion (see development of impactless loop 2 in **Figure 22**, where clearance r is repeatedly increased for Δr and two penetrations per stop are allowed). This process is explained in more detail in **Figures 21D** and **21F** and **Figure 22** by the:

1. development of the position of extremes 1–4;
2. appearance of new extreme 5;
3. development of impact velocities v, μ,
4. disappearance of impact μ.

An additional impact, which is not of the grazing character, turns the system motion more or less into

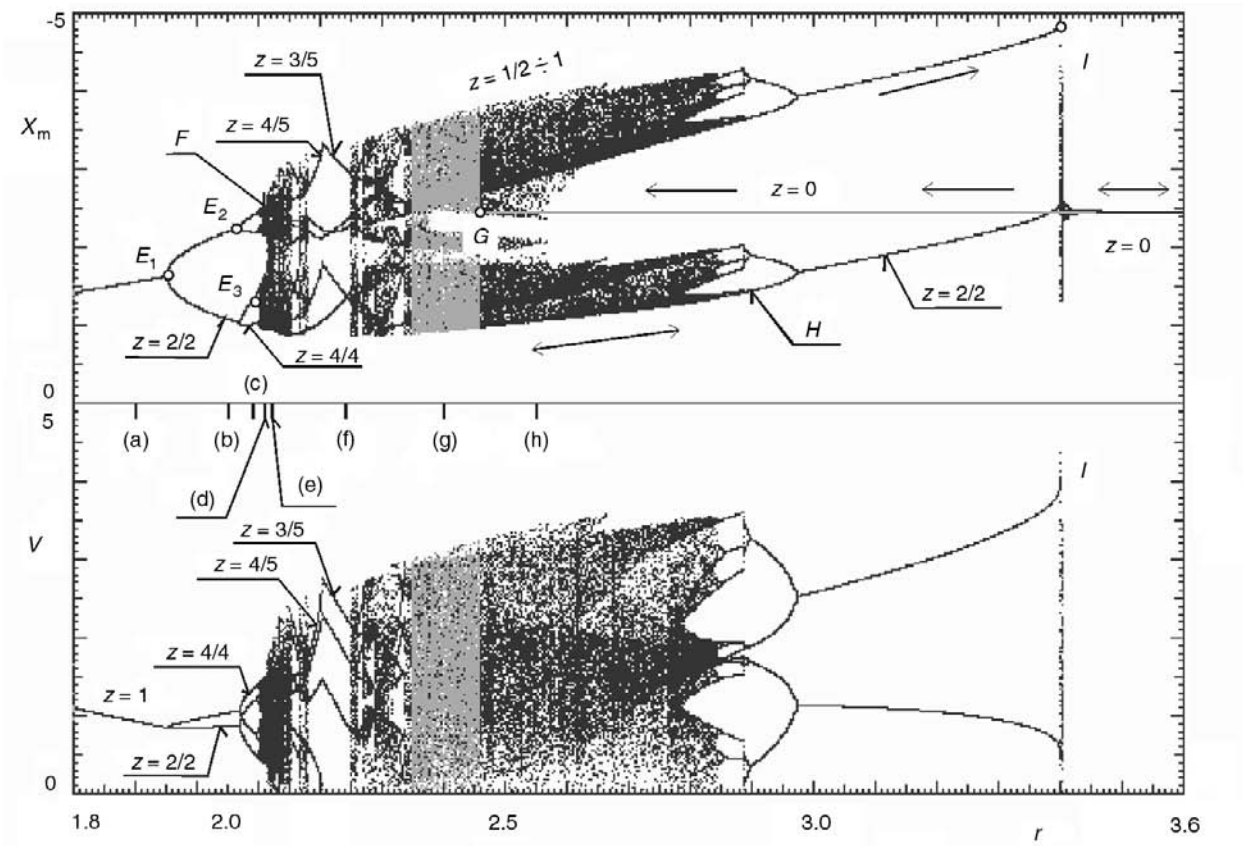


Figure 18 Bifurcation diagrams along line *i* in **Figure 17**.

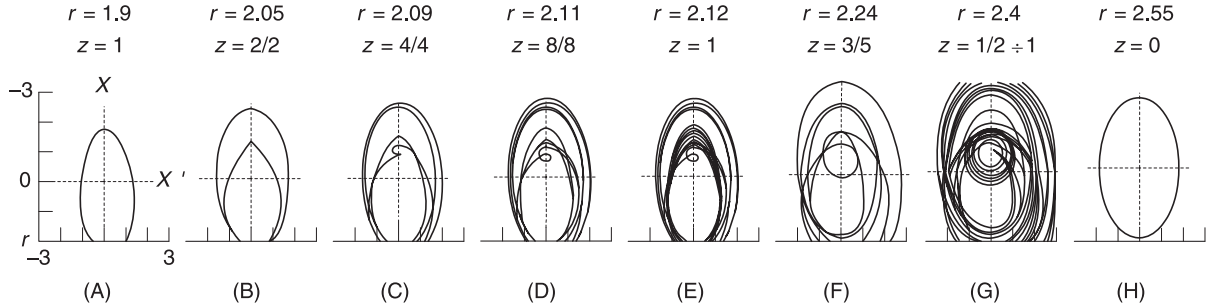


Figure 19 Phase trajectories of motions along line *i* in **Figure 17A**.

the state before the stability loss (**Figure 21D**), similarly as in the case of the interruption of the Feigenbaum cascade (see way C in **Figure 17**), and the instability of $z = 2/3$ impact motion develops to new additional impact. The intensity and appearance of an additional impact are unpredictable and the chaotic motion of the intermittency character arises (see **Figure 23A**), where time series of extremes **1–4** and impact velocities μ, v are displayed in the time interval $(0 < T < 500)$.

Time intervals of $z = 2/3$ impact motion during the intermittency are longer, the nearer are system parameters to the saddle-node stability boundary $(s_{+1})_{2/3}$. For example, point L on this boundary (**Figures 17B** and **20**) has coordinate $r = 3.3342$ and the intermittency in **Figure 23A** was simulated for $r = 3.334$. The chaotic impact motion in **Figure 23B** corresponds to point $\varepsilon(r = 3.3)$ and time intervals of $z = 2/3$ impact motion are short.

This way into the chaos can be found in other $z = 2/n$ $(n > 3)$ subharmonic impact motions. It is characterized by very sharp boundary $(s_{+1})_{2/n}$ between periodic $z = 2/n$ and chaotic $z = 1/(n-1) \div 1$ impact motions and quantity z decreases.

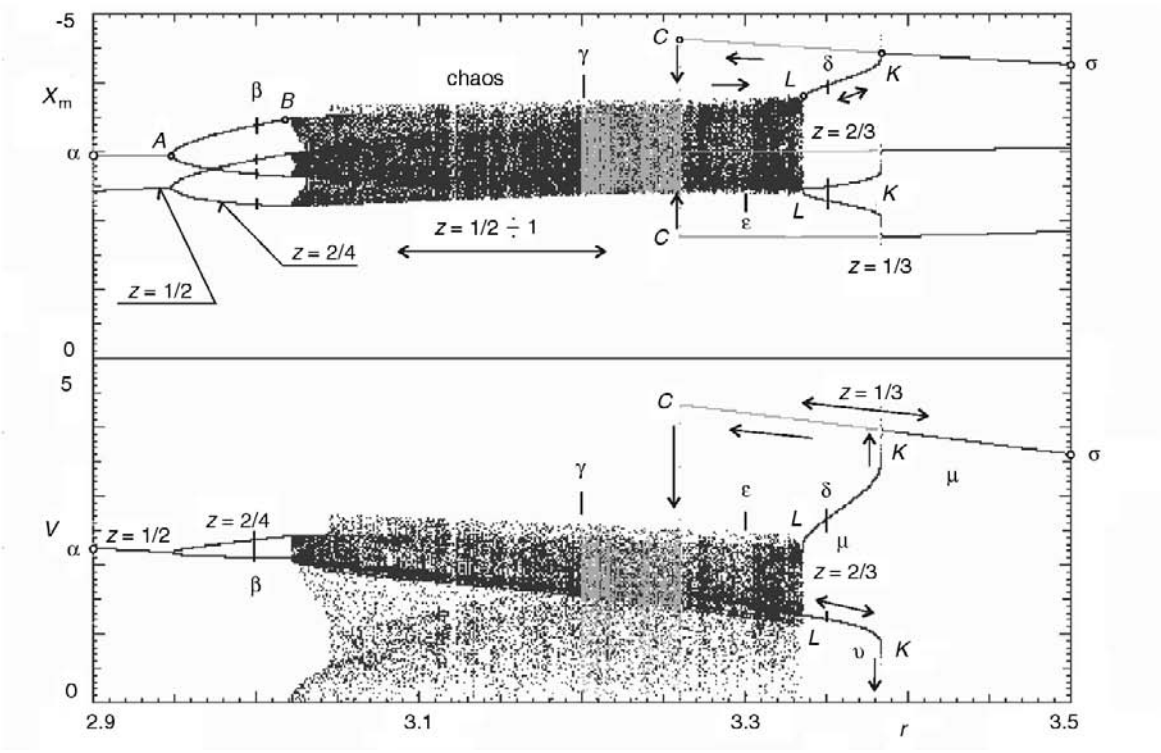


Figure 20 Bifurcation diagrams along line *k* in **Figure 17B**.

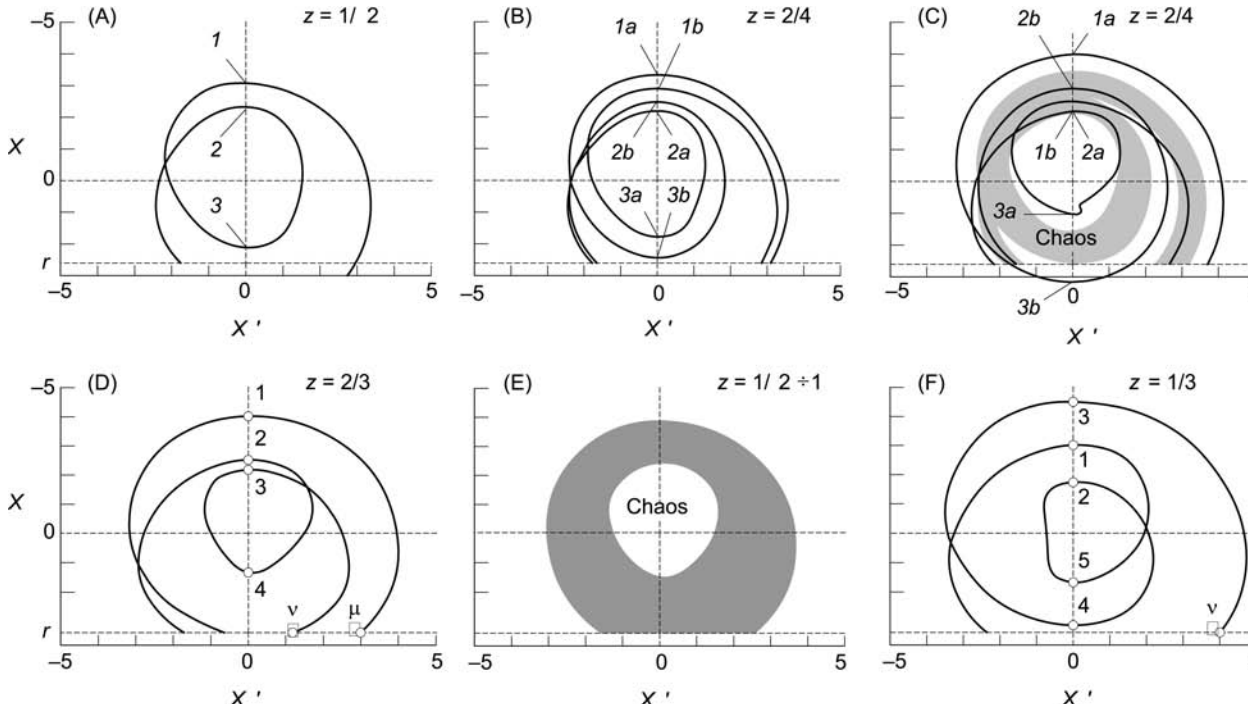


Figure 21 Phase trajectories of motions along line *k* in **Figure 17**.

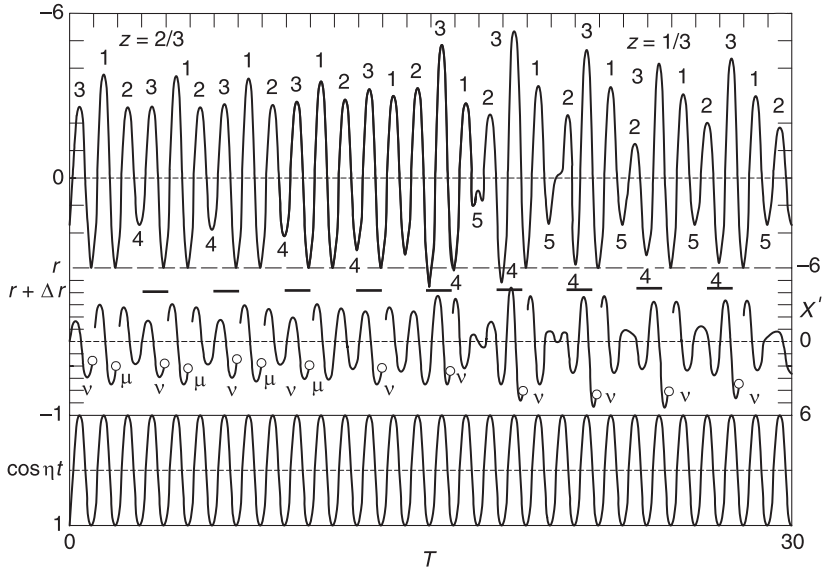


Figure 22 The last stage of development of saddle-node bifurcation and the elision of additional impacts.

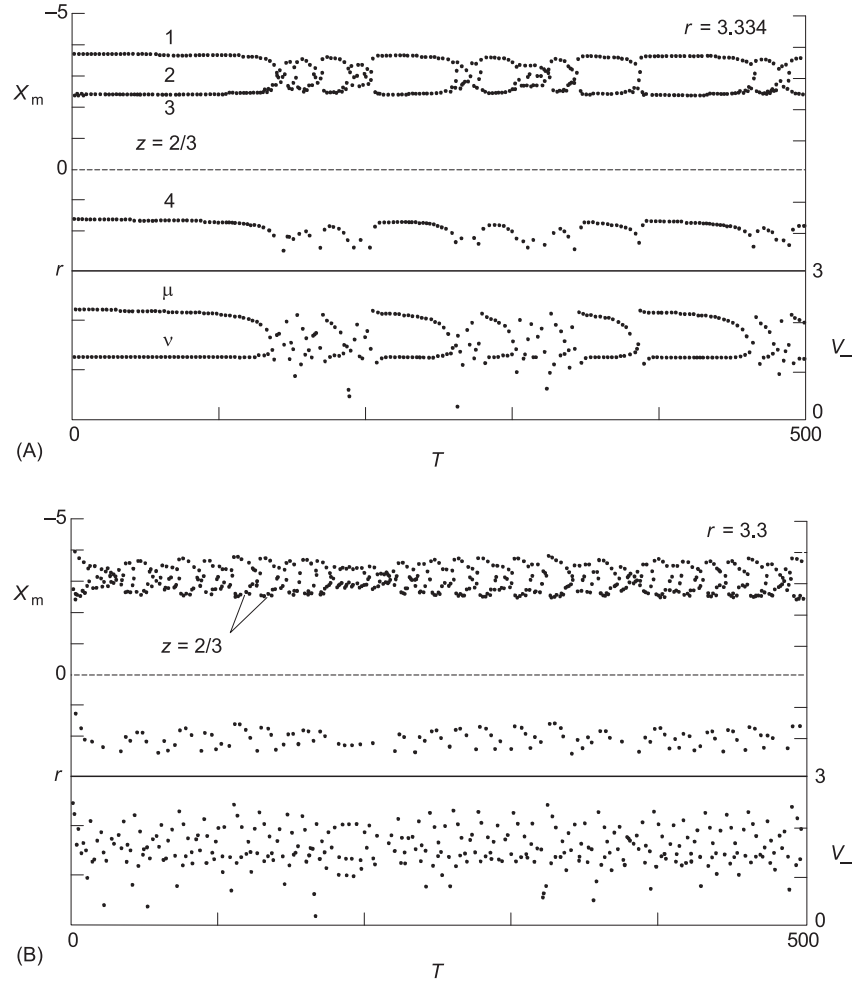


Figure 23 Intermittency (A) near point *L* and (B) in point ε in **Figure 17B**.

When clearance r decreases, e.g., from point σ in **Figure 17B**, then $z = 1/3$ impact motion (**Figure 21F**) ends its existence in point C on grazing bifurcation boundary $\rho_{1/3}$ and the system jumps inside the region of chaotic $z = 1/2 - 1$ motion (**Figure 21E**). It corresponds to way B (see **Figure 17**) into the chaos (see also points C in **Figure 20**).

There are other procedures, which throw light on the chaotic motion, e.g., stroboscopic or Poincaré's mappings, Lyapunov's exponents, autocorrelation functions, frequency power spectra, chaotic attractors and their dimensions, etc.

Conclusion

Explained dynamics of the simplest impact oscillator has shown the complexity and diversity of its behavior. The more complex the mechanical system and the higher the number of impacting bodies, the less and smaller are regions of periodic impact motions and the larger are regions of chaotic impact motions. Theoretical analysis of complicated impact oscillators is difficult and the effective tools for their investigation are simulations of the systems motion. They show the real behavior of chosen mathematical models of the mechanical system with impacts.

See Plates 52, 53, 54, 55.

See also: **Chaos**; **Dynamic stability**; **Nonlinear systems analysis**; **Nonlinear systems, overview**.

Further Reading

Babitsky VI (1998) *Theory of Vibro-Impact Systems*. Berlin: Springer.

Babitsky VI (ed.) (1999) *Dynamics of Vibro-Impact Systems*. Berlin: Springer.

Bansevičius R, Ragulskis K (1981) *Vibromotors*. Vilna (in Russian): Mokslas.

Brach RM (1991) *Mechanical Impact Dynamics*. New York: John Wiley

Brogliato B (1999) *Nonsmooth Mechanics: Models, Dynamics and Control*. Berlin: Springer.

Fejgin MI (1994) *Forced Oscillations in Systems with Discontinuous Nonlinearities*. Moscow (in Russian): Nauka.

Kobrinsky AE (1969) *Dynamics of Mechanisms with Elastic Connections and Impact Systems*. London: Iliffte Book.

Moon FC (1999 Ed.) *New Applications of Nonlinear and Chaotic Dynamics in Mechanics*. Dordrecht: Kluwer Academic Publishers.

Peterka F (1981) *Introduction to Vibration of Mechanical Systems with Internal Impacts*. Prague (in Czech): Academia.

Pfeiffer F, Glocker C (1996) *Multibody Dynamics with Unilateral Contacts*. New York: John Wiley.

Ragulskene VL (1974) *Vibro-Shock Systems*. Vilno: Mintis.

Silas G, Grindeu L (1986) *Vibro-Impact Systems*. Bucharest (in Rouman): *Editura Tehnica*.

Thompson JMT, Bishop SR (1994 eds.) *Nonlinearity and Chaos in Engineering Dynamics*. Chichester: John Wiley.

Viba JA (1988) *Optimalization and Synthesis of Vibro-Impact Systems*. Riga: Zinatne.

Wiercigroch M, Kraker A (2000 eds) *Applied Nonlinear Dynamics and Chaos of Mechanical Systems with Discontinuities*. Singapore: World Scientific.

VISCOUS DAMPING

F Gandhi, The Pennsylvania State University, University Park, PA, USA

Copyright © 2001 Academic Press

doi:10.1006/rwvb.2001.0016

Vibratory systems with discrete degrees-of-freedom are typically comprised of inertial, elastic, and viscous elements, and can undergo oscillatory motions under transient or periodic loading conditions. The inertial element (mass) stores kinetic energy, and the elastic element (spring) stores strain energy. In the absence of a viscous element (dashpot or damper), which generates a force proportional to velocity, the system would in principle continue to oscillate indefinitely when subjected to an initial perturbation. However, if a viscous dashpot was present, it would dissipate the energy in the system, thereby causing the oscillations to decay with time (see **Critical damping**).

When the vibratory system is subjected to a sustained sinusoidal excitation force, it will eventually reach a steady-state oscillatory behavior, with the force of the viscous damper $C\dot{x}$ (C is the viscous damping constant), influencing the amplitude and the phase of the steady-state response. For the vibratory system:

$$m\ddot{x} + C\dot{x} + Kx = F(t) = F_0 \sin \Omega t \qquad [1]$$

it can be shown that the steady-state response x is given as:

$$x(t) = x_0 \sin(\Omega t - \phi) \qquad [2]$$

where

$$x_0 = \frac{F_o}{\sqrt{\left((K - m\Omega^2)^2 + (C\Omega)^2\right)}} \quad \phi = \tan^{-1}\frac{C\Omega}{K - m\Omega^2} \qquad [3]$$

Away from the resonance condition (when the excitation frequency Ω is not close to the system's natural frequency), the $K - m\Omega^2$ term is large (and overshadows the $C\Omega$ term associated with viscous damping). In that case, viscous damping has little influence on the amplitude, x_0, and the phase, ϕ, of the response (eqn [3]). However, near resonance conditions, viscous damping has a significant influence on both the response amplitude and the phase. Since $(K - m\Omega^2) \rightarrow 0$, it is seen from the expression for x_0 that in the absence of viscous damping the oscillation amplitude could become extremely large; and it is in fact the viscous damping in the system that attenuates the resonant amplitude (**Figure 1A**). The phase difference between the excitation force and the response amplitude, ϕ (which assumes a value of 0° or 180° in the absence of viscous damping), varies continuously with excitation frequency, Ω, when viscous damping is present in the system (**Figure 1B**).

Once the system with viscous damping has reached steady-state oscillatory behavior under the harmonic excitation force ($F_0 \sin \Omega t$), the work done by this force over every cycle can be calculated as follows:

$$\begin{aligned} W &= \int_0^{2\pi/\Omega} F\,\mathrm{d}x = \int_0^{2\pi/\Omega} F\dot{x}\,\mathrm{d}t \\ &= \int_0^{2\pi/\Omega} \{F_0 \sin \Omega t\}\{x_0\Omega \cos(\Omega t - \phi)\}\mathrm{d}t \\ &= \pi F_0 x_0 \sin\phi = \pi C\Omega x_0^2 \end{aligned} \qquad [4]$$

and this is equal to the energy dissipated over the cycle by the viscous damper. The energy dissipated could also be calculated as the work done over any cycle by the viscous damping force (rather than the excitation force). Thus:

$$\begin{aligned} W &= \int_0^{2\pi/\Omega} C\dot{x}\,\mathrm{d}x = \int_0^{2\pi/\Omega} C\dot{x}^2\,\mathrm{d}t \\ &= \int_0^{2\pi/\Omega} C\Omega^2 x_0^2 \cos^2(\Omega t - \phi)\mathrm{d}t = \pi C\Omega x_0^2 \end{aligned} \qquad [5]$$

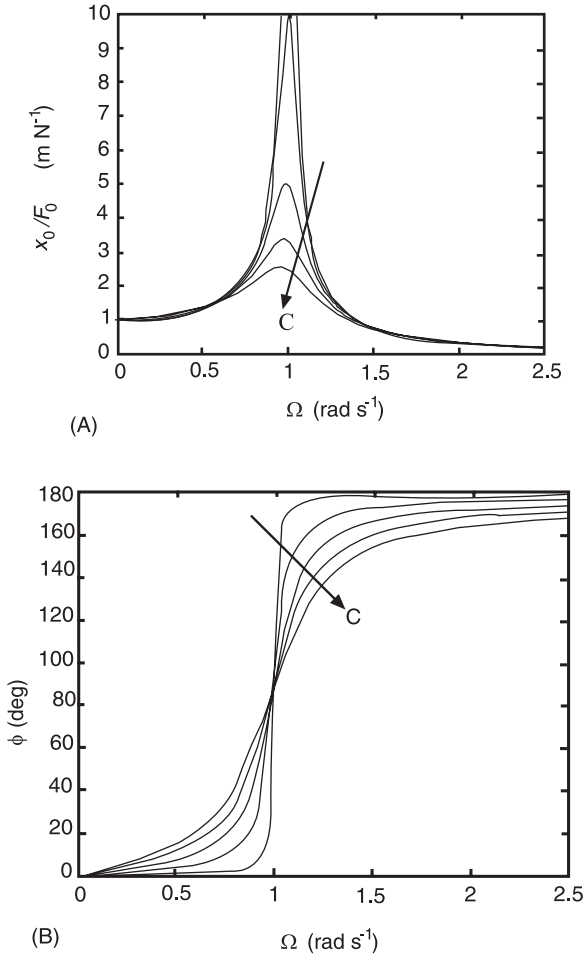


Figure 1 Response amplitude under harmonic excitation force. ($m = 1\,\mathrm{kg}$, $K = 1\,\mathrm{N\,m^{-1}}$, $C = 0.02$, 0.1, 0.2, 0.3 and $0.4\,\mathrm{Ns\,m^{-1}}$.)

While the work done or the energy pumped into the system by the external excitation force is dissipated by the viscous damper, the remaining stored energy in the system switches between kinetic and potential over every oscillatory cycle in the steady state.

For a harmonic excitation force, $F_0 \sin \Omega t$, and a steady-state harmonic response (eqns [2] and (3)), eqn [1] can also be expressed as:

$$F = (K - m\Omega^2)x \pm (C\Omega)\sqrt{(x_0^2 - x^2)} \qquad [6]$$

This expression for force as a function of displacement produces the hysteresis loops shown in **Figure 2**. This is a fairly typical hysteresis cycle associated with oscillatory systems subjected to a steady harmonic excitation force. The area enclosed in the hysteresis loops is simply a measure of the energy dissipated per cycle, $\pi C\Omega x_0^2$, due to the viscous damping in the system.

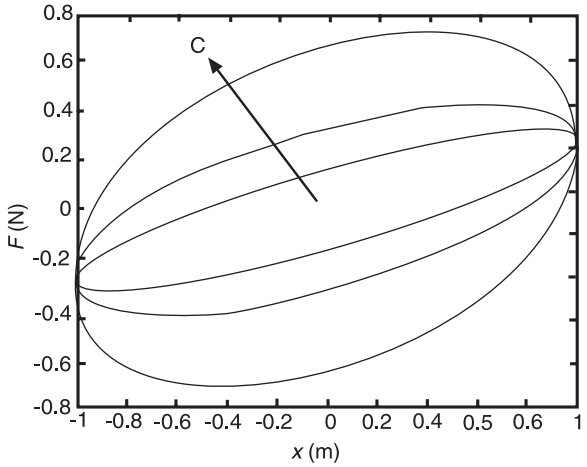


Figure 2 Hysteresis loop under harmonic excitation. ($m = 1$ kg, $K = 1\,\mathrm{N\,m^{-1}}$, $C = 0.2,\ 0.4$ and $0.8\,\mathrm{Ns\,m^{-1}}$, $\Omega = 0.85\,\mathrm{rad\,s^{-1}}$.)

The transient response of a system in the presence of viscous damping is not addressed in this article as it has been extensively covered elsewhere (see **Critical damping**).

See also: **Critical damping**.

Further Reading

Flugge W (1967) *Viscoelasticity*. Blaisdell.

Inman DJ (1996) *Engineering Vibration*. Englewood Cliffs, NJ: Prentice Hall.

Lazan BJ (1969) *Damping of Materials and Members in Structural Mechanics*. Oxford: Pergamon Press.

Nashif AD, Jones DIG, Henderson JP (1985) *Vibration Damping*. New York: Wiley.

W

WAVE PROPAGATION

Guided Waves in Structures

M J S Lowe, Imperial College of Science, Technology and Medicine, London, UK

Copyright © 2001 Academic Press

doi:10.1006/rwvb.2001.0173

Definition of Guided Waves (and Guided-wave Modes)

A guided wave is one whose propagation is guided by a structural form or boundary. The structure both guides the direction of the wave and determines its characteristics. In the context which is discussed here, the guided waves are elastodynamic; their propagation characteristics therefore depend on the density and the elastic properties of the material, as well as on the nature of the boundaries. A well-known example of such waves is the seismic wave created by an earthquake, which propagates along the surface of the earth. The sound (or vibration) which can easily be made to propagate along a tensioned wire is also a guided wave, as are the 'whispering gallery' waves which are guided around a circular enclosure by the wall.

Guided waves are natural properties of a structure, and are directly analogous to the natural vibration properties of a structure. The natural vibration properties of a plate of certain dimensions of thickness, length, and width are the unforced natural frequencies and mode shapes and can readily be calculated. For example, these natural vibration modes include a series of bending modes and in-plane extensional modes. But if the plate is assumed to be infinite in length and width, then these natural frequencies and mode shapes do not exist in the same way. Instead then, the natural properties of the plate are the guided waves which can propagate indefinitely along the plate. These, again, are unforced properties. They also have particular characteristics of spatial form (shape), such as bending and extension, which are found in the vibration modes of a finite bounded structure, and they are often referred to as the guided-wave modes. So, a guided-wave mode is a particular type of wave which has its own properties of frequency, velocity, and shape and which can travel indefinitely in an elastic structure. Indeed, it is reverberation of these guided-wave modes back and forth between the ends of the finite plate which sets up what is referred to as the vibration modes. From a theoretical point of view, both kinds of properties are the unforced steady-state solutions to the elastodynamic equations of motion, the difference coming simply from the different boundary conditions (see **Mode of vibration**).

An important feature of guided waves is that they may propagate over very long distances because the structure, or waveguide, retains the energy by its boundaries, so that it does not spread out as it would in an unbounded volume of material. For example, the waves which are guided along a tensioned wire propagate in only a single dimension, the direction along the wire. In contrast, the waves which propagate from a point source in an unbounded volume of material spread out in all three dimensions, so that the amplitude then diminishes with the distance of propagation. This is why the surface wave in an earthquake can be more damaging than the compression waves which reflect from deep strata; the surface wave is guided by the surface and so spreads in only two dimensions rather than three. The property of long-distance propagation is one reason why guided ultrasonic waves have become popular for nondestructive testing.

Another key characteristic of guided waves is that they exhibit dispersion. The velocity of a guided wave, in general, varies with its frequency. Consequently, the shape of the signal of a wave packet (a short-time wave train) may vary with the distance and time of propagation. The short time signal contains a finite band of frequencies; if the low-frequency components of the signal travel at different speeds from the high-frequency components, then the signal shape must change with time. In fact, what happens is that the wave packet spreads out and its amplitude

diminishes. It is important to appreciate that this dispersion is not a function of the material properties (at least for linear elastic materials) but is caused by the properties of the guided wave. It is therefore essentially a result of the boundary conditions which are imposed by the waveguide structure.

Theoretical Basis

The primary property of a guided wave which needs to be calculated is the velocity–frequency relationship, that is, the variation of the velocity of the mode with the frequency. This relationship is known as a dispersion curve. There can be many different modes which may propagate in a given structure; each has its own dispersion curve, so that at any chosen frequency the velocity can be read off the curve. The curves are continuous and they represent two-dimensional eigenvalues of the modal equations. Thus, whereas a natural vibration mode of a finite plate has its value of natural frequency, a guided-wave mode in a plate has its frequency–velocity curve.

The guided-wave modes also have their eigenvectors, that is, their mode shapes. The mode shapes of a guided wave which are of interest are the distributions of the displacements and stresses in the directions normal to the direction of propagation; in the example of a plate, the mode shapes are the profiles of these quantities through the thickness. In the direction of propagation the mode shapes are simply harmonic functions: thus a displacement or stress quantity at any location in the thickness of the structure additionally varies sinusoidally in time and in the direction of propagation. The mode shapes of a mode vary, in general, from one location to another along the dispersion curve. Another interesting feature is that the wave crests of a guided wave are straight and aligned exactly at right angles to the direction of propagation for all modes in which there is no attenuation (modes with attenuation will be discussed later in this entry).

There are various ways to approach the problem of calculation of the dispersion curves. One approach, which has the benefit of being rather physical, is to compose the field in the waveguide from a superposition of bulk waves (waves which could propagate in an unbounded medium), the sum of the bulk waves being such that the boundary conditions are satisfied. Such an approach is illustrated for the example of a plate in **Figure 1**. The plate is assumed to be infinite in extent, both in the direction of propagation of the wave and in the direction normal to the plane of the illustration. Four waves are shown in the plate: longitudinal and shear waves traveling in downward directions and a similar pair traveling in upward directions. Each of these partial waves is a continuous plane wave, such as would travel in an unbounded medium. The task then is to find the angles of propagation, the amplitudes and the phases of all of these modes such that when they are superposed the surfaces of the plate are traction-free. This is done by applying Snell's law to relate the stress components of all of the waves at the surfaces of the plate. It turns out that, in order to satisfy the traction-free condition at all positions along the surfaces, the partial waves must all have the same frequency and their directions must be fixed in relation to each other. The angles defining the directions of the partial waves in fact relate to a value of velocity in the direction along the plate, which will be the velocity of the guided mode.

For a given structural geometry and material properties, the mathematical problem then becomes the solution of a characteristic function $f(\,)$ of the form:

$$f(\omega, C) = 0 \qquad [1]$$

where ω is the frequency and C is the velocity of the guided wave. The numerical solutions of this function are the frequency–velocity dispersion curves. At any location on a dispersion curve, the distributions of the displacements and stresses through the thickness of

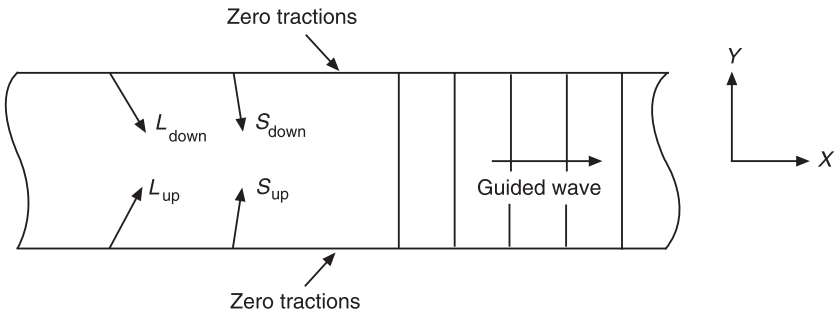


Figure 1 Guided wave in plate composed by superposition of partial waves.

the structure (the wave mode shapes) are simply found by summing the contributions from the four partial waves at that location. To complete the description, the propagation of the wave along the structure is described by a harmonic wave equation in much the same form as that for a wave in an unbounded medium (see **Wave propagation**, Waves in an unbounded medium). Taking, for example, the particle displacement in the Y direction, the space–time equation for the propagation is:

$$u_Y = A\mathrm{e}^{\mathrm{i}(k_X x - \omega t)} \qquad [2]$$

where k_X is the wavenumber in the direction along the structure, which is related to the velocity of the wave by:

$$C = \frac{\omega}{k_X} = \frac{\omega * \text{wavelength}}{2\pi} \qquad [3]$$

The dispersion curves and mode shapes of some of the best known guided waves will now be presented in the following several sections.

Waves which are Guided along a Flat Boundary

The surface wave which was mentioned earlier in the earthquake example is in fact the Rayleigh wave which is one of the simplest guided wave modes. The Rayleigh wave exists at the free surface of a semi-infinite half-space of an isotropic solid material. Strictly speaking, the half-space should be bounded by a vacuum in order for the surface to be perfectly traction-free. However, in practice, the tractions at the boundary between typical structural materials and air are virtually zero. Also, a thick plate can act effectively as a semi-infinite half-space provided that the thickness is very much larger than the near-surface region in which the wave propagates; this depends on the wavelength being short enough and thus on the frequency being high enough.

The characteristic function of a Rayleigh wave is a cubic expression:

$$p^3 - 8p^2 + (24 - 16a)p + 16(a - 1) = 0 \qquad [4]$$

with:

$$p = \left(\frac{\omega}{k_X C_S}\right)^2 \text{ and } a = \left(\frac{1 - 2v}{2(1 - v)}\right) \qquad [5]$$

in which k_X is the wavenumber of the Rayleigh wave, C_S is the bulk velocity of shear waves in an unbounded volume of the material, and v is Poisson's ratio.

The solution of the Rayleigh wave function shows the Rayleigh wave to be nondispersive with a velocity just below the velocity of the bulk shear wave. In steel, for example, the bulk shear wave velocity is about $3.25\,\mathrm{km\,s^{-1}}$ and the Rayleigh wave velocity is about $3.0\,\mathrm{km\,s^{-1}}$.

The displacement and stress mode shapes of the Rayleigh wave in steel are shown in **Figure 2** for a frequency of 1 MHz, in which case the wavelength is about 3 mm. If the frequency was to be increased then the depth scale of the mode shape plot would be reduced in linear proportion. Thus, it can be seen that the Rayleigh wave exists effectively just in the material within two or three wavelengths of the surface. The shear stress and the stress normal to the surface can both be seen to be zero at the surface, as is the necessary boundary condition for the solution.

If the vacuum is replaced by another solid material, so that the geometry consists of two semi-infinite half-spaces meeting at a flat interface, then another type of guided wave may exist. This is the Stoneley or interface wave. In this case the boundary condition is not traction-free but instead the condition is imposed that the tractions in the two materials must balance at the interface and the displacements must be continuous. Again, the solution, when one exists, yields a velocity which does not vary with frequency. However, a solution only exists within certain ranges of the properties of the two materials. As with the Rayleigh wave, the mode shapes are dominant in the material close to the interface, in this case existing on both sides of the interface.

Waves which are Guided along a Plate

The Lamb waves which are guided along a simple isotropic plate are perhaps the best known guided waves in structures. Strictly speaking, Lamb's theory for these waves requires the surfaces of the plate to be traction-free, that is to say the plate should be in vacuum. In practice however, as with the Rayleigh wave, the Lamb wave solutions are valid for any typical structural material in air.

The solutions of the characteristic functions for Lamb waves can be calculated separately for symmetric and for antisymmetric modes, all modes having shapes which are either perfectly symmetric or perfectly antisymmetric with regard to the midplane of the plate. The characteristic function for the symmetric Lamb waves is:

$$(B^2 - k_X^2)^2 \tan(Ah) + (4k_X^2 AB)\tan(Bh) = 0 \qquad [6]$$

and for antisymmetric waves:

$$(B^2 - k_X^2)^2 \cot(Ah) + (4k_X^2 AB)\cot(Bh) = 0 \quad [7]$$

in which:

$$A = \sqrt{\left[\left(\frac{\omega}{C_L}\right)^2 - k_X^2\right]} \text{ and } B = \sqrt{\left[\left(\frac{\omega}{C_S}\right)^2 - k_X^2\right]} \quad [8]$$

C_S and C_L are the velocities of bulk shear and longitudinal waves respectively, and the thickness of the plate is $2h$.

Figure 3 shows the Lamb wave dispersion curves for a steel plate. The horizontal axis shows the frequency–thickness product because the results can be scaled linearly in this way. Thus, for example, these curves could represent the modes in a 1-mm-thick plate for the frequency range up to 10 MHz or, equally, for a 2-mm-thick plate up to 5 MHz. The vertical axis shows the phase velocity, that is, the velocity of the wave crests. The modes are labeled in the conventional way for Lamb waves: the '*s*' modes are the symmetric modes and the '*a*' modes are the antisymmetric modes. The subscripts, 0,1,2 ..., indicate the series of these two types, the complexity of the mode shapes increasing with the increasing mode number. The fundamental modes, s_0 and a_0, are very easily understood as extensional and bending modes when the frequency is low, as illustrated in the exaggerated displaced shape sketches in the figure. As the frequency is increased, the velocities of both modes change, until ultimately, at the high-frequency end of the plot, they converge to the same value. This is the velocity of the Rayleigh wave and, indeed, the solution is asymptotic to the Rayleigh wave solution at high frequency. Looking at the mode shapes at high frequency, it can be seen that the motion is concentrated more and more at the surfaces of the plate so that in the limit a Rayleigh wave propagates simultaneously on both surfaces. In the case of the s_0 mode, these two Rayleigh waves have the same phase, and in the case of the a_0 mode, they are in opposite phase. The particle motion of all Lamb modes is in the plane defined by the direction of the guided-wave propagation and the normal to the surface of the plate.

Another way in which the Lamb wave dispersion curves are often presented is by wavenumber instead of phase velocity. The relationship between wavenumber and phase velocity is the simple expression in eqn [3]. The wavenumber curves are shown in **Figure 4**.

The phase velocity curves present the velocity of the wave crests but this is not in fact the velocity at which a pulse or other short-time wave signal (wave packet) travels. A wave packet travels at the group velocity which is obtained by taking the derivative of the frequency with respect to the wavenumber:

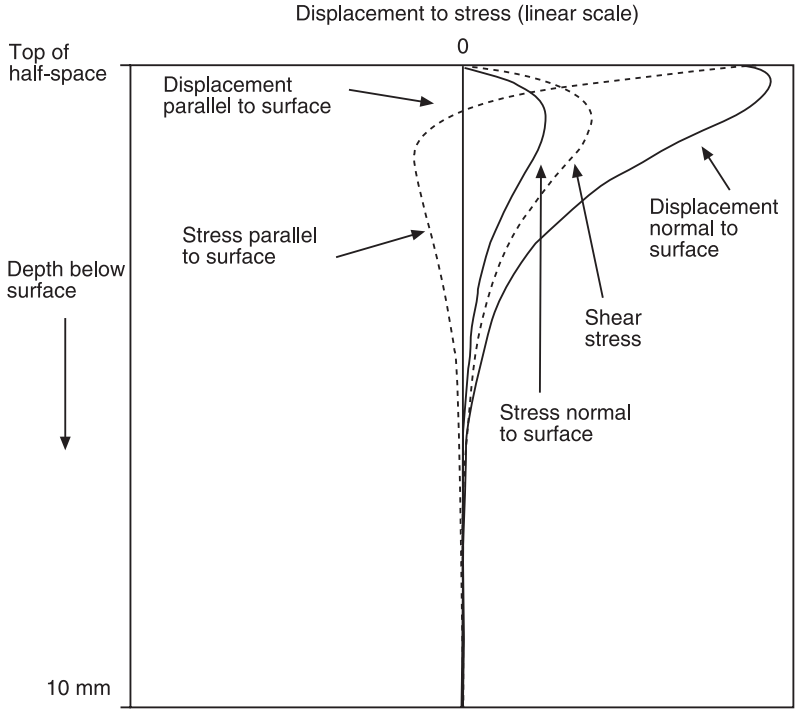


Figure 2 Mode shapes of 1 MHz Rayleigh wave in steel.

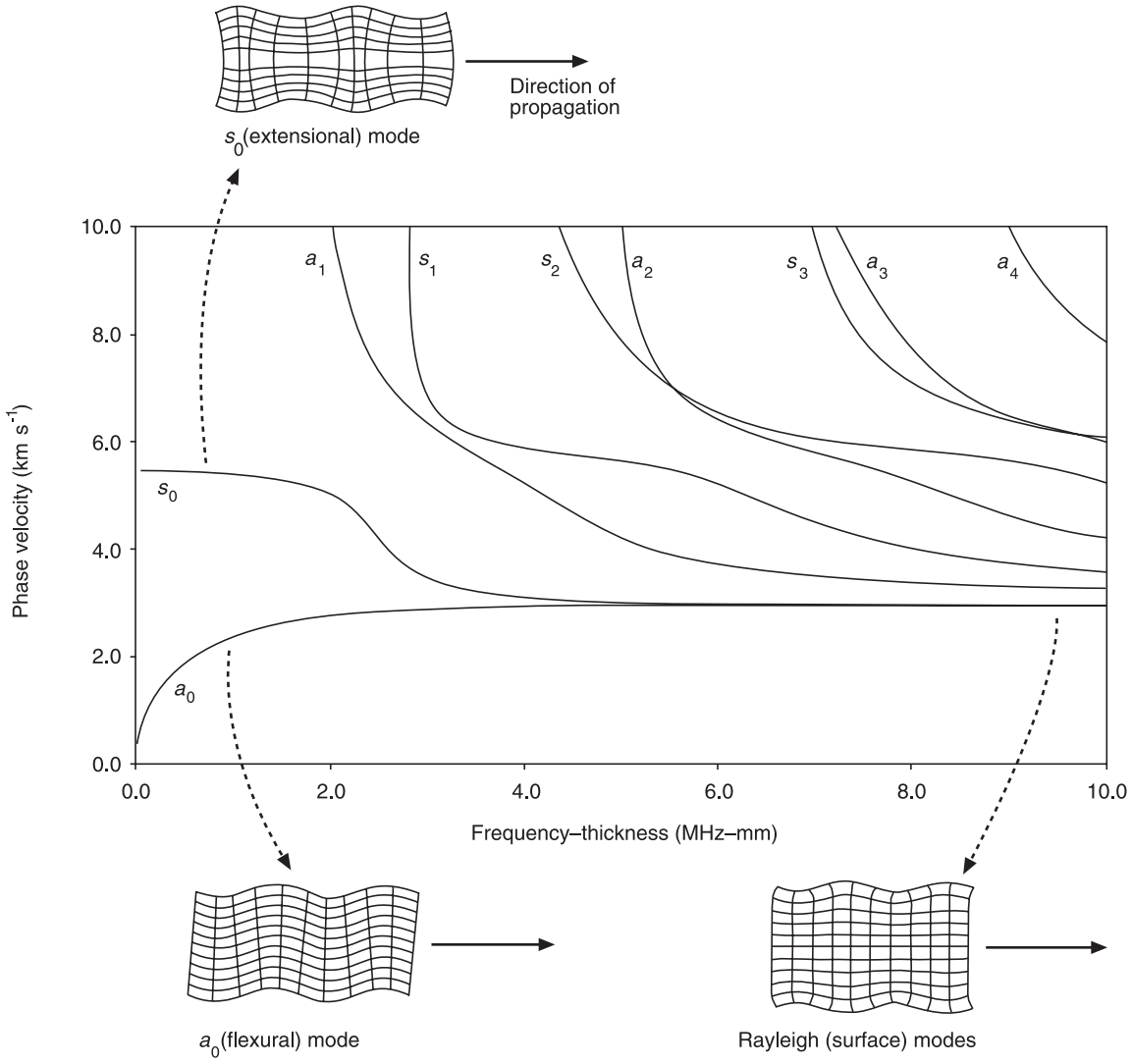


Figure 3 Phase velocity dispersion curves for Lamb waves in steel plate, showing shapes of fundamental modes.

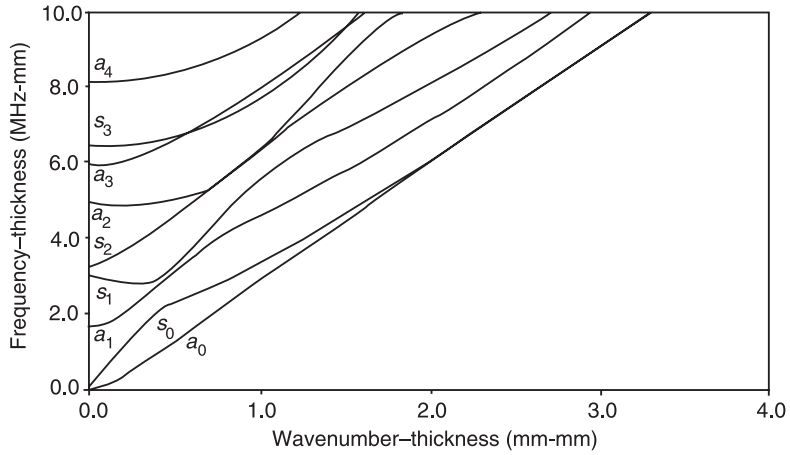


Figure 4 Wavenumber dispersion curves for Lamb waves in steel plate.

$$\text{Group velocity} = \frac{d\omega}{dk_X} \qquad [9]$$

Therefore if, for example, a wave packet signal consists of a sinusoidal tone windowed by an envelope function, then the envelope travels at the group velocity whereas the crests of the sinusoidal signal within the envelope travel at the phase velocity for that particular frequency. The value of calculating the group velocity is that this gives the important information for long-range propagation about the arrival times of the wave packets. **Figure 5** shows the group velocity dispersion curves for the steel plate.

Finally, there is one more family of modes which can propagate in a plate which are quite different from the Lamb modes. These are the Love modes, or shear horizontal (SH) modes and they differ from the Lamb modes in the direction of their particle motion. In this case the particle motion is entirely in the direction which is normal to the direction of propagation and parallel to the surface of the plate. **Figure 6** shows the Love mode dispersion curves for the steel plate. The displacement mode shapes are illustrated on the figure in an exaggerated scale for the first two modes. The fundamental mode has a very simple mode shape, with no variation of the displacement through the thickness of the plate; therefore, the only variation is the distance–time harmonic variation along the axis of propagation. Consequently it travels at exactly the velocity of shear bulk waves. The next mode, SH_1, has a variation of the displacement through the thickness which follows the shape of half a sine wave; the displacement profile is antisymmetric with a positive value at one surface and negative at the other. Higher-numbered modes have profiles with increasing numbers of half-waves through the thickness. Interestingly, the mode shapes for each SH mode remain identical for all locations on the curve; this is very much the exception since the mode shapes vary considerably along the curves for most types of guided waves.

Waves in a Bar or Hollow Cylinder

All kinds of beams, rods, and cylinders make excellent waveguides, and of course they occur frequently in engineering structures. Guided waves in these objects can propagate for extremely long distances. The dispersion curves for a cylindrical object are calculated in the same way as for the flat geometries discussed above, except that the partial waves must be expressed in the form for propagation in a cylindrical coordinate system; specifically, the harmonic exponential functions are replaced here by Bessel functions. The resulting dispersion curves differ conceptually from the flat-geometry case in that there now exist multiple families of modes, each family corresponding to a different circumferential order of the Bessel functions.

An example, using a solid steel bar, is given in **Figure 7**. The horizontal axis shows the frequency–radius product; thus, the upper limit could be, for example, 5 MHz for a 1-mm-radius bar or 10 MHz for a 0.5-mm-radius bar. The dispersion curves show the conventional labels for cylindrical geometry: '*L*' denotes the axially symmetric modes, '*T*' denotes torsional, and '*F*' denotes flexural. The first index of each label denotes the circumferential order and the second index is simply a sequence identifier. The order 0 modes have mode shapes which are constant

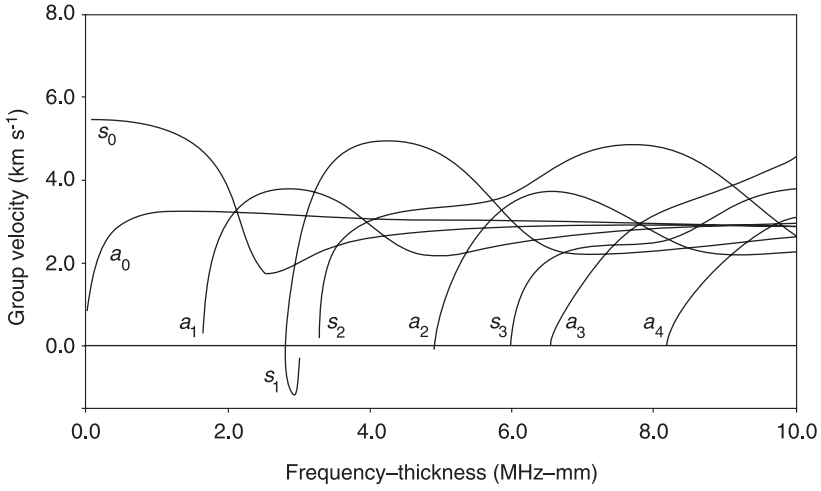


Figure 5 Group velocity dispersion curves for Lamb waves in steel plate.

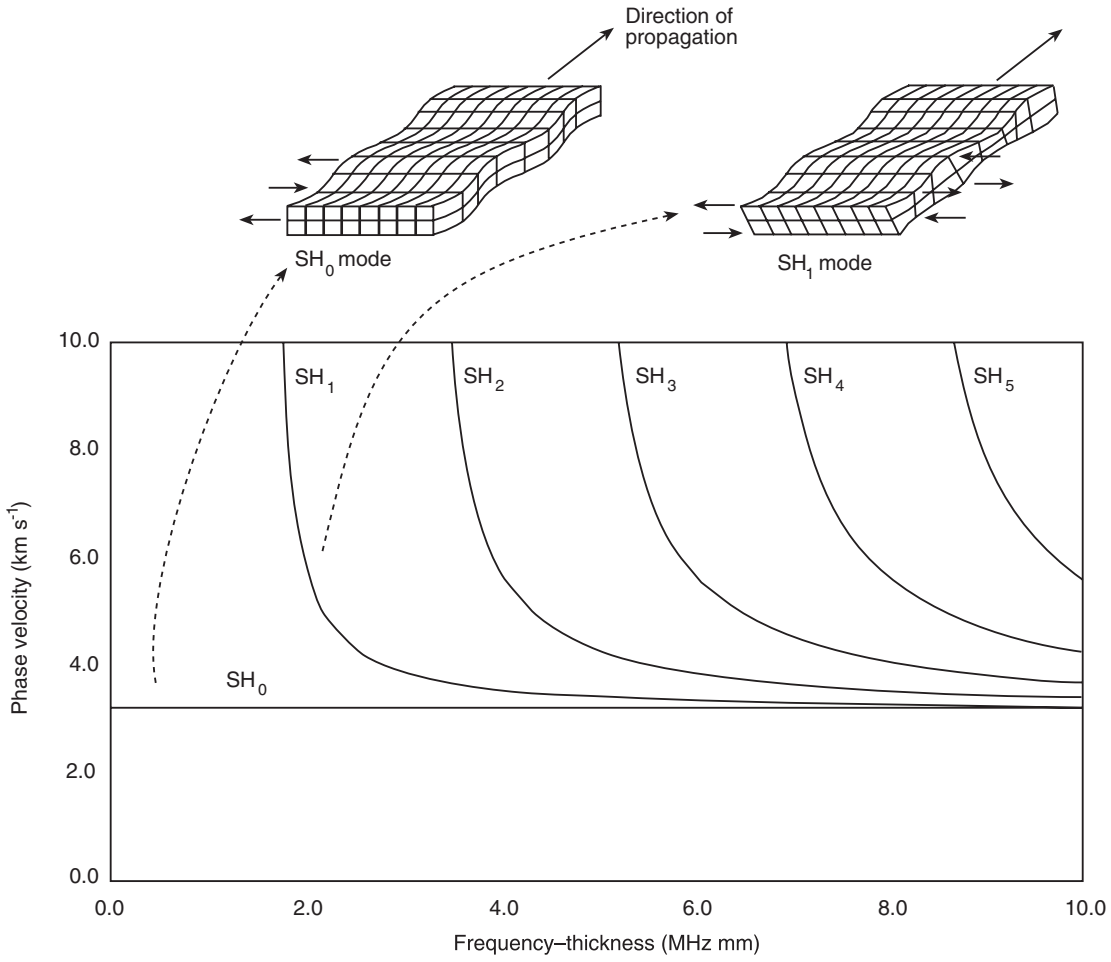


Figure 6 Phase velocity dispersion curves for Love waves in steel plate.

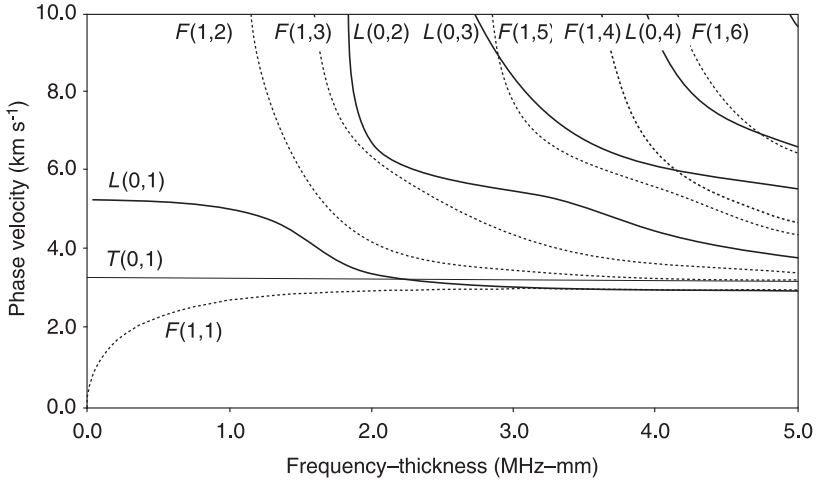


Figure 7 Phase velocity dispersion curves for waves which propagate along a solid steel cylinder (bar).

around the circumference of the cylinder. The $L(0, \ldots)$ modes are therefore essentially axial extensional modes, although with various different mode shape profiles across the radius. The $T(0, 1)$ mode is pure torsion of the cylinder, with displacements only in the tangential direction, and accordingly it travels at exactly the bulk shear velocity. The $F(1, \ldots)$ modes have mode shapes which vary sinusoidally in the circumferential direction, the circumferential order of 1 indicating that in these cases there is exactly one sinusoid around the circumference. Higher orders $(2, 3, 4, \ldots)$ may also exist but are not shown here. The fundamental flexural mode, $F(1, 1)$, is thus a bending mode as, for example its axial stress would be positive at one circumferential location and negative at 180° around the circumference. It is therefore analogous to the a_0 mode in the plate, and, indeed, its dispersion curve is rather similar.

Attenuation of Guided Waves

Guided waves are attenuated by the mechanisms of scattering, absorption, and leakage.

Scattering and absorption of guided waves are no different conceptually with guided waves than with bulk waves: scattering losses occur when some of the energy of the waves is lost because of partial reflections from features such as inhomogeneities or inclusions in the material, or roughness of the surface; absorption occurs when the material has damping properties, this is the case for example with plastic materials.

Leakage is quite a different phenomenon which is peculiar to guided waves. Leakage occurs when a waveguide structure is in contact with another medium so that some of the energy is able to leak from the waveguide into the surrounding material. An example of this is 'leaky Lamb waves' the Lamb waves which propagate in a plate that is immersed in a fluid. The dispersion curves for leaky Lamb waves in a steel plate immersed in water are almost the same as those for the strict Lamb waves (in fact, this is to be expected because the acoustic impedance of the water is very much lower than that of the steel). However, there is an additional attenuation associated with each location on each dispersion curve. The attenuation is very much a part of the modal properties of the plate–water system and the attenuation curves can be calculated along with the dispersion curves. **Figure 8** shows the attenuation curves for this example. The attenuation is exponential with distance so it may be expressed by multiplying the wave propagation eqn [2] by an exponential with a real negative argument. Another consistent form of expression is to add an imaginary part to the wavenumber of the guided wave. The attenuation in the figure is expressed in the converted units of $\mathrm{dB\,mm^{-1}}$, using also the attenuation–thickness scaling relationship; thus, the attenuation at the top of the scale could be, for example, $2\ \mathrm{dB\,mm^{-1}}$ traveled in a 1-mm-thick plate or $1\ \mathrm{dB\,mm^{-1}}$ traveled in a 2-mm-thick plate.

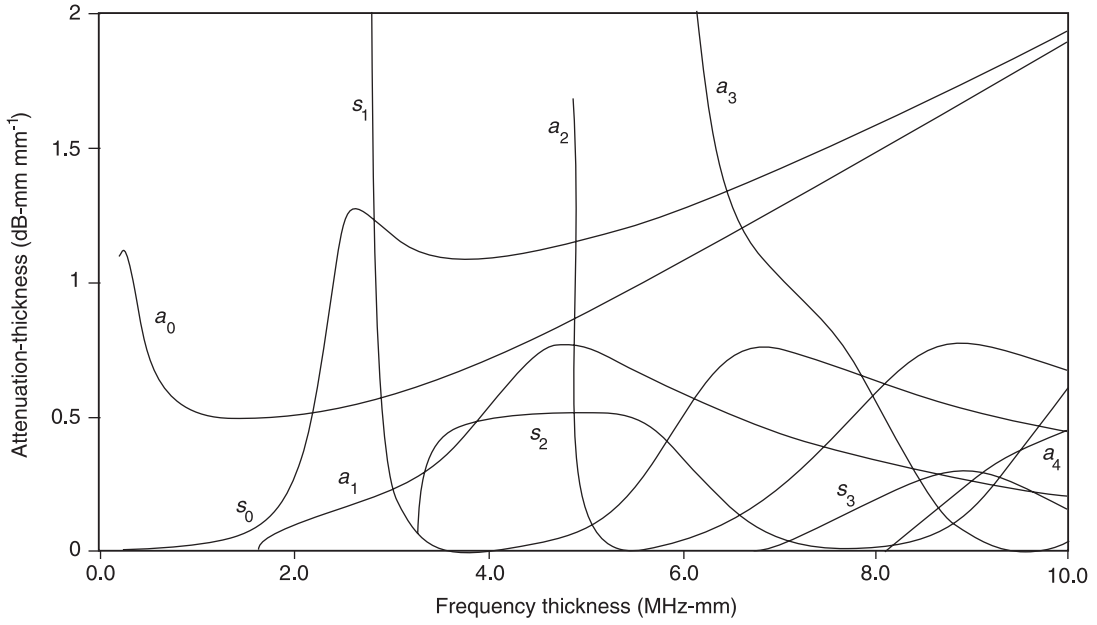


Figure 8 Attenuation curves for leaky Lamb waves in a steel plate immersed in water.

The curves show significant variations of attenuation, and this can be understood by examining the mode shapes. For example, the s_0 mode at low frequency has very little displacement in the direction normal to the surface of the plate, and therefore it leaks very little; on the other hand, the a_0 mode has significant lateral motion and so it has high attenuation. The attenuations of the s_0 and a_0 modes can be seen to be converging towards a straight line. In the high-frequency limit these modes both become the Rayleigh mode, for which the attenuation per unit distance increases linearly with frequency, or this can alternatively be expressed as a constant attenuation per wavelength. In the case of a steel half-space in contact with water, the attenuation is 0.58 dB per wavelength.

Guided Waves in Engineering

Guided waves occur in several diverse instances in engineering. Already briefly mentioned are the examples of earthquakes and the field of acoustics, but there are others. At the very low-frequency end of the scale, seismic exploration has for many years used guided waves to survey, particularly for oil reserves. A point source (for example, an explosion) is used to generate waves, then multiple receivers are used to detect the arrivals of waves; these include waves which are guided by the rock strata. Accordingly, much of the research literature for guided waves is focused on modeling such phenomena. At higher frequencies, typically between about 50 kHz and 10 MHz, guided waves are used for nondestructive testing. For example, surface waves may be used to detect microcracking of the surface of a material, or to measure the properties of thin electroplated or painted layers deposited on a much thicker object. Waves which are guided in plates, bars, and pipes may be used to detect regions where there is material thinning, cracking or corrosion. At very high frequency, in the GHz range, surface-guided waves are used in many electronic surface acoustic wave (SAW) devices, for example, for performing operations in signal processing, such as frequency filtering.

See also: **Mode of vibration**; **Nondestructive testing**, Ultrasonic; **Wave propagation**, Waves in an unbounded medium.

Further Reading

Achenbach JD (1984) *Wave Propagation in Elastic Solids*. New York: North-Holland.

Auld BA (1990) *Acoustic Waves and Fields in Solids*, 2nd edn. Florida: Robert E Kreiger.

Brekhovskikh LM (1960) *Waves in Layered Media*. New York: Academic Press.

Kennett BLN (1983) *Seismic Wave Propagation in Stratified Media*. Cambridge: Cambridge University Press.

Kino CS (1987) *Acoustic Waves: Devices, Imaging and Digital Signal Processing*. New Jersey: Prentice-Hall, Englewood Cliffs.

Kolsky H (1963) *Stress Waves in Solids*. New York: Dover Publications.

Malvern LE (1969) *Introduction to the Mechanics of a Continuous Medium*. New Jersey: Prentice-Hall.

Nayfeh AH (1995) *Wave Propagation in Layered Anisotropic Media, with Applications to Composites*. Amsterdam: North-Holland.

Redwood M (1960) *Mechanical Waveguides*. New York: Pergamon Press.

Rose JL (1999) *Ultrasonic Waves in Solid Media*. Cambridge: Cambridge University Press.

Viktorov IA (1967) *Rayleigh and Lamb Waves – Physical Theory and Applications*. New York: Plenum Press.

Interaction of Waves with Boundaries

M J S Lowe, Imperial College of Science, Technology and Medicine, London, UK

Copyright © 2001 Academic Press

doi:10.1006/rwvb.2001.0172

Introduction

When an elastic wave which is traveling in a fluid or solid medium is incident at a boundary of the material, then it may be partially reflected or transmitted, the characteristics of the interaction depending on the nature of the boundary. Additional waves may also be generated. This entry addresses the physics of this wave interaction. The focus is on the interaction of plane waves with a flat boundary between two materials, although there is some discussion about the interaction of waves with boundaries of arbitrary shapes, which has relevance to the topics of sound scattering and nondestructive testing (NDT).

The understanding of these reflection and transmission phenomena is important in several areas. In the subject of ultrasonic NDT, for example, the interaction of the ultrasound waves with features of the structure is the key to the technique. The ultrasound reflects from boundaries of the body as well as from any defects such as cracks, and the measurement of these reflections reveals the desired informa-

tion. In another example, the understanding of structure-guided elastic waves relies very much on the interaction characteristics at the waveguide boundaries as these determine the properties of the guided waves. In considering shock and vibration problems, it can be useful to examine the internal reflections of waves within a body. Or, in acoustics studies, it is useful to determine the extent to which sound is reflected and transmitted at structural boundaries such as partitions.

Reflection and Transmission of a Plane Wave Normally Incident at a Boundary

Consider a flat interface between two half-spaces, as illustrated in **Figure 1**. The two half-spaces are composed of materials $M1$ and $M2$ – they may be either fluid or solid materials, both of which have the same solution for the normal incidence case. A continuous elastic compression wave is incident from material $M1$ at the boundary; its direction of propagation, X, is normal to the interface.

The particle displacement, u_X, and the stress in the direction normal to the interface, σ_{XX}, of the incident wave are given by the expressions:

$$u_X = I\,\mathrm{e}^{\mathrm{i}(kx-\omega t)} \qquad [1]$$

$$\sigma_{XX} = \mathrm{i}\omega C_{M1}\rho_{M1}u_X \qquad [2]$$

where I is the amplitude of the particle displacement (I for incident wave), k is the wavenumber, x is the distance from the interface along the path of propagation, C_{M1} is the wave speed, ρ_{M1} is the density of material $M1$, and i is $\sqrt{(-1)}$ (see **Wave propagation**, Waves in an unbounded medium).

At the interface it is now assumed that some of the energy of this wave is transmitted into medium $M2$ and some is reflected. The transmitted and reflected waves are both of the same type as the incident wave (in this case, compression) and have amplitudes, not yet known, of T and R respectively. The particle displacement and stress equations for T and R are the same as eqns [1] and [2] except for these different amplitudes and the fact that the harmonic exponent of the R wave is in negative X (opposite direction of travel).

The amplitudes of T and R are found by satisfying the boundary conditions at the interface. These conditions are the continuity of the particle displacement and the equilibrium of the stress across the boundary. Specifically, at $x = 0$, $u_{X(M1)} = u_{X(M2)}$ and $\sigma_{XX(M1)} = \sigma_{XX(M2)}$. These lead to the two equations:

$$I + R = T \qquad [3]$$

$$Z_{M1}(I - R) = Z_{M2}T \qquad [4]$$

in which Z is the product of the density and the wave speed, $Z = \rho C$; this is a property of the material and is known as the acoustic impedance (SI units rayls). The

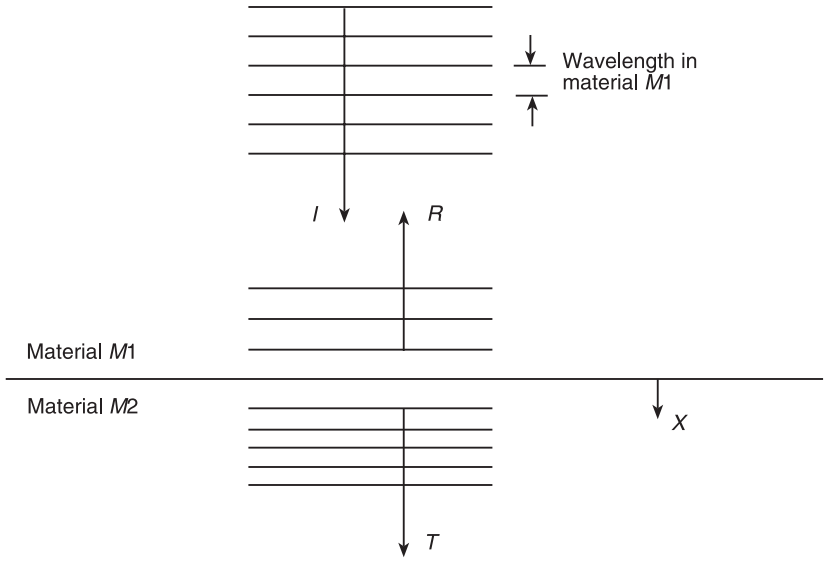


Figure 1 Interface between two media, showing incident (I), reflected (R), and transmitted (T) waves.

reflection and transmission coefficients for particle displacements are then:

$$\frac{u_{X(R)}}{u_{X(I)}} = \frac{R}{I} = \frac{Z_{M1} - Z_{M2}}{Z_{M1} + Z_{M2}} \quad [5]$$

$$\frac{u_{X(T)}}{u_{X(I)}} = \frac{T}{I} = \frac{2Z_{M1}}{Z_{M1} + Z_{M2}} \quad [6]$$

The reflection and transmission coefficients for the stresses are not the same as those for the displacements, essentially because of the phase difference between displacement and stress, but are:

$$\frac{\sigma_{XX(R)}}{\sigma_{XX(I)}} = \frac{Z_{M2} - Z_{M1}}{Z_{M1} + Z_{M2}} \quad [7]$$

$$\frac{\sigma_{XX(T)}}{\sigma_{XX(I)}} = \frac{-2Z_{M2}}{Z_{M1} + Z_{M2}} \quad [8]$$

Finally, the reflection and transmission can be expressed in terms of the energy in the waves, which is proportional to the product of the displacement and the stress, by:

$$\frac{\text{Energy}_{(R)}}{\text{Energy}_{(I)}} = \left(\frac{Z_{M2} - Z_{M1}}{Z_{M1} + Z_{M2}}\right)^2 \quad [9]$$

$$\frac{\text{Energy}_{(T)}}{\text{Energy}_{(I)}} = \frac{4Z_{M1}Z_{M2}}{(Z_{M1} + Z_{M2})^2} \quad [10]$$

These equations apply equally to the compression waves used in this derivation or to shear waves, provided that the materials are solids so that they can support shear waves.

In the special case of reflection from a free surface, when the second material is absent, the acoustic impedance Z_{M2} is zero. Then it can be seen from these equations that there is total reflection; that is to say, the amplitude of the reflection coefficient is unity and this is true whether one looks at displacement, stress, or energy. Also, the particle displacement at the boundary is twice the displacement of the incident wave; this is the sum of the displacements of the incident and reflected waves, which are in the same phase. However, the stress at the boundary is zero; this is again the sum of the stresses of the incident and reflected waves but now the phase differences lead to cancellation rather than addition. One other point worth mentioning in regard to this case is standing waves. In the steady state, when there is perfect reflection from the boundary and the reflected wave is equal to the incident wave, there is no net transport of energy, and the resulting field in the material no longer shows the wave propagation characteristic of phase motion. Instead, the field is composed only of standing waves. The displacement field is then of the same form as the displacement mode shapes of a vibrating body; indeed, it is reflections such as this which initiate vibrations.

The acoustic impedance is clearly an important property, since it determines how much reflection and transmission takes place at an interface. Values of acoustic impedance for a few common materials are given in **Table 1**, and it is worth considering a couple of examples. If a sound wave in air is incident at a concrete wall then, according to eqns [9] and [10], 99.98% of the energy is reflected. If a sound wave in water is incident at an interface with steel, then 12% of the energy is transmitted into the steel (and only 88% is reflected).

Reflection and Transmission of Obliquely Incident Plane Waves

Consider the interface between two media once again, but this time with a wave which is obliquely incident at an angle θ_{IL}, as shown in **Figure 2**. The materials, $M1$ and $M2$, are both solids, and the incident wave is longitudinal. In general, now, the interaction of the incident wave results in two reflected waves, a longitudinal wave (RL) and a shear wave (RS). Similarly there are two transmitted waves, longitudinal (TL) and shear (TS). This would also happen if the incident wave was a shear wave. The angle of reflection of the longitudinal wave is the same as the angle of incidence, but all the other angles

Table 1 Example values of acoustic impedance for some common materials

Material name	*Density* (kg m^{-3})	*Longitudinal velocity* (m s^{-1})	*Acoustic impedance* (rayl)
Air	1.21	343	415
Aluminum	2700	6320	17×10^6
Concrete	2200	3900–4700	$8.6–10.3 \times 10^6$
Copper	8900	4700	42×10^6
Epoxy resin	1100–1250	2400–2900	$2.6–3.6 \times 10^6$
Glass	3600	4260	15×10^6
Perspex (acrylic resin)	1180	2730	3.2×10^6
Rubber (soft)	900	1480	1.3×10^6
Steel	7800	5960	46×10^6
Water	998.2	1478	1.48×10^6

depend on the material properties of $M1$ and $M2$, according to Snell's law:

$$\frac{C_{L(M2)}}{\sin(\theta_{TL})} = \frac{C_{S(M2)}}{\sin(\theta_{TS})} = \frac{C_{S(M1)}}{\sin(\theta_{RS})} = \frac{C_{L(M1)}}{\sin(\theta_{IL})} \qquad [11]$$

where each of the angles θ_{TL}, θ_{TS}, θ_{RS} is the angle which the wave defined by the respective subscript makes with the normal to the interface. Physically, this equation corresponds to the phase matching of the wave crests along the interface, as illustrated for two of the waves on the right-hand side of the figure.

If the bulk velocities of material $M2$ are faster than those of material $M1$, then there are limiting angles for the transmission, known as the critical angles. Consider again the incident longitudinal wave and the two transmitted waves in **Figure 2**. The waves in material $M2$ are indeed faster than those in material $M1$ in this example because the angles of TL and TS are larger than the angle of IL. If the angle of IL is now increased, then the angle of TL approaches 90° when TL becomes parallel to the interface. At this particular angle, the angle of the incident wave IL is said to be the critical angle for longitudinal waves in medium $M2$. Similarly, there is a second (larger) critical angle for which the transmitted shear wave is parallel to the interface. At all angles larger than the critical angle, the transmitted wave travels parallel to the interface, and has a profile of exponential decay in the direction normal to the interface. This is illustrated in **Figure 3** and is known as an inhomogeneous or evanescent wave. The depth of the decay decreases as the angle of the incident wave is increased. If both of the transmitted waves are evanescent then in the steady state there is in fact no transmission of energy into medium $M2$ so all of the energy which is incident at the interface is reflected. This is the same phenomenon which is known as total reflection in optics.

The calculation of the amplitudes of the reflected and transmitted waves follows the same approach as that which was taken for the normally incident waves; that is to say, displacement and stress boundary conditions must be satisfied. In this case, there are two displacements which must be continuous: the displacement normal to the interface and the displacement parallel to the interface. Similarly, there are two stress components which must be balanced: the stress normal to the interface and the shear stress in the plane of the figure (these are the two tractions at the interface). These four conditions are sufficient to calculate the four unknown amplitudes.

Two examples of the reflection and transmission coefficients for an obliquely incident wave follow. In the first example, medium $M1$ is steel and medium $M2$ is vacuum. Thus, the transmitted waves TL and TS are already known to be zero and the task is to find the amplitudes of the reflected waves RL and RS. **Figure 4** shows these amplitudes vs the angle of incidence θ_{IL}. The amplitudes are expressed as reflection coefficients, that is, the ratio of the particle displacement in the reflected wave to that in the incident wave.

The second example takes medium $M1$ to be water and medium $M2$ to be steel. In this case the reflected shear wave is known to be zero (there is no shear wave in the fluid), and the task is to find the amplitude of the reflected longitudinal wave RL. **Figure 5** shows this vs the angle of incidence θ_{IL}. Also identified on the plot are the two critical angles. The

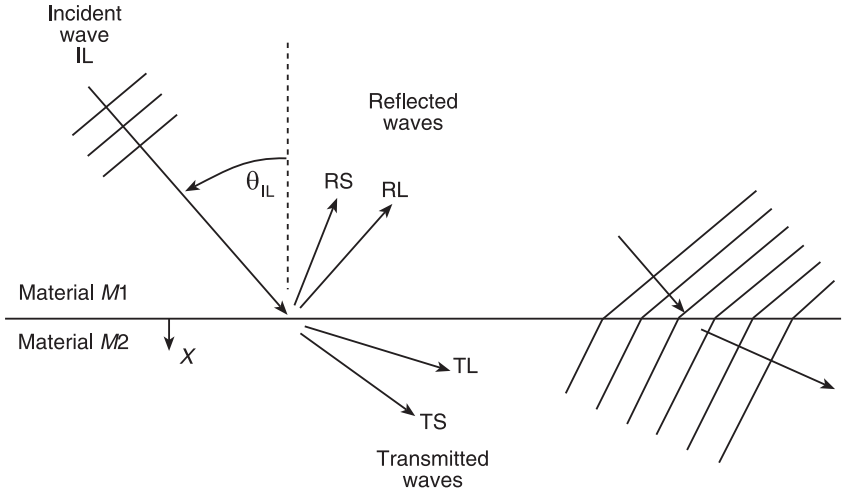


Figure 2 Reflection and transmission at an interface when a wave is incident at an oblique angle.

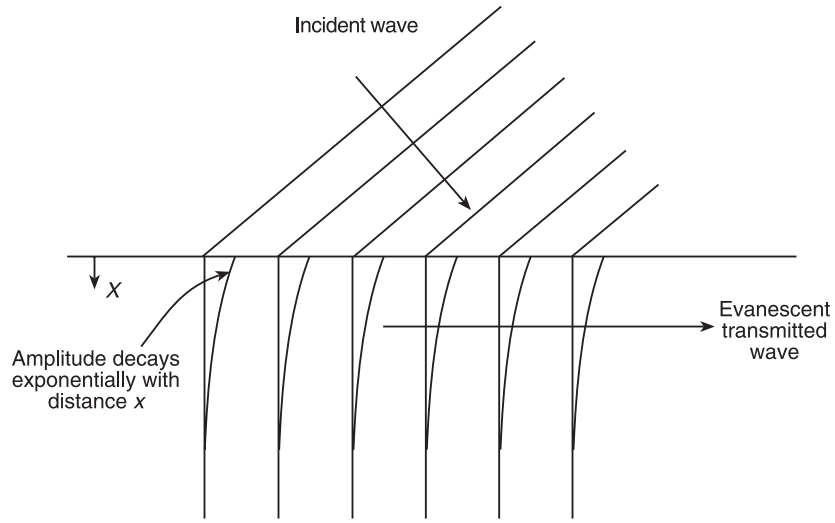


Figure 3 Evanescent waves generated at an interface between two materials when the angle of the incident wave is greater than

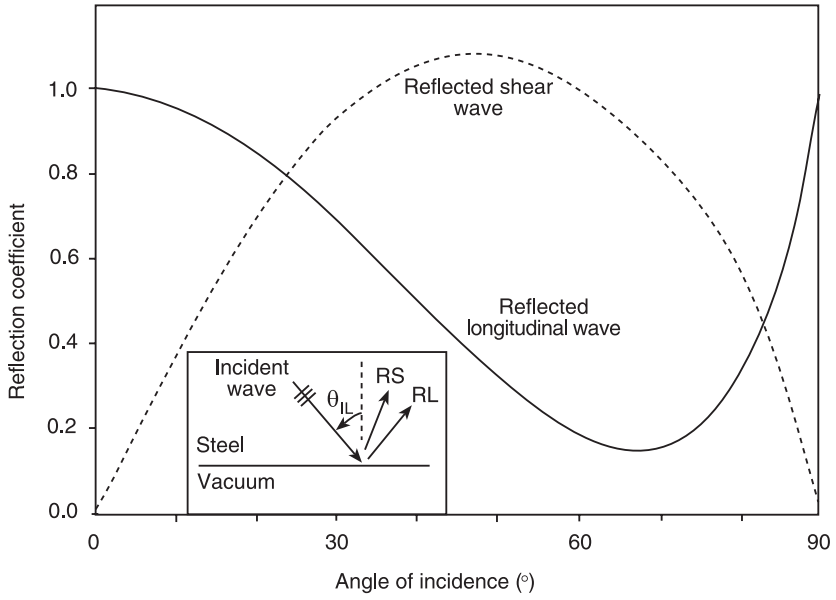


Figure 4 Reflection coefficients of longitudinal and shear waves from a free surface of steel when a longitudinal wave within the steel is incident at the surface at an oblique angle.

reflection coefficient can be seen to be unity at all angles greater than the shear critical angle.

Interaction of Waves with Discrete Structural Features

There are many circumstances where the concepts which have been explained here may be applied directly, such as the example already given of a sound wave incident at a solid wall. In geomechanics, the reflection and transmission of seismic waves across boundaries between different strata may be studied with these relationships. In ultrasonic NDT, the need to consider reflection and transmission at flat boundaries is commonplace. For example, water is often used as a coupling medium because its impedance is so much higher than that of air, easing the task of getting sound into the structure. Then a transducer which is placed in the water emits ultrasound waves which travel through the water, then arrive at the flat surface of a structure, enter the structure, and finally reflect from any defects or perhaps other surfaces. The full signal which is

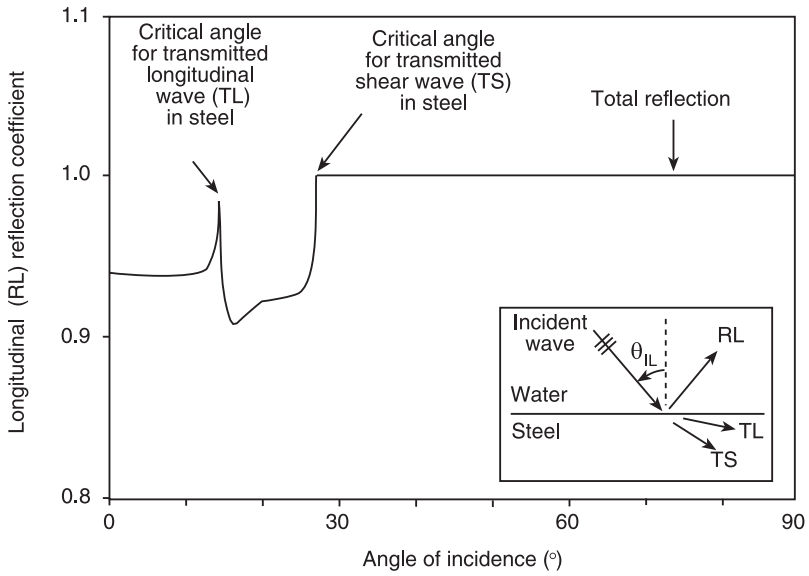


Figure 5 Reflection coefficient when a longitudinal wave in water is incident at an interface with steel.

reflected from the structure thus includes reflections from these various boundaries.

However there are also circumstances where it is necessary to understand the interaction of waves with bodies which are not flat but of arbitrary shapes, for example, the interaction of ultrasonic waves with discrete defects such as cracks, voids, or inclusions. This is a large and complex research topic, particularly the so-called inverse problem of determining the sizes and distributions of such features from the reflected signals. In fact, there are several regimes of scattering, associated with the scale of the interaction; specifically, the ratio of the wavelength of the sound to the characteristic dimension of the scatterer. As a very general rule, if the wavelength is much shorter than the dimension of the scatterer, then it is permissible to take a ray-tracing approach (Kirchoff approximation). In this, the incidence of a beam (or ray) of sound which arrives at the surface of the scatterer is treated using the plane reflection concepts explained above; if it arrives at an angle to the surface, it is reflected and transmitted according to those equations. The total reflection and transmission fields are then calculated as the sum of the actions of all of the rays. This approach is often taken when studying ultrasonic NDT, looking for cracks with high-frequency signals. In the other limit, when the wavelength is much larger than the characteristic size of the scatterer, these techniques are wholly inaccurate. For example, the scattering of a sound wave from a spherical inclusion in a solid, when the inclusion is significantly smaller than the wavelength, is understood much more realistically by studying the displacement response of the whole inclusion to the presence of the passing stress field than by the ray approach. This is an issue, for example, when studying the scattering of ultrasound from materials containing small-scale porosity.

Nomenclature

C	wave speed
I	incident wave
k	wave number
R	reflected wave
T	transmitted wave
Z	product of density and wave speed
ρ	density

See also: **Nondestructive testing**, Sonic; **Nondestructive testing**, Ultrasonic; **Wave propagation**, Guided waves in structures; **Wave propagation**, Waves in an unbounded medium.

Further Reading

Achenbach JD (1984) *Wave Propagation in Elastic Solids*. New York: North-Holland.

Auld BA (1990) *Acoustic Waves and Fields in Solids*, 2nd edn. Florida: Robert E Kreiger.

Halmshaw R (1987) *Non-destructive Testing*. London: Edward Arnold.

Kolsky H (1963) *Stress Waves in Solids*. New York: Dover Publications.

Rose JL (1999) *Ultrasonic Waves in Solid Media*. Cambridge: Cambridge University Press.

Waves in an Unbounded Medium

M J S Lowe, Imperial College of Science, Technology and Medicine, London, UK

Copyright © 2001 Academic Press

doi:10.1006/rwvb.2001.0140

Background

This entry introduces the propagation of elastic waves in an infinite expanse of a fluid or solid material. The nature and basic equations of elastic waves are explained, together with their relevance to other topics in vibration engineering.

Wave propagation differs from vibration fundamentally according to the structural boundary conditions. A structure which has no boundaries, that is to say, which is infinite in spatial extent, has no natural modes of vibration in the usual sense. It does, however, have the natural properties that waves with particular characteristics may propagate indefinitely in the material in the steady state. These waves in the unbounded space, often known as the bulk waves, depend on the properties of the material and are, indeed, precisely the elastodynamic modal properties of the medium. On the other hand, the natural properties of a body which has boundaries all around it are its modes of vibration; the steady-state solutions to its unforced equations of motion do not include wave propagation. However, as will be illustrated in the following discussion, the modes of wave propagation are closely linked to the natural modes of vibration: it is the creation of standing wave patterns of these wave modes which leads to vibrations.

The consideration of waves in an unbounded medium may appear at first to be rather abstract, since real structures always have boundaries. However, there are several good reasons for starting to look at wave theory from this viewpoint.

First, there are in fact very real circumstances in which the theory of waves in an infinite medium is directly useful. A good example is the propagation of sound waves in air. When someone speaks, the sound which travels through the air to the listener can be considered to be traveling through an infinite expanse of air. This is because the waves are not yet influenced by any boundaries, such as the walls of the room, as they travel through the open space; the boundaries only become important when the waves arrive at them and are reflected or absorbed. A similar example is the propagation of ultrasonic waves in a solid material: after leaving the transducer and before arriving at a boundary of the material or a scattering feature, these waves may be considered to be traveling in an infinite volume of the solid material. Therefore, good use may be made of the theory of the properties of waves in an infinite medium in order to understand the characteristics of a wave while it is in transit between the source and the destination. These characteristics may include its speed, its frequency and wavelength, its intensity, or the rate at which it decays due to material damping or scattering phenomena (see **Nondestructive testing**, Sonic; **Nondestructive testing**, Ultrasonic; **Ultrasonics**).

A second reason for studying waves in an unbounded medium is that this provides a building block for the consideration of waves in more complicated structures when they reflect and reverberate within the boundaries of the body. Thus, although the wave fields which develop in the structure may be rather complicated, they can be understood by studying the properties of waves which could exist in an unbounded medium and then by examining how these interact with the boundaries. To make this concept more concrete, consider the initiation of vibration in a solid body when it is impacted, for example, by a hammer. The hammer blow sets up waves within the body which reflect internally from the boundaries, reverberate, and ultimately set up standing waves. As stated earlier, once a steady state has been reached, these standing waves define the natural vibration modes of the body. Thus it is possible to study the natural frequencies and mode shapes of the body by considering the characteristics of the unbounded waves together with the patterns of their reverberations which arise (see **Wave propagation**, Interaction of waves with boundaries).

Another closely related consideration is the study of more complicated wave propagation phenomena, such as waves which are guided by a structure. Well-known examples of these are the Rayleigh wave which propagates along the surface of a structure, such as the earthquake wave which is guided along the surface of the earth, and the Lamb waves which are guided along a plate. The common feature of these guided waves is that the structure is partially, but not completely, bounded. The plate has two surfaces but is considered to be infinite in the other directions – its length and width. There thus arise wave fields in which there is no propagation through the thickness of the plate but there is propagation along the plate; in other words, the behavior in the

through-thickness direction can be understood in the way in which one thinks about natural vibration, whereas the behavior along the plate is characteristic of the behavior of propagating waves. These wave fields may be considered as a superposition of several unbounded waves in proportions and phases such that the necessary conditions at the boundaries are satisfied (see **Wave propagation**, Guided waves in structures).

Theoretical Basis

Elastic waves are physically no different from seismic, sound, or ultrasound waves, other than in their respective ranges of frequencies. Sound waves conventionally cover the human audible range of frequencies (from about 50 Hz to 20 kHz), ultrasound waves cover frequencies above the audible range (from 20 kHz up to around 1 GHz may be encountered), and seismic waves exist at very low frequencies, significantly lower than the audible range. Therefore, the concepts which are presented here for elastic waves are equally applicable to these specific subject areas, and they differ only by the matter of scale.

The properties of elastic waves depend on the elastic properties of the material in which they propagate. This includes the number of different modes which can propagate and their velocities. Consider, to begin with, as is usually done in this subject, an infinitesimally small cube of the material. This will provide the basis for developing the equation of motion and the wave equation as its solutions. This rather general starting point could be applied to all sorts of materials; in the following subsections, some specific solutions will be examined.

An infinitesimal cube of a material is shown in **Figure 1**. Its dimensions are δx, δy, δz in the Cartesian coordinate system XYZ with spatial location given by xyz. The material has density, ρ, and the analysis here is additionally limited to consideration of an isotropic material so that only two elastic constants are needed. These are defined by the Lamé constants, λ and μ, which are of course easily expressed as functions of Young's modulus and Poisson's ratio. The stresses acting on the cube are defined by the vector $\boldsymbol{\sigma}$, some of which components are shown in the figure, and the displacements of the cube as the vector $\mathbf{u}$.

Consideration of the stresses acting on the faces of the cube, and of the inertia of the cube, leads to the force differential equation of motion in its general form:

$$\rho \frac{\partial^2 \mathbf{u}}{\partial t^2} = (\lambda+\mu)\nabla(\nabla \cdot \mathbf{u}) + \mu \nabla^2 \mathbf{u} \qquad [1]$$

where ∇ is the vector operator $(\partial/\partial X, \partial/\partial Y, \partial/\partial Z)$ and ∇^2 is the scalar operator:

$$\left(\frac{\partial^2}{\partial X^2} + \frac{\partial^2}{\partial Y^2} + \frac{\partial^2}{\partial Z^2}\right)$$

Any permissible nontrivial solutions to this equation

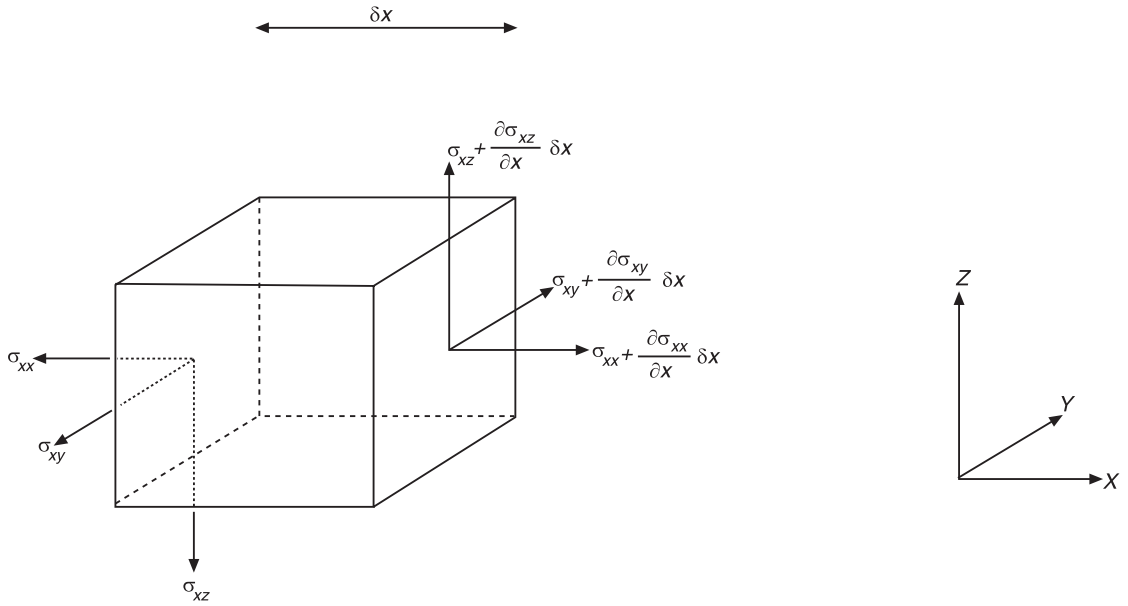


Figure 1 Infinitesimal cube, showing stresses on faces.

will define the motion of the waves in the material. Thus the material properties which affect the properties of the waves are the density, ρ, and the two elastic constants, λ and μ.

Plane Waves in a Perfect Inviscid Fluid or Gas

A perfect inviscid fluid or gas does not support shear stresses and so the Lamé constant μ is zero in this case, thus simplifying eqn [1]. Further simplification is achieved by considering solutions for plane waves in a chosen direction; since the medium is infinite, the direction which is taken for illustration is arbitrary. Taking the direction of travel of the wave to be the X direction, the plane wave assumption imposes the condition that there is no variation of the field in the Y or Z directions. A valid solution to eqn [1] is now given by:

$$u_X = A\mathrm{e}^{\mathrm{i}(kx-\omega t)} \qquad [2]$$

where A is an arbitrary constant and k is the wavenumber, defined in the following expression:

$$C = \text{wavespeed} = \frac{\omega}{k} = \frac{\omega * \text{wavelength}}{2\pi} = \left(\frac{\lambda}{\rho}\right)^{1/2} \qquad [3]$$

The pressure of the wave is given by:

$$\sigma_{XX} = i\omega C\rho u_X \qquad [4]$$

Eqn [2] shows that the wave motion is defined by a function which is harmonic in both time and space. Thus the variation of the particle displacement u_X takes the form of a sine wave, whether observing the wave passing a particular location over a period of time, or observing a length of the wave train in space at a particular moment in time. Furthermore the wave propagates without loss of amplitude. The wave speed is the phase speed, that is the speed of a crest of the harmonic function. **Figure 2** shows the harmonic waveform which would be seen; in this case the axes are labeled to represent the spatial observation at a moment in time. Also shown on the figure, for illustration, is the same wave train a moment later in time. Eqn [4] shows that the pressure is represented by the same form of function but its phase differs by 90° from that of the particle displacement.

Another feature of the solution is that the particle motion of the wave is parallel to the direction of motion; there is neither strain nor displacement in either direction normal to the direction of motion. Therefore, physically, one can imagine the cube of material being compressed and dilated along the direction of the wave propagation; indeed, the Lamé constant, λ, is the compression stiffness of the fluid or gas when the sample is compressed on one axis and constrained on the other two. The wave thus exists as a propagating cycle of compression and dilation of the material.

Eqn [3] shows that the wave speed in the material is a constant for given values of the material properties and does not vary with frequency. Also, it can be seen that the wave speed is large if the stiffness is large and is small if the density is large. The wavelength is, of course, inversely proportional to the frequency.

Plane Waves in an Elastic Isotropic Solid

An elastic solid does support shear and so both of the Lamé constants must be retained in the solution for this case. Consider again solutions for plane waves which travel in the X direction. The plane wave assumption imposes the condition that there is no variation of the field in the Y or Z directions. However, particle motion in either of those directions

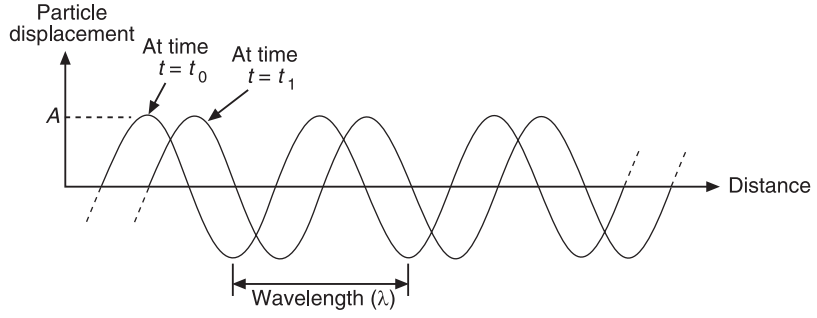


Figure 2 Harmonic motion of elasic wave, showing spatial variation of displacement at two moments in time.

would not violate that condition so long as it does not vary in that direction. Therefore, for this example, the possibility of particle motion in the Y direction will be allowed. There are now two possible solutions to eqn [1]:

$$u_X = A\mathrm{e}^{\mathrm{i}(k_L x - \omega t)} \quad [5]$$

$$u_Y = A\mathrm{e}^{\mathrm{i}(k_S x - \omega t)} \quad [6]$$

where K_L and K_S are wavenumbers, defined by:

$$C_L = \text{longitudinal wave speed} = \frac{\omega}{k_L} = \left(\frac{\lambda + 2\mu}{\rho}\right)^{1/2} = \left[\frac{E(1-v)}{\rho(1+v)(1-2v)}\right]^{1/2} \quad [7]$$

$$C_S = \text{shear wave speed} = \frac{\omega}{k_S} = \left(\frac{\mu}{\rho}\right)^{1/2} = \left[\frac{E}{2\rho(1+v)}\right]^{1/2} \quad [8]$$

in which for completeness the wave speeds are additionally given in terms of Young's modulus, E, and Poisson's ratio, v.

Eqns [5] and (7) define the wave motion for the longitudinal wave (subscript L), sometimes known as the compression wave or P wave. As with the fluid wave, it can be seen that the particle motion is parallel to the direction of propagation and the material compresses and dilates as the wave propagates. In fact, the particle motion characteristics of the longitudinal wave are the same as those of the fluid wave; the difference is just in the form of the elastic constants which define the speed.

Eqns [6] and (8) define the shear wave (subscript S), sometimes known as the transverse wave or S wave, and this is somewhat different. In this case the displacement is in the Y direction, and so is normal to the direction of propagation. There is no displacement in the X or Z directions. Thus the material is deformed in a shearing motion as the wave propagates, and there is no change of its volume. Clearly, this introduces the need for another qualification when defining a shear motion because it is now necessary to define the polarization of the wave. In this particular example the shearing motion is defined by the XY plane (or by a polarization vector in the Z direction), but in general it could be in any plane in which the X-axis lies. The speed of the shear wave can be seen, according to the material constants in eqns [7] and [8], to be lower than that of the longitudinal wave. In typical structural materials, the shear wave speed is a little over half of the longitudinal wave speed.

Waves in Absorbing Isotropic Materials

The discussion up until now has assumed an ideal homogeneous elastic material, in which there is no loss of energy from the propagating waves. In practice, these assumptions are often perfectly workable, for example in many structural materials such as steel, aluminum, or glass. However, there are mechanisms for loss of energy which can be significant and which should be taken into account.

If a material is not homogeneous, then waves propagating through it may lose energy through scattering. When incident at an inhomogeneity the waves may partially reflect, perhaps at an oblique angle, according to the shape of the inhomogeneity. The wave which continues along the original direction must then reduce in amplitude. Strictly speaking, the energy is not lost from the body but is partitioned from one wave into multiple waves. However, from the point of view of following the original wave, the interactions can be considered to be attenuative. Scattering occurs at inclusions of air or other materials within a body, at cracks, or at fibers or grain boundaries. It increases as the frequency is increased, being low when the wavelength is much larger than the scatterers and high when it is of comparable size or shorter. Scattering from fibres is an important consideration when ultrasonic nondestructive (NDT) techniques are applied to carbon fibre composites. Losses from the scattering (and also viscous losses; see next paragraph) typically limit the upper testing frequency to around 10 MHz. The scattering from grain boundaries in metals sets the upper limit for ultrasonic NDT of metal structures. Test frequencies in aluminum and carbon steel are typically limited to around 100 MHz (although this is not a precise figure because it depends on the distance of propagation which is required as well as the particular constitution of the metal), maximum test frequencies in stainless steel can be considerably lower. In practice these limits are rarely a concern; the majority of testing is in any case done at much lower frequencies, typically between 1 and 10 MHz. The ultrasonic testing of concrete illustrates well the problems of scattering: test frequencies are normally limited to around 50–100 kHz to avoid excessive scattering from the aggregate.

The other important mechanism of loss is absorption. This is effectively material damping through

phenomena such as hysteresis and viscoelasticity. In this case the energy is converted to heat in the material. The attenuation again increases with the frequency. All materials exhibit this effect to some extent but often the losses are not significant. The significance depends, of course, on the frequency of the wave and the distance of travel being considered. For practical ultrasonic testing in steel or aluminum at 1–10 MHz the damping is negligible. However, waves in plastic materials such as polyethylene suffer from quite considerable damping.

Attenuation is very often modeled by introducing an extra term, α, in the wave propagation eqn [2]:

$$u_X = A e^{i(kx-\omega t)} e^{-\alpha x} \qquad [9]$$

where the attenuation is included by the real exponential product in which α is the attenuation constant. This equation can also be rearranged to express the attenuation by an imaginary part to the wavenumber. Such a model has the benefit of simplicity, but it limits the attenuation such that the loss is a constant quantity per wavelength traveled. It happens that this is a workable assumption for the absorption losses in many typical structural materials at ultrasonic test frequencies. However, it is not representative of the more complex loss mechanisms such as are encountered in the earlier scattering examples.

The Effects of Material Anisotropy

The study of elastic waves in anisotropic materials is a complex and specialist subject. However, it is important to mention it here briefly because it is a topic which appears in the literature and in some practical applications. In particular, there is increasing use of ultrasonic techniques to inspect or to measure the elastic properties of fiber composite structures. The anisotropy of granular metals or of crystal structures can also be significant. In brief, when the equation of motion [1] is derived using the anisotropic elastic constants, its solution differs in two principal regards with respect to the solutions for an isotropic material. First, there exists the possibility in general of three bulk waves, rather than two, and second, the velocity of each of these waves varies according to the direction of travel. These velocities, which are properties of the material, are therefore often presented in a graphical way. **Figure 3** shows a typical representation of the properties of a unidirectional graphite epoxy. The slowness (inverse of the velocity) is plotted as a function of the angle for each of the three waves.

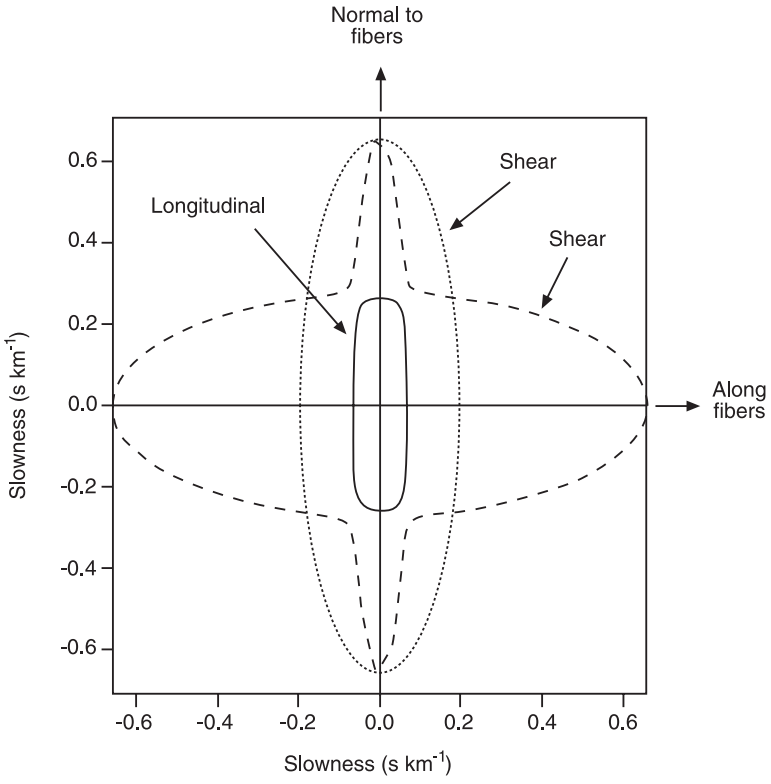


Figure 3 Slowness curves for bulk waves in a unidirectional graphite epoxy composite.

Cylindrical and Spherical Waves

Although it is convenient to consider waves to have plane wave fronts because it reduces any analysis to one dimension in Cartesian space, it should be recognized that this does not represent all practical wave phenomena. Waves which radiate from a point source (spherical waves) or from a line source (cylindrical waves) occur moderately often. Good examples are noise sources in acoustics or seismic sources in geomechanics. In practice, one may make the assumption that the waves are approximately plane when the distance from the source is much greater than the wavelength. However, this is not reasonable in the near field. Strictly, the wave equation must be derived in cylindrical or spherical coordinates, thereby modifying the wave propagation eqn [1]. Practically, this may not be necessary because, apart from in the immediate vicinity of the source, the resulting equation differs significantly from the plane wave equation only in the amplitude of the wave. From simple energy conservation considerations it is straightforward to show that the amplitude of the particle displacement must be inversely proportional to the radius for spherical waves and to the square root of the radius for cylindrical waves (the energy is proportional to the square of the particle displacement).

Nomenclature

A	arbitrary constant
E	Young's modulus
k	wavenumber
λ	Lané constant
μ	elastic constant
ν	Poisson's ratio
ρ	density

See also: **Nondestructive testing**, Sonic; **Nondestructive testing**, Ultrasonic; **Ultrasonics**; **Wave propagation**, Guided waves in structures; **Wave propagation**, Interaction of waves with boundaries

Further Reading

Achenbach JD (1984) *Wave Propagation in Elastic Solids*. New York: North Holland.
Auld BA (1990) *Acoustic Waves and Fields in Solids*, 2nd edn. Florida: Robert E Kreiger.
Brekhovskikh LM, Goncharov V (1985) *Mechanics of Continua and Wave Dynamics*. Berlin: Springer-Verlag.
Graff KF (1991) *Wave Motion in Elastic Solids*. New York: Dover Publications.
Halmshaw R (1987) *Non-destructive Testing*. London: Edward Arnold.
Kolsky H (1963) *Stress Waves in Solids*. New York: Dover Publications.
Krautkramer J, Krautkramer H (1983) *Ultrasonic Testing of Materials*. Berlin: Springer-Verlag.
Malvern LE (1969) *Introduction to the Mechanics of a Continuous Medium*. New Jersey: Prentice-Hall.
Porges G (1977) *Applied Acoustics*. London: Edward Arnold.
Rose JL (1999) *Ultrasonic Waves in Solid Media*. Cambridge: Cambridge University Press.

WAVELETS

See **TRANSFORMS, WAVELETS**

WHOLE-BODY VIBRATION

M J Griffin, Institute of Sound and Vibration Research, The University of Southampton, Southampton, UK

Copyright © 2001 Academic Press

doi:10.1006/rwvb.2001.0082

Introduction

Whole-body vibration occurs when the human body is supported on a surface that is vibrating (e.g., sitting on a seat, standing on a floor, or lying on a bed). Whole-body vibration occurs in transport (e.g., road, off-road, rail, air, and marine transport) and when near some machinery. Whole-body vibration affects human comfort, the performance of activities, and health.

The acceptability of vibration in many environments is determined by human responses to vibration. Vibration becomes annoying before it damages a building; the vibration in transport can cause dis-

comfort or interfere with activities when it does not damage the vehicle; the vibration of tools and machines produces injuries and disease without breaking the tool or machinery.

The responses of the body differ according to the direction of the motion (i.e., axes of vibration). The three principal directions of whole-body vibration for seated and standing persons are: fore-and-aft (x-axis), lateral (y-axis) and vertical (z-axis). The vibrations to which the body is exposed are measured at the interfaces between the body and the surfaces supporting the body (e.g., on the seat beneath the ischial tuberosities, at a backrest or at the feet for a seated person; beneath the feet for a standing person). **Figure 1** illustrates the relevant translational and rotational axes for a seated person.

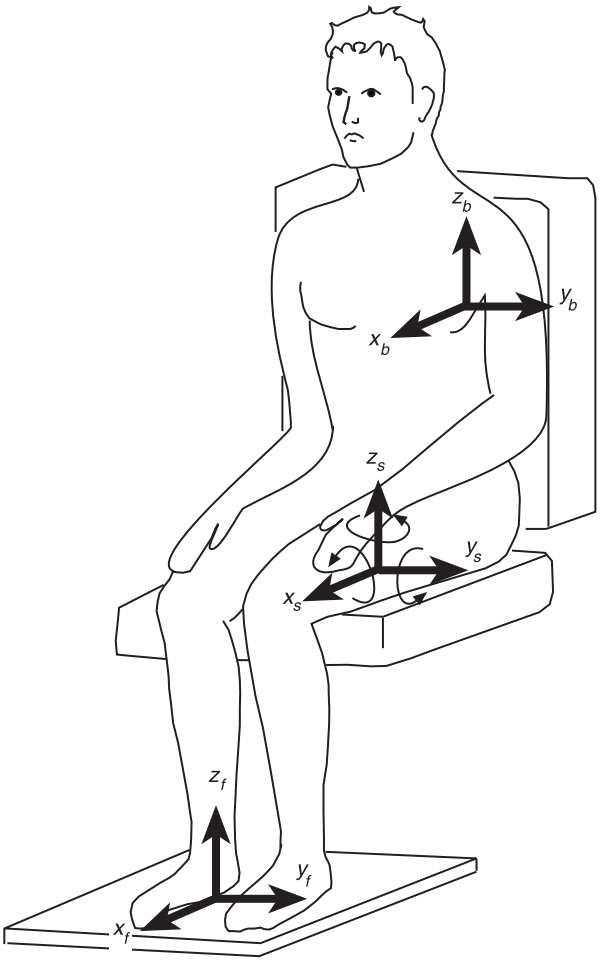


Figure 1 Axes of vibration used to measure exposures to whole-body vibration.

Biodynamics

The human body is a complex mechanical system which does not, in general, respond to vibration in the same manner as a rigid mass: there are relative motions between the body parts that vary with the frequency and the direction of the applied vibration. Although there are resonances in the body, it is oversimplistic to summarize the dynamic responses of the body by merely mentioning one or two resonance frequencies. The dynamics of the body affect all human responses to vibration, but the effects of vibration on discomfort, and the interference with activities and health cannot be predicted solely by considering the body as a mechanical system.

Transmissibility of the Human Body

The extent to which the vibration at an input to the body (e.g., the vertical vibration at a seat) is transmitted to a part of the body (e.g., vertical vibration at the head or the hand) is described by the transmissibility. At low frequencies of oscillation (e.g., below about 1 Hz), the vertical oscillations of a seat and the body parts are very similar and so the transmissibility is approximately unity. With increasing frequency of oscillation, the motions on the body increase above those measured at the seat and the transmissibility reaches a peak at one or more frequencies (i.e., resonance frequencies). At high frequencies the motion on the body is less than that at the seat.

The resonance frequencies, and the transmissibilities at resonance, vary according to the direction (i.e., axis) of vibration, vary according to where the vibration is measured on the body, and vary according to the posture of the body. There can be large differences between subjects. For seated persons, there may be resonances in transmissibilities measured to the head and the hand at frequencies in the range 4–12 Hz for vertical vibration, below 4 Hz with fore-and-aft (i.e., x-axis) vibration and below 2 Hz with lateral (i.e., y-axis) vibration. The backrest of a seat can increase the transmission of x-axis vibration to the upper body and bending of the legs can affect the transmission of vertical vibration to the head of a standing person.

Mechanical Impedance of the Human Body

Mechanical impedance reflects the relation between the driving force at the input to the body and the resultant movement of the body. If the human body were rigid, the ratio of force to acceleration applied to the body would be constant and indicate the mass of the subject. Because the body is not rigid, the ratio of force to acceleration is only close to the body mass at very low frequencies (below about 2 Hz with vertical vibration; below about 1 Hz with horizontal vibration).

Measures of mechanical impedance show a principal resonance for vertical vibration of seated subjects at about 5 Hz, and sometimes a second resonance in

the range 7–12 Hz. The large difference in impedance between that of a rigid mass and that of the human body means that the body cannot usually be represented by a rigid mass when measuring the vibration transmitted through seats (see below). The mechanical impedance of the body is generally nonlinear: the resonance frequency reduces when the vibration magnitude increases.

Biodynamic Models

A simple model with one or two degrees-of-freedom can represent the point mechanical impedance of the body and a dummy can be constructed to represent this impedance for seat testing. The transmissibility of the body is affected by many more variables and requires a more complex model reflecting the posture of the body and the translation and rotation associated with the various modes of vibration.

Vibration Discomfort

The relative discomfort caused by different vibrations can be predicted from suitable measurements and an appropriate evaluation of the vibration. Limits to prevent vibration discomfort vary between environments (e.g., between buildings and transport) and between types of transport (e.g., between cars and trucks) and within types of vehicle (e.g., between sports cars and limousines). The design limit depends on external factors (e.g., cost and speed) and the comfort in alternative environments (e.g., competitive vehicles).

Effects of Vibration Magnitude

As an approximate guide, the threshold for perception of vertical whole-body vibration in the frequency range 1–100 Hz is approximately $0.01\,\mathrm{ms}^{-2}$ r.m.s., while $0.1\,\mathrm{ms}^{-2}$ is easily noticeable, $1.0\,\mathrm{ms}^{-2}$ r.m.s. is uncomfortable and $10\,\mathrm{ms}^{-2}$ r.m.s. is potentially dangerous. The precise values depend on vibration frequency and exposure duration and differ for other axes of vibration.

Doubling the vibration magnitude (when expressed in ms^{-2}) produces an approximate doubling of the sensation of discomfort. Halving the vibration magnitude can therefore produce a considerable improvement in comfort. For some types of whole-body vibration, differences in vibration magnitude greater than about 10% may be detectable.

Effects of Vibration Frequency and Direction

The extent to which vibration causes effects on the body at different frequencies is reflected in frequency weightings: frequencies capable of causing the greatest effect are given the greatest weight and others are attenuated in accord with their decreased importance. Two different frequency weightings (one for vertical and one for horizontal vibration of seated or standing persons) were presented in International Standard 2631 (1974, 1985) and reproduced in other standards. Although International Standard 2631 was revised in 1997 to use different methods, the revision is difficult to comprehend. One reasonable interpretation is that it is broadly similar to British Standard 6841 (1987), and so this standard will be explained here.

Frequency weightings W_b to W_f, as defined in British Standard 6841 (1987), are shown in **Figure 2** as they may be implemented by analog or digital filters (International Standard 2631 (1997) defines similar weightings and also an additional weighting, W_k, which might be used as an alternative to W_b). **Table 1** defines simple asymptotic (i.e. straight-line) approximations to these weightings. **Table 2** shows how the weightings should be applied to the 12 axes of vibration illustrated in **Figure 1** and multiplying factors for each axis. (The weightings W_g and W_f are not required to predict vibration discomfort: W_g is similar to the weighting for vertical vibration in the old ISO 2631 (1974, 1985); W_f is used to predict motion sickness caused by vertical oscillation.)

The r.m.s. value of the weighted acceleration (i.e., after frequency weighting and after being multiplied by the multiplying factor) is sometimes called a component ride value. Vibration occurring in several axes is more uncomfortable than vibration occurring in a single axis. In order to obtain an overall ride

Table 1 Asymptotic approximations to frequency weightings, $W(f)$, in BS 6841 (1987) for comfort, health, activities, and motion sickness

	Weighting name	*Weighting definition*
W_b	$0.5 < f < 2.0$	$W(f) = 0.4$
	$2.0 < f < 5.0$	$W(f) = f/5.0$
	$5.0 < f < 16.0$	$W(f) = 1.00$
	$16.0 < f < 80.0$	$W(f) = 16.0/f$
W_c	$0.5 < f < 8.0$	$W(f) = 1.0$
	$8.0 < f < 80.0$	$W(f) = 8.0/f$
W_d	$0.5 < f < 2.0$	$W(f) = 1.00$
	$2.0 < f < 80.0$	$W(f) = 2.0/f$
W_e	$0.5 < f < 1.0$	$W(f) = 1.00$
	$1.0 < f < 20.0$	$W(f) = 1.00/f$
W_f	$0.100 < f < 0.125$	$W(f) = f/0.125$
	$0.125 < f < 0.250$	$W(f) = 1.0$
	$0.250 < f < 0.500$	$W(f) = (0.25/f)^2$
W_g	$1.0 < f < 4.0$	$W(f) = (f/4)^{1/2}$
	$4.0 < f < 8.0$	$W(f) = 1.00$
	$8.0 < f < 80.0$	$W(f) = 8.0/f$

f, frequency in, Hz; $W(f)$, 0 where not defined.

Table 2 Application of frequency weightings for the evaluation of vibration with respect to discomfort

Input position	*Axis*	*Frequency weighting*	*Axis multiplying factor*
Seat	x_s	W_d	1.0
	y_s	W_d	1.0
	z_s	W_b	1.0
	r_x (roll)	W_e	0.63
	r_y (pitch)	W_e	0.40
	r_z (yaw)	W_e	0.20
Seat back	x_b	W_c	0.80
	y_b	W_d	0.50
	z_b	W_d	0.40
Feet	x_f	W_b	0.25
	y_f	W_b	0.25
	z_f	W_b	0.40

value, the root-sums-of-squares of the component ride values is calculated:

$$\text{overall ride value} = \left(\sum (\text{component ride values})^2\right)^{1/2}$$

Overall ride values from different environments can be compared: a vehicle having the highest overall ride value would be expected to be the most uncomfortable with respect to vibration.

Effects of Vibration Duration

Vibration discomfort tends to increase with increasing duration of exposure to vibration. The rate of increase may depend on many factors but a simple fourth-power time dependency is used to approximate how discomfort varies with duration of exposure from the shortest possible shock to a full day of

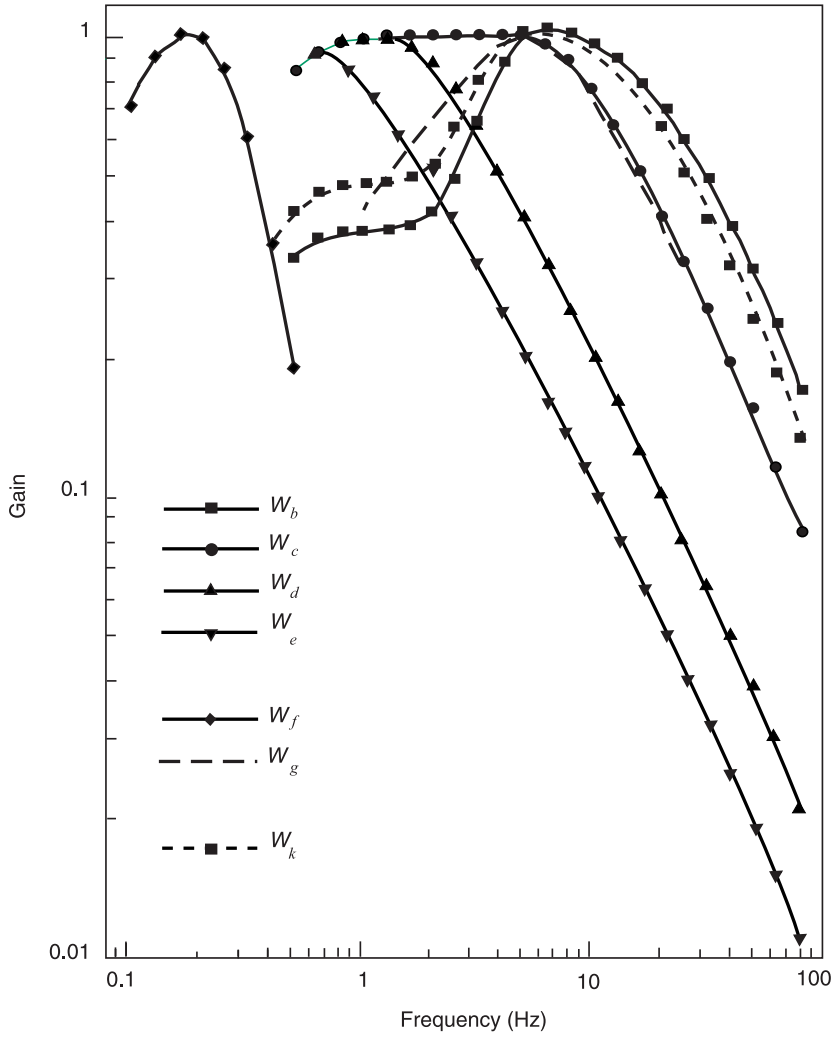


Figure 2 Acceleration frequency weightings for whole-body vibration and motion sickness (as defined in British Standard 6841, 1987 and ISO 2631, 1997).

vibration exposure (i.e., $(\text{acceleration})^4 \times \text{duration} = \text{constant}$; see below).

Interference with Activities

Whole-body vibration can influence input processes (especially vision) and output processes (especially continuous hand control). In both cases there may be a disturbance occurring entirely outside the body (e.g., vibration of a display or vibration of a hand-held control), a disturbance at the input or output (e.g., movement of the eye or hand), and a disturbance within the body affecting the peripheral nervous system (i.e., afferent or efferent system). Central processes (e.g., learning, memory, decision making) may also be affected by vibration but understanding is currently too limited to make confident generalized statements.

Effects of vibration on vision and manual control are most usually caused by the movement of the affected part of the body (i.e., eye or hand). The effects may be decreased by reducing the transmission of vibration to the eye or to the hand, or by making the task less susceptible to disturbance (e.g., increasing the size of a display or reducing the sensitivity of a control). Consequently, the effects of vibration on vision and manual control can often be reduced by redesigning the task. The effects of vibration on task performance are therefore highly task-specific and generalized vibration limits are not useful.

Effects of Vibration on Vision

When an observer sits or stands on a vibrating surface, the effects of vibration on vision depend on the extent to which the vibration is transmitted to the head and eyes. The motions most affecting vision may be the vertical and pitch movements of the head. The pitch motion of the head is compensated by the vestibulo-ocular reflex which serves to stabilize the line of sight of the eyes at frequencies below about 10 Hz. The effects of translational motion of the head depend on viewing distance: the effects are greatest when close to a display. Consequently, the greatest problems with vibration occur with pitch head motion when the display is attached to the head (e.g., a virtual reality display) and with translational head motion when viewing near displays not fixed to the head.

When an observer and a display oscillate together in phase at low frequencies (below about 5 Hz), the retinal image motions (and decrements in visual performance) are less than when either the observer or the display oscillate separately. The advantage is lost as the vibration frequency is increased since there is then an increasing phase difference between the motion of the head and the motion of the display.

The absolute threshold for the visual detection of the vibration of an object by a stationary observer occurs when the peak-to-peak oscillatory motion gives an angular displacement at the eye of approximately 1 min arc. The acceleration required to achieve this threshold can be low at low frequencies but increases in proportion to the square of the frequency to become very high at high frequencies. If the vibration displacement is above the visual detection threshold there may be perceptible blur; the effects of vibration on visual performance (e.g., effects on reading speed and reading accuracy) may then be estimated from the maximum time that the image spends over some small area of the retina (e.g., the period of time spent near the nodes of the motion with sinusoidal vibration). For sinusoidal vibration this time decreases (and so reading errors increase) in linear proportion to the frequency of vibration and in proportion to the square root of the displacement of vibration. With dual-axis vibration (e.g., combined vertical and lateral vibration of a display) this time is greatly reduced and so reading performance is worse than with single-axis vibration. With narrow-band random vibration there is a greater probability of low image velocity than with sinusoidal vibration of the same magnitude and predominant frequency, so reading performance tends to be less affected by random vibration than by sinusoidal vibration.

Manual Control

The mechanical jostling of the hand caused by vibration produces unwanted movement of a control. The gain (i.e., sensitivity) of a control determines the control output. The optimum gain in static conditions (high enough not to cause fatigue but low enough to prevent inadvertent movement) is greater than the optimum gain during exposure to vibration when inadvertent movement is more likely.

Some control errors may increase in linear proportion to vibration magnitude. There is no simple relation between the frequency of vibration and its effects on control performance: the effects of frequency depend on the control order (which varies between tasks) and the biodynamic responses of the body (which vary with posture and between operators). With zero-order tasks and the same magnitude of acceleration at each frequency, the effects of vertical seat vibration may be greatest in the range 3–8 Hz since transmissibility to the shoulders is greatest in this range. In the horizontal axes (i.e., the x- and y-axes of the seated body) the greatest effects appear to occur at lower frequencies: around 2 Hz or below.

The effects of vertical whole-body vibration on spilling liquid from a hand-held cup tend to be great-

est at 4 Hz and the effects of vibration on writing speed and subjective estimates of writing difficulty are most affected by vertical vibration in the range 4–8 Hz. Vibration may affect the performance of tracking tasks by reducing the visual performance of the operator. Collimating a display by means of a lens so that it appears to be at infinity can reduce, or even eliminate, errors with some tasks.

Cognitive Performance

Simple cognitive tasks (e.g., simple reaction time) appear to be unaffected by vibration, other than by changes in arousal or motivation or by direct effects on input and output processes. This may also be true for some complex cognitive tasks. However, the scarcity and diversity of experimental studies allow the possibility of real and significant cognitive effects of vibration.

Health Effects

It is believed that disorders of the back (back pain, displacement of intervertebral discs, degeneration of spinal vertebrae, and osteoarthritis) may be associated with vibration exposure. There may be several alternative causes of an increase in disorders of the back among persons exposed to vibration (e.g., poor sitting posture, heavy lifting). It is not always possible to conclude confidently that a back disorder, or any other complaint, is solely, or primarily, caused by whole-body vibration.

Methods of Vibration Evaluation and Assessment

The manner in which the health effects of oscillatory motions depend upon the frequency, direction, and duration of motion is currently assumed to be similar to that for vibration discomfort (see above). However, it is assumed that the total exposure, rather than the average exposure, is important and so a dose measure is used.

National and international standards British Standard 6841 (1987) defines an action level for vertical vibration based on vibration dose values. The vibration dose value uses a fourth-power time dependency to accumulate vibration severity over the exposure period from the shortest possible shock to a full day of vibration:

$$\text{vibration dose value} = \left[\int_{t=0}^{t=T} a^4(t)\mathrm{d}t\right]^{1/4}$$

where $a(t)$ is the frequency-weighted acceleration. If the exposure duration (t, s) and the frequency-weighted r.m.s. acceleration (a_{rms}, ms^{-2}r.m.s.) are known for conditions in which the vibration characteristics are statistically stationary, it can be useful to calculate the estimated vibration dose value or eVDV:

$$\text{estimated vibration dose value} = 1.4 a_{\text{rms}} t^{1/4}$$

The eVDV is not applicable to transients, shocks, and repeated shock motions in which the crest factor (peak value divided by the r.m.s. value) is high.

No precise limit can be offered to prevent disorders caused by whole-body vibration, but standards define useful methods of quantifying vibration severity. British Standard 6841 (1987) offers the following guidance:

> High vibration dose values will cause severe discomfort, pain and injury. Vibration dose values also indicate, in a general way, the severity of the vibration exposures which caused them. However there is currently no consensus of opinion on the precise relation between vibration dose values and the risk of injury. It is known that vibration magnitudes and durations which produce vibration dose values in the region of $15\,\text{ms}^{-1.75}$ will usually cause severe discomfort. It is reasonable to assume that increased exposure to vibration will be accompanied by increased risk of injury.

An action level might be set higher or lower than $15\,\text{ms}^{-1.75}$. **Figure 3** compares this action level with exposure limits suggested in the old version of ISO 2631 (1974, 1985).

In International Standard 2631 (1997) two different methods of evaluating vibration severity with respect to health effects are defined, and for both methods there are two boundaries. When evaluating vibration using the vibration dose value, it is suggested that below a boundary corresponding to a vibration dose value of $8.5\,\text{ms}^{-1.75}$ 'health risks have not been objectively observed' between 8.5 and $17\,\text{ms}^{-1.75}$ 'caution with respect to health risks is indicated' and above $17\,\text{ms}^{-1.75}$ 'health risks are likely'. The two boundaries define a VDV health guidance caution zone. The alternative method of evaluation uses a time dependency in which the acceptable vibration does not vary with duration between 1 and 10 min and then decreases in inverse proportion to the square root of duration from 10 min to 24 h. This method suggests an r.m.s. health guidance caution zone, but the method is not fully defined in the text, it allows very high accelerations at short durations, it conflicts dramatically with the

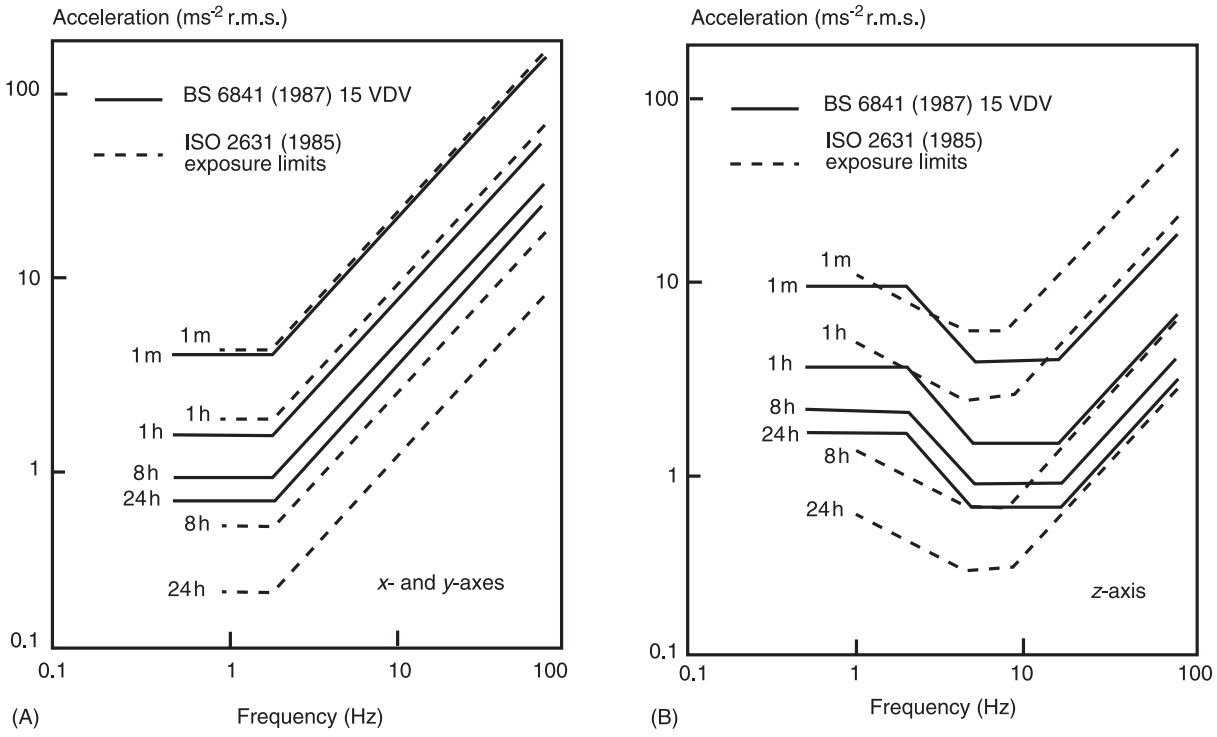


Figure 3 (A, B) Comparison of International Standard 2631 (1985) exposure limits with an action level based on a vibration dose value (VDV) of 15 $ms^{-1.75}$ from British Standard 6841 (1987), When seated: x-axis = fore-and-aft; y-axis = lateral; z-axis = vertical). (Reproduced with permission from Griffin, 1990).

vibration dose value method, and it cannot be extended to durations below 1 min.

With severe vibration exposures, prior consideration of the fitness of the exposed persons and the design of adequate safety precautions may be required. The need for regular checks on the health of routinely exposed persons may also be considered.

Figure 4 illustrates the VDV health guidance caution zone, the root-mean-square health guidance caution zone, and the accelerations corresponding to the 15.0 $ms^{-1.75}$ action level for exposure durations between 1 s and 24 h. Any exposure to continuous vibration, intermittent vibration, or repeated shock may be compared with either the action level or the VDV health guidance caution zone by calculating the vibration dose value. It would be unwise to exceed the appropriate action level without considering the possible health effects of an exposure to vibration or shock.

EU Machinery Safety Directive The Machinery Safety Directive of the European Community (89/392/EEC) states: 'machinery must be so designed and constructed that risks resulting from vibrations produced by the machinery are reduced to the lowest level, taking account of technical progress and the availability of means of reducing vibration, in particular at source'. Instruction handbooks for machinery causing whole-body vibration should specify the frequency-weighted acceleration if it exceeds a stated value (currently a frequency-weighted acceleration of 0.5 ms^{-2} r.m.s.). Standardized test procedures are being prepared but the values currently quoted may not always be representative of the operating conditions in the work for which the machinery is used.

Proposed EU Physical Agents Directive The opening principles of a proposed Council Directive on the minimum health and safety requirements regarding hand-transmitted vibration are: 'Taking account of technical progress and of the availability of measures to control the physical agent at source, the risks arising from exposure to the physical agent must be reduced to the lowest achievable level, with the aim of reducing exposure to below the threshold level ...'.

A proposed EU Directive has been drafted based on 8-h energy-equivalent acceleration magnitudes (called A(8) values). The proposed Directive identifies a threshold level (A(8) = 0.25 ms^{-2} r.m.s.), an action level (A(8) = 0.5 ms^{-2} r.m.s.), and an exposure limit value (A(8) = 0.7 ms^{-2} r.m.s.). When exposures exceed the threshold level it is proposed that workers must receive information concerning the potential

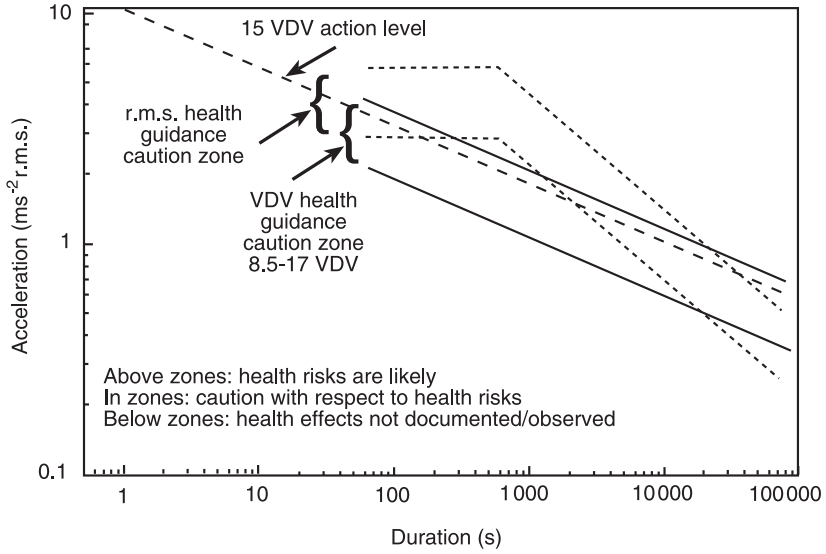


Figure 4 Action level corresponding to a vibration dose value (VDV) of $15\,ms^{-1.75}$ (see British Standard 6841, 1987) compared with r.m.s. and VDV health guidance caution zones suggested in ISO 2631 (1997).

risk of exposure to whole-body vibration. The action level is intended to identify the conditions in which training in precautionary measures is required, an assessment of the vibration is to be made, and a program of preventive measures is to be instituted. The proposed Directive also indicates that when the action level is exceeded workers shall have the right to regular health surveillance, including routine examinations designed for the early detection of disorders caused by whole-body vibration. If the exposure limit value is exceeded, health surveillance must be carried out and member states of the Community will be expected to control the harmful effects. This draft is not consistent with current standards and may be expected to be modified prior to finalization.

Seating Dynamics

Seating dynamics influence the vibration responsible for discomfort, interference with activities, and injury. Most seats exhibit a resonance at low frequencies which results in higher magnitudes of vertical vibration occurring on the seat than on the floor. At high frequencies there is usually attenuation of vibration.

Seat transmissibility may be measured on laboratory simulators with volunteer subjects, but precautions are required to protect subjects from injury. Measurements may also be performed with drivers or passengers in vehicles. Anthropodynamic dummies are being developed to represent the average mechanical impedance of the human body so that laboratory and field studies can be performed without exposing people to vibration. Seat transmissibility may also be predicted using measurements of the impedance of a seat and the known mechanical impedance of the human body.

The suitability of a seat for a specific vibration environment depends on: (1) the vibration spectra present in the environment, (2) the transmissibility of the seat; and (3) the sensitivity of the human body to the different frequencies of vibration. These three functions of frequency are contained within a simple numerical indication of the isolation efficiency of a seat called the seat effective amplitude transmissibility or SEAT. In concept, the SEAT value compares the vibration severity on a seat with the vibration severity on the floor beneath the seat:

$$\text{SEAT}\ (\%) = \frac{\text{ride comfort on seat}}{\text{ride comfort on floor}} \times 100$$

A SEAT value greater than 100% indicates that, overall, the vibration on the seat is worse than the vibration on the floor beneath the seat; SEAT values below 100% indicate that the seat has provided some useful attenuation. The optimization of seating dynamics may be both the cheapest and the most effective method of improving vehicle ride and reducing any associated hazard.

The SEAT value may be calculated from either the frequency-weighted r.m.s. values (if the vibration does not contain transients) or the vibration dose values of the frequency-weighted acceleration on the seat and the floor:

$$\text{SEAT}\ (\%) = \frac{\text{vibration dose value on seat}}{\text{vibration dose value on floor}} \times 100$$

Conventional seating (comprising some combination of foam, rubber, or metal springing) usually has a resonance at about 4 Hz and therefore provides no attenuation at frequencies below about 6 Hz). Attenuation can be provided at frequencies above about 2 or 3 Hz using a separate suspension mechanism beneath the seat pan (i.e., sometimes called a suspension seat).

Disturbance in buildings

Acceptable magnitudes of vibration in some buildings are close to vibration perception thresholds. The acceptability of vibration in buildings depends on the use of the building in addition to the vibration frequency, direction, and duration. Using the guidance contained in ISO 2631 part 2 (1989) it is possible to summarize the acceptability of vibration in different types of building in a single table of vibration dose values (**Table 3**). The vibration dose values in **Table 3** are applicable irrespective of whether the vibration occurs as a continuous vibration, intermittent vibration, or repeated shocks.

See also: **Ground Transportation Systems**; **Motion Sickness**; **Ship Vibrations**; **Tire Vibrations**.

Table 3 Vibration dose values at which various degrees of adverse comment may be expected in buildings.

Place	*Low probability of adverse comment*	*Adverse comment possible*	*Adverse comment probable*
Critical working areas	0.1	0.2	0.4
Residential	0.2–0.4	0.4–0.8	0.8–1.6
Office	0.4	0.8	1.6
Workshops	0.8	1.6	3.2

Based on International Standard 2631 Part 2 (1989) and British Standard 6472 (1992). See Griffin (1990).

Further Reading

Bongers PM and Boshuizen HC (1990) *Back Disorders and Whole-body Vibration at Work*. Thesis, University of Amsterdam.

Bovenzi M and Zadini A (1992) Self-reported back symptoms in urban bus drivers exposed to whole-body vibration. *Spine* 17(9): 1048–1059.

British Standards Institution (1987) *Measurement and Evaluation of Human Exposure to Whole-body Mechanical Vibration and Repeated Shock*. London: British Standard BS 6841.

British Standards Institution (1992), *Evaluation of Human Exposure to Vibration in Buildings (1 Hz to 80 Hz)*. London: British Standard BS 6472.

Commission of the European Communities (1994) Amended proposal for a council directive on the minimum health and safety requirements regarding the exposure of workers to the risks arising from physical agents – individual directive in relation to article 16 of directive 89/391/EEC. *Official Journal of the European Communities* C 230, 19.8.94, 3–29.

Council of the European Communities (Brussels) (1989) On the approximation of the laws of the member states relating to machinery. Council directive (89/392/EEC). *Official Journal of the European Communities* June: 9–32.

Griffin MJ (1990) *Handbook of Human Vibration*. London: Academic Press.

Griffin MJ (1998) A comparison of standardized methods for predicting the hazards of whole-body vibration and repeated shocks. *Journal of Sound and Vibration* 215(4): 883–914.

International Organization for Standardization (1974) *Guide for the Evaluation of Human Exposure to Whole-body Vibration*. Geneva: International Standard ISO 2631.

International Organization for Standardization (1989) *Evaluation of Human Exposure to Whole-body Vibration – Part 2: Continuous and Shock-induced Vibration in Buildings*. Geneva: International Standard ISO 2631-2.

International Organization for Standardization (1997) *Mechanical Vibration and Shock-Evaluation of Human Exposure to Whole-body Vibration – Part 1: General Requirements*. Geneva: International Standard ISO 2631-1.

WIND-INDUCED VIBRATIONS

T Kijewski, F Hann, and A Kareem, University of Notre Dame, Notre Dame, IN, USA

Copyright © 2001 Academic Press

doi:10.1006/rwvb.2001.0155

Introduction

As modern structures move toward taller and more flexible designs, the problems of wind effects on structures – those compromising structural integrity

and those inducing human discomfort – have become increasingly apparent. To fully address this problem, a diverse collection of contributions must be considered, as illustrated in **Figure 1**. It is the complexity and uncertainty of the wind field and its interaction with structures that necessitates such an interdisciplinary approach, involving scientific fields such as meteorology, fluid dynamics, statistical theory of turbulence, structural dynamics, and probabilistic methods. The following sections will describe the contributions from each of these areas, beginning with a description of the wind field characteristics and the resulting wind loads on structures. Subsequent sections will then address procedures for determining wind-induced response, including traditional random vibration theory and code-based approximations, with an example to illustrate the application of both approaches. The treatment of wind effects on structures will conclude with a discussion of aeroelastic effects, wind tunnel testing, and the evolving numerical approaches.

Wind Characteristics

Civil engineering structures are immersed in the earth's atmospheric boundary layer, which is characterized by the earth's topographic features, e.g., surface roughness. The most common description of the wind velocity within this boundary layer superimposes a mean wind component, described by a mean velocity profile, with a fluctuating velocity component. The vertical variation of the mean wind velocity, $\bar{U}$, can be represented by a logarithmic relationship, or by a power law given as:

$$\bar{U}(z) = \bar{U}_{\text{ref}} \left(\frac{z}{z_{\text{ref}}} \right)^{\alpha} \qquad [1]$$

where z_{ref} is the reference height, $\bar{U}_{\text{ref}}$ is the mean reference velocity, and α is a constant that varies with the roughness of the terrain, with specific values defined in fundamental texts.

The fluctuating wind field is characterized by temporal averages, variances of velocity components, probabilities of exceedance, energy spectra, associated length scales, and space-time correlations. One important measure is the total energy of the wind fluctuations, expressed as the standard deviation of the velocity fluctuations normalized by the mean wind velocity, and referred to as turbulence intensity. The energy spectra describe the distribution of energy at each frequency, whereas the space–time correlation describes the degree to which velocity fluctuations are correlated in space and/or time. A measure of the average size of turbulent eddies, the length scale, can be then estimated by integrating velocity cross-correlation functions.

Wind Loads on Structures

Just as the most elementary description of the velocity of the oncoming wind field superimposes a mean component, $\bar{U}(z)$, increasing with height according

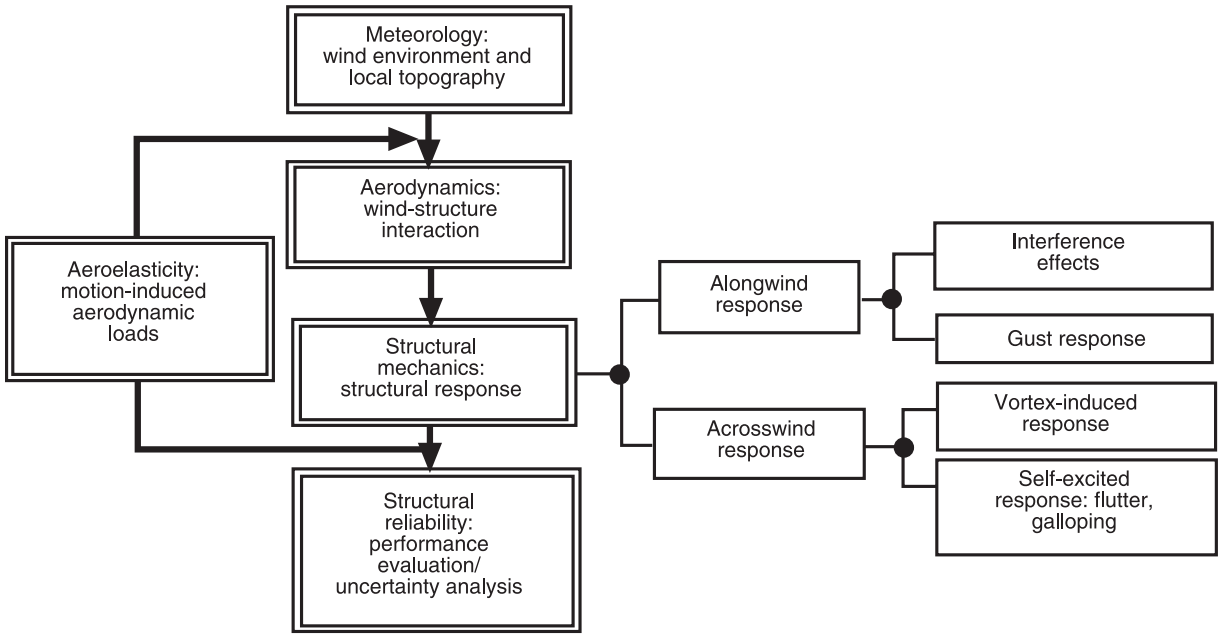


Figure 1 Overview of scheme to determine wind effects on structures.

to the power law given in eqn [1], with a randomly fluctuating component, $u(z, t)$, the oncoming wind will impose loads on the structure that vary both spatially and temporally. The fluctuating wind velocity translates directly into fluctuating positive pressures ($p_w(z, t)$) distributed across the building's windward face, as shown in **Figure 2**. Corresponding negative pressures, $p_l(z, t)$, result on the leeward face of the structure.

Upon impacting the windward face, the wind is then deflected around the structure and accelerated such that it cannot negotiate the sharp corners and thus separates from the building, leaving a region of high negative pressure, also shown in **Figure 2**. This separated flow forms a shear layer on each side, and subsequent interaction between the layers results in the formation of discrete vortices, which are shed alternately. This region is generally known as the wake region.

The three-dimensional simultaneous loading of the structure due to its interaction with the wind results in three structural response components, illustrated in **Figure 2**. The first, termed the alongwind component, primarily results from pressure fluctuations in the approach flow, leading to a swaying of the structure in the direction of the wind. The acrosswind component constitutes a swaying motion perpendicular to the direction of the wind and is introduced by side-face pressure fluctuations primarily induced by the fluctuations in the separated shear layers, vortex shedding and wake flow fields. The final torsional component results from imbalances in the instantaneous pressure distribution on the building surfaces. These wind load effects are further amplified on asymmetric buildings as a consequence of inertial coupling in the building's structural system.

As the wind pressures vary spatially over the face of the structure, there is the potential for regions of high localized pressures, of particular concern for the design of cladding systems; however, it is their collective effect that results in the integral loads used for the design of the structural system, which will be of primary interest in this discussion.

Since the alongwind motion primarily results from the fluctuations in the approach flow, its load effects have been successfully estimated using quasi-steady and strip theories, which imply that the fluctuating pressure field is linearly related to the fluctuating velocity field at any level on the building. Although the alongwind response may also include interference effects due to the buffeting of the structure by the wake of upstream obstacles, it is the gust response due to the oncoming wind that is primarily considered. Thus, the aerodynamic loads, $F(t)$, considering only this component, are expressed in terms of velocity fluctuations as:

$$F(t) = \tfrac{1}{2}\rho A C_D \left(\bar{U} + u(t)\right)^2 \approx \tfrac{1}{2}\rho A C_D \bar{U}^2 + \rho A C_D \bar{U} u(t) \qquad [2]$$

in which $\rho =$ air density, $A =$ projected area of the structure loaded by the wind, and $C_D =$ drag coefficient. This expression is approximated by ignoring the generally small term containing the square of the fluctuating velocity.

The preceding expression implicitly assumes that the velocity fluctuations approaching a structure are fully correlated over the entirety of the structure and these are transformed linearly to force fluctuations. This assumption may be valid for very small structures, but fails to hold for structures with larger spatial dimensions and leads to overestimation of

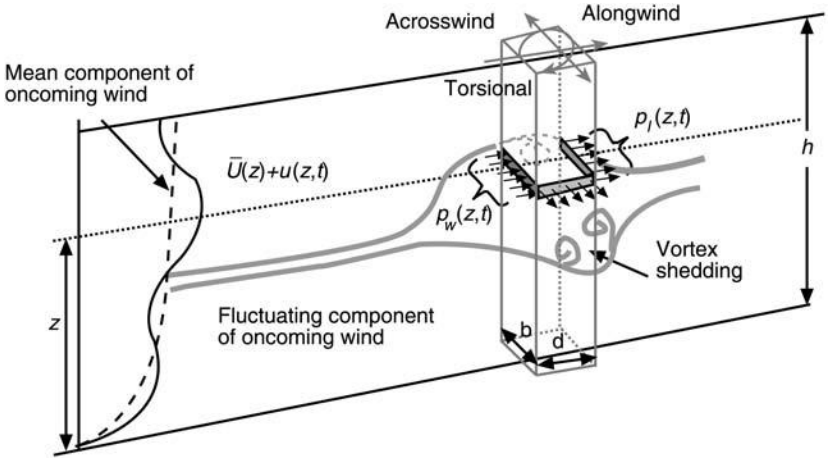


Figure 2 Description of oncoming wind field and resulting wind-induced effects on structure.

loads. In this case, the effect of imperfect correlation of wind fluctuations is conveniently introduced through an aerodynamic admittance function. As this loading scenario is described relatively easily in the frequency domain, eqn [2] is accordingly transformed and the aerodynamic admittance, $\chi^2(f)$, is introduced:

$$S_F(f) = (\rho C_D)^2 \chi^2(f) S_u(f) \qquad [3]$$

where $S_F(f)$, $S_u(f) =$ power spectral density (PSD) of wind loads and wind fluctuations, respectively. Ideally, $\chi^2(f)$ not only represents the lack of correlation in the approach flow, but it also captures any departure from quasi-steady theory that may result from complex nonlinear interactions between the fluctuating wind and the structure. The transformation of wind velocity fluctuations to wind force fluctuations is illustrated in the frequency domain in **Figure 3**. For simple rectangular plates and prisms, both experimental and theoretical information concerning $\chi^2(f)$ is available. For typical buildings that are aerodynamically bluff, one needs to resort to wind tunnel tests to directly obtain the PSD of the aerodynamic force. Alternatively, one can invoke the strip and quasi-steady theories with an appropriate correlation structure of the approaching flow field to estimate $\chi^2(f)$ and hence $S_F(f)$; however, this may introduce some uncertainty in the estimates, as this approach may not fully capture all the features of the wind-structure interactions.

The approach described above has served as a building block for the 'gust loading factor' used in most building codes. However, the acrosswind and torsional responses cannot be treated in terms of these gust factors inasmuch as they are induced by the unsteady wake fluctuations, which cannot be conveniently expressed in terms of the incident turbulence. As a result, experimentally derived loading functions have been introduced. Accordingly, the acrosswind and torsional load spectra obtained by synthesizing the surface pressure fields on scale models of typical building shapes are available in the literature. In a recent study, scale models of a variety of basic building configurations, with a range of aspect ratios, were exposed to simulated urban and suburban wind fields to obtain mode-generalized loads.

Wind-induced Response: Theory

In order to derive the structural response from aerodynamic loads, basic random vibration theory is utilized. The equations of motion of a structure represented by a discretized lumped-mass system are given by:

$$\mathbf{M}\ddot{x}(t) + \mathbf{C}\dot{x}(t) + \mathbf{K}x(t) = F(t) \qquad [4]$$

in which $\mathbf{M}$, $\mathbf{C}$, and $\mathbf{K}$ are the assembled mass, damping and stiffness matrices of the discretized system, respectively, x is the displacement, and $\dot{x}$ and $\ddot{x}$ are the first two time derivatives of x, representing velocity and acceleration, respectively. In general, these equations are derived to provide two translations and one rotation per story level; however, for the sake of illustration, it is assumed here that the structure is uncoupled in each direction. By employing the standard transformation of coordinates, the following modal representation is obtained for one of the translation directions:

$$\ddot{q}_j + 2\zeta_j(\omega_n)_j\dot{q}_j + (\omega_n)_j^2 q_j = P_j(t) \qquad [5]$$

in which $P_j(t) = [\phi_j]^{\mathrm{T}} F(t)$ where $[\ ]^{\mathrm{T}}$ denotes transpose, ϕ_j, ζ_j and $(\omega_n)_j = 2\pi(f_n)_j$ are the jth mode shape, modal critical damping ratio and natural frequency, respectively, and q and its derivatives now represent modal response quantities related to x and its derivatives, respectively, by $x(t) = [\phi_j]q_j(t)$. The PSD of response, $Sq_j^{(r)}$ is given by:

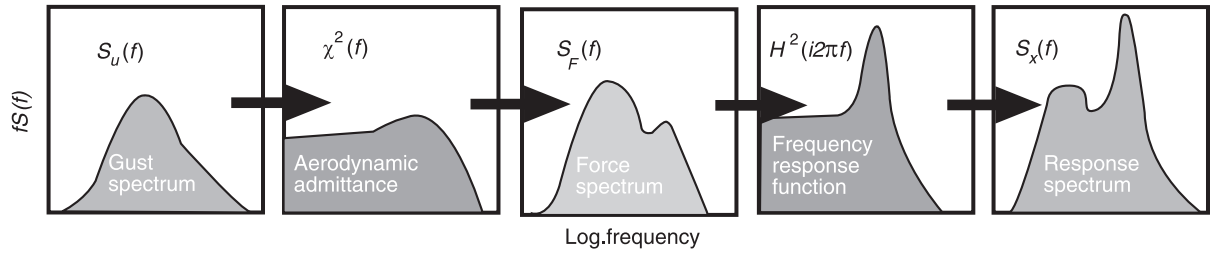


Figure 3 Procedure for determination of response spectrum.

$$Sq_j^{(r)}(f) = \left|H_{j^{(r)}}^2(i2\pi f)\right| S_{P_j}(f) \quad [6]$$

$$S_{P_j}(f) = \left[\phi_j\right]^{\mathrm{T}} S_F(f)\, \phi_j \quad [7]$$

in which $|H_{j^{(r)}}^2(i2\pi f)|$ is the jth-mode frequency response function (FRF). The superscript r indicates the derivative of response, i.e., $r = 0, 1, 2, 3$ denotes displacement, velocity, acceleration and jerk. Determination of wind-induced response by this approach is summarized in **Figure 3**.

The root mean square (RMS) value of response in physical coordinates, $\sigma_{x^{(r)}}^2$, is then given by the weighted superposition of all N modal contributions:

$$\sigma_{x^{(r)}}^2 = \sum_{j=1}^{N} \frac{\phi_j^2 \pi (f_n)_j S_{P_j}(f_n)_j \left(2\pi (f_n)_j\right)^{2r}}{4\left(2\pi (f_n)_j\right)^4 \zeta_j m_j^2} + \sum_{j=1}^{N} \frac{\phi_j^2 \int_0^{(f_n)_j} S_{P_j}(f)\mathrm{d}f \left(2\pi (f_n)_j\right)^{2r}}{\left(2\pi (f_n)_j\right)^4 m_j^2} \quad [8]$$

where m_j is the jth modal mass, $m_j = [\phi_j]^{\mathrm{T}}\mathbf{M}$, and the first term of eqn [8] represents the resonant component, and the second term, the background component. The preceding equation is an approximation of the area under the response PSD, which is very close to exact for most lightly damped structures.

Wind-induced Response: Codes and Standards

International codes and standards have simplified the random vibration-based response analysis described in the previous section through the use of simplified algebraic expressions and the statistically derived gust effect factor, which accounts for the gustiness of the wind by providing equivalent static loads. Both time and spatial averaging play an important role in the development of gust factors, as does the site terrain, structure size, and dynamic characteristics.

Through the use of random vibration theory, the dynamic amplification of loading or response, represented by the gust effect factor, can be readily defined. For example, the expected peak response $y_{\max}^{(r)}$ can be estimated from the RMS value $\sigma_{y^{(r)}}$ and mean value $\bar{y}^{(r)}$ by the following expression, based on the probabilistic description of peak response during an interval T:

$$y_{\max}^{(r)} = \bar{y}^{(r)} + g^{(r)}\sigma_{y^{(r)}} \quad [9]$$

The peak factor $g^{(r)}$ varies between 3.5 and 4 and is given by:

$$g = \frac{\sqrt{\left(2\ln((f_n)_1 T)\right)} + 0.5772}{\sqrt{\left(2\ln((f_n)_1 T)\right)}} \quad [10]$$

The gust effect factor (GEF) G is then defined as the ratio of the maximum expected response to the mean response:

$$G = \frac{y_{\max}^{(r)}}{\bar{y}^{(r)}} = 1 + g^{(r)}\frac{\sigma_{y^{(r)}}}{\bar{y}^{(r)}} \quad [11]$$

The RMS response represents the area under the power spectral density of $y^{(r)}$, which can be described in terms of a background component Q, representing the response due to quasi-steady effects, and a resonant contribution R to account for dynamic amplification. To simplify the determination of these terms, international standards provide a series of simplified algebraic expressions. Typically G is defined in terms of the displacement response:

$$G = 1 + 2g_{y^{(0)}} I_H \sqrt{(Q + R)} \quad [12]$$

where $I_H =$ turbulence intensity at the top of the structure. Q and R, respectively, represent the contributions of the background and resonant components approximated in eqn [8].

Most major codes and standards around the world account for the dynamic effects of wind in terms of the equivalent static loads F_{eq} through the use of the GEF:

$$F_{eq}(z) = GC_{fx}\bar{q}(z)A \quad [13]$$

where the mean wind pressure is $\bar{q} = \frac{1}{2}\rho\bar{U}^2$ and $C_{fx} =$ the mean alongwind aerodynamic force coefficient. Each international standard uniquely defines G based on the form in eqn [12]. For example, in the ASCE 7-98 Standard the gust factor is defined as:

$$G = 0.925\left(\frac{1 + 1.7I_{\bar{z}}\sqrt{\left(g_Q^2 Q^2 + g_R^2 R^2\right)}}{1 + 1.7g_v I_{\bar{z}}}\right) \quad [14]$$

where three peak factors are defined: g_Q and g_v are taken as 3.4 for simplicity and g_R is determined from eqn [10] with $T = 3600\,\mathrm{s}$, and $I_{\bar{z}}$ is the turbulence intensity at the equivalent height of the structure, $\bar{z}$, is determined by a code-specified expression.

The background and resonant response components are similarly defined by approximate expressions:

$$Q^2 = \frac{1}{1 + 0.63\left(\frac{b+h}{L_{\bar{z}}}\right)^{0.63}} \quad [15]$$

$$R^2 = \frac{1}{\beta} R_n R_h R_b (0.53 + 0.47 R_L) \quad [16]$$

where b and h are the width and height, respectively, of the structure, shown in **Figure 2**, and $L_{\bar{z}}$ is the integral length scale of turbulence at the equivalent height. The resonant component involves four factors (R_n, R_h, R_b, R_L) which are dependent upon the first mode natural frequency, defined as n_1 in ASCE 7-98, and the damping ratio, defined in the standard as β, as well as the dimensions of the structure, the mean wind speed at the equivalent height, $\bar{V}_{\bar{z}}$, and the wind field's characteristics. Expressions for these terms may be found in ASCE 7-98.

Following the determination of the gust effect factor, the maximum alongwind displacement $X_{\max}$ and RMS accelerations $\sigma_{\ddot{x}}$ may be calculated directly:

$$X_{\max}(z) = \frac{\phi(z)\rho b h C_{fx} \hat{V}_{\bar{z}}^2}{2m_1(2\pi n_1)^2} KG \quad [17]$$

$$\sigma_{\ddot{X}}(z) = \frac{0.85\phi(z)\rho b h C_{fx} \bar{V}_{\bar{z}}^2}{m_1} I_{\bar{z}} KR \quad [18]$$

where $\hat{V}_{\bar{z}}$ is the 3-s gust at the equivalent height, $\phi(z)$ is assumed to be the fundamental mode shape, m_1 is the first mode mass and K is a coefficient representative of the terms resulting from the integration of the mode shape and wind profile in the determination of the RMS response. Expressions for these terms are also provided in ASCE 7-98. Note that, in the case of the acceleration response, background effects are not considered, thus the GEF is not directly used as defined in eqn [14]. Instead it is replaced with a collection of terms analogous to using a GEF with only a resonant component.

Example of Wind-induced Response

To illustrate the determination of wind-induced response by both random vibration theory and by the code-based procedure, the following example is provided. **Table 1** lists the assumed properties of the structure, which is located in a city center. The basic wind speed, measured as a 3-s gust, at the reference height of 33 ft (10 m) in open terrain, is taken as 90 mph (40.23 ms^{-1}). For the sake of brevity, only acceleration response will be provided, considering only the first mode with an assumed linear mode shape. To further simplify the analysis, the response will only be calculated at the structure's full height, at which point the mode shape given in **Table 1** would equal unity.

The RMS accelerations in the alongwind direction were first determined in accordance with ASCE 7-98, by eqn [18], with all calculated parameters listed in **Table 2**. Unfortunately, as discussed previously, acrosswind and torsional responses cannot be determined by the same analytical procedure and are thus omitted from the ASCE 7 Standard. However, these response components, as well as the alongwind response, can readily be determined by eqn [8] with the aid of the wind tunnel data provided in **Figure 4**. Note that it is common practice to plot these load spectra in a nondimensional form, S^*, as defined in **Figure 4**, where $\bar{U}_H$ is the mean wind velocity at the height of the building, in urban terrain. A power law

Table 1 Assumed structural properties

h	600 ft (182.88 m)
b	100 ft (30.48 m)
d	100 ft (30.48 m)
ρ	0.0024 slugs ft^{-3} (1.25 kg m^{-3})
C_{fx}	1.3
$(f_n)_1$: alongwind, acrosswind, torsion	0.2 Hz, 0.2 Hz, 0.35 Hz
ρ_B: building density	12 lb ft^{-3} = 0.3727 slugs ft^{-3} (192.22 kg m^{-3})
β	0.01
First mode shape	$\phi(z) = (z/H)$

Table 2 Values calculated from ASCE 7-98

$I_{\bar{z}}$	0.302
$L_{\bar{z}}$	594.52 ft
Q^2	0.589
R_n	0.111
R_h	0.146
R_b	0.555
R_L	0.245
R^2	0.580
g_Q, g_v	3.4 (assumed)
g_R	3.787
G	1.01
K	0.502
m_1	745 400 slugs (10 886 129 kg)
$\bar{V}_{\bar{z}}$	87.83 ft s^{-1} (26.77 m s^{-1})
U_H	102.36 ft s^{-1} (31.20 m s^{-1})
$S^*_{Fx}(n_1)$[a]	0.000 48
$S^*_{Fy}(n_1)$[a]	0.0023
$S^*_{Mz}(n_1)$[a, b]	0.000 025

[a] Spectral values in nondimensional form (see **Figure 4**).
[b] $S_{Mz}(n_1)$ should be multiplied by a correlation factor of 0.7042.

relationship (eqn [1]) can be used to translate the reference wind velocity of 90 mph (40.23 m s^{-1}) from open terrain at 33 ft (10 m) to urban terrain at the buiding height.

In the case of acceleration response, $r = 2$ and $N = 1$ in eqn [8], as only first mode contributions are considered. Note also that in eqn [8], m_j is defined as the modal mass for the alongwind and acrosswind directions, taken as the total mass of the building, divided by three; however, for the torsional response, this modal mass term must be replaced by the first mode mass moment of inertia determined by: $(1/12)m_1(b^2 + d^2)$, where d is the depth of the structure as shown in **Figure 2**. In addition, the torsional analysis requires the multiplication of the spectral density by a reduction factor to account for the assumption of a constant mode shape inherent in force-balance experimental measurements.

Examining first the properties in **Table 2**, a comparison of R^2 and Q^2 reveals that this particular structure receives nearly equal contributions from the background and resonant components. For the alongwind response, shown in **Table 3**, the simplified response estimate given by ASCE 7-98 compares well with the wind tunnel data. Also note that the acrosswind accelerations are twice that of the alongwind response, illustrating that acrosswind response components have a greater role in determining the habitability performance of a structure. On the other hand, the structure's torsional response is slightly less than the alongwind, which should be no surprise considering that the structure has no geometric or structural asymmetries and that the loading data from the wind tunnel was obtained using an isolated building model.

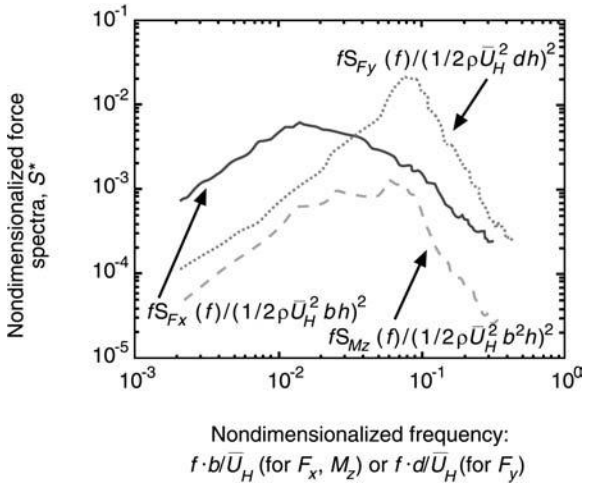


Figure 4 Aerodynamic load spectra obtained via force-balance tests in a wind tunnel. (—) Alongwind; (. . .) acrosswind; (- - -) torsional.

Table 3 Calculated RMS lateral accelerations (in milli-g).

	Alongwind	*Acrosswind*	*Torsional*[a]
ASCE 7-98 (eqn [18])	5.90	N/A	N/A
Experimental (eqn [8])	6.17	13.5	5.05

[a] Torsion-induced lateral accelerations at building corner.

Aeroelastic Effects

The determination of wind-induced loads and response discussed previously did not account for aeroelastic effects, which can sometimes have significant contributions to the structural response. Response deformations can alter the aerodynamic forces, thus setting up an interaction between the elastic response and aerodynamic forces commonly referred to as aeroelasticity. Aeroelastic contributions to the overall aerodnamic loading are distinguished from other unsteady loads by recognizing that aeroelastic loads vanish when there is no structural motion. Different types of aeroelastic effects are commonly distinguished from each other. They include vortex-induced vibration, galloping, flutter, and aerodynamic damping.

As alluded to earlier, aerodynamically bluff cross-sections shed vortices at a frequency governed by the nondimensional Strouhal number, *St*:

$$St = \frac{f_s b}{\bar{U}} \qquad [19]$$

where f_s is the shedding frequency (in Hz). The shedding of vortices generates a periodic variation in the pressure over the surface of the structure. When the frequency of this variation approaches one of the natural frequencies of a structure, vortex-induced vibration can occur. The magnitudes of these vibrations are governed both by the structure's inherent damping characteristics and by the mass ratio between the structure and the fluid it displaces. These two effects are often combined in the Scruton number defined as:

$$Sc = \frac{4\pi\zeta m}{\rho b^2} \qquad [20]$$

where m is the mass per unit length of the structure.

Vortex-induced vibration is more complex than a mere resonant forcing problem. Nonlinear interaction between the body motion and its wake results in the 'locking in' of the wake to the body's oscillation frequency over a larger velocity range than would be predicted using the Strouhal number. Vortex-induced

vibration, therefore, occurs over a range of velocities that increases as the structural damping decreases.

Galloping occurs for structures of certain cross-sections at frequencies below those of vortex-induced vibration. One widely known example of galloping is the large acrosswind amplitudes exhibited by power lines when freezing rain has resulted in a change of their cross-section. Analytically, galloping is considered a 'quasisteady' phenomenon because knowledge of the static aerodynamic coefficients of a given structure (i.e., mean lift and drag forces on a stationary model) allows quite reliable prediction of galloping behavior.

Stability of aeroelastic interactions is of crucial importance. The attenuation of structural oscillations by both structural and aerodynamic damping characterizes stable flow-structure interactions. In an unstable scenario, the motion-induced loading is further reinforced by the body motion, possibly leading to catastrophic failure. Such unstable interactions involve extraction of energy from the fluid flow such that aerodynamic effects cancel structural damping. Flutter is the term given to this unstable situation, which is a common design issue for long-span bridges.

Depending on the phase of the force with respect to the motion, self-excited forces can be associated with the displacement, the velocity, or the acceleration of the structure. Because of these associations, these forces can be thought of as 'aerodynamic contributions' to stiffness, damping, and mass, respectively. In addition to stiffness and damping, aeroelastic effects can couple modes that are not coupled structurally. Whenever the combined aeroelastic action on various modes results in negative damping for a given mode, flutter occurs. By means of structural dynamics considerations and aerodynamic tailoring, flutter must be avoided for the wind velocity range of interest. Even without resulting in flutter, aeroelastic effects can have a significant effect on response.

Wind Tunnel Testing

Despite the obvious advances of computational capabilities over the years, the complexity of the bluff body fluid-structure interaction problems concerning civil engineering structures has precluded numerical solutions for the flow around structures. Thus, wind tunnels remain, at this juncture, the most effective means of estimating wind effects on structures. However, it should be noted that not all structures require wind tunnel testing. For many conventional structures, for example, low-rise buildings, code-based estimates may well suffice. Wind tunnel testing may be necessary, however, when dealing with a novel design or a design for which dynamic and aeroelastic effects are difficult to anticipate. Examples of such structures include, but are not limited to, long-span bridges and tall buildings.

Wind tunnel testing of a given structure first involves appropriate modeling of the wind environment, necessitating various scaling considerations. Geometric scaling is based on the boundary layer height, the scale of turbulence, and the scale of the surface roughness all constrained by the size of the wind tunnel itself. Ideally, these lengths should hold to the same scaling ratio – a performance that can be approached when the boundary layer is simulated over a long fetch with scaled floor roughness. Dynamic scaling requires Reynolds number equality between the wind tunnel and the prototype. Without extraordinary measures, this is most often not possible and must be kept in mind when interpreting results. Velocity scaling is most often obtained from elastic forces of the structure and inertial forces of the flow. Kinematic scaling involves appropriate distributions of the mean velocity and turbulence intensity and can be achieved with flow manipulation in the wind tunnel.

Both active and passive means are available to generate turbulent boundary layers. While active devices such as air jets, flapping vanes and airfoils are capable of generating a wide range of turbulence parameters, passive devices are cheaper and more efficient to implement. Passive devices include spires, fences, grids, and floor roughness. Depending on the length and cross-sectional size of the tunnel, surrounding terrain may also be modeled.

Once an appropriate incident flow has been generated, there are several options for obtaining aerodynamic load data for the structure of interest. Pressure measurements can be performed on the surface of a model, forces can be quantified from the base of a lightweight, rigid model, or forces can be obtained from an aeroelastic model of the structure. Pressure measurements are capable of quantifying localized loading on a structure's surface. Issues such as fatigue loads for cladding panels and panel anchor and glass failure require such localized analysis.

Integrated loads on a structure are often estimated with high-frequency base balances. These devices are generally integrated into a rotating section of the floor of a wind tunnel. A lightweight model of the structure is mounted on the balance for measuring wind loads over a range of incidence angles. The low mass of the model is necessary to ensure that the natural frequency of the model-balance system is well above any expected wind forcing frequency. A primary advantage of this approach is that modal force spectra are obtained directly and can be used in subsequent analytical estimations of building response. As long as the structural geometry does

not change, the forces can be used to analyze the effects of internal structural design changes without the need for further wind tunnel tests.

Aeroelastic models allow interaction between structural motion and aerodynamic forces. Such models can be constructed as continuous or discrete models. Continuous models require specialized materials having structural properties matching those of the prototype. Discrete models are simpler to implement and consist of an internal spine to account for structural dynamic feature, with an external cladding that maintains proper geometric scaling with the prototype. Dynamic response of both buildings and bridges can be estimated utilizing such models.

Numerical Methods

With the evolution of computer capabilities, numerical methods have presented another option for the analysis of fluid-structure interactions. A host of simulation schemes to generate wind fields and the associated response, in a probabilistic framework, are currently available. However, these schemes rely on quasisteady formulations to transform wind fluctuations into load fluctuations. A welcome departure from the limitations of such approaches is offered by the field of computational fluid dynamics (CFD), serving as a promising alternative to wind tunnel testing. One of the more attractive approaches within this area involves the solution of the Navier–Stokes equations in the large eddy simulation (LES) framework to simulate pressure fields around structures that convincingly reproduce the experimentally measured pressure distributions in both the mean and RMS, as well as replicating the aerodynamic forces and flow re-attachment features. Coupled with computer-aided flow visualization, which provides visual animation, this numerical simulation may serve as a useful tool to analyze the evolution of flow fields around structures and estimate the attendant loads. This approach definitely has merit, and as computational capacity increases, these schemes will eventually become the methods of choice.

Nomenclature

A	projected area of building exposed to wind
b	width of structure
$\mathbf{C}$	structural damping matrix
C_{fx}	alongwind aerodynamic force coefficient
C_D	drag coefficient
d	depth of structure
f	frequency
f_n	natural frequency in Hertz
f_s	vortex shedding frequency in Hertz
F	force (or load), in physical coordinates
F_{eq}	equivalent static load
g	peak factor
G	gust effect factor
h	height of structure
H	frequency response function
I_H	turbulence intensity at top of structure
$I_{\bar{z}}$	turbulence intensity at equivalent height
j	subscript denoting modal index
K	integration constant (ASCE 7-98)
$\mathbf{K}$	structural stiffness matrix
$L_{\bar{z}}$	integral length scale of turbulence at equivalent height
$\mathbf{M}$	structural mass matrix
m	structural mass per unit height
m_j	jth modal mass
n_1	fundamental natural frequency (ASCE 7-98)
N	total number of modal components
P	force (or load), in modal coordinates
p_l	wind pressure on leeward face of building
p_w	wind pressure on windward face of building
Q	background component
$\overline{q}$	mean wind pressure
q	modal displacement
$\dot{q}$	modal velocity
$\ddot{q}$	modal acceleration
r	superscript denoting derivative order
R	resonant component
R_n, R_h, R_b, R_L	terms for approximation of resonant component (ASCE 7-98)
Sc	Scruton number
S_F	power spectral density of wind loads, in physical coordinates
S_P	power spectral density of wind loads, in modal coordinates
S_q	power spectral density of response, in modal coordinates
St	Strouhal number
S_u	power spectral density of wind fluctuations
S^*	nondimensionalized load spectra
t	time
T	time interval
u	longitudinal velocity fluctuations
$\overline{U}$	mean wind velocity
$\overline{U}_{\text{ref}}$	mean wind velocity at reference height
$\overline{U}_H$	wind velocity at building height
$\overline{V}_{\bar{z}}$	mean wind velocity at equivalent height
$\widehat{V}_{\bar{z}}$	3–s gust at equivalent height
$\dot{x}$	structural displacement, in physical coordinates

$\dot{x}$	structural velocity, in physical coordinates
$\ddot{x}$	structural acceleration, in physical coordinates
$X_{\max}$	maximum alongwind displacement (ASCE 7-98)
$\overline{y}$	mean response
$y_{\max}$	expected peak response
z	vertical position
$\overline{z}$	equivalent height
z_{ref}	reference height
$[\,]^{\text{T}}$	transpose operator
α	power law exponent
β	critical damping ratio (ASCE 7-98)
ρ	air density
ρ_b	building density
σ	root mean square
ϕ	mode shape
χ^2	aerodynamic admittance function
ω_n	natural frequency in rad s^{-1}
ζ	critical damping ratio

See also: **Stochastic analysis of nonlinear systems**; **Stochastic systems**;

Further Reading

ASCE (1999) *Minimum Design Loads for Buildings and Other Structures*, ASCE7-98. Reston, VA: American Society of Civil Engineers.

Cermak JE (1976) Aerodynamics of buildings. *Annual Review of Fluid Mechanics*, vol. 8, pp. 75–106. Palo Alto, CA: Annual Reviews Inc.

Cermak JE (1987) Advances in physical modeling for wind engineering. *Journal of Engineering Mechanics* 113(5): 737–756.

Kareem A (1987) Wind effects on structures: a probabilistic viewpoint. *Probabilistic Engineering Mechanics* 2(4): 166–200.

Kareem A, Kijewski T, Tamura Y (1999), Mitigation of motions of tall buildings with specific examples of recent applications. *Wind & Structures* 2(3): 201–251.

Kijewski T, Kareem, A (1998) Dynamic wind effects: a comparative study of provisions in codes and standards with wind tunnel data. *Wind & Structures* 1(1): 77–109.

Lutes LD, Sarkani S (1997) *Stochastic Analysis of Structural and Mechanical Vibrations*. Englewood Cliffs, NJ: Prentice Hall.

Murakami S (1998) Overview of turbulence models applied in CWE-1997. *Journal of Wind Engineering and Industrial Aerodynamics* 74–76: 1–24.

Simiu E, Scanlan R (1996) *Wind Effects on Structures*, 3rd edn. New York: Wiley.

Solari G, Kareem A (1998) On the formulation of ASCE7-95 gust effect factor. *Journal of Wind Engineering and Industrial Aerodynamics* 77/78: 673–684.

Sutro D (2000) Into the tunnel. *Civil Engineering Magazine* 71(6): 37–41.

Zhou Y, Kijewski T, Kareem A (2001) Aerodynamic loads on tall buildings: an interactive database. *Journal of Structural Engineering*, ASCE (in press).

WINDOWS

S Braun, Technion - Israel Institute of Technology, Haifa, Israel

Copyright © 2001 Academic Press

doi:10.1006/rwvb.2001.0052

General

Signal patterns are often investigated in the dual domains of time and frequency. Windows are functions multiplying the signal functions resulting in improved analysis results. While multiplying window functions exist for both the time and frequency domain signal functions, this entry will only deal with the first type.Given a time signal $x(t)$, a window $w(t)$ is applied as follows, resulting in the modified signal $x'(t)$:

$$x'(t) = w(t)x(t) \qquad [1a]$$

The window $w(t)$, and hence $x'(t)$, are time limited, even if $x(t)$ is a continuous power signal. An equivalent windowing operation can be performed in the frequency domain, by applying a Fourier transform (FT) to eqn [1a]. This results in the convolution:

$$X'(\omega) = W(\omega) \otimes X(\omega) \qquad [1b]$$

The use of these windows usually occurs in one of the following applications:

- Spectral analysis – reduction of leakage
- Spectral analysis – rotating machines, reduction of effect of speed fluctuation
- Spectral analysis – smoothing of spectral estimates
- Spectral analysis – overlapped processing
- Impulse testing – improvement of signal to noise ratio
- Digital filter design – the so-called 'window' method

Control of Leakage Error in Spectral Analysis

(see **Spectral analysis**, classical methods)

Leakage

Leakage is an error noticable in the frequency description of signals: power (or energy) appears in frequency regions outside those where the actual physical phenomena occur. In the analysis, power has 'leaked' to neighboring regions.While leakage can occur in general cases of signals, it is the easiest to demonstrate for the specific case of harmonic signals.

Measurements are taken in a finite time. Analyzing via the discrete Fourier transform (DFT) imposes periodicities both in the time as well as in the frequency domain (see **Transform methods**). The respective periods are $N\Delta t$ and $1/\Delta t$, with Δt the sampling interval, and N the number of samples analyzed (**Figure 1**).

Two cases of harmonic signals are shown in **Figure 2A** and **2D**. Only in the first case are an integral number of periods spanned by the observation interval. Noting the effect of the periodicity imposed by the DFT operation, this results in discontinuities only in the second case, where a non-integral number of periods are spanned by the observation interval (**Figures 2B, 2D**). This results in high-frequency components, hence the leakage occurrence (**Figures 2C, 2F**).

Multiplying windows can be applied, giving gradually less weight to both end regions of the signal. The discontinuities due to the periodic extension of the signal can thus be avoided. To avoid the loss in the total signal power induced by this type of weighing, a correction factor needs to be applied.

A multitude of windows can be used in order to control leakage, but only a handful are used by practitioners of vibration analysis.

The rectangular window

This is defined as:

$$w_{\mathrm{R}}(n) = \begin{cases} 1 & 0 \le n \le N-1 \\ 0 & \text{otherwise} \end{cases} \qquad [2]$$

Thus $x'(t) = x(t)$, and the unmodified signal is analyzed. The leakage can be understood by using the convolution of eqn [1b]. **Figure 3** shows the Fourier transformation of the rectangular window $W(\omega)$. This is characterized by a main lobe and decreasing sidelobes, with zeros at multiples of $1/N\Delta t$.

Figure 4 shows the convolution for two cases: denoting the signal's period by $M\Delta t$ with M the number of points per period, and $p = N/M$ periods spanned in the time interval, the location of the signal on the frequency scale will be $p/N\Delta t$. For the case of

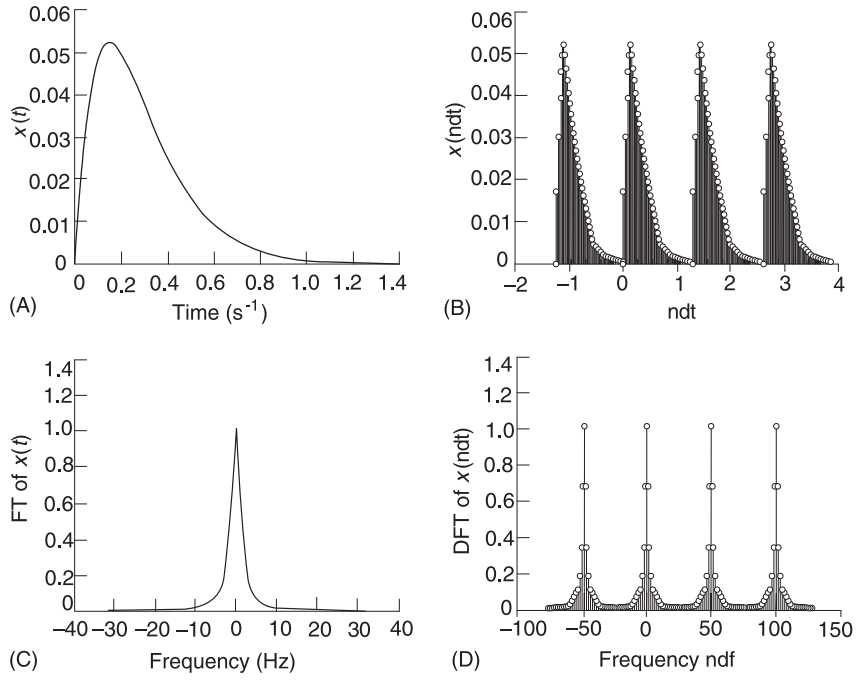


Figure 1 Periodic extension of the discrete Fourier transform. (A) Signal in time domain; (B) extended discrete time domain signal; (C) signal in frequency domain; (D) extended discrete frequency domain signal.

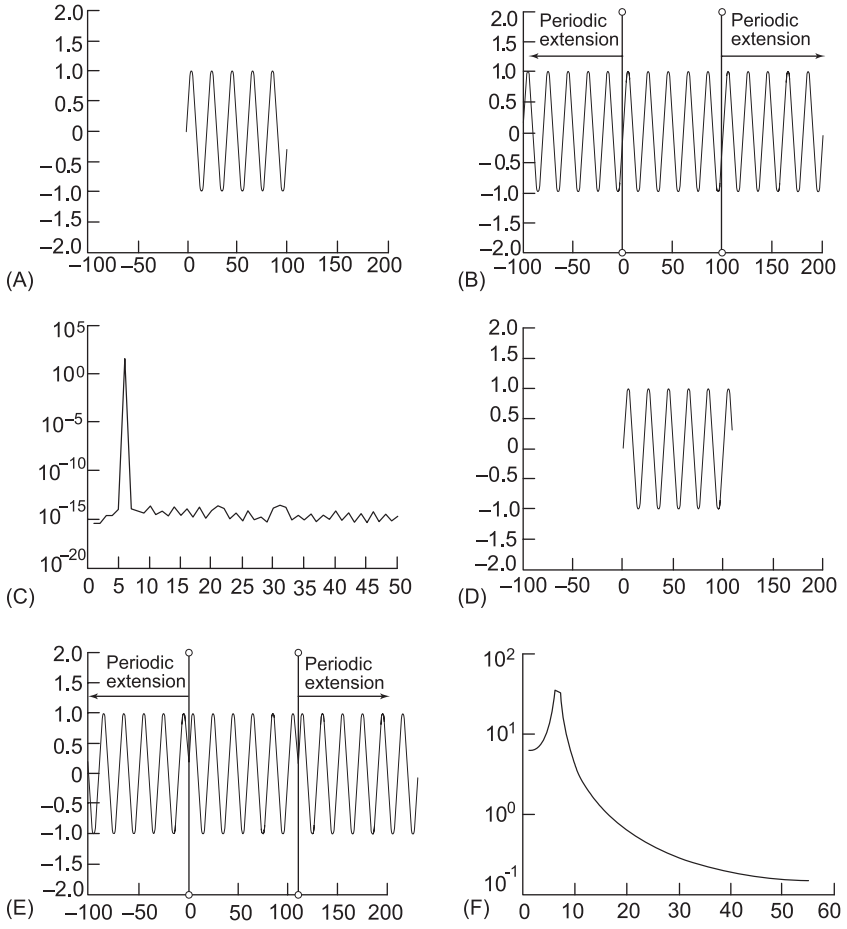


Figure 2 Discrete Fourier transform analysis of a harmonic signal. (A) Signal 1 = integer number of periods; (B) periodic extension of signal 1; (C) signal 1 = magnitude of DFT; (D) signal 2 = odd number of half periods; (E) periodic extension of signal 2; (F) signal 2 = magnitude of DFT.

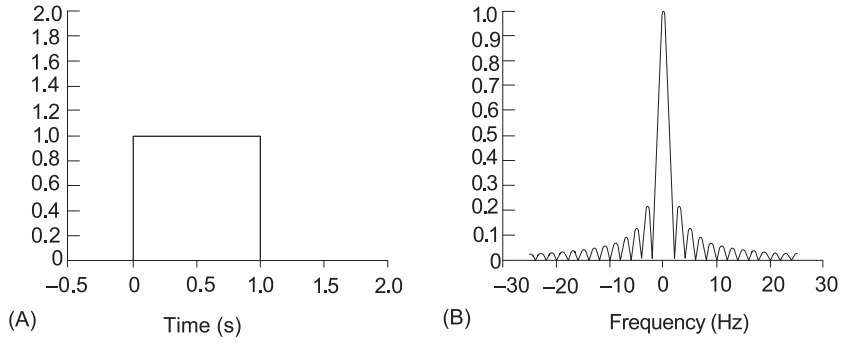


Figure 3 Rectangular window: (A) time domain; (B) magnitude in frequency domain.

Figure 2A, p is an integer, and the convolution, with discrete steps of $1/N\Delta t$, will result in zero, except at the location $p/N\Delta t$. For the case of **Figure 2B**, p is an odd multiple of $\frac{1}{2}$, and the convolution with steps of $1/N\Delta t$ is nonzero for a wide range of frequencies, hence the leakage effect (**Figure 4**).The main characteristics of the window affecting the leakage effect are:

1. Sidelobe characteristics: the maximum sidelobe, and their attenuation as a function of frequency
2. Scallop loss: the attenuation of signal at frequencies not at the center of the main lobe
3. The correction factor needed in order to preserve the total power.

These are compared later for some popular windows.

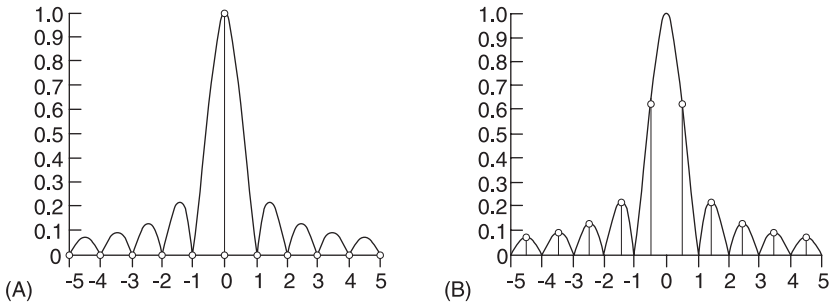


Figure 4 Leakage for the case of harmonic signals, rectangular window: (A) signal spanning an integer number of periods; (B) signal spanning an odd number of half periods.

The Hanning window

This is defined by:

$$w_{\mathrm{H}}(n) = \begin{cases} 0.5\left[1 - \cos\left(2\pi\dfrac{n}{N}\right)\right] & 0 \le n = N-1 \\ 0 \qquad \text{otherwise} \end{cases} \qquad [3]$$

This is probably the most popular window, with very good overall performance. **Figure 5** and **Table 1** enable a comparison between the Hanning and rectangular (and other) windows.The general shape obviously gradually attenuates both the signals end region. In the frequency domain, the maximum sidelobe is significantly reduced, the side lobe attenuation as a function of frequency has much higher slope and the scallop loss is also lower.

Figure 6 shows a signal composed of three harmonic components of frequencies. For this case, 10, 12.25, and 14.5 periods respectively are spanned by the analysis interval. Also shown is the spectrum using a rectangular as well as a Hanning window (the third window showing the flat top, is addressed in a later paragraph). Note the reduced scallop losses for the Hanning window compared with the rectangular one.The Hanning window is sometimes easier to implement directly in the frequency domain eqn [1b], as the convolution with W_H is one with a sequence of $[-\frac{1}{4}, \frac{1}{2}, -\frac{1}{4}]$ (which in some computer languages can be implemented via summations and binary shifts).

Table 1 Comparisons of some window properties

Window	*Highest side lobe level* (dB)	*Flow of sidelobe maxima* (dBoct)	*Scallop loss* (dB)
Rectangular	−13	06	3.92
Hanning	−32	−18	1.42
Hamming	−43		1.78
Flat top	−95		0.01

Additional windows for leakage control

Hamming window:

$$w_{\mathrm{HM}}(n) = \begin{cases} 0.54 + 0.46\cos\left(2\pi\dfrac{n}{N}\right) & 0 \le n \le N-1 \\ 0 \qquad \text{otherwise} \end{cases} \qquad [4a]$$

Kaiser window:

$$w_{\mathrm{HK}}(n) = \frac{I_0\left[2\beta\sqrt{(N-N^2)}\right]}{I_0(\beta)} \qquad [4b]$$

where I_0 is the modified Bessel function of the first

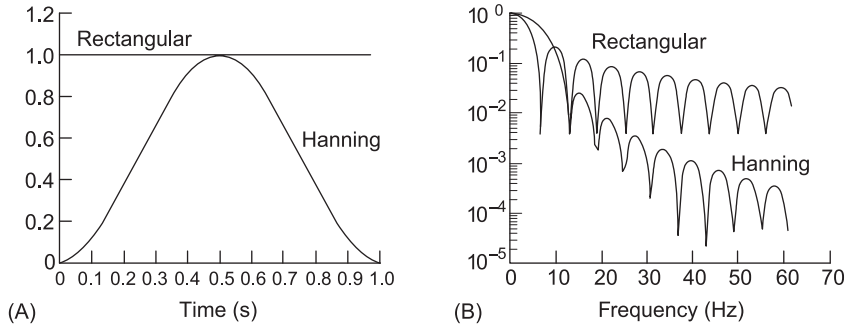


Figure 5 Rectangular and Hanning windows: (A) time domain windows; (B) magnitude in frequency domain.

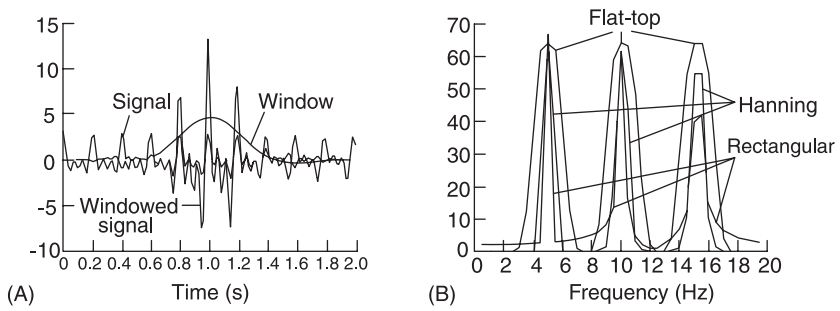


Figure 6 Signal with three components – scallop loss: (A) windowing in the time domain; (B) scallop loss for various windows.

kind, zero order. This window is optimal in the sense that it has a large main lobe together with a sharpest transition beyond it.

Correction Factor

The application of a window decreases the total power of the signal, and a correction scaling factor is thus needed. Unfortunately it is not possible to find an exact correction factor, as this depends on the type of signal, wideband/narrowband, or often random continuous vs harmonic. For a random continuous signal, the correction factor depends on the noise bandwidth of the window. For the Hanning window, the power spectral density (PSD) should thus be multiplied by a factor of 8/3. For a harmonic signal, the correction factor depends on the exact frequency. For a signal spanning an integral number of periods (i.e., no leakage), the correction of the magnitude of the FT is 2. For a harmonic signal, the correction factor can be in the range, 1.5–2, depending on the exact frequency.

Leakage Reduction Choice of Window

The Hanning window is usually a good choice. The main advantage of controlling the leakage is an increase in the dynamic range of the analysis, as leakage may swamp signal components of close frequencies and much smaller magnitudes. **Figure 7** is an example. For signals with closely spaced line spectra (like rotating machinery vibrations), the use of the

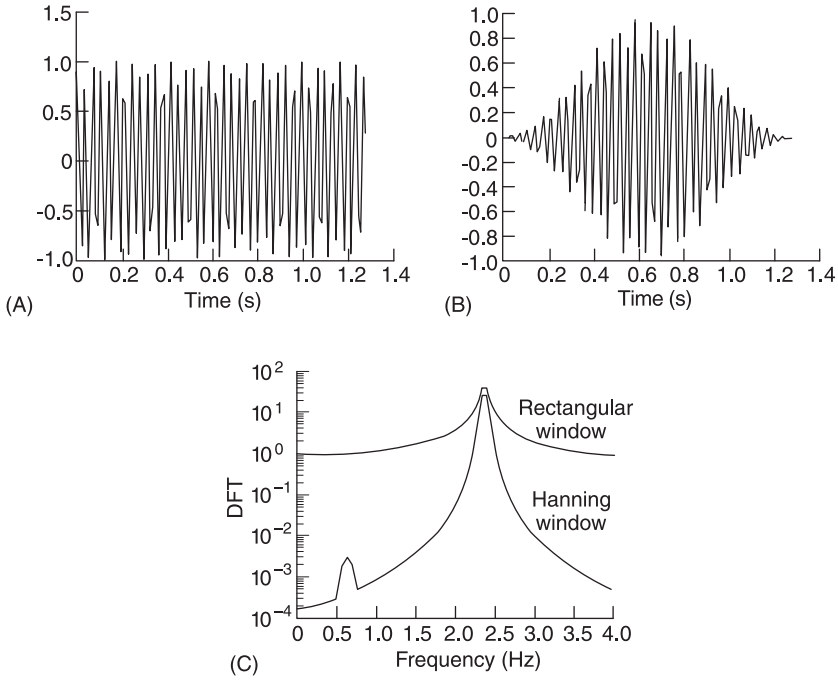


Figure 7 Effect of window on dynamic range: (A) composite signal, rectangular window; (B) composite signal, Hanning window; (C) magnitude of DFT, effect of windows.

Hanning window is almost always recommended. Due to the much smaller secondary lobe, the Hamming window may sometimes be more useful.The Hanning window (and most windows) are not useful however if the frequency spacing between components is less than the window's bandwidth. Unless a longer duration signal can be analyzed, a rectangular window would then perform better. **Table 1** summarizes the main characteristics of some popular windows.

Flat-top Window

Spectral analysis of periodic phenomena results in a discrete spectrum, with spectral 'lines' at discrete frequencies. Unless an integral number of periods are spanned by the analysis interval for all existing spectral lines, the leakage error discussed in the prior paragraph results in underestimated magnitudes. The exact underestimation will vary with the line frequency.

In vibration analysis, line spectra are typical of measurements on rotating machinery. The frequencies involved depend on the geometry and kinematics of the rotating elements, but are basically proportional to the machine's rotating speed. In practice there will always exist some fluctuations in this speed. The location of the line spectra within the main lobe of the analysis window will thus fluctuate, with corresponding varying magnitudes. A window with a 'flat' characteristic shape is then of advantage.

Some invariance of the analyzed spectrum to these speed fluctuations can be achieved. **Table 1** summarizes the main caracteristics of some popular windows. A typical flat-top window is:

$$w_{\mathrm{FT}}(n) = a_0 + 2\left[2a_1\cos\left(2\pi\frac{n}{N}\right) + a_2\cos\left(4\pi\frac{n}{N}\right) + a_3\cos\left(6\pi\frac{n}{N}\right)\right] \quad [5]$$

where:

$$a_0 = 0.9945, \quad a_1 = 0.95573,$$
$$a_2 = 0.53929, \quad a_3 = 0.09158$$

and its characteristics are shown in **Figure 8**. The negligible scallop loss is also evident in **Figure 6**. Due to the large width of the main lobe, the window may not be suitable for signals with very close spectral lines.

Another use of the flat-top window is for calibration purposes (obviously in the frequency domain) using harmonic signals.

Control of Variance in Spectral Analysis Random Data

(see **Spectral analysis**, classical methods)

Spectral Estimation via Autocorrelation Functions

While computations of the PSD are now mainly undertaken directly in the frequency domain via the FFT, the classic method of computations via the autocorrelation function appear in the literature. The PSD $S(\omega)$ is computed as the Fourier transform of the autocorrelation function $R(t)$ as (see **Correlation functions**):

$$S(\omega) = \int_{-\infty}^{\infty} R(\tau)\exp(-\mathrm{j}\omega\tau)\,\mathrm{d}t \quad [6a]$$

$R(\tau)$ is statistically consistent, i.e., converges to the true value by using an increasing number of signal samples N. The variance of $S(\omega)$ as computed via eqn. [6a] can be controlled by applying a window to $R(\tau)$, resulting in the estimate:

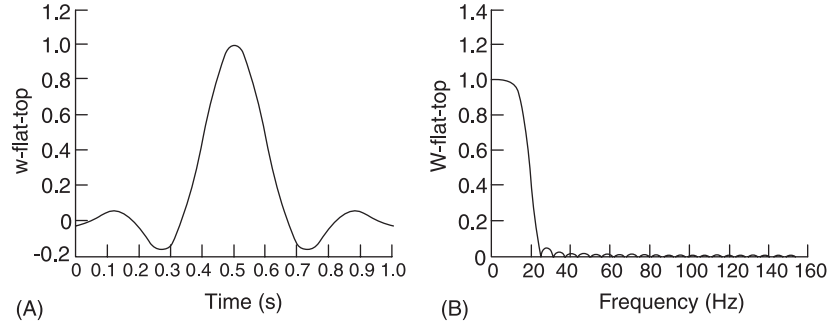


Figure 8 Flat-top window: (A) time domain; (B) magnitude, frequency domain.

$$S'(\omega) = \int_{-\infty}^{\infty} w(\tau)R(\tau)\exp(-j\omega\tau)\,d\tau \qquad [6b]$$

Possible windows are those already mentioned, i.e., the Hanning window. As the windowing decreases resolution due to their increased main lobe width, it is sometimes claimed that the actual choice of a specific window is not very critical.

Overlap Processing and Windows

In the spectral analysis of random signals, the high variance of the spectral estimates is often controlled by averaging spectral estimates from sections of the signal. For constant signal duration, the number of segments used for this averaging operation can be increased by overlapping these segments. The variance is reduced when such sections are uncorrelated. To avoid the correlation between the signal points of the end of each section and the beginning of the next one due to the overlap, a Hanning window is usually applied to each section before the overlapping operation (**Figure 9**). This gives less weight to the correlated signal points and results in a higher variance reduction. Comparing for example 50 percent overlap in conjunction with a rectangular and Hanning window, the variance of the estimator for the first case would be approximately 40 percent higher. The method using a rectangular window is sometimes called the Bartlett method, that with a Hanning window, the Welch method. It is also possible to cast the formulation of the overlapped based PSD estimation as one of windowing like eqn [6b].

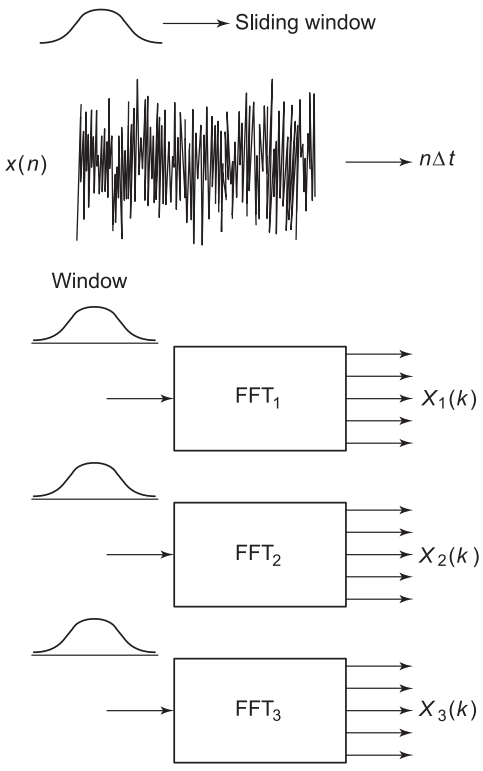


Figure 9 Overlap processing.

Overlapped analysis can be useful for a random continuous signal. There is no advantage in applying it to cases where close harmonic signals (and their spectral lines) are sought, as the increased bandwidth of the window could be detrimental. It is also not recommended for signals having sharp spiky transient components, as the overlapping in conjunction with a Hanning window could suppress some of these transients.

Windowing Used in Impulse Testing/ Transient Analysis

Windowing transients can improve the signal to noise ratio. The basic idea is to weight the signal according to the certainty associated with it. Assuming a stationary additive random noise, less weight is given to the signal points of lesser magnitude. The specific weighting is a function of the signal shape.

Force Window

This type of window is applied to transients spanning only a part of the analysis duration. This can occur in multichannel data acquisition tasks, where the duration of the acquisition is equal in all channels, and hence dictated by the channel with the longest transient. One example is that of impulse testing where a short impact excites a structure, with a decaying response of longer duration. The window applied to the force is hence often called a force window. It is a rectangular window, of duration spanning at least the force duration. Its approximate form is hence:

$$w_F(n) = \begin{cases} 1 & 0 \le n < N_T - 1 \\ 0 & \text{otherwise} \end{cases} \qquad [7]$$

where N is the number of samples acquired and N_T is slightly larger than the number of samples spanning the signal. A gradual transition towards zero around N_T is usually preferred, and eqn [7] is thus only approximate.

The noise variance is obviously reduced by the factor N_T/N, and the signal/noise ratio (RMS/RMS) is improved by $(N/N_T)^{1/2}$ (**Figure 10**).

Exponential Window

Still assuming stationary continuous noise, then an exponentially decreasing weight is indicated for

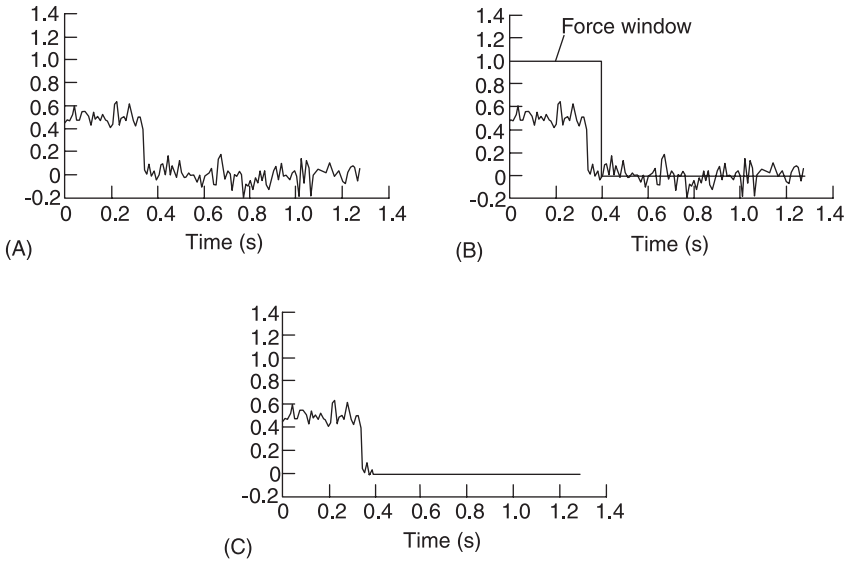


Figure 10 Force window: (A) noisy transient signal; (B) location of window; (C) windowed transient.

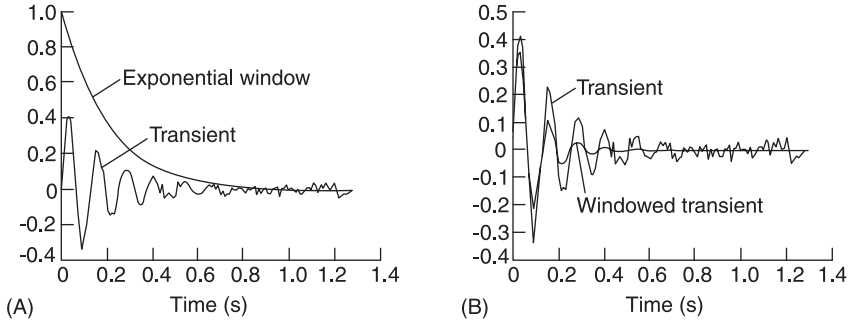


Figure 11 Exponential window: (A) noisy oscillating decaying transient and window; (B) transient original and windowed.

exponentially decaying oscillations. Thus the window is of the form (**Figure 11**):

$$w_{\exp}(n) = \exp(-an) \qquad 0 \le n < N \qquad [8]$$

The parameter a is chosen so as to have a decay to zero for $n = N$. The noise variance is then approximately reduced by a factor of 3, the signal/noise improved by 1.7. The effect of the windowing is to have a faster effective decay than the one due to the physical situation. Any damping factors extracted from the decaying oscillations must be corrected, as its value has been increased artificially. Assuming that the decaying oscillations are a combination of components of the form:

$$x(t) = A_{\exp}(-\zeta\omega_n t)\sin\left[\omega_n\left(1-\zeta^2\right)^{1/2}t\right] \qquad [9a]$$

where ζ is the physical damping ratio and ω_n the corresponding natural frequency. Then the computational equivalent damping is:

$$\zeta_{\text{eff}} = \zeta + \frac{a}{\omega_n} \qquad [9b]$$

The a/ω_n factor must be used for correction. The exponential window is also used for situations where the signal has not decayed to zero in the analyzing window (a common situation when very light damping exists). The truncation at the end, with the resulting discontinuity and leakage, is avoided by using this window.

Design of Digital FIR Filters

There exists one easily implemented method of designing digital finite impulse response (FIR) filters. The filters are based on a moving average (MA) operation:

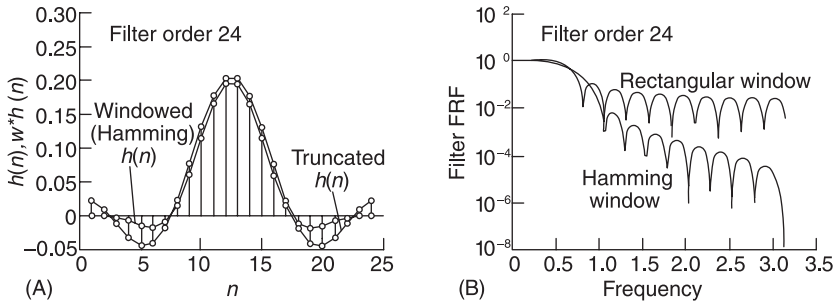


Figure 12 Design of FIR filters: (A) desired impulse response, truncated and windowed; (B) FRF of filter, rectangular (truncated) and windowed.

$$y(n) = \sum_{i=0}^{m} b_i x(n-i) \qquad [10]$$

where the coefficients b_i are actually the impulse response of the digital filter. The desired impulse response is basically computed as the inverse Fourier transform of a desired transfer function of the filter.

The design attempts to approximate the performance of ideal filters. The theoretical impulse response of ideal filters is usually of infinite duration. A practical implementation, necessitating a limited impulse response, should not be based on a simply truncated impulse response. Such a discontinuity in the impulse response, a case causing the Gibbs phenomenon, would result in unfavorable filtering characteristics, far from approximating those of the ideal filters. The solution is to apply a suitable window to the ideal impulse response:

$$h'(n) = w(n)h(n) \qquad [11]$$

Some of the windows used for this filter design are the general ones like the Hanning window. The worst one is the rectangular window, i.e., one resulting in the unmodified impulse response. An example of the improvement of the filter's performance is shown in **Figure 12**. Depending on specific desired filter characteristics, others like the Kaiser, Chebyshev, and Blackman windows can be used. The literature dealing with digital filter describes these in detail (see **Digital filters**).

Nomenclature

I	modified Bessel function
M	number of points per period
N	number of samples
$R(\tau)$	autocorrelation function
$w(t)$	window
w_{F}	force window
w_{HK}	Kaiser window
w_{HM}	Hamming window
$x(t)$	time signal
Δt	sampling interval

See also: **Digital filters**; **Correlation functions**; **Spectral analysis, classical methods**; **Transform methods**

Further Reading

Polock DSG (1999) *A Handbook of Time-Series Analysis, Signal Processing and Dynamics*. Academic Press.

Rabiner LR, Gold B (1975) *Theory and Applications of Digital Signal Processing*. Englewood Cliffs, NJ: Prentice Hall.

Z

Z TRANSFORMS

See **TRANSFORM METHODS**

GLOSSARY

absorber, vibration:
- **damped vibration absorber:** an added device which introduces damping to a structure at a point by providing an inertial sprung mass against which an added damper can react, thereby introducing damping to a specifically targeted mode of vibration
- **undamped vibration absorber:** an added device which provokes an antiresonance at the point of attachment at a preselected frequency of forced vibration

accelerance: one of the family of different frequency response functions: the harmonic acceleration response in one degree-of-freedom to a single harmonic excitation force applied in the same or another degree-of-freedom. Also known as **inertance** (although this name is not approved by ISO). See also **mobility** and **receptance**

acceleration: see **displacement**

aliasing: the phenomenon in digital signal processing, due to inadequate sampling frequency, whereby a signal with a frequency f_N which is higher than half the digitization sampling frequency, f_S, appears in the resulting spectrum as if it were a signal with a frequency (f_{S-N}), which is lower than its actual value

analysis, modal: a procedure which extracts the normal mode properties of a system, either by analyzing measured response functions (experimental modal analysis — EMA) or by performing an eigensolution on the system's mass and stiffness matrices (analytical modal analysis)

antialiasing filter: signal conditioning or processing device which provides a low-pass filtering effect to reduce in a signal to be analyzed those frequency components which are higher than one-half the sampling frequency (the Nyquist frequency)

antiresonance: a condition in forced vibration whereby a specific point or DOF has zero amplitude at a specific frequency of vibration

Argand diagram: see **diagram**

autocorrelation function: (see **power spectral density**) the signal average of the product of the signal with a delayed version of itself. The inverse Fourier transform of the power spectral density function

balancing: the procedure of adjusting the mass distribution of a rotor so that vibrations or forces reactions during rotation are minimized

bandwidth: strictly, the frequency span encompassed by a resonance curve (Bode diagram of the modulus of a frequency response function) at the level which is 0.707 times the peak value. Alternatively, the frequency range of excitation and measurement during a vibration test

Bode diagram/plot: see **diagram**

burst random: see **signal**

burst sine: see **signal**

coherence: a measure of the degree of correlation between two signals presented in the frequency domain (i.e., a form of spectrum). Has a real value and is normalized between 0 and 1.

coordinate (or co-ordinate): strictly, the location of a point on a structure in space. Often used to mean a degree-of-freedom
- **principal** (or **modal**) **coordinate:** a time-varying quantity which describes the extent (amount) of motion in one of the systems modes of vibration. Sometimes referred to as **modal coordinate**

correlation: the systematic quantitative comparison of two sets of like data, such as time histories, or modal properties, resulting in a numerical measure of the degree of similarity or dissimilarity. See **coherence**

critical speed: speed of a rotating rotor that corresponds to a resonance

damping: any of several physical mechanisms whereby mechanical energy (i.e., kinetic or strain) is converted into heat and thereby removed from a vibrating system. In the absence of a steady input of energy, such as is achieved through continuous excitation of the system, the vibration will decay to rest as a direct consequence of the damping mechanisms
- **hysteretic** (also **structural**): a type of damping for which the mathematical model used to describe it is based on observation of the characteristics of damping due to internal hysteresis of materials
- **proportional:** refers to the distribution (rather than the type) of damping in a structure whereby the damping elements are assumed to be distributed in a way which reflects the distribution of stiffness, and/or mass, of the structure. Has the convenient property that the mode shapes (q.v.) of a proportionally damped structure are identical to the mode shapes of the undamped version of the same

structure, and are therefore real in a mathematical sense

structural: see **damping hysteretic**

viscous: a type of damping in which the damper force is proportional to velocity and whose mathematical description is easily accommodated in the models used to describe a structure's dynamics, especially for time domain analysis

critical: a level of viscous damping above which free oscillatory motion does not take place: it is common practice to define practical levels of damping (usually much lower than critical) as a fraction of critical damping (damping ratio)

dB: the dB (or decibel) is a unit for describing ratio of quantities, based on a logarithmic scale in which x described in dB = 20 log x. Thus, 0 dB represents a value of unity (1.0) while 20 dB represents a value of 10.0. Also used to describe ratio of power or energy quantities, in which case a power level P is described as 10 log P. Absolute values need to be related to a reference unit

degree-of-freedom: used to define the location and direction of the motion of a specific point of a system or structure. Sometimes called a **coordinate**. Each point on a structure has six degrees of freedom (three translation and three rotation directions)

diagram:

Argand: a plot of a complex function, such as an FRF, in which the x–y axes are the real and imaginary parts of the function, respectively. The corresponding data, plotted as modulus and phase on polar axes, result in an identical plot. Also known as a **Nyquist diagram**

Bode: a form of presentation of a complex function, such as an FRF, in which there are two graphs: the first presenting the log-modulus of the function against log-frequency, and a second plot of the phase (of the complex function) against log-frequency. Used to convey information covering a wide frequency range

Nyquist: see **diagram, Argand**

discrete Fourier transform (DFT): see **transform**

displacement: change of position of element. Often measured in conjunction with rotating rotors and active control tasks. The measurement and use of velocity and acceleration, the first and second derivative of displacement prevail in vibration task. Off-the-shelf acceleration-measuring systems comprise the majority used by practitioners (see **jerk**)

dynamic range: response range of a transducer or data acquisition system between maximum-level noise level: often expressed as a ratio in dB

eigenvalue: mathematical term for a root of the characteristic equation of a dynamic system: generally equal to the square of one of the system's natural frequencies

eigenvector (see **mode shape**): mathematical term for one of the vectors of the characteristic equation of a dynamic system: describes one of the system's normal mode shapes. The matrix product of the eigenvector (transposed) times the mass matrix times the eigenvector is equal to the **modal mass** (q.v.); when the modal mass is unity, the eigenvector is said to be mass-normalized

fast Fourier transform (FFT): see **transform**

forced vibration: see **vibration**

Fourier: see **transform**

free vibration: see **vibration**

frequency:

excitation: the frequency at which a system is made to vibrate under the influence of an external harmonic force

natural (undamped, damped): a frequency at which a structure will vibrate when given an initial disturbance from its equilibrium position and then left to move under free vibration conditions. If the structure is damped, the mathematical description of this frequency will be complex, having an imaginary part which describes the oscillation rate and a real part which defines the decay rate

resonance (sometimes, inaccurately, **resonant**): a frequency at which an FRF or other response curve reaches a local maximum value in the vicinity of a natural frequency. This resonance frequency will often be very close to, but not necessarily equal to, the corresponding natural frequency

sampling: the frequency at which a signal is digitized (sampled, discretized) for the purpose of digital spectral analysis

Nyquist: half the sampling frequency used to discretize a signal prior to digital spectral analysis

frequency response function (FRF): see **function**

forced vibration: see **vibration**

function:

frequency response (FRF): the ratio between the steady-state harmonic response in one degree of freedom of a structure (j, say) to the similarly steady-state harmonic force

applied at another degree of freedom of the structure (such as k)

point: a particular FRF in which the excitation and response degrees of freedom are the same (i.e., $j = k$).

transfer: an FRF in which the excitation and response degrees of freedom are not the same (i.e., $j \neq k$).

impulse response function (IRF): The response time history of a system, measured in one particular degree of freedom to a unit impulse excitation applied at another degree of freedom

harmonic: (*n.*) an integer multiple of a fundamental sinusoidal signal to which it is related
(*adj.*) equivalent to 'sinusoidal' in describing signal type

Hilbert transform: see **transform**

impedance, mechanical: one of the family of inverse frequency response functions: the ratio between the single harmonic excitation force applied in one degree of freedom to the harmonic velocity response in the same or another degree of freedom.

impulse response function (IRF): see **function**

inertance: see **accelerance**

isolation, vibration: a feature of forced vibration in which vibration levels in certain regions of a structure are constrained to be much lower than at other regions by suitable distribution of mass and stiffness

jerk: derivative of acceleration, used in conjunction with responses to shock excitations

leakage: a phenomenon which arises during digital spectral analysis of continuous signals as a result of the finite duration of the sampled signal and its relationship with the frequencies present in the original signal. Often, leakage occurs because the signal being analyzed is not periodic with respect to the sample length (duration, period) used for the analysis. The consequence of leakage is that a computed spectrum may indicate the presence of signal components which are not in the original signal and it may not accurately indicate those which are. Windows are used to reduce the effects of leakage

linearity: a characteristic often assumed to be present in structures subjected to vibration analysis or testing techniques: the primary assumption is essentially that the response of the structure to two forces applied simultaneously will be identical to that derived by adding the responses of the structure to each force applied individually. Other definitions can also be applied

line spectrum: see **spectrum**

MAC or **modal assurance criterion:** a simple parameter used to measure the degree of correlation between two vectors of the same length: usually eigenvectors, or mode shapes. A MAC value of 100% indicates that the two vectors being compared are parallel, or are perfectly correlated. MAC values of greater than 80% generally indicate 'similar' mode shapes

mass, modal: a quantity which relates to a given mode shape and which is computed from that mode shape vector and the mass matrix of the system model. The modal mass is automatically unity for mass-normalized mode shapes

mobility: one of the family of frequency response functions: the harmonic velocity response in one degree of freedom to a single harmonic excitation force applied in the same or another degree of freedom

modal coordinate: see **coordinate**

modal mass: see **mass, modal**

modal stiffness: see **stiffness, modal**

mode, mode shape (see **eigenvector**): strictly, a pattern of vibration exhibited by a structure or system. Generally, described as a vector of values, defining the relative displacement amplitudes and phases of each degree of freedom, which describes the motion of the system

complex: a mode of vibration in which the relative displacements exhibit phase differences between one degree of freedom and the next which are not always 0 or 180° (situation which applies in a real mode). Complex modes do not exhibit modal lines

mass-normalized (see **eigenvector**)

normal, damped: the vector of relative amplitudes for the vibration of a damped system in one of its natural modes of free vibration. These modes are the modes which the structure assumes in the absence of any external excitation. In this case, the structure is assumed to possess arbitrary damping and, as a result, the normal modes are complex

normal, undamped: the vector of relative amplitudes for the vibration of the undamped system in one of its natural modes of free vibration. These modes are the modes which the structure assumes in the absence of any external excitation. In this case, the structure is assumed to possess no damping and, as a result, the normal modes are real

real: a mode of vibration in which the relative displacements exhibit phase differences between one degree of freedom and the next

which are always 0 or 180°. Real modes exhibit modal lines

mode indicator function: a function which is used to indicate the existence of global system modes (those which are observed throughout the structure) as opposed to local modes (which are only visible in a small region of the structure)

model (mathematical): a mathematical description of a system or structure in a form which can be described by equations of motion which can then be solved analytically or numerically to describe that system's dynamic behavior

- **continuous:** a mathematical model which describes the system or structure as a continuous medium, using partial differential equations with, typically, transcendental expressions for the solutions
- **discrete, lumped parameter:** an alternative type of mathematical model (to the continuous type) in which the mass, stiffness, and damping properties of the structure are discretized so that the behavior can be described by a finite series of ordinary differential equations leading to finite discrete solutions
- **modal:** a model which is defined in terms of eigenvalues and eigenvectors, or natural frequencies and mode shapes. Usually presented as eigenvalue and eigenvector matrices
- **response:** a model which is defined in terms of some characteristic response functions, such as FRFs, or IRFs, or equivalent
- **spatial:** a model which is defined in terms of the system's distribution of mass, stiffness, and damping in space. Usually described as mass, stiffness, and damping matrices

multiple-degrees-of-freedom (MDOF) system (see **single-degree-of-freedom (SDOF) system**): a system for which two or more coordinates or degrees of freedom are needed to define completely the position of the system at any instant

natural frequency: see **frequency**

node: 1. a DOF which has zero amplitude of vibration; used when describing a mode shape or an operating deflection shape

2. a specific grid point in a discrete (lumped parameter) model of a structure

nonlinearity: a form of structural behavior which does not conform to the definition of linearity (see **linearity**)

normal mode: see **mode**

Nyquist diagram: see **diagram**

operating deflection shape: see **mode shape**

pole: mathematical term which is equivalent to eigenvalue or to (square of) natural frequency. For systems describable by a ratio of rational polynomials in a transform domain, the value of the transform variable for which the denominator polynomial equals zero

power spectral density (PSD): (see **autocorrelation function**) the distribution of the squared signal (acceleration, velocity, etc.) with frequency (in squared units per Hz, i.e., g^2/Hz). The Fourier transform of the autocorrelation function

principal coordinate: see **coordinate**

receptance: one of the family of frequency response functions: the harmonic displacement response in one degree of freedom to a single harmonic excitation force applied in the same or another degree of freedom. See also **mobility** and **accelerance**

resonance (see **frequency**): a phenomenon associated with forced vibration which relates to a narrow range of frequencies in which the response amplitude of a system attains levels which are much higher than elsewhere

sampling (see **frequency**)

series, Fourier: a method of representing a periodic signal as the sum of separate sinusoids whose frequencies are integer multiples of the fundamental period of the original signal. See also **transform, Fourier**

signal (time history): a time-varying quantity which describes the excitation or response of a vibrating system. In vibration testing, a quantity which is used either to drive the excitation of a system into vibration or to represent the measurement of one of the vibration forces or responses which are used to describe the system's movement. Types of signal commonly encountered include:

- **burst:**
  - **random:** a signal which consists of two sections, the first being a finite duration of a stationary random signal followed by a second section which is zero
  - **sine:** a signal which consists of two sections, the first being a finite duration of a steady sinusoid followed by a second section which is zero
- **chirp:** a signal comprising a single rapidly swept sine wave between a minimum and maximum frequency
- **harmonic:** a sinusoidal signal at a single frequency
- **periodic:** A signal which repeats itself indefinitely after a period, T. In signal analysis or processing, the period of the repeating signal is not necessarily the same as the period over which the signal is measured or analyzed

and in such a situation, analysis of the signal may not yield a true indication of its form (see also **leakage**)

periodic random: a signal which consists of a succession of records (sometimes called 'samples'), each of finite length, T, which is usually selected to suit the sampling period of a means of analyzing the signal. Each of the first few records is identical to each other and thus represent a periodic signal, even though an individual period appears to be very complex, almost random. Then the next few records consist of several repetitions of another 'complex' record. This pattern is repeated for as long as the signal is required

pseudorandom: a periodic signal for which the basis record is very complex, and appears to be random. However, this record is repeated indefinitely and so forms a periodic signal

random: a nondeterministic signal. No analytical expression predicting future values can exist. It is defined only in terms of statistical functions and parameters, for example an amplitude probability function

sine, sinusoid, discrete sine: a signal which consists of a pure, single, sinusoidal or harmonic component; also **stepped sine**

sine sweep: a signal which comprises a sinusoid whose frequency is varied slowly so that a range of frequencies is covered throughout the duration of the signal

stepped sine: a signal which comprise a series of discrete sinusoids, one after the other

transient: a signal which lasts a finite length of time, being zero before and after that period, and which is fully defined within the record length

white noise: a signal with a constant **power spectral density**, independent of frequency. In practice a signal can have white noise characteristics only in a finite frequency range

single-degree-of-freedom (SDOF) system (see also: **multiple-degrees-of-freedom (MDOF) system**): a system for which only one coordinate is needed to define completely the position of the system at any instant

spectrum: description of the essential elements of a signal (or time history) in terms of constituent sinusoidal components

continuous: nonzero in a continuous range of frequencies. Typical for **random signals**

discrete: a spectrum computed only at discrete frequencies. These frequencies are usually equi-spaced, a result of using the **fast Fourier transform** algorithm. Sometimes synonymous with **line spectrum**

line: a discrete spectrum, with nonzero values only at discrete frequencies. Typical of vibrations generated by rotating machinery

stiffness, modal: a quantity which relates to a given mode shape and which is computed from that mode shape vector and the stiffness matrix of the system model. The modal stiffness is equal to the eigenvalue for a mass-normalized mode shape

time history (see **signal**): description of a time-varying quantity, such as displacement or force, as a direct function of time

transducer: a device which transforms one form of energy into another, practically used synonymously with the term sensor

transform

discrete (DFT): a discrete transform which converts a a discrete (usually time domain) sequence into another discrete (usually frequency domain) sequence. With correct sampling, the DFT approximates samples of the (continuous) Fourier transform In the DFT, the continuous time-varying signal is approximated by a discrete number of sampled values taken from the original data. The resulting spectrum has exactly the same number of components as the number of sampled data points, although not all of these may be displayed

fast Fourier transform (FFT): a computer algorithm for the efficient computation of the DFT of a sampled signal. The algorithm takes advantage of the symmetry of the transform and is very efficient when applied to a data set containing 2^N values

Fourier: a continuous transform between two domains, usually time and frequency. One of the most basic mathematical tools for representing the relevant features of a time history signal in terms of its constituent frequency components, and of reconstructing a time record from a knowledge of the frequency (or spectral) components. For periodic signals, the transform exists only at discrete frequencies (see **line spectrum**), and is more conveniently represented via the **Fourier** series

Hilbert: a type of transform for converting a function from one form to another which, unlike the Fourier transform, derives a transformed function in the same domain as the original (i.e., a time signal transforms to another time signal, a frequency function to another frequency function)

validation: the process of demonstrating the adequacy of the performance of a given prediction capability, usually that of a finite element model constructed to predict the vibration properties of the structure

velocity (see **displacement**)

verification: the process(es) used to demonstrate that an algorithm or other procedure has been correctly implemented in a computer program or test sequence

vibration

forced: the vibration structure which is the direct result of an applied excitation force, or forces. Although there will be an initial transient response which is governed by the free vibration characteristics of the system, this will die away, leaving only the steady response due entirely to the externally applied excitation. This motion can be described completely in terms of the free vibration normal modes of the system

free: the type of vibration which ensues when a system or structure is set into motion by an initial disturbance and then left to vibrate under the influence only of the internal forces due to its own stiffness, inertia, and damping. This motion can be described completely in terms of the free vibration normal modes of the system

white noise: see **signal**

window: an approach used in signal processing to minimize the approximations introduced when using a discrete Fourier transformation on a continuous signal. Usually applied in the time domain, as a multiplying function applied to the time signal. Various shapes of window functions have been developed to produce optimum frequency information for particular types of signal

APPENDICES

1. STANDARD NOMENCLATURE

2. ABBREVIATIONS

3. UNITS AND CONVERSION FACTORS
   Common units used in engineering and vibration control
   Conversion factors

4. PHYSICAL PROPERTIES OF SOME COMMON SUBSTANCES
   Solids
   Liquids
   Gases

5. VIBRATION MODES OF CLASSICAL ELEMENTS

6. STANDARDS AND GUIDELINES

7. FREQUENCY RESPONSE FUNCTIONS

1. STANDARD NOMENCLATURE

Matrices and vectors

$\mathbf{A}$	Matrix
$\mathbf{a}$	vector
a_{jk}	matrix element (row j; column k)
$\mathbf{A}^{\mathrm{T}}$	transpose
$\mathbf{A}^{\mathrm{H}}$	Hermetian transpose
$\mathbf{A}^{+}$	generalized inverse

Physical parameters

m	mass element
k	stiffness element
c	viscous damping element
$\mathbf{M}$	mass matrix
$\mathbf{K}$	stiffness matrix
$\mathbf{C}$	viscous damping matrix
ζ	damping ratio
η	structural damping loss factor
$x(t)$ or x	displacement
$v(t)$ or v or $\dot{x}$	velocity
$a(t)$ or a or $\dot{v}$	acceleration
$f(t)$ or f	force
t	time
Δt	sampling interval
s	Laplace operator
ω	frequency (rad s^{-1})
ω_{n}	undamped natural frequency
ω_{d}	damped natural frequency
ω_{R}	resonant frequency
Ω	rotation speed
$H(\omega)$	frequency response function
$h(t)$	impulse response function
E	energy; modulus
P	power
p, $P(..)$	probability density, probability distribution
$R(\tau)$	correlation function
$R_{xx}(\tau), R_{xy}(\tau)$	auto- and cross-correlation
$S(\omega)$	spectral density
$S_{xx}(\omega), S_{xy}(\omega)$	auto- and cross-spectral density
i, j	$\sqrt{-1}$
$\otimes$	convolution
$k_{..} = f(K_{..})$	dots denote indices, i.e. $k_{12} = f(K_{12})$, etc.
x^*	complex conjugate (of x)

Transforms

$\mathrm{F}[\ ]$, $\mathrm{F}^{-1}[\ ]$	Fourier transform, inverse Fourier transform
$\mathrm{L}[\ ]$, $\mathrm{L}^{-1}[\ ]$	Laplace transform, inverse Laplace transform
$\mathrm{Z}[\ ]$, $\mathrm{Z}^{-1}[\ ]$	Z transform, inverse Z transform
$\mathrm{H}[\ ]$, $\mathrm{H}^{-1}[\ ]$	Hilbert transform, inverse Hilbert transform

2. ABBREVIATIONS

ADC	analog-to-digital converter
ARMA	autoregressive moving average
CAD	computer-aided design
CFD	computational fluid dynamics
CG	center of gravity
CWT	continuous wavelet transform
DAC	digital-to-analog converter
DOF	degree of freedom
DFT	discrete Fourier transform
DSP	digital signal processing
DWT	discrete wavelet transform
EOM	equation of motion
EU	engineering units; European Union
FEA	finite element analysis
FEM	finite element method
FFT	fast Fourier transform
FIR	finite impulse response
FPE	final prediction error
FRF	frequency response function
IC	integrated circuit
IIR	infinite impulse response
IRF	impulse response function
ISO	International Standards Organization
LDV	laser Doppler vibrometer
LQ	linear quadratic
LSB	least significant bit
LVDT	linear voltage differential transformer
MAC	modal assurance criteria (also FMAC, AUTOMAC, FDAC, FRAC ...)
MDOF	multi-degree-of-freedom
MEMS	microelectromechanical systems
MIFs	mode indicator functions
MIMO	multi-input multi-output
MISO	multi-input single-output
NDT	nondestructive testing
NVH	noise, vibration, harshness
ODS	operating deflection shape
PCB	printed circuit board
PDF	probability density function
PSD	power spectral density
QA	quality assurance
RMS	root mean square
SDOF	single-degree-of-freedom
SEA	statistical energy analysis
S/H	sample and hold
SIMO	single-input multi-output
SISO	single-input single-output
SLDV	scanning laser Doppler vibrometer
SNR	signal-to-noise ratio
STFT	short-time (term) Fourier transform
SVD	singular value decomposition
TDA	time domain (synchronous) averaging
WVD	Wigner-Ville distribution
YW	Yule Walker

3. UNITS AND CONVERSION FACTORS

Common units used in engineering noise and vibration control

Primary units

length metre (m)
mass kilogramme (kg)
quantity of a substance mol
temperature kelvin (K)
time second (s)

Secondary units

energy joule ($J \equiv Nm \equiv Ws$)
force newton ($N \equiv kg\,m\,s^{-2}$)
frequency hertz (s^{-1})
molecular weight mol^{-1}
power watt ($W \equiv J\,s^{-1} \equiv Nm\,s^{-1}$)
pressure Pascal ($Pa \equiv N\,m^{-1}$)
radian frequency rad s^{-1}

Derived units

acceleration $m\,s^{-2}$
acoustic (radiation) impedance[a] (force per unit area/volume velocity per unit area) $Ns\,m^{-1}$
acoustic intensity $W\,m^{-2}$
autospectral density (power spectral density) units^2 Hz^{-1}
energy density $J\,m^{-3}$
energy spectral density units^2 $s\,Hz^{-1}$
entropy $J\,kg^{-1}\,K^{-1}$
gas constant $J\,kg^{-1}\,K^{-1}$
mechanical impedance (force/velocity) $N\,s\,m^{-1}$
mechanical stiffness $N\,m^{-1}$
mobility $m\,N^{-1}\,s^{-1}$
modulus of elasticity, adiabatic bulk modulus $N\,m^{-2}$
quefrency s
specific acoustic impedance (pressure/velocity) $N\,s\,m^{-3}$
surface density $kg\,m^{-2}$
universal gas constant $J\,mol^{-1}\,K^{-1}$
velocity $m\,s^{-1}$
viscosity $N\,s\,m^{-2}$
viscous damping $N\,s\,m^{-1}$
volume density $kg\,m^{-3}$
volume velocity $m^3\,s^{-1}$

Conversion factors

Length

1 ft = 0.3048 m
1 in = 25.4 mm
1 mile = 1.609344 km
1 mph = 1.6093 km h^{-1} = 0.44704 m s^{-1}
1 nautical mile = 1.852 km
1 knot = 1 nm h^{-1} = 0.5144 m s^{-1}

Area

1 ft^2 = 0.09290304 m^2
1 in^2 = 0.00064516 m^2
1 acre = 4046.86 m^2
1 hectare = 10^4 m^2

Volume

1 ft^3 = 28.3168 litre
1 litre = 10^{-3} m^3
1 UK gal = 4.54609 litre
1 UK pint = 0.568261 litre
1 US gal = 3.7853 litre

Mass

1 lb = 0.45359237 kg
1 oz = 28.3495 g
1 ton = 1.01605 tonne
1 lb ft^{-3} = 16.0185 kg m^{-3}

[a] Acoustic impedance is sometimes defined as pressure/volume velocity.

Force (N, kg m s^{-2})

1 lbf = 4.44822 N
1 kgf = 1 kp = 9.80665 N
1 bar = 14.50 psi = 10^6 dyne cm^{-1}
= 10^5 Pa = 10^{-5} N m^{-2}

1 psi = 6.89476 kPa
1 mm H_2O = 9.80665 Pa
1 mm Hg = 133.322 Pa
1 atm = 101.325 kPa

Energy (J, Nm, Ws)

1 ft-lbf = 1.355818 J
1 Btu = 1055.06 J

1 kWh = 3.6 MJ
1 kcal = 4.1868 kJ

Power (W, J s^{-1}, N m s^{-1})

1 ft-lbs s^{-1} = 1.355818 W
1 hp = 745.7 W

1 kcal h^{-1} = 1.163 W

Temperature

a °C = *b* K − 273.15
a °C = (*b* F − 32)/1.8

b °F = (1.8 × *a* °C) + 32

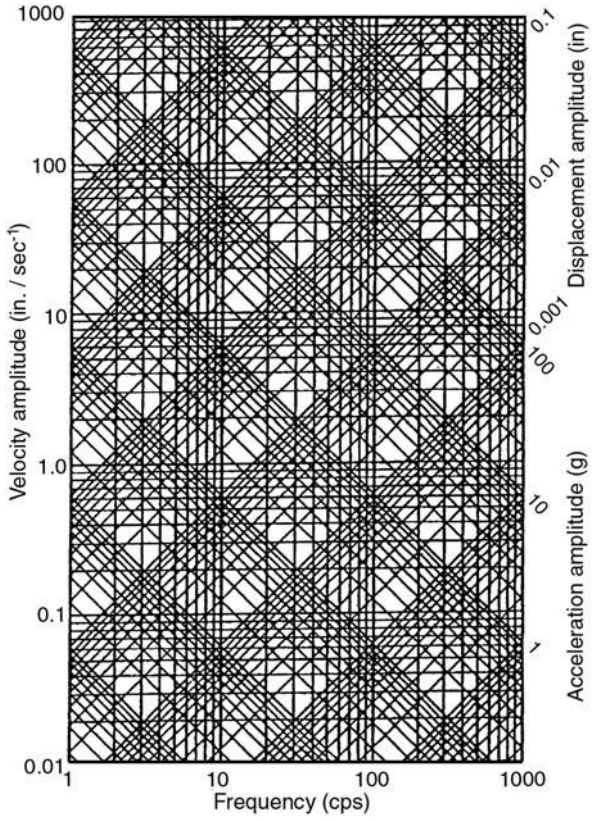
Units and conversion factors (vibration-oriented)

Conversion factors for rotational velocity and acceleration

Multiply value in or by → → / *to obtain value in* ↓	*rad s^{-1}* *rad s^{-2}*	*degree s^{-1}* *degree s^{-2}*	*rev s^{-1}* *rev s^{-2}*	*rev min^{-1}* *rev min s^{-1}*
rad s^{-1} rad s^{-2}	1	0.01745	6.283	0.1047
degree s^{-1} degree s^{-2}	57.30	1	360	6.00
rev s^{-1} rev s^{-2}	0.1592	0.00278	1	0.0167
rev min^{-1} rev min s^{-1}	9.549	0.1667	60	1

Conversion factors for simple harmonic motion

Multiply numerical value in terms of → *by* / *to obtain value in terms of* ↓	*Amplitude*	*Average value*	*Root-mean-square value (rms)*	*Peak-to-peak value*
Amplitude	1	1.571	1.414	0.500
Average value	0.637	1	0.900	0.318
Root-mean-square value (rms)	0.707	1.111	1	0.354
Peak-to-peak value	2.000	3.142	2.828	1



Relation of frequency to the amplitudes of displacement, velocity, and acceleration in harmonic motion.

4. PHYSICAL PROPERTIES OF SOME COMMON SUBSTANCES

Solids

Solid	*Density*, ρ_0 (kg m^{-3})	*Young's modulus*, E (Pa)	*Poisson's ratio*, ν	*Wavespeed*, c_L		*Product of critical frequency* (f_c) and bar thickness[a] (m s^{-1})
				Bar (m s^{-1})	Bulk (m s^{-1})	
Aluminum	2700	7.1×10^{10}	0.33	5150	6300	12.7
Brass	8500	10.4×10^{10}	0.37	3500	4700	18.7
Concrete (dense)	2600	$\sim 2.5 \times 10^{10}$	–	–	3100	21.1
Copper	8900	12.2×10^{10}	0.35	3700	5000	17.7
Cork	250	6.2×10^{10}	–	–	500	130.7
Cast iron	7700	10.5×10^{10}	0.28	3700	4350	17.7
Glass (Pyrex)	2300	6.2×10^{10}	0.24	5200	5600	12.6
Gypsum (plasterboard)	650	–	–	–	6800	9.61
Lead	11300	1.65×10^{10}	0.44	1200	2050	54.5
Nickel	8800	21×10^{10}	0.31	4900	5850	13.3
Particle board	750	–	–	–	669	97.7
Polyurethane	72	1.9×10^{7}	–	–	513	127.4
Polystyrene	42	1.1×10^{7}	–	–	512	127.6
PVC	66	5.5×10^{7}	–	–	913	71.6
Plywood	600	–	–	–	3080	21.2
Rubber (hard)	1100	2.3×10^{9}	0.4	1450	2400	45.1
Rubber (soft)	950	5×10^{6}	–	–	1050	62.2
Silver	10500	7.8×10^{10}	0.37	2700	3700	24.2
Steel	7700	19.5×10^{10}	0.28	5050	6100	12.9
Tin	7300	4.5×10^{10}	0.33	2500	–	26.1
Wood (hard)	650	1.2×10^{10}	–	4300	–	15.2

[a] Where a bar thickness does not apply, the thickness of the bulk material is used.

Liquids

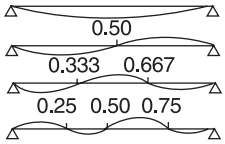
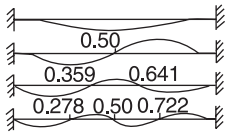
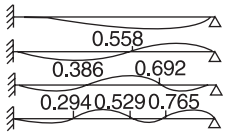
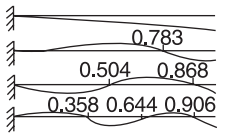
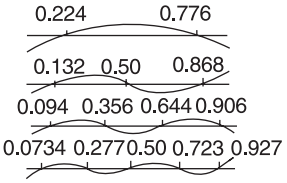
Liquid	*Density* ρ_0 (kg m^{-3})	*Temperature* (°C)	*Specific heat ratio*, γ	*Wavespeed*, c (m s^{-1})
Castor oil	950	20	–	1540
Ethyl alcohol	790	20	–	1150
Fresh water	998	20	1.004	1483
Fresh water	998	13	1.004	1441
Glycerin	1260	20	–	1980
Mercury	13600	20	1.13	1450
Petrol	680	20	–	1390
Sea water	1026	13	1.01	1500
Turpentine	870	20	1.27	1250

Gases

Gas	*Density* ρ_0 (kg m^{-3})	*Temperature* (°C)	*Specific heat ratio*, γ	*Wavespeed*, c (m s^{-1})
Air	1.293	0	1.402	332
Air	1.21	20	1.402	343
Carbon dioxide	1.84	20	1.40	267
Hydrogen	0.084	0	1.41	1270
Hydrogen	0.084	20	1.41	1330
Nitrogen	1.17	20	1.40	349
Oxygen	1.43	0	1.40	317
Oxygen	1.43	20	1.40	326
Steam	0.6	100	1.324	405

5. VIBRATION MODES OF CLASSICAL ELEMENTS

Natural frequencies and normal modes of uniform beams

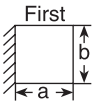
Supports	*Mode n*	*(A) Shape and nodes (numbers give location of nodes in fraction of length from left end)*	*(B) Boundary conditions*	*(C) Frequency equation*	*(D) Constants*	*(E) kl* $w_n = k^2\sqrt{\frac{EIg}{Ay}}$	*(F) R Ratio of nonzero constants column (D)*
Hinged-hinged	1		$x=0\ \{x=0,\ x''=0$ $x=l\ \{x=0,\ x''=0$	$\sin kl=0$	$A=0$ $B=0$ $\frac{C}{D}=1$	3.1416 6.283 9.425 12.566 $\approx n\pi$	1.0000 1.0000 1.0000 1.0000 1.0000
	2						
	3						
	4						
	n>4						
Clamed-clamped	1		$x=0\ \{x=0,\ x'=0$ $x=l\ \{x=0,\ x'=0$	$(\cos kl)(\cosh kl)=1$	$A=0$ $C=0$ $\frac{D}{B}=R$	4.730 7.853 10.996 14.137 $\approx\frac{(2n+l)\pi}{2}$	–0.9825 –1.0008 –1.0000– –1.0000+ –1.0000–
	2						
	3						
	4						
	n>4						
Clamed-hinged	1		$x=0\ \{x=0,\ x'=0$ $x=l\ \{x=0,\ x''=0$	$\tan kl=\tanh kl$	$A=0$ $C=0$ $\frac{D}{B}=R$	3.927 7.069 10.210 13.352 $\approx\frac{(4n+l)\pi}{4}$	–1.0008 –1.0000+ –1.0000 –1.0000 –1.0000
	2						
	3						
	4						
	n>4						
Clamped-free	1		$x=0\ \{x=0,\ x''=0$ $x=l\ \{x''=0,\ x'''=0$	$(\cos kl)(\cosh kl)=-1$	$A=0$ $C=0$ $\frac{D}{B}=R$	1.875 4.694 7.855 10.996 $\approx\frac{(2n-l)\pi}{2}$	–0.7341 –1.0185 –0.9992 –1.0000+ –1.0000–
	2						
	3						
	4						
	n>4						
Free-free	1		$x=0\ \{x''=0,\ x''=0$ $x=l\ \{x''=0,\ x'''=0$	$(\cos kl)(\cosh kl)=-1$	$B=0$ $D=0$ $\frac{C}{A}=R$	0 (represents translation) 4.730 7.853 10.996 14.137 $\approx\frac{(2n-l)\pi}{2}$	 –0.9825 –1.0008 –1.0000– –1.0000+ –1.0000–
	2						
	3						
	4						
	5						
	n>5						

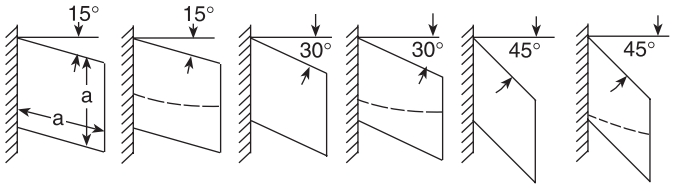
Natural frequencies and nodal lines of square plates with various edge conditions (after D. Young. *J. Appl. Mechanics*, 17:448 (1950))

	1st mode	*2nd mode*	*3rd mode*	*4th mode*	*5th mode*	*6th mode*
$\omega_n\sqrt{Da/\gamma ha^4}$	3.494	8.547	21.44	27.46	31.17	
Nodal lines						
$\omega_n\sqrt{Da/\gamma ha^4}$	35.99	73.41	108.27	131.64	132.25	165.15
Nodal lines						
$\omega_n\sqrt{Da/\gamma ha^4}$	6.958	24.08	26.80	48.05	63.14	
Nodal lines						

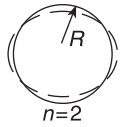
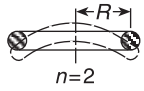
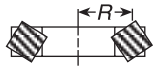
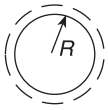
$\omega_n = 2\pi f_n$; $D = Eh^3/12(1-\mu^2)$; γ = weight density; h = plate thickness; a = plate length.

Natural frequencies and nodal lines of cantilevered rectangular and skew rectangular plates ($\mu = 0.3$)* (after Barton, M.V. *J. Appl. Mechanics*, 1951; 18:129)

Mode \ *a/b*	1/2	1	2	5
First 	3.508	3.494	3.472	3.450
Second 	5.372	8.547	14.93	34.73
Third 	21.96	21.44	21.61	21.52
Fourth 	10.26	27.46	94.49	563.9
Fifth 	24.85	31.17	48.71	105.9

Mode	*First*	*Second*	*First*	*Second*	*First*	*Second*
$\omega_n\sqrt{Dg/\gamma ha^4}$	3.601	8.872	3.961	10.190	4.824	13.75
Nodal lines						

Natural frequencies of complete circular rings whose thickness in radial direction is small compared to radius

Type of vibration	*Shape of lowest mode*	*Rectangular cross-section*	*Circular cross-section*
		ω_n	ω_n
Flexural in plane of ring with *n* complete wavelength in circumference		$\sqrt{\frac{Eg}{\gamma}\frac{I}{AR^4}\frac{n^2(n^2-1)^2}{n^2+1}}$ *n* any integer > 1	$\sqrt{\frac{E\pi r^4}{4mR^4}\frac{n^2(n^2-1)^2}{n^2+1}}$ *n* any integer > 1
Flexural normal to plane of ring			$\sqrt{\frac{E\pi r^4}{4mR^4}\frac{n^2(n^2-1)^2}{n^2+1+\mu}}$ *n* any integer > 1
Torsional		First mode $\sqrt{\frac{Eg}{\gamma R^2}\frac{Ix}{Ip}}$	$\sqrt{\frac{G\pi r^2}{mR^2}(n^2+1+\mu)}$ *n*=0, or any integer
Extensional		$\sqrt{\frac{Eg}{\gamma R^2}}$	$\sqrt{\frac{E\pi r^2}{mR^2}(1+n^2)}$ *n*=0, or any integer

E=modulus of elasticity; *G*=modulus of rigidity; γ= weight density; *n*: defined for each type of vibration; *r*=radius of ring; μ=Poisson's ratio. Properties of cross-sections: *I*= moment of inertia with respect to axis of section; I_x=moment of inertia with respect to radial line; I_p=polar moment of inertia; *A*=area; *r*=radius; *m*=mass per unit of length.

6. STANDARDS AND GUIDELINES

ISO 10055:1996 Mechanical vibration – vibration testing requirements for shipboard equipment and machinery components

ISO 10068:1998 Mechanical vibration and shock – free, mechanical impedance of the human hand–arm system at the driving point

ISO 10137:1992 Bases for design of structures; serviceability of buildings against vibration

ISO 10142:1996 Carbonaceous materials for use in the production of aluminium – calcined coke – determination of grain stability using a laboratory vibration mill

ISO 10326–1:1992 Mechanical vibration; laboratory method for evaluating vehicle seat vibration; part 1: basic requirements

ISO/TS 10811–1:2000 Mechanical vibration and shock – vibration and shock in buildings with sensitive equipment – part 1: measurement and evaluation

ISO/TS 10811–2:2000 Mechanical vibration and shock – vibration and shock in buildings with sensitive equipment – part 2: classification

ISO 10814:1996 Mechanical vibration – susceptibility and sensitivity of machines to unbalance

ISO 10815:1996 Mechanical vibration – measurement of vibration generated internally in railway tunnels by the passage of trains

ISO 10816–1:1995 Mechanical vibration – evaluation of machine vibration by measurements on non-rotating parts – part 1: general guidelines

ISO 10816–2: 1996 Mechanical vibration – evaluation of machine vibration by measurements on non-rotating parts – part 2: large land-based steam turbine generator sets in excess of 50 MW

ISO 10816–3: 1998 Mechanical vibration – evaluation of machine vibration by measurements on non-rotating parts – part 3: industrial machines with nominal power above 15 kW and nominal speeds between 120 r/min and 15000 r/min when measured in situ

ISO 10816–4:1998 Mechanical vibration – evaluation of machine vibration by measurements on non-rotating parts – part 4: gas turbine driven sets excluding aircraft derivatives

ISO 10816–5:2000 Mechanical vibration – evaluation of machine vibration by measurements on non-rotating parts – part 5: machine sets in hydraulic power generating and pumping plants

ISO 10816–6:1995 Mechanical vibration – evaluation of machine vibration by measurements on non-rotating parts – part 6: reciprocating machines with power ratings above 100 kW

ISO 10817–1:1998 Rotating shaft vibration measuring systems – part 1: relative and absolute sensing of radial vibration

ISO 10819:1996 Mechanical vibration and shock – hand–arm vibration – method for the measurement and evaluation of the vibration transmissibility of gloves at the palm of the hand

ISO 10846–1:1997 Acoustics and vibration – laboratory measurement of vibro-acoustic transfer properties of resilient elements – part 1: principles and guidelines

ISO 10846–2:1997 Acoustics and vibration – laboratory measurement of vibro-acoustic transfer properties of resilient elements – part 2: dynamic stiffness of elastic supports for translatory motion – direct method

ISO 11342:1998 Mechanical vibration – methods and criteria for the mechanical balancing of flexible rotors

ISO 11342:1998/Cor 1:2000 Mechanical vibration – methods and criteria for the mechanical balancing of flexible rotors

ISO 13090-1:1998 Mechanical vibration and shock – guidance on safety aspects of tests and experiments with people – part 1: exposure to whole-body mechanical vibration and repeated shock

ISO 13753:1998 Mechanical vibration and shock – hand-arm vibration – method for measuring the vibration transmissibility of resilient materials when loaded by the hand-arm system

ISO 14964:2000 Mechanical vibration and shock – vibration of stationary structures – specific requirements for quality management in measurement and evaluation of vibration

ISO 16063–1: 1998 Methods for the calibration of vibration and shock transducers – part 1: basic concepts

ISO 16063–11: 1999 Methods for the calibration of vibration and shock transducers – part 11: primary vibration calibration by laser interferometry

ISO 1925: 2001 Mechanical vibration – balancing – vocabulary

ISO 1940–1: 1986 Mechanical vibration; balance quality requirements of rigid rotors; part 1: determination of permissible residual unbalance

ISO 1940–2: 1997 Mechanical vibration – balance quality requirements of rigid rotors – part 2: balance errors

ISO 2017: 1982 Vibration and shock; isolators; procedure for specifying characteristics

ISO 2247:2000 Packaging – complete, filled transport packages and unit loads – vibration tests at fixed low frequency

ISO 2247:1985 Packaging; complete, filled transport packages; vibration test at fixed low frequency

ISO 2631–1:1997 Mechanical vibration and shock – evaluation of human exposure to whole-body vibration – part 1: general requirements

ISO 2631–2:1989 Evaluation of human exposure to whole-body vibration; part 2: continuous and shock-induced vibration in buildings (1 to 80 Hz)

ISO 2631–4:2001 Mechanical vibration and shock – evaluation of human exposure to whole-body vibration – part 4: guidelines for the evaluation of the effects of vibration and rotational motion on passenger and crew comfort in fixed-guideway transport systems

ISO 2671:1982 Environmental tests for aircraft equipment; part 3.4: acoustic vibration

ISO 2953:1999 Mechanical vibration – balancing machines – description and evaluation

ISO 2954:1975 Mechanical vibration of rotating and reciprocating machinery; requirements for instruments for measuring vibration severity

ISO 3046–5:1978 Reciprocating internal combustion engines – performance – part 5: torsional vibrations

ISO 4548–7:1990 Methods of test for full-flow lubricating oil filters for internal combustion engines; part 7: vibration fatigue test

ISO 4866:1990 Mechanical vibration and shock; vibration of buildings; guidelines for the measurement of vibrations and evaluation of their effects on buildings

ISO 4866:1990/Amd.1:1994 Mechanical vibration and shock – vibration of buildings – guidelines for the measurement of vibrations and evaluation of their effects on buildings; amendment 1

ISO 4866:1990/Amd.2:1996 Mechanical vibration and shock – vibration of buildings – guidelines for the measurement of vibrations and evaluation of their effects on buildings; amendment 2

ISO 5007:1990 Agricultural wheeled tractors; operator's seat; laboratory measurement of transmitted vibration

ISO 5008:1979 Agricultural wheeled tractors and field machinery; measurement of whole-body vibration of the operator

ISO 5344:1980 Electrodynamic test equipment for generating vibration; Methods of describing equipment characteristics

ISO 5347–10:1993 Methods for the calibration of vibration and shock pick-ups; part 10: primary calibration by high impact shocks

ISO 5347–11:1993 Methods for the calibration of vibration and shock pick-ups; part 11: testing of transverse vibration sensitivity

ISO 5347–12:1993 Methods for the calibration of vibration and shock pick-ups; part 12: testing of transverse shock sensitivity

ISO 5347–13:1993 Methods for the calibration of vibration and shock pick-ups; part 13: testing of base strain sensitivity

ISO 5347–14:1993 Methods for the calibration of vibration and shock pick-ups; part 14: resonance frequency testing of undamped accelerometers on a steel block

ISO 5347–15:1993 Methods for the calibration of vibration and shock pick-ups; part 15: testing of acoustic sensitivity

ISO 5347–16:1993 Methods for the calibration of vibration and shock pick-ups; part 16: testing of mounting torque sensitivity

ISO 5347–17:1993 Methods for the calibration of vibration and shock pick-ups; part 17: testing of fixed temperature sensitivity

ISO 5347–18:1993 Methods for the calibration of vibration and shock pick-ups; part 18: testing of transient temperature sensitivity

ISO 5347–19:1993 Methods for the calibration of vibration and shock pick-ups; part 19: testing of magnetic field sensitivity

ISO 5347–20:1997 Methods for the calibration of vibration and shock pick-ups – part 20: primary vibration calibration by the reciprocity method

ISO 5347–22:1997 Methods for the calibration of vibration and shock pick-ups – part 22: accelerometer resonance testing – general methods

ISO 5347–3:1993 Methods for the calibration of vibration and shock pick-ups; part 3: secondary vibration calibration

ISO 5347–4:1993 Methods for the calibration of vibration and shock pick-ups; part 4: secondary shock calibration

ISO 5347–5:1993 Methods for the calibration of vibration and shock pick-ups; part 5: calibration by earth's gravitation

ISO 5347–6:1993 Methods for the calibration of vibration and shock pick-ups; part 6: primary vibration calibration at low frequencies

ISO 5347–7:1993 Methods for the calibration of vibration and shock pick-ups; part 7: primary calibration by centrifuge

ISO 5347–8:1993 Methods for the calibration of vibration and shock pick-ups; part 8: primary calibration by dual centrifuge

ISO 5348:1998 Mechanical vibration and shock – mechanical mounting of accelerometers

ISO 5349:1986 Mechanical vibration; guidelines for the measurement and the assessment of human exposure to hand-transmitted vibration

ISO 5982:1981 Vibration and shock; mechanical driving point impedance of the human body

ISO 6070:1981 Auxiliary tables for vibration generators; methods of describing equipment characteristics

ISO 6267:1980 Alpine skis; measurement of bending vibrations

ISO 6721–3:1994 Plastics – determination of dynamic mechanical properties – part 3: flexural vibration – resonance-curve method

ISO 6721–3:1994/Cor 1:1995 Plastics – determination of dynamic mechanical properties – part 3: flexural vibration – resonance-curve method

ISO 6721–4:1994 Plastics – determination of dynamic mechanical properties – part 4: tensile vibration – non-resonance method

ISO 6721–5:1996 Plastics – determination of dynamic mechanical properties – part 5: flexural vibration – non-resonance method

ISO 6721–6:1996 Plastics – determination of dynamic mechanical properties – part 6: shear vibration – non-resonance method

ISO 6721–7:1996 Plastics – determination of dynamic mechanical properties – part 7: torsional vibration – non-resonance method

ISO 6721–8:1997 Plastics – determination of dynamic mechanical properties – part 8: longitudinal and shear vibration – wave-propagation method

ISO 6721–9:1997 Plastics – determination of dynamic mechanical properties – part 9: tensile vibration – sonic-pulse propagation method

ISO 6954:2000 Mechanical vibration – guidelines for the measurement, reporting and evaluation of vibration with regard to habitability on passenger and merchant ships

ISO 7096:2000 Earth-moving machinery – laboratory evaluation of operator seat vibration

ISO 7096:1994 Earth-moving machinery – laboratory evaluation of operator seat vibration

ISO 7505:1986 Forestry machinery; chain saws; measurement of hand-transmitted vibration

ISO 7626–1:1986 Vibration and shock; experimental determination of mechanical mobility; part 1: basic definitions and transducers

ISO 7626–5:1994 Vibration and shock – experimental determination of mechanical mobility – part 5: measurements using impact excitation with an exciter which is not attached to the structure

ISO/TR 7849:1987 Acoustics; estimation of airborne noise emitted by machinery using vibration measurement

ISO 7916:1989 Forestry machinery; portable brush-saws; measurement of hand-transmitted vibration

ISO 7919–1:1996 Mechanical vibration of non-reciprocating machines – measurements on rotating shafts and evaluation criteria – part 1: general guidelines

ISO 7919–2:1996 Mechanical vibration of non-reciprocating machines – measurements on rotating shafts and evaluation criteria – part 2: large land-based steam turbine generator sets

ISO 7919–3:1996 Mechanical vibration of non-reciprocating machines – measurements on rotating shafts and evaluation criteria – part 3: coupled industrial machines

ISO 7919–4:1996 Mechanical vibration of non-reciprocating machines – measurements on rotating shafts and evaluation criteria – part 4: gas turbine sets

ISO 7919–5:1997 Mechanical vibration of non-reciprocating machines – measurements on rotating shafts and evaluation criteria – part 5: machine sets in hydraulic power generating and pumping plants

ISO 7962:1987 Mechanical vibration and shock; mechanical transmissibility of the human body in the *z* direction

ISO 8002:1986 Mechanical vibrations; land vehicles; method for reporting measured data

ISO 8041:1990 Human response to vibration; measuring instrumentation

ISO 8041:1990/Amd 1:1999 Human response to vibration – measuring instrumentation – amendment 1

ISO 8041:1990/Cor 1:1993 Human response to vibration; measuring instrumentation; technical corrigendum 1

ISO 8042:1988 Shock and vibration measurements; characteristics to be specified for seismic pick-ups

ISO 8318:2000 Packaging – complete, filled transport packages and unit loads – sinusoidal vibration tests using a variable frequency

ISO 8318:1986 Packaging; complete, filled transport packages; vibration tests using a sinusoidal variable frequency

ISO 8528–9:1995 Reciprocating internal combustion engine driven alternating current generating sets – part 9: measurement and evaluation of mechanical vibration

ISO 8569:1996 Mechanical vibration and shock – measurement and evaluation of shock and vibration effects on sensitive equipment in buildings

ISO 8579–2:1993 Acceptance code for gears; part 2: determination of mechanical vibrations of gear units during acceptance testing

ISO 8608:1995 Mechanical vibration – road surface profiles – reporting of measured data

ISO 8626:1989 Servo-hydraulic test equipment for generating vibration; method of describing characteristics

ISO 8662–1:1988 Hand-held portable power tools; measurement of vibrations at the handle; part 1: general

ISO 8662–10:1998 Hand-held portable power tools – measurement of vibrations at the handle – part 10: nibblers and shears

ISO 8662–11:1999 Hand-held portable power tools – measurement of vibrations at the handle – part 11: fastener driving tools – ISO 8662–11:1999

ISO 8662–12:1997 Hand-held portable power tools – measurement of vibrations at the handle – part 12: saws and files with reciprocating action and saws with oscillating or rotating action

ISO 8662–13:1997 Hand-held portable power tools – measurement of vibrations at the handle – part 13: die grinders

ISO 8662–13:1997/Cor.1:1998 Hand-held portable power tools – measurement of vibrations at the handle – part 13: die grinders; technical corrigendum 1

ISO 8662-14:1996 Hand-held portable power tools – measurement of vibrations at the handle – part 14: stone-working tools and needle scalers

ISO 8662–2:1992 Hand-held portable power tools; measurement of vibrations at the handle; part 2: chipping hammers and riveting hammers

ISO 8662–3:1992 Hand-held portable power tools; measurement of vibrations at the handle; part 3: rock drills and rotary hammers

ISO 8662–4:1994 Hand-held portable power tools – measurement of vibrations at the handle – part 4: grinders

ISO 8662–5:1992 Hand-held portable power tools; measurement of vibrations at the handle; part 5: pavement breakers and hammers for construction work

ISO 8662–6:1994 Hand-held portable power tools – measurement of vibrations at the handle – part 6: impact drills

ISO 8662–7:1997 Hand-held portable power tools – measurement of vibrations at the handle – part 7: wrenches, srewdrivers and nut runners with impact, impulse or ratched action

ISO 8662–8:1997 Hand-held portable power tools – measurement of vibrations at the handle – Part 8: Polishers and rotary, orbital and random orbital sanders

ISO 8662–9:1996 Hand-held portable power tools – measurement of vibrations at the handle – part 9: rammers

ISO 8727:1997 Mechanical vibration and shock – human exposure – biodynamic coordinate systems

ISO 8821:1989 Mechanical vibration; balancing; shaft and fitment key convention

ISO 9022–10:1998 Optics and optical instruments – environmental test methods – part 10 combined sinusoidal vibration and dry heat or cold

ISO 9022–15:1998 Optics and optical instruments – environmental test methods – part 15: combined digitally controlled broad-band random vibration and dry heat or cold

ISO 9022–19:1994 Optics and optical instruments – environmental test methods – part 19:

temperature cycles combined with sinusoidal or random vibration

ISO 9688:1990 Mechanical vibration and shock; analytical methods of assessing shock resistance of mechanical systems; information exchange between suppliers and users of analyses

ISO 9996:1996 Mechanical vibration and shock – disturbance to human activity and performance – classification

Vibration severity ranges and examples of their application (after ISO IS 2372: Mechanical vibration of machines with operating speeds from 10 to 200 rps – basis for specifying evaluation standards)

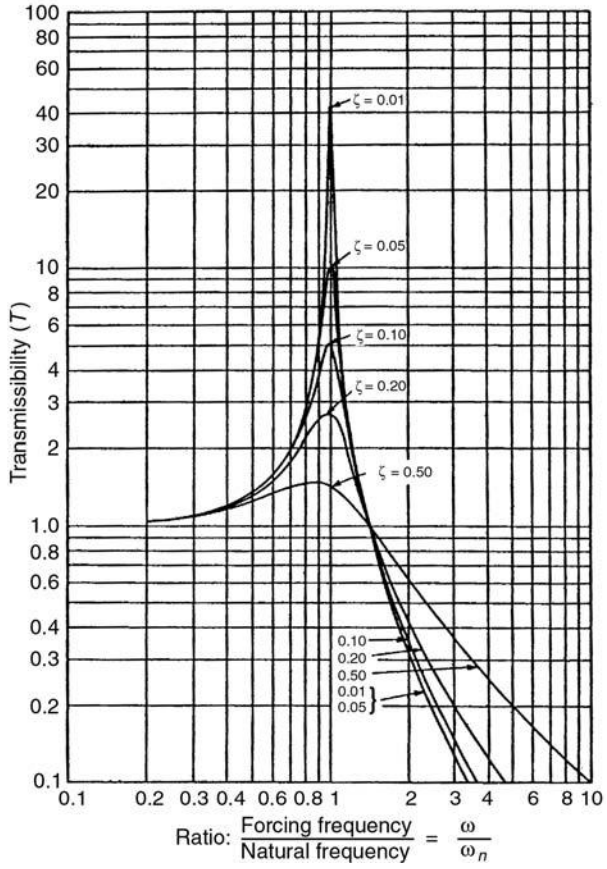
Range of vibration severity	Examples of quality judgement for seperate classes of machines			
Limits of range, mm /s^{-1}	Small machines, class I	Medium machines, class II	Large machines, class III	Turbo-machines, class IV
0.28	A	A	A	A
0.45				
0.71				
1.12	B			
1.8		B		
2.8	C		B	
4.5		C		B
7.1	D		C	
11.2				C
18		D	D	
28				D
45				

The letters A, B, C and D represent machine vibration quality grades, ranging from good (A) to unacceptable (D).

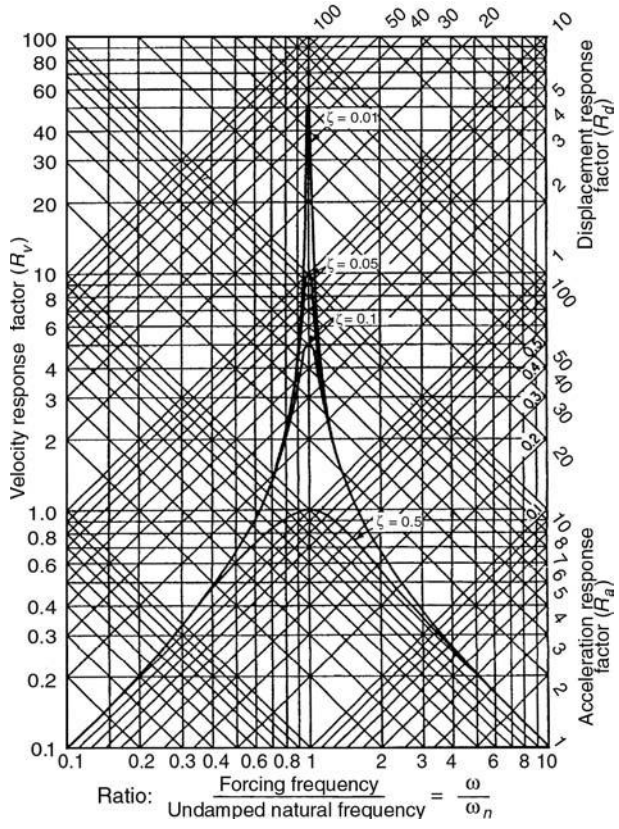
Quality judgement of vibration severity (after ISO IS 3945: The measurement and evaluation of vibration severity of large rotating machines, in situ; operating at speeds from 10 to 200 rps)

Vibration severity		Support classification	
in. /s^{-1}	mm /s^{-1}	Hard supports	Soft supports
0.017	0.45	Good	Good
0.028	0.71		
0.044	1.12		
0.071	1.8		
0.11	2.8	Satisfactory	
0.18	4.5		Satisfactory
0.28	7.1	Unsatisfactory	
0.44	11.2		Unsatisfactory
0.71	18.0	Impermissible	
1.10	28.0		Impermissible
2.80	71.0		

7. FREQUENCY RESPONSE FUNCTIONS



Transmissibility of a viscous-damped system. Force transmissibility and motion transmissibility are identical numerically. The fraction of critical damping is denoted by ζ.



Response factors for a viscous-damped single-degree-of-freedom system excited in forced vibration by a force acting on the mass.

INDEX

NOTE

Page numbers in **bold** refer to major discussions. Page numbers suffixed by *T* refer to Tables; page numbers suffixed by *F* refer to Figures. vs denotes comparisons

This index is in letter-by-letter order, whereby hyphens and spaces within index headings are ignored in the alphabetization. Terms in parentheses are excluded from the initial alphabetization.

Cross-reference terms in *italics* are general cross-references, or refer to subentry terms within the same main entry (the main entry is not repeated to save space).

Readers are also advised to refer to the end of each article for additional cross-references – not all of these cross-references have been included in the index cross-references.

A

ABAQUS 246–247, 305
absorbers **1–26**
  attenuation capabilities 22–23, 23*F*, 25*F*
  AVA 4*F*, 5–6, 7*F*, 8*F*
  dynamic **9–26**
  future perspectives 24, 25*F*
  piezoelectricity and 1–3, 1*F*, 3*F*
  positive position feedback 3–5, 4*F*, 5*F*, 6*F*
  special configurations of 18–21, 20*T*, 20*F*, 21*F*, 22*F*
  undamped 10–17, 10*F*, 11*F*, 12*F*, 14*F*, 15*F*, 16*T*, 16*F*, 18*T*, 18*F*, 19*F*
Absorbers, Active **1–9**
Absorbers, Vibration **9–26**
acausal filters **1196**
accelerance 1129
acceleration 604
accelerograms 439–441, 440*T*, 443–446
accelerometers
  absolute motion and 1383, 1390–1392, 1395–1396
  ADXL50 772, 773*F*
  bearing diagnostics and 151
  calibration of 1130–1132
  cross-axis sensitivity and 1121–1122
  environmental testing and 491
  location 495
  MEMS and 772–774
  rotation 1080–1081
acceptance testing 490
acoustics
  aerodynamics and 93
acoustics
  boundary integral formulation and 1278–1279
  excitation and 897
  external problem and 1279
  FEM and 1277–1278
  fluid/structural interaction and 545–550
  internal problem 1279–1282
  MEMS and 774, 775*F*
  noise and **887–898**
  parallel processing and 1000
  radiation impedance and 891
  SPL 1268, 1268*F*
  structural interactions and **1265–1283**
  subsonic waves and 897
  tire vibration and 1375–1376
  See also sound
active constrained layer (ACL) 361*F*, 362*F*, 363*F*, 656–658
active constrained layer damping (ACLD) 353–360, 355*F*, 356*F*, 359*T*, 359*F*,
active control
  active suspensions 38, 39*F*
  adjustable suspensions 38, 38*F*
  applications 28–33, 29*T*, 29*F*, 30*F*, 31*F*, 32*F*, 33*F*, 34*F*, 35*F*, 36*F*
  civil structures **26–36**
  damping and 28–33, **342–351**
  fuzzy logic and 43–45
  groundhook 41
  hybrid 26–28, 27*F*, 42
  isolation **46–48**
  optimal 55
  passive suspensions 37, 37*F*
  semiactive 26–28, 27*F*, 37*F*, 38–44, 40*F*, 41*F*, 42*F*, 43*F*, 44*F*
active control (*continued*)
  skyhook 38–41
  suppression **48–58**
  vehicles 37–45, 37*F*
Active Control of Civil Structures **26–36**
Active Control of Vehicle Vibration 37–45
Active Isolation **46–48**
  actuation 47–48, 47*T*
  feedback 46–47, 47*F*
  feedforward 46–47, 46*F*
actively controlled response of buffet affected tails (ACROBAT) 78
active-passive devices 653–658
active piezoelectric damping composites (APDC) 354
active states 925–926
Active Vibration Suppression **48–57**
  compensators and 55–56
  control and 53, 55
  degree of freedom and 49–51, 49*F*, 50*F*
  limitations of 57
  modal control and 51–52
  pole placement 54
  spillover 53–54
  stability and 56–57
actuated joints 1059
actuators 79–81
  active isolation and 47–48
  active materials 58–61, 60*F*, 61*F*
  configurations 759–760
  distributed 1134–1138
  effective implementation of 68–70, 68*F*, 69*F*, 70*F*, 71*F*
  electrical input 71–72, 72*F*, 73*F*, 74*F*
  electrostriction and 482–490

actuators (*continued*)
energy extraction 70
magnetostrictive materials 64–65, **753–762**
MEMS and 771–779
piezoelectricity and 61–64, 62*F*, 63*F*
proof-mass 653
RMA 48
sensitivity and 1140–1141
shape memory alloys and 65–68, 65*F*, 66*F*, 67*F*, 1147
structonic cylindrical shells and 1138–**1141**
See also MEMS; smart structures
Actuators and Smart Structures **58–81**
Adaptive Filters **81–87**
convergence coefficients 86–87
LMS algorithm 82, 83*F*, 84–86
RLS algorithm 84
steepest descent algorithm 81–82, 82*F*
See also optimal filters
adaptive resonance theory (ART) 866
ADAPTx Automated System Identification Software 682
A/D converters 368–373
additive noise 666–668
Ader, Clement 1065
ADINA 305
ADXL50 accelerometer 772, 773*F*
aerodynamics
ACROBAT and, 78
blades and **174–178**
buffeting and, 92
continuous turbulence and, 91
flutter and **553–565**, **565–577**
gusts and, 89–91, 92
maneuvering and, 89–93
sound 878
vibration origins 1191
aeroelastic effects 1584–1586
aeroservoelasticity 95, 95*F*
control surface buzz 96, 96*F*
dynamic maneuvers 89–93, 90*F*, 91*F*, 92*F*, 93*F*
flight loads 88–89, 88*F*, 89*F*
ground loads 93–95
limit cycle oscillations 95, 95*F*
negative damping 97
panel flutter 96, 96*F*
stall flutter 96, 97*F*
vortex shedding 97
Aeroelastic Response, **87–97**
aerospace
acoustic tests and 494
SNDT and 905
Agnes, G **1–9**
Ahmadian, M **37–45**
airbags 283*F*, 285
Akaike Information Criterion (AIC) 682, 1205
algorithms
back propagation 873–874
contact 308
algorithms (*continued*)
differentiation/integration and **1193–1199**
DYNA3D and 305–312
Gauss-Seidel 995
hourglassing 305, 308
least mean squares 82–84, 86
Levenberg-Marquart 866
model updating 834
neural networks and 871–872
recursive least square 84
steepest descent 81–82
aliasing errors 670
A/D converters and 368
antialiasing filters and 367–368
data acquisition and 365–369
differentiation/integration and 1195
parameters and 369
American Beauty 1064
American National Standards Institute (ANSI) 245, 1224
American Petroleum Institute (API) 1081, 1224
Ampere's law 755
analytic signals 643*F*
Hilbert transform and 643–646
Anderson, PW 744
Andronov, AA 431
animation 415, 416
annular fluid flow 1023
ANSYS 247, 305
a posteriori verification 463
a priori reasoning 135, 632, 637, 1266, 1268
Arabs 112
arbitrary Eulerian Lagrangian (ALE) formulation 251*T*, 252
DYNA3D and 306
meshes and 281–282
Aristotle 126
ARMA (autoregressive moving average) process 1202–1203, 1203*F*
Arnold VI 432
ARTeMIS Extractor 682
ASCE 7–98 tabular values 1583, 1583*T*, 1584
asymptotic modal analysis (AMA) 1269
asymptotic techniques
nonlinear systems and 957–962
attenuation 1558–1559
attractors
chaos and **227–236**
austenite *See* shape memory alloys
Austrian Standards Organization (ON) 1224
auto-associative neural network (ANN) 864–865
autocorrelation function 977–978, 1592
adaptive filters and **81–87**
cepstral analysis and 217–218
columns and 241
model-based identification and 675
PSD 297*F*
autocorrelation function (*continued*)
rain-on-the-roof excitation and 241
signal processing and 1200–1204
spectral density and 296
AutoMAC 270
automobiles
bridges and **202–207**
ground transportation systems and **603–620**
tire vibrations and **1369–1379**
vehicular vibrations **37–45**
See also crash
AutoRegressive model 674, 675, 902
AutoRegressive Model with eXogenous input (ARX) model 677, 679, 684
model-based identification and 675, 677, 679–680, 682, 684–685, 685*F*
AutoRegressive Moving Average (ARMA) model 675
model-based identification and 674
AutoRegressive Moving Average with eXogenous input (ARMAX) model 675, 679, 684
model-based identification and 675, 679–680, 682, 684–685, 684*F*, 685*F*
Averaging **98–110**
basic operations 98–101, 98*F*, 99*F*, 100*F*, 101*F*
exponential 103
frequency domain 108–109, 110*F*
jitter effects 102*F*, 103–108, 108*F*, 109*F*
moving average (MA) 99–100, 99*F*, 100*F*,
PSD 108–109
recursion 100–101, 100*F*, 102
TDA 101–108, 102*F*, 103*F*, 104*F*, 105*F*, 106*F*, 107*F*, 108*F*, 109*F*
axial loading
columns and **236–243**
crash and 310*F*
See also loading

B

back propagation algorithm 873–874
baffled plate 889*F*
Bajaj, A **928–943**, **952–966**
Balancing **111–124**
calculations of 88
coupled rotation and 111*F*, 112–113, 112*F*, 113*F*
flexible state and 118–119
influence coefficients and 119–123, 120*F*, 122*F*, 124*T*
rigid states and 113–118, 114*F*, 115*F*, 116*F*, 117*F*, 118*F*
rotor-stator interactions 1107–1121
tire vibrations 1370
torsion and 112–113
Banks, HT **658–664**
bar plots 413

bars 1125–1127
Barton, J 971
basic linear algebra subprograms (BLAS) 991
Basic Principles **124–137**
  calculus of variations 126
  Dunkerley's method 135–136, 136*F*
  Euler's equations 126–130, 129*F*
  flexural motion 130, 131*F*
  Galerkin's method 135
  generalized system coordinates 130–131
  Hamilton's principle 131
  Lagrange equations 131
  Maxwell's theorem of reciprocity 136, 136*F*
  parameters 125, 125*F*
  Rayleigh's Principle 131*F*, 132–134, 133*F*, 134*F*
  Ritz method 134
  vectors 125–126, 127*F*, 128*F*
Bauchau, O **461–467**
Bayesian Information Criterion (BIC) 682
Baz, A **351–364**, **1144–1155**
Beams **137–143**, 1329–1330, 1330*F*, 1331*F*
  Bernoulli-Euler 748*F*
  boundary conditions and 181*F*, 183–185, 184*F*, 184*T*, 185*T*
  continuous systems and 1312–1317
  cross-axis contamination and 1122
  Duffing's equation and 233–235
  Dunkerley method and 135–136
  Euler-Bernoulli theory and 137–141, 140*F*
  feedforward control 517
  flexural radiation and 1458, 1468
  Gelerkin method and 135
  localization and **741–751**, 748*F*
  magnetically buckled 234*F*
  MEMS 787–789
  natural frequencies and 414–415
  piezoelectric damping and 354–360
  shape memory alloys and 1147–1148
  shells and **1155–1167**
  ship vibrations **1167–1173**
  sound and 885–886
  time frequency and 1366*F*
  Timoshenko theory and 142
  transmissibility and 1523–1527
  transverse vibrations and 137–142, 138*T*, 139*T*, 140*F*, 140*T*, 141*F*, 141*T*, 142*T*, 143*F*
  vibration intensity and 1483–1484, 1486–1487
Bearing Diagnostics **143–152**
bearings 1078
  bicoherence 148
  cage fault 149
  cepstral analysis and 147, 218–220
  coupling 163, 163*F*, 164*F*
  distributed defects 149–151
  diversity 154*F*, 156–157, 156*F*
  failure modes 143
bearings (*continued*)
  fault 1083
  fluids and 153–155, 153*F*, 154*F*, 155*F*
  functions and 152–153
  HFRT 146, 146*F*
  journal bearing 150*F*, 151
  localized defects 144–151, 144*T*, 145*F*, 146*F*, 148*F*, 149*F*, 150*T*, 150*F*
  magnetic links 158–161, 159*F*, 160*F*, 161*F*
  misalignment and 1116–1118, 1186
  property comparison 155*F*, 161*T*, 161
  roller bearing 143, 157–158
  rolling faults and 1187–1188
  sealing systems 161–162, 162*F*,
  shock pulse counting 146
  signature generation 144–145, 144*T*, 145*F*
  statistical parameters 145–146
  synchronized averaging 147
  time-frequency distribution 147
  wavelet transform 147
  See also rotor dynamics; standards
Bearing Vibrations **152–165**
Bellville spring 755, 1181, 1181*F*
Belts **165–174**
  drives 170–174, 171*F*, 172*F*, 173*F*,
  moving 166–170, 166*F*, 167*F*, 168*F*, 170*F*
  stationary 166, 166*F*
Belytschko-Tsy shell 305
Belytshco-Shwer beam 305
bending moment sensitivity 1125–1127
bending strains 1136
Bendixson's theorem 593
Benson, DJ **278–286**
Bernoulli, John 124, 1344
Bernoulli-Euler beams 748*F*
Bert, CW **236–243**, **286–294**
Bessel function 729
Bessel functions 288
Betti's principle 197–198
bias error 670
bicoherence 145*F*, 147–149, 149*F*
bifurcation
  center manifold theory and 962
  eigenvalues and 818
  Hopf 435
  local 963
  nonlinear analysis and 962–965
  normal form theory 963
  parametric excitation and 1003, 1006
  perturbation methods and **1009–1011**
  vibro-impact systems and 1533–1536, 1539, 1543
Bigret, R **111–124**, **152–165**, **174–180**, **1064–1069**, **1069–1077**, **1078–1084**, **1085–1106**, **1107–1120**
biharmonic operator 1331
bilinear transformation 393–394
  time frequency and 1360–1361
binary representation 232
biodynamics 1571
  mechanical impedance and 1571
  models for 1572
  transmissibility and 1571
bioengineering
  crashworthiness and 308–311
biorthogonality 1074
biotechnology 778
birdstrike 93
Birkhoff, George 228, 233
Blades and Bladed Disks **174–180**, 415
  breakdowns and 176
  instability and 175
  localization and 741*F*, 745, 750*F*, 751*F*
  propellers 1170
  pulsations and 177, 177*F*
  resonance 179*F*
  rotation vs. rest 177–178
  signal generation and 1191
  strain and 175*T*, 178*F*
  strains and 175
  technology and 176
  See also disks; helicopter damping; rotation
blanching 622
block diagrams 686*F*, 687*F*
block-Lanczos algorithm 695–696
Blue Wave Ultrasonics 759
Bode plots 122, 418, 421*F*, 757, 758*F*
Boltzmann superposition model 661–662
Bond number 739, 739*F*
Booch, G 969, 975*F*
Book, W **1055–1063**
Boolean matrices 997–1000
Borel measure 664
bounce transmissibility 610
Boundary Conditions **180–191**
  beams 181*F*, 183–185, 184*F*, 184*T*, 185*T*, 1329–1330
  cables and 211
  continuous methods and 288
  coupled systems and 186, 187*F*, 188*F*, 189*F*
  DYNA3D and 306
  equations of motion and 1329, 1329*F*
  external problem and 1279
  FEA software and 253
  field dynamics and 492–493, 495
  finite element methods 531–533
  guided waves and **794–805**
  integral formulation 1278–1279, 1282–1285
  internal problem and 1279–1282
  liquid sloshing and **726–740**
  longitudinal waves 181–183, 181*F*
  membranes and plates 1331
  moving 190
  noise and 888–889
  nonlinear analysis and 945
  nonreflecting 190

Boundary Conditions (*continued*)
radiation efficiency 894*F*, 895*F*, 896*F*, 897*F*
semidefinite systems 191
shells 1159
sound pressure and 888–889
three-dimensional 186–188
tire vibration and 1378
torsion 183
waves and **1559–1564**
Boundary Element Methods **192–202**, 201*F*, 1279–1282
eigenvalues and 198
elasticity and 197
Fourier transforms 201
fundamental solutions 192–195, 192*F*, 193*F*
harmonic oscillations and 195–198
Helmholtz equation and 195
Kirchhoff plates and 197
Laplace transforms 201
symmetry and 194–195
transient problems and 198–201
Box-Jenkins method 677
Bragg cell 702, 1404
Branca, Giovanni 1064
Braun, S **98–110**, **294–302**, **665–672**, **1208–1223**, **1406–1419**, **1587–1595**
Breguet, Louis 1065
Bresse-Timoshenko theory 239
Bridges **202–207**
dynamic response of 203
frequencies of 202–203, 203*F*, 204*F*
railroad tracks and 206
traveling load and 204*F*, 205, 205*F*, 206*F*
British Standards Institution (BSI) 1224
6841 860, 1572
6842 625
broad-band random excitations 1266
Broyden-Fletcher-Goldfarb-Shanno algorithm 637
Bubnov-Galerkin method 240
buckling 238
columns and 241
buffeting 92
buildings 1578
See also active control
bulk waves 908
Burg's method 1203
Butterworth filters 703

C

C++ 971–972
numerical efficiency and 972–973
Cables **209–216**, 209*F*
chains and 213
linear theory and 210–215, 211*F*
modal analysis of 211–215
noise 1133
nonlinear model of 209–210, 214*F*
shallow sag 210–213
Cables (*continued*)
suspended 209–210, 210*F*
tangential displacement and 211
cage fault 145, 149
Cai, GQ **1238–1246**
calculus of variations 126, 1344–1346, 1345*T*
Euler's equations 126–130
finite element methods 533
flexural motion 130, 131*F*
calibration 818
Campbell diagram 414, 415*F*
cantilevers
beam model 692*F*, 693*F*, 694*F*
Duffing's equation and 233–235
pipes 1021–1022
plates 1028, 1028*F*
time frequency and 1367*F*
Cantor set 233
capacitive displacement sensors 1399–1400
capacitor sensors 1398*F*, 1399*F*
Cardona, A **967–976**
Cartwright, ML 228
cascade spectrum plot 385, 428*F*
CATIA 305
Cauchy principal value 642
cavities 1078, 1170
dimensions 1265
SEA and 1268
center manifold theory 432–435, 962
center of gravity 1490–1493
Centre Technique des Industries Mecaniques 1078
Cepstrum Analysis **216–227**, 747–748
ballpass frequency and 220*F*
bearing diagnostics and 145*F*, 147
bearing outer race fault 219*F*
complex applications 222–227
definitions for 216–218
echo removal 225*F*
editing effects 223*F*
forcing function 226*F*
FRFs 226*F*
liftering and 224, 226*F*
power spectrum and 218–222, 221*F*
terminology of 216
unwrapped phase 218, 218*F*
zoom spectra 224*F*
ceramic actuators 482–488
CFRF matrix 276*F*, 277*F*
chains 213
Chaos **227–236**
bifurcation and 435
Duffing's equation 233–235
history of 228
initial conditions 229–232, 1097–1098
invariant manifolds and 228–229
Melnikov's method and 232
nonlinearity sources of 235
Poincare maps and 228
rotor dynamics 1097–1098
rotor-stator interactions 1112–1115
Smale's horseshoe and 232–233
strange attractors and 233–235
Chaos (*continued*)
symbolic dynamics and 229–232
vibro-impact systems and 1531–1548
chatter 589
chemical reactions 1440
Chladni figures 414
Choi-Williams distribution (CWD) 147, 148*F*, 598, 600*F*, 1364–1366, 1365*F*
time-frequency and 600
Cholesky factorization 52, 712–713
circle-fitting method 822–823
circular plates 416*F*, 1026–1027
civil engineering
SNDT and 905
clamped-clamped plate 1025*F*
classes 969
diagram 970*F*
hierarchy and 974–976
closed loop control 50
Coad, P 969, 971
coaxiality fault 1083, 1099
cognition
whole-body vibration and 1575
Cohen's class of distributions 1362–1366
collaboration diagrams 970
Columns **236–243**
dimensionless frequency 237*T*
end conditions 237*T*
free lateral vibration and 237–239
nonlinear vibration of 240–241
random vibration of 241–242
stepped 239
tapered 239
thin-walled 239–240
transverse shear flexibility and 239
Commercial Software **243–256**
dynamic applications and 244–245
history of 244
quality assurance and 245–246
Comparison of Vibrational Properties
modal properties **265–272**
response properties **272–277**
spatial properties and **256–264**
compass plots 418*F*
compensators 55–56
complementary energy method 289, 290, 1320
complex envelope displacement analysis (CEDA) 1269, 1271–1274, 1273*F*
complex exponential method 821
complex exponential model class 675
complex mode indicator function (CMIF) 425, 429, 429*F*
component diagrams 971, 972*F*
component mode synthesis 1334–1335
composite FRF 425
compound FRF matrices 274, 275, 278
compound modes 417
compression 887
columns and **236–243**
packaging and **983–988**

compression (*continued*)
plate vibration and 1029
computational methods
averaging and **98–110**
correlation functions and 298–299
eigenproblems and 463
computational model updating (CMU) 851–854
Computation for Transient and Impact Dynamics **278–286**
computers
classes and 969
crashworthiness and 304
DYNA3D and 305–312, 305*T*
improvement of 968*T*
localization and 749
nonlinear systems and 953
object oriented programming and **967–976**
parallel processing and **990–1001**
tasks 968*T*
See also MEMS
cone kernel distribution (CKD) 1364–1366
Constantinides, AG 380–395
constitutional white finger 621
contact algorithms 280–281, 308
Continuous Methods **286–294**
complementary energy method 289–290
differential transformation method 291–292
formulation and solution 287–288
Galerkin method 290, 292–293
lower-bound approximations 291
Rayleigh method and 288–289
Ritz method 290
continuous systems 1312–1317, 1327–1332
variational methods and 1350–1354
continuum mechanics 973–974
contour maps 416
control *See* active control
controlled numerical center (CNC) tools **1379–1380**
control surface buzz 96
convergence 466*F*
convolution 381, **1304–1308**
Cooper, JE **87–97**
coordinate measuring machines (CMMs) 1490
See also isolation theory
Coordinate Modal Assurance Criterion (COMAC) 270–271, 270*F*, 275, 276
coordinate orthogonality check (CORTHOG) 271
coordinates 130–131
Co-Quad plots 418
Coriolis effects 409–410, 857, 860
Correlation Functions **294–302**, 680
computational aspects of 298–299
flow propagation 299*F*, 300*F*,
matrices and 298, 299–302
nonstationary signals and 296
random signals and 297–298
Correlation Functions (*continued*)
stochastic processes and 296
COSMOS/M 247–248
cost function 977
helicopter damping and 633
neural networks 870
Coulomb forces 636
damping 337
energy 475
friction 582–583
shock isolation and **1180–1183**
coupled analyses 254*T*, 255
coupled systems 1080
balancing and **111–124**
bearing vibration and 163
boundary conditions 186, 187*F*, 188*F*, 189*F*
differentiation/integration and 1194
equations of motion and 1326
gyroscopic 1097, 1099–1101, 1099*F*, 1100*F*
isolation theory and 1490–1494
magnetostrictive materials **753–762**
power balance and 1267
rotation and 112–113, 1068–1069
SEA and 1266
standards and 1231–1232
variational methods and 1354
couple unbalance 1185
crack propagation 509–512, 1083
Craig, RR Jr. **691–698**
Crash 302–314
application examples 312
axial loading 310*F*
bioengineering and 310–311
component roles and 308
contact algorithms and 308
DYNA3d 305–312, 305*T*, 307*T*
economic elements and 308
human head impact 312*F*
impact crushing 309*F*
safety standards 303*T*
solid mechanics and 304–305
supercomputers and 304
vehicle collision 304, 310*F*, 311*F*, 312*F*
CRAY supercomputer 304–312, 305*T*
Critical Damping **314–319**
definition of 315–317
distributed parameters 318–321
initial conditions and 315*F*
lumped parameters and 317–318
critical moment theorem 1070–1071
cross-axis sensitivity 1131–1132
cross flow 1023
cross-generalized mass (CGM) matrix 267
cross-orthogonality (XOR) matrices 267
crystalline growth 754
Curie brothers 1011, 1014
Curie-Weiss law 476, 478
current analysis 378
current sensor 1399–1400, 1400*F*
curse of dimensionality 902, 902*F*
CuZnAl 660
cycle limits 1095–1097
rotor-stator interactions 1107–1110
cyclostationary phenomenon 602
cylinders
bearings vibrations and 153–155
flexural radiation and 1460–1463, 1465–1468

D

d'Albans, Marquis de Jouffroy 1064
d'Alembert 1099, 1344
principle 126, 131, 607
rotation and 1070
rotor dynamics 1085
variational methods and 1355
Dalpiaz, G **1184–1193**
D'Ambrogio, W **1253–1264**
damping 344*F*, 413, 414*F*, 424*F*, 426*F*
absolute motion transducers and 1383
active **351–364**
active constrained layer (ACLD) 353–360, 355*F*, 356*F*, 359*T*, 359*F*, 361*F*, 362*F*, 363*F*
active mass driver (AMD) system 30, 33*F*
active/semi-active 347–349
advanced concepts 640–641
augmentation 630
chaos and 228
classical 723–725
complex modulus 338–339
Coulomb 337
critical **314–319**
directly-coupled 344*F*
discrete elements and **395–402**
dual frequency 638–639
Duffing's equation and 233
Duhamel's Principle and 1308
earthquakes and 442*F*, 449–460, 451*F*, 460*F*
elastically coupled 345–346, 346*F*
elastomeric testing and 631–632
equations of motion and 1324–1332
equivalent viscous 340–341, 341*F*, 721–722
in FE models **321–327**
fluids and **467–475**
fluid-structure interactions and 551
flutter and **553–565**
fractional derivative 325
friction and **582–589**, 590–592
fundamental theory and **1290–1299**
helicopter **629–642**
hybrid 28–30, 30*F*, 31*F*, 32*F*, 353–360
hysteretic 323–324, 646, **658–664**
impulse response function 1338–1339
isochrones and 420
isolation theory and **1487–1506**, **1507–1521**

damping (*continued*)
Krylov-Lanczos methods and 691–697
linear matrix methods **721–726**
liquid sloshing and 734–740
localization and 747
magnetic constrained layer (MCLD) 352, 353*F*
mass-spring system and 687*F*, 689, 689*F*
materials **327–331**, 329*F*, 331*F*, 337–338
matrices 360–363
maximum control voltage and 360, 360*T*
measurement of **332–335**
membranes and **762–770**
MEMS 779–781, 780*F*, 783–784, 784*T*
modal analysis and **820–824**
modal properties and 324–325
modulus 338–339
mounts and 342–349
negative 97
nonclassical 725–726
nonlinearity and 420
nonlinear resonance and 932–934
passive 343–345, 351–352
physical mechanisms of 321*F*
piezoelectric 352, 352*F*, 353*F*, 354–360
plate vibration and 889–890
proportional 723
residuals and 848–850
resonance and **1046–1055**
robots and 1056–1057, 1063
rotor dynamics 1085–1088, 1092
rotor-stator interactions 1107–1121
semiactive 30–33, 33*F*, 34*F*, 35*F*, 36*F*
shape memory alloys and 352, 353*F*, **1146**, 1149–1151
ship vibrations 1168
signal generation and 1184–1185
single frequency 632–637
structural 323–324
suspension and 37–38, 616
tires and 618
treatment types 351–354, 352*F*, 353*F*, 354*F*,
vehicular vibration and, 38–44
viscoelastic 325–326, 326*F*, 339–340, 649, 656–658
viscous 321–323, 324–325, 336–337, 340–341, 344*F*, 633–634, 636–637, 1294–1295, 1496–1501, **1548–1551**
wind and 1583
See also absorbers
Damping, Active **351–364**
Damping in FE models **321–327**
viscous 321–323
Damping Materials **327–331**
Damping Measurement **332–335**
Damping Models **335–342**
Damping Mounts **342–351**
damping ratios 413
Danish Standards Association (DS) 1224
dashpot
damping measurement and 332–333
Duhamel's Principle and 1308
parameters 636, 661
viscous damping and 336–337
data 365*F*
acquisition **364–376**
aliasing 365–369, 365*F*, 366*F*, 367*F*, 369*F*
basic diagnostics and 377
cleansing and 901
discretization errors and 369–371, 370*F*,
displays and **413–431**
environmental testing and 491–492
external sampling and 373–375, 373*F*
feature processing and 901–904
modal 413–417
neural networks and **863–868**
periodic 491
random 491
resampling schemas 374*F*, 375, 375*F*
sigma-delta converters 371–372, 371*F*, 372*F*
Simpson's rule 1197–1198
SNDT and 900–904
transient 491
triggering and 373, 373*F*
See also modal analysis
Data Acquisition **364–376**
data set 674, 676*F*
David, A **1001–1009**
da Vinci, Leonardo 125–126
deformable mirrors 483–485, 485*F*
degrees of freedom (DOF) 1326*F*, 1327*F*, 1332
absorbers and 15–18
active suppression and 49–51
averaging method and 960–961
cepstral analysis and 217*F*
chaos and **227–236**
critical damping and 315*F*
damping measurement and 332–333
damping mounts and **342–351**
direct problem and 1254–1259, 1257*F*, 1258*F*, 1259*F*
Duhamel's Principle and 1308
earthquakes and 444, 447–460, 447*F*
environmental testing and 498
equations of motion and 1291–1293, 1324–1327
FEA software and 245
finite difference methods and 524–525
flutter 567–570
forced vibration and 1295–1299
force transducers and 1123, 1125, 1126, 1130
degrees of freedom (DOF) (*continued*)
FRF data and 418, 420
ground transportation and 605–613
impulse response function **1335–1343**
inverse problem and 1259–1265
isolation theory and 1488–1490, 1494–1501
Krylov-Lanczos methods and 691–697
modal analysis and 828
modal properties and 269–271
model updating and 852, 854
NNM and 919–920, 919*F*
nonlinear system resonance and **928–943**
Nyquist plot of 424*F*
parallel processing and 992, 995
piezoelectric damping and 358
Rayleigh method and 1309–1312
residuals and 848–851
resonance and 1047–1055, 1048*F*, 1049*F*, 1050*F*, 1051*T*, 1053*F*
robots 1060
Schur method and 995–1000
signal representation and 645
SNDT and 899, 899*F*
spatial properties and 257, 258
stochastic analysis and 1240–1242, 1250–1252
structure-acoustic interaction and 1265
substructuring and 1333–1335, 1333*F*
superposition and 1300–1301
translation and 1325*F*
variational methods and 1357–1359
viscous damping and 324–325
See also boundary conditions
De Laval, Carl Gustav 112, 1064, 1065
De Laval model 1070–1071, 1072, 1085–1088, 1092, 1102–1103, 1110, 1112
chaos and 1112–1115
Den-Hartog's implementation 2
deployment diagrams 970, 972*F*
design optimization tools (DOT) 637
deterioration 376, 376*F*
deterministic models 1200, 1203–1204
detuning 404
Deutches Institut fur Normung (DIN) 1224
development testing 490
Devloo, P **967–976**
Devonshire theory 476–477
Diagnostics and Condition Monitoring, Basic Concepts **376–380**
detection and 381
deterioration time and 376*F*
general principles of 376–378, 377*F*
rotation and 379, 379*T*
signal generation and **1184–1193**
vibration signatures and 379

differential transformation method 291–292, 291*T*
differentiation 1195–1196, 1198
Digital Filters 380–395, 392*F*
acausal 1196
bilinear transformation and 393–394, 393*T*, 394*T*, 395*F*
canonic realization and 385, 385*F*
differentiation/integration and 1193–1199
discrete-time systems and 381–382, 381*F*
finite impulse response 385–387, 387*T*, 387*F*
frequency sampling and 389–390, 390*F*, 393*F*
infinite impulse response 391–394
minimax design and 390, 391*T*, 392*F*
seven-point 1196
signal flow and 383–385, 383*F*, 384*F*, 390*F*
suppression and 385
windows and 387–389, 388*F*
See also signals
digital signal processing (DSP) 367
dimension reduction 432–435
Dimentberg, MF 1033–1039, 1040–1046, 1246–1252
dipole sound 880–882
Dirac's delta function 1336, 1336*F*
direct problem 1254–1259, 1257*F*, 1258*F*, 1259*F*
direct solvers 992
Dirichlet preconditioner 999–1000
Discrete Elements 395–404
damping and 402
mass/inertia 396–397, 397*F*
modeling of 396
springs 396*F*, 398, 398*F*, 400*T*
torsional systems and 396
discrete Fourier transform (DFT)
See Fourier transforms
discrete systems 1309–1311
time 381–382
variational methods and 1355–1359
discretization 369–371, 973
Disks 404–413, 405*F*
asymmetric 408
axisymmetric 404–407
gyroscopic couple and 1099–1101
nodal diameter 405–411
rotating 409–410
symmetric 407–408
types of 404
vibration response and 405*F*, 410–413
See also rotation
displacement
beam vibration and 1330
equations of motion and 1324–1332
displacement sensors
capacitive 1399–1400
eddy current 1400
LVDT 1400–1401
displays 413–431
frequency response data 417–420
frequency spectra 420–421
modal data 413–417
model order indication and 425–429
Displays of Vibration Properties 413–431
distributed parameter systems (DPSs) 318–321
sensor/actuators and 1134–1143
Doebling, S 898–906
domains *See* parallel processing
Dongarra, JJ 973
Donnell-Mushtari-Vlasov equations 1159–1160, 1161–1162
Donnel's theory 353
Doppler effect 700, 700*F*
laser vibrometers and 700–706
double modes 416, 419*F*
chaos and 229–232
doubling map 230*F*
Drew, SJ 1443–1455, 1456–1480
drop test 617
Dubois-Pelerin principle 973
Dubuisson, B 869–877
Duffing's equation 227, 228, 233–235, 235*F*, 1110
Duhamel's Principle 444, 1305–1308, 1306*F*
Duncan, Dowson 1070
Dunkerley method 112, 135–136
Durbin's method 1203
DYNA3D 305–312, 305*T*
codes for 305–307
dynamic analysis
bearings 143–152
bifurcation theory and 435
cables and 209
classification and unfolding 435
dimension reduction and 432–435
displacement fields 200
displays and 413–431
earthquakes and 439–461
FEA software and 243–256
finite element methods 535
fluids and 467–475
impact 278–286
isolation theory and 1487–1506, 1507–1521
laboratory vs. field 492–493
MEMS 779–781
normal form simplification and 435
robots 1055–1063
rotors 1085–1106
shape memory alloys and 1144–1155
stability and 431–438, 433*F*, 435*F*, 436*F*, 437*F*
structural modifications and 1253–1264
transient 278–286
See also active control; rotation; structural analysis
Dynamic Stability 431–438
dynamic systems
basic principles of 125–126
blades and 174–178
coordinates for 130–131
fundamental theory and 1290–1299
nonlinear systems and 952–966
object oriented programming and 974–975
packaging and 983–989
parametric excitation and 1001–1009
rotor-stator interactions 1107–1120
tire vibrations 1369–1379
variational formulations in 1322–1324
vibro-impact systems and 1531–1548
dynamic unbalance 1186
Dyne, S 1193–1199

E

Earthquake Excitation and Response of Buildings 439–461, 441*F*
attenuation and 440*T*
damping and 451*T*, 451*F*, 460*F*
elastic MDOF systems 449–453
elastic SDOF system and 447–448
Fourier amplitude spectrum and 444*F*, 445*F*
ground motion and 439–446, 441*F*, 442*F*, 443*F*, 444*F*, 445*F*, 446*F*
MDOF systems and 455–459
SDOF systems 444, 447–455, 447*F*, 452*F*
shape functions and 453*F*
spectra smoothing and 450*F*
tripartite response and 449*F*
eccentricity 112–113
rigid states and 115
echo removal 225*F*
economic elements 308
eddy current sensors 1400
efficiency
modal radiation 892–894
Eigensystem Realization Algorithm (ERA) 673, 677–682
Eigenvalue Analysis 461–467
computational methods for 463
inverse problems 686–691
Rayleigh quotient and 462
Rayleigh-Ritz analysis and 462–463
similarity transformation methods 461, 464
Sturm sequence property and 463
vector iteration methods and 464–466
eigenvalues 424*F*
4 DOF pitch plane model 608
bifurcations and 818
boundary element methods 198
chaos and 228
continuous systems and 1312–1317
damping and 322–323
FEA software and 255*T*, 256

eigenvalues (*continued*)
finite element methods 530–533
hysteretic damping and 323–324
localization and 744
model validation and 851–854
nonlinear systems and 953
normal form simplification and 435
plate vibration and 889
residuals and 848–851
rotation and 1071–1072
structural-acoustic interactions 1281
See also rotation
elasticity
aeroelastic effects and **87–97**, 1584–1586
boundary element methods 196, 196*F*
bulk waves and 908
cables and 210, 213
columns and 238
damping materials and **327–330**
discrete elements and 398, 398*F*, 399*T*, 400*T*
FEA software and 251*T*
fluid/structural interaction and 545–550
flutter and **553–565**, **565–577**
hysteretic damping and 659–660
isolation theory and **1487–1506**
lag dampers and **629–642**
noise and **887–898**
nonlinear analysis and 948*F*, 1110–1111
piezoelectricity and 1013
potential energy and 1346–1347
sensor/actuators and 1134–1143
shape memory alloys and **1144–1155**
shock isolation and **1180–1184**
transmissibility 1522–1527
vibration intensity and **1480–1487**
viscoelastic dampers and 649, 656–658
waves and 1566–1568
See also boundary conditions; damping
elastic modulus 1329
Electricite de France (EDF) 220
Electric Power Research Institute 1078
electrodynamic shaker 494
electromagnetic acoustic transducers (EMATS) 913
electromagnetic damping composites (EMDC) 354, 354*F*
electromagnetic sensors 1401–1402, 1402*F*
electronic speckle pattern interferometry (ESPI) 699, 705, 706*F*, 709*F*
full field measurement and 707–709
electronic vibration origins 1191
Electrorheological and Magnetorheological Fluids **467–475**
electrorheological (ER) fluids 640
actuators and 58–72
new applications of 474–475
semiactive control and 467–468
smart fluids and 468–474, 468*F*, 469*F*, 470*F*, 471*F*, 472*F*, 473*F*
electrostatic field
MEMS 785–787, 785*F*, 791*T*
Electrostrictive Materials **475–490**, 476*F*, 488*F*
actuator classification and 484*F*
applications of 482–490
deformable mirrors and 483–485, 485*F*, 486*F*, 487*F*
flapper 489*F*
interferograms and 486*F*
ion rattling and 480*F*
microscopic origins of 475–476
multimorph mirror and 485*F*
oxide perovskites and 477–482, 479*T*, 479*F*, 481*F*
phenomenology of 476–477
servo valve 489*F*
temperature and 477, 478*F*, 480–482, 482*F*, 483*F*, 484*F*
elementary run out 112
element technology 282–283
Elishakoff, I **236–243**
Elliott, SJ **81–87**, **977–982**
encapsulation 969
Energenics, Inc. 759
energy
absorption 308
actuators and 70–72
basic principles of 124, 125–126
FEA 1320–1322
flow 1266–1267, 1267*F*, 1269*F*
fundamental theory and **1290–1299**
Hamilton's Principle and 131
hybrid control and **649–658**
magnetostrictive materials 754–755
operator 601
Rayleigh's method 1309–1317
resonance and 1047–1048
Ritz method 1318–1319
SEA and 1266
shape memory alloys and 1148
stochastic systems and 1250–1252
time-average 1268
variational formulations 1322–1324
See also spectra
engineering units (EU) 1209–1211
ensemble average response 1268
envelopes 493–494
environmental testing **490–496**, 492*F*, **496–504**
correlation and 497*F*, 499*F*, 500*F*, 503*F*
envelopes and 493–494
field dynamic 492–493, 498–500, 499*F*
fixture design and 495–496
force identification and 502–503
frequency domain and 497–498
environmental testing (*continued*)
input-output relationships 497–498, 497*F*
laboratory dynamic and 492–493, 500–502
LDVs and 1406
measurement locations and 494
motion control and 493
seismic instruments and **1121–1134**
test methods and 490–491, 494–495
use identification and 491–492
Environmental Testing, Implementation **496–504**
Environmental Testing, Overview **490–496**
EPROM circuits 779
equations
2SLS method 679
absolute motion 1382–1395
active absorbers 1–6
active damping 356–359, 360–364
active isolation 46
active suppression 49–57
actuators and smart structures 62–63, 65, 66, 70–72
adaptive filters 82–86
aeroelasticity 89
ARX models 677
autocorrelation function 977–978, 1592
averaging methods **98–110**, 1244–1246
balancing 112–117, 118–121
basic principles **124–136**
bearings 145, 147, 148, 155–156, 160
belts 166–169, 170–172
bending strains 1136
biharmonic differential operator 1024
blades 175, 177, 178
boundary conditions 181–188
boundary element methods 192–201
bounded waves 1560–1562
Bresse-Timoshenko 239
bridges 203–206
cables 209–213
calculus of variations 126, 130
capacitance 1399
CEDA 1271
cepstral analysis 217, 222
chaos 228–234
circle-fitting method 822
circular plates 1026
civil structures 28
classical damping 723
columns 237–238, 239–242
complex exponential method 821
continuous methods 287–293
correlation functions 295–301
correlation methods 680
cost function 977
crack propagation 510–511
crashworthiness 306–308

equations (*continued*)
critical damping 315–316, 317–321
Curie-Weiss 476, 478
D'Alembert 1322
damping in FE models 321–325
damping materials 327–329
damping models 336–341
damping mounts 343–348
data acquisition 370–372
data set 674
digital filters 381–382, 385–393
Dirac's delta function 1336
direct problem 1254–1259
discrete elements 396–402
disks 404–405, 413
dissipated power 1266
distributed actuation 1136–1137
Donnell-Mushtari-Vlasov 1159–1162
Doppler frequency 1404
Duffing 228
Duhamel's Principle 1305–1308
Dunkerley's method 135–136
DYNA3D and 306–307
dynamics 279–281, 283
dynamic stability 432–435
earthquake excitation 444–459
eigenvalue analysis 461–463, 464–465, 466
electromagnetic sensors 1402
electrostriction 475–479, 484
energy flow exchange 1266
energy operator 601
environmental testing 492–493, 497–502
ERA 680–681
Euler-Bernoulli beam theory 137–142
Euler's 126–130, 878
exponential window 1594
external problem 1277
FEA software and 255*T*
feedforward control 513–516
finite difference methods 520–528
finite element methods 531–543, 1322
FIR filters 1594
flexural motion 130
flexural radiation 1457–1465
fluids 470, 473
fluid/structure interaction 545–551
flutter 556–559, 566–570
FM0 601
FM4 601
Fokker-Planck-Kolmogorov 1238, 1248–1249
forced problem 1281–1282
forced response 579–581
forced vibration 894–896
force window 1593
Fourier-based identification 666–667, 668–671
free vibration 1029, 1293–1295
friction 583–587, 591–593
Galerkin's method 135
gear diagnostics 597–598, 600–602
equations (*continued*)
generalized inverses 720
Green's 879, 888
ground transportation 603, 608–621
guided wave 1552, 1553, 1554
Hamilton's principle 131, 1322–1323, 1328
hand-transmitted vibration 626
Hanning window 1590
helicopter damping 631–635, 636–637
Helmholtz 195, 878
Hilbert transforms 642, 643
Hohenemser/Prager 238
Hooke's 1012
Hu-Washizu stationary principle 1321
hybrid control 650–654
hysteretic damping 659–660, 661–664
Ibrahim time domain method 821
impulse response function 1336–1343
input power vector 1267
internal problem 1279–1282
inverse iteration of rigid body modes 718–719
inverse problems 686–688, 1259–1264
isolation theory 1491–1505, 1509–1512, 1514, 1517–1518, 1521
Kaiser window 1590
Kirchhoff-Helmholtz 888, 1457
Kolomogorov 1249
Krylov-Lanczos methods 691–696
Lagrange 131, 240, 721, 1323
Laplace transforms 1336–1338, 1407–1409
laser vibrometry 700, 701, 702, 703, 704, 707
Lenz's law 1402
liquid sloshing 727–735, 736, 737–740
LMS method 679
Love-type 1155–1159, 1159*T*, 1160–1161
magnetostrictive materials 754–755
Mathieu 730, 1111
Maxwell 136, 1135
Melnikov's method 232
membranes 763–769, 1135
MEMS 780, 782–783, 785, 787–789
minimum total complementary energy 1320
minimum total potential energy 1320
modal analysis 824–828
modal density 1266
modal directivity 890
modal parameters 683
modal properties 266–269, 270–271
modal radiation efficiency 892–894
mode acceleration 719
equations (*continued*)
model based identification 674–683
model class 674–676
model order selection 682
model updating 845, 847–851
mode of vibration 838, 840–843
Moore-Penrose generalized inverse 717–718
motion 1291–1293, 1325, 1326, 1327, 1328, 1329, 1331
NA4 601
narrow-band demodulation 602
Navier's 911
neural networks 869–876
NNM 918–920, 921–922
noise 878–886, 888–895
nonclassical damping 725
nonlinear analysis 945, 947–949, 953–956, 957–964
nonlinear system resonance and 929–941
nonsingular linear systems 711–713
nullspace 320
optimal filters 977–981
packaging 984
parallel processing 990, 992–999
parametric excitation 1002, 1003–1006
Parseval's 388, 445
perturbations 232
piezoelectric materials 1012–1013, 1013*T*, 1015–1017
pipes 1019–1022
plate vibration 889–890, 892, 1024
Poisson's ratio 327
principle of least action 1323
production error 676
Prony method 678–679
proportional damping 723
random processes 1033–1037, 1040–1041, 1043–1045
rational fraction polynomial method 823
Rayleigh integral 889
Rayleigh method 1309–1317
Rayleigh quotient 462
Rayleigh-Ritz analysis 462
Rayleigh's Principle 132–134
Rayleigh wave 1553
reciprocity 1267
rectangular plates 1026
rectangular window 1588
response properties 274–278
Ritz method 134, 1322–1319
robot vibrations 1060
rotation 1070–1077, 1083–1084
rotor dynamics 1085–1095, 1097–1106
rotor-stator interactions 1107, 1110–1119
running sum 1196–1197
Scruton number 1584
SEAT 1577
seismic instruments 1121–1132
shape memory alloys 1145–1153
shells 1155–1165

equations (*continued*)
ship vibrations 1168
shock 1173–1174
signal generation 1185, 1188–1191
signal integration/differentiation 1193–1198
signal processing, model based 1199–1205
similarity transformations 461, 464, 471
Simpson's rule 1197–1198
singular systems 714–716
Smale's horseshoe 233
SNDT 899
sound 1444–1446, 1451–1452
sound power 890–891
sound pressure with boundaries 888–889
spatial properties 257–258, 260–262
spectral analysis and 1209–1211, 1213–1221
spectral coherence function (SCF) 602
standard wave 1329
statistical moments 1243–1244
steady-state power balance 1267
stochastic analysis 1238–1246
stochastic differential calculus 1246–1252
stochastic systems 1246–1252
strain-life method 507
Stribeck 1188
Strouhal number 1584
structonic cylindrical shells 1139
structural-acoustic interactions 1275–1282
structural dynamic modifications 1254–1264
structural system parameters 823
Sturm sequence property 463
substructuring 1333–1335
Succi method 1281
superposition 1300–1304
SVD 716–717
synchronized averaging 598
system coordinates 130–131
Taylor series 210
time frequency methods 1360–1364
Timoshenko beam theory 142
tire vibrations 1373–1377
transmissibility 343, 348, 1522–1527
trapezium rule 1197
ultrasonics 212–213, 908–909, 910–911, 1437–1438
unbound waves 1566–1567, 1569
undamped vibration 722–723
variational methods 1344–1359
vectorial approach 125–126
vector iteration 464–466
vehicular vibration 38–42
vibration absorbers 10–23
vibration dose value 1575
vibration intensity 1480–1487
vibro-impact 1532–1540
equations (*continued*)
virtual work principle 1320
viscous damping 721, 722, 1548–1549
wavelet transformation 600, 1420–1428
wave number 891
Weiner-Khintchine theorem 1361
wind 1579, 1580, 1581–1583, 1584
windows 1587–1590, 1592–1594
Z transforms 1409–1411
See also Fourier transforms
equations of motion (EOM) 1324
beams and 1329–1330
continuous system models and 1327–1331
membranes and 1331
multiple DOF 1326–1327
plates and 1331
rods and 1328–1329
shafts and 1328–1329
single DOF 1324–1325
strings and 1328–1329
equilibrium
averaging method and 960–962
basic principles of 125–126
cables and 209–210
chaos and **227–236**
curvature 209
discrete elements and 396
eigenspaces and 953
environmental testing and 498–500
equations of motion and 1327
invariant manifolds and 955–956
nonlinear systems and **952–966**
point classification and 953
rotor dynamics 1096*F*, 1097–1098
variational methods and 1355
See also chaos; parametric excitation; stability
equipartition 1266
error
Fourier-based identification and 666–671
modal analysis and 834
model-based identification and 676–677
model updating and 845
neural networks 870
spectral analysis and 1222–1223
ETREMA Products, Inc. 759
Euler 1099
Bernoulli beam theory 137–142, 166, 338
field equations 878
Lagrange equations 1344–1346, 1345*T*
relations 316
EU Machinery Safety Directive 626, 1576
EU Physical Agents Directive 627–628, 1576
Ewins, DJ 332–335, 404–413, 805–813, 829–838, 838–844
excitation
acoustic 897
aerodynamics and 1191
aliasing error and 670
averaging methods 1244–1246
balancing and **112–123**
bias error and 670
blades and 174–178
capacitance and 1399
complex stiffness and 338–339
Duffing equation and 228
Duhamel's Principle and 1304–1308
earthquakes and **439–461**
environmental testing and 497–498
fluid/structural interaction and 545–551
forced response 579–581
Fourier-based identification and 665–671
ground transportation and 605–621
hydraulics and 1191
identification and **673–685**
impulse response function 1335–1343
isolation theory and **1507–1521**
leakage errors and 671
localization and 747
MEMS 779–781
modal 814*F*, 815, 816–817
model-based identification and **673–685**
noise and 887–898
nonlinear resonance and **928–943**
nonlinear systems and 956
oil film 1191
parametric **1001–1009**
periodic 1296–1297
random errors and 671
random processes **1040–1046**
resonance and **1046–1055**
rotor dynamics 1102
rotor-stator interactions 1107–1121
ship vibrations **1167–1173**
stochastic analysis and **1238–1246**, 1247–1252
time frequency and 1366–1368
transverse vibration and 169
vibration isolation and 1501–1504
viscous damping and **1548–1551**
See also active control; damping
exponential model class 676
external problem 1276*F*, 1279

F

failure models 143, 252*T*
Faraday-Lenz law 755, 761
far-field approach 890
Farhat, C **710–720**
Farrar, C **898–906**
Fassois, SD **673–685**
fast oscillating function 1273*F*
Fatigue **505–512**
classical approach to 508

Fatigue (*continued*)
crack propagation analysis 509–512, 509*T*, 510*F*, 511*F*
estimation 647
strain-life method 505–508, 506*F*, 507*T*, 508*F*, 509*T*
faults
bearings and 1083, 1187–1188
coaxiality 1083, 1099
gears and 1189–1191, 1191*F*, 1192*T*
FDAC matrix 275*F*
Federal Aviation Administration (FAA) 245
feedback 3–5, 28
feedforward control 28, 46–47
applications of 516–519, 518*F*, 519*F*, 520*F*
beams and 517
description of 513–516, 513*F*, 514*F*
networks 866
Feedforward Control of Vibration, 513–520
Feeny, BF **924–928**
Feigenbaum's cascade 1543–1544
Feldman, M **642–648**
FETI (dual Schur complement method) 997–1000
field dynamic
boundary conditions and 492–493, 495
environment 492–493, 498–500
measurement location and 494
filters
acausal 1196
adaptive **81–87**
antialiasing 367–368
Butterworth 703
digital **380–395**
FIR 385–387, 977–978, 978*F*, 1594
IIR 1594
minimax, 390
optimal **977–982**
recursion 100–101
spectral analysis and 1216–1218
Weiner, 978–981
final prediction error (FPE) 1205
Finite Difference Methods **520–530**
central 525–527, 526*F*
formulas 521, 521*F*, 522*T*, 523*T*
forward 524–525
operators 522, 524*T*,
partial differential equations 528, 529*F*
finite element analysis (FEA)
ABAQUS 246–247
ANSYS 247
boundary conditions 253
COSMOS/M 247–248
coupled analyses 255
dynamic applications and 244–245
energy methods and 1320–1322
geometric nonlinearity 252
history of 244
linear analyses 253–255
materials and 252–253
finite element analysis (FEA) (*continued*)
meshing and 250
MSC/NASTRAN 248–249
nonlinear analyses 254
nonstandard elements 250
object oriented programming and **967–976**
SAMCEF 249–250
software quality assurance and 245–246
solution methods and 255–256
standard elements 250
Finite Element Methods 243–244, 250–253, **530–544**, 1332
basic approach to 531–533, 541*T*, 542*T*
crash and **302–314**
damping in **321–327**
dynamic problems 535
eigenvalues 533
error analysis 540–543, 543*F*
modal properties and 265, 266–267, 269
model updating and 844–847, 852
nonlinear analysis 536–538, 536*F*, 538*F*, 539*F*
nonstructural problems 539, 541*T*
piezoelectric damping and 352–358
propagation 534
spatial properties and **256–264**
static problems 534
structural-acoustic interactions 1277–1278
structural problems 536–539, 536*F*, 538*F*, 539*F*
substructuring and 1333–1334
finite impulse response (FIR) filters 385–387, 977, 978*F*, 1594
time domain formulation and 977–978
Wiener 978–981
finite spherical monopole 1447
Fisher's discriminant 903
fixed references 1398, 1398*F*
fixture design 495
Flanagan-Belytschko constant 305
flap 629–630
flappers 485–488
Flatau, A **753–762**
flexibility 118–119, 209
columns and 239
isolation theory and **1487–1506**
plate vibration and 1033
robots 1056–1057
sound and **1443–1455**
spatial properties and 260–264
tire vibration and 1374–1375
flexural motion 130, **1456–1480**
basic theory of 1456–1463, 1456*F*, 1458*T*, 1459*F*, 1459*T*, 1460*F*, 1461*F*, 1461*T*, 1462*T*, 1463*F*
boundary conditions and 186, 187*F*, 188*F*, 189*F*
MEMS 787–789
Ritz method and 134
flexural motion (*continued*)
sound and **1456–1480**
source ratios 1463–1468, 1464*F*, 1466*F*, 1467*F*, 1468*F*, 1469*F*, 1470*F*, 1471*F*, 1472*F*, 1473*F*, 1474*F*, 1475*F*, 1476*F*, 1477*F*, 1478*F*, 1479*F*, 1480*F*
transmissibility 1523–1527
Floquet theory 338, 960, 1002
shape memory alloys and 1151–1152
fluids 887, 949
acoustic radiation and 545–550, 545*F*, 546*F*, 547*F*, 548*F*, 549*F*, 551*F*, 552*F*
bearings and 152–165
damping modes 469, 469*F*, 470*F*, 551
electrorheological (ER) **467–475**, 640
excitation and 473*F*
force feedback and 474, 474*F*
force/velocity form 472*F*
ideal Bingham 469*F*
lag dampers and 629–641
liquid sloshing **726–740**
lumped model 472*F*
magnetorheological (MR) 467–475, 640–641
particle orientation and 468*F*
pipes and **1019–1024**
plate vibration and 1033
Reynolds number and 472*F*
semiactive dampers and 31–33
shock isolation and 1183
signal generation and 1191
smart **467–475**
sound and **1443–1455**
structure interaction and 544–553
ultrasonics and **1437–1441**
whirl and 1191
Fluid/Structure Interaction 544–553
Flutter 553–565
active pylons 574, 575*F*
aeroelasticity and 553–560, 553*F*, 554*F*, 555*F*, 556*F*, 557*F*, 558*F*, 559*F*, 560*F*
binary 561
modal properties 566–567, 567*F*
model of 555–559, 567
panel 96
simulation 570–571, 571*F*, 572*F*
smart wings 575–576, 576*F*
solution 559–560
suppression 572–573, 573*F*, 574*F*
test validation 561–563, 562*F*, 563*F*
torsion 561
transfer function 569
types of 560–561
Flutter, Active Control 565–577
FM0 601
FM4 601
foam blocks 1182
Fokker-Planck-Kolmogorov equations 1238, 1248–1249

forced problem 1281–1282
Forced Response **578–582**
base excitation 580–581, 580*F*, 581*F*
harmonic excitation 579–580, 579*F*, 580*F*
resonance 581–582, 581*F*
forced vibration 1295–1299
friction damping and 585–586
modes of 843–844
force transducers 1123
bending moment sensitivity and 1125–1127
hammer attachment and 1124
loading effects and 1128–1130
rigid foundation 1123
stinger and 1124–1125
Forde, BWR 972
Fortran 973
Fourier, Joseph 1065
Fourier analysis
earthquakes and 443–445
helicopter damping and 634, 639
time frequency and 1360–1361
Fourier transforms 1411–1419, 1412*F*, 1414*F*, 1415*F*, 1416*F*, 1418*F*
adaptive filters 84–86
averaging and 109
boundary element methods 201
bridges and 203
CEDA and 1271, 1272*F*
correlation function and 296
differentiation/integration and **1193–1199**
Duhamel's Principle 1305
impulse response function 1339–1343
influence coefficients and 122
linearity 1413
MDL criterion and 1205
modal analysis 815
nonlinear testing and 1287
properties of 1412–1419
spectral analysis and **1208–1223**
wavelets and 1420–1423
windows and 1588–1592, 1588*F*, 1589*F*
See also cepstral analysis
fractals **1191**
fractional derivative models 325
free-free planar truss 420*F*
free vibration
complex 842–843
continuous methods and 287–293
friction damping and 584–585
origins of 840–841
orthogonality and 841–842
structonic shell systems and 1139–1140
frequency
actuator sensitivity and 1140–1141
aliasing and 365–369
averaging and 99–100, 108–109
basic diagnostics and 379–381
basic principles of 124
frequency (*continued*)
bearing diagnostics and **143–152**
Bragg cell 1404
bridges and **202–207**
cables and 211–215
capacitance and 1399
columns and **236–243**, 237*T*
convergence coefficients and 86–87
critical damping and **314–319**
cycle limits and 1107–1110
damping in FE models and **321–327**
damping materials and **327–331**
damping models and **335–342**
damping mounts and **342–351**
digital filters and **380–395**
disks and **404–413**
Domain Assurance Criterion (FDAC) 275–276
domain methods 822–823
earthquakes and **439–461**
energy methods and **1308–1324**
environmental testing **496–504**
equations of motion and 1324–1332
Euler-Bernoulli beam theory 137–141
excitation 414
force transducers and 1123–1132
Fourier-based identification and 665–671
FRF data and 417–420, 421*F*
fundamental theory and **1290–1299**
gear diagnostics and **741–751**
ground transportation **603–620**
hand-transmitted vibration and 623*F*
helicopter damping and **629–642**
Hilbert transforms and **642–648**
identification and **673–685**
index 274*F*, 275*F*
input-output domain 497–498
instantaneous 644
isolation theory and **1487–1506**, **1507–1521**
LDVs and 1403–1406
liquid sloshing and 736–739
localization and **741–751**
membranes and 763–767
MEMS 779, 783–784, 784*T*
misalignment and 1186
MMIF and 425–429
modal analysis and **820–824**
modal indicators and 425–429
model-based analysis and **673–685**, 1204–1205
motion sickness and **856–861**, 859*F*
moving belts and 166–170
neural networks and 867–868
noise and **877–887**, **887–898**
nondimensional 1026*T*, 1027*T*, 1028*T*, 1029*T*
nonlinear stiffness and 425*F*
nonlinear system resonance and **928–943**
nonlinear testing and 1286*F*
Nyquist 445
frequency (*continued*)
plate vibration and 414–415, 889–890, **1024–1031**
plotting of 413–414
residuals 850
resonance **1046–1055**, 1285
response function (FRF) 646, 1366
ride natural 614
Ritz method and 290
rotor dynamics and 1088–1090
rotor-stator interactions 1107–1121
SEA and 1265–1272
shape memory alloys and 1148–1153
shells and 1160–1163
shifting devices 702–703
sigma-delta converters and 371–372
signal generation and 1185–1192
signal integration/differentiation **1193–1199**
spectra 420–421, 428*F*, **1208–1223**
stationary belts and 166
structure-acoustic interaction and **1265–1274**
time methods and **1360–1369**
tire vibrations **1369–1379**
transduction and 755–759, 755*F*, 756*F*, 757*F*, 758*F*
ultrasonic **906–918**, **1437–1441**
vibro-impact systems and **1531–1548**
weighting 625–626, 626*F*, 627*F*
weightings 1572, 1572*T*, 1573*T*
whole-body vibrations and **1570–1578**
windows and **1587–1595**
See also rotation
frequency response functions (FRFs) 820
absolute motion transducers and 1382
Assurance Criterion (FRAC) 274, 276
averaging and 100
cepstral analysis and 217, 218, 222–227
compound matrix 274, 278
cross-axis contamination and 1122
direct problem 1254–1259, 1257*F*, 1258*F*, 1259*F*
environmental testing and 299–302, 497–498
flutter and 563
forced response and 579
force transducers and 1128–1130
Fourier-based identification and 665–671
impulse response function 1341–1342
inverse problem 1259–1265, 1259*F*, 1262*F*, 1263*F*, 1264*F*
modal analysis **813–820**, 824–828
model updating and 852
neural networks and 864
residuals and 848–850
resonance and 1053–1054

frequency response functions (FRFs) (*continued*)
response properties and **272–277**
shape memory alloys and 1150–1151, 1152*F*
Fresnel equations 182
friction 589–590, 950
base isolators 587–589, 587*F*, 588*F*
counter-clockwise rotation 595*F*
damping and 335, **582–589**
dry 583–584, 583*F*, 584*F*, 586*F*
element acceleration 594*F*
forced vibration and 585–586
free vibration and 584–585, 584*F*
limit cycle and 592–593
links and 153–161
misalignment and 1186
negative damping and 590–592
PDF 594*F*
rotor dynamics 1095
snubber 1181, 1182*F*
Spurr's sprag-slip and 593–597
static vs. kinetic 582
stochastic systems and 1250–1252
time history 594*F*
velocity curve 591*F*
Friction Damping **582–589**
Friction Induced Vibrations **589–596**
Froude scale 630
Fuller, CR **513–520**
full-field measurement 707–708
fuzzy logic 43–45

G

Galerkin method 135, 239, 240, 290, 292–293, 1332
dimension reduction and 432–435
Galilean referential 1085, 1086, 1106
Galilei, Galileo 124–125
galloping 1585
Gamma, E 969
Gandhi, F **1548–1551**
Gaussian classifiers 872
Gaussian elimination 711, 711*F*, 715
Gaussian theory 1135
time frequency and 1362
Gaussian white noise 1238–1240, 1241–1246
Gauss-Newton method 677
Gauss-Seidel algorithm 995
Gauss's law 755
Gabor, Denis 642
Gear Diagnostics **597–602**, 1080
algorithms for 598–603
cepstral analysis and 218–220
Choi-Williams distribution 600*F*
disks and **404–413**
failure modes and 597
planetary system 597*F*
signal generation and 1189–1191, 1191*F*, 1192*T*
standards and 1232–1233
tooth averaging 599*F*
vibration model of 597–598
General Problem of the Stability of Motion (Lyapnuov) 1097
geometry
eccentricity and 112–113
isolation theory and 1490
membranes and 763–767
nonlinear systems and 251*T*, 252, 947, 953
piezoelectricity and 1015
rotating line 1067, 1068*F*
rotation and 112
run out and 112–113
shape memory alloys and 1151
structure-acoustic interaction and 1265
Gern, FH **565–576**
Gibbs energy 476
Giurgiutiu, V **58–80**
Gladwell, GML 691
glass transition region 329
global error indicator 273
global positioning systems (GPS) 774
global sonic nondestructive testing (GSNDT) 899, 906
aerospace and 905
basis of 899
civil engineering and 905
data processing and 900–904
history of 904–905
operational evaluation and 900
rotation and 905
Goldman, Paul 1112
Golubitsky, M 432
Graeffe's root-squaring method 463
Gram-Schmidt orthogonalization 691
graphical comparison 266
gravimetric calibration 1131
gravity
equations of motion and 1325
liquid sloshing and 739–740
Green function 879, 888, 889, 1281
Griffin, MJ **621–629**, **856–861**, **1570–1578**
Griffin, S **46–48**
Groundhook control 41
Ground Transportation Systems **603–620**
2 DOF pitch plane 609–610, 611*F*, 612*F*
2 DOF quarter car 612–613, 614*F*
4 DOF pitch plane ride 608
7 DOF 606*F*
analysis models 605–621, 607*F*, 608*F*
damping 616, 617*F*
deflection ratio 613, 613*F*
driver/passenger sensitivity 603–604, 605*F*, 619*T*
fatigue time 604*F*
guidelines 614
loading 616*F*
mass transmissibility 613, 613*F*
parameter determination 614–621, 619*T*, 620*T*
PSD 618–621, 618*F*
ride natural frequency 614
Ground Transportation Systems (*continued*)
suspension springs 615, 616*F*,
tires 617*F*, 618
weight 615, 615*F*, 615*T*
Guckel rings 788
guided waves **1551–1559**
attenuation of 1558–1559
bars and 1556
cylinders and 1556
definition of 1551
engineering and 1559
flat boundary and 1553
plates and 1552*F*, 1553–1556
theory 1552–1553
Guyan reduction method 258, 1333
Gyration 239
gyroscopes 19–21, 1332
gyroscopic couple 1097, 1099–1101, 1099*F*, 1100*F*

H

Haddow, A **1285–1289**
Hagg's number 1088
Hall probe 761
Hallquist, J **278–286**
Hamiltonian mechanics 228
bifurcation and 435
distributed actuation and 1136
energy methods and 1322–1323
nonlinearity and 235
piezoelectricity and 1014, 1015–1017
Ritz method and 290
Hamilton's principle 131, 358, 1328
variational methods 1344, 1348–1349, 1355
hammers 1121, 1124
Han, RPS 972
Hand-Transmitted Vibration **621–629**
band spectra 623*F*
blanching 624*F*, 626*T*
dangerous processes 622*T*
disorders of 621*T*
effects of 621–625, 624*T*
evaluation standards for 625–628
frequency-weighted 626*F*, 627*F*
preventive measures 625, 625*T*
sources of 621
Stockholm Workshop scale 622*T*
threshold level 628*F*
white finger 627*F*
whole-body vibration 1574
Hann, F **1578–1587**
Hanning window 389, 672*F*, 1216–1219, 1218*F*, 1590–1591, 1590*F*
harmonics 1270
boundary element methods 195–198, 1279–1282
bridges and **202–207**
chaos and **227–236**
continuous systems and 1312–1317
flexural radiation and **1456–1480**
forced problem 1281–1282

harmonics (*continued*)
forced response 579–581
forced vibration and 1291–1296
free vibration and 1293
friction and **589–596**
impulse response function 1341–1342
nonlinear resonance and **928–943**
resonance and **1046–1055**, 1288
response and 1286
rotor dynamics 1085–1088, 1097
rotor-stator interactions 1107–1121
signal integration/differentiation **1193–1199**
sonic **898–906**
superposition and 1301–1304
ultrasonic **906–918**
windows and 1216–1218
See also excitation; oscillation; sound
Hartmann, F **192–202**
Hayek, S **544–553**, **1480–1487**, **1522–1531**
Heckl, M 1265
Helicopter Damping **629–642**
advanced concepts 640–641
augmentation and 630
dual frequency characterization 638–639, 638*F*, 639*F*, 640*F*
elastomeric testing 630*F*, 631–632, 631*F*
hysteresis modeling and 633*F*, 636–637, 638*F*, 639, 640*F*
rotary hub 629*F*, 630*F*
single frequency characterization 632–637, 634*F*, 635*F*, 636*F*
stiffness and 633–635, 633*F*, 636*F*, 637*F*, 638*F*
viscous 633–634, 641*F*
Helmholtz equation 878
boundary element methods 195
parallel processing and 1000
Hessenberg form 467
heteroclinic point 229
high frequency resonance technique (HFRT)
bearing diagnostics and 146, 146*F*, 1188
Hilbert Transforms **642–648**, 642*F*, 648*F*
analytic signals and 643–646
CEDA and 1271
cepstral analysis and 218, 222
notation 642
properties of 642–643
transformers and 647–648
vibration systems and 646–647
Hodges, CH 744
Hohenemser-Prager equations 238, 241
Holmes, PH 431
Holmes, PJ **227–236**
homoclinic loop 231*F*
homoclinic points 229
Smale's horseshoe and 232–233
Hooke's equations 660, 754, 1012
Hopf bifurcation 435
horseshoe maps 232–234
hourglassing 305, 308
Householder's method 467
Hubble Space Telescope 485, 488*F*
Hughes shells 305
hull wake 1169
human body
crashworthiness and 308–311
energy absorption and 308
force transducer and 1124
ground transportation **603–620**
See also neural networks
Hu-Washizu stationary principle 1321
Hybrid Control **649–658**
active-passive devices 653–658, 654*F*, 655*F*, 656*F*, 657*F*
design strategies 650–652, 650*F*, 651*F*
piezoelectric network 653–655
proof-mass actuator 652*F*, 653
stiffness and 658, 658*F*
viscoelastic layer 656–658
hybrid damping 353–354
characteristics of 354–360
control law and 358
motion equations and 358
hybrid-discrete-continuous model 172
Hybrid III Family 311
Hydraulic Institute 1225
hydraulics 1191, 1232
hyperstaticity 1116–1118
hyper-surfaces 228
hysteresis
double frequency 639
magnetostrictive materials 759
single frequency 636–637
transduction and 757
Hysteretic Damping 323, 325, **658–664**
Boltzmann superposition model 661–662
definition of 659–660
frequency-dependent 323
isolation theory and 1494–1501
Kelvin model 660–661, 660*F*
loading 659*F*
material complex modulus 323–324
nested loops and 662*F*
nonlinear models 662–664
relay operators 663*F*,
resonance and 1050

I

Ibn-al-Razzaz 112
Ibrahim, R **582–589**, **589–596**, **726–740**
Ibrahim time domain method 821–822, 823
IC technology *See* MEMS
IDEAS-MS 305
Identification, Fourier-Based Methods **665–672**
additive noise 667*F*, 668*F*
error mechanisms and 669–671
frequency domain and 666, 666*F*
MIMO systems 669, 669*F*
MISO systems 668–669, 669*F*
noise-corrupted signals and 666–668
response decomposition 667*F*, 669*F*
schema for 668*F*
test 665*F*
windows 672*F*
Identification, Model Based Methods **673–685**, 673*F*, 674*F*
ARMAX responses 684*F*, 685*F*
AR order 684*F*
Blackman-Tukey method 685*F*
classification and 673–674
continuous line response 684*F*, 685*F*
data set and 674
elements of 673
estimation criterion and 676–682
example of 684
frequency response 685*F*
frequency stabilization and 684*F*
least squares methods 678–680
modal parameters and 683
model class and 674–676
order and 682–683, 684*F*
parameter extraction and 683
schema for 674*F*, 676*F*
SISO system, 676*F*
validation and 683
impacts **1531–1548**, 1532*F*, 1533*F*
bearing faults and 1187–1188
bifurcation and 1533–1536, 1535*F*, 1539, 1539*F*
chaos and 1542–1548, 1542*F*, 1545*F*, 1546*F*, 1547*F*
classification and 1536, 1537*F*
dynamics 278–286, 953
examples of 1533, 1533*F*, 1534*F*, 1535*F*
noise 1449–1452
periodic stability and 1535*F*, 1538*F*, 1539–1542, 1539*F*, 1541*F*
stability regions and 1536, 1538*F*
subharmonic regions and 1536–1539, 1538*F*
impedance 1444–1445, 1444*T*
bearings vibrations and 153–155
direct problem and 1254–1259
influence coefficients and 120–123
inverse problem and 1259–1265
rotor dynamics 1093
improved reduced system (IRS) 258
impulse response functions (IRFs) 820
cepstral analysis and 217–218
time frequency and 1366–1368, 1366*F*, 1367*F*
vibration isolation and 1504–1505
inchworm motor 759
indicator function plot 430*F*

inertia 1325
basic principles of 124, 125–126
belt drives and 170–172
columns and 239–240
coupling and 1326
discrete elements and 396–397, 396*F*, 397*F*,
fluid-structure interactions and 549–550
force transducers and 1123–1132
isolation theory and 1490, **1507–1521**
model updating and 845
plate vibration and 1033
rotor dynamics **1085–1106**, 1329
shear flexibility and 239
shells and 1159
unbalance and 1185–1186
vector iteration and 464–466
vibration isolation and **1487–1506**
See also damping; mass; rotation
infinite impulse response (IIR) 391–394
infinitesimal cube 1566*F*
influence coefficients 119–123
infrared analysis 378
inheritance diagrams 969, 975*F*
initial peak 1098
Inman, D **278–286**, **314–319**
instability diagram 414
instantaneous frequency 644–645
instantaneous phase 643, 644*F*
Institute of Electrical and Electronic Engineers (IEEE) 245
Instrumental Variable (IV) method 675–676, 680
integration **1196–1198**
intelligent transportation systems (ITS) 771
intelligent vehicle systems (IVS) 773
interaction diagrams 968*F*
interface force 1124
interference diagrams 414
interferometers 701–702
See also laser based measurements
interlaminar stress 787–789
internal problem 1276*F*, 1279–1282
International Electro-technical Commission (IEC) 1224
International Road Traffic Accident Database (IRTAD) 302
International Standards Organization (ISO) 245, 604, 1081–1082, 1224–1225
2631 1572, 1575
5349 625, 626*T*
nonrotating parts and 1226–1232
standards and 1228–1232
invariant manifolds 228–229, 955–956
inverse iteration 718–719
Inverse Problems **686–690**
classical 686–688
structural dyanmics and 1259–1264, 1259*F*, 1262*F*, 1263*F*, 1264*F*
Inverse Problems in Vibration (Gladwell) 691
ion propulsion 771
isochrones 420, 426*F*, 1093
isolation theory 1507
ambient vibrations 1507–1508, 1508*F*
coupled systems 1490–1493, 1494*F*, 1496*F*, 1497*F*, 1498*F*, 1499*F*
criteria of 1508*F*, 1509*F*, 1510–1512, 1511*T*
degrees of freedom (DOF) and 1494–1501, 1494*F*, 1496*F*, 1497*F*, 1498*F*, 1499*F*, 1500*F*, 1501*F*
detrimental effects and 1508–1509
dynamic systems 1512, 1513*F*
elastic mounts 1490
experimental selection 1521
general purpose machines 1517–1519, 1518*F*, 1519*F*
geometric properties 1490
impacts 1515
impulse excitation 1502–1504, 1503*F*, 1504*F*
inclined mounts 1493
inertia and 1490, 1515–1517, 1516*T*, 1516*F*
mounting conditions 1517–1518, 1518*F*
nonlinearity 1504–1505
nonrigid structures and 1520
polyharmonic excitations 1515
precision and 1513–1514
random excitation 1501–1502
single frequency excitations and 1514–1515
transmission model 1509–1510, 1509*F*, 1510*F*
wave effects 1505, 1506*F*
isotropic links 1093–1097
iteration
eigenproblems and 463
inverse 465–466, 466*F*
solvers 993–994
subspace 466
vector methods and 464–466
See also chaos

J

Jacobi method 464, 467
jitter 102*F*, 103–108, 108*F*, 109*F*
Joule effect 754

K

Kaiser window 1590
Kajima Shizuoka Building 30, 34*F*, 35*F*
Kane's method 1060
Kapania, RK **1335–1343**
Kareem, A **1578–1587**
Karman-type nonlinearity 1015
Kelvin model 660–661, 662
Kelvin-Voigt damping 338–339
kernel design 1363
Kijewski, T **1578–1587**
Kimball-Love observation 338
kinematic conditions
equations of motion and 1324–1332
fundamental theory and **1290–1299**
kinetic energy 1266
columns and 240
discrete elements and 395–397
equations of motion and 1327
friction and **589–596**
Hamilton's Principle and 131
piezoelectric damping and 357
resonance and 1047
rotor dynamics 1102
time-average energy and 1268
variational methods and 1350, 1353
See also energy
Kirchhoff-Helmholtz equation 888
Kirchhoff plates 197
Klapka, I **967–976**
Kobayashi, AS **505–512**
Kolmogorov-Arnold-Moser theorem 235
Kolmogorov equation 1249
Krasnosel'skii-Pokrovskii kernels 664
Krishnan, R **629–642**
Kronecker delta function 186, 1275
Krousgrill, CM **928–943**
Krylov-Lanczos Methods **691–698**
block-Lanczos algorithm and 695–696
modes of 692–694
other applications 697
physical meaning of vectors 691–695
Krylov subspaces 467
Kunaporn, S 512
Kyobashi Seiwa Building 30

L

laboratory dynamic 492–493, 500–501, 500*F*
LADWP Receiving Station 442
lag 629–630
See also helicopter damping
Lagrangian mechanics
DYNA3D and 305
energy methods and 290, 1323
FETI and 997–1000
formulation 131, 1324, 1344–1346, 1345*T*
interpolation 389
motion 1327
Lame coefficients 186, 1567
Lame parameter 1136, 1137
Lanczos method
FEA software and 256
vectors 692–694
See also Krylov-Lanczos methods

Laplace transforms 1407–1409
boundary element methods 201
identification and 673
impulse response function 1336–1338
membranes and plates 1331
Laser Based Measurements **698–710**, 703*F*, 1403*F*, 1403–1404
applications of 705–706
Doppler vibrometer techniques 700–706, 704*F*, 705*F*
full-field measurement and 707–709
geometric properties and 707*F*
holographs and 699, 708*F*
non-Doppler techniques 706–707
scanning systems 703*F*, 704*F*
speckle noise and 705
laser Doppler vibrometer (LDV) 1403–1406
LDL super T factorization 712–713
lead magnesium niobates (PMNs) 660
leakage 671, 1588–1591
windows and 1216–1218
learning algorithm 871–872
least-squares method 677, 678–680, 1203
Leissa, AW **762–770**, **1024–1031**
Lenz's law 1402
Lesieutre, GA **321–327**
Levenberg-Marquart (LM) algorithm 866
Levinson recursion 1203
Li, CJ **143–152**, **597–603**
Liapunov-Floquet transformations 1004–1005
Lieven, NAJ **578–582**
limit cycle 592–593, 592*F*
Lin, YK **1238–1246**
Linear Algebra **710–720**
BLAS 991
Moore-Penrose generalized inverse 717–719
nonsingular systems 710–714
singular systems 714–716
SVD 716–717
linear analyses 252–255, 253*T*, 254*T*
cables and 210–215
Fourier-based identification and **665–672**
Linear Damping Matrix Methods **721–726**
linear dependence 295*F*
linear interpolation function 282
linear least squares method 677
Linear Multi Stage (LMS) method 674–680
linear systems
Duhamel's Principle and **1304–1308**
stochastic analysis and 1247–1252
superposition and **1299–1304**
linear variable differential transformer (LVDT) 1193, 1398, 1400–1401, 1401*F*
Link, M **844–856**
links 152–153
bearings 153–165
fluid 153–155
isotropic 1093–1097
kinematic 1060
magnetic 158–161
misalignment and 1116–1118
rotation and 1068–1069
Liquid Sloshing **726–740**
Bond number 739*F*
coordinates 728*F*
damping 851
free and forced 727–729
gravitational field 739–740
mechanical models 731–734
modeling 731*F*, 732*F*, 733*F*
parametric 730
rigid moment of inertia 733*F*, 734*F*
road tankers 735–738, 737*F*, 738*F*, 739*F*
surface motion 731*F*
tank shapes 735*T*
liquid spring 1182
Littlewood, JE 228
Liu shells 305
loading 253*T*
bending moment sensitivity 1125–1127
bridges and **202–207**
columns and **236–243**
crash and 310*F*
earthquakes and 446–460
flight 88–89
force transducers and 1123–1132
ground 93–95
gunfire 93
hysteretic damping 659–660, 659*F*
impulse response function **1335–1343**
isolation theory and 1518–1520
noise and **887–898**
packaging and **983–989**
shape memory alloys and 1147–1148
signature generation and 144–145, 144*T*
suspension 37–38
Localization **741–751**
bladed disk assembly 741*F*, 745, 750*F*, 751*F*
coupled oscillators and 746*F*, 747*F*
engineering significance of 748–749
forced response and 750*F*
gear faults and 598
harmonic frequency and 745*F*
history of 744–745
key results of 745–748
mode 742–744, 743*F*, 746*F*, 748*F*, 749*F*
NN and 922
truss beams and 741*F*, 749
logarithmic decrement method 617
logarithms *See* cepstral analysis
looping
hybrid control and 650–652
Love-type equations of motion 1155–1159, 1159*T*, 1160–1161
Lowe, MJS **1437–1441**, **1551–1559**, **1559–1564**, **1565–1570**
low oscillating function 1273*F*
LQG/LTR controller 1147
LU factorization 711–712
lumped parameter approach 887
classification and 1290–1291
critical damping and 317–318
sensor/actuators and 1134–1143
superposition and **1300–1304**
Lyapunov 1097
Lyon, RH 1265

M

Ma, F **721–726**
McConnell, KG **1121–1134**, **1381–1397**, **1398–1406**
Mach numbers 563
Mach-Zehnder interferometer 701–702, 702*F*, 1404, 1404*F*
Macjkie, RI 972
McKee, K **143–152**
MACSYMA 1010
MAC values 852–854, 853*T*
Maddux, GE **1398–1406**
MADYMO 305, 311
magnetorheological (MR) fluids **467–475**, 640–641
actuators and, 58–72
new applications of 474–475
semiactive control and 467–468
smart fluids and 468–474, 468*F*, 469*F*, 470*F*, 471*F*, 472*F*, 473*F*
magnetic constrained layer damping (MCLD) 352, 353*F*
magnetic links 158–161
magnetic systems 1088
Magnetostrictive Materials 660, **753–762**
actuation configurations 58–72, 759, 760*F*
magnetism and 753–755, 754*T*
sensing configurations 760–761, 761*F*
transduction 755–759, 756*F*, 757*F*, 758*F*
Maia, NMM **820–824**, **824–829**
MA (moving average) modeling 1199, 1203*F*, 1203
manifolds 229*F*, 955–956
center 962
Duffing's equation and 233–235
invariant 228–229
Melnikov's method and 232
Maple 1010, 1340
Marcondes, J **983–989**, **1173–1180**
Markov theory 677
stochastic systems and 1246–1252
martensite *See* shape memory alloys
mass
balancing and **111–124**
basic principles of 124, 125–126

mass (*continued*)
continuous systems and 1312–1317
discrete elements and 396–397, 396*F*, 397*F*,
Dunkerley's method and 135–136
eigenvalue analysis and **461–467**
equations of motion and 1324–1332
forced response and 581–582
force transducers and 1123–1132
isolation theory and **1507–1521**
MEMS 781–782
model updating and 845
Rayleigh method and 1309–1312
Ritz method and 1318–1319
robots and 1062
sensor/actuators and 1134–1143
transmissibility 1522–1527
unbalance and 1185–1186
variational methods and 1355
vehicular vibration and, **37–45**
vibration isolation and **1487–1506**
See also inertia; rotation
mass-spring model 687*F*, 689, 689*F*, 733*F*, 734
dashpot system 591*F*
discrete elements and 398, 398*F*, 399*T*, 400*T*
resonance and 1047–1048
shock isolation and **1180–1184**
superposition and 1300–1301
See also boundary conditions; damping
material anistropy 251*T*
acoustic impedance and 1561*T*, 1562*F*
damping and **327–331**
effects of 1569
evanescent waves and 1563*F*
facilities 252*T*
guided waves and 1551–1559
plate vibration and 1029
Rayleigh waves and 1554*F*
robots and 1063
unbound waves and **1565–1570**
material complex modulus 323–324
material damping 337–338
material properties
actuators and 58–72
MEMS and 797, 798*T*
shape memory alloys **1144–1155**
shock absorption and 1174
ultrasonics and 1439
Mathematica 1010, 1340, 1343
mathematics
autocorrelation functions 977–978, 1592
averaging methods **98–110**, 1244–1246
basic principles **124–137**
Bendixson's theorem 593
Bessel function 729
block-Lanczos algorithm 695–696
Bond number 739*F*, 739
Broyden-Fletcher-Goldfarb-Shanno algorithm 637
mathematics (*continued*)
Cantor set 233
chaos theory 227–235
classes 975
continuum mechanics 973–974
cost function 977
Dirac's delta function 1336
Duffing's equation 233–235
eigenvalue analysis 461–467
equations of motion 1324–1332
expectation operator 345
external problem 1279
finite difference methods **520–528**
Floquet theory 338, 1002
fundamental equations of motion 1291–1293
fuzzy logic **43–45**
Gaussian theory 1135
gear diagnostics and 598–602
Hilbert transforms **642–648**
Jacobi method 464, 467
Kolmogorov-Arnold-Moser theorem 235
Krylov-Lanczos methods and 691–697
Krylov subspaces 467
Lame' constants 1567
Lenz's law 1402
linear algebra **710–720**
Mathieu equations 228, 730, 1110, 1111
Maxwell equation 1135
Melnikov's method 232
model updating 847
numerical efficiency and 972–973
parallel processing **990–1001**
Poisson ratio 889, 1331, 1568
QR algorithm 467
random processes **1033–1039**
Rayleigh quotient 462
Rayleigh-Ritz analysis 462–463
root mean square 245
running sum 1196–1197
Schur method and 995–1000
Scruton number 1584
SEA 1265–1272
segment averaging 1219–1221
sensor/actuators and 1141
signal integration/differentiation **1193–1199**
similarity transformation methods 461, 464
Simpson's rule 1197–1198
Smale-Birkhoff homoclinc theorem 233
Smale's horseshoe 232–233
SRSS 245
statistical moments 1243–1244
Strouhal number 1584
Sturm sequence property 463, 467
Succi method 1281–1285
Taylor series 1325
trapezium rule 1197
van der Pol equations 227–228
vector iteration methods 464–466
wind 1586
mathematics (*continued*)
windows **1587–1595**
Young's modulus 889, 1567
Mathieu equations 228, 730, 1110, 1111
MathWorks 682
MATLAB 682, 1343
matrices 1267
active suppression 51–55
adaptive filters **81–87**
CFRF 274, 276*F*, 277*F*, 278
CGM 267
classes 975*F*
correlation 298, 299–302
critical damping and 317–318
cross-sensitivity 1126
damping 321–324, 346–347, 356–358, **721–726**
direct problem and 1254–1259
elemental 363
environmental testing and **496–504**
FDAC 275*F*
FETI and 997–1000
flutter 567–570
forced problem 1281–1282
FRF 274–278
influence coefficients and 120–123
inverse problems 465–466, 686–688
laboratory vs. field 492–493
Lanczos 694–695
linear algebra and **710–720**
linear damping **721–726**
lumped mass 279–280
MAC 268*F*, 269, 269*F*
mass 260–264
model-based identification and 673, 673*F*
piezoelectric damping and 356–358
Poincare' method and 957–959
random processes 1041, 1043
Rayleigh method and 1309–1312
rigidity 363
rotation 1070–1077
rotor dynamics 1085–1088, 1091–1092, 1102
RVAC 274*F*, 275–277
sensitivity 847
shape memory alloys and 1147–1148
signal processing 1201–1203
singular 714–715, 720
skyline storage and 714*F*
sparse 713–714
stiffness error 260–264
stochastic systems 1247–1252
structural dynamic modifications and **1253–1264**
Sturm sequence property 463
submatrices 360
subspace iteration and 466
TOR 257
transformation 360
XOR 257, 267
See also eigenvalue analysis
MATRIXx 682

Maxwell, James Clerk 1065
equation of 1135
model of 337
theorem of reciprocity 136, 819
mean time before failure (MTBF) 1249
mean-value method 1269
measurement
damping **332–335**
full field 707–709
influence coefficients and 122
packaging 984–987, 984*F*, 984*T*, 985*F*, 985*T*, 986*F*,
rotation 1080–1081
standards for **1224–1238**
See also Laser-Based Measurements; modal analysis
mechanical impedance 1571
mechanical shock 1228
Melnikov's method 232, 233
Membranes **762–770**
circular 765, 765*F*, 765*T*, 766*T*
complicating effects 769, 769*F*, 770*F*
other shapes 764*F*, 765*T*, 767, 767*F*, 768*F*
rectangular 763, 764*F*
shells and **1155–1167**
strain 1135–1136
vibration 1331
See also cables
MEMS, Applications **771–779**
MEMS, Dynamic Response **779–794**
MEMS, General Properties **794–805**
MEMS (microelectromechanical systems) 771, 1011, 1017, 1142
acoustic microsensors 774, 775*F*
applications of 760*F*, 771, 772*T*, 777–778
damping 783–784, 784*T*
design 803–804, 803*T*, 804*F*
dynamic response **779–794**
electrostatic field 785–787, 785*F*, 791*T*
fabrication technology 798–801, 799*T*, 801*T*, 802*T*, 803*F*, 803*T*
general properties of **794–805**
interlaminar stress 787–789, 788*F*, 789*F*
machining 795*F*, 796, 797
mass 781, 782*F*, 782*T*
material choice 797, 798*T*
measurement 796, 796*T*
microaccelerometers 772–774, 772*T*, 773*F*, 774*F*
microactuators 775–777, 776*F*, 777*T*
micropumps 777, 777*F*, 778*F*
microsensors 771–772, 773*F*, 774, 775*F*
microvalves 777, 777*F*, 778*F*
packaging 801
signal conditioning 789–790
stiffness 782–783, 783*T*
voltage conversions 786*T*, 790–793, 793*F*
meshing 249*T*, 250, 601
mapping solutions from 281–282
See also gear diagnostics
metglas amorphous ribbons 761
Michelson interferometer 701*F*, 701–702, 1404*F*, 1404
microelectromechanical systems *See* MEMS
MILSpecs 1225
MIMO (multi-input, multi-output) method 821–823
Mindlin-Reissner plates 197
minimax filters 390
minimum complementary energy 1347
minimum description length (MDL) criterion 1205–1206, 1206*F*
misalignment 1116–1118, 1186
Modal Amplitude Coherence (MAC) 683
modal analysis **805–813**, **820–823**
applications **829–838**
calibration 818
damping and 826–828
data processing 815–816, 816*F*
error location 834
excitation 808–809, 809*F*, 814*F*, 815, 816–817
frequency-domain methods 822–823
history of 806
mathematical construction 811–813
measurement **813–820**
method classification and 820
model construction 824–829
multipoint testing 817–818
NN and 922
parameter quality and 823
pretesting 819
procedures of 806
property comparison 830–832, 831*F*, 833*F*
response properties 824–826, 824*F*, 837–838
sensing mechanism 815, 815*F*
signal processing 810, 811*F*
spatial models 824–826, 824*F*
structural analysis 834–837, 836*F*
support conditions 818–819
theory of 807–808
time-domain methods 821–822
transducers 809
troubleshooting 829
updating 832–834
validation 819, 830
Modal Analysis, Experimental, Applications **829–838**
Modal Analysis, Experimental, Basic principles **805–813**
Modal Analysis, Experimental, Construction of models from tests **824–829**
Modal Analysis, Experimental, Measurement techniques **813–820**
Modal Analysis, Experimental, Parameter extraction methods **820–824**
Modal Assurance Criterion (MAC) 268*F*, 269*F*, 274–276
COMAC and 267–271
correlation functions and 296
numerical comparison and 266
SNDT and 903
vector correlation and 267–270
modal properties 889–890
active suppression and 51–52
actuator sensitivity and 1140–1141
balancing and **111–124**
blades and 177
BLAS 991
boundary element methods **192–202**
cables and 211–215
COMAC 275, 276
comparison of **265–272**
complex plot 429*F*
continuous methods and **286–294**
continuum mechanics and 973–974
damping and **321–327**, 721–726
density 1266, 1268
direct graphical comparison 266
direct numerical comparison 266
disks and **404–413**
displays and 413–417
DOF correlation 270–271
double 419*F*
earthquakes and 458–460
energy 1266–1267
equations of motion and 1326
Euler-Bernoulli theory and 137–141
experimental analysis and **805–813**
FEA software and 244
F-F-F-F square plates 1027*F*
finite element methods **530–544**
flutter and 566–567
Fokker-Planck-Kolmogorov equations 1248–1249
forced problem 1281–1282, 1298–1299
free-free planar truss 420*F*
free vibration frequencies and 1026*T*
gear diagnostics and **597–603**
geometric nonlinearity 252
indicator function 425–429, 430*F*
influence coefficients and 119–123
inverse problem 1259–1264, 1259*F*, 1262*F*, 1263*F*, 1264*F*
Krylov-Lanczos methods and 691–697
localization and **741–751**
membranes and **762–770**
model-based identification and **673–685**
multivariate 429*F*
near-field approach 891
noise and **887–898**
nonlinear normal **918–924**
nonlinear system resonance and **928–943**

modal properties (*continued*)
nonlinear testing and 1286, 1289
optimal filters and **977–982**
order selection and 682–683
orthogonality criteria 266–267
overlap and 1265
parameter extraction and 683–685
planar flexural shapes 418*F*
plate vibration and 889–890
radiation efficiency 892–894, 893*F*
Rayleigh's Principle and 132–134
Rayleigh waves and 1554*F*
rotation 1071–1072, 1075–1076
rotor dynamics 419*F*, **1085–1106**, 1090
scale factor (MSF) 266
SEA and 1266–1267
shape memory alloys and **1144–1155**
shells and **1155–1167**
sound radiation and 891–892
stochastic differential calculus 1246–1252
structural dynamics and **1253–1264**
structural modes and 683
superposition and 1302–1304
three-dimensional plot of 423*F*
validation and 683
vector correlation 267–270
wave number and 891
weak elements 418*F*
wind and **1578–1587**
mode acceleration method 719
Mode Indicator Functions (MIFs) 425–429
modeling
absolute motion and 1382–1395
additional methods for 1207
antiresonances 848
AR 1201–1203, 1202*F*
ARMA 1201, 1203
basic principles **124–137**
biodynamics and 1572
classes of 674–676
continuous system 1327–1331
damping **321–327**, **332–335**, **335–342**, 850–851
deterministic 1200
discrete elements 396
equations of motion and 1324–1332
finite element method and 844–845
flutter and 555–565
gear vibration 597–598, 599, 1189–1191, 1190*F*, 1191*F*
hysteresis 636–637, 639
identification methods and **673–685**
liquid sloshing and 731–734
MA 1199, 1203, 1203*F*
mass-spring 733*F*, 733–734
modal analysis and **824–829**, 829–838
normal mode 848–849
parameter identification and 847–848
parametric methods 1203
modeling (*continued*)
pendulum 732–738, 732*F*
pseudoresponse 849–850
quality and 847
robots **1055–1063**
rotor-stator interactions 1107–1121
selection and 1205–1206, 1206*F*
sequential methods 1203
ship vibrations **1167–1173**
signals and **1184–1193**, **1199–1208**
spectra and 1204–1205, 1205*F*
stochastic 1199–1200
superposition and 1300–1301
symptom-based 1185
test/analysis residuals 848–851
tool wear and 1380
transverse vibration and 169
updating of **844–856**
validation of 851–855, 852*F*, 853*F*, 853*T*, 854*F*, 855*F*
Model Updating and Validating **844–856**
Mode of Vibration **838–844**
complex 842–843
definition of 838, 839*F*
essential features of 839–840, 839*F*, 840*F*
forced 843–844
free 840–843
orthogonality 841–842
types of 839
mode shape plots 415–417
mode synthesis 1334–1335
modulus damping 338–339
modulus difference 271
momentum conservation principle 307
monopole sound 880
Monte Carlo simulation 740, 1046
localization and 746
Moon, FC 233
Moore-Penrose generalized inverse 717–719
Moors 112
motion
control 493
envelopes and 493–494
friction and **589–596**
sprag-slip 593–597
transducers for **1398–1406**
See also oscillation
Motion Sickness **856–861**
causes of 857
dose value (MSDV) 859, 860
nonvertical oscillatory motion 859–860
vertical oscillatory motion and 857–859
Motor Vehicle Safety Standard (MVSS) 303*T*, 304
mounts 343*F*, 344*T*
active/semi-active damping and 347–349
basic concepts of 342–343
dynamically coupled 347*F*
elastically coupled damping and 345–346
mounts (*continued*)
fluid-elastic 347*F*
multidirectional 346
multiple DOF 348*F*
passive damping and 343–345
SDOF 345*F*, 346*F*
See also damping
MSC/NASTRAN 248–249
Mucino, VH **302–314**
Mullins effect 631
multi degrees of freedom (MDOF) 820
multilayer feed forward (MLFF) networks 866, 867
multilayer neural networks (MLNN) 864, 872–875
multipath propagation 299–301, 299*F*, 300*F*
multiple input/single output (MISO) systems 665, 668–669, 669*F*
multiple input/multiple output (MIMO) systems 665, 669, 669*F*
feedforward control **513–520**
multiple instructions/multiple data (MIMD) processors 990
multivariate mode indicator function (MMIF) 425–429, 429*F*
MUMPS 795
Muszynska, Agnes 1112

N

NA4 601
Naeim, F **439–461**
Nanjing Communication Tower 30
narrow-band demodulation 602
NASTRAN 405
National Agency for Finite Elements and Standards (NAFEMS) 245
National Highway Traffic Safety Administration (NHTSA) 303*T*, 304
Natori, MC **1011–1018**
natural frequencies
of plates and beams 414–415
plotting of 413–414
Navier's equations 911
NB4 601
near-field approach 891
Neumann preconditioner 1000
neural networks
architecture and 870, 871*F*
assessment and 867–868
error and 870
faults and 865–867
learning and 871–872, 874
monitoring and 864–867
multilayer 872–875, 873*F*, 875*F*
neurons 869–870, 869*F*
patterns and 874
perceptron 871–872
processing tasks and 863*T*
radial basis function 875–877
Neural Networks, diagnostic applications **863–868**

Neural Networks, general principles **869–877**
neurological disorders 622
Newkirk effect 1107–1110
Newton, Isaac 124, 1099, 1344
  law of motion 1324, 1325, 1329
  rotation and 1070, 1085
Newton-D'Alembert principle 1112
Niemkiewicz, J **1224–1238**
Nitinol 660
  See also shape memory alloys
nodes
  circular plates and 1026–1027
  diameter (ND) 405–413
  laboratory vs. field testing 492–493
  line indices and 414–415
  modal shape plots and 415–417
  rotation and 1073
noise **887–898**, 887–888, 896–898
  baffled plates and 889*F*, 891–896, 896*F*, 897*F*
  boundary conditions and 888–889
  cable 1133
  corrupted signals 666–668
  dipole sources 882*F*
  Green's functions and 879
  Huygen's source 884–885, 885*F*
  monopole sources 885*F*, 886*F*, 887*F*
  neural networks and 867
  plate vibration and 889–891, 893*F*, 894*F*, 895*F*
  power and 883–884
  quadrupole sources 883*F*, 884*T*
  radiating field and 879–882
  sigma-delta converters and 372
  sound power and 890–891
  sound pressure with boundaries 888–889
  spherical harmonics and 881*T*
  superposition and 884–886
  waves and 878–879
Noise Radiated by Baffled Plates **887–898**
Noise Radiated from Elementary Sources **877–887**
nonconservative forces 1332
Nondestructive Testing, Sonic **898–906**
Nondestructive Testing, Ultrasonic **906–918**, 1439
nondestructive testing (NDT) 378, 1559, 1563–1564, 1568
nonlinear analysis 252, 254*T*, 255*T*, 953
  asymptotic techniques and 957–962
  averaging method and 960–962
  backlash and 951*F*
  bifurcations and 963–965, 964*F*, 965*F*
  classes and 947–953
  Coulomb friction law and 950*F*
  dimension reduction and 962–965
  effects of 944
  equilibrium and 953–957, 954*F*, 955*F*, 956*F*
nonlinear analysis (*continued*)
  finite element methods 536–538
  Hilbert transforms and 646
  neural networks and **869–877**
  overview of **944–951**
  parametric excitation and 1003–1009
  perturbation and 957–962
  Poincare' method and 957–959
  resonance and 1054–1055
  rotor dynamics 1094*F*, 1095–1097, 1095*F*
  sources and 945–947
  stability and 953–957
  stochastic analysis and **1238–1246**
  vortices and 949*F*
  See also chaos
Nonlinear Normal Modes (NNM) **918–924**
  applications of 921–924
  cyclic assembly and 921*F*
  definition of 918–921
  degrees of freedom (DOF) and 919*F*, 920
  resonance and 921–922, 923*F*
  stiffness and 425*F*, 920*F*
Nonlinear System Identification **924–928**
Nonlinear System Resonance Phenomena **928–943**
  cubic 940–943
  quadratic 937–939
  response curves 932*F*, 933*F*, 935*F*, 936*F*, 938*F*, 939*F*, 940*F*, 941*F*, 942*F*, 943*F*
  single degree of freedom and 930–937
  two degrees of freedom and 937–943
nonlinear systems 924–925, 928, 1332
  active states and 925–926
  elastic recall 1110–1111
  hysteretic damping 662–664
  misalignment and 1116
  nonparametric identification and 926–927
  overview of **944–951**
  parametric identification and 927
  perturbation methods and **1010**
  piezoelectricity and 1015–1017
  transverse vibration and 167–169
  von Karman 1136
  See also chaos
Nonlinear Systems Analysis **952–966**
Nonlinear Systems, Overview **944–951**
nonsingular linear systems 710–714
nonstationary signals 296
nonvertical oscillatory motion 859–860
normal form theory 963, 1005
normalized cross-orthogonality (NCO) 270, 271
Norton, MP **877–887**, 887–898, **1443–1455**, **1456–1480**
nuclear radiation 1133
Nuclear Regulatory commission (NRC) 245
nullspace 714–715, 720
Nyquist plots 418–420
  CEDA and 1271
  damping measurement and 333
  DOF 424*F*
  frequency 445
  influence coefficients and 122
  modal analysis and 822*F*
  receptance 423*F*
  sigma-delta converters and 371–372

O

object oriented programming
  class diagram 969
  collaboration diagrams 970
  component diagrams 971
  continuum mechanics and 973–974
  criteria of 968–969
  deployment diagrams 970
  dynamic systems and 974–975
  language of 971–972
  methodology of 969
  numerical efficiency and 972–973
  sequence diagrams 970
  software design and 967–968
  state transition diagram 970
  vs. procedural programming 968*F*
Object Oriented Programming in FE Analysis **967–976**
odd-odd plate mode 892–893
oil analysis 378
oil film excitation 1191
oil-pressure servo valves 485–488
oil whip 1085
online systems 1082, 1083
open loop control 49–50
Operating Deflection Shapes (ODSs) 272, 275
optical heterodyning 1404–1405
Optimal Filters **977–982**, 978*F*, 981*F*
  time domain formulation and 977–978
  Wiener 978–981
optimization
  hybrid control and 650–652
  rotor dynamics 1095
  structural modifications and 1262–1264
orthogonality 266–267, 270, 271
  basic principles of 124
  biorthogonality 1074
  forced vibration and 1298–1299
  inverse problems 688
  isolation theory and 1514
  iterative solvers and 994
  mode of vibration and 841–842
  nonlinear systems and 926
  Rayleigh's method and 1317
  shells and 1155
  TAM and 259–260
  Zernlike polynomials 484
orthonormality 461

oscillation
averaging method and 960–962
bearings vibrations and 152–161
boundary element methods 195–198
chaos and **227–236**
critical damping and **314–319**
fast function 1273*F*
FEA software and 245
flutter and **553–565**
friction and **589–596**
fundamentals of **1290–1299**
gear diagnostics and **597–603**
helicopter damping and **629–642**
liquid sloshing and **726–740**
limit cycle 95
localization and **741–751**, 746*F*
low function 1273*F*
motion sickness and **856–861**, 857*F*, 858*F*, 859*F*
NNM and **918–924**
noise and **877–887**, 887–898
nonlinear analysis and **952–966**
nonlinear resonance and **928–943**
nonvertical motion and 859–860
Poincare' method and 957–959
power balance and 1267
resonance and **1046–1055**
SEA and 1266–1267
stick-slip 589, 590*F*
time frequency and **1360–1369**
tire vibrations **1369–1379**
vector iteration and **464–466**
vertical motion and 857–859
vibro-impact systems and **1531–1548**
viscous damping and **1548–1551**
whole-body vibrations and **1570–1578**
See also absorbers; boundary conditions
Output Error method 677
overdamped system 316
overlap processing 1593
oxide perovskites 477–482

P

Packaging **983–989**
loading and 988*F*
measurement and 984–987, 984*F*, 984*T*, 985*F*, 985*T*, 986*F*
MEMS and 801
structural design and 983–987, 983*F*, 983*T*
testing of 988
transmissibility and 987*F*,
Pade matching 1200, 1204
PAM-CRASH 305
Pan, J 877–887, 887–898
parallelograms 126
Parallel Processing **990–1001**
direct solvers and 992
domain decomposition 992*F*, 994–1000
Parallel Processing (*continued*)
FETI method 997–999
gradient iteration and 994, 994*T*
iterative methods and 993–994
network topology and 990, 991*F*
Schur methods 995–1000, 997*T*, 998*F*
parameters
4 DOF pitch plane model 608
analog inputs and 369
averaging method and 960–962
basic principles of 124
bearing diagnostics and 145–151
bifurcation and 435
chaos and 1112–1115
critical damping and **314–319**
damping materials and **327–331**
damping measurement and **332–335**
distributed 318–321
earthquakes and **439–461**
equations of motion and 1292–1293
extraction of 683
feedforward control **513–520**
ground transportation **603–620**
inverse problems 686–688
Lame 1014, 1015
lumped 317–318
Markov 677
modal analysis and 821*F*
model-based identification and **673–685**
model updating and 845–848
neural networks and 864
NNM and 919
noise and **887–898**
nonlinear systems and **952–966**
signal processing and **1199–1208**
SNDT and 899
stochastic analysis and **1238–1246**
structural dynamic modifications **1253–1264**
updating 847–848
Parametric Excitation **1001–1009**, 1332
cables and 214*F*
Floquet theory and 1002, 1004–1005
nonlinear analysis and 1003–1009
perturbation methods and 1010
point-mapping and 1006
problem formulation and 1002
resonance and 1054
transverse vibration and 169
See also excitation
parametric identification 673
cables and 212*F*, 213*F*
Fourier-based **665–672**
modal analysis and **820–824**
nonlinear systems and 926–927
nonlinear testing and 1288
Parseval's theorem 388, 445
Pascal, Blaise 1064
passband patterns 745*F*, 748*F*
passive damping 351–352
PATRAN 305
pendulum model 732, 732*F*, 734, 736
absorbers and, 22
chaos and 228
equations of motion and 1325*F*, 1325
localization and 743*F*, 745
road tanker and 735–738
perceptron 871
perfect inviscid fluid 1567
periodic data 491
periodic orbits 230*T*
chaos and **227–236**
periodic rezoning 282
periodic truss beam 741*F*
Perkins, NC **209–216**, **944–951**
perovskites 477–482
perturbation methods, 232, 957–962
bifurcation and 1003*F*
nonlinear systems and 1010
parametric excitation and 1003–1004, 1009
rotation and 1002*F*
See also chaos
Perturbation Techniques for Nonlinear Systems 1010
Peterka, IF **1531–1548**
phase space 228
phase unwrapping 218
phasors 1270
physical classes 975
Pierre, C **741–751**
piezoelectric actuators 482–488
absolute motion sensing and 1385–1387
hybrid control and 653–656
viscoelastic layer and 656–658
piezoelectric materials 1011–1012, 1012*T*, 1017
active absorbers and, 1–3, 2
active damping and 352, 352*F*
active isolation and, 47, 48
actuators and 58–72, 61*T*
advanced theory 1014–1015
applications 1013
damping and 353*F*, 354–360
feedforward control 519
flappers 485–488
four fundamental equations of 1013, 1013*T*
hysteretic damping and 660
linearity and 1012
sensor/actuators and 1134–1143
shells and 358–360
thermoelasticity and 1013
thermoelectromechanical coupling 1015–1017
Piezoelectric Materials and Continua **1011–1018**
Pipes **1019–1024**
annular fluid flow and 1023
cross flow 1023
external fluid flow and 1022
internal fluid flow and 1019–1022
pistons **1445–1445**

pitch 629–630
  excitation 610
pitch-catch setup 906, 907*F*
pitchfork bifurcation 215, 930
pitch plane model
  2 DOF 609–610
  2 DOF quarter car model 612–613
  4 DOF 608
  road excitation and 606–607, 618–621
  suspension and 615–616
  weight and 615
plasticity 252*T*
Plates **1024–1031**, 1331
  acoustic radiation and 545–550
  baffled 887–898
  cantilevered skew 1028*F*
  circular 1026–1027, 1027*T*, 1027*F*, 1028*T*, 1028*F*
  complicating effects 1029–1033
  continuous systems and 1316–1317
  flexural radiation and 1459, 1463–1465
  forced vibration and 894–896
  Kirchhoff 197
  MEMS 787
  modal properties and 889–890
  modal radiation efficiency 892–894, 896*F*, 897*F*
  model updating and 845
  natural frequencies and 414–415
  rectangular 1026
  SEA and 1267
  sensor/actuators and 1134–1143
  sound power and 890
  triangular 1030*F*
  ultrasonic waves and 910
  vibration intensity and 1484–1485, 1487
plotting
  bar plots 413
  Campbell diagrams 414
  compass 416
  FRF data and 417–420
  indicator function 430*F*
  instability diagram 414
  interference diagrams 414
  mode shape 415–417
  root-locus diagrams 413
  singular value 425, 428*F*
  spectrum 420–421, 428*F*
pneumatic spring 1183
Poincare, Henri 228, 431
Poincare map 228, 232, 235*F*
Poincare' method 957–959
point-mapping 1006
Poisson's ratio 327, 889, 1331, 1567
  shells and 1156
polar notation 643
pole placement 54
polymorphism 969
polynomial model classes 675
positive position feedback 3–5
potential energy 1266
  columns and 239
  equations of motion and 1327
potential energy (*continued*)
  Hamilton's Principle and 131
  minimum 1346–1347
  minimum total 1320
  piezoelectric damping and 357
  Rayleigh method and 132–134, 288
  resonance and 1047
  viscous damping and 336
  See also energy
potential mode identifier 429
power balance
  modal groups and 1266–1267
  oscillators and 1266, 1267
  WIA and 1269
power spectral density (PSD) 245, 1581
  cepstral analysis and **216–227**
  classical analysis and 595*F*, 1210–1211, 1212*F*, 1214, 1219–1221
  correlation functions and 296–299, 297*F*
  random signals and 1219–1223
  road excitation and 618–621
  windows and 1591
Pozo, R 973
Prasad, MG **1299–1304**
prediction error method 676–677
Preisach plane 664
prescribed conditions 252*T*
Principal Response Functions (PRFs) 272, 278
Principia Mathematica (Newton) 124
principle of least action 1323
probability 1238–1242
Prony method 678–679, 682, 1200, 1204
proof-mass actuators 653
propellers 1170–1172
proper orthogonal decomposition (POD) 926
proper orthogonal values (POVs) 926
pseudoresponse residual 849–850
pseudo-velocity (PSV) 444
pulleys *See* belts
P-waves 913, 913*F*
pylons 574
pyrotechnic shock 495
Pythagoras' theorem 579

Q

QR algorithm 467
quadrupole sound 882, 883*F*
qualification testing 490
quasiharmonic motion 590*F*
quefrency 216
  bearings and 218–220

R

Rade, D **9–26**
Rades, M **256–264**, 265–272, 272–277, **413–431**, **1046–1055**, **1180–1184**
radial based function (RBF) 864, 875–877
Radiation by Flexural Elements 130, **1456–1480**
  basic theory of 1456–1463, 1456*F*, 1458*T*, 1459*F*, 1459*T*, 1460*F*, 1461*F*, 1461*T*, 1462*T*, 1463*F*
  boundary conditions and 186, 187*F*, 188*F*, 189*F*
  MEMS 787–789
  Ritz method and 134
  sound and **1456–1480**
  source ratios 1463–1468, 1464*F*, 1466*F*, 1467*F*, 1468*F*, 1469*F*, 1470*F*, 1471*F*, 1472*F*, 1473*F*, 1474*F*, 1475*F*, 1476*F*, 1477*F*, 1478*F*, 1479*F*, 1480*F*
  transmissibility 1523–1527
rahmonics 218–220
  complex cepstrum and 222–227
rain-on-the-roof excitation 241
Ram, YM **686–690**
Randall, RB **216–227**, **364–376**
random data 491
random error 671
  spectral analysis and 1222–1223
Random Processes **1033–1039**
  autocorrelation function 1037, 1037*F*
  damping 1037, 1038*F*
  Fourier transforms and 1033
  normalization and 1033
  singularities 1034, 1035*F*
random signals 297–298, 644*F*, 1185
  generation of 1185–1192
  spectral analysis and 1219–1223
  stochastic analysis and **1238–1246**
Random Vibration, Basic Theory **1040–1046**
  central limit theorem and 1044, 1044*F*
  degrees of freedom (DOF) 1040–1042
  Gaussian noise and 1045–1046
  mean square response 1042, 1042*F*
range charts 1405*F*
Rankine, William 112
Rao, SS **202–207**, **395–404**, **520–530**, **530–544**, **1019–1024**, **1308–1324**, **1344–1360**
Rateau, Edmond 1065
rational fraction polynomial method 823
Rayleigh's method
  basics of 132–134
  columns and 238, 239
  continuous systems 1312–1317
  discrete systems 1309–1311
  finite element methods 533
  integral 889, 890
  MEMS 787
  noninteger power 289
  ordinary 288–289
  quotient 462
  random processes 1038
  substructuring 1332

Rayleigh-Ritz analysis 290, 462–463, 691
iterative solvers and 993
Rayleigh waves 1553, 1554*F*
ultrasonic testing and 908
Raynaud's disease 621
receptance 421*F*, 423*F*
reciprocity 136, 1267
modal analysis and 819
rectangular plates 1026
recurrent neural networks (RNN) 867
recursion 100–101, 108
Reissner energy 1344, 1347
residuals 848–850
resonance
actuators and 482–489
antiresonance and **1046–1055**
bearing diagnostics and 146, 146*F*
cubic systems 940–943
degrees of freedom (DOF) and 930–943, 1047–1055, 1048*F*, 1049*F*, 1050*F*, 1051*T*, 1053*F*
electrostriction and **475–490**
forced response and 581–582
forced vibration and 1296
location 1051
mass-spring damping 1047–1048, 1048*F*, 1049*F*, 1050*F*
MEMS 779
NNM and 921–922
nonlinear systems and **928–943**, 944, 1054–1055
parameter sweep through 1288
phase method 1052–1053
primary 931–934, 938–939
quadratic systems 937–939
residuals and 848
rotor dynamics 1097
secondary 934–937
sharpness of 1051
ship vibrations 1170–1171
sub-harmonic 1288
testing 1052
transduction and 755–759, 755*F*, 756*F*, 757*F*, 758*F*
viscous damping and **1548–1551**
whole-body vibrations and **1570–1578**
See also frequency; harmonics
Resonance and Antiresonance **1046–1055**
response properties **272–277**
aeroelastic **87–97**
bridges and **202–207**
CFRF matrices 276*F*, 277*F*
FDAC matrices 275*F*
forced 1075–1076
free 1072–1073
FRFs 273*F*
individual 272–273
MEMS **779–794**
modal analysis 824–826, 837–838
parameters 1267–1268
principal 277–278
pseudoresponse 849–850
residuals 848–850
response properties (*continued*)
RVAC matrices 274*F*
sets 274–277
transduction and 755*F*, 755–759, 756*F*, 757*F*, 758*F*
See also active control; modal analysis
Response Vector Assurance Criterion (RVAC) 274*F*, 275–277
Reynolds number 1585
ride natural frequency 614
rigidity 113–118, 166, 1373–1374
RISK processors 990
Ritz method 290, 1332
basics of 134
energy and 1318–1320
finite element methods 533
MEMS 787
substructuring 1332
vectors 691
Rivin, E **1487–1506**, **1507–1521**
Rixen, Daniel **710–720**, **990–1001**
RMS acceleration 604
RMS value 1582, 1583
windows and 1593
road excitations 618–620
Robert, G **243–256**
Robot Vibrations **1055–1063**
actuated joints 1059
altered operational strategies 1063
arm improvement 1062
commanded motion 1057, 1058*F*, 1059*F*, 1063
components 1059
damping 1063
degrees of freedom (DOF) 1060, 1060*F*, 1061*F*
flexibility and 1056*F*, 1057
kinematic linkages 1060, 1060*F*
mass allocation 1062
material selection 1063
modeling 1057
See also MEMS
Rochelle salt 1013
rockets 1265
rod vibration 1328–1329, 1328*F*, 1329*F*, 1330*F*
rigid state 118–119
rolling bearing faults 1187–1188
root-finding methods 463
root-locus diagrams 413
root mean square (RMS) 145
averaging and 98
Rosenhouse, G **124–137**, **180–191**, **1304–1308**
Rotating Machinery, Essential Features **1064–1069**
Rotating Machinery, Modal Characteristics **1069–1077**
Rotating Machinery, Monitoring **1078–1084**
rotation 414
abnormal situations 1078–1080, 1082–1083
balancing and **111–124**
basic diagnostics and 379, 379*T*
rotation (*continued*)
bearing faults and 1187–1188
bearing vibration and 152–163
biorthogonality 1074, 1074*F*
blades and **174–180**
columns and 239–240
coupled 112–113, 1068–1069
data collection 1082
definitions 1069
disks and 409–410
eccentricity and 112–113
equations of motion and 1325
flexible state and 118–119
fluid-structure interactions and 549–550
forced responses 1071–1076
formulations 1070–1071
free responses 1072–1073
friction and **589–596**
helicopter damping and **629–642**
historical studies of 1064–1066
influence coefficients and 119–123
limits 1081–1082, 1081*F*
links and 1068–1069
liquid sloshing and **726–740**
localization and 741–751
machines and **1064–1069**, 1067*F*, 1068*F*,
maintenance 1078, 1079*F*
misalignment and 1186
monitoring 1078–1084
motion sickness and **856–861**
natural frequencies 1071
natural modes 1071–1072
nodal points 1073, 1073*F*
nonlinear systems and 956
online systems 1082
resetting sensitivity 1077
rigid states and 113–118
sensing and measurement 1080–1081, 1080*F*
shells and 1159
signal generation and **1184–1193**
signals and 1192*T*
SNDT and 905
spectral analysis and 1218
speed and 118–119
sprag-slip 593–597
standards 1082, **1224–1238**
transient analysis 1083–1084
unbalance and 1185–1186
rotor-bearing systems 413, 414*F*, 417, 420*F*
helicopters **629–642**
unbalance plot 420
Rotor Dynamics **1085–1106**
chaos 1096*F*, 1097–1098
coaxiality fault 1098*F*, 1099
De Laval's model 1085–1088
formulation 1102
gyroscopic couple 1099–1101, 1099*F*, 1100*F*
initial peak 1098
isotropic links 1093–1097, 1094*F*
modal properties 1090

Rotor Dynamics (*continued*)
modeling 1085–1088, 1086*F*, 1087*F*
natural frequencies 1088–1090, 1089*F*, 1090*T*
temporary rates of flow 1102–1103, 1103*F*, 1104*F*, 1105*F*
torsion 1105–1106, 1106*F*
unbalance 1086*F*, 1091–1092, 1091*F*, 1098
Rotor-Stator Interactions 1107–1120
chaos 1112–1115, 1113*F*, 1114*F*, 1117*T*
contact at reducing speed 1107
cycle limits 1107–1110, 1108*F*, 1109*F*
deterministic contacts 1109*F*, 1110–1112, 1110*F*, 1111*F*
misalignment 1116*T*, 1116–1118, 1117*F*, 1118*F*
support deterioration 1118
tremors 1118–1121, 1119*F*
roughness index (RI) 618–621
Routh-Hurwitz stability 23
Rubbing Shafts Above and Below the Resonance (Critical Speed) (Taylor) 1107
Rumbaugh, J 969, 971
Runge-Kutta-Gill method 1119
running sum 1196–1197
run out 112–113, 1099–1101, 1099*F*, 1100*F*
RVAC matrices 274*F*, 275–277, 278

S

Saddles 229, 1544–1548
SAMCEF 248–249
sampling
data acquisition and **364–376**
digital filters and 389–391
external 373–375
sigma-delta converters and 371–372
Simpson's rule 1197–1198
software resampling and 375
satellite ultraquiet isolation technology experiment (SUITE) 48
scanning laser Doppler vibrometer (SLDV) 700, 703, 704*F*, 1403
full-field measurement and 707–709
scattering 1568
SCE Lucerne Valley Station 443
Schmerr, LW Jr. **906–918**
Schur method
FETI 997–1000, 998*F*, 999*F*
primal complement 995–997
Schwarz method 995
Sciulli, D **46–48**
Scott, RZ **137–143**
Scruton number 1584
sealing 161–162, 1088
seating dynamics 1577
segment averaging 1219–1221
Seismic Instruments, Environmental Factors 1121–1134
absolute motion transducers and 1381–1396
bending moment sensitivity 1125–1127
calibration 1130–1132
cross-axis sensitivity and 1121–1122, 1122*F*, 1123*F*
environmental factors 1132–1133
force transducers and 1123–1132, 1123*F*, 1124*F*, 1125*F*, 1126*F*, 1127*F*, 1128*F*, 1129*F*, 1131*F*, 1132*F*
loading effects 1128–1130
seizure 151
self-organizing feature maps (SOFM) 865
semi-iterative solvers 994–1000
Sendagay INTES building 30, 30*F*
Sensors and Actuators 1134–1144
distributed 1134–1138
magnetostrictive materials **753–762**
MEMS and 771–779
sensitivity and 1140–1141
structonic cylindrical shells and 1138–1141
See also MEMS
separatrices 232
sequence diagrams 970, 971*F*
servo valves 485–488
Sestieri, A **1253–1264**, **1275–1283**
shaft encoder 375
Shaft Rubbing (Newkirk) 1107
shaft vibration 1191, 1328–1329, 1330*F*
standards and 1228–1232
shallow sag cable 210–213
Shape Memory Alloys (SMAs) 660, 1144–1155, 1146*T*
active damping augmentation 1149–1150, 1150*F*, 1151*F*, 1152*F*
active impedance and 1151–1153, 1153*F*, 1154*F*, 1155*F*
actuators and 65–68
control actuators 1147, 1147*F*
fibers 352, 353*F*
passive damping 1146, 1147*F*
properties of 1145*F*, 1145–1146, 1146*F*
smart structures and 75–77
stiffness and 1147–1148, 1147*F*, 1148*F*, 1149*F*, 1150*F*
Shaw, S 1010
shear 887, 1135
beam vibration and 1330
bending moment sensitivity and 1125–1127
boundary conditions and 183
columns and 239–240
damping materials and **327–331**
flexibility 239
fluid-structure interactions and 545–552
piezoelectic damping and 354–360
shear (*continued*)
shells and 1159, 1161–1162
sheetmetal 286
Shells 1155–1167
curvilinear surface coordinates 1155, 1156*T*
damping and 1165
Donnell-Mushtari-Vlasov equations 1159–1162
forced vibrations and 1163–1165
frequency and 1160–1163, 1163*F*, 1164*F*
Love-type equations of motion 1155–1159, 1159*T*, 1160–1161
membranes and **762–770**, 1159–1160
piezoelectricity and 358–360, 1014–1015
rotary inertia and 1159, 1161*T*
sensor/actuators and 1134–1143
shear and 1159
vibration intensity and 1485
shimmy 358
Ship Vibrations 1167–1173
background of 1168, 1168*F*
damping and 1171
excitation and 1168–1170
resonance and 1170–1171
Shock 1173–1180
absorption 1174, 1175*F*, 1176*F*, 1177–1180, 1177*F*, 1178*F*, 1179*F*
bearing diagnostics and 146
distribution 1174–1176, 1174*F*, 1175*F*
fragility and 1177, 1177*F*
hammershock 93
packaging and **983–989**
springs and 1180–1181
viscosity 283
Shock Isolation Systems 1180–1184
short term Fourier transform (STFT) 1364
Shteinhauz, GD **1369–1379**
Sidahmed, M **376–380**, **1184–1193**, **1379–1380**
side force coefficient 738*F*
Sieg, T **629–642**
sigma-delta converters 371–372
signal envelope 644
Signal Generation Models for Diagnostics 1184–1193
Signal Integration and Differentiation 1193–1199
Signal Processing, Model Based Methods 1199–1208
signals
aerodynamics and 1191
bearings and 146, 146*F*, 1187–1188
continuous 1193–1194, 1194*F*, 1195*F*
decomposition and 647
demodulation and 647
deterministic 1203–1204
digital filters **380–395**
DSP 367

signals (*continued*)
electric origins 1191
feedforward control **513–520**
frequency shifting and 702–703
gears and 1189–1191, 1191*F*, 1192*T*
Hilbert transforms and **642–648**
hybrid control **649–658**
hydraulics and 1191
integration/differentiation and **1193–1199**
mechanical origins and 1185–1191, 1186*F*, 1187*T*, 1187*F*, 1188*T*, 1188*F*, 1189*F*, 1190*F*, 1191*F*
MEMS 789–793
misalignment and 1186
modal properties and 810
model based processing and **1199–1208**
noise-corrupted 666–668
optimal filters and **977–982**, 981*F*
parametric methods 1203–1204
rotation and 1192*T*
running sum and 1196, 1197*F*
sampled 1196*F*
samples 1195–1197
Simpsons's rule and 1197–1198, 1197*F*
spectral analysis and **1208–1223**
three component 1591*F*
trapezium rule and 1197, 1197*F*
unbalance and 1185–1186
vibration characteristics and 1184–1185, 1185*F*
windows and **1587–1595**
signal-to-noise ratios
discretization and 369–371
Fourier-based identification and 666–668
model processing and 1204
signature generation 144–145, 144*T*
Silva, JMM **813–820**
similarity transformation methods 461, 464
simply-supported plates 1026, 1028*T*
Simpson's rule 1197–1198
single-input multiple output (SIMO) systems
cepstral analysis and 222–227
method 820–821
modal anaylsis and 820–823
single input/single output (SISO) systems 665
data set 674, 676*F*
feedforward control **513–520**
modal anaylsis and 820–823
model-based identification and 674–685
single instruction/multiple date (SIMD) processors 990
single layer feed forward (SLFF) networks 866
single value decomposition (SVD) 425
singular systems 714–716
singular value decomposition (SVD) 716–717
singular vectors 425
Sinha, SC **1001–1009**
sinusoidal displacement 635
skyhook control 38–41
skyline storage 714*F*
sliding friction 335
Smale, S 228
Smale's horsehoe 232–233, 232*F*, 234
Smale-Birkhoff homoclinic theorem 233
Smallwood, D **490–496**
smart fluids 468–474
smart structures 73, 80
adaptive actuation 74, 76*F*
electroactive materials 77–78, 78*F*, 79*F*
magnetoactive materials 77–79, 78*F*, 79*F*
sensory 74, 75*F*
shape memory alloys and 75–77
smart wing technology 575–576
S-N diagram 505–507
Snell's law 1552
Snyder, R **629–642**
Society of Automotive Engineers 604
Soedel, W **1155–1167**
software 243
ABAQUS 246–247
analyses 253–255
ANSYS 247
COSMOS/M 247–248
dynamic applications of 244–245
history of 244
influence coefficients and 119–123
MSC/NASTRAN 248–249
quality assurance and 245–246
resampling 375
SAMCEF 249–250
solution methods and 255–256
technical description of 250–253
solvers 256
direct 992
iterative 993–994
semi-iterative 994–1000
somatosensory system 857
sonic nondestructive testing (SNDT) 898, 899, 906
aerospace and 905
civil engineering and 905
curse of dimensionality and 902, 902*F*
data acquisition and 900–901
degrees of freedom (DOF) and 899*F*
feature extraction and 901–904, 901*F*, 904*F*
global 899–904
history of 904–905
model building and 903–904
operational evaluation 900
rotation and 905
Soong, TT **26–36**
sound 1443–1444, 1452–1453
basic theory of 1444–1446, 1446*F*
boundary pressures and 888–889
sound (*continued*)
compact sources 1447–1452, 1448*T*, 1449*F*, 1450*F*, 1451*F*, 1452*F*, 1453*F*, 1453*T*, 1454*F*, 1455*F*
feedforward control 519–520
flexural radiation and **1456–1480**
Green's equations and 879
impedance and 1444–1445, 1444*T*
multipole 1535–1536
plate vibration and 890–891, 894–896
power radiation and 883–884
pressure level 1268, 1268*F*
radiation ratio 1446
sources 878–879
structural-acoustic interactions **1275–1283**
superposition and 884–886
wave number of 891
See also noise
Spatial Properties **256–264**
hybrid TAM 262*F*
mass and 260–264
reduced mass matrices and 257–260
static TAM 259*F*, 260*F*, 261*F*
stiffness and 260–264, 263*F*
specialized elements 250*T*
speckle noise 705, 706*F*, 709*F*
full field measurement and 707–709
spectra
aerodynamic load 1584*F*
bandwidth 646*T*
cable in plane 212*F*
central frequencies 645*T*
cepstral analysis and **216–227**, 221*F*
coherence function 602
correlation functions and 296
earthquakes and **439–461**
engineering units and 1209–1211, 1210*F*, 1212*F*, 1213*T*
frequency display and 420–421
frequency domain representation and 1208
gear diagnostics and 599–600
leakage error and 1588–1591
model-based analysis and 1204–1205
periodic signals and 1214–1218, 1215*T*, 1215*F*, 1216*F*, 1217*F*, 1218*F*, 1223
plots 428*F*
PSD 245, 1581, 1591
random signals and 1219–1223, 1220*F*, 1221*T*, 1221*F*, 1222*F*
signal representation and 645–646
stochastic analysis and **1238–1246**
time frequency and 1364
transient analysis and 1213–1214, 1223
uncertainty principle and 1212–1213
variance control and 1592–1593
wind and 1581*F*, 1583*T*
windows and **1587–1594**

spectra (*continued*)
zero padding and 1213–1214, 1214*F*
zoom 222, 224*F*
See also frequency
Spectral Analysis, Classical Methods **1208–1223**
Spencer, BF Jr. **26–34**
spillover 53–54
sprag-slip mechanism 593–597, 593*F*
springs
belt drives and 170–172
model updating and 845
shock isolation and **1180–1184**
superposition and 1300–1301
suspension 37–38
transmissibility and 1523–1527
See also mass-spring model
sprung mass 604, 605
2 DOF pitch plane model 609–610
2 DOF quarter car model 612–613
4 DOF pitch plane model 608
excitation and 605–607
suspension and 37–38, 615–616
weight and 615
Spurr's sprag-slip mechanism 593–597, 593*F*
Square Root of Sum Squares (SRSS) 245
squeal 589
squeeze flow devices 473
stability
active suppression and 56–57
misalignment and 1116–1118
nonlinear systems and 953–956
rotor dynamics 1088–1090, 1093–1095, 1097–1098
rotor-stator interactions 1107–1121
Routh-Hurwitz 23
tremors 1118–1121
vibro-impact systems and 1536–1548
stability, dynamic **431–438**
stabilization diagrams 429
stall flutter 96
standard finite elements 250*T*
standard linear model 660–661, 662
standards 1224
balancing and 117–118, 117*F*
broadband 1226
condition monitoring 1233–1237, 1234*F*, 1235*T*, 1235*F*, 1236*T*
gears 1232–1233, 1234*F*
machinery 1225
measurement 1226, 1226*F*
non-rotating parts 1226–1228, 1227*T*, 1228*T*, 1229*T*, 1229*F*
organizations for 1224–1225
rotating parts 1081, 1082, 1228–1232, 1230*T*, 1231*F*, 1231*T*, 1232*F*
Standards for Vibrations of Machines and Measurement Procedures **1224–1238**
standard wave equation 1329
state condensation 258
state diagrams 970, 971*F*
state space model class 676
static condensation 1333
static loading 209
static unbalance 1185
stationary probability 1239–1242
statistical energy analysis (SEA) 1265–1266
alternatives to 1269–1272
description of 1268
modal groups and 1266–1267
stators *See* rotor-stator interactions
steady states 1285
Steffen, V Jr. **9–26**
Steiglitz-McBride method 1203
Steindland, A **431–438**
stick-slip motion 583, 590*F*
stiffness
columns and 241
complex 338–339, 634–635
continuous systems and 1312–1317
damping and 321–325, **327–331**, 632–641, 638*F*
eigenvalue analysis and **461–467**
equations of motion and 1292–1293, 1324–1332
ground transportation and 607
gyroscopic couple and 1099–1101
helicopter damping and 632–641, 638*F*
hybrid control and 658, 658*F*
isolation theory and 1493–1506, **1507–1521**
Krylov-Lanczos methods and 691
lag dampers and 629–641
matrix 712, 715
MEMS 782–783, 783*T*
model updating and 845
NNM and 920*F*
plate vibration and 1029
Rayleigh method and 1309–1312
robots and 1062
rotor dynamics 1085–1088, 1092, 1102
rotor-stator interactions 1107–1121
Schur method and 995–1000
sensor/actuators and 1134–1143
shape memory alloys **1144–1155**
shells and **1155–1167**
signal generation and 1184–1185
SNDT and 899
spatial properties and 260–262, 263*F*
structural modifications and 1262–1264
superposition and 1300–1301
tire vibration and 617–618, 1374–1375
viscosity-elasto-slide (SVES) 636–637
See also absorbers
Stiharu, I 771–779, 779–794, 794–805
stingers 1124–1125
stochastic analysis 744, 1238
approximate probability solutions 1241–1242
stochastic analysis (*continued*)
averaging methods 1244–1246
differential calculus (SDE) 1246–1252
exact probability solutions 1238–1240, 1241*F*
models 1199, 1201–1203
processes 296
statistical moments 1243–1244
Stochastic Analysis of Non-Linear Systems **1238–1246**
Stochastic Systems **1246–1252**, 1248*F*, 1249*F*, 1251*F*
Stoneley wave 1553
stopband patterns 745*F*
storage modulus 327
strain
columns and 239
damping models and **335–342**
finite element methods 536–538
flutter and **553–565**
motion sensors and 1388–1389
piezoelectic damping and 353
shape memory alloys 1145
variational methods and 1350, 1350*F*, 1353
See also actuators
strain-life method 507–508
strength of materials theory 1328, 1330, 1331
stress
Boltzmann model and 661–662
damping models and **335–342**
finite element methods 536–538
flutter and **553–565**
interlaminar 787–789
Kelvin model and 660–661, 662
piezoelectricity and 1012–1013
screening 490
shape memory alloys and 1145
stress-life method 505–507
Stribech, Richard 153
Stribeck equation 1188
string vibration 591, 1328–1329, 1330*F*
continuous systems and 1315
taut 213
transverse vibration and 167
Strouhal number 1584
Stroustrup, B 972
structonic shell systems 1135*F*, 1137*F*, 1138–1141, 1138*F*, 1139*F*, 1140*F*, 1141*F*, 1142*F*, 1143*F*, 1144*F*
structural analysis
boundary integral formulation and 1278–1279
external problem and 1279
FEM and 1277–1278
internal problem 1279–1282
seismic instruments **1121–1134**
shape memory alloys and **1144–1155**
substructuring **1332–1335**
Structural Dynamic Modifications **1253–1264**

structural dynamics 256*T*, 490
acoustic radiation and 545–550, 545*F*, 546*F*, 547*F*, 548*F*, 549*F*, 551*F*, 552*F*
actuators and, 58–72
bounded waves and 1563–1564
bridges and **202–207**
damping and 323–324, 551
direct problem and 1254–1259, 1257*F*, 1258*F*, 1259*F*
disks and **404–413**
earthquakes and **439–461**
finite element methods 534–539
fluid interaction and **544–553**, 949
flutter and **553–565**, 565–577
forced response **578–582**
ground transportation and **603–620**
guided waves and **1551–1559**
impulse response function **1335–1343**
inverse problem 1259–1265, 1259*F*, 1262*F*, 1263*F*, 1264*F*
isolation theory and **1487–1506**, 1507–1521
Krylov-Lanczos methods and 691–697
localization and **741–751**
MEMS and **771–779**, 779–794, 794–805
model-based identification and **673–685**
model updating and **844–856**
modification **1253–1264**
neural networks and **869–877**
noise and **877–887**, 887–898
packaging and **983–989**
periodic truss beam 741*F*
response properties 272
robots **1055–1063**
smart structures and 73–80
SNDT and **898–906**
sound **1443–1455**
vehicular vibration **37–45**
vibration intensity and 682, **1480–1487**
wind and **1578–1587**, 1579*F*, 1580*F*, 1583*T*
See also boundary conditions; modal analysis
structural reduction *See* Krylov-Lanczos methods
structure-acoustic interaction 1265
boundary integral formulation and 1278–1279
energy balance with two oscillators 1266
envelope method 1271–1272
external problem and 1279
FEM and 1277–1278
internal problem 1279–1282
power balance in two modal groups 1266–1267
power balance with oscillators 1267
response parameters 1267–1268
SPL 1268*F*, 1268
structure-acoustic interaction (*continued*)
statistical energy analysis and 1265–1266, 1268–1274
structural interactions and **1275–1283**
thermal methods 1270–1271
WIA and 1269
Structure-Acoustic Interaction, High Frequencies **1265–1274**
Structure-Acoustic Interaction, Low Frequencies **1275–1283**
structure under test (SUT) 1124–1125
Sturm sequence property 463, 467
Su, Tsu-Jeng 697
subharmonic instability 421
substructuring 256, **1332–1335**
Succi method 1280*F*, 1281–1285, 1281*F*, 1282*F*
Sun, J-Q **342–351**
Sunar, M **1332–1335**
supercomputers 304–312, 305*T*
superposition 1286, 1300
applications of 1300*F*, 1301–1304, 1301*F*, 1302*F*, 1303*F*, 1304*F*
linearity and 1300–1301, 1300*F*, 1301*F*
suspended cable 209–210
suspension 615
2 DOF pitch plane model 609–610
2 DOF quarter car model 612–613
4 DOF pitch plane model 608
active 38
adjustable 38
damping and 616
passive 37
semiactive 38
springs and 615
tire vibrations 1371–1372
weight and 615
See also ground transportation systems
symbolic dynamics 229–232
symmetry
bifurcation and 435
boundary element methods 194–195
cables and 212–213
columns and 239, 241
disks and **404–413**
inverse problems 686–688
isolation theory and 1490
iterative solvers and 994
modal shape plots and 416
NNM and 919
stochastic analysis and 1238–1240
synchronized averaging 147, 598
system coordinates 130–131

T

tandem systems 696*F*
tangential displacement 211
taut string 213
Taylor, HD 1107
Taylor series 1325
beam vibration and 1329
cables 210
chaos and 228
friction and 591
normal form theory and 1007
Technical Committees 1225
temperature
damping materials and 329–330
electrostriction and 475, 477, 478*F*, 480–482, 482*F*, 483*F*, 484*F*
frequency equivalence concept 329
piezoelectricity and 1013, 1014–1017
shape memory alloys and **1144–1155**
transducers and 1133
tensile stress 1029
tension 166
belt drives and 170–172
shallow sag and 210–213
suspension 209–210
Terfenol-D 47, 48, 660, 753, 759
test-analysis model (TAM) 265, 269, 272
hybrid 258, 262*F*
IRS 260*F*
modal 258, 261*F*
orthogonality and 259–260
spatial properties and **256–264**
static 259*F*
Testing, Non-Linear Systems **1285–1289**
linear/nonlinear response 1285–1287
procedures for 1287–1289
testing methods
accelerated 495
environmental 494–495
packaging and 988–989
Theory of Vibration, Duhamel's Principle and Convolution **1304–1308**
Theory of Vibration, Equations of Motion **1324–1332**
Theory of Vibration, Energy Methods **1308–1324**
continuous systems 1312–1317, 1316*F*
discrete systems 1309–1311, 1311*F*, 1312*F*
FEA 1320–1322
Rayleigh's method and 1309–1317
Ritz method and 1318–1319
variational formulations 1322–1324
Theory of Vibration, Fundamentals **1290–1299**
classification and 1290–1291
equations of motion 1291–1293, 1291*F*, 1292*F*, 1293*F*
forced vibration and 1296*F*, 1297*F*
free vibration and 1293–1299, 1294*F*, 1295*F*

Theory of Vibration, Impulse Response Function **1335–1343**
Fourier transforms 1339–1343
initial condition response 1339
Laplace transformation method 1336–1338, 1337*T*, 1338*F*
Theory of Vibration, Substructuring **1332–1335**
Theory of Vibration, Superposition **1299–1304**
applications of 1300*F*, 1301–1302, 1301*F*, 1302*F*, 1303*F*, 1304*F*
linearity and 1300–1301, 1300*F*, 1301*F*
Theory of Vibration, Variational Methods **1344–1360**
applications 1350–1358
calculus 126, 1344–1346
Hamilton's principle 1348–1349, 1355
solid mechanics 1346–1348
thermal analogy methods 1269, 1270–1271
thermal equilibrium 631
thermographic analysis 378
thickness 1033
Thom, R 432
three-node bending mode 417
time
average energy 1268, 1270
domain analysis displays 429
domain formulation 977–978
domain methods 821–822
Duhamel's Principle and 1308
DYNA3D and 306
dynamics and **278–286**
earthquake history and 447–453
frequency distribution 147
gear diagnostics and 600
Hilbert transforms and 648
integration 256, 256*T*
normal form theory and 1005, 1007
periodic center manifold reduction 1005
perturbation methods and 1003–1004, 1009
transient dynamics and 278
windows and **1587–1595**
See also parametric excitation
time domain averaging (TDA) 101
performance of 103–108
periodic extraction and 109
recursion 102
regular 101
Time Frequency Methods **1360–1369**, 1368*F*
applications of 1366–1368
bilinear 1367*F*
Cohen's class and 1362–1366
Fourier analysis and 1360–1361
spectrogram and 1364
Wigner-Ville distribution 1361–1363
Timoshenko beam model 142, 1329
tire properties 617–618
Tire Vibrations **1369–1379**, 1370*F*
frequency influences 1378–1379
responses 1372–1377, 1374*F*, 1375*F*, 1376*F*
sources of 1370–1371
suspension and 1371–1372, 1371*T*, 1372*F*
tire construction and 1371, 1371*F*
Toeplitz structure 1203
Tomasini, EP **698–710**
Tonpilz 759
tools classes 974
Tool Wear Monitoring **1379–1380**
tooth averaging 598, 599*F*
See also gear diagnostics
Tordan, MJ **364–376**
torsion 112–113, 396
belts and 169
boundary conditions and 183
columns and 239–240
continuous systems and 1315
isolation theory and 1493
MEMS 782–783, 783*T*
moving belts and 166–170
rotor dynamics 1105–1106
standards and 117–118
transmissibility 1523
transducers 755–759, 755*F*, 756*F*, 757*F*, 758*F*, 1398
accelerometers 1383, 1390–1392, 1390*F*, 1391*F*, 1392*F*, 1395–1396, 1396*T*, 1397*T*
calibration of 1130–1132
capacitive 1390, 1390*F*
data acquisition and **364–376**
displacement sensors and 1399–1401
electromagnetic sensors 1402
environmental factors and 1132–1133
force 1123–1132
LDVs 1403–1406
magnetostrictive materials 755–761
modal properties and 809
mounting and 1133
piezoelectric 1385–1387, 1385*F*, 1386*F*, 1387*F*, 1388*F*, 1389*T*
pressure 1384
seismic displacement 1383
seismic force 1384
seismic velocity 1383
standards and 1226*F*, 1232–1238
strain gauge 1388–1389, 1389*F*
transient response 1393–1395, 1393*F*, 1394*F*, 1395*T*
ultrasonic 912–917
velocity and 1402–1406
Transducers for Absolute Motion **1381–1397**
Transducers for Relative Motion **1398–1406**
Transform Methods **1406–1419**
differentiation/integration and **1193–1199**
Fourier 1411–1419, 1414*F*, 1415*F*, 1416*F*, 1418*F*
Transform Methods (*continued*)
Laplace 1407–1409
spectral analysis and **1208–1223**
Z-transforms 1409–1411, 1410*F*, 1412*F*
See also Fourier transforms
Transforms, Wavelets **1419–1435**
continuous wavelet 1423–1425, 1424*F*, 1425*F*
discrete wavelet 1427–1433, 1429*F*, 1430*F*, 1431*F*, 1432*F*
distribution sampling 1425–1427, 1426*F*
Fourier 1420–1422, 1421*F*, 1422*F*
performance of 1433, 1433*F*, 1434*F*
transient analysis 1209, **1213–1214**, 1223
absolute motion and 1393–1395
boundary element methods 198–201
data 491
dynamics 278–286
rotation 1083–1084
translation 1325*F*, 1326
motion sickness and **856–861**
whole body vibration and 1574
transmissibility 343, 1522
active/semi-active damping and 347–349
biodynamics and 1571
bounce 610
elastically coupled damping and 345–346
flexural 1523–1531, 1525*F*, 1526*F*, 1527*F*, 1528*F*, 1529*F*, 1530*F*, 1531*F*
gear diagnostics and **597–603**
longitudinal 1522
multidirectional mounts and 346
passive damping and 343–345
seat dynamics and 1577
torsion and 1523
See also boundary conditions
transport speed 166
transverse shear flexibility 239
transverse vibration
continuous systems and 1315–1317
moving belts and 166–170
nonlinear effects of 167–169
variational methods and 1352–1353, 1352*F*
trapezium rule 1197
tremors 1118–1121
Trevithick, Richard 1064
triangular plates 1030*F*
triboelectric effects 1133
triggering 373
Trigger Scuba, Inc. 759
Troger, H **431–438**
truncation 1256
tuned mass dampers *See* absorbers
turbulence *See* wind
turbines 1191, 1229
turbomachines 220, 1191

two-state least squares (2SLS) method 679
Tzou, HS 1011–1017, 1134–1153

U

Uchino, K 475–490
Ueda, Y 228
ultrasonic nondestructive testing 906–918, 1439–1440
  acoustic impedance and 911*T*
  A-scan 906
  attenuation and 911
  B-scan 906, 907*F*
  bulk waves and 908
  C-scan 907, 907*F*
  displacement and 909*F*
  Lamb waves and 909*F*
  material density and 908*T*
  plate waves and 909
  pulse-echo inspection 906, 907*F*
  Rayleigh waves and 908
  reflection/refraction and 910–911, 910*F*
  testing system of 907*F*
  transducers and 912–916, 912*F*, 913*F*, 914*F*, 915*F*, 916*F*, 917*F*, 1439
Ultrasonics 1437–1441
  acoustic emission and 1440
  chemical reactions and 1440
  cleaning and 1439
  definition of 1437
  electronics and 1440
  features of 1437–1439, 1438*T*
  generation of 1440–1443
  imaging and 1439
  magnetostrictive materials 759
  material properties and 1439
  welding and 1440
U-Mode Indicator Function (UMIF) 278, 429
unbalance 112–113, 1185–1186
  flutter and 553–565
  rotor dynamics 1091–1092, 1095, 1098–1098
  rotor-stator interactions 1107–1121
uncertainty principle 1212–1213
Ungar, EE 327–331
unified matrix polynomial approach (UMPA) 823
unified modeling language (UML) 969
unperturbed phase portrait 235*F*
unsprung mass *See* sprung mass

V

Vakakis, AF 918–924
van der Pol equations 227–228
variational principle
  columns and 240
Varoto, PS 496–504
Vecelic's system 689*F*
vectors
  basic principles of 125–126, 127*F*
  critical damping and 317–318
  iteration methods and 464–466
  Krylov-Lanczos methods and 691–695, 697
  modal correlation and 267–270
  neural networks and 871–872
  nonlinear systems and 953–956
  Poincare' method and 957–959
  Rayleigh quotient 462
  Rayleigh-Ritz analysis 462–463, 691
Veldvizen, T 973
velocity
  actuator sensitivity and 1140–1141
  electromagnetic sensors and 1402
  friction and 583–584, 589–597
  LDVs and 1403–1404, 1405–1406
  optical heterodyning and 1404–1405
vertical oscillatory motion 857–859, 860*F*
vestibular system 857
vibrational properties
  absorbers 1–9, 9–26
  active damping and 351–364
  actuators and smart structures 58–81
  adaptive filters 81–87
  active isolation 46–48
  active suppression of 48–58
  aeroelasticity 87–97
  averaging and 98–110
  balancing and 111–124
  basic diagnostics and 376–380
  basic principles of 124–137
  beams and 137–143
  bearings and 143–152, 152–165
  belts and 165–174
  boundary conditions and 180–191
  boundary element methods and 192–202
  bounded waves 1559–1564
  bridges and 202–207
  cables and 209–216
  civil structures and 26–36
  columns and 236–243
  continuous methods 286–294
  damping measurement and 332–335, 342–351, 1548–1551
  damping models and 321–327, 335–342
  data acquisition 364–376
  digital filters and 380–395
  discrete elements and 395–404
  disks and 404–413
  displays and 413–431
  dose value (VDV) 1575–1576, 1576*F*, 1577*F*
  Duhamel's Principle 1304–1308
  dynamic systems and 431–438, 433*F*, 435*F*, 436*F*, 437*F*
  earthquakes and 439–461
  eigenvalue analysis 461–467
  electrostriction 475–490
vibrational properties (*continued*)
  energy methods 1308–1324
  environmental testing 490–496, 496–504
  equations of motion and 1324–1332
  fatigue and 505–512
  feedforward control of 513–520
  finite difference methods 520–530
  finite element methods 530–544
  flexural radiation and 1456–1480
  fluids and 467–475, 544–553
  flutter and 553–565
  forced response and 578–582
  Fourier-based identification 665–672
  friction 582–589, 589–596
  fundamentals of 1290–1299
  gear diagnostics 597–603
  ground transportation and 603–620
  guided waves 1551–1559
  hand-transmitted 621–629
  helicopter damping 629–642
  Hilbert transforms and 642–648
  hybrid control and 649–658
  hysteretic damping 658–664
  identification methods and 673–685
  impact and 1531–1548
  impulse response function 1335–1343
  intensity and 1480–1487
  inverse problems 686–690
  isolation theory 1487–1506, 1507–1521
  linear algebra and 710–720
  linear damping matrix methods 721–726
  liquid sloshing 726–740
  localization and 741–751
  magnetostrictive materials 753–762
  magnitude 1572
  membranes and 762–770
  MEMS 771–779, 779–794
  modal analysis 265–272, 805–813, 820–824, 824–829, 829–838
  model-based identification and 673–685
  model updating/validating and 844–856
  mode of 838–844
  motion sickness and 856–861
  neural networks and 869–877
  noise and 877–887, 887–898
  nonlinear normal modes and 918–924
  nonlinear systems and 928–943, 952–966
  nonlinear testing and 1285–1289
  optimal filters and 977–982
  packaging and 983–989
  parallel processing and 990–1001
  parametric excitation and 1001–1009
  perturbation methods and 1009–1011

vibrational properties (*continued*)
piezoelectric materials and **1011–1018**
pipes and **1019–1024**
plates and **1024–1031**
random processes **1033–1039**, **1040–1046**
resonance and **1046–1055**
response property comparison and 272–277
robots and **1055–1063**
rotation **1064–1069**, **1069–1077**, **1078–1084**
rotor dynamics **1085–1106**
rotor-stator interactions **1107–1120**
seismic instruments and **1121–1134**
sensors and actuators **1134–1144**
shape memory alloys and **1144–1155**
shells and **1155–1167**
ship vibrations **1167–1173**
shock and **1173–1180**
signal generation **1184–1193**
signal integration/differentiation and **1193–1199**
signal processing and **1199–1208**
sound and **1443–1455**
spatial comparison and **256–264**
spectral analysis and **1208–1223**
standards for **1224–1238**
stochastic analysis and **1238–1246**, **1246–1252**
structural-acoustic interactions **1265–1274**, **1275–1283**
structural dynamics and **1253–1264**
substructuring **1332–1335**
superposition and **1299–1304**
time frequency and **1360–1369**
tires and **1369–1379**
tool wear and **1379–1380**
transducers and **1381–1397**, **1398–1406**
transmission **1522–1531**
ultrasonic **906–918**, **1437–1441**
unbounded waves **1565–1570**
variational methods **1344–1360**
vehicular **37–45**
whole body **1570–1578**
wind induced **1578–1587**
windows and **1587–1595**
vibration exciter 1124–1125
Vibration Generated Sound, Fundamentals **1443–1455**
Vibration Generated sound, Radiation by Flexural Elements **1456–1480**
vibration-induced white finger (VWF) 621–622, 625
Vibration Intensity **1480–1487**
beams 1484, 1486
complex 1482
flexural waves 1483–1485
plates 1484–1485, 1487
rods 1486
shells 1485
waves in elastic media 1482–1483
Vibration Isolation, Applications and Criteria **1507–1521**
Vibration Isolation Theory **1487–1506**
ambient vibrations 1507–1508, 1508*F*
coupled systems 1490–1493, 1494*F*, 1496*F*, 1497*F*, 1498*F*, 1499*F*
criteria of 1508*F*, 1509*F*, 1510–1512, 1511*T*
degrees of freedom (DOF) and 1494–1501, 1494*F*, 1496*F*, 1497*F*, 1498*F*, 1499*F*, 1500*F*, 1501*F*
detrimental effects and 1508–1509
dynamic systems 1512, 1513*F*
elastic mounts 1490
experimental selection 1521
general purpose machines 1517–1519, 1518*F*, 1519*F*
geometric properties 1490
impacts 1515
impulse excitation 1502–1504, 1503*F*, 1504*F*
inclined mounts 1493
inertia and 1490, 1515–1517, 1516*T*, 1516*F*
mounting conditions 1517–1518, 1518*F*
nonlinearity 1504–1505
nonrigid structures and 1520
polyharmonic excitations 1515
precision and 1513–1514
random excitation 1501–1502
single frequency excitations and 1514–1515
transmission model 1509–1510, 1509*F*, 1510*F*
wave effects 1505, 1506*F*
Vibration Transmission **1522–1527**
See also transmissibility
Vibro-Impact Systems **1531–1548**, 1532*F*, 1533*F*
bifurcation and 1533–1536, 1535*F*, 1539*F*, 1539
chaos and 1542–1548, 1542*F*, 1545*F*, 1546*F*, 1547*F*
classification and 1536, 1537*F*
examples of 1533, 1533*F*, 1534*F*, 1535*F*
periodic stability and 1535*F*, 1538*F*, 1539–1542, 1539*F*, 1541*F*
stability regions and 1536, 1538*F*
subharmonic regions and 1536–1539, 1538*F*
vibrometers 700–706, 704*F*, 705*F*
in-plane 703–704
rotational 704–705
SLDV 703, 1403
Villari effect 754, 761
virtual work principle 1320
variational methods and 1353
viscoelastic damping 325–326, 649, 656–658
viscoelastic damping (*continued*)
materials and **327–331**
measurement and 334
models of 339–340
passive 351–352
transverse vibration and 169
viscoplasticity 252*T*
viscosity
damping 321–323, 344*F*, 633–634
SVES 636–637
Viscous Damping **1548–1551**, 1549*F*, 1550*F*
equivalent 340–341
isolation theory and 1496–1501
models of 336–337
See also damping
visual system 857
motion sickness and 859, 860
whole body vibration and 1574
Voigt model 660
voltage conversion
MEMS 790–793
Volterra series 926
volute spring 1181, 1182*F*
von Karman geometric nonlinearity 1136
vortices
shedding 97
wind and 1584–1585
Vorus, WS **1167–1173**

W

Wagner function 558
Waizuddin Ahmed, **603–620**
Wang, KW **649–658**
Watt, James 112, 1064, 1064
wave intensity analysis (WIA) 1269
wavelet transformations (WT) 598, 600
bearing diagnostics and 147, 148*F*
continuous 1423–1425, 1427
discrete 1427–1433
performance of 1433
signal generation and 1191
STFT 1420–1423
wave number 895*F*
boundary conditions and 894*F*
plate vibration and 893
Wave Propagation, Guided Waves in Structures **1551–1559**
Wave Propagation, Interaction of Waves with Boundaries **1559–1564**
Wave Propagation, Waves in an Unbounded Medium **1565–1570**
waves
acoustic impedance and 1561*T*, 1562*F*
with boundaries **1559–1564**
boundary element methods 200
bulk 908
cables and 210–215
cylindrical 1557*F*, 1570
discrete structures and 1563–1564

waves (*continued*)
DYNA3D and 307
elasticity and 1566, 1567–1568
evanescent 1563*F*
flexural radiation and 887, **1456–1480**
guided **1551–1559**
harmonic motion 1567*F*
isotropic materials and 1568–1569
Lamb 1555*F*, 1556*F*, 1558*F*
localization and **741–751**
Love 1557*F*
media interference and 1560*F*
noise and **877–887**, **887–898**
plane 1560–1562, 1567–1568
Rayleigh 908, 1553, 1554*F*
reflection and 1560–1562, 1563*F*, 1564*F*
scattering and 1568
shape memory alloys and 1148–1153
slowness curves and 1569*F*
sonic **898–906**
spherical 1570
Stoneley 1553
structural-acoustic interactions **1274–1285**
subsonic 897
superposition and 1301–1304
tire vibration and 1376–1377
transducers and 912–916
ultrasonic **906–917**, **1437–1443**
in unbound medium **1565–1570**
vibration isolation and 1505
vibration intensity and 1482–1487
See also boundary conditions; transmissibility
weighted residual approach 533
Weiner-Khintchine theorem 1361
Weiner series 926
Welch method 1219
welding 1440
Wereley, NM **629–641**
WHAMS 305
Wheatstone bridge 1388, 1389*F*
whirl 1191
White, P **1360–1369**, **1420–1434**
white noise
stochastic systems and 1247–1252
Whole-Body Vibration **1570–1578**
acceleration frequency and 1573*F*
axis measurement of 1571*F*
biodynamics 1571–1572
building disturbance and 1578
discomfort 1572–1573
exposure limit comparison 1576*F*
frequency weightings 1572*T*, 1573*T*
health and 1575–1576
interference 1574–1574
seating dynamics 1577
VDV 1577*F*, 1578*T*
vision and 1574
Wickert, J **1324–1332**
wide-band demodulation 602
Wiener filter 978–979
causally constrained 980–981
unconstrained 979
Wigner-Ville distributions (WVDs) 598, 1361–1363, 1363*F*
Wilson, Ed 691
wind **1578–1587**
aerodynamic load 1584*F*
aeroelastic effects and 1584–1586
characteristics of 1579
continuous turbulence and, 91
gusts and, 89–91, 92
induced response and 1581–1584, 1581*F*
numerical methods and 1586
response theory and 1581–1582
shedding 97
structures and 1579–1581, 1579*F*, 1580*F*
tunnel testing 1585–1586
vortices and, 97, 1584–1585
Wind Induced Vibrations **1578–1587**
Windows **1587–1595**
digital filters and 387–389
dynamic range effects and 1591*F*
exponential window 1594, 1594*F*
FIR filters and 1594
flat-top 1592, 1592*F*
force window 1593, 1594*F*
Hanning 524–525, 1590*F*, 1591
impulse testing and 1593–1594
Kaiser 1590
leakage and 1590*F*
overlap processing and 1593, 1593*F*
property comparison 1590*T*
Windows (*continued*)
rectangular 1588, 1589*F*, 1590*F*
spectral analysis and 1216–1218
transient analysis and 1593–1594
wire frame format 415, 416
Wishbone suspension 615
Wohler diagram 505–507
Wright, J **553–565**

X

XOR matrices 267

Y

Yang, B **1290–1299**
Yokohama Landmark Tower 30
Young's modulus 889, 1136, 1567
boundary conditions and 182, 183
continuous systems and 1313
Euler-Bernoulli beam theory 137–141
hysteretic damping and 659
model updating and 845, 847
Rayleigh's Principle and 132
shape memory alloys 1145, 1151
shells and 1156
Yourdon, E 969, 971
YW method 1203

Z

Zacksenhouse, M **863–868**
Zeglinski, GW 972
Zernlike polynomials 484
zero-energy mode control 283
zero padding 1213–1214
Zimmermann, T 972
zoom spectra 222, 224*F*
Z transforms 1409
cepstral analysis and 217, 218
differentiation/integration and 1195
digital filters and 387–389
inversion 1411
MA modeling and 1199
properties of 1409–1410
spectral analysis and 1208
windows and 1216–1218
Zu, JW **165–174**